European Community on Computational Methods in Applied Sciences

ECCOMAS Congress 2016

VII European Congress

on Computational Methods in Applied Sciences and Engineering

PROCEEDINGS

Volume III

M. Papadrakakis, V. Papadopoulos, G. Stefanou, V. Plevris (Eds)

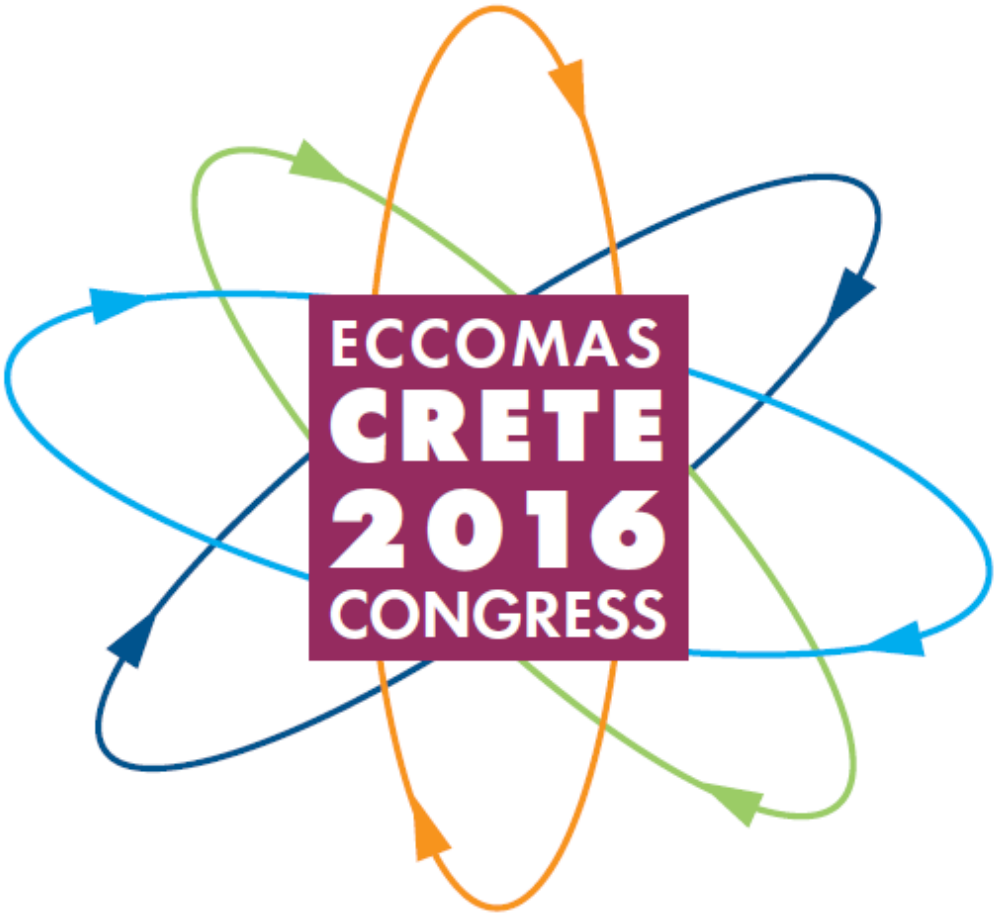

ECCOMAS Congress 2016

Proceedings of the VII European Congress on Computational Methods
in Applied Sciences and Engineering
Held in Crete, Greece
5-10 June 2016

Edited by:

M. Papadrakakis
National Technical University of Athens, Greece

V. Papadopoulos
National Technical University of Athens, Greece

G. Stefanou
Aristotle University of Thessaloniki, Greece

V. Plevris
Oslo and Akershus University College of Applied Sciences, Oslo, Norway

A publication of:

Institute of Structural Analysis and Antiseismic Research
School of Civil Engineering
National Technical University of Athens (NTUA)
Greece

ECCOMAS Congress 2016
M. Papadrakakis, V. Papadopoulos, G. Stefanou, V. Plevris (Eds)

First Edition, September 2016

© The authors

ISBN: **978-618-82844-0-1**

PREFACE

This volume contains the full-length papers presented at the **VII European Congress on Computational Methods in Applied Sciences and Engineering** (ECCOMAS Congress 2016) that was held on June 5-10, 2016 on the Crete Island, Greece.

The main objective of the quadrennial ECCOMAS Congresses is to provide a forum for presentation and discussion of state-of-the-art advances in computational methods in applied sciences and engineering, including basic methodologies, scientific developments and industrial applications and to serve as a platform for establishing links between research groups of academia and industry with common as well as complementary activities. About 2,200 papers were presented at the ECCOMAS Congress by authors from 53 countries around the world. This volume, consists of 667 full length accepted papers which will be indexed by SCOPUS database with access to the pdf file of the paper.

The ECCOMAS Congress 2016 is organized by the Institute of Structural Analysis and Antiseismic Research of the National Technical University of Athens under the support of the Greek Association for Computational Mechanics (GRACM), the Institute of Research and Development for Computational Methods in Engineering Sciences (ICMES) and the Computer Applications and Education in Engineering Sciences (CAEES).

The editor of this volume would like to thank all authors for their contributions. Special thanks go to the colleagues who contributed to the organization of the Minisymposia and to the reviewers who, with their work, contributed to the scientific quality of this e-book.

M. Papadrakakis
National Technical University of Athens, Greece

V. Papadopoulos
National Technical University of Athens, Greece

G. Stefanou
Aristotle University of Thessaloniki, Greece

V. Plevris
Oslo and Akershus University College of Applied Sciences, Oslo, Norway

ACKNOWLEDGEMENTS

The conference organizers acknowledge the support towards the organization of the 7th European Congress on Computational Methods in Applied Sciences and Engineering, to the following organizations:

- Greek Association for Computational Mechanics (GRACM)
- Institute of Structural Analysis and Antiseismic Research, National Technical University of Athens
- John Argyris Foundation
- Institute of Research and Development for Computational Methods in Engineering Sciences (ICMES)
- Computer Applications and Education in Engineering Sciences (CAEES)
- Region of Crete
- Municipality of Hersonissos

Plenary Speakers

We would also like to thank the Plenary and Semi-Plenary Speakers for their help in the setting up of a high standard Scientific Programme.

Plenary Speakers: Alexandre Ern, Charbel Farhat, Gerhard A. Holzapfel, Antonio Huerta, Thomas J.R. Hughes, Alfio Quarteroni, Ole Sigmund, Theodosios P. Tasios

Semi-Plenary Speakers: Assyr Abdulle, Olivier Allix, Lourenco Beirao da Veiga, Andreas G. Boudouvis, Annalisa Buffa, Ramon Codina, Laura De Lorenzis, Bernard Geurts, Kyriakos Giannakoglou, Antonio J. Gil, Dan Givoli, Anthony Gravouil, George Karniadakis, Mats G. Larson, Kim Meow Liew, Wing Kam Liu, Federico Negri, Shinji Nishiwaki, Ursula Rasthofer, Ernst Rank, Cord-Christian Rossow, Giancarlo Sangalli, Jörg Schröder, Bert Sluys, Christian Soize, Roberto Verzicco, Barbara Wohlmuth

SUMMARY

Preface..... iii

Acknowledgements..... iv

Contents..... xvii

VOLUME I

SEMI-PLENARY LECTURES 1

MINISYMPOSIA

MS 102 - COMPUTATIONAL MODELS IN BIOMECHANICS AND MECHANOBIOLOGY 27
Organized by Estefania Peña, Renato Natal Jorge, Miguel A. Martínez, Pedro S. Martins

MS 103 - MECHANICS OF BIOLOGICAL TISSUES 55
Organized by Markus Böl, Gerhard A. Holzapfel

MS 105 - SIMULATION OF CARDIOVASCULAR PROCEDURES AND DEVICES 81
Organized by Ferdinando Auricchio, Michele Conti, Simone Morganti, Alessandro Reali, Alessandro Veneziani

MS 106 - DIRECT AND INVERSE METHODS FOR CARDIOVASCULAR AND PULMONARY BIOMECHANICS 98
Organized by Wolfgang A. Wall, C. Alberto Figueroa, Marek Behr

MS 108 - NUMERICAL METHODS FOR COUPLED PROBLEMS IN BIOMEDICAL APPLICATIONS 105
Organized by Martina Bukac, Annalisa Quaini

MS 111 - POPULATION BALANCE MODELING: CURRENT STATUS, FUTURE PROSPECTS AND NOVEL APPLICATIONS FROM NANOPARTICLES' SYNTHESIS TO (LUNG) CANCER 120
Organized by Georgios Lolas, Georgios Bourantas, Panagiotis Gavriliadis, Konstantinos Syrigos

MS 112 - ANEURYSMS: SOLID MECHANICS, FLUID MECHANICS, AND MECHANOBIOLOGY 137
Organized by Christian J. Cyron, Sven Hirsch, Philippe Bijlenga, Roland C. Aydin, Anne M. Robertson, Gerhard A. Holzapfel

MS 113 - MATHEMATICAL AND NUMERICAL MODELING OF THE HEART 155
Organized by Luca Dede', Luca Pavarino, Alfio Quarteroni

MS 115 - TUMOR GROWTH MODELING AND THE MECHANICAL ASPECTS OF CANCER 178
Organized by Hector Gomez, Assad Oberai, Krishna Garikipati, Kristen Mills, Thomas J.R. Hughes

MS 201 - MICROSTRUCTURE-DRIVEN DEFORMATION AND FAILURE IN CRYSTALLINE MATERIALS 188
Organized by Pilar Ariza, Lucia Nicola, Angelo Simone

MS 202 - CIVIL ENGINEERING MATERIALS AND STRUCTURES UNDER EXTREME LOADINGS 216
Organized by Fabrice Gatuingt, Frédéric Dufour, Panagiotis Kotronis

MS 203 - COMPUTATIONAL METHODS FOR MODELLING INSTABILITIES IN SOLIDS & STRUCTURES 254
Organized by Spyros A. Karamanos

MS 204 - IMPACT AND CRASH MECHANICS 273
Organized by Manfred Bischoff, Fabian Duddeck

MS 205 - PROBABILISTIC APPROACH TO NUMERICAL SIMULATION OF FRACTURE 323
Organized by Alexander V. Gerasimov

MS 301 - METHODS FOR CUT AND COMPOSITE MESHES: THEORY, ALGORITHMS AND APPLICATIONS 373
Organized by Mats G. Larson, André Massing

MS 302 - MESH GENERATION AND ADAPTION 384
Organized by Josep Sarrate, Xevi Roca, Rafael Montenegro, Eloi Ruiz

MS 303 - CURVED MESH GENERATION FOR HIGH-ORDER METHODS 417
Organized by Xevi Roca, Josep Sarrate

MS 304 - COMPUTATIONAL MODELLING OF ADDITIVE PRODUCTION PROCESSES 469
Organized by Dirk Hartmann, Stefan Kollmannsberger, Ernst Rank, Utz Wever

MS 305 - ADVANCED MESHING METHODS FOR INDUSTRIAL APPLICATIONS 480
Organized by Frederic Alauzet, Thierry Coupez, Alain Dervieux, Adrien Loseille

MS 306 - LATTICE SPRING METHODS FOR LINEAR AND NONLINEAR CONTINUA 511
Organized by Ioannis Doltsinis

MS 403 - PARTICLE-BASED METHODS IN FLUID MECHANICS 539
Organized by Sergio Idelsohn, Eugenio Oñate

MS 404 - SIMULATION OF ENVIRONMENTAL FLOWS 650
Organized by Pablo Ortiz, Piotr K. Smolarkiewicz, Joanna Szmelter

MS 405 - COMPUTATIONAL MODELING OF MULTIPHASE FLOWS: ADVANCED METHODS, INTERFACE PHENOMENA AND ENVIRONMENTAL APPLICATIONS 750
Organized by Adeline Montlaur, Santiago Arias Calderón, Martin Kronbichler

MS 406 - ADVANCES IN COMPUTATIONAL METHODS FOR GAS-LIQUID TWO-PHASE FLOW 788
Organized by Byeong Rog Shin, Takeo Kajishima

MS 408 - MANIPULATION AND CONTROL OF TURBULENT FLOW 831
Organized by Markus Rütten, Christina Voß

MS 409 - CURRENT TRENDS IN MODELLING AND SIMULATION OF TURBULENT FLOWS 865
Organized by Suad Jakirlić

MS 410 - COMPLEX FLUID FLOWS IN ENGINEERING: MODELLING, SIMULATION AND OPTIMIZATION 949
Organized by Stefanie Elgeti, Philipp Knechtges

MS 411 - NON-NEWTONIAN HEAT AND FLUID FLOW SUBJECTED TO MAGNETIC FORCES 1061
Organized by Laszlo Konozsy, Dimitris Drikakis

MS 412 - NUMERICAL METHODS FOR WAVES AND FLOWS IN COASTAL AND DEEP WATER HYDRODYNAMICS 1093
Organized by Nina Shokina, Yuri Shokin, Leonid Chubarov, Gayaz Khakimzyanov, Vadym Aizinger, Denys Dutykh

MS 414 - NEW TRENDS IN NUMERICAL METHODS FOR MULTI-MATERIAL COMPRESSIBLE FLUID FLOWS 1139
Organized by Andy Barlow, Michael Dumbser, Raphaël Loubère, Pierre-Henri Maire, Rob Rieben, Mikhail Shashkov, François Vilar

MS 415 - COMPUTATIONAL NON-NEWTONIAN FLUID MECHANICS 1205
Organized by Georgios Georgiou, John Tsamopoulos

MS 501 - ALGORITHMIC ASPECTS OF HIGH-PERFORMANCE COMPUTING FOR MECHANICS AND PHYSICS 1237
Organized by Santiago Badia, Victor Calo, Javier Principe

MS 503 - HPC-BASED SIMULATIONS FOR THE ENGINEERING REALM AND INDUSTRIAL APPLICATIONS 1277
Organized by Makoto Tsubokura, Mariano Vázquez, Takayuki Aoki

MS 504 - NUMERICAL METHODS AND TOOLS FOR KEY EXASCALE COMPUTING CHALLENGES IN ENGINEERING AND APPLIED SCIENCES 1352
Organized by Eugenio Oñate, Manolis Papadrakakis, Peter Wriggers

MS 505 - INTERACTIVE SIMULATIONS IN COMPUTATIONAL ENGINEERING 1392
Organized by Adrian Harwood, Petra Wenisch

MS 506 - ACCURACY AND EFFICIENCY OF APPROXIMATE COMPUTATIONS IN SCIENCE AND ENGINEERING 1409
Organized by Aram Soroushian

MS 601 - SHOCK WAVE-BOUNDARY LAYER INTERACTION AND ITS CONTROL 1455
Organized by Piotr Doerffer, George Barakos

MS 602 - INNOVATIVE METHODS FOR FLUID-STRUCTURE-INTERACTION 1498
Organized by E. Harald van Brummelen, Roger Ohayon, Trond Kvamsdal

MS 603 - COMPUTATIONAL METHODS IN FLUID-STRUCTURE INTERACTION WITH IMPACT ON INDUSTRIAL APPLICATIONS 1582
Organized by Elisabeth Longatte, Yannick Hoarau, Marianna Braza

MS 605 - FRICTIONAL CONTACTS WITH LUBRICATION – BASICS AND APPLICATIONS 1623
Organized by Michael Müller, Thomas Hagemann

MS 606 - COMPUTATIONAL MODELING OF HYDRAULIC FRACTURING 1637
Organized by Gianluca Cusatis, Gilles Pijaudier-Cabot, Günther Meschke

MS 607 - ADVANCES IN COMPUTATIONAL METHODS FOR LIQUID-VAPOR FLOWS WITH PHASE TRANSFER PROCESSES 1672
Organized by Rémi Abgrall, Pietro M. Congedo, Tore Flåtten, Bernhard Müller, Marica Pelanti, Maria Giovanna Rodio

MS 608 - ADVANCES IN TIME INTEGRATION FOR SOLID, FLUID AND COUPLED SYSTEMS 1709
Organized by Ilinca Stanciulescu, Peter Betsch

MS 609 - ADVANCED COMPUTATIONAL MODELING OF BATTERIES AND FUEL CELLS 1838
Organized by Edwin Knobbe, Wolfgang A. Wall

MS 610 - NUMERICAL METHODS TO STUDY THE CONTACT MECHANICS OF DRY, ADHESIVE AND LUBRICATED ROUGH SURFACES 1850
Organized by Carmine Putignano, Daniele Dini

MS 612 - NUMERICAL SIMULATIONS FOR SMART-CITY APPLICATIONS 1876
Organized by Julien Waeytens, Rachida Chakir

MS 615 - COMPUTATIONAL MODELS IN MAGNETOHYDRODYNAMICS 1886
Organized by Oleg Zikanov

MS 701 - ADVANCED MATERIALS: COMPUTATIONAL ANALYSIS OF PROPERTIES AND PERFORMANCE 1893
Organized by Vadim V. Silberschmidt, Valery P. Matveenko

MS 702 - MODELING OF NANOFILLED COMPOSITES 1971
Organized by Konstantinos I. Tserpes

MS 705 - IDENTIFICATION OF MATERIAL MODELS 2003
Organized by Danuta Szeliga, Wacław Kuś, Tadeusz Burczyński, Jan Kusiak

MS 706 - MODELING OF FIBER-BASED STRUCTURES - TEXTILES AND TEXTILE REINFORCED COMPOSITES 2010
Organized by Yordan Kyosev, Philippe Boisse, Nahiene Hamila, Damien Durville

MS 707 - MICROMECHANICAL MODELLING: COMPETITION BETWEEN ANALYTICAL AND NUMERICAL METHODS 2039
Organized by Siegfried Schmauder, Vera Petrova

MS 711 - FOURIER-BASED METHODS FOR COMPUTING THE BEHAVIOR OF HETEROGENEOUS MATERIALS DEVELOPMENTS, EXTENSIONS AND APPLICATIONS 2099
Organized by Lionel Gélébart, Hervé Moulinec, Franz Roters, François Willot

MS 712 - SMART MATERIAL SYSTEMS AND STRUCTURES 2110
Organized by Mieczysław Kuczma, Pavel Krejči, Jörg Schröder, Georgios E. Stavroulakis, Gwidon Szefer

MS 713 - MICROSTRUCTURE-BASED MODELLING OF HETEROGENEOUS MATERIALS 2134
Organized by Jan Zeman, Jan Novak, Guillermo Díaz

MS 714 - STRENGTH, FATIGUE AND STABILITY OF COMPOSITE STRUCTURES 2182
Organized by Raimund Rolfes, Martin Ruess, Kai-Uwe Schröder

VOLUME II

MINISYMPOSIA

MS 715 - COMPUTATIONAL ANALYSIS OF COMPOSITE STRUCTURES 2210
Organized by Efstathios E. Theotokoglou

MS 801 - MULTISCALE COMPUTATIONAL HOMOGENIZATION FOR BRIDGING SCALES IN THE MECHANICS AND PHYSICS OF COMPLEX MATERIALS 2266
Organized by Julien Yvonnet, Kenjiro Terada, Peter Wriggers, Marc Geers

MS 802 - ADVANCES IN THE MODELLING OF MULTI-SCALE, MULTI-PHYSICS AND MULTI-UNCERTAINTY PROBLEMS 2323
Organized by Francisco M. Andrade Pires, Chengfeng Li

MS 805 - ADVANCED MULTI-PHYSICS AND MULTI-SCALE TECHNIQUES FOR MODELING INELASTIC PROCESSES IN SOLIDS: DAMAGE, FRACTURE AND CONTACT MECHANICS 2353
Organized by Mauro Corrado, Marco Paggi, José Reinoso

MS 806 - MULTISCALE MODELLING OF MATERIALS AND STRUCTURES 2363
Organized by Tadeusz Burczyński, Xavier Oliver, Maciej Pietrzyk, Alfredo Huespe

MS 807 - ADVANCED COMPUTATIONAL STRATEGIES FOR MODELLING, SIMULATION AND CHARACTERISATION OF MULTI-SCALE HETEROGENEOUS MATERIALS 2449
Organized by Stéphane Bordas, Daniel Dias-da-Costa, Fabrice Pierron, Timon Rabczuk, Pierre Kerfriden, Pascal Lava

MS 808 - MULTISCALE AND MULTIPHYSICS MODELING OF CEMENTITIOUS MATERIALS 2460
Organized by Jörg F. Unger, Thomas Titscher

MS 809 - MULTISCALE STOCHASTIC FINITE ELEMENT METHODS 2471
Organized by George Stefanou, Xi Frank Xu, Yu Ching Wu

MS 811 - MULTISCALE MODELING OF CONCRETE AND CONCRETE STRUCTURES 2501
Organized by Herbert Mang, Yong Yuan

MS 901 - ISOGEOMETRIC METHODS 2514
Organized by Yuri Bazilevs, David J. Benson, Rene De Borst, Thomas J.R. Hughes, Trond Kvamsdal, Alessandro Reali, Giancarlo Sangalli, Clemens V. Verhoosel

MS 902 - INNOVATIVE NUMERICAL APPROACHES FOR MULTI-PHYSICS PROBLEMS 2558
Organized by Anna Pandolfi, Laurent Stainier, Kerstin Weinberg

MS 903 - ADVANCES IN FICTITIOUS DOMAIN METHODS FOR SOLID MECHANICS 2566
Organized by Alexander Düster, Ernst Rank, Stefan Kollmannsberger, Andreas Schröder

MS 905 - DISCONTINUOUS GALERKIN METHODS: NEW TRENDS AND APPLICATIONS 2614
Organized by Sonia Fernández-Méndez, Nicoletta Franchina

MS 906 - MATHEMATICAL ADVANCES IN ISOGEOMETRIC ANALYSIS 2715
Organized by Annalisa Buffa, John A. Evans, Thomas J.R. Hughes, Giancarlo Sangalli

MS 907 - REGULARIZED ENRICHED APPROXIMATIONS AND QUADRATURE FOR DISCONTINUITIES, SINGULARITIES AND CONTINUOUS-DISCONTINUOUS TRANSITION 2726
Organized by Elena Benvenuti, Giulio Ventura, José M.A. César de Sá

MS 908 - VERIFICATION AND VALIDATION OF STRUCTURAL MECHANICS SIMULATION MODELS 2734
Organized by George Lampeas

MS 910 - HIGH ORDER CFD METHODS: CONCLUSIONS AND OUTLOOK 2843
Organized by Koen Hillewaert, John Ekaterinaris, Peter Vincent, Norbert Kroll, Norbert Huynh, Z.J. Wang

MS 911 - NUMERICAL METHODS IN THE MECHANICS OF GENERALIZED CONTINUA 2869
Organized by Elena Atroshchenko, Jack S. Hale, George Bourantas, Stéphane P.A Bordas

MS 912 - HIGH-ORDER METHODS, SENSITIVITY ANALYSIS AND ADAPTATION FOR THE NAVIER STOKES EQUATIONS 2883
Organized by Vincent Couaillier, Rémi Abgrall, Eusebio Valero

MS 913 - HIGH-ORDER METHODS FOR POLYGONAL AND POLYHEDRAL MESHES 2930
Organized by Lourenço Beirao da Veiga, Franco Brezzi, Donatella Marini, Alessandro Russo

MS 916 - DIRECT METHODS FOR LIMIT STATES OF MATERIALS AND STRUCTURES 2971
Organized by Konstantinos V. Spiliopoulos, Dieter Weichert

MS 917 - MESOSCOPIC METHODS FOR COMPLEX FLUIDS AND SOFT MATTER 3026
Organized by Zhen Li, Wenxiao Pan, Igor V. Pivkin

MS 918 - COMPUTER ALGEBRA SYSTEMS IN MODELLING STATIC AND DYNAMIC PROBLEMS IN MECHANICS OF SOLIDS 3045
Organized by Alexander V. Matrosov, Dmitriy P. Goloskokov

MS 919 - RECENT ADVANCES IN NUMERICAL SIMULATION AND ANALYSIS OF KINETIC MODELS 3113
Organized by E. Harald van Brummelen, Manuel Torrilhon

MS 921 - RECENT ADVANCES IN BOUNDARY ELEMENT METHODS 3139
Organized by Gernot Beer, Luiz Wrobel, Martin Schan

MS 922 - HIGH-ORDER METHODS FOR ELASTIC WAVES AND THEIR APPLICATION 3211
Organized by Thomas Hagstrom, Daniel Appelo

MS 923 - NOVEL DISCRETIZATION METHODS – MATHEMATICAL AND MECHANICAL ASPECTS 3224
Organized by Jörg Schröder, Peter Wriggers, Ferdinando Auricchio, Carsten Carstensen

MS 1001 - STRUCTURAL AND MULTIDISCIPLINARY OPTIMIZATION 3239
Organized by J.F. Aguilar Madeira, Helder C. Rodrigues

MS 1002 - EVOLUTIONARY ALGORITHMS AND METAHEURISTICS IN CIVIL ENGINEERING AND CONSTRUCTION MANAGEMENT 3473
Organized by Jorge Magalhaes-Mendes, David Greiner

MS 1003 - ADVANCES IN DESIGN OPTIMIZATION OF STRUCTURES AND MATERIALS 3534
Organized by Zhen Luo, Zhan Kang

MS 1004 - AERODYNAMIC STRATEGIES FOR THE GLOBAL OPTIMIZATION OF FLYING CONFIGURATIONS IN SUPERSONIC FLOW 3596
Organized by Adriana Nastase, Catalin Nae

MS 1005 - MONITORING AND CONTROL OF STRUCTURES 3630
Organized by Resat Oyguc

MS 1006 - PARAMETER IDENTIFICATION IN SOLID MECHANICS 3652
Organized by A. Gil Andrade-Campos, Marco Rossi, Sandrine Thuillier, Franck Toussaint, Marta C. Oliveira

MS 1007 - ADDITIVE MANUFACTURING AND OPTIMIZATION 3689
Organized by Ekkehard Ramm, Ole Sigmund, Pierre Duysinx, Wing Kam Liu

MS 1008 - ULTRASONIC GUIDED WAVES TESTING AND MONITORING 3753
Organized by Yaacoubi Slah, Nico Declercq

MS 1009 - ADJOINT METHODS FOR STEADY & UNSTEADY OPTIMIZATION 3770
Organized by Kyriakos C. Giannakoglou, Jens Dominik Mueller

MS 1010 - INVERSE PROBLEMS, DESIGN AND OPTIMIZATION 4061
Organized by Marcelo J. Colaço, Helcio R. B. Orlande, George S. Dulikravich

MS 1011 - SURROGATE-ASSISTED EVOLUTIONARY ALGORITHMS IN AERODYNAMIC DESIGN/OPTIMIZATION 4082
Organized by Varvara Asouti, Esther Andrés, Emiliano Iuliano

MS 1013 - SOLUTION OF LARGE-SCALE INVERSE PROBLEMS 4164
Organized by Clint Dawson, Steve Mattis, Troy Butler, Lindley Graham

MS 1014 - DESIGN OPTIMIZATION AND INVERSE PROBLEMS FOR WAVE PROPAGATION PROBLEMS 4178
Organized by Martin Berggren

MS 1101 - REDUCED BASIS, POD AND PGD MODEL ORDER REDUCTION TECHNIQUES 4187
Organized by

MS 1103 - MATHEMATICAL SURROGATE MODELLING IN ELECTROMAGNETICS 4284
Organized by Francisco Chinesta, Elias Cueto, Antonio Huerta, Pierre Ladeveze, Gianluigi Rozza

MS 1201 - COMPUTATIONAL STRUCTURAL DYNAMICS 4351
Organized by
Evangelos J. Sapountzakis, Andreas E. Kampitsis

VOLUME III

MINISYMPOSIA

MS 1202 - ADVANCED BEAM MODELS 4445
Organized by Dinar Camotim, Zuzana Dimitrovová, Rodrigo Gonçalves

MS 1203 - THE MODELS AND INVESTIGATIONS METHODS OF DYNAMICS OF THE SOLIDS SYSTEMS WITH DRY FRICTION 4553
Organized by Alexey A. Kireenkov, Alexander V. Karapetyan

MS 1204 - NONLINEAR DYNAMICS OF ROTATING STRUCTURES 4611
Organized by Evangeline Capiez-Lernout, Marc P. Mignolet, Christian Soize

MS 1206 - ADVANCES IN NUMERICAL METHODS FOR LINEAR AND NON-LINEAR DYNAMICS AND WAVE PROPAGATION 4674
Organized by Alexander Idesman

MS 1207 - COMPUTATIONAL SIMULATION OF SMART STRUCTURES AND MATERIALS 4728
Organized by Ruediger Schmidt, Kai-Uwe Schröder

MS 1208 - BIFURCATIONS AND STABILITY 4741
Organized by Pekka Neittaanmäki, Nikolay Banichuk, Juha Jeronen, Tero Tuovinen

MS 1209 - DYNAMIC ANALYSIS OF BEAMS UNDER MOVING VEHICLES: APPLICATION TO RAILWAY TRACK MODELLING, DESIGN AND REHABILITATION 4780
Organized by Fernardo Simões, Antonio Pinto da Costa

MS 1210 - ADVANCES IN MODELING AND ANALYSIS OF FGM STRUCTURES 4810
Organized by Justin Murin, Stephan Kugler, Mehdi Aminbaghai

MS 1211 - COMPUTATIONAL STRATEGIES FOR STRUCTURAL ROBUSTNESS ASSESSMENT 4900
Organized by Domenic Asprone, Fulvio Parisi

MS 1212 - DYNAMICS AND SEISMIC RESPONSE OF ROCKING AND SELF-CENTERING STRUCTURES..... 4959
Organized by Matthew DeJong, Elias Dimitrakopoulos, Michalis Fragiadakis

MS 1213 - INNOVATIVE STRUCTURAL SYSTEMS FOR SEISMIC RESISTANT BUILDINGS 5142
Organized by Carlo Castiglioni

MS 1214 - HISTORIC MASONRY STRUCTURES: MODELLING, ASSESSMENT & RETROFIT 5172
Organized by Panagiotis Asteris, Charilaos Maniatakis, Constantine Spyrakos

MS 1215 - NONLINEAR VIBRATIONS OF CONSERVATIVE AND NONCONSERVATIVE SYSTEMS: PHENOMENA AND ADVANCED NUMERICAL METHODS 5396
Organized by Malte Krack, Ludovic Renson, Gaëtan Kerschen

MS 1216 - STRUCTURAL ANALYSIS AND VIBRATIONS 5444
Organized by Diana V. Bambill, Carlos A. Rossit

MS 1217 - COMPUTATIONAL METHODS IN EARTHQUAKE ENGINEERING AND STRUCTURAL DYNAMICS 5464
Organized by Vagelis Plevris, Georgia Kremmyda, Yasin Fahjan

MS 1218 - STABILITY AND CONTROL OF FLEXIBLE STRUCTURES 5646
Organized by Ilaria Venanzi, Marco Lepidi

MS 1220 - DYNAMICS OF STRUCTURES SUBJECT TO SEISMIC EXCITATIONS 5712
Organized by Michel Géradin, Evtim Zahariev, Evangelos J. Sapountzakis

MS 1221 - COMPUTATIONAL STRUCTURAL STABILITY 5768
Organized by Herbert A. Mang, Yeon-Bin Yang

MS 1222 - INFLUENCE OF LIQUEFIABLE SOIL ON SINGLE AND CLOSELY CLUSTERED STRUCTURES 5817
Organized by Nawawi Chouw, Rolly Orense, Tam Larkin

MS 1224 - INNOVATIVE SOLUTIONS FOR THE SEISMIC PROTECTION OF INDUSTRIAL BUILDINGS 5834
Organized by Walter Salvatore, Carlo Castiglioni, Francesco Morelli, Nikolaos Bakas

MS 1225 - SEISMIC PERFORMANCE ASSESSMENT OF STRUCTURES AND SEISMIC RISK MITIGATION STRATEGIES 5934
Organized by Marco Vona

MS 1301 - THE STOCHASTIC COMPUTER METHODS IN MECHANICS 6029
Organized by Marcin Kamiński, Takahiko Kurahashi

MS 1303 - ANALYSIS AND DESIGN OF SAFETY CRITICAL SYSTEMS UNDER UNCERTAINTY 6091
Organized by Edoardo Patelli, Michael Beer, Matteo Broggi, Francisco Alejandro Díaz De la O

MS 1304 - STOCHASTIC MODELING AND IDENTIFICATION OF UNCERTAINTIES IN COMPUTATIONAL MECHANICS 6136
Organized by Johann Guilleminot, Maarten Arnst, Christian Soize

MS 1306 - ERCOFTAC SIG-45: UNCERTAINTY QUANTIFICATION IN CFD AND FLUID STRUCTURE INTERACTION 6196
Organized by Didier Lucor, Sunetra Sarkar

MS 1307 - NON-INTRUSIVE SURROGATE MODELS FOR UNCERTAINTY QUANTIFICATION IN HIGH DIMENSIONS 6250
Organized by Bruno Sudret, Eleni Chatzi, Jean-Marc Bourinet, Nicolas Gayton

MS 1308 - MODELLING AND INVERSE METHODS IN NONLINEAR DYNAMICAL SYSTEMS 6316
Organized by Sotirios Natsiavas, Costas Papadimitriou, Eleni Chatzi, Dimitrios Giagopoulos

MS 1309 - SCALABLE MULTI-FIDELITY MODELING FOR DESIGN, UNCERTAINTY QUANTIFICATION, AND INVERSE PROBLEMS 6383
Organized by Paris Perdikaris, George Em. Karniadakis

MS 1310 - COMPUTATIONAL METHODS FOR THE SOLUTION OF STOCHASTIC DIFFERENTIAL EQUATIONS 6398
Organized by Jianbing Chen, Ioannis Kougioumtzoglou, Vissarion Papadopoulos

MS 1401 - TOICA: THERMAL OVERALL INTEGRATED CONCEPT AIRCRAFT 6420
Organized by Pierre Arbez, Jean-Claude Dunyach

STS 3 - INNOVATIVE DESIGN OPTIMIZATION TOOLS LINKED TO INDUSTRIAL AERONAUTICAL APPLICATIONS: TARGETING GREENER PERFORMANCES 6471
Organized by Jacques Periaux, Gabriel Bugeda

STS 5 - TRANSITION LOCATION EFFECT ON SHOCK WAVE BOUNDARY LAYER INTERACTION 6485
Organized by Piotr Doerffer, Pawel Flaszynski

STS 7 - MORPHING TECHNOLOGIES FOR AIRCRAFT WINGS 6496
Organized by Hans Peter Monner

STS 9 - ADVANCED WING HIGH-LIFT SYSTEMS 6505
Organized by Jochen Wild

YOUNG INVESTIGATORS MINISYMPOSIUM 6515
Organized by Jaan-Willem Simon, Alexander Popp, Joan Baiges

ECCOMAS OLYMPIAD MINISYMPOSIUM 6526

VOLUME IV

CONTRIBUTED SESSIONS

CS 110 - NUMERICAL MODELS IN BIOMECHANICS 6539

CS 210 - NUMERICAL SIMULATION OF COMPOSITE MATERIALS 6637

CS 211 - CRACK PROPAGATION 6688

CS 212 - NUMERICAL MODELING OF DAMAGE, FAILURE AND FRACTURE 6699

CS 230 - DYNAMIC FAILURE AND FRACTURE 6799

CS 310 - CAD, CAM AND CAE 6847

CS 320 - GRID GENERATION AND ADAPTIVE TECHNIQUES 6911

CS 410 - COMPUTATIONAL FLUID MECHANICS 6955

CS 420 - MULTI-PHASE AND CHEMICALLY REACTING FLOWS 7138

CS 450 - NUMERICAL METHODS AND CONVERGENCE ACCELERATION IN CFD 7274

CS 460 - UNSTEADY FLOW COMPUTATION 7390

CS 500 - HIGH PERFORMANCE COMPUTING 7572

CS 610 - AERO-ACOUSTICS 7589

CS 620 - COMPUTATIONAL CONTACT MECHANICS 7628

CS 630 - SIMULATION OF FLUID-STRUCTURE INTERACTION 7640

CS 720 - COMPUTATIONAL MATERIALS SCIENCE 7711

CS 750 - COMPUTATIONAL MODELING OF COMPOSITES 7765

CS 751 - SMART MATERIALS AND STRUCTURES 7853

CS 830 - COMPUTATIONAL NANOTECHNOLOGY 7875

CS 840 - MULTI-SCALE COMPUTATIONAL METHODS FOR SOLIDS AND FLUIDS 7886

CS 930 - HIGH-ORDER DISCRETIZATION METHODS 7956

CS 940 - EXTENDED DISCRETIZATION METHODS 8066

CS 960 - MESHLESS METHODS 8115

CS 980 - NUMERICAL AND SYMBOLIC COMPUTATION 8162

CS 990 - PARTICLE-BASED METHODS 8196

CS 1010 - COMPUTATIONAL INVERSE PROBLEMS AND OPTIMIZATION 8247

CS 1020 - EVOLUTIONARY AND DETERMINISTIC METHODS FOR DESIGN, OPTIMIZATION AND CONTROL 8391

CS 1100 - REDUCTION ORDER METHODS 8539

CS 1200 - STRUCTURAL DYNAMICS 8597

CS 1201 - COMPUTATIONAL SOIL MECHANICS 8708

CS 1202 - STRUCTURAL ANALYSIS AND MULTIBODY DYNAMICS 8739

CS 1300 - UNCERTAINTY QUANTIFICATION AND ERROR ESTIMATION 8769

CONTENTS

Semi-plenary Lectures

NONPARAMETRIC PROBABILISTIC APPROACH OF MODEL UNCERTAINTIES INTRODUCED BY A PROJECTION-BASED NONLINEAR REDUCED-ORDER MODEL 1
Christian Soize, Charbel Farhat

Minisymposia

100 BIOLOGICAL SYSTEMS

MS 102: COMPUTATIONAL MODELS IN BIOMECHANICS AND MECHANOBIOLOGY

THE INFLUENCE OF MECHANICAL STIMULUS ON NUTRIENT TRANSPORT AND CELL GROWTH IN ENGINEERED CARTILAGE: A FINITE ELEMENT APPROACH 27
S. Cortez, A. Completo, J.L. Alves

HYBRID CELL CENTRED/VERTEX MODEL FOR LARGE TISSUE DEFORMATIONS 37
José J. Muñoz, Payman Mosaffa, Yanlan Mao, Rob Tetley, Nina Asadipour, Antonio Rodríguez-Ferran

SENSITIVITY OF TEMPERATURE FIELD IN THE SYSTEM PROTECTIVE CLOTHING - FOREARM WITH RESPECT TO PERTURBATIONS OF EXTERNAL HEATING CONDITIONS 46
Bohdan Mochnacki, Mariusz Ciesielski

MS 103: MECHANICS OF BIOLOGICAL TISSUES

INFLUENCE OF MUSCLE COMPRESSION ON DYNAMIC MUSCLE PERFORMANCE 55
Tobias Siebert, Norman Stutzig, Olaf Till, Christian Rode

A 3D ELECTROMECHANICAL FEM-BASED MODEL FOR CARDIAC TISSUE 63
Minh Tuan Duong, Alexander Jung, Ralf Frotscher, Manfred Staat

BIOMECHANICAL PROPERTIES OF CORNEAL EXTRACELLULAR MATRIX USING EXPERIMENTAL AND COMPUTATIONAL METHODS 74
Hamed Hatami-Marbini

MS 105: SIMULATION OF CARDIOVASCULAR PROCEDURES AND DEVICES

MODELLING OF PATIENT-SPECIFIC CASES OF ATHEROSCLEROSIS IN CAROTID ARTERIES 81
Timur Gamilov, Roman Pryamonosov, Sergey Simakov

PERSONALIZED COMPUTATION OF FRACTIONAL FLOW RESERVE IN CASE OF TWO CONSECUTIVE STENOSES ... 90
Yuri Vassilevski, Timur Gamilov, Philip Kopylov

MS 106: DIRECT AND INVERSE METHODS FOR CARDIOVASCULAR AND PULMONARY BIOMECHANICS

BLOOD FLOW IN THE COMMON CAROTID ARTERY WITH STENOSIS 98
Helena Henriques, Luisa Sousa, Catarina Castro, Carlos António, Rosa Santos, Pedro Castro, Elsa Azevedo

MS 108: NUMERICAL METHODS FOR COUPLED PROBLEMS IN BIOMEDICAL APPLICATIONS
A FENICS-HPC FRAMEWORK FOR MULTI-COMPARTMENT BLOCH-TORREY MODELS 105
Dang Van Nguyen, Johan Jansson, Johan Hoffman

MS 111: POPULATION BALANCE MODELING: CURRENT STATUS, FUTURE PROSPECTS AND NOVEL APPLICATIONS FROM NANOPARTICLES' SYNTHESIS TO (LUNG) CANCER
THERMODYNAMICS OF IRREVERSIBLE AGGREGATION 120
Themis Matsoukas

MS 112: ANEURYSMS: SOLID MECHANICS, FLUID MECHANICS, AND MECHANOBIOLOGY
RELATIVE ROLES OF MECHANICS AND BIOCHEMISTRY IN THE INITIATION AND PROGRESSION OF CEREBRAL ANEURYSM THROMBOSIS 137
Malebogo Ngoepe, Yiannis Ventikos

TECHNIQUES TO INTEGRATE PATIENT-SPECIFIC SIMULATION OF ANEURYSMAL BLOOD FLOW INTO THE CLINICAL WORKFLOW 147
Gábor Závodszky, Roland Joó-Kovács, György Paál, István Szikora

MS 113: MATHEMATICAL AND NUMERICAL MODELING OF THE HEART
PROXIMAL ISOVELOCITY SURFACE FOR DIFFERENT MITRAL VALVE HOLE GEOMETRIES 155
Alexandre This, Hernán G. Morales, Odile Bonnefous

COMPARISON OF TETRAHEDRAL AND HEXAHEDRAL MESHES FOR FINITE ELEMENT SIMULATION OF CARDIAC ELECTRO-MECHANICS 164
Bernardo Lino De Oliveira, Joakim Sundnes

MS 115: TUMOR GROWTH MODELING AND THE MECHANICAL ASPECTS OF CANCER
A PARAMETRIC STUDY OF A MULTIPHASE POROUS MEDIA MODEL FOR TUMOR SPHEROIDS AND ENVIRONMENT INTERACTIONS 178
P. Mascheroni, D.P. Boso, C. Stigliano, M. Carfagna, L. Preziosi, P. Decuzzi, B.A. Schrefler

200 DAMAGE, FRACTURE AND FAILURE

MS 201: MICROSTRUCTURE-DRIVEN DEFORMATION AND FAILURE IN CRYSTALLINE MATERIALS
STABILITY OF ASYMMETRIC GRAIN BOUNDARIES IN GRAPHENE 188
J.P. Mendez, F. Arca, M.P. Ariza

DEFORMATION-DIFFUSION COUPLED ANALYSIS OF LONG-TERM HYDROGEN DIFFUSION IN NANOFILMS 197
Xingsheng Sun, Pilar Ariza, Kevin Wang

MESH OBJECTIVE DAMAGE MODELING OF DUCTILE FRACTURE AT VISCO-PLASTIC CONTINUUM RESPONSE ... 209
Senad Razanica, Ragnar Larsson, B. Lennart Josefson

MS 202: CIVIL ENGINEERING MATERIALS AND STRUCTURES UNDER EXTREME LOADINGS

EQUIVALENT SDOF MODEL FOR ESTIMATING BLAST-INDUCED DYNAMIC REACTIONS OF EQUILATERAL TRIANGULAR HARDENED WALL ELEMENTS 216
Sebastian Mendes, Liling Cao, Douglas Heinze, Elisabeth Malsch

MODELLING STRATEGIES OF PRESTRESSING TENDONS AND REINFORCEMENT BARS IN CONCRETE STRUCTURES 234
Antoine Llau, Ludovic Jason, Frédéric Dufour, Julien Baroth

MODELING AND SIMULATION FOR AN OPTIMIZED DESIGN OF A DYNAMIC BEND TEST. 242
Rana Akiki, Fabrice Gatuingt, Cédric Giry, Nicolas Schmitt, Lavinia Stéfan

MS 203: COMPUTATIONAL METHODS FOR MODELLING INSTABILITIES IN SOLIDS & STRUCTURES

ON STABILITY LOSS OF A THIN-WALLED SPHERICAL SHELL SUBJECTED TO EXTERNAL PRESSURE AND INTERNAL HOMOGENEOUS CORROSION 254
Emmanuel Gutman, Rudolf Bergman, Semyon Levitski

EFFICIENCY OF DAMAGE-PLASTICITY MODELS IN CAPTURING COMPACTION-EXPANSION TRANSITION OF CONCRETE UNDER DIFFERENT COMPRESSION LOADING CONDITIONS 261
Reza Mousavi, Masoud D. Champiri, Kaspar J. Willam

MS 204: IMPACT AND CRASH MECHANICS

A SIMPLIFIED MODEL OF A STEEL COLUMN SUBJECTED TO IMPACT 273
Piseth Heng, Mohammed Hjiaj, Jean-Marc Battini

MATERIAL MODELLING OF CAST ALUMINIUM BY APPLICATION OF THE WILKINS DAMAGE MODEL 287
Christian Mühlstätter, Matthias Hartmann

FINITE ELEMENT SIMULATION OF CRACK PROPAGATION AND DELAMINATION IN LAYERED SHELLS DUE TO BLADE CUTTING 295
Federica Confalonieri, Aldo Ghisi, Umberto Perego

EVOLUTIONARY LEVEL SET METHOD FOR CRASHWORTHINESS TOPOLOGY OPTIMIZATION 309
Mariusz Bujny, Nikola Aulig, Markus Olhofer, Fabian Duddeck

MS 205: PROBABILISTIC APPROACH TO NUMERICAL SIMULATION OF FRACTURE

NUMERICAL SIMULATION OF HIGH-VELOCITY INTERACTION ELEMENTS WITH THIN-WALLED STRUCTURES ... 323
Alexander V. Gerasimov, Sergey V. Pashkov

NUMERICAL SIMULATION OF MULTILAYER COMPOSITES FAILURE UNDER DYNAMIC LOADING 334
Sergey A. Zelepugin, Aleksey S. Zelepugin, Vladimir F. Tolkachev

SIMULATION OF MECHANICAL PROPERTIES OF CERAMIC PARTS PRODUCED BY ADDITIVE TECHNOLOGIES IN WIDE RANGE OF LOADING RATES 341
Vladimir A. Skripnyak, Evgeniya Skripnyak, Vladimir V. Skripnyak, Irina K. Vaganova

FRACTURE OF THIN METAL SHEETS WITH DISTRIBUTION OF GRAIN SIZES IN THE LAYERS 355
Natalia V. Skripnyak, Vladimir V. Skripnyak, Vladimir A. Skripnyak

BRITTLE OR QUASI-BRITTLE FRACTURE OF CERAMIC NANOCOMPOSITES UNDER DYNAMIC LOADING 366
Evgeniya G. Skripnyak, Vladimir A. Skripnyak, Vladimir V. Skripnyak, Natalia V. Skripnyak, Irina K. Vaganova

300 DISCRETIZATION METHODS, GRID, MESH AND SOLID GENERATION

MS 301: METHODS FOR CUT AND COMPOSITE MESHES: THEORY, ALGORITHMS AND APPLICATIONS
REMOVING THE STABILIZATION PARAMETER IN FITTED AND UNFITTED SYMMETRIC NITSCHE FORMULATIONS 373
Christoph Lehrenfeld

MS 302: MESH GENERATION AND ADAPTION
A SEMI-UNSTRUCTURED TURBOMACHINERY MESHING LIBRARY WITH FOCUS ON MODELING OF SPECIFIC GEOMETRICAL FEATURES 384
Marco Stelldinger, Thomas Giersch, Felix Figaschewsky, Arnold Kühhorn

CARTESIAN MESHES WITH DYNAMIC LOCAL WAVELET-BASED REFINEMENT FOR FLOW AROUND BODY PROBLEMS. 402
Kirill Merkulov, Igor Menshov, Andrew Plenkin

A MESH GENERATION METHOD FOR HISTORICAL MONUMENTAL BUILDINGS: AN INNOVATIVE APPROACH ... 409
Giovanni Castellazzi, Antonio Maria D'Altri, Stefano De Miranda, Francesco Ubertini, Gabriele Bitelli, Alessandro Lambertini, Ilenia Selvaggi, Antonio Tralli

MS 303: CURVED MESH GENERATION FOR HIGH-ORDER METHODS
HIGH-ORDER CURVED MESH GENERATION BY USING A FINE LINEAR TARGET MESH 417
Verena Schmid, Hadrien Beriot, Onur Atak, Gwenael Gabard

AUTOMATIC GENERATION OF 3D UNSTRUCTURED HIGH-ORDER CURVILINEAR MESHE 428
Michael Turner, David Moxey, Spencerj.Sherwin, Joaquim Peiro

MESH GENERATION FOR THE 2D NURBS-ENHANCED FINITE ELEMENT METHOD 444
Ruben Sevilla, Luke Rees, Oubay Hassan

IMAGE SEGMENTATION TECHNIQUES FOR BIOMEDICAL MODELING: ELECTROPHYSIOLOGY AND HEMODYNAMICS 454
Alexander Danilov, Roman Pryamonosov, Alexandra Yurova

A CONSISTENTLY LINEARISED SOLID MECHANICS BASED MESH DEFORMATION TECHNIQUE FOR HIGH ORDER CURVED ELEMENTS 462
Roman Poya, Ruben Sevilla, Antonio Gil

MS 304: COMPUTATIONAL MODELLING OF ADDITIVE PRODUCTION PROCESSES
VALIDATION OF MODELLING ASSUMPTIONS FOR THE BUILDUP SIMULATION OF LASER BEAM MELTING ON THE BASIS OF THE RESIDUAL STRESS DISTRIBUTION 469
Fabian Bayerlein, Christian Zeller, Martin Wunderer, Johannes Weirather, Michael F. Zäh, Markus Schmid, Georg Schlick, Roland Hessert, Michael Hofmann, Thomas Uihlein

MS 305: ADVANCED MESHING METHODS FOR INDUSTRIAL APPLICATIONS
MESHING OCEAN DOMAINS FOR COASTAL ENGINEERING APPLICATIONS 480
Alexandros Avdis, Christian Jacobs, Simon Mouradian, Jon Hill, Matthew Piggott

HIGH-ORDER TRACKING METHOD FOR THE SIMULATION OF BURNING FRONTS IN 3D 493
Denis Gueyffier, Bastien Andrieu

SINGULAR MESH GENERATION FROM MULTIPLE OVERSET MESHES: A TOOL FOR INDUSTRIAL APPLICATIONS...501
Gennaro Abbruzzese, Marta Cordero Gracia, Mariola Gómez López, Nuno Vinha

MS 306: LATTICE SPRING METHODS FOR LINEAR AND NONLINEAR CONTINUA
GENERATING TRIANGULAR LATTICES FOR SURFACES WITH IRREGULAR BOUNDARY 511
Tatiana Sá Marques, Vitor Dias Da Silva

WAVE TRANSMISSION THROUGH NONLINEAR IMPACTING METAMATERIAL UNIT 526
Arnab Banerjee, Raj Das, Emilio Calius

400 FLOW PROBLEMS

MS 403: PARTICLE-BASED METHODS IN FLUID MECHANICS
A PARTICLE FINITE ELEMENT METHOD FOR MACHINING SIMULATIONS 539
Juan Manuel Rodríguez Prieto, Pär Jonsén, Ales Svoboda

DYNAMICS OF DUST PARTICLES NEAR THE ROUND BELL SUCTION INLET 554
Olga Averkova, Konstantin Logachev, Artur Logachev, Elena Tolmacheva

RECOVERY OF DIFFERENTIATION/INTEGRATION COMPATIBILITY OF MESHLESS OPERATORS VIA LOCAL ADAPTATION OF THE POINT CLOUD IN THE CONTEXT OF NODAL INTEGRATION 568
Gabriel Fougeron, Guillaume Pierrot, Denis Aubry

MODELING OF NON-SPHERICAL, ELONGATED PARTICLES FOR INDUSTRIAL SUSPENSION FLOW SIMULATION ... 586
Jakob Dominik Redlinger-Pohn, Lisa Maria König, Christoph Kloss, Christoph Goniva, Stefan Radl

A LAGRANGIAN FINITE ELEMENT METHOD FOR THE SIMULATION OF 3D COMPRESSIBLE FLOWS 600
Massimiliano Cremonesi, Attilio Frangi

A LAGRANGIAN PFEM APPROACH TO THE NUMERICAL SIMULATION OF 3D LARGE SCALE LANDSLIDES IMPINGING IN WATER RESERVOIRS 608
Massimiliano Cremonesi, Francesco Ferri, Umberto Perego

A NUMERICAL INVESTIGATION OF FLOW DYNAMICS OVER A TRAPEZOIDAL SMOOTH OPEN CHANNEL ……..... 619
Giacomo Viccione

A NUMERICAL INVESTIGATION OF LIQUID IMPACT ON PLANAR SURFACES. …….. 627
Giacomo Viccione, Vittorio Bovolin, Eugenio Pugliese Carratelli

AERODYNAMICS OF AN UNSTEADY PARTICLE FLOW IN THE CHUTE …….. 638
Olga Averkova, Ivan Logachev, Konstantin Logachev

MS 404: SIMULATION OF ENVIRONMENTAL FLOWS
PROJECTION-BASED MODEL REDUCTION FOR FINITE ELEMENT APPROXIMATION OF SHALLOW WATER FLOWS …….. 650
Matthew Farthing, Alexander Lozovskiy, Christopher Kees

EFFICIENT TWO-DIMENSIONAL SIMULATION MODELS FOR HYDRAULIC AND MORPHODYNAMIC TRANSIENTS..670
Pilar Garcia-Navarro, Javier Murillo, Mario Morales-Hernandez, Carmelo Juez, Asier Lacasta

ADDRESSING THE CHALLENGES OF IMPLEMENTATION OF HIGH-ORDER FINITE-VOLUME SCHEMES FOR ATMOSPHERIC DYNAMICS ON UNSTRUCTURED MESHES …….. 684
Panagiotis Tsoutsanis, Dimitris Drikakis

MODELLING OF LONG WAVES (SEICHES) IN CASCAIS BAY …….. 709
Vera Bras, Antonio Trigo-Teixeira

A MESHLESS METHOD FOR SIMULATION OF PARTICLE-DRIVEN GRAVITY CURRENTS WITH OBSTACLES ……. 720
Karel Kovářík, Jozef Mužík, Dana Sitányiová

APPLICATION OF THE SHALLOW WATER EQUATIONS TO REAL FLOODING CASE …….. 735
Hani Ali, Pierre-Yves Lagrée, Jose-Maria Fullana

MS 405: COMPUTATIONAL MODELING OF MULTIPHASE FLOWS: ADVANCED METHODS, INTERFACE PHENOMENA AND ENVIRONMENTAL APPLICATIONS
A MULTIPHASE MODEL FOR THE NUMERICAL SIMULATION OF ICE-FORMATION IN SEA-WATER …….. 750
Vanessa Covello, Antonella Abbà, Luca Bonaventura, Alessandro Della Rocca, Lorenzo Valdettaro

A 3D CFD NUMERICAL STUDY OF THE BUBBLE GENERATION PROCESS INTO A BUBBLE T-JUNCTION GENERATOR AND ITS COMPARISON WITH EXPERIMENTAL DATA: PART I …….. 772
Santiago Arias, Adeline Montlaur

MS 406: ADVANCES IN COMPUTATIONAL METHODS FOR GAS-LIQUID TWO-PHASE FLOW
COUPLING OF FLUID STUCTURE INTRACTION SOLVER WITH A VOF METHOD FOR MULTIPHASE STRUCTURE INTERACTION …….. 788
Daniele Cerroni, Roberto Da Via', Sandro Manservisi, Filippo Menghini

A METHOD OF CHAINED ANALYTICAL WAVE STRUCTURES FOR LARGE SCALE STRATIFIED TWO-PHASE PIPE FLOWS …….. 806
Andreas Holm Akselsen

MS 408: MANIPULATION AND CONTROL OF TURBULENT FLOW
MODELING OF EXCITATION OF CONTROLLING DISTURBANCES IN SWEPT WING BOUNDARY LAYER BY MEANS OF PLASMA ACTUATORS 831
Sergey Chernyshev, Andrey Kiselev, Aleksandr Kuryachii

NUMERICAL SIMULATION OF INTERACTION PROCESS BETWEEN DIELECTRIC BARRIER DISCHARGE AND DUCT FLOW 844
Pavel Semenev, Dmitriy Pudovikov, Pavel Toktaliev

IMPLEMENTATION OF POD AND DMD METHODS IN APACHE SPARK FRAMEWORK FOR SIMULATION OF UNSTEADY TURBULENT FLOW IN THE MODEL COMBUSTOR 857
Mikhail Kalugin, Sergei Strijhak

MS 409: CURRENT TRENDS IN MODELLING AND SIMULATION OF TURBULENT FLOWS
NUMERICAL VALIDATION OF A FOUR PARAMETER LOGARITHMIC TURBULENCE MODEL 865
Daniele Cerroni, Roberto Da Vià, Sandro Manservisi, Filippo Menghini

LARGE-EDDY SIMULATION AND FAR FIELD ACOUSTICS OF A SUBSONIC HOT JET 878
O. Labbé

ON THE APPLICATION OF MODERN TURBULENCE MODELS IN THE FLOW LAMINARIZATION PROBLEMS 893
Sergey Chernyshev, Aleksander Ivanov, Andrey Kiselev, Dmitriy Sboev, Leonid Teperin, Petr Vorotnikov, Valeriy Vozhdaev

ASSESSMENT OF RANS AND DES METHODS FOR THE AHMED BODY 912
Emmanuel Guilmineau, Gan Bo Deng, Alban Leroyer, Patrick Queutey, Michel Visonneau, Jeroen Wackers

A WAY TO IMPROVE JET MODELING WITHIN RANS EQUATION SYSTEM 922
Alexey Troshin

A MODIFIED SSG/LLR-ω REYNOLDS STRESS MODEL FOR PREDICTING BLUFF BODY AERODYNAMICS 936
Csaba Klajbár, László Könözsy, Karl W. Jenkins

MS 410: COMPLEX FLUID FLOWS IN ENGINEERING: MODELLING, SIMULATION AND OPTIMIZATION
NUMERICAL ANALYSIS OF RAREFIED GAS FLOWS USING THE ACADEMIC CFD CODE GALATEA 949
Angelos Klothakis, Georgios Lygidakis, Ioannis Nikolos

TOPOLOGY OPTIMIZATION FOR FLUID FLOW EMPLOYING LOCAL OPTIMALITY CRITERIA 967
Philip Sarstedt, Gerhard Kachel, Jörg Ettrich, Karl Bühler

NUMERICAL SIMULATION OF THE CONJUGATE HEAT TRANSFER IN THE COOLING SYSTEM OF THE COMBUSTION CHAMBERS OF THE AVIATION RAMJET ON THE ENDOTHERMIC FUELS 979
Vadim Volokhov, Pavel Toktaliev, Sergei Martynenko

SENSITIVITY STUDY OF THE NUMERICAL SETUP FOR AN AUTOMATIC OPTIMIZATION PROCEDURE FOR A HYDRAULIC MACHINE 992
Alexander Tismer, Markus Schlipf, Stefan Riedelbauch

ADVANCES IN GEOMETRICAL PARAMETRIZATION AND REDUCED ORDER MODELS AND METHODS FOR COMPUTATIONAL FLUID DYNAMICS PROBLEMS IN APPLIED SCIENCES AND ENGINEERING: OVERVIEW AND PERSPECTIVES 1013
F. Salmoiraghi, F. Ballarin, G. Corsi, A. Mola, M. Tezzele, G. Rozza

NEAR WALL BEHAVIOR OF IMPLICIT LARGE EDDY SIMULATIONS 1032
Ioannis Kokkinakis, Dimitris Drikakis

VALIDATION AND VERIFICATION OF A 2D LATTICE BOLTZMANN SOLVER FOR INCOMPRESSIBLE FLUID FLOW 1046
Tamás István Józsa, Máté Szőke, Tom-Robin Teschner, László Könözsy, Irene Moulitsas

MS 411: NON-NEWTONIAN HEAT AND FLUID FLOW SUBJECTED TO MAGNETIC FORCES
VALIDATION OF A MAGNETO- AND FERRO-HYDRODYNAMIC MODEL FOR NON-ISOTHERMAL FLOWS IN CONJUNCTION WITH NEWTONIAN AND NON-NEWTONIAN FLUIDS 1061
László Könözsy, Pietro Scienza, Dimitris Drikakis

NUMERICAL STUDY OF MAGNETIC PARTICLES CONCENTRATION IN BIOFLUID (BLOOD) UNDER THE INFLUENCE OF HIGH GRADIENT MAGNETIC FIELD IN MICROCHANNEL 1084
Vassilios Loukopoulos, George Bourantas, Dimitrios Labropoulos, Vassilios-Martin Nikiforidis, Stéphane Bordas, George Nikiforidis

MS 412: NUMERICAL METHODS FOR WAVES AND FLOWS IN COASTAL AND DEEP WATER HYDRODYNAMICS
NEW ALGORITHM FOR NUMERICAL SIMULATION OF SURFACE WAVES WITHIN THE FRAMEWORK OF THE FULL NONLINEAR DISPERSIVE MODEL 1093
Zinaida Fedotova, Oleg Gusev, Gayaz Khakimzyanov

NUMERICAL MODELLING OF SURFACE WAVES IN THE FRAMEWORK OF THE SHALLOW WATER MODEL 1104
Nina Shokina, Gayaz Khakimzyanov

ON NUMERICAL METHODS FOR SOLVING RUN-UP PROBLEMS. COMPARATIVE ANALYSIS OF NUMERICAL ALGORITHMS AND NUMERICAL RESULTS. 1127
Leonid Chubarov, Alexandr Rychkov, Gayaz Khakimzyanov, Yurii Shokin

MS 414: NEW TRENDS IN NUMERICAL METHODS FOR MULTI-MATERIAL COMPRESSIBLE FLUID FLOWS
EULERIAN CALCULATIONS OF MULTIMATERIAL FLOWS WITH SUB-CELL RECONSTRUCTION OF INTERFACES ... 1139
Igor Menshov, Pavel Zakharov

SOME ACOUSTIC-TRANSPORT SPLITTING SCHEMES FOR TWO-PHASE COMPRESSIBLE FLOWS 1151
Simon Peluchon, Gérard Gallice, Pierre-Henri Maire

LAGRANGE-FLUX EULERIAN SCHEMES FOR COMPRESSIBLE MULTIMATERIAL FLOWS 1165
Florian De Vuyst, Thibault Gasc, Renaud Motte, Mathieu Peybernes, Raphael Poncet

ISOTROPY–PRESERVING SLOPE LIMITERS FOR FINITE VOLUME METHODS ON SQUARE MESHES 1179
Jan Velechovsky, Marianne Francois

BUILDING A MORE EFFICIENT LAGRANGE-REMAP SCHEME THANKS TO PERFORMANCE MODELING 1191
Thibault Gasc, Florian De Vuyst, Mathieu Peybernes, Raphaël Poncet, Renaud Motte

MS 415: COMPUTATIONAL NON-NEWTONIAN FLUID MECHANICS
DEVELOPMENT OF CONFINED VISCOPLASTIC FLOWS WITH HETEROGENEOUS WALL SLIP 1205
Pandelitsa Panaseti, Maria Philippou, Zacharias Kountouriotis, Georgios Georgiou

SQUEEZE FLOW OF VISCOPLASTIC BINGHAM MATERIAL 1215
Larisa Muravleva

500 HIGH PERFORMANCE COMPUTING

MS 501: ALGORITHMIC ASPECTS OF HIGH-PERFORMANCE COMPUTING FOR MECHANICS AND PHYSICS
PSEUDOMULTIGRID GAUSS–SEIDEL METHOD FOR LARGE SCALE AND HIGH PERFORMANCE COMPUTING 1237
Sergey Martynenko, Vadim Volokhov, Pavel Toktaliev

ALGORITHM FOR FAST SIMULATIONS OF SPACE-TIME FINITE ELEMENT METHOD 1260
Marcin Skotniczny, Anna Paszynska, Maciej Paszynski

HYBRID PARALLELISATION OF AN ALGORITHMICALLY DIFFERENTIATED ADJOINT SOLVER 1268
Pavanakumar Mohanamuraly, Jan Christian Huckelheim, Jens-Dominik Mueller

MS 503: HPC-BASED SIMULATIONS FOR THE ENGINEERING REALM AND INDUSTRIAL APPLICATIONS
EFFICIENT PARALLEL GEOMETRY DISTRIBUTION FOR THE SIMULATION OF COMPLEX FLOWS 1277
Andreas Lintermann

LARGE-SCALE FREE-SURFACE FLOW SIMULATION USING LATTICE BOLTZMANN METHOD ON MULTI-GPU CLUSTERS 1294
Naoyuki Onodera, Kunihide Ohashi,

LARGE-SCALE LES ANALYSIS OF AUTOMOTIVE ENGINE COOLING FAN 1305
Yuji Kobayashi, Kenji Yoshida, Itsuhei Kohri, Masaharu Sakai, Hideo Asano

DIRECT AEROACOUSTIC SIMULATION RELATED WITH MODE CHANGE IN A RECORDER 1315
Hiroshi Yokoyama, Ryoma Hamasuna, Akira Miki, Hirofumi Onitsuka, Akiyoshi Iida

NUMERICAL ANALYSIS OF RADIO FREQUENCY BLACKOUT FOR ATMOSPHERIC REENTRY VEHICLE USING CFD-CEM COMBINED METHOD 1325
Yusuke Takahashi, Reo Nakasato, Nobuyuki Oshima

DIRECT FEM LARGE SCALE COMPUTATION OF TURBULENT MULTIPHASE FLOW IN URBAN WATER SYSTEMS AND MARINE ENERGY 1339
Ezhilmathi Krishnasamy, Johan Hoffman, Johan Jansson

MS 504: NUMERICAL METHODS AND TOOLS FOR KEY EXASCALE COMPUTING CHALLENGES IN ENGINEERING AND APPLIED SCIENCES
KINETIC MODELS AND ALGORITHMS FOR SOLUTION OF THE MAGNETOGASDYNAMIC PROBLEMS ON THE MODERN SUPERCOMPUTING SYSTEMS 1352
Boris Chetverushkin, Nicola D'Ascenzo, A. Saveliev, Valeri Saveliev

ERROR ANALYSIS AND QUANTIFICATION IN NEURON SIMULATIONS 1366
Francesco Casalegno, Francesco Cremonesi, Stuart Yates, Michael L. Hines, Felix Schürmann, Fabien Delalondre

EVALUATION OF SPARSE LINEAR ALGEBRA OPERATIONS IN TRILINOS 1381
Mohammad Siahatgar, Gabriele Von Voigt

MS 505: INTERACTIVE SIMULATIONS IN COMPUTATIONAL ENGINEERING
AUTOMATIC VISUALIZATION AND CONTROL OF ARBITRARY NUMERICAL SIMULATIONS 1392
Jan P. Springer, Helen Wright

MS 506: ACCURACY AND EFFICIENCY OF APPROXIMATE COMPUTATIONS IN SCIENCE AND ENGINEERING
DIRECT TIME-DOMAIN INTEGRATION APPROACH FOR VISCOELASTIC SYSTEMS INVOLVING VARIOUS DAMPING MODELS 1409
Zhe Ding, Li Li, Yujin Hu

ON THE PERFORMANCE OF A COMPUTATIONAL COST REDUCTION TECHNIQUE APPLIED TO COOLING TOWERS TRANSIENT ANALYSIS 1421
Aram Soroushian, Amin Jahani Mehrnoosh, Yalda Zarabimanesh, Mohammad Hadi Ghondaghsaz, Ali Baiani, Ali Zakizade

A DIFFERENT LOOK AT THE RICHARDSON EXTRAPOLATION LEADING TO A NEW PROPOSITION 1432
Aram Soroushian

ON THE FREQUENCY CONTENT OF ERRORS ORIGINATED IN A TIME INTEGRATION COMPUTATIONAL COST REDUCTION TECHNIQUE 1443
Aram Soroushian, Mahmood Hosseini, Seyed Mohammad Khalkhali

600 INTERDISCIPLINARY COUPLED AND CONTACT PROBLEMS

MS 601: SHOCK WAVE-BOUNDARY LAYER INTERACTION AND ITS CONTROL
NUMERICAL SIMULATION OF TRANSONIC BUFFET AND ITS CONTROL USING TANGENTIAL JET BLOWING 1455
Ksenia Abramova, Kamil Khairullin, Alexander Ryzhov, Vitaly Soudakov

SHOCK WAVE BOUNDARY LAYER INTERACTION IN PROFILE CASCADES REPRESENTING ROTOR BLADINGS OF THE LAST STAGE OF LARGE OUTPUT STEAM TURBINES 1464
Martin Luxa, David Simurda, Jaromir Prihoda, Jana Vachova

SHOCK WAVE BOUNDARY LAYER INTERACTION INVESTIGATION: CONTROL BY ROD VORTEX GENERATORS AND THEIR APPLICATION ON HELICOPTER ROTOR BLADES 1474
Fernando Tejero Embuena, Piotr Doerffer, Pawel Flaszynski

ANALYSIS OF EFFECTS OF SHAPE AND LOCATION OF MICRO - TURBULATORS ON UNSTEADY SHOCKWAVE - BOUNDARY LAYER INTERACTION IN TRANSONIC FLOW 1484
Janusz Sznajder, Tomasz Kwiatkowski

MS 602: INNOVATIVE METHODS FOR FLUID-STRUCTURE-INTERACTION
ASSESSMENT OF THE FLUID-STRUCTURE INTERACTION CAPABILITIES FOR AERONAUTICAL APPLICATIONS OF THE OPEN-SOURCE SOLVER SU2. 1498
Ruben Sanchez, Heather L. Kline, David Thomas, Anil Variyar, Marcello Righi, Thomas D. Economon, Juan J. Alonso, Rafael Palacios, Grigorios Dimitriadis, Vincent Terrapon

CONVERGENCE ANALYSIS OF COUPLING ITERATIONS FOR THE UNSTEADY TRANSMISSION PROBLEM WITH MIXED DISCRETIZATIONS 1530
Azahar Monge, Philipp Birken

USING IMPROVED RADIAL BASIS FUNCTIONS METHODS FOR FLUID-STRUCTURE COUPLING AND MESH DEFORMATION 1545
Giorgos Strofylas, Georgios Mazanakis, Sotirios Sarakinos, Georgios Lygidakis, Ioannis Nikolos

A MONOLITHIC FLUID-STRUCTURE INTERACTION METHOD, APPLICATION TO A PISTON PROBLEM 1564
Felix Ischinger, Martijn Anthonissen, Barry Koren

MS 603: COMPUTATIONAL METHODS IN FLUID-STRUCTURE INTERACTION WITH IMPACT ON INDUSTRIAL APPLICATIONS
SLAMMING IMPACT SIMULATION OF 2D WATER ENTRY FOR RIGID STRUCTURES 1582
Omar Hashim Hassoon, Mostapha Tarfaoui, A. El Malki

A MESH MORPHING BASED FSI METHOD USED IN AERONAUTICAL OPTIMIZATION APPLICATIONS 1594
Matej Andrejašič, David Eržen, Emiliano Costa, Stefano Porziani, Marco Evangelos Biancolini, Corrado Groth

A PATH-CONSERVATIVE OSHER-TYPE SCHEME FOR AXIALLY SYMMETRIC COMPRESSIBLE FLOWS IN FLEXIBLE TUBES 1613
Julia Leibinger, Michael Dumbser, Uwe Iben

MS 605: FRICTIONAL CONTACTS WITH LUBRICATION – BASICS AND APPLICATIONS
LIMITING SHEAR STRESS FORMULATION FOR TEHL SIMULATION 1623
Thomas Lohner, Klaus Michaelis, Karsten Stahl

MS 606: COMPUTATIONAL MODELING OF HYDRAULIC FRACTURING
THE XFEM FOR A SIMPLIFIED MODEL IN HYDRAULIC FRACTURING 1637
Markus Schätzer, Thomas-Peter Fries

SENSITIVITY ANALYSIS OF HYDRAULIC FRACTURING USING AN EXTENDED FINITE ELEMENT METHOD FOR THE PKN MODEL 1647
Hasini Garikapati, Clemens V. Verhoosel, Harald Van Brummelen, Pedro Diez

NUMERICAL MODELLING OF COUPLED HYDRO-THERMAL PROCESSES OF THE SOULTZ HETEROGENEOUS GEOTHERMAL SYSTEM 1659
Musa Dahiru Aliyu, Hua-Peng Chen

MS 607: ADVANCES IN COMPUTATIONAL METHODS FOR LIQUID-VAPOR FLOWS WITH PHASE TRANSFER PROCESSES
A LOW DIFFUSIVE APPROACH FOR TWO PHASE FLOWS 1672
Alberto Beccantini

A LARGE TIME STEP ROE SCHEME APPLIED TO TWO-PHASE FLOW 1693
Sofia Lindqvist, Halvor Lund

MS 608:ADVANCES IN TIME INTEGRATION FOR SOLID, FLUID AND COUPLED SYSTEMS
ENERGY CONSERVING TIME INTEGRATION BASED ON GALERKIN-VARIATIONAL INTEGRATORS WITH CONSTRAINTS 1709
Matthias Bartelt, Michael Groß

MIXED INTEGRATORS FOR STRUCTURE-PRESERVING SIMULATIONS IN NONLINEAR STRUCTURAL DYNAMICS 1736
Alexander Janz, Peter Betsch, Christian Hesch

ENERGY AND MOMENTUM CONSERVING VARIATIONAL BASED TIME INTEGRATION OF ANISOTROPIC HYPERELASTIC CONTINUA 1765
Michael Groß, Rajesh Ramesh, Julian Dietzsch

STRUCTURE-PRESERVING OPTIMAL CONTROL OF DISCRETE MECHANICAL SYSTEMS 1789
Peter Betsch, Christian Becker

VARIATIONAL INTEGRATORS OF MIXED ORDER FOR DYNAMICAL SYSTEMS WITH MULTIPLE TIME SCALES AND SPLIT POTENTIALS 1818
Theresa Wenger, Sina Ober-Blöbaum, Sigrid Leyendecker

CO-SIMULATION OF LARGE MBD, FEA AND DEM SYSTEMS 1832
Jose Ortiz, Neil Macdonald

MS 609: ADVANCED COMPUTATIONAL MODELING OF BATTERIES AND FUEL CELLS
STOCHASTIC 3D MODELING OF AMORPHOUS MICROSTRUCTURES - A POWERFUL TOOL FOR VIRTUAL MATERIALS TESTING 1838
Matthias Neumann, Volker Schmidt

MS 610: NUMERICAL METHODS TO STUDY THE CONTACT MECHANICS OF DRY, ADHESIVE AND LUBRICATED ROUGH SURFACES
PERCOLATION PROPERTIES OF THE FREE VOLUME GENERATED BY TWO ROUGH SURFACES IN CONTACT 1850
Paolo Cinat, Marco Paggi, Claudia Borri

A PARAMETRICALLY TIME-DEPENDENT METHODOLOGY FOR RECIPROCATING CONTACT MECHANICS BETWEEN VISCOELASTIC SOLIDS 1856
Carmine Putignano, Giuseppe Carbone, Daniele Dini

STATISTICAL AND GEOMETRICAL CHARACTERISTICS OF RANDOMLY ROUGH SURFACES USED FOR CONTACT SIMULATIONS. 1864
Rafael Schouwenaars, Carlos G. Figueroa, Víctor Hugo Jacobo, Armando Ortiz

MS 612: NUMERICAL SIMULATIONS FOR SMART-CITY APPLICATIONS
NUMERICAL OPTIMIZATION OF NEAR-ROAD VEGETATION BARRIERS 1876
Ludek Benes, Viktor Sip

MS 615: COMPUTATIONAL MODELS IN MAGNETOHYDRODYNAMICS
LARGE EDDY SIMULATIONS OF MAGNETIC FIELD EFFECT ON TURBULENT FLOW IN A SQUARE DUCT 1886
Jie Mao, Kunlei Zhang, Zhongquan Tan, Ke Liu

700 MATERIALS

MS 701: ADVANCED MATERIALS: COMPUTATIONAL ANALYSIS OF PROPERTIES AND PERFORMANCE
OPTIMAL DESIGN AND ADDITIVE MANUFACTURING OF NOVEL REINFORCING ELEMENTS FOR COMPOSITE MATERIALS 1893
Francesco Fabbrocino, Ilenia Farina, Ada Amendola, Luciano Feo, Fernando Fraternali

A TEMPERATURE SENSITIVE CRYSTAL PLASTICITY MODEL FOR THE PREDICTION OF HIGH TEMPERATURE MECHANICAL BEHAVIOUR OF MULTI-PHASE TIAL ALLOY 1909
M. Umer Ilyas, M. Rizviul Kabir

LAYOUT OPTIMIZATION OF PIEZOELECTRIC ELEMENTS WITH EXTERNAL ELECTRIC CIRCUITS IN SMART CONSTRUCTIONS BASED ON SOLUTION OF THE NATURAL VIBRATIONS PROBLEM 1920
Nataliia Iurlova, Valerii P. Matveenko, Dmitriy A. Oshmarin, Nataliya V. Sevodina, Maksim A. Yurlov

DETERMINATION OF OPTIMAL PARAMETERS FOR A PASSIVE RL-CIRCUIT BY SOLVING THE PROBLEM ON NATURAL VIBRATIONS OF ELECTROELASTIC BODIES 1930
Maksim Yurlov, Valerii P. Matveenko, Dmitriy A. Oshmarin, Nataliya V. Sevodina, Nataliya A. Iurlova

COMPUTATIONAL MODELLING OF MECHANICAL BEHAVIOR OF BIOLOGICAL TISSUES FOR BIOMEDICAL APPLICATIONS 1940
Simin Li, Yang Liu, Juan Du, Begum Zeybek, Lorenzo Zani, Mark P. Lewis, Vadim V. Silberschmidt

ANALYSIS OF FIBRE BRAGG GRATINGS SENSORS OPTIMAL PLACEMENT FOR MONITORING OF DAMAGE PROPAGATION IN LAMINATE COMPOSITES 1950
Mikhail Tashkinov

SEVEN DIFFERENT WAYS TO MODEL VISCOELASTICITY IN A GEOMETRICALLY EXACT SETTING 1959
Alexey Shutov

MS 702: MODELING OF NANOFILLED COMPOSITES
SIMULATING ATOMIC FORCE MICROSCOPY FOR THE DETERMINATION OF THE ELASTIC PROPERTIES OF NANOPARTICLE REINFORCED EPOXY RESIN 1971
Johannes Fankhänel, Andreas Kempe, Raimund Rolfes

MULTI-SCALE FINITE ELEMENT ANALYSIS OF GRAPHENE/POLYMER NANOCOMPOSITES ELECTRICAL PERFORMANCE 1984
Asimina Manta, Matthieu Gresil, Constantinos Soutis

MS 705: IDENTIFICATION OF MATERIAL MODELS
THE BOOTSTRAP APPROACH TO THE STATISTICAL SIGNIFICANCE OF PARAMETERS IN RSM MODEL 2003
Jacek Pietraszek, Leszek Wojnar

MS 706: MODELING OF FIBER-BASED STRUCTURES - TEXTILES AND TEXTILE REINFORCED COMPOSITES
INVERSE IDENTIFICATION OF THE BENDING STIFFNESS OF A BRAIDED POLYETHYLENE TWINE SUBJECT TO LARGE DEFORMATION: APPLICATION TO THE IDENTIFICATION OF THE MESH OPENING RIGIDITY OF FISHING NETS 2010
Barthélémy Morvan, Guilhem Bles, Nicolas Dumergue, Daniel Priour

MULTI-SCALE FRAMEWORK FOR MODELLING CARBON FIBRE WEAVES BASED ON STOCHASTIC REINFORCEMENT GEOMETRY 2029
Andy Vanaerschot, Karen Soete, Stepan Lomov, Dirk Vandepitte

MS 707: MICROMECHANICAL MODELLING: COMPETITION BETWEEN ANALYTICAL AND NUMERICAL METHODS
MULTISCALE MODELING OF THERMO-ELASTIC PROPERTIES OF MICROCRACKED MATERIAL 2039
Antonino Favata, Patrizia Trovalusci, Renato Masiani

EFFECTIVE ELASTICITY COEFFICIENTS IN DRY POROUS MATERIALS. NUMERICAL AND SEMI-ANALYTICAL APPROACHES 2050
Vladimir Sladek, Bruno Musil, Jan Sladek

INFLUENCE OF MICRO CRACKS ON EFFECTIVE MATERIAL PROPERTIES IN FIBER REINFORCED SMART COMPOSITE MATERIALS 2073
Michael Wünsche, Jan Sladek, Vladimir Sladek

DEFECT ACCUMULATION IN NANOPOROUS WEAR-RESISTANT COATINGS UNDER COLLECTIVE RECRYSTALLIZATION. SIMULATION BY HYBRID CELLULAR AUTOMATON METHOD 2080
Dmitry Moiseenko, Pavel Maksimov, Sergey Panin, Viktor Panin

MS 711: FOURIER-BASED METHODS FOR COMPUTING THE BEHAVIOR OF HETEROGENEOUS MATERIALS DEVELOPMENTS, EXTENSIONS AND APPLICATIONS
NONLINEAR COMPOSITE VOXELS AND FFT-BASED HOMOGENIZATION 2099
Matthias Kabel, Andreas Fink, Felix Ospald, Matti Schneider

MS 712: SMART MATERIAL SYSTEMS AND STRUCTURES
A THERMODYNAMICALLY CONSISTENT FINITE STRAIN MICRO-SPHERE FRAMEWORK FOR PHASE-TRANSFORMATION 2110
Richard Ostwald, Thorsten Bartel, Andreas Menzel

OPTIMAL CONTROL TUNNING IN SMART STRUCTURES WITH DELAMINATIONS 2123
Panos Koutsianitis, Amalia Moutsopoulou, Georgios Drosopoulos, Georgios Tairidis, Georgia Foutsitzi, Georgios Stavroulakis

MS 713: MICROSTRUCTURE-BASED MODELLING OF HETEROGENEOUS MATERIALS
DEPENDENCE OF THE MECHANICAL PROPERTIES OF PENTAMODE MATERIALS ON THE LATTICE MICROSTRUCTURE 2134
Ada Amendola, Francesco Fabbrocino, Luciano Feo, Ferdinando Auricchio, Fernando Fraternali

HOMOGENIZATION TECHNIQUES FOR ACCURATE AND APPROXIMATE ESTIMATES FOR OVERALL PROPERTIES OF MICROCRACKED VISCOELASTIC MASONRIES 2151
Amna Rekik, Alain Gasser

APPLICATION OF POLAR ELASTICITY TO THE PROBLEM OF PURE BENDING OF A THICK PLATE 2162
Svitlana Fedorova, Jiří Burša

ARTIFICIAL MICROSTRUCTURE GENERATOR FOR DUAL-PHASE STEELS 2172
Yuliang Hou, Alexandre Dumon, Pièrre Culière, Mohamed Rachik

MS 714: STRENGTH, FATIGUE AND STABILITY OF COMPOSITE STRUCTURES
ON THE STRUCTURAL DESIGN OF IMPERFECTION SENSITIVE LAMINATED COMPOSITE SHELL STRUCTURES SUBJECTED TO AXIAL COMPRESSION 2182
Linus Friedrich, Pawel Lyssakow, Garth Pearce, Martin Ruess, Chiara Bisagni, Kai-Uwe Schröder

STRENGTH AND WEIGHT EQUIVALENT SUBSTITUTION OF LARGE SANDWICH PANELS BY MONOLITHIC CFRP STRUCTURES 2190
Martin Meindlhumer, Martin Schagerl

ROBUST INTEGRAL COMPOSITE AIRCRAFT STRUCTURES 2202
Tamas Havar

MS 715: COMPUTATIONAL ANALYSIS OF COMPOSITE STRUCTURES
MINIMAL MASS DESIGN OF STRENGTHENING TECHNIQUES FOR PLANAR AND CURVED MASONRY STRUCTURES 2210
Gerardo Carpentieri, Francesco Fabbrocino, Mariella De Piano, Valentino Paolo Berardi, Luciano Feo, Fernando Fraternali

MODELING OF FIBER-REINFORCED PLASTICS TAKING INTO ACCOUNT THE MANUFACTURING PROCESS …….. 2220
Cherry Ann Reclusado, Sumito Nagasawa

CONVERGENCE ANALYSIS OF STRESS FIELDS TO HOMOGENIZATION PREDICTIONS IN OPTIMAL PERIODIC COMPOSITE DESIGN …….. 2236
Pedro Coelho, Rui Reis, José Guedes

A NUMERICAL STUDY FOR THE BUCKLING CAPACITY OF WIND TURBINE BLADES: GEOMETRY, LOADING AND MATERIAL INFLUENCE …….. 2247
Efstathios E. Theotokoglou, George A. Balokas, Evgenia K. Savvaki

800 MULTISCALE PROBLEMS

MS 801: MULTISCALE COMPUTATIONAL HOMOGENIZATION FOR BRIDGING SCALES IN THE MECHANICS AND PHYSICS OF COMPLEX MATERIALS

A SEMI-IMPLICIT MICROPLAR DISCRETE-TO-CONTINUUM METHOD FOR GRANULAR MATERIALS …….. 2266
Kun Wang, Waiching Sun

MODELING OF LOW-ALLOYED TRIP-STEELS BASED ON DIRECT MICRO-MACRO SIMULATIONS …….. 2280
Stefan Prüger, Ashutosh Gandhi, Daniel Balzani

HOMOGENIZATION METHOD FOR DESIGNING NOVEL ARCHITECTURED CELLULAR MATERIALS …….. 2292
Zheng-Dong Ma

A HOMOGENIZATION TECHNIQUE FOR ELASTO-PLASTIC COMPOSITES …….. 2316
Federica Covezzi, Stefano De Miranda, Sonia Marfia, Elio Sacco

MS 802: ADVANCES IN THE MODELLING OF MULTI-SCALE, MULTI-PHYSICS AND MULTI-UNCERTAINTY PROBLEMS

THEORETICAL PREDICTION OF PLASTIC INSTABILITY FOR ASYMMETRICAL MATERIALS …….. 2323
Shenghua Wu, Nannan Song, F. M. Andrade Pires

MULTISCALE SIMULATION OF THREE-DIMENSIONAL UNSTEADY GAS FLOWS IN MICROCHANNELS OF TECHNICAL SYSTEMS …….. 2331
Viktoriia Podryga, Yury Karamzin, Tatiana Kudryashova, Sergey Polyakov

HIGHER-ORDER ASYMPTOTIC HOMOGENIZATION OF PERIODIC MATERIALS WITH LOW SCALE SEPARATION …….. 2346
M. Mohammed Ameen, R.H.J. Peerlings, M.G.D. Geers

MS 805: ADVANCED MULTI-PHYSICS AND MULTI-SCALE TECHNIQUES FOR MODELING INELASTIC PROCESSES IN SOLIDS: DAMAGE, FRACTURE AND CONTACT MECHANICS

MESO-SCALE MODELING OF HYBRID INDUSTRIAL/RECYCLED STEEL FIBER-REINFORCED CONCRETE …….. 2353
Antonio Caggiano, Diego Said Schicchi, Guillermo Etse, Enzo Martinelli

MS 806: MULTISCALE MODELLING OF MATERIALS AND STRUCTURES
THE KIRKENDALL SHIFT AND FRENKEL EFFECT DURING MULTI-COMPONENT DIFFUSION PROCESS 2363
Bartek Wierzba

CRACK PATH FIELD AND STRAIN INJECTION TECHNIQUES IN DYNAMIC FRACTURE SIMULATIONS 2372
Oriol Lloberas-Valls, Alfredo E. Huespe, Javier Oliver, Ivo F. Dias

HYBRID FE/XFE FINITE ELEMENT MODEL FOR SIMULATION OF BRITTLE-DUCTILE FRACTURES IN DUAL-PHASE STEEL GRADES. 2390
Konrad Perzynski, Lukasz Madej

EFFECTIVE MESO AND MACRO PROPERTIES FOR FIBRE-REINFORCED-POLYMER CURING COUPLED TO VISCO-ELASTICITY 2398
Rolf Mahnken, Christian Dammann

ON APPLICATION OF THE MESHLESS FINITE DIFFERENCE METHOD TO NUMERICAL HOMOGENIZATION 2417
Irena Jaworska

A MESOSCALE STUDY OF DEFORMATION AND FAILURE OF ANGLE-PLY LAMINATES UNDER TENSILE LOADING BY MEANS OF NUMERICAL HOMOGENIZATION 2426
Marek Romanowicz

MODELING OF PHASE CHANGES IN MICRO-DOMAIN INDUCED BY AN ULTRASHORT LASER PULSE 2437
Ewa Majchrzak, Lukasz Turchan, Jolanta Dziatkiewicz

MS 807: ADVANCED COMPUTATIONAL STRATEGIES FOR MODELLING, SIMULATION AND CHARACTERISATION OF MULTI-SCALE HETEROGENEOUS MATERIALS
VALIDATION OF A DISCRETE CRACK MODEL FOR LIGHTWEIGHT AGGREGATE CONCRETE BEAMS 2449
D. Dias-Da-Costa, R. Graça-E-Costa, R.N.F. Carmo

MS 808: MULTISCALE AND MULTIPHYSICS MODELING OF CEMENTITIOUS MATERIALS
REINFORCEMENT CORROSION IN CONCRETE DUE TO CARBONATION AND CHLORIDE INGRESS UP AND BEYOND INDUCTION PERIOD 2460
Karolina Hájková, Libor Jendele, Vit Šmilauer, T. Sajdlová, Jan Červenka

MS 809: MULTISCALE STOCHASTIC FINITE ELEMENT METHODS
THE STOCHASTIC FINITE ELEMENT METHOD FOR NUCLEAR APPLICATIONS 2471
José David Arregui Mena, Lee Margetts, Llion Evans, D. V. Griffiths, Anton Shterenlikht, Luis Cebamanos, Paul M Mummery

DETERMINATION OF MESOSCALE RANDOM FIELDS FOR THE APPARENT PROPERTIES OF SPATIALLY RANDOM COMPOSITES 2484
Dimitrios Savvas, George Stefanou

MS 811: MULTISCALE MODELING OF CONCRETE AND CONCRETE STRUCTURES
NUMERICAL SIMULATION OF THE AUTOGENOUS SHRINKAGE OF HARDENING PORTLAND CEMENT PASTE ... 2501
Peng Gao, Guang Ye, Jiangxiong Wei, Qijun Yu

900 NUMERICAL SIMULATION METHODS

MS 901: ISOGEOMETRIC METHODS
ANALYSIS OF LAMINATED COMPOSITE PLATES USING ISOGEOMETRIC COLLOCATION METHOD 2514
G. S. Pavan, K. S. Nanjunda Rao

MODELLING STIFFENED LIGHTWEIGHT STRUCTURES WITH ISOGEOMETRIC ANALYSIS VIA MORTAR METHODS 2531
Malte Woidt, Kay Sommerwerk, Matthias C. Haupt, Peter Horst

DOMAIN DECOMPOSITION SOLUTION SCHEMES FOR LARGE-SCALE IGA PROBLEMS 2541
George Stavroulakis, Dimitris Tsapetis, Manolis Papadrakakis

MS 902: INNOVATIVE NUMERICAL APPROACHES FOR MULTI-PHYSICS PROBLEMS
NUMERICAL PROPERTIES OF A DISCONTINUOUS GALERKIN FOMULATION FOR ELECTRO-THERMAL COUPLED PROBLEMS 2558
Lina Homsi, Christophe Geuzaine, Ludovic Noels

MS 903: ADVANCES IN FICTITIOUS DOMAIN METHODS FOR SOLID MECHANICS
TOWARDS LATTICE-BOLTZMANN ON DYNAMICALLY ADAPTIVE GRIDS — MINIMALLY-INVASIVE GRID EXCHANGE IN ESPRESSO 2566
Michael Lahnert, Carsten Burstedde, Christian Holm, Miriam Mehl, Georg Rempfer, Florian Weik

AUTOMATIC CONFORMAL DECOMPOSITION OF ELEMENTS CUT BY NURBS 2591
Jakob W. Steidl, Thomas-Peter Fries

A DESIGN-THROUGH-ANALYSIS APPROACH USING THE FINITE CELL METHOD 2601
Benjamin Wassermann, Tino Bog, Stefan Kollmannsberger, Ernst Rank

MS 905: DISCONTINUOUS GALERKIN METHODS: NEW TRENDS AND APPLICATIONS
DISCONTINUOUS GALERKIN COMPUTATION OF GASEOUS MIXTURE COAXIAL JETS 2614
Nicoletta Franchina, Marco Savini, Francesco Bassi

DISCONTINUOUS GALERKIN SOLUTION OF THE REYNOLDS-AVERAGED NAVIER–STOKES AND KL-KT-LOG(W) TRANSITION MODEL EQUATIONS 2632
A. Bassi, Alessandro Colombo, Antonio Ghidoni, Marco Lorini, Gianmaria Noventa

A STUDY OF MULTIGRID SMOOTHERS USED IN COMPRESSIBLE CFD BASED ON THE CONVECTION DIFFUSION EQUATION 2648
Philipp Birken, Jonathan Bull, Antony Jameson

HIGH-ORDER LINEARLY IMPLICIT TWO-STEP PEER METHODS FOR THE DISCONTINUOUS GALERKIN SOLUTION OF THE INCOMPRESSIBLE RANS EQUATIONS 2664
Francesco Carlo Massa, Gianmaria Noventa, Francesco Bassi, Alessandro Colombo, Antonio Ghidoni, Marco Lorini
OUTPUT-BASED SPACE-TIME ADAPTATION WITH NON-VARIATIONAL TIME INTEGRATION 2684
Krzysztof Fidkowski

MATRIX-FREE MODIFIED EXTENDED BACKWARD DIFFERENTIATION FORMULAE APPLIED TO THE DISCONTINUOUS GALERKIN SOLUTION OF COMPRESSIBLE UNSTEADY VISCOUS FLOWS 2697
Alessandra Nigro, Carmine De Bartolo, Andrea Crivellini, Francesco Bassi

MS 906: MATHEMATICAL ADVANCES IN ISOGEOMETRIC ANALYSIS
PRECONDITIONERS FOR ISOGEOMETRIC ANALYSIS BASED ON SOLVERS FOR SYLVESTER EQUATION 2715
Giancarlo Sangalli, Mattia Tani

MS 907: REGULARIZED ENRICHED APPROXIMATIONS AND QUADRATURE FOR DISCONTINUITIES, SINGULARITIES AND CONTINUOUS-DISCONTINUOUS TRANSITION
EFFECTIVE 3D REGULARIZED XFEM FOR PULL-OUT OF STEEL BARS IN CONCRETE, BENDING AND SHEAR TESTS ON FRP-REINFORCED CONCRETE BEAMS 2726
Elena Benvenuti, Nicola Orlando

MS 908: VERIFICATION AND VALIDATION OF STRUCTURAL MECHANICS SIMULATION MODELS
EXPERIMENTAL VALIDATION OF COMPOSITE STRUCTURES IN EXPLICIT IMPACT ANALYSIS 2734
Konstantinos Fotopoulos, George Lampeas

CODE VERIFICATION IN SHELL ANALYSIS BY THE METHOD OF MANUFACTURED SOLUTIONS 2745
Michael Gfrerer, Martin Schanz

EXPERIMENTAL VALIDATION OF A MODEL UPDATE PROCEDURE FOCUSING ON SMALL GEOMETRIC DEVIATIONS 2757
Thomas Maywald, Arnold Kühhorn, Sven Schrape

OPTIMUM DESIGN, FINITE ELEMENT MODEL UPDATING AND DYNAMIC ANALYSIS OF A FULL LAMINATED GLASS PANORAMIC CAR ELEVATOR 2774
Dimitrios Giagopoulos, Iraklis Chatziparasidis

INVESTIGATION IN THE MECHANICAL BEHAVIOUR OF LOW-VELOCITY IMPACTED CFRP PLATES UNDER DIFFERENT BOUNDARY CONDITIONS 2786
Süleyman Arslan, Zamaan Sadeghi, Athanasios Dafnis, Kai-Uwe Schröder

A NEW SHELL FINITE ELEMENT WITH DRILLING DEGREES OF FREEDOM AND ITS RELATION TO EXISTING FORMULATIONS 2803
Robert Winkler, Dimitrios Plakomytis

MS 910: HIGH ORDER CFD METHODS: CONCLUSIONS AND OUTLOOK
CURVED GRID GENERATION AND DG COMPUTATION FOR THE DLR-F11 HIGH LIFT CONFIGURATION 2843
Ralf Hartmann, Harlan Mcmorris, Tobias Leicht

BS1 - DNS OF THE TAYLOR-GREEN VORTEX AT RE = 1600 2859
Andrea Mastellone, Luigi Cutrone, Francesco Capuano

MS 911: NUMERICAL METHODS IN THE MECHANICS OF GENERALIZED CONTINUA
THE STRUCTURAL SYMMETRY WITHIN THE CONTEXT OF NONLOCAL ELASTICITY 2869
Aurora Angela Pisano, Paolo Fuschi

ISOGEOMETRIC GALERKIN METHODS FOR GRADIENT-ELASTIC BARS, BEAMS, MEMBRANES AND PLATES 2876
Jarkko Niiranen, Sergei Khakalo, Viacheslav Balobanov, Josef Kiendl, Antti H. Niemi, Bahram Hosseini, Alessandro Reali

MS 912: HIGH-ORDER METHODS, SENSITIVITY ANALYSIS AND ADAPTATION FOR THE NAVIER STOKES EQUATIONS
ADAPTIVE MESH REFINEMENT TECHNIQUES FOR HIGH-ORDER FINITE-VOLUME WENO SCHEME 2883
Harshavardhana Srinivasan, Panagiotis Tsoutsanis

IMPLEMENTATION OF A LOW-MACH NUMBER MODIFICATION FOR HIGH-ORDER FINITE-VOLUME SCHEMES FOR ARBITRARY HYBRID UNSTRUCTURED MESHES 2900
Nicholas Simmonds, Panagiotis Tsoutsanis, Adrian Gaylard

APPROPRIATE COMBINATIONS OF CONTROLLER PARAMETERS FOR UNSTEADY FLOW SIMULATIONS WITH ADAPTIVE TIME STEP CONTROL 2916
Kathrin Kozulovic, Graham Ashcroft

MS 913: HIGH-ORDER METHODS FOR POLYGONAL AND POLYHEDRAL MESHES
ADAPTIVE BEM-BASED FEM ON POLYGONAL MESHES FROM VIRTUAL ELEMENT METHODS 2930
Steffen Weißer

VEM AND TOPOLOGY OPTIMIZATION ON POLYGONAL MESHES 2941
Paola F. Antonietti, Matteo Bruggi, Simone Scacchi, Marco Verani

THE VIRTUAL ELEMENT METHOD FOR DISCRETE FRACTURE NETWORK FLOW AND TRANSPORT SIMULATIONS 2953
Matias Fernando Benedetto, Stefano Berrone, Andrea Borio, Sandra Pieraccini, Stefano Scialo

MS 916: DIRECT METHODS FOR LIMIT STATES OF MATERIALS AND STRUCTURES
COMPOSITE FEM MODELS FOR LIMIT AND SHAKEDOWN ANALYSIS 2971
Leonardo Leonetti, Giovanni Garcea, Hung Nguyen-Xuan

ON SHAKEDOWN OF ELASTIC-PLASTIC BODIES WITH TEMPERATURE DEPENDENT PROPERTIES 2983
Michael Peigney

A NUMERICAL STUDY ON THE ENDURANCE LIMIT OF PARTICULATE REINFORCED METAL MATRIX COMPOSITES (PRMMCS) USING THE DIRECT METHOD AND THE STATISTICAL LEARNING 2994
Geng Chen, Bezold Alexander, Christoph Broeckmann, Dieter Weichert

SHAKEDOWN ANALYSIS OF PLATE BENDING UNDER STOCHASTIC UNCERTAINTY BY CHANCE CONSTRAINED PROGRAMMING 3007
Ngoc Trinh Tran, Thanh Ngoc Tran, H.G. Matthies, G.E. Stavroulakis, M. Staat

LIMIT ANALYSIS LOCUS OF HIGH STRENGTH STEEL PLATES UNDER NON-QUADRATIC YIELD CRITERIA 3020
Konstantinos Nikolaou, Christos Bisbos

MS 917: MESOSCOPIC METHODS FOR COMPLEX FLUIDS AND SOFT MATTER
PARTICLE BASED SIMULATION OF FLUID FLOW IN PERIODICALLY GROOVED CHANNELS 3026
Dorothea Kasiteropoulou, Theodoros Karakasidis, Antonios Liakopoulos

MS 918: COMPUTER ALGEBRA SYSTEMS IN MODELLING STATIC AND DYNAMIC PROBLEMS IN MECHANICS OF SOLIDS
HIGH COMPUTATIONAL EFFICIENCY THROUGH GENERIC ANALYTICAL FORMULATION FOR LINEAR SOIL PRESSURE DISTRIBUTION OF RIGID SPREAD RECTANGULAR FOOTINGS 3045
John Bellos, Nikolaos P. Bakas

A REAL-SPACE MODAL ANALYSIS METHOD FOR NON-PROPORTIONAL DAMPED STRUCTURES 3065
Evgueni Stanoev

A FORCE-BASED FORMULATION FOR THE ANALYSIS OF 3-DIMENSIONAL INELASTIC STRUCTURAL FRAMES ... 3091
Theodoros Patsios, Konstantinos Spiliopoulos

THE FEATURES OF ANALYTICAL SOLUTIONS OF BOUNDARY VALUE PROBLEMS OF THE ELASTICITY THEORY FOR FINITE DOMAINS WITH ANGULAR POINTS OF A BOUNDARY 3107
Alexander Kerzhaev, Mikhail Kovalenko, Irina Menshova

MS 919: RECENT ADVANCES IN NUMERICAL SIMULATION AND ANALYSIS OF KINETIC MODELS
DISCRETE VELOCITY MODELS: A STUDY OF THE HYDRODYNAMIC LIMIT 3113
Hans Babovsky

MESO - MACRO MODELS FOR A HARD SPHERE GAS 3121
Sergey Bogomolov, Natalya Esikova, Artem Kuvshinnikov

MS 921: RECENT ADVANCES IN BOUNDARY ELEMENT METHODS
ADVANCES IN THE BOUNDARY ELEMENT METHOD IN GEOMECHANICS 3139
Gernot Beer

ENERGETIC BEM FOR THE NUMERICAL SOLUTION OF DAMPED WAVE PROPAGATION EXTERIOR PROBLEMS 3159
Alessandra Aimi, Mauro Diligenti, Chiara Guardasoni

MODELLING THE PROCESS OF SEQUENTIAL EXCAVATION WITH THE BOUNDARY ELEMENT METHOD 3168
Christian Duenser, Gernot Beer

GREEN'S FUNCTION FOR THE EVALUATION OF ANCHOR LOSSES IN MEMS 3181
Attilio Frangi, Massimiliano Cremonesi

EFFICIENT BOUNDARY ELEMENT FORMULATION OF THERMOELASTICITY 3190
Relindis Rott, Martin Schanz

A CHEBYSHEV INTERPOALTION-BASED FAST MULTIPOLE METHOD FOR POROELASTICITY 3201
Barbara Knöbl, Thomas Traub, Martin Schanz

MS 922: HIGH-ORDER METHODS FOR ELASTIC WAVES AND THEIR APPLICATION
ENERGY STABLE HIGH ORDER FINITE DIFFERENCE METHODS ON STAGGERED GRIDS: AN INITIAL INVESTIGATION 3211
Ossian O'Reilly, Tomas Lundquist, Jan Nordström

MS 923: NOVEL DISCRETIZATION METHODS – MATHEMATICAL AND MECHANICAL ASPECTS
ALTERNATIVE TO RETURN -MAPPING ALGORITH FOR COMPUTING PLASTIC STRAIN. APPLICATION TO DILATANT MATERIALS 3224
Siegfried Maiolino

DISCONTINUOUS GALERKIN METHOD WITH REDUCED INTEGRATION SCHEME FOR THE BOUNDARY TERMS IN ALMOST INCOMPRESSIBLE LINEAR ELASTICITY 3231
Hamid Reza Bayat, Stephan Wulfinghoff, Stefanie Reese

1000 OPTIMIZATION, INVERSE PROBLEMS AND CONTROL

MS 1001: STRUCTURAL AND MULTIDISCIPLINARY OPTIMIZATION
A METHOD FOR BI-DIRECTIONAL COUPLING OF STRUCTURE AND SYSTEM IN THE OPTIMISATION OF MULTI-FUNCTIONAL COMPONENTS 3239
Ajit Panesar, Ian Ashcroft, Ricky Wildman, Richard Hague

SHAPE-TOPOLOGY OPTIMIZATION FOR DESIGNING SHELL STRUCTURES 3249
Hirotaka Nakayama, Masatoshi Shimoda

ON A NASH GAME FOR TOPOLOGY OPTIMIZATION UNDER LOAD-UNCERTAINTY – FINDING THE WORST LOAD 3259
Carl-Johan Thore

ANALYSIS AND DESIGN OF REINFORCED CONCRETE STRUCTURES AS A TOPOLOGY OPTIMIZATION PROBLEM 3271
Matteo Bruggi

ADJOINT OPTIMAL CONTROL PROBLEMS FOR FLUID-STRUCTURE INTERACTION SYSTEMS 3280
Daniele Cerroni, Roberto Da Vià, Sandro Manservisi, Filippo Menghini, Luca Zaniboni

APPLICATION OF WHIRL FLUTTER OPTIMIZATION-BASED SOLUTION TO FULL-SPAN MODEL OF TWIN TURBOPROP AIRCRAFT 3293
Jiri Cecrdle

ON THE CONSIDERATION OF UNCERTAINTY IN DESIGN: OPTIMIZATION – RELIABILITY – ROBUSTNESS 3310
Nicolas Lelièvre, Pierre Beaurepaire, Cécile Mattrand, Nicolas Gayton, Abdelkader Ostmane

A NEW OPTIMIZED ANISOTROPIC MOVING LEAST SQUARES SURROGATE MODEL WITH MAXIMIZED PROGNOSIS 3321
Kevin Cremanns, Dirk Roos

LATIN HYPERCUBE SAMPLING BASED ON ADAPTIVE ORTHOGONAL DECOMPOSITION 3333
Dirk Roos

A BENCHMARK OF CONTEMPORARY METAMODELING ALGORITHMS 3344
Can Bogoclu, Dirk Roos

TOPOLOGY OPTIMIZATION USING A KRIGING-ASSISTED GENETIC ALGORITHM WITH A NOVEL LEVEL SET REPRESENTATION APPROACH 3361
Mitsuo Yoshimura, Koji Shimoyama, Takashi Misaka, Shigeru Obayashi

TOPOLOGY OPTIMIZATION OF CONTACT PROBLEMS BASED ON ALLEN CAHN APPROACH 3377
Andrzej Myslinski

ON THE OPTIMAL DESIGN OF CABLE-STAYED BRIDGES 3386
Gerardo Carpentieri, Mariano Modano, Francesco Fabbrocino, Luciano Feo, Fernando Fraternali

A MIXED-INTEGER LINEAR PROGRAMMING APPROACH FOR GLOBAL DISCRETE SIZE OPTIMIZATION OF FRAME STRUCTURES 3395
Roxane Van Mellaert, Kristo Mela, Teemu Tiainen, Markku Heinisuo, Geert Lombaert, Mattias Schevenels

A SUPER-STRUCTURE BASED OPTIMISATION APPROACH FOR BUILDING SPATIAL DESIGNS 3409
Koen Van Der Blom, Sjonnie Boonstra, Hèrm Hofmeyer, Michael Emmerich

BENDING STIFFNESS OF A MULTILAYERED PLATE 3423
Petr Tovstik, Tatiana M. Tovstik

EFFICIENT SIZING OF STRUCTURES UNDER STRESS CONSTRAINTS 3436
Zhi Hong, Mostafa Abdalla

TOPOLOGY OPTIMIZATION OF WAVE BARRIERS FOR RAILWAY INDUCED VIBRATIONS IN BUILDINGS 3461
Cédric Van Hoorickx, Mattias Schevenels, Geert Lombaert

MS 1002: EVOLUTIONARY ALGORITHMS AND METAHEURISTICS IN CIVIL ENGINEERING AND CONSTRUCTION MANAGEMENT

MULTIOBJECTIVE OPTIMIZATION USING GENETIC ALGORITHMS IN TIME-COST CONSTRUCTION PROJECT SCHEDULING PROBLEM 3473
Jorge Magalhães-Mendes

APPLICATION OF GENETIC ALGORITHMS TO STRUTTED SHEET PILE WALL DESIGN OPTIMIZATION 3485
Mohamed Eid, Remon Isaac

NASH EVOLUTIONARY ALGORITHMS: TESTING PROBLEM SIZE IN RECONSTRUCTION PROBLEMS IN FRAME STRUCTURES 3493
David Greiner, Jacques Periaux, Jose M. Emperador, Blas Galván, Gabriel Winter

OPTIMUM DESIGN OF REINFORCED CONCRETE FRAMES ACCORDING TO EC8 AND MC2010 WITH GENETIC ALGORITHMS 3505
Panagiotis Mergos

CALIBRATION OF THE NUMERICAL MODEL OF A STAND IN DRAGÃO STADIUM BASED ON GENETIC ALGORITHMS 3519
Jorge Leite, Diogo Ribeiro, Hugo Marques, Rui Calçada

MS 1003: ADVANCES IN DESIGN OPTIMIZATION OF STRUCTURES AND MATERIALS
DESIGN OF ISOTROPIC MICROSTRUCTURES VIA A TWO-SCALE APPROACH 3534
Alexis Faure, Georgios Michailidis, Rafael Estevez, Guillaume Parry, Grégoire Allaire

SHAPE OPTIMIZATION OF GRAPHENE SHEETS FOR MAXIMUM FUNDAMENTAL FREQUENCY 3546
Jin-Xing Shi, Masatoshi Shimoda

TOPOLOGY OPTIMIZATION WITH AN IMPLICIT FUNCTION AND PARAMETERIZED CUTTING SURFACE 3553
Peter Dunning

TOPOLOGY OPTIMIZATION OF PERIODIC STRUCTURES FOR COUPLED ACOUSTIC-STRUCTURE SYSTEMS 3565
William Martins Vicente, Renato Picelli, Renato Pavanello, Yi Min Xie

BESO APPROACH TO TOPOLOGY OPTIMIZATION OF GAN PHONONIC CRYSTALS 3583
Luca D'Alessandro, Bichoy Bahr, Luca Daniel, Dana Weinstein, Raffaele Ardito

MS 1004: AERODYNAMIC STRATEGIES FOR THE GLOBAL OPTIMIZATION OF FLYING CONFIGURATIONS IN SUPERSONIC FLOW
LOW BOOM / LOW DRAG SMALL SIZE SUPERSONIC AIRCRAFT DESIGN 3596
Atsushi Ueno, Yasushi Watanabe, Itham Salah El Din, Richard Grenon, Gerald Carrier

DEVELOPMENT OF PHYSICAL METHODS OF THE SUPERSONIC AIRPLANE NEAR-FIELD INVESTIGATION AIMED AT THE SONIC BOOM MINIMIZATION 3612
Sergey Chernyshev, Alexander Ivanov, Andrey Kiselev, Vladimir Mosharov, Leonid Teperin

GLOBAL OPTIMIZATION OF THE SHAPE OF AN AEROSPACE VEHICLE, VIA ITERATIVE OPTIMUM-OPTIMORUM STRATEGY 3621
A. Nastase

MS 1005: MONITORING AND CONTROL OF STRUCTURES
SHAPE IDENTIFICATION ANALYSIS OF CAVITY IN RESIN STRUCTURE BASED ON THERMAL NONDESTRUCTIVE TESTING METHOD 3630
Kotaro Maruoka, Takahiko Kurahashi, Tetsuro Iyama

DESIGN AND INSTALLATION OF A PERMANENT MONITORING SYSTEM FOR PALAZZO LOMBARDIA IN MILANO, ITALY 3640
Marta Berardengo, Alfredo Cigada, Stefano Manzoni, Marcello Vanali

MS 1006: PARAMETER IDENTIFICATION IN SOLID MECHANICS
AN INVERSE PROBLEM STRATEGY BASED ON FORWARD MODEL EVALUATIONS: GRADIENT-BASED OPTIMIZATION WITHOUT ADJOINT SOLVES 3652
Miguel Aguilo

COHESIVE ZONE MODEL IDENTIFICATION WITH DCB TEST PARAMETER ESTIMATION SENSITIVITY 3676
Racine Ly, Julien Jumel, Martin Shanahan, Florian Lavelle

MS 1007: ADDITIVE MANUFACTURING AND OPTIMIZATION
TOPOLOGY OPTIMIZATION FOR ADDITIVE MANUFACTURING WITH CONTROLLABLE SUPPORT STRUCTURE COSTS 3689
Matthijs Langelaar

STUDY OF TOPOLOGY OPTIMIZATION PARAMETERS AND SCAFFOLD STRUCTURES IN ADDITIVE MANUFACTURING 3700
Alain Garaigordobil, Ruben Ansola, Estrella Veguería

FINITE ELEMENT APPROXIMATION OF A TIME-DEPENDENT TOPOLOGY OPTIMIZATION PROBLEM 3711
Matteo Bruggi, Nicola Parolini, Francesco Regazzoni, Marco Verani

DESIGNING MANUFACTURABLE VISCOELASTIC DEVICES USING A TOPOLOGY OPTIMIZATION APPROACH WITHIN A TRULY-MIXED FEM FRAMEWORK 3724
Paolo Venini, Marco Pingaro, Carlo Cinquini

ISO-XFEM FOR TOPOLOGY OPTIMIZATION OF STRUCTURES UNDER MULTIPLE LOAD CASES AND ACCELERATION LOADING 3739
Meisam Abdi, Ian Ashcroft, Ricky Wildman

MS 1008: ULTRASONIC GUIDED WAVES TESTING AND MONITORING
LAMINATE ELEMENT METHOD AND ITS APPLICATION TO THE STUDY OF GUIDED WAVE RESONANCE PHENOMENA IN LAYERED ELASTIC STRUCTURES WITH DEFECTS 3753
Evgeny Glushkov, Natalia Glushkova, Artem Eremin, Rolf Lammering

INVESTIGATIONS OF MECHANICAL GUIDED WAVES PROPAGATION IN PIPES REPAIRED LOCALLY BY COMPOSITE PATCHES 3761
Slah Yaacoubi, Weina Ke, F. Dahmene, M. El Mountassir

MS 1009: ADJOINT METHODS FOR STEADY & UNSTEADY OPTIMIZATION

TWO-STEPS SHAPE OPTIMIZATION ALGORITHM IMPROVING HYDRODYNAMICS STABILITY 3770
Takashi Nakazawa

ON THE CORRECT APPLICATION OF AD CHECKPOINTING TO ADJOINT MPI-PARALLEL PROGRAMS 3778
Ala Taftaf, Laurent Hascoët

SPHERICITY: MESH OPTIMIZATION FOR ARBITRARY ELEMENT TOPOLOGY 3797
Pavlos Alexias, Eugene De Villiers

LINKING PARAMETRIC CAD WITH ADJOINT SURFACE SENSITIVITIES 3812
Ilias Vasilopoulos, Dheeraj Agarwal, Marcus Meyer, Trevor T. Robinson, Cecil G. Armstrong

A CODE-COUPLING APPROACH TO THE IMPLEMENTATION OF DISCRETE ADJOINT SOLVERS BASED ON AUTOMATIC DIFFERENTIATION 3828
Jan Backhaus, Anna Engels-Putzka, Christian Frey

CAD KERNEL AND GRID GENERATION ALGORITHMIC DIFFERENTIATION FOR TURBOMACHINERY ADJOINT OPTIMIZATION 3843
Ismael Sanchez Torreguitart, Tom Verstraete, Lasse Mueller

ALTERNATIVE SOLUTION ALGORITHMS FOR PRIMAL AND ADJOINT INCOMPRESSIBLE NAVIER-STOKES 3858
Mattia Oriani, Guillaume Pierrot

DEFROSTER NOZZLE SHAPE OPTIMIZATION USING THE CONTINUOUS ADJOINT METHOD 3883
Lefki Germanou, Evangelos Papoutsis-Kiachagias, Antoine Delacroix, Kyriakos Giannakoglou

SENSITIVITY ANALYSIS FOR FORCED RESPONSE IN TURBOMACHINERY USING AN ADJOINT HARMONIC BALANCE METHOD 3893
Anna Engels-Putzka, Christian Frey

A TWO-LEVEL HYBRID APPROACH FOR OPTIMAL ACTIVE FLOW CONTROL ON A THREE-ELEMENT AIRFOIL 3912
Anil Nemili, Emre Özkaya, Nicolas R. Gauger, Felix Kramer, Frank Thiele

TRANSITION FROM 2D CONTINUOUS ADJOINT LEVEL SET TOPOLOGY TO SHAPE OPTIMIZATION 3928
J.R.L. Koch, E.M. Papoutsis-Kiachagias, K.C. Giannakoglou

AERODYNAMIC SHAPE OPTIMIZATION USING THE TRUNCATED NEWTON METHOD AND CONTINUOUS ADJOINT 3942
Mehdi Ghavami Nejad, Evangelos M. Papoutsis-Kiachagias, Kyriakos C. Giannakoglou

UNSTEADY ADJOINT TO THE CUT-CELL METHOD USING MESH ADAPTATION ON GPU'S 3957
Konstantinos Samouchos, Stergios Katsanoulis, Kyriakos Giannakoglou

SHAPE OPTIMIZATION OF TURBOMACHINERY ROWS USING A PARAMETRIC BLADE MODELLER AND THE CONTINUOUS ADJOINT METHOD RUNNING ON GPUS 3972
K.T. Tsiakas, F. Gagliardi, X.S. Trompoukis, K.C. Giannakoglou

GEOMETRIC CONTINUITY CONSTRAINTS FOR ADJACENT NURBS PATCHES IN SHAPE OPTIMISATION 3985
Xingchen Zhang, Yang Wang, Mateusz Gugala, Jens-Dominik Mueller

TOWARDS MULTIDISCIPLINARY ADJOINT OPTIMIZATION OF TURBOMACHINERY COMPONENTS 3999
Marc Schwalbach, Tom Verstraete

TOWARDS AN OUTPUT-BASED RE-MESHING FOR TURBOMACHINERY APPLICATIONS 4011
Mateusz Gugala, Marcus Meyer, Jens-Dominik Mueller

OPTIMISATION OF A U-BEND USING A CAD-BASED ADJOINT METHOD WITH DIFFERENTIATED CAD KERNEL 4023
Salvatore Auriemma, Mladen Banovic, Orest Mykhaskiv, Herve Legrand, Jens-Dominik Mueller, Tom Verstraete, Andrea Walther

A CONTINUOUS ADJOINT APPROACH FOR VEHICLE INTERIOR NOISE REDUCTION 4035
Christos Kapellos, Michael Hartmann

A MIXED OPERATOR OVERLOADING AND SOURCE TRANSFORMATION APPROACH FOR ADJOINT CFD COMPUTATION 4047
Zahrasadat Dastouri, Sinan Gezgin, Uwe Naumann

MS 1010: INVERSE PROBLEMS, DESIGN AND OPTIMIZATION

EFFICIENT CALIBRATION OF DISCRETE ELEMENT MATERIAL MODEL PARAMETERS USING LATIN HYPERCUBE SAMPLING AND KRIGING 4061
Michael Rackl, Carolin D. Görnig, Kevin J. Hanley, Willibald A. Günthner

UPDATING PRIOR PARAMETERS BASED ON LIKELIHOOD FUNCTION-BAYESIAN METHOD FOR PARAMETER ESTIMATION AT HIGH MEASUREMENT UNCERTAINTY 4073
Sankaran Somasundharam, K Srinivas Reddy

MS 1011: SURROGATE-ASSISTED EVOLUTIONARY ALGORITHMS IN AERODYNAMIC DESIGN/OPTIMIZATION

CONSTRAINED MULTI-POINT AERODYNAMIC SHAPE OPTIMIZATION OF THE VISCOUS DPW WING THROUGH EVOLUTIONARY PROGRAMMING AND SUPPORT VECTOR MACHINES 4082
Daniel González Juárez, Esther Andrés Pérez, Mario Jaime Martin Burgos

SURROGATE-BASED GLOBAL OPTIMIZATION OF A CYLINDER BY THE USE OF EVOLUTIONARY ALGORITHMS, SUPPORT VECTOR MACHINES AND NON UNIFORM B-SPLINES 4092
Eesther Andrés-Pérez, Daniel González-Juárez, Mario J. Martin-Burgos, Leopoldo Carro-Calvo, Sancho Salcedo-Sanz

PERFORMANCE COMPARISON OF KRIGING AND SVR SURROGATE MODELS APPLIED TO THE OBJECTIVE FUNCTION PREDICTION WITHIN AERODYNAMIC SHAPE OPTIMIZATION 4104
Daniel Viúdez-Moreiras, Esther Andrés-Pérez, Daniel González-Juárez, Mario J. Martin Burgos

HEAT TRANSFER OPTIMIZATION OF A RIBBED SURFACE USING SURROGATE-ASSISTED GENETIC ALGORITHMS 4117
Panagiotis Tsirikoglou, Ghader Ghorbaniasl, Simon Abraham, Chris Lacor

MULTI-FIDELITY EXTENSION TO NON-INTRUSIVE PROPER ORTHOGONAL DECOMPOSITION BASED SURROGATES 4129
Tariq Benamara, Piotr Breitkopf, I. Lepot, Caroline Sainvitu

EVOLUTIONARY AERODYNAMIC SHAPE OPTIMIZATION THROUGH THE RBF4AERO PLATFORM 4146
Dimitrios Kapsoulis, Varvara Asouti, Kyriakos Giannakoglou, Stefano Porziani, Emiliano Costa, Corrado Groth, Ubaldo Cella, Marco Evangelos Biancolini

THE RBF4AERO BENCHMARK TECHNOLOGY PLATFORM 4156
Massimo Bernaschi, Alessandro Sabellico, Giorgio Urso, Emiliano Costa, Stefano Porziani, Fabrizio Lagasco, Corrado Groth, Ubaldo Cella, Marco Evangelos Biancolini, Dimitrios H.Kapsoulis, Varvara G. Asouti, Kyriakos C. Giannakoglou

MS 1013: SOLUTION OF LARGE-SCALE INVERSE PROBLEMS
DATA ASSIMILATION USING MRI DATA 4164
Geir Nævdal, Ove Sævareid, Rolf J. Lorentzen

MS 1014: DESIGN OPTIMIZATION AND INVERSE PROBLEMS FOR WAVE PROPAGATION PROBLEMS
FULL-WAVEFORM INVERSION FOR THE RECONSTRUCTION OF ELECTROMAGNETIC PROPERTY PROFILES USING PLANE MICROWAVES 4178
Namho Joh, Jun Won Kang

1100 REDUCTION METHODS

MS 1101: REDUCED BASIS, POD AND PGD MODEL ORDER REDUCTION TECHNIQUES
REDUCED BASIS METHOD FOR POISSON-BOLTZMANN EQUATION 4187
Cleophas Kweyu, Martin Hess, Lihong Feng, Matthias Stein, Peter Benner

AN ITERATIVE MODEL ORDER REDUCTION SCHEME FOR A SPECIAL CLASS OF BILINEAR DESCRIPTOR SYSTEMS APPEARING IN CONSTRAINT CIRCUIT SIMULATION 4196
Pawan Goyal, Peter Benner

ELECTRICAL FIELDS SIMULATION IN HETEROGENOUS DOMAINS USING THE PROPER GENERALIZED DECOMPOSITION 4213
Chady Ghnatios, Francisco Chinesta, Anais Barasinski

MODEL ORDER REDUCTION IN STRUCTURAL DYNAMICS 4221
Raul Rodriguez Sanchez, Martin Buchschmid, Gerhard Müller

TOWARDS A NON-INTRUSIVE PROPER GENERALIZED DECOMPOSITION SCHEME FOR MODEL ORDER REDUCTION 4248
Xi Zou, Pedro Díez, Michele Conti, Ferdinando Auricchio

A PGD-BASED TIME SPACE DECOMPOSITION FOR THE UNSTEADY NAVIER-STOKES EQUATIONS APPLIED TO INCOMPRESSIBLE FLOWS 4263
Michel Visonneau

MS 1103: MATHEMATICAL SURROGATE MODELLING IN ELECTROMAGNETICS

RATIONAL MODELING OF MULTIVARIATE MULTI-FIDELITY DATA 4284
Elizabeth Rita Samuel, Dirk Deschrijver, Luc Knockaert, Tom Dhaene, Annie Cuyt

ON THE USE OF S-PARAMETER TRANSFORMATIONS TO IMPROVE SURROGATE MODEL BEHAVIOUR OF MULTIPORT NETWORKS 4295
Petrie Meyer

RECENT ADVANCES IN SURROGATE MODELLING OF REFLECTOR ANTENNA SYSTEMS 4302
Dirk De Villiers

A SHORT-TIME PRONY METHOD FOR THE DETECTION OF TRANSIENTS 4313
Annie Cuyt, Wen-Shin Lee, Min-Nan Tsai

SURROGATE MODELING OF ANTENNA RADIATION CHARACTERISTICS BY GAUSSIAN PROCESSES 4322
Jan Pieter Jacobs, Dirk De Villiers

ACCELERATION OF MESH-BASED PHYSICAL OPTICS FOR ELECTROMAGNETIC SCATTERING ANALYSIS 4330
Dao P. Xiang, Matthys M. Botha

DESIGN OF AXIALLY SYMMETRIC POWER COMBINERS USING SURROGATE BASED OPTIMIZATION 4339
Ryno Beyers, Dirk De Villiers

1200 STRUCTURAL STABILITY AND DYNAMICS

MS 1201: COMPUTATIONAL STRUCTURAL DYNAMICS

FLEXURAL VIBRATION ANALYSIS OF GRAPHENE NANOPLATELETS REINFORCED NANOCOMPOSITE BEAMS 4351
Jie Yang, Chuang Feng

DYNAMIC RESPONSE OF REAL OFFSHORE WIND TURBINES ON MONOPILES IN STRATIFIED SEABED 4361
Guillermo M. Álamo, Juan J. Aznárez, Luis A. Padrón, Alejandro E. Martínez-Castro, Rafael Gallego, Orlando Maeso

DYNAMIC ANALYSIS OF SPECIAL CARS ON UNEVEN ROADS 4377
Szymon Tengler

STRUCTURED SPATIAL DISCRETIZATION OF DYNAMICAL SYSTEMS 4398
Marko Jokic, Andrej Jokic, Bruno Dogancic

WAVE PROPAGATION IN THIN PRETWISTED ANISOTROPIC STRIPS 4406
Maloth Thirupathi, Mira Mitra, P J Guruprasad

NUMERICAL ROUTINE FOR DYNAMIC ANALYSIS OF TRANSMISSION LINES GUYED TOWERS SUBMITTED TO BROKEN CABLE 4416
Thiago Brazeiro Carlos, João Kaminski Jr.

INVARIANCE OF EIGENFREQUENCIES AND EIGENMODES UNDER GEOMETRIC TRANSFORMATION IN ELONGATED ELASTIC STRUCTURES 4436
Maryam Morvaridi, Michele Brun

MS 1202: ADVANCED BEAM MODELS

A COMPUTATIONALLY EFFECTIVE FORMULATION TO FINITE ROTATIONS - SMALL STRAINS DESCRIPTION OF BEAM ELEMENTS 4445
Salvatore Lopez

A COROTATIONAL FINITE ELEMENT TO MODEL BENDING VIBRATIONS OF METALLIC STRANDS 4455
Francesco Foti

3D BEAM-COLUMN FINITE ELEMENT UNDER NON-UNIFORM SHEAR STRESS DISTRIBUTION DUE TO SHEAR AND TORSION 4467
Paolo Di Re, Daniela Addessi, Filip C. Filippou

SINGULARLY PERTURBED PROBLEMS IN MECHANICS (SOME FUNDAMENTAL ASPECTS OF DESIGNING AND COMPUTING) 4481
Lyudmila K. Kuzmina

A DEGENERATE-CONTINUUM BASED TIMOSHENKO BEAM APPROACH FOR THE AEROELASTIC ANALYSIS OF THE WIND TURBINE BLADES 4488
Anthoula Panteli, Dimitris Manolas, Konstantinos Spiliopoulos

DYNAMICS OF WIND TURBINE BLADES USING A GEOMETRICALLY-EXACT BEAM FORMULATION 4503
Celso Faccio Junior, Alfredo Gay Neto

EXTENDED FORMULA FOR THE CRITICAL VELOCITY OF A LOAD MOVING ON A BEAM SUPPORTED BY A FINITE DEPTH FOUNDATION 4520
Zuzana Dimitrovová

FIRST-ORDER DISPLACEMENT-BASED ZIGZAG THEORIES FOR COMPOSITE LAMINATES AND SANDWICH STRUCTURES: A REVIEW 4528
Marco Di Sciuva

MS 1203: THE MODELS AND INVESTIGATIONS METHODS OF DYNAMICS OF THE SOLIDS SYSTEMS WITH DRY FRICTION

VIRTUAL TESTBENCH FOR THE OMNI WHEEL DYNAMICS SIMULATION: NEW CONTACT TRACKING ALGORITHM 4553
Ivan Kosenko, Sergey Stepanov, Kirill Gerasimov, Mikhail Stavrovskiy

MODEL AND INVESTIGATION OF DYNAMICS OF SOLID SYSTEM WITH TWO MASSIVE ECCENTRICS ON A ROUGH PLANE 4572
Sergey Semendyaev, Alexey Tsyganov

NON-REGULAR VEHICLE DYNAMICS. APPLICATION TO COLLISION 4584
Ahmed Bouzar Essaidi, Bachir Menkouz, Moussa Haddad, Taha Chettibi

TESTING, SIMULATING AND UNDERSTANDING UNDER-PLATFORM DAMPER DYNAMICS 4599
Chiara Gastaldi, Muzio M. Gola

MS 1204: NONLINEAR DYNAMICS OF ROTATING STRUCTURES
A NEW DYNAMIC SUBSTRUCTURING METHOD FOR NONLINEAR AND DISSIPATIVE SYSTEMS 4611
Colas Joannin, Benjamin Chouvion, Fabrice Thouverez

SOME REMARKS ON TIME INTEGRATION OF 3D ROTOR-STATOR ASSEMBLY 4624
Benoit Prabel

DELAYED FEEDBACK CONTROL METHOD FOR CALCULATING SPACE-TIME PERIODIC SOLUTIONS OF VISCOELASTIC PROBLEMS 4638
Ustim Khristenko, Patrick Le Tallec

COMBINING FINITE ELEMENT ANALYSIS AND ANALYTICAL MODELLING FOR EFFICIENT SIMULATIONS OF NON-LINEAR GEAR DYNAMICS 4655
Shadi Sweiki, Jakub Korta, Antonio Palermo, Rocco Adduci, Domenico Mundo

DAMPING INDUCED BY DRY FRICTION: ANALYSES AND EXPERIMENTS FOR MODELING IMPROVEMENT 4664
Marc-André Douville, Béatrice Faverjon, Eric Chatelet, Georges Jacquet-Richardet

MS 1206: ADVANCES IN NUMERICAL METHODS FOR LINEAR AND NON-LINEAR DYNAMICS AND WAVE PROPAGATION
RAYLEIGH METHOD APPLIED TO A 46-M-HIGH CONCRETE MAST 4674
Alexandre De M. Wahrhaftig, Reyolando M. L. R. F. Brasil

A DISPERSION MINIMIZED MIMETIC METHOD FOR A COLD PLASMA MODEL 4682
Vrushali A. Bokil, Vitaliy Gyrya, Duncan A. Mcgregor

A VOLUME-AGGLOMERATION MULTIRATE TIME ADVANCING APPROACH 4703
Emmanuelle Itam, Stephen Wornom, Bruno Koobus, Alain Dervieux

THERMOMECHANICAL NUMERICAL SIMULATION OF IMPACTS ON ELASTIC-PLASTIC SOLIDS WITH THE FINITE VOLUME METHOD 4717
Thomas Heuzé

MS 1207: COMPUTATIONAL SIMULATION OF SMART STRUCTURES AND MATERIALS
TRANSVERSE WAVE PROPAGATION IN A ONE-DIMENSIONAL STRUCTURE COUPLED TO ITS ELECTRICAL ANALOGUE: COMPARISON OF TRANSFER MATRIX MODELS 4728
Boris Lossouarn, Mathieu Aucejo, Jean-François Deü

MS 1208: BIFURCATIONS AND STABILITY
BUCKLING OF ANNULAR PLATE JOINT WITH CIRCULAR BEAM 4741
Sergei Filippov, Maria Boyarskaya

THE CURL AND FLUTING OF PAPER: THE EFFECT OF ELASTO-PLASTICITY 4752
Anna-Leena Erkkilä, Teemu Leppänen, Tero Tuovinen

STABILITY OF STEEL STRUCTURES WITH CLEARANCES AND IMPERFECTION 4770
Katarzyna Rzeszut, Andrzej Garstecki

MS 1209: DYNAMIC ANALYSIS OF BEAMS UNDER MOVING VEHICLES: APPLICATION TO RAILWAY TRACK MODELLING, DESIGN AND REHABILITATION
NUMERICAL ANALYSIS FOR THE DYNAMIC RESPONSE CHARACTERISTICS OF THE PRESTRESSED CONCRETE SLEEPER 4780
Tsutomu Watanabe, Kodai Matsuoka, Shintaro Minoura

NUMERICAL DYNAMIC ANALYSIS OF BEAMS ON NONLINEAR ELASTIC FOUNDATIONS UNDER HARMONIC MOVING LOAD 4794
Diego Froio, Roberto Moioli, Egidio Rizzi

MS 1210: ADVANCES IN MODELING AND ANALYSIS OF FGM STRUCTURES
ELASTOSTATIC AND MODAL AND BUCKLING ANALYSIS OF SPATIAL FGM BEAM STRUCTURES 4810
Justin Murin, Mehdi Aminbaghai, Juraj Hrabovsky, Vladimir Kutis, Juraj Paulech, Stephan Kugler

THERMO-ELASTICITY IN SHELL STRUCTURES MADE OF FUNCTIONALLY GRADED MATERIALS 4838
Stephan Kugler, Peter Fotiu, Justin Murin

FINITE BEAM ELEMENT WITH PIEZOELECTRIC LAYERS AND FUNCTIONALLY GRADED MATERIAL OF CORE 4863
Vladimír Kutiš, Justín Murín, Juraj Paulech, Juraj Hrabovský, Roman Gogola, Jakub Jakubec

NUMERICAL SOLUTION OF DIFFERENTIAL EQUATIONS WITH NON-CONSTANT COEFFICIENTS 4878
Juraj Hrabovský, Justín Murín, Mehdi Aminbaghai, Vladimír Kutiš, Juraj Paulech

TWO-WAY COUPLED ELECTRO-THERMAL ANALYSIS OF FGM SYSTEM CALCULATED BY THE NEW LINK FINITE ELEMENT 4888
Juraj Paulech, Vladimír Kutiš, Juraj Hrabovský, Justín Murín, Roman Gogola, Tibor Sedlár, Gabriel Gálik

MS 1211: COMPUTATIONAL STRATEGIES FOR STRUCTURAL ROBUSTNESS ASSESSMENT
PROGRESSIVE COLLAPSE FRAGILITY MODELS OF RC FRAMED BUILDINGS BASED ON PUSHDOWN ANALYSIS 4900
Emanuele Brunesi, Roberto Nascimbene, Fulvio Parisi

MECHANICAL PROPERTIES OF S355 UNDER EXTREME COUPLED EFFECT OF HIGH TEMPERATURES AND HIGH STRAIN RATES 4920
Daniele Forni, Bernardino Chiaia, Ezio Cadoni

IMPLEMENTATION OF PROGRESSIVE DAMAGE IN FINITE ELEMENT CODES FOR THE ASSESSMENT OF ROBUSNTESS 4928
Domenico Asprone, Bernardino Chiaia, Valerio De Biagi, Gaetano Manfredi, Fulvio Parisi

SEISMIC RESIDUAL CAPACITY ASSESSMENT OF FRAMED STRUCTURES DAMAGED BY EXCEPTIONAL ACTIONS 4942
Antonio Formisano, Giuseppe Iazzetta, Giuseppe Marino, Francesco Fabbrocino, Raffaele Landolfo

MS 1212: DYNAMICS AND SEISMIC RESPONSE OF ROCKING AND SELF-CENTERING STRUCTURES
ROCKING RESPONSE OF MASONRY BLOCK STRUCTURES USING MATHEMATICAL PROGRAMMING 4959
Francesco Portioli, Lucrezia Cascini, Raffaele Landolfo

CONTROLLED ROCKING, DISSIPATIVE CONTROLLED ROCKING AND MULTI-HIERARCHICAL ACTIVATION: NUMERICAL ANALYSIS AND EXPERIMENTAL TESTING 4969
Royce Liu, Alessandro Palermo

THE ROLE OF THE PRESTRESSED TENDONS ON THE SEISMIC PERFORMANCE OF HYBRID ROCKING BRIDGE BENTS 4983
Anastasios I. Giouvanidis, Elias G. Dimitrakopoulos

MODELLING CONTACT IN ROCKING STRUCTURES WITH A NONSMOOTH DYNAMICS APPROACH 4997
Anastasios I. Giouvanidis, Elias G. Dimitrakopoulos

A SIMPLE ANALYTICAL MODEL FOR THE ROCKING PREWEC SYSTEM 5010
Dimitrios Kalliontzis, Sri Sritharan

AN ANALYTICAL MODEL FOR DYNAMIC RESPONSE OF AN ELASTIC SDOF SYSTEM FIXED ON TOP OF A ROCKING SINGLE-STORY FRAME STRUCTURE: EXPERIMENTAL VALIDATION 5023
Jonas A. Bachmann, Christoph Jost, Quentin Studemann, Michalis F. Vassiliou, Bozidar Stojadinovic

SMOOTH-ROCKING OSCILLATOR UNDER NATURAL ACCELEROGRAMS 5063
Blerta Lipo, Gianmarco De Felice

EXPERIMENTAL INVESTIGATION OF THE SEISMIC RESPONSE OF A COLUMN ROCKING AND ROLLING ON A CONCAVE BASE 5074
Jonas A. Bachmann, Patrick Blöchlinger, Matthias Wellauer, Michalis F. Vassiliou, Bozidar Stojadinovic

SEISMIC ASSESSMENT OF MASONRY ROCKING COLUMNS AND FRAMES UNDER GROUND MOTION EXCITATIONS 5098
Ioannis Kavvadias, Lazaros Vasiliadis

PARAMETRIC INVESTIGATION OF THE DYNAMIC RESPONSE OF RIGID BLOCKS SUBJECTED TO SYNTHETIC NEAR-SOURCE GROUND MOTION RECORDS 5113
Michalis Fragiadakis, Ioannis Psycharis, Yenan Cao, George P. Mavroeidis

A MACRO-ELEMENT FORMULATION FOR ROCKING FLEXIBLE BODIES WITH A DEFORMABLE BASE 5129
Evangelos Avgenakis, Ioannis N. Psycharis

MS 1213: INNOVATIVE STRUCTURAL SYSTEMS FOR SEISMIC RESISTANT BUILDINGS

NONLINEAR ANALYSIS AND EXPERIMENTAL BEHAVIOUR OF AN INNOVATIVE STEEL FRAME WITH REINFORCED CONCRETE INFILL WALLS 5142
Andrea Dall'Asta, Graziano Leoni, Francesco Morelli, Walter Salvatore, Alessandro Zona

MODAL PROPERTIES AND SEISMIC RESPONSE OF EXISTING BUILDING RETROFITTED BY EXTERNAL BRACINGS WITH VISCOUS DAMPERS 5156
Laura Gioiella, Enrico Tubaldi, Fabrizio Gara, Andrea Dall'Asta

MS 1214: HISTORIC MASONRY STRUCTURES: MODELLING, ASSESSMENT & RETROFIT

SIMPLE CLOSED FORM HOMOGENIZATION MODEL FOR THE NON LINEAR STATIC AND DYNAMIC ANALYSIS OF RUNNING BOND MASONRY WALLS IN AND OUT OF PLANE LOADED 5172
Elisa Bertolesi, Gabriele Milani

CONSTRUCTION PHASES ANALYSIS OF UNREINFORCED MASONRY BUILDINGS THROUGH EQUIVALENT FRAME MODEL 5190
Francesco Pugi, Alessio Francioso, Giacomo Sevieri

A COMBINED EXPERIMENTAL AND NUMERICAL STUDY OF THE PULL-OUT MECHANISM OF THREADED TITANIUM BARS EMBEDDED IN MARBLE BLOCKS 5207
Stavros K. Kourkoulis, Aikaterini Marinelli, Ioanna Dakanali

FINITE-DISCRETE ELEMENT MODELLING OF MASONRY INFILL WALLS SUBJECTED TO OUT-OF-PLANE LOADS 5219
Laura Liberatore, Marta Bruno, Omar Al Shawa, Monica Pasca, Luigi Sorrentino

PALAZZO LA SAPIENZA IN PISA: STRUCTURAL ASSESSMENT AND RETROFIT OF AN HISTORICAL MASONRY BUILDING IN ITALY 5230
Silvia Caprili, Federico Mangini, Nicola Mussini, Walter Salvatore

THREE-DIMENSIONAL NONLINEAR BEHAVIOUR OF MASONRY WALLS MODELLED WITH DISCRETE ELEMENTS 5248
Daniele Baraldi, Antonella Cecchi

NUMERICAL VALIDATION OF EQUIVALENT-FRAME MODELS FOR URM WALLS 5262
Rossella Siano, Guido Camata, Vincenzo Sepe, Enrico Spacone, Pere Roca, Luca Pelà

SEISMIC ASSESSMENT OF HISTORICAL MASONRY TOWERS IN THE NORTH-EAST REGION OF ITALY 5274
Marco Valente, Gabriele Milani

NATIVITY CHURCH IN BETHLEHEM: FULL 3D NON-LINEAR FE APPROACH FOR STRUCTURAL DAMAGE PREDICTION 5287
Gabriele Milani, Marco Valente, Claudio Alessandri

DYNAMIC BEHAVIOUR AND EARTHQUAKE PERFORMANCE OF GREEK BASILICA CHURCHES WITH FOUNDATION DEFORMABILITY 5301
George Manos, Evaggelos Kozikopoulos, Lambros Kotoulas

PROBLEMS RELATED TO THE USE OF FIBER REINFORCED CEMENTITIOUS MATERIALS AS STRENGTHENING OF MASONRY MEMBERS 5314
Daniela Sinicropi, Antonio Borri, Marco Corradi, Michele Paradiso

FAST KINEMATIC LIMIT ANALYSIS OF FRP REINFORCED MASONRY VAULTS THROUGH A NEW GENETIC ALGORITHM NURBS-BASED APPROACH 5326
Andrea Chiozzi, Gabriele Milani, Antonio Tralli

THE ROLE OF RESTORATION MORTARS IN THE EARTHQUAKE PROTECTION OF KAISARIANI MONASTERY 5340
Antonia Moropoulou, Maria Apostolopoulou, Petros Moundoulas, Eleni Aggelakopoulou, Louiza Siouta, Asterios Bakolas, Maria Douvika, Panagiotis Karakitsios, Panagiotis G. Asteris

FIRST RESULTS OF THE VIBRATION-BASED STRUCTURAL HEALTH MONITORING OF A MASONRY DOME 5359
Nicola Cavalagli, Gabriele Comanducci, Massimiliano Gioffrè, Vittorio Gusella, Filippo Ubertini

BEHAVIOR OF SINGLE STORY BEARING WALL MASONRY STRUCTURES IN VARIOUS CONDITIONS 5373
Abdelraouf Kassem

SEISMIC PROTECTION OF MONUMENTS AND HISTORIC STRUCTURES – THE SEISMO RESEARCH PROJECT 5382
Constantine Spyrakos, Charilaos Maniatakis

MS 1215: NONLINEAR VIBRATIONS OF CONSERVATIVE AND NONCONSERVATIVE SYSTEMS: PHENOMENA AND ADVANCED NUMERICAL METHODS

FORCED RESPONSE OF SHROUDED BLADES WITH VARIABLE OPERATING POINTS 5396
Ferhat Kaptan, Lars Panning-Von Scheidt, Jörg Wallaschek, Victor Salit

GEOMETRY EFFECTS ON THE NONLINEAR OSCILLATIONS OF VISCOELASTIC CYLINDRICAL SHELLS 5406
Zenon Del Prado, Marco Amabili, Paulo Gonçalves, Frederico Da Silva

REDUCED ORDER MODELS FOR DYNAMIC BEHAVIOR OF PRESTRESSED ELASTOMER DAMPING DEVICES 5417
Antoine Legay, Jean-François Deü, Benjamin Morin

LOCALIZATION OF VIBRATORY ENERGY OF A LINEAR SYSTEM IN A CHAIN OF FOUR NONLINEAR OSCILLATORS 5427
Simon Charlemagne, Claude-Henri Lamarque, Alireza Ture Savadkoohi

CONTINUATION OF QUASI-PERIODIC SOLUTIONS WITH TWO-FREQUENCY HARMONIC BALANCE METHOD .. 5438
Louis Guillot, Pierre Vigué, Christophe Vergez, Bruno Cochelin

MS 1216: STRUCTURAL ANALYSIS AND VIBRATIONS

ASYMPTOTIC ANALYSIS OF DEFORMATIONS OF THE SLIGHTLY ORTHOTROPIC SPHERICAL LAYER UNDER NORMAL PRESSURE 5444
Andrei L. Smirnov, Svetlana M. Bauer, Liudmila A. Venatovskaia, Eva B. Voronkova

EXPERIMENTAL VALIDATION OF FINITE ELEMENT MODELS FOR REINFORCED CONCRETE BEAMS WITH AND WITHOUT DISCONTINUITIES 5454
Marios Filippoupolitis, Carl Hopkins, Siu-Kui Au

MS 1217: COMPUTATIONAL METHODS IN EARTHQUAKE ENGINEERING AND STRUCTURAL DYNAMICS

SEISMIC BEHAVIOR INDICES OF OLD TYPE REINFORCED CONCRETE MEMBERS 5464
Anthos Ioannou, Stavroula J. Pantazopoulou

EFFECT OF SOIL SPATIAL VARIABILITY ON THE DYNAMIC BEHAVIOR OF A SLOPE 5483
Michael Michael, Tamara Al-Bittar, Abdul-Hamid Soubra

ENERGY-MOMENTUM METHOD FOR NONLINEAR DYNAMIC OF 2D COROTATIONAL BEAMS 5496
Sophy Chhang, Mohammed Hjiaj, Jean-Marc Battini, Carlo Sansour

THE INFLUENCE OF UNCERTAINTY OF DESIGN PARAMETERS ON DYNAMIC CHARACTERISTICS OF STRUCTURE WITH DAMPERS 5507
Magdalena Lasecka-Plura, Roman Lewandowski

FINITE-DISCRETE NUMERICAL MODELLING OF REINFORCED CONCRETE STRUCTURES 5523
Nikolina Zivaljic, Zeljana Nikolic, Hrvoje Smoljanovic, Ivan Balic

BEAM DYNAMIC STRESSES INCREMENTS AFTER PARTIAL DECONSTRUCTION OF FOUNDATION 5533
Vladimir Gordon, Olga Pilipenko, Timur Gasimov

RELIABILITY OF SYSTEMS EQUIPPED WITH VISCOUS DAMPERS WITH VARIABLE PROPERTIES 5550
Andrea Dall'Asta, Laura Ragni, Fabrizio Scozzese, Enrico Tubaldi

AN INVESTIGATION ON EFFECT OF SUBGRADE REACTION MODULUS OF SOIL ON NATURAL PERIOD OF LOW RISE BUILDINGS 5567
Rafet Sisman, Abdurrahman Sahin

A PROBABILISTIC APPROACH TOWARDS AN EVALUATION OF EXISTING CODE PROVISIONS FOR SEISMICALLY ISOLATED STRUCTURES 5574
Anastasios Tsiavos, Bozidar Stojadinovic

EFFECT OF THE SEISMIC EXCITATION'S INCIDENCE ANGLE ON THE NONLINEAR BEHAVIOR OF BASE ISOLATED BUILDINGS CONSIDERING POUNDING TO ADJACENT MOAT WALLS 5585
Eftychia A. Mavronicola, Panayiotis C. Polycarpou, Petros Komodromos

NUMERICAL NON-LINEAR SIMULATION OF THE IN-PLANE BEHAVIOUR OF R/C FRAMES WITH MASONRY INFILLS UNDER SEISMIC TYPE LOADING 5598
George Manos, Vasilios Soulis

MODELING THE MECHANICAL RESPONSE OF A LEAD-CORE BEARING DEVICE: DAMAGE MECHANICS APPROACH 5613
Todor Zhelyazov, Rajesh Rupakhety, Simon Olafsson

INVESTIGATION OF THE PERFORMANCE OF VARIOUS MODAL CORRELATION CRITERIA IN STRUCTURAL DAMAGE IDENTIFICATION 5626
Manolis Georgioudakis, Vagelis Plevris

MS 1218: STABILITY AND CONTROL OF FLEXIBLE STRUCTURES

EXPLOITING MULTIPLE REFERENCE MODELS FOR ADAPTIVE CONTROL OF FLEXIBLE STRUCTURES 5646
Ilaria Venanzi, Laura Ierimonti

PASSIVE CONTROL OF WAVE PROPAGATION IN PERIODIC ANTI-TETRACHIRAL META-MATERIALS 5658
Marco Lepidi, Andrea Bacigalupo

FLEXIBLE COMPLEX SYSTEM OF A DOUBLE-STRING UNDER EXTREME MOVING LOADS 5670
Jarosław Rusin

ON THE MODELING OF SELF-DAMPING IN STRANDED CABLES 5680
Francesco Foti, Luca Martinelli, Federico Perotti

COMPUTATIONAL EFFECTIVENESS OF LMI DESIGN STRATEGIES FOR VIBRATION CONTROL OF LARGE STRUCTURES 5689
Francisco Palacios-Quiñonero, Josep Rubió-Massegú, Josep M. Rossell, Hamid Reza Karimi

A SMART BASE RESTRAINT FOR WIND TURBINES TO MITIGATE UNDESIRED EFFECTS DUE TO STRUCTURAL VIBRATIONS 5702
Nicola Caterino, Christos T. Georgakis, Mariacristina Spizzuoco, Antonio Occhiuzzi

MS 1220: DYNAMICS OF STRUCTURES SUBJECT TO SEISMIC EXCITATIONS

NONLINEAR DYNAMIC BEHAVIOUR OF BASE-ISOLATED BUILDINGS WITH THE FRICTION PENDULUM SYSTEM SUBJECTED TO NEAR-FAULT EARTHQUAKES 5712
Fabio Mazza, Sandro Sisinno

ABSOLUTE FINITE ELEMENT COORDINATES IN THE DYNAMICS OF LARGE FLEXIBLE STRUCTURES 5726
Evtim Zahariev

MODAL ANALYSIS OF A FRAME MODEL UNDER UNMEASURED SEISMIC INPUT 5742
Claudio Valente, Vincenzo Sepe, Marco Di Pilla, Fabrizio Iezzi, Rossella Siano, Luigia Zuccarino

EQUIVALENT UNIAXIAL ACCELEROGRAM FOR CSS-BASED ISOLATION SYSTEMS ASSESSMENT UNDER TWO-COMPONENTS SEISMIC EVENTS 5753
Marco Furinghetti, Alberto Pavese

MS 1221: COMPUTATIONAL STRUCTURAL STABILITY

MIXED SOLID MODELS IN NUMERICAL ANALYSIS OF SLENDER STRUCTURES 5768
Domenico Magisano, Leonardo Leonetti, Giovanni Garcea

COMPUTATIONAL ANALYSIS OF THE COLLAPSE BEHAVIOUR OF THIN-WALLED POLYGONAL STEEL BEAMS 5789
Raffaele Ardito

INFLUENCE OF STRAIN DEFINITIONS ON TRUSSES CRITICAL LOADS 5799
Reyolando Brasil, Jose Balthazar

ULTIMATE STRENGTH ANALYSIS OF STIFFENED PANELS OF SHIP STRUCTURES UNDER COMBINED LOAD 5810
Li Hong, Meng Linghua, Qin Zhongwen, Zhang Enguo, Li Li

MS 1222: INFLUENCE OF LIQUEFIABLE SOIL ON SINGLE AND CLOSELY CLUSTERED STRUCTURES
NUMERICAL ANALYSES OF THE INFLUENCE OF STRUCTURAL SLENDERNESS ON THE SEISMIC RESPONSE OF SINGLE AND CLUSTERED STRUCTURES 5817
Gonzalo Barrios, Tam Larkin, Nawawi Chouw

EFFECT OF HIGHER MODES ON STRUCTURAL RESPONSE WITH NONLINEAR SOIL-FOUNDATION-STRUCTURE INTERACTION 5826
Xiaoyang Qin, Nawawi Chouw, Tam Larkin

MS 1224: INNOVATIVE SOLUTIONS FOR THE SEISMIC PROTECTION OF INDUSTRIAL BUILDINGS
SEISMIC RETROFIT OF AN INDUSTRIAL STRUCTURE THROUGH AN INNOVATIVE SELF-CENTERING HYSTERETIC DAMPER: MODELLING, ANALYSIS AND OPTIMIZATION. 5834
Francesco Morelli, Andrea Piscini, Walter Salvatore

PERFORMANCE ASSESSMENT OF SEISMIC RETROFITTING MEASURES ON SILO STRUCTURES USING INNOVATIVE SEISMIC PROTECTION SYSTEMS 5851
Marius Pinkawa, Benno Hoffmeister, Markus Feldmann

SEISMIC RETROFIT OF INDUSTRIAL SILOS BY MEANS OF BASE ISOLATION DEVICES 5868
Alper Kanyilmaz, Carlo Andrea Castiglioni, Julia Georgi

EFFICIENCY OF SEISMIC ISOLATION ON INDUSTRIAL PLANTS - CASE STUDY OF A GAS TANK 5896
José Henriques, Francesco Morelli, Bram Vandoren, Walter Salvatore, Hervé Degée

PERFORMANCE-BASED NONLINEAR RESPONSE HISTORY ANALYSIS FRAMEWORK FOR THE "PROINDUSTRY" PROJECT CASE STUDIES 5912
Marco Faggella, Raffaele Laguardia, Rosario Gigliotti, Francesco Morelli, Franco Braga, Walter Salvatore

PERFORMANCE BASED EARTHQUAKE ASSESSMENT OF AN INDUSTRIAL SILOS STRUCTURE AND RETROFIT WITH SLIDING ISOLATORS 5926
Edoardo Rossi, Michelangelo Ventrella, Marco Faggella, Rosario Gigliotti, Franco Braga

MS 1225: SEISMIC PERFORMANCE ASSESSMENT OF STRUCTURES AND SEISMIC RISK MITIGATION STRATEGIES
A CRITICAL REVIEW OF FRAGILITY CURVES FOR EXISTING RC BUILDINGS 5934
Monica Mastroberti, Marco Vona

DYNAMIC IDENTIFICATION AND MODELLING OF A RC HOSPITAL BUILDING 5942
Giorgio Lacanna, Pauline Deguy, Maurizio Ripepe, Massimo Baglione, Marco Tanganelli, Stefania Viti, Mario De Stefano

SEISMIC HAZARD OF URBAN AREAS: A CASE-STUDY 5952
Giorgio Lacanna, Pauline Deguy, Maurizio Ripepe, Massimo Coli, Barbara Paoletti, Sara Barducci, Marco Tanganelli, Stefania Viti, Mario De Stefano

SPO2FRAG V1.0: SOFTWARE FOR PUSHOVER-BASED DERIVATION OF SEISMIC FRAGILITY CURVES 5962
Iunio Iervolino, Georgios Baltzopoulos, Dimitrios Vamvatsikos, Roberto Baraschino

COMPUTER-AIDED SEISMIC RISK ASSESSMENT AT URBAN SCALE. MODEL DEFINITION AND VALIDATION ON A CASE STUDY 5977
Alberto Basaglia, Alessandra Aprile, Francesco Pilla, Enrico Spacone

TOWARDS INTEGRATED SEISMIC RISK ASSESSMENT IN PALESTINE - APPLICATION TO THE CITY OF NABLUS ... 5987
Ricardo Monteiro, Paola Ceresa, Vania Cerchiello, Jamal Dabeek, Antonella Di Meo, Barbara Borzi

REASSESS V1.0: A COMPUTATIONALLY-EFFICIENT SOFTWARE FOR PROBABILISTIC SEISMIC HAZARD ANALYSIS 5999
Iunio Iervolino, Eugenio Chioccarelli, Pasquale Cito

SIMPLIFIED PERIOD ESTIMATION OF ITALIAN RC BRIDGES FOR LARGE-SCALE SEISMIC ASSESSMENT 6013
C. Zelaschi, R. Monteiro, R. Pinho

1300 UNCERTAINTY QUANTIFICATION AND ERROR ESTIMATION

MS 1301: THE STOCHASTIC COMPUTER METHODS IN MECHANICS
FLOW FIELD ESTIMATION IN OPEN CHANNEL BASED ON KALMAN FILTER FINITE ELEMENT METHOD 6029
Taichi Yoshiara, Takahiko Kurahashi, Yasuhide Kobayashi, Toshihiko Eto

STOCHASTIC TECHNIQUES FOR THE NUMERICAL SOLUTION OF ENGINEERING BOUNDARY VALUE PROBLEMS 6041
Victor Maceiras, Manuel Casteleiro

THE BOOTSTRAP APPROACH TO THE STATISTICAL SIGNIFICANCE OF PARAMETERS IN THE FIXED EFFECTS MODEL 6061
Jacek Pietraszek, Renata Dwornicka, Agnieszka Szczotok

ON FULLY COUPLED THERMO-ELASTO-PLASTIC STOCHASTIC FINITE ELEMENT ANALYSIS OF STEEL STRUCTURES 6069
Marcin Kaminski, Michał Strakowski

AN INTRODUCTION TO STOCHASTIC FINITE ELEMENT METHOD ANALYSIS OF HYPERELASTIC STRUCTURES ... 6078
Marcin Kamiński, Damian Sokołowski

MS 1303: ANALYSIS AND DESIGN OF SAFETY CRITICAL SYSTEMS UNDER UNCERTAINTY
IDENTIFICATION OF INTERVAL FIELDS FOR SPATIAL UNCERTAINTY REPRESENTATION IN FINITE ELEMENT MODELS 6091
Matthias Faes, Jasper Cerneels, Dirk Vandepitte, David Moens

INTRODUCTION OF BEAD INGS INTO A CRASH TUBE USING A ROBUST OPTIMISATION APPROACH 6099
Stefan Scheiblhofer

DYNAMICAL ANALYSIS OF PLATE MODELS WITH UNCERTAIN STRUCTURAL PROPERTIES USING THE INTERVAL FIELD METHOD 6107
Maurice Imholz, Dirk Vandepitte, David Moens

POWER GRID ROBUSTENSS TO SEVERE FAILURES: TOPOLGICAL AND FLOW BASED METRICS COMPARISION 6121
Roberto Rocchetta, Edoardo Patelli

MS 1304: STOCHASTIC MODELING AND IDENTIFICATION OF UNCERTAINTIES IN COMPUTATIONAL MECHANICS
MULTILEVEL STOCHASTIC REDUCED-ORDER MODEL IN LINEAR STRUCTURAL DYNAMICS FOR COMPLEX STRUCTURES 6136
Olivier Ezvan, Anas Batou, Christian Soize

TO ESTIMATE NON-STATIONARY STOCHASTIC DISTRIBUTED LOAD ON A BEAM STRUCTURE FROM RESPONSE SAMPLES 6148
S.Q. Wu, J. Zhu

A ROBUST POLYNOMIAL CHAOS KALMAN FILTER FRAMEWORK FOR CORROSION DETECTION IN REINFORCED CONCRETE STRUCTURES 6160
Wael Slika, George Saad

ANALYSIS OF STOCHASTIC DYNAMIC SOIL-STRUCTURE INTERACTION PROBLEMS BY MEANS OF COUPLED FINITE ELEMENTS-PERFECTLY MATCHED LAYERS 6172
Manthos Papadopoulos, Stijn François, Geert Degrande, Geert Lombaert

A MULTISCALE FRAMEWORK FOR THE STOCHASTIC ASSIMILATION AND MODELING OF UNCERTAINTY ASSOCIATED NCF COMPOSITE MATERIALS 6186
Loujaine Mehrez, Roger Ghanem, Colin Mcauliffe, William R. Rodgers, Venkat Aitharaju

MS 1306: ERCOFTAC SIG-45: UNCERTAINTY QUANTIFICATION IN CFD AND FLUID STRUCTURE INTERACTION
A MULTI-FIDELITY ADAPTIVE SAMPLING METHOD FOR METAMODEL-BASED UNCERTAINTY QUANTIFICATION OF COMPUTER SIMULATIONS 6196
Riccardo Pellegrini, Cecilia Leotardi, Umberto Iemma, Emilio Campana, Matteo Diez

A LEAST-SQUARES, ADAPTIVE UNCERTAINTY PROPAGATION APPROACH FOR A PLASMA-COUPLED COMBUSTION SYSTEM 6213
Kunkun Tang, Luca Massa, Jonathan Wang, Jonathan Freund

UNCERTAINTY QUANTIFICATION IN NUMERICAL SIMULATIONS OF THE FLOW IN THORACIC AORTIC ANEURYSMS 6226
Alessandro Boccadifuoco, Alessandro Mariotti, Simona Celi, Nicola Martini, Maria Vittoria Salvetti

MS 1307: NON-INTRUSIVE SURROGATE MODELS FOR UNCERTAINTY QUANTIFICATION IN HIGH DIMENSIONS
OPTIMIZATION OF A PHOTOACOUSTIC GAS SENSOR USING MULTIFIDELITY RBF METAMODELING 6250
Cedric Durantin, Justin Rouxel, Jean-Antoine Desideri, Alain Gliere

BEARING CAPACITY OF STRIP FOOTINGS ON SPATIALLY RANDOM SOILS USING KRIGING AND MONTE CARLO SIMULATION 6260
Jawad Thajeel, Tamara Al-Bittar, Nour Issa, Abdul Hamid Soubra

AN OPTIMAL SENSOR PLACEMENT METHOD FOR SHM BASED ON BAYESIAN EXPERIMENTAL DESIGN AND POLYNOMIAL CHAOS EXPANSION 6272
Giovanni Capellari, Eleni Chatzi, Stefano Mariani

CALIBRATION OF NESTED COMPUTER MODELS 6283
Sophie Marque-Pucheu, Guillaume Perrin, Josselin Garnier

A STATISTICAL APPROACH FOR BUILDING SPARSE POLYNOMIAL CHAOS EXPANSIONS 6307
Simon Abraham, Ghader Ghorbaniasl, Chris Lacor

MS 1308: MODELLING AND INVERSE METHODS IN NONLINEAR DYNAMICAL SYSTEMS
FINITE ELEMENT METAMODELING OF UNCERTAIN STRUCTURES 6316
Vasilis Dertimanis, Dimitris Giagopoulos, Eleni Chatzi

DYNAMICS OF MULTIBODY SYSTEMS SUBJECT TO UNILATERAL MOTION CONSTRAINTS USING A NEW NUMERICAL ALGORITHM FOR CONTACT DETECTION 6328
Antonios Pournaras, Fotios Karaoulanis, Sotirios Natsiavas

EQUATIONS OF MOTION FOR MECHANICAL SYSTEMS SUBJECT TO ACATASTATIC CONSTRAINTS 6342
Elias Paraskevopoulos, Sotirios Natsiavas

PARAMETER ESTIMATION OF NONLINEAR LARGE SCALE SYSTEMS THROUGH STOCHASTIC METHODS AND MEASUREMENT OF ITS DYNAMIC RESPONSE 6369
Dimitrios Giagopoulos, Alexandros Arailopoulos

MS 1309: SCALABLE MULTI-FIDELITY MODELING FOR DESIGN, UNCERTAINTY QUANTIFICATION, AND INVERSE PROBLEMS
VARIABLE FIDELITY MODELLING IN MODERN AIRCRAFT DESIGN 6383
Marian Zastawny

MS 1310: COMPUTATIONAL METHODS FOR THE SOLUTION OF STOCHASTIC DIFFERENTIAL EQUATIONS
FOUR-DIMENSIONAL PATH INTEGRATION METHOD FOR ESTIMATING THE STOCHASTIC ROLL RESPONSE 6398
Wei Chai, Arvid Naess, Bernt Leira

SEISMIC RELIABILITY ASSESSMENT OF FRAME STRUCTURES WITH FLEXIBILITY-BASED STOCHASTIC BEAM-COLUMN ELEMENTS 6407
Georgios Balokas, Michalis Fragiadakis

1400 SPECIAL TECHNOLOGICAL SESSIONS

MS 1401: TOICA: THERMAL OVERALL INTEGRATED CONCEPT AIRCRAFT
THERMAL TRADE OFF SUSTAINED BY MULTI DISCIPLINARY AND MULTI LEVEL OPTIMIZATION 6420
Olivier Tabaste, Cedric Campguilhem

COLLABORATIVE ENGINEERING TECHNOLOGIES ENABLING MULTI-PARTNER THERMAL ANALYSIS IN EARLY DESIGN STAGES OF AIRCRAFT 6436
Erik Baalbergen, Wim Lammen, Bert De Wit, Robert Maas, Marie Moghadasi, Johan Kos, Fabio Chiacchio

VISUAL ANALYTICS FOR EVALUATION OF VALUE IMPACT IN ENGINEERING DESIGN 6461
Timoleon Kipouros, Ola Isaksson

STS 3: INNOVATIVE DESIGN OPTIMIZATION TOOLS LINKED TO INDUSTRIAL AERONAUTICAL APPLICATIONS: TARGETING GREENER PERFORMANCES
COMBINING AN RBF-BASED MORPHER WITH CONTINUOUS ADJOINT FOR LOW-SPEED AERONAUTICAL OPTIMIZATION APPLICATIONS 6471
Evangelos Papoutsis-Kiachagias, Matej Andrejasic, Stefano Porziani, Corrado Groth, David Erzen, Marco Evangelos Biancolini, Emiliano Costa, Kyriakos Giannakoglou

STS 5: TRANSITION LOCATION EFFECT ON SHOCK WAVE BOUNDARY LAYER INTERACTION
LOAD CONTROL OF NATURAL-LAMINAR-FLOW WING VIA BOUNDARY LAYER CONTROL 6485
Wieńczysław Stalewski, Janusz Sznajder

STS 7: MORPHING TECHNOLOGIES FOR AIRCRAFT WINGS
AN ADAPTIVE TRAILING EDGE FOR LARGE COMMERCIAL AIRCRAFT 6496
Antonio Concilio, Ignazio Dimino, Rosario Pecora

STS 9: ADVANCED WING HIGH-LIFT SYSTEMS
APPLICATION OF SYNTHETIC JETS ACTUATORS IN WING-PYLON JUNCTION AREA TO IMPROVE THE HIGH LIFT PERFORMANCES 6505
Petr Vrchota

YOUNG INVESTIGATORS MINISYMPOSIUM
A NANO-MACRO BOTTOM-UP APPROACH TOWARDS BRITTLE FRACTURE 6515
Sandeep Patil, Yousef Heider, Carlos Hernandez Padilla, Eduardo Cruz Chu, Bernd Markert

ECCOMAS OLYMPIAD MINISYMPOSIUM
INTEGRATION OF DESIGN AND ANALYSIS THROUGH BOUNDARY INTEGRAL EQUATIONS 6526
Benjamin Marussig, Jürgen Zechner, Gernot Beer, Thomas-Peter Fries

Contributed Sessions

CS 110: NUMERICAL MODELS IN BIOMECHANICS

EVALUATION OF ANGULAR KINEMATICS OF LOWER LIMB AMPUTEES USING QUANTITATIVE FLUOROSCOPIC IMAGING 6539
Alexander Breen, Mihai Dupac

PRELIMINARY STUDY TO INVESTIGATE THE EFFECT OF PISTON-LIKE AND ROCKING MOTIONS OF THE STAPES FOOTPLATE ON THE BASILAR MEMBRANE VIBRATION 6547
Philipp Wahl, Sebastian Ihrle, Pascal Ziegler, Peter Eberhard

IN-HOUSE MULTIBODY HUMAN MODEL BASED ON EULER PARAMETERS FOR THE FAST IMPACT SCENARIO CALCULATION 6556
Jan Spicka, Michal Hajzman, Tomasz Bonkowski

EXPERIMENTAL STUDY ON THE FUZZY-PID HYBRID CONTROL ALGORITHM FOR UNLOADING SYSTEM IN MECHATRONIC DEVICE FOR GAIT RE-EDUCATION 6567
Slawomir Duda, Grzegorz Gembalczyk

FE BONE STRUCTURAL ANALYSIS WITH CT MAPPING OF INHOMOGENEOUS MATERIAL PROPERTIES 6574
Miguel Tobias Bahia, Emílio Graciliano Ferreira Mercuri, Mildred Ballin Hecke

SOLVING THE INVERSE PROBLEM OF ESTIMATING FUZZY VISCOELASTIC CONSTITUTIVE PARAMET ERS 6588
Ruifei Peng, Haitian Yang

DEVELOPMENT OF A CENTRIFUGAL BLOOD PUMP FOR ECMO AND VAD OPERATIONS 6606
Shinhwa Choi, Nahmkeon Hur, Mohammad Moshfeghi, Seongwon Kang, Wonjung Kim

EFFECT OF PERIVASCULAR TISSUE ON INFLATION-EXTENSION BEHAVIOR OF ABDOMINAL AORTA 6616
Tereza Voňavková, Lukáš Horný, Jan Veselý, Tomáš Adámek, Rudolf Žitný

EFFECT OF STERILIZATION ON MECHANICAL PROPERTIES OF BIOLOGICAL COMPOSITE 6625
Jan Vesely, Hynek Chlup, Rudolf Zitny, Tomas Grus

FINITE-ELEMENT MODEL OF INTRAOCULAR PRESSURE MEASUREMENT BY MAKLAKOV APPLANATION TONOMETER 6631
Dmitry V. Franus

CS 210: NUMERICAL SIMULATION OF COMPOSITE MATERIALS

MOMENT-CURVATURE DIAGRAMS FOR EVALUATION OF SECOND ORDER EFFECTS IN RC ELEMENTS 6637
Helena Barros, Carla Ferreira, Tatiana Marques

INVESTIGATIONS ON AN INNOVATIVE METAL-THERMOPLASTIC COMPOSITE ASSEMBLY 6652
Simon Paroissien, Patrick Rozycki, Thierry Renault

A FAILURE CRITERIA FOR UNIDIRECTIONAL FIBER REINFORCED COMPOSITES BASED ON MICROMECHANICS BY ASYMPTOTIC HOMOGENIZATION 6664
Rafael Quelho De Macedo, José Miranda Guedes, Rafael Thiago Luiz Ferreira, Maurício Vicente Donadon

EVOLUTION EQUATIONS BASED APPROACH FOR MODELING FATIGUE IN AMORPHOUS GLASSY POLYMERS. ON THE INVESTIGATION OF FATIGUE DAMAGE DEVELOPMENT IN POLYCARBONATE 6675
Sami Holopainen

CS 211: CRACK PROPAGATION
ULTRASONIC GUIDED WAVES INSPECTION OF PIPES FROM ONE END TO THE FIRST BENT 6688
Mihai Valentin Predoi, Marian Soare, Ovidiu Vasile, Mihail Boiangiu

CS 212: NUMERICAL MODELING OF DAMAGE, FAILURE AND FRACTURE
DUCTILE FRACTURE CRITERIA IN PREDICTION OF SLANT FRACTURE 6699
Petr Kubik, Frantisek Sebek, Jindrich Petruska

DAMAGE MODELING USING STRAIN GRADIENT BASED FINITE ELEMENT FORMULATION 6711
Filip Putar, Jurica Soric, Tomislav Lesicar, Zdenko Tonkovic

RELIABILITY ANALYSIS IN FRACTURE MECHANICS ACCORDING TO COMBINED FAILURE CRITERIA 6721
Rudy Chocat, Paul Beaucaire, Loïc Debeugny, Jean-Pierre Lefebvre, Caroline Sainvitu, Piotr Breitkopf, Eric Wyart

NEW BENCHMARK FOR THE LIFE ASSESSMENT OF A THIN-WALLED PIPE SUBJECTED TO STRESS ASSISTED CORROSION 6734
Yulia Pronina, Elena Sedova

A HIGHER ORDER PHASE-FIELD APPROACH TO FRACTURE FOR FINITE-DEFORMATION CONTACT PROBLEMS 6741
Marlon Franke, Christian Hesch, Maik Dittmann

MODELLING THERMAL BARRIER COATINGS AND THEIR INFLUENCE ON THE LIFETIME OF ROCKET ENGINE NOZZLE STRUCTURES 6764
Marek Fassin, Stephan Wulfinghoff, Stefanie Reese

ANALYTICAL SOLUTION FOR DYNAMIC FRACTURE OF TWO COPLANAR LIMITED-PERMEABLE CRACKS IN MAGNETO-ELECTRO-ELASTIC MATERIAL 6774
Peiwei Zhang

DAMAGE DETECTION OF A BRIDGE BY PARAMETRIC STATISTICAL MOMENT METHOD 6788
Isabella Failla, Nicola Impollonia, Giuseppe Ricciardi

CS 230: MODELLING OF CONCRETE AND MEASURING
A COHESIVE ZONE MODEL FOR THE CHARACTERISATION OF THE INTERFACIAL TRANSITION ZONE (ITZ) BETWEEN CEMENT PASTE AND AGGREGATE 6799
Etienne Malachanne, Marie Salgues, Mouad Jebli, Frederic Jamin

AN EXACT SHEAR STRAIN APPROACH FOR RC FRAME ELEMENTS WITH AXIAL-SHEAR INTERACTION 6810
Alexander Kagermanov, Paola Ceresa

CROSS-SECTIONAL FAILURE CRITERION COMBINED WITH STRAIN-HARDENING DAMAGE MODEL FOR SIMULATION OF THIN-WALLED TEXTILE-REINFORCED CONCRETE SHELLS 6823
Ehsan Sharei, Rostislav Chudoba, Alexander Scholzen

SEISMIC ASSESSMENT OF A 5-STOREY RETROFITTED RC BUILDING 6832
Hussein Bark, George Markou, Christos Mourlas, Manolis Papadrakakis

CS 310: CAD, CAM AND CAE
VECTOR FIELD GUIDED TOOL PATHS FOR FIVE-AXIS MACHINING 6847
Stanislav Makhanov

AN 'A PRIORI' MODEL REDUCTION FOR ISOGEOMETRIC BOUNDARY ELEMENT METHOD 6882
Shengze Li, Jon Trevelyan, Weihua Zhang, Zhuxuan Meng

RESEARCH OF DEFORMATION QUALITIES OF POROUS MATERIALS ENHANCING COMPUTER DESIGN OF WETSUIT 6892
Irina Cherunova, Elena Sirota, Nikolai Kornev, Mathias Paschen, Sebastian Schreier, Tatyana Lesnikova, Pavel Cherunov

MATHEMATICAL MODELLING OF CITY AERODYNAMICS 6900
Svetlana Valger, Natalya Fedorova, Alexander Fedorov

CS 320: GRID GENERATION AND ADAPTIVE TECHNIQUES
A STABLE AND CONSERVATIVE TIME-DEPENDENT INTERFACE FORMULATION ON SUMMATION-BY-PARTS FORM: AN INITIAL INVESTIGATION 6911
Samira Nikkar, Jan Nordström

A LAPLACIAN MESH DEFORMATION TECHNIQUE FOR SIMULATION-DRIVEN DESIGN OPTIMIZATION 6928
Mario J. Martin-Burgos, Daniel González-Juárez, Esther Andrés-Pérez

AN INTEGRATED FRAMEWORK FOR WRAPPING AND MESH GENERATION OF COMPLEX GEOMETRIES 6938
David Martineau, Jeremy Gould, Jacques Papper

CS 410: COMPUTATIONAL FLUID MECHANICS
THE VORTICITY CREATION PROCESS AT PHYSICAL SURFACES 6955
Horia Dumitrescu, Vladimir Cardos

HEAT RECOVERY BY CROSS FLOW 6966
Karel Adamek, Jan Kolar, Pavel Peukert

THE INLET AND OUTLET BOUNDARY PROBLEM WITH THE PREFERENCE OF MASS FLOW 6979
Martin Kyncl, Jaroslav Pelant

BUDGET ANALYSIS OF TURBULENT KINETIC ENERGY IN CORNER SEPARATION : RANS VS LES 6999
Jean-François Monier, Feng Gao, Jérôme Boudet, Liang Shao, Lipeng Lu

A SHALLOW WATER EQUATION BASED ON DISPLACEMENT AND PRESSURE AND THE ZU-CLASS SYMPLECTIC METHOD 7014
Feng Wu, Wan-Xie Zhong

IMMERSED BOUNDARY METHODS FOR COMPRESSIBLE LAMINAR FLOWS 7029
Rakesh Ramakrishnan, Anant Girdhar, Santanu Ghosh

IMPACT OF EXTERNAL SURROUNDINGS ON NATURAL CONVECTION IN A VERTICAL CHANNEL ASYMMETRICALLY HEATED 7045
Delphine Ramalingom, Alain Bastide

INFLUENCE OF ADJACENT ROOMS ON THE DEVELOPMENT OF GAS EXPLOSION 7056
Iurii Polandov, Sergei Dobrikov

DOMAIN DECOMPOSITION APPROACH FOR NEAR-WALL TURBULENCE MODELING 7066
Sergey Utyuzhnikov

LARGE EDDY SIMULATION OF SALTATION OVER GAUSSIAN HILLS 7074
Gang Huang, Catherine Le Ribault, Serge Simoëns, Ivana Vinkovic, J.M.Vignon

AN EXPERIMENTAL AND NUMERICAL STUDY ON THE PERFORMANCE OF AN INNOVATIVE VERTICAL-AXIS WIND TURBINE 7087
Katarzyna Kludzinska, Krzysztof Tesch, Piotr Doerffer

NUMERICAL SIMULATION OF NONLINEAR FREE SURFACE WATER WAVES USING A COUPLED POTENTIAL FLOW-URANS/VOF APPROACH 7095
Bulent Duz, Tim Bunnik, Geert Kapsenberg

THE OPTIMAL CONTROL OF A MULTI-MASS VIBRATION PROPULSION SYSTEM IN A VISCOUS INCOMPRESSIBLE FLUID 7121
Artem Nuriev, Olga Zakharova

HIGH-RESOLUTION SIMULATION OF INTERNAL WAVES ATTRACTORS AND IMPACT OF INTERACTION OF HIGH AMPLITUDE INTERNAL WAVES WITH WALLS ON DYNAMICS OF WAVES ATTRACTORS 7130
Ilias Sibgatullin, Michael Kalugin

NUMERICAL SIMULATION OF HEAT AND MASS TRANSFER PROCESSES IN LARGE-SCALE FLUIDIZED BED COMPLEX STRUCTURE APPARATUS AS AN EXAMPLE OF THE REACTOR OF ISOPARAFFINS DEHYDROGENATION 7138
Sergei Solovev, Svetlana Egorova, Alexander Lamberov, Olga Soloveva

CS 420: MULTI-PHASE AND CHEMICALLY REACTING FLOWS

SHOCK CAPTURING COMPUTATIONS WITH STABILIZED POWELL-SABIN ELEMENTS 7149
Giorgio Giorgiani, Herve Guillard, Boniface Nkonga

NUMERICAL INVESTIGATION OF METASTABLE CONDENSING FLOWS WITH AN IMPLICIT UPWIND METHOD ... 7165
Lucia Azzini, Teus Van Der Stelt, Matteo Pini

LEVEL SET METHOD FOR SIMULATING THE INTERFACE KINEMATICS: APPLICATION OF A DISCONTINUOUS GALERKIN METHOD 7182
Roozbeh Mousavi, Florian Kummer, Martin Oberlack, Peter F. Pelz

LARGE EDDY SIMULATION OF TURBULENT COMPRESSIBLE FLOWS USING THE CHARACTERISTIC BASED SPLIT SCHEME AND MESH ADAPTATION 7222
Renato Linn, Armando Awruch

NUMERICAL SIMULATION OF HYDROGEN JET INJECTION AND IGNITION IN SUPERSONIC FLOW 7237
Yulia Zakharova, Natalya Fedorova, Svetlana Valger, Marat Goldfeld, Olga Vankova

A 3D UNSTEADY NUMERICAL SIMULATION OF THE REFRIGERANT FLOW EVAPORATION IN A PLATE HEAT EXCHANGER 7247
Mirza Popovac, Gerwin Schmid, Michael Lauermann

RESEARCH OF UNSTEADY FLOW REGIMES IN CHANNEL OF HYPERSONIC INLET 7255
Natalya Fedorova, Marat Goldfeld

EXPLICIT DARCY'S LAW BOUNDARY CONDITION WITH COMBINED CONTINUUM AND DISCRETE MODEL FOR PRESSURE DRIVEN MEMBRANE APPLICATIONS 7266
Tomi Naukkarinen, Teemu Turunen-Saaresti

CS 450: NUMERICAL METHODS AND CONVERGENCE ACCELERATION IN CFD

A MULTIGRID FORMULATION FOR FINITE DIFFERENCE METHODS ON SUMMATION-BY-PARTS FORM: AN INITIAL INVESTIGATION 7274
Andrea Alessandro Ruggiu, Per Weinerfelt, Tomas Lundquist, Jan Nordström

IMPROVED DUAL TIME–STEPPING USING SECOND DERIVATIVES 7285
Jan Nordström, Andrea Ruggiu

A DIRECT SOLVER FOR THE ADVECTION-DIFFUSION EQUATION USING GREEN'S FUNCTIONS AND LOW-RANK APPROXIMATION 7302
Jonathan Bull

AN IMPROVED DISCRETIZATION METHOD FOR BOUNDED CONVECTIVE SCHEMES ON UNSTRUCTURED CO-LOCATED GRIDS 7317
Vlado Przulj

A LOW-MACH, LOW-REYNOLDS PRECONDITIONING SCHEME WITH PARTICULAR ATTENTION TO VISCOUS TIME-STEPPING 7334
Jens Fiedler, Graham Ashcroft

PERFORMANCE IMPROVEMENT OF FLOW COMPUTATIONS WITH AN OVERSET-GRID METHOD INCLUDING BODY MOTIONS USING A FULL MULTIGRID METHOD 7347
Kunihide Ohashi, Hiroshi Kobayashi

SOLVING LINEAR SYSTEMS WITH MULTIPLE RIGHT-HAND SIDES WITH GMRES : AN APPLICATION TO AIRCRAFT DESIGN 7358
Aloïs Bissuel, Grégoire Allaire, Laurent Daumas, Frédéric Chalot, Michel Mallet

COMPARISON OF DIFFERENT SPATIAL/ANGULAR AGGLOMERATION MULTIGRID SCHEMES FOR RADIATIVE HEAT TRANSFER COMPUTATIONS 7372
Georgios Lygidakis, Ioannis Nikolos

CS 460: UNSTEADY FLOW COMPUTATION
LINEARISED FREQUENCY DOMAIN GUST ANALYSIS OF LARGE CIVIL AIRCRAFT 7390
Philipp Bekemeyer, Reik Thormann, Sebastian Timme

CONSISTENT NON-REFLECTING BOUNDARY CONDITIONS FOR BOTH STEADY AND UNSTEADY FLOW SIMULATIONS IN TURBOMACHINERY APPLICATIONS 7403
Daniel Schlüß, Christian Frey, Graham Ashcroft

REDUCED ORDER MODELLING OF GUST ANALYSIS USING COMPUTATIONAL FLUID DYNAMICS 7423
Reik Thormann, Philipp Bekemeyer, Sebastian Timme

ON THE REGULARISATION OF NON-REFLECTING BOUNDARY CONDITIONS NEAR ACOUSTIC RESONANCE 7435
Christian Frey, Hans-Peter Kersken

ON GRID RESOLUTION REQUIREMENTS FOR LES OF WALL-BOUNDED FLOWS 7454
Saleh Rezaeiravesh, Mattias Liefvendahl, Christer Fureby

A HYBRID MESH HARMONIC BALANCE SOLVER FOR THE AEROELASTIC ANALYSIS OF TURBOMACHINERY 7466
Hans-Peter Kersken, Graham Ashcroft, Christian Frey

NUMERICAL AND EXPERIMENTAL INVESTIGATIONS OF DYNAMIC STALL PROBLEM ON A 2D HELICOPTER ROTOR BLADE SECTION 7477
Antonello Marino, Serena Russo, Giovanni Paolo Reina, Gennaro Esposito, Francesco Capizzano, Carlo De Nicola

INVESTIGATION OF A MODERN & HYBRID TURBULENCE MODELLING APPROACH FOR TRANSIENT AUTOMOTIVE AERODYNAMICS SIMULATIONS 7488
Rene Devaradja, Petr Simanek, Jacques Papper, Pavla Policka

FREE-SURFACE FLOW SIMULATIONS FOR MOORED AND FLOATING OFFSHORE PLATFORMS 7515
Arthur Veldman, Roel Luppes, Peter Van Der Plas, Henri Van Der Heiden, Bulent Duz, Henk Seubers, Joop Helder, Tim Bunnik, Rene Huijsmans

MODELLING OF UNSTEADY SECONDARY VORTICES GENERATED BEHIND THE RADIAL GAP OF THE AXIAL TURBINE BLADE WHEEL 7532
Petr Straka

PATHWAYS TO IMPROVED AERODYNAMIC DESIGN 7544
James Page, Paul Hield, Callum Mantell, Paul Tucker

SIMULATIONS OF BLAST WAVE PROPAGATION IN OPEN AND CLOSED SPACE 7557
Natalya Fedorova, Svetlana Valger, Yulia Zakharova

CS 500: HIGH PERFORMANCE COMPUTING
ON A DYNAMIC SCHEDULING ALGORITHM FOR MASSIVELY PARALLEL COMPUTATIONS OF ATOMIC ISOTOPE 7572
Elizaveta Dorofeeva, Jatin Arora, Stefan Typel, Gevorg Poghosyan, Peter Sanders, Achim Streit

APPLICATION THE SPARSE MATRIX METHOD TO CALCULATE THE METAL ELASTIC STRESS-STRAIN STATE, USING THE FINITE ELEMENT METHOD 7581
Inna Barankova, Uliana Mikhailova, Victor Demidovich

CS 610: AERO-ACOUSTICS
FLUID ANALYSIS USING FICTITIOUS DOMAIN FINITE ELEMENT METHOD 7589
Yukihiro Terakado, Tahahiko Kurahashi

ON THE SIMULATION OF AERODYNAMIC NOISE WITH DIFFERENT TURBULENCE MODELS 7599
Xin Huang, Michael Schäfer

NUMERICAL INVESTIGATION OF THERMOACOUSTIC ENGINE USING IMPLICIT LARGE EDDY SIMULATION 7609
Mustapha Mahdaoui, Rachid Bennacer, Smaïne Kouidri, N. Martaj

SEMI-DISCRETE COINCIDENCE IN THE MID-FREQUENCY SOUND TRANSMISSION THROUGH RIB-STIFFENED PANELS 7620
Edwin Reynders, Cédric Van Hoorickx, Arne Dijckmans

CS 620: COMPUTATIONAL CONTACT MECHANICS
SOLVING UNILATERAL CONTACT PROBLEMS IN MULTIBODY DYNAMICS USING A PRIMAL-DUAL INTERIOR POINT METHOD 7628
Dario Mangoni, Alessandro Tasora

CS 630: SIMULATION OF FLUID-STRUCTURE INTERACTION
3D DRBEM MODELING FOR ROTATING INITIALLY STRESSED ANISOTROPIC FUNCTIONALLY GRADED PIEZOELECTRIC PLATES 7640
Mohamed Abdelsabour Fahmy

DIRECT EDDY CURRENT METHOD FOR VOLUMETRIC FLAWS OF CYLINDRICAL SHAPE 7659
Valentina Koliskina, Andrei Kolyshkin, Rauno Gordon, Olev Märtens

NUMERICAL SIMULATION OF BUOYANT PLUMES USING A FIXED POINT ITERATIVE METHOD 7666
Blanca Bermúdez, Alejandro Rangel-Huerta, W. Fermín Guerrero S., José David Alanis Urquieta

INVESTIGATION OF THE FLOW OVER AN OSCILLATING CYLINDER WITH A VERY LARGE EDDY SIMULATION MODEL 7674
Anastasia Kondratyuk, Michael Schäfer, Awais Ali

NUMERICAL STUDY OF TWO OPTIMIZED COUPLING INTERFACE TREATMENTS FOR STEADY CONJUGATE HEAT TRANSFER PROBLEMS 7682
Marc Paul Errera, Roch Roukoz El Khoury

EFFECT OF DISC GEOMETRY ON THE DYNAMIC STABILITY OF DIRECT SPRING OPERATED PRESSURE RELIEF VALVES 7695
István Erdődi, Csaba Hős

CFD SIMULATION OF THERMO- AERODYNAMIC INTERACTION IN A SYSTEM HUMAN-CLOTH-ENVIRONMENT UNDER VERY LOW TEMPERATURE AND WIND CONDITIONS 7703
Irina Cherunova, Sina Samarbaksch, Nikolai Kornev

CS 720: COMPUTATIONAL MATERIALS SCIENCE
ON THE INFLUENCE OF THE INCLUSIONS' MORPHOLOGY ON THE ACCURACY OF THE PREDICTION OF REINFORCED COMPOSITES MECHANICAL BEHAVIOUR 7711
Viwanou Hounkpati, Vladimir Salnikov, Philippe Karamian-Surville, Alexandre Vivet

NUMERICAL SIMULATION OF ADVANCED PULTRUSION PROCESSES WITH MICROWAVE HEATING 7720
Evgeny Barkanov, Pavel Akishin, Rudolf Emmerich, Matthias Graf

EFFICIENT NUMERICAL SIMULATION OF INDUSTRIAL SHEET METAL BENDING PROCESSES 7739
Christian Zehetner, Paula Reimer, Franz Hammelmüller, Hans Irschik, Wolfgang Kunze

NUMERICAL MODELLING AND SIMULATION OF SHEET METAL CUTTING PROCESSES 7749
Paula Reimer, Christian Zehetner, Franz Hammelmüller, Wolfgang Kunze

SIMULATION OF PRECIPITATION IN V-CONTAINING HSLA STEEL FOR THE STRENGTHENING ENHANCEMENT 7757
Piyada Suwanpinij, Paolo Massaro, Annalisa Pola, Prasonk Srichareonchai

CS 750: COMPUTATIONAL MODELING OF COMPOSITES
NUMERICAL ANALYSIS OF SANDWICH PANELS SUBJECTED TO POINT LOADS 7765
Zbigniew Pozorski, Jolanta Pozorska

BOND OF REINFORCEMENT IN REACTIVE POWDER CONCRETE: EXPERIMENTAL STUDY 7771
Mingde Sun, Ri Gao, Aili Li, Yongjing Wang

MODELLING SOIL-FIBRE COMPOSITE BEHAVIOUR USING A MICROMECHANICAL APPROACH 7779
Thomas Bower, Anthony Jefferson, Peter Cleall, Paul Lyons

NUMERICAL SIMULATION OF MECHANICAL BEHAVIOR OF WOVEN COMPOSITE AT DIFFERENT STRAIN RATE BY A COLLABORATIVE ELASTO-PLASTO-DAMAGE MODEL WITH FRACTIONAL DERIVATIVES 7786
Alina Krasnobrizha, Patrick Rozycki, Laurent Gornet, Pascal Cosson

NUMERICAL SIMULATION OF MECHANICAL BEHAVIOUR OF COMPOSITE SANDWICH PANELS WITH DEFECTS 7800
Aleksandr Anoshkin, Valerii Zuiko, Mikhail Alikin, Anna Tchugaynova

TIMOSHENKO BEAM ELEMENT WITH ANISOTROPIC CROSS-SECTIONAL PROPERTIES ……. 7810
Alexander R. Stäblein, Morten H. Hansen

STABILIZATION OF THE NUMERICAL PRIMING TO STABILIZATION PHENOMENON IN THE CRUSHING OF A COMPOSITE PANEL USING LOCAL AND DIFFUSE DAMAGE LAWS …….. 7820
Christine Espinosa, Floran Tostain, Samuel Rivallant

STRUCTURAL ANALYSIS OF ADHESIVE BONDING FOR THICK-WALLED TUBULAR COMPOSITE PROFILES …….. 7837
Geminiano Mancusi, Agostina Orefice, Luciano Feo, Fernando Fraternali

CS 751: SMART MATERIALS AND STRUCTURES
TOWARDS REAL-TIME STRUCTURAL HEALTH MONITORING DAMAGE DETECTION WITHOUT USER INPUT ….. 7853
Mohmmad Salmanpour, Zahra Sharif Khodaei, Ferri Aliabadi

FIBROUS TECTONICS:A RETHINKING OF COMPOSITE PRODUCTION THROUGH INNOVATION AND EXPLORATION OF MOLDING TECHNIQUES AND METHODOLOGIES …….. 7863
David Costanza

CS 830: COMPUTATIONAL NANOTECHNOLOGY
EFFECT OF NANOSIZED ASPERITIES AT THE SURFACE OF A NANOHOLE …….. 7875
Mikhail Grekov, Aleksandra Vakaeva

CS 840: MULTI-SCALE COMPUTATIONAL METHODS FOR SOLIDS AND FLUIDS
THE GEMA FRAMEWORK – AN INNOVATIVE FRAMEWORK FOR THE DEVELOPMENT OF MULTIPHYSICS AND MULTISCALE SIMULATIONS …….. 7886
Carlos Augusto Teixeira Mendes, Marcelo Gattass, Deane Roehl

NONLINEAR PATCH METHOD AND APPLICATION …….. 7895
Antoine Brunet, Pierre Sarrailh, François Rogier, Jean-François Roussel, Denis Payan

ASSESSMENT OF A CONTINUUM MICROMECHANICS-BASED MULTISCALE MODEL FOR CONCRETE BY MEANS OF SENSITIVITY ANALYSIS AND UNCERTAINTY PROPAGATION …….. 7905
Luise Göbel, Andrea Osburg, Tom Lahmer

SPATIAL CLUSTERING STRATEGIES FOR HIERARCHICAL MULTI-SCALE MODELLING OF METAL PLASTICITY …… 7922
Md Khairullah, Jerzy Gawad, Dirk Roose, Albert Van Bael

BLACK-BOX SOLVER FOR ONE-DIMENSIONAL MULTISCALE MODELLING USING THE QTT FORMAT …….. 7938
Ivan Oseledets, Maxim Rakhuba, Andrei Chertkov

SCALE EFFECT IN MICROFLOWS MODELLING WITH THE MICROPOLAR FLUID THEORY …….. 7948
Anna Kucaba-Pietal

CS 930: HIGH-ORDER DISCRETIZATION METHODS

A COMPARISON OF VARIOUS NODAL DISCONTINUOUS GALERKIN METHODS FOR THE 3D EULER EQUATIONS 7956
Michael Bergmann, Svetlana Drapkina, Graham Ashcroft, Christian Frey

A 3D ISOGEOMETRICAL BOUNDARY ELEMENT ANALYSIS FOR NON-LINEAR GRAVITY WAVE PROPAGATION ... 7967
Jorge Maestre, Jordi Pallarés, Ildefonso Cuesta

HYBRID OPENMP/MPI PARALLELIZATION OF A HIGH–ORDER DISCONTINUOUS GALERKIN CFD SOLVER 7992
Francesco Bassi, Alessandro Colombo, Andrea Crivellini, Matteo Franciolini

ON THE CHOICE OF SHOCK CAPTURING SCHEMES FOR THE SOLUTION OF THE LWR TRAFFIC FLOW EQUATION USING A HIGH ORDER MODAL DISCONTINUOUS GALERKIN DISCRETIZATION 8013
Alberto Costa Nogueira Junior, João Lucas De Sousa Almeida, Cláudio Alessandro De Carvalho Silva

COMPARISON OF FINITE VOLUME HIGH-ORDER SCHEMES FOR THE WO-DIMENSIONAL EULER EQUATIONS 8033
Jens Wellner

NURBS-BASED ISOGEOMETRIC ANALYSIS FOR BALLISTIC EVALUATION OF TITANIUM PLATES 8047
Mattia Montanari, Petros Siegkas, Antonio Pellegrino, Nik Petrinic

HYBRID RIEMANN SOLVERS FOR LARGE SYSTEMS OF CONSERVATION LAWS 8057
Birte Schmidtmann, Mariia Astrakhantceva, Manuel Torrilhon

CS 940: EXTENDED DISCRETIZATION METHODS

THE USE OF ENRICHED BASE FUNCTIONS IN THE THREE-DIMENSIONAL SCALED BOUNDARY FINITE ELEMENT METHOD 8066
Sascha Hell, Wilfried Becker

METHODOLOGY OF COMBINED APPLICATION OF DIRECTIONAL DERIVATIVES AND THE EXTENDED FINITE ELEMENT METHOD (X-FEM) FOR SOLVING VIBRATION EIGENVALUE PROBLEMS 8085
Daria Serbichenko, Pascal Cosson, Patrick Rozycki

XFEM ANALYSIS – INCLUDING BUCKLING – OF COMPOSITE SHELLS CONTAINING DELAMINATION 8103
Wilhelm J.H. Rust, Saleh Yazdani, Peter Wriggers

CS 960: MESHLESS METHODS

THREE-DIMENSIONAL CRACK PROPAGATION ANALYSIS USING MESHLESS POINT COLLOCATION METHOD 8115
Eiji Tanaka

A CELL-BASED SMOOTHED POINT INTERPOLATION METHOD FOR AXISYMMETRIC PROBLEMS 8133
Arash Tootoonchi, Arman Khoshghalb

EFFICIENT SHAPE FUNCTION COSTRUCTION OF EFG MESHLESS METHOD 8142
P. Metsis, M. Papadrakakis

CS 980: NUMERICAL AND SYMBOLIC COMPUTATION
MODERNIZING SOFTWARE IN SCIENCE AND ENGINEERING: FROM C/C++ APPLICATIONS TO MOBILE PLATFORMS 8162
Liliana Favre, Claudia Pereira, Liliana Martinez

NEW EDUCATIONAL MATLAB TOOL TO EXPLAIN TWO DIMENSIONAL FINITE ELEMENT METHOD TO GRADUATE STUDENTS 8177
Rafet Sisman, Abdurrahman Sahin

CONTRIBUTION OF NUMERICAL THERMAL SIMULATION OF MASONRY TO THE GLOBAL OBJECTIVE OF BUILDINGS ENERGY EFFICIENCY 8187
Hipólito Sousa, Rui Sousa, Luís Silva, Gonçalo Sousa

CS 990: PARTICLE-BASED METHODS
TOWARDS MULTIPHYSICS SIMULATION OF DEEP PENETRATION LASER WELDING USING SMOOTHED PARTICLE HYDRODYNAMICS 8196
Haoyue Hu, Peter Eberhard, Florian Fetzer, Peter Berger

MULTIPLE TIMESCALE MODELLING OF PARTICLE SUSPENSIONS IN METAL MELTS SUBJECTED TO EXTERNAL FORCES 8207
Anton Manoylov, Georgi Djambazov, Valdis Bojarevics, Koulis Pericleous

STATISTICAL DISTRIBUTION FUNCTION OF CHARGED PARTICLES IN MAGNETIC FIELD 8224
B.Chetverushkin, Nicola D'Ascenzo, Valeri Saveliev

A STABILISED TOTAL LAGRANGIAN CORRECTED SMOOTH PARTICLE HYDRODYNAMICS TECHNIQUE IN LARGE STRAIN EXPLICIT FAST SOLID DYNAMICS 8231
Giorgio Greto, Sivakumar Kulasegaram, Chun H. Lee, Antonio J. Gil, Javier Bonet

BLOOD FLOW SIMULATION USING SMOOTHED PARTICLE HYDRODYNAMICS 8241
Mohammed Al-Saad, Sivakumar Kulasegaram, Stephane P.A. Bordas

CS 1010: COMPUTATIONAL INVERSE PROBLEMS AND OPTIMIZATION
ON THE VALIDITY OF TIDAL TURBINE ARRAY CONFIGURATIONS OBTAINED FROM STEADY-STATE ADJOINT OPTIMISATION 8247
Christian T. Jacobs, Matthew D. Piggott, Stephan C. Kramer, Simon W. Funke

DEVELOPMENT OF ACCURATE PNEUMATIC TYRE FINITE ELEMENT MODELS BASED ON AN OPTIMISATION PROCEDURE 8262
Chrysostomos-Alexandros Bekakos, George Papazafeiropoulos, Dan J. O'Boy, Jan Prins

METEOROLOGICAL DATA ASSIMILATION USING AN ADJOINT PROGRAM GENERATED BY AUTOMATIC DIFFERENTIATION 8275
Yasuyoshi Horibata

EVOLUTIONARY TOPOLOGY OPIMIZATION USING PARAMETERIZED B-SPLINE SURFACE 8283
Igor Pehnec, Damir Vucina, Frane Vlak

GEARBOX DESIGN VIA MIXED-INTEGER PROGRAMMING 8294
Bastian Dörig, Thorsten Ederer, Peter F. Pelz, Marc E. Pfetsch, Jan Wolf

A FRAMEWORK FOR THE DESIGN BY OPTIMIZATION OF HYDROFOILS UNDER CAVITATING CONDITIONS 8305
Paolo Olivucci, Stefano Gaggero

A COMPUTATIONAL STRATEGY FOR TRAJECTORY OPTIMIZATION OF UNDERACTUATED MULTIBODY SYSTEMS WITH CONTACTS 8324
Silvia Manara, Alessio Artoni, Marco Gabiccini

ANALYSIS OF NON-LINEAR ENVIRONMENTAL LOAD COMBINATIONS BY EXTENDED CONTOUR-LINE ALGORITHMS 8337
Bernt Leira

ADJOINT-BASED ROBUST OPTIMIZATION USING POLYNOMIAL CHAOS EXPANSIONS 8351
Joao Miranda, Dinesh Kumar, Chris Lacor

APPLICATION OF THE DECONVOLUTION METHODS FOR PROCESSING OF MEASUREMENT SIGNALS IN THE FAST PROCESSES 8365
Marat Goldfeld, Valery Pickalov

INVERSION METHODS BASED ON KALMAN FILTERING FOR IDENTIFICATION IN TUNNELING PROBLEMS 8378
Tamara Nestorović, Luan T. Nguyen

CS 1020: EVOLUTIONARY AND DETERMINISTIC METHODS FOR DESIGN, OPTIMIZATION AND CONTROL
EVALUATION OF DIFFERENT APPROACHES FOR THE OPTIMIZATION OF LAYOUT AND CONTROL OF BOOSTER STATIONS 8391
Philipp Pöttgen, Peter F. Pelz

MANIFESTATION OF ASCENDANCY OF EXTINCTION-REIGNITION ON SOUNDING HYBRID ROCKET USING DESIGN INFORMATICS 8403
Kazuhisa Chiba, Masahiro Kanazaki, Toru Shimada

COMPUTING AN OPERATING STRATEGY FOR AN ACTIVE BODY CONTROL WITH DYNAMIC PROGRAMMING IN THE AUTOMOTIVE AREA 8419
Marlene Utz, Phillipp Hedrich, Peter F. Pelz

SEISMIC RELIABILITY-BASED DESIGN OF STRUCTUTRES ISOLATED BY FPS 8431
Paolo Castaldo, Guglielmo Amendola, Bruno Palazzo

SEISMIC RETROFIT OF EXISTING BUILDINGS THROUGH THE DISSIPATIVE COLUMNS 8445
Paolo Castaldo, Bruno Palazzo, Francesco Perri, Ivana Marino, Marco Maria Faraco

AN EXAMPLE OF ENERGY DISSIPATION OPTIMIZATION FOR STEEL MRFS WITH PIN-JOINTED COLUMN BASES 8460
Elide Nastri, Annabella Paciello

ECCENTRICALLY BRACED FRAMES DESIGNED FOR THE ENERGY DISSIPATION OPTIMIZATION 8476
Elide Nastri

AN EXAMPLE OF COLUMN DESIGN OPTIMIZATION FOR FAILURE MODE CONTROL OF REINFORCED CONCRETE FRAMES 8492
Roberta Muscati

A COMPARISON OF MILP AND MINLP SOLVER PERFOMANCE ON THE EXAMPLE OF A DRINKING WATER SUPPLY SYSTEM DESIGN PROBLEM 8509
Lea Rausch, Philipp Leise, Thorsten Ederer, Lena C. Altherr, Peter F. Pelz

RELIABILITY TEST DEMONSTRATION METHOD FOR EXPONENTIAL LIFE SYSTEM WITH RELIABILITY GROWTH UNDER THE CONDITION OF IN-TIME CORRECTIVE STRATEGY 8528
Yunyan Xing, Ping Jiang, Feng Yao, Zhiwei Yang, Michael Emmerich, Thomas Bäck

CS 1100: REDUCTION ORDER METHODS
EVALUATION OF LINE-FITTING METHOD OF MODEL ORDER REDUCTION 8539
Valery Makhavikou, Roland Kasper, Dmitry Vlasenko

AN EFFICIENT ORDER REDUCTION STRATEGY IN EARTHQUAKE NONLINEAR RESPONSE ANALYSIS OF STRUCTURES 8552
Franz Bamer, Abbas Kazemi Amiri, Christian Bucher

ACTIVE SUBSPACES FOR THE PRELIMINARY FLUID DYNAMIC DESIGN OF UNCONVENTIONAL TURBOMACHINERY 8572
Juan S. Bahamonde, Matteo Pini, Piero Colonna

EXTENSION AND APPLICATION OF A NONLINEAR REDUCED ORDER MODEL TO GUST LOAD PREDICTION IN TIME DOMAIN 8587
Christoph Strobach, Klemens Lindhorst, Matthias Haupt, Peter Horst

CS 1200: STRUCTURAL DYNAMICS
RESEARCH ON HYSTERETIC BEHAVIORS OF A SAPARATED SHOCK ABSORBER APPLIED IN RAILWAY BRIDGE 8597
Aili Li, Ri Gao, Mingde Sun, Jilei Zhang

FINITE ELEMENT ANALYSIS OF TIMBER BEAMS WITH FLAWS 8606
Janka Kovacikova, Mats Ekevad, Olga Ivankova, Sven Berg

NONLINEAR FORCED RESPONSE OF A STATOR VANE WITH MULTIPLE FRICTION CONTACTS USING A COUPLED STATIC/DYNAMIC APPROACH 8612
Marco Lassalle, Christian Maria Firrone

COMPUTATIONAL METHOD OF DETERMINATION OF INTERNAL EFFORTS IN LINKS OF MECHANISMS AND ROBOT MANIPULATORS WITH STATICALLY DEFINABLE STRUCTURES CONSIDERING THE DISTRIBUTED DYNAMICALLY LOADINGS 8627
Zhumadil Baigunchekov, Muratulla Utenov, Nurzhan Utenov, Saltanat Zhilkibayeva

FE MODELLING OF SFRC BEAMS UNDER IMPACT LOADS 8640
Pegah Behinaein, Ali Abbas, Demetris Cotsovos

AN APROXIMATE ANALYTICAL SOLUTION FOR NONLINEAR FGM SHELL STRUCTURE WITH VARIABLE IN TIME PARAMETERS 8654
Victor Gristchak, Yuliia Fatieieva

UNCERTAINTY OF MODELS IN INTELLIGENT SYSTEMS UNDER STOCHASTIC LOADING 8665
Amalia Moutsopoulou, Georgios Stavroulakis, Tasos Pouliezos

COMPUTATIONAL MODELLING OF COLD-FORMED STEEL SCREWED CONNECTIONS AT AMBIENT AND ELEVATED TEMPERATURES 8678
Luis Mesquita, Rui Dias, Armandino Parente, Paulo Piloto

MONITORING AND ANALYSIS OF STRESS FIELD FOR ORTHOTROPIC STEEL DECK OF DASHENGGUAN YANGZTE RIVER BRIDGE 8691
Ying Wang, Y.S. Song

CS 1201: COMPUTATIONAL SOIL MECHANICS
A MORE COMPREHENSIVE MODELING OF CONTACT FORCE DURING SHEAR TESTING USING DEM 8708
Varvara Roubtsova, Mohamed Chekired

THREE-DIMENSIONAL BE-FE MODEL OF BUCKET FOUNDATIONS IN POROELASTIC SOILS 8725
Jacob D. R. Bordón, Juan J. Aznárez, Orlando F. Maeso

CS 1202: STRUCTURAL ANALYSIS AND MULTI BODY DYNAMICS
ON THE NUMERICAL INFLUENCES OF INERTIA REPRESENTATION FOR RIGID BODY DYNAMICS 8739
Xiaoming Xu, Wanxie Zhong

APPROACHES TO THE CREATION OF MULTIBODY MODELS OF THE VVER 1000 NUCLEAR REACTOR CONTROL ASSEMBLY 8756
Pavel Polach, Michal Hajžman

CS 1300: UNCERTAINTY QUANTIFICATION AND ERROR ESTIMATION
THE UPLIFT CAPACITY OF HORIZONTAL PLATE ANCHORS IN SPATIALLY VARIABLE CLAY USING SPARSE POLYNOMIAL CHAOS EXPANSIONS 8769
Tom Charlton, Mohamed Rouainia

FATIGUE RELIABILITY OF AGEING RAILWAY BRIDGES: FEASIBILITY OF PROBABILISTIC APPROACH 8778
Nirosha D. Adasooriya

AN EFFICIENT AERODYNAMIC SHAPE OPTIMIZATION FRAMEWORK FOR ROBUST DESIGN OF AIRFOILS USING SURROGATE MODELS 8787
Daigo Maruyama, Dishi Liu, Stefan Görtz

QUANTIFICATION OF SPATIAL VARIABILITY FOR TRANSVERSE ELASTIC MODULUS OF SPRUCE WOOD …….. 8801
Alireza Farajzadeh Moshtaghin, Steffen Franke, Thomas Keller, Anastasios Vassilopoulos

COMPARISON BETWEEN A POLYNOMIAL CHAOS SURROGATE MODEL AND MARKOV CHAIN MONTE CARLO FOR INVERSE UNCERTAINTY QUANTIFICATION BASED ON AN ELECTRIC DRIVE TEST BENCH …….. 8809
Philipp Glaser, Michael Schick, Kosmas Petridis, Vincent Heuveline

ECCOMAS Congress 2016
VII European Congress on Computational Methods in Applied Sciences and Engineering
M. Papadrakakis, V. Papadopoulos, G. Stefanou, V. Plevris (eds.)
Crete Island, Greece, 5–10 June 2016

A COMPUTATIONALLY EFFECTIVE FORMULATION TO FINITE ROTATIONS - SMALL STRAINS DESCRIPTION OF BEAM ELEMENTS

S. Lopez

Dipartimento di Ingegneria Civile, Università della Calabria
87030 Rende, Italy
e-mail: salvatore.lopez@unical.it

Keywords: Nonlinear three-dimensional beam analysis, finite elements, finite rotations, spatial dome structures.

Abstract. *In the context of three-dimensional elastic frame structures analysis with small strains and in the presence of large rotations we present a computationally effective model for the Euler-Bernoulli beam element. Actually, kinematical and strain measures of the beam element are completely defined by referring to boundary nodal displacements and one finite rotation parameter solely. In particular, the director along axis of the beam is defined directly by nodal positions while directors along the principal axes of the cross-section are detected by referring to the related orthogonal plane and the used rotation parameter. The definition of local rotations, required for the evaluation of torque and flexural deformation components, is obtained by imposing rotational compatibility and equilibrium conditions across inter-element boundaries. The description of the finite three-dimensional rotations is well posed under widely applicable hypotheses. The analysis of complex spatial dome structures, where matrices with large dimension and bandwidth occur, now proves a remarkable reduction of the required arithmetical operations with respect to the classical approaches.*

1 Introduction

Considerable work has been devoted to develop models for three-dimensional elastic frame structures for small strains and in the presence of large rotations. In this context the co-rotational, with minimal set parametrizations and multiplicative representations of rotations, is the most widely exploited approach. Indeed, the large-scale calculations required by these formulations have encouraged efficient treatments of the finite rotations. Then, those treatments, typically based on the rotation vector of the Euler theorem to describe finite rotations, have an economical definition of the rotated local reference system because only three parameters are used while evaluations of the coefficients in the force vector and in the tangent stiffness matrix are inexpensive. The evolution of the co-rotational approach can be traced by referring to the works of Stuelpnagel [1], Belytschko and Hsieh [2], Goldstein [3], Argyris [4], Rankin and Nour-Omid [5], Cardona and Geradin [6], Crisfield [7], Atluri and Cazzani [8], Geradin and Rixen [9], Ibrahimbegović et al. [10] and Felippa [11].

In this context here we present an alternative and computationally effective approach. Actually, kinematical and strain measures of the beam element are completely defined by referring to boundary nodal displacements and one finite rotation parameter. In particular, the director along axis of the beam is defined directly by nodal positions while directors along the principal axes of the cross-section are detected by referring to the related orthogonal plane and the only used rotation parameter. The definition of local rotations, required for the evaluation of torque and flexural deformation components, is obtained by imposing rotational compatibility and completeness conditions across inter-element boundaries. Finally, the description of the finite three-dimensional rotations is well posed under widely applicable hypotheses.

Being the infinitesimal nodal rotations computed by vectorial operations among the adjacent elements, such a formulation requires the extra storage of an integer matrix for the node - connected elements recognition. These connections, furthermore, increase the dimension of elemental force vector and tangent stiffness matrix and lead to complex programming for the imposition of rotational boundary conditions and linked applied moments. In contrast, by retaining similar approximation properties, the discretization uses one rotational unknown for each element instead of three required by the classical approaches.

As regards beam element modeling, here we use a small strain - finite displacement formulation of a two-node finite element based on the Euler-Bernoulli beam theory. The actual configuration of the element is rigidly translated and rotated, and deformed according to linear interpolations for axial displacements and quadratic interpolations for torque and flexural modes. The nonlinear motion is recovered by referring to the nodes at the boundaries of the element with three unknown displacements per node plus one unknown rotation per element. We note that boundary conditions on rotations are imposed by assuming as known the related nodal slopes or applied moments. It follows that, as will be discussed later, treatment of rotational boundary conditions and external moments proves to be more complex with respect to typical co-rotational formulations. Furthermore, the incremental rotations are restricted to the range of validity of the described formulation. Overall the use of the presented approach requires more implementation effort but less arithmetical operations with respect to the classical one.

2 Treatment of finite rotations

In the following, we denote with Greek indices the components of vectors and matrices while Latin indices are reserved to nodes and elements identification. Let $\mathbf{g}_\alpha = \{g_{\alpha\beta}\}$ and $\hat{\mathbf{g}}_\alpha = \{\hat{g}_{\alpha\beta}\}$ be, respectively, the actual and the initial configuration of three unit mutually orthogonal vectors

in the inertial reference basis $\mathbf{k}_\alpha = \{k_{\alpha\beta}\} = \{\delta_{\alpha\beta}\}$, where $\delta_{\alpha\beta}$ is the Kronecker delta. Then, matrix $\hat{\mathbf{G}} = [\hat{\mathbf{g}}_1|\hat{\mathbf{g}}_2|\hat{\mathbf{g}}_3]$ links $\hat{\mathbf{g}}_\alpha$ and $\mathbf{k}_\alpha$ vectors by $\hat{\mathbf{g}}_\alpha = \hat{\mathbf{G}}\mathbf{k}_\alpha$ while $\mathbf{G} = [\mathbf{g}_1|\mathbf{g}_2|\mathbf{g}_3]$ maps $\mathbf{k}_\alpha$ into $\mathbf{g}_\alpha$ vectors by $\mathbf{g}_\alpha = \mathbf{G}\mathbf{k}_\alpha$.

To obtain the updated treatment of rotations we refer to the $\mathbf{g}_{\alpha(k)} = \mathbf{G}_{(k)}\mathbf{k}_\alpha$, $\mathbf{G}_{(k)} = \mathbf{E}_{(k)}\bar{\mathbf{G}}_{(k)}$, expression for the actual configuration of the $\mathbf{g}_\alpha$ orthonormal triad at the k-th step. Vectors $\mathbf{e}_{\alpha(k)}$ defining $\mathbf{E}_{(k)} = [\mathbf{e}_1|\mathbf{e}_2|\mathbf{e}_3]$ represent the incremental rotation from the $\bar{\mathbf{g}}_{\alpha(k)}$ previously computed configuration. The subsequent $k+1$ step, afterward, refers to the $\bar{\mathbf{G}}_{(k+1)} = \mathbf{E}^*_{(k)}\bar{\mathbf{G}}_{(k)}$ updated configuration with the $\mathbf{e}^*_{\alpha(k)}$ established configuration of $\mathbf{e}_\alpha$. The process is initialized by $\bar{\mathbf{G}}_{(0)} = \hat{\mathbf{G}}$.

Classically, the treatment of rotations is based on the recursive composition $\mathbf{g}_{\alpha(k)} = \mathbf{E}_{(k)}\bar{\mathbf{G}}_{(k)}\hat{\mathbf{g}}_\alpha$, $\mathbf{E}_{(k)} = \mathbf{E}(\boldsymbol{\psi}_{(k)})$, where ψ_α components of $\boldsymbol{\psi}$ are the unknown rotation parameters. Following the description given before, $\mathbf{E}_{(k)}$ is the incremental rotation matrix which maps the updated frame $\bar{\mathbf{g}}_{\alpha(k)}$ into the actual frame $\mathbf{g}_{\alpha(k)}$ while $\bar{\mathbf{G}}_{(k)} = \bar{\mathbf{G}}_{(k)}(\bar{\boldsymbol{\psi}}_{(k)})$ maps the initial frame $\hat{\mathbf{g}}_\alpha$ into the updated frame $\bar{\mathbf{g}}_{\alpha(k)}$. Based on the rotation vector $\boldsymbol{\psi} = \varphi\boldsymbol{\phi}$, $\boldsymbol{\phi}^T\boldsymbol{\phi} = 1$, of the Euler theorem to describe finite rotations, a representation of rotation operators is:

$$\mathbf{G}(\boldsymbol{\psi}) = \mathbf{I} + \frac{\sin\varphi}{\varphi}\boldsymbol{\psi}_\times + \frac{1-\cos\varphi}{\varphi^2}\boldsymbol{\psi}^2_\times. \tag{1}$$

where $\mathbf{I}$ is the identity matrix. In (1) $\boldsymbol{\psi}_\times$ denotes the skew symmetric tensor obtained by the components of vector $\boldsymbol{\psi}$:

$$\boldsymbol{\psi}_\times = \mathbf{Skew}(\boldsymbol{\psi}) = \begin{bmatrix} 0 & -\psi_3 & \psi_2 \\ \psi_3 & 0 & -\psi_1 \\ -\psi_2 & \psi_1 & 0 \end{bmatrix}. \tag{2}$$

The $\boldsymbol{\psi} = \mathbf{axial}(\boldsymbol{\psi}_\times)$ is the converse operation of (2) that extracts the $\boldsymbol{\psi}$ vector from the skew symmetric tensor $\boldsymbol{\psi}_\times$.

In the use of the $\mathbf{G} = \mathbf{E}\bar{\mathbf{G}}$ composition of rotation operators, however, we stress that $\boldsymbol{\psi}_G \neq \boldsymbol{\psi} + \bar{\boldsymbol{\psi}}$ successive rotations cannot be obtained by simply adding their corresponding rotation vectors but the solution of the inverse $\boldsymbol{\psi}_G = G^{-1}(\mathbf{G})$ problem is required. Such a problem is defined as the operation of obtaining the $\boldsymbol{\psi}_G$ rotation vector based on the knowledge of the $\mathbf{G}$ rotation matrix and can be solved by the no ill-conditioning Spurrier algorithm [12]. By referring to the established configuration $\boldsymbol{\psi}^*_{(k)}$, afterwards, the updated configuration is achieved in the subsequent $k+1$ step as

$$\mathbf{G} = \mathbf{E}^*_{(k)}\bar{\mathbf{G}}_{(k)}, \quad \boldsymbol{\psi}_G = G^{-1}(\mathbf{G}), \quad \bar{\mathbf{G}}_{(k+1)} = \mathbf{G}(\boldsymbol{\psi}_G). \tag{3}$$

The process is initialized by $\bar{\mathbf{G}}_{(0)} = \mathbf{I}$.

In the presented finite rotations formulation let respectively $\overset{i}{\mathbf{u}}$ and $\overset{j}{\mathbf{u}}$ displacement vectors at the i and j boundary nodes of the element with lengh h, while discrete operators s and d rest defined by $s\mathbf{u} = (\overset{i}{\mathbf{u}} + \overset{j}{\mathbf{u}})/2$ and $d\mathbf{u} = (\overset{j}{\mathbf{u}} - \overset{i}{\mathbf{u}})/h$. Then, by evaluating the vector connecting the i and j nodes, we refer to

$$\mathbf{p}_1 = d\mathbf{u} + \hat{\mathbf{g}}_1, \quad \check{\mathbf{g}}_1 = \mathbf{p}_1/||\mathbf{p}_1|| \tag{4}$$

for the first actual vector of the orthonormal basis. By referring to the given unit vector $\bar{\mathbf{g}}_2$ we define the vectors

$$\mathbf{p}_2 = \bar{\mathbf{g}}_2 - \check{\mathbf{g}}_1 \cdot \bar{\mathbf{g}}_2 \ \check{\mathbf{g}}_1, \qquad \check{\mathbf{g}}_2 = \mathbf{p}_2/||\mathbf{p}_2|| \tag{5}$$
$$\check{\mathbf{g}}_3 = \check{\mathbf{g}}_1 \times \check{\mathbf{g}}_2$$

such that the basis $\check{\mathbf{G}} = [\check{\mathbf{g}}_1|\check{\mathbf{g}}_2|\check{\mathbf{g}}_3]$ is orthonormal and coincides with the principal axes of the beam element. The additional rotation in the reference space characterized by the angle r about the $\check{\mathbf{g}}_1$ axis

$$\mathbf{G}_r = \mathbf{I} + \sin r\check{\mathbf{g}}_{1\times} + (1-\cos r)\check{\mathbf{g}}_{1\times}^2 \tag{6}$$

completes now the definition of the rotation operator $\mathbf{G} = \mathbf{G}_r\check{\mathbf{G}}$ that links $\mathbf{g}_\alpha$ and $\mathbf{k}_\alpha$ vectors.

We note that, in the definition of the $\check{\mathbf{g}}_2$ vector in (5), the vectors $\check{\mathbf{g}}_1$ and $\bar{\mathbf{g}}_2$ have to form a linearly independent set. However this is not an actual limitation for the incremental rotation $\mathbf{E}_{(k)}$. Furthermore, rotation $\mathbf{G}_r$ defined in (6) preserves the linearity of the vector space operations because it has as axis of rotation the component $\check{\mathbf{g}}_1 = \mathbf{g}_1$ of $\mathbf{G}$.

3 Kinematics and energetic quantities of the beam element

Let ξ be the referential coordinate along the beam element centerline $-h/2 \le \xi \le +h/2$. Global displacement vector $\mathbf{u}(\xi)$ of the e element is composed of rigid and deformation components by

$$\overset{e}{\mathbf{u}}(\xi) = \overset{e}{\mathbf{u}} + (\overset{e}{\mathbf{g}}_1 - \overset{e}{\hat{\mathbf{g}}}_1)\xi + \overset{e}{\mathbf{G}}\overset{e}{\tilde{\mathbf{u}}}(\xi), \tag{7}$$

where

$$\begin{aligned}
\overset{e}{\tilde{u}}_1(\xi) &= \overset{e}{\varepsilon}\xi \\
\overset{e}{\tilde{u}}_2(\xi) &= -\frac{h^2}{8}\overset{e}{\chi}_3 - \frac{h^2}{24}\overset{e}{\gamma}_2\xi + \frac{1}{2}\overset{e}{\chi}_3\xi^2 + \frac{1}{6}\overset{e}{\gamma}_2\xi^3 \\
\overset{e}{\tilde{u}}_3(\xi) &= \frac{h^2}{8}\overset{e}{\chi}_2 + \frac{h^2}{24}\overset{e}{\gamma}_3\xi - \frac{1}{2}\overset{e}{\chi}_2\xi^2 - \frac{1}{6}\overset{e}{\gamma}_3\xi^3.
\end{aligned} \tag{8}$$

Then, local transverse rotations in the $\overset{e}{\mathbf{G}}$ basis are computed by

$$\begin{aligned}
\overset{e}{\varphi}_2(\xi) &= -\overset{e}{\tilde{u}}_{3,\xi}(\xi) = -\frac{h^2}{24}\overset{e}{\gamma}_3 + \overset{e}{\chi}_2\xi + \frac{1}{2}\overset{e}{\gamma}_3\xi^2 \\
\overset{e}{\varphi}_3(\xi) &= \overset{e}{\tilde{u}}_{2,\xi}(\xi) = -\frac{h^2}{24}\overset{e}{\gamma}_2 + \overset{e}{\chi}_3\xi + \frac{1}{2}\overset{e}{\gamma}_2\xi^2,
\end{aligned} \tag{9}$$

while local axial rotation is now defined by the expression

$$\overset{e}{\varphi}_1(\xi) = \overset{e}{\chi}_1\xi + \frac{1}{3}\overset{e}{\gamma}_1\xi^2. \tag{10}$$

By evaluating above relations for nodal coordinates we deduce that

$$\overset{e}{\varepsilon} = \overset{e}{\mathbf{g}}_1 \cdot \overset{e}{\mathbf{p}}_1 - 1 \tag{11}$$

is the expression of the axial deformation and

$$\overset{e}{\boldsymbol{\chi}} = d\overset{e}{\boldsymbol{\varphi}}, \qquad \overset{e}{\boldsymbol{\gamma}} = \frac{6}{h^2}s\overset{e}{\boldsymbol{\varphi}}, \tag{12}$$

are the expressions of torque and shear deformations as a function of nodal displacement and local rotations.

In the following, we refer to the m and p elements respectively adjacent of the current e element at the nodes i and j. Let, furthermore, $\overset{em}{\hat{\mathbf{P}}} = \overset{e}{\hat{\mathbf{G}}} \cdot \overset{m}{\hat{\mathbf{G}}}$ and $\overset{ep}{\hat{\mathbf{P}}} = \overset{e}{\hat{\mathbf{G}}} \cdot \overset{p}{\hat{\mathbf{G}}}$ rotation matrices

that carry out the representations of vector respectively in the $\overset{m}{\hat{\mathbf{g}}}_\alpha$ and $\overset{p}{\hat{\mathbf{g}}}_\alpha$ basis with respect to $\overset{e}{\hat{\mathbf{g}}}_\alpha$. By referring to the $\overset{ei}{\boldsymbol{\varphi}}$ and $\overset{ej}{\boldsymbol{\varphi}}$ nodal local rotations, nodal director components are now calculated by the vectorial operations

$$\overset{ei}{\mathbf{G}} = \overset{e}{\mathbf{G}}(\mathbf{I} + \overset{ei}{\boldsymbol{\varphi}}_\times), \qquad \overset{ej}{\mathbf{G}} = \overset{e}{\mathbf{G}}(\mathbf{I} + \overset{ej}{\boldsymbol{\varphi}}_\times). \tag{13}$$

We note that the first order accuracy of the (13) representations leads to local evaluations consistent with the small strains hypotheses. Rotational compatibility conditions at the boundary nodes, then, are obtained by imposing

$$\overset{m}{\mathbf{G}}(\mathbf{I} + \overset{mj}{\boldsymbol{\varphi}}_\times) = \overset{e}{\mathbf{G}}(\mathbf{I} + \overset{ei}{\boldsymbol{\varphi}}_\times)\overset{em}{\hat{\mathbf{P}}}, \qquad \overset{p}{\mathbf{G}}(\mathbf{I} + \overset{pi}{\boldsymbol{\varphi}}_\times) = \overset{e}{\mathbf{G}}(\mathbf{I} + \overset{ej}{\boldsymbol{\varphi}}_\times)\overset{ep}{\hat{\mathbf{P}}}. \tag{14}$$

Now we also define respectively the local rotations $\overset{em}{\boldsymbol{\theta}}$ and $\overset{ep}{\boldsymbol{\theta}}$ connecting directly the $\overset{m}{\mathbf{g}}_\alpha$ and $\overset{p}{\mathbf{g}}_\alpha$ bases with $\overset{e}{\mathbf{g}}_\alpha$ by the relations:

$$\overset{e}{\mathbf{G}} = \overset{m}{\mathbf{G}}\overset{em}{\hat{\mathbf{P}}} \cdot (\mathbf{I} + \overset{em}{\boldsymbol{\theta}}_\times), \qquad \overset{e}{\mathbf{G}} = \overset{p}{\mathbf{G}}\overset{ep}{\hat{\mathbf{P}}} \cdot (\mathbf{I} + \overset{ep}{\boldsymbol{\theta}}_\times). \tag{15}$$

Then by (14) and (15) we can evaluate at the first order:

$$\overset{mj}{\boldsymbol{\varphi}} = \overset{em}{\hat{\mathbf{P}}} \cdot (\overset{ei}{\boldsymbol{\varphi}} + \overset{em}{\boldsymbol{\theta}}), \qquad \overset{pi}{\boldsymbol{\varphi}} = \overset{ep}{\hat{\mathbf{P}}} \cdot (\overset{ej}{\boldsymbol{\varphi}} + \overset{ep}{\boldsymbol{\theta}}), \tag{16}$$

with

$$\overset{em}{\boldsymbol{\theta}}_\times = \overset{em}{\hat{\mathbf{P}}}\overset{m}{\mathbf{G}} \cdot \overset{e}{\mathbf{G}} - \mathbf{I}, \qquad \overset{ep}{\boldsymbol{\theta}}_\times = \overset{em}{\hat{\mathbf{P}}}\overset{p}{\mathbf{G}} \cdot \overset{e}{\mathbf{G}} - \mathbf{I}. \tag{17}$$

We note that rotations $\overset{em}{\boldsymbol{\theta}}$ and $\overset{ep}{\boldsymbol{\theta}}$ are in function of the assumed nodal displacements and elemental rotations unknowns. To recover expressions for the rotational deformations in (12), here we impose equilibrium equations or consistence conditions at the nodes.

Twisting and bending moments $\mathbf{m}_\alpha$ at the i node due to the e element can be expressed by the formula

$$\overset{ei}{\mathbf{m}}_\alpha = \overset{e}{H}_{\alpha\alpha}\overset{ei}{\varphi}_{\alpha,\xi}\overset{ei}{\mathbf{g}}_\alpha. \tag{18}$$

In (18) we denote with $\mathbf{H} = \mathbf{diag}[GJ_1, EJ_2, EJ_3]$ the elastic constitutive matrix of torsional and bending stiffnesses about the principal axes. Let $\overset{i}{\mathbf{m}}$ the applied vector moment at the i node, then related equilibrium equation is:

$$\overset{ei}{\mathbf{m}} = \overset{i}{\mathbf{m}} + \overset{mj}{\mathbf{m}}, \qquad \overset{ei}{\mathbf{m}} = \sum_\alpha \overset{e}{H}_{\alpha\alpha}\overset{ei}{\varphi}_{\alpha,\xi}\overset{ei}{\mathbf{g}}_\alpha, \quad \overset{mj}{\mathbf{m}} = \sum_\alpha \overset{m}{H}_{\alpha\alpha}\overset{mj}{\varphi}_{\alpha,\xi}\overset{mj}{\mathbf{g}}_\alpha. \tag{19}$$

For clarity of presentation, in the following we refer to the case $\overset{i}{\mathbf{m}} = \mathbf{0}$. Then, for the β component of equilibrium equation (19) we have

$$\overset{m}{H}_{\beta\beta}\overset{mj}{\varphi}_{\beta,\xi} = \sum_\alpha \overset{e}{H}_{\alpha\alpha}\overset{ei}{\varphi}_{\alpha,\xi}\overset{mj}{\mathbf{g}}_\beta \cdot \overset{ei}{\mathbf{g}}_\alpha. \tag{20}$$

By proceeding in a similar way for the equilibrium equation at the j node and by writing relations (20) in the matrix form we obtain

$$\overset{m}{\mathbf{H}}\overset{mj}{\boldsymbol{\varphi}}_{,\xi} = \overset{mj}{\mathbf{G}} \cdot \overset{ei}{\mathbf{G}}\overset{e}{\mathbf{H}}\overset{ei}{\boldsymbol{\varphi}}_{,\xi}, \qquad \overset{p}{\mathbf{H}}\overset{pi}{\boldsymbol{\varphi}}_{,\xi} = \overset{pi}{\mathbf{G}} \cdot \overset{ej}{\mathbf{G}}\overset{e}{\mathbf{H}}\overset{ej}{\boldsymbol{\varphi}}_{,\xi}. \tag{21}$$

By inserting compatibility conditions $\overset{ei}{\mathbf{G}}\overset{em}{\hat{\mathbf{P}}} = \overset{mj}{\mathbf{G}}$ and $\overset{ej}{\mathbf{G}}\overset{ep}{\hat{\mathbf{P}}} = \overset{pi}{\mathbf{G}}$ in the (21) relations we have:

$$\overset{m}{\mathbf{H}}\overset{mj}{\boldsymbol{\varphi}}_{,\xi} = \overset{em}{\hat{\mathbf{P}}} \cdot \overset{e}{\mathbf{H}}\overset{ei}{\boldsymbol{\varphi}}_{,\xi}, \qquad \overset{p}{\mathbf{H}}\overset{pi}{\boldsymbol{\varphi}}_{,\xi} = \overset{ep}{\hat{\mathbf{P}}} \cdot \overset{e}{\mathbf{H}}\overset{ej}{\boldsymbol{\varphi}}_{,\xi}. \tag{22}$$

In the cases of constant bending state, $\overset{e}{\boldsymbol{\gamma}} = \mathbf{0}$ and $\overset{m}{\boldsymbol{\gamma}} = \mathbf{0}$ in (12) expressions imply that $\overset{ej}{\boldsymbol{\varphi}} = -\overset{ei}{\boldsymbol{\varphi}}$ and $\overset{mi}{\boldsymbol{\varphi}} = -\overset{mj}{\boldsymbol{\varphi}}$, respectively, and

$$\overset{ei}{\boldsymbol{\varphi}}_{,\xi} = \overset{e}{\boldsymbol{\chi}} = -\frac{2}{\overset{e}{h}}\overset{ei}{\boldsymbol{\varphi}}, \qquad \overset{mj}{\boldsymbol{\varphi}}_{,\xi} = \overset{m}{\boldsymbol{\chi}} = \frac{2}{\overset{m}{h}}\overset{mj}{\boldsymbol{\varphi}}. \tag{23}$$

Finally, by (16), (22) and (23), for the i node we obtain

$$\overset{em}{\mathbf{A}}\overset{ei}{\boldsymbol{\varphi}} = -\frac{1}{\overset{m}{h}}\overset{em}{\hat{\mathbf{P}}}\overset{m}{\mathbf{H}}\overset{em}{\hat{\mathbf{P}}} \cdot \overset{em}{\boldsymbol{\theta}}, \qquad \overset{em}{\mathbf{A}} = \frac{1}{\overset{e}{h}}\overset{e}{\mathbf{H}} + \frac{1}{\overset{m}{h}}\overset{em}{\hat{\mathbf{P}}}\overset{m}{\mathbf{H}}\overset{em}{\hat{\mathbf{P}}} \cdot . \tag{24}$$

Similarly, for the j node:

$$\overset{ep}{\mathbf{A}}\overset{ej}{\boldsymbol{\varphi}} = -\frac{1}{\overset{p}{h}}\overset{ep}{\hat{\mathbf{P}}}\overset{p}{\mathbf{H}}\overset{ep}{\hat{\mathbf{P}}} \cdot \overset{ep}{\boldsymbol{\theta}}, \qquad \overset{ep}{\mathbf{A}} = \frac{1}{\overset{e}{h}}\overset{e}{\mathbf{H}} + \frac{1}{\overset{p}{h}}\overset{ep}{\hat{\mathbf{P}}}\overset{p}{\mathbf{H}}\overset{ep}{\hat{\mathbf{P}}} \cdot . \tag{25}$$

By the (24) and (25) definitions of the local rotations we can obtain the computation of the (12) element beam deformations in function of the assumed unknowns. We note that the $\mathbf{A}$ matrices are defined by fixed quantities of the problem. Then such quantities can be computed, for each node, at the preprocessing procedure.

If we want to achieve the complete consistence at the generic i node, together with (16) expressions we must impose the $\sum_\alpha \overset{ei}{\varphi}_{\alpha,\xi}\overset{ei}{\mathbf{g}}_\alpha = \sum_\alpha \overset{mj}{\varphi}_{\alpha,\xi}\overset{mj}{\mathbf{g}}_\alpha$ and $\sum_\alpha \overset{ei}{\varphi}_{\alpha,\xi\xi}\overset{ei}{\mathbf{g}}_\alpha = \sum_\alpha \overset{mj}{\varphi}_{\alpha,\xi\xi}\overset{mj}{\mathbf{g}}_\alpha$ continuity conditions that, at the first order of approximation, lead to the relations:

$$\overset{mj}{\boldsymbol{\varphi}}_{,\xi} = \overset{em}{\hat{\mathbf{P}}} \cdot \overset{ei}{\boldsymbol{\varphi}}_{,\xi} \qquad \text{and} \qquad \overset{mj}{\boldsymbol{\varphi}}_{,\xi\xi} = \overset{em}{\hat{\mathbf{P}}} \cdot \overset{ei}{\boldsymbol{\varphi}}_{,\xi\xi} \tag{26}$$

respectively, while for the j node

$$\overset{pi}{\boldsymbol{\varphi}}_{,\xi} = \overset{ep}{\hat{\mathbf{P}}} \cdot \overset{ej}{\boldsymbol{\varphi}}_{,\xi} \qquad \text{and} \qquad \overset{pi}{\boldsymbol{\varphi}}_{,\xi\xi} = \overset{ep}{\hat{\mathbf{P}}} \cdot \overset{ej}{\boldsymbol{\varphi}}_{,\xi\xi}. \tag{27}$$

After algebraic manipulations by the above expressions the following relations are obtained:

$$-\frac{2\overset{m^2}{h} + 3\overset{m}{h}\overset{e}{h} + \overset{e^2}{h}}{\overset{e^2}{h}}s\overset{e}{\boldsymbol{\varphi}} + \frac{\overset{m}{h} + \overset{e}{h}}{2}d\overset{e}{\boldsymbol{\varphi}} = \overset{em}{\boldsymbol{\theta}}, \qquad -\frac{2\overset{p^2}{h} + 3\overset{p}{h}\overset{e}{h} + \overset{e^2}{h}}{\overset{e^2}{h}}s\overset{e}{\boldsymbol{\varphi}} - \frac{\overset{p}{h} + \overset{e}{h}}{2}d\overset{e}{\boldsymbol{\varphi}} = \overset{ep}{\boldsymbol{\theta}}. \tag{28}$$

Also here, by the (28) definitions of the local rotations, we can achieve the computation of the element beam deformations in function of the assumed unknowns.

4 Boundary conditions, multiple connections and solution scheme

Boundary conditions imposition implies a case depending implementation of the solution process. In effect, conditions involving rotations and moments given at boundary nodes are imposed by specializing related elements by following the formulation described in Section

3 because we have worked with global rotation and curvature definitions. Furthermore, we remark that only the external work of forces can be defined in the described formulation so that moments can be modelled as forces following the motion of points of the beam element. In particular, let vector $\overset{n}{\mathbf{m}}$ be the spatially fixed moment applied in the n node of the e element and $\overset{en}{\mathbf{g}}_\alpha$ the related nodal basis. As described in [13], we refer to three force vectors $\mathbf{p}_{(\alpha)}$ applied to n and compute the external work as

$$W_{\mathbf{m}} == \sum_\alpha \mathbf{p}_{(\alpha)} \cdot (\overset{en}{\mathbf{g}}_\alpha - \overset{en}{\hat{\mathbf{g}}}_\alpha). \tag{29}$$

The variation of the functional $W_{\mathbf{m}}$ is carried out on the $\overset{en}{\mathbf{g}}_\alpha$ vectors by considering $\mathbf{p}_{(\alpha)}$ as constants. Then, after variation of (29), we define the $\mathbf{p}_{(\alpha)}$ force vectors by

$$\mathbf{p}_{(\alpha)} = -\frac{1}{2}\sum_{\beta\kappa} e_{\alpha\beta\kappa} p_\beta \overset{en}{\mathbf{g}}_\kappa, \qquad \sum_\alpha \overset{en}{\mathbf{g}}_\alpha \times \mathbf{p}_{(\alpha)} = \overset{n}{\mathbf{m}}. \tag{30}$$

As can be observed in (30), applied forces are such that the resulting moment in the n node is the given $\overset{n}{\mathbf{m}}$ vector. Simple algebraic manipulations, finally, lead to the $p_\alpha = \overset{n}{\mathbf{m}}^T \overset{en}{\mathbf{g}}_\alpha$ components. We note that, the definitions given in (29) and (30) imply that the external force vectors are a function of the assumed unknowns.

In the case of more elements connected to the i node, the relations in (19) of the (*EF*) equilibrium based formulation become

$$\overset{ei}{\mathbf{m}} = \overset{i}{\mathbf{m}} + \sum_m \overset{mj}{\mathbf{m}}, \quad \text{or} \quad \sum_\alpha \overset{e}{H}_{\alpha\alpha} \overset{ei}{\varphi}_{\alpha,\xi} \overset{ei}{\mathbf{g}}_\alpha = \overset{i}{\mathbf{m}} + \sum_m \sum_\alpha \overset{m}{H}_{\alpha\alpha} \overset{mj}{\varphi}_{\alpha,\xi} \overset{mj}{\mathbf{g}}_\alpha. \tag{31}$$

Being $\overset{ei}{\mathbf{G}}\overset{em}{\hat{\mathbf{P}}} = \overset{mj}{\mathbf{G}}$, $\forall m$ and by assuming $\overset{mi}{\boldsymbol{\varphi}} = -\overset{mj}{\boldsymbol{\varphi}}$, $\forall m$ we obtain:

$$\overset{em}{\mathbf{A}}\overset{ei}{\boldsymbol{\varphi}} = -\sum_m \frac{1}{\overset{m}{h}} \overset{em}{\hat{\mathbf{P}}} \overset{m}{\mathbf{H}} \overset{em}{\hat{\mathbf{P}}} \cdot \overset{em}{\boldsymbol{\theta}}, \qquad \overset{em}{\mathbf{A}} = \frac{1}{\overset{e}{h}} \overset{e}{\mathbf{H}} + \sum_m \frac{1}{\overset{m}{h}} \overset{em}{\hat{\mathbf{P}}} \overset{m}{\mathbf{H}} \overset{em}{\hat{\mathbf{P}}} \cdot, \tag{32}$$

and the analogous for the j node. From the implementation point of the view, at the current e element, multiple connections are carried out by repeating m times the assembling of internal force vectors and stiffness matrices for each connected element. For the (*CF*) consistence based formulation, instead, a master element must be assigned at the multiply connected node as reference of related continuity conditions.

The definition of equilibrium equations is based on the classical stationary problem for the energy functional. Because a multiplicative approach is here exploited, admissible variational formulation and linearization must be carried out at the solution point in the respect of the $\delta\mathbf{G} = \delta\boldsymbol{\varphi}_\times \mathbf{G}$ consistent condition, where $\delta\boldsymbol{\varphi}$ is the spatial component of the angular variation. A predictor-corrector scheme as described in [14] for the equilibrium path individualization is used in the analysis. It is characterized by a predictor step obtained by the linear extrapolation of the previously computed two solution points when $k > 0$, while the first order asymptotic extrapolation is used when $k = 0$. Furthermore, the corrector is accomplished by a Newton method based corrector scheme with minimization of the distance between the approximate and equilibrium points as a constraint equation.

5 Numerical examples

Equilibrium curve of the framed dome shown in Figure 1 and analyzed in Battini [15], Kouhia and Tuomala [16], was calculated with both *EF* and *CF* approaches. By assuming ε=0 or ε=0.0001 two different behaviours of the structure have been considered. The dome has been modelled by using N_{mb}=4,8 elements for each member, i.e. totally 18N_{mb} elements.

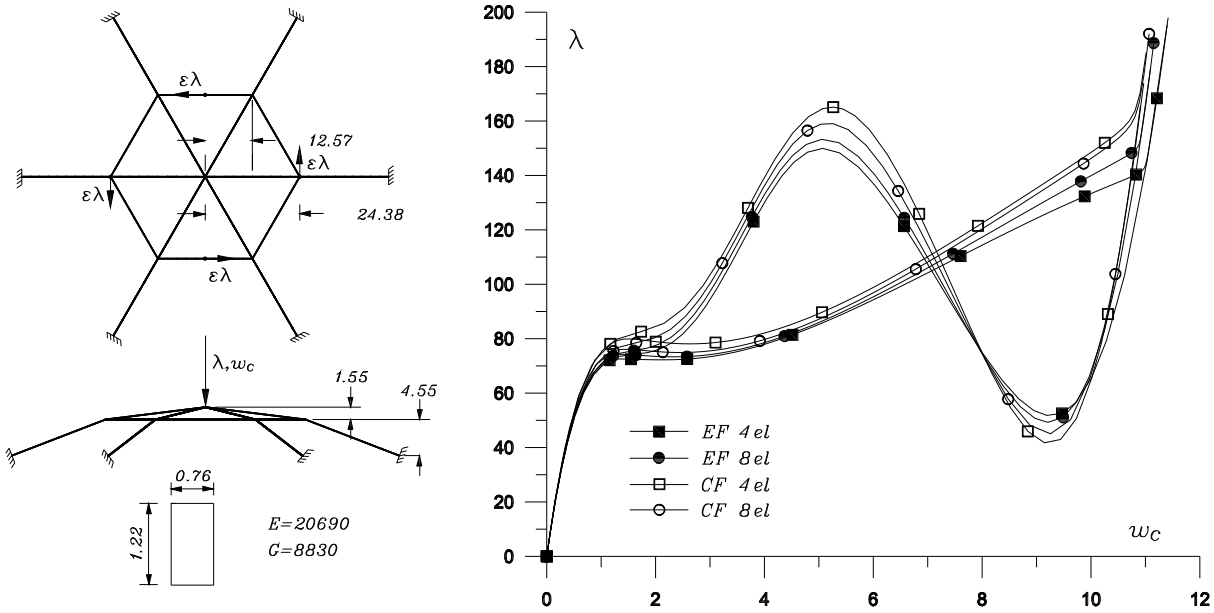

Figure 1: Framed dome: problem definition and equilibrium paths.

In Figure 1 the fundamental path and the secondary path branching out at the lowest bifurcation point are also displayed. Significant deformed configurations are shown in Figure 2 for both loadings. In particular, the perfect case (a) is characterized by a symmetric behaviour while the post-buckling mode (b) is a rotation around the central vertical axis. The detected computational performances indicate that the presented formulation requires more implementation effort but less arithmetical operations with respect to the classical rotation vector based approach.

6 Conclusions

In the hypothesis of large displacements and rotations and small strains, a technique to analyze the behaviour of three-dimensional finite element beam frames has been presented. The approach is based on an updated Lagrangian description of rotations and the presented formulations do not use angle measures. By adopting the Euler-Bernoulli beam model, a computationally effective beam element is obtained because kinematical and strain measures are completely defined by referring to boundary nodal displacements and one finite rotation parameter solely. The treatment of rotational boundary conditions and external moments proves to be more complex with respect to the co-rotational formulations. Nevertheless, the description of the finite three-dimensional rotations is well posed under widely applicable hypotheses, while the analysis of complex spatial dome structures, where matrices with large dimension and bandwidth occur, now proves a remarkable reduction of the required arithmetical operations with respect to the classical approaches.

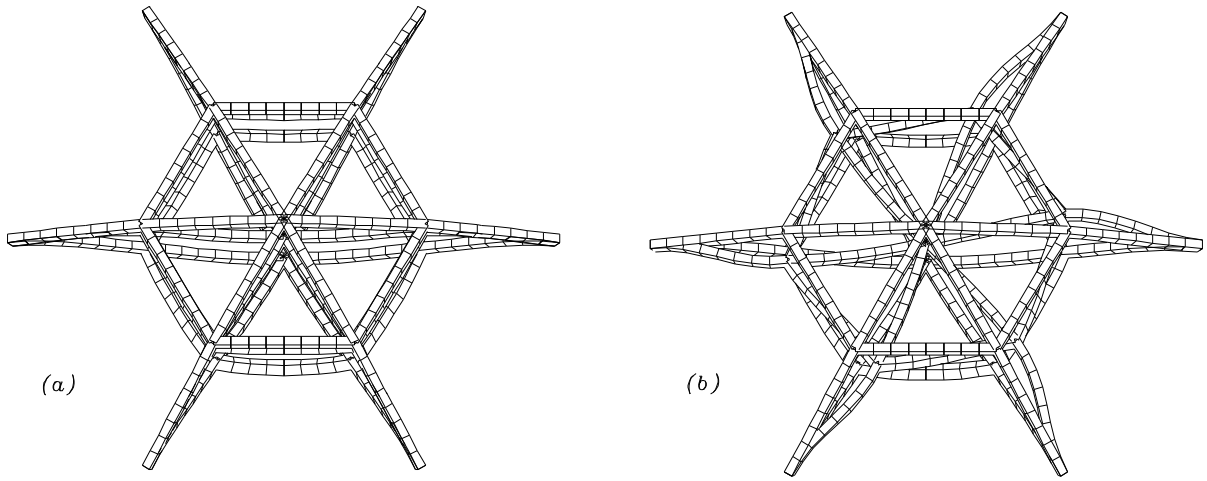

Figure 2: Framed dome: deformed configurations for N_{mb}=8.

REFERENCES

[1] J. Stuelpnagel, On the parameterization of the three-dimensional rotation group, *SIAM Review*, **6**, 422–430, 1964.

[2] T. Belytschko, B.J. Hsieh, Non-linear transient finite element analysis with convected co-ordinates, *Int. J. Numer. Meth. Engrg.*, **7**, 255–271, 1973.

[3] H. Goldstein, *Classical mechanics*. Addison-Wesley, Reading, Massachusetts, 1980.

[4] J. Argyris, An excursion into large rotations, *Comput. Meth. Appl. Mech. Engrg.*, **32**, 85–155, 1982.

[5] C.C. Rankin, B. Nour-Omid, The use of projectors to improve finite element performance, *Computers and Structures*, **30**, 257–267, 1988.

[6] A. Cardona, M. Geradin, A beam finite element non-linear theory with finite rotations, *Int. J. Numer. Meth. Engrg.*, **26**, 2403–2438, 1988.

[7] M.A. Crisfield, A consistent co-rotational formulation for nonlinear three-dimensional beam elements, *Comput. Meth. Appl. Mech. Engrg.*, **81**, 131–150, 1990.

[8] S.N. Atluri, A. Cazzani, Rotations in computational solid mechanics, *Arc. Comput. Methods Eng.*, **2**, 49–138, 1995.

[9] M. Geradin, D. Rixen, Parametrization of finite rotations in computational dynamics: a review, *Revue europeenne des elements finis*, **4**, 497–553, 1995.

[10] A. Ibrahimbegović, H. Shakourzadeh, J.L. Batoz, M. Al Mikdad, Y.Q. Guo, On the role of geometrically exact and second-order theories in buckling and post-buckling analysis of three-dimensional beam structures, *Computers and Structures*, **61**, 1101–1114, 1996.

[11] C.A. Felippa, A systematic approach to the element-independent corotational dynamics of finite elements, *Technical Report CU-CAS-95-06 Center for Aerospace Structures Dept of Aerospace Engineering*, Univ. Colorado Boulder, 2000.

[12] R.A. Spurrier, Comments on singularity-free extraction of a quaternion from a director-cosine matrix, *J. Spacecraft*, **15**, 255–256, 1978.

[13] S. Lopez, Three-dimensional finite rotations treatment based on a minimal set parametrization and vector space operations in beam elements, *Comput. Mech.*, **52**, 377-399, 2013.

[14] S. Lopez, An effective parametrization for asymptotic extrapolations, *Comput. Meth. Appl. Mech. Engrg.*, **189**, 297–311, 2000.

[15] J.M. Battini, Co-rotational beam elements in instability problems, *Royal Institute of Technology Department of Mechanics*, Stockholm, Sweden, 2002.

[16] R. Kouhia, M. Tuomala, Static and dynamic analysis of space frames using simple Timoshenko type elements, *Int. J. Num. Meth. Engng.*, **36**, 11891221, 1993.

ECCOMAS Congress 2016
VII European Congress on Computational Methods in Applied Sciences and Engineering
M. Papadrakakis, V. Papadopoulos, G. Stefanou, V. Plevris (eds.)
Crete Island, Greece, 5–10 June 2016

A COROTATIONAL FINITE ELEMENT TO MODEL BENDING VIBRATIONS OF METALLIC STRANDS

Francesco Foti[1]

[1] Politecnico di Milano, Dep. of Civil and Environmental Engineering
P.zza L. Da Vinci 32, 20133, Milano, Italy
e-mail: francesco.foti@polimi.it

Keywords: Corotational finite elements, cable dynamics, hysteretic bending, friction.

Abstract. *A new formulation to model the mechanical response of metallic strands undergoing a combination of axial load and planar bending is developed. Each wire of the strand is modeled as an elastic curved thin rod. A kinematic model is then introduced to relate the generalized strain variables of the strand to those of the wires. The stress-strain state of the wires is evaluated starting from the analysis of the internal contact conditions. Friction is modeled through the classic Amontons-Coulomb law and the elastic tangential compliance of contact patches is accounted for. A non-holonomic material constitutive law in terms of the cross sectional generalized stresses and strains of the Euler-Bernoulli beam theory is obtained and implemented within a corotational beam element explicitly conceived for nonlinear static and dynamic analyses of flexible structures. Numerical applications are presented to highlight the role of the tangential compliance mechanism on the hysteretic bending behavior of a typical steel strand.*

1 INTRODUCTION

Metallic strands can be regarded as composite elements which are made of helical wires twisted around a straight core and grouped in concentric layers. They are widespread structural members, used in many engineering applications, e.g. overhead electrical lines, tensile structures, guyed masts and towers.

When a strand is bent, wires tend to slip relatively one to each other, as a consequence of the axial force gradient generated along their length. The relative displacements are contrasted by friction forces, which are a function of the geometry of the internal structure, the material properties of the wires and the intra- and inter-layer contact pressures. If the forces which tend to activate sliding are greater than the friction ones, then a generic wire can experience relative displacements with respect to the neighbors. Interwire sliding phenomena makes the bending behavior of strands inherently non-linear and can significantly affect both the local response of the elements under cyclic loading (e.g. leading to the occurrence of fretting fatigue and wear [11, 18]) as well as the overall structural response. In fact, bending vibrations of metallic strands are characterized by an hysteretic damping mechanism, as it can be inferred from both quasi-static [17] as well as dynamic tests [21].

In the present paper, a new formulation to model the mechanical response of metallic strands undergoing a combination of axial load and planar bending is developed. Each wire of the strand is modeled as an elastic curved thin rod. A kinematic model is then introduced to relate the generalized strain variables of the strand to those of the wires. The stress-strain state of the wires is then evaluated starting from the analysis of the internal contact conditions. Friction is modeled through the classic Amontons-Coulomb law and the elastic tangential compliance of contact patches is accounted for, aiming at extending a previous authors' model taking into account the gross sliding only [3, 5, 7-9]. A non-holonomic material constitutive law in terms of the cross sectional generalized stress and strains of the Euler-Bernoulli beam theory is obtained, which can be exploited to describe cables as structural members reacting to a generic combination of axial force and bending. The sectional constitutive law is then implemented within a corotational beam element, previously developed and able to deal with large displacements and rotations and explicitly conceived for the nonlinear static and dynamic analysis of flexible structures [3, 6, 10].

The new mechanical model developed in this work is presented with reference to a simple strand made of a single layer of wires, in order to focus on the most important aspects of the proposed approach, while avoiding additional difficulties and cumbersome calculations stemming from a more complex internal geometry.

Numerical applications of the proposed cross sectional and finite element formulations are then presented for the case of a well documented steel strand, extensively studied in literature both for a combination of axial-torsional loads [4, 15, 16, 19, 20] as well as under the combined action of axial load and planar bending [9].

Within this context, systematic comparisons are carried out among the predictions of the new formulation and those of the model previously developed by the author and neglecting the interwire tangential contact compliance. The aim is to assess the effects of the tangential contact compliance on the hysteretic bending behavior of the strand. The latter, in turn, plays a key role in the modeling of the flexural vibrations of metallic strands.

2 GEOMETRY OF THE STRAND

A strand made of a single layer of six round wires, wrapped around an initially straight core wire, is considered in this work (Figure 1). The core and external wires have diameters d_0 and d_1, respectively. Each wire can be described as a curved thin rod, defined by the position of the centerline within a reference system attached to the strand centerline (axes $\{x_i\}$ (i=1, 2, 3)) as depicted in Figure 1. The centerline of the external wires is a circular helix spanned by the position vector:

$$\mathbf{x}(\theta) = \frac{R}{\tan(\alpha)}(\theta - \theta_0)\mathbf{e}_1 + R\cos(\theta)\mathbf{e}_2 + R\sin(\theta)\mathbf{e}_3 \tag{1}$$

where: $\{\mathbf{e}_i\}$ are the unit vectors of the axes $\{x_i\}$, R is the *helix radius*, i.e. the distance measured on the plane (x_2, x_3) from the centroid of the wire to that of the strand, α is the lay angle, i.e. the constant angle which the tangent vector to the helix defines with the strand centerline (axis x_1), and θ is the *swept angle*, i.e. the angle which the projection of the position vector $\mathbf{x}$ on the plane x_1=0 makes with the axis x_1 (see Figure 1(b)). The symbol θ_0 is adopted to denote the value of the swept angle at the strand cross section identified by the coordinate: x_1=0.

The external wires are assumed in contact with the core, but not among them. This condition, commonly referred to as *radial contact* condition (e.g. [1]), is typical of metallic strands.

As a consequence the helix radius in the reference (undeformed) configuration of the strand is the sum of the wire radii: R=0.5(d_0+d_1). The lay angle must be smaller than the maximum value α_{max}, that causes contact among the wires of a layer (see e.g. [2]).

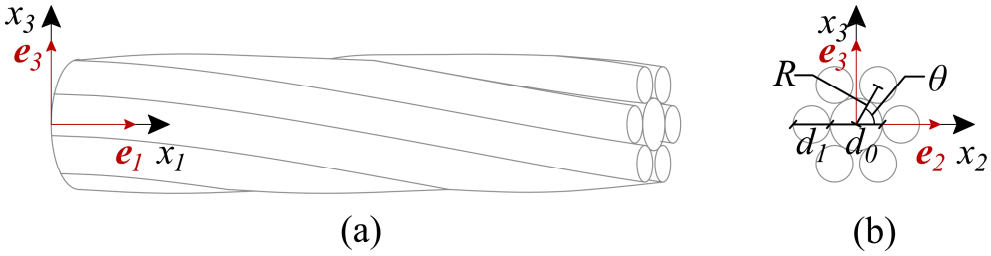

Figure 1: Geometry of the strand. (a) Side view. (b) Cross section.

3 MECHANICAL MODEL OF THE STRAND

The response of the strand to a constant axial force F_s and bending moment distribution M_s is first studied. The geometric nonlinearities, which typically affect the behavior of such slender structural elements, then, are fully considered within the framework of the corotational beam element formulation.

A “two-stage” approach is adopted in this work to tackle the axial-bending problem. As outlined e.g. in [1], the solution of the bending problem is superimposed on the initial state of stress and deformation due to the axial load. The axial force in a generic wire of the layer (tangent to the wire centerline), hence, can be expressed through the sum of a first contribution due to the axial load ($F_{w1,a}$) and a second one due to the bending of the strand ($F_{w1,b}$):

$$F_{w1} = F_{w1,a} + F_{w1,b} \tag{2}$$

3.1 Solution of the axial problem

The axial response of small-diameter metallic strands is substantially linear for a broad range of loads corresponding to typical service conditions (see e.g. the experimental results in [19] and the numerical simulations in [4, 9]). Accordingly, geometric nonlinearities due to the variation of the internal strand geometry, such as the contraction of the wire diameters (Poisson's effect) and the wire flattening (normal deformation of internal contact surfaces), can be practically neglected without significantly affecting the results.

A model for the linear coupled axial-torsional response of strands has been presented in [3, 9]. Whenever an axial load F_s is applied to the simple strand considered in the present paper, the axial elongation of the strand can be evaluated (under the assumption of zero torsional rotations of the cross sections) as:

$$\varepsilon_s = \frac{F_s}{EA_s} \tag{3}$$

where EA_s is the direct axial stiffness of the strand. By denoting as EA_0 and EA_1 the axial stiffness of the core and external wires, respectively, the strand stiffness EA_s is given by:

$$EA_s = EA_0 + 6EA_1 \cos^3(\alpha) \tag{4}$$

The axial force in the wires of the layer, then, can be expressed as:

$$F_{w1,a} = \cos^2(\alpha)\frac{EA_1}{EA_s}F_s \tag{5}$$

The axial force $F_{w1,a}$ is the same for all wires of the layer and constant along their length.

3.2 The contact model

The external wires are in contact with the core along a continuous helix (linear contact) with the same pitch of the wire centerline (see [8, 9] for more details). A system of radial (P) and tangential (T) forces per unit length of the wire centerline is first defined to model the interaction between a generic wire and the core, as shown in Figure 2. Then, the indefinite equilibrium equations of the wire in radial and tangential direction are written as:

$$\begin{cases} \dfrac{F_{w1,a} + F_{w1,b}}{\rho} - P = 0 \\ \dfrac{dF_{w1,b}}{dS} - T = 0, \ \text{ with: } \ T \le \mu P \end{cases} \tag{6a, b}$$

where ρ is the curvature radius of the wire centerline, which can be evaluated starting from equation (1) as: $\rho = R/\sin^2(\alpha)$ and μ is the friction coefficient of the contact interface.

The radial contact force P can be obtained by solving equation (6a). By neglecting the contribution $F_{w1,b}/\rho$ due to the bending of the strand, the following expression is obtained:

$$P \simeq \frac{F_{w1,a}}{\rho} \tag{7}$$

While introducing a great simplification in the analysis of the interwire contact conditions, the approximation introduced in (7) doesn't affect significantly the solution of the bending problem, as it has been shown numerically in [3] and analytically in [8] for the more general case of multi-layer metallic strands.

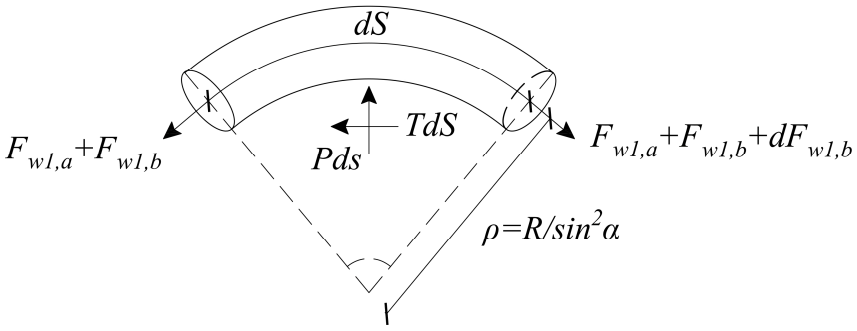

Figure 2: Equilibrium of an infinitesimal segment of the wire.

The tangential force T is related to the gradient of the wire axial force through the tangential equilibrium equation (6b). Since the term $F_{w1,a}$ stemming from the solution of the axial problem is constant along the length of the wire (see equation (5)), only the gradient of the bending contribution $F_{w1,b}$ to the total wire axial force is present in (6b).

The axial force gradient gives the wires the trend to slip with respect to the underlying core. This relative displacement is contrasted by the tangential contact force T, whose values are bounded by the Amontons-Coulomb inequality: $T \leq \mu P$. As long as $T < \mu P$, the sliding between the wire and the core is prevented (*no-sliding regime*). Relative displacements between the wire centerline (which will be denoted in the following as u_t) and the core, however, are present also in the no-sliding regime because of the tangential compliance of the contact surface. Goudreau et al. [12] studied the tangential compliance mechanism between the external wires and the core of a strand by exploiting the solution of the Hertzian contact problem for two parallel cylinders, made of the same material and pressed together. Accordingly, they introduced a non-linear relation between the relative displacement u_t and the tangential force per unit length T, herein re-stated as follows:

$$u_t = u_t^{gs}(P)\left(1-\left(1-\frac{T}{\mu P}\right)^{\frac{2}{3}}\right), \quad \text{with: } T \leq \mu P \tag{8}$$

where $u_t{}^{gs}(P)$ is the value of the relative displacement at the onset of gross sliding. The displacement $u_t{}^{gs}$ is a function of the normal contact force P. By denoting as $C_{Ti}(P)$ the initial value of the tangential compliance of the contact surface, $u_t{}^{gs}$ can be expressed as:

$$u_t^{gs} = \frac{3C_{Ti}(P)}{2\mu P} \tag{9}$$

The initial tangential compliance, in turn, depends upon the normal contact compliance $C_n(P)$ of the surface, according to the following relation, first proposed by Hobbs and Raoof [13] and later adopted also by Goudreau et al.:

$$C_{Ti}(P) = \frac{C_n(P)}{2(1-\nu)} \tag{10}$$

where ν is the Poisson coefficient of the material. A closed-form expression of the normal contact compliance $C_n(P)$ has been also derived by Goudreau et al. for the special case of ν=0.3, herein re-written, by denoting as E the Young modulus of the material, as:

$$C_n(P) = \frac{1}{E}\left(0.068505 + 1.1586 \ln\left(\sqrt{0.54945 \frac{E d_0}{P}\left(1 + \frac{d_1}{d_0}\right)}\right)\right) \tag{11}$$

A linear approximation of the model by Goudreau et al. is adopted in this work to characterize the tangential compliance between wires and core in the no-sliding regime. Based on the initial value of the tangential compliance, the following relation is introduced:

$$T \simeq \frac{1}{C_{Ti}(P)} u_t \leq \mu P \tag{12}$$

3.3 Solution of the bending problem

The nonlinear bending of multilayer strands has been studied in [3, 5, 7-9], starting from a description of the wire kinematics which accounts for the possible activation of gross-sliding phenomena, but neglects the effects of the tangential contact compliance. The aforementioned kinematic model will be augmented to account for the tangential compliance with the core wire.

By recalling equation (1) and assuming all wires as linearly elastic, the axial strain of a generic wire, ε_{w1}, can be expressed as the sum of the strain due to the axial load and to the bending, i.e.:

$$\varepsilon_{w1} = \frac{F_{w1}}{EA_1} = \frac{F_{w1,a}}{EA_1} + \frac{F_{w1,b}}{EA_1} = \varepsilon_{w1,a} + \varepsilon_{w1,b} \tag{13}$$

Two limit kinematic hypothesis can be introduced to evaluate $\varepsilon_{w1,b}$, which will be referred in the following as: *full-stick* and *full-slip* assumption. In the first case the tangential force T, due to the friction between the wire and the core, is assumed to be large enough to prevent the gross-sliding and the effect of the tangential compliance is neglected. As a consequence, the wire behaves as a part of an ideal planar cross section and the term $\varepsilon_{w1,b}$ can be simply evaluated according to the well-known Euler-Bernoulli kinematic model:

$$\varepsilon_{w1,b}^{full-stick} = \cos^2(\alpha) R \sin(\theta) \chi_s \tag{14}$$

where χ_s is the bending curvature with respect to the axis x_2 (see Figure 1).

In the second case, instead, the wire is free to slide with respect to the core and can be considered as individually bent. Under the full-slip assumption, hence, the term $\varepsilon_{w1,b}$ is identically equal to zero. By neglecting the tangential compliance, hence, the following incremental alternatives can be introduced to account for the possible transition between the no-sliding and the gross-sliding regime:

$$\dot{\varepsilon}_{w1,b} = \begin{cases} \dot{\varepsilon}_{w1,b}^{no-sliding} = \dot{\varepsilon}_{w1,b}^{full-stick} \\ \dot{\varepsilon}_{w1,b}^{gross-sliding} = 0 \end{cases} \tag{15a, b}$$

where a dot is adopted to denote the derivative with respect to a time variable t.

Equation (15a) can be modified in order to account for the effect of the tangential compliance between the external wires and the core, based on the solution of the bending problem in no-sliding regime which will be detailed in the following.

By recalling the definition of the relative displacement u_t introduced in Section 3.2, the term $\varepsilon_{w1,b}$ can be evaluated as:

$$\varepsilon_{w1,b}^{no-sliding} = \varepsilon_{w1,b}^{full-stick} + \frac{du_t}{dS} \tag{16}$$

By observing that $\sin(\alpha)\mathrm{d}S = R\mathrm{d}\theta$ (see e.g. [8]), from equations (6b), (12), (13) and (16) it's easy to derive the following equation for the axial force $F_{w1,b}$ in the *no-sliding* regime:

$$\frac{d^2 F_{w1,b}^{no-sliding}(\theta)}{d\theta^2} - \frac{R^2}{C_{Ti} EA_1 \sin^2(\alpha)} F_{w1,b}^{no-sliding}(\theta) = -\frac{R^3 \cos^2(\alpha)\chi_s}{C_{Ti}\sin^2(\alpha)}\sin(\theta) \tag{17}$$

The equation above can be easily solved under the assumption of constant curvature of the strand. The following expression is obtained:

$$F_{w1,b}^{no-sliding}(\theta) = \frac{\cos^2(\alpha) R\, EA_1\, \chi_s}{1 + \dfrac{C_{Ti}(P) EA_1 \sin^2(\alpha)}{R^2}}\sin(\theta) \tag{18}$$

Once the function $F_{w1,b}^{no-sliding}(\theta)$ is known, the corresponding axial strain can be evaluated and used in (15, a).

A numerical strategy to evaluate the wire axial force $F_{w1,b}(\theta)$, accounting for the possible transition between *no-sliding* and *gross-sliding* regime has been developed by the author in [3, 5, 7-9] and is adopted also in this work. The numerical procedure is based on a classic *Return-Map algorithm*, based on a "*no-sliding* prediction" and a "*gross-sliding* correction" (according to the alternative kinematic equations previously discussed). The Return-Map algorithm delivers the value of the gradient of the wire axial force which satisfies equation (16b), over a discrete set of control points defined along the pitch of the wire. Then, the wire axial force is obtained through numerical integration along the wire length.

Finally, starting from the knowledge of the wire axial force in all the wires of the layer the cross sectional moment of the strand can be evaluated, through simple equilibrium considerations, as:

$$M_s = M_s^{ind} + M_s^{add} = EI_{\min}\chi_s + M_s^{add} \tag{20}$$

The first term, M_s^{ind}, in (20) is linear and stems from the individual bending of the wires. It can be simply calculated as the product of the strand curvature and the minimum bending stiffness of the strand $EI_{\min}$. The latter can be evaluated by modeling the strand as a bundle of elastic curved thin rods, individually bent. The following expression can be obtained from [8]:

$$EI_{\min} = EI_0 + 6\cos^3(\alpha) EI_1 \tag{21}$$

The second term in (20), instead, accounts for the additional moment due to the bending contribution $F_{w1,b}(\theta)$ to the total axial force of the wires and can be evaluated (see e.g. [8]) as:

$$M_s^{add} = \sum_{i=1}^{6} R\cos(\alpha) F_{w1,b}(\theta_i)\sin(\theta_i) \tag{22}$$

3.4 The corotational beam element

The equations (3) and (20) fully define the relation between generalized stress and strain variables of the strand cross section, herein regarded as a plane Euler-Bernoulli beam. The proposed constitutive equations have been implemented within a corotational beam element

previously developed [3, 6, 10] to study the static and dynamic response of flexible structures taking into account geometrical and material nonlinearities.

4 NUMERICAL APPLICATION

The proposed strand mechanical model and beam finite element formulation are applied in this section to investigate the bending response of a strand made of steel wires, already studied in [9]. The geometric and material properties of the element are listed in Table 1.

d_0 (mm)	d_1 (mm)	α (deg)	E (GPa)	ν (-)
3.94	3.73	11.8	188	0.3

Table 1: Geometric and material parameters from [15].

The wire axial force in the no-sliding regime is shown in Figure 3 in terms of the amplification factor q_F of the force equivalent to $F_{w1,b}^{no-sliding}$ but obtained (under the full-stick assumption) by neglecting the tangential compliance. The factor q_F is plotted in Figure 3 as a function of the non-dimensional axial load parameter η, defined as the ratio between the axial load F_s and the Rated Tensile Strength of the element (here 137 kN – see [19]). From Figure 3, it can be observed that the inclusion of the tangential compliance mechanism in the strand mechanical model leads to a reduction of 10% of the maximum value which can be attained by the wire axial force $F_{w1,b}$ in the no-sliding regime with respect to the full-stick solution. The value of q_F depends on the non-dimensional loading parameter η. By increasing the axial load, indeed, the tangential compliance is reduced, as predicted by equations (10) and (11). As a consequence the axial force $F_{w1,b}$ tends toward the full-stick solution $F_{w1,b}^{full-stick}$ for increasing values of axial load. However, it's worth noting that the ratio q_F: (a) doesn't reach the unit value, even for very large values of the axial load, close to the RTS of the strand (for which, however, the assumption of linearly elastic material adopted in the proposed formulation ceases to be valid), and (b) is only slightly dependent on the axial load for the particular strand under consideration (variations of q_F are in the order of 3% for axial loads ranging from zero to the RTS value).

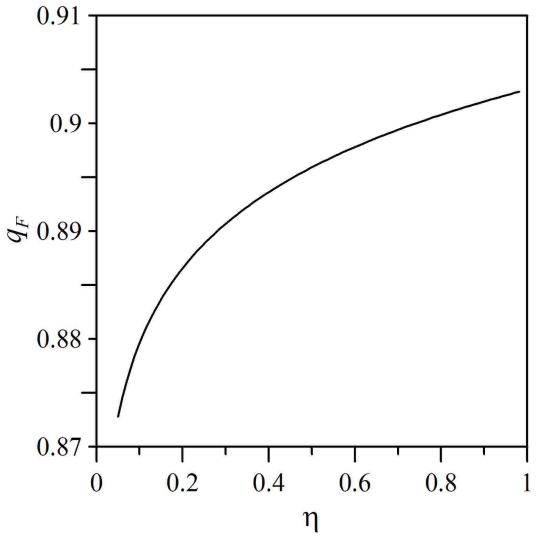

Figure 3: Ratio q_F vs. the non-dimensional axial load η.

Figure 4 shows a comparison among the moment-curvature diagrams of the strand cross section obtained with the proposed formulation, accounting for the tangential compliance of the internal contact surfaces, and those obtained by considering a full-stick initial behavior of the wires. Results are plotted for different values of the axial load parameter η in the range 0.1-0.25 (Figure 4(a)) and for different values of the friction coefficient μ in the range 0.3-0.7 (Figure 4(b)), in order to cover the interval of values typically considered in literature (e.g.: [8, 9, 14, 17]).

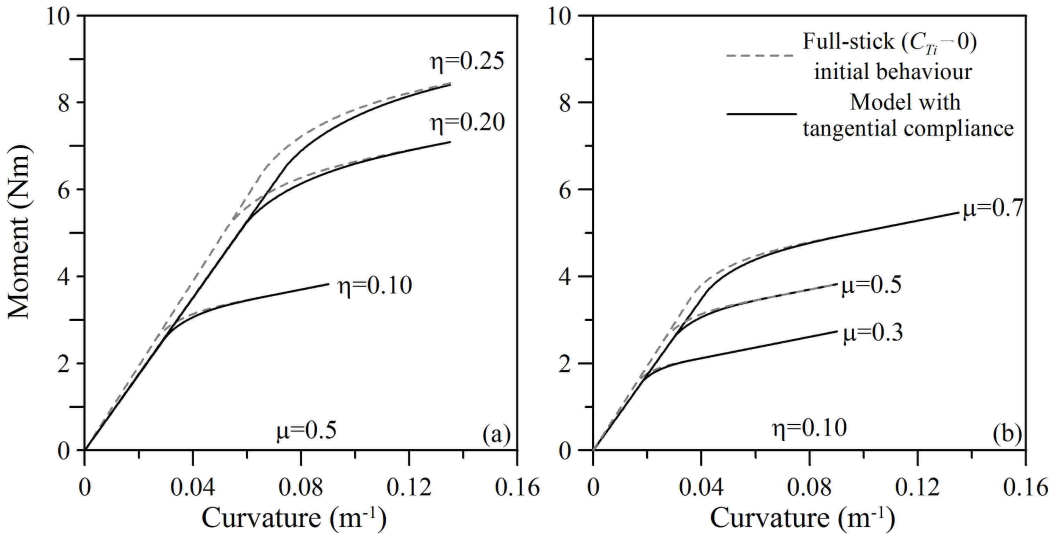

Figure 4: Moment-curvature diagrams. (a) Variation of the non-dimensional axial load η. (b) Variation of the friction coefficient μ.

The moment-curvature diagrams obtained with or without accounting for the tangential compliance mechanism are very similar, for the special strand considered in this work. In particular, the two models exhibit a similar dependency on the axial loading parameter η and on the friction coefficient μ. These parameters strongly influence the hysteretic bending behavior of metallic strands, as it has been extensively discussed e.g. in [8, 9]. The major effect of the tangential compliance between the core and the external wires is recognized in a reduction of about 10% of the value of the initial bending stiffness (i.e. the maximum bending stiffness of the strand section: $EI_{\max}$) of the cross section.

A typical experimental test setup for the characterization of the hysteretic bending behavior of metallic strands has been numerically simulated, in order to investigate the effect of the tangential contact compliance on the overall behavior of a strand specimen. A schematic representation of the numerical test setup is reported in Figure 5. The specimen is first loaded in the axial direction and then subjected to a transverse quasi-static load F. A mesh of 32 equally spaced corotational beam finite elements is adopted to represent the strand. Mesh refinements have been also considered in preliminary calculations to check the accuracy of the numerical model. A friction coefficient equal to 0.5 has been assumed in all the analyses.

Figures 6(a) and 6(b) show the load-displacement curves of the strand for a monotonically increasing vertical load and two different values of axial load, namely: η=0.1 (Figure 6(a)) and η=0.2 (Figure 6(b)). The load-displacement curves obtained both with and without considering the tangential compliance are plotted in Figures 6(a) and 6(b), together with the reference elastic solutions (plotted with red dashed lines) calculated under the full-stick ($EI_{\max}^{full-stick}$) and the full-slip ($EI_{\min}$) kinematic assumptions. The main effect of the tangential

compliance mechanism can be recognized in a reduction of the initial stiffness of the load-displacement curves, of about 10% for the slacker strand (η=0.1) and 1% in the other case (η=0.2). The influence of the tangential compliance mechanism on the specimen behavior, hence, is similar to the influence on the cross sectional response. However, a more pronounced dependency on the value of the axial load is observed for the overall specimen response than for the individual cross section behavior.

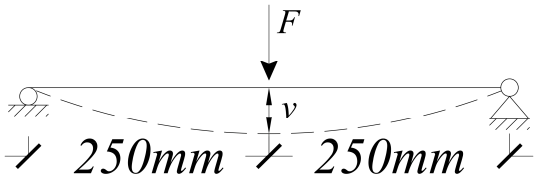

Figure 5: Structural scheme of the setup.

Additional numerical tests under cyclic vertical loading have shown that, for the special strand considered in this paper, the tangential compliance mechanism affects very slightly both the shape as well as the area of the hysteresis loops.

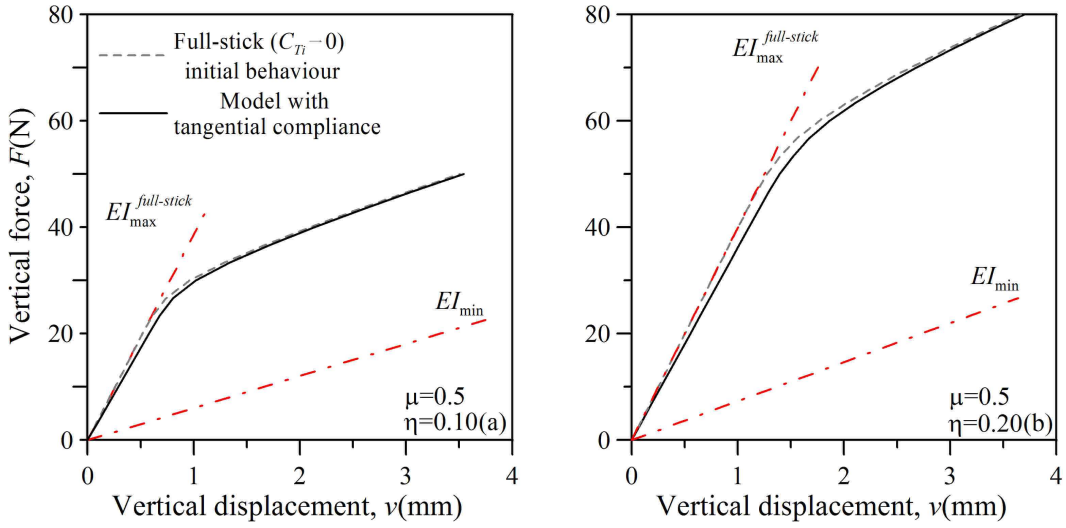

Figure 6: Bending behavior of the strand. (a) Monotonic loading. Load vs. displacement curve, μ=0.5 and η=0.10. (b) Monotonic loading. Load vs. displacement curve, μ=0.5 and η=0.20.

5 CONCLUSIONS

A new mechanical model to study the mechanical response of metallic cables undergoing a combination of axial load and planar bending has been developed for a single-layer strand. The proposed formulation is based on a detailed analysis of the internal contact conditions between the external wires and the core of the strand. Friction is modeled through the classic Amontons-Coulomb law and the elastic tangential compliance of contact patches is accounted for, aiming at extending a previous authors' model taking into account the gross sliding only. A nonlinear and non-holonomic relation between the sectional generalized stress and strains of the Euler-Bernoulli beam theory is formulated and implemented in a corotational beam element suitable for nonlinear static and dynamic analyses of flexible structures.

The proposed strand mechanical model and finite element formulation have been applied to characterize the hysteretic bending behavior of a common structural steel strand. Numerical

analyses have been carried out to show the influence of the tangential contact compliance mechanism between the external wires and the core, both on the cross sectional behavior as well as on the overall response of a strand specimen tested on a typical experimental test rig.

For the particular strand considered in this work, it is found that the tangential contact compliance mainly influence the initial bending stiffness of the strand, while it has only a small effect on the shape of the cross sectional moment-curvature diagrams and on the overall hysteretic behavior. Ongoing research is devoted to the extension of the proposed formulation to other strand geometries, including the case of multi-layer elements.

REFERENCES

[1] A. Cardou, C. Jolicoeur, Mechanical models of helical strands, *Applied Mechanics Reviews* (ASME), **50**, 1-14, 1997.

[2] G.A. Costello, *Theory of wire ropes*, Springer-Verlag, New York (USA), 1990.

[3] F. Foti, *A corotational beam element and a refined mechanical model for the nonlinear dynamic analysis of cables*, Doctoral Dissertation, Politecnico di Milano, Milan (Italy), 2013.

[4] F. Foti, A. de Luca di Roseto, Analytical and Finite Element modelling of the elastic-plastic behaviour of metallic strands under axial-torsional loads, Submitted to: *International Journal of Mechanical Sciences*, 2016.

[5] F. Foti, L. Martinelli, A model for the cyclic biaxial bending of stranded ropes (in Italian), *XX Congresso AIMETA 2011*, Bologna (Italy), (ISBN:9788890634017) 2011.

[6] F. Foti, L. Martinelli, Dynamics of co-rotational beam elements – some aspects on the kinetic energy and the integration of the equations of motion. J. Eberhardsteiner et.al. eds. *Proceedings of the 6th European Congress on Computational Methods in Applied Sciences and Engineering (ECCOMAS)*, Vienna (Austria), (ISBN:978-3-9502481-9-7) 2012.

[7] F. Foti, L. Martinelli, A corotational beam element to model the hysteretic bending behavior of metallic wire ropes, *The 4th Canadian Conference on Nonlinear Solid Mechanics (CanCNSM 2013)*, Montreal (Canada), 2013.

[8] F. Foti, L. Martinelli, An analytical approach to model the hysteretic bending behavior of spiral strands, *Applied Mathematical Modelling*. in press (http: //dx.doi.org/ 10.1016/j.apm.2016.01.063), 2016.

[9] F. Foti, L. Martinelli, Mechanical modeling of metallic strands subjected to tension, torsion and bending, Submitted to: *International Journal of Solids and Structures*, 2016.

[10] F. Foti, L. Martinelli, F. Perotti, Numerical integration of the equations of motion of structural systems undergoing large 3D rotations: dynamics of corotational slender beam elements, *Meccanica*, **50**, 751-765, 2015.

[11] M Giglio, A Manes, Bending fatigue on a metallic wire rope for aircraft rescue hoist, *Engineering Failure Analysis*, **10**, 223-235, 2003.

[12] S Goudreau, F Charette, C Hardy, L Cloutier, Bending Energy Dissipation of Simplified Single-Layer Stranded Cable, Journal of Engineering Mechanics (ASCE), **124**, 811-817, 1998.

[13] R.E. Hobbs, M. Raoof, Interwire slippage and fatigue prediction in stranded cables for TLP tethers. C. Chryssostomiolis and J.J. Connor eds. *Proceedings of the 3rd International Conference on Behaviour of offshore structures*, Vol. 2, Hemisphere Publishing/McGraw-Hill, New York (USA), 77-99, 1982.

[14] K.J. Hong, A. Der Kiureghian, J.L. Sackman, Bending behavior of helically wrapped cables, Journal of Engineering Mechanics (ASCE), **131**, 500-511, 2005.

[15] W.G. Jiang, M.S. Yao, J.M. Walton, A concise finite element model for simple straight wire rope strand, *International Journal of Mechanical Sciences*, 41, 143-161, 1999.

[16] R. Judge, Z. Yang, S.W. Jones, G. Beattie, Full 3D finite element modelling of spiral strand cables, *Construction and Building Materials*, **35**, 452-459, 2012.

[17] K.O. Papailiou, On the bending stiffness of transmission line conductors, *IEEE Transaction on Power Delivery*, **12**, 1576-1588, 1997.

[18] M.A. Urchegui, W. Tato, X. Gómez, Wear Evolution in a Stranded Rope Subjected to Cyclic Bending, *Journal of Materials Engineering and Performance*, **17**, 550-560, 2008.

[19] W.S. Utting, N. Jones, The response wire rope strands to axial tensile loads – Part I. Experimental results and theoretical predictions, *International Journal of Mechanical Sciences*, **29**, 605-619, 1987.

[20] W.S. Utting, N. Jones, Response of wire rope strands to axial tensile loads. Part II: comparisons of experimental results and theoretical predictions, *International Journal of Mechanical Sciences*, **29**, 621-636, 1987.

[21] Z.H. Zhu, S.A. Meguid, Nonlinear FE-based investigation of flexural damping of slacking wire cables, *International Journal of Solids and Structures*, **44**, 5122–5132, 2007.

ECCOMAS Congress 2016
VII European Congress on Computational Methods in Applied Sciences and Engineering
M. Papadrakakis, V. Papadopoulos, G. Stefanou, V. Plevris (eds.)
Crete Island, Greece, 5–10 June 2016

3D BEAM-COLUMN FINITE ELEMENT UNDER NON-UNIFORM SHEAR STRESS DISTRIBUTION DUE TO SHEAR AND TORSION

Paolo Di Re[1], Daniela Addessi[1] and Filip C. Filippou[2]

[1]Department of Structural and Geotechnical Engineering, University of Rome, Sapienza
via Eudossiana 18, Rome, 00184, Italy
e-mail: {paolo.dire,daniela.addessi}@uniroma1.it

[2] Department of Civil and Environmental Engineering, University of California, Berkeley
731 Davis Hall, Berkeley, CA, United States
e-mail: filippou@berkeley.edu

Keywords: Fiber section models, Mixed Formulation, Warping, Shear and torsion, Damage.

Abstract. *The paper discusses the application of a 2-node, three-dimensional (3D) beam-column finite element with an enhanced fiber cross-section model to the inelastic response analysis of concrete members. The element accounts for the local distribution of strains and stresses under the coupling of axial, flexural, shear, and torsional effects with an enriched kinematic description that accounts for the out-of-plane deformations of the cross-section. To this end the warping displacements are interpolated with the addition of a variable number of local degrees of freedom. The material response is governed by a 3D nonlinear stress-strain relation with damage that describes the degrading mechanisms of typical engineering materials under the coupling of normal and shear stresses. The element formulation is validated by comparing the numerical results with measured data from the response of two prismatic concrete beams under torsional loading and with standard beam formulations.*

1 INTRODUCTION

Beam-column finite elements are widely used for describing the inelastic response of structural members in large scale simulations, because of the optimal balance between accuracy and computational efficiency they offer.

Among the different beam finite element models *force-based* and *mixed* formulations [1, 2, 3, 4] have proven superior to the classical *displacement-based* models under large inelastic, cyclic deformations, even with the slight increase in computational cost for the element state determination. In this framework, many researchers focused their efforts on the development of an efficient, discrete *fiber cross-section model* [5, 6] for effectively capturing the multi-axial coupling of the beam stress resultants under general constitutive material relations. While classical Euler-Bernoulli beam formulations assume that plane sections remain plane and normal to the axis and are unable to capture the effect of shear and torsion, recent studies have proposed enhanced models that account for these effects [7, 8, 9, 10]. Nonetheless, no existing model appears to give a complete and realistic representation of the cross-section warping with the resulting shear stresses and strains. According to [11] existing models fail to reproduce accurately the interaction of the shear and normal stresses along the beam axis, the local response near the boundaries, and the shear lag phenomenon.

This paper extends the 2-node 3D beam-column finite element (FE) in [12] to reinforced concrete beams. The formulation by LeCorvec is based on a modified Hu-Washizu variational potential that leads to the definition of a four-field mixed formulation. With respect to the standard Hu-Washizu mixed formulation with only three independent fields, LeCorvec's formulation introduces as fourth additional field the out-of-plane displacements due to warping of the element cross-section [12]. These displacements are interpolated at two independent levels: along the axis and over the cross-section. The degrees of freedom associated with the resulting interpolation functions constitute additional independent variables of the element allowing it to capture the evolution of the warping displacements during the loading process, and the coupling between the shear and torsion with the normal stress components.

To correctly reproduce the nonlinear behavior of the cross-section, a fiber discretization is introduced. Hence, stress and strain variables are determined at each discrete fiber and then integrated over the area to obtain the generalized section quantities. To describe the damaging mechanisms typical of brittle-like engineering materials, the isotropic 3D damage model in [15] is adopted. This considers the non-symmetric response, in tension and compression, and the unilateral effect, observed during cyclic load patterns for this material type.

The proposed FE is validated by comparing the numerical results of plain concrete (PC) and reinforced concrete (RC) beams under end torque with experimental measurements and by confronting these results with those of standard FE beam models.

2 FINITE ELEMENT FORMULATION

This section summarizes the salient features of the 3D beam-column FE formulation in [12] with the description of the warping displacements for the cross section under inelastic nonlinear material response.

The FE element formulation is based on the assumption of small end node displacements and small strains, because nonlinear geometry effects are accounted for with the corotational formulation during the transformation of the nodal response variables.

Figure 1 shows the global FE reference system (O, X, Y, Z) together with the nodal displacement vector components. These are the twelve degrees of freedom (DOFs) of a standard 3D

beam-column element, that is three translations (listed in the vectors $\mathbf{u}_{I/J}$) and three rotations (listed in the vectors $\boldsymbol{\theta}_{I/J}$) at each node:

$$\mathbf{u} = \left\{\mathbf{u}_I^T \;\; \boldsymbol{\theta}_I^T \;\; \mathbf{u}_J^T \;\; \boldsymbol{\theta}_J^T\right\}^T \tag{1}$$

The corresponding nodal force components are collected in the vector:

$$\mathbf{p} = \left\{\mathbf{p}_I^T \;\; \mathbf{m}_I^T \;\; \mathbf{p}_J^T \;\; \mathbf{m}_J^T\right\}^T \tag{2}$$

with $\mathbf{p}_{I/J}$ and $\mathbf{m}_{I/J}$ being the force and moment vectors at node I/J.

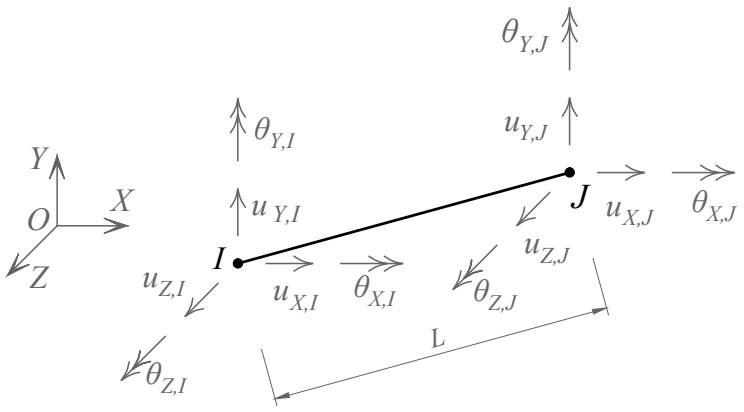

Figure 1: Global FE reference system (undeformed configuration): nodal traslation and rotation components.

By restraining the rigid body motions of the element, the basic reference system (I, x, y, z) is introduced (Figure 2), with x parallel to the axis directed from node I to node J and y and z lying in the plane of the element cross-section. Hence, the basic displacement vector $\mathbf{v}$, also called the element deformation vector, can be defined:

$$\mathbf{v} = \{u_{x,J} \quad \theta_{z,I} \quad \theta_{z,J} \quad \theta_{x,J} \quad \theta_{y,I} \quad \theta_{y,J}\}^T \tag{3}$$

where $u_{x,J}$ is the translation of node J parallel to the local axis x, $\theta_{z,I/J}$ and $\theta_{y,I/J}$ are the rotations at node I/J about the z and y–axis, respectively, and $\theta_{x,J}$ is the rotation at node J about the x–axis. The basic displacement vector $\mathbf{v}$ is obtained from the global vector $\mathbf{u}$ according to:

$$\mathbf{v} = \mathbf{a}_g\,\mathbf{u} \quad with \quad \mathbf{a}_g = \begin{bmatrix} -1 & 0 & 0 & 0 & 0 & 0 & 1 & 0 & 0 & 0 & 0 & 0 \\ 0 & 1/L & 0 & 0 & 0 & 1 & 0 & -1/L & 0 & 0 & 0 & 0 \\ 0 & 1/L & 0 & 0 & 0 & 0 & 0 & -1/L & 0 & 0 & 0 & 1 \\ 0 & 0 & 0 & -1 & 0 & 0 & 0 & 0 & 0 & 1 & 0 & 0 \\ 0 & 0 & -1/L & 0 & 1 & 0 & 0 & 0 & 1/L & 0 & 0 & 0 \\ 0 & 0 & -1/L & 0 & 0 & 0 & 0 & 0 & 1/L & 0 & 1 & 0 \end{bmatrix} \tag{4}$$

where $\mathbf{a}_g$ is the kinematic matrix and L is the undeformed element length. The basic force vector $\mathbf{q}$, corresponding to the deformation vector $\mathbf{v}$, is defined as:

$$\mathbf{q} = \{p_{x,J} \quad m_{z,I} \quad m_{z,J} \quad m_{x,J} \quad m_{y,I} \quad m_{y,J}\}^T \tag{5}$$

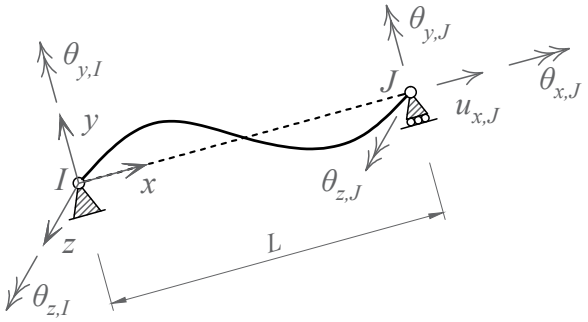

Figure 2: Basic FE reference system (deformed configuration): basic displacement components.

where $p_{x,J}$ is the force at node J in the direction of the local x–axis, $m_{z,I/J}$ and $m_{y,I/J}$ are the moments at node I/J about the z and y–axis, respectively, and $m_{x,J}$ is the moment at node J about the x–axis.

Because of the virtual work equivalence, the element stiffness matrix $\hat{\mathbf{k}}$ and the element force vector $\mathbf{p}$ in the global system can be defined through the transpose of the matrix $\mathbf{a}_g$, [2]:

$$\hat{\mathbf{k}} = \mathbf{a}_g^T \, \mathbf{f}^{-1} \, \mathbf{a}_g \qquad \text{and} \qquad \mathbf{p} = \mathbf{a}_g^T \, \mathbf{q} \tag{6}$$

where $\mathbf{f}$ is the element basic flexibility matrix, whose derivation is discussed next.

Under the assumption of the cross-section remaining rigid in plane and out of plane, the generalized section displacement vector $\mathbf{u}_s(x)$ is defined in the basic coordinate system as:

$$\mathbf{u}_s(x) = \{u(x) \quad \theta_z(x) \quad v(x) \quad \theta_x(x) \quad \theta_y(x) \quad w(x)\}^T \tag{7}$$

where $u(x)$, $v(x)$ and $w(x)$ are the translation components of the beam axis, and $\theta_x(x)$, $\theta_y(x)$ and $\theta_z(x)$ are the rotations of the cross-section (Figure 3(a)).

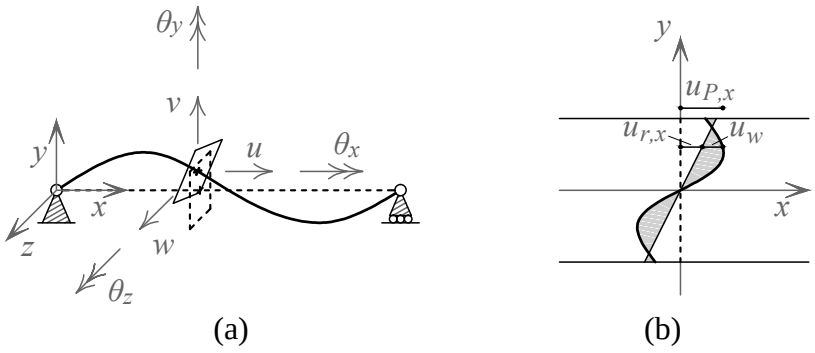

Figure 3: Cross-section rigid (a) and warping (b) displacements.

To describe the warping of the cross-section, the assumption of a rigid cross section is partially removed, by accounting for the out-of-plane deformations of the cross section, which still remains rigid in its plane. Hence, the displacement $\mathbf{u}_P(x, y, z)$ at the generic point P is expressed as the composition of the rigid part $\mathbf{u}_r(x, y, z) = \mathbf{a}_s(y, z) \, \mathbf{u}_s(x)$ and the displacement

$\mathbf{u}_w(x,y,z)$ due to the warping (Figure 3(b)):

$$\mathbf{u}_P(x,y,z) = \left\{ \begin{array}{c} u_{P,x}(x,y,z) \\ u_{P,y}(x,y,z) \\ u_{P,z}(x,y,z) \end{array} \right\} = \mathbf{a}_s(y,z)\,\mathbf{u}_s(x) + \mathbf{u}_w(x,y,z) \tag{8}$$

where $\mathbf{a}_s(y,z)$ is the compatibility operator, defined as:

$$\mathbf{a}_s(y,z) = \left[\begin{array}{cccccc} 1 & -y & 0 & 0 & z & 0 \\ 0 & 0 & 1 & -z & 0 & 0 \\ 0 & 0 & 0 & y & 0 & 1 \end{array} \right] \tag{9}$$

By applying the same operator, the strain vector is also evaluated as the sum of the rigid part $\boldsymbol{\epsilon}_r(x,y,z) = \mathbf{a}_s(y,z)\,\mathbf{e}(x)$ and that associated to the warping $\boldsymbol{\epsilon}_w(x,y,z)$:

$$\boldsymbol{\epsilon}(x,y,z) = \left\{ \begin{array}{c} \epsilon_x(x,y,z) \\ \gamma_{xy}(x,y,z) \\ \gamma_{xz}(x,y,z) \end{array} \right\} = \mathbf{a}_s(y,z)\,\mathbf{e}(x) + \boldsymbol{\epsilon}_w(x,y,z) \tag{10}$$

The generalized section deformation vector $\mathbf{e}(x)$ is:

$$\mathbf{e}(x) = \left\{ \begin{array}{c} \epsilon_G(x) \\ \chi_z(x) \\ \gamma_y(x) \\ \chi_x(x) \\ \chi_y(x) \\ \gamma_z(x) \end{array} \right\} = \left\{ \begin{array}{l} u'(x) \\ \theta'_z(x) \\ v'(x) - \theta_z(x) \\ \theta'_x(x) \\ \theta'_y(x) \\ w'(x) + \theta_y(x) \end{array} \right\} \tag{11}$$

where $\epsilon_G(x)$ is the axial strain, $\chi_z(x)$ and $\chi_y(x)$ are the curvatures, $\chi_x(x)$ the torsion rate of twist, and $\gamma_y(x)$ and $\gamma_z(x)$ the shear strains. As a consequence of the assumption that the section remains rigid in its plane, the warping displacement field has non-zero values only in the x direction, i.e.

$$\mathbf{u}_w(x,y,z) = \left\{ u_w(x,y,z) \quad 0 \quad 0 \right\}^T$$

Hence, the vector $\boldsymbol{\epsilon}_w(x,y,z)$ of the strains due to the warping displacements $u_w(x,y,z)$ becomes:

$$\boldsymbol{\epsilon}_w(x,y,z) = \left\{ \begin{array}{ccc} \frac{\partial u_w(x,y,z)}{\partial x} & \frac{\partial u_w(x,y,z)}{\partial y} & \frac{\partial u_w(x,y,z)}{\partial z} \end{array} \right\}^T \tag{12}$$

The stress components that are work conjugate with the strain quantities in $\boldsymbol{\epsilon}(x,y,z)$ are collected in the stress vector $\boldsymbol{\sigma}(x,y,z) = \left\{ \sigma_x(x,y,z) \quad \tau_{xy}(x,y,z) \quad \tau_{xz}(x,y,z) \right\}^T$, where σ_x is the normal stress along the beam axis direction, and τ_{xy} and τ_{xz} are the shear stresses in the plane of the cross-section parallel to the y and z–axis, respectively. With the virtual work equivalence the generalized stress vector $\mathbf{s}(x)$ is:

$$\mathbf{s}(x) = \int_A \mathbf{a}_s^T(y,z)\,\boldsymbol{\sigma}(x,y,z)\,dA = \left\{ \begin{array}{c} N(x) \\ M_z(x) \\ T_y(x) \\ M_x(x) \\ M_y(x) \\ T_z(x) \end{array} \right\} \tag{13}$$

where A is the cross-section area, $N(x)$ the axial stress, $M_z(x)$ and $M_y(x)$ are the bending moments, $M_x(x)$ the torsional moment, and $T_y(x)$ and $T_z(x)$ the generalized shear stresses.

From the element equilibrium in the undeformed configuration the stress vector $\mathbf{s}(x)$ can be expressed in terms the basic element force vector $\mathbf{q}$:

$$\mathbf{s}(x) = \mathbf{b}(x)\,\mathbf{q} + \mathbf{s}_p(x) \quad , \quad \mathbf{b}(x) = \begin{bmatrix} 1 & 0 & 0 & 0 & 0 & 0 \\ 0 & \frac{x}{L}-1 & \frac{x}{L} & 0 & 0 & 0 \\ 0 & -\frac{1}{L} & -\frac{1}{L} & 0 & 0 & 0 \\ 0 & 0 & 0 & 1 & 0 & 0 \\ 0 & 0 & 0 & 0 & \frac{x}{L}-1 & \frac{x}{L} \\ 0 & 0 & 0 & 0 & \frac{1}{L} & \frac{1}{L} \end{bmatrix} \tag{14}$$

where $\mathbf{b}(x)$ is the equilibrium matrix and $\mathbf{s}_p(x)$ the generalized section stresses under element loading. In addition to these forces, the force field $p_w(x, y, z)$ is work conjugate with the warping displacement $u_w(x, y, z)$ and arises at cross-sections with constrained warping displacements. In the element formulation in [12] the warping displacements u_w are treated as internal DOFs that are condensed out during the element state determination, as described in the next section. Consequently, only the standard twelve DOFs in (1) are associated with the global DOFs of the structural model.

2.1 Warping displacement interpolation

The study in [12] interpolates the warping displacement field $u_w(x, y, z)$ along the element axis x independently from the interpolation over the cross-section. The Gauss-Lobatto integration rule is used along the element axis using n_w points and 1D Lagrange polynomials $\mathrm{N}_i(x)$. At each Gauss-Lobatto point x_i, the warping displacements are interpolated over the cross-section by subdividing it into several rectangular patches with a regular distribution of interpolation points in each, for a total of s_w points (Figure 4). This approach defines a set of m_w 2D interpolation functions $\mathrm{M}_j(y, z)$ for the warping DOFs.

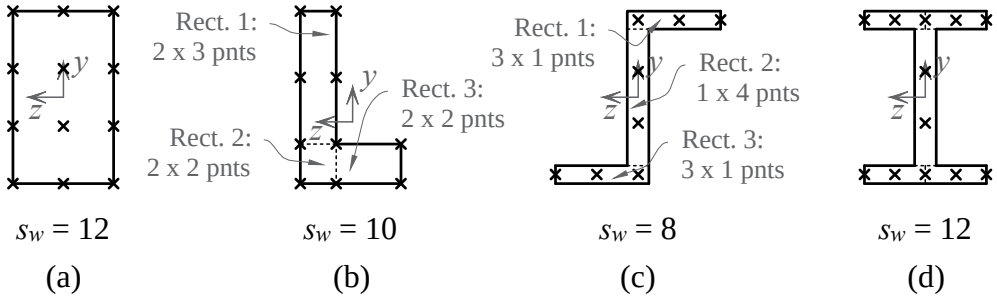

Figure 4: Warping interpolation points over the element cross-section.

This study explores the use of Hermite polynomials for the warping displacements in addition to the Lagrange polynomials used in [12]. For the Lagrange polynomials only one internal DOF is required at each integration point of the warping displacement u_w (Figure 5(a)) and the total number m_w of warping DOFs is equal to the number s_w of integration points. In contrast, Hermite polynomials required three internal DOFs at each integration point, one for the warping displacement u_w, and two for the derivatives $\partial u_w/\partial y$ and $\partial u_w/\partial z$ (Figure 5(b)). In this

case the total number m_w of warping DOFs is equal to three times the number s_w of integration points, $m_w = 3\,s_w$.

Henceforth, $u_{w,ij}$ denotes the generic j-th warping DOF at section x_i, coinciding with the displacements u_w for Lagrange polynomials, and with the displacements u_w and their derivatives for Hermite polynomials:

$$\begin{aligned} \{u_{w,1}, \quad u_{w,2}, \quad u_{w,3}, \ldots\} &= \{u_w^{pnt\,1}, \quad u_w^{pnt\,2}, \quad u_w^{pnt\,3}, \ldots\} \quad Lagrange \\ \{u_{w,1}, \quad u_{w,2}, \quad u_{w,3}, \ldots\} &= \{u_w^{pnt\,1}, \quad \tfrac{\partial u_w^{pnt\,1}}{\partial y}, \quad \tfrac{\partial u_w^{pnt\,1}}{\partial z}, \ldots\} \quad Hermite \end{aligned} \tag{15}$$

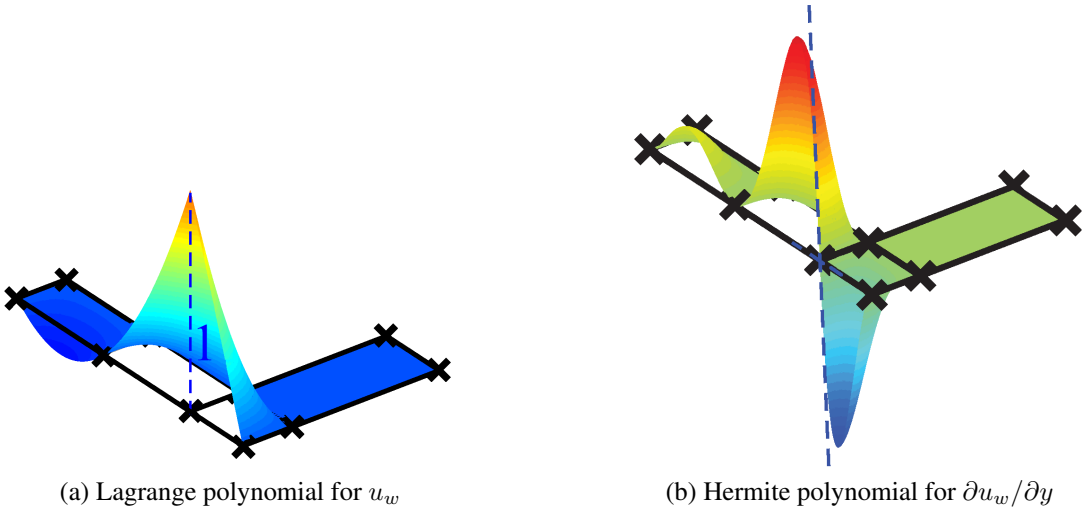

(a) Lagrange polynomial for u_w (b) Hermite polynomial for $\partial u_w/\partial y$

Figure 5: Example of polynomial interpolation function in a cross-section composed by a set of rectangular portions: L-shaped section of Figure 4(b), $m_w = 10$ for Lagrange and $m_w = 30$ for Hermite.

The interpolation of the warping displacement field $u_w(x, y, z)$ thus is:

$$u_w(x, y, z) = \sum_{i=1}^{n_w} \mathrm{N}_i(x)\, u_{w,i}(x_i, y, z) = \sum_{i=1}^{n_w} \mathrm{N}_i(x)\, \mathbf{M}(y, z)\, \mathbf{u}_{w,i} \tag{16}$$

with the following expression for the interpolation of $u_{w,i}(x_i, y, z)$ at section i:

$$u_{w,i}(x_i, y, z) = \sum_{j=1}^{m_w} \mathrm{M}_j(y, z)\, u_{w,ij} = \mathbf{M}(y, z)\, \mathbf{u}_{w,i} \tag{17}$$

$\mathbf{u}_{w,i}$ is a column vector with all m_w warping DOFs $u_{w,ij}$ at section i (following the order in Equation (15)) and $\mathbf{M}(y, z)$ is a row vector with all m_w shape functions $M_j(y, z)$ defined over the cross-section.

It is important to point out the following difference between Lagrange and Hermite polynomials. Because for the Lagrange polynomials all warping DOFs correspond to warping displacement values the condition of warping restraint $u_{w,ij} = 0$ can be applied to each polynomial separately, so that even a single point or a specific portion of the cross-section can be restrained. In contrast, for the Hermite polynomials some of the warping DOFs are the derivatives of the warping displacement field in the cross-section. This requires the restraint of all displacements of the particular cross-section at the same time, thus ensuring that $u_w = \partial u_w/\partial y = \partial u_w/\partial z = 0$ is satisfied on the cross-section.

The vector $\mathbf{p}_{w,i}$ collecting the warping forces $p_{w,i}$ at the points located on the i-th section can be defined, which is work conjugated with $\mathbf{u}_{w,i}$.

2.2 Element variational formulation

This section describes the main aspects of the element formulation and focuses on the role played by the warping DOFs in the governing equations.

The equations governing the element state determination are derived on the basis of a modified Hu-Wahizu variational principle, depending on the four independent fields $\mathbf{u}_s(x)$, $\mathbf{e}(x)$, $\boldsymbol{\sigma}(x,y,z)$ and $u_w(x,y,z)$ [12]:

$$\Pi(\mathbf{u}_s, \mathbf{e}, \boldsymbol{\sigma}, u_w) = \int_V \boldsymbol{\sigma}^T \mathbf{a}_s \left[\mathbf{e}(\mathbf{u}_s) - \mathbf{e}\right] dV + \int_V W(\mathbf{e}, \boldsymbol{\epsilon}_w)\, dV - \mathbf{u}^T \mathbf{p} - \int_0^L \mathbf{u}_s^T \mathbf{p}_s\, dx \quad (18)$$

where $W(\mathbf{e}, \boldsymbol{\epsilon}_w)$ is the internal potential energy and $\mathbf{p}_s$ denotes the loads along the element axis. The stationarity of Π with respect to the four independent fields gives the following governing equations:

Stationarity with respect to:	Governing equation:	
$\mathbf{u}_s(x)$	$\mathbf{a}_g^T \mathbf{q} = \mathbf{p} + \mathbf{p}_{rp}$	(19a)
$\mathbf{e}(x)$	$\boldsymbol{\sigma}(x,y,z) = \hat{\boldsymbol{\sigma}}[\boldsymbol{\epsilon}(x,y,z)]$	(19b)
$\boldsymbol{\sigma}(x,y,z)$	$\mathbf{v} = \int_0^L \mathbf{b}^T(x)\, \mathbf{e}(x)\, dx$	(19c)
$u_w(x,y,z)$	$\mathbf{p}_{w,i} = \int_0^L \frac{\partial \mathrm{N}_i}{\partial x} \mathbf{s}_w^x\, dx + \int_0^L \mathrm{N}_i\, \mathbf{s}_w^{yz}\, dx$	(19d)

The first three (19a), (19b) and (19c) are the equations of the standard three-field mixed formulation [4], and govern the element equilibrium, the material constitutive law and the element compatibility, respectively. The vector $\mathbf{p}_{rp}$ collects the nodal forces under element loading. Equation (19d), represents the section equilibrium equation under warping displacements. The stresses $\mathbf{s}_w^x$ and $\mathbf{s}_w^{yz}$ are the generalized stresses due to section warping, as defined by the integral of the material stresses $\boldsymbol{\sigma}(x,y,z)$ over the cross-section:

$$\mathbf{s}_w(x) = \left\{ \begin{array}{c} \mathbf{s}_w^x(x) \\ \mathbf{s}_w^{yz}(x) \end{array} \right\} = \left\{ \begin{array}{c} \int_A \left[\mathbf{a}_w^x(y,z)\right]^T \boldsymbol{\sigma}(x,y,z)\, dA \\ \int_A \left[\mathbf{a}_w^{yz}(y,z)\right]^T \boldsymbol{\sigma}(x,y,z)\, dA \end{array} \right\} \quad (20)$$

with $\mathbf{a}_w^x(y,z)$, $\mathbf{a}_w^{yz}(y,z)$ being $3 \times m_w$ matrices of the following form:

$$\mathbf{a}_w^x(y,z) = \left[\begin{array}{c} \mathbf{M}(y,z) \\ \mathbf{0} \\ \mathbf{0} \end{array} \right] \quad , \quad \mathbf{a}_w^{yz}(y,z) = \left[\begin{array}{c} \mathbf{0} \\ \frac{\partial \mathbf{M}(y,z)}{\partial y} \\ \frac{\partial \mathbf{M}(y,z)}{\partial z} \end{array} \right] \quad (21)$$

The nonlinear system of equations (19) are solved by iteration of their linearized form [12].

3 CORRELATION STUDIES

This section discusses the correlation study of two specimens for validating the 3d beam formulation. The Matlab toolbox FEDEASLab [16] is used for investigating the capability of the

model to represent the damage evolution of frame members when relevant warping deformations arise. To this end, two different prismatic beams under end torsional loads are considered, from the experimental tests of plain concrete specimens by [17] and of RC specimens by [18]. In this framework, advantages and disadvantages of the use of Hermite polynomials vs. Lagrange polynomials for the warping interpolation functions are discussed.

The Gauss-Lobatto integration rule is adopted for the integrals along the element axis together with a fiber discretization of the cross-section using the mid-point rule [6]. The nonlinear material relation of the following section is used for each concrete fiber and the classical J2 plasticity model is used for the steel bars.

3.1 Damage model

In this study the constitutive behavior of concrete is described with the damage material model in [15]. The model uses a scalar damage variable D to define the relation between the strain tensor $\mathbf{E}$ and the stress tensor $\mathbf{\Sigma}$:

$$\mathbf{E} = \frac{(1+\nu)\mathbf{\Sigma} - \nu\,\mathrm{tr}(\mathbf{\Sigma})\,\mathbf{I}}{E(1-D)} \tag{22}$$

where E in the material Young modulus and ν the Poisson ratio, and $\mathbf{I}$ is the second order identity tensor. The damage variable D, bounded in the range $[0 \quad 1]$, where $D = 0$ correponds to initial undamaged state and $D = 1$ to the complete degraded state, is a function of a single variable Y, which is the combination of two strain measures Y_t and Y_c for cracking (tensile state) and crushing (compressive state), respectively. The combination gives:

$$Y = r\,Y_t + (1-r)\;Y_c \qquad \text{with} \quad r = \frac{\sum \left\langle \hat{\bar{\sigma}}_i \right\rangle_+}{\sum |\hat{\bar{\sigma}}_i|} \in [0;1] \tag{23}$$

where $\hat{\bar{\sigma}}_i$ are the principal effective stresses.

The evolution law for D is defined by the following exponential relation:

$$D = 1 - \frac{Y_0(1-A)}{Y} - A\,e^{-B(Y-Y_0)} \tag{24}$$

where $Y_0 = r\,\epsilon_{0,t} + (1-r)\;\epsilon_{0,c}$ is the initial threshold for Y and A and B are material parameters, also defined from the combination of the tensile and compressive parameters, $A_{t/c}$ and $B_{t/c}$, respectively according to:

$$A = A_t\left(2\,r^2\,(1-2k) - r\,(1-4k)\right) + A_c\left(2\,r^2 - 3\,r + 1\right) \tag{25}$$

$$B = r^q B_t + (1-r^q)\,B_c \qquad \text{with} \quad q = r^2 - 2r + 2 \tag{26}$$

k is a parameter for calibrating the asymptotic stress value at large shear deformations and is set equal to 0.7 throughout the following simulations.

Figure 6(a) and 6(b) shows the resulting stress-strain constitutive relation and the damage evolution law with the material parameters in the first row of Table 1.

3.2 Plain concrete and RC beams subjected to end torsional loads

Two prismatic beams under pure torsion are used for the validation of the 3d beam formulation. Both specimens have a total length of 160 cm, and are divided into three parts: two end

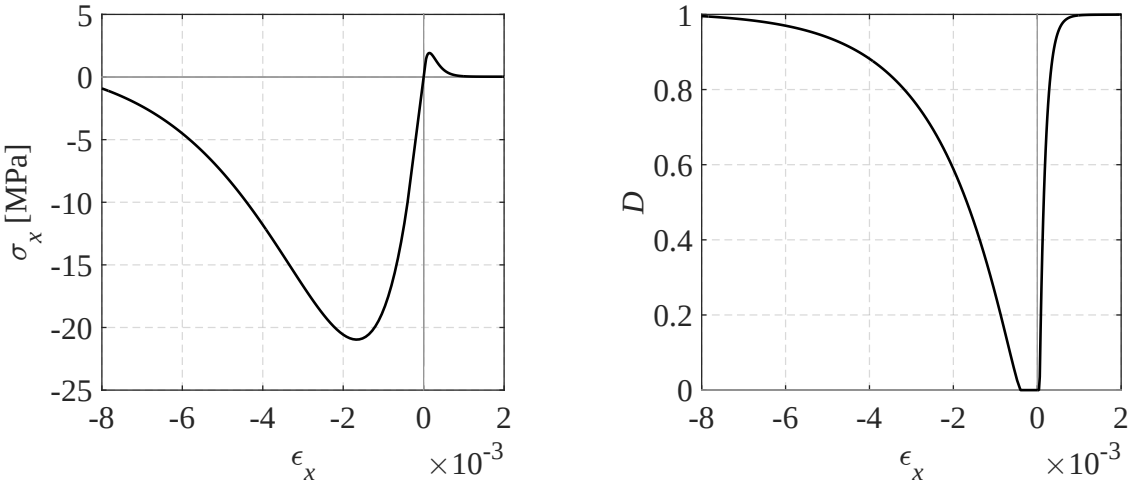

(a) Uniaxial stress-strain relation. (b) Damage evolution law.

Figure 6: Damage constitutive law for concrete.

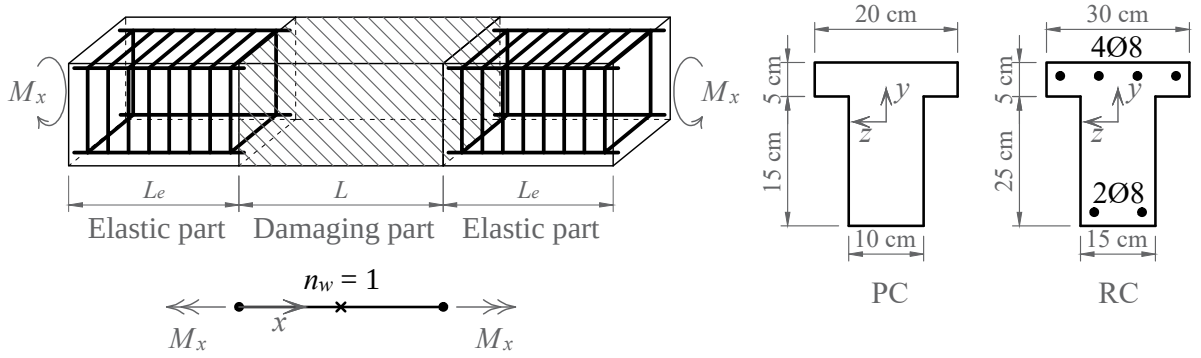

Figure 7: Beams subjected to end torsional loads: specimens geometry.

regions of length L_e, reinforced so as to remain elastic, and a middle part of length L undergoing cracking and damage (Figure 7). For pure torsion a torsional moment M_x is applied at both ends with a particular arrangement that allows the beam cross-sections to undergo warping.

The plain concrete (PC) and the reinforced concrete (RC) cross-section in Figure 7 are considered for the central damaging part of the beam. The geometrical parameters are: $L = 60$ cm for the former one ($L_e = 50$ cm) and $L = 100$ cm for the latter one ($L_e = 30$ cm). Only the middle part is modeled in the numerical analysis, using one FE with one warping interpolation point located along the axis, $n_w = 1$ (Figure 7), as a uniform warping distribution is expected in this direction. Three Gauss-Lobatto quadrature points are used for the integration along the FE with a uniform fiber discretization made of 86 fibers at each point. The material parameters are given in Table 1. Modulus E is not specified in the two reference papers, thus it is adjusted to reproduce the measured initial stiffness. For the steel bars, which are modeled as additional fibers, the following material parameters are used: Young modulus $E = 210000\,\mathrm{MPa}$, Poisson coefficient $\nu = 0.3$, yield stress $f_y = 560\,\mathrm{MPa}$, isotropic hardening $H_i = 0.001\,E$ and kinematic hardening $H_k = 0.01\,E$.

Four different warping DOFs distributions in Figure 8 are considered. The first two adopt Lagrange polynomials, L1(12) and L2(30) and the other two use Hermite polynomials, H1(12) and H2(30) with the total number of internal DOFs in parentheses.

	E [MPa]	ν	$\varepsilon_{0,t}$	A_t	B_t	$\varepsilon_{0,c}$	A_c	B_c
PC	25 000	0.20	0.000055	0.98	7 000	0.000200	1.30	600
RC	30 000	0.20	0.000100	0.98	11 000	0.000200	1.50	600

Table 1: Beams subjected to end torsional loads: material parameters for concrete.

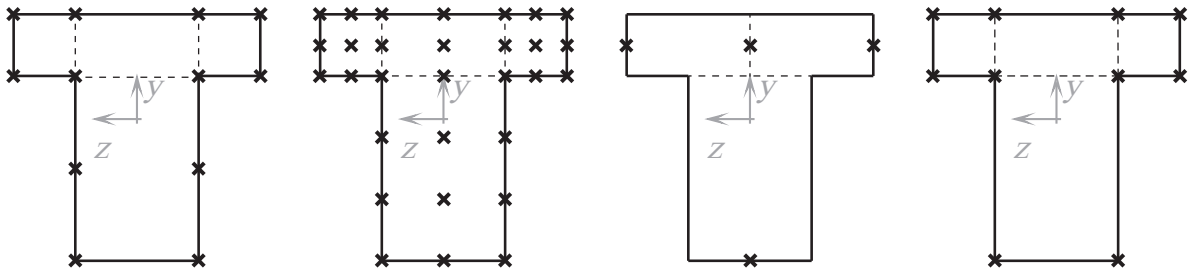

(a) L1(12) (b) L2(30) (c) H1(12) (d) H2(30)

Figure 8: Warping DOFs distribution over the cross-section of the T-shaped beams ("L" = Lagrange interpolation functions, "H" = Hermite interpolation functions and the number in the parentheses indicates the total number m_w of warping DOFs).

Figure 9(a) compares the global response for the four warping distributions with the experimental results for the plain concrete beam. The H2(30) model gives the best solution, since it adopts cubic interpolation functions in the y and z direction. The L2(30) model uses the same number of warping DOFs and, although it provides parabolic interpolation functions (cubic only in the y direction for the web), it gives a solution that agrees very well with the solution of the H2(30) model. The L1(12) model with linear interpolation functions, slightly overestimates the element strength, with a significantly smaller number of warping DOFs. Finally, the H1(12) model, which uses the same number of warping DOFs with linear interpolation functions as the L1(12) model, underestimates both the stiffness and the strength of the element. These results lead to the conclusion that Lagrange polynomials are a good compromise between accuracy and computational efficiency. In fact, with a small number of warping DOFs these interpolation functions give satisfactory solutions, whereas for the Hermite polynomials high order interpolation polynomials are required over the cross section. For sections composed of thin rectangular segments, as is the case for the commercial steel profiles, linear Lagrange polynomial prove computationally superior (see [12]) to the Hermite polynomials which require many warping DOFs for good results.

Figure 9(b) compares the results of the H2(30) model with the experimental results in [17] and with the analytical results of the same study under the assumption of a rigid cross-section. The response under the assumption of a rigid cross-section results from a value of $J = 6\,774\,\mathrm{cm}^4$ for the polar moment of area based on the semi-analytical solution with Fourier series.

Figure 9(b) shows that the rigid section assumption overestimates the peak load, since the damage distribution over the cross-section is not captured correctly. In fact, Figure 10 shows that the distribution of damage variable D is similar to that for a circular section where warping is not possible. Instead, in the presence of warping the damage distribution is much more diffused over the whole cross-section. Figure 11 shows the γ_{xy} distribution. Note that the section warping gives rise to parabolic distributions of the shear strains γ_{xy} and γ_{xz} over the section. In contrast, the rigid section assumption is associated with in a linear distribution of

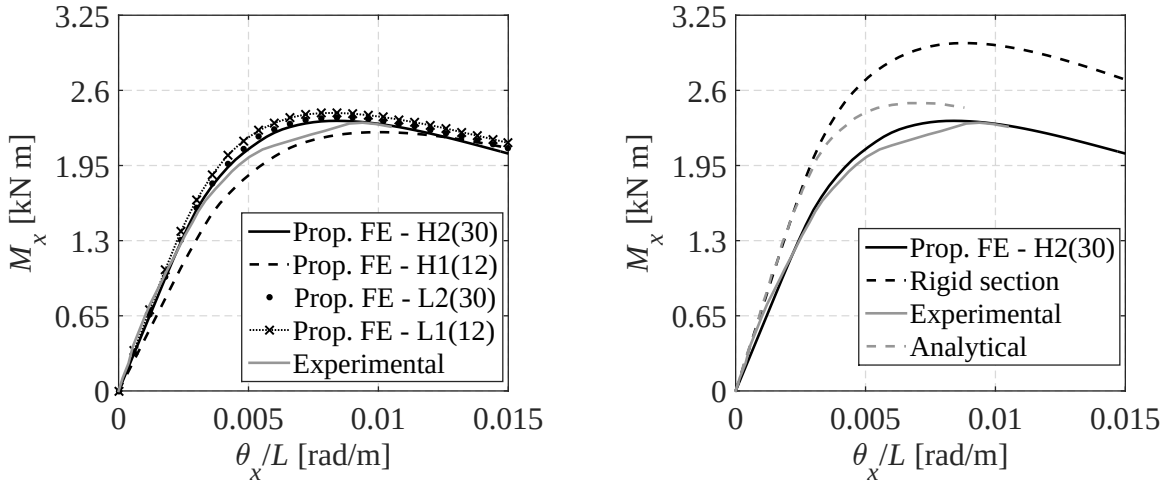

(a) Comparison between the different warping distributions.

(b) Numerical vs experimental response.

Figure 9: Response of the T-shaped plain concrete beam: moment vs rotation per unit length.

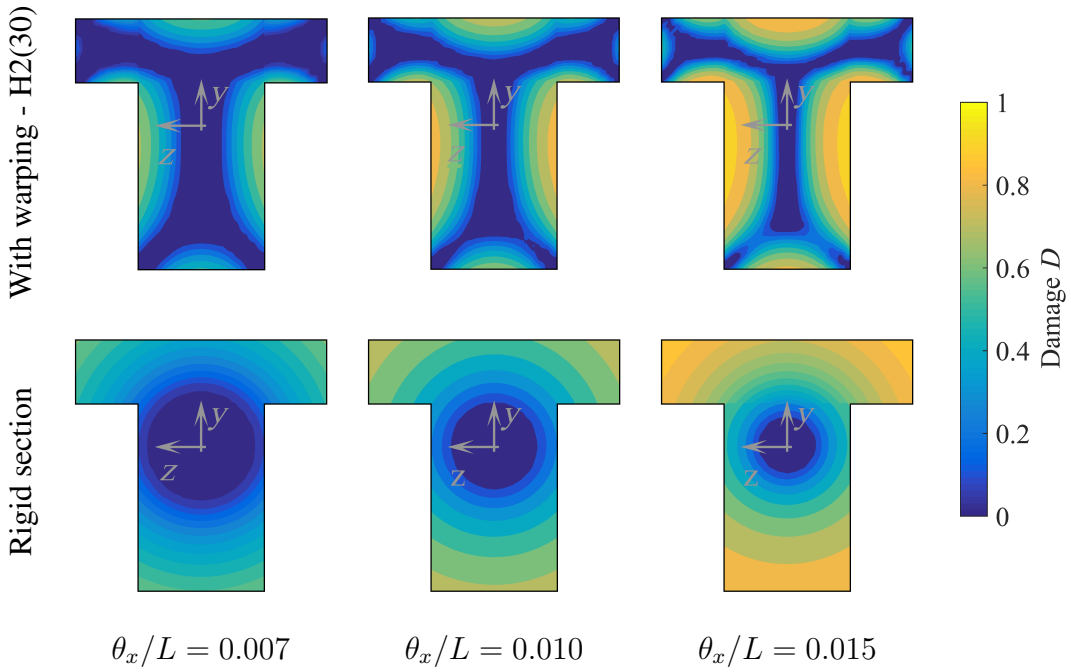

Figure 10: Evolution of the damage over the plain concrete T-shaped cross-section with and without warping.

these strains in the y and z direction.

Similar observations result for the RC beam whose global response is shown in Figure 12. The response under the assumption of a rigid cross-section results from a value of $J = 32\,642\,\mathrm{cm}^4$ for the polar moment of area based on the semi-analytical solution with Fourier series. The response of the plain concrete beam with the H2(30) model is superimposed on the same figure for contrast. The comparison shows that the reinforcing bars increase the member strength slightly under high values of torsional deformation, when the concrete is completely damaged. The experimental response shows greater strength under intermediate deformations, as the beam transitions from the uncracked to the fully cracked state, but this transitory behavior

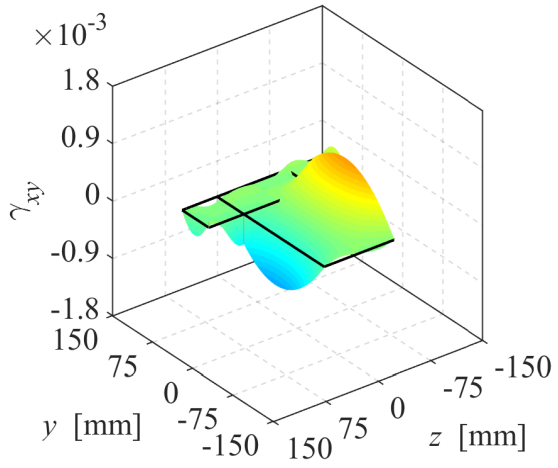

Figure 11: Shear strain in the plain concrete section - Model with warping, H2(30) - $\theta_x/L = 0.007$.

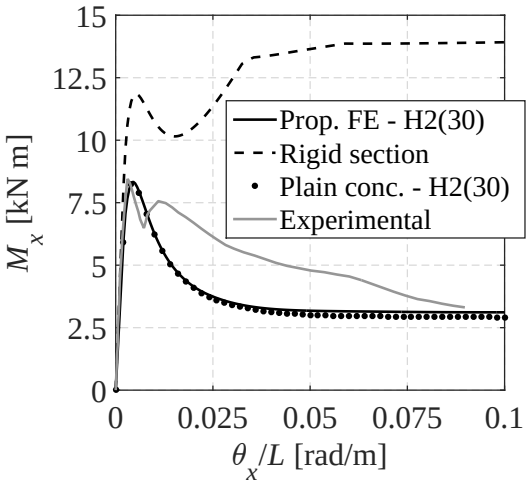

Figure 12: Numerical vs experimental response for the RC beam: moment vs rotation per unit length.

due to rough cracks and dowel action is not accounted for in the present numerical model.

4 CONCLUSIONS

- The paper extends an existing 3d enhanced fiber beam element formulation with warping degrees of freedom to the analysis of concrete beams under torsion with warping by incorporating a constitutive material law with damage.
- Two examples demonstrate the capabilities of the element for describing the inelastic response of plain concrete and RC members under torque, as well as the resulting shear strain-stress and damage distributions over the cross-section.
- The numerical analyses show the importance of the interaction between the warping deformations and the damage progression. In fact, the standard elements, that account for the torsional effects in a simplified way, give unrealistic results and overestimate both the strength and the ductility of the structure.
- The 3d enhanced fiber beam element proves to be robust and accurate and has significantly lower computational cost than shell and brick finite elements, while delivering results of excellent accuracy for the local response of the structural members.

REFERENCES

[1] V. Ciampi, L. Carlesimo .A nonlinear beam element for seismic analysis of structures, *Proceedings of the Eighth European Conference on Earthquake Engeneering*, Laboratorio Nacional de Engenharia, Lisbon, 1986.

[2] A. Neuenhofer, F.C. Filippou. Evalutation of nonlinear frame finite-element models, *Journal of Structural Engineering*, **123**, 958–966, 1997.

[3] D. Addessi, V. Ciampi. A regularized force-based beam element with a damage-plastic section constitutive law, *International Journal for Numerical Methods in Engineering*, **70**, 610–629, 2007.

[4] A. Saritas, O. Soydas. Variational base and solution strategies for non-linear force-based beam finite elements, *International Journal of Non-Linear Mechanics*, **47**, 54–64, 2012.

[5] M.H. Scott, G.L. Fenves. Plastic hinge integration methods for force-based beam-column elements, *Journal of Structural Engineering*, **132**, 244-252, 2006.

[6] S.M. Kostic, F.C. Filippou. Section discretization of fiber beam-column elements for cyclic inelastic response, *Journal of Structural Engineering*, **138**, 592–601, 2012.

[7] J. M. Bairan Garcia, A. R. Mari Bernat. Coupled model for the non-linear analysis of anisotropic sections subjected to general 3D loading. Part 1: Theoretical formulation, *Computers and Structures*, **84**, 2254–2263, 2006.

[8] J. N. Gregori, P. M. Sosa, M.A. F. Prada, F. C. Filippou. A 3D numerical model for reinforced and prestressed concrete elements subjected to combined axial, bending, shear and torsion loading. *Engineering Structures*, **29**, 3404–3419, 2007.

[9] A. Saritas, F.C. Filippou. Inelastic axial-flexure shear coupling in a mixed formulation beam finite element, *International Journal of Nonlinear Mechanics*, **44**, 913-922, 2009.

[10] S. Mohr, J. M. Bairan Garcia, A. R. Mari Bernat. A frame element model for the analysis of reinforced concrete structures under shear and bending, *Engineering Structures*, **32**, 3936–3954, 2010.

[11] S. Zhou. Finite beam element considering shear-lag effect in box girder, *Journal of Engineering Mechanics*, **136**, 11151122, 2010.

[12] V. Le Corvec. Nonlinear 3d frame element with multi-axial coupling under consideration of local effects, *UC Berkeley Electronic Theses and Dissertations Degree: Ph.D.*, Civil and Environmental Engineering, UC Berkeley, 2012.

[13] V. Le Corvec, F.C. Filippou. Enhanced 3D Fiber beam-column element with warping displacements. *Proceedings 3rd International Conference on Computational Methods in Structural Dynamics and Earthquake Engineering COMPDYN, ECCOMAS*, Corfu, Greece, 2011.

[14] D. Addessi, P. Di Re. A 3D mixed frame element with multi-axial coupling for thin-walled structures with damage, *Frattura ed Integrità Strutturale*, **29**, 178-195, 2014.

[15] J. Mazars, F. Hamon, S. Grange. A new 3D damage model for concrete under monotonic, cyclic and dynamic loadings, *Materials and Structures*, DOI 10.1617/s11527-014-0439-8, 2014.

[16] F. C. Filippou, M. Constantinides. Fedeaslab getting started guide and simulation examples, *Technical Report 22, NEESgrid*, www.nees-grid.org, 2004.

[17] C. J. Karayannis, C. E. Chalioris. Experimental validation of smeared analysis for plain concrete in torsion, *Journal of Structural Engineering*, **126**, 646–653, 2000.

[18] C. E. Chalioris. Torsional strengthening of rectangular and flanged beams using carbon fibre-reinforced-polymers Experimental study, *Construction and Building Materials*, **22**, 21–29, 2008.

ECCOMAS Congress 2016
VII European Congress on Computational Methods in Applied Sciences and Engineering
M. Papadrakakis, V. Papadopoulos, G. Stefanou, V. Plevris (eds.)
Crete Island, Greece, 5–10 June 2016

Singularly Perturbed Problems in Mechanics (some fundamental aspects of designing and computing)

Lyudmila K.Kuzmina
KNRTU - KAI
RUSSIA
Lyudmila.Kuzmina@kpfu.ru

Abstract. It is important study, that is concerned with the development of the concepts and methods of classical stability theory in reference to the problems of designing and computing for singularly perturbed class systems , generated by engineering practice. The various aspects of complex systems dynamics are considered. Methods of the modelling and analysis on the generalized methodology base, coupling the stability theory ideas and asymptotic theory manners, are elaborated. Non-traditional, extended approach, formed on A.M.Lyapunov's theory methods, on brilliant ideas of N.G.Chetayev, P.A.Kuzmin, V.V. Rumyantsev, K.P.Persidskiy, is worked out. It gives universal tool that makes it possible to come near to the solving of fundamental problems in general modelling theory, in designing/computing. The effective algorithm of engineering level is constructed, which is perspective for multidisciplinary systems. Besides all investigated objects are interpreted from unified positions as singular ones; effectual non-traditional technology of modelling, that uses *principally non-linear approach*, is established; the simple schemes of *decomposition of original systems (models) and of dynamic properties* are worked out; *the generalization of the reduction principle,* well-known in stability theory, is got for general qualitative analysis. This manner is permitting to construct the hierarchical sequence of simplified systems (and models) as comparison ones; to determine the conditions of the qualitative equivalence between original and shortened systems; to find the areas of their acceptability for analytical or computer- analytical analysis in designing of engineering objects.

Keywords: Complex Systems, Stability Theory, Singularity, Modelling.

Author is grateful to Russian Foundation of Fundamental Investigations for support of this research (grant 15-08-00393).

1 INTRODUCTION

The first fundamental rigorous results in this direction were obtained by H.Poincare and by A.M.Lyapunov. In classical works of A.M.Lyapunov the comparison method (general method of qualitative analysis) was developed with the strong justification for the solving of stability problems. This method led to the reduction principle, well-known one in stability theory (A.M.Lyapunov, K.P.Persidskiy,…), and to the comparison principle (R.Bellman-V.Matrosov).

There is the direct methodological connection between stability theory and singular perturbations theory (I.S.Gradstein, N.G.Chetayev); between modelling problems and parametric stability theory (N.G.Chetayev, P.A.Kuzmin). With reference to Mechanics problems, formulated here, it leads to the singularly perturbed problems, with various singularities types, with specific critical cases. This research is formed on accepted here basic proposition about global, in-depth fundamental, connection between the singularly perturbed problems (and modelling problems in Mechanics) and the stability methods of Lyapunov's theory. Such tenet is ascending to well-known stability postulate (N.G.Chetayev), and singularity postulate (L.K.Kuzmina), with the extending statement about stability with parametric perturbations on singular case. All original objects may be treated from unified

view point of systems of singularly perturbed class. The object state may be described by the equations with small (or big) parameters. The original mathematical model (as example, in Lagrange's form) may be represented in standard form, as singular model, with small parameters in different powers. For this it is necessary to construct the corresponding non-linear, non-singular, evenly-regular transformation of variables. It is postulated (L.K.Kuzmina), that such suitable transformation exists always, and it may be constructed by special, non-formal manners. Besides the original dynamic problems are solved as singular ones; shortened (approximate) systems are introduced as subsystems of *s*-level (*s*-systems); *reduced models are obtained as asymptotic s-models*. Here these *s*-systems are also singularly perturbed ones. It is non-traditional approach, combining the methods of stability theory and perturbations theory that allows to come near to the solving fundamental problem of modelling ,designing, computing in Mechanics via understanding it as problem of singularly perturbed class.

Following to ideas of N.G.Chetayev's, in accordance with Lyapunov's methods, the singular problems may be solved (stability, proximity, optimality, quickness,…) both for non-critical and for critical cases; with simple and multiple roots;… Also for singular systems with the peculiarities (critical spectrums) the reduction conditions may be determined. In these cases the direct use of known results of singular perturbations theory (A.N.Tikhonov, A.Naifeh,…) is non-suitable: eigen-values of corresponding matrices are zero- and imaginary ones. Mechanical systems, modelling the technical objects, are "quasi-Tikhonov's systems" (N.N.Moiseev). *Therefore special, novel, manners are necessary*. Methods, based on Lyapunov's methodology, Chetayev's ideas, elaborated here, give powerful tool; bring new interesting results, perspective both for perturbations theory (singular problems in specific, critical cases are solvable) and for applications to Mechanics, for general modelling theory.

2 INITIAL GENERAL PRINCIPLES OF METHODOLOGY

It is well known [1-16], many applied investigations lead to the mathematical problems, having important general features: the reduction of the order of the differential equations, the loss of continuity, boundary condition. We shall call the singular systems such ones, when the transition to the reduced system is accompanied by the lowering of the model order, with the structural change. For these systems the initial mathematical model may be presented in standard form of system with the singular perturbations. It enables to consider the original objects on typical scheme, to construct by regular manners the "idealized" mechanical-mathematical models, that are interesting for engineering applications, to get strict conditions of their acceptability in dynamics.

For singularly perturbed objects a motion consists of components of various multi-scale classes, from fast to slow, and their differential equations (mathematical models) can be led to the form of equations with small parameters before higher derivatives. Therefore in practice for analysis of such systems the reduced models of lower order are being used as working models. Let the differential equations of the perturbed motion of considered system can be led to a form (let consider the systems with the steady states set)

$$M(m)\frac{dy}{dt} = Y(t, m, y) \tag{1}$$

where $y = \|z, x\|^T$, z, x are m-, n-dimensional vectors; $m > 0$ is a small dimensionless parameter; $M(m) = \|M_{i,j}(m)\|$; $Y(t,m,y) = \|Z(t,m,y); P(m)x + X(t,m,y)\|^T$; $P(m) = \|P_{i,j}(m)\|$;

$M_{i,j}$, $P_{i,j}$ are submatrices of the appropriate sizes; $Z(t, m, y)$, $X(t, m, y)$ are non-linear vector-functions, holomorphic (in appropriate domain) on the totality of variables z, x, in which coefficients are continuous, limited functions of t, m; $Z(t, m, z, 0)= 0$, $X(t, m, z, 0)= 0$; $M_{i,j}(m) = m^{a_i} I$, $0 \le a_i \le r$; I are identity matrices. We shall be able to consider the critical cases of system (1), where z are critical variables [1]. Taking into consideration in (1) only members containing m in power not more than s, $s < r$, we shall receive the shortened approximate system of type

$$M_s(m)\frac{dy}{dt} = Y_s(t, m, y) \tag{2}$$

We shall call (2) the shortened system of s-level, s-system (s-approximation on m). For singularly perturbed systems that are considered here, the order of system (2) is lower than order of full system (1). In applications to mechanics this shortened system leads to the reduced model as the asymptotic model of s-level. From the point of view of mechanics a transition to the reduced model is accompanied by a decrease of freedom degrees number. The system (2) is system of differential-algebraic equations.

We shall be able to obtain the sequence of asymptotic models (as designing-basic models) in mechanics, corresponding the sequence of shortened s-systems (s=0,1,2,…r-1). The following problem is important both for the theory and applications: in which cases and under what conditions it is possible to reduce the system (1)analysis to shortened s-system? The similar problem for equations with small parameter under higher derivatives was considered by many authors [2-8]. We shall show the solving of some concrete problems of mechanics on examples of systems with big and small papameters, that lead to particular cases of the system (1) of special class, that are not embraced by already known fundamental results. This methodology allows to realize the parallel computing in engineering for original very complex system.

3 MECHANICAL SYSTEMS WITH NONRIGID ELEMENTS

As an example of such technical/mechanical system we shall consider the systems of gyrostabilization, modelling ones as mechanical (or electromechanical) systems with controlling gyroscopic elements. Here there is a critical case of zero roots. We shall solve a stability problem of the steady motion for such system, supposing that the elements of the system are not absolutely rigid (we neglect the mass of elastic elements). Differential equations of perturbed motion we shall accept in a form of Lagrange's equations (as in [5, 15])

$$\frac{d}{dt} a\dot{q}_M + (b+g)\dot{q}_M + cq_M = Q''_M, \quad \frac{dq_M}{dt} = \dot{q}_M \tag{3}$$

Here $q_M = \|q_1, q_2, q_3, q_4\|^T$ is n - dimensional vector of mechanical generalized coordinates, where q_1 is l-dimensional vector of the gyroscopes precessions angles; q_2 is (m-l)-dimensional vector of angles deviations of own rotations of gyroscopes from their values in steady motion; q_3 is (s-m)-dimensional vector of stabilization angles, s=m+l; q_4 is (n-s)-dimensional vector of elastic elements deformations; a, b, g are square $n\times n$ - matrices of forms of the system kinetic energy, dissipative function of friction forces, gyroscopic coefficients accordingly; $c = \|c_{i,j}\|$, $b = \|b_{i,j}\|$ (i, j=1,...,4), c_{ij} and b_{ij} are submatrices of an appropriate sizes; b_{44} is square (n-s)×(n-s) -matrix of dissipative

function of internal friction forces in material of elastic bodies; c_{44} is square $(n\text{-}s)\times(n\text{-}s)$ -matrix, corresponding to potential energy of elasticity forces.

We assume that all functions in (3) are holomorphic (on the totality of their variables) in certain area.

For solving of this problem (and choosing of a reduced model) we shall lead equations (3) to a form (1) with singular perturbations. For this, first, we must introduce in equations (3) a small parameter, using physical considerations. We suppose, that the elements of the considered systems are of a sufficiently high rigidity and according to that $c_{44} = c_{44}^* / m^2$, $b_{44} = b_{44}^* / m$, where $m>0$ is a small parameter. Now, using the constructed transformation of variables

$$z = \|a_1, a_2\|^T q_M + \|b_1^0 + g_1^0,\ b_2^0 + g_2^0\|^T q_M,\ k_1 = \|a_1, a_2, a_3\|^T q_M,\quad k_2 = a_4 q_M,\quad q_j = q_j,\quad (j = 1, 4)$$

where a_i, b_i, g_i (i = 1,…,4) are submatrices of matrices a, b, g correspondingly, we shall lead equations (3) to the singularly perturbed form. This transformation is the non-linear, non-singular under condition that $\left|b_{i,j}^0 + g_{i,j}^0\right|_{i=1,2}^{j=2,3} \neq 0$, evenly regular [6], not changing the statement of the stability problem. System (3) in new variables has a form (1)

$$\frac{dz}{dt} = Z(t, m, z, x), \qquad M(m)\frac{dx}{dt} = P(m) + X(t, m, z, x) \tag{4}$$

where $x = \|x_1, x_2, x_3\|^T$, $x_1 = \|k_1, q_1\|^T$, $x_2 = k_2$, $x_3 = q_4$; $a_1 = 0$, $a_2 = 2$, $a_3 = 0$; $P_{2i}(m) = mP'_{2i}(m)$ (i=1,2).

The characteristic equation has m zero-roots. Other roots can be found from the equation $d(l, m)=0$. We assume the shortened system of 0-level (degenerated system) as an approximate one for a system (4), marking it (4′) without writing. In old variables it is the system

$$\frac{d}{dt}a^* q + (b^* + g^*)q + c^* q = Q^*,\quad \frac{dq}{dt} = q \tag{5}$$

where $q = \|q_1, q_2, q_3\|^T$ is s-dimensional vector of generalized coordinates, describing the state of an absolutely rigid system; a^*, b^*, c^*, g^* are $s\times s$-matrices of absolutely rigid system.

The equation (5) describes a motion of an idealized model of mechanical system. This model corresponds to an approximate system (4′) of 0-level. We shall call it a “limit model”. A problem: in what conditions a transition from the initial model (3) to its idealized model (to absolutely rigid system) is possible in qualitative analysis, designing, computing? Using methods of stability theory [1, 2], combined with the singular perturbations methods [7,8] and introducing the differential equations for deviations that respond to non-critical (basic) variables x, we can find out the acceptability conditions for transition validity from system (4) to the system (4′) in concrete dynamical problems. After returning to old variables, taking into account the properties of the considered mechanical system, we receive the corresponding statements.

3.1 Stability problem

When the stability property for reduced model (5) will be ensuring same property for original (full) model (3)?

Theorem 1. If $\left|b_{i,j}^0 + g_{i,j}^0\right|_{i=1,2}^{j=2,3} \neq 0$, $\left|c_{31}^0\right| \neq 0$ and all roots (except m zero roots) of characteristic equation of reduced system (5) have negative real parts, then with sufficiently small values of μ (sufficiently high rigidity of the system elements) the zero solution stability of the full system will be succeeding from the zero solution stability of reduced system (5). And reduced system (5) has integral

$$\left\|\begin{matrix} a_1^* \\ a_2^* \end{matrix}\right\| \dot{q} + \left\|\begin{matrix} b_1^{*0} + g_1^{*0} \\ b_2^{*0} + g_2^{*0} \end{matrix}\right\| q + j\,(q, \dot{q}) = B$$

and full system (3) has integral of Lyapunov:

$$\left\|\begin{matrix} a_1 \\ a_2 \end{matrix}\right\| \dot{q}_M + \left\|\begin{matrix} b_1^0 + g_1^0 \\ b_2^0 + g_2^0 \end{matrix}\right\| q_M + F(q_M, \dot{q}_M) = A\,.$$

3.2 Estimations of approximate solutions

Let $q_i = q_i(t,m)$, $\dot{q}_i = \dot{q}_i(t,m)$, $(i = 1...4)$ be the solution of system (3) with the initial conditions $q_{i0} = q_i(t_0,m)$, $\dot{q}_{i0} = \dot{q}_i(t_0,m)$;we shall designate $q_i^* = q_i^*(t)$, $q_i^{\cdot *} = q_i^{\cdot *}(t)$, ($i$ =1,…4) as the solution of approximate system (5), defined by the initial conditions $q_{j0}^* = q_j^*(t_0)$, $\dot{q}_{j0}^* = \dot{q}_j^*(t_0)$ (j=1, 2, 3), where $q_4^* \equiv 0$, $\dot{q}_4^* \equiv 0$.

Making use of stability theory methods we can prove the following statement:

Theorem 2. If the characteristic equation for system (5) has all roots in the left half-plane (except m zero roots) for $d(0, 0)\neq 0$, then under sufficiently big stiffness of the system elements (i.e. m is sufficiently small) there exists such a m_*-value for $x>0$, $h>0$, $g>0$ given in advance (no matter how small x and g are), that in a perturbed motion: $\left\|q_i - q_i^*\right\| < x$, $\left\|\dot{q}_i - \dot{q}_i^*\right\| < x$ (i=1,…,4) when $0<m<m_*$ for $t \geq t_0+g$, if $q_{j0} = q_{j0}^*$, $\dot{q}_{j0} = \dot{q}_{j0}^*$, ($j$=1,2,3) $\left\|q_{40}\right\| < h$, $\left\|\dot{q}_{40}\right\| < h$.

It should be pointed out that while demonstrating and using variables z, x we introduce deviations $a=z-z^*$, $b=x-x^*$ and consider a differential equation for b. The analysis of these equations as well as the integral structure enable to derive the statement of Theorem.

These results, complementing already known [9], justify for the systems, considered here, admissibility of approximate limit model (as asymptotic model of 0-level) and determine the conditions, under which the considered transition is correct (in a meaning, adopted here).

Remark. According to this we can introduce other approximate model (as designing-basic model) for (3). This is asymptotic model of 1-level (m-approximation), that has (s+(n-s)/2) of freedom degrees (if in (4) take into consideration members containing μ in power not more than 1). This model is new one (it is very interesting result).

System (4) belongs to the special critical case, when all eigenvalues of matrix P_{22}, corresponding to the fast x_2, are zero.

4 SYSTEMS WITH FAST ROTORS

Using the same asymptotic approach, we can solve a problem of the transition strict substantiation to a reduced (approximate) model for the mechanical systems with the fast rotors (gyroscopes) [13]. No-giving the formulas and computations here, we note only the some results. In this case original mathematical model is accepted in a form of Lagrange's equations [5]; big parameter is introduced through gyroscopic forces [5, 13]; the necessary transformation of state variables is constructed; the initial equations are reduced to standard form (1). The reduced models are got on our scheme. According to elaborated method, by strict mathematical manner we obtained the known (precessional) model and new («limit») model (as shortened model of 1-st level and 0-level, correspondingly). The conditions of acceptability of these models are determined.

5 SYSTEMS WITH SMALL DELAY TIME

Here the electromechanical systems (EMS), modelling the gyrostabilization systems, are investigated. Original model is presented in general form of Lagrange-Maxwell (Gaponov) equations [14]. The problems: the constructing of reduced model; and their acceptability (in corresponding sense) for these systems. For case of fast-acting systems, interpreting ones as singularly perturbed system, according to our method, we solve these problems. The required transformation is constructed; the reduced models (two types) are obtained; the domains of acceptability are determined.

6 CONCLUSION

In the applications to engineering practice the elaborated methods are very effective, those are enabling to construct the acceptable shortened submodels(as *s-approximations*) by strict mathematical way; to substantiate strongly their correctness in dynamics, including Lyapunov's critical cases; to consider specific cases, inherent for mechanical systems; to evaluate the corresponding errors in such transition-simplifying. It is allowing to realize the using of parallel supercomputing in designing processes on modern computing machines .

The elaborated methods are illustrated on examples from engineering practice, from Mechanics. In framework of this approach it is considered actual problems for fast gyros theory, electromechanical systems, robotic systems; mechanical systems with the friction, non-holonomic systems; Newton's model of point mass dynamics,…

New elegant outcomes are obtained, that are interesting both for theory and for applications, both in general theory of singularly perturbed systems and in applied engineering problems. Also this approach is very perspective from gnosiological view point, for general knowledge theory, with revealing interesting new models, with possibility for investigation of the original complex multi-scale system **with using analytical or computer- analytical parallel methods from first steps of engineering designing**.

Finally as some additional remarks we notice that by analogy with these systems, using the same methods, other singularly perturbed problems and systems of mechanics may be considered.

The subject-matter of investigations is general problem of modelling in mechanics. *The development of mathematical modelling questions of mechanics is closely concerned with actual tasks of mechanical systems dynamics, of differential equations theory* ***with big and small parameters,*** *of stability theory.* In one's turn it is generating new trends in mathematics, interesting mathematical and mechanical problems.

The received results are generalizing and supplementing ones, known in theory of perturbations; these results are developing interesting applications in engineering. With reference to Mechanics and engineering applications the rigorous theoretic justification is

obtained for considered approximate models and theories, both traditional (K.Magnus, A.Andronov, D.Merkin,…) and *new ones*; the separation of state variables on different-frequency groups is developed from first stages of designing; the acceptability of approximate theories, models is discussed, including "exotic" Aristotle's model in Dynamics.
Deep philosophical aspect of idealization problem in Mechanics is highlighted.

The author is grateful to Russian Foundation of Fundamental Investigation for support in this research.(15-08-00393).

REFERENCES

[1] A.M.Lyapunov, *The general problem of motion stability*. Moscow, USSR AS Coll. of papers, vol.2, pp.7-264, 1956.
[2] N.G.Chetayev, *Appl. Math. and Mech.* Vol.21, No.3, pp.419-421, 1957.
[3] L.K.Kuzmina, Proceedings of 9-th National All-Russian Congress on Theor. and Appl. Mech. Nizh.Novgorod, vol.1, p.76, 2006.
[4] N.N.Moiseev, Mathematical Problems of Systems Analysis. Moscow, Nauka 1981.
[5] L.K.Kuzmina, *Appl. Math. and Mech.* Vol.46, No.3, pp.382-388, 1982.
[6] S.Lefshetz, Differential Equations: geometric theory. New York, 1957.
[7] I.M.Gradstein, *Math. Rev.* Vol.32, No.3, pp.533-544, 1953.
[8] A.N.Tikhonov, *Math. Rev.* Vol.31, No.3, pp.575-586, 1953.
[9] F.L.Chernousko, A.S.Shamaev, *Proc. USSR AS, Mech. of Solid Body*. No.3, pp.33-42, 1983.
[10] Y.Z.Tsypkin, P.V.Bromberg, *Izv.AS USSR, OTS*. No.2, pp.1163-1167, 1945.
[11] A.A.Feldbaum, *Avtomatika and telemech.* No.4, pp.253-279, 1948.
[12] A.A.Voronov, Introduction in dynamics of complex controlled systems. Moscow, Nauka. 1985.
[13] D.R.Merkin, *Gyroscopic systems.* Moscow, 1956.
[14] L.K.Kuzmina, *Appl. Math. and Mech.* Vol.55, No.4, pp.594-601, 1991.
[15] L.K.Kuzmina, *Applied Mechanics in the Americas* Vol.12, AAM, USA, 178-181 2008.
[16]Lyudmila K.Kuzmina. Lyapunov theory methods in stability problems of singular systems. Nonlinear analysis: Theory, Methods and Applications, Elsevier, 2009, v.71, No.12, 2481-2485.

ECCOMAS Congress 2016
VII European Congress on Computational Methods in Applied Sciences and Engineering
M. Papadrakakis, V. Papadopoulos, G. Stefanou, V. Plevris (eds.)
Crete Island, Greece, 5–10 June 2016

A DEGENERATE-CONTINUUM BASED TIMOSHENKO BEAM APPROACH FOR THE AEROELASTIC ANALYSIS OF THE WIND TURBINE BLADES

Anthoula N. Panteli[1], **Dimitris I. Manolas**[2], **and Konstantinos V. Spiliopoulos**[1]

[1]School of Civil Engineering, Institute of Structural Analysis and Antiseismic Research,
National Technical University of Athens, Zografou Campus, 157-80 Athens, Greece
e-mail: {anpanteli, kvspilio} @central.ntua.gr

[2] School of Mechanical Engineering, Section of Fluids,
National Technical University of Athens, Zografou Campus, 157-80 Athens, Greece
e-mail: manolasd@fluid.mech.ntua.gr

Keywords: aeroelasticity, wind turbine blades, large displacements, finite rotations, geometrically non-linear effects, Total Lagrangian formulation

Abstract. *Due to the substantial increase of the size of current and future wind turbine designs, the blades tend to be quite flexible, resulting to large displacements and finite rotations under the action of the aerodynamic loading. As a result, the geometry of the blades changes, in some cases the flap deflection exceeds* 10% *of the blade radius, and thus, geometrically non-linear effects of significant importance take place.*
Two geometrically non-linear models are available in the multi-body hydro-servo-aeroelastic tool hGAST [1, 2], the first employs a 2nd order Euler-Bernoulli beam approach and the second is based on a non-linear sub-body modeling of the blades. In the present paper, a degenerate-continuum based Timoshenko beam approach is presented, which has been implemented in the code. The main kinematic assumptions are that the cross-section remains plane and rigid in its own plane, hence, the cross-sectional out-of-plane and in-plane warpings are neglected. The material is assumed homogeneous, isotropic, linear and elastic.
Comparisons between the non-linear models and the linear one are presented. The basic outcome from the analysis of a three-bladed rotor, with aerodynamic and structural properties same to the 5MW NREL reference wind turbine, is that the non-linear models result to a significant difference in torsional response compared to the linear model, due to the bending-torsion non-linear coupling. This could be an important aspect for the design of the blades, since it contributes to passive load reduction strategies.

1 INTRODUCTION

In bibliography, geometrically non-linear beam theories could be separated into two categories: a degenerate-continuum beam theory [3, 4, 5] and a geometrically exact beam theory [6, 7]. The first category, which has been inspired by the work done for shells (first introduced in 1968 by Ahmad et al. [8]), is directly derived from the 3D-continuum. The strain-displacement relations used are written in a strong sense, i.e. at the material particle level. The second category, which has been introduced by Reissner [6] for the plane case and by Simo [7] for the spatial case, deals with the problem formulation at a beam theory level. The strain-displacement relations used are written in a weak sense, i.e. at the reference point of the beam. These *generalized* strain measures do not spoil the geometric exactness, as this is expressed via the resultant form of the differential equilibrium equations at the deformed state. Actually, Reissner [9] had proposed a formulation in 3D before Simo, but, using a rotation matrix simplification to derive the required strain-displacement relations, he spoiled the geometric exactness [10]. Many finite-element developers of the beam theories, e.g. Jelenić & Crisfield [10], Cardona & Geradin [11], Ibrahimbegović [12], based their approach on the geometrically exact beam theory.

The more flexible wind turbine blades of modern design lead to a strong coupling between aerodynamics and structural dynamics, namely the aeroelasticity. Thus, the structural models used in aeroelasticity of the blades need to account for the exact geometry of the deformed shape, so that an accurate input for the aerodynamics load estimation may be provided. A review on the structural models used in aeroelasticity of the blades is given in [13]. As far as the 1D structural models are concerned, linear beam models had been used for long. Important terms which consider certain non-linearities were included, i.e. coupling-type terms associated with the centrifugal forces. Today, two non-linear beam theory models for rotor blades are used: One is the moderate deflection beam model [9, 14] based on ordering schemes, and, the other is the large deflection beam model [15, 16] developed according to the aforementioned geometrically exact beam theory.

As far as the aerodynamics is concerned, the aerodynamic model, used to transform the wind flow field to loads on the blades, is a (BEM) Blade-Element Momentum model, which accounts for dynamic inflow, yaw misalignment, and dynamic stall effects [17].

In this work, a Total Lagrangian beam approach based on the degenerate-continuum concept, for using it in aeroelasticity, is presented. The difference compared to the beam theory model presented in [3, 4, 5] is that before the element interpolation is performed, an analytical integration over the cross-section is carried out to reduce the 3D integration to a 1D integration. The same procedure is followed in [18] for an Updated Lagrangian formulation. The paper outline is as follows: In section 2, the kinematics and kinetics of the degenerate-continuum based beam formulation are presented. An important issue is how to represent the finite rotations of the cross-section. In the present work, the rotational vector representation technique is used to avoid the non-uniqueness problem associated to the Euler angles one [19]. The exponential mapping of the skew-symmetric matrix of the rotational vector is evaluated to update the cross-sectional orientation. Consistent linearization of the configuration state is presented in the following, needed to construct a step-by-step analysis, in the context of a Total Lagrangian formulation. In section 3, the linearized equilibrium equation is presented, from which the beam matrices are derived after the discretization procedure, using the finite element method. In section 4, the numerical results from the three-bladed 5MW NREL [20] rotor motion, under uniform inflow conditions, are presented. Comparisons are given between the three options of the geometrically non-linear modeling (degenerate-continuum based, 2nd order Euler-Bernoulli, sub-body

approach models) and the linear one.

2 DEGENERATE-CONTINUUM BASED TIMOSHENKO BEAM APPROACH

2.1 Assumptions

- The cross-section of the beam remains plane and rigid inside its own plane, hence, warping is not included. However, the warping displacement behavior could be added to the assumed deformations.
- Shear deformation is taken into account, and, it is assumed constant in the cross-section as a consequence of the previous non-warping assumption.
- The initial reference line of the beam is assumed, for the sake of simplicity, straight.
- The material is homogeneous, isotropic and linear elastic.

2.2 Basic kinematics

The reference bases used in kinematics are (fig. 1),

- $\boldsymbol{E_j}, j = 1 - 3$, is the orthonormal body-attached reference basis (which is rotating in the context of the blade dynamics)
- $\boldsymbol{V_i}(\xi), i = r, s, t$, is the orthonormal moving basis, attached to each cross-section

where, ξ is the arc-length variable along the reference line of the beam.

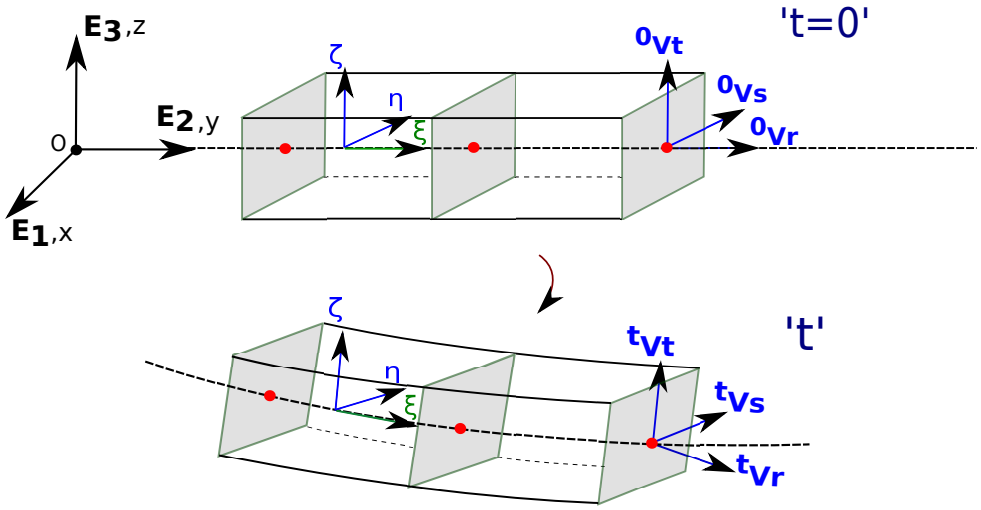

Fig. 1: Initial and deformed configuration of the beam.

2.2.1 Initial configuration state

The initial cross-sectional orientation is expressed via the initial orthogonal transformation $\xi \rightarrow {}^0\mathbf{\Lambda}(\xi) \in SO(3)$, $SO(3)$ is the special orthogonal group, thus, the moving frame basis at the initial (undeformed) state (fig. 1) is given by,

$$ {}^0\boldsymbol{V_i}(\xi) = {}^0\Lambda_{ij}(\xi)\boldsymbol{E_j} \tag{1}$$

The triads ${}^0\boldsymbol{V_i}(\xi), i = r, s, t$ are directed along the axes shown in fig. 1, which are parallel to the reference basis $\boldsymbol{E_j}, j = 1 - 3$, (in blade dynamics the origin of these triads is located on the pitch axis of the blade). The basis vectors ${}^0\boldsymbol{V_i}(\xi)$, in general, depend on ξ due to the presence of initial curvatures and/or twist. In the present, because of the straight beam assumption, these vectors are constant along the beam. The corresponding position vector $\boldsymbol{R}$ of an arbitrary material particle (ξ, η, ζ) of the undeformed beam is given by,

$$ \boldsymbol{R}(\xi, \eta, \zeta) = \boldsymbol{R_0}(\xi) + {}^0\mathbf{\Lambda^T} \cdot \begin{Bmatrix} 0 \\ \eta \\ \zeta \end{Bmatrix} = \boldsymbol{R_0}(\xi) + \eta \cdot {}^0\boldsymbol{V_s} + \zeta \cdot {}^0\boldsymbol{V_t} \tag{2}$$

where, $\boldsymbol{R_0}(\xi)$ is the position vector of the undeformed beam reference point.

2.2.2 Current configuration state

In a similar way, the deformed cross-sectional orientation is expressed via the orthogonal transformation $\xi \rightarrow {}^t\mathbf{\Lambda}(\xi) \in SO(3)$, thus, the moving frame basis at the current (deformed) state (fig. 1) is given by,

$$ {}^t\boldsymbol{V_i}(\xi) = {}^t\Lambda_{ij}(\xi)\boldsymbol{E_j} \tag{3}$$

The Bernoulli hypothesis of the plane cross-sections remaining planar after deformation and retaining their shape and area is assumed to hold, thus, the corresponding position vector ${}^t\boldsymbol{r}$ of an arbitrary material particle (ξ, η, ζ) of the deformed beam is given by,

$$ {}^t\boldsymbol{r}(\xi, \eta, \zeta) = {}^t\boldsymbol{r_0}(\xi) + {}^t\mathbf{\Lambda^T}(\xi) \cdot \begin{Bmatrix} 0 \\ \eta \\ \zeta \end{Bmatrix} = {}^t\boldsymbol{r_0}(\xi) + \eta \cdot {}^t\boldsymbol{V_s}(\xi) + \zeta \cdot {}^t\boldsymbol{V_t}(\xi) \tag{4}$$

where, ${}^t\boldsymbol{r_0}(\xi)$ is the position vector of the deformed beam reference point.

2.3 Updated (trial) configuration state

The update of the configuration state w.r.t. the displacements is conventional, i.e. additive, due to their vectorial nature. To update the configuration state w.r.t. the rotations, the cross-sectional orientation at configurations $t + \Delta t$ and t are related via the rotational (pseudo)-vector $\boldsymbol{\theta}(\xi)$ (fig. 2), which rotates the base vectors ${}^t\boldsymbol{V_i}(\xi)$ into the base vectors ${}^{t+\Delta t}\boldsymbol{V_i}(\xi)$ around the axis $\frac{1}{\theta(\xi)} \cdot \boldsymbol{\theta}(\xi)$ for the angle $\theta(\xi)$, through

$$ {}^{t+\Delta t}\boldsymbol{V_i}(\xi) = \mathbf{\Lambda}(\xi)\ {}^t\boldsymbol{V_i}(\xi) = exp(\hat{\boldsymbol{\theta}}(\xi))\ {}^t\boldsymbol{V_i}(\xi), \quad i = r, s, t \tag{5}$$

where, the rotation matrix $\mathbf{\Lambda}(\xi)$ is given by,

$$ \mathbf{\Lambda}(\xi) = exp(\hat{\boldsymbol{\theta}}(\xi)) = \boldsymbol{I} + \frac{sin\theta}{\theta}\hat{\boldsymbol{\theta}} + \frac{1 - cos\theta}{\theta^2}\hat{\boldsymbol{\theta}}\hat{\boldsymbol{\theta}} \tag{6}$$

where $\hat{\boldsymbol{\theta}}(\xi)$ is the skew-symmetric matrix formed by the components of the rotational vector $\boldsymbol{\theta}(\xi)$ ($\hat{\boldsymbol{\theta}}(\xi) = -e^{ij}_k \theta^k \boldsymbol{E_i} \boldsymbol{E_j^T}$; e^{ij}_k is the permutation symbol). The above formula is the well-known Rodrigues formula. Details about the derivation of the formula one could find at [3, 21].

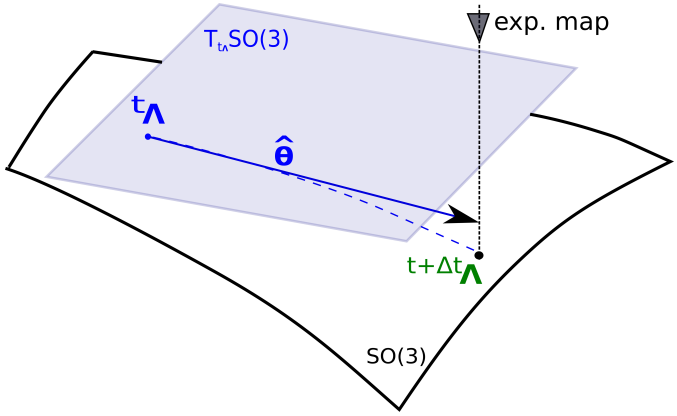

Fig. 2: Geometric interpretation of the exponential map, $T_{{}^t\Lambda}SO(3)$: tangent plane at ${}^t\boldsymbol{\Lambda}$ [22].

2.3.1 Strain and stress measures at the updated (trial) configuration state

By subtracting the position vector at $t = 0$, given in eq. (2), from the position vector at $t + \Delta t$, given in eq. (4) for $t = t + \Delta t$, for an arbitrary material particle (ξ, η, ζ) of the beam, the displacement field at $t + \Delta t$ is written as follows,

$$ {}^{t+\Delta t}\boldsymbol{u}(\xi,\eta,\zeta) = {}^{t+\Delta t}\boldsymbol{u}_0(\xi) + \eta \cdot {}^{t+\Delta t}\boldsymbol{\Delta V_s}(\xi) + \zeta \cdot {}^{t+\Delta t}\boldsymbol{\Delta V_t}(\xi) \tag{7} $$

where, ${}^{t+\Delta t}\boldsymbol{u}_0(\xi)$ is the updated displacement of the beam reference point, and, ${}^{t+\Delta t}\boldsymbol{\Delta V_s}(\xi)$, ${}^{t+\Delta t}\boldsymbol{\Delta V_t}(\xi)$ are the differences between the initial and the updated cross-sectional directors.

To know the stress condition contributing to the geometric stiffness in the context of the Newton-Raphson iterative procedure, the internal forces and moments of the beam at the trial state $t + \Delta t$ need to be evaluated. To do so, the steps below are followed (for convenience, the variables ξ, η, ζ are omitted from the RHS),

1. The material particle (ξ, η, ζ) global displacement gradients are evaluated,

$$ \left\{ {}^{t+\Delta t}u_{,x}\ {}^{t+\Delta t}u_{,y}\ {}^{t+\Delta t}u_{,z}\ {}^{t+\Delta t}v_{,x}\ {}^{t+\Delta t}v_{,y}\ {}^{t+\Delta t}v_{,z}\ {}^{t+\Delta t}w_{,x}\ {}^{t+\Delta t}w_{,y}\ {}^{t+\Delta t}w_{,z} \right\}^T $$

   where, ${}^{t+\Delta t}u$, ${}^{t+\Delta t}v$, ${}^{t+\Delta t}w$ are the components of the updated displacement (eq. 7) w.r.t. the reference basis $\boldsymbol{E}$, while, (,) denotes the spatial derivative relative to the x, y, z coordinates.

2. Using the coordinate transformation of a 2nd order tensor [23], the global displacement gradients are rotated to get the initial local ones, i.e. relative to the initial cross-sectional basis ${}^0\boldsymbol{V}$.

3. The components of the Green strain tensor [3, 4] are evaluated. Because of the assumption that the cross-sectional shape does not change during deformation, the only remaining

components of the Green strain tensor are,

$$
\begin{aligned}
{}^{t+\Delta t}\epsilon_{\xi\xi}(\xi,\eta,\zeta) &= {}^{t+\Delta t}u_{\xi,\xi} + \frac{1}{2}({}^{t+\Delta t}u_{\xi,\xi})^2 + \frac{1}{2}({}^{t+\Delta t}v_{\eta,\xi})^2 + \frac{1}{2}({}^{t+\Delta t}w_{\zeta,\xi})^2 \\
{}^{t+\Delta t}\epsilon_{\xi\eta}(\xi,\eta,\zeta) &= \frac{1}{2}({}^{t+\Delta t}u_{\xi,\eta} + {}^{t+\Delta t}v_{\eta,\xi} + {}^{t+\Delta t}u_{\xi,\xi}{}^{t+\Delta t}u_{\xi,\eta} + {}^{t+\Delta t}v_{\eta,\xi}{}^{t+\Delta t}v_{\eta,\eta} \\
&\qquad + {}^{t+\Delta t}w_{\zeta,\xi}{}^{t+\Delta t}w_{\zeta,\eta}) \\
{}^{t+\Delta t}\epsilon_{\xi\zeta}(\xi,\eta,\zeta) &= \frac{1}{2}({}^{t+\Delta t}u_{\xi,\zeta} + {}^{t+\Delta t}w_{\zeta,\xi} + {}^{t+\Delta t}u_{\xi,\xi}{}^{t+\Delta t}u_{\xi,\zeta} + {}^{t+\Delta t}v_{\eta,\xi}{}^{t+\Delta t}v_{\eta,\zeta} \\
&\qquad + {}^{t+\Delta t}w_{\zeta,\xi}{}^{t+\Delta t}w_{\zeta,\zeta}) \qquad (8)
\end{aligned}
$$

where, ${}^{t+\Delta t}u_{\xi}, {}^{t+\Delta t}v_{\eta}, {}^{t+\Delta t}w_{\zeta}$ are the updated displacements of an arbitrary material particle w.r.t. the cross-sectional basis ${}^{\mathbf{0}}\boldsymbol{V}$, while, (,) denotes the spatial derivative relative to the ξ, η, ζ coordinates.

4. The internal forces/moments that arise in the geometric stiffness due to the 2nd Piola-Kirchhoff normal stress ${}^{t+\Delta t}S_{\xi\xi}(\xi,\eta,\zeta)$ are defined as,

$$
\begin{aligned}
{}^{t+\Delta t}F_{\xi\xi}(\xi) &= \int_{{}^0A} {}^{t+\Delta t}S_{\xi\xi}\, d^0A, & {}^{t+\Delta t}M_{\eta\eta}(\xi) &= \int_{{}^0A} \zeta \cdot {}^{t+\Delta t}S_{\xi\xi}\, d^0A \\
{}^{t+\Delta t}M_{\zeta\zeta}(\xi) &= \int_{{}^0A} \eta \cdot {}^{t+\Delta t}S_{\xi\xi}\, d^0A, & {}^{t+\Delta t}M_{\xi\xi 1}(\xi) &= \int_{{}^0A} \eta^2 \cdot {}^{t+\Delta t}S_{\xi\xi}\, d^0A \\
{}^{t+\Delta t}M_{\xi\xi 2}(\xi) &= \int_{{}^0A} \zeta^2 \cdot {}^{t+\Delta t}S_{\xi\xi}\, d^0A, & {}^{t+\Delta t}M_{\xi\xi 3}(\xi) &= \int_{{}^0A} \eta\zeta \cdot {}^{t+\Delta t}S_{\xi\xi}\, d^0A \qquad (9)
\end{aligned}
$$

where, ${}^0A$ is the initial cross-sectional area, ${}^{t+\Delta t}S_{\xi\xi}(\xi,\eta,\zeta) = E \cdot {}^{t+\Delta t}\epsilon_{\xi\xi}$, E is the Young's modulus, ${}^{t+\Delta t}F_{\xi\xi}(\xi)$ is the normal force, ${}^{t+\Delta t}M_{\eta\eta}(\xi)$, ${}^{t+\Delta t}M_{\zeta\zeta}(\xi)$ are the bending moments, and, ${}^{t+\Delta t}M_{\xi\xi 1-3}(\xi)$ lead to the effective torsional moment components due to the bending, all referred to the initial state. A geometrical interpretation of the last internal moment is given in [24].
The internal forces/moments that arise in the geometric stiffness due to the 2nd Piola-Kirchhoff shear stress ${}^{t+\Delta t}S_{\xi\eta}(\xi,\eta,\zeta), {}^{t+\Delta t}S_{\xi\zeta}(\xi,\eta,\zeta)$ are defined as,

$$
\begin{aligned}
{}^{t+\Delta t}F_{\xi\eta}(\xi) &= \int_{{}^0A} {}^{t+\Delta t}S_{\xi\eta}\, d^0A, & {}^{t+\Delta t}F_{\xi\zeta}(\xi) &= \int_{{}^0A} {}^{t+\Delta t}S_{\xi\zeta}\, d^0A \\
{}^{t+\Delta t}M_{\xi\xi 4}(\xi) &= \int_{{}^0A} \zeta \cdot {}^{t+\Delta t}S_{\xi\eta}\, d^0A, & {}^{t+\Delta t}M_{\xi\xi 5}(\xi) &= \int_{{}^0A} \eta \cdot {}^{t+\Delta t}S_{\xi\zeta}\, d^0A \qquad (10)
\end{aligned}
$$

where, ${}^{t+\Delta t}S_{\xi\eta}(\xi,\eta,\zeta) = G \cdot (2^{t+\Delta t}\epsilon_{\xi\eta})$, ${}^{t+\Delta t}S_{\xi\zeta}(\xi,\eta,\zeta) = G \cdot (2^{t+\Delta t}\epsilon_{\xi\zeta})$, G is the shear modulus, ${}^{t+\Delta t}F_{\xi\eta}(\xi)$, ${}^{t+\Delta t}F_{\xi\zeta}(\xi)$ are the shear forces, and, ${}^{t+\Delta t}M_{\xi\xi 4-5}(\xi)$ lead to the torsional moment components, all referred to the initial state.

By performing the cross-sectional integration analytically, the internal forces and moments are derived in relation with the cross-sectional properties and a resultant form of the strain measures.

Remark: At the updated configuration $t + \Delta t$,

- *'Rotations'* contribute in the internal elastic energy are depicted in the difference

$$
{}^{t+\Delta t}\boldsymbol{\Delta V_i}(\xi) = {}^{t+\Delta t}\boldsymbol{V_i}(\xi) - {}^0\boldsymbol{V_i}, i = s, t \qquad (11)
$$

- *'Curvature' measures* contribute in the internal elastic energy are depicted in the derivative of the above difference along the beam arc-length, $\frac{\vartheta^{t+\Delta t}\boldsymbol{\Delta V_i}(\xi)}{\vartheta\xi}, i = s, t$:

$$\frac{\vartheta({}^{t+\Delta t}\boldsymbol{V_i}(\xi) - {}^{0}\boldsymbol{V_i})}{\vartheta\xi} = \frac{\vartheta(exp(\hat{\boldsymbol{\theta}}(\xi))\,{}^{t}\boldsymbol{V_i}(\xi))}{\vartheta\xi} \tag{12}$$

where the orientation update relation (5) has been used.

For the differentiation of the exponential mapping we refer to [25], where a family of trigonometric functions, that have been used, facilitate the procedure significantly.

2.4 Perturbation of the configuration state at $t + \Delta t$

To construct the perturbed configuration state at $t + \Delta t$,

- The perturbed position of the reference line relative to ${}^{t+\Delta t}\boldsymbol{r_0}(\xi)$ is constructed as,

$${}^{t+\Delta t,\epsilon}\boldsymbol{r_0}(\xi) = {}^{t+\Delta t}\boldsymbol{r_0}(\xi) + \epsilon\,\delta\boldsymbol{u_0}(\xi) \tag{13}$$

where, $\delta\boldsymbol{u_0}(\xi) = \delta u_{0i}(\xi)\boldsymbol{E_i}$ is a vector field, interpreted, for $\epsilon > 0$, as superposed infinitesimal displacement onto the reference line [22].

- The perturbed orthogonal transformation relative to ${}^{t+\Delta t}\boldsymbol{\Lambda}(\xi)$, which consists of the cross-sectional basis ${}^{t+\Delta t}\boldsymbol{V}(\xi)$ as given in eq. (5), is constructed by two ways (fig. 3),

a)

$${}^{t+\Delta t,\epsilon}\boldsymbol{\Lambda}(\xi) = exp(\epsilon\boldsymbol{\delta\Psi}(\xi))^{t+\Delta t}\boldsymbol{\Lambda}(\xi) = exp(\epsilon\boldsymbol{\delta\Psi}(\xi))exp(\hat{\boldsymbol{\theta}}(\xi))\,{}^{t}\boldsymbol{\Lambda}(\xi) \tag{14}$$

where, $\boldsymbol{\delta\Psi}(\xi)$ is a skew-symmetric tensor field, interpreted, for $\epsilon > 0$, as superposed infinitesimal rotation (spin) onto the moving frame [22]. The eq. (5) has been used above, in the form ${}^{t+\Delta t}\boldsymbol{\Lambda}(\xi) = exp(\hat{\boldsymbol{\theta}}(\xi))\,{}^{t}\boldsymbol{\Lambda}(\xi)$.

b)

$${}^{t+\Delta t,\epsilon}\boldsymbol{\Lambda}(\xi) = exp(\hat{\boldsymbol{\theta}}(\xi) + \epsilon\delta\hat{\boldsymbol{\theta}}(\xi))\,{}^{t}\boldsymbol{\Lambda}(\xi) \tag{15}$$

where, $\delta\hat{\boldsymbol{\theta}}(\xi)$ is a skew-symmetric tensor field, interpreted, for $\epsilon > 0$, as infinitesimal rotation that can be added to the previous rotation.

To get a relation between the axial vectors $\boldsymbol{\delta\psi}(\xi)$ and $\delta\boldsymbol{\theta}(\xi)$ of the skew-symmetric matrices $\boldsymbol{\delta\Psi}(\xi)$ and $\delta\hat{\boldsymbol{\theta}}(\xi)$ respectively, the Rodrigues formula is used in eqs. (14, 15) and then, the derivative with respect to the scalar parameter ϵ is taken, for $\epsilon = 0$ [26],

$$\boldsymbol{\delta\psi}(\xi) = \boldsymbol{T(\theta)}\delta\boldsymbol{\theta}(\xi) \tag{16}$$

where,

$$\boldsymbol{T(\theta)} = \frac{sin\theta}{\theta}\boldsymbol{I} + \frac{1 - cos\theta}{\theta^2}\hat{\boldsymbol{\theta}} + \frac{\theta - sin\theta}{\theta^3}\boldsymbol{\theta}\otimes\boldsymbol{\theta} \tag{17}$$

For the derivation of the transformation $\boldsymbol{T(\theta)}$ (named as the tangential transformation because is a linear map between tangent spaces, fig. 3) see [3, 11, 27].

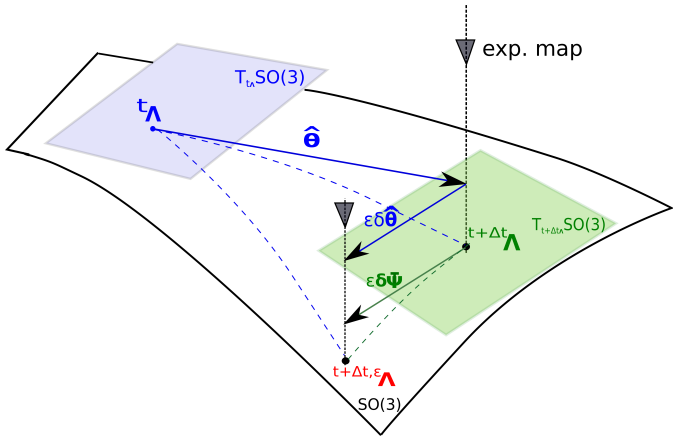

Fig. 3: Rotation increments and their projection onto the manifold SO(3) [11, 26].

2.4.1 Virtual strain measures

By employing the directional derivative onto the perturbed configuration state (eqs. 13, 14), the variation of the configuration state $(\delta \boldsymbol{r_0}(\xi), \delta \boldsymbol{\Lambda}(\xi))$ is derived,

$$\delta \boldsymbol{r_0}(\xi) = \frac{d}{d\epsilon}\bigg|_{\epsilon=0} {}^{t+\Delta t,\epsilon}\boldsymbol{r_0}(\xi) = \delta \boldsymbol{u_0}(\xi) \tag{18}$$

$$\delta \boldsymbol{\Lambda}(\xi) = \frac{d}{d\epsilon}\bigg|_{\epsilon=0} {}^{t+\Delta t,\epsilon}\boldsymbol{\Lambda}(\xi) = \boldsymbol{\delta\Psi}(\xi)\, {}^{t+\Delta t}\boldsymbol{\Lambda}(\xi) \tag{19}$$

Thus, the virtual displacement for an arbitrary material particle (ξ, η, ζ) is written as,

$$\delta \boldsymbol{u}(\xi,\eta,\zeta) = \delta \boldsymbol{u_0}(\xi) + \eta \cdot \delta \boldsymbol{V_s}(\xi) + \zeta \cdot \delta \boldsymbol{V_t}(\xi) \tag{20}$$

where, $\delta \boldsymbol{u_0}(\xi)$ is the virtual displacement of the beam reference point and $\delta \boldsymbol{V_i}(\xi) = \delta \boldsymbol{\Lambda_{ij}}(\xi)\boldsymbol{E_j}$, $i = r, s, t, j = 1-3$. Specifically, by using eqs. (16, 17, 19), the virtual cross-sectional directors are given as follows,

$$\delta \boldsymbol{V_s}(\xi) = \boldsymbol{\delta\Psi}(\xi)^{t+\Delta t}\boldsymbol{V_s}(\xi) = \boldsymbol{\delta\psi}(\xi) \times {}^{t+\Delta t}\boldsymbol{V_s}(\xi) = (\boldsymbol{T(\theta)}\delta\boldsymbol{\theta}(\xi)) \times {}^{t+\Delta t}\boldsymbol{V_s}(\xi) \tag{21}$$

$$\delta \boldsymbol{V_t}(\xi) = \boldsymbol{\delta\Psi}(\xi)^{t+\Delta t}\boldsymbol{V_t}(\xi) = \boldsymbol{\delta\psi}(\xi) \times {}^{t+\Delta t}\boldsymbol{V_t}(\xi) = (\boldsymbol{T(\theta)}\delta\boldsymbol{\theta}(\xi)) \times {}^{t+\Delta t}\boldsymbol{V_t}(\xi) \tag{22}$$

By substituting eq. (21) and eq. (22) in eq. (20), the material particle virtual displacement is written in relation with the unknown variables $\delta \boldsymbol{u_0}(\xi)$ and $\delta\boldsymbol{\theta}(\xi)$. The steps (1) and (2) from the section 2.3.1 are followed to get the initial local infinitesimal displacement gradients. Following [4] for a Total Lagrangian formulation, the corresponding components of Green-Lagrange strain tensor are given by,

- The linear virtual strain components are (for convenience the variables ξ, η, ζ are omitted from the RHS),

$$\begin{aligned}
\delta e_{\xi\xi}(\xi,\eta,\zeta) &= \delta u_{\xi,\xi} + {}^{t+\Delta t}u_{\xi,\xi}\,\delta u_{\xi,\xi} + {}^{t+\Delta t}v_{\eta,\xi}\,\delta v_{\eta,\xi} + {}^{t+\Delta t}w_{\zeta,\xi}\,\delta w_{\zeta,\xi} \\
\delta e_{\xi\eta}(\xi,\eta,\zeta) &= \frac{1}{2}(\delta u_{\xi,\eta} + \delta v_{\eta,\xi} + {}^{t+\Delta t}u_{\xi,\xi}\,\delta u_{\xi,\eta} + {}^{t+\Delta t}v_{\eta,\xi}\,\delta v_{\eta,\eta} + {}^{t+\Delta t}w_{\zeta,\xi}\,\delta w_{\zeta,\eta} \\
&\quad + {}^{t+\Delta t}u_{\xi,\eta}\delta u_{\xi,\xi} + {}^{t+\Delta t}v_{\eta,\eta}\,\delta v_{\eta,\xi} + {}^{t+\Delta t}w_{\zeta,\eta}\,\delta w_{\zeta,\xi}) \\
\delta e_{\xi\zeta}(\xi,\eta,\zeta) &= \frac{1}{2}(\delta u_{\xi,\zeta} + \delta w_{\zeta,\xi} + {}^{t+\Delta t}u_{\xi,\xi}\,\delta u_{\xi,\zeta} + {}^{t+\Delta t}v_{\eta,\xi}\,\delta v_{\eta,\zeta} + {}^{t+\Delta t}w_{\zeta,\xi}\,\delta w_{\zeta,\zeta} \\
&\quad + {}^{t+\Delta t}u_{\xi,\zeta}\,\delta u_{\xi,\xi} + {}^{t+\Delta t}v_{\eta,\zeta}\,\delta v_{\eta,\xi} + {}^{t+\Delta t}w_{\zeta,\zeta}\,\delta w_{\zeta,\xi})
\end{aligned} \tag{23}$$

where, $\delta u_\xi, \delta v_\eta, \delta w_\zeta$ are the components of the virtual displacement for the material particle (ξ, η, ζ), eq. (20), rotated to the cross-sectional basis ${}^{\mathbf{0}}\boldsymbol{V}$, and, (,) denotes the spatial derivative relative to the ξ, η, ζ coordinates.

- The non-linear virtual strain components are (for convenience the variables ξ, η, ζ are omitted from the RHS),

$$\begin{aligned}
\delta\eta_{\xi\xi}(\xi,\eta,\zeta) &= \frac{1}{2}(\delta u_{\xi,\xi}^2 + \delta v_{\eta,\xi}^2 + \delta w_{\zeta,\xi}^2) \\
\delta\eta_{\xi\eta}(\xi,\eta,\zeta) &= \frac{1}{2}(\delta u_{\xi,\xi}\delta u_{\xi,\eta} + \delta v_{\eta,\xi}\delta v_{\eta,\eta} + \delta w_{\zeta,\xi}\delta w_{\zeta,\eta}) \\
\delta\eta_{\xi\zeta}(\xi,\eta,\zeta) &= \frac{1}{2}(\delta u_{\xi,\xi}\delta u_{\xi,\zeta} + \delta v_{\eta,\xi}\delta v_{\eta,\zeta} + \delta w_{\zeta,\xi}\delta w_{\zeta,\zeta})
\end{aligned} \tag{24}$$

3 VIRTUAL WORK EQUATION FOR A TOTAL LAGRANGIAN FORMULATION

The equilibrium equation of the body at $(t + \Delta t, \epsilon)$ is given by [4],

$$\int_{{}^0V} {}^0\rho\, {}^{t+\Delta t,\epsilon}\ddot{r}_{Gk}\, \delta u_k d^0V + \int_{{}^0V} {}^{t+\Delta t,\epsilon}S_{ij}\, \delta^{t+\Delta t,\epsilon}\epsilon_{ij}\, d^0V = \int_{{}^0V} {}^{t+\Delta t}f_k^G\, \delta u_k\, d^0V + \int_{{}^{t+\Delta t}S_f} {}^{t+\Delta t}f_k^S\, \delta u_k^S\, d^{t+\Delta t}S \tag{25}$$

where, ${}^0V$ is the initial volume, ${}^0\rho$ is the mass density referred to the initial state, ${}^{t+\Delta t,\epsilon}\ddot{r}_{Gk}$, $k = \xi, \eta, \zeta$ is the acceleration of the particle due to all the inertia effects [2], i.e. the acceleration of the body origin, the Coriolis acceleration, and, the acceleration due to the body deformation, $\delta u_k = \left\{\delta u_\xi, \delta v_\eta, \delta w_\zeta\right\}^T$ are the virtual displacements, ${}^{t+\Delta t,\epsilon}S_{ij}$, $i, j = \xi, \eta, \zeta$, are the 2nd Piola-Kirchhoff stress components, $\delta^{t+\Delta t,\epsilon}\epsilon_{ij}$ are the virtual strains, ${}^{t+\Delta t}f_k^G$ is the gravitational load and ${}^{t+\Delta t}f_k^S$ is the surface aerodynamic load, where ${}^{t+\Delta t}S_f$ corresponds to the last calculated surface area.

For the linearization of the internal virtual work (2nd term of the LHS of the above relation 25), the iterative decompositions for stresses and strains are used,

$${}^{t+\Delta t,\epsilon}S_{ij} = {}^{t+\Delta t}S_{ij} + dS_{ij} \tag{26}$$

$${}^{t+\Delta t,\epsilon}\epsilon_{ij} = {}^{t+\Delta t}\epsilon_{ij} + d\epsilon_{ij},\ d\epsilon_{ij} = de_{ij} + d\eta_{ij} \tag{27}$$

where, ${}^{t+\Delta t}S_{ij} = C_{ijrs}\,{}^{t+\Delta t}\epsilon_{ij}$, C_{ijrs} expresses the material constitutive behaviour, ${}^{t+\Delta t}\epsilon_{ij}$ are given by eq. (8), $dS_{ij} = C_{ijrs}\, d\epsilon_{ij}$, de_{ij} is the linear strain part, given by the same relations as the corresponding virtual strain components (eqs. 23), and $d\eta_{ij}$ is the non-linear strain part, the variation of which is related to the geometrical stiffness. While variation and linearization can commute, the variation $\delta d\eta_{ij}$ is given by the chain-differentiation of eqs. (24).

Substituting in relation (25) the iterative decompositions (26) and (27), and following the

linearization process as it is presented in [4], the linearized equilibrium equation is derived,

$$\int_{{}^0V} {}^0\rho\, {}^{t+\Delta t,\epsilon}\ddot{r}_{Gk}\, \delta u_k d^0V + \left\{ \underbrace{\int_{{}^0V} C_{ijrs}\, de_{rs}\, \delta e_{ij}\, d^0V}_{\Rightarrow \boldsymbol{K_{mat}}} + \underbrace{\int_{{}^0V} {}^{t+\Delta t}S_{ij}\, \delta d\eta_{ij}\, d^0V}_{\Rightarrow \boldsymbol{K_{geom}}} \right\} =$$

$$\int_{{}^0V} {}^{t+\Delta t}f_k^G\, \delta u_k\, d^0V + \int_{{}^{t+\Delta t}S_f} {}^{t+\Delta t}f_k^S\, \delta u_k^S\, d^{t+\Delta t}S - \left(\underbrace{\int_{{}^0V} {}^{t+\Delta t}S_{ij}\, \delta e_{ij} d^0V}_{\Rightarrow \boldsymbol{F_{int}}} \right) \tag{28}$$

To construct the under-braced integrals, one has to substitute the strain components de_{rs}, δe_{ij} and $\delta d\eta_{ij}$ in eq. (28). By performing analytical integration over the cross-sectional area, the 1D form of the linearized virtual work is derived. After discretization, the matrices $\boldsymbol{K_{mat}}$, $\boldsymbol{K_{geom}}$ and the vector $\boldsymbol{F_{int}}$ are constructed. The first matrix refers to the resistance due to the linear constitutive behaviour of the material, while, the second one refers to the resistance due to the non-linear geometrical stiffness.

As far as the numerical implementation is concerned, one has to note two issues. The first is that the developed finite element is based on a quadratic interpolation, using a 2nd order Lagrange polynomial, of both the displacement and the rotation parameters, while, the second is that the mass matrix is evaluated using the initial configuration of the body, and thus, it is calculated prior to the step-by-step solution. Time integration is performed using the Newmark 2nd order implicit method [4].

4 NUMERICAL RESULTS

Time domain non-linear aeroelastic simulations for the isolated rotor of the 5MW NREL reference wind turbine [20] are performed, using the multi-body hydro-servo-aeroelastic tool hGAST [1, 2]. The present non-linear Degenerate-Continuum based Timoshenko beam model (non-linear DC) is compared to the 2nd order Euler-Bernoulli beam model (non-linear EB), the sub-body beam model (non-linear SB) and the linear one (linear). The transverse shear effect was neglected in view of enabling direct comparison with the 2nd order Euler-Bernoulli model. The 2nd order Euler-Bernoulli beam model accounts for moderate deflections by using an ordering scheme acted on the cross-sectional rotations [14, 28]. The sub-body modeling is an extension of the multi-body formulation to the body level. It consists of dividing the body (blade) into sub-bodies, which are subsequently treated as beam elements. At the sub-body level, local deflections and rotations are assumed small, and thus, the use of a linear Timoshenko beam model is justified, while by imposing kinematic and dynamic continuity between consecutive sub-bodies at their connection points, large deflections and rotations are gradually built [28]. The linear model accounts for the non-linear tension-bending coupling effect, which is added in the analysis of rotating bodies, since the centrifugal force increases their bending stiffness.

Uniform inflow conditions are considered at the rated wind speed of $11.4m/s$, where the deflections are expected to attain their maximum value and, in turn, the non-linear effects will be more pronounced. The rotor is operated at fixed rotational speed of $12rpm$ and at zero pitch angle (open loop operation, i.e. the controller is not active), corresponding to average operating conditions at the rated wind speed. The results are presented in terms of time histories, after the initial transients are damped.

In fig. 4, the blade tip twist angle is presented. The three non-linear models (non-linear DC, non-linear EB, non-linear SB) predict higher amplitudes of the twist angle variation as compared with the linear model. This is linked to the bending-torsion coupling effect [28] which is predicted only by the non-linear models. Although the twist angle amplitude as predicted by the non-linear SB model is $\sim 20\%$ reduced compared to the other two non-linear models, the phase of the signal is in perfect agreement between the three of them. Moreover, the non-linear models result to an increase of the twist angle mean value ($\sim 0.4^o$ for the non-linear SB model and $\sim 0.25^o$ for the other two non-linear models) compared to the linear model ($\sim 0.1^o$).

The increase in the amplitude of the twist angle affects the flapwise deflection (fig. 5) through the corresponding change in the effective angle of attack. So, in fig. 5, the three non-linear models depict a phase shift of the flapwise deflection signal compared to the linear model, following the phase of the torsion angle. Moreover, the non-linear DC and non-linear EB models predict the same amplitude of the flapwise deflection variation, although the non-linear DC model results to a slightly reduced mean value compared to the non-linear EB model. The non-linear SB model shows reduced amplitude of the variation ($\sim 25\%$) compared to the other two non-linear models, and slightly reduced compared to the linear model. The flapwise deflection mean value predicted by the non-linear SB model is identical to this of the linear modeling.

In fig. 6, the blade tip edgewise deflections are presented. As expected, the agreement between the four models is good, since the edgewise direction of the blade is stiff compared to the flapwise one, and, the corresponding loads are driven just by the gravity. In fig. 7, the blade tip extension is presented. The linear model predicts a positive extension due to the centrifugal force, while, the three non-linear models consistently predict the virtual axial shortening of the blade due to the bending.

Regarding the loads, the non-linear models predict considerably higher amplitude of the blade root torsion moment due to the bending-torsion coupling, as seen in fig. 8. The linear model results to an almost constant torsion moment, independent of the azimuth position of the blade. Its mean value is reduced about 40% compared to all the non-linear beam models, which predict almost the same mean values of the torsion moment. The amplitude of the variation is identical for the non-linear DC and non-linear EB models, while, the non-linear SB model predicts reduced amplitude ($\sim 30\%$).

In similar with the flapwise deflections (fig. 5), the amplitude of the flapwise bending moment at the blade root (fig. 9) is clearly affected by the increase in the amplitude of the twist angle (fig. 4). This is depicted in the results of all the non-linear models. Specifically, the non-linear DC model predicts a slightly increased amplitude of the variation ($\sim 5\%$) compared to the non-linear EB model, while, the other models follow with $\sim 20\%$ reduced amplitude for the non-linear SB model and $\sim 70\%$ reduced amplitude for the linear one, compared to the non-linear DC model. The mean value of the flapwise moment is almost the same for the non-linear DC, the non-linear EB and the linear model, while, the non-linear SB model predicts slightly increased mean value. A good agreement between the three non-linear models is obtained in the phase of the signal (which again follows the phase of the twist angle variation).

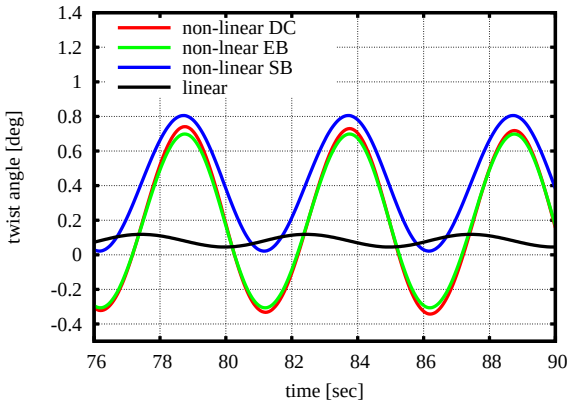

Fig. 4: Time history of the tip twist angle.

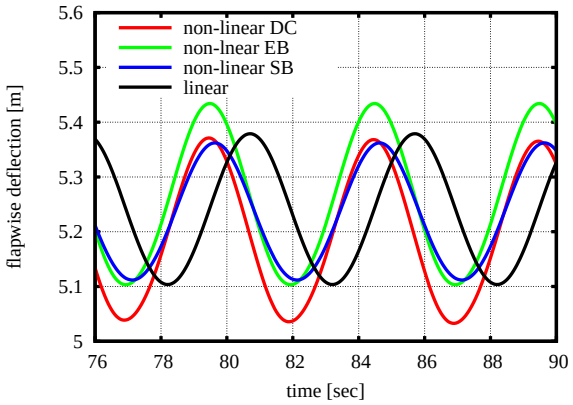

Fig. 5: Time history of the tip flapwise displacement.

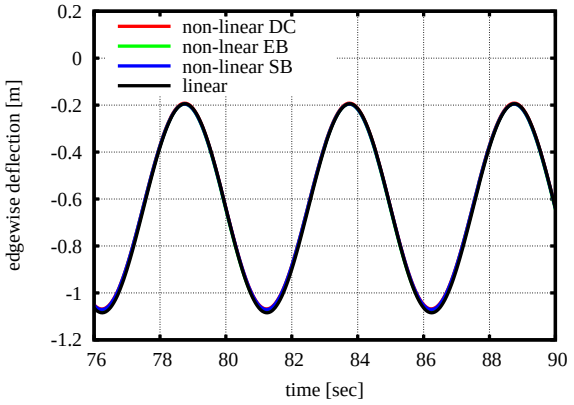

Fig. 6: Time history of the tip edgewise displacement.

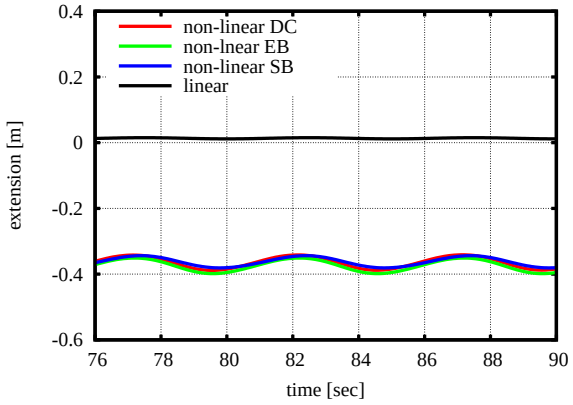

Fig. 7: Time history of the tip extension.

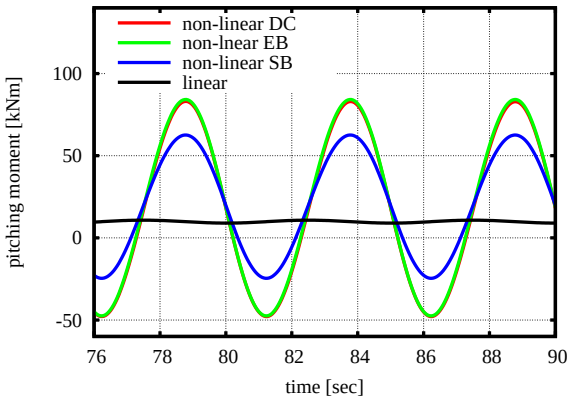

Fig. 8: Time history of the root pitching moment.

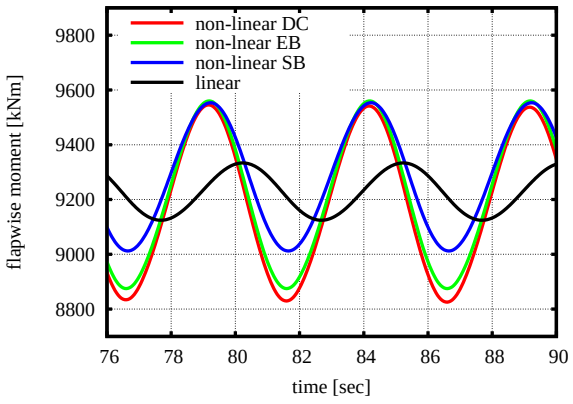

Fig. 9: Time history of the root flapwise bending moment

5 CONCLUDING REMARKS

A Total Lagrangian degenerate-continuum based Timoshenko beam approach was presented. The important features are that there is no constraint in the magnitude of displacements and rotations and that the beam model may be easily extended to a general curved beam. The main kinematic assumption is that the cross-sectional plane remains planar and rigid during deformation, although warping can be included in the formulation.

The present beam approach was implemented in the multi-body hydro-servo-aeroelastic tool hGAST. The stiffness of the beam is derived by retaining all the geometrical non-linear terms from the Green strain tensor, while, the beam inertia is taken into account using the initial configuration. The aeroelastic analysis of the three-bladed rotor of the 5MW NREL reference wind turbine was performed. The numerical results compare four modelings, the present beam approach, the 2nd order Euler-Bernoulli, the sub-body and the linear one, to assure the validity of the present formulation. The comparisons show that the present formulation works well, while the non-linear coupling effects compare well with the 2nd order Euler-Bernoulli beam theory model. The basic outcome from the analyses is that the geometrical non-linearity is significant w.r.t. the torsion-bending coupling terms and this is shown mainly in the torsional response, which is the basic factor for the determination of the aerodynamic loading.

ACKNOWLEDGMENT

The first author wishes to acknowledge the funding received towards the present work from the Fanourakis Foundation fellowship and Leventis Foundation fellowship. She also wishes to thank MSc. Structural Engineer Evangelos Katsavrias for his support in programming and for helpful discussions.

REFERENCES

[1] V. Riziotis, S. Voutsinas, GAST: A general aerodynamic and structural prediction tool for wind turbines, *EWEC Conference*, Dublin Castle, Ireland, 1997.

[2] D. Manolas, Hydro-aero-elastic analysis of offshore wind turbines, *PhD Thesis*, NTUA, Athens, 2015.

[3] M. A. Crisfield, *Non-linear finite element analysis of solids and structures, Vol. 2: Advanced topics*. John Wiley & Sons Ltd., 1997.

[4] K-J. Bathe, *Finite Element Procedures*. Prentice-Hall, Inc., 1996.

[5] E. N. Dvorkin, E. Oñate, J. Oliver, On a non-linear formulation for curved Timoshenko beam elements considering large displacement/rotation increments, *International Journal for Numerical Methods in Engineering*, **26**, 1597-1613, 1988.

[6] E. Reissner, On one-dimensional finite-strain beam theory: the plane problem, *Journal of applied mathematics and physics (ZAMP)*, **23**, 795-804, 1972.

[7] J. C. Simo, A finite strain beam formulation. The three-dimensional dynamic problem. Part I, *Computer Methods in Applied Mechanics and Engineering*, **49**, 55-70, 1985.

[8] S. Ahmad, B. M. Irons, O. C. Zienkiewicz, Curved thick shell and membrane elements with particular reference to axi-symmetric problems, *Proc. 2nd Conf. Matrix Methods in Structural Mechanics.* Wright-Patterson Air Force Base, Ohio, 1968.

[9] E. Reissner, On finite deformations of space-curved beams, *Journal of applied mathematics and physics (ZAMP)*, **32**, 734-744, 1981.

[10] G. Jelenić, M. A. Crisfield, Geometrically exact 3D beam theory: implementation of a strain-invariant finite element for statics and dynamics, *Computer Methods in Applied Mechanics and Engineering*, **171**, 141-171, 1999.

[11] A. Cardona, M. Geradin, A beam finite element non-linear theory with finite rotations. *International Journal for Numerical Methods in Engineering*, **26**, 2403-2438, 1988.

[12] A. Ibrahimbegocić, On finite element implementation of geometrically nonlinear Reissner's beam theory: three-dimensional curved beam elements, *Computer Methods in Applied Mechanics and Engineering*, **122**, 11-26, 1995.

[13] P. Zhang, S. Huang, Review of aeroelasticity for wind turbine: Current status, research focus and future perspectives, *Frontiers in Energy*, **5(4)**, 419-434, 2011.

[14] D. H. Hodges, E. H. Dowell, Nonlinear equations of motion for the elastic bending and torsion of twisted nonuniform rotor blades, *NASA TN D-7818*, 1974.

[15] D. H. Hodges, *Nonlinear Composite Beam Theory, Volume 213 Progress in Astronautics and Aeronautics*. American Institute of Aeronautics and Astronautics Inc., 2006.

[16] P. F. Pai, *Highly Flexible Structures: Modeling, Computation, and Experimentation*. American Institute of Aeronautics and Astronautics Inc., 2007.

[17] S. G. Voutsinas, V. A. Riziotis, P. Chaviaropoulos, Non-linear aerodynamics and fatigue loading on wind turbines operating at extreme sites, *AIAA Paper* No. 97-0935, 1997.

[18] Z. Q. Chen, T. J. A. Agar, Geometric nonlinear analysis of flexible spatial beam structures, *Computers & Structures*, **49(6)**, 1083-1094, 1993.

[19] H. Goldstein, C. Poole, J. Safko, *Classical mechanics*. Third edition, Addison Wesley, 2001.

[20] J. Jonkman, S. Butterfield, W. Musial, G. Scott, Definition of a 5-MW Reference Wind Turbine for Offshore System Development. *Technical Report, NREL/TP-500-38060*, February 2009.

[21] J. Argyris, An excursion into large rotations. *Computer Methods in Applied Mechanics and Engineering*, **32**, 85-155, 1982.

[22] J. C. Simo, L. Vu-Quoc, A three-dimensional finite-strain rod model. Part II: Computational aspects, *Computer Methods in Applied Mechanics and Engineering*, **58**, 79-116, 1986.

[23] M. Papadrakakis, *Analysis of Structures with the Finite Element Method (in Greek)*, Papasotiriou Publics, 2001.

[24] C. J. Houbolt, W. G. Brooks, Differential equations of motion for combined flapwise bending, chordwise bending, and torsion of twisted nonuniform rotor blades, *NACA Technical Note 3905*, 1958.

[25] M. Ritto-Corrêa, D. Camotim, On the differentiation of the Rodrigues formula and its significance for the vector-like parameterization of Reissner-Simo beam theory, *International Journal for Numerical Methods in Engineering*, **55**, 1005-1032, 2002.

[26] A. Ibrahimbegović, F. Frey, I. Kožar, Computational aspects of vector-like parametrization of three-dimensional finite rotations, *International Journal for Numerical Methods in Engineering*, **38**, 3653-3673, 1995.

[27] J. C. Simo, L. Vu-Quoc, On the dynamics in space of rods undergoing large motions - A geometrically exact approach, *Computer Methods in Applied Mechanics and Engineering*, **66**, 125-161, 1988.

[28] D. I. Manolas, V. A. Riziotis, S. G. Voutsinas, Assessing the importance of geometric nonlinear effects in the prediction of wind turbine blade loads, *Journal of Computational and Nonlinear Dynamics*, **20(4)**, ASME, 2015.

ECCOMAS Congress 2016
VII European Congress on Computational Methods in Applied Sciences and Engineering
M. Papadrakakis, V. Papadopoulos, G. Stefanou, V. Plevris (eds.)
Crete Island, Greece, 5–10 June 2016

DYNAMICS OF WIND TURBINE BLADES USING A GEOMETRICALLY-EXACT BEAM FORMULATION

Celso Jaco Faccio Júnior[1], **Alfredo Gay Neto**[1]

[1]Polytechnic School at University of São Paulo
Av. Prof. Almeida Prado tv. 2, n. 83
celsojf@gmail.com, alfredo.gay@usp.br

Keywords: Wind Turbine, Blade, Beam, Finite Element Method.

Abstract. *On wind energy context, the blades of horizontal axes wind turbines have, in their majority, a closed multicellular thin-walled cross section, which varies along the blade length due to aerodynamic requirements. If one wants to analyze the structural behavior of such blades, a dynamic model is necessary. Such models are desirable, since it is important the development of lighter and more flexible wind turbine designs. The desirable results of the models include evaluating the possible large deflections along time, the internal loads along the blade length and natural frequencies experimented by the structure. Moreover, one can address the magnitude and frequency of the reactions lying at the top of the turbine tower structure, due to the action of the blades. In order to model the blades with a small number of degrees of freedom, geometrically-exact beam elements are employed. The equivalent properties to be input in the model, however, are not straightforward to be obtained. This is one of the goals of the present work. A pre-processor was developed to evaluate the cross sections properties of a wind turbine blade. It calculates all the necessary input data to represent the blade as an equivalent beam and, generates an input file with data of the model to be solved in the geometrically-exact GIRAFFE dynamic simulator. Since dealing with multicellular thin-walled cross section, it is important to evaluate the centroid, the barycenter, the shear center, the inertia properties, and the equivalent specific mass. All these properties may vary along the blade length. It is possible to manipulate the blade profile, changing the number of cells, thickness, materials involved, shape of the external shell and webs positioning. The developed pre-processor, together with the dynamic simulator, can be used to predict large displacements in a dynamic simulation of wind turbines.*

1 INTRODUCTION

The idea of using the kinetic energy provided from wind is not new. There are registers of windmills dated even from medieval times. However, the current increase for energy demand, has made of the wind energy one of the most important renewable energy resources. One of the issues raised during the last years is the structural design that best fits on the role of extracting the kinetic energy from wind. Although many innovative designs are being proposed, the most common still used is the horizontal axis wind turbine (HAWT).

HAWT are structures which usually are made by some slender bodies, composed mainly by a foundation, a tower, a nacelle a rotorhub and blades. It comes that HAWT have been presenting good results on energy production. Although many issues, such as the local wind flow may affect an HAWT, it has been seen that the energy production is directly associated with the diameter of the rotor and the design of the blades. As expected, a large rotor diameter produces more energy. For example, a HAWT 41 m rotor diameter may produce 600 kW, while a 66 m rotor may produce up to 1500 kW (Hau, 2013). Unlikely the rotor diameter, there is no straightforward relation between the blades airfoil design and the energy production. In fact, the relation between the shape of the blade and the energy production is much more complex and plays a major role, since it is the structure responsible for extracting the wind energy. The blade shape is influenced by aspects such as:

- Rotor diameter;
- Aerodynamic loads;
- Gravitational loads;
- Fluid structure interaction;
- Others.

An accurate modeling of those aspects should result in a structure able not just to resist to internal and external forces, but also that has the best use of the materials and gives the minimum maintenance. It follows that modern blade of HAWT's are becoming more slender, more flexible and composite made. All of those questions lead to a huge complexity when modeling and simulating HAWT. These models should be able to handle dynamics, nonlinearities and instability.

Deal with all the variables that compose the problem on a high-hierarchy context (e.g.: finite elements solids) may result on non-practical solution time and on hard to evaluate inputs and outputs. On the other hand, beam-like modeling presents, generally, fast solution time and easier to handle inputs and outputs. Although beam-like models present some simplifications, a huge amount of works proves that they are very representative and still useful.

Despite of the inherent simplifications, there are different beams theories that may apply, accordingly to the problem to be solved. Depending on the slenderness and on the cross section characteristics, one may choose to represent the structure using the Bernoulli-Euler beam, the Timoshenko beam, the Vlasov's beam (when warping plays a role), among other theories - refer to (Gere and Timoshenko, 1997), (Timoshenko and Goodier, 1951) and (Vlasov, 1961) for the classical theories here referenced.

1.1 The geometrically-exact beam model

When presenting the distinct beam theories, always one has a kinematic assumption regarding the behavior of the beam cross-sections. The Bernoulli-Euler beam theory is known as the classic beam theory. Their main assumption is that the beam cross-section moves as a rigid body and that it keeps orthogonal to the beam axis. On the Timoshenko beam theory the beam cross-section has rotation degrees of freedom around the beam axis, leading to distortion due to shear. The Timoshenko-Vlasov theory has the non-uniform Vlasov torsion in addition to the Timoshenko beam theory hypothesis. Therefore, it is necessary to introduce the concept of bimoment and bishear as a consequence of the non-uniform torsion of the beam.

The geometrically-exact beam theory may consider Bernoulli-Euler, Timoshenko or more elaborated kinematic assumptions of the cross-section. The main feature of such model is that the cross-section movement may present finite rotations and large translations in space. We here mention some works, basis of current developments: the first developments on this theory were presented on Simo (1985), Simo and Vu Quoc (1991) and Pimenta and Yojo (1993). Although the rotation tensors were expressed by Yojo (1993) using the Euler parameters, the development using Rodrigues parameters were after presented on Pimenta and Campello (2001).

The geometrically-exact beam theory plays a very important role on high-nonlinear engineering structures, such as offshore risers and slender wind turbines. A geometrically-exact model for static offshore risers for oil exploitation was presented by Gay Neto et al. (2014a), which was used to study the riser stability under torsion by Gay Neto and Martins (2013), Gay Neto et al. (2014b) and Wriggers et al. (2015). On these models, the contact between the riser and the seabed is considered, and in some cases a rolling beam to flat surface contact model is used, as presented by Gay Neto et al. (2014a).

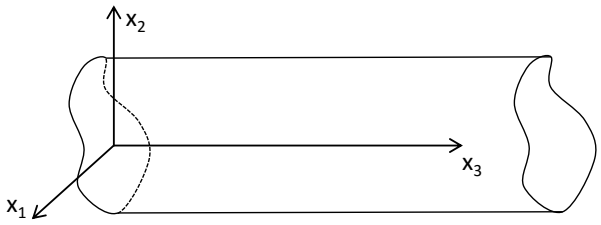

Figure 1: Beam axis notation.

Although all the complexity involved on the development of the geometrically-exact beam formulation, a linear constitutive equation regarding the cross section of a warping-free beam element is given by:

$$\boldsymbol{\sigma} = \boldsymbol{D}\boldsymbol{\varepsilon}, \tag{1}$$

where $\boldsymbol{\sigma}$ is a vector that collects the generalized stresses (internal loads) of the beam and is defined as:

$$\boldsymbol{\sigma} = \begin{bmatrix} N_1 \\ N_2 \\ N_3 \\ M_1 \\ M_2 \\ M_3 \end{bmatrix}, \tag{2}$$

where N_1, N_2 and N_3 are the components of the internal force and M_1, M_2 and M_3 are the components of the internal moment. The variable $\boldsymbol{\varepsilon}$ is a vector that collects the generalized strains of the beam and is defined as

$$\boldsymbol{\varepsilon} = \begin{bmatrix} \eta_1 \\ \eta_2 \\ \eta_3 \\ \kappa_1 \\ \kappa_2 \\ \kappa_3 \end{bmatrix}, \tag{3}$$

and $\boldsymbol{D}$ is the constitutive matrix of the beam as follows

$$\boldsymbol{D} = \begin{bmatrix} GA & 0 & 0 & 0 & 0 & G(S_1^s - S_1) \\ 0 & GA & 0 & 0 & 0 & G(-S_2^s + S_2) \\ 0 & 0 & EA & ES_1 & -ES_2 & 0 \\ 0 & 0 & ES_1 & EI_{11} & -EI_{12} & 0 \\ 0 & 0 & -ES_2 & -EI_{12} & EI_{22} & 0 \\ G(S_1^s - S_1) & G(-S_2^s + S_2) & 0 & 0 & 0 & GI_t \end{bmatrix}, \tag{4}$$

where E is the material Young Modulus, G is the material Shear Modulus, A is the beam cross-section area, S is the first order moment of inertia, I is the second order moment of inertia, I_t is the torsion stiffness and S_1^s and S_2^s are given by:

$$S_1^s = A(g_2 - s_2) \tag{5}$$

$$S_2^s = A(g_1 - s_1), \tag{6}$$

where the (g_1, g_2) are cross-section centroid coordinates and (s_1, s_2) are the shear center coordinates. The subscript numbers indicate from which axis the property is calculated and the 12 subscript is used to refer to the product of inertia. Figure 2 presents a generic beam section located at an arbitrary point $\boldsymbol{O}$, the centroid $\boldsymbol{g}$ in green and the shear center $\boldsymbol{s}$ in red.

1.2 Wind Turbine Blade Cross-Section Profiles

As commented in Section 1, HAWT blades design may be very complex due to all the requirements that it should satisfy such as the dynamic loads, the materials involved, the manufacturing process and others. Due to all of these needs it is very common to have blades with varying cross sections along their length. This solution permits each blade section to be designed according to their specific requirements. It is also very common the usage of two webs,

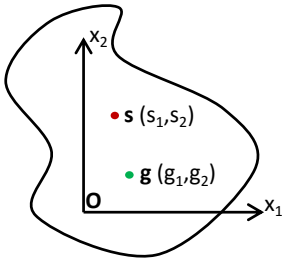

Figure 2: Beam cross-section.

in order to improve the mechanical properties of the cross section. A typical HAWT blade profile is presented in Figure 3, where one may observe an outer shell in black color and two webs in red color.

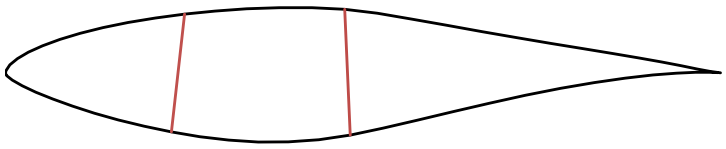

Figure 3: Typical HAWT blade profile.

The first profiles used on HAWT blades were designed by the Nation Advisory Committee for Aeronautics (NACA). The results, however, were not as expected. It was proved then that an aeronautical profile is not necessarily the best profile for an HAWT (Burton et al., 2011).

The early developments of profiles for specific use on HAWT began with a partner work with the National Renewable Energy Laboratory (NREL) and Tangler and Somers (1995). This work produced some families of profiles for specific stall-regulated, variable pitch and variable-rpm wind turbines. Some of the NREL profiles information is available on their website (`https://wind.nrel.gov/airfoils/`). Other families of airfoils designed for HAWT are the Risø airfoils family (Fugslang and Bak, 2004) and the Delft airfoils family (Timmer and van Rooij, 2003).

1.3 Shear Center and Shear Stresses on Thin-Walled Beams

As presented on subsection 1.1, a necessary property to evaluate the constitutive matrix $\boldsymbol{D}$ is the shear center of the beam cross-section. The shear center is a specific point in the cross section where shear forces may be applied, producing no twist. Although this simple definition, the distribution of the shear stresses may be very complex regarding the material of the cross section, thickness considerations and the number of cells. More definitions about the shear center are found in works such as Pilkey (2002) and Fung (1993). The shear center referred to an arbitrary origin $\boldsymbol{O}$ may be defined, assuming the known shear stresses distribution $\boldsymbol{q} = \hat{\boldsymbol{q}}(A)$ from an applied shear force magnitude V, with components V_1 and V_2, in the cross-section plane. It is also possible to calculate each coordinate of the shear center separately. To calculate

the s_1 it is necessary to apply a shear force parallel to the axis 2 such as V_2. An analogue process also applies for the other beam section axis. Therefore, the shear center coordinates are:

$$s_1 = \frac{1}{V_2} \int_A |\boldsymbol{r} \times \boldsymbol{q}| dA \tag{7}$$

$$s_2 = \frac{1}{V_1} \int_A |\boldsymbol{r} \times \boldsymbol{q}| dA, \tag{8}$$

where $\boldsymbol{r}$ measures the distance between the origin $\boldsymbol{O}$ to the s element. Figure 4 presents a beam section, an arbitrary origin $\boldsymbol{O}$ and a thin-walled element s of the beam.

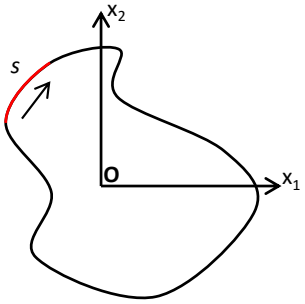

Figure 4: Beam thin-walled section and element s.

Thus, the major difficult arises from finding the shear stress distribution on the cross section of the beam. On this work, in order to reduce the complexity on finding the shear stress distribution, the thin-walled hypothesis is adopted. Furthermore, on this work the shear center follows the definition presented on Megson (2014) and expands it to a multicellular profile. The hypothesis adopted is that since the force is applied at the shear center each cell should have zero twist.

The thin-walled approach allows the consideration of constant stresses across the thickness of the beam. Other simplifications of this hypothesis is that squares and higher order terms of t are neglected on the section properties calculations and that the section is represented by its mid-line. Regarding the thin-walled assumption, according to Megson (2005) there is no exactly definition for a thin-walled structure, however it is pointed that the approximations are reasonably accurate for section which the ratio

$$\frac{t_{max}}{b} < 0.1 \tag{9}$$

where t_{max} is the maximum thickness of the section and b is a typical cross section dimension.

1.4 Torsion on Thin-Walled Beams

The last missing parameter for the constitutive matrix $\boldsymbol{D}$ presented on Subsection 1.1 is the torsion stiffness I_t. The torsion stiffness may be interpreted as the axial rotation stiffness of a given beam cross-section to an applied pure torque. It is defined as

$$GI_t = \frac{T}{\theta} \tag{10}$$

where T is the applied torque, G is the Shear Modulus and θ is the rate of twist of the section. Moreover, in order to calculate the torsion stiffness it is necessary to evaluate the rate of twist response to an applied torque. It is possible to prove, by equilibrium conditions, that a closed section thin-walled beam subject to a pure torque T, without axial constraints, has solution only for a constant shear flow q. On the case of a constant shear flow the rate of twist per unit length may be expressed as

$$\theta = \frac{q}{2GA} \oint \frac{ds}{t}, \tag{11}$$

where A is the enclosed area of the cell, ds is the differential thin-walled element and t is the thickness of the s element. Therefore, the torsion stiffness calculation of a single thin-walled profile may be summarized as:

1. Define a convenient rate of twist θ.
2. Calculate the equivalent shear flow q.
3. Calculate the torsion equivalent T.
4. Use equation 10 to calculate the torsion stiffness GI_t.

Although this simple process for the calculation of a single cell torsion stiffness, the multi-cellular torsion stiffness calculations are quite more complex. This work follows the the multi-cellular torsion stiffness definition presented by Shama (2010). The main hypothesis presented on this work is that each cell has the same twist per unit length. This condition generates one additional equation for each cell and makes the problem determined.

2 WIND TURBINE FEM MODEL

2.1 GIRAFFE

The GIRRAFE platform represents an advance on a previous finite element code named "FemCable", which main motivation was a finite element simulation of offshore structures, more specifically, the simulation of oil explotation risers. More information about the FemCable and their use is available at Gay Neto (2012).

The Generic Interface Readily Accessible for Finite Elements (GIRAFFE) is a generic platform for finite element analysis specially suitable for structural problems which may include translational and rotational DOFs and possible multiphysics applications (Gay Neto, 2015). Although GIRAFFE is not a fully generic platform, it was developed using the C++ object oriented language in a such way that new formulations, including translational and rotational DOFs, may be easily incorporated.

Furthermore, one of the finite element formulations available in GIRAFFE is the geometrically-exact beam presented on the subsection 1.1 which makes it a properly tool for the analysis of a highly nonlinear problem such as an HAWT dynamic simulation.

2.2 Wind Turbine Program

Although the simplicity of an beam-like model, some difficulties may arise to the assembly of an HAWT blade model. Some of the possible difficulties are:

- Varying airfoil shape along the blade.
- Calculation of geometric properties such as torsion stiffness and shear center of each cross-section.

The varying airfoil shape nature of an HAWT blade maybe an important issue since it has a huge variation along the length due to all structural requirements. Furthermore, the common use of webs on the cross section of HAWT blades may turn the calculation of the geometric properties such as the torsion stiffness and the shear center into a very laborious task.

In order to help on these issues it was developed a C# program with a GUI that helps on the geometric description of the blades for an HAWT. The program uses the thin-walled approximation and defines the profile by a set of points and the webs by the index of these points. The program interface is presented on Figure 5.

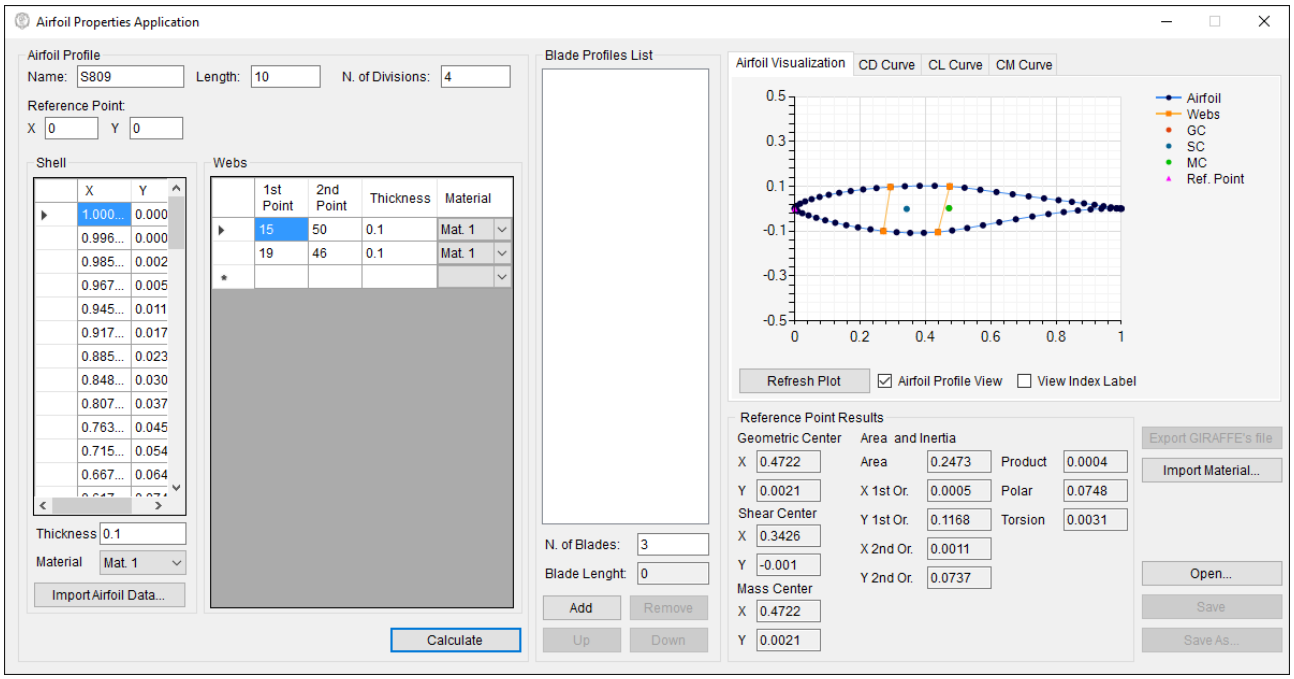

Figure 5: Wind Turbine GUI.

Some of the main features of the program are:

- Instant calculation of airfoil profile geometric properties.
- Permits the creation of a group of airfoil profiles.
- Permits the definition of any point as the beam axis.
- Exports all the necessary information to build the constitutive matrix for the GIRAFFE geometrically-exact beam formulation.

2.3 FEM Model Description

The aim of this subsection is to describe, in detail, all the characteristics that defines the wind turbine finite element model in analysis. This work presents dynamic simulation of the blades of an HAWT based on gravitational loads and a prescribed rotation on the central node of the wind turbine.

Some characteristics of the finite element model are:

- 3 equally-spaced wind turbine blades;
- 9 m length blade;
- 30 equally-spaced nodes per blade, total of 91 nodes;
- 3-node beam elements, total of 45 beam elements;
- 100 s simulation with integration time step of 0.01 s;
- 9.81 m/s^2 gravity acceleration to the negative z direction;
- Newmark integration method as presented on Ibrahimbegovic and Mikdad (1998) and Ibrahimbegovic and Mamouri (2000) with $\beta = 0.28$ and $\gamma = 0.54$.

In order to have a more realistic model, the local axis of each blade section is rotated on its containing plane. Table 1 summarizes the local vectors $\boldsymbol{e_1}$ and $\boldsymbol{e_3}$ that defines the local orientation of the cross-sections.

Blade	$\boldsymbol{e_1}$	$\boldsymbol{e_3}$
1	$(0, 0.9701, 0.2425)$	$(1, 0, 0)$
2	$(-0.2100, 0.9701, -0.1212)$	$(-0.5, 0, 0.8660)$
3	$(0.2100, 0.9701, -0.1212)$	$(-0.5, 0, -0.8660)$

Table 1: Local axis orientation of the blades.

The material properties of the blades has the following characteristics

- Young Modulus $E = 200$ GPa;
- Poisson coefficient $\nu = 0.3$;
- Density $\rho = 7500$ kg/m^3;

Although there is a known airfoil profile variation along the length of an HAWT blade, this work describes the blade using 4 profiles. The selection of these profiles is based on the NREL typical blades profiles described on Burton et al. (2011) for an stall regulated HAWT with diameter from 10 to 20 m. All the airfoil information used is available at the NREL website (`http://wind.nrel.gov/airfoils/`). The adopted thickness of the outer shell and the webs is 0.05 m. Table 2 summarize the profiles used on each beam section from 1 to 15 of the blade starting from the central node to the tip of the blade.

Beam	Airfoil Profile
1-2	16 point discrete circle (0.5 diameter)
3-7	NREL S807
8-12	NREL S805A
13-15	NREL S806A

Table 2: HAWT blade profiles.

Figure 6 presents the profiles used along the blade's length, their webs in red and the beam axis in green. The horizontal axis of of the profiles on Figure 6 represent the beam axis 1 and the vertical axis represent the beam axis 2 (see notation in Figure 1).

In order to evaluate the dynamics of the wind turbine structure some elements of the model will be monitored. In other words, these elements will have their displacements and reactions monitored on every time step of the simulation. On this work the monitored elements will be:

- Central wind turbine node (node 1);
- Tip node of each blade (nodes 31, 61 and 91);
- Beam element number 12;

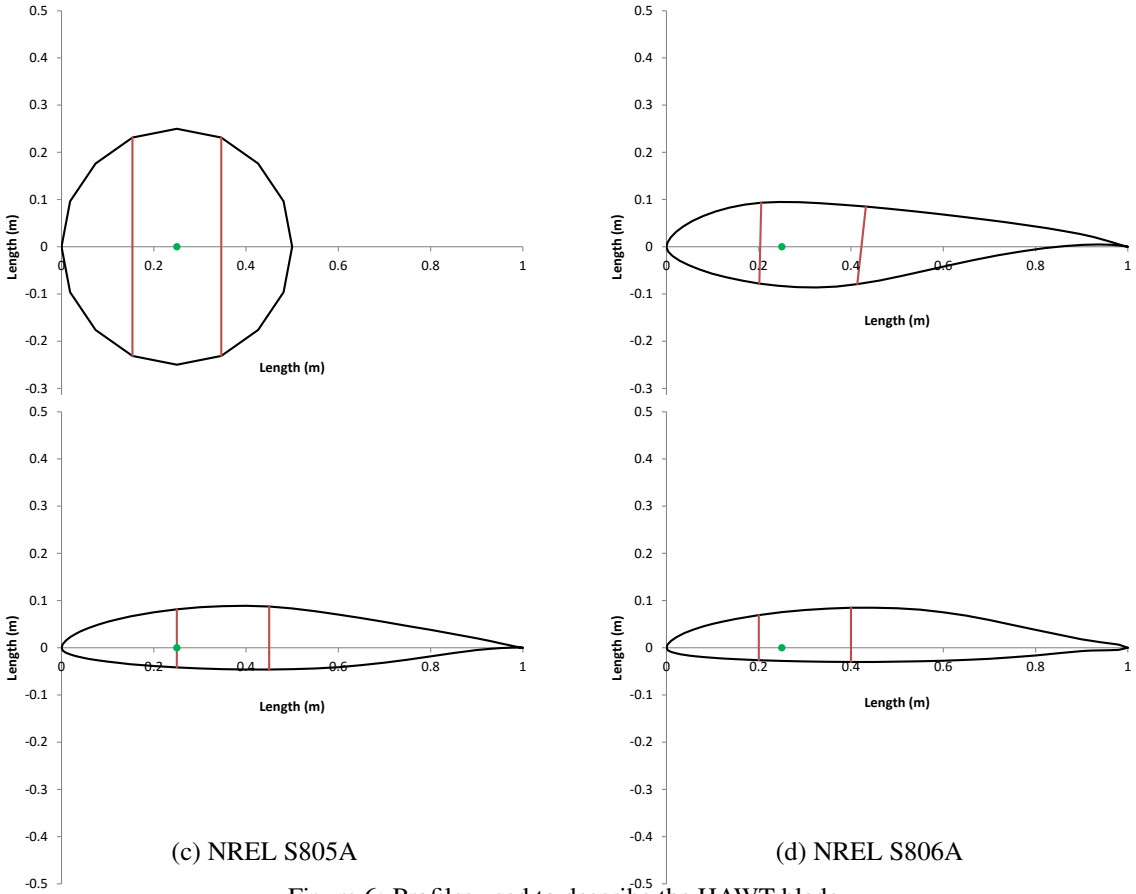

(c) NREL S805A (d) NREL S806A

Figure 6: Profiles used to describe the HAWT blade.

Figure 7 presents the wind turbine model and the monitors highlighted in red. The horizontal axis represents the x global orientation while the vertical axis represents the z global orientation and node 1 is at $(0, 0, 0)$.

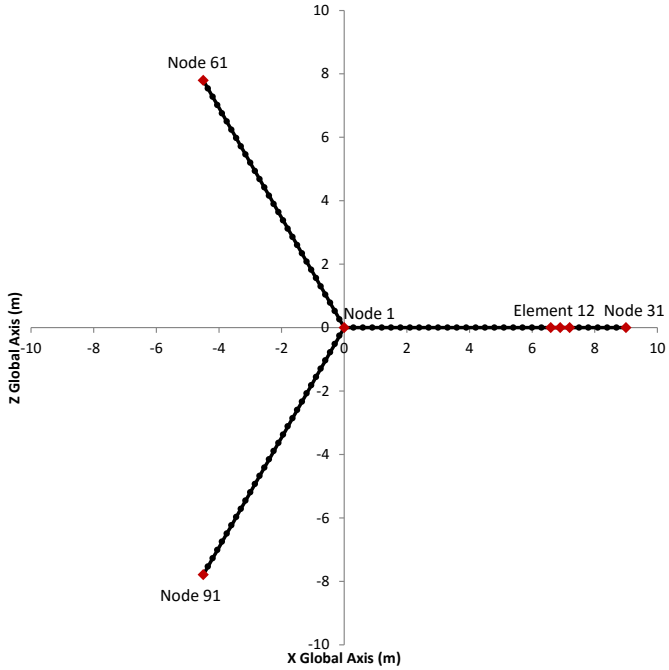

Figure 7: Wind turbine finite element model with monitors in red.

3 RESULTS

As previously described this dynamic simulation is induced by a prescribed rotation on the central node of the wind turbine. Although this simplification, the node 1 prescribed rotation expressed in radians is divided in 4 steps, described as follows:

- Step 1 - The rotation velocity increases from $t = 0s$ to $t = 20s$ according to the function $\phi_1(t) = 15\sin(0.025\pi t - \pi/2) + 15$;
- Step 2 - The rotation is velocity is maintained constant from $t = 20s$ to $t = 60s$, $\phi_2 = 15 + 1.2(t - 20)$;
- Step 3 - The rotation decreases from $t = 60s$ to $t = 80s$ according to the function $\phi_3(t) = 15\sin(0.025\pi t - \pi/2) + 63$;
- Step 4 - The rotation ceases from $t = 80s$ to $t = 100s$, $\phi_4 = 78$

Figure 8 presents a graphic that describes the node 1 rotation versus time. It is possible to note on this graph all the steps described previously.

On wind turbines the rotation of the blades yields on very important dynamic loads for the tower. These loads have huge influence on the structural behavior of an HAWT since they are crucial to evaluate aspects such as peak loads and fatigue. On this simulation the interface between the tower and the blades is monitored on node 1. Although the gravitational and inertial loads acting on the xz plane that contains the wind turbine blades, the axial peak forces occurred on the y direction. Figure 9 presents the y forces along time for node 1.

These peak loads may come from the way that the geometry of the blades was described. It follows that the centroid of each blade may not lie on the xz plane and that the axis of each blade is twisted on the plane of its cross section.

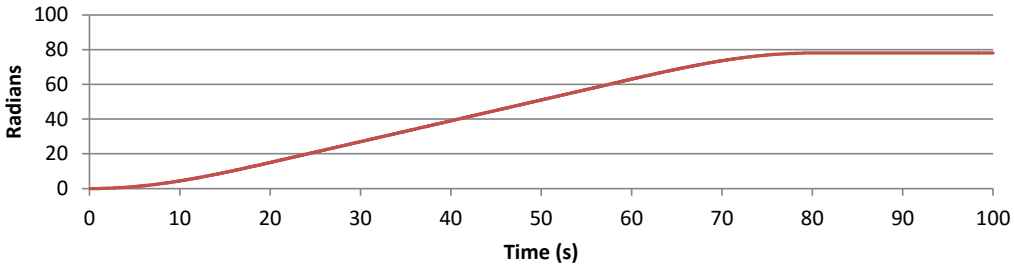

Figure 8: Node 1 rotation versus time.

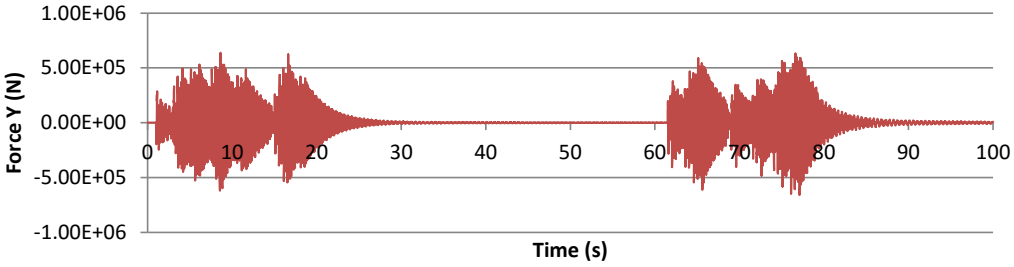

Figure 9: Force y along time.

It is also important to note that the peak loads occurs on step 1 and 3 that are the ones where there is change on the rotation velocity. This result is very interesting since the energy of a wind turbine comes from the motion resistance of the turbine inside the nacelle. Moreover, large force peaks may come from a severe acceleration/breaking operation applied to the rotor.

Figure 10 presents the z forces along time. It is seen on this graphic that the loads on the z direction are very relevant and include a non-null average, due to the structure self-weight. On steps 3 and 4 when the turbine is at a constant rotation speed and the turbine is stopped, the z direction force is the main force acting on node 1.

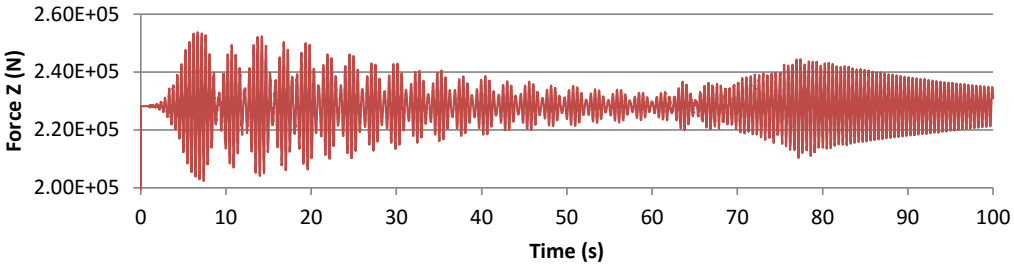

Figure 10: Force z along time.

Figure 11 presents the node 1 x forces along time. This graphic shows that although there are peak loads on steps 1 and 3, the highest peak loads are on step 4. The peak loads experienced

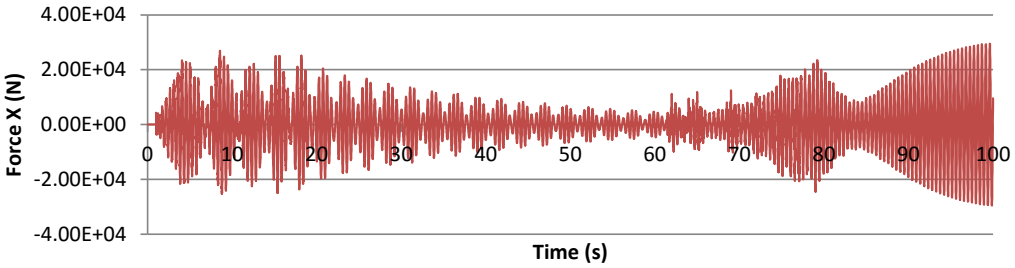

Figure 11: Force x along time.

on step 4 occurs due to the excitation of the blade tip and is considerably relevant.

One way to confirm the cyclic behavior of the dynamic model is by the analysis of the nodal displacement of each blade's tip. Figure 12 presents the x direction displacement of the nodes 31, 61 and 91.

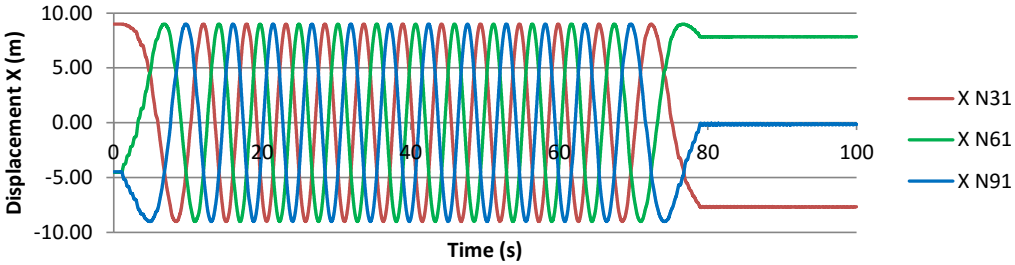

Figure 12: Displacement x along time of nodes 31, 61 and 91.

It is possible to note from this graphic that the turbine behaves as expected regarding the cyclic position of the coordinates. It is also interesting to note the node displacements when the turbine stops. Figure 13 presents a graphic of the x displacement of node 91 from $t = 80s$ to $t = 100s$. On this graphic is seen that the node position still oscillating, however tending to stop. This behavior was expected since there is an inherent numerical dumping on the simulation process due to the choice of Newmark integration parameters.

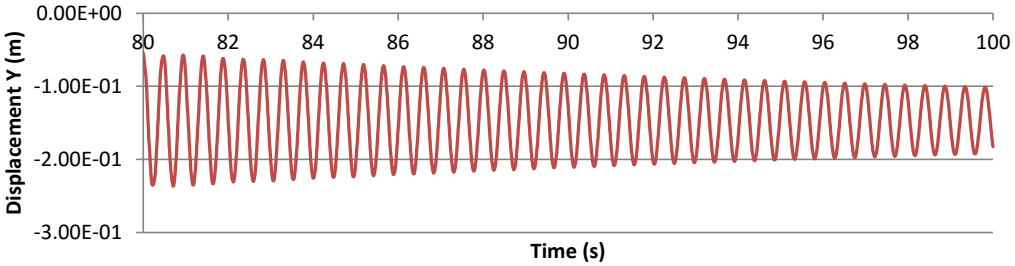

Figure 13: X displacement of node 91 from $t = 80$ to $t = 100$.

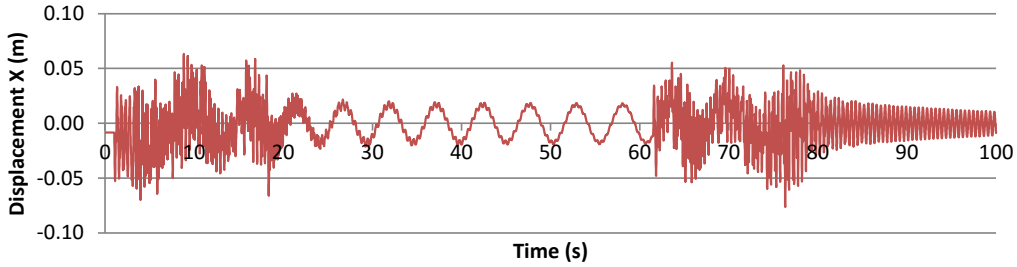

Figure 14: Y displacement of node 91 .

It is also interesting to see that the tip of the blade has out of plane displacements that appears from the geometry issues already discussed. Figure 14 presents the graphic that shows the out of plane displacement y of node 91. It seen that even when the wind turbine is at constant speed (step 2), there is an out of plane oscillating behavior of the node.

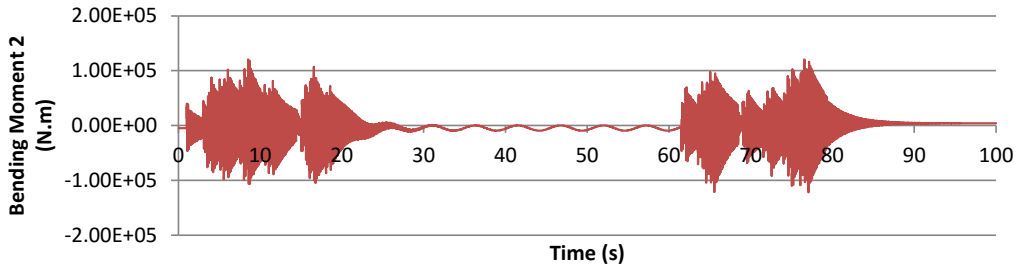

Figure 15: Bending moment around element axis 2 along time.

Despite of all the possible analysis of an HAWT dynamic simulation, the main usual goal is to evaluate the generalized stresses (tension, bending moment and torsion moment) acting on a specific part of the blade. On this simulation the part of interest on the blade structure is represented by the beam element 12. The bending moments around element axis 2 along time is shown on Figure 15. On this graphic is possible to note that the peak loads occurs when there is change on the rotation velocity of the wind turbine. It is also interesting to note that this bending moment still oscillating even when the rotation speed is constant (step 2).

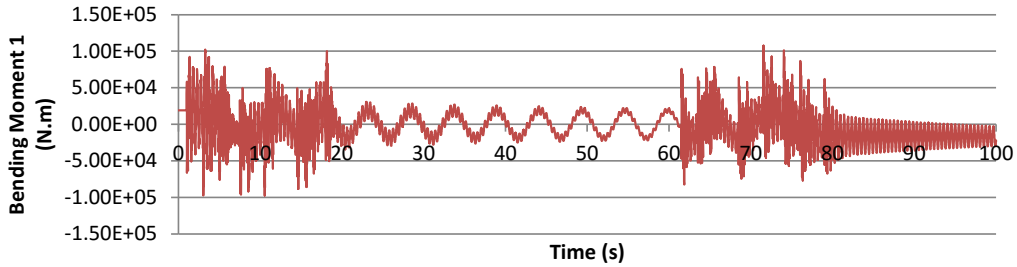

Figure 16: Bending moment around element axis 1 along time.

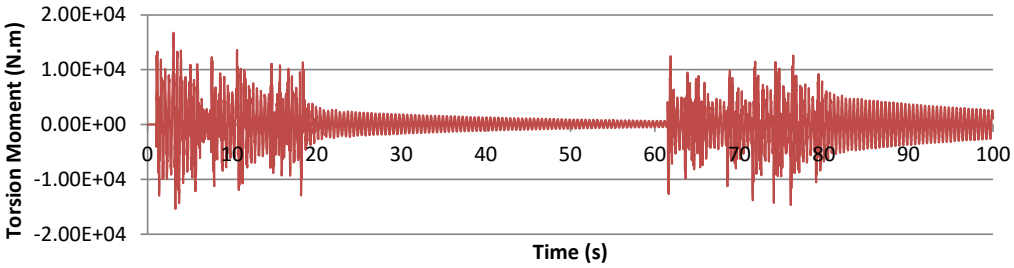

Figure 17: Torsion moment along time.

The bending moment around element axis 1 along time is presented on Figure 16. As other results, the peak loads are on steps 1 and 3. However the oscillating moment on step 4 indicates that the beam is still in movement.

Finally, the torsion moments along time is presented on Figure 17. Despite of the peak loads on steps 1 and 3, the torsion moments on step 4 are very relevant. Therefore, it is possible to assume that the stopping process of an wind turbine should be soft enough to avoid the possible high torsion moments on the blade.

4 CONCLUSION

The main conclusion of this work is that the GIRAFFE platform and the Wind Turbine program are very promising tools to evaluate the dynamics of an HAWT. The GIRAFFE geometrically-exact beam regarding the possibility of any cross section and beam axis position turns it into a very suitable tool for this kind of simulation. Furthermore, the user-friendliness of the Wind Turbine Program on handling defined cross sections and geometric properties calculations on a GUI is a very helpful tool for HAWT simulations.

Although on this simulation the aerodynamic loads were not included, it was seen that the variation of speed of an HAWT induces very relevant internal loads on the structure.

4.1 Future Works

Some of the possible advances regarding this work are:

- Verification of the thin-walled hypothesis;
- Verification of the shear center precision using shell elements;
- Verification of the torsion stiffness precision using shell elements;
- Inclusion of the aerodynamic loads.

4.2 Acknowledgments

The authors acknowledge FAPESP for funding this project under the grant number 2015/11655-3.

References

Burton, T., Jenkins, N., Sharpe, D., and Bossanyi, E. (2011). *Wind Energy Handbook*. John Wiley & Sons, Inc.

Fugslang, P. and Bak, C. (2004). Development of the risø wind turbine airfoils. *Wind Energy*, 7:142–162.

Fung, Y. C. (1993). *An Introduction to the Theory of Aeroelasticity*. Dover Publications Inc.

Gay Neto, A. (2012). Estabilidade estrutural da configuração estática de risers em catenária. Master's thesis, University of São Paulo.

Gay Neto, A. (2015). *Giraffe User's Manual*. University of São Paulo, v 1.0.100 edition.

Gay Neto, A. and Martins, C. A. (2013). Structural stability of flexible lines in catenary configuration under torsion. *Marine Structures*, 34:16–40.

Gay Neto, A., Pimenta, P. M., and Wriggers, P. (2014a). Contact between rolling beams and flat surfaces. *International Journal for Numerical Methods in Engineering*, 97(9):683–706.

Gay Neto, A., Pimenta, P. M., and Wriggers, P. (2014b). Self-contact modeling on beams experiencing loop formation. *Computational Mechanics*, 55:193–208.

Gere, J. M. and Timoshenko, S. (1997). *Mechanics of Materials*. PWS Publishing Company.

Hau, E. (2013). *Wind Turbines*. Springer.

Ibrahimbegovic, A. and Mamouri, S. (2000). On rigid components and joint constraints in nonlinear dynamics of flexible multibody systems employing 3d geometrically exact beam model. *Computer Methods in Applied Mechanics and Engineering*, 188(805-831).

Ibrahimbegovic, A. and Mikdad, M. A. (1998). Finite rotations in dynamics of beams and implicit timestepping schemes. *International Journal for Numerical Methods in Engineering*, 41(781-814).

Megson, T. H. G. (2005). *Structural and Stress Analysis*. ELSEVIER.

Megson, T. H. G. (2014). *Introduction to Aircraft Structural Analysis*. ELSEVIER.

Pilkey, W. D. (2002). *Analysis and Design of Elastic Beams*. John Wiley & Sons, Inc.

Pimenta, P. M. and Campello, E. (2001). Geometrically nonlinear analysis of thin-walled space frames. In *2nd European Congress on Computational Mechanics*.

Pimenta, P. M. and Yojo, T. (1993). Geometrically-exact analysis of spatial frames. *App. Mechanics Reviews*, 46(11):118–128.

Shama, M. (2010). *Torsion and Shear Stresses in Ships*. Springer.

Simo, J. C. (1985). A finite strain beam formulation. three-dimensional dynamic problem. part i. *Comp. Methods in App. Mech. and Eng.*, 49:55–70.

Simo, J. C. and Vu Quoc, L. (1991). A geometrically exact rod model incorporating shear and torsion-warping deformation. *Comp. Methods in App. Mech. and Eng*, 27(3):371–393.

Tangler, J. L. and Somers, D. M. (1995). *NREL Airfoil Families for HAWTs*. AWEA, Washington , DC.

Timmer, W. A. and van Rooij, R. P. J. O. M. (2003). ummary of the delft university wind turbine dedicated airfoils. *Journal of Solar Energy Engineering*, 125:488–496.

Timoshenko, S. and Goodier, J. N. (1951). *Theory of Elasticity*. McGraw-Hill.

Vlasov, V. Z. (1961). *Thin-Walled Elastic Beams*. Israel Program for Scientific Translations.

Wriggers, P., Gay Neto, A., and Pimenta, P. M. (2015). Modellierung von kabelstrukturen und deren verhalten bei kontakt und torsion. *Bauingenieur-Germany*, 90(193-199).

Yojo, T. (1993). *Análise Não-Linear Geometricamente Exata de Pórticos Espaciais*. PhD thesis, Polytechnic School at University of São Paulo.

ECCOMAS Congress 2016
VII European Congress on Computational Methods in Applied Sciences and Engineering
M. Papadrakakis, V. Papadopoulos, G. Stefanou, V. Plevris (eds.)
Crete Island, Greece, 5–10 June 2016

EXTENDED FORMULA FOR THE CRITICAL VELOCITY OF A LOAD MOVING ON A BEAM SUPPORTED BY A FINITE DEPTH FOUNDATION

Zuzana Dimitrovová

Departamento de Engenharia Civil, Faculdade de Ciências e Tecnologia, Universidade Nova de Lisboa and IDMEC, Instituto Superior Técnico, Universidade de Lisboa, Lisboa, Portugal
e-mail: zdim@fct.unl.pt

Keywords: Critical velocity, Finite soil depth, Moving load, Integral transforms, Analytical solution, Moving window method.

Abstract. *In this paper, an extended formula for the critical velocity of a uniformly moving load is derived. It is assumed that the load is traversing an infinite beam supported by finite depth foundation under plane strain condition. The critical velocity is extracted by parametric analysis applied on the analytical solution of the steady state deflection beam shape. Results obtained are compared with the previously published results of this author, where simplified assumptions were implemented on the shear contribution. It is confirmed that there is an interaction between the beam and the foundation and thus the critical velocity is dependent on the mass ratio defined as the square root of the fraction of the foundation mass to the beam mass. Several options for damping are also analysed and results of displacement fields are compared with finite element simulations. In order to obtain steady-state form of the finite element results, the enhanced moving widow method is implemented in software ANSYS.*

1 INTRODUCTION

The response of rails to moving loads is important research topic of high-speed railway transportation. If simple geometries of the track and subsoil are considered, it can be assumed that the track structure acts as a continuously supported beam resting on a uniform layer of springs. Two distinct interpretations are used, either the beam is modelled by the rail and the layer of springs represents the underlying remainder of the track structure, or an equivalent beam encompassing the whole track is used and the spring layer stands for the subgrade or foundation. The stiffness of the spring layer along the length of the beam is named as the track modulus and defines Winkler's model, which is often referred to as a "one-parameter model". Such a simplified model was traditionally used to estimate the critical velocity of moving trains.

The first solution of steady-state dynamic response of an infinite beam on elastic foundation traversed by moving load was presented by Timoshenko [1]. In [2], the moving coordinate system is introduced to convert the governing equation to ordinary differential equation that can be solved by the Fourier integral transform. In [3], the concept of the dynamic stiffness matrix is implemented. Two semi-infinite beams are solved for and connected by continuity equations. Then the critical velocity can be determined as the velocity that ensures the nullity of the determinant of the dynamic stiffness matrix. This concept was extended to finite and infinite beams with sudden change in foundation stiffness [4].

If the beam is modelled as the rail, the classical formula, predicts very high critical velocity, giving impression that is unreachable by high-speed trains and consequently no attention was paid to this fact during expansions of high-speed railway network. Unfortunately, practical experience showed that the realistic critical velocity can be much lower [5] and should be related to the wave-velocity of propagation in the foundation. Therefore, in further investigations the spring layer was replaced by elastic half-space and the critical velocity was determined as the Rayleigh-wave velocity of propagation [6].

Nevertheless, it is important to release, that only finite active depth of the foundation soils should be included in the analysis. Under such assumption, it was shown in [7] that there is an interaction between the beam and the foundation. In [7] only simplified plane models of the foundation were used for analyses of finite and infinite beams, but it was confirmed that the critical velocity is not given either by the classical formula from [2] or by the lowest wave-velocity of propagation in the foundation, but there is a smooth transition between these two extreme values governed by the mass ratio. For a low mass ratio, the critical velocity approaches the classical formula and for a higher mass ratio, it approaches the lowest wave-velocity of propagation in the foundation. In this paper generalizations, in conformity with [8] are derived. It is proven that in such extension, the final results depend on the interface condition between the beam and the foundation.

2 CRITICAL VELOCITY

The critical velocity of the load traversing an infinite Euler-Bernoulli beam on an elastic foundation is given by the classical formula [2]

$$v_{cr} = \sqrt[4]{\frac{4kEI}{m^2}} \tag{1}$$

where m and EI stand for the mass per unit length and the bending stiffness of the beam, respectively, and k for the Winkler constant of the foundation. If the beam is modelled by the rail, then Eq. (1) predicts a critical velocity that is generally much higher than the one ob-

served in reality. The main reason is related to the fact that there is no mass in the foundation and thus no wave propagation is possible. Several works have been published on this subject replacing the spring layer by an elastic half-space and concluding that the critical velocity corresponds to the Rayleigh-wave velocity of propagation, which is the slowest wave-velocity [6].

Nevertheless, better estimation should account for the active finite depth of the foundation, which can either be the actual depth at which a stiff substratum is located or a depth after which no appreciable soil deformations occur. Under simplified assumptions on a plane model under plane strain conditions, it was derived in [7] that the critical velocity is governed by the mass ratio according to approximately

$$V_{cr} = v_{cr}\left[\left(1-\vartheta_s\right)\sqrt{\frac{2}{2+M^{2+\sqrt{\vartheta_s}}}}+\vartheta_s\right] \tag{2}$$

where V_{cr} is the new value of the critical velocity, ϑ_s is the shear ratio defined as $\vartheta_s = v_s / v_{cr}$ with v_s being the shear-wave velocity, and M is the mass ratio defined as the square root of the foundation mass to the beam mass. Thus, for a low mass ratio, the critical velocity approaches the classical value v_{cr} and for a higher mass ratio, it approaches the velocity of propagation of shear waves in the foundation. In this simplified model horizontal displacements were neglected and therefore the Rayleigh velocity could not be detected. Due to the proximity of these two velocities defined by the approximate formula

$$\frac{v_R}{v_s} = \frac{0.87+1.12\upsilon}{1+\upsilon} \tag{3}$$

where υ is the soil Poisson ratio and v_R is the Rayleigh-wave velocity, this does not have to be considered a disadvantage.

In this paper new results are derived in conformity with [8]. Deductions from [8] are simplified by considering only a constant moving force, thus the analytical solution can be restricted only to its steady-state part. Final results of the critical velocity, which can then be extracted by parametric analyses, are dependent on the interface condition between the beam and the foundation. However, there is only a small difference between the three possibilities: the previously published approximate formula (2) and results according to two options for the interface condition. Namely, results with the interface condition in form of zero horizontal displacement give values very similar to Eq. (2) and results obeying the zero shear stress condition have the asymptotic tendency to slightly lower velocity, the velocity of propagation of Rayleigh waves.

Deflection shapes and adequacy of the interface condition are analysed by finite element results. In order to obtain steady-state form of the finite element results, the enhanced moving widow method is implemented in software ANSYS as described in [9].

3 THE MODEL AND ITS SOLUTION

It is assumed that the load is traversing an infinite beam supported by a foundation of finite depth *H*, as depicted on Figure 1. It is further assumed that: (i) the beam obeys linear elastic Euler-Bernoulli theory; (ii) the beam vertical displacement is measured from the equilibrium deflection caused by the beam weight; (iii) the foundation is represented by a finite strip of width *b* under plane strain condition; (iv) the foundation soil is linear elastic homogeneous material.

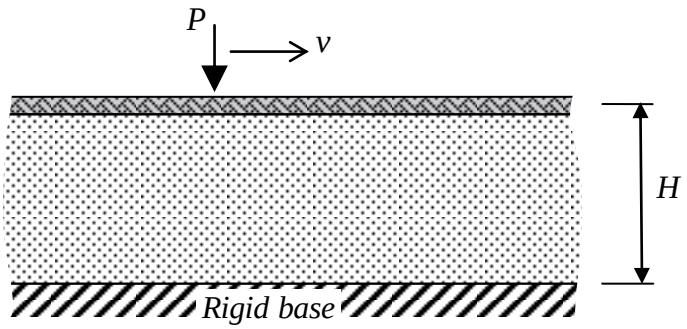

Figure 1: Infinite beam on an elastic foundation of finite depth subjected to a moving load.

The governing equations for determination of the beam deflection shape and displacement fields in the foundation soil are given by

$$\mu\Delta\mathbf{u}+\left(\lambda+\mu\right)\nabla\left(\nabla\cdot\mathbf{u}\right)=\rho\mathbf{u}_{,tt} \tag{4}$$

$$EIw_{,xxxx}\left(x,t\right)+c_b w_{,t}\left(x,t\right)+mw_{,tt}\left(x,t\right)+p\left(x,t\right)=P\delta\left(x-vt\right) \tag{5}$$

where $\mathbf{u}=\left(u_x,u_z\right)$ is the displacement field in the foundation, λ, μ are Lame's constants of the soil, ρ is the soil density and t is the time. Overall this paper, derivatives will be designated by the corresponding variable symbol in the subscript position, preceded by a comma. Moreover, ∇ is the gradient and Δ is the Laplace operators applied on spatial variables x, z. Further, P is the moving load, v is its velocity, p is the foundation pressure and c_b is the viscous damping coefficient of the beam. The unknown beam deflection $w\left(x,t\right)$, spatial coordinate z and P are assumed positive when acting downward. Spatial coordinate x is positive to the right, the load travels from the left to the right and finally, δ is the Dirac delta function.

Damping in the soil can be assumed as hysteretic

$$\lambda=\lambda_0\left(1+\mathrm{i}\eta_h\right),\ \mu=\mu_0\left(1+\mathrm{i}\eta_h\right) \tag{6}$$

or viscous

$$\lambda=\lambda_0\left(1+c_s\bullet_{,t}\right),\ \mu=\mu_0\left(1+c_s\bullet_{,t}\right) \tag{7}$$

where η_h is the loss factor of the soil and c_s is the coefficient of the viscous damping in the soil.

The solution method follows these steps: firstly, the governing equations for the soil layer are expressed in terms of displacement potentials. Then all equations are simplified by introduction of moving coordinates and leaving only the terms that contribute to the steady-state part of the solution. After that several dimensionless variables are introduced to facilitate the equations manipulation and posterior results analyses. The main solution method is the single Fourier transform, which allows analytical solution of all displacement and stress components in the frequency domain. The inverse transform is accomplished numerically. Dimensionless variables allow identifying results for all possible input data combinations. Except for the damping values, which define viscous damping in the beam, viscous and hysteretic damping in the foundation, results depend only on the mass ratio M, the velocity ratio $\alpha=v/v_{cr}$, the shear ratio ϑ_s and soil Poisson's ratio υ.

4 THE ENHANCED MOVING WINDOW METHOD

Finite element confirmation of steady-state analytical predictions in infinite media is generally a complicated issue because it is difficult to choose the correct (i) size of the model, (ii) size of the finite elements; (iii) type of the boundary conditions and (iv) a method that would allow deflection fields stabilization. The model itself must be large enough in order to eliminate satisfactorily transient effects due to a sudden placement of the load on the structure and, on the other hand, small enough to be computationally accessible. The edges of the finite elements must be sufficiently small in order to represent adequately propagating waves. The boundary conditions are even more delicate issue. The dynamic analysis of solids of infinite dimensions with discrete methods such as finite elements calls for the use of special boundary that are normally referred to as absorbing, non-reflecting or transmitting boundaries. The purpose of these special boundaries is to prevent wave reflections at the edges of the mathematical models used, which, by necessity, must remain finite in size. A number of these boundaries have been proposed in the past with recourse to various mathematical or physical principles. Unfortunately, none of the transmitting boundaries can fully prevent all possible reflections under the full range of possible incident angles.

Some of the difficulties named above could be overcome by implementation of the moving window method. In the moving window method the load is kept still, and the finite element model of the railway track moves in the direction opposing the originally assumed load movement. This can be achieved by several ways. Either the finite elements are altered in order to implement the effect of the load velocity [10], or results are shifted against the load.

A shift of results is impossible in commercial finite element software, because such an operation is usually protected against inappropriate usage. Implementation of the enhanced moving window method in commercial finite element software ANSYS is described in [9]. The method is tested on one-, two- and three-dimensional models. It is shown that the steady-state response of an infinite structure can be obtained with sufficient accuracy, which significantly reduces the calculation time by reduction of both, the model size and the analysis time.

When the model is large enough, periodic boundary conditions can be used on the front and rear faces of the model. Regarding the bottom face, other considerations must be taken. A reduction of the model depth by representative springs and viscous boundary is used here according to [11]. These distributed elastic springs are defined as:

$$k_n = \frac{\lambda_0 + 2\mu_0}{H - h},\ k_t = \frac{\mu_0}{H - h} \tag{8}$$

where k_n and k_t are spring stiffnesses in the normal and tangential directions, respectively and h is the depth that is modelled by finite elements. These elastic boundaries allows introduction of absorbing boundaries, which help to stabilization of the results.

5 NUMERICAL RESULTS

Final results are shown in Figure 2 for shear ratio 0.5 and soil Poisson ratio 0.2. It is seen that results from [7] and new results with zero displacement interface condition are quite proximate, especially regarding the asymptotic value for higher mass ratio. When zero shear is admitted at the interface, than the asymptotic tendency directs to lower velocity. In such a case the ratio given by Eq. (2) indicates that this velocity is the Rayleigh-wave velocity of propagation.

Deflection shapes were confirmed by the finite element results exploiting the enhanced moving window method. One case is shown in Figure 3. The case presented considers two

rails supported by soft foundation with input data summarized in Table 1. In the first part of Figure 3 finite element solution is compared to the analytical solution with zero horizontal displacement interface condition. It is seen that the coincidence is very good. The other part compares the analytical solutions for the two interface conditions. It can be observed that the zero shear condition allows for higher displacements.

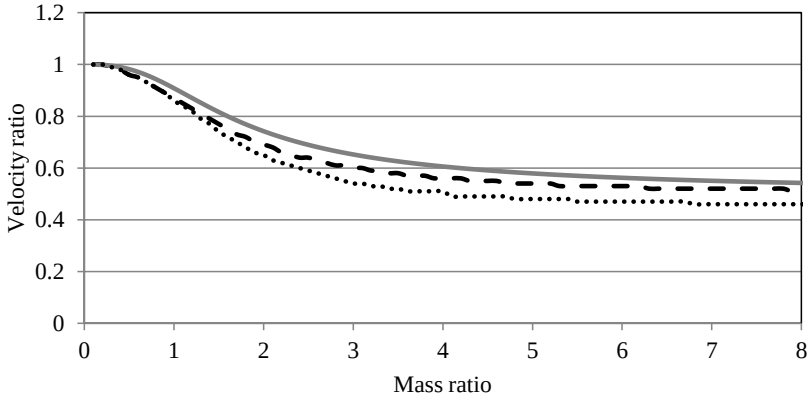

Figure 2: Critical velocity as a function of the mass ratio for shear ratio 0.5: previous estimate according to Eq. (2) (grey), solution with zero displacement interface condition (black dashed), solution with zero shear interface condition (black dotted).

Property	Value
Beam bending stiffness EI (MN·m^2)	12.8
Beam mass per unit length m (kg·m^{-1})	120
Soil Young's modulus E_s (MN·m^{-2})	10
Soil Poisson's ratio υ	0.3
Soil density ρ (kg·m^{-3})	1850
Active depth H (m)	12
Moving force P (kN)	200
Velocity v (m·s^{-1})	50

Table 1: Numerical data used with a unit strip width of the soil.

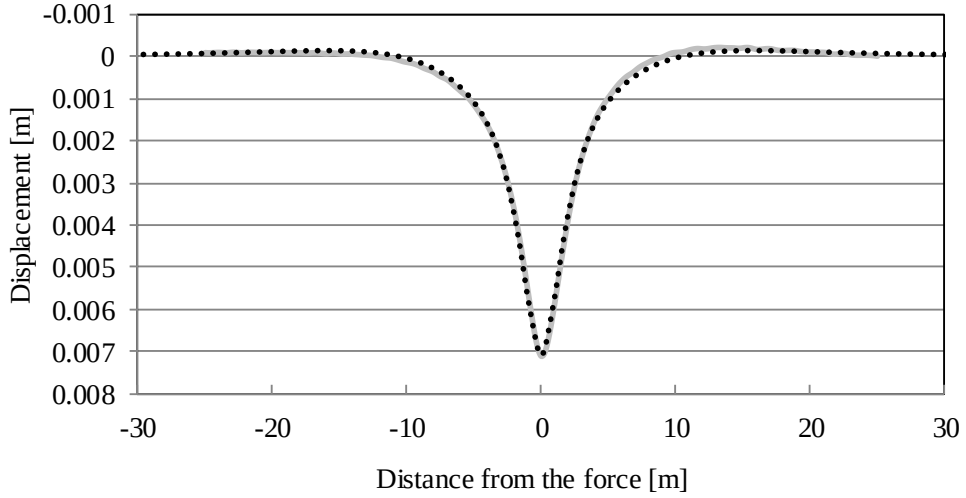

a)

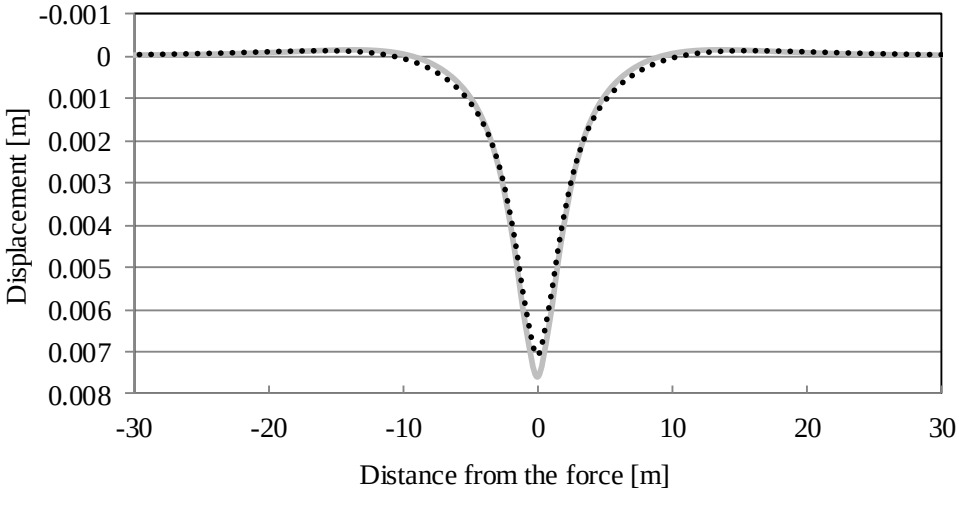

Figure 3: Deflection shapes comparison: a) finite element solution (grey) and solution with zero displacement interface condition (black dotted); b) solution with zero shear interface condition (grey) and solution with zero displacement interface condition (black dotted).

In addition, shear stress and horizontal displacement were extracted in the vertical cut below the load from the finite element solution. It is seen that it is more adequate to assume zero horizontal displacement at the interface between the beam and the foundation.

6 CONCLUSIONS

In this contribution, the critical velocity of a uniformly moving load on a beam supported by a finite depth foundation was analysed. Generalizations of the method published in [7] were derived. The new approach follows developments in [8] but simplifies the analysis by admitting only a constant moving force. Analytical results for the deflection beam shape and displacement fields in the foundation are obtained by the Fourier transform. The inverse transform is accomplished numerically.

Final results of the critical velocity are then extracted by parametric analyses. It is confirmed that there is an interaction between the beam and the foundation, and thus there is a smooth transition between the classical value of the critical velocity and the lowest velocity of wave propagation in the foundation, depending on the assumptions adopted. However, the new results are dependent on the interface condition between the beam and the foundation. Only small differences occur between the three possibilities: the previously published results in [7] and results according to two options for the interface condition. Results with the interface condition in form of zero horizontal displacement give values very similar to the ones published in [7] and results obeying the zero shear stress condition have the asymptotic tendency to slightly lower velocity, the velocity of propagation of Rayleigh waves.

Deflection shapes and adequacy of the interface condition were analysed by finite element results exploiting the enhanced moving widow method implemented in software ANSYS. It was confirmed that, if the model considers the beam axis coincident with the soil upper surface, which is the common finite element approach, then it is more adequate to assume that the horizontal displacements are zero at the interface.

7 ACKNOWLEDGEMENTS

This work was supported by FCT, through IDMEC, under LAETA, project UID/EMS/50022/2013.

REFERENCES

[1] S.P. Timoshenko, Statical and dynamical stresses in rails. *2nd International Congress for Applied Mechanics*, Zürich, Switzerland, September 12-17, 1926, 407-418.

[2] L. Frýba, *Vibration of solids and structures under moving loads*, Research Institute of Transport, Prague (1972), 3rd edition. Thomas Telford, London, 1999.

[3] Y.H. Chen, Y.-H. Huang, Dynamic stiffness of infinite Timoshenko beam on viscoelastic foundation in moving co-ordinate. *International Journal for Numerical Methods in Engineering*, **48**, 1-18, 2000.

[4] Z. Dimitrovová, A.S.F. Rodrigues: Critical velocity of a uniformly moving load. *Advances in Engineering Software*, **50**, 44–56, 2012.

[5] C. Madshus, A.M. Kaynia, High-speed railway lines on soft ground: dynamic behaviour at critical train speed. *Journal of Sound and Vibration*, **231,** 689-701, 2000.

[6] V.V. Krylov, A.R. Dawson, M.E. Heelis, A.C. Collop, Rail movement and ground waves caused by highspeed trains approaching track-soil critical velocities. *Proceedings of the Institution of Mechanical Engineers, Part F: Journal of Rail and Rapid Transit*, **214**, 107-116, 2000.

[7] Z. Dimitrovová, Critical velocity of a uniformly moving load on a beam supported by a finite depth foundation. *Journal of Sound and Vibration*, **366,** 325–342, 2016.

[8] J. Náprstek, C. Fischer, Interaction of a Beam and Supporting Continuum under a Moving Periodic Load. B.H.V. Topping, J.M. Adam, F.J. Pallarés, R. Bru, M.L. Romero eds. Civil-Comp Press, Stirlingshire, UK. *10th International Conference on Computational Structures Technology (CST2010),* Valencia, Spain, September 14-17, 2010.

[9] Z. Dimitrovová, A.F.S. Rodrigues, An Enhanced Moving Window Method: Applications to High-Speed Tracks. B.H.V. Topping, Y. Tsompanakis eds. Civil-Comp Press, Stirlingshire, UK. *13th International Conference on Civil, Structural and Environmental Engineering Computing* (CC2011), Chania, Crete, Greece, September 6-9, 2011.

[10] A.W.M. Kok, Finite element models for the steady state analysis of moving loads. *Heron*, **45**, 53-61, 2000.

[11] Z. Dimitrovová, A.F.S. Rodrigues, Critical velocity obtained by simplified models of the railway track: viability and applicability. B.H.V. Topping, J.M. Adam, F.J. Pallarés, R. Bru, M.L. Romero eds. Civil-Comp Press, Stirlingshire, UK. *10th International Conference on Computational Structures Technology (CST2010),* Valencia, Spain, September 14-17, 2010.

ECCOMAS Congress 2016
VII European Congress on Computational Methods in Applied Sciences and Engineering
M. Papadrakakis, V. Papadopoulos, G. Stefanou, V. Plevris (eds.)
Crete Island, Greece, 5–10 June 2016

FIRST-ORDER DISPLACEMENT-BASED ZIGZAG THEORIES FOR COMPOSITE LAMINATES AND SANDWICH STRUCTURES: A REVIEW

M. Di Sciuva[1]
[1] Politecnico di Torino
Department of Mechanical and Aerospace Engineering
Corso Duca degli Abruzzi, 24 10129 TORINO (I)

marco.disciuva@polito.it

Keywords: Zigzag theory, multilayer plates, sandwich plates.

Abstract. *The paper gives a critical review and new accomplishments of the displacement-based zigzag theories for laminated composite and sandwich structures, with special emphasis to the underlying ideas, relative strengths and weaknesses. Some numerical results substantiate the conclusions.*

1. INTRODUCTION

Composite laminates and sandwich structures are characterized by high stiffness-to-weight and strength-to-weight ratios and by the possibility to be tailored according to the particular application. Sandwich structures exhibit further promising properties such as high-energy absorption, impact resistance, noise and vibration reduction, excellent damping behavior, [1, 2]**.** Due to these appealing properties, in the last thirty years an increasing number of high-performance and lightweight primary load-bearing structures in the aerospace, automotive, nuclear, naval and civil constructions, are comprised of relatively thick composite laminates and sandwich structures with one hundred or more layers. Such structures are inherently heterogeneous and anisotropic and may suffer unwanted failure due to transverse shearing and out-of-plane stretching.

As failure predictions call for an accurate evaluation of the stress field within each layer of laminated composite and sandwich structures, affordable computational costs for these structures are the main concern. In order for the computational costs to be affordable, accurate computational models for multilayered composite and sandwich structures need to be independent of number of layers and of their micro-structure.

Different approaches have been adopted to face these modeling challenges [3]. A first broad classification could be the following one: three-dimensional (3D) models and two-dimensional (2D) models. Example of 3D models can be found in [4,5,6,7,8,9]. The reduction of the 3D model to the 2D model rely generally on the use of the *axiomatic approach*, that is, on the a-priori assumed trough-the-thickness distribution of the primary variables. In the *displacement-based approach* [10,11], the primary variables are generalized displacements (displacement, rotation, etc.); in the *mixed approach* [12], both generalized displacements and stresses (generally, out-of-plane stresses) are adopted as primary variables.

Following [3], the 2D plate/shell models can be divided into Equivalent Single Layer (ESL) models (also known as Smeared Laminate models) and Layer-wise (LW) models according to the type of kinematics assumed.

Equivalent Single Layer (ESL) (also known as Smeared Laminate) models are generally based on a smooth expansion (generally, a power series expansion) over the whole laminate thickness of the displacement field in terms of the thickness-wise co-ordinate. This means that the kinematics along the thickness is assumed to be at least C^1-continuous and independent of the laminate lay-up. As a consequence, the multilayer structure is substituted with a plate/shell made by an equivalent single layer. While computationally not expensive, ESL models are generally not accurate, especially when through-the-thickness distribution of strains and stresses are the main concern and the laminate is highly heterogeneous.

Among the displacement-based ESL models, the most popular are the Classical Lamination Plate Theory (CLPT), based on the Kirchhoff's plate theory [13] and the First-order Shear Deformation Theory (FSDT), based on the Mindlin's and Reissner's plate theories [14,15] . Both CLPT and FSDT make use of a linear expansion of the in-plane displacement. In addition to the weaknesses of the ESL models, it is well-know that FSDT needs ad hoc shear correction factors to yield accurate results [14,15,16,17,18]. As well-known, CLPT and FSDT perform relatively well in predicting global quantities, such as, transverse displacement, fundamental natural frequency and buckling load for thin and moderately thick laminates that have a relatively low degree of transverse heterogeneity; however, their accuracy diminishes rapidly when they are used to predict the displacement and stress fields in highly heterogeneous and/or thick composite and sandwich laminates [11,19,16,20,21]. Improved predictions can be obtained using higher order through-the-thickness expansions of the displacements and/or stresses [22]. Computationally efficient analytical models for beams,

plates and shells that account for transverse shear and thickness-stretch deformations have recently been advanced in [23,24,25]. Reviews on the ESL theories are given in [26,27,28].

Contrary to the ESL models, Layer-wise (LW) models [3,29,30,31,32,33,34,35,36] make a-priori assumptions on the distribution of the displacement and stress fields within each layer. Limiting the discussion to the displacement-based approach, LW models postulates a C^0-continuous kinematics, that is a distribution of displacements (first of all, in-plane displacements) continuous along the thickness with first derivative showing a jump at layer interfaces (the reason of this discontinuity will be explained hereinafter). According to [26], the LW models are further divided into (i) *layer dependent models*, wherein the number of kinematic variables increases with the number of layers; and (ii) *layer independent models*, wherein the number of variables remains constant and independent on the number of layers. Hereafter in this paper, the terminology Layer-wise (LW) models will be adopted only to indicate the layer dependent LW models, while the terminology Zigzag (ZZ) models will be adopted for the layer independent LW models.

Layer dependent LW models [29,30,31,34] are generally very accurate but computationally costly; in these models the number of unknowns increases with the number of layers, as in 3D models. As we said, in order for the computational costs to be affordable (this is especially relevant for nonlinear and/or progressive failure analysis of thick laminates made up of hundreds of layers), computational models for multilayered composite and sandwich structures need to be independent of number of layers and of their micro-structure, while preserving the ability to take into account the distortion of cross-section typical in composite laminate and sandwich structures.

From the above, we easily understand the strong interest for computational models allowing to take into account the layered nature of the composite laminates and sandwich structures, while preserving the affordable computational cost of the ESL models.

To date, ZZ models seem to be the best candidates to meet these requirements, [37,38,39,40,41,42,43,44,45,46,47,48,49,50,51,52,53,54,55,56,57,58,59,60,61,62,63,64,65,66,67]. In fact, they attempt to combine the advantages of ESL and LW models. In the ZZ models (as in ESL models), the number of kinematic unknowns does not depend on the number of layers. The in-plane displacements combine the smooth (generally, polynomial) functions defined across the entire laminate thickness (linear [37,38,39,40,41,52,55,56,57] or higher-order polynomial, [42,43,44,45,46,51,53,58,59] with the piecewise linear (i.e., zigzag) distributions. The zigzag contributions enable a more realistic modeling of the in-plane cross-sectional distortion in multilayered composites, giving rise to a computationally efficient theory for the modeling of relatively thick laminated composite and sandwich structures. The zigzag model predictions are often as accurate as those obtained by the computationally expensive LW and higher-order models. LW-based zigzag models have also been explored in [30,31].

Extensions of the kinematics of the Di Sciuva's First-order zigzag theory (linear zigzag model) include, among other: (i) extension to the linear [41] and nonlinear [48] multilayered shell theory; (ii) general lamination lay-up [42,47,49]; (iii) satisfaction of the shear stress-free boundary conditions on the top and bottom surfaces [44,46,50]; (iv) polynomial expansion of the global part to any degree [47,49]; (v) extension to the dynamics, buckling [16,47,49,48]; (vi) thermal effects [68],[69]; (vii) sublaminates approach [68,69,70,71,72,73,74]; (viii) inclusion of von Kármán geometrically nonlinear effects [16,48,49]; (ix) extension to the nonlinear theory of laminated composites with damaged interfaces [49,68,69,74,75,76]; (x) inclusion of the transverse normal strain and stress [74,77,78]; (xi) visco-elastic effects [79]; (xii) active control of beams, plates and shells [80].

Averill [55] pointed out two drawbacks of the classical zigzag models, (1) the transverse shear stresses derived from the constitutive equations vanish erroneously along clamped boundaries, and that (2) C^1-continuous finite element approximations are required for the transverse deflection variable leading to a type of approximation that is particularly undesirable for plate and shell finite elements.

In an attempt to resolve the aforementioned drawbacks of the classical zigzag models, Tessler, Di Sciuva and Gherlone developed the Refined Zigzag Theory (RZT), [61,62,63,64,65,66,67] that makes use of a set of novel zigzag functions and uses FSDT as a baseline. The transverse shear stresses are allowed to be discontinuous along the ply interfaces; this relaxation of stress continuity permits more accurate predictions of all response quantities including the transverse shear stresses that provide accurate average values of the ply-level stresses. RZT overcomes the key drawbacks of the original zigzag theories, i.e., (1) transverse shear stresses and forces do not vanish erroneously along clamped edges, and (2) since the strains are defined in term of first derivatives of the kinematic variables, computationally efficient C^0-continuous finite elements are readily formulated. The RZT has shown to be very accurate over a wide range of aspect ratios and material systems, including thick laminates with a high degree of transverse shear flexibility and heterogeneity [61,62,63,64,65,66,67].

Another first-order zigzag theory largely used in the literature [53,58,81,82,83,84,85] is the Murakami's zigzag theory [52], which shares with RZT the same kinematics, but different zigzag functions. As will be seen later, Murakami's zigzag functions are basically of geometrical nature, in the sense that the jump in their thickness-wise derivative depends only on the thickness of each layer, when the same jump in the derivative of the RZT zigzag functions depends on the lay-up and on the transverse shear elastic compliance of the layers.

In closing this introductory overview of the zigzag approaches for the analysis of laminated composite laminates and sandwich structures, it should be noted that they belong to the more general modern approaches, known either as Multi-scale or Global-local approaches [86,87,88,89,90,91,92], where the displacement field within each layeris represented as a superposition of a layer-wise field, defined over each layer, and a global field spanning the entire laminate. Thus, the governing equations exhibit explicit coupling between effects associated with different (global and local) length scales. This multi-scale representation allows the accuracy of layer-wise theories to be achieved at a reduced computational cost [88]. It also facilitates the use of highly refined kinematic descriptions in regions of critical interest with reduced-order descriptions elsewhere in the structure, and affords a straight-forward means of transitioning between such descriptions. The distribution of available computational resources in this manner can improve both accuracy and efficiency, and can be carried out adaptively to maximize its potential benefits.

Aim of this paper is to give a review of the first-order displacement-based zigzag theories for composite laminates and sandwich structures, with special emphasis to the underlying ideas, relative strengths and weaknesses. First, the basic ideas on which rests the first-order Di Sciuva's zigzag theory are presented. This will serve as a starting point for introducing the main concern of the paper: a rewiev and comparison of the first-order Refined Zigzag Theory (RZT) and the first-order Murakami's Zigzag theory. The paper ends with the presentation of some Numerical results and the Conclusions.

2. GEOMETRICAL PRELIMINARIES

We consider a multi-layered plate of constant thickness $2h$, built-up of a finite number N of linearly elastic anisotropic layers, each of them exhibiting different mechanical properties, see Figure 1. The layers are joined by N-1 interfaces and may be either perfectly bonded or have displacement jumps across the interface due to interfacial damage. The points of the plate are referred to a global orthogonal Cartesian co-ordinate system (**x**,,z), with $\mathbf{x} \equiv (x_\alpha, \alpha = 1,2)$ the reference plane of the plate and z the thickness-wise co-ordinate. In the body of paper, Italic indices range from 1 to 3, Greek indices range from 1 to 2 and the summation convention on the repeated indices on a monomial expression is adopted. In general, superscript (k) placed in brackets on the right of any quantity identifies its affiliation to the layer *k*. The layer *k* has a constant thickness, $2h^{(k)}$. The coordinates of the bottom and top faces and of the mid-surface of the k*th* layer are denoted by $z_B^{(k)}$, $z_T^{(k)}$ and $z_M^{(k)}$, respectively. The interfacial coordinate between the k*th* and (k+1)*th* layers is denoted by $z^{(k)}$. $z_{(k)}$, so that $z_{(k)} = z_T^{(k)} = z_B^{(k+1)}$.

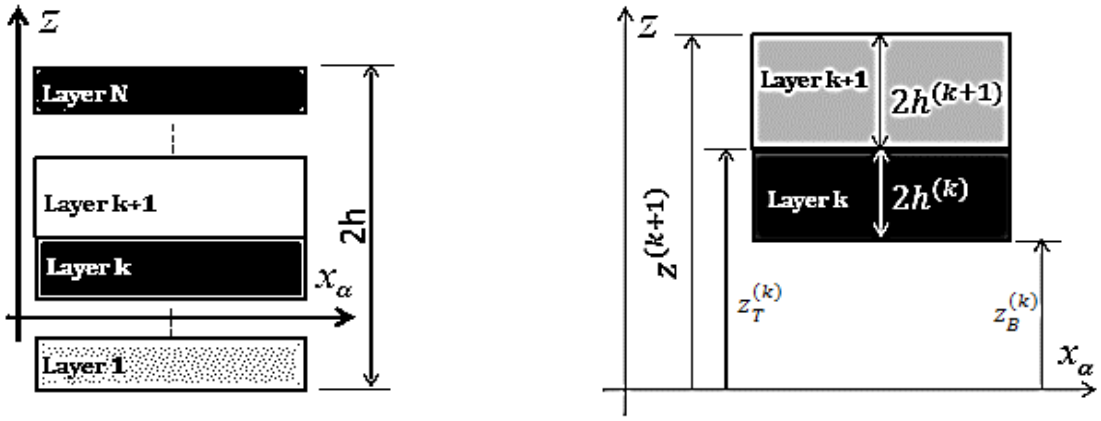

Fig. 1-Geometry and layer numbering of the multilayered plate.

For further convenience, we introduce non-dimensional local layer coordinates, $\zeta^{(k)}$, such that $\zeta^{(k)} \in [-1, +1]$, and k=1,...,N,

$$\zeta^{(k)} = \frac{z^{(k)} - z_M^{(k)}}{h^{(k)}} = \frac{z^{(k)} - z_B^{(k)}}{h^{(k)}} - 1 \text{ with } z^{(k)} \equiv z \in [z_B^{(k)}, z_T^{(k)}].$$

The origin of this local layer coordinate is located $z_M^{(k)}$abroad the coordinate system.

3. CONTACT AND BOUNDARY CONDITIONS

In order to understand the assumed kinematics of zigzag models for multilayered plates, we recall some important issues from 3D theory of elasticity. From 3D theory of elasticity it is well known that displacements and stresses must satisfy interlayer continuity conditions at the interface between two perfectly bonded layers and boundary conditions on the top and bottom surfaces.

3.1 Interlayer continuity or contact conditions

(i) continuity of the displacement field (geometric)

$$U_i^{(k)}\left(\boldsymbol{x}, z_T^{(k)}\right) = U_i^{(k+1)}\left(\boldsymbol{x}, z_B^{(k+1)}\right) \tag{1}$$

(ii) continuity of the transverse shear and normal stresses and of the gradient of the transverse normal stress (static)

$$\sigma_{iz}^{(k)}\left(\boldsymbol{x}, z_T^{(k)}\right) = \sigma_{iz}^{(k+1)}\left(\boldsymbol{x}, z_B^{(k)}\right) \tag{2}$$

$$\partial_z\sigma_{zz}^{(k)}\left(\boldsymbol{x}, z_T^{(k)}\right) = \partial_z\sigma_{zz}^{(k+1)}\left(\boldsymbol{x}, z_B^{(k)}\right) \tag{3}$$

where $U_i^{(k)}(\boldsymbol{x}, z)$ is the displacement component along the x_i $(i = 1,2,z)$ co-ordinate axis, and σ_{iz} are the components of the stress tensor.

3.2 Boundary conditions on the top (T) and bottom (B) surfaces

If the bottom and top surfaces of the laminate are loaded only by the pressure $\bar{p}_z^{(B)}(\boldsymbol{x}, -h)$ and $\bar{p}_z^{(T)}(\boldsymbol{x}, +h)$, then on the bottom (B) and top (T) surfaces of the laminate the following boundary conditions apply:

(i) On the transverse shear stresses (free-transverse shear stresses boundary conditions)

$$\sigma_{\alpha z}^{(1)}\left(\boldsymbol{x}, z_B^{(1)}\right) = \sigma_{\alpha z}^{(N)}\left(\boldsymbol{x}, z_T^{(N)}\right) = 0 \tag{4}$$

(ii) On the transverse normal stress and its gradient

$$\sigma_{zz}^{(1)}\left(\boldsymbol{x}, z_B^{(1)}\right) = \bar{p}_z^{(B)}(\boldsymbol{x}, -h); \qquad \sigma_{zz}^{(N)}\left(\boldsymbol{x}, z_T^{(N)}\right) = \bar{p}_z^{(T)}(\boldsymbol{x}, +h) \tag{5}$$

$$\partial_z\sigma_{zz}^{(1)}\left(\boldsymbol{x}, z_B^{(1)}\right) = \partial_z\sigma_{zz}^{(N)}\left(\boldsymbol{x}, z_T^{(N)}\right) = 0 \tag{6}$$

i.e., the transverse normal stresses must be equals to the applied pressure and the transverse shear stresses and the gradient of the transverse normal stress must vanishe.

4. EQUIVALENT SINGLE LAYER (ESL) THEORIES

As we said, Equivalent Single Layer (ESL) theories are generally based on a smooth expansion (generally, a power series expansion) over the whole laminate thickness of the displacement field in terms of the thickness-wise co-ordinate.

As a general expression for the expansion, we can assume the following one [41],

$$U_i\ (\mathbf{x},z) = \mathcal{Z}_{r(i)}(z)\widehat{U}_i^{(r(i))}(\mathbf{x}) = (\mathbf{x},z)\ \ (i = 1,2,3),\ \ r(i) = 0,1,2,\dots,R_i \tag{7}$$

where $\mathcal{Z}_{r(i)}(z)$ stands for any set of a-priori chosen linearly independent functions. Generally, they are assumed to be a power series of z,

$$\mathcal{Z}_{r(i)}(z) = z^r\ ,\quad r = 0,1,2,..,R_i \tag{8}$$

or their orthogonal corresponding Legendre's polynomial of first kind. They are known as polynomial theories.

This means that the kinematics along the thickness is assumed to be at least C^1-continuous and independent of the laminate lay-up. As a consequence, the multilayer structure is substituted with a plate/shell made by an equivalent single layer.

Almost all the polynomials theories assume

$$R_1 = R_2 > R_3 \tag{9}$$

In addition, many theories make the further assumption, $R_1 = R_2 > R_3 = 0$. In order to emphasize the order of expansion adopted for the in-plane displacement (i=1,2) and the transverse displacement (i=3), the following notation is adopted, $\{R, R_3\} -$ order polynomial theory.

4.1 ESL First-order Shear Deformation Theory-FSDT

This theory assumes the following kinematics [3,14,15],

$$\begin{aligned} U_\alpha\ (\mathbf{x},z) &= \widehat{U}_\alpha^{(0)}(\mathbf{x}) + z\widehat{U}_\alpha^{(1)}(\mathbf{x}) \qquad (\alpha = 1,2),\ \ R_\alpha = 1 \\ U_3\ (\mathbf{x},z) &= \widehat{U}_3^{(0)}(\mathbf{x}) = w^{(0)}(\mathbf{x}) \qquad\qquad\qquad\quad R_3 = 0 \end{aligned} \tag{10}$$

Following the previous terminology, this ESL First-order shear deformation theory is a $\{1,0\} -$ order polynomial theory.

4.2 ESL Third-order Shear Deformation Theory-TSDT

Most of the third-order shear deformation theories start by assuming the following kinematics [10]

$$\begin{aligned} U_\alpha\ (\mathbf{x},z) &= \widehat{U}_\alpha^{(0)}(\mathbf{x}) + z\widehat{U}_\alpha^{(1)}(\mathbf{x}) + z^2\widehat{U}_\alpha^{(2)}(\mathbf{x}) + z^3\widehat{U}_\alpha^{(3)}(\mathbf{x}) \qquad (\alpha = 1,2),\ \ R_\alpha = 3 \\ U_3\ (\mathbf{x},z) &= \widehat{U}_3^{(0)}(\mathbf{x}) = w^{(0)} \qquad\qquad\qquad\qquad\qquad\qquad\qquad\qquad\qquad\quad R_3 = 0 \end{aligned} \tag{11}$$

Following the previous terminology, this ESL Third-order shear deformation theory is a $\{3,0\} -$ order polynomial theory.

Requiring the transverse shear stresses to vanish on the top and bottom surfaces of the plate ($z = \pm h$), the number of generalized in-plane displacements reduces from 4 to 2. For example, one well-known TSDT is Reddy's TSDT [3,22]. In this theory, for the in-plane displacements the following expression is assumed

$$U_\alpha(\mathbf{x},z) = \widehat{U}_\alpha^{(0)}(\mathbf{x}) + z\widehat{U}_\alpha^{(1)}(\mathbf{x}) + z^3\widehat{U}_\alpha^{(3)}(\mathbf{x}) \tag{12}$$

where

$$\widehat{U}_\alpha^{(3)}(\mathbf{x}) = -\frac{1}{3h^2}\left(\partial_\alpha w^{(0)}(\mathbf{x}) + \widehat{U}_\alpha^{(1)}(\mathbf{x})\right) \tag{13}$$

In Eq.(13) and in the following, $\partial_i\ (.) = \frac{\partial(.)}{\partial x_i}$.

While computationally not expensive, ESL models are generally not accurate, especially when through-the-thickness distribution of strains and stresses are the main concern and the laminate is highly heterogeneous.

5. FIRST-ORDER DI SCIUVA's ZIGZAG THEORY-DSCZZT

Guided by these constraints, the majority of zigzag theories attempt to model accurately the transverse shear deformability and cross-section warping by satisfying the continuity constraints on the displacement field (Fig.2a) and on the inter-laminar shear stresses (Fig.2b). In other words, the displacement field is C^0 -continuous across the plate thickness, as well as the transverse shear stresses.

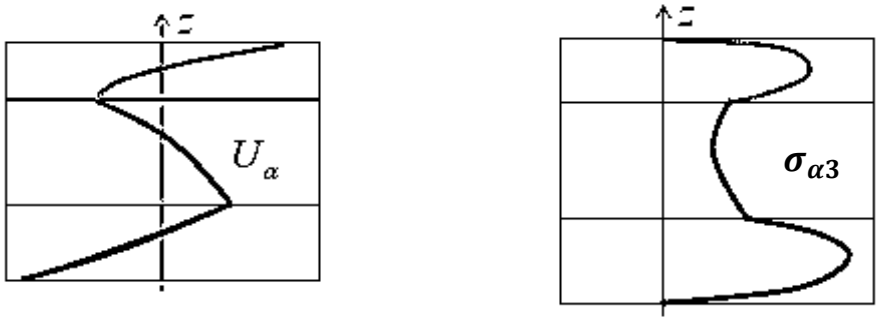

Fig. 2 - Thickness-wise distribution of the (a) in-plane displacements and (b) transverse shear stresses. Both the distributions are of the zigzag type, that is, their derivative along z is discontinuous at the interface (zigzag behavior).

As most of the plate theories assume constant transverse displacement in the z-direction and zero transverse normal stress, the contact conditions on the transverse normal stress and its gradient (Eqs. 5-6) are a-priori satisfied, thus reducing the interface static contact conditions to the transverse shear stresses (Eq. 4). For material possessing a plane of elastic symmetry parallel to the reference plane of the plate, Hooke's law allows to write these contact conditions in terms of transverse shear elastic coefficients and transverse shear strains.

$$C_{\alpha 3}^{\beta 3(k)}\epsilon_{\beta 3}^{(k)}\left(\mathbf{x}, z_T^{(k)}\right) = C_{\alpha 3}^{\beta 3(k+1)}\epsilon_{\beta 3}^{(k+1)}\left(\mathbf{x}, z_B^{(k+1)}\right) \tag{14}$$

where $2\epsilon_{\beta 3} = \partial_z\ U_\alpha\ + \partial_\alpha\ U_z$ are the transverse shear components of the strain tensor and and $C_{\alpha 3}^{\beta 3(k)}$ the transverse shear components of the elasticity tensor.

From Eq. (14) we easily deduce that in general the contact conditions on the transverse shear stresses cannot be met when the transverse shear elastic coefficients vary between two adjacent layers. Usually, the thickness-wise distribution of the elastic coefficients in

laminated plates are piecewise constant functions of the thickness coordinate. Then, if the through-the-thickness distribution of the in-plane displacements are assumed to be smooth functions, i.e., at least C^1 -continuous functions of the z-coordinate, the transverse shear stress will have jumps across the interfaces proportional to the jumps in the transverse shear elastic coefficients. We conclude that in order to be the **transverse shear stresses continuous at the interfaces, the transverse shear strains must have a jump at the interfaces.**

By taking into account the expression of the transverse shear strain, we conclude that the **gradient of the in-plane displacements must be discontinuous at the interfaces,** that is the **in-plane displacements need to be $\boldsymbol{C^{(0)}}$ −continuous,** that is, $\partial_z\, U_\alpha^{(k)}(\mathbf{x}, z_T^{(k)}) \neq \partial_z\, U_\alpha^{(k+1)}\left(\mathbf{x}, z_B^{(k+1)}\right)$. Figure 4 shows graphically this.

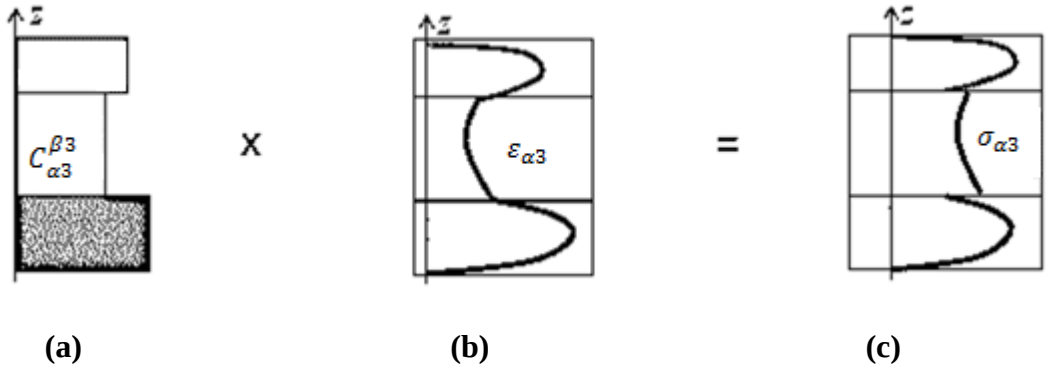

(a) **(b)** **(c)**

Fig. 3 - Typical thickness-wise distributions of (a) transverse shear elastic stiffness coefficients, (b) transverse shear strains, and (c) transverse shear stresses, in a laminated structures if the in-plane displacements are assumed to be at least C^1 -continuous functions of the z-coordinate.

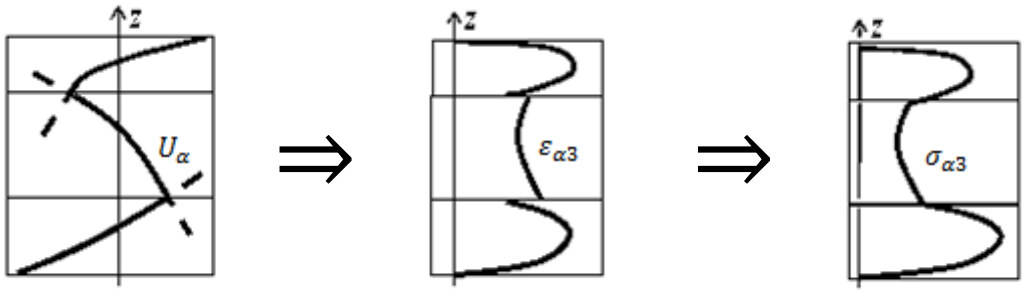

(a) **(b)** **(c)**

Fig. 4 - (a) C^0 -continuous in-plane displacements (zig-zag pattern); (b) Jumps in the transverse shear strains; (c) C^0 -continuous transverse shear stresses (zig-zag pattern).

Zigzag theories seek to meet this requirements by adopting a kinematics having a number of generalized displacements as the corresponding ESL theory [16,37,38,40]. To do this, the in-plane displacement field within each layer is taken to be composed of the superposition of

global and local contributions, while the transverse displacement is assumed to be constant over the thickness.

$$U_\alpha^{(k)}(\mathbf{x},z) = \widehat{U}_\alpha^{(k)}(\mathbf{x},z) + \breve{U}_\alpha^{(k)}(\mathbf{x},z) \;\; (\alpha = 1,2)$$
$$U_z \;(\mathbf{x},z) = w(\mathbf{x}) \tag{15}$$

In Eq.(15) $\widehat{U}_\alpha^{(k)}(\mathbf{x},z)$ gives the global kinematics (see, Eq. 7) and $\breve{U}_\alpha^{(k)}(\mathbf{x},z)$ the local enrichment.

In order to introduce the underlying ideas of the zigzag theories without excessive mathematical formalism, I will refer to the First-order zigzag plate theory.

In this zigzag theory, the Global kinematics is the same as that of the ESL First-Order Shear Deformation Theory (Eq. 10), that is, a linear expansion of the in-plane displacements (Figure 5(a)) [16,37,38,40].

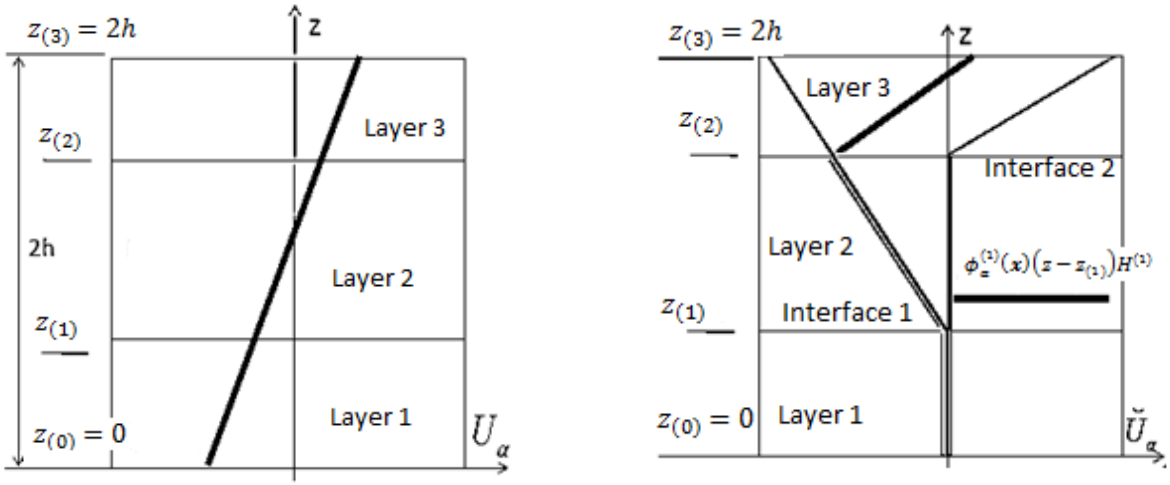

(a) **(b)**

Fig. 5 - (a) Global ESL FSDT and (b) local enrichment in the Di Sciuva's FSDZZT.

The local enrichment, known as ***zigzag function***, is given by the expression

$$\breve{U}_\alpha^{(k)}(\mathbf{x},z) = \sum_{q=1}^{k-1} \emptyset_\alpha^{(q)}(\mathbf{x})(z - z_{(q)})H^{(q)} \tag{16}$$

where $\emptyset_\alpha^{(q)}$ are unknown generalized displacements and

$$H^{(q)} = H\left(z - z_{(q)}\right) = \begin{cases} 0 & z \le z_{(q)} \\ 1 & z > z_{(q)} \end{cases}$$

is the Heaviside unit function.

Eq. (16) is the expansion for the local enrichment used to model multilayered plates by enforcing the continuity of the transverse shear stresses at the interfaces (C^0 – contribution),

as is evident from the analytical expression and from the graphs shown in figure 5(b) for the case of a three-layer laminate.

It is easy to convince that the zigzag local enrichment,

(a) is a continuous piece-wise linear function of the z coordinate (it satisfy a-priori the interface continuity conditions on the displacements);

(b) has piece-wise constant first derivative;

(c) adds N-1 unknown generalized displacements $\emptyset_\alpha$ for each coordinate directions;

(d) is zero on the first layer.

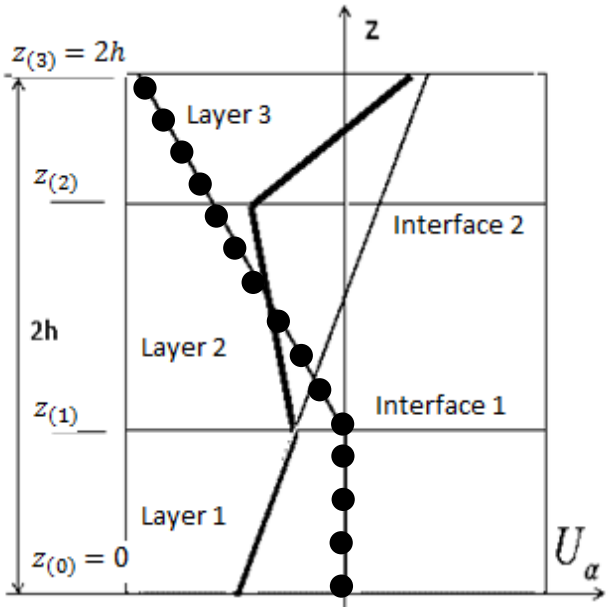

Fig. 6 - Global ESL FSDT (———), local zigzag enrichment (●—●—●) and resulting kinematics (⟶) of Di Sciuva's FSDZZT.

Figure 6 shows the global contribution (ESL FSDT), the zigzag function relative to the contrivìbution of the first interface (see, Fig. 5(b)) and the resulting kinematics adopted in First-order Di Sciuva's zigzag theory-FSDZZT, [16,37,38,40].

Since this zigzag function satisfy a-priori the interface continuity conditions on the displacements, it adds N-1 unknown generalized displacements for each co-ordinate directions. By taking into account that there are N-1 interface continuity conditions on the transverse shear stresses to be satisfied, it follows that, by satisfying these contact conditions, we can compute the N-1 unknowns generalized displacements $\emptyset_\alpha$ in terms of the global generalized displacements.

For example, for laminates with layers of orthotropic materials, the result is the following one,[16,37,38,40]

$$\widehat{U}_\alpha^{(k)}(\mathbf{x},z) = \widehat{U}_\alpha^{(0)}(\mathbf{x}) + z\widehat{U}_\alpha^{(1)}(\mathbf{x}); \qquad \breve{U}_\alpha^{(k)}(\mathbf{x},z) = f_{DSC\alpha}^{(k)}(z)\gamma_\alpha(\mathbf{x}) \tag{17}$$

where

$$\gamma_\alpha = \widehat{U}_\alpha^{(1)}(\mathbf{x}) + \partial_\alpha w(\mathbf{x}) \tag{18}$$

is the shear strain at reference plane and the zigzag function has the following very simple expression

$$f_{DSC\alpha}^{(k)}(z) = \sum_{q=1}^{k-1} a_{\alpha}^{(q)}(z - z_{(q)})H^{(q)} \tag{19}$$

where

$$a_{\alpha}^{(q)} = \left(\frac{C_{\alpha 3}^{\alpha 3(q)}}{C_{\alpha 3}^{\alpha 3(q-1)}} - 1\right)\left(1 + \sum_{j=1}^{q-1} a_{\alpha}^{(j)}\right) \tag{20}$$

are the ***interface continuity constants***. They are functions only of the transverse shear elastic coefficients.

Note that this first-order zigzag plate theory as five unknowns, as in ESL FSDT! This is the strength of the Di Sciuva's zigzag theory. On the other hand, because of the fulfilment of the continuity conditions the model estimates constant transverse shear stresses across the plate thickness. Thus, it is not able to fulfill the conditions of zero transverse shear stresses on the top and bottom plate surfaces. This is the weakness of this zigzag theory.

6. FIRST-ORDER REFINED ZIGZAG THEORY-RZT

As anticipated in the Introduction, in addition to the advantages highlighted above, and to the following ones (i) no shear correction factors are required, (ii) very accurate distribution of the transverse shear stresses are obtained from the integration of the local equilibrium equations, (iii) finite elements based on the First-order Shear Deformation Zigzag Theory are free from shear locking effects, the Di Sciuva's First-order Shear Deformation Zigzag Theory also suffers some deficiencies due to the fulfillment of the contact conditions of the transverse shear stresses. These weaknesses can be summarized as follows, (i) constant transverse shear stresses distribution along the plate thickness, (ii) classical clamped boundary conditions give zero transverse shear strains and, thus, zero transverse shear stresses at the clamped edges, when these last are obtained from the constitutive equations, (iii) due to the presence of $\partial_{\alpha} w$ (see, Eqs. (17) and (18)) in the in-plane displacement field, C^1 shape functions are required, in formulating beam, plate and shell finite elements. FSDT requires C^0 shape functions.

The first and third deficiency are specific of the First-order Shear Deformation Zigzag theory, i.e., higher-order zigzag theories does not suffer of these drawbacks. The second apply in the general case. The third deficiency, concerning the need for C^1 finite elements, has been addressed and solved in [93] in the framework of the Third-order Shear Deformation Zigzag theory.

To overcome the first two drawbacks, Tessler, Di Sciuva and Gherlone in a series of recent papers [61,62,63,64,65] advanced a new version of the first-order zigzag theory, named Refined Zigzag Theory-RZT.

Concerning the kinematics, the starting point is the same as in the Di Sciuva's first-order shear deformation zigzag plate theory, that is, Eq.(15), as the same is the global contribution, Eq. (17a) (that of the first-order shear deformation theory) and the local enrichment, that is, a piecewise linear zigzag function, whose starting mathematical expression is

$$\breve{U}_{\alpha}\left(\mathbf{x}, \zeta^{(k)}\right) = L_B\left(\zeta^{(k)}\right)\breve{U}_{\alpha B}^{(k)}(\mathbf{x}) + L_T\left(\zeta^{(k)}\right)\breve{U}_{\alpha T}^{(k)}(\mathbf{x}) \tag{20}$$

where $\breve{U}_{\alpha B}^{(k)}(\mathbf{x})$ and $\breve{U}_{\alpha T}^{(k)}(\mathbf{x})$ stand for the displacements on the bottom and top surfaces of the layer *k*, and

$$L_B(\zeta^{(k)}) = \frac{1}{2}\left(1-\zeta^{(k)}\right); \quad L_T(\zeta^{(k)}) = \frac{1}{2}\left(1+\zeta^{(k)}\right) \qquad -1 \le \zeta^{(k)} \le +1 \tag{21}$$

are linear Lagrange's interpolation polynomials.
So, the zigzag enrichment adds 2N unknowns generalized displacements for each co-ordinate directions, $\breve{U}_{\alpha}^{(B,k)}(\mathbf{x})$ and $\breve{U}_{\alpha}^{(T,k)}(\mathbf{x})$.

Let us summarize what has been achieved. For each co-ordinate directions, we have 2N unknown generalized displacements and 2(N-1) constraints (interface continuity conditions). This result in 2 free generalized displacements. In RZT this freedom has been exploited by adding the condition that the local contribution is zero on the top and bottom surfaces of the whole plate, as depicted in figure 7 for a three-layer laminate.

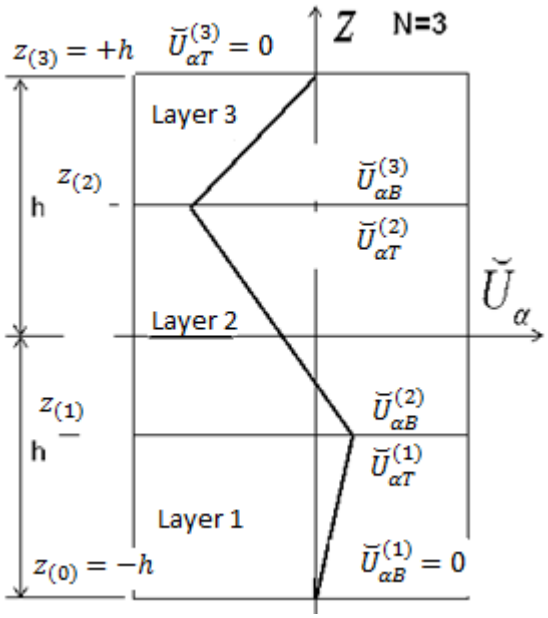

Fig. 7 – Refined Zigzag function for a three-layer laminate.

Where is the difference? The difference is in the expression of the refined zigzag function, $f_{RZT}(z)$.

In an attempt to overcome the drawbacks of Di Sciuva's first-order zigzag theory, i.e., transverse shear stresses are constant over the whole thickness of the plate, transverse shear stresses vanish at clamped end and C^1 shape functions are required in the finite element formulation, in the Refined zigzag theory the continuity conditions on the transverse shear stresses are partially relaxed.

Generalizing the previous results of the Di Sciuva's first-order zigzag theory, FSDZZT, Eq. (17b), RZT starts by writing the local kinematics in the following way

$$\breve{U}_{\alpha}^{(k)}(\mathbf{x}, z) = f_{RZT\alpha}^{(k)}(z)\psi_{\alpha}(\mathbf{x}) \tag{22}$$

where $\psi_\alpha(\mathbf{x})$ is the amplitude of the zigzag function. Note that it is independent of the other kinematic variables, then in RZT the number of independent generalized kinematic variables is greater than that of the ESL FSDT; specifically, they are 4 for the beam and 7 for the plate and shell.
As a consequence, transverse shear stress reads (orthotropic material)

$$\sigma_{\alpha 3}^{(k)} = C_{\alpha 3}^{\alpha 3(k)} \epsilon_{\alpha 3}^{(k)} \left(\mathbf{x}, z^{(k)}\right) = \frac{1}{2} C_{\alpha 3}^{\alpha 3(k)} \left(\gamma_\alpha(\mathbf{x}) + \psi_\alpha(\mathbf{x}) \partial_z f_{RZT\alpha}^{(k)}(z)\right) \tag{23}$$

with γ_α given by Eq. (18). Now we introduce the auxiliary transverse shear strain measure [61],

$$\eta_\alpha(\mathbf{x}) = \gamma_\alpha(\mathbf{x}) - \psi_\alpha(\mathbf{x}) \tag{24}$$

Note that when

$$\eta_\alpha(\mathbf{x}) = 0 \quad \Rightarrow \quad \psi_\alpha(\mathbf{x}) = \gamma_\alpha(\mathbf{x}) \tag{25}$$

and RZT reduces to Di Sciuva's FSDZZT.

Substituting Eq. (24) into Eq. (23), yields

$$\sigma_{\alpha 3}^{(k)} = \frac{1}{2} C_{\alpha 3}^{\alpha 3(k)} \eta_\alpha(\mathbf{x}) + \underline{\frac{1}{2} C_{\alpha 3}^{\alpha 3(k)} \left(1 + \partial_z f_{RZT\alpha}^{(k)}(z)\right) \psi_\alpha(\mathbf{x})} \tag{26}$$

As anticipated, instead to require the transverse shear stress to be continuous at the interfaces, in the Refined Zigzag Theory we require to be continuous only the underlined term in Eq. (26), that is

$$C_{\alpha 3}^{\alpha 3(k)} \left(1 + \partial_z f_{RZT\alpha}^{(k)}(z)\right) \tag{27}$$

Satisfying the interface static continuity condition, Eq. (2), yields

$$\partial_z f_{RZT\alpha}^{(k)}(z) = \frac{G_{\alpha 3}}{C_{\alpha 3}^{\alpha 3(k)}} - 1 \tag{28}$$

As before, there are two free additional conditions to uniquely determine the zigzag function. As we said, in the RZT the following two additional conditions

$$\breve{U}_\alpha^{(1)}(\mathbf{x}, z_B) = \breve{U}_\alpha^{(N)}(\mathbf{x}, z_T) = 0 \tag{29}$$

are imposed (see, Fig. 7). As a consequence, we obtain

$$\frac{2h}{G_{\alpha 3}} = \int_{-h}^{h} \frac{1}{C_{\alpha 3}^{\alpha 3(k)}} dz = \sum_{k=1}^{N} \frac{2h^{(k)}}{C_{\alpha 3}^{\alpha 3(k)}} \tag{30}$$

Note that the slope of zigzag function depends on the lay-up and on the transverse shear elastic compliance of the layers.

7. FIRST-ORDER MURAKAMI'S ZIGZAG THEORY-MZT

A first-order zigag theory formally identical to the first-order ZZT has been advanced by Murakami [52].

Murakami's zigzag theory (MZT) shares with the RZT the same global displacement field, Eq. (18a) and a formally identical local enrichment, Eq. (22), the difference being in the expression of the zigzag functions. Following Eq. (22), we write the local contribution as

$$\breve{U}_{\alpha}^{(k)}(\mathbf{x},z) = f_{MZT\alpha}^{(k)}(z)\psi_{\alpha}(\mathbf{x}) \tag{31}$$

where

$$\partial_z f_{MZT\alpha}^{(k)}(z) = \frac{(-1)^{(k)}}{h^{(k)}} \quad \Rightarrow \quad f_{MZT\alpha}^{(k)}(z) = (-1)^{(k)}\frac{z-z_M^{(k)}}{h^{(k)}} \tag{32}$$

So, RZT and MZT have the same number of independent kinematic variables. From the above, it is evident that Murakami's zigzag function depends only on the thickness of each layer; it is independent on the mechanical properties of layers. Figure 8 gives plots of the global contribution (ESL FSDT), the zigzag function and the resulting kinematics, for RZT and MZT, for a three-layer symmetric laminate.

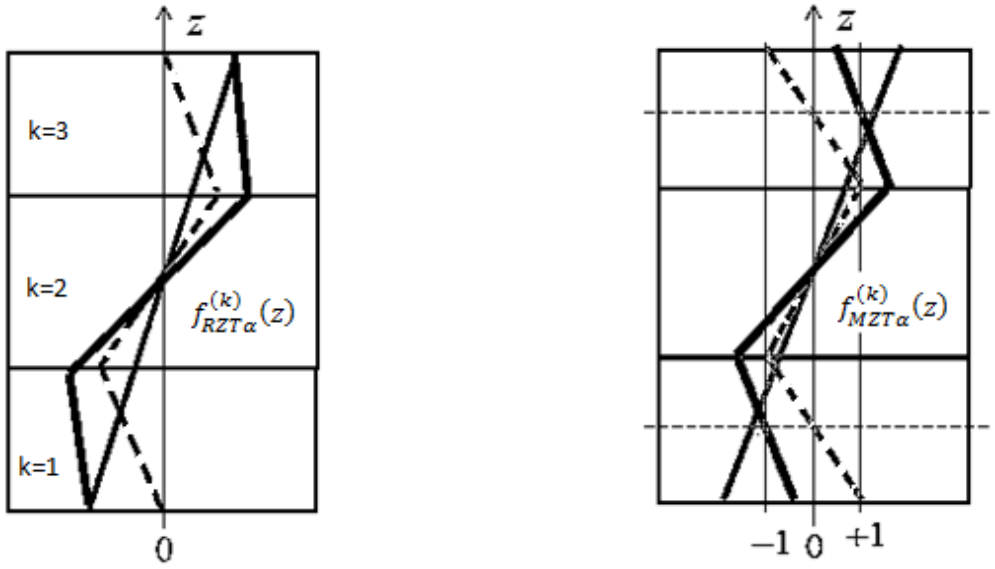

(a) **(b)**

Fig. 8 – Kinematics of (a) RZT and (b) MZT. (⟶ global contribution (ESL FSDT), (– – –) local contribution (zigzag function), (▬▬) resulting kinematics, for a three-layer symmetric laminate.

8. NUMERICAL RESULTS

In order to substantiate the accuracy of the first-order zigzag theory and show the relative performances of RZT and MZT, in this Section some numerical results are quoted. Further comparisons can be found in [84,85,94,[95].

All the numerical results presented in this Section refer to the bending, under transverse bi-sinusoidal loading, and natural frequencies of symmetric (0/90/core/90/0) square sandwich plates of side a. The faces are comprised of two-layer regular cross-ply laminate (0/90) having thickness equal to 0.1 times the total thickness of the sandwich plate.

Table 1 gives the mechanical properties of unidirectional lamina with respect to the corresponding mechanical properties of core, the geometry and the boundary conditions of the sandwich plates under investigation.

	$E_1^{(f)}/E_1^{(c)}$	$E_2^{(f)}/E_2^{(c)}$	$a/2h$	$t^{(c)}/t^{(f)}$	Boundary conditions
Sandwich (1)	$5x10^5$	$1x10^5$	6	8	Simply supported
Sandwich (2)	$4.8x10^2$	$1.2x10$	10	8	Fully clamped

Table 1- Geometry, material data and boundary conditions of the sandwich plates.

8.1 Bending of sandwich plate

Figures 8 and 9 refer to sandwich plate (1) under transverse sinusoidal loading

$$\bar{p}_z^{(T)}(\mathbf{x}) = \bar{p}_0 \sin\frac{\pi x_1}{a}\sin\frac{\pi x_2}{a} \tag{33}$$

Numerical results as estimated by the 3D theory of elasticity [4], [5], the ESL FSDT, the RZT, and the MZT are compared.

Figure 9 shows estimates for the normalized transverse deflection at the center of the plate as a function of the span-to-thickness ratio a/2h and figure 10 shows the normalized in-plane displacements and transverse shear stresses. With the exception of 3D, the transverse shear stresses are evaluated by integration of the 3D local equilibrium equations. Concerning shear correction factors, as noted in the Introduction, no shear correction factors have been used in RZT and MZT, i.e., $k_x^2 = k_y^2 = 1$. In the ESL FSDT, in addition to the case, $k_x^2 = k_y^2 = 1$, ad hoc shear correction factors are used, $k_x^2 = 0.0242, k_y^2 = 0.0225$. They have been evaluated following the approach proposed by Ferreira [98]. It is of interest to note that these values are very different from those usually adopted in ESL FSDT, $k = \frac{5}{6};\ 1;\ \frac{\pi^2}{12}$. Moreover, in order to enhance some weakness of the MZT, the unidirectional orthotropic lamina is assumed to have equal transverse shear stiffness in the principal orthotropic directions 1 and 2, that is, $G_{13} = G_{23}$.

It is concluded that, (i) RZT is very accurate in predicting global (transverse displacement) and local (thickness-wise distribution) of displacement and normal in-plane stresses (not shown in figure). Even when considering the integrated shear stresses, clearly emerges the greater accuracy of the predictions made by RZT than MZT and ESL FSDT. Moreover, these results show that (i) ESL FSDT improves its accuracy if a suitable shear correction factor is

adopted (fig. 9); (ii) MZT predicts the same deflections of the FSDT model with unitary shear correction factors (fig. 9).

A point of interest is the behavior of MZT for this specific sandiwch construction. As we said, the orthotropic unidirectional lamina constituting the faces has $G_{13} = G_{23}$. This means that the faces are free of zigzag effect (that is, the actual in-plane displacement doesn't change slope in the faces), while the zigzag effect will be present at the interface between core and face. This behavior is very well caught by RZT theory, while MZT completely fails (fig. 10, top). What happens is this. Having to vanish the zigzag effect in the case of two adjacent layers having the same transverse shear stiffness (this is the case for the faces in our sandwich), since the MZZ functions are independent of the transverse shear stiffness of the layers (see, Eq. (32)), in order to vanish the zigzag effect in the faces, the amplitude of the zigzag function, i.e., $\psi_\alpha(\mathbf{x})$ in Eq. (31), should be zero. This implies zero contribution of the zigzag effect on the whole thickness and, as a consequence, the same trend of the in-plane displacements provided by ESL FSDT (Fig. 10, top). This deficiency also affects the distribution prediction of transverse shear stresses (Fig. 10, bottom).

8.2 Natural frequencies of square sandwich plate

Aim of this investigation is to assess the reliability of the RZT changing the problem under investigation. Here we investigate the natural frequencies of sandwich plate (2), which is different from sandwich plate (1) for material characteristics of the faces and core, aspect ratio and boundary conditions (table 1). Note that in this sandwich the core is stiffer than sandwich (1) and the plate is fully clamped. As a consequence, the ad hoc shear correction factors are changed. They are $k_x^2 = 0.0825, k_y^2 = 0.1446$.

Figure 11 show the estimated free undamped frequencies for the lowest six modes (m is the number of half waves in the x_1 direction and n that in the x_2 direction). As for the bending problem of sandwich (1), RZT provides estimates very close to the 3D elasticity for all modes. FSDT with ad-hoc shear correction factors is also accurate, even if its accuracy decreases for higher modes (fifth and sixth), indicating the need to introduce other values of the correction factors as the modal number increases.

9. CONCLUDING REMARKS

Aim of this paper is to give a review of the first-order displacement-based zigzag theories for composite laminates and sandwich structures, with special emphasis to the underlying ideas, relative strengths and weaknesses. To do this, the Di Sciuva's first-order zigzag theory, the first-order Refined Zigzag Theory, and the Murakami's first-order zigzag theory have been reviewed and numerically compared. It is shown that RZT and Murakami's Zigzag theory share the same kinematics, but different zigzag functions. Specifically, unlike RZT zigzag functions, Murakami's zigzag functions are basically of geometrical type, in the sense that the jump in their thickness-wise derivative depends only on the thickness of each layer (see, Eq. (32)), when the same jump in the derivative of the RZT zigzag functions depends on the lay-up and on the transverse shear elastic compliance of the layers (see, Eq. (28)). This makes Murakami's zigzag functions approach generally unreliable, especially when the laminate does not present a repetitive or periodic lay-up, as pointed out by the same Murakami [52] and recently also by Gherlone [84], Iurlaro et al [85], [94] and Iurlaro [95]. In extreme cases, like that of sandwich taken used for the numerical assessment presented in this paper, the Murakami's zigzag approach completely fails, in the sense that Murakami's zigzag

functions do not give any contribution and Murakami's approach provides the same incorrect results of FSDT with unitary shear correction factors. On the contrary, also for this sandwich plates, RZT provides a very accurate estimates.

From the present numerical investigation and others available in the open literature [61, 62,63,64,65,66,67], it seems reasonable to draw the conclusion that RZT is very accurate in predicting global (transverse displacement) and local (thickness-wise distribution) of displacement and normal in-plane stresses.

By taking into account the additional strength of RZT, mainly, the possibility to develop C^0 beam [97,98,99,100,101,102,103], plate and shell finite elements, [104,105,106,107,108], like ESL FSDT, in my opinion RZT represents, among the first-order zigzag theories, the best compromise between computational efficiency and numerical accuracy.

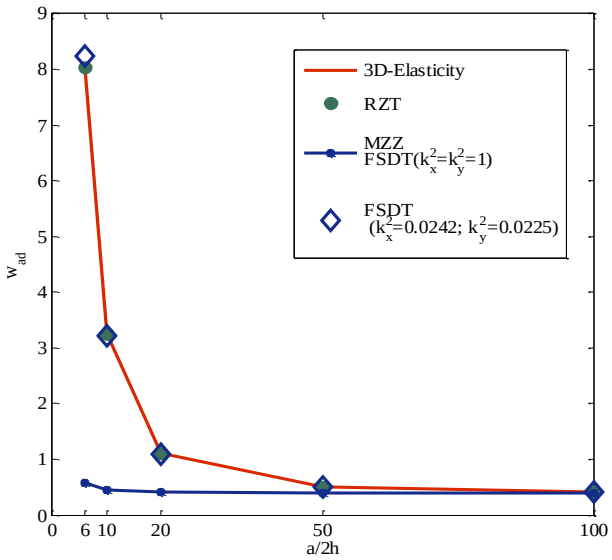

Fig. 9 - Normalized transverse deflection at the center of the plate as a function of the span-to-thickness ratio a/2h.

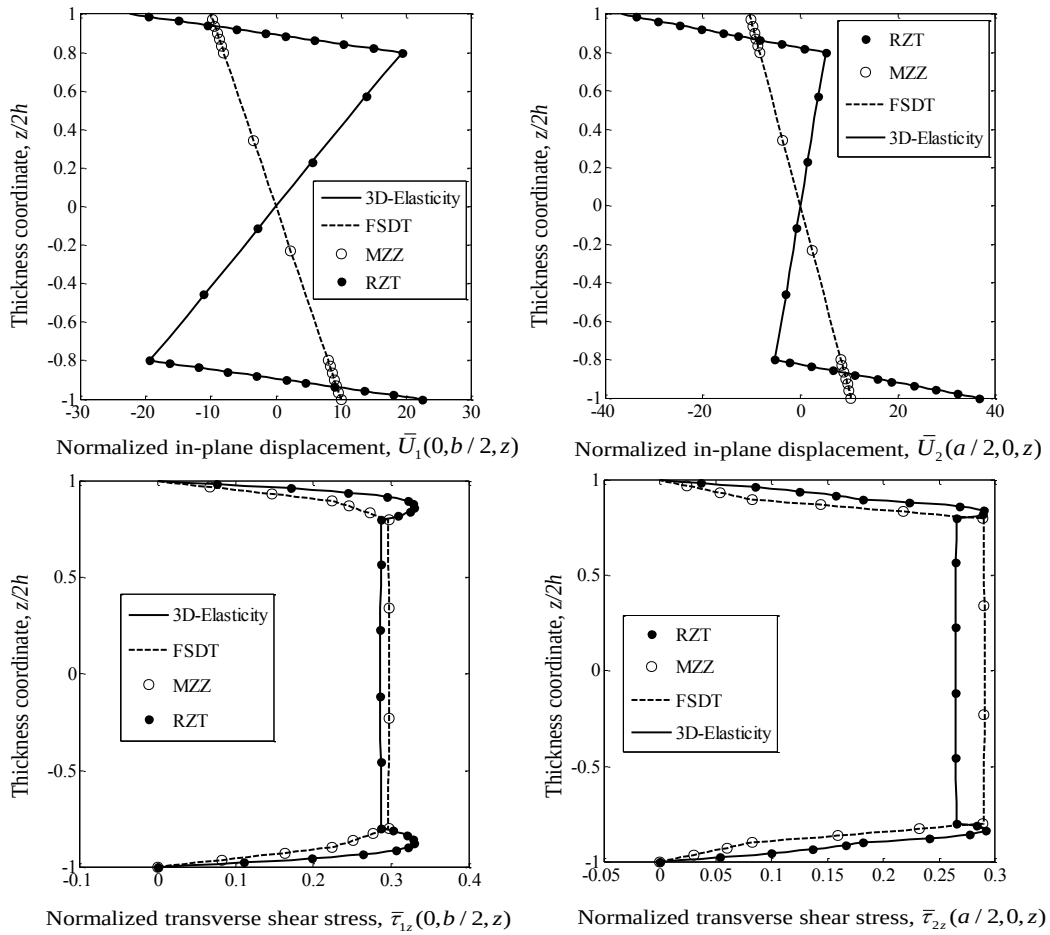

Fig. 10 – Normalized in-plane and transverse shear stresses. With the exception of 3D, the transverse shear stresses are evaluated by integration the 3D local equilibrium equations.

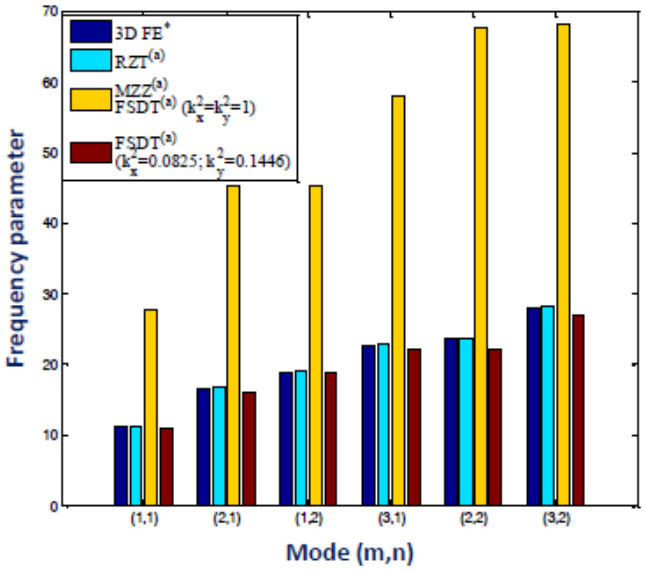

Fig. 11 – Natural frequencies for sandwich plate (2).

REFERENCES

[1] J.R. Vinson, Sandwich Structures: past, present, and future. O. T. Thomsen, E. Bozhevolnaya, A. Lyckegaard, Eds., *Sandwich structures 7: Advancing with sandwich structures and materials.* Aalborg, Denmark, 29-31 August, 2005.

[2] A.S. Herrmann, P.C. Zahlen, I. Zuardy, Sandwich Structures Technology in Commercial Aviation-Present Applications and Future Trends. O. T. Thomsen, E. Bozhevolnaya, A. Lyckegaard, Eds., *Sandwich structures 7: Advancing with sandwich structures and materials.* Aalborg, Denmark, 29-31 August, 2005.

[3] J. N. Reddy, *Mechanics of laminated composite plates and shells*. *Theory and analysis*, CRC Press, Inc., 2004.

[4] N.J. Pagano, Exact solutions for composite laminates in cylindrical bending. *Journal of Composite Materials*, **3**(3), 398-411, 1969.

[5] N.J. Pagano, Exact solutions for rectangular bidirectional composites and sandwich plates. *Journal of Composite Materials*, **4**(1), 20-34, 1970.

[6] S. Srinivas, A.K. Rao, Bending, vibration and buckling of simply supported thick orthotropic rectangular plates and laminates. *International Journal of Solids and Structures*, **6**(11), 1463-1481, 1970.

[7] S. Srinivas, A.K. Rao, A three-dimensional solutions for plates and laminates. *Journal of Franklin Institute*, **291**(6), 469-481, 1971.

[8] A.K. Noor, W.S. Burton, Three dimensional solutions for antisymmetrically laminated anisotropic plates. *Journal of Applied Mechanics*, **57**(1), 182-188, 1990.

[9] M. Savoia, J.N. Reddy, A variational approach to three-dimensional elasticity solutions of laminated composite plates. *Journal of Applied Mechanics*, **59**(2), 166-175, 1992.

[10] K. H. Lo, R. M. Christensen, E. M. Wu, A high-order theory of plate deformation—Part 1: Homogeneous plates. *Journal of Applied Mechanics*, **44**(4), 663–668, 1977.

[11] D. Liu and X. Li, An overall view of laminate theories based on displacement hypothesis. *Journal of Composite Materials*, **30**(14), 1539–1561, 1996.

[12] E. Reissner, On a certain mixed variational theorem and a proposed application. *International Journal for Numerical Methods in Engineering*, **20**, 1366–1368, 1984.

[13] E. Reissner and Y. Stavsky, Bending and stretching of certain types of heterogeneous aeolotropic elastic plates. *Journal of Applied Mechanics*, **28**(3), 402–408, 1961.

[14] R. D. Mindlin, Influence of rotatory inertia and shear deformation on flexural motions of isotropic elastic plates. *Journal of Applied Mechanics*, **18**, 31–38, 1951.

[15] J. M. Whitney, N. J. Pagano, Shear deformation in heterogeneous anisotropic plates. *Journal of Applied Mechanics*, **37**(4), 1031–1036, 1970.

[16] M. Di Sciuva, Bending, vibration and buckling of simply-supported thick multilayered orthotropic plates. An evaluation of a new displacement model. *Journal of Sound and Vibration*, **105**(3), 425-442, 1986.

[17] V. Birman, C.W. Bert, On the choice of shear correction factor in sandwich structures. Journal of Sandwich Structures and Materials, **4**, 83–95, 2002.

[18] L. Iurlaro, M. Gherlone, M. Di Sciuva, A. Tessler, Assessment of the refined zigzag theory for bending, vibration, and buckling of sandwich plates: a comparative study of different theories. *Composite Structures*, **106,** 777–792, 2013.

[19] E. Reissner, Reflections on the theory of elastic plates. *Applied Mechanics Reviews*, **38(**11), 1453–1464, 1985.

[20] L. Librescu, A. Khdeir, J.N. Reddy, A comprehensive analysis of the state of stress of elastic anisotropic flat plates using refined theories. *Acta Mechanica*, **70**, 57–81, 1987.

[21] A.K. Noor, W.S. Burton, Assessment of shear deformation theories for multilayered composite plates. *Applied Mechanics Reviews*, **42**(1), 1–13, 1989.
[22] J. N. Reddy, A simple higher-order theory for laminated composite plates. *Journal of Applied Mechanics*, **51(**4), 745–752, 1984.
[23] A. Tessler, An improved plate theory of 1,2-order for thick composite laminates. *International Journal of Solids and Structures*, **30**(7), 981–1000, 1993.
[24] G. M. Cook, A. Tessler, A 3,2-order bending theory for laminated composite and sandwich beams. *Composites Part B: Engineering*, **29**(5), 565–576, 1998.
[25] A. Barut, E. Madenci, T. Anderson, A. Tessler, Equivalent single-layer theory for a complete stress field in sandwich panels under arbitrarily distributed loading. *Composite Structures*, **58**(4), 483 – 495, 2002.
[26] Y.M. Ghugal, R.P. Shimpi, A review of refined shear deformation theories of isotropic and anisotropic laminated plates. *Journal of Reinforced Plastics and Composites*, **21**, 775-813, 2002.
[27] C.Wanji, W. Zhen, A selective review on recent development of displacement-based laminated plate theories. *Recent Patents on Mechanical Engineering*, **1**(1), 29-44, 2008.
[28] R. Khandan, S. Noroozi, P. Sewell, J. Vinney, The development of laminated composite plate theories: a review. *Journal of Material Science*, **47**, 5901-5910, 2012.
[29] J.N. Reddy, A generalization of two-dimensional theories of laminated composite plates. *Communications in Applied Numerical Methods*, **3**, 173–180, 1987.
[30] A. Toledano, H.Murakami, A composite plate theory for arbitrary laminate configurations. *Journal of Applied Mechanics*, **54**(1), 181–189, 1987.
[31] A. Toledano, H. Murakami, A high-order laminated plate theory with improved in-plane responses. *International Journal of Solids and Structures*, **23(**1), 111–131, 1987.
[32] E.J. Barbero, J.N. Reddy, J.L. Teply, General two-dimensional theory of laminated cylindrical shells. *AIAA Journal*, **28,** 544–553, 1990.
[33] J. Aboudi, Mechanics of Composite Materials—A Unified Micromechanical Approach. *Studies in Applied Mechanics*, **29**, Elsevier, Amsterdam. 1991.
[34] X. Lu, D. Liu, An interlaminar shear stress continuity theory for both thin and thick composite laminates. *Journal of Applied Mechanics*, **59**(3), 502–509, 1992.
[35] K.P. Soldatos, Vectorial approach for the formulation of variationally consistent higher-order plate theories. *Composite Engineering*, **3**, 3–17, 1993.
[36] K.P. Soldatos, Generalization of variationally consistent plate theories on the basis of a vectorial formulation. *Journal of Sound and Vibration*, **183**, 819–839, 1995.
[37] M. Di Sciuva, A refinement of the transverse shear deformation theory for multilayered orthotropic plates. *VII National Conference AIDAA*, Naples, Italy, 25-28 October, 1983. Also, in *AEROTECNICA, MISSILI E SPAZIO*, **2**, 84-92, 1984.
[38] M. Di Sciuva, A refined transverse shear deformation theory for multilayered anisotropic plates. *Atti Accademia delle Scienze di Torino*, Italy, Classe di Scienze Fisiche, Matematiche e Naturali, **118**, 279-295, 1984.
[39] M. Di Sciuva, Development of an anisotropic, multilayered, shear-deformable rectangular plate element. *Computers & Structures*, **21**, 789–796, 1985.
[40] M. Di Sciuva, Evaluation of some multilayered, shear-deformable plate elements. *Proceedings of 26th Structures, Structural Dynamics and Materials Conference*, AIAA/ASME/ASCE/AHS-Paper 85-0717, 394 – 400, 1985.
[41] M. Di Sciuva, An improved shear-deformation theory for moderately thick multilayered anisotropic shells and plates. *Journal of Applied Mechanics*, **54(**3), 589–596, 1987.

[42] M. Di Sciuva, Further refinement in the transverse shear deformation theory for multilayered composite plates. *Atti Accademia delle Scienze di Torino*, Italy, Classe di Scienze Fisiche, Matematiche e Naturali, **124**(5-6), 248–268, 1990.
[43] M. Di Sciuva, Improved third-order shear deformation theory for multilayered anisotropic plate. Analytical and Fem results. Proceedings of *European Conference on New Advances in Computational Structural Mechanics*, Giens (France), April 1991.
[44] M. Di Sciuva, Multilayered anisotropic plate models with continuous interlaminar stresses. *Composite Structures*, **22**(3), 149 – 167, 1992.
[45] M. Di Sciuva M, A general quadrilateral multilayered plate element with continuous interlaminar stresses. *Computers & Structures*, **47**(1), 91-105, 1993.
[46] M. Di Sciuva, U. Icardi (1993) Discrete-layer models for multilayered shells accounting for interlayer continuity. *MECCANICA*, **28**(4), 281-291, 1993.
[47] M. Di Sciuva, A generalization of the zig-zag plate models to account for general lamination configuration. *Atti Accademia delle Scienze di Torino*, Italy, Classe di Scienze Fisiche, Matematiche e Naturali, **128**(3-4), 81–103, 1994.
[48] L. Librescu, W. Lin, M. Di Sciuva, U. Icardi, Postbuckling of laminated composite and sandwich-type plates and shells: on the significance of the fulfilment of static interlayer continuity conditions. 20th *Congress of the International Council of the Aeronautical Sciences*, Sorrento (Italy), 8-13September, 1996.
[49] M. Di Sciuva, Geometrically nonlinear theory of multilayered plates with interlayer slips. *AIAA Journal*, **35**, 1753–1759, 1997.
[50] M. Di Sciuva, U. Icardi, On modeling of global and local response of sandwich plates with laminated faces. *Journal of Sandwich Structures and Materials*, **2**(4), 350-378, 2000.
[51] M. Di Sciuva, M. Gherlone, L. Librescu, Implications of damaged interfaces and of other non-classical effects on the load carrying capacity of multilayered composite shallow shells. *International Journal of Non-Linear Mechanics*, **37**(4-5), 851–867, 2002.
[52] H. Murakami, Laminated composite plate theory with improved in-plane responses. *Journal of applied Mechanics*, **53**, 661–666, 1986.
[53] T.K. Varadan, K. Bhaskar, A higher-order theory for bending analysis of laminated shells of revolution. Computers and Structures, 40, 815–819, 1991.
[54] M. Cho, R. R. Parmenter, Efficient higher order composite plate theory for general lamination configurations. *AIAA Journal*, vol. 31, no. 7, pp. 1299–1306, 1993.
[55] R. C. Averill, Static and dynamic response of moderately thick laminated beams with damage. *Composites Engineering*, **4**(4), 381–395, 1994.
[56] R. C. Averill, Y. C. Yip, Development of simple, robust finite elements based on refined theories for thick laminated beams. *Computers and Structures*, **59**(3), 529–546, 1996.
[57] Z.Q. Cheng, A.K. Jemah, F.W. Williams, Theory for multilayered anisotropic plates with weakened interfaces. *Journal of applied Mechanics*, **63**, 1019–1026, 1996.
[58] J.S.M. Ali, K. Bhaskar, T.K. Varadan, A new theory for accurate thermal/mechanical flexural analysis of symmetric laminated plates, Composite Structures, 45, 227–232, 1999.
[59] P. Umasree and K. Bhaskar, Analytical solutions for flexure of clamped rectangular cross-ply plates using an accurate zig-zag type higher-order theory. *Composite Structures*, **74**(4), 426 – 439, 2006.
[60] S. Kapuria, S.D. Kulkarni, An improved discrete Kirchhoff quadrilateral element based on third-order zigzag theory for static analysis of composite and sandwich plates. *International Journal for Numerical Methods in Engineering*, **69**, 1948–1981, 2007.

[61] A. Tessler, M. Di Sciuva, M. Gherlone, Refinement of Timoshenko beam theory for composite and sandwich beams using zigzag kinematics. *NASA/TP-2007-215086*, 2007.
[62] A. Tessler, M. Di Sciuva, M. Gherlone, A refined zigzag beam theory for composite and sandwich beams. *Journal of Composite Materials*, **43**(9), 1051–1081, 2009.
[63] A. Tessler, M. Di Sciuva, M. Gherlone, Refined zigzag theory for laminated composite and sandwich plates. *NASA/TP-2009-215561*, January 2009.
[64] M. Di Sciuva, M. Gherlone, A.Tessler, A robust and consistent first-order zigzag theory for multilayered beams. R. Gilat, L. Banks-Sills Eds. *Advances in Mathematical Modelling and Experimental Methods for Materials and Structures: The Jacob Aboudi Volume*, Springer, N.Y., 255-268. 2010.
[65] A. Tessler, M. Di Sciuva, M. Gherlone, A consistent refinement of first-order shear-deformation theory for laminated composite and sandwich plates using improved zigzag kinematics. *Journal of Mechanics of Materials and Structures*, **5**(2), 341–367, 2010.
[66] A. Tessler, M. Di Sciuva, M. Gherlone, Refined zigzag theory for homogeneous, laminated composite, and sandwich plates: a homogeneous-limit methodology for zigzag function selection. *NASA/TP-2010-216214*, 2010.
[67] A. Tessler, M. Di Sciuva, M. Gherlone, A homogeneous limit methodology and refinements of computationally efficient zigzag theory for homogeneous, laminated composite, and sandwich plates. *Numerical Methods for Partial Differential Equations*, **27**(1), 208–229, 2011.
[68] M. Gherlone, M. Di Sciuva, Thermo-mechanics of undamaged and damaged multilayered composite plates: a sub-laminates finite element approach. *Composite Structures*, 81(1), 125-136, 2007.
[69] M. Gherlone, M. Di Sciuva, Thermo-mechanics of undamaged and damaged multilayered composite plates: assessment of the fem sub-laminates approach. *Composite Structures*, 81(1), 137-155, 2007.
[70] R. C. Averill, Y. C. Yip, Thick beam theory and finite element model with zig-zag sublaminate approximations. *AIAA Journal*, **34**(8), 1627–1632, 1996.
[71] Y.-B. Cho and R. C. Averill, "An improved theory and finite-element model for laminated composite and sandwich beams using first-order zig-zag sublaminate approximations. *Composite Structures*, **37**(3), 281–298, 1997.
[72] Y. B. Cho, R. C. Averill, First-order zig-zag sublaminate plate theory and finite element model for laminated composite and sandwich panels. *Composite Structures*, **50**(1), 2000.
[73] D. Eby, R. C. Averill, Zigzag sublaminate model for nonlinear analysis of laminated panels. *Journal of Aerospace Engineering*, **13**(3), 100–109, 2000.
[74] U. Icardi, Layerwise mixed element with sublaminates approximation and 3D zig-zag field, for analysis of local effects in laminated and sandwich composites. International Journal for Numerical Methods in Engineering, **70(**1), 94–125, 2007.
[75] M. Di Sciuva, L. Librescu, Contribution to the nonlinear theory of multilayered composite shells featuring damaged interfaces. *Composites Part B*, **32**, 219-227, 2001.
[76] M. Di Sciuva, M. Gherlone, Quasi-3D static and dynamic analysis of undamaged and damaged sandwich beams. *Journal of Sandwich Structures and Materials*, 7(1), 31-52, 2005.
[77] U. Icardi, A three-dimensional zigzag theory for the analysis of thick laminated beams. *Modern Trends in the Theory and Behavior of Structures Symposium*, 1999 ASME Mechanics and Materials Conference, Virginia Polytechnic Institute and State University, Blacksburg, VA, USA, 1999 June 27-30.

[78] M. Di Sciuva, U. Icardi, Numerical assessment of the core deformability effect on the behaviour of sandwich beams. *Composite Structures*, **52**, 41-53, 2001.
[79] N.N. Sy, J. J. Lee, M. Cho, Viscoelastic response of higher order zigzag model of laminated composite/sandwich plates. *WCCM XI-Minisymposium on New Trends in Zigzag Theories for Multilayered and Sandwich Beams, Plates and Shells*, Barcelona, Spain, 20-25 July 2014.
[80] M. Di Sciuva, U. Icardi, Actively controlled beams with damaged interfaces. 1999 *ASME Mechanics and Materials Conference*, June 27-30, 1999, Virginia Tech, Blacksburg, VA 24061 USA.
[81] E. Carrera, On the use of the Murakami's zig-zag function in the modeling of layered plates and shells. *Computers and Structures*, **82,** 541–554, 2004.
[82] S. Brischetto, E. Carrera, L. Demasi, Improved bending analysis of sandwich plates using a zig-zag function. *Composite Structures*, **89**(3), 408–415, 2009.
[83] D. A. Maturi, A. J. M. Ferreira, A. M. Zenkour, D. S. Mashat, Analysis of laminated shells by Murakami's zig-zag theory and radial basis functions collocation. *Journal of Applied Mathematics*, Volume 2013, Article ID 123465, 14 pages, 2013.
[84] M. Gherlone, On the use of zigzag functions in equivalent single layer theories for laminated composite and sandwich beams: a comparative study and some observations on external weak layers. *Journal of Applied Mechanics*, **80**(6), 061004-1-19, 2013.
[85] L. Iurlaro, M. Gherlone, M. Di Sciuva, A comparison of zigzag functions for the bending, vibration and buckling analysis of multilayered composite and sandwich plates. WCCM XI, Barcelona, Spain, 2014.
[86] D.H. Robbins Jr., J.N. Reddy, Variable kinematic modeling of laminated composite plates. *International Journal for Numerical Methods in Engineering*, **39**, 2283–2317, 1996.
[87] T.O.Williams, A generalized multilength scale nonlinear composite plate theory with delamination. *International Journal of Solids and Structures*, **36**, 3015–3050, 1999.
[88] T.O. Williams, Efficiency and accuracy considerations in a unified plate theory with delamination. *Composite Structures*, **52**, 27–40, 2001.
[89] T.O. Williams, A generalized, multilength scale framework for thermo-diffusional-mechanically coupled, nonlinear, laminated plate theories with delaminations. *International Journal of Solids and Structures*, **42**, 1465–1490, 2005.
[90] T.O. Williams, A new theoretical framework for the formulation of general, nonlinear, multi-scale plate theories. *International Journal of Solids and Structures*, **45**, 2534–2560, 2008.
[91] A.Tessler, M. Gherlone, D. Versino, M. Di Sciuva, Analytic and computational perspectives of multi-scale theory for homogeneous, laminated composite, and sandwich beams and plates. *NASA/TP-2012-217573*, 2012.
[92] L. Iurlaro, M. Gherlone, M. Di Sciuva, A. Tessler, A multi-scale refined zigzag theory for multilayered composite and sandwich plates with improved transverse shear stresses. S. Idelsohn, M. Papadrakis, B. Schrefler, Eds. *V International Conference COUPLED PROBLEMS 2013 in Science and Engineering*, Ibiza, June 2013.
[93] W. Zhen, C. Wanji, A C^0-type higher-order theory for bending analysis of laminated composite and sandwich plates. *Composite Structures*, **92**, 653-661, 2010.
[94] L. Iurlaro, M. Gherlone, M. Di Sciuva, A. Tessler, Assessment of the Refined Zigzag Theory for bending, vibration, and buckling of sandwich plates: a comparative study of different theories. *Composite Structures*, **106,** 777–792, 2013.

[95] L. Iurlaro, Development of refined models for multilayered composite and sandwich structures. Analytical formulation, FEM implementation and experimental assessment. *Ph.D. thesis*, Politecnico di Torino, Italy, 2015.
[96] A.J.M. Ferreira, A formulation of the multiquadratic radial basis function method for the analysis of laminated composite plates. *Composite Structures*, **59**, 385–392, 2003.
[97] E. Oñate, A. Eijo, S. Oller, Two-noded beam element for composite and sandwich beams using Timoshenko theory and Refined Zigzag kinematics. *Publication CIMNE* no. 346, 2010.
[98] M. Gherlone, A. Tessler, M. Di Sciuva, C^0 beam elements based on the refined zigzag theory for multilayered composite and sandwich laminates. *Composite Structures*, **93**(11), 2882 – 2894, 2011.
[99] E. Oñate, A. Ejio, S. Oller, Simple and accurate two-noded beam element for composite laminated beams using a refined zigzag theory. *Computers Methods in Applied Mechanics and Engineerig*, **213-216**, 362-382, 2012.
[100] A. Ejio, E. Oñate, S. Oller, A numerical model of delamination in composite laminated beams using the LRZ beam element based on the refined zigzag theory. *Composite Structures*, **104**, 270-280, 2013.
[101] E. Oñate *Structural Analysis with the Finite Element Method; Linear statics. Vol. 2 Beams, Plates and Shells.* Springer, 2013.
[102] D. Di Capua, E. Oñate, Two-noded zigzag beam element accounting for shear effects based on an extended Euler Bernoulli theory. *Composite Structures*, **132**, 1192-1205, 2015.
[103] M. Di Sciuva, M. Gherlone, L. Iurlaro, A. Tessler, A class of higher-order C^0 composite and sandwich beam elements based on the Refined Zigzag Theory. *Composite Structures*, **132**, 784–803, 2015.
[104] A. Eijo, E. Oñate, S. Oller, A four-noded quadrilateral element for composite laminated plates/shells using the refined zigzag theory. *International Journal for Numerical Methods in Engineering*, **95**, 631-660, 2013.
[105] A. Eijo, E. Oñate, S. Oller, Delamination in laminated plates using the 4-noded quadrilateral QLRZ plate element based on the Refined Zigzag Theory. *Composite Structures*, **108**, 456-471, 2013.
[106] D. Versino, Refined theories and discontinuous Galerkin methods for the analysis of multilayered composite structures. *Ph.D. thesis*, Politecnico di Torino, Italy, 2012.
[107] D. Versino, M. Gherlone, M. Mattone, M. Di Sciuva, A. Tessler, An efficient, C^0 triangular elements based on the Refined Zigzag Theory for multilayered composite and sandwich plates. *Composites Part B*, **44B**(1), 218–230, 2013.
[108] D. Versino, M. Gherlone, M. Di Sciuva, Four-node shell element for doubly curved multilayered composites shells based on the Refined Zigzag Theory. *Composite Structures*, **118**, 392-402, 2014.

ECCOMAS Congress 2016
VII European Congress on Computational Methods in Applied Sciences and Engineering
M. Papadrakakis, V. Papadopoulos, G. Stefanou, V. Plevris (eds.)
Crete Island, Greece, 5–10 June 2016

VIRTUAL TESTBENCH FOR THE OMNI WHEEL DYNAMICS SIMULATION: NEW CONTACT TRACKING ALGORITHM

Ivan Kosenko[1], **Sergey Stepanov**[2], **Kirill Gerasimov**[3], **and Mikhail Stavrovskiy**[4]

[1]Moscow Aviation Institute (National Research University)
Volokolamskoe shosse 4, 125993, Moscow, Russia
e-mail: kosenko@ccas.ru

[2]Dorodnicyn Computing Centre of Russian Academy of Sciences
Vavilov street 40, 119333, Moscow, Russia
e-mail: stepsj@ccas.ru

[3]Lomonosov Moscow State University
GSP-1, 1-52, Leninskie Gory, 119991, Moscow, Russia
e-mail: kiriger@gmail.com

[4]STAN Group
1 Vadkovsky lane, 127994, Moscow, Russia
e-mail: stavrov@list.ru

Keywords: Object-Oriented Modeling, Modeling of Mechanical Constraint, Omni Wheel, Contact Tracking, Unilateral Constraint, Roller Inclination, Model of Friction.

Abstract. *General approach for constructing the computer models of the multibody system dynamics with unilateral constraints and friction is under consideration. Base dynamical abstractions, classes, are described which provide a model building using object-oriented paradigm for the design of dynamic objects virtual prototypes.*

Contact tracking block is the most important one of any algorithm for simulation the mechanical contact. This block provides permanent computations of the contact point/patch where the process of bodies mechanical interaction takes place. A general formulation of contact in algebraic and/or differential forms is under analysis.

The omni directional wheel dynamical testbench is under construction then. This model is built in a way such that the wheel disc equipped by rollers along its rim keeps its vertical orientation permanently. Such an arrangement of the virtual testbench provides indeed the simulation of the wheel motion like it is a part of any virtual omni vehicle.

Using the omni wheel permanent vertical orientation we are able to build up an efficient algorithm for contact tracking between the roller and the floor. The case of so-called angled (being preliminarily rotated) rollers is also included. The angle of roller inclination to the wheel plane is possible to be varied, as a parameter of the dynamical problem, in frame of wide range of its values. This approach is a natural generalization of its previous version which was implemented for the case of zero angle of the roller prerotation.

1 INTRODUCTION

A construct of the omni vehicle dynamical model has been presented in [1], see also papers [2, 3]. Concept of an omni wheel was proposed in [4]. Simplified model for mounting of roller on the wheel disk has been considered there: the roller axis of symmetry assumed to belong to the disk, or equivalently an angle of inclination, denote it by ψ, for the roller axis to the wheel plane is equal to zero.

In engineering applications nevertheless one may encounter frequently a situation with $\psi > 0$. We proposed in [1] fast algorithm for tracking a contact provided the omni wheel keeps vertical orientation of its plane (in frame of the whole vehicle construct). Thus actual is a task for building up the contact tracking algorithm also for the case of $\psi > 0$. This task has been completed in this paper. To reach this goal we accept the working model of a virtual testbench consisting of one wheel equipped by rollers along its rim. One can see easily this simplification has mostly methodical nature and does not prevent us to integrate all the construct back into the whole vehicle having generally several omni wheels already analyzed previously [1].

2 GENERAL DESCRIPTION OF THE MULTIBODY DYNAMICS MODEL ARCHITECTURE

2.1 Object-oriented concept

First of all, in frame of the general approach let us build up the multibody system (MBS) dynamical model using object-oriented paradigm with Modelica language [5]. Consider the MBS consisting of $m+1$ bodies $B_0, \ldots, B_m$. Represent it as a set $\mathcal{B} = \{B_0, \ldots, B_m\}$. Here B_0 assumed to be a base body. We suppose B_0 to be connected with an inertial frame of reference, or to have a known motion with respect to the inertial frame of reference. For example one can imagine the base body as a rotating platform, or as a vehicle performing its motion according to a given law. For definiteness and simplicity we suppose in the following text that all state variables describing the rigid bodies motion always refer to one fixed inertial coordinate system connected to the base body by default.

Some bodies of the MBS assumed connected by mechanical constraints. Suppose all constraints compose the set $\mathcal{C} = \{C_1, \ldots, C_n\}$. We include in our considerations constraints of the following types: holonomic/nonholonomic, scleronomic/rheonomic, bilateral/unilateral.

Thus one can uniquely represent a structure of the MBS via a undirected graph $G = (\mathcal{B}, \mathcal{C}, \mathcal{I})$. Here $\mathcal{I} \subset \mathcal{C} \times \mathcal{B}$ is an incidence relation setting in a correspondence the vertex incident to every edge $C_i \in \mathcal{C}$ of the graph. According to physical reasons it is easy to see that for any mechanical constraint C_i there exist exactly two bodies $B_k, B_l \in \mathcal{B}$ connected by this constraint.

It is clear that consideration of the graph G does not provide a structural information sufficient for the MBS dynamics description. Indeed, in addition to the force interaction represented usually by wrenches between bodies B_k, B_l through the constraint C_i there exist kinematic conditions specific for different kinds of constraints. Wrenches themselves can be represented in turn by constraint forces and constraint torques couples. These forces and couples are connected by virtue of Newton's third law of dynamics.

Thus if the system of ODEs for translatory-rotary motion can be associated with the object of a model corresponding to rigid body, then the system of the algebraic equations can be naturally associated with the object of a model corresponding to constraint. Note that according to above consideration the set of algebraic equations comprises relations for constraint wrenches, and kinematic relations depending on the certain type of constraints.

Thus all the "population" of any MBS model is reduced to objects of two classes: *RigidBody*

(objects $B_0, \ldots, B_m$), *Constraint* (objects $C_1, \ldots, C_n$). According to this approach simulation of the whole system behavior reduces to permanent information interaction between the objects of two considered types. Within the frame of Newton's laws of dynamics one can construct the MBS as a communicative network for this interaction. In this case the objects of bodies "feel" the action of other ones through corresponding objects of constraints.

Physical interactions are conducted in models due to objects splitted also in two classes of ports: *WrenchPort, KinematicPort*. The first one is to be used to transfer wrench. In addition, *WrenchPort* has to be used for transferring the information about current location of the point constraint force acts upon.

In our idealized model the force interaction between bodies supposed exactly at a geometric point. Its coordinates are fed outside constraint object through *WrenchPort* permanently in time.

Now it is possible to describe an architecture of information interactions within the particular constraint C_i corresponding to an individual edge of graph G, see Figure 1.

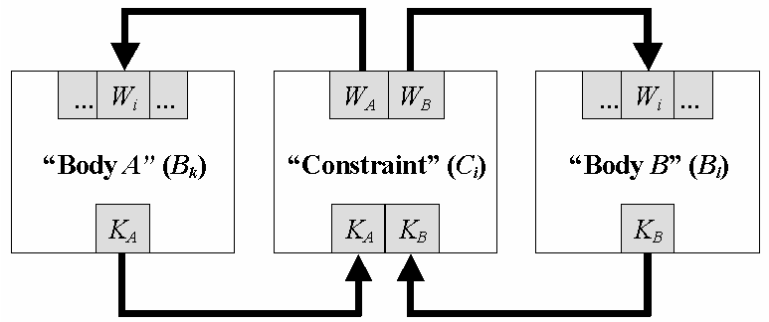

Figure 1: Architecture of constraint

KinematicPort is to be used to transfer the data of rigid body kinematics: configuration (position of center of mass, orientation), velocity (velocity of the center of mass, angular rate), and acceleration (acceleration of the center of mass, angular acceleration) containing in particular information about twist. When getting force information through ports $W_1, \ldots, W_s$ from the incident objects of class *Constraint* the object of class *RigidBody* simultaneously generates, due to an integrator, kinematic information being fed outside through the port K. On the other hand every object of class *Constraint* gets kinematic data from the objects corresponding to bodies connected by the constraint under consideration through its two "input" ports K_A, K_B. Simultaneously using the system of algebraic equations this object generates information concerning wrenches, and transmits the data to "output" ports W_A, W_B for the further transfer to objects of bodies under constraint.

In base class *RigidBody* dynamics of rigid body is described here by means of Newton's differential equations for the body mass center, and by Euler's differential equations for the rotary motion. Note that to be able to have an invariant description of the rotary motion one can use an excellent tool: quaternion algebra $\mathbf{H}$. In this case we "lift" the configuration manifold from $SO(3)$ to $S_3 \subset \mathbf{H}$ and then implement dynamics of rotation in flat space $\mathbf{H} \cong \mathbf{R}^4$ taking into account that S_3 is an invariant manifold of the rotary dynamics redefined on $\mathbf{H}$. In this way we have only one flat chart $\mathbf{H}$ for the underlying due to double covering configuration manifold $SO(3)$, and need not in any special choices of the configuration angles or anything like that.

The double covering $S_3 \to SO(3)$, $\mathbf{q} \mapsto T$ mentioned implemented inside the *RigidBody*

class by the known formula

$$T = \frac{1}{|\mathbf{q}|^2} \cdot \begin{bmatrix} q_0^2 + q_1^2 - q_2^2 - q_3^2 & 2\,(q_1 q_2 - q_0 q_3) & 2\,(q_1 q_3 + q_0 q_2) \\ 2\,(q_0 q_3 + q_1 q_2) & q_0^2 - q_1^2 + q_2^2 - q_3^2 & 2\,(q_2 q_3 - q_0 q_1) \\ 2\,(q_1 q_3 - q_0 q_2) & 2\,(q_0 q_1 + q_2 q_3) & q_0^2 - q_1^2 - q_2^2 + q_3^2 \end{bmatrix},$$

where q_0, q_1, q_2, q_3 are the Euclidean coordinates of the quaternion $\mathbf{q}$ and $|\mathbf{q}|$ is its Euclidean norm. The rotation matrix T is fed outside the object through the *KinematicPort* permanently in time. The Euler equations are constructed using quaternion algebra in a way described in [6].

Note that according to our technology of the constraint construction two connected bodies are identified by convention with the letters A and B fixed for each body. All kinematic and dynamic variables and parameters concerned one of the bodies are equipped with the corresponding letter as a subscript.

All objects of the class *Constraint* must have classes-inheritors as subtypes of a corresponding base class. According to Newton's third law this superclass must contain the equations of the form

$$\mathbf{F}_A + \mathbf{F}_B = \mathbf{0}, \quad \mathbf{M}_A + \mathbf{M}_B = \mathbf{0}. \tag{1}$$

in its behavioral section. Here arrays $\mathbf{F}_A$, $\mathbf{M}_A$ and $\mathbf{F}_B$, $\mathbf{M}_B$ represent constraint forces and torques "acting in directions" of bodies A and B correspondingly. Kinematic equations for different types of constraints are to be added to Eqs. (1) in different classes-inheritors corresponding to these particular types of constraints.

2.2 Example of a joint constraint

Class *Joint* plays an important auxiliary role in the future model of an omni wheel we will build. *Joint* is a model derived from the base class *Constraint*. Remind [7] that in order to make a complete definition of the constraint object behavior for the case of rigid bodies one has to compose a system of twelve algebraic equations with respect to (w. r. t.) twelve coordinates of vectors $\mathbf{F}_A$, $\mathbf{M}_A$, $\mathbf{F}_B$, $\mathbf{M}_B$ constituting the wrenches acting upon the connected bodies.

First six equations (1) always present in the base model *Constraint* due to Newton's third law. For definiteness suppose these six equations are used to express six components of $\mathbf{F}_B$, $\mathbf{M}_B$ depending on $\mathbf{F}_A$, $\mathbf{M}_A$. Thus six components of $\mathbf{F}_A$, $\mathbf{M}_A$ remain unknown. To determine them each constraint of rigid bodies need in six additional independent algebraic equations. These equations can include components of force and torque directly, or be derived from the kinematic relations corresponding to specific type of the constraint.

In the case of the joint constraint being investigated here let us represent the motion of the body B as a compound one consisting of the body A convective motion w. r. t. an inertial frame of reference, and a relative motion w. r. t. the body A. An absolute motion is one of the body B w. r. t. the inertial system.

Define the joint constraint with help of the following parameters: (a) a unit vector $\mathbf{n}_A$ defining in the body A an axis of the joint; (b) a vector $\mathbf{r}_A$ fixed in the body A and defining a point which constantly stays on the axis of the joint; (c) a vector $\mathbf{r}_B$ fixed in the body B and defining a point which also constantly stays on the axis of the joint. The main task of the base joint class is to keep always in coincidence the geometric axes fixed in each of the bodies.

First of all one has to compute the radii vectors of the points fixed in the bodies w. r. t. inertial system

$$\mathbf{R}_\alpha = \mathbf{r}_{O_\alpha} + T_\alpha \mathbf{r}_\alpha \quad (\alpha = A, B),$$

where [7] $\mathbf{r}_{O_\alpha}$ is the position of the α-th body center of mass, T_α is its current matrix of rotation. The joint axis has the following components

$$\mathbf{n}_{Ai} = T_A \mathbf{n}_A$$

in the inertial frame of reference. According to the equation for relative velocity for the marked point of the body B defined by the position $\mathbf{R}_B$ we have

$$\mathbf{v}_{Ba} = \mathbf{v}_{Be} + \mathbf{v}_{Br}, \quad \mathbf{v}_{Ba} = \mathbf{v}_{O_B} + [\boldsymbol{\omega}_B, T_B \mathbf{r}_B], \quad \mathbf{v}_{Be} = \mathbf{v}_{O_A} + [\boldsymbol{\omega}_A, \mathbf{R}_B - \mathbf{r}_{O_A}], \tag{2}$$

where $\mathbf{v}_{Ba}$, $\mathbf{v}_{Be}$, $\mathbf{v}_{Br}$ are an absolute, convective, and relative velocities of the body B marked point, $\boldsymbol{\omega}_A$, $\boldsymbol{\omega}_B$ are the bodies angular velocities.

Furthermore, according to the computational experience of the dynamical problems simulation the precompiler work is more regular if the kinematic equations are expressed directly through accelerations. Indeed, otherwise the compiler tries to perform the formal differentiation of equations for the velocities when reducing an index of the total DAE system. Frequently this leads to the problems either in time of translation or when running the model.

Thus using the known Euler formulae for the rigid body kinematics and the Coriolis theorem we obtain an equations for the relative linear acceleration in the form

$$\begin{aligned} &\mathbf{a}_{Ba} = \mathbf{a}_{O_B} + [\boldsymbol{\varepsilon}_B, T_B \mathbf{r}_B] + [\boldsymbol{\omega}_B, [\boldsymbol{\omega}_B, T_B \mathbf{r}_B]], && \mathbf{a}_{Ba} = \mathbf{a}_{Be} + 2[\boldsymbol{\omega}_A, \mathbf{v}_{Br}] + \mathbf{a}_{Br}, \\ &\mathbf{a}_{Be} = \mathbf{a}_{O_A} + [\boldsymbol{\varepsilon}_A, \mathbf{R}_B - \mathbf{r}_{O_A}] + [\boldsymbol{\omega}_A, [\boldsymbol{\omega}_A, \mathbf{R}_B - \mathbf{r}_{O_A}]], && \mathbf{a}_{Br} = \mu \mathbf{n}_{Ai}, \end{aligned} \tag{3}$$

where $\mathbf{a}_{Ba}$, $\mathbf{a}_{Be}$, $\mathbf{a}_{Br}$ are an absolute, convective, and relative accelerations of the body B marked point, $\boldsymbol{\varepsilon}_A$, $\boldsymbol{\varepsilon}_B$ are the bodies angular accelerations, $\mathbf{v}_{Br}$ is a relative velocity of the body B marked point, $\boldsymbol{\omega}_A$, $\boldsymbol{\omega}_B$ are the bodies angular velocities.

We also need in an analytic representation of the conditions that the only projections of the bodies angular velocities and accelerations having a differences are ones onto the joint axis. Corresponding equations have the form

$$\boldsymbol{\omega}_B = \boldsymbol{\omega}_A + \boldsymbol{\omega}_r, \quad \boldsymbol{\varepsilon}_B = \boldsymbol{\varepsilon}_A + [\boldsymbol{\omega}_A, \boldsymbol{\omega}_r] + \boldsymbol{\varepsilon}_r, \quad \boldsymbol{\varepsilon}_r = \lambda \mathbf{n}_{Ai}, \tag{4}$$

where $\boldsymbol{\omega}_r$, $\boldsymbol{\varepsilon}_r$ are the relative angular velocities and accelerations.

Besides the kinematic scalars μ, λ we will need in their reciprocal values $F = (\mathbf{F}_A, \mathbf{n}_{Ai})$, $M = (\mathbf{M}_A, \mathbf{n}_{Ai})$ correspondingly. Note that the class described above is a partial one (doesn't yet complete the constraint definition) and can be used to produce any imaginable model of the joint type constraint. To obtain a complete description of the joint model one has to add to the behavioral section exactly two equations. One of them is to define one of the values μ, F (translatory case). Other equation is intended to compute one of the values λ, M (rotary case).

Consider one example of joint classes among others being derived from the *Joint* model for the particular, revolute, type of joint being applied in the omni wheel construct. This model *FixedIdealJoint* is defined by the equations

$$\mu = 0, \quad M = 0$$

and prevents the relative motion along the joint axis but allows free rotation about it. It is exactly a revolute joint without any control for the rotary motion.

It is clear one can create a lot of other different combinations of equations to construct the joint constraints of any desirable type needed in engineering applications. The only issue one

has to take into account when constructing the kinematic pair that if there exists an obstacle for the relative motion eliminating one DOF then it causes an additional scalar kinematic equation "lifted" to the level of accelerations. Reciprocally if the corresponding motion is possible then the developer has to include the scalar equation instead imposing the condition on the matching generalized effort, force or torque what applicable.

2.3 Bond graph concept

Referring for the details to the papers [8, 9] let us give here a brief outline of the multibond graph scheme concerning the general constraint architecture under consideration, see Figure 2. Remind that each multibond is a pair comprising twist as its flow component, while the wrench plays a role of the effort component.

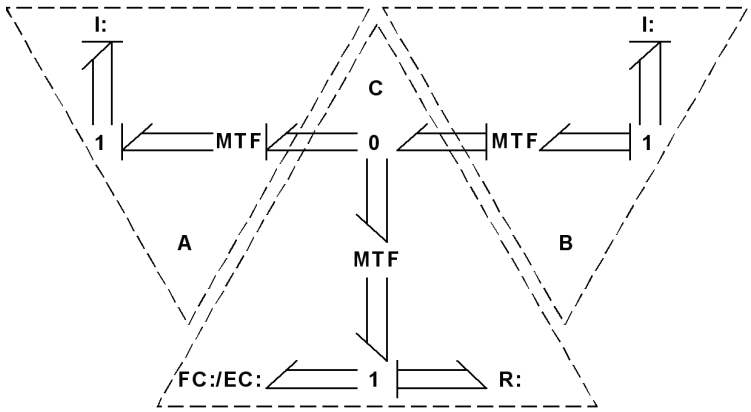

Figure 2: Architecture of constraint: bond graph representation

Describing Figure 2 first of all one has to highlight the multibond true nature. Considering the rigid body as a mechanical system with six degrees of freedom (DOFs) we note that the flow part, twist, of any multibond represents an object tangent to configuration manifold $\mathcal{D} = \mathbf{R}^3 \times SO(3)$ which is in turn the rigid body displacement group [10]. In such a way the multibond effort component representing the wrench of reaction forces is indeed the cotangent object, 1–form, at the same point of $\mathcal{D}$. Thus the multibond power is a natural pairing, the value of 1–form, wrench, evaluated on the configuration manifold tangent vector, twist.

In the way under description we follow the ideas of the paper [10] leaving the rigid body kinematics unsplitted to its translatory and rotary parts. To this end we go farther than the usual approach for the bond graph applications when frequently the developer first keeps in his mind the equations and then builds up the corresponding bond graph. Unlike to this we first construct the bond graph connecting it to the physical nature of the problem, and then the system of DAEs is to be assembled mostly by compiler without any participation of the developer. In this latter case physical invariance of the model independent on the choice of (generalized) coordinates is maintained.

Regarding the general scheme depicted in Figure 2 with its connection to the family of the joint constraint classes we can conclude that the equations (3), (4) together implement implicitly the constraint transformer, central modulated transformer in triangle C of Figure 2, to the joint local coordinate system and four scalar flow constraints forbidding relative translatory and rotary motions in the direction orthogonal to the joint axis. For derived classes only two free scalar bonds remain.

Here we encounter the known complementarity rules [11] in a way similar to one described in [8, 7]. In our context the variables in the pairs (μ, F), (λ, M) are mutually complement, where one of μ, λ is to be utilized for the flow constraint and one of F, M is used to compose the effort constraint. All the variables mentioned complete the set of constraints for the remaining yet unused joint axis creating thus two final scalar constraint elements in the bond graph of Figure 2.

Namely, equations (3) implementing the Coriolis theorem for accelerations simultaneously implement, in an implicit manner, two scalar flow constraints, FC-elements, from the bottom left corner of the multibond graph model in Figure 2. These flow constraints are constructed, due to compiler restrictions, using accelerations instead of velocities being used in a classic bond graph approach. The constraints have an obvious kinematic sense: they prevent the relative motion of the body B marked point in two directions normal to the joint axis fixed in the body A.

In addition, the equations (4) implement two other scalar flow constraints, this time for the rotary motion. These constraints forbid the relative rotation of the body B w. r. t. body A about two axes each normal to the joint axis mentioned above which is rigidly connected with the body A.

Note, that the construct of equations (3) and (4) is such that they allow the body B relative motion along and about the joint axis of the body A thus implementing the kinematic pair with two DOFs. Returning to Figure 2 of the general constraint multi-bondgraph we can conclude that the vertical multibond attached to 0-junction implements flow variables corresponding to the relative body B motion w. r. t. body A in inertial coordinates. Such a description supposes an existence of the special coordinates reference frame connected with the body A at its joint constraint marked point. The transformation to these coordinates is implemented exactly via corresponding transformer, central in the triangle block C. The transformer itself nests in formulae of equations (3) and (4).

The derived joint class example described above is to close the system of kinematic equations (3) and (4) completing them by two scalar additional equations, each playing a role of an either FC-element, like $\mu = 0$, or EC-element, like $M = 0$. Any time to be able to construct a consistent system of equations for the total model we have to follow the guidelines similar to ones of the complementarity rules.

These latter correspond to the notions of the bond graph theory in a natural way. Indeed, the theory of bond graphs is based on the energy interactions. Every our multibond being an energy/power conductor reflects complementarity by its twist/wrench duality. To close the total DAE system for the model under development we have to "close" or rather to "seal" each free scalar bond in EC/FC-element of the block C in Figure 2 by the corresponding one scalar equation for flow or effort variable. Thus here we outline the main rule to compose equations for the models of constraints for MBS of any type in a consistent way when applying the object-oriented approach.

3 GENERAL DESCRIPTION OF THE CONTACT TRACKING ALGORITHM

We outline here general approach for implementing contact tracking algorithm in case of the unilateral constraint. As it was already mentioned we use the so called complementarity rules [11] as a base for the unified description of the unilateral constraint. Taking into account complementarity rules one can see easily that any constraint always is defined by the three scalar equations. To derive these equations consider first local geometry of the problem, see Figure 3.

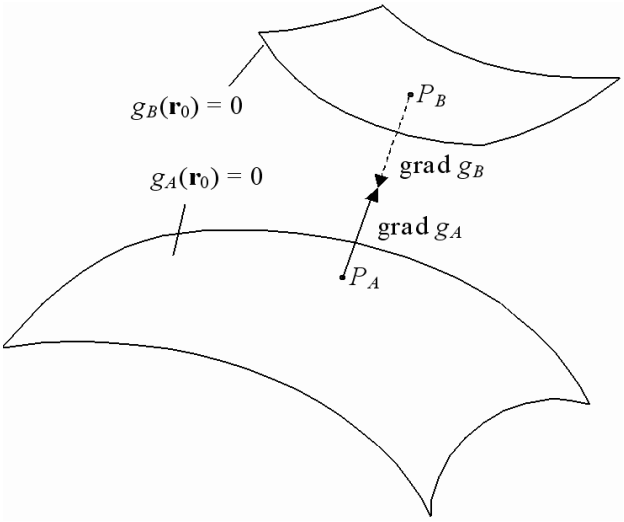

Figure 3: Area of Constraint

Outer surfaces supposed to be defined with respect to principal central axes of corresponding bodies by the equations

$$f_\alpha\left(\mathbf{r}_\alpha\right) = 0 \quad (\alpha = A, B).$$

Then in inertial frame of reference for the whole MBS these equations will take the form

$$g_\alpha(\mathbf{r}_0) = 0 \quad (\alpha = A, B),$$

where

$$g_\alpha\left(\mathbf{r}_0\right) = f_\alpha\left[T_\alpha^*\left(\mathbf{r}_0 - \mathbf{r}_{O_\alpha}\right)\right] \quad (\alpha = A, B),$$

with $\mathbf{r}_{O_A}$, $\mathbf{r}_{O_B}$ being a vectors of masscenters positions O_A, O_B for the bodies A and B, and T_A, T_B mean an orthogonal matrices for current bodies orientations. An asterisk denotes conjugating what equivalent to inverting of matrix for the case of orthogonality. Thus the functions $g_A(\mathbf{r}_0)$, $g_B(\mathbf{r}_0)$ depend upon the time indirectly through the variables $\mathbf{r}_A$, $\mathbf{r}_B$, T_A, T_B.

Constraint object of our model is to compute at each current instant positions of the points P_A and P_B which are the nearest ones for interacting bodies A and B. By virtue of above assumptions such points are to be evaluated in a unique way. Denote the radii vectors of these points with respect to inertial frame of reference by $\mathbf{r}_{P_A}$, $\mathbf{r}_{P_B}$. Then using simple geometric considerations for the coordinates of the mentioned vectors one can derive the following system of algebraic equations

$$\begin{aligned} \operatorname{grad} g_A\left(\mathbf{r}_{P_A}\right) &= \lambda \cdot \operatorname{grad} g_B\left(\mathbf{r}_{P_B}\right), \\ \mathbf{r}_{P_A} - \mathbf{r}_{P_B} &= \mu \cdot \operatorname{grad} g_B\left(\mathbf{r}_{P_B}\right), \\ g_A\left(\mathbf{r}_{P_A}\right) &= 0, \\ g_B\left(\mathbf{r}_{P_B}\right) &= 0. \end{aligned} \tag{5}$$

Here the first equation is a condition of the collinearity for the normals to outer surfaces at the points being computed. The second condition requies the points P_A, P_B to be relocated on the straight line collinear to the normals above.

One can verify easily that one can compute the gradients using the formulae

$$\operatorname{grad} g_\alpha\left(\mathbf{r}_{P_\alpha}\right) = T_\alpha \operatorname{grad} f_\alpha\left[T_\alpha^*\left(\mathbf{r}_{P_\alpha} - \mathbf{r}_{O_\alpha}\right)\right], \tag{6}$$

where $\alpha = A, B$. It easy to see the system (5) consists of eight scalar equations and has eight scalar unknown variables: x_{P_A}, y_{P_A}, z_{P_A}, x_{P_B}, y_{P_B}, z_{P_B}, λ, μ. Variables λ, μ are an auxiliary ones. And the variable μ plays a role of contact detector at that: if $\mu > 0$ then bodies are disconnected, otherwise if $\mu \leq 0$ then bodies are in contact. Equations (5) one uses either without or with a presence of the contact of bodies A, B. In a latter case one uses the equation $\mu = 0$ instead of one of the surfaces equations.

According to computational experience it is more reliable and convenient if one use equations of constraint in a differential form than in an algebraic one (5) instead. Such an approach is used frequently also when analyzing the properties of mechanical systems.

Analytical computations show that one can substitute the equations (5) by the differential ones of the form

$$\frac{d\mathbf{r}_{P_A}}{dt} = \mathbf{v}_A, \quad \frac{d\mathbf{r}_{P_B}}{dt} = \mathbf{v}_B, \quad \frac{d\lambda}{dt} = v_\lambda, \quad \frac{d\mu}{dt} = v_\mu, \tag{7}$$

where the variables of right hand sides are calculated implicitly by help of system of linear algebraic equations of the form

$$\begin{aligned}
[\boldsymbol{\omega}_A, \operatorname{grad} g_A] + T_A \operatorname{Hess} f_A T_A^* (\mathbf{v}_A - \mathbf{v}_{P_A}) - \\
\lambda \{[\boldsymbol{\omega}_B, \operatorname{grad} g_B] + T_B \operatorname{Hess} f_B T_B^* (\mathbf{v}_B - \mathbf{v}_{P_B})\} - \\
v_\lambda \operatorname{grad} g_B &= \mathbf{0}, \\
\mathbf{v}_A - \mathbf{v}_B - \\
\mu \{[\boldsymbol{\omega}_B, \operatorname{grad} g_B] + T_B \operatorname{Hess} f_B T_B^* (\mathbf{v}_B - \mathbf{v}_{P_B})\} - \\
v_\mu \operatorname{grad} g_B &= \mathbf{0}, \\
\operatorname{grad} g_A \cdot \mathbf{v}_A - \operatorname{grad} f_A T_A^* \mathbf{v}_{P_A} &= 0, \\
\operatorname{grad} g_B \cdot \mathbf{v}_B - \operatorname{grad} f_B T_B^* \mathbf{v}_{P_B} &= 0.
\end{aligned} \tag{8}$$

When using this latter, i. e. differential form of a constraint one needs to set a consistent initial values for the variables $\mathbf{r}_{P_A}$, $\mathbf{r}_{P_B}$, λ, μ at the start time instant of simulation. Vectors $\mathbf{v}_{P_A}$ and $\mathbf{v}_{P_B}$ in the system (8) of algebraic linear equations are the velocities of a nearest points of the bodies and are computed according to Euler's formula

$$\mathbf{v}_{P_\alpha} = \mathbf{v}_{O_\alpha} + [\boldsymbol{\omega}_\alpha, \mathbf{r}_{P_\alpha} - \mathbf{r}_{O_\alpha}] \quad (\alpha = A, B). \tag{9}$$

Matrices $\operatorname{Hess} f_A$, $\operatorname{Hess} f_B$ are ones of Hesse for corresponding functions and have the form

$$\operatorname{Hess} f_\alpha = \begin{pmatrix} \dfrac{\partial^2 f_\alpha}{\partial x_\alpha^2} & \dfrac{\partial^2 f_\alpha}{\partial x_\alpha \partial y_\alpha} & \dfrac{\partial^2 f_\alpha}{\partial x_\alpha \partial x_\alpha} \\ \dfrac{\partial^2 f_\alpha}{\partial y_\alpha \partial y_\alpha} & \dfrac{\partial^2 f_\alpha}{\partial y_\alpha^2} & \dfrac{\partial^2 f_\alpha}{\partial y_\alpha \partial z_\alpha} \\ \dfrac{\partial^2 f_\alpha}{\partial z_\alpha \partial x_\alpha} & \dfrac{\partial^2 f_\alpha}{\partial z_\alpha \partial y_\alpha} & \dfrac{\partial^2 f_\alpha}{\partial z_\alpha^2} \end{pmatrix},$$

with $\alpha = A, B$. Normal vector

$$\mathbf{n}_A = \frac{\operatorname{grad} g_A}{|\operatorname{grad} g_A|} \tag{10}$$

will play an important role in the further course. Normal for an outer surface of the body A is chosen here for definiteness. One can use the vector $\mathbf{n}_B$ as well.

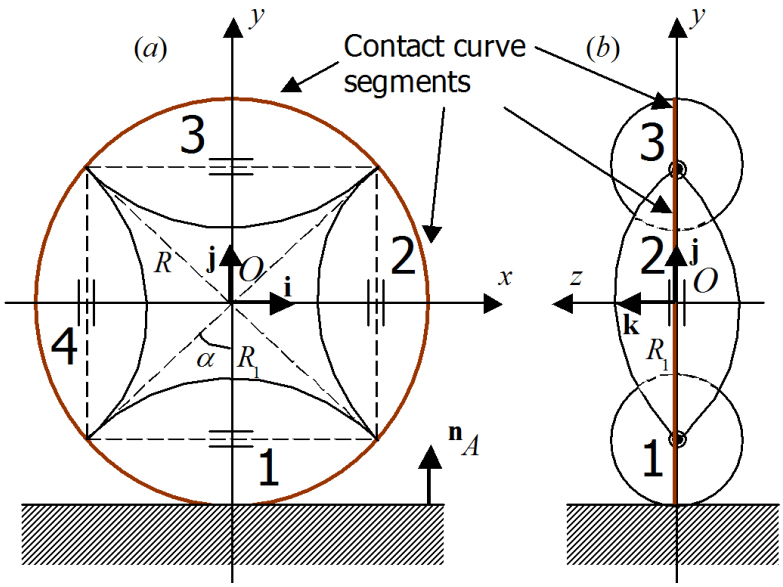

Figure 4: The omni wheel vertically aligned: (a) lateral view; (b) front view.

4 VIRTUAL OMNI WHEEL TESTBENCH ARRANGEMENT

4.1 Preliminaries

Let us consider an omni wheel now. Omni wheel for the case of $\psi = 0$ is shown in Figure 4. There one can see the lateral view, fragment (a), of the wheel being equipped by four axisymmetrical rollers, each having a shape of the circular spindle. These rollers have been enumerated by their numbers. Each roller is connected to the wheel by a joint which axis coincides with the roller axis of rotation. These latter axes both are orthogonal to the wheel radius exiting from the central point O and passing through the the roller central point. So it is possible for the wheel to have a free rolling in direction perpendicular to its plane. Corresponding contacting curve with respect to the wheel coordinate system, being a circle in the case shown, has a coloured highlighting. This curve has a circular shape provided the wheel plane keeps its vertical orientation. Front view of the omni wheel is shown in fragment (b).

For the case of $\psi = 0$ being shown in Figure 4 a roller outer profile, generatrix, along its axis of rotation has evidently a circular shape, see Figure 4, fragment (a), again. This shape provides smooth transfer from one roller to another while the motion occurs. Evidently if $\psi \neq 0$ then it is not the case. Thus, the contact tracking algorithm for the case of $\psi = 0$ implemented in [1] turned out to be simple enough. In the case of $\psi > 0$ it becomes visibly complicated. And its implementation on Modelica language is the main goal of this paper.

Other details of Figure 4 are the following: R is the omni wheel radius, R_1 is the distance between the wheel central point O and the roller central point, α is the half roller angular length from the viewpoint O. Unit vectors $\{\mathbf{i}, \mathbf{j}, \mathbf{k}\}$ of the base being connected with the wheel are shown in their initial positions.

In engineering applications one may encounter frequently a situation with $\psi > 0$. We proposed in [1] fast algorithm for tracking a contact provided the omni wheel keeps vertical orientation of its plane (in frame of the whole vehicle construct). Thus the task for building up the contact tracking algorithm also for the case of $\psi > 0$ is of interest. This task has been completed

in this paper. To reach this goal we accept the working model of a virtual testbench consisting of one wheel equipped by rollers along its rim. One can see easily that this simplification has mostly methodical nature and does not prevent us from integrating all the construct back into the whole vehicle having generally several omni wheels previously analyzed [1].

So let us consider an omni wheel, see Figure 4 its lateral and front views with four rollers, which is able to keep vertical orientation of its plane. We will see later how to arrange an implementation of such a servo-constraint. Note in addition, that in the case of $\psi > 0$ a generatrix of the roller outer surface will not be a segment of the circle anymore. It is represented by a more complicated curve. Moreover, point break of contact on the roller surface does not correspond to the surface tip for the case of $\psi > 0$ as it took place for the simple case of $\psi = 0$. To arrange correct simulation on event of the contact exchange between rollers one has to truncate the roller surface properly.

4.2 Model of the omni wheel dynamics

Vehicle equipped by omni wheels might be replaced by a wrench consisting of force and torque in the multibody, rigid, representation. The force supposed to act at the wheel center. Thus approximately we can analyze the omni wheel dynamics with the wrench applied instead of a remainder of the vehicle.

Moreover, the vehicle, or a separated wheel, performs in our example motion on the horizontal floor for simplicity. Thus, the wheel being embedded into the vehicle in the simplest case should be aligned vertically. To express such an alignment analytically we can connect with the wheel the base $\{\mathbf{i}, \mathbf{j}, \mathbf{k}\}$ originating from the wheel center. Both unit vectors $\mathbf{i}, \mathbf{j}$ lie in the wheel plane, and unit vector $\mathbf{k}$ is normal to it. Thus the vertical alignment of the wheel is equivalent to horizontal alignment for the vector $\mathbf{k}$. Analytical condition for this is

$$\mathbf{k} \cdot \mathbf{n}_A = 0,$$

where unit vector $\mathbf{n}_A$ is vertical, or normal to the floor. In other words, let $T \in SO(3)$ be the matrix of transformation from base $\{\mathbf{i}, \mathbf{j}, \mathbf{k}\}$ to the inertial absolute coordinate system. Then components of vector $\mathbf{k}$ are exactly the components of the matrix $T = (t_{ij})_{i,j=1}^{i,j=3}$ third column. Thus one can express condition of the wheel vertical alignment in the form

$$t_{23} = 0.$$

This latter equation shows that the omni wheel multibody system undergoes the geometrical servo constraint. It is easy to see that this constraint may be implemented via control effort, rotating torque $\mathbf{M}$ directed such as to prevent rotation of the wheel plane w. r. t. horizontal line belonging to this plane.

For details of the torque vector $\mathbf{M}$ computation note that this vector has to be directed along horizontal line passing through the wheel center and belonging to its plane. Directing unit vector $\mathbf{l}$ for this line has to satisfy the equation

$$\mathbf{l} = \mathbf{k} \times \mathbf{n}_A / |\mathbf{k} \times \mathbf{n}_A|.$$

Hence

$$\mathbf{M} = \lambda \mathbf{l}$$

and the multiplier λ is simply a value of torque balancing the wheel vertical orientation. In the wheel model torque $\mathbf{M}$ has to be added to other torques applied to the wheel under simulation. The value λ is exactly the Lagrange multiplier corresponding to the servo-constraint above.

It is easy to see the servo-constraint plays here a role of the virtual testbench for investigating the omni wheel dynamics. The remainder of the whole vehicle model is replaced simplistically by the wrench being applied to the wheel. The whole omni wheel dynamics visual model is seen in Figure 5

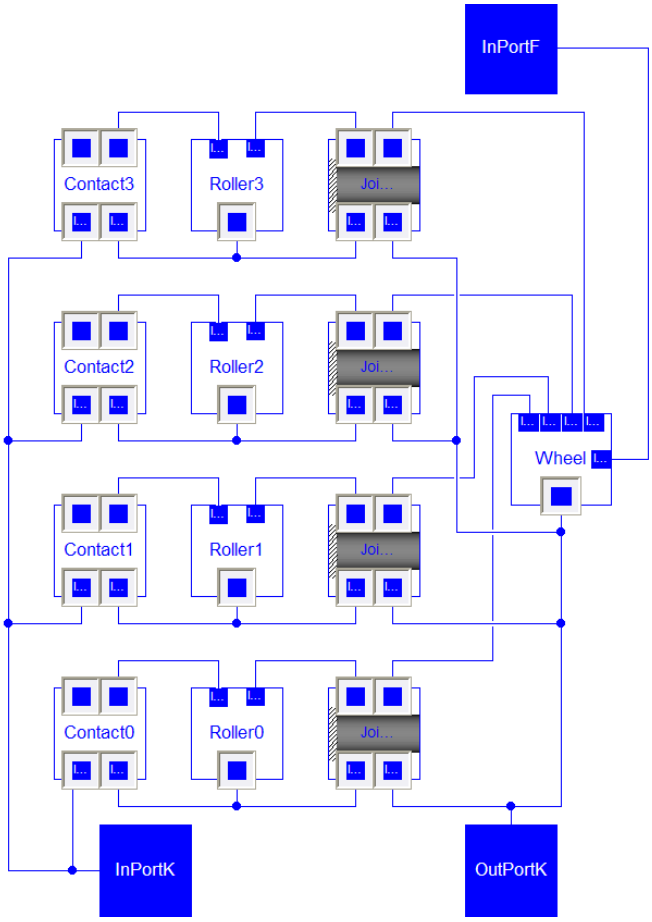

Figure 5: The omni wheel dynamics visual model.

As one can detect here the model of the omni wheel multibody system has been implemented using original multibody dynamics class library developed previously [7, 9]. One can use this library independently or with help of the knowm Modelica Standard Multibody class library or with any other Modelica library. The better way being recommended for such use is the following one. Firstly, one can implement mechanical subsystems of the whole system under implementation. For instance, mechanisms having tree structure are modeled in a better way using Modelica Standard Multibody Library while mechanical subsystems including unilateral constraints with friction are better implemented using the aforementioned library of classes. Secondly, the only issue remained is to implement proper interfaces using models of ports mapping corresponding signals being tranferred from one subsystems to another.

5 IMPROVED CONTACT TRACKING ALGORITHM

5.1 Implicit contact tracking algorithm

We will assume in the further course that the wheel plane keeps its vertical orientation permanently. We have to introduce auxiliary orthonormal bases: $b_1 = \{\mathbf{i}_1, \mathbf{j}_1, \mathbf{k}_1\}$ and $b_2 = \{\mathbf{i}_2, \mathbf{j}_2, \mathbf{k}_2\}$. Intermediate base b_2 characterises partially position and orientation of the roller, while the base b_1 relates to the omni wheel.

The base b_2 coordinate system has its origin O_B at the roller central point. The unit vector $\mathbf{i}_2$ is directed along the roller axis of rotation, see Figure 6, fragment (a). The unit vector $\mathbf{j}_2$ is directed orthogonally to $\mathbf{i}_2$ and lies simultaneously in the vertical plane. The third unit vector $\mathbf{k}_2$ of the base b_2 is defined in a natural way as

$$\mathbf{k}_2 = \mathbf{i}_2 \times \mathbf{j}_2.$$

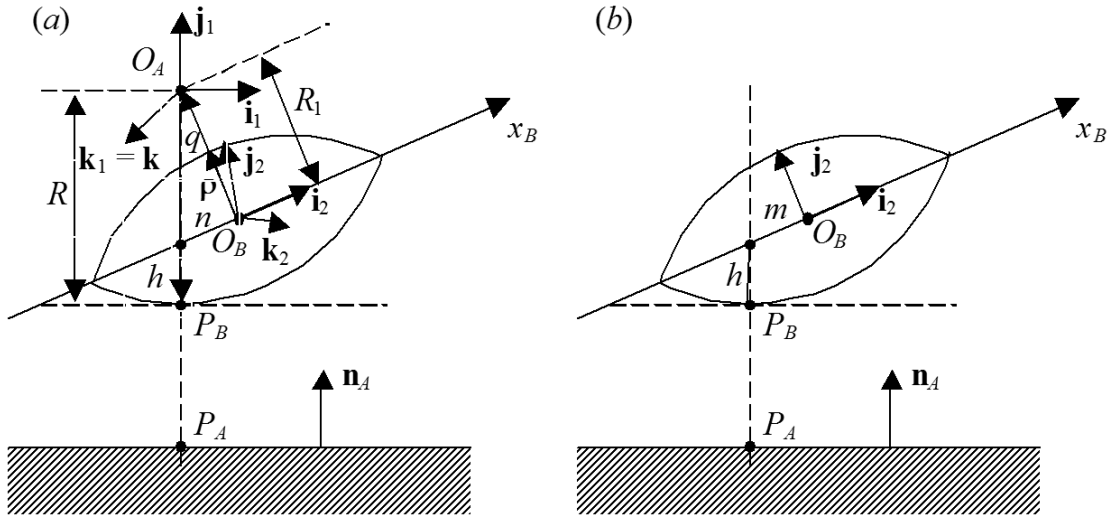

Figure 6: Contact tracking scheme: (a) lateral view of the omni wheel with a roller has been rotated about line O_AO_B by the angle ψ, (b) lateral view of the individual roller.

Remind here that all unit vectors are computed w. r. t. given fixed (absolute) coordinate system. We assume that positions and orientations are known for all bodies belonging to the multibody system for any instant $t \in [t_0, t_1]$ of simulation process. Therefore, we have

$$\mathbf{i}_2 = T_B \cdot (1,0,0)^T, \quad \boldsymbol{\rho} = (\mathbf{r}_{O_A} - \mathbf{r}_{O_B}) \,/\, |\mathbf{r}_{O_A} - \mathbf{r}_{O_B}|\,,$$

where T_B is the roller current orientation matrix.

Origin of the base b_1 coordinate system is located at the point O_A ($= O$ in Figure 4) of the wheel center. The unit vector $\mathbf{i}_1$ is oriented horizontally and belongs to the wheel plane. The unit vector $\mathbf{k}_1$ is orthogonal to the wheel plane and is identical to one of the wheel connected base vectors. We assume that using a controller the vector $\mathbf{k}_1$ permanently maintains its horizontal state. Supposing vector $\mathbf{k}_1(t)$ known we also have $\mathbf{j}_1(t) = (0,1,0)^T$ and $\mathbf{i}_1(t) = \mathbf{j}_1(t) \times \mathbf{k}_1(t)$.

Consider now relations providing base b_2 construction. Unit vector $\mathbf{i}_2$ has been built above. During roller and the floor contact the vector $\mathbf{i}_2(t)$ can not become vertical. Moreover, if the

roller distortion takes place, its angle of rotation $\psi > 0$ about axis $O_A O_B$ is fixed non-zero, then the condition $\mathbf{i}_2 \neq (0,1,0)^T$ is fulfilled permanently. So we can assume that the condition

$$\mathbf{c} = \mathbf{i}_2 \times (0,1,0)^T \neq \mathbf{0}$$

is also fulfilled.

Thus, we can define $\mathbf{k}_2 = \mathbf{c}/|\mathbf{c}|$. And after this we can set $\mathbf{j}_2 = \mathbf{k}_2 \times \mathbf{i}_2$. Geometrical constraints, conditions of orthogonality to be exact, play important role in the omni wheel kinematics

$$\boldsymbol{\rho} \cdot \mathbf{i}_2 = 0, \quad \boldsymbol{\rho} \cdot \mathbf{k}_1 = 0.$$

These equations actually apply to computing the unit vector $\boldsymbol{\rho}$ and we have their differential versions

$$\frac{d}{dt}\boldsymbol{\rho} \cdot \mathbf{i}_2 + \boldsymbol{\rho} \cdot \frac{d}{dt}\mathbf{i}_2 = 0, \quad \frac{d}{dt}\boldsymbol{\rho} \cdot \mathbf{k}_1 + \boldsymbol{\rho} \cdot \frac{d}{dt}\mathbf{k}_1 = 0.$$

The value $c_\beta = \cos\beta = \mathbf{i}_2 \cdot (0,1,0)^T$ of cosine for the angle β of the roller axis inclination to vertical $(0,1,0)^T$ plays also an important role in the contact tracking algorithm. If current value of the variable c_β is less than some limiting parameter $c_{\beta\max}$, and simultaneously if an altitude of the point O_B defining position of the roller center is less than value R of the wheel radius then the contact takes place. Otherwise no contact occurs.

Note here that in order to arrange the unilateral constraint in the multibody system dynamics model the developer usually has to implement something like hybrid automata construct. In our omni wheel model, on the contrary, this is not the case. It turned out sufficient to implement "simple" "`if`" construct to switch states "contact" and "no contact" for each individual roller, and simultaneously to advance forward "contact" state from one roller to its neighbour. The whole picture looks like from time to time neighbouring rollers mutually exchange their states. One can find details of the unilateral constraint implementation in [1]. Merely note that "`if`"-alternatives are the following: (a) "contact" state corresponds to zero-valued relative acceleration of two contacting surfaces at the point of contact, (b) "no contact" branch corresponds to the zero-valued reaction mutual for both bodies at contact. All this is according to the Signorini rule. "`if`"-condition depends on the roller orientation variables.

Essential role in all these computations plays a contact tracking algorithm. Generally, its implementation reduces to computation of the contact point/patch which enables computing forces at contact. Usually, one considers contact of two surfaces participating in rigid/elastic interaction of two massive bodies. As a rule, such algotithms are pretty expensive and noticeably slow the whole simulation process. Fortunately, in case of omni wheels we found here the simplest way to make this computation as fast as possible using "elementary" geometric considerations.

We can also easily see from the Figure 6 that the point P_B of contact between roller and floor is obtained using formula

$$\mathbf{r}_{P_B} = \mathbf{r}_{O_B} + R_1\boldsymbol{\rho} - R\mathbf{j}_1 + \mu\mathbf{k}_1,$$

where the scalar μ is to be computed. Here the value R_1 is the distance between points O_A and O_B. The scalar μ can be computed if we multiply the last equation by $\mathbf{k}_2$ using dot-product. Thus we have

$$\mu = \left[R\mathbf{j}_1 \cdot \mathbf{k}_2 - R_1\boldsymbol{\rho} \cdot \mathbf{k}_2\right] / \mathbf{k}_1 \cdot \mathbf{k}_2$$

since the vector $\mathbf{r}_{P_B} - \mathbf{r}_{O_B}$ lies in vertical section of axis-symmetrical surface of the roller, and the vector $\mathbf{k}_2$ by construction is orthogonal to this section. As a result the position $\mathbf{r}_{P_B}$ of the contact point P_B is uniquely computed.

5.2 Explicit contact tracking algorithm

Yet another way to obtain current position $\mathbf{r}_{P_B}$ of the contact point P_B, or more accurately: the roller point closest to the floor, is an application of the following chain of equations. This chain is simply understood from geometrical scheme shown in Figure 6, (a) and (b).

$$\mathbf{r}_{P_B} = \mathbf{r}_{O_B} - m\mathbf{i}_2 - h\mathbf{j}_1,$$

where $m = R_1 \sin q / \cos q / \cos\psi$, $h = R - R_1 / \cos q$, q is the current value for angle of deviation of the vector $\boldsymbol{\rho}$ from direction of the vector $\mathbf{j}_1$. So we have

$$\cos q = \boldsymbol{\rho} \cdot \mathbf{n}_A, \quad \sin q = (\mathbf{n}_A \times \boldsymbol{\rho}) \cdot \mathbf{k}_1.$$

Here we give explanations of some details of Figure 6. Fragment (a) corresponds to the lateral projection of the wheel and likewise the distorted roller projection. This latter object is shown here in a general position. Furthermore, P_B is the current contact point between the roller and the horizontal floor, n is a projection of the roller axial line segment onto the wheel plane. We can see easily that this projection is computed by the formula $n = m\cos\psi$ because the roller axis is turned about $O_A O_B$ by the angle ψ, see fragment (b) for the roller axial vertical lateral section. Thus, we have to pass two straight line segments from the roller center O_B to reach the point P_B: (a) the segment of the roller axis of length m; (b) the segment down the vertical of length h. As we already mentioned above all variables needed are computed through known variables using explicit formulae.

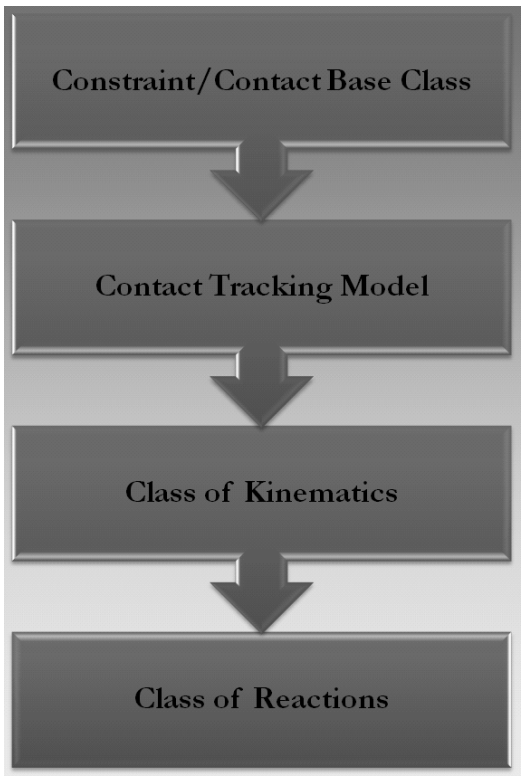

Figure 7: Contact model by stages of inheritance.

In case of $\psi > 0$, distortion exists, for both implicit and explicit algorithms not all the length of the roller surface generatrix is necessarily in contact. So really we have to cut tips of rollers

to provide regular simulation process. Length of the tip to be cut we can obtain for instance empirically or compute it explicitly. Indeed, one can easily see from Figure 6 that the real roller length should be computed by the formula

$$L = 2R \sin\alpha / \cos\psi.$$

"Ideal" switching of contact takes place in this case: exactly at the instant of contact loss for current roller a contact immediately arises for the "next" roller in direction of the wheel rolling.

5.3 Computer implementation

Model of the omni wheel testbench virtual prototype is a container class including the following objects instantiated: (a) disk of the wheel; (b) objects of rollers mounted along the wheel rim; (c) objects of joints connecting rollers and the wheel disk; (d) objects of contacts connecting objects of rollers and the object of the horizontal floor surface; (e) model of base body as a horizontal floor.

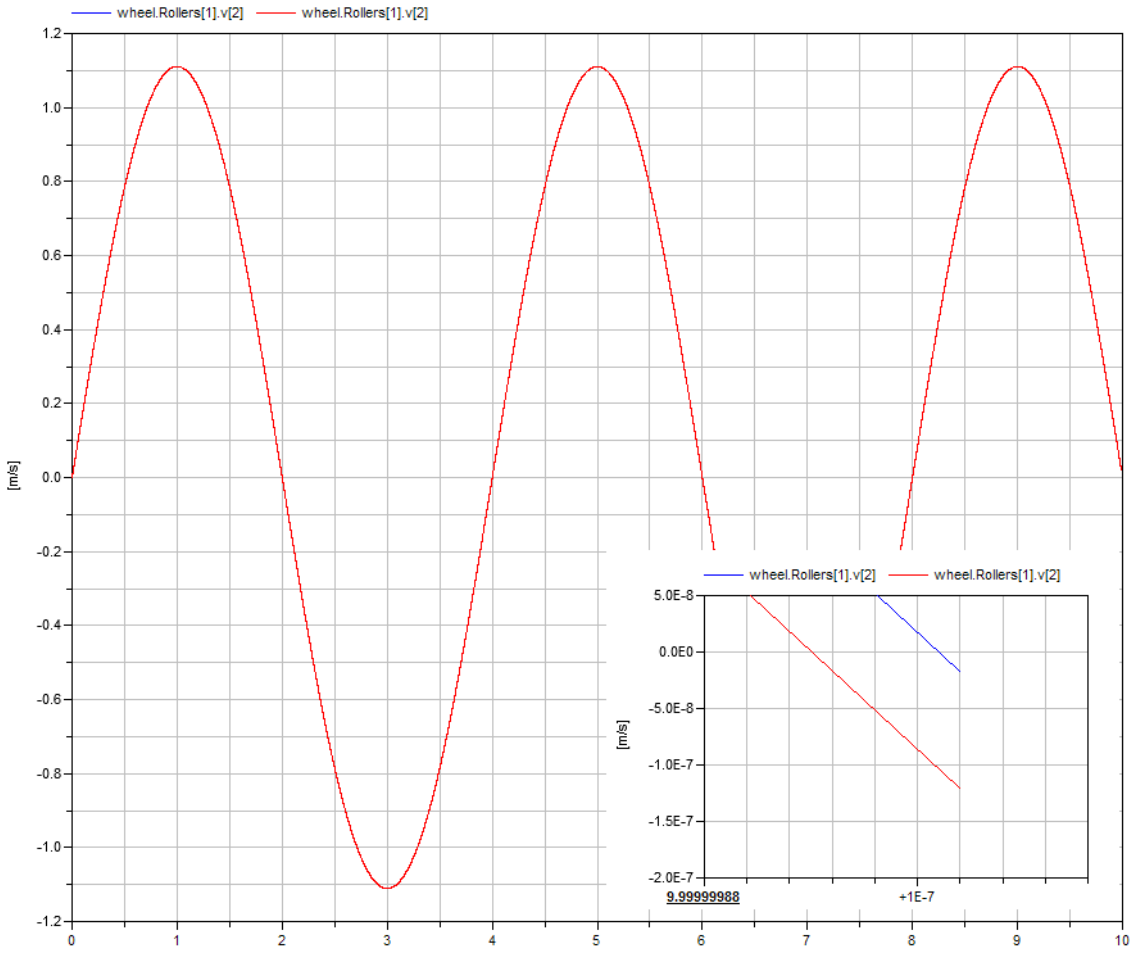

Figure 8: Comparison of dynamics for the roller No. 1 central point, its velocity y-coordinate, for cases of: explicit (blue curve) and implicit (red curve) algorithm of contact tracking.

Let us analyse in more details a structure of contact model. This model has many similarities with contact models previously considered [7]. Nevertheless important differencies exist. One of them mentioned above with regard to organization of the contact class using simple and

efficient construct [1]. Note that in case of $\psi > 0$ the point of contact creates a curve with discontinuities at instances of rollers changes. However, this circumstance does not prevent the process of regular simulation.

Finally, we apply rigid point contact model as part of the simplest omni wheel model. For this we use the base class for constraint/contact models having only equations of Newton's third law as a behavioral section [9].

We use class of the contact tracking model on the second stage of inheritance, see Figure 7. Cases of this class organization have been analysed above. Coordinates of nearest points P_A and P_B at contact for each pair (floor, roller) are computed as a result for this class functionality.

Class for computing all kinematical characteristics at contact needed "works" in case of contact existence on the next stage of inheritance. On the third stage class for computing the reactions at contact is "turned on". Reactions are the following: (a) normal reaction; (b) tangent force of friction; (c) torque of reactions (zero in the current consideration though it is not difficult to compute torque for several contact models).

To verify an approach for building up the models under analysis we compare the omni wheel dynamics in cases of implicit and explicit algorithms. The wheel performs free motion (combining rotation and sliding) with the only restriction: keep vertical alignment of the wheel disk.

Roller No. 1 central point, its mass center, altitude was analyzed and verified. More accurately we examine y-coordinate of the point velocity. Both models turned out almost identical: in the worst case we have a divergence: in accelerations of order 10^{-8}, in velocities of order 10^{-7}, in position of order 10^{-6} over the time span being equal to 10 units of time. Results of simulation for velocities are shown in Figure 8. Other divergencies for the roller No. 1 central point acceleration and position at time = 10units are shown in Figure 9 and 10 respectively. As expected the model with explicit contact tracking algorithm is faster approximately in 1.5 times.

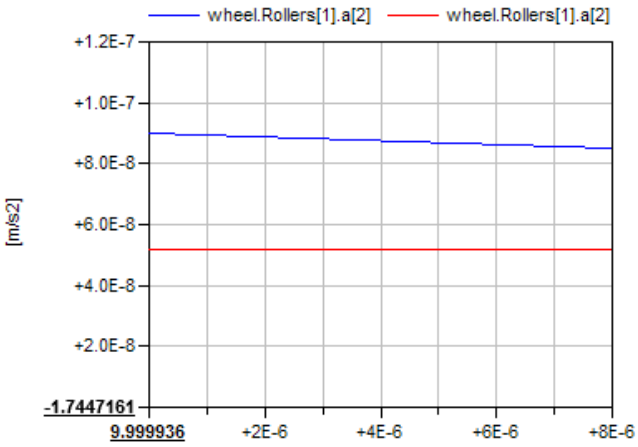

Figure 9: Divergence for y-components of acceleration.

6 CONCLUSIONS

- Two contact tracking algorithms were proposed: implicit and explicit. As expected the second algorithm turned out to be faster almost in 1.5 times. Both algorithms are simple (and efficient) even in simpler case of rollers without any distortion.

- In case of distorted rollers contact curve becomes discontinuous at instants of rollers

Figure 10: Divergence for y-components of position.

change. But simulation process maintains its regularity.

- Both algorithms generate identical dynamics.
- Process of the contact model design using technology of "vertical separation" outlined above has an evident motivation and allows a simple generalization both for the normal force computation and for the tangent friction force model.

7 ACKNOWLEDGMENT

The investigation was performed in MAI under financial support provided by RSF, project 14-21-00068.

REFERENCES

[1] I. Kosenko, K. Gerasimov, Object-oriented implementation of a unilateral point-contact constraint model with friction in frame of the omni vehicle multibody system. *Proceedings of the jointly organized 11th World Congress on Computational Mechanics – WCCM XI, 5th European Congress on Computational Mechanics – ECCM V, 6th European Congress on Computational Fluid Dynamics – ECFD VI*, Barcelona, Spain, July 20–25, 2014, pp. 4452–4463.

[2] V. Kálmán, Controlled braking for omnidirectional wheels. *International Journal of Control Science and Engineering*, **3**, 48–57, 2013.

[3] J. Tobolár, F. Herrmann, and T. Bünte. Object-oriented modelling and control of vehicles with omni-directional wheels. *Computational Mechanics 2009*, November 2009.

[4] B. E. Ilon. Wheels for a course stable selfpropelling vehicle movable in any desired direction on the ground or some other base. *Technical report, US Patents and Trademarks office*, Patent 3,876,255, 1975.

[5] I. I. Kosenko, Physically oriented approach to construct multibody system dynamics models using Modelica language. *Proceedings of Multibody 2007, Multibody Dynamics 2007.*

An ECCOMAS Thematic Conference, Politecnico di Milano, Milano, Italy, June 25–28, 2007, 20 pp.

[6] I. I. Kosenko, Integration of the equations of a rotational motion of a rigid body in quaternion algebra. The Euler case. *Journal of Applied Mathematics and Mechanics*, **62**:193–200, 1998.

[7] I. I. Kosenko, Implementation of unilateral multibody dynamics on Modelica. *Proceedings of the 4th International Modelica Conference*, Hamburg University of Technology, Hamburg–Harburg, Germany, March 7–8, 2005, pp. 13–23.

[8] I. Kosenko, Implementation of unilateral constraint model for multibody systems dynamics on Modelica language. *Proceedings of ACMD2006, The Third Asian Conference on Multibody Dynamics 2006*, Institute of Industrial Science, The University of Tokyo, Tokyo, Japan, August 1–4, 2006.

[9] I. I. Kosenko, M. S. Loginova, Ya. P. Obraztsov, M. S. Stavrovskaya, Multibody systems dynamics: Modelica implementation and bond graph representation. *Proceedings of the 5th International Modelica Conference*, arsenal research, Vienna, Austria, September 4–5, 2006, pp. 213–223.

[10] D. P. Chevallier, On acceleration analysis in multibody dynamics. C. Soize and G. Schueller eds. *Structural Dynamics. EURODYN 2005. Vol. 1.*, Millpress, Rotterdam, The Netherlands, 2005, pp. 587–592.

[11] F. Pfeiffer. Unilateral multibody dynamics. *Meccanica*, **34**:437–451, 1999.

ECCOMAS Congress 2016
VII European Congress on Computational Methods in Applied Sciences and Engineering
M. Papadrakakis, V. Papadopoulos, G. Stefanou, V. Plevris (eds.)
Crete Island, Greece, 5–10 June 2016

MODEL AND INVESTIGATION OF DYNAMICS OF SOLID SYSTEM WITH TWO MASSIVE ECCENTRICS ON A ROUGH PLANE

Sergey V. Semendyaev[1], **Alexey A. Tsyganov**[1]

[1] Moscow Institute of Physics and Technology
9 Institutskiy per., Dolgoprudny, Moscow Region, 141700, Russian Federation
e-mail: {semendyaevsergey, lesha.tsyganov}@gmail.com

Keywords: Solid System, Internal Movers, Dry Friction, Mathematical Modeling, Tracking.

Abstract. *In this paper we investigate the solid system with internal rotating eccentrics as a movers. The system moves in plane with dry friction. Massive eccentrics rotating with variable angular velocity convert rotational motion into uneven translational. The motion is caused by inertia forces and friction between the system and the rough surface and occurs in short steps or slides. The equations of motion are derived under assumption of decreasing linear dependence of electric motor torque on angular velocity. We consider the motion of the platform and the pendulum, and then the resulting system is presented in a convenient form for numerical integration in MatLab. Runge–Kutta fourth-order method is used. Tracking of labels applied to the system is performed using time-lapse video and Adobe After Effects. The results of numerical integration of math model are presented and compared with experimental data obtained using a tracking program.*

1 INTRODUCTION

An interest in solid systems driven by inner movements of masses without outer movers, such as wheels, chain tracks, or legs, arises in last decade. A new class of mechanisms (robots, mechatronic systems) able to move in a resisting medium without external movers due to movement of internal bodies attracts attention [1-12].

In study [1] there is a very simple mechanical model: an absolutely rigid body that can move along a horizontal line; inside the body, there is a movable mass that also moves horizontally. Such a motion realized as a result of the specific periodic relative motions of a material point inside the body. The internal motion parameters providing for a maximum average velocity of the system as a whole are determined.

In paper [2] they deal with a class of vibration-driven models that simulate the dynamics of vibration-driven mobile robots, which mean autonomous mechanisms consisting of a body and movable internal masses. Moving under the action of drives, the internal masses interact with the robot body and the body, in turn, interacts with the external environment. By controlling the motion of internal masses, they can control the force of reaction of the external environment acting on the robot body, providing its motion in the desired direction and regulating the velocity. Vibration-driven robots are simple in design and do not require special limbs, such as wheels, chain tracks, or legs. In particular, this makes them promising for movement not only on surfaces but also within dense media resisting pressure (e.g., in soil), as well as in pipes. Presumably, micro robots of this type can be applied in medicine in order to deliver drugs or a diagnostic sensor to an affected area.

In work [3] the controlled horizontal motion of a body in the presence of dry friction forces is investigated. Control is accomplished by means of a movable mass that can move within the body in a bounded range.

In study [4] for three forms of resistance forces they have calculated the periodic translational motion of a two-mass system consisting of the main body (the container), interacting with the medium, and an internal moving mass. They have considered simple motions of the internal mass with respect to the container, called two-phase motion, and a corresponding piecewise-constant relative velocity of the internal mass. They have shown that as a result of simple motions of the internal mass with respect to the body, the system is displaced as a whole. The principle of motion considered in this paper was realized in a number of experimental models. The internal displacements were obtained by means of a pendulum system and a rotating mass. Mobile mini-robots, moving inside a tube, have been designed and successfully tested. Experiments have confirmed the practical realizability of the principle described above for displacing bodies in resistant media.

In paper [5] the dynamical system consisting of a rigid body and an internal mass is investigated. The rigid body can move along a rough horizontal plane with a piece-wise linear resistance law due to the special periodic internal motions. A three-phase control is constructed and the motion of the body relative to the environment is controlled by varying the relative acceleration of the internal mass. The relationships between the control parameters for the realization of a directed velocity-periodic motion of the rigid body are established through both theoretical and numerical methods. Optimal and practical parameters of the internal motion, at which the maximal mean velocity of the body is reached, are determined.

In work [6] a periodic motion of the internal body relative to the main body, which generates the motion of the main body with periodically changing velocity and the maximum displacement for the period, is constructed for a wide class of laws of resistance of the environment to the motion of the main body. The principle of motion considered is appropriate for mobile mini- and micro-robots. The body (housing) of such robots can be hermetically

sealed and smooth, without protruding parts, which enables these robots to be used for the non-destructive inspection of miniature engineering structures such as thin pipe-lines, as well as in medicine.

In study [7], optimal control problems are solved for two types of vibrationally excited mobile systems. First, a three-body articulated system moving in a horizontal plane is considered. The system consists of a rigid body (main body) to which two links are attached by revolute joints. All three bodies interact with the environment with the forces depending on the velocity of motion of these bodies relative to the environment. The system is controlled by highfrequency periodic angular oscillations of the links relative to the main body. This system models the swimming of some animals. The equation of motion of this system is derived and analyzed. Second, a two-body system moving along a horizontal line in a nonlinear resistive medium is considered. One of the bodies (the main body) interacts with the environment and with the other body (internal body), which interacts with the main body but does not interact with the environment. The environment resists the motion of the main body with a force that depends on the velocity of the main body relative to the environment. A periodic optimal motion of the internal body relative to the main body is defined by solving an optimal control problem.

In paper [8] they investigate two systems consisting of a spherical shell rolling without slipping on a plane and a moving rigid body fixed inside the shell by means of two different mechanisms. In the former case the rigid body is attached to the center of the ball on a spherical hinge. They show an isomorphism between the equations of motion for the inner body with those for the ball moving on a smooth plane. In the latter case the rigid body is fixed by means of a nonholonomic hinge. Equations of motion for this system have been obtained and new integrable cases found.

Paper [9] is concerned with the motion of a cubic rigid body (cube) with a rotor, caused by a sudden brake of the rotor, which imparts its angular momentum to the body. This produces an impulsive reaction of the support, leading to a jump or rolling from one face to another. The robot, called by them M-block, is 4 cm in size and uses an internal flywheel mechanism rotating at 20 000 rev/min. Initially the cube rests on a horizontal plane. When the brake is set, the relative rotation slows down, and its energy is imparted to the case.

This paper [10] deals with the problem of a spherical robot propelled by an internal omniwheel platform and rolling without slipping on a plane. The problem of control of spherical robot motion along an arbitrary trajectory is solved within the framework of a kinematic model and a dynamic model. A number of particular cases of motion are identified, and their stability is investigated. An algorithm for constructing elementary maneuvers (gaits) providing the transition from one steady-state motion to another is presented for the dynamic model. A number of experiments have been carried out confirming the adequacy of the proposed kinematic model.

In work [11] they consider the motion of a system consisting of a rigid body and internal movable masses on a rough surface. The possibility of rotation of the system around its center of mass due to the motion of internal movable masses is investigated. To describe the friction between the body and the reference surface, a local Amontons-Coulomb law is selected. To determine the normal stress distribution in the contact area between the body and the surface, a linear dynamically consistent model is used. As examples they consider two configurations of internal masses: a hard horizontal disk and two material points, which move parallel to the longitudinal axis of the body symmetry in the opposite way. Motions of the system are analyzed for selected configurations.

In work [12] the two-dimensional motion of a system consisting of a hollow rigid body, resting on a rough plane, and two internal mobile point masses, capable of moving parallel to

the longitudinal axis of symmetry of the body is considered. Friction in the contact area is modelled by a local Amontons–Coulomb law. A dynamically matched linear model is used to describe the normal stress distribution. The possibility of achieving rotation of the system by a certain relative motion of internal masses is investigated. Two control laws for the movable masses are considered: piecewise-linear and harmonic, for which the equations of motion are integrated numerically for different values of the parameters of the control laws.

In our work we consider solid system consisting of a rigid nesting frame with two internal masses in the form of eccentrics (unbalanced massive wheels). Eccentrics rotate with variable angular velocity and have no contact with external medium. Nesting frame has a contact with a rough surface with dry friction and moves short steps (or slides) in plane due to rotating eccentrics.

2 EXPERIMENTS

We constructed a model of solid system with two unbalanced wheels in Moscow Institute of Physics and Technology at the Chair of Theoretical Mechanics.

The solid system was designed in SolidWorks program. From a practical point of view, we decided to use open-source building platform (Makeblock, mechanical parts and motors). The result of modeling is presented on Fig.1.

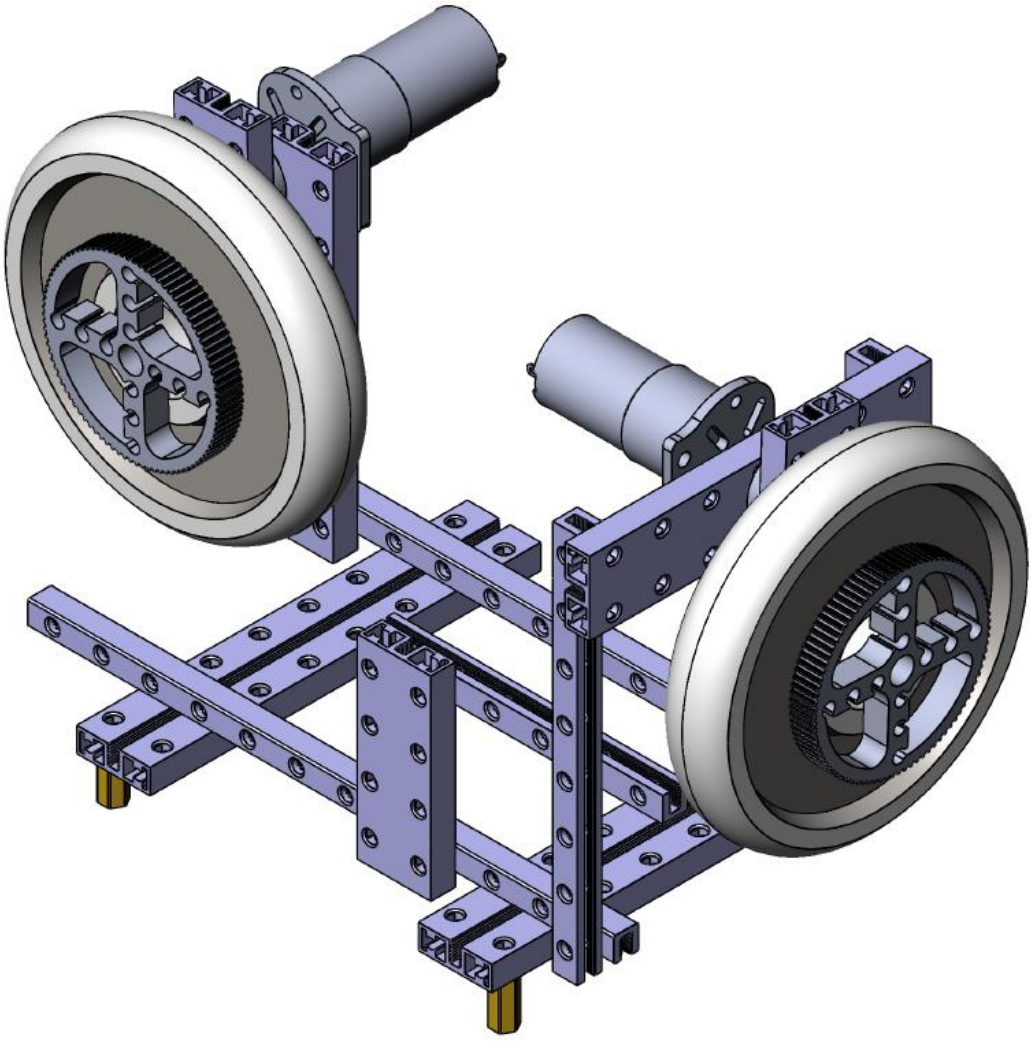

Figure 1: CAD-model of the solid system.

Assembly of the system has led to the result shown in the Fig. 2. Open-source microcontroller (Arduino) sets the velocities of motors rotating two eccentrics. Rigid nesting frame stays on four legs with rounded plastic foots.

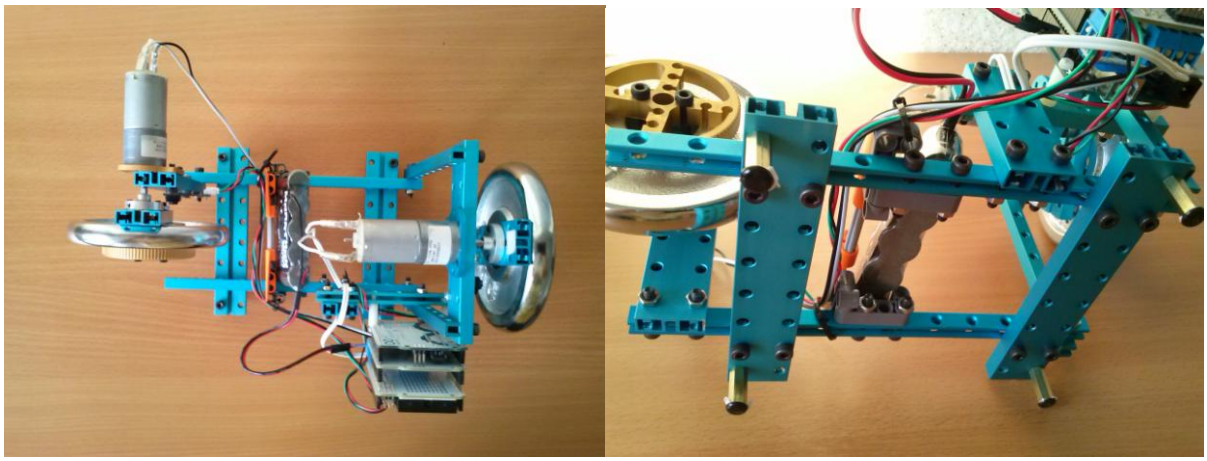

Figure 2: Experimental-model of the solid system (view from above, bottom view).

One of the wheels is placed along the longitudinal axis of symmetry, another one – in transversal position. The main parameters of the model are presented in Table 1.

Characteristics	Value
Total weight	1.825 kg
Weight of wheels	0.5 kg
Average angular speed of the wheels	125 rpm
Eccentricity of longitudinal wheel	3.5 cm
Eccentricity of transversal wheel	2.5 cm
The longitudinal distance between the points of contact with the surface	13.1 cm
The transversal distance between the points of contact with the surface	11.3 cm

Table 1: Parameters of the model.

First part of experiment was devoted to testing of the system on different rough surfaces. Characteristics of surfaces are presented in Table 2.

№	Type	Characterisation	Coef. of friction
1	Laminated chipboard 1	Smooth, with microscopic uniform embossing	0.31
2	Glass	Smooth	0.52
3	Laminated chipboard 2	Smooth, with the moth-eye pattern "under the tree"	0.35
4	Plywood	Very rough, non-uniform	0.34
5	Plastic	Slightly rough, uniform	0.32

Table 2: Characteristics of surfaces.

Two series of experiments were conducted. First, the longitudinal motion of the body was studied (the transversal wheel does not rotate) for two types of rotation (back and forth). The results are shown in Fig. 3, where all measurements were made for 11 revolutions of the

wheel with average angular velocity 125 rpm. In the second series, the rotational motion was experienced (only the transversal wheel is rotating) in similar conditions. The results are presented in Fig. 4.

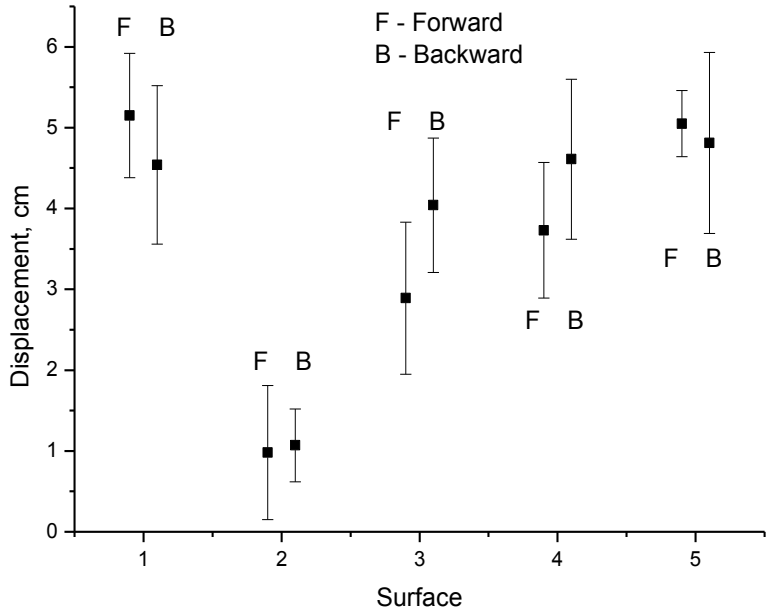

Figure 3: Longitudinal displacement of the body (back and forth) on different surfaces.

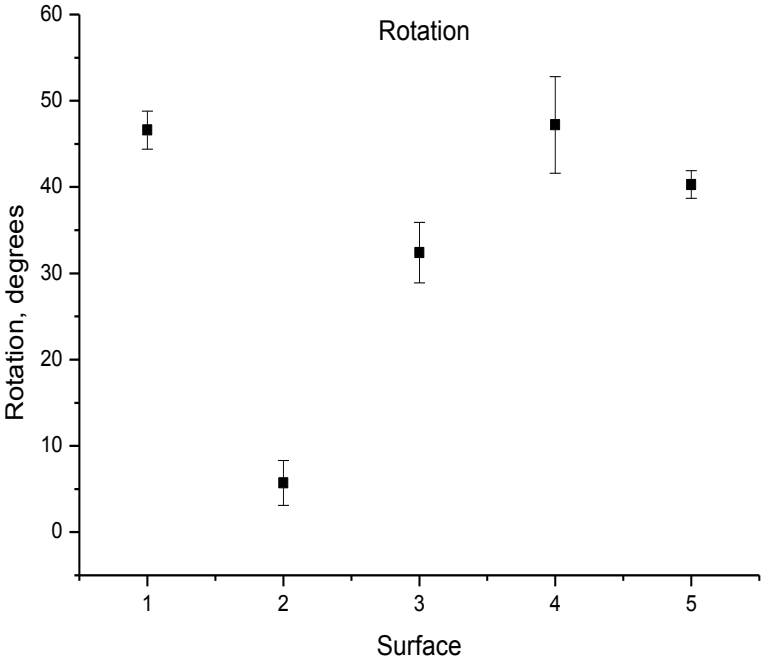

Figure 4: Rotational motion of the body on different surfaces.

It can be seen that both displacement and rotation angle are diminishing with increasing of the coefficient of friction. Note that if this coefficient were zero, no displacement would occur.

In this series of experiments the glass was the most difficult material in terms of repeatability – relative measurement error was the highest compared to other materials. Conversely, the most predictable was the laminated chipboard surface. That is why in the second part of experiments, we decided to use laminated chipboard only.

Second part of experiment was devoted to tracking of the system on the rough surface. The longitudinal motion of the body was studied (the transversal wheel does not rotate) for one type of rotation (forth).

Tracking of labels applied to the system is performed using time-lapse video and Adobe After Effects program. Video frame rate was 60 frames per second. The results of tracking experiments are presented on Fig. 5 (displacement of the system body in meters, time in seconds). Observation of the movement is accomplished by means of contrasting markers on the system components. Recording is done on camera. The resulting video is processed in the software. It uses the standard function "Tracking". In the case of tracking robot position output data are contingent pixels that are converted into millimeters (60 px = 10 mm). To control the time periods and synchronization in the experiment it was used a stopwatch accurate to hundredths of a second.

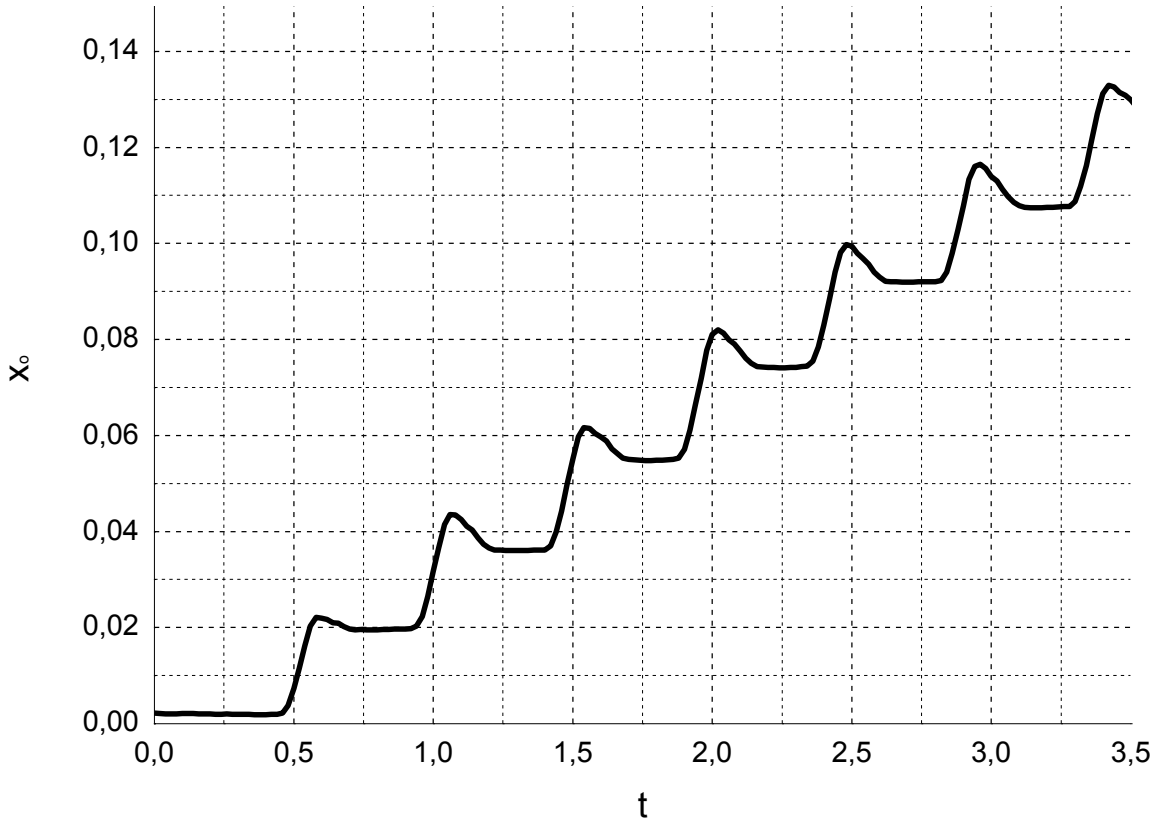

Figure 5: Experimental data obtained using a tracking system in Adobe After Effects program, displacement of body in dependence of time

As we can see, the movement takes place at a constant average speed. Approximately periodic movement occurs sliding forward with some setback.

Such movement can be explained qualitatively as follows. Wheel rotates with variable angular velocity. There are two phases: first, when wheel moves same direction as acceleration of gravity; and the second, vice versa. In first case wheel is accelerated, in second – slows down. Uneven rotational movement of the wheel is converted into a non-uniform translational movement of the base frame, since there are unequal movement pulses differently compensated by friction forces between foots and surface.

The nature of the movement is in good agreement with the results of mathematical modeling, which are presented in the next section.

3 MATHEMATICAL MODELING

First consider the simplified system, shown in Fig.6. A hollow case of mass *m* with flat basement carries a mathematical pendulum of mass m_1 and length *a*, suspended at the point O'. The external forces include normal reaction *N*, friction force *F*, and moment *M*, applied to the pendulum. Note that while the reaction forces *N* and *F* have passive character, the moment *M* is created by a motor, attached to the case, and ensures the movement of the system.

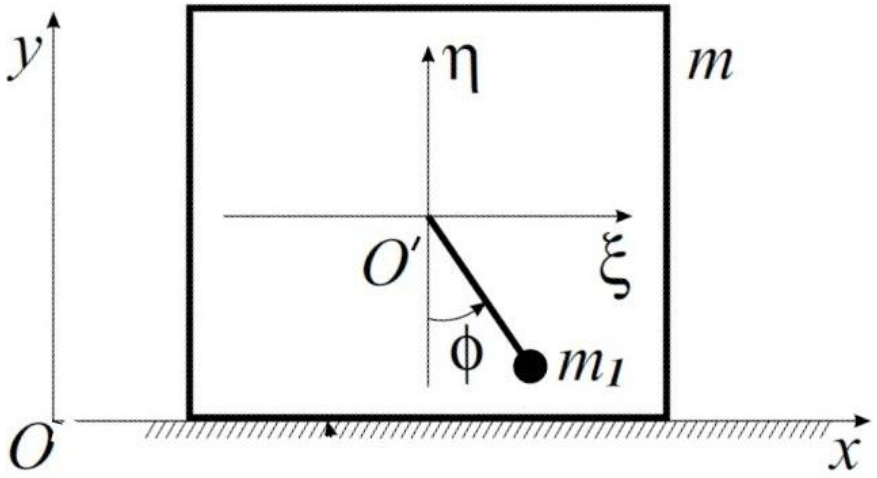

Figure 6: Mechanical model of the system with single unbalanced wheel.

We set coordinates *x* and *y* of point O' and angle ϕ between the pendulum axle and vertical as generalized coordinates. The equations of motion in the Lagrangian form are:

$$\frac{d}{dt}\left(\frac{\partial T}{\partial \dot{x}}\right)=F,\ \frac{d}{dt}\left(\frac{\partial T}{\partial \dot{y}}\right)=N-(m+m_1)g,\quad \frac{d}{dt}\left(\frac{\partial T}{\partial \dot{\phi}}\right)-\frac{\partial T}{\partial \phi}=-\frac{\partial \Pi}{\partial \phi}+M,$$

$$T=\frac{1}{2}(m+m_1)\left(\dot{x}^2+\dot{y}^2\right)+\frac{1}{2}m_1\left(a^2\dot{\phi}^2+2a\dot{x}\dot{\phi}\cos\phi+2a\dot{y}\dot{\phi}\sin\phi\right), \tag{1}$$

$$\Pi=-m_1 ag\cos\phi,\quad F=-\mu N\operatorname{sign}\dot{x}.$$

Since *y=const*, the second equation (1) follows:

$$N=(m+m_1)g+am_1\left(\ddot{\phi}\sin\phi+\dot{\phi}^2\cos\phi\right). \tag{2}$$

A physically plausible form of system (1) is:

$$(m+m_1)\frac{dv_0}{dt}=F,\quad \frac{d}{dt}(T+\Pi)=F\dot{x}+M\dot{\phi},\quad v_0=\dot{x}+a\xi\dot{\phi}\cos\phi,\quad \xi=\frac{m_1 a}{m+m_1}, \tag{3}$$

where v_0 is velocity of the centre of gravity.

We will make the assumption of a decreasing linear relationship between torque of the motor and the angular velocity of its rotation (Fig. 7):

$$M=M_0-k|\omega|,\quad M_0,k=const,\quad M_0,k>0. \tag{4}$$

This kind of dependence usually takes place in direct current motors as in our work.

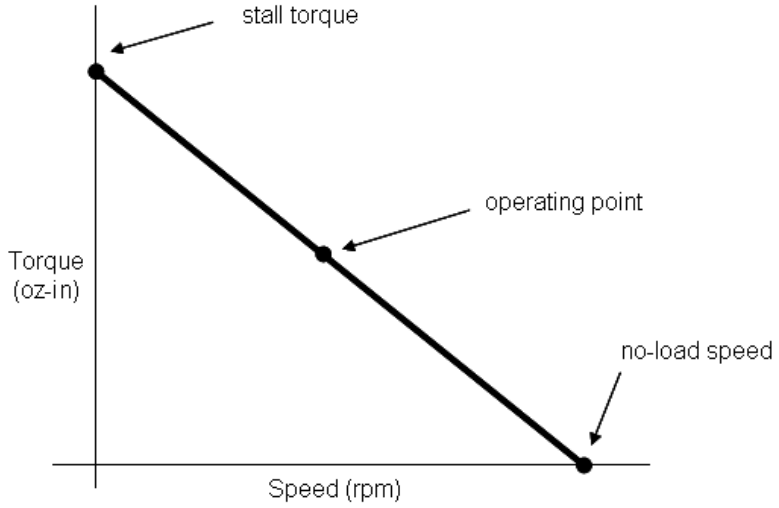

Figure 7: The dependence of the torque of the motor from its angular velocity.

As a result, we obtain the following system of equations for the motion of the platform and the pendulum:

$$\begin{gathered}\left(m+m_1\right)\dot{\upsilon}+am_1\left(\ddot{\varphi}\cos\varphi-\dot{\varphi}^2\sin\varphi\right)=-\mu N\frac{\upsilon}{|\upsilon|},\\ N=\left(m+m_1\right)g+m_1a\left(\ddot{\varphi}\sin\varphi+\dot{\varphi}^2\cos\varphi\right),\\ m_1a^2\ddot{\varphi}+m_1a\dot{\upsilon}\cos\varphi=M_0-k|\dot{\varphi}|-m_1ag\sin\varphi.\end{gathered}\tag{5}$$

The system is represented as (if $\upsilon\neq 0$):

$$\dot{\upsilon}=\frac{\Delta_1}{\Delta},\quad \ddot{\varphi}=\frac{\Delta_2}{\Delta},\tag{6}$$

where:

$$\begin{gathered}\Delta=mm_1a^2+a^2m_1^2\sin^2\varphi-\mu a^2m_1^2\sin\varphi\cos\varphi\frac{\upsilon}{|\upsilon|},\\ \Delta_1=\left(-\mu\left(m+m_1\right)g\frac{\upsilon}{|\upsilon|}+am_1\dot{\varphi}^2\left(\sin\varphi-\mu\cos\varphi\frac{\upsilon}{|\upsilon|}\right)\right)m_1a^2-\\ -am_1\left(\cos\varphi+\mu\sin\varphi\frac{\upsilon}{|\upsilon|}\right)\left(M_0-k|\dot{\varphi}|-m_1ag\sin\varphi\right),\\ \Delta_2=\left(m+m_1\right)\left(M_0-k|\dot{\varphi}|-m_1ag\sin\varphi\right)-\\ -\left(-\mu\left(m+m_1\right)g\frac{\upsilon}{|\upsilon|}+am_1\dot{\varphi}^2\left(\sin\varphi-\mu\cos\varphi\frac{\upsilon}{|\upsilon|}\right)\right)m_1a\cos\varphi.\end{gathered}\tag{7}$$

Then the system (6, 7) (taking into account also the case $\upsilon=0$) is solved numerically in MatLab program. Runge–Kutta fourth-order method is used. The results are shown in Fig. 8.

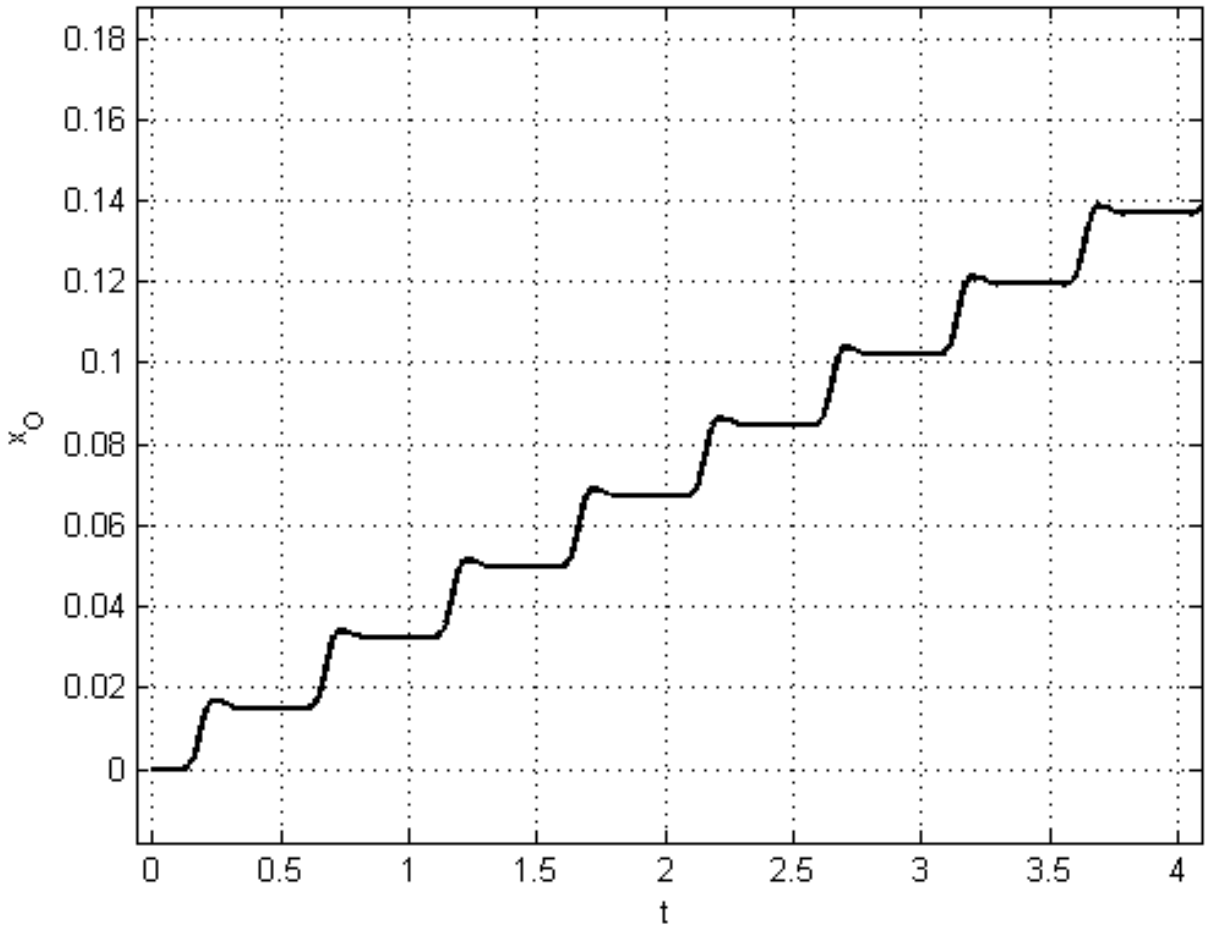

Figure 8: Numerical integration in MatLab, displacement of body in dependence of time.

Graph of body diplacement x (meters) from the time t (seconds) in Fig. 8 is obtained by numerical integration at the following conditions (Table 3):

Parameter	Value
The reduced length of the pendulum	0.06 m
Body weight (without pendulum)	1.325 kg
The pendulum weight	0.5 kg
The coefficient of friction	0.3
Acceleration of gravity	9.8 m/s^2
M_0	0.341 N·m
k	0.020 N·m·s

Table 3: Parameters in numerical integration.

Though this model can move, it has visible shortcomings. First of all, the rectilinear trajectory is unstable: due to unaccounted disbalances the body will deviate. Obviously, in practice, it is impossible to attach a cargo to the body, keeping ideal symmetry. Further, the practical needs are not restricted by rectilinear motion: usually mobile devises move along a prescribed curve. Our aim is to create a robot which could perform stable rectilinear or curvilinear motion. The key problem is to let the body move more accurately and to adapt to the surfaces with different coefficients of friction. This problem can be described in next paper.

4 CONCLUSIONS

- The motion of body with rotating internal wheels in interaction with external environment in form of rough surface can be used as the principle for the motion of mobile robots.
- Robotic mechanisms of this class, being isolated from external environment in shell, can be used in extreme conditions, with strong pollution of surrounding space, in aggressiveness of environment (for example, on another planet or in chemically active environment).
- The movement of the system is studied with the help of mathematical modeling and numerical integration and is compared with experimental data obtained by tracking method.

ACKNOWLEDGEMENTS

We thank PhD A.V. Sakharov and Professor A.P. Ivanov for a discussion of certain questions and cooperation.

This research was supported by the basic part of a State grant in the sphere of scientific activity (No. 2014/120 "Investigation of the regularities of the dynamics of systems with friction and the development of mobile robots without external motors", (NIR No. 2583) and the Russian Foundation for Basic Research (14-01-00432)).

REFERENCES

[1] F.L. Chernous'ko, On a motion of a body containing a movable internal mass. *Doklady Physics*, **50** (11), 593-597, 2005.

[2] N.N. Bolotnik, I.M. Zeidis, K. Zimmermann, S.F. Yatsun, Dynamics of controlled motion of vibration-driven systems. *Journal of Computer and Systems Sciences International*, **45** (5), 831-840, 2006.

[3] F.L. Chernous'ko, Analysis and optimization of the motion of a body controlled by a movable internal mass. *Journal of Applied Mathematics and Mechanics*, **70** (6), 819-842, 2006.

[4] F.L. Chernous'ko, The optimal periodic motions of a two-mass system in a resistant medium. *Journal of Applied Mathematics and Mechanics*, **72**, 116–125, 2008.

[5] H.B. Fang, J. Xu, Dynamic analysis and optimization of a three-phase control mode of a mobile system with an internal mass. *Journal of Vibration and Control*, **17** (1), 19–26, 2011.

[6] N.N. Bolotnik, T.Yu. Figurina, F.L. Chernous'ko, Optimal control of the rectilinear motion of a two-body system in a resistive medium. *Journal of Applied Mathematics and Mechanics*, **76**, 1-14, 2012

[7] F.L. Chernousko, N.N. Bolotnik, T.Yu. Figurina, Optimal control of vibrationally excited locomotion systems. *Regular and Chaotic Dynamics*, **18** (1-2), 85-99, 2013

[8] I.A. Bizyaev, A.V. Borisov, I.S. Mamaev, The dynamics of nonholonomic systems consisting of a spherical shell with a moving rigid body inside. *Regular and Chaotic Dynamics*, **19** (2), 198-213, 2014.

[9] A.P. Ivanov, On the impulsive dynamics of M-blocks. *Regular and Chaotic Dynamics*, **19** (2), 214-225, 2014.

[10] Yu.L. Karavaev, A.A. Kilin, The dynamics and control of a spherical robot with an internal omniwheel platform. *Regular and Chaotic Dynamics*, **20** (2), 134-152, 2015.

[11] A.V. Sakharov, Rotation of the body with movable internal masses around the center of mass on a rough plane. *Regular and Chaotic Dynamics*, **20** (4), 428-440, 2015.

[12] A.V. Sakharov, Rotation of a body with two movable internal masses on a rough plane. *Journal of Applied Mathematics and Mechanics*, (in press), 2015.

ECCOMAS Congress 2016
VII European Congress on Computational Methods in Applied Sciences and Engineering
M. Papadrakakis, V. Papadopoulos, G. Stefanou, V. Plevris (eds.)
Crete Island, Greece, 5–10 June 2016

NON-REGULAR VEHICLE DYNAMICS. APPLICATION TO COLLISION

A. BOUZAR ESSAIDI, B. MENKOUZ, M. HADDAD and T. CHETTIBI

Laboratoire Mécanique des Structures

Ecole Militaire Polytechnique

BP 17 Bordj El Bahri Algiers, Algeria

bouzaressaidiahmed@gmail.com

Keywords: Non-Regular, Dynamic, Vehicle, Linear Model, Holding Contact, Collision, Fixed Obstacle.

Abstract. *The principal aim of this paper is to evaluate the non-regular dynamic behavior of a vehicle involved in a collision with a fixed obstacle. Firstly, the model used for the wheels/ground interaction is the linear model. In addition, we established the constraints equations relating to holding contact with the ground and those concerning conditions of Ackermann. The obtained results had been compared with those given by the Pc-Crash software. We noted a good correlation for various scenarios. After validation, we used this model in the case of collision vehicle/fixed obstacle. A comparison of the simulation and experimental results confirmed the good agreement between the model and the real system of Crash-Test.*

1 INTRODUCTION

The modeling and simulation of the dynamic behavior of vehicle today are a scientific theme that has progressed rapidly under the impetus of vehicles industries. Thanks to their potential, this discipline has become an indispensable tool for improving the performance of vehicle.

However, in some situations, particularly those characterized by a non-regular vehicles dynamics (rollover, crash, sudden change in certain parameters of the roadway, demining operation by an intervention vehicle ...), the equations governing the movement of system lead to differential and algebraic equations are difficult to solve.

Most mechanical systems subjected to non-permanent excitations can be modeled by non-smooth dynamical systems. This non-regularity can originate in the batch-term control, in the interaction of the environment with the system and in problems of sudden change in system parameters. This loss of regularity, in the late 1970s, Michelle Schatzman [1] and Jean Jacques Moreau [2] started researching a mathematically consistent formulation for modeling the dynamic behavior of non-regular mechanisms.

In the case of vehicle, the non-regular dynamic situations can be classified into three categories:

i) Non-regular dynamic situations caused by discontinuities of control parameters (sudden change of steering angle, sudden braking action...).

ii) Non-regular dynamic situations caused by discontinuities in the system/environment interaction (collision vehicle/fixed barrier, collision vehicle/vehicle, rollover, skidding, ground roughness, slope change in a way, sudden change in the parameters road…).

iii) Non-regular dynamic situations caused by discontinuities of some parameters of the vehicle (sudden change of the damping coefficient or stiffness of the suspension system ...).

The objective of this work is the development of a comprehensive approach to dynamic behavior modeling of the vehicle taking into account the problems of irregular dynamics in collision between the vehicle and a fixed obstacle. In addition, the validation of the results of this approach compared with those given by appropriate software.

2 VEHICLE DYNAMIC MODEL

2.1 Geometric description of the system

In the present study, the structure of the considered mobile robot is composed of a vehicle (Figure 1) which is supposed rigid body fixed to the chassis and suspended via the suspension system composed of a spring and damper (*ki* is the stiffness and *bi* is the damping coefficient). Unsuspended masses are negligible compared to the suspended masse. In addition, the caster, toe and tilt angles of the kingpin are not considered. The anti-roll bar is not modeled. The braking is applied to all wheels and the load transfer is considered.

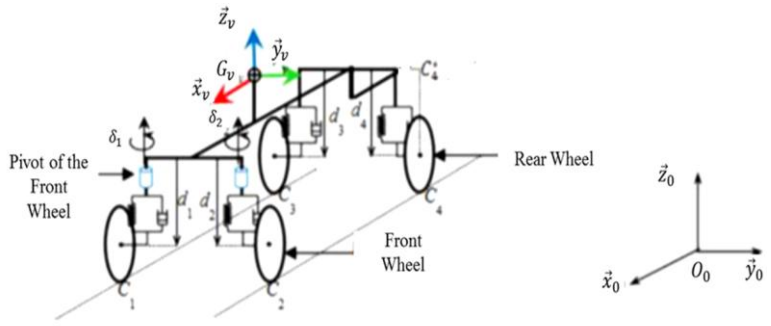

Figure 1: Vehicle model.

The system is moving on a road to which is attached a frame $\Re_0 = \left(O_0, \vec{x}_0, \vec{y}_0, \vec{z}_0\right)$. Let $\Re_v = \left(G_v, \vec{x}_v, \vec{y}_v, \vec{z}_v\right)$ be the mobile frame linked to the robot chassis, G_v the original center of gravity of the robot. The axis $\vec{x}_v$ is perpendicular to the plane of longitudinal symmetry of the vehicle, facing the left side, the axis is perpendicular to $\vec{y}_v$ and directed towards the front of the vehicle.

The configuration of the vehicle frame versus the fixed reference $\Re_0$ is defined by six parameters: three cartesian coordinates (x, y, z) of the center of gravity and the three angles (φ_1: roll, φ_2: pitching and φ_3: yaw) orientation of the $\Re_v$ with respect to reference $\Re_0$. The rotation matrix of $\Re_v$ relatively to $\Re_0$ is:

$$ {}^{0}P_{v} = \begin{bmatrix} c_2c_3 & s_1s_2c_3 - c_1s_3 & c_1s_2c_3 + s_1s_3 \\ c_2s_3 & s_1s_2s_3 + c_1c_3 & c_1s_2s_3 - s_1s_3 \\ -s_2 & s_1c_2 & c_1c_2 \end{bmatrix} \tag{1} $$

With: $c_i = \cos\left(\varphi_i\right), s_i = \sin\left(\varphi_i\right), i = 1..3$.

The kinematic wrenches of the vehicle frame relative to the reference, expressed in the vehicle frame are given by the following relationships:

$$ {}^{v}\vec{V}_{Gv} = {}^{v}P_0 \begin{pmatrix} \dot{x} \\ \dot{y} \\ \dot{z} \end{pmatrix} \text{ and } {}^{v}\vec{w}_v = \begin{pmatrix} w_{xv} \\ w_{yv} \\ w_{zv} \end{pmatrix} = \begin{bmatrix} 1 & 0 & -s_2 \\ 0 & c_1 & s_1c_2 \\ 0 & -s_1 & c_1c_2 \end{bmatrix} \begin{pmatrix} \dot{\varphi}_1 \\ \dot{\varphi}_2 \\ \dot{\varphi}_3 \end{pmatrix} \tag{2} $$

In order to take into account the efforts of wheels/ground interaction, we attach to each wheel, a frame $\Re_i = \left(C_i, \vec{e}_{xi}, \vec{e}_{yi}, \vec{e}_{zi}\right)$ placed at the wheel/ground contact point. The unit vectors of $\Re_i$ are defined, according to the normal $\vec{n}_i$ of the wheel i contact with the ground plane and its steering angle, by the following expressions:

$$For\ \ i=1...4\ \left\{\begin{array}{c} {}^{0}\vec{e}_{zi}={}^{0}\vec{n}_i \\ {}^{0}\vec{e}_{xi}=\dfrac{({}^{0}P_v\cdot{}^{v}\vec{v}_i)\wedge{}^{0}\vec{e}_{zi}}{\left|({}^{0}P_v\cdot{}^{v}\vec{v}_i)\wedge{}^{0}\vec{e}_{zi}\right|} \\ {}^{0}\vec{e}_{yi}={}^{0}\vec{e}_{zi}\wedge{}^{0}\vec{e}_{xi} \end{array}\right\} \tag{3}$$

With $\vec{n_i}$ the vector normal to the wheel plane. These vectors are defined by ${}^{v}\vec{v}_i=\begin{pmatrix}-\sin\delta_i & \cos\delta_i & 0\end{pmatrix}^T$ for the front wheels of the vehicle and ${}^{v}\vec{v}_i=\begin{pmatrix}0 & 1 & 0\end{pmatrix}^T$ for the other wheels.

The transition matrix of the wheel/ground interaction frame ($\mathcal{R}_i/\mathcal{R}_0$) is defined by the following relationship:

$${}^{0}P_i=\left[\begin{array}{c|c|c} {}^{0}\vec{e}_{xi} & {}^{0}\vec{e}_{yi} & {}^{0}\vec{e}_{zi} \end{array}\right]\quad for\ \ i=1...4 \tag{4}$$

In this, the elongations of the springs are modeled by the variables d_i, for i = 1...4. The vector of the generalized coordinates $\vec{q}$ contains the kinematic variables of translation and orientation of the vehicle, the variables characterizing the elongation of the springs and the two front wheels steering angles δ_1 and δ_2. The vector $\vec{q}$ is thus defined as follows:

$$\vec{q}=\left(x,y,z,\varphi_1,\varphi_2,\varphi_3,d_1,d_2,d_3,d_4,\delta_1,\delta_2\right)$$

2.2 Constraints equations

The constraints equations of a vehicle are defined by the conditions linked to Ackermann steering system and the wheels/ground holding contact conditions of the vehicle. They are developed bellows.

2.2.1 Ackermann Conditions

During the movement of the vehicle along a curve, the steering angles are linked to the existing of yaw speed w_{zv} and the radius of curvature of this curve by the following equations:

$$\begin{array}{l} if\ \ w_{zv}=0\Rightarrow\left\{\begin{array}{l}\delta_1=0\\ \delta_2=0\end{array}\right. \\ if\ \ w_{zv}\neq 0\Rightarrow\left\{\begin{array}{l}\delta_1=\tan^{-1}\left(\dfrac{L_v}{R+L_w/2}\right)\\ \delta_2=\tan^{-1}\left(\dfrac{L_v}{R-L_w/2}\right)\end{array}\right. \end{array} \tag{5}$$

With: L_v: vehicle wheelbase; L_w: rear track; $R=V_{xv}/w_{zv}$ The curvature radius calculated on the rear track of the robot center and V_{xv}: longitudinal velocity.

2.2.2 Wheels/ground holding contact conditions (WGHCC)

WGHCCs of a vehicle are defined by the following algebraic equations:

$$\left({}^{0}\overrightarrow{O_0C_i} - {}^{0}\overrightarrow{O_0G_v} - {}^{0}\overrightarrow{G_vC_i}^{*} + r_w\,{}^{0}\vec{n}_i \right) {}^{0}\vec{z}_v + d_i = 0 \quad for\ i = 1...4 \tag{6}$$

With r_w: the radius of the wheels.

The conditions (6), derived twice with respect to time, can be expressed as follows:

$$\left[J_v \right] \cdot \ddot{\vec{X}} + \overrightarrow{B_{cv}} = \vec{0} \tag{7}$$

With: $\left[J_v \right]$ is the Jacobean matrix inherent to the **WGHCC** of the vehicle;

$\overrightarrow{B_{cv}}$ are the acceleration constraints vector of **WGHCC** of the vehicle.

$$\ddot{\vec{X}} = \left(\ddot{x}, \ddot{y}, \ddot{z}, \dot{w}_{xv}, \dot{w}_{yv}, \dot{w}_{zv}, \ddot{d}_1, \ddot{d}_2, \ddot{d}_3, \ddot{d}_4 \right)^T \tag{8}$$

$$\left[J_v \right] = \begin{bmatrix} {}^{0}\overrightarrow{n_1}^{T} & -{}^{0}\overrightarrow{n_1}^{T}\left({}^{0}P_v \left[* {}^{v}\overrightarrow{G_vC_1} \right] \right) & -{}^{0}\overrightarrow{n_1}^{T}\,{}^{0}\overrightarrow{z_v} & 0 & 0 & 0 \\ {}^{0}\overrightarrow{n_2}^{T} & -{}^{0}\overrightarrow{n_2}^{T}\left({}^{0}P_v \left[* {}^{v}\overrightarrow{G_vC_2} \right] \right) & 0 & -{}^{0}\overrightarrow{n_2}^{T}\,{}^{0}\overrightarrow{z_v} & 0 & 0 \\ {}^{0}\overrightarrow{n_3}^{T} & -{}^{0}\overrightarrow{n_3}^{T}\left({}^{0}P_v \left[* {}^{v}\overrightarrow{G_vC_3} \right] \right) & 0 & 0 & -{}^{0}\overrightarrow{n_3}^{T}\,{}^{0}\overrightarrow{z_v} & 0 \\ {}^{0}\overrightarrow{n_4}^{T} & -{}^{0}\overrightarrow{n_4}^{T}\left({}^{0}P_v \left[* {}^{v}\overrightarrow{G_vC_4} \right] \right) & 0 & 0 & 0 & -{}^{0}\overrightarrow{n_4}^{T}\,{}^{0}\overrightarrow{z_v} \end{bmatrix} \tag{9}$$

$$\overrightarrow{B_{cv}}(i) = {}^{0}\overrightarrow{n_i}^{T}\left[{}^{0}P_v \left(2 \cdot {}^{v}\overrightarrow{w_v} \wedge \left(-\dot{d}_i \cdot {}^{v}z_v \right) + {}^{v}\overrightarrow{w_v} \wedge \left({}^{v}\overrightarrow{w_v} \wedge {}^{v}\overrightarrow{G_vC_i} \right) \right) \right] \quad for\ i = 1...4 \tag{10}$$

$\left[* {}^{0}\overrightarrow{G_vC_i} \right]$: The operator of the vector cross product.

2.3 Motions equations

The main forces acting on a vehicle in motion are wheels/ground interaction forces, the dynamic forces, gravity and the aerodynamic forces. In this model, we consider only the dynamic forces, gravity, and wheel/ground interaction efforts for simplification reasons.

Interaction efforts applied to each wheel of the system are represented in the reference related to wheels by the vector $\left(F_{xi} \quad F_{yi} \quad F_{zi} \right)$. These three components are linked together by a dependency relationship defined by the wheels/ground interaction efforts of the linear model [3] [4] [5] [10] [22]. Taking account of the forces applied on the vehicle, the twelve following equations of motion is obtained as follows:

$$\begin{cases} m \begin{pmatrix} \ddot{x} \\ \ddot{y} \\ \ddot{z} \end{pmatrix} = m \cdot {}^{0}\vec{g} + \sum_{i=1}^{4} {}^{0}\vec{F}_i + {}^{0}\vec{F}_{out} \\ {}^{v}\mathbb{I}_{Gv}\,{}^{v}\overrightarrow{\dot{w}_v} + {}^{v}\overrightarrow{w_v} \wedge \left({}^{v}\mathbb{I}_{Gv}\,{}^{v}\overrightarrow{w_v} \right) = \sum_{i=1}^{4} {}^{v}\overrightarrow{G_vC_i} \wedge {}^{v}\vec{F}_i + {}^{v}\vec{M}_{out} \end{cases} \tag{11}$$

With ${}^{0}\vec{g}$: the gravitational acceleration; ${}^{v}\overrightarrow{\dot{w}_v}$: Angular acceleration of the vehicle expressed in $\mathcal{R}_v$ frame; ${}^{v}\mathbb{I}_{Gv}$ is the tensor of inertia of the robot; m_v is the mass.

and:

$$\left({}^{v}P_i \cdot {}^{i}\vec{F}_i \right) \cdot {}^{v}\vec{z}_v = -k_i \left(d_i - L_{0i} \right) - b_i \cdot \dot{d}_i \qquad for\ i = 1...4 \tag{12}$$

With L_{0i}: Initial spring length of the wheel *i*.

By grouping the various equations of constraints and motion of the system (car-like robot), we obtain the following differential-algebraic system describing the dynamics of our system:

$$[A]\cdot\ddot{\vec{X}} = \vec{B} \tag{13}$$

$$[A] = \begin{bmatrix} [M_v]_{6\times10} \\ [J_v]_{4\times10} \end{bmatrix} with: [M_v] = \begin{bmatrix} m\cdot I_{3\times3} & 0_{3\times3} & 0_{3\times4} \\ 0_{3\times3} & {}^{v}\mathbb{I}_{Gv} & 0_{3\times4} \end{bmatrix}$$

$$\vec{B} = \begin{pmatrix} \vec{B}_{mv} \\ -\vec{B}_{cv} \end{pmatrix}, \text{ with}: \vec{B}_{mv} = \begin{pmatrix} m\cdot\vec{g} + \sum_{i=1}^{4}\left({}^{0}P_i\cdot{}^{i}\vec{F}_i\right) + {}^{0}\vec{F}_{out} \\ -{}^{v}\vec{w}_v \wedge \left({}^{v}\mathbb{I}_{Gv}\cdot{}^{v}\vec{w}_v\right) + \sum_{i=1}^{4}{}^{v}\overrightarrow{G_vC_i} \wedge \left({}^{0}P_i\cdot{}^{i}\vec{F}_i\right) + {}^{v}\overrightarrow{M}_{out} \end{pmatrix}$$

The numerical integration equations, with the consideration of the initial conditions, describe the dynamic behavior of the vehicle for a given time history of acceleration (or braking) and steering data. In this work, we used the Euler method for integrating these differential equations.

3 RESULTS

To discuss the reliability of obtained results we will validate them by comparison with those given by Pc-crash® accidents simulator [21]. Then, we will present some examples of applications of the modeling approach for different complex scenarios. In these examples, the applied geometrical and inertial parameters of the vehicle are summarized in Table 1.

Parameters	Car like robot
Mass *m*	950 *Kg*
Moment of inertia *Ixx*	1072 *Kg/m²*
Moment of inertia *Iyy*	1342 *Kg/m²*
Moment of inertia *Izz*	1342 *Kg/m²*
Height of center of gravity	0.50 *m*
Front track	1.41 *m*
Rear track	1.41 *m*
front wheelbase	1.04 *m*
Rear wheelbase	1.50 *m*
Front suspension stiffness	9.97 *KN/m*
Rear suspension stiffness	6.79 *KN/m*
Front dumping	897.28 *N.s/m*
Rear dumping	611.01 *N.s/m*
Coefficient of friction	0.70
Radius wheel	0.25 m

Table 1: Geometrical and inertial parameters of the vehicle.

Scenario 1: Acceleration and deceleration on a straight path:

This scenario is described as follows (Figure 2): *i)* an acceleration phase for 4 seconds; *ii)* a constant speed phase for 2 seconds and *iii)* a deceleration for 4 seconds (the braking is distributed on the front and rear wheels). The simulation results by the developed application and those given by PC-Crash are illustrated in figures 3 and 4. These figures show a good correlation between the results obtained by the dynamic model developed and those given by the software of Pc-Crash.

Scenario 2: Dynamics of the robot during the course of a turn:

This scenario is described as follows: *i)* linear movement for 2 seconds at constant speed $S = 15\ m/s$ and *ii)* turning for 8 seconds with 100m of curvature radius. The obtained simulation results are illustrated in figures 5 to 6. The curves plotted in these figures show a very satisfactory correlation between the results of our developed model and those given by Pc-Crash.

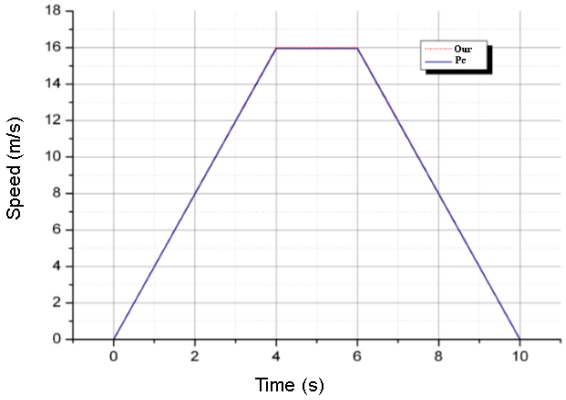

Figure 2: Speed of the vehicle.

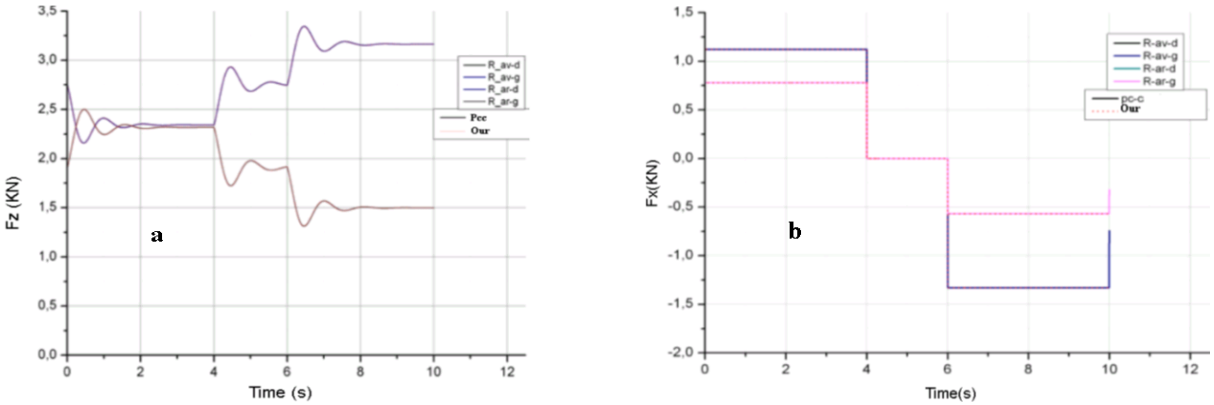

Figure 3: (a) Vertical and (b) longitudinal forces wheels

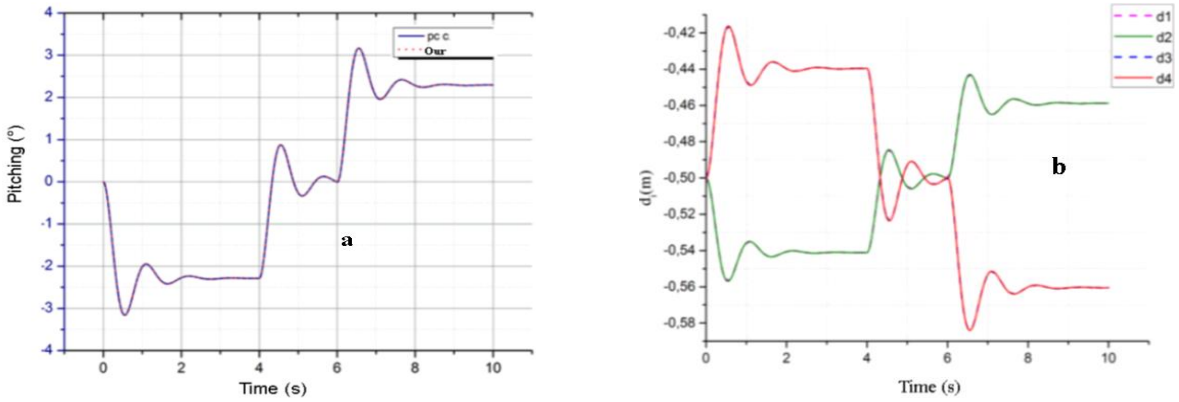

Figure 4: (a) Pitching angle and (b) elongation of spring of suspension

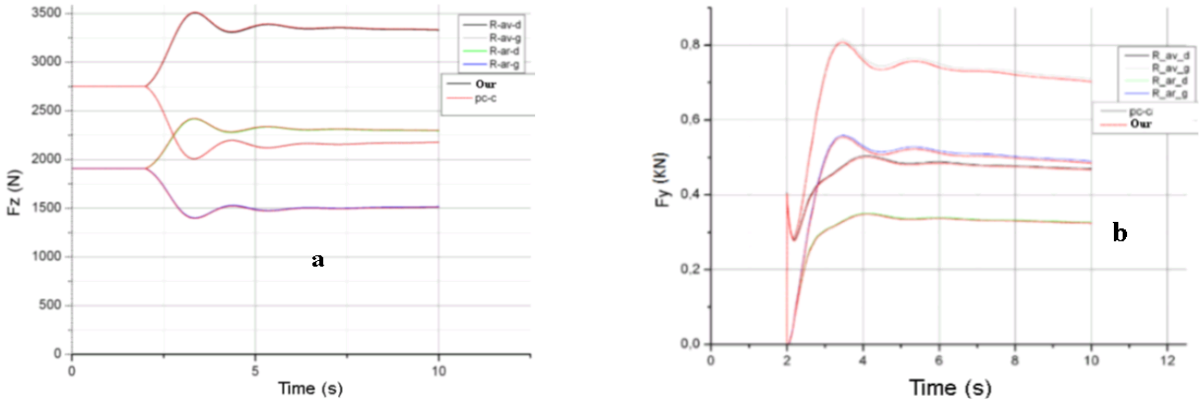

Figure 5: (a) Vertical and (b) longitudinal forces wheels

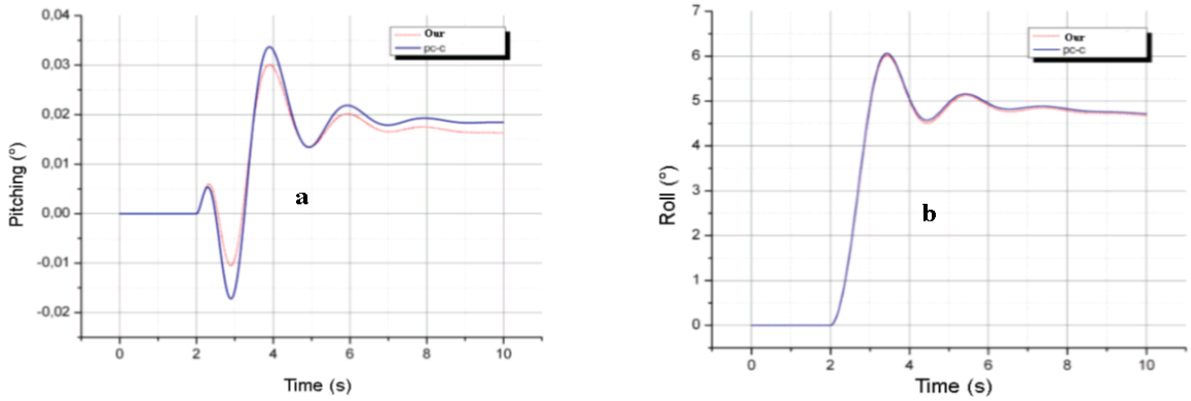

Figure 6: (a) Pitching angle and (b) roll angle

In the results for these two scenarios, we have already met with non-regularities of certain parameters (Figure 3b and 5b). In the first scenario, the irregular dynamic is caused by discontinuities of longitudinal acceleration, while for the second scenario; is approved by the sudden change in curvature radius.

4 APPLICATION TO COLLISION

Vehicle dynamic in normal operating mode remains predominant in the literature because it is usually sufficient to study a wide operating range, for this; we found a very little literature treating the irregular dynamic of the vehicle. However, the modeling of non-regular dynamic

behavior of the vehicle will explain the phenomena which are introduced into the phase of an accident (the investigation of road accidents), and the operation of these models in vehicle construction or in mission planning an intervention autonomous vehicles.

To find a solution to our problems, we will be simply made to realize, first, an analytical study of the constraints equations and motions equations and, secondly, the resolution process. The approach should ensure convergence and allow the user to obtain the desired response at the instants for any case.

Simulate a collision type of accident is to replicate the response of the vehicle involved in the accident, before, during and after the collision. This simulation requires the development and implementation of three models:

i) The collision detection model.
ii) The collision force calculate model.
iii) The model of the dynamic behavior of objects (vehicle, pedestrians ...) colliding.

In this work, we opted for a representation, not polyhydric, very simple based on modeling of vehicle and obstacles in the form of rectangular objects. The algorithm that we used for collision detection is based on the calculation of the distance between the rectangular objects. The distance between parallelepipeds is the smallest between the edges of the facets with respect to each other. The distance in the configuration illustrated in Figure 7, is given by:

$$L_{i/j} = \left({}^{j}R_i \cdot {}^{i}P_2 - {}^{j}P_5 \right) \cdot z_i \tag{14}$$

Either $L_{i/j}$ the smallest distance between the two parallelepipeds, whichever is negative, the objects collide. Otherwise, the objects are separated.

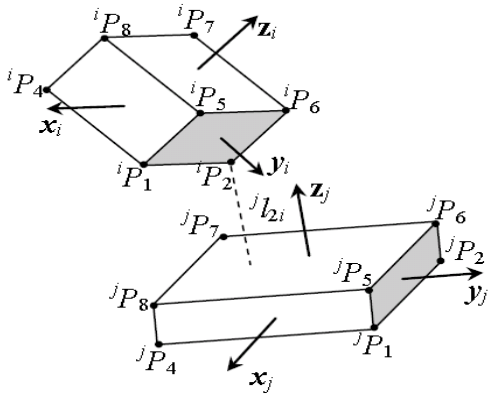

Figure 7: Calculating the distance between two parallelepipeds.

The second step of processing a collision problem is to calculate the collision forces. The methods used to assess these forces can be classified into three categories: the constraints methods, pulse-based methods and penalties methods. We chose a penalty method for the following reasons: *i)* penalties methods are implemented in several simulation software and *ii)* simplicity implementation. In this method, the collision force applied by the object *i* on the *j* item to the collision point, is given by:

$$F_{i/j} = -\left(k_{i/j} \cdot l_{i/j} + b_{i/j} \cdot \dot{l}_{i/j} \right) \left(\vec{n}_{i/j} - \mu_{i/j} \frac{\vec{v}_{i/j}}{\left\| \vec{v}_{i/j} \right\|} \right) \text{ and } F_{i/j} = -F_{j/i} \tag{15}$$

With $\vec{n}_{i/j}$ the common normal to the contact surfaces; $k_{i/j}$ and $b_{i/j}$ are the coefficients of stiffness and damping of the two objects at the point of collision; $\vec{v}_{i/j}$ the relative sliding velocity

at the contact point; $\dot{l}_{i/j} = l_{i/j}/dt$: is the velocity of interpenetration. The value of this speed is calculated by a numerical derivation of $l_{i/j}$.

$$l_{i/j}(t+dt) = \left(l_{i/j}(t+dt) - l_{i/j}(t)\right)/dt \tag{16}$$

4.1 Simulation algorithm of vehicle's collision

The simulation process starts with the initial conditions (position, orientation and vehicle velocity). During its movement, the vehicle is subjected to the force of gravity, the wheels/ground interaction efforts and inertia forces. The collision forces are not taken into account if there is a collision between the vehicle and its environment. It is therefore necessary to detect whether there is a collision or not. In a collision, it is necessary to calculate the impact point, the normal to the surfaces in this point and the interpenetration distance, and evaluate the collision forces. Then, these forces are taken into account in the vehicle dynamics. Once the full dynamic is calculated, the overall configuration system is updated.

4.2 Simulation of collision vehicle/fixed obstacle

To simulate the non-regular dynamic behavior of a vehicle collision phase. The vehicle in rectilinear motion with constant speed, it collides with a fixed obstacle (a wall) considered a perfectly rigid body. The angle α is the orientation between the vehicle speed and the normal to the wall (Figure 8), we considered two cases of collision:

Case 1: a frontal collision for α = 180 °

Case 2: an oblique collision for α = 170 °.

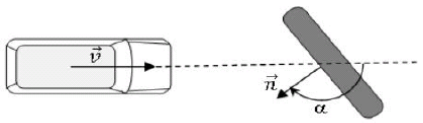

Figure 8: Collision of a vehicle with the wall.

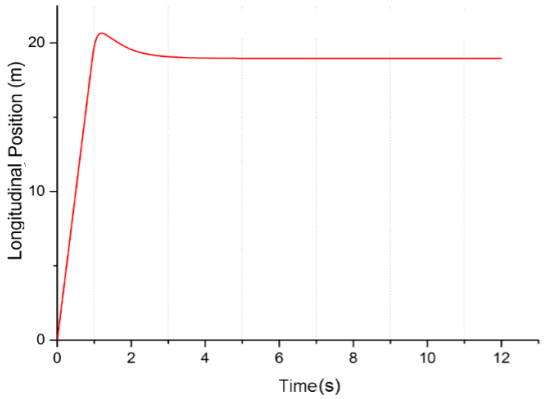

a) Longitudinal position

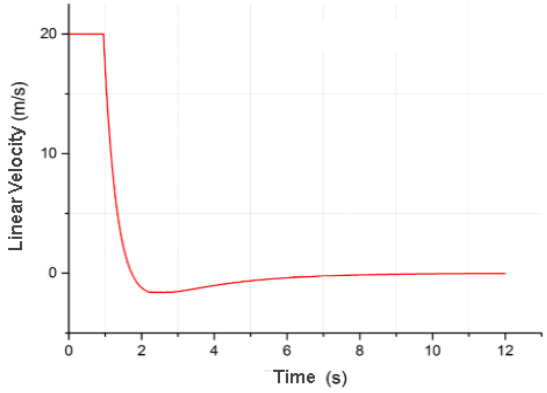

b) Linear velocity

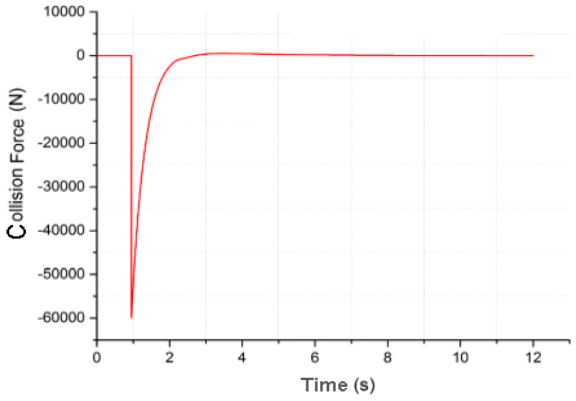

c) Collision forces

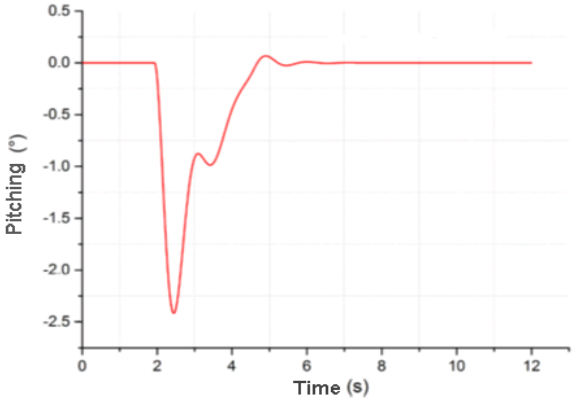

d) Pitching angle

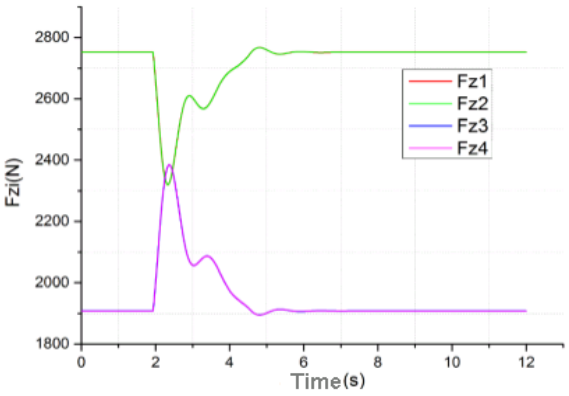

e) Vertical forces

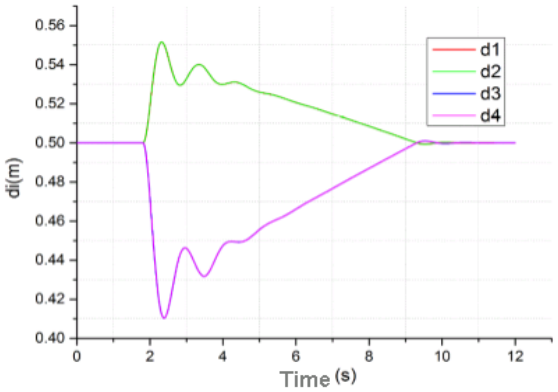

f) Elongation of springs

Figure 9**:** Results obtained of frontal collision vehicle/wall.

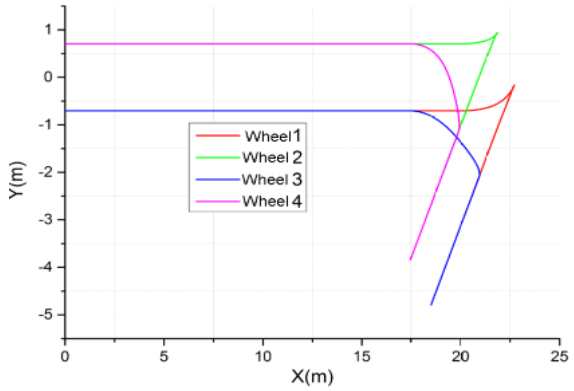

a) Vehicle trajectory

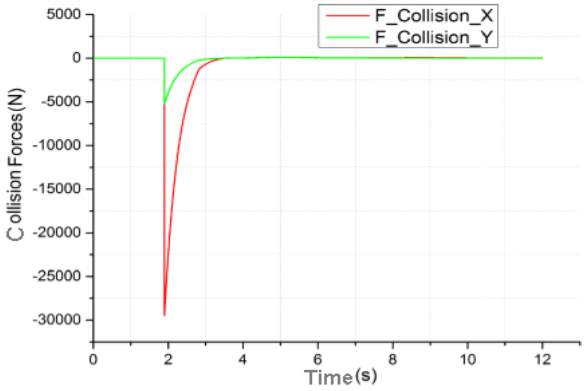

b) Collision forces

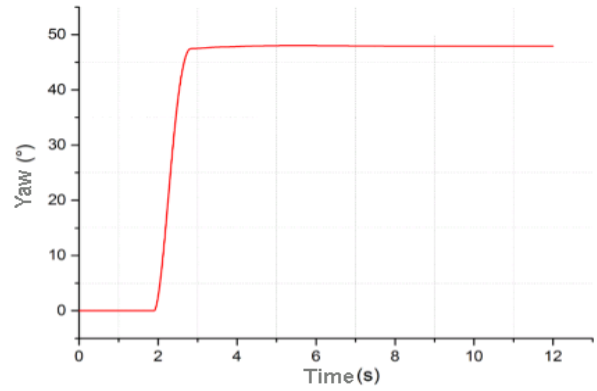

c) Yaw angle

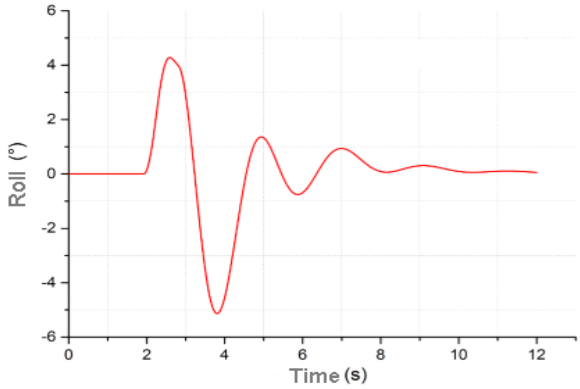

d) Roll angle

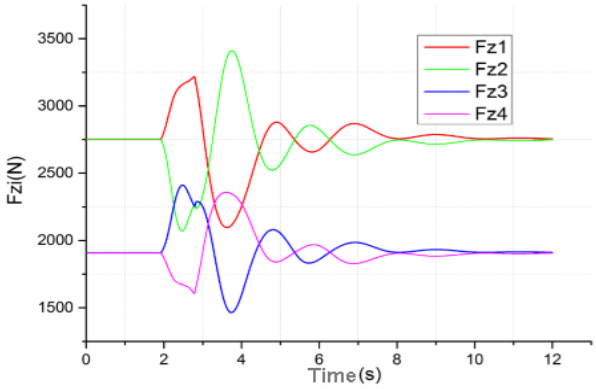

e) Vertical forces

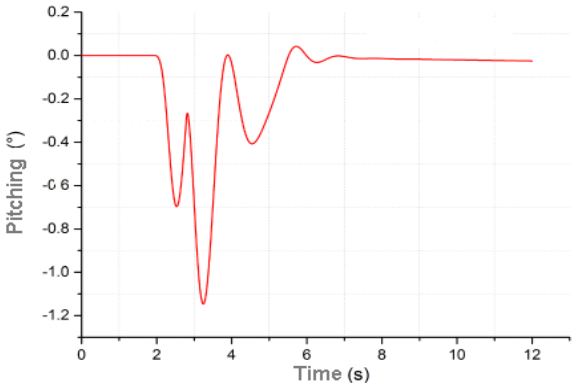

f) Pitching angle

Figure 10: Results obtained of an oblique collision vehicle/wall.

The results obtained for the first case are illustrated in Figure 9. We note, in phase collision, a sharp decrease of the robot speed (Figure b). Then after the crash phase, a movement of the vehicle to the rear until the stoppage of vehicle (Figure 9a). This frontal collision, causes an inclination of the vehicle backward (change in the negative pitch angle (Figure 9d)), which causes an increase of the vertical forces applied to the rear wheel and a decrease in those front wheels (Figure 9f).

In the second case, the vehicle changes its direction after the collision (Figure 10a) and obviously, the longitudinal component of force is higher than that of the transversal component (Figure 10b). The vehicle is moving at an angle of 50 ° with respect to the yaw axis and then stabilizes at that angle (Figure 10c), and unlike the first case, we observe a change in the roll angle due to the orientation of the wall (Figure 10d).

Before the collision, the vertical forces applied on the same axle are identical. After that, we find that the vertical forces on the right side conversely increases the left side (Figure 10f), which shows that the point of application of the collision is in the driver's side.

4.3 Validation results of the frontal collision vehicle/wall

The validation of the collision model was performed by comparison with those given experimentally Crash-test [24]. For this, we have considered a vehicle of mass m = 2000 Kg in rectilinear motion with constant velocity v = 13.42 m/s. In this validation, we considered that the collision vehicle/wall is composed of two phases:

i) A deformation phase with stiffness $K_1 = 1.243\ 10^6\ N/m^2$.

ii) A restitution phase with a stiffness $K_2 = 896.6\ 10^3\ N/m^2$.

The collision force applied by the wall on the vehicle, is defined by the following relationship:

$$F_{w/v} = \begin{cases} -\left(k_1 \cdot l_{w/v}\right) x_v & if\ \dot{l}_{w/v} > 0 \\ -k_2 \cdot \left(l_{w/v} - l_p\right) x_v & if\ \dot{l}_{w/v} \le 0 \end{cases} \quad (17)$$

With $l_{w/v}$ the penetration distance of the vehicle in the wall; l_p : Distance from permanent deformation.

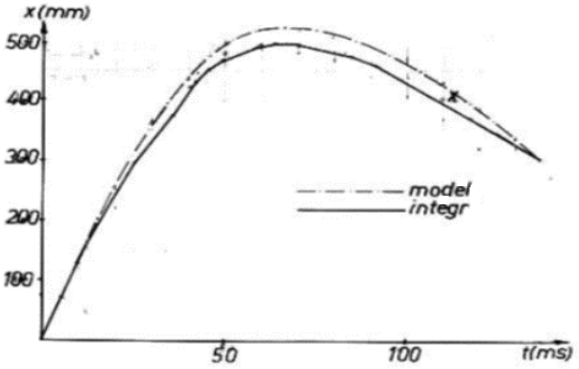

a) Penetration distance (Crash-test) **[24]**

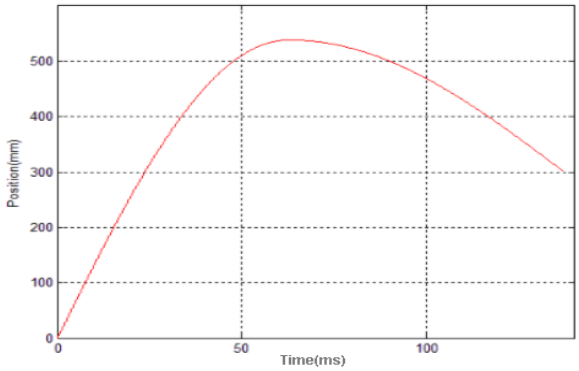

b) Penetration distance (our model)

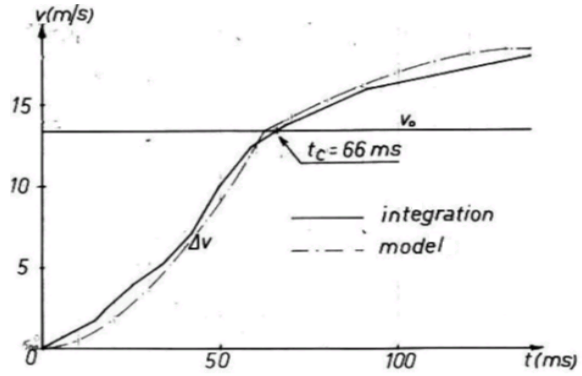

c) Penetration velocity (Crash-test) **[24]**

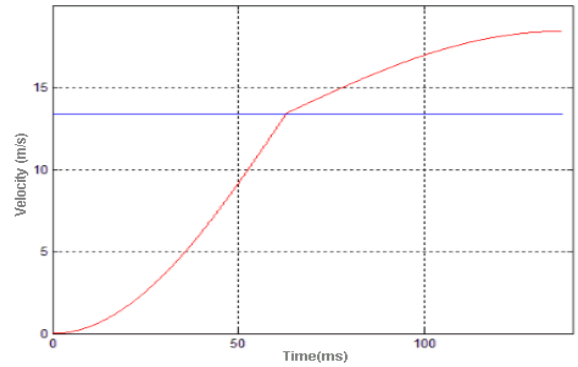

d) Penetration velocity (our model)

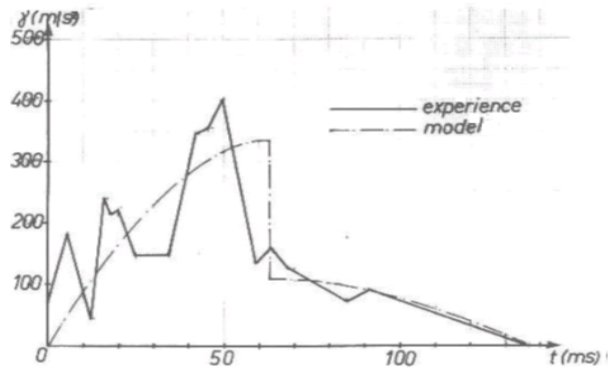

e) Penetration acceleration (Crash-test) **[24]**

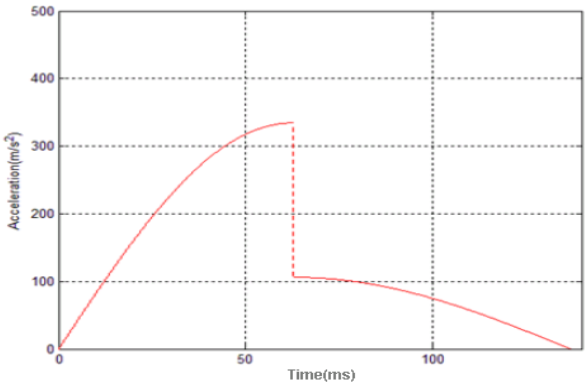

f) Penetration acceleration (our model)

Figure 11: Validation results of the collision model vehicle/wall.

Our simulation results and those given by experimental measurement Crash test are presented in Figure 11. We find, from these results, that the curves of the displacement, velocity and

acceleration of penetration are substantially the same compared with those of the experiment. We can say that the modeling of the head-on collision of a vehicle against a wall is correct.

5 CONCLUSION

In this work, we introduced the steps necessary for dynamic modeling of the vehicle. The first step relates to the mechanical system description. In this step, the vehicle is considered as a rigid body connected to the ground via the suspension system. The second step is devoted to the generation of system constraints equations to know the wheels/ground holding contact conditions and the Ackermann steering. The third step relates to the generation of the motions equations. While the final step is devoted to solving the system of differential and algebraic equations by the Euler explicit method. The validation results of the developed dynamic model was carried out by comparison with those given by the PC-Crash software. We show that the results are very satisfactory. Subsequently, we focused our study on the non-regular behavior of a vehicle during a collision with a fixed obstacle. We have proposed a method based on the evaluation of the distance to vehicle /obstacle interpenetration. The collision force is calculated, thereafter, via a penalty method. The results of this method are validated experimentally with those given by Crash-test. These results show the affinity of the developed model. Moreover, the choice of model validation was not trivial but rather conditioned by the availability of middle address the same problems.

REFERENCES

[1] C. Bardo, M. Lasry, M. Schatzman. *Bifurcation and Nonlinear Eigenvalue Problems*. 1978.

[2] J.J. Moreau, P.D. Panagiotopoulos. *Nonsmooth Mechanics and Applications*, 1988.

[3] A. Bouzar Essaidi, M. Haddad, T. Chettibi. *Dynamics of car-like robots with trailers, application to skid*. International Conference on Automatic Control, Telecomunication and Signals. Annaba, Algeria, 2015.

[4] A. Bouzar Essaidi, B. Menkouz, M. Haddad, T. Chettibi. *Dynamics of car-like robots with trailers, application to skid and jackknife*. The 4th International Conference on Electrical Engineering- ICEE'15. Boumerdes. Almgeria, 2015.

[5] A. Bouzar Essaidi and M. Haddad. *Modélisation Dynamique Des Véhicules Avec Remorque.* 22ème Congrès Français de Mécanique. Lyon, Août 2015.

[6] J. Brossad. *Dynamique des véhicules. Modélisation des systèmes complexes,* Collection des sciences appliquées de Lyon, France, 2006.

[7] B. Chazelle, D. Dobkin, N. Shouraboura, A. Tal. *Strategies for Polyhedral Surface Decomposition: An Experimental Study*, 11th Symposium on Computational Geometry, 297-305, 1995.

[8] JR. Chardonnet. *Modèle Dynamique Temps-Réel Pour l'Animation d'Objets Poly-Articulés Dans des Environnement Contraints, Prise en Compte des Contact Frottants et des Déformations Locales : Application en Robotique Humanoïde et Aux Avatars Virtuels*. Thèse, UMII, 2009.

[9] D. Dobkin, D. Kirkpatrick. *Determining the Separation of Preprocessed Polyhedra*: A Unified Approach, ICALP, p. 400-413, 1990.

[10] H. Dugoff, P.S. Fancher, L. Segel. *An Analysis of Tire Traction Properties and Their Influence on Vehicle Dynamic Performance.* SAE Transaction, vol. 3. 1219–1243, 1970.

[11] E. Gilbert, D. Johnson, S. Keerthi. *A Fast Procedure for Computing the Distance Between Complex Objects in Three-dimensional Space,* IEEE Journal of Robotics and Automation, vol. RA-4, p. 193-203, 1988.

[12] B. Heibing, M. Ersoy. *Chassis handbook. Fundamentals, Driving dynamics, Components, Mechatronics,* Perspectives,ATZ, Germany, 2011.

[13] U. Kiencke, L. Nielsen. *Automative control systems, Springer Verlag,* SAE, 2000.

[14] M. Lin, J. Canny. *A Fast Algorithm for Incremental Distance Calculation,* IEEE International Conference on Robotics and Automation, 1991.

[15] Reza N. Jazar. *Vehicle Dynamics: Theory and Applications.* School of Aerospace. Mechanical and Manufacturing Engineering.RMIT University. Austria, 2009.

[16] H.B. Pacejka, E. Bakker, L. Lidner. *A New Tire Model with an Application in Vehicle Dynamics Studies,* SAE paper 890087, 1989.

[17] H.B. Pacejka, E. Bakker. *The Magic Formula Tyre Model. Proceedings of the first International Colloquium on Tyre Models for Vehicle Dynamics Analysis,* 1-18, 1991.

[18] H.B. Pacejka. *The Tyre as a Vehicule Component*. Delft University of technology & TNO-Delft. Netherlands, 1996.

[19] H. B. Pacejka. *Tyre and Vehicle Dynamics*. Second edition, Heinemann, UK, 2006.

[20] S. Datentechnik. *A Simulation program for Vehicle Accidents, Technical Manual of PC-CRASH*, Linz, Austria, 2006.

[21] H. Steffan, A. Moser, G. Kasanický. *The Pedestrian Model in PC-Crash –The Introduction of a Multi Body System and its Validation*, International Congress and Exposition Detroit, Michigan, March 1-4, SAE 01-0445, 1999.

[22] J. Stephant, A. Charara, D. Meizel. *Contact roue-sol : comparaison de modèles d'efforts*, Journées automatique et automobile, Bordeaux, France, 2001.

[23] A. Stefan, M. Druzhinina, L. Moklegaard. *Adaptive continuously variable compression braking control for heavy-duty vehicles*. Journal of Dynamic Systems Measurement and Control, 124(3):406, 2002.

[24] P. Rapin. *La mécanique du choc*. Technical report, Conférence du C.E.S.I.A., 1966.

[25] H. Wolfgang. *User-Appropriate Tyre-Modelling for Vehicle Dynamics in Standard and Limit Situations, Vehicle System Dynamics*, Swets & Zeitlinger, Vol.38, No.2, pp.103-125, 2002.

[26] A. Yerlan. *Contrôle Global de Châssis Appliqué à la Sécurité Active des Véhicules*. Thèse, INSA de Lyon, 2011.

ECCOMAS Congress 2016
VII European Congress on Computational Methods in Applied Sciences and Engineering
M. Papadrakakis, V. Papadopoulos, G. Stefanou, V. Plevris (eds.)
Crete Island, Greece, 5–10 June 2016

TESTING, SIMULATING AND UNDERSTANDING UNDER-PLATFORM DAMPER DYNAMICS

C. Gastaldi, Muzio M. Gola

Politecnico di Torino
Corso Duca degli Abruzzi 24, Torino, Italy
e-mail: {chiara.gastaldi,muzio.gola}@polito.it

Keywords: under-platform damper, friction, damping, contact parameters

Abstract. *Underplatform dampers (UPDs) are widely used as a source of friction damping and are frequently incorporated into compressors and turbines for both aircraft and power-plant applications to mitigate the effects of resonant vibrations on fatigue failure.*
The need for reliable models of UPDs has led to a considerable amount of literature in the last three decades. The standard approach is to fine-tune and experimentally validate the UPDs models by comparing measured and calculated vibration response of blade pairs. With this approach one cannot investigate the damper behaviour directly and no measurements of the contact parameters can be undertaken. The experimental-numerical method proposed by these authors overcomes this problem through the combined use of purposely developed tools:

- *a test rig capable of measuring directly the damper working parameters (i.e. damper hysteresis cycle and kinematics);*
- *error estimates of measured and derived forces and displacements ;*
- *a numerical routine representing the damper between the platforms solved either in the time or in the frequency domain;*
- *a robust procedure for the estimation of friction and stiffness parameters at the contact from experimental data.*

These tools combined together offer concrete prospects of success in damper simulation and design. On one hand, they allow mapping the values of contact parameters under different working conditions (i.e. frequency, centrifugal load and presence/absence of damper rolling), thus ensuring valuable predictions both at the design and at the simulation stage. On the other hand the experimental-numerical method offers a clear understanding of all contact events (stick, slip, lift) which take place during the cycle, and on how they influence the damping performance. This deeper insight is the basis to actual design and optimization criteria.
Purpose of the paper is to illustrate the tools and methods through the analysis of a family of rigid bar dampers with a curved-flat cross section. A series of diagrams fit to describe the damper behaviour will be presented and used to estimate relevant friction contact parameters.

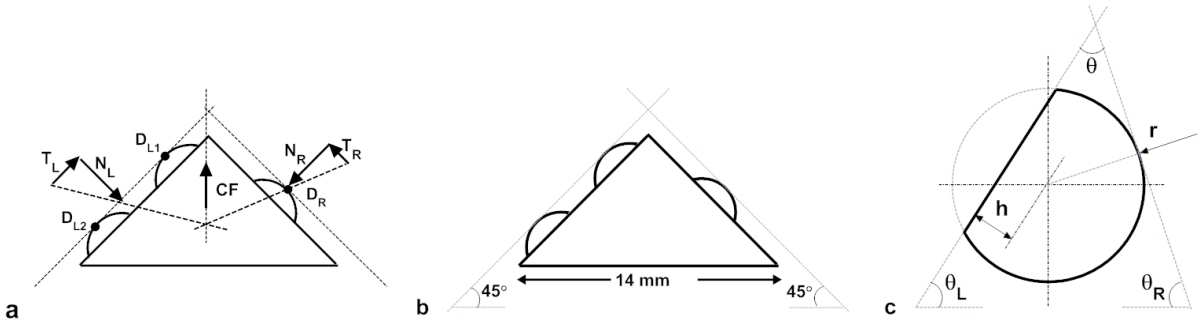

Figure 1: Laboratory three-point damper a- IP hysteresis cycle b- Tangential/Normal force ratio during the cycle c- Contact Forces Diagram

1 INTRODUCTION

The dedicated damper routine developed by the AERMEC group [1, 2, 3] combines numerical simulation with a trustworthy experimental approach for these reasons:

- experimental observations can be used as a benchmark to draw the appropriate values of contact parameters (local friction coefficients and contact stiffness) to be used as input to a numerical model which represents the dynamics of the damper between the two platforms.
- the validated routine becomes a design and optmization tool.

The outcome of the design and optimization tool are highly dependent on friction interface parameters, as demonstrated in [4]. Trustworthy predictions cannot prescind from the experimental investigation of friction interface parameters, and studies on the measurement of friction coefficients and contact stiffness values appear in the literature to this day [5].
The first part of the paper will illustrate the test rig and the numerical model applied to a three-point laboratory damper shown in Fig. 1a-b. It will be shown how experimental data can be used to understand the damper behaviour and then to estimate friction contact parameters. Moreover, it will be highlighted how the simplified configuration of the three-point laboratory damper (three equal non-conforming contacts with known positions) makes the tuning process easier.
The second part of the paper will instead focus on two real optimized curved-flat dampers, whose configurations (i.e. angles and depth of cut) were chosen following the pre-optimization technique presented in [6]. The purpose of the paper is to highlight the additional effort necessary to correctly model differenct contact interfaces (both conforming and non-conforming) and to propose a robust data-processing technique to estimate contact parameters.

2 THE TEST RIG

The experimental investigation here summarized takes advantage of a test rig (Fig.2) purposely developed at the AERMEC lab [1] representing a damper between two platforms.
The damper is loaded by a deadweight simulating the centrifugal force. The cable holes are properly oriented and pass through the damper center of mass: their sections shrink down to match the cables' diameter in correspondence of the center of mass to exactly reproduce the loading conditions encountered on a bladed disk.

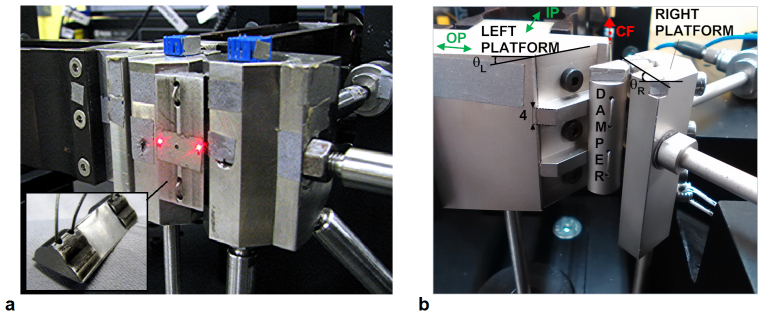

Figure 2: Experimental setup featuring a- the three point laboratory damper and b- a curved-flat damper

Table 1: Uncertainty on experimental data

Quantity	Standard deviation
Right contact force (N_R,T_R)	$3\%(0.5N)$
Left contact force (N_L,T_L)	$3-5\%(0.7-0.9N)$
Left c. force application point	0.5 mm
Platforms relative movement ($w_{LP}-w_{RP}$)	$0.08\mu m$
Rotation (β)	$5\%(0.6\cdot 10^{-4}rad)$

The left blade platform, which serves as input motion to the system, is connected to two perpendicular piezoelectric actuators. The actuators are capable of reproducing any in-plane periodic displacement, however the cases analyzed in this paper all reproduce the typical blades' In-Phase (IP) motion. The right blade platform, connected, by means of a tripod, to two force sensors measures the contact forces transmitted between the platforms, through the damper. A laser head measures the platforms' relative displacement and damper kinematics.
The forces transmitted between the platforms through the damper are measured and related to the measured relative platform movement in order to record the damper hysteresis loop (e.g shown in Fig.3).
A complete description of the test rig components, calibration procedures and the error estimation techniques can be found in [1, 7]. Table 1 lists all the measured and derived quantities together with their level of uncertainty. These results led the authors to believe that the accuracy of force and kinematic measurements offers a trustworthy basis on which to build the contact parameter estimation technique.

3 UNDERSTANDING AND SIMULATING A LABORATORY THREE-POINT DAMPER

3.1 Relevant Diagrams

The hysteresis cycle in Fig.3a plots the force (vertical componentin the I-P case) transmitted to the right platform plotted as a function of the corresponding component of the relative displacement between platforms. Reference points on the hysteresis loop have been marked by a symbol and a number, repeated on the corresponding points on other diagrams: they are useful to guide the analysis of the cycle by cross-comparison.
For each hysteresis cycle (Fig.3a) a set of experimental diagrams can be produced to investigate the damper behavior. Numerical results (dashed line) are shown together with their experimental match (solid line). The experimental results allow to validate the numerical model (by

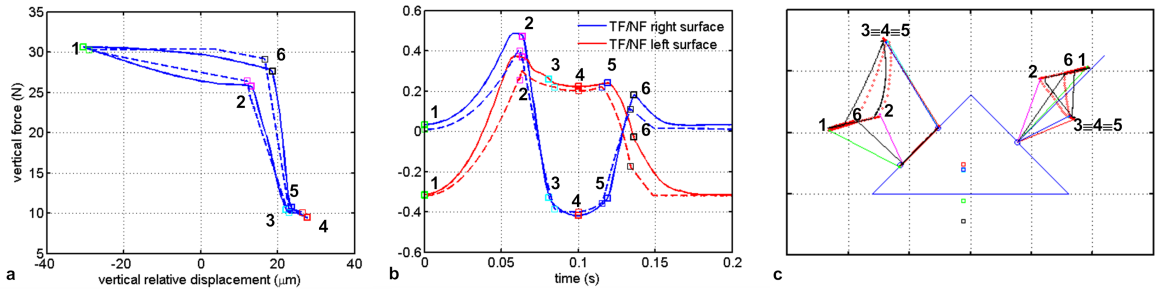

Figure 3: Laboratory three-point damper a- IP hysteresis cycle b- Tangential/Normal force ratio during the cycle c- Contact Forces Diagram

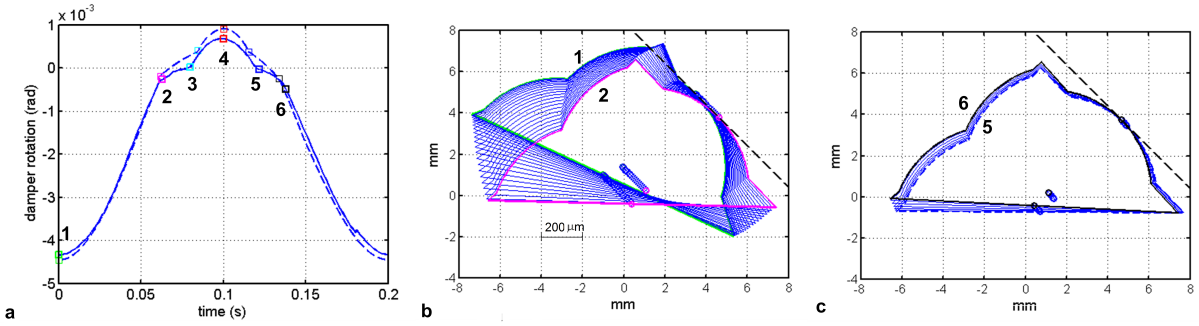

Figure 4: Laboratory three-point damper a- Rotation against time. b- Kinematic reconstruction from marker 1 to 2 . c- Kinematic reconstruction from marker 5 to 6

comparing the two sets of results) and to estimate the contact parameters used to obtain the simulated cycle. These diagrams are:

- T/N force ratios (Fig. 3b) : it represents the ratio of the total tangential and normal force components on the left and right contact surfaces plotted as a function of time. The flat portions of each line may indicate a slip phase subject to cross-confirmation by other diagrams - on an interface: in such case the ratio T/N will represent a friction coefficient.
- Contact forces diagram (Fig. 3c): it represents -) the vectors of forces transmitted between the platforms -) the damper surfaces and their points of application.
- Damper rotation (b) against time (Fig. 4a).
- Damper kinematic reconstruction (i.e. Fig. 4b-c): a visual representation of damper positions with magnified (x 100) displacements and rotation.

3.2 The damper numerical routine

The interpretation of experimental results is quite complex because it requires to relate the behaviour of forces and motions in order to assess the working mode in each part of the hysteresis cycle. A numerical model is then necessary to analyze each tract of the hysteresis cycle by precisely identifying stick or slip conditions and the related exchanged forces, as shown in

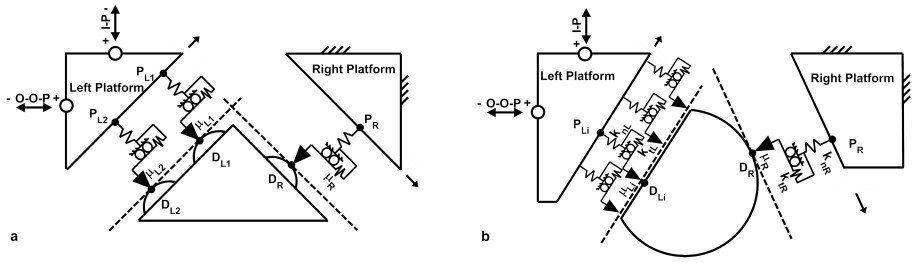

Figure 5: Damper numerical routine featuring a Laboratory damper b Curved-flat damper

Table 2: Step by step analysis of the cycle in Fig. 3-4

Stage	T_L/N_L	N_L position	D_{L1}	D_{L2}	T_R/N_R	D_R
1-2	Varying	on D_{L2}	Separation	Stick	Varying	Stick
2-3	$\approx$ Constant	b/w D_{L1} and D_{L2}	Slip_+	Slip_+	Varying	Stick
3-4	Constant	on D_{L1}	Slip_+	Separation	Constant	Slip_-
4-5	Constant	on D_{L1}	Slip_+	Separation	Varying	Stick
5-6	Varying	b/w D_{L1} and D_{L2}	Slip_+	Stick	Varying	Stick
6-1	Constant	on D_{L2}	Separation	Slip_+	Varying	Stick

Table 2. A functional scheme of the numerical model adapted to both damper configurations is shown in Fig. 5. All contact interfaces are modeled using an Iwan-type contact model which requires three contact parameters: normal and tangential contact stiffness and friction coefficient. A complete description of the damper numerical routine, which can be solved either in the time or in the frequency domain, can be found in [1] and [2].

3.3 Estimation of contact parameters

3.3.1 Friction coefficients

Friction coefficients are estimated using the T/N force ratios (Fig. 3b). The right one poses no problem since there is only one contact point on that side of the damper. The left surface is, on the other hand, the result of the combination of the two contact points. Initially $\mu_{L1} = \mu_{L2}$ is assumed, and by considering in addition another tract where only one of the left contact points is actually in contact and is slipping (e.g. stage 3-4 for μ_{L1} and stage 6-1 for μ_{L2} referring to Fig. 3b-c) μ_{L1} and μ_{L2} can be determined. The resulting values of friction coefficients are in this case : μ_{L1} = 0.22, μ_{L2} = 0.34 and $\mu_R = 0.4$.

3.3.2 Contact stiffness values

Since all contact points share the same geometry it is here assumed that they all share the same normal and tangential stiffness values k_n and k_t. The **normal contact stiffness** k_n was estimated using the normal displacement-normal force curve of a cylinder pressed against a plane[9]-[10].
The **tangential contact stiffness** was estimated using the full-stick (all contact points in contact and in stick) cycle slope of the OP hysteresis cycles (here not shown)[1]. It shold be noted that this slope is the same in all investigated cases and does not change when the platform starts closing. This due to the fact that during that stage all contact points are repeatably in the same

contact condition. The cycle slope is a composite effect of normal and tangential stiffness values at all contacts. The resulting values of contact stiffness are in this case : $k_n = 2.4N/\mu m$, $k_t = 1.6N/\mu m$.

4 LIMITS OF THE CURRENT PRACTICE ON LABORATORY UPDs INVESTIGATION

The methods developed for the three-point laboratory damper are successful in exploring and understanding its behaviour, however several shortcomings still remain to be tackled.

1. The laboratory damper here analyzed is a non-optimized configuration (i.e. large rolling motion caused by contact point lift-off minimizes the dissipated energy per cycle).

2. In order for the design tool to be effective, its simulation capabilities have to include dampers with other geometries (i.e. curved-flat damper as shown in Fig.1)

These authors have tackled point 1 in [6], by proposing a pre-optimization method for curved-flat UPDs. This method was successful in identifying and excluding those damper configurations (choice of θ_L, θ_R and h shown in Fig. 1c) leading to undesirable damper behaviour (contact point lift-off, jamming etc.).
Concerning point 2, a few successful attempts to model curved-flat UPDs have been presented by these authors [2, **?**]. However some of the assumptions made for the three-point laboratory damper are not valid for other damper geometries, for instance:

- number of contact points on the flat side;
- position of the contact points on the flat side;
- contact stiffness values of the flat side are potentially different from those representing the cylindrical contact point.

These differences make the tuning procedure described in 3.3 not completely suitable when estimating contact parameters relative to the curved-flat dampers-platforms interface. The purpose of this paper is to overcome these shortcomings by proposing a new method with a solid experimental basis and a fine data processing technique.

5 EXPLORING CURVED-FLAT DAMPERS

5.1 Selected configurations

As mentioned before the selected damper configurations are the result of a pre-optimization process which aims at maximizing the dissipated energy [6]. The parameters which influence the damper behaviour are (see Fig.1):

- the non-dimensional "residual radius" h/r;
- the angles of the platforms θ_R and θ_L.
- the value of the friction coefficients μ_R and μ_L;

The selected damper configurations are:

- A: $\theta_L = 55^0$, $\theta_R = 65^0$, $h/2 = 0.2$

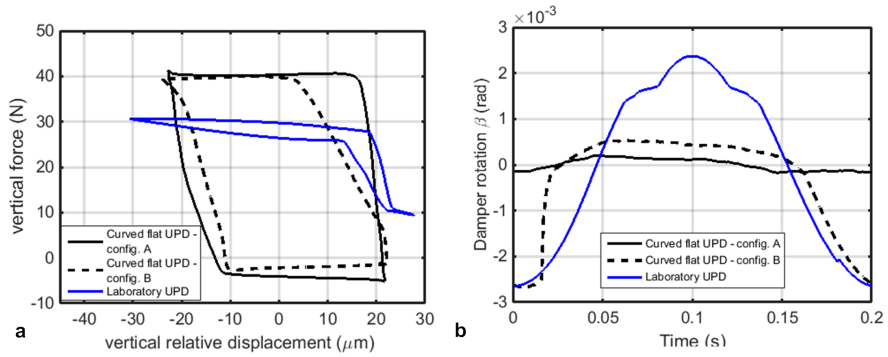

Figure 6: a Hysteresis cycles and b Damper rotation signals for an applied centrifugal load of $CF = 4.65kg$ and a 5 Hz $\pm 30\mu m$ IP imposed displacement

- B: $\theta_L = 35^0$, $\theta_R = 65^0$, $h/2 = 0.2$

While h/r,θ_L and θ_R are parameters the designer can act upon, friction coefficients are unknown constraints measured a-posteriori.
Figure 6 shows the hysteresis cycles and the rotation signals for the two curved-flat damper configurations and for the above mentioned laboratory damper. The boundary conditions imposed to the dampers (i.e. centrifugal load, imposed displacement and frequency) are the same for all three cases. The results shown here were produced by a 5 Hz excitation because the signals are cleaner and easier to manipulate. However, it should be noted that contact stiffness values did not change for all investigated frequencies (i.e. up to 160 Hz).
Severe differences are noted among the three configurations:

- **force levels**: the curved-flat damper which display a set of friction coefficients ($\mu_R = 0.65$, $\mu_L = 0.5$) and ($\mu_R = 0.78$, $\mu_L = 0.5$) for configurations A and B respectively, ensure slip force levels higher than those encountered for the laboratory damper ($\mu_R = 0.4$, $\mu_L \approx 0.3$).

- Configuration A (i.e. choice of angles and parameter h/r) manages to avoid lift-off completely, as shown by the rotation signal in Fig. 6, and thus to maximize the dissipated energy.

- Configuration B does encouter some lift-off and therefore a larger rotation, it is however a significant improvement if compared to the laboratory damper.

6 CONTACT PARAMETERS ESTIMATION FOR CURVED-FLAT DAMPERS

Both the pre-optimization technique presented in [6] and the damper numerical routine itself need a robust model of contact interfaces. The purpose of this section is to present the new configuration introduced in the numerical routine to model a curved-flat damper and the new experimental capabilities developed at AERMEC to estimate the relevant contact parameters.
This section will focus on the contact point position and on the contact stiffness values. The technique to estimate friction coefficients developed for the three-point laboratory damper can be applied without further modifications to any other damper configuration.

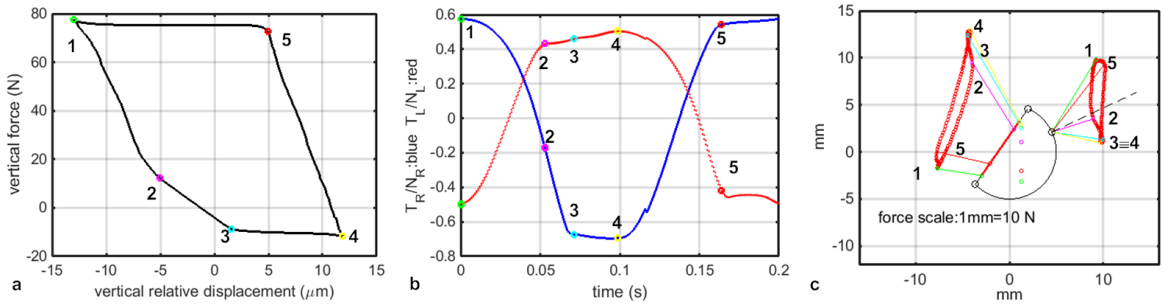

Figure 7: Curved-flat damper a- IP hysteresis cycle b- Tangential/Normal force ratio during the cycle c- Contact Forces Diagram

6.1 Contact points number and position

While the number and position of contact points used to model the laboratory UPD (see Fig. 5a) was determined by the damper configuration itself, while the flat portion of the curved-flat damper requires additional attention. A few successful attempts to model a curved-flat UPD using only two contact points on the left side have been carried out in the past [2]. However, without additional experimental evidence the system is under-determined and selecting the position of the contact points and the contact stiffness values requires a cumbersome case-by-case fine-tuning procedure. Section 6.1.2 proposes a novel method to estimate the normal contact stiffness per unit length. Therefore it is sensible to envision a series of contact points uniformly distributed over the contact interface, the higher the number of contact points, the finer the representation of the interface.

6.1.1 Contact stiffness values

As mentioned before the contact stiffness tuning technique developed for the laboratory damper is not valid anymore. While the normal contact stiffness on the right (i.e. cylindrical) side can still be deduced using the normal displacement-normal force curve of a cylinder pressed against a plane[9]-[10], the remaining unknowns (k_{tL}, k_{tR} and k_{nL}) need additional information which can only be provided by a robust experimental basis.

6.1.2 Normal contact stiffness at the flat interface

Referring to Fig. 8 it is possible to write the expression of the rotation β at a given instant in time as:

$$\beta = \frac{n(x)}{x - (\frac{L}{2} - 3a)} \tag{1}$$

where $n(x)$ is the displacement in the normal direction at a given position x of the flat interface. The reference system x is parallel to the contact and its origin lies in the middle of the flat interface. Let us divide the flat interface into k segments each Δx long. If the normal stiffness is uniformly distributed the normal stiffness pertaining to one of these segments is:

$$k_{ni} = \frac{dk_{nL}}{dx} \cdot \Delta x \qquad 1 \leq i \leq k \tag{2}$$

If the force per unit length q(x) is known, e.g. $q(x) = \frac{q_{max}}{3a} \cdot (x - (\frac{L}{2} - 3a))$, it is possible to substitute the expression of $n(x)$ inside Eq. 1.

$$\beta = \frac{q(x) \cdot \Delta x}{\frac{dk_{nL}}{dx} \Delta x \cdot (x - (\frac{L}{2} - 3a))} \tag{3}$$

where a represents the distance between N_L application point and the nearest flat surface edge, as shown in Fig. 8b. If the force is uniformly distributed $q(x)$ will act on a portion of flat surface 3a long.
It is possible to express $q(x)$ as a function of the moment M produced by the resultant N_L around the origin shown in Fig. 8a.

$$\begin{aligned} M &= \int_{\frac{L}{2}-3a}^{\frac{L}{2}} \frac{q_{max}}{3a}(x - (\frac{L}{2} - 3a)) \cdot x \cdot dx \\ &= \frac{3}{2} q_{max} \cdot a \cdot (\frac{L}{2} - a) \end{aligned} \tag{4}$$

Substituting Equ. 4 in Equ. 3, it is possible to express $\frac{dk_{nL}}{dx}$ as:

$$\frac{dk_{nL}}{dx} = \frac{q(x)}{\beta} \tag{5}$$

$$= \frac{2M}{9a^2 \cdot (\frac{L}{2} - a)} \tag{6}$$

Figure 8c plots $2 \cdot M$ against $9a^2 \cdot (\frac{L}{2} - a)$ for the case shown in Fig. 7. The slope highlighted in the figure is the normal contact stiffness per unit length. The shape is slightly distorted:

- for low values of rotation/moment: this is due to the fact that the assumption made in Equ. 3 (i.e. that rotation and moment signals in time are synchronous) is not perfectly true due to minor distorsions caused by spurious movements of the left platform;
- close to markers 1/5: during those stages the left contact force resultant N_L application point is close to the lower edge, a situation similar to lift-off where the length of $a- > 0$.

The resulting values of $\frac{dk_{nL}}{dx}$ for both configurations of curved-flat UPDs are reported in Table 6.1.2. The results have been repeated on both tracts (i.e. ascending and descending) of the shape in Fig. 8c and repeated using repeated independent measurements.

6.1.3 Tangential Contact Stiffness values

The tangential contact stiffness values are derived directly from experimental data. The available laser heads are pointed on damper and platform protrusions purposely machined to be perpendicular to the contact surfaces, as shown in Fig. 9a.
The laser signal is then plotted against the corresponding tangential force (T_R or T_L respectively), as shown in Fig. 9 b and c for the curved-flat damper (configuration A). It should be noted that the tangential force on the cylindrical side T_R is measured using the load cells, while the tangential force resultant on the flat side T_L is reconstructed using the procedure described

Table 3: Flat interface normal contact stiffness per unit length

Damper configuration	Centrifugal Load	Repetition	$\frac{dk_{nL}}{dx}$ (N/mm^2)	$\sigma(N/mm^2)$
A	4.65 kg	1	18900	1387
A	4.65 kg	2	19004	1831
A	8.65 kg	1	18054	847
A	8.65 kg	2	19393	669
B	4.65 kg	1	1334	362
B	4.65 kg	2	1231	79
B	8.65 kg	1	6412	558
B	8.65 kg	2	6586	581

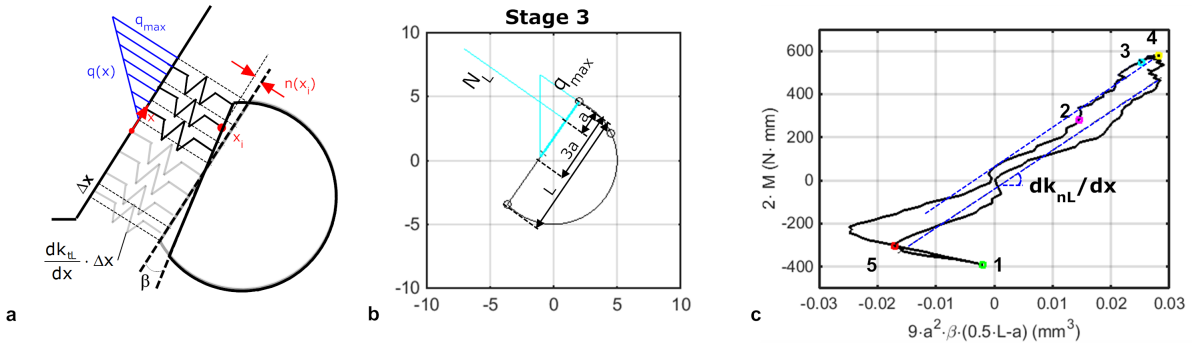

Figure 8: a- Scheme representing the flat surface model. b- Force component N_L and corresponding force per unit-length on the flat surface at marker 3 for the cycle in Fig. 7a. c- Flat interface normal contact stiffness per unit length relative to the cycle shown in Fig. 7.

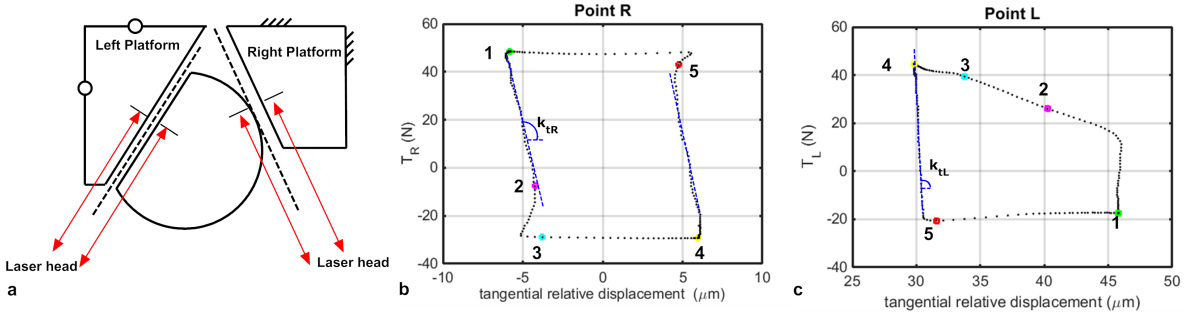

Figure 9: a- Functional scheme representing the experimental procedure used to estimate the tangential contact stiffness values b- Hysteresis at the right contact c- Hysteresis at the left interface

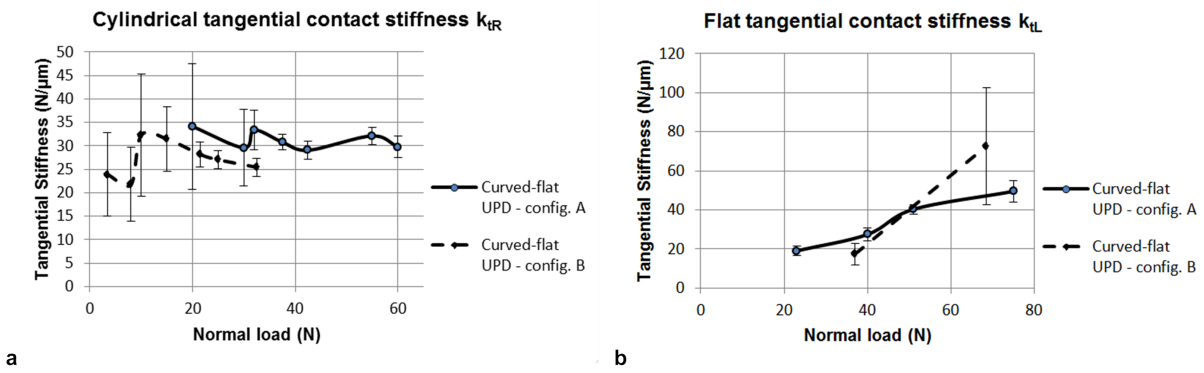

Figure 10: Curved-flat damper a- IP hysteresis cycle b- Tangential/Normal force ratio during the cycle c- Contact Forces Diagram

in Fig.1a.

For each contact interface the stages corresponding to a stick state are identified using the Tangential/Normal force ratio diagram (i.e. in Fig. 7b). The stages are "1-3" and "4-5" for the right interface and "1-2" and "4-5" for the left one. Out of these tracts only those highlighted in Fig. 9 b-c are used to estimate the tangential stiffness values. In particulare stage $2-3$ for the right interface and stage "1-2" for the left one are neglected due to spurious platforms' movements.
For each identified tract the central portion of the slope is singled out and fitted using a least square method. The resulting values are plotted against their respective normal load levels at the interface (see Fig. 10) , together with their standard deviation.
It should be noted how the right tangential stiffness (i.e. on the cylindrical side) is not influenced by variations of the normal load, while the one on the flat side increases with increasing normal load. This may be due to the conforming nature of the flat contact interface.

7 CONCLUSIONS

This paper focuses on a coupled experimental-numerical approach to investigate, simulate and understand under-platform dampers behaviour. The paper highilights the strengths of this method, but also its limits concerning the estimation of friction contact parameters, with a particular emphasis on contact stiffness values.
A novel procedure and data processing technique is therefore proposed to overcome these limits and give reliable indications to the damper designer concerning the values of contact parameters to be used as input to the damper numerical routine. A sample of results is discussed in order to show, in practice, the technique to estimate the contact parameters (tangential stiffness on the cylindrical side and both tangential and normal contact stiffness on the flat interface) starting from the experimental results. Each measured quantity is assigned a level of uncertainty and the data processing technique gives an indication of the reliability of each derived quantity. These authors believe that this work constitutes a reliable basis to build a design tool (i.e. validated damper numerical routine) capable of giving trustworthy predictions in the frame of asymmetrical damper design and optimization.

REFERENCES

[1] Gola, M. M., Liu, T. A direct experimental-numerical method for investigations of a laboratory under-platform damper behavior. *International Journal of Solids and Structures*, **51(25-26)**, pp. 4245-4259, 2014.

[2] Gastaldi, C., Gola, M. M., Understanding Complexities in Underplatform Damper Mechanics. *In Proc. ASME Turbo Expo 2014*, **GT2014-25240**, 2014.

[3] Gastaldi, C., Gola, M. M., A Random Sampling Strategy for Tuning Contact Parameters of Underplatform Dampers. *In Proc. ASME Turbo Expo 2015*, **GT2015-42834**, 2015.

[4] Schwingshackl, C.W., Petrov, E.P., and Ewins, D.J., Effects of Contact Interface Parameters on Vibration of Turbine Bladed Disks With Underplatform Dampers. *Journal of Engineering for Gas Turbines and Power*, **134**(3), 2012.

[5] Schwingshackl, C.W., Petrov, E.P., and Ewins, D.J., Measured and estimated friction interface parameters in a nonlinear dynamic analysis. *Mechanical Systems and Signal Processing*, **28**, pp.574-584.

[6] Gastaldi, C., Gola, M. M., Pre-optimization of Asymmetrical Underplatform Dampers. *Accepted at ASME Turbo Expo 2016*, **GT2016-57359**, 2016.

[7] Gola, M. M., Bragas Dos Santos, M., Liu, T., 2012. Measurement of the scatter of underplatform damper hysteresis cycle: experimental approach. *In Proc. of ASME IDET*, **DETC2012-70269**, pp. 359-369.

[8] Gola, M. M., Liu, T., M. Bragas Dos Santos M., Investigation of under-platform damper kinematics and its interaction with contact parameters (nominal friction coefficient)". *In Proc. of World Tribology Congress*, 2013.

[9] T.Harris, Rolling Bearing Analysis, *3rd Edition, John Wiley and Sons*, 1991.

[10] Brändlein J., Ball and Roller Bearings : Theory, Design, and Application, *John Wiley and Sons*, 1999.

[11] Gola, M. M., Gastaldi, C., An improved Microslip Model for variable normal Loads, *In Proc. of 9th IFToMM International Conference on Rotor Dynamics*, IFToMM ICORD 2014.

ECCOMAS Congress 2016
VII European Congress on Computational Methods in Applied Sciences and Engineering
M. Papadrakakis, V. Papadopoulos, G. Stefanou, V. Plevris (eds.)
Crete Island, Greece, 5–10 June 2016

A NEW DYNAMIC SUBSTRUCTURING METHOD FOR NONLINEAR AND DISSIPATIVE SYSTEMS

Colas Joannin[1,2], **Benjamin Chouvion**[2], **and Fabrice Thouverez**[2]

[1]Turbomeca, Safran group
Avenue Joseph Szydlowski, 64510 Bordes, France
e-mail: colas.joannin@doctorant.ec-lyon.fr

[2] Laboratoire de Tribologie et Dynamique des Systèmes, École Centrale de Lyon
36 avenue Guy de Collongue, 69134 Écully, France
e-mail: {benjamin.chouvion,fabrice.thouverez}@ec-lyon.fr

Keywords: Reduced-Order Model, Nonlinear Mode, Component Mode Synthesis, Mistuning.

Abstract. *This work is devoted to the development of a new dynamic substructuring method inspired by classic fixed-interface component mode synthesis, in order to compute the steady-state vibrations of dissipative, nonlinear structures. For each substructure, the displacement field is sought as a multiharmonic oscillation made of standard static mode shapes, supplemented by the eigenvectors of the nonlinear complex modes of the substructure computed with fixed-boundary conditions. The method eventually leads to a strongly reduced nonlinear algebraic system, easily solved by iterative solvers. The procedure is tested on a lumped parameter model of bladed disk subjected to dry friction nonlinearities, with or without structural mistuning, and proves very efficient in terms of computational cost. These results emphasize the promising capabilities of this new reduced-order modeling technique to tackle such nonlinear systems exhibiting high modal density.*

1 INTRODUCTION

Reduced-order modeling has always been a key problematic in computational mechanics. Despite the soaring hardware and software capabilities offered by modern electronics and computing, finite element analysis of large scale industrial systems remains challenging when some complex and nonlinear phenomena are to be included in the design process. Component mode synthesis (CMS) methods [1, 2, 3, 4] have been widely used in structural dynamics, but can unfortunately prove ill-suited to the study of nonlinear systems when a large number of degrees-of-freedom (DOF) are impacted by strong nonlinear effects. For such systems, standard techniques may indeed fail to find a satisfying compromise between order-reduction and accuracy, due to the lack of representativity of the reduction basis. From this perspective, owing to their ability to capture the essence of the nonlinearities [5, 6], nonlinear complex modes are interesting candidates in devising new effective and efficient approaches to reduce nonlinear models.

In bladed-disk dynamics, the loss of cyclic symmetry of the structures, referred to as mistuning, has been a leading subject of research, first tackled by a few authors in the 1960s [7, 8, 9, 10] and widely studied since then [11]. This phenomenon mainly denotes the discrepancies between the blades of the assembly, resulting for instance from the manufacturing process and in-operation wear, but which can also be intentionally introduced in the nominal design. Even though the mistuning of cyclic structures is known to potentially induce a significant increase in the vibration level, it has also proved, indeed, to improve the robustness of the design against hazardous instabilities such as flutter. In order to perform quantitative analyses on industrial models, several mistuning dedicated reduced-order modeling techniques have been devised to efficiently handle large scale systems [12, 13, 14, 15]. Unfortunately, most of them are not applicable in the presence of nonlinearities, hence the need for further endeavours devoted to the reduced-order modeling of nonlinear, mistuned cyclic structures.

In the present paper, a new approach is proposed to build reduced-order models of nonlinear and dissipative systems. The method does not require any cyclic or nearly-cyclic symmetry assumption, and can thus be directly applied to the study of strongly mistuned bladed-disks. The procedure mimics a standard Craig-Bampton CMS, but makes use of the notion of nonlinear complex modes to build nonlinear superelements, including all internal nonlinear DOFs in the reduction basis. The resulting algebraic system can thus be much smaller than that of a standard harmonic balance method (HBM), which requires to retain all nonlinear DOFs as master coordinates. The flexibility of nonlinear complex modes [5, 6, 16] makes this reduction technique suitable for the study of a broad range of nonlinearities, dissipative and non-smooth ones included.

In Section 2, the main steps of the computation of nonlinear complex modes are first reminded, and the nonlinear superelement equations are derived. A lumped-parameter model of bladed-disk exhibiting dry friction nonlinear elements is then used in Section 3 to illustrate the capability of this new technique. First, the method is tested on a tuned system, and is then used to synthesise the response after application of a random mistuning pattern. Section 4 presents the performance of the procedure, and its potential limitations.

2 NONLINEAR COMPONENT MODE SYNTHESIS

This section aims at summarizing the main steps to build a nonlinear superelement. The computation of nonlinear complex modes is briefly reminded in Section 2.1, and the notion is illustrated on a basic 2-DOFs system. In Section 2.2, the system of equations defining a nonlinear superelement are then derived. As mentioned in the introduction, this new reduced-order modeling procedure shares some similarities with classic CMS methods, and is hereafter referred to as CNCMS, for component nonlinear complex mode synthesis.

2.1 Nonlinear complex modes

The concept of nonlinear mode is nowadays well established in the community of nonlinear dynamicists. A comprehensive review listing all major contributions and techniques applicable to structural dynamics is proposed in [17]. Nonlinear complex modes are an extension of nonlinear normal modes to dissipative systems, that aims at taking advantage of numerical and frequency-based formulation such as the harmonic balance method to compute the free vibrations of damped nonlinear structures. First introduced in [5], they have proved tremendously interesting to study all sorts of nonlinear systems [6, 16, 18], and are fundamentals to the reduced-order modeling technique presented here. Only a brief reminder is provided here to introduce some notations, but more details can be found in [5, 6, 16, 18].

Nonlinear complex modes refer to pure or pseudo-oscillations of the system of nonlinear differential equations (1). The terms are defined in a classic manner, with $\mathbf{M}$ the mass matrix, $\mathbf{C}$ the viscous damping matrix, $\mathbf{K}$ the linear stiffness matrix, and $\mathbf{f}_{nl}$ a term of nonlinear restoring and dissipative forces.

$$\mathbf{M}\ddot{\mathbf{x}}(t) + \mathbf{C}\dot{\mathbf{x}}(t) + \mathbf{K}\mathbf{x}(t) + \mathbf{f}_{nl}(\mathbf{x}, \dot{\mathbf{x}}) = \mathbf{0} \tag{1}$$

The n-th mode $\mathbf{x}_n$ is approximated by a truncated series of damped oscillations of fundamental frequency ω_n and modal damping β_n, such that with $\lambda_n = -\beta_n + i\omega_n$ and $c.c.$ referring to the complex conjugate terms,

$$\mathbf{x}_n(t) = \frac{1}{2}\left\{\sum_{k=1}^{n_h} \hat{\mathbf{x}}_{n,k} e^{kt\lambda_n} + c.c.\right\} \tag{2}$$

Similarly to standard Galerkin methods, the approximation (2) is then substituted into the governing equations (1), and the orthogonality of the residual to the subspace spanned by the functions $\{e_k = e^{ikt\omega_n}\}$, $\forall k \in [\![1, n_h]\!]$, is enforced, with respect to the inner product (3) where $\overline{g(t)}$ is the complex conjugate of $g(t)$. In order to take advantage of the orthogonality property of the complex exponential functions, the solution is assumed to be undamped over the period T used in the inner product, which has proved to have a negligible effects on the accuracy of the results (see [5] for further information).

$$\langle f|g\rangle = \frac{2}{T}\int_0^T f(t)\overline{g(t)}dt \text{ , with } T = \frac{2\pi}{\omega_n} \tag{3}$$

The resulting algebraic system (4) is the eigenproblem corresponding to the nonlinear complex mode $\mathbf{x}_n$, where the term $\langle \mathbf{f}_{nl}|e_k\rangle$ potentially couples all the equations. This system is underdetermined and must be supplemented with two equations, classically in the form of a

phase condition and a continuation scheme, which are not detailed here. The interested reader is referred to [18] for further information.

$$\begin{aligned} &\forall k \in [\![1, n_h]\!] : \\ &\left[(k\lambda_n)^2\mathbf{M} + (k\lambda_n)\mathbf{C} + \mathbf{K}\right] \hat{\mathbf{x}}_{n,k} + \langle \mathbf{f}_{nl} | e_k \rangle = \mathbf{0} \end{aligned} \tag{4}$$

The flexibility of nonlinear complex modes arises, among other things, from their applicability to a broad range of nonlinearities, including non-smooth forces. This is made possible and easy to implement by means of the alternating frequency-time scheme (AFT) proposed in [19], and widely used in conjunction with harmonic balance methods [5, 16, 18]. This procedure uses direct ($\mathcal{F}$) and inverse ($\mathcal{F}^{-1}$) Fourier transforms to compute $\langle \mathbf{f}_{nl} | e_k \rangle$ from the time-domain definition of the nonlinear terms.

To exemplify nonlinear complex modes, let us now consider the academic system on Figure 1 subjected to a dry friction force, with the lumped-parameters taking their values in Table 1. Figure 2 shows the variations of the first natural frequency and corresponding modal damping as a function of the displacement amplitude $|x_1|$. These so-called backbones are thoroughly explained in previous papers [5, 6, 18] and will not be discussed here. However, it should be remembered in the following sections that nonlinear complex modes are functions of a parameter describing the intensity of the nonlinear effects, here the amplitude of vibration $|x_1|$, and that the modes of friction-damped systems exhibit an optimum damping point, corresponding to a maximum dissipation arising from the nonlinearity.

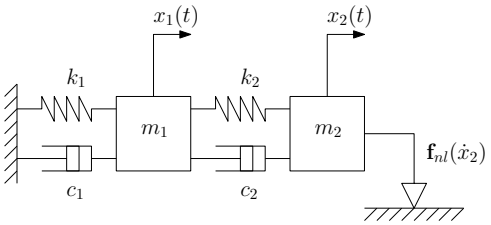

Figure 1: 2-DOFs dry-friction damped model

– (unit)	m (kg)	c (Ns/m)	k (N/m)
DOF1	1	0.5	640
DOF2	0.02	0.5	40

Table 1: Values of the lumped-parameters for the 2-DOFs system

2.2 Nonlinear superelement

This section is dedicated to the derivation of the equations governing one superelement, built by means of nonlinear complex modes. Each substructure being treated indepedently, the nonlinear superelement could be perfectly used in conjunction with standard CMS superelements

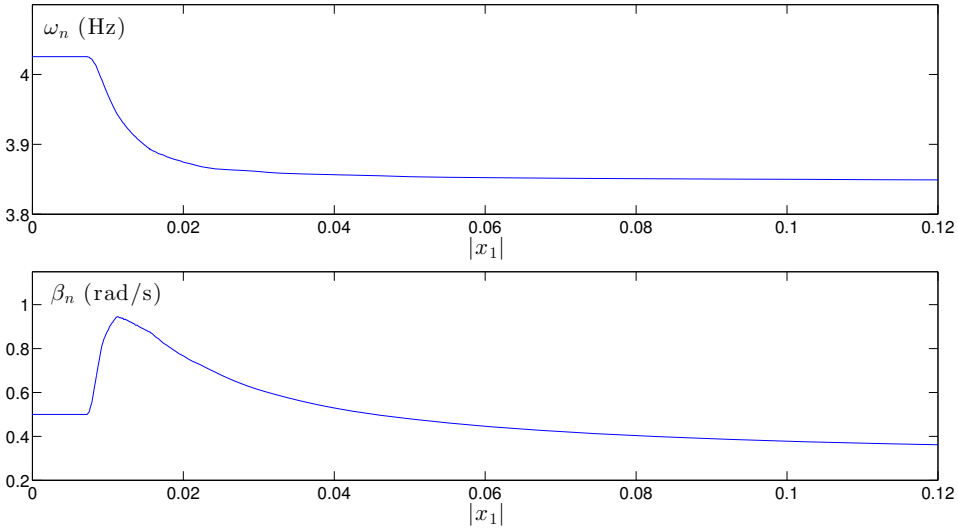

Figure 2: Nonlinear natural frequency and modal damping of the 2-DOFs model

using linear modes. This reduced-order model is devoted to the study of forced vibrations arising from harmonic or multi-harmonic excitations, of the form given in Eq. (5) where Ω is the fundamental forcing frequency.

$$\mathbf{f}_e(t) = \frac{1}{2}\left(\sum_k \langle \mathbf{f}_e | e_k \rangle e^{ik\Omega t} + c.c.\right) \tag{5}$$

The displacement of the substructure is sought as a multi-harmonic oscillation (6) made of nonlinear eigenvectors $\boldsymbol{\varphi}_{n,k}$ corresponding to fixed-interface nonlinear complex modes, supplemented by linear static modes $\boldsymbol{\psi}_{s,k}$ as in a standard fixed-interface CMS [1]. The generalized coordinates q_n and p_s corresponding to the nonlinear complex modes and static modes, respectively, are the new unknowns of the problem.

$$\mathbf{x}(t) = \frac{1}{2}\left(\sum_n q_n \sum_k \boldsymbol{\varphi}_{n,k}(|q_n|)e^{ik\Omega t} + \sum_s p_s \sum_k \boldsymbol{\psi}_{s,k} e^{ik\Omega t} + c.c.\right) \tag{6}$$

The relation between the nonlinear eigenvectors $\boldsymbol{\varphi}_{n,k}$ and the k-th harmonics $\hat{\mathbf{x}}_{n,k}$ in Eq. (2) is given by Eq. (7).

$$\hat{\mathbf{x}}_{n,k} = q_n \boldsymbol{\varphi}_{n,k} \tag{7}$$

In the following, the vectors $\boldsymbol{\psi}_{s,k}$ are all taken equal to the standard static modeshapes of a Craig-Bampton CMS, given by Eq. (8) when the DOFs are partitionned into a set of internal (subscript i) and boundary (subscript b) DOFs, although different vectors could be used.

$$\begin{aligned} &\forall k \in [\![1, n_h]\!] : \\ &\boldsymbol{\psi}_{s,k} = -\mathbf{K}_{ii}^{-1}\mathbf{K}_{ib} \quad \text{with} \quad \mathbf{K} = \begin{bmatrix} \mathbf{K}_{ii} & \mathbf{K}_{ib} \\ \mathbf{K}_{bi} & \mathbf{K}_{bb} \end{bmatrix} \end{aligned} \tag{8}$$

As mentioned in Section 2.1 for the 2-DOFs model, the modal parameters $\boldsymbol{\varphi}_{n,k}$ and λ_n are functions of a parameter describing the activation of the nonlinearity. In Eq. (6), this parameter is the amplitude $|q_n|$ of the coordinate of the corresponding mode. In theory, since the mode is complex, two variables should be used to describe its variations (*i.e.* the real and imaginary parts of q_n), but it was shown in [5] that chosing only the amplitude $|q_n|$ yields excellent results for dry-friction nonlinearities. In the following equations, the dependency of $\boldsymbol{\varphi}_{n,k}$ and λ_n on $|q_n|$ is implied.

In accordance with Galerkin methods, the approximation (6) is substituted into Eq. (1), after addition of the external forcing $\mathbf{f}_e$ from Eq. (5) on the right hand side, and the residual is orthogonalized to the subspace spanned by the functions $\{e_k = \mathrm{e}^{ik\Omega t}\}$ with respect to the inner product (3). The operation yields,

$$\begin{aligned} &\forall k \in [\![1, n_h]\!] : \\ &\left[(ik\Omega)^2\mathbf{M} + (ik\Omega)\mathbf{C} + \mathbf{K}\right] \left\{ \sum_n q_n \boldsymbol{\varphi}_{n,k} + \sum_s p_s \boldsymbol{\psi}_{s,k} \right\} + \langle \mathbf{f}_{nl} | e_k \rangle = \langle \mathbf{f}_e | e_k \rangle \end{aligned} \tag{9}$$

As performed in [6] in a modal synthesis procedure, the term $\langle \mathbf{f}_{nl} | e_k \rangle$ is replaced by the sum of the analogous vectors in the eigenproblem (4), which yields the set of equations (10), where the second line accounts now for $\langle \mathbf{f}_{nl} | e_k \rangle$. The matrix $\tilde{\mathbf{K}}$ differs from the matrix $\mathbf{K}$ owing to the fixed boundary conditions enforced during the computation of the modes.

$$\begin{aligned} &\forall k \in [\![1, n_h]\!] : \\ &\sum_n \left[(ik\Omega)^2\mathbf{M} + (ik\Omega)\mathbf{C} + \mathbf{K}\right] q_n \boldsymbol{\varphi}_{n,k} \\ -&\sum_n \left[(k\lambda_n)^2\mathbf{M} + (k\lambda_n)\mathbf{C} + \tilde{\mathbf{K}}\right] q_n \boldsymbol{\varphi}_{n,k} \\ +&\sum_s \left[(ik\Omega)^2\mathbf{M} + (ik\Omega)\mathbf{C} + \mathbf{K}\right] p_s \boldsymbol{\psi}_{s,k} \\ -&\langle \mathbf{f}_e | e_k \rangle \approx \mathbf{0} \end{aligned} \tag{10}$$

Finally, the residuals (10) are orthogonalized to the subspace spanned by the basis vectors $\boldsymbol{\varphi}_{n,k}$ and $\boldsymbol{\psi}_{s,k}$ with respect to the classic Hermitian form in $\mathbb{C}^n$. The whole process leads to the set of algebraic equations (11) governing the motion of a substructure, where $\bullet^\dagger$ refers to the Hermitian transpose.

$$\begin{aligned} &\forall k \in [\![1, n_h]\!] : \\ &\boldsymbol{\rho}_k = \begin{bmatrix} \boldsymbol{\Phi}_{n,k}^\dagger \left(\mathbf{Z}_k \boldsymbol{\Phi}_{n,k} - \boldsymbol{\xi}_k\right) & \boldsymbol{\Phi}_{n,k}^\dagger \mathbf{Z}_k \boldsymbol{\Psi}_{s,k} \\ \boldsymbol{\Psi}_{s,k}^\dagger \left(\mathbf{Z}_k \boldsymbol{\Phi}_{n,k} - \boldsymbol{\xi}_k\right) & \boldsymbol{\Psi}_{s,k}^\dagger \mathbf{Z}_k \boldsymbol{\Psi}_{s,k} \end{bmatrix} \begin{Bmatrix} \mathbf{q} \\ \mathbf{p} \end{Bmatrix} - \begin{Bmatrix} \boldsymbol{\Phi}_{n,k}^\dagger \langle \mathbf{f}_e | e_k \rangle \\ \boldsymbol{\Psi}_{s,k}^\dagger \langle \mathbf{f}_e | e_k \rangle \end{Bmatrix} = \mathbf{0} \end{aligned} \tag{11}$$

with $\mathbf{Z}_k = \left[(ik\Omega)^2\mathbf{M} + (ik\Omega)\mathbf{C} + \mathbf{K}\right]$ and $\boldsymbol{\xi}_k = \left[\mathbf{M}\boldsymbol{\Phi}_{n,k}\boldsymbol{\Lambda}_n^2 k^2 + \mathbf{C}\boldsymbol{\Phi}_{n,k}\boldsymbol{\Lambda}_n k + \tilde{\mathbf{K}}\boldsymbol{\Phi}_{n,k}\right]$ the dynamic stiffness matrix and the term arising from the substitution of each $\langle \mathbf{f}_{nl} | e_k \rangle$ from the eigenproblems, $\boldsymbol{\Phi}_{n,k}$ and $\boldsymbol{\Psi}_{s,k}$ the matrices made of the column vectors $\boldsymbol{\varphi}_{n,k}$ and $\boldsymbol{\psi}_{s,k}$, $\boldsymbol{\Lambda}_n$ a diagonal matrix made of the nonlinear eigenvalues distributed along the diagonal, and $\mathbf{q}$ and $\mathbf{p}$ the column vectors listing the general coordinates q_n and p_s respectively.

The reduced-order order model of the global system is eventually built by coupling the substructures through the generalized coordinates corresponding to the static modeshapes, p_s. If more than one harmonic is kept in the series expansion (2), which is typically the case for strong and non-smooth nonlinearities such as contact and friction, the resulting system is over-determined. However, one could, as a first approximation, discard the equations for which $\langle \mathbf{f}_e | e_k \rangle = \mathbf{0}$, which has proved to have a neglictible impact on the accuracy of the results. In the case of a mono-harmonic excitation, as in Section 3, the resulting system of equations is thus square.

Whether the system dealt with is over-determined or square, it is clearly nonlinear due to the dependency of the modes over the amplitude of their coordinates $|q_n|$, and must be solved iteratively by standard routines available in most commercial computing softwares. In practice, $\boldsymbol{\varphi}_{n,k}$ and λ_n are known for discrete values of $|q_n|$ from the nonlinear mode computation performed beforehand, and it requires now that they be interpolated at each iteration of the solver, which is readily achieved by linear or cubic interpolations.

3 NUMERICAL EXAMPLES

The dynamic substructuring method derived in Section 2 is now tested on a lumped-parameter model of bladed-disk, first on a tuned system, and then on the mistuned model, in order to demonstrate its efficiency in dealing with such complex and rich systems.

3.1 Lumped-parameter model

The cyclic model devised in this section aims at being representative of the phenomenology encountered in bladed-disk dynamics. It consists of identical sectors such as shown on Figure 3, with structural parameters taking the values reported in Table 2. The viscous damping parameters are defined so as to set the linear modal damping ratio of the first mode to 0.1%. Throughout the study, the maximum harmonic number n_h is set to 5, which has proved to provide a sufficient accuracy for the purpose of such analyses, and the nonlinear force arising from the dry-friction element is modeled by a hyperbolic tangent law [18].

– (unit)	Tip	Middle	Root	Disk	Ground
m (kg)	0.2	0.3	0.4	1.2	–
c (Ns/m)	1.3	0.7	26.7	33.3	0.4
k (10^6·N/m)	2	1	40	50	0.6

Table 2: Values of the parameters for the fundamental sector

In order to obtain clear and legible response curves for the mistuned system in Section 3.3, a model with only 12 sectors is used throughout Section 3.2 and Section 3.3. However, the performance of the method are appraised in Section 4.1 for 72 sectors, so as to deal with a more significant number of nonlinear DOFs, and thus assess the practical capabilities of the CNCMS.

3.2 Tuned system

The superelement of one sector is built from one nonlinear complex mode and two static modeshapes. Of course, for this tuned case, cyclic boundary conditions could have been applied

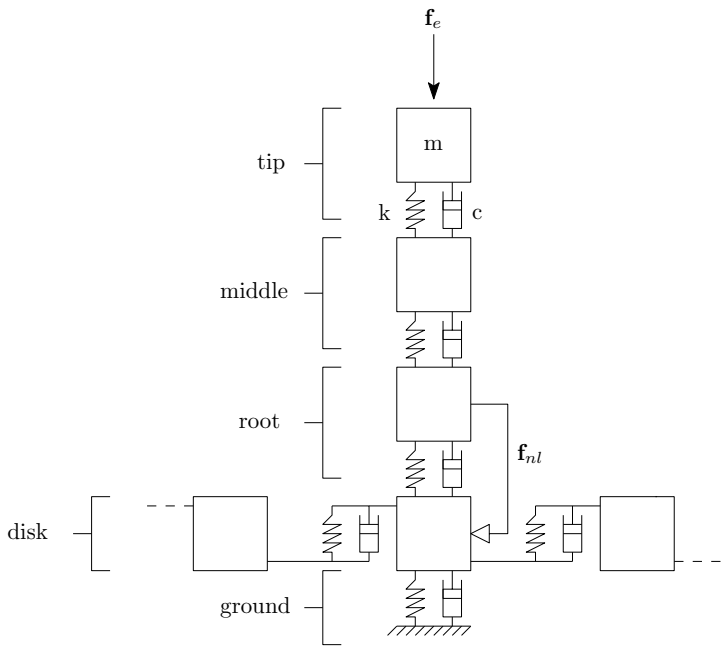

Figure 3: Fundamental sector of the cyclic model

to compute the mode, thus restricting the study to cyclic solutions. The system is first subjected at the blade tips to a travelling wave excitation, standard in bladed-disk dynamics, with 6 nodal parameters and for various excitation levels. In accordance with the linear theory of cyclic systems, the frequency response exhibits one resonance corresponding to the double mode with 6 nodal diameters. Figure 4 shows the perfect agreement of the solution obtained by CNCMS with the reference, computed by means of a classic harmonic balance method (HBM), even for a strong activation of the nonlinearities. The shift of the resonance toward lower frequencies as the amplitude of the response increases is characteristic of friction damped systems, and is a direct consequence of the evolution of the nonlinear natural frequencies that can be observed on Figure 2.

3.3 Mistuned system

An interesting application of the reduced-order modeling technique presented in this paper is the study of nonlinear and mistuned cyclic structures. In order to prove that the method can effectively handle such systems, the lumped-parameter model of Section 3.1 is modified by defining a new type of sector, with different tip and middle stiffness values, so as to shift the first natural frequency by 5% from that of the initial sector. The values taken by the structural parameters of this new sector are reported in Table 3. The fundamental sector A of the tuned model and this new sector B are then distributed according to a randomly generated pattern given in Table 4. The first nonlinear complex mode of each sector type is computed and used to build two different nonlinear superelements, which are then assembled in accordance with the mistuning pattern to build the reduced-order model.

The response of the mistuned system is computed for a travelling wave excitation with 6 nodal diameters, at a strong nonlinear level, and compared to the reference on Figure 5. As a consequence of the mistuning pattern, the response non longer exhibits one single peak, the

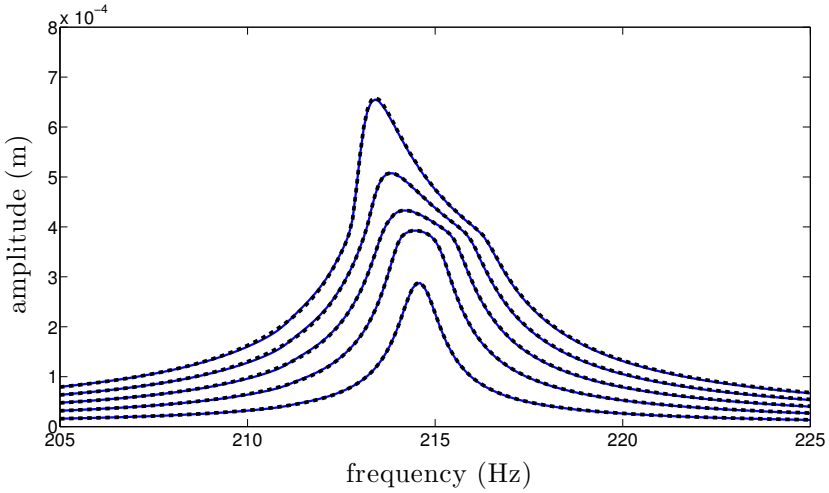

Figure 4: Response to a travelling wave excitation with 6 nodal diameters, for 5 excitation amplitudes (CNCMS in blue solid lines and HBM in black dashed lines)

– (unit)	Tip	Middle	Root	Disk	Ground
m (kg)	0.2	0.3	0.4	1.2	–
k (10^6·N/m)	1.8	0.9	40	50	0.6

Table 3: Values of the parameters of sector B

Sector	1	2	3	4	5	6	7	8	9	10	11	12
Type	A	B	A	A	B	B	B	A	A	B	A	B

Table 4: Mistuning pattern

travelling wave exciting now all the modes in the frequency range. Even though some small differences can be observed, the accuracy of the solution synthesised by CNCMS is very satisfactory. The origin of these differences is adressed in Section 4.2, and should be put in perspective with the complexity of the response and the computational efficiency of the method, discussed in Section 4.1.

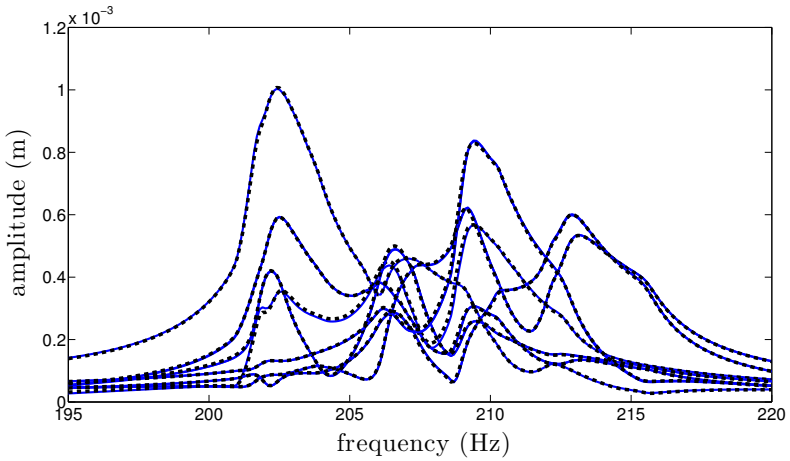

Figure 5: Response of all the blades of the mistuned system for a travelling wave excitation with 6 nodal diameters (CNCMS in blue solid lines, HBM black dashed lines)

4 DISCUSSION

This section briefly discusses the performance of the proposed reduced-order modeling technique. The efficiency of the method in terms of computational effort is first appraised, as well as the actual order-reduction obtained. The range of validity of the assumptions made is also adressed.

4.1 Performance

Figure 6 shows the ratio of the time required to compute the solution on a model with 72 sectors by HBM, normalized by the time required by CNCMS, for different excitation amplitudes F. Even close to the linear domain (F=1N), the CNCMS is about already 80 times faster than the HBM, and is up to 190 times faster when the system is extremely nonlinear (F=10N). Close to the optimum damping point (F=5N), mentioned in Section 2.1 and where it can be interesting to operate industrial systems, the ratio is close to 135, which highlights the outstanding potential of the CNCMS. The local maximum observed for F=4N also points out that the pattern of the nonlinear effects, besides the excitation level, can impact the performance of standard HBM methods when compared to the CNCMS.

The computational efficiency of the method clearly stands out in this study. It should however be pointed out that on the relatively small lumped-parameter model used here, the reduction capability of the CNCMS was not fully taken advantage of. On a larger model, the reduction arising from the use of nonlinear complex modes, allowing to drop all internal DOFs, would indeed be significantly more effective, and the computational performance of the method might prove even more impressive.

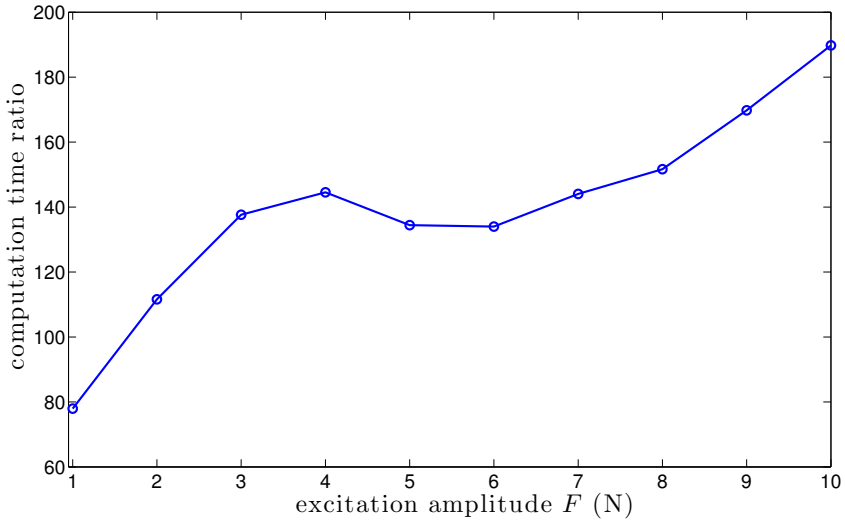

Figure 6: Computation time ratio between HBM and CNCMS

4.2 Limitations

In Section 3, some very small differences between the results obtained by CNCMS and the HBM reference could be observed. This could be explained by the fact that the model used here does not fully satisfy the assumptions made to derive the nonlinear superelement equations. In Eq. (6), the approximation of the displacement field for a given substructure uses indeed linear static modeshapes to account for the motion of the boundaries, which is quite understandable when it comes to actual blade-disk friction. On the lumped-parameter model of Section 3, however, the dry-friction elements are directly linked to the boundaries, which makes this approximation a bit bold. Nevertheless, the HBM reference curve is accurately approximated eventually, which allows to appraise the robustness of this new method.

5 CONCLUSION

The dynamic substructuring technique presented in this paper, the CNCMS, proved very promising for the study of forced vibrations in nonlinear structures. The method proved to handle quite well cases of neighboring resonant modes, and excellent computational performance has been obtained on a phenomenological model of mistuned bladed-disk, with a computation time about 135 times smaller than with standard and state-of-the-art HBM methods. Although devised initially in order to provide a new and efficient way to tackle problematics in bladed-disk dynamics, and allow to combine the presence of nonlinearities and mistuning, the procedure is flexible and could be applied to other types of nonlinear systems. Furthermore, the similarities between the CNCMS and the classic fixed-interface CMS perfectly allow to combine the two methods to build nonlinear and linear superelements, respectively, and build a hybrid reduced-order model by assembling these superelements.

Future prospects of this work could involve testing the procedure on other kind of nonlinearities, such as large deformation, or extend it to other CMS methods such as free-interface CMS. The implementation of the method on a large-scale 3D-model is an ongoing project of the authors, in view of assessing its potential for real, industrial structures.

REFERENCES

[1] M. C. C. Bampton, R. R. Craig, Jr., Coupling of substructures for dynamic analyses, AIAA Journal 6 (7) (1968) 1313–1319. doi:10.2514/3.4741.

[2] R. Craig, C. J. Chang, Free-interface methods of substructure coupling for dynamic analysis, AIAA Journal 14 (11) (1976) 1633–1635. doi:10.2514/3.7264.

[3] D. D. Klerk, D. J. Rixen, S. N. Voormeeren, General framework for dynamic substructuring: History, review and classification of techniques, AIAA Journal 46 (5) (2008) 1169–1181. doi:10.2514/1.33274.

[4] K. Bathe, Finite Element Procedures, Prentice Hall, 2006.

[5] D. Laxalde, F. Thouverez, Complex non-linear modal analysis for mechanical systems: Application to turbomachinery bladings with friction interfaces, Journal of Sound and Vibration 322 (4–5) (2009) 1009–1025. doi:10.1016/j.jsv.2008.11.044.

[6] M. Krack, L. P. von Scheidt, J. Wallaschek, A method for nonlinear modal analysis and synthesis: Application to harmonically forced and self-excited mechanical systems, Journal of Sound and Vibration 332 (25) (2013) 6798–6814. doi:10.1016/j.jsv.2013.08.009.

[7] D. S. Whitehead, Effect of mistuning on the vibration of turbo-machine blades induced by wakes, Journal of Mechanical Engineering Science 8 (1) (1966) 15–21. doi:10.1243/JMES_JOUR_1966_008_004_02.

[8] J. T. Wagner, Coupling of turbomachine blade vibrations through the rotor, Journal of Engineering for Gas Turbines and Power 89 (4) (1967) 502. doi:10.1115/1.3616718.

[9] R. C. F. Dye, T. A. Henry, Vibration amplitudes of compressor blades resulting from scatter in blade natural frequencies, Journal of Engineering for Power 91 (3) (1969) 182–187. doi:10.1115/1.3574726.

[10] D. Ewins, The effects of detuning upon the forced vibrations of bladed disks, Journal of Sound and Vibration 9 (1) (1969) 65–79. doi:10.1016/0022-460X(69)90264-8.

[11] M. P. Castanier, C. Pierre, Modeling and analysis of mistuned bladed disk vibration: Current status and emerging directions, Journal of Propulsion and Power 22 (2) (2006) 384–396. doi:10.2514/1.16345.

[12] M. P. Castanier, G. Óttarsson, C. Pierre, A reduced order modeling technique for mistuned bladed disks, Journal of Vibration and Acoustics 119 (3) (1997) 439–447. doi:10.1115/1.2889743.

[13] R. Bladh, M. P. Castanier, C. Pierre, Reduced order modeling and vibration analysis of mistuned bladed disk assemblies with shrouds, Journal of Engineering for Gas Turbines and Power 121 (3) (1999) 515–522. doi:10.1115/1.2818503.

[14] M. T. Yang, J. H. Griffin, A reduced-order model of mistuning using a subset of nominal system modes, Journal of Engineering for Gas Turbines and Power 123 (4) (1999) 893–900. doi:10.1115/1.1385197.

[15] M. Mbaye, C. Soize, J.-P. Ousty, E. Capiez-Lernout, Robust analysis of design in vibration of turbomachines, Journal of Turbomachinery 135 (2) (2012) 021008–021008. doi:10.1115/1.4007442.

[16] M. Krack, L. P. von Scheidt, J. Wallaschek, On the computation of the slow dynamics of nonlinear modes of mechanical systems, Mechanical Systems and Signal Processing 42 (1–2) (2014) 71–87. doi:10.1016/j.ymssp.2013.08.031.

[17] G. Kerschen, M. Peeters, J. Golinval, A. Vakakis, Nonlinear normal modes, part i: A useful framework for the structural dynamicist, Mechanical Systems and Signal Processing 23 (1) (2009) 170–194. doi:10.1016/j.ymssp.2008.04.002.

[18] C. Joannin, B. Chouvion, F. Thouverez, M. Mbaye, J.-P. Ousty, Nonlinear modal analysis of mistuned periodic structures subjected to dry friction, Journal of Engineering for Gas Turbines and Powerdoi:10.1115/1.4031886.

[19] T. M. Cameron, J. H. Griffin, An alternating frequency/time domain method for calculating the steady-state response of nonlinear dynamic systems, Journal of Applied Mechanics 56 (1) (1989) 149–154. doi:10.1115/1.3176036.

ECCOMAS Congress 2016
VII European Congress on Computational Methods in Applied Sciences and Engineering
M. Papadrakakis, V. Papadopoulos, G. Stefanou, V. Plevris (eds.)
Crete Island, Greece, 5–10 June 2016

SOME REMARKS ON TIME INTEGRATION OF 3D ROTOR-STATOR ASSEMBLY

B. Prabel[1]

[1] CEA, DEN, DANS, DM2S, SEMT, DYN - CEA Saclay, F-91191 France
e-mail: benoit.prabel@cea.fr

Keywords: Time integrators, Rotordynamics, Model reduction, Nonlinear vibrations, FEM

Abstract. *This paper focuses on the application of time integration methods to rotor-stator assembly modeled by Finite Element Method. In particular the average acceleration method (which is implicit) and the central differences method (which is explicit) are examined. Both belong to the Newmark's time integrator family and are widely used. It is found that the first one is unstable due to the periodic kinematic constraints linking the rotating to the non rotating parts of the structure. A proposed remedy is to add numerical damping leading to the implicit HHT and α-generalized schemes. Concerning the integration with an explicit scheme, it is demonstrated that a classical implementation lead to a vanishingly small critical time step because of the strong gyroscopic effects. An exact implementation of this kind of scheme is proved to maintain the value of the critical time step.*

1 INTRODUCTION

The need to fully control the dynamical behavior of rotors is motivated by rotors machinery more and more complex operating in more and more severe conditions. Modeling capacities are often wished to ensure the lowest cost of design and maintenance and the highest safety margins.

To this end, this work focuses on the computation of the time response of a three-Dimensional Finite Element model (3D-FE model) enabling to represent the behavior of a complex rotor-stator assembly.

First, a three-Dimensional modelin the Finite Element software Cast3M [1] is considered, following the work of Combescure and Lazarus [2]. As pointed out by Geradin and Kill [3] and Chatelet *et al.* [4], compared to one-dimensional models (1D models), 3D-FE models exhibit better accuracy for evaluating stiffness of disc and wheel-shaft assembly. They are also required when dealing with non-axisymmetric geometry like bladed disc. They however imply an higher computational cost and some reduction techniques are necessary in industrial cases.

Time integration methods is widely viewed as the more direct manner to predict the dynamic response of a mechanical structure to a given loading in presence of some non-linearities. This general fact remains true in rotordynamics as pointed out by Genta [5] Alternatives in the frequency domain (like the Harmonic Balance Method for example) exist but their use is not always straightforward.

Hence, the present paper aims at presenting the specificity of time-integration methods when applied to a 3D rotor-stator assembly, exhibiting some little known numerical instabilities and their possible remedies.

2 MODELING 3D ROTOR-STATOR ASSEMBLY

2.1 Equation of motion of a 3D rotor-stator assembly

The more "natural" approach to model the vibrations of a rotor discretized by non-beam-element is to consider its motion in the rotating frame $\mathcal{R}' = \{O', \underline{e}'_1, \underline{e}'_2, \underline{e}'_3\}$. This one is represented on figure 1. A simple rotation defined by the angular velocity Ω around the first axis ($\underline{e}_1 = \underline{e}'_1$), links this frame to the non-rotating Galilean frame $\mathcal{R}$.

The position and displacement of a point P defined in the rotating frame by its relative coordinate can be expressed in the inertial frame by the rotation of angle $\underline{\Omega} t$ and the translation of the origin $\underline{s} = \underline{OO'}$. Following Argyris [6] for example, the position $\underline{y}$ of P is given by the coordinate $x + u$ in $\mathcal{R}'$, and the coordinate y of this point in $\mathcal{R}$ are expressed by:

$$\begin{aligned} \underline{y} &= \underline{OP} = \underline{OO'} + \underline{O'P} \\ y &= s + [R](x + u) \end{aligned} \tag{1}$$

where $[R] = \begin{bmatrix} \underline{e}'_1 & \underline{e}'_2 & \underline{e}'_3 \end{bmatrix}$ is the orthonormal matrix of the basis vectors of $\mathcal{R}'$ expressed in $\mathcal{R}$, and s is the coordinate of $\underline{OO'}$ in $\mathcal{R}$.

To deal with vibrations, velocity and acceleration have to be computed. The derivation of basis vector is simply:

$$\dot{\underline{e}}'_i = \underline{\Omega} \wedge \underline{e}'_i \tag{2}$$

Then velocity and acceleration in the inertial frame can be derived as:

$$\begin{aligned} \dot{\underline{y}} &= \dot{\underline{s}} + \dot{\underline{x}} + \dot{\underline{u}} \\ \dot{y} &= \dot{s} + [R]\dot{u} + \underline{\Omega} \wedge ([R]\,(x + u)) \end{aligned} \tag{3a}$$

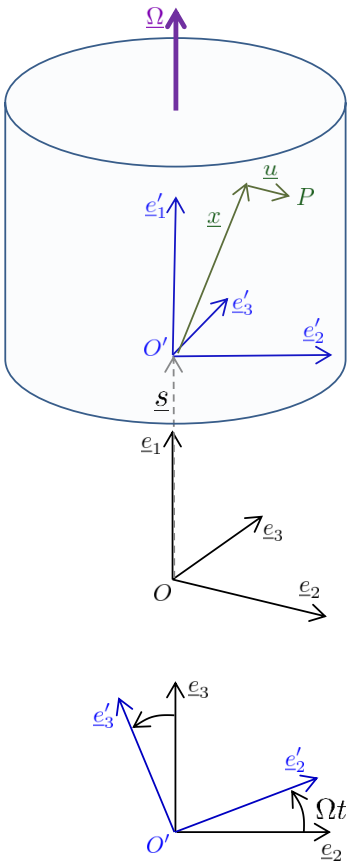

Figure 1: Definition of non-rotating (also called inertial) and rotating frames

$$\begin{aligned} \ddot{y} =& \ddot{s} + [R]\ddot{u} + \dot{\underline{\Omega}} \wedge ([R]\,(x+u)) + \underline{\Omega} \wedge \underline{\Omega} \wedge ([R]\,(x+u)) + 2\underline{\Omega} \wedge ([R]\dot{u}) \\ [R]^T\ddot{y} =& [R]^T\ddot{s} + \ddot{u} + \dot{\Omega}\wedge(x+u) + \Omega \wedge \Omega\wedge(x+u) + 2\Omega\wedge\dot{u} \end{aligned} \tag{3b}$$

The third term of the Right-Hand-side of Eq. (3b) is the Euler term and is zero as long as the spin speed is constant. The fourth term refers to the centrifugal effect acting in the radial direction. The last therm of the RHS is the probably the most characteristic of Rotordynamics as it refers to the Coriolis effect which produces a pseudo-acceleration in a direction perpendicular to the relative velocity.

The geometry of the rotor is discretized in the rotating frame with standard finite element shape functions:

$$\underline{x} = \sum_i N_i(x)\underline{x}_i \tag{4}$$

Isogeometric element are considered and displacements, velocity and acceleration are approximated in the same space of functions:

$$\begin{aligned} \underline{u}(\underline{x},t) &= \sum_i N_i(x)\underline{u}_i(t) \\ \dot{\underline{u}}(\underline{x},t) &= \sum_i N_i(x)\dot{\underline{u}}_i(t) \\ \ddot{\underline{u}}(\underline{x},t) &= \sum_i N_i(x)\ddot{\underline{u}}_i(t) \end{aligned} \tag{5}$$

The weak form of the mechanical problem for the domain $\mathcal{D}$ of boundary $\partial\mathcal{D} = \partial\mathcal{D}_F \cup \partial\mathcal{D}_u$ is given by Eq. (6).

$$\begin{aligned} &\forall \delta\underline{v} \in V^0 = \{\delta\underline{v}, \text{ so that } \delta\underline{v} = 0 \text{ sur } \partial\mathcal{D}_u\}, \\ &\int_{\mathcal{D}} \rho\underline{\ddot{u}} \cdot \delta\underline{v}\, d\mathcal{D} + \int_{\mathcal{D}} \underline{\underline{\sigma}} : \delta\underline{\underline{e}}(\underline{v})\, d\mathcal{D} = \int_{\mathcal{D}} \underline{f}_d \cdot \delta\underline{v}\, d\mathcal{D} + \int_{\partial\mathcal{D}_F} \underline{F}_d \cdot \delta\underline{v}\, d\Gamma \end{aligned} \tag{6}$$

Injecting the kinematic of the rotor in the weak form of the problem, supposing that equilibrium due to centrifugal forces is verified by a static motion generating a constant state of stress σ^0, and using the discretized approximation of these quantities, dynamic equilibrium is obtained:

$$[M]\underline{\ddot{u}}' + [\Omega G + C_{visc}]\underline{\dot{u}}' + [K_{elas} + \Omega^2 K_{cent} + K(\sigma^0)]\underline{u}' = F'_{ext} \tag{7}$$

where the Coriolis effect is G.

For the non-rotating part (i.e. the stator), the geometry and displacement are expressed in the inertial frame. Then, the discretized equations of motion reduce to :

$$[M]\underline{\ddot{u}} + [C_{visc}]\underline{\dot{u}} + [K_{elas}]\underline{u} = F_{ext} \tag{8}$$

2.2 Linking the rotating to the non-rotating frame

As depicted by figure 1, a simple change of frame enables to establish the constraint equation between the degrees of freedom of the rotor and ones of the stator. to equal their relative displacements :

$$\begin{pmatrix} U1 \\ U2 \\ U3 \end{pmatrix} = \begin{bmatrix} 1 & 0 & 0 \\ 0 & \cos\Omega t & -\sin\Omega t \\ 0 & \sin\Omega t & \cos\Omega t \end{bmatrix} \cdot \begin{pmatrix} U1' \\ U2' \\ U3' \end{pmatrix} \tag{9}$$
$$U \quad = \quad R(\Omega t) \quad \cdot \quad U'$$

A Lagrange multiplier Λ is introduced to recast the constraint :

$$\begin{pmatrix} 0 & -I & R \\ -I^T & 0 & 0 \\ R^T & 0 & 0 \end{pmatrix} \cdot \begin{bmatrix} \Lambda \\ U \\ U' \end{bmatrix} = \begin{pmatrix} 0 \\ 0 \\ 0 \end{pmatrix} \tag{10}$$
$$\text{soit} \qquad L(\Omega t) \quad \cdot \quad q \quad = \quad 0$$

3 NEWMARK TIME INTEGRATION SCHEMES

3.1 Basic equations of the Newmark scheme

A large number of literature exists about time integration scheme and the Newmark's scheme that seems to be one of the most used in structural dynamic community (see the books of Hughes [7], Géradin [8], Argyris [6] or Zienkiewicz [9] for example). It is often presented as a truncated Taylor development of local quantities which is not presented here for sake of clarity.

A recurrence formula links displacement, velocity and acceleration at time t_{n+1} :

$$\begin{aligned} \ddot{u}_{n+1} &= \frac{1}{\beta\Delta t^2}(u_{n+1} - u_n) - \frac{1}{\beta\Delta t}\dot{u}_n + (1 - \frac{1}{2\beta})\ddot{u}_n \\ \dot{u}_{n+1} &= \frac{\gamma}{\beta\Delta t}(u_{n+1} - u_n) + (1 - \frac{\gamma}{\beta})\dot{u}_n + \Delta t(1 - \frac{\gamma}{2\beta})\ddot{u}_n \end{aligned} \tag{11}$$

Introducing these expressions in the dynamic equilibrium, one gets :

$$\left[\frac{1}{\beta\Delta t^2}M + \frac{\gamma}{\beta\Delta t}C + K\right](u_{n+1} - u_n) = F^{ext}_{n+1} - Ku_n \\ - C\left((1-\frac{\gamma}{\beta})\dot{u}_n + \Delta t(1-\frac{\gamma}{2\beta})\ddot{u}_n\right) \\ - M\left(-\frac{1}{\beta\Delta t}\dot{u}_n + (1-\frac{1}{2\beta})\ddot{u}_n\right) \tag{12}$$

3.2 Properties of the Newmark scheme

The accuracy and stability of the Newmark scheme depend on the value of the parameters γ and β. Table 1 sums up the stability conditions of some different schemes for a 1-dof system subjected to no external loading.

Scheme	γ	β	$\Delta t_c/\Delta t^e$
Central difference	$1/2$	0	2
Fox and Goodwin	$1/2$	$1/12$	2.45
Linear acceleration	$1/2$	$1/6$	3.46
Average acceleration	$1/2$	$1/4$	∞
Modified average acceleration	$1/2+\alpha$	$1/4(1+\alpha)^2$	∞
Runge-Kutta 4	-	-	$2\sqrt{2}$
Fu-De Vogelaere	-	-	$2\sqrt{2}$

Table 1: Critical time step of some time integration schemes

where $\Delta t^e = \frac{min(\Delta x^e)}{\sqrt{E/\rho}}$ is the caracteristic time of an element of Young modulus E, density ρ and internodal distance Δx^e.

The application of the central difference method to rotordynamic will be presented in the next section. Then, the average acceleration method will be considered in section §5.

4 AN EXPLICIT SCHEME : THE CENTRAL DIFFERENCE METHOD

4.1 Classical approximation of the central difference method

Choosing $\gamma = \frac{1}{2}, \beta = 0$, the displacement at time $n+1$ only depends on quantities at time n :

$$u_{n+1} = u_n + \Delta t\dot{u}_n + \frac{\Delta t^2}{2}\ddot{u}_n \tag{13}$$

Introducing the velocity at the mid step :

$$\dot{u}_{n+\frac{1}{2}} = \frac{u_{n+1} - u_n}{\Delta t} \tag{14}$$

which enables to write :

$$\dot{u}_{n+1} = \frac{\Delta t}{2}\ddot{u}_{n+1} + \dot{u}_{n+\frac{1}{2}} \tag{15}$$

the equation of motion to solve at each time step is simply :

$$\left[M + \cancel{\frac{\Delta t}{2}C}\right] \ddot{u}_{n+1} = F^{ext}_{n+1} - Ku_{n+1} - C\dot{u}_{n+\frac{1}{2}} \tag{16}$$

A very common practice in code implementation is to neglect the term $\frac{\Delta t}{2}C$ on the Left-Hand-Side of equation (16). This leads to the "classical" central difference scheme. This assumption is generally justified by the relatively low effect of damping compared to the inertial one and to the stiffness. Combined to a lumping technique, it has the advantage to keep the operator diagonal, so that no matrix has to be inverted.

However in the case of rotordynamics, the matrix C includes viscous and gyroscopic (Coriolis matrix) effects. That is why it is proposed here to consider the "Full" central difference scheme which does not neglect the participation of this term and compute the inverse of $\left[M + \frac{\Delta t}{2}C\right]$. This strategy is adopted only in the case where the spatial description is reduced by modal approach.

The effect on the performance of the scheme is evaluated on the basis of the following example.

4.2 Application to a rotor modeled by 3D FE

A rotor constituted of a shaft and four short blades is considered (see figure 2.

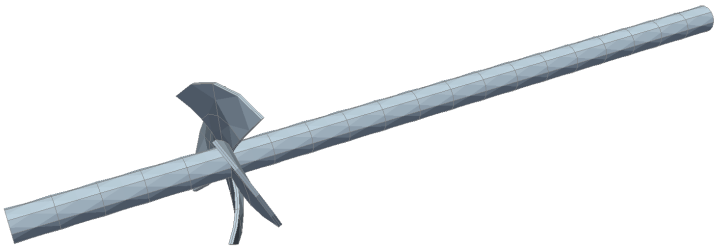

Figure 2: 3D mesh of the rotor test case

An unbalance excitation generated by a blade loss is simulating by applying an equivalent force to the model. Displacement evolution with time for different time step Δt are given figure 3a.

Figure 3a demonstrates that the application of the "Full" central difference scheme maintain the critical time step to an acceptable value, whereas the "classical" assumption that neglect C on the LHS drastically decrease it and causes unstable behavior for $\Delta t \geq \frac{T}{256}$ (where $T = 2\pi/\Omega$).

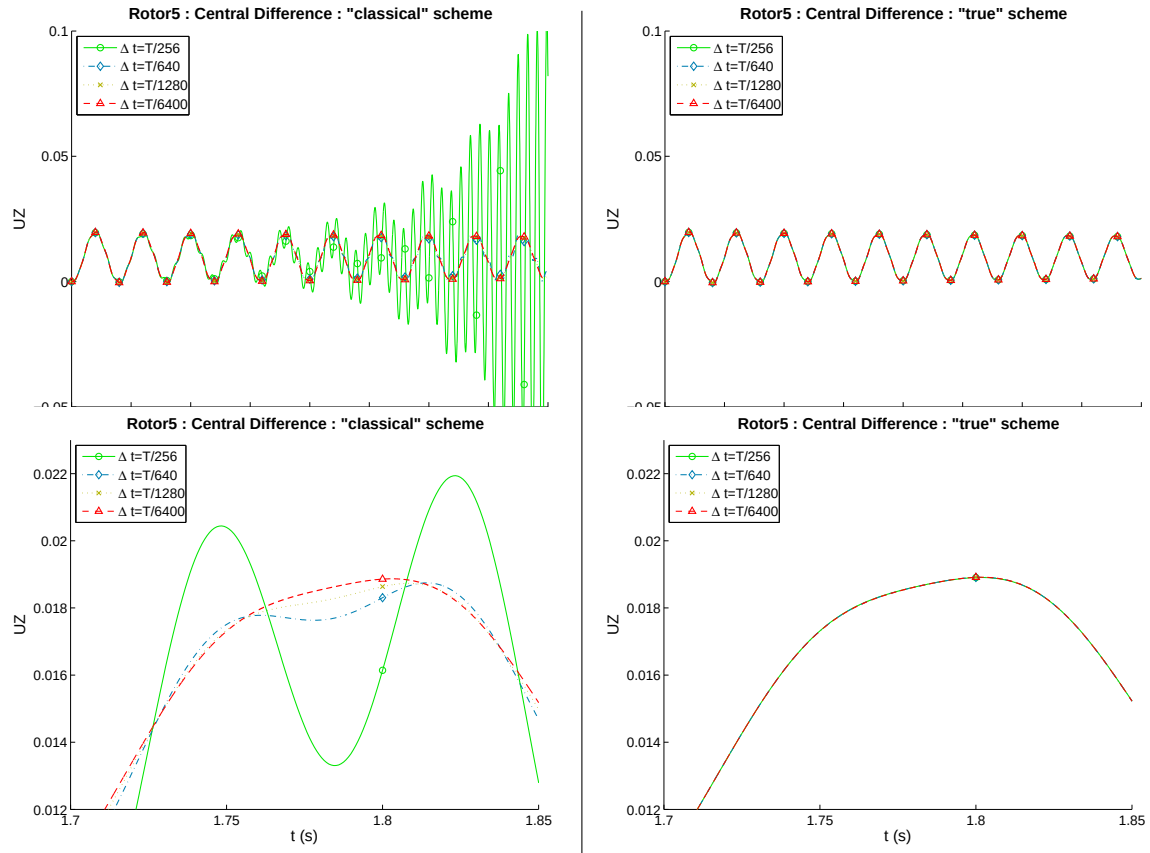

(a) "Classical" central difference scheme

(b) "Full" central difference scheme

Figure 3: Displacement evolution with time for various time step and the explicit central difference method

5 AN IMPLICIT SCHEME : THE AVERAGE ACCELERATION METHOD

5.1 Application to a 4 degree of freedom problem

A very simple model with 4 degree of freedom is presented here to illustrate the behavior of the average acceleration scheme when used to compute the response of a rotor-stator assembly. The model is depicted on figure 4.

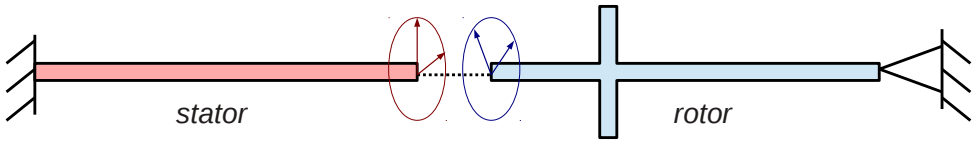

Figure 4: 4 dof rotor-stator system

Only the first modes are considered for the rotor and the stator (respectively the first flexural modes along y and z and the rigid body mode along y' and z'). The introduction of the two kinematic constraints linking rotating to non-rotating parts adds two Lagrange multipliers to the system. Hence, the vector of unknown is :

$$q^T = \begin{pmatrix} \lambda_y & \lambda_z & u_y & u_z & u'_y & u'_z \end{pmatrix} \tag{17}$$

and the equation of motion is :

$$Kq + C\dot{q} + M\ddot{q} = F \tag{18}$$

$$\text{with } K = \begin{bmatrix} 0 & 0 & 1 & 0 & -\cos\Omega t & \sin\Omega t \\ & 0 & 0 & 1 & -\sin\Omega t & -\cos\Omega t \\ & & k & 0 & 0 & 0 \\ & & & k & 0 & 0 \\ & & & & k' & 0 \\ \textit{sym} & & & & & k' \end{bmatrix} \quad C = \begin{bmatrix} 0 & 0 & 0 & 0 & 0 & 0 \\ & 0 & 0 & 0 & 0 & 0 \\ & & c & 0 & 0 & 0 \\ & & & c & 0 & 0 \\ & & & & c' & 0 \\ \textit{sym} & & & & & c' \end{bmatrix}$$

$$\text{and } M = \begin{bmatrix} 0 & 0 & 0 & 0 & 0 & 0 \\ & 0 & 0 & 0 & 0 & 0 \\ & & m & 0 & 0 & 0 \\ & & & m & 0 & 0 \\ & & & & m' & 0 \\ \textit{sym} & & & & & m' \end{bmatrix}$$

An unbalance loading is applied to the rotor along the y'-direction :

$$F = (2\pi\Omega)^2 \cdot r(t) \cdot \begin{pmatrix} 0 & 0 & 0 & 0 & f & 0 \end{pmatrix}^T \tag{19}$$

with a linear ramp variation during the half of the first period :

$$r(t) = \begin{cases} 2\Omega t & \text{if} \quad 0 \leq t < \frac{1}{2\Omega} \\ 1 & \text{else} \end{cases} \tag{20}$$

Numerical values used in for this test case are given table 2.

m	m'	k	k'	c	c'	f	Ω
1E3	1E3	6E6	0	31E3	0	$\frac{1}{(2\pi\Omega)^2}$	5 Hz

Table 2: Numerical value of the 4-dof system

Solving equation (19) with the average acceleration method lead to the results of figure 5.

As there is no physical source of instability in the proposed model, the simple 4-dof example presented here proved the instability of the Newmark average acceleration method for this class of linear but with periodic constraints problem ! This is contradictory with the unconditionally stable reputation of this scheme for linear problem. Evolution of Lagrange multipliers suggests that the periodic constraint is the source of numerical divergence of the solution.

A single article of 1989 written by Cardona and Géradin [12] demonstrates that some kinematics constraints may lead to infinite eigenvalues of the amplification matrix. Time integration of systems with a relative important participation of kinematic constraints is then not an easy task. This explains why a great amount of literature can be found about time-integration in flexible multibody dynamics [13].

Three solutions can be adopted to treat this problem :

- When possible, eliminate the constraints (and the associated variables),
- Derive two times the constraint equation and add mass and damping terms so that the constraint becomes an overdamped system,

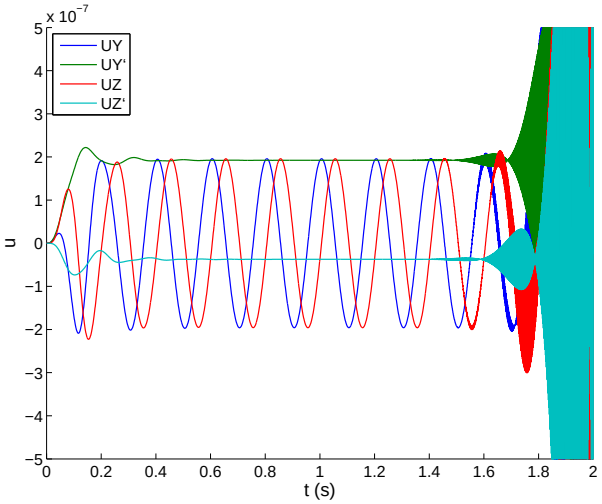

(a) Displacement time evolution up to 2 s

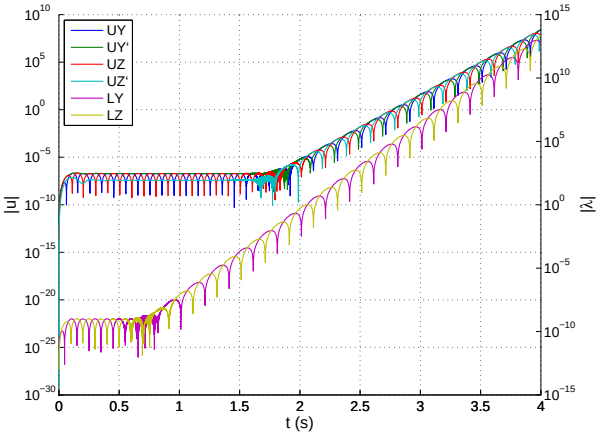

(b) Lagrange multipliers time evolution

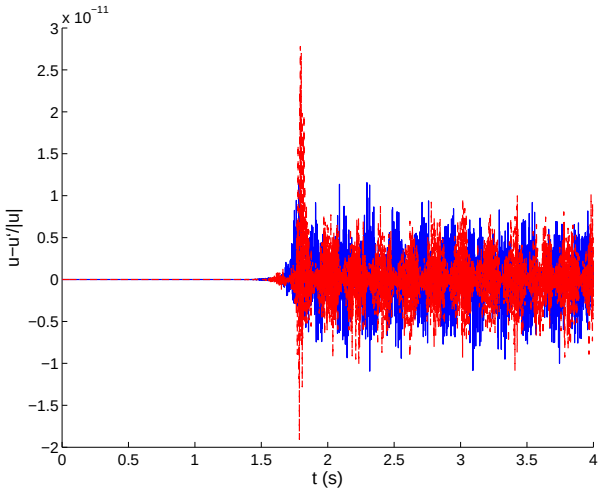

(c) Relative validity of the constraint rotor-stator

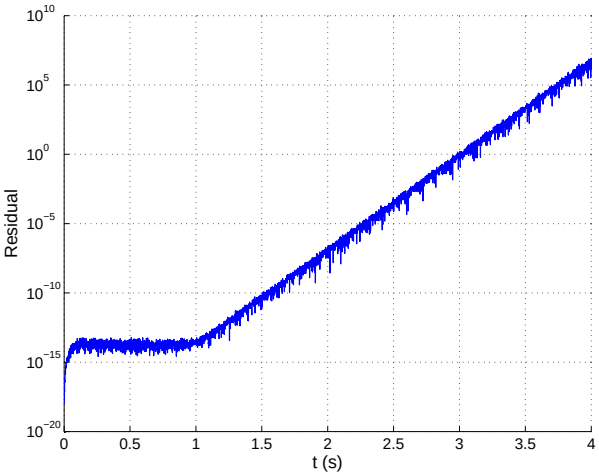

(d) Evolution of the residual of the dynamic equilibrium

Figure 5: Results of the average acceleration method for the 4-dof system

- Use a scheme which presents naturally numerical damping.

The last one will be discussed in the following subsection.

5.2 Adding numerical damping to the scheme

Three scheme with numerical damping have been implemented in Cast3M and tested on the 4-dof test case :

- Modified average acceleration with α=0.05
- HHT with α=0.05
- α-generalized with ρ_∞=0.9048

The spectral radius (identified as the highest eigenvalue of the amplification matrix) and the numerical damping are plotted for these scheme figure 6. Figure 6 shows that high frequencies

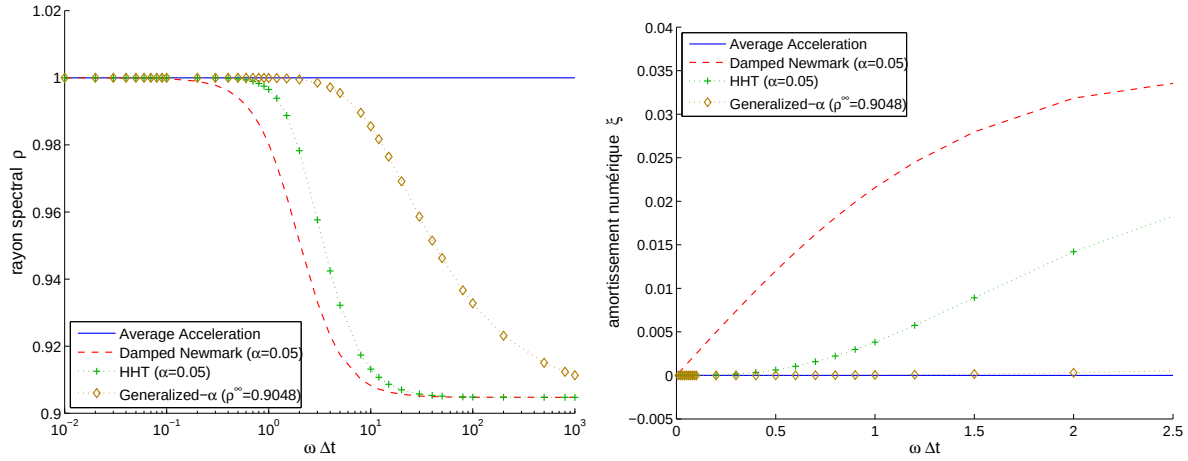

(a) Spectral raidus (b) Damping

Figure 6: Characteristics of some schemes

are considered as spurious and attenuated by these schemes.

The HHT (from Hilber-Hughes-Taylor [10]) and the α-generalized [11] methods are methods closed to the Newmark's one, but a weighting of elastic, viscous and inertial forces over time step is performed in order to control the damping. The general equation of motion to solve is no more (8) but :

$$(1-\alpha_m)M\ddot{u}_{n+1} + \alpha_m M\ddot{u}_n + (1-\alpha_f)C\dot{u}_{n+1} + \alpha_f C\dot{u}_n + (1-\alpha_f)Ku_{n+1} + \alpha_f Ku_n = (1-\alpha_f)F^{ext}_{n+1} + \alpha_f F^{ext}_n \quad (21)$$

where $\alpha_m = 0$ for the HHT method. The Newmark parameters are adjusted to maintain second order accuracy :

$$\gamma = \frac{1}{2} + \alpha_f - \alpha_m \quad \text{et} \quad \beta = \frac{1}{4}(1+\alpha_f-\alpha_m)^2 \quad (22)$$

For the α-generalized method, the spectral radius ρ_∞ $\omega\Delta t \to \infty$ can be chosen and the coefficients α_m and α_f deduced as :

$$\alpha_m = \frac{2\rho_\infty - 1}{\rho_\infty + 1} \quad \text{et} \quad \alpha_f = \frac{\rho_\infty}{\rho_\infty + 1} \quad (23)$$

Using one of the three aforementioned scheme leads to a slightly damped stable solution as depicted by figure 7a.

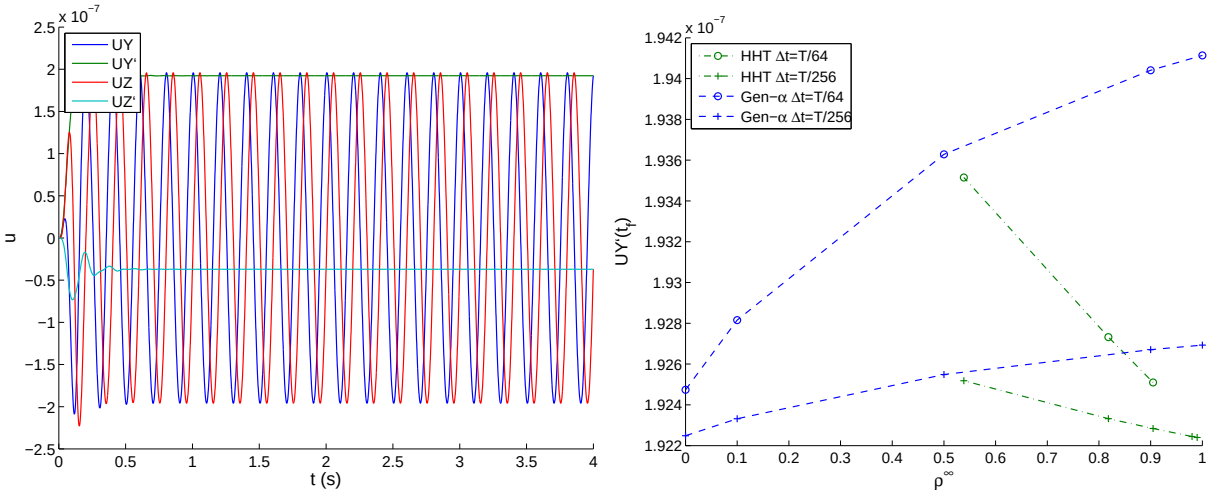

(a) Time evolution of displacements obtained with the HHT scheme (α=0.05)

(b) Displacement UY' at th eend of simulation

Figure 7: Results obtained with numerical damping

The stationary value of the UY' displacement as a function of the spectral radius for the HHT and α-generalized methods and for two values of time step is given figure 7b. For this very simple 4-dof system, the analytic solution at steady state is UY'=1.922E-7. Observation of this figure indicates that :

- with the HHT scheme, instability is observed for too small values of α_f and this critical value depends on time step,
- with the HHT scheme, the amplitude of vibration tends to decrease with the spectral radius, which is counter-intuitive !
- with the α-generalized scheme, the system is always stable even if $\rho^\infty = 1$ (no dissipation) !
- with the α-generalized scheme, the finale amplitude increase with the spectral radius but remains a finite value,
- a better solution is found for smaller time step and for respectively large and small radius for HHt and α-generalized schemes.

5.3 Application to 3D rotor-stator assembly

A system very close to the 4-dof previously studied system is considered. The 3D FE mesh of this system is given figure 8.

Average acceleration method is first used with two spatial discretization :

- FE dof : the Finite Element degree of freedom,
- CMS dof : a Component Mode Synthesis method (Craigh Brampton) is used to reduce the number of dof.

Mode shapes used in CMS are plotted figure 9.

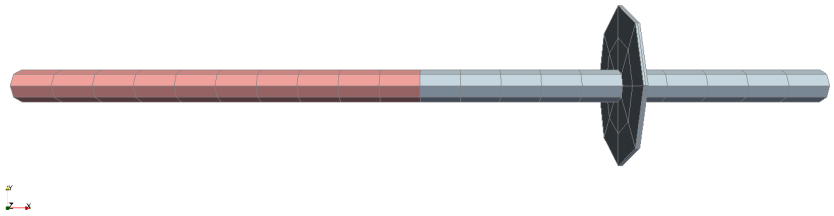

Figure 8: FE mesh : the stator is on the left (pink) and the rotor is on the right (light blue)

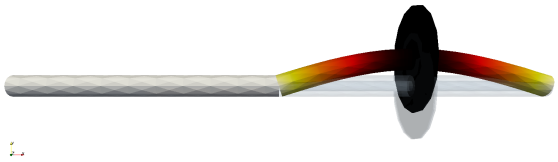

(a) Eigenmode (first flexion of the rotor)

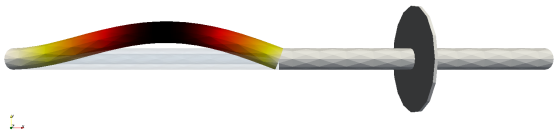

(b) Eigenmode (first flexion of the stator)

(c) Static solution (lateral displacement imposed to the rotor)

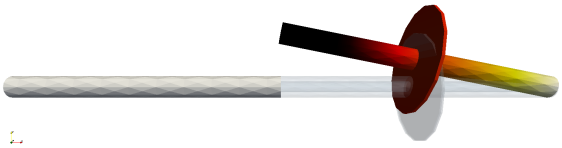

(d) Static solution (lateral displacement imposed to the stator)

Figure 9: Mode shape constituting the CMS base

The displacement evolution with time for both spatial discretization is given figure **??**. Whereas FE-dof based response remains stable, it seems that CMS-dof based solution become unstable like the 4-dof system.

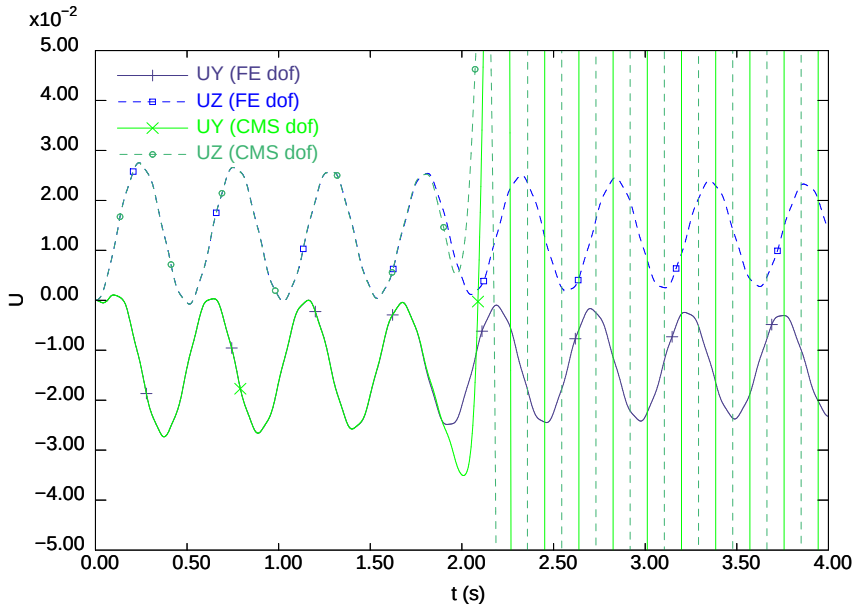

transitoire (Ω=5Hz) − DYNAMOI physique: acc moy. − modal: HHT α_F=0

Application of the numerically damped HHT and α-generalized methods enables to get ride

of this instability as it is shown on figures 10.

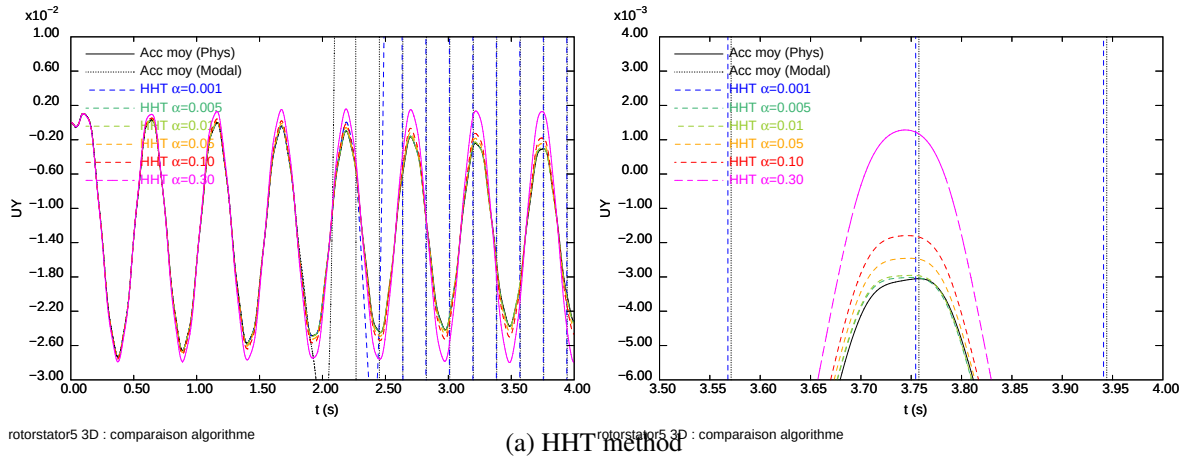

(a) HHT method

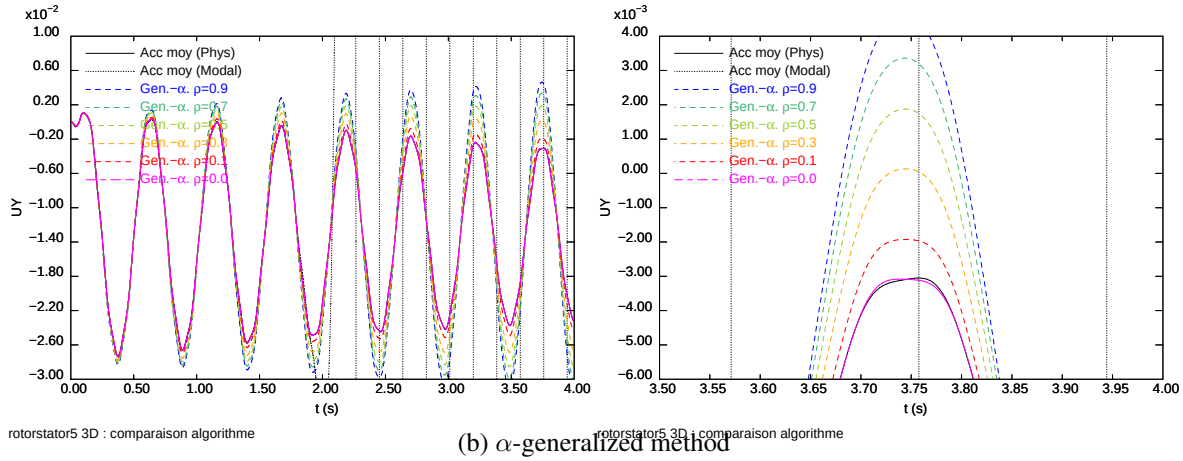

(b) α-generalized method

Figure 10: Results of time integration applied to 3D rotor-stator assembly

Once again, the HHT method seems efficient for a "just stable" value of parameter $\alpha_f = 0.005$, whereas the α-generalized method is the closest to the reference for an high damping value ($\rho^\infty = 0$).

6 CONCLUSIONS AND PERSPECTIVES

Two kinds of numerical instabilities have been highlighted for both the central difference and the average acceleration method.

The first one concerns the drop of the critical time step when neglecting the gyroscopic term in the operator computing the acceleration at the next time step. A simple remedy is to use the full formulation but it could be expensive if the inversion of a large matrix have to be performed.

For implicit scheme, matrix inversion is naturally done and the time step is expected to be greater. However the kinematic constraints to link the rotating to the non-rotating parts introduce a numerical instability which has to be dissipated. HHT and α-generalized methods have been found to do this task under the condition to choose appropriately the numerical damping.

As this choice may not be obvious in every situations, combination of an explicit integrator with a component mode synthesis method seems to be the most attractive way to model complex 3D rotor-stator assembly.

Future development will concern the integration of nonlinear component (bearing, squeeze-film, rotor-stator contact, ...) in the models.

REFERENCES

[1] Cast3M Finite Element software, CEA, `http://www-cast3m.cea.fr`, 2015.

[2] D. Combescure, A. Lazarus, Refined finite element modelling for the vibration analysis of large rotating machines: Application to the gas turbine modular helium reactor power conversion unit. *Journal of Sound and Vibration*, 318(4), 1262-1280, 2008.

[3] M. Geradin, N. Kill, A new approach to finite element modelling of flexible rotors. *Engineering Computations*, 1(1), 52-64, 1984.

[4] E. Chatelet, F. D?Ambrosio, G. Jacquet-Richardet, Toward global modelling approaches for dynamic analyses of rotating assemblies of turbomachines. *Journal of Sound and Vibration*, 282(1), 163-178, 2005.

[5] G. Genta, *Dynamics of rotating systems*. Springer, 2005.

[6] J. H. Argyris and H.-P. Mlejnek, *Dynamics of structures*. North-Holland Amsterdam, 1991.

[7] T. J. Hughes, *The Finite Element Method: Linear Static and Dynamic - Finite Element Analysis*. Prentice-Hall International, Inc., 1987.

[8] M. Géradin and D. Rixen, *Théorie des vibrations: application à la dynamique des structures*. Masson Paris, 1993.

[9] O. Zienkiewicz, R. Taylor, and J. Zhu, *The Finite Element Method: Its Basis And Fundamentals*. Butterworth-Heinemann, 6th edition ed., 2005.

[10] H. M. Hilber, T. J. Hughes, and R. L. Taylor, Improved numerical dissipation for time integration algorithms in structural dynamics, *Earthquake Engineering & Structural Dynamics*, vol. 5, no. 3, pp. 283–292, 1977.

[11] J. Chung and G. Hulbert, A time integration algorithm for structural dynamics with improved numerical dissipation: the generalized-α method, *Journal of applied mechanics*, vol. 60, no. 2, pp. 371–375, 1993.

[12] A. Cardona and M. Géradin, Time integration of the equations of motion in mechanism analysis, *Computers & Structures*, vol. 33, no. 3, pp. 801–820, 1989.

[13] O. A. Bauchau, *Flexible multibody dynamics*, vol. 176. Springer, 2010.

ECCOMAS Congress 2016
VII European Congress on Computational Methods in Applied Sciences and Engineering
M. Papadrakakis, V. Papadopoulos, G. Stefanou, V. Plevris (eds.)
Crete Island, Greece, 5–10 June 2016

DELAYED FEEDBACK CONTROL METHOD FOR CALCULATING SPACE-TIME PERIODIC SOLUTIONS OF VISCOELASTIC PROBLEMS

Ustim Khristenko[1,2], **Patrick Le Tallec**[1]

[1]LMS Ecole Polytechnique
91128 Palaiseau, France
e-mail: khristen@lms.polytechnique.fr, patrick.letallec@polytechnique.edu

[2] Manufacture Francaise des Pneumatiques Michelin
Place des Carmes Dechaux, 63040 Clermont-Ferrand Cedex 9, France
e-mail: khristen@lms.polytechnique.fr

Keywords: Optimal control, Delayed feedback control, Space-time periodic solution, Viscoelasticity, Steady rolling.

Abstract. *We are interested in fast techniques for calculating a periodic solution to viscoelastic evolution problems with a space-time periodic condition of "rolling" type. Such a solution is usually computed as an asymptotic limit of the initial value problem with arbitrary initial data. We want to invent a control method, accelerating the convergence. The main idea is to modify our problem by introducing a feedback control term, based on a periodicity error, in order to accelerate the convergence to the desired periodic solution of the problem.*

First, an abstract evolution problem has been studied. From the analytic solution of the modified (controlled) problem, an efficient control has been found, optimizing the spectrum of the problem. The proposed control term can be mechanically interpreted, and its efficiency increases with the relaxation time.

In order to confirm numerically the theoretical results, a finite element simulation has been carried out on a full 2D model for a steady rolling of a viscoelastic tyre with periodic sculpture. It has demonstrated that the controlled solution converges indeed faster than the non-controlled one, and that the efficiency of the method increases with the problem's relaxation time, that is when the memory of the underlying problem is large.

1 INTRODUCTION

In industrial applications, in order to avoid the inversion of very large matrices, dynamic periodic state are often computed as the asymptotic limit solution of an initial value evolution problem with arbitrarily chosen initial data. In such cases, one is not really interested in the evolution history, but only in convergence time. Computations can take a lot of time for "viscous" problems, when memory effects are very large. Then the convergence time becomes a significant parameter for industrial implementations, and developing methods accelerating convergence is of current interest.

For such problems, even if the asymptotic limit is periodic, the solution of the initial value evolution problem is not. Thus the periodicity of the desired solution can be considered as an extra information (observation), which makes possible to apply control techniques. In other words, we want to use this information to construct a filter for the evolution problem. This modifies the original evolution problem through a control term based on the observation error. In this framework, the present work is dedicated to the development of acceleration methods for the solution of periodic problems. This kind of problems can be faced, for instance, in the cardiac contractions modeling [2]. Another example is a steady rolling of a viscoelastic tyre [1] with a periodic sculpture. In this case, the steady state satisfies a "rolling" periodicity condition: the state at any point is the same that at the corresponding point of the next sculpture motive but one time period ago. It means the periodicity condition includes shift both in time and space. For such problems, we consider such a space-time periodicity as an observation and we use it for developing an accelerating method. The main idea is to modify the original problem by introducing a feedback control term [2, 3, 4] based on a periodicity error,which accelerates convergence to the stable periodic solution of the problem.

In the following section, we present an analytical analysis of an abstract problem, in order to find out an optimal form of the control. After introducing a delayed feedback control term based on the observation error (in an abstract form), we find the solution to the modified problem, in order study the influence of the control on the convergence rate. Then, we propose the optimal control, optimizing the spectrum of the problem and minimizing the convergence time. The proposed control can be mechanically interpreted. And the efficiency of the method increase with the convergence time of the problem.

The last section applies the technique to a full viscoelastic problem. There we consider the steady rolling of the viscoelastic tyre with a periodic sculpture. The numerical simulation results are presented, comparing both controlled and non-controlled solutions in a simplified 2D framework.

2 ANALYTICAL ANALYSIS

2.1 General problem

Let us consider a general evolution problem with space-time periodic condition:

$$\partial_t u + Au = f \tag{1}$$
$$u(t) = Hu(t-T) \tag{2}$$

defined on a Hilbert space V with scalar product $\langle \cdot, \cdot \rangle$. We make two fundamental assumptions which are usually satisfied for time periodic viscoelastic problems:

- the operator A is V-elliptic, namely there exists a constant $C > 0$ such that $\forall u \in V$ $\langle Au, u \rangle \geq C\|u\|^2$
- the operators A and the space shift H can be diagonalized in the same basis.

In practice, the solution of such problems is usually computed as an asymptotic limit of the solution to the initial value evolution problem (1) with an arbitrary initial condition. Due to the ellipticity condition, this asymptotic limit exists. In the frame of this work, we are going to propose an optimal control method, accelerating the convergence of the initial value problem solution to the solution of (1)-(2).

2.2 Controlled problem

We can consider the condition (2) as an observation and use it to construct a control method. So we modify the initial value problem by introducing a feedback control term [3, 4], based on the observation error, as follows:

$$\partial_t u(t) + Au(t) + \overbrace{G\Big(u(t) - Hu(t-T)\Big)}^{\text{control term}} = f, \tag{3}$$
$$u(t) = \phi(t), \quad t \leq 0. \tag{4}$$

Above $\phi(t)$ represents the initial data, and $u(t) - Hu(t-T)$ is the observation error. Moreover, the gain operator G which acts on this observation error has to be properly identified. It is clear that the solution $u(t,x)$ to the modified problem (3) converges to the solution of the original problem (1). The question is whether there exists a gain operator G, providing the fastest convergence to the time periodic asymptotic limit. This amounts to analyze the influence of the gain operator G on the (vanishing) asymptotic behavior of the homogeneous solution of (3). Thus we have to find the solution of the homogeneous controlled problem as a function of G, which will yield the optimal choice of G by minimizing the real part of the spectrum of the problem. We assume that the gain operator can be expressed as an analytical function $G(A, H)$ of the evolution and shift operators. Then if A and H are diagonalizable in the same base, G is also diagonalizable in this base.

Theorem 1. *Since A, G and H are diagonalizable in the same base $\{v_p(x)\}_{p\in\mathbb{Z}}$, the homogeneous solution to the controlled problem (3) is simply given by*

$$u(t,x) = \sum_{p,k\in\mathbb{Z}} c_{p,k}\, e^{\lambda_{p,k} t} v_p(x) \tag{5}$$

where the coefficients $c_{p,k}$ are defined from the initial data, and the inverse relaxation time $\lambda_{p,k}$ can be expressed in terms of eigenvalues of A, G and H.

Proof. We write the solution $u(t,x)$ in the base $\{v_p(x)\}_{p\in\mathbb{Z}}$, where A, G and H are diagonalizable:

$$u(t,x) = \sum_{p\in\mathbb{Z}} u_p(t) v_p(x) \tag{6}$$

where $u_p(t)$ are the coordinates of $u(t,x)$ in this base. Let α_p, γ_p and σ_p be the eigenvalues of A, G and H respectively, associated to the same eigenfunction $v_p(x)$. Then $u_p(t)$ satisfies

$$\partial_t u_p(t) + (\alpha_p + \gamma_p)\, u_p(t) - (\gamma_p \sigma_p) u_p(t-T) = 0, \qquad \forall p \in \mathbb{Z} \tag{7}$$

This is a simple delay-differential equation [5, 6, 7]. We are looking for its solution in the exponential form $u_p(t) = e^{\lambda_p t}$. The characteristic equation for λ_p is

$$\lambda_p + (\alpha_p + \gamma_p) - (\gamma_p \sigma_p)\, e^{-T\lambda_p} = 0. \tag{8}$$

Multiplying this by $Te^{T(\lambda_p+\alpha_p+\gamma_p)}$, this characteristic equation takes the form:

$$T\,(\lambda_p + \alpha_p + \gamma_p)\, e^{T(\lambda_p+\alpha_p+\gamma_p)} = T\,(\gamma_p\sigma_p)\, e^{T(\alpha_p+\gamma_p)} \tag{9}$$

To represent a solution of this equation, one have to introduce a Lambert W function [8, 10, 11, 7]. It is a complex-valued function denoted by $W\,[z]$ and satisfying $W\,[z]\, e^{W[z]} = z$ $(\forall z \in \mathbb{C})$. The Lambert W function will be described in more details in the next paragraph. For the time being, simply note that the Lambert function W is multivalued and has an infinite number of branches W_k, $k \in \mathbb{Z}$. Then, we can rewrite the equation (9) in terms of W_k as :

$$T\,(\lambda_p + \alpha_p + \gamma_p) = W_k\left[T\,(\gamma_p\sigma_p)\, e^{T(\alpha_p+\gamma_p)}\right], \qquad k \in \mathbb{Z}. \tag{10}$$

So the characteristic equation (8) has an infinite number of roots, corresponding to different branches W_k of the Lambert function :

$$\lambda_{p,k} = -\,(\alpha_p + \gamma_p) + \frac{1}{T} W_k\left[T\,(\gamma_p\sigma_p)\, e^{T(\alpha_p+\gamma_p)}\right], \qquad k \in \mathbb{Z}, \quad p \in \mathbb{Z}. \tag{11}$$

Thus, the general solution to (7) is

$$u_p(t) = \sum_{k\in\mathbb{Z}} c_{p,k} e^{\lambda_{p,k} t}, \qquad \forall p \in \mathbb{Z} \tag{12}$$

Assembling all components of the eigenbase, we then obtain the solution (6) to the controlled problem (3):

$$u(t,x) = \sum_{p\in\mathbb{Z}} \sum_{k\in\mathbb{Z}} e^{\lambda_{p,k} t} c_{p,k} v_p(x) \tag{13}$$

with $\lambda_{p,k}$ as defined by (11). Coefficients $c_{p,k}$ are to be found from the initial data.

□

2.3 A few properties of the Lambert W function

Let us take a brief overview on the Lambert W function [8, 9, 10, 11, 7] with its infinite number of branches $W_k,\ k \in \mathbb{Z}$. For any branch, its first derivative is given by

$$\frac{d}{dz} W_k [z] = \frac{W_k [z]}{z(W_k [z] + 1)}, \qquad k \in \mathbb{Z} \tag{14}$$

Their real values have some order [10, 11]. The rightmost value corresponds to the so called principal branch W_0:

$$\max_{k \in \mathbb{Z}} \Re W_k [z] = \Re W_0 [z], \quad \forall z \in \mathbb{C}. \tag{15}$$

This real value of this principal branch is bounded from below by -1 and reaches the minimum at $z = -\frac{1}{e}$, i.e.

$$\Re W_0 [z] \geq -1, \quad \forall z \in \mathbb{C}, \tag{16}$$

$$W_0 \left[-\tfrac{1}{e}\right] = -1. \tag{17}$$

Inside the circle $|z| < \frac{1}{e}$, the principal branch can be decomposed in power series [9]

$$W_0 [z] = \sum_{n=1}^{\infty} \frac{(-n)^{n-1}}{n!} z^n, \qquad |z| < \frac{1}{e} \tag{18}$$

The real part of the principal branch $\Re W_0$ is plotted on Figure 1 (in this section, all plots are extracted from Mathematica 10.0).

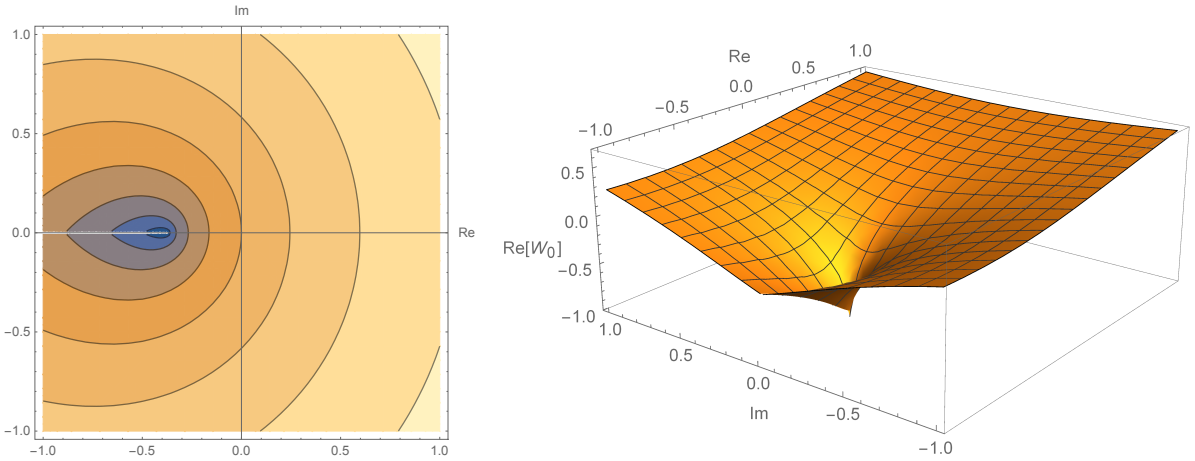

Figure 1: Real part of the principal branch of Lambert W function.

We can also define a Lambert operator W as follows : for any linear operator A, the Lambert W operator function of A is a linear operator $W[A]$, such that $W[A]\, e^{W[A]} = A$. Under minor assumptions on the operator A, one can also prove that this operator has an infinite number of branches W_k, $k \in \mathbb{Z}$, with a principal branch W_0.

2.4 Main result: the optimal control

The next theorem presents the main result of the current paper, namely the characterization of the optimal control for the problem (3).

Theorem 2. *Under the assumptions of paragraph 2.1, the optimal gain operator for the problem (3), providing the fastest convergence to the asymptotic solution, is given by*

$$G = \frac{1}{T} W_0 \left[-\tfrac{1}{e} e^{-TA} H^{-1} \right], \tag{19}$$

where W_0 denotes the operator form of the principal branch of the Lambert W function.

Proof. According to Theorem 1, the solution of the controlled problem takes the exponential form (5) with inverse (complex) relaxation time defined by (11). When all $\lambda_{k,p}$ have negative real part, the solution converges in time to the asymptotic limit, corresponding to the periodic solution of the problem. By properly constructing the eigenvalues of G in (11), we can control the problem's inverse relaxation times $\lambda_{k,p}$. Decreasing their real part, we accelerate the convergence. The optimal control, providing the fastest convergence, moves all eigenvalues $\lambda_{k,p}$ on the left as much as possible. According to (15), for any $p \in \mathbb{Z}$ we have $\Re\lambda_{0,p} = \max_{k\in\mathbb{Z}} \Re\lambda_{k,p}$. Therefore, we need to optimize the principal branches $\lambda_{0,p}$:

$$\lambda_{0,p} = -\alpha_p + \underbrace{\frac{1}{T}\left(W_0 \left[T\sigma_p\gamma_p \, e^{T(\gamma_p+\alpha_p)} \right] - T\gamma_p \right)}_{\text{control term}}, \qquad p \in \mathbb{Z}. \tag{20}$$

The second term in the right part characterizes the convergence rate of the controlled problem. For the non-controlled solution ($\gamma_p = 0, \ \forall p$), this term is equal to zero. Convergence slows down, if it is real value is positive, and accelerates, if it is negative. When its real value is minimal, $\lambda_{0,p}$ is moved to the left as much as possible, and the associated γ_p is optimal. Therefore, for each $p \in \mathbb{Z}$ we need to compute γ_p, which minimizes the control term:

$$\gamma_p = \arg\min_{\gamma} \Re \left(W_0 \left[T\gamma \, e^{T\gamma} \sigma_p e^{T\alpha_p} \right] - T\gamma \right), \qquad p \in \mathbb{Z}. \tag{21}$$

Let us fix p and make the change of variable:

$$\gamma_p = \frac{1}{T} W_0 \left[z \right], \text{ yielding } z = T\gamma_p e^{T\gamma_p}. \tag{22}$$

We therefore have to solve the following minimization problem:

$$\begin{gathered} \text{Find } \ z \in \mathbb{C} \ \text{ minimizing } \ \Re\, J(z), \\ J(z) = W_0 \left[\eta z \right] - W_0 \left[z \right], \end{gathered} \tag{23}$$

where $\eta = \sigma_p e^{T\alpha_p}$ is a given complex number constructed from the eigenvalues of A and H. The minimizers cancel the derivatives of the cost function J, which from formula (14) satisfy :

$$\begin{aligned} \tfrac{d}{dz} J(z) &= \frac{W_0 \left[\eta z \right]}{z(W_0 \left[\eta z \right] + 1)} - \frac{W_0 \left[z \right]}{z(W_0 \left[z \right] + 1)} && (24) \\ &= \frac{J(z)}{z(W_0 \left[\eta z \right] + 1)(W_0 \left[z \right] + 1)} && (25) \end{aligned}$$

There are two candidates, where the derivative takes infinite values:

$$W_0\left[z\right] = -1 \qquad \Leftrightarrow \qquad z = -\tfrac{1}{e} \tag{26}$$

or

$$W_0\left[\eta z\right] = -1 \qquad \Leftrightarrow \qquad z = -\tfrac{1}{\eta e} \tag{27}$$

The point $z = 0$ makes no interest, since it corresponds to the non-controlled case. From (16) we also have

$$\Re J(-\tfrac{1}{e}) = \quad \Re\, W_0\left[-\tfrac{\eta}{e}\right] + 1 \quad \geq 0 \tag{28}$$

$$\Re J(-\tfrac{1}{\eta e}) = \; -\left(1 + \Re\, W_0\left[-\tfrac{1}{\eta e}\right]\right) \; \leq 0 \tag{29}$$

Hence we conclude that the solution of the minimization problem (23) is given by the critical point $z = -\frac{1}{\eta e}$, that is

$$\gamma_p = \frac{1}{T} W_0\left[-\tfrac{1}{e}\,\sigma_p^{-1} e^{-T\alpha}\right] \tag{30}$$

In operator terms, this yields

$$G = \frac{1}{T}\, W_0\left[-\tfrac{1}{e}\, H^{-1} e^{-TA}\right]. \tag{31}$$

□

Corollary 2.1. *If the inverse of the shift H is weakly contracting $\|H^{-1}\| \leq 1$, the optimal control takes the explicit form*

$$G = -\frac{1}{T}\sum_{n=1}^{\infty} c_n \cdot \left(H^{-1} e^{-TA}\right)^n \quad \textit{with} \;\; c_n = \frac{n^{n-1}}{n!\, e^n}. \tag{32}$$

Proof. Since A is elliptic, then $\Re\alpha_p > 0$ and $|e^{-\alpha_p}| \leq 1$. If $\|H^{-1}\| \leq 1$, then $|\sigma_p^{-1}| \leq 1$. Therefore

$$|-\tfrac{1}{e}\,\sigma_p^{-1} e^{-\alpha_p}| < \tfrac{1}{e}, \qquad \forall p \in \mathbb{Z}. \tag{33}$$

So γ_p in (30) can be decomposed in the power series (18):

$$\gamma_p \;=\; \frac{1}{T} W_0\left[-\tfrac{1}{e}\,\sigma_p^{-1} e^{-T\alpha}\right] \tag{34}$$

$$\;=\; \frac{1}{T}\sum_{n=1}^{\infty} \frac{(-n)^{n-1}}{n!}\left(-\tfrac{1}{e}\,\sigma_p^{-1} e^{-T\alpha}\right)^n \tag{35}$$

$$\;=\; -\frac{1}{T}\sum_{n=1}^{\infty} \frac{n^{n-1}}{n!\, e^n}\left(\sigma_p^{-1} e^{-T\alpha}\right)^n \tag{36}$$

yielding the claimed statement. □

Remark 2.1. *In practice, the norm of the shift operator or of its inverse is unity. We can therefore use (32) for calculating G, usually restricting ourselves to the first five terms.*

Remark 2.2. *Note that $e^{-t\mathcal{A}}$ is a fundamental solution of the non-controlled problem, i.e. $u(t,x) = e^{-t\mathcal{A}}u(0,x)$, when $G = 0$. That is e^{-TA} plays role of the T-shift in time for the non-controlled solution. Thus the proposed control can be interpreted as a correction of the present solution by canceling all the future T-shifted periodicity errors :*

$$\mathcal{G}\Delta u(t) \simeq -\frac{1}{T}\sum_{n=1}^{\infty} c_n\, H^{-n}\Delta u(t+nT) \tag{37}$$

where the periodicity error

$$\Delta u(t) = u(t) - Hu(t-T) \tag{38}$$

2.5 Efficiency of the method

We have developed an optimal control for an abstract evolution problem, accelerating convergence to the periodic solution. Now we want to estimate the efficiency of the proposed control, that is how fast does the controlled solution converge in comparison with the non-controlled one. This is based on a direct calculation yielding

$$\begin{aligned}
\lambda_{0,p} &= -\alpha_p + \frac{1}{T}\left(W_0\left[T\gamma_p\sigma_p e^{T(\alpha_p+\gamma_p)}\right] - T\gamma_p \right) && (39)\\
&= -\alpha_p - \frac{1}{T}\left(1 + W_0\left[-\tfrac{1}{e}\sigma_p^{-1}e^{-T\alpha_p}\right] \right) && (40)\\
&= -\alpha_p - \frac{1}{T}\, g\left(\log\sigma_p + T\alpha_p\right) && (41)
\end{aligned}$$

where we define the spectral control term by

$$g(z) = 1 + W_0\left[-\tfrac{1}{e}\, e^{-z}\right] \tag{42}$$

The real part of $g(z)$, $z \in \mathbb{C}$ on the right half-plane $\Re z \geq 0$ is represented on Figure 2, and its restriction on the real axis is detailed on Figure 3.

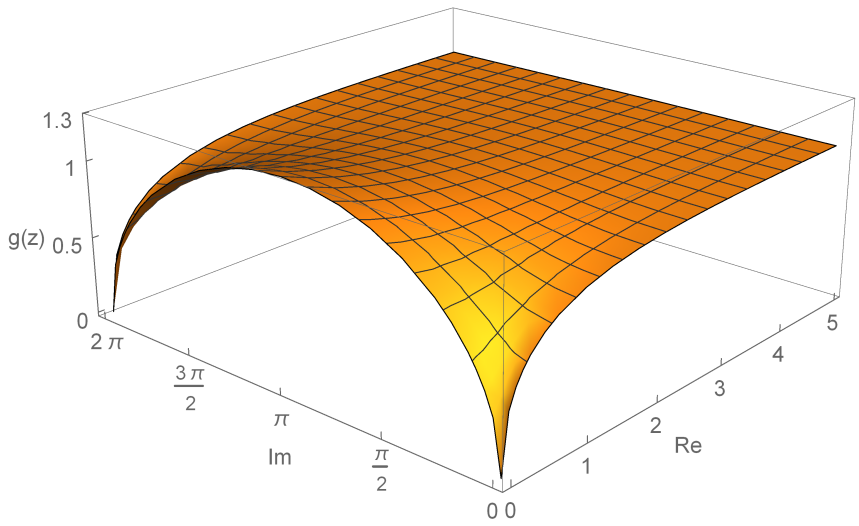

Figure 2: Real part of $g(z)$ on the complex right half-plane $z \in \mathbb{C}$, $\Re z \geq 0$.

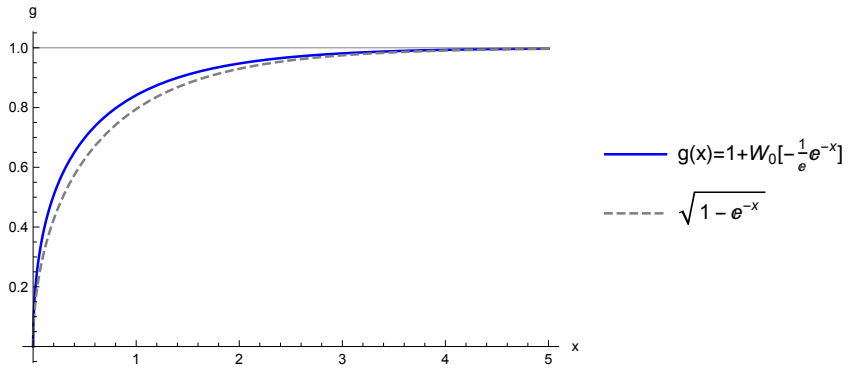

Figure 3: Function $g(x) = 1 + W_0\left[-\frac{1}{e}\, e^{-x}\right]$ on the real half-line $x \geq 0$.

A direct calculation then yields

$$1 + \frac{g(\Re(\log \sigma_p + T\alpha_p))}{T\Re\alpha_p} \leq \left|\frac{\Re\lambda_{0,p}}{\Re\alpha_p}\right| \leq 1 + \frac{g(\Re(\log \sigma_p + T\alpha_p) + i\pi)}{T\Re\alpha_p} \tag{43}$$

For the proposed optimal control, we therefore see that the gain increases when the real part of the spectrum of the operator A goes to zero (see Figure 4). In other words, the method gets more and more efficient when the problem gets more and more viscous, as represented on Figure 4, which computes the approximate minimal gain as the function of the eigenvalues of A, obtained by replacing the control term g by its real approximation $\sqrt{1 - e^{-x}}$.

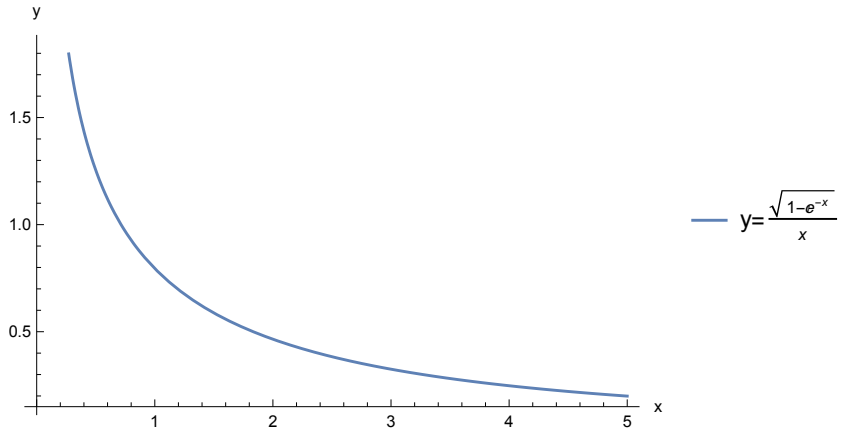

Figure 4: Estimation of the slowest convergence rate: y - gain, x - spectrum of A.

3 APPLICATION: STEADY ROLLING OF A VISCOELASTIC PERIODIC WHEEL

3.1 Model problem

The present section is dedicated to the application of the developed control method to a model problem, in order to justify on practice the theoretical results discussed in the previous section. It considers a steady rolling problem of a 2D viscoelastic tyre [1] presenting a space periodic sculpture. In our approach the periodicity of the sculpture is represented not by a modification of the geometry but by a space periodic modification of the Young's modulus. Thus our model problem considers the steady rolling of a simple viscoelastic ring, with a Young's modulus periodic as a function the angle. We apply a rotating lateral force, representing the contact force applied by the soil. In contrast with the real contact model, we suppose herein that this lateral force is a given function of time and space. Viscoelasticity implies that we deal with an evolution problem in terms of strains. We are interested in the established space-time periodic state, which is the asymptotic limit of the initial value problem with an arbitrary initial state. Applying the optimal control method described in the previous section, we expect to accelerate the convergence to the desired periodic solution.

In more details, let us consider a steady rolling of a wheel (Figure 5, left) with an angular velocity ω. A given force, presenting a ground contact pressure, is applied to the outer border Γ_1 and normal to its surface. In Lagrange (material) configuration, it moves along the exterior boundary with angular velocity $-\omega$. In a Lagrangian frame, its normal component takes the form $f(t, \underline{x}) = f(R_{\omega t}\underline{x})$, with $f(\underline{x})$ quadratic on part of the boundary and zero elsewhere as shown on Figure 5, right. The notation $R_{\omega t}$ represents a rotation of angle ωt around the origin.

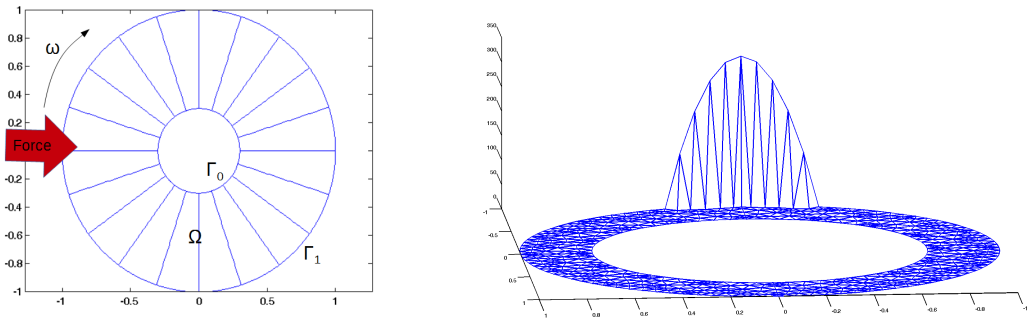

Figure 5: Left: 2D tyre. Right: Normal pressure

On the inner boundary Γ_0, a zero displacement condition is imposed. Thus, in the absence of mass forces, the momentum conservation law writes:

$$\operatorname{div} \underline{\underline{\sigma}} = 0, \qquad \text{in } \Omega \tag{44}$$

$$\underline{\underline{\sigma}}\, \underline{n}\,|_{\Gamma_1} = f\, \underline{n}, \qquad \underline{u}|_{\Gamma_0} = 0, \tag{45}$$

where $\underline{u}$ is the displacement field and $\underline{\underline{\sigma}}$ is a Cauchy stress tensor, $\underline{n}$ denotes a unit normal to the boundary.

The material is considered to be viscoelastic and nearly incompressible. We assume that we are in small strains. The viscoelastic constitutive law is of Kelvin-Voight type :

$$\underline{\underline{\sigma}}\,(t, x) = \eta\, \partial_t \underline{\underline{\varepsilon}}\,(t, \underline{x}) + \underline{\underline{\underline{\underline{K}}}}(\underline{x})\, \underline{\underline{\varepsilon}}\,(t, \underline{x}) \tag{46}$$

where $\underline{\underline{\varepsilon}}$ is the strain tensor

$$\underline{\underline{\varepsilon}} = \frac{1}{2}\left(\nabla \underline{u} + (\nabla \underline{u})^{\top}\right) = \nabla_s \underline{u}, \tag{47}$$

η is a scalar viscosity coefficient; $\underline{\underline{\underline{\underline{K}}}}$ is the fourth-order elasticity tensor:

$$\underline{\underline{\underline{\underline{K}}}}\,\underline{\underline{\varepsilon}} = \lambda \operatorname{tr}\underline{\underline{\varepsilon}}\,\underline{\underline{\mathbb{1}}} + 2\mu\underline{\underline{\varepsilon}}, \tag{48}$$

where Lamé coefficients λ and μ are expressed via Young's modulus E and Poisson's ratio ν:

$$\lambda = \frac{E\nu}{(1+\nu)(1-2\nu)}, \qquad \mu = \frac{E}{2(1+\nu)} \tag{49}$$

Given a nearly incompressible material, the Poisson's ratio is taken close to 0.5. As it was mentioned above, the periodic structure of the wheel is represented by the angular periodicity of the Young's modulus $E(\underline{x})$. Namely, there is an angle $\omega T = 2\pi/M$ (where M is the number of sculpture motives), such that

$$E(\underline{x}) = E(R_{\omega T}\underline{x}). \tag{50}$$

Herein, we have simply taken $E(\underline{x}) = E_0\left(1 + \cos\left[\frac{2\pi}{\omega T}\arg \underline{x}\right]\right)$, where E_0 is the mean of Young's modulus. We are looking for a "rolling" periodic solution, i.e. a solution satisfying the following space-time periodicity condition:

$$\underline{u}(t, \underline{x}) = R_{\omega T}^{-1}\,\underline{u}(t - T, R_{\omega T}\underline{x}). \tag{51}$$

In other words, the state at any point is the same that the one at the corresponding point of the next sculpture motive but one time period ago. Let us therefore define the space shift

$$H = R_{\omega T}^{-1}\,\underline{u}(t - T, R_{\omega T}\underline{x}) \tag{52}$$

Altogether, we are looking for the displacement field $\underline{u}(t, \underline{x})$ which satisfies :

$$\begin{aligned} \operatorname{div}\left[\eta\,\nabla_s \partial_t \underline{u} + \underline{\underline{\underline{\underline{K}}}}\,\nabla_s \underline{u}\right] &= 0, && \text{in } \Omega \\ \left[\eta\,\nabla_s \partial_t \underline{u} + \underline{\underline{\underline{\underline{K}}}}\,\nabla_s \underline{u}\right]\cdot \underline{n} &= f\,\underline{n}, && \text{on } \Gamma_1 \\ \underline{u} &= 0, && \text{on } \Gamma_0 \\ \underline{u}(t) &= H\underline{u}(t - T). \end{aligned} \tag{53}$$

3.2 Controlled problem

Let us introduce the space $V_0 = \{\underline{v} \in H^1(\Omega)^2 \mid \underline{v} = 0 \text{ on } \Gamma_0\}$ and let us define the operators $\mathcal{C}$ and $\mathcal{K}$ as follows: $\forall \underline{v} \in V_0$

$$\int_\Omega \mathcal{C}\underline{u}\cdot\underline{v} = \int_\Omega \eta\,\nabla_s \underline{u} : \nabla_s \underline{v} \tag{54}$$

$$\int_\Omega \mathcal{K}\underline{u}\cdot\underline{v} = \int_\Omega \underline{\underline{\underline{\underline{K}}}}\,\nabla_s \underline{u} : \nabla_s \underline{v} \tag{55}$$

Then the system (53) writes:

$$\int_\Omega (\mathcal{C}\partial_t \underline{u} + \mathcal{K}\underline{u}) \cdot \underline{v} = \int_{\Gamma_1} f\, \underline{n} \cdot \underline{v}, \qquad \forall \underline{v} \in V_0, \tag{56}$$
$$\underline{u}(t) = H\underline{u}(t-T).$$

The associated controlled problem is

$$\int_\Omega \Big(\mathcal{C}\partial_t \underline{u} + \mathcal{K}\underline{u} + \mathcal{G}\left(\underline{u}(t) - H\underline{u}(t-T)\right)\Big) \cdot \underline{v} = \int_{\Gamma_1} f\, \underline{n} \cdot \underline{v}, \qquad \forall \underline{v} \in V_0 \tag{57}$$
$$\underline{u}(t) = \underline{u}_0(t), \qquad t \leq 0$$

with arbitrary initial data $\underline{u}_0$. According to Theorem 2, the optimal gain operator takes the form

$$\mathcal{G} = -\frac{1}{T}\mathcal{C} \sum_{n=1}^{\infty} c_n\, e^{-nT\left(\mathcal{C}^{-1}\mathcal{K}\right)} H^{-n}, \qquad c_n = \frac{n^{n-1}}{n!\, e^n}. \tag{58}$$

If we proceed with the finite element discretization, it can be quite expensive to compute an exponential of the matrix associated to the operator $\mathcal{C}^{-1}\mathcal{K}$. So we need to simplify this expression.

3.3 Simplified controlled problem

Let $\underline{u}_*$ be the periodic solution of the problem (53), that is the true displacement, and $\underline{\underline{\sigma}}_* = \eta\, \nabla_s \partial_t \underline{u}_* + \underline{\underline{\underline{\underline{K}}}}\, \nabla_s \underline{u}_*$ be the true Cauchy stress. Associated to this true stress tensor $\underline{\underline{\sigma}}_*$, the true strain tensor $\underline{\underline{\varepsilon}}_* = \nabla_s \underline{u}_*$ is the solution of the first order differential equation

$$\eta\, \partial_t \underline{\underline{\varepsilon}} + \underline{\underline{\underline{\underline{K}}}}\, \underline{\underline{\varepsilon}} = \underline{\underline{\sigma}}_* \tag{59}$$
$$\underline{\underline{\varepsilon}}\,(t) = H\underline{\underline{\varepsilon}}\,(t-T) \tag{60}$$

If we suppose that we know the true stress tensor $\underline{\underline{\sigma}}_*$, we can apply the optimal feedback control of the previous section to this problem, leading to the associated controlled problem:

$$\eta\, \partial_t \underline{\underline{\varepsilon}} + \underline{\underline{\underline{\underline{K}}}}\, \underline{\underline{\varepsilon}} + \eta\, \underline{\underline{\underline{\underline{G}}}} \left(\underline{\underline{\varepsilon}} - H\underline{\underline{\varepsilon}}(t-T)\right) = \underline{\underline{\sigma}}_* \tag{61}$$
$$\underline{\underline{\varepsilon}}(t) = \nabla_s \underline{u}_0(t), \quad t \leq 0$$

with arbitrary initial data $\underline{u}_0$. According to Theorem 2, the optimal gain operator has the form

$$\underline{\underline{\underline{\underline{G}}}} = -\frac{1}{T} \sum_{n=1}^{\infty} c_n\, e^{-nT\left(\eta^{-1}\underline{\underline{\underline{\underline{K}}}}\right)} H^{-n}, \qquad c_n = \frac{n^{n-1}}{n!\, e^n}, \tag{62}$$

Note that the strain estimator $\underline{\underline{\varepsilon}}$ is not necessarily a displacement symmetric gradient any more and that we do not know the value of the true periodic stress. However, its initial value and its asymptotic limit is a gradient, and we know the divergence of the true stress field. Hence, we decide to decompose the strain estimator into a symmetric gradient and a zero divergence field

$$\underline{\underline{\varepsilon}} = \nabla_s \underline{u} + \underline{\underline{\tilde{\varepsilon}}}, \tag{63}$$

and to take the divergence of the strain controlled problem, omitting all terms in $\underline{\underline{\tilde{\varepsilon}}}$, which leads to the new controlled system

$$\begin{aligned}
\text{div}\,\Big[\eta\,\partial_t\nabla_s\underline{u} + \underline{\underline{\underline{\underline{K}}}}\;\nabla_s\underline{u} + \eta\,\underline{\underline{\underline{\underline{G}}}}\,\Big(\nabla_s\underline{u} - H\nabla_s\underline{u}(t-T)\Big)\Big] &= 0 \\
\Big[\eta\,\partial_t\nabla_s\underline{u} + \underline{\underline{\underline{\underline{K}}}}\;\nabla_s\underline{u} + \eta\,\underline{\underline{\underline{\underline{G}}}}\,\Big(\nabla_s\underline{u} - H\nabla_s\underline{u}(t-T)\Big)\Big]\cdot\underline{n} &= f\,\underline{n}, \qquad \text{on } \Gamma_1 \\
\underline{u} &= 0, \qquad \text{on } \Gamma_0 \\
\underline{u}(t) &= \underline{u}_0(t), \quad t \le 0
\end{aligned} \tag{64}$$

It is seen that $\underline{u}_*$ is the asymptotic limit for this problem, i.e. $\underline{u} \to \underline{u}_*$, and thus (64) is a controlled system associated to the initial model problem (53) with a simplified gain operator, applied to the strain field and computed by the formula

$$\underline{\underline{\underline{\underline{G}}}} = -\frac{1}{T}\sum_n c_n\, e^{-nT\left(\eta^{-1}\underline{\underline{\underline{\underline{K}}}}\right)} H^{-n}, \qquad c_n = \frac{n^{n-1}}{n!\,e^n}. \tag{65}$$

In this way, we have applied the developed optimal control method to the viscoelastic constitutive law. We may have sacrificed a part of the control "optimality" to the simplicity of its form. In practice, for a plane strain problem, introducing the reduced Lamé coefficients $\tilde{\lambda} = -nT\lambda/\eta$ and $\tilde{\mu} = -nT\mu/\eta$, the exponential coefficients in the gain operator (65) are defined by

$$e^{-nT\eta^{-1}\underline{\underline{\underline{\underline{K}}}}}\begin{bmatrix} \varepsilon_{11} & \varepsilon_{12} \\ \varepsilon_{12} & \varepsilon_{22} \end{bmatrix} = e^{\tilde{\lambda}+2\tilde{\mu}}\sinh\tilde{\lambda}(\varepsilon_{11}+\varepsilon_{22})\underline{\underline{\underline{\underline{\mathbb{1}}}}} + e^{2\tilde{\mu}}\begin{bmatrix} \varepsilon_{11} & \varepsilon_{12} \\ \varepsilon_{12} & \varepsilon_{22} \end{bmatrix} \tag{66}$$

3.4 Numerical results

The controlled and non-controlled evolution problems have been solved numerically, in order to compare their rates of convergence and to justify in practice that the controlled one is really faster. The numerical simulation has been carried out in MatLab R2014a by the finite elements method with $P1$ elements on a conforming triangular mesh (Figure 6), ωT-periodic with respect to rotation. It represents a tyre with 15 motives, i.e. $\omega T = 2\pi/15$. The periodic Young's modulus is in the form: $E(\underline{x}) = E_0\,(1 + \cos[15\arg\underline{x}])$, where E_0 is a homogeneous stiffness. An undeformed state is taken as initial data, that is $\underline{u}(0,\underline{x}) = 0$.

We carry out several pairs of simulations (controlled and non-controlled cases) with different values of viscosity coefficient, in order to verify if the efficiency estimation from paragraph 2.5 holds. The gain of the control method is represented by ratio n_0/n_c of the iteration numbers for non-controlled and controlled problem respectively. The gain values corresponding to distinct viscosity coefficients are presented in Table 1. These results are depicted on Figure 7. We can see that the efficiency indeed increases with the viscosity coefficient.

On Figure 8 there are plotted some simulation results: l_2-norm evolution of numerical solution (left column) and periodicity error (right column) with distinct viscosity coefficients ($\eta = E_0, 3E_0, 8E_0$ respectively). The abscissa ticks correspond to the number of ωT-periods. Dashed vertical lines mark the convergence time, that is the moment when the periodicity error becomes less than the specified accuracy. The large visible oscillations of the solution are associated with 2π-periodicity of the tyre, while the oscillations associated with ωT-periodicity are of a much smaller scale and aren't quite visible on the plot.

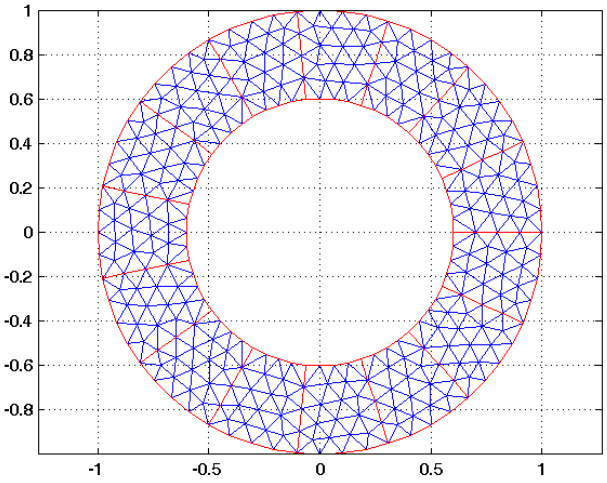

Figure 6: Periodic mesh, representing a tyre with 15 motives

Viscosity η	relax.time^{-1} E_0T/η	Gain n_0/n_c
$0.1E_0$	8.378	1.19
$0.5E_0$	1.676	1.38
E_0	0.838	1.62
$2E_0$	0.419	2.05
$3E_0$	0.279	2.41
$4E_0$	0.209	2.72
$5E_0$	0.168	2.97
$8E_0$	0.105	3.33

Table 1: Convergence time ratio with respect to viscosity coefficient.

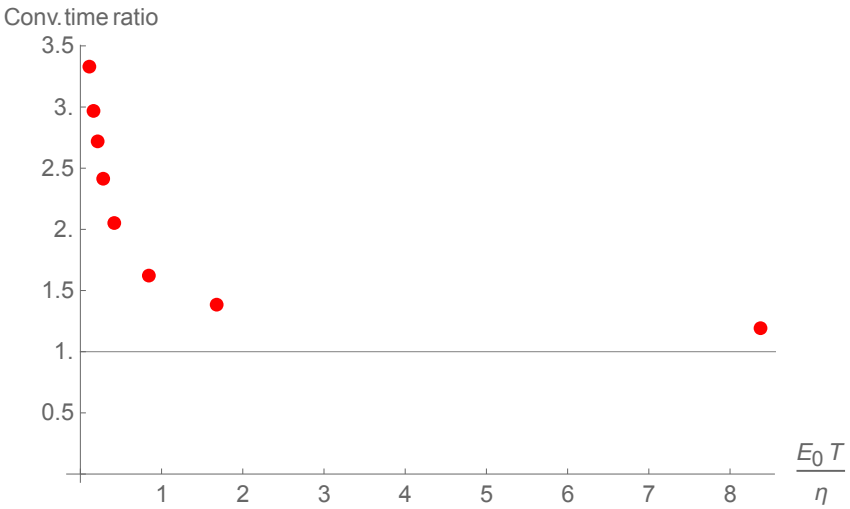

Figure 7: Convergence time ratio (gain) as the function of the inverse relaxation time.

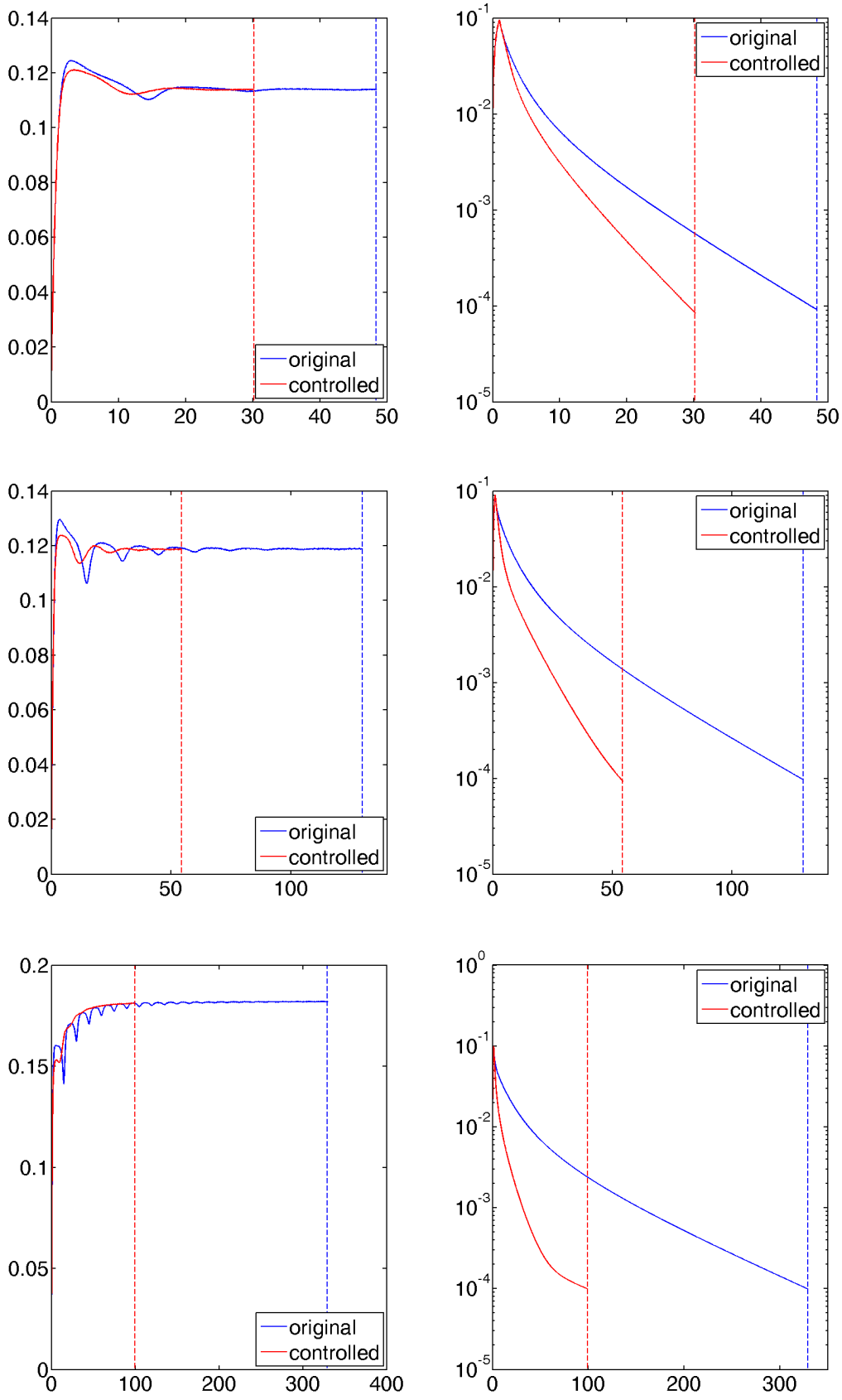

Figure 8: Results: l_2-norm of the numerical solution (left) and of the periodicity error (right) for $\eta = E_0, 3E_0, 8E_0$ respectively.

4 CONCLUSION

In this paper, we have developed a new control method for calculating viscoelastic evolution problems while accelerating the convergence of its solution to the asymptotic limit, which is time periodic. The method is similar to the feedback control methods, using the eigenvalue assignment technique [3, 4]. From another perspective, it can be interpreted as an observer-controller filtering method, where the space-time periodicity condition plays the role of the observation [2]. It turns out that the proposed control term actually acts like the correction of the present solution by the future periodicity errors (37).

As seen from the construction of the optimal control, its mathematical properties use the Lambert W function. In this way, we have estimated the dependence of the convergence acceleration on the relaxation rate. In fact, the acceleration increases with the memory of the problem. So the developed method might not be efficient for fast converging problems (which is not really of interest) but becomes more and more efficient for the slowly converging problems.

The developed control method has been tested on a full 2D model problem. It has been applied to the steady rolling of a viscoelastic tyre with a periodic sculpture. An approach, when the optimal control is applied to the viscoelastic evolution law, has been formulated. In this case, the control term is quite simple and cheap to compute. The numerical solution of the problem has justified the theoretical results: for a very viscous material, we have indeed obtained a significant acceleration of convergence.

ACKNOWLEDGMENTS

The work is supported by MFP Michelin. We also thank Jean François Deldon and Thomas Homolle for fruitful discussions.

REFERENCES

[1] P. Le Tallec, C. Rahier, Numerical models of steady rolling for nonlinear viscoelastic structures in finite deformations. *International Journal for Numerical Methods in Engineering*, **37**, 1159-1186, 1994.

[2] P. Moireau, *Assimilation de donnees par filtrage pour les systemes hyperboliques du second ordre. Applications à la mecanique cardiaque*. PhD thesis, Ecole Polytechnique, 2008.

[3] P. Hovel, E. Scholl, Control of unstable steady states by time-delayed feedback methods. *Physical Review E*, **72**, 046203, 2005.

[4] K. Pyragas, Analytical properties and optimization of time-delayed feedback control. *Physical Review E*, **66**, 026207, 2002.

[5] R. Bellman, K.L. Cooke, *Differential-Difference Equations*. Academic Press, New York, 1963.

[6] F.M. Asl, A.G. Ulsoy, Analysis of a System of Linear Delay Differential Equations. *ASME J. Dynamic Systems, Measurement and Control*, Vol. **125**, No. 2, p. 215-223, 2003.

[7] S. Yi, A.G. Ulsoy, Solution of a System of Linear Delay Differential Equations Using the Matrix Lambert Function, *Proceedings of American Control Conference*, 2433-2438, 2006.

[8] R.M. Corless, G.H. Gonnet, D.E.G. Hare, D.J. Jeffrey, D.E. Knuth, On the Lambert W Function. *Advances in Computational Mathematics*, **5**, 329–359, 1996

[9] R.M. Corless, D.J. Jeffrey, D.E. Knuth, A Sequence of Series for the Lambert Function. *Proceedings of the 1997 international symposium on Symbolic and algebraic computation*, pp. 197–204, 1997.

[10] H. Shinozaki, *Lambert W Function Approach to Stability and Stabilization Problems for Linear Time-Delay Systems*, Kyoto Institute of Technology, 2007

[11] H. Shinozaki, T. Mori, Robust stability analysis of linear time-delay systems by Lambert W function: Some extreme point results. *Automatica*, **42**, 1791-1799, 2006.

ECCOMAS Congress 2016
VII European Congress on Computational Methods in Applied Sciences and Engineering
M. Papadrakakis, V. Papadopoulos, G. Stefanou, V. Plevris (eds.)
Crete Island, Greece, 5–10 June 2016

COMBINING FINITE ELEMENT ANALYSIS AND ANALYTICAL MODELLING FOR EFFICIENT SIMULATIONS OF NON-LINEAR GEAR DYNAMICS

Shadi Shweiki[1], Jakub Korta[1], Antonio Palermo[1], Rocco Adduci[1] and Domenico Mundo[1]

[1] Department of Mechanical, Energy and Management Engineering, Università della Calabria
Cubo 45C, 87036, Rende, Italy
{shadi.shweiki, jakub.korta, antonio.palermo, domenico.mundo}@unical.it

Keywords: gear dynamics, meshing stiffness, 1D modelling, finite element simulation

Abstract. *Although gears have been used in mechanical industry for a long time and first systematic research activities, aimed at understanding gear meshing, started in the '50s, still nowadays a lack of accurate description for several physical phenomena represents a limitation for transmission design. One of the main causes of such limitations is the three-dimensional (3D), local and non-linear nature of contact problems. Given the complexity of these problems, a variety of modelling techniques with different levels of fidelity and required computational effort have been set up. Among the available methodologies, analytical modelling, which has been developed for a vast variety of applications from the early days of gear dynamics research, still attracts the interest of researchers thanks to the low computational requirements and to the capability to efficiently describe specific phenomena.*
Among analytical models, one-dimensional (1D) description aims at studying the torsional gear vibrations around the rotational axes and can be used to simulate either gear whine or gear rattle phenomena.
The aim of this paper is to illustrate a numerical approach, based on 3D (Finite Element) FE simulations, to estimate the mass and inertia properties of a 1D gear pair model. The proposed approach is based on pre-strained modal analyses, carried out on the 3D FE model of a pair of meshing gears, from which the variable meshing stiffness and modal mass values in a given system configuration are derived and used to calibrate the equivalent 1D model. An application example of the proposed method is provided by analyzing a pair of identical spur gears, for which the 1D model is created and used to estimate the dynamic TE at different rotation speeds and under constant external load in steady-state conditions.

1 INTRODUCTION

In the field of mechanical transmissions, simulation tools are acquiring ever more importance in the industrial development process that aims at achieving products of high quality at affordable costs, as to stand the competitive pressure of globalized markets. The dynamic behavior of gears has a direct influence on the performance of the entire system in terms of acoustic emissions and durability. The recent trend for lightweight design stresses even more the necessity to include a proper dynamic behavior as one of the main design targets. The gears themselves bring different challenging problems and difficulties at the design stage [1]. Typical non-linear phenomena [2] due to contact stiffness and clearance has to be well predicted in the initial design phase in order to reduce the development time and increase product quality. Given the complexity of these phenomena, a variety of modelling techniques with different levels of fidelity and required computational effort have been developed in the last decades. Three are the main model categories which can be identified: analytical, Finite Element (FE) and Multibody. Analytical models have been developed for a vast variety of applications[3-6]. They started from the early days of gear dynamics research, with a single gear pair and a single degree of freedom (DoF), and evolved until today's more refined 3D formulations. Ongoing research is still exploring analytical models since they provide low computational requirements, thanks to their lumped parameter formulation, and can be tailored to efficiently describe specific applications.

For these reasons, analytical formulations can be usefully employed, especially for analyses involving long operational time, where the simulation time and cost required by more detailed simulations would be prohibitively high. To achieve an analytical formulation of gear meshing, a one-dimensional (1D) description can be used with the aim of studying the torsional gear vibrations around the rotational. Such a simplified representation can be used to simulate either gear whine or gear rattle phenomena. Rotating masses are lumped into inertia moments and associated to the related rotational DoFs. Connectivity between the DoFs can be set by means of translational spring-damper elements by expressing rotations as equivalent displacements along the line of action, which represents the so called Transmission Error (TE) between the meshing gears. A 1D analytical model, which considers both clearance-type nonlinearity due to backlash and angle-varying mesh stiffness was proposed by Blankenship and Kahraman [3] to address the contact loss phenomenon in steady-state forced response.

When a 1D modeling approach for gear meshing analysis is used, simulation results can be found in a significantly shorter simulation time, as compared to the detailed FE simulations, but a higher approximation level in the description of the dynamic behavior of the engaging gears is paid. This means that, in order to use in a proficient way an analytical model, an a-priori knowledge of the system is required to prevent from neglecting important effects [7] or wasting efforts in modelling irrelevant phenomena.

The dynamic behavior of two engaging gears is strongly related to the variable meshing stiffness of the teeth in contact[8, 9]: a poorly approximated representation of the meshing stiffness in the simulation model causes poor results in terms of accurate prediction of the real behavior. In particular, an inaccurate representation of the meshing stiffness can result in a poor prediction of the dynamic response excited by orders coexisting with the fundamental meshing order in the system.

The purpose of this works is not to develop new analytical models but to present an alternative approach to improve the predictive accuracy of an existing 1D model without increasing its computational cost. From the simulation point of view, FE formulations proved a reliable tool in predicting the static and dynamic behavior of mechanical system

in a detailed manner, at the cost of high computational times. For this reason, the idea behind this work is to combine 3D FE modeling with a one DoF analytical model for dynamic simulation of gear meshing. This way, computationally demanding FE simulations are used in a model preparation phase to derive the gear pair meshing stiffness and resonance frequencies with high accuracy for a discrete number of different positions of the gears along the meshing cycle. A modal mass value is also then derived from the previous estimated quantities for each analyzed position along the meshing cycle. Model data derived from FE simulation is then used to define the parameters (equivalent inertia and instantaneous meshing stiffness) defining the 1D analytical model. The resulting 1D model is then used to simulate the dynamic behavior of a pair of identical gears in different operating conditions.

2 ANALYTICAL MODEL

One of the simplest models that allow predicting the dynamic torsional behavior of a pair of cylindrical gears is proposed in [3] and shown in Figure 1.

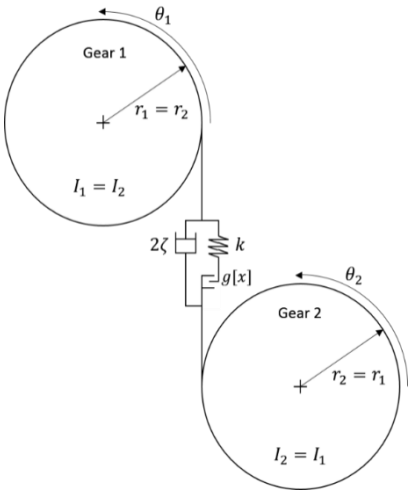

Figure 1: Dynamic representation of the 1D model of meshing cylindrical gears.

The dynamic behavior of this one DoF system, which considers a pair of identical gears, is ruled by the following equation of motion:

$$\ddot{x} + 2\zeta\dot{x} + k[POS(t)]g[x(t)] = F(t) \tag{1}$$

where x is the linear relative displacement of the contact points on the two meshing teeth along the line of action and represents the dynamic Transmission Error (*DTE*) in the system, $\dot{x}$ and $\ddot{x}$ are its first and second time derivatives; ζ is a damping coefficient introduced in the model in order to take into account friction losses between the teeth; the model parameter $k[POS(t)]$ is intended to represent the variable meshing stiffness as function of the instantaneous position of the teeth in the meshing cycle *POS(t)*, which is computed *a priori* with non-linear FE simulations and stored in a mono dimensional look-up table with the corresponding position in the meshing cycle[10, 11].

With this formulation it is also possible to model the backlash b between the gears introducing the restoring function $g[x(t)]$ which is the following function of the relative displacement between the teeth:

$$g[x(t)] = \begin{cases} x(t) - b, & x(t) > b, \\ 0, & |x(t)| \leq b, \\ x(t) + b, & x(t) < -b. \end{cases} \quad (2)$$

The restoring function acts as a switch for the meshing stiffness, by bringing its value to zero when the relative displacement is below the backlash threshold. This situation means that there is no contact between the teeth and consequently no elastic meshing force. When the instantaneous relative displacement assumes a value higher than the imposed backlash, the restoring function allows to consider only the effective penetration between the teeth in contact, subtracting the backlash from the estimated relative displacement.
The external force $F(t)$ in equation (1) represents the loading force in the system. In general, a time-varying load can be considered in the model, but it is considered to be constant in the work presented in this paper, based on the assumption that the imposed value of torque transmitted by the gears is constant.
The instantaneous acceleration value $\ddot{x}$ is computed numerically by using a Runge-Kutta algorithm, implemented in a Simulink model, that solves the following equation:

$$F - (kg + c\dot{x}) = M_{eq}\ddot{x} \quad (2)$$

The relative gear velocity and displacement are obtained by integrating acceleration and velocity respectively. The terms on the left side of equation 2 represent the force contribution due to external excitation, elastic force and damping force. The values of the last two contributions are calculated at each time step by multiplying the relative speed and penetration by the damping coefficient, assumed constant, and by the actual value of meshing stiffness respectively, which instead is dependent on the actual position of the gears along the meshing cycle. The latter is calculated, along with the equivalent mass M_{eq}, through a series of FE dynamic analyses of the two gears in different positions along the meshing cycle, as it will be illustrated in section 3.

3 FE MODEL

In order to enable the use of the analytical model described in section 2 and illustrated in Figure 1, the values of model parameters, such as meshing stiffness, damping coefficient and equivalent mass must be determined before the simulation starts.
The approach proposed in this work to obtain an estimate of these parameters is based on detailed static and dynamic FE simulations[12].
As illustration example, a simple mechanical transmission, consisting of a pair of identical gears already analyzed in [3] and with main geometric properties listed in table 1, is analyzed.

Parameter	Value
Normal module	3 mm
Normal pressure angle	20 deg
Pitch diameter	150 mm
Root diameter	142.5 mm
Facewidth	25.4 mm

Table 1: Gears specifications.

The proposed approach is based on a pre-processing phase in which the variable stiffness, and equivalent mass are computed from FE simulations, for different positions along the meshing stiffness. The 3D gear geometry was generated according to the geometrical parameters listed in table 1 and discretized with hexagonal elements for the FE analyses [13], as shown in figure 2. Data needed for 1D simulation are calculated using the pre-strained modal approach, carried out on a series of models, which represent the gears in discrete angular positions along the meshing cycle. In every position, a two-step FE simulation is carried out, starting from calculating teeth static deflection resulting from the application of a 300 Nm torque on the driving gear and by fixing all the DoFs of the center of rotation of the driven gear. This way, the static deflection of the teeth for different gear pair configurations is obtained, which is later used in combination with the results of a modal analysis, aimed at calculating the fundamental rotational resonant frequency of the system, to estimate the 1D model parameters.

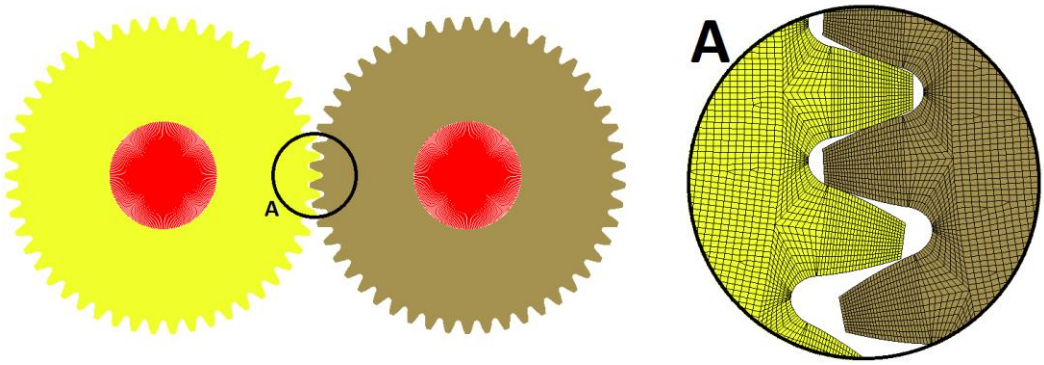

Figure 2: FE model of the analyzed gear pair, used to derive parameter values to be used in the 1D model.

The rotational (torsional) stiffness of the 1D model is calculated according as:

$$k_{\emptyset} = \frac{T}{\emptyset} \tag{3}$$

where T is the applied torque and $\emptyset$ the angular displacement of the statically loaded gear along the rotational axis. Another parameter derived from the simulation results is the equivalent mass, which is calculated as modal mass in the 1D model by using the following equation:

$$M_{eq} = \frac{k_{\emptyset}}{\omega^2} \tag{4}$$

where ω^2 is the square of fundamental torsional frequency estimated for the 3D model. Using this expression, M_{eq} and $k_{\emptyset}$ have been computed, which are used as model parameter data for the 1D model at the later stage. Figure 3 shows the calculated rotational stiffness and first resonant frequency estimated for the gear pair model in different angular positions along the meshing cycle. From these simulation results, it appears clear that the static and dynamic characteristics of a meshing gear pair depend very strongly on the instantaneous configuration. Figure 4 shows the first mode shape of the gears in two different angular positions, in which one and two teeth pairs are in contact. The figure shows also the frequency values of the first resonance in the two configurations, which were identified for these models through a pre-strained modal analysis. It can be seen that the difference is as high as 400 Hz, which is about 20% of the lower value.

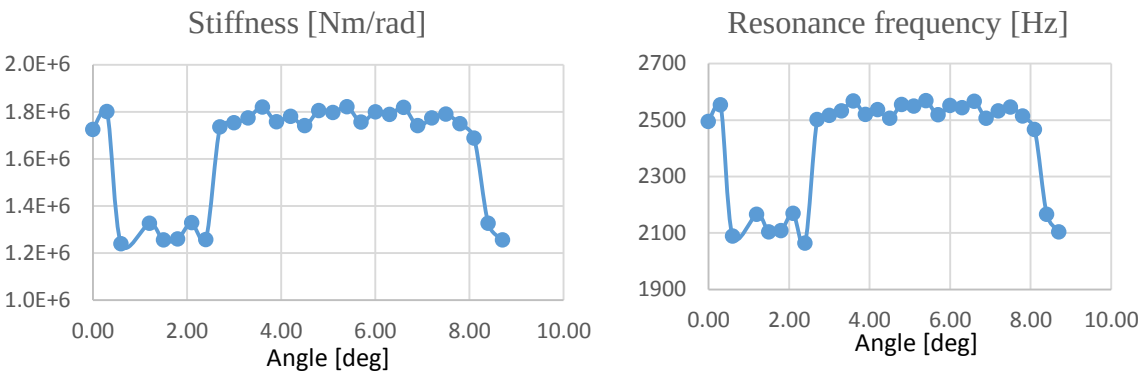

a b

Figure 3. Rotational stiffness (a) and fundamental frequency (b) values for the analyzed gear pair.

Figure 4. First resonant frequency and mode shape for a gear pair in two different angular configurations

4 RESULTS

Once the 1D model parameters are calculated, different analyses can be carried out by solving equation 2 and predict the dynamic behavior of the gear pair. In this paper we show the results of analyses that have been performed by operating the input gear with a constant speed until steady state was obtained. This process was repeated for different increasing and decreasing rotational velocities. Figure 5 shows a comparison between the DTE computed for an angular velocity of 600 rpm (a) and of 4200 rpm (b). The different shape of the two curves proves that this model is able to catch dynamic effects of gear meshing on DTE, which are not relevant at low rotational speed. The figure shows also that when the meshing frequency is close to the resonant frequency of the system, as in the case of figure 5-b, the DTE signal is dominated by the meshing order. In this case the first order of the rotational speed corresponds to the natural frequency of the gear pair.

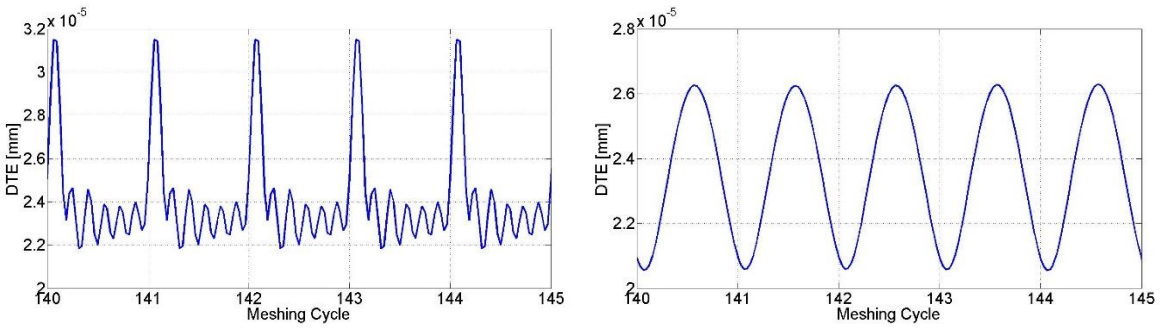

a b

Figure 5. Dynamic transmission error (DTE) for different angular speeds: 600 rpm (a) and 4200 rpm (b)

Effects of system non-linearity due to backlash between the meshing teeth is visible in figure 6, where the contact force along different meshing cycle is plotted. Contact losses between the teeth are shown by values of the meshing force close to 0 in figure 6-a, where elastic force is imposed to be zero by to the restoring function, while the damping force is still acting. Figure 6-b shows the trend of the contact force when no contact loss occurs, and minimum values are far away from zero.

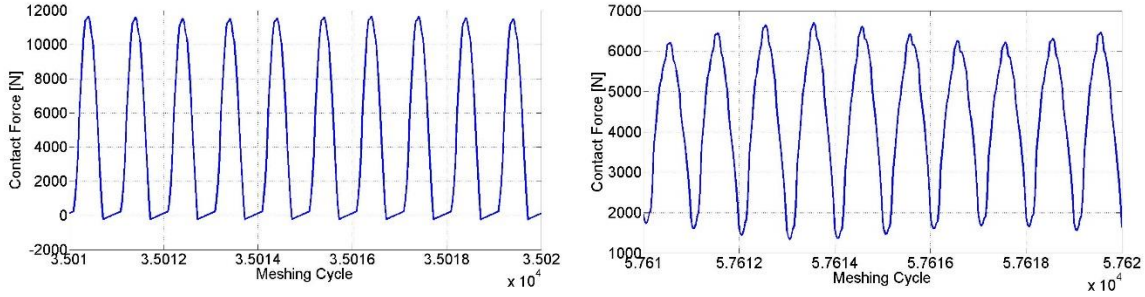

a b

Figure 6: Dynamic meshing force for in case of contact loss a) and without contact loss b)

Other effects that can be analyzed using this proposed simulation approach are the jump phenomena in the RMS value of the computed DTE, due to the clearance type non-linearity (Figure 7).

Due to the backlash between the gear teeth, different branches of RMS curves for the computed DTE are obtained when the rotational velocity changes, corresponding to different states of the system. The lower branch is obtained for slightly increasing speed while the upper branch is obtained for decreasing speed.

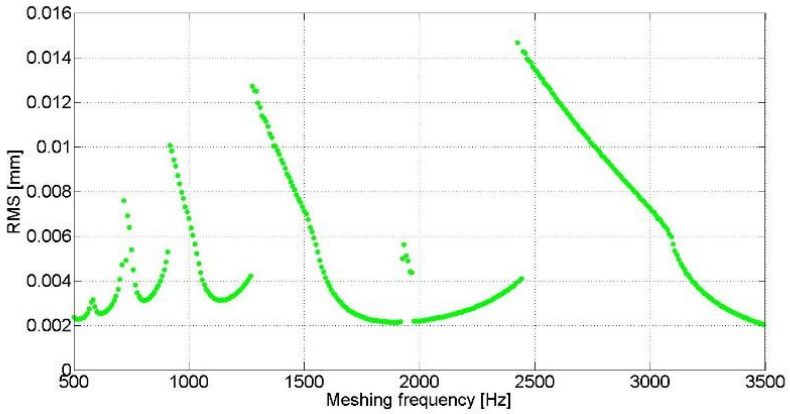

Figure 7: RMS of DTE plotted against meshing frequency

By considering the curves reported in figure 7 it is possible to recognize an almost-linear trend in the regions distant from the jumps frequency. The onset of contact loss causes a knee in the curve, recognizable as a softening effect compared to the almost-linear trend, which is a well-known behavior described in literature [3].

5 CONCLUSIONS

This work shows the possibility to use analytical model to describe complex phenomena related to gear dynamics. In the proposed approach the lack of accuracy of analytical and semi-analytical meshing stiffness formulations is covered by the use of FE

simulations which allow to have a realistic description of the meshing process. A high computational efficiency is reached by limiting the FE simulations in a preparation phase. The simplicity of the analytical formulation makes this model suitable for computationally efficient analyses, in those cases where the numerical complexity of FE-based models requires unaffordable computational time.
Classical jump-up phenomena are predicted by the model and agree with the classical trend shown in literature.
The 1D model described in this work takes into account only the relative rotation between the two gears bodies, under the assumption that the other relative displacements can be neglected during the simulation. The flexibility of the proposed approach for FE-based estimation of model parameters makes it applicable also to more complex analytical models for gear dynamic simulations, which allow taking into account additional relative displacements between the gears.

6 ACKNOWLEDGMENT

The research activities described in this paper were funded within the People Programme (Marie Curie Actions) of the 7th Framework Programme of the European Union FP7/2007-2013, under the contract with the Research Executive Agency (REA) n. 324336 and the related research project DEMETRA Design of Mechanical Transmissions: Efficiency, Noise and Durability Optimization (www.fp7demetra.eu).

7 REFERENCES

[1] S. Shweiki, A. Palermo, A. Toso, D. Mundo, and W. Desmet, “Effects of center distance and microgeometry on the dynamic behaviour of a spur gear pair,” in Proceedings of the International Conference on Engineering Vibration (ICOEV 2015) September 7–10, 2015, Ljubljana, Slovenia, 2015, pp. 119–130.
[2] K. L. Johnson and K. L. Johnson, Contact mechanics. Cambridge
university press, 1987.
[3] G. W. Blankenship, A. Kahraman, Steady state forced response of a mechanical oscillator with combined parametric excitation and clearance type non-linearity, Journal of Sound and Vibration, 185, 5 (1995) 743-765.
[4] H. N. Ozguven and D. R. Houser, “Dynamic analysis of high speed gears by using loaded static transmission error,” Journal of Sound and Vibration, vol. 125.1, 1988, pp. 71–83, ISSN: 0022-460X.
[5] G. Liu and R. G. Parker, “Dynamic modeling and analysis of tooth profile modification for multimesh gear vibration,” Journal of Mechanical Design, vol. 130, no. 12, 2008, p. 121402.
[6] D. R. Houser, J. Harianto, and Y. Ueda, “Determining the source of gear whine noise,”Gear Solutions, vol. 1623, 2004, pp. 17 – 22.
[7] J. D. Smith, Gear noise and vibration. CRC Press, 2003.
[8] R. G. Parker, S. M. Vijayakar, and T. Imajo, “Non-linear dynamic response of a spur gear pair: modelling and experimental comparisons,” Journal of sound and vibration, vol. 237, no. 3, 2000, pp. 435–455.
[9] V. K. Tamminana, A. Kahraman, and S. Vijayakar, “A study of the relationship between the dynamic factors and the dynamic transmission error of spur gear pairs,” Journal of Mechanical Design, vol. 129, 2007,pp. 75–84.

[10] A. Palermo, D. Mundo, R. Hadjit, and W. Desmet, “Multibody element for spur and helical gear meshing based on detailed three-dimensional contact calculations,” Mechanism and Machine Theory, vol. 62, 2013, pp. 13–30.
[11] A. Palermo, D. Mundo, R. Hadjit, and Desmet, “Effects of variable loads and misalignments on gear noise and vibration through multibody simulation based on transmission error,” in Proceedings of the International Conference on Noise and Vibration Engineering (ISMA2012) and 4th International Conference on Uncertainty in Structural Dynamics (USD2012) September 17–19, 2012, Leuven, Belgium, 2012, pp. 3995–4006.
[12] R. Version, “5.1, radioss theory manual, altair engineering,” Inc., Troy,MI, 2008.
[13] F. L. Litvin and F. A., Eds., Gear geometry and applied theory.Cambridge University Press, 2004, ISBN: 0-521-81517-7.

ECCOMAS Congress 2016
VII European Congress on Computational Methods in Applied Sciences and Engineering
M. Papadrakakis, V. Papadopoulos, G. Stefanou, V. Plevris (eds.)
Crete Island, Greece, 5–10 June 2016

DAMPING INDUCED BY DRY FRICTION: ANALYSES AND EXPERIMENTS FOR MODELING IMPROVEMENT

M.A. Douville, B. Faverjon, E. Chatelet, G. Jacquet-Richardet

[1] Université de Lyon, CNRS, INSA-Lyon, LaMCoS,
UMR5259, France F-69621LaMCoS
e-mail: georges.jacquet@insa-lyon.fr

Keywords: Vibration, Friction, Nonlinear behavior, Experiment, Modelling.

Abstract. *The present study deals with the effects of contact characteristics on the vibratory response of a beam associated with several rubbing devices. Experimentally different contact configurations are tested by varying the contact area size and roughness of samples. For each tests, the frequency response functions (FRF) are measured and compared. Numerically, temporal calculations are presented and compared to measured data, using Masing's contact model with updated parameter values and averaged estimated values.*

1 INTRODUCTION

The optimization of the vibratory response of structures in presence of rubbing is always very delicate due to the highly nonlinear behavior induced by dry friction occurring at the interfaces. Sticking, macro or micro slipping between interfaces have major effects on both natural frequencies and damping properties.
Due to the diversity of contact configurations, friction models are often very case dependent and cannot be efficiently used without identifying: the type of friction occurring at the interfaces (based on the shape of the hysteresis curve) and contact parameters such as friction coefficient or joint stiffness. Those information may be obtained from specific experimental analyses or from available databases. In [1] for example, the authors propose estimated friction coefficients and contact stiffness values based on a very large experimental campaign they carried.

There is always a need for better understanding of rubbing mechanisms leading to optimal configurations and for more physics-based models than the classical and simple Coulomb or Masing models. A promising way concerns models that take into account material and geometrical properties of contacting surfaces, surface roughness data, and contact loading [2-4]. These models are based on the pioneer work of Greenwood and Williamson on rough contacts [5]. Knowing the behavior of an individual spherical asperity pressed against a flat surface it is possible, thanks to statistical summation, to simulate the global behavior of two rough flat-on-flat rubbing surfaces.

In the present study, a test rig has been developed to measure the dynamic response of a steel beam associated with several friction configurations. The set-up allows punctual or surface to surface contact cases. In the case of surface to surface contact, devices with various area size, shape and roughness were tested in order to assess their influence on the overall response. Numerically, temporal calculations are presented and compared to the measured data using different contact models with updated parameter values and averaged estimated values.

2 THE TEST RIG

The studied structure is a cantilever steel beam with a rectangular cross section of 0.008 m by 0.04 m and a length of 0.50 m. At the free end, the beam may be associated with different rubbing devices (Figure 1).

The experimental set-up allows the measurement of the displacement at 0.35 m of the clamped end of the beam by mean of an accelerometer (measured signal integrated twice). The excitation force provided by a shaker is measured by a force sensor located at the end of the shaker's push rod. The normal and tangential contact forces are also given by a force sensor. Two categories of devices were chosen in order to allow punctual contacts or surface to surface contacts (Figure 2). Sine sweeps (harmonic excitation) were performed at constant excitation force amplitude within the [15-130] Hz frequency range and for various normal contact forces.

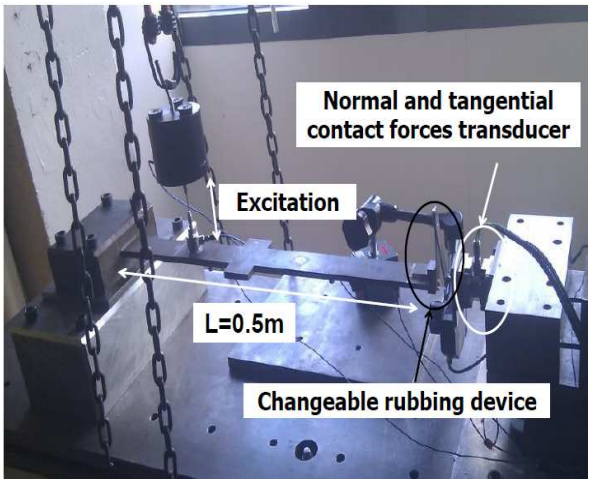

Figure 1: Experimental set up – cantilever steel beam.

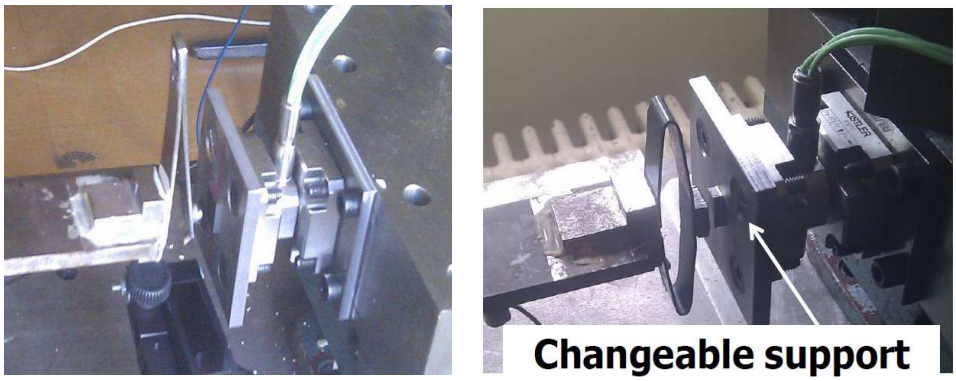

a) Punctual contact b) Surface to surface contact

Figure 2: Rubbing devices.

Figure 3 gives an example of typical measured FRFs for the punctual contact case. The classical influence of normal contact load is exhibited.

For a high normal load (Fn=40N associated to an excitation force of 2 N) contact is stuck. The FRF exhibits a linear behaviour with a peak resonance at 86 Hz. As the normal load is lowered (from 30 N to 0.25 N) relative displacement is allowed at the contact (presence of stick/slip) and vibrational amplitudes around the 86 Hz resonance peak are damped, becoming nearly flat. Finally, for Fn=0.1 N contact is in a slip state and a high resonance peak is again observed at 24Hz (free configuration).

In Figure 4, an example of the measured tangential forces in stick and stick/slip states is shown. When contact is stuck, the tangential force is proportional to displacement (sinusoidal signal). On the other hand, when contact is in a stick/slip state, the tangential force is proportional to displacement in the stuck phase and keep the limit value of $\pm\mu Fn$ (μ friction coefficient) in the slip phase.

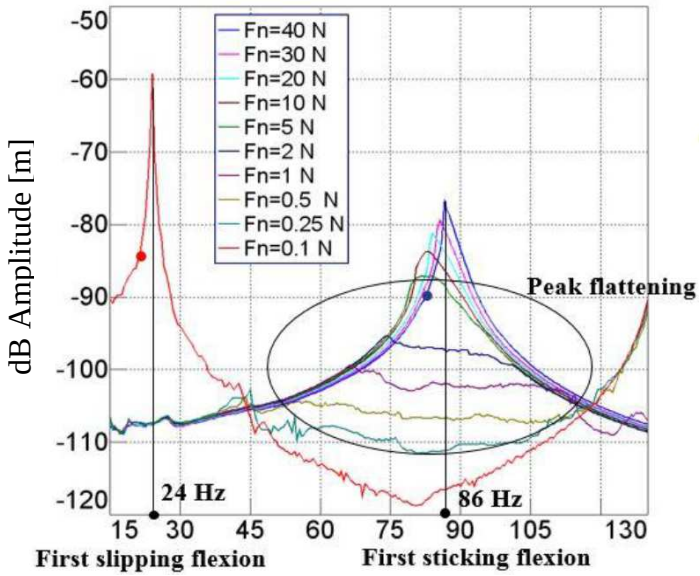

Figure 3: FRF vs normal load.

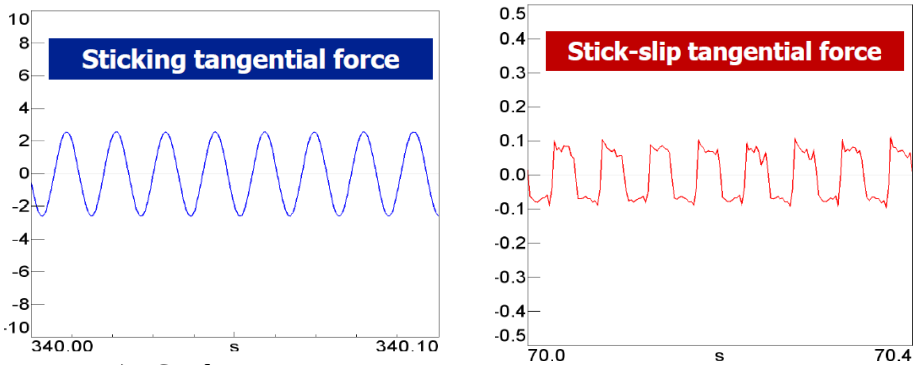

a) Stick contact state b) Stick/slip contact state

Figure 4 : Measured tangential force.

3 DYNAMIC RESPONSE OF THE STRUCTURE

Only the results associated to surface to surface contact configurations are presented here. The different samples considered were made of various contact areas (13x13 mm^2, 9x9 mm^2, 13x5 mm^2, 5x5 mm^2, Figure 5) and two surface finish, one rough and one smooth. Surface finish is described by the average roughness (Ra) defined in [6]:

$$R_a = \frac{1}{L}\int_0^L |z(x)|dx \tag{1}$$

where $z(x)$ represents the height of asperities and L the sampling length.

In Figure 6, the profiles of the 13x13 mm^2 samples are presented. The smooth one has a Ra of 0.714 µm while the rough one has a Ra of 3.76 µm. Regarding the external forces, nor-

mal loads were varied within the range [0.1 – 80] N and the excitation force amplitude remained at 2N.

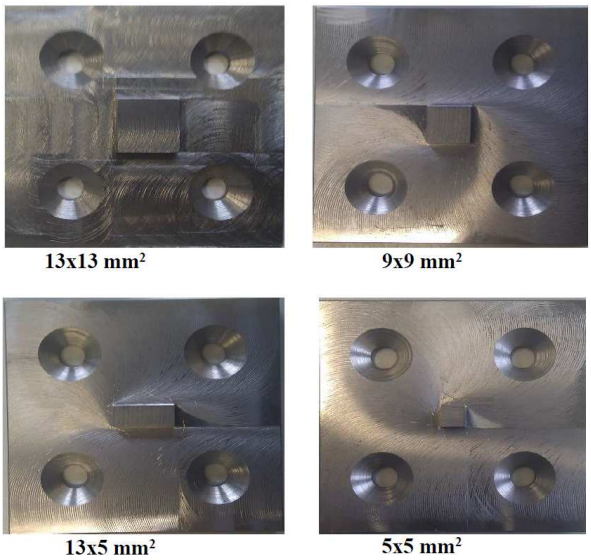

Figure 5: Samples

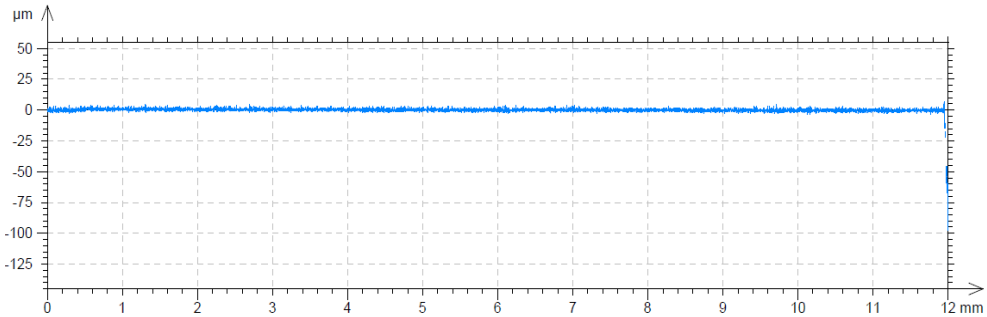

a) Profile of the smooth 13x13 mm^2 sample : Ra=0.714 µm

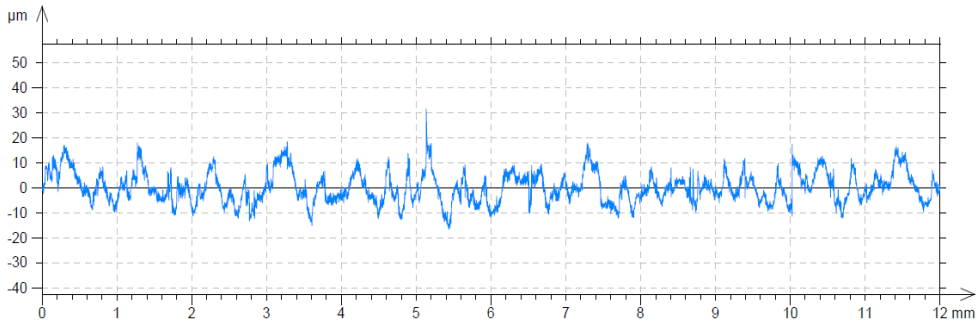

b) Profile of rough 13x13 mm^2 sample : Ra=3.76 µm

Figure 6: Profiles of the 13x13 mm^2 specimens.

Figure 7 gives the FRFs associated to the four smooth samples for a normal load of 2N. As clearly shown responses are identical and contact area size does not affect significantly the dynamics of the assembly. The same observations were made when assessing the influence of surface roughness.

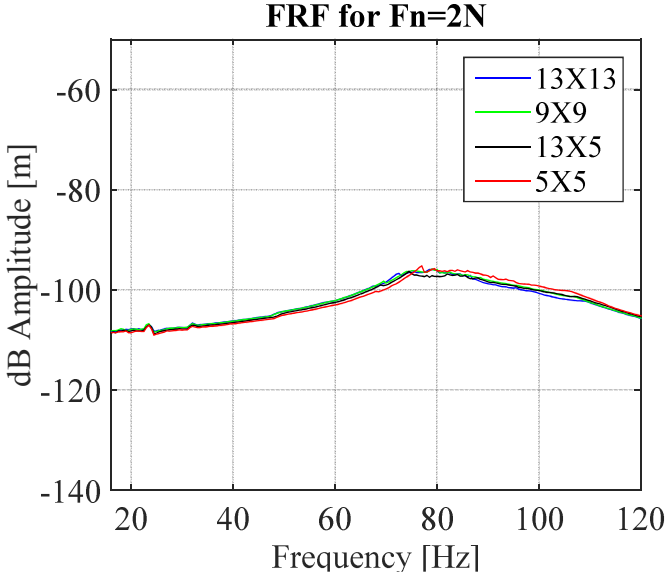

Figure 7: Area size influence on the FRFs for the smooth samples with Fn=2 N.

The overall effect of area size is illustrated in Tables 1 and 2 while the effect of roughness is shown in Tables 3 and 4. Results reported concern surfaces 13x13 mm^2 and 5x5 mm^2. Discrepancies are illustrated via three quantities: maximum displacement amplitudes, frequency at which the maximum amplitudes are obtained and damping ratios.

	Fn=0.1 N	Fn=2 N	Fn=10 N	Fn=80 N
Amplitude differences.	-5.2 %	0.7 %	1.5 %	0.8 %
Frequency at max amplitudes.	0 %	3 %	-1.1 %	0 %
Damping ratio differences.		-0.44 %	0.91 %	0.27 %

Table 1: Effect of area size: 13x13 mm^2 smooth versus 5x5 mm^2 smooth.

	Fn=0.1 N	Fn=2 N	Fn=10 N	Fn=80 N
Amplitude differences.	4 %	1.7 %	1.3 %	3.3 %
Frequency at max amplitudes.	0 %	0 %	0 %	1.6%
Damping ratio differences.		6.9 %	0.59 %	0.81 %

Table 2: Effect of area size: 13x13 mm^2 rough versus 5x5 mm^2 rough.

As shown in Tables 1 and 2, discrepancies between surfaces 13x13 and 5x5 are limited. Variation in maximum displacement amplitudes does not exceed 5.2 % and frequencies of the

maximum amplitudes as well as damping are not affected significantly, with one exception for Fn=2 N with 6.9 % discrepancy on damping.

	Fn=0.1 N	Fn=2 N	Fn=10 N	Fn=80 N
Amplitude differences.	-0.31 %	2.4 %	0.85 %	-0.2 %
Frequency of the maximum amplitudes.	0 %	5.8 %	2.8 %	1.6 %
Damping ratio differences.		-11.3 %	-1 %	0 %

Table 3: Influence of roughness: 13x13 mm^2 smooth versus 13x13 mm^2 rough.

	Fn=0.1 N	Fn=2 N	Fn=10 N	Fn=80 N
Amplitude differences.	8.4 %	-1.5 %	-1 %	2.32 %
Frequency of the maximum amplitudes.	0 %	5.8 %	4 %	1.6 %
Damping ratio differences.		-4.1 %	-1.36 %	0.81 %

Table 4: Influence of roughness: 5x5 mm^2 smooth versus 5x5 mm^2 rough.

The former conclusions remain when considering the effects of roughness on the dynamics of the assembly as shown in Tables 3 and 4.

4 NUMERICAL MODELLING

A finite element model of the structure has been constructed using beam, shell and 8 nodes brick elements. For the contact interface, zero thickness elements are used with Masing's tangential contact model. Masing's model is a combination of a Coulomb's contact model with a spring representing contact stiffness as illustrated in Figure 8 for a single dof mass-spring system. The tangential contact force Ft is given by:

$$\begin{aligned} F_t &= sgn(\dot{x})\mu Fn \quad \text{for slipping contact} \\ F_t &= -sgn(\dot{x})\mu Fn + k_d(x-z) \quad \text{for sticking contact} \end{aligned} \tag{2}$$

where μ is the friction coefficient, F_n the normal contact load, k_d the contact stiffness, x the mass displacement, $\dot{x}$ its velocity and z the internal slipping variable.

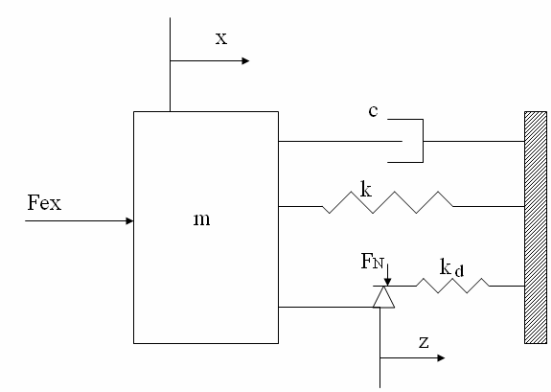

Figure 8: Masing's contact model in case of a 1 dof mass-spring system

Due to nonlinearity, solutions are obtained using a Newmark time integration scheme with Newton-Raphson iterations. Two different set of parameters (μ and k_d) are considered. The first is obtained using model updating from experimental data. The second considers estimated averaged values obtained from [2], as in this reference authors suggest values representing a best compromise when experimental data are not available: friction coefficient of 0.66 and contact stiffness of 3e7 N/m. Table 5 gives the parameters used for the smooth surface with an area of 13x13 mm^2 for models 1 and 2. Parameters suggested in [2] are higher than the identified values.

	Friction coefficient	**Contact stiffness**
Model 1	0.45	3.9e5 N/m
Model 2	0.66	3e7 N/m

Table 5: Parameter for the smooth 13x13 mm^2 surface

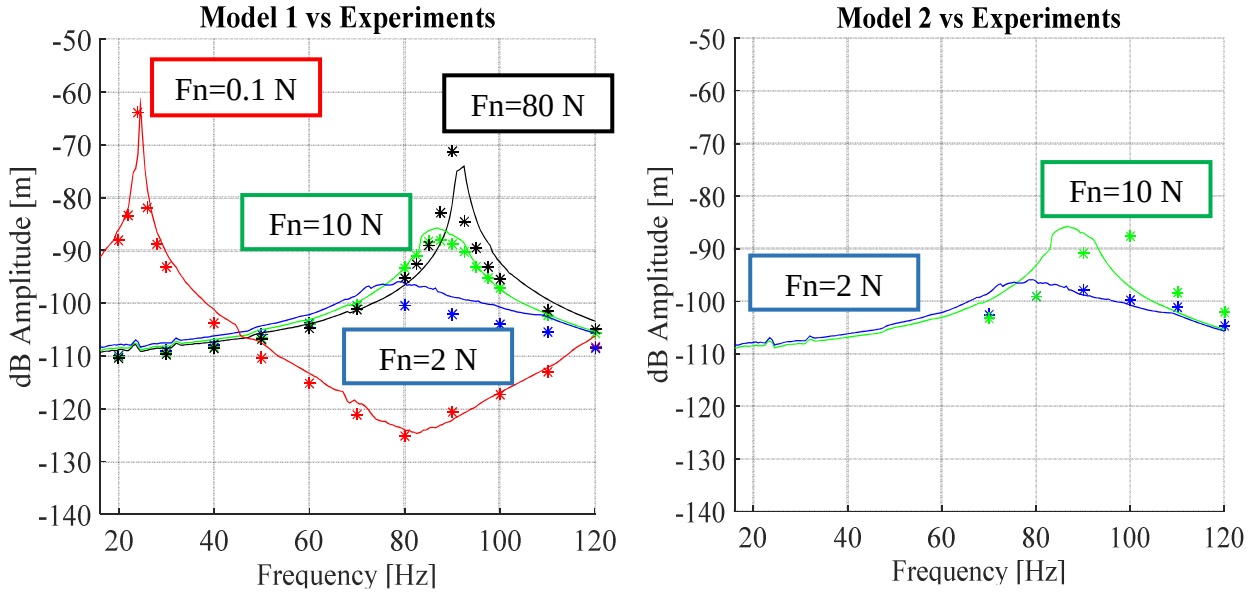

Figure 9: Models 1 and 2 versus experiments

Figure 9 gives numerical and experimental results. In the case of model 2, comparisons are limited to two normal loads, due to calculation time. Results clearly show that model 1 reproduces with good accuracy the experimental FRFs while there is a shift of 10 Hz between model 2 and experiments. Minimal discrepancy is obtained when reaching the maximal displacement amplitudes for both models. A 10 Hz frequency shift is not dramatic considering that no experimental data is available, but illustrates the need for accurate parameter estimation.

Numerical studies were made for the other configurations of contact area size and roughness and confirm little to no influence of these parameters on the dynamic response of the assembly. An example of comparison between surface 13x13 and 5x5 is shown in Table 6.

	Fn=0.1 N	Fn=2 N	Fn=10 N	Fn=80 N
Amplitude differences.	0 %	1.4 %	2.2 %	-3.1 %
Frequency of max amplitudes.	0 %	0 %	0 %	0 %
Damping ratio differences.		1.7 %	1.6 %	0.23 %

Table 6: Contact area size effect on the FRF – smooth 13x13mm^2 versus smooth 5x5 mm^2

In order to examine a broader range of configurations, numerical calculations were performed for higher normal loads (120 – 160 – 200 N) and excitation loads (2 – 20 – 40 - 100 N). In Figure 10, smooth surface 13x13 and rough surface 13x13 are compared for Fn=120 N and Fex=40 N. The maximal amplitude discrepancy is 6.1 % and it appears that the smooth surface dissipates significantly more energy than the rough one. Other calculations show an increase of the influence of contact characteristics for higher external loads (Fn and Fex). However, the observed discrepancies for maximum amplitude remain limited and do not exceed 10% for instance.

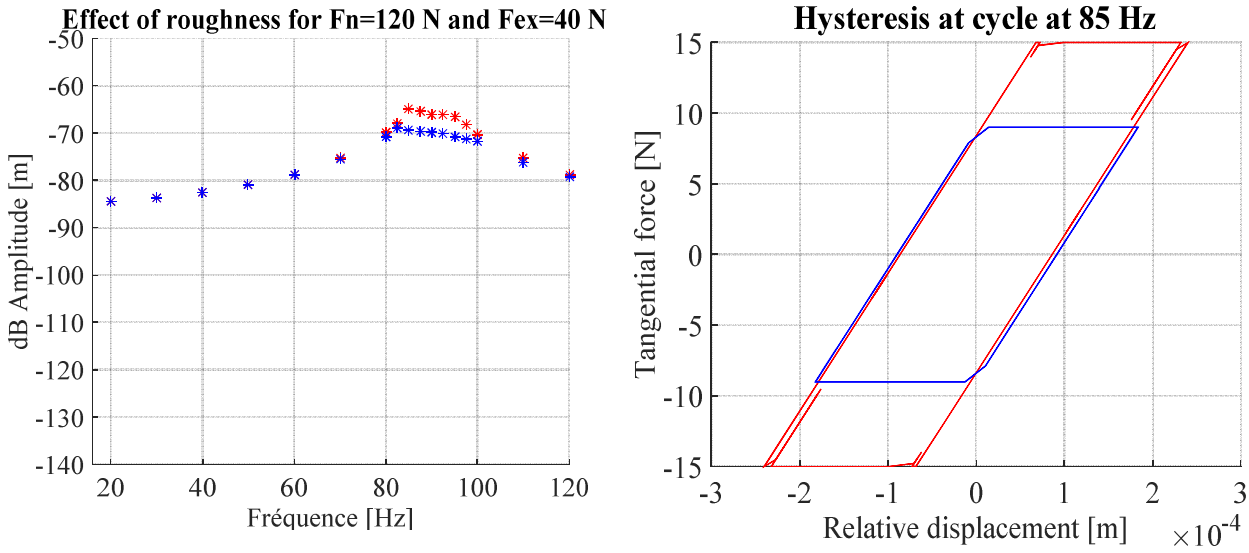

Figure 10: Smooth surfaces (red) versus rough surface (blue)
for 13x13 sample, Fn=120 N and Fex=40 N.

5 CONCLUSIONS

This study focuses on the dynamics of a beam associated with rubbing devices. Both experimental and numerical results are presented. Different configurations were tested in order to assess the effect of contact area size and roughness of the assembly. It was shown that the influence of such characteristics is limited when considering the discrepancies on maximum amplitude of displacements, frequencies of peak displacements and damping ratios. For the configurations considered, the behaviour remain globally in the frame of macro-slip.

Numerically, calculations with Masing's model were done. In the case where experimental data is available, the numerical model and experiments agree very well and confirm the fact that contact area and roughness have limited effects on the FRFs. On the other hand, when measured data are not available, the correlation between the model (using averaged estimated values) and experiments is more delicate as a shift between the peak frequencies is observed. This is due to the fact that the contact stiffness estimation is too high. However a good agreement was noticed for maximum amplitudes. This last results emphasize that work for a better estimation of contact parameters is still needed. A model which does not require prior experimental friction tests such as in [5] is under development.

6 ACKNOWLEDGMENT

This work has been carried out in the context of the FUI 2012-2015 SICODYN Project (pour des Simulations crédibles via la COrrélation calculs-essais et l'estimation d'incertitudes en DYNamique des structures). The authors would like to gratefully acknowledge the support of the FUI (Fonds Unique Interministériel).

REFERENCES

[1] C.W. Schwingshackl, E.P. Petrov, D.J. Ewins, Measured and estimated friction interface parameters in a nonlinear dynamic analysis. *Mechanical Systems and Signal Processing*, **28**, 574–584, 2012.

[2] M. Eriten, A.A. Polycarpou, L.A. Bergman, Physics-based modeling for partial slip behavior of spherical contacts. *International Journal of Solids and Structures*, **47**, 2554–2567, 2010.

[3] M. Eriten, A.A. Polycarpou, L.A. Bergman, Physics-based modeling for fretting behavior of nominally flat rough surfaces. *International Journal of Solids and Structures*, **48**, 1436–1450, 2011.

[4] M. Eriten, A.A. Polycarpou, L.A. Bergman, A Physics-Based Friction Model and Integration to a Simple Dynamical System. *Journal of Vibration and Acoustics*, **134**, 051012, 2012.

[5] J. A. Greenwood, J. B. P. Williamson, *Contact of Nominally Flat Surfaces.* Proc. R. Soc. A, **295** (1442), 300–319, 1966.

[6] K. Johnson, *Contact Mechanics*, Cambridge University Press, Cambridge, 1985.

ECCOMAS Congress 2016
VII European Congress on Computational Methods in Applied Sciences and Engineering
M. Papadrakakis, V. Papadopoulos, G. Stefanou, V. Plevris (eds.)
Crete Island, Greece, 5–10 June 2016

RAYLEIGH METHOD APPLIED TO A 46-M-HIGH CONCRETE MAST

Alexandre de M. Wahrhaftig[1], **and Reyolando M. L. R. F. Brasil** [2]

[1] Federal University of Bahia (UFBa), Polytechnic School, Department of Construction and Structures
Rua Aristides Novís, Nº 02, 5º andar, Federação, Salvador – BA, Brazil, CEP: 40210-910
alixa@ufba.br

[2] University of São Paulo (USP), Polytechnic School, Dep. of Structural and Geotechnical Engineering
Av. Prof. Almeida Prado, tv. 2, n[br] 83, Cidade Universitária, São Paulo – SP, Brazil, CEP: 05508-900
reyolando.brasil@poli.usp.br

Keywords: Rayleigh method, Geometric nonlinearity, Material nonlinearity, Slenderness system, Geometric stiffness, Finite element method.

Abstract. *In this study, an analytical approach based on the Rayleigh method is adopted to calculate the first resonant frequency of a 46-m-high concrete mobile phone mast system, by considering the geometric stiffness, functions of the concentrated forces, and self-weight of the structure. It is important to bear in mind that actual structures are more complex than simple systems such as beams and columns because the properties of actual structures vary with their length. The mast is done in concrete its nonlinear behavior is linearized reducing the flexural stiffness and the ground is taken into account as distributed springs. Under geometric nonlinearity, the vibration frequency of the fundamental mode is calculated analytically and, for comparison, a finite element method (FEM)-based computer simulation is performed. Finally, the structural stiffness is evaluated. The results of the analytical approach are found to differ slightly from those of the FEM-based model.*

1 INTRODUCTION

Lee [1] relates that because beams are basic structural components, studies on free vibration of linear elastic beams under various conditions have been extensively reported for several decades. Accurate prediction of the natural frequencies of structures or structural components is important, especially in the design of structures subjected to dynamic loads. In various structural engineering fields, including civil, architectural, mechanical, and aeronautical engineering, tapered members, for example, are frequently used in structural designs for economical, aesthetic and geometrical reasons, goes on he.

The dynamic bending of such systems, which mingles with the flexural vibration of beams/columns, was initially investigated by Daniel Bernoulli in the late 18th century. The vibrations of Euler–Bernoulli beams have long been studied, since around 1750, Strutt [2]. As a beam, a column represents a continuous structural member, and its vibrations are governed by nonlinear partial differential equations, relates Norouzi [3], for which exact analytical solutions cannot be found, Awrejcewicz [4].

To investigate of the behavior of a continuous system with infinite degrees of freedom requires discretization techniques in which the structure is transformed into subsystems defined by points called joints. The discretization of differential equations was initialized by Euler through the first order discrete approximation. The Euler method is a one-step discrete method. Eventhough, this method provides a very low computational accuracy, one still used such a method in numerical computations because it is very simple to use, affirm Guo [5]. In fact, the discretization methods lead to the resolution of an algebraic problem for an initial continuous eigenvalue problem. The possibility to solve automatically the algebraic problem using a computer makes the discretization approach advantageous as compared to the initial continuous one, comments Challamel et al [6].

However, continuum systems can be associated with a system having a single degree of freedom, thereby restricting the mode in which the system will deform, and express the properties of such a system as functions of the generalized coordinates. This technique was adopted by Rayleigh [7] in his classic study of elastic system vibration, and his equations were found to be valid in the entire domain of the problem. However, actual structures are more complex than simple beams and columns, because their properties vary with their length and apply that method require a special attention. In order to evaluate the application of the Rayleigh method to an actual structure was selected one piece of concrete with high slenderness, for which the frequency of the first vibration mode was calculated analytically and by a computational model using the finite element method (FEM)**.**

2 CHARACTERISTICS OF THE 46-M-HIGH CONCRETE MAST

The structure is a concrete pole with high slenderness (slenderness of 334) with 46 m high. It has a hollow circular section of external diameter ϕ_{ext} and thickness of the wall of each segment *t*. The geometric details can be seen in shown in Figure 1 and Figure 2. In the structure there is a set of antennas and one platform on top, which totalize a mass of 1097.76 kg. There is even ladder, cables and guardrail, from 6 up to 46 m of height, which gives the structure an additional mass distributed of 40 kg/m. The lateral soil was represented by distributed spring stiffness (K_m) equal to 2668.93 kN/m^3. The density adopted for reinforced concrete foundation was 2500 kg/m^3, while the superstructure is considered to 2600 kg/m^3 concrete to be centrifuged. The foundation is of the kind shaft, relatively deep, with the following characteristics: base diameter 140 cm, shaft diameter 80 cm, length of shaft 580 cm and 20 cm base height. The concrete resistance is 45 MPa for the post, and 20 MPa for the foundation. Because the material has a nonlinear behavior or physical nonlinearity of concrete for is neces-

sary take it into account. What will be done following the recommendations from Brazilian Association for Standardization [8], which preconize um reducer factor of 0.5.

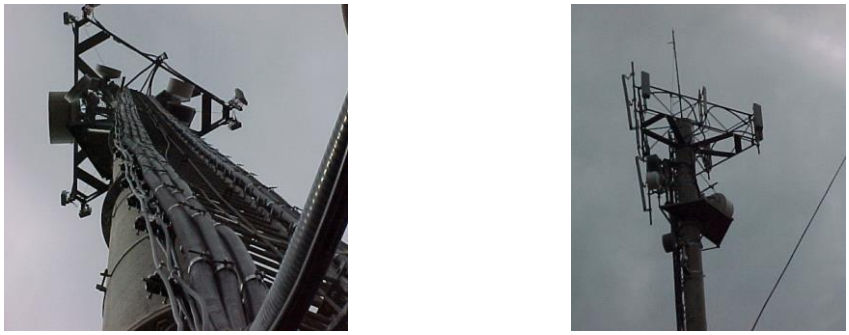

Figure 1: Mobile phone mast system (46 m high).

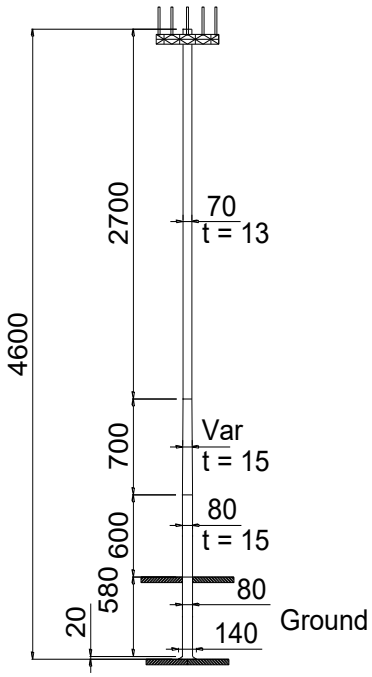

Figure 2: Geometric of the 46-m-high concrete mast (measurements in centimeters).

3 SYNTHETIC MATHEMATICAL DESCRIPTION

Below is described synthetically the mathematical bases of the Rayleigh Method. The basic concept underlying that method is the principle of conservation of energy in mechanical systems; therefore, it is applicable to linear and nonlinear structures according to Clough [9]. Temple [10] suggested that the fundamental principles developed by Rayleigh are applicable to both linear and nonlinear continuous systems with finite degrees of freedom. The purpose is to determine the fundamental period of vibration and to analyze the stability of elastic systems with the precision required for engineering problems. Toward this end, the principle of virtual work must be described by adequately chosen generalized coordinates and by a functional form that describes the first mode of vibration. At the end of the calculation, the equation of motion is written in terms of the generalized coordinates, from which one can extract the generalized elastic and geometric properties of the system. However, it is important to have in mind that for actual structure the integrals obtained by the method should be resolved within the limits established for each interval, i.e., the generalized properties calculated for

each segment of the structure, with special attention to the geometric stiffness because each part must consider the normal force distributed in its range as well as forces that operate in the upper segments.

Consider the well-known trigonometric function

$$\phi(x) = 1 - \cos\left(\frac{\pi x}{2L}\right). \tag{1}$$

Applying the principle of virtual work and its adequate derivations, the dynamic properties of interest of the system can be obtained as follows. The conventional stiffness is given by

$$K_0 = \int_0^L EI\left(\frac{d^2\phi(x)}{dx^2}\right)^2 dx, \tag{2}$$

where *E* is the elastic modulus and *I* is the inertia of the section. The geometrical stiffness appears as a function of the axial load, which includes the self-weight, and it is expressed as

$$K_g = \int_0^L N(x)\left(\frac{d\phi(x)}{dx}\right)^2 dx, \tag{3}$$

where *N(x)* is a function of the normal force given by $N(x) = \left[m_0 + \bar{m}\left(L - x\right)\right]g.$

If is necessary to consider the soil participation on the vibration of the system, one way is to associate it as distributed springs along of the height, for that should take the Eq.(4), where *k(x)* is the spring parameter.

$$K_m = \int_0^L k(x)\phi(x)^2 dx. \tag{4}$$

The total generalized mass is given by $M = m_0 + m,$ where m_0 is the tip lumped mass at the element joint and

$$m = \int_0^L \bar{m}\left[\phi(x)\right]^2 dx, \text{ where } \bar{m} \text{ is the mass per unit length} \tag{5}$$

Finally, the natural cyclical frequency should be calculated as

$$\omega = \sqrt{\frac{K}{M}}, \text{since } K = K_0 - K_g + K_m, \tag{6}$$

For further details on the development of this specific analytical procedure, readers may refer to our previous work, Wahrhaftig [11].

4 RESULTS AND DISCUSSION

4.1 Geometric definitions and parameters of the Rayleigh method

The following ordered referring to the heights in the structure are defined: $L_1 = 0.2$ m, $L_2 = 6.0$ m, $L_3 = 12.0$ m, $L_4 = 19.0$ m, $L_5 = 46.0$ m. On the base foundation, one has: $D_1 = 140$ cm, $A_1 = \frac{\pi}{4}D_1^{\,2}$, $I_1 = \frac{\pi}{64}D_1^{\,4}$. On the shaft $D_2 = 80$ cm, $A_2 = \frac{\pi}{4}D_2^{\,2}$, $I_2 = \frac{\pi}{64}D_2^{\,4}$. The variable diameter on the segment between the base and the shaft is obtained by linear interpolation on the variable segment, doing: $D_1(x) = \frac{D_2 - D_1}{L_1}x + D_1$. So, the area and inertia of the section are given by $A_1(x) = \frac{\pi}{4}D_1(x)^2$ and $I_1(x) = \frac{\pi}{64}D_1(x)^4$. Being D_3 and e_3 the ex-

ternal diameter and thickness of the initial section, one has $D_3 = 80$ cm and $t_3 = 13$ cm. Then, the internal diameter, area and inertia of the section are: $d_3 = D_3 - 2t_3$, $A_3 = \frac{\pi}{4}\left(D_3^{\,2} - d_3^{\,2}\right)$ and $I_3 = \frac{\pi}{64}\left(D_3^{\,4} - d_3^{\,4}\right)$. Similarly, D_5, t_5, d_5, A_5 and I_5 are the external diameter, the thickness, area and inertia to the last segment. Between these two segments there is a segment with variable section, of thickness equal to the previous ($t_4 = t_3$), such diameter can be obtained by linear interpolation similarly as done previously, using the expression $D_4(x) = \frac{D_4 - D_3}{L_4 - L_3}\left(x - L_3\right) + D_3$. Therefore, $d_4(x) = D_4(x) - 2t_4$, $A_4(x) = \frac{\pi}{64}\left(D_4(x)^4 - d_4(x)^4\right)$ and $I_4(x) = \frac{\pi}{64}\left(D_4(x)^4 - d_4(x)^4\right)$ are, respectively, the internal diameter , the area and the inertia of the variable section on that correspondent segment.

The parameters of the analytical procedure are listed in Table 1.

Table 1. Parameters of analytical procedure.

Parameter	Value
Elastic modulus of the mast concrete reduced	E = 18782971011 MPa
Elastic modulus of the foundation concrete reduced	E_1 = 12521.98 MPa
Density of structure and foundation concrete	ρ = 2600 kg/m^3, ρ_1 = 2500 kg/m^3
Lumped mass at the top	m_0 = 1097.76 kg
Additional distributed mass per unit height	$\bar{m}_e$ = 40 kg/m
Spring parameter	k_s = 2668.93 kN/m^3
Gravitational acceleration	g = 9.806650 m/s^2

4.2 Calculation of generalized mass of the Rayleigh method

Sub-indices in Roman numerals are introduced from this point on to prevent ambiguity in notation. The generalized mass is calculated using the following integrals.

$$m_1 = \int_0^{L_1} m_I(x)\phi(x)^2\,dx, \text{ where } m_I(x) = \left(\frac{A_2 - A_1}{L_1} + A_1\right)\rho_1;$$

$$m_2 = \int_{L_1}^{L_2} m_{II}\phi(x)^2\,dx, \text{ where } m_{II} = A_2\rho_1;\ m_3 = \int_{L_2}^{L_3} m_{III}\phi(x)^2\,dx, \text{ where } m_{III} = A_3\rho + \bar{m}_e; \tag{7}$$

$$m_4 = \int_{L3}^{L_4} m_{IV}(x)\phi(x)^2\,dx, \text{ where } m_{IV} = A_4(x)\rho + \bar{m}_e \text{ and } A_4(x) = \frac{\pi}{4}\left(D_4(x)^2 - d_4(x)^2\right);$$

$$\text{and } m_5 = \int_{L_4}^{L} m_V\phi(x)^2\,dx, \text{ where } m_V = A_5\rho + \bar{m}_e.$$

The generalized distributed mass is given by $m = \sum_{i=1}^{5} m_i$ and the total generalized mass is given by $M = m_0 + m$. The total generalized mass of the structure is 7848.06 kg.

4.3 Calculation of generalized geometric stiffness by Rayleigh method

To compute the generalized geometric stiffness, it is necessary to determine the normal forces for the parts defined in the geometry. From the top to the bottom of the structure, the axial forces are

$$\begin{gathered} F_0 = m_0 g,\ \ F_5 = \int_{L_4}^{L} m_V g dx,\ F_4 = \int_{L_3}^{L_4} m_{IV}(x) g dx, \\ F_3 = \int_{L_2}^{L_3} m_{III} g dx,\ F_2 = \int_{L1}^{L_2} m_{II} g dx,\ \text{and}\ F_1 = \int_{0}^{L_1} m_I(x) g dx, \end{gathered} \tag{8}$$

where g is the gravitational acceleration. The generalized axial force F is given by $F = \sum_{i=0}^{5} F_i$, and the geometric stiffness is calculated as follows:

$$\begin{gathered} K_{g5} = \int_{L_4}^{L} \left[F_0 + m_V (L-x) g \left(\frac{d}{dx}\phi(x) \right)^2 \right], \\ K_{g4} = \int_{L_3}^{L_4} \left[F_0 + F_5 + m_{IV}(x)(L_4 - x) g \left(\frac{d}{dx}\phi(x) \right)^2 \right], \\ K_{g3} = \int_{L_2}^{L_3} \left[F_0 + F_5 + F_4 + m_{III}(L_3 - x) g \left(\frac{d}{dx}\phi(x) \right)^2 \right], \\ K_{g2} = \int_{L_2}^{L_3} \left[F_0 + F_5 + F_4 + F_3 + m_{II}(L_2 - x) g \left(\frac{d}{dx}\phi(x) \right)^2 \right], \ \text{and} \\ K_{g1} = \int_{L_2}^{L_3} \left[F_0 + F_5 + F_4 + F_3 + F_3 + m_I(x)(L_1 - x) g \left(\frac{d}{dx}\phi(x) \right)^2 \right]. \end{gathered} \tag{9}$$

Thus, the generalized geometric stiffness K_g of the structure is given by $K_g = \sum_{i=1}^{5} K_{gi}$. The generalized geometric stiffness of the structure is 2.630744 kN/m.

4.4 Calculation of generalized conventional stiffness by Rayleigh method

The elastic geometric components are

$$K_{01} = \int_{0}^{L_1} E_1 I_1(x) \left(\frac{d^2}{dx^2}\phi(x) \right)^2 dx,\ K_{02} = \int_{L_1}^{L_2} E_1 I_2 \left(\frac{d^2}{dx^2}\phi(x) \right)^2 dx,$$

$$\begin{gathered} K_{03} = \int_{L_2}^{L_3} EI_3 \left(\frac{d^2}{dx^2}\phi(x) \right)^2 dx,\ K_{04} = \int_{L_3}^{L_4} EI_4(x) \left(\frac{d^2}{dx^2}\phi(x) \right)^2 dx, \\ \text{and}\ K_{05} = \int_{L_4}^{L} EI_5 \left(\frac{d^2}{dx^2}\phi(x) \right)^2 dx. \end{gathered} \tag{10}$$

The generalized elastic stiffness is given by the sum of the above components, as $K_0 = \sum_{i=1}^{5} K_{0i}$ .The generalized conventional stiffness is 8.068271 kN/m.

4.5 Calculation of generalized spring stiffness by Rayleigh method

Once that k_s is the spring factor, such value, for this specific case, is k_s = 2669 kN/m^3, the distributed springs, in the first and second segments are given by $k_1(x) = k_s D_1(x)$ and $k_2(x) = k_s D_2$. The generalized spring stiffness, designed by K_m, is calculated by means of follow equations:

$$K_m = \int_0^{L_1} k_1(x)\phi(x)^2 dx + \int_{L_1}^{L_2} k_2(x)\phi(x)^2 dx. \tag{11}$$

So, the generalized stiffness of the structure can be finally determined by the algebraic sum of the precedents parcels, so that is the total stiffness obtained by: $K = K_0 - K_g + K_m$. The generalized total stiffness is 6.560661 kN/m.

4.6 Calculation of frequency by Rayleigh method

The frequency of the first mode calculated numerically using Eq. (8) is 0.132477 Hz. If the geometric stiffness is not considered, linear analysis, the frequency is 0.172238 Hz.

4.7 Solution from a computational model based on the fem

The formulation corresponding to the finite element method (FEM) in relation to the mathematical procedure is the *geometric nonlinear formulation*. Then, the problem representing the modal analysis is resolved as

$$\det\left[\left[K\right] - \omega^2\left[M\right]\right] = 0 \tag{12}$$

with [*K*] being the stiffness matrix, composed by the conventional and geometric parcels and [*M*] is the mass matrix. In the classical modal analysis, this information is related to the natural frequencies of the system (eigenvalues), clears Shiki [12]. For comparison, a computational model based on the FEM was developed according to SAP2000 (Integrated software for structural analysis and design, Analysis Reference Manual, Computer and Structures, Inc., Berkeley, California, USA), a commercial software packed. The forces and parameters listed in Table 1 were applied to the model with the corresponding masses. The material was assumed to be isotropic, homogeneous, elastically linear, and with the parameters used in the analytical investigation in addition to a Poisson's ratio of 0.2. The spring value also was assigned to the foundation. The structures analyzed were modeled using 40 bar elements with constant and variable cross sections, as appropriate.

The modal analysis was performed over the stiffness came from a nonlinear static preprocessing. The first natural frequency calculated by FEM without geometric nonlinearity is 0.169961 Hz, and with geometric and material nonlinearity is 0.141285 Hz.

5 CONCLUSIONS

- This study employed an analytical procedure based on the Rayleigh method to calculate the initial undamped frequency of a 46-m-high concrete mast under geometric nonlinearity. Computational modeling based on finite element method (FEM) was performed for comparison.
- It was observed that the geometric stiffness represents 32.61% of the conventional stiffness. This implies that the reduction in the stiffness reduces the frequency in 15.51%. The same analysis using the FEM represents a reduction of 30.28%.

- When calculated analytically by the Rayleigh method, under geometric nonlinearity, the vibration frequency of the first natural mode was only 3% greater than that obtained by the FEM using a compatible formulation (0.145517 Hz for the former and 0.141285 Hz for latter). When computed without the geometric stiffness component, this frequency was 0.172238 Hz and 0.184065 Hz for both methods. So, one notes that the analytically solution based on the Rayleigh method has a good approximation with the nonlinear formulation based on the geometric matrix from the FEM. The results showed that there were no absolute differences between both solutions.

REFERENCES

[1] B. K. Lee, S. J. Oh, T. E. Lee, Free Vibration Of Tapered Timoshenko Beams By Deformation Decomposition, International Journal of Structural Stability and Dynamics, Vol. 13, No. 2 (2013) 1250057 (20 pages), doi:10.1142/S0219455412500575.

[2] J. W. Strutt, R. B. Lindsay, The Theory of Sound, second ed., Dover Publications, vol. 1, New York, 1945.

[3] H. Norouzi, D. Younesian, Chaotic vibrations of beams on nonlinear elastic foundations subjected to reciprocating loads, Mech. Res. Commun. 69 (2015) 121–128, doi:10.1016/j.mechrescom.2015.07.001.

[4] J. Awrejcewicz, A.V. Krysko, N.A. Zagniboroda, V.V. Dobriyan, V.A. Krysko, On the general theory of chaotic dynamics of flexible curvilinear Euler–Bernoulli beams, Nonlinear Dyn. 79 (2015) 11–29, doi: 10.1007/s11071-014-1641-5.

[5] Y. Guo, A. C.J. Luo, On complex periodic motion sand bifurcations in a periodically forced, damped, hardening Duffing oscillator, Chaos, Solitons and Fractals81(2015) 378–399, doi: 10.1016/j.chaos.2015.10.004.

[6] N. Challamel, V. Picandet, I. Elishako, C. M. Wang, B. Collet, T. Michelitsch, On Nonlocal Computation of Eigenfrequencies of Beams Using Finite Difference and Finite Element Methods, International Journal of Structural Stability and Dynamics, Vol. 15, No. 7 (2015) 1540008 (18 pages), doi:10.1142/S0219455415400088.

[7] Rayleigh, Theory of Sound (two volumes), Dover Publications, New York, re-issued. 1877.

[8] Brazilian Association for Standardization (ABNT) — Design of structural concrete - Procedure, NBR6118/14, Rio de Janeiro, (2014).

[9] R.W. Clough, J. Penzien, Dynamic of Structures, second ed., McGraw Hill International Editions, Taiwan, 1993.

[10] G. Temple, W.G. Bickley, Rayleigh´s Principle and its Applications to Engineering, Oxford University Press, Humphrey Milford, London, 1933.

[11] A.M. Wahrhaftig, R. M. L. R. F. Brasil, J.M. Balthazar, The first frequency of cantilever bars with geometric effect: a mathematical and experimental evaluation, J. Braz. Soc. Mech. Sci. Eng., 35 (2013) 457-467, doi:10.1007/s40430-013-0043-9.

[12] S. B. Shiki, V. Lopes Jr., S. da Silva, Identification of nonlinear structures using discrete-time Volterra series, J. Braz. Soc. Mech. Sci. Eng. 36 (3) (2014) 523-532, doi: 10.1007/s40430-013-0088-9.

ECCOMAS Congress 2016
VII European Congress on Computational Methods in Applied Sciences and Engineering
M. Papadrakakis, V. Papadopoulos, G. Stefanou, V. Plevris (eds.)
Crete Island, Greece, 5–10 June 2016

A DISPERSION MINIMIZED MIMETIC METHOD FOR A COLD PLASMA MODEL

Vrushali A. Bokil[1], Vitaliy Gyrya[2], and Duncan A. McGregor[1]

[1]Oregon State University
Department of Mathematics, Corvallis, OR 97331
e-mail: {bokilv,mcgregod}@math.oregonstate.edu

[2] Los Alamos National Laboratory
T-5, Applied Mathematics and Plasma Physics, Los Alamos, NM
e-mail: vitaliy_gyrya@lanl.gov

Keywords: Maxwell's Equations, Mimetic Methods, Cold Plasma, Exponential Time Differencing, Numerical Dispersion Relation, Yee Scheme.

Abstract. *In this paper we consider the lowest edge-based mimetic finite difference (MFD) discretization in space for Maxwell's equations in cold plasma on rectangular meshes. The method uses a generalized form of mass lumping that, on one hand, eliminates a need for linear solves at every iteration while, on the other hand, retains a set of free parameters of the MFD discretization. We perform an optimization procedure, called m-adaptation, that identified a set of free parameters that lead to the smallest numerical dispersion. The choice of the time stepping proved to be critical for successful optimization. Using exponential time differencing we were able to reduce the numerical dispersion error from second to fourth order of accuracy in mesh size. It was not possible to achieve this order of magnitude reduction in numerical dispersion error using the standard leapfrog time stepping. Numerical simulations independently verify our theoretical findings.*

1 Introduction

A variety of numerical techniques are available in the literature for the simulation of Electromagnetic (EM) wave propagation in linear dispersive media, the gold standard being the Yee Finite difference Time Domain (FDTD) method [6]. EM wave propagation in a medium is modeled by Maxwell's Equations, a vector system of Partial Differential Equations (PDEs), that govern the evolution of the EM field, along with appropriate constitutive equations for the response of the medium to the EM field. The Yee scheme is a FDTD method that simultaneously discretizes Maxwell's equations along with the constitutive laws for the medium to produce a second order accurate discretization in space and time. However, the second order numerical dispersion errors that arise in the discrete solution obtained using the Yee scheme can lead to large errors over long time integration on electrically large domains. Thus, the construction of numerical methods with high order numerical dispersion errors for linear dispersive media, which is the goal of this paper, is crucial to the accurate simulation of EM waves in such media.

In this paper, we consider the simulation of EM waves in a cold isotropic plasma, a type of linear dispersive medium. The model for cold plasma is based on the Auxiliary Differential Equation (ADE) approach in which an Ordinary Differential Equation (ODE) for the evolution of the time derivative of the macroscopic polarization (polarization current density) is appended to Maxwell's equations to produce a hybrid PDE-ODE system. The evolution ODE for the polarization current density models the averaged response of the material to the electromagnetic field. We present the construction of a dispersion minimized numerical method for Maxwell's equations in a cold plasma by performing a novel optimization procedure, called *m-adaptation*, on a family of numerical methods for the cold plasma model based on the Mimetic Finite Difference (MFD) method in space and Exponential Time Differencing (ETD) in time.

MFD methods are a flexible family of methods that are based on general polygonal and polyhedral meshes, see [7] for a comprehensive review. The word mimetic indicates the fact that they mimic/preserve in the discrete settings some properties of the continuous equations. The MFD construction is generally non-unique and leads to a parameterized family of methods with equivalent properties, such as stencil size and base convergence rate among others. Many of the classical discretizations are contained within the MFD family, e.g. Yee scheme on rectangular elements. The number of parameters characterizing the scheme grows rapidly with the dimension, the number of vertices in a polygonal element, and the order of the discretization. The parameterized nature of the family of MFD methods presents an opportunity for optimization for some desired properties. M-adaptation, as introduced in [4, 5], is the process of selecting an optimal member of the family of mimetic schemes for a selected optimization criteria (in this case, minimization of numerical dispersion). In [5] other optimization criteria were analysed.

We have previously considered the problem of optimizing numerical dispersion error in models of electromagnetic wave propagation in free space [1]. In this earlier work, we started with the parameterized family of MFD schemes that all have second (base) order of numerical dispersion error on rectangular meshes. Through m-adaptation we produced a method that has fourth order numerical dispersion error. The present paper extends our prior work to a cold plasma model which, as discussed above, appends an additional evolution equation for the polarization current density to Maxwell's equations. The extension of m-adaptation to the cold plasma model proved to be non-trivial, as illustrated by our first failed attempt presented in the appendix section of this paper. It turns out, that for linear dispersive media, the choice of the time discretization scheme is critical for the m-adaptation technique to produce a high order method. The Leapfrog time differencing method, which we previously employed in [1] for the

case of EM propagation in free space, does not allow m-adaptation to produce a higher order method for the cold plasma model. Instead, replacing the Leapfrog time differencing with ETD allows for successful optimization over the family of fully discrete MFD schemes. The optimal Exponential Time Mimetic Finite Difference (ETMFD) method, produced by m-adaptation, has a fourth order numerical dispersion error as compared to the (base) second order error for the rest of the ETMFD schemes in this family on rectangular meshes.

The ETD method was originally introduced in computational electromagnetism as a scheme for handling stiff problems, such as computing the electric and magnetic fields in a box surrounded by perfectly matched layers [2]. For these problems, explicit time-stepping, for example the Leapfrog time differencing method, requires an extremely small time step in order to be stable. On the other hand implicit schemes that are unconditionally stable can be costly to implement in three dimensions. ETD involves an exact integration of some of the lower order linear terms in the governing equations, and higher order accuracy can be obtained by using a higher order discretization of the resulting integral terms. However, the ETD approach has been shown to offer no major advantages over the time averaging of the lower order linear terms in the Yee scheme, for alleviating stiffness. In some cases, ETD may be less efficient by necessitating smaller step sizes [8].

We would like to emphasize that the reason for the choice of ETD in our work is not for handling stiffness, but rather that it is a good candidate for a time discretization method which allows for successful optimization in the m-adaptation technique. In contrast to other numerical methods for the cold plasma model that use ETD discretization only for the equation of polarization current density [3], our ETMFD method is a discretization of a hyrbrid PDE-ODE system modeling the evolution of the polarization current density and electric field forced by spatial derivatives of field variables.

The outline of the paper is as follows. In Section 2 we present first and second order PDE models for cold plasma, and the corresponding weak formulations. The lowest order edge based MFD discretization for the electric field and current density on rectangular meshes is presented in Section 3, while the exponential time difference discretization for scalar and vector equations is presented in Section 4. In Section 5 we present a fully discrete ETMFD family of discretizations that employs a generalized form of mass-lumping to produce a fully explicit scheme to avoid the need for linear solves at every time step. In Section 5.1 we derive the numerical dispersion relation for this family of discrete schemes and choose the set of MFD parameters that produces a method with the lowest numerical dispersion error. This optimization requires numerical dispersion properties derived in Sections 3 and 4. In Section 6 we present results of numerical simulations that independently validate our theoretical results. In Section 7 we present some concluding remarks. Finally, in Appendix A, we demonstrate that a straightforward extension of our ideas developed in [1] does not allow the m-adaptation process to reduce numerical dispersion error, thus, demonstrating the novelty of the ETMFD method presented in this paper.

2 Maxwell's Equations in a Cold Plasma

The Cold Plasma (CP) model is a special case of the Lorentz model [6] governing the evolution of electromagnetic waves in partially ionized gases without magnetization effects. It consists of Maxwell's equations along with evolution equations for the time derivative of the macroscopic electric polarization field. This time derivative is called the polarization current density. Suppose $\Omega \subset \mathbb{R}^2$ and $T > 0$. Maxwell's equations governing the evolution of wave propagation on $\Omega \times [0, T]$ relate the electric field intensity $\mathbf{E}$, and the magnetic flux density B

as

$$\frac{\partial}{\partial t}\mathbf{E} = c_0^2\ \mathbf{curl}\ B - \frac{1}{\epsilon_0}\mathbf{J}, \tag{2.1a}$$

$$\frac{\partial}{\partial t}B = -\text{curl}\ \mathbf{E}, \tag{2.1b}$$

where c_0, and ϵ_0, are the speed of light, and the electric permittivity of free space, respectively. The vector $\mathbf{J}$ is the polarization current density and is modeled by the evolution equation

$$\frac{\partial}{\partial t}\mathbf{J} + \omega_i \mathbf{J} = \epsilon_0 \omega_P^2 \mathbf{E}. \tag{2.2}$$

Here ω_i is the ion collision frequency and ω_P is the plasma frequency. For a vector field $\mathbf{f} = (\mathbf{f}_x, \mathbf{f}_y)^T$ and for a scalar field f we define the scalar (curl) and vector (**curl**) curl operators as follows,

$$\text{curl}(\mathbf{f}) := \frac{\partial}{\partial x}\mathbf{f}_y - \frac{\partial}{\partial y}\mathbf{f}_x, \qquad \mathbf{curl}(f) := \left(\frac{\partial}{\partial y}f, -\frac{\partial}{\partial x}f\right)^T.$$

All the fields in the system (2.1)-(2.2) are functions of position $\mathbf{x} = (x, y)^T$ and time $t \in [0, T]$. We also assume perfect electrical conductor (PEC) boundary conditions.

$$\mathbf{E} \times \mathbf{n} = 0, \text{ on } \partial\Omega \times [0, T], \tag{2.3}$$

where $\mathbf{n}$ is a unit outward vector to the boundary Ω. The equations (2.1) and (2.2) are subject to appropriate initial conditions.

The first order equations (2.1-2.2) can be written in an equivalent second order formulation, which we call the **Maxwell-CP Model**, by eliminating the magnetic flux density field B as

$$\begin{cases} \dfrac{\partial^2}{\partial t^2}\mathbf{E} = -\dfrac{1}{\epsilon_0}\dfrac{\partial}{\partial t}\mathbf{J} - c_0^2\ \mathbf{curl}\ \text{curl}\ \mathbf{E}, & \text{in} \quad \Omega \times (0, T], \\ \dfrac{\partial}{\partial t}\mathbf{J} = -\omega_i \mathbf{J} + \epsilon_0 \omega_p^2 \mathbf{E}, & \text{in} \quad \Omega \times (0, T], \\ \mathbf{E} \times \mathbf{n} = 0, & \text{on } \partial\Omega \times (0, T], \end{cases} \tag{2.4}$$

along with appropriate initial conditions. We will construct a MFD discretization based on this second order formulation.

2.1 Variational Formulation

The MFD discretization, just like a finite element formulation, will be constructed based on the weak form of (2.4). To this end, we consider the Sobolev spaces

$$\begin{aligned} \mathbf{L}^2(\Omega) &= [L^2(\Omega)]^2, \\ \mathbf{H}(\text{curl}, \Omega) &= \{\mathbf{v} \in \mathbf{L}^2(\Omega) : \text{curl}\ \mathbf{v} \in L^2(\Omega)\}, \\ \mathbf{H}_0(\text{curl}, \Omega) &= \{\mathbf{v} \in \mathbf{H}(\text{curl}, \Omega), \mathbf{v} \times \mathbf{n} = 0, \text{ on } \partial\Omega\}. \end{aligned}$$

The weak formulation of (2.4) is obtained in a standard way. Multiply the first, and the second equation, in (2.4) by test functions, $\boldsymbol{\phi} \in \mathbf{H}_0(\text{curl}, \Omega)$, and $\psi \in \mathbf{L}^2(\Omega)$, respectively, and integrate over the domain Ω. The weak formulation reads

Find $\mathbf{E} \in C^2([0,T];\mathbf{H}_0(\text{curl},\Omega))$, *and* $\mathbf{J} \in C^1([0,T];\mathbf{L}^2(\Omega))$, *subject to appropriate initial conditions, such that for all* $\boldsymbol{\phi} \in \mathbf{H}_0(\text{curl},\Omega)$ and $\psi \in \mathbf{L}^2(\Omega)$ we have

$$[\mathbf{E}_{tt},\boldsymbol{\phi}]_E + c_0^2\,[(\text{curl }\mathbf{E}),(\text{curl }\boldsymbol{\phi})]_F + \frac{1}{\epsilon_0}\,[\mathbf{J}_t,\boldsymbol{\phi}]_E = 0, \tag{2.5}$$

$$[\mathbf{J}_t,\psi]_E + \omega_i\,[\mathbf{J},\psi]_E - \epsilon_0\omega_p^2\,[\mathbf{E},\psi]_E = 0, \tag{2.6}$$

where the bilinear forms are defined as follows:

$$[\mathbf{J},\mathbf{E}]_E := \int_\Omega \mathbf{J}\cdot\mathbf{E}\,d\Omega, \qquad [J,E]_F := \int_\Omega J\,E\,d\Omega. \tag{2.7}$$

Here $(\mathbf{J},\mathbf{E})$ are vector functions, and (J,E) are scalar functions.

2.2 Dispersion Relation

In this paper our aim is to construct a numerical method for the Maxwell-CP model (2.4) that is the optimal method chosen from a family of schemes by minimizing for numerical dispersion error. Thus, in this section, we present a brief overview of continuous and numerical dispersion relations and their connections to symbols of differential operators.

Given a plane wave

$$\mathbf{u}(t,\mathbf{x}) := \mathrm{e}^{\mathrm{i}(\mathbf{k}\cdot\mathbf{x}-\omega t)}\mathbf{u}_0, \tag{2.8}$$

a continuous or discrete *dispersion relation* is a relation between the frequency ω and the wave vector $\mathbf{k}$, under which $\mathbf{u}$, or its restriction to a discrete grid, is a solution of a continuum PDE, or its discrete approximation, respectively.

Consider an abstract linear equation

$$\mathcal{L}_t\{\mathbf{u}\} = \mathcal{L}_\mathbf{x}\{\mathbf{u}\}, \tag{2.9}$$

where $\mathcal{L}_t$ and $\mathcal{L}_x$ are linear operators corresponding to time and space, respectively, and $\mathbf{u}$ is either a continuous plane wave (2.8) or its discrete representation. For example, $\mathcal{L}_t$ and $\mathcal{L}_\mathbf{x}$ could be the continuous differential operators $\mathcal{L}_t\{\mathbf{u}\} = \frac{\partial^2}{\partial t^2}\mathbf{u}$ and $\mathcal{L}_\mathbf{x}\{\mathbf{u}\} = \triangle\mathbf{u}$ or their discrete approximations.

As it turns out, for all linear operators $\mathcal{L}_t$ and $\mathcal{L}_x$ (continuous or discrete) considered in this paper the plane wave (2.8) is a generalized eigenfunction, i.e.

$$\mathcal{L}_t\{\mathbf{u}\} = \mathcal{T}(\omega)\mathbf{u} \qquad \text{and} \qquad \mathcal{L}_x\{\mathbf{u}\} = \mathcal{S}(\mathbf{k})\mathbf{u}, \tag{2.10}$$

where $\mathcal{T}(\omega)$ and $\mathcal{S}(\mathbf{k})$ are square matrices acting on $\mathbf{u}_0$, i.e.

$$\mathcal{T}(\omega)\mathbf{u} = \mathrm{e}^{\mathrm{i}(\mathbf{k}\cdot\mathbf{x}-\omega t)}\,\mathcal{T}(\omega)\mathbf{u}_0 \qquad \text{and} \qquad \mathcal{S}(\mathbf{k})\mathbf{u} = \mathrm{e}^{\mathrm{i}(\mathbf{k}\cdot\mathbf{x}-\omega t)}\,\mathcal{S}(\mathbf{k})\mathbf{u}_0.$$

If $\mathcal{T}(\omega)$ and $\mathcal{S}(\mathbf{k})$ were scalars, they would be eigenvalues and $\mathbf{u}$ would be the eigenfunction of $\mathcal{L}_t$ and $\mathcal{L}_x$. Since, in general, they are not scalars we refer to $\mathbf{u}$ as a generalized eigenfunction and call $\mathcal{T}(\omega)$ and $\mathcal{S}(\mathbf{k})$ - symbols of linear operators $\mathcal{L}_t$ and $\mathcal{L}_x$, respectively.

Substituting (2.10) into (2.9) and cancelling the exponential terms $\mathrm{e}^{\mathrm{i}(\mathbf{k}\cdot\mathbf{x}-\omega t)}$ on both sides we obtain a dispersion relation written in terms of symbols of linear operators

$$\mathcal{T}(\omega)\mathbf{u}_0 = \mathcal{S}(\mathbf{k})\mathbf{u}_0. \tag{2.11}$$

In this work we are primarily concerned with *dispersion error*, which can be defined as the absolute value of the difference between the frequency $\omega(\mathbf{k})$, solution to the continuous dispersion relation, and its discrete counterpart, $\omega_{\Delta t,h}(\mathbf{k})$, solution to the discrete dispersion relation. There are other ways in which the dispersion error can be defined as discussed in Section 6. Dispersion error is the result of frequency dependent speed of propagation of plane waves in the discretized grid regardless of whether the continuum solution has such frequency dependent propagation or not. In particular, the speed of propagation of waves in the discrete grid always differs from that in the continuum case and is commonly observed as non-physical oscillations in discrete solutions. Thus, if $\mathcal{T}_{\Delta t}$ is a discrete approximation of $\mathcal{T}$, and $\mathcal{S}_h$ is a discrete approximation of $\mathcal{S}$ then we have

$$\mathcal{T}_{\Delta t} - \mathcal{S}_h = \mathcal{T} - \mathcal{S} + \mathcal{O}(h^\alpha). \tag{2.12}$$

Where $\Delta t > 0, h > 0$ are mesh resolution parameters. It will be our goal to find $\mathcal{T}_{\Delta t}$ and $\mathcal{S}_h$ so that α is as large as possible reducing the discrepancy in wave speed.

3 Mimetic Finite Difference Discretization in Space

A mimetic finite difference discretization of the continuous variational formulation (2.5-2.6) has the form

$$[(\mathbf{E}_h)_{tt}, \boldsymbol{\phi}_h]_{\mathscr{E}} + c_0^2 \left[(\text{curl}_h\ \mathbf{E}_h), (\text{curl}_h\ \boldsymbol{\phi}_h)\right]_{\mathscr{F}} + \frac{1}{\epsilon_0}\left[(\mathbf{J}_h)_t, \boldsymbol{\phi}_h\right]_{\mathscr{E}} = 0, \tag{3.1}$$

$$[(\mathbf{J}_h)_t, \psi_h]_{\mathscr{E}} + \omega_i \left[\mathbf{J}_h, \psi_h\right]_{\mathscr{E}} - \epsilon_0 \omega_p^2 \left[\mathbf{E}_h, \psi_h\right]_{\mathscr{E}} = 0. \tag{3.2}$$

Here $\mathbf{E}_h$, and $\mathbf{J}_h$, are discrete approximations of the solutions $\mathbf{E}$, and $\mathbf{J}$, respectively; $\boldsymbol{\phi}_h$ and ψ_h are discrete test functions; curl_h is a discrete linear operator approximating its continuous counterpart curl. The bilinear forms $[\cdot,\cdot]_{\mathscr{E}}$ and $[\cdot,\cdot]_{\mathscr{F}}$ are discrete approximations of the continuous bilinear forms $[\cdot,\cdot]_E$ and $[\cdot,\cdot]_F$ defined in (2.7). We will now make all of the above precise.

3.1 Discrete Spaces and Interpolation

Let $\mathscr{T}$ be a polygonal partitioning (mesh) of the domain Ω. Let $\mathscr{E}$, and $\mathscr{F}$, be the set of all edges e, and faces (cells) f, respectively, of the mesh $\mathscr{T}$. In the discrete form every function will be represented in terms of a finite number of values called degrees of freedom (DoF) assembled into a vector (e.g. $\mathbf{E}_h$, $\mathbf{J}_h$) assuming some ordering of these DoF. Each DoF will be associated either to an edge or to a face/element. The DoF of scalar functions (e.g. $\text{curl}\,\mathbf{E}$) will be associated with faces only (one DoF per face) and can be interpreted as an average value of the function over the face/cell. The DoF of vector functions (e.g. $\mathbf{E}$ and $\mathbf{J}$) will be associated with edges only (one DoF per edge) and can be interpreted as an average value of the tangential component of the vector function along the edge. See Figure 1 for illustration.

We will denote the discrete space corresponding to vector functions as $\mathscr{E}_h$ and the discrete space corresponding to scalar functions as $\mathscr{F}_h$. We define interpolation operators $\mathcal{I}^{\mathscr{E}_h}$, and $\mathcal{I}^{\mathscr{F}_h}$, as linear operators that for each function in $\mathbf{H}(\text{curl}, \Omega)$, and L^2, assigns a vector of DoF in $\mathscr{E}_h$, and $\mathscr{F}_h$, respectively.

The interpolation operator $\mathcal{I}^{\mathscr{E}_h}$, and the vector of DoF for vector functions are defined as

$$\mathcal{I}^{\mathscr{E}_h} : \mathbf{H}(\text{curl}, \Omega) \to \mathscr{E}_h, \qquad \mathbf{E}_e := \frac{1}{|e|}\int_e \mathbf{E}\cdot\boldsymbol{\tau}_e\, de, \tag{3.3}$$

$$\mathcal{I}^{\mathscr{E}_h}(\mathbf{E}) = \mathbf{E}_h := \left(\mathbf{E}_e\right)_{e\in\mathscr{E}}, \tag{3.4}$$

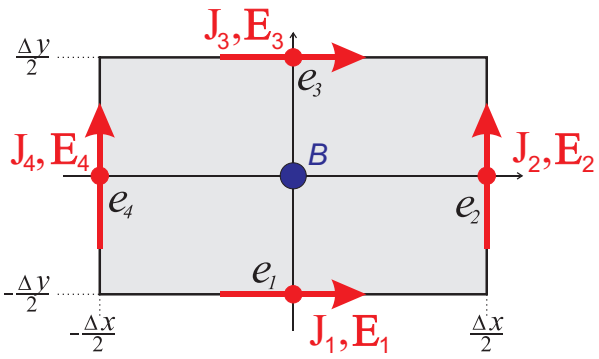

Figure 1: Illustration of DoF for vector functions, marked as $\mathbf{E}$, and scalar functions, marked as B on a rectangular element centered at the origin.

where $\boldsymbol{\tau}_e$ is a counter-clockwise tangent to the edge e. The interpolation operator $\mathcal{I}^{\mathscr{F}_h}$ for scalar functions, and the vector of DoF for scalar functions are defined as

$$\mathcal{I}^{\mathscr{F}_h} : L^2 \to \mathscr{F}_h, \qquad B_f := \frac{1}{|f|}\int_f B\, df, \tag{3.5}$$

$$\mathcal{I}^{\mathscr{F}_h}(B) = B_h := \big(B_f\big)_{f\in\mathscr{F}}. \tag{3.6}$$

3.2 Discrete Inner Products and the Adjoint Curl

Discrete bilinear forms $[\cdot,\cdot]_{\mathscr{E}}$ and $[\cdot,\cdot]_{\mathscr{F}}$ can be represented by square matrices and are defined through a standard assembly process

$$(\mathbf{E}_h)^T\mathbb{M}_{\mathscr{E}}\mathbf{D}_h = [\mathbf{E}_h,\mathbf{D}_h]_{\mathscr{E}} := \sum_{f\in\mathscr{F}}[\mathbf{E}_h,\mathbf{D}_h]_{\mathscr{E},f} = \sum_{f\in\mathscr{F}}(\mathbf{E}_{h,f})^T\mathbb{M}_{\mathscr{E},f}\mathbf{D}_{h,f}, \tag{3.7}$$

$$(B_h)^T\mathbb{M}_{\mathscr{F}}M_h = [B_h,M_h]_{\mathscr{F}} := \sum_{f\in\mathscr{F}}[B_h,M_h]_{\mathscr{F},f} = \sum_{f\in\mathscr{F}}(B_{h,f})^T\mathbb{M}_{\mathscr{F},f}M_{h,f}, \tag{3.8}$$

where $[\mathbf{E}_h,\mathbf{D}_h]_{\mathscr{E},f}$ and $[B_h,M_h]_{\mathscr{F},f}$ are to be defined locally on each face f.

For scalar functions the definition for the local bilinear form is the simplest

$$[B_h,M_h]_{\mathscr{F},f} := |f|B^T_{h,f}M_{h,f}, \qquad \text{i.e.} \quad \mathbb{M}_{\mathscr{F},f} = |f|, \tag{3.9}$$

where $|f|$ is the area of the face f.

Next, we define the discrete curl_h operator as a mapping from the discrete space $\mathscr{E}_h$, approximating vector functions, to the discrete space $\mathscr{F}_h$, approximating scalar functions. The definition will be made locally on each face f through the identity

$$[\psi_h,\mathrm{curl}_h\mathbf{E}_h]_{\mathscr{F},f} = \int_f \psi\,\mathrm{curl}(\mathbf{E})\, df, \tag{3.10}$$

which must hold for any constant ψ and any vector function $\mathbf{E}$ whose local discrete representation on the face f is $\mathbf{E}_{h,f}$. Identity (3.10) defines curl_h uniquely since the RHS of (3.10) can be expressed in terms of the vector of DoF $\mathbf{E}_{h,f}$ of $\mathbf{E}$ on the face f only using integration by parts

$$\int_f \psi\,\mathrm{curl}(\mathbf{E})\, df = \psi\sum_{e\in\partial f}\int_e \mathbf{E}\cdot\boldsymbol{\tau}_e\, de, \tag{3.11}$$

where $\boldsymbol{\tau}_e$ is a counter-clockwise tangent to the edge e of the face f. The edge integrals in (3.11) are exactly the DoF of $\mathbf{E}$, defined in (3.3), up to orientation of the edges. On a rectangular element the local matrix curl_h is a column vector of length four given by

$$\text{curl}_{h,f} = \frac{1}{\Delta x \Delta y}(\Delta x, \Delta y, -\Delta x, -\Delta y)^T. \tag{3.12}$$

The construction of the mass matrix $\mathbb{M}_{\mathscr{E}}$ contains many details that are not necessary for performing dispersion reduction analysis that is the center point of this paper. Therefore, we limit ourselves to presenting the final form of the matrix on a rectangular mesh and refer interested readers to [1] for all details.

In fact, instead of computing $\mathbb{M}_{\mathscr{E},f}$ we compute an approximation to its inverse

$$\mathbb{W}_{\mathscr{E},f} \approx \mathbb{M}^{-1}_{\mathscr{E},f}, \qquad \mathbb{W}_{\mathscr{E},f} = \frac{1}{4\Delta x \Delta y}\begin{pmatrix} 1+4w_1 & 4w_2 & 1-4w_1 & -4w_2 \\ 4w_2 & 1+4w_3 & -4w_2 & 1-4w_3 \\ 1-4w_1 & -4w_2 & 1+4w_1 & 4w_2 \\ -4w_2 & 1-4w_3 & 4w_2 & 1+4w_3 \end{pmatrix}. \tag{3.13}$$

Here w_1, w_2 and w_3 are free parameters. Different values of these parameters give rise to different numerical schemes, as discussed in [1]. In particular, this family of matrices $\mathbb{W}_{\mathscr{E},f}$ contains the Yee-scheme as one of its members. In order to recover the famous Yee-FDTD stencil, $\mathbb{W}_{\mathscr{E}} = \frac{1}{2\Delta x \Delta y}\mathbb{I}$, one has to take $w_1 = w_3 = \frac{1}{4}$ and $w_2 = 0$.

Our global matrices are then assembled in the usual way for every face f. As we are considering a second order formulation we introduce the following discrete curl-curl operator,

$$\mathbb{A}_h = (\text{curl}_h)^T \mathbb{M}_{\mathscr{F}} \text{curl}_h. \tag{3.14}$$

This matrix can be assembled from local matrices $(\text{curl}_{h,f})^T \Delta x \Delta y \, \text{curl}_{h,f}$.

3.3 Discrete in Space Continuous in Time Formulation on Rectangular Meshes

A discrete in space continuous in time formulation of the second order Maxwell-CP system is as follows:
Find $\mathbf{E}_h \in C^2([0,T], \mathscr{E}_h \cap \mathbf{H}_0(\text{curl}, \Omega))$ *and* $\mathbf{J}_h \in C^1([0,T], \mathscr{E}_h)$ *such that:*

$$\begin{cases} \dfrac{\partial^2}{\partial t^2}\mathbf{E}_h + \dfrac{1}{\epsilon_0}\dfrac{\partial}{\partial t}\mathbf{J}_h = -c_0^2 \mathbb{W}_{\mathscr{E}} \mathbb{A}_h \mathbf{E}_h, \\ \dfrac{\partial}{\partial t}\mathbf{J}_h = -\omega_i \mathbf{J}_h + \epsilon_0 \omega_P^2 \mathbf{E}_h. \end{cases} \tag{3.15}$$

3.4 Dispersion Analysis for Discrete in Space Continuous in Time Formulation

To obtain dispersion relations we assume plane wave solutions for the electric field and the polarization current density. Thus, in the discrete in space and continuous in time formulation (3.15), we represent the spatially discrete electric field, $\mathbf{E}_h(t)$, and polarization current density, $\mathbf{J}_h(t)$, as

$$\begin{aligned} \mathbf{E}_h(t) &= \mathcal{I}^{\mathscr{E}_h}\left(\mathbf{E}_0 e^{\mathrm{i}(\mathbf{k}\cdot\mathbf{x})}\right) E(t), \\ \mathbf{J}_h(t) &= \mathcal{I}^{\mathscr{E}_h}\left(\mathbf{J}_0 e^{\mathrm{i}(\mathbf{k}\cdot\mathbf{x})}\right) J(t). \end{aligned} \tag{3.16}$$

Here $\mathbf{E}_0$ and $\mathbf{J}_0$ are two-dimensional vectors that specify the initial intensity and the orientation of the corresponding vector fields. The continuous plane wave vector fields are characterized

by the wave vector $\mathbf{k}$ (whose magnitude we refer to as the wave number k) and the vectors $\mathbf{E}_0$ and $\mathbf{J}_0$. In the spatially discrete setting a similar characterization is made. We use U_i to denote a DoF for either the electric field or polarization current density. The role of the vectors $\mathbf{E}_0$ and $\mathbf{J}_0$ is assumed by two DoF associated with two adjacent orthogonal edges, as depicted in Figure 2. The DoF U_1 is associated to a horizontal edge, while the DoF U_2 is associated to a vertical edge. Other DoF, U_i, for the waves of the form (3.16) can be written in terms of U_1, U_2, and the exponent $e^{\mathrm{i}(\mathbf{k}\cdot\boldsymbol{\Delta}\mathbf{x_i})}$ as

$$\begin{aligned} U_i &= U_1 e^{\mathrm{i}(\mathbf{k}\cdot\boldsymbol{\Delta}\mathbf{x_i})} \qquad \text{for a horizontal edge } e_i, \\ U_i &= U_2 e^{\mathrm{i}(\mathbf{k}\cdot\boldsymbol{\Delta}\mathbf{x_i})} \qquad \text{for a vertical edge } e_i, \end{aligned} \tag{3.17}$$

where $\boldsymbol{\Delta}\mathbf{x_i}$ is the "shift"-vector from the center of the edge e_1 or e_2 to the center of the edge e_i, respectively. In particular, the vector of four DoF $(U_1, U_2, U_3, U_4)^T$, corresponding to the element f, can be written in terms of the vector of the first two DoF $(U_1, U_2)^T$ and $\mathbf{k} = (k_x, k_y)^T$ as follows:

$$\begin{pmatrix} U_1 \\ U_2 \\ U_3 \\ U_4 \end{pmatrix} = \mathbb{S} \begin{pmatrix} U_1 \\ U_2 \end{pmatrix}, \qquad \text{where} \quad \mathbb{S} = \begin{pmatrix} 1 & 0 \\ 0 & 1 \\ \mathrm{e}^{\mathrm{i}k_y\Delta y} & 0 \\ 0 & e^{-\mathrm{i}k_x\Delta x} \end{pmatrix}. \tag{3.18}$$

In the semi-discrete formulation (3.15), we perform several multiplications of waves of the form (3.16) by global matrices $\mathbb{A}$ and $\mathbb{W}$ assembled from identical local matrices $\mathbb{A}^f$ and $\mathbb{W}^f$. The following result presents a simple way of performing such a multiplication.

Lemma 1. *Consider the result of multiplication*

$$\mathbf{V} = \mathbb{Z}\mathbf{U}, \tag{3.19}$$

where the global matrix $\mathbb{Z}$ is assembled from identical local matrices $\mathbb{Z}^f$ and the vector of DoF $\mathbf{U}$ *has the form* (3.17) *Then the vector of DoF* $\mathbf{V}$ *also has the form* (3.17) *The vector of two DoF $(V_1, V_2)^T$ characterizing the vector* $\mathbf{V}$ *depends linearly on the vector of two DoF $(U_1, U_2)^T$ characterizing the vector* $\mathbf{U}$*; the two-by-two matrix corresponding to the linear mapping has the form $(\mathbb{S}^*\mathbb{Z}^f\mathbb{S})$:*

$$\begin{pmatrix} V_1 \\ V_2 \end{pmatrix} = (\mathbb{S}^*\mathbb{Z}^f\mathbb{S}) \begin{pmatrix} U_1 \\ U_2 \end{pmatrix}, \tag{3.20}$$

where $\mathbb{S}$ was defined in (3.18) *and $\mathbb{S}^*$ is a conjugate transpose of $\mathbb{S}$.*

Proof. The fact that $\mathbf{V}$ satisfies (3.17) follows immediately from the fact that $\mathbf{U}$ satisfies (3.17). The linear relation between $(V_1, V_2)^T$ and $(U_1, U_2)^T$ is a direct consequence of the linear relation (3.19). The main point of the lemma is to show that the linear relation (3.20) is given by the two-by-two matrix $(\mathbb{S}^*\mathbb{Z}^f\mathbb{S})$.

Consider the two elements f_1 and f_2 that determine the value of V_1 and the two elements f_1 and f_3 that determine the values of V_2, as shown in Figure. 2. The value of V_1 is a sum of the contributions from the elements f_1 and f_2

$$\begin{aligned} V_1 &= \begin{bmatrix} 1 & 0 & 0 & 0 \end{bmatrix} \mathbb{Z}^f\mathbb{S} \begin{bmatrix} U_1 \\ U_2 \end{bmatrix} + \begin{bmatrix} 0 & 0 & 1 & 0 \end{bmatrix} \mathbb{Z}^f\mathbb{S} \begin{bmatrix} e^{-\mathrm{i}k_2\Delta y}U_1 \\ e^{-\mathrm{i}k_2\Delta y}U_2 \end{bmatrix} = \\ &= \begin{bmatrix} 1 & 0 & e^{-\mathrm{i}k_2\Delta y} & 0 \end{bmatrix} \mathbb{Z}^f\mathbb{S} \begin{bmatrix} U_1 \\ U_2 \end{bmatrix}. \end{aligned} \tag{3.21}$$

Here the product $\mathbb{Z}^f\mathbb{S}(U_1,U_2)^T$ is a size four vector of contributions from the element to the four DoF of $\mathbf{V}$, while multiplication on the left by $(1,0,0,0)$ extracts the first component of this vector.

Similarly, to (3.21) we get the expression for V_2

$$\begin{aligned} V_2 &= \begin{bmatrix} 0 & 1 & 0 & 0 \end{bmatrix} \mathbb{Z}^f\mathbb{S} \begin{bmatrix} U_1 \\ U_2 \end{bmatrix} + \begin{bmatrix} 0 & 0 & 0 & 1 \end{bmatrix} \mathbb{Z}^f\mathbb{S} \begin{bmatrix} e^{-\mathrm{i}k_1\Delta x}U_1 \\ e^{-\mathrm{i}k_1\Delta x}U_2 \end{bmatrix} = \\ &= \begin{bmatrix} 0 & 1 & 0 & e^{-\mathrm{i}k_1\Delta x} \end{bmatrix} \mathbb{Z}^f\mathbb{S} \begin{bmatrix} U_1 \\ U_2 \end{bmatrix}. \end{aligned} \tag{3.22}$$

Combining (3.21) and (3.22) and recalling the definition (3.18) of the transformation matrix $\mathbb{S}$ we obtain the final result (3.20). □

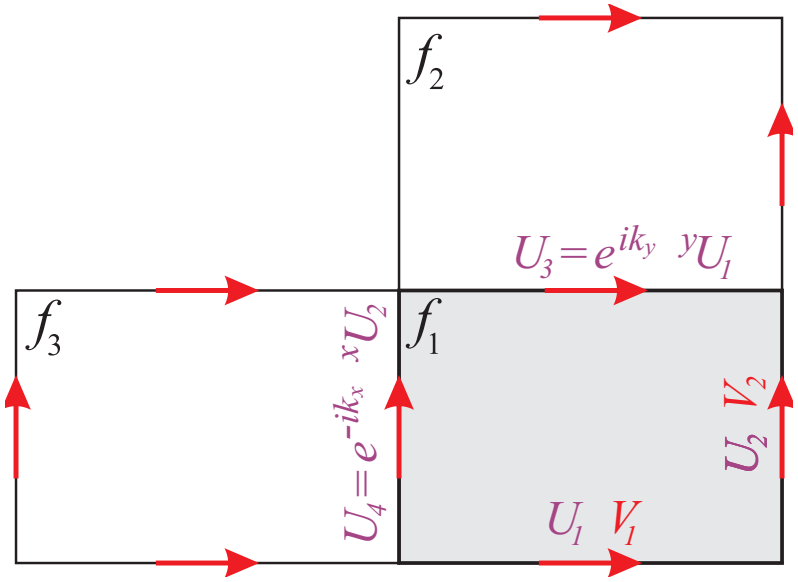

Figure 2: Three cells used to assemble the contributions after multiplication by a uniform matrix.

For a rectangular mesh the two discretization parameters are $h = \Delta x$, which without loss of generality we assume to be the smallest of Δx and Δy, and the aspect ratio of the elements

$$\gamma = \frac{\Delta y}{\Delta x}. \tag{3.23}$$

The characterization of waves by two DoF (3.17) and the wave vector $\mathbf{k}$ together with Lemma 1 suggests rewriting the first equation in (3.15), only in terms of two DoF associated to two orthogonal edges e_1 and e_2, as

$$\frac{\partial^2}{\partial t^2}\mathbf{E}_{(e_1,e_2)} + \frac{1}{\epsilon_0}\frac{\partial}{\partial t}\mathbf{J}_{(e_1,e_2)} = -c_0^2\overline{\mathbb{W}}_{\mathscr{E}}\overline{\mathbb{A}}_h\mathbf{E}_{(e_1,e_2)}. \tag{3.24}$$

In the above we use the DoF notation introduced in (3.3), with $\mathbf{U}_{(e_1,e_2)} := (U_{e_1},U_{e_2})^T$, for $\mathbf{U} = \mathbf{E}$ or $\mathbf{U} = \mathbf{J}$. Here $\overline{\mathbb{W}}_{\mathscr{E}}$ and $\overline{\mathbb{A}}_h$ are 2×2 matrices defined as

$$\overline{\mathbb{W}}_{\mathscr{E}} = \mathbb{S}^\star\mathbb{W}_{\mathscr{E},f}\mathbb{S} \qquad \text{and} \qquad \overline{\mathbb{A}}_h = \mathbb{S}^\star\mathbb{A}_{h,f}\mathbb{S}. \tag{3.25}$$

Performing dispersion analysis on the semi-discrete system (3.24) yields a 2×2 eigenvalue problem. The matrix $\mathbb{A}_h$ has rank one, thus the product $\overline{\mathbb{W}}_{\mathscr{E}}\overline{\mathbb{A}}_h$ is at most rank one. This implies

that one of two eigenvalues is zero. This eigenvalue corresponds to evanescent waves, which are not of interest as they do not propagate in space. We focus on the non-zero eigenvalue of the matrix $\overline{\mathbb{W}}_{\mathscr{E}}\overline{\mathbb{A}}_h$. The non-zero eigenvalue corresponds to transient waves. Since one of the eigenvalues of this matrix is zero, the symbol is given by the trace of the matrix as

$$\begin{aligned}\mathcal{S}_h(\mathbf{k}) &= -c_0^2\mathrm{Tr}(\overline{\mathbb{W}}_{\mathscr{E}}\overline{\mathbb{A}}_h)\\ &= -\frac{4c_0^2}{h^2}\sin^2\frac{k_x h}{2}\left(1+(1-4w_3)\sin^2\frac{k_x h}{2}\right)\\ &- \frac{32c_0^2}{\gamma h^2}w_2\sin^2\frac{k_x h}{2}\sin^2\frac{k_y\gamma h}{2}\\ &- \frac{4c_0^2}{\gamma^2 h^2}\sin^2\frac{k_y\gamma h}{2}\left(1+(1-4w_1)\sin^2\frac{k_y\gamma h}{2}\right).\end{aligned} \tag{3.26}$$

The difference between the continuous and the discrete symbols, in the case of exact time integration, defines the order of numerical dispersion. Therefore, we are interested in making this difference, $\mathcal{S}(\mathbf{k})-\mathcal{S}_h(\mathbf{k})$, as small as possible. For a general member of the MFD family this difference is second order in h. This can be seen by taking $\mathbf{k} = k(\cos\theta, \sin\theta)^T$ and expanding $\mathcal{S}_h(\mathbf{k})$ in a Taylor series in h as

$$\begin{aligned}\mathcal{S}_h(\mathbf{k}) = -(c_0k)^2\Big\{1+\Big(&\tfrac{(3w_3-1)}{3}\cos^4\theta + 2\gamma w_2\cos^2\theta\sin^2\theta+\\ &+\tfrac{\gamma^2(3w_1-1)}{3}\sin^4\theta\Big)k^2h^2+\mathcal{O}(h^4)\Big\}.\end{aligned} \tag{3.27}$$

We observe that we can eliminate the angular (θ) dependence of the h^2 term in (3.27) through the following choice of free parameters in the MFD scheme

$$\tfrac{\gamma^2(3w_1-1)}{3} = \gamma w_2 = \tfrac{(3w_3-1)}{3}, \quad \text{e.g. by taking} \quad \begin{cases} w_1 = \frac{3w_2\gamma^{-1}+1}{3},\\ w_3 = \frac{3w_2\gamma+1}{3}.\end{cases} \tag{3.28}$$

This yields the following discrete symbol

$$\mathcal{S}_h(\mathbf{k}) = -(c_0k)^2\left\{1+\gamma w_2k^2h^2+\mathcal{O}(h^4)\right\}. \tag{3.29}$$

Taking $w_2 = 0$ we can eliminate the second order difference between the continuous and discrete symbols, thus making the numerical dispersion fourth order accurate. Then by using a fourth order discretization in time, we could arrive at a method with fourth order dispersion error. This approach has its advantages especially at low spatial resolution. Unfortunately, the storage necessary for these schemes may be prohibitive for large problems. We will instead focus on choosing a second order time integrator so that w_2 can eliminate all second order dispersion errors.

4 Exponential Time Differencing

Exponential differencing is a time integration technique commonly used for lossy dielectrics. The idea is as follows. Consider a time dependent ODE of the form

$$\dot{u} = cu + F(u,t). \tag{4.1}$$

To create the exact solution of (4.1) one exploits the fact that

$$\frac{d}{dt}\left(e^{-ct}u\right) = e^{-ct}\left(\dot{u}-cu\right). \tag{4.2}$$

Multiply (4.1) by e^{-ct}, integrate from t_n to t_{n+1} and divide by $e^{-ct_{n+1}}$

$$u(t_{n+1}) - \mathrm{e}^{c\Delta t}u(t_n) = \int_{t_n}^{t_{n+1}} F(u(s),s)\mathrm{e}^{c(\Delta t - s)}\, ds. \tag{4.3}$$

Formula (4.3) is exact. Thus, in principle, higher order accuracy can be obtained by using higher order discretization of the integral term, c.f. [2]. In practice, due to specifics of definitions of $F(u(s),s)$, it could be convenient to use the following approximation to the integral in (4.3)

$$\int_{t_n}^{t_{n+1}} F(u(s),s)\mathrm{e}^{c(\Delta t - s)}\, ds \approx F^{n+1/2}\int_{t_n}^{t_{n+1}} \mathrm{e}^{c(\Delta t - s)}\, ds = c^{-1}(\mathrm{e}^{c\Delta t}-1)F^{n+1/2}, \tag{4.4}$$

where $F^{n+1/2}$ is an approximation of $F(u(t_{n+1/2}), t_{n+1/2})$. When F depends on u then this approach may be implicit. However, in our case F depends only on t as we employ a staggering technique so this quantity is computed explicitly. This approach can be generalized to vector valued ODE in time

$$\dot{\mathbf{u}} = \mathbb{X}\mathbf{u} + \mathbf{F}(\mathbf{u}, t) \tag{4.5}$$

to produce the following discretization when $\mathbb{X}$ is invertible

$$\mathbf{u}^{n+1} - \mathrm{e}^{\mathbb{X}\Delta t}\mathbf{u}^n = \mathbb{X}^{-1}(\mathrm{e}^{\mathbb{X}\Delta t} - \mathbb{I})\mathbf{F}^{n+1/2}. \tag{4.6}$$

4.1 Continuous in Space Discrete in Time Formulation

Rewrite the first order PDEs (2.1-(2.2)) as

$$\begin{cases} \dot{\mathbf{u}} = \mathbb{X}\mathbf{u} + \mathbf{F}, \\ \dot{B} = -\mathrm{curl}\mathbf{E}, \end{cases} \tag{4.7}$$

where

$$\mathbf{u} = \begin{pmatrix} \mathbf{E} \\ \mathbf{J} \end{pmatrix}, \qquad \mathbb{X} = \begin{pmatrix} 0 & -\dfrac{1}{\epsilon_0} \\ \epsilon_0\omega_P^2 & -\omega_i \end{pmatrix}, \qquad \mathbf{F} = \begin{pmatrix} c_0^2\, \mathbf{curl} B \\ 0 \end{pmatrix}. \tag{4.8}$$

We will consider a time discretization $\mathbf{E}^n$ and $\mathbf{J}^n$ of $\mathbf{E}$ and $\mathbf{J}$ on integer time steps $t_n := n\Delta t$ and $B^{n+1/2}$ of B on staggered half-integer time steps $t_{n+1/2} := (n+1/2)\Delta t$.

For the first equation in (4.8) we use the ETD scheme (4.6), where we define the matrix

$$\mathbb{Y} := \mathbb{X}^{-1}(\mathrm{e}^{\mathbb{X}\Delta t} - \mathbb{I}). \tag{4.9}$$

For the second equation we use the standard time-staggered leap-frog. Thus, the semi-discrete scheme for (4.8) reads

$$\begin{cases} \begin{pmatrix} \mathbf{E}^{n+1} \\ \mathbf{J}^{n+1} \end{pmatrix} = \mathrm{e}^{\mathbb{X}\Delta t}\begin{pmatrix} \mathbf{E}^{n} \\ \mathbf{J}^{n} \end{pmatrix} + \mathbb{Y}\begin{pmatrix} c_0^2\, \mathbf{curl}\, B^{n+1/2} \\ 0 \end{pmatrix}, \\ B^{n+1/2} = B^{n-1/2} - \Delta t\ \mathrm{curl}\ \mathbf{E}^n. \end{cases} \tag{4.10}$$

In order to obtain from (4.10) an appropriate second order formulation we proceed similarly to how we obtained (2.4) from (2.1-(2.2)) by eliminating the magnetic induction B from the evolution equation. We do this by applying a leap-frog step to both sides of the first equation in (4.10). This yields a continuous in space discrete in time discretization

$$\begin{pmatrix} \mathbf{E}^{n+1} \\ \mathbf{J}^{n+1} \end{pmatrix} = (\mathbb{I} + e^{\mathbb{X}\Delta t})\begin{pmatrix} \mathbf{E}^{n} \\ \mathbf{J}^{n} \end{pmatrix} - \mathrm{e}^{\mathbb{X}\Delta t}\begin{pmatrix} \mathbf{E}^{n-1} \\ \mathbf{J}^{n-1} \end{pmatrix} - c_0^2\Delta t\mathbb{Y}\begin{pmatrix} \mathbf{curl}\ \mathrm{curl}\ \mathbf{E}^n \\ 0 \end{pmatrix}. \tag{4.11}$$

4.2 Dispersion Analysis for Continuous in Space Discrete in Time Formulation

To obtain a discrete in time dispersion relation we divide both sides of (4.11) by the exponential integrator $\mathbb{Y}$ to get

$$\frac{1}{\Delta t}\mathbb{Y}^{-1}\left[\begin{pmatrix}\mathbf{E}^{n+1}\\ \mathbf{J}^{n+1}\end{pmatrix} - (\mathbb{I}+e^{\mathbb{X}\Delta t})\begin{pmatrix}\mathbf{E}^{n}\\ \mathbf{J}^{n}\end{pmatrix} + \mathrm{e}^{\mathbb{X}\Delta t}\begin{pmatrix}\mathbf{E}^{n-1}\\ \mathbf{J}^{n-1}\end{pmatrix}\right] = \begin{pmatrix}-c_0^2\,\mathbf{curl}\,\mathrm{curl} & 0\\ 0 & 0\end{pmatrix}\begin{pmatrix}\mathbf{E}^{n}\\ \mathbf{J}^{n}\end{pmatrix}. \tag{4.12}$$

Assuming time-harmonic solutions in the above equation we produce the system

$$\mathbb{Y}^{-1}\frac{\mathrm{e}^{-\mathrm{i}\omega\Delta t}\mathbb{I} - (\mathbb{I}+\mathrm{e}^{\mathbb{X}\Delta t}) + \mathrm{e}^{\mathrm{i}\omega\Delta t}\mathrm{e}^{\mathbb{X}\Delta t}}{\Delta t} = \begin{pmatrix}-c_0^2\,\mathbf{curl}\,\mathrm{curl} & 0\\ 0 & 0\end{pmatrix}. \tag{4.13}$$

Defining the discrete symbol in time to be

$$\mathcal{T}_{\Delta t}(\omega) = \mathbb{Y}^{-1}\frac{\mathrm{e}^{-\mathrm{i}\omega\Delta t}\mathbb{I} - (\mathbb{I}+\mathrm{e}^{\mathbb{X}\Delta t}) + \mathrm{e}^{\mathrm{i}\omega\Delta t}\mathrm{e}^{\mathbb{X}\Delta t}}{\Delta t}, \tag{4.14}$$

and expanding $\mathcal{T}_{\Delta t}$ in a Taylor Series in the variable Δt we obtain

$$\mathcal{T}_{\Delta t}(\omega) = (-\omega^2\mathbb{I} + \mathrm{i}\omega\mathbb{X}) + \frac{\Delta t^2}{12}(-\omega^2\mathbb{I} + \mathrm{i}\omega\mathbb{X})^2 + \mathcal{O}(\Delta t^4). \tag{4.15}$$

We will make use of this expansion in our method optimization proceedure.

5 Exponential Time Mimetic Finite Difference Method (ETMFD) for Cold Plasma

We now present the fully discrete **Exponential Time Mimetic Finte Difference (ETMFD)** method for the Maxwell-CP model, based on MFD in space and ETD in time. Our fully discrete problem is:
Given $\mathbf{E}_h^\ell, \mathbf{J}_h^\ell \in \mathscr{E}_h$ for $\ell \in \{0,1\}$, find $\mathbf{E}_h^n, \mathbf{J}_h^n \in \mathscr{E}_h \quad \forall n \geq 0$ such that

$$\begin{pmatrix}\mathbf{E}_h^{n+1}\\ \mathbf{J}_h^{n+1}\end{pmatrix} = (\mathbb{I}+\mathrm{e}^{\mathbb{X}\Delta t})\begin{pmatrix}\mathbf{E}_h^{n}\\ \mathbf{J}_h^{n}\end{pmatrix} - \mathrm{e}^{\mathbb{X}\Delta t}\begin{pmatrix}\mathbf{E}_h^{n-1}\\ \mathbf{J}_h^{n-1}\end{pmatrix} - c_0^2\Delta t\mathbb{Y}\begin{pmatrix}\mathbb{W}_{\mathscr{E}}\mathrm{curl}_h^T\mathbb{A}_h\mathbf{E}^n\\ 0\end{pmatrix}. \tag{5.1}$$

5.1 M-Adaptation of the ETMFD

To perform m-adaptation for the ETMFD we must first find its discrete dispersion relation. Intuitively the dispersion relation for (5.1) would be determined by equality between the space discrete symbol $\mathcal{S}_h$ and the time discrete symbol $\mathcal{T}_{\Delta t}$. However, the temporal symbol as defined is matrix valued while the spatial symbol is scalar. Consider our space discretization of the first row of (2.4) assumuing $\mathbf{E}_h$ and $\mathbf{J}_h$ are appropriate transient plane waves as discussed in (3.26)

$$\frac{\partial^2}{\partial t^2}\mathbf{E}_{(e_1,e_2)} + \frac{1}{\epsilon_0}\frac{\partial}{\partial t}\mathbf{J}_{(e_1,e_2)} = \mathcal{S}_h(\mathbf{k}_h)\mathbf{E}_{(e_1,e_2)}, \tag{5.2}$$

This evolution equation implies that $\mathbf{E}_{(e_1,e_2)}$ and $\mathbf{J}_{(e_1,e_2)}$ must be colinear as $\mathcal{S}_h$ is scalar. We therefore define the quantities

$$E_0 = |\mathbf{E}_{(e_1,e_2)}|, \qquad J_0 = |\mathbf{E}_{(e_1,e_2)}|. \tag{5.3}$$

Thus, the spatial symbol of the ETMFD must be some 2x2 matrix multiplied by $\mathcal{S}_h(\mathbf{k})$ acting on the vector $(E_0, J_0)^T$. However as $\mathcal{S}_h(\mathbf{k})$ does not depend on J_0 and has no influence on the second row of the system (4.13) so this matrix must be

$$\mathbb{P}_1 = \begin{pmatrix}1 & 0\\ 0 & 0\end{pmatrix}. \tag{5.4}$$

Given that $\mathcal{S}_h\mathbb{P}_1$ is matrix valued we can now pose the discrete dispersion relation as a 2×2 eigenvalue problem on the initial orientations of the fields $\mathbf{E}_0$ and $\mathbf{J}_0$, which must be non-zero eigenvectors of the matrix $\overline{\mathbb{W}}_{\mathscr{E}}\,\overline{\mathbb{A}}_h$. The discrete dispersion relation for (5.1) is then given by

$$\mathcal{T}_{\Delta t}(\omega)\begin{pmatrix}E_0\\J_0\end{pmatrix} = \mathcal{S}_h(\mathbf{k})\mathbb{P}_1\begin{pmatrix}E_0\\J_0\end{pmatrix}. \tag{5.5}$$

To perform m-adaptation we begin by choosing w_1, w_3 as defined in (3.28) which eliminates dependence on angle of propagation and leaves us with one free parameter w_2, i.e.

$$w_1 = \frac{3w_2\gamma^{-1}+1}{3}, \qquad w_3 = \frac{3w_2\gamma+1}{3}. \tag{5.6}$$

In order to relate time and space discretization sizes we introduce the Courant number

$$\nu = \frac{c_0\Delta t}{h}. \tag{5.7}$$

By moving both terms in (5.5) to the left side and expanding in a Taylor series in h we get

$$\begin{aligned} 0 &= \Big(\mathcal{T}_\Delta t(\omega) - \mathcal{S}_h(\mathbf{k})\mathbb{P}_1\Big)\begin{pmatrix}E_0\\J_0\end{pmatrix} = \\ &= \left(\big(-\omega^2\mathbb{I} + \mathrm{i}\omega\mathbb{X} + c_0^2k^2\mathbb{P}_1\big) + \frac{h^2}{12c_0^2}\Big(\nu^2(-\omega^2\mathbb{I}+\mathrm{i}\omega\mathbb{X})^2 + 12\gamma w_2 c_0^4k^4\mathbb{P}_1^2\Big)\right)\begin{pmatrix}E_0\\J_0\end{pmatrix} + \\ &\quad + \mathcal{O}(h^4)\begin{pmatrix}E_0\\J_0\end{pmatrix}. \end{aligned} \tag{5.8}$$

As $(\omega, \mathbf{k})$ is a solution of the discrete dispersion relation we have

$$c_0^2k^2\mathbb{P}_1\begin{pmatrix}E_0\\J_0\end{pmatrix} = \big(\omega^2\mathbb{I} - \mathrm{i}\omega\mathbb{X} + \mathcal{O}(h^2)\big)\begin{pmatrix}E_0\\J_0\end{pmatrix}. \tag{5.9}$$

Substituting this into the order h^2 term in (5.8) we have

$$\frac{h^2}{12c_0}\left(\nu^2 + 12\gamma w_2\right)c_0^4k^4\mathbb{P}^2 + \mathcal{O}(h^4). \tag{5.10}$$

We can eliminate order h^2 term entirely by a proper choice of the parameter w_2

$$\left(\nu^2 + 12\gamma w_2\right) = 0 \qquad \Rightarrow \qquad w_2 = -\frac{\nu^2}{12\gamma}. \tag{5.11}$$

Under the choice (5.11) the dispersion error is

$$\Big(\mathcal{T}_{\Delta t}(\omega) - \mathcal{S}_h(\mathbf{k})\mathbb{P}_1\Big)\begin{pmatrix}E_0\\J_0\end{pmatrix} = \big(-\omega^2\mathbb{I} + \mathrm{i}\omega\mathbb{X} + c_0^2k^2\mathbb{P}_1 + \mathcal{O}(h^4)\big)\begin{pmatrix}E_0\\J_0\end{pmatrix}. \tag{5.12}$$

For convenience we explicitly write out the the choice of the optimal matrix $\mathbb{W}_{\mathscr{E},f}$

$$\mathbb{W}_{\mathscr{E},f} = \frac{1}{12\Delta x\Delta y}\begin{pmatrix} 7-\nu_y^2 & -\nu_x\nu_y & \nu_y^2-1 & \nu_x\nu_y \\ -\nu_x\nu_y & 7-\nu_x^2 & \nu_x\nu_y & \nu_x^2-1 \\ \nu_y^2-1 & \nu_x\nu_y & 7-\nu_y^2 & -\nu_x\nu_y \\ \nu_x\nu_y & \nu_x^2-1 & -\nu_x\nu_y & 7-\nu_x^2 \end{pmatrix}, \qquad \begin{aligned}\nu_x &= \frac{c_0\Delta t}{\Delta x},\\ \nu_y &= \frac{c_0\Delta t}{\Delta y}.\end{aligned} \tag{5.13}$$

6 Numerical Simulations for Specific Media

For our experiments we introduce a change of variables for $\mathbb{X}$ which allows for an easier formulation of the matrix exponential.

$$\mathbb{X} = \begin{pmatrix} 0 & -\epsilon_0^{-1} \\ \epsilon_0(\alpha^2+\beta^2) & 2\alpha \end{pmatrix}, \quad \alpha = -\frac{\omega_i}{2},\ \beta = \frac{\sqrt{4\omega_P^2 - \omega_i^2}}{2}. \tag{6.1}$$

The ODE system governing the cold plasma model is a classical damped, driven oscillator. For different values of the parameters the character of the system changes. We present results for the case when the system is under damped ($\omega_i^2 < 4\omega_p^2$). The matrix exponential for $\mathbb{X}\Delta t$ is given by

$$\mathrm{e}^{\mathbb{X}\Delta t} = \mathrm{e}^{\alpha\Delta t}\begin{pmatrix} \cos(\beta\Delta t) - \alpha\dfrac{\sin(\beta\Delta t)}{\beta} & -\dfrac{\sin(\beta\Delta t)}{\epsilon_0\beta} \\ \epsilon_0(\alpha^2+\beta^2)\dfrac{\sin(\beta\Delta t)}{\beta} & \cos(\beta\Delta t) + \alpha\dfrac{\sin(\beta\Delta t)}{\beta} \end{pmatrix} := \begin{pmatrix} \alpha_1 & \alpha_2 \\ \beta_2 & \beta_1 \end{pmatrix}. \tag{6.2}$$

The integral of this matrix is given by

$$\int_0^{\Delta t} \mathrm{e}^{\mathbb{X}s}\, ds = \begin{pmatrix} \alpha_3 & \alpha_4 \\ \beta_3 & \beta_4 \end{pmatrix}, \tag{6.3}$$

where the coefficients in the matrix above are defined as

$$\alpha_3 := \frac{1}{\beta}\left(\frac{\mathrm{e}^{\alpha\Delta t}(2\alpha\beta\cos(\beta\Delta t) + (\beta^2-\alpha^2)\sin(\beta\Delta t)) - 2\alpha\beta}{\alpha^2+\beta^2}\right), \tag{6.4}$$

$$\alpha_4 := \frac{1}{\beta}\left(-\frac{\beta - \mathrm{e}^{\alpha\Delta t}(\alpha\sin(\beta\Delta t) - \beta\cos(\beta\Delta t))}{\epsilon_0(\alpha^2+\beta^2)}\right), \tag{6.5}$$

$$\beta_3 := \frac{1}{\beta}\left(\epsilon_0(\beta + \mathrm{e}^{\alpha\Delta t}(\alpha\sin(\beta\Delta t) - \beta\cos(\beta\Delta t)))\right), \tag{6.6}$$

$$\beta_4 := \frac{1}{\beta}\left(\mathrm{e}^{\alpha\Delta t}\sin(\beta\Delta t)\right). \tag{6.7}$$

The second order formulation for the discrete electric field $\mathbf{E}$ and polarization current density $\mathbf{J}$, as introduced in Section 5.1, was a convenient formulation of the discrete ETMFD method for the analysis of numerical dispersion. However, in our numerical experiments we have found that L^2 errors in the second order system for $\mathbf{E}$ and $\mathbf{J}$ are very sensitive to the choice of initial conditions. Thus, for our numerical simulations we will use a different formulation of the discrete ETMFD method, with an equivalent numerical dispersion relation, that retains the second order discrete evolution equation for the electric field, but uses a first order discrete evolution equation for the polarization current density $\mathbf{J}$. Since the focus of this paper is on numerical dispersion optimized methods, we do not investigate the appropriate initialization of the discrete ETMFD scheme here. We defer this investigation to future work.

The hybrid second order evolution equation for the discrete electric field $\mathbf{E}$ and first order evolution equation for the polarization density $\mathbf{J}$ is given as

$$\mathbf{E}_h^{n+1} = (1+\alpha_1)\mathbf{E}_h^n + \alpha_2\mathbf{J}_h^n - \alpha_1\mathbf{E}_h^{n-1} - \alpha_2\mathbf{J}_h^{n-1} - c_0^2\Delta t\alpha_3\mathbb{W}_{\mathscr{E}}\mathbb{A}_h\mathbf{E}_h^n \qquad n \geq 2, \tag{6.8}$$

$$\mathbf{J}_h^{n+1} = \beta_1\mathbf{J}_h^n + \beta_2\mathbf{E}_h^n + \frac{\beta_3}{\alpha_3}(\mathbf{E}_h^{n+1} - \alpha_1\mathbf{E}_h^n - \alpha_2\mathbf{J}_h^n) \qquad n \geq 1. \tag{6.9}$$

This formulation is explicit when we compute $\mathbf{E}^{n+1}$ before $\mathbf{J}^{n+1}$. It requires three initial conditions given by

$$\mathbf{E}_h^0 = \mathcal{I}^{\mathscr{E}_h}(\mathbf{E}(0)), \qquad \mathbf{E}_h^1 = \mathcal{I}^{\mathscr{E}_h}(\mathbf{E}(\Delta t)), \qquad \mathbf{J}_h^0 = \mathcal{I}^{\mathscr{E}_h}(\mathbf{J}(0)). \tag{6.10}$$

In our numerical simulations we used a midpoint quadrature on every edge for $\mathbf{E}_h$ and computed $\mathbf{J}_h$ exactly; i.e.,

$$\mathbf{E}_{h|e}^j = \boldsymbol{\tau}_e \cdot \mathbf{E}(x_c, y_c, j\Delta t), \;\; j = \{0, 1\}, \qquad \mathbf{J}_{h|e}^0 = \frac{1}{|e|}\int_e \mathbf{J}(x, y, 0) \cdot \boldsymbol{\tau}_e ds. \tag{6.11}$$

Experiment 1. In our first experiment we investigate the numerical anisotropy of our method. If $(\omega_n, \mathbf{k}_n)$ are solutions of the numerical dispersion relation, then as eigenvalue pairs they satisfy the relation

$$\det\left(\mathcal{T}_{\Delta t}(\omega_n) - \mathcal{S}_h(\mathbf{k}_n)\mathbb{P}_1\right) = 0. \tag{6.12}$$

The continuous dispersion relation between ω and $\mathbf{k}$ can be written as

$$-\mathrm{i}\omega^3 + \omega_i\omega^2 - \mathrm{i}(\omega_p^2 + c_0^2k^2)\omega - \omega_i c_0^2 k^2 = 0. \tag{6.13}$$

Assume that $\mathbf{k}$ is fixed and real valued. Let $(\omega, \mathbf{k})$ be a solution to (6.13). We define the relative dispersion error as

$$\mathcal{E}(\omega) = \frac{1}{|\omega|}\det\left(\mathcal{T}_{\Delta t}(\omega) - \mathcal{S}_h(\mathbf{k})\mathbb{P}_1\right) \tag{6.14}$$

which is analogous to a local truncation error, i.e., we measure how close the true root ω of the continuous dispersion relation (6.13) is to being a root of the numerical dispersion relation (6.12). We parameterize the wave vector as $\mathbf{k} = 4(\cos\theta, \sin\theta)$. For this experiment we will also choose $\omega_i = 1$ and $\omega_p = 1$. In Figure 3 we plot $\mathcal{E}(\omega)$ as a polar function of θ on a log scale. A perfect circe in this diagram indicates isotropic error, otherwise the error shows the directional dependence of dispersion. For the purpose of comparison we also include the relative dispersion error of ETD in time and Yee like staggering in space, which we refer to as the ET-Yee scheme.

Figure 3 illustrates that while the dispersion error of our method is anisotropic it is significantly reduced compared to that of the ET-Yee scheme. By varying the aspect ratio we find that we can reduce dispersion error in the direction of increased refinement at the expense of increased dispersion error in the less refined direction.

Experiment 2. In our second experiment we will investigate the accuracy of our ETMFD method for discretizing problems with a known exact solution. For $\mathbf{k} = (k_x, k_y)^T$ with $k_x, k_y \in \pi\mathbb{Z}$, let $a + \mathrm{i}b = \omega$ be a (complex) root of the dispersion relation (6.13). We consider the exact solution for the Maxwell-CP model given by

$$\mathbf{E}(x, y, t) = \mathrm{e}^{at}\cos(bt)\begin{pmatrix} -k_y\cos(k_x x)\sin(k_y y) \\ k_x\sin(k_x x)\cos(k_y y)\end{pmatrix}, \tag{6.15}$$

$$\mathbf{J}(x, y, t) = \epsilon_0\omega_p^2\mathrm{e}^{at}\frac{(a+\omega_i)\cos(bt) + b\sin(bt)}{b^2 + (a+\omega_i)^2}\begin{pmatrix} -k_y\cos(k_x x)\sin(k_y y) \\ k_x\sin(k_x x)\cos(k_y y)\end{pmatrix}. \tag{6.16}$$

For our experiments we consider $\omega_P = \omega_i = \epsilon_0 = c = 1$ and $k_x = k_y = \pi$. For this we have $a \approx 0.023$ and $b \approx 4.55$. We choose the final time to be $T = 4$. To calculate relative L^2 errors we use an appropriate inner product, based on our mimetic discretization, which is defined as

$$\mathcal{E}_{L^2}^h(\mathbf{F}_h^n) := \frac{\sqrt{(\mathbf{F}_h^n - \mathcal{I}^{\mathscr{E}_h}(\mathbf{F}(n\Delta t))^T\mathbb{M}_{\mathscr{E}}(\mathbf{F}_h^n - \mathcal{I}^{\mathscr{E}_h}(\mathbf{F}(n\Delta t))}}{\sqrt{\mathcal{I}^{\mathscr{E}_h}(\mathbf{F}(n\Delta t))^T\mathbb{M}_{\mathscr{E}}\mathcal{I}^{\mathscr{E}_h}(\mathbf{F}(n\Delta t))}}, \tag{6.17}$$

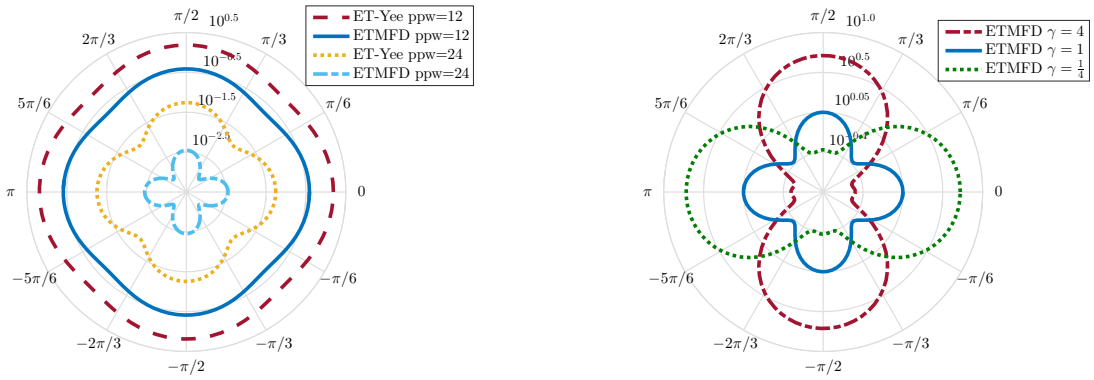

(a) (b)

Figure 3: We consider a cold isotropic plasma with $\omega_P = 1$ and $\omega_i = 1$. Figure (a) plots relative dispersion error for a wave with $k = 4$ and resolved at 12 and 24 points per wavelength on a mesh with an aspect ratio $\gamma = 1$ for both the ET-Yee and ETMFD schemes. We choose the Courant number to be $\nu = \frac{1}{2}$. Figure (b) plots the relative dispersion error for a cell with $\Delta x \Delta y = 12^{-2}$ for the aspect ratios $\gamma = 4, 1, \frac{1}{4}$. In this case we choose the Courant number to be $\nu = \frac{1}{2}\min\{\gamma^3, 1\}$.

Table 1: Relative L^2 Errors for Experiment 2.

	Electric Field, **E**				Current Density, **J**			
$\log_2(h)$	ET-Yee	rate	ETMFD	rate	ET-Yee	rate	ETMFD	rate
-4	1.1024e-02		4.8495e-05		3.0064e-02		1.3322e-04	
-5	2.7237e-03	2.0170	3.0206e-06	4.0049	7.4940e-03	2.0042	8.3901e-06	3.9890
-6	6.7826e-04	2.0057	1.8844e-07	4.0026	1.8704e-03	2.0024	5.3485e-07	3.9715
-7	1.6931e-04	2.0021	1.1767e-08	4.0013	4.6717e-04	2.0013	3.4784e-08	3.9426
-8	4.2303e-05	2.0009	7.3501e-10	4.0008	1.1674e-04	2.0007	2.3361e-09	3.8963

where $\mathbf{F}_h^n = (\mathbf{E}_h^n, \mathbf{J}_h^n)^T$ and the interpolation $\mathcal{I}^{\mathscr{E}_h}$ operator is defined in (3.3).

To define the dispersion error we fit an appropriate temporal function, $F(t : \omega_h)$, to temporal grid data $\{\mathbf{E}_{h,e_i}^n\}_{n=0}^N$ at some edge e_i to find the best discrete frequency w_h. To calculate the relative dispersion errors, we perform the following procedure. If (a_h, b_h) is the result of the non-linear least squares fitting of time tracking data $\{\mathbf{F}_{h|e}^n\}_{n=1}^N$ to the appropriate function $(\exp(a_h t)\cos(b_h t)$ for the electric field and $\epsilon_0\omega_p^2 \mathrm{e}^{a_h t}\frac{(a_h+\omega_i)\cos(b_h t)+b_h \sin(b_h t)}{b_h^2+(a_h+\omega_i)^2}$ for the current density) then we define the relative dispersion error by

$$\mathcal{E}_d^h(\mathbf{F}_h) := \sqrt{\frac{(a-a_h)^2 + (b-b_h)^2}{a^2+b^2}}, \tag{6.18}$$

where a, b are the true data. For comparison, we have also performed our simulations with the corresponding ET-Yee scheme (i.e., Yee spatial staggering with ETD), which is second order accurate in space and time. In Table 1 we present relative L^2 errors in the electric field and polarization density, while in Table 2 we present relative dispersion errors for the electric field and polarization density, respectively. Figures 4, and 5 plot the results of Tables 1-2. Our results indicate fourth order dispersion and L^2 error convergence for the ETMFD as compared to the corresponding (well known) second order convergence for the ET-Yee scheme.

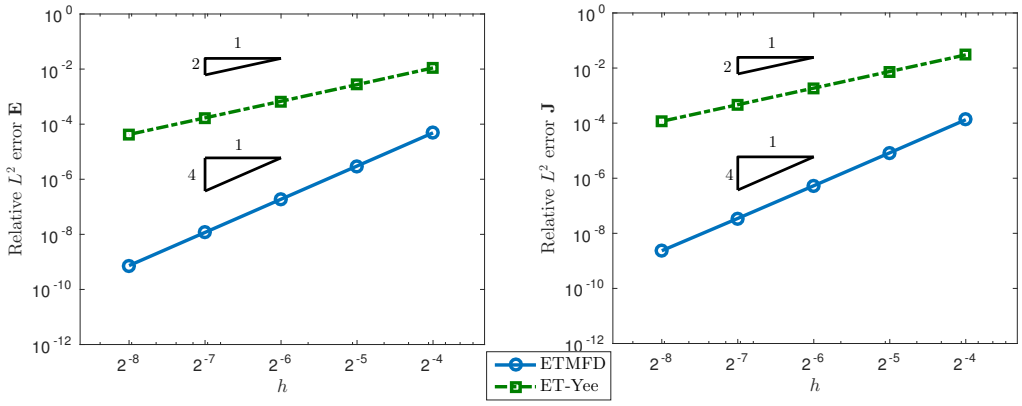

Figure 4: Relative L^2 errors for Experiment 2.

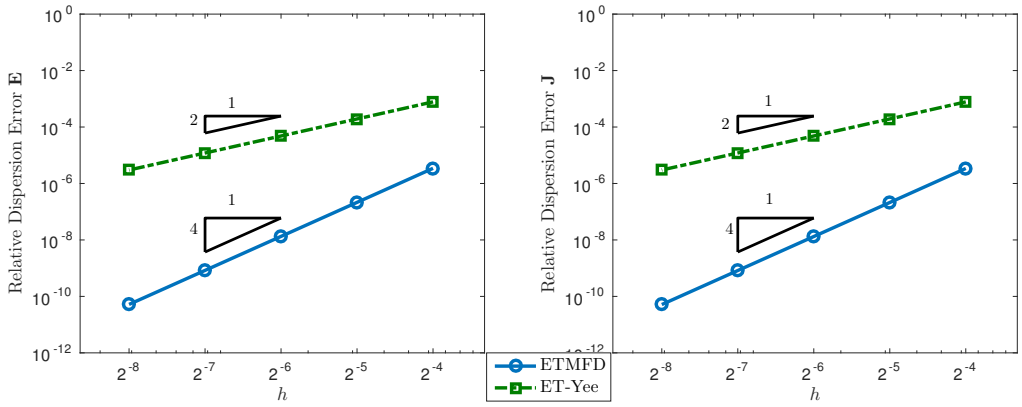

Figure 5: Relative dispersion errors for Experiment 2.

Table 2: Relative Dispersion Errors for Experiment 2.

	Electric Field, $\mathbf{E}$				Current Density, $\mathbf{J}$			
$\log_2(h)$	ET-Yee	rate	ETMFD	rate	ET-Yee	rate	ETMFD	rate
-4	7.7638e-04		3.4427e-06		8.7152e-04		3.4530e-06	
-5	1.9280e-04	2.0129	2.1407e-07	4.0080	2.1720e-04	2.0045	2.1487e-07	4.0063
-6	4.8070e-05	2.0066	1.3345e-08	4.0042	5.4246e-05	2.0014	1.3399e-08	4.0032
-7	1.2002e-05	2.0033	8.3287e-10	4.0021	1.3557e-05	2.0005	8.3655e-10	4.0016
-8	2.9985e-06	2.0017	5.1994e-11	3.9892	3.3886e-06	2.0003	5.2097e-11	4.0052

7 Conclusions

We have constructed a new successful m-adaptation of Mimetic Finite Difference (MFD) method for Maxwell's equations in a cold plasma. We started from a second order edge based family of MFD discretizations in space. We used a generalized form of mass lumping. This was done, on one hand, to obtain a fully explicit scheme, thus avoiding linear solves at every time step. As a result the new scheme is highly efficient. On the other hand, the generalized form of mass lumping preserves free parameters in the MFD discretization. This allows for further optimization within the family.

We demonstrated that using the standard leapfrog time stepping does not allow reduce the numerical dispersion within the MFD family. Fortunately, using exponential time differencing

allows for a successful m-adaptation of the MFD family. For the optimal choice of parameters in the exponential time MFD (ETMFD) discretization the numerical dispersion errors were shown to be fourth order as opposed to second order for a general member of the ETMFD family. Numerical simulations independently verified our theoretical results showing fourth order numerical dispersion and L^2-errors for some special solutions.

One of the advantages of our m-adapted ETMFD method over other fourth order methods, that have been constructed in the literature using the modified equation approach (see e.g. [9]), is smaller stencil size as compared to those of other fourth order methods. This is due to the low order base discredization. Higher order approximation is a result m-adaptation procedure, which is possible due to mesh regularity and symmetry.

The use of ETD offers a number of advantages in complex dispersive media. First, it allows for an explicit staggering of the electric field and current density from the magnetic field. This is in contrast to time averaging schemes which are semi-implicit with spatial staggering. Though ETD may require smaller time steps than a semi-implicit approach, linear dispersive media such as a cold isotropic plasma are stiff media requiring very small time steps in numerical discretizations in order to capture the fast decaying transients in the media. Thus a cheaper explicit scheme is preferable to a more expensive implicit scheme when run with comparable time steps.

Finally, our approach can be interpreted as a generalization (though non-trivial) of m-adaptation in vacuum. It inherits a similar structure for its discrete symbol in time and allows for successful optimization over numerical dispersion errors. As a consequence, the optimal choice of free MFD parameters and the corresponding local mass matrices turn out to be the same in the case of vacuum and Maxwell-CP model. In the future we will investigate the sensitivity of errors to initial conditions and extend the ideas and techniques considered here to other types of linear and nonlinear dispersive materials.

Maxwell's equations include divergence constraints on the electric and magnetic flux densities. It is well known that if solutions satisfy these divergence constraints initially then the curl equations guarantee that these conditions are satisfied at later times. Thus, the divergence constraints are redundant in the continuum equations as long as they are satisfied by initial conditions. This property may or may not hold for solutions to discrete approximations of Maxwell's equations. We are currently working on understanding the divergence properties of our ETMFD method along with a stability analysis of our schemes. These and related issues will be part of a future paper that will address the construction of ETMFD schemes for a large class of linear dispersive models.

8 Acknowledgments

V. Gyrya's work was carried out under the auspices of the National Nuclear Security Administration of the U.S. Department of Energy at Los Alamos National Laboratory under Computing Research (ASCR) Program in Applied Mathematics Research.

D. A. McGregor's work is supported by the U.S. Department of Energy National Energy Technology Laboratory Graduate Professional Internship Program.

REFERENCES

[1] Vrushali A. Bokil, Nathan L. Gibson, Vitaliy Gyrya, and Duncan A. McGregor. Dispersion reducing methods for edge discretizations of the electric vector wave equation. *J. Comput. Phys.*, 287:88–109, 2015.

[2] Steven M. Cox and Paul C. Matthews. Exponential time differencing for stiff systems. *J. Comput. Phys.*, 176(2):430–455, 2002.

[3] Steven A. Cummer. An analysis of new and existing fdtd methods for cold plasma and a method for improving accuracy. *IEEE Trans. Antennas Propag.*, 45(3):392–400, 1997.

[4] Lourenço Beirão da Veiga, Konstantin Lipnikov, and Gianmarco Manzini. *The Mimetic Finite Difference Method for Elliptic Problems*, volume 11. Springer, 2014.

[5] Vitaliy Gyrya, Konstantin Lipnikov, Gianmarco Manzini, and Daniil Svyatskiy. M-adaptation in the mimetic finite difference method. *Math. Mod. Meth. Appl. S.*, 24(08):1621–1663, 2014.

[6] Tatsuya Kashiwa and Ichiro Fukai. A treatment by the fd-td method of the dispersive characteristics associated with electronic polarization. *Microwave Opt. Technol. Lett.*, 3(6):203–205, 1990.

[7] Konstantin Lipnikov, Gianmarco Manzini, and Mikhail Shashkov. Mimetic finite difference method. *J. Comput. Phys.*, 257(part B):1163–1227, 2014.

[8] Peter G. Petropoulos. Analysis of exponential time-differencing for fdtd in lossy dielectrics. *IEEE Trans. Antennas Propag.*, 45(6):1054–1057, 1997.

[9] Jeffrey L. Young. A higher order fdtd method for em propagation in a collisionless cold plasma. *IEEE Trans. Antennas Propag.*, 44(9):1283–1289, 1996.

A M-Adaptation for leapfrog time stepping

We demonstrate the need for exponential time differencing in the spatially discretized cold plasma model to produce a fully discrete method with high order numerical dispersion by first considering the case of a simple conductive medium. A conductive medium is a special case of CP where we take $\omega_i \to \infty$ and assume the ratio $\epsilon\omega_P^2/\omega_i \to \sigma$ as $\omega_i \to \infty$. A conductive medium is modeled by the second order PDE

$$\frac{\partial^2}{\partial t^2}\mathbf{E} + \frac{\sigma}{\epsilon_0}\frac{\partial}{\partial t}\mathbf{E} = -c_0^2\mathbf{curl}\ \mathrm{curl}\mathbf{E}, \tag{A.1}$$

in which σ is the electrical conductivity. Let $\tau = \frac{\epsilon_0}{\sigma}$. The standard Leapfrog discretization in time with semi-implicit time averaging of the low order term gives us the scheme

$$\frac{\mathbf{E}^{n+1} - 2\mathbf{E}^n + \mathbf{E}^{n-1}}{\Delta t^2} + \frac{\mathbf{E}^{n+1} - \mathbf{E}^{n-1}}{2\tau\Delta t} = -c_0^2\mathbf{curl}\ \mathrm{curl}\mathbf{E}^n. \tag{A.2}$$

The symbol of the time discretization and its expansion in ω is given by

$$\frac{-4\sin^2\frac{\omega\Delta t}{2}}{\Delta t^2} - \frac{\mathrm{i}}{\tau}\frac{\sin\omega\Delta t}{\Delta t} = -\omega^2 - \frac{\mathrm{i}}{\tau}\omega + \frac{\Delta t^2}{12}\omega^2\left(\omega^2 + \frac{2\mathrm{i}}{\tau}\omega\right) + \mathcal{O}(\Delta t^4). \tag{A.3}$$

Defining the Courant number to be $\nu = \frac{c\Delta x}{\Delta t}$, and discretizing in space using the MFD for a rectangular mesh gives us a discrete dispersion relation of the form

$$0 = \frac{-4\sin^2\frac{\omega\Delta t}{2}}{\Delta t^2} - \frac{\mathrm{i}}{\tau}\frac{\sin\omega\Delta t}{\Delta t} - \mathcal{S}_h(\mathbf{k}) \tag{A.4}$$

$$= -\omega^2 - \frac{\mathrm{i}}{\tau}\omega + c_0^2k^2 + \frac{h^2}{12c_0^2}\left(\nu^2\omega^2\left(\omega^2 + \frac{2\mathrm{i}}{\tau}\omega\right) + 12\gamma w_2 c_0^4 k^4\right) + \mathcal{O}(h^4). \tag{A.5}$$

As the whole series must be equal to zero, we have that

$$c_0^2 k^2 = \omega^2 + \frac{\mathrm{i}}{\tau}\omega + \mathcal{O}(h^2). \tag{A.6}$$

Substituting this into the Δx^2 term of the Taylor series we arrive at

$$0 = \frac{h^2}{12c_0^2}\left(\nu^2\omega^2\left(\omega^2 + \frac{2\mathrm{i}}{\tau}\omega\right) - 12\gamma w_2\left(\omega^2 + \frac{\mathrm{i}}{\tau}\omega\right)^2\right) + \mathcal{O}(h^4). \tag{A.7}$$

As

$$\omega^2\left(\omega^2 + \frac{2\mathrm{i}}{\tau}\omega\right) \neq \left(\omega^2 + \frac{\mathrm{i}}{\tau}\omega\right)^2, \forall\omega, \tag{A.8}$$

we cannot choose w_2 independent of ω to eliminate this term in the dispersion error. We consider this a failure as we are interested in time domain schemes that have higher order numerical dispersion error rather than schemes that reduce or eliminate numerical dispersion at a design frequency (though such schemes are of interest in their own right).

ECCOMAS Congress 2016
VII European Congress on Computational Methods in Applied Sciences and Engineering
M. Papadrakakis, V. Papadopoulos, G. Stefanou, V. Plevris (eds.)
Crete Island, Greece, 5–10 June 2016

A VOLUME-AGGLOMERATION MULTIRATE TIME ADVANCING APPROACH

E. Itam[1], S. Wornom[2], B. Koobus[1] and A. Dervieux[3]

[1] IMAG, Université de Montpellier, Montpellier, France
e-mail: {emmanuelle.itam,bruno.koobus}@umontpellier.fr

[2] LEMMA, 2000 route des Lucioles, Sophia-Antipolis, France
stephen.wornom@inria.fr

[3] INRIA, 2204 route des Lucioles, Sophia-Antipolis, France
alain.dervieux@inria.fr

Keywords: computational fluid dynamics, multirate time advancing, explicit scheme, volume agglomeration, unstructured grid, hybrid turbulence model.

Abstract. *A frequent configuration in computational fluid mechanics combines an explicit time advancing scheme for accuracy purposes and a computational grid with a very small portion of much smaller elements than in the remaining mesh. Examples of such situations are the traveling of a discontinuity followed by a moving mesh, and the large eddy simulation of high Reynolds number flows around bluff bodies where together very thin boundary layers and vortices of much more important size need to be captured. For such configurations, explicit time advancing schemes with global time stepping are very costly. In order to overcome this problem, the multirate time stepping approach represents an interesting improvement. The objective of such schemes, which allow to use different time steps in the computational domain, is to avoid penalizing the computational cost of the time advancement of unsteady solutions which can become large due to the use of small global time steps imposed by the smallest elements such as those constituting the boundary layers. In the present work, a new multirate scheme based on control volume agglomeration is proposed for the solution of the compressible Navier-Stokes equations possibly equipped with turbulence models. The method relies on a prediction step where large time steps are performed with an evaluation of the fluxes on macro-cells for the smaller elements for stability purpose, and on a correction step in which small time steps are employed only for the smaller elements. The efficiency of the proposed method is evaluated on several benchmarks flows: the problem of a moving contact discontinuity (inviscid flow), the computation with hybrid turbulence model of flows around bluff bodies like a tandem cylinders at Reynolds number* 1.66×10^5 *, a circular cylinder at Reynolds number* 8.4×10^6*, and a flow around a space probe model at Reynolds number* 1×10^6.

1 INTRODUCTION

A frequent configuration in CFD calculations combines an explicit time advancing scheme for accuracy purpose and a computational grid with a very small portion of much smaller elements than in the remaining mesh. Examples of such situations are isolated traveling shock and large eddy simulation of high Reynolds number flows around bluff bodies where very thin boundary layers and vortices of much more important size need to be captured.

For such configurations, explicit time advancing schemes with global time stepping are very costly. In order to overcome this problem, the multirate time stepping approach represents an interesting alternative. By using several different timestep sizes on different subdomains, multirate timestepping avoids to apply too small timesteps in regions where the mesh is rather coarser. Then it avoids to use the small timesteps of boundary layer on the whole domain and thus penalize the global computational cost of the advancement in time of unsteady solutions. Many works have been published on multirate methods in the field of ODE, see for example [1, 2, 3, 4, 5, 6, 7, 8, 9, 10, 11, 12], but only few works were conducted on multirate time advancing schemes for the solution of PDE and hyperbolic conservation laws [13, 14, 15, 16, 18, 17], and rare applications were performed in Computational Fluid Dynamics (CFD), for shock propagation in [17] and for shallow water computations in [18, 19]. Therefore, there is still much work to do to provide a viable multirate method for CFD applications. In this work, we propose a new multirate scheme based on control volume agglomeration which is well suited to our numerical framework using a mixed finite volume/finite element formulation. The method relies on a prediction step where large time steps are used with an evaluation of the fluxes performed on the macro-cells for the smaller elements, and on a correction step in which small time steps are employed only for the smaller elements. Target applications are three-dimensional unsteady flows modeled by the compressible Navier-Stokes equations equipped with turbulence models and discretized on unstructured possibly deformable meshes.

2 Multirate time advancing by volume agglomeration

In this section, we present a multirate time advancing scheme based on volume agglomeration which is currently being developed for the solution of the three-dimensional compressible Navier-Stokes equations. The finite-volume spatial discretization combined with an explicit forward-Euler time-advancing is written:

$$vol_i \; w_i^{n+1} = vol_i \; w_i^n \; + \; \Psi_i, \quad \forall \, i = 1, ..., ncell,$$

where vol_i is the volume of $cell_i$, $w_i^n = (\rho_i^n, (\rho u)_i^n, (\rho v)_i^n, (\rho w)_i^n, E_i^n, (\rho k)_i^n, (\rho \varepsilon)_i^n)$ are as usually the density, moments, total energy, turbulent energy and turbulent dissipation at $cell_i$ and time level t^n, and $ncell$ the total number of cells in the mesh.

We assume that we can define a maximal stable time step (*local timestep*) $\Delta t_i, i = 1, ..., ncell$ on each node. This can be based on a stability analysis which in practice takes into account advective terms (condition of Courant-Friedrichs-Lewy or CFL) and diffusive terms of the discrete PDE under study, together with the type of explicit time advancing scheme. In short, using Δt_i is advancing at $CFL = 1$. A consistent time advancing should use for stability a *global time step* $\Delta t = \min_{1,ncell} \; \Delta t_i$. The user is supposed to choose a (integer) *timestep factor* $K \; > \; 1$.

We first define the inner zone and the outer zone, the coarse grid, and the construction of the fluxes on the coarse grid, ingredients on which our multirate time advancing scheme is based.

- **Definition of the Inner and Outer zones** :
  - We define the **outer zone** as the set of cells i for which the explicit scheme is stable for a time step $K\Delta t$
$$\Delta t_i \ \geq \ K\Delta t,$$
  - the **inner zone** is the set of cells for which
$$\Delta t_i \ < \ K\Delta t.$$

- **Definition of the coarse grid** :
  - **Objective** :
    - Advancement in time is performed with time step $K\Delta t$
    - Advancement in time preserves accuracy in the outer zone (space order of 3, Runge-Kutta 4)
    - Advancement in time is consistent in the inner zone
  - A **coarse grid** is defined on the inner zone by applying cell agglomeration in such a way that on each macro-cell, the maximal local time step is at least $K\Delta t$. Agglomeration consists in considering each cell and aggregating to it neigboring cells which are not yet aggregated to an other one (Figure 1). Agglomeration into macro cell is re-iterated until macro-cells with maximal timestep smaller then $K\Delta t$ have disappeared.
  - **Time-advancing on the macro-cells** :
    - We advance in time the chosen explicit scheme (Runge-Kutta 4 in our examples) on the coarse grid with $K\Delta t$ as time step
    - A flux smoothing can be performed on the macro cells for stability purpose.

- **Construction of the flux on the coarse grid**
  - The nodal fluxes Ψ_i are assembled on the fine cells (as usual)
  - Fluxes are summed on the macro-cells I (inner zone) :
$$\Psi^I = \sum_{k \in I} \Psi_k \tag{1}$$
  - Possibly smoothing of the coarse flux (inner zone) :
$$\Psi^I = (\sum_{K \in \mathcal{V}(I)} \Psi^K vol^K)/(\sum_{K \in \mathcal{V}(I)} vol^K) \tag{2}$$

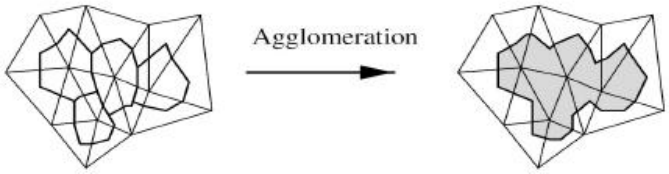

Figure 1: Sketch (in 2D) of the agglomeration of 4 cells into a macro-cell. Cells are dual cells of triangles, bounded by sections of triangle medians.

The multirate algorithm is then based on a **prediction step** and a **correction step** as defined hereafter :

Step 1 (prediction step) :
The solution is advanced in time with time step $K\Delta t$, on the macro cells in the inner zone and on the fine cells in the outer zone :

For $\alpha = 1, RKstep$

$$\text{outer zone :} \quad vol_i w_i^{(\alpha)} = vol_i w_i^{(0)} + b_\alpha K\Delta t \; \Psi_i^{(\alpha-1)} \tag{3}$$

$$\text{inner zone :} \quad vol^I w^{I,(\alpha)} = vol^I w^{I,(0)} + b_\alpha K\Delta t \; \Psi^{I,(\alpha-1)} \tag{4}$$

$$w_i^{(\alpha)} = w^{I,(\alpha)} \quad \text{for } i \in I \tag{5}$$

EndFor α.

Step 2 (correction step) :

- The unknowns are frozen in the outer zone at level $t^n + K\Delta t$.
- The outer unknowns near the boundary of the outer zone which are necessary for advancing the inner zone are interpolated in time.
- In the inner zone, using these interpolated values, the solution is advanced in time with the chosen explicit scheme and time step Δt.

Remark: The complexity, proportional to the number of points in the inner zone, is therefore mastered.

3 Applications

The multirate algorithm introduced in the previous section was implemented in the parallel CFD code AIRONUM shared by INRIA Sophia-Antipolis, LEMMA company and University of Montpellier. The parallelism relies on mesh partitioning and MPI. A description of this tool, which solves with a mixed element/volume method on unstructured meshes the compressible Euler and Navier-Stokes equations possibly equipped with a turbulence model, can be found in [20] and [21]. When computing hybrid RANS-LES flows, an important part of the mesh is dedicated to the boundary layer and involved possibly very small cells. Another important part of the mesh is dedicated to the capture of vortices with many cells of medium size (possibly 10-100 larger than smaller cells of the boundary layers). In introducing the multirate algorithm, attention was paid to several issues related to parallelism, and in particular a macro-cell belongs to only one subdomain of the partition, and we have optimized the evaluation of the fluxes on the macro-cells located at the boundary between neighboring subdomains. However, in the present phase of the study, no optimization of the MPI partitions for balancing the load in the inner zone has been done.

3.1 Contact discontinuity

In this first example, we consider the case of a moving contact discontinuity. For this purpose, the compressible Euler equations are solved in a rectangular parallelepiped as computational domain where the density is initially discontinuous at its middle (see Figure 2) while moments and pressure are uniform.

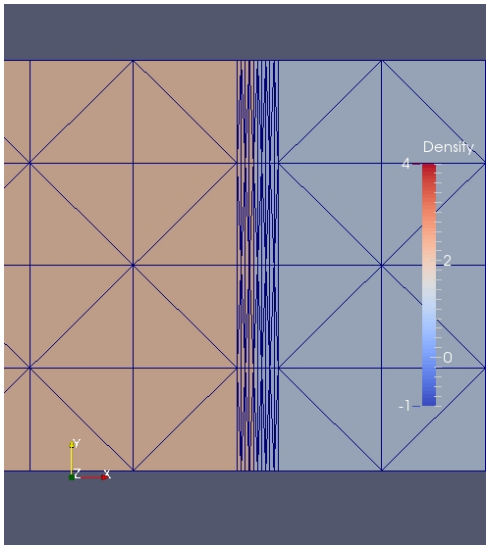

Figure 2: ALE calculation of a traveling contact discontinuity. Instantaneous mesh with mesh concentration in the middle of zoom and corresponding advected discontinuous fluid density.

The uniform velocity is a purely horizontal one. As can be seen in Figure 2, small cells are present on either side of the disconstinuity. The mesh moves during the computation in such a way that the nodes located at the discontinuity are still the same, and that the number of small cells are equally balanced on either side of the discontinuity. An Arbitrary Lagrangian-Eulerian formulation is then used to solve the Euler equations on the resulting deforming mesh. Our long term objective is to combine the multirate time advancing with a mesh adaptation algorithm in such a way that the small time steps imposed by the necessary good resolution of

the discontinuity remain of weak impact on the global computational time.

The mesh used in this simulation contains 25000 nodes and 96000 tetrahedra. The computational domain is decomposed into 2 subdomains. When integer K, used for the definition of the inner and outer zones, is set to 5, 10 and 15, the percentage of nodes located in the inner zone is always 1.3%, which corresponds to the vertices of the small cells located on either side of the discontinuity.

The multirate scheme with the aforementioned values of K, as well as a 4-stage Runge-Kutta method, are used for the computation. Each simulation was run over an elapsed time of 10 minutes, and 2 cores were used on a Bullx B720 cluster. This elapsed time corresponds to 2390 time steps for the explicit scheme, and 268, 365 and 536 times steps for K equals 15, 10 and 5, respectively. An improvement in the efficiency of about 1.75, 1.58 and 1.15 is observed when K is set to 15, 10 and 5, respectively.

3.2 Tandem cylinders

Our main study concerning the application of multirate is the calculation of a flow around a tandem cylinders at Reynolds number 1.66×10^5. This was a test case of an AIAA workshop, see [22]. It is a challenging computation since several complex flow features need to be captured around multiple bodies (stagnation zones, boundary layers, shear layers, separations, laminar-turbulent transition, recirculations, vortex sheddings, wakes). Furthermore, small cells are necessary for a proper prediction of the very thin boundary layers, which implies very small global time steps so that classical explicit calculations become very costly. The application of our multirate scheme to the tandem cylinders benchmark is also made more difficult by the fact that we use a hybrid turbulence model based on RANS and VMS-LES approaches, so that additional equations associated with turbulent variables need to be advanced in time.

In order to illustrate the quality of resolution, the Q-criterion isosurfaces are shown in Figure 3. It shows the complex flow features and the very small structures that need to be captured by the numerical model and the turbulence model, which renders this simulation particularly challenging. Further information concerning the comparison between computation and experiments are available in [21].

Two meshes were used for this study : a coarse mesh which contains 2.6 million nodes and 15 million tetrahedra, and a fine mesh with 16 million nodes and 96 million tetraedra. For both the smallest cell thickness is $1.2.10^{-4}$.

- **Coarse mesh**

  The computational domain is decomposed into 192 subdomains. When integer K, used for the definition of the inner and outer zones, is set to 2, 5 and 10, the percentage of nodes located in the inner zone is 4%, 16% and 25%, respectively.

  The lift curve obtained by the multirate scheme with $K = 10$ and the explicit scheme corresponding to half of a period of vortex shedding for the first cylinder is given in Figure 4. The underlying explicit scheme is the 4-stage Runge-Kutta method and the CFL number was set to 1. Each simulation was left running over an elapsed time of 40 hours. A number of 192 cores on a Bullx B720 cluster was used to perform these computations. One can check that the responses given by the two schemes are close to each other, except for the oscillations at the top of the lift curve for the multirate method that are an unproperly controlled restart in the simulation. The number of time steps is 15284 for the multirate

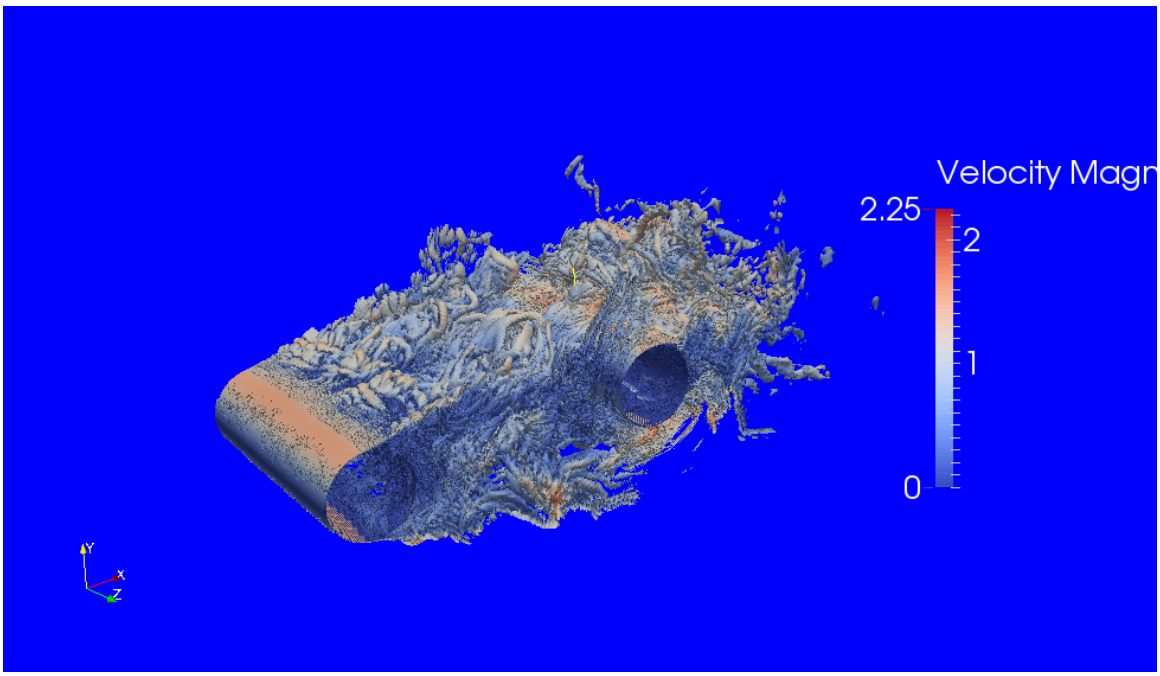

Figure 3: Tandem cylinders at Reynolds number 1.66×10^5: instantaneous Q-criterion isosurfaces (coloured with velocity modulus).

scheme and 132531 for the classical explicit scheme. From Figure 4, an improvement in the efficiency of about 1.14 is observed when the multirate scheme is used in our parallel solver. This rather slight improvement in efficiency can be explained by the fact that some of the subdomains almost contain only inner nodes so that workload is not equally shared by each computer core when the proposed multirate approach is used. Indeed, in our parallel strategy which is based on a decomposition of the computational domain in subdomains, designed to minimize the inter-core communications, and on a message passing parallel programming (MPI) model, each subdomain is assigned to a computer core. It is clear that in order to further increase the efficiency of the multirate approach in our parallel computing framework, the domain decomposition needs to be adapted.

Based on the fact that the cost per node in these explicit simulations is essentially due to the computation of the convective and diffusive fluxes, we can deduce that, for the multirate simulation that was performed and which involves $K = 10$ and 25% of the nodes located in the inner zone, the benefit-cost ratio between the multirate scheme and the classical 4-stage Runge-Kutta method would be 3 from a sequential computation.

In a second step, the multirate simulation is carried out with $K = 5$ for the same benchmark, which means that the RK4 scheme is now performed with time steps $5\Delta t$ and Δt for the nodes located in the outer zone and the nodes located in the inner zone, respectively. The lift curve obtained by the multirate scheme with $K = 5$ and $K = 10$ for the first cylinder is depicted in Figure 5. Both simulations were left running over an elapsed time of 20 hours, which allows to simulate a quarter of a period of vortex shedding with a CFL number set to 1. One can notice that the response is similar, as expected, for both values of K, and that the efficiency is improved by a factor 1.09 when the multirate scheme is used with $K = 10$ in our parallel solver. From a sequential point of view, we can also deduce that the cost of the multirate scheme with $K = 5$ and $K = 10$ would be

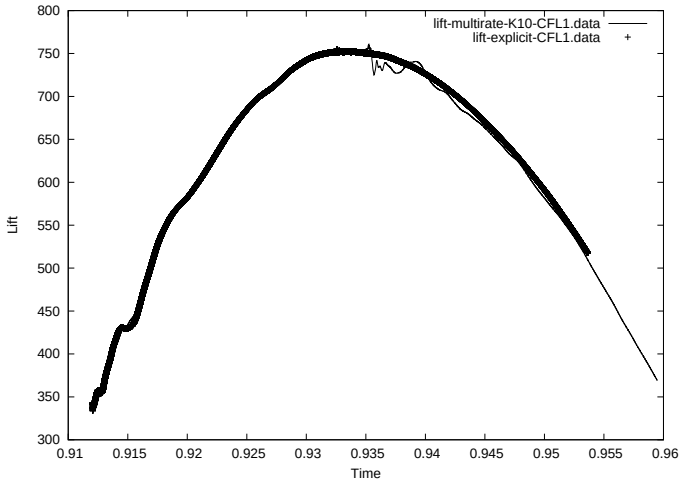

Figure 4: Coarse mesh - Tandem cylinders at Reynolds number 1.66×10^5 : lift curve for the first cylinder, multirate scheme (K=10) and explicit RK4 scheme, corresponding to an elapsed time of 40 hours.

of the same order.

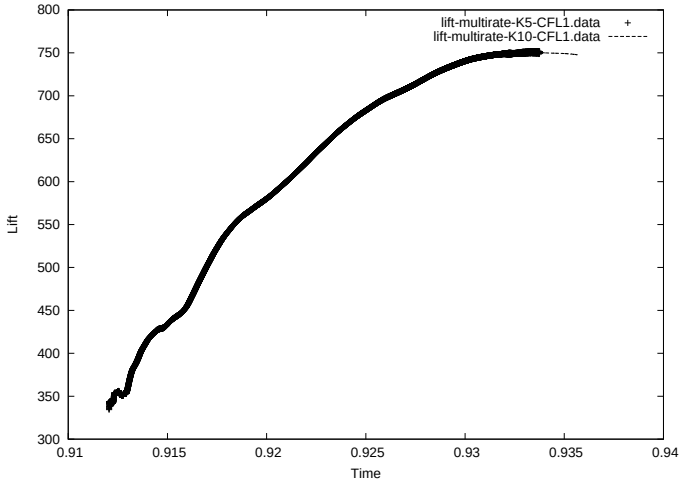

Figure 5: Coarse mesh - Tandem cylinders at Reynolds number 1.66×10^5 : lift curve for the first cylinder, multirate scheme with K=5 and K=10, corresponding to an elapsed time of 20 hours.

- **Fine mesh:**

The computational domain is decomposed into 768 subdomains. When integer K, used for the definition of the inner and outer zones, is set to 5, 10 and 20, the percentage of nodes located in the inner zone is 18%, 24% and 35%, respectively.

The lift curve obtained by the multirate scheme with $K = 5$, $K = 10$, and $K = 20$, and by the explicit scheme, is shown in Figure 6. The underlying explicit scheme is the 4-stage

Runge-Kutta method and the CFL number was set to 1. Each simulation was left running over an elapsed time of 1 hour. A number of 768 cores on the Bullx cluster was used to perform these computations.

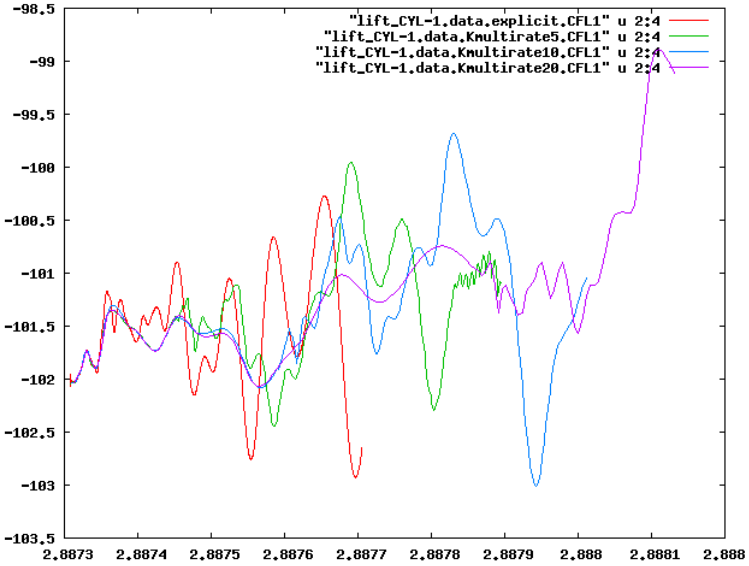

Figure 6: Fine mesh - Tandem cylinders at Reynolds number 1.66×10^5 : lift curve for the first cylinder, multirate scheme ($K = 5$, $K = 10$, $K = 20$) and explicit RK4 scheme, corresponding to an elapsed time of 1 hour.

One can observe that the lift curves quickly become different between the various options because of differences in the time step size and the rapidly fluctuating small scales that can be captured by this fine mesh. These differences affect the instantaneous solution but do not notably affect the flow statistics. From this Figure, an improvement in the efficiency of a factor slightly greater than 2 is observed when the multirate option is used with $K = 20$ compared to the classical 4-stage Runge-Kutta explicit scheme. For $K = 5$ and $K = 10$ this improvement becomes 1.5 and 1.8, respectively (see Figure 7). The better efficiency observed with the fine mesh compared to the coarse mesh is certainly due to a better distribution of the workload among the cores when the multirate approach is used.

As for the coarse mesh, the benefit-cost ratio between the multirate scheme and the classical 4-stage Runge-Kutta method would be 3 from a sequential point of view.

3.3 Circular cylinder

The third application concerns the simulation of the flow around a circular cylinder at Reynolds number 8.4×10^6. As for the previous benchmark, the computational domain is made of small cells around the body in order to allow a proper representation of the very thin boundary layer that occurs at such a high Reynolds number. On the other hand, the same hybrid RANS/VMS-LES model as that of the previous benchmark is used to compute this flow, which implies again that both the fluid and turbulent variables need to be advanced by the time integration scheme, and therefore also the multirate method.

Figure 8 depicts the Q-criterion isosurfaces and shows the very small and complex structures that need to be captured by the numerical and the turbulence models, which renders this simulation very challenging.

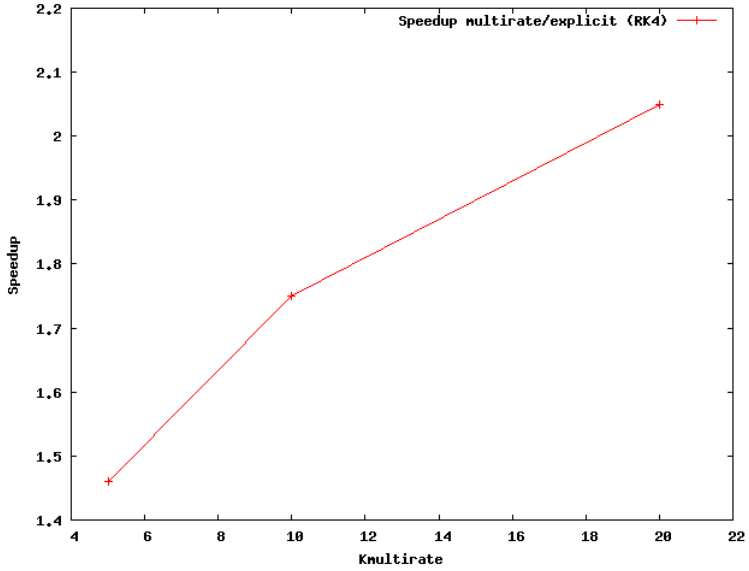

Figure 7: Fine mesh - Tandem cylinders at Reynolds number 1.66×10^5 : speedup multirate/explicit (RK4).

The mesh used in this simulation contains 4.3 million nodes and 25 million tetrahedra. The smallest cell thickness is $2.5.10^{-6}$. The computational domain is decomposed into 768 subdomains. When integer K, used for the definition of the inner and outer zones, is set to 5, 10 and 20, the percentage of nodes located in the inner zone is 15%, 19% and 24%, respectively.

The lift curve corresponding to the explicit scheme and the multirate option with $K = 20$ is shown in Figure 9. The explicit scheme is the 4-stage Runge-Kutta method. Each simulation was left running over an elapsed time of 20 minutes, and 768 cores were used on a Bullx B720 cluster. The number of time steps is 175 for the multirate scheme and 2153 for the explicit method. From Figure 9, we deduce an improvement in the efficiency of about 1.62 when the multirate scheme is used with $K = 20$, as compared with 3 which would be, from a sequential point of view, the ideal benefit-cost ratio between the multirate scheme, with $K = 20$ and 24% of the nodes located in the inner zone, and the explicit scheme. This result in efficiency is pretty good, considering the fact that the domain decomposition does not equally share the number of inner nodes between the subdomains, as noticed in the previous section.

The multirate simulation was also carried out for $K = 5$ and $K = 10$, which means that the time step ratio between the outer zone and the inner zone is 5 and 10, respectively. The efficiency is then improved by a factor 1.25 ($K = 5$), 1.46 ($K = 10$) and 1.62 for $K = 20$.

3.4 Spatial probe

The last case is the supersonic flow around a probe model for Exomars (see for example [23]). We choose a Reynolds number of 1 million. Delicate features in this simulation are a separation arising on a highly curved wall and relatively large recirculation zone at afterbody. Hybrid RANS-LES calculation brings more information than pure RANS does. The mesh involves $4,380000$ cells and the smallest mesh thickness is 2.10^{-5}. A sketch of this flow is presented in Figure 10. The impact of multirate on accuracy is very low (Figure 11). The gain in efficiency varies from 2.18 with $K = 10$ and 56 cells in the inner zone to a maximum of 2.89 with $K = 40$ and 151 cells in the inner zone. For $K = 40$, only 15 subdomains have inner cells (mean number 15 inner cells).

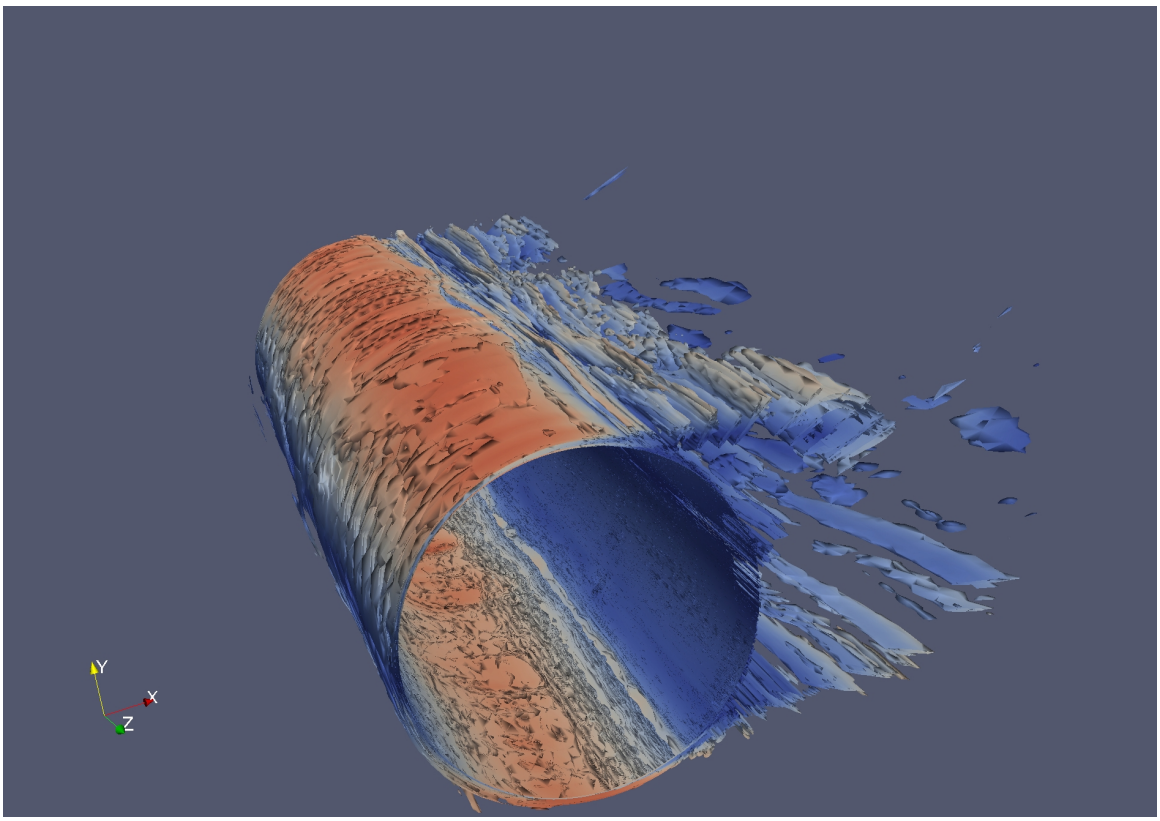

Figure 8: Circular cylinder at Reynolds number 8.4×10^6 : instantaneous Q-criterion isosurfaces (coloured with velocity modulus).

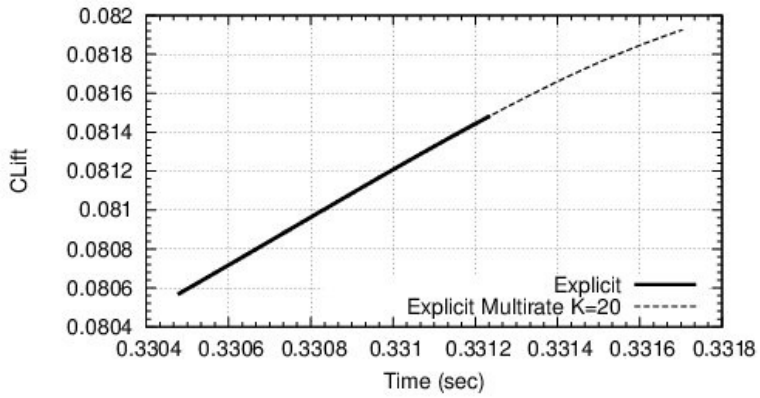

Figure 9: Circular cylinder at Reynolds number 8.4×10^6 : comparison of lift coefficient curves for explicit (bold line) and multirate (dashes) .

4 Conclusion

A new multirate strategy is proposed in this work. The method is based on control volume agglomeration, and relies on a prediction step where large time steps are used and where the fluxes for the smaller elements are evaluated on macro cells for stability purpose. A correction step follows in which only the smaller elements are advanced in time with a small time step. Preliminary results are given. They show that the proposed multirate strategy can be applied in complex CFD problems such as the prediction of three-dimensional flows around bluff bodies with complex hybrid turbulence models. Nevertheless, there is still work to do to obtain an

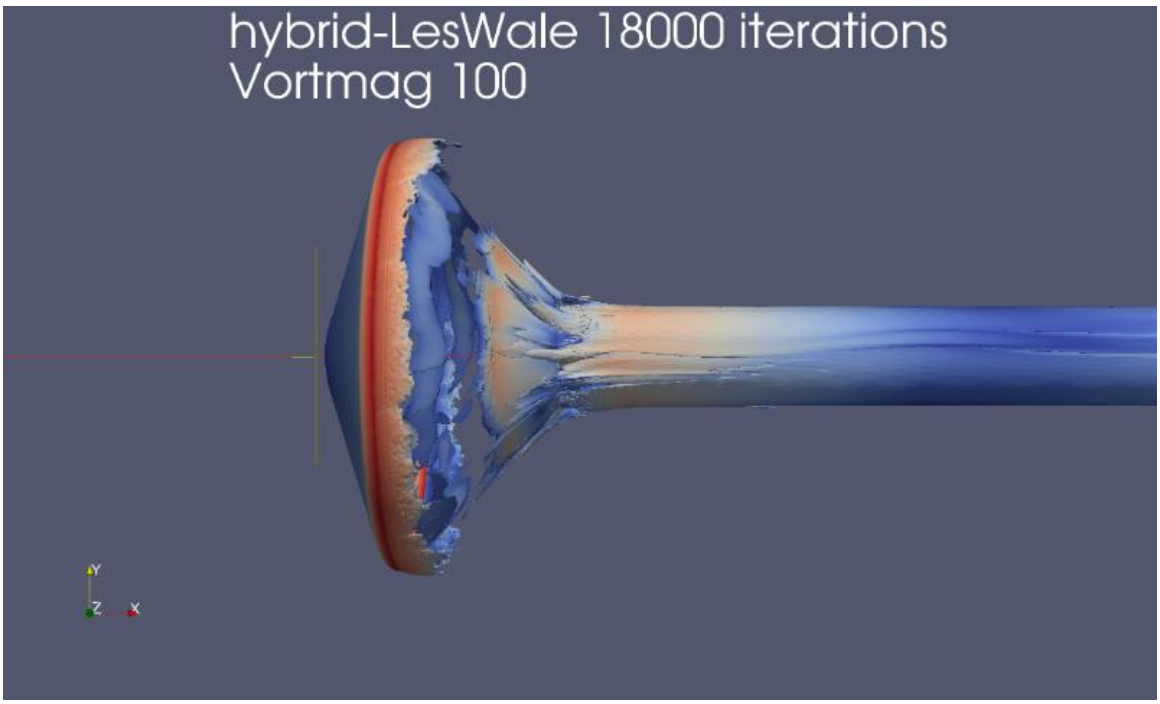

Figure 10: Flow around a probe model at Reynolds number 1 million. Q criterion.

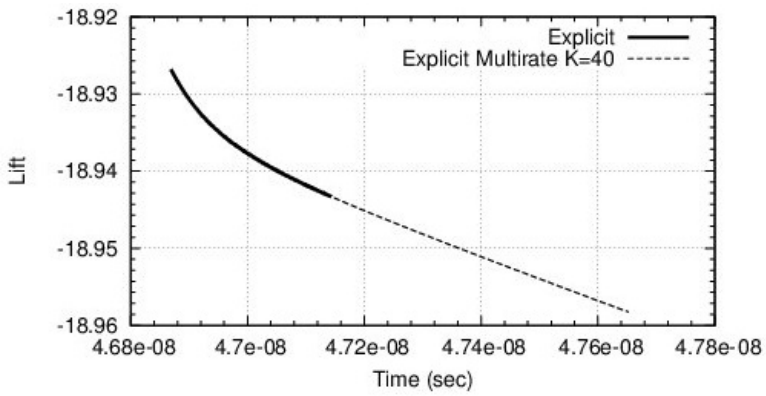

Figure 11: Flow around a probe model at Reynolds number 1 million. Impact of multirate on instantaneous lift accuracy.

efficient multirate method in a parallel numerical framework. Indeed, at the present time, the domain decomposition into subdomains is designed to minimize the inter-core communications. We need to adapt the domain decomposition in such a way that the workload becomes shared equally for both Step1 and Step2 of the multirate.

Acknowledgments

This work has been supported by French National Research Agency (ANR) through “Modèle numérique” program (projet MAIDESC n^0 ANR-13-MONU-0010).

HPC resources from GENCI-[CINES] (Grant 2014-c20142a5067 and 2014-x20142a6386) are also gratefully acknowledged.

REFERENCES

[1] J. R. Rice, Split Runge-Kutta Method for Simultaneous Equations, *Journal of Research of the National Bureau of Standards - B. Mathematics and Mathematical Physics*, Vol. 64B, No3, 1960.

[2] J.F. Andrus, Numerical solution of systems of ordinary differential equations separated into subsystems, *SIAM J. Numerical Analysis*, Vol.16, No 4, 1979.

[3] C.W. Gear and D.R. Wells, Multirate linear multistep methods, *BIT*, 484-502, 1984.

[4] S. Skelboe, Stability properties of backward differentiation multirate formulas, *Applied Numerical Mathematics*, 5, 151-160, 1989.

[5] J. Sand and S. Skelboe, Stability of backward Euler multirate methods and convergence of waveform relaxation, *BIT*, 32, 350-366, 1992.

[6] J.F. Andrus, Stability of a multi-rate method for numerical integration of ODE'S, *Computers Math. Applic.*, Vol. 25, No 2, pp. 3-14, 1993.

[7] M. Günther and P. Rentrop, Multirate ROW methods and latency of electric circuits, *Applied Numarical Mathematics*, 13, 83-102, 1993.

[8] C. Engstler and C. Lubich, MUR8: a multirate extension of the eight-order Dormer-Prince method, *Applied Numerical Mathematics*, 25, 185-192, 1997.

[9] C. Engstler and C. Lubich, Multirate Extrapolation Methods for Differential Equations with Different Time Scales, *Computing*, 58, 173-185, 1997.

[10] M. Günther, A. Kvaerno and P. Rentrop, MultA. Guelhan, J. Klevanski and S. Willems,irate partitioned Runge-Kutta methods, *BIT*, Vol. 38, No 2, pp. 101-104, 1998.

[11] M. Günther, A. Kvaerno and P. Rentrop, Multirate partitioned Runge-Kutta methods, *BIT*, Vol. 41, No 3, pp. 504-514, 2001.

[12] V. Savcenco, W. Hundsdorfer and J.G. Verwer, A multirate time stepping strategy for stiff ordinary differential equations, *BIT*, Vol. 47, pp. 137-155, 2007.

[13] E. Constantinescu and A. Sandu, Multirate Timestepping Methods for Hyperbolic Conservation Laws, *J. sci. Comp*, 33(3), 239-278, 2007.

[14] A. Sandu and E. Constantinescu, Multirate Explicit Adams Methods for Time Integration of Conservation Laws, *J. Sci. Comp*, 38: 229-249, 2009.

[15] P.R. Mugg, Construction and analysis of multi-rate partitioned Runge-Kutta methods, *Thesis*, Naval Postgraduate School, Monterey, California, June 2012.

[16] R. Kirby, On the convergence of high resolutin methods with multiple time scales for hyperbolic laws, *Mathematics of Computation*, Vol. 72, Number 243, 129-1250, 2002.

[17] R. Löhner, K. Morgan and O.C. Zienkiewicz, The use of domain splitting with an explicit hyperbolic solver, *Comput. Methods Appl. Mech. Engrg.*, 45, 313-329, 1984.

[18] B. Seny, J. Lambrechts, T. Toulorge, V. Legat, J.-F. Remacle, An efficient parallel implementation of explicit multirate Runge-Kutta schemes for discontinuous Galerkin computations, *J. of Comp. Phys.*, Vol. 256, pp. 135-160, 2014.

[19] B. Seny, J. Lambrechts, V. Legat, J.-F. Remacle, YIC2013, Second ECCOMAS Young Investigators Conference 2 6 September 2013, Bordeaux, France.

[20] C. Moussaed, M.V. Salvetti, S. Wornom, B. Koobus and A. Dervieux, "Simulation of the flow past a circular cylinder in the supercritical regime by blending RANS and variational-multiscale LES models", *Journal of Fluids and Structures*, Volume 47, May 2014, pages 114-123.

[21] E. Itam, S. Wornom, B. Koobus, B. Sainte-Rose, A. Dervieux, Simulation of multiple blunt-body flows with a hybrid variational multiscale model, Conference on Modelling Fluid Flow (CMFF 15) The 16th International Conference on Fluid Flow Technologies Budapest, Hungary, September 1-4, 2015

[22] D. Lockard, Summary of the Tandem Cylinder Solutions from the Benchmark Problems for Airframe Noise Computations-I, Proceedings of Workshop AIAA-2011-353 (2011).

[23] A. Guelhan, J. Klevanski and S. Willems, Experimental Study of the Dynamic Stability of the Exomars Capsule. In: Proceedings of 7th European Symposium on Aerothermodynamics. ESA Communications. 7th European Symposium on Aerothermodynamics, 9.-12. Mai 2011, Brugge, Belgium (2011).

ECCOMAS Congress 2016
VII European Congress on Computational Methods in Applied Sciences and Engineering
M. Papadrakakis, V. Papadopoulos, G. Stefanou, V. Plevris (eds.)
Crete Island, Greece, 5–10 June 2016

THERMOMECHANICAL NUMERICAL SIMULATION OF IMPACTS ON ELASTIC-PLASTIC SOLIDS WITH THE FINITE VOLUME METHOD

Thomas Heuzé[1]

[1]Research Institute in Civil and Mechanical Engineering (GeM, UMR 6183 CNRS)
École Centrale de Nantes, 1 rue de la Noë, F-44321 Nantes, France
e-mail: thomas.heuze@ec-nantes.fr

Keywords: Thermomechanics, Finite volume method, Impacts, Thermo-elastic-plastic solids.

Abstract. *We present in this work two implementation schemes of the finite volume method for the numerical simulation of impacts on thermo-elastic-plastic solids within the small strain framework for one dimension (bar) solid media, based on the Lax-Wendroff and high (second) order TVD methods. A strong thermomechanical coupling and adiabatic conditions are assumed. Comparison is performed with results obtained with the classical finite element method and an analytical solution on a test case involving a discontinuous solution. The finite volume methods (mainly the high order TVD one) improve both the track of the shock wave path, even after many reflexions of waves, and the computation of plastic strains and temperature.*

1 INTRODUCTION

The modelling and numerical simulation of hyperbolic initial boundary value problems including extreme loading conditions such as impacts require the ability to accurately capture and track the wave front of shock waves induced in the medium. Indeed, this permits to both understand correctly the path of waves and assess accurately the field of plastic strains and hence that of residual stresses within a structure. These problems require therefore numerical schemes able to meet high orders of accuracy and a high resolution of discontinuity without any spurious oscillations.

The numerical simulation of impacts on dissipative solids has been and is again mainly performed with the classical finite element method implemented in many industrial codes. However, finite elements do not use any feature of the characteristic structure of the set of hyperbolic equations, and the amount of artificial viscosity added to numerical time integrators is hard to assess properly in order to remove the sole spurious oscillations. Hence, a poor resolution of discontinuity and track of the wave path is generally achieved.

The finite volume method, initially developed for the simulation of gas dynamics [1], has gained recently more and more interest for problems involving impacts on solid media. The characteristic structure of the set of hyperbolic equations can be accounted for by the solution of a Riemann problem at interfaces between cells, and the same order of convergence is achieved for both the displacement and stress fields [2]. Several authors [3, 4, 5, 6, 7] have proposed many ways to simulate impacts on dissipative solid media such that elastic-plastic solids.

In this work, we use the finite volume method for the numerical simulation of impacts on thermo-elastic-plastic solids within the small strain framework in one dimension (actually bars here), and compare it to results obtained with the classical finite element method. First, the set of equations considered are presented in section 2. Since the material is deformed at high strain rate, adiabatic conditions are assumed to compute the rise of temperature, and the thermal softening is accounted for. Next, two implementations schemes of the finite volume method for this kind of material are presented in section 3: the Lax-Wendroff method and a high-order TVD method using the Superbee limiter. Then, the finite volumes numerical solutions are compared to the results of the finite element method and to an analytical solution of a test case involving a discontinuous solution in section 4.

2 INITIAL BOUNDARY VALUE PROBLEM FOR A THERMO-ELASTIC-PLASTIC MATERIAL IN ONE DIMENSION

We consider in this work a unidimensional initial boundary value problem written for a thermo-elastic-plastic material within the linearized small strain framework. The set of conservation laws reads:

$$\frac{\partial \mathbf{u}}{\partial t} + \frac{\partial \mathbf{f}(\mathbf{u})}{\partial x} = \mathbf{0} \quad \forall x \in]0, L[\tag{1}$$

within a domain of length L, the unknown vector $\mathbf{u}$ and the flux $\mathbf{f}(\mathbf{u})$ are defined as

$$\mathbf{u} = \begin{bmatrix} \sigma \\ v \end{bmatrix} \; ; \quad \mathbf{f} = \begin{bmatrix} -Hv \\ -\sigma/\rho \end{bmatrix} \tag{2}$$

where ρ is the mass density, and σ and v denote the axial stress and velocity components respectively. The conservations laws (1) should be supplemented with appropriate boundary and initial conditions. For a purely elastic material, the modulus H is equal to the Young's modulus

E. For an elastic-plastic material, the modulus H stands for the tangent modulus:

$$\frac{d\sigma}{d\varepsilon} = \frac{EQ}{E+Q} \tag{3}$$

In this work, an elastic-plastic material with a linear isotropic material is considered. Moreover, the influence of the thermal part on the mechanical part is accounted for through thermal softening via a linear decrease of the tensile yield stress with the temperature. The constitutive set of equations are listed below:

$$\dot{\varepsilon} = \dot{\varepsilon}^e + \dot{\varepsilon}^p \tag{4}$$

$$\dot{\sigma} = E\dot{\varepsilon}^e \tag{5}$$

$$\dot{\varepsilon}^p = \dot{p}\ \text{sign}(\sigma) \tag{6}$$

$$f = |\sigma| - (\sigma_0 + Qp)\left(1 - A\frac{(T-T_0)}{T_0}\right) \leq 0 \tag{7}$$

$$\dot{p} \geq 0;\ f \leq 0; f\dot{p} = 0 \tag{8}$$

where the equations (4), (5), (6), (7) and (8) refer to the additive partition of the total strain rate ($\dot{\varepsilon}$) into elastic ($\dot{\varepsilon}^e$) and plastic ($\dot{\varepsilon}^p$) parts, the elastic law, the plastic flow rule, the criterion and the Kuhn-Tucker complementary conditions. In (6), $\dot{p}$ denotes the rate of cumulated plastic strain. The tensile yield stress in (7) involve the initial tensile yield stress σ_0, a strain hardening modulus Q, a decrease coefficient A and the reference temperature T_0. The temperature is solution of the heat equation, assuming adiabatic conditions, written with the sole mechanical dissipation on the right hand side:

$$\rho C\dot{T} = \sigma\dot{\varepsilon}^p - Qp\dot{p} \tag{9}$$

where C is the thermal heat capacity.

3 FINITE VOLUME METHODS

The finite volume methods are based on subdividing the spatial domain into grid cells [1] of length Δx, and defining the approximation $\mathbf{U}_i$ of $\mathbf{u}$ within the i^{th} grid cell by integral averaging. These are then updated using the conservation laws (2) written in integral form on one cell, generally coupled with an explicit time integration scheme. We present here the application of the Lax-Wendroff method and a high-order Total Variation Diminishing (TVD) method using the Superbee limiter, to a thermo-elastic-plastic material.

3.1 LAX-WENDROFF

The Lax-Wendroff method is a second order accurate method, presented here in its Richtmyer two-steps version. The first step amounts to approximate $\mathbf{u}$ at the midpoint in time $t_{n+1/2} = t_n + \Delta t/2$ (n referring to the time step number) by:

$$\mathbf{U}_{i+\frac{1}{2}}^{n+\frac{1}{2}} = \frac{\mathbf{U}_i^n + \mathbf{U}_{i+1}^n}{2} + \frac{\Delta t}{2\Delta x}(\mathbf{F}_i^n - \mathbf{F}_{i+1}^n) \tag{10}$$

The second step requires to evaluate the flux at this point

$$\mathbf{F}_{i+\frac{1}{2}}^n = \mathbf{f}\left(\mathbf{U}_{i+\frac{1}{2}}^{n+\frac{1}{2}}\right) \tag{11}$$

in order to update the unknowns at time t_{n+1} with the following conservative scheme:

$$\mathbf{U}_i^{n+1} = \mathbf{U}_i^n - \frac{\Delta t}{\Delta x}\left(\mathbf{F}_{i+\frac{1}{2}}^n - \mathbf{F}_{i-\frac{1}{2}}^n\right) \tag{12}$$

For implementing a thermo-elastic-plastic material, a dedicated Riemann solver should be considered. First, at each step of the Richtmyer algorithm, a prediction-correction scheme should be set in order to handle the Kuhn-Tucker complementary conditions (8). An elastic constitutive behaviour is first assumed, leading to an elastic trial solution. For the first Richtmyer step, it comes:

$$\left(\sigma_{i+\frac{1}{2}}^{n+\frac{1}{2}}\right)^{\text{trial}} = \frac{\sigma_i^n + \sigma_{i+1}^n}{2} + \frac{c_e^2 \Delta t}{2\Delta x}(\rho v_{i+1}^n - \rho v_i^n) \tag{13}$$

$$v_{i+\frac{1}{2}}^{n+\frac{1}{2}} = \frac{v_i^n + v_{i+1}^n}{2} + \frac{\Delta t}{2\Delta x}\left(\frac{\sigma_{i+1}^n - \sigma_i^n}{\rho}\right) \tag{14}$$

where c_e stands for the elastic sound speed defined by $c_e = \sqrt{E/\rho}$, generally set to $\Delta t/\Delta x$ if the Courant number is set at one. Then, the criterion (7) is computed with that trial state within the grid cells i and $i+1$, provided their respective cumulated plastic strain values p_i^n and p_{i+1}^n and temperature values T_i^n and T_{i+1}^n at time t_n. Two cases thus arise for each grid cell: either the plastic criterion is satisfied, and hence the evolution is actually elastic $\sigma_{i+1/2}^{n+1/2} = \left(\sigma_{i+1/2}^{n+1/2}\right)^{\text{trial}}$, or the plastic criterion is violated $f\left(\left(\sigma_{i+1/2}^{n+1/2}\right)^{\text{trial}}\right) > 0$, and a plastic correction needs to be carried out. In the latter case, the plastically admissible stress state should be computed by matching the elastic-plastic Riemann invariants defined on the two integral curves passing by the states of the grid cells i and $i+1$ at time t_n:

$$v_{i+\frac{1}{2}}^{n+\frac{1}{2}} = v_i^n + \frac{\Delta x}{\Delta t}\left(\int_{\sigma_i^n}^{\sigma_i^*} \frac{d\sigma}{\rho c^2} + \int_{\sigma_i^*}^{\sigma_{i+\frac{1}{2}}^{n+\frac{1}{2}}} \frac{d\sigma}{\rho c^2}\right) \tag{15}$$

$$v_{i+\frac{1}{2}}^{n+\frac{1}{2}} = v_{i+1}^n - \frac{\Delta x}{\Delta t}\left(\int_{\sigma_{i+1}^n}^{\sigma_{i+1}^*} \frac{d\sigma}{\rho c^2} + \int_{\sigma_{i+1}^*}^{\sigma_{i+\frac{1}{2}}^{n+\frac{1}{2}}} \frac{d\sigma}{\rho c^2}\right) \tag{16}$$

where σ_i^* and σ_{i+1}^* stand for the tensile yield stress in each grid cell at time t_n if the trial state did not satisfy the plastic criterion, or are equal to σ_i^n (resp. σ_{i+1}^n) if the plastic criterion has been satisfied. At one cell interface $i+1/2$, the plasticity can develop from its left side, from its right side, or from both. Hence the stress at this interface is updated based on the criterion assessed at the two grid cells:

$$\sigma_{i+\frac{1}{2}}^{n+\frac{1}{2}} = \frac{1}{\frac{1}{\rho c_i^2} + \frac{1}{\rho c_{i+1}^2}}\left(\frac{\sigma_i^*}{\rho c_i^2} + \frac{\sigma_{i+1}^*}{\rho c_{i+1}^2} + \frac{1}{\rho c_e^2}(\sigma_i^n + \sigma_{i+1}^n - \sigma_i^* - \sigma_{i+1}^*) + \frac{\Delta t}{\Delta x}(v_{i+1}^n - v_i^n)\right) \tag{17}$$

where c_i and c_{i+1} denote the sound speed at grid cell i and $i+1$. These are equal to c_e if the evolution is elastic, or c_p the plastic sound speed ($= \sqrt{(d\sigma/d\varepsilon)/\rho}$) if the evolution is elastic-plastic. The second step of the Richtmyer algorithm is also based on a prediction-correction scheme; the trial state is obtained via the conservative formula (12). This trial state is also tested with the plastic criterion within each grid cell provided its cumulated plastic strain value

p_i^n and temperature value T_i^n, and the same reasoning is applied. Once the stress have been updated at time t_{n+1}, the cumulated plastic strain are updated using the criterion (7), and hence the plastic strains through the plastic flow rule (6). The temperature is updated at the end of the time step through an implicit time discretization of (9):

$$T_i^{n+1} = T_i^n + \frac{1}{\rho C}(\sigma_i^{n+1}\Delta\varepsilon_i^p - Qp_i^{n+1}\Delta p_i) \tag{18}$$

3.2 HIGH-ORDER TVD METHODS

The high order Total Variation Diminishing methods enable to meet both high order of accuracy in smooth regions and a high resolution of discontinuity without any spurious oscillations where shocks arise in the solution. Their strength relies on their ability to introduce a controlled amount of numerical viscosity locally, so that to adapt to the local regularity of the solution. Following [1] and [4], the conservative formula (12) can be rewritten in term of flux-difference splitting, plus some additional flux to reach higher order of accuracy:

$$\mathbf{U}_i^{n+1} = \mathbf{U}_i^n - \frac{\Delta t}{\Delta x}\left(\mathcal{A}^+\mathbf{U}_{i-\frac{1}{2}}^n + \mathcal{A}^-\mathbf{U}_{i+\frac{1}{2}}^n\right) - \frac{\Delta t}{\Delta x}\left(\tilde{\mathbf{F}}_{i+\frac{1}{2}}^n - \tilde{\mathbf{F}}_{i-\frac{1}{2}}^n\right) \tag{19}$$

where $\mathcal{A}^+\mathbf{U}_{i-1/2}^n = \sum_{p=1}^m (\lambda_{i-1/2}^{(p)})^+ \mathcal{W}_{i-1/2}^{(p)}$ and $\mathcal{A}^-\mathbf{U}_{i+1/2}^n = \sum_{p=1}^m (\lambda_{i+1/2}^{(p)})^- \mathcal{W}_{i-1/2}^{(p)}$ are the right-going and left-going fluctuations respectively, provided $\mathbf{U}_{i-1/2}^n = \mathbf{U}_i^n - \mathbf{U}_{i-1}^n$, $\mathcal{W}_{i-1/2}^{(p)} = \alpha_{i-1/2}^{(p)}\mathbf{K}^{(p)}$ are the waves formed of the wave strength coefficient $\alpha_{i-1/2}^{(p)}$ weighting the right eigenvectors $\mathbf{K}^{(p)}$ of the jacobian matrix $\mathbf{A} = \partial\mathbf{f}/\partial\mathbf{u}$, and $(\lambda_{i-1/2}^{(p)})^\pm$ are the characteristic speeds (the eigenvalues of $\mathbf{A}$) travelling rightward or leftward respectively. In addition, $\tilde{\mathbf{F}}_{i+1/2}^n$ and $\tilde{\mathbf{F}}_{i-1/2}^n$ stand for limited additional correction fluxes designed so that the method achieves a high order of accuracy in smooth regions and a high resolution of discontinuity in rough ones. These limited fluxes are expressed as a function of limited waves $\tilde{\mathcal{W}}_{i-1/2}^{(p)} = \tilde{\alpha}_{i-1/2}^{(p)}\mathbf{K}^{(p)}$, $1 \leq p \leq m$:

$$\tilde{\mathbf{F}}_{i-\frac{1}{2}}^n = \frac{1}{2}\sum_{p=1}^m |\lambda_p|\left(1 - \frac{\Delta t}{\Delta x}|\lambda_p|\right)\tilde{\alpha}_{i-1/2}^{(p)}\mathbf{K}^{(p)} \tag{20}$$

These waves are limited based on an upwind ratio $\theta_{i-1/2}^{(p)}$ defined for the $p-$wave as:

$$\theta_{i-1/2}^{(p)} = \frac{\mathcal{W}_{I-1/2}^{(p)}}{\mathcal{W}_{i-1/2}^{(p)}} = \frac{\alpha_{I-1/2}^{(p)}}{\alpha_{i-1/2}^{(p)}} \tag{21}$$

where the index I denotes the upwind interface of that located at $x_{i-1/2}$, that is I equals $i-1$ if $\lambda_{i-1/2}^{(p)} > 0$, $i+1$ if $\lambda_{i-1/2}^{(p)} < 0$. This ratio may be understood as a certain measure of the local regularity of the solution, the $p-$wave strength may thus be limited as a function of this measure:

$$\tilde{\alpha}_{i-1/2}^{(p)} = \phi(\theta_{i-1/2}^{(p)})\alpha_{i-1/2}^{(p)} \tag{22}$$

where $\phi(\theta_{i-1/2}^{(p)})$ is a limiting function. Among many others, Lax-Wendroff is found for $\phi(\theta) = 1$, and for instance Superbee is obtained for $\phi(\theta) = \max(0, \min(1, 2\theta), \min(2, \theta))$.

Implementing a thermo-elastic-plastic material also requires a special elastic-plastic Riemann solver. This is also based on a prediction-correction scheme. First, an elastic trial solution

$(\sigma_{i+1/2})^{\text{trial}}$ is computed at each interface, solution of an elastic Riemann problem consisting of two elastic (discontinuous) waves travelling at speeds $-c_e$ and c_e. Then, this trial stress state is tested against the yield criterion in both grid cells i and $i+1$, being given their respective cumulated plastic strain values (p_i^n, p_{i+1}^n) and temperature values (T_i^n, T_{i+1}^n). In each of these grid cells, either the plastic yield criterion is satified, and then only one elastic wave occurs, or the criterion is violated, and then a plastic wave travelling at speed $\pm c_p$ should be added to the elastic one. In all, the characteristic spectrum solution of the elastic-plastic Riemann problem may consist of (i) two elastic waves if the trial stress state satisfies the yield criterion in both adjacent grid cells, (ii) two elastic waves plus one left or right plastic (discontinuous) wave if the trial stress state has violated the yield criterion in the sole left of right grid cell adjacent to the interface, or (iii) two elastic waves plus two plastic waves if the trial stress state violates the yield criterion in both grid cells i and $i+1$, as shown in figure 1. Notice that the plastic

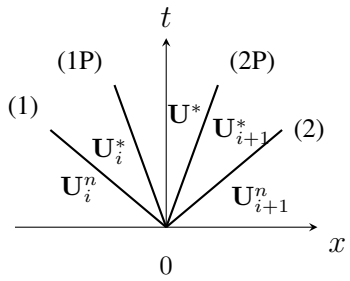

Figure 1: Characteristic structure of the elastic-plastic Riemann problem.

waves here involved in the solution of the elastic-plastic Riemann problem are actually strong discontinuous waves since a linear hardening is considered in this work. A nonlinear hardening would yield weak discontinuous plastic centered rarefaction waves: this case will be treated in a latter work.

It remains to compute the strength $\alpha_{i+1/2}^{(p)}$ of each of these waves. This is based on the decomposition of $\mathbf{U}_{i+1/2}$ on the eigenbasis of the jacobian matrix $\mathbf{A} = \partial \mathbf{f} / \partial \mathbf{u}$:

$$\mathbf{U}_{i+\frac{1}{2}} = \mathbf{U}_{i+1}^n - \mathbf{U}_i^n = \sum_{p=1}^{m} \alpha_{i+1/2}^{(p)} \mathbf{K}^{(p)} \tag{23}$$

The strength of elastic waves are first computed since the stresses in areas $\mathbf{U}_i^*$ and $\mathbf{U}_{i+1}^*$ are known and equal to the respective tensile yield stresses. Then, the strengths of plastic waves are computed by forming a system of equations with the two remaining waves. For example, if plasticity occurs from both sides, the two plastic wave strength are computed by:

$$\left[\mathbf{K}^{(1P)}\,,\,\mathbf{K}^{(2P)}\right] \begin{bmatrix} \alpha_{i+1/2}^{(1P)} \\ \alpha_{i+1/2}^{(2P)} \end{bmatrix} = \mathbf{U}_{i+1}^n - \mathbf{U}_i^n - \alpha_{i+1/2}^{(1)} \mathbf{K}^{(1)} - \alpha_{i+1/2}^{(2)} \mathbf{K}^{(2)} \tag{24}$$

The fluctuations $\mathcal{A}^+ \mathbf{U}_{i+1/2}^n$ and $\mathcal{A}^- \mathbf{U}_{i+1/2}^n$ are then computed, and the unknowns $\mathbf{U}_i^{n+1}$ are hence updated at time t_{n+1} through the formula (19). The thermomechanical coupling is treated as discussed in section 3.1.

4 SUDDEN UNLOADING OF STRONG-DISCONTINUOUS LOADING WAVE IN A LINEAR HARDENING BAR

We consider a semi-infinite bar made of a linear hardening material, in an initial natural state, suddenly loaded on its left side at time $t = 0$ with a constant tensile stress value σ^* sufficiently large to deform the bar plastically. After time t_u, the applied load is suddenly released to zero. The analytical solution of this problem can be found in [8], and is summarized in figure 2. A

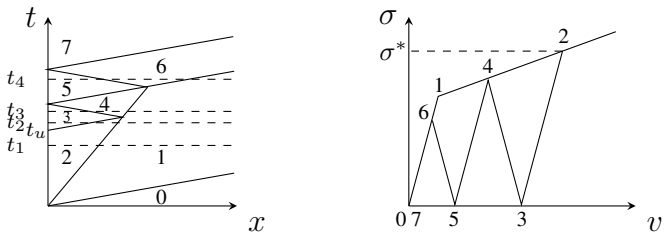

Figure 2: Analytical solution of a semi-infinite bar suddenly plastically loaded then unloaded on its end, plotted with two strain strong-discontinuities here.

stationary strong-discontinuous strain interface is formed at each unloading cycle, the righward plastic wave being weakened until it disappears. Introducing the parameter β defined by:

$$\beta = \frac{c_e + c_p}{c_e - c_p} > 1 \tag{25}$$

the length of the $(n+1)$th stationary strain-discontinuous interfaces, l_{n+1}, and its stress associated are given by:

$$\begin{aligned} l_{n+1} &= \beta l_n \\ \sigma_{2(n+1)} &= \frac{\sigma_{2n}}{\beta} \end{aligned} \qquad (n = 1, 2, \ldots) \tag{26}$$

where l_n the length of the nth stationary strain-discontinuous interfaces and σ_{2n} the stress associated.

4.1 COMPARISON WITH THE FINITE ELEMENT METHOD FOR AN ELASTIC-PLASTIC MATERIAL

The numerical results obtained for a steel (see table 1 for numerical values of parameters) with the Lax-Wendroff and the second-order TVD Superbee finite volume methods are compared here to the analytical solution of this test case and to the results obtained with the finite element method coupled with an explicit time integrator. The constitutive equations in the latter solution is integrated with a radial return algorithm [9], and the solution is computed within a larger domain than that shown in figures 3 to mimic a semi-infinite bar. For the finite volume solutions, transmittive boundary conditions have been set on the right side of the bar.

Both the stress and plastic strain fields are compared at instants t_1, t_2, t_3 and t_4 (see figure 2), in figures 3. When the bar is loaded, an elastic precursor travels at the elastic sound speed (see figure 3(a)), followed by a plastic wave. Since the Courant number has been set at one, the three numerical methods fit perfectly the analytical solution. However, the plastic wave travels slower, numerical oscillations appears for the Finite Element (the largest ones) and Lax-Wendroff solutions. For the latter one, this is due to the fact that Lax-Wendroff is not a monotone

$E = 2 \cdot 10^{11}$ Pa	$\sigma_0 = 400 \cdot 10^6$ Pa	$L = 6$ m
$\rho = 7800$ kg.m^{-3}	$A = 4$	number of grid cells/elements = 100
$C = 450$ J.kg^{-1}.K^{-1}	$T_0 = 293$ K	$t_u = 1.2 \cdot 10^{-3}$ s
$Q = 10 \cdot 10^9$ Pa	$\sigma^* = 900 \cdot 10^6$ Pa	

Table 1: Numerical values of parameters

method nor a TVD one. Moreover, the Finite element solution overestimates the plastic strain value closed to the boundary, though reduces to the right values when it departs. Superbee achieves the best resolution of the plastic wave on five cells here.

Then, the prescribed load is released to zero, and an unloading wave pursues the forerunning plastic loading disturbance (see figure 3(b)). Strong oscillations appears at integration points within the unloaded area in the Finite Element solution. Many solutions can be used to reduce these oscillations, among others (i) unload in two time steps rather than in one, (ii) reaverage at integration points the stress moved at nodes using the finite element shape functions or (iii) adding some additional numerical viscosity. Superbee achieves a proper elastic unload, superposed with the analytical solution, while Lax-Wendroff is not so bad.

When the unloading wave catches up with the plastic wave, a discontinuity of the (plastic) strain appears at this point due to the strain history difference on both sides (see figure 3(c)). Thus, a stationary discontinuous interface is generated, as well as internal reflective waves, so that the plastic strain continues to propagate rightward, but with a smaller value. The resolution of these two plastic strain fronts is quite close for these three numerical methods.

A second unload disturbance is required here to stop the progession of plastic strain (see figure 3(d)). The stress front is poorly solved by the finite element method, Lax-Wendroff has also difficulties with the left front. Only Superbee gives acceptable results after several reflexions of plastic waves.

4.2 COMPARISON WITH THE FINITE ELEMENT METHOD FOR A THERMO-ELASTIC-PLASTIC MATERIAL

The thermomechanical coupling is here added, with numerical parameters listed in table 1. Since on the one hand a linear hardening is considered in this work, and the other hand the thermal part influences the mechanical one through the sole yield stress, the plastic sound speed is not affected by the temperature here, but the stress and the plastic strain actually depend on the temperature. With the numerical values of parameters listed in table 1, the stress does not change much with respect to figure 3 at the beginning, though more after many wave reflexions. The change in plastic strain is much pronounced. The thermo-elastic-plastic (TEP) numerical solutions are plotted in figure 4, and the plastic strains superposed with the (isothermal) elastic-plastic (EP) analytical solution to observe the effect of the thermomechanical coupling. The decrease of the tensile yield stress through thermal softening leads to an increase of the plastic flow, and hence to an increase of temperature (figures 4(a) and 4(b)). Recall that adiabatic conditions have been assumed so that no conduction effects are here accounted for. This explains why the temperature and plastic strain profiles are similar.

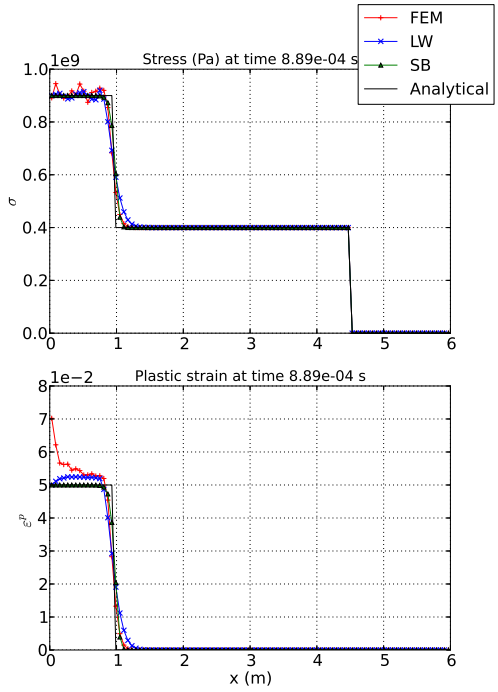

(a) Time $t_1 = 8.89 \cdot 10^{-4}$ seconds.

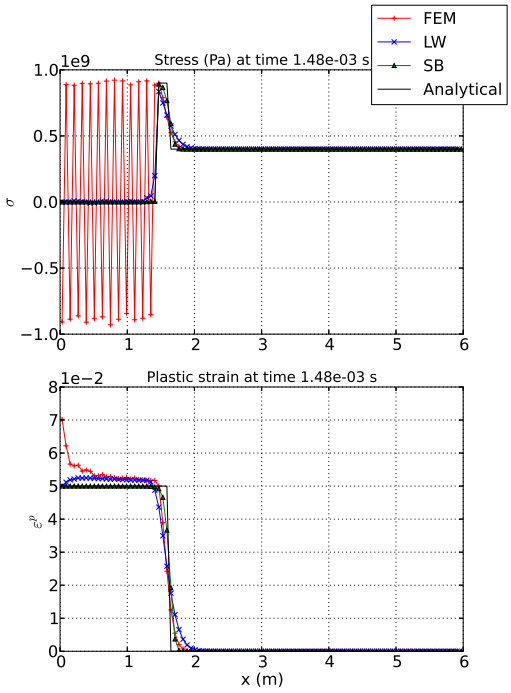

(b) Time $t_2 = 1.48 \cdot 10^{-3}$ seconds.

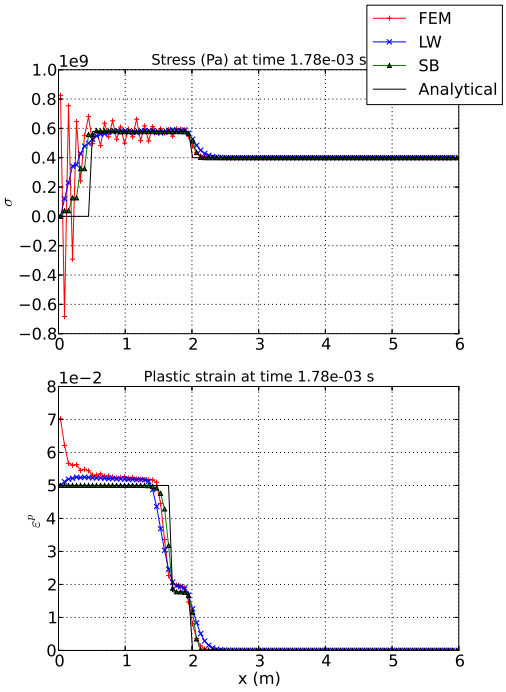

(c) Time $t_3 = 1.78 \cdot 10^{-3}$ seconds.

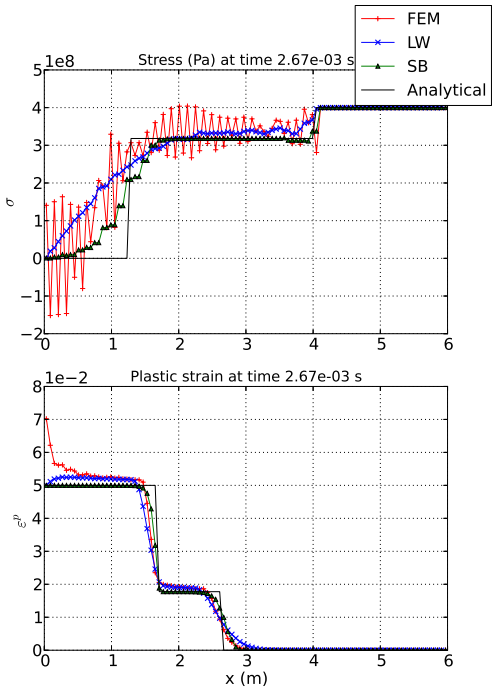

(d) Time $t_4 = 2.67 \cdot 10^{-3}$ seconds.

Figure 3: Comparison of the analytical, Finite Element (FEM), Lax-Wendroff (LW) and Superbee (SB) stress and plastic strain fields at different times.

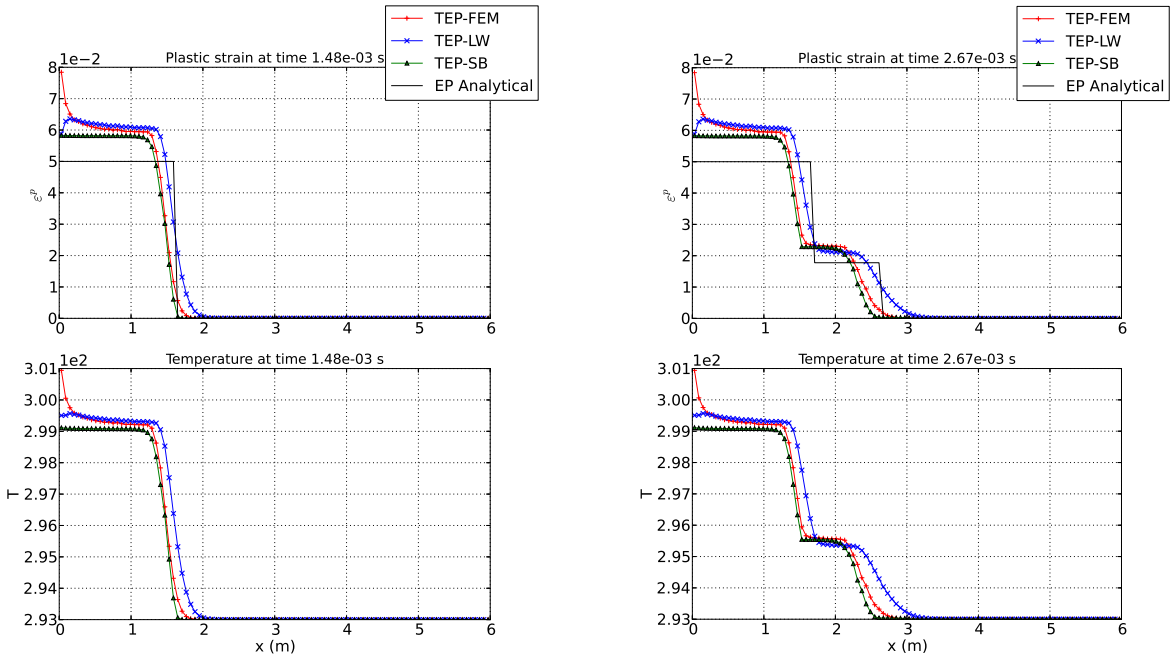

(a) Time $t_2 = 1.48 \cdot 10^{-3}$ seconds.

(b) Time $t_4 = 2.67 \cdot 10^{-3}$ seconds.

Figure 4: Comparison of the analytical, Finite Element (FEM), Lax-Wendroff (LW) and Superbee (SB) plastic strain and temperature fields at different times.

5 CONCLUSIONS

In this work, two schemes of the finite volume methods (namely the Lax-Wendroff and the Superbee TVD limiter) have been implemented for the numerical simulation of impacts on thermo-elastic-plastic bars. These methods were tested against an analytical solution and the finite element method on a test case involving strong discontinuous waves. The Superbee TVD limited solution has been shown to be the best in term of accuracy, so that it improves both the track of the shock wave path, even after many reflexions of waves, and the computation of plastic strains and temperature.

REFERENCES

[1] R. Leveque, *Finite volume methods for hyperbolic problems.* Cambridge University PressMcGraw Hill, 2002.

[2] C. Lee, A. Gil, J. Bonet, (2013). Development of a cell centred upwind finite volume algorithm for a new conservation law formulation in structural dynamics. *Computers and Structures*, **118**, 13–38, 2013.

[3] G. Miller, P. Collela, A high-order eulerian Godunov method for elastic-plastic flow in solids. *Journal of Computational Physics*, **167**, 131–176, 2001.

[4] T. Fogarty. Finite volume methods for acoustics and elasto-plasticity with damage in a heterogeneous medium. PhD thesis, University of Washington, 2001.

[5] P. Barton, R. Deiterding, D. Meiron, D. Pullin, Eulerian adaptive finite-difference method for high-velocity impact and penetration problems. *Journal of Computational Physics*, **240**, 76–99, 2013.

[6] A.L. Ortega, M. Lombardini, D. Pullin, D. Meiron, Numerical simulation of elastic-plastic solid mechanics using an eulerian stretch tensor approach and HLLD Riemann solver. *Journal of Computational Physics*, **257**, 414–441, 2014.

[7] M. Aguirre, A. Gil, J. Bonet, C. Lee, An upwind vertex centred finite volume solver for lagrangian solid dynamics. *Journal of Computational Physics*, **300**, 387–422, 2015.

[8] L. Wang, *Foundations of stress waves.* Elsevier, 2011.

[9] J.C. Simo, T.J.R. Hughes. Computational Inelasticity. Springer, 1997.

ECCOMAS Congress 2016
VII European Congress on Computational Methods in Applied Sciences and Engineering
M. Papadrakakis, V. Papadopoulos, G. Stefanou, V. Plevris (eds.)
Crete Island, Greece, 5–10 June 2016

TRANSVERSE WAVE PROPAGATION IN A ONE-DIMENSIONAL STRUCTURE COUPLED TO ITS ELECTRICAL ANALOGUE: COMPARISON OF TRANSFER MATRIX MODELS

B. Lossouarn[1], **M. Aucejo**[1], **J.-F. Deü**[1]

[1]Structural Mechanics and Coupled Systems laboratory, Conservatoire National des Arts et Métiers
2 rue Conté, Paris, France
e-mail: {boris.lossouarn,mathieu.aucejo,jean-francois.deu}@cnam.fr

Keywords: Wave Propagation, Transfer Matrix, Piezoelectric Coupling, Electrical Network.

Abstract. *Wave propagation in mechanical structures can be controlled by a coupling to an electrical network exhibiting a similar dispersion relation. The energy transfer between the two media is maximized on a broad frequency range when choosing a network that is the electrical analogue of the structure to control. In terms of structural vibration, this strategy is equivalent to a multimodal tuned mass damping. Indeed, the control is implemented thanks to a multimodal electrical network, whose modes are close enough to those of the mechanical structure. The electromechanical coupling can be achieved by using an array of piezoelectric patches, which are small enough compared to the smallest wavelength to control. Then, when considering interconnected patches, wave propagation occurs simultaneously in the mechanical and electrical media. Wave propagation in one-dimensional periodic structures can be analyzed with the transfer matrix method. In this paper, the definition of an electromechanical unit cell gives a relation between state vectors involving both mechanical and electrical degrees of freedom. As an extension of a previous work focusing on longitudinal propagation, four transfer matrix models are defined in order to describe the piezoelectric coupling of a beam to its discrete electrical analogue. Indeed, the beam can be approximated either by its discrete equivalent, a fully homogenized model, a piecewise homogenized model or a finite element model. Offering an increasing complexity, those formulations are compared in order to determine their respective limits. Depending on the frequency range of interest, it then becomes possible to choose a suitable model for the analysis of structures involving a piezoelectric coupling to their electrical analogues.*

1 INTRODUCTION

Multimodal vibration control can be implemented by coupling a mechanical structure to its electrical analogue. A practical solution is to cover the structure to control with an array of piezoelectric patches that are interconnected with a suitable electrical network. From a finite difference method applied to the continuous equations describing the mechanical medium, an electromechnical analogy provides the suitable electrical topology [1, 2]. This method was applied to the control of a beam and it led to a passive electrical network made of inductors and transformers [3, 4]. A periodic layout of the electromechanical structure allows using the transfer matrix method [5, 6]. This method has often been implemented in problems involving independent piezoelectric shunts [7, 8, 9] but rarely with an interconnection of successive patches [10]. This last case requires the definition of state vectors that combine both mechanical and electrical degrees of freedom, because a real electromechanical waveguide is considered. The electrical part is described with the discrete equations governing the lumped electrical components but the continuous mechanical medium can be approximated by various models.

The present contribution extends previous models and results that were initially dedicated to the analysis of longitudinal wave propagation in coupled analogous waveguides [11]. When considering transverse propagation, the transfer matrices are obviously different, but the methods remain the same. A first section presents the electromechanical unit cell including a beam segment and a portion of the analogous electrical network, which was presented in [4]. Then, a model describing a pair of piezoelectric patches subjected to bending motion is proposed. In a second section, we recall the transfer matrices that were obtained in [4] when considering either a discrete or a fully homogenized beam coupled to the discrete electrical analogue. Two new models are added: a piecewise homogenized model and a finite element model, which both take into account the mechanical discontinuity induced by the addition of piezoelectric patches. The last section compares the propagation constants and the frequency response functions obtained with the four transfer matrix models, which offer an increasing complexity. The main objective is to define their respective limits and to select the most appropriate depending on the frequency range of interest and the required accuracy.

2 ANALOGOUS PIEZOELECTRIC NETWORK ON BEAM

A beam is coupled to its analogous electrical network through a periodic array of piezoelectric patches. A unit cell is defined by considering both mechanical and electrical propagation media. Then, the linear piezoelectricity theory gives a model describing a pair of piezoelectric patches subjected to bending motion.

2.1 Electromechanical unit cell

A periodic array of piezoelectric patches is distributed on an homogeneous beam. An electrical network interconnects the patches, which creates an electrical waveguide. The chosen network is the periodic electrical analogue of a beam [3, 4] because it was shown that this solution can lead to a broadband control of transverse waves. As seen in Fig. 1, an electromechanical periodic structure is obtained, so that a unit cell of length a can be defined. The thickness of the main structure is h_{s} and its width is b. The piezoelectric patches have a thickness h_{p}, a width b and a length l_{p}, with $l_{\mathrm{p}} \leq a$. Then, $\dot{q}_{\mathrm{I}}$ is the current flowing from the network to the pair of patches and V_{I} is the voltage on the electrodes connected to the network. The two piezoelectric patches need to be transversely polarized in identical directions in order to generate a non-zero voltage when bending excitation occurs [12].

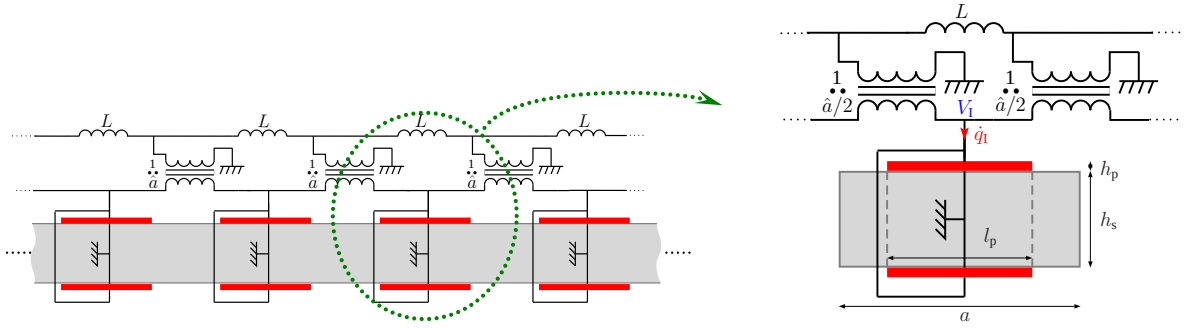

Figure 1: Beam segment coupled to its analogous electrical network through a periodic array of piezoelectric patches and corresponding electromechanical unit cell.

2.2 Bending model for a pair of thin piezoelectric patches

For a thin piezoelectric patch under plane-stress assumption and polarized in transverse direction [13], the 3D linear piezoelectricity theory is simplified into the one-dimensional formulation

$$\begin{aligned} \sigma_\mathrm{p} &= Y_\mathrm{p}^E \varepsilon_\mathrm{p} - \bar{e}_{31} E_\mathrm{p} \\ D_\mathrm{p} &= \bar{e}_{31} \varepsilon_\mathrm{p} + \bar{\epsilon}_{33}^\varepsilon E_\mathrm{p} \end{aligned}, \quad \text{where} \quad Y_\mathrm{p}^E = \frac{1}{s_{11}^E}, \quad \bar{e}_{31} = \frac{d_{31}}{s_{11}^E}, \quad \text{and} \quad \bar{\epsilon}_{33}^\varepsilon = \epsilon_{33}^\sigma - \frac{d_{31}^2}{s_{11}^E}. \tag{1}$$

ε_p and σ_p are respectively the strain and stress in the axial direction '1' of the piezoelectric patch. D_p and E_p are the electric displacement and electric field in the transverse direction '3'. s_{11}^E is the elastic compliance at constant electric field, d_{31} is the piezoelectric charge constant and ϵ_{33}^σ is the permittivity at constant stress. If we consider that the stress is constant along the thickness, the normal force N_p is obtained by multiplying σ_p by the patch cross-section area $S_\mathrm{p} = bh_\mathrm{p}$. For a thin piezoelectric patch, the electric field E_p can be seen as constant along the thickness [13], which means that E_p is equal to $-V_\mathrm{p}/h_\mathrm{p}$, where V_p is the voltage between the two electrodes. Finally, the electric charge q_p comes from the integration of $-D_\mathrm{p}$ all over the surface of the patch. It is thus found from Eq. (1) that

$$\begin{aligned} N_\mathrm{p} &= Y_\mathrm{p}^E S_\mathrm{p} \varepsilon_\mathrm{p} - e_\mathrm{p} V_\mathrm{p} \\ q_\mathrm{p} &= e_\mathrm{p} \Delta U_\mathrm{p} + C_\mathrm{p}^\varepsilon V_\mathrm{p} \end{aligned}, \quad \text{where} \quad e_\mathrm{p} = -b\bar{e}_{31}, \quad C_\mathrm{p}^\varepsilon = \frac{\bar{\epsilon}_{33}^\varepsilon A_\mathrm{p}}{h_\mathrm{p}} \quad \text{and} \quad A_\mathrm{p} = bl_\mathrm{p}. \tag{2}$$

$\Delta U_\mathrm{p} = U_\mathrm{pR} - U_\mathrm{pL}$ is the difference between the right and left end displacements of the patch and C_p^ε is the capacitance of the patch when no strain is allowed along the direction '1'.

Regarding the bending of thin piezoelectric patches, we consider that the electrical variables only depend on axial deformations [13]. Then, for two patches that offer a symmetrical positioning with respect to the neutral axis, their contribution to the bending moment, M_2p, is equal to the integration of the stress times the distance to the central axis z over the two cross-section areas. Furthermore, it is seen from the parallel electrical connection in Fig. 1 that $V_\mathrm{I} = V_\mathrm{p}$ and $q_\mathrm{I} = 2q_\mathrm{p}$. So, with $\varepsilon_\mathrm{p} = \theta_\mathrm{p}' z$, Eqs. (1) and (2) give

$$\begin{aligned} M_\mathrm{2p} &= 2Y_\mathrm{p}^E I_\mathrm{p} \theta_\mathrm{p}' - e_\mathrm{p}(h_\mathrm{s} + h_\mathrm{s}) V_\mathrm{I} \\ q_\mathrm{I} &= e_\mathrm{p}(h_\mathrm{s} + h_\mathrm{s}) \Delta\theta_\mathrm{p} + 2C_\mathrm{p}^\varepsilon V_\mathrm{I} \end{aligned}, \quad \text{where} \quad 2I_\mathrm{p} = \frac{b(h_\mathrm{s} + 2h_\mathrm{p})^3}{12} - \frac{bh_\mathrm{s}^3}{12}, \tag{3}$$

$\Delta\theta_\mathrm{p} = \theta_\mathrm{pR} - \theta_\mathrm{pL}$ is the difference between the right and left rotations at the ends of the patches and θ_p' corresponds to their curvature.

3 TRANSFER MATRIX MODELS FOR TRANSVERSE WAVE PROPAGATION

Four transfer matrix models are proposed to describe the considered electromechanical unit cell. All of them take into account a discrete electrical network but they differ in the definition of the mechanical medium. The first model consider a lumped beam, whereas the second is fully homogenized. Then, the discontinuity induced by the piezoelectric patches is introduced in a piecewise homogenized model. This third transfer matrix model is validated by the last one, which is based on a finite element method.

3.1 Discrete model based on global properties

The mechanical part of the unit cell in Fig. 1(b) is an elastic beam segment symmetrically covered with two piezoelectric patches. This structure can be firstly seen as an homogenized medium governed by a global piezoelectric coupling similar to Eq. (3). Then, if the considered wavelength is considerably longer than the length of the unit cell, the curvature can be approximated by $\theta' \approx \Delta\theta/a$, where $\Delta\theta = \theta_{\mathrm{R}} - \theta_{\mathrm{L}}$ is the difference between the right and left rotations at the ends of the unit cell. Consequently, the bending moment M depends on a global bending stiffness K_θ^E, which gives the discrete model

$$\begin{array}{l} M = K_\theta^E \Delta\theta - e_\theta V_{\mathrm{I}} \\ q_{\mathrm{I}} = e_\theta \Delta\theta + C^\varepsilon V_{\mathrm{I}} \end{array}, \quad \text{where} \quad \frac{1}{K_\theta^E} = \frac{l_{\mathrm{p}}}{Y_{\mathrm{s}} I_{\mathrm{s}} + 2 Y_{\mathrm{p}}^E I_{\mathrm{p}}} + \frac{a - l_{\mathrm{p}}}{Y_{\mathrm{s}} I_{\mathrm{s}}} \quad \text{and} \quad I_{\mathrm{s}} = \frac{b h_{\mathrm{s}}^3}{12}. \tag{4}$$

K_θ^E is obtained directly from the geometry and the material properties of the unit cell. However, the coupling e_θ and the blocked capacitance C^ε depend on global 3D considerations. C^ε is the capacitance of the pair of piezoelectric patches when $\Delta\theta = 0$. This does not mean that the patches are fixed because $\Delta\theta$ is not equal to $\Delta\theta_p$ when the patches do not cover the whole unit cell ($a \neq l_{\mathrm{p}}$). Consequently, C^ε is not equal to $2C_p^\varepsilon$ as it depends on the ratio a/l_{p}. On the other hand, C^σ is the capacitance of the pair of patches when no bending moment is applied at the ends of the unit cell ($M = 0$). This free capacitance is easier to handle because it is directly related to the free capacitance of a single piezoelectric patch: $C^\sigma = 2C_{\mathrm{p}}^\sigma$, which can be measured or approximated from 3D calculations [12]. Another global constant that can be easily obtained is K_θ^D, the stiffness in open circuit ($q_{\mathrm{I}} = 0$). It is computed in the same way as K_θ^E in Eq. (4) with Y_{p}^D instead of Y_{p}^E . Y_{p}^D is the Young modulus at constant electric displacement, which is defined from Eq. (1) by $Y_{\mathrm{p}}^D = Y_{\mathrm{p}}^E + \bar{e}_{31}^2/\bar{\epsilon}_{33}^\varepsilon$. Then, from the definition of C^σ and K_θ^D, Eq. (4) gives $C^\sigma = C^\varepsilon + e_\theta^2/K_\theta^E$ and $K_\theta^D = K_\theta^E + e_\theta^2/C^\varepsilon$. Those two equations are reorganized to finally get the global constants appearing in Eq. (4):

$$\begin{array}{l} e_\theta = \sqrt{K_\theta^E \left(1 - \dfrac{K_\theta^E}{K_\theta^D}\right) C^\sigma} \\ C^\varepsilon = C^\sigma \dfrac{K_\theta^E}{K_\theta^D} \end{array}. \tag{5}$$

The mechanical part of the discrete model is illustrated in Fig. 2(a), where the torsional spring refers to the bending stiffness and the lumped mass m is the mass of the unit cell. If ρ_{s} is the density of the beam and ρ_{p} is the density of the piezoelectric material, $m = \rho_{\mathrm{s}} S_{\mathrm{s}} a + 2\rho_{\mathrm{p}} S_{\mathrm{p}} l_{\mathrm{p}}$. The shear force is not represented because it does not depend directly on the piezoelectric coupling, contrary to the total bending moment, which is increased by $e_\theta V_{\mathrm{I}}$ according to Eq. (4). When the discrete mechanical unit cell is coupled to its analogous electrical network, the resulting electromechanical unit cell can be represented by the electric scheme in Fig. 3 [4]. The relation

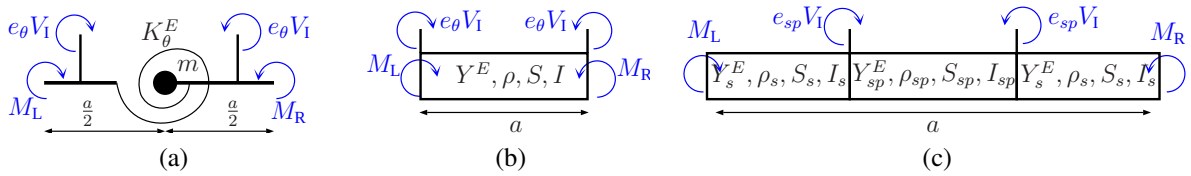

Figure 2: Three models for the mechanical part of the unit cell: (a) Discrete model. (b) Fully homogenized model. (c) Piecewise homogenized model.

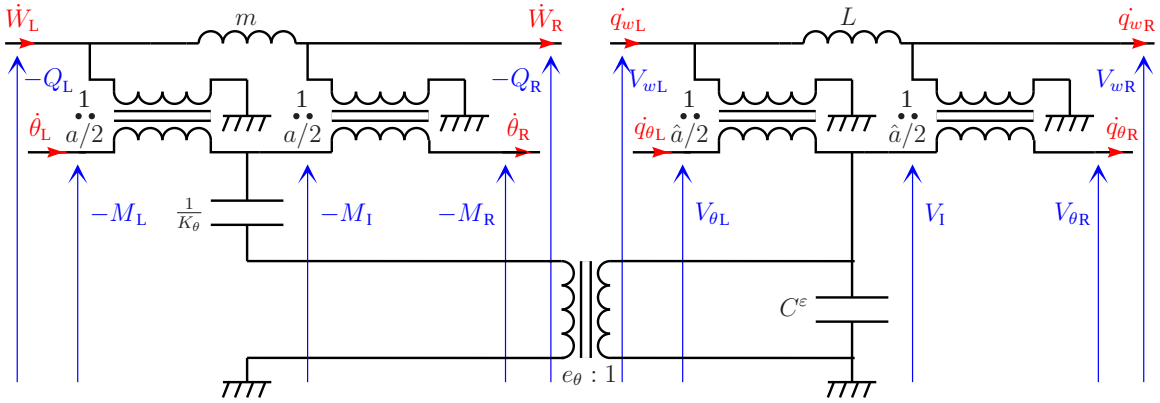

Figure 3: Electrical model of the discrete electromechanical unit cell.

between the electromechanical state vectors at the right and left ends of the unit cell is thus given by the following transfer matrix formulation [4]:

$$\begin{bmatrix} W_\mathrm{R}^\star \\ \theta_\mathrm{R}^\star \\ q_{w\mathrm{R}}^\star \\ q_{\theta\mathrm{R}}^\star \\ M_\mathrm{R}^\star \\ Q_\mathrm{R}^\star \\ V_{\theta\mathrm{R}}^\star \\ V_{w\mathrm{R}}^\star \end{bmatrix} = \begin{bmatrix} 1 & 1 & 0 & 0 & \frac{1}{2} & -\frac{1}{4} & \frac{\Lambda}{2e_\theta} & -\frac{\Lambda}{4e_\theta} \\ 0 & 1 & 0 & 0 & 1 & -\frac{1}{2} & \frac{\Lambda}{e_\theta} & -\frac{\Lambda}{2e_\theta} \\ 0 & 0 & 1 & 1 & -\frac{e_\theta}{2} & \frac{e_\theta}{4} & -\frac{1+\Lambda}{2} & \frac{1+\Lambda}{4} \\ 0 & 0 & 0 & 1 & -e_\theta & \frac{e_\theta}{2} & -(1+\Lambda) & \frac{1+\Lambda}{2} \\ \frac{f}{2} & \frac{f}{4} & 0 & 0 & 1 & -1 & 0 & 0 \\ -f & -\frac{f}{2} & 0 & 0 & 0 & 1 & 0 & 0 \\ 0 & 0 & -\frac{\tilde{f}}{2} & -\frac{\tilde{f}}{4} & 0 & 0 & 1 & -1 \\ 0 & 0 & \tilde{f} & \frac{\tilde{f}}{2} & 0 & 0 & 0 & 1 \end{bmatrix} \begin{bmatrix} W_\mathrm{L}^\star \\ \theta_\mathrm{L}^\star \\ q_{w\mathrm{L}}^\star \\ q_{\theta\mathrm{L}}^\star \\ M_\mathrm{L}^\star \\ Q_\mathrm{L}^\star \\ V_{\theta\mathrm{L}}^\star \\ V_{w\mathrm{L}}^\star \end{bmatrix}, \tag{6}$$

where $f = \omega^2 m a^2 / K_\theta^E$, $\tilde{f} = \omega^2 L C^\varepsilon \hat{a}^2$ and $\Lambda = e_\theta^2 / (K_\theta^E C^\varepsilon)$. The symbol "$\star$" denotes dimensionless state variables, which are highlighted for the sake of conciseness of the transfer matrix: $W^\star = W/a$, $\theta^\star = \theta$, $M^\star = M/K_\theta^E$, $Q^\star = aQ/K_\theta^E$, $q_w^\star = q_w/\hat{a}$, $q_\theta^\star = q_\theta$, $V_\theta^\star = C^\varepsilon V_\theta$ and $V_w^\star = \hat{a} C^\varepsilon V_w$.

3.2 Fully homogenized model for the mechanical part

When considering wavelengths that are not considerably longer than the length of the unit cell, the assumption $\theta' \approx \Delta\theta / a$ is no more valid and the mechanical model involving lumped mass and stiffness needs to be improved. A first solution is to ensure the continuity of the mechanical structure by considering an homogenized beam segment as the one represented in Fig. 2(b). The electrical network is still discrete, which gives a semi-continuous model, where

the definition of e_θ and C^ε remains the same as in the discrete model:

$$\begin{array}{l} M = Y^E I\theta' - e_\theta V_\mathrm{I} \\ q_\mathrm{I} = e_\theta \Delta\theta + C^\varepsilon V_\mathrm{I} \end{array}, \quad \text{where} \quad Y^E I = K_\theta^E a. \tag{7}$$

Figure 2(b) shows that a bending moment $M_\mathrm{R} + e_\theta V_\mathrm{I}$ is applied to the right side of the beam segment and a bending moment $-(M_\mathrm{L} + e_\theta V_\mathrm{I})$ is applied to its left side. After a modification of the state vector, a purely mechanical transfer matrix $\boldsymbol{T_m}$ can thus be used to described the relation between the dimensionless forces and displacements at both ends as

$$\begin{bmatrix} W_\mathrm{R}^\star \\ \theta_\mathrm{R}^\star \\ M_\mathrm{R}^\star + \dfrac{\Lambda}{e_\theta} V_\mathrm{I}^\star \\ Q_\mathrm{R}^\star \end{bmatrix} = \boldsymbol{T_m} \begin{bmatrix} W_\mathrm{L}^\star \\ \theta_\mathrm{L}^\star \\ M_\mathrm{L}^\star + \dfrac{\Lambda}{e_\theta} V_\mathrm{I}^\star \\ Q_\mathrm{L}^\star \end{bmatrix}, \quad \text{where} \quad V_\mathrm{I}^\star = C^\varepsilon V_\mathrm{I}. \tag{8}$$

Here, we focus on an homogeneous Euler-Bernouilli beam segment [10, 4], which means that the mechanical transfer matrix is

$$\boldsymbol{T_m} = \begin{bmatrix} \frac{\mathrm{c}+\mathrm{ch}}{2} & \frac{1}{ka}\frac{\mathrm{s}+\mathrm{sh}}{2} & -\frac{1}{(ka)^2}\frac{\mathrm{c}-\mathrm{ch}}{2} & \frac{1}{(ka)^3}\frac{\mathrm{s}-\mathrm{sh}}{2} \\ -ka\frac{\mathrm{s}-\mathrm{sh}}{2} & \frac{\mathrm{c}+\mathrm{ch}}{2} & \frac{1}{ka}\frac{\mathrm{s}+\mathrm{sh}}{2} & \frac{1}{(ka)^2}\frac{\mathrm{c}-\mathrm{ch}}{2} \\ -(ka)^2\frac{\mathrm{c}-\mathrm{ch}}{2} & -ka\frac{\mathrm{s}-\mathrm{sh}}{2} & \frac{\mathrm{c}+\mathrm{ch}}{2} & -\frac{1}{ka}\frac{\mathrm{s}+\mathrm{sh}}{2} \\ -(ka)^3\frac{\mathrm{s}+\mathrm{sh}}{2} & (ka)^2\frac{\mathrm{c}-\mathrm{ch}}{2} & ka\frac{\mathrm{s}-\mathrm{sh}}{2} & \frac{\mathrm{c}+\mathrm{ch}}{2} \end{bmatrix}, \tag{9}$$

where $\mathrm{c} = \cos(ka)$, $\mathrm{ch} = \cosh(ka)$, $\mathrm{s} = \sin(ka)$, $\mathrm{sh} = \sinh(ka)$. The wave number k is obtained from the beam dispersion relation $k = \omega\sqrt[4]{\rho S/Y^E I}$, where $\rho = m/(aS_\mathrm{s} + 2l_\mathrm{p}S_\mathrm{p})$ is the homogenized density of the unit cell. Concerning the electrical part, note from Fig. 3 that

$$V_\mathrm{I}^\star = \begin{bmatrix} 0 \\ 0 \\ 1 \\ -\frac{1}{2} \end{bmatrix}^T \begin{bmatrix} q_{w\mathrm{L}}^\star \\ q_{\theta\mathrm{L}}^\star \\ V_{\theta\mathrm{L}}^\star \\ V_{w\mathrm{L}}^\star \end{bmatrix} \tag{10}$$

Furthermore, Fig. 3 shows that the electrical propagation results from the superposition of a purely electrical contribution, involving a transfer matrix $\boldsymbol{T_e}$, and a second contribution due to the coupling e_θ:

$$\begin{bmatrix} q_{w\mathrm{R}}^\star \\ q_{\theta\mathrm{R}}^\star \\ V_{\theta\mathrm{R}}^\star \\ V_{w\mathrm{R}}^\star \end{bmatrix} = \boldsymbol{T_e} \begin{bmatrix} q_{w\mathrm{L}}^\star \\ q_{\theta\mathrm{L}}^\star \\ V_{\theta\mathrm{L}}^\star \\ V_{w\mathrm{L}}^\star \end{bmatrix} + e_\theta(\theta_\mathrm{L}^\star - \theta_\mathrm{R}^\star) \begin{bmatrix} \frac{1}{2} \\ 1 \\ 0 \\ 0 \end{bmatrix}, \quad \text{where} \quad \boldsymbol{T_e} = \begin{bmatrix} 1 & 1 & -\frac{1}{2} & \frac{1}{4} \\ 0 & 1 & -1 & \frac{1}{2} \\ -\frac{\tilde{f}}{2} & -\frac{\tilde{f}}{4} & 1 & -1 \\ \tilde{f} & \frac{\tilde{f}}{2} & 0 & 1 \end{bmatrix}. \tag{11}$$

Finally, Eqs. (8), (10) and (11) give a transfer matrix formulation between the left and right electromechanical state vectors, which can be written as

$$\begin{bmatrix} W_\mathrm{R}^\star \\ \theta_R^\star \\ M_\mathrm{R}^\star \\ Q_\mathrm{R}^\star \\ q_{w\mathrm{R}}^\star \\ q_{\theta\mathrm{R}}^\star \\ V_{\theta\mathrm{R}}^\star \\ V_{w\mathrm{R}}^\star \end{bmatrix} = \begin{bmatrix} \boldsymbol{I_4} & \boldsymbol{0_4} \\ -e_\theta \begin{bmatrix} \begin{bmatrix} 0 & \frac{1}{2} \\ 0 & 1 \end{bmatrix} & \boldsymbol{0_2} \\ \boldsymbol{0_2} & \boldsymbol{0_2} \end{bmatrix} & \boldsymbol{I_4} \end{bmatrix} \begin{bmatrix} \boldsymbol{T_m} & \dfrac{\Lambda}{e_\theta}(\boldsymbol{T_m} - \boldsymbol{I_4}) \begin{bmatrix} \boldsymbol{0_2} & \boldsymbol{0_2} \\ \boldsymbol{0_2} & \begin{bmatrix} 1 & -\frac{1}{2} \\ 0 & 0 \end{bmatrix} \end{bmatrix} \\ e_\theta \begin{bmatrix} \begin{bmatrix} 0 & \frac{1}{2} \\ 0 & 1 \end{bmatrix} & \boldsymbol{0_2} \\ \boldsymbol{0_2} & \boldsymbol{0_2} \end{bmatrix} & \boldsymbol{T_e} \end{bmatrix} \begin{bmatrix} W_\mathrm{L}^\star \\ \theta_\mathrm{L}^\star \\ M_\mathrm{L}^\star \\ Q_\mathrm{L}^\star \\ q_{w\mathrm{L}}^\star \\ q_{\theta\mathrm{L}}^\star \\ V_{\theta\mathrm{L}}^\star \\ V_{w\mathrm{L}}^\star \end{bmatrix}. \tag{12}$$

3.3 Piecewise homogenized model for the mechanical part

The previous homogenized model does not take into account the mechanical discontinuity induced by the addition of piezoelectric patches on the beam. This can be rectified by discriminating the purely elastic segments "s" from the segments "sp" involving a piezoelectric contribution. The piecewise homogenized model is thus made of three beam segments, as presented in Fig. 2(c). In the "sp" segment covered by the pair of piezoelectric patches, the problem can be expressed under the same form as in Eq. (7):

$$\begin{array}{l} M_{\text{sp}} = Y_{\text{sp}}^{E} I_{\text{sp}} \theta_{\text{p}}' - e_{sp} V_{\text{I}} \\ q_{\text{I}} = e_{\text{sp}} \Delta\theta_{\text{p}} + C_{\text{sp}}^{\varepsilon} V_{\text{I}} \end{array}, \quad \text{where} \quad Y_{\text{sp}}^{E} I_{\text{sp}} = Y_{\text{s}} I_{\text{s}} + 2 Y_{\text{p}}^{E} I_{\text{p}}. \tag{13}$$

The "sp" constants appearing in the previous system of equations are not equal to the ones in Eq. (7) because they refer to the central segment of the unit cell, without considering the purely elastic segments. Nevertheless, e_{sp} and $C_{\text{sp}}^{\varepsilon}$ can be computed with the same method as in Eq. (5) by considering a global stiffness that refer to the sole "sp" segment.

As the problem focusing on the "sp" beam segment is equivalent to the one presented in Sec. 3.2, a 8×8 transfer matrix $\boldsymbol{T}_{\text{sp}}$ is built on the same form as Eq. (12) but with homogenized constants referring to the "sp" segment. The two "s" beam segments are purely elastic, so that their 4×4 mechanical transfer matrices $\boldsymbol{T}_{\text{s}}$ are obtained as $\boldsymbol{T_m}$ but with the use of the constants Y_{s}, ρ_{s}, S_{s} and I_{s}. At the end, the piecewise homogenized model of the electromechanical unit cell is given by

$$\begin{bmatrix} W_{\text{R}}^{\star} \\ \theta_{\text{R}}^{\star} \\ M_{\text{R}}^{\star} \\ Q_{\text{R}}^{\star} \\ q_{w\text{R}}^{\star} \\ q_{\theta\text{R}}^{\star} \\ V_{\theta\text{R}}^{\star} \\ V_{w\text{R}}^{\star} \end{bmatrix} = \begin{bmatrix} \boldsymbol{T}_{\text{s}} & \boldsymbol{0} \\ \boldsymbol{0} & \boldsymbol{I_4} \end{bmatrix} \boldsymbol{T}_{\text{sp}} \begin{bmatrix} \boldsymbol{T}_{\text{s}} & \boldsymbol{0} \\ \boldsymbol{0} & \boldsymbol{I_4} \end{bmatrix} \begin{bmatrix} W_{\text{L}}^{\star} \\ \theta_{\text{L}}^{\star} \\ M_{\text{L}}^{\star} \\ Q_{\text{L}}^{\star} \\ q_{w\text{L}}^{\star} \\ q_{\theta\text{L}}^{\star} \\ V_{\theta\text{L}}^{\star} \\ V_{w\text{L}}^{\star} \end{bmatrix}, \quad \text{where} \quad \boldsymbol{I_4} = \begin{bmatrix} 1 & 0 & 0 & 0 \\ 0 & 1 & 0 & 0 \\ 0 & 0 & 1 & 0 \\ 0 & 0 & 0 & 1 \end{bmatrix}. \tag{14}$$

3.4 Finite element model

A convenient finite element model was proposed by Thomas et al. [13], who focused on thin piezoelectric patches shunted with independent electrical circuits. The model is based on a condensation of the electrical degrees of freedom in order to recast the system into a standard elastic vibration problem. However, this method is not applicable when considering connections of different patches with an electrical network. There are electrical nodes that interconnect successive unit cells, which means that the corresponding electrical degrees of freedom cannot be condensed. Before condensation, the finite element formulation is expressed as follows

$$\begin{bmatrix} \boldsymbol{M_m} & \boldsymbol{0} \\ \boldsymbol{0} & 0 \end{bmatrix} \begin{bmatrix} \ddot{\boldsymbol{q}}_{\boldsymbol{m}} \\ \ddot{V}_{\text{I}} \end{bmatrix} + \begin{bmatrix} \boldsymbol{K_m} & \boldsymbol{K_c} \\ -\boldsymbol{K_c}^{\boldsymbol{T}} & C_{\text{sp}}^{\varepsilon} \end{bmatrix} \begin{bmatrix} \boldsymbol{q_m} \\ V_{\text{I}} \end{bmatrix} = \begin{bmatrix} \boldsymbol{F_m} \\ q_{\text{I}} \end{bmatrix}, \tag{15}$$

where $\boldsymbol{M_m}$, $\boldsymbol{K_m}$ and $\boldsymbol{K_c}$ are respectively the mass, stiffness and coupling matrices that are defined in [13]. The electric charge q_{I} flowing toward the pair of piezoelectric patches is obtained from the topology of the analogous network as

$$q_{\text{I}} = \boldsymbol{S_q q_e} \quad \text{where} \quad \boldsymbol{S_q} = \begin{bmatrix} 0 & 1 & 0 & -1 \end{bmatrix} \quad \text{and} \quad \boldsymbol{q_e} = \begin{bmatrix} q_{w\text{L}} & q_{\theta\text{L}} & q_{w\text{R}} & q_{\theta\text{R}} \end{bmatrix}^{T} \tag{16}$$

By analogy with the force vector $\boldsymbol{F_m}$ and the displacement vector $\boldsymbol{q_m}$, the voltage vector $\boldsymbol{F_e} = \begin{bmatrix} V_{w\mathrm{L}} & V_{\theta\mathrm{L}} & -V_{w\mathrm{R}} & -V_{\theta\mathrm{R}} \end{bmatrix}^T$ is defined as the dual of the electric charge vector $\boldsymbol{q_e}$. The principle of superposition allows considering that the voltage vector $\boldsymbol{F_e}$ is a sum of two contributions. The first contribution is obtained when no mechanical displacement is allowed ($\boldsymbol{q_m} = \boldsymbol{0}$) and the second contribution excludes external charge displacements ($\boldsymbol{q_e} = \boldsymbol{0}$): $\boldsymbol{F_e} = \boldsymbol{F_e^e} + \boldsymbol{F_e^m}$. The purely electrical contribution $\boldsymbol{F_e^e}$ only depends on the choice of the electrical network. Similarly to established practices in mechanical problems, we define the electrical matrices $\boldsymbol{K_e}$ and $\boldsymbol{M_e}$ as equivalents of stiffness and mass matrices:

$$\boldsymbol{F_e^e} = \left[\boldsymbol{K_e} - \omega^2 \boldsymbol{M_e}\right] \boldsymbol{q_e} \tag{17}$$

When considering the electrical analogue of a beam, $\boldsymbol{M_e}$ can be found from the network in Fig. 3 with $e_\theta = 0$ and $C^\varepsilon \to \infty$, i.e. $V_\mathrm{I} = 0$. However, the matrix $\boldsymbol{K_e}$ cannot be obtained directly from Fig. 3 with $e_\theta = 0$ and $L = 0$. Actually, $\boldsymbol{K_e}$ is not defined, unless we introduce additional degrees of freedom. This is performed by adding two virtual capacitors $C_0/2$ in the "θ" electrical line, on both sides of the unit cell. In the end, we get

$$\boldsymbol{K_e} = \frac{4}{\hat{a}^2 C_0} \begin{bmatrix} 1 & \frac{\hat{a}}{2} & -1 & \frac{\hat{a}}{2} \\ \frac{\hat{a}}{2} & \frac{\hat{a}^2}{4}\frac{C_{\mathrm{sp}}^\varepsilon + 2C_0}{C_{\mathrm{sp}}^\varepsilon + C_0} & -\frac{\hat{a}}{2} & \frac{\hat{a}^2}{4}\frac{C_{\mathrm{sp}}^\varepsilon}{C_{\mathrm{sp}}^\varepsilon + C_0} \\ -1 & -\frac{\hat{a}}{2} & 1 & -\frac{\hat{a}}{2} \\ \frac{\hat{a}}{2} & \frac{\hat{a}^2}{4}\frac{C_{\mathrm{sp}}^\varepsilon}{C_{\mathrm{sp}}^\varepsilon + C_0} & -\frac{\hat{a}}{2} & \frac{\hat{a}^2}{4}\frac{C_{\mathrm{sp}}^\varepsilon + 2C_0}{C_{\mathrm{sp}}^\varepsilon + C_0} \end{bmatrix} \quad \text{and} \quad \boldsymbol{M_e} = \frac{L}{2} \begin{bmatrix} 1 & \frac{\hat{a}}{2} & 0 & 0 \\ \frac{\hat{a}}{2} & \frac{\hat{a}^2}{4} & 0 & 0 \\ 0 & 0 & 1 & -\frac{\hat{a}}{2} \\ 0 & 0 & -\frac{\hat{a}}{2} & \frac{\hat{a}^2}{4} \end{bmatrix}. \tag{18}$$

Note that the capacitance C_0 is a numerical parameter that has to be small compared to $C_{\mathrm{sp}}^\varepsilon$. A good practice is to set C_0 between $C_{\mathrm{sp}}^\varepsilon \times 10^{-3}$ and $C_{\mathrm{sp}}^\varepsilon \times 10^{-9}$ to conceal its influence on electrical propagation and to avoid numerical issues.

The contribution $\boldsymbol{F_e^m}$ is equal to $\boldsymbol{F_e}$ when $\boldsymbol{q_e} = \boldsymbol{0}$. Fig. 3 shows that $\boldsymbol{q_e} = \boldsymbol{0}$ induces that $q_\mathrm{I} = 0$. Then, $q_\mathrm{I} = 0$ induces that $V_{w\mathrm{L}} = V_{w\mathrm{R}} = 0$ and $V_{\theta\mathrm{L}} = V_{\theta\mathrm{R}} = V_\mathrm{I}$. Furthermore, Eq. (15) gives $V_\mathrm{I} = \boldsymbol{K_c}^{\boldsymbol{T}} \boldsymbol{q_m} / C_{\mathrm{sp}}^\varepsilon$ when $q_\mathrm{I} = 0$. As a consequence,

$$\boldsymbol{F_e^m} = \frac{1}{C_{\mathrm{sp}}^\varepsilon} \boldsymbol{S_V} \boldsymbol{K_c}^{\boldsymbol{T}} \boldsymbol{q_m} \quad \text{where} \quad \boldsymbol{S_V} = \begin{bmatrix} 0 & 1 & 0 & -1 \end{bmatrix}^T. \tag{19}$$

Finally, Eqs. (15), (16), (17), (18) and (19) lead to the following dynamic stiffness matrix formulation involving a combination of mechanical and electrical degrees of freedom:

$$\left[\begin{bmatrix} \boldsymbol{K_m} + \frac{1}{C_{\mathrm{sp}}^\varepsilon} \boldsymbol{K_c} \boldsymbol{K_c}^{\boldsymbol{T}} & \frac{1}{C_{\mathrm{sp}}^\varepsilon} \boldsymbol{K_c} \boldsymbol{S_q} \\ \frac{1}{C_{\mathrm{sp}}^\varepsilon} \boldsymbol{S_V} \boldsymbol{K_c}^{\boldsymbol{T}} & \boldsymbol{K_e} \end{bmatrix} - \omega^2 \begin{bmatrix} \boldsymbol{M_m} & \boldsymbol{0} \\ \boldsymbol{0} & \boldsymbol{M_e} \end{bmatrix} \right] \begin{bmatrix} \boldsymbol{q_m} \\ \boldsymbol{q_e} \end{bmatrix} = \begin{bmatrix} \boldsymbol{F_m} \\ \boldsymbol{F_e} \end{bmatrix}, \tag{20}$$

With a restriction to the transverse case, $\boldsymbol{q_m} = \begin{bmatrix} W_\mathrm{L} & \theta_\mathrm{L} & \boldsymbol{q_\mathrm{I}} & W_\mathrm{R} & \theta_\mathrm{R} \end{bmatrix}^T$ and $\boldsymbol{F_m} = \begin{bmatrix} -Q_\mathrm{L} & -M_\mathrm{L} & \boldsymbol{0} & Q_\mathrm{R} & M_\mathrm{R} \end{bmatrix}^T$, where $\boldsymbol{q}_\mathrm{I}$ is the mechanical displacement vector of the internal nodes of the unit cell [13]. So, the dynamic stiffness matrix in Eq. (20) can be reorganized in order to distinguish the left, right and internal degrees of freedom:

$$\begin{bmatrix} \boldsymbol{\tilde{D}_{LL}} & \boldsymbol{\tilde{D}_{LI}} & \boldsymbol{\tilde{D}_{LR}} \\ \boldsymbol{\tilde{D}_{IL}} & \boldsymbol{\tilde{D}_{II}} & \boldsymbol{\tilde{D}_{IR}} \\ \boldsymbol{\tilde{D}_{RL}} & \boldsymbol{\tilde{D}_{RI}} & \boldsymbol{\tilde{D}_{RR}} \end{bmatrix} \begin{bmatrix} \boldsymbol{q}_\mathrm{L} \\ \boldsymbol{q}_\mathrm{I} \\ \boldsymbol{q}_\mathrm{R} \end{bmatrix} = \begin{bmatrix} \boldsymbol{F}_\mathrm{L} \\ \boldsymbol{0} \\ \boldsymbol{F}_\mathrm{R} \end{bmatrix} \quad \text{where} \quad \boldsymbol{F}_\mathrm{L} = \begin{bmatrix} -Q_\mathrm{L} \\ -M_\mathrm{L} \\ V_{w\mathrm{L}} \\ V_{\theta\mathrm{L}} \end{bmatrix}, \quad \boldsymbol{F}_\mathrm{R} = \begin{bmatrix} Q_\mathrm{R} \\ M_\mathrm{R} \\ -V_{w\mathrm{R}} \\ -V_{\theta\mathrm{R}} \end{bmatrix}, \tag{21}$$

$\boldsymbol{q}_{\mathrm{L}} = \left[\begin{array}{cccc} W_{\mathrm{L}} & \theta_{\mathrm{L}} & q_{w\mathrm{L}} & q_{\theta\mathrm{L}} \end{array}\right]^T$ and $\boldsymbol{q}_{\mathrm{R}} = \left[\begin{array}{cccc} W_{\mathrm{R}} & \theta_{\mathrm{R}} & q_{w\mathrm{R}} & q_{\theta\mathrm{R}} \end{array}\right]^T$. With this partitioning, the waveguide finite element methods [6] can be applied. First, the internal degrees of freedoms are eliminated through

$$\left[\begin{array}{cc} \boldsymbol{D_{LL}} & \boldsymbol{D_{LR}} \\ \boldsymbol{D_{RL}} & \boldsymbol{D_{RR}} \end{array}\right] \left[\begin{array}{c} \boldsymbol{q}_{\mathrm{L}} \\ \boldsymbol{q}_{\mathrm{R}} \end{array}\right] = \left[\begin{array}{c} \boldsymbol{F}_{\mathrm{L}} \\ \boldsymbol{F}_{\mathrm{R}} \end{array}\right], \quad \text{where} \quad \begin{array}{l} \boldsymbol{D_{LL}} = \tilde{\boldsymbol{D}}_{\boldsymbol{LL}} - \tilde{\boldsymbol{D}}_{\boldsymbol{LI}}\tilde{\boldsymbol{D}}_{\boldsymbol{II}}^{-1}\tilde{\boldsymbol{D}}_{\boldsymbol{IL}} \\ \boldsymbol{D_{LR}} = \tilde{\boldsymbol{D}}_{\boldsymbol{LR}} - \tilde{\boldsymbol{D}}_{\boldsymbol{LI}}\tilde{\boldsymbol{D}}_{\boldsymbol{II}}^{-1}\tilde{\boldsymbol{D}}_{\boldsymbol{IR}} \\ \boldsymbol{D_{RL}} = \tilde{\boldsymbol{D}}_{\boldsymbol{RL}} - \tilde{\boldsymbol{D}}_{\boldsymbol{RI}}\tilde{\boldsymbol{D}}_{\boldsymbol{II}}^{-1}\tilde{\boldsymbol{D}}_{\boldsymbol{IL}} \\ \boldsymbol{D_{RR}} = \tilde{\boldsymbol{D}}_{\boldsymbol{RR}} - \tilde{\boldsymbol{D}}_{\boldsymbol{RI}}\tilde{\boldsymbol{D}}_{\boldsymbol{II}}^{-1}\tilde{\boldsymbol{D}}_{\boldsymbol{IR}} \end{array}. \tag{22}$$

Then, the condensed dynamic stiffness matrix is transformed into a transfer matrix [6, 8]:

$$\left[\begin{array}{c} W_{\mathrm{R}} \\ \theta_{\mathrm{R}} \\ q_{w\mathrm{R}} \\ q_{\theta\mathrm{R}} \\ Q_{\mathrm{R}} \\ M_{\mathrm{R}} \\ -V_{w\mathrm{R}} \\ -V_{\theta\mathrm{R}} \end{array}\right] = \left[\begin{array}{cc} -\boldsymbol{D_{LR}^{-1}D_{LL}} & \boldsymbol{D_{LR}^{-1}} \\ -\boldsymbol{D_{RL}} + \boldsymbol{D_{RR}D_{LR}^{-1}D_{LL}} & -\boldsymbol{D_{RR}D_{LR}^{-1}} \end{array}\right] \left[\begin{array}{c} W_{\mathrm{L}} \\ \theta_{\mathrm{L}} \\ q_{w\mathrm{L}} \\ q_{\theta\mathrm{L}} \\ Q_{\mathrm{L}} \\ M_{\mathrm{L}} \\ -V_{w\mathrm{L}} \\ -V_{\theta\mathrm{L}} \end{array}\right]. \tag{23}$$

4 COMPARISON OF THE TRANSFER MATRIX MODELS

The propagation constants of the proposed transfer matrices are compared. Depending on the frequency range of interest, we note differences between the models. Those differences are confirmed by the observation of frequency response functions, which lead to guidelines concerning the choice of a suitable model.

4.1 Propagation constants

The computation of the eigenvalues λ of a transfer matrix gives access to the propagation constants $\mu = \ln(\lambda) = \delta + i\eta$ [5, 8]. The real part δ is the attenuation constant, which represents the exponential decay of the amplitude of a wave propagating along one unit cell. The imaginary part η is the phase constant, i.e. the phase shift between the two ends of the unit cell. Table 1 gives the geometry and the material properties of the considered unit cell. Concerning the electrical network, the transformer ratio $\hat{a}$ is set arbitrarily to 1 and the inductance value is tuned to $L = a^2 m/(\hat{a}^2 K_\theta^E C^\varepsilon)$ in order to satisfy the multimodal coupling condition defined in [4]. This condition induces that the electrical network approximates the dispersion relation

	Beam (Aluminum 2017)	Patches (PZT)
Length (mm)	$a = 50$	$l_{\mathrm{p}} = 30$
Width (mm)	$b = 20$	$b = 20$
Thickness (mm)	$h_{\mathrm{s}} = 20$	$h_{\mathrm{p}} = 5$
Density (kg/m^3)	$\rho_{\mathrm{s}} = 2780$	$\rho_{\mathrm{p}} = 7800$
Young modulus (GPa)	$Y_{\mathrm{s}} = 73.9$	$1/s_{11}^E = 66.7$
Charge constant (pC/N)	-	$d_{31} = -210$
Permittivity (nF/m)	-	$\epsilon_{33}^\sigma = 21.2$

Table 1: Geometry and material properties of the beam and the piezoelectric patches.

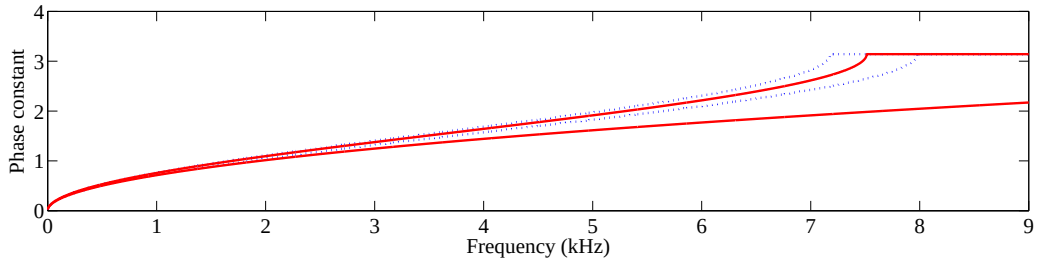

Figure 4: Phase constants - ($\cdots$) for the discrete model, (—) for the piecewise homogenized model.

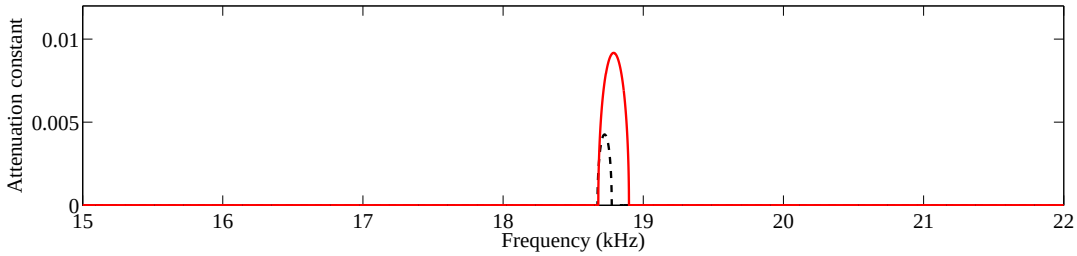

Figure 5: Attenuation constants - ($--$) for the fully homogenized model, (—) for the piecewise homogenized model.

of the beam segment, which is required to implement the analogous coupling. Once the mechanical and electrical properties are defined, the propagation constants of the transfer matrices in Eqs.(6), (12), (14) and (23) can be compared. For each model, the 8×8 transfer matrices give eight propagation constants μ. Two opposite sets of four constants refer to propagation in opposite directions of the electromechanical waveguide. So, only four propagations constants need to be considered to analyze the phase or the attenuation.

First, the phase constants in Fig. 4 show that, below 9 kHz, the discrete model differs significantly from the other ones. Note that the finite element model tends to the piecewise homogenized model when increasing the number of elements. Furthermore, the results obtained with the fully homogenized model are very close to those of the piecewise homogenized model over the frequency range of interest. This is the reason why the fully homogenized and finite element models are not represented in Fig. 4. For each of the other models, only two phase constants are represented because the two other ones are equal to zero. For the piecewise homogenized model, one phase constant approaches a classical beam dispersion relation while the other phase constant reach a step when $\eta = \pi$. This last phase constant thus represents a propagation in a discrete medium [14], which is actually the discrete electrical network. On the other hand, the discrete model offers two phase constants related to discrete waveguides, i.e. with a step at $\eta = \pi$. This is simply explained by the fact that, in the discrete model, the mechanical medium is also represented by a lumped model. Around 7.5 kHz, $\eta = \pi$ means that the wavelength is equal to two unit cells and Fig. 4 shows large differences between the models. So, the discrete model is no more valid when the considered wavelength approaches the length of the unit cell.

The difference between the piecewise homogenized model and the fully homogenized model clearly appears when looking at the smallest attenuation constant for each model around 19 kHz, as seen in Fig. 5. Over this frequency range, the discrete electrical network does not influence

the results anymore because no ellectrical propagation occurs above 7.5 kHz, which was predicted from Fig. 4. However the effect of the mechanical discontinuity induced by the addition of piezoelectric patches creates a stop band for transverse propagation in the beam. Note that a stop band also appears with the fully homogenized model. This is explained by the fact that, even without considering structural discontinuity, the patches induces additional moments on both sides of the unit cell, as represented in Fig. 2(b). This generates a periodic discontinuity that leads to a moderate stop band effect. This stop band is not negligible compared to the one obtained with the piecewise homogenized model because the effect of the mechanical discontinuity is actually quite small in the present example. With the same geometry, the stop band for longitudinal waves was significant [11], but a similar effect for transverse wave would require a considerably thicker discontinuity. In conclusion, strong structural modification would be needed to benefit from structural stop bands in transverse propagation and, anyway, this effect does not occur on the same frequency range as the proposed analogous control.

4.2 Frequency response functions

Frequency response functions (FRFs) are compared for a free-free beam, which is periodically covered with 20 pairs of piezoelectric patches. The two electrical lines of the network needs to be short-circuited at both ends in order to satisfy analogous boundary conditions [4]. Then, the modal coupling condition tunes the electrical modes to the modes of the discrete mechanical model. A tuned mass control is then observed on several modes together and the vibration amplitude is reduced by introducing damping in the network. Here, a resistance $R_s = 20\ \Omega$ is added in series to the inductors by replacing L by $L - jR_s/\omega$, where $j^2 = -1$. The finite electromechanical structure consists of $n = 20$ identical unit cells. A solution to get the relation between the state vectors at both ends of the beam is to raise the transfer matrix to the power of n [4]. The only excitation is a transverse force at one end of the beam. All the other forces, moments and voltages at the ends of the structure are equal to zero. This simplify the problem and it becomes possible to get FRFs as the ratio of the velocity at one end over the excitation force at the other end.

The models are first compared in a low-frequency range. The FRFs obtained with the discrete and the piecewise homogenized model are represented in Fig 6 from 0 to 3.3 kHz. This frequency range covers the first eight bending modes of the beam when no coupling occurs. Again, the FRFs obtained with the homogenized and the finite element model are not represented because they cannot be distinguished from the piecewise homogenized model. As predicted by Fig 4, it is observed that the discrete model is no more reliable when the wavelength approaches the length of the unit cell. A limit of validity can be set to 1 kHz, which corresponds to about ten

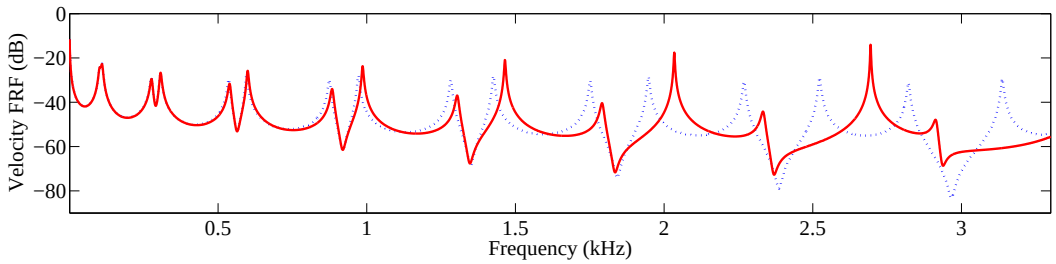

Figure 6: Frequency response functions at low frequencies - (· · ·) for the discrete model, (—) for the piecewise homogenized model.

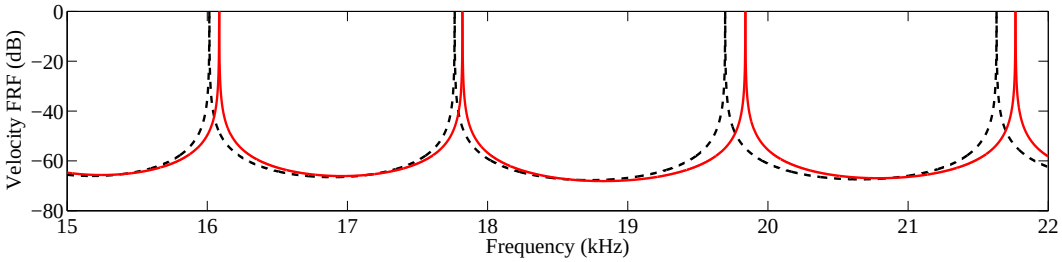

Figure 7: Frequency response functions at higher frequencies - (− −) for the fully homogenized model, (—) for the piecewise homogenized model.

unit cells per wavelength according to Fig 4. With the discrete model, the position of the mechanical resonances are shifted because the mechanical medium is modeled by a lattice. Thus, it does not take into account the increasing mistuning between the continuous and the discrete media.

The second comparison is performed at higher frequencies. Actually, we want to observe the FRFs when the wavelength in the beam is close to two times the length of a unit cell ($\eta = \pi$). This condition occurs between 18 and 19 kHz and it comes with the stop band effect, which was shown in the analysis of the attenuation constants in Fig 5. The finite element model still tends to the piecewise homogenized model, but the homogenized model now presents a slightly different response, as seen in Fig 7. Below 18 kHz, there is already a difference in the positioning of the resonances, but it is even more pronounced after the stop band, which is larger with the piecewise homogenized model. Nevertheless, the effect of the stop band is quite negligible, especially when considering that the approximations of the Euler-Bernoulli model are questionable at such high frequencies. It is also remarked that the considered frequency range is clearly beyond the last electrical resonances. Here, the control strategy involving an analogous discrete network has no effect and the FRFs are essentially due to propagation in the mechanical waveguide.

5 CONCLUSIONS

- Four transfer matrix models are proposed and compared. They differ in the definition of the mechanical medium which can be discrete, fully homogenized, piecewise homogenized or based on a finite element model.
- The finite element model tends to the piecewise homogenized model which is the most accurate because it takes into account the mechanical discontinuity induced by the piezoelectric patches.
- For problems involving analogous control with a discrete electrical network, the fully homogenized model is generally sufficient because the eventual stop band effects occur at frequencies where the proposed control is no more efficient.
- The discrete model is convenient because of its easy implementation but it should be limited to wavelength above ten times the length of the unit cell.
- A future work will consist in the extension of the proposed finite element model to the case of a plate coupled to an analogous electrical network.

REFERENCES

[1] A. Bloch, Electromechanical analogies and their use for the analysis of mechanical and electromechanical systems. *Journal of the Institution of Electrical Engineers-Part I: General*, **92**, 157–169, 1945.

[2] R.H. MacNeal, *The solution of partial differential equations by means of electrical networks*. California Institute of Technology, 1949.

[3] M. Porfiri, F. Dell'Isola, F.M. Frattale Mascioli, Circuit analog of a beam and its application to multimodal vibration damping, using piezoelectric transducers. *International Journal of Circuit Theory and Applications*, **32**, 167–198, 2004.

[4] B. Lossouarn, J.-F. Deü, M. Aucejo, Multimodal vibration damping of a beam with a periodic array of piezoelectric patches connected to a passive electrical network. *Smart Materials and Structures*, **24**, 115037, 2015.

[5] D.M. Mead, Wave propagation in continuous periodic structures: research contribution from Southampton. *Journal of Sound and Vibration*, **190**, 495–524, 1996.

[6] B.R. Mace, D. Duhamel, M.J. Brennan, L. Hinke, Finite element prediction of wave motion in structural waveguides. *The Journal of the Acoustical Society of America*, **117**, 2835–2843, 2005.

[7] L. Airoldi, M. Ruzzene, Design of tunable acoustic metamaterials through periodic arrays of resonant shunted piezos. *New Journal of Physics*, **13**, 113010, 2011.

[8] L. Airoldi, M. Ruzzene, Wave Propagation Control in Beams Through Periodic Multi-Branch Shunts. *Journal of Intelligent Material Systems and Structures*, **22**, 1567–1579, 2011.

[9] G. Wang, S. Chen, J. Wen, Low-frequency locally resonant band gaps induced by arrays of resonant shunts with Antoniou's circuit: experimental investigation on beams. *Smart Materials and Structures*, **20**, 015026, 2011.

[10] Y. Lu, J. Tang, Electromechanical tailoring of structure with periodic piezoelectric circuitry. *Journal of Sound and Vibration*, **331**, 3371–3385, 2012.

[11] J.-F. Deü, B. Lossouarn, M. Aucejo, Comparison of electromechanical transfer matrix models for passive damping involving an array of shunted piezoelectric patches. *22nd International Congress on Sound and Vibration 2015 (ICSV 22)*, Florence, Italy, June 12-16, 2015.

[12] C. Maurini, J. Pouget, F. Dell'Isola, Extension of the Euler-Bernoulli model of piezoelectric laminates to include 3D effects via a mixed approach. *Computers and Structures*, **84**, 1438–1458, 2006.

[13] O. Thomas, J.-F. Deü, J. Ducarne, Vibrations of an elastic structure with shunted piezoelectric patches: efficient finite element formulation and electromechanical coupling coefficients. *International Journal for Numerical Methods in Engineering*, **80**, 235–268, 2009.

[14] L. Brillouin, *Wave propagation in periodic structures*. McGraw-Hill, 1946.

ECCOMAS Congress 2016
VII European Congress on Computational Methods in Applied Sciences and Engineering
M. Papadrakakis, V. Papadopoulos, G. Stefanou, V. Plevris (eds.)
Crete Island, Greece, 5–10 June 2016

BUCKLING OF ANNULAR PLATE JOINT WITH CIRCULAR BEAM

Sergei B. Filippov[1], **Maria L. Boyarskaya**[2]

[1]Saint Petersburg State University
St. Petersburg State University, 7/9 Universitetskaya nab., St. Petersburg, 199034 Russia
e-mail: s_b_filippov@mail.ru

[2] Saint Petersburg State University
St. Petersburg State University, 7/9 Universitetskaya nab., St. Petersburg, 199034 Russia
e-mail: marusya1904@mail.ru

Keywords: Buckling, Annular Plate, Eigenvalue Problem, Asymptotic Technique, The Ritz Method.

Abstract. *Buckling of an annular elastic thin plate joint with circular beam under the action of radial stresses is studied. Such plate can be considered as a model of the supporting ring of a cylindrical shell in the case when the ring has a T-shaped cross-section. First the initial stress-resultants are found. Then assuming that the plate is narrow buckling equations and boundary conditions are simplified by means of an asymptotic technique. The approximate eigenvalue problem has analytical solutions for particular cases. In the general case, for its solution the Rayleigh-Ritz method and the shooting procedure are used.*

1 INTRODUCTION

The external pressure acting on a circular cylindrical shell may cause buckling of the shell. Reinforcing of the shell by rings leads to raising its critical pressure. If the width of the rings is sufficiently small the buckling mode is similar to the buckling mode of the shell without rings, and the shell surface is covered by a series of pits stretched along the generatrix of the cylinder. In the case of this typical buckling the rings may be considered as circular beams. Almost in all studies of ring-stiffened shells the beam model of the ring is used (see [1]-[3] and references there).

If the width of a ring grows, the critical pressure increases until the typical buckling mode will be replaced with the buckling mode consisting of small pits formed on the surface of the ring while the cylindrical shell itself does not actually deform (see, [4]). The buckling of the plate occurs under the action of radial stresses arising on the plate edge joined with the cylindrical shell. These stresses are caused by the pressure acting on a circular cylindrical shell. The beam model can not be used for studying the buckling of the wide ring which should be considered as an annular plate. Buckling of annular thin plates is well enough studied (see, for example, [5]-[7]). The aim of this paper is the solution of the buckling problem for the annular plate stiffened by a circular beam.

In [8] by means of an asymptotic analysis the approximate boundary conditions on the plate edge joined with the cylindrical shell are obtained. If the plate is thin these conditions coincide with the conditions on the clamped edge. In the paper [4] for the ring with the rectangular cross-section on the other plate edge the free edge conditions were introduced. The approximate values of the critical pressure found by the solution of the eigenvalue problem for the annular plate are in good agreement with the numerical ones obtained by FEM for the ring-stiffened shell.

In this paper we consider buckling under the action of radial stresses of the ring with the T-shaped cross-section joined with the cylindrical shell and located outside the shell. As a model of such a ring we use a circular plate. We assume that the edge joined with the shell is clamped and the other plate edge is stiffened by the circular beam.

Two cases are analyzed. In the first case the shell is under the internal pressure p (see Figure $1a$) and in the second case the pressure is external (see Figure $1b$).

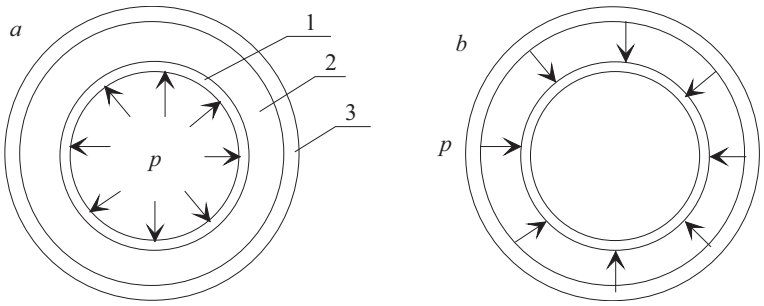

Figure 1: Pressure acting on the shell; 1 — shell, 2 — plate, 3 — beam.

In the work [9] the buckling of a circular plate under the action of radial stresses on the inner edge was considered. For the specific pre-buckling stresses the analytical solution was obtained.

2 BASIC EQUATIONS

Let r be the radial coordinate on the middle surface of the plate and σ_0 the radial stress at the edge $r = r_0$ causing buckling, where r_0 is the radius of the shell. The compressive stresses are regarded as positive. After separation of variables equations describing the buckling of the annular plate can be written in the following form

$$\begin{gathered} Q_1' + \frac{1}{r}Q_1 + \frac{m}{r}Q_2 = T_1 w'' + T_2\left(\frac{w'}{r} - \frac{m^2}{r^2}w\right), \\ Q_1 = M_1' + \frac{1}{r}(M_1 - M_2) + 2\frac{m}{r}H, \quad Q_2 = -\frac{m}{r}M_2 + \frac{2}{r}H, \\ M_1 = D(\kappa_1 + \nu\kappa_2), \quad M_2 = D(\kappa_2 + \nu\kappa_1), \quad H = D(1-\nu)\kappa_{12}, \quad D = \frac{Eh^3}{12(1-\nu^2)}, \\ \kappa_1 = -w'', \quad \kappa_2 = \frac{m^2}{r^2}w - \frac{w'}{r}, \quad \kappa_{12} = \left(\frac{m}{r}w\right)', \end{gathered} \tag{1}$$

where $(')$ denotes the derivative with respect to the radial coordinate r, m is the circumferential wave number, w is the normal deflection, Q_1, Q_2 and M_1, M_2, H are the stress-resultants and stress-couples, T_1 and T_2 are the pre-buckling stress-resultants, E is Young's modulus, h is the plate thickness, ν is Poisson's ratio, κ_1, κ_2, κ_{12} are the changes of curvature.

We assume that the loaded edge of the plate $r = r_0$ is clamped:

$$w = w' = 0, \quad r = r_0. \tag{2}$$

At the other plate edge $r = r_1$ stiffened by the circular beam the boundary conditions have the form

$$M_1 = \frac{EJ_r}{r_0^2}w', \quad Q_1 = T_1 w', \quad r = r_1, \tag{3}$$

where J_r is the moment of inertia of the beam cross-section. For the beam with rectangular cross-section $J_r = a^3 b/12$ (see Figure 2).

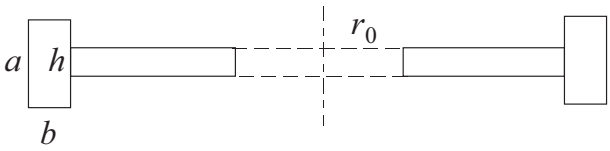

Figure 2: The cross-section of the annular plate joint with the beam

System (1) can be reduced to the equation

$$\frac{d^4w}{ds^4} + \frac{2}{s}\frac{d^3w}{ds^3} - \frac{2m^2 + 1 - \beta t_1}{s^2}\frac{d^2w}{ds^2} + \frac{2m^2 + 1 + \beta t_2}{s^3}\frac{dw}{ds} + \frac{m^2(m^2 - 4 - \beta t_2)}{s^4}w = 0, \tag{4}$$

where

$$\beta = \frac{h\sigma_0 r_0^2}{D}$$

is the buckling stress parameter,

$$s = \frac{r}{r_0}, \quad t_k = \frac{r^2 T_k}{h\sigma_0 r_0^2}, \quad k = 1, 2. \tag{5}$$

3 PRE-BUCKLING STRESS-RESULTANTS

To find the pre-buckling stress-resultants T_1 and T_2 we use equations of axisymmetric tangential deformation of the plate:

$$T_1' + \frac{1}{r}(T_1 - T_2) = 0, \quad T_1 = B\left(u' + \nu\frac{u}{r}\right), \quad T_2 = B\left(\frac{u}{r} + \nu u'\right), \tag{6}$$

where u is the radial displacement and $B = Eh/(1-\nu^2)$. The general solution of equations (6) has the form

$$u = C_1 r + \frac{C_2}{r}, \quad T_{1,2} = B\left(\gamma_0 C_1 \mp \delta_0 \frac{C_2}{r^2}\right), \tag{7}$$

where $\gamma_0 = 1 + \nu$, $\delta_0 = 1 - \nu$.

In the first case corresponding to the Figure 1a the boundary conditions for equations (6) are

$$T_1(r_0) = h\sigma_0, \quad T_1(r_1) = -\frac{ES}{r_1^2}u(r_1), \tag{8}$$

where S is the area of the ring cross-section. Substituting solution (7) into boundary conditions (8) we get

$$(\gamma_0 + \delta_0 S_0)C_1 - \frac{\delta_0(1-S_0)}{r_1^2}C_2 = 0, \quad \gamma_0 C_1 - \frac{\delta_0}{r_0^2}C_2 = \frac{(1-\nu^2)\sigma_0}{E}, \tag{9}$$

where $S_0 = (1+\nu)S/(hr_1)$. The solution of equations (9) has the form

$$C_1 = \frac{(1-S_0)(1-\nu^2)\sigma_0}{dr_1^2 E}, \quad C_2 = \frac{(\gamma_0 + \delta_0 S_0)(1-\nu^2)\sigma_0}{d\delta_0 E}, \quad d = \frac{(1-S_0)\gamma_0}{r_1^2} - \frac{\gamma_0 + \delta_0 S_0}{r_0^2}.$$

Taking into account formulas (7) we obtain

$$T_{1,2} = \frac{h\sigma_0 r_0^2}{r^2}\left(\frac{r^2(1-S_0)\gamma_0 \mp r_1^2(\gamma_0 + \delta_0 S_0)}{r_0^2(1-S_0)\gamma_0 - r_1^2(\gamma_0 + \delta_0 S_0)}\right). \tag{10}$$

In the second case corresponding to the Figure 1b the stresses are tensile. We get the pre-buckling stress-resultants for the second case substituting $-\sigma_0$ instead σ_0 in formulas (10).

If $S_0 = 1$ then

$$T_{1,2} = \pm\frac{h\sigma_0 r_0^2}{r^2}. \tag{11}$$

The analytical solution of equations (1) for the pre-buckling stress-resultants (11) was obtained in [9], however the condition $S_0 = 1$ is unlikely in a real structure.

Taking $S_0 = 0$ in formulas (10), we get the pre-buckling stress-resultants for the plate without the beam which corresponds to a ring with the rectangular cross-section.

4 APPROXIMATE SOLUTION FOR THE FIRST CASE

Consider the buckling of the annular plate under the action of compressive radial stresses applied to the inner clamped plate edge (see Figure 1a). The outer plate edge is joined with circular beam.

Let us suppose that the plate is narrow, i.e. the non-dimensional width of the plate is $\varepsilon = r_1/r_0 - 1 \ll 1$. Usually this condition holds for the rings supporting a shell.

Assume that $m \sim 1$. Then after replacing the variable

$$s = 1 + \varepsilon x \tag{12}$$

in equations (4) and neglecting small terms we get the approximate equation

$$\frac{d^4w}{dx^4} + \beta\varepsilon^2 t_1 \frac{d^2w}{dx^2} + \beta\varepsilon^3 t_2 \frac{dw}{dx} = 0. \tag{13}$$

Replacing variable in relations (2) and (3) according to (12) we obtain the following approximate boundary conditions

$$\begin{gathered} w = w' = 0, \quad x = 0, \\ w'' + cw' = 0, \quad w''' + \beta\varepsilon^2 t_1 w' = 0, \quad x = 1, \end{gathered} \tag{14}$$

where

$$c = \frac{12\varepsilon(1-\nu^2)J_n}{h_n^3}, \quad J_n = \frac{J_r}{r_0^4}, \quad h_n = \frac{h}{r_0}.$$

In the case $S_0 = 1$ it follows from (11) and (5) that $t_{1,2} = \pm 1$. Hence in the first approximation equation (13) and boundary conditions (14) can be written as

$$\frac{d^4w}{dx^4} + \beta_0^2 \frac{d^2w}{dx^2} = 0, \quad \beta_0^2 = \beta\varepsilon^2 \tag{15}$$

$$\begin{gathered} w = w' = 0, \quad x = 0, \\ w'' + cw' = 0, \quad w''' + \beta_0^2 w' = 0, \quad x = 1. \end{gathered} \tag{16}$$

Substituting the general solution of equation (15)

$$w(x) = C_1 \sin\beta_0 x + C_2 \cos\beta_0 x + C_3 x + C_4$$

into boundary conditions (16) we obtain that eigenvalue problem (15), (16) has a nontrivial solution if

$$\beta_0 \cos\beta_0 + c \sin\beta_0 = 0. \tag{17}$$

The non-dimensional critical load β_c may be found by means of the formula

$$\beta_c = \beta_0^2/\varepsilon^2, \tag{18}$$

where β_0 is the minimal positive root of equation (17).

In the case of arbitrary S_0 we get the following approximate expressions for the narrow plate taking into account formulas (10), (5) and (12):

$$t_1 = 1 - \frac{\varepsilon h_n x}{\varepsilon h_n + S_n}, \quad t_2 = \frac{\nu S_n - h_n}{\varepsilon h_n + S_n}, \quad S_n = \frac{S}{r_0^2} = \frac{h_n r_{1n} S_0}{1+\nu}. \tag{19}$$

Equation (13) and boundary conditions (14) take the form

$$\frac{d^4w}{dx^4} + \beta_0^2 t_1(x) \frac{d^2w}{dx^2} + \varepsilon\beta_0^2 t_2 \frac{dw}{dx} = 0. \tag{20}$$

$$\begin{gathered} w = w' = 0, \quad x = 0, \\ w'' + cw' = 0, \quad w''' + \beta_0^2 t_1(1) w' = 0, \quad x = 1. \end{gathered} \tag{21}$$

Eigenvalue problem (20), (21) does not have an analytical solution. To find an approximate value of β_0 we use the Rayleigh-Ritz method. Multiplying equations (20) by w and integrating by parts over the interval $[0, 1]$ we obtain

$$[w'''w - w''w']_0^1 + \int_0^1 (w'')^2\, dx + \beta_0^2 \int_0^1 t_1 w''w\, dx + \varepsilon\beta_0^2 t_2 \int_0^1 w'w\, dx = 0. \tag{22}$$

Taking into account boundary conditions (21) from equation (22) we find

$$\beta_0^2 = \frac{G_1 + I_1}{G_2 + I_2 + I_3}, \tag{23}$$

where

$$\begin{gathered} G_1 = c[w'(1)]^2, \quad G_2 = t_1(1)w'(1)w(1), \quad I_1 = \int_0^1 (w'')^2\, dx, \\ I_2 = -\varepsilon t_2 \int_0^1 w'w\, dx, \quad I_3 = -\int_0^1 t_1 w''w\, dx. \end{gathered} \tag{24}$$

The substituting in formulas (23), (24) instead exact solution $w(x)$ an arbitrary function $W(x)$ satisfying boundary conditions $W(0) = W'(0) = 0$ get an approximate value of β_0. Accuracy of the approximation will be high if we take the function $W(x)$ close to $w(x)$. To choose the function $W(x)$ we consider solutions of eigenvalue problem (15), (16). If $c = 0$ then the minimal positive root of equation (17) is $\beta_1 = \pi/2$. Corresponding to $\beta_1 = \pi/2$ buckling mode has the form $W_1(x) = 1 - \cos(\pi x/2)$. In the case $c = \infty$ the buckling mode is $W_2(x) = 1 - \cos(\pi x)$. Let for any dimensionless stiffness c

$$W(x) = 1 - \cos kx, \tag{25}$$

where $k(c) = \pi(c + 1)/(c + 2)$, $k(0) = \pi/2$, $k(\infty) = \pi$.

Formula (23) for eigenvalue problem (15), (16) after sustituting function (25) in relation (24) and neglecting small terms may be written in the form

$$\beta_0^2 = \frac{4ck \sin k + k^2(2k + \sin 2k)}{2k - \sin 2k}. \tag{26}$$

Comparison of the minimal positive roots of equation (17) and the approximate values of β_0 obtained from formula (26) for $c \in [0, 10]$ shows that the relative error of approximate results is less than 0.1%.

We use function (25) also for the calculation eigenvalues of buckling problem (20), (21). Substituting this function instead $w(x)$ in relations (24), we obtain

$$\begin{gathered} G_1 = c(k \sin k)^2, \quad G_2 = \frac{S_n k \sin k(1 - \cos k)}{S_n + \varepsilon}, \\ I_1 = \frac{k^3}{4}(2k + \sin 2k), \quad I_2 = \varepsilon \frac{1 - \nu S_n}{2(S_n + \varepsilon)}(1 - \cos k)^2, \\ I_3 = \frac{2k^2(2S_n + \varepsilon) - 2kS_n(4 \sin k - \sin 2k) - \varepsilon(7 - 8 \cos k + \cos 2k)}{8(S_n + \varepsilon)}. \end{gathered} \tag{27}$$

Formulas (23) and (27) get an approximate minimal positive eigenvalue β_0 of problem (20), (21). The non-dimensional critical load β_c may be found by means of relation (18).

Consider an annular plate with the parameters $\varepsilon = 0.1$, $\nu = 0.3$, $h_n = h_p/r_0 = 0.01$, which outer edge is stiffened by the circular beam of a rectangular cross-section. The width and height of the beam cross-section are $a = a_n r_0$ and $b = b_n r_0$ correspondingly (see Figure 2). Then $S_n = a_n b_n / h_n$, $J = a^3 b/12$. Values of the dimensionless stiffness c and the non-dimensional critical load β_c for different values of a_n and b_n are given in the Table 1. The last column of

a_n	b_n	c	Values of β_c	
			Ritz method	Shooting
0	0.0	0	830	784
0.01	0.01	0.001	685	663
0.04	0.01	0.058	520	515
0.05	0.02	0.227	448	447
0.06	0.03	0.590	469	468
0.07	0.04	1.248	542	541
0.08	0.05	2.330	640	639
0.10	0.07	6.370	816	816
0.12	0.09	14.15	915	915

Table 1: Results of calculation for various dimensions of beam cross-section.

the Table 1 contains values β_c obtained by the numerical solution of eigenvalue problem (20), (21). These results are found by means of the initial-value or shooting procedure represented in [10]. The approximate results calculated from formula (23) are given in the penultimate column. Comparison of the numerical and the approximate results shows that the relative error of the approximate results is less than 6%.

In Fig. 3, for the plate stiffened by the beam of a square cross-section the parameter β_0 vs. $a_n = b_n$ is plotted.

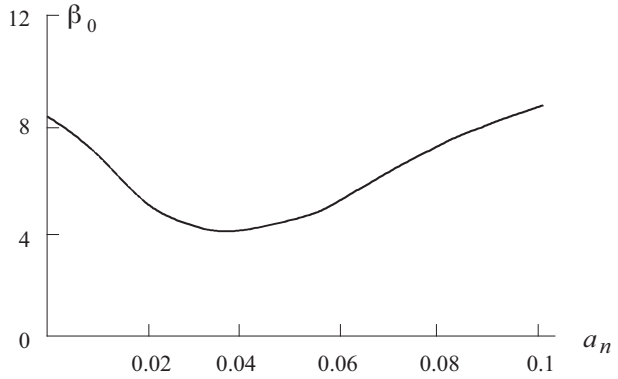

Figure 3: Parameter β_0 vs. dimension of beam cross-section a_n.

At increase in the sizes of the beam cross-section section the parameter of the critical load $\beta_c = \beta_0^2/\varepsilon^2$ decreases, and then increases. Decrease of the critical load β_c with growth of the sizes a_n and b_n is connected with increase in the pre-buckling stress-resultants t_1 at the external

edge of the plate, and its increase is caused by increase in stiffness of a beam c. Hence, by the local buckling under an internal pressure the ring with the rectangular cross-section for which $a_n = b_n = 0$ is more effective than the ring with the T-shaped cross-section.

5 APPROXIMATE SOLUTION FOR THE SECOND CASE

The second case differs from the first case only in that the radial stress at the edge $r = r_0$ is tensile i.e. its has opposite sign. Therefore to obtain in the second case an approximate equation and boundary conditions for the narrow plate and $m \sim 1$ we should change β to $-\beta$ in formulas (13) and (14). Then for $m \sim 1$ by means of relation (23) we obtain that $\beta < 0$, and plate buckling does not occur.

Consider the case of the large circumferential wave number: $m \sim 1/\varepsilon$. Then for a narrow plate the approximate buckling equation and the boundary conditions are

$$\frac{d^4w}{dx^4} - (2m_0^2 + \beta_0 t_1)\frac{d^2w}{dx^2} + m_0^2(m_0^2 + \beta_0 t_2)w = 0, \tag{28}$$

$$\begin{gathered} w = w' = 0, \quad x = 0, \\ w'' + cw' - \nu m_0^2 w = 0, \quad w''' - [(2-\nu)m_0^2 + \beta_0 t_1]w' = 0, \quad x = 1. \end{gathered} \tag{29}$$

where

$$m_0 = \varepsilon m, \quad \beta_0 = \varepsilon^2 \beta, \quad t_1 = 1 - \frac{\varepsilon h_n x}{\varepsilon h_n + S_n}, \quad t_2 = \frac{\nu S_n - h_n}{\varepsilon h_n + S_n}, \quad S_n = \frac{h_n r_{1n} S_0}{1+\nu}.$$

Equation (28) has analytical solutions only in the cases $S_0 = 0$ and $S_0 = 1$ (see [4] and [9]). In the general case we search approximate value of β_0 by means of the Rayleigh-Ritz method. We multiply equations (28) by w, integrate by parts over the interval $[0, 1]$ and obtain

$$[w'''w - w''w']_0^1 + I_2 + 2m_0(I_1 - [w'w]_0^1) - \beta_0 I_3 + m_0^2(m_0^2 + \beta_0 t_2)I_0 = 0. \tag{30}$$

Here

$$I_2 = \int_0^1 (w'')^2\,dx, \quad I_1 = \int_0^1 (w')^2\,dx, \quad I_0 = \int_0^1 w^2\,dx, \quad I_3 = \int_0^1 t_1 w''w\,dx.$$

Using boundary conditions (29) from equation (30) we find

$$\beta_0 = \frac{I_2 + m_0^2 I_1 + m_0^4 I_0 - 2\nu m_0^2 w(1)w'(1) + c(w'(1))^2}{I_3 - t_2 m_0^2 I_0 - t_1(1)w(1)w'(1)}. \tag{31}$$

As a Ritz function $W(x)$ we use the solution of following eigenvalue problem

$$\frac{d^4w}{dx^4} - (2m_0^2 + \beta_0)\frac{d^2w}{dx^2} + m_0^2(m_0^2 + \beta_0 t_2)w = 0, \tag{32}$$

$$\begin{gathered} w = w' = 0, \quad x = 0, \\ w'' + cw' - \nu m_0^2 w = 0, \quad w''' - [(2-\nu)m_0^2 + \beta_0 t_1]w' = 0, \quad x = 1. \end{gathered} \tag{33}$$

Substituting $w = e^{\lambda x}$ into equation (32) we obtain the biquadratic equation

$$\lambda^4 - (2m_0^2 + \beta_0)\lambda^2 + m_0^2(m_0^2 + \beta_0 t_2) = 0$$

which has the following roots:

$$\lambda_{1,2} = \pm\sqrt{b_0 - a_0}, \quad \lambda_{3,4} = \pm\sqrt{b_0 + a_0},$$

where

$$a_0 = \sqrt{(1 - t_2)m_0^2\beta_0 + \beta_0^2/4}, \quad b_0 = m_0^2 + \beta_0/2.$$

In the case $\beta_0 \le m_0^2/t_2$ all roots are real and eigenvalue problem (32), (33) does not have a nontrivial solution. Let us search $\beta_0 > m_0^2/t_2$. Then equation (32) has the general solution

$$w = C_1 \sin\alpha x + C_2 \cos\alpha x + C_3 \sinh\gamma x + C_4 \cosh\gamma x,$$

where C_k, $k = 1, 2, 3, 4$ are arbitrary constants,

$$\alpha = \sqrt{a_0 - b_0}, \quad \gamma = \sqrt{a_0 + b_0}.$$

To obtain the constants C_k we substitute the general solution into boundary conditions (33) and get a system of linear homogeneous algebraic equations. The determinant of this system may be written as

$$D(\beta_0) = \begin{vmatrix} 0 & 1 & 0 & 1 \\ \alpha & 0 & \gamma & 0 \\ (A-\alpha^2)s_1 + c\alpha c_1 & (A-\alpha^2)c_1 - c\alpha s_1 & (A+\gamma^2)s_2 + c\gamma c_2 & (A+\gamma^2)c_2 + c\gamma s_2 \\ \alpha(B-\alpha^2)c_1 & -\alpha(B-\alpha^2)s_1 & \gamma(B+\gamma^2)c_2 & \gamma(B+\gamma^2)s_2 \end{vmatrix}$$

where

$$A = -\nu_0^2, \quad B = m_0^2(\nu - 2) - \beta_0 t_1(1),$$

$$s_1 = \sin\alpha, \quad s_2 = \sinh\gamma, \quad c_1 = \cos\alpha, \quad c_2 = \cosh\gamma.$$

After transformations, we get

$$D(\beta_0) = Fs_1s_2 + Gc_1c_2 + H + c\alpha\gamma(\alpha^2 + \gamma^2)(\alpha s_1c_2 + \gamma c_1s_2).$$

Here

$$F = \gamma^2(A-\alpha^2)(B+\gamma^2) - \alpha^2(A+\gamma^2)(B-\alpha^2),$$
$$G = -\alpha\gamma[(A-\alpha^2)(B+\gamma^2) + (A+\gamma^2)(B-\alpha^2)],$$
$$H = \alpha\gamma[(A+\gamma^2)(B+\gamma^2) + (A-\alpha^2)(B-\alpha^2).$$

If $\beta_0(m_0)$ is the minimal positive root of equation $D(\beta_0) = 0$ then we can find the parameter of the critical load β_c from the following formulas

$$\beta_c = \beta_m/\varepsilon^2, \quad \beta_m = \min_{m_0} b_0(m_0). \tag{34}$$

Since $D(\beta_m) = 0$, the system of linear homogeneous algebraic equations with the unknowns C_k has nontrivial solution for $\beta_0 = \beta_m$. As such solution we take the minors of elements of the third row of a determinant $D(\beta_m)$:

$$C_1^* = \alpha\gamma(B-\alpha^2)s_1 + \gamma^2(B+\gamma^2)s_2, \quad C_2^* = \alpha\gamma(B-\alpha^2)c_1 - \alpha\gamma(B+\gamma^2)c_2,$$
$$C_3^* = -\alpha^2(B-\alpha^2)s_1 - \alpha\gamma(B+\gamma^2)s_2, \quad C_4^* = -\alpha\gamma(B-\alpha^2)c_1 + \alpha\gamma(B+\gamma^2)c_2,$$

Hence, the buckling mode of the problem (32), (33) is

$$W = C_1^* \sin\alpha x + C_2^* \cos\alpha x + C_3^* \sinh\gamma x + C_4^* \cosh\gamma x.$$

Substituting in formula (30) instead the exact solution $w(x)$ the function $W(x)$ we obtain the approximate value of the non-dimesion critical load of problem (28), (29):

$$\beta_0 = \frac{I_2 + m_0^2 I_1 + m_0^4 I_0 - 2\nu m_0^2 W(1)W'(1) + c(W'(1))^2}{I_3 - t_2 m_0^2 I_0 - t_1(1)W(1)W'(1)}, \tag{35}$$

where

$$I_2 = \int_0^1 (W'')^2\,dx, \quad I_1 = \int_0^1 (W')^2\,dx, \quad I_0 = \int_0^1 W^2\,dx, \quad I_3 = \int_0^1 t_1 W''W\,dx.$$

The relative error of approximate results, obtain from formula (28), in comparison with numerical results, found by means of the shooting procedure, is less than 0.1%.

In Fig. 4, for the plate with the parameters $\varepsilon = 0.1$, $\nu = 0.3$, $h_n = 0.01$ stiffened by the beam of a square cross-section the critical load β_0 vs. the dimensionless sizes of the beam cross-section a_n is plotted.

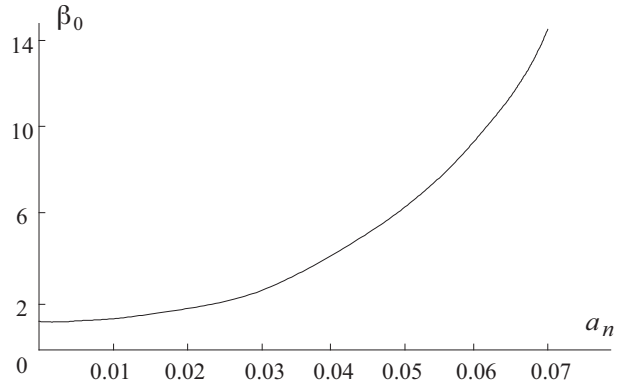

Figure 4: Parameter β_0 vs. sizes of beam a_n.

At increase in the sizes of the beam cross-section the parameter of critical load $\beta_c = \beta_0^2/\varepsilon^2$ increases. Therefore, by the local buckling under an external pressure the ring with the T-shaped cross-section is more effective than the ring with rectangular cross-section.

6 CONCLUSIONS

We discussed buckling of rings with the T-shaped cross-section supporting a circular cylindrical shell. The cases of internal and external uniform pressures acting on the shell are analyzed. As a model of the ring the annular thin narrow plate joint with a circular beam is used. Buckling equations and boundary conditions are simplified by means of an asymptotic technique. To find the approximate critical load the Rayleigh-Ritz method is used. The solutions of the approximate eigenvalue problems are obtained in closed form. Comparison of the numerical results found by means of the shooting procedure and the approximate results shows that the relative error of the approximate results is small.

The dependence of the critical load on the dimensions of the beam cross-section is studied. In case of the internal pressure with the increase in these dimensions the critical load decreases, and then increases. Therefore, by the local buckling under an internal pressure the ring with the rectangular cross-section is more effective than the ring with the T-shaped cross-section. If the pressure is external then the increase in the dimensions of beam cross-section caused the

increase of critical load, and the ring with the T-shaped cross-section is more effective than the ring with rectangular cross-section.

The results obtained in the current paper may be used for optimal design of the cylindrical shell stiffened by rings.

7 ACKNOWLEDGEMENT

This research was partially supported by grant from the Russian Foundation for Basic Research 16-01-00580.

REFERENCES

[1] Dai H. L., Qi L. L., Zheng H. Y., Buckling Analysis for a Ring-Stiffened FGM Cylindrical Shell Under Hydrostatic Pressure and Thermal Loads. *Journal of Mechanics*, **30**, 403-410, 2014.

[2] Pulletikurti V. Manikanta, P. Ranga Raju, Y. Appa Rao, Computer Aided Design and Analysis of Ring Stiffened Cylindrical Shell for Underwater Applications. *Engineering Science and Technology Journal* **2**, 632-640, 2012.

[3] Teng, J.G., Rotter, J.M., *Buckling of Thin Metal Shells*. CRC Press, 2003.

[4] Filippov, S. B., Buckling of circular ring joint with cylindrical shell. *Shell Structures Theory and Applications, Proc. of the 9th SSTA Conference*, Poland, **2**, 109–112, 2009.

[5] Bauer S.M., Voronkova E.B., On the Unsymmetrical buckling of the nonuniform orthotropic circular plates. *Lecture Notes in Computer Science. Numerical analysis and its Applications*, 198-205, 2013.

[6] Koohkan H., Kimiaeifar A., Mansourabadi A., Vaghefi R., An analytical approach on the buckling analysis of circular, solid and annular functionally graded thin plates. *Journal of Mechanical Engineering*, **41**, 7-14, 2010.

[7] Coman C. D., Haughton D. M., Localized wrinkling instabilities in radially stretched annular thin films *Acta Mechanica*, **185**, 179-200, 2006.

[8] Filippov, S. B., Optimal design of stiffened cylindrical shells based on an asymptotic approach. *Technische Mechanik*, **24**, 221–230, 2004.

[9] Mansfield, E. H.: On the buckling of an annular plate. *Quart. J. Mech. and Applied Math.*, **13**, 16–23, 1960.

[10] Ng B., Reid W., An initial-value method for eigenvalue problems using compound matrices. *J. Comp. Phys*, **30**, 125–136, 1979.

ECCOMAS Congress 2016
VII European Congress on Computational Methods in Applied Sciences and Engineering
M. Papadrakakis, V. Papadopoulos, G. Stefanou, V. Plevris (eds.)
Crete Island, Greece, 5–10 June 2016

THE CURL AND FLUTING OF PAPER: THE EFFECT OF ELASTO-PLASTICITY

Anna-Leena Erkkilä[1], **Teemu Leppänen**[2] **and Tero Tuovinen**[1]

[1]University of Jyväskylä
PO Box 35, FI-40014 Jyväskylä, Finland
{anna-leena.erkkila, tero.tuovinen}@jyu.fi

[2] LUT Savo Sustainable Technologies, Lappeenranta University of Technology, Varkaus unit
Opiskelijankatu 3, FI-78210 Varkaus, Finland
teemu.leppanen@lut.fi

Keywords: Elasto-plasticity, Hygroexpansivity, Paper, Finite Element Method, Curl, Fluting.

Abstract. *An in-plane elasto-plastic material model and a hygroexpansivity model were applied for paper. The input parameters for both models are fiber orientation and dry solids content. A finite element model was constructed offering possibilities for studying different structural variations of an orthotropic sheet as well as buckling behavior and internal stress situations under through-thickness strain differences. Examples related to the curl and web-fluting phenomena of paper are presented. Both studied cases presented in this paper indicates the usefulness of the hygro-elasto-plastic model in predicting the challenging deformation phenomena of orthotropic paper sheets. The application possibilities of the hygro-elasto-plastic model are diverse, including the investigation into several phenomena and defects appearing in drying, converting and printing process conditions.*

1 INTRODUCTION

There are several undesired phenomena that can be considered to be connected to hygroscopic and stress-strain behavior of the paper web or sheet during production processes and in end-use. Examples of such phenomena are the development of shrinkage profiles, loose edges of web, baggy paper web causing possible wrinkling and misregistration in printing, out-of-plane deformations such as cockling, curl and fluting in heatset-web-offset (HSWO) printing process or distortion of shape of product such as sheet or box (see Fig. 1). Natural fibers and their treatments, bonds between fibers and their orientation in the fiber network, additives and manufacturing conditions all affect the sorption based dimensional instability and the mechanical properties of paper or board [1, 2, 3, 4, 5, 6, 7, 8, 9, 10].

Several models to predict in-plane mechanical and rheological properties, shrinkage and hygroexpansivity of paper and board have been introduced. Nonlinear elastic models, orthotropic elasto-plastic approaches and viscoelastic models have been used for studying bending, buckling, failure, tensile response, and creep and relaxation behavior of paper sheet, see, for example [11, 12, 13, 14, 15, 16] and [17, 18, 19, 20, 21, 22, 23, 24]. The formula for the hygroexpansion of paper has been derived from the hygroexpansion of a single fiber and the efficiency of the stress transfer between fibers in [25]. In the reference [26], the traditional theory for linear thermoelasticity was applied to estimate hygroexpansion strains. An orthotropic hypoelastic constitutive model has been proposed for studies of phenomena behind the shrinkage profile [27]. In that model, the total strain including the hygroscopic strain component and the elastic modulus dependent on the moisture ratio are described by an exponential relation. The relation between strain history and tensile stiffness was assumed to be linear, and the model and isotropic inputs were calibrated by laboratory scale experiments. In the reference [28], the measured moisture dependency of material constants was utilized in the nonlinear elastic model to investigate the effect of moisture on mechanical behavior. Some studies on the buckling of paper have been introduced in [12, 29, 30]. Low tension streaks, having longer dimension, appear as buckling to baggy embodiment and may cause runnability problems [31, 32]. Plastic strains caused by moisture streaks or some mechanical unevenness result in uneven tension profiles of the web. Buckling streakiness i.e. bagginess of paper web has been simulated using hygro-elasto-plastic model (LE-model) introduced in [33]. In the LE-model, the in-plane elasto-plastic constitutive material model and hygroexpansivity model as a function of dry solids content (DSC) and the anisotropy index of fiber orientation are applied for numerical solutions of the finite element method. The use of the anisotropy index parameter instead of the traditional fiber orientation anisotropy simplifies the handling of different directions in the case of anisotropic sheet and, for example, the determination of Hill's yield surface for the finite element approach is straightforward.

In this study, the LE-model is utilized to simulate results connected to two out-of-plane deformations: curl and fluting. Paper or board curl is the tendency of a flat paper or board sheet to distort and form curved surfaces of cylindrical shape (see Fig. 1). Although the basic cause of curl is simply a deformation variation of paper in its thickness direction, the processes causing the different deformations in different layers are complex and variable [34]. In the references [35] and [34], an analytical equation for sheet curl resulting from the hygroexpansion coefficients and elastic properties of the layers using elastic lamination theory has been derived. In the studies [36], [37] and [38], the hygroscopic out-of-plane deformations using the elastic constitutive model have been presented, while the elasto-plastic model has been applied in [39]. Twisted or diagonal curl modes are usually considered very harmful; an analytical equation is

Figure 1: Examples of out-of-plane deformations of paper: picture of fine paper curl (left) and fluting in a printed area of a HSWO printed product (right).

given by Uesaka, see, for example [40]. In this paper, the LE-model is utilized to study the effect of through-thickness variation of fiber orientation and dry solids content on curl amplitude and mode.

Fluting appears as permanent, regularly spaced waves arising during heatset-web-offset printing process in the running direction of the printing machine and the machine direction (MD) of paper, see Fig. 1. Generally, two stages can be distinguished in the fluting phenomenon: fluting formation and fluting retention. There is, however, no final conclusion of the mechanisms of these two stages. For fluting formation, at least three more or less different explanations have been offered. A phenomenon related to tension wrinkles [41, 42] and differential shrinkage of inked and non-inked areas due the moisture difference [43, 44] are two of the proposed reasons. The occurrence of moisture difference is also confirmed by measurements [45, 46]. Thirdly, small local in-plane moisture content variations have been linked to the formation of fluting [47]. It has been suggested that the ink layer has an effect on the permanency of fluting [41, 43]. However, in [47] it has been estimated that ink stiffening alone cannot explain the amplitudes observed in practice. Based on simulations and experimental study, he suggests that irreversible shrinkage and thermal plastic deformations of paper may be additional mechanisms for fluting to achieve a required retention. Earlier simulation studies concerning the fluting phenomenon are based on elastic material models, see for example [44, 38, 47]. However, when fluting retention and trough-thickness moisture gradients are concerned, an elasto-plastic modeling approach could be very convenient, as simulation results of the LE-model presented in this paper indicates.

2 MEASUREMENTS

2.1 Fiber orientation anisotropy

The fiber orientation parameters are measured using the layered fiber orientation method developed by Erkkilä [48, 49, 50]. Adhesive or lamination tape splitting was applied to paper sheet to separate approximately 10 individual layers from a paper sheet. Then the sample layers were placed against a black background, and an image of a suitable area was captured by scanner using reflective illumination. In analyzing the layer images, the aim is to detect the edges of fibers or fiber bundles and to determine their orientations. The detection of edges is based on the computation of image gradients in every image element. For a discrete digital image, the derivatives $\frac{\partial f}{\partial x}$ and $\frac{\partial f}{\partial y}$ can be approximated through a discrete differentiation operator. The operator uses two kernels $k_x(i,j)$ and $k_y(i,j)$ that are convolved with the original image $f(x,y)$ to calculate approximations of the horizontal and vertical derivatives by

$$\frac{\partial f(x,y)}{\partial x} \approx D_x(x,y) = (f * k_x)(x,y), \tag{1}$$

$$\frac{\partial f(x,y)}{\partial y} \approx D_y(x,y) = (f * k_y)(x,y), \tag{2}$$

where $*$ denotes the 2-dimensional convolution operation. The coefficients of the kernels used are based on the principle of binomial filter design [50]. The magnitude (length) $|\nabla f(x,y)|$ and direction $\theta_f(x,y)$ of gradient vectors at each local image point are calculated by applying Eqs. (3) and (4)

$$|\nabla f(x,y)| = \sqrt{D_x^2 + D_y^2}, \tag{3}$$

$$\theta_f(x,y) = \tan^{-1}\frac{D_y}{D_x}. \tag{4}$$

The magnitude of gradient vector is directly related to the probability that the part of the image examined represents the edge of the fiber. At the fiber edge, the direction of the gradient corresponds to the direction normal to that segment of fiber edge. The discrete orientation distribution is then formed as a weighted probability density function of the local orientations $P(\theta_P)$, where the weighting factor is the gradient magnitude $|\nabla f(x,y)|$. The direction histogram is

$$P(\theta_P) = \frac{\Sigma_{x,y}\left(|\nabla f(x,y)|\,\delta_{\theta_{f(x,y)},\theta_P}\right)}{\Sigma_{x,y}\,|\nabla f(x,y)|} \tag{5}$$

where $\delta_{\theta_{f(x,y)},\theta_P}$ is Kronecker's delta function and $\{\theta_P, \theta_f \in Z : 0 \leq \theta_P, \theta_f < 360\}$. The main direction of the orientation (orientation angle) θ is defined as the deviation of the longer symmetry axis from the machine direction. The anisotropy of the fiber orientation distribution ξ is defined as a ratio of the maximum distribution value $P(\theta)$ and the value in the perpendicular direction to the maximum value $P(\theta + 90)$. Examples of the layer image, the gradient magnitude, and the direction histogram are presented in Fig. 2.

2.2 Hygroexpansion coefficient measurements

A mixture of two pulps containing 71% thermomechanical pulp and 29% bleached softwood draft pulp was used in this study. The oriented laboratory sheets were formed using a dynamic sheet former with the target basis weight 65 g/m^2. The sheets were wet-pressed according to ISO5269-1:2005, and then were either air-dried freely or under restraint in standard atmosphere conditions (23 Celsius, 50% RH). The procedure for the hygroexpansivity measurements followed the general guidelines stated in ISO 8226-1:1994 for maximum relative humidity up to 68%. According to ISO 8226-1:1994, the hygroexpansive strain X is

$$X = \frac{l_{66} - l_{33}}{l_{50}} 100\% \tag{6}$$

where l is the length in the specific RH% indicated by the subscript. However, the hygroexpansion coefficient β (%/%), defined as

$$\beta = \frac{X}{\Delta M} \tag{7}$$

where ΔM (%) is the moisture content change, was used in this study. At least seven parallel samples were measured in each anisotropy level. The same image analysis based method

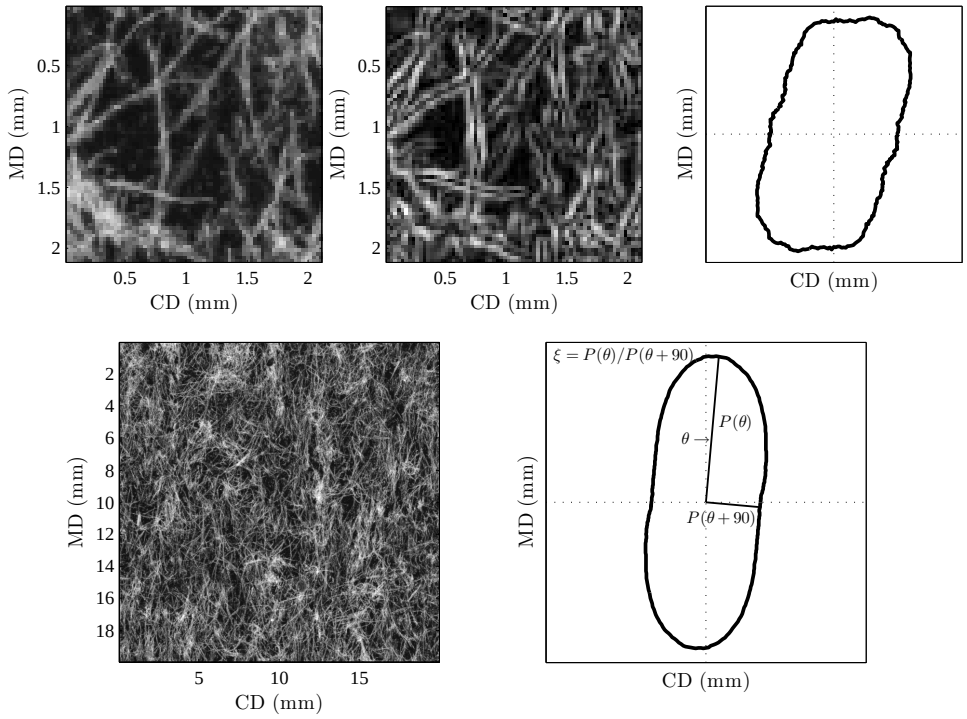

Figure 2: A 2.1 mm $\times$ 2.1 mm region of newsprint layer image (top left), corresponding magnitude of gradient (top middle) and orientation distribution i.e. direction histogram (top right). A 20 mm $\times$ 20 mm region of layer image (bottom left) and corresponding direction histogram, direction 1 (P(θ)), direction 2 (P(θ + 90)), orientation angle θ and anisotropy ξ (bottom right).

was also applied to determine the drying shrinkage of freely dried samples as a percent relative in-plane dimensional change (%) during drying. Sheet forming and measurements of hygroexpansivity as well as drying shrinkage are described in detail in [51].

2.3 Stress-strain tests

The fine paper samples with three different fiber orientation anisotropy levels were produced by pilot machine. The measured averaged anisotropy values of the studied samples was 1.20, 1.51 and 2.02. The dry solids contents varied from 53% to 56% at the initial stage. The basis weight of samples was from 77 g/m^2 to 80 g/m^2. The stress-strain curves were measured from paper strips (width 20 mm) with a span length of 180 mm. Strips were cut from the long side along four different in-plane directions γ: 0, 45, 70 and 90 degrees in relation to cross direction (CD) perpendicular to MD. The samples were dried in a tensile test machine to five target DSC levels: 55%, 65%, 75%, 85% and 95%. However, the measured DSC values during each measurement were read and used in studies instead of the target DSC values. Drying shrinkage was prevented in the loading direction. The tensile stress caused by restrained shrinkage was, however, released by unloading a tensile test specimen before the load-elongation measurement was started. Three repetitions of measurements on each anisotropy, cutting direction and dry solids content combinations were performed. A description of the measuring method is presented in reference [39]. In this study, the parallel results were used as individual test points so that the total amount of data in the fitting procedure was 180 individual stress-strain curves.

Table 1: The fitting parameters of Eq. (10) for the yield stress σ_y, the yield strain ε_y and the hardening constant H [33].

	A_1	A_2	A_3	n
σ_y	-5.9030 (Pa^n)	3.1959 (Pa^n)	18.3077 (Pa^n)	0.1760 (-)
ε_y	380.4181 (-)	14.3408 (-)	-269.8327 (-)	-0.7720 (-)
H	-0.6021 (Pa^{2n})	4.0423 (Pa^{2n})	11.3795 (Pa^{2n})	0.0715 (-)

3 MODELS FOR MATERIAL BEHAVIOR

Material behavior under external and internal tensions and dry solids content changes are described by elasto-plastic material model and the hygroexpansivity model. Elasto-plastic material model is based on the curve fittings presented in [52] where equation

$$\sigma = \begin{cases} E\varepsilon & \text{if} \quad \varepsilon \leq \varepsilon_y \\ E\varepsilon_y - \frac{H}{2E} + \sqrt{H\left(\frac{H}{4E^2} + \varepsilon - \varepsilon_y\right)} & \text{if} \quad \varepsilon > \varepsilon_y \end{cases} \tag{8}$$

was found suitable for describing all the uniaxial stress-strain relationships considered. In Eq. (8), σ and ε are the stress and strain, respectively; the dry solids content $R_{sc} = [0, 1]$ and the anisotropy index ϕ dependent fitting parameters are the elastic modulus E, the yield strain ε_y and the hardening constant H. The anisotropy index ϕ is defined as [52]

$$\phi = \sqrt{\frac{1 - \xi^2}{\xi + \tan^2 \gamma / \xi} + \xi} \tag{9}$$

where ξ is the fiber orientation anisotropy and γ is the angle from the minor axis of the fiber orientation distribution [52]. The material model was constructed by fitting the equation [33]

$$P = (A_1 + A_2\phi + A_3 R_{sc})^{1/n} \quad P = \{\sigma_y, \varepsilon_y, H\} \tag{10}$$

for the dry solids content and the anisotropy index dependence. In Eq. (10), the parameters A_1, A_2, A_3 and n are the fitting constants, see Table 1.

The hygroexpansivity model is based on the measurements and fitting procedures presented in [53] and [33]. The hygroexpansion coefficients β for every in-plane direction are defined by the equation

$$\beta = \frac{k\phi^v}{R_{sc}^2} \exp\left(\frac{k\phi^v}{-\frac{1}{a}k\phi^v + \frac{b}{a}\left(1 - \exp\left(-100\frac{k\phi^v}{a}\right)\right)}\left(\frac{1}{R_{sc}} - 1\right)\right) \tag{11}$$

where the fitting parameters have values $k = 0.0439$, $v = -0.9015$, $a = 2.5054$ and $b = 0.0250$ [33].

In the continuum mechanical model, plane stress is assumed and the yield surface is described by the Hill's yield function [54]. When the Hoffman's approximation is used as in [39] the yield surface has the form

$$f(\sigma) = \sqrt{\sigma_1^2 - \sigma_1\sigma_2 + \left(\frac{\sigma_{y,1}}{\sigma_{y,2}}\right)^2(\sigma_2^2 - \sigma_{12}^2) + \left(\frac{2\sigma_{y,1}}{\sigma_{y,45°}}\right)^2\sigma_{12}^2} \tag{12}$$

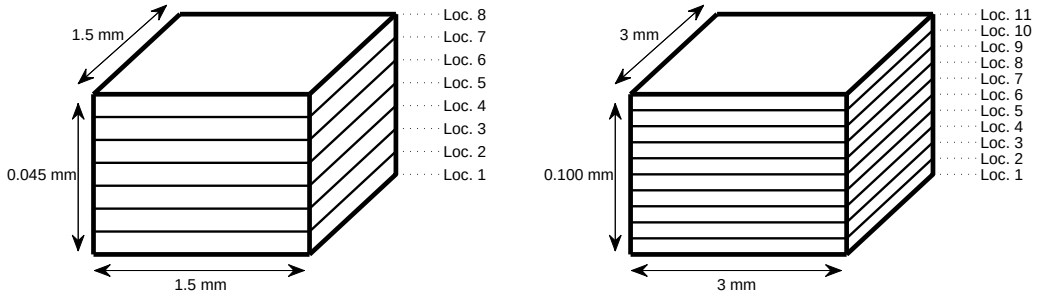

Figure 3: Elements used for the fluting (left) and the curl (right) simulations. Thickness directional DSC profile is defined by the locations shown.

where σ_1, σ_2 and σ_{12} are the stress tensor components and $\sigma_{y,1}$, $\sigma_{y,2}$ and $\sigma_{y,45^\circ}$ are the yield stresses in the main direction, cross direction and the direction deviating 45 degrees from the main direction, respectively. The elastic modulus is defined for directions 1, 2 and 45° by the yield stresses $\sigma_{y,i}$ and the yield strains $\varepsilon_{y,i}$ as

$$E_i = \frac{\sigma_{y,i}}{\varepsilon_{y,i}}. \tag{13}$$

The direction is specified by the subscript i. The in-plane yield stress and yield strain parameters are defined by Eq. (10) and the shear modulus is approximated by the equation [55]

$$G_{12} = \frac{1}{\left(\frac{4}{E_{45^\circ}} - \frac{1}{E_1} - \frac{1}{E_2} - \frac{2\nu_{12}}{E_1}\right)} \tag{14}$$

where ν_{12} is the Poisson ratio defined as

$$\nu_{12} = \left(0.015\left(1 - R_{sc}\right) + 0.15\right)\phi_1. \tag{15}$$

In Eq. (15), ϕ_1 is the anisotropy index of the main direction. The dependence of ν_{12} on the anisotropy index and dry solids content is roughly based on the results presented in [28] and by Maxwell relation the Poisson ratio ν_{21} is defined as $\nu_{21} = \nu_{12}E_2/E_1$.

4 NUMERICAL SOLUTION AND SAMPLE SETUP

Finite element method (FEM) was used to obtain the numerical solutions. Simulations were performed by the commercial software ABAQUS/Standard using shell element S4R with composite structure, see [56]. Two different phenomena were considered: fluting and curl of paper. The element size and thickness of the simulated sample are given in Fig. 3. In both cases, one element is used in the thickness direction of the sample. In the fluting simulations, the element was divided in the thickness direction into 7 layers with equal thicknesses, whereas in the curl simulations, the element was divided into 10 layers. The in-plane layouts used in the simulations are shown in Fig. 4. Automatic incrementation control and volume-proportional damping were utilized to obtain the numerical solutions [56]. For the fluting and curl simulations the damping factors 10^{-8} and 10^{-12} were used, respectively.

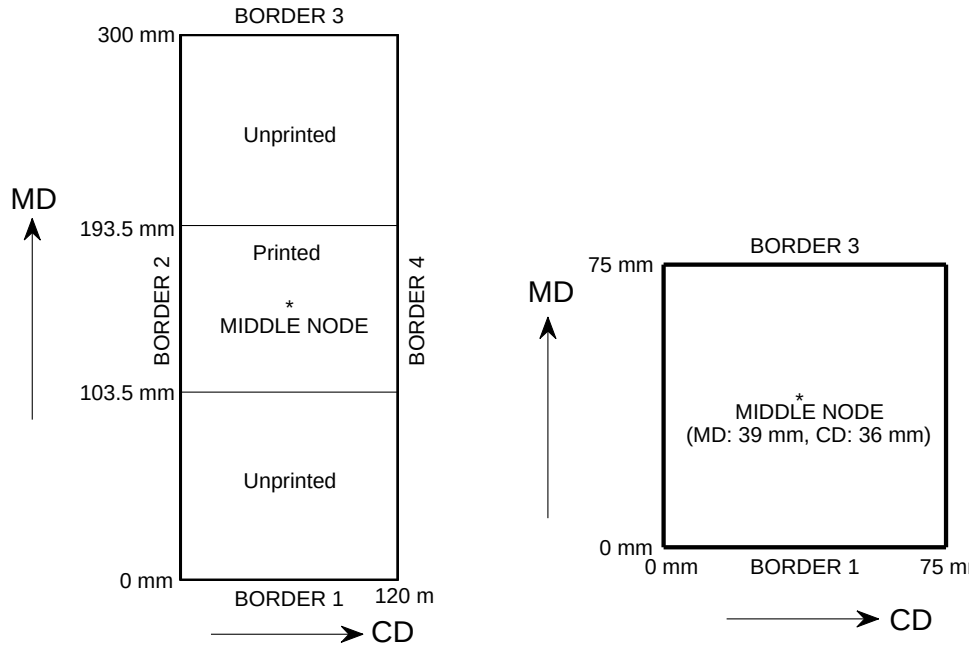

Figure 4: Layouts for fluting (left) and curl (right) simulations.

4.1 Curl simulations

The through-thickness variation of the fiber orientation of the samples is presented in Fig. 5. The initial DSC was 85% throughout the sample. In step 1, MD tension 200 N/m was applied via borders 1 and 3 and the following boundary conditions were applied:

- Boundary condition 1: Out-of-plane displacement (u_3) was restrained in all nodes.
- Boundary condition 2: In the middle node (not located into geometrical middle point, see Fig. 4) all displacements and rotations were restrained.

In step 2, the DSC profile were applied to the sample. Different DSC profiles used in step 2 are presented in Fig. 6. In step 3, the whole sample was dried into DSC 95%. In step 4, the external tension was removed and in step 5, the boundary condition 1 was removed.

4.2 Fluting simulations

In the fluting simulations, a homogeneous strongly MD-orientated sample ($\theta = 0$, $\xi = 4$) was used. The initial DSC was 96% throughout the sample. In the following, the displacements and the rotations are marked as u_1 (coincides with the MD when $\theta = 0$), u_2 (coincides with the CD when $\theta = 0$), u_3 and ur_1, ur_2, ur_3, respectively, see [56]. The boundary conditions were defined as (see Fig. 4):

- Out-of-plane displacement (u_3) was restrained in the borders 1, 2, 3 and 4.
- The rotation ur_1 was restrained in the borders 2 and 4.
- The rotation ur_2 was restrained in the borders 1 and 3.
- In the middle node the displacements u_1 and u_2 and rotation ur_3 were restrained.

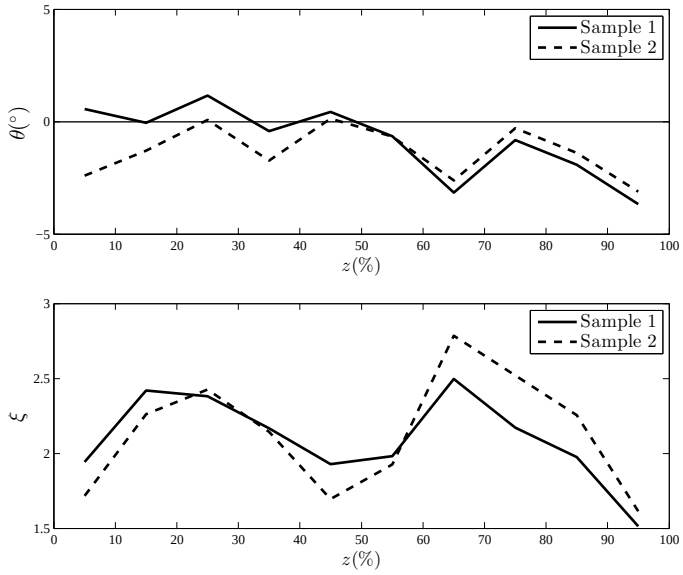

Figure 5: Through-thickness (z) variation of the orientation angle θ (top) and the anisotropy ξ (bottom) of the samples used in the curl simulations.

In step 1, the DSC profile (see Fig. 7) was applied to the printed area and the through-thickness symmetry was nullified by setting the out-of-plane directional force with value 10^{-3} N to the node located at position MD = 190.5 mm, CD = 42 mm. In step 2, this force was removed. In step 3, MD tension 400 N/m was applied via borders 1 and 3 and in step 4, the DSC profile applied to the printed area in step 1 was replaced by the initial dry solids content 96 %. The simulations were ended by step 5 where the external tension was removed from borders 1 and 3.

5 RESULTS AND DISCUSSION

Curl may have different modes: curl toward surface 1 or surface 2 and cylindrical shape main axis along MD (MD curl), along CD (CD curl) or to some other angle (diagonal curl).

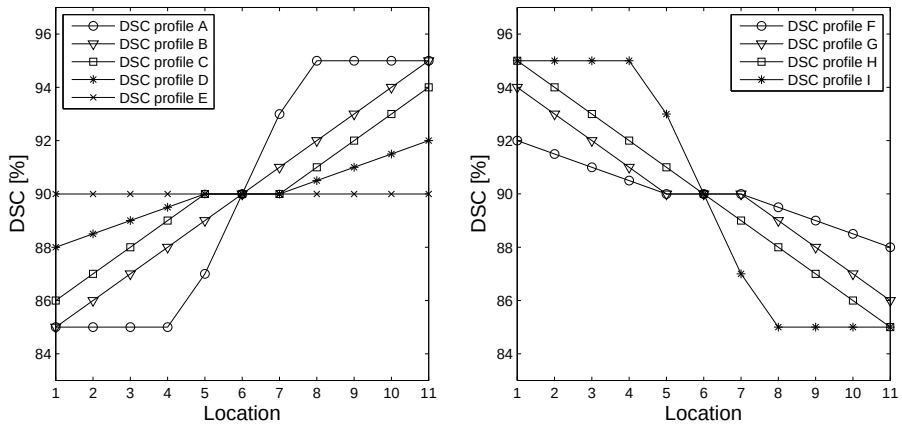

Figure 6: Curl simulations: DSC profiles.

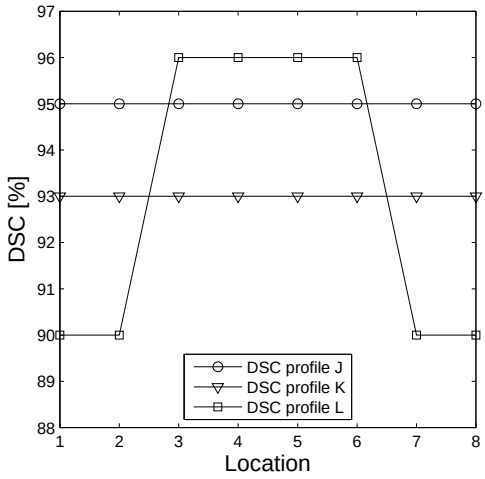

Figure 7: Fluting simulations: DSC profiles.

The simulated curl of samples 1 and 2 with all DSC profiles A-I is presented in Figs. 8 and 9. With flat drying profile E, the curl amplitude of both samples is minor, because of fairy symmetrical anisotropy profile between sides of the samples. When drying includes profiles D or F no significant change in curl can be detected. This indicates that no plastic strains either at surface 1 or 2 have been induced. However, higher gradient in DSC profiles (A-C and G-I) generates plastic strains that change the curl. Generally, paper curls toward the surface dried last [9], i.e. dryings using DSC profiles A, B and C turn curl more toward surface 1 and DSC profiles G, H, I toward surface 2. The equivalency of strain at both sides of samples can be adjusted by drying two-sidedness. However, near the equivalent strain condition, the sample is at risk to manifest diagonal or CD mode of curl. Diagonal and CD curl are harmful modes of curl in many applications and there have been attempts to control this by adjusting the two-sidedness of orientation angle. Obviously, zero orientation angles at both sides of samples would provide the best results, but even when there is only minor orientation angle two-sidedness, as in sample 2, there is no guarantee of maintaining MD curl mode at every drying profile. The clearest example of this phenomenon can be observed in tests carried out in single-sided and double-sided printing by either side toward heated roller of the copier or printer, see, for example [57].

Out-of-plane deformations of steps 3, 4 and 5 of fluting simulation with DSC profile L are presented in Fig. 10. Corresponding plastic deformations in MD and CD at step 5 are presented in Fig. 11. Due to the higher moisture content the printed area expands according to the hygroexpansion tendency. The tension and dryer unprinted areas constrain the printed area in CD and force it to buckle to a wavy form. The strong waviness at the printed area in step 3 can generate plastic strain especially to concave positions of waves. The leveling of the moisture difference in step 4 does not remove the plastic deformations formed already and permanent wavy deformations are produced to the sample. A higher moisture difference between printed and unprinted areas and unevenness of the moisture content profile increase severity of fluting waviness, see Fig. 12. The wavelength of simulated fluting is around 20 mm (see Fig. 12), which fit into the range of typically observed fluting wavelength approximately between 5 and 30 mm, see, for example [58]. However, the wavelength is dependent on boundary conditions, sample and element size, disturbances, etc.

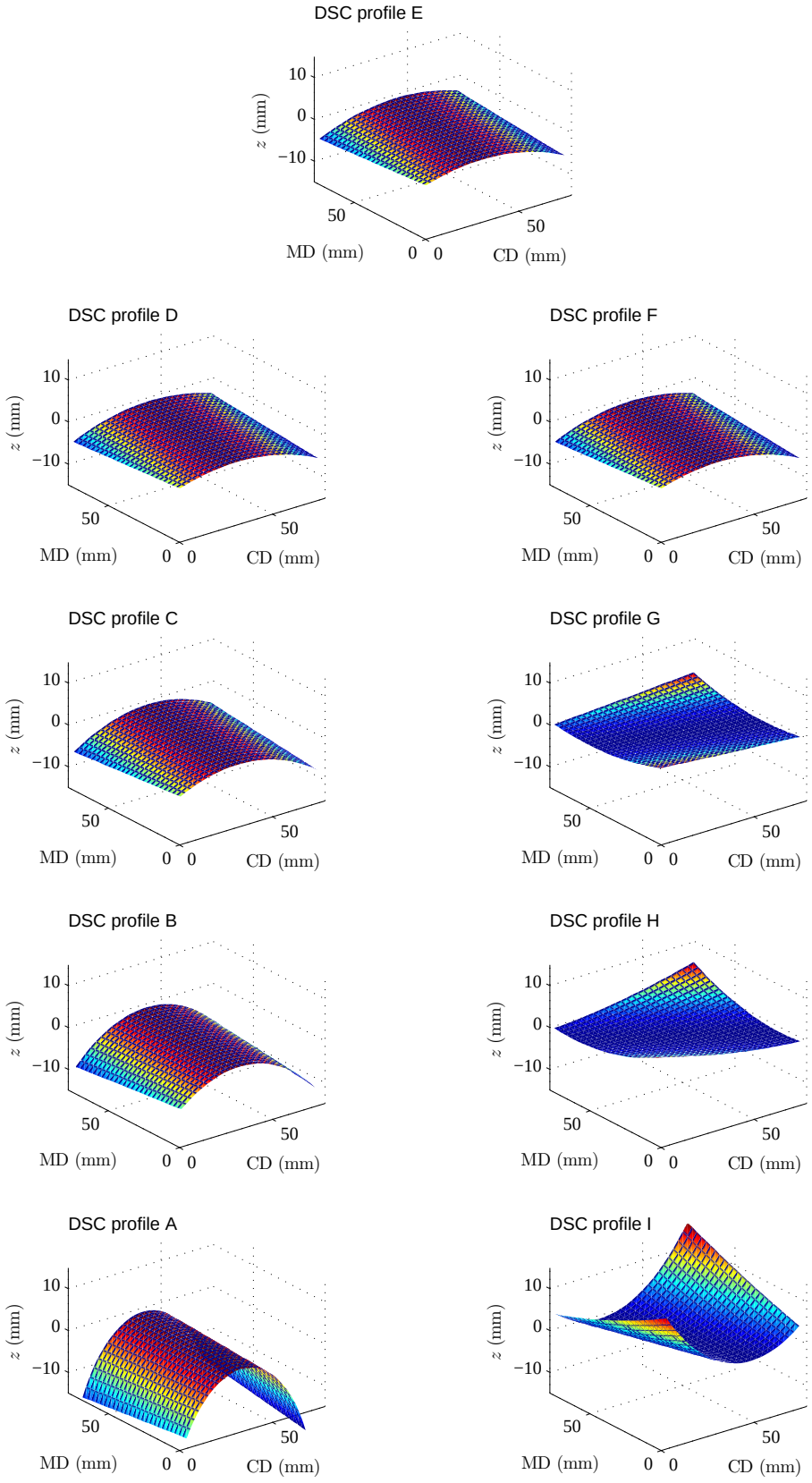

Figure 8: Simulated curl of sample 1.

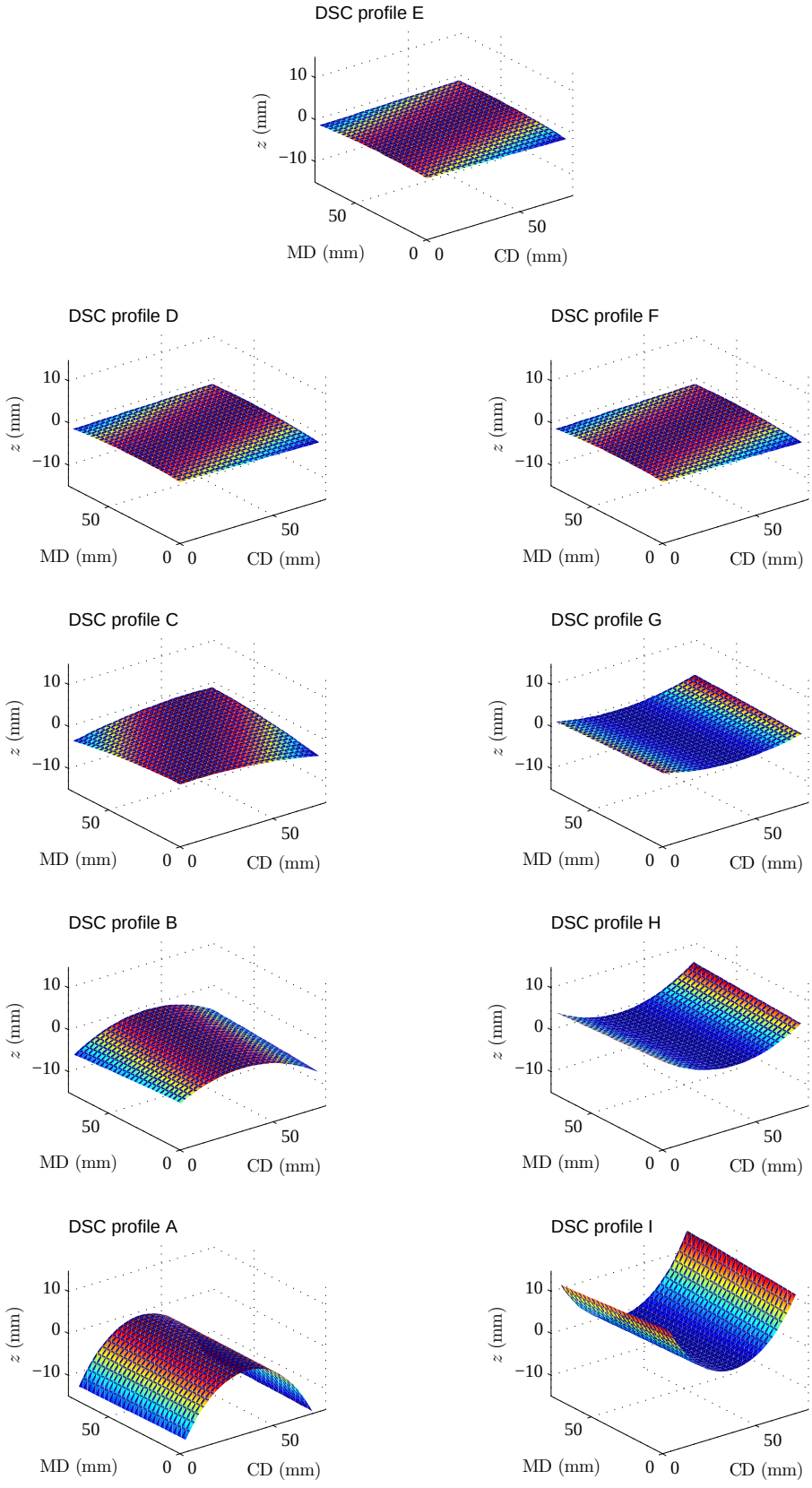

Figure 9: Simulated curl of sample 2.

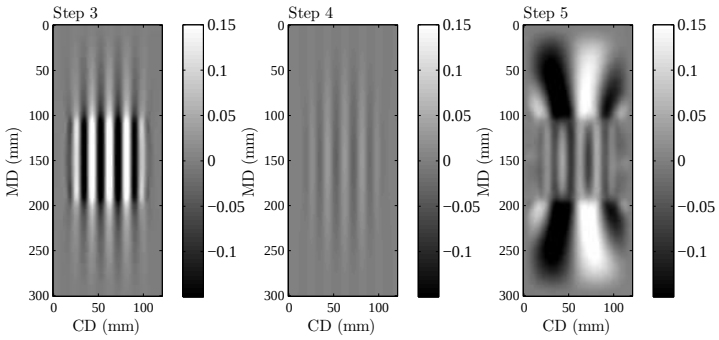

Figure 10: Simulated fluting with DSC profile L. In step 3 (left) both the external tension and the DSC profile are valid. In step 4 (middle) the DSC profile is removed and in step 5 (right) also the external tension is nullified.

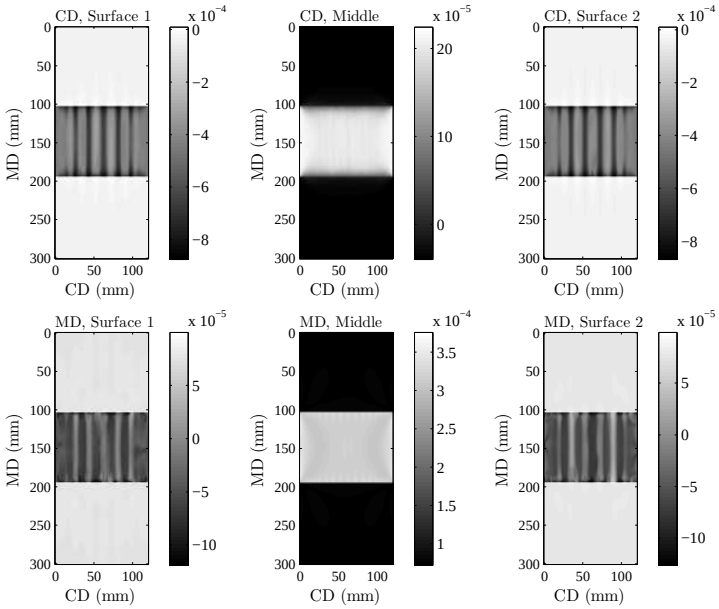

Figure 11: Plastic CD (top) and MD (bottom) strains for the layers: Surface 1 (left), Middle (middle) and Surface 2 (right). Simulations were performed with DSC profile L.

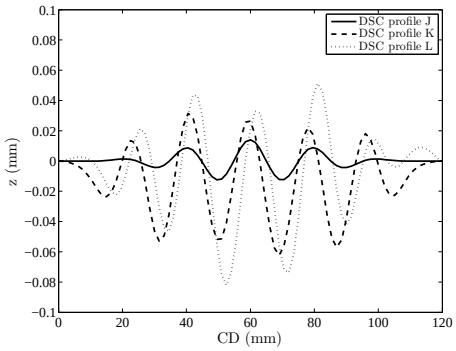

Figure 12: Cross-sections of the simulated fluting from the middle (MD = 150 mm) of the sample.

6 CONCLUSIONS

There are several undesired phenomena that can be considered to be connected to hygroscopic and stress-strain behavior of paper web or sheet during production processes and in end-use. Out-of-plane deformation defects such as curl and fluting in heatset-web-offset printing have been studied widely by different experimental and modeling approaches, but there are still features left unknown.

The objective of this work was to apply a hygro-elasto-plastic model to the out-of-plane deformation phenomenon corresponding to copy curl and HSWO fluting conditions. In both cases, the simulations predict the behavior of hygroscopic orthotropic sheet under moisture change during different external in-plane stretch or stress conditions. The model includes two experimental models: elasto-plastic material model and hygroexpansivity model. In both models, the structural properties of the sheet are described by fiber orientation probability distribution, and both models are functions of the dry solids content and fiber orientation anisotropy index. The anisotropy index simplifies the procedure of determining the constitutive parameters of the material model and hygroexpansion coefficients in different directions of an anisotropic sheet. For studies of the combined and more complicated effects of hygro-elasto-plastic behavior, these two models were implemented in a finite element program for numerical solution.

The behavior of two orientated structures was simulated using different z-directional DSC profiles. The plastic strains were generated at least 8% and higher differences between surfaces in DSC profiles. It has been noticed that DSC differences between surfaces of paper can reach over 10% in a paper machine drying [59, 60]. The equivalency of strain at both sides of samples can be adjusted by drying two-sidedness. This is a practically utilized method to control curl amplitude, but has not been predicted by simulation before. Near the equivalent strain condition, however, the sample is at risk to manifest diagonal or CD mode of curl. Results also predict phenomena that are commonly observed in copier printing tests.

Although the generation of HSWO fluting have been successfully predicted by modeling, the mechanisms behind permanency of HSWO fluting has been a demanding task to solve. The presented elasto-plastic model indicated that permanent waviness/fluting can be generated with elasto-plastic model simulations. Both studied cases presented in this paper, together with earlier studies at [33], proved the usefulness of the model in predicting the challenging deformation phenomena of orthotropic paper sheets.

7 ACKNOWLEDGEMENTS

Simulations were performed by a commercial software ABAQUS which was licensed to CSC (the Finnish IT center for science).

REFERENCES

[1] M. Alava, K. Niskanen, The physics of paper. *Reports on Progress in Physics*, **69**, 669–723, 2006.

[2] L.S. Nordman, Laboratory investigations into the dimensional stability of paper. *Tappi*, **41**, 23–50, 1958.

[3] D.J. Fahey, W.A. Chilson, Mechanical treatments for improving dimensional stability of paper. *Tappi*, **46**, 393–399, 1963.

[4] L. Salmen, C. Fellers, M. Htun, The development and release of dried-in stresses in paper. *Nordic Pulp and Paper Research Journal*, **2**, 44–48, 1987.

[5] T. Uesaka, D. Qi, Hygroexpansivity of paper: effects of fibre-to-fibre bonding. *Journal of Pulp and Paper Science*, **20**, 175–179, 1994.

[6] Å. Lyne, C. Fellers, P. Kolseth, The effect of filler on hygroexpansivity. *Nordic Pulp and Paper Research Journal*, **11**, 152–163, 1996.

[7] A. de Ruvo, S. Lundberg, S. Martin-Löf, C. Södermark, Influence of temperature and humidity on the elastic and expansional properties of paper and the constituent fibre. *The Fundamental Properties of Paper Related to Its Uses, Transactions of the Symposium*, London, England, 1976.

[8] V. Setterholm, E.W. Kuenzi, Fiber orientation and degree of restraint during drying – effect of tensile anisotropy of paper handsheet. *Tappi*, **53**, 1915–1920, 1970.

[9] P. Glynn, H.W.H. Jones, W. Gallay, Drying stresses and curl in paper. *Pulp and Paper Magazine of Canada*, **62**, 39–48, 1961.

[10] T. Leppänen, A.-L. Erkkilä, J. Hämäläinen, Effect of fiber orientation structure on simulated cockling of paper. *Pulp and Paper Canada*, **109**, 31–38, 2008.

[11] M.W. Johnson, T.J. Urbanik, A nonlinear theory for elastic plates with application to characterizing paper properties. *Journal of Applied Mechanics*, **51**, 146–152, 1984.

[12] M.W. Johnson, T.J. Urbanik, Buckling of axially loaded, long rectangular paperboard plates. *Wood and Fiber Science*, **19**, 135–146, 1987.

[13] J.C. Suhling, R.E. Rowlands, M.W. Johnson, D.E. Gunderson, Tensorial strength analysis of paperboard. *Experimental Mechanics*, **25**, 75–84, 1985.

[14] C. Fellers, B. Westerlind, A. de Ruvo, An investigation of the biaxial failure envelope of paper – experimental study and theoretical analysis. *Proceedings of Fundamental Research Symposium*, Cambridge, England, 1983.

[15] J. Castro, M. Ostoja-Starzewski, Elasto-plasticity of paper. *International Journal of Plasticity*, **19**, 2083–2098, 2003.

[16] P. Mäkelä, S. Östlund, Orthotropic elastic-plastic material model for paper materials. *International Journal of Solids and Structures*, **40**, 5599–5620, 2003.

[17] Q.S. Xia, M.C. Boyce, D.M. Parks, A constitutive model for the anisotropic elastic-plastic deformation of paper and paperboard. *International Journal of Solids and Structures*, **39**, 4053–4071, 2002.

[18] J.P. Brezinski, The creep properties of paper. *Tappi*, **39**, 116–128, 1956.

[19] J. Lif, S. Östlund, C. Fellers, Applicability of anisotropic viscoelasticity of paper at small deformations. *Mechanics of Time-Dependent Materials*, **2**, 245–267, 1999.

[20] W. Lu, L.A. Carlsson, Influence of viscoelastic behavior on curl of paper. *Mechanics of Time-Dependent Materials*, **5**, 79–100, 2001.

[21] M.G. Pecht, M.W. Johnson, R.E. Rowlands, Constitutive equations for the creep of paper. *Tappi Journal*, **67**, 106–108, 1984.

[22] M.G. Pecht, M.W. Johnson, The strain response of paper under various constant regain states. *Tappi Journal*, **68**, 90–93, 1985.

[23] J.L. Rand, A nonlinear viscoelastic creep model. *Tappi Journal*, **78**, 178–182, 1995.

[24] T. Uesaka, K. Murakami, R. Imamura, Two-dimensional linear viscoelasticity of paper. *Wood Science and Technology*, **14**, 131–142, 1980.

[25] T. Uesaka, General formula for hygroexpansion of paper. *Journal of Material Science*, **29**, 2373–2377, 1994.

[26] S. Lavrykov, B.V. Ramarao, Å.L. Lyne, The planar transient hygroexpansion of copy paper: experiments and analysis. *Nordic Pulp and Paper Research Journal*, **19**, 183–190, 2004.

[27] T. Wahlström, K. Adolfsson, S. Östlund, C. Fellers, Numerical modelling of the cross direction shrinkage profile in a drying section: a first approach. *Proceedings of the 1999 TAPPI International Paper Physics Conference*, San Diego, USA, 1999.

[28] K.C. Yeh, J.M. Considine, J.C. Suhling, The influence of moisture content on the nonlinear constitutive behavior of cellulosic materials. *Tappi Proceedings: 1991 International Paper Physics Conference*, Havaii, USA, 1991.

[29] N. Banichuk, J. Jeronen, M. Kurki, P. Neittaanmäki, T. Saksa, T. Tuovinen, On the limit velocity and buckling phenomena of axially moving orthotropic membranes and plates. *International Journal of Solids and Structures*, **48**, 2015–2025, 2011.

[30] A. Kulachenko, P. Gradin, H. Koivurova, Modelling the dynamical behaviour of a paper web. Part I. *Computers & structures*, **85**, 131–147, 2007.

[31] C. Land, T. Wahlström, L. Stolpe, Moisture streaks and their relation to baggy paper webs. *Journal of Pulp and Paper Science*, **34**, 234–239, 2008.

[32] D. Roisum, The mechanics of wrinkling. *Tappi Journal*, **79**, 217–226, 1996.

[33] A.-L. Erkkilä, T. Leppänen, J. Hämäläinen, T. Tuovinen, Hygro-elasto-plastic model for planar orthotropic material. *International Journal of Solids and Structures*, **62**, 66–80, 2015.

[34] J. Pijselman, J. Poustis, Curl of multiply papers – an analytical study. *Svensk Papperstidning*, **85**, 177–184, 1982.

[35] L. Carlsson, C. Fellers, M. Htun, Curl and two-sidedness of paper. *Svensk Papperstidning*, **83**, 194–197, 1980.

[36] F. Bloom, D.W. Coffin, Modelling the hygroscopic buckling of layered paper sheets. *Mathematical and Computer Modelling*, **31**, 43–60, 2000.

[37] T. Leppänen, J. Sorvari, A.-L. Erkkilä, J. Hämäläinen, Mathematical modelling of moisture induced out-of-plane deformation of a paper sheet. *Modelling and Simulation in Materials Science and Engineering*, **13**, 841–850, 2005.

[38] A. Kulachenko, P. Gradin, T. Uesaka, Tension wrinkling and fluting in heatset web offset printing process – post-buckling analysis. *Proceedings of 13th Pulp and Paper Fundamental Research Symposium*, Cambridge, England, 2005.

[39] P. Lipponen, T. Leppänen, J. Kouko, J. Hämäläinen, Elasto-plastic approach for paper cockling phenomenon: on the importance of moisture gradient. *International Journal of Solids and Structures*, **45**, 3596–3609, 2008.

[40] T. Uesaka, Dimensional stability and environmental effects on paper properties. *Handbook of physical testing of paper, Vol I*. New York: Marcel Dekker, 2002.

[41] C.C. Habeger, Tension wrinkling and the fluting of light-weight coated papers in web-offset printing. *Journal of Pulp and Paper Science*, **19**, 214–218, 1993.

[42] J.Y. Hung, Paper fluting – results of TEC studies. *TEC Systems, DePere*. Wisconsin, USA, 1984.

[43] T. Hirabayashi, S. Fujiwara, T. Fukui, Factors of the fluting of coated paper in web-offset printing. *Proceedings of Pan-Pacific and International Printing and Graphic Arts Conference*, Montreal, Canada, 1998.

[44] D. Coffin, A buckling analysis corresponding to the fluting of lightweight coated webs. *Proceedings of International Paper Physics Conference*, Victoria, B.C., Canada, 2003.

[45] J. MacPhee, V. Bellini, B.E. Blom, A.D. Cieri, V. Pinzone, R.S. Potter, The effect of certain variables on fluting in heatset web offset printing. *Web Offset Assosiation, Affiliate of Printing Industries of America Inc.*, USA, 2000.

[46] S. Simmons, B. Blom, C. Dreher, D. Dewildt, D. Coffin, Parametric evaluation of web offset fluting. *Proceedings of TAGA's 53rd Annual Technical Conference*, San Diego, CA, USA, 2001.

[47] A. Kulachenko, P. Gradin, T. Uesaka, Basic mechanisms of fluting formation and retention in paper. *Mechanics of materials*, **39**, 643–663, 2007.

[48] A.-L. Erkkilä, Mechanism and measurements of the layered orientation structure of paper sheets. *Licentiate Thesis*, University of Jyväskylä, Jyväskylä, Finland, 1995.

[49] A.-L. Erkkilä, P. Pakarinen and M. Odell, Sheet forming studies using layered orientation analysis. *Pulp & Paper Canada*, **99**, 81–85, 1998.

[50] P. Lipponen, A.-L. Erkkilä, T. Leppänen and J. Hämäläinen, On the importance of in-plane shrinkage and through-thickness moisture gradient during drying on cockling and curling phenomena. *Transactions of the 14th Fundamental Research Symposium*, Oxford, England, 2009.

[51] C. Hii, Hygroexpansivity of paper. *M.Sc. Thesis*, Helsinki University of Technology, Espoo, Finland, 2008.

[52] A.-L. Erkkilä, T. Leppänen, J. Hämäläinen, Empirical plasticity models applied for paper sheets having different anisotropy and dry solids content levels. *International Journal of Solids and Structures*, **50**, 2151–2179, 2013.

[53] A.-L. Erkkilä, T. Leppänen, M. Ora, T. Tuovinen, A. Puurtinen, Hygroexpansivity of anisotropic sheets. *Nordic Pulp and Paper Research Journal*, **30**, 325–334, 2015.

[54] R. Hill, A theory of the yielding and plastic flow of anisotropic metals. *Proceedings of the Royal Society of London. Series A, Mathematical and Physical Sciences 191*, London, England, 1948.

[55] R.F. Gibson, *Principles of composite material mechanics*, McGraw-Hill Inc., 1994.

[56] ABAQUS, *Abaqus documentation*, Dassault Systèmes, Providence, RI, USA, 2013.

[57] M.A. Evans, B.A. LeMaire, *An investigation into papers for digital printing*, Printing Industry Center, Rochester, NY, USA, 2006.

[58] J.-E. Nordström, S. Lindberg, A. Lundström, Human perception and optical measurement of HSWO waviness. *International Printing & Graphics Arts Conference*, Bordeaux, France, 2002.

[59] J. Keränen, O. Timofeev, R. Talja, Simulated combined air-cylinder drying process. *Proceedings of 3rd Nordic Drying Conference*, Karlstad, Sweden, 2005.

[60] S.G. Harding, D. Wessman, S. Stenström, L. Kenne, Water transport during the drying of cardboard studied by NMR imaging and diffusion techniques. *Chemical Engineering Science*, **56**, 5269–5281, 2001.

ECCOMAS Congress 2016
VII European Congress on Computational Methods in Applied Sciences and Engineering
M. Papadrakakis, V. Papadopoulos, G. Stefanou, V. Plevris (eds.)
Crete Island, Greece, 5–10 June 2016

STABILITY OF STEEL STRUCTURES WITH CLEARANCES AND IMPERFECTIONS

Katarzyna Rzeszut[1], **Andrzej Garstecki**[2]

[1] Faculty of Civil and Environmental Engineering, Poznan University of Technology
Piotrowo 5, 60-965 Poznan, Poland
e-mail: katarzyna.rzeszut@put.poznan.pl

[2] Polytechnic Institute, Stanislaw Staszic, University of Applied Sciences in Pila
Podchorazych 10, 64-920 Pila, Poland
e-mail: Andrzej.garstecki@put.poznan.pl

Keywords: Stability analysis, Steel structures, Imperfections, Clearances.

Abstract. *This paper deals with statics and stability problems of steel structures with the emphasis on their sensitivity to initial imperfections and clearances. The main aim is to performed an indication as the state of stress, displacement and the critical load. The paper presents theoretical studies involving linear and nonlinear behavior of thin-walled steel structures with a special reference to the interactive buckling, initial geometric imperfections and clearances which is in the scope of the modern approach to design. For this purpose authors proposed model structures composed of rigid bars where strains are concentrated in connecting elastic joints These model structures enable to derive nonlinear algebraic equilibrium equations which strictly describe pre- and post-buckling behavior of structures with various combinations of imperfections and clearances. Numerous examples demonstrate variable types of structural response depending on the modes and amplitudes of imperfections in relation with clearances. In the case of large clearances the model structure behaves like a typical Euler column characterized by a stable and symmetric bifurcation point. However, clearances combined with certain patterns of imperfections can result in unstable post buckling behavior and also in snap through phenomena. The developed model structures, which illustrate complex structural stability response accounting for initial geometric imperfections and clearances, due to its simplicity makes possibility to describe the exact close form solutions for both linear and nonlinear stability analysis. Based on the proposed model structure it is shown, that interaction between initial clearances and initial geometric imperfections can strongly affect the structural stability response.*

1 INTRODUCTION

In the last decades permanent development of light-weight structures is observed. They are esthetic and economic. Important is also that small weight of structural materials well matches the requirements of sustainable development. From among structural materials steel is particularly attractive in application to light weight-structures. A great variety of hot- and cold-formed steel sections is at designers' disposal. Modern highly automated cutting, drilling welding and corrosion protection make possible to design and prefabricate optimal structural elements, which can be easily assembled using pre-stressed bolts. It must be underlined here that two special aspects in design of light-weight steel structures must be seriously taken into account, namely fire protection and protection against local and global instability.

The fact that steel structures are apt to fail by loss of stability belongs to the textbook's knowledge for decades. This tendency towards instability is a direct consequence of high slenderness of steel structural elements. Designers can find practical recommendations in design codes [3, 4, 5] with theoretical and experimental background in the literature [6, 12] how to overcome the problems of instability. Professional computer programs supporting design of steel structures implement many of these recommendations. However, modern light-weight steel structures gave rise to new stability problems. Application of thin-walled cold formed sections and welded I sections with slender webs increased the importance of local instability phenomena which often appeared at a similar load level as global instability. The case when two or more different modes in stability and dynamic analyses are associated with the same or similar eigenvalues is termed a bimodal or multimodal solution. Designers' concern is that these solutions are very sensitive to imperfections. Design codes and scientific papers [1, 2, 7,13] contain recommendations with respect to forms and magnitude of global geometric imperfections which can be taken into account. There is definitely not so much information and recommendations with respect to local imperfections .

New stability problems were also originated when roof cladding elements were assumed to provide support for compressed top flanges of purlins or beams of frames [8, 9, 10, 11]. Roof cladding are often made of profiled steel plates. They are point-wise connected to the beams by self-tapping screws or by rivets. Thickness of steel plates is small, therefore variable loads and hence variable interaction forces often result in increasing diameter of the holes in thin walls of the plate. In this case we have slotted connections with unilateral constraints. Similar type of unilateral constraints can also appear in a bolted connection with a clearance between structural elements. These imperfect connections can strongly influence the structural response. Moreover, there can be unfavorable combinations of clearances and initial geometric imperfections.

Economic and safe design must be based on a reliable structural analysis where all essential imperfections are taken into consideration. On the other hand a numerical model of the actual structure cannot be too complicated. Otherwise computer time would be too great. Keeping this in mind, the author presents in this book stability behavior of structures with various combinations of global and local initial geometric imperfections, combinations of clearances and simultaneous appearance of geometric imperfections and clearances. Of course, in order to demonstrate these phenomena nonlinear stability problems must be formulated and solved. The author proposed model structures composed of rigid bars where strains are concentrated in connecting elastic joints. These model structures make possible to derive nonlinear algebraic equations which strictly describe pre- and post-buckling behavior of structures with various combinations of imperfections and clearances. By the way of numerous examples influence of imperfections and clearances on the structural behavior is discussed.

`

2 THEORETICAL BACKGROUND

In order to illustrate the phenomenon of the interaction of initial geometric imperfections and clearances a model structure is developed. It consists of *n* incompressible rods connected by elastic hinges with the rotational stiffness k_n [N·m/rad]. At the position of internal hinges the elastic intermediate supports with the stiffness $k_{n\Delta}$ [N/m] and clearances Δ_0 are imposed. Now Δ_0 *i* Δ denote, respectively, the clearance and the total transverse displacement of the structures at the position of internal hinges. This model enables the derivation of the exact nonlinear equilibrium equations, taking into account large displacements. At the same time, this simple model well illustrates the real structural response in terms of its stability problems. The geometry of the proposed model structure shows Figure 1.

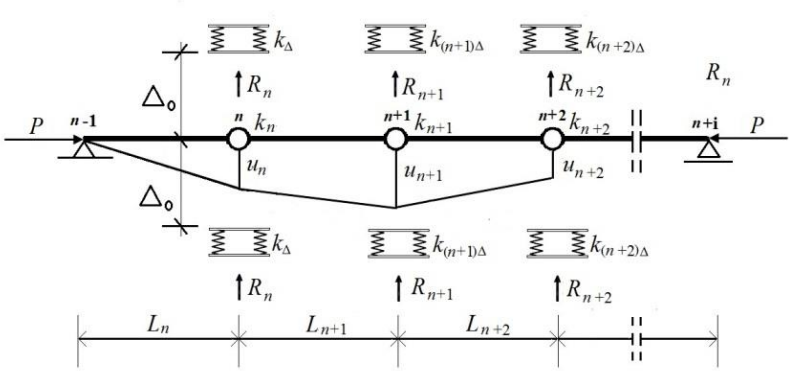

Figure 1: Geometry of the proposed model structure

2.1 Eigenvalue problem

At the first stage, the initial clearance is very large and the gap remains open: $|u_n| < \Delta_0$. Then the supports positioned at the elastic hinges do not switch on to cooperate with the bar, which is supported only at its ends. At this stage, the equation describing displacement u_n and rotation angles of nodes ϕ_n may be derived from geometries that are illustrated graphically in Figure 2.

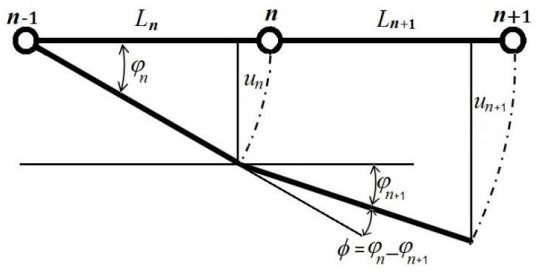

Figure 2: Geometric relation of the model structure

Hence we obtain the following geometrical relationships:

$$\varphi_n = \arcsin\frac{u_n - u_{n-1}}{L_n} \quad and \quad \phi_n = \arcsin\frac{u_n - u_{n-1}}{L_n} - \arcsin\frac{u_{n+1} - u_n}{L_{n+1}}, \tag{1}$$

where: φ_n – rotation of angle *n*-th bar. The set of equilibrium equations takes the form:

$$k_n \cdot \phi_n^{\,e} = P \cdot u_n . \tag{2}$$

Equation (2) can be written in matrix form:

$$\left(\boldsymbol{K} - PL\boldsymbol{I}\right)\bar{u} = 0, \tag{3}$$

where $\boldsymbol{I}$ is a unit matrix. The solution of (3) are the eigenvalues λ_n^{cr} and associated with it the normalized eigenvectors $\boldsymbol{u}_n^{\mathrm{cr}}$.

2.2 Initial imperfections

The initial geometric imperfections u_n^i are introduced in to the model as a linear combination of eigenvectors u_n^{cr} derived from the solution of the linear eigenvalue problem:

$$u_n^i = \alpha_m \cdot u_m^{\mathrm{cr}} . \tag{4}$$

By changing the value of the proportionality factor α_m, associated with various forms of buckling modes, enables to obtain all possible combinations of imperfection. It is worth to note that imperfections developed as the linear combinations of the eigenvectors are considered as the most dangerous.

The displacement caused by geometrical imperfections u_n^i induce initial rotations of the bars φ_n^i and rotations of the hinges ϕ_n^i. These deformations are kinematically admissible and does not induce any stress.

As a result of the action of the external load elastic part of displacements and rotations, represent by the superscript *e*, appeared. They are inducing elastic internal moments at the elastic hinges $M_n = k_n \phi_n^e$. In the initial phase, when the external load $P = 0$, the geometric relationships shown in Figure 3 take the form:

$$\varphi_n^i = \arcsin\frac{u_n^{\,i} - u_{n-1}^{\,i}}{L_n} \quad and \quad \phi_n^i = \arcsin\frac{u_n^{\,i} - u_{n-1}^{\,i}}{L_n} - \arcsin\frac{u_{n+1}^{\,i} - u_n^{\,i}}{L_{n+1}} . \tag{5}$$

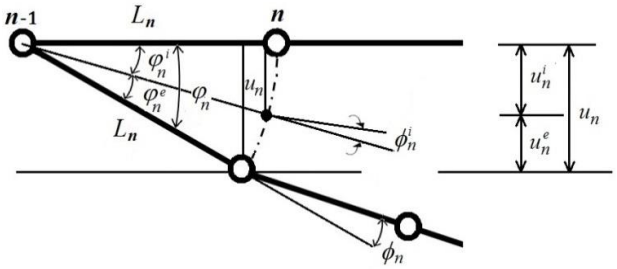

Figure 3: Geometric imperfections in model structure

In the next phase, when the load $P > 0$, it is obtained:

$$u_n = u_n^{\,i} + u_n^e \quad \text{and} \quad M_n = k_n \cdot \phi_n^{\,e} = P \cdot \left(u_n^{\,i} + u_n^e\right) \tag{6}$$

$$\varphi_n = \varphi_n^{\,i} + \varphi_n^{\,e} \quad \text{and} \quad \phi_n = \phi_n^i + \phi_n^e . \tag{7}$$

`

Now the set of nonlinear equilibrium equations takes the form:

$$k_n \cdot \varphi_n^{\,e} = P \cdot \left(u_n^{\,i} + u_n^e \right) \tag{8}$$

of unknowns elastic part of displacements u_n^e. Elastic part of hinge rotation ϕ_n^e is determine using the following relationship:

$$\phi_n^e = \phi_n - \phi_n^i. \tag{9}$$

2.3 Nonlinear equilibrium equations

In the second stage, depending on the value of the initial clearance Δ_0 and total lateral displacement of structures u_n, at the points of elastic hinges presence the cooperation with the intermediate supports is observed. When the gap is closing ($|u_n| \geq \Delta_0$), then the appropriate intermediate support with the stiffness $k_{n\Delta}$ is switched on to the cooperation. Hence, the equilibrium equation should be written in the general form. Until now, the bending moment in the elastic joint has been described as $M = k_n \cdot \phi_n^{\,e} = P \cdot u_n$. Now, in equilibrium equations must be taken into account the reactions of intermediate supports $R_n = k_{n\Delta}\left(u_n - \Delta_0\right)$. Equilibrium equations will be written in the form of an equation of virtual work. For this purpose, the virtual displacement δu_n is introduced to the model, so that the hinge No. *n* moves vertically and horizontally, while the hinge No. *n+2* moves only in the horizontal direction (Fig. 4).

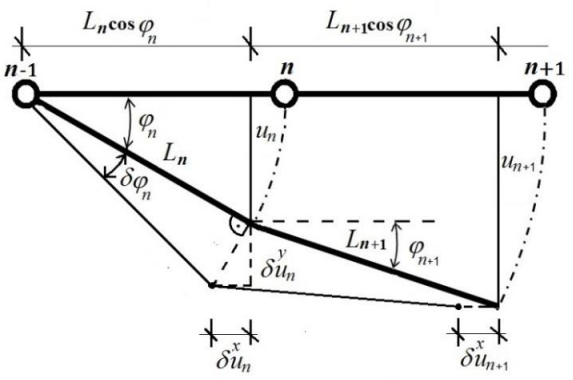

Figure 4: Geometric relation of the model structure - virtual displacement δu_n

Thus, the virtual displacement of the hinge No. *n+1* in the vertical direction $\delta^y u_{n+1} = 0$. The vertical $\delta^y u_n$ and horizontal $\delta^x u_n$ components of virtual displacement of the hinge No. *n* can be determined using the following relationship:

$$\delta^y u_n = L_n \cos\varphi_n \delta\varphi_n, \tag{10}$$

$$\delta^x u_n = L_n \sin\varphi_n \delta\varphi_n = u_n \delta\varphi_n. \tag{11}$$

The horizontal component of virtual displacement $\delta^x u_{n+1}$ of hinge No. *n+1* is calculated from the kinematic chain relation in the following form:

$$\delta^x u_{n+1} = \delta^x u_n + L_{n+1} \sin\varphi_{n+1} \delta\varphi_{n+1}. \tag{12}$$

The unknown value of the virtual rotation $\delta\varphi_{n+1}$ can be determined from the kinematic chain of vertical displacement:

$$\delta^y u_{n+1} = L_n \cos\varphi_n \delta\varphi_n + L_{n+1} \cos\varphi_{n+1} \delta\varphi_{n+1}. \tag{13}$$

Hence:

$$\delta\varphi_{n+1} = -\frac{L_n \cos\varphi_n}{L_{n+1} \cos\varphi_{n+1}} \delta\varphi_n. \tag{14}$$

For $L_n = L_{n+1}$ equation (14) takes the form:

$$\delta\varphi_{n+1} = -\frac{\cos\varphi_n}{\cos\varphi_{n+1}} \delta\varphi_n. \tag{15}$$

Thus, the horizontal displacement hinge No. *n+1* can be written as:

$$\delta^x u_{n+1} = u_n \delta\varphi_n + \left(u_{n+1} - u_n\right)\left(-\frac{\cos\varphi_n}{\cos\varphi_{n+1}}\right)\delta\varphi_n. \tag{16}$$

The equilibrium equations are derived in a week form and take into consideration the moments in hinges, reactions R_n and compressive force P:

$$M_n \delta\phi_n + M_{n+1}\delta\phi_{n+1} = P\ \delta^x u_{n+1} - R_n \delta^y u_n, \tag{17}$$

where: $M_n = k_n \phi_n^e$ i $M_{n+1} = k_{n+1}\phi_{n+1}^e$ and $\delta^y u_n$ is vertical displacement of hinge No. n which amplitude exceeds the respective value of the clearance Δ_0.

Total rotation of the hinge can be expressed as $\phi_n = \varphi_n - \varphi_{n+1}$, thus similarly total virtual rotation of the hinge can be obtained as:

$$\delta\phi_n = \delta\varphi_n - \delta\varphi_{n+1} = \left(1 + \frac{\cos\varphi_n}{\cos\varphi_{n+1}}\right)\delta\varphi_n \tag{18}$$

and

$$\delta\phi_{n+1} = \delta\varphi_{n+1} = -\frac{\cos\varphi_n}{\cos\varphi_{n+1}} \delta\varphi_n. \tag{19}$$

Thus, the equation of virtual work takes the form:

$$\begin{aligned} &k_n \phi_n^e \left(1 + \frac{\cos\varphi_n}{\cos\varphi_{n+1}}\right)\delta\varphi_n + k_{n+1}\phi_{n+1}^e \left(-\frac{\cos\varphi_n}{\cos\varphi_{n+1}}\right)\delta\varphi_n = \\ &= P\left[u_n\left(1 + \frac{\cos\varphi_n}{\cos\varphi_{n+1}}\right)\delta\varphi_n - u_{n+1}\frac{\cos\varphi_n}{\cos\varphi_{n+1}}\right]\delta\varphi_n - R_n L_n \cos\varphi_n \delta\varphi_n\ . \end{aligned} \tag{20}$$

It is worth to note that equation (20) is a set of n equilibrium equations. The type of equilibrium path can be evaluated using the energy approach involving the analysis of the variation of potential energy:

`

$$\delta \Pi = 0 \quad \text{oraz}$$
$$\delta^2 \Pi \begin{cases} > 0 & \text{stan stateczny} \\ = 0 & \text{stan krytyczny} \\ < 0 & \text{stan niestateczny.} \end{cases} \tag{21}$$

3 NUMERICAL EXAMPLES

Numerical examples are solved for various amplitudes of initial imperfections α_m, normalized amplitudes of clearances $\overline{\Delta}_0 = \Delta_0 / L$ and elastic supports stiffness k_Δ, where L is taken as the unit value.

The first example refers to a structure with initial imperfection pattern developed according to first buckling mode with small amplitude $\alpha_1 = 0{,}001$ (Fig. 5). At nodes 1, 2 and 3 with the initial intermediate support clearances of two different amplitudes $\overline{\Delta}_0^1 = 0{,}13\overline{u_2}$ and $\overline{\Delta}_0^2 = 0{,}5\overline{u_2}$ were introduced. The curve *m1* shows the equilibrium path obtained for the structure without intermediate supports (solid line – stable; dashed line - unstable equilibrium path). On the other hand, curves *1a, b, c* and *2a, b, c* represent behavior of structures with intermediate supports in distances of a clearance $\overline{\Delta}_0^1$ and $\overline{\Delta}_0^2$. Symbols *a, b* and *c* refer to increasing value of intermediate support stiffness, expressed as a relation $\eta = k_1 / k_\Delta$, where k_1 is elastic rotational hinge stiffness and k_Δ is elastic intermediate supports stiffness (a – $\eta_1 = 0{,}4$, b – $\eta_2 = 0{,}5$, c – $\eta_3 = 1$). In the first case the clearance $\overline{\Delta}_0^1$ is so small that the intermediate supports switch on before the bifurcation point, so all equilibrium paths are stable.

In the second case the clearance $\overline{\Delta}_0^2$ is large, so there is possible stable and unstable post-buckling behavior as well. It is worth to note that for both small and large clearance the cooperation with intermediate supports resulting in increased stiffness of whole structure in proportion to the supports stiffness.

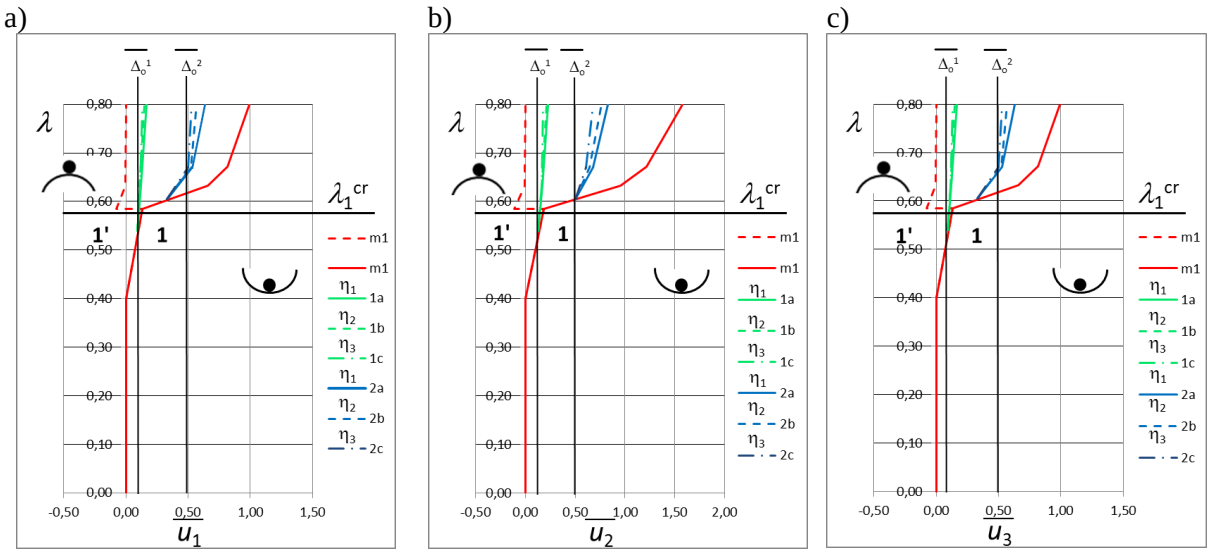

Figure 5: Equilibrium path for the initial geometric imperfections $\alpha_1 = 0{,}001$ and clearances $\overline{\Delta}_0^1 = 0{,}13\overline{u_2}$, $\overline{\Delta}_0^2 = 0{,}5\overline{u_2}$; displacement of the hinge: a) No. 1, b) No. 2, c) No. 3

Figure 6 shows the displacement obtained for the model structure with geometric imperfections pattern developed according to second buckling mode with small amplitude $\alpha_2 = 0{,}001$. Since the displacement of the bar is asymmetrical due to the asymmetric shape of imperfections, positive and negative value of the clearances have to be taken into consideration. One can notice that in this case both stable and unstable equilibrium path may occur. The last example refers to the initial geometric imperfections developed according to three different buckling modes with amplitudes $\alpha_1 = 0{,}001$, $\alpha_2 = 0{,}1$ i $\alpha_3 = 0{,}045$. The curve *(m1d2s3)* shows the equilibrium path obtained for the structure without intermediate supports. In this case several bifurcation points associated with the three buckling modes and stable and unstable post-buckling behavior is observed. Small amplitude of clearance (Δ_0) result in switching on the intermediate supports into cooperation before the bifurcation point, then all equilibrium paths are stable paths and increase of whole structure stiffness occurs (Fig. 7).

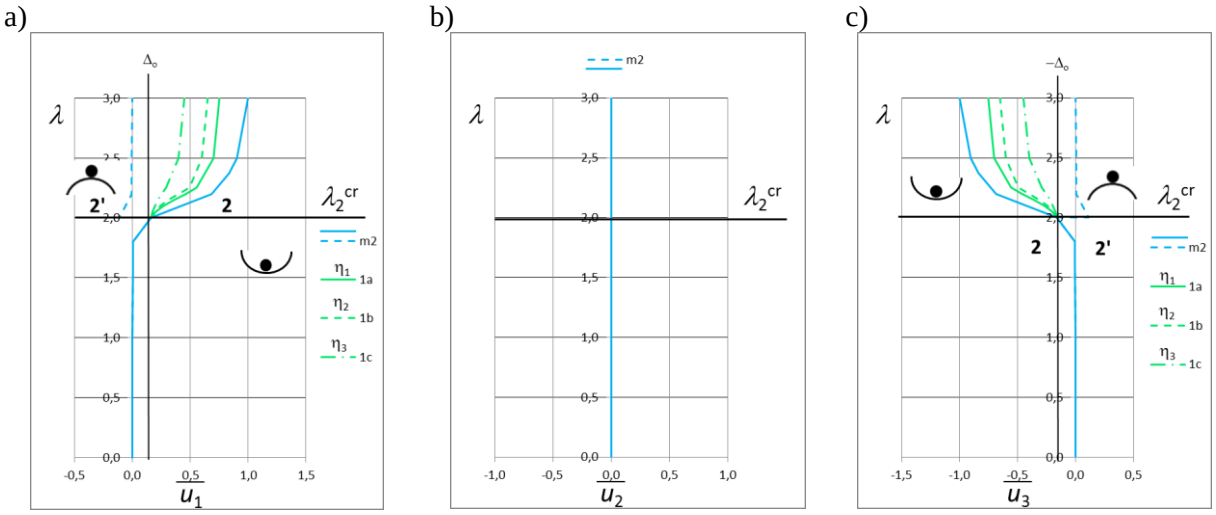

Figure 6: Equilibrium path for the initial geometric imperfections $\alpha_2 = 0{,}001$ and clearance $\overline{\Delta}_0 = \pm 0{,}18\overline{u}_1$; displacement of the hinge: a) No. 1, b) No. 2, c) No. 3

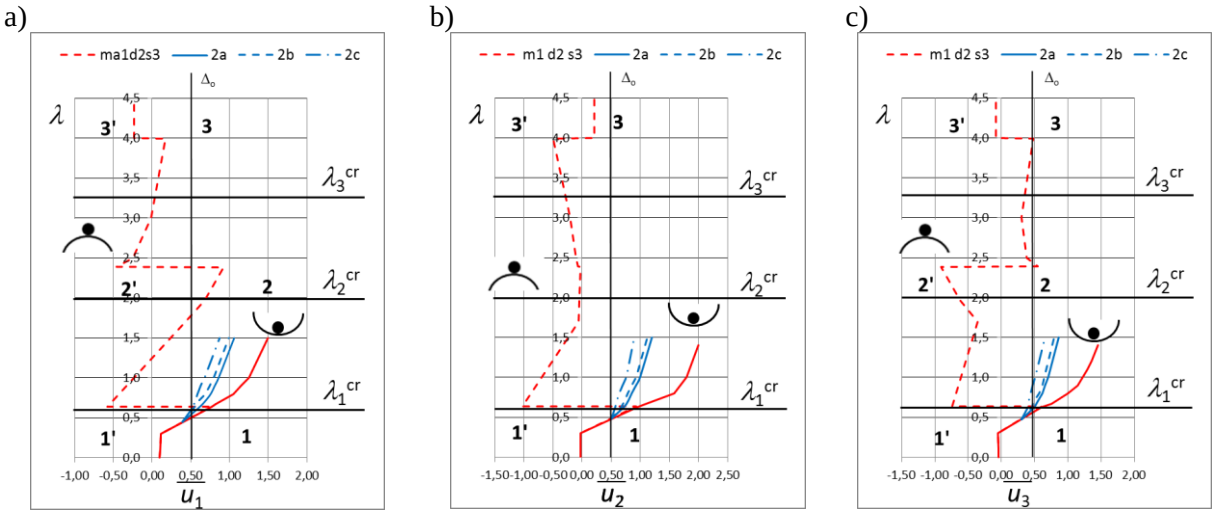

Figure 7: Equilibrium path for the initial geometric imperfections $\alpha_2 = 0{,}001$, $\alpha_2 == 0{,}1$, $\alpha_2 = 0{,}45$ and clearance $\overline{\Delta}_0 = 0{,}5\overline{u}_2$; displacement of the hinge: a) No. 1, b) No. 2, c) No. 3

`

4 CONCLUSIONS

In the paper interaction of initial geometric imperfections and clearances for the structural model consisting of *n*-compressible bars connected by means of elastic hinges is discussed. The proposed model illustrates the behavior of real structures in terms of stability and enables the derivation of exact nonlinear equilibrium equations taking into account large displacements.

In summary the following conclusions can be drawn:

- In the first stage, when the initial clearance is very large, intermediate supports do not switch on to cooperate and the stable equilibrium path is observed.
- For the very small amplitudes of geometric imperfections, developed according first, second or third buckling mode, single points of bifurcation accompanied by the unstable equilibrium path appeared.
- The increase in the amplitude of the initial geometric imperfection results in an increase in the value of the critical load defining the bifurcation point, where it is possible the snap through to the configuration described by unstable equilibrium path.
- The observed snap through is caused by transition of the structure from a high to a low level of potential energy. In this case, the initial geometric imperfections play a positive role resulting in a stable post-buckling behavior.
- In the case of small clearance, depending on the shape of initial geometric imperfections and intermediate supports stiffness, different equilibrium paths are possible. If clearance is very small and intermediate supports switch on before the bifurcation point, all equilibrium path are stable. When the intermediate supports switch on after bifurcation point both stable and unstable post-buckling behavior of the structure is observed.
- It is shown, that interaction between initial clearances and initial geometric imperfections can strongly affect the structural stability response. Therefore, the proper design of clearance, taking into account the initial geometric imperfection, is extremely important in order to obtain a safe the structure characterized by stable equilibrium paths.

REFERENCES

[1] Dubina D., Ungureanu V., Effect of imperfections on numerical simulation of instability behaviour of cold-formed steel members, Thin-Walled Structures, 2002, Vol. 40 (3), s. 239–262.

[2] EN 10162:2005. Cold Rolled Steel Sections - Technical Delivery Conditions - Dimensional And Cross-sectional Tolerances.

[3] EN 1993-1-1. Design of steel structures - Part 1-1: General rules and rules for builings.

[4] EN 1993-1-3. Design of steel structures - Part 1-3: General rules - Supplementary rules for cold-formed members and sheeting.

[5] EN 1993-1-8. Design of steel structures - Part 1-8: Design of joints.

[6] Rzeszut K., Garstecki A., Coupled instability of thin walled structures with slotted connections, w: Proceedings of Fifth International Conference on Coupled Instabilities in Metal Structure, 2008, s. 157–164.

[7] Rzeszut K., Garstecki A., Initial imperfections and clearances in stability analysis of thin walled steel structures, w: European Conference on Computational Mechanics, 2010, s. 16–21.

[8] Rzeszut K., Garstecki A., Parameter identification in FEM models of thin-walled purlins restrained by sheeting, Recent Advances in Computational Mechanics, CRC Press/Balkema, 2014, s. 121–128.

[9] Sokol L., Lateral stabilization by steel sheeting of structural members Thin-Walled Structures, 1996, Vol. 25 (3), s. 207–217.

[10] Vraný T., Effect of loading on the rotational restraint of cold-formed purlins, Thin-Walled Structures, 2006, Vol. 44 (12), s. 1287–1292.

[11] Wald F., Sokol Z., Moal M., Mazura V., Muzeau J.P., Stiffness of cover plate connections with slotted holes, Journal of Constructional Steel Research, 2004, Vol. 60, s. 621–634.

[12] Yu C., Schafer B.W., Simulation of cold-formed steel beams in local and distortional buckling with applications to the direct strength method, Journal of Constructional Steel Research, 2007, Vol. 63, s. 581–590.

[13] Zeinoddini V., Schafer B.W., Global imperfections and dimensional variations in cold-formed steel members, International Journal of Structural Stability and Dynamics, 2011, Vol. 1 (5), s. 829–854.

ACKNOWLEDGMENT

Financial support by the grant 01/11/DSPB/0605/2016 DSPB is kindly acknowledged.

`

ECCOMAS Congress 2016
VII European Congress on Computational Methods in Applied Sciences and Engineering
M. Papadrakakis, V. Papadopoulos, G. Stefanou, V. Plevris (eds.)
Crete Island, Greece, 5–10 June 2016

NUMERICAL ANALYSIS FOR THE DYNAMIC RESPONSE CHARACTERISTICS OF THE PRESTRESSED CONCRETE SLEEPER

Tsutomu Watanabe[1], **Kodai Matsuoka**[1], **and Shintaro Minoura**[1]

[1] Railway Technical Research Institute
address 2-8-38 Hikari-cho Kokubunnji-shi Tokyo Japan
e-mail: watanabe.tsutomu.30@rtri.or.jp

Keywords: Prestressed concrete sleeper, Railway track, Rail joint, Impact load, Numerical analysis, Dynamic interaction.

Abstract. *The Prestressed concrete sleeper (PC sleeper) has many advantages over the wooden sleeper in terms of maintenance, load bending capacity, weight and lateral ballast resistance force. In Japan, the PC sleeper has been widely used since 1951. The PC sleeper is designed in consideration of the impact wheel load which is mainly caused by a rail joint or wheel flat. This research focused on the impact wheel load at rail joints. By field measurements in an operating line and numerical analyses, the dynamic response characteristic of the PC sleeper was clarified. The field measurement of PC sleeper behavior shows that the maximum bending moment of a PC sleeper with a rail joint during train running is almost 4 times larger than that in plain sections, and the maximum bending moment of the PC sleeper adjacent to the rail joint is almost 2.7 times larger than that in plain sections. The numerical analysis shows that support condition has the greatest influence on the bending moment of the PC sleeper among various parameters. Furthermore, the impact wheel load caused by a rail joint affects dynamic behavior of PC sleepers within 4m from the rail joint.*

1 INTRODUCTION

A prestressed concrete sleeper (PC sleeper) is designed mainly in consideration of an impact wheel load during the train running. The impact load is generally caused by the wheel flat, the rail joint, the welded joint irregularity of the rail and the railhead corrugation. Among those defects, the wheel flat and the rail joint have the greatest the influence on the dynamic response of the PC sleeper. At the beginning of the development of the PC sleeper, it had been thought that the enormous impact wheel load was mainly induced by the wheel flat [1, 2]. For this reason, a large number of researches into the wheel flat have been conducted [3, 4]. Through the running test and the impact load examination of the PC sleepers, these researches made clear that the design load of the PC sleeper shall be the 4 times larger than the static load in order to allow no tensile stress (full prestressing) under the assumed maximum impact load by wheel flat. Such knowledge and information have been used for the design of PC sleepers in Japan [1]. Recently, various kings of research and development have been promoted from the viewpoint of the optimization of the sleeper [5-10].

On the other hand, particularly in Japan, though the rail joint has been recognized as another serious source of the impact wheel load, the research into the effect of the impact wheel load generated by the rail joint has been insufficient. This is due to the fact that the suspended rail joint, that is, the rail joint installed between adjacent two sleepers has been widely introduced in an attempt to prevent the impact wheel load as a standard installation method of the rail with wooden or PC sleepers. For example, though the PC sleepers that are adjacent to the rail joint are affected by the impact wheel load caused by the rail joint, the longitudinal span of the influence of the impact wheel load and the effect of the rail joint irregularity have not been sufficiently investigated. Recently, in Japan, a specified type of PC sleeper which is installed directly under the rail joint has been increasingly used. Thus, the phenomenon elucidation of the dynamic response of the PC sleepers at or adjacent to the rail joint is required. Furthermore, the most suitable design of the PC sleeper according to the track condition is also being required [11].

The dynamic response of the PC sleeper at rail joints includes a high frequency phenomenon within 1/1000 seconds. Recently, tools for the phenomenon elucidation of the dynamic response of the PC sleeper at rail joints are gradually being provided such as high quality measurement systems (high frequency and multi-channel synchronized measurement) of the spread of high spec. supercomputers.

Against these backgrounds, this research focused on the impact wheel load at rail joints paying attention to the following points.

(1) Conduct the field measurement in an operating line in order to elucidate the bending moment of the PC sleeper during the train running at rail joints and in plain track sections.
(2) Develop three dimensional numerical analysis models by a finite element method.
(3) Evaluate the effect of the various parameters of the vehicle or track on the bending moment of the PC sleeper quantitatively.
(4) Evaluate the longitudinal span of the influence of the impact wheel load at rail joints.

2 INVESTIGATION METHOD

2.1 Field measurement method

Figure 1 shows the outline of the track. In this section, standard rails of 25m in length and 60kg/m in weight are used and there are rail joints at an interval of 25m. PC sleepers are type-6 PC sleepers in the plain section and PC sleepers at the rail joints are those standardized in Japanese Industrial Standard (JIS). The numbers of PC sleepers per rail (25m in length) is 41.

The field measurement of the bending moment of PC sleepers during the train passing was conducted on two rail joint PC sleepers (Joint 1, Joint 2), two type-6 PC sleepers adjacent to the rail joint (A and B) and two type-6 PC sleepers (C and D). The type-6 PC sleepers C and D are in the plain section. Trains running in this section are Japanese standard commuter trains with the static nominal wheel load of almost 50kN.

Figure 2 shows the positions of strain gauge on the PC sleeper. In total, four strain gauges per sleeper were used, two of which were attached on the side of the PC sleeper (one at an upper position and the other at a lower position) at its longitudinal center and the other two strain gauges were attached in the same manner at its rail seat position. Strain gauges made in KYOWA ELECTRONIC INSTRUMENTS CO. were used for the field measurement, and a built-in chassis made in NATIONAL INSTRUMENTS CO. were used to acquire the experimental signals from 32-channel strain gauge units. The sampling rate is 5000Hz.

Figure 3 shows the measurement method of the vibration mode of the PC sleeper. Seven piezoelectric accelerometers were installed on the top of the PC sleeper. The piezoelectric accelerometers were made in RION CO. (PV-85). Measured response of the accelerometer was recorded in a laptop PC with 5000Hz sampling via preamplifier and A/D converter. Vibration characteristics were identified by the ERA (Eigensystem Realization Algorithm) method [12, 13], which can identify the character matrix of linear time-invariant systems with the principles of minimal realization. The MAC (Modal Amplitude Coherence) value on the controllability was applied to the accuracy evaluation of the vibration characteristics. 40 degrees of freedom were set in order to identify the major modes of the PC sleeper. When the MAC value is 0.99 or more, it is judged to be the vibration mode characteristic of the PC sleeper.

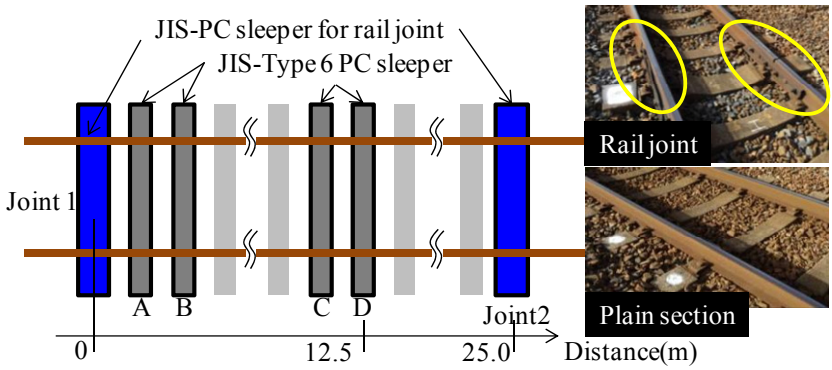

Figure 1: Outline of the track.

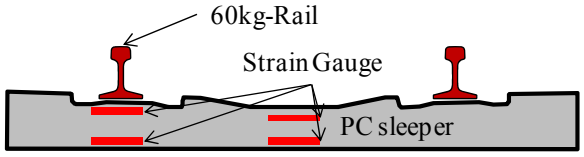

Figure 2: Positions at which to attach the strain gauges to the PC sleeper.

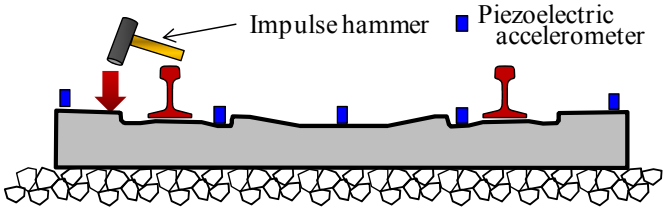

Figure 3: Measurement method of the vibration mode of the PC sleeper on the impulse hammer test.

2.2 Numerical analysis method

(1) Dynamic model of the track

Figure 4 shows the outline of the three dimensional numerical analysis model of the target track. The DIASTARSIII program developed by the Railway Technical Research Institute was used for numerical analysis [14, 15].

The track was modeled using the finite element method. Assembling all elements in the total model, the equation of motion of the track is obtained in a standard matrix form as

$$M^B\ddot{X}^B + C^B\dot{X}^B + K^BX^B = F_L^B + F_I^B(X^V, X^B) + F_N^B(X^B) \quad (1)$$

where X^B is the displacement vector of the track, and M^B, C^B and K^B are the mass, damping and stiffness matrices, respectively; F_L^B is load vectors; $F_I^B(X^V, X^B)$ is the interaction force between the rail and the car, $F_N^B(X^B)$ is the load vectors of non-linear spring force in the track.

As shown in Figure 4, the rail and sleepers were modeled using beam elements, and the rail pads, the ballast and the roadbed were modeled using spring elements. The basic rail mesh size was set at 35mm and the PC sleeper mesh size was set at 55mm. The total number of nodal points is 8338 and the total numbers of elements is 13012.

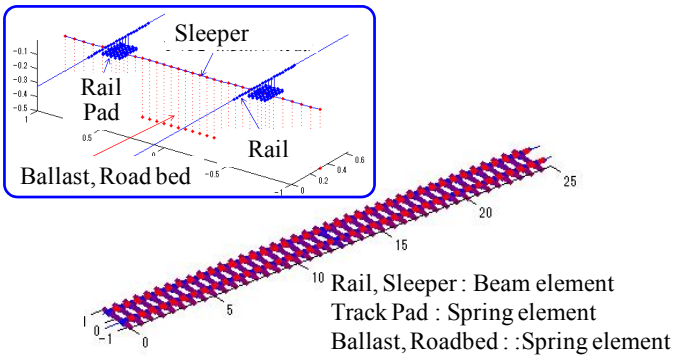

Figure 4: Outline of the three dimensional numerical analysis model of the target track.

(2) Dynamic model of the vehicle

Figure 5 shows the dynamic model of the vehicle assuming that a body, bogies and wheelsets are rigid. These three-dimensional rigid elements are linked by springs K_N and dampers C_N (N is a suffix in Figure 5) according to their respective characteristics. The train has 31 degrees of freedom (5 degrees of freedom for the body, 5 degrees of freedom for the bogies, and 4 degrees of freedom for the wheelset) per one car. The train consists of multiple vehicle models linked together by springs K_C and dampers C_C attached to the ends of the vehicle models. Assuming that the train runs at a constant speed, the equation of three dimensional motion of the train with N vehicles is written in a matrix form as shown in reference [16].

$$M^V\ddot{X}^V + C^V\dot{X}^V + K^VX^V = F_L^V + F_I^V(X^V, X^B) + F_N^V(X^V) \quad (2)$$

where, superscript V and B are the vehicle and the track, respectively; X^V is the displacement vector of the vehicle; M^V, C^V and K^V are the mass, damping and stiffness matrices of the vehicle, respectively; F_L^V is load vectors; $F_I^V(X^V, X^B)$ is the interaction force between the rail and the vehicle, $F_N^V(X^V)$ is the load vectors of non-linear spring force in the car. In this research, the train consists of six Japanese standard commuter vehicles with a length of 20 m and an axle load of almost 50 kN.

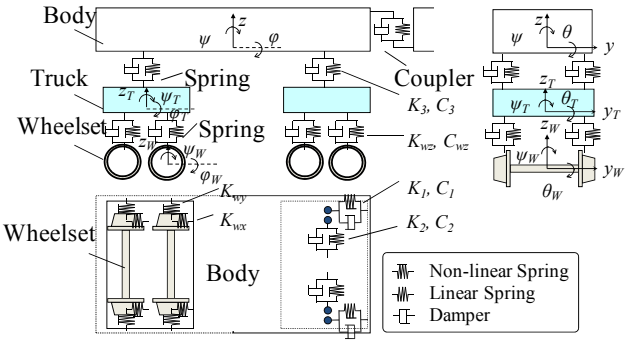

Figure 5: Dynamic model of vehicle.

(3) Dynamic model of the interaction force between the wheel and the rail

Figure 6 shows the wheel/rail model. We focused on relative displacement between the wheel and the rail. The vertical interaction force between these components was modeled by *Hertzian* contact springs so that it is possible to judge the contact condition between the wheel and rail. The vertical relative displacement between the rail and the wheel δ_z is expressed by equation (3).

$$\delta_z = z_R - z_W + e_Z + e_{z0}(y) \tag{3}$$

where z_R is the rail vertical displacement, z_W is the wheel vertical displacement, e_Z is the vertical track irregularity. $e_{z0}(y)$ is the wheel radius variation in the current wheel contact point. When $\delta_Z \geq 0$, the wheel is in contact with the rail, and $\delta_Z \leq 0$, the wheel is loss of contact with the rail. The z-direction interaction force H produced due to the contact of the wheel and the rail is expressed by equation (4).

$$H = H(\delta_Z) \tag{4}$$

The interaction force in the horizontal direction is expressed as creep force in the case that the wheel flange has no contact with the rail. In contract, if the wheel flange is in contact with the rail, the wheel load and horizontal pressure act on the rail, causing the rail crown to move in the horizontal direction. In this case, torsion of the rail occurs. The torsion resistance generated by the rail and the rail fastener is expressed by a spring element.

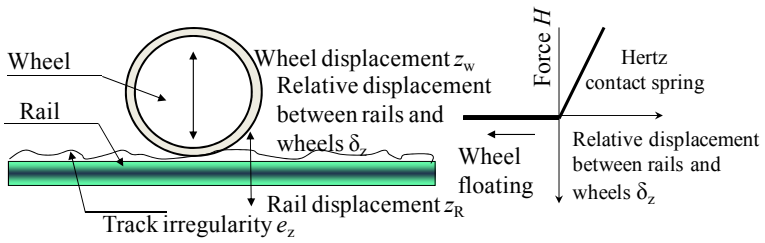

Figure 6: Wheel/ rail model.

Figure 7 shows the irregularities used for the numerical analysis. These irregularities consist of the combination of the rail irregularity and the wheel irregularity. The rail irregularity was measured on the track by a measuring device of 1m-chord versine and as for the wheel we referred to a previous research [17].

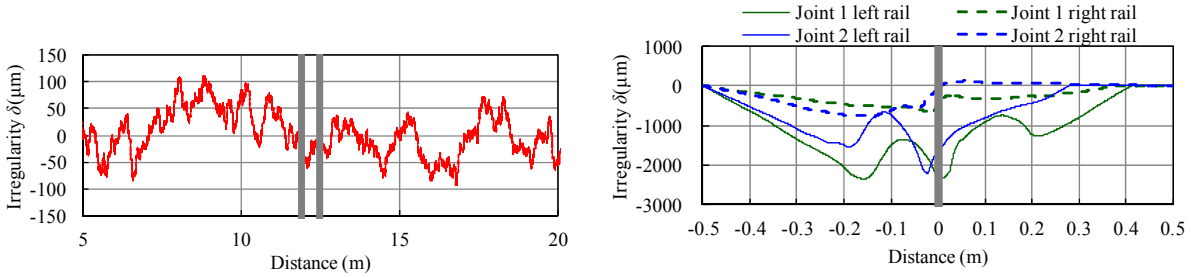

(a) Plain section (b) Rail joint section

Figure 7: Irregularities used for numerical analysis.

(4) Solution method

In the previous paragraph, the equation of motion of the vehicle and that of the track are derived in the vehicle's coordinate system and the global coordinate system respectively. Coupling of these equations is conducted by applying the compatibility and equilibrium conditions to the sub region where both systems are connected with each other. At every moment during the train moving, the compatibility condition is evaluated using a fictitious nodal point at the center of the left and right rails where the wheelset exists.

In order to carry out efficient numerical analysis, the equations of motion concerning the vehicle and track described as equation (1) and equation (2) are transformed to modal coordinate system. The resultant equations are progressively solved in time increment Δt by using the *Newmark* method. However, because the equation of motion is non-linear, iterative calculation has to be carried out within Δt until the unbalanced force becomes sufficiently small. The mode order in the analysis is set at a value that enabled vibration up to about 2000Hz to be reproduced, and the analysis time step is set at 0.0001 sec.

(5) Numerical analysis condition

Table 1 shows the material dimensions and properties. Though basically the values used in the numerical analysis were derived from the Japanese design standards and the nominal values [18, 19], the spring constant of the rail pad was set at two times larger than the nominal value because of the degree of the agreement between the numerical analysis result and the measurement result of bending moment of the PC sleeper. The PC sleeper support condition was not assumed to be uniform over the whole length of the sleeper but to be nonuniform as shown in Figure 8.

Table 2 shows the numerical analysis cases. The numerical analyses were conducted with a focus on the effect of the various parameters. Basic case is underlined. The sleeper support conditions 2 and 4 were considered to be roughly corresponding to that immediate after the track maintenance. On the other hand, the sleeper support conditions 1 and 3 were considered to be corresponding to that a few days after the track maintenance.

Rail	60kg rail Young modulus E_S = 200MPa
Rail Pad	Spring constant D_P = 220MN/m (Nominal value = 110MN/m)
PC sleeper	Type-6 PC sleeper PC wire = φ2.9mm 3-strand cable 12-wires Length L_P = 2000mm, Width B_P = 240mm Height H_P = 170mm(Rail seat), 150mm(Center) Concrete Young modulus E_C = 33MPa
	Rail joint PC sleeper PC wire = φ2.9mm 3-strand cable 16-wires Length L_P = 2000mm, Width B_P = 300mm Height H_P = 170mm(Rail seat), 145mm(Center) Concrete Young modulus E_C = 33MPa
Ballast	Thickness h = 250mm Support spring constant D_B = 180MN/m(1 rail)
Roadbed	Coefficient of subgrade reaction K_{30} = 110MN/m^3 Support spring constant D_S = 111MN/m(1 rail) $D_T = 1/((1/D_B)+(1/D_S))$

Table 1: Material properties.

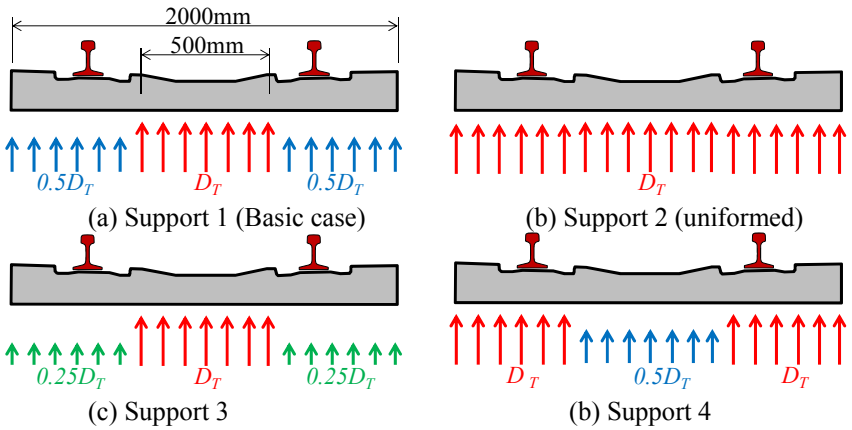

Figure 8: PC sleeper support condition.

PC sleeper	Type-6 PC sleeper, Rail joint PC sleeper
Train speed V	40~130km/h per 10 km/h (Basic case is *80km/h*.)
Vehicle mass M_V (Passenger occupancy)	0% occupancy (= Empty) *50% occupancy* 100% occupancy
Wheelset mass M_W	M_W, 1.5M_W, 2.0M_W
Irregularity	*Plain section*, *Joint 1* (see figure 7) Joint2, No-joint
Spring constant of rail pad (MN/m)	110, *220*
PC sleeper support condition	Support *1*, 2, 3, 4 (see figure 8)

Table 2: Numerical analysis cases.

3 INVESTIGATION RESULT

3.1 Vibration mode of PC sleeper

Table 3 shows the comparison of natural frequencies of the PC sleeper vibration modes. The natural frequencies given by the numerical analyses are coincident with the measurement results excluding the rotation mode. In order to decrease this discrepancy, the accurate evaluation of the PC sleeper support condition is in need. As might be expected, the natural frequency of the rail joint PC sleeper is higher than that of the type-6 PC sleeper because the cross section and the PC wire volume of the rail joint PC sleeper are larger than that of the type-6 PC sleeper.

Mode	Type-6 PC sleeper		Rail joint PC sleeper	
	Measurement (Hz)	Numerical analysis (Hz)	Measurement (Hz)	Numerical analysis (Hz)
Vertical rigid mode	92	86	101	105
Rotation mode	102	86	74	95
1st bending mode	173	174	202	203
2nd bending mode	497	478	534	520
3rd bending mode	813	817	907	939

Table 3: Comparison of the natural frequencies of the PC sleeper vibration modes.

3.2 Bending moment of the PC sleeper

Figures 9 and 10 show the comparison of the bending moments of the PC sleeper during the train running. Numerical analyses were conducted under the condition that the train speed is 80km/h and the passenger occupancy is 50%. From these figures, it can be seen that the absolute value of negative bending moments of the center of the PC sleeper are larger than that of positive bending moments of the rail seat of the PC sleeper.

Regarding the positive bending moment, the differences between “Support 1” and “Support 2” is not clear. On the other hand, regarding the negative bending moment, the bending moment of “Support 1” is almost two times larger than that of “Support 2”. In addition, the negative bending moment of “Support 1” is also coincident with the measurement result. One possible reason may be that more than one year has passed since the track maintenance, and therefore, the PC sleeper support condition has been gradually transferring from “Support 1” to “Support 2” due to the dynamic interaction between the PC sleeper and the ballast.

Figure 11 shows the relation between the train speed and the maximum bending moment of the PC sleeper during the train running. From the field measurement results, the maximum bending moment of the PC sleeper at the rail joint generated during the train running is almost 4 times larger than that in the plain section, and the maximum bending moment of the PC sleeper adjacent to the rail joint is also almost 2.7 times larger than that in the plain section. Furthermore, the bending moments of the type-6 PC sleeper are different depending on its installation section.

Regarding the comparison of the negative bending moments between “Joint 1” and “Joint 2” obtained by the numerical analyses, it can be seen that “Joint 2” is 1.5 times larger than “Joint 1”. This is due to the difference of the support condition between “Joint 1” and “Joint 2”. From the numerical analyses, it can be seen that regarding the dynamic response amplification ratio from 40km/h to 130km/h of the train speed, the rail joint PC sleeper is larger than

type-6 PC sleeper. Concretely, the ratio of the rail joint PC sleeper is 1.4 and that of the type-6 PC sleeper is 1.2.

In figure 11, the design limit values under the allowable stress design method in cases where the design wheel load is 80kN, the impact factor is 2.0, the load dispersion coefficient is 0.5, and the allowable tensile stress is 2.0N/mm^2 are indicated. The actual generated bending moments are under the design value.

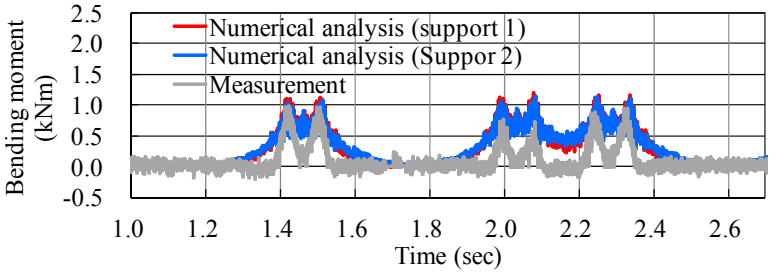

(a) Positive bending moment

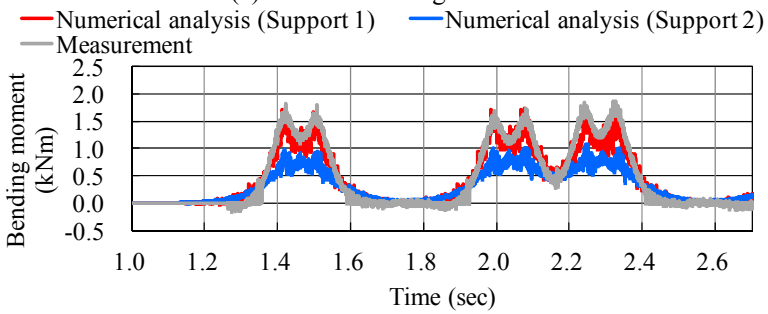

(b) Negative bending moment

Figure 9: Comparison of the bending moment of the type-6 PC sleeper during the train running.

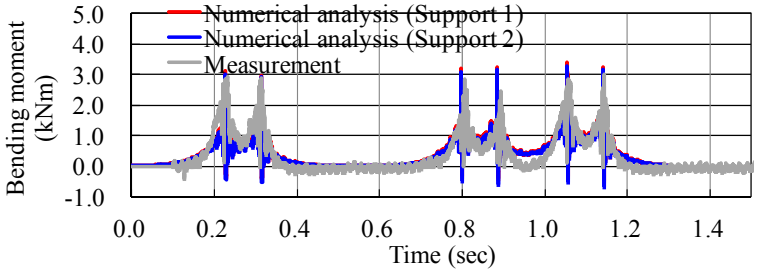

(a) Positive bending moment

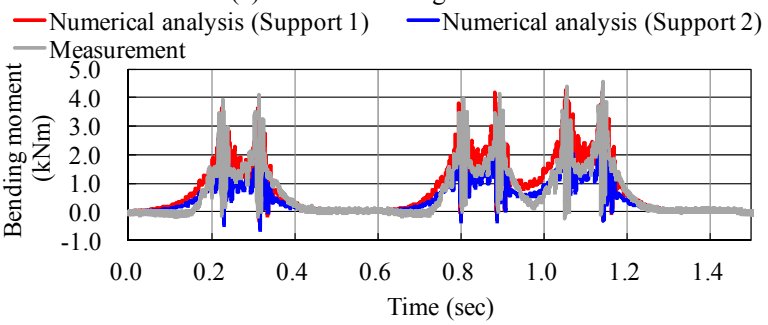

(b) Negative bending moment

Figure 10: Comparison of the bending moment of the rail joint PC sleeper during the train running.

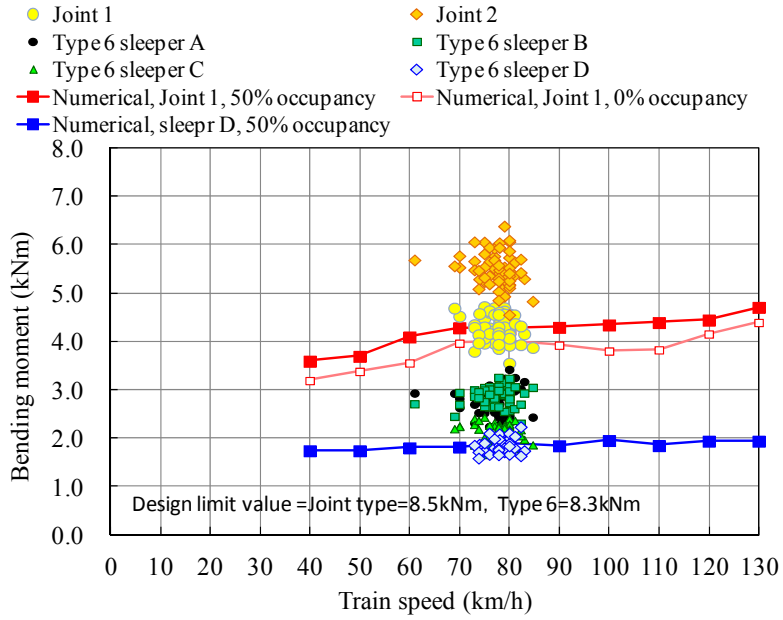

(a) Positive bending moment

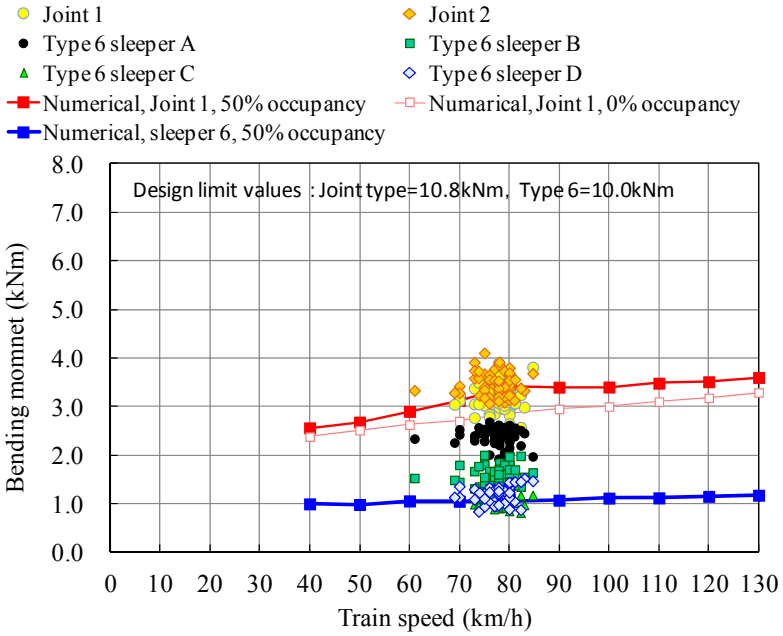

(b) Negative bending moment

Figure 11: Relation between the train speed and the maximum bending moment of the PC sleeper during the train running.

3.3 Influence of various parameters

Figure 12 shows the effect of the various parameters on the bending moment of the PC sleeper during the train running. The knowledge and findings obtained by the numerical analyses in this research are shown below.

As for the passenger occupation variation, when the passenger occupation ratio increases from 50% to 100%, the bending moment increases by up to 1.2 times.

As for the wheelset mass variation, when the wheelset mass increases by 2 times, the bending moment increases by up to 1.5 times. It can be seen that negative bending moment especially is largely affected.

As for the irregularity variation, the bending moment of the PC sleeper at "Joint 1" or "Joint 2" is up to 3.4 times larger than that at "No-joint".

Concerning the rail pad stiffness, when the spring constant of the rail pad decreases by half, the bending moment decreases by up to 20%. Furthermore, it can be seen that the bending moment in the case of "Support 3" is up to 4 times larger than that in the case of "Support 4".

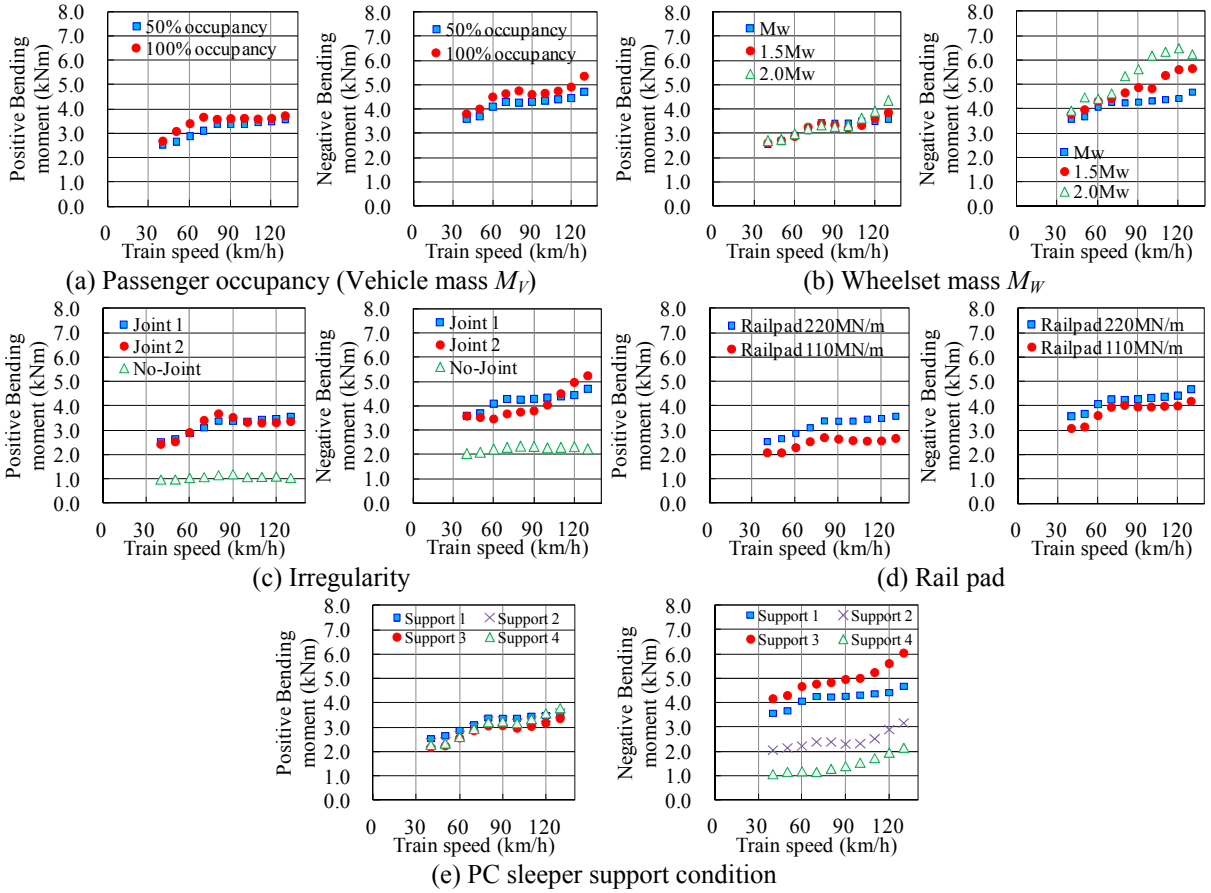

(a) Passenger occupancy (Vehicle mass M_V)

(b) Wheelset mass M_W

(c) Irregularity

(d) Rail pad

(e) PC sleeper support condition

Figure 12: Effect of the various parameters on the bending moment of the PC sleeper during the train running.

3.4 Influence of the rail joint

Figure 13 shows the longitudinal span of the influence due to the impact wheel load at the rail joint. It can be seen that the longitudinal span of the influence is almost 4m, and there are not much difference between each case. Based on these results, the plain section, i.e. the section which is not affected by the rail joint, can be defined as a section more than a span of 4m away from the rail joint. Though length of this span absolutely depends on the given condition, this span is one of the reference values about the rail joint section. In the future, we must clarify the generality of the longitudinal span of the influence of the impact wheel load at the rail joint by increasing the sample of the irregularity and the analysis parameters.

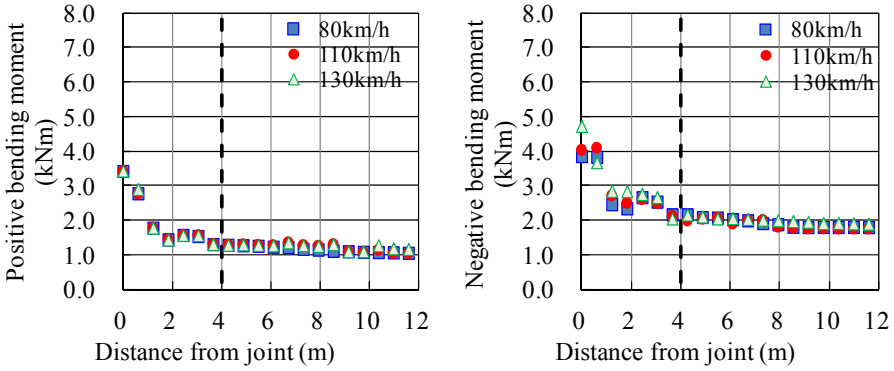

(a) Basic case (80,110,130km/h)

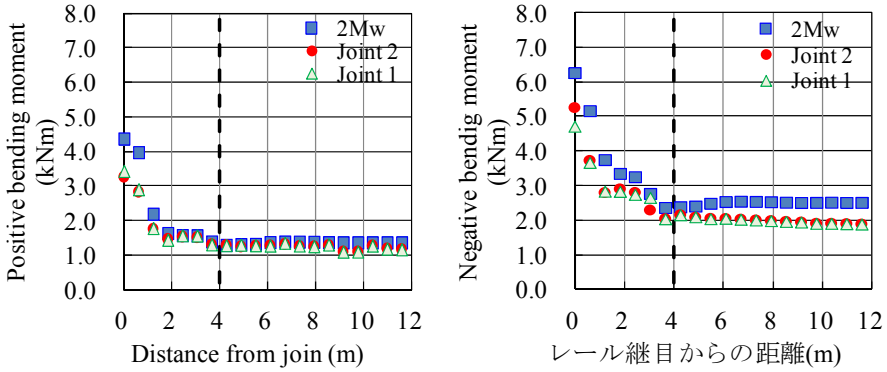

(b) Effect of wheelset mass and PC sleeper support condition (130km/h)

Figure 13: Longitudinal span of the influence of the impact wheel load at rail joint.

4 CONCRUSIONS

This research focused on the impact wheel load at the rail joints. We carried out field measurement in an operating line and numerical analyses, in order to reveal the dynamic response characteristics of the PC sleeper. The knowledge and findings obtained in this research are summarized as below.

- The field measurement results shows that the maximum bending moment of the PC sleeper at the rail joint during the train passing is almost four times larger than that in the plain section, and the maximum bending moment of the PC sleeper adjacent to the rail joint is almost 2.7 times larger than that in the plain section. Furthermore, the bending moment of type-6 PC sleeper varies depending on the measurement section.
- The absolute value of negative bending moment at the center of the PC sleeper was larger than that of the positive bending moment at the rail seat of the PC sleeper.

- Results of the numerical analyses indicate that the dynamic amplification ratio of the rail joint PC sleeper at from 40km/h to 130km/h is larger than type-6 PC sleeper. Concretely, the rail joint PC sleeper was 1.4 times, type-6 PC sleeper was 1.2 times.
- The longitudinal span of the influence of the impact wheel load at the rail joint is almost 4m.

In the future, we will reflect the concept of these knowledge and findings in the design of the PC sleeper.

REFERENCES

[1] H. Wakui, H. Okuda, A study on limit-state design method for prestressed concrete sleepers, *Concrete Library of JSCE*, **33**, 1-25, 1999.

[2] H. Wakui, H. Okuda, Effects of wheel-flats on concrete sleepers, *International Symposium on precast concrete railway sleepers*, Madrid, 287-299, 1991

[3] Joint Committee on Relation between Track and Equipment of the Mechanical and Engineering Divisions, AAR, Effect of Flat Wheels on Track and Equipment, *American Railway Engineering Association*, **53**, 1952.

[4] ORE D 161.1 rp3, The Influence of Wheel Flats on the Track with 20 and 22.5 t Axle Loads, Utrecht, 1986.

[5] Sakdirat Kaewunruen, Experimental and numerical studies for evaluating dynamic behavior of prestressed concrete sleepers subject to severe impact loading, *Ph.D. Thesis*, *Department of Civil and Mining Engineering*, *University of Wollongong*, 2007.

[6] Javad Sadeghi, Investigation of Characteristics and Modelling of Railway Track System, *Ph.D. Thesis*, *Department of Civil and Mining Engineering*, *University of Wollongong*, 1997.

[7] Zijian Zhang, Sihang Wei, Bassem Andrawes, Daniel A. Kuchma, J. Riley Edwards, Numerical and experimental study on dynamic behavior of concrete sleeper track caused by wheel flat, *International Journal of rail Transportation*, **4:1**, 1-19, 2016.

[8] NS Vyas, AK Gupta, Modeling rail wheel-flat dynamics, *Proceedings of the 1st World Congress on Engineering Asset Management (WCEAM)*, 11-14, 2006.

[9] J. Bian, Y.T. Gu, M. Murray, Numerical Study of Impact Forces on Railway Sleepers under Wheel Flat, *Advances in Structural Engineering*, **16:1**, 2013.

[10] D.Kishore Kumar, K.Sambasivarao, Static and Dynamic Analysis of Railway Track Sleeper, *International Journal of Engineering Research and General Science*, **2:6**, 2014.

[11] Masaki Sue, Yuki Okumura, Yuichiro Hori, Takayuki Onodera, Development of an Ideal Sleeper, *JR EAST Technical Review*, 29, 2015.

[12] Kodai Matsuoka, Kiyoyuki Kaito, Hidekazu Ishii, Statistical consideration regarding the vibration characteristics and variation factors of 24-span steel railway bridge in 86 years in service, *Japan Society of Civil Engineers*, **68:3**, 157-174, 2012(In Japanese).

[13] Tomonori NAGAYAMA, Masato ABE, Yozo FUJINO, Kenji IKEDA, Non-iterative identification of non-proportionally damped system from ambient vibration measure-

ment and analysis of dynamic properties of a long span suspension bridge, *Japan Society of Civil Engineers*, **745**, 155-169, 2003.

[14] H. Wakui, N. Matsumoto, M. Tanabe, A Study on Dynamic Interaction Analysis for Railway Vehicle and Structures, QR of RTRI, **35:2**, 96-104, 1994.

[15] M. Tanabe, N. Matsumoto, H. Wakui, M. Sogabe, Simulation of a Shinkansen train on the railway structure during an earthquake, Japan Journal of Industrial and Applied Mathematics, **28-1**, 223-236, 2011.

[16] M. Tanabe, S. Komiya, H. Wakui, N. Matsumoto, M. Sogabe, Simulation and visualization of high-speed Shinkansen train on the railway structure, Japan Journal of Industrial and Applied Mathematics, **17**, 309-320, 2000.

[17] Toshiki Kitagawa, Kaoru Murata, Kiyoshi Nagakura, Roughnesses on the wheel and rail surfaces for conventional narrow-gauge lines, J-rail2007, 515-518, 2007(In Japanese).

[18] Railway Technical Research Institute. Design Standards for Railway Structures and Commentary (Concrete Structures), 2007.

[19] Railway Technical Research Institute. Design Standards for Railway Structures and Commentary (Track structures), 2012.

ECCOMAS Congress 2016
VII European Congress on Computational Methods in Applied Sciences and Engineering
M. Papadrakakis, V. Papadopoulos, G. Stefanou, V. Plevris (eds.)
Crete Island, Greece, 5–10 June 2016

NUMERICAL DYNAMIC ANALYSIS OF BEAMS ON NONLINEAR ELASTIC FOUNDATIONS UNDER HARMONIC MOVING LOAD

D. Froio[1], **R. Moioli**[1], **E. Rizzi**[1*]

[1]Università degli Studi di Bergamo, Dipartimento di Ingegneria e Scienze Applicate
viale G. Marconi 5, I-24044, Dalmine (BG), Italy
e-mail: diego.froio@unibg.it
r.moioli@studenti.unibg.it
*Corresponding Author, egidio.rizzi@unibg.it

Keywords: Dynamic response of beams and railways; Nonlinear Winkler elastic foundation; Harmonic moving load; Numerical Finite Element Method implementation; Critical velocities.

Abstract. *As a main background practical context of the present numerical investigation, the appropriate description of track vibrations induced by high-speed trains looks crucial in contemporary railway engineering. The present paper is concerned with the modelization of the transient dynamic response of a simply-supported Euler-Bernoulli beam resting on a homogeneous in space Winkler elastic foundation, under the action of a transverse concentrated load with harmonic-varying magnitude, moving at constant velocity along the beam. Two types of constitutive laws are considered for the foundation subgrade reaction: (a) a linear law and (b) a nonlinear, cubic law. The governing linear/non-linear partial differential equation of motion is first semi-discretized in space with a Finite Element Method approach, by using cubic Hermitian polynomials as interpolation functions for the unknown deflection. Then, the dynamic solution is obtained numerically by a direct integration method, with focus on determining several characteristic response features, such as the critical velocities of the moving load, leading to high transverse deflections. Extensive numerical analyses are finally performed, with the following two main goals: (1) to demonstrate the reliability, consistency and accuracy of the present implementation, specifically by the comparison of the obtained numerical critical velocities with previously-published analytical and numerical results; (2) to investigate how the frequency of the harmonic moving load as well as its velocity do influence the response of the whole beam-foundation system, with or without taking viscous damping into account. Results show that such goals have been consistently achieved and outline new interesting trends, like the appearance of two critical velocities also for the nonlinear foundation, the first of which gets close to zero as the frequency of the load approaches the first natural frequency of the beam. The present outcomes reveal potential implications in practical terms, especially in lowering the ranges of admissible train speeds, as for structural requirement or for preventing passenger discomfort.*

1 INTRODUCTION

The observed ground, beam and track vibrations, induced by rapidly-growing high-speed railway networks and the considerable evolution of train vehicles capable to travel at more than 500 km/h may degrade rolling equipment and track and raise questions about vehicle stability, maintenance costs and possible passenger discomfort. For these reasons many studies have been carried out in the last few decades towards the prediction of the dynamic behavior of railway beams and tracks. Amongst the prevailing models, the most diffused one considers the train vehicle as a single load traveling at constant velocity on a beam supported by an elastic foundation (see Kerr [13]). Comprehensive literature reviews about the problem of moving loads acting on beams may be found in Beskou and Theodorakopoulos [2], Frýba [11], Kerr [13] and Wang et al. [20].

The main scope of the elastic foundation model is that of providing a simplified description of the contact between the rail and the sleepers-ballast-ground system. Based on the well-known Winkler model, the foundation is represented as a uniform layer of infinitely closely-spaced springs, which, according to its original formulation, push up/pull down the beam with a force linearly-proportional to the beam deflection (see e.g. Froio and Rizzi [9] and wide state of the art review, with historical perspective, presented therein).

Concerning the analysis of beams lying on a damped or undamped Winkler elastic foundation, excited by a moving load, different approaches have been adopted so far. One of the most common modelizations is to consider the steady-state response of infinite beams subjected to a constant magnitude moving load (see e.g. Frýba [11]), as well as to a moving load with harmonically-varying amplitude, as reported by Bogacz et al. [3]. Similar results were also obtained by Chen et al. [6], by using the dynamic stiffness matrix method in the description of the influence of the structural parameters and of the load frequency on the critical velocities of the beam. A further extension of this work was then reported by Chen and Huang [7], for the case of a beam of finite length.

Besides analytical solutions and other numerical methods, in the past two decades the Finite Element Method (FEM) has been widely used for solving structural dynamic problems involving moving loads. Combined with the Finite Element Method, the numerical direct integration in time appears one of the most common approaches for the solution of the equations of motion in the time domain. For instance, FEM and Newmark method were applied successfully by Thambiratnam and Zhuge [19] for a constant amplitude moving load and by Kien and Hai [14] for a harmonic moving load. Following a FEM approach, Andersen et al. [1] treated the steady-state response of an infinite Euler-Bernoulli beam lying on a viscoelastic foundation, subjected to a harmonic point load moving with uniform velocity.

Regarding beams of finite length, simply-supported beams on nonlinear viscoelastic foundations were tackled by Castro et al. [4, 5]. Critical velocities were determined and the effects of load intensity and foundation stiffness on both beam displacements and critical velocity were investigated. The results they presented were in agreement to those shown earlier by Dimitrovová and Rodrigues [8] for a linear elastic foundation.

The present paper is concerned with the transient dynamic response of a simply-supported Euler-Bernoulli beam resting on a homogeneous in space Winkler elastic foundation under the action of a transverse concentrated load with harmonic-varying magnitude, moving at constant velocity along the beam. Two types of constitutive laws are considered for the foundation subgrade reaction: (a) a linear law and (b) a nonlinear, cubic law. The dynamic response is obtained numerically by using a FEM implementation and a HHT-α algorithm for the time

integration. Then, critical velocities are determined for both types of foundation, by considering different values of the frequency of the moving load.

The purpose of the present paper is two-fold. Firstly, this work aims at demonstrating the reliability, consistency and accuracy of the present implementation, by the comparison of the obtained numerical critical velocities to results reported by earlier Castro et al. [4] and by Chen et al. [6]. Secondly, extensive numerical analyses are performed to study the effects of the frequency of the moving load, of its velocity and of the foundation behavior, on the response of the whole beam-foundation system, with or without viscous damping, outlining here new results for the nonlinear foundation case.

The paper is organized as follows. Section 2 presents the governing boundary value problem for the linear/nonlinear partial differential equation of motion of a simply-supported beam on elastic foundation and its semi-discretization in space through a FEM formulation and implementation. In Section 3 the outcomes of a series of independent numerical analyses relative to the case of a constant amplitude moving load are presented and consistently compared to results reported in the literature. Section 4 provides the outcomes of a vast numerical investigation on the dynamic response of beams lying on visco-elastic foundations, subjected to a force which moves along the beam axis at constant velocity and simultaneously varies its amplitude in time on the basis of a harmonic law. In particular, the relationship between the amplitude frequency of the moving load and the critical velocity of the beam-foundation system is explicitly depicted in appropriate bifurcation curves, for both linear and nonlinear elastic foundations. Finally, main conclusions are outlined in closing Section 5.

2 MODEL EQUATION AND FINITE ELEMENT FORMULATION

Consider the idealized system shown in Fig. 1, consisting of a simply-supported finite beam lying on a Winkler elastic foundation under the action of a concentrated force of magnitude F (either constant or variable in time), moving with constant velocity v. The force is assumed positive if directed upward. The following assumptions are adopted throughout the formulation:

1. Euler-Bernoulli beam model with Young's modulus (E), cross section area (A), moment of inertia (I) and mass density (ρ), assumed constant along the beam axis;
2. Viscous damping smeared onto both the beam and the foundation, with constant damping coefficient (c);
3. Beam at rest with zero initial deflection and velocity at the instant when the force leaves from the left support of the beam.

From these assumptions, the equation of motion describing the transverse deflection of the beam is (see Frýba [11]):

$$EI\frac{\partial^4 w(x,t)}{\partial x^4}+\rho A\frac{\partial^2 w(x,t)}{\partial t^2}+c\frac{\partial w(x,t)}{\partial t}+r\big(w(x,t)\big)=F(t)\delta(x-vt);\ 0<x<l,\ t>0; \quad (1)$$

where x is the axial coordinate, with the origin fixed on the left end of the beam, t is the time coordinate, with the origin at the instant on which the force starts its motion from the left extreme of the beam ($x=0$), $w(x,t)$ is the vertical deflection of the beam (positive if upward), measured from the static equilibrium position of the beam subjected to its self-weight only, acting downward, and $r(w)$ is the reaction force per unit length supplied by the foundation. The right hand side of Eq. (1) represents, by means of the Dirac delta function δ, the unit

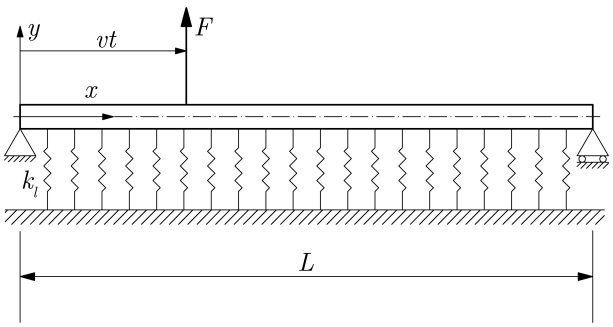

Figure 1: *Simply-supported finite beam lying on an elastic foundation subjected to a moving force.*

concentrated moving load acting at time t at relative position vt, with either constant $F(t) = F$ or variable amplitude $F(t) = F\cos(\Omega t)$, where F is its reference amplitude and Ω is the angular frequency of the harmonic amplitude variation in time.

According to Castro et al. [4] and many other authors the adopted force-displacement relation for the foundation may be described by the following polynomial cubic law:

$$r\big(w(x,t)\big) = k_l\, w(x) + k_{nl}\, w(x)^3; \tag{2}$$

where k_l is a classical linear Winkler coefficient and k_{nl} describes an additional nonlinear stiffness coefficient attached to the cubic term.

By means of cubic Hermitian polynomials as interpolation functions and by the application of Galerkin Finite Element Method, equation of motion (1) may be rewritten for an arbitrary finite element in semi-discretized form. Then, by assembling the contributions from all of the finite elements and imposing the boundary conditions of zero transverse displacements at the two extreme nodes of the beam, the global equations of motion are obtained as:

$$\mathbf{M}\ddot{\mathbf{q}} + \mathbf{C}\dot{\mathbf{q}} + \mathbf{K}\mathbf{q} + \mathbf{Q}_{nl}(\mathbf{q}) = F\boldsymbol{\Psi}(x_c); \tag{3}$$

where $\mathbf{M}$ and $\mathbf{K}$ are the global structural mass and stiffness matrices, $\mathbf{Q}_{nl}$ is the global vector of the nonlinear forces, $\boldsymbol{\Psi}(x_c)$ is the vector deriving from the assembly of the element-wise vectors of equivalent external forces produced by the Dirac delta function, $\mathbf{q}$, $\dot{\mathbf{q}}$ and $\ddot{\mathbf{q}}$ are the global vectors of the generalized displacements, velocities and accelerations, respectively. Both mass and stiffness matrices are symmetric and positive definite. The previously-defined matrices and vectors have been obtained according to the work of Castro et al. [4, 5].

The viscous damping term $\mathbf{C}\dot{\mathbf{q}}$ has been added to Eq. (3) to account for smeared damping. Rayleigh-type damping is assumed, e.g. the damping matrix $\mathbf{C}$ is defined as a linear combination of the mass and stiffness matrices:

$$\mathbf{C} = a_0\mathbf{M} + a_1\mathbf{K}. \tag{4}$$

The values of the coefficients a_0 and a_1 have been chosen accordingly to Dimitrovová and Rodrigues [8] as follows:

$$a_0 = 2\xi\sqrt{\frac{2k_l}{\rho A}}; \qquad a_1 = 0;$$

where ξ is the damping factor. Coefficient a_1 is taken null, meaning that a mass-proportional viscous damping is considered.

Hence, the semi-discrete equations of motion (3) represent a coupled system of linear second-order differential equations with constant coefficients, whose solution, given the initial conditions, represents the transient response of the beam. In this work, the following homogeneous initial conditions are assumed:

$$\mathbf{q}(0) = \mathbf{0}; \quad \dot{\mathbf{q}}(0) = \mathbf{0}. \tag{5}$$

The numerical solution of the initial-value problem satisfying Eqs. (3), (5) has been achieved through a HHT-α implementation (see Hilber et al. [12]). The main methodologies and computational details about the implementation will be reported elsewhere (Froio et al. [10]).

3 CONSTANT AMPLITUDE MOVING LOAD: VALIDATION OF THE FEM FORMULATION

In this section, a concentrated load of constant magnitude $F(t) = F$, namely $\Omega = 0$, moving along the beam axis with constant velocity v, is considered. A consistent validation comparison between the present numerical analyses, in terms of maximum upward and downward beam displacements versus load velocity, and analogous studies proposed in the literature is performed. In particular, results obtained by Castro et al. [4] for both linear and nonlinear foundation behaviors have been taken as reference outcomes, since their work has been lying at the basis of the present investigation.

The type of analyzed beam is a UIC60 rail (see Fig. 2a), one of the most diffused steel profiles in railway tracks. Its mechanical properties are reported in Fig. 2b. A beam length (L) of 200 m has been selected in order to reasonably represent the limit case of a beam of an infinite length. The assumed load magnitude is 83.4 kN, corresponding to a locomotive of the Thalys high-speed train (EU), which has a total axle mass of about 17000 kg (see Castro et al. [4]). The number of adopted finite elements is 200, i.e the spatial discretization consists of finite elements with a length of 1 m.

Computations are performed for velocities of the moving load varying between 50 m/s and 300 m/s with a step variation of 1 m/s. For each simulation performed at a certain value of the moving load velocity, the maximum upward (positive) and downward (negative) displace-

(a)

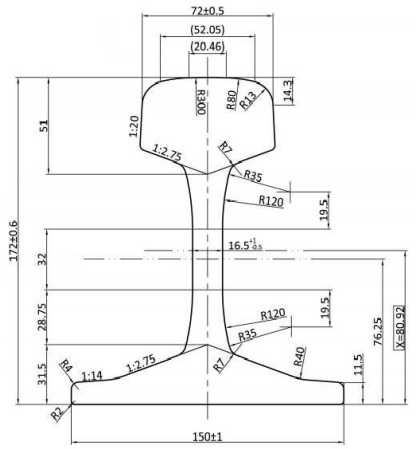

(b)

Mechanical properties:			
Young's modulus	E	210	GPa
Cross-sectional area	A	7684×10^{-6}	m^2
Area moment of inertia	I	3055×10^{-8}	m^4
Mass per unit length	μ	60	kg/m

Figure 2: *UIC60 rail profile (taken from the internet), quotes in millimeters (a) and mechanical properties of UIC60 rail (b).*

ments of the beam have been recorded. Then, these values have been plotted as a function of the moving load velocity. From such curves the critical velocity for a finite beam may be detected as the velocity of the moving load at which maximum displacements are attained (see Dimitrovová and Rodrigues [8]).

Regarding aspects of numerical integration, the time span taken throughout the integration process corresponds to the amount of time along which the moving load is really acting along the beam, that is $\tau = L/v$. The adopted time step corresponds to the time taken by the load to travel a distance of 0.2 m, namely a fifth of the finite element length. The HHT-α parameter expressing the numerical dissipation rate is chosen equal to -0.1. The finite element program has been implemented within a MatLab environment [16].

3.1 Beams lying on a linear elastic foundation

A uniform linear elastic foundation is considered, with two different values of Winkler's elastic coefficient equal to $k_l = 250$ kN/m^2 and $k_l = 500$ kN/m^2, respectively. Both undamped and damped behaviors are taken into account, assuming the damping factor ζ in the amount of 2%. As already noticed by Dimitrovová and Rodrigues [8], both foundation stiffness values are actually not that realistic, but they may be adopted in order to achieve a more direct inspection of the critical behavior of the system. The results obtained for the case of a beam on an undamped foundation with the two linear Winkler stiffness coefficients are shown in Fig. 3a. The same results for the damped case are reported in Fig. 3b.

From the observation of these plots, the critical velocity may be clearly detected and the corresponding maximum and minimum displacements are indicated in Tables 1 and 2. It appears that the value of the critical velocity is weakly sensitive to the damping factor, while it affects more the magnitude of the maximum and minimum displacements. From Figs. 3a and 3b, it appears clear that increasing the stiffness of the foundation causes a shift in the position of the critical velocities towards higher values, in addition to the expected effect of decreasing the deflection amplitudes.

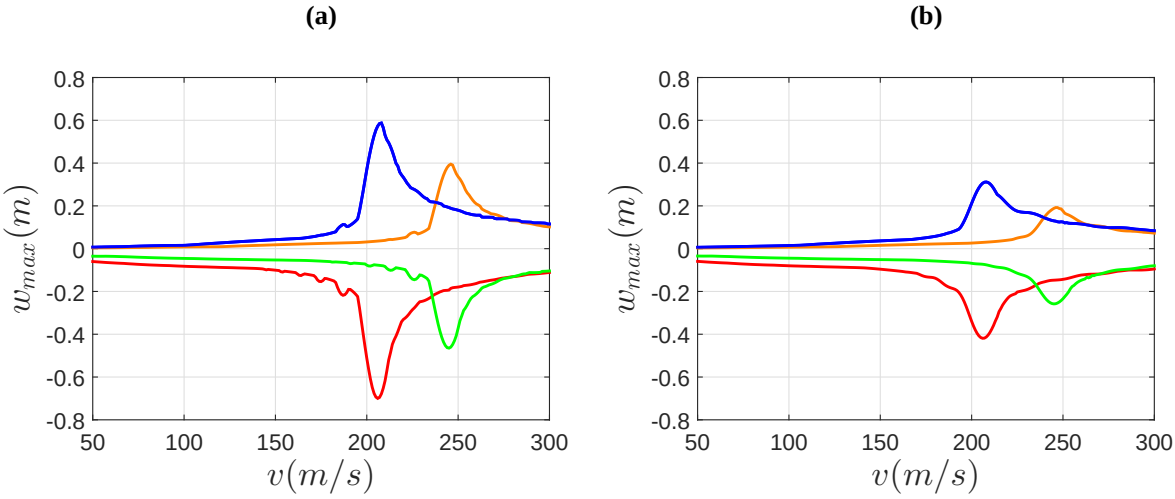

Figure 3: *Representation of beam maximum displacements as a function of load velocity for linear elastic foundations with stiffnesses of* $k_l = 250\,\text{kN/m}^2$ *(— upward and — downward displacements) and* $k_l = 500\,\text{kN/m}^2$ *(— upward and — downward displacements), undamped case* $\zeta = 0\%$ *(a) and damped case* $\zeta = 2\%$ *(b).*

	v_{cr} (m/s)			w_{max} (m)		
ζ	Present work	Ref. [4]	Error	Present work	Ref. [4]	Error
0%	206	206	$0.00\,\%$	-0.6999	-0.700	$-0.01\,\%$
	208	208	$0.00\,\%$	0.5873	0.587	$0.05\,\%$
2%	206	206	$0.00\,\%$	-0.4189	-0.419	$-0.02\,\%$
	208	208	$0.00\,\%$	0.3117	0.312	$-0.01\,\%$

Table 1: *Maximum displacements and critical velocities for a linear foundation with stiffness* $k_l = 250\,\text{kN/m}^2$. *Percentage relative error with respect to Castro et al. [4].*

	v_{cr} (m/s)			w_{max} (m)		
ζ	Present work	Ref. [4]	Error	Present work	Ref. [4]	Error
0%	245	245	$0.00\,\%$	-0.4649	-0.465	$-0.02\,\%$
	246	246	$0.00\,\%$	0.3950	0.395	$0.00\,\%$
2%	245	245	$0.00\,\%$	-0.2582	-0.258	$0.08\,\%$
	246	246	$0.00\,\%$	0.1922	0.192	$0.10\,\%$

Table 2: *Maximum displacements and critical velocities for a linear foundation with stiffness* $k_l = 500\,\text{kN/m}^2$. *Percentage relative error with respect to Castro et al. [4].*

The comparisons between the outcomes depicted in Figs. 3a and 3b and gathered in Tables 1 and 2, if compared to those reported in Castro et al. [4], reveal a very good agreement, for both damped and undamped cases. Furthermore, in view of the results above, it may be noticed that a good degree of consistency has been also achieved with respect to the analytical solution proposed by Dimitrovová and Rodrigues [8].

3.2 Beams lying on a nonlinear elastic foundation

Two examples of nonlinear foundations are examined in this section: one with a nonlinear component of foundation stiffness $k_{nl} = 2500\,\text{kN/m}^4$ and another with $k_{nl} = 25000\,\text{kN/m}^4$. The assumed linear component of foundation stiffness is $k_l = 250\,\text{kN/m}^2$ for both examples. The computed results are shown in Fig. 4a and 4b for both undamped and damped ($\zeta = 2\%$) cases.

Comparing these plots to those depicted for a linear foundation, it can be seen that the addition of the nonlinear contribution to the foundation stiffness results in an increment of the critical velocities. Moreover, a decrease of the maximum upward and downward displacements is detected. The inclusion of damping brings a further decrease of the maximum displacements entity, together with a small decrease of the critical velocities.

For the nonlinear type of foundation the values of the critical velocities are not explicitly indicated by Castro et al. [4]. Nonetheless, the results obtained with the implemented method are matching the deflection curves and the maximum values of displacements reported in that work. The values of critical velocities, maximum displacements and percentage relative errors upon the latter are reported in Table 3, for a foundation with nonlinear stiffness $k_{nl} = 2500\,\text{kN/m}^4$, and in Table 4, for a foundation with nonlinear stiffness $k_{nl} = 25000\,\text{kN/m}^4$.

The results reported in this section are preliminary to the analysis with a harmonic moving load, which represents the core of this work and will be presented in Section 4. In fact, first the concept of critical velocity of a constant amplitude moving load for a finite simply-supported beam has been again outlined and its dependence on the mechanical parameters of the systems,

already reported in the literature, has been confirmed. Second, thanks to the previously-reported results, the present finite element implementation reveals to be fully reliable with respect to the outcomes presented by Castro et al. [4] and by Dimitrovová and Rodrigues [8], proving its correctness.

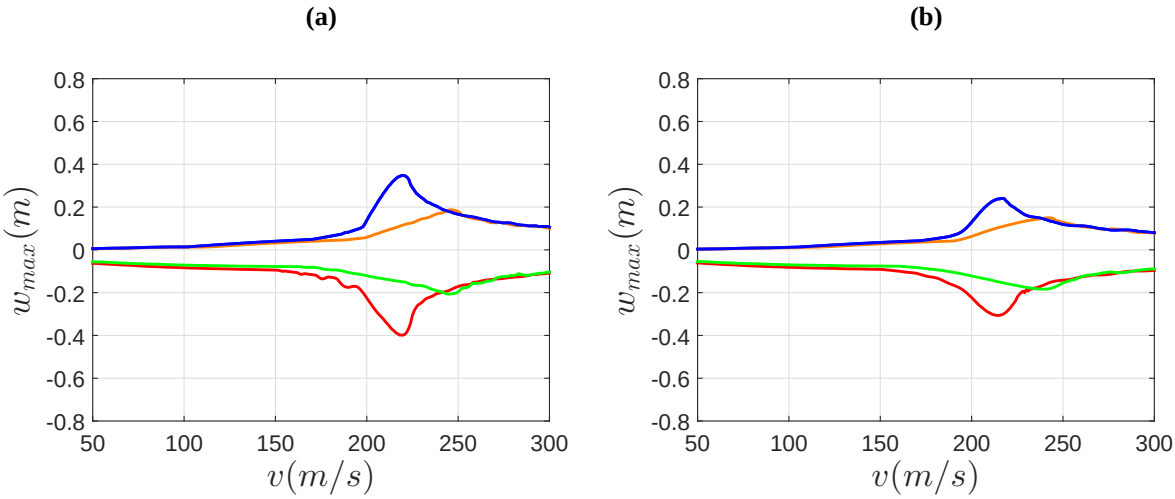

Figure 4: *Representation of beam maximum displacements as a function of load velocity for nonlinear elastic foundations with linear stiffness coefficient* $k_l = 250\,\mathrm{kN/m^2}$ *and nonlinear stiffness coefficients* $k_{nl} = 2500\,\mathrm{kN/m^4}$ *(— upward and — downward displacements) and* $k_{nl} = 25000\,\mathrm{kN/m^4}$ *(— upward and — downward displacements), undamped case* $\zeta = 0\%$ *(a) and damped case* $\zeta = 2\%$ *(b).*

ζ	v_{cr} (m/s)	w_{max} (m)		
		Present work	Ref. [4]	Error
0%	220	-0.3999	-0.400	$-0.02\,\%$
	220	0.3497	0.349	$0.20\,\%$
2%	215	-0.3064	-0.306	$0.10\,\%$
	217	0.2421	0.242	$0.04\,\%$

Table 3: *Maximum displacements and critical velocities for a nonlinear elastic foundation with* $k_l = 250\,\mathrm{kN/m^2}$ *and* $k_{nl} = 2500\,\mathrm{kN/m^4}$*. Percentage relative error with respect to Castro et al. [4].*

ζ	v_{cr} (m/s)	w_{max} (m)		
		Present work	Ref. [4]	Error
0%	245	-0.2042	-0.204	$0.10\,\%$
	246	0.1861	0.186	$0.05\,\%$
2%	241	-0.1832	-0.183	$0.10\,\%$
	242	0.1497	0.150	$-0.20\,\%$

Table 4: *Maximum displacements and critical velocities for a nonlinear elastic foundation with* $k_l = 250\,\mathrm{kN/m^2}$ *and* $k_{nl} = 25000\,\mathrm{kN/m^4}$*. Percentage relative error with respect to Castro et al. [4].*

4 HARMONIC MOVING LOAD

In the present section the main effects of the load frequency of the harmonic-varying magnitude of the moving load on the displacements of the beam and on the critical velocities are outlined. In order to obtain values of beam displacements and critical velocities representative of real railway supports, more realistic values of foundation stiffness have been adopted for the numerical simulations presented herein, with respect to those reported in Section 3.

Regarding the load frequency range, according to Chen et al. [6] the frequency (Ω) shall be always lower than 420 rad/s in nowadays engineering problems. Consequently, the computations have been performed in the range from 0 rad/s to 440 rad/s, with intervals of 40 rad/s. For each of these frequencies, the maximum upward and downward beam displacements have been computed, for velocities of the moving load starting from 10 m/s to 600 m/s, at speed intervals of 10 m/s. Then, when the neighborhood of the position of the critical velocity has been approximately recognized, the velocity step is further refined to 1 m/s, for reaching locally a better accuracy. Although the upper bound of the selected range of moving load velocity is clearly unattainable by today railway transports, its adoption looks necessary in order to properly capture more than one critical velocity.

The number of adopted finite elements is 400 (twice as in the previous analyses), each one with a length of 0.5 m. It is worth to point out that for some of the simulations presented in this section, the results retrieved with a time step chosen accordingly to the criterion given by Castro et al. [4], namely choosing the time step as the time taken by the load to travel a fifth of a finite element length, are actually characterized by a low accuracy. Therefore, a lower time step, equal to 10^{-4} s, has been adopted for all the numerical analyses presented in this section. Further information and data are extensively reported in Moioli [17].

4.1 Beams lying on a linear elastic foundation

First, a uniform linear elastic foundation is considered, with a value of Winkler linear elastic coefficient (k_l) equal to 10^4 kN/m^2. The relationship between beam maximum upward and downward displacements and load velocities, retrieved for an undamped and a damped foundation, is shown in Fig. 5.

It is noticeable that, as the amplitude of the moving load starts oscillating with frequency Ω, the critical velocities might be either one or two within the displayed range of velocities. In particular, the higher critical velocity (v_{cr2}) increases and quickly moves towards the upper limit of the plot as the load frequency increases. Conversely, the lower critical velocity (v_{cr1}) decreases until reaching zero at a very high load frequency. Such value corresponds to the lowest natural frequency of a simply-supported beam lying on a linear elastic foundation, which is defined as (see Frýba [11]):

$$\omega_1 = \sqrt{\frac{\pi^4}{L^4}\frac{EI}{m} + \frac{k_l}{m}} = 408.5\,\text{m/s}.$$

The interpretation of this result is straightforward: in fact, it is well known that a fixed load oscillating at the same natural frequency of the beam causes the resonance of the system.

A comparison between the results for the undamped foundation and those for the damped foundation reveals that, as for the case of a moving load with constant magnitude, the maximum beam displacements of the damped foundation are much smaller and much more difficult to be defined, with respect to those computed for the undamped foundation. The latter observation may be clearly visualized in Fig. 5, where multiple little peaks appear in the neighborhood of

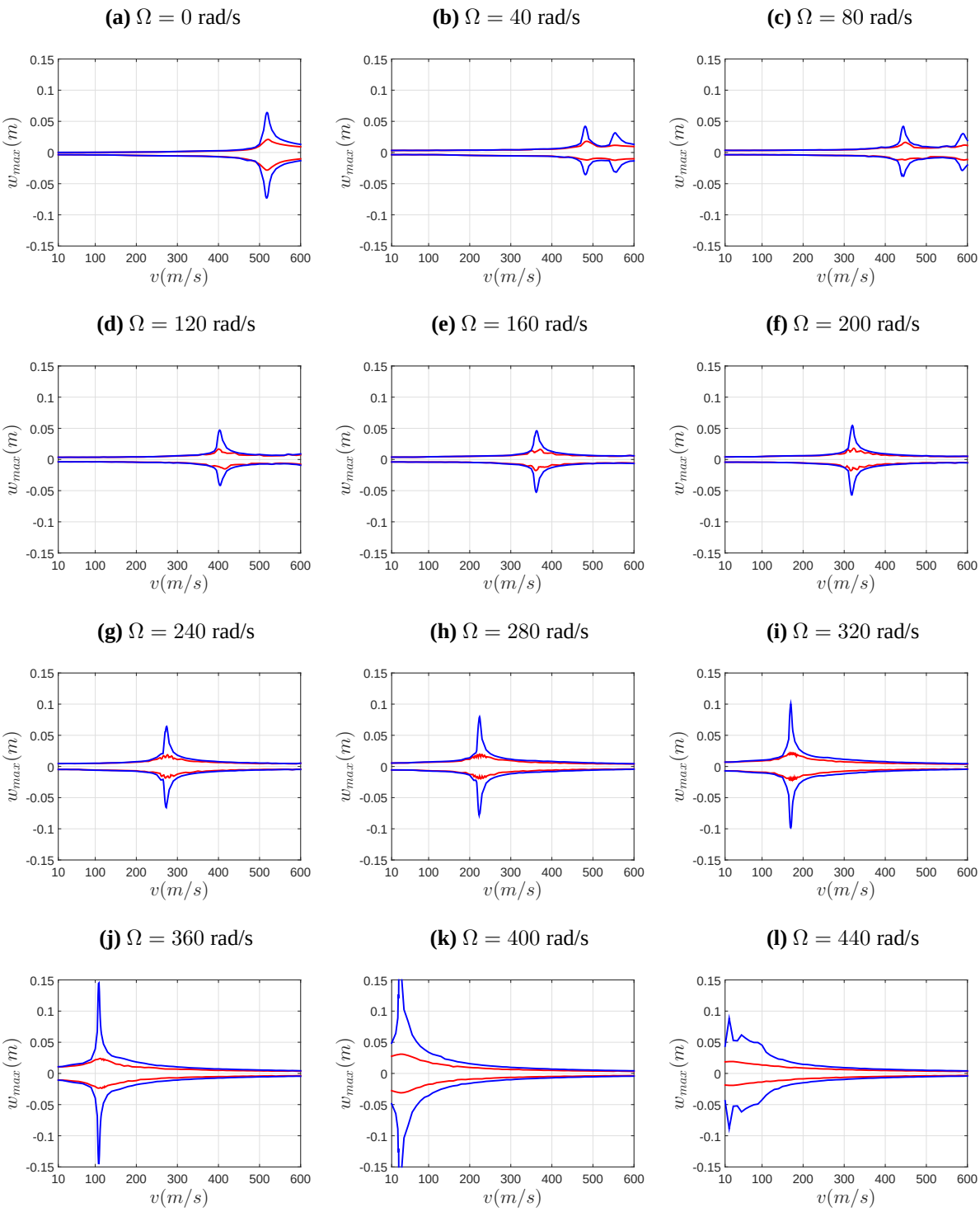

Figure 5: *Representation of beam maximum displacements as a function of load velocity and frequency for undamped (—) and damped (—) linear elastic foundations with stiffness of* $k_l = 10^4\,\mathrm{kN/m^2}$.

the critical velocity. These oscillations point out that an even more refined time step is needed for obtaining a better accuracy in the local definition of the peaks. Critical velocities are instead much less affected by damping.

The relationship between the frequency of oscillation of the moving load and the critical

velocity is explicitly depicted in Figs. 6a and 6b. These bifurcation curves have been established by fitting the values of the critical velocity computed at the different frequencies of the load. The fitting is performed by adopting the following proposed models for the lower and higher critical velocities, respectively:

$$v_{cr1} = a_1 + a_2\,\Omega + a_3\,e^{a_4\Omega}; \tag{6}$$

$$v_{cr2} = b_1 + b_2\,\Omega + b_3\,\Omega^2. \tag{7}$$

The four coefficients of the first expression are retrieved with a nonlinear least squares regression method, while the three of the second expression are achieved with a linear least squares regression method, performed by using the curve fitting built-in function in MatLab. The computed values of the coefficients in Eq. (6) and Eq. (7) for the undamped system are:

$$a_1 = 521.8 \text{ m/s}, \quad a_2 = -0.9206 \text{ m/rad}, \quad a_3 = -2.694 \text{ m/s}, \quad a_4 = 9.559 \times 10^{-3} \text{ s/rad};$$
$$b_1 = 516.9 \text{ m/s}, \quad b_2 = \quad 0.9750 \text{ m/rad}, \quad b_3 = -1.250 \times 10^{-3} \text{ ms/rad}^2.$$

The fitted curves for the undamped linear elastic foundation are plotted in Fig. 6a. This figure shows also bifurcation curves computed in accordance with the analytical solution developed by Chen et al. [6]. The comparison between the fitted curves and the analytical result reveals a very good agreement, providing a further verification of the reliability of the present finite element implementation, even for the case of a variable load.

Even though the determination of the coefficients in Eqs. (6), (7) require a significant amount of computational time, they show explicitly the critical velocities as a function of the load frequency, differently from the implicit formulation developed by Chen et al. [6]. Furthermore, the obtained models for the critical velocity/load frequency pairs are much simpler than their analytical counterparts proposed by Chen et al. [6], which involve cumbersome complex irrational fractions of polynomials containing the mechanical parameters of the system.

It is important to notice that the solution by Chen et al. [6] presents a third branch, on the right of the first natural frequency of the beam (408 rad/s). Nevertheless, as already proven by

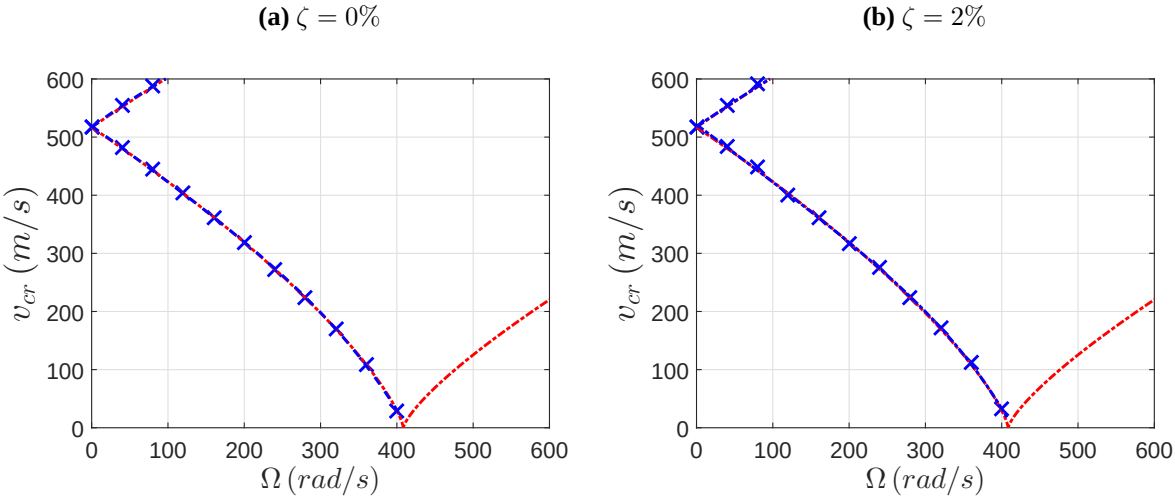

Figure 6: *Critical velocity and load frequency pairs for undamped and damped linear elastic foundations with stiffness of* $k_l = 10000\,kN/m^2$. *Results computed with: (*$\times$*) finite element implementation; (-·-) fitted curves; (-·-) analytical solution by Chen et al. [6].*

Kim [15], the critical velocities represented by such a branch cannot be detected from the plots of the maximum displacements versus load velocity, because no peak of displacement corresponds to these velocities in a finite beam. Therefore, it is not necessary to perform numerical simulations for load frequencies higher than the first natural frequency of the beam.

Bifurcation curves for critical velocity and frequency pairs have also been obtained for the case of a damped ($\zeta = 2\%$) linear elastic foundation. The adopted fitting models have been the same as those employed for the undamped foundation, i.e. those defined by Eq. (6) and Eq. (7). The coefficients computed for the damped foundation are:

$$a_1 = 522.6 \text{ m/s}, \quad a_2 = -0.9698 \text{ m/rad}, \quad a_3 = -0.9883 \text{ m/s}, \quad a_4 = 1.116 \times 10^{-2} \text{ s/rad};$$
$$b_1 = 517.9 \text{ m/s}, \quad b_2 = \quad 0.8875 \text{ m/rad}, \quad b_3 = -3.125 \times 10^{-3} \text{ ms/rad}^2.$$

The corresponding curves are plotted in Fig. 6b. In this case the critical velocity has not been reported by Chen et al. [6]. Nonetheless, comparing the curves obtained in accordance to Chen et al. [6] for the undamped case to those fitted from the numerical results, it can be seen that the level of damping is almost ineffective on the value of the critical velocity.

4.2 Beams lying on a nonlinear elastic foundation

For the nonlinear foundation model the assumed linear and nonlinear parameters defining the foundation stiffness are $k_l = 5 \times 10^3$ kN/m^2 and $k_{nl} = 2 \times 10^6$ kN/m^4, respectively. These values are selected in such a way that to provide a foundation model that is more compliant with respect to that of the linear elastic foundation for small beam displacements and, at the same time, stiffer for large displacements, as proposed by many authors (see e.g. Nguyen and Duhamel [18]).

Fig. 7 shows the retrieved results for damped and undamped nonlinear elastic foundations. It can be seen that, as in the case of a linear foundation, a second critical velocity appears for a harmonic variation of the moving load amplitude. A comparison between the graphs in Fig. 7 and their counterparts in Fig. 5 for the linear foundation, reveals that lower critical velocities and associated smaller maximum deflections are retrieved for the case of a nonlinear elastic foundation. For a foundation with viscous damping, a decrease of the maximum displacements can be observed, together with a small decrease of the critical velocities.

Bifurcation curves describing the relationship between critical velocities and load frequency are established in an analogous way as for the case of a linear elastic foundation. The adopted models for the higher and the lower critical velocity curves are the same as those employed for the linear foundation, in Eqs. (6)-(7). The coefficients computed for the undamped nonlinear elastic foundation are:

$$a_1 = 459.6 \text{ m/s}, \quad a_2 = -1.139 \text{ m/rad}, \quad a_3 = -4.5089 \text{ m/s}, \quad a_4 = 8.007 \times^{-3} \text{ s/rad};$$
$$b_1 = 456.9 \text{ m/s}, \quad b_2 = \quad 0.8082 \text{ m/rad}, \quad b_3 = \quad 4.018 \times 10^{-4} \text{ ms/rad}^2;$$

and, for the damped ($\zeta = 2\%$) nonlinear elastic foundation are:

$$a_1 = 452.1 \text{ m/s}, \quad a_2 = -1.084 \text{ m/rad}, \quad a_3 = -4.991 \text{ m/s}, \quad a_4 = 0.089 \text{ s/rad};$$
$$b_1 = 443.9 \text{ m/s}, \quad b_2 = \quad 1.078 \text{ m/rad}, \quad b_3 = -8.929 \times 10^{-4} \text{ ms/rad}^2.$$

Fig. 8 shows the curves retrieved for the undamped and the damped nonlinear foundation. Comparing these plots to those reported previously in Fig. 6, it is clear that the relationship between the critical velocities and the load frequency for linear and nonlinear elastic foundations displays similar features. Nonetheless, in contrast with the case of a linear foundation, the curves for the damped nonlinear foundation are slightly shifted downward, with respect to the undamped ones.

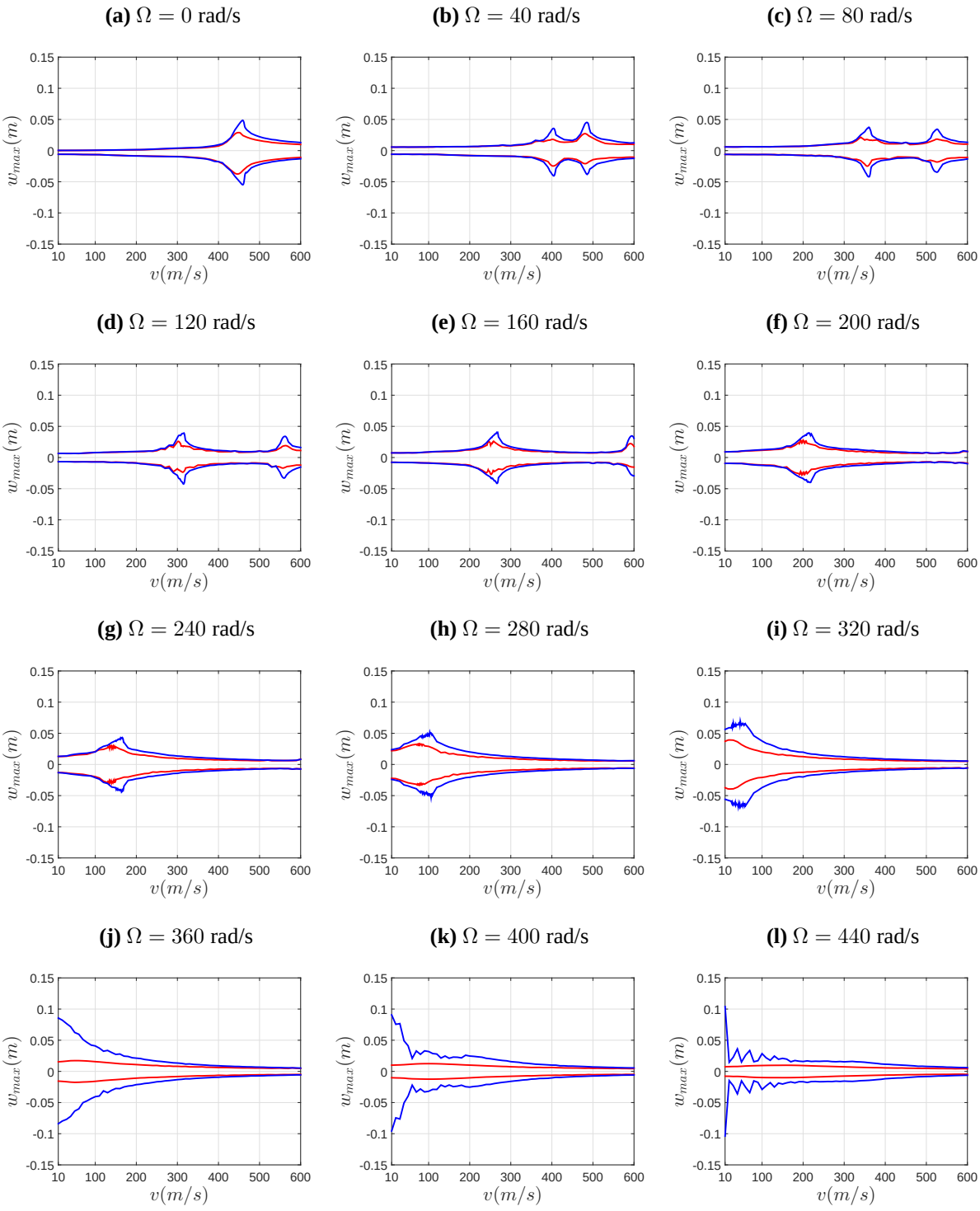

Figure 7: *Representation of beam maximum displacements as a function of load velocity and frequency for undamped (—) and damped (—) nonlinear elastic foundations with stiffnesses of* $k_l = 5 \times 10^3\,\mathrm{kN/m^2}$ *and* $k_{nl} = 2 \times 10^6\,\mathrm{kN/m^4}$.

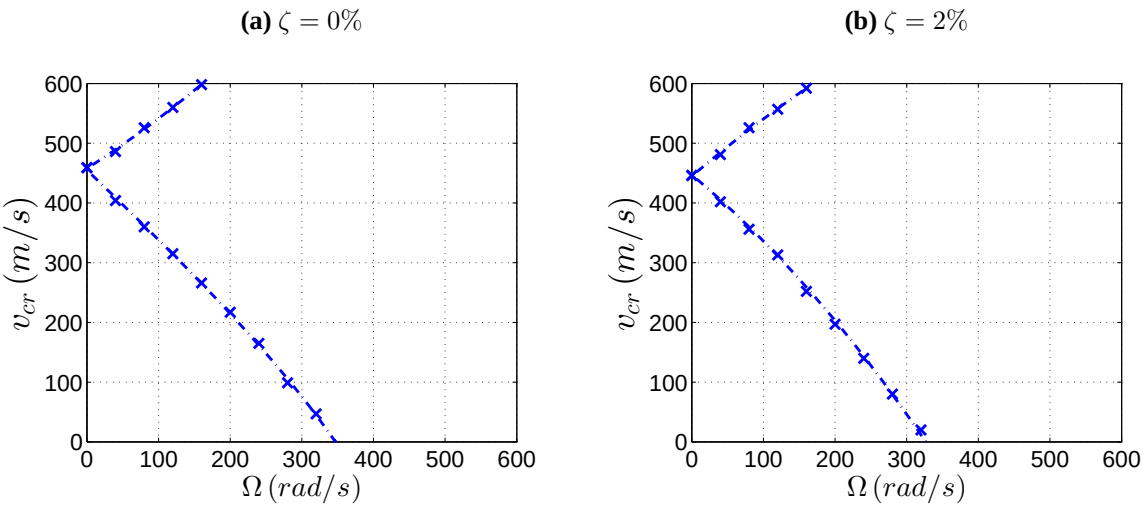

Figure 8: *Critical velocity and load frequency pairs for undamped and damped nonlinear elastic foundations with stiffnesses of* $k_l = 5 \times 10^3$ kN/m^2 *and* $k_{nl} = 2 \times 10^6$ kN/m^4. *Results computed with: (*$\times$*) finite element implementation; (- - -) fitted curves.*

5 CONCLUSIONS

In this work a finite element approach has been developed within a MatLab environment to analyze the dynamic transient response of a simply-supported beam lying on linear or nonlinear Winkler elastic foundation, subjected to a concentrated load moving at constant velocity with either constant or harmonically-varying amplitude.

The extensive performed campaign of numerical simulations provided several interesting findings and new outcomes about the behavior of high-speed rail tracks. The most significant results may be summarized in the following itemized list:

- When the amplitude of the moving load is constant, the present finite element implementation has been proven to provide results that appear fully consistent to those reported by Castro et al. [4].

- For all types of foundation, the beam maximum displacements at the critical velocities initially decrease with the load amplitude frequency, before increasing sharply near the natural frequency of the beam. Furthermore, when damping is included in the analysis, no significant effects on the critical velocities are detected, while the amplitude of displacements is lowered.

- When the beam is subjected to a moving harmonic load, two critical velocities are detected, independently from the considered type of foundation behavior, either linear or nonlinear. The two critical velocities tend to separate as the loading frequency increases. The higher critical velocity v_{cr2} increases, starting from the value of the critical velocity obtained for a constant magnitude load. On the contrary, the lower critical velocity v_{cr1} decreases, until it reaches zero for a frequency of the load equal to the first natural frequency of the beam. This behavior may reveal potential implications in practical terms, especially in lowering down the ranges of admissible train speeds, when the frequency of oscillation of the moving load amplitude becomes high.

- The relationship between the moving load amplitude frequency and the critical velocity of

the beam is portrayed in appropriate analytical bifurcation curves. These curves have been achieved by fitting the values of the critical velocity computed at different frequencies of the load variation, according to proposed variations with the amplitude frequency, with calibrated best-fitted coefficients.

- For the case of a linear foundation, the obtained bifurcation curves show a very good agreement to those available from the analytical approaches by Chen et al. [6]. In addition, the employed models for the description of the analytical bifurcation curves are explicit and much simpler than those exact proposed by Chen et al. [6].

- The employed models for the description of the bifurcation curves are also appropriate for the nonlinear case, with or without damping. The derived formulas are simple and possibly workable in practice; they may supply a guideline for the design of railway tracks when the magnitude of the moving load is oscillating in time.

It must be recognized that, in order to obtain a more realistic dynamic response of the system, some further improvements of the modelization could be made. Real applications usually require extensions to infinite beams; it is then necessary to eliminate the effect of the supports, to mitigate the perturbation induced by the boundary conditions and to prevent the reflection of the traveling waves. This could be achieved by using appropriate absorbing boundaries. Furthermore, a real vehicle spring-mass-damper system interacting with the rail should be considered, instead of a simple moving force. Finally, the assumption of symmetric behavior in tension and compression for the foundation stiffness should also be relaxed, leading to the analysis of a bilinear foundation. These issues will be the subject of on-going (Froio et al. [10]) and future investigations.

Acknowledgments

The Authors wish to acknowledge public research funding from "*Fondi di Ricerca d'Ateneo ex 60%"* and a ministerial doctoral grant and funds at the ISA Doctoral School, University of Bergamo, Department of Engineering and Applied Sciences (Dalmine). The Authors are very grateful to Prof. Fernando Simões and Prof. António Pinto da Costa, IST, University of Lisbon, for their helpful comments and suggestions, which have greatly helped in the development of this work.

REFERENCES

[1] L. Andersen, S.R.K. Nielsen, P.H. Kirkegaard, Finite element modelling of infinite Euler beams on Kelvin foundations exposed to moving loads in convected co-ordinates. *Journal of Sound and Vibration*, **241(4)**, 587–604, 2001.

[2] N.D. Beskou, D.D. Theodorakopoulos, Dynamic effects of moving loads on road pavements: a review. *Soil Dynamics and Earthquake Engineering*, **31(4)**, 547–567, 2011.

[3] R. Bogacz, T. Krzyỳski, K. Popp, On the generalization of Mathews problem of the vibrations of a beam on elastic foundation. *ZAMM - Journal of Applied Mathematics and Mechanics / Zeitschrift für Angewandte Mathematik und Mechanik*, **69(8)**, 243–252, 1989.

[4] P. Castro Jorge, F.M.F. Simões, A. Pinto da Costa, Dynamics of beams on non-uniform nonlinear foundations subjected to moving loads. *Computers & Structures*, **148**, 26–34, 2014.

[5] P. Castro Jorge, A. Pinto da Costa, F.M.F. Simões, Finite element dynamic analysis of finite beams on a bilinear foundation under a moving load. *Journal of Sound and Vibration*, **346**, 328–344, 2014.

[6] Y.H. Chen, Y.H. Huang, C.T. Shih, Response of an infinite Timoshenko beam on a viscoelastic foundation to a harmonic moving load. *Journal of Sound and Vibration*, **241(5)**, 809–824, 2001.

[7] Y.H. Chen, Y.H. Huang, Dynamic characteristics of infinite and finite railways to moving loads. *Journal of Engineering Mechanics*, **129(9)**, 987–995, 2003.

[8] Z. Dimitrovová, A.F.S. Rodrigues, Critical velocity of a uniformly moving load. *Advances in Engineering Software*, **50(1)**, 44–56, 2012.

[9] D. Froio, E. Rizzi, Analytical solution for the elastic bending of beams lying on a variable Winkler support. *Acta Mechanica*, DOI: 10.1007/s00707-015-1508-y, 1–23, 2015.

[10] D. Froio, R. Moioli, E. Rizzi, A. Pinto da Costa, F.M.F. Simões, Dynamics of beams on a bilinear elastic foundation under harmonic moving load, in preparation.

[11] L. Frýba, *Vibration of Solids and Structures under Moving Loads, 3rd Edition*. Research Institute of Transport, 1972.

[12] H.M. Hilber, T.J.R. Hughes, R.L. Taylor, Improved numerical dissipation for time integration algorithms in structural dynamics. *Earthquake Engineering and Structural Dynamics*, **3(10)**, 283–292, 1977.

[13] A.D. Kerr, Continuously supported beams and plates subjected to moving loads: a survey. *Solid Mechanics Archives*, **6(4)**, 401–449, 1981.

[14] N.D. Kien, L.T. Ha, Dynamic characteristics of elastically supported beam subjected to a compressive axial force and a moving load. *Vietnam Journal of Mechanics*, **33(2)**, 113–131, 2011.

[15] S.M. Kim, Vibration and stability of axial loaded beams on elastic foundation under moving harmonic loads, *Engineering Structures*, **26(1)**, 95–105, 2004.

[16] The MathWorks, Inc. MatLab. http://www.mathworks.com/products/matlab; 2016.

[17] R. Moioli, *Numerical Analysis of Beams on Nonlinear Winkler Elastic Foundations under Moving Load*, M.Sc. Thesis in Mechanical Engineering, Advisor E. Rizzi, Co-Advisor D. Froio, Università di Bergamo, Scuola di Ingegneria, 201 pages, 31 March 2016.

[18] V.H. Nguyen, D. Duhamel, Finite element procedures for nonlinear structures in moving coordinates, Part II: Infinite beam under moving harmonic loads. *Computers & Structures*, **86(21)**, 2056–2063, 2008.

[19] D. Thambiratnam, Y. Zhuge, Dynamic analysis of beams on an elastic foundation subjected to moving loads. *Journal of Sound and Vibration*, **198(2)**, 149–169, 1996.

[20] Y.H. Wang, L.G. Tham, Y.K. Cheung, Beams and plates on elastic foundations: a review. *Progress in Structural Engineering and Materials*, **7(4)**, 174–182, 2005.

ECCOMAS Congress 2016
VII European Congress on Computational Methods in Applied Sciences and Engineering
M. Papadrakakis, V. Papadopoulos, G. Stefanou, V. Plevris (eds.)
Crete Island, Greece, 5–10 June 2016

ELASTOSTATIC AND MODAL AND BUCKLING ANALYSIS OF SPATIAL FGM BEAM STRUCTURES

Justín Murín[1], Mehdi Aminbaghai[2], Juraj Hrabovský[1],

Vladimír Kutiš[1], Juraj Paulech[1], Stephan Kugler[3]

[1]Slovak University of Technology in Bratislava, Faculty of Electrical Engineering and Information Technology, Ilkovicova 3, 812 19 Bratislava, Slovakia,
justin.murin@stuba.sk
[2]Institute for Mechanics of Materials and Structures Karlsplatz 13, A-1040 Vienna, Austria,
mehdi.aminbaghai@tuwien.ac.at
[3]University of Applied Sciences Wiener Neustadt, Johannes Gutenberg-Strasse 3, A/2700 Wiener Neustadt, Austria,
kugler@fhwn.ac.at

Keywords: Functionally graded materials, Homogenization of material properties, FGM finite 3D beam element, Static and modal and buckling analysis, Spatially varying material properties.

Abstract. *In this contribution, a homogenized beam finite element of double symmetric cross-section made of a Functionally Graded Material (FGM) is presented, which can be used for static, modal and buckling analysis of single beams and beam structures with three directional variation of material properties. The material properties in a real beam can vary continuously in longitudinal direction while the variation with respect the transversal and lateral directions is assumed to be symmetric in a continuous or discontinuous manner. The shear force deformation effect and the effect of inertia and rotary inertia are taken into account. Additionally, the longitudinally varying Winkler elastic foundation and the effect of axial force are included by the finite element equations as well. Homogenization of spatially varying material properties to effective quantities with a longitudinal variation is done by the extended mixture rules and multilayer method (MLM). For the homogenized beam the 12×12 finite element effective matrix, consisting of the linearized stiffness and consistent mass inertia terms, is established. Numerical experiments are made concerning static, modal and buckling analyses of single FGM beam and beam structures to show the accuracy and effectiveness of the proposed FGM beam finite element.*

1 INTRODUCTION

Important classes of structural components, where FGM is used, are beams and beam structures. FGM beams play an important role not only in classical structural applications, but we can find many applications in thermal, electric-thermal or electric-thermal-structural systems (e.g. micro-electro-mechanical systems (MEMS) as sensors and actuators and other mechatronic devices). In all these applications, using new materials like FGM can greatly improve the efficiency of the systems. FGM is built as a mixture of two or more constituents whose particles have almost the similar form and dimensions (powder, plasma particles, etc.). The continuous or multilayered variation of macroscopic material properties can be caused by varying the volume fraction of the constituents or by varying the constituent's material properties (e.g. by a non-homogeneous temperature field). In the literature a huge amount of papers can be found which deal with modeling and simulation of static and dynamic problems of FGM beams.

The latest results of theoretical research on statics and vibration and loss of stability of FGM and composite beams are presented for example in the articles [1-13].The first significant feature of the references [1-8] (and also of those published in the previous period) is that variation of material properties is considered only in one direction, usually along the beam thickness, and exceptionally in the longitudinal direction of the beam. The second feature of these works is that they are analyzed only a simple planar beams with rectangular cross-section. The third feature of most of these works is that their fundamental equations are based on the equations of plane stress state in a continuum with varying material properties which are simplified for the solution of the beams. In [9-12], general formulations for non-uniform shear warping are presented and an advanced 20×20 stiffness matrix and the corresponding nodal load vector of a member of arbitrary composite cross section is developed, taking shear lag effects into account due to both flexure and torsion. In [13], a static analysis of three-dimensional FGM beams by hierarchical modeling and a collocation meshless solution method is presented.

With regard to our work in the past period in the field, we presented in [14-16] a solution of free vibration of a single 2D FGM beam with continuous planar polynomial variation of material properties (in axial and transversal direction) by a fourth-order differential equation of second order beam theory. The focus of these publications is laid on a new concept for expanding the second order bending beam theory considering the shear deformation according to Timoshenko beam theory. There, the shear deformation effect in FGM beams with planar continuous variations of material properties is originally included by means of the average shear correction factor that has been obtained by an integration of the shear correction function [17]. A continuous polynomial variation of the effective elastic modulus and the mass density is considered by continuous polynomial planar variation of both the volume fraction and material properties of the FGM constituents. The choice of a polynomial gradation of material properties enables an easier integration of the derived differential equation and allows to model practically realizable variations of material properties. The effect of consistent inertia and rotary inertia, and the effect of axial forces are taken into account as well.

As mentioned above, many time published papers registered e.g. in the Web of Science database, deal with static and dynamic and buckling analysis of the FGM single planar beam with transverse variation of material properties only. Less attention is paid on both the longitudinal and lateral variations of material properties. The authors failed in finding more papers which deal with analysis of single beams or spatial beam structures made of FGM with spatial variation of material properties (in three directions).

The proposed contribution is a continuation of our previous papers [14-18]. The derivation of the FGM beam finite element equations suitable for static, modal and buckling analyses of single beams or spatial beam structures made of spatially varying FGM (in longitudinal and transversal and lateral direction) is presented. From the differential equations of axial, flexural and torsional deformation of the FGM beam with longitudinally varying material properties the transfer relations and following the local and global finite beam element matrices are established. Effects of axial and shear forces are included as well as the longitudinally varying Winkler elastic foundation and inertia loads. Homogenization of the spatially varying material properties in the real FGM beam and calculation of their effective values are done by extended mixture rules and by the multilayer method (MLM) [18,25]. This method can also be used in the homogenization of multilayer beams with symmetrically discontinuous (multilayered) variation of material properties in transversal and lateral direction. In the modal and buckling analysis an eigenvalue problem is solved. Numerical experiments are performed to calculate the elastostatic and modal response and the critical buckling force of chosen FGM beams and beam structures with rectangular and hollow cross-sections with spatial variations of material properties. The solution results are discussed and compared to those obtained by means of very fine 3D – solid and beam finite element meshes of the software ANSYS Workbench [34].

The novel aspects of the current paper are:

- extension of the MLM to homogenization of the spatially (polynomial) varying material properties (continuously in longitudinal and symmetrically in transversal and lateral direction (continuously or multilayered)) for calculation of the effective longitudinally varying elasticity modules for axial and flexural and torsional loading, and the competent effective mass-densities;
- extension of the second order beam theory and the uniform torsion theory on static, modal and buckling analysis of FGM beams with spatial variation of material properties (in three directions);
- including the effects of the shear and axial forces, as well as the longitudinally varying Winkler elastic foundations;
- derivation of the transfer relations for the 3D straight FGM beam (with homogenized longitudinal variation of the effective material properties) of doubly symmetric cross-section;
- establishing of the 12×12 effective finite element matrix of the 3D FGM beam (with homogenized longitudinal variation of the effective material properties) consisting of the linear and linearized geometric stiffness and consistent mass inertia terms;
- performing of the numerical experiments concerning the static and modal and buckling analysis of the FGM beams and beam structures with spatially varying material properties.

2 FINITE ELEMENT EQUATIONS OF THE 3D FGM BEAM

Let us consider a straight beam element of doubly symmetric cross-section – Figure 1. The degrees of freedom at node *i* are: the displacements u_i, v_i, w_i in the local directions *x*, *y*, *z*, and the cross-sectional area rotations about the *x*, *y*, *z* directions - $\varphi_{x,i}, \varphi_{y,i}, \varphi_{z,i}$. The degrees of freedom at the node *j* are denoted in a similar manner. The internal forces at node *i* are: the axial force N_i, the transversal forces $R_{y,i}$ and $R_{z,i}$, the bending moments $M_{y,i}$ and, the torsion moment $M_{x,i}$.

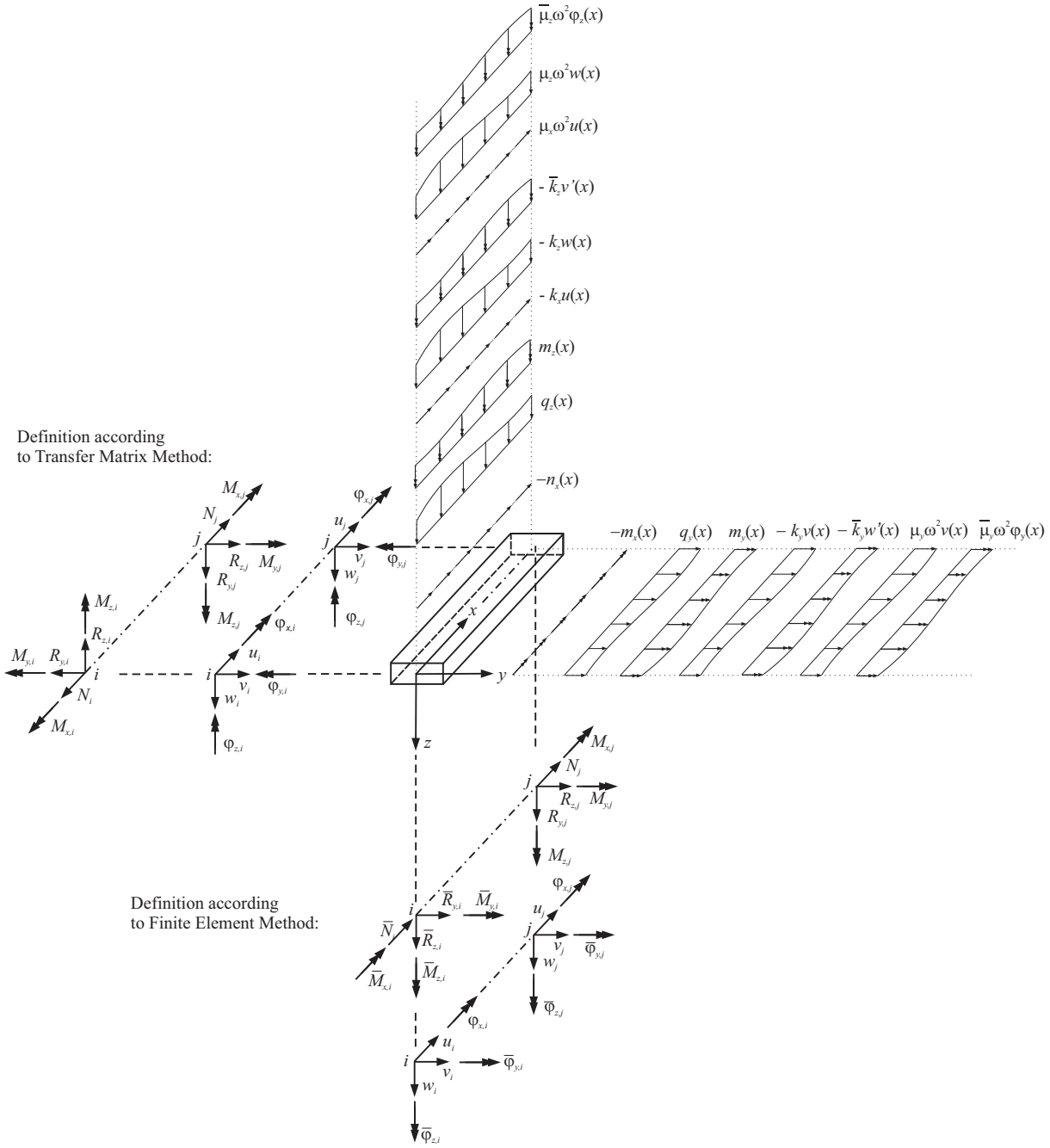

Figure 1: The local internal variables, static and inertia and loads for transfer matrix and finite element methods.

Furthermore, $n_x = n_x(x)$ denotes the axial force distribution, $q_z = q_z(x)$ and $q_y = q_y(x)$ are the transversal and lateral force distributions, $m_x = m_x(x)$, $m_y = m_y(x)$ and $m_z = m_z(x)$ are the distributed moments, $\mu_x = \rho A = \mu_y = \mu_z = \mu$ denote the mass distribution, $\overline{\mu}_y = \rho I_y$, $\overline{\mu}_z = \rho I_z$ and $\overline{\mu}_{xT} = \rho I_p$ refer to the distributions of mass moments of inertia, $\rho = \rho_L^H(x) \equiv \rho_L^H$ is the homogenized effective mass density distribution, A is the cross-sectional area, I_y and I_z are the second moments of area, $I_p = I_y + I_z$ denotes the polar moment of area, $k_x = k_x(x)$, $k_y = k_y(x)$, $k_z = k_z(x)$, $\overline{k}_y = \overline{k}_y(x)$, $\overline{k}_z = \overline{k}_z(x)$ are the elastic foundation modules

(the torsional elastic foundation is not considered), and ω is the circular frequency. The effective homogenized and longitudinally varying stiffness reads as follows: $EA = E_L^{NH}(x)A$ is the axial stiffness ($E_L^{NH}(x) \equiv E_L^{NH}$ is the effective elastic modulus for axial loading), $EI_y = E_L^{M_yH}(x)I_y$ is the flexural stiffness about the *y*-axis ($E_L^{M_yH}(x) \equiv E_L^{M_yH}$ is the effective elastic modulus for bending about axis *y*), $EI_z = E_L^{M_zH}(x)I_z$ is the flexural stiffness in axis *z*, ($E_L^{M_zH}(x) \equiv E_L^{M_zH}$ is the effective elastic modulus for bending about axis *z*), $G\bar{A}_y = G_{Ly}^{H}(x)k_y^{sm}A$ is the reduced shear stiffness in *y*-direction ($G_{Ly}^{H}(x) \equiv G_{Ly}^{H}$ is the effective shear modulus and k_y^{sm} is the average shear correction factor in *y*-direction), $G\bar{A}_z = G_{Lz}^{H}(x)k_z^{sm}A$ is the reduced shear stiffness in *z* – direction ($G_{Lz}^{H}(x) \equiv G_{Lz}^{H}$ is the effective shear modulus and k_z^{sm} is the average shear correction factor in *z* - direction), $G_L^{M_xH}(x)I_T$ is the effective torsional stiffness, $G_L^{M_xH}(x) = G_L^{M_xH}$ is the torsional elastic modulus and I_T is the torsion constant – $I_p = I_T$ for the circular and ring cross-section). The derivatives with respect to *x* of the relevant variable is denoted with an apostrophe " ′ " throughout the article.

The differential equations for axial, transversal, lateral and torsional deformation and their solution are established according the Figure 1: Definition according the Transfer Matrix Method. The finite element equations of the 3D FGM beam are established from the transfer matrix relations according Figure 1: Definition according the Finite Element Method.

2.1 Axial deformation

Equation (1) results from the axial deformation problem of the FGM beam, including the specific case of harmonic oscillations ($u = u(x)$ is the axial displacement distribution, $u' = u'(x)$ is its first derivative and $u'' = u''(x)$ is its second derivative):

$$N' = n_x + \left(k_x - \mu_x \omega^2\right)u\,, \tag{1}$$

$$u' = \frac{N}{EA}, \tag{2}$$

By combination of (1) and (2) we get the differential equation with non-constant polynomial coefficients

$$\eta_{2u}u'' + \eta_{1u}u' + \eta_{0u}u = n_x\,, \tag{3}$$

with $\eta_{2u} = EA,\ \eta_{1u} = E'A,\ \eta_{0u} = \mu\omega^2 - k_x$, and $E \equiv E_L^{NH}(x)$. The polynomial distributed axial force is: $n_x = \sum_{k=0}^{p_n} n_{x,k}x^k = n_{x,0}x^0 + n_{x,1}x^1 + n_{x,2}x^2 + \ldots + n_{x,p_n}x^{p_n}$, where $n_{x,k}$ are the values of the *k*-th derivative of the axial force n_x at the beam node *i*. For the modal analysis of axial vibration the right hand side of (3) vanishes.

The solution of (3) can be expressed by the polynomial transfer functions $\bar{b}_{kN} = \bar{b}_{kN}(x)$, ($k \in \langle 0, p_n + 2\rangle$) for axial loading [19, 20]:

$$\begin{bmatrix} u(x) \\ u'(x) \end{bmatrix} = \begin{bmatrix} \bar{b}_{0N} & \bar{b}_{1N} \\ \bar{b}'_{0N} & \bar{b}'_{1N} \end{bmatrix} \cdot \begin{bmatrix} u_i \\ u'_i \end{bmatrix} + \begin{bmatrix} \sum_{k=0}^{p_n} n_{x,k} \bar{b}_{k+2N} \\ \sum_{k=0}^{p_n} n_{x,k} \bar{b}'_{k+2N} \end{bmatrix}. \tag{4}$$

Here, u_i is the axial displacement and u'_i is the value of first derivative of $u(x)$ at node *i*.

If the $u'(x)$ and u'_i are replaced with the constitutive equation of the FGM beam (2), we get

$$\begin{bmatrix} u(x) \\ N(x) \end{bmatrix} = \begin{bmatrix} A_{1,1} = \bar{b}_{0N} & A_{1,2} = \dfrac{\bar{b}_{1N}}{E_i A} \\ A_{2,1} = EA\bar{b}'_{0N} & A_{2,2} = \dfrac{EA}{E_i A}\bar{b}'_{1N} \end{bmatrix} \cdot \begin{bmatrix} u_i \\ N_i \end{bmatrix} + \begin{bmatrix} A_{1,3} = \sum_{k=0}^{p_n} n_{x,k} \bar{b}_{k+2N} \\ A_{2,3} = EA \sum_{k=0}^{p_n} n_{x,k} \bar{b}'_{k+2N} \end{bmatrix}, \tag{5}$$

where E_i is the initial value of the homogenized elastic modulus $E_L^{NH}(x)$ at node *i*.

By setting $x = L$ in (5), the dependence of the nodal variables at node *j* on the nodal variables at node *i* are obtained. By appropriated mathematical operations and by considering the altered orientation of the local internal variables in FEM formulation (see Fig. 1), the local finite element equation for the axial loading (including the particular case of axial harmonic vibrations) are obtained (with $\bar{N}_i = -N_i$):

$$\begin{bmatrix} \bar{N}_i \\ N_j \end{bmatrix} = \begin{bmatrix} B_{1,1} = \dfrac{A_{1,1}}{A_{1,2}} & B_{1,7} = -\dfrac{1}{A_{1,2}} \\ B_{7,1} = A_{2,1} - \dfrac{A_{1,1}A_{2,2}}{A_{12}} & B_{7,7} = \dfrac{A_{2,2}}{A_{1,2}} \end{bmatrix} \cdot \begin{bmatrix} u_i \\ u_j \end{bmatrix} + \begin{bmatrix} F_1 = \dfrac{A_{1,3}}{A_{1,2}} \\ F_7 = A_{2,3} - \dfrac{A_{1,3}A_{2,2}}{A_{1,2}} \end{bmatrix}. \tag{6}$$

It can be easy shown that the matrix *B* is symmetric. The terms of the matrix *B*and the loads vector *F* are calculated numerically using MATHEMATICA [21]. Their indices are deliberately numbered in order to indicate the position of the components in the local matrix and loads vector of the 3D beam finite element, which is established later.

2.2 Flexural deformation about the *y* and *z* axis

The differential equation of 4th order with non-constant coefficients of the homogenized FGM beam flexural transversal deformation (including the particular case of flexural harmonic vibrations) in the *x*-*z* plane (Figure 1) has the form [15]:

$$\eta_{4w} w'''' + \eta_{3w} w''' + \eta_{2w} w'' + \eta_{1w} w' + \eta_{0w} w = \eta_{Lxz}(x) \tag{7}$$

with polynomial loads acting in the *x*-*z* plane

$$\eta_{Lxz}(x) = \sum_{s=0}^{\max s} \eta_{Lxz,s} x^s = \sum_{k=0}^{p_{qz}} q_{z,k} x^k + \sum_{k=1}^{p_{qz}} k q_{z,k} x^{k-1} + \sum_{k=2}^{p_{qz}} k(k-1) q_{z,k} x^{k-2} + \sum_{k=0}^{p_{my}} m_{y,k} x^k + \sum_{k=1}^{p_{my}} k m_{y,k} x^{k-1}, \tag{8}$$

where: $\eta_{Lxz,s}$ are the values of the *k*-th derivative of load polynomial (8) at the beam node *i* (*s* is the maximum degree of the polynomial); $q_{z,k}$ are the values of the *k*-th derivative of the

polynomial transversal force $q_z = q_z(x)$, and $m_{y,k}$ are the values of the *k*-th derivative of the polynomial moment $m_y = m_y(x)$ at the beam node *i* (p_{qz} and p_{my} is the maximum degree of the polynomials).For the modal analysis of flexural vibration the right hand side of (7) vanishes. Again, $w = w(x)$ refers to the deflection curve in the $x-z$ plane. The derivation of the non-constant coefficients η_{0w} to η_{4w} and appropriated parameters of the differential equation (7) from the main coupled equations (9) and (10) of the 2nd order beam theory (including the inertia forces, shear and axial force) using the relation between the transversal and shear force (11) is described in [15, 17].

$$R_z' = -q_z + k_z w - \mu\omega^2 w \qquad M_y' = Q_z + m_y + \overline{\mu_y}\omega^2\varphi_y \tag{9}$$

$$\varphi_y' = -\frac{M_y}{EI_y} \Rightarrow M_y = -EI_y\varphi_y'^{\,e} \quad w' = \varphi_y + \frac{Q_z}{G\overline{A}_z} \Rightarrow Q_z = G\overline{A}_z w' - G\overline{A}_z\varphi_y \tag{10}$$

$$Q_z = -\left(\overline{k_z} + N^{II}\right)w' + R_z \tag{11}$$

Here, Q_z is the shear force and $N^{II} \equiv N$ is the resultant axial force of the 2nd order beam theory (it has a system character and has to be known). In our case, $E \equiv E_L^{M_y H}$ is the homogenized elastic modulus for bending about *y* and $G \equiv G_{Lz}^{H}$ is the shear modulus in *z*-direction. Further, $\varphi_y = \varphi_y(x)$ denotes the angle of cross-section rotation about the*y*-axis.

If the variation of the beam parameters is polynomial, the solution of the differential equation (7) based on the transfer functions [20] can be written as,

$$\begin{bmatrix} w(x) \\ w'(x) \\ w''(x) \\ w'''(x) \end{bmatrix} = \begin{bmatrix} b_{0w} & b_{1w} & b_{2w} & b_{3w} \\ b_{0w}' & b_{1w}' & b_{2w}' & b_{3w}' \\ b_{0w}'' & b_{w1}'' & b_{2w}'' & b_{3w}'' \\ b_{0w}''' & b_{1w}''' & b_{2w}''' & b_{3w}''' \end{bmatrix} \cdot \begin{bmatrix} w_i \\ w_i' \\ w_i'' \\ w_i''' \end{bmatrix} + \begin{bmatrix} \sum_{s=0}^{max\,s} \eta_{Lxz,s} b_{s+4w} \\ \sum_{s=0}^{max\,s} \eta_{Lxz,s} b_{s+4w}' \\ \sum_{s=0}^{max\,s} \eta_{Lxz,s} b_{s+4w}'' \\ \sum_{s=0}^{max\,s} \eta_{Lxz,s} b_{s+4w}''' \end{bmatrix}. \tag{12}$$

There, b_{jw}, b_{jw}', b_{jw}'' and b_{jw}''' with ($j \in \langle 0,3 \rangle$),and b_{s+4w}, b_{s+4w}', b_{s+4w}'' and b_{s+4w}''' are the solution functions (so called the transfer functions for bending) of the differential equation (7). The dependence of the $w' = w'(x)$, $w'' = w''(x)$ and $w''' = w'''(x)$ on the $\varphi_y = \varphi_y(x)$, $M_y = M_y(x)$ and $R_z = R_z(x)$ is described in [648], from which the transfer matrix expression is obtained

$$\begin{bmatrix} w(x) \\ \varphi_y(x) \\ M_y(x) \\ R_z(x) \end{bmatrix} = \begin{bmatrix} A_{1,1} & A_{1,2} & A_{1,3} & A_{1,4} \\ A_{2,1} & A_{2,2} & A_{2,3} & A_{2,4} \\ A_{3,1} & A_{3,2} & A_{3,3} & A_{3,4} \\ A_{4,1} & A_{4,2} & A_{4,3} & A_{4,4} \end{bmatrix} \cdot \begin{bmatrix} w_i \\ \varphi_{y,i} \\ M_{y,i} \\ R_{z,i} \end{bmatrix} + \begin{bmatrix} A_{1,5} \\ A_{2,5} \\ A_{3,5} \\ A_{4,5} \end{bmatrix}. \tag{13}$$

The kinematical and kinetic variables at node *I* are denoted by index *i* in (12). The terms *A* in (12) are established semi analytically using MATHEMATICA [21].

By setting $x = L$ in (13) the dependence of the nodal variables at node *j* on the nodal variables at node *i* are obtained. Then, using appropriate mathematical operations and by considering the altered orientation of the local internal variables in FEM formulation (see Fig. 1), the local finite element equations for the deflection (in particular case for the flexural free vibration) about the *y*-axis read (with $\bar{R}_{z,i} = -R_{z,i}$, $\bar{M}_{y,i} = -M_{y,i}$, $\bar{\varphi}_{y,i} = -\varphi_{y,i}$ and $\bar{\varphi}_{y,j} = -\varphi_{y,j}$),

$$\begin{bmatrix} \bar{R}_{z,i} \\ \bar{M}_{y,i} \\ R_{z,j} \\ M_{y,j} \end{bmatrix} = \begin{bmatrix} B_{3,3} & B_{3,6} & B_{3,9} & B_{3,12} \\ B_{5,2} & B_{5,5} & B_{5,8} & B_{5,11} \\ B_{9,3} & B_{9,6} & B_{9,9} & B_{9,12} \\ B_{11,2} & B_{11,5} & B_{11,8} & B_{11,11} \end{bmatrix} . \begin{bmatrix} w_i \\ \bar{\varphi}_{y,i} \\ w_j \\ \bar{\varphi}_{y,j} \end{bmatrix} + \begin{bmatrix} F_3 \\ F_5 \\ F_9 \\ F_{11} \end{bmatrix} . \tag{14}$$

Indices in matrix B and $F$are deliberately numbered to indicate the position of members of the components in the local matrix of 3D beam finite element, which is shown later. The terms of matrix B and F have to be evaluated numerically. It can be easy shown that the matrix *B* is symmetric.

The differential equation of 4th order with non-constant coefficients for the homogenized FGM beam flexural deformation (including the particular case of lateral flexural harmonic vibrations) in the *x*-*y* plane (Figure 1), can be derived similarly to the previous case:

$$\eta_{4v} v'''' + \eta_{3v} v''' + \eta_{2v} v'' + \eta_{1v} v' + \eta_{0v} v = \eta_{Lxy}(x), \tag{15}$$

with polynomial loads acting in the *x*-*y* plane

$$\eta_{Lxy}(x) = \sum_{s=0}^{\max s} \eta_{Lxy,s} x^s = \sum_{k=0}^{p_{qz}} q_{y,k} x^k + \sum_{k=1}^{p_{qz}} k q_{y,k} x^{k-1} + \sum_{k=2}^{p_{qz}} k(k-1) q_{y,k} x^{k-2} + \sum_{k=0}^{p_m} m_{z,k} x^k + \sum_{k=1}^{p_m} k m_{z,k} x^{k-1}, \tag{16}$$

where: $\eta_{Lxy,s}$ are the values of the *k*-th derivative of load polynomial (16) at the beam node *i* (*s* is the maximum degree of the polynomial); $q_{y,k}$ are the values of the *k*-th derivative of the polynomial transversal force $q_y = q_y(x)$ and $m_{z,k}$ are the values of the *k*-th derivative of the polynomial moment $m_z = m_z(x)$ at the beam node *i* (p_{qy} and p_{mz} is the maximum degree of the polynomials).). For the modal analysis of flexural vibration the right hand side of (15) vanishes.

Again, $v = v(x)$ is the deflection curve in $x - y$ plane. Its derivatives with respect to *x* are denoted by an apostrophe.

By appropriated mathematical operations (similarly to the previous case) the local finite element equations for the flexural lateral deflection (in *x*-*y* plane) are obtained,

$$\begin{bmatrix} \bar{R}_{y,i} \\ \bar{M}_{z,i} \\ R_{y,j} \\ M_{z,j} \end{bmatrix} = \begin{bmatrix} B_{2,2} & B_{2,6} & B_{2,8} & B_{2,12} \\ B_{6,2} & B_{6,6} & B_{6,8} & B_{6,12} \\ B_{8,2} & B_{8,6} & B_{8,8} & B_{8,12} \\ B_{12,2} & B_{12,6} & B_{12,8} & B_{12,12} \end{bmatrix} . \begin{bmatrix} v_i \\ \bar{\varphi}_{z,i} \\ v_j \\ \bar{\varphi}_{z,j} \end{bmatrix} + \begin{bmatrix} F_2 \\ F_6 \\ F_8 \\ F_{12} \end{bmatrix} . \tag{17}$$

It can be easy shown that the matrix *B* is symmetric.

2.3 Uniform torsional deformation

The differential equations of uniform torsion of a beam are formulated according the Figure 1 and have a form,

$$M_x' = m_x - \rho_L^H I_p \omega^2 \varphi_x, \tag{18}$$

$$\varphi_x' = \frac{M_x}{GI_T}. \tag{19}$$

Here, $\varphi_x = \varphi_x(x)$ is the angle of twist about x - axis and $\varphi_x' = \varphi_x'(x)$ is its first derivative.

By a combination of equations (18) and (19) and after some mathematical manipulations the differential equation for uniform torsion (including the particular case of torsional harmonic vibrations) has been obtained

$$\eta_{2T}\varphi_x'' + \eta_{1T}\varphi_x' + \eta_{0T}\varphi_x = m_x, \tag{20}$$

with non-constant parameters $\eta_{1T} = GI_T$, $\eta_{2T} = G'I_T$, $\eta_{0T} = \rho_L^H I_p \omega^2$ and $G \equiv G_L^{M_x H}$. Further, $\varphi_x'' = \varphi_x''(x)$ is the second derivative of the angle of twist. The polynomial distributed axial force is: $m_x = \sum_{k=0}^{p_n} m_{x,k} x^k = m_{x,0}x^0 + m_{x,1}x^1 + m_{x,2}x^2 + ... + m_{x,p_n} x^{p_{mx}}$, where $m_{x,k}$ are the values of the k-th derivative of the distributed torsional moment m_x at the beam node i. For the modal analysis of axial vibration the right hand side of (3) vanishes. According to [19], the solution of the differential equation (20) reads:

$$\begin{bmatrix} \varphi_x(x) \\ \varphi_x'(x) \end{bmatrix} = \begin{bmatrix} \bar{b}_{0T} & \bar{b}_{1T} \\ \bar{b}_{0T}' & \bar{b}_{1T}' \end{bmatrix} \cdot \begin{bmatrix} \phi_{x,i} \\ \phi_{x,i}' \end{bmatrix} + \begin{bmatrix} \sum_{k=0}^{p_{mx}} m_{x,k} \bar{b}_{k+2T} \\ \sum_{k=0}^{p_{mx}} m_{x,k} \bar{b}_{k+2T}' \end{bmatrix}. \tag{21}$$

In equation (21), the $\bar{b}_{kT}$ and $\bar{b}_{kT}'$, $(k \in \langle 0, p_{mx} + 2 \rangle)$, are the transfer functions for torsion and their first derivatives, respectively and represent the solution functions of the differential equation (20). The transfer functions depend on the longitudinal variation of the torsional shear modulus, the natural frequency, the polar moment of inertia, the torsion constant and the consistent mass density. They are calculated in a similar way as is shown in the previous loading cases. By inserting (18) and (19) into (21) and after some mathematical manipulations the transfer matrix relations (22) for the particular case of uniform torsion harmonic free vibration are obtained,

$$\begin{bmatrix} \varphi_x(x) \\ M_x(x) \end{bmatrix} = \begin{bmatrix} \bar{b}_{0T} & \dfrac{\bar{b}_{1T}}{G_i I_T} \\ GI_T \bar{b}_{0T}' & \dfrac{GI_T}{G_i I_T} \bar{b}_{1T}' \end{bmatrix} \cdot \begin{bmatrix} \phi_{x,i} \\ M_{x,i} \end{bmatrix} + \begin{bmatrix} A_{1,3} = \sum_{k=0}^{p_{mx}} m_{x,k} \bar{b}_{k+2T} \\ A_{2,3} = GI \sum_{k=0}^{p_{mx}} m_{x,k} \bar{b}_{k+2T}' \end{bmatrix}. \tag{22}$$

By setting $x = L$ in (22) a dependence of the state variables at point j on the state variables at initial point i for modal analysis reads

$$\begin{bmatrix} \varphi_{x,j} \\ M_{x,j} \end{bmatrix} = \begin{bmatrix} \left[\bar{b}_{0T}\right]_{x=L} & \dfrac{\left[\bar{b}_{1T}\right]_{x=L}}{G_i I_T} \\ G_j I_T \left[\bar{b}'_{0T}\right]_{x=L} & \dfrac{G_j I_T}{G_i I_T}\left[\bar{b}'_{1T}\right]_{x=L} \end{bmatrix} \cdot \begin{bmatrix} \varphi_{x,i} \\ M_{x,i} \end{bmatrix} + \begin{bmatrix} \sum_{k=0}^{p_{mx}} m_{x,k}\, \bar{b}_{k+2T}\big|_{x=L} \\ GI \sum_{k=0}^{p_{mx}} m_{x,k}\, \bar{b}'_{k+2T}\big|_{x=L} \end{bmatrix}. \tag{23}$$

By simple mathematical manipulations we get the local finite element equation for uniform torsion (with $\bar{M}_{x,i} = -M_{x,i}$):

$$\begin{bmatrix} \bar{M}_{x,i} \\ M_{x,j} \end{bmatrix} = \begin{bmatrix} B_{4,4} & B_{4,10} \\ B_{10,4} & B_{10,10} \end{bmatrix} \cdot \begin{bmatrix} \varphi_{x,i} \\ \varphi_{x,j} \end{bmatrix} + \begin{bmatrix} F_4 = \dfrac{A_{1,3}}{A_{1,2}} \\ F_{10} = A_{2,3} - \dfrac{A_{1,3}A_{2,2}}{A_{1,2}} \end{bmatrix}. \tag{24}$$

The transfer constants $\left[\bar{b}_{kT}\right]_{x=L}$ and $\left[\bar{b}'_{kT}\right]_{x=L}$, $\left(k \in \langle 0, p_{mx}+2\rangle\right)$, can be calculated with a simple numerical algorithm [20] which we programmed using software[21]. The variables G_i and G_j correspond to the values of the homogenized torsional shear modulus at point *i*and*j*. It can be easy shown that the matrix *B* is symmetric. The case of non-uniform torsion will be considered in our future work.

2.4 Local FGM beam finite element equation

The local equation of the FGM finite beam element is obtained by superposition of the equations for axial, flexural, lateral and torsional deformation, and it reads,

$$\begin{bmatrix} \bar{N}_i \\ \bar{R}_{y,i} \\ \bar{R}_{z,i} \\ \bar{M}_{x,i} \\ \bar{M}_{y,i} \\ \bar{M}_{z,i} \\ N_j \\ R_{y,j} \\ R_{z,j} \\ M_{x,j} \\ M_{y,j} \\ M_{z,j} \end{bmatrix} = \begin{bmatrix} B_{1,1} & 0 & 0 & 0 & 0 & 0 & B_{1,7} & 0 & 0 & 0 & 0 & 0 \\ & B_{2,2} & 0 & 0 & 0 & B_{2,6} & 0 & B_{2,8} & 0 & 0 & 0 & B_{2,12} \\ & & B_{3,3} & 0 & B_{3,5} & 0 & 0 & 0 & B_{3,9} & 0 & B_{3,11} & 0 \\ & & & B_{4,4} & 0 & 0 & 0 & 0 & 0 & B_{4,10} & 0 & 0 \\ & S & & & B_{5,5} & 0 & 0 & 0 & B_{5,9} & 0 & B_{5,11} & 0 \\ & & Y & & & B_{6,6} & 0 & B_{6,8} & 0 & 0 & 0 & B_{6,12} \\ & & & M & & & B_{7,7} & 0 & 0 & 0 & 0 & 0 \\ & & & & M & & & B_{8,8} & 0 & 0 & 0 & B_{8,12} \\ & & & & & E & & & B_{9,9} & 0 & B_{9,11} & 0 \\ & & & & & & T & & & B_{10,10} & 0 & 0 \\ & & & & & & & R & & & B_{11,11} & 0 \\ & & & & & & & & Y & & & B_{12,12} \end{bmatrix} \cdot \begin{bmatrix} u_i \\ v_i \\ w_i \\ \varphi_{x,i} \\ \bar{\varphi}_{y,i} \\ \bar{\varphi}_{z,i} \\ u_j \\ v_j \\ w_j \\ \varphi_{x,j} \\ \bar{\varphi}_{y,j} \\ \bar{\varphi}_{z,j} \end{bmatrix} + \begin{bmatrix} F_1 \\ F_2 \\ F_3 \\ F_4 \\ F_5 \\ F_6 \\ F_7 \\ F_8 \\ F_9 \\ F_{10} \\ F_{11} \\ F_{12} \end{bmatrix}. \tag{25}$$

The local finite element matrix *B* in (25) consists formally of the linear stiffness matrix K_L and the linearized geometric stiffness matrix K_N (containing the terms with second order axial force N^{II} that has to be known or has to be evaluated by a linear elastic-static calculation) and the consistent mass matrix *M*:

$$[B] = \left[K_L + K_N - \omega^2 M\right]. \tag{26}$$

The terms B and F correspond to the previously derived terms of the local beam element matrices and load vectors in (6), (14), (17) and (24). In the modal analysis of a single straight beam the global finite element matrix coincides with the local matrix. For a general case, the global matrix of the beam and the beam structure are established in the usual finite element method way. In the modal and buckling analysis the eigenvalue problem is solved. In modal analysis, for given or calculated axial forces N^{II} and defined geometrical parameters and homogenized material properties and the global boundary conditions, the circular frequency ω is increased until the determinant of the global beam structure matrix tends to zero. This circular frequency is the natural circular frequency from which the natural frequency (eigenfrequency) can be calculated. In buckling analysis, the circular frequency ω is set to zero, and the second order beam theory axial force N^{II} is increased until the determinant of the global beam structure matrix tends to zero. Then, the axial force represents the buckling force N_{Ki}^{II}.Further, the mode or buckling shapes can be calculated by the transfer relations (5), (13), and (22). In static analysis, the circular frequency ω is set to zero and the load vector hast be established. The global and local displacements and rotations at the nodes are calculated from those the local internal forces and moments in the homogenized beam elements cross-sections are evaluated. After that the normal and shear stress is calculated in the beam cross sections with real distribution of material properties. The solution approach we have implemented into the software MATHEMATICA [21] by which the numerical calculations presented in the chapter 4 were done.

3 HOMOGENIZATION OF IN THREE DIRECTIONS VARYING MATERIAL PROPERTIES

One important goal of mechanics of heterogeneous materials is to derive their effective properties from the knowledge of the constitutive laws and complex micro-structural behavior of their components. Microscopic modeling expresses the relation between the characteristics of the components and the average (effective) properties of composites. In the case of FGM it is the relation between the characteristics of the components and the effective properties of FGM.

The methods based on homogenization theories (e.g. the mixture rules [22,23]; self-consistent methods [24]) have been designed and successfully applied to determine the effective material properties of heterogeneous materials from the corresponding material behavior of the constituents (and of the interfaces between them) and from the geometrical arrangement of the phases. In this context, the microstructure of the material under consideration is basically taken into account by a representative volume element (RVE).

Mixture rules are one of the methods for micromechanical modeling of heterogeneous materials. Extended mixture rules [25] are based on the assumption that the constituents volume fractions, formally denoted as fibers – f and matrix – m (the notation is very often used in the literature also for the FGM constituents, although this material is point wise isotropic and the reinforcing constituents are not of several forms and dimensions) vary continuously as polynomial functions, $v_f(x,y,z)$ and $v_m(x,y,z)$. The condition $v_f(x,y,z)+v_m(x,y,z)=1$ has to be fulfilled. The appropriated material property distribution in the real FGM beam (Figure 2a) then reads

$$p(x,y,z)=v_f(x,y,z)\,p_f(x,y,z)+v_m(x,y,z)\,p_m(x,y,z). \tag{27}$$

Here, $p_f(x,y,z)$ and $p_m(x,y,z)$ are the spatial distribution of material properties of the FGM constituents. The extended mixture rule (27) can be analogically used for FGM made of more than two constituents. The assumption of a polynomial variation of the constituent's volume fractions and material properties enables an easier establishing of the main field equations and allows the modeling of many common realizable variations.

In the research studies and in practical applications, the one directional variation of the FGM properties is mostly considered. For the FGM beams and shells the transversal variation (continuously or discontinuously, symmetrically or asymmetrically) has been mainly considered. There, an exponential law for variation of the constituents volume fractions through the beam's height is often presented, e.g. in [26-28] and in references therein. The homogenization of such variations is relatively simple. If the material properties vary only with respect to the longitudinal direction, the homogenization is frequently not needed since there are the FGM beam and link finite elements established that consider such variations in a very accurate and effective way [29-31]. The more complicated case is, when the material properties vary in three directions - namely in transversal, lateral and longitudinal directions of the FGM beam.

In this contribution, the homogenization techniques of spatially varying (continuously or discontinuously and symmetrically in transversal and lateral direction, and continuously in longitudinal direction) material properties of FGM beams of selected doubly-symmetric cross-sections are presented. The expressions are proposed for the evaluation of effective elastic modules for axial loading and for transversal and lateral bending complemented with the shear modules for transversal and lateral shear and uniform torsion and for themass density by the extended mixture rules (EMR) and the multilayer method (MLM).

Let us consider a two node straight beam element with predominantly rectangular cross-sectional area *A* (Figure 2). The composite material of this beam arises from mixing two constituents. The continuous polynomial spatial variation of the elastic modules and mass density can be caused by continuous polynomial spatial variation of both the volume fractions ($v_f(x,y,z)$ and $v_m(x,y,z)$) and the material properties ($p_f(x,y,z)$ and $p_m(x,y,z)$) of the FGM constituents.

In our case the elastic modulus $E(x,y,z)$, the Poisson ratio $\nu(x,y,z)$, and mass density $\rho(x,y,z)$ are calculated by expression (27). The FGM shear modulus is calculated by expression:

$$G(x,y,z)=\frac{E(x,y,z)}{2(1+\nu(x,y,z))} \tag{28}$$

If the Poisson's ratio of the constituents is approximately of the same value and the constituents volume fraction variation is not strong, then the FGM shear modulus can by calculated using a simplification

$$G(x,y,z)=\frac{E(x,y,z)}{\xi}, \tag{29}$$

where ξ is an average value of the function $\xi(x,y,z)=2(1+\nu(x,y,z))$

$$\xi=\frac{1}{L}\int_0^L\left(\frac{1}{A}\int_{(A)}\xi(x,y,z)dA\right)dx. \tag{30}$$

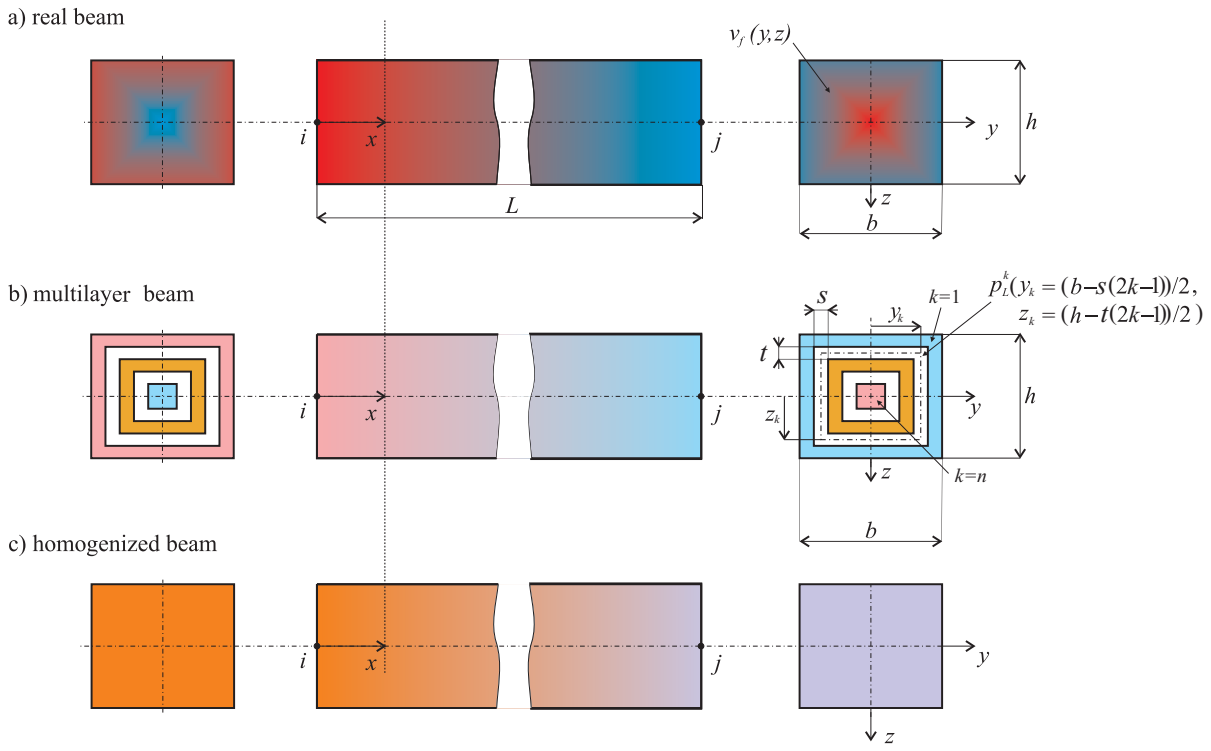

Figure 2: FGM beam with rectangular cross-section.

Homogenization of the spatially varying material properties (the reference volume is the volume of the whole beam) is done in two steps. In the first step, the real beam (Figure 2a) is transformed into a multilayer beam (Figure 2b). Homogenized material properties of the layers are calculated with the EMR [30]. Competent homogenized layer *k* at position *x* has a constant volume fractions and the material properties of the constituents in the *y* and *z* direction. They are calculated as an average value from their values at the boundaries of the respective layer. Polynomial variation of these parameters appears with respect to the longitudinal direction of the layer. Sufficient accuracy of the proposed substitution of the continuous transversal and lateral variation of material properties by the layer-wise constant distribution of material properties is reached if the division to layers is fine enough. In the second step, the effective longitudinal material properties of the homogenized beam are derived using the MLM. These homogenized material properties are constant through the beam's height and depth but they vary continuously along the longitudinal beam axis. Accordingly, the beam finite element equations are established for the homogenized beam (Figure 2c) in order to calculate the primary effective beam unknowns (the displacements, temperatures, electric potential, eigenfrequency, buckling force, etc…). The secondary variables, for example the mechanical stress, have to be calculated from the internal local forces and moments on the real beam [29].

The homogenized elastic modules for tension-compression - $E_L^{NH}(x)$, bending about axis *y* - $E_L^{M_yH}(x)$, bending about axis *z* - $E_L^{M_zH}(x)$, shear in *y* direction - $G_{Ly}^{H}(x)$, shear in *z* direction - $G_{Lz}^{H}(x)$, torsion $G_L^{M_xH}(x)$, and the homogenized mass density for axial loading $\rho_L^{NH}(x)$ and torsion $\rho_L^{M_xH}(x)$ can be calculated using the following expressions:

$$E_L^{NH}(x)=\frac{\sum_{k=1}^{n}E_k(x)A_k}{A},\quad E_L^{M_yH}(x)=\frac{\sum_{k=1}^{n}E_k(x)I_{y,k}}{I_y},\quad E_L^{M_zH}(x)=\frac{\sum_{k=1}^{n}E_k(x)I_{z,k}}{I_z},\tag{31}$$

$$G_{Ly}^{H}(x)=\frac{\sum_{k=1}^{n}k_{y,k}^{sm}G_k(x)A_k}{k_y^{sm}A},\quad G_{Lz}^{H}(x)=\frac{\sum_{k=1}^{n}k_{z,k}^{sm}G_k(x)A_k}{k_z^{sm}A},\tag{32}$$

$$G_L^{M_xH}(x)=\frac{\sum_{k=1}^{n}G_k(x)I_{T,k}}{I_T},\quad \rho_L^{NH}(x)=\frac{\sum_{k=1}^{n}\rho_k(x)A_k}{A},\ \rho_L^{M_xH}(x)=\frac{\sum_{k=1}^{n}\rho_k(x)I_{p,k}}{I_p}.\tag{33}$$

Here, A_k denotes the cross-sections area, $E_k(x)$is the elastic modulus, $I_{y,k}$ and $I_{z,k}$ are the second moments of area, $G_k(x)$ is the shear modulus, $I_{T,k}$ is the torsion constant and $\rho_k(x)$ is the mass density, $I_{p,k}$ is the polar moment of area of the kth layer. The exact expressions for homogenization of spatial varying (continuously or discontinuously and symmetrically in transversal and lateral direction, and continuously in longitudinal direction) material properties for the FGM beams depend on the form of the cross-section. For rectangular hollow cross-sections we present the corresponding expressions in the following chapters.

3.1 Hollow cross-section

A straight beam of hollow cross-sectional area $A=b_1h_1-b_nh_n$(Figure 3) is made of a FGM whose properties vary in the y and z direction continuously and symmetrically according the main inertial planes, $x-y$ and $x-z$, and continuously in longitudinal beam direction x. Further, $I_y=\frac{b_1h_1^3}{12}-\frac{b_nh_n^3}{12}$ and $I_z=\frac{h_1b_1^3}{12}-\frac{h_nb_n^3}{12}$ are the second moments of area, $I_p=I_y+I_z$ is the polar moment of area, $\overline{A}_y=k_y^{sm}A$ and $\overline{A}_z=k_z^{sm}A$ refer to the reduced cross-sectional areas – by the average shear correction factors k_y^{sm} and k_z^{sm} [17,32,75], and $I_T=\frac{2(h_1-t)^2(b_1-s)^2}{\frac{h_1-t}{s}+\frac{b_1-s}{t}}$ is the torsion constant. Here, s and t refer to the thicknesses of the cross-section walls.

For the homogenization of spatially varying material properties the hollow cross-sectional area is divided into n hollow parts, where $t_k=(h_1-h_n)/2n$ is the flange thickness and $s_k=(b_1-b_n)/2n$ is the web thickness (Figure 3), respectively. The hollow area of the kth part $(k\in\langle 1,\ n\rangle)$ is: $A_k=2t_k(b_1-s_k(2k-1))+2s_k(h_1-t_k(2k-1))$. The second moments of area of the kth part are: $I_{y,k}=(b_1-s_k(2k-2))(h_1-t_k(2k-2))^3/12-(b_1-2ks_k)(h-2kt_k)^3/12$, $I_{z,k}=(b_1-s_k(2k-2))^3(h_1-t_k(2k-2))/12-(b_1-2ks_k)^3(h_1-2kt_k)/12$ .The polar moment of area of kth part is $I_{p,k}=I_{y,k}+I_{z,k}$.

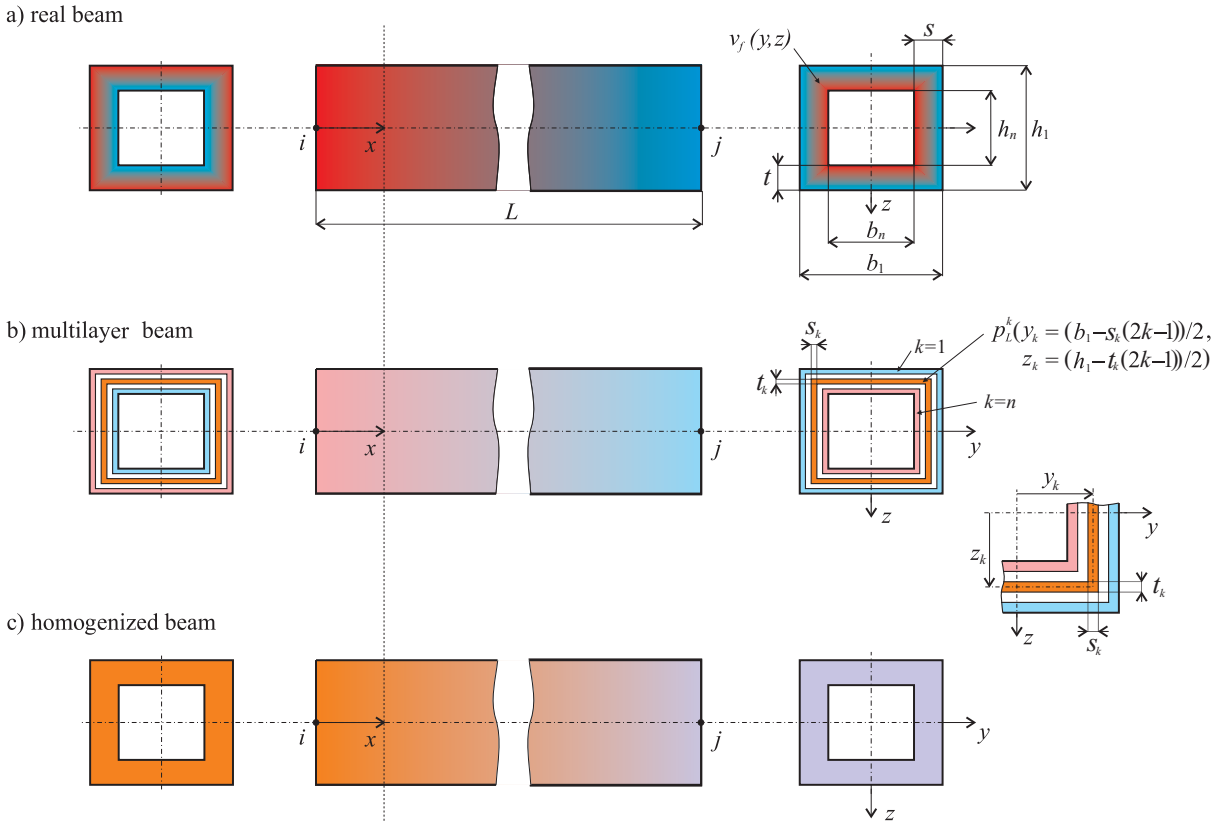

Figure 3: A straight FGM beam of hollow cross-section.

According to (27) and (28) the real material properties are: $E(x,y,z)$ is the elastic modulus, $\nu(x,y,z)$ is the Poisson's ratio, $G(x,y,z)=E(x,y,z)/(2(1+\nu(x,y,z)))$ is the shear modulus and $\rho(x,y,z)$ is the mass density: $(x\in<0,L>, y\in<\pm h_n/2, \pm h_1/2>, z\in<\pm b_n/2, \pm b_1/2>)$. The effective homogenized material properties, like the elastic modules, are calculated under assumption, that the relevant stiffness of the homogenized beam is equal to the stiffness of the real beam virtually divided on the hollow parts. Thus, we get the effective elastic modulus for axial loading

$$E_L^{NH}(x)=\frac{\sum_{k=1}^{n-1}E_k(x)A_k}{A}, \tag{34}$$

with $E_k(x)=\left[E(x,y,z)\right]_{\substack{y=y_k\\z=z_k}}$ and the effective elastic modules for bending about the y and z axis,

$$E_L^{M_yH}(x)=\frac{\sum_{k=1}^{n}E_k(x)I_{y,k}}{I_y},\quad E_L^{M_zH}(x)=\frac{\sum_{k=1}^{n}E_k(x)I_{z,k}}{I_z}. \tag{35}$$

The effective elastic modulus for uniform torsion reads,

$$G_L^{M_xH}(x)=\frac{\sum_{k=1}^{n}G_k(x)I_{T,k}}{I_T}, \tag{36}$$

with $G_k(x) = \left[G(x,y,z)\right]_{\substack{y=y_k \\ z=z_k}}$. The torsion constant of the kth hollow part $\left(k \in \langle 1,\ n\rangle\right)$ can be evaluated as

$$I_{T,k} = \frac{2\left(b_1 - s_k(2k-1)\right)^2 \left(h_1 - t_k(2k-1)\right)^2}{\dfrac{\left(b_1 - s_k(2k-1)\right)}{t_k} + \dfrac{\left(h_1 - t_k(2k-1)\right)}{s_k}}. \tag{37}$$

The effective shear modulus in y direction is given by,

$$G_{Ly}^H(x) = \frac{\sum_{i=1}^{n} k_{y,k}^{sm} G_k(x) A_k}{k_y^{sm} A}, \tag{38}$$

with the average shear correction factors: k_y^{sm} for whole rectangular cross-section and $k_{y,k}^{sm}$ for kth part.
The shear modulus in z direction then reads,

$$G_{Lz}^H(x) = \frac{\sum_{k=1}^{n} k_{z,k}^{sm} G_k(x) A_k}{k_z^{sm} A}, \tag{39}$$

with the average shear correction factors: k_z^{sm} for whole rectangular cross-section and $k_{z,k}^{sm}$ for kth part.
The effective mass density for tension - $\rho_L^{NH}(x)$ and torsion $\rho_L^{M_xH}(x)$ is

$$\rho_L^H(x) = \frac{\sum_{k=1}^{n} \rho_k(x) A_k}{A}, \qquad \rho_L^{M_xH}(x) = \frac{\sum_{k=1}^{n} \rho_k(x) I_{p,k}}{I_p}, \tag{40}$$

with $\rho_k(x) = \left[\rho(x,y,z)\right]_{\substack{y=y_k \\ z=z_k}}$.It should be noted, that the effective mass density for tension has been taken also for the lateral and transversal bending.

4 NUMERICAL INVESTIGATIONS

4.1 Example 1: FGM beam structure - hollow cross-section

The FGM beam structure with a constant rectangular hollow cross-section is considered (Figure 4), which consists of two parts – Beam1 and Beam2. Its geometry is given byh_1 = 0.005 m, h_n = 0.00375 m, b_1 = 0.01 m, b_n = 0.0075 m and L = 0.1 m. The angle between the beams is $\theta = 150°$. The cross-sectional area is $A = 2.1875\times10^{-5}$ m^2, the second moments of area are $I_{y'} = 7.12077\times10^{-11}$ m^4 and $I_{z'} = 2.84831\times10^{-10}$ m^4, the polar moment of area is $I_p = I_{y'} + I_{z'} = 3.56038\times10^{-10}$ m^4 and the torsion constant is $I_T = 1.6748\times10^{-10}$ m^4.

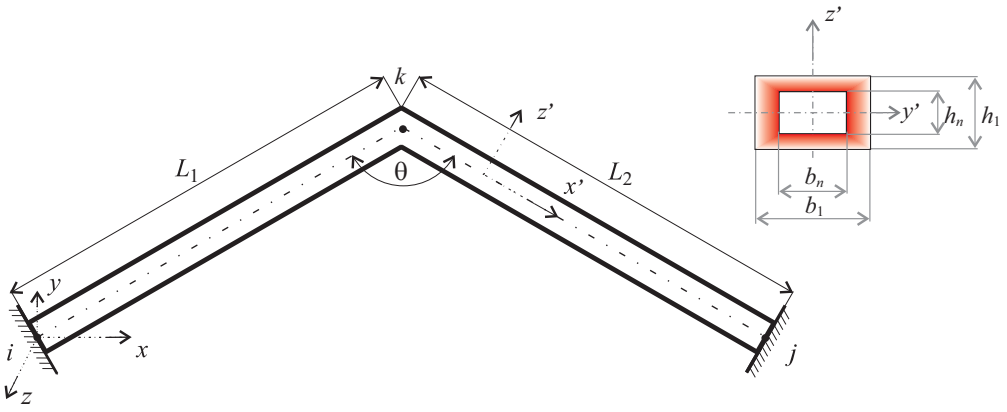

Figure 4: FGM beam structure in global (*x*, *y*, *z*) coordinate system.

The material of the beam consists of two components: Aluminum Al6061-TO – denoted with index *m* and Titanium carbide TiC – denoted with index *f*. The material properties of the components are assumed to be constant and their values are: Aluminum Al6061-TO – the elasticity modulus $E_m = 69.0\,\text{GPa}$, the mass density $\rho_m = 2700$ kgm^{-3}, the Poisson's ratio $\nu_m = 0.33$; Titanium carbide TiC – the elasticity modulus $E_f = 480.0\,\text{GPa}$, the mass density $\rho_f = 4920$ kgm^{-3}, the Poisson's ratio $\nu_f = 0.20$.

The TiC volume fraction varies in the local y' and z' direction linearly and symmetrically according to the $x'-y'$ and $x'-z'$ planes: $\left[v_f\left(y',z'\right)\right]_{\substack{y'=\pm h_n/2\\ z'=\pm b_n/2}} = 0$, $\left[v_f\left(y',z'\right)\right]_{\substack{y'=\pm h_1/2\\ z'=\pm b_1/2}} = 1$ - the inner edges of the cross-sectional area are made of pure Al6061-TO –and the outer cross-section edges are made of pure TiC. Constant effective material properties are considered in the local x' – direction of both beams. Using EMR and MLM the effective elastic modulus (in [GPa]) for axial loading E_L^{NH}, for bending about axis y' - $E_L^{M_yH}$ and about axis z' - $E_L^{M_zH}$ the shear moduli G_{Ly}^{H} and G_{Lz}^{H}, the torsional shear modulus $G_L^{M_xH}$, and the mass density ρ_L^{NH} [kgm^{-3}] for tension and $\rho_L^{M_xH}$ [kgm^{-3}] for torsion have been calculated by equations (34 - 40). The influence of the number of divisions *n* to the layers on the homogenized material properties [32, 33] is shown in Table 1. The average shear correction factors k_y^{sm} and k_z^{sm} for $n = 20$ layers are $k_y^{sm} = 0.4712$ and $k_z^{sm} = 0.2910$ [32, 33]. For homogeneous hollow cross-section, following shear correction factors are obtained: $k_y = 0.5081$ and $k_z = 0.3291$ (calculated e.g. with ANSYS [34], for rectangular hollow beam-section).

layers *n*	E_L^{NH}	$E_L^{M_yH} = E_L^{M_zH}$	$G_{Ly}^{H} = G_{Lz}^{H}$	$G_L^{M_xH}$	ρ_L^{NH}	$\rho_L^{M_xH}$
2	281.839	296.151	112.716	120.614	3849.643	3926.946
5	283.894	302.229	113.901	124.066	3860.743	3959.777
10	284.188	303.098	114.071	124.561	3862.328	3964.469
15	284.242	303.259	114.102	124.653	3862.222	3965.339
20	284.261	303.315	114.113	124.685	3862.725	3965.643

Table 1: Influence of the number of division *n* to the layers on the homogenized material properties.

Modal analysis

The FGM beam structure, clamped at the node *i* and *j*, is studied by modal analysis. The effect of axial force is not considered by this example. The first six eigenfrequencies *f* [Hz] are given in Table 2 using the new FGM beam finite element (NFE) and homogenized material properties for $n = 20$. Only two of our proposed FGM finite element are used – one for each part. For comparison purposes, the same problem is solved using a very fine mesh – 21600 of SOLID186 elements of the FEM program ANSYS [34]. The average relative difference Δ[%] between eigenfrequencies calculated by our method (NFE) and the ANSYS solution is evaluated.

eigenfrequencies *f* [Hz]		NFE without shear	NFE with shear	ANSYS	Δ[%] without shear	Δ[%] with shear
1st	flexural – *xz* plane	2392.0	2361.1	2343.6	2.07	0.75
2nd	flexural – *xy* plane	3859.1	3765.4	3798.8	1.65	0.82
3rd	flexural – *xy* plane	4444.0	4384.0	4341.1	2.37	0.99
4th	flexural – *xz* plane	7391.0	7123.3	7182.5	2.96	0.77
5th	flexural – *xy* plane	9147.1	9027.1	8928.4	2.57	1.23
6th	torsional	10051.1	10013.4	9896.8	1.56	1.18

Table 2: Eigenfrequencies of the FGM beam structure.

A comparison of 1st,2nd and 3rd eigenforms of the FGM beam structure evaluated by the new FGM beam finite element and FEM program ANSYS is shown in Figures 5 - 7.

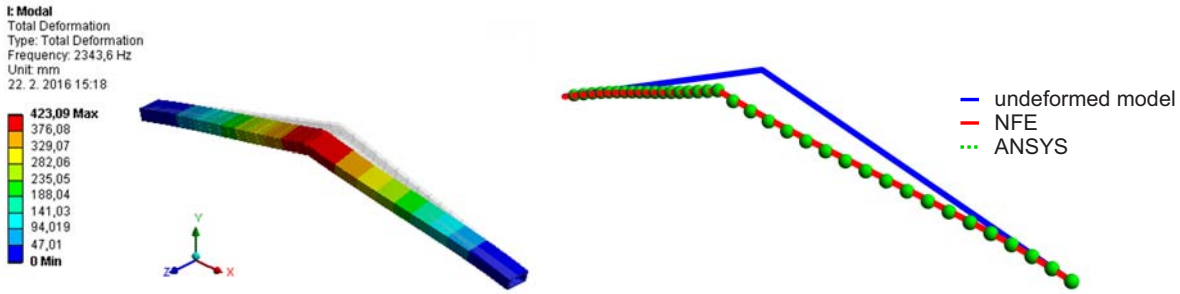

Figure 5: The 1st eigenform of the FGM beam structure displayed by the ANSYS postprocessor and comparison of NFE and ANSYS.

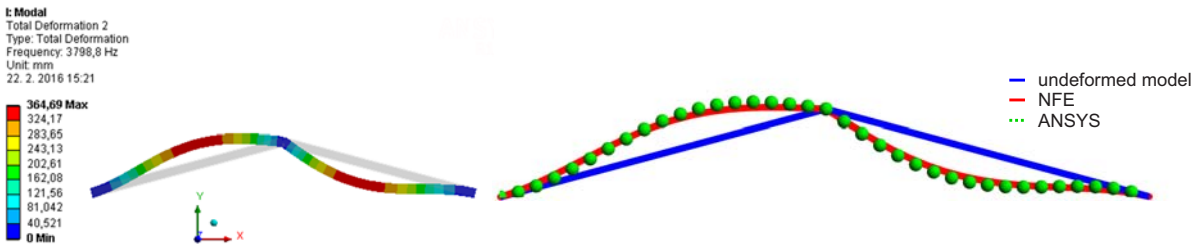

Figure 6: The 2nd eigenform of the FGM beam structure displayed by the ANSYS postprocessor and comparison of NFE and ANSYS.

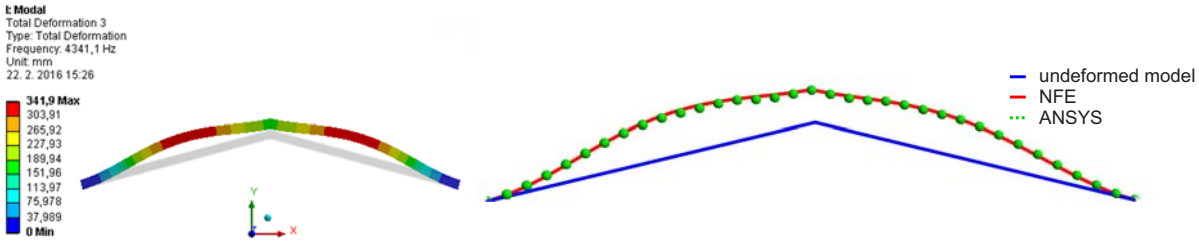

Figure 7: The 3rd eigenforms of the FGM beam structure displayed by the ANSYS postprocessor and comparison of NFE and ANSYS.

Elasto-static analysis

The FGM beam structure, clamped at the node *i* and *j*, loaded by the vertical force $F_{ky} = 100$ N in the global negative *y* direction and the torsion moment $M_{kx} = 100$ Nm about global *x*-axis at point *k*, is studied by elasto-static analysis. The effects of axial forces is not considered by this example. The displacements according the global coordinate system at the point *k* are given in Table 3 using the new FGM beam finite element (NFE) and homogenized material properties for *n* = 20. Only two of the herein proposed new FGM finite elements were used – one for each part. For comparison purposes, the same problem is solved using a very fine mesh – 21600 of SOLID186 elements of the FEM program ANSYS [34]. The average relative difference Δ[%] between displacements calculated by our method and the ANSYS solution is evaluated.

Displacements [mm], [rad]	NFE without shear correction	NFE with shear correction	ANSYS	Δ[%] without shear correction	Δ[%] with shear correction
v_k	-0.01135	-0.01137	-0.01140	0.39	0.27
w_k	-2.56285	-2.56285	-2.58651	0.91	0.91
φ_{xk}	0.19804	0.19804	0.20030	1.13	1.13

Table 3: Global displacements at point *k*.

The total deformation of the FGM beam structure is shown in Figure 8.

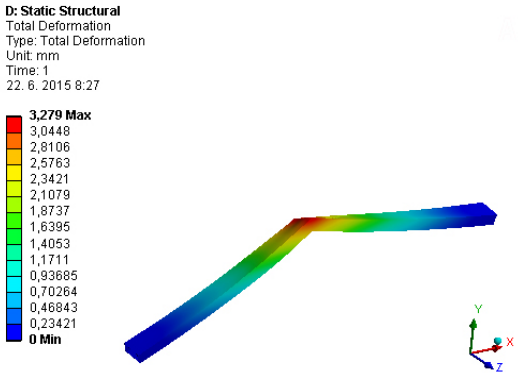

Figure 8: Total deformation of the FGM beam structure.

As can be seen in Table 4, a very good agreement of our results is obtained.

4.2 Example 2: FGM beam – spatial variation of material properties

The cantilever FGM beam on varying horizontal and vertical Winkler foundation is considered (as shown in Figure 9). Its rectangular cross-section is constant with height h = 0.005 m and width b = 0.01 m. The length of the beam is L = 0.1 m.

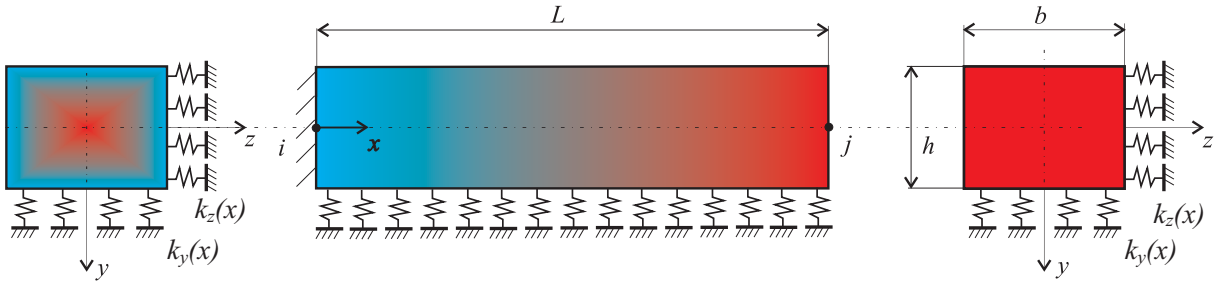

Figure 9: Clamped beam on elastic foundation with spatially varying material properties.

The beam is made of a mixture of two components: Aluminum Al6061-TO and Titanium Carbide TiC, their constant constituent's material properties are given in Case I. The Aluminum volume fraction, in this case, varies linearly and symmetrically according to the $x-y$ and $x-z$ planes: At node i is $\left\lfloor v_{fi}(y,z)\right\rfloor_{\substack{y=0\\z=0}}=1, \left\lfloor v_{fi}(y,z)\right\rfloor_{\substack{y=\pm h/2\\z=\pm b/2}}=0$ and then vary continuous linearly in the longitudinal direction to the constant value at node j ($v_{fj}=1$).

Using EMR and MLM with n = 20 layers the effective elastic modulus for axial loading E_L^{NH}, for bending about axis y - $E_L^{M_yH}$ and about axis z - $E_L^{M_zH}$, shear modules G_{Ly}^{H} and G_{Lz}^{H}, torsional shear modulus $G_L^{M_xH}$, and mass density ρ_L^{NH} for tension and $\rho_L^{M_xH}$ for torsion are evaluated as:

$$E_L^{NH}=342.109-2731.095x\ \text{GPa};$$

$$E_L^{M_yH}=E_L^{M_zH}=396.429-3274.293x\ \text{GPa};$$

$$G_{Ly}^{H}=G_{Lz}^{H}=138.581-1129.418x\ \text{GPa};$$

$$G_L^{M_xH}=162.233-1362.936x\ \text{GPa};$$

$$\rho_L^{NH}=4175.19-14751.9x\ \text{kgm}^{-3};$$

$$\rho_L^{M_xH}=4468.34-17683.43x\ \text{kgm}^{-3}.$$

Modal analysis

The FGM cantilever beam, clamped at the node i, and resting on varying Winkler elastic foundation $k_y(x)$=5000-30000x+60000x^2 kN/m^2 and $k_z(x)$=5000-1000x+6000x^2 kN/m^2 is studied by modal analysis. The average shear correction factors in y' – direction $k_y^{sm}=5/6$ and in z' – direction $k_z^{sm}=5/6$ are used [35]. The first nine eigenfrequencies f [Hz] are evaluated as shown in Table 4. It is use only one of our proposed finite element. The effect of axial force was not considered in this example. The same problem is solved using a very fine mesh – 32000 of SOLID186 elements of the FEM program ANSYS [34]. The results of ANSYS as

well as the results of the NFE are presented in Table 4. The average relative difference $\Delta[\%]$ between eigenfrequencies calculated by our method and the ANSYS solution is evaluated.

eigenfrequencies f [Hz]		NFE without foundation	ANSYS without foundation	$\Delta[\%]$	NFE with foundation	ANSYS with foundation	$\Delta[\%]$
1st	flexural - axis y	838.9	844.9	0.71	1356.1	1365.3	0.67
2nd	flexural - axis z	1660.0	1674.4	0.86	1896.3	1911.3	0.78
3rd	flexural - axis y	4329.5	4301.7	0.65	4433.4	4413.5	0.45
4th	flexural - axis z	8288.5	8228.8	0.73	8332.2	8275.1	0.69
5th	flexural - axis y	11046.0	10920.0	1.15	11125.8	10961.0	1.50
6th	torsional	11182.0	10926.0	2.34	11048.0	10969.0	0.72
7th	flexural - axis z	20023.0	19907.0	0.58	20051.0	19925.0	0.63
8th	flexural - axis y	20379.0	20312.0	0.33	20397.1	20333.0	0.32
9th	axial	22212.6	22213.0	0.01	22212.7	22213.0	0.01

Table 4: Eigenfrequencies of the FGM beam with and without elastic foundation.

Again, a very good agreement of our results compared to ANSYS is indicated in Table 4. For instance, the 1st, 6th and 9th mode of the FGM beam structure displayed by ANSYS is shown in Figure 10.

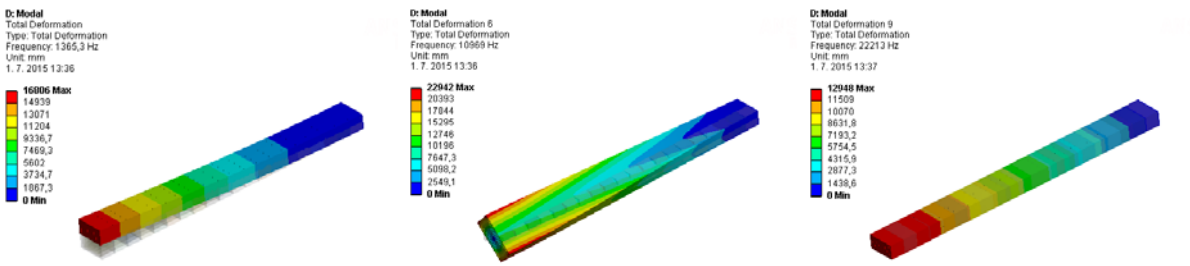

Figure 10: The 1th and 6th and 9th eigenforms of the beam (with Winkler elastic foundations).

Buckling and elastic-static analysis

The FGM cantilever beam, clamped at the node i, has been studied by buckling and elastic-static analysis. All the calculations were done with our 3D FGM beam finite element (NFE) which we have implemented into the code MATHEMATICA [21]. Additionally, the effect of axial force was considered. It has to be pointed out that the entire structure is discretized using only one herein proposed finite element.

The critical buckling force calculated by our 3D FGM beam finite element is $N_{Ki}^{II} = 7.171$ kN and calculated by ANSYS (with 50 of BEAM188 elements) is $N_{Ki}^{II} = 7.081$kN. The first buckling form is shown in Figure 11. In the elasto-static analysis the axial force $N^{II} \equiv N$ have been chosen as a part of the critical buckling force N_{Ki}^{II}.

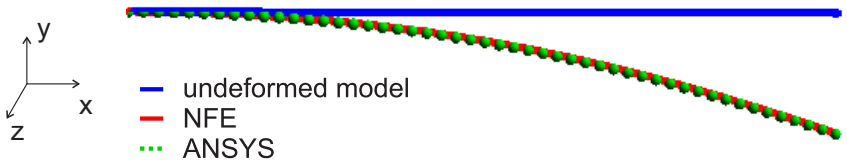

Figure 11: The first buckling form.

In the elastic-static analysis, the cantilever FGM beam resting on varying vertical Winkler elastic foundation $k_y = 5000 - 30000x + 600000x^2$ kN/m^2 is loaded by forces $F_y = F_z = 50$ N and $F_x = -2$ kN at node j (Figure 12). The average shear correction factors in y' – direction $k_y^{sm} = 5/6$ and in z' – direction $k_z^{sm} = 5/6$ are used [35]. The displacements at node j are evaluated using the only one new FGM beam finite element (NFE). The same problem is solved using a very fine mesh – 23015 of SOLID186 elements of the FEM program ANSYS [34]. The results of ANSYS as well as the results of the NFE are presented in Table 5. The average relative difference Δ[%] between displacements calculated by our method and the ANSYS solution is evaluated.

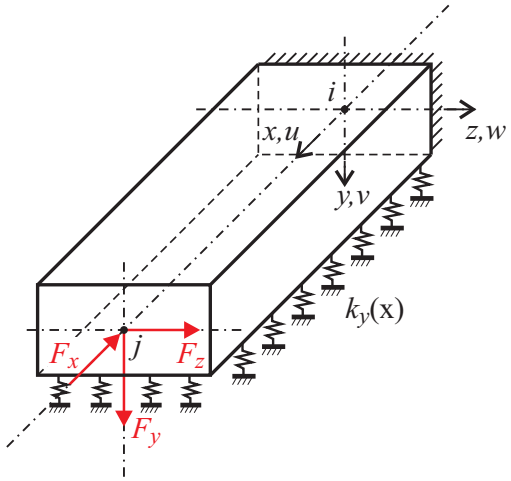

Figure 12: Loaded FGM beam.

Displacements at node j [mm], [rad]	NFE with foundation	ANSYS with foundation	NFE without foundation	ANSYS without foundation
u_j	-0.02445	-0.02507	-0.02445	0.02507
v_j	0.24641	0.24933	0.74414	0.75348
w_j	0.14452	0.14791	0.14452	0.14791
φ_{yj}	-0.00247	-0.00256	-0.00247	-0.00256
φ_{zj}	0.00503	0.00527	0.1304	0.01321

Table 5: Displacements at node j with and without elastic foundation.

The comparison of the vertical beam deflection curve with and without elastic foundation is shown in Figure 13.

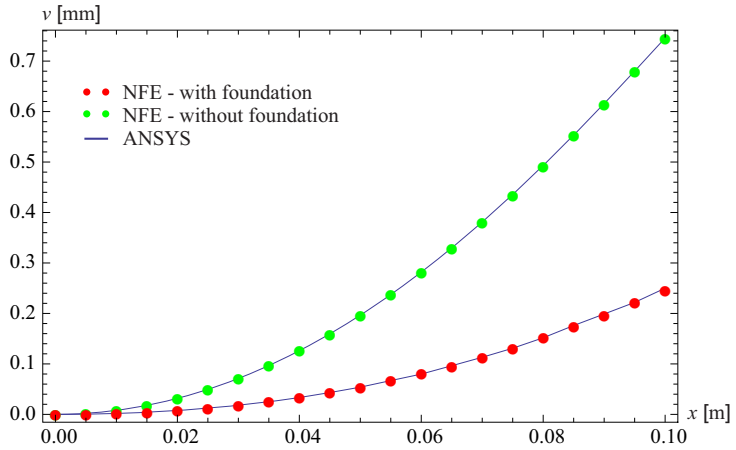

Figure 13: Vertical beam deflection curve with and without elastic foundation.

The bending moments about the *y* and *z* – axis for case without elastic foundation are shown in Figures 14 and 15, respectively. The Figures 16 and 17 show the transversal force in *y* and *z* – axis. The comparison of the bending moments $M_y(x=0)$, $M_z(x=0)$ and transversal forces $R_y(x=L)$, $R_{yz}(x=L)$ for the case F_x = -2 kN calculated by our approach and by ANSYS are compared in Table 6.

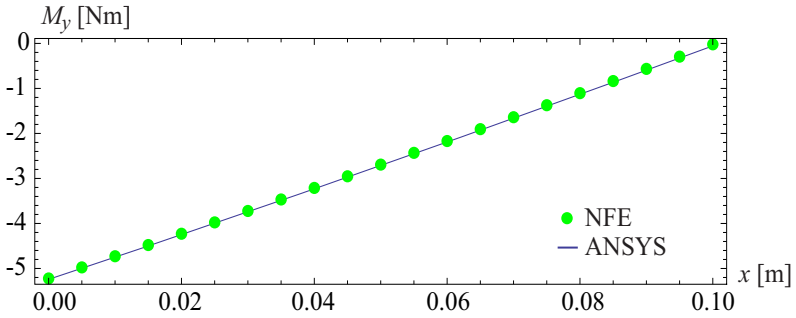

Figure 14: Bending moment about the *y* – axis (without elastic foundation).

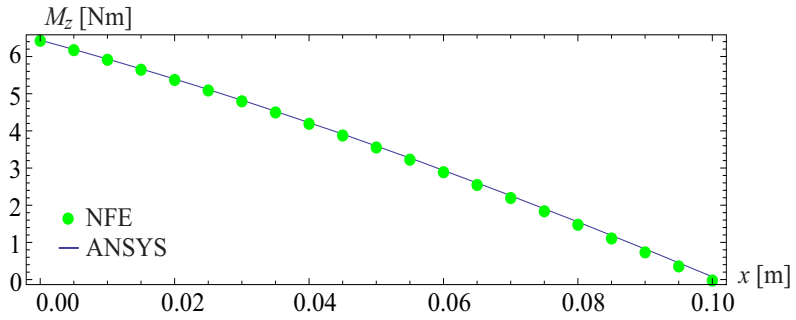

Figure 15: Bending moment about the *z* – axis (without elastic foundation).

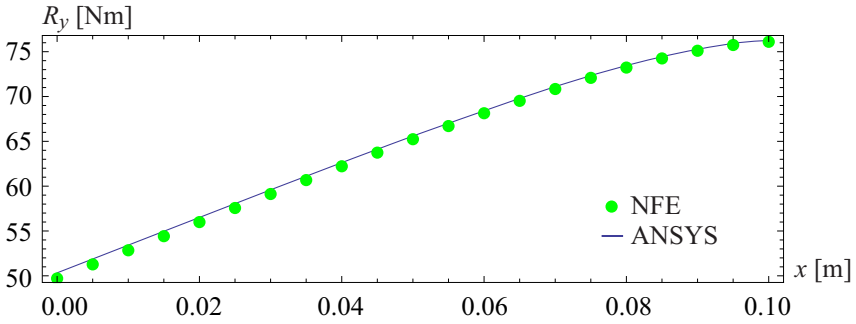

Figure 16: Transversal force in y – axis (without elastic foundation).

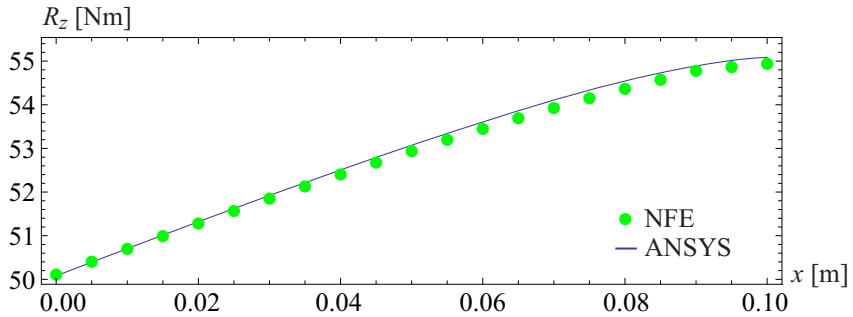

Figure 17: Transversal force in z – axis (without elastic foundation).

	NFE Fx = -2 kN	ANSYS Fx = -2 kN	Δ[%]
$M_y(x=0)$ [Nm]	-5.2182	-5.2416	0.45
$M_z(x=0)$ [Nm]	6.4691	6.4404	0.45
$R_y(x=L)$ [N]	54.9472	55.0873	0.25
$R_z(x=L)$ [N]	76.2088	76.2251	0.02

Table 6: Bending moments and transversal forces.

In Figure 18, the resultant normal stress, caused by axial, transversal and lateral forces, in the clamped cross-section is shown that was calculated by our approach [18] extended here for variation of material properties in three directions.

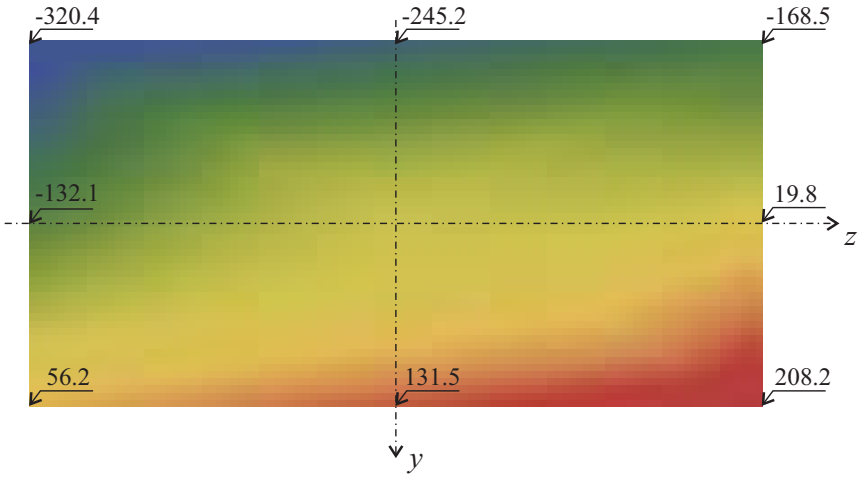

Figure 18: Resultant normal stress $\sigma(x, y, z)$ [MPa] at position $x = 0$ calculated by our approach [18].

In Figure 19, the resultant normal stress, caused by axial, transversal and lateral forces, in the clamped cross-section is shown that was calculated by ANSYS (using a very fine mesh – 23015 of SOLID186). As can be seen, a very good agreement of both solution method has been obtained at all marked points excluding the corners. As is well known, the solutions with 3D solid finite elements produce in the sharp corners incorrect stress first of all by the very fine meshes. In the nearby points of the sharp corners is the match of the results very good (see the details in Figure 19). More detailed description of the stress calculation for the FGM beam with spatial variation of material properties will be given in our newly prepared paper.

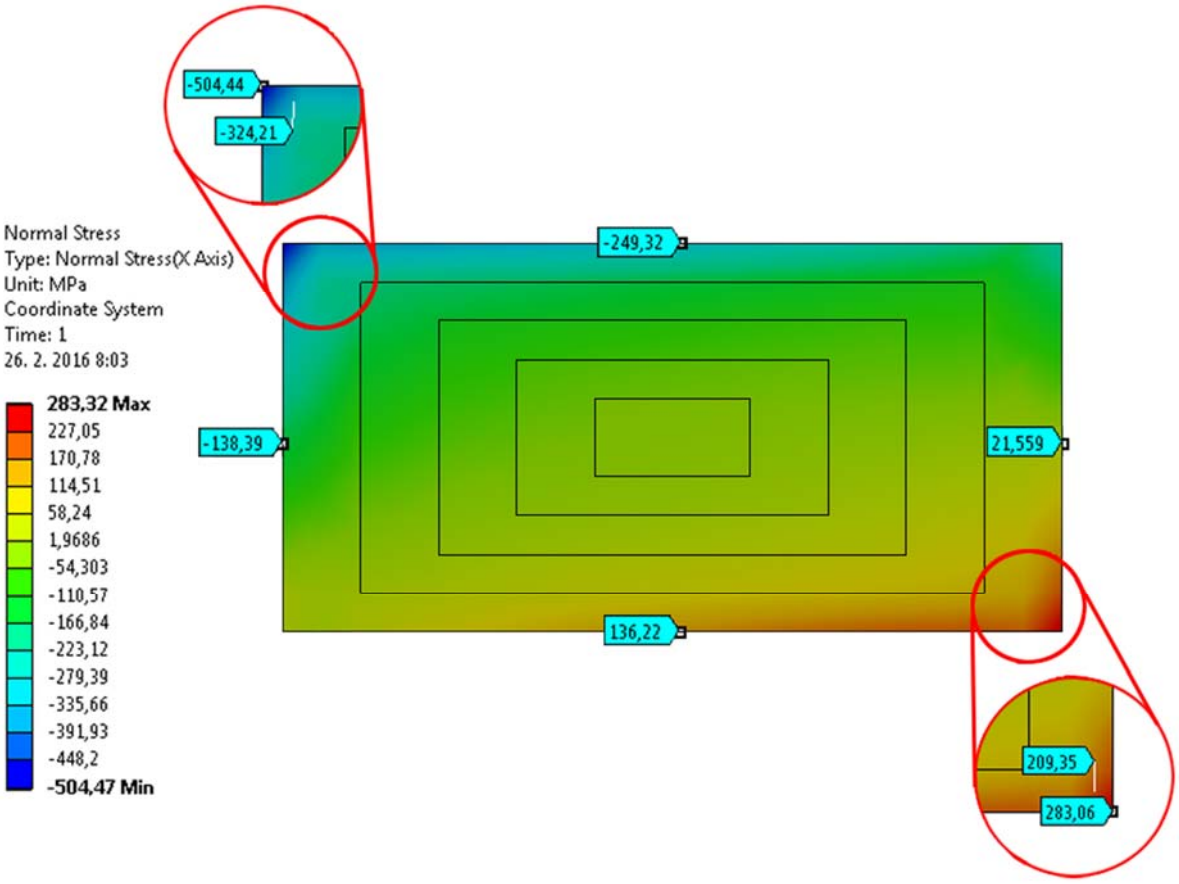

Figure 19: Normal stress $\sigma(x, y, z)$ [MPa] at position $x = 0$ calculated by ANSYS (SOLID186)

5 CONCLUSION

On base of the transfer relations for the 3D straight FGM beam of doubly symmetric cross-section with longitudinal polynomial variation of the effective material properties, the effective matrix of the 3D beam finite element for static, modal and buckling analysis of the FGM single beams and beam structures is established in this contribution. Symmetrically transversal and lateral, and continuously longitudinal variation of material properties is considered in the real beam. Homogenization of the spatially varying material properties in the real FGM beam and the calculation of effective parameters of the homogenized beam are done by the extended mixture rules and the multilayer method (MLM). Effects of the varying planar Winkler elastic foundations and the shear force deformation (by means of the average shear correction factors) and the consistent mass and mass moment of inertia distribution are

taken into account. The effect of axial force is included for the flexural deformations as well that allows performing of analysis within the 2nd order beam theory. All the derived equations were programmed through the software MATHEMATICA [21] and the numerical calculations were carried out. In modal and buckling analysis, the eigenvalue problem is solved. In buckling analysis, the circular frequency ω is set to zero and axial force N is increased the determinant of the global matrix of the beam structure tends to zero. This axial force corresponds to the critical buckling force. In modal analysis, for given internal axial forces N in the competent beams and geometrical parameters and material and boundary conditions, the circular frequency ω is increased until the determinant of the global matrix of the beam structure tends to zero. This circular frequency corresponds to the natural circular frequency from which the natural frequency (eigenfrequency) is calculated. In linearized elastostatic analysis (according the second order beam theory), the internal axial forces have to be evaluated that input in the linearized geometric stiffness matrix. By the linear beam theory only linear stiffness matrix is established. The load vector is established and the local and global displacements and internal forces are calculated. After that, as usually, the secondary variables like eigen- and buckling- forms, and the stress are calculated. The main issue of numerical investigations is the modal, buckling and elastostatic analysis of FGM beam structures (single beams and spatial beam structures) with spatial variation of material properties. By selected numerical examples the effect of axial and shear forces is evaluated. The results carried out by our approach are compared with results obtained using very fine beam and continuum meshes in the FEM program ANSYS [34]. An excellent agreement of our solution results is obtained, which confirms respectable accuracy and effectiveness of our approach.

The main advantage of the new beam finite element is that the individual beams of the beam structure with spatial variation of material properties (continuous or layered but symmetrically in transversal and lateral direction, and continuous polynomial in longitudinal direction) can be modeled with only one beam finite element, because the variation of the material properties is relatively accurately included into the finite element matrix. Another advantage is that the beam finite element can be very effectively used also for the modeling of spatial beam structures.

Disadvantage of this approach is that by more complicated variation of material properties some problems arise by the transfer constants calculation. This problem can be solved by the dividing of the definition domain of the transfer functions [20]. Another problems comparing to continuum approach can arise by the beams with complex cross-sectional area.

Acknowledgement: This work was financially supported by grants of Science and Technology Assistance Agency no. APVV-0246-12 and Scientific Grant Agency of the Ministry of Education of Slovak Republic and the Slovak Academy of Sciences and VEGA No. 1/0453/15.

REFERENCES

[1] F. Ebrahimi, E. Salari, Size-dependent free flexural vibrational behavior of functionally graded nanobeams using semi-analytical differential method. *Composite Part B,* **79**: 156-169, 2015.

[2] F. Ebrahimi, E. Salari, Nonlocal thermo-mechanical vibration analysis of functionally graded nanobeams in thermal enviroment. *ActaAstronautika*; **113**: 29-50, 2015.

[3] S.E. Ghiasian, Y. Kiani, M.R. Eslami, Nonlinear thermal dynamic buckling of FGM beams. *European Journal of Mechanics A/Solids*, **54**: 232-242, 2015.

[4] U. Eroglu, In-plane free vibration of circular beams made of functionally graded material in thermal environment: Beam theory. *Composite Structures*, **122**: 217-228, 2015.

[5] M. Meradjah, A. Kaci, M.S.A. Houari, A. Tounsi, S.R. Mahmoud, A new higher order shear and normal theory of fuctionaly graded beams. *Steel and Composite Structures*, **18**: 793-809, 2015.

[6] N. Wattanasakulpong, Q. Mao, Dynamic response of Timoshenko fuctionally graded beams with classical and non-classical boundary conditions using Chebyshev collocation method. *Composite Structures*, **119**: 346-354, 2015.

[7] R. Bennai, H.A. Atmane, A. Tounsi, A new higher-order shear and normal deformation theory for functionally graded sandwich beams. *Steel and Composite Structures*, **19**: 521-546, 2015.

[8] S. El-Borgi, R. Fernandes, J.N. Reddy, Non-local free and forced vibrations of graded nanobeams resting on a non-linear elastic foundation. *Int. J. of Non-Linear Mechanics*, **77**: 348-363, 2015.

[9] I.C. Dikaros, E.J. Sapountzakis, Non-uniform shear warping effect in the analysis of composite beams by BEM. *Engineering Structures*, **76**: 215 – 234, 2014.

[10] I.C. Dikaros, E.J. Sapountzakis, Generalized warping analysis of composite beams of an arbitrary cross-section by BEM. I: Theoretical considerations and numerical implementation. *Engineering Mechanics* 2014; DOI: 10.1061/(ASCE) EM.1943-7889.0000775.

[11] I.C. Dikaros, E.J. Sapountzakis, Generalized warping analysis of composite beams of an arbitrary cross-section by BEM. II: Numerical applications. *Engineering Mechanics* 2014; DOI: 10.1061/(ASCE)EM.1943-7889.0000776.

[12] E.J. Sapountzakis, I.C. Dikaros, Advanced 3D beam element of arbitrary composite cross-section including generalized warping effect. *Int. J. for Numerical Methods in Engineering*, 2015, DOI: 10.1002/nme.4849.

[13] G. Giunta, S. Belourttar, A.J.M. Ferreira, A static analysis of three-dimensional functionally graded beams by herarchical modelling and collocation meshless solution method. *ActaMechanica*, 2015; DOI 10.1007/s00707-1503-3.

[14] J. Murin, M. Aminbaghai, V. Kutis, Exact solution of the bending vibration problem of the FGM beam with variation of material properties. *Engineering Structures*, **32**: 1631 – 1640, 2010.

[15] M. Aminbaghai, J, Murin, V. Kutis, Modal analysis of the FGM-beams with continuous transversal symmetric and longitudinal variation of material properties with effect of large axial force. *Engineering Structures*, **34**: 314 – 329, 2012.

[16] J. Murin, M. Aminbaghai, V. Kutis, J. Hrabovsky, Modal analysis of the FGM beams with effect of axial force under longitudinal variable elastic Winkler foundation. *Engineering Structures*, **49**: 234 – 247, 2013.

[17] J. Murin, M. Aminbaghai, J. Hrabovsky, V. Kutis, S. Kugler, Modal analysis of the FGM beams with effect of the shear correction function. *Composites: Part B*, **45**:1575–1582, 2013.

[18] V. Kutis, J. Murin, R. Belak, J. Paulech,Beam element with spatial variation of material properties for multiphysics analysis of functionally graded materials. *Computers and Structures*, **89**: 1192 – 1205, 2011.

[19] H. Rubin, Analytische Berechnung von Stäben und Stabwerken mit stetiger Veränderlichkeit von Querschnitt, elastischer Bettung und Massenbelegung nach

Theorie erster und zweiter Ordnung, *Baustatik - Baupraxis 7. Berichte der 7. Fachtagung "Baustatik - Baupraxis"* Aachen/Deutschland 18.-19. März 1999. Balkema 1999, Abb., Tab.S.135-145, in German.

[20] H. Rubin, Solution of differential equations of arbitrary order with polynomial coefficients and application to a statics problem. *ZAMM* **76**, 105 – 117, 1996.

[21] Wolfram S. MATHEMATICA 5, Wolfram research, Inc., 2003.

[22] H. Altenbach, J. Altenbach, W. Kissing,*Mechanics of composite structural elements*. Springer Verlag, 2003.

[23] J.C. Halpin, J.L. Kardos, The Halpin-Tsai equations. A review, *Polymer Engineering and Science*, **16**(5): 344 – 352, 1976.

[24] T. Reuter, G.J. Dvorak, Micromechanical models for graded composite materials: Ii. Thermomechanical loading, *Mechanics and Physics of Solids*, **46**: 1655 – 1673, 1998.

[25] J. Murin, V. Kutis, Improved mixture rules for composite (FGMs) sandwich beam finite element. *In Computational Plasticity IX. Fundamentals and Applications*. Barcelona, Spain 2007: 647 – 650.

[26] A.E. Alshorbagy, M.A. Eltaher, F.F. Mahmoud, Free vibration of a functionally graded beam by finite element method. *Applied Mathematical Modelling*, **35**: 412 – 425, 2010.

[27] M. Simsek, Vibration analysis of a functionally graded beam under a moving mass by using different beam theories, *Composite Structures*, **92**: 904 – 917, 2010.

[28] T. Rout, On the dynamic stability of functionally graded material under parametric excitation. PhD thesis. National Institute of Technology Rourkela, India. 2012.

[29] V. Kutis, J. Murin, R. Belak, J. Paulech, Beam element with spatial variation of material properties for multiphysics analysis of functionally graded materials. *Computers and Structures*, **89**: 1192 – 1205, 2010.

[30] J. Murin, S. Kugler, M. Aminbaghai, J. Hrabovsky, V. Kutis, J. Paulech, Homogenization of material properties of the FGM beam and shells finite elements. In.: *11th World Congress on Computational mechanics (WCCM XI)*, Barcelona, 20-25 July, 2014.

[31] J. Murin, M. Aminbaghai, J. Hrabovsky, V. Kutis, J. Paulech, S. Kugler, A new FGM beam finite element for modal analysis. In.: *11th World Congress on Computational mechanics (WCCM XI)*, Barcelona, 20-25 July, 2014.

[32] J. Murín, J. Hrabovský, V. Kutiš, J. Paulech, Shear correction function derivation for the FGM beams. In: *2nd International Conference on Multi-scale Computational Methods for solid and Fluids*, Sarajevo, Bosnia and Hercegovina, 10–12 June, 2015.

[33] J. Murin, M. Aminbaghai, J. Hrabovsky, V. Kutis,S. Kugler, Effect of the Shear Correction Function in the FGM Beams Modal Analysis. *In Proceedings of the 15th European Conference on Composite Materials*, Venice, Italy, 24-28 June, 2012, ISBN 978-88-88785-33-2.

[34] ANSYS Swanson Analysis System, Inc., 201 Johnson Road, Houston, PA 15342/1300, USA.

[35] H. Mang, G. Hoffstetter,*Festigkeitslehre*. Springer Verlag; 2000.

ECCOMAS Congress 2016
VII European Congress on Computational Methods in Applied Sciences and Engineering
M. Papadrakakis, V. Papadopoulos, G. Stefanou, V. Plevris (eds.)
Crete Island, Greece, 5–10 June 2016

THERMO-ELASTICITY IN SHELL STRUCTURES MADE OF FUNCTIONALLY GRADED MATERIALS (ECCOMAS CONGRESS 2016)

Stephan Kugler[1], Peter A. Fotiu[1], and Justin Murin[2]

[1]Department of Applied and Numerical Mechanics,
University of Applied Sciences Wiener Neustadt,
Johannes Gutenbergstraße 3, Wiener Neustadt, Austria
e-mail: {kugler,fotiu}@fhwn.ac.at

[2] Department of Applied Mechanics and Mechatronics,
Institute for Automotive Mechatronics,
Faculty of Electrical Engineering and Information Technology,
Slovak University of Technology in Bratislava, Slovakia
Ilkovicova 3, 81219 Bratislava, Slovakia
e-mail: justin.murin@stuba.sk

Keywords: Thermo-Elasticity, FGM-Shell-Structures, Drilling degrees of freedom, Two-Step-Algorithm.

Abstract. *An efficient low order finite shell element is derived for the thermo-elastic analysis of shell structures made of functionally graded materials or multilayer composites. It is based on a one-way coupling between the thermal and the mechanical analysis. The thermal quantities are evaluated using a new iterative scheme that properly accounts for convection boundary conditions and large gradients of the thermal conductivity. The resulting non-constant temperature field with respect to the thickness direction gives nodal forces and couples, which are applied on a shear weak six parameter shell formulation. Here, drill rotations are included, supplemented with a proper method for calculating effective elastic properties. Numerical results indicate efficiency and accuracy of the proposed approach.*

1 Introduction

This paper focuses on the analysis of thermo-elastic effects in shell structures of functionally graded materials (FGM) or multilayer composites (MLC). The constitutive model is characterized by a variation of material properties, which is continuous in FGMs and discontinuous in MLCs. We focus only on arbitrary variations in transverse direction. Variations with respect to the membrane directions can be modeled easily using a discretization scheme with elements each showing constant transverse variations. FGM and MLC structures play an important role in the development of sensors and actuators (see [1] and references therein) and accurate virtual analysis procedures are required.

Many papers deal with the static and dynamic analysis of FGM beams with transverse variations of material properties. In [2] elasticity solutions for simply supported FGM beams are given using the Euler-Bernoulli beam theory. Chakraborty et al. [3] discuss thermo-elastic beam problems based on the first order shear theory. Mahi et al. [4] consider free vibrations of symmetric FGM beams subjected to an initial thermal stress. In case of combined variations of material properties in transverse and longitudinal directions, many achievements are due to Murin et al. [5, 6, 7]. The amount of literature dealing with FGM shells is also overwhelming. In Shen [8] special attention is put onto the nonlinear response of FGM plates. In [9, 10] electro-mechanical analyses of FGM shells with piezo-electric layers are proposed. Thermo-elastic analysis procedures of FGM plate and shell structures are discussed in [11]. There, a higher order shell formulation is used. However, only little literature is found if drill rotations (i.e. the rotation about the shell's normal) are to be included. This frequently missing sixth nodal degree of freedom gets important if shell structures are combined with beam structures. There, any torsional moment within the beam directly activates drill rotations if the beam axis is perpendicular to the shell's membrane. In that field many achievements are due to Kugler et al. [12, 13], where references to earlier procedures [14] can be found. A generalization of those procedures to FGMs and MLCs are given in [15, 16] where elasticity is described using effective elastic properties derived in [15].

In this paper we discuss a numerical framework to analyze thermo-elastic effects in FGM and MLC shells. Frequently, the variation of Poisson's ratio in FGMs and MLCs does not show large gradients - therefore, we assume Poisson's ratio to be constant. As boundary conditions we consider the following cases:

- Nodal temperatures (Dirichlet-type): The mean temperature at any node is prescribed.
- Convection on top- and bottom-surface (von Neumann-type): Convection is applied independently onto the top- and bottom-surface prescribing the gradient of the non-constant transverse temperature distribution.
- Nodal displacements and rotations (Dirichlet-type): Displacements and rotations are prescribed.
- Mechanical loads (von Neumann-type): Any transverse and in-plane mechanical loads can be applied onto the finite element model.

The present paper is organized as follows: In Sect. 2 the details of the proposed numerical framework is discussed. We start with describing the thermal analyses in Sect. 2.1. The temperature field in FGM and MLC shells is found for an arbitrary variation of thermal conductivity and convection conditions. Non-constant temperature distributions with respect to the thickness

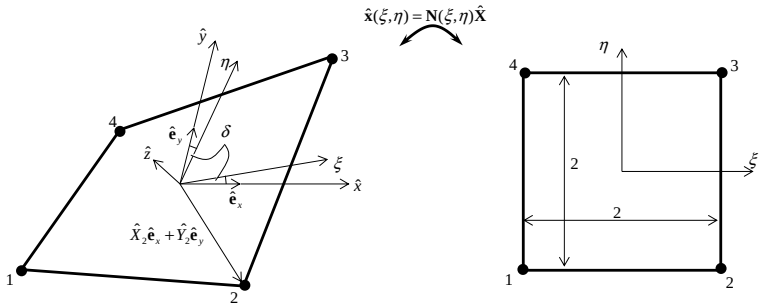

Figure 1: Plane quadrilateral with skew angled element coordinates ξ and η

direction require an iterative solution scheme. The mechanical analysis is discussed in Sect. 2.2. There, a quadrilateral six parameter shell element is described, where drilling rotations are included within the membrane part of the stiffness matrix. The bending part of the stiffness matrix incorporates a shear elastic behavior with an exact thin plate limit. A projection procedure for arbitrarily warped element geometries is included. Arbitrary variations of the Young's modulus require four effective elastic properties, i.e. the offset of a mechanical neutral surface from the discretized mid-surface, effective moduli for membrane and bending properties and a shear correction factor. In Sect. 2.3 an efficient one-way coupling scheme between the thermal and the mechanical field is proposed. Based on the evaluated temperature distributions internal nodal forces and couples are calculated, which are applied onto the mechanical model. The numerical accuracy and the effectiveness of the proposed formulation is discussed in Sect. 3. There, solutions based on the proposed framework are compared to continuum solutions found with ANSYS an to reference solutions found in literature. Finally, in Sect. 4 conclusions are drawn.

2 Numerical procedure

Consider a curved FGM or MLC shell geometry of thickness h, where the geometrical mid-surface is discretized by four noded shell elements. Thus, the element configuration could possibly be warped. Any warped surface geometries do not pose a problem if scalar fields like temperature distributions are analyzed (see Sect. 2.1). However, in mechanical analyses warped shell elements lead to a coupling between membrane and bending properties, which can be circumvented by special projection schemes (see Sect. 2.2). Within each element we assume material properties to be constant in membrane directions $\hat{x}$ - $\hat{y}$ and variable in transverse direction $\hat{z}$.

Since both the thermal analysis and the mechanical analysis is based on a four noded finite element, we introduce a two dimensional element kinematics. The nodal coordinates of the i-th node ($i = 1, 2, 3, 4$) read $\hat{\mathbf{r}}_i = \hat{X}_i\hat{\mathbf{e}}_x + \hat{Y}_i\hat{\mathbf{e}}_y$ and the mapping (Fig. 1) between the Cartesian and the parameter coordinates is carried out using the classical bilinear shape functions [17],

$$\begin{bmatrix} \hat{x} \\ \hat{y} \end{bmatrix} = \begin{bmatrix} \mathbf{N} & \mathbf{0} \\ \mathbf{0} & \mathbf{N} \end{bmatrix} \begin{bmatrix} \hat{\mathbf{X}} \\ \hat{\mathbf{Y}} \end{bmatrix} \tag{1}$$

with

$$\mathbf{N} = \begin{bmatrix} N_1 & N_2 & N_3 & N_4 \end{bmatrix}$$

$$N_1 = \frac{1}{4}(1-\xi)(1-\eta) \quad , \quad N_2 = \frac{1}{4}(1+\xi)(1-\eta) \ ,$$

$$N_3 = \frac{1}{4}(1+\xi)(1+\eta) \quad , \quad N_4 = \frac{1}{4}(1-\xi)(1+\eta) \ . \tag{2}$$

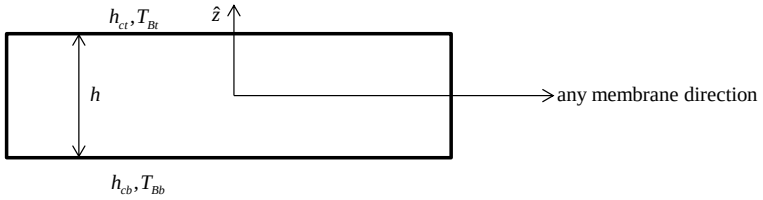

Figure 2: Description of the thermal field problem

In (1) the nodal coordinates are arranged as $\hat{\mathbf{X}} = \left[\begin{array}{cccc} \hat{X}_1 & \hat{X}_2 & \hat{X}_3 & \hat{X}_4 \end{array} \right]^T$ and $\hat{\mathbf{Y}} = \left[\begin{array}{cccc} \hat{Y}_1 & \hat{Y}_2 & \hat{Y}_3 & \hat{Y}_4 \end{array} \right]^T$. An alternative formulation [18] of the shape functions (2) is

$$\mathbf{N} = \boldsymbol{\Delta} + \mathbf{b}_x \hat{x} + \mathbf{b}_y \hat{y} + \boldsymbol{\gamma} \xi \eta, \tag{3}$$

with

$$\mathbf{b}_x = \frac{1}{2A_e} \left[\begin{array}{cccc} \hat{y}_{24} & \hat{y}_{31} & \hat{y}_{42} & \hat{y}_{13} \end{array} \right], \; \mathbf{b}_y = \frac{1}{2A_e} \left[\begin{array}{cccc} \hat{x}_{42} & \hat{x}_{13} & \hat{x}_{24} & \hat{x}_{31} \end{array} \right], \tag{4}$$

$$\boldsymbol{\gamma} = \frac{1}{4A_e} \left[\begin{array}{c} \hat{X}_2 \hat{y}_{34} + \hat{X}_3 \hat{y}_{42} + \hat{X}_4 \hat{y}_{23} \\ \hat{X}_1 \hat{y}_{43} + \hat{X}_3 \hat{y}_{14} + \hat{X}_4 \hat{y}_{31} \\ \hat{X}_1 \hat{y}_{24} + \hat{X}_2 \hat{y}_{41} + \hat{X}_4 \hat{y}_{12} \\ \hat{X}_1 \hat{y}_{32} + \hat{X}_2 \hat{y}_{13} + \hat{X}_3 \hat{y}_{21} \end{array} \right]^T, \tag{5}$$

$$\boldsymbol{\Delta} = \frac{1}{4} \left[\mathbf{t} - \left(\sum_{i=1}^{4} \hat{X}_i \right) \mathbf{b}_x - \left(\sum_{i=1}^{4} \hat{Y}_i \right) \mathbf{b}_y \right], \tag{6}$$

$$\mathbf{t} = \left[\begin{array}{cccc} 1 & 1 & 1 & 1 \end{array} \right], \tag{7}$$

$$\hat{x}_{IJ} = \hat{X}_I - \hat{X}_J \,, \; \hat{y}_{IJ} = \hat{Y}_I - \hat{Y}_J \,, \; A_e = \frac{1}{2} \left(\hat{x}_{24} \hat{y}_{31} + \hat{x}_{31} \hat{y}_{42} \right). \tag{8}$$

2.1 Thermal analysis

In this section we evaluate the temperature field $T(\hat{x}, \hat{y}, \hat{z})$ within the shell's volume. Consider a FGM or MLC shell structure of thickness h with a transversely varying thermal conductivity k, where convection is applied onto the outer surfaces. Figure 2 shows a cut through the shell structure, where convection is applied independently onto the top- and bottom-surface, i.e.

$$\hat{z} = -h/2: \;\; q_n^b = h_{cb}(T(\hat{z} = -h/2) - T_{Bb}), \tag{9}$$

$$\hat{z} = h/2: \;\; q_n^t = h_{ct}(T(\hat{z} = h/2) - T_{Bt}). \tag{10}$$

In (9) and (10) h_{ct} and h_{cb} denote the convection coefficient on the top and bottom surface, while T_{Bt} and T_{Bb} are the temperatures of the adjacent fluid. We decompose $T(\hat{x}, \hat{y}, \hat{z})$ according to

$$T(\hat{x}, \hat{y}, \hat{z}) = \bar{T}(\hat{x}, \hat{y}) + \widetilde{T}(\hat{z}), \tag{11}$$

where

$$\bar{T}(\hat{x}, \hat{y}) = 1/h \int_h T(\hat{x}, \hat{y}, \hat{z}) \, d\hat{z}, \tag{12}$$

is the mean temperature, while $\widetilde{T}(\hat{z})$ describes the unknown temperature distribution in transverse direction. The iterative solution strategy consists of two steps:

1. Evaluation of the mean temperature $\bar{T}(\hat{x},\hat{y}) = {}^1\!/_h \int_h T(\hat{x},\hat{y},\hat{z})\, d\hat{z}$ in membrane direction.
2. Estimate $\widetilde{T}(\hat{z})$ based on a mean temperature $\bar{T}$.

An iterative procedure with iteration number I is required since the shell's surface temperatures are initially unknown. Hence, (9) and (10) cannot be satisfied exactly, and we rewrite (9) and (10) according to

$$\hat{z} = -{}^h\!/_2 : \quad q_n^{b\,I+1} = h_{cb}(\bar{T}^{I+1} - T_{Bb}^{*I}),$$

$$\hat{z} = {}^h\!/_2 : \quad q_n^{t\,I+1} = h_{ct}(\bar{T}^{I+1} - T_{Bt}^{*I}), \tag{13}$$

with

$$T_{Bb}^{*I} = T_{Bb} - \widetilde{T}^I(\hat{z} = -{}^h\!/_2),$$

$$T_{Bt}^{*I} = T_{Bt} - \widetilde{T}^I(\hat{z} = {}^h\!/_2). \tag{14}$$

The **global iterative algorithm** can be summarized as follows:

1. $I = 0$
2. $\widetilde{T}^{I=0}(\hat{z} = \pm {}^h\!/_2) = 0$
3. WHILE $\frac{\bar{T}^{I+1} - \bar{T}^I}{\bar{T}^{I+1}} <$ tol (tol = tolerance limit)
   (a) $T_{Bb}^{*I} = T_{Bb} - \widetilde{T}^I(\hat{z} = -{}^h\!/_2)$ and $T_{Bt}^{*I} = T_{Bt} - \widetilde{T}^I(\hat{z} = {}^h\!/_2)$
   (b) FIND $\bar{T}^{I+1}$ according to Sect. 2.1.1 using convection boundary condition (13) and (14).
   (c) FIND $\widetilde{T}^{I+1}$ according to Sect. 2.1.2
   (d) $I = I + 1$

2.1.1 Evaluation of mean temperature

In this section we discuss a suitable procedure to evaluate the mean temperature $\bar{T}$. The strong form of the corresponding boundary value problem [19] reads

$$\bar{k}\bar{T}_{,ii} = 0, \tag{15}$$

$$\bar{T} = T_0 \ \text{ at } \ \Gamma_T, \tag{16}$$

$$q_0 = q_n = -\bar{k}\bar{T}_{,i} n_i \ \text{ at } \ \Gamma_q. \tag{17}$$

where a comma within an index denotes a partial derivative and Einstein's summation convention is understood ($i = \hat{x},\hat{y}$). The Dirichlet boundary condition (16) prescribes a given value T_0 at the boundary Γ_T, while the von Neumann boundary condition prescribes the heat flux $q_i n_i$

along Γ_q. In (17) $-\bar{k}\bar{T}_{,i} = \bar{q}_i$ is the mean heat flux, while $\bar{k}$ denotes the mean value of thermal conductivity,

$$\bar{k} = \frac{1}{h}\int_h k(\hat{z})d\hat{z}. \tag{18}$$

The weak form of (15)-(17) is given by,

$$\int_V \bar{k}\bar{T}_{,ii}\delta\bar{T}dV - \int_{\Gamma_q}(q_0 - q_n)\delta\bar{T}d\Gamma = 0, \tag{19}$$

where the weighting function $\delta\bar{T}$ is a virtual temperature distribution that has to satisfy the Dirichlet boundary condition $\delta\bar{T} = 0$ at Γ_T. Applying the Gaussian theorem to the first integral leads to

$$\int_V \bar{k}\bar{T}_{,i}\delta\bar{T}_{,i}dV + \int_{\Gamma_q} q_0\delta\bar{T}d\Gamma = 0. \tag{20}$$

We use bilinear interpolations (2) for the mean temperature fields

$$\bar{T} = \mathbf{N}\bar{\mathbf{T}}^e \;\text{ and }\; \delta\bar{T} = \mathbf{N}\delta\bar{\mathbf{T}}^e\ , \tag{21}$$

where $\bar{\mathbf{T}}^e$ and $\delta\bar{\mathbf{T}}^e$ denote the corresponding nodal values. Introducing this into (20) yields

$$\begin{aligned}\left(\delta\bar{\mathbf{T}}^e\right)^T \Bigg[&\underbrace{\bar{k}h\int_{-1}^{1}\int_{-1}^{1}\mathbf{B}^T\mathbf{B}\det\mathbf{J}\,d\xi d\eta}_{\mathbf{K}_T^e}\bar{\mathbf{T}}^e + \\ &+\underbrace{\int_{-1}^{1}\int_{-1}^{1}\left(h_{ct}+h_{cb}\right)\mathbf{N}^T\mathbf{N}\det\mathbf{J}\,d\xi d\eta}_{\mathbf{K}_{Tc}^e}\bar{\mathbf{T}}^e - \\ &-\underbrace{\int_{-1}^{1}\int_{-1}^{1}\left(h_{ct}T^*_{Bt}+h_{cb}T^*_{Bb}\right)\mathbf{N}^T\det\mathbf{J}\,d\xi d\eta}_{\mathbf{F}_{Tc}^e}\Bigg] = 0,\end{aligned} \tag{22}$$

with $\mathbf{B}$ referring to the gradient of the shape functions,

$$\mathbf{B} = \begin{bmatrix}\mathbf{B}_{\hat{x}}\\ \mathbf{B}_{\hat{y}}\end{bmatrix} = \begin{bmatrix} N_{1,\hat{x}} & N_{2,\hat{x}} & N_{3,\hat{x}} & N_{4,\hat{x}} \\ N_{1,\hat{y}} & N_{2,\hat{y}} & N_{3,\hat{y}} & N_{4,\hat{y}}\end{bmatrix}. \tag{23}$$

We assume that $\widetilde{T}(\hat{z})$ is constant within one element, thus, T^*_{Bt} and T^*_{Bb} from (14) is also elementwise constant and is evaluated at each element's center. The differential volume of a shell structure is given by $dV = hdA = h\det\mathbf{J}\,d\xi d\eta$, where $\det\mathbf{J}$ denotes the determinant of the element Jacobian. With (22) we finally obtain

$$\left(\mathbf{K}_T^e + \mathbf{K}_{Tc}^e\right)\bar{\mathbf{T}}^e = \mathbf{F}_{Tc}^e, \tag{24}$$

Equations (24) have to be assembled to a global system in a standard manner [20]. All integrations over the element domain are carried out numerically by a 2×2 Gauss integration.

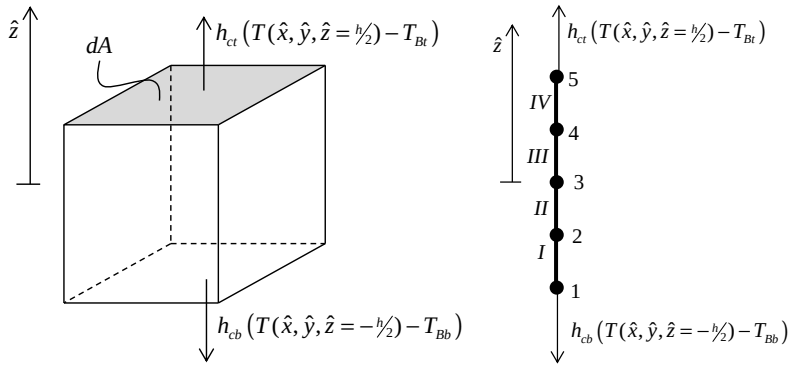

(a) Problem of transverse temperature distribution

(b) Discretized problem of transverse temperature distribution ($n = 4$)

Figure 3: Transverse temperature distribution

2.1.2 Evaluation of transverse temperature distribution

Once the mean temperature $\bar{T}(\hat{x},\hat{y})$ is evaluated at every point of the shell's structure, the temperature distribution with respect to the thickness direction is calculated. Thereby, we analyze the problem depicted in Fig. 3(a) showing an infinitesimal volume portion of cross section dA and a height of h where a convection boundary condition on the top and bottom surface is applied. In what follows we discuss a procedure where the temperature distribution with respect to the thickness direction is found from a thermal conduction problem with two Neumann conditions. At every location $\hat{x}$ and $\hat{y}$ the following system of equations holds[1]

$$\frac{d}{d\hat{z}}\left(k(\hat{x},\hat{y},\hat{z})\frac{d}{d\hat{z}}T(\hat{x},\hat{y},\hat{z})\right)+K^*=0\ , \tag{25}$$

$$\hat{z}=h/2:\ -k(\hat{x},\hat{y},\hat{z}=h/2)\left.\frac{dT(\hat{x},\hat{y},\hat{z})}{d\hat{z}}\right|_{\hat{z}=h/2}-h_{ct}\left(T(\hat{x},\hat{y},\hat{z}=h/2)-T_{Bt}\right)=0\ , \tag{26}$$

$$\hat{z}=-h/2:\ -k(\hat{x},\hat{y},\hat{z}=-h/2)\left.\frac{dT(\hat{x},\hat{y},\hat{z})}{d\hat{z}}\right|_{\hat{z}=-h/2}-h_{ct}\left(T(\hat{x},\hat{y},\hat{z}=-h/2)-T_{Bb}\right)=0\ . \tag{27}$$

In (25) K^* is given by

$$K^*=Kk(\hat{z}), \tag{28}$$

where K represents an unknown constant. The inclusion of (28) in (25) is mandatory for accurate results and is in contrast to [11] where a similar strong form is used without K^*. The inclusion of K^* can be motivated by the following thought experiment: Within a shell's section of constant conductivity the transverse temperature distribution is expected to be parabolic with prescribed gradients at the top and bottom surface. In absence of K^* the solution of (25) leads to a linear distribution and (26) and (27) cannot be satisfied exactly. The introduction of a non-vanishing constant K^* avoids such a deficiency. The unknown constant K is found from the

[1] Within one element the thermal conduction coefficient k is assumed to be constant, however, k can be discontinuous from element to element.

constraint that the mean value of $T(\hat{x},\hat{y},\hat{z})$ must equal $\bar{T}(\hat{x},\hat{y})$ from (12). Rewriting (25)-(27) with $T(\hat{x},\hat{y},\hat{z}) = \bar{T}(\hat{x},\hat{y}) + \widetilde{T}(\hat{z})$ leads to

$$\frac{d}{d\hat{z}}\left(k(\hat{x},\hat{y},\hat{z})\frac{d}{d\hat{z}}\widetilde{T}(\hat{z})\right) + Kk(\hat{z}) = 0\ , \tag{29}$$

$$\hat{z} = {}^{h}/_{2}:\ -k(\hat{x},\hat{y},\hat{z}={}^{h}/_{2})\left.\frac{d\widetilde{T}(\hat{z})}{d\hat{z}}\right|_{\hat{z}={}^{h}/_{2}} - h_{ct}\left(\bar{T}(\hat{x},\hat{y}) + \widetilde{T}(\hat{z}=-{}^{h}/_{2}) - T_{Bt}\right) = 0\ , \tag{30}$$

$$\hat{z} = -{}^{h}/_{2}:\ -k(\hat{x},\hat{y},\hat{z}=-{}^{h}/_{2})\left.\frac{d\widetilde{T}(\hat{z})}{d\hat{z}}\right|_{\hat{z}=-{}^{h}/_{2}} - h_{ct}\left(\bar{T}(\hat{x},\hat{y}) + \widetilde{T}(\hat{z}=-{}^{h}/_{2}) - T_{Bb}\right) = 0\ , \tag{31}$$

$$\int_{h}\widetilde{T}(\hat{z})\,d\hat{z} = 0\ . \tag{32}$$

An analytical solution of (29)-(32) can be given in case of a constant conductivity, i.e. $k(\hat{z}) = k$, however, for arbitrary variations of $k(\hat{z})$ we propose a FEM like solution procedure using a discretization with n linear elements of length $l_e = {}^{h}/_{n}$, see Fig. 3(b). Hence, we find for interior elements

$$dA\int_{l_e} k(\hat{z})\widetilde{T}_{,\hat{z}}\delta\widetilde{T}_{,\hat{z}}\,d\hat{z} = dAK\int_{l_e} k(\hat{z})\delta\widetilde{T}\,d\hat{z}, \tag{33}$$

and for the top and bottom elements

$$\text{bottom}\ (\hat{z}=-{}^{h}/_{2}):\ dA\int_{l_e} k(\hat{z})\widetilde{T}_{,\hat{z}}\delta\widetilde{T}_{,\hat{z}}\,d\hat{z} = dA\int_{l_e} K^{*}\delta\widetilde{T}\,d\hat{z} - \left(h_{cb}dA\left(\bar{T}+\widetilde{T}-T_{Bb}\right)\delta\widetilde{T}\right)\Big|_{\hat{z}=-{}^{h}/_{2}}, \tag{34}$$

$$\text{top}\ (\hat{z}={}^{h}/_{2}):\ dA\int_{l_e} k(\hat{z})\widetilde{T}_{,\hat{z}}\delta\widetilde{T}_{,\hat{z}}\,d\hat{z} = dA\int_{l_e} K^{*}\delta\widetilde{T}\,d\hat{z} - \left(h_{ct}dA\left(\bar{T}+\widetilde{T}-T_{Bt}\right)\delta\widetilde{T}\right)\Big|_{\hat{z}={}^{h}/_{2}}, \tag{35}$$

where $k(\hat{z})$ is assumed to the be the value of thermal conductivity at each element's center, being constant throughout each element. This finally leads to the following system of equations

$$\left\{\frac{n}{h}\begin{bmatrix} k_1 & \cdots & 0 & 0\\ \vdots & \ddots & \vdots & \vdots\\ 0 & \cdots & k_{n-1} & -k_n\\ 0 & \cdots & -k_n & k_n\end{bmatrix} + \begin{bmatrix} h_{cb} & \cdots & 0 & 0\\ \vdots & \ddots & \vdots & \vdots\\ 0 & \cdots & 0 & 0\\ 0 & \cdots & 0 & h_{ct}\end{bmatrix}\right\}\begin{bmatrix}\vartheta_1\\ \vdots\\ \vartheta_n\\ \vartheta_{n+1}\end{bmatrix} =$$

$$= \frac{K\,h}{2n}\begin{bmatrix} k_1\\ \vdots\\ k_{n-1}\\ k_n\end{bmatrix} + \begin{bmatrix} h_{cb}\left(T_{Bb}-\bar{T}\right)\\ \vdots\\ 0\\ h_{ct}\left(T_{Bt}-\bar{T}\right)\end{bmatrix}, \tag{36}$$

where ϑ_i for $i = 1...n+1$ denotes the nodal value of $\widetilde{T}$ and k_i for $i = 1...n$ refers to the thermal conductivity at the i-th element's center. Equation (36) can be rewritten according to

$$\mathbf{K}\boldsymbol{\vartheta} = K\mathbf{F} + \mathbf{F}_c, \tag{37}$$

and represents a linear algebraic system of equations approximating (29)-(31). Equation (32) is modeled as

$$\frac{1}{2}\left(\vartheta_1 + \vartheta_{n+1}\right) + \sum_{i=2}^{n} \vartheta_i = \left[\begin{array}{cccc} 1/2 & \cdots & 1 & 1/2 \end{array}\right] \left[\begin{array}{c} \vartheta_1 \\ \vdots \\ \vartheta_n \\ \vartheta_{n+1} \end{array}\right] = \mathbf{L}\boldsymbol{\vartheta} = 0, \tag{38}$$

and can be used to evaluate the unknown constant K,

$$K = -\frac{\mathbf{L}\mathbf{K}^{-1}\mathbf{F}_c}{\mathbf{L}\mathbf{K}^{-1}\mathbf{F}}, \tag{39}$$

consequently, the nodal values $\boldsymbol{\vartheta}$ read

$$\boldsymbol{\vartheta} = -\frac{\mathbf{L}\mathbf{K}^{-1}\mathbf{F}_c}{\mathbf{L}\mathbf{K}^{-1}\mathbf{F}}\mathbf{K}^{-1}\mathbf{F} + \mathbf{K}^{-1}\mathbf{F}_c. \tag{40}$$

2.2 Mechanical analysis

The derivation of a six parameter shell element is based on four steps. In Sect. 2.2.1 we present useful equations for evaluating effective elastic quantities. Arbitrary warped element geometries show a computationally expensive coupling between membrane and bending properties. In order to avoid the derivation of those coupling matrices, we describe in Sect. 2.2.2 a projection scheme, which extracts a plane element configuration. Using that projection the derivation of the stiffness matrix can be separated into a membrane (Sect. 2.2.3) and a bending part (Sect. 2.2.4).

2.2.1 Effective elastic quantities

The element formulation requires four effective quantities that are directly related to the distribution of Young's modulus $E(\hat{z})$. We present here only the main results and refer to [15] for details. In case of unsymmetrical variations of E the offset $\overline{z}$ of a neutral surface from the discretized mid-plane is evaluated as

$$\overline{z} = \frac{\int_{-h/2}^{h/2} E(\hat{z})\hat{z}d\hat{z}}{\int_{-h/2}^{h/2} E(\hat{z})d\hat{z}}. \tag{41}$$

With respect to this plane, membrane and bending deformations are decoupled and an arbitrary normal strain reads

$$\varepsilon_{ij}(\hat{z}') = \varkappa_{ij}\hat{z}' + \varepsilon_{ij}^{(0)}, \tag{42}$$

with $\hat{z}' = \hat{z} - \overline{z}$. In (42) $\varepsilon_{ij}^{(0)}$ denotes the strain in the neutral surface and $\varkappa_{ij}$ refers to a curvature. The effective moduli for membrane (E_m) and bending (E_b) read

$$E_m = \frac{1}{h}\int_{-h/2-\overline{z}}^{h/2-\overline{z}} E(\hat{z}')d\hat{z}', \tag{43}$$

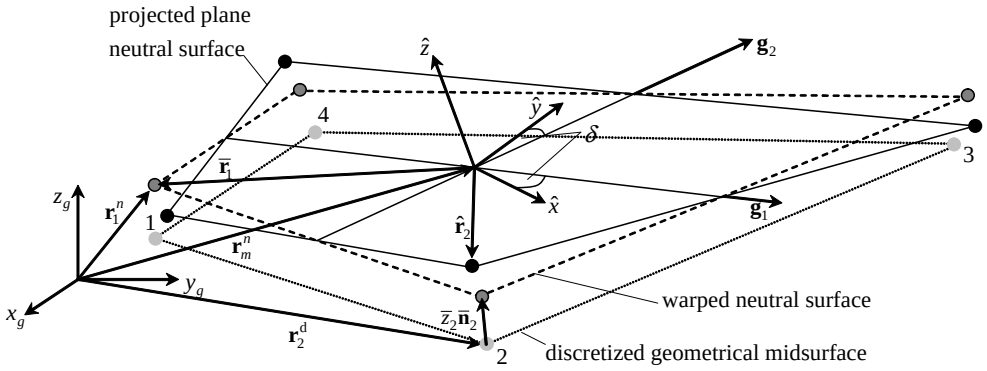

Figure 4: Discretized mid-surface, warped neutral surface, projected plane neutral surface

$$E_b = \frac{12}{h^3} \int_{-h/2-\overline{z}}^{h/2-\overline{z}} E(\hat{z}')\hat{z}'^2 d\hat{z}'. \tag{44}$$

Since shear deformations are accounted for, a shear correction factor α_s is to be introduced. For homogenous shells $\alpha_s = 5/6$, while in case of varying $E(\hat{z})$ one finds [15]

$$\frac{1}{\alpha_s} = \frac{144}{E_b h^5} \int_{-h/2-\overline{z}}^{h/2-\overline{z}} \frac{1}{E(\hat{z}')} \left[\int_{\hat{z}'}^{h/2-\overline{z}} E(\zeta)\zeta d\zeta \right]^2 d\hat{z}'. \tag{45}$$

2.2.2 A projection scheme

We decouple the membrane and bending properties in two steps. Firstly, we shift the element configuration, which is discretizing the geometrical mid-plane to the mechanical neutral surface (41). According to Fig. 4 this is done via

$$\mathbf{r}_i^n = \mathbf{r}_i^d + \overline{z}_i \overline{\mathbf{n}}_i \quad \text{no sum on } i, \tag{46}$$

where $\mathbf{r}_i^d$ and $\mathbf{r}_i^n$ denote the coordinates of the i-th node ($i = 1, 2, 3, 4$) of the discretized and the neutral surface. The projection is carried out along a nodal fiber direction $\overline{\mathbf{n}}_i$, which can be extracted from the preprocessor or can be found with the aid of an algorithm discussed in [15]. Since the element configuration discretizing the neutral surface may be warped, we extract a plane element configuration as shown in Fig. 4. A local Cartesian coordinate system $\hat{x} - \hat{y} - \hat{z}$ is placed at the element's center point with $\mathbf{r}_m^n = \frac{1}{4}\sum_{i=1}^4 \mathbf{r}_i^n$. The base vectors $\mathbf{e}_{\hat{x}}$ and $\mathbf{e}_{\hat{y}}$ share an equal angle δ to $\mathbf{g}_1$ and $\mathbf{g}_2$, which join the center and the mid-side points (Fig. 4). Finally, the nodes are projected onto the $\hat{\mathbf{e}}_x - \hat{\mathbf{e}}_y$ plane giving a plane element with local nodal vectors $\hat{\mathbf{r}}_i = \begin{bmatrix} \hat{X}_i & \hat{Y}_i & 0 \end{bmatrix}^T$ as depicted in Fig. 1. The proposed projection scheme may introduce some rigid body error. This problem is indicated by many authors, e.g. [21, 22] and can easily be corrected by a method proposed by Rankin and Nour-Omid [23]. The details of this procedure are discussed in [12, 24], we only give the final result

$$\hat{\mathbf{K}}_{proj} = \hat{\mathbf{P}}_R^T \hat{\mathbf{K}} \hat{\mathbf{P}}_R, \tag{47}$$

with $\hat{\mathbf{P}}_R = \left[\mathbf{I}_{(24\times24)} - \hat{\mathfrak{R}}\left(\hat{\mathfrak{R}}^T\hat{\mathfrak{R}}\right)^{-1}\hat{\mathfrak{R}}^T\right]$ denoting the projection with

$$\hat{\mathfrak{R}} = \begin{bmatrix} \hat{\mathfrak{R}}_1 \\ \hat{\mathfrak{R}}_2 \\ \hat{\mathfrak{R}}_3 \\ \hat{\mathfrak{R}}_4 \end{bmatrix} \quad \text{with} \quad \hat{\mathfrak{R}}_i = \begin{bmatrix} 1 & 0 & 0 & 0 & \hat{Z}_i & -\hat{Y}_i \\ 0 & 1 & 0 & -\hat{Z}_i & 0 & \bar{X}_i \\ 0 & 0 & 1 & \hat{Y}_i & -\bar{X}_i & 0 \\ 0 & 0 & 0 & 1 & 0 & 0 \\ 0 & 0 & 0 & 0 & 1 & 0 \\ 0 & 0 & 0 & 0 & 0 & 1 \end{bmatrix}. \tag{48}$$

The parts of the element stiffness matrix

$$\hat{\mathbf{K}} = \begin{bmatrix} \hat{\mathbf{K}}_{membrane} & \mathbf{0} \\ \mathbf{0} & \hat{\mathbf{K}}_{plate} \end{bmatrix} \tag{49}$$

are derived in Sect. 2.2.3 and Sect. 2.2.4, while the global stiffness matrix $\widetilde{\mathbf{K}}$ is assembled after a transformation of $\hat{\mathbf{K}}_{proj}$ to the global Cartesian coordinate system. Note that $\widetilde{\mathbf{K}}$ refers to the mechanical neutral surface (41), while the load vector is usually applied onto the discretized mid-plane. Therefore, an element load vector applied onto the mid-surface $\left[\begin{array}{cc}\mathbf{F}^d & \mathbf{M}^d\end{array}\right]^T$ has to be reduced to a force vector, which refers the neutral surface $\left[\begin{array}{cc}\mathbf{F}^n & \mathbf{M}^n\end{array}\right]^T$ via

$$\mathbf{F}^n = \mathbf{F}^d \quad \text{and} \quad \mathbf{M}^n = \mathbf{M}^d - \overline{z}_i\overline{\mathbf{n}}_i \times \mathbf{F}^d. \tag{50}$$

After solving the global system of equations the resulting displacements $\mathbf{U}^n$ and rotations $\boldsymbol{\phi}^n$ also refer to the neutral surface. During post-processing at the discretized configuration, a transformation according to

$$\mathbf{U}^d = \mathbf{U}^n + \overline{z}_i\overline{\mathbf{n}}_i \times \boldsymbol{\phi}^n \quad \text{and} \quad \boldsymbol{\phi}^d = \boldsymbol{\phi}^n \tag{51}$$

has to be carried out [15].

2.2.3 The membrane part

The inclusion of drill rotations, i.e. the rotation about the shell's normal, is a main issue of this paper. These in-plane rotational degrees of freedom are introduced using a recently proposed Cosserat-type functional [13, 12],

$$\delta\Pi_{membrane} = h\int_{\Omega}\delta\hat{\overline{\boldsymbol{\varepsilon}}}_s^T\hat{\mathbf{C}}_m\hat{\overline{\boldsymbol{\varepsilon}}}_s dA_e + 2\alpha h\int_{\Omega}\delta\hat{\overline{\varepsilon}}_a\hat{\overline{\varepsilon}}_a dA_e. \tag{52}$$

In (52), $\hat{\overline{\boldsymbol{\varepsilon}}}_s$ and $\hat{\overline{\varepsilon}}_a$ denote the symmetric and the antimetric part of the membrane strain tensor, respectively. The overbar indicates assumed strains, which can be assumed independently and are not directly related to prescribed deformations and rotations,

$$\hat{\boldsymbol{\varepsilon}}_s = \left[\begin{array}{ccc} u_{\hat{x},\hat{x}} & u_{\hat{y},\hat{y}} & u_{\hat{x},\hat{y}} + u_{\hat{y},\hat{x}}\end{array}\right]^T \quad \text{and} \quad \hat{\varepsilon}_a = {}^1\!/_2\left(u_{\hat{x},\hat{y}} - u_{\hat{y},\hat{x}}\right) + \varphi_{\hat{z}}. \tag{53}$$

For sake of convenience the direct strain-displacement-relation is given in (53), where u_i for $i = \hat{x}, \hat{y}$ and $\varphi_{\hat{z}}$ refer to membrane displacements and drill rotations, respectively. In (52) A_e denotes the area of the element (8) and $\hat{\mathbf{C}}_m$ refers to the plane stress elasticity matrix (43)

$$\hat{\mathbf{C}}_m = \frac{E_m}{1-\nu^2}\begin{bmatrix} 1 & \nu & 0 \\ \nu & 1 & 0 \\ 0 & 0 & \frac{1-\nu}{2} \end{bmatrix}. \tag{54}$$

The variable α represents an additional material constant relating the skew symmetric parts of stresses and strains. As frequently recommended (e.g. [14]), this constitutive parameter can be related to the shear modulus of the corresponding material,

$$\alpha = \overline{\alpha}\frac{E_m}{2\left(1+\nu\right)}, \tag{55}$$

where $\overline{\alpha}$ denotes an additional scaling factor. The present formulation can be optimized according to accuracy and efficiency, while avoiding any internal (incompatible) degrees of freedom to circumvent membrane shear locking in low order elements [18]. The predictive quality is nearly independent of $\overline{\alpha}$ and suitable scaling factors are discussed in [12]. The assumed strain fields are related to nodal displacements and rotations, i.e.

$$\hat{\overline{\boldsymbol{\varepsilon}}}_s = \hat{\overline{\mathbf{B}}}_{su0}\begin{bmatrix}\mathbf{U}_{\hat{x}}\\ \mathbf{U}_{\hat{y}}\end{bmatrix} + \hat{\overline{\mathbf{B}}}_{suH}\begin{bmatrix}\boldsymbol{\gamma} & \mathbf{0}\\ \mathbf{0} & \boldsymbol{\gamma}\end{bmatrix}\begin{bmatrix}\mathbf{U}_{\hat{x}}\\ \mathbf{U}_{\hat{y}}\end{bmatrix}, \tag{56}$$

$$\hat{\overline{\varepsilon}}_a = \frac{1}{2}\left(\hat{\overline{\mathbf{B}}}_{au0}\begin{bmatrix}\mathbf{U}_{\hat{x}}\\ \mathbf{U}_{\hat{y}}\end{bmatrix} + \hat{\overline{\mathbf{B}}}_{auH}\begin{bmatrix}\boldsymbol{\gamma} & \mathbf{0}\\ \mathbf{0} & \boldsymbol{\gamma}\end{bmatrix}\begin{bmatrix}\mathbf{U}_{\hat{x}}\\ \mathbf{U}_{\hat{y}}\end{bmatrix}\right) + \overline{\mathbf{N}}_{\varphi}\hat{\boldsymbol{\Phi}}, \tag{57}$$

where $\mathbf{U}_{\hat{x}} = \begin{bmatrix}\mathbf{U}_{\hat{x}1} & \cdots & \mathbf{U}_{\hat{x}4}\end{bmatrix}^T$ and $\mathbf{U}_{\hat{y}} = \begin{bmatrix}\mathbf{U}_{\hat{y}1} & \cdots & \mathbf{U}_{\hat{y}4}\end{bmatrix}^T$ are the inplane nodal displacements while $\hat{\boldsymbol{\Phi}} = \begin{bmatrix}\phi_{\hat{z}1} & \cdots & \phi_{\hat{z}4}\end{bmatrix}$ contains the drill rotation angles. The corresponding $\hat{\overline{\mathbf{B}}}$-matrices and the shape functions $\overline{\mathbf{N}}_{\varphi}$ read

$$\hat{\overline{\mathbf{B}}}_{su0} = \sqrt{\frac{j_0}{j}}\begin{bmatrix}\mathbf{b}_x & \mathbf{0}\\ \mathbf{0} & \mathbf{b}_y\\ \mathbf{b}_y & \mathbf{b}_x\end{bmatrix}, \quad \hat{\overline{\mathbf{B}}}_{suH} = \sqrt{\frac{j}{j_0}}\begin{bmatrix}\left(\xi\eta\right)_{,\hat{x}} & -\nu\left(\xi\eta\right)_{,\hat{y}}\\ -\nu\left(\xi\eta\right)_{,\hat{x}} & \left(\xi\eta\right)_{,\hat{y}}\\ 0 & 0\end{bmatrix}, \tag{58}$$

$$\hat{\overline{\mathbf{B}}}_{au0} = \sqrt{\frac{j_0}{j}}\begin{bmatrix}\mathbf{b}_y & -\mathbf{b}_x\end{bmatrix}, \quad \hat{\overline{\mathbf{B}}}_{auH} = 2\sqrt{\frac{j}{j_0}}\begin{bmatrix}\left(\xi\eta\right)_{,\hat{y}} & -\left(\xi\eta\right)_{,\hat{x}}\end{bmatrix}, \tag{59}$$

$$\overline{\mathbf{N}}_{\varphi} = \sqrt{\frac{j_0}{j}}\begin{bmatrix}N_1 & N_2 & N_3 & N_4\end{bmatrix}, \tag{60}$$

where $j = \det\mathbf{J}$ and $j_0 = \det\mathbf{J}_0 = \det\mathbf{J}(\xi=\eta=0)$ (see (2) - (8)). The prefactors $\sqrt{j/j_0}$ and $\sqrt{j_0/j}$ enable an analytical integration of all parts of the membrane stiffness matrix avoiding a four point Gaussian quadrature. The resulting membrane part of the stiffness matrix may be found in [25].

2.2.4 The bending part

The bending part of the stiffness matrix is based on the Mindlin-Reissner hypothesis and is valid for thin to moderately thick shell structures [17, 24, 12]. Equilibrium requires the potential Π_{plate} to be a minimum, i.e.

$$\Pi_{plate} = \Pi_b + \Pi_s - \Pi_{ext} \;\rightarrow \min, \tag{61}$$

with

$$\Pi_b = \frac{1}{2}\int_{\Omega}\hat{\overline{\boldsymbol{\epsilon}}}_b^T\hat{\mathbf{C}}_b\hat{\overline{\boldsymbol{\epsilon}}}_b d\Omega,$$

$$\Pi_s = \frac{1}{2}\alpha_s h \frac{E_b}{2(1+\nu)} \int\limits_{A_e} \hat{\overline{\boldsymbol{\gamma}}}_s^T \hat{\overline{\boldsymbol{\gamma}}}_s dA,$$

$$\Pi_{ext} = \int\limits_{A_e} p u_{\hat{z}} dA. \tag{62}$$

An overbar again indicates that the corresponding field can be interpolated independently, i.e. without any relation to strain displacement equations. The subscripts b and s indicate that the corresponding quantity refers to bending and shear, respectively, and Π_{ext} is due to the externally applied pressures p. The variables $\hat{\overline{\boldsymbol{\epsilon}}}_b$ and $\hat{\overline{\boldsymbol{\gamma}}}_s$ denote bending and transverse shear strains. In (62) $\hat{\mathbf{C}}_b$ refers to the bilinear plane stress elasticity matrix (44)

$$\hat{\mathbf{C}}_b = \frac{E_b}{1-\nu^2} \begin{bmatrix} 1 & \nu & 0 \\ \nu & 1 & 0 \\ 0 & 0 & \frac{1-\nu}{2} \end{bmatrix}, \tag{63}$$

while α_s denotes the shear correction factor (45). Following the procedure in [12, 24], the corresponding interpolations read

$$\hat{\overline{\boldsymbol{\epsilon}}}_b = \hat{\overline{\mathbf{B}}}_{b0} \begin{bmatrix} \boldsymbol{\Phi}_{\hat{x}} \\ \boldsymbol{\Phi}_{\hat{y}} \end{bmatrix} + \hat{\overline{\mathbf{B}}}_{bH} \begin{bmatrix} \boldsymbol{\gamma} & \mathbf{0} \\ 0 & \boldsymbol{\gamma} \end{bmatrix} \begin{bmatrix} \boldsymbol{\Phi}_{\hat{x}} \\ \boldsymbol{\Phi}_{\hat{y}} \end{bmatrix}, \tag{64}$$

with

$$\hat{\overline{\mathbf{B}}}_{b0} = \hat{z}\sqrt{\frac{j_0}{j}} \begin{bmatrix} \mathbf{0} & \mathbf{b}_x^T \\ -\mathbf{b}_y^T & \mathbf{0} \\ -\mathbf{b}_x^T & \mathbf{b}_y^T \end{bmatrix}, \quad \hat{\overline{\mathbf{B}}}_{bH} = \hat{z}\sqrt{\frac{j}{j_0}} \begin{bmatrix} \nu\,(\xi\eta)_{,\hat{y}} & (\xi\eta)_{,\hat{x}} \\ -\,(\xi\eta)_{,\hat{y}} & -\nu\,(\xi\eta)_{,\hat{x}} \\ 0 & 0 \end{bmatrix}, \tag{65}$$

and

$$\hat{\overline{\boldsymbol{\gamma}}}_s = \mathbf{J}_0^{-1} \mathbf{N}_s \boldsymbol{\Gamma} \tag{66}$$

with

$$\mathbf{N}_s = \sqrt{\frac{j_0}{j}} \begin{bmatrix} \frac{1}{2}(1-\eta) & 0 & \frac{1}{2}(1+\eta) & 0 \\ 0 & \frac{1}{2}(1+\xi) & 0 & \frac{1}{2}(1-\xi) \end{bmatrix}$$

and $\boldsymbol{\Gamma} = \mathbf{A}_{uz}\mathbf{U}_{\hat{z}} + \mathbf{A}_{\varphi x}\boldsymbol{\Phi}_{\hat{x}} + \mathbf{A}_{\varphi y}\boldsymbol{\Phi}_{\hat{y}}$. The coefficients $\mathbf{A}_{uz}$, $\mathbf{A}_{\varphi x}$ and $\mathbf{A}_{\varphi y}$ only depend on the element's geometry and read

$$\mathbf{A}_{uz} = \frac{1}{2} \begin{bmatrix} -1 & 1 & 0 & 0 \\ -1 & 0 & 0 & 1 \\ 0 & 0 & 1 & -1 \\ 0 & -1 & 1 & 0 \end{bmatrix},$$

$$\mathbf{A}_{\varphi x} = \frac{1}{4} \begin{bmatrix} \hat{y}_{12} & \hat{y}_{12} & 0 & 0 \\ \hat{y}_{14} & 0 & 0 & \hat{y}_{14} \\ 0 & 0 & \hat{y}_{43} & \hat{y}_{43} \\ 0 & \hat{y}_{23} & \hat{y}_{23} & 0 \end{bmatrix}, \; \mathbf{A}_{\varphi y} = \frac{1}{4} \begin{bmatrix} \hat{x}_{21} & \hat{x}_{21} & 0 & 0 \\ \hat{x}_{41} & 0 & 0 & \hat{x}_{41} \\ 0 & 0 & \hat{x}_{34} & \hat{x}_{34} \\ 0 & \hat{x}_{32} & \hat{x}_{32} & 0 \end{bmatrix}, \tag{67}$$

leading to a formulation, which ensures the satisfaction of the Kirchhoff patch test [26, 27]. Again, the prefactors $\sqrt{j/j_0}$ and $\sqrt{j_0/j}$ enable an analytical integration of all parts of the plate bending stiffness matrix, see e.g. [25].

2.3 Weak one-way coupling

The finite element formulation discussed in Sect. 2.2 is based on a weak form of the equilibrium conditions,

$$\delta\Pi = \int (\delta\boldsymbol{\varepsilon})^T \boldsymbol{\sigma} dV - \delta\Pi_{ext} = 0, \tag{68}$$

where any external loads are neglected in this paper[2]. The strain field in membrane directions reads

$$\begin{aligned}
\varepsilon_{\hat{x}\hat{x}} &= \frac{1}{E(\hat{z})}(\sigma_{\hat{x}\hat{x}} - \nu\sigma_{\hat{y}\hat{y}}) + \alpha(\hat{z})\Delta T(\hat{z}),\\
\varepsilon_{\hat{y}\hat{y}} &= \frac{1}{E(\hat{z})}(\sigma_{\hat{y}\hat{y}} - \nu\sigma_{\hat{x}\hat{x}}) + \alpha(\hat{z})\Delta T(\hat{z}),\\
\varepsilon_{\hat{z}\hat{z}} &= \frac{-\nu}{E(\hat{z})}(\sigma_{\hat{x}\hat{x}} + \sigma_{\hat{y}\hat{y}}) + \alpha(\hat{z})\Delta T(\hat{z}),\\
\gamma_{\hat{x}\hat{y}} &= \frac{2(1+\nu)}{E(\hat{z})}\sigma_{\hat{x}\hat{y}},
\end{aligned} \tag{69}$$

where we adopted a plane stress constraint, i.e. $\sigma_{\hat{z}\hat{z}} = 0$. The thermal expansion coefficient shows an arbitrary variation with respect to the thickness direction and is denoted by $\alpha(\hat{z})$. Solving (69) for the stresses yields

$$\begin{aligned}
\sigma_{\hat{x}\hat{x}} &= \frac{E(\hat{z})}{1-\nu^2}(\varepsilon_{\hat{x}\hat{x}} + \nu\varepsilon_{\hat{y}\hat{y}}) - \frac{E(\hat{z})\alpha(\hat{z})\Delta T(\hat{z})}{1-\nu},\\
\sigma_{\hat{y}\hat{y}} &= \frac{E(\hat{z})}{1-\nu^2}(\varepsilon_{\hat{y}\hat{y}} + \nu\varepsilon_{\hat{x}\hat{x}}) - \frac{E(\hat{z})\alpha(\hat{z})\Delta T(\hat{z})}{1-\nu},\\
\sigma_{\hat{x}\hat{y}} &= \frac{E(\hat{z})}{2(1+\nu)}\gamma_{\hat{x}\hat{y}},
\end{aligned} \tag{70}$$

or in matrix notation

$$\begin{bmatrix} \sigma_{\hat{x}\hat{x}} \\ \sigma_{\hat{y}\hat{y}} \\ \sigma_{\hat{x}\hat{y}} \end{bmatrix} = \frac{E(\hat{z})}{1-\nu^2}\begin{bmatrix} 1 & \nu & 0 \\ \nu & 1 & 0 \\ 0 & 0 & \frac{1-\nu}{2} \end{bmatrix}\begin{bmatrix} \epsilon_{\hat{x}\hat{x}} \\ \epsilon_{\hat{y}\hat{y}} \\ \epsilon_{\hat{x}\hat{y}} \end{bmatrix} - \frac{E(\hat{z})\alpha(\hat{z})\Delta T(\hat{z})}{1-\nu}\begin{bmatrix} 1 \\ 1 \\ 0 \end{bmatrix},$$

$$\boldsymbol{\sigma} = \mathbf{C}\boldsymbol{\varepsilon} - \frac{E(\hat{z})\alpha(\hat{z})\Delta T(\hat{z})}{1-\nu}\begin{bmatrix} 1 \\ 1 \\ 0 \end{bmatrix}. \tag{71}$$

Within the proposed weak one way coupling procedure we introduce (71) into (68) obtaining

$$\delta\Pi = \delta\Pi_m - \delta\Pi_t = \int\limits_{V_e} (\delta\boldsymbol{\varepsilon})^T \mathbf{C}\boldsymbol{\varepsilon} dV - \int\limits_{V_e} (\delta\boldsymbol{\varepsilon})^T \frac{E(\hat{z})\alpha(\hat{z})\Delta T(\hat{z})}{1-\nu}\begin{bmatrix} 1 \\ 1 \\ 0 \end{bmatrix} dV = 0. \tag{72}$$

[2]The inclusion of external loads can be done in a standard manner [18] and does not introduce any complications.

The first term on the RHS is devoted to the element stiffness matrix (Sect. 2.2.3 and Sect. 2.2.4), while the second part refers to internal forces and couples caused by thermal loading, which can be simplified according to

$$\delta\Pi_t = \int\limits_{V_e} \left[\begin{array}{cc} \delta\epsilon_{\hat{x}\hat{x}} & \delta\epsilon_{\hat{y}\hat{y}} \end{array}\right] \frac{E(\hat{z})\alpha(\hat{z})\Delta T(\hat{z})}{1-\nu} \left[\begin{array}{c} 1 \\ 1 \end{array}\right] dV. \tag{73}$$

The virtual normal-strain field is related to virtual displacements and rotations according to $\left[\begin{array}{cc} \delta\epsilon_{\hat{x}\hat{x}} & \delta\epsilon_{\hat{y}\hat{y}} \end{array}\right] = \left[\begin{array}{cc} \delta u_{\hat{x},\hat{x}} + \hat{z}\varphi_{\hat{y},\hat{x}} & \delta u_{\hat{y},\hat{y}} - \hat{z}\varphi_{\hat{x},\hat{y}} \end{array}\right]$. Interpolating the displacement and rotation field with classical bilinear shape-function (2),

$$\left[\begin{array}{c} u_{\hat{x}} \\ u_{\hat{y}} \end{array}\right] = \left[\begin{array}{cc} \mathbf{N} & \mathbf{0} \\ \mathbf{0} & \mathbf{N} \end{array}\right] \left[\begin{array}{c} \mathbf{U}_{\hat{x}} \\ \mathbf{U}_{\hat{y}} \end{array}\right] \text{ and } \left[\begin{array}{c} \varphi_{\hat{x}} \\ \varphi_{\hat{y}} \end{array}\right] = \left[\begin{array}{cc} \mathbf{N} & \mathbf{0} \\ \mathbf{0} & \mathbf{N} \end{array}\right] \left[\begin{array}{c} \mathbf{\Phi}_{\hat{x}} \\ \mathbf{\Phi}_{\hat{y}} \end{array}\right], \tag{74}$$

leads to

$$\delta\Pi_t = \left[\begin{array}{cc} \delta\mathbf{U}_{\hat{x}}^T & \delta\mathbf{U}_{\hat{y}}^T \end{array}\right] \left[\begin{array}{c} \mathbf{F}_{\hat{x}} \\ \mathbf{F}_{\hat{y}} \end{array}\right] + \left[\begin{array}{cc} \delta\mathbf{\Phi}_{\hat{x}}^T & \delta\mathbf{\Phi}_{\hat{y}}^T \end{array}\right] \left[\begin{array}{c} \mathbf{M}_{\hat{x}} \\ \mathbf{M}_{\hat{y}} \end{array}\right], \tag{75}$$

with

$$\begin{aligned} \mathbf{F}_{\hat{x}} &= \int\limits_{V_e} \mathbf{N}_{,\hat{x}} \frac{E(\hat{z})\alpha(\hat{z})\Delta T(\hat{z})}{1-\nu} dV \quad , \quad \mathbf{F}_{\hat{y}} = \int\limits_{V_e} \mathbf{N}_{,\hat{y}} \frac{E(\hat{z})\alpha(\hat{z})\Delta T(\hat{z})}{1-\nu} dV, \\ \mathbf{M}_{\hat{x}} &= -\int\limits_{V_e} \mathbf{N}_{,\hat{y}} \hat{z} \frac{E(\hat{z})\alpha(\hat{z})\Delta T(\hat{z})}{1-\nu} dV \quad , \quad \mathbf{M}_{\hat{y}} = \int\limits_{V_e} \mathbf{N}_{,\hat{x}} \hat{z} \frac{E(\hat{z})\alpha(\hat{z})\Delta T(\hat{z})}{1-\nu} dV. \end{aligned} \tag{76}$$

Differentiating the shape functions indicates that the integral over the element area can be carried out analytically, if the distributions of Young's modulus E, thermal expansion α and temperature ΔT are assumed to be constant. Thus, we get

$$\begin{aligned} \mathbf{F}_{\hat{x}} &= \frac{1}{2} \left[\begin{array}{c} \hat{y}_{24} \\ \hat{y}_{31} \\ \hat{y}_{42} \\ \hat{y}_{13} \end{array}\right] \int\limits_{-h/2}^{h/2} \frac{E(\hat{z})\alpha(\hat{z})\Delta T(\hat{z})}{1-\nu} d\hat{z} \quad , \quad \mathbf{F}_{\hat{y}} = \frac{1}{2} \left[\begin{array}{c} \hat{x}_{42} \\ \hat{x}_{13} \\ \hat{x}_{24} \\ \hat{x}_{31} \end{array}\right] \int\limits_{-h/2}^{h/2} \frac{E(\hat{z})\alpha(\hat{z})\Delta T(\hat{z})}{1-\nu} d\hat{z}, \\ \mathbf{M}_{\hat{x}} &= \frac{1}{2} \left[\begin{array}{c} \hat{x}_{24} \\ \hat{x}_{31} \\ \hat{x}_{42} \\ \hat{x}_{13} \end{array}\right] \int\limits_{-h/2}^{h/2} \hat{z} \frac{E(\hat{z})\alpha(\hat{z})\Delta T(\hat{z})}{1-\nu} d\hat{z} \quad , \quad \mathbf{M}_{\hat{y}} = \frac{1}{2} \left[\begin{array}{c} \hat{y}_{24} \\ \hat{y}_{31} \\ \hat{y}_{42} \\ \hat{y}_{13} \end{array}\right] \int\limits_{-h/2}^{h/2} \hat{z} \frac{E(\hat{z})\alpha(\hat{z})\Delta T(\hat{z})}{1-\nu} d\hat{z}. \end{aligned} \tag{77}$$

These element forces and couples refer to the discretized mid-surface and have to be transformed to the neutral surface by (50).

2.4 Stress evaluation

The stress components are evalutated element-wise at $\xi = \eta = 0$ based on an a posteriori procedure, requiring the nodal displacement and rotation vector in the elemental Cartesian base. The membrane strains at the elements center are evaluated with respect to the nodal degrees of freedom by

$$\left[\begin{array}{c} \epsilon_{\hat{x}\hat{x}} \\ \epsilon_{\hat{y}\hat{y}} \\ \gamma_{\hat{x}\hat{y}} \end{array}\right] = \left[\begin{array}{cc} \mathbf{b}_x & \mathbf{0} \\ \mathbf{0} & \mathbf{b}_y \\ \mathbf{b}_y & \mathbf{b}_x \end{array}\right] \left[\begin{array}{c} \mathbf{U}_{\hat{x}} \\ \mathbf{U}_{\hat{y}} \end{array}\right] + \hat{z}' \left[\begin{array}{cc} \mathbf{0} & \mathbf{b}_x^T \\ -\mathbf{b}_y^T & \mathbf{0} \\ -\mathbf{b}_x^T & \mathbf{b}_y^T \end{array}\right] \left[\begin{array}{c} \mathbf{\Phi}_{\hat{x}} \\ \mathbf{\Phi}_{\hat{y}} \end{array}\right]. \tag{78}$$

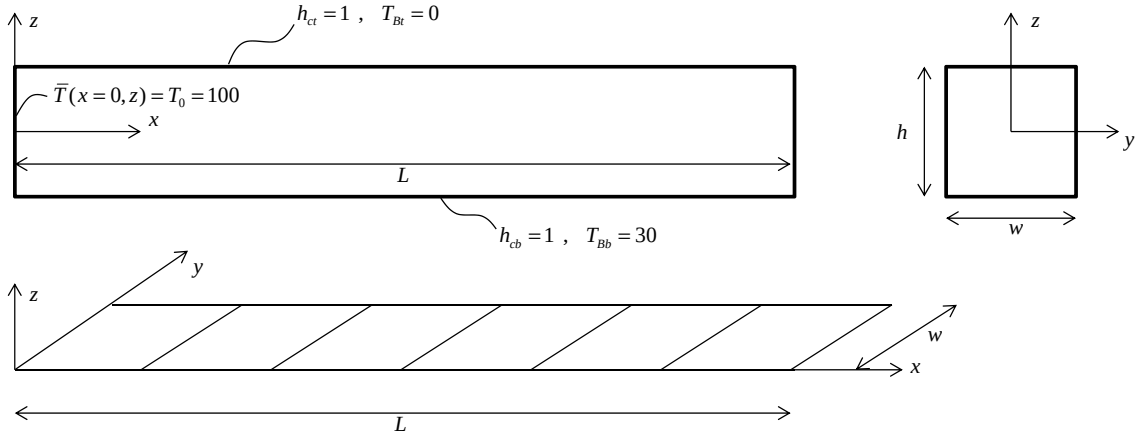

Figure 5: FGM fin with a discretization of $N = 6$

Consequently, the membrane stresses are found by applying the constitutive relation (71),

$$\begin{bmatrix} \sigma_{\hat{x}\hat{x}} \\ \sigma_{\hat{y}\hat{y}} \\ \sigma_{\hat{x}\hat{y}} \end{bmatrix} = \frac{E(\hat{z}')}{1-\nu^2} \begin{bmatrix} 1 & \nu & 0 \\ \nu & 1 & 0 \\ 0 & 0 & \frac{1-\nu}{2} \end{bmatrix} \begin{bmatrix} \epsilon_{\hat{x}\hat{x}} \\ \epsilon_{\hat{y}\hat{y}} \\ \epsilon_{\hat{x}\hat{y}} \end{bmatrix} - \frac{E(\hat{z}')\alpha(\hat{z}')\Delta T(\hat{z}')}{1-\nu} \begin{bmatrix} 1 \\ 1 \\ 0 \end{bmatrix}.$$

The definition of transverse shear strains read $\gamma_{\hat{x}\hat{z}} = u_{\hat{z},\hat{x}} + \varphi_{\hat{y}}$ and $\gamma_{\hat{y}\hat{z}} = u_{\hat{z},\hat{y}} - \varphi_{\hat{x}}$. The transverse displacement and the two bending angles are interpolated with classical bilinear shape functions yielding to the following estimates of the averaged shear strains

$$\begin{bmatrix} \overline{\gamma}_{\hat{x}\hat{z}} \\ \overline{\gamma}_{\hat{y}\hat{z}} \end{bmatrix} = \begin{bmatrix} \mathbf{b}_x \\ \mathbf{b}_y \end{bmatrix} \mathbf{U}_{\hat{z}} + \begin{bmatrix} 1/4 \sum_{i=1}^{4} \phi_{\hat{y}i} \\ -1/4 \sum_{i=1}^{4} \phi_{\hat{x}i} \end{bmatrix}. \tag{79}$$

Accordingly, the averaged shear stresses read $\overline{\tau}_{i\hat{z}} = \frac{E_b(\xi=\eta=0)}{2(1+\nu)}\overline{\gamma}_{i\hat{z}}$ for $i = \hat{x}, \hat{y}$, and the integrated shear force is given by $s_i = \alpha_s h \overline{\tau}_{i\hat{z}}$. Finally, we evaluate the shear stress distribution from

$$\tau_{i\hat{z}}(\hat{z}') = \frac{12 s_i}{E_b h^3} \int_{\hat{z}'}^{h/2-\overline{z}} E(\zeta)\zeta d\zeta \quad , \quad \gamma_{i\hat{z}}(\hat{z}') = \frac{2(1+\nu)\tau_{i\hat{z}}(\hat{z}')}{E(z')}, \tag{80}$$

see [15]

3 Benchmark examples

In this Section we compare the proposed formulation to continuum solutions evaluated by ANSYS. A main issue of this paper is the correct estimation of temperature distributions based on the procedures discussed in Sect. 2.1. Consequently, a pure thermal problem is discussed in Sect. 3.1, which shows interesting results for two MLC structures with the same mean value of thermal conductivity. More examples can be found in [25].

3.1 Temperature distributions in a MLC fin

Consider a rectangular MLC structure of length $L = 10$, width $w = 1$ and height $h = 1$ shown in Fig. 5, which is discretized with N elements. On the top and bottom surface ($z = \pm h/2$) there is convection with $h_{ct} = h_{cb} = 1$ and a fluid temperature $T_{Bt} = 0$ and $T_{Bb} = 30$, while at the left end $x = 0$ the temperature is set to $\bar{T}(x = 0, z) = T_0 = 100$.

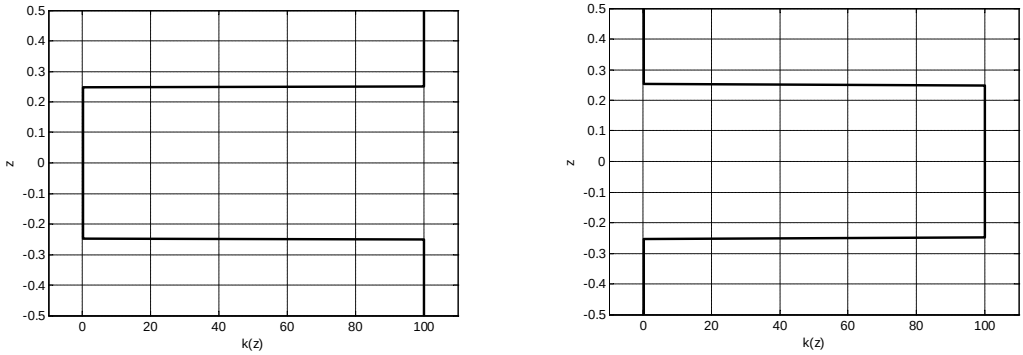

(a) Configuration 1 (b) Configuration 2

Figure 6: Distribution of thermal conductivity of layered fin

Interval in transverse direction	Configuration 1	Configuration 2
$-0.5 \leq z \leq -0.25$	$k = 100$	$k = 0.1$
$-0.25 \leq z \leq 0$	$k = 0.1$	$k = 100$
$0 \leq z \leq 0.25$	$k = 0.1$	$k = 100$
$0.25 \leq z \leq 0.5$	$k = 100$	$k = 0.1$

Table 1: Conductivity distribution

The fin is composed of four equidistant layers of height $h_L = {}^{h}/_{4}$, with two different thermal conductivities. We compare two symmetric configurations (i.e. Configuration 1 and Configuration 2) according to Tab. 1 (see Fig. 6). Configuration 1 is characterized by a high thermal conductivity on the top and bottom layer, while Configuration 2 has nearly isolating outside layers. The mean value $\overline{k}$ of thermal conductivity is equal for both configurations and classical approaches from literature assuming a constant temperature in thickness direction lead to equal temperature distributions in membrane direction for both configurations. The reference results are evaluated using ANSYS by discretizing the $x - z$ plane with 500×100 PLANE55 elements [28]. The application of the Dirichlet boundary condition, i.e. $T(x = 0, z) = T_0$, is in contrast to the applied convection boundary conditions at $x = 0$, $z = \pm {}^{h}/_{2}$, since the thermal gradient with respect to the thickness direction is not vanishing on the top and bottom side. Therefore, we apply a von Neumann boundary condition onto the ANSYS model based on Fourier's law, i.e.

$$q_n(x = 0,\, z) = -k(z)\bar{T}_{,x} = Ck(z), \tag{81}$$

where the constant C is found iteratively so that the evaluated mean value of the temperature distribution at $x = 0$ equals T_0. By this we obtain

$$\text{Config. 1: } q_n^{(1)}(x = 0,\, z) = -16.3613k(z), \tag{82}$$

$$\text{Config. 2: } q_n^{(2)}(x = 0,\, z) = -8.7069k(z). \tag{83}$$

The distribution of the mean value of temperature is depicted in Fig. 7, where we used $N = 20$ shell elements in membrane direction and ten elements through each layer in transverse direction ($n = 40$). The solid line corresponds to the present approach, while the dots refer to the ANSYS solution. Figure 7 indicates excellent accuracy of the proposed solution algorithm for

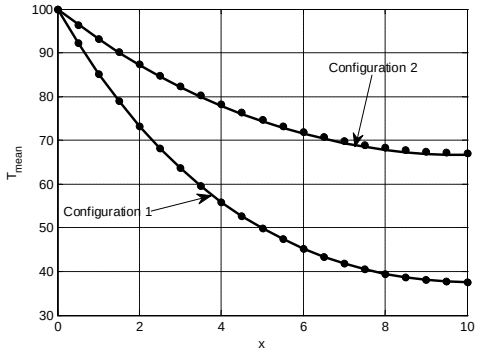

Figure 7: Mean temperature distribution of both configurations $N = 20,\ n = 40$

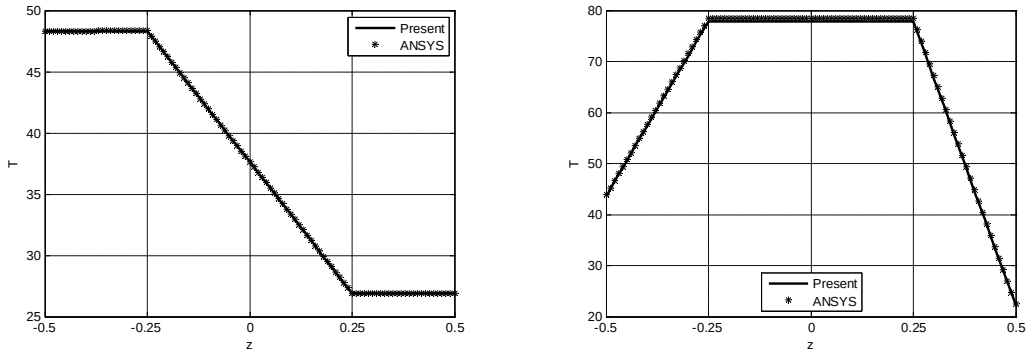

(a) Configuration 1 (b) Configuration 2

Figure 8: Temperature distribution in transverse direction at $x = L$, ($N = 20,\ n = 40$)

both configurations, and we observe large differences between the two configurations, even if the average value of the thermal conductivity is identical. The temperature distribution in transverse direction is shown in Fig. 8, and, again, indicates a good predictive quality of the proposed approach. The crucial step in our derivation is the iterative solution procedure discussed on page 5. The convergence rate is depicted in Fig. 9 for both configurations. We observe that in case of Configuration 2 (low conductivity on the top and bottom layer) about ten iterations are required to get accurate results, while Configuration 1 requires only two iterations.

3.2 Thermo-elastic analysis of a bi-quadratic FGM beam

In this example, originated by Lü et al. [29], a bi-directional FGM beam ($L = 0.1,\ h = w = 0.01$) depicted in Fig. 10 is analyzed. The state equations vary exponentially along the axial and transverse direction,

$$E(x, z) = E_0 e^{\alpha_1 x + \alpha_3 (z + h/2)}, \tag{84}$$

$$\beta(x, z) = \beta_0 e^{ax + b(z + h/2)}, \tag{85}$$

where β denotes the thermal stress constant,

$$\beta(x, z) = \frac{E(x, z)\alpha(x, z)}{1 - \nu}. \tag{86}$$

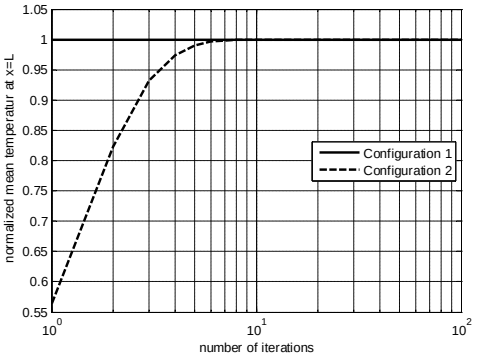

Figure 9: Convergence with respect to the number of iterations at $x = L$, ($N = 20$, $n = 40$)

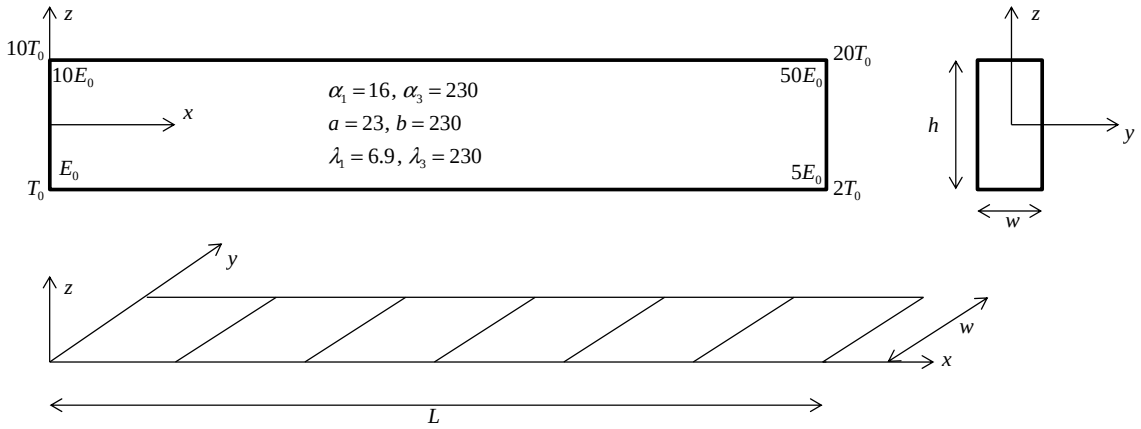

Figure 10: The schematic representation of a bi-quardratic FGM beam

Poisson's ratio is assumed to be constant $\nu = 0.25$ and the temperature field is prescribed by

$$T(x, z) = T_0 e^{\lambda_1 x + \lambda_3 (z + h/2)}. \tag{87}$$

We choose $E_0 = 1$, while β_0 is defined by $\beta_0 T_0 = \frac{10^{-4} E_0}{1-\nu}$. A clamped-clamped situation is analyzed. This example is solved analytically by Lü et al. [29] based on a two-dimensional thermo-elastic model. Lezgy-Nazargah [30] analyzed the same problem using a fully coupled isogeometric two-dimensional finite element approach. For sake of comparison we consider an ANSYS solution with a very fine mesh (1000x100) of fully integrated quadrilateral plane stress elements. A study of the transverse displacements is depicted in Fig. 11. We observe a close agreement of the evaluated bending line compared to ANSYS (Fig. 11(a)). A convergence study with respect to the number of elements over the length N and thickness n is given in Fig. 11(b), indicating a fast rate of convergence. For $N = n \geq 6$ a relative error of less than $\pm 3\%$ is provided, while the present approach converges to a 3% stiffer solution compared to ANSYS. In Fig. 12 the stress distributions at $x = L/2$ are compared to ANSYS and to the solutions published in [29, 30]. The axial thermal stress distribution σ_{xx} is in good agreement compared to the reference solutions (see Fig. 12(a)). The transverse shear stress distributions τ_{xz} are less accurate (see Fig. 12(b)). Considering the maximum shear the analytical solutions of Lü et al. are in good agreement to ANSYS, Lezgy-Nazargah's results show a relative error of 13%, while our proposed algorithm delivers a relative error of 10%. A qualitative comparison indicates that our peak stress is located at $z = 0.0018$ (neutral plane) while the continuum solutions show a

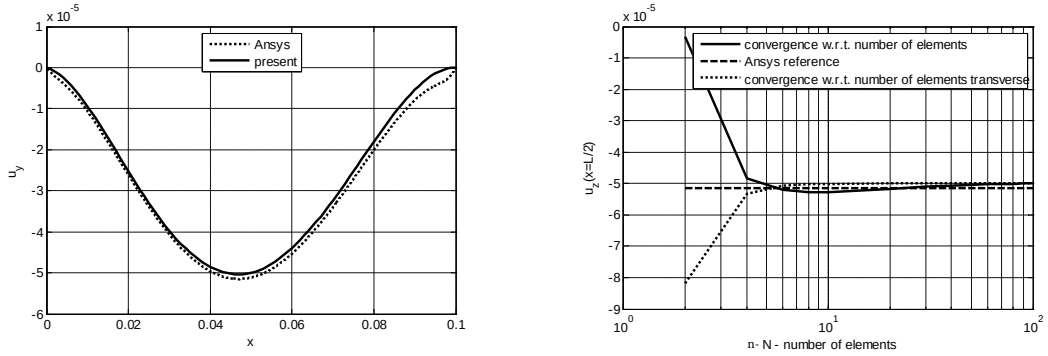

(a) Comparison of transverse displacement $u_z(x)$ with $N = n = 100$

(b) Convergence study of transverse displacement $u_z(x = {}^{L}/_{2})$ with respect to number of shell elements N ($n = 100$) and discretization in transverse direction n ($N = 100$)

Figure 11: Transverse displacement of bi-directional thermo-elastic beam

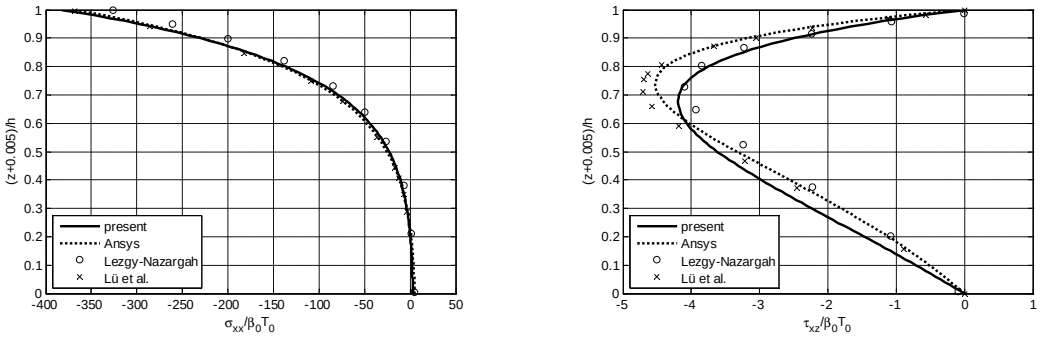

(a) Axial stress distribution

(b) Shear stress distribution

Figure 12: Stress analysis of bi-directional thermo-elastic beam at $x = {}^{L}/_{2}$ with $N = n = 100$ subjected to a non-uniform temperature field

peak-location of $z = 0.0023$. This may stem from stress rearrangements in the two-dimensional regime which are not covered in our proposed approach.

3.3 FGM shell structure

Consider a hemisphere with a radius $R = 10$ and a thickness of $h = 0.5$ (Fig. 13(a)). Due to symmetry only one quarter of the structure is discretized by a mesh according to Fig. 13(b). The material properties and boundary conditions depend only on the radial coordinate r, thus, only one quarter of the structure needs to be analyzed[3]. The model is loaded at the inner and outer surface with a convection boundary condition,

$$h_{ct} = h_{cb} = 10 \ , \ \ T_{Bt} = 0 \ , \ \ T_{Bb} = 300. \tag{88}$$

At the equator the mean temperature is kept at $\overline{T} = 500$. Due to these thermal boundary conditions we expect strong variations of temperature in thickness direction $\hat{z}$ and in membrane

[3]This axisymmetric problem could be analyzed with less than a quarter, however, in order to check the performance of the proposed formulation regarding warped element configurations, we use on quarter of the structure.

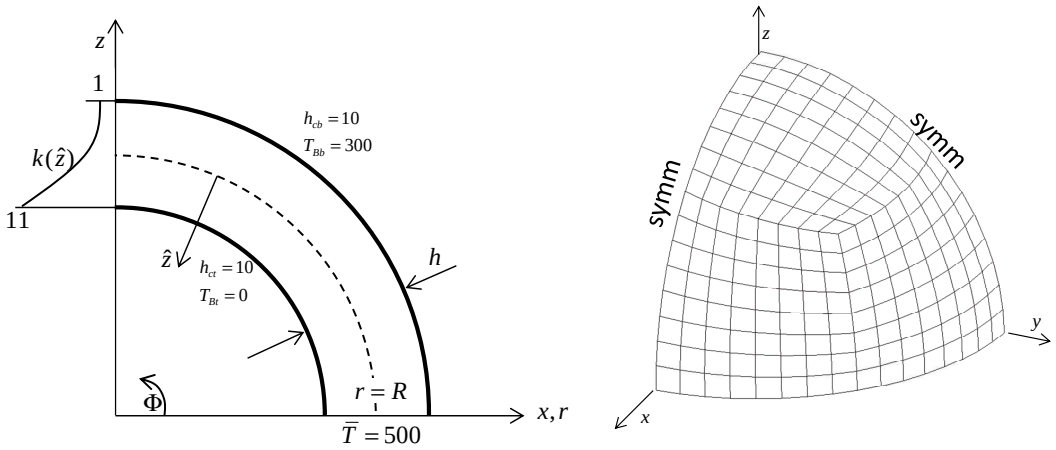

(a) FGM shell structure (b) Shell mesh: $N = 192$

Figure 13: Problem description - FGM shell structure

	u_r	u_z	Error in u_r	Error in u_z
ANSYS	0.2104	-0.1256	-	-
Present $N = 48$ elements	0.2646	-0.1216	25.7%	3.2%
Present $N = 192$ elements	0.2261	-0.1211	7.5%	3.6%
Present $N = 768$ elements	0.2100	-0.1210	0.2%	3.7%

Table 2: Displacements of FGM shell structure

direction ϕ. The material parameters show only spatial variations of the thermal conductivity,

$$k(\hat{z}) = 3.5 + 20\hat{z} + 40\hat{z}^2, \tag{89}$$

representing a parabolic distribution with low conductivity at the outside, $k(\hat{z} = -h/2) = 1$, and high conductivity at the inner surface, $k(\hat{z} = h/2) = 11$. Since we focus mainly on temperature effects Young's modulus E, Poisson's ratio ν and thermal expansion α are assumed constant with respect to the thickness direction, i.e.

$$E = 10 \ , \ \ \nu = 0.3 \ , \ \ \alpha = 1 \cdot 10^{-4}. \tag{90}$$

Elastic solutions of an FGM hemisphere with a varying Young's modulus can be found in [16]. The reference results are evaluated using an axisymmetric model in ANSYS with the fully coupled PLANE 13 element and a very fine discretization of 100×500. For sake of convenience we apply a thermal Dirichlet boundary condition of $T(R - h/2 \leq x \leq R + h/2) = 500$ accepting some error discussed in Sect. 3.1. The temperature distributions with respect to the meridian $0 \leq \phi \leq 90$ are shown in Fig. 14(a). Due to high[4] convection coefficients $h_{cb} = h_{ct} = 10$ the results do not show any variations for $\phi > 20$. The temperature field with respect to the thickness direction is depicted in Fig. 14(b). The distributions evaluated with the present formulation (solid lines) are compared to the ANSYS solutions, indicting a good accuracy. The displacements in radial direction u_r and in height direction u_z are listed in Tab. 2 for different numbers of shell elements. We observe a clear convergence with respect to N for displacements

[4]The term "high" can not be seen absolutely, however, it causes large thermal gradients with respect to the meridian direction ϕ.

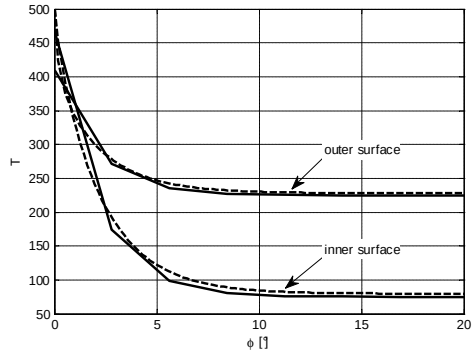

(a) Temperature distribution along the meridian

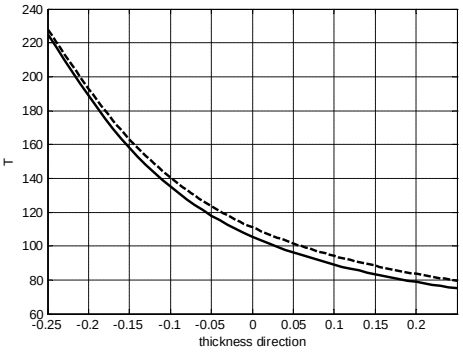

(b) Temperature distribution with respect to $\hat{z}$ at $\phi = 90$

Figure 14: Temperature distributions in FGM shell structure (Solid line: Present formulation, Dashed line: ANSYS) - $N = 768$, $n = 50$, $I = 10$

in radial direction leading to very accurate results for $N = 768$. In terms of displacements in height direction some error of $< 4\%$ has to be accepted. Since a main issue of the proposed

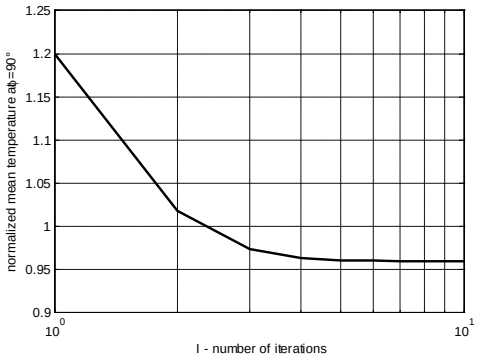

(a) Convergence of $\overline{T}$ at $\phi = 90$ with respect to I

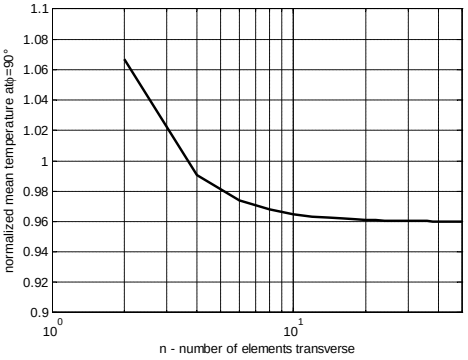

(b) Convergence of $\overline{T}$ at $\phi = 90$ with respect to n

Figure 15: Convergence issues in FGM shell structure

procedure is the iterative strategy discussed on page 5, the convergence of mean temperature $\overline{T}$ (normalized to the ANSYS result) at $\phi = 90$ with respect to the number of iterations I is studied in Fig. 15(a). There, a stable value is reached after six iterations. A final error of less than four percent is also indicated in Fig. 14 and stems from the large temperature gradient in meridian direction at the equator, which may not be resolved properly with low numbers of N. Figure 15(b) indicates convergence with respect to the number of elements discretizing the transverse direction. Obviously, using fifty elements in transverse direction leads to accurate solutions.

4 Conclusion

In this paper a novel approach to the evaluation of thermo-elastic effects in FGM or multi-layer shell structures is proposed. The temperature field is evaluated by an iterative procedure assuming non-constant temperature variations with respect to the thickness direction. A key issue is the decomposition of $T(\hat{x}, \hat{y}, \hat{z})$ according to (11). The resulting displacement fields are evaluated with the aid of a quadrilateral shell element based on effective elastic quantities.

Suitable projection schemes enable an independent derivation of the membrane and the plate bending part. Drilling rotations are included based on an enlarged functional, where the symmetry of stress and strain is enforced only in a weak sense. Special strain field interpolations ensure that all parts of the stiffness matrix can be given analytically even for arbitrarily shaped element configurations, thus, any Gaussian quadrature is avoided. It is shown that thermal expansion causes internal forces and couples, which are applied onto the proposed shell element. The resulting analysis procedure can be termed efficient and leads to accurate results compared to ANSYS solutions where continuum formulations are used.

5 Acknowledgment

This work has been supported by grants of Science and Technology Assistance Agency no. APVV-0246-12 and Scientific Grant Agency of the Ministry of Education of Slovak Republic and the Slovak Academy of Sciences and VEGA No. 1/0453/15.

REFERENCES

[1] B. Abbasnejad, G. Rezazadeh, Mechanical behavior of a fgm micro-beam subjected to a nonlinear electrostatic pressure, International Journal of Materials and Design 8 (2012) 381–392.

[2] B. Sankar, An elasticity solution for functionally graded beams, Composites Science and Technology 61 (2001) 689–696.

[3] S. Chakraborty, S. Gopalakrishnan, J. Reddy, A new beam finite element for the analysis of functionally graded materials, International Journal of Mechanical Sciences 45 (2003) 519–539.

[4] A. Mahi, E. A. Bedia, A. Tounsi, I. Mechab, An analytical method for temperature-dependent free vibration analysis of functionally graded beams with general boundary condition, Composite Structures 92 (2010) 1877–1887.

[5] J. Murin, V. Kutis, Improved mixture rules for the composite (fgm s) sandwich beam finite element, Proceedings IX international conference on compotational plasticity (COMPLAS IX), Barcelona.

[6] J. Murin, V. Kutis, An effective multilayered sandwich beam-link finite element for solution of the electro-thermo-structural problems, Computers & Structures 87 (2009) 1496–1507.

[7] J. Murin, M. Aminbaghai, V. Kutis, Exact solution of the bending vibration problem of fgm beams with variation of material properties, Engineering Structures 32 (2010) 1631–1640.

[8] S. Shen, Functionally graded materials - Nonlinear analysis of shear deformable FGM plates and shells, Taylor and Francis Group, 2009.

[9] K. Liew, X. He, S. Kitipornchai, Finite element method for feedback control of fgm shells in the frequency domain via piezoelectric sensors and actuators, Computer Methods in Applied Mechanics and Engineering 193 (2004) 257–273.

[10] A. Alibeigloo, Static analysis of a functionally graded cylindrical shell with piezoelectric layers as sensor and actuator, Smart Materials and Structures 18 (2009) 12pp.

[11] R. Naghdabadi, S. H. Kordkheili, A finite element formulation for analysis of functionally graded plates and shells, Archive of applied mechanics 74 (2005) 375–386.

[12] S. Kugler, Development of a laterally pressed quadrilateral shell element, Ph.D. thesis, STU Bratislava (2010).

[13] S. Kugler, P. Fotiu, J. Murin, A highly efficient membrane finite element with drilling degrees of freedom, Acta Mechanica 213 (2010) 323–348.

[14] T. J. Hughes, F. Brezzi, On drilling degrees of freedom, Computer Methods in Applied Mechanics and Engineering 72 (1989) 105–121.

[15] S. Kugler, P. Fotiu, J. Murin, The numerical analysis of fgm shells with enhanced finite elements, Engineering Structures 49 (2013) 920–935.

[16] S. Kugler, P. Fotiu, J. Murin, Enhanced functionally graded material shell finite elements, ZAMM Z. Angew. Math. Mech. (2013) 1–13.

[17] O. C. Zienkiewicz, R. L. Taylor, Finite Element Method: Volume 2, Solid Mechanics (Finite Element Method), Butterworth-Heinemann, 2000.

[18] T. Belytschko, W. Liu, B. Moran, Nonlinear Finite Elements for Continua and Structures, Wiley, 2000.

[19] A. Mills, Basic Heat and Mass Transfer, Prentice Hall, 1999.

[20] O. C. Zienkiewicz, R. L. Taylor, Finite Element Method: Volume 1, The Basis (Finite Element Method), Butterworth-Heinemann, 2000.

[21] T. Belytschko, I. Leviathan, Projection schemes for one-point quadrature shell elements, Computer Methods in Applied Mechanics and Engineering 115 (1994) 277–286.

[22] T. Belytschko, I. Leviathan, Physical stabilization of the 4-node shell element with one point quadrature, Computer Methods in Applied Mechanics and Engineering 113 (1994) 321–350.

[23] C. Rankin, B. Nour-Omid, The use of projectors to improve finite element performance, Computers & Structures 30 (1988) 257–267.

[24] S. Kugler, P. Fotiu, J. Murin, Advances in quadrilateral shell elements with drilling degrees of freedom, H. Altenbach and V. Eremeyev (eds.) Shell-like Structures - Advanced Structured Materials Vol. 15 (2011) 307–328.

[25] S. Kugler, P. Fotiu, J. Murin, Thermo-elasticity in shell structures made of functionally graded materials, Acta Mechanica (2016) 10.1007/s00707–015–1550–9.

[26] K. Bathe, E. Dvorkin, A formulation of general shell elements - the use of mixed interpolation of tensorial components, International Journal for Numerical Methods in Engineering 22 (1986) 697–722.

[27] E. Dvorkin, K. Bathe, A continuum mechanics based four-node shell element for general non-linear analysis, Eng. Comput. 1 (1984) 77–88.

[28] ANSYS, Ansys V11 Documentation.

[29] C. Lü, W. Chen, R. Xu, C. Lim, Semi-analytical elasticity solutions for bi-directional functionally graded beams, International Journal of Solids and Structures 45 (2008) 258–275.

[30] M. Lezgy-Nazargah, Fully coupled thermo-mechanical analysis of bi-directional fgm beams using nurbs isogeometric finite element approach, Aerospace Science and Technology 45 (2015) 154–164.

ECCOMAS Congress 2016
VII European Congress on Computational Methods in Applied Sciences and Engineering
M. Papadrakakis, V. Papadopoulos, G. Stefanou, V. Plevris (eds.)
Crete Island, Greece, 5–10 June 2016

FINITE BEAM ELEMENT WITH PIEZOELECTRIC LAYERS AND FUNCTIONALLY GRADED MATERIAL OF CORE

Vladimír Kutiš[1], Justín Murín[1], Juraj Paulech[1], Juraj Hrabovský[1], Roman Gogola[1] and Jakub Jakubec[1]

[1]Department of Applied Mechanics and Mechatronics
Institute of Automotive Mechatronics
Faculty of Electrical Engineering and Information Technology
Slovak University of Technology in Bratislava
Ilkovičova 3, 812 19 Bratislava, Slovak Republic
e-mail: vladimir.kutis@stuba.sk, justin.murin@stuba.sk, juraj.paulech@stuba.sk,
juraj.hrabovsky@stuba.sk, roman.gogola@stuba.sk, jakub.jakubec@stuba.sk

Keywords: Piezoelectric Material, FGM, FEM, Beam Element, Transient Analysis

Abstract. *New smart materials have been developed in material science, that are suitable for mechatronic applications. Modern mechatronic systems are focusing on minimizing size, active control and low energy consumption. All this attributes can be incorporated into term Micro Electro Mechanical Systems (MEMS). To improve performance of MEMS system, new materials and technologies are developed - one of them, which found broad application usage is Functionally graded material (FGM). MEMS application usually contains multilayer structure and in some application class MEMS systems contain piezoelectric layers. Piezoelectric structures offer facilities to make motions. Piezoelectric layers can be also used to damp vibrations as an active damping or as an active sensor. For better understanding these multiphysical problems new mathematical models are developed.*

The paper deals with finite beam element with piezoelectric layers and functionally graded material of core. In the paper homogenization of FGM material properties and homogenization of core and piezoelectric layers is presented. In the process of homogenization direct integration method and multilayer method is used. There is also presented the derivation of individual submatrices of local stiffness and mass matrix, where concept of transfer constants is used. Functionality of new FGM finite beam with piezoelectric layers is presented by numerical experiments.

1 INTRODUCTION

New materials have been introduced in the area of mechanisms and mechatronic applications. Contemporary mechanical systems are focusing on minimizing size, active control and low energy consumption. All these attributes can be incorporated into term Micro Electro Mechanical System (MEMS). MEMS applications usually contain multilayer structure and some of these layers can have piezoelectric properties. Piezoelectric structures offer facilities to make motions or they can be used to damp vibrations as an active damper or as an active sensor.

2 PIEZOELECTRIC CONSTITUTIVE EQUATIONS

Piezoelectric constitutive equations describe the relationship between mechanical and electrical quantities [1]. This relationship is derived in tensor notation, but for practical usage it can be rewritten into matrices notation.

2.1 Tensor notation of piezoelectric constitutive equations

The form of the constitutive equations depends on chosen mechanical and electrical quantities and can be expressed in two basic configurations [2]. The first configuration is expressed by mechanical stress tensor components σ_{kl} and vector components of electric intensity E_k and has a form

$$D_i = \epsilon^{\sigma}_{ik} E_k + d_{ikl}\sigma_{kl} \tag{1}$$

$$\varepsilon_{ij} = d_{ijk} E_k + s^{E}_{ijkl}\sigma_{kl} \tag{2}$$

where ε_{ij} are strain tensor components, D_i are components of electric displacement vector, d_{ikl} are tensor components of piezoelectric constants, ϵ^{σ}_{ik} are components of permittivity tensor under constant mechanical stress and s^{E}_{ijkl} are components of compliance tensor under constant electric intensity.
The constitutive equations can be also expressed by strain tensor components ε_{kl} and vector components of electric intensity E_k and has a form

$$\sigma_{ij} = c^{E}_{ijkl}\varepsilon_{kl} - e_{ijk} E_k \tag{3}$$

$$D_i = e_{ikl}\varepsilon_{kl} + \epsilon^{\varepsilon}_{ik} E_k \tag{4}$$

where new quantities are components of stiffness tensor under constant electric intensity c^{E}_{ijkl} and components of piezoelectric modulus tensor e_{ijk}.

2.2 Matrix notation of piezoelectric constitutive equations

If we use symmetric properties of individual tensor in constitutive tensor equations, we can rewrite constitutive equations into matrix notation [3]. Then equations (1) and (2) have a form

$$D_i = \epsilon^{\sigma}_{ik} E_k + d_{iq}\sigma_q \tag{5}$$

$$\varepsilon_p = d_{pk} E_k + s^{E}_{pq}\sigma_q \tag{6}$$

and equations (3) and (4) can be rewritten in the form

$$\sigma_p = c^{E}_{pq}\varepsilon_q - e_{pk} E_k \tag{7}$$

$$D_i = e_{iq}\varepsilon_q + \epsilon^{\varepsilon}_{ik} E_k \tag{8}$$

D_i and E_k are vectors with three components, σ_q and ε_q are vectors with six components, matrices s^E_{pq} and c^E_{pq} have dimension 6×6, matrices d_{iq} and e_{pk} have dimension 3×6 and matrix $\epsilon^{\varepsilon}_{ik}$ has dimension 3×3. Constitutive equations (5) and (6) written in a component form can be rewritten as

$$\boldsymbol{\varepsilon} = \mathbf{s}^E \boldsymbol{\sigma} + \mathbf{d}^T \mathbf{E} \tag{9}$$

$$\mathbf{D} = \mathbf{d}\boldsymbol{\sigma} + \boldsymbol{\epsilon}^{\sigma} \mathbf{E} \tag{10}$$

and equations (7) and (8) can be rewritten as

$$\boldsymbol{\sigma} = \mathbf{c}^E \boldsymbol{\varepsilon} - \mathbf{e}^T \mathbf{E} \tag{11}$$

$$\mathbf{D} = \mathbf{e}\boldsymbol{\varepsilon} + \boldsymbol{\epsilon}^{\varepsilon} \mathbf{E} \tag{12}$$

3 BASIC FEM EQUATIONS FOR PIEZOELECTRIC STRUCTURE

To obtain basic FEM equations for piezoelectric structure, the Hamilton's principle is used and can be expressed in the form

$$\int_{t_1}^{t_2} (\delta L + \delta W)\, dt = 0 \tag{13}$$

where L is Lagrangian, W is work of external mechanical and electrical forces and t_1 and t_2 defined considered time interval.
Lagrangian of piezoelectric structure is given by

$$\begin{aligned} L =& T - U + W_e = \\ &= \int_V \frac{1}{2} \rho \dot{\mathbf{u}}^T \dot{\mathbf{u}} dV - \int_V \frac{1}{2} \boldsymbol{\varepsilon}^T \boldsymbol{\sigma} dV + \int_V \frac{1}{2} \mathbf{E}^T \mathbf{D} dV \end{aligned} \tag{14}$$

where T is kinetic energy of structure, U is potential energy of structure and W_e is electric energy stored in piezoelectric material. In kinetic energy term $\dot{\mathbf{u}}$ represents velocity vector.
Virtual work of external mechanical and electrical forces can be expressed as

$$\delta W = \sum \left(\delta \mathbf{u}^T \mathbf{F}\right) - \sum \left(\delta \boldsymbol{\phi}^T \mathbf{Q}\right) \tag{15}$$

where $\mathbf{F}$ and $\mathbf{Q}$ represents discrete forces and electric charges, respectively and $\mathbf{u}$ and $\boldsymbol{\phi}$ are displacement vector and scalar electric potential, respectively.
Equation (13) can be rewritten using (14) and (15)

$$\begin{aligned} \int_{t_1}^{t_2} \Bigg[& \delta \int_V \frac{1}{2} \rho \dot{\mathbf{u}}^T \dot{\mathbf{u}} dV - \delta \int_V \frac{1}{2} \boldsymbol{\varepsilon}^T \boldsymbol{\sigma} dV + \delta \int_V \frac{1}{2} \mathbf{E}^T \mathbf{D} dV + \\ & + \sum \left(\delta \mathbf{u}^T \mathbf{F}\right) - \sum \left(\delta \boldsymbol{\phi}^T \mathbf{Q}\right) \Bigg] dt = 0 \end{aligned} \tag{16}$$

After some manipulation and using constitutive equations (11) and (12) Hamilton's principle for piezoelectric system can be expressed in form

$$\begin{aligned} \int_{t_1}^{t_2} \Bigg[& - \int_V \rho \delta \mathbf{u}^T \ddot{\mathbf{u}} dV - \int_V \delta \boldsymbol{\varepsilon}^T \mathbf{c}^E \boldsymbol{\varepsilon} dV + \int_V \delta \boldsymbol{\varepsilon}^T \mathbf{e}^T \mathbf{E} dV + \int_V \delta \mathbf{E}^T \mathbf{e} \boldsymbol{\varepsilon} dV + \\ & + \int_V \delta \mathbf{E}^T \boldsymbol{\epsilon}^{\varepsilon} \mathbf{E} dV + \sum \left(\delta \mathbf{u}^T \mathbf{F}\right) - \sum \left(\delta \boldsymbol{\phi}^T \mathbf{Q}\right) \Bigg] dt = 0 \end{aligned} \tag{17}$$

Using shape functions ($\mathbf{N}_u$, $\mathbf{N}_\phi$), we can write relationship between displacement of point and nodal displacement of finite element and between scalar electric potential of point and nodal scalar electric potential of finite element

$$\mathbf{u} = \mathbf{N}_u \mathbf{u}^e \tag{18}$$

$$\boldsymbol{\phi} = \mathbf{N}_\phi \boldsymbol{\phi}^e \tag{19}$$

Relationship between components of strain and components of nodal displacements has form

$$\boldsymbol{\varepsilon} = \mathbf{B}_u \mathbf{u}^e \tag{20}$$

Similarly relationship between components of electric field intensity and components of nodal potential can be written as

$$\mathbf{E} = -\mathbf{B}_\phi \boldsymbol{\phi}^e \tag{21}$$

Virtual strain and virtual electric field intensity can be expressed as

$$\delta\boldsymbol{\varepsilon} = \mathbf{B}_u \delta\mathbf{u}^e \tag{22}$$

$$\delta\mathbf{E} = -\mathbf{B}_\phi \delta\boldsymbol{\phi}^e \tag{23}$$

Equation (17) can be modified using equations (18)-(23)

$$\begin{aligned}
&\int_{t_1}^{t_2} \delta(\mathbf{u}^e)^T \left[-\left(\int_{V^e} \mathbf{N}_u^T \rho \mathbf{N}_u dV \right) \ddot{\mathbf{u}}^e - \left(\int_{V^e} \mathbf{B}_u^T \mathbf{c}^E \mathbf{B}_u dV \right) \mathbf{u}^e - \right. \\
&\left. - \left(\int_{V^e} \mathbf{B}_u^T \mathbf{e}^T \mathbf{B}_\phi dV \right) \boldsymbol{\phi}^e + \mathbf{N}_u^T \mathbf{F} \right] dt + \\
&+ \int_{t_1}^{t_2} \delta(\boldsymbol{\phi}^e)^T \left[\left(-\int_{V^e} \mathbf{B}_\phi^T \mathbf{e} \mathbf{B}_u dV \right) \mathbf{u}^e + \left(\int_{V^e} \mathbf{B}_\phi^T \boldsymbol{\epsilon}^\varepsilon \mathbf{B}_\phi dV \right) \boldsymbol{\phi}^e - \mathbf{N}_\phi^T \mathbf{Q} \right] dt = 0
\end{aligned} \tag{24}$$

From equations (24) we obtain finite element equations for piezoelectric analysis

$$\begin{bmatrix} \mathbf{M}_{uu}^e & \mathbf{0} \\ \mathbf{0} & \mathbf{0} \end{bmatrix} \begin{bmatrix} \ddot{\mathbf{u}}^e \\ \ddot{\boldsymbol{\phi}}^e \end{bmatrix} + \begin{bmatrix} \mathbf{C}_{uu}^e & \mathbf{0} \\ \mathbf{0} & \mathbf{0} \end{bmatrix} \begin{bmatrix} \dot{\mathbf{u}}^e \\ \dot{\boldsymbol{\phi}}^e \end{bmatrix} + \begin{bmatrix} \mathbf{K}_{uu}^e & \mathbf{K}_{u\phi}^e \\ \mathbf{K}_{\phi u}^e & \mathbf{K}_{\phi\phi}^e \end{bmatrix} \begin{bmatrix} \mathbf{u}^e \\ \boldsymbol{\phi}^e \end{bmatrix} = \begin{bmatrix} \mathbf{F}^e \\ \mathbf{Q}^e \end{bmatrix} \tag{25}$$

where

$$\mathbf{M}_{uu}^e = \int_V \mathbf{N}_u^T \rho \mathbf{N}_u dV \tag{26}$$

$$\mathbf{K}_{uu}^e = \int_V \mathbf{B}_u^T \mathbf{c}^E \mathbf{B}_u dV \tag{27}$$

$$\mathbf{K}_{u\phi}^e = \int_V \mathbf{B}_u^T \mathbf{e}^T \mathbf{B}_\phi dV \tag{28}$$

$$\mathbf{K}_{\phi u}^e = \int_V \mathbf{B}_\phi^T \mathbf{e} \mathbf{B}_u dV \tag{29}$$

$$\mathbf{K}_{\phi\phi}^e = -\int_V \mathbf{B}_\phi^T \boldsymbol{\epsilon}^\varepsilon \mathbf{B}_\phi dV \tag{30}$$

$$\mathbf{F}^e = \mathbf{N}_u^T \mathbf{F} \tag{31}$$

$$\mathbf{Q}^e = -\mathbf{N}_\phi^T \mathbf{Q} \tag{32}$$

4 FEM EQUATIONS OF FGM BEAM WITH PIEZOELECTRIC LAYERS

2D beam element with piezoelectric layers, where beam core is made from functionally graded material is shown in Figure 1, where all degrees of freedom are depicted. Mechanical degrees of freedom in each node are two displacements (in direction x a y) and rotation (in plane $x-y$) [6]. Electric degrees of freedom are electric potentials ϕ_i on 4 electrodes. The height of beam core made from FGM is h, the height of piezoelectric layer is h_p, the depth and the length of the beam element are b and L, respectively.
Material properties of FGM core are function of longitudinal and transversal coordinate x and y, material properties of piezoelectric layers are constants.

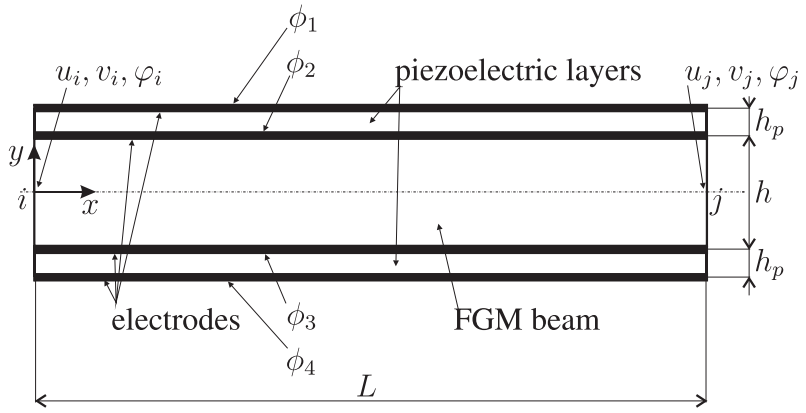

Figure 1: Electric DOF in 2D beam element

In order to derive individual submatrices of the beam element with piezoelectric layers and FGM core, two steps in homogenization process have to be performed. At first, homogenization of material properties of FGM core have to be performed, where direct integration method is used [6]. In the next step, homogenization of piezoelectric layers and homogenized FGM core (from step one) is performed. After these two operations, homogenized material properties of the beam vary through the length of the beam as a function of longitudinal coordinate x and are constant in transversal direction.

4.1 Equations for structural analysis

The structural submatrix $\mathbf{K}^e_{uu}$ for the beam element with piezoelectric layers can be expressed in a form

$$\mathbf{K}^e_{uu} = \begin{bmatrix} k'_u & 0 & 0 & -k'_u & 0 & 0 \\ & k'_{v2} & k'_{v3} & 0 & -k'_{v2} & k_{v2} \\ \mathrm{S} & & k'_{v33} & 0 & -k'_{v3} & k_{v3} \\ & \mathrm{Y} & & k'_u & 0 & 0 \\ & & \mathbf{M} & & k'_{v2} & -k_{v2} \\ & & & & & k_{v23} \end{bmatrix} \tag{33}$$

where individual components contain the influence of FGM core stiffness and also the influence of piezoelectric layers stiffness. The calculation of components is identical for classical multilayer or FGM beam without piezoelectric layer and is described in [6]. Mass matrix $\mathbf{M}^e_{uu}$ can be calculated numerically using classical shape functions and homogenized density of FGM beam with piezoelectric layers according equation (26).

4.2 Equations for electric analysis

Electric field intensity in piezoelectric layer is constant and for top layer can by expressed as [4, 5]

$$E_1 = -\frac{\partial \phi}{\partial y} = \frac{\phi_2 - \phi_1}{h_p} \tag{34}$$

and for bottom layer as

$$E_2 = -\frac{\partial \phi}{\partial y} = \frac{\phi_4 - \phi_3}{h_p} \tag{35}$$

Both components of electric field intensity can be written in a form

$$\mathbf{E} = \begin{bmatrix} E_1 \\ E_2 \end{bmatrix} = -\begin{bmatrix} 1/h_p & -1/h_p & 0 & 0 \\ 0 & 0 & 1/h_p & -1/h_p \end{bmatrix} \begin{bmatrix} \phi_1 \\ \phi_2 \\ \phi_3 \\ \phi_4 \end{bmatrix} = -\mathbf{B}_\phi \boldsymbol{\phi}^e \tag{36}$$

For 1D problems the matrix of material properties for electric field – permittivity is reduced to only one material property ϵ^ε, but because the beam element contains two identical layers, we can write

$$\boldsymbol{\epsilon}^{\boldsymbol{\varepsilon}} = \begin{bmatrix} \epsilon^\varepsilon & 0 \\ 0 & \epsilon^\varepsilon \end{bmatrix} \tag{37}$$

Then the equation (30) has a form

$$\mathbf{K}^e_{\phi\phi} = -\int_V \mathbf{B}^T_\phi \boldsymbol{\epsilon}^\varepsilon \mathbf{B}_\phi dV = -\int_L \mathbf{B}^T_\phi \boldsymbol{\epsilon}^\varepsilon \mathbf{B}_\phi A_p dx \tag{38}$$

where A_p is cross-section of one piezoelectric layer, i.e. $A_p = bh_p$.
After some mathematical manipulations the equation (38) can be expressed as

$$\mathbf{K}^e_{\phi\phi} = \begin{bmatrix} -\frac{A_p L \epsilon^\varepsilon}{h_p^2} & \frac{A_p L \epsilon^\varepsilon}{h_p^2} & 0 & 0 \\ \frac{A_p L \epsilon^\varepsilon}{h_p^2} & -\frac{A_p L \epsilon^\varepsilon}{h_p^2} & 0 & 0 \\ 0 & 0 & -\frac{A_p L \epsilon^\varepsilon}{h_p^2} & \frac{A_p L \epsilon^\varepsilon}{h_p^2} \\ 0 & 0 & \frac{A_p L \epsilon^\varepsilon}{h_p^2} & -\frac{A_p L \epsilon^\varepsilon}{h_p^2} \end{bmatrix} \tag{39}$$

4.3 Coupling of structural and electrical analysis

Piezoelectric material properties express coupling between mechanical and electrical field - matrices $\mathbf{e}$ or $\mathbf{d}$. The relationship between these two matrices can be expressed by elasticity matrix. In 1D problem in $x - y$ plane (in index notation $x_1 - x_2$) we have only one material property – e_{21} or d_{21}, where index 2 represents direction of piezoelectric layer polarization and also the direction of electric field intensity vector and index 1 defines direction of mechanical deformation. The relationship between these two quantities is reduced to expression $e_{21} = d_{21}E_p$ [7, 8], where E_p is Young modulus of elasticity of piezoelectric material. In reality, relationship between matrices $\mathbf{e}$ and $\mathbf{d}$ is more complicated and the quantity e_{21} computed from matrix $\mathbf{d}$ and elastic matrix for 3D system and the quantity e_{21} computed from d_{21} and E_p have

different values. Therefore if we have quantities e_{21} and d_{21} computed from matrix relationship, it is better to used them then simplified relationship.
Piezoelectric material properties of both piezoelectric layers are defined as

$$\mathbf{e} = \begin{bmatrix} e_{21} & 0 & -ye_{21} \\ e_{21} & 0 & -ye_{21} \end{bmatrix} \tag{40}$$

The expression $\mathbf{e}^T\mathbf{E}$ defines mechanical stress caused by piezoelectric effect. In the beam elements, internal quantities are not mechanical stress but internal forces and moments, then the first and the third column of matrix (40) multiplied by corresponding components of $\mathbf{B}_u$ and $\mathbf{B}_\phi$ as well as corresponding components of displacement $\mathbf{u}$ and potential $\boldsymbol{\phi}$ represents axial forces and bending moments, respectively.
Description of piezoelectric behaviour by e_{21} is more suitable for sensor equation – matrix $\mathbf{K}^e_{\phi u}$, description by d_{21} is more suitable for actuator equation – matrix $\mathbf{K}^e_{u\phi}$, i.e.

$$\mathbf{e} = \begin{bmatrix} d_{21}E_p & 0 & -yd_{21}E_p \\ d_{21}E_p & 0 & -yd_{21}E_p \end{bmatrix} \tag{41}$$

Using equations (40) and (41) we can write (28) and (29) in form

$$\mathbf{K}^e_{u\phi} = \begin{bmatrix} -\frac{A_p d_{21} E_p}{h_p} & \frac{A_p d_{21} E_p}{h_p} & -\frac{A_p d_{21} E_p}{h_p} & \frac{A_p d_{21} E_p}{h_p} \\ 0 & 0 & 0 & 0 \\ \frac{A_y d_{21} E_p}{h_p} & -\frac{A_y d_{21} E_p}{h_p} & \frac{A_y d_{21} E_p}{h_p} & -\frac{A_y d_{21} E_p}{h_p} \\ \frac{A_p d_{21} E_p}{h_p} & -\frac{A_p d_{21} E_p}{h_p} & \frac{A_p d_{21} E_p}{h_p} & -\frac{A_p d_{21} E_p}{h_p} \\ 0 & 0 & 0 & 0 \\ -\frac{A_y d_{21} E_p}{h_p} & \frac{A_y d_{21} E_p}{h_p} & -\frac{A_y d_{21} E_p}{h_p} & \frac{A_y d_{21} E_p}{h_p} \end{bmatrix} \tag{42}$$

and

$$\mathbf{K}^e_{\phi u} = \begin{bmatrix} -\frac{A_p e_{21}}{h_p} & 0 & \frac{A_y e_{21}}{h_p} & \frac{A_p e_{21}}{h_p} & 0 & -\frac{A_y e_{21}}{h_p} \\ \frac{A_p e_{21}}{h_p} & 0 & -\frac{A_y e_{21}}{h_p} & -\frac{A_p e_{21}}{h_p} & 0 & \frac{A_y e_{21}}{h_p} \\ -\frac{A_p e_{21}}{h_p} & 0 & \frac{A_y e_{21}}{h_p} & \frac{A_p e_{21}}{h_p} & 0 & -\frac{A_y e_{21}}{h_p} \\ \frac{A_p e_{21}}{h_p} & 0 & -\frac{A_y e_{21}}{h_p} & -\frac{A_p e_{21}}{h_p} & 0 & \frac{A_y e_{21}}{h_p} \end{bmatrix} \tag{43}$$

where parameter A_y represents first moment of cross-section of piezoelectric layer

$$A_y = \frac{1}{2} A_p (h + h_p) \tag{44}$$

4.4 FEM equations for the beam element with piezoelectric layers

FEM equations for beam element with piezoelectric layers and FGM core for transient analysis have classical form

$$\begin{bmatrix} \mathbf{M}^e_{uu} & \mathbf{0} \\ \mathbf{0} & \mathbf{0} \end{bmatrix} \begin{bmatrix} \ddot{\mathbf{u}}^e \\ \ddot{\boldsymbol{\phi}}^e \end{bmatrix} + \begin{bmatrix} \mathbf{C}^e_{uu} & \mathbf{0} \\ \mathbf{0} & \mathbf{0} \end{bmatrix} \begin{bmatrix} \dot{\mathbf{u}}^e \\ \dot{\boldsymbol{\phi}}^e \end{bmatrix} + \begin{bmatrix} \mathbf{K}^e_{uu} & \mathbf{K}^e_{u\phi} \\ \mathbf{K}^e_{\phi u} & \mathbf{K}^e_{\phi\phi} \end{bmatrix} \begin{bmatrix} \mathbf{u}^e \\ \boldsymbol{\phi}^e \end{bmatrix} = \begin{bmatrix} \mathbf{F}^e \\ \mathbf{Q}^e \end{bmatrix} \tag{45}$$

where individual submatrices are defined by (33), (39), (42) and (43), vector of nodal unknowns is defined as

$$\begin{bmatrix}\mathbf{u}^e\\ \boldsymbol{\phi}^e\end{bmatrix} = \begin{bmatrix}u_i & v_i & \varphi_i & u_j & v_j & \varphi_j & \phi_1 & \phi_2 & \phi_3 & \phi_4\end{bmatrix}^T \tag{46}$$

and vector of nodal loads is defined as

$$\begin{bmatrix}\mathbf{F}^e\\ \mathbf{Q}^e\end{bmatrix} = \begin{bmatrix}F_{xi} & F_{yi} & M_i & F_{xj} & F_{yj} & M_j & Q_1 & Q_2 & Q_3 & Q_4\end{bmatrix}^T \tag{47}$$

where Q_1, Q_2, Q_3 and Q_4 are electric charge on electrodes 1, 2, 3 and 4, respectively.

5 NUMERICAL EXAMPLES

All derived equations for FGM beam with piezoelectric layers were implemented in our FEM code MultiFEM.
In this section three numerical examples are presented:

- Example 1 – considered simple beam is made from FGM with attached piezoelectric layers, only static analysis is considered
- Example 2 – the same simple beam as in Example 1 is considered, but analysis is transient
- Example 3 – considered structure contains three beam parts with partially attached piezoelectric layers, two beam parts are made from FGM and one beam part has constant material properties

5.1 Material properties of FGM structure and piezoelectric layers

In all three examples, the same functionally graded material is considered. Material of matrix (index m) is NiFe with constant density and Young's modulus and material of fibre (fibre – index f) is tungsten with constant density and Young's modulus:

- Young's modulus: $E_m = 255$ GPa, $E_f = 400$ GPa
- density: $\rho_m = 9200$ kg/m^3, $\rho_f = 19300$ kg/m^3

Volume fractions of both constituents $v_m(x,y)$ and $v_f(x,y)$ vary along the length (axis x) and height (axis y) of beams according equations:

$$v_m(x,y) = -1.\overline{3}\times 10^8 x^3y^2 + 1333.\overline{3}x^3 + 2.\times 10^7 x^2y^2 - 200.x^2 - 40000.y^2 + 1. \quad [\text{-}] \tag{48}$$

$$v_f(x,y) = 1.\overline{3}\times 10^8 x^3y^2 - 1333.\overline{3}x^3 - 2.\times 10^7 x^2y^2 + 200.x^2 + 40000.y^2 \quad [\text{-}] \tag{49}$$

Both functions of volume fractions for beam with length 0.1 m and height 0.01 m are shown in Figure 2.

Effective material properties of FGM are defined by material properties of constituents and their variations and Young's modulus and density of considered FGM have form

$$\begin{aligned}E_{\text{FGM}}(x,y) =& 1.9\overline{3}\times 10^{19}x^3y^2 - 1.9\overline{3}\times 10^{14}x^3 - 2.9\times 10^{18}x^2y^2 + \\ &+ 2.9\times 10^{13}x^2 + 5.8\times 10^{15}y^2 + 2.55\times 10^{11} \quad [\text{Pa}]\end{aligned} \tag{50}$$

$$\begin{aligned}\rho_{\text{FGM}}(x,y) =& 1.34667\times 10^{12}x^3y^2 - 1.34667\times 10^{7}x^3 - 2.02\times 10^{11}x^2y^2 + \\ &+ 2.02\times 10^{6}x^2 + 4.04\times 10^{8}y^2 + 9200. \quad [\text{kg/m}^3]\end{aligned} \tag{51}$$

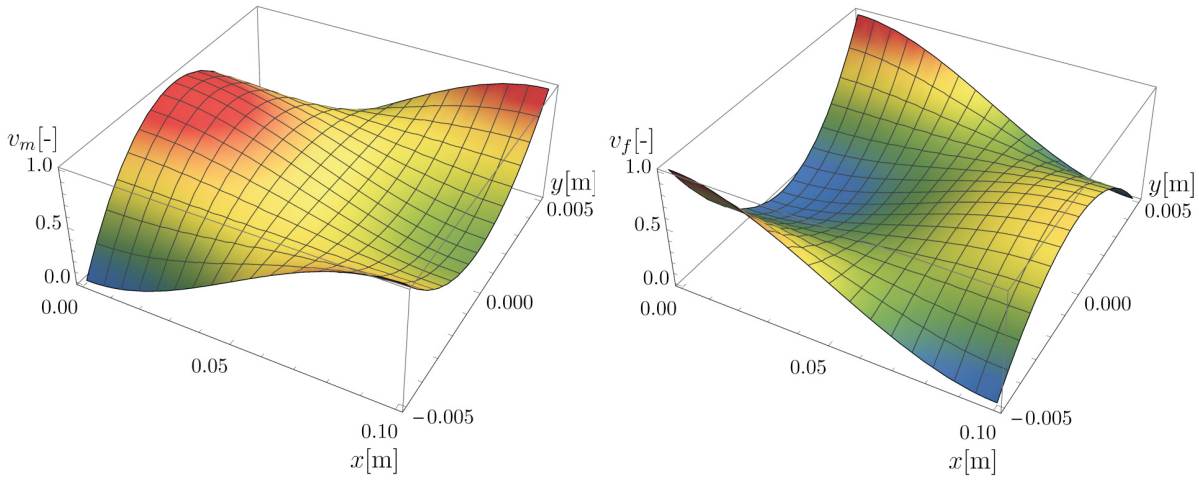

Figure 2: Left – volume fraction of matrix, right – volume fraction of fibre

In all three examples, height and depth of beam cross-section is 0.01m. Homogenized material properties of investigated FGM beams can be calculated by defined cross-section parameters of beams and by effective material properties and have following forms:

$$E^N_{\text{FGM}}(x) = -3.\overline{2} \times 10^{13}x^3 + 4.8\overline{3} \times 10^{12}x^2 + 3.0\overline{3} \times 10^{11} \quad \text{[Pa]} \tag{52}$$

$$E^M_{\text{FGM}}(x) = 9.\overline{6} \times 10^{13}x^3 - 1.45 \times 10^{13}x^2 + 3.42 \times 10^{11} \quad \text{[Pa]} \tag{53}$$

$$\rho_{\text{FGM}}(x) = -2.2\overline{4} \times 10^{6}x^3 + 33666.\overline{6}x^2 + 12566.\overline{6} \quad \text{[kg/m}^3\text{]} \tag{54}$$

$E^N_{\text{FGM}}(x)$ and $E^M_{\text{FGM}}(x)$ represent homogenized Young's modulus for axial loading and for bending, respectively.

Piezoelectric layers in investigated beams are made from PZT5A piezoelectric material. PZT5A is orthotropic material and has following material properties (direction of poling has index 3):

- mechanical properties:
  - Young's moduli: $E_1 = 61$ GPa, $E_2 = 61$ GPa, $E_3 = 53,2$ GPa
  - Poisson numbers: $\mu_{12} = 0.35$, $\mu_{13} = 0.38$, $\mu_{23} = 0.38$
  - shear moduli: $G_{12} = 22.6$ GPa, $G_{13} = 21.1$ GPa, $G_{23} = 21.1$ GPa
  - density: 7750 kg/m^3
- piezoelectric properties: $d_{31} = -171 \times 10^{-12}$ C/N, $d_{33} = 374 \times 10^{-12}$ C/N, $d_{15} = 584 \times 10^{-12}$ C/N, $d_{24} = 584 \times 10^{-12}$ C/N
- relative permittivity: $\epsilon^{\sigma}_{11} = 1728.8$, $\epsilon^{\sigma}_{22} = 1728.8$, $\epsilon^{\sigma}_{33} = 1694.9$

5.2 Example 1 – static analysis of piezoelectric beam

Figure 3 shows simple cantilever made of FGM with piezoelectric layers, which is loaded by transversal force F at free end. Electrodes on top and bottom piezoelectric layers are short circuited. The goal of analysis is to investigate static responds of structure on prescribed loading and compare results of 1D model with results of 2D model.

Geometry parameters of beam are:

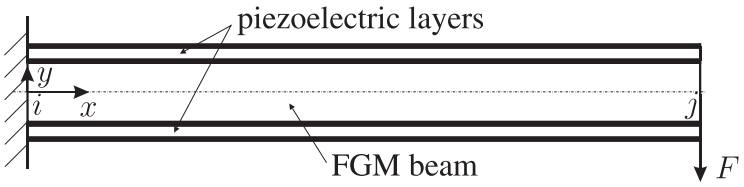

Figure 3: Example 1: static analysis of FGM beam with piezoelectric layers

- length 0.1 m
- height of FGM core 0.01 m, height of piezoelectric layer 0.001 m
- depth of beam 0.01 m

Material of beam:

- core of beam is made from FGM (NiFe-tungsten) and its effective and homogenized material properties are described by equations (50)-(54)
- piezoelectric layers are made from PZT5A – reduced properties $\overline{e}_{31} = \dfrac{d_{31}}{s^E_{11}} = -10.43$ C/m^2

Using multilayered method homogenized Young's modulus for axial loading and for bending and homogenized density of whole beam can be calculated using homogenized material properties of FGM core and constant material properties of piezoelectric layers and they have form

$$E^N(x) = -2.68519 \times 10^{13}x^3 + 4.02778 \times 10^{12}x^2 + 2.62944 \times 10^{11} \quad \text{[Pa]} \tag{55}$$

$$E^M(x) = 5.59414 \times 10^{13}x^3 - 8.3912 \times 10^{12}x^2 + 2.23616 \times 10^{11} \quad \text{[Pa]} \tag{56}$$

$$\rho(x) = -1.87037 \times 10^{6}x^3 + 280556.x^2 + 11763.9 \quad \text{[kg/m}^3\text{]} \tag{57}$$

Boundary conditions:

- left end – fixed
- right end – transversal force $F = 10$ N

The static analysis of system was performed by new FGM beam element with piezoelectric layers. The analysis was performed by 1, 2, 4 and 10 elements – see Figure 4 left.

Deformed shape of beam is shown in Figure 4 right. Displacement in y direction of free end is -10.63×10^{-6} m. Electric charge on top electrodes for FEM models with different number of elements are summarized in Table 1.

The same problem was analyzed by FEM code ANSYS, where two types of plane elements were used – PLANE223 with piezoelectric capabilities and PLANE183. Because material properties of FGM core vary along the length and height of beam, discretized 2D model contains 6400 elements. Displacement in y direction of free end was -10.70×10^{-6} m and total electric charge on top electrode was 9.2715×10^{-8} C.
As we can see from obtained results, new FGM beam element with piezoelectric layers is very accurate and effective in static analysis, because variation of material properties of FGM core of beam is directly incorporated into stiffness matrix.

Figure 4: Example 1: left – discretized beam with node and element numbers, right – deformation of beam

Number of elements	1	2	4	10
$Q_{\text{elem 1}}$ [C]	9.2650×10^{-8}	6.8159×10^{-8}	3.9209×10^{-8}	1.6939×10^{-8}
$Q_{\text{elem 2}}$ [C]		2.4491×10^{-8}	2.8950×10^{-8}	1.5256×10^{-8}
$Q_{\text{elem 3}}$ [C]			1.8203×10^{-8}	1.3624×10^{-8}
$Q_{\text{elem 4}}$ [C]			6.2883×10^{-9}	1.1998×10^{-8}
$Q_{\text{elem 5}}$ [C]				1.0343×10^{-8}
$Q_{\text{elem 6}}$ [C]				8.6318×10^{-9}
$Q_{\text{elem 7}}$ [C]				6.8450×10^{-9}
$Q_{\text{elem 8}}$ [C]				4.9743×10^{-9}
$Q_{\text{elem 9}}$ [C]				3.0245×10^{-9}
$Q_{\text{elem 10}}$ [C]				1.0157×10^{-9}
Q_{SUM} [C]	9.2650×10^{-8}	9.2650×10^{-8}	9.2650×10^{-8}	9.2650×10^{-8}

Table 1: Example 1: Electric charge on individual electrodes

5.3 Example 2 – transient analysis of piezoelectric beam

In Example 2 transient analysis of FGM beam with piezoelectric layers with the same geometry and material parameters as in Example 1 was performed. Electrodes on top and bottom piezoelectric layers are short circuited. The goal of analysis is to investigate free vibration of structure without considering damping.
Boundary conditions:

- left end – fixed
- right end – free

Initial conditions:

- initial displacement of nodes – initial deformation of system is defined by prescribed displacement of free end in vertical direction $+0.01$m
- initial velocity of nodes – all nodes have zero initial velocities

The transient analysis of system was performed by new FGM beam element with piezoelectric layers. In the analysis Newmark integration scheme was used. Total simulation time was 5 ms

and number of equidistant substeps was 80. 1D model of system was discretized by 10 elements – see Figure. 4 left.
Displacement of nodes 4, 8 and 11 in direction y as function of time are shown in Figure 5 left. Time variations of electric charge in top electrode on elements 2 and 4 are shown in Figure 5 right.

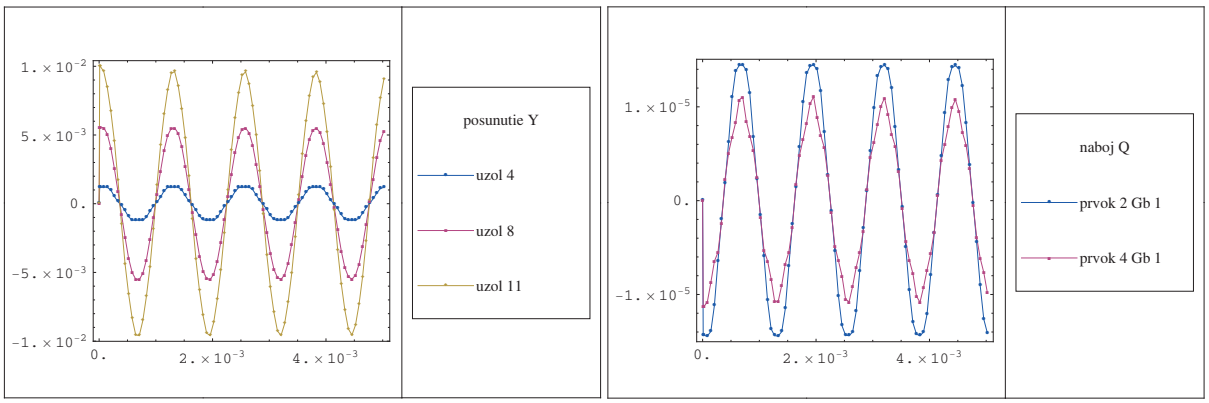

Figure 5: Example 2: left – Y displacement time variation of nodes (4, 8, 11), right – charge time variation of top electrodes on elements (2, 4)

5.4 Example 3 – transient analysis of simple structure

Figure 6 shows simple structure, which contains three beams. Piezoelectric layers are partially attached to the beam 1 and 2. Electrodes on top and bottom piezoelectric layers are short circuited. The goal of analysis is to investigate free vibration of structure with considering damping.

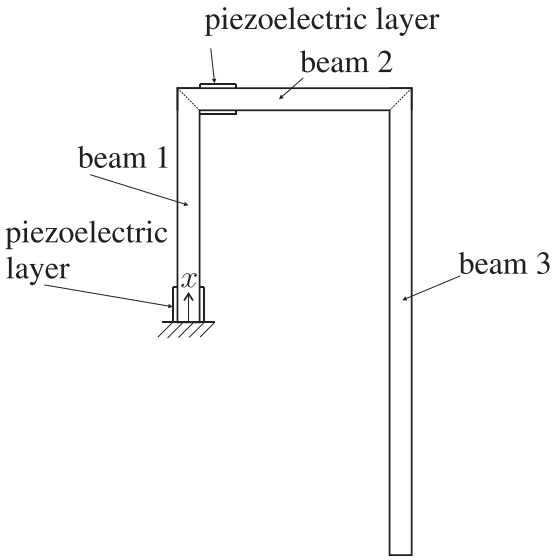

Figure 6: Example 3: free vibration of structure with piezoelectric elements

Geometry parameters of beams are:

- cross-section – all beams have height and depth of cross-section 0.01 m, height of piezoelectric layers is 0.001 m and its depth is 0.01 m
- length – beam 1 and 2 have length 0.05 m and beam 3 has length 0.1 m, length of piezoelectric layers is 0.01 m

Material parameters of beam are:

- core of beam – beam 1 and 2 are made from FGM, homogenized material properties are defined by equations (52)-(54), beam 3 has constant material properties: $E = 319.4$ GPa, $\rho = 13989.6$ kg/m^3
- piezoelectric layer – PZT5A

Three different types of beam finite elements were used in transient analysis of system: FGM beam element, FGM beam element with piezoelectric layers and beam element with Hermite shape functions. Discretized 1D model of system is shown in Figure 7, where nodes and element types are depicted.

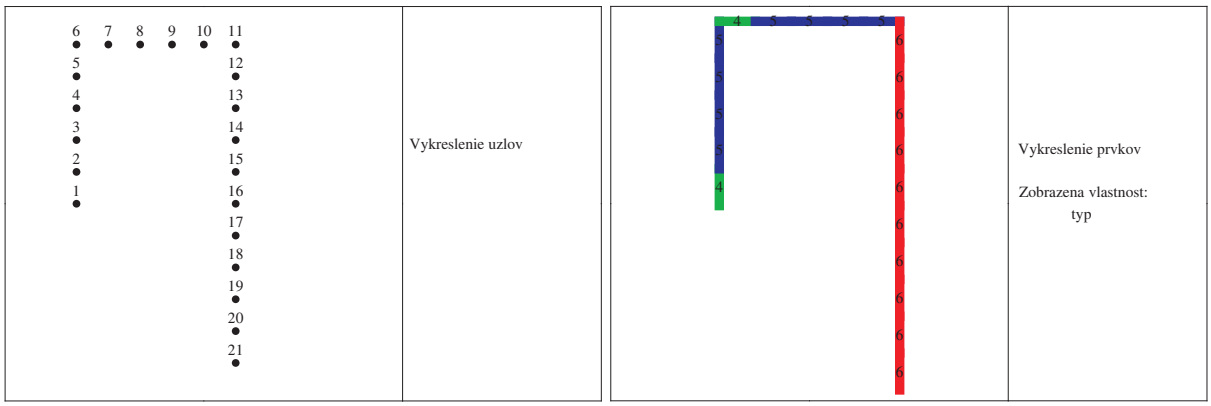

Figure 7: Example 3: left – nodes, right – elements with element types numbering

Boundary conditions:

- left end – fixed
- right end – free

Initial conditions:

- initial displacement of nodes – initial deformation of system is defined by prescribed displacement of free end in horizontal direction $+0.01$m
- initial velocity of nodes – all nodes have zero initial velocities

In the analysis Newmark integration scheme was used. Total simulation time was 7.5 ms and number of equidistant substeps was 400. In the analysis Rayleigh damping was used. Mass-proportional damping coefficient and stiffness-proportional damping coefficient had the same value 1×10^{-5}.
Deformed shape of system at the end of simulation time (7.5 ms) is shown in Figure 8 left. Figure 8 right shows time variation of electric charge in top electrode on elements 1 and 6. Displacements of nodes 8 and 21 as function of time in direction x and y are shown in Figure 9 left and right, respectively.

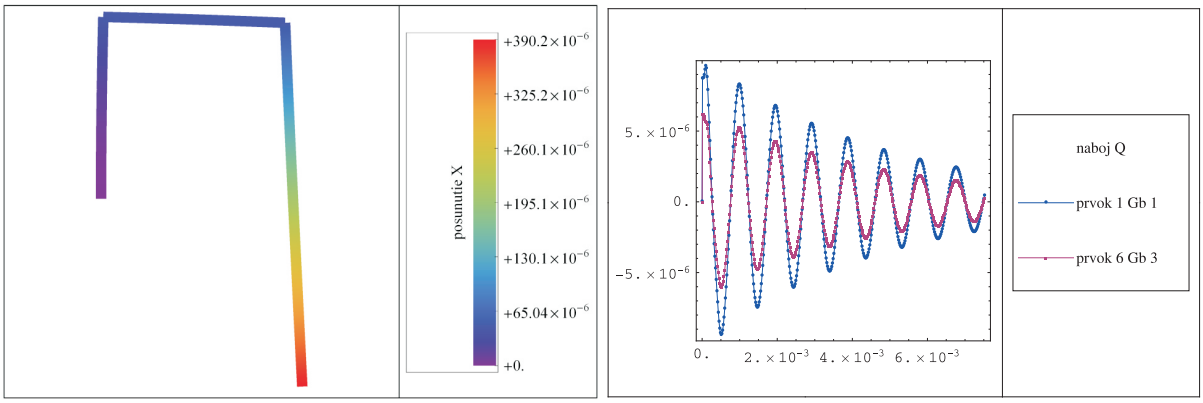

Figure 8: Example 3: left – X displacement of structure at time 7.5ms, right – charge time variation of top electrode on element 1 and 6

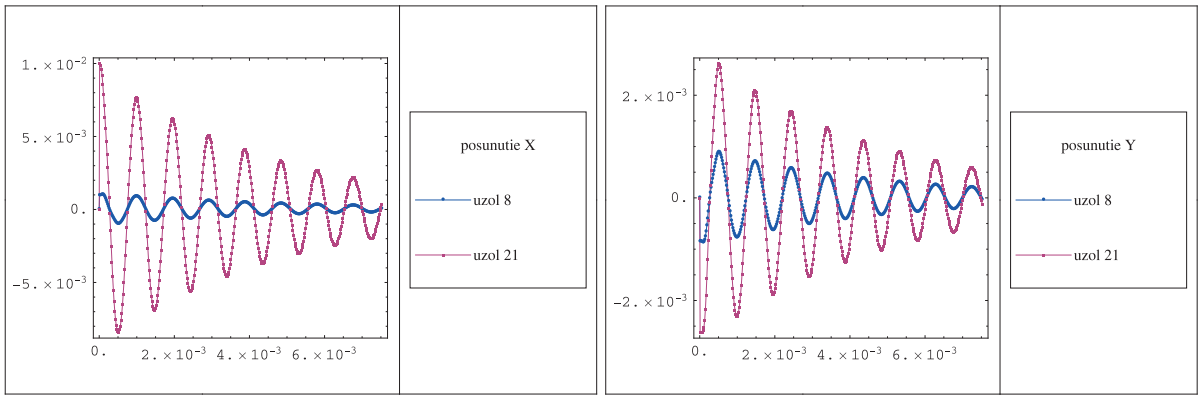

Figure 9: Example 3: left – X displacement time variation of nodes (8, 21), right – Y displacement time variation of nodes (8, 21)

6 CONCLUSIONS

The paper presents new beam finite element with piezoelectric layers, where core of the beam can be made of FGM materials. Such combination of materials is very attractive for mechatronic applications, because material composition of FGM core can be optimized for design stress state and deformation can be controlled by voltages on electrodes. The beam finite element can be used for analysis of such systems very effectively and accurately.

ACKNOWLEDGEMENT

This work was supported by the Slovak Research and Development Agency under the contract No. APVV-14-0613 and APVV-0246-12, by Grant Agency VEGA, grant No. 1/0228/14 and 1/0453/15.

REFERENCES

[1] Moheimani, S.O.R. and Fleming, A.J.. *Piezoelectric Transducers for Vibration Control and Damping*. Springer, (2006).

[2] Ballas, R.G. *Piezoelectric Multilayer Beam Bending Actuators*, Springer, (2007).

[3] Barnett, A.R., Peelamedu, S.M., Dukkipati, R.V. and Naganathan, N.G. Finite Element Approach to Model and Analyze Piezoelectric Actuators. *JSME International Journal*, (2001) **44**:476–485.

[4] I. Bruant, G. Coffignal, F. Lene, M. Verge. Active control of beam structures with piezoelectric actuators and sensors: modeling and simulation. *Smart Material Structures* (2001) **10**:404–408.

[5] Q. Luo, L. Tong. An accurate laminated element for piezoelectric smart beam including peel stress. *Computational Mechanics* (2004) **33**:108–120.

[6] Kutiš, V., Murín, J., Belák, R., Paulech, J. Beam element with spatial variation of material properties for multiphysics analysis of functionally graded materials. *Computers & Structures*, (2011) **89**:1192–1205.

[7] Preumont, A. *Mechatronics Dynamics of Electromechanical and Piezoelectric Systems*, Springer, (2006).

[8] Preumont, A. *Vibration Control of Active Structures*, Kluwer, (2002).

ECCOMAS Congress 2016
VII European Congress on Computational Methods in Applied Sciences and Engineering
M. Papadrakakis, V. Papadopoulos, G. Stefanou, V. Plevris (eds.)
Crete Island, Greece, 5–10 June 2016

NUMERICAL SOLUTION OF DIFFERENTIAL EQUATIONS WITH NON-CONSTANT COEFFICIENTS

Juraj Hrabovsky[1], Justin Murin[1], Mehdi Aminbaghai[2], Vladimir Kutis[1], and Juraj Paulech[1]

[1]Slovak University of Technology in Bratislava
Faculty of Electrical Engineering and Information Technology
Ilkovicova 3, 812 19 Bratislava, Slovakia
e-mail: juraj.hrabovsky@stuba.sk

[2] Vienna University of Technology
Institute for Mechanics of Materials and Structures
Karlsplatz 3, A/1040 Vienna, Austria
e-mail: mehdi.aminbaghai@tuwien.ac.at

Keywords: differential equation with non-constant coefficients, transfer functions, transfer constants, Functionally Graded Material

Abstract. *Nowadays, new materials like Functionally Graded Material (FGM) are necessary for sophisticated structures like MEMS systems, advanced electronic devices, etc. Computer modelling of such complex systems, like structures with spatial variation of material properties (e.g. FGM) are, using commercial FEM code with classic elements, needs remarkable effort during preparation phase and sufficient computer equipment for solution phase because of necessity the numbers of elements and material models. Therefore new methods for modeling and simulation of FGM beams with spatial variation of material properties are developed.*

In the proposed contribution, semi-analytical method (based on calculation of transfer functions and transfer constants) for solution of differential equation with non-constant polynomial coefficients, is presented. This method is used in derivation process (for setting up the transfer matrix) of our new beam finite elements for modeling and simulation of Functionally Graded Material (FGM) beam structures (e.g. new 3D FGM beam finite element for modal and structural analysis, new FGM beam finite elements for coupled electro-thermo-mechanical analysis). Numerical experiments are made to show the accuracy and effectiveness of this method.

1 INTRODUCTION

Physical processes in materials, such as heat transfer, conduction of electric current, mechanical stress, etc., are often described by partial differential equations or by system of partial differential equations. An exact analytical solution is usually possible only for simplified investigated domains (e.g. one dimensional link parts - bars) and simple boundary conditions of the investigated system, where the geometry allows to reduce the partial differential equations into ordinary differential equations. The geometry of the bar, as well as the boundary conditions fulfil the requirements that are needed to apply analytical methods for solving the differential equations.

One example, let us write general partial differential equation for heat transfer in considered domain:

$$\frac{\partial T(x,y,z,\tau)}{\partial \tau} = \frac{\lambda}{c\rho} \bigtriangledown^2 T(x,y,z,\tau) + \frac{Q}{c\rho} \tag{1}$$

Quantity $T(x,y,z,\tau)$ [K] is the unknown temperature of the system, τ [s] is the time, λ [$\mathrm{Wm^{-1}K^{-1}}$] is the thermal conductivity of considered material, c [$\mathrm{Jkg^{-1}K^{-1}}$] is its specific heat, ρ [$\mathrm{kgm^{-3}}$] is the density of the material and Q [$\mathrm{Wm^{-3}}$] is the volume heat sources in the system. For steady state and for 1D geometry (bar construction) we can simplify this partial differential equation into the form of ordinary differential equation:

$$\frac{d^2T(x)}{dx^2} = -\frac{Q}{c\lambda} \tag{2}$$

with two boundary conditions, e.g.:

$$\begin{aligned} T(0) &= T_0 \\ T(L) &= T_L \end{aligned} \tag{3}$$

It is possible to write similar ordinary differential equations also for other physical fields (e.g. electric field, structural analysis, etc.). When we consider variable material properties of the bar (e.g. Functionally Graded Material - FGM) the ordinary differential equations contain variable (nonconstant) coefficients.

In this contribution, semi-analytical method based on calculation of transfer functions (transfer constants), for solution of differential equation with polynomial coefficients [1] is presented. This method is used in derivation process (for setting up the transfer matrix) of our new beam finite elements for modeling and simulation of FGM beam structures with 3D spatial variation of material properties (e.g. new 3D FGM beam finite element for modal, structural and buckling analysis [2][3], new FGM beam finite elements for coupled electro-thermo-mechanical analysis[4]).

2 SEMI-ANALYTICAL METHOD FOR SOLUTION OF LINEAR DIFFERENTIAL EQUATION WITH NON-CONSTANT COEFFICIENTS

There will be set out a procedure for solving differential equations with variable coefficients and right-hand side, which is taken from Rubins article [1]. These differential equations must fulfil the following requirements:

- differential equation of one independent variable
- polynomial character of variable coefficients and right side of the differential equation

- known interval of the independent variable, where the solution of the differential equation needs to be determined ($x \in \langle 0, L \rangle$)

The order of differential equation and also the order of its right side are arbitrary.

2.1 Solving of the differential equation with non-constant coefficients

Let us consider 1D differential equation with non-constant coefficients and the right side in the form:

$$\sum_{u=0}^{m} \eta_u(x)\, y^{(u)}(x) = \sum_{j=0}^{g} q_j\, a_j(x) \tag{4}$$

where m is a order of the differential equation, $y(x)$ is an unknown function of independent variable x, $y^{(u)}(x)$ is u^{th} derivative of the unknown function $y(x)$ $\left(y^{(u)}(x) = d^u y(x)/dx^u\right)$, $\eta_u(x)$ is a polynomial variable coefficient for u^{th} derivation of the differential equation, g is the order of a polynomial on the right side of the differential equation, q_j is a constant coefficient for j^{th} power of the right side polynomial. Function $a_j(x)$ is an auxiliary function for polynomial formulation

$$\begin{aligned} a_j(x) &= \frac{x^j}{j!} \qquad j > 0 \\ a_j(x) &= 1 \qquad j = 0 \\ a_j(x) &= 0 \qquad j < 0 \end{aligned} \tag{5}$$

Polynomial coefficients $\eta_u(x)$ of the differential equation (4) for $u = \{0; m\}$ can be written as:

$$\begin{aligned} \eta_u(x) &= \sum_{r=0}^{p_u} \rho_{ur}(x) \\ \rho_{ur}(x) &= \eta_{ur}\, a_r(x) \end{aligned} \tag{6}$$

where η_{ur} is a constant coefficient for r^{th} power of polynomial for u^{th} derivation, p_u is an order of polynomial for u^{th} derivation and $a_r(x)$ is an auxiliary function according to (5) for polynomial formulation.
According to this notation, derivation and integration of polynomial can be written in general form:

$$\begin{aligned} a_j^{'}(x) &= a_{j-1}(x) \\ \int_0^x a_j(x) &= a_{j+1}(x) \end{aligned} \tag{7}$$

Then the solution of the differential equation (4) has according to [1] the form:

$$y(x) = \sum_{j=0}^{m-1} y_0^{(j)}\, c_j(x) + \sum_{j=0}^{g} q_j\, b_{j+m}(x) \tag{8}$$

where $y_0^{(j)}$ is j^{th} derivative of the function $y(x)$ at the position $x = 0$ $\left(y_0^{(j)} = y^{(j)}(x)|_{x=0}\right)$, $c_j(x)$ is a transfer function for uniform solution of the differential equation and $b_{j+m}(x)$ is a

transfer function for particular solution of the differential equation (4).
Then the derivative of the solution (8) has a form:

$$y^{(u)}(x) = \sum_{j=0}^{m-1} y_0^{(j)}\, c_j^{(u)}(x) + \sum_{j=0}^{g} q_j\, b_{j+m}^{(u)}(x) \tag{9}$$

For $u = 0$ is Eq. (9) equal to Eq. (8). The solution (8) of the differential equation (4) and its derivatives (9) can be written in the matrix form:

$$\begin{aligned}\begin{bmatrix} y(x) \\ y'(x) \\ y''(x) \\ \vdots \\ y^m(x) \end{bmatrix} &= \begin{bmatrix} c_0 & c_1 & c_2 & \dots & c_{m-1} \\ c_0' & c_1' & c_2' & \dots & c_{m-1}' \\ c_0'' & c_1'' & c_2'' & \dots & c_{m-1}'' \\ \vdots & \vdots & \vdots & \ddots & \\ c_0^m & c_1^m & c_2^m & \dots & c_{m-1}^m \end{bmatrix} \cdot \begin{bmatrix} y_0 \\ y_0' \\ y_0'' \\ \vdots \\ y_0^m \end{bmatrix} \\ &+ \begin{bmatrix} b_m & b_{m+1} & b_{m+2} & \dots & b_{j+m} \\ b_m' & b_{m+1}' & b_{m+2}' & \dots & b_{j+m}' \\ b_m'' & b_{m+1}'' & b_{m+2}'' & \dots & b_{j+m}'' \\ \vdots & \vdots & \vdots & \ddots & \\ b_m^m & b_{m+1}^m & b_{m+2}^m & \dots & b_{j+m}^m \end{bmatrix} \cdot \begin{bmatrix} q_0 \\ q_1 \\ q_2 \\ \vdots \\ q_g \end{bmatrix}\end{aligned} \tag{10}$$

The solution (8) and its derivatives (9) of the differential equation (4) are based on determination of the transfer functions generally labelled $c(x)$ and $b(x)$. The calculation of functions $b_{j+m}^{(u)}(x)$ is based on the use of power series and recursive process, considering $u = \{0; m\}$ and $j = \{0; g\}$. It is necessary to guarantee the convergence of the series for a given interval $x \in \langle 0; L\rangle$ for successful calculation of these functions. It is always fulfil for differential equation with constant coefficients η_u but for differential equation with variable (polynomial) coefficients $\eta_u(x)$ it is often necessary to divide the interval of x into the shorter sections (in our case the independent variable is geometric variable, for example $x = L$ is the length of the bar), and thus determine the solution also for inner region of the bar (where $x \in (0; L)$). This division of the interval is implemented in an algorithm. Calculated functions $b_{j+m}^{(u)}(x)$ are used for next calculation of the functions $c_j^{(u)}(x)$, where $u = \{0; m\}$ and $j = \{0; m-1\}$.

2.2 Recursive calculation of the transfer functions using the power series

We can write (6) again:

$$\rho_{ur}(x) = \eta_{ur}\, a_r(x) \tag{11}$$

with assumption for $u = \{0; m\}$ and $r = \{0; p_u\}$.
Let us introduce the following equation:

$$\widetilde{\rho}_{ur}(x) = \rho_{m-u,r}(x)\frac{x^u}{\eta_{m0}} \tag{12}$$

where $u = \{0; m\}$ and $r = \{0; p_{m-u}\}$.
The calculation itself is based on determining of the power series members $e_s^{(u)}$:

$$b_j^{(u)} = \sum_{s=0}^{\infty} e_s^{(u)}(x) \tag{13}$$

where $j = \{m; \max j\}$ and $u = \{0; m\}$. The value max$j$ = max(j_e, j_g) where $j_e = m+g$ ensures correct calculation for the high order of the polynomial on the right-hand side of the differential equation (order of the right-hand side polynomial is higher than order of any polynomial on the left-hand side of the differential equation) and the value $j_g = \max(p_t - t + 2m - 1)$ where $t = \{0; m-1\}$ ensures correct calculation for the high order of the polynomials for derivatives on the left-hand side of the differential equation.
First members of the series $(s = 0)$ are:

$$e_0^{(u)}(x) = \frac{a_{j-u}(x)}{\eta_{m0}} \tag{14}$$

Next members for $s = 0$ are calculated using matrix $\varepsilon_{s,ur}(x)$ where $u = \{0; m\}$ and $r = \{0; p_{m-u}\}$. For the members of matrix $\varepsilon_{0,ur}(x)$ it holds:

$$\begin{aligned} \varepsilon_{0,00}(x) &= e_0^{(m)}(x) \\ \varepsilon_{0,ur}(x) &= 0 \end{aligned} \tag{15}$$

For the rest of series members where $s > 0$ we can write a recursive rule:

$$\begin{aligned} \varepsilon_{s,ur}(x) &= \varepsilon_{s-1,u,r-1}(x); \quad u = \{0; m\}, r = \{1; p_{m-u}\} \\ \varepsilon_{s,u0}(x) &= \frac{\varepsilon_{s-1,u-1,0}(x)}{j - m + s}; \quad u = \{1; m\} \\ \varepsilon_{s,00}(x) &= -\Big(\sum_{u=1}^{m} \varepsilon_{s,u0}(x)\widetilde{\rho}_{u0}(x) + \sum_{u=0}^{m} \sum_{r=1}^{p_{m-u}} \varepsilon_{s,ur}(x)\widetilde{\rho}_{ur}(x) \Big) \end{aligned} \tag{16}$$

Backward recursion has then a form:

$$\begin{aligned} e_s^{(m)}(x) &= \varepsilon_{s,00}(x) \\ e_s^{(m)}(x) &= \frac{x}{j + s - u} e_s^{(u+1)}(x) \end{aligned} \tag{17}$$

where $u = \{m-1; 0\}$.

Equation (13) then can be used for calculation the functions $b_j^{(u)}(x)$. But we can see that $s \in \langle 0; \infty \rangle$ so it is necessary to choose maximum permissible limit for s. The fact of lack of convergence or divergence of the series is accepted when this limit is reached. In that case it is necessary to determine the functions $b_j^{(u)}(x)$ using shorter interval, so primary interval $x \in \langle 0; L \rangle$ needs to be divided.

The functions of uniform solution of the differential equation are calculated as follows:

$$c_j^{(u)}(x) = a_{j-u}(x) - \sum_{t=0}^{j} \sum_{r=0}^{p_t} \binom{j-t+r}{r} \eta_{tr} b_{j-t+r+m}^{(u)}(x) \tag{18}$$

where $u = \{0; m-1\}$ and $j = \{0; m-1\}$.

2.3 Characteristics of the algorithm for solving of the differential equations

The result of the calculation of the differential equation with variable coefficients and the right-hand side is the solution according to the equation (8). It should be noted that this is a solution for selected point x of the considered interval of the independent variable, so the

program is designed for calculation of values $c_j(x)$ in given point x for $j = \{0; m-1\}$ where m is the order of the differential equation. The values $b_{j+m}(x)$ for selected point x are also calculated for $j = \{0; g\}$ where g is order of the right-hand side polynomial of the differential equation. It means that functions $c(x)$ and $b(x)$ cannot be calculated analytically but only at discrete points x, where x is from interval $\langle 0; L\rangle$.

The algorithm calculates matrices of discrete values $c_j^{(u)}(x)$ and $b_{j+m}^{(u)}(x)$ in defined point x where $u = \{0; m-1\}$ represents derivative for calculations according to (9). It always holds:

$$\begin{aligned} c_j^{(u)}(x)|_{x=0} &= 1; \quad \text{if } i = u \\ c_j^{(u)}(x)|_{x=0} &= 0; \quad \text{if } i \neq u \\ c_{j+m}^{(u)}(x)|_{x=0} &= 0; \quad \text{forall } j = \{0; g\} \end{aligned} \tag{19}$$

For the calculation of $c_j^{(u)}(x)$ and $b_{j+m}^{(u)}(x)$ we do not need to know the the polynomial functions of the right side (does not enter into calculation) of the differential equation but only the degree of the right side polynomial. Its coefficients q_j are used only in the solution (8) and its derivatives (9). So we can use calcualted $c_j^{(u)}(x)$ and $b_{j+m}^{(u)}(x)$ for different coefficients q_j of the right side polynomial if its degree does not change.

Using power series gives us exact solution and because advanced numerical operations as numerical integration are not required in the calculation of the transfer functions $c_j^{(u)}(x)$ and $b_{j+m}^{(u)}(x)$ this procedure is fast and can be easy implemented into the FEM code. Only the differential equations with one independent variable can be solved and the variable coefficients and the term on the right side of the differential equation has to be polynomial.

The whole procedure of calculation transfer functions $c_j^{(u)}(x)$ and $b_{j+m}^{(u)}(x)$ is described in [1] in detail - the block diagram of this procedure is shown in Figure 1. This approach for calculation differential equation with non-constant parameters was implemented into the software Mathematica [5].

3 NUMERICAL EXAMPLE

Let us consider differential equation of 2^{nd} order on the interval $y \in \langle 0, L\rangle$, $L = 0.1$ with non-constant polynomial coefficients:

$$\eta_2(x)y''(x) + \eta_1(x)y'(x) + \eta_0(x)y(x) = q \tag{20}$$

where

$$\begin{aligned} \eta_0 =& -637\,500\,000\,000x^4 + 146\,625\,000\,000x^3 - 10\,965\,000\,000x^2 \\ &+ 267\,750\,000x + 60\,000 \\ \eta_1 =& \frac{129\,417\,900}{121}x^2 - \frac{12\,941\,790}{121}x \\ \eta_2 =& \frac{43\,139\,300}{121}x^3 - \frac{6\,470\,895}{121}x^2 + \frac{2\,217\,793}{7\,260} \\ q =& -6\,375\,000\,000\,000x^4 + 1\,459\,950\,000\,000x^3 - 109\,650\,000\,000x^2 + \\ &+ 2\,742\,500\,000x + 610\,000 \end{aligned} \tag{21}$$

with boundary conditions:

$$y[0] = y_0 = 10 \qquad y'[L] = y_L = -122.623 \tag{22}$$

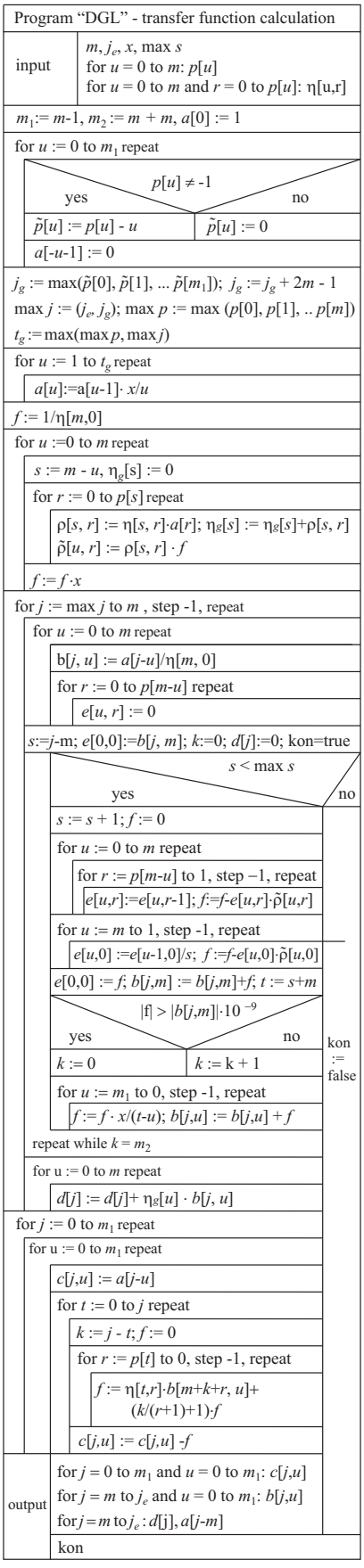

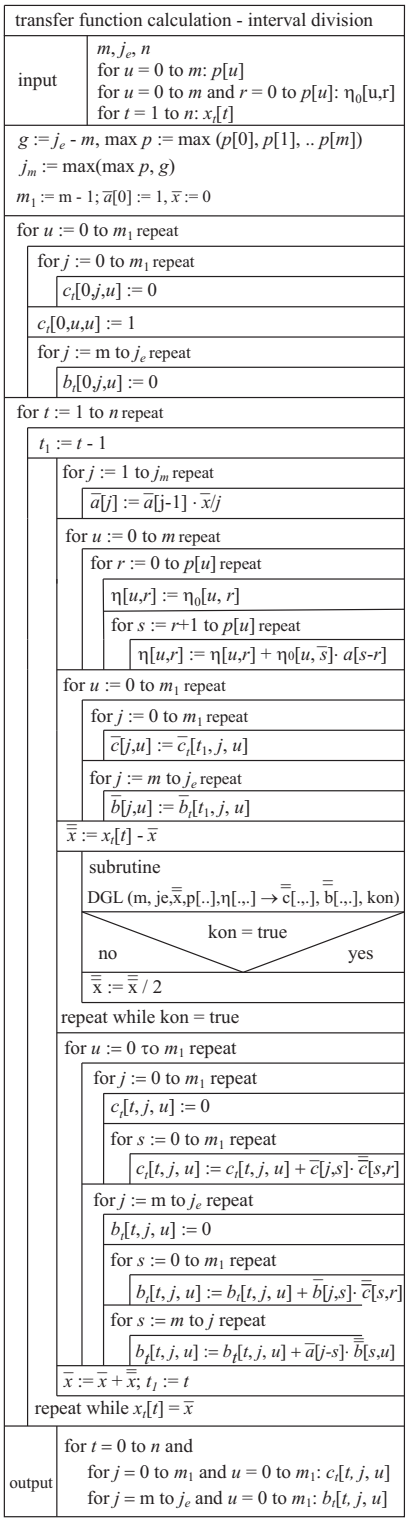

Figure 1: Block diagram of calculation transfer functions [1]

This differential equation can represent differential equation for heat transfer (consideration of the convective effect and internal heat generation) in the form:

$$-\lambda(x)\frac{d^2T(x)}{dx^2} - \frac{d\lambda}{dx}\frac{xT(x)}{dx} + \alpha(x)T(x)\frac{o}{A} = Q(x) + \alpha(x)T_{amb}\frac{o}{A} \tag{23}$$

where we consider that thermal conductivity $\lambda(x)$ [Wm^{-1}K^{-1}], coefficient of convective heat transfer $\alpha(x)$ [Wm^{-2}K^{-1}] and volume heat $Q(x)$ [Wm^{-3}] are polynomial functions. A is a cross-section of the bar, o is a perimeter ot the bar ant T_{amb} is a constant ambient temperature.

The solution of differential equation (20) according to (8) is:

$$y(x) = \sum_{j=0}^{m-1=1} y_0^{(j)} c_j(x) + \sum_{j=0}^{g=4} \varepsilon_j b_{j+2}(x) = c_0(x)y_0 + c_1(x)y_0' + \sum_{j=0}^{g=4} \varepsilon_j b_{j+2}(x) \tag{24}$$

where $m = 2$ and $g = 4$. The transfer functions $c_j^{(u)}(x = L)$ and $b_{j+m}^{(u)}(x = L)$ for differential equation (20) with non-constant coefficient (21) according the proposed method have a form:

$$c_j^{(u)}(x = L) = \begin{bmatrix} c_0 & c_1 \\ c_0' & c_1' \end{bmatrix} = \begin{bmatrix} 202.258 & 3.33436 \\ 9722.66 & 160.297 \end{bmatrix} \tag{25}$$

$$b_{j+m}^{(u)}(x = L) = \begin{bmatrix} b_2 & b_3 & b_4 & b_5 & b_6 \\ b_2' & b_3' & b_4' & b_5' & b_6' \end{bmatrix} = \tag{26}$$

$$= \begin{bmatrix} -0.000159832 & -2.67325 \times 10^{-6} & -4.87898 \times 10^{-8} & -8.52047 \times 10^{-10} & -1.33152 \times 10^{-11} \\ -0.007846 & -0.000141612 & -2.89679 \times 10^{-6} & -5.68637 \times 10^{-8} & -9.91117 \times 10^{-10} \end{bmatrix}$$

The solution of differential equation (20) according the proposed method for $n = 50$ internal points compared with solution obtained by numerical solution in software Mathematica [5](explicit RungeKutta method) is shown in Figure 2 and its first derivative is shown in Figure 3.

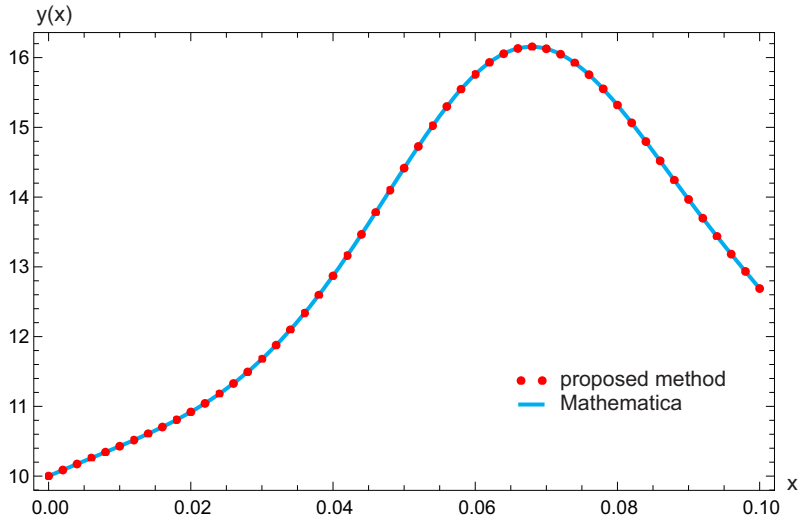

Figure 2: The solution of differential equation

As it can be seen in Figures 2 and 2, a very good agreement of both solution results has been obtained.

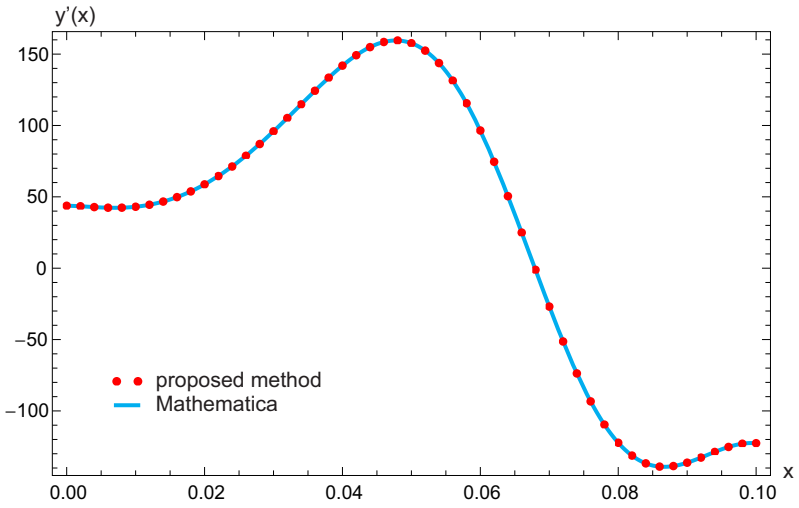

Figure 3: The 1^{st} derivation of the solution of differential equation

4 CONCLUSIONS

In this contribution the approach for solving differential equation with non-constant (polynomial) coefficient has been presented. The general solution of the homogeneous differential equation is formulated with the transfer functions $c_j^{(u)}(x)$ and the particular solution with $b_{j+m}^{(u)}(x)$. The transfer functions $b_{j+m}^{(u)}(x)$ are calculated with the help of series formulas and then the functions $c_j^{(u)}(x)$ may be determined with these $b_{j+m}^{(u)}(x)$.

The numerical example solution of differential equation of $2^n d$ order with non-constant polynomial coefficients using proposed approach and comparison with results obtained in software Mathematica have been . On base of the transfer relations the effective matrix of the 3D beam finite elements for modal, structural and buckling analysis [2][3] or coupled electro-thermo-mechanical analysis [4] of the FGM single beams and beam structures can be established. Material properties of the FGM can vary in all three direction x, y, z. Homogenization of the spatially varying material properties in the real FGM beam (material properties vary in all three direction) and the calculation of effective parameters of the homogenized beam (material properties vary only in longitudinal direction) are done by the extended mixture rules and the multilayer method.

Acknowledgement: This work was supported by the Slovak Research and Development Agency under the contract No. APVV-0246-12 and APVV-14-0613, by Grant Agency VEGA, grant No. 1/0228/14 and 1/0453/15.

REFERENCES

[1] H. Rubin, Analytische Lsung linearer Differentialgleichungen mit vernderlichen Koeffizienten und baustatische Anwendung. *Bautechnik*, **76**, 225–231, 1999.

[2] Murin, J., Aminbaghai, M., Hrabovsky, J., Kutis, V., Paulech, J., Kugler, S. A new FGM beam finite element for modal analysis. *11th World Congress on Computational mechanics (WCCM XI)*, Barcelona, July 20-25, 2014

[3] Murin, J., Aminbaghai, M., Hrabovsky, J., Kutis, V., Paulech, J. 3D beam finite element for elastic-static analysis of the FGM structures. *8th ICCSM: International congress of croatian society of mechanics*. Opatija, Croatia. September 29 - October 2, 2015, ISBN 978-953-7539-21-9.

[4] Paulech, J. ,Hrabovsky, J., Murin, J., Kutis, V. Analysis of actuator system made of FGM using new electro-thermo-mechanical finite elements. *Coupled problems in science and engineering VI. Coupled problems 2015: 6th International conference on computational methods for coupled problems in science and engineering*. Venice, Italy, May 18-20, 2015. ISBN 978-84-943928-3-2.

[5] Wolfram S. MATHEMATICA 5, Wolfram research, Inc., 2003.

ECCOMAS Congress 2016
VII European Congress on Computational Methods in Applied Sciences and Engineering
M. Papadrakakis, V. Papadopoulos, G. Stefanou, V. Plevris (eds.)
Crete Island, Greece, 5–10 June 2016

TWO-WAY COUPLED ELECTRO-THERMAL ANALYSIS OF FGM SYSTEM CALCULATED BY THE NEW LINK FINITE ELEMENT

Juraj Paulech[1], Vladimír Kutiš[1], Juraj Hrabovský[1], Justín Murín[1], Roman Gogola[1], Tibor Sedlár[1], Gabriel Gálik[1]

[1] Department of Applied Mechanics and Mechatronics, Institute of Automotive Mechatronics, Faculty of Electrical Engineering and Information Technology, Slovak University of Technology in Bratislava
Ilkovičova 3, 812 19 Bratislava, Slovakia
e-mail: juraj.paulech@stuba.sk

Keywords: Thermoelectric Analysis, FGM Link Finite Element, ANSYS.

Abstract. *The paper deals with derivation process of new FEM equations for steady thermoelectric two-way coupled analysis of link conductor made of Functionally Graded Material (FGM). One example of coupled analysis will be introduced to demonstrate accuracy and effectiveness of our new approach in computer modelling of such systems.*

INTRODUCTION

Nowadays, new materials are necessary for sophisticated structures like MEMS systems, advanced electronic devices, etc. Computer modelling of such complex systems, like structures with spatial variation of material properties (e.g. FGM) are, using commercial FEM code with classic elements, needs remarkable effort during preparation phase and sufficient computer equipment for solution phase because of necessity the numbers of elements and material models.

Finite elements for electric-thermal analyses of FGM materials considering Joule heat have been developed in [1]. This paper deals with derivation of new link finite element for two-way coupled static thermoelectric analyses considering Joule heat and also thermoelectric effects like Seebeck and Peltier effects. These effects describe direct conversion of thermal energy into electric energy (Seebeck effect) and conversion of electric energy into the temperature difference within the system (Peltier effect).

Let us consider straight link conductor, the conductor is a slender construction. Let the conductor is made of a mixture of two or more materials so its thermal, electric and thermoelectric material properties change according to chosen function. Under these conditions, we can consider one-dimensional system of differential equations and original method further explained in [2] for solving the differential equations for thermoelectric coupled analysis.

HOMOGENIZATION OF MATERIAL PROPERTIES

Let us consider FGM conductor with length L [m], and rectangular cross-section area A [m^2] (height h [m] and width b [m]) with nodes symbolically denoted "0" and "L", see Figure 1.

Let the conductor is made of mixture of two component materials – matrix (index m) and fibre (index f). Let the change of material properties is only in longitudinal and transversal direction (2D change). Let the thermal conductivities λ_m and λ_f, and electric conductivities σ_m and σ_f are known values for matrix and fibre, respectively. Then, according to the homogenization process described in [1] we can calculate homogenized thermal and electric conductivities for whole conductor. These homogenized material properties need to be polynomials.

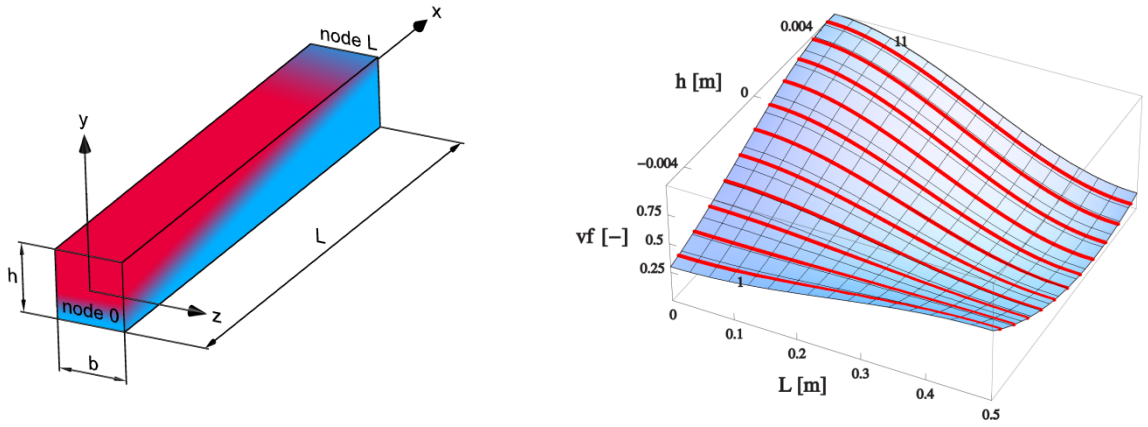

Figure 1: FGM conductor (left) and fibre volume fraction in the conductor – division into layers (right)

Homogenization process supposes that volume fractions of matrix and fibre are known and have also polynomial form, see Figure 1. Then, homogenization includes two steps:

- In the first step the real link is transformed to a multilayered link, real link is divided into chosen number of layers in transversal direction ($N = 11$ for the case shown in Figure 1). The extended mixture rule [3] is used for calculation of material properties of the layers. Then, each layer will have constant volume fraction and material properties of the constituents through its height, see Figure 2. Polynomial variation of these parameters will appear only in the longitudinal direction of the layers.
- In the next step, these layers will be used for calculation of homogenized material properties for whole link (see Figure 2) according to laminate theory described in [4]. This homogenized material properties will interpret material changes in the whole FGM link and they will have polynomial form with just one independent variable (x).

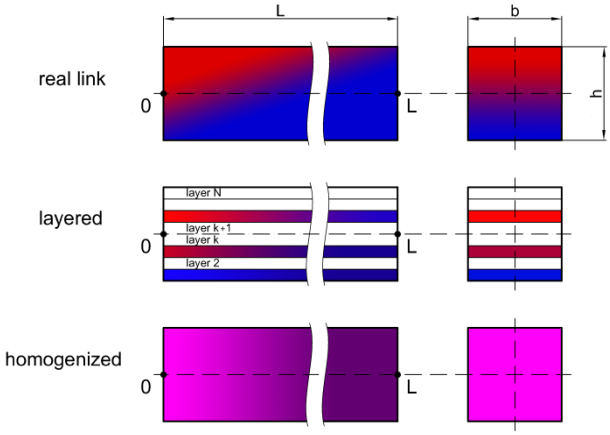

Figure 2: Graphic form of the homogenization process

For thermoelectric coupling that results in Seebeck and Peltier effects, Seebeck coefficient $\alpha(x, y)$ of the whole conductor needs to be known. This material property cannot be calculated according to the homogenization process based on extended mixture rule and laminate theory, because this material property is not given according to volume fractions of individual material components (expect the Joule heat, thermoelectric effects are significant especially for semiconductor materials and the behaviour of the semiconductors is given according to atomic structure, not according to volume fraction of individual admixtures). Moreover, the value of Seebeck coefficient can also be negative number. The determination of final Seebeck coefficient according to material properties of individual components is beyond the scope of this article. For our model case the final Seebeck coefficient will be chosen as a polynomial function $\alpha(x)$ for longitudinal direction of the homogenized conductor.

MATHEMATICAL BACKGROUND FOR TWO-WAY COUPLED THERMOELECTRIC ANALYSIS

Thermoelectric and electric-thermal effects like Joule heat, Seebeck, Peltier and Thomson effects are described by set of two thermoelectric constitutive equations (static analysis) [5]:

$$\begin{aligned} \mathbf{q} &= [\![\Pi]\!] \cdot \mathbf{J} - [\![\lambda]\!] \cdot \nabla T \\ \mathbf{J} &= [\![\sigma]\!] \cdot (\mathbf{E} - [\![\alpha]\!] \cdot \nabla T) \end{aligned} \tag{1}$$

where $\mathbf{q}$ [Wm^{-2}] is heat flux vector, $\mathbf{J}$ [Am^{-2}] is electric current density vector, $[\![\Pi]\!]$ [V] is Peltier coefficient matrix, $[\![\lambda]\!]$ [Wm^{-1}K^{-1}] is thermal conductivity matrix, T [K] is absolute

temperature, $\mathbf{E}$ [Vm^{-1}] is electric field intensity vector, $[\![\sigma]\!]$ [Sm^{-1}] is electric conductivity matrix and $[\![\alpha]\!]$ [VK^{-1}] is Seebeck coefficient matrix.

These constitutive equations are coupled by set of governing equations for static thermal and electric fields:

$$\begin{aligned} \nabla \cdot \mathbf{q} &= P \\ \nabla \cdot \mathbf{J} &= 0 \end{aligned} \tag{2}$$

where P [Wm^{-3}] is heat generation per volume unit.

In general, we can write for electric field intensity, Peltier coefficient and heat generation:

$$\begin{aligned} \mathbf{E} &= -\nabla\varphi & P &= P_J + P_{aux} \\ [\![\Pi]\!] &= T[\![\alpha]\!] & P_J &= [\![\sigma]\!]^{-1}\mathbf{J}^2 \end{aligned} \tag{3}$$

where φ [V] is electric potential, P_J [Wm^{-3}] is Joule heat per volume unit and P_{aux} [Wm^{-3}] is auxiliary heat generation per volume unit.

Applying (1) and (3) into (2) we can write for 1D system (longitudinal direction x):

$$\begin{aligned} \frac{d}{dx}[T(x)\alpha(x)J(x)] - \frac{d}{dx}\left[\lambda(x)\frac{dT(x)}{dx}\right] &= \frac{J^2(x)}{\sigma(x)} + P_{aux}(x) \\ \frac{d}{dx}\left[\sigma(x)\frac{d\varphi(x)}{dx}\right] + \frac{d}{dx}\left[\sigma(x)\alpha(x)\frac{dT(x)}{dx}\right] &= 0 \end{aligned} \tag{4}$$

DERIVATION OF NEW FGM EQUATIONS FOR FGM LINK CONDUCTOR

We can use the method for solving 1D differential equation with non-constant coefficients and with right-hand side described in [2] for our system of equations (4). But all non-constant coefficients on the left-hand side and right-hand side itself have to be in polynomial form (it is the condition of used approach). So general formulation of one-dimensional differential equation suitable for the method has the form:

$$\sum_{u=0}^{m} \eta_u(x) y^{(u)}(x) = \sum_{j=0}^{g} \varepsilon_j a_j(x) \tag{5}$$

where:

m	– degree of the differential equation
$y(x)$	– unknown function of independent variable x
$y^{(u)}(x)$	– u^{th} derivation of the unknown function
$\eta_u(x)$	– polynomial variable coefficient for u^{th} derivation on the left-hand side of the differential equation
g	– degree of a polynomial on the right-hand side of the differential equation
ε_j	– constant coefficient for j^{th} power of the right-hand side polynomial
$a_j(x) = \frac{x^j}{j!}$	– auxiliary function for the right-hand side polynomial formulation

at which $x \in \langle 0; L \rangle$, where L is the length of considered interval of unknown solution.

Considering function $a_j(x)$ for formulation the polynomials, we can write general rules for derivation and integration of such function:

$$\begin{aligned} a_j'(x) &= a_{j-1}(x) \\ \int_0^x a_j(x)\,dx &= a_{j+1}(x) \end{aligned} \tag{6}$$

According to [2] the solution of the differential equation (5) has the form:

$$y(x) = \sum_{i=0}^{m-1} y_0^{(i)} c_i(x) + \sum_{j=0}^{g} \varepsilon_j b_{j+m}(x) \tag{7}$$

where:

$y_0^{(i)}$ i^{th} derivation of the function y in $x = 0$, thus $y_0^{(i)} = y^{(i)}(x)\big|_{x=0}$

$c_i(x)$ function for uniform solution of the differential equation

$b_{j+m}(x)$ function for particular solution of the differential equation

And derivation of the solution (7) is in the form:

$$y^{(u)}(x) = \sum_{i=0}^{m-1} y_0^{(i)} c_i{}^{(u)}(x) + \sum_{j=0}^{g} \varepsilon_j b_{j+m}^{(u)}(x) \qquad u = \{0, m-1\} \tag{8}$$

The solution of differential equation (7) lies in determining the functions generally labelled $c(x)$[1] and $b(x)$ that appear in the solution.

The result of calculation of the differential equation with variable coefficients and the right-hand side is the solution according to equation (7). It should be noted that this is a solution for selected point x of the considered interval of independent variable, so the program is designed for calculation of values $c_i(x)$ in given point x for $i = \{0, m-1\}$ where m is the degree of the differential equation. Then the values $b_{j+m}(x)$ for selected point x are also calculated for $j = \{0, g\}$ where g is degree of the right-hand side polynomial of the differential equation. It means that functions $c(x)$ and $b(x)$ cannot be calculated analytically but only at discrete points x, where x is from interval $\langle 0; L \rangle$.

The program algorithm, also described in [2], efficiently calculates matrixes of discrete values $c_i^{(u)}(x)$ and $b_{j+m}^{(u)}(x)$ for user defined point x where $u = \{0, m-1\}$ represents derivation for calculations according to (8).

It should be noted that the polynomial function of the right-hand side of the differential equation itself does not enter into the calculation. For the calculation of $c(x)$ and $b(x)$ it is only necessary to know the degree of the right-hand side polynomial. The values of the coefficients ε_j of the right-hand side only enter into the final equation – solution (7) or derivation (8), respectively.

Programming code offers the possibility of automatic uniform interval division calculation, and the values of $c(x)$ and $b(x)$ for interval dividing points are included in the output. So during single run of the program we can get all the necessary values to solve the differential equation also for selected internal points in the interval $x \in (0; L)$, in our case for conductor inner region.

This program for solving differential equations is used in process of deriving new FEM equations for two-way coupled thermoelectric analysis in FGM link conductor mentioned above. Figure 3 shows geometry and physical quantities used during the derivation process.

[1] denoting is symbolical – general; correctly it should be mentioned that it is a set of values $c_i(x)$ within the range $i = \{0, m-1\}$; it is also similar for $b_j(x)$ with the range $j = \{0, m-1\}$

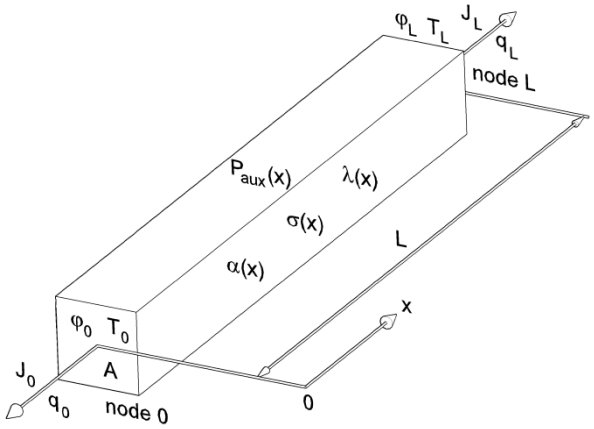

Figure 3: Two-nodal conductor for thermoelectric analysis

Let us write the governing function (4) for heat flux in the form suitable for calculation according [2]. Comparing the general form of the differential equation (5) with governing function (4) in expanded form:

$$\sum_{u=0}^{m} \eta_u(x) y^{(u)}(x) = \sum_{j=0}^{g} \varepsilon_j a_j(x) \tag{9}$$

$$-\lambda(x)T''(x) + [\alpha(x)J(x) - \lambda'(x)]T'(x) + \left[\alpha'(x)J(x) + \alpha(x)J'(x)\right]T(x) = \frac{J^2(x)}{\sigma(x)} + P_{aux}(x)$$

we get:

$m = 2$ – degree of the differential equation

$y(x) \equiv T(x)$ – unknown function of independent variable x is function of temperature

$y^{(u)}(x) \equiv T^{(u)}(x)$ – u^{th} derivation of unknown temperature

$\eta_0(x) = \alpha'(x)J(x) + \alpha(x)J'(x)$ – 0^{th} derivation of the temperature on the left-hand side of the differential equation

$\eta_1(x) = \alpha(x)J(x) - \lambda'(x)$ – non-constant coefficient of the 1st derivation of the temperature

$\eta_2(x) = -\lambda(x)$ – non-constant coefficient of the 2nd derivation

$g > 0$ – degree of the polynomial on the right-hand side

ε_j – constant coefficient of the j^{th} power of the right-hand side polynomial

$a_j(x) = \frac{x^j}{j!}$ – auxiliary function for formulation of polynomial

Now, we can rewrite the solution of the differential equation for our case and its derivation:

$$T(x) = \sum_{i=0}^{1} T_0^{(i)} c_i(x) + \sum_{j=0}^{g} \varepsilon_j b_{j+2}(x) = c_0(x)T_0 + c_1(x)T_0' + \sum_{j=0}^{g} \varepsilon_j b_{j+2}(x) \tag{10}$$

$$T'(x) = c_0'(x)T_0 + c_1'(x)T_0' + \sum_{j=0}^{g} \varepsilon_j b_{j+2}'(x) \tag{11}$$

Let us write again the constitutive equation (1) for 1D heat flux:

$$q(x) = T(x)\alpha(x)J(x) - \lambda(x)T'(x) \tag{12}$$

Let the boundary conditions for thermal field are:

$$T(L) = T_L \qquad q(0) = q_0 \tag{13}$$

Then we can put together equation (12) expressed for position $x = 0$ (position at node 0) and equation (10) expressed for $x = L$ (node L), and using boundary conditions (13) after some mathematical operations we can write in matrix form (lower index "0" and "L" for used physical quantities means that concerned quantity is evaluated for position $x = 0$ or $x = L$, respectively):

$$\begin{bmatrix} c_0(L) + \frac{\alpha_0 J_0}{\lambda_0} c_1(L) & -1 \end{bmatrix} \begin{bmatrix} T_0 \\ T_L \end{bmatrix} = \left[\frac{c_1(L)}{\lambda_0} q_0 - \sum_{j=0}^{g} \varepsilon_j b_{j+2}(L) \right] \tag{14}$$

Now, let the boundary conditions are changed:

$$T(0) = T_0 \qquad q(L) = q_L \tag{15}$$

Then we can put together equation (12) expressed for position $x = L$, equation (11) expressed for node L and equation (10) expressed for node L, and using boundary conditions (15) after some mathematical operations we can write in matrix form:

$$\begin{bmatrix} c_0(L) - \frac{c_1(L) c_0'(L)}{c_1'(L)} & \frac{c_1(L)\alpha_L J_L}{c_1'(L)\lambda_L} - 1 \end{bmatrix} \begin{bmatrix} T_0 \\ T_L \end{bmatrix} = \left[\frac{c_1(L)}{c_1'(L)} \left(\frac{q_L}{\lambda_L} + \sum_{j=0}^{g} \varepsilon_j b_{j+2}'(L) \right) - \sum_{j=0}^{g} \varepsilon_j b_{j+2}(L) \right] \tag{16}$$

The matrixes (14) and (16) can be put together. Comparing mathematical formulation and FEM formulation of our task we can find out, that there is sign difference in heat flux at node L (heat flux at node L for FEM formulation has opposite direction than it is in mathematical formulation). Considering these facts we get the system of FEM equations for thermal field in the conductor:

$$\begin{bmatrix} c_0(L) + \frac{\alpha_0 J_0}{\lambda_0} c_1(L) & -1 \\ c_0(L) - \frac{c_1(L) c_0'(L)}{c_1'(L)} & \frac{c_1(L)\alpha_L J_L}{c_1'(L)\lambda_L} - 1 \end{bmatrix} \begin{bmatrix} T_0 \\ T_L \end{bmatrix} = \begin{bmatrix} \frac{c_1(L)}{\lambda_0} q_0 - \sum_{j=0}^{g} \varepsilon_j b_{j+2}(L) \\ \frac{c_1(L)}{c_1'(L)} \left(\frac{-q_L}{\lambda_L} + \sum_{j=0}^{g} \varepsilon_j b_{j+2}'(L) \right) - \sum_{j=0}^{g} \varepsilon_j b_{j+2}(L) \end{bmatrix} \tag{17}$$

We can also evaluate the temperature within the range of the conductor. Using equation (12) expressed for node 0 and substituting it into equation (10) then we can write:

$$T(x) = c_0(x) T_0 + c_1(x) \frac{T_0 \alpha_0 J_0 - q_0}{\lambda_0} + \sum_{j=0}^{g} \varepsilon_j b_{j+2}(x) \tag{18}$$

Now, comparing the general form of the differential equation (5) with governing function (4) for electric current density in expanded form:

$$\sum_{u=0}^{m} \eta_u(x) y^{(u)}(x) = \sum_{j=0}^{g} \varepsilon_j a_j(x) \tag{19}$$

$$\sigma(x)\varphi''(x) + \sigma'(x)\varphi'(x) = -\alpha'(x)\sigma(x)T'(x) - \alpha(x)\sigma'(x)T'(x) - \alpha(x)\sigma(x)T''(x)$$

we get:

$m = 2$ – degree of the differential equation
$y(x) \equiv \varphi(x)$ – unknown function of independent variable x is function of el. potential
$y^{(u)}(x) \equiv \varphi^{(u)}(x)$ – u^{th} derivation of unknown electric potential
$\eta_0(x) = 0$ – 0^{th} derivation of the potential is not present on the left-hand side

$\eta_1(x) = \sigma'(x)$ – non-constant coefficient of the 1st derivation of the potential
$\eta_2(x) = \sigma(x)$ – non-constant coefficient of the 2nd derivation of the potential
$g > 0$ – degree of the polynomial on the right-hand side
ε_j – constant coefficient of the j^{th} power of the right-hand side polynomial
$a_j(x) = \frac{x^j}{j!}$ – auxiliary function for formulation of polynomial of the right side

Similar to the derivation process for thermal field we can derive also FEM equations for electric field:

$$\begin{bmatrix} -c_0(L) & 1 \\ -c_0(L) + \dfrac{c_1(L)c_0'(L)}{c_1'(L)} & 1 \end{bmatrix} \begin{bmatrix} \varphi_0 \\ \varphi_L \end{bmatrix} = \begin{bmatrix} -\dfrac{c_1(L)}{\sigma_0} J_0 - c_1(L)\alpha_0 T_0' + \displaystyle\sum_{j=0}^{g} \varepsilon_j b_{j+2}(L) \\ -\dfrac{c_1(L)}{c_1'(L)} \left(\dfrac{-J_L}{\sigma_L} + \alpha_L T_L' + \displaystyle\sum_{j=0}^{g} \varepsilon_j b_{j+2}'(L) \right) + \displaystyle\sum_{j=0}^{g} \varepsilon_j b_{j+2}(L) \end{bmatrix} \tag{20}$$

And similar to the equation (18) for thermal field we can also evaluate the electric potential within the range of the conductor:

$$\varphi(x) = c_0(x)\varphi_0 - c_1(x)\left(\frac{J_0}{\sigma_0} + \alpha_0 T_0'\right) + \sum_{j=0}^{g} \varepsilon_j b_{j+2}(x) \tag{21}$$

The temperature and electric potential are primary variables for thermal and electric field analyses, respectively. Calculating the secondary variables, like heat flux and electric current density, is possible using equation (1) expressed for one-dimensional task. But this is suitable only for 1D model where we calculate one longitudinal distribution of the heat flux or electric current density for homogenized model, respectively. However, our 1D model results from real 3D FGM conductor, so it is more realistic to calculate the secondary variables in layers that were considered during homogenization process (see [1] for details).

FEM equations for two-way coupled thermoelectric analysis are equations (17) and (20). They are solved using iterative algorithm. During iteration process it is necessary to find substitutional functions for results obtained from FEM equations (results of these FEM equations are not continuous functions but only sets of discrete values) and also it is necessary to convert non-polynomials into polynomials (e.g. see P_J in equation (3)). Iteration process can be set ahead by evaluating equations (1) expressed for one-dimensional task also within individual iterative steps.

THERMOELECTRIC ANALYSIS OF FGM LINK CONDUCTOR - NUMERICAL EXPERIMENT

In this chapter there will be one academic example of thermoelectric analysis of given FGM link conductor presented. The task will be solved using our new approach, by commercial FEM code ANSYS and also by numerical solution of differential equations in software Mathematica due to comparison reasons.

Let us consider electric conductor with rectangular cross-section according to Figure 1. Its length is $L = 500$ [mm], height $h = 10$ [mm] and width $b = 20$ [mm]. Let the conductor consists of mixture of two component materials – matrix (index m) with constant electric conductivity $\sigma_m(x, y) = 1.429 \times 10^6$ [Sm^{-1}] and thermal conductivity $\lambda_m(x, y) = 2$ [$\text{Wm}^{-1}\text{K}^{-1}$], and fibre (index f) with electric conductivity $\sigma_f(x, y) = 1.111 \times 10^7$ [Sm^{-1}] and thermal conductivity $\lambda_m(x, y) = 400$ [$\text{Wm}^{-1}\text{K}^{-1}$]. Volume fraction of individual com-

ponents is functionally changed according to chosen polynomial, graphically shown in Figure 1:

$$v_f(x,y) = 0.7125 - 7.2214x^2 + 9.6286x^3 + 92.500y - 1658.57x^2y + 2211.43x^3y - 2500y^2 + 1.5514 \times 10^5 x^2y^2 - 2.0686 \times 10^5 x^3y^2 - 9 \times 10^5 y^3 + 1.08 \times 10^7 x^2y^3 - 1.44 \times 10^7 x^3y^3 \ [-]$$

$$v_m(x,y) = 1 - v_f(x,y) \ [-]$$

Using extended mixture rule for chosen number of layers ($N = 11$) we get longitudinal variation of effective electric and thermal conductivities for individual layers and using laminate theory we can calculate also homogenized electric and thermal conductivity of FGM conductor, see Figure 4.

The equations of homogenized electric and thermal conductivities are:

$$\sigma^H(x) = 8.1273 \times 10^6 - 5.7507 \times 10^7 x^2 + 7.6676 \times 10^7 x^3 \ [\mathrm{Sm^{-1}}]$$

$$\lambda^H(x) = 277.352 - 2363.82x^2 + 3151.77x^3 \ [\mathrm{Wm^{-1}K^{-1}}]$$

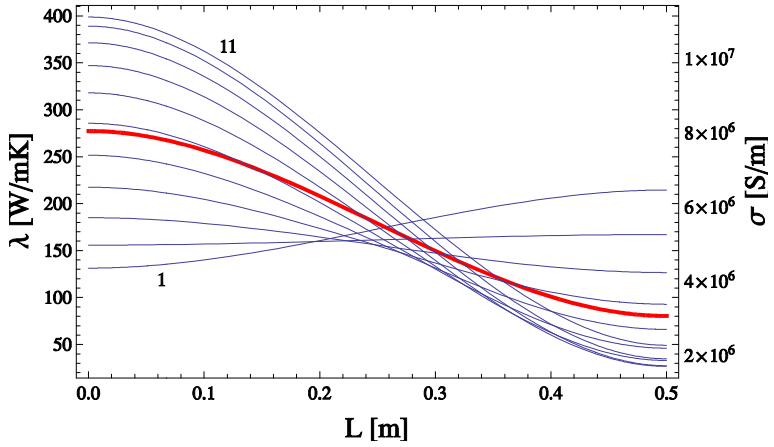

Figure 4: Longitudinal distribution of the homogenized electric and thermal conductivity (red) and the effective electric and thermal conductivities in respective layers for $N = 11$ (blue)

Let us consider final Seebeck coefficient for whole conductor according to chosen polynomial function (academic example, without considering homogenization process based on mixture of the components):

$$\alpha(x) = -4 \times 10^{-4} + 28 \times 10^{-4} x^2 \ [\mathrm{VK^{-1}}]$$

We assume static state for thermoelectric analysis. In nodes 0 and L there are electric potentials and temperatures specified and there is variable auxiliary heat generation in the conductor, so boundary conditions (see Figure 5) are:

$$\varphi(0) = 0.11 \ [\mathrm{V}]; \quad T(0) = 273 \ [\mathrm{K}]$$

$$\varphi(L) = 0 \ [\mathrm{V}]; \quad T(L) = 283 \ [\mathrm{K}]$$

$$P_{aux}(x) = 2 \times 10^5 - 6.4 \times 10^6 x^5 \ [\mathrm{Wm^{-3}}]$$

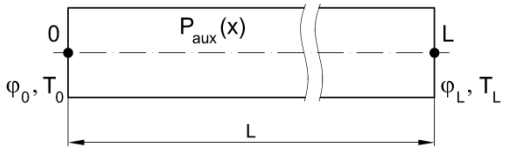

Figure 5: Boundary conditions of the model

We also created 2D model in code ANSYS [6], we used 55 000 PLANE223 elements (8 node quad-elements). The task was also solved in software Mathematica [7], where the differential equations (4) with specified boundary conditions and homogenized material properties were numerically solved using iterative algorithm. Finally, the task was also solved by only one our new developed two-nodal link element using FEM equations (17) and (20) for nodal points of the link and with equations (18) and (21) for chosen points within the link. In Figure 6 and Figure 8 we can see calculated longitudinal distribution of the electric potential and temperature in the conductor, respectively. In Figure 7 and Figure 9 there are shown distributions of the electric current densities and heat fluxes for chosen layers (1st, 6th and 11th layer), respectively. Summary of calculated results is in Table 1.

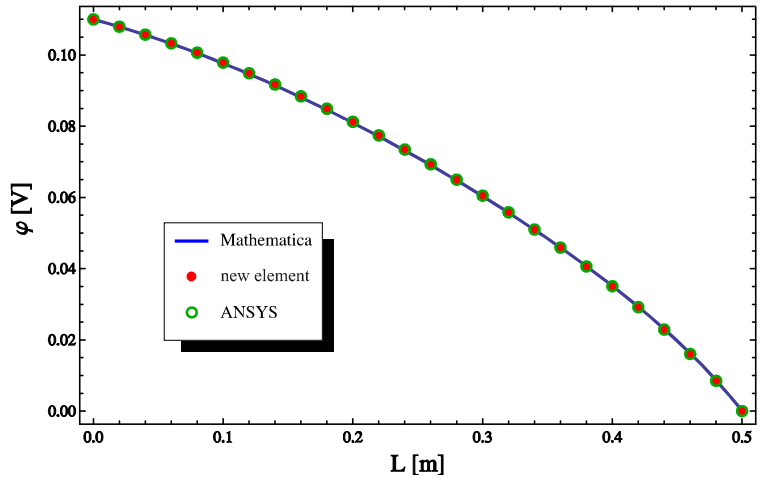

Figure 6: Distribution of the electric potential through the length of conductor

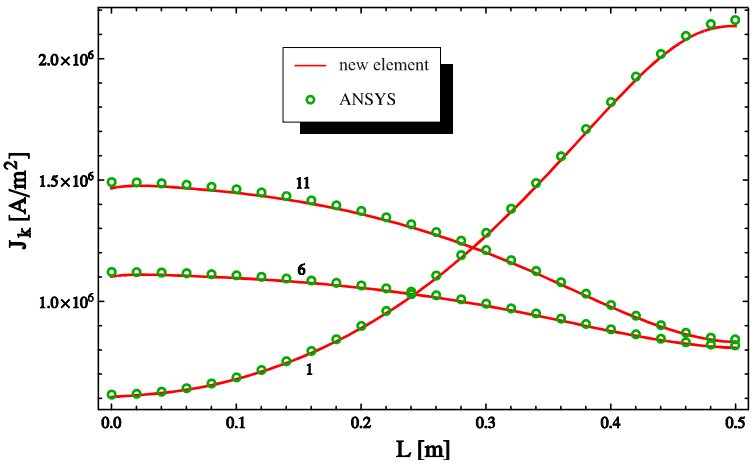

Figure 7: Longitudinal distribution of the current densities in the chosen layers of conductor

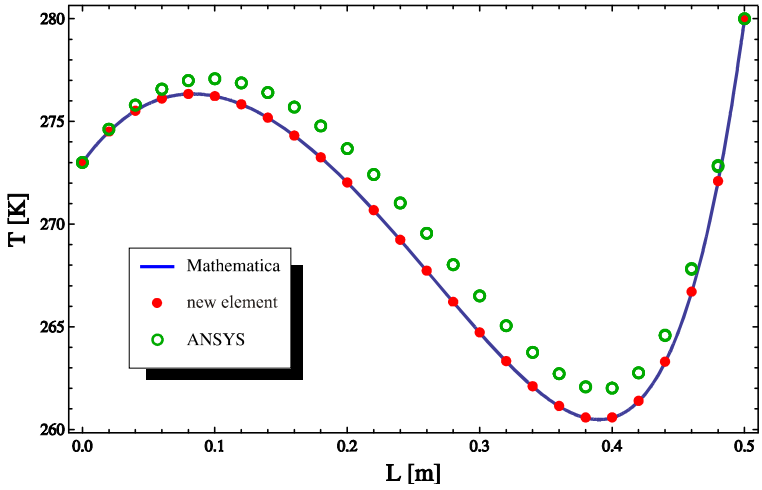

Figure 8: Distribution of the temperature through the length of conductor

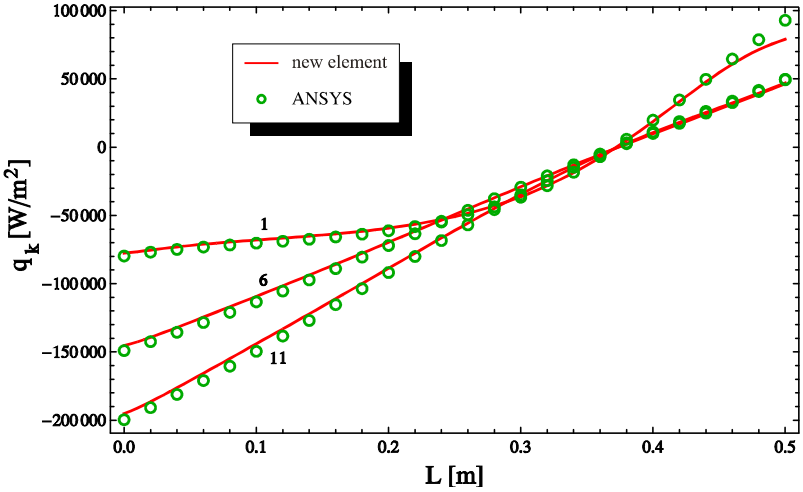

Figure 9: Longitudinal distribution of the heat fluxes in the chosen layers of conductor

$J_{\text{layer,node}}$ $\times 10^5$ [Am^{-2}]	$J_{1,0}$	$J_{1,L}$	$J_{6,0}$	$J_{6,L}$	$J_{11,0}$	$J_{11,L}$	J_0^H	J_L^H
new element	6.0532	21.3455	11.0189	8.0888	14.6612	8.3291	10.8288	10.8288
ANSYS	6.1584	21.5903	11.2089	8.1852	14.9130	8.4328	-	-
Mathematica	-	-	-	-	-	-	10.8274	10.8274
$q_{\text{layer,node}}$ $\times 10^4$ [Wm^{-2}]	$q_{1,0}$	$q_{1,L}$	$q_{6,0}$	$q_{6,L}$	$q_{11,0}$	$q_{11,L}$	q_0^H	q_L^H
new element	-7.7619	7.9057	-14.5377	4.6420	-19.5074	4.7011	-14.2730	5.2933
ANSYS	-7.9756	9.2951	-14.9012	4.9339	-19.9653	4.9732	-	-
Mathematica	-	-	-	-	-	-	-14.1887	5.2594

Table 1: Comparison of calculated electric and thermal quantities for chosen layers and homogenized values in nodal points of the conductor

There is small difference in the results (secondary variables) between ANSYS solution and calculation using the new approach in nodal points because of substitutional functions used for conversion non-polynomials into polynomials during iterative process. But we can see

from Figure 6 – Figure 9 that obtained results correspond to ANSYS 2D simulation very well. Differences in the results for primary variables in the conductor inner region are due to fact that our approach is based on reduction of the real 3D system into 1D problem.

CONCLUSIONS

New finite link element for two-way coupled static thermoelectric analyses has been developed in this contribution. New FEM equations with consideration Joule heat, auxiliary heat, and thermoelectric effects, like Seebeck and Peltier effects, were derived. Numerical example with good agreement between calculations with just only one new link element and commercial FEM code that uses numbers of classic elements have been presented. The new approach fully agrees with numerical solution for 1D differential equation of thermal and electric fields calculated using iterative algorithm. So, effectiveness and accuracy of the new developed link element for these analyses are excellent.

ACKNOWLEDGEMENT

This work was supported by the Slovak Research and Development Agency under the contract No. APVV-0246-12 and APVV-14-0613, by Grant Agency VEGA, grant No. 1/0228/14 and 1/0453/15.

REFERENCES

Murín, J. et al.: Electric-Thermal Link Finite Element Made of a FGM with Spatial Variation of Material Properties. *In: Composites Part B: Engineering*. ISSN 1359-8368. Vol. 42 (2011), p. 1966-1979.

Rubin, H.: Analytische Lösung linearer Differentialgleichungen mit veränderlichen Koeffizienten und baustatische Anwendung. *Bautechnik 76*. (1999)

Murín, J., Kutiš, V.: Improved mixture rules for the composite (FGM's) sandwich beam finite element. *In: Computational Plasticity IX. Fundamentals and Applications*. Barcelona. (2007), p. 647-650

Altenbach, H. et al.: Mechanics of composite structural elements. *Springer-Verlag*. Berlin. (2003), 468 p.

Antonova, E., Looman, D.: Finite Elements for Thermoelectric Device Analysis in ASNYS. *In: ICT International Conference*. Clemson SC USA. (2005), p. 215-218

ANSYS Swanson Analysis System, Inc., 201 Johnson Road, Houston, PA 15342/1300, USA.

S. Wolfram MATHEMATICA 5, Wolfram research, Inc., (2003)

ECCOMAS Congress 2016
VII European Congress on Computational Methods in Applied Sciences and Engineering
M. Papadrakakis, V. Papadopoulos, G. Stefanou, V. Plevris (eds.)
Crete Island, Greece, 5–10 June 2016

PROGRESSIVE COLLAPSE FRAGILITY MODELS OF RC FRAMED BUILDINGS BASED ON PUSHDOWN ANALYSIS

Emanuele Brunesi[1], Roberto Nascimbene[1], and Fulvio Parisi[2]

[1] EUCENTRE, European Centre for Training and Research in Earthquake Engineering
Via Ferrata 1, 27100 Pavia, Italy
{emanuele.brunesi, roberto.nascimbene}@eucentre.it

[2] Dept. of Structures for Engineering and Architecture, University of Naples Federico II
Via Claudio 21, 80125 Naples, Italy
fulvio.parisi@unina.it

Keywords: RC buildings, robustness, progressive collapse, fragility analysis, fiber modeling, pushdown analysis.

Abstract. *Partial or total progressive collapse under abnormal loading conditions (e.g. deliberate terrorist attacks, uncontrolled gas releases, and vehicle or aircraft impacts) is one of the most vivid examples of low probability-high consequence (LPHC) event that may occur in the lifetime of a structure. Despite this, structural safety for extreme loads that may lead to disproportionate (or progressive) collapse has been probabilistically assessed and controlled in a few cases, thus neglecting uncertainties in loads and system capacity. As such, this paper moves from a deterministic to a probabilistic framework, proposing fragility models at multiple damage states for low-rise reinforced concrete (RC) framed bare structures which may be applied for progressive collapse risk assessment and management. Two building classes representative of structures designed for either gravity loads or earthquake resistance in accordance with current European rules were investigated. Monte Carlo (MC) simulation was used to generate random realizations of two-dimensional (2D) and three-dimensional (3D) structural models. Their fiber-based finite element (FE) representations were developed within an open source platform for nonlinear static pushdown analysis. The output consisted of fragility functions for each damage state of interest. Such fragility models were then compared to those derived through incremental dynamic analysis (IDA) in a previous study. IDA-based and pushdown-based capacities were additionally used to propose regression models for quick estimation of dynamic amplification factor (DAF) at a given displacement/drift target. The analysis results show a significant influence of both seismic design/detailing and secondary beams on robustness of the case-study building classes.*

1 INTRODUCTION

Accidental and man-made extreme events such as impacts, fires or explosions can induce abnormal loads on building structures, which in turn may suffer heavy damage and finally experience a partial or total building collapse. This depends on the fact that structural systems designed according to conventional approaches are not necessarily able to withstand extreme loads. To confirm this scenario, several residential, iconic and public buildings resulted in significant casualties and property loss as a consequence of a disproportionately high propagation of direct damage to their key components [1-5].

Following the early interest in blast- and progressive collapse-resistant building analysis and design, which was triggered by the 1968 partial collapse of Ronan Point tower in UK, the occurrence of further dramatic accidents and deliberate attacks either in urban or industrial environments has led homeland security to become a primary concern for public authorities and stakeholders, causing the protection of structures against extreme loads to have a larger and larger impact on economy and society. Several definitions of progressive collapse, the most known of which is based on the significant disproportion in size between the initial and final damage configurations, have appeared in the literature [6-12]. Acting on building exposure, the contribution of nonstructural protective measures such as barriers, sacrificial elements and limitation or control of public access have been reaffirmed to be crucial in order to increase structural safety and to mitigate progressive collapse-related risk in a cost-effective manner. Moving from passive to active strengthening strategies, extensive efforts have been more recently made in design and simulation [13-35] to propose approaches and rules for structural integrity and robustness against abnormal loads. Codified methodologies [13-16] have emerged in the last two decades providing design guidelines to inhibit cascade or domino effects as a result of a local failure, which progresses in time to a collapse encompassing the entire structure or essential parts of it. Focusing on performance of structures and structural components, the key role played by requirements such as robustness, integrity, continuity, redundancy and ductility has been recognized [17-19]. Besides direct and indirect design provisions prescribed in codes and standards [13-16], a huge amount of analytical studies on blast and progressive collapse phenomena have been done [11, 12, 17-35], thus quantifying the influence of modeling assumptions and analysis techniques. Solid or shell FE [25, 28, 33, 34], lumped-plasticity [18, 22-24, 26, 27] and spread-plasticity [11, 12, 17, 19, 25, 29-32, 35] approaches have been examined for progressive collapse analysis of different building typologies ranging from civilian to strategic and military facilities. In this respect, conventional or alternative pushdown procedures and implicit or explicit nonlinear dynamic analyses have been explored using general purpose codes or open platforms.

Despite the large number of deterministic investigations, probabilistic approaches have been applied to a lesser extent in this field and a few research works have appeared in the literature so far (see e.g. [1, 6, 36-41]), emphasizing the need for probabilistic risk assessment and management of disproportionate collapse under blast loads and/or sudden column loss scenarios. In light of this, a framework for fragility analysis of European RC framed buildings was implemented, integrating fiber-based FE modeling with Monte Carlo simulation for random realizations of structural prototypes and pushdown analysis techniques for progressive collapse assessment. Two 4-story building populations, each of which analyzed using two types of numerical representation (i.e. 2D models and 3D models), were studied in a probabilistic fashion in order to propose fragility models at multiple damage states. The former class was designed only for gravity loads according to Eurocode 2 (EC2) [42], and the latter was designed for earthquake resistance in compliance with Eurocode 8 (EC8) [43]. For each building class under consideration (i.e. EC2-compliant structures and EC8-compliant structures),

fragility analysis was based on (i) the random generation of 2D and 3D fiber-based models through MC simulation, (ii) pushdown analysis of each structural model including dynamic effects in a simplified manner [15], and (iii) derivation of fragility functions for each structural model and damage state of interest. Considering design criteria and structural idealizations, four groups of fragility models were presented, thus quantifying the sensitivity of progressive collapse to design rules (i.e. seismic or non-seismic) and redistribution capacity of secondary beam systems. A comparison was then provided between such pushdown-based fragility models and those obtained by Brunesi et al. [40] using incremental-mass nonlinear dynamic analysis. Finally, the influence of dynamic effects on progressive collapse potential was estimated by taking advantage of IDA-based predictions [40] and pushdown capacity curves, which were determined without introducing any aprioristic amplification factor for specific structural portions. Pushdown and IDA estimates resulting from the application of the same uniform mass/load distribution over the entire structure were normalized in order to construct a set of DAF-vertical displacement/drift curves and to fit a corresponding regression model for each building class and structural representation under study, thus permitting a quick analytical assessment of DAF at a given displacement/drift design target.

2 FRAGILITY ANALYSIS: METHODOLOGY AND PROCEDURES

In a general framework for probabilistic risk analysis (PRA) using either hazard- or scenario-based approaches, the annual probability of disproportionate collapse can obtained through the conditional probabilities of two limit states: (1) local damage given an extreme event, and (2) global (structural) collapse given a local damage [6]. These two conditional probabilities can be in turn quantified using a multilevel analysis where uncertainties related to abnormal loading and structural system are modeled and propagated. The probability of damage to structural components and systems can be then obtained by means of reliability computations in which demand is convolved with capacity [44]. As such, PRA is a quantitative and rational tool for an effective risk-informed decision making process in case of LPHC events and fragility analysis can be considered as one of its fundamental components, which is indeed used in conventional risk management techniques to investigate and describe the physical vulnerability of a population of buildings or structural assemblies to specific damage scenarios. Although such concepts currently pertain to a well-established approach for disaster mitigation in earthquake engineering (see e.g. [45-50]), only a few applications have been recently presented for disproportionate collapse under blast loads and/or sudden column loss scenarios [36-41].

Several methodologies may be proposed to provide a mathematical formulation to vulnerability, either in terms of damage probability matrices or vulnerability curves, and there cannot be a unanimous consensus on a unique approach for derivation of vulnerability models to be implemented in PRA, due to a variety of structural modeling options, analysis techniques, and damage criteria. Even though any model with its level of sophistication presents peculiar advantages and drawbacks, the development of fragility models is recognized to be a key aspect for disaster mitigation actions, as those functions characterize the conditional probability of exceeding a certain damage level for a prescribed load intensity. The conditional probability may be defined as follows:

$$P_{ik} = P\left[D \geq d_i \middle| S = s_k\right] \tag{1}$$

where D is the damage measure (DM) used to describe structural or nonstructural damage, S is the scalar or vector-valued intensity measure (IM) used to describe the load intensity, and P_{ik} is the probability that the damage level d_i is reached or exceeded for a given IM level s_k.

Therefore, vulnerability to progressive collapse may be regarded as a measure of how prone a building is to damage for a given severity of the selected column removal scenario and the corresponding fragility models at multiple damage states may be regarded as a graphical representation of vulnerability to this type of mechanism, providing estimates of the proportion of a building class falling within discrete damage bands from a specified IM.

In light of the aforementioned considerations, this study presents a probabilistic mechanics-based assessment procedure for fragility analysis of structures subjected to disproportionate collapse. Analytical fragility curves were derived in case of gravity-load designed [42] and earthquake resistant [43] RC framed buildings. As discussed in the following, concepts of methodologies developed for earthquake engineering applications [45-50] and recently applied in this field [39, 40] were integrated with specific analysis techniques for progressive collapse simulation. A flowchart presenting the proposed routine and their prevailing components is shown in Fig. 1, while the rationale behind this framework is summarized hereafter.

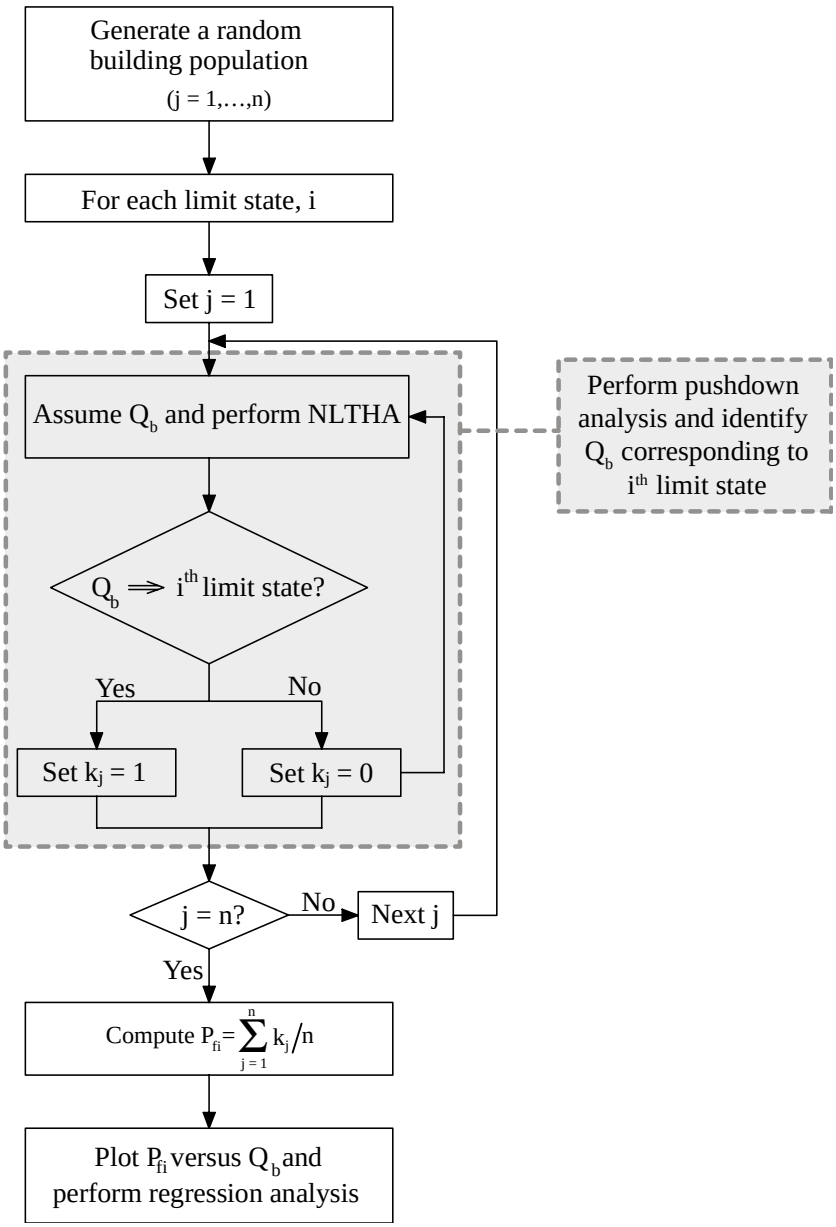

Figure 1: Flowchart for derivation of progressive collapse fragility models.

According to Brunesi et al. [40], fragility was estimated by means of a MC simulation consisting of the following three steps:

1) Generation of the building population which implied modeling of random variables (RVs) in compliance with statistics and probability distribution functions for material properties, geometrical parameters and design loads.
2) Damage analysis of each random realization which implied identifying simulated design criteria and numerical modeling strategies to predict progressive collapse potential and assess whether a prescribed amount of damage at a given IM level is reached or not.
3) Analytical derivation of progressive collapse fragility which implied adopting procedures for nonlinear regression analysis in order to fit cumulative fragility points, after that capacity and demand were convolved.

In this latter step, the distribution of buildings in each damage state of interest was used to derive the statistical parameters – i.e. mean (μ), standard deviation (σ) and coefficient of determination (R^2) – of each lognormal fragility function, fitting discrete points from damage probability matrices through the least squares technique. To evaluate progressive collapse fragility, several thousands of structural prototypes for each building class were randomly generated on the basis of statistics and probability distributions for each RV, as specified in Section 3, and their capacity was estimated by means of classical fiber force-based [51] FE approaches commonly adopted in earthquake [46, 48, 50, 52] and progressive collapse analysis [11, 12, 17, 19, 25, 29-32, 35, 40]. To this aim, pushdown simulation techniques [11, 17, 18, 23, 24, 31] rather than IDA procedures [19, 26, 40] were implemented and the downward load on beams (Q_b) was assumed as reference IM. Three criteria, either at local/sectional or global/structural levels, were selected for the identification of limit states corresponding to slight damage (LS1), significant damage (LS2) and complete damage (LS3), thus allowing the evaluation of structural performance. Based on capacity/demand convolution, fragility models for EC2-compliant [42] and EC8-compliant [43] buildings analyzed using either 2D or 3D prototypes were finally computed, allowing a two-way comparison between functions obtained (i) by different design solutions for the same type of structural representation (i.e. EC2-conforming versus EC8-conforming), and (ii) by different modeling types for the same design rules (i.e. 2D versus 3D).

3 UNCERTAINTY MODELING AND COMPUTATIONAL STRATEGY

Pushdown analysis was implemented in a fragility analysis framework to provide the probability of exceedance of different damage states induced by column loss events. In this study, two design rules (i.e. according to EC2 [42] and EC8 [43]) and two structural idealizations (i.e. 2D and 3D models) were considered, resulting in four types of structural models each of them characterized by different kinds of uncertainty. Thousands of samples of RC framed structures were randomly generated for each of the two building populations (i.e. gravity-load and earthquake resistant prototypes). Uncertainties in geometry, material properties and loads were modeled according to Brunesi et al. [40], as a further aim of this paper is to compare IDA-based and pushdown-based fragility models, thus quantifying the mismatch between the two analysis methods. As discussed in Section 6, corrective coefficients were proposed for the statistical parameters (i.e. μ and σ) of each lognormal fragility function derived from the latter approach in direct relation to those computed through nonlinear dynamic simulations. As such, every simulation realization analyzed herein was assumed to be equal to the corresponding random idealization studied in the comparative research [40]. A summary of selected RVs with their peculiar probabilistic features was provided in the following, while more compre-

hensive details regarding the statistical background of MC sampling can be found in [40]. A similar consideration can be drawn in terms of FE idealization of each case-study of the two building classes, as specified in the upcoming discussion.

As shown in Fig. 2, the structures under study were 4-story, 4×4-bay RC framed buildings, which had a lateral force-resisting system (LFRS) composed of five primary frames connected each other by one-way RC joist slabs and continuous cast-in-situ secondary beams. Following typical layouts and building practice, the span lengths in both longitudinal and transverse directions, namely L_x and L_y, were assumed as RVs with uniform distribution in the range [4.0 m, 6.0 m]. A similar criterion was applied in past studies for random sampling associated with seismic vulnerability analysis of RC structures (see e.g. [45, 46, 48, 50]). The center-to-center plan dimensions were equal at any floor, but varied in length (*x*-direction) and width (*y*-direction) according to different random combinations of column spacing in the two directions. As progressive collapse resistance was found to be almost insensitive to changes in the interstory height [19], the latter was considered as a deterministic parameter equal to 3.0 m. Material uncertainties were taken into account by randomly selecting steel yielding strengths of 380 MPa and 450 MPa and cubic concrete strengths of 25 MPa, 30 MPa and 35 MPa, each of them assumed to have the same probability of occurrence [48]. Those values were considered as nominal strengths which were then multiplied by a normally distributed (dimensionless) RV with mean equal to 1.1 in case of reinforcing steel and 1.5 in case of concrete, and with coefficient of variation (CoV) equal to 10%. Finally, a normal distribution was assigned to dead load (DL) with mean of 3.0 kN/m^2 and CoV = 17%, whereas live load (LL) was considered as a deterministic parameter equal to 2.0 kN/m^2 because the case-study buildings were assumed to be employed for housing. In order to permit a representation of the sample in the low probability region of the distribution, the Latin Hypercube algorithm was adopted for MC sampling of RVs with normal distribution [40, 48].

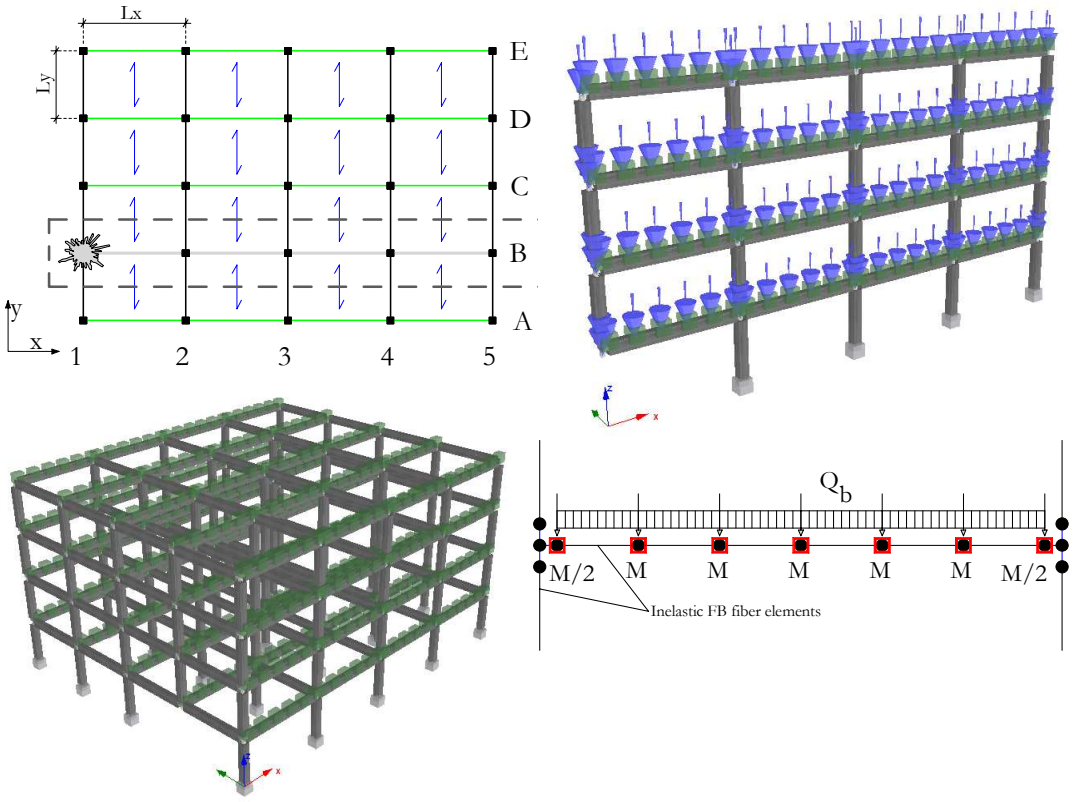

Figure 2: Example of a representative structural prototype.

Fig. 2 shows isometric and plan views of a representative building model used for damage analysis through distributed-plasticity approach and pushdown simulation techniques. While high-definition solid FE models based on classical principles of nonlinear fracture mechanics [53-55] represent an attractive solution for interpreting the evolution of crack patterns and damage mechanisms of RC structures at a local level [25, 33, 34], fiber-based idealizations were shown to be a transparent and viable approach to accurately characterize the inelastic response of such building typology in a computationally efficient manner [32]. To this aim, the open FE platform SeismoStruct [56] was adopted to prepare 2D and 3D models of EC2-compliant and EC8-compliant structures and to play out the series of pushdown analyses explicitly including material and geometric nonlinearities. Potential large displacements/rotations and P-Delta effects were taken into account using a total corotational transformation [52] and the spreading of inelasticity over the member length and cross section was reproduced through a direct integration of the uniaxial material response of individual fibers. Each inelastic beam-column element had 5 integration points and each cross section was discretized in 400 fibers to accurately represent its stress/strain state during incremental monotonic loading. A one-to-six correspondence between structural members and model elements was assumed to reduce numerical instability and accommodate the deformed shape during progressive collapse analysis (Fig. 3). A simple bilinear constitutive rule with isotropic strain hardening was assigned to reinforcing steel, whereas the uniaxial uniform confinement model proposed by Mander et al. [57] was assumed to simulate the inelastic behavior of concrete, explicitly accounting for tension softening [40].

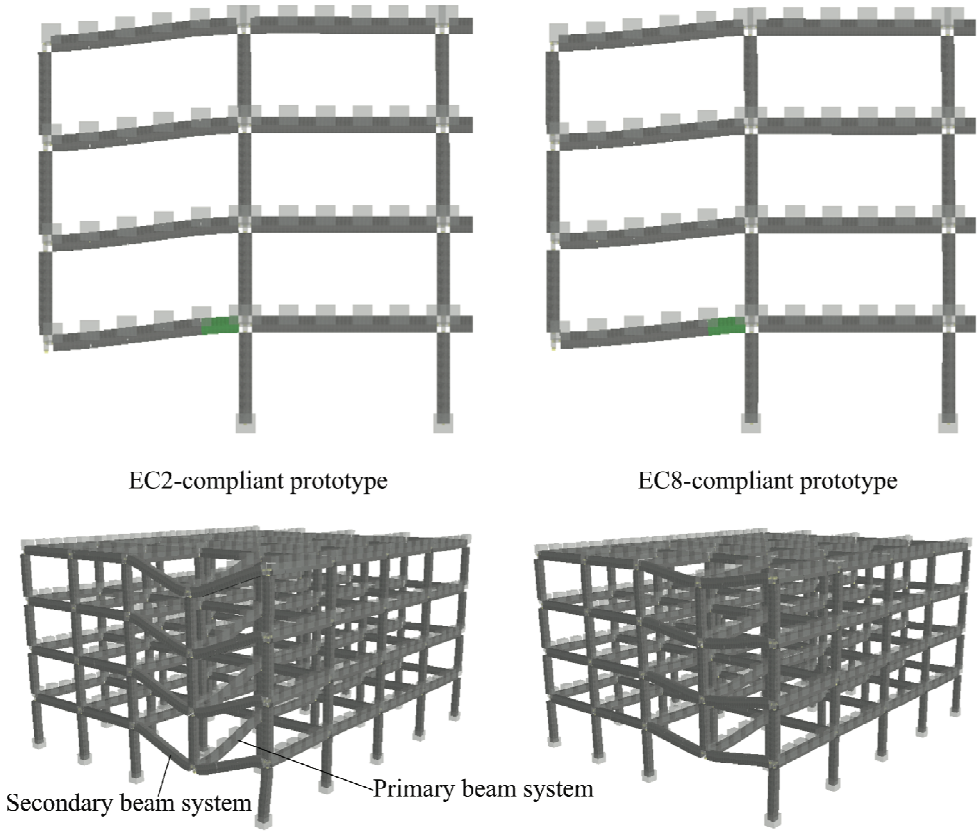

Figure 3: Deformed shapes at ultimate conditions of EC2-compliant and EC8-compliant buildings.

In order to characterize the nonlinear response of random populations of case-study buildings, two analysis types can be used in both direct and indirect progressive collapse-resistant

assessment procedures: nonlinear static (or pushdown) analysis, and nonlinear dynamic analysis. The former is a relatively simple approach and provides a load-displacement capacity curve that, similarly to seismic analysis, permits one identifying whether a structure has adequate capacity to withstand extreme loads or not, in a static fashion. Material and geometric nonlinearities such as large displacements/rotations (i.e. beam-catenary action), second order effects, coupled axial-flexural inelastic behavior and plastic hinge formation (i.e. stiffness/strength degradation and ductility exploitation) can be included in the analysis using a nonlinear static method. Nonetheless, the main disadvantage of a static simulation is the inability to take into account the dynamic behavior of a structure in case that one or more bearing elements are instantaneously removed from the frame. This loading condition may cause highly dynamic effects which in turn may lead a statically safe structure to become dynamically unsafe due to the fact that time-dependent overloads produced by column loss may induce a progressive fracture of other members before a new equilibrium state is achieved [19, 22, 29, 34, 40]. As a result of this cascade effect, a different dissipative mechanism and related propagation of damage through the cross section depth may be predicted to occur by different analysis methods. If pushdown analysis is based on the application of a monotonically increased downward load or load distribution, during dynamic analysis the structure is damaged under cyclic reversals, as it oscillates upward and downward in such a way that more closely reflects the physical nature of progressive collapse.

In light of those considerations, procedures were proposed to equivalently include dynamic effects in a static fashion whether pushdown techniques are adopted for progressive collapse assessment [14, 15, 26]. In particular, the new Unified Facility Criteria (UFC) released in 2009 [15] prescribed the application of a non-uniform downward load distribution to the structure, explicitly identifying structural portions characterized by different levels of dynamic amplification (i.e. adjacent spans and areas away from the removed column). As such, this code-compliant approach was integrated within the probabilistic simulations performed to carry out fragility analysis, thus accounting for the dynamic nature of progressive collapse phenomena in a simplified and computationally efficient manner. As discussed in [40], fragility analysis needs an iterative procedure in case of dynamic analysis because a step function with monotonically increasing magnitude is required for an aprioristic factorization of Q_b that is able to simulate the different dynamic loading conditions corresponding to attainment of each limit state for each structure realization (Fig. 1). On the other hand, a single incremental analysis can be more rapidly performed in a static fashion and directly provides a set of displacement-controlled Q_b values for each building prototype which allows one evaluating multiple damage states at once.

The effectiveness of this equivalent nonlinear static procedure [15] was evaluated in comparison with IDA estimates [40] and a further set of standard pushdown analyses [14] was carried out assuming a uniform downward load distribution consistent with that selected for vertical mass when performing dynamic simulations. Therefore, pushdown capacity curves obtained by this latter approach were normalized with respect to IDA envelopes in order to compute a series of specific force-based DAFs for the two populations of EC2-conforming and EC8-conforming case-study buildings. Regression analyses were then performed using predictions for both 2D and 3D structural models and simplified equations were proposed to allow DAF to be estimated as a function of vertical displacement/beam drift. Furthermore, sensitivity of progressive collapse potential to simulation techniques with different levels of sophistication (i.e. IDA [40] versus pushdown [15]) was probabilistically assessed in terms of fragility functions.

The prevailing trends emerged from pushdown analysis with and without consideration of equivalent dynamic effects [15], namely P1 and P2, are discussed in the following.

4 PUSHDOWN ANALYSIS OF EC2-CONFORMING STRUCTURES

In the first stage of this research, progressive collapse capacity of EC2-compliant buildings was predicted by means of 2D and 3D structural models in combination with pushdown analysis techniques including or not dynamic effects in a static fashion (i.e. P1 and P2). This allowed the authors to carry out a two-way comparison between response predictions obtained (i) by different types of structural idealization for the same type of analysis (i.e. 2D versus 3D models), and (ii) by different analysis types for the same structural representation (i.e. P1 versus P2). Thus, the influence of dynamic effects and secondary beam systems on robustness of EC2-conforming case-study prototypes was quantified. The conclusions drawn from capacity curves presented in this section were then compared to those derived for earthquake resistant building class examined in Section 5 and finally extended in terms of fragility models, as discussed in Section 6.

4.1 Two-dimensional versus three-dimensional models: EC2-compliant buildings

To assess and compare the progressive collapse potentials of gravity-load designed structures in terms of analysis method and structural modeling, an internal 2D frame was first extracted from each 3D model and then analyzed by removing the leftmost ground column. That scenario was considered as it is the most demanding single column-removal condition in case of framed buildings [19]. As shown in Fig. 4, response estimates for the 2D models were then collected and compared to those provided by nonlinear static analysis of 3D models, in order to quantify the effects of secondary beam systems in the redistribution of gravity loads from a removed column. This sensitivity was initially investigated considering the results of standard pushdown analysis (i.e. P2) and the trends observed were then compared to those obtained by pushdown assuming a non-uniform load distribution (i.e. P1), thus exploring the influence of dynamic effects and corresponding equivalent load pattern on the resisting/redistribution mechanisms enforced in both primary and secondary frames.

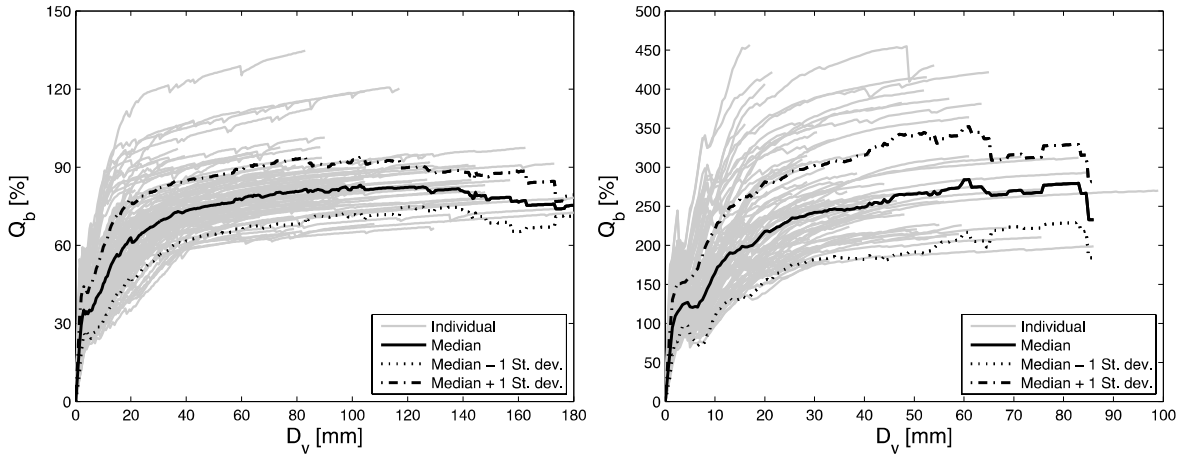

Figure 4: Pushdown (P2) curves of EC2-conforming buildings using 2D models (left) and 3D models (right).

Fig. 4 presents the set of downward load-vertical displacement curves predicted for 2D and 3D models, revealing a maximum progressive collapse capacity of about $1.35Q_b$ in case of the most resistant 2D structure. Peaks of up to $0.83Q_b$ can be observed if the median is considered, and capacities approximately lying within a ± 12% fork were shown when referring to median ± 1 standard deviation. The set of numerical predictions obtained by 3D models confirmed the significant influence of secondary framing beams on progressive collapse potential of the sys-

tem, as they provide a rationally-controlled alternative load path for the unbalanced demand induced by a column loss scenario. Given that one-way slabs were assumed according to construction practice for such buildings, secondary beams were supposed to resist only their self-weight so they were designed to comply with minimum reinforcement requirements by current European standards [42] and, hence, they can be considered as a latent resource of stiffness and strength. The redundancy provided by secondary beams or "secondary-beam effect" visibly improved the robustness of case-study prototypes, being their contribution effective in controlling the overall structural response. As a result, capacities approximately 3 times higher than those shown for 2D models were predicted in this case considering either maximum or median resistance of the EC2-compliant buildings. Slightly more scattered estimates were determined as a wider fork of up to ± 24% resulted when computing median ± 1 standard deviation. As discussed by Brunesi et al. [40], predictions suggested that these secondary members may be actively used to interact with the primary frame systems, resulting in a stiffer, stronger and more stable response under column loss-induced overloads. Due to their visible participation in primary mechanism, vertical displacement peaks more than halved can be shown when 3D and 2D models are compared (Fig. 4).

4.2 Uniform versus non-uniform load distributions: EC2-compliant buildings

In this subsection, the sensitivity of progressive collapse resistance to analysis method was investigated, focusing on gravity-load designed 2D and 3D structural models. In detail, Fig. 5 collects the series of downward load-vertical displacement capacity curves determined for the EC2-conforming population of structures by means of pushdown analysis based on the application of code-compliant [15] non-uniform load distributions able to account for different levels of dynamic amplification in specific portions of the structure. Peculiar behavioral aspects of obtained response (i.e. P1) were examined. In addition, a comparison was provided with those discussed in subsection 4.1 for conventional pushdown analysis approach (i.e. P2).

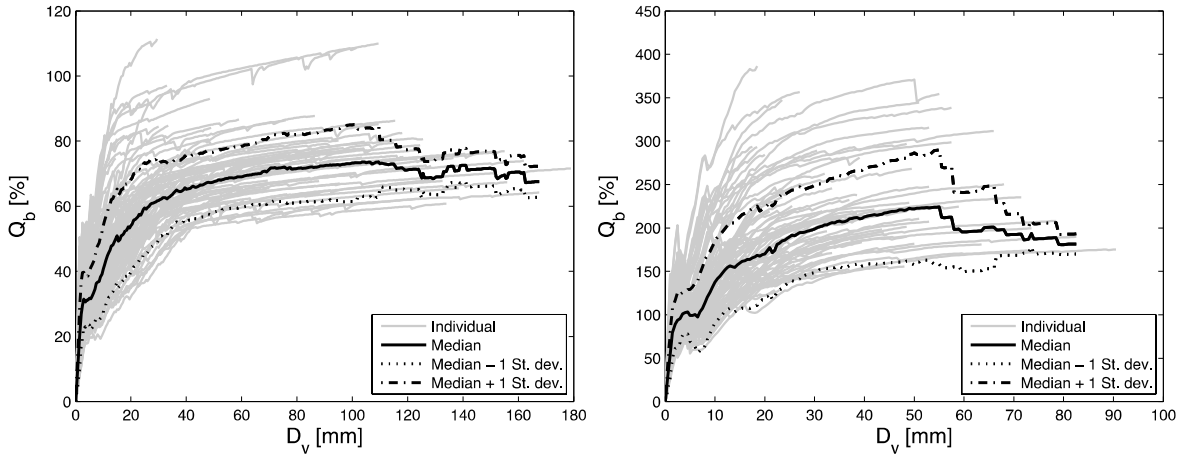

Figure 5: Pushdown (P1) curves of EC2-compliant buildings using 2D models (left) and 3D models (right).

Such an approach explicitly includes dynamic effects in a nonlinear static analysis using an equivalent/global procedure that provides a constant amount of overload dependent on plastic and yielding rotational capacity to be applied to specific structural portions more sensitive to a sudden column removal than others (adjacent spans versus areas away from the removed column). Therefore, predictions more conservative than those resulting from P2 were achieved in this case either for 2D or 3D models. Peaks of about $1.11Q_b$ and $3.86Q_b$ were predicted for the most resistant 2D and 3D structure, respectively. Such an outcome confirms the considerable

contribution provided by secondary frame elements for gravity load redistribution as a consequence of a sudden column-removal condition. As previously mentioned, 3D models resulted in capacities approximately 3 times larger than those determined in case of 2D models. Compared to P2, estimates roughly 10%-20% smaller can be observed as a consequence of equivalent dynamic effects. By contrast, similar considerations can be drawn in terms of median and standard deviation.

4.3 Regression models for DAF estimation: EC2-compliant buildings

DAF can be considered as a mechanical measure that permits one to quantify the inaccuracy of pushdown analysis in comparison with IDA for different design targets beyond the elastic range of the structure. As such, DAF was obtained as the ratio between static and dynamic capacities in terms of vertical peak resistance of the 2D or 3D structural model at a given vertical displacement. Fig. 6 presents the series of force-based DAF versus vertical displacement curves of the population of gravity-load designed structures.

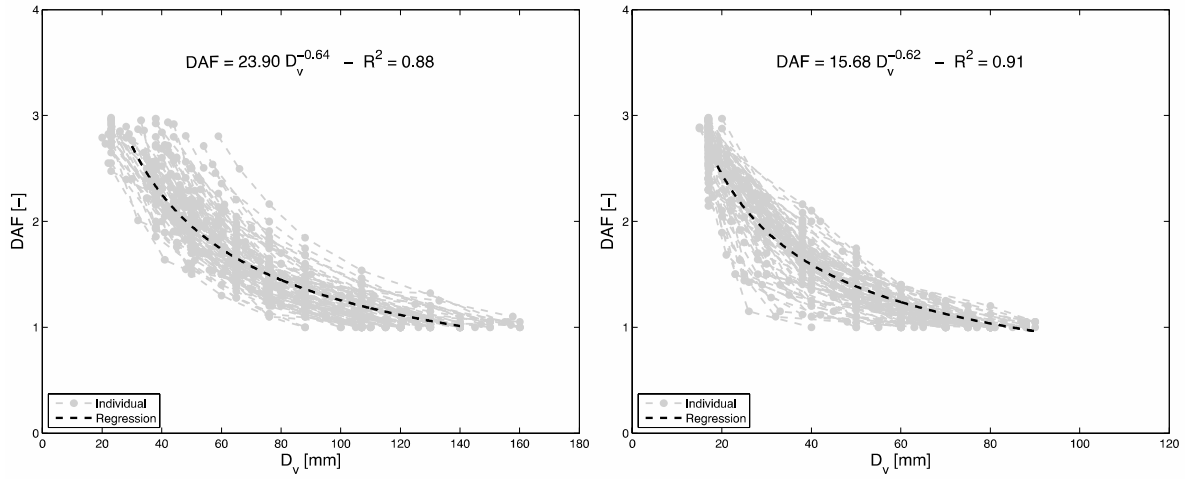

Figure 6: DAF estimates for EC2-conforming building class using 2D models (left) and 3D models (right).

To get a reliable estimate of this quantity, standard pushdown analysis (P2) was used as it is based on the application of a uniform downward load distribution, according to that assumed for nonlinear dynamic simulations [40]. The set of static-to-dynamic capacity ratios of 2D and 3D models collected in Fig. 6 were then used to conduct a regression analysis, which is aimed at providing specific analytical expressions for a quick assessment of DAF at a given vertical displacement/drift target. Accurate predictions were observed for both 2D and 3D models, as the coefficient of determination (R^2) was equal to 0.88 and 0.91, respectively.

5 PUSHDOWN ANALYSIS OF EC8-CONFORMING STRUCTURES

The procedures assumed to perform progressive collapse analysis of EC2-compliant building class were then applied to the population of EC8-compliant structures. As before, numerical simulations were carried out considering either 2D or 3D models. Pushdown analysis with and without consideration of dynamic effects was performed on prototype buildings having the same overall geometry in accordance with MC random sampling of RVs but different detailing as they were separately designed in compliance with EC2 [42] and EC8 [43]. In particular, the population EC8-conforming structures was designed for a medium-high seismicity, assuming the PGA at bedrock to be 0.30g for life safety limit state. A type C ground was selected to perform design in medium ductility class by response spectrum analysis on 3D mod-

els, incorporating accidental eccentricity of the center of mass. Further and more comprehensive details regarding simulated design criteria and related sectional properties/reinforcement layouts may be found in Brunesi et al. [40], while the prevailing numerical observations resulting from the series of pushdown analyses carried out are summarized hereafter, in direct relation to those derived for EC2-conforming case-study buildings.

5.1 Two-dimensional versus three-dimensional models: EC8-compliant buildings

The set of pushdown capacity curves obtained by 2D and 3D models are collected in Fig. 7, and reflected a visible benefit from seismic design/detailing rules. Peak force capacities 50%-70% larger than those observed in case of gravity-load designed structures were predicted for earthquake-resistant framed buildings.

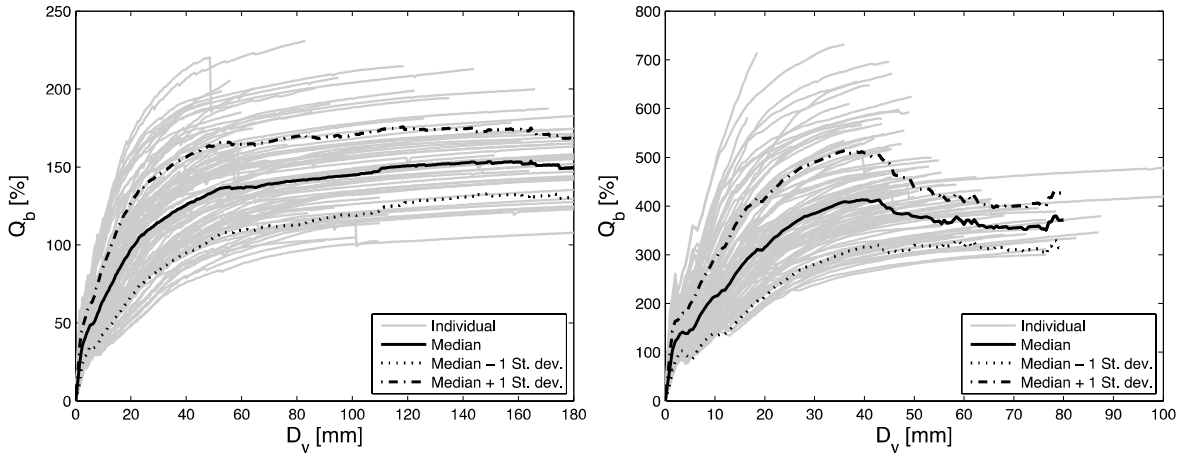

Figure 7: Pushdown (P2) curves of EC8-compliant buildings using 2D models (left) and 3D models (right).

Such an outcome is mostly due to more stable and robust flexural hinging mechanisms and arch effects/catenary actions developed in the critical portions of EC8-compliant structures, as a result of minimum seismic requirements and symmetrical arrangement of longitudinal reinforcement [43]. Compared to EC2-conforming buildings, their collapse modes were characterized by different levels of resistance, robustness, rationale and control. The EC8-conforming prototypes can displace further in the nonlinear regime of their response, or alternatively carry higher loads for a given vertical displacement. Maxima of about $2.31Q_b$ and $7.31Q_b$ were determined using 2D and 3D models, respectively. Hence, the trends emerged by comparing the responses of 2D and 3D gravity-load resistant framed structures were confirmed and corroborated even further by the series of pushdown curves shown in Fig. 7.

5.2 Uniform versus non-uniform load distributions: EC8-compliant buildings

Dynamic effects were included in progressive collapse analysis according to the equivalent procedure proposed in UFC [15], thus permitting one to evaluate their influence on robustness of EC8-conforming building class. In Fig. 8, the downward load-vertical displacement curves predicted by means of 2D models were compared to those obtained using a 3D structural idealization. The peak progressive collapse resistance was found to be equal to $2.09Q_b$ and $6.77Q_b$ in case that the strongest 2D and 3D prototypes are considered, respectively. Compared to Fig. 7, Fig. 8 reveals 10%-15% lower capacities, thus reaffirming the key role played by this code-compliant procedure in controlling the unsafety level of a standard pushdown approach. When considering the median of EC8-compliant buildings, the maximum load carrying capacity was approximately $1.39Q_b$ in case of 2D models and a ± 15% fork was observed whether referring

to median ± 1 standard deviation. On the other hand, a more than doubled peak resistance resulted from the median of 3D models, in combination with a ± 10% wider fork for median ± 1 standard deviation.

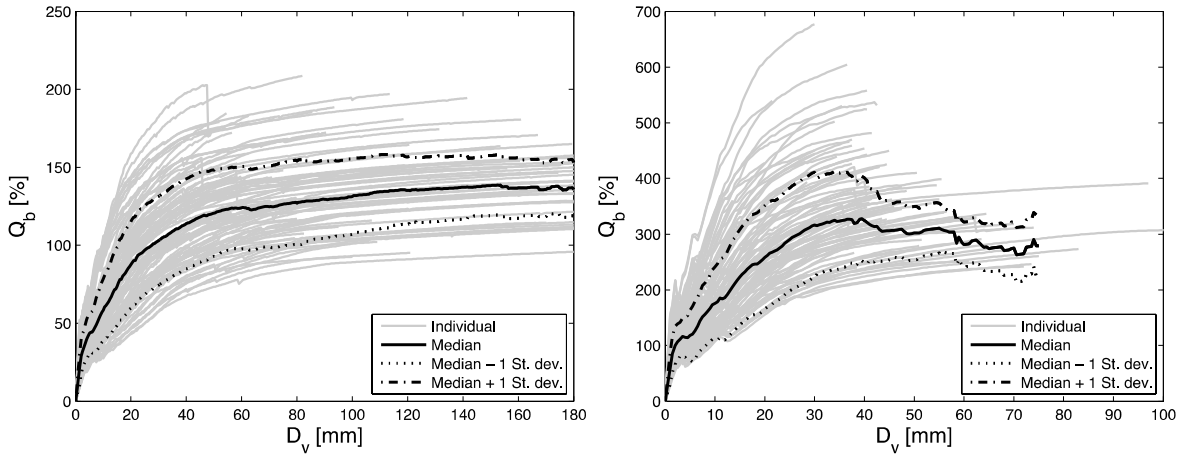

Figure 8: Pushdown (P1) curves of EC8-conforming buildings using 2D models (left) and 3D models (right).

The comparison between pushdown capacity curves of EC2-compliant and EC8-compliant random realizations (i.e. Fig. 5 versus Fig. 8) revealed trends similar to those evidenced when comparing the results of standard pushdown simulations (i.e. Fig. 4 versus Fig. 7). The significant benefit from seismic design/detailing criteria, which was highlighted for either 2D models or 3D models, can be therefore reaffirmed.

5.3 Regression models for DAF estimation: EC8-compliant buildings

Conventional pushdown predictions (i.e. P2) and IDA estimates [40] were used to quantify the discrepancy between the two simulation techniques at different levels of inelastic demand for column loss-induced overloads. As done in case of EC2-conforming prototypes, an exponentially decaying model was fitted to the series of static-to-dynamic capacity ratios obtained by 2D and 3D models (see Fig. 9), thus proposing simplified equations for quick analytical assessment of DAF for earthquake resistant buildings.

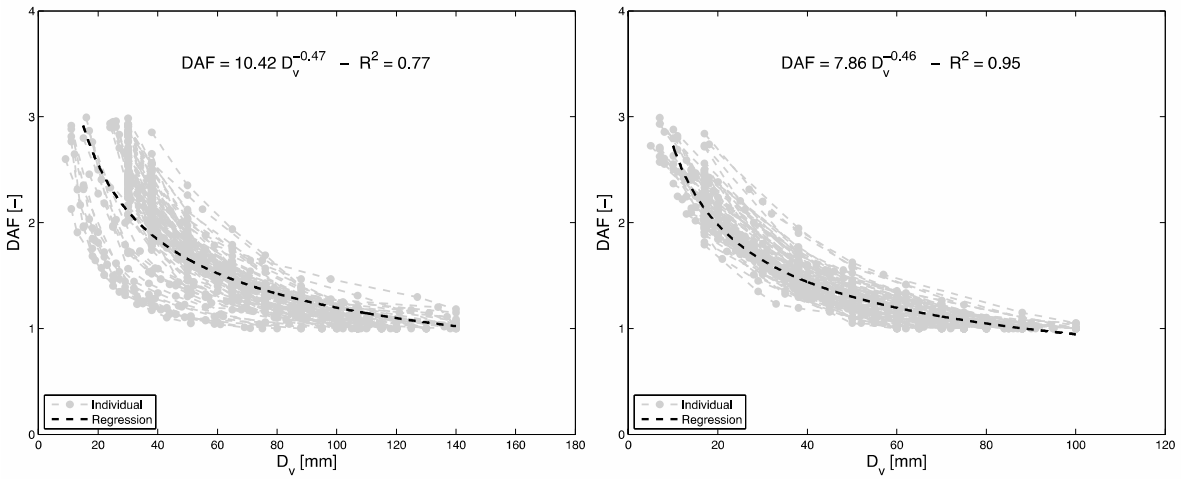

Figure 9: DAF estimates for EC8-compliant building class using 2D models (left) and 3D models (right).

The scatter is very low in case of 3D structural models, as the resulting regression function is characterized by a coefficient of determination equal to 0.95. Conversely, regression analysis provided a less accurate fit using capacities from 2D models (i.e. $R^2 = 0.77$), particularly in the small displacement range, that is when structural performance was characterized by minor or moderate damage.

6 DERIVATION OF FRAGILITY MODELS

To convolve capacity and demand under progressive collapse scenario, the following three criteria were introduced – either at global/structural (i.e. vertical drifts) or local/sectional (i.e. concrete and steel strains) levels – for limit states definition: slight (LS1), significant (LS2) and complete (LS3) damage. As discussed in [40], slight damage limit condition refers to a situation in which the building can be immediately used after an event with minor repair or strengthening only, so it can be regarded as a sort of serviceability limit state. Conversely, complete damage can be considered as an ultimate limit state beyond which the structure is close to collapse, being no longer able to deform and to sustain any further load increment nor the gravity loads for which it has been designed. Significant damage can be regarded as an intermediate case beyond which the building becomes unsafe for its occupants, being the majority of its source of nonlinearity yet fully in use. Therefore, LS2 may be identified as a sort of life safety limit state.

To determine whether a structural element reaches a limit condition, strains and drifts experienced in the critical portion of the skeletal frame where the progressive collapse mechanism was forced to occur were compared with conventionally identified limit capacities [40]:

- LS1 was defined by steel and concrete strains for both EC8- and EC2-compliant building classes. For each randomly generated structure, the yielding strain of steel bars was computed as the ratio between yielding strength and Young's modulus, while concrete strain at peak strength was determined in accordance with Mander et al. [57].
- LS2 was supposed to occur when the vertical drift, obtained as the ratio between the peak displacement above the column removed and the beam span length, exceeded a deterministic threshold. In detail, that drift was assumed to be equal to 0.5% and 1.0% in case of EC2-conforming and EC8-conforming building classes, respectively.
- LS3 was characterized in terms of ultimate steel strain and ultimate concrete strain. For each randomly generated structure, the ultimate concrete strain was calculated according to different material properties and reinforcement arrangement, whereas the buckling/fracture strain of steel bars was set to 4% and 6% in the case of EC2-conforming and EC8-conforming building classes, respectively.

Therefore, a multiplier of Q_b was identified on each pushdown (P1) curve for each damage state, in order to assemble a damage probability matrix. The latter contained fractions of sampled structures in each damage state, for a set of increasing Q_b levels. The cumulative fraction of buildings in each damage state was then computed, summing up the percentages of frames pertaining to each of them according to MC simulation. Finally, a lognormal cumulative distribution function was fitted to fragility points through regression analysis, thus providing the probability of exceeding each damage state in a continuous fashion.

Fragility functions for each structure typology are shown in Figs. 10 and 11, while their parameters, in terms of mean, standard deviation and coefficient of determination, are collected in Table 1. A good match with fragility points from pushdown analysis was observed for each limit state (i.e. LS1, LS2 and LS3), design approach (i.e. EC2- and EC8-compliant structures) and structural idealization (i.e. 2D and 3D models), being R^2 in the range 0.972-0.999.

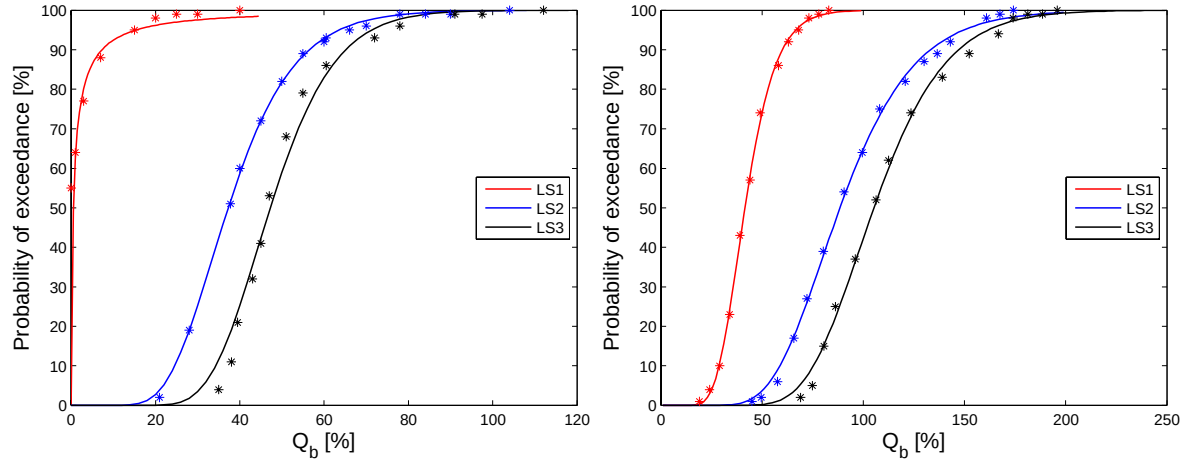

Figure 10: Fragility models of EC2-compliant (left) and EC8-compliant (right) building classes – 2D prototypes.

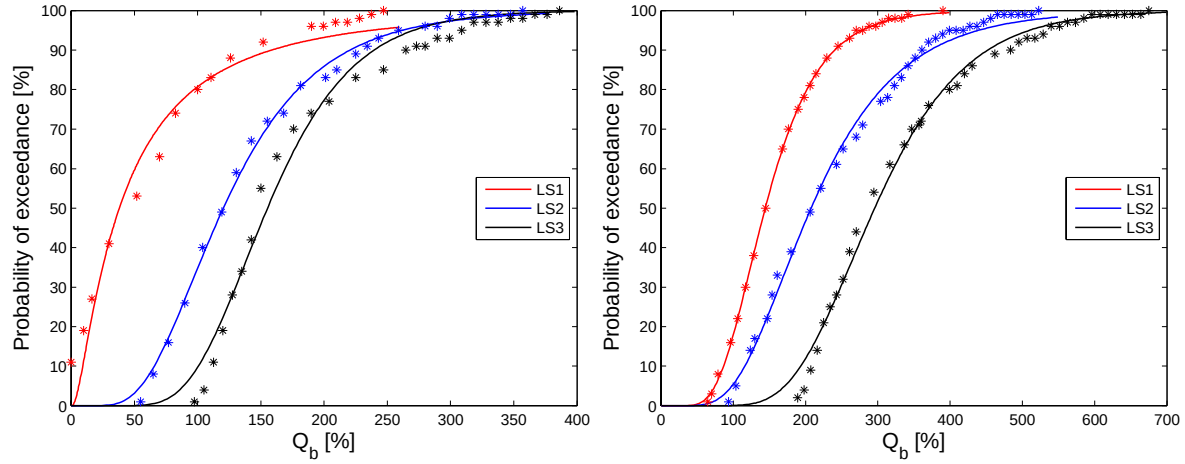

Figure 11: Fragility models of EC2-compliant (left) and EC8-compliant (right) building classes – 3D prototypes.

		LS1			LS2			LS3		
Class	**Model**	μ	σ	R^2	μ	σ	R^2	μ	σ	R^2
EC2-conf.	2D	-5.243	2.053	0.985	-0.987	0.325	0.999	-0.749	0.240	0.985
	3D	-0.964	1.112	0.972	0.186	0.472	0.997	0.440	0.338	0.982
EC8-conf.	2D	-0.880	0.288	0.999	-0.122	0.319	0.998	0.051	0.261	0.996
	3D	0.367	0.399	0.999	0.731	0.456	0.995	1.084	0.332	0.994

Table 1: Pushdown analysis (P1) – μ, σ and R^2 of fragility functions in terms of Q_b.

A very low scatter can be observed in case of EC8-conforming structures, as their fragility models are characterized by a coefficient of determination close to unity ($0.995 < R^2 < 0.999$) for both 2D and 3D models. As far as the EC2-compliant building class is concerned, an identical accuracy was obtained for LS2 and LS3, considering both 2D and 3D models, while the goodness of fit for LS1 was slightly lower as R^2 equals 0.985 and 0.972 for 2D and 3D models, respectively. Nonetheless, that limit state (i.e. slight damage condition) is less crucial than others for progressive collapse applications, in which (i) moderate damage is likely to occur

as a consequence of redistribution of vertical loads from a removed column and (ii) an optimal design target is the life safety or collapse prevention limit state in light of classical performance-based design principles. Moreover, the fragility models proposed in this study reaffirm the key role played by secondary framing beams and seismic design/detailing rules for a cost-effective progressive collapse vulnerability mitigation of RC structures. In fact, a symmetrical reinforcement configuration is effective for the creation of a rationally-controlled primary resisting mechanism, whereas redundancy added by secondary beam systems (designed to satisfy minimum reinforcement requirements prescribed in current code regulations) is crucial to ensure alternative load paths under abnormal loading conditions. In this respect, it can be emphasized that the additional robustness resources provided by secondary frame systems can be predicted at the design stage, for instance through a correlation between the maximum vertical displacement of the 3D model normalized to that of the equivalent 2D model ($D_{max,3D}/D_{max,2D}$) and the maximum demand-to-capacity ratio of beams [19].

Finally, the set of fragility models at multiple damage states derived and commented in this research were compared to the corresponding set of IDA-based functions proposed by Brunesi et al. [40]. Table 2 presents ratios of mean ($\chi_\mu = \mu_{IDA}/\mu_{P1}$) and standard deviation ($\chi_\sigma = \sigma_{IDA}/\sigma_{P1}$) of IDA-based and pushdown-based fragility functions for each damage state, design approach and structural representation of interest.

		LS1		**LS2**		**LS3**	
Class	**Model**	χ_μ	χ_σ	χ_μ	χ_σ	χ_μ	χ_σ
EC2-conf.	2D	1.249	1.132	1.224	1.205	1.158	1.038
	3D	1.528	1.182	0.232	1.169	0.789	1.073
EC8-conf.	2D	1.321	1.459	2.015	1.225	-0.511	1.075
	3D	0.344	1.208	0.822	1.192	0.909	1.040

Table 2: IDA vs. P1 – ratios of mean ($\chi_\mu = \mu_{IDA}/\mu_{P1}$) and standard deviation ($\chi_\sigma = \sigma_{IDA}/\sigma_{P1}$) of fragility functions.

Pushdown analysis was therefore confirmed to be unconservative for vulnerability assessment of RC framed structures subjected to progressive collapse, as detailed from a deterministic standpoint in past studies [19, 40]. In light of this, ad hoc countermeasures are likely to be implemented in current regulations for progressive collapse scenario loss modeling.

7 CONCLUSIONS

In this work, a modeling procedure for large displacement inelastic pushdown analysis was integrated in a probabilistic framework for the derivation of fragility functions for RC framed structures under extreme loads resulting from a threat-independent sudden column loss. Two low-rise RC building classes were studied, namely gravity-load designed buildings and earthquake resistant buildings. The case-study structures were investigated using two analysis methods, i.e. pushdown analysis with and without consideration of equivalent dynamic effects, and two modeling strategies, i.e. 2D and 3D fiber-based models. The progressive collapse fragility was evaluated for both case-study building classes, considering both structural idealizations as well as uncertainties related to geometry of structural elements, material properties and gravity loads. Classical performance-based assessment principles assumed in earthquake engineering were extended to define demand and capacity at local and global structural levels. A set of fragility models were then derived, allowing the following conclusions to be drawn:

- The fragility models proposed in this study are optimally fitted to discrete fragility estimates provided by pushdown analysis combined with MC simulation, particularly for life safety and total collapse prevention limit states which are crucial for progressive collapse assessment.
- Different fragility levels are associated with multiple damage states, depending on the building class and modeling strategy considered in probabilistic progressive collapse assessment.
- Considerable benefits from seismic design and secondary beams on the actual robustness level of RC bare building structures are confirmed and quantified by the fragility models proposed herein.
- Incremental-mass nonlinear dynamic analysis is suggested to be implemented in progressive collapse-resistant building analysis and design, as pushdown analysis was proven to underestimate the fragility level associated with this type of structures in case of progressive collapse.

REFERENCES

[1] B.R. Ellingwood, E.V. Leyendecker, Approaches for design against progressive collapse. *J Struct Div ASCE*, **104**(3), 413-423, 1978.

[2] J.L. Gross, W. McGuire, Progressive collapse resistant design. *J Struct Eng ASCE*, **109**(1), 1-15, 1983.

[3] W.G. Corley, P.F. Mlakar, M.A. Sozen, C.H. Thornton, The Oklahoma city bombing: summary and recommendations for multihazard mitigation. *J Perform Constr Fac ASCE*, **12**(3), 100-112, 1998.

[4] C. Pearson, N. Delatte, Ronan Point Apartment tower collapse and its effect on building codes. *J Perform Constr Fac ASCE*, **19**(2), 172-177, 2005.

[5] Z.P. Bažant, M. Verdure, Mechanics of progressive collapse: Learning from World Trade Center and building demolitions. *J Eng Mech ASCE*, **133**(3), 308-319, 2007.

[6] B.R. Ellingwood, Mitigating risk from abnormal loads and progressive collapse. *J Perform Constr Fac ASCE*, **20**(4), 315-323, 2006.

[7] O.A. Mohamed, Progressive collapse of structures: Annotated bibliography and comparison of codes and standards. *J Perform Constr Fac ASCE*, **20**(4), 418-425, 2006.

[8] R.S. Nair, Preventing disproportionate collapse. *J Perform Constr Fac ASCE*, **20**(4), 309-314, 2006.

[9] U. Starossek, Typology of progressive collapse. *Eng Struct*, **29**(9), 2302-2307, 2007.

[10] U. Starossek, M. Haberland, Disproportionate collapse: terminology and procedures. *J Perform Constr Fac ASCE*, **24**(6), 519-528, 2010.

[11] G. Xu, B.R. Ellingwood, An energy-based partial pushdown analysis procedure for assessment of disproportionate collapse potential. *J Constr Steel Res*, **67**, 547-555, 2011.

[12] B. Santafé Iribarren, P. Berke, Ph. Bouillard, J. Vantomme, T.J. Massart, Investigation of the influence of design and material parameters in the progressive collapse analysis of RC structures. *Eng Struct*, **33**(10), 2805-2820, 2011.

[13] National Institute of Standards and Technology (NIST). *Best practices for reducing the potential for progressive collapse in buildings*. US Department of Commerce. Washington, DC; 2007.

[14] General Services Administration (GSA). *Progressive collapse analysis and design guidelines for new federal office buildings and major modernization project*. Washington, DC; 2003.

[15] Department of Defense (DoD). Unified Facilities Criteria (UFC): *Design of structures to resist progressive collapse*. Washington, DC; 2009.

[16] ASCE 7-02. *Minimum design loads for buildings and other structures*. American Society of Civil Engineers. Reston, VA; 2002.

[17] K. Khandelwal, S. El-Tawil, Pushdown resistance as a measure of robustness in progressive collapse analysis. *Eng Struct*, **33**(9), 2653-2661, 2011.

[18] F. Parisi, N. Augenti, Influence of seismic design criteria on blast resistance of RC framed buildings: A case study. *Eng Struct*, **44**, 78-93, 2012.

[19] E. Brunesi, R. Nascimbene, Extreme response of reinforced concrete buildings through fiber force-based finite element analysis. *Eng Struct*, **69**, 206-215, 2014.

[20] S.M. Marjanishvili, Progressive analysis procedure for progressive collapse. *J Perform Constr Fac ASCE*, **18**(2), 79-85, 2004.

[21] B.M. Luccioni, R.D. Ambrosini, R.F. Danesi, Analysis of building collapse under blast loads. *Eng Struct*, **26**(1), 63-71, 2004.

[22] G. Kaewkulchai, E.B. Williamson, Beam element formulation and solution procedure for dynamic progressive collapse analysis. *Comput Struct*, **82**(7-8), 639-651, 2004.

[23] B.A. Izzuddin, A.G. Vlassis, A.Y. Elghazouli, D.A. Nethercot, Progressive collapse of multi-storey buildings due to sudden column loss - part I: simplified assessment framework. *Eng Struct*, **30**(5), 1308-1318, 2008.

[24] A.G. Vlassis, B.A. Izzuddin, A.Y. Elghazouli, D.A. Nethercot, Progressive collapse of multi-storey buildings due to sudden column loss - part II: application. *Eng Struct*, **30**(5), 1424-1438, 2008.

[25] Y. Bao, S.K. Kunnath, S. El-Tawil, H.S. Lew, Macromodel-based simulation of progressive collapse: RC frame structures. *J Struct Eng ASCE*, **134**(7), 1079-1091, 2008.

[26] M.-H. Tsai, B.-H. Lin, Investigation of progressive collapse resistance and inelastic response for an earthquake-resistant RC building subjected to column failure. *Eng Struct*, **30**(12), 3619-3628, 2008.

[27] M. Sasani, Response of a reinforced concrete infilled-frame structure to removal of two adjacent columns. *Eng Struct*, **30**(9), 2478-2491, 2008.

[28] C.H. Lee, S. Kim, K.H. Han, K. Lee, Simplified nonlinear progressive collapse analysis of welded steel moment frames. *J Constr Steel Res*, **65**(5), 1130-1137, 2009.

[29] H.S. Kim, J. Kim, D.W. An, Development of integrated system for progressive collapse analysis of building structures considering dynamic effects. *Adv Eng Softw*, **40**(1), 1-8, 2009.

[30] F. Fu, 3-D nonlinear dynamic progressive collapse analysis of multi-storey steel composite frame buildings - Parametric study. *Eng Struct*, **32**(12), 3974-3980, 2010.

[31] H.R. Valipour, S.J. Foster, Finite element modelling of reinforced concrete framed structures including catenary action. *Comput Struct*, **88**(9-10), 529-538, 2010.

[32] Y. Li, X.Z. Lu, H. Guan, L.P. Ye, An improved tie force method for progressive collapse resistance design of reinforced concrete frame structures. *Eng Struct*, **33**(10), 2931-2942, 2011.

[33] P.X. Dat, T.K. Hai, Membrane actions of RC slabs in mitigating progressive collapse of building structures. *Eng Struct*, **55**, 107-115, 2013.

[34] L. Kwasniewski, Nonlinear dynamic simulations of progressive collapse for a multistory building. *Eng Struct*, **32**(5), 1223-1235, 2010.

[35] S. Szyniszewski, T. Krauthammer, Energy flow in progressive collapse of steel framed buildings. *Eng Struct*, **42**, 142-153, 2012.

[36] R.M. Bennett, Formulations for probability of progressive collapse. *Struct Safety*, **5**(1), 66-77, 1988.

[37] J. Agarwal, D.I. Blockley, N.J. Woodman, Vulnerability of structural systems. *Struct Safety*, **25**(3), 263-286, 2003.

[38] J.W. Baker, M. Schubert, M.H. Faber, On the assessment of robustness. *Struct Safety*, **30**, 253-267, 2008.

[39] J. Park, J. Kim, Fragility analysis of steel moment frames with various seismic connections subjected to sudden loss of a column. *Eng Struct*, **32**(6), 1547-1555, 2010.

[40] E. Brunesi, R. Nascimbene, F. Parisi, N. Augenti, Progressive collapse fragility of reinforced concrete framed structures through incremental dynamic analysis. *Eng Struct*, **104**, 65-79, 2015.

[41] F. Parisi, Blast fragility and performance-based pressure-impulse diagrams of European reinforced concrete columns. *Eng Struct*, **103**, 285-297, 2015.

[42] CEN, European Committee for Standardization. EN 1992-1-1. Eurocode 2 (EC2): *Design of concrete structures - Part 1.1: General rules and rules for buildings*. Brussels, 2004.

[43] CEN, European Committee for Standardization. EN 1998-1-5. Eurocode 8 (EC8): *Design of structures for earthquake resistance - Part 1.5: specific rules for concrete buildings*. Brussels, 2004.

[44] M.G. Stewart, M.D. Netherton, D.V. Rosowsky, Terrorism risks and blast damage to built infrastructure. *Nat Hazard Rev*, **7**(3), 114-122, 2006.

[45] G.M. Calvi, A displacement-based approach for vulnerability evaluation of classes of buildings. *J Earthq Eng*, **3**(3), 411-438, 1999.

[46] H. Crowley, R. Pinho, J.J. Bommer, A probabilistic displacement-based vulnerability assessment procedure for earthquake loss estimation. *Bull Earthq Eng*, **2**(2), 173-219, 2004.

[47] T. Rossetto, A. Elnashai, A new analytical procedure for the derivation of displacement-based vulnerability curves for populations of RC structures. *Eng Struct*, **27**(3), 397-409, 2005.

[48] B. Borzi, R. Pinho, H. Crowley, Simplified pushover-based vulnerability analysis for large-scale assessment of RC buildings. *Eng Struct*, **30**(3), 804-820, 2008.

[49] K. Porter, R. Kennedy, R. Bachman, Creating fragility functions for performance-based earthquake engineering. *Earthq Spectra*, **23**(2), 471-89, 2007.

[50] V. Silva, H. Crowley, R. Pinho, H. Varum, Extending displacement-based earthquake loss assessment (DBELA) for the computation of fragility curves. *Eng Struct*, **56**, 343-356, 2013.

[51] E. Spacone, F.C. Filippou, F.F. Taucer, Fibre beam-column model for non-linear analysis of RC frames: Part I. Formulation. *Earthquake Eng Struct Dyn*, **25**, 711-725, 1996.

[52] E. Brunesi, R. Nascimbene, G.A. Rassati, Seismic response of MRFs with partially-restrained bolted beam-to-column connections through FE analyses. *J Constr Steel Res*, **107**, 37-49, 2015.

[53] R. De Borst, Smeared cracking, plasticity, creep and thermal loading – A unified approach. *Comp Meth Appl Mech Eng*, **62**(1), 89-110, 1987.

[54] C.-C. Hung, S. El-Tawil, Hybrid rotating/fixed-crack model for high performance fiber reinforced cementitious composites. *ACI Mater J*, **107**(6), 568-576, 2010.

[55] E. Brunesi, R. Nascimbene, Numerical web-shear strength assessment of precast prestressed hollow core slab units. *Eng Struct*, **102**, 13-30, 2015.

[56] Seismosoft. SeismoStruct – A computer program for static and dynamic nonlinear analysis of framed structures. Available from URL: www.seismosoft.com.

[57] J.B. Mander, M.J.N. Priestley, R. Park, Theoretical stress-strain model for confined concrete. *J Struct Eng ASCE*, **114**(8), 1804-1826, 1988.

ECCOMAS Congress 2016
VII European Congress on Computational Methods in Applied Sciences and Engineering
M. Papadrakakis, V. Papadopoulos, G. Stefanou, V. Plevris (eds.)
Crete Island, Greece, 5–10 June 2016

MECHANICAL PROPERTIES OF S355 UNDER EXTREME COUPLED EFFECT OF HIGH TEMPERATURES AND HIGH STRAIN RATES

Daniele Forni[1,2], **Bernardino Chiaia**[2], **Ezio Cadoni**[1]

[1]DynaMat Lab, University of Applied Sciences of Southern Switzerland
CH-6952 Canobbio, Switzerland
e-mail: daniele.forni@supsi.ch
e-mail: ezio.cadoni@supsi.ch

[2] Department of Structural, Geotechnical and Building Engineering, Politecnico di Torino
Torino, Italy
e-mail: bernardino.chiaia@polito.it

Keywords: Robustness, fire induced progressive collapse, S355 structural steel, high strain-rates, high temperatures, Johnson-Cook constitutive law.

Abstract. *With the intention of focusing the attention on the extreme combined effects of temperature and dynamic loadings, the high strain rate behaviour in tension of the widely used S355 structural steel in a wide range of elevated temperatures is presented.*
By means of a Split Hopkinson Tensile Bar (SHTB) equipped with a water-cooled induction heating system, the main mechanical properties as well as different strain energy densities have been evaluated. The reduction factors for the main mechanical properties, in which the novelty of our data is the addition of the strain rate dependency to the temperature, are reported as well. Lastly, a critic review of the Johnson-Cook constitutive law has been reported, highlighting that the use of single averaged thermal softening parameter (m) could lead to considerable errors. These results could be of great interest for the assessment of robustness in structures subjected to fire induced progressive collapse.

1 INTRODUCTION

An extended exposure to high temperatures may severely influence the performance of the steel framed structures triggering for example a fire induced progressive collapse.

Even if the progressive collapse became an important topic after the partial collapse of the Ronan Point Building (UK) in 1968 [1, 2, 3], only after the 9/11 World Trade Center tragedy [4, 5] a significant amount of research has been carried out to assess the fire resistance and to predict the blast response of steel structures. But, only uncorrelated effects of dynamic loadings and high temperatures have been considered [6]. For that reason the mechanical response of steel structures subjected to extreme combined effects has still criticisms open to investigation.

With the intention of fulfilling these criticisms, the mechanical behaviour of a widely used structural steel, namely S355, in a wide range of temperatures (200 °C, 400 °C, 550 °C, 700 °C and 900 °C) and high strain rates will be presented. The results can be of great interest for the assessment of robustness in structures where a progressive collapse is triggered by a coupled effect of fire and dynamic loadings.

2 PROGRESSIVE COLLAPSE: CHOICE OF THE APPROACH

Two approaches are known for studying the progressive collapse, namely the indirect and the direct methods. While for the first, the designers may use an implicit design, in the second the designers need to perform a structural analysis. Two typical used direct methods are the *specific local resistance method* (known also as *key element design*) and the *alternate load path*.

Another approach that should be followed is based on the employment of discrete element method (DEM) models. An extensive research in this field has been performed by Masoero *et al*. [7, 8, 9], that demonstrated the DEM's applicability to progressive collapse by simulating the behaviour of 2D and 3D framed structures after a sudden damage.

Focusing the attention on the direct methods we should not forget the analytical procedure that can be used to model the problem. Although simplified hypotheses are supposed, like *linear static* or *non-linear static* analysis as well as *linear dynamic* analysis, the most rigorous approach for evaluating a progressive collapses is through the use of an explicit *non-linear dynamic* procedure. But, even if the *non-linear dynamic* procedure is the most accurate approach, another fundamental aspect should be taken into consideration: the real mechanical properties of the material subjected to extreme combined loadings [10].

With the intention of evaluating the structural performance in response of a coupled effect of fire and blast loading, one of the most commonly implemented [11, 12, 13] and easy-to-use constitutive relationships in the finite element programs is here considered. This constitutive model has been proposed by Johnson and Cook during the eighties [14] and is widely used to describe the material strength in numerical simulations of dynamic events. The flow stress can be expressed as:

$$\sigma = (A + B \cdot \epsilon_p^n) \cdot (1 + c \cdot ln\frac{\dot{\epsilon}}{\dot{\epsilon}_0}) \cdot (1 - T^{*m}) \tag{1}$$

where ϵ_p is the true plastic strain, $\dot{\epsilon}$ is the considered strain rate, $\dot{\epsilon}_0$ is the reference strain rate (taken as 1 s^{-1}) and T^* is a dimensionless temperature. In order to find the Johnson-Cook parameters A, B and n [15], representing the strain hardening effects of the material in quasi-static conditions, c [15] representing the strain rate sensitivity and m [16] representing the thermal softening sensitivity, a mechanical characterisation in a wide range of temperatures and high strain rates is necessary.

3 MECHANICAL CHARACTERISATION AT HIGH STRAIN-RATES AND HIGH TEMPERATURES

The mechanical characterisation at high strain-rates was carried out by means of a Split Hopkinson Tensile Bar (SHTB) installed at the DynaMat Laboratory [17]. The tests at elevated temperatures were performed by using an Ambrell compact EASYHEAT induction water-cooled heating system (Figure 1). A detailed description of the functioning of the SHTB equipped with the induction water-cooled heating system has been given in [16].

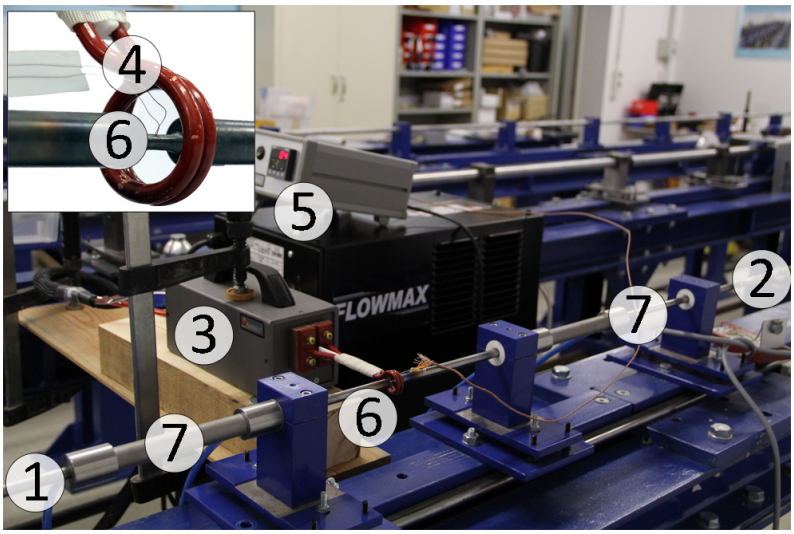

Figure 1: Setup for the high strain rate tests at elevated temperature: (1) the input bar, (2) the output bar, (3) the heating system, (4) the water-cooled induction coil, (6) the sample to be tested connected by means of a thermocouple to a (5) thermal controller and (7) the cooling system for the input and output bars, respectively.

The specimens for the mechanical characterisation were obtained in the longitudinal direction from an hot-rolled wide-flange section HE A [18]. Starting from the initial section geometry, wire electrical discharge machining (WEDM) was used in order to obtain small prismatic samples, that where turned in order to obtain round samples with 3 mm in diameter and 5 mm of gauge length. A full description of the geometry is reported in [19, 20].

In order to understand the effect of the temperature on the dynamic mechanical properties of the S355 structural steel, the high strain rate tests at elevated temperatures were performed with the same testing conditions adopted at room temperature. With these testing conditions and at 20 °C, the obtained averaged strain rates were approximately 300 s^{-1} ($v_1 = 2.30$ m/s), 500 s^{-1} ($v_2 = 2.90$ m/s) and 850 s^{-1} ($v_3 = 4.00$ m/s). The corresponding particle velocities in the input bar, used as a reference for the testing condition, are reported within brackets.

Additional tests were also performed by compensating the preload with the intention of obtaining tests with comparable effective strain rate. This has been helpful for the calibration of the Johnson-Cook thermal softening sensitivity parameter (m).

4 RESULTS

Due to the different mechanical properties of steel at elevated temperatures, an increase of the reflected pulses is noted for increasing temperatures (Figure 2 left). This lead to a noticeable increase in the averaged strain rate at different temperatures (Figure 2 right).

The temperature effect on the mechanical properties of the S355 structural is represented in Figure 3, where the engineering stress versus strain and the true stress versus strain represen-

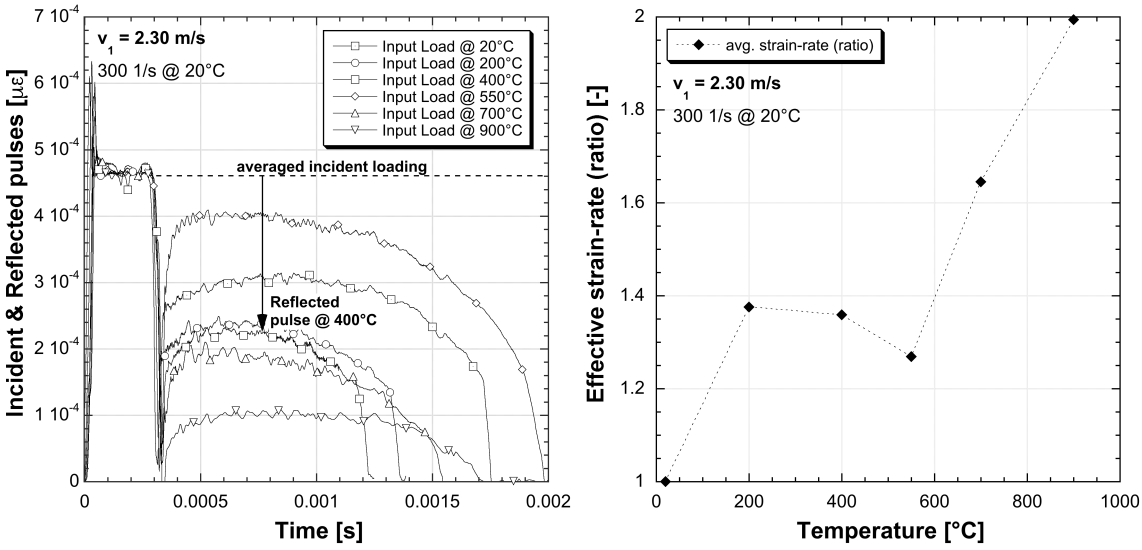

Figure 2: Comparison of reflected pulses at increasing temperatures (left) and effective strain-rate for increasing temperatures (rigth) for a fixed testing condition ($v_1 = 2.30$ m/s).

A (MPa)	**B** (MPa)	**n** (-)	**c** (-)
448	782	0.562	0.0247

Table 1: Johnson-Cook parameters obtained at room temperature [15].

tative plots are depicted. In Figure 4 the post-mortem images of the samples tested at different temperatures are reported.

Another way of comparing the tensile properties at different temperatures is by means of a reduction factor determined as the ratio of the value at elevated temperatures to the corresponding value at room temperature. The reduction factors for the proof strength and the ultimate tensile strength evaluated at high strain rates are reported in Figure 5. It is possible to observe that the reduction factor proposed by the Eurocode 3 [21] for the proportional limit in quasi-static conditions is not applicable for the high strain-rate tests, while the reduction factors seem not to be strongly different for the three testing conditions. The reduction factors for the other mechanical properties are reported in [16].

5 CONSTITUTIVE MODEL

The Johnson-Cook parameters evaluated by means of tests at room temperature are reported in Table [15], while the experimental data at different temperatures and for a fixed strain rate ($450\,s^{-1}$) were used to determine [16] the thermal softening sensitivity parameters (Table 2).

In a previous study by the current authors [16], a thermal softening factor obtained experimentally at different temperatures was defined (R^*). In Figure 6 a comparison between this

m ($450\,s^{-1}$)				
200 °C (-)	400 °C (-)	550 °C (-)	700 °C (-)	900 °C (-)
0.551	0.675	0.988	0.953	0.454

Table 2: Johnson-Cook thermal softening sensitivity parameters at different temperatures [16].

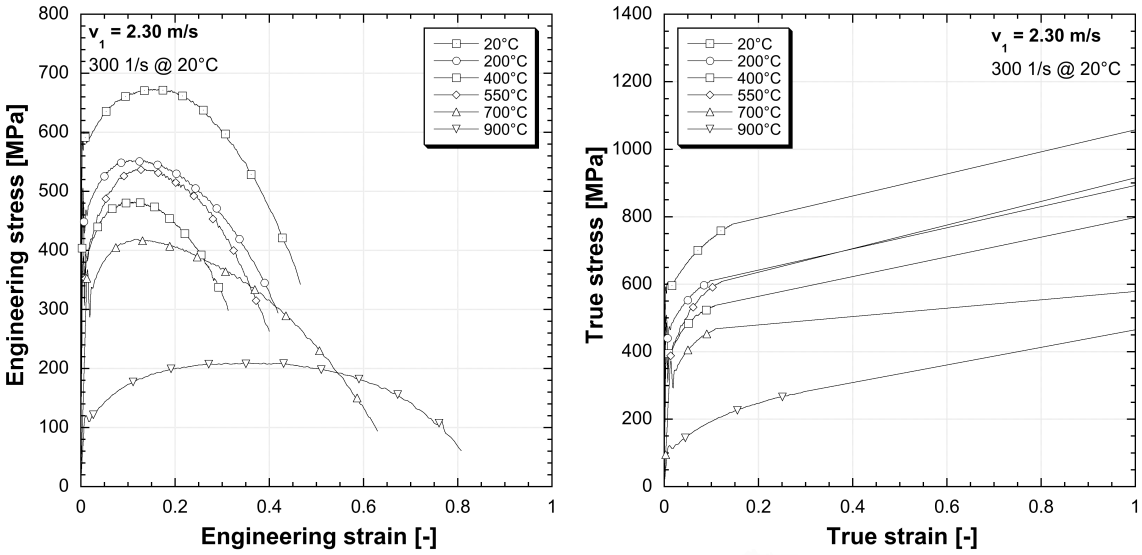

Figure 3: Comparison of engineering stress-strain curves (left) and true stress-strain curves (right) at different temperatures.

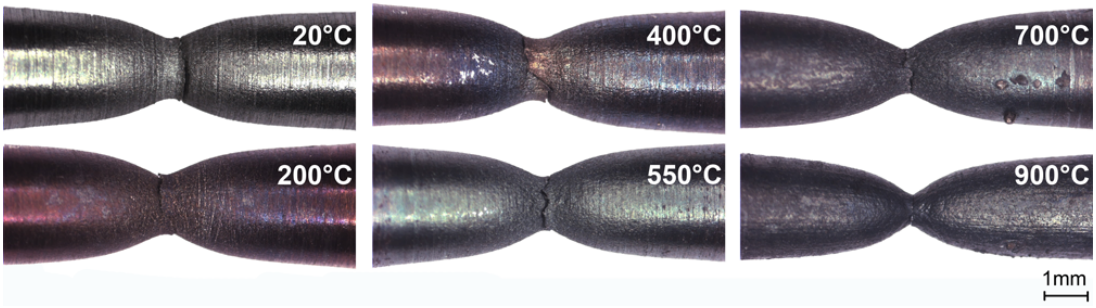

Figure 4: Reduction of area of samples tested at elevated temperatures.

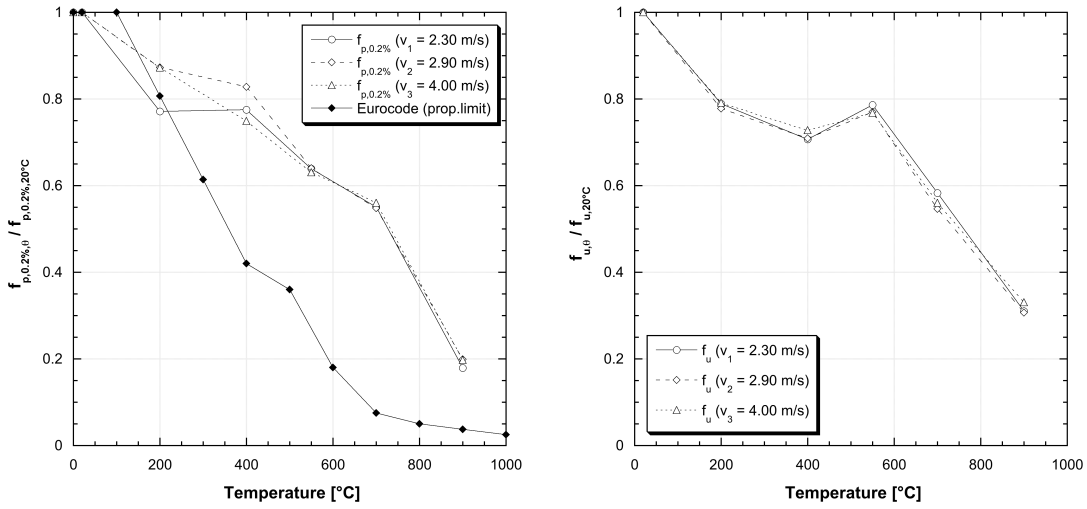

Figure 5: Reduction factors for the proof strength (left) and the ultimate tensile strength (right).

factor and the thermal factor of the Johnson-Cook constitutive law $(1 - T^{*m})$ with fixed single values of m is reported. It is possible to observe that single averaged values of m obtained by comparing only two sets of data from room temperature and a single high temperature, could lead to considerable errors.

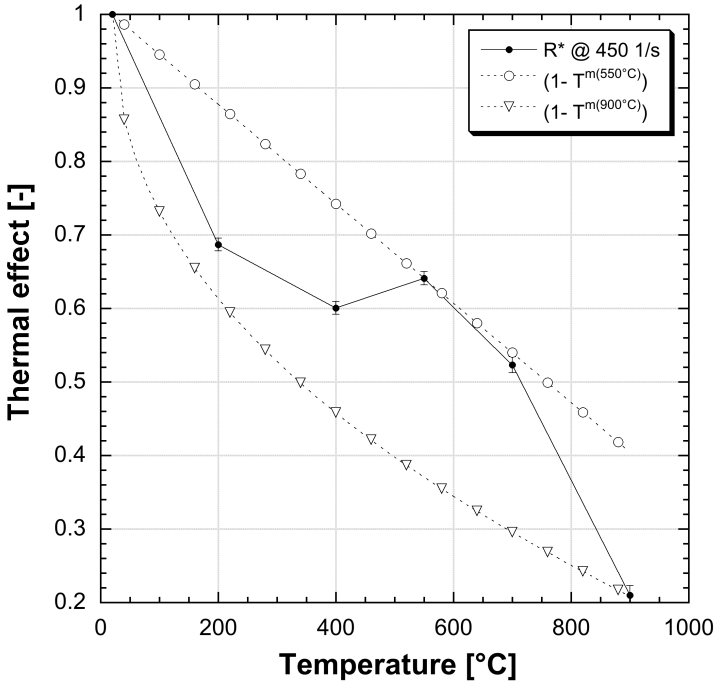

Figure 6: Comparison between the thermal softening factors obtained experimentally and the thermal factor of the Johnson-Cook constitutive law with fixed single values of m.

6 CONCLUSIONS

In this paper the high strain rate behaviour in tension of the widely used S355 structural steel in a wide range of elevated temperatures has been presented.

- Due to the different mechanical properties of steel at elevated temperatures, a perceptible increase in the effective strain rate was observed.
- The tensile properties were not significantly influenced by the different dynamic testing conditions.
- A remarkable difference between quasi-static and high strain rate reduction factors was highlighted.
- A perceptible variation of the thermal softening parameter (m) was highlighted.
- Using a single averaged value of m could lead to considerable errors.

These findings could be helpful in order to simulate the effect of a dynamic loading, e.g. an explosion, on steel structural elements under different temperatures. As a future development a numerical simulation will be implemented in Ls-Dyna considering the material properties of the structural steel S355 at high temperatures and high loading rates.

7 ACKNOWLEDGEMENTS

This work is part of research project *Behaviour of structural steels under fire in a wide range of strain rate* founded by the State Secretariat for Education, Research and Innovation of the Swiss Confederation (project C12.0051), in the frame of the *COST ACTION TU0904 - Integrated Fire Engineering and Response (IFER).*

REFERENCES

[1] C. Pearson and N. Delatte. Ronan point apartment tower collapse and its effect on building codes. *Journal of Performance of Constructed Facilities*, 19(2):172–177, 2005.

[2] J.B. Menzies and D.A. Nethercot. Progressive collapse - preventive measures in the united kingdom. *Proceedings of the Structural Engineers World Congress, San Francisco, USA*, 1998.

[3] A. Longinow and B.R. Ellinwood. The impact of the ronan point collapse - 25 years after. *Proceedings of the Structural Engineers World Congress, San Francisco, USA*, 1998.

[4] Z.P. Bazant and Y. Zhou. Why did the world trade center collapse? - Simple analysis. *Journal of Engineering Mechanics*, 128(1):2–6, JAN 2002.

[5] Z.P. Bazant and M. Verdure. Mechanics of progressive collapse: Learning from world trade center and building demolitions. *Journal of Engineering Mechanics*, 133(3):308–319, MAR 2007.

[6] J.Y. Richard Liew. Survivability of steel frame structures subject to blast and fire. *Journal of Constructional Steel Research*, 64(7–8):854 – 866, 2008.

[7] E. Masoero, F.K. Wittel, H.J. Herrmann, and B.M. Chiaia. Progressive collapse mechanisms of brittle and ductile framed structures. *Journal of Engineering Mechanics*, 136(8):987–995, 2010.

[8] E. Masoero, F.K. Wittel, H.J. Herrmann, and B.M. Chiaia. Hierarchical structures for a robustness-oriented capacity design. *Journal of Engineering Mechanics*, 138(11):1339–1347, 2012.

[9] E. Masoero, P. Darò, and B.M. Chiaia. Progressive collapse of 2d framed structures: An analytical model. *Engineering Structures*, 54:94–102, 2013.

[10] H.M. Elsanadedy, T.H. Almusallam, Y.R. Alharbi, Y.A. Al-Salloum, and H. Abbas. Progressive collapse potential of a typical steel building due to blast attacks. *Journal of Constructional Steel Research*, 101(0):143 – 157, 2014.

[11] E. Cadoni, M. Dotta, D. Forni, and S. Bianchi. Strain-rate effect on the tensile behaviour of high strength alloys. *Applied Mechanics and Materials*, 82:124–129, 2011.

[12] E. Cadoni, M. Dotta, D. Forni, and N. Tesio. Dynamic behaviour of reinforcing steel bars in tension. *Applied Mechanics and Materials*, 82:86–91, 2011.

[13] E. Cadoni, M. Dotta, D. Forni, and N. Tesio. High strain rate behaviour in tension of steel B500A reinforcing bar. *Materials and Structures*, pages 1–11, 2015.

[14] G.R. Johnson and W.H. Cook. Fracture characteristics of three metals subjected to various strains, strain rates, temperatures and pressures. *Engineering Fracture Mechanics*, 21(1):31–48, 1985.

[15] D. Forni, B. Chiaia, and E. Cadoni. Strain rate behaviour in tension of S355 steel: base for progressive collapse analysis. *Submitted to Engineering Structures (2015)*, 2015.

[16] D. Forni, B. Chiaia, and E. Cadoni. High strain rate response of S355 at high temperatures. *Materials & Design*, 94:467 – 478, 2016.

[17] E. Cadoni, M. Dotta, D. Forni, N. Tesio, and C. Albertini. Mechanical behaviour of quenched and self-tempered reinforcing steel in tension under high strain rate. *Materials & Design*, 49(0):657 – 666, 2013.

[18] M. Knobloch, J. Pauli, and M. Fontana. Influence of the strain-rate on the mechanical properties of mild carbon steel at elevated temperatures. *Materials & Design*, 49:553 – 565, 2013.

[19] E. Cadoni, M. Dotta, D. Forni, and P. Spaetig. Strain-rate behavior in tension of the tempered martensitic reduced activation steel EUROFER97. *Journal of Nuclear Materials*, 414(3):360 – 366, 2011.

[20] E. Cadoni, L. Fenu, and D. Forni. Strain rate behaviour in tension of austenitic stainless steel used for reinforcing bars. *Construction and Building Materials*, 35(0):399 – 407, 2012.

[21] Eurocode 3 (2005) - Design of steel structures. Part 1-2: General rules - Structural fire design. 2005.

ECCOMAS Congress 2016
VII European Congress on Computational Methods in Applied Sciences and Engineering
M. Papadrakakis, V. Papadopoulos, G. Stefanou, V. Plevris (eds.)
Crete Island, Greece, 5–10 June 2016

IMPLEMENTATION OF PROGRESSIVE DAMAGE IN FINITE ELEMENT CODES FOR THE ASSESSMENT OF ROBUSTNESS

D. Asprone[1], **B. Chiaia**[2], **V. De Biagi**[2], **G. Manfredi**[1], **F. Parisi**[1]

[1]Università degli Studi "Federico II"
via Claudio 21, 80125 Napoli, Italy
e-mail: {d.asprone,g.manfredi,f.parisi}@unina.it

[2] Politecnico di Torino
C.so Duca degli Abruzzi 24, 10129, Torino, Italy
e-mail: {bernardino.chiaia,valerio.debiagi}@polito.it

Keywords: Robustness, Progressive Damage, Nonlinear FEM, Commercial software.

Abstract. *Different procedures for assessing the robustness of a reinforced concrete (RC) frame under progressive damage are proposed and compared. The removal of a column in a RC frame structure is modeled with a commercial nonlinear finite element software according to three alternative strategies: (i) reduction of mechanical properties of the damaged column, (ii) incremental loading of the structure after total removal of the damaged column, and (iii) incremental unloading of internal forces on the damaged column. Nonlinear analysis is performed under a prescribed load combination on three concrete frames designed with three Italian building codes in force in different periods. Despite the differences in the strategies for damage modeling, similarities between structural response predictions are highlighted. In addition, it is shown that seismic design provisions for RC building structures increase the ductility of the structure but do not guarantee the robustness against the removal of a column.*

1 INTRODUCTION

Structural engineers have been concerned with the resistance of building structures to disproportionate collapse since Ronan Point accident in 1968. In 2001, the catastrophic failures of WTC towers in New York showed the true effects of progressive collapse and raised the public interest on such topic. Specific guidelines have been developed and robustness requirements have been inserted in building codes and laws. Eurocode 0, which is the document at the base of the modern European national regulations on constructions, states that *a localised failure due to accidental actions may be acceptable, provided it will not endanger the stability of the whole structure, and that the overall load-bearing capacity of the structure is maintained and allows necessary emergency measures to be taken*.

In such framework, the researches conducted since the second half of the last century have focused the attention on sudden element removals [1, 2, 3]. Basically, such situations are induced by explosions and impact loads [4]. For ensuring structural robustness in constructions, the modern design philosophies switch from being reliability-based to accounting for consequences of local failure. In this sense, Gudmundsson and Izzuddin [5] argued that the scenario of sudden column loss is an effective and straightforward strategy for integrity assessment. Various design guidelines implement such approach through linear/nonlinear static or nonlinear dynamic analysis [6, 7]. On one side, static analysis with dynamic increase factor may lead to conservative rather than unsafe design depending on the structural behaviour and configuration [8]. On the other, a large computational effort is required for detailed nonlinear dynamic analyses [9].

Despite the previous scenario are the ones that have engendered and still cause many fatalities for building occupants, the attention has recently switched on other sources of degradation and damage [10, 11]. For example, Sun and others dealt with the progressive collapse of steel frames due to fire [12, 13] modifying a FEM code developed at the University of Sheffield. Others used commercial FEA software ABAQUS for investigating the behaviour of steel structures and connections subjected to fire loads, e.g., [14]. Fang and others [15] proposed a simplified energy-based robustness assessment approach in which the maximum temperature is unknown (i.e., this represents an event-independent local damage scenario); they assess the integrity of the steel structure subjected to fire through a multistage procedure implemented on ADAPTIC code.

The robustness of concrete buildings subjected to element removal has been usually assessed through numerical, experimental and analytical strategies (see, for example, [16, 17, 18]). In addition, theoretical [19, 20, 21, 22] and probabilistic approaches [23, 24, 25] as well as scenario analyses have been already formulated and proposed [26].

The aim of the research herein presented is to model in a simple and feasible way a progressive damage acting on concrete frame structure through a commercial software. This is fundamental for assessing the robustness of a construction in such unexpected scenarios [27].

2 METHODS

A progressive damage acting on a column of the first level of a reinforced concrete structure is simulated. The structure is subjected to the following load combination

$$1.50\,(DL + 0.25LL)\,, \tag{1}$$

where DL represents the dead load, i.e., the weight of the structural and nonstructural components; LL is the live load, i.e., the moving loads. This load combination is suggested in GSA

[28]; the term 1.50 is the dynamic amplification factor [29].

The test structure is represented by a 14×30 m reinforced concrete frame structure made of 140 beams and 160 columns distributed in five levels. The columns are disposed along the nodes of a grid, as depicted in the schematic of Figure 1(a). The plan position of each column is identified by means of a letter (from A to H) and a number (from 1 to 4) As can be observed in Figure 1(b), at each level, each node is connected with the neighboring ones through an orthogonal mesh of beams (28 beams per level). The levels are labelled by Roman numbers from I (ground level at +0.00 m) to VI (top level at +15.20 m). The interstorey height is 3.20 m for level II and 3.00 m for the remaining levels. The elevation of the levels is reported in Table 1. The bottom nodes, i.e., the foundation nodes, are rigidly constrained.

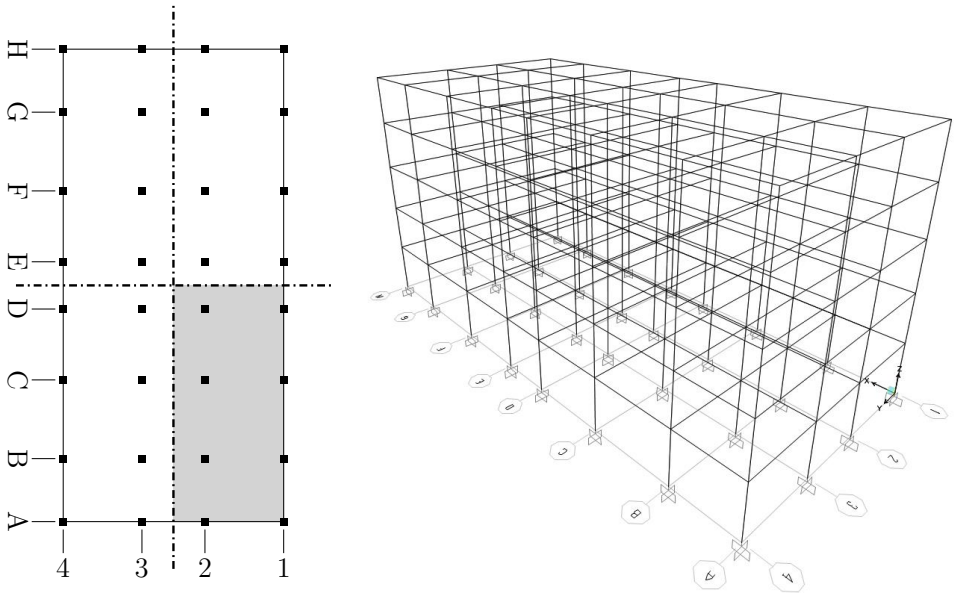

(a) (b)

Figure 1: (a) Plan view of the schematic of the reinforced concrete frame structure; (b) prospective of the frame structure.

Level	Elevation	Level	Elevation
I	0 m	IV	9.2 m
II	3.2 m	V	12.2 m
III	6.2 m	VI	15.2 m

Table 1: Elevations of the levels of the structure.

In the following, the nodes are identified by the sequence N:[plan position(level)]; for example, the node set at the fourth level at the position identified by letter E and number 3 is written as "N:E3(IV)". The beams are identified by the sequence B:[position of the initial node]:[position of the final node]; in this sense, for example, the beam of the third level (+9.20 m) connecting the nodes N:C2(III) and N:D2(III), is named as "B:C2(III):D2(III)". The columns are identified by the sequence C:[position of the bottom node]:[position of the top node]; for example, the column between the nodes N:F2(II) and N:F2(III) is denoted as "C:F2(II):F2(III)". The structure is doubly symmetrical in plan. Thus, the right-hand side lower quarter is considered in the present paper. The results are replicable to the other corresponding parts of the structure.

Referring to the amount of reinforcement within the elements, the structural safety (of the undamaged structure) has been guaranteed through three different design philosophies. In the first case (named "D+HoR" in the following), ultimate limit state semi-probabilistic approach accounting for ductility and hierarchy of resistances has been implemented; in the second case (named "D" in the following), only ductility requirements are satisfied; in the third case (named "S" in the following), only static design accounting for dead and live loads (with basic seismic design requirements) has been performed. The previous design philosophies correspond to present and early Italian building laws, i.e., [31], [32], [33], respectively. Following the well-known structural mechanics rules, the bending moment-curvature relationships for each of the three structural schemes previously illustrated has been computed and the nonlinear flexure relationships have been implemented in the corresponding Finite Element models.

The effects of progressive column removal have been analyzed through the implementation of three different numerical strategies, described in detail in the following subsections.

In all simulations, eight columns, corresponding to the bottom column of the studied quarter of the construction, are alternatively considered. The identification codes and sizes of the columns are reported in Table 2. The behavior of the structure to the progressive damage is evaluated through the maximum vertical drift of all the beams converging in the top node of the damaged element. In reference to Figure 2 in which two horizontal beams converge in node N, the vertical drift, v_{N}, is

$$v_{\mathrm{N}} = \max\left\{\frac{\Delta_1}{\ell_1}; \frac{\Delta_2}{\ell_2}\right\}. \tag{2}$$

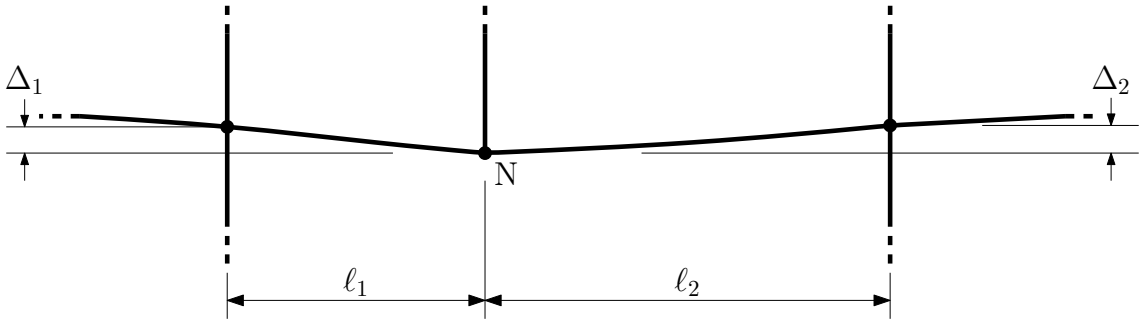

Figure 2: Scheme for the evaluation of vertical drift.

Progressive number	Identification code	Size (cm^2)	Progressive number	Identification code	Size (cm^2)
#1	C:A1(I):A1(II)	30x50	#5	C:A2(I):A2(II)	30x65
#2	C:B1(I):B1(II)	60x30	#6	C:B2(I):B2(II)	65x40
#3	C:C1(I):C1(II)	60x30	#7	C:C2(I):C2(II)	65x40
#4	C:D1(I):D1(II)	50x30	#8	C:D2(I):D2(II)	30x60

Table 2: Damaged elements.

The simulations were performed on an Intel i7, 3.60 GHz, 64-bit computer with 16 GB RAM. A specific MATLAB script controlled a SAP2000 solver and stored the displacement of the monitored nodes on a database file. The computation times related to each simulation are evaluated through MATLAB software.

2.1 Damage model A

The damage model A implemented a progressive reduction of the cross-section area and inertia. As implemented by Lematre and Chaboche [30], the degradation of the structural element was controlled by a damage parameter d varying from 0, in case of no damage, to 1, in case of total damage. If $d = 1$ the element is totally removed. The geometrical properties of the i-th element, i.e., the damaged element, of the RC frame were

$$\begin{aligned} A_{id} &= A_{i0}\,(1-d) \\ J_{id} &= J_{i0}\,(1-d)^2\,, \end{aligned} \tag{3}$$

where A_{i0} and J_{i0} are the cross-section area and inertia. The damage model acted on the size of the concrete cross section, not on the area of the rebar.

The eight columns previously identified were alternatively subjected to the damage, and the overall response of the frame structure was monitored. The simulations (21 in total) were performed at the following values of the damage parameter d:

- from d = 0.000 to d = 0.700, with step of 0.100;
- from d = 0.700 to d = 0.850, with step of 0.050;
- from d = 0.850 to d = 0.950, with step of 0.025;
- from d = 0.950 to d = 0.990, with step of 0.010;
- at d = 0.995 and d = 1.000.

For each value of the damage parameter, the reduced geometrical properties, i.e., the ones derived from Eqn. (3), are automatically assigned to the damaged element. For sake of simplicity, a unique undamaged scheme was considered as a basis for all the simulations. The external load was applied to the damaged structure with its nominal value, see load combination detailed in Eqn. (1). SAP2000 solver was set as static nonlinear. Meanwhile, the vertical displacements of the top node of the damaged column (i.e., the node set at level II, i.e., at +3.20 m), as well as the boundary nodes at the same level, were monitored. In addition, the axial force in the damaged element was recorded. This allowed to rapidly estimate the vertical drift of the beams at +3.20 m, assessing the amount of damage on the floor. The results associated with each value of damage parameter were independent one from each other. No previous damage history is considered was each simulation.

2.2 Damage model B

The damage model B considered the total removal of the damaged element and the progressive loading of the structure. Before the incremental loading of the structure, no additional loads were acting on the scheme. The loading process was controlled by the vertical displacement of the top node of the damaged element (i.e., the node set at +3.20 m). Because of that, the loading process might be related to an incremental "pushdown" analysis. In order to monitor the effective load on the structure at each loading step, the total base vertical reaction was considered. The reference base reaction value in the undamaged scheme was determined before the removal of the element and, then, the corresponding values at each loading step were recorded.

2.3 Damage model C

The damage model C considered the substitution of the damaged element with a set of forces that simulate its presence. The forces are then progressively reduced to zero. The simulations accounting for this damage model were implemented as follows, see Figure 3 for visual details. First, (i) the undamaged structure was loaded with the external loads with the load combination into Eqn. (1). A nonlinear solver was considered and the displacements and the forces in the elements were evaluated. In particular, the forces acting in the potentially damaged element were recorded, i.e., the red forces in Figure 3(a). In the present paper, only the forces acting at the top end of the element were considered; the bottom end of the element, being a base column, was restraint. Then, (ii) the damaged element was removed and a set of external forces, F^*, were added to the scheme, black forces in Figure 3(b). Such forces are opposite to the ones of the previous step, i.e., $F^* = -F$. A nonlinear run was made and the nodal displacements were read and it resulted that were approximatively equal to the ones computed at step (i). In the following (iii), a system of forces f opposite to the ones derived in the previous step (ii) was added on the node, as sketched in blue in Figure 3(c). The purpose of the model was to progressively reduce the effects of forces F^*, which means damaging the i-th element. Thus, forces f were progressively increased from zero to F following a displacement controlled incremental scheme (see Damage model B for details on the control node). Therefore, it results

$$\begin{aligned} f &: 0 \to F \\ F^* + f &: F^* \to 0. \end{aligned} \tag{4}$$

It might happen that it was not possible to increment the forces f to their nominal value F because a failure occurs in the loading process. In this case, the ultimate value of f was considered in the analysis.

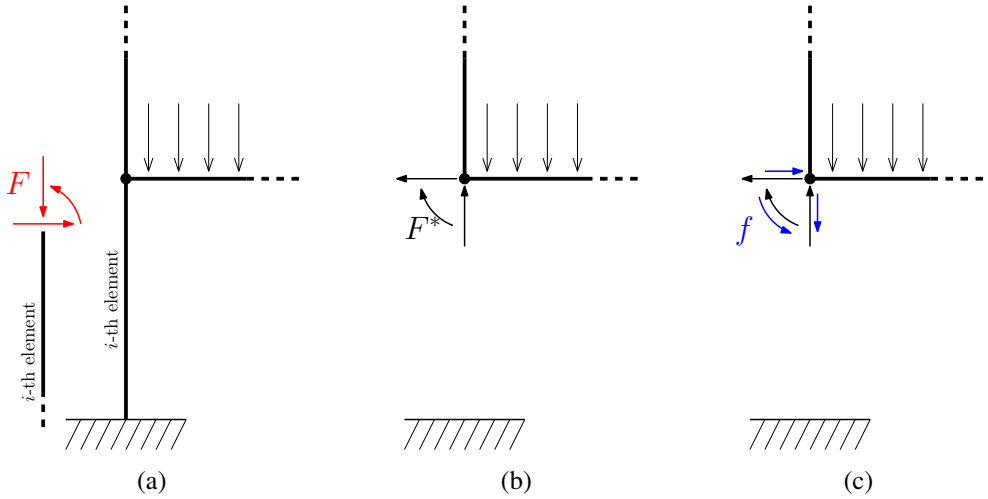

Figure 3: Damage model C. The details are reported in section 2.3.

3 RESULTS

The observed behavior modes of the three structures subjected to the three damage models are presented in the following. Figure 4 displays the values of vertical drift as much as the

damage parameter d increases. If figure panels are observed, it emerges that the trends obtained for the three structures designed with different standards ("S", "D" or "D+HoR") are similar. The increment of the vertical drift is relatively small for low values of damage parameter, while it sharply increases as much as d tends to unity. The behaviors of the three different structures to damage are compared observing the ranges of the damage parameter at equal vertical drift. For the structure able to support static loads only, see Figure 4(a), a vertical drift of 10^{-3} is given for values of d ranging between 0.65 and 0.85 (depending from the damaged element). A narrow range of values of the damage parameter are found for the same vertical drift in the other two structures: 0.84 – 0.91 in ductile only schemes ("D") and 0.86 – 0.92 in "D+HoR" structures.

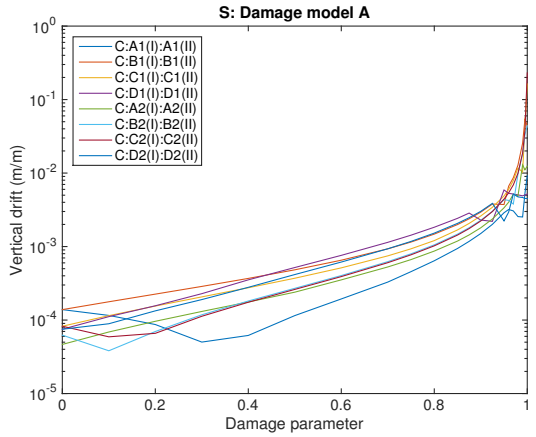

(a) "S": static design

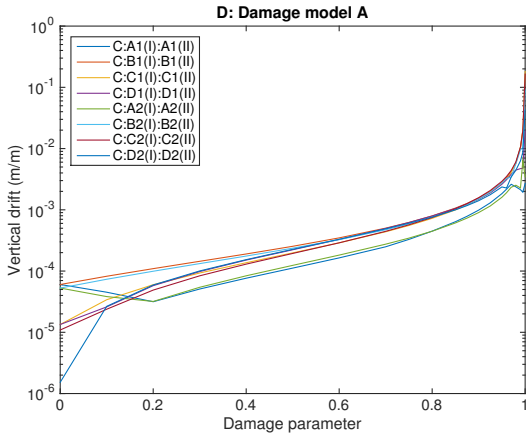

(b) "D": ductility design

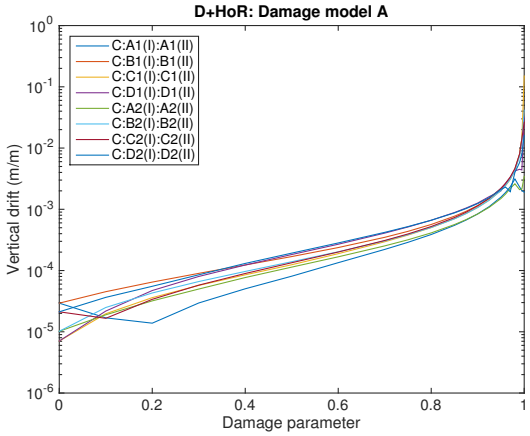

(c) "D+HoR": ductility + hierarchy of resistances design

Figure 4: Vertical drifts as functions of the damage parameter d for the Damage model A.

Figure 5 gives the outputs of pushdown analysis illustrated in the framework of Damage model B. The loading percentage is plotted with reference to the vertical drift. It is observed that the overall response varies depending on the structural design and on the damaged element. In none of the considered cases, the values attain 100%, i.e., it is not possible to apply on the structure the loading combination reported in Eqn. (1). The inspection of Figure 5(a) indicates that the response of the structure "S" is variable: the maximum loading allowed on the damaged scheme is about 50% in case of the removal of column C:A2(I):A2(II). Lower values, i.e.,

between 25% and 30% of the nominal loading expressed by Eqn. (1), are found in case of damage of the remaining elements. Different trends are observed for the structures designed with ductility. The behaviors of "D" and "D+HoR" schemes under damage are essentially the same. The maximum loading related to the tests performed on columns C:D1(I):D1(II) and C:D2(I):D2(II), i.e., the violet and blue curves in Figures 5(b) and 5(c), is larger than 80% of the nominal value. In the tests performed on the other columns, the maximum load ranges between 40% and 60%. The plateau in some curves on "D" and "D+HoR" structures confirm that, before failure, plastic hinges form and the structure dissipate energy in order to support larger loads.

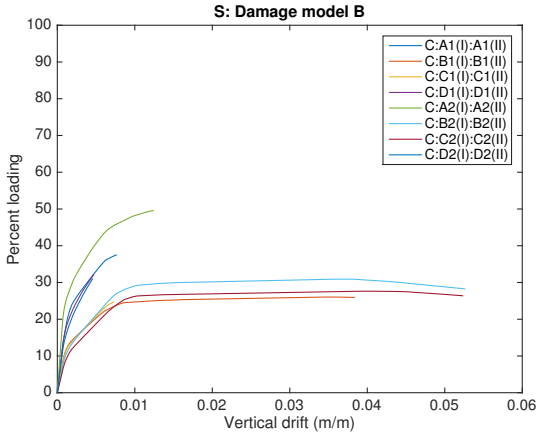

(a) "S": static design

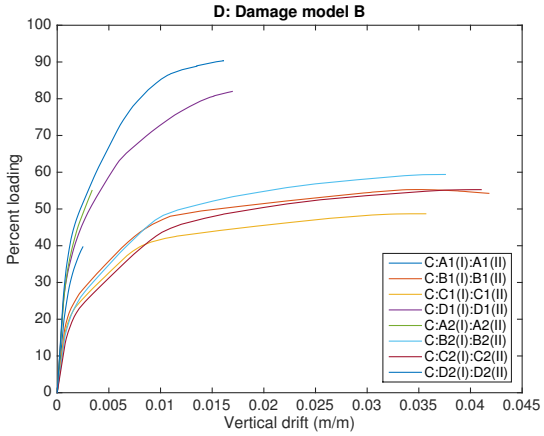

(b) "D": ductility design

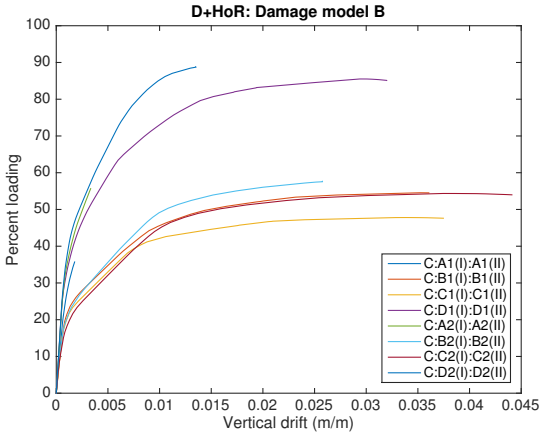

(c) "D+HoR": ductility + hierarchy of resistances design

Figure 5: Vertical drifts and percentage of unloading for Damage model B.

Consistent results are found if Damage model C (Figure 6) is considered. Despite the loading on the structure is different from the previous damage model, the results are quite similar. The tests conducted on the structure designed to support static loads show that the unloading ranges between 20% and 50%, as displayed in Figure 6(a). Meanwhile, the remaining schemes confirm that it is not possible to add the nominal value of f in order to set to cancel the force F^*. Ranges between 40% and 90% are observed in Figures 6(b) and 6(c).

Both Damage model B and C identify the behavior of the damaged structure through values of vertical drift and loading/unloading percentages. Therefore, a relationship between the two

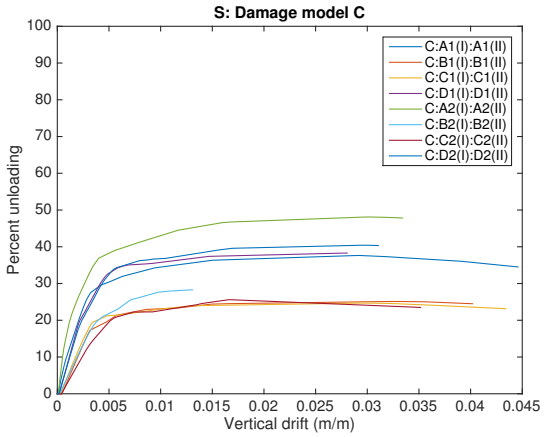

(a) "S": static design

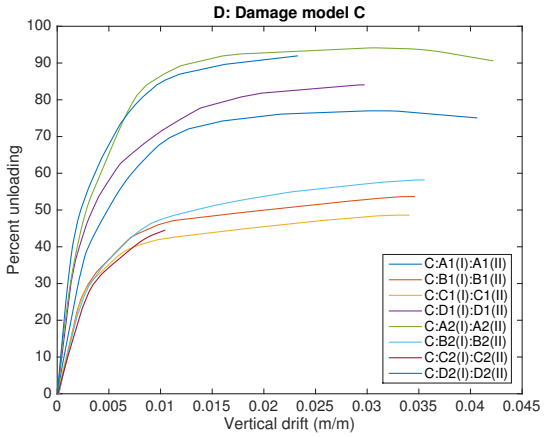

(b) "D": ductility design

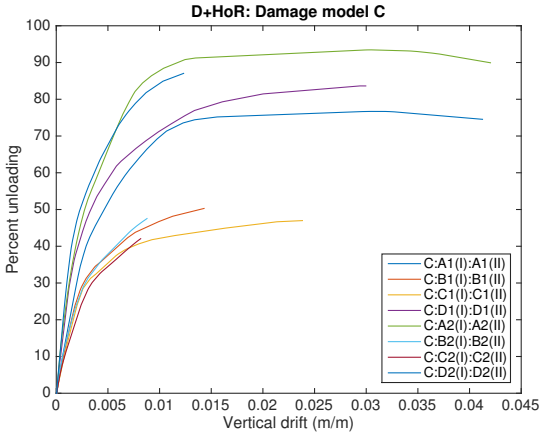

(c) "D+HoR": ductility + hierarchy of resistances design

Figure 6: Vertical drifts and percentage of loading for Damage model C.

different approaches is investigated. The coupling between the results of the two damage models is made through the value of the vertical drift. The loading percentages of Damage model B are interpolated at the values of the drifts corresponding to the computed unloading percentages of Damage model C. In Figure 7 the correlation points are plot. It results that at 0% in Damage model B, positive percentages are evaluated in Damage model C. This is due to the fact that at the beginning of the simulation in Damage model B the structure is unloaded, i.e., no vertical drift is recorded, while it is loaded (and, thus, deformed) at the initial step of the simulations with Damage model C.

Fair correlation is seen in any of the considered structures for loading/unloading percentages smaller than roughly 35%. In the schemes designed with ductility requirements (i.e., both "D" and "D+HoR") better results are observed in some tests for percentages larger than 50%.

In order to assess the computational effort for performing the simulations, the computation times needed for getting the results herein presented have been recorded. As emerges in Table 3, the time needed for the calculations related to Damage model A is one order of magnitude larger than the one necessary to perform the robustness analysis on Damage models B and C.

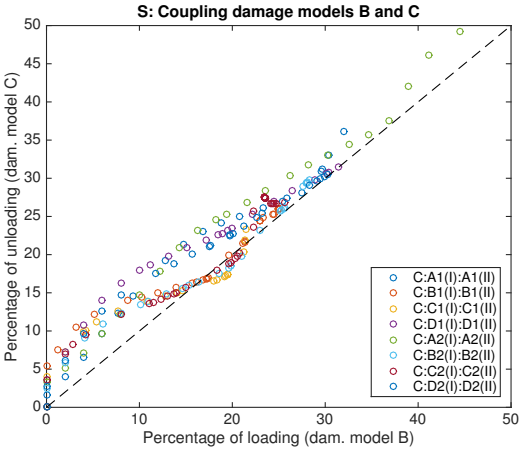

(a) "S": static design

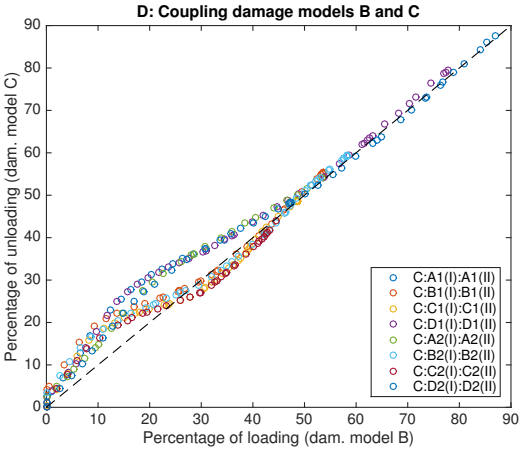

(b) "D": ductility design

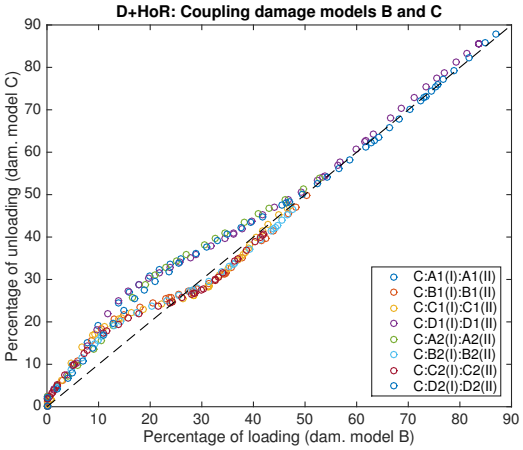

(c) "D+HoR": ductility + hierarchy of resistances design

Figure 7: Coupling between Damage model B and Damage model C. The dashed line is the bisector of the quarter, identifying the perfect correlation between the two damage models.

4 DISCUSSION AND CONCLUSIONS

A literature overview has highlighted that no detailed researches were conducted on the ways to implement a damage condition in a commercial FEM software in order to assess the structural robustness of a construction. The present approach deals with three different strategies that do not expressly consider the damage from a local (microscopic effects on the damaged element) to a global (the whole construction) scale. The first damage model evaluates the response of the structure for various levels of cross-section reduction in selected damaged elements. The second damage model presupposes that selected elements are removed and the structure is incrementally loaded. In the last damage model, the damaged element is replaced by an additional system of forces equivalent to the ones that it experiences in the undamaged structure; then, forces are progressively reduced. In real situations, the external loads (gravity + dead load) are always present throughout all the duration of the damage process. Because of that, we think that Damage model C can provide a good representation of what might happen on a real damaged structure. Meanwhile, we observe that a damage on a column is monitored through geometrical and mechanical data (carbonation depth, spalling, aging): in this case, there are no clear connec-

Scheme	Dam. model A	Dam. model B	Dam. model C
S	6h 12m	0h 24m	0h 31m
D	5h 52m	0h 38m	0h 37m
D+HoR	3h 40m	0h 27m	0h 17m

Table 3: Computation times.

tions between the percentage of unloading and the amount of damage on the element. Although Damage model A tries to overcome this problem through the damage parameter, its inadequacy is highlighted by the fact that at the beginning of each simulation the structure is unloaded. Damage model B does not consider neither the presence of the element during the damage process nor the loads acting on the structure. However, it is the simplest to be implemented in the analysis since no iterative calculations or advanced modeling are required.

We believe that the Damage model C can be the most accurate among the three proposed strategies for assessing the structural robustness of a structure. However, at present, its implementation in a commercial code is not simple because programming abilities are required. Usually, softwares does not allow to control single loadcases, except those related to seismic horizontal force in push-over analyses. The implementation of Damage model C in the commercial softwares would require a specific plug-in able to perform such kind of analyses.

Anyway, the results of Damage models B and C are comparable, as found in Figure 7. That is why we believe that Damage model B, which is the simplest and the quickest to be implemented among the three proposed strategies, can give insights on the structural robustness of a scheme. This choice is supported by the fact that there are no substantial differences in the computational effort in choosing Damage model B or C for assessing the robustness of the structure.

In general, we found that none of the three structures designed with different standard requirements are safe in case of the removal of a column at the bottom level. This confirms that seismic design guidelines and principles do not necessarily ensure the structural robustness of a building.

Future developments of the research would deal with the correlation between the physical damage and the parameters to be used in the numerical simulation. This would permit to assess the reliability of a structure onto which a progressive damage is acting.

ACKNOWLEDGEMENTS

The present work was done under in framework of ReLUIS project 2014/2016 “Supporto alle attività di gestione tecnica dell’emergenza e connesse ai programmi di prevenzione sismica, per lo sviluppo della conoscenza e l’assistenza alla redazione di norme tecniche, per la collaborazione alle attività di formazione, comunicazione e divulgazione – ReLUIS. Linea di ricerca Cemento Armato”.

REFERENCES

[1] J. Kim, T. Kim. Assessment of progressive collapse-resisting capacity of steel moment frames. *Journal of Constructional Steel Research*, **65**,169–179, 2009.

[2] B.A. Izzuddin, A.G. Vlassis, A.Y. Elghazouli, D.A. Nethercot. Progressive collapse of multi-storey buildings due to sudden column loss? Part I: simplified assessment framework. *Engineering Structures*, **30**, 1308–1318, 2008.

[3] A.G. Vlassis, B.A. Izzuddin, A.Y. Elghazouli, D.A. Nethercot. Progressive collapse of multi-storey buildings due to sudden column loss? Part II: application. *Engineering Structures*, **30**, 1424–1438, 2008.

[4] F. Parisi, C. Balestrieri, D. Asprone. Blast resistance of tuff stone masonry walls. *Engineering Structures*, **113**, 233–244, 2016.

[5] G.V. Gudmundsson, B.A. Izzuddin. The 'sudden column loss idealisation' for disproportionate collapse assessment. *The Structural Engineer*, **88**, 22–26, 2010.

[6] British Standards Institution. *BS 5950: Structural use of steelwork in buildings, Part 1: code of practice for design ? rolled and welded sections*. London, 2001.

[7] Unified Facilities Criteria. *Design of buildings to resist progressive collapse*. Department of Defense, Virginia, USA, 2009.

[8] H. Zolghadr Jahromi, A.G. Vlassis, B.A. Izzuddin. Modelling approaches for robustness assessment of multi-storey steel-composite buildings. *Engineering Structures*, **51**, 287–294, 2013.

[9] L. Kwasniewski. Nonlinear dynamic simulations of progressive collapse for a multistory building. *Engineering Structures*, **32**, 1223–35, 2010.

[10] D. Asprone, F. Jalayer, A. Prota, G. Manfredi. Proposal of a probabilistic model for multi-hazard risk assessment of structures in seismic zones subjected to blast for the limit state of collapse. *Structural Safety*, **32**, 25–34, 2010.

[11] E. Nigro, A. Bilotta, D. Asprone, F. Jalayer, A. Prota, G. Manfredi. Probabilistic approach for failure assessment of steel structures in fire by means of plastic limit analysis. *Fire Safety Journal*, **68**, 16–29, 2014.

[12] R.R. Sun, Z.H. Huang, I.W. Burgess. Progressive collapse analysis of steel structures under fire conditions. *Engineering Structures*, **34**. 400–413, 2012.

[13] R.R. Sun, Z.H. Huang, I.W. Burgess. The collapse behaviour of braced steel frames exposed to fire. *Journal of Constructional Steel Research*, **72**, 130–142, 2012.

[14] K.T. Ng, L. Gardner. Buckling of stainless steel columns and beams in fire. *Engineering Structures*, **29**, 711–30, 2007.

[15] C. Fang, B.A. Izzuddin, A.Y. Elghazouli, D.A. Nethercot. Simplified energy-based robustness assessment for steel-composite car parks under vehicle fire. *Engineering Structures*, **49**, 719–732, 2013.

[16] J.L. Le, B. Xue. Probabilistic analysis of reinforced concrete frame structures against progressive collapse. *Engineering Structures*, **76**, 313–323, 2014.

[17] S. Sagiroglu, M. Sasani. Progressive collapse-resisting mechanisms of reinforced concrete structures and effects of initial damage locations. *Journal of Structural Engineering*, **140**, 04013073-1–12, 2014.

[18] A. Fascetti, K.S. Kunnath, N. Nisticò. Robustness evaluation of RC frame buildings to progressive collapse. *Engineering Structures*, **86**, 242–249, 2015.

[19] V. De Biagi, B. Chiaia. Complexity and robustness of frame structures. *International Journal of Solids and Structures*, **50**, 3723–3741, 2013.

[20] C. Cennamo, B. Chiaia, V. De Biagi, L. Placidi. Monitoring and compartmentalized structures. *Zeitschrift für Angewandte Mathematik und Mechanik*, **95**, 638–648, 2015.

[21] V. De Biagi. Structural behavior of a metallic truss under progressive damage. *International Journal of Solids and Structures*, **82**, 56–64, 2016.

[22] V. De Biagi, B. Chiaia. Damage tolerance in parallel systems. *International Journal of Damage Mechanics*, 1–20, 2016. (DOI: 10.1177/1056789516630777)

[23] P. Russo, F. Parisi. Risk-targeted safety distance of reinforced concrete buildings from natural-gas transmission pipelines. *Reliability Engineering and System Safety*, **148**, 57–66, 2016.

[24] E. Brunesi, R. Nascimbene, F. Parisi, N. Augenti. Progressive collapse fragility of reinforced concrete framed structures through incremental dynamic analysis. *Engineering Structures*, **104**, 65–79, 2015.

[25] F. Parisi F. Blast fragility and performance-based pressure?impulse diagrams of European reinforced concrete columns. *Engineering Structures*, **103**, 285–297, 2015.

[26] F. Parisi, N. Augenti. Influence of seismic design criteria on blast resistance of RC framed buildings: a case study. *Engineering Structures*, **44**, 78–93, 2012.

[27] V. De Biagi, B. Chiaia, B. Frigo. Impact of snow avalanche on buildings: Forces estimation from structural back-analyses. *Engineering Structures*, **92**, 15–28, 2015.

[28] General Services Administration, *Alternate Path Analysis & Design Guidelines For Progressive Collapse Resistance*. Washington, DC, 2013.

[29] P. Ruth, K.A. Marchand, E.B. Williamson. Static equivalency in progressive collapse alternate path analysis: reducing conservatism while retaining structural integrity. *Journal of Performance of Constructed Facilities*, **20**, 349–364, 2006.

[30] J. Lemaître, J.-L. Chaboche, *Mechanics of Solid Materials*. Cambridge University Press, 1994.

[31] Repubblica Italiana, Decreto Ministeriale 14/01/2008 – Norme tecniche per le costruzioni. *Gazzetta Ufficiale della Repubblica Italiana*, **29**, S.O. 30, 2008

[32] Repubblica Italiana, Decreto Ministeriale 16/01/1996 – Norme tecniche relative ai criteri generali di verifica di sicurezza delle costruzioni e dei carichi e sovraccarichi. *Gazzetta Ufficiale della Repubblica Italiana*, **29**, S.O. 19, 1996.

[33] Regno d'Italia, Regio decreto-legge 3/04/1930 – Nuove norme tecniche ed igieniche di edilizia per le localit sismiche. *Gazzetta Ufficiale del Regno di Italia*, **133**, 2236–2258, 1930.

ECCOMAS Congress 2016
VII European Congress on Computational Methods in Applied Sciences and Engineering
M. Papadrakakis, V. Papadopoulos, G. Stefanou, V. Plevris (eds.)
Crete Island, Greece, 5–10 June 2016

SEISMIC RESIDUAL CAPACITY ASSESSMENT OF FRAMED STRUCTURES DAMAGED BY EXCEPTIONAL ACTIONS

A. Formisano[1], G. Iazzetta[2], G. Marino[3], F. Fabbrocino[4] and R. Landolfo[5]

[1,2,3,5]Department of Structures for Engineering and Architecture
Piazzale Tecchio 80, 80125 Naples
e-mail: [1]antoform@unina.it, [2]peppe.iazzetta@libero.it, [3]gmarino1986@libero.it, [5]landolfo@unina.it,

[4]Department of Engineering, Pegaso Telematic University
Centro Direzionale, Isola A3, 80143 Naples
e-mail: [4]francesco.fabbrocino@unipegaso.it

Keywords: Framed structures, Exceptional actions, Fire damage, Seismic response, Residual capacity, Theoretical model.

Abstract. *The effect of natural or man-made disasters, especially when they assume exceptional character, on the urban habitat (buildings, infrastructures, etc.) can result in damages and losses for billions of dollars. In case of cascading events, the residual capacity of a construction damaged from a first threat is not evaluated through suitable calculation procedures neither well codified in actual standards.*

In this framework and with reference to framed structure buildings, the current research activity has the task to provide a tool which helps structural engineers to make a fast evaluation of the buildings performance after exceptional loading actions. Specifically, a theoretical formulation based on the results provided by pushover analyses for the assessment of the residual seismic capacity of buildings after damage produced by exceptional actions is herein presented. The theoretical method presented is basically applied to some case studies of steel framed buildings aiming at showing its effectiveness. To this purpose, a general analysis methodology, with the aim to show the procedure for the practical application of the theoretical formulation, is shown. Such a methodology has been applied to two steel framed buildings designed according to both the old and the new seismic Italian codes. After these frames have been subjected to a fire analysis at different temperatures, non-liner static analyses including P-Δ effects have been carried out with the aim to estimating both the force-displacement curves and the plasticity distribution in the structures. The analyses have provided the tangible application of the procedure, giving the structural parameters accounting for the structure damage status at the end of the exceptional loading action.

1 INTRODUCTION

Disasters occur under many different forms and have duration ranging from a hourly disruption to days or weeks of ongoing destruction. They can be either natural [1] or produced by people, both of them having a great impact on the community.

Hurricanes [2, 3] and tropical storms are among the most powerful natural disasters because of their size and destructive potential. Tornadoes are relatively brief but violent and, together with earthquakes, strike suddenly without warning. Flooding is the most common of natural hazards and requires an understanding of the environment natural systems.

Disasters can also be caused by humans. Hazardous materials emergencies include chemical spills and groundwater contamination. Workplace fires are more common and can cause significant property damage and loss of life. Communities are also vulnerable to threats posed by extremist groups, who use violence against both people and property. High-risk targets include military and civilian government facilities, international airports, large cities and high-profile landmarks. Cyber-terrorism involves attacks against computers and networks done to intimidate or coerce a government or its people for political or social objectives.

After constructions are subjected to a first extreme event, the structural performance evaluation should be related to the building response under gravity loads. After this step, the structure should be checked with reference to the seismic actions used in the design phase.

For example, considering fire exposure as a damage event, few studies have been developed and implemented to assess the residual seismic capacity of framed structures after the above exceptional action.

Among the limited researches available in literature, it was found that Mostafei et al. provided a study on the seismic resistance of fire-damaged reinforced concrete columns [4]. Analytical results show that the main seismic resistance properties of two reinforced concrete columns, namely the lateral load capacity and ductility, decreased substantially due to fire exposure. Mostafei also performed a structural test for evaluating the residual lateral load resistance of a reinforced concrete structure after fire damage [5]. Results of this test showed a reduction of both residual lateral stiffness and lateral load capacity of the structure after fire damage.

In the framework of this research activity, in the first part of this study, a theoretical formulation (based on pushover curves) for the assessment of seismic residual capacity of framed structure after extreme load action has been proposed. Instead, in the second part, related to the numerical investigation on moment resisting steel frames after fire damage, an analysis methodology able to validate the equations given in the first part has been proposed.

More in detail, based on the results provided in first part of this paper, with the aim to show a numerical procedure able to evaluate the functions $k_\delta(\phi)$, $k_F(\phi)$ used to measure the reduction of structural performance after an exceptional action, numerical non-linear seismic analyses on two steel structures, before subjected to fire and designed according to both the old [6] and the new [7] seismic Italian codes, have been performed.

2 THEORETICAL PREDICTION OF THE SEISMIC RESPONSE OF DAMAGED FRAMED STRUCTURES

In the last few decades, with the development of Performance-Based Design procedures, the need of simplified methods to estimate with an adequate confidence level the seismic demand for structures is increased. Non-linear static procedures appear as one of the most attractive analysis tool due to both their ease of use and also for the simple and effective graphical representation of the structural response by means of the so-called pushover curve.

The procedure of a conventional pushover analysis [8] is an incremental-iterative solution of the static equilibrium equations. The forcing function is a set of displacements or forces that are necessarily kept constant during the analysis. During an increment of displacement or force, the resistance of the structure is evaluated from the internal equilibrium conditions and the stiffness matrix is updated under certain conditions dependent on the iterative scheme adopted. The unbalanced forces are re-applied if they are deemed large until a convergence criterion is satisfied. At convergence, the stiffness matrix is reorganised and another increment of displacements or forces is applied.

In order to evaluate the seismic capacity of a framed structure before damaged by extreme actions, a theoretical formulation based on the *F*-δ pushover curve is herein proposed. The proposed formulation allows to evaluate the seismic response by determining three significant points of the cited response curve.

With reference to the Figure 1, which schematically illustrates the results provided by a push-over analysis carried out on a generic undamaged framed structure, it is possible to identify the following points:

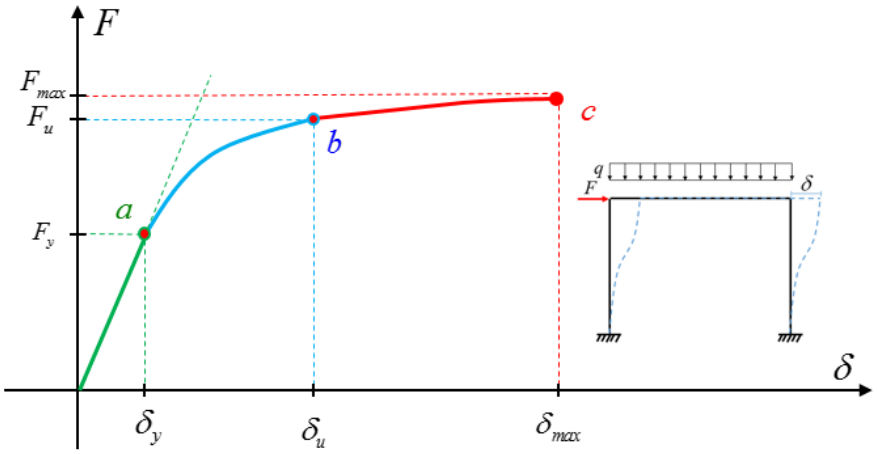

Figure 1: General force-displacement curve.

- Point a (F_y; δ_y) = seismic base shear and top horizontal displacement values corresponding to the first yielding;
- Point b (F_u; δ_u) = seismic base shear and top horizontal displacement values corresponding to the structure excursion in the elasto-plastic field;
- Point c (F_{max}; δ_{max}) = seismic base shear and top horizontal displacement values corresponding to the collapse.

So, when the following conditions are met:

$$\begin{aligned} F &\in \left[0; F_y\right] \\ \delta &\in \left[0; \delta_y\right] \end{aligned} \tag{1}$$

the structure is in the elastic range.

Instead, when:

$$\begin{aligned} F &\in \left[F_y; F_u\right] \\ \delta &\in \left[\delta_y; \delta_u\right] \end{aligned} \tag{2}$$

the structure is in the elastic-plastic range and, finally, when:

$$\begin{aligned} F &\in \left[F_u ; F_{max}\right] \\ \delta &\in \left[\delta_u ; \delta_{max}\right] \end{aligned} \tag{3}$$

the structure is in the plastic range up to the collapse condition (robustness field).

The quantities shown in Figure 1, useful for the assessment of seismic capacity of undamaged framed structure, can also be used to determine the residual capacity of buildings damaged by exceptional loading actions.

To this purpose, the mentioned quantities must be corrected to take into account the damage produced by an extreme load acting before the earthquake. In particular, in order to determine the seismic capacity of a framed structure damaged by an exceptional action, it is necessary to calculate the points *a*, *b* and *c* of the *F*-δ curve corresponding to each damage level induced by external (natural or man-made) actions. Consequently, the following relationships have to be considered:

$$\begin{cases} F_y \rightarrow F_y\left(\phi\right) \\ F_u \rightarrow F_u\left(\phi\right) \\ F_{max} \rightarrow F_{max}\left(\phi\right) \end{cases} \tag{4}$$

$$\begin{cases} \delta_y \rightarrow \delta_y(\phi) \\ \delta_u \rightarrow \delta_u(\phi) \\ \delta_{max} \rightarrow \delta_{max}(\phi) \end{cases} \tag{5}$$

where (F_y, F_u, F_{max}) and (δ_y, δ_u, δ_{max}) are parameters representative of the seismic behaviour of the original structure (without damage), while the corresponding ($F_y(\phi)$, $F_u(\phi)$, $F_{max}(\phi)$) and ($\delta_y(\phi)$, $\delta_u(\phi)$, $\delta_{max}(\phi)$) are indicative of the structural seismic behaviour after induced damage. The parameter ϕ has to be seen as "the value of a generic parameter correlated to a specific damage state produced by an assigned external action acting before the seismic event". Table 1 shows some meanings assumed by the damage parameter ϕ corresponding to different types of exceptional actions considered.

Exceptional Load	**Φ**
Fire	Temperature, Exposure time [4], [5], [9]
Hurricane, Tornado	Wind speed [2]
Blast load, Explosion	Wave front speed; Peck static overpressure; Maximum dynamic pressure [10], [11], [12]
Volcanic Ash Fall	Ash thickness; Ash density; Ash temperature [13]
Volcanic Pyroclastic Flow	Flow temperature; Flow dynamic pressure; Flow speed [13]
Volcanic Lahar	Lahar speed; Lahar hydrodynamic pressure [13]
Volcanic Earthquake	Earthquake Peak Ground Acceleration (PGA) [13]

Table 1: Examples of damage parameters corresponding to various types of exceptional actions.

Once ϕ is defined and assuming known the values of the following functions:

$$\begin{aligned}\alpha_y(\phi) &= \left[F_y(\phi)/F_y\right] \\ \alpha_u(\phi) &= \left[F_u(\phi)/F_u\right] \\ \alpha_{max}(\phi) &= \left[F_{max}(\phi)/F_{max}\right]\end{aligned} \tag{6}$$

$$\begin{aligned}\xi_y(\phi) &= \left[\delta_y(\phi)/\delta_y\right] \\ \xi_u(\phi) &= \left[\delta_u(\phi)/\delta_u\right] \\ \xi_{max}(\phi) &= \left[\delta_{max}(\phi)/\delta_{max}\right]\end{aligned} \tag{7}$$

the values of displacements and forces after damage can be expressed in the following way:

$$\begin{aligned}\delta_y(\phi) &= \delta_y \cdot \xi_y(\phi) \\ \delta_u(\phi) &= \delta_u \cdot \xi_u(\phi) \\ \delta_{max}(\phi) &= \delta_{max} \cdot \xi_{max}(\phi)\end{aligned} \tag{8}$$

$$\begin{aligned}F_y(\phi) &= F_y \cdot \alpha_y(\phi) \\ F_u(\phi) &= F_u \cdot \alpha_u(\phi) \\ F_{max}(\phi) &= F_{max} \cdot \alpha_{max}(\phi)\end{aligned} \tag{9}$$

From these general relationships it is possible to extrapolate a more compact formulation, thereby expressing the six constants (F_y, F_u, F_{max}, δ_y, δ_u, δ_{max}) as a function of only two maximum parameters (F_{max}, δ_{max}) of the curve. This is shown in Figure 2, where the dimensionless pushover curve obtained for a generic ϕ parameter is plotted.

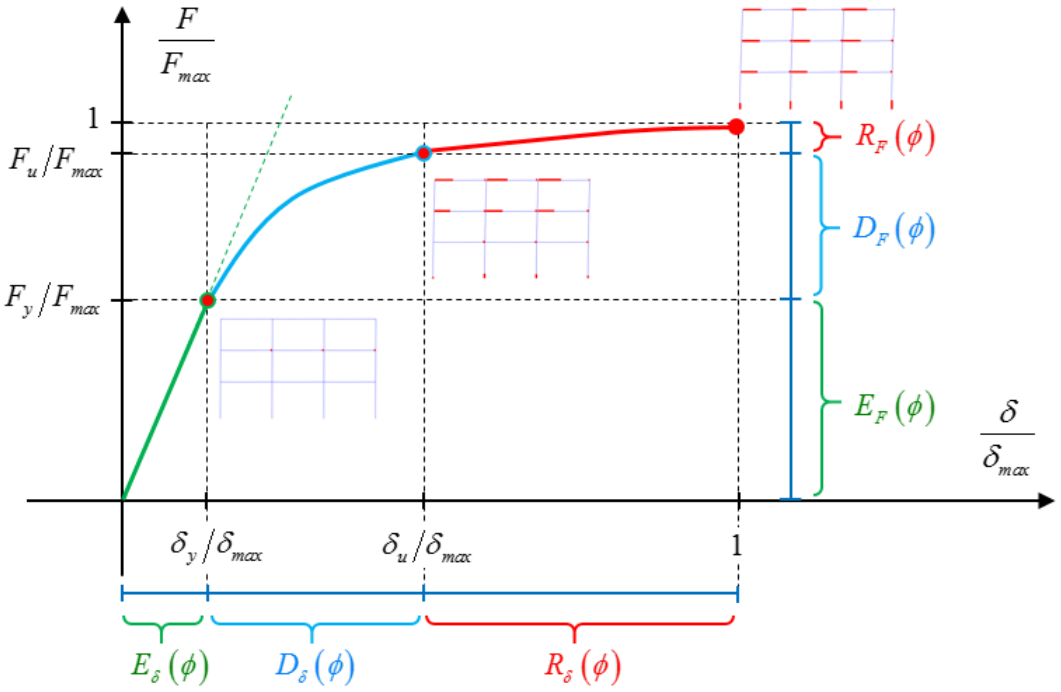

Figure 2: Dimensionless pushover curve.

Assuming once again known the functions described in equations (6) and (7), it is possible to write:

$$E_\delta(\phi) = \left[\frac{\delta_y}{\delta_{max}} \cdot \frac{\xi_y(\phi)}{\xi_{max}(\phi)} \right] \tag{10}$$

$$D_\delta(\phi) = \left\{ \left[\frac{\delta_u}{\delta_{max}} \cdot \frac{\xi_u(\phi)}{\xi_{max}(\phi)} \right] - \left[\frac{\delta_y}{\delta_{max}} \cdot \frac{\xi_y(\phi)}{\xi_{max}(\phi)} \right] \right\} \tag{11}$$

$$R_\delta(\phi) = \left\{ 1 - \left[\frac{\delta_u}{\delta_{max}} \cdot \frac{\xi_u(\phi)}{\xi_{max}(\phi)} \right] \right\} \tag{12}$$

These functions must satisfy the following conditions:

$$\begin{cases} E_\delta(\phi) \\ D_\delta(\phi) \in [0;1] :\rightarrow E_\delta(\phi) + D_\delta(\phi) + R_\delta(\phi) = 1 \\ R_\delta(\phi) \end{cases} \tag{13}$$

$E_\delta(\phi)$, $D_\delta(\phi)$ and $R_\delta(\phi)$ are parameters that can be seen as distribution coefficients of the seismic capacity of structures in terms of horizontal displacement. In particular, $E_\delta(\phi)$ refers to the elastic field, $D_\delta(\phi)$ to the ductile field and $R_\delta(\phi)$ to the robustness field.

Multiplying the expressions (10), (11) and (12) for the quantity ($\delta_{max} \cdot \xi_{max,}$), the following equations can be derived:

$$\delta_{max} \cdot \xi_{max}(\phi) \cdot E_\delta(\phi) = \Delta\delta_y(\phi) \tag{14}$$

$$\delta_{max} \cdot \xi_{max}(\phi) \cdot D_\delta(\phi) = \Delta\delta_u(\phi) \tag{15}$$

$$\delta_{max} \cdot \xi_{max}(\phi) \cdot R_\delta(\phi) = \Delta\delta_{max}(\phi) \tag{16}$$

where $\Delta\delta_i(\phi)$ (i=y, u, max) are the displacement increment necessary for the transition from a behavioural phase to the following one.

Through the equations (14), (15) and (16), it is possible to write:

$$\delta_y(\phi) = 0 + \Delta\delta_y(\phi) \tag{17}$$

$$\delta_u(\phi) = \delta_y(\phi) + \Delta\delta_u(\phi) \tag{18}$$

$$\delta_{max}(\phi) = \delta_u(\phi) + \Delta\delta_{max}(\phi) \tag{19}$$

where $\delta_i(\phi)$ (i=y,u,max) are the basic displacements required to determine the seismic response in the displacement field.

Placing the equations (14), (15), (16) in the equations (17), (18), (19), it is possible to write:

$$\delta_y(\phi) = 0 + \delta_{max} \cdot \xi_{max}(\phi) \cdot E_\delta(\phi) \tag{20}$$

$$\delta_u(\phi) = \left[\delta_{max} \cdot \xi_{max}(\phi) \cdot E_\delta(\phi) \right] + \left[\delta_{max} \cdot \xi_{max}(\phi) \cdot D_\delta(\phi) \right] \tag{21}$$

$$\delta_{max}(\phi) = \left[\delta_{max} \cdot \xi_{max}(\phi) \cdot E_\delta(\phi) \right] + \left[\delta_{max} \cdot \xi_{max}(\phi) \cdot D_\delta(\phi) \right] + \left[\delta_{max} \cdot \xi_{max}(\phi) \cdot R_\delta(\phi) \right] \tag{22}$$

Grouping the equations (20), (21) and (22) with respect to (δ_{max} . $\xi_{max}(\phi)$), the following relationships are achieved:

$$k_{y,\delta}(\phi) = \xi_{max}(\phi) \cdot E_{\delta}(\phi) \tag{23}$$

$$k_{u,\delta}(\phi) = \xi_{max}(\phi) \cdot \left[E_{\delta}(\phi) + D_{\delta}(\phi) \right] \tag{24}$$

$$k_{max,\delta}(\phi) = \xi_{max}(\phi) \cdot \left[E_{\delta}(\phi) + D_{\delta}(\phi) + R_{\delta}(\phi) \right] = \xi_{max}(\phi) \tag{25}$$

where $k_{i,\delta}(\phi)$ (i= y, u, max) are the reduction factors of seismic performance of the structure in the displacement field, which take implicitly into account the repartition of the capacity itself.

Definetively, it is possible to write:

$$\delta_{y}(\phi) = \left[\delta_{max} \cdot k_{y,\delta}(\phi) \right] \tag{26}$$

$$\delta_{u}(\phi) = \left[\delta_{max} \cdot k_{u,\delta}(\phi) \right] \tag{27}$$

$$\delta_{max}(\phi) = \left[\delta_{max} \cdot k_{max,\delta}(\phi) \right] \tag{28}$$

Instead the equations (26), (27) and (28) show that the basic displacements $\delta_{y}(\phi)$, $\delta_{u}(\phi)$ and $\delta_{max}(\phi)$ belonging to the $F(\phi)$–$\delta(\phi)$ curve can be calculated starting from the displacement value δ_{max} only, therefore neglecting the δ_{u} and δ_{y} values.

Equivalently, the trends of $F_{y}(\phi)$, $F_{u}(\phi)$ and $F_{max}(\phi)$ can be expressed as a function of the F_{max} value only by considering the $k_{F,y}(\phi)$, $k_{F,u}(\phi)$ and $k_{F,max}(\phi)$ parameters as follows:

$$F_{y}(\phi) = \left[F_{max} \cdot k_{y,F}(\phi) \right] \tag{29}$$

$$F_{u}(\phi) = \left[F_{max} \cdot k_{u,F}(\phi) \right] \tag{30}$$

$$F_{max}(\phi) = \left[F_{max} \cdot k_{max,F}(\phi) \right] \tag{31}$$

where:

$$k_{y,F}(\phi) = \alpha_{max}(\phi) \cdot E_{F}(\phi) \tag{32}$$

$$k_{u,F}(\phi) = \alpha_{max}(\phi) \cdot \left[E_{F}(\phi) + D_{F}(\phi) \right] \tag{33}$$

$$k_{max,F}(\phi) = \alpha_{max}(\phi) \cdot \left[E_{F}(\phi) + D_{F}(\phi) + R_{F}(\phi) \right] = \alpha_{max}(\phi) \tag{34}$$

Definitively, all the previous relationships provide a theoretical formulation for the calculation of the seismic response of a framed structure previously damaged by an extreme event.

Unfortunately, into equations (8), (9), (26), (27), (28), (29), (30) and (31), the values of the functions $\alpha(\phi)$, $\xi(\phi)$, $k_{\delta}(\phi)$ and $k_{F}(\phi)$ are not known a priori (see respectively equations (6), (7), (23), (24), (25), (32), (33), (34)) .

Basically, the main issue consists on the determination of the structure damage status at the end of the exceptional loading action. In this framework, Table 2 shows some of the variables, other than the building properties, which influence the structural response.

Exceptional Load	Influential variables
Fire	Fire scenario, Fire model, Fire Proofing
Hurricane, Tornado	Wind speed
Blast load, Explosion	Explosive characteristic, Detonation scenario, Blast Proofing
Volcanic Ash Fall	Ash thickness, Ash density, Ash temperature , Roof configuration
Volcanic Pyroclastic Flow	Flow dynamic pressure, Building shape, Topographical configuration of the site
Volcanic Lahar	Structural typology, Impact Angle with structure, Lahar temperature, Impact surface, Flow density
Volcanic Earthquake	Earthquake Response Spectrum, Soil-Structure Interaction.

Table 2: List of various variables influencing different types of exceptional actions.

The variables listed into the above table must be considered in order to provide useful values of the functions $\alpha(\phi)$ and $\xi(\phi)$ and, consequently, of the functions $k_\delta(\phi)$ and $k_F(\phi)$ for design purposes. This aim can be accomplished through a comprehensive numerical and experimental investigation campaign by taking into account at least the variability of the above mentioned influential variables.

Once known these functions and the undamaged structure capacity (F_{max}; δ_{max}), a simplified check of the seismic capacity of a given framed structure after an exceptional loading action can be executed without performing sequential non-linear analyses.

3 THE CASE STUDIES

In order to show the effectiveness of the theoretical method presented above, starting from the general equations described in Section 2, it can be possible to replace the dependence of the functions from "ϕ" with the specified damage parameter that, in the specific case, consists on the temperature value "θ" inside the structural members.

Practically, starting from the following general equations:

$$\begin{aligned} F(\phi) &= F_{max} \cdot k_F(\phi) \\ \delta(\phi) &= \delta_{max} \cdot k_\delta(\phi) \end{aligned} \tag{35}$$

it is possible to express the study significant parameters as a function of the parameter θ as follows:

$$\begin{aligned} \alpha(\phi) &\rightarrow \alpha(\theta) \\ \xi(\phi) &\rightarrow \xi(\theta) \end{aligned} \tag{36}$$

$$\begin{aligned} k_F(\phi) &\rightarrow k_F(\theta) \\ k_\delta(\phi) &\rightarrow k_\delta(\theta) \end{aligned} \tag{37}$$

which give rise to the following relationships:

$$F(\phi) = F_{max} \cdot k_F(\theta)$$
$$\delta(\phi) = \delta_{max} \cdot k_\delta(\theta) \tag{38}$$

that are used to examine the structural seismic behaviour of steel MRF after fire.

3.1 Geometrical and mechanical features

In this study, two different types of steel framed structures have been analysed aiming at evaluating their seismic capacity after fire actions. The choice of the frame types has been done according to a previous study performed by the first Author [14, 15, 16].

The first framed structure has been designed according to the old Seismic Italian Code (M.D., 1996), while the second one has been designed according to the new Seismic Italian Code (M.D., 2008). Both structures are subjected to permanent and variable loads of 5.15 kNm^{-2} and 2 kNm^{-2}, respectively.

Both framed structures have the same geometric configuration with three 5m bays and three levels (H=3.50 m at 1st floor; H=3.00 m at 2nd and 3rd floor).

Figure 3 shows the geometrical properties of the steel framed structures inspected.

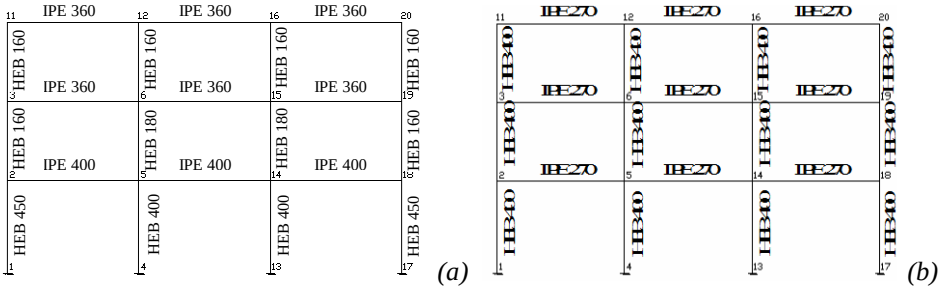

Figure 3: The examined steel framed structures designed according to M.D. 1996 (a) and M.D. 2008 (b).

The selected framed buildings are made of S275JR steel profiles.

Figure 4a shows the stress-strain relationships of the steel material used in this study, while figure 4b shows the reduction factors of the material mechanical properties at elevated temperatures [17].

In particular, six uniform temperature fields (θ= 20°C, 100°C, 200°C, 300°C, 400°C, 500°C) have been applied to the structures before seismic loads have been considered.

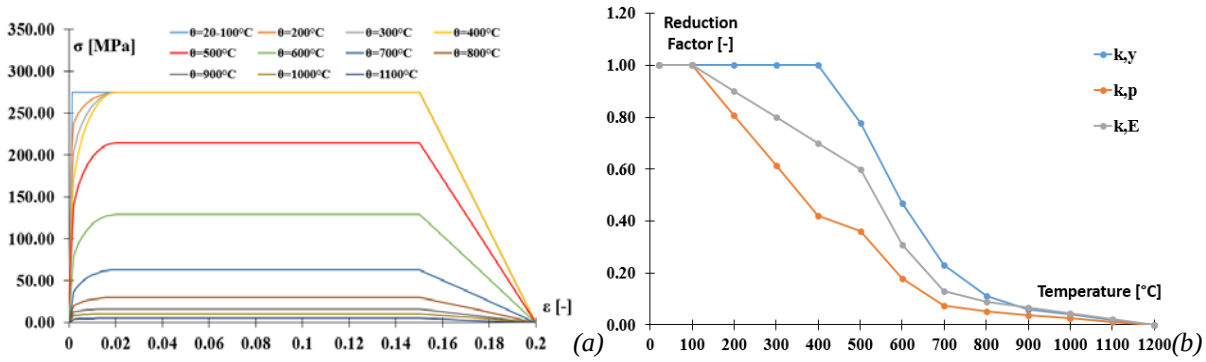

Figure 4: Mechanical properties of S275JR steel: constitutive laws (a) and reduction factors (b) at different temperatures.

3.2 The FEM models

Non-linear static analyses including *P-Δ* effects have been performed by means of the FE software "ABAQUS v.6.10-1" [18] in order to estimate both the force-displacements pushover curves and the plasticity distribution in the inspected structures.

Figure 5a and b show the details of the typical finite element model based on beam elements used for modelling the generic frame. In particular, columns and beams have been modelled by using into a 2D model the beam elements type B21. Second-order elements, like B22 ones, have been avoided owing to the so-called 'volumetric locking' problem, which is induced by the large strains in the frame deformed configuration. Firstly, the effect of different number of constitutive elements for columns and beams has been investigated in order to provide accurate results with a reduced computational time. It was found that 80 elements are sufficient for a reliable analysis of the 2D plane frame model.

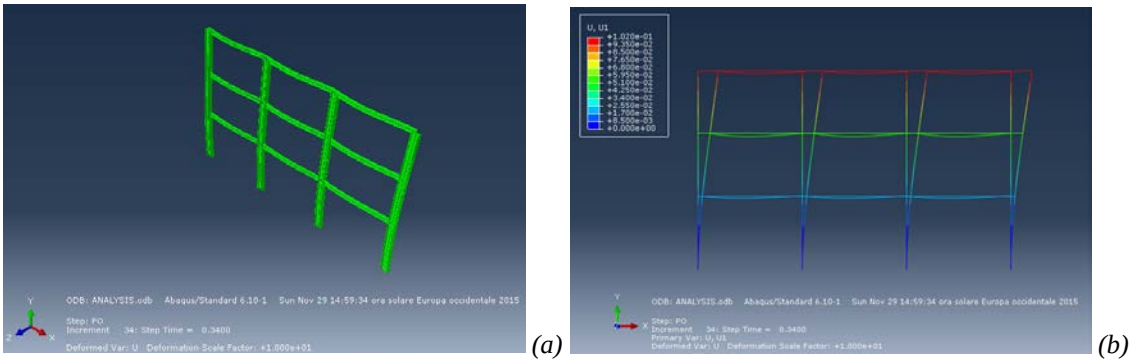

Figure 5: Deformed FEM model under gravity loads of one of the tested frames (a) and horizontal displacements under seismic actions (b).

The column bases of the steel framed structures are fixed (fully rigid column bases). For the sake of simplicity, rotational stiffness of beam-column joints have not been modelled, but the full continuity between beams and columns at their intersections has been considered. In the Abaqus numerical models, the non-linear stress-strain material curves have been modelled. Since the analysis involves large inelastic strains, the engineering stress-strain curves have been converted into true stresses vs. logaritmic plastic strains at different temperatures. In fact, in order to simulate the effect of fire, a simplified hypothesis has been done: only the mechanical property variation has been considered, neglecting thermal expansions and the related phenomena. So, mechanical properties change due to temperature has been considered constant through the cross-sections and applied to all structural members.

3.3 Numerical results at θ = 20 - 100°C

The analyses performed with the Abaqus software on the examined structures at the environment condition (θ = 20°C) have shown that their behaviour is analogous to that of the same structures at θ = 100°C. The numerical analysis results in the non-linear field on the case studies in terms of diplacements and force-displacement pushover curves are illustrated in Figures 6a and b, respectively.

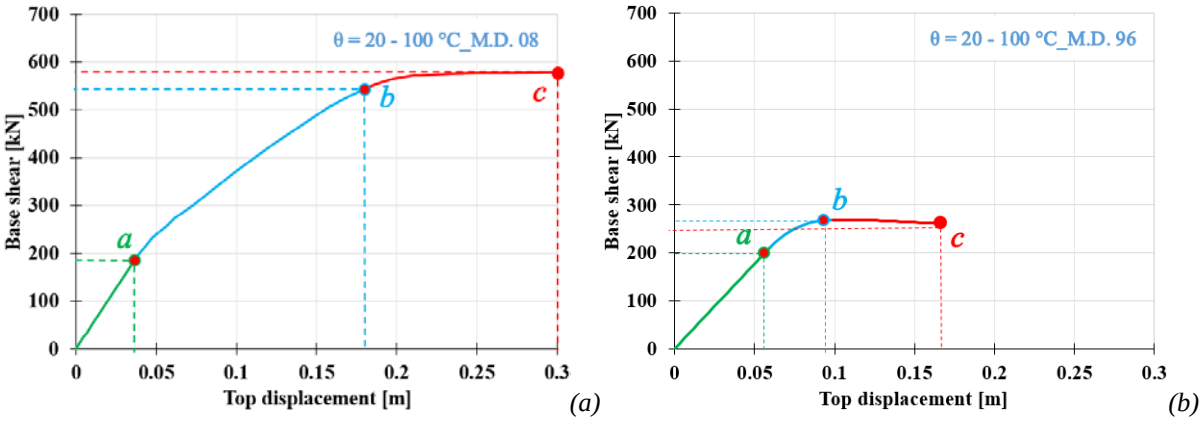

Figure 6: Force-displacement pushover curves at θ = 20 – 100°C for frames designed with M.D. 08 (a) and M.D. 96 (b) codes.

The points highlighted in Figure 6 have been determined starting from the study of plasticity distribution within the structures subjected to horizontal incremental loads [19, 20]. In order to better understand this aspect, firstly reference is made to the Figures 7a and 8a, where the damage state corresponding to the first yelding phenomena due to horizontal loads in the structures designed according to M.D. 08 and M.D. 96, respectively, is plotted. This plasticity distribution corresponds to the points “a” of the force-displacement curves of Figures 6a and 6b.

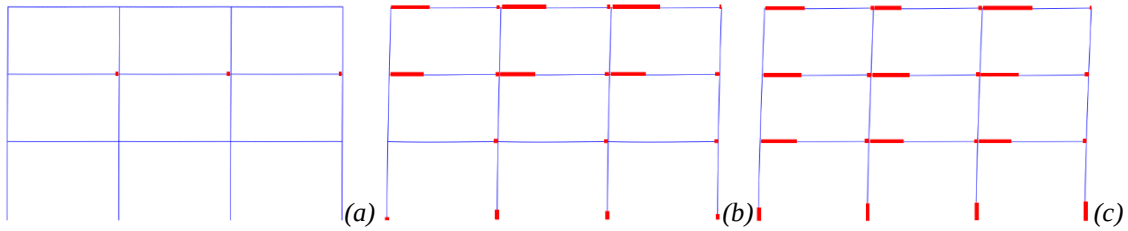

Figure 7: Plasticity distribution at θ = 20 – 100°C for the M.D. 08 frame: (a) first yielding; (b) mechanism activation; (c) collapse.

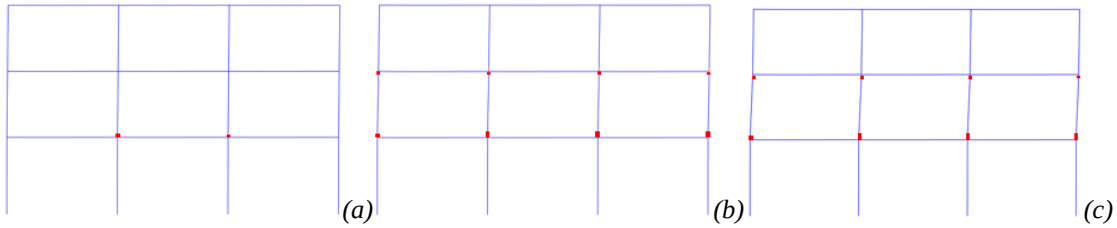

Figure 8: Plasticity distribution at θ = 20 – 100°C for the M.D. 06 frame: (a) first yielding; (b) mechanism activation; (c) collapse.

Figures 7b and 8b provide a snapshot of the plasticity distribution at the time of the mechanism activation for M.D. 08 frame and M.D. 96 one, respectively. This condition is reached when a quasi-global collapse mechanism for M.D. 08 frame and a soft-storey mechanism for M.D. 96 frame are attained. In this condition, the points "b" of the curves in Figures 6a and 6b are reached.

Finally, Figures 7c and 8c show the distribution and the extension of the yielded zone at collapse for the examined structures. This condition occurs when the extension of the plastic zones in the columns is equal to the cross-section height. Therefore, the parameters F_{max} and δ_{max} are attained, they providing the points "c" of the curves in Figures 6a and 6b.

3.4 Numerical results at high temperatures

Following the procedure described in the previous section and considering different temperature values up to 500°C, the non-linear force-displacement curves of the investigated frames have been obtained. These curves, which are representative of the seismic capacity of the Italian frames under examination, are shown in Figures 9a and 9b.

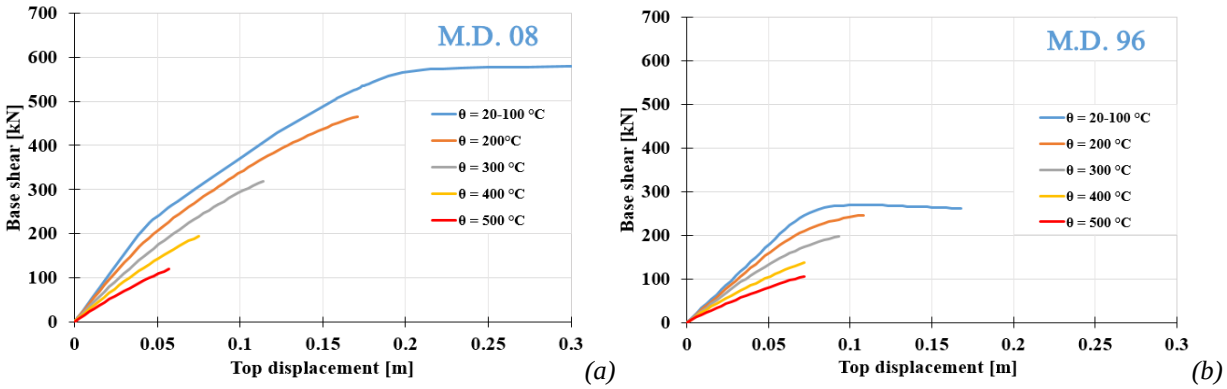

Figure 9: Force-displacement curves obtained from non-linear analyses on M.D. 08 (a) and M.D. 96 (b) frames.

The analysis of results describing the plasticity evolution within the study framed structures has allowed to redact the Tables 3 and 4, where the lists of variables describing the seismic response curves are plotted. In such tables, the zero values are indicative of the incapacity of structures to withstand seismic actions after fire.

From the analysis of results, it is highlighted that, at the same value of temperature, a substantial behavioural difference between the framed structure designed according to the new Seismic Italian Code (M.D., 2008) and the one designed according to the old Seismic Italian Code (M.D., 1996) exists.

M.D. 08						
θ [°C]	F_y [kN]	F_u [kN]	F_{max} [kN]	δ_y [m]	δ_u [m]	δ_{max} [m]
20	196.12	543.75	579.00	0.0386	0.180	0.300
100	196.12	543.75	579.00	0.0386	0.180	0.300
200	83.40	422.47	466.10	0.0180	0.141	0.170
300	0	297.10	319.50	0	0.104	0.114
400	0	177.70	192.20	0	0.066	0.075
500	0	120.00	120.00	0	0.060	0.060

Table 3: Numerical results obtained from analyses on the structure designed according to the M.D. 08 code.

M.D. 96						
θ [°C]	F_y [kN]	F_u [kN]	F_{max} [kN]	δ_y [m]	δ_u [m]	δ_{max} [m]
20	212.99	269.12	261.10	0.060	0.099	0.168
100	212.99	269.12	261.10	0.060	0.099	0.168
200	143.43	230.58	246.00	0.045	0.087	0.108
300	76.34	177.57	198.33	0.027	0.075	0.093
400	22.25	129.13	137.14	0.009	0.066	0.072
500	0	103.13	108.80	0	0.066	0.072

Table 4: Numerical results obtained from analyses on the structure designed according to the M.D. 96 code.

In order to quantify the above detected differences, the pictures reported in Figures 10a and 10b need to be considered.

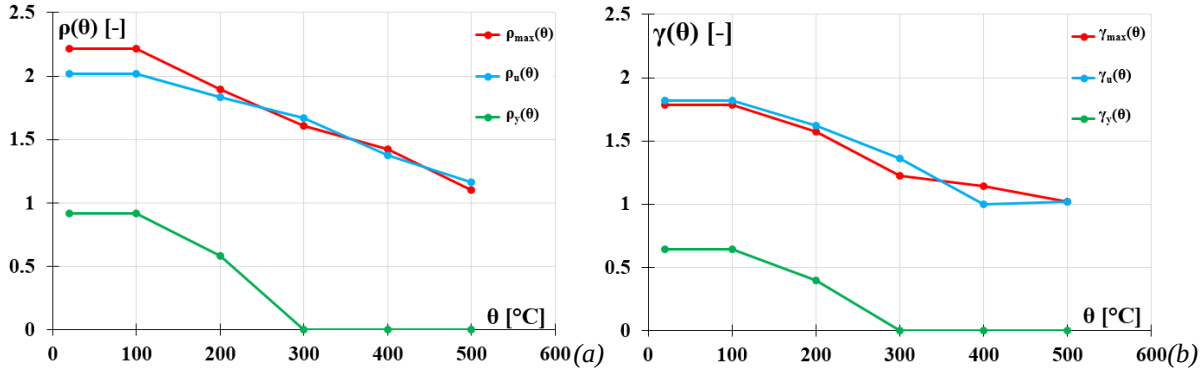

Figure 10: Behavioural trends of the $\rho - \theta$ (a) and $\gamma - \theta$ (b) curves.

The above graphs are representative of the following functions:

$$\begin{aligned}
\rho_y(\theta) &= \left[F_y(\theta)_{M.D.08} / F_y(\theta)_{M.D.96}\right] \\
\rho_u(\theta) &= \left[F_u(\theta)_{M.D.08} / F_u(\theta)_{M.D.96}\right] \\
\rho_{max}(\theta) &= \left[F_{max}(\theta)_{M.D.08} / F_{max}(\theta)_{M.D.96}\right]
\end{aligned} \tag{39}$$

$$\begin{aligned}
\gamma_y(\theta) &= \left[\delta_y(\theta)_{M.D.08} / \delta_y(\theta)_{M.D.96}\right] \\
\gamma_u(\theta) &= \left[\delta_u(\theta)_{M.D.08} / \delta_u(\theta)_{M.D.96}\right] \\
\gamma_{max}(\theta) &= \left[\delta_{max}(\theta)_{M.D.08} / \delta_{max}(\theta)_{M.D.96}\right]
\end{aligned} \tag{40}$$

From the reported trends it can be observed that, at the same temperature, structure designed according to the M.D. 08 code always shows a seismic performance in the elastic-plastic and plastic ranges greater than that of the frame designed according to the M.D. 96 code. This occurs in terms of both forces and displacements up to 400 °C.

Analogously to the design philosophy at basis of the two codes, the detected situation changes in the elastic range. In fact, it can be noted that the M.D. 96 frame, being designed to remain mainly in the elastic range under applied loads, has shown an elastic performance better than that of the M.D. 08 frame, which is designed particularly to dissipate the amount of the seismic energy input in the elastic-plastic range, showing greater excursions in the plastic field. To confirm this, it can be observed that, starting from a temperature of 300 °C, the formation of plastic zones in the M.D. 08 structure occurs already for vertical loads, while this condition for the other structure happens at a temperature of 500 °C.

Regarding the degradation of forces and displacements with the temperature, reference is made to the trends shown in Figures 11a and 11b, which represent the functions described in the equation (6), for M.D.08 frame and M.D. 96 one, respectively. On the other hand, the variation of the parameter ξ with temperature θ is shown in Figures 12a and 12b.

As it can be observed, at the same temperature, force and displacement parameters undergo significant reductions, particularly in the elastic field, for the structure designed according to the M.D. 08 code.

This condition can be explained considering the reduced seismic capacity of the old structure compared to the new one, as well as the different collapse mechanisms attributable to the two structures analysed (floor mechanism for the M.D. 96 frame and column

mechanism at their base for the M.D. 08 frame, neglecting in both cases the beam mechanisms).

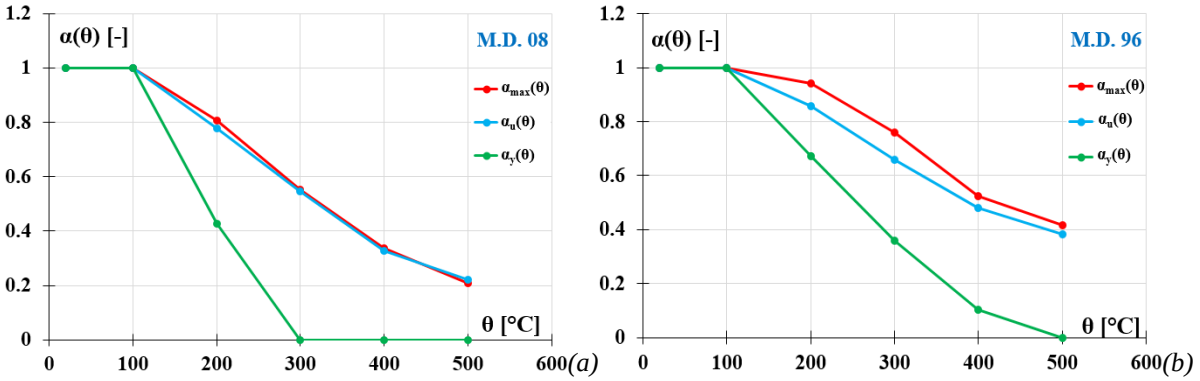

Figure 11: $\alpha - \theta$ curves for M.D. 08 (a) and M.D. 96 (b) frames.

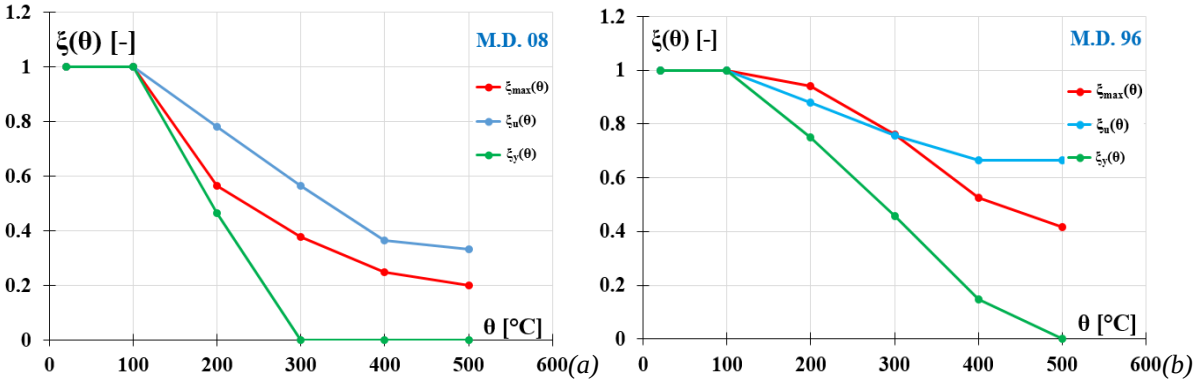

Figure 12: $\xi - \theta$ curves for M.D. 08 (a) and M.D. 96 (b) frames.

3.5 Calculation of $k_F(\theta)$ and $k_\delta(\theta)$ functions

Starting from the results provided by the numerical analyses performed on the two steel frames, the functions described by equations (6) and (7) in Section 2 have been calculated.

Once evaluated the pushover response parameters at θ=20°C, combining them with the functions cited above, the $k_F(\theta)$ and $k_\delta(\theta)$ functions are achieved.

Figures 13, 14 and 15 show the trends of the functions described above for the two frames designed with different seismic design codes.

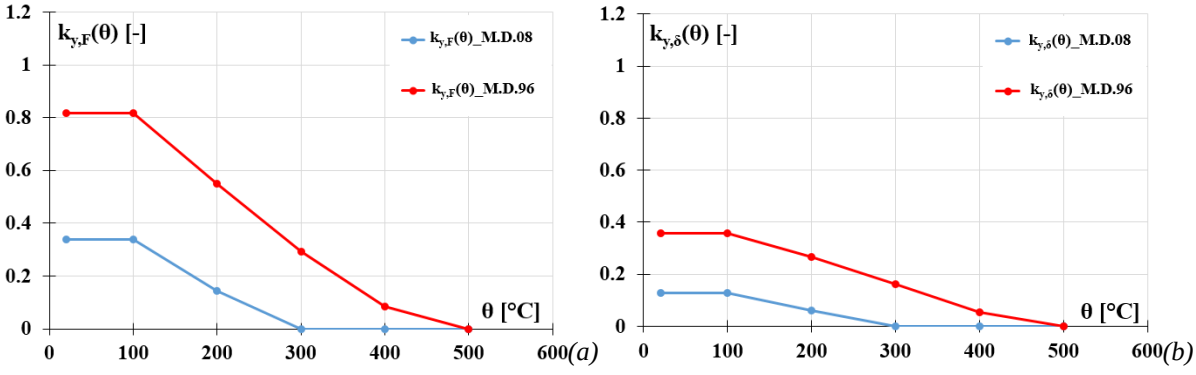

Figure 13: $k_{y,F} - \theta$ (a) and $k_{y,\delta} - \theta$ (b) curves of the inspected framed structures.

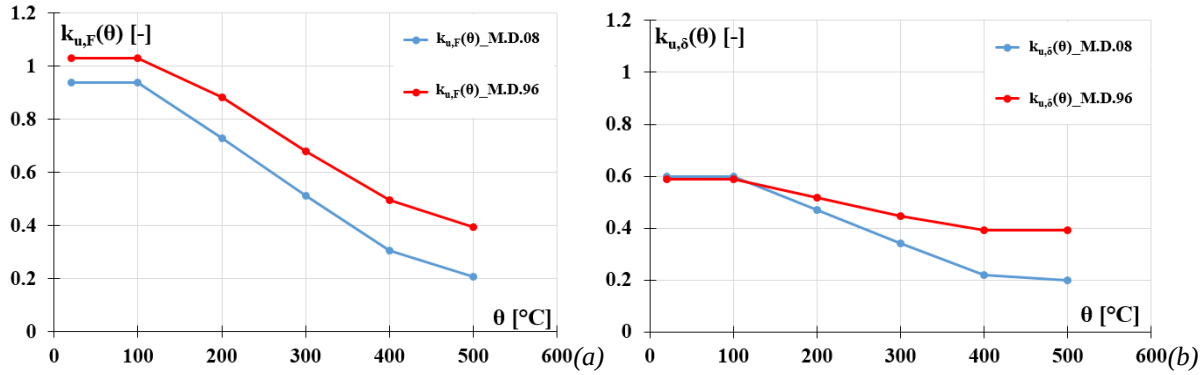

Figure 14: $k_{u,F} - \theta$ (a) and $k_{u,\delta} - \theta$ (b) curves of the inspected framed structures.

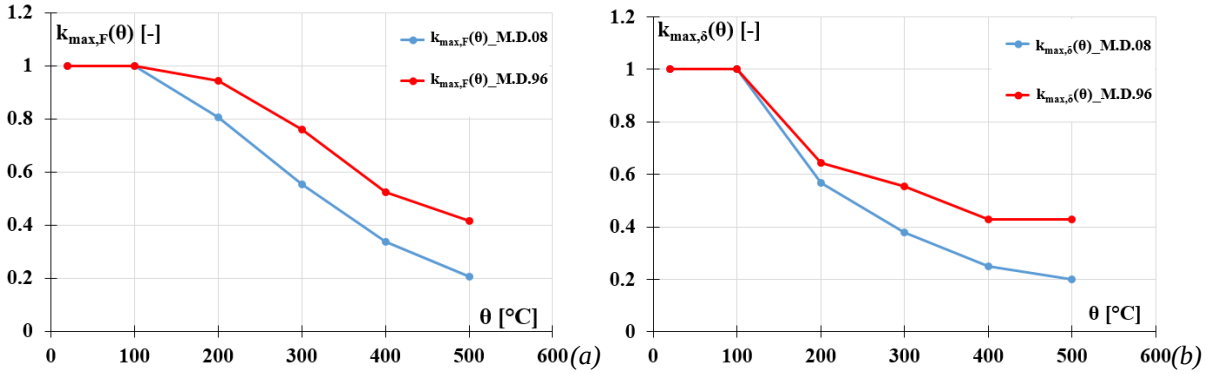

Figure 15: $k_{max,F} - \theta$ (a) and $k_{max,\delta} - \theta$ (b) curves of the inspected framed structures.

As already detected in the previous section for the functions $\xi(\theta)$ and $\alpha(\theta)$, at the same temperature, the most significant reduction of the functions k_δ and k_F with the temperature θ, especially in the elastic field, is detected for the M.D. 08 frame.

Finally, it should be noted that, by multiplying the values of F_{max} and δ_{max} at 20°C for the appropriate values of the above functions, it is possible to fully reconstruct the values of Tables 3 and 4.

4 CONCLUSIVE REMARKS AND FURTHER DEVELOPMENTS

In this study, a research activity concerning the seismic behaviour of framed structures after damages deriving from application of an exceptional load has been carried out.

Based on the results of a pushover analysis, a theoretical formulation to evaluate a simplified force-displacement curve for seismic appraisement of a structure damaged from an extreme event is reported.

However, after the basic non-linear behaviour of the undamaged structure is estimated, the concrete application of the method requires the *a priori* knowledge of some functions depending on the structure damage status at the end of the exceptional loading action. This can be attained by means of a widespread experimental-numerical examination campaign for evaluating the damages deriving from some variables influencing the effects of a given exceptional action.

An effective and practical way to apply the proposed method is provided in the Section 3 of the paper, where the residual seismic capacity of steel Moment Resisting Frames (designed according to both the new and the old seismic Italian codes) subjected to a preliminary fire action is estimated.

Numerical analysis results have shown that the reduction of mechanical properties of steel material due to fire can drastically affect the seismic response of investigated structures.

Results of this numerical investigation have shown that the structure designed according to the M.D. 08 code shows a seismic capacity in the post-elastic range greater than that designed according to the M.D. 96 code. Contrary, in the elastic field, the old frame behaves better than the new one. This is mainly due to the different design approaches used for the inspected frames. In fact the M.D. 96 structure is mainly designed to withstand applied loads without energy dissipation in the post-elastic range (no "capacity design" approach). This means that the first yielding in the old structure develops for base shear values greater than the new frame ones.

Finally, it is perceived that at the room temperature, the base shear capacity of the M.D. 08 frame is at least two times greater than the M.D. 96 structure one. Starting from this condition, the difference between the base shears drastically decreases after fire action. However, it can be noted that the force reduction trend shows a linear gradient with temperature, reaching its lower value at the temperature of 500 °C. The same behaviour is also observed for displacements. These trends are mainly due to the different distribution of damage under seismic loads, which appears to be more distribuited for the M.D. 08 frame, while it is localised at a certain storey for the M.D. 96 structure.

As a further development of the research activity, in order to both better understand the seismic behaviour of steel MRF before and after fire and validate the theoretical formulations given, an exhaustive campaign of numerical and experimental investigations is strongly needed. Some of the aspects that need to be more investigated are:

- The influence of the structure seismic response before fire damage, taking into account different geometrical configurations and any structural irregularities.
- The influence of the fire model and location.
- The influence of structural response at high temperatures, i.e. thermal expansions and related phenomena, as well as the actual temperature distribution in the cross-sections and along the structural elements.

REFERENCES

[1] Raizer V., Natural disasters and structural survivability, *R&RATA #3 (Vol.2)*, San Diego , California. September, 2009.

[2] Yue Li, Ellingwood Bruce R., Hurricane damage to residential construction in the US: Importance of uncertainty modeling in risk assessment, *Engineering Structures 28 pp. 1009-1018, Elsevier.* 2006.

[3] Jordan James W. and Paulius Saul L., Lessons Learned from Hurricane Katrina, *American Society of Civil Engineers (ASCE),* Proceedings of the Fourth Forensic Engineering Congress, held in Cleveland, Ohio from October 6-9, 2006

[4] Mostafei H., Vecchio F.J., Benichou N., Seismic resistance of fire damaged reinforced concrete columns, Conference on Improving the Seismic Performance of Existing Buildings and other structures, by *the Applied Technology Council and the Structural Engineering Institute of ASCE,* San Francisco, pp 12. December 9-11, 2009.

[5] Mostafei H., A new testing Capability for Seismic Resistance Assessment of Structures Damaged Due to a Fire, *15 WCEE LISBOA*, 2012.

[6] Ministerial Decree of Public Works (M. D.), Technical codes for constructions in seismic zones (in Italian), *Official Gazette of the Italian Republic published on January 16th*, 1996.

[7] Ministerial Decree of Public Works emanated on 2008, January 14th (M.D. 08), New technical codes for constructions (in Italian), *Official Gazette of the Italian Republic n. 29 published on 2008 February 4th*, 2008.

[8] Elnashai Amr S., Advanced inelastic static (pushover analysis for earthquake applications, *Structural Engineering & Mechanics pp. 51-69*, July, 2001

[9] Nigro E., Cefarelli G., Pustorino S., Princi P., Progettazione di strutture in acciaio e composte acciaio-calcestruzzo in caso di incendio secondo gli Eurocodici e le Norme Tecniche per le costruzioni, Hoepli, 2010.

[10] Draganić H., Sigmund V., Blast loading on structures, *Technical Gazette 19*, pp. 643-652. March, 2012.

[11] Luccioni B.M., Ambrosini R.D., Danesi R.F., Analysis of building collapse under blast load, *Engineering Structures 26 pp. 63-71, Elsevier.* 2004.

[12] Ngo T., Mendis P., Gupta A., Ramsay J., Blast loading and blast effect on structures-An overwiew, *EJSE International Special Issue: Loading on structures pp. 76-91*, 2007.

[13] De Gregorio D., Mazzolani F.M., Faggiano B., Vulnerabilità vulcanica dei centri urbani in zone ad elevato rischio: il caso Vesuvio, *Tesi di dottorato in Ingegneria delle Costruzioni XIII ciclo*, 2010.

[14] Formisano A., Mazzolani F.M., On the catenary effect of steel buildings, *Proc. of the COST ACTION C26 Final Conference "Urban Habitat Constructions under Catastrophic Events"*, Naples, Italy, 16-18 September, pp. 619-624, 2010.

[15] Formisano A., Mazzolani F.M., Progressive collapse and robustness of steel framed structures, *Civil-Comp Proceedings*, paper 99, 2012.

[16] Formisano A., Landolfo R., Mazzolani F.M., Robustness assessment approaches for steel framed structures under catastrophic events, *Computers and Structures*, 147, pp. 216-228, 2015.

[17] EN 1993-1-2, *Eurocode 3 – Design of steel structures – Part 1-2: General Rules-Structural Fire Design*, April, 2005.

[18] Simulia, *Abaqus Analysis User's Manual (version 6.10-1)*, Dassault Systemés, Vélizy-Villacoublay, France, 2010.

[19] Formisano A., Faggiano B., Landolfo R., Mazzolani F.M., Ductile behavioural classes of steel members for seismic design, *Proc. of the 5th Int. Conference on Behaviour of Steel Structures in Seismic Areas (Stessa 2006)*, Yokohama, Japan, 14-17 August, pp. 225-232, 2006.

[20] Formisano A., Gamardella F., Mazzolani F.M., Capacity and demand ductility for shear connections in steel MRF structures, *Civil-Comp Proceedings*, paper 102, 2013.

ECCOMAS Congress 2016
VII European Congress on Computational Methods in Applied Sciences and Engineering
M. Papadrakakis, V. Papadopoulos, G. Stefanou, V. Plevris (eds.)
Crete Island, Greece, 5–10 June 2016

ROCKING RESPONSE OF MASONRY BLOCK STRUCTURES USING MATHEMATICAL PROGRAMMING

Francesco Portioli[1], Lucrezia Cascini[2] and Raffaele Landolfo[2]

[1] University of Naples Federico II, Department of Structures for Engineering and Architecture
Via Forno Vecchio 36, 80134 Naples
e-mail: fportiol@unina.it

[2] University of Naples Federico II, Department of Structures for Engineering and Architecture
Via Forno Vecchio 36, 80134 Naples
{lucrezia.cascini, landolfo}@unina.it

Keywords: Masonry block structures, Non-smooth contact dynamics, Rigid blocks, Mathematical programming.

Abstract. *In this paper a variational formulation for dynamic analysis is adopted to investigate rocking behaviour of masonry block structures under lateral loads. The model is composed of rigid bodies interacting at potential contact points located at the vertexes of the bock interfaces. A no-tension and associative frictional behaviour with infinite compressive strength is assumed at contact interfaces. The contact dynamic problem is governed by equilibrium equations, which relate external, inertial and contact forces, and by kinematic equations, which ensure compatibility between contact displacement rates and block degrees of freedom. Mathematical programming is used to solve the optimization problem arising from the formulation of the variational problem associated to dynamics of the block assemblages. To evaluate the accuracy and computational efficiency of the implemented formulation, a validation study is presented for rigid blocks subjected to rocking behaviour under different acceleration pulse types and for an in-plane wall panel problem from the literature. A good agreement in terms of failure mechanism and response time histories was observed. The computational efficiency and the stability of the implemented procedure were found to be encouraging, thus suggesting that the proposed model may be used to model dynamic behaviour of masonry block assemblages with a large number of rigid bodies.*

1 INTRODUCTION

In case of seismic events, the response of masonry structures, such as historical monuments made of stone blocks or facades in masonry buildings subjected to local failure mechanism, is typically characterized by rocking behaviour [1-3].

Different modelling approaches are available in the literature to investigate the dynamic response of masonry block structures subjected to rocking. Among those, non-smooth contact dynamics (NSCD) represents an alternative modelling approach to discontinuous finite element modelling as well as to the discrete element method (DEM) [4-8].

The NSCD method has been applied to masonry block structures since the beginning of its development and it is now receiving a growing attention in the research community on masonry structures [9-11]. This is due to different reasons, also including the availability of fast and accurate algorithm for the numerical solution of the formulations which have been proposed in the literature for the mathematical programming problem arising from the conditions governing the contact dynamics [12-15].

In this paper a simple formulation for dynamic analysis of masonry block structures is adopted to investigate rocking behaviour of masonry block structures. The aim of the study was to evaluate its accuracy and computational efficiency when applied to in-plane loaded wall panels. The adopted modelling approach for contact interfaces represents an extension to dynamics of the point-based formulation used in the rigid block model which has been developed for limit analysis of masonry block structures in [16-18].

The static and kinematic variables as well as the relationships governing the behaviour of the rigid block model and the limit analysis formulation are presented in Sections 2 and 3. In Section 4 we present a validation study on single rigid block subjected to free rocking motion and to different acceleration pulse types. Finally, an application to a numerical case study of an in-plane wall panel considered in the literature is illustrated to show the ability of the implemented formulation to capture rocking behaviour of multi-block assemblages.

2 THE RIGID BLOCK DYNAMIC MODEL

We consider a multi-body assemblage made of rectangular rigid blocks *i* interacting at potential contact points *k* located at the vertexes of the interface *j* (Fig. 1).

A no-tension and associative frictional behaviour with infinite compressive strength is assumed at contact interfaces.

The dynamic model is formulated following the approach proposed in [19, 20] for granular materials, though now detailed for two-dimensional assemblages of rectangular blocks.

The contact variables are the internal forces acting at each contact point *k*, which are located at a vertex of interface *j* of block *i* (Fig. 2a). These variables are collected in vector **c** and include the shear force component t_k and the normal force n_k along the local coordinate axes.

The kinematic variables associated in a virtual work sense to the contact forces are the relative displacement rates at the contact points, namely the tangential and normal displacement rates Δu_{tk} and Δu_{nk} (Fig. 2b), which are collected in the vector $\Delta \boldsymbol{u}$.

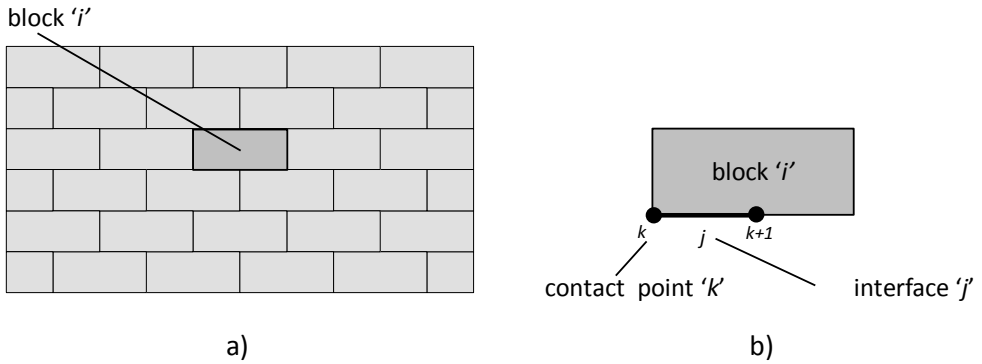

Figure 1: a) Rigid block assemblage; b) Rigid block *i* , interface *j* and contact point *k*.

External loads applied to the centroid of rigid block *i* are collected in vector of external forces $\boldsymbol{f}_{ext}$ (Fig. 2a).
The position at the centroid of block *i* is collected in the vector $\boldsymbol{x}_i$:

$$\boldsymbol{x}_i(t) = \left[x_i(t) \quad z_i(t) \quad \alpha_i(t) \right]^{\mathrm{T}} \tag{1}$$

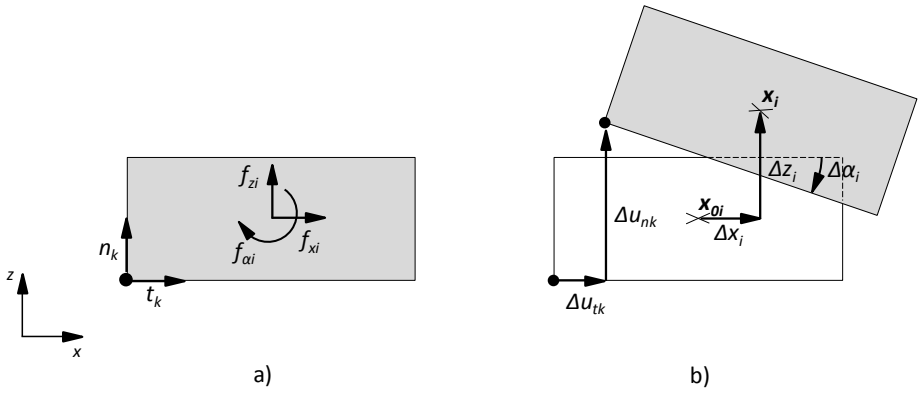

Figure 2: a) Contact forces and b) kinematic variables at block centroid *i*, and contact point *k*.

The equations of motions are discretized with respect to time using the θ-method and assuming:

$$\dot{\boldsymbol{x}}(t) = \frac{1}{\theta}\left[\frac{\Delta \boldsymbol{x}}{\Delta t} - (1-\theta)\,\dot{\boldsymbol{x}}_0 \right] \tag{2}$$

where $\Delta \boldsymbol{x} = \boldsymbol{x} - \boldsymbol{x}_0$ is the displacement vector, $\boldsymbol{x}_0$ and $\dot{\boldsymbol{x}}_0$ are the known position and velocity at time t_0 and $\theta \geq 0.5$.

On the basis of the incremental expression (2), the equations of motion of the rigid block assemblage interacting at potential contact points can be posed as follows:

$$\bar{\boldsymbol{M}} \Delta \boldsymbol{x} + \boldsymbol{A}_0 \boldsymbol{c} = \bar{\boldsymbol{f}}_0 \tag{3}$$

where $\boldsymbol{A}_0$ is the equilibrium matrix corresponding to contact forces;

$\bar{\boldsymbol{M}} = \dfrac{1}{\theta \Delta t^2} \boldsymbol{M}$;

$\boldsymbol{M}$ is the mass matrix collecting the mass m_i and the mass moment of inertia J_i of each block*;*

$\bar{\boldsymbol{f}}_0 = \boldsymbol{f}_{ext} + \bar{\boldsymbol{M}}\dot{\boldsymbol{x}}_0 \Delta t$.

The non-penetration condition at potential contact point *k* is formulated in a linearized explicit form, that is assuming that the geometry is the same for two subsequent time steps.

In matrix form, the condition can be expressed imposing that the normal component of the relative displacement at a contact point *k* has not to be greater than the initial gap g_{0k}, as follows:

$$\boldsymbol{N}_0^{\mathrm{T}} \Delta \boldsymbol{u} \le \boldsymbol{g}_0 \tag{4}$$

where $\boldsymbol{N}_0^{\mathrm{T}}$ is the matrix collecting the initial normal associated with surfaces *j* and $\boldsymbol{g}_0$ is the vector of initial gaps.

For contact interactions, a complementarity condition is also included which ensures that contact forces are positive only if the gap is closed otherwise are zero:

$$\begin{aligned} &\boldsymbol{n} \ge \boldsymbol{0} \\ &\mathrm{diag}(\boldsymbol{n})\left(\boldsymbol{N}_0^{\mathrm{T}} \Delta \boldsymbol{u} - \boldsymbol{g}_0 \right) = \boldsymbol{0} \end{aligned} \tag{5}$$

The behaviour at contact interfaces undergoing sliding failure is governed by failure conditions which are expressed according to the Coulomb friction law.

In vector notation, the limit conditions for sliding failure can be written as:

$$\pm \boldsymbol{t} \le \mu \boldsymbol{n} \tag{6}$$

where μ is the friction coefficient.

3 FORMULATION AND IMPLEMENTATION OF THE VARIATIONAL PROBLEM OF RIGID BLOCK DYNAMICS

Under the assumption of associative flow rule for displacement rates, the equilibrium equations (3), kinematic conditions (4-5) and sliding friction conditions (6) are equivalent to the following discrete mixed force–displacement problem [19, 20]:

$$\begin{aligned} &\min_{\Delta x} \ \max_{c} \ \frac{1}{2} \Delta \boldsymbol{x}^{\mathrm{T}} \bar{\boldsymbol{M}} \Delta \boldsymbol{x} - \Delta \boldsymbol{x}^{\mathrm{T}} \bar{\boldsymbol{f}}_0 + \Delta \boldsymbol{x}^{\mathrm{T}} \boldsymbol{A}_0 \boldsymbol{c} - \boldsymbol{g}_0 \\ &\text{subject to} \quad \pm \boldsymbol{t} - \mu \boldsymbol{n} \le \boldsymbol{0} \qquad \boldsymbol{n} \ge \boldsymbol{0} \end{aligned} \tag{7}$$

The problem (7) can be uncoupled into two dual quadratic programming problems, corresponding to the kinematic and force-based formulation of the contact dynamic problem.

To calculate and update positions of the blocks and contact gaps, an iterative procedure was implemented to solve the mathematical program (7).

The procedure was implemented in a computer code, *DynoBlock_2D*, which provides as outputs the time histories of contact forces and kinematic variables as well as the plots of the failure mechanisms at different time steps.

The quadratic programming problems associated to (7) were solved using the primal–dual interior-point solver in MOSEK [23].

The analyses were carried out using a PC containing a 3.3GHz Intel Xeon E3-1245 processor with 8 GB of RAM. The value of algorithm parameter θ for time discretization was set equal to 0.7 and time increment was set equal to 0.002 s.

4 DYNAMICS OF THE SINGLE RIGID BLOCK

To validate the proposed formulation, the case study of a single rigid block subjected to free rocking motion and to ground acceleration pulses was considered.

The rigid block dimensions are 0.20×1.00m and the unit weight is 18.0 kN/m^3 (Fig. 3). The friction coefficient μ adopted at the contact interface is equal to 0.7.

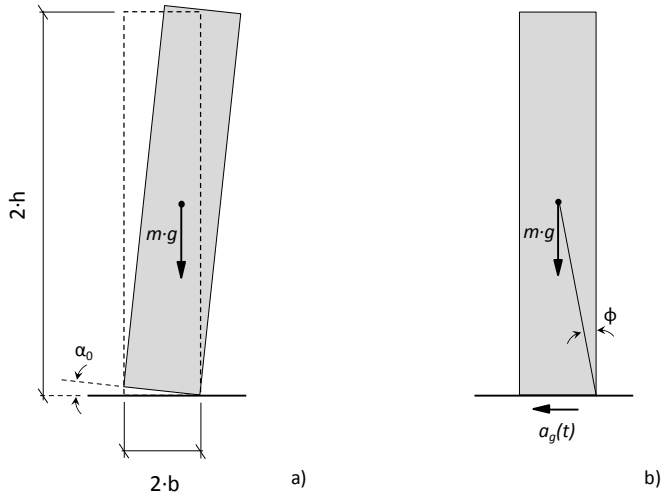

Figure 3: Rigid block subjected to free rocking motion and to ground acceleration pulses.

To analyze the free rocking motion response of the block subjected to gravity acceleration g an initial angle α_0=0.01 rad was considered.

The rotation time history of rigid block obtained from the proposed formulation is shown in Fig. 4. The comparison with closed form solution, which is referred to a value of the coefficient of restitution $\sqrt{r} = 0.925$ relating the reduction of the angular velocity before and after the impact, shows a good agreement [21].

The response obtained for the rigid block resting on the base and subjected to a constant horizontal ground acceleration a_g was investigated as well for validation. The objective of this set of simulations was to test the accuracy of the formulation in predicting the minimum value of the horizontal acceleration for the motion to be initiated and the magnitudes of rectangular pulse excitations with duration of 1.0s needed for overturning.

The numerical simulations showed that the minimum value of the horizontal acceleration a_g to begin tilting of the block was 0.20g. As expected, this value is in accordance with the condition $a_g / g \geq \varphi$, corresponding to the simple condition that the overturning moment induced by the lateral force on the contact has to be greater than the corresponding resistant moment related to the weight.

The rotation time histories for different values of ground accelerations in the case of rectangular pulse excitations are shown in Figure 5.

Case study	Model size ($b \times c$)	a_g (g)					
		Acceleration value for rocking initiation		Overturning acceleration amplitude for constant pulse with duration 1.0 s		Overturning acceleration amplitude for a sinusoidal pulse with duration 1.0 s	
		Differential equations	Proposed	Differential equations	Proposed	Differential equations	Proposed
Single block	1 × 2	0.200	0.201	0.204	0.204	0.237	0.237

Table 1: Single rigid block: acceleration values for overturning and CPU times.

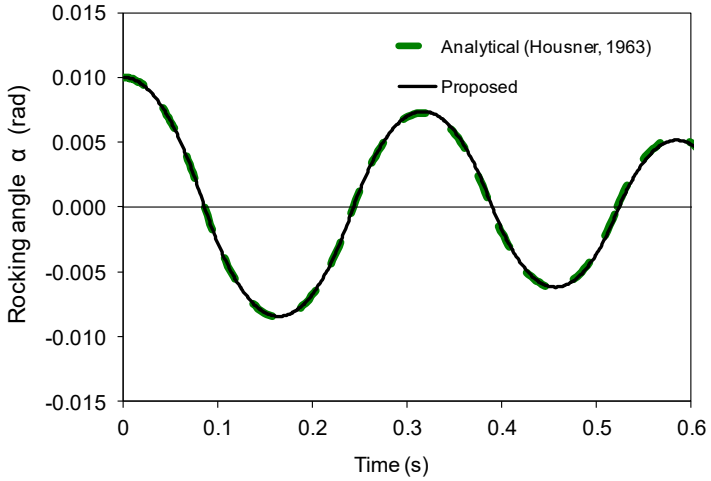

Figure 4: Rotation time history of the rigid block subjected to free rocking motion: comparison of proposed and analytical formulations.

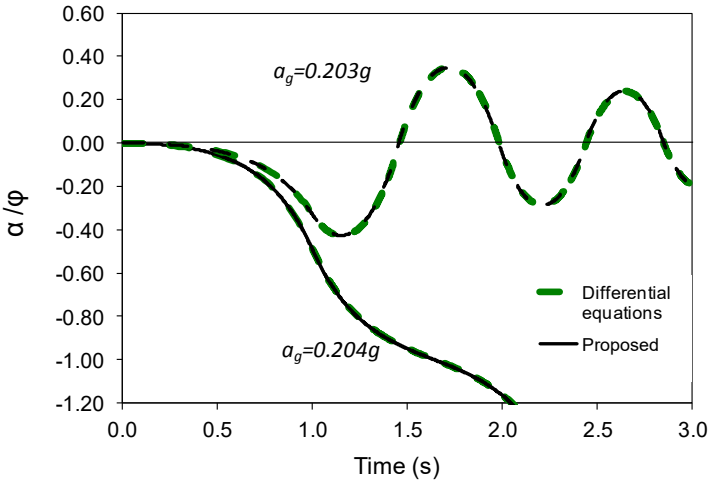

Figure 5: Rotation time histories of the rigid block subjected to constant (rectangular) acceleration pulses with duration of 1.0 s.

A similar study was carried out for sinusoidal pulse excitation. Also in this case the results are in good agreement with the response obtained from numerical integration of the differential equation of motion (see Table 1).

5 APPLICATION TO IN-PLANE LOADED MASONRY WALL

In this section we consider for validation a block panel analysed by Ferris and Tin-Loi [22] using mathematical programming with equilibrium constraints (MPEC) for computational limit analysis and subsequently investigated in [16] using a second order cone programming formulation (SOCP) .

The main goal of this study was to compare results from the present QP dynamic formulation with those obtained from previously developed limit equilibrium analysis (LA) procedures and to illustrate the ability of the proposed formulation in capturing the rocking response in case of rectangular pulse excitation.

The wall panel under investigation is illustrated in Figure 6 (example no.3 in [22]). The size of a full block is 0.4×0.175m, the friction coefficient is 0.65 and the unit weight is 1.0kN/m^3. To simulate the load cases of the limit analysis formulation, in the contact dynamic QP formulation the blocks are subject to a constant value of horizontal acceleration and to the gravity acceleration. The analysis is repeated increasing the horizontal acceleration by step of 0.001g until rocking motion is initiated. Once the minimum value of acceleration is obtained, a constant acceleration pulse with duration of 1.1 seconds is applied to the panel to analyze the evolution of the failure mechanism over time.

The sizes of the numerical model, expressed as the number of blocks b and contact points c, are reported in Table 2, together with the numerical results in terms of accelerations and ultimate load factors obtained from limit equilibrium analysis, as well as CPU times.

The computed acceleration magnitude to initiate rocking motion is in good agreement with the load factors obtained using previously presented limit equilibrium formulations (Table 2). Indeed, the computed acceleration values are comprised in the range of associative and non-associative solutions from limit analysis problems.

Case study	Model size ($b \times c$)	Limit equilibrium analysis using SOCP [16]				Dynamic analysis using QP (proposed)	
		Associative friction solutions		Non-associative friction solutions			
		λ	CPU Time (s)	λ	CPU Time (s)	a_g (g)	CPU Time* (s)
Example no. 3 [22]	46 × 240	0.404	0.1	0.356	0.9	0.387	97.5

*Referred to 3.3GHz CPU, per unit time duration of dynamic analysis (second) in the case of QP formulation.

Table 2. In-plane loaded masonry wall: comparison of collapse load factors from LA formulations and acceleration obtained from CD-QP problems.

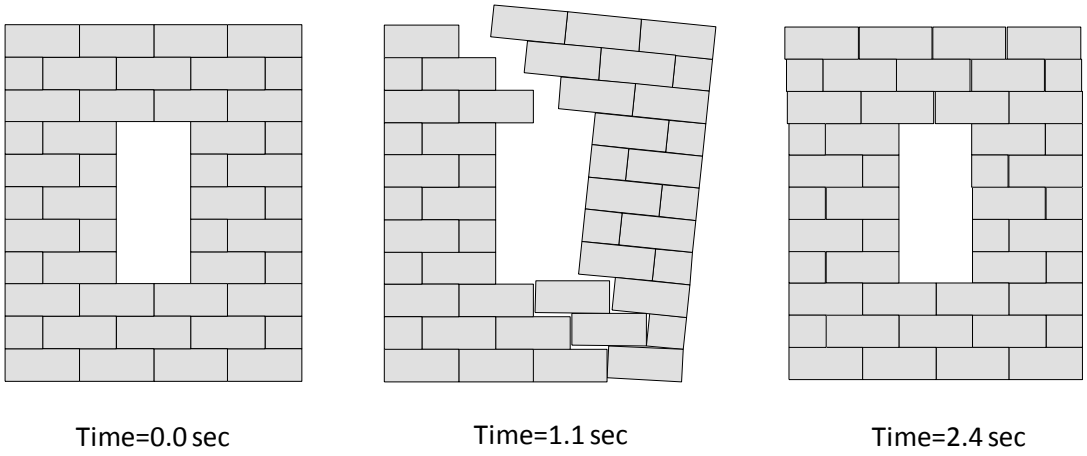

Figure 6: Wall sample n.3 [22]: failure mechanism time history obtained from the contact dynamic formulation under a rectangular pulse excitation of 0.387g with duration of 1.1s.

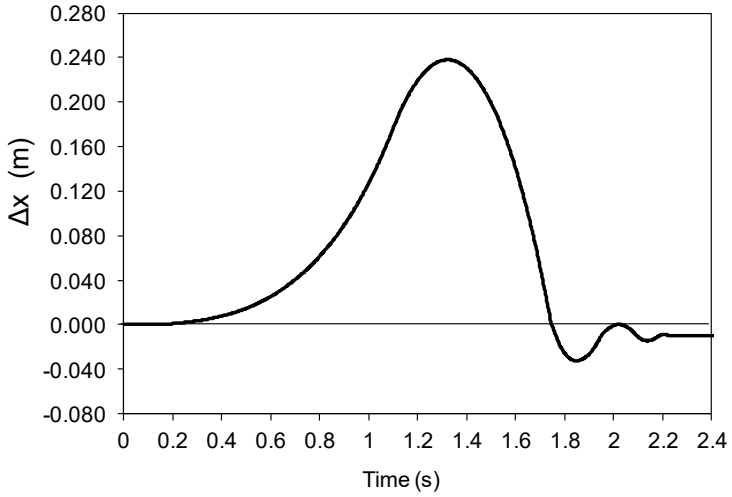

Figure 7: Time history of the top drift displacement.

The time history of the failure mechanism and the drift displacement at the top for the rectangular pulse excitation with duration of 1.1 s are shown in Figures 6 and 7.

It is interesting to point out the residual drift after pulse excitation and the stability of the predicted response, which shows no chattering effect and is only slightly affected by the few mechanical and algorithm parameters inherent the numerical model, namely the friction coefficient, the θ factor and the size of time step.

6 CONCLUSIONS

- A 2D formulation for contact dynamic analysis of block masonry structures with no-tension and associative frictional joints and infinite compressive strength was presented. The formulation is based on the contact point model for interfaces and uses QP programming to solve the discretized equation of motion under kinematic and static constraints.

- The model was validated against numerical case studies from the literature involving single and multi-block assemblages and a good agreement in terms of failure mechanism and response time histories was observed.
- The computational efficiency and the convergence stability of the implemented procedure were found to be encouraging, also considering the small number of mechanical and algorithm parameters associated to the adopted formulation.

REFERENCES

[1] S. Lagomarsino, Seismic assessment of rocking masonry structures, *Bulletin of Earthquake Engineering*, 13 (1), 97-128, 2015.

[2] M.J. DeJong, E.G. Dimitrakopoulos, Dynamically equivalent rocking structures, *Earthquake Engineering and Structural Dynamics*, 43 (10), 1543-1563, 2014.

[3] O.A. Shawa, G. de Felice, A. Mauro, L. Sorrentino, Out-of-plane seismic behaviour of rocking masonry walls, *Earthquake Engineering and Structural Dynamics*, 41 (5), 949-968, 2012.

[4] P. Lötstedt, Mechanical systems of rigid bodies subject to unilateral constraints, *SIAM Journal on Applied Mathematics*, 42(2):281–296, 1982.

[5] J.J. Moreau, Unilateral contact and dry friction in finite freedom dynamics, In: Moreau, Panagiotopoulos, editors. *Non-smooth mechanics and applications*. CISM courses and lectures, vol. 302, 1–82, 1988.

[6] M. Jean, The non–smooth contact dynamics method, *Comput Meth Appl Mech. Eng*;177:235–57, 1999.

[7] V. Acary, B. Brogliato, *Numerical methods for nonsmooth dynamical systems*, Springer, Berlin, 2008.

[8] J.V. Lemos, Discrete element modeling of masonry structures, Int J Archit Herit 1(2):190–213, 2007.

[9] B. Chetouane, F. Dubois, M. Vinches, C. Bohatier, NSCD discrete element method for modeling masonry structures, *Int. Journal for Numerical Methods in Engineering*, 64, pp.65-94, 2005.

[10] A. Rafiee, M. Vinches, C. Bohatier, Modelling and analysis of the Nîmes arena and the Arles aqueduct subjected to a seismic loading, using the Non-Smooth Contact Dynamics method, *Engineering Structures*, 30 (12), pp. 3457-3467, 2008.

[11] G. Lancioni, S. Lenci, Q. Piattoni, E. Quagliarini, Dynamics and failure mechanisms of ancient masonry churches subjected to seismic actions by using the NSCD method: The case of the medieval church of S. Maria in Portuno, *Engineering Structures*, 56, 1527-1546, 2013.

[12] M. Anitescu, F.A. Potra, A time-stepping method for stiff multibody dynamics with contact and friction, *Int. J. Numer. Meth. Eng.* 55: 753–784, 2002.

[13] D.E. Stewart, J.C. Trinkle, An implicit time-stepping scheme for rigid body dynamics with inelastic collisions and coulomb friction, *Int. J. Numer. Meth. Eng.* 39(15): 2673-2691, 1996.

[14] A. Tasora, M. Anitescu, A matrix-free cone complementarity approach for solving large-scale, nonsmooth, rigid body dynamics, *Computer Methods in Applied Mechanics and Engineering*, 200 (5-8), 439-453, 2011.

[15] E.D. Andersen, C. Roos, T. Terlaky, On implementing a primal-dual interior-pointmethod for conic quadratic optimization, *Math. Programming*, 95(2), 2003.

[16] F. Portioli, C. Casapulla, M. Gilbert, L. Cascini, Limit analysis of 3D masonry block structures with non-associative frictional joints using cone programming, *Computers and Structures*, 143: 108-121, 2014.

[17] F. Portioli, C. Casapulla, L. Cascini, An efficient solution procedure for crushing failure in 3D limit analysis of masonry block structures with non-associative frictional joints, *International Journal of Solids and Structures*, 69-70, 252-266, 2015.

[18] F. Portioli, L. Cascini, Assessment of masonry structures subjected to foundation settlements using rigid block limit analysis, *Engineering Structures*, 113, 347-361, 2016.

[19] K. Krabbenhoft, A.V. Lyamin, J. Huang, M. Vicente da Silva, Granular contact dynamics using mathematical programming methods, *Computers and Geotechnics*, 43, 165-176, 2012.

[20] K.W. Lim, K. Krabbenhoft, J.E. Andrade, A contact dynamics approach to the Granular Element Method, *Computer Methods in Applied Mechanics and Engineering*, 268, 557-573, 2014.

[21] G. W. Housner, The behavior of inverted pendulum structures during Earthquakes, *Bull. Seism. Soc. Am.*, Vol. 53, 404-417, 1963.

[22] M.C. Ferris, F. Tin-Loi, Limit analysis of frictional block assemblies as a mathematical program with complementarity constraints, *Int. Journal of Mechanical Sciences*, 43 (1), pp. 209-224, 2001.

[23] The MOSEK optimization tools manual (2011). Version 6.0. MOSEK ApS, Denmark 2011. http://www.mosek.com

ECCOMAS Congress 2016
VII European Congress on Computational Methods in Applied Sciences and Engineering
M. Papadrakakis, V. Papadopoulos, G. Stefanou, V. Plevris (eds.)
Crete Island, Greece, 5–10 June 2016

CONTROLLED ROCKING, DISSIPATIVE CONTROLLED ROCKING AND MULTI-HIERARCHICAL ACTIVATION: NUMERICAL ANALYSIS AND EXPERIMENTAL TESTING

Royce Liu & Alessandro Palermo

University of Canterbury
Private Bag 4800, Christchurch 8140, New Zealand
royce.liu@pg.canterbury.ac.nz
alessandro.palermo@canterbury.ac.nz

Keywords: pier, bridge, experimental, unbonded post-tensioning, controlled rocking, PRESSS.

Abstract. *The earliest modern work on rocking focussed on pure rocking structures. That is, structures that are able to uplift and where the tendency to self-centre is purely provided by self-weight. Since then, free rocking has evolved into a multitude of new design strategies due to the addition of elements such as post-tensioning (controlled rocking) or having multiple interfaces in a single element where uplift can occur (segmental rocking). Although these new design strategies evolved from free rocking, there is little clarity in current literature about the differences in dynamic behaviour which is important in seismic design. A specific example of this, is that, the PRESSS system also known as DCR (dissipative controlled rocking: the combination of post-tensioning, dissipative devices and free rocking) and free rocking are usually mistaken to reduce damage to a structure through the same mechanism of gap opening and hence that the dynamic behaviours are the same. This paper looks to give a short modern history of the evolution the rocking structure and argue that design strategies based on rocking may not have the same dynamic response as pure rocking through comparison of the results of non-linear response history analyses of a SDOF structure utilizing pure rocking, controlled rocking, and dissipative controlled rocking strategies. Following on the theme of the evolution of the rocking structure, at the University of Canterbury, unidirectional, quasi-static, cyclic, tests were conducted on a 1/3 scale two span bridge utilising a single cantilever controlled rocking pier which was designed to operate in three different configurations: without dissipative devices, with one set of hysteretic dissipative devices, and with two sets of hysteretic dissipative devices. The very last configuration is a new design strategy proposed by the authors as "hierarchical DCR" where there are two sets of dissipative devices across the rocking interface and where one set is activated at a later pier displacement to the other. The concept behind this idea is to increase structural robustness of the DCR system as a means of collapse prevention due to subsequent or unusually rare events such as the maximum credible earthquake. This paper will also present the results of this testing.*

1 INTRODUCTION

Past major earthquakes have shown significant drawbacks related to bridges using conventionally designed RC piers. These include: residual drift, which affects post-earthquake functionality and speed of reinstatement; physical damage from non-linear material behaviour, which not only affects post-earthquake functionality and the speed of reinstatement, but also, the remaining life of the bridge; and major indirect losses, from down time of the bridge caused by the aforementioned consequences of allowing non-linear material behaviour within the pier member. An alternative to conventional RC design, whose aim is to minimise and or eliminate the aforementioned performance issues related to member plastic hinging, are a family of design strategies based on rocking. These include free rocking, controlled rocking and dissipative controlled rocking (DCR) also known as hybrid PRESSS [1] and are all shown in Figure 1. Controlled rocking is free rocking with the addition of unbonded post-tensioning (Fig. 1b). Instead of wholly relying on self-weight to provide self-centering, where the tendency to self-centre reduces with displacement (Fig. 1a), controlled rocking also relies upon both the initial post-tensioning force and elongation of the tendons to provide self-centering. The name of this design strategy was coined from the fact that there is greater control over the tendency to self-centre due to the adjustable nature of the post-tensioning. This combination results in a bilinear elastic force-displacement plot with positive stiffness after uplift initiates (Fig. 1b).

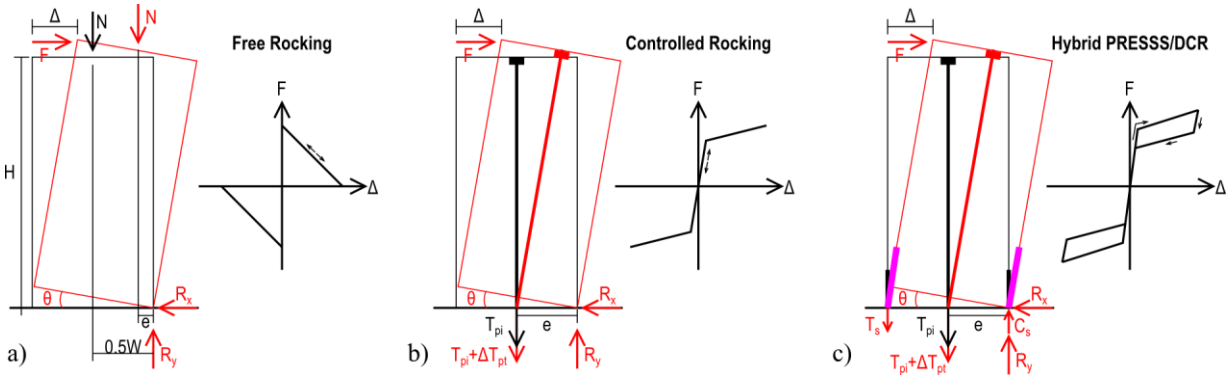

Figure 1: Free body diagrams and force displacement plots for a rigid block on rigid foundation utilising: **a)** free rocking; **b)** controlled rocking; and **c)** hybrid PRESSS/DCR.

The further addition of dissipative devices (usually metal hysteretic) across the rocking interface (internal or external to the member) results in the design strategy of dissipative controlled rocking (Fig. 1c). The dissipative devices add to the moment capacity and or damping of the structure resulting in a flag shaped hysteresis loop (Fig. 1c).

This contribution focusses on rocking bridge structures and has three main aims. The first is to elaborate more on the variety and development of rocking solutions in order to show the evolution of the rocking structure and the reasoning associated with it. The second is to argue that not all design strategies based on rocking exhibit the same dynamic behaviour which is a common misconception. And the third is to present the concepts for a new design strategy called Multi-Performance DCR (MDCR) developed by the authors, in addition to results from experimental testing as proof of concept.

2 LITERATURE REVIEW: EVOLUTION OF ROCKING APPLIED TO BRIDGES

Two main streams of design strategies for bridges based on rocking have evolved in parallel, namely, uplifting and jointed structures. Major interest in the use of rocking as a seismic design strategy stems from Housner [2] where he observed that water towers which were able to rock

on their foundations during the May 1960 Chilean Earthquake survived relatively undamaged compared to their monolithic counterparts.

Uplifting structures encompass two types of foundation rocking: uplifting shallow foundation (Fig. 2a, right) and pile cap rocking on supporting piles (Fig. 2a, left); and stepping (Fig. 2b). These types of structures are the closest to classical free rocking structures due to their reliance on self-weight for self-centering. Of the uplifting structures, the rocking shallow foundation [3–6] and stepping structures were the first to be investigated [7,8]. While the rocking pile foundation was investigated later on [9,10] but more as a solution to geotechnical constraints imposed by poor soil conditions.

Uplifting is a form of seismic isolation because seismic demands are reduced to the supported structure through period elongation [2,3,6,11–14]. However, the amount of period elongation is dependent on the amplitude of rocking displacement [2,6]. In addition to this, soil–structure interaction effects for foundation rocking structures also contribute to reducing seismic demands [15].

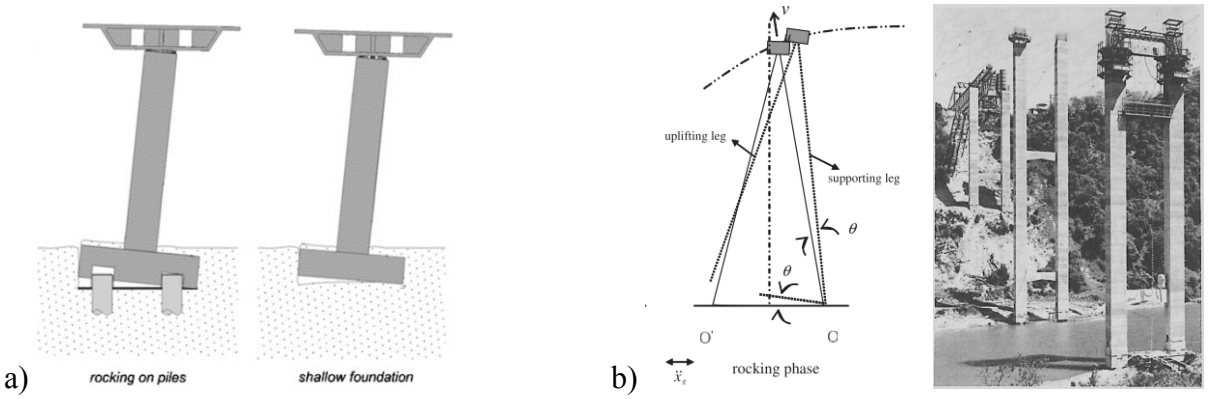

Figure 2: a) Examples of foundation rocking structures [9]. Left, rocking on piles and right, rocking shallow foundation. **b)** Examples of stepping structures. Left, displaced structure showing mode of movement [11]. Right, Rangitikei viaduct NZ a bridge using stepping piers [16].

The other stream of design strategies based on rocking are jointed structures, where, locations of plastic hinges are replaced with rocking joints as a means of reducing seismically induced damage. This type of design strategy was initially developed for precast concrete buildings under the US PRESSS program where both a crude controlled rocking solution [17] and the present day hybrid PRESSS/ dissipative controlled rocking (DCR) [1] solution were developed. The first application of a jointed rocking structure to bridges was proposed by [18]. Mander and Cheng [18] envisioned both free and controlled rocking bridge piers (cantilever and pier bent) with steel armouring at the rocking interfaces to prevent damage to the edges of the rocking sections (Fig. 3a).

The proposed application of the hybrid PRESSS system to bridges (Fig. 3b) was only made some years later by Palermo et al. [19] as a means of achieving improved seismic performance compared to monolithic construction. Initially the PRESSS system in bridges used internal dissipative devices in the form of debonded mild steel reinforcement [20] (Fig. 3c). This then changed into the use of external dissipative devices [21] to facilitate easy observation and replacement (Fig 4a). Then Kam et al. [22] proposed improvement of the response of the DCR connection to both near and far field earthquakes through combining velocity (fluid viscous dampers) and displacement dependent dissipators (metal hysteretic) to produce an advanced flag shape hysteresis curve (Figs. 4b & c).

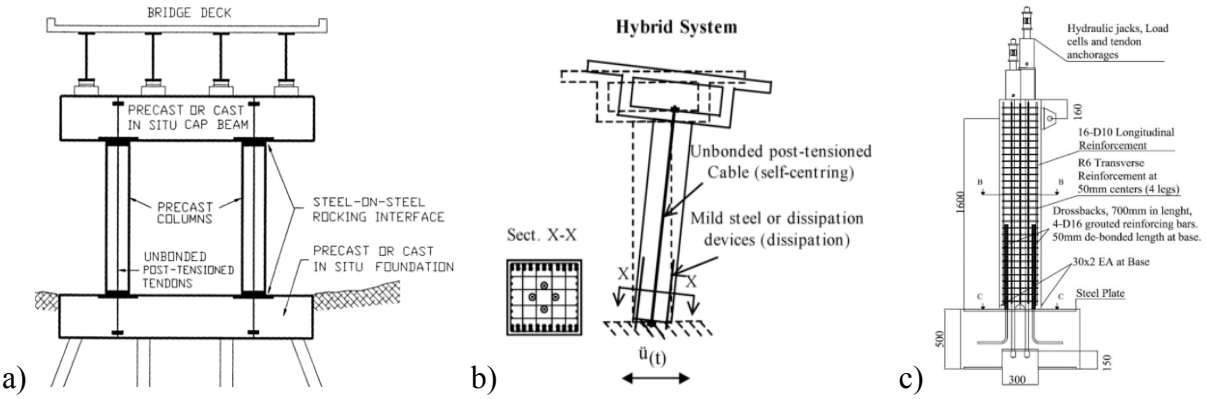

Figure 3: a) Controlled rocking pier bent [18]. **b)** Proposed application of PRESSS to bridges showing possible design [19]. **c)** Design schematic of a cantilever PRESSS column used in experimental testing [20].

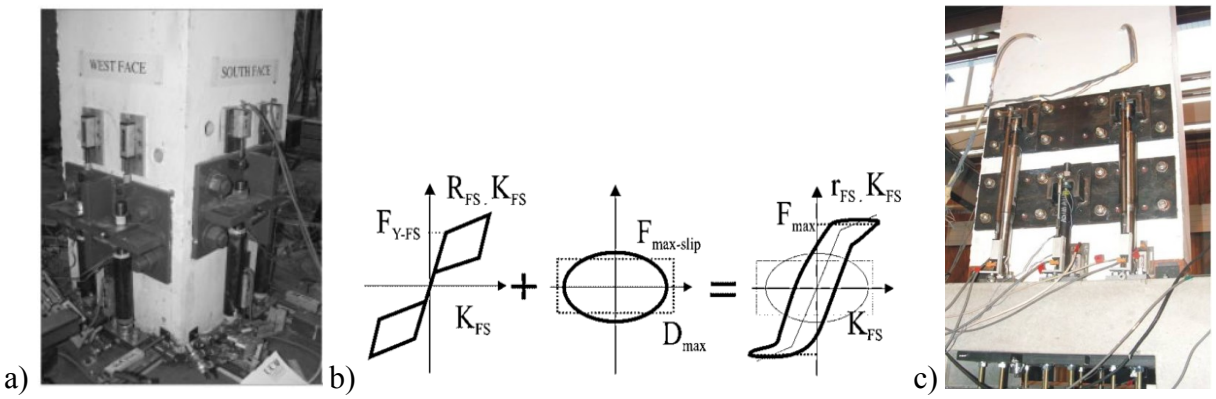

Figure 4: a) PRESSS/DCR column using external dissipators [21]. **b)** Advanced flag shape (AFS) hysteresis [22]. **c)** Experimental testing of the AFS concept showing the combination of viscous and metal hysteretic devices to achieve the advanced flag shape [23].

Most of the previously described developments on DCR applied to bridges were made at the University of Canterbury, New Zealand. Outside this institution, research has been more focussed on applying low damage technologies to accelerated bridge construction (especially in the US) and the application of DCR to tall segmental concrete bridge piers (Fig. 5) as a means of increasing the dissipative capacity of the pier [24–26].

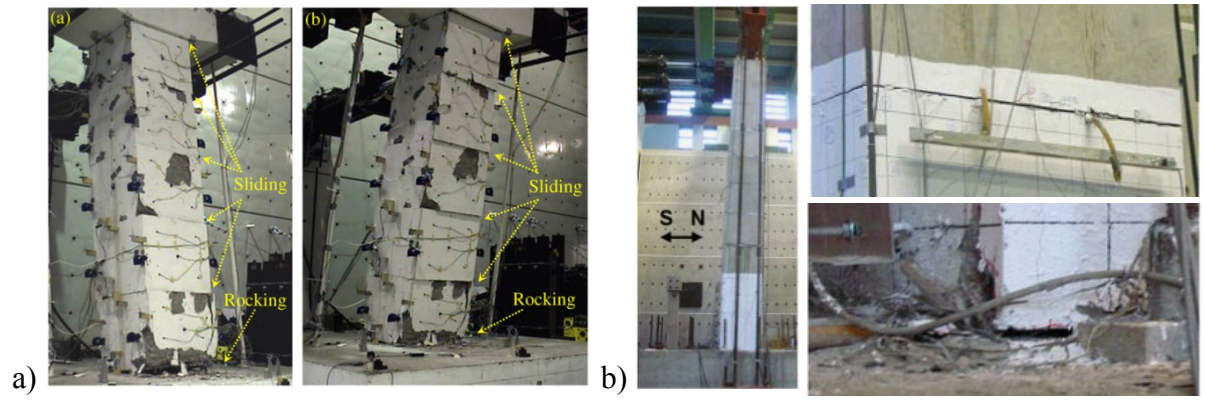

Figure 5: a) Segmental pier combining controlled rocking with frictional means of energy dissipation from sliding [27]. **b)** Segmental pier tested by Wang [24] using internal debonded reinforcement for energy dissipation.

Today, the authors of this paper see the DCR solution evolve into "Multi-Performance Dissipative Controlled Rocking" (MDCR) [28]. Further explanation of this concept is given later in this paper.

3 DISCUSSION: WHY FREE ROCKING AND HYBRID PRESSS ROCKING DO NOT WORK IN THE SAME WAY

There is a common misconception that Dissipative Controlled Rocking (DCR) and free rocking have similar dynamic behaviours and that their treatment in design can be considered similar. This misconception arises from the assumption that the addition of post tensioning, and dissipative devices to a free rocking structure does not change the dynamic behaviour of the free rocking structure. However, other than the obvious similarities, these two design strategies exhibit very different dynamic behaviours which is an extremely important consideration for design.

Consider for example the free vibration (Fig.7) and ground motion response (Fig. 8) of the HBD5/PT2 pier specimen (Fig. 6, right) taken from Marriott [29] and modelled in OpenSees using a simple 2 spring SDOF (Fig. 6, left) in three different configurations: free rocking of the pier, post-tensioning only (controlled rocking), and post-tensioning with metal hysteretic dissipators (DCR).

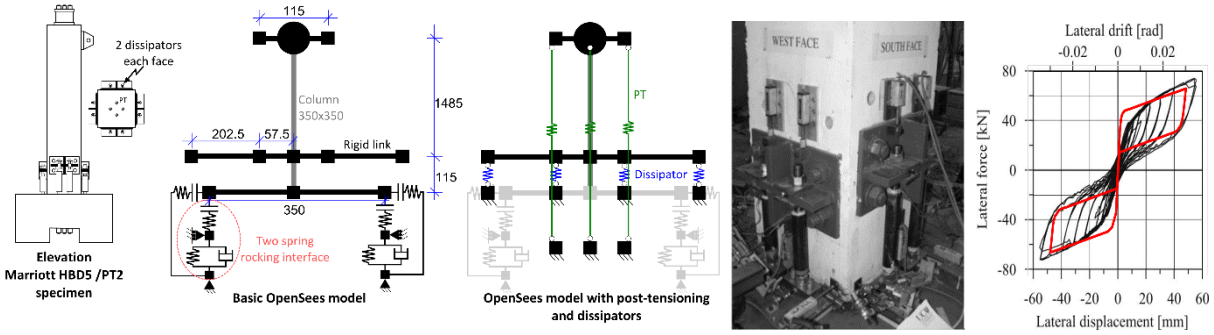

Figure 6: Left, OpenSees models of test specimens HBD5/PT2 taken from [29]. Middle, photo of HBD5 specimen from [29] with external buckling restrained fuse dissipators, and concrete to steel rocking interface. Right, comparison of the model and experimental flag shaped hysteresis curves.

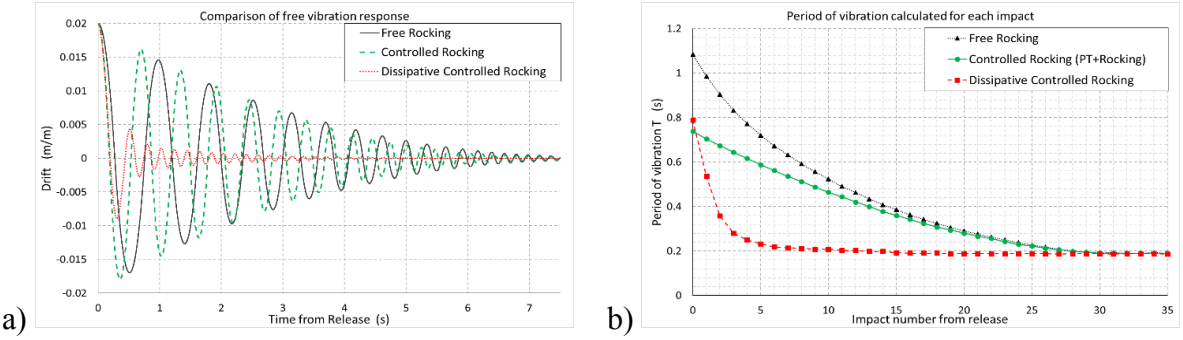

Figure 7: a) Free vibration response since release from 2% drift. **b)** Variation in the period of vibration as a function of the number of rocking impacts since release.

It can be seen in Figure 7a that the addition of post-tensioning immediately reduces the initial period of vibration due to the additional restoring force provided by tendon elongation. Figure 7b shows that the addition of post-tensioning has little effect on the damping of the system which is expected due to it behaving in the elastic range. This means that controlled rocking

mainly relies on contact damping for energy dissipation. Finally, with the further addition of metal hysteretic dissipators, the pier will tend to behave as a fixed base structure. This is due to the continuous supplemental damping provided by the dissipators quickly reducing the amplitude of vibration so that the displacements of the dissipators are below yield and the pier no longer rocks due to the high elastic stiffness of the dissipators (Fig's. 7a &b).

Inspecting the response history (Fig. 8) of the same pier, in the same three configurations, subject to seven different ground motions (Fig. 8, top left) scaled to have the same PGA (0.365g) as the design spectrum, a similar trend in behaviour is apparent. The displacement response of the different configurations (Fig. 8) clearly shows the period elongation effects of free rocking which are not observed for the controlled rocking (post-tensioning plus rocking) or DCR configurations. Hence, controlled rocking and DCR do not display seismic isolation properties and should therefore be treated more like fixed base structures in terms of seismic design.

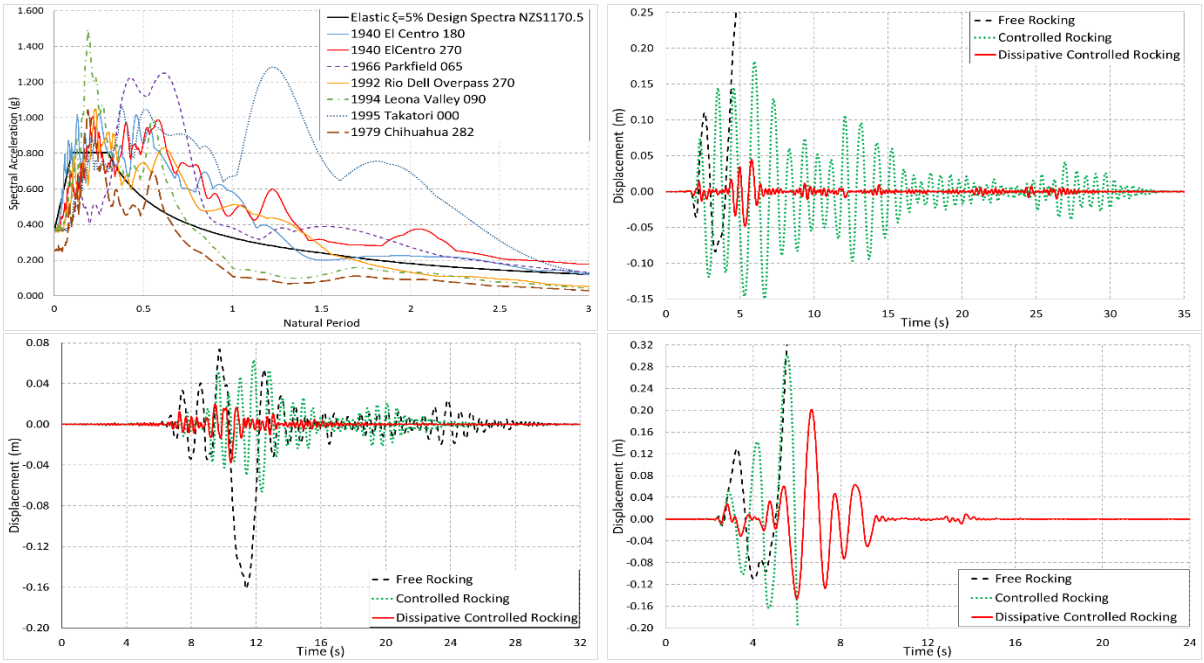

Figure 8: Top left, 5% damped elastic acceleration spectra used for nonlinear response history analysis. Top right, bottom left, and bottom right, displacement response of the three pier configurations subject to the 1940 ElCentro 180, 1994 Leona Valley 090, and 1995 Takatori 000 records respectively. The 1994 Leona Valley 090 record was the only record which did not result in overturning of the free rocking configuration.

4 IMPROVING THE STRUCTURAL REDUNDANCY OF DCR: MULTI-PERFORMANCE DISSIPATIVE CONTROLLED ROCKING (MDCR)

In the context of cantilever bridge piers, the plastic hinging mechanism is of column sway, where, collapse prevention is dependent upon the ductility capacity of the plastic hinge at the base. In DCR cantilever bridge piers the rotational ductility against overturning is dependent upon the dissipators and post-tensioning. Currently, all the dissipators are designed to activate at a set level of earthquake loading and all have the same ultimate capacities. Hence, currently the robustness of DCR is purely provided by multiplicity in the number of dissipators and post-tensioning. Once rupture of a few dissipators and yielding of the post-tensioning occurs, the pier would lose significant stiffness and would be prone to P-Δ effects which would eventuate in collapse of the structure (Fig. 9a).

To mitigate this issue, research is being conducted by the authors on a new design strategy based on dissipative controlled rocking called "Multi-Performance Dissipative Controlled

Rocking" (MDCR). The concept is to delay the onset of collapse through discretizing the capacity of the structure provided by dissipative devices and or mechanisms (rocking), such that, the devices and or mechanisms are activated in a hierarchical manner under increasing levels of shaking. The authors have proposed three methods of achieving this [28], however, only one is explained in detail here due to its relation to the experimental results being presented

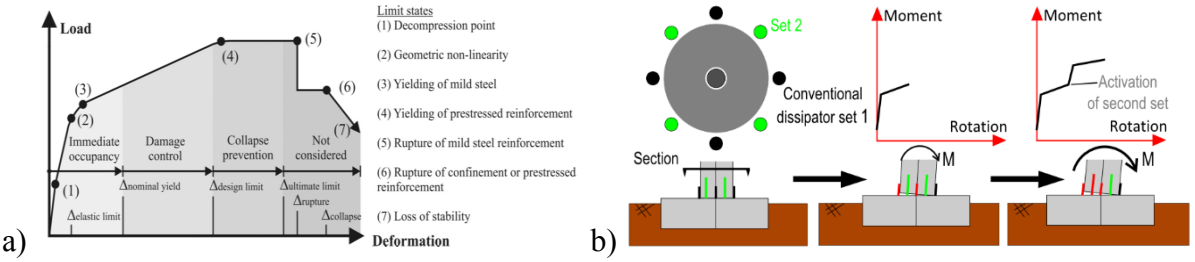

Figure 9: a) Performance objectives and limits for a DCR pier [29]. **b)** Example of hierarchical activation used.

The method of achieving hierarchical activation focussed on in this paper, is to have two sets of dissipators across one rocking interface (Fig. 9b). One set, is directly attached to the members either side of the rocking interface, while, the other is attached in such a way that it is only engaged when uplift at the rocking interface exceeds a specified value. The purpose of this arrangement, is that under frequent seismic loading (return period less than ULS) only one set of dissipative devices is relied upon and if the intensity of the ground motion exceeds that of the ULS ground motion then the second set of dissipative devices is activated in addition to the first set. In this way, after a ULS ground motion, even though one set of dissipators may be spent, the vulnerability of a DCR pier to a sequential significant ground motion (if the first set is not immediately replaced) is lessened due to the presence of the second unused set on standby. In addition to this, in extreme events where both sets contribute to resisting the ground motion, the onset of yielding of the post-tensioning and major P-Δ effects are delayed due to the activation of the second set reducing overall displacements.

5 EXPERIMENTAL INVESTIGATION INTO MDCR

Experimental testing was carried out on a 1/3 scale precast concrete bridge with single cantilever, post-tensioned, rocking pier designed to operate in controlled rocking, DCR, and MDCR configurations. The same pier was also tested in isolation after removal of the decks in DCR and MDCR configurations. The aim of the testing was to physically test the MDCR concept and compare it to a conventional DCR benchmark.

5.1 Specimen overview

The specimen is based on a prototype structure (Fig. 10) typical of a two lane, short-span, reinforced concrete, New Zealand Highway Bridge. The prototype consists of two, 13m simple spans; a single, 1.5m diameter circular pier; and hammer head type cap beam, supporting, a precast superstructure made of standard design double hollow core units. The test specimen, is a fully precast concrete structure (design f'c = 40MPa) and is 1:3 scale. Like the prototype, it is a two span simply supported bridge (Fig. 11). The decks are hollow core slabs each nominally 4222mm long by 2400mm wide and rest on rectangular UHMWPE bearings.

The pier is 500mm in diameter, and has a clear length of 2140mm. The armouring at the base of the pier is a custom made, 500 x 10 CHS with an annular steel ring welded to the base (Fig. 12c).Shear studs welded to the inside of the CHS ensure composite action with the pier. Shear and torsion restraint of the pier base is provided by external shear and torsion keys (Fig.

12b). Pier post-tensioning is provided by a single 26.5mm diameter Macalloy bar of 3182mm unbonded length. Grooved type dissipators were used. The dissipators had 4 grooves, are 16mm in diameter, have a design fuse length of 185mm, a design fuse area of 135mm^2 and are made from mild steel (Fig. 12e) The pier base accommodates a maximum of 8 dissipators (Fig. 12a) which are evenly distributed around the pier (Fig. 9b): 4 for conventional PRESSS hybrid configuration and 4 for hierarchical activation ($\theta_{engagement}$ =2.5% so that yielding would occur prior to θ_{MCE} =2.75%). The dissipator to dissipator circle diameter is 570mm.

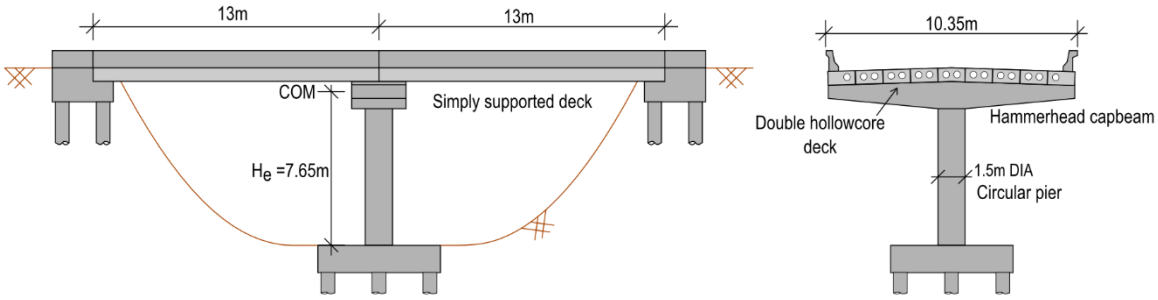

Figure 10: Prototype bridge.

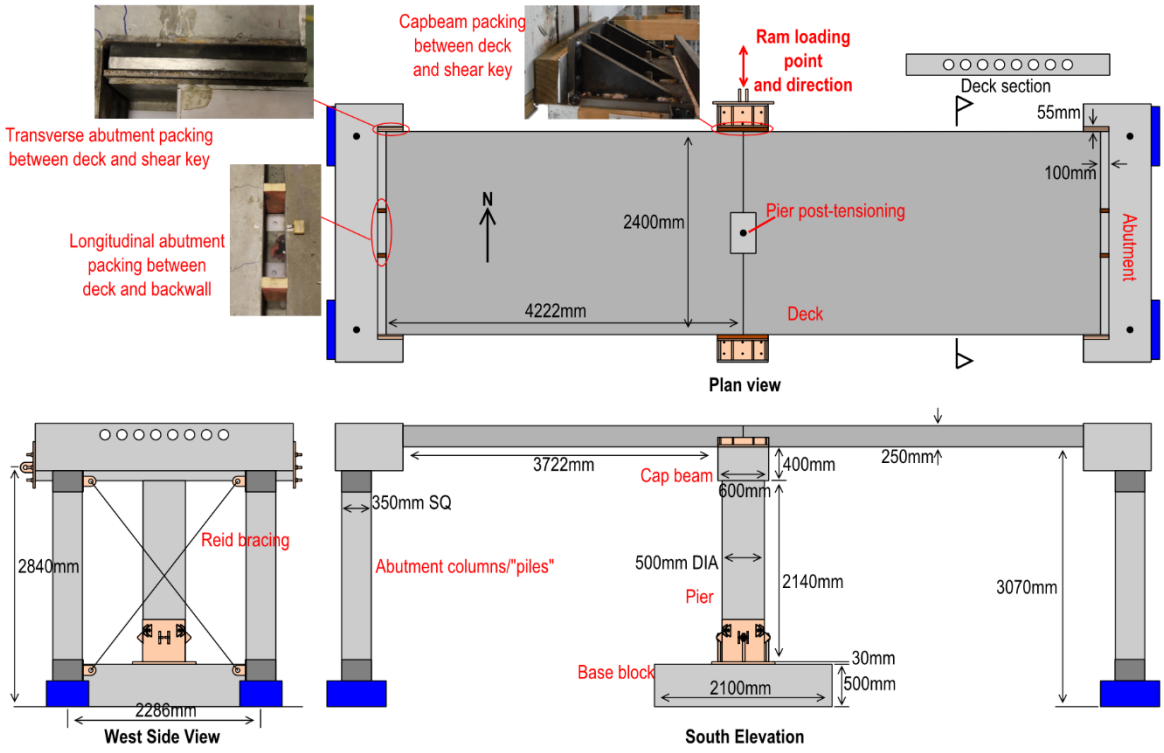

Figure 11: Overall specimen dimensions and detail regarding the boundary conditions around the decks.

5.2 Pier details: hierarchical activation of two sets of dissipators

In the experimental testing shown here, hierarchical activation, involved two sets of dissipators, where, one set is engaged at a later pier displacement to the other. Many options for achieving this were investigated, however, most were either infeasible or impractical. The final option chosen, consists of dissipators being connected by pins to the foundation and pier (Fig. 12a), but where, the pinned bracket connecting the dissipator to the pier has a slotted hole (Fig. 12d).

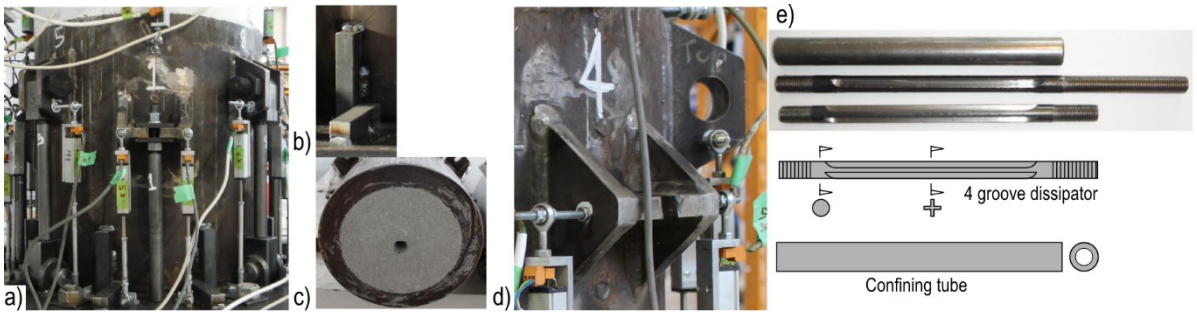

Figure 12: a) Pier with all dissipators attached; **b)** Shear and torsion keys; **c)** Pier base rocking interface; **d)** Dissipator bracket detail, pinned dissipator bracket in background; **e)** Groove type dissipator and confining tube.

At zero lateral pier displacement, the pin in the slotted hole is designed to sit at the top of the slot. Then as the pier uplifts, the dissipator bracket with slotted hole moves upwards and relative to this the pin approaches the bottom of the slot. Only when the uplift is sufficient for the pin to engage with the bottom of the slot, is the dissipator pulled upon. This option for producing hierarchical activation was chosen for three reasons: the pins allow the dissipator to be pulled on axially, despite, the arced uplift movement of the pier; the slotted hole allows the dissipator to undergo compression once it has been extended, whilst, also providing vertical and horizontal restraint of the dissipator ends; and this option was reasonably practical to implement, along with the spent dissipators being accessible for replacement.

5.3 Specimen design

In terms of seismic action design parameters, the prototype was assumed to be of importance level 2; sited in Christchurch, with a hazard factor of 0.3; constructed on non-liquefiable soil of class C; and not subject to near fault effects. Seismic design was only conducted in the transverse direction due to this direction of loading being the governing load case for the pier. Displacement based design was used to determine the seismic design parameters for the prototype pier which were then scaled for specimen design. Table 1 below summarizes the salient pier seismic design parameters calculated.

Table 1: Summary of specimen seismic design parameters from displacement based design.

Specimen ULS design actions and dimensions	**Units**	**Value**
Design gravity load, W_{scaled}	kN	195
Design lateral load, V_{scaled}	kN	42.9
Effective height of equivalent SDOF, $H_{e,\ scaled}$	mm	2550
Pier diameter, D_{scaled}	mm	500
Design base moment, M_{scaled}	kNm	109.4
Design displacement, Δds	mm	52
MCE displacement, $\Delta MCEs$ (ADRS assuming EPP F-Δ)	mm	81.4

5.4 Test setup and loading regime

The test set up consisted of a single 300kN ram, loading the bridge transversely at the cap beam level 2310mm above the base of the pier (Fig. 13). The position and direction of loading were chosen to simulate transverse seismic loading of the bridge and to allow later pier only tests to be conducted. Loading of the bridge was cyclic, displacement controlled, and quasi-static. The loading protocol used for testing was derived from ACI T1.1-01 [30]: three fully reversed cycles are applied at each drift ratio; the first drift ratio is within the linear elastic

response range; subsequent drift ratios are between 1.25 and 1.5 times the previous value. Lateral drifts of 0.1%, 0.125%, 0.175%, 0.25%, 0.35%, 0.5%, 0.75%, 1.0%, 1.5%, 2.0% 2.75% 3.5%, and 4.5% were imposed. However, only during testing of the pier in isolation were all of the drift ratios imposed. During bridge testing, the maximum applied drift ratio was 2.75% due to safety reasons and the load capacity of the ram to cap beam loading attachment.

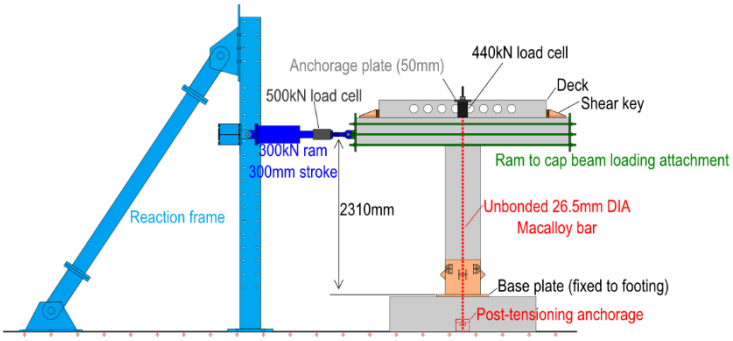

Figure 13: Experimental test set up showing that the bridge was loaded by a single ram at the cap beam level

5.5 Testing schedule

The bridge and pier only test configurations relevant for comparing the performance of DCR and MDCR are summarized in Table 2 below.

Table 2: Selected bridge and pier test schedules. No deck post-tensioning or deck dissipators were used in tests 1,3 and 4.

Test	Pier post-tensioning kN	Conventional pier dissipators	Pinned dissipators
1: Bridge, no pier dissipators	89.2	-	-
3: Bridge, 8 pier dissipators (MDCR)	91.37	4	4
4: Bridge, 4 pier dissipators (PRESSS)	92.3	4	0
12: Pier only (decks removed), $\lambda(\theta=2\%)$ =1.33	154.7	4	0
13: Pier only (decks removed), $\lambda(\theta=2\%)$ =0.75	155.3	4	4

5.6 Experimental results and analysis

In the very first test of the bridge system (Test 1), energy dissipation was found to be significant despite the source only being from friction (Fig. 14a). The self-centering characteristic of the pier combined with the frictional hysteresis produced a flag shaped response. The addition of 4 dissipators in Test 4 so the pier would be in a conventional PRESSS hybrid configuration increased both the stiffness and damping of the entire system (Fig. 14a). In Test 3, the bridge was tested with the pier utilising hierarchical activation. However, due to the activation drift being just over 2% and the maximum drift applied being 2.75% the contribution made was small (Fig. 14a). In tests 3 and 4 no failure of the dissipators occurred.

Testing of the pier in isolation, allowed the full effect of hierarchical activation (Test 13) to be observed (Fig. 14b). Compared to the conventional PRESSS arrangement (Test 12), the activation of the second set of dissipators increased the amount of energy able to dissipated (Fig. 15) in addition to the pier stiffness. In test 12, during unloading from the peak positive displacement of the second cycle at 3.5% drift, failure of one dissipator on the extreme tension side of

the pier occurred. The dissipator failed due to shear failure of the dissipator threads engaged with the nut below the dissipator bracket. This caused that particular dissipator to work in tension only for the following load cycles resulting in pinching of the hysteresis loops.

Further evaluation of the changes in damping between tests 12 and 13 was undertaken through evaluation and comparison of the area based hysteretic damping from these two tests (Fig. 16a).The area based hysteretic damping was computed using equation 1. Where: ED is the area enclosed in one cycle of a hysteresis loop; F_{pp} and F_{pn} are the signed peak positive and negative forces measured during that cycle; U_{pp} and U_{pn} are the signed peak positive and negative displacements for the same cycle; K_{eff}, is the effective secant stiffness; and U_o is the average peak displacement.

$$\xi_A = \frac{ED}{2\pi K_{eff} U_o^2} \quad where, \quad K_{eff} = \frac{F_{PP}-F_{PN}}{U_{PP}-U_{pn}} \; and \; U_o = \frac{U_{pp}-U_{pn}}{2} \tag{1}$$

Figure 16a compares the area based damping averaged over the repeated cycles for each drift level for tests 12 (conventional PRESSS) and 13 (MDCR). It can be seen that past a drift of 1.5% for test 13, that the hysteretic damping is less than that for test 12 until failure of the thread on one dissipator occurred. This reduced hysteretic damping can be explained as follows: because the experiment was displacement controlled U_o is very much the same for both tests 12 and 13, therefore, comparing the difference between the two tests in terms of the area based damping is effectively the average ratio of the energy dissipated per cycle (ED) to the effective stiffness K_{eff}. Although, ED for test 13 is larger than the corresponding cycle in test 12 once activation occurs (Fig. 15), this increase in ED is not as large as the increase in Keff therefore resulting in a reduced value of area based damping when compared to test 12. The implications of this reduced area based hysteretic damping combined with increased secant stiffness with respect to transient seismic response is currently unknown and further work will be conducted to numerically assess such impacts.

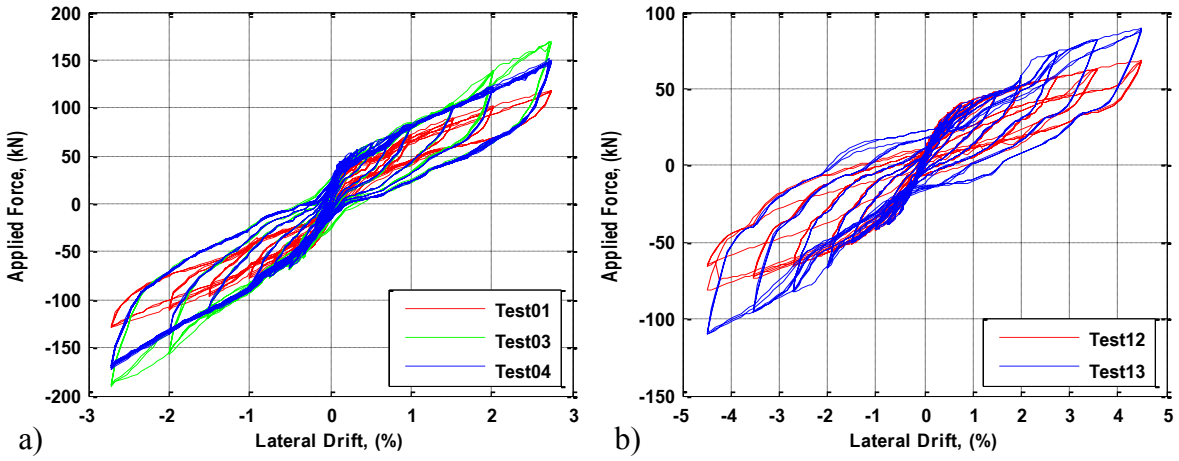

Figure 14: a) Comparison of the force displacements of tests 1, 3 and 4; **b)** Comparison of force-displacement behaviour of tests 12 and 13 showing effect of hierarchical activation during a pier only test.

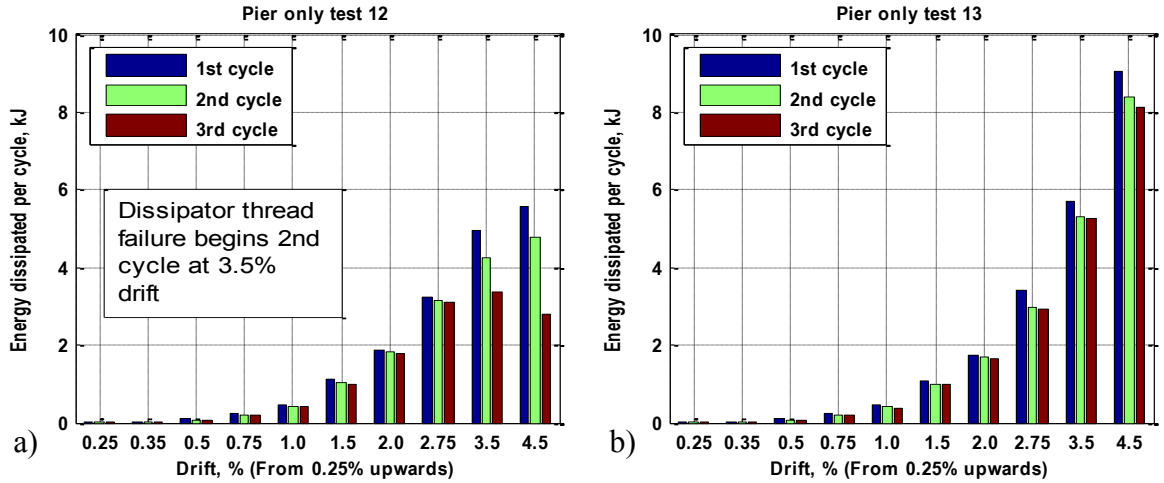

Figure 15: a) Energy dissipated per cycle for pier only test 12 – PRESSS configuration. **b)** Energy dissipated per cycle for pier only test 13 – MDCR configuration.

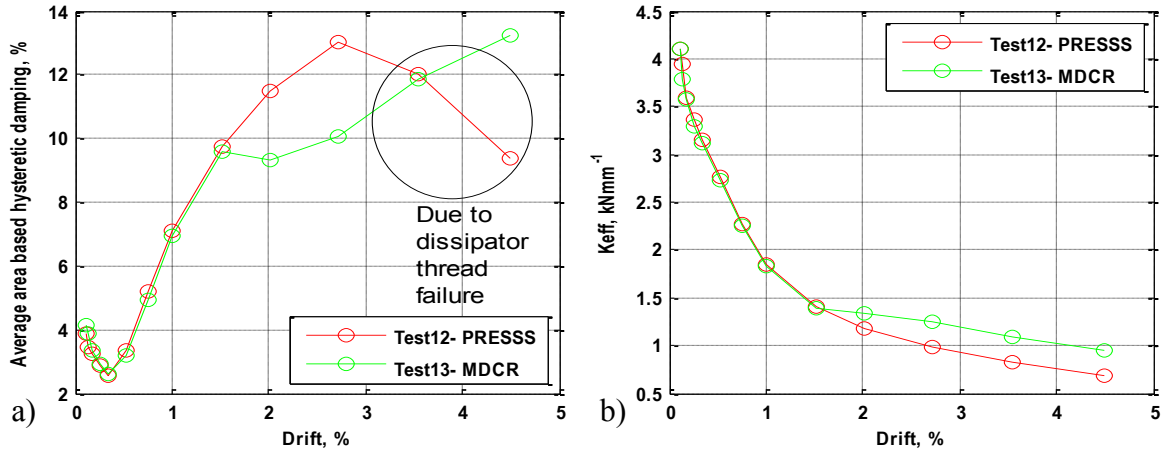

Figure 16: a) Comparison of the average corrected hysteretic damping for tests 12 and 13 as a function of ductility. **b)** Average effective stiffness for each drift level of tests 12 and 13. Activation of the second set of dissipators increases the effective stiffness.

6 CONCLUSION

In conclusion, a brief literature review was given outlining the family of rocking structures and their relation to one another. The literature review showed the progressive development and changes of rocking structures with time. The distinction in dynamic behaviour between free rocking, controlled rocking, and DCR was shown through the results of preliminary numerical analysis in OpenSees. A possible future evolution of PRESSS hybrid rocking was suggested in the form of hierarchical activation (MDCR) and description of this new design strategy given. Finally, results from experimental testing, focussing, on the comparison of DCR against MDCR were given. The results prove the concept of MDCR, however, the unexpected effect on area based hysteretic damping will require further investigation to ascertain whether this is detrimental to transient response.

REFERENCES

[1] Priestley, M.J.N. (1996) The PRESSS Program Current Status and Proposed Plans for Phase III. *PCI Journal*, **41**, 22–40.

[2] Housner, G.W. (1963) The Behaviour of Inverted Pendulum Structures during Earthquakes. *Bulletin of the Seismological Society of America*, **53**, 403–17.

[3] Evision, R.J. (1977) Rocking Foundations. Christchurch, N.Z.

[4] Bartlett, P.E. (1976) Foundation Rocking On a Clay Soil. Auckland, N.Z.

[5] Wiessing, P.R. (1979) Foundation Rocking on Sand. Auckland, N.Z.

[6] McManus, K.J. (1980) The Seismic Response of Bridge Structures Free to Rock on their Foundations.

[7] Muto, K., Umemura, H. and Sonobe, Y. (1960) Study of the overturning vibrations of slender structures. *Proceedings of the 2nd World Conference on Earthquake Engineering Tokyo, Japan*, p. 1239–61.

[8] Beck, J.L. and Skinner, R.I. (1974) Seismic response of a reinforced concrete bridge pier designed to step. *Earthquake Engineering and Structural Dynamics*, **2**, 343–58.

[9] Antonellis, G. and Panagiotou, M. (2014) Seismic Response of Bridges with Rocking Foundations Compared to Fixed-Base Bridges at a Near-Fault Site. *Journal of Bridge Engineering*, **19**.

[10] Allmond, J. and Kutter, B. (2012) Centrifuge Testing of Rocking Foundations on Saturated Sand and Unconnected Piles: The Fluid Response. *GeoCongress 2012*, American Society of Civil Engineers. p. 1760–9. http://dx.doi.org/doi:10.1061/9780784412121.181

[11] Chen, Y.H., Liao, W.H., Lee, C.L. and Wang, Y.P. (2006) Seismic isolation of viaduct piers by means of a rocking mechanism. *Earthquake Engineering & Structural Dynamics*, John Wiley & Sons, Ltd. **35**, 713–36.

[12] Anastasopoulos, I., Loli, M., Georgarakos, T. and Drosos, V. (2013) Shaking Table Testing of Rocking-Isolated Bridge Pier on Sand. *Journal of Earthquake Engineering*, **17**, 1–32.

[13] Ma, Q.T.M. (2010) The Mechanics of Rocking Structures Subjected to Ground motion. The University of Auckland.

[14] Mergos, P.E. and Kawashima, K. (2005) Rocking isolation of a typical bridge pier on spread foundation. *Journal of Earthquake Engineering*, **9**, 395–411.

[15] Anastasopoulos, I., Gazetas, G., Loli, M., Apostolou, M. and Gerolymos, N. (2009) Soil failure can be used for seismic protection of structures. *Bulletin of Earthquake Engineering*, **8**, 309–26. http://dx.doi.org/10.1007/s10518-009-9145-2

[16] Robinson, W.H. (1985) Hysteretic dampers for protecting structures during earthquakes. *Journal De Physique*, **46**, 421–4.

[17] Priestley, M.J.N. and Tao, J.R. (1993) Seismic response of precast prestressed concrete frames with partially debonded tendons. *PCI Journal*, **38**, 58–69.

[18] Mander, J.B. and Cheng, C.T. (1997) Seismic resistance of bridge piers based on damage avoidance design. National Center for Earthquake Engineering Research, New York.

[19] Palermo, A., Pampanin, S. and Calvi, G.M. (2005) Concept and development of hybrid solutions for seismic resistant bridge systems. *Journal of Earthquake Engineering*, **9**, 899–921.

[20] Marriott, D., Pampanin, S. and Palermo, A. (2006) Experimental Validation of High-Performance Hybrid Bridge Piers. *2006 NZSEE Conference*, Napier, New Zealand.

[21] Marriott, D., Pampanin, S. and Palermo, A. (2009) Quasi-static and pseudo-dynamic

testing of unbonded post-tensioned rocking bridge piers with external replaceable dissipaters. *Earthquake Engineering and Structural Dynamics*, **38**, 331–54.
[22] Kam, W.Y., Pampanin, S., Palermo, A. and Carr, A.J. (2010) Self-centering structural systems with combination of hysteretic and viscous energy dissipations. *Earthquake Engineering & Structural Dynamics*, **39**, 1083–108. http://dx.doi.org/10.1002/eqe
[23] Marriott, D., Pampanin, S., Palermo, A. and Bull, D. (2008) Shake-table testing of hybrid post-tensioned precast wall systems with alternative dissipating solutions. *NZSEE Conference*,.
[24] Wang, J.C., Ou, Y.C., Chang, K.C. and Lee, G.C. (2008) Large-scale seismic tests of tall concrete bridge columns with precast segmental construction. *Earthquake Engineering & Structural Dynamics*, John Wiley & Sons, Ltd. **37**, 1449–65. http://dx.doi.org/10.1002/eqe.824
[25] Sideris, P., Aref, A.J. and Filiatrault, A. (2014) Quasi-Static Cyclic Testing of a Large-Scale Hybrid Sliding-Rocking Segmental Column with Slip-Dominant Joints. *Journal of Bridge Engineering*,. http://dx.doi.org/10.1061/(ASCE)BE.1943-5592.0000605
[26] Hewes, J.T. and Priestley, M.J.N. (2002) Seismic design and performance of precast concrete segmental bridge columns.
[27] Sideris, P., Aref, A.J. and Filiatrault, A. (2014) Large-scale seismic testing of a hybrid sliding-rocking posttensioned segmental bridge system. *Journal of Structural Engineering*, **140**. http://dx.doi.org/10.1061/(ASCE)ST
[28] Liu, R. and Palermo, A. (2015) Low Damage Design and Seismic Isolation : What's the difference ? *2015 NZSEE Conference*, Rotorua, New Zealand.
[29] Marriott, D. (2009) The Development of High-Performance Post-Tensioned Rocking Systems for the Seismic Design of Structures. University of Canterbury.
[30] ACI Innovation Task Group 1. (2001) Acceptance criteria for moment frames based on structural testing. American Concrete Institute, Farmington Hills, Michigan, USA.

ECCOMAS Congress 2016
VII European Congress on Computational Methods in Applied Sciences and Engineering
M. Papadrakakis, V. Papadopoulos, G. Stefanou, V. Plevris (eds.)
Crete Island, Greece, 5–10 June 2016

THE ROLE OF THE PRESTRESSED TENDONS ON THE SEISMIC PERFORMANCE OF HYBRID ROCKING BRIDGE BENTS

Anastasios I. Giouvanidis[1], **Elias G. Dimitrakopoulos**[2]

[1]Department of Civil and Environmental Engineering, The Hong Kong University of Science and Technology
Kowloon Bay, Hong Kong
e-mail: agiouvanidis@connect.ust.hk

[2] Department of Civil and Environmental Engineering, The Hong Kong University of Science and Technology
Kowloon Bay, Hong Kong
e-mail: ilias@ust.hk

Keywords: rocking bridges, flag-shaped hysteretic behavior, self-centering, prestressed tendons.

Abstract. *Allowing structural members to uplift and rotate around pre-defined pivot points isolates and relieves the structure from deformation and damage during strong earthquakes. Such rocking behavior has been examined as damage avoidance seismic design for bridges. Rocking structures, either freestanding or hybrid (supplemented with energy dissipation and re-centering devices), have been proposed by several researchers as high-performance systems that can survive major earthquakes without substantial damage. This paper investigates, analytically and numerically, the seismic performance of a hybrid rocking bridge bent which exhibits flag-shaped hysteretic behavior. The rocking frame is enhanced with elastic prestressed central tendons to provide re-centering capacity and hysteretic buckling restrained braces to dissipate energy. The present study examines its seismic behavior under both pulse-type and non-pulse-type ground motions. The focus of the present analysis is on the role of the prestressing force on the seismic performance. The results reveal the diverse influence of prestress. Specifically, prestress is beneficial for small rocking rotations, but could become detrimental when the frame sustains large rotations and as the size of the columns increases. Finally, the results reveal the sensitivity of the different rocking design solutions to the characteristics of the considered ground motion. As a consequence, none of the examined rocking frames can be considered as the optimal design solution under all ground motions.*

1 INTRODUCTION

Rocking as a means of seismic isolation is attracting the interest of researchers for almost a century (see [18, 16, 29, 6, 13, 9, 10, 30, 8, 39, 34] and references therein). Recently, there is an increasing need to examine the dynamics of progressively more complicated and realistic structures ([1, 2, 40, 38] among others). Of particular interest for bridge engineering is the rocking frame configuration of Fig. 1 proposed originally by [22] as a "damage avoidance design" for bridges. The existing bridges designed to rock remain scarce (see [11] and references therein), even though, an increasing number of studies illustrate their high seismic performance. In particular, [7, 33, 35, 36] revealed that rocking piers can exhibit large drifts (around 6% to 10%) with minor damage and/or residual displacements. Recent experimental studies [37, 27] showed that the residual drifts of posttensioned rocking columns are negligible (0.4%) compared to the pertinent drifts of conventional monolithic columns (6.8%) with the same peak drift ratios; in accordance with [32]. Further, [19, 20] showed that the stability of the rigid rocking frame is enhanced, the more heavy its cap-beam is, regardless of the rise of its center of mass; a counter-intuitive behavior.

Such self-centering systems aim to eliminate residual drifts after strong earthquakes. Many researchers [25, 26, 28, 23, 17, 43] combine the use of additional re-centering with energy dissipation devices, to propose "hybrid rocking systems" which exhibit flag-shaped hysteretic behavior (FSHB). In this context [26, 23, 17] compared numerically and experimentally the seismic performance of rocking versus conventionally designed monolithic piers. The rocking piers showed higher self-centering capacity and lower residual displacements compared to the monolithic solution. [11] examined a hybrid rocking frame with asymmetric configuration (with columns unequal in height), and compared its stability with the pertinent symmetric configuration. That study unveiled the marginal influence of the asymmetry on the stability despite the very different kinematics between the two configurations. Building on previous work on hybrid rocking structures [17, 21, 11], the present work investigates the effect of the prestressing force on the seismic performance of hybrid FSHB rocking frames, and compares different rocking design solutions.

2 ANALYTICAL MODELLING

This section examines (analytically) a rocking bridge bent which exhibits flag-shaped hysteretic behavior. The present study considers structures designed to exhibit planar rocking and it assumes no sliding between the contacting bodies takes place [5]. Consider the rocking frame of Fig. 1 enhanced with central (linear-elastic) prestressed tendons and (nonlinear-hysteretic) buckling restrained braces (BRBs) at the bottom of the piers. Note that, this study ignores the fracture of the tendons and the dissipaters, which is discussed in [11]. To describe the hysteretic behavior of the BRBs, the Bouc-Wen model [4, 42] is adopted. The restoring dissipating force is expressed as:

$$F_D = \varepsilon k_d u\left(t\right) + \left(1-\varepsilon\right) k_d u_y z\left(t\right) \tag{1}$$

where ε is the post-yield to pre-yield elastic stiffness (k_d) ratio, $u\left(t\right)$ is the axial deformation of the brace, u_y is the yield displacement equal with $u_y = 4b\sin\left(\phi_y/2\right)$ with $2b$ the width of the base of the column of the frame and ϕ_y the yield rotation (Fig. 1). $z\left(t\right)$ is a dimensionless hysteretic parameter that is governed by:

$$\dot{z}(t) = \frac{1}{u_y}\left[\dot{u}(t) - \gamma\left|\dot{u}(t)\right| z\cdot\left|z\right|^{n-1} - \beta\dot{u}(t)\left|z\right|^{n}\right] \tag{2}$$

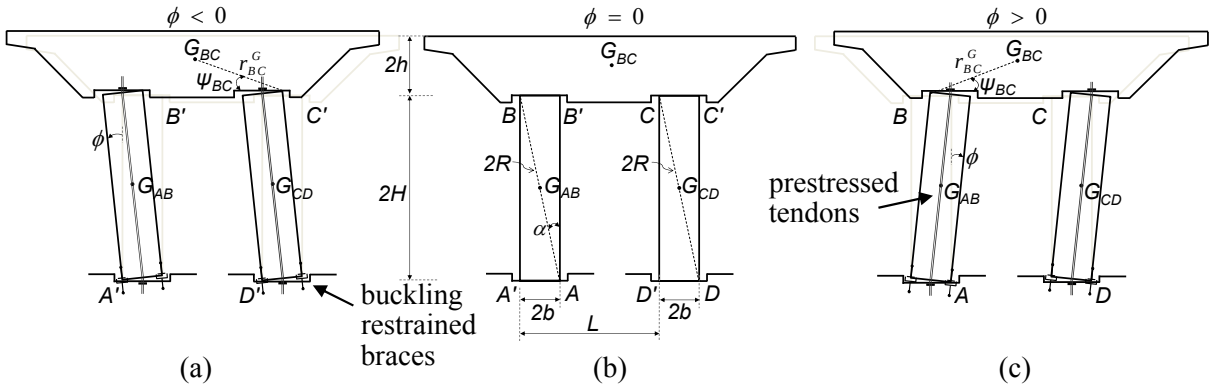

Figure 1: The examined hybrid rocking bridge bent (a) during counter-clockwise rotation, (b) at rest position and (c) during clockwise rotation.

Parameters β, γ and n control the shape of the hysteretic loop. Following [3], $\beta = 0.55$, $\gamma = 0.45$, $n = 1$, $\varepsilon = 0.025$ and $u_y = 3.5\,mm$.

2.1 Flag-shaped hysteretic behavior (FSHB)

Assuming positive (clockwise) rotations, the restoring moment offered by the weight of the two columns and the cap-beam is equal with:

$$\frac{M_R^{gr}}{2\left(m_{AB}+m_{BC}\right)gR} = \sin\left(\alpha-\phi\right) \tag{3}$$

where m_{AB} and m_{BC} are the masses of the column AB and the cap-beam BC respectively, R is the half diagonal of the column of the frame, g is the gravitational acceleration, and α is the slenderness of the column. ϕ is the generalized coordinate which describes the rocking motion of the frame (Fig. 1). The additional re-centering and energy dissipation devices offer a total restoring moment M_R^{hyb}:

$$\begin{aligned}\frac{M_R^{hyb}}{2(m_{AB}+m_{BC})gR} &= 4\left(\rho_t+\varepsilon\rho_d\right)\sin\phi + 2\sin\alpha p_{str}\cos\tfrac{\phi}{2} \\ &+8\left(1-\varepsilon\right)\rho_d\sin\tfrac{\phi_y}{2}\cos\tfrac{\phi}{2}z(t)\end{aligned} \tag{4}$$

The dimensionless parameters ρ_d, ρ_t and p_{str} control the stiffness of the dissipaters k_d, of the tendons k_t and the initial prestressing force P_0 respectively:

$$\rho_d = \frac{k_d b^2}{\left(m_{AB}+m_{BC}\right)gR},\quad \rho_t = \frac{k_t b^2}{\left(m_{AB}+m_{BC}\right)gR},\quad p_{str} = \frac{P_0}{\left(m_{AB}+m_{BC}\right)g} \tag{5}$$

The present study assumes that the design parameters ρ_d, ρ_t and p_{str} vary within $0 \le \rho_d \le 5.0$, $0 \le \rho_t \le 0.7$ and $0 \le p_{str} \le 0.1$ respectively. The total restoring moment becomes:

$$\begin{aligned}\frac{M_R}{2(m_{AB}+m_{BC})gR} &= \sin\left(\alpha-\phi\right) + 4\left(\rho_t+\varepsilon\rho_d\right)\sin\phi + 2\sin\alpha p_{str}\cos\tfrac{\phi}{2} \\ &+8\left(1-\varepsilon\right)\rho_d\sin\tfrac{\phi_y}{2}\cos\tfrac{\phi}{2}z(t)\end{aligned} \tag{6}$$

On the other hand, the overturning moment induced by the ground excitation ($\ddot{u}_g$) becomes:

$$\frac{M_{OT}}{2\left(m_{AB}+m_{BC}\right)\ddot{u}_g R} = \cos\left(\alpha-\phi\right) \tag{7}$$

Rocking initiates when the overturning moment of Eq. (7) becomes equal with the total restoring moment of Eq. (6). This equality yields the minimum ground acceleration necessary for rocking initiation:

$$\ddot{u}_{g,\min} = g \tan\alpha \, (1 + 2p_{str}) \tag{8}$$

Eq. (8) shows that increase of the prestressing force, causes increase in the ground acceleration necessary to initiate rocking. During rocking, the motion of the frame is interrupted by non-smooth impacts. At each impact, a part of the total kinetic energy is lost and the frame continues its motion with a ratio between the angular velocity after and before the impact (coefficient of restitution) equal with [11]:

$$\eta = \frac{\dot{\phi}^{+}}{\dot{\phi}^{-}} = \frac{1 - \frac{3}{2}\sin^2\alpha + 3\gamma_m \cos 2\alpha}{1 + 3\gamma_m} \tag{9}$$

The present study assumes the coefficient of restitution η to be 0.92.

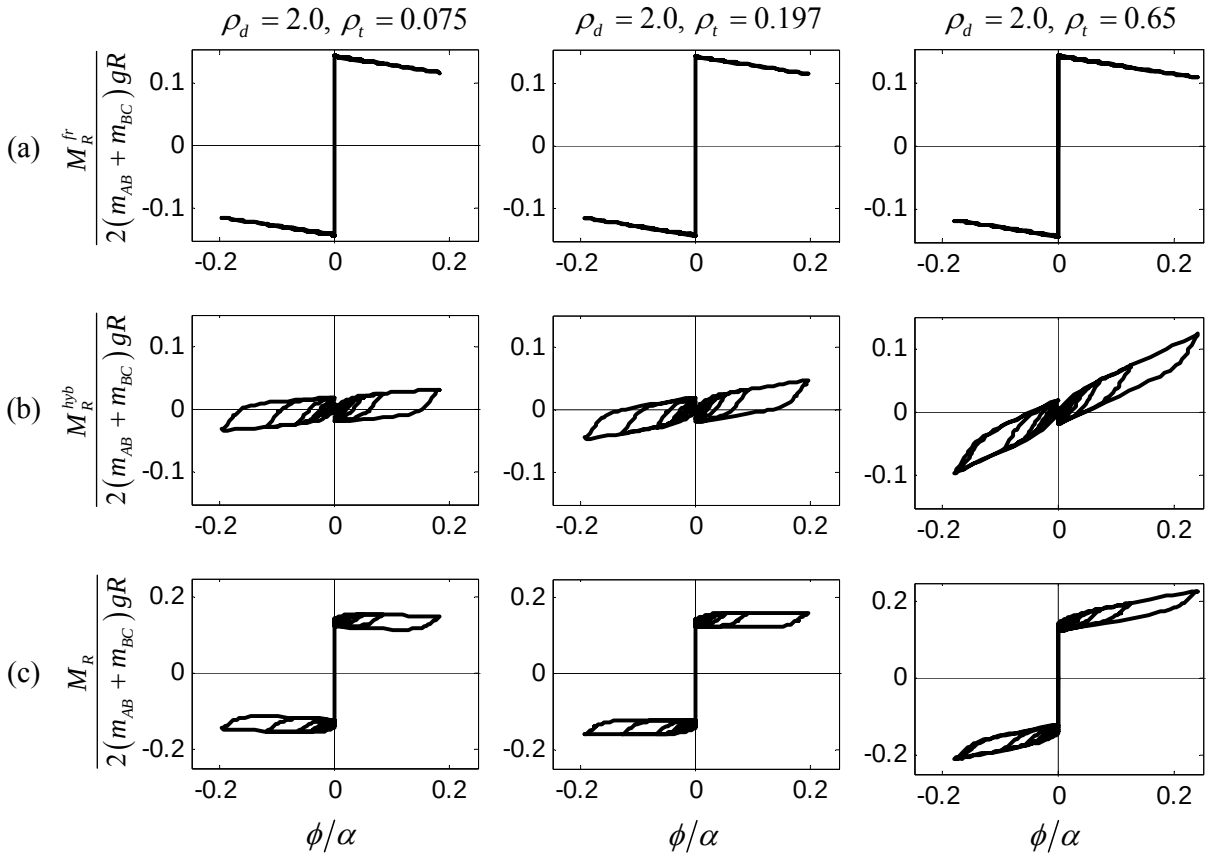

Figure 2: Restoring moments due to (a) gravitational forces, (b) the presence of tendon and dissipater and (c) total restoring moment for the rocking frame subjected to M&P pulse with $\nu_g = 45°$, $\gamma_g = 2.0$, $\alpha_g = 0.6g$ and $\omega_g = 6.09\, rad/s$.

The moment-rotation relationship follows the curves shown in Fig. 2. Observe that, the restoring moment due to the gravitational forces of the columns and the cap-beam do not enclose any area under the moment-rotation curve (Fig. 2(a)) since energy is dissipated only during impact. The presence of buckling restrained braces provides additional energy dissipation, equal with the enclosed area in Fig. 2(b). When tendons and dissipaters are combined, the hysteretic

behavior of the rocking bridge bent becomes flag-shaped (Fig. 2(c)). Note that, increase in the tendon's and the dissipater's stiffness causes increase in the overall lateral stiffness of the structure. For positive stiffness systems, it holds:

$$\rho_t + \varepsilon\rho_d > \frac{1}{4} \tag{10}$$

2.2 Equation of motion (EOM)

Fig. 1 illustrates the examined hybrid FSHB rocking frame. The equation of motion is derived using Lagrange's equation:

$$\frac{d}{dt}\left(\frac{\partial L}{\partial \dot{\phi}}\right) - \frac{\partial L}{\partial \phi} = Q \tag{11}$$

where $L = T - V$, with T the kinetic energy, V the potential energy and Q the generalized force. The kinetic energy of the system is:

$$\begin{aligned} T = I_{AB}^{pivot}\dot{\phi}^2 + m_{AB}\left[\dot{u}_g^2 + 2\dot{u}_g R\cos\left(\alpha \mp \phi\right)\dot{\phi}\right] \\ +\tfrac{1}{2}m_{BC}\left[\dot{u}_g^2 + 4R^2\dot{\phi}^2 + 4R\dot{u}_g\cos\left(\alpha \mp \phi\right)\dot{\phi}\right] \end{aligned} \tag{12}$$

where I_{AB}^{pivot} is the mass moment of inertia of the AB column with respect to the pivot point. For a rectangular column is equal with $I_{AB}^{pivot} = (4/3)\, m_{AB}R^2$. The double sign in Eq. (12) and throughout the present study denotes the sign of rotation. In particular, the upper sign corresponds to clockwise (positive) rotations and the bottom to counter-clockwise (negative) rotations.

The potential energy of the hybrid FSHB rocking frame is defined as a contribution from the gravitational and the elastic forces from the tendons. Before rocking starts, the initial prestressing force (P_0) induces an initial elongation (δl_0) to the tendon equal with $\delta l_0 = P_0/k_t$, where $k_t = EA/l$ is the elastic stiffness of the tendon with E being the Young's modulus, A the cross-sectional area and l the length of each tendon. During rocking, each tendon deforms. The elongation of each tendon is equal to the sum of the elongations at the base and the top of each tendon: $\delta l = 4b\sin\left(\phi/2\right)$. Hence, the total elongation of each tendon is $\Delta l = \delta l + \delta l_0$. Therefore, the potential energy of the hybrid FSHB rocking frame takes the form:

$$V = 2m_{AB}gR\cos\left(\alpha - \phi\right) + m_{BC}g\left[2R\cos\left(\alpha - \phi\right) + r_{BC}^{G}\sin\psi_{BC}\right] + k_t\left(4b\sin\frac{\phi}{2} + \frac{P_0}{k_t}\right)^2 \tag{13}$$

where r_{BC}^{G} is the distance from the pivot point B (or C') to the center of mass G_{BC} and the angle ψ_{BC} is shown in Fig. 1.

The calculation of the non-conservative forces Q is based on the virtual work principle $\delta W_D = Q\delta\phi$ and yields:

$$Q = -4b\cos\frac{\phi}{2}\left[\varepsilon k_d u\left(t\right) + \left(1-\varepsilon\right)k_d u_y z\left(t\right)\right] \tag{14}$$

Therefore, Eq. (11) gives:

$$\ddot{\phi} = -\frac{1+2\gamma_m}{1+3\gamma_m}p^2\left[\begin{array}{l} \sin\left(\alpha\mathrm{sgn}\left(\phi\right) - \phi\right) + \frac{\ddot{u}_g}{g}\cos\left(\alpha\mathrm{sgn}\left(\phi\right) - \phi\right) + 4\left(\rho_t + \varepsilon\rho_d\right)\sin\phi \\ +2\sin\alpha p_{str}\cos\frac{\phi}{2} + 8\left(1-\varepsilon\right)\rho_d\sin\frac{\phi_y}{2}\cos\frac{\phi}{2}z\left(t\right) \end{array}\right] \tag{15}$$

where p is the frequency parameter of the column of the frame, which for rectangular columns becomes $p = \sqrt{3g/4R}$. $\mathrm{sgn}(\phi)$ is the sign function and $\gamma_m = m_{BC}/2m_{AB}$ is the mass ratio. Ignoring the presence of the dissipater and of the prestressing force, Eq. (15) verifies the equation of motion of the symmetric rocking frame enhanced with slack (unbonded) central tendons [14], and for $\gamma_m = 0$ the pertinent equation of motion of the anchored rocking block [10].

3 SEISMIC PERFORMANCE OF THE HYBRID FSHB ROCKING BRIDGE BENT

This section examines the seismic response of the planar (freestanding and hybrid FSHB) rocking bent of Fig. 1. Consider a cap-beam 13 m wide with height $2h$ = 2 m. Assume a two-(square)-column frame with $2b$ = 1.4 m base width, same density and height $2H$ = 9.8 m each. Both columns have the same slenderness $\alpha = 8.1^\circ$ and frequency parameter $p = 1.22\ rad/s$, while the distance L is 8 m. The cap-beam/column mass ratio (γ_m) is taken as 5. The yield displacement (u_y) of the braces is assumed 3.5 mm [3], which corresponds to a yield rotation $\phi_y/\alpha = 0.018$. The present section focuses on the influence of the prestressing force on the seismic performance of the hybrid FSHB frame, while it ignores the deformation of its structural members.

3.1 Pulse-type ground motions

This study considers first pulse-type ground motions to examine the seismic performance of the hybrid FSHB rocking frame. Various mathematical expressions have been proposed in the literature that can capture the long distinct pulses of near-fault ground excitations ([41] among others). The present study adopts the Mavroeidis and Papageorgiou (M&P) [24] wavelet according to which the frequency of the pulse (ω_g), the acceleration amplitude (α_g), the number (γ_g) and the phase angle (ν_g) of half cycles are the four parameters which can idealize a wide range of near-fault ground excitations. Eq. (16) provides the expression for the ground velocity of the M&P pulse [24] with parameter A to control the velocity amplitude of the envelope of the signal.

$$\dot{u}_g(t) = \begin{cases} \frac{A}{2}\left[1+\cos\left(\frac{\omega_g}{\gamma_g}(t-t_0)\right)\right]\cos\left[\omega_p(t-t_0)+\nu_g\right], & t_0 - \frac{\pi\gamma_g}{\omega_g} \le t \le t_0 + \frac{\pi\gamma_g}{\omega_g} \\ 0 \qquad\qquad\qquad\qquad\qquad\qquad\qquad\qquad\qquad\qquad , & otherwise \end{cases} \tag{16}$$

This analysis compares the seismic performance of the freestanding and the hybrid FSHB rocking bridge bent focusing on the influence of the prestressing force. In other words, the study examines structural systems with fundamentally different behavior (i.e. negative, zero and positive post-uplift lateral stiffness) under two levels of the rocking rotation, (i) for small "safe" rotations $\phi/\alpha = 0.1$ and (ii) large "critical" rotations $\phi/\alpha = 1.0$. Recall that, $\phi/\alpha = 1.0$ represents the "critical" rotation under which the freestanding frame is considered to become unstable. In the hybrid FSHB frame the "critical" rotation increases due to the presence of the tendons and the braces. The exact "critical" rotation (ϕ_{cr}) is given by the solution of the nonlinear equation:

$$\left.\frac{\partial V_{tot}}{\partial \phi}\right|_{\phi=\phi_{cr}} = 0 \tag{17}$$

Contrary to Eq. (13), in Eq. (17) the potential energy accounts also for the presence of the braces by simplifying their behavior from nonlinear hysteretic to bilinear elastic. Thus, the total

potential energy of the system becomes [15]:

$$V_{tot} = 2m_{AB}gR\cos(\alpha-\phi) + m_{BC}g\left[2R\cos(\alpha-\phi) + r_{BC}^{G}\sin\psi_{BC}\right] \\ +k_t\left(4b\sin\tfrac{\phi}{2} + \tfrac{P_0}{k_t}\right)^2 + 16(1-\varepsilon)k_d b^2\sin\tfrac{\phi_y}{2}\sin\tfrac{\phi}{2} + 8\varepsilon k_d b^2\sin^2\tfrac{\phi}{2} \tag{18}$$

Therefore, Eq. (17) gives:

$$\sin(\alpha-\phi_{cr}) + 4\rho_t\sin\phi_{cr} + 2\varepsilon\rho_d\sin\phi_{cr} + 4(1-\varepsilon)\rho_d\sin\frac{\phi_y}{2}\cos\frac{\phi_{cr}}{2} + \frac{2b}{R}p_{str}\cos\frac{\phi_{cr}}{2} = 0 \tag{19}$$

Eq. (19) provides the "critical" rotation of hybrid FSHB rocking bridge bents for various values of the (dimensionless) design parameters ρ_d, ρ_t and p_{str}. The combination of the design parameters ρ_t and ρ_d, yield structural systems with (i) tendons flexible enough, such that the frame maintains its negative stiffness, (ii) zero overall stiffness and (iii) stiffer tendons so that the rocking frame exhibits positive post-uplift lateral stiffness. Recall that, the fracture of the tendons and braces is ignored, hence hybrid rocking frames with zero or positive lateral stiffness theoretically will not overturn.

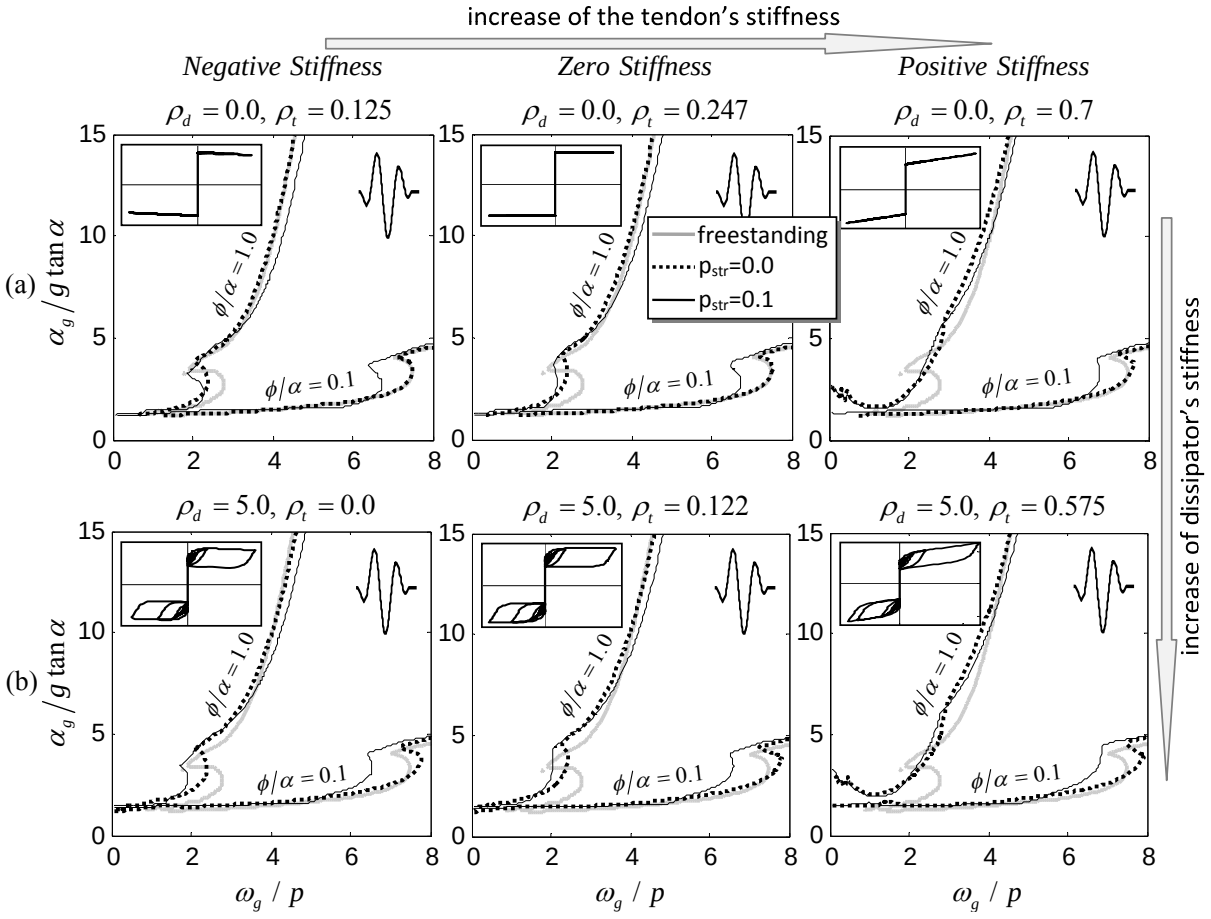

Figure 3: Seismic performance of the rocking bridge bent subjected to M&P pulse with $\nu_g = 45°$, $\gamma_g = 2.0$ for different levels of prestress and for the following dissipation parameters (a) $\rho_d = 0.0$ and (b) $\rho_d = 5.0$.

Fig. 3 compares rocking frames with negative, zero and positive post-uplift lateral stiffness under pulse-type ground motions. Fig. 3 unveils the diverse role of the prestressing force on

the seismic performance of the hybrid FSHB rocking frame. In particular, for large rocking rotations ($\phi/\alpha = 1.0$) and as the size of the columns increases ($\omega_g/p > 3$), the prestressing force has negative effect on the stability of the frame; the lower the prestress the higher the seismic stability. This is true regardless of the sign of the lateral stiffness, but more pronounced to negative stiffness systems. Overall for large rocking rotations, both the freestanding and the hybrid with zero prestressing force exhibit the highest seismic rotation. On the contrary, for either small-sized rocking columns ($\omega_g/p < 3$) and large rotations ($\phi/\alpha = 1.0$) or large rocking columns ($\omega_g/p > 6$) and small rotations ($\phi/\alpha = 0.1$), the prestressing force has beneficial influence on the performance.

Further, note that each column of Fig. 3 considers frames with the same (negative, zero, or positive) lateral stiffness. The ρ_d increase effect is slightly favorable regardless of the sign of the overall stiffness. In addition, increasing the stiffness of the tendons (i.e. increasing ρ_t), the overall lateral stiffness of the system increases. However, Fig. 3 shows that this increase doesn't lead to superior seismic performance (e.g. Fig. 3(a)).

3.2 Historic excitations

The present section examines the seismic response of the hybrid FSHB rocking frame to historic ground motions, regardless of whether they contain distinguishable pulses or not. It employs a well-known set of historic ground motions scaled to yield a probability of exceedance of 2% in 50 years [31].

Number	Record	Magnitude	Scale factor	dt(s)	Duration(s)	PGA(cm/s^2)
SE21	1992 Mendocino	7.1	0.98	0.02	59.98	741.13
SE22	1992 Mendocino	7.1	0.98	0.02	59.98	476.22
SE23	1992 Erzincan	6.7	1.27	0.005	20.775	593.60
SE24	1992 Erzincan	6.7	1.27	0.005	20.775	529.06
SE25	1949 Olympia	6.5	4.35	0.02	79.98	878.23
SE26	1949 Olympia	6.5	4.35	0.02	79.98	805.68
SE27	1965 Seattle	7.1	10.04	0.02	81.82	1722.40
SE28	1965 Seattle	7.1	10.04	0.02	81.82	1364.70
SE29	1985 Valpariso	8.0	2.9	0.025	99.975	1605.50
SE30	1985 Valpariso	8.0	2.9	0.025	99.975	1543.50
SE31	1985 Valpariso	8.0	3.96	0.025	99.975	1246.20
SE32	1985 Valpariso	8.0	3.96	0.025	99.975	884.43
SE35	1978 Miyagi-oki	7.4	1.78	0.02	79.98	595.07
SE36	1978 Miyagi-oki	7.4	1.78	0.02	79.98	768.62

Table 1: Earthquake records with probability of exceedance of 2% in 50 years (adapted from [31].

Figs 4, 5 compare the response of the examined rocking frames in terms of peak rotation and time history analysis respectively. Both Figs 4, 5 verify the high seismic performance of the examined rocking frames, since all of them survive the excitations even though the earthquake records are scaled to the maximum credible earthquake level. Note that, according to the assumptions of the present analysis, when the structure survives the excitation, it eventually re-centers with no permanent displacement and/or expected damage. In particular, Fig. 4 confirms the influence of the prestressing force on the seismic behavior. Prestressing the tendons

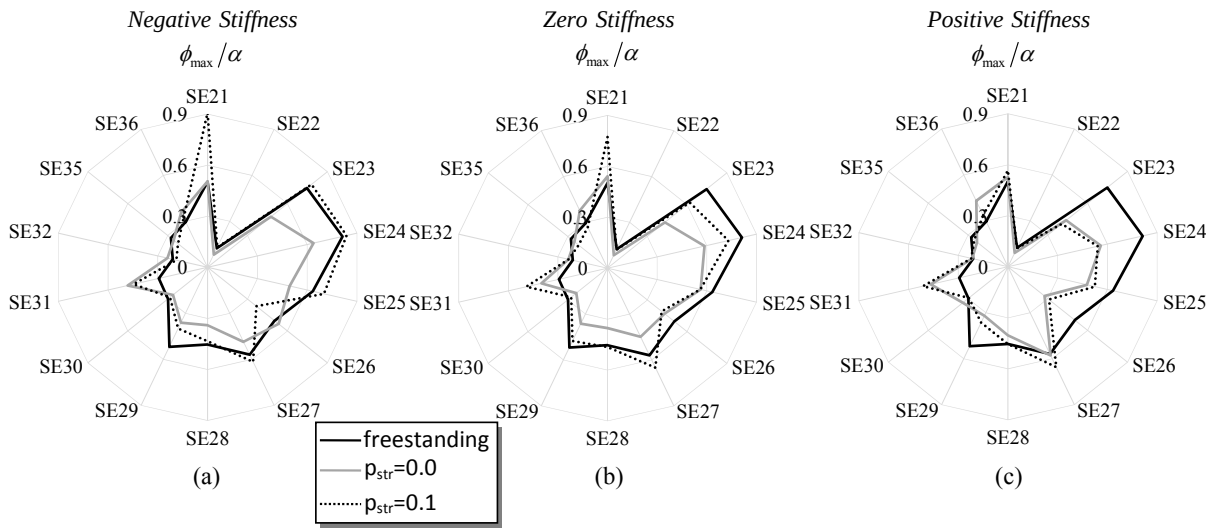

Figure 4: Maximum rotations for the freestanding and hybrid FSHB rocking bridge bent with (a) negative ($\rho_t = 0.075$), (b) zero ($\rho_t = 0.197$), (c) positive ($\rho_t = 0.65$) stiffness, $\rho_d = 2.0$ and different levels of prestress.

deteriorates the seismic performance of the hybrid FSHB rocking frame regardless of the sign of the overall stiffness. This degrading effect becomes even more pronounced on negative stiffness systems when the frame sustains large rocking rotations (see for instance $SE21$, $SE23$, $SE24$ $SE25$, $SE27$ in Figs 4(a), 5). In that cases, both the freestanding and the hybrid frame with slack tendons ($p_{str} = 0$) outperform the hybrid FSHB with $p_{str} = 0.1$. On the contrary, when the frame undergoes small rotations, the prestressing force has indeed beneficial effect (e.g. $SE30$, $SE32$, $SE35$, $SE36$ in Figs 4(a), 5).

Further, Fig. 4 shows that increase of the stiffness of the structure (i.e. from negative to positive) has beneficial effect on the seismic performance of the hybrid FSHB without however changing the effect of the prestress, which remains detrimental regardless of the sign of the lateral stiffness. This (slight) enhancement though, comes at the cost of higher energy demands by the buckling restrained braces (as Fig. 6 shows). Specifically, Fig. 6 compares hybrid FSHB rocking frames with negative, zero and positive overall lateral stiffness, in terms of the net dissipated hysteretic energy. Fig. 6 shows that negative stiffness systems yield the lowest energy demands. This is attributed to the fact that a negative stiffness system cannot resonate (in a classical sense). Overall, positive stiffness systems exhibit the highest energy needs. In other words, the rocking rotation mitigation due to the increased stiffness, comes at the cost of higher energy demands by the dissipaters. Fig. 6 shows that increase of the prestress does not lead to higher energy demands, since for most records the energy dissipated by the braces is slightly lower for prestressed hybrid FSHB frames ($p_{str} \neq 0$) than for slack hybrid FSHB frames ($p_{str} = 0$).

In summary Figs. 3, 4, 5 and 6 show that depending on the characteristics of the examined earthquake record, a different rocking design solution (i.e. freestanding or hybrid with negative, zero, or positive post-uplift lateral stiffness) might yield the optimal rocking design solution in terms of seismic performance. Therefore, the assessment of the seismic performance of hybrid FSHB rocking bridge bents beckons for a probabilistic evaluation [12], which is not however the scope of the present study.

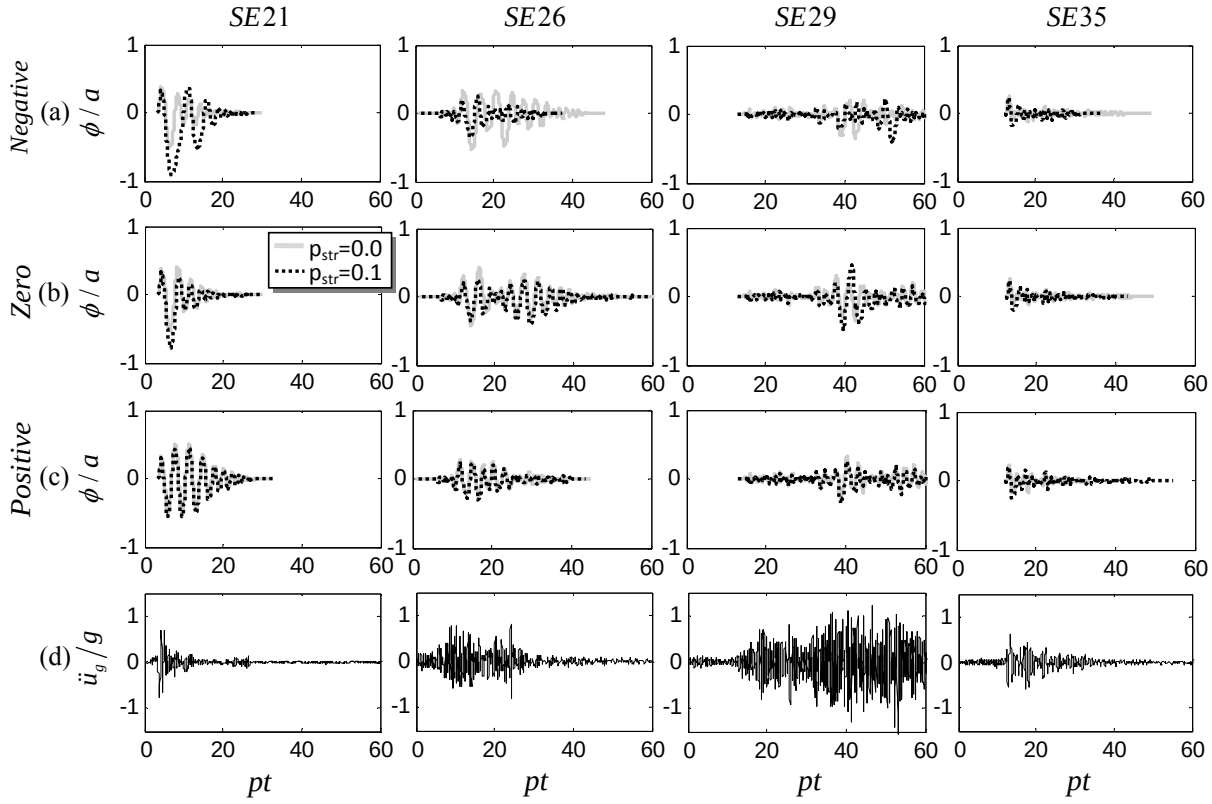

Figure 5: Time history analysis for the hybrid FSHB rocking bridge bent with (a) negative ($\rho_t = 0.075$), (b) zero ($\rho_t = 0.197$), (c) positive ($\rho_t = 0.65$) stiffness, $\rho_d = 2.0$ and different levels of prestress.

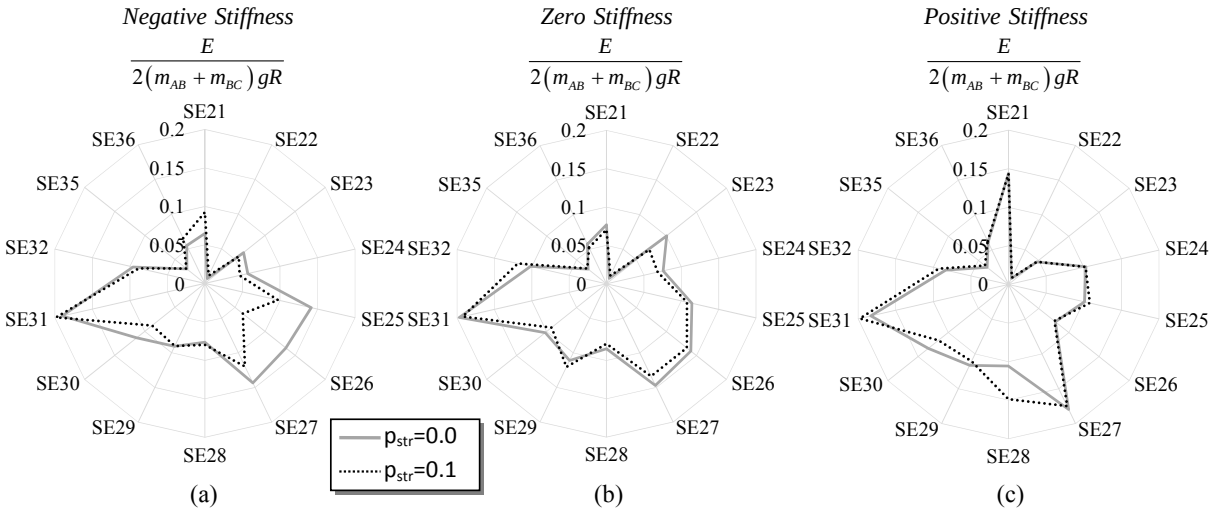

Figure 6: Net dissipated energy for the hybrid FSHB rocking bridge bent with (a) negative ($\rho_t = 0.075$), (b) zero ($\rho_t = 0.197$), (c) positive ($\rho_t = 0.65$) stiffness $\rho_d = 2.0$ and different levels of prestress.

4 CONCLUSIONS

This study investigates the seismic performance of planar freestanding and hybrid rocking frames with flag-shaped hysteretic behavior. This work demonstrates the diverse role of the prestressing force on the performance of the hybrid FSHB rocking bents. Prestressing the tendons deteriorates the frame's seismic performance when it sustains large rocking rotations and as the size of the columns increases; a counter-intuitive conclusion. On the contrary, either for small-sized rocking columns and large rocking rotations or for large-sized rocking columns and small rocking rotations, the influence of the prestress becomes beneficial in restoring the frame. The analysis also confirms the beneficial influence of the dissipater, which is more pronounced for negative stiffness rocking frames. Increasing the overall stiffness, the seismic performance of the frame is slightly enhanced at the expense, however, of higher energy demands by the dissipaters. This is not the case for the prestressing force, since increasing the prestress does not lead to higher energy demands. Finally, this work confirms the sensitivity of the examined rocking frames (freestanding and hybrid FSHB) to the characteristics of the adopted earthquake records, and that none of the rocking design solutions examined is optimal in all cases.

5 ACKNOWLEDGMENTS

Financial support was provided by the Research Grants Council of Hong Kong, under grant reference number ECS 639613.

REFERENCES

[1] Acikgoz, S., DeJong, M. J., The interaction of elasticity and rocking in flexible structures allowed to uplift. *Earthquake Engineering & Structural Dynamics*, **41**(15), 2177–2194, 2012.

[2] Acikgoz, S., DeJong, M. J., The rocking response of large flexible structures to earthquakes. *Bulletin of earthquake engineering*, **12**(2), 875–908, 2014.

[3] Black, C. J., Makris, N., Aiken, I. D., Component testing, seismic evaluation and characterization of buckling-restrained braces. *Journal of Structural Engineering*, **130**(6), 880–894, 2004.

[4] Bouc, R., Forced vibration of mechanical systems with hysteresis. *Proceedings of the fourth conference on non-linear oscillation*, Prague, Czechoslovakia, 1967.

[5] Brogliato, B., Zhang, H., Liu, C., Analysis of a generalized kinematic impact law for multibody-multicontact systems, with application to the planar rocking block and chains of balls. *Multibody System Dynamics*, **27**(3), 351–382, 2012.

[6] Chen, Y. H., Liao, W. H., Lee, C. L., Wang, Y. P., Seismic isolation of viaduct piers by means of a rocking mechanism. *Earthquake engineering & structural dynamics*, **35**(6), 713–736, 2006.

[7] Cheng, C. T., Shaking table tests of a self-centering designed bridge substructure. *Engineering Structures*, **30**(12), 3426–3433, 2008.

[8] DeJong, M. J., Dimitrakopoulos, E. G., Dynamically equivalent rocking structures. *Earthquake Engineering & Structural Dynamics*, **43**(10), 1543–1563, 2014.

[9] Dimitrakopoulos, E. G., DeJong, M. J., Revisiting the rocking block: closed-form solutions and similarity laws. *Proceedings of the Royal Society A: Mathematical, Physical and Engineering Science*, **468**(2144), 2294–2318, 2012.

[10] Dimitrakopoulos, E. G., DeJong, M. J., Overturning of retrofitted rocking structures under pulse-type excitations. *Journal of Engineering Mechanics*, **138**(8), 963–972, 2012.

[11] Dimitrakopoulos, E. G., Giouvanidis, A. I., Seismic response analysis of the planar rocking frame. *Journal of Engineering Mechanics*, **141**(7), 04015003, 2015.

[12] Dimitrakopoulos, E. G., Paraskeva, T. S., Dimensionless fragility curves for rocking response to near-fault excitations. *Earthquake Engineering & Structural Dynamics*, **44**(12), 2015-2033, 2015.

[13] ElGawady, M. A., Ma, Q., Butterworth, J. W., Ingham, J., Effects of interface material on the performance of free rocking blocks. *Earthquake Engineering & Structural Dynamics*, **40**(4), 375–392, 2011.

[14] Giouvanidis, A. I., Dimitrakopoulos, E. G., Seismic analysis of hybrid rocking bridge bents. *Second European Conference on Earthquake Engineering and Seismology*, Istanbul, Turkey, 2014.

[15] Giouvanidis, A. I., Dimitrakopoulos, E. G., Seismic performance of rocking frames with flag-shaped hysteretic behavior. *Journal of Engineering Mechanics*, **under review**, 2016.

[16] Housner, G. W., The behavior of inverted pendulum structures during earthquakes. *Bulletin of the seismological society of America*, **53**(2), 403–417, 1963.

[17] Kam, W. Y., Pampanin, S., Palermo, A., Carr, A. J., Self-centering structural systems with combination of hysteretic and viscous energy dissipations. *Earthquake Engineering & Structural Dynamics*, **39**(10), 1083–1108, 2010.

[18] Kirkpatrick, P., Seismic measurements by the overthrow of columns. *Bulletin of the Seismological Society of America*, **17**(2), 95–109, 1927.

[19] Makris, N., Vassiliou, M. F., Planar rocking response and stability analysis of an array of free-standing columns capped with a freely supported rigid beam. *Earthquake Engineering & Structural Dynamics*, **42**(3), 431–449, 2012.

[20] Makris, N., Vassiliou, M. F., Are Some Top-Heavy Structures More Stable?. *Journal of Structural Engineering*, **140**(5), 06014001, 2014.

[21] Makris, N., Vassiliou, M. F., Dynamics of the rocking frame with vertical restrainers. *Journal of Structural Engineering*, **141**(10), 04014245, 2014.

[22] Mander, J. B., Cheng, C.-T., *Seismic resistance of bridge piers based on damage avoidance design, Report No. NCEER-97-0014*, University at Buffalo, 1997.

[23] Marriott, D., Pampanin, S., Palermo, A., Quasi-static and pseudo-dynamic testing of unbonded post-tensioned rocking bridge piers with external replaceable dissipaters. *Earthquake Engineering & Structural Dynamics*, **38**(3), 331–354, 2009.

[24] Mavroeidis, G. P., Papageorgiou, A. S., A mathematical representation of near-fault ground motions. *Bulletin of the Seismological Society of America*, **93**(3), 1099–1131, 2003.

[25] Palermo, A., Pampanin, S., Calvi, G. M., Concept and development of hybrid solutions for seismic resistant bridge systems. *Journal of Earthquake Engineering*, **9**(6), 899–921, 2005.

[26] Palermo, A., Pampanin, S., Marriott, D., Design, modeling, and experimental response of seismic resistant bridge piers with posttensioned dissipating connections. *Journal of Structural Engineering*, **133**(11), 1648–1661, 2007.

[27] Panagiotou, M., Trono, W., Jen, G., Kumar, P., Ostertag, C. P., Experimental seismic response of hybrid fiber-reinforced concrete bridge columns with novel longitudinal reinforcement detailing. *Journal of Bridge Engineering*, **20**(7), 04014090, 2014.

[28] Pollino, M., Bruneau, M., Seismic retrofit of bridge steel truss piers using a controlled rocking approach. *Journal of Bridge Engineering*, **12**(5), 600–610, 2007.

[29] Psycharis, I. N., Jennings, P. C., Rocking of slender rigid bodies allowed to uplift. *Earthquake Engineering & Structural Dynamics*, **11**(1), 57–76, 1983.

[30] Psycharis, I. N., Fragiadakis, M., Stefanou, I., Seismic reliability assessment of classical columns subjected to near-fault ground motions. *Earthquake Engineering & Structural Dynamics*, **42**(14), 2061–2079, 2013.

[31] S.A.C., *Suites of earthquake ground motions, Structural Engineers Association of California (SEA), Applied Technology Council (ATC) and Consortium of Universities for Research in Earthquake Engineering (CUREE)*, <http://nisee.berkeley.edu> 1997.

[32] Sakai, J., Mahin, S. A., Mitigation of residual displacements of circular reinforced concrete bridge columns. *13th World Conference on Earthquake Engineering Proceedings*, Vancouver, Canada, 2004.

[33] Schaefer, J. A., Kennedy, B., Eberhard, M. O., Stanton, J. F., *Unbonded pretensioned bridge columns with rocking detail, Report No. PEER 2014/08*, University of Washington, 2014.

[34] Sritharan, S., Aaleti, S., Henry, R. S., Liu, K. Y., Tsai, K. C., Precast concrete wall with end columns (PreWEC) for earthquake resistant design. *Earthquake Engineering & Structural Dynamics*, **44**(12), 2075–2092, 2015.

[35] Stathas, N., Skafida, S., Bousias, S. N., Fardis, M. N., Digenis, S., Palios, X., Hybrid simulation of bridge pier uplifting. *Bulletin of Earthquake Engineering*, **DOI:10.1007/s10518-015-9822-2**, 1–14, 2015.

[36] Thonstad, T., Mantawy, I. M., Stanton, J. F., Eberhard, M. O., Sanders, D. H., Shaking Table Performance of a New Bridge System with Pretensioned Rocking Columns. *Journal of Bridge Engineering*, **21**(4), 04015079, 2016.

[37] Trono, W., Jen, G., Panagiotou, M., Schoettler, M., Ostertag, C. P., Seismic response of a damage-resistant recentering posttensioned-hyfrc bridge column. *Journal of Bridge Engineering*, **20**(7), 04014096, 2014.

[38] Truniger, R., Vassiliou, M. F., Stojadinovic B., An analytical model of a deformable cantilever structure rocking on a rigid surface: experimental validation. *Earthquake Engineering & Structural Dynamics*, **44**(15), 2795–2815, 2015.

[39] Vassiliou, M. F., Mackie, K. R., Stojadinovic B., Dynamic response analysis of solitary flexible rocking bodies: modeling and behavior under pulse-like ground excitation. *Earthquake Engineering & Structural Dynamics*, **43**(10), 1463–1481, 2014.

[40] Vassiliou, M. F., Truniger, R., Stojadinovic B., An analytical model of a deformable cantilever structure rocking on a rigid surface: development and verification. *Earthquake Engineering & Structural Dynamics*, **44**(15), 2775–2794, 2015.

[41] Voyagaki, E., Mylonakis, G., Psycharis, I. N., Rigid block sliding to idealized acceleration pulses. *Journal of Engineering Mechanics*, **138**(9), 1071–1083, 2012.

[42] Wen, Y.-K., Method for random vibration of hysteretic systems. *Journal of the engineering mechanics division*, **102**(2), 249–263, 1976.

[43] White, S., Palermo, A., Quasi-Static Testing of Posttensioned Nonemulative Column-Footing Connections for Bridge Piers. *Journal of Bridge Engineering*, **DOI:10.1061/(ASCE)BE.1943-5592.0000872**, 04016025, 2016.

ECCOMAS Congress 2016
VII European Congress on Computational Methods in Applied Sciences and Engineering
M. Papadrakakis, V. Papadopoulos, G. Stefanou, V. Plevris (eds.)
Crete Island, Greece, 5–10 June 2016

MODELLING CONTACT IN ROCKING STRUCTURES WITH A NONSMOOTH DYNAMICS APPROACH

Anastasios I. Giouvanidis[1], **Elias G. Dimitrakopoulos**[2]

[1]Department of Civil and Environmental Engineering, The Hong Kong University of Science and Technology
Kowloon Bay, Hong Kong
e-mail: agiouvanidis@connect.ust.hk

[2] Department of Civil and Environmental Engineering, The Hong Kong University of Science and Technology
Kowloon Bay, Hong Kong
e-mail: ilias@ust.hk

Keywords: rocking, nonsmooth dynamics, linear complementarity problem, impact, flexible rocking structures.

Abstract. *Rocking action isolates the structure from excessive lateral loads and relieves it from deformation and damage. A complete description of the dynamics of a rocking structure entails, apart from the equation of motion, an appropriate treatment of the contact phenomenon. To date, most analytical and numerical investigations of rocking behavior treat contact with the classical impact model or with ad-hoc assumptions. This paper revisits the contact process adopting a nonsmooth dynamics approach. More specifically, it treats impact through a system of inequalities, which is known as the linear complementarity problem (LCP). Throughout the study, impact is considered to be instantaneous. Set-valued contact laws model the behavior in the normal direction of the (unilateral) contact. The analysis assumes that sliding in the tangential direction is prevented. The present study demonstrates the ability of the proposed methodology to capture the impact behavior of different structures rocking on a rigid base. The results show that the proposed LCPs verify the corresponding results of other methodologies. In addition, the proposed nonsmooth dynamics approach offers a more concise description of the impact problem in rocking structures and it contributes to a more realistic treatment and better understanding of the contact phenomenon during rocking.*

1 INTRODUCTION

Rocking action relieves the structure from deformation and damage during strong earthquakes, offering a favorable seismic isolation effect (e.g.[15]). As a consequence, it attracts the attention of researchers which examine the dynamic behavior of rocking structures either experimentally [17] or analytically [25, 10, 24, 28]. While most studies ignore the (e.g. flexural) deformation of the rocking structures, [6, 23] studied the dynamics of flexible (deforming) rocking structures. Those studies compared flexible base-fixed structures with flexible structures allowed to uplift, and showed that in most cases base-fixed structures sustain larger deformations than rocking structures, verifying the earlier results of [19]. They also highlighted the sensitivity of the characteristics of the rocking systems and of the excitation considered on the response. Recent studies [20, 1, 2, 29, 27] revisited the stability of flexible rocking structures sustaining large rotations. They unveiled that for large flexible rocking structures, the effect of flexibility is not detrimental to the stability.

However, a complete description of the dynamics of a rocking structure requires, apart from the equation of motion, an appropriate treatment of the impact. During rocking, the motion of the structure is interrupted by nonsmooth impacts at the contact points. To date, most analytical studies on the rocking behavior treat impacts with ad-hoc assumptions which usually hinge on the conservation of angular momentum (e.g. [15, 18, 12, 13]). The classical approach results in a coefficient of restitution, usually defined as the angular velocity ratio after and before impact [15], which provides the unknown post-impact state. While such approach can provide dependable results for very simple rigid rocking structures, the investigation of progressively more realistic and more complicated rocking structures, creates incentive for more sophisticated analysis/simulation methods of the involved contact/impact phenomenon. More systematic approaches have been proposed in the context of nonsmooth dynamics [4, 14, 16, 21] or finite elements [26]. These methodologies rely on either a rigid multibody approach [5], or assume deformable contact formulations [3], or utilize compliant contact elements between the contacting bodies [30].

The present study describes the impact event adopting a nonsmooth dynamics approach. The aim of this paper is (i) to present briefly the nonsmooth approach, (ii) to treat impact (without sliding) between unilateral contacts and (iii) to evaluate its implementation to various rocking structures.

2 PROPOSED NONSMOOTH ANALYSIS APPROACH

2.1 Nonsmooth dynamics

The proposed herein nonsmooth dynamics approach assumes that the response can be decomposed into *smooth motion* and *nonsmooth events* [4, 14, 16, 8, 9, 11]. The present study examines the impact phenomenon in two archetypal rocking structures (Fig. 2): (i) the rigid block, and (ii) the flexible oscillator. The proposed approach originates from multibody dynamics with unilateral contacts [22, 16]. Specifically, impact, between rigid bodies which cannot overlap (impenetrability constraint), is considered instantaneous. Subsequently, all non-impulsive forces are considered negligible. Under these assumptions, instantaneous contacts (i.e. impacts) induce sudden, velocity changes ("jumps") making the response discontinuous (nonsmooth). The focus of the present study is on structures designed to exhibit planar rocking. Hence, this study assumes that sliding between contacting bodies is prevented, either by proper detailing of the contact connections to act as shear keys or by sufficient friction coefficient.

2.2 Linear complementarity problem (LCP) for impact

In general, the LCP is based on determining from a system of linear equations $\mathbf{y} = \mathbf{A}\mathbf{x} + \mathbf{b}$, with the matrices $\mathbf{A}$ and $\mathbf{b}$ known, the two unknown non-negative vectors $\mathbf{x} \geq 0$ and $\mathbf{y} \geq 0$ satisfying the complementarity condition: $\mathbf{y}^T\mathbf{x} = 0$. The LCP encapsulates a great variety of contact states, such as impact, "flight" (detachment/separation), bouncing and full contact [4].

The (Newton-Euler) equation of motion for a multibody system with unilateral contacts can be written as:

$$\mathbf{M}\ddot{\mathbf{q}} - \mathbf{h}(\mathbf{C}, \mathbf{K}, \ddot{u}_g(t)) - \mathbf{W}_N\lambda_N - \mathbf{W}_T\lambda_T = \mathbf{0} \tag{1}$$

where $\mathbf{q}$ is the generalized coordinates vector. $\mathbf{M}$, $\mathbf{C}$ and $\mathbf{K}$ are the mass, the damping and the stiffness matrices respectively, and $\mathbf{h}$ is the vector containing all the non-impulsive forces e.g. external excitation ($\ddot{u}_g(t)$), dissipating and elastic forces. $\mathbf{W}$ are the direction matrices of the contact forces in the normal (subscript '*N*') and the tangential (subscript '*T*') direction of contact respectively, and λ are the pertinent contact force vectors. To capture the impact-induced velocity jumps, we integrate the equation of motion (Eq. (1)) over the time interval of impact. Let t^- (and superscript $^-$) and t^+ (and superscript $^+$) denote the time at the beginning and at the end of impact respectively.

$$\lim_{t^-\to t^+}\int_{t^-}^{t^+}\mathbf{h}(\mathbf{C}, \mathbf{K}, \ddot{u}_g)dt = \mathbf{0}, \quad \lim_{t^-\to t^+}\int_{t^-}^{t^+}\lambda_N dt = \mathbf{\Lambda}_N, \quad \lim_{t^-\to t^+}\int_{t^-}^{t^+}\lambda_T dt = \mathbf{\Lambda}_T \tag{2}$$

Eq. (1) becomes:

$$\dot{\mathbf{q}}^+ + \dot{\mathbf{q}}^- = \mathbf{M}^{-1}\mathbf{W}_N\mathbf{\Lambda}_N + \mathbf{M}^{-1}\mathbf{W}_T\mathbf{\Lambda}_T \tag{3}$$

where vector $\dot{\mathbf{q}}$ denotes the generalized velocities. Pre-multiplying Eq. (3) by $\mathbf{W}_N^T$ (and $\mathbf{W}_T^T$) returns the vectors of the relative contact velocities in the normal $\dot{\mathbf{g}}_N = \mathbf{W}_N^T\dot{\mathbf{q}}$ (and in the tangential $\dot{\mathbf{g}}_T = \mathbf{W}_T^T\dot{\mathbf{q}}$) direction accordingly:

$$\begin{aligned}\dot{\mathbf{g}}_N^+ - \dot{\mathbf{g}}_N^- &= \mathbf{G}_{NN}\mathbf{\Lambda}_N + \mathbf{G}_{NT}\mathbf{\Lambda}_T \\ \dot{\mathbf{g}}_T^+ - \dot{\mathbf{g}}_T^- &= \mathbf{G}_{TN}\mathbf{\Lambda}_N + \mathbf{G}_{TT}\mathbf{\Lambda}_T\end{aligned} \tag{4}$$

where the $\mathbf{G}$ matrices are:

$$\begin{aligned}\mathbf{G}_{NN} &= \mathbf{W}_N^T\mathbf{M}^{-1}\mathbf{W}_N, \quad \mathbf{G}_{NT} = \mathbf{W}_N^T\mathbf{M}^{-1}\mathbf{W}_T \\ \mathbf{G}_{TN} &= \mathbf{W}_T^T\mathbf{M}^{-1}\mathbf{W}_N, \quad \mathbf{G}_{TT} = \mathbf{W}_T^T\mathbf{M}^{-1}\mathbf{W}_T\end{aligned} \tag{5}$$

This study assumes that sliding is prevented, therefore the tangential relative (contact) velocity is zero $\dot{\mathbf{g}}_T = \mathbf{0}$, and Eq. (4) gives:

$$\mathbf{\Lambda}_T = -\mathbf{G}_{TT}^{-1}\mathbf{G}_{TN}\mathbf{\Lambda}_N \tag{6}$$

Newton's impact law : Newton's law defines the ratio of the relative normal contact velocities, before ($\dot{g}_N^-$) and after impact ($\dot{g}_N^+$), as the coefficient of restitution ε_N:

$$\dot{\mathbf{g}}_N^+ = -\bar{\bar{\varepsilon}}_N\dot{\mathbf{g}}_N^- \tag{7}$$

$\bar{\bar{\varepsilon}}_N$ is the diagonal matrix of the dissipative coefficient of restitution ε_N, and varies from zero for perfectly inelastic (plastic) impact to one for perfectly elastic impact. The velocity jump along the normal direction of impact is:

$$\mathbf{v}_N = \dot{\mathbf{g}}_N^+ + \bar{\bar{\varepsilon}}_N\dot{\mathbf{g}}_N^- \tag{8}$$

then, Eq. (4) yields a system of linear equations:

$$\mathbf{v}_N = \left(\mathbf{G}_{NN} - \mathbf{G}_{NT}\mathbf{G}_{TT}^{-1}\mathbf{G}_{TN}\right)\boldsymbol{\Lambda}_N + \left(\mathbf{E} + \overline{\overline{\varepsilon}}_N\right)\dot{\mathbf{g}}_N^- \tag{9}$$

for which the additional complementarity conditions hold:

$$\mathbf{v}_N \geq \mathbf{0},\ \boldsymbol{\Lambda}_N \geq \mathbf{0},\ \mathbf{v}_N^T\boldsymbol{\Lambda}_N = 0 \tag{10}$$

In Eq. (9), $\mathbf{E}$ is the identity matrix. Eqs (9), (10) define a LCP which treats (non-sliding) impacts according to Newton's law. The complementarity conditions (Eq. 10) reflect the inequality character of (dry) contacts. Fig. 1 illustrates this complementary relationship; the positive part of the horizontal axis allows positive normal impulses with zero velocities, while the vertical axis allows positive relative velocities with zero normal impulses.

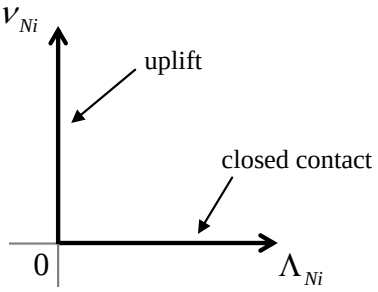

Figure 1: The inequality character of contact [22].

3 REVIEW OF THE ROCKING BLOCK USING THE PROPOSED APPROACH

The present section revisits the impact behavior of the rigid rocking block of Fig. 2(a) adopting the proposed nonsmooth dynamics approach. Consider a rigid block with base width $2b$ and height $2H$ as in Fig. 2(a). The generalized coordinates vector for the planar rocking motion of the block is: $\mathbf{q}^T = \begin{bmatrix} x & y & \phi \end{bmatrix}$, where x and y are the translations along the pertinent axes, and ϕ is the planar rocking rotation. Assume that the two closed contact points (pivot points "1" and "2") produce two forces/impulses in the normal direction of contact (one force per point), but only one force in the tangential direction of contact, the resultant of the two tangential forces at the two pivot points (e.g. as in Fig. 3). The consideration of the resultant tangential force (instead of its constituents) is eligible by the rigid body assumption (the two constituents are linearly dependent) and most importantly, does not overconstraint the problem [8, 9, 11]. Thus, the mass matrix and the direction matrices in the normal and tangential direction of contact become respectively:

$$\mathbf{M} = \begin{bmatrix} m & 0 & 0 \\ 0 & m & 0 \\ 0 & 0 & I_0 \end{bmatrix},\ \mathbf{W}_N = \begin{bmatrix} 0 & 0 \\ 1 & 1 \\ -b & b \end{bmatrix},\ \mathbf{W}_T = \begin{bmatrix} 1 \\ 0 \\ H \end{bmatrix} \tag{11}$$

where I_0 is the mass moment of inertia with respect to the center of mass of the block. For a rectangular block $I_0 = (1/3)\,mR^2$, where m is the mass of the block and R is the half diagonal distance (Fig. 2(a)).

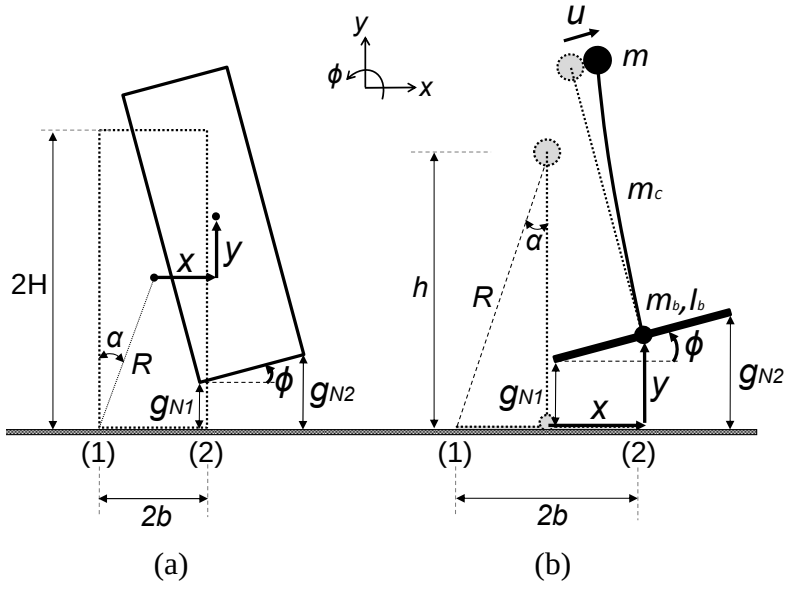

Figure 2: The examined rocking structures: (a) rigid block, (b) flexible oscillator.

3.1 Analysis of all physically feasible post-impact states

With reference to Fig. 3, consider a rigid block performing pure rotation (without sliding) about pivot point "1" ($g_{N1}^- = \dot{g}_{N1}^- = 0$). Impact takes place at pivot point "2" at the moment $g_{N2}^- = 0$ and with pre-impact contact velocity $\dot{g}_{N2}^- = 2b\dot{\phi}^- < 0$. There are four possible (post-impact) states (Fig. 3(E)): (i) full contact ($E_{1/1}$), (ii) bouncing ($E_{1/2}$), (iii) rocking ($E_{2/1}$), and (iv) "flight" ($E_{2/2}$). This section examines all physically feasible post-impact states, and determines the conditions under which each (post-impact) state occurs.

Full contact ($A \to E_{1/1}$) or bouncing ($A \to E_{1/2}$) (Fig. 3): When after impact, point "1" remains in contact with the ground ($\dot{g}_{N1}^+ = 0$), point "2" might stay in contact or not ($\dot{g}_{N2}^+ \geq 0$). The corresponding velocity jumps at the two contact points are (Eqs (7), (8)):

$$\begin{aligned} \nu_{N1} &= \dot{g}_{N1}^+ + \varepsilon_N \dot{g}_{N1}^- = \dot{g}_{N1}^+ = 0 \\ \nu_{N2} &= \dot{g}_{N2}^+ + \varepsilon_N \dot{g}_{N2}^- = -\varepsilon_N \dot{g}_{N2}^- + \varepsilon_N \dot{g}_{N2}^- = 0 \end{aligned} \tag{12}$$

Eq. (12) implies that the block bounces at point "2" with a contact velocity $\dot{g}_{N2}^+ = -\varepsilon_N \dot{g}_{N2}^- > 0$ for a nonzero (Newton) coefficient of restitution $\varepsilon_N > 0$, and it stays in full contact at point "2" ($\dot{g}_{N2}^+ = 0$) for $\varepsilon_N = 0$. In either case, both velocity jumps are zero (Eq. (12)) and thus known. It follows (Eq. 10) that the remaining two unknowns, the normal impulses Λ_{N1} and Λ_{N2}, are both positive. The solution of the LCP of Eq. (9) yields their values:

$$\begin{aligned} \frac{\Lambda_{N1}}{m\dot{g}_{N2}^-} &= (1+\varepsilon_N)\left(\frac{1}{3\sin^2\alpha} - \frac{1}{2}\right) \\ \frac{\Lambda_{N2}}{m\dot{g}_{N2}^-} &= -(1+\varepsilon_N)\frac{1}{3\sin^2\alpha} \end{aligned} \tag{13}$$

with the help of which, Eq. (6) gives the (dimensionless) tangential impulse:

$$\frac{\Lambda_T}{m\dot{g}_{N2}^-} = (1+\varepsilon_N)\frac{\cot\alpha}{2} \tag{14}$$

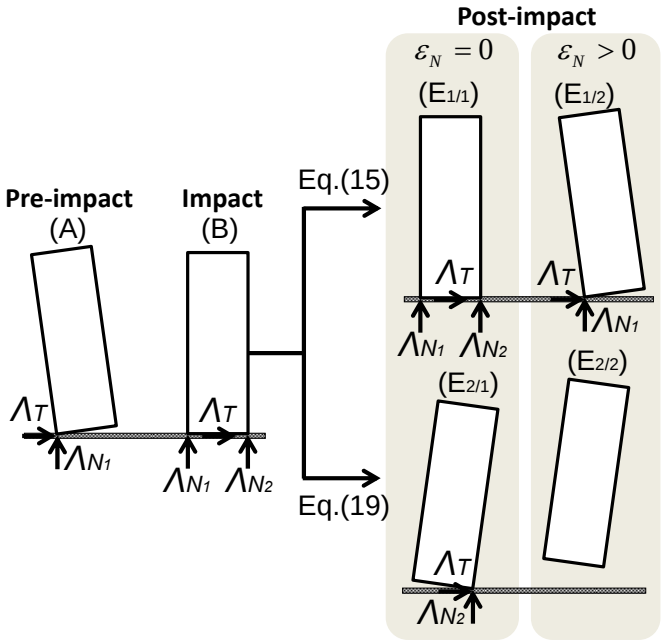

Figure 3: Post-impact states for the rocking block according to Newton's law.

Note that, all unknowns (contact velocities and/or impulses) are given in dimensionless terms.

The inequality character of contact determines the (existential) conditions under which each post-impact state occurs. Specifically, the $\Lambda_{N1} > 0$ condition and Eq. (13) show that the block can bounce or remain in full contact with the ground after impact when:

$$\frac{H}{b} < \frac{1}{\sqrt{2}} \tag{15}$$

in agreement with [5].

Rocking ($A \rightarrow E_{2/1}$) or "flight" ($A \rightarrow E_{2/2}$) (Fig. 3): Assume that after impact the block changes pivot point. Hence, contact at point "1" is lost $\dot{g}_{N1}^{+} > 0$, while the new contact at point "2" is either maintained $\dot{g}_{N2}^{+} = 0$, or also lost $\dot{g}_{N2}^{+} > 0$. The velocity jumps for the two contact points are (Eqs (7), (8)):

$$\begin{aligned} \nu_{N1} &= \dot{g}_{N1}^{+} + \varepsilon_N \dot{g}_{N1}^{-} = \dot{g}_{N1}^{+} > 0 \\ \nu_{N2} &= \dot{g}_{N2}^{+} + \varepsilon_N \dot{g}_{N2}^{-} = 0 \end{aligned} \tag{16}$$

The velocity jumps of Eq. (16) give $0 = \nu_{N2} = \varepsilon_N \dot{g}_{N2}^{-}$. When ε_N is nonzero, contact at point "2" is lost ($\dot{g}_{N2}^{+} = -\varepsilon_N \dot{g}_{N2}^{-} > 0$) and uplifting (detachment) of both contact points takes place. The former case ($\varepsilon_N = 0$) leads to pure rocking behavior while the latter ($\varepsilon_N > 0$) to "flight" behavior. For velocity jumps $\nu_{N1} > 0$ and $\nu_{N2} = 0$, the complementarity conditions (Eq. (10)) return $\Lambda_{N1} = 0$ and $\Lambda_{N2} > 0$. The solution of the LCP of Eq. (9) yields the remaining two unknowns, the normal impulse Λ_{N2} at point "2", and the post-impact normal contact velocity $\dot{g}_{N1}^{+}$ of point "1":

$$\begin{aligned} \frac{\Lambda_{N2}}{m\dot{g}_{N2}^{-}} &= (1+\varepsilon_N)\left(\frac{3\sin^2\alpha}{4} - 1\right) \\ \frac{\dot{g}_{N1}^{+}}{\dot{g}_{N2}^{-}} &= (1+\varepsilon_N)\left(\frac{3\sin^2\alpha}{2} - 1\right) \end{aligned} \tag{17}$$

and from Eq. (6), the tangential impulse becomes:

$$\frac{\Lambda_T}{m\dot{g}_{N2}^-} = \frac{3}{4}(1+\varepsilon_N)\sin\alpha\cos\alpha \tag{18}$$

Again, the inequality character of contact dictates the (existential) conditions under which each post-impact state occurs. Specifically, when contact at point "1" is lost ($\Lambda_{N1} = 0$), the complementary behavior (Fig. 1) requires $\dot{g}_{N1}^+ > 0$. Hence, Eq. (17) shows that the block exhibits rocking or "flight" post-impact behavior when [5]:

$$\frac{H}{b} > \frac{1}{\sqrt{2}} \tag{19}$$

In summary, Eqs (12) to (19) describe completely all possible post-impact states for the rigid rocking block. Thus, the proposed methodology verifies the corresponding results from other methodologies, while at the same time encapsulates all physically feasible post-impact states. Specifically, the geometric slenderness criterion, derived by [5], is in agreement with Eqs (15), (19). For non-sliding (sticking) impacts, a rocking block is considered "stocky" when Eq. (15) is satisfied, whereas when Eq. (19) holds, the block is regarded as "slender". In many studies, including past work of the authors ([10, 7, 12, 13] among others), the ratio $\eta = \dot{\phi}^+ \big/ \dot{\phi}^-$ defines a coefficient of restitution with respect to the angular velocities. When a (slender) block rocks or separates ("flight" mode) from the ground after impact (Fig. 3($E_{2/1}$/$E_{2/2}$)), Eq. (3) with the aid of Eqs (17), (18) shows that the relationship between pre- and post-impact angular velocity ratio is:

$$\eta = \frac{\dot{\phi}^+}{\dot{\phi}^-} = 1 - \frac{3}{2}\sin^2\alpha - \frac{3}{2}\varepsilon_N\sin^2\alpha \tag{20}$$

Eq. (20) verifies the pertinent equation derived by [25, 17]. For perfectly inelastic (plastic) impact ($\varepsilon_N = 0$), the block exhibits pure rocking behavior, and Eq. (20) agrees with the Housner's angular coefficient of restitution [15].

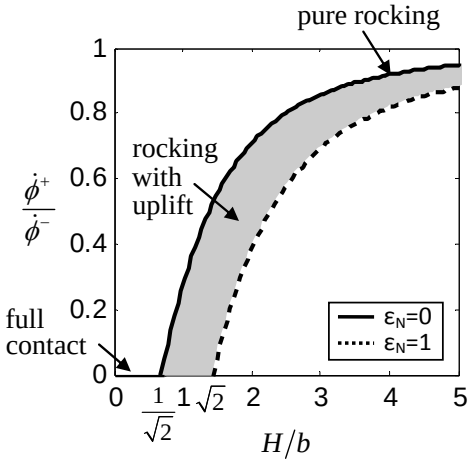

Figure 4: Admissible regions for all the post-impact states for the rocking block.

Eqs (13), (14) treat the bouncing and full contact behavior of the block (Fig. 3($E_{1/1}$/$E_{1/2}$)), with the help of which Eq. (3) gives:

$$\eta = \frac{\dot{\phi}^+}{\dot{\phi}^-} = -\varepsilon_N \tag{21}$$

Eq. (21) shows that for $\varepsilon_N = 0$ the block remains in full contact after impact ($\dot{\phi}^+ \big/ \dot{\phi}^- = 0$), while for perfectly elastic impact ($\varepsilon_N = 1$), the rocking block bounces without any loss of kinetic energy.

Fig. 4 illustrates the admissible regions of all the examined post-impact states of the rigid rocking block. For non-sliding impacts, Fig. 4 shows the admissible domain when rocking occurs. A slender block exhibits pure rocking motion (Eq. (20)) when $\varepsilon_N = 0$. The grey area in Fig. 4 describes the rocking behavior of the block which is accompanied by uplifts/jumps of the pivot points immediately after impact occurs [25, 17]. Note that, the higher the slenderness ratio H/b, the less energy is dissipated during impact, and, in the limit, as this ratio becomes (theoretically) infinite, the block rocks without any energy loss.

4 NUMERICAL EVALUATION OF THE PROPOSED APPROACH

This section illustrates the versatility of the proposed approach by examining (numerically) the behavior of a rigid rocking block and a flexible oscillator in terms of time history analysis (Fig. 2). Consider (i) a stocky block with $2b$ = 1.4 m base width and $H/b = 1\big/\sqrt{2}$ (Eq. (15), Fig. 5(a)) and (ii) a slender block with the same base width but $H/b = 7.0$ (Eq. (19), Fig. 5(b)). The frequency parameter of a rocking block is $p = \sqrt{3g/4R}$, where g is the gravitational acceleration and R is the half-diagonal distance (Fig. 2(a)). Fig. 5 plots the free rocking response of both a stocky and a slender block (Fig. 5(a) and Fig. 5(b) respectively). Specifically, Fig. 5(a)(top) plots the response of the block for three different (Newton) coefficients of restitution. Both blocks have an initial rotation equal with $\alpha/3$, where α denotes the slenderness of the block (Fig. 2(a)). The stocky block does not change pivot point after impact and hence, exhibits bouncing behavior. When $\varepsilon_N = 0$ the impact is considered totally inelastic (plastic) and the block remains in full contact after impact with the ground. On the contrary, for totally elastic impacts ($\varepsilon_N = 1$) the stocky block bounces without any energy loss at impact. The slender block though, changes pivot point after each impact and exhibits pure rocking motion for $\varepsilon_N = 0$ (Fig. 5(b)(top)). Fig. 5(bottom) shows the normal relative distance g_N of the two contact points (as Fig. 2 shows) for both the bouncing and the rocking motion of the two blocks. It is important to note, that both bouncing and rocking behavior are captured numerically with the aid of the same LCP.

Fig. 6 plots the response of the slender rocking block by comparing the proposed nonsmooth dynamics approach for $\varepsilon_N = 0$ with the classical impact model [15] assuming an angular coefficient of restitution equal with 0.97 (according to Eq. (20)). The two (identical) blocks exhibit pure rocking motion and are subjected to the same sine pulse excitation with $\alpha_g/g = 0.45$ and $\omega_g/p = 5.75$. Fig. 6 shows that the results derived by the proposed methodology are in complete agreement with the classical impact model. In addition, the proposed methodology encapsulates all physically feasible post impact states; something that is not feasible with the classical impact model.

Further, the proposed approach is also applicable to more complicated rocking structures. Consider the flexible rocking oscillator of Fig. 2(b) with slenderness $\alpha = 0.1\ rad$ and $H/b = 10$ [29]. The oscillator has a deformable column with mass m_c uniformly distributed along its length. Assume the concentrated (lumped) mass m on the top has zero moment of inertia, whereas the base mass m_b gives moment of inertia $I_b = (1/3)\, m_b b^2$ with respect to its center of mass. The generalized coordinates vector for the planar rocking motion of the flexible rocking oscillator is: $\mathbf{q}^T = \begin{bmatrix} u & x & y & \phi \end{bmatrix}$, where x and y are the translations of the base mass along the pertinent axes, u is the elastic relative translation of the lumped mass and ϕ is the planar

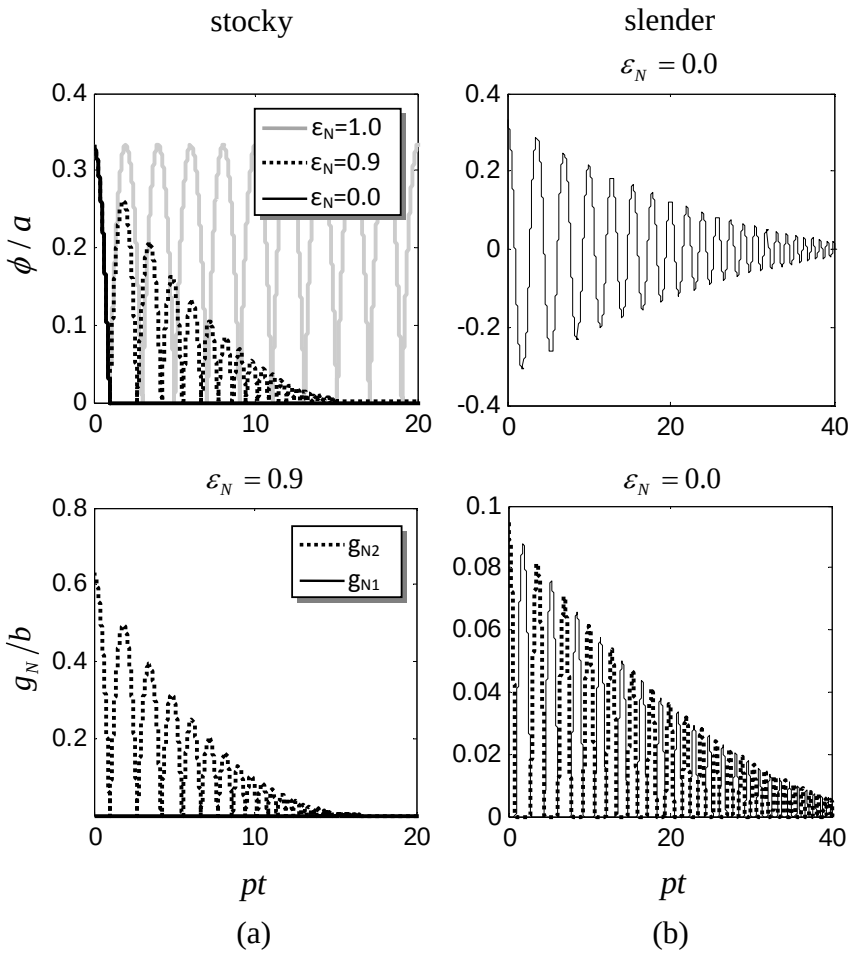

Figure 5: Free rocking response for (a) a stocky and (b) a slender block.

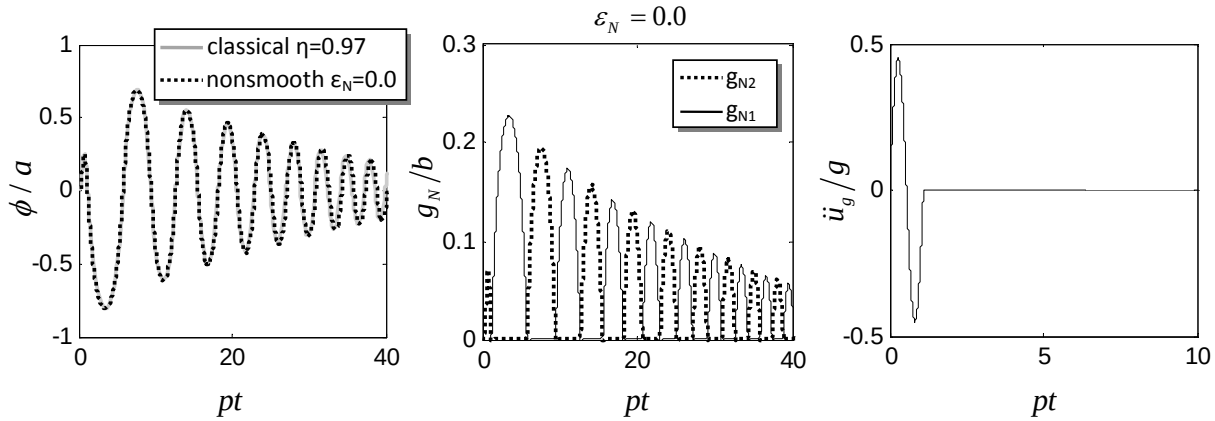

Figure 6: Comparison between the nonsmooth dynamics approach and the classical impact model for a (slender) rocking block subjected to sine pulse with $\alpha_g = 0.45g$ and $\omega_g = 5.75p$.

rocking rotation (Fig. 2(b)). Following [29], the present study assumes $\gamma_{m_b} = m_b/m = 2$ and $\gamma_{m_c} = m_c/m = 1$. Further, the damping ratio is taken as 1%, while the natural frequency ω_n/p is considered as 5, with p being the frequency parameter of the oscillator equal with $p = \sqrt{g/R}$.

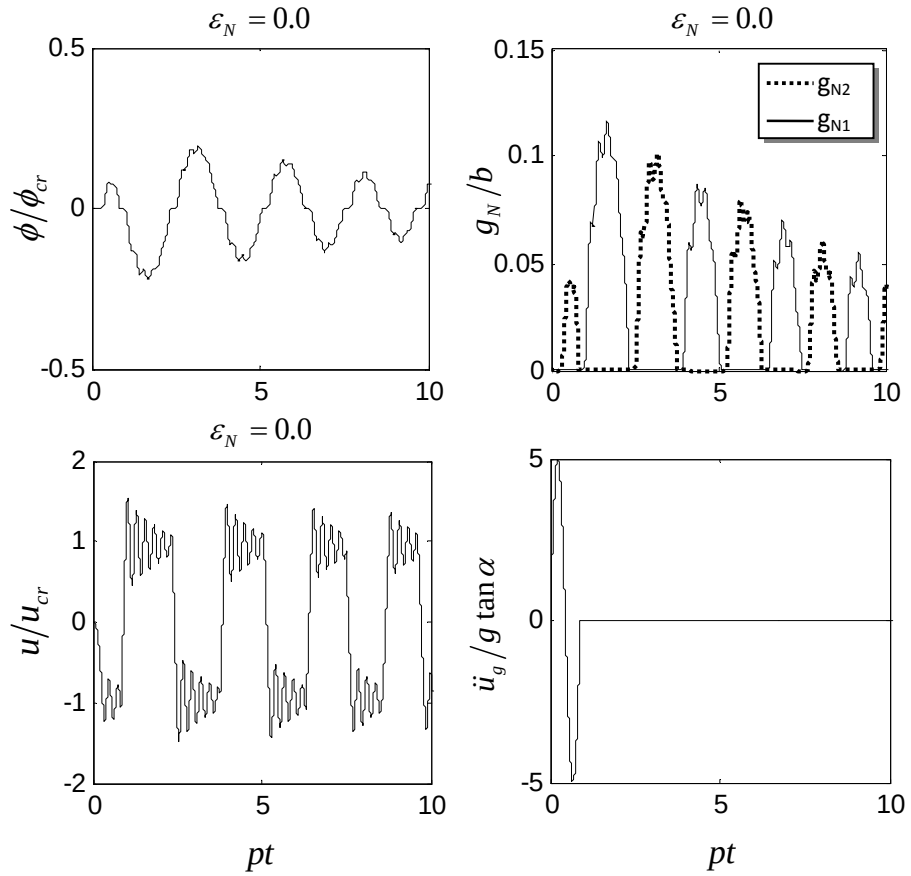

Figure 7: Time history response of the (slender) flexible rocking oscillator subjected to sine pulse with $\alpha_g = 5g\tan\alpha$ and $\omega_g = 7p$.

Fig. 7 shows that subjected to a sine pulse excitation with $\alpha_g/g\tan\alpha = 5$ and $\omega_g/p = 7$, the flexible rocking oscillator of Fig. 2(b) exhibits pure rocking motion, which is in good agreement with the pertinent results from [29]. Note that, ϕ_{cr} denote the "critical" rocking angle of unstable equilibrium for the rigid rocking oscillator, and u_{cr} the "critical" relative displacement of the mass m at the time-instant rocking initiates [29].

5 CONCLUSIONS

The present study revisits the contact/impact phenomenon encountered in rocking structures adopting a nonsmooth dynamics approach. In particular, it formulates the impact problem as a system of inequalities, known as linear complementarity problem (LCP), and examines the impact of two archetypal rocking structures: the rigid rocking block and the flexible rocking oscillator. In the normal direction of contact, the present analysis adopts the Newton's contact law, while in the tangential direction sliding is prevented (non-sliding contact). The analysis shows that the results from the proposed LCPs are in total agreement with the pertinent results

of other methodologies. Overall, this work demonstrates the ability of the proposed nonsmooth dynamics approach to capture all physically feasible post-impact states in a systematic and condensed manner; at least for the rocking systems examined.

6 ACKNOWLEDGMENTS

Financial support was provided by the Research Grants Council of Hong Kong, under grant reference number ECS 639613.

REFERENCES

[1] Acikgoz, S., DeJong, M. J., The interaction of elasticity and rocking in flexible structures allowed to uplift. *Earthquake Engineering & Structural Dynamics*, **41**(15), 2177–2194, 2012.

[2] Acikgoz, S., DeJong, M. J., The rocking response of large flexible structures to earthquakes. *Bulletin of earthquake engineering*, **12**(2), 875–908, 2014.

[3] Andreaus, U., Casini, P., Dynamics of three-block assemblies with unilateral deformable contacts. Part 1: contact modelling. *Earthquake engineering & structural dynamics*, **28**(12), 1621–1636, 1999.

[4] Brogliato, B., *Nonsmooth mechanics: models, dynamics and control*. Springer, 1999.

[5] Brogliato, B., Zhang, H., Liu, C., Analysis of a generalized kinematic impact law for multibody-multicontact systems, with application to the planar rocking block and chains of balls. *Multibody System Dynamics*, **27**(3), 351–382, 2012.

[6] Chopra, A. K., Yim, S. C. S., Simplified earthquake analysis of structures with foundation uplift. *Journal of Structural Engineering*, **111**(4), 906–930, 1985.

[7] DeJong, M. J., Dimitrakopoulos, E. G., Dynamically equivalent rocking structures. *Earthquake Engineering & Structural Dynamics*, **43**(10), 1543–1563, 2014.

[8] Dimitrakopoulos, E. G., Analysis of a frictional oblique impact observed in skew bridges. *Nonlinear Dynamics*, **60**(4), 575–595, 2010.

[9] Dimitrakopoulos, E. G., Seismic response analysis of skew bridges with pounding deck-abutment joints. *Engineering Structures*, **33**(3), 813–826, 2011.

[10] Dimitrakopoulos, E. G., DeJong, M. J., Revisiting the rocking block: closed-form solutions and similarity laws. *Proceedings of the Royal Society A: Mathematical, Physical and Engineering Science*, **468**(2144), 2294–2318, 2012.

[11] Dimitrakopoulos, E. G., Nonsmooth analysis of the impact between successive skew bridge-segments. *Nonlinear Dynamics*, **74**(4), 911–928, 2013.

[12] Dimitrakopoulos, E. G., Giouvanidis, A. I., Seismic response analysis of the planar rocking frame. *Journal of Engineering Mechanics*, **141**(7), 04015003, 2015.

[13] Giouvanidis, A. I., Dimitrakopoulos, E. G., Seismic performance of rocking frames with flag-shaped hysteretic behavior. *Journal of Engineering Mechanics*, **under review**, 2016.

[14] Glocker, C., *Set-valued force laws: dynamics of non-smooth systems*. Springer, 2001.

[15] Housner, G. W., The behavior of inverted pendulum structures during earthquakes. *Bulletin of the seismological society of America*, **53**(2), 403–417, 1963.

[16] Leine, R. I., Van Campen, D. H., Glocker, C. H., Nonlinear dynamics and modeling of various wooden toys with impact and friction. *Journal of vibration and control*, **9**(1-2), 25–78, 2003.

[17] Lipscombe, P. R., Pellegrino, S., Free rocking of prismatic blocks. *Journal of engineering mechanics*, **119**(7), 1387–1410, 1993.

[18] Makris, N., Vassiliou, M. F., Planar rocking response and stability analysis of an array of free-standing columns capped with a freely supported rigid beam. *Earthquake Engineering & Structural Dynamics*, **42**(3), 431–449, 2012.

[19] Meek, J. W., Effects of foundation tipping on dynamic response. *Journal of the Structural Division*, **101**(7), 1297–1311, 1975.

[20] Oliveto, G., Calio, I., Greco, A., Large displacement behaviour of a structural model with foundation uplift under impulsive and earthquake excitations. *Earthquake engineering & structural dynamics*, **32**(3), 369–393, 2003.

[21] Payr, M., Glocker, C., Oblique frictional impact of a bar: analysis and comparison of different impact laws. *Nonlinear Dynamics*, **41**(4), 361–383, 2005.

[22] Pfeiffer, F., Glocker, C., *Multibody dynamics with unilateral contacts*. Springer Science & Business Media, 2000.

[23] Psycharis, I. N., Effect of base uplift on dynamic response of SDOF structures. *Journal of Structural Engineering*, **117**(3), 733–754, 1991.

[24] Psycharis, I. N., Fragiadakis, M., Stefanou, I., Seismic reliability assessment of classical columns subjected to near-fault ground motions. *Earthquake Engineering & Structural Dynamics*, **42**(14), 2061–2079, 2013.

[25] Shenton III, H. W., Jones, N., P., Base excitation of rigid bodies. I: Formulation. *Journal of Engineering Mechanics*, **117**(10), 2286–2306, 1991.

[26] Theodosiou, C., Natsiavas, S., Dynamics of finite element structural models with multiple unilateral constraints. *International Journal of Non-Linear Mechanics*, **44**(4), 371–382, 2009.

[27] Truniger, R., Vassiliou, M. F., Stojadinovic B., An analytical model of a deformable cantilever structure rocking on a rigid surface: experimental validation. *Earthquake Engineering & Structural Dynamics*, **44**(15), 2795–2815, 2015.

[28] Vassiliou, M. F., Mackie, K. R., Stojadinovic B., Dynamic response analysis of solitary flexible rocking bodies: modeling and behavior under pulse-like ground excitation. *Earthquake Engineering & Structural Dynamics*, **43**(10), 1463–1481, 2014.

[29] Vassiliou, M. F., Truniger, R., Stojadinovic B., An analytical model of a deformable cantilever structure rocking on a rigid surface: development and verification. *Earthquake Engineering & Structural Dynamics*, **44**(15), 2775–2794, 2015.

[30] Yilmaz, C., Gharib, M., Hurmuzlu, Y., Solving frictionless rocking block problem with multiple impacts. *Proceedings of the Royal Society A: Mathematical, Physical and Engineering Science*, **10.1098/rspa.2009.0273**, 2009.

ECCOMAS Congress 2016
VII European Congress on Computational Methods in Applied Sciences and Engineering
M. Papadrakakis, V. Papadopoulos, G. Stefanou, V. Plevris (eds.)
Crete Island, Greece, 5–10 June 2016

A SIMPLE ANALYTICAL MODEL FOR THE ROCKING PREWEC SYSTEM

Dimitrios Kalliontzis[1] **and Sri Sritharan**[2]

[1] Ph.D. student in the Dept. of Civil, Environmental & Geo-Eng., Univ. of Minnesota-Twin Cities, Minneapolis 55455
kalli072@umn.edu

[2] Wilson Engineering Professor in the Dept. of Civil, Construction & Environmental Engineering, Iowa State University,
Ames, 50011
sri@iastate.edu

Keywords: Rocking, Concrete, Dynamics, Modelling, O-connectors, PreWEC

Abstract. *A simple analytical model for simulating a controlled rocking system consisting of a Precast Wall with End Columns (named as PreWEC) has been developed and compared against experimental results. The wall panel and end columns are secured to the foundation using prestressing, allowing PreWECs to experience rocking motions. The proposed model accounts for its predominant rotational degree of freedom formulation based on existing knowledge and adds new features to accurately capture the measured responses. They include a migrating rotation center that recognizes the variation in the contact length and its effect on the elongation in the post-tensioned tendons. Supplemental energy dissipation in PreWEC is provided by steel O-connectors, which horizontally join the wall panel to the end columns. These connectors are modelled using a system of nonlinear springs. Two different experiments were used to demonstrate the accuracy of the model validation, which include: a) a 5/18-scale PreWEC subjected to shake table motions; and b) a 1/5-scale PreWEC subjected to free vibration motions. It is shown that rotation responses and associated peaks experienced by the PreWEC rocking system can be accurately predicted using a simplified model.*

1 BACKGROUND

Rocking is a phenomenon that can influence the response of structures, which are allowed to uplift from their base. The eminent work by Housner [1] provided the fundamental knowledge and first steps towards modelling free rocking response of rigid members.

The topic of rocking response has received significant attention in recent years when vertical post-tensioning is introduced along the member length to control the rocking response and allow structural members to re-center upon removal of the lateral load [7, 10]. A simple form of a controlled rocking system is shown in **Fig. 1**, which shows the post-tensioning tendons anchored at the top of the member and the foundation. This concept has paved the way for developing new seismic resilient structural systems that are able to minimize both structural damage and residual drifts when subjected to earthquake input motions.

As part of the *NEES* Rocking Wall Project, a shake table testing of four controlled rocking concrete walls has been recently conducted by Nazari et al. [8] at 1/3.6 scale. As expected, the walls experienced negligible residual displacements and minimal damage that was mainly concentrated at wall compression toes. In another study, Ma [5] followed the original theory of Housner and extended it to modelling of controlled rocking systems as guided by experimental results from a rocking post-tensioned masonry wall. Ma observed from the experimental data that the assumption made in the Housner model of stationary pivot points at the bottom corners of the block did not hold for this controlled rocking unit. Instead, it was noted that the wall developed a contact over a finite area with the foundation surface, which was varying as a function of its angular displacement. This variation led to a continuously migrating rotation center residing within the contact area. The empirical model by Ma, therefore, accounted for this behavior by tracking the correct location of the pivot point. A method that provides a good estimate for the variation in the contact area of a controlled rocking body was suggested by Aaleti and Sritharan [1].

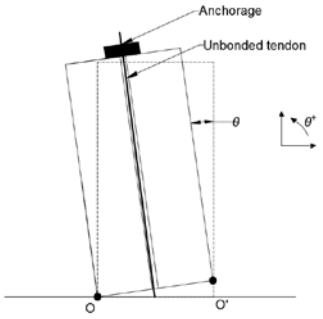

Figure 1: An idealized controlled rocking block.

2 RESEARCH SIGNIFICANCE

The focus of this paper is on modelling of a specific controlled rocking unit, as the PreWEC system. This system, shown schematically in **Fig. 2**, is one of the latest improvements in controlled rocking systems that incorporate supplemental hysteric damping. The PreWEC system consists of a precast wall with end columns with the wall panel and the end columns being individually anchored to the foundation using unbonded post-tensioned tendons [11]. The end columns are horizontally connected to the wall with mild steel O-connectors, which can be tailed to the strain and displacement demands [2]. This study presents analytical results from a model developed for the PreWEC system and compares them with experimental results obtained from shake table testing of PreWEC[1] [9] as well as from free vibration tests of another unit conducted by Twigden et al. [12].

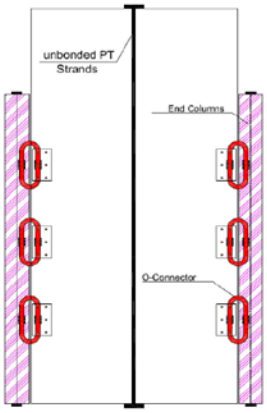

Figure 2: A schematic representation of the PreWEC System [9].

3 SUMMARY OF EXPERIMENTAL STUDIES

3.1 PreWEC system from *NEES* Rocking Wall Project

Test Setup

The unit designated as PreWEC[1] used twelve O-connectors and a wall specimen that was 1.524 mm long, 4,876.8 mm tall and 127 mm thick. The wall was post-tensioned to the foundation with five 270 Grade centrally placed steel strands. The total initial prestressing force applied through these strands was 865.18 kN.

The PreWEC[1] system was placed within a small pocket on top of the foundation with a layer of grout ensuring full contact between the prefabricated members. This unit was tested using a shake table, whose base was attached to the laboratory strong floor using tie-downs. A seismic mass consisting of a frame and two mass blocks (each block being 2,489.2 mm tall with a square cross-section of 1,219.2 x 1,219.2 mm^2) was used outside of the shake table, as shown in **Fig. 3**, connected to the wall panel using a rigid link beam.

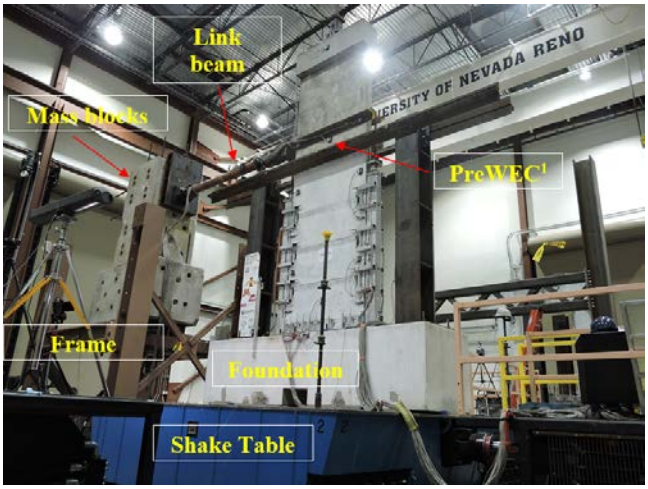

Figure 3: Test Setup for the PreWEC[1] [9].

Input Motions

The PreWEC[1] was subjected to a series of 42 test runs consisted of several input motions, including recorded earthquake excitations with varying intensities. Analysis of the PreWEC[1]

response in this study focused on the 23 first test runs, during which the O-connector experienced no deterioration or fracture. More information regarding the test setup, type of O-connectors, instrumentation and input motions are available on *NEEShub* by Nazari et al. [9].

3.2 PreWEC system tested by Twigden et al. [12]

Test Setup

The unit was 800 mm long, 3,000 mm high and 125 mm thick. The wall was anchored to the foundation with three steel strands of 15.2 mm diameter, each prestressed to $0.5\,f_{py}$. As shown in the test setup of **Fig 4**, this wall base was also placed in a grout pocket on the top of a foundation. Concrete mass blocks were placed on top of the wall to provide additional seismic mass. A lateral support frame was employed to minimize any out-of-plane motion of the system.

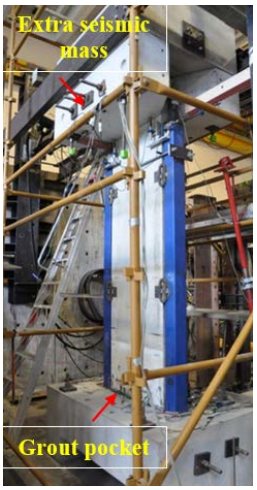

Figure 4: Test Setup for the PreWEC by Twigden et al. [10].

Input Motions

Two free vibration test runs were conducted on this specimen using: a) four (system designated as PreWEC-1); and b) six (system designated as PreWEC-2) O-connectors joining each end column with the wall panel. The specimen was tilted laterally using a hydraulic actuator and quickly released at the desired top lateral displacement level (i.e., 60 mm). More information about these experiments can be found in the paper by Twigden et al. [12], while information about the O-connectors used in this study can be found in Twigden and Henry [13].

4 MODELLING OF THE PREWEC SYSTEM

4.1 Equation of motion for PreWEC[1]

A dynamic system consisting of two generalized coordinates (q_1 and q_2) was built for simulating the response of PreWEC[1], where q_1 corresponds to the wall rotation and q_2 represents the rotation of the mass blocks with respect to the frame as observed from test videos. A schematic representation of this model is shown in **Fig. 5**. It is noted that the end columns were not included in this model and the contribution of O-connectors was included by assuming that the displacement demand imposed on the connectors was equal to the uplift of the wall panel

at one end and compression of the wall toes at the other end. This is consistent with experimental observations [11].

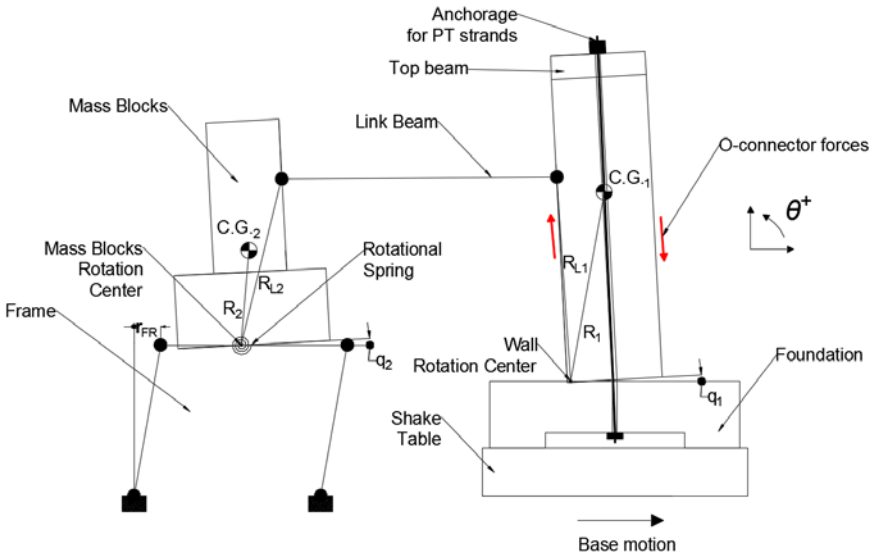

Figure 5: A schematic view of the model developed for PreWEC[1].

Modelling of the PreWEC[1] followed the Housner approach. However, the rotation center was assumed to be located in the middle of the wall contact length at the foundation interface and is, therefore, migrating as a function of the rotation q_1. The simplified method proposed by Aaleti and Sritharan [1] was employed to compute the expected contact length at 2% top lateral drift of the wall, assuming properties of confined concrete and an equivalent stress block at the wall toes. The variation of contact length from $0 \rightarrow 2\,\%$ drift was modified from the original method using the Meregotto-Pinto equation [6] as shown in **Fig. 6**.

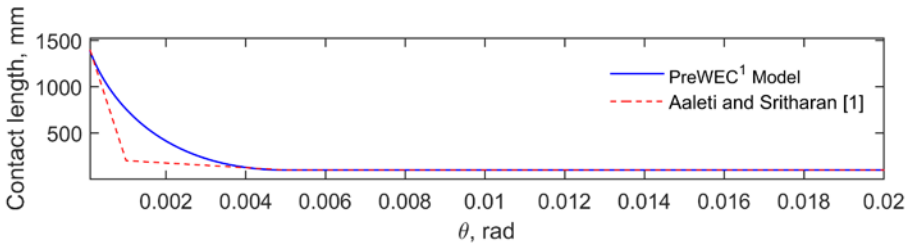

Figure 6: Contact length variation for PreWEC[1] model.

Similarly, the degree of freedom, q_2, corresponding to the mass concrete block rotation was modelled assuming an inverted pendulum, in which a linear rotational spring was used to capture the observed rotation of the mass blocks with respect to the supporting frame (see **Fig. 5**). The rotation center of the block was also modelled to vary as a function of its rotation in a similar fashion with **Fig. 6** with a minimum distance of 495 mm from its bottom corner being reached at $\theta = 0.005\,\text{rad}$.

In addition to the hysteric dissipation provided by the O-connectors, the system's energy dissipation included three damping components. As shown below, these components were provided by: a) the rocking wall panel; b) mass blocks; and c) frame supporting the mass blocks.

$$M_{damp,wall} = c_1 \dot{q}_1 \tag{1}$$

$$M_{damp,blocks} = c_2 \dot{q}_2 \tag{2}$$

$$F_{damp,\,frame} = sign\left(\dot{r}_{FR}\right) c_3 \sqrt{\left|\dot{r}_{FR}\right|} \tag{3}$$

where c_1, c_2 and c_3 were damping coefficients which were trained in an error minimization process using a set of two test runs (i.e., Test#4 and Test#18) [9]. Variables $M_{damp,wall}$ and $M_{damp,blocks}$ also served as numerical damping parameters in the numerical ODE solver.

Estimation of energy dissipation due to impact followed an approach described in Kalliontzis et al. [4]. Their proposed expression assume that the rotation centers of a rocking member just before and just after impact are as shown in **Fig. 7**. Using conservation of angular momentum before and after impact about the rotation center after impact, the equation for the coefficient of restitution (*COR*) in this approach is expressed as:

$$COR = \left[\frac{1 + \frac{MR^2}{I_{cm}} \left(1 - \left(\sin a\right)^2 \left(1 + k^2\right)\right)}{1 + \frac{MR^2}{I_{cm}} \left(1 - \left(\sin a\right)^2 \left(1 - k^2\right)\right)} \right]^2 \tag{4}$$

where k is a factor defining the location of rotation centers just before and just after impact; and I_{cm} denotes the mass moment of inertia of the block with respect to its gravitational center. With respect to Eq. 4, in the absense of a suitable value, $k = 0.72$ is recommended for concrete rocking members, which is used in this study.

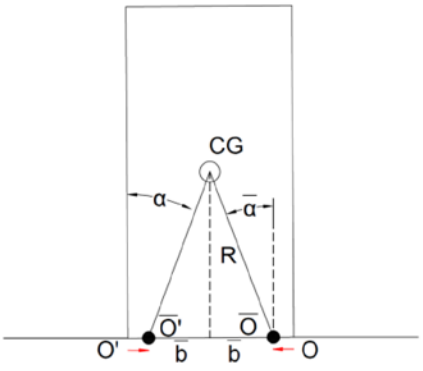

Figure 7: Rocking block with rotation centers $\bar{O}$ and $\bar{O}'$ just before and just after impact, respectively; where $\bar{b} = kb$ with $0 \le k \le 1$ and b is the block half-width [4].

Assuming the two rotational degrees of freedom shown in **Fig. 5** (i.e., one for the wall panel and the other for the mass blocks), two equations of motion were derived and they are presented in **Eqs. 5** and **6**.

$$\left(I_o + M_{EM}L_{L_1}{}^2 - \frac{M_{EM}{}^2}{\bar{I}_{o,b}}\left(L_{L_1}L_{L_2}\right)^2\right)\ddot{q}_1 = -p_1{}^2\left[\frac{\ddot{u}_g}{g}\cos\left(a_1 - |q_1|\right) + sign(q_1)\sin\left(a_1 - |q_1|\right)\right]$$
$$-sign(q_1)F_{PT}\left[\frac{W}{2} - \frac{C}{2}\right] - sign(q_1)\left[F_{down}\left(W - \frac{C}{2}\right) + F_{up}\frac{C}{2}\right] - M_{damp,wall} \quad (5)$$
$$-M_{EM}L_{L_1}\left(\ddot{u}_g + R_{L_1}\dot{q}_1{}^2\sin\left(a_{L,1} + q_1\right) + R_{L_2}\dot{q}_2{}^2\sin\left(a_{L,2} - q_2\right) + L_{L_2}\ddot{q}_{2,1}\right) - F_{damp,\,frame}L_{L_1}$$

$$\left(I_{o,b} + M_{EM}L_{L_2}{}^2\right)\ddot{q}_2 = -p_2{}^2 sign(q_2)\sin\left(a_2 - |q_2|\right) - M_{damp,blocks} - k_r q_2$$
$$-M_{EM}L_{L_2}\left(\ddot{u}_g + R_{L_1}\dot{q}_1{}^2\sin\left(a_{L,1} + q_1\right) + R_{L_2}\dot{q}_2{}^2\sin\left(a_{L,2} - q_2\right)\right) - F_{damp,\,frame}L_{L_2} \quad (6)$$
$$-M_{EM}\left(L_{L_1}L_{L_2}\right)\ddot{q}_1$$

with,

$$\ddot{q}_{2,1} = \frac{\begin{bmatrix} -p_2{}^2 sign(q_2)\sin\left(a_2 - |q_2|\right) - M_{damp,blocks} - k_r q_2 \\ -M_{EM}L_{L_2}\left(\ddot{u}_g + R_{L_1}\dot{q}_1{}^2\sin\left(a_{L,1} + q_1\right) + R_{L_2}\dot{q}_2{}^2\sin\left(a_{L,2} - q_2\right)\right) - F_{damp,\,frame}L_{L_2} \end{bmatrix}}{\left(I_{o,b} + M_{EM}L_{L_2}{}^2\right)} \quad (7)$$

$$L_{L_1} = -R_{L_1}\cos\left(a_{L,1} + q_1\right) \quad (8)$$

$$L_{L_2} = -R_{L_2}\cos\left(a_{L,2} - q_2\right) \quad (9)$$

$$p_1 = \sqrt{M_w g R_1} \quad (10)$$

$$p_2 = \sqrt{\frac{2}{3}M_{EM}gR_2} \quad (11)$$

$$\bar{I}_{o,b} = I_{o,b} + M_{EM}L_{L_2}{}^2 \quad (12)$$

In the above equations, $a_{L,1}$ and $a_{L,2}$ are the "slenderness" ratios with respect to the link beam location on the wall and mass blocks, respectively, which are updated with respect to the rotation center location; R_{L_1}, R_{L_2}, R_1 and R_2 are as identified in **Fig. 5**; F_{PT} represents the total force applied through the post-tensioned strands to the wall panel and it was estimated as per the Aaleti and Sritharan approach [1]; and F_{down} and F_{up} denote the O-connector forces, respectively, on the the uplift and compression sides of the wall panel due to the wall rotation.

In addition, the response of the wall system was also computed by using the experimentally recorded force applied through the link beam to the wall as the input parameter. In this case, the dynamic system consisted of a single degree of freedom, q_1, and its equation of motion is described in **Eq. 13**.

$$I_o\ddot{q}_1 = -p_1{}^2\left[\frac{\ddot{u}_g}{g}\cos\left(a_1 - |q_1|\right) + sign(q_1)\sin\left(a_1 - |q_1|\right)\right] - sign(q_1)F_{PT}\left[\frac{W}{2} - \frac{C}{2}\right]$$
$$-sign(q_1)\left[F_{down}\left(W - \frac{C}{2}\right) + F_{up}\frac{C}{2}\right] - M_{damp,wall} - F_{LinkBeam}L_{L_1} \quad (13)$$

where $F_{LinkBeam}$ represents the experimentally obtained link beam forces recorded using a load cell.

4.2 Modelling of O-connectors

Fig. 8a presents experimental data obtained from a quasi-static cyclic reversal test on the O-connector used in PreWEC[1] (Courtesy of Nazari Maryam, Ph. D. candidate at Iowa State University). Using a similar test setup to the one described by Henry et al. [2], the two pairs of O-connectors were subjected to the vertical displacement history shown in **Fig. 8b**.

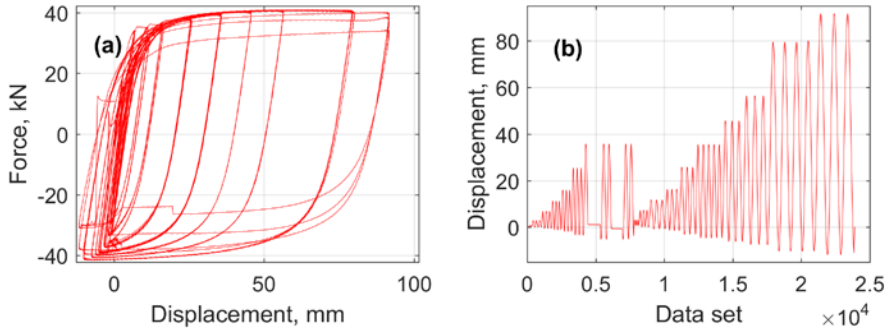

Figure 8: O-connector used in PreWEC[1] (a) measured force vs displacement response of one connector; and (b) applied displacement history protocol.

The recorded O-connector data was used to develop a numerical model for simulating the resistance of the connectors in the simulation of the PreWEC system. This model used the Meregotto-Pinto equation [6] to develop rules for the envelope, load reversals and reloading branches of the connector responses. **Fig. 9** compares model response with the experimental data, showing satisfactory agreement including the strength degradation experienced by the connector toward the end of testing.

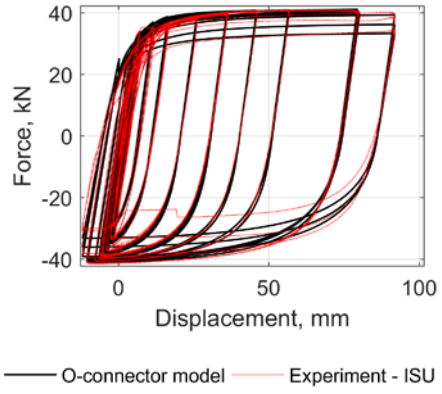

Figure 9: Comparison of force-displacement responses produced by the O-connector model and experimental data.

4.3 Initiation of rocking motion

Previous research studies that employed the Housner model for investigating free rocking motion routinely assumed that a free-standing rigid block is expected to uplift once the overturning moment produced by the ground acceleration exceeds the moment resistance of

the block, which depends on its mass and geometric properties. Considering the case of PreWEC[1], this limit is expressed as follows:

$$\frac{\ddot{u}_g}{g}+\frac{F_{LinkBeam}L_{L_1}}{Mgh}\geq\left[1+\frac{F_{PT,i}}{Mg}\right]\frac{b}{h} \tag{14}$$

with h representing the height of the gravity center of the system; and $F_{PT,i}$ is the initial post-tensioning force in the strands of the wall panel. While the above limit may accurately predict the initiation of controlled rocking of systems that can be reliably idealized as rigid blocks, its application to systems influenced by a migrating rotation center may not be satisfactory. Considering such a system at an initial rest condition being subjected to a horizontal ground motion, its imminent rotation point is unlikely to be located at its bottom corner. Hence, the moment equilibrium about this point is inapprorpiate without taking into account of the reaction forces at the wall base. To overcome this concern, the moment equilibrium may be taken about the correct rotation center, assuming that the rotation center coincides with the resultant compression force at the base.

Fig. 10 shows an example based on the PreWEC[1] model that the limiting expression in **Eq. 14** will not accurately capture when the rocking motion will initiate. The figure compares two analytical solutions established for the PreWEC[1] response assuming the aforementioned limit. The first case assumed a migrating rotation center during rocking motion as described in section 4.1, while the second case assumes that the rotation center is always located at one of the bottom wall corners (i.e., the wall is fully rigid). The corresponding experimental rotation time history is also plotted in the figure. It is seen that the two models fail to detect the beginning of rocking motion by approximately 2 seconds, while the first case predicts a significantly higher peak angular displacement response compared to the experimental observation. On the contrary, due to the higher moment resistance resulting from a fully rigid wall assumption, the second case significantly underestimates the peak displacement.

In order to tackle this issue associated with the initiation of rocking motion, the proposed model does not include a lower-bound limit for the overturning moment by assuming that the rotation center is located at the center of the wall base when the wall is at an initial rest mode. It is shown in the next section that this choice significantly contributes to accurately capturing the wall response for very small and large rotations.

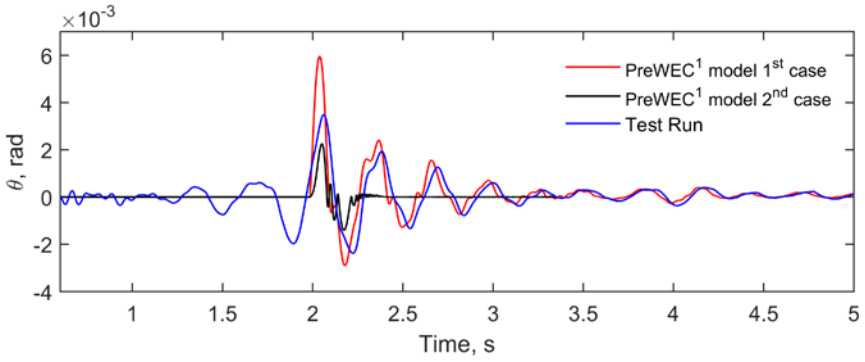

Figure 10: Measured rotation vs time of PreWEC[1] in the second input motion of Test#4 compared with analytical responses based on the limit of **Eq. 14**.

4.4 Modelling of PreWEC-1 and PreWEC-2 systems

Modelling of these systems followed the same approach as that described for PreWEC[1]. Variation of contact length in these systems was similarly estimated using the simplified

method proposed by Aaleti and Sritharan [1]. Moreover, these PreWECs used O-connectors with different dimensions and thus, the modelling rules were modified accordingly.

5 COMPARISON WITH EXPERIMENTAL RESPONSES

5.1 PreWEC[1] system

Fig. 11 presents several comparisons of PreWEC[1] model as per **Eq. 13**, with measured rotation time histories using $c_1 = 5I_o$. It is seen that the model is able to accurately reproduce the experimental responses for earthquake excitations of various intensities. Similar results were obtained with the use of the 2DOF system of **Eqs. 5-6** with suitable selections of the stiffness and damping parameters characterizing the seismic mass (i.e., $k_r = 39.63^5$ kN-mm; $c_2 = 6I_{o,b}$; $c_3 = 0.88$ kN$\sqrt{\text{s/mm}}$). These results are shown in Fig. 12.

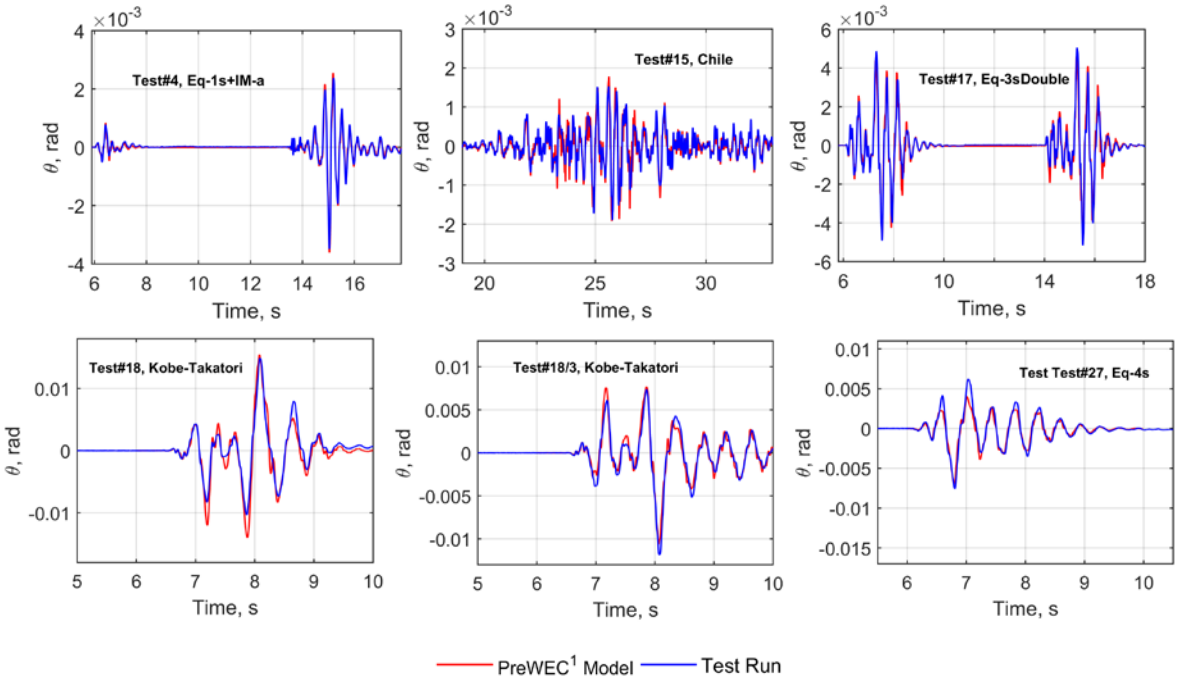

Figure 11: PreWEC[1] rotation time history responses from experimental and analytical results

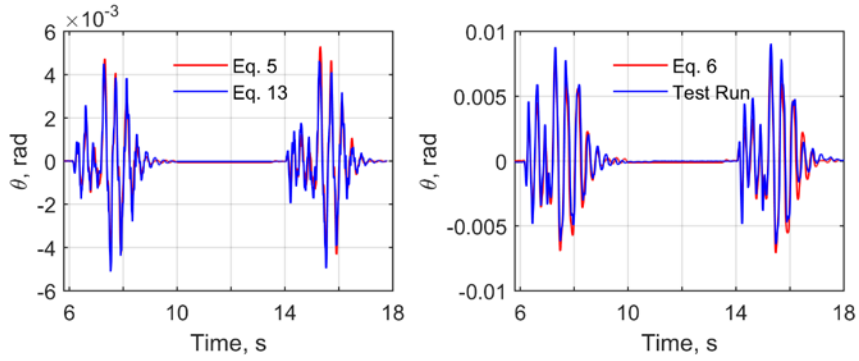

(a) (b)

Figure 12: Rotation time history responses of a) the PreWEC[1] using analytical results of **Eq. 5** and **Eq. 13**; and b) the mass blocks using analytical results of **Eq. 6** and experimental data (Test#17).

In **Fig. 13**, typical force-displacement responses are also presented for both the analytical and experimental data, showing that the numerical model can accurately follow the experimentally observed behavior.

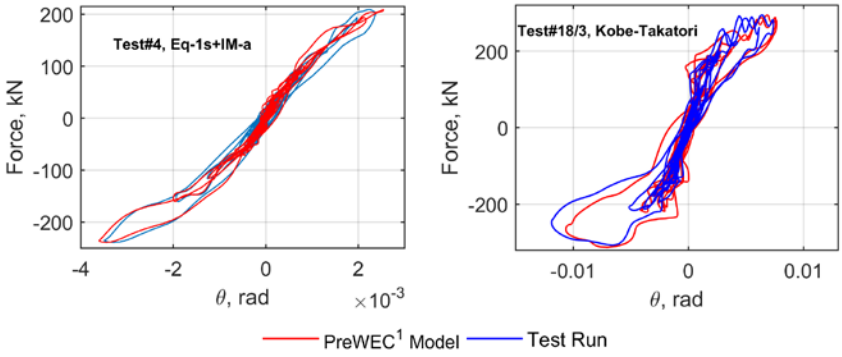

Figure 13: Comparison of force-displacement responses of the PreWEC[1] system

Finally, **Fig. 14** presents the error obtained between peak rotation responses as computed by the model of **Eq. 13** and experimental data, where positive values correspond to underestimation of the peaks while the negative peaks reflect overestimation of the peak responses. It is seen that the model is able to accurately capture the maximum responses established from the shake table tests, while the measured error remains below 10% for most of the cases. A mean value computed from all the absolute error measures was found to be approximately 5%.

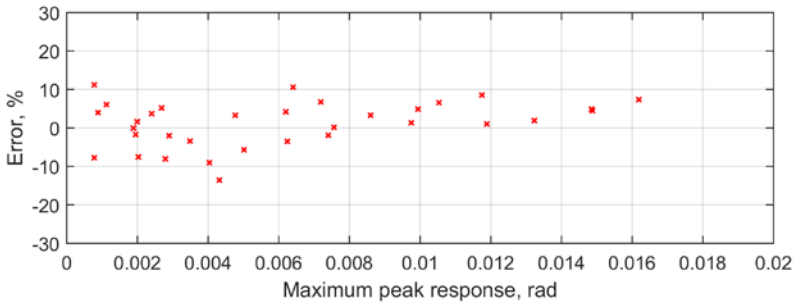

Figure 14: Estimated error for the maximum peak responses predicted by the analytical model

5.2 PreWEC-1/2 systems

Fig. 15 presents the analytical solutions for the free vibration motion of these PreWECs conducted by the model of **Eq. 13** (where $F_{LinkBeam} = 0$ and $\ddot{u}_g = 0$) using a) four, and b) six O-connectors. Note that a value of $c_1 = 2.5I_o$ was selected in this case. Also included in this figure are experimentally recorded responses. For both cases, the free vibration responses closely match measured responses.

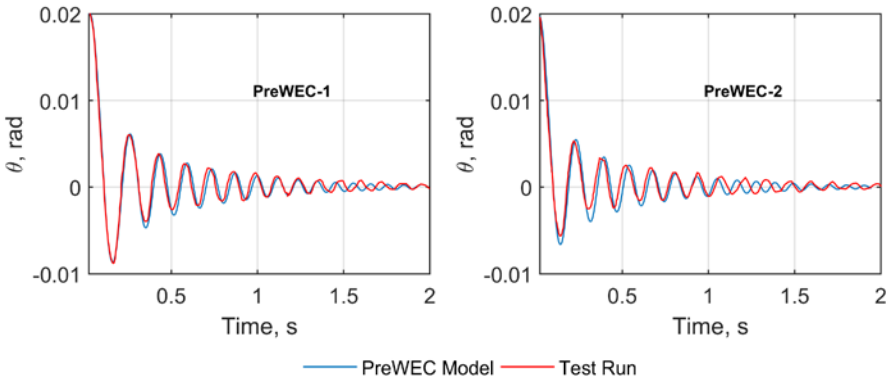

Figure 15: PreWEC-1 and PreWEC-2 Models vs experimental results of free vibration tests.

6 CONCLUSIONS

An analytical approach for estimating the dynamic response of PreWEC systems is introduced in this paper. The proposed method uses the Housner's model as the basis for developing the equation of motion, while allowing a migrating rotation center that was defined based on the contact length-rotation relationship by the Aaleti and Sritharan method [1]. Energy dissipation in the proposed model consisted of a) an impact mechanism that was expressed per the Kalliontzis et al. approach [4], b) hysteric dissipation provided by the O-connectors, and c) empirically selected continuous damping mechanisms, which additionally served as numerical damping parameters for solving the equation of motion.

Validation of the analytical model used two independent experimental investigations conducted using: a) shake table, and b) free vibration testing. Comparison with these experimental results show that the model developed for the PreWEC with hysteric energy dissipation is appropriate for both cases.

7 ACKNOWLEDGEMENTS

The work presented in the paper was undertaken as part of the "*NEES* Rocking Wall" Project with funding from the National Science Foundation (NSF) under Grant No. 1041650. The authors would like to thank Maryam Nazari, Ph.D. candidate and Lin Shibin, Postdoctoral Research Associate, both at Iowa State University, for their help with the experimental data analyses. Any opinions, findings and conclusions or recommendations expressed in this material are those of the authors and do not necessarily reflect the views of NSF.

REFERENCES

[1] S. Aaleti, S. Sritharan, A simplified analysis method for characterizing unbonded post-tensioned precast wall systems. *Engineering Structures*, **31**(12), 2966-2975, 2009.

[2] Henry R. S., S. Aaleti, S. Sritharan, J. M. Ingham, Concept and finite-element modelling of new steel shear connectors for self-centering wall systems. *J. Engineering Mechanics*, ASCE, **136**(2), 220-229, 2010.

[3] G. W. Housner, The behaviour of inverted pendulum structures during earthquakes. *Bull. Seismol. Soc. Am.*, **53**(2), 403-417, 1963.

[4] D. Kalliontzis, S. Sritharan, A. Schultz, Modified coefficient of restitution model for free rocking members. *J. Struct. Eng.*, ASCE, under review.

[5] Q. T. M. Ma, The mechanics of rocking structures subjected to ground motion. *PhD Thesis*, The University of Auckland, New Zealand, 2009.

[6] M. Meregotto, P. Pinto, Method of analysis for cyclically loaded reinforced concrete plane frames including changes in geometry and nonelastic behaviour of elements under combined normal force and bending, *Proc. Symp. Resistance Ultim. Deformability Struct. Acted Well-defined Repeated Loads*, IASBE, Lisbon, Portugal, 1973.

[7] S. D. Nakaki, J. F. Stanton, S. Sritharan, An overview of the PRESSS five-story precast test building, *PCI J.*, March-April, 1999.

[8] M. Nazari, S. Aaleti, S. Sritharan, Shake table testing of unbonded post-tensioned precast concrete walls. *10th U.S. National Conf. Earthquake Eng.*, Alaska, 2014.

[9] M. Nazari, S. Aaleti, S. Sritharan, Shake table testing of single rocking wall 1 (SRW1) @ UNR. *Network for Earthquake Eng. Simulation (distributor)*, DOI: 10.4231/D3D29P75Z, 2015.

[10] M J N Priestley, S Sritharan, J R Conley, S Pampanin, Preliminary results and conclusions from the PRESSS five-story precast concrete test bulding. *PCI J.*, **44**(6), 42-67, 1999.

[11] S. Sritharan, S. Aaleti, R. H. Henry, K. Y. Liu, K. C. Tsai, Precast concrete wall with end columns (PreWEC) for earthquake resistant design. *Earthquake Eng. Struct. Dyn.*, published online, 2015.

[12] K. M. Twigden, R. S. Henry, Q. T. Ma, Pseudo-static cyclic, snap back and shake table testing of PreWEC self-centering wall systems. *10th U.S. National Conf. Earthquake Eng.*, Alaska, 2014.

[13] K. M. Twigden, R. S. Henry, Experimental response and design of O-connectors for rocking wall systems. *Structures*, **3**, 261-271, 2015.

ECCOMAS Congress 2016
VII European Congress on Computational Methods in Applied Sciences and Engineering
M. Papadrakakis, V. Papadopoulos, G. Stefanou, V. Plevris (eds.)
Crete Island, Greece, 5–10 June 2016

AN ANALYTICAL MODEL FOR THE DYNAMIC RESPONSE OF AN ELASTIC SDOF SYSTEM FIXED ON TOP OF A ROCKING SINGLE-STORY FRAME STRUCTURE: EXPERIMENTAL VALIDATION

Jonas A. Bachmann, Christoph Jost, Quentin Studemann, Michalis F. Vassiliou, Božidar Stojadinović

Swiss Federal Institute of Technology (ETH) Zürich
Stefano-Franscini-Platz 5, 8093 Zürich, Switzerland
e-mail: bachmann@ibk.baug.ethz.ch
{cjost, qstudem} @student.ethz.ch
{vassiliou, stojadinovic} @ibk.baug.ethz.ch

Keywords: Rocking, Uplift, Seismic Isolation, Earthquake Engineering.

Abstract. *It has been shown that assemblies of large rocking bodies have remarkable seismic stability and minimal residual displacement. Such dynamic response characteristics make freely rocking systems desirable for their superior seismic performance, but challenging to design. In Russia and the former Soviet Union structures have been constructed with an intentionally "soft story" that comprises rocking columns able to take the seismic displacement. The uplift of the columns works as a mechanical fuse and limits the forces transmitted to rest of the structure. This paper describes an experimental investigation of the dynamic response of specimens comprising an elastic single-degree-of-freedom system fixed to a rigid beam that is rocking on rigid columns. The goal of the tests is to verify and validate the dynamic rocking model of a two-degree-of-freedom system of such rocking podium structures. The time history responses computed using the numerical model are in good agreement with the results obtained in the experimental tests. Furthermore, the model predicts both the rocking column rotations and the superstructure deformation relatively well. The prediction is better for smaller tilt angles.*

1 INTRODUCTION

Base isolation has been used for decades. It decreases the design forces of the superstructure and takes most of the displacement demand through a soft and specially designed layer between the structure and the ground. Usually this soft layer comprises either rubber or (concave) sliding bearings. Simplified models, experimental validation of them, and code provisions have resulted in the increasing use of seismic isolation.

In Russia and the former Soviet Union states another method of seismic isolation has been used. The soft layer does not comprise bearings placed under the base slab, but the entire bottom story intentionally designed as "soft". Its concrete columns are designed to uplift and sustain rocking motion during an earthquake. Thus, the design forces of the superstructure are controlled by the uplift force of the bottom story. The critical design parameters for such podium building structure are the geometric properties of the columns. Column ends are protected by steel plates to avoid concrete crushing when they uplift (Figure 1). Unlike for concave or lead-rubber bearings (which have a hysteretic form of damping that results in residual displacements) energy dissipation due to uplift and rocking is instantaneous and happens at every impact. Therefore the rocking podium system has minimal (if any) residual deformation and has a resilient behavior. Added dampers can be used to diminish the magnitude of the rocking motion. Interestingly, full-scale dynamic tests of rocking podium structures have been performed on real structures. The structures were excited using a hydraulic jack to push the structure to an initial displacement and then release it [1, 2]. It should be mentioned that this system does not rely on the size of the rocking elements for its stability, as the rocking isolation techniques proposed for solitary columns or rocking assemblies do [3–60].

The force-displacement response of concave friction-pendulum and lead-rubber bearings can be approximated by a bilinear envelope curve with positive stiffnesses. This allows for a rough approximation of the base isolated structure response using a secant stiffness linear model with viscous damping [61, 62]. On the contrary, a rocking podium structure has negative post-uplift stiffness (the restoring force decreases as the lateral displacement increases). It has been proven that these kind of systems cannot be approximated by a SDOF elastic systems and, hence, the widely used elastic response spectra are not applicable [12].

This paper presents a simplified model to describe the behavior of an elastic structure sitting on a rocking podium. The model was validated using the results from small-scale experiments performed in the Swiss Federal Institute of Technology (ETH) in Zurich, in the context of the Masters Semester project of the 2nd and 3rd author.

Figure 1: Left: Basement with rocking columns. Right: Close up of a column out of reinforced concrete. [1]

2 DYNAMIC MODEL

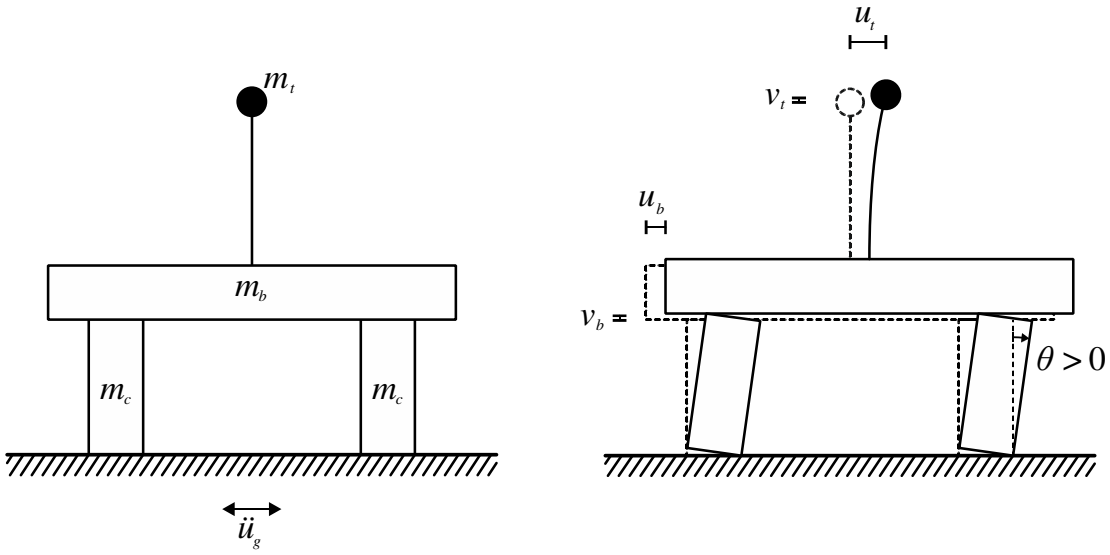

Figure 2: Dynamic model of a rocking podium structure. Left: Initial position. Right: Rocking position.

In order to gain insight into the behavior of rocking podium structure, an elementary planar analysis can be performed using a simple 2-DOF model. The parameters of the model are shown in Figure 2. It comprises two rocking columns (N = 2), one cap beam, and a SDOF system fixed to the beam. The elastic behavior of a more complex superstructure is described using an equivalent SDOF elastic system, thus neglecting any higher modes effects. The columns and the slab are assumed to behave rigidly. Two dimensionless parameters γ and η are introduced.

$$\gamma = \frac{m_b}{N m_c} = \frac{m_b}{2m_c}$$
$$\eta = \frac{m_t}{N m_c} = \frac{m_t}{2m_c} \tag{1}$$

The SDOF system on top with the mass m_t has a fixed-base natural frequency ω_s and a viscous damping ratio ζ. Using a Lagrangian formulation, the following equations of motion are obtained:

$$\ddot{u}_t + \omega_s^2 \left(u_t - u_b\right) + \ddot{u}_g + 2\zeta\omega_s \left(\dot{u}_t - \dot{u}_b\right) = 0 \tag{2}$$

$$\begin{aligned} &\ddot{\theta}\left[\gamma + \frac{I_C}{4R^2 m_c} + \frac{1}{4} + \eta \sin\left(\pm\alpha - \theta\right)\right]\frac{2R}{g} - \dot{\theta}^2\eta\left[\cos\left(\pm a - q\right)\sin\left(\pm a - q\right)\right]\frac{2R}{g} + \\ &+\left(\gamma + \frac{1}{2} + \eta\right)\sin\left(\pm\alpha - \theta\right) + \frac{\ddot{u}_g}{g}\left(\gamma + \frac{1}{2}\right)\cos\left(\pm\alpha - \theta\right) + \\ &-\frac{\omega_s^2\eta}{g}\left(u_t - u_b\right)\cos\left(\pm\alpha - \theta\right) - \frac{2\zeta\omega_s\eta}{g}\cos\left(\pm\alpha - \theta\right)\left(\dot{u}_t - \dot{u}_b\right) = 0 \end{aligned} \tag{3}$$

where I_C is the rotational moment of inertia of one column around its center of mass. The slenderness α of the column (Figure 3a) controls the magnitude of the forces transferred to the

superstructure. The ground acceleration that leads to the uplift of a single rigid column, and therefore initiates rocking motion, is:

$$\ddot{u}_{g,uplift} = g\tan(\alpha)$$
$$\tan(\alpha) = \frac{2B}{2H} = \frac{B}{H} \tag{4}$$

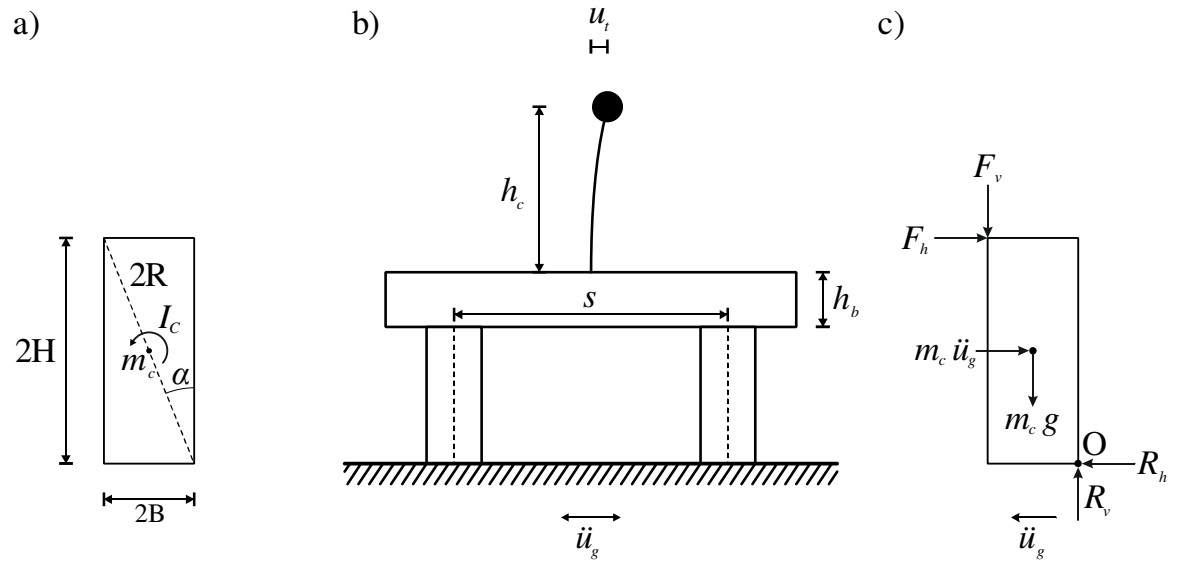

Figure 3: a) Column. b) State of the structure at incipient uplift. c) Forces at incipient uplift.

The contact forces acting on a single column right at the verge of uplift, rotating around point O, are shown in Figure 3c and given in equation (5).

$$F_h = \frac{m_t\left(\omega_s^2 u_t + 2\zeta\omega_s\dot{u}_t\right)}{2} - \frac{m_b\ddot{u}_g}{2}, \quad F_v = \frac{\left(m_t + m_b\right)g}{2} \pm \frac{m_t\left(\omega_s^2 u_t + 2\zeta\omega_s\dot{u}_t\right)\left(h_c + h_b\right)}{s} \tag{5}$$

For the model under consideration, the principle of virtual work at incipient uplift gives:

$$\delta\theta\left(Hm_c + 2Hm_b\right)\ddot{u}_g - \delta\theta\left(\omega_s^2 m_t u_t + 2\zeta\omega_s m_t\dot{u}_t\right)2H - \delta\theta\left[Bm_c + 2Bm_b + 2Bm_t\right]g = 0 \tag{6}$$

The SDOF superstructure will always start to oscillate before the columns start to rock because rocking starts only when the ground acceleration reaches the uplift limit of the podium structure. This limit not only depends on the ground acceleration $\ddot{u}_g$ but also on the actual displacement u_t of the top mass (Figure 3b). Equation (6) leads to the two following thresholds for the podium structure uplift acceleration $\ddot{u}_g$:

$$\ddot{u}_g \geq g\tan(\alpha)\left[\frac{1+2\gamma+2\eta}{1+2\gamma}\right] + \omega_s^2 u_t\left[\frac{2\eta}{1+2\gamma}\right] + 2\zeta\omega_s\left[\frac{2\eta}{1+2\gamma}\right]$$
$$\ddot{u}_g \leq -g\tan(\alpha)\left[\frac{1+2\gamma+2\eta}{1+2\gamma}\right] + \omega_s^2 u_t\left[\frac{2\eta}{1+2\gamma}\right] + 2\zeta\omega_s\left[\frac{2\eta}{1+2\gamma}\right] \tag{7}$$

Hence, the uplift acceleration for the podium structure can be higher or lower than $g\tan(\alpha)$, the uplift acceleration for a single rocking column (equation (4)).

As soon one of the thresholds in equation (7) is reached, the rocking motion of the podium structure starts. When the structure rocks back and hits the ground it is assumed to have

stopped rocking until equation (7) is fulfilled again – this could happen instantly, or not at all. There are limitations for this assumption: if the top mass is light a structure might not start rocking again in the numerical model although it could do so in reality. This, however, was not the case in the conducted experiments since only relatively top-heavy superstructures were used. A different approach is needed to model the response of rocking podium structures with light superstructures.

The model dissipates input energy through structural damping of the SDOF model of the superstructure and through rocking impacts. Since the podium structure model has two degrees of freedom, two equations are necessary to formulate the energy loss. The model proposed by Housner [63] assumes that impact happens instantaneously and that the contact forces are concentrated at the new pivot point. For a solitary column this means that the angular momentum about the new pivot point is conserved. Applying Housner's assumptions to the 2-DOF model led to the first equation. The second equation was derived by assuming that the horizontal velocity of the top mass m_t stays the same before and after impact [13, 43]. Thus, the coefficient of restitution for the 2-DOF system was derived:

$$c = \frac{\dot{\theta}_{after}^2}{\dot{\theta}_{before}^2} = \left[1 - \frac{\sin^2(\alpha)\left(2\gamma + 2\eta + \frac{1}{2}\right)}{\frac{1}{4} + \frac{I_C}{4m_c R^2} + \gamma + \eta} \right]^2 \tag{8}$$

Equation (8) can be compared to the expressions for coefficient of restitution of other, simpler, systems. With $\eta = \gamma = 0$ it yields exactly what Housner proposed for his rigid block, and with $\eta = 0$ it yields the solution of Makris and Vassiliou [39] for an array of free-standing columns capped with a free-standing rigid beam.

Uplift of the podium structure affects the vibration properties of the SDOF superstructure [7, 27, 58]. An eigenfrequency analysis reveals that there are two distinct mode shapes of the podium structure: one is overturning of the rocking frame structure with a natural frequency of 0 Hz, and the other is the vibration of the SDOF system when the rocking frame structure is uplifted. In this state the natural frequency of the SDOF $f_{s,u}$ is amplified compared to its fixed-base counterpart, f_s, and is given by equation (9):

$$f_{s,u} = \sqrt{\frac{3\gamma + 3\eta + 1}{3\gamma + 3\eta \sin^2(\alpha) + 1}}\, f_s \tag{9}$$

For top-heavy structures ($\eta \to \infty$) the amplification factor simplifies to $\sin^{-1}(\alpha)$.

3 SPECIMEN AND TEST SETUP

The 2-DOF model presented in the previous section was instantiated in the lab using two frames on top of each other, the first representing the rocking podium, and the second one representing the elastic SDOF system (Figure 4). In order to allow for replacements or improvements during the testing campaign, the specimen was screwed together. The base plate was fixed to the shake table. The material used for the specimens and the setup, apart from the steel masses on top, was aluminum (EN AW-6060).

The rocking podium structure (i.e. the first story) has a total height of 500 mm and a column slenderness α of 0.1385 rad, determined by the column width of 69.7 mm. The two 480 mm tall columns are identical, and stiff enough to be modelled as rigid. To achieve a high stiffness, each column is built out of two hollow 60 mm x 60 mm x 4 mm sections. Rectangular plates (5 mm x 50 mm x 400 mm), two at the bottom and two at the top of the columns are

used to connect the columns into a rigid frame. When rocking, the frame is assumed to rotate around the outer edges of these plates.

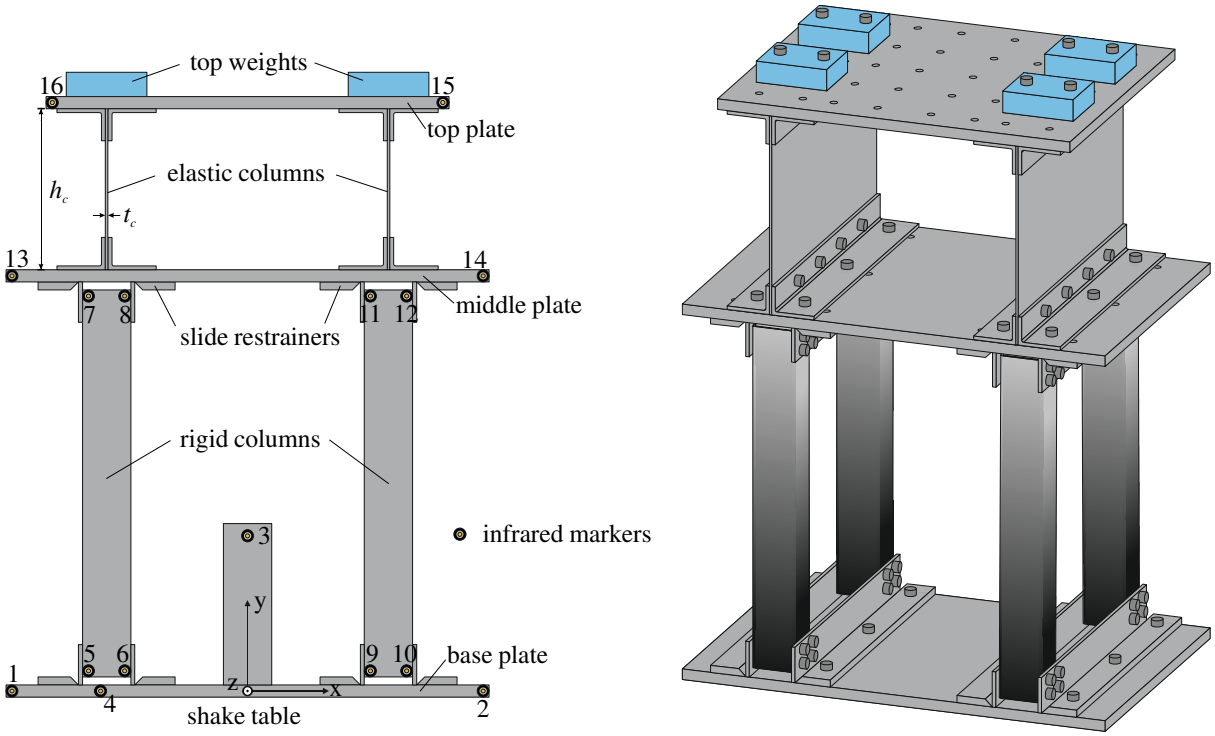

Figure 4: Left: front view of the specimen with locations of the infrared markers. Right: 3D view of the specimen.

The elastic SDOF superstructure was fixed to the aluminum plate positioned on top of the rocking columns. It comprises two elastic columns, the top plate, the top weights, and the connecting L-sections. The height of an aluminum sheet representing the elastic column is 441 mm, the thickness is 3 mm and the depth is 400 mm. The connecting extruded L sections have a length of 400 mm and a cross section of 60 mm x 40 mm x 5 mm.

Part	**Mass** [kg]	**Quantity** [-]	**Ground** [kg]	**Columns** [kg]	**Beam** [kg]	**Top** [kg]
base plate	10.96	1	10.96			
slide restrainers	0.54	8	2.16		2.16	
1 rigid column setup	3.94	2		7.88		
middle plate	11.09	1			11.09	
L section	0.56	8			2.24	2.24
1 elastic column	1.56	2			1.56	1.56
top plate	7.88	1				7.88
top weights	7.92	2				15.84
Total	65.57		13.12	7.88	17.05	27.52

Table 1: Masses of the different parts.

Table 1 shows the weights of the different parts of the experimental setup, including screws and other small parts. The mass of the elastic columns of the superstructure is evenly distributed to the top and bottom mass.

Then the mass ratios are:

$$\gamma = \frac{m_b}{N m_c} = \frac{17.05kg}{7.88kg} = 2.16$$
$$\eta = \frac{m_t}{N m_c} = \frac{27.52kg}{7.88kg} = 3.49 \quad (10)$$

3.1 Similitude Analysis

The above mentioned model dimensions were chosen so that it reproduces, as closely as possible, a typical full size prototype podium structure. The main laboratory constraint was the size of the model, which resulted in a scaling down of the rocking column length dimension by a factor of 6 (given that a typical floor would have a height of 3.0 m). The other properties of the model were chosen so that similitude is maintained. The similitude analysis between the Prototype full-scale podium structure and the Model is shown in Table 2.

Parameter	**Prototype**	**Model**
Story height	3.0 m	500 mm
Excitation frequency	f_p	$\sqrt{6}\,f_p$
Superstructure period	0.544 s	0.222 s
Mass ratio γ	2.16	2.16
Mass ratio η	3.49	3.49

Table 2: Properties of the Prototype and Model podium structures.

The fundamental vibration of the prototype superstructure was targeted to be in the range between 0.5 s and 0.6 s, chosen as typical for a 5-story masonry building. The fundamental vibration period of the fixed-base superstructure model was 0.222 s, corresponding to a fundamental period of 0.544 s for the prototype. The mass ratio $\gamma = 2.16$ (Table 1) is larger than what may be expected (as the slab weight would be much larger than the total column weight) but lower values were not possible in the lab, given that the model column had to be practically undeformable under its loads. The uplifted period was measured at 0.145 s which is 1.53 times smaller than the fixed-base natural period of 0.222 s, confirming the value that equation (9) predicts, namely 1.53.

3.2 Experimental Setup

The experimental setup is shown in Figure 5. To avoid sliding, restrainers were added to the baseplate. The green steel columns and plywood plates were used for safety reasons and to prevent the specimen from collapsing.

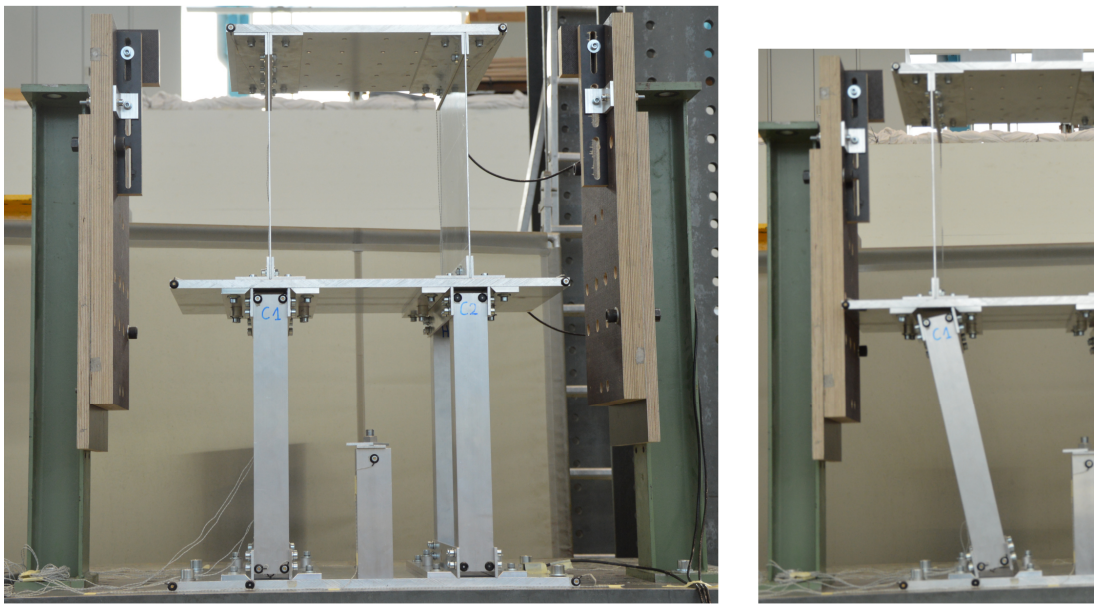

Figure 5: Left: Front view of the specimen. Right: Overturned specimen at the end of the test.

3.3 Excitation

The ETH 1-D shaking table was used to apply a base motion to the specimen. It is supported by roller bearings and actuated using servo-hydraulic actuators to move only in one horizontal direction. The stroke of the table is 250 mm, and the maximum velocity is 225 mm/s. Each specimen was tested using 12 different symmetric Ricker wavelets and 12 different antisymmetric Ricker wavelets.

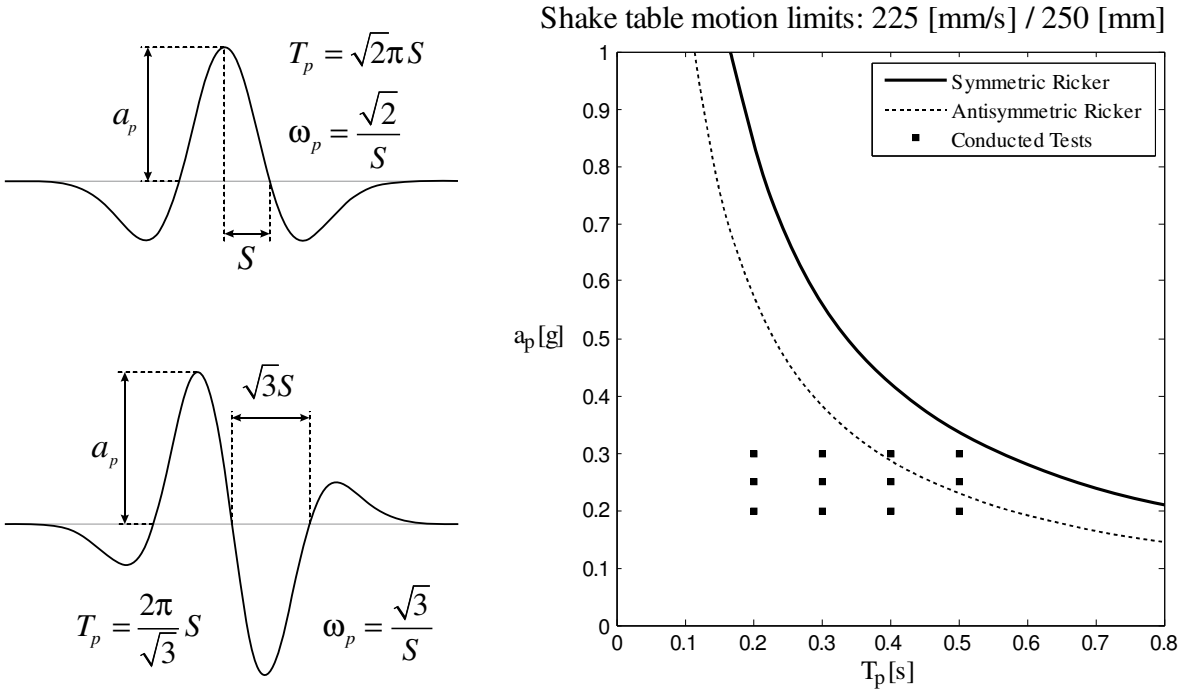

Figure 6: Left: Symmetric and antisymmetric Ricker wavelets. Right: Shake table motion limits

A Ricker wavelet approximates the main pulse of pulse-type ground motions [64]. Typical symmetric and antisymmetric Ricker wavelets are shown in Figure 6. The acceleration amplitude, a_p, and period, T_p, of a Ricker wavelet are discussed further in [33, 65]. The Ricker wavelets used in this study had acceleration amplitudes of a_p = {0.20, 0.25, 0.30}g and the pulse periods of T_p = {0.20, 0.30, 0.40, 0.50}s. At the Prototype scale these values correspond to periods of {0.49, 0.74, 0.98, 1.23}s.

For 3 out of the 24 different Ricker wavelets the shake table would reach its motion limits (Figure 6), namely the velocity limit of 225 mm/s. For our study this did not pose any problems. The acceleration and displacement output of the shake table was measured in all tests and subsequently used as input for the numerical model for comparison. Unfortunately, the shaking table reproduced the command motions with different degrees of accuracy during the test campaign, depending on the characteristics of the motion and numerous factors associated with the state of the shaking table.

3.4 Data Acquisition System

An Optotrak Certus System, manufactured by Northern Digital Inc., was used to track the position of the specimens during the tests. This system uses active infrared-emitting diodes as markers and a trinocular camera system to determine the position of the markers (Figure 4). Three markers (1, 2, 3) were placed on the shake table and parts of the specimen rigidly connected to the shake table. These markers were used to define a rigid plane; the displacements measured during the tests were relative to marker 1. Eight other markers (5-8 & 13-16) were placed on the moving parts of the specimen to measure their position. The built-in tools of the Optotrak Certus System software were able to measure angles, either in 2D or 3D, between lines defined by two markers. Lines defined by markers 1-2 and 5-7 were used to identify the rocking angle in real time during the experiments. Other output parameters were defined to show the out-of-plane behavior of the specimen, to measure the differential rotation of the middle and top plate compared to the base plate. The position sampling frequency was 250 Hz.

The accuracy of the system has been determined in previous experiments [56]. In the x- and y-directions in the plane where rocking motion takes place, the accuracy is about 0.02 mm. In the z-direction, perpendicular to the plane of motion, the accuracy is about 0.10 mm.

3.5 Experiment Outcomes and Observations

Table 3 lists the 24 tests with Ricker wavelets, numbered for reference.

No.	Excitation type	a_p [g]	T_p [s]	Exp.	Num.
1	Antisymmetric Ricker	0.20	0.20		
2	Antisymmetric Ricker	0.20	0.30		
3	Antisymmetric Ricker	0.20	0.40		
4	Antisymmetric Ricker	0.20	0.50	overturn	overturn
5	Antisymmetric Ricker	0.25	0.20		
6	Antisymmetric Ricker	0.25	0.30		
7	Antisymmetric Ricker	0.25	0.40		
8	Antisymmetric Ricker	0.25	0.50	overturn	overturn
9	Antisymmetric Ricker	0.30	0.20		
10	Antisymmetric Ricker	0.30	0.30		

No.	Excitation type	a_p [g]	T_p [s]	Exp.	Num.
11	Antisymmetric Ricker	0.30	0.40		
12	Antisymmetric Ricker	0.30	0.50		overturn
13	Symmetric Ricker	0.20	0.20		
14	Symmetric Ricker	0.20	0.30		
15	Symmetric Ricker	0.20	0.40		
16	Symmetric Ricker	0.20	0.50		
17	Symmetric Ricker	0.25	0.20		
18	Symmetric Ricker	0.25	0.30		
19	Symmetric Ricker	0.25	0.40		
20	Symmetric Ricker	0.25	0.50		
21	Symmetric Ricker	0.30	0.20		
22	Symmetric Ricker	0.30	0.30		
23	Symmetric Ricker	0.30	0.40		
24	Symmetric Ricker	0.30	0.50	overturn	

Table 3: List of tests with Ricker wavelet excitation

Typical test response is one where the frame uplifts and rocks without overturning, without out-of-plane motion, or stepping or sliding on the rocking surface, and where the superstructure SDOF vibrates in its uplifted frequency. The following deviations in specimen response were observed:

- Sliding:
  Two different types of sliding were observed. One type was sliding occurring at every impact during rocking and the other type was sliding occurring when there was no rocking. The amount of sliding during the rocking motion was small, and very difficult to detect in measured data (the transition from one edge of the rocking column to the other was usually fast and clear). Sliding while the columns were not rocking was significantly larger and could be detected in measurements. Such sliding occurs because the still-vibrating SDOF superstructure excites the podium frame, causing the relatively light columns to overcome friction at their bases and slide. Restrainers were placed near the column bases to keep such sliding to a minimum (< 0.3 mm) for small and light specimens tested in this study.
- Out-of-plane movement:
  The large number of rocking interfaces (2 rocking columns with 4 rocking edges each) accompanied by unnoticeable but still present imperfections and asymmetry caused small out-of-plane movements during a few tests, accumulating to 2 mm in the worst case.

4 COMPARISON BETWEEN EXPERIMENTAL AND ANALYTICAL RESULTS

The objective of the experimental campaign was to validate the analytical model of a rocking podium structure presented in the Section 2. The specimen was tested against 12 different symmetric and antisymmetric Ricker pulses. Figures 9-32 compare the numerical and experimental time histories of the normalized tilt angle (θ/α), the absolute and relative top mass displacement (u_T and u_T-u_B), and the accelerations of the ground, beam, and the top mass (a_{ground}, a_{beam}, and a_{top}). For the numerical solution, the measured shaking table (i.e. ground) acceleration was used as input.

Even though some tilt angle time histories were captured very well by the numerical solution, it is generally difficult to predict the entire time history correctly. Unlike elastic systems, the "period" of rocking oscillators strongly depends on their amplitude of vibration. In turn, the amplitude depends on the energy dissipated at each impact. Therefore, any error introduced grows larger, since the solution goes out of phase with the experiment. This confirms the observations of many researchers and suggests that a stochastic (rather than a deterministic) treatment of the rocking problem should be employed.

Nevertheless, for analytical pulses, where the maximum tilt angle occurs in the beginning of the time history, the matching in terms of tilt angle maxima is generally good, even though the shake table controller was not able to enforce a clear pulse motion. Figures 7 and 8 demonstrate this match by comparing the maximum tilt angles. For small absolute tilt angles ($\theta/\alpha < 0.5$) the results compare better. As the tilt angles increase, the negative post-uplift stiffness of the rocking structure affects the highly nonlinear behavior more and more, leading to larger discrepancies between the computed and measured maximum tilt angles.

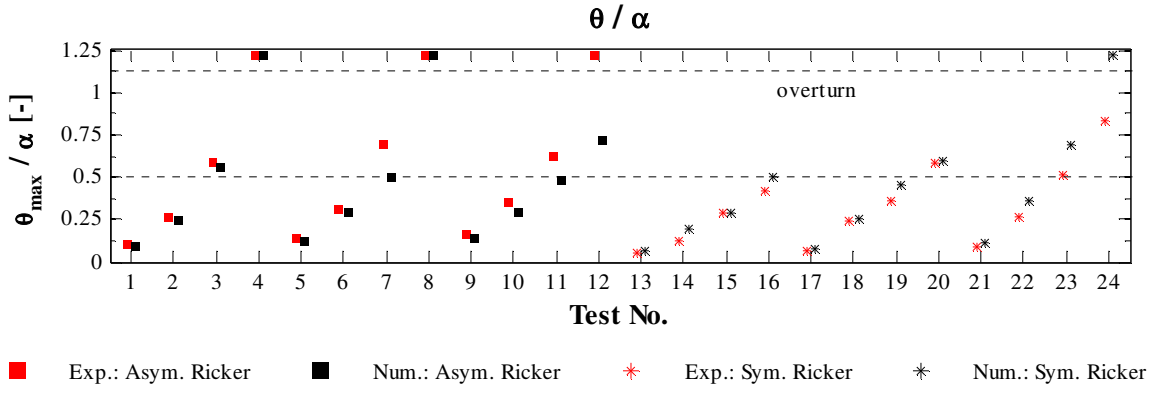

Figure 7: Comparison of computed and measured maximum normalized tilt angle θ/α

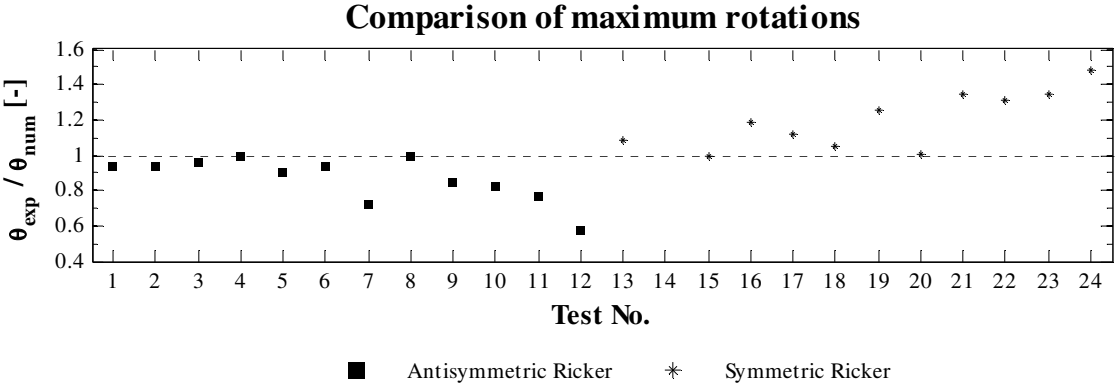

Figure 8: Comparison of computed and measured maximum tilt angle θ

The maximum superstructure deformation (u_T-u_B) is also captured quite well, with an average error of 8% (Table 4). The tests highlighted in gray were not taken into account because in these tests either the numerical and/or the experimental model overturned.

Antisymmetric Ricker			**Symmetric Ricker**		
No.	**Exp.**	**Num.**	**No.**	**Exp.**	**Num.**
[-]	[mm]	[mm]	[-]	[mm]	[mm]
1	5.03	6.09	13	4.61	4.39
2	6.48	6.20	14	5.92	6.53
3	8.27	7.49	15	8.14	7.26
4	*5.83*	*4.47*	16	8.51	7.60
5	5.93	5.82	17	5.54	4.53
6	8.79	7.77	18	6.57	6.14
7	8.63	7.51	19	8.34	7.10
8	*4.54*	*4.50*	20	7.74	7.15
9	6.46	6.16	21	6.69	5.30
10	7.83	6.49	22	8.35	6.82
11	8.55	8.40	23	8.02	7.40
12	*8.44*	*3.74*	*24*	*6.63*	*7.43*

Table 4: Comparison of computed and measured superstructure deformation u_T-u_B [mm]. Overturning occurred in tests highlighted in gray.

The recorded motions of the top mass and have a pronounced high frequency component. This component is attributed to the rocking impacts. It cannot be captured by the analytical model, since the impacts excite higher modes of vibration which are not taken into account in the analytical model.

5 CONCLUSIONS

A small-scale model of a rocking podium structure was constructed and tested. A 2-DOF analytical model of a rocking podium structure was derived and verified and validated against the test results. The computed responses compare well to the test results in terms of the maximum tilt angle and peak superstructure deformation, as well as in terms of the eigenfrequency of the superstructure in the uplifted state. The computed and measured response time histories generally do not match equally well because rocking motion is very sensitive to imperfections at the rocking surfaces, imperfections in the specimens and errors in applying the excitation. The above observation urges for a probabilistic treatment of the rocking problem.

6 TIME HISTORIES

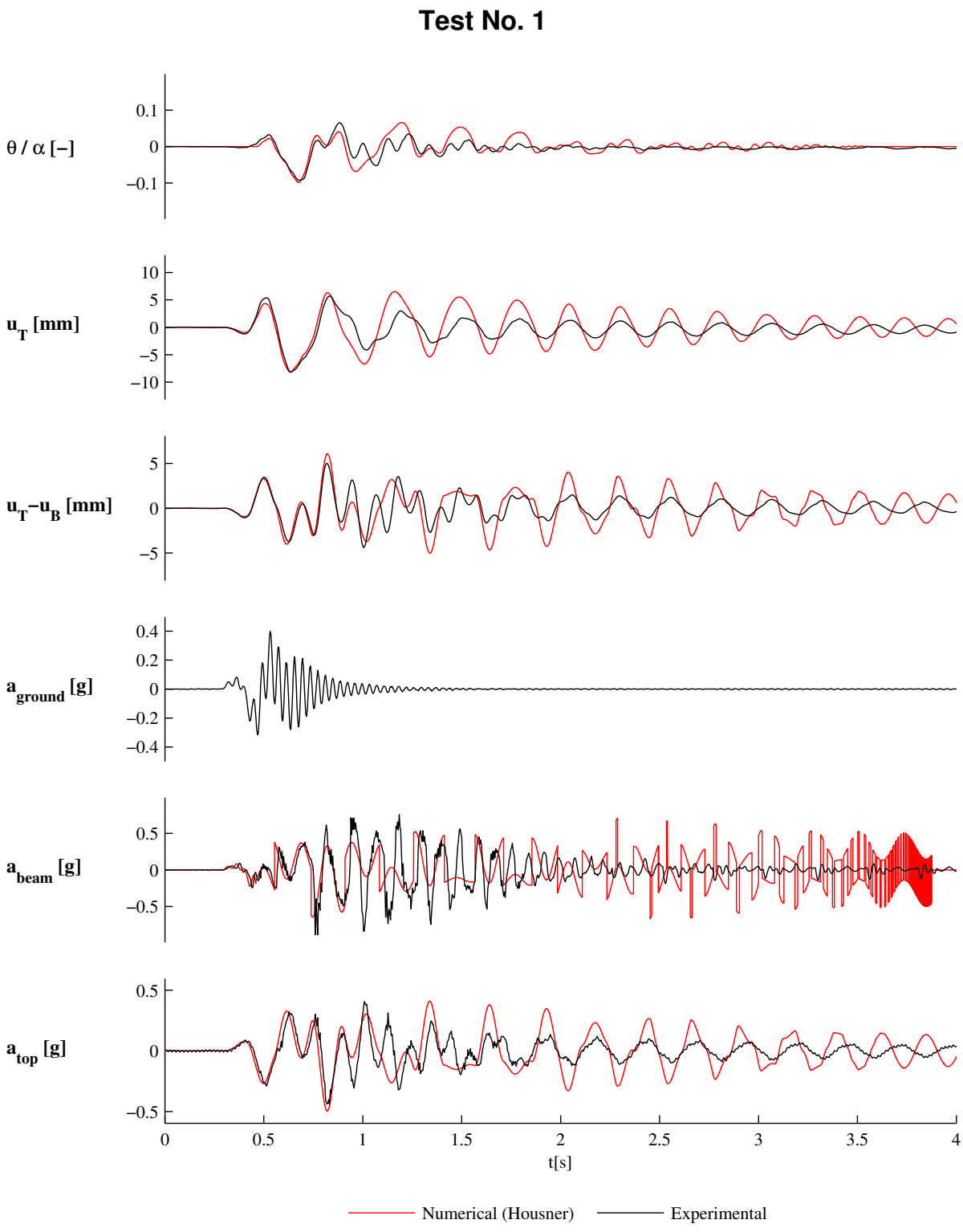

Figure 9: Test No. 1: Time histories for: tilt angle θ/α, top displacement u_T, relative top displacement u_T-u_B, ground acceleration, beam acceleration, top mass acceleration

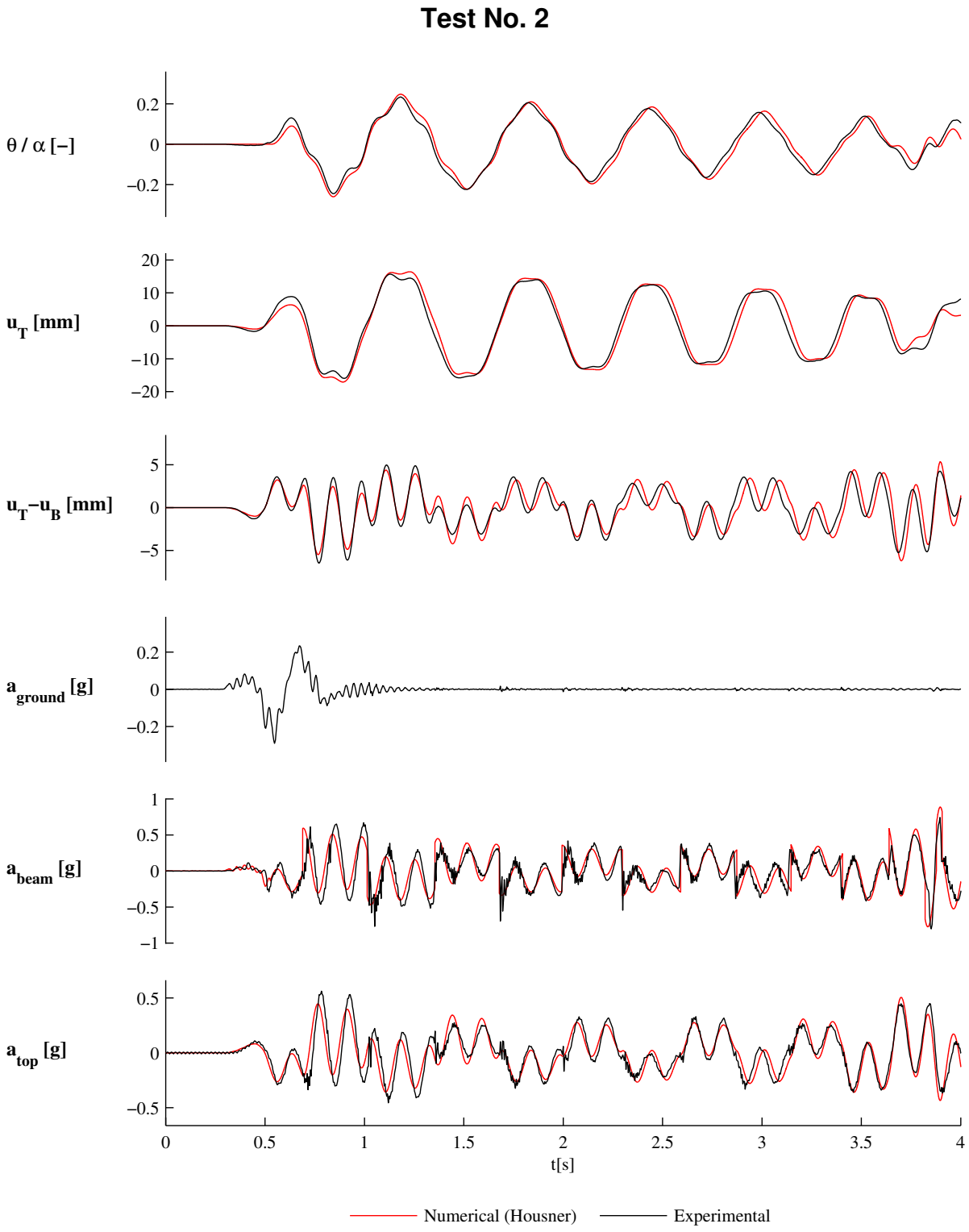

Figure 10: Test No. 2: Time histories for: tilt angle θ/α, top displacement u_T, relative top displacement u_T-u_B, ground acceleration, beam acceleration, top mass acceleration

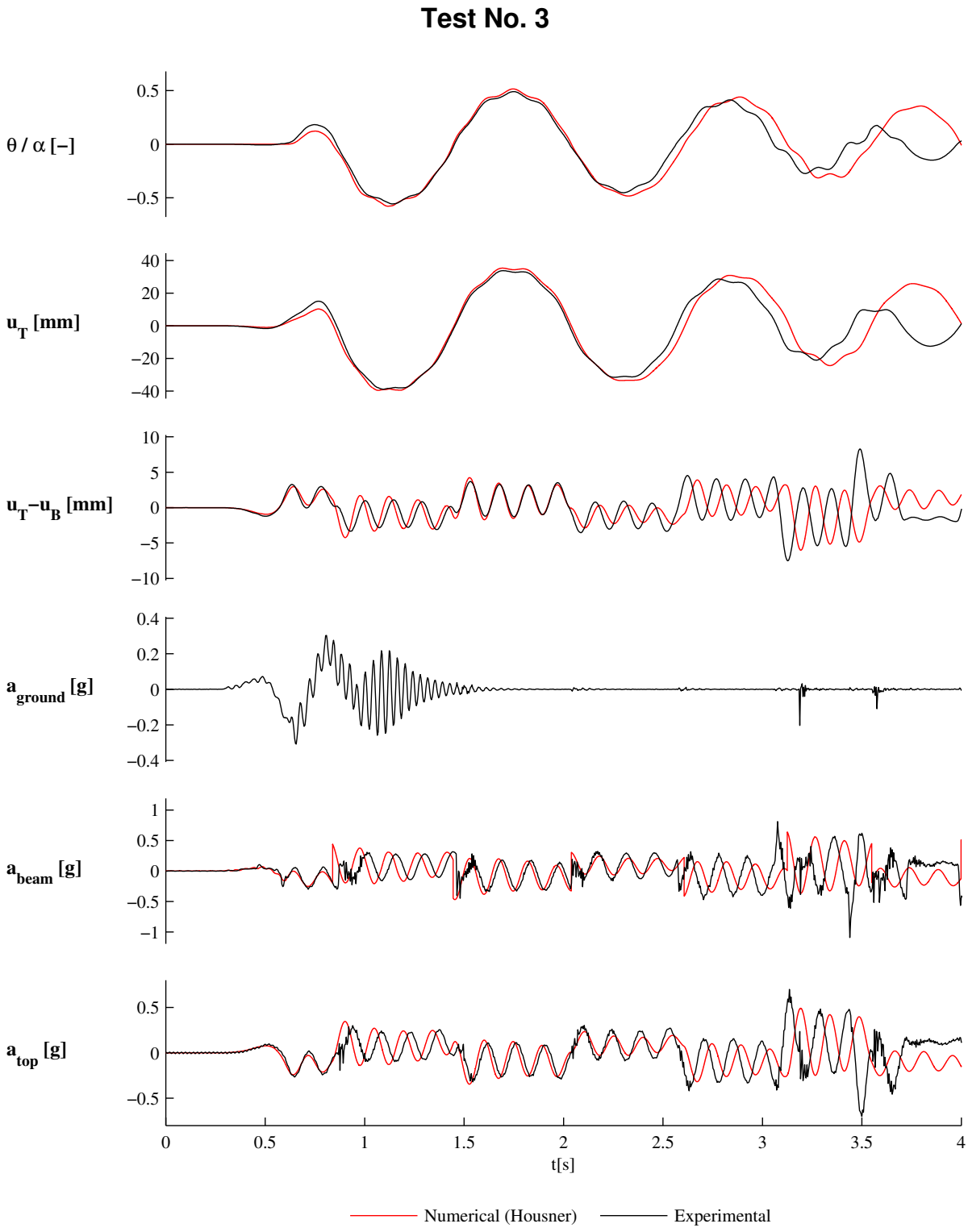

Figure 11: Test No. 3: Time histories for: tilt angle θ/α, top displacement u_T, relative top displacement u_T-u_B, ground acceleration, beam acceleration, top mass acceleration

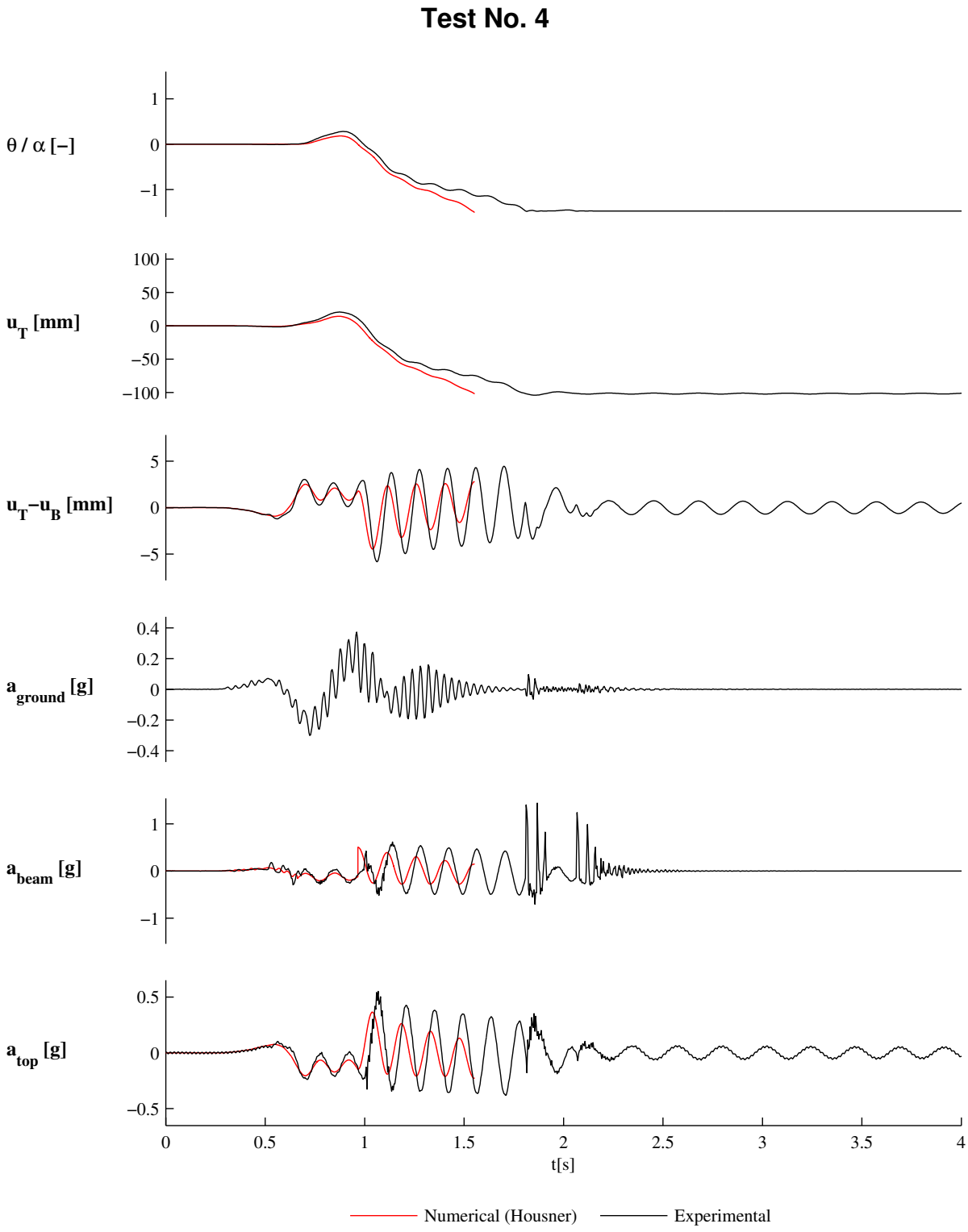

Figure 12: Test No. 4: Time histories for: tilt angle θ/α, top displacement u_T, relative top displacement u_T-u_B, ground acceleration, beam acceleration, top mass acceleration

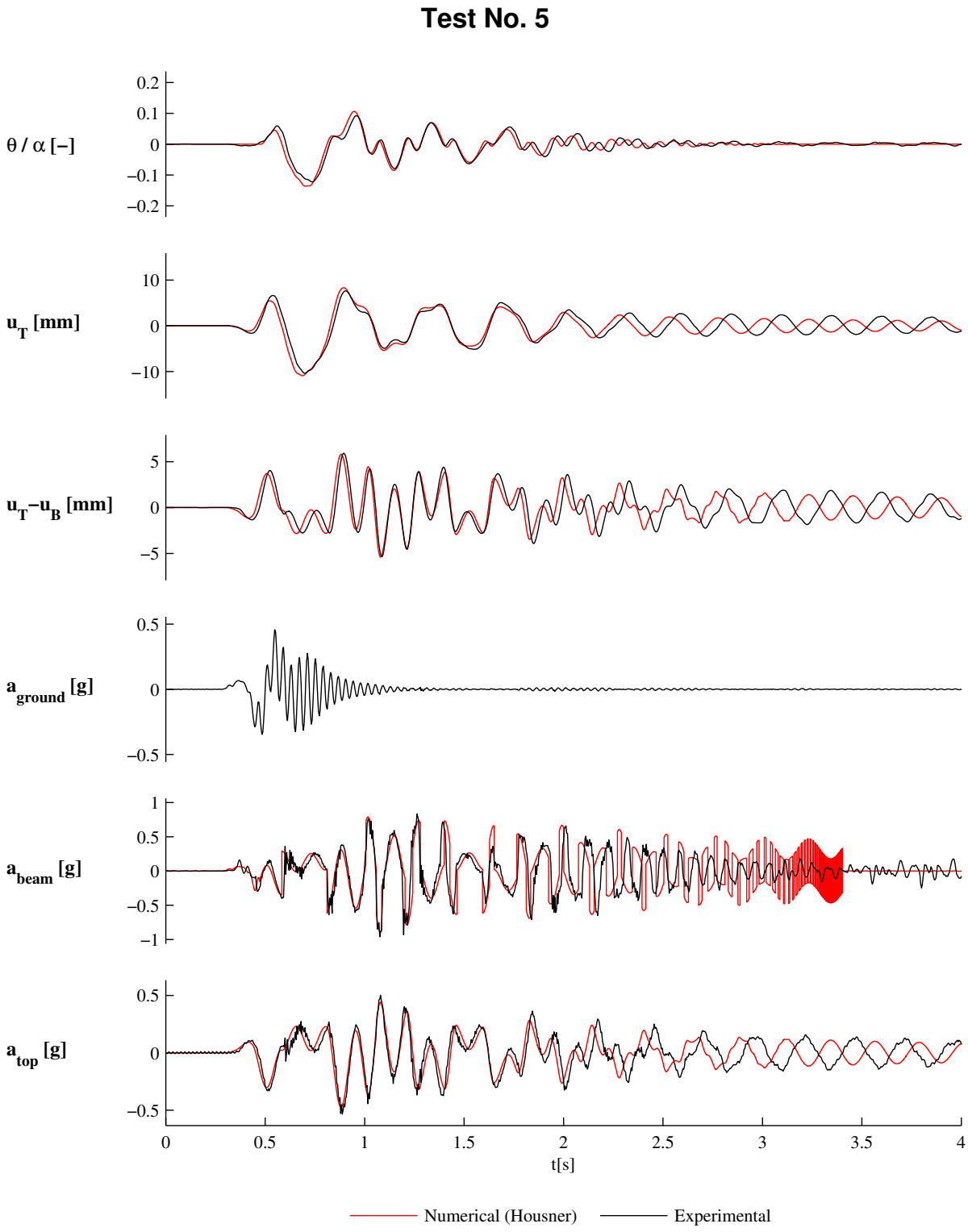

Figure 13: Test No. 5: Time histories for: tilt angle θ/α, top displacement u_T, relative top displacement u_T-u_B, ground acceleration, beam acceleration, top mass acceleration

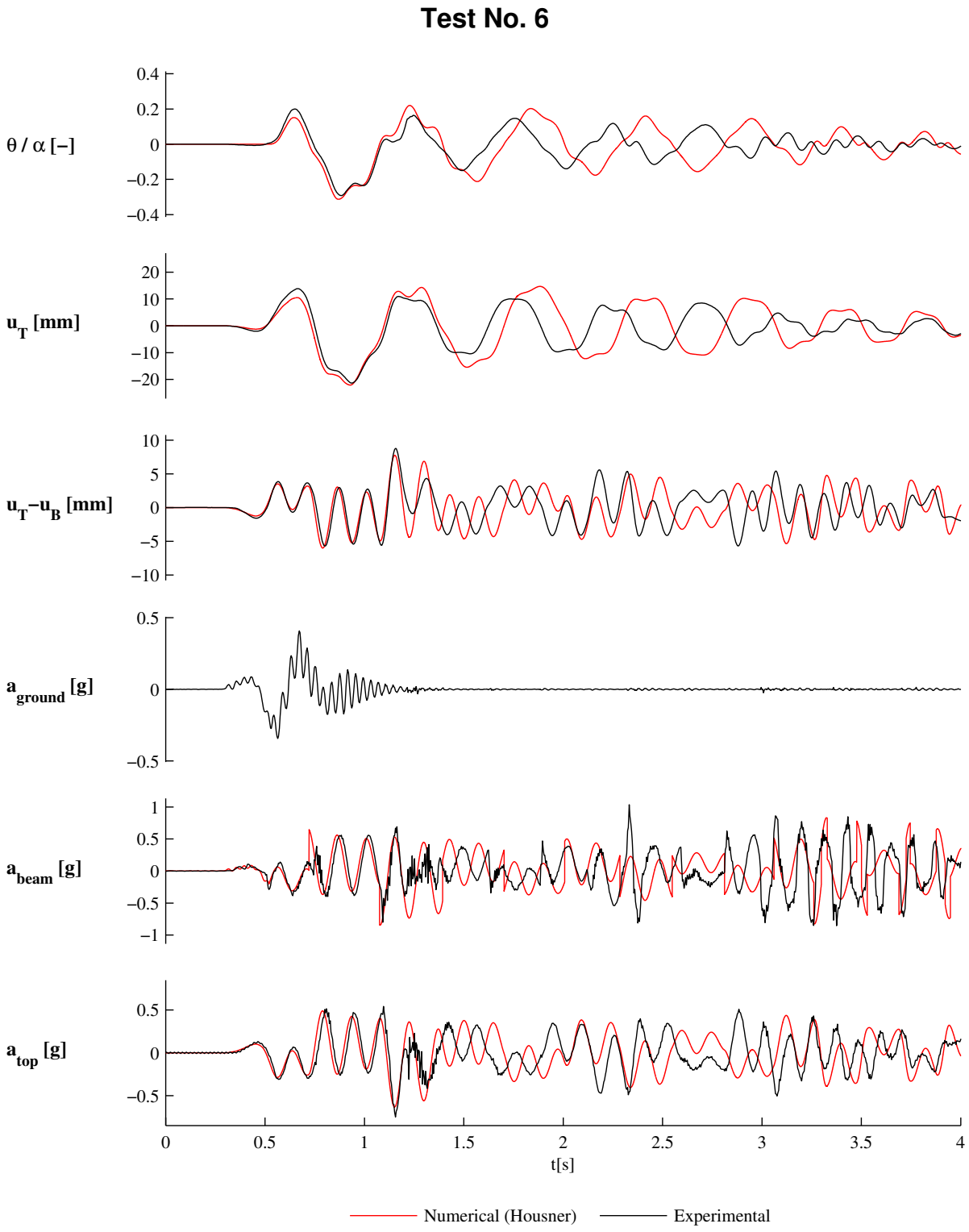

Figure 14: Test No. 6: Time histories for: tilt angle θ/α, top displacement u_T, relative top displacement u_T-u_B, ground acceleration, beam acceleration, top mass acceleration

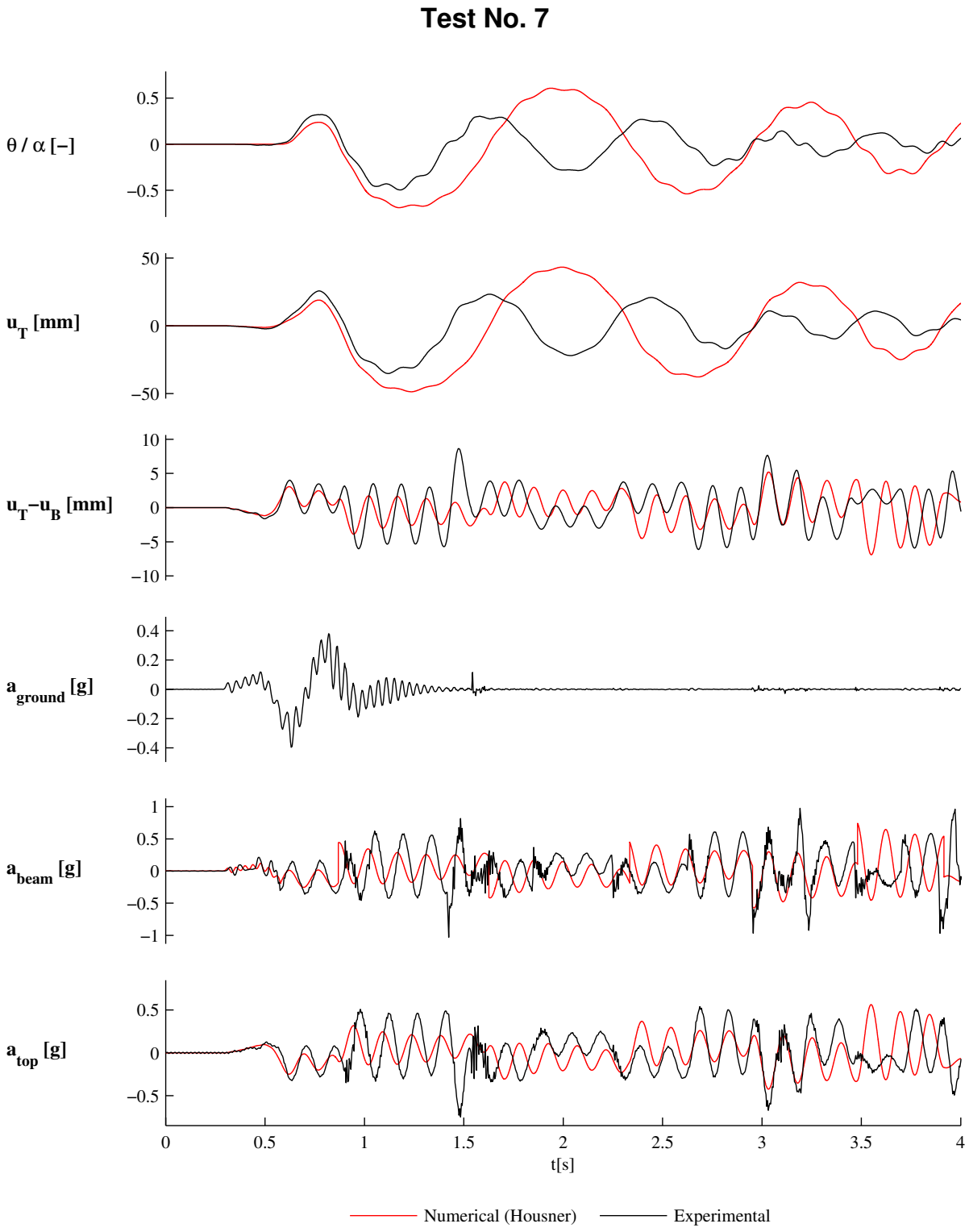

Figure 15: Test No. 7: Time histories for: tilt angle θ/α, top displacement u_T, relative top displacement u_T-u_B, ground acceleration, beam acceleration, top mass acceleration

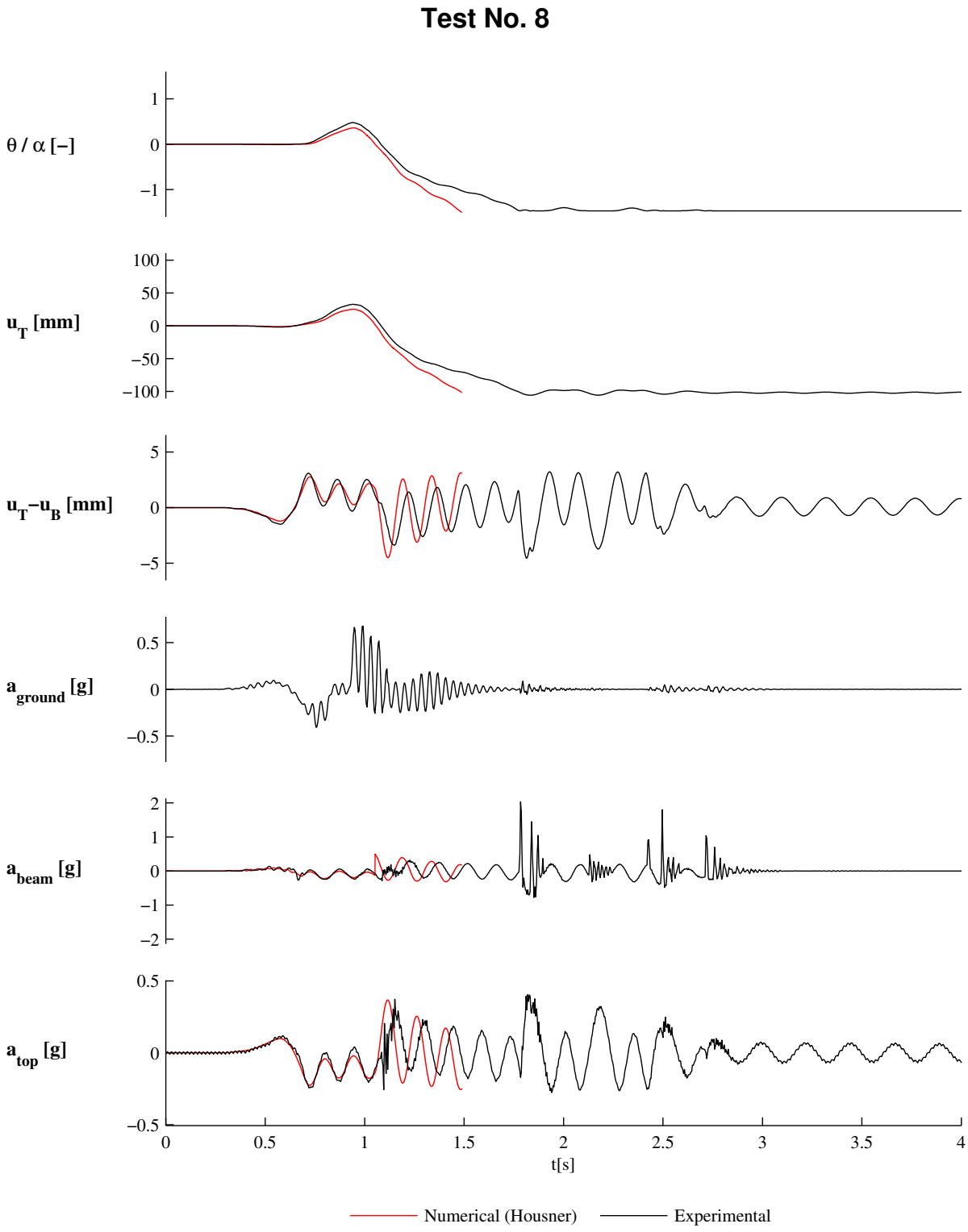

Figure 16: Test No. 8: Time histories for: tilt angle θ/α, top displacement u_T, relative top displacement u_T-u_B, ground acceleration, beam acceleration, top mass acceleration

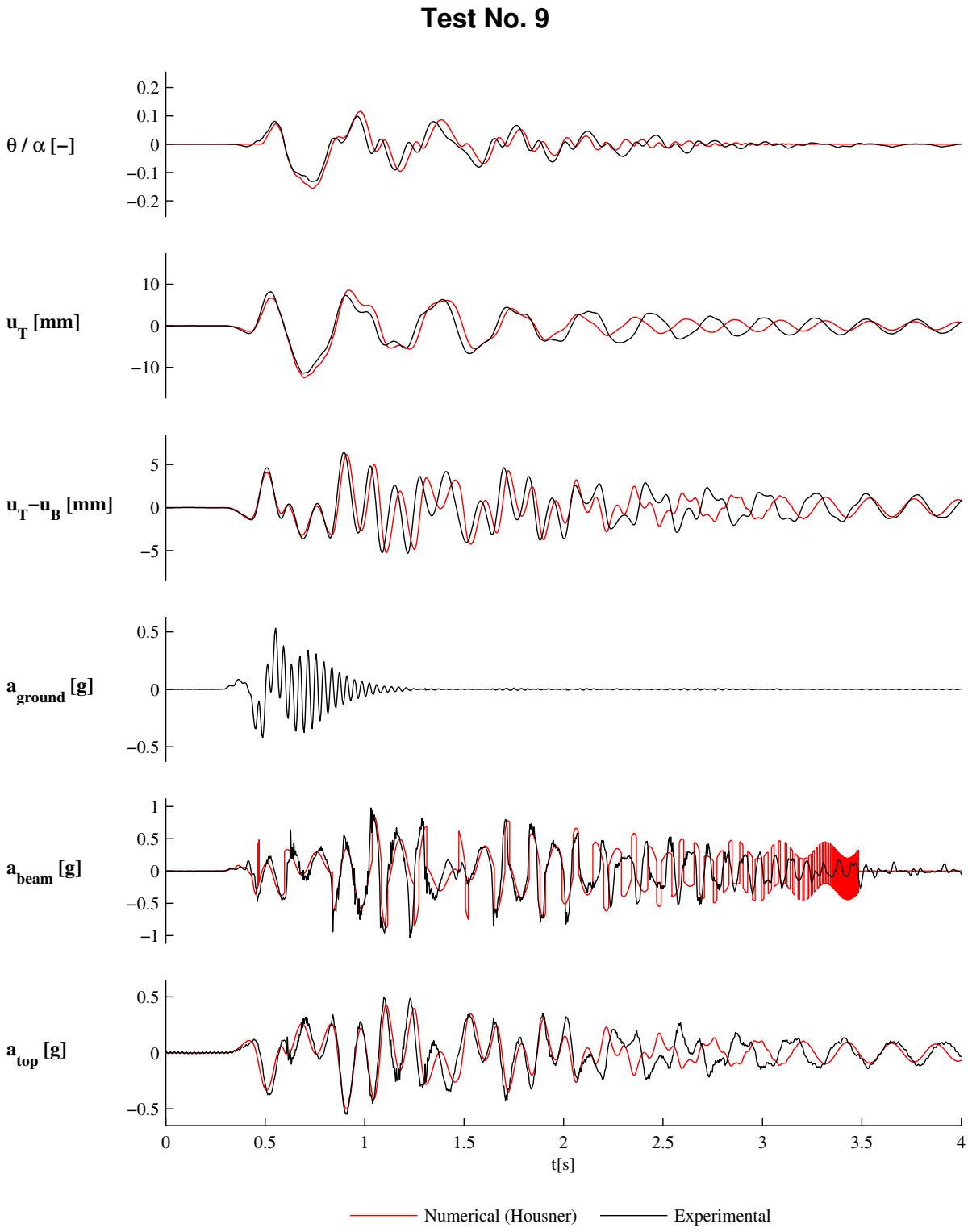

Figure 17: Test No. 9: Time histories for: tilt angle θ/α, top displacement u_T, relative top displacement u_T-u_B, ground acceleration, beam acceleration, top mass acceleration

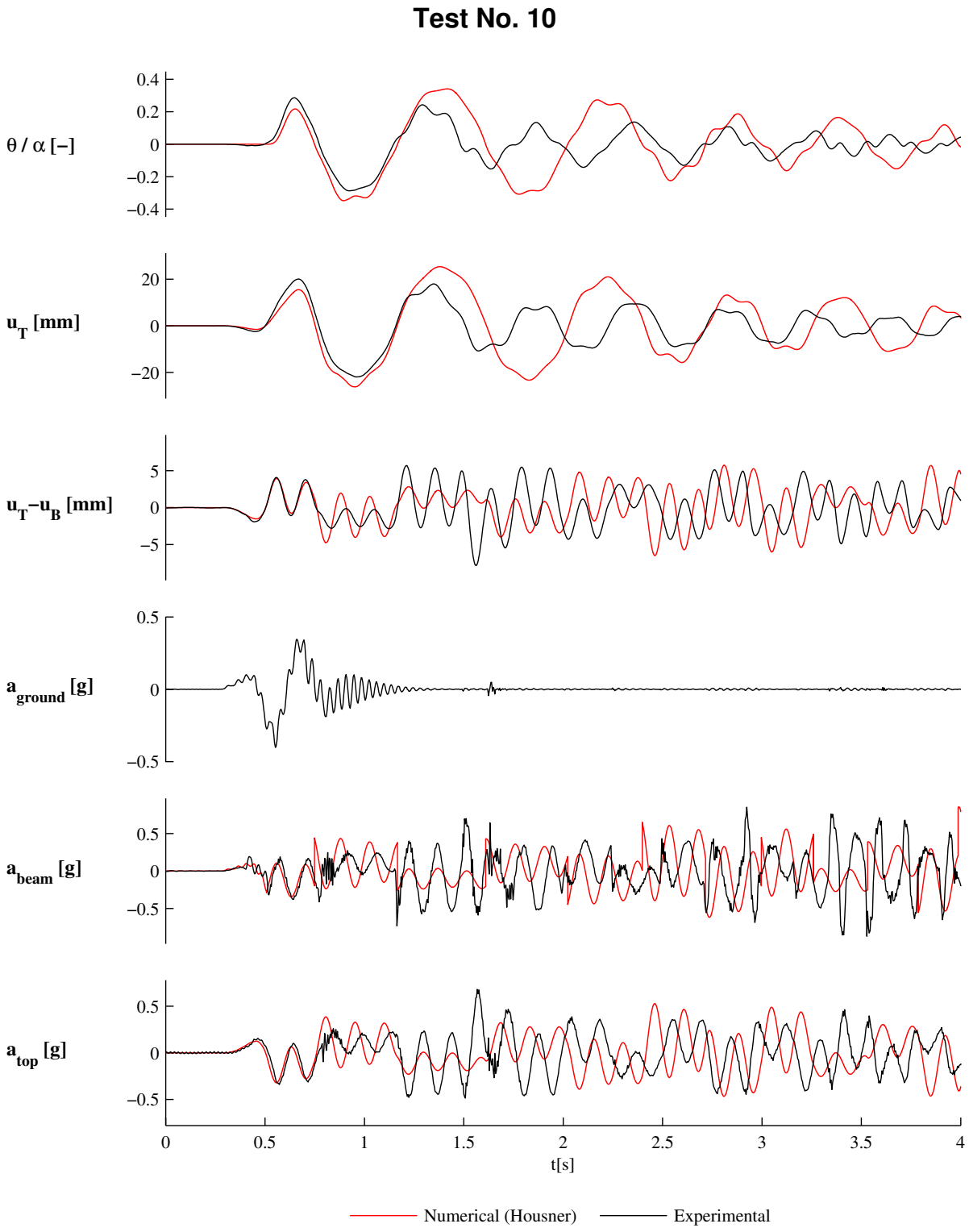

Figure 18: Test No. 10: Time histories for: tilt angle θ/α, top displacement u_T, relative top displacement u_T-u_B, ground acceleration, beam acceleration, top mass acceleration

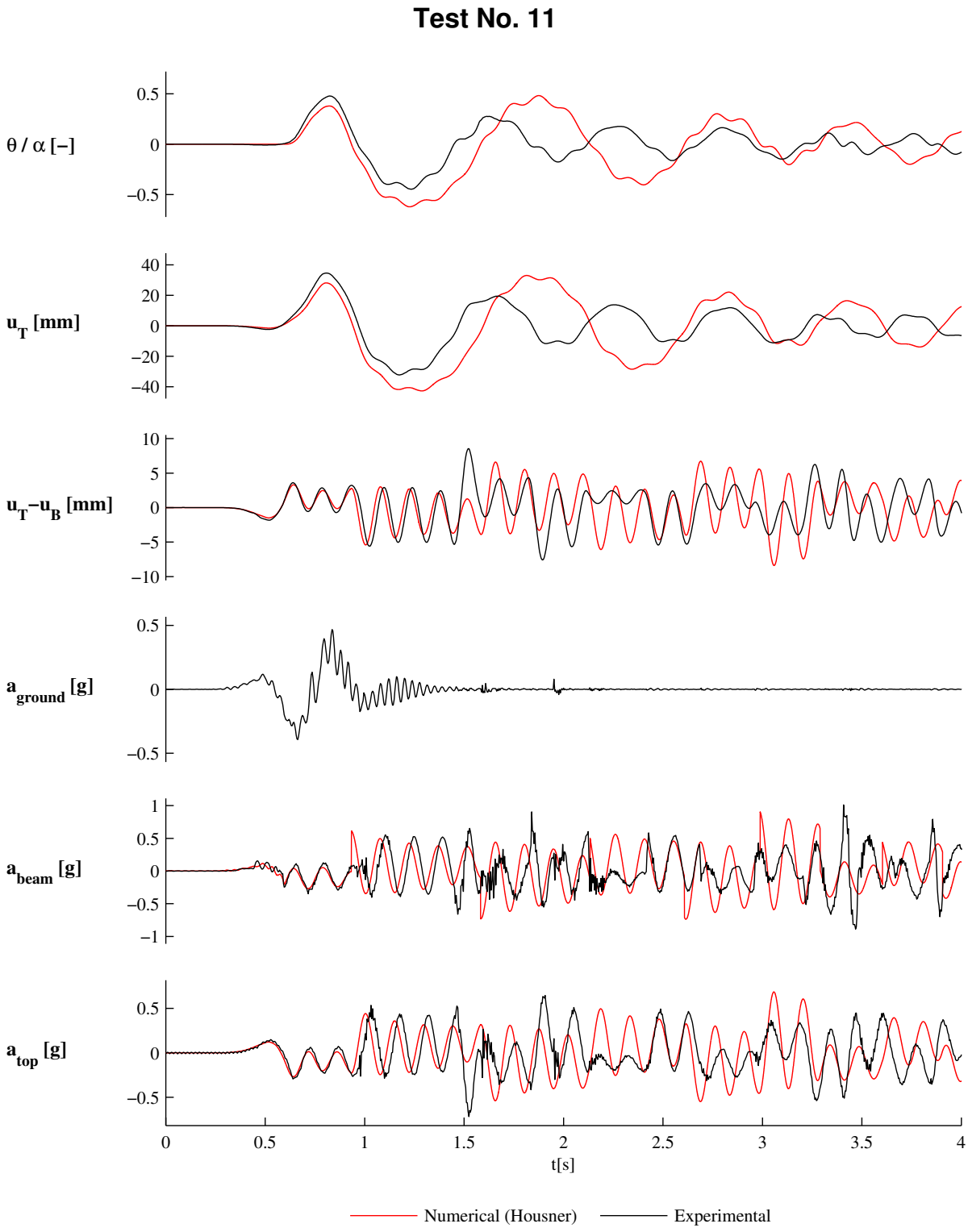

Figure 19: Test No. 11: Time histories for: tilt angle θ/α, top displacement u_T, relative top displacement u_T-u_B, ground acceleration, beam acceleration, top mass acceleration

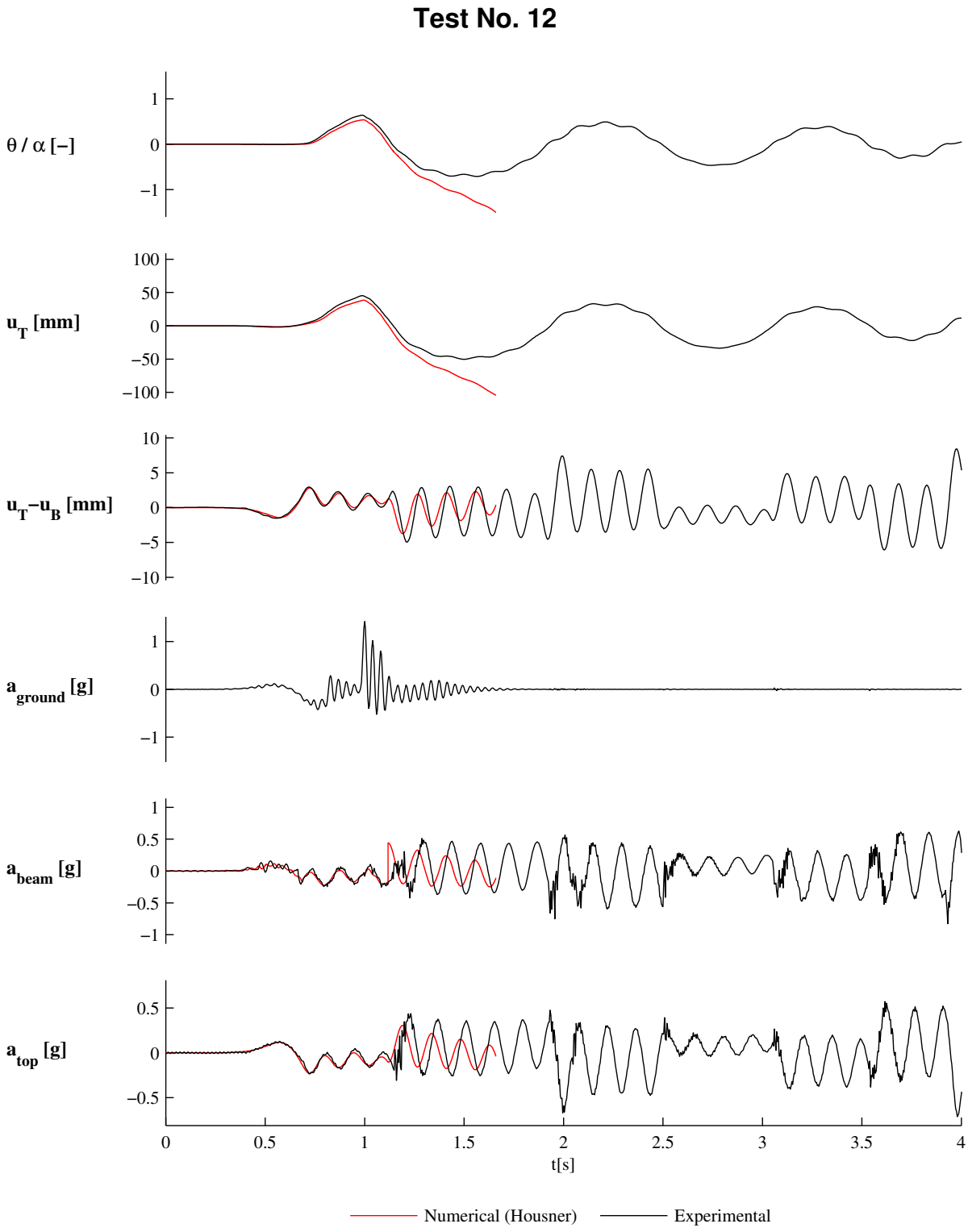

Figure 20: Test No. 12: Time histories for: tilt angle θ/α, top displacement u_T, relative top displacement u_T-u_B, ground acceleration, beam acceleration, top mass acceleration

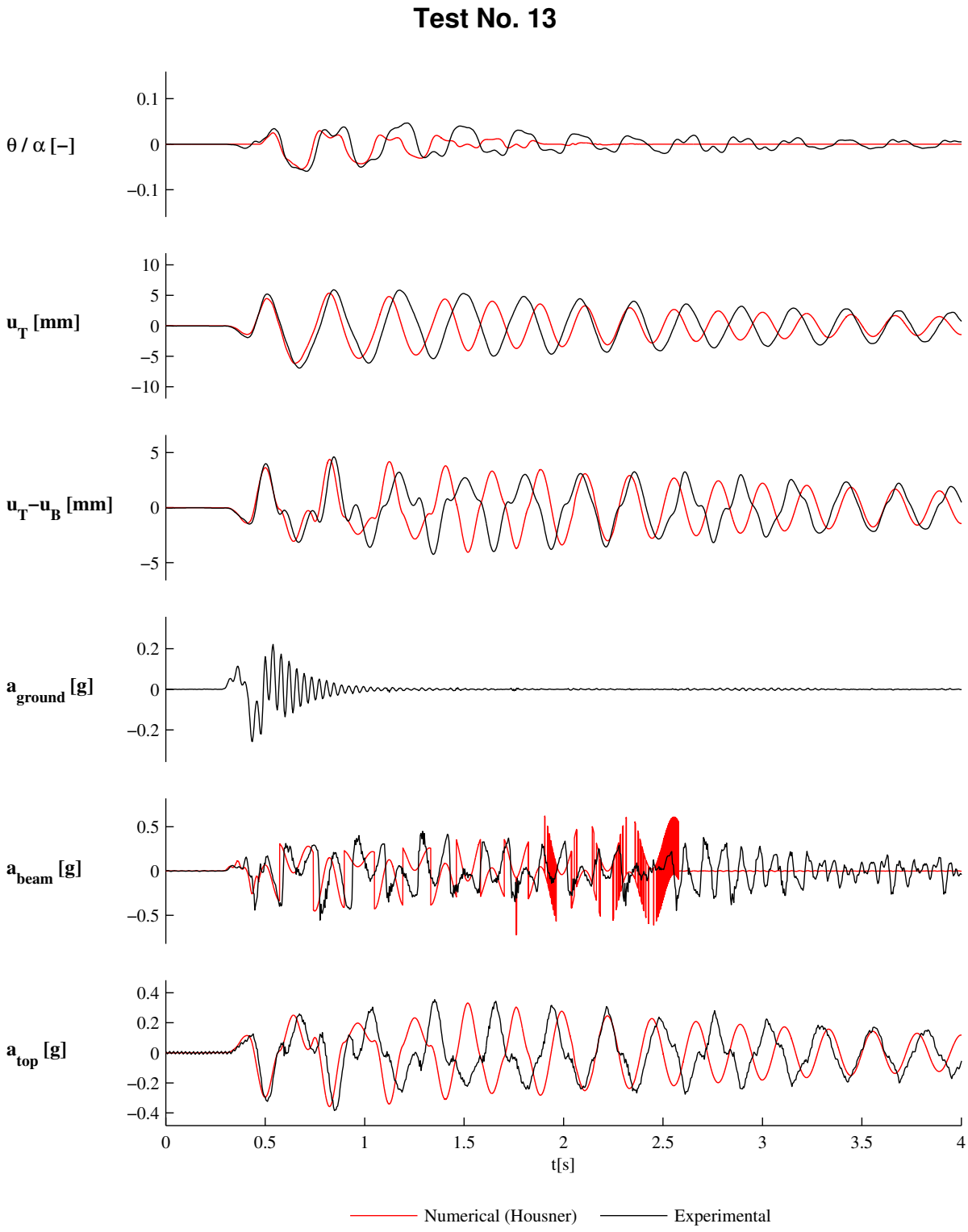

Figure 21: Test No. 13: Time histories for: tilt angle θ/α, top displacement u_T, relative top displacement u_T-u_B, ground acceleration, beam acceleration, top mass acceleration

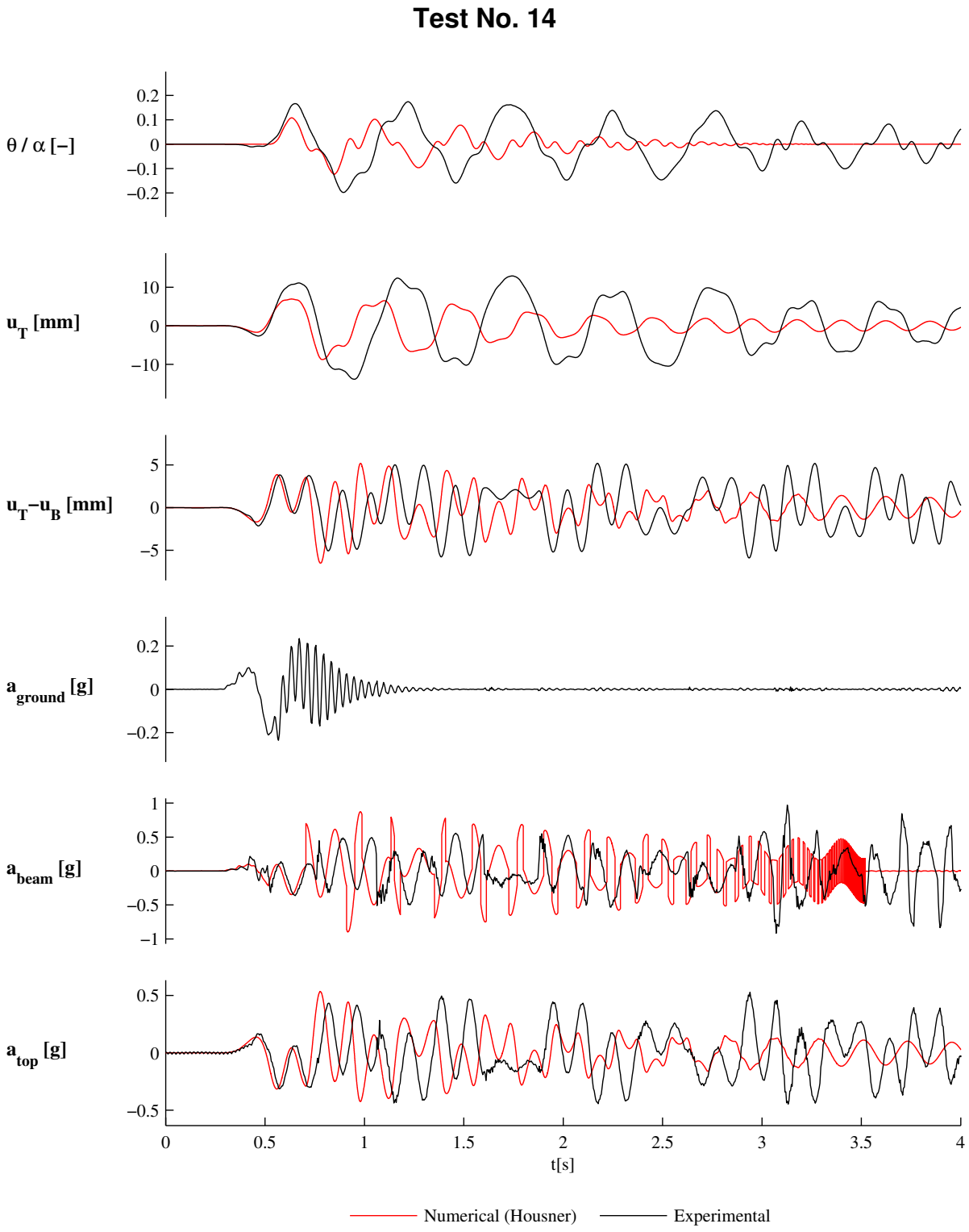

Figure 22: Test No. 14: Time histories for: tilt angle θ/α, top displacement u_T, relative top displacement u_T-u_B, ground acceleration, beam acceleration, top mass acceleration

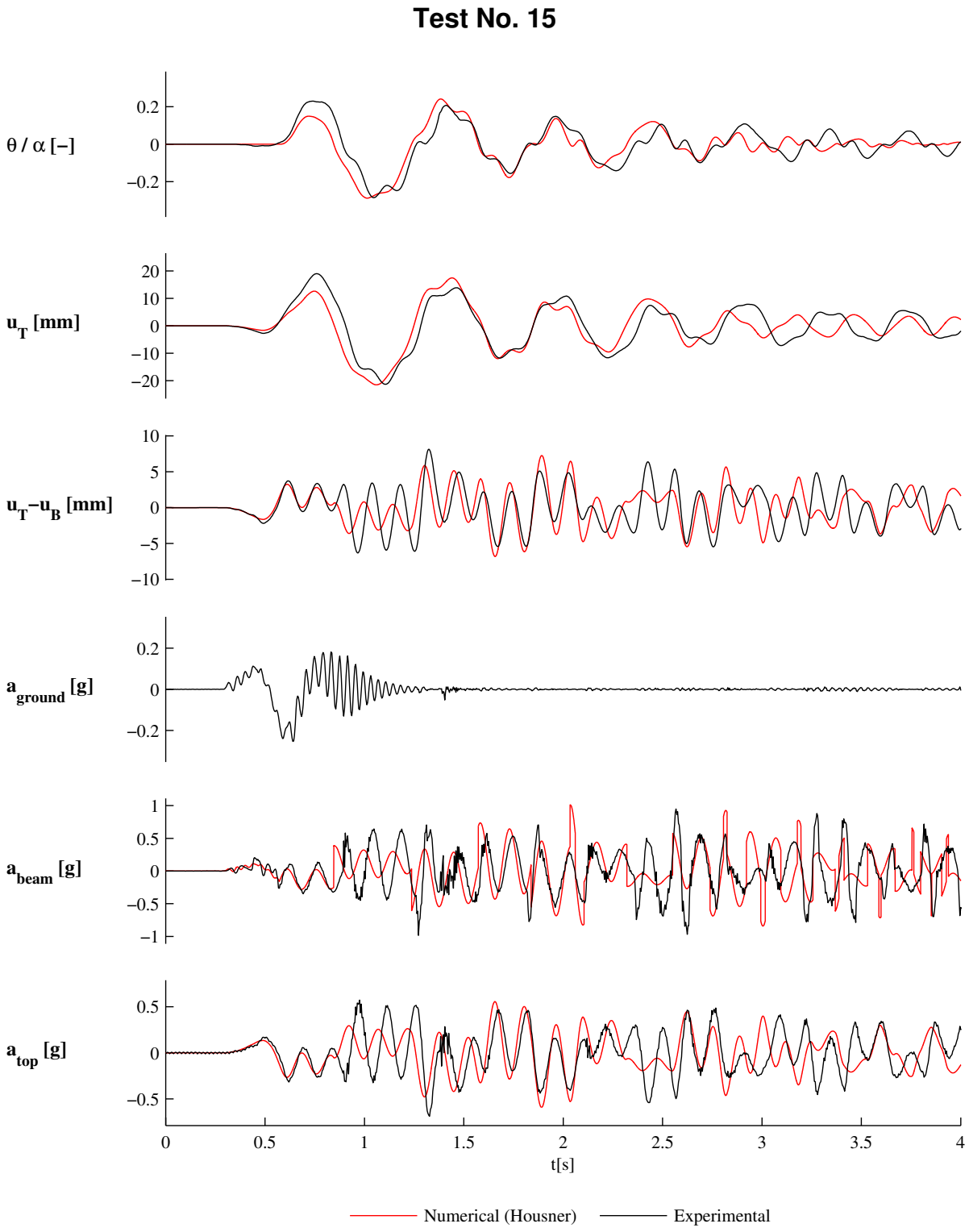

Figure 23: Test No. 15: Time histories for: tilt angle θ/α, top displacement u_T, relative top displacement u_T-u_B, ground acceleration, beam acceleration, top mass acceleration

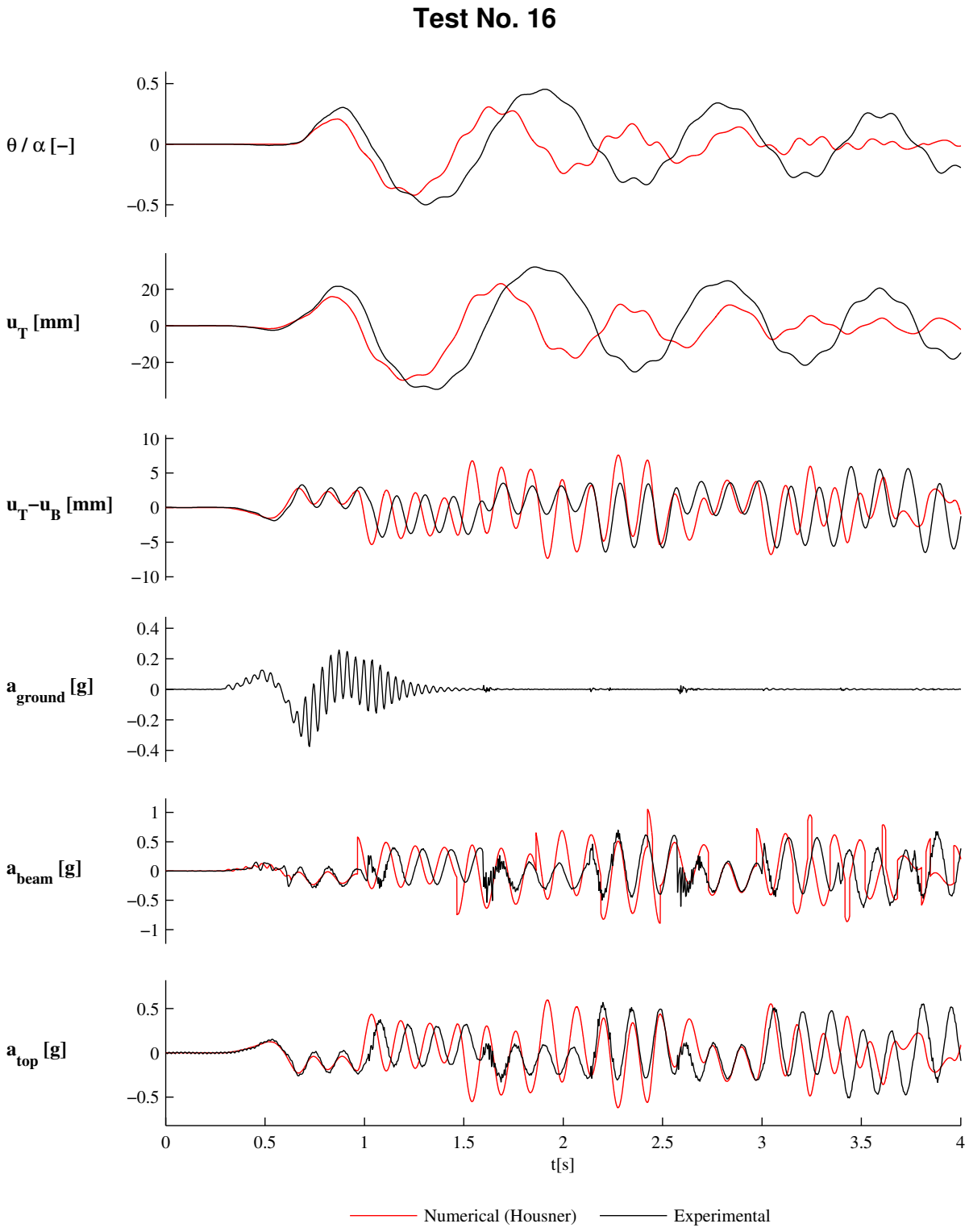

Figure 24: Test No. 16: Time histories for: tilt angle θ/α, top displacement u_T, relative top displacement u_T-u_B, ground acceleration, beam acceleration, top mass acceleration

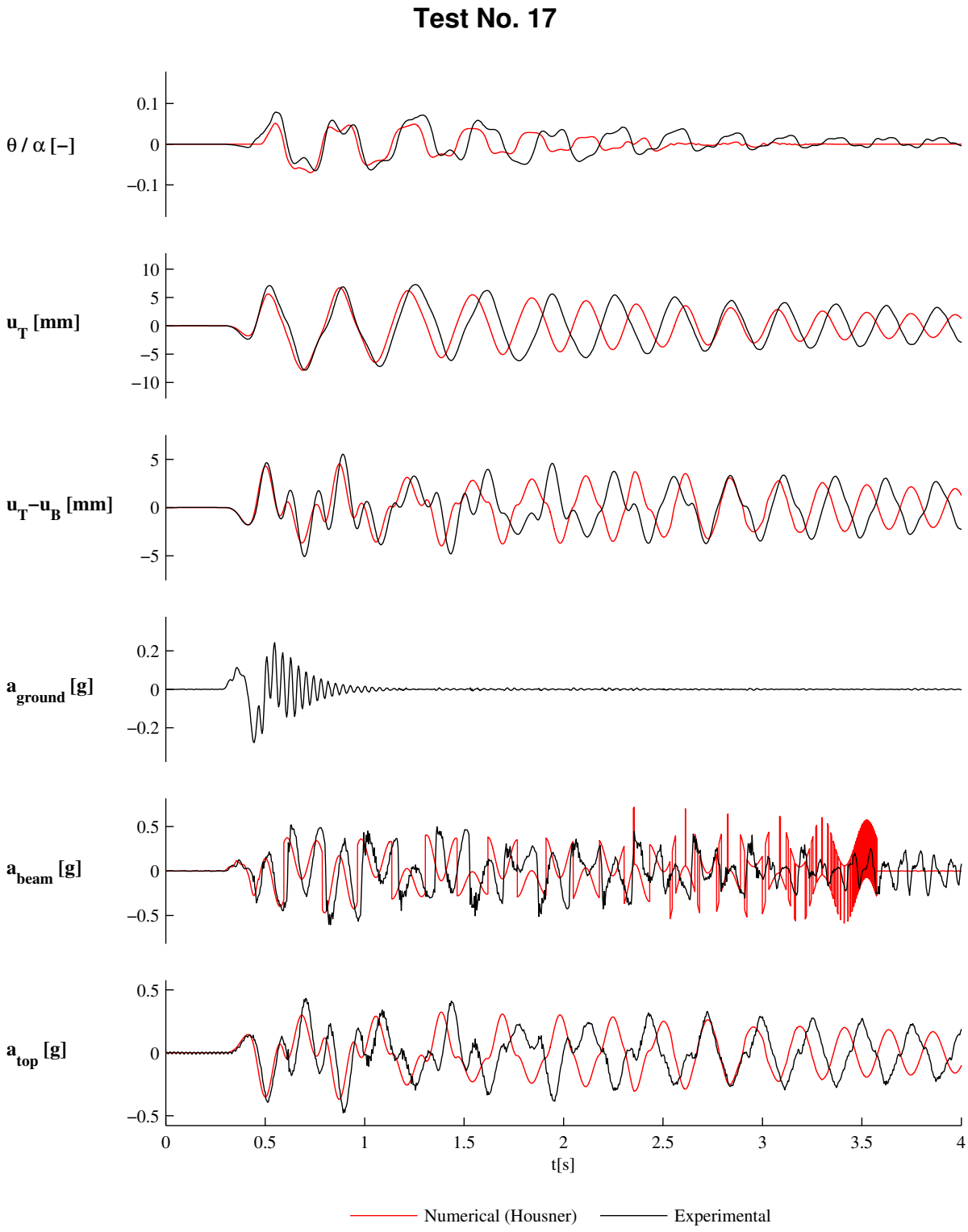

Figure 25: Test No. 17: Time histories for: tilt angle θ/α, top displacement u_T, relative top displacement u_T-u_B, ground acceleration, beam acceleration, top mass acceleration

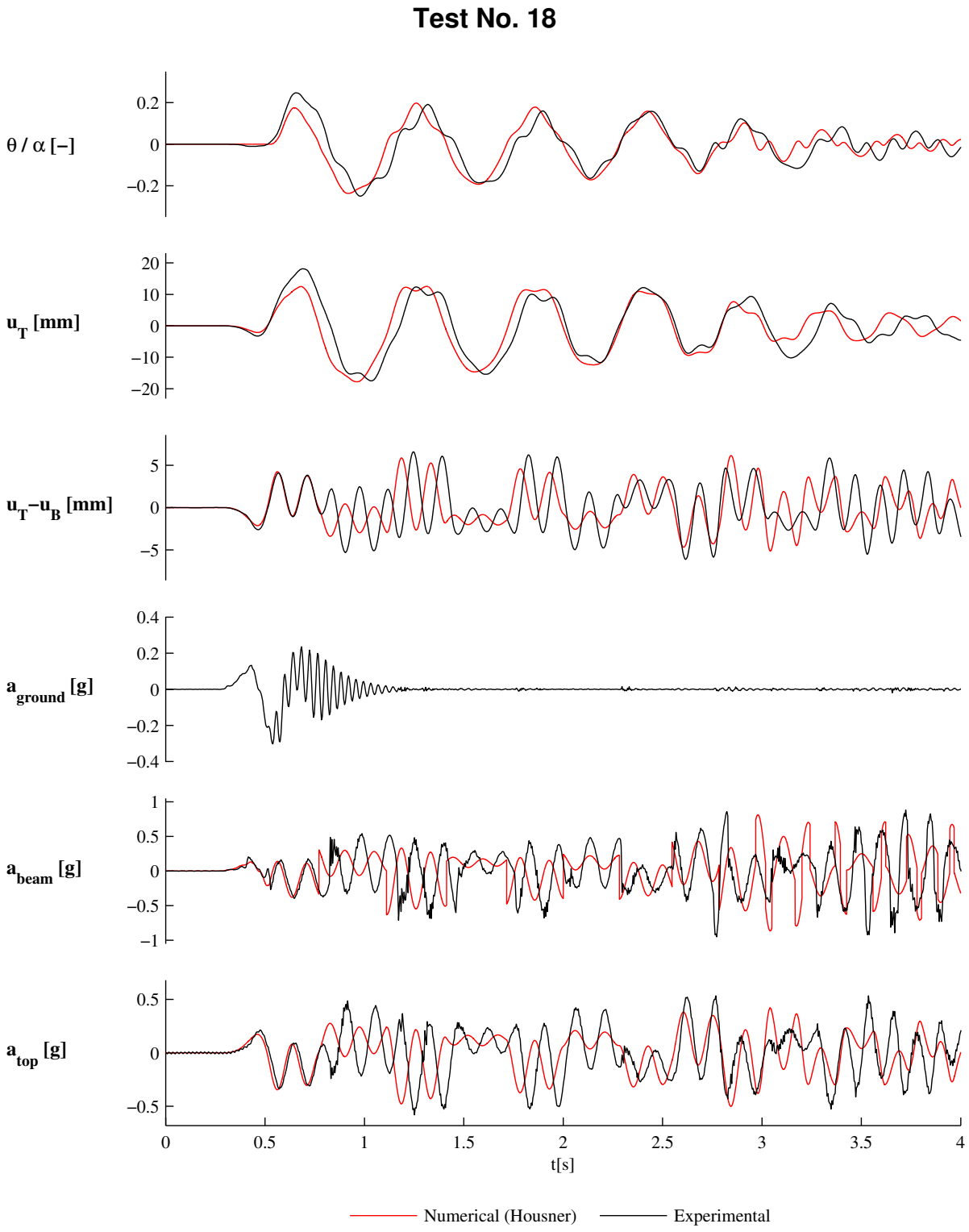

Figure 26: Test No. 18: Time histories for: tilt angle θ/α, top displacement u_T, relative top displacement u_T-u_B, ground acceleration, beam acceleration, top mass acceleration

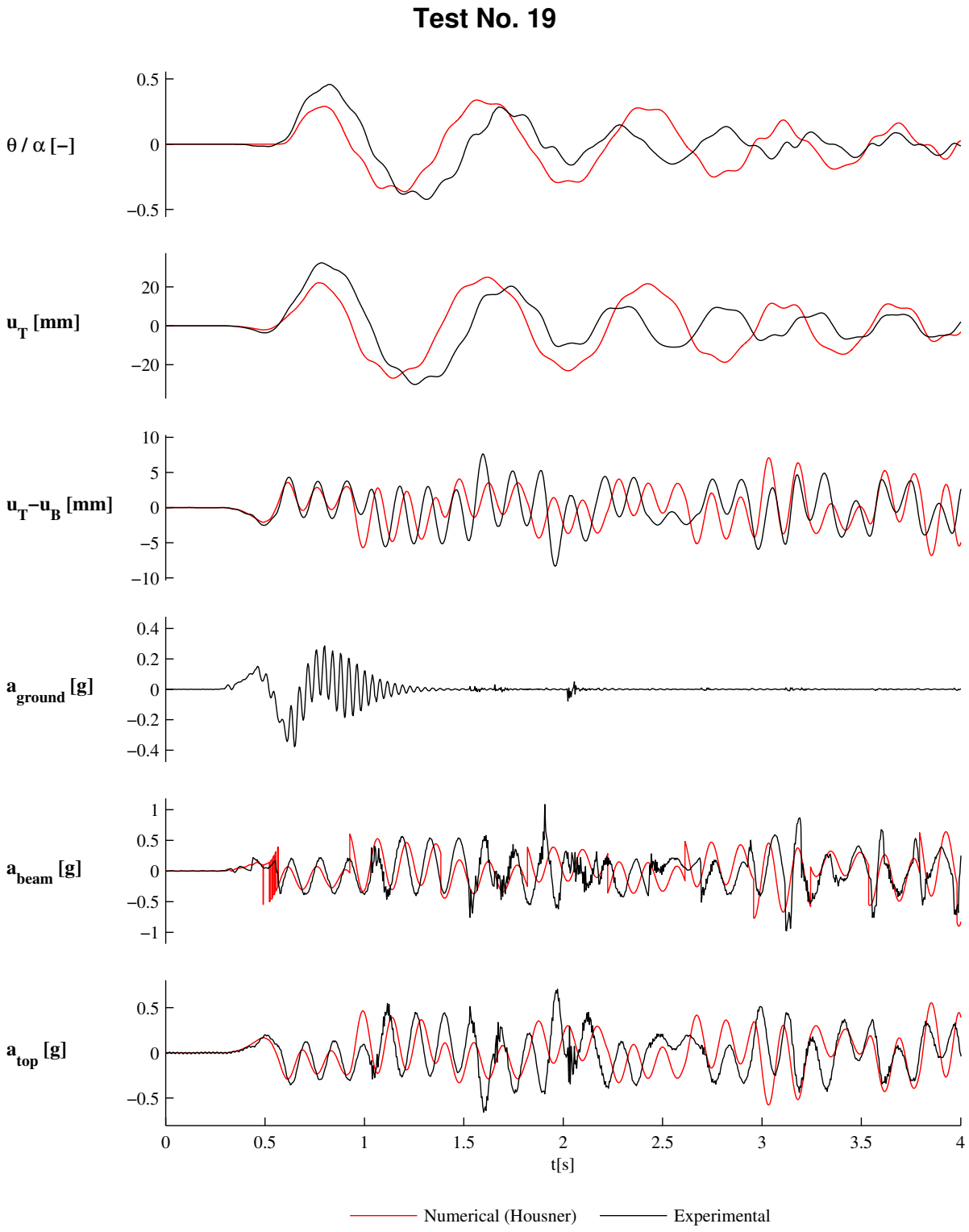

Figure 27: Test No. 19: Time histories for: tilt angle θ/α, top displacement u_T, relative top displacement u_T-u_B, ground acceleration, beam acceleration, top mass acceleration

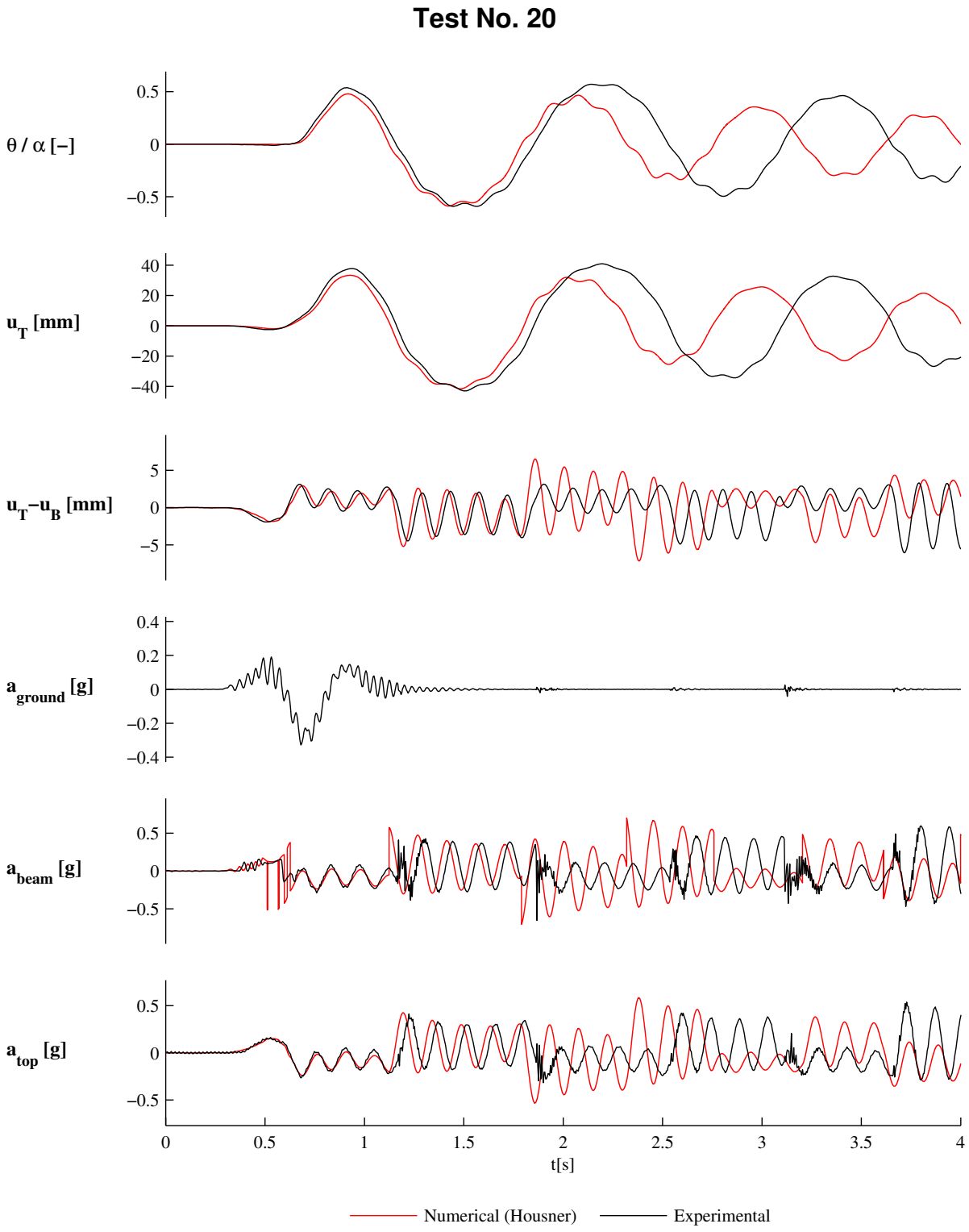

Figure 28: Test No. 20: Time histories for: tilt angle θ/α, top displacement u_T, relative top displacement u_T-u_B, ground acceleration, beam acceleration, top mass acceleration

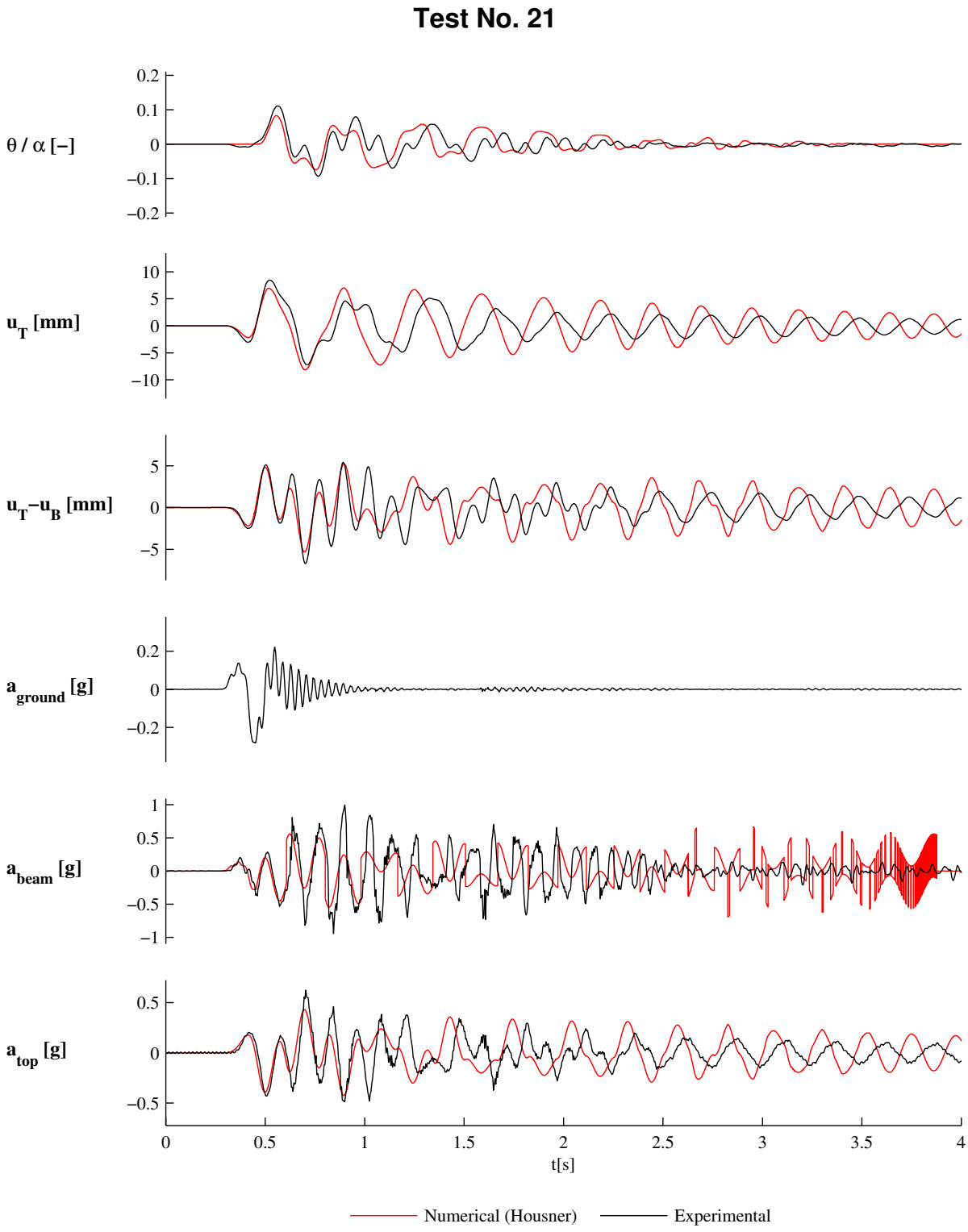

Figure 29: Test No. 21: Time histories for: tilt angle θ/α, top displacement u_T, relative top displacement u_T-u_B, ground acceleration, beam acceleration, top mass acceleration

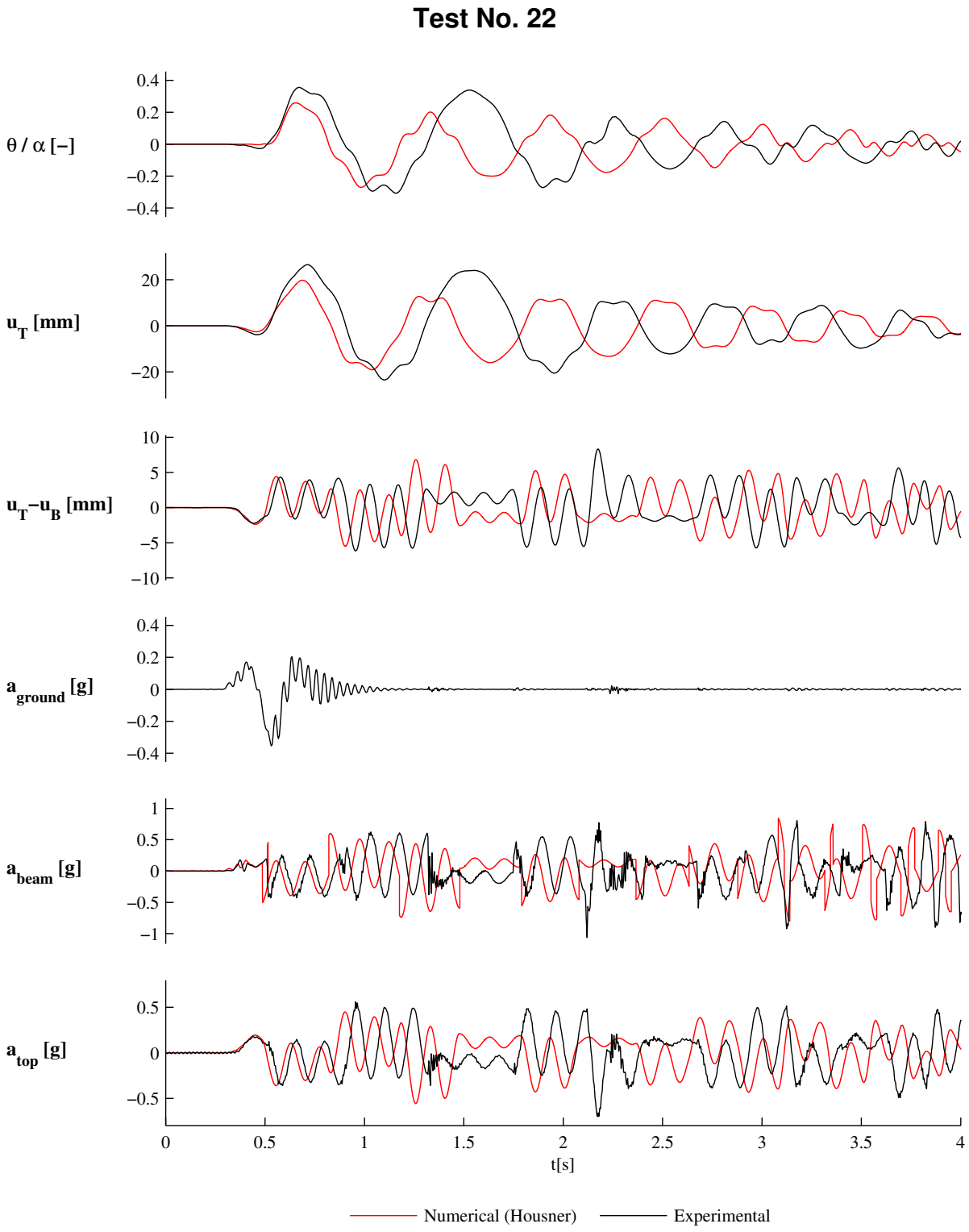

Figure 30: Test No. 22: Time histories for: tilt angle θ/α, top displacement u_T, relative top displacement u_T-u_B, ground acceleration, beam acceleration, top mass acceleration

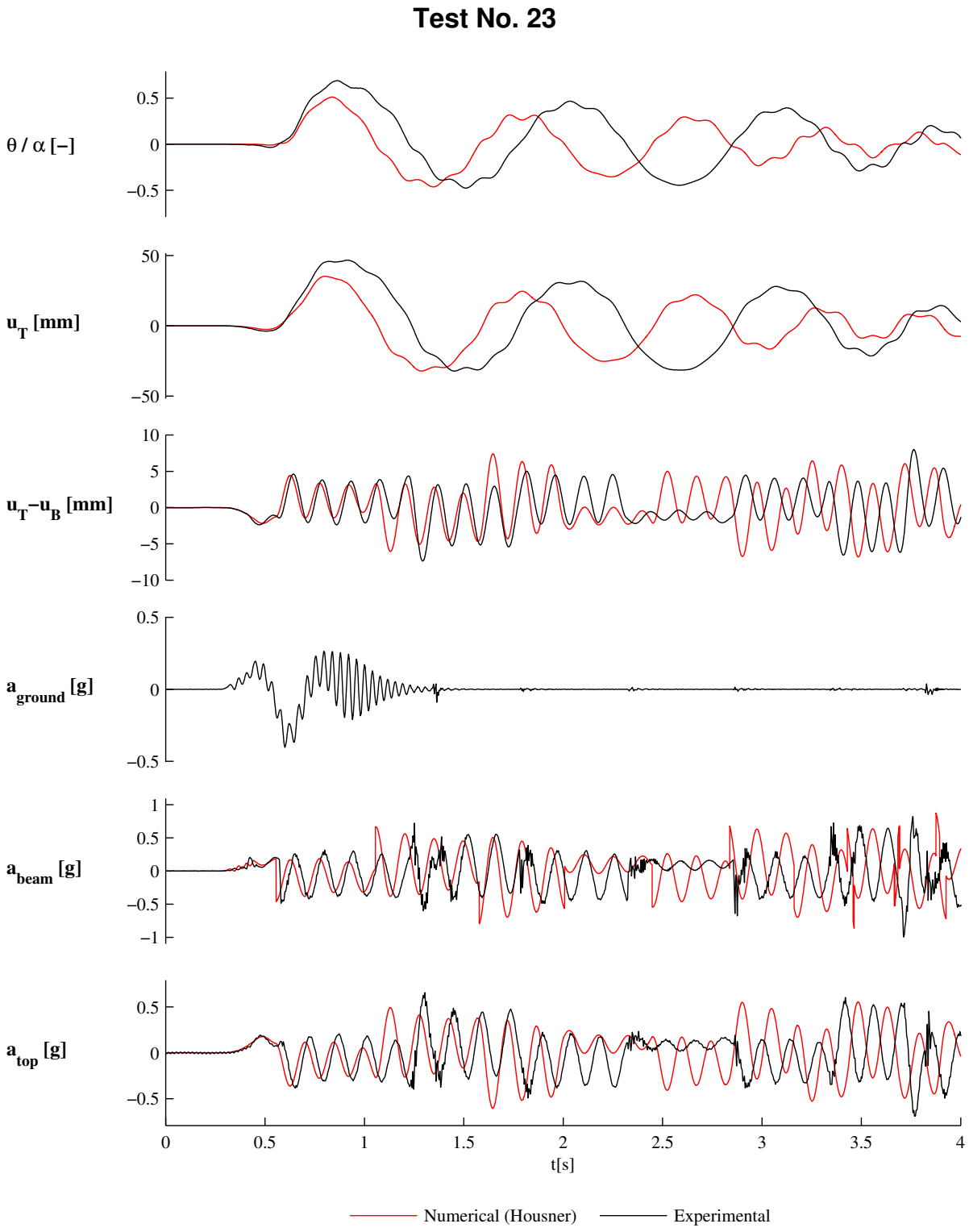

Figure 31: Test No. 23: Time histories for: tilt angle θ/α, top displacement u_T, relative top displacement u_T-u_B, ground acceleration, beam acceleration, top mass acceleration

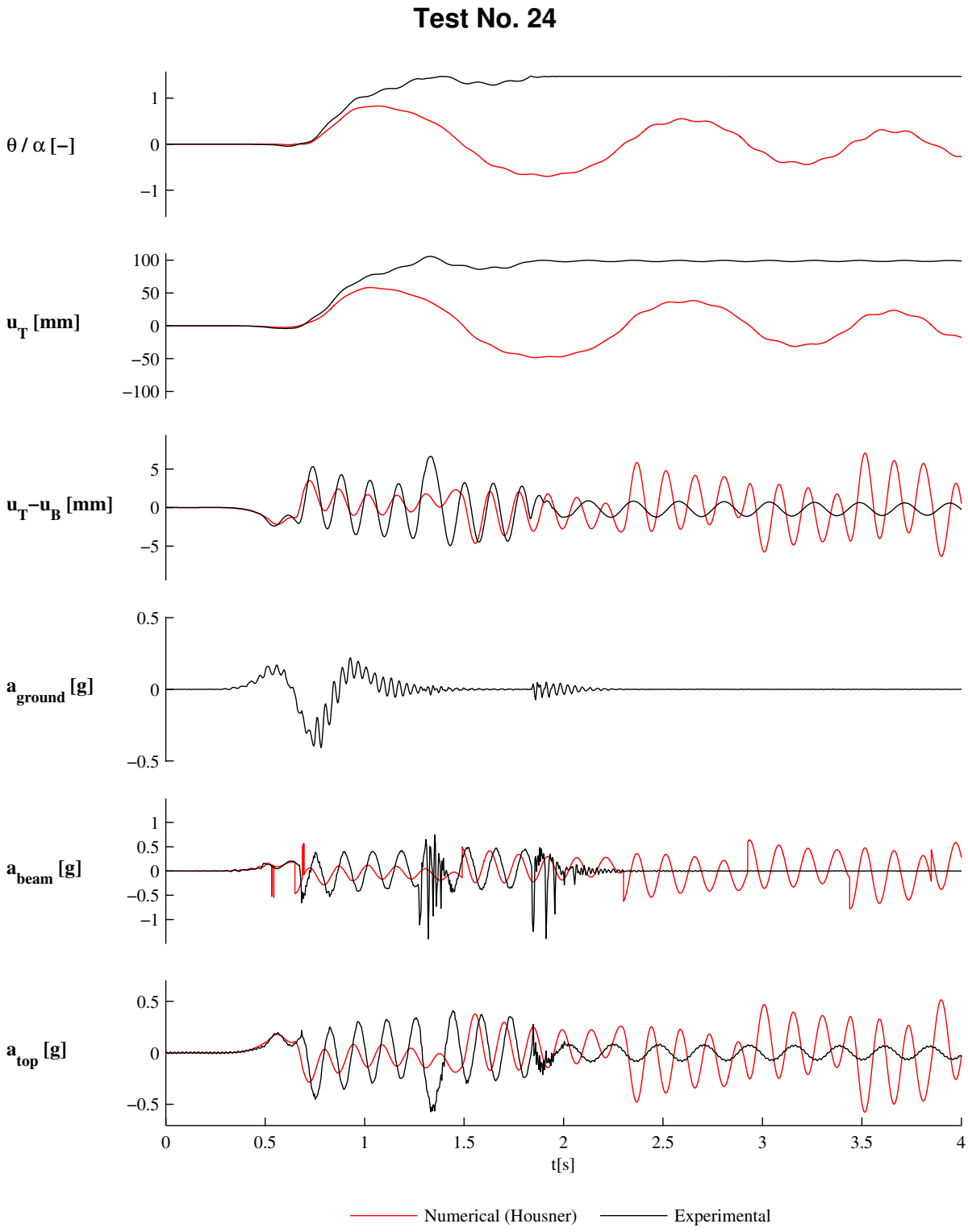

Figure 32: Test No. 24: Time histories for: tilt angle θ/α, top displacement u_T, relative top displacement u_T-u_B, ground acceleration, beam acceleration, top mass acceleration

REFERENCES

[1] С. Семенов (S. Semenov), "Kinematic base isolation," 2011. [Online]. Available: https://www.youtube.com/watch?v=Tqr0k4Dw2FM, accessed on 03/2016.

[2] С. Семенов (S. Semenov), "Сейсмоизоляция Protection against earthquake," 2015. [Online]. Available: https://www.youtube.com/watch?v=sZ5KCX2wMd0, accessed on 03/2016.

[3] J. L. Beck and R. I. Skinner, "The seismic response of a reinforced concrete bridge pier designed to step," *Earthq. Eng. Struct. Dyn.*, vol. 2, no. 4, pp. 343–358, 1973.

[4] C.-S. Yim, A. K. Chopra, and J. Penzien, "Rocking response of rigid blocks to earthquakes," *Earthq. Eng. Struct. Dyn.*, vol. 8, no. 6, pp. 565–587, 1980.

[5] I. N. Psycharis and P. C. Jennings, "Rocking of slender rigid bodies allowed to uplift," *Earthq. Eng. Struct. Dyn.*, vol. 11, no. 1, pp. 57–76, Jan. 1983.

[6] R. D. Sharpe and R. I. Skinner, "The seismic design of an industrial chimney with rocking base," *Bull. New Zeal. Natl. Soc. Earthq. Eng.*, vol. 16, no. 2, pp. 98–106, 1983.

[7] A. K. Chopra and S. C. S. Yim, "Simplified Earthquake Analysis of Structures with Foundation Uplift," *J. Struct. Eng.*, vol. 111, no. 4, pp. 906–930, Apr. 1985.

[8] S. J. Hogan, "The many steady state responses of a rigid block under harmonic forcing," *Earthq. Eng. Struct. Dyn.*, vol. 19, no. 7, pp. 1057–1071, Oct. 1990.

[9] I. N. Psycharis, "Effect of Base Uplift on Dynamic Response of SDOF Structures," *J. Struct. Eng.*, vol. 117, no. 3, pp. 733–754, Mar. 1991.

[10] N. Makris and Y. Roussos, "Rocking response and overturning of equipment under horizontal pulse-type motion," *Rept. No. PEER Report-98/05*, 1998.

[11] J. Zhang and N. Makris, "Rocking Response of Free-Standing Blocks under Cycloidal Pulses," *J. Eng. Mech.*, vol. 127, no. 5, pp. 473–483, May 2001.

[12] N. Makris and D. Konstantinidis, "The rocking spectrum and the limitations of practical design methodologies," *Earthq. Eng. Struct. Dyn.*, vol. 32, no. 2, pp. 265–289, Feb. 2003.

[13] G. Oliveto, I. Caliò, and A. Greco, "Large displacement behaviour of a structural model with foundation uplift under impulsive and earthquake excitations," *Earthq. Eng. Struct. Dyn.*, vol. 32, no. 3, pp. 369–393, Mar. 2003.

[14] F. Prieto, P. B. Lourenço, and C. S. Oliveira, "Impulsive Dirac-delta forces in the rocking motion," *Earthq. Eng. Struct. Dyn.*, vol. 33, no. 7, pp. 839–857, Jun. 2004.

[15] D. Konstantinidis and N. Makris, "Seismic response analysis of multidrum classical columns," *Earthq. Eng. Struct. Dyn.*, vol. 34, no. 10, pp. 1243–1270, Aug. 2005.

[16] M. Apostolou, G. Gazetas, and E. Garini, "Seismic response of slender rigid structures with foundation uplifting," *Soil Dyn. Earthq. Eng.*, vol. 27, no. 7, pp. 642–654, Jul. 2007.

[17] D. Konstantinidis and N. Makris, "The dynamics of a rocking block in three dimensions," *8th Hell. Soc. Theor. Appl. Mech. Int. Congr. Mech. Patras, Greece*, no. September 2015, pp. 12 – 14, 2007.

[18] F. Peña, F. Prieto, P. B. Lourenço, A. Campos Costa, and J. V. Lemos, "On the dynam-

ics of rocking motion of single rigid-block structures," *Earthq. Eng. Struct. Dyn.*, vol. 36, no. 15, pp. 2383–2399, Dec. 2007.

[19] Q. T. M. Ma and M. H. Khan, "Free vibration tests of a scale model of the South Rangitikei Railway Bridge," in *New Zealand Society for Earthquake Engineering Annual Conference*, 2008.

[20] A. Contento and A. Di Egidio, "Investigations into the benefits of base isolation for non-symmetric rigid blocks," *Earthq. Eng. Struct. Dyn.*, vol. 38, no. 7, pp. 849–866, Jun. 2009.

[21] D. Konstantinidis and N. Makris, "Experimental and analytical studies on the response of freestanding laboratory equipment to earthquake shaking," *Earthq. Eng. Struct. Dyn.*, vol. 38, no. 6, pp. 827–848, May 2009.

[22] L. Papaloizou and P. Komodromos, "Planar investigation of the seismic response of ancient columns and colonnades with epistyles using a custom-made software," *Soil Dyn. Earthq. Eng.*, vol. 29, no. 11–12, pp. 1437–1454, Nov. 2009.

[23] D. Konstantinidis and N. Makris, "Experimental and analytical studies on the response of 1/4-scale models of freestanding laboratory equipment subjected to strong earthquake shaking," *Bull. Earthq. Eng.*, vol. 8, no. 6, pp. 1457–1477, Dec. 2010.

[24] Q. T. M. Ma, "The mechanics of rocking structures subjected to ground motion," 2010.

[25] M. F. Vassiliou, "Analytical investigation of the dynamic response of a pair of columns capped with a rigid beam and of the effect of seismic isolation on rocking structures," Doctoral dissertation, Dept. of Civil Engineering, Univ. of Patras, Greece (in Greek), 2010.

[26] M. A. ElGawady, Q. Ma, J. W. Butterworth, and J. Ingham, "Effects of interface material on the performance of free rocking blocks," *Earthq. Eng. Struct. Dyn.*, vol. 40, no. 4, pp. 375–392, Apr. 2011.

[27] S. Acikgoz and M. J. DeJong, "The interaction of elasticity and rocking in flexible structures allowed to uplift," *Earthq. Eng. Struct. Dyn.*, vol. 41, no. 11, pp. 1–18, Mar. 2012.

[28] E. G. Dimitrakopoulos and M. J. DeJong, "Revisiting the rocking block: closed-form solutions and similarity laws," *Proc. R. Soc. A Math. Phys. Eng. Sci.*, vol. 468, no. 2144, pp. 2294–2318, Aug. 2012.

[29] E. G. Dimitrakopoulos and M. J. DeJong, "Overturning of Retrofitted Rocking Structures under Pulse-Type Excitations," *J. Eng. Mech.*, vol. 138, no. 8, pp. 963–972, Aug. 2012.

[30] F. Gelagoti, R. Kourkoulis, I. Anastasopoulos, and G. Gazetas, "Rocking isolation of low-rise frame structures founded on isolated footings," *Earthq. Eng. Struct. Dyn.*, vol. 41, no. 7, pp. 1177–1197, Jun. 2012.

[31] R. Kourkoulis, I. Anastasopoulos, F. Gelagoti, and P. Kokkali, "Dimensional Analysis of SDOF Systems Rocking on Inelastic Soil," *J. Earthq. Eng.*, vol. 16, no. 7, pp. 995–1022, Oct. 2012.

[32] N. Makris and M. F. Vassiliou, "Sizing the slenderness of free-standing rocking columns to withstand earthquake shaking," *Arch. Appl. Mech.*, vol. 82, no. 10–11, pp. 1497–1511, Oct. 2012.

[33] M. F. Vassiliou and N. Makris, "Analysis of the rocking response of rigid blocks standing free on a seismically isolated base," *Earthq. Eng. Struct. Dyn.*, vol. 41, no. 2, pp. 177–196, Feb. 2012.

[34] D. Zulli, A. Contento, and A. Di Egidio, "3D model of rigid block with a rectangular base subject to pulse-type excitation," *Int. J. Non. Linear. Mech.*, vol. 47, no. 6, pp. 679–687, Jul. 2012.

[35] S. Acikgoz and M. J. DeJong, "Analytical and experimental observations on vibration modes of flexible rocking structures," in *Society for earthquake and civil engineering dynamics (SECED) young engineer's conference, Newcastle, UK*, 2013.

[36] S. Acikgoz and M. J. DeJong, "Linearization and Modal Analysis of Flexible Rocking Structures," in *NZSEE 2013*, 2013, pp. 1–8.

[37] G. Antonellis and M. Panagiotou, "Seismic Response of Bridges with Rocking Foundations Compared to Fixed-Base Bridges at a Near-Fault Site," *J. Bridg. Eng.*, vol. 19, no. 5, p. 04014007, May 2014.

[38] E. G. Dimitrakopoulos and M. J. De Jong, "Seismic overturning of rocking structures with external viscous dampers," in *Computational methods in earthquake engineering*, Springer, 2013, pp. 243–258.

[39] N. Makris and M. F. Vassiliou, "Planar rocking response and stability analysis of an array of free-standing columns capped with a freely supported rigid beam," *Earthq. Eng. Struct. Dyn.*, vol. 42, no. 3, pp. 431–449, Mar. 2013.

[40] A. Sextos, S. Nalmpantis, P. Faraonis, D. Skiada, and K. Stylianidis, "Probabilistic Seismic Hazard Assessment Through Geometrically Non-Linear Back-Analysis of Byzantine and Roman Monuments," in *10th HSTAM International Congress on Mechanics. Chania, Greece*, 2013.

[41] M. F. Vassiliou, K. R. Mackie, and B. Stojadinović, "Rocking Response of Slender, Flexible Columns under Pulse Excitation," in *COMPDYN 2013*, 2013, no. June.

[42] H. Zhang, B. Brogliato, and C. Liu, "Dynamics of planar rocking-blocks with Coulomb friction and unilateral constraints: comparisons between experimental and numerical data," *Multibody Syst. Dyn.*, vol. 32, no. 1, pp. 1–25, Jun. 2014.

[43] S. Acikgoz and M. J. DeJong, "The rocking response of large flexible structures to earthquakes," *Bull. Earthq. Eng.*, vol. 12, no. 2, pp. 875–908, Apr. 2014.

[44] M. J. DeJong and E. G. Dimitrakopoulos, "Dynamically equivalent rocking structures," *Earthq. Eng. Struct. Dyn.*, vol. 43, no. 10, pp. 1543–1563, Aug. 2014.

[45] V. Drosos and I. Anastasopoulos, "Shaking table testing of multidrum columns and portals," *Earthq. Eng. Struct. Dyn.*, vol. 43, no. 11, pp. 1703–1723, Sep. 2014.

[46] N. Makris, "The Role of the Rotational Inertia on the Seismic Resistance of Free-Standing Rocking Columns and Articulated Frames," *Bull. Seismol. Soc. Am.*, vol. 104, no. 5, pp. 2226–2239, Oct. 2014.

[47] N. Makris and M. F. Vassiliou, "Are Some Top-Heavy Structures More Stable?," *J. Struct. Eng.*, vol. 140, no. 5, p. 06014001, May 2014.

[48] N. Makris and M. F. Vassiliou, "Dynamics of the Rocking Frame with Vertical Restrainers," *J. Struct. Eng.*, vol. 141, no. 10, p. 04014245, Oct. 2015.

[49] R. E. Truniger, M. F. Vassiliou, and B. Stojadinović, "Experimental Study on the Interaction between Elasticity and Rocking," in *10th U.S. National Conference on Earthquake Engineering*, 2014.

[50] M. F. Vassiliou, K. R. Mackie, and B. Stojadinović, "Dynamic response analysis of solitary flexible rocking bodies: modeling and behavior under pulse-like ground excitation," *Earthq. Eng. Struct. Dyn.*, vol. 43, no. 10, pp. 1463–1481, Aug. 2014.

[51] E. G. Dimitrakopoulos and A. I. Giouvanidis, "Seismic Response Analysis of the Planar Rocking Frame," *J. Eng. Mech.*, vol. 141, no. 7, p. 04015003, Jul. 2015.

[52] E. G. Dimitrakopoulos and T. S. Paraskeva, "Dimensionless fragility curves for rocking response to near-fault excitations," *Earthq. Eng. Struct. Dyn.*, vol. 44, no. 12, pp. 2015–2033, Sep. 2015.

[53] N. Makris, "A half-century of rocking isolation," *Earthquakes Struct.*, vol. 7, no. 6, pp. 1187–1221, Dec. 2014.

[54] N. Makris and M. F. Vassiliou, "The dynamics of the rocking frame," in *Seismic Assessment, Behavior and Retrofit of Heritage Buildings and Monuments*, Springer, 2015, pp. 37–59.

[55] N. Makris and M. F. Vassiliou, "Seismic Response and Stability of the Rocking Frame," in *Computational Methods, Seismic Protection, Hybrid Testing and Resilience in Earthquake Engineering*, Springer, 2015, pp. 249–273.

[56] R. E. Truniger, M. F. Vassiliou, and B. Stojadinović, "An analytical model of a deformable cantilever structure rocking on a rigid surface: experimental validation," *Earthq. Eng. Struct. Dyn.*, vol. 44, no. 13, 2015.

[57] M. F. Vassiliou and N. Makris, "Dynamics of the Vertically Restrained Rocking Column," *J. Eng. Mech.*, vol. 141, no. 12, p. 04015049, Dec. 2015.

[58] M. F. Vassiliou, R. E. Truniger, and B. Stojadinović, "An analytical model of a deformable cantilever structure rocking on a rigid surface: development and verification," *Earthq. Eng. Struct. Dyn.*, vol. 44, no. 13, 2015.

[59] N. Makris and G. Kampas, "Size Versus Slenderness: Two Competing Parameters in the Seismic Stability of Free□Standing Rocking Columns," *Bull. Seismol. Soc. Am.*, vol. 106, no. 1, pp. 104–122, Feb. 2016.

[60] E. Bakhtiary and P. Gardoni, "Probabilistic seismic demand model and fragility estimates for rocking symmetric blocks," *Eng. Struct.*, vol. 114, pp. 25–34, 2016.

[61] J. Kelly, "Earthquake-resistant design with rubber," 1993.

[62] N. Makris and C. J. Black, "Dimensional Analysis of Bilinear Oscillators under Pulse-Type Excitations," *J. Eng. Mech.*, vol. 130, no. 9, pp. 1019–1031, Sep. 2004.

[63] G. W. Housner, "The Behavior of inverted Pendulum Structures during Earthquakes," *Bull. Seismol. Soc. Am.*, vol. 53, no. 2, pp. 403–417, 1963.

[64] N. Ricker, "Further developments in the wavelet theory of seismogram structure," *Bull. Seismol. Soc. Am.*, vol. 33, no. 3, pp. 197–228, 1943.

[65] M. F. Vassiliou and N. Makris, "Estimating time scales and length scales in pulselike earthquake acceleration records with wavelet analysis," *Bull. Seismol. Soc. Am.*, vol. 101, no. 2, pp. 596–618, 2011.

ECCOMAS Congress 2016
VII European Congress on Computational Methods in Applied Sciences and Engineering
M. Papadrakakis, V. Papadopoulos, G. Stefanou, V. Plevris (eds.)
Crete Island, Greece, 5–10 June 2016

SMOOTH-ROCKING OSCILLATOR UNDER NATURAL ACCELEROGRAMS

Blerta Lipo[1], **Gianmarco de Felice**[2]

[1] University Roma Tre
e-mail: blerta.lipo@uniroma3.it

[2] University Roma Tre
e-mail: gianmarco.defelice@uniroma3.it

Keywords: Rocking, masonry, seismic analyses.

Abstract. *Following the work by Psycharis [1], in this paper we study the dynamic behavior of a rocking block resting on an elastic Winkler-type foundation for the out-of-plane seismic assessment of masonry walls. The equations of motion are derived and implemented for the simple smooth-rocking block and the calibration of the Winkler-type foundation stiffness is carried out according to the experimental results available in the literature. The dynamic response under natural seismic records is evaluated and the effect of the stiffness on the overall response is analyzed for different natural accelerograms. Both demand and capacity are calculated with reference to the kinetic and potential energies of the system and different intensity measures are considered with the aim of identifying the most representative one for the rocking motion. Finally, a comparison between non-linear time history analyses and a possible energy-based approach is discussed.*

1 INTRODUCTION

The out-of-plane rocking of masonry walls is the most recurrent mechanism triggered by earthquake shocks in historical constructions. This is why, increasing interest is shown in the study of this type of mechanism for the purpose of predicting existing buildings responses during a seismic event. Even though this behavior is complicated to capture, it is seen that could be well represented by means of a single degree of freedom oscillator. This simple approach has been often preferred to more complex models, which, while having greater chance to better grasp the response, may present inherent difficulty in the choice of inputs parameters.
The first major study on the behavior of slender structures subjected to rocking motion was carried out by Housner [2] in the well known “The behavior of inverted pendulum structures

during earthquakes". He described the rocking motion with a model that included a linear force-displacement relation for the block and damping concentrated at impacts. Thanks to this simple but powerful approach, which proved able to reproduce the main feature of rocking behavior, Housner was the first to point up that a gravity structure can exhibit significant capacity towards overturning by tilting/rocking. Recently it has been demonstrated that the same model may be extended also to study the response of a wider set of mechanisms developed by masonry constructions (Mauro et al. [3]). After Housner fundamental study, many other authors have defined different force-displacement relationships for describing the motion of the block from the triggering of the mechanism until the out-of-plane collapse. In 2002 Doherty et al. [4] presented a trilinear curve used to reproduce the nonlinear force–displacement relationship obtained experimentally for unreinforced brick masonry walls. In Shawa et al. [5], starting from existing rocking models, a new three-branch model is formulated which takes into account the asymmetry resulting from the restraint provided by transverse walls and the out-of-plumb of the block. Ferreira et al. [6] proposed a simplified analytical approach based on a linearized four-branch model used to characterize the response of stone masonry s*acco* walls in terms of overturning moment-rotation relationship. The models adopted so far in literature proved able to reproduce the rocking of masonry blocks tested in laboratory. Nevertheless, their main drawback depends on the fact that, in order to increase the accuracy, the number of parameters is increased and that these parameters may lack a physical meaning.

In this paper, a smooth single degree of freedom model is presented for reproducing the rocking behavior of masonry walls. With respect to the Housner model, only one parameter is added which consists in the stiffness of the foundation represented with a set of unilateral springs.

2 GENERAL FORMULATION OF THE PROBLEM

As mentioned before, the most known rocking block in literature is the one developed by Housner [2] that can only oscillate alternatively around the two pivot points O and O' (Figure 1, a). Therefore it is assumed that the static friction coefficient between the block and its base is high enough for sliding to be negligible, verified hypothesis for adequately slender objects.

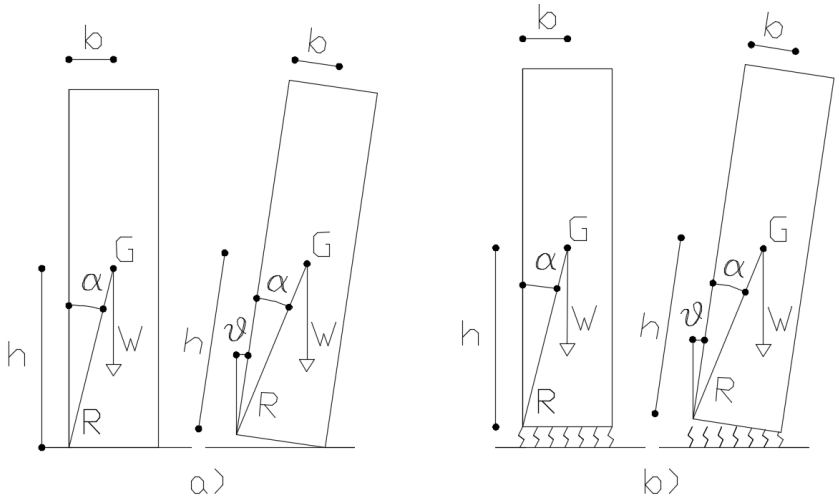

Figure 1. Comparison between the rigid model (a) and the smooth-rocking model (b).

This inverted pendulum has only one degree of freedom, the tilting angle θ from the vertical position and its motion under a horizontal ground acceleration $\ddot{u}_g$ can be described by equation 1. The significant parameters are the moment of inertia of the block I_0 about the point 0, the restoring moment M_R, that depends on wall geometry and self-weight W=g m, and the ground acceleration $\ddot{u}_g$. Symbols are depicted in Figure 1.

$$I_0\,\ddot{\theta} + \; M_R(\theta, sign(\theta)) = -m\,\ddot{u}_g R\,cos(\alpha\,sign(\theta) - \theta) \tag{1}$$

The block will initiate rocking only if the ground acceleration is greater than a threshold value depending on its slenderness α. During rocking, motion is interrupted by subsequent impacts at the pivot points with consequently dissipation of energy [7]. In this paper, such phenomenon is treated as in Housner [2], by reducing the angular velocity when the block passes the resting position, as shown in eq. (2).

$$\dot{\theta}^{+} = \eta\,\dot{\theta}^{-} \tag{2}$$

where $\dot{\theta}^{+}$ and $\dot{\theta}^{-}$ are the angular velocities before and after impact, respectively. The equation of motion (1), together with the impact treatment, equation (2), have been implemented in Matlab R2015b and integrated numerically using a Runge-Kutta algorithm with integration step and tolerances sufficiently appropriate to guarantee an adequate accuracy of the solution.

2.1 The smooth-rocking moment-rotation relationship

Various experimental evidences ([4]) have shown that the actual response of masonry walls loaded out-of-plane may be far different from the rigid (bilinear) moment-rotation relationship assumed by Housner [2]. More precisely, when dealing with brick or stone masonries, a smoother response has been observed ([6]). In this paper, in order to better simulate the actual behavior of masonry walls, a smooth restoring moment-rotation is obtained by considering a rigid block resting on a Winkler-type foundation (Figure 1b). This approach makes it possible to introduce only one additional parameter with respect to those defined by Housner, precisely the stiffness k of the springs on which the wall is resting.
The equations relative to the Winkler-type foundation, derived in Shawa et al [6] for the case of one-sided rocking, are here reported for the two-sided case (eq. 3) where M_R is the restoring moment, θ_{cr} is the relative rotation corresponding to lift-off of the block, the other symbols have the same meaning as in Housner [2] (Figure 1b).

$$M_R = WR\,sin(\alpha\,sign(\theta) - \theta) - Wb\,sign(\theta) + \frac{2}{3}\,k\,b^3\theta \qquad for\ \theta \le \theta_{cr}$$

$$M_R = WR\,sin(\alpha\,sign(\theta) - \theta) - \frac{1}{6}\,k\,\theta\sqrt{\left[\frac{2\,W}{k\,\theta\,sign(\theta)}\right]^3} \qquad for\ \theta > \theta_{cr} \tag{3}$$

$$\theta_{cr} = \frac{W}{2b^2k}$$

The vertical component of the displacement is neglected during the motion of the block and the rotations instead are considered sufficiently small. In order to model the inability of the ancient mortar to sustain tensile stresses, it is assumed that the block is just resting on the springs, without any bond between them. In particular, the moment-rotation curve presents two fictitious branches corresponding to the case where the coupling of the springs is perfectly reagent ($\theta \leq \theta_{cr}$), and the case where contact is lost in one of the base edges and a limited portion only of the base section is reacting ($\theta > \theta_{cr}$).

In Figure 2 the moment-rotation relationship for a block having 2b = 0.25 m and 2h = 3 m and a specific weight of 12.06 kN/m^3 is presented, comparing the results for different values of the stiffness k. For finite values of k, a linear behavior is exhibited until $\theta \leq \theta_{cr}$, then the response suddenly curves to the maximum allowable restoring moments and then goes to an almost linear branch with negative stiffness until the ultimate rotation is reached. Noteworthy, the maximum rotation the block can bear without overturning is not reached for $\theta = \alpha$ as in the Housner [2] oscillator but it also depends on the stiffness of the springs and is derived here numerically starting from equation 3b). When the foundation springs are very stiff, the block is expected to behave as if it was rocking on a rigid foundation, therefore, for $k \rightarrow \infty$, the second branch of the restoring moment-rotation curve ($\theta > \theta cr$) tends to WR sin($\alpha - \theta$) and the first branch tends to infinity in the vertical direction.

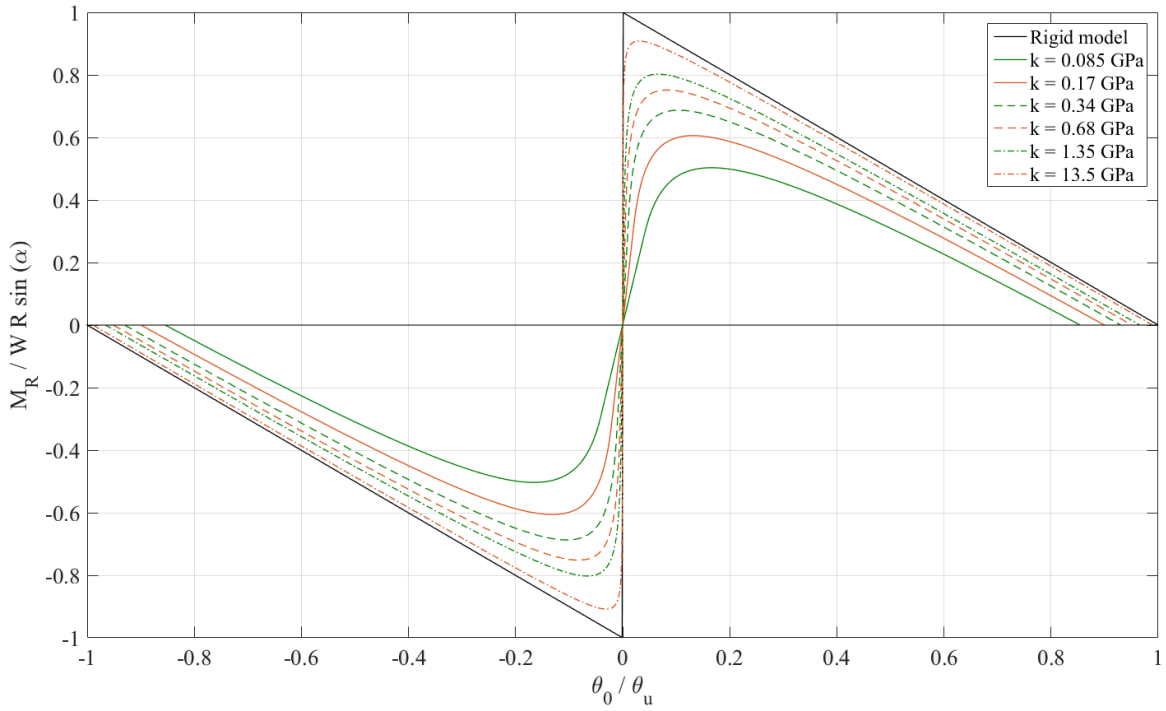

Figure 2. Moment rotation variation for different stiffness values.

It is worth underlining that the curves represented in Figure 2 by varying the values of k resemble those obtained by de Felice [8] for multi-leaf walls exhibiting failure for disaggregation because of the absence of connection throughout the thickness of the wall. Accordingly, the introduction of the parameter k would make it possible to fictitiously account for any losses of monoliticity of the wall by reducing its restoring moment and ultimate displacement capacity.

The free oscillatory motion of a block occurs with a period which, as known, is a function of the maximum angle of rotation that is reached during the motion. In Figure 3, there are shown the values of the period of a block, obtained numerically according to the maximum rotation θ_u referring to different value of stiffness k. For initial rotation $\theta_0 < \theta_{cr}$ the period T is constant and corresponds to oscillations without partialization of the base joints. When approaching the overturning rotation periods tends to infinity.

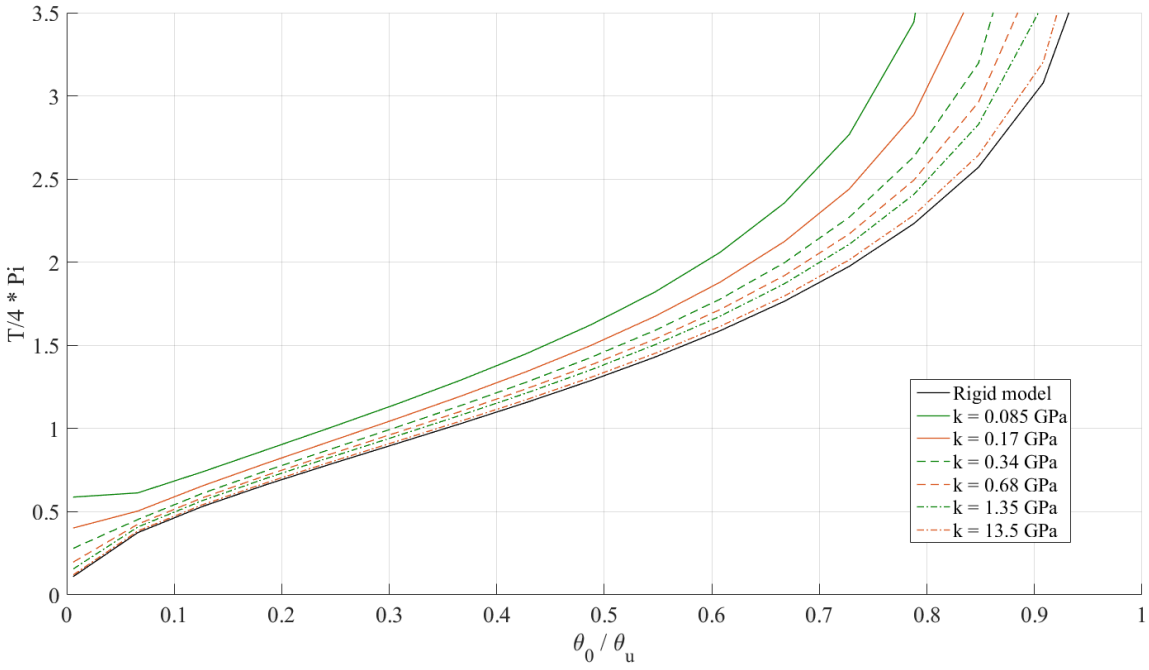

Figure 3. Period T of block laying in different stiffness layer rocking with amplitude θ_0.

3 CALIBRATION OF THE STIFFNESS K BASED ON EXPERIMENTAL DATA

The equations of motions (eq. 3 and eq. 2) have been implemented in Matlab R2015b and integrated using the ode solver. Different integration options have been considered in order to better evaluate the response of the block. Aiming at investigating the feasibility of the proposed approach some comparisons with experimental data are briefly reported.

3.1 Static tests

The first comparison is made with respect to the experimental results presented by Ferreira et al. [6] which have performed static tests on six full-scale (1.3m x 0.65m x 2.50 m) unreinforced regular *sacco* stone masonry specimens subjected to horizontal out-of-plane loading and three different vertical loadings N. Here are compared the results of the wall without force on the top (N = 0 kN) undergoing a uniform pressure applied by means of an airbag. Among the others setups tested, the wall selected exhibited a cracking pattern which is more in line with the assumption made in the present work, *i.e* characterized by a single crack at the base, while the other tests yielded to a bending-rocking pattern. The results reported in Figure 4, confirms that the proposed approach is able to fit reasonably well the response of a masonry wall undergoing static overturning forces. The image representing the cracking pattern is taken from [12].

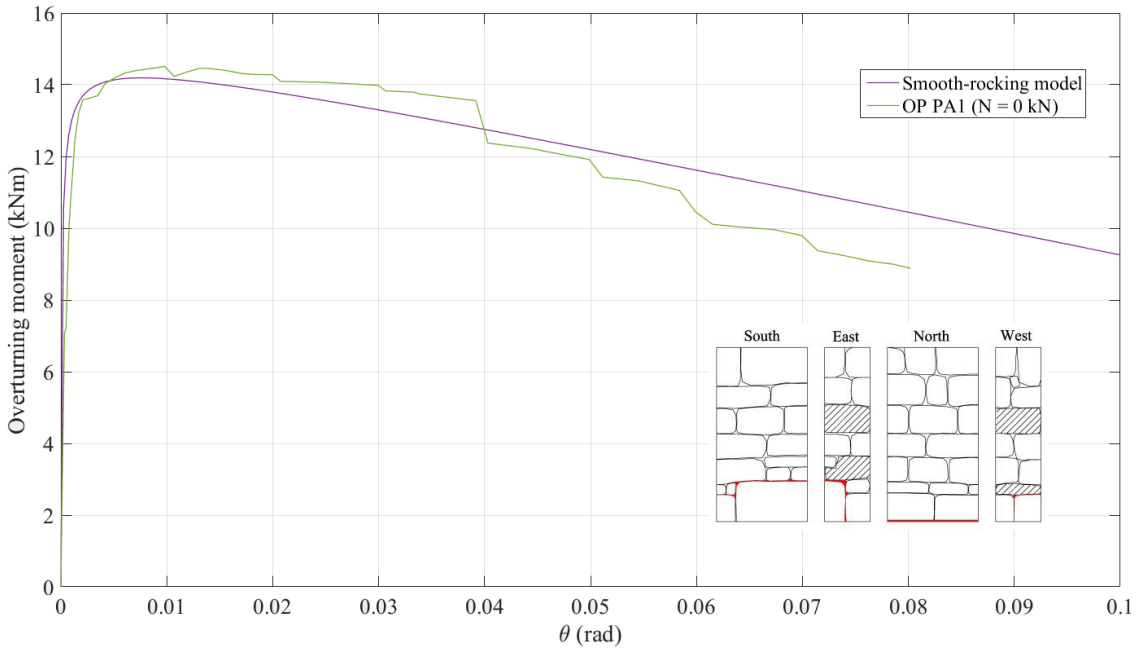

Figure 4. Overturning moment-rotation curves for airbag tests compared to the smooth model.

3.2 Dynamic tests

El Gawady et al. [9] performed some free rocking experimental tests of walls rocking on foundations made of different materials. Each block was initially tilted to an angle θ_0, held still, and then released with zero angular velocity at time t = 0, thereafter rocking back and forth freely. In order to validate the equations of motion derived for free vibrations, we are comparing here the results for three different interface material: concrete, 4-layer rubber and timber for a block with aspect ratio 5. The parameters to calibrate for fitting the curves are two: the stiffness k and the coefficient of restitution η because they both depend on the foundation material. The parameter k has been calibrated referring to the half-period – rotation graphics starting from typical stiffness values for each interface material. Then the coefficient of restitution η is calibrated in order to better fit the rest of the experimental data. The results in figure 5 demonstrate that the proposed model can fit rationally well the free vibration of blocks resting on foundation made by different materials.

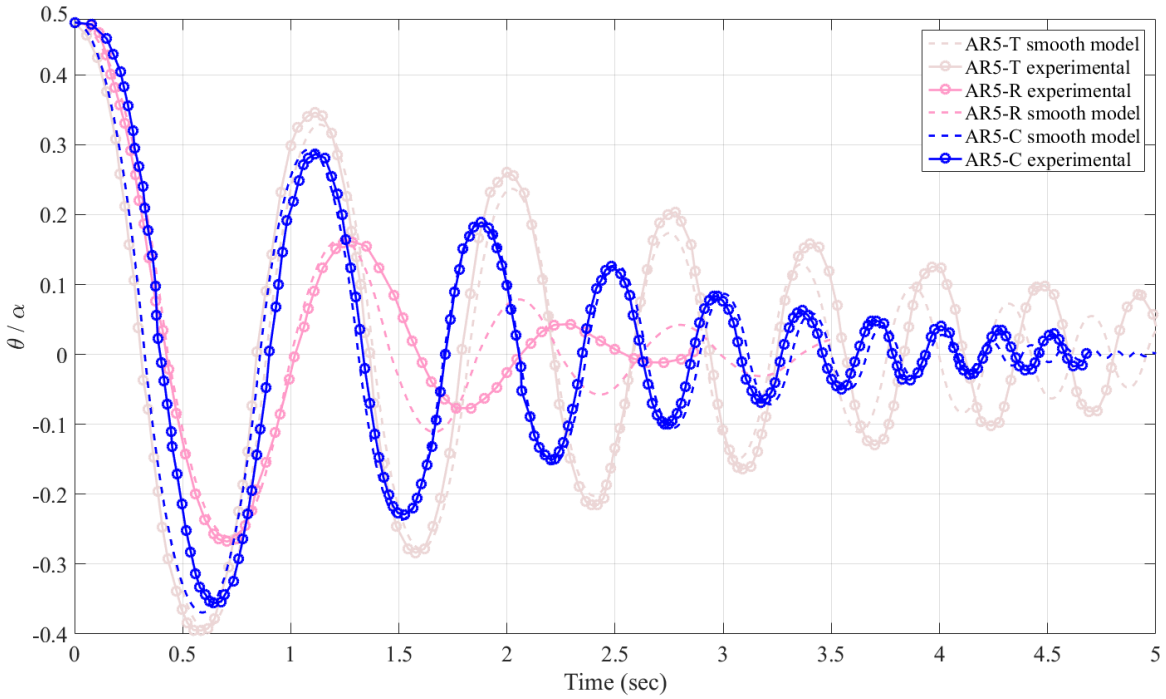

Figure 5. Comparison between experimental results and smooth model free oscillations on different interface material.

4 ASSESSMENT STRATEGIES FOR THE SMOOTH-ROCKING BLOCK

For the purpose of understanding how actual walls behave during the rocking motion, in this section we compare the non-linear time-history analyses of the smooth-rocking block with Italian code-procedures [10] and a possible energy-based approach [11]. Given the strong numerical integration sensitivity, a parametric analysis varying from time to time the accelerograms is performed. The latter varies in a purely random way by multiplying both the time-axis and the acceleration-axis with random coefficients belonging to a normal distribution having 3% coefficient of variation and unity mean [5]. Four walls, having (2b, 2h) = (0.125, 1.5), (0.20, 3.0), (0.25, 3.0), (0.375, 3.0) m, are considered. The four accelerograms of table 1 are used, whose amplitudes are scaled with ten coefficients varying from 0.2 to 2.0.

Earthquake	Year	Mw	Station	Soil type	Record	PGA (g)	PGV (m/s)
Irpinia	1980	6.9	Bagnoli Irpino	A	BagnirWE	0.167	0.377
Umbria-Marche	1997	6.0	Nocera Umbra	B	R1168EW	0.438	0.280
Irpinia	1980	6.9	Calitri	B	CalitWe	0.181	0.317
Irpinia	1980	6.9	Sturno	B	SturWE	0.313	0.700

Table 1: Accelerograms selected to perform numerical analyses.

From each dynamic analysis an energy demand/capacity ratio, ED/EC, is obtained as originally proposed by Shawa et al. [5] for the rigid model while closed form solution equations are derived for the smooth model. In particular, the capacity EC is evaluated as the area underneath the restoring-moment – rotation curve and differs from block to block (Fig.

6b). The demand ED is evaluated as the maximum potential energy recorded during the motion if $\theta < \theta_u$, or otherwise, as the sum of potential and kinetic energies evaluated at $\theta = \theta_u$. Moreover, a reduced coefficient of restitution, $\eta = 0.85$, which multiplies angular velocity before impact to give angular velocity after impact, is used, based on experimental results. Each *dot* in the following figures represents the median demand/capacity ratio out of one hundred time histories, in order to account for the scatter of the response. A total of 16 000 time history analyses have been performed.
The demand/capacity ratio of the smooth-rocking block is then compared with force-based and displacement based procedures. In particular, for the force-based assessment procedure it is checked ED/EC in comparison to PGA/($2a_0^*$) where PGA is the Peak Ground Acceleration, 2 is a behavior factor and a_0^* is defined in equation 4, where λ_0 is the static collapse load multiplier of the mechanism at rest and its value is calculated as tan(α), while $e^* = 1$ defines the participating mass and CF = 1 is a confidence factor.

$$a_0^* = \frac{\lambda_0 g}{e^* \, CF} \tag{4}$$

As far as regards the displacement-based procedure, the comparison is made between the demand/capacity ratio and the fraction between the spectral demand evaluated for the secant period $S_{De}(T_s)$ and the displacement capacity d_u^*.

Then, a possible energy based verification is considered as initially introduced by Sorrentino et al. in [11]. In this case, the verification is satisfied if the kinetic energy KE, multiplied by 2, is not larger that the area below the skeleton moment-rotation curve (E0) of the rigid block. The kinetic energy of the system is defined considering instead of the translational velocity v, the Peak Ground Velocity (PGV) of each accelerogram reported in table 1. Bearing in mind that the block motion is rotational, its kinetic energy depends on the angular velocity $\dot{\theta}$ instead of the translational one.
The first comparison is made between the smooth block and the rigid one in terms of demand/capacity ratios (Figure 6). As it can be seen from the graph, the smooth model is probably more realistic since it reacts even in the field of small oscillations differently from the rigid block that starts rocking only if it is exceeded a certain threshold. Moreover the smooth model is less conservative as it has a smaller capacity as also shown in Figure 6b) which compares the various capacity curves between the four block studied, normalized with respect to block 4.

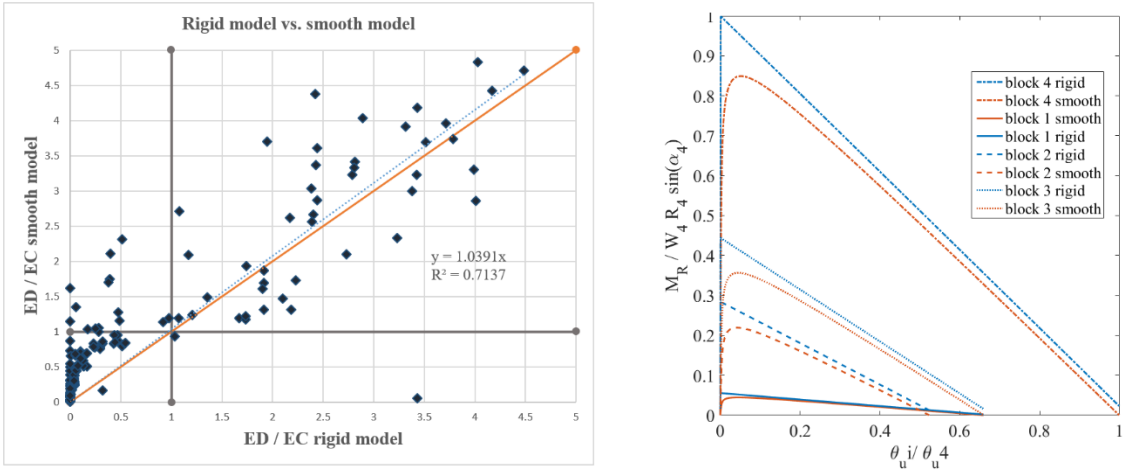

Figure 6. Comparison between the smooth and rigid model in terms of demand/capacity ratios (a) capacity curves for the four blocks considered (b).

In the following, the behavior of masonry walls subjected to out-of-plane loads predicted by the proposed model is compared to the one predicted by the force-based (fig. 7a) and displacement-based procedures (fig. 7b) reported in the Italian code [10]. The discussion of the results is made in terms of conservativeness of the procedure and scatter of the response, measured through the coefficient of correlation R^2 for a linear regression passing through the origin. When neglecting the results in which the block overturns for both numerical analysis and code-based procedures, force and displacement-based approaches seem very conservative while the energy-based approach (see fig. 8) seems less conservative also showing a slightly less scatter response. Currently there is a considerable scatter between non linear numerical analyses and simplified approaches models offset by adequate safety margins. This confirms the fact that the non-linear analysis prove valuable for a more physical representation of the phenomenon and also that the accuracy of the predictions using linear elastic spectra for rocking structures will always be very limited [13].
Anyway, further numerical analysis, considering a wider range of signals and blocks, should be done to better assess the level of reliability of the approaches proposed in the Italian code [10].

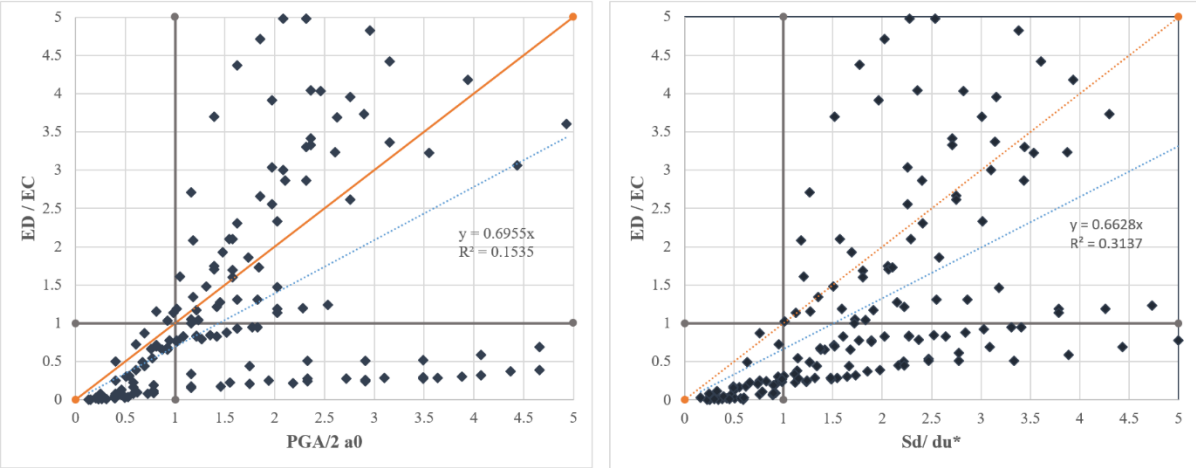

Figure 7. Comparison between the smooth model and code demand/capacity ratios (a) force-based and (b) displacement-based.

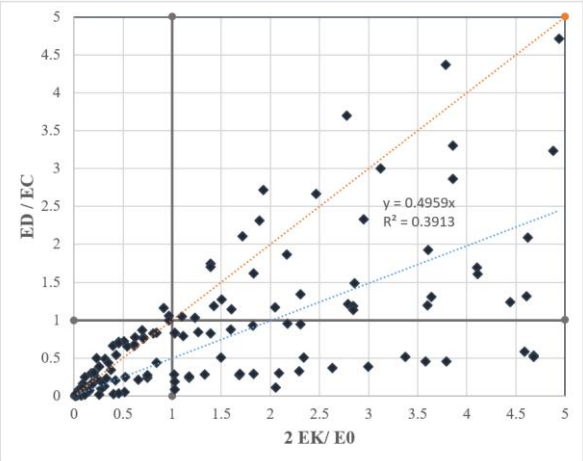

Figure 8. Comparison between the smooth model and the energy-based approach.

5 CONCLUSIONS

- In this paper, a smooth moment-rotation relationship for describing the response of a block subjected to rocking motion is presented and the most significant aspects of its behavior have been highlighted.
- The replicated experimental tests have evidenced that the model is able to capture quite well the skeleton curve of the block in static conditions and the response under free oscillations, taking into account the stiffness of the foundation.
- Preliminary results suggest that the model may be able to be adopted for simulating the behavior of walls with loss of monoliticity, but this issue should be still addressed in detail.
- Comparing the results of the parametric analysis in terms of energy based ratios between the rigid and smooth block, it seems that the latter could be a good model to describe the behavior of rocking structures given that it reacts also in the field of small oscillations. Further numerical analysis should be done to better assess the reliability of code approaches.

REFERENCES

[1] I.N. Psycharis, *Dynamic behaviour of rocking structures allowed to uplift*, California Institute of Technology, Pasadena, California, 1982.

[2] GW Housner, *The behaviour of inverted pendulum structures during earthquakes.* Bull Seismol Soc AM 1963;53(2):402-17.

[3] A. Mauro, G. de Felice, M. J. DeJong, *The relative dynamic resilience of masonry collapse mechanisms*. Engineering Structures, 85, 182-194, 2015. DOI:10.1016/j.engstruct.2014.11.021.

[4] K. Doherty, M. Griffith, N. Lam, J. Wilson, Displacement-based analysis for out-of-plane bending of seismically unreinforced masonry walls. Earthquake Engineering and Structural Dynamics 2001; 31 (4): 833-50.

[5] O.A. Shawa, G. de Felice, A. Mauro, L. Sorrentino, *Out-of-plane seismic behaviour of rocking masonry walls.* Earthquake Engineering and Structural Dynamics, 41, 949-968, 2012. DOI: 10.1002/eqe.1168.

[6] T.M. Ferreira, A. A. Costa, R. Vicente, H. Varum, *A simplified four-branch model for the analytical study of the out-of-plane performance of regular stone URM walls*. Engineering Structures, 83 (2015) 140-153.

[7] E. Dimitrakopoulos, M.J. DeJong, *Revisiting the rocking block: closed-form solutions and similarity laws*. Proc R Soc A 2012:468:2294-318.

[8] G. de Felice, *Out-of-plane seismic capacity of masonry depending on wall section morphology*. Int J Architect Herit 2011; 5 (4-5):466-82.

[9] M.A. ElGawady, Ma Quincy, J.W. Butterworth, J. Ingham, *Effects of interface material on the performance of free rocking block*. Earthquake Engineering and Structural Dynamics 2011; 40(4):375-392.

[10] Consiglio Superiore dei Lavori Pubblici. *Circolare 02 febbraio 2009 n.617 Istruzioni per l'applicazione delle "Nuove norme tecniche per le costruzioni" di cui al DM 14 gennaio 2008.* Gazzetta Ufficiale della Repubblica Italiana n.47, Supplemento Ordinario n.27, C8.A.4. Roma 2009; (in Italian).

[11] L. Sorrentino, D. DAyala, G. de Felice, M. Griffith, S. Lagomarsino, G. Magenes, *Review of out-of-plane seismic assessment techniques applied to existing masonry building.* International Journal of Architectural Heritage, submitted 2015.

[12] A. Costa, A. Arede, AA. Costa, TM Ferreira, A Gomes, H Varum. *Experimental study of the out-of-plane behaviour of unreinforced sacco stone mansonry walls: Comparative analysis of two different test setups.* In: 9th International masonry conference – 9IMC, Paper ID: 1467, 7-9 July, Guimaraes, Portugal;2014.

[13] N. Makris, D. Konstantinidis. *The rocking spectrum and the limitations of practical design methodologies.* Earthquake Engineering and Structural Dynamics 2003; 32(2):265-89.

ECCOMAS Congress 2016
VII European Congress on Computational Methods in Applied Sciences and Engineering
M. Papadrakakis, V. Papadopoulos, G. Stefanou, V. Plevris (eds.)
Crete Island, Greece, 5–10 June 2016

EXPERIMENTAL INVESTIGATION OF THE SEISMIC RESPONSE OF A COLUMN ROCKING AND ROLLING ON A CONCAVE BASE

Jonas A. Bachmann[1], Patrick Blöchlinger[2], Matthias Wellauer[2], Michalis F. Vassiliou, and Božidar Stojadinović

[1] Swiss Federal Institute of Technology (ETH) Zürich
Stefano-Franscini-Platz 5, 8093 Zürich, Switzerland
e-mail: bachmann@ibk.baug.ethz.ch
{patricbl, wellauem} @student.ethz.ch
{vassiliou, stojadinovic}@ibk.baug.ethz.ch

Keywords: Rocking structures, Earthquake Engineering, Experimental Testing, Uplifting Structures

Abstract. *Rocking modifies the seismic response of structures, because uplifting works as a mechanical fuse and limits the forces transmitted to the structure. However, the engineering community is in general reluctant to let a structure uplift because it can overturn, and, more important, an unanchored structure has no redundancy against this failure mode. Using a safety factor for the design of a flat rocking foundation (i.e. designing it larger than minimum required to prevent overturning) goes against the essence of the rocking seismic isolation method, as the structure would end up behaving as fixed to the ground. To protect against overturning but preserve the ability to uplift we propose to extend the flat rocking foundation using curved wedges at its ends. This paper presents the results of dynamic tests of small bodies rocking on curved foundations. The results compare relatively well with the analytical solutions, but they are shown to be very sensitive to the coefficient of restitution.*

1 INTRODUCTION

Since Housner published his seminal paper [1] on rocking of rigid blocks, a plethora of studies on uplifting structures has been published [2-60]. The remarkable property of rocking blocks is that, for a given height to base slenderness ratio, they become more stable as their size increases. There are even cases when out of two columns with the same base, the taller one survived an earthquake while the shorter one did not [60]. It has also been proven that the presence of a cap beam atop of rocking columns, like in the case of the ancient Greek and Roman temples, increases the stability of the system [12, 38, 46]. These results have led researchers to propose rocking as a seismic isolation technique, as the uplift works as a mechanical fuse and limits the forces transmitted to the structures. However, even though some rocking structures have been built in New Zealand [2, 5], the former Soviet Union and Russia [63] and Greece [64], practicing engineers are generally reluctant to apply this method. One reason for that is the lack of codes and simplified methods of analysis. However, this reluctance also stems on the inherent fear of engineers to design unanchored structures that may overturn. Engineers are used to the safety factors, where all the material, geometric, modelling and loading uncertainties are "hidden".

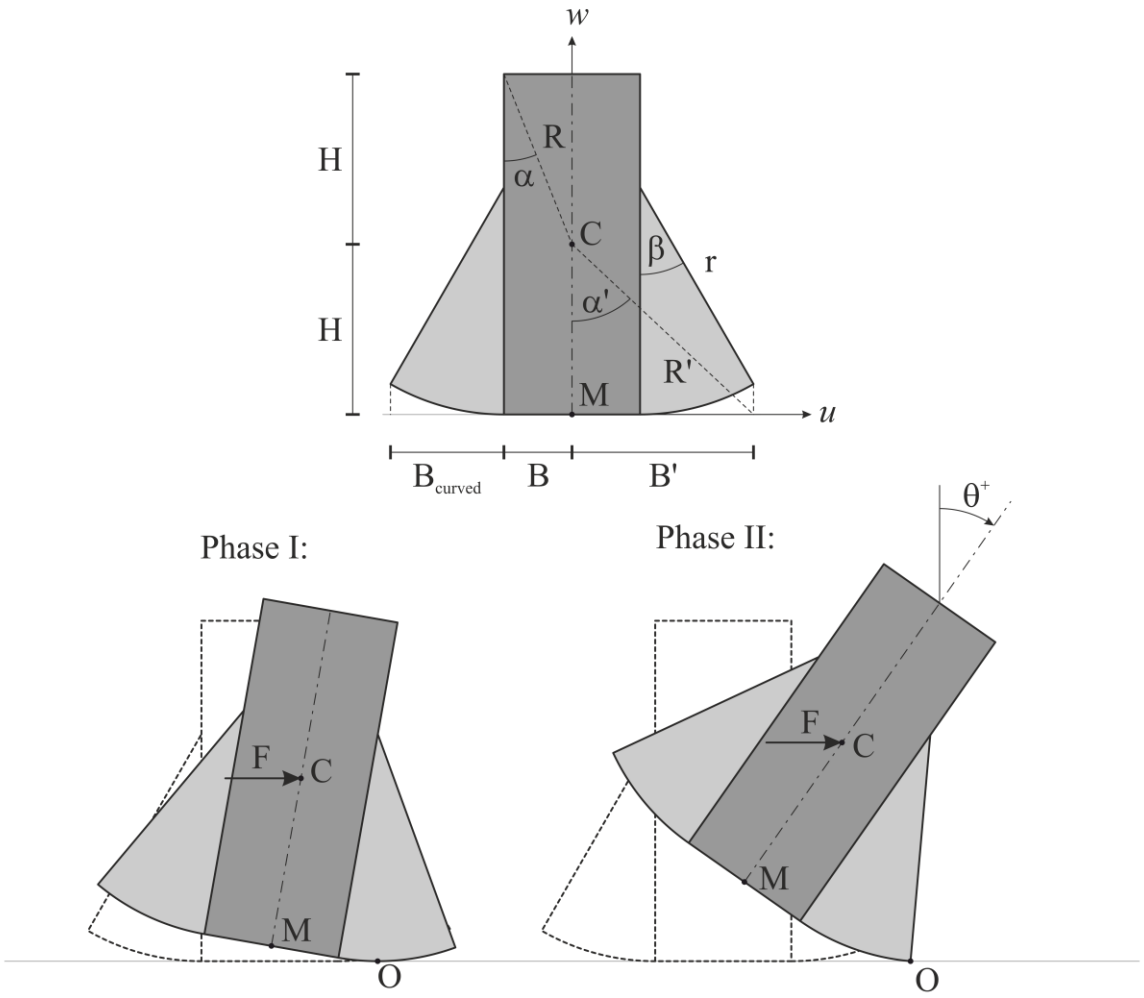

Figure 1. Top: Rigid block with curved wedges - resting position [65]
Bottom: Rigid block with curved wedges - Phase I (rolling) and Phase II (rocking)

In the case of rocking foundations, when it comes to overturning "resistance", the application of a safety factor would simply mean that the foundation should become larger. This goes against the essence of the rocking seismic isolation method, as the structure would end up behaving as fixed to the ground. To protect against overturning but preserve the ability to uplift we propose to extend the flat rocking foundation using curved wedges at its ends [65] (Figure 1). This paper presents the results of dynamic tests of small bodies rocking on curved foundations. The tests were performed in the ETH Zurich within the semester project of the second and third author. The results compare relatively well with the analytical solutions, but they are shown to be very sensitive to the coefficient of restitution.

2 REVIEW OF THE ROCKING RESPONSE OF A RIGID BLOCK.

With reference to Figure 2 and assuming that the coefficient of friction is large enough so that there is no sliding, the equation of motion of a rocking block with size $R=\sqrt{h^2+b^2}$ and slenderness α = arctan(b/h) for rotation around O and O' respectively is (Yim et al. [3], Makris and Roussos [9], Zhang and Makris [10] among others)

$$I_O\ddot{\theta}(t)+mgR\sin\left[-\alpha-\theta(t)\right]=-m\ddot{u}_g(t)R\cos\left[-\alpha-\theta(t)\right],\quad \theta(t)<0 \tag{1}$$

$$I_O\ddot{\theta}(t)+mgR\sin\left[\alpha-\theta(t)\right]=-m\ddot{u}_g(t)R\cos\left[\alpha-\theta(t)\right],\quad \theta(t)>0 \tag{2}$$

Where I_o is the moment of inertia of the block around the pivot point.

For rectangular blocks, $I_O=(4/3)mR^2$, and the above equations can be expressed in the compact form

$$\ddot{\theta}(t)=-p^2\left\{\sin\left[\alpha\,\mathrm{sgn}\left(\theta(t)\right)-\theta(t)\right]+\frac{\ddot{u}_g}{g}\cos\left[\alpha\,\mathrm{sgn}\left(\theta(t)\right)-\theta(t)\right]\right. \tag{3}$$

The oscillation frequency of a rigid block under free vibration is not constant, because it strongly depends on the vibration amplitude (Housner [1]). Nevertheless, the quantity

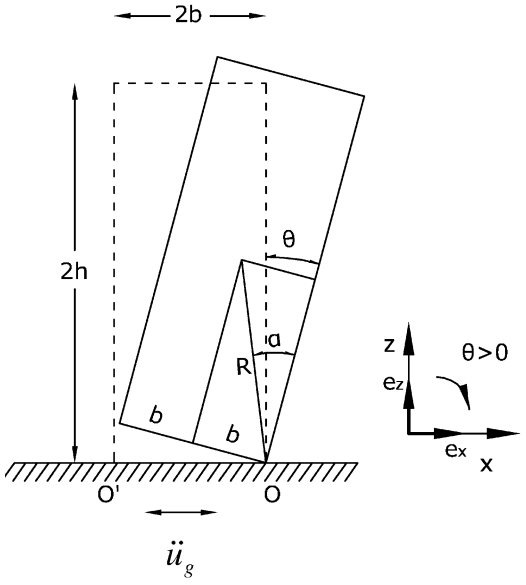

Figure 2. Geometric characteristics of the rocking body model

$p = \sqrt{\frac{3g}{4R}}$ is a measure of the dynamic characteristics of the block. For the 2.0m×0.5m block shown in Figure 2 (e.g. a modern refrigerator), p = 2.67 *rad/s*, while $p \approx 8$ *rad/s* for a typical clay masonry brick. When the angle of rotation reverses, it is assumed that the rotation continues smoothly from points *O* to *O'* and that the impact force is concentrated at the new pivot point, *O'*. The ratio of angular velocity after and before the impact is $\varepsilon = \dot{\theta}_2 / \dot{\theta}_1$. Assuming (a) that the impact is instantaneous and (b) that all the impact forces are concentrated at the new pivot point, one can apply conservation of angular momentum about the new pivot point (Housner, [1]). This gives the following coefficient of restitution

$$\varepsilon = 1 - \frac{3}{2}\sin^2 \alpha \tag{4}$$

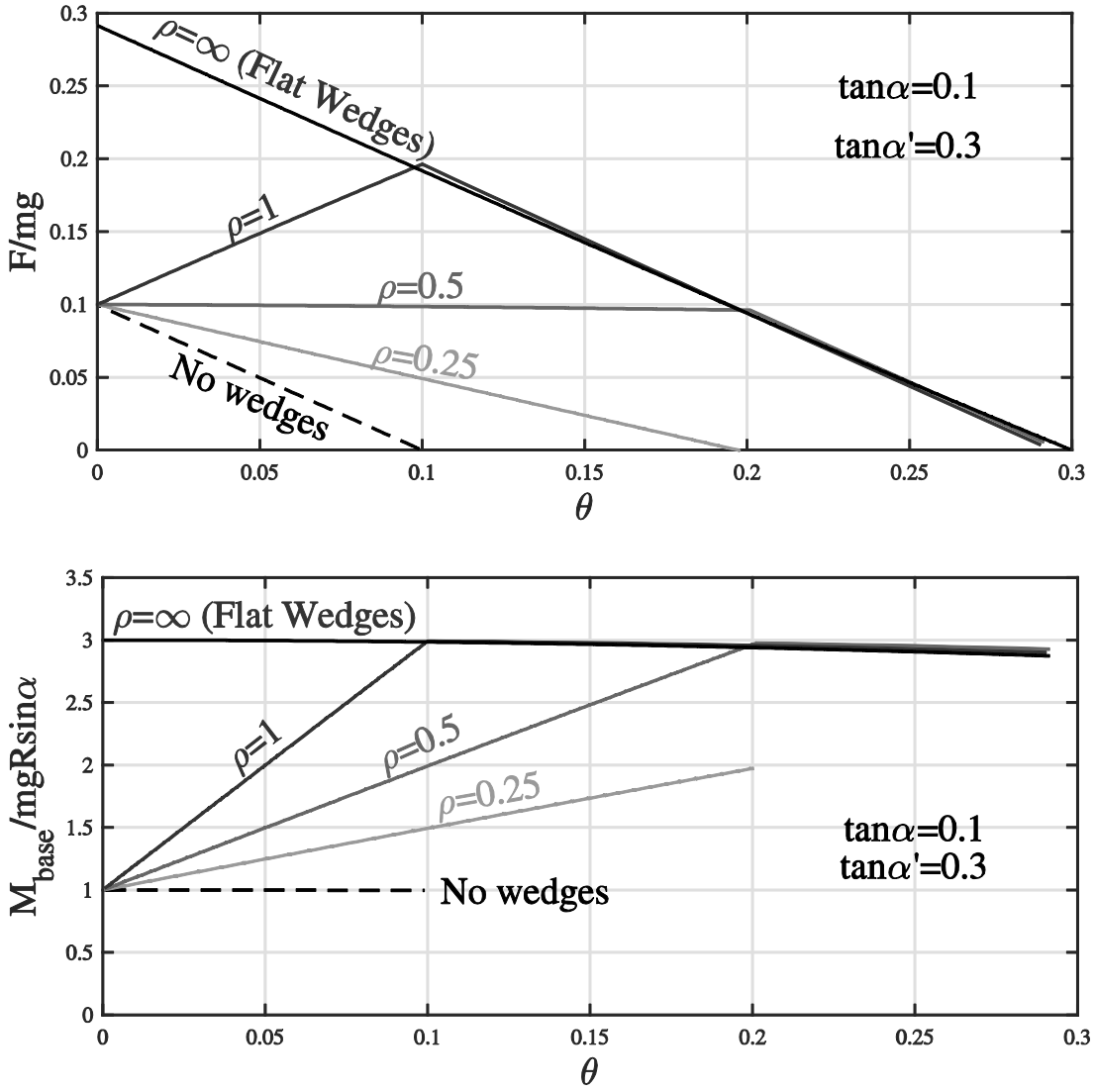

Figure 3 Response of blocks with different wedge curvature. Top: Lateral force – base rotation pushover response curves; Bottom: Base moment – base rotation pushover response curves.

Under the action of a horizontal force F is applied at the center of mass of the block a rigid block does not displace until the force reaches the uplift equilibrium value. The force – rotation pushover response curve of a rigid block is

$$F = mg\tan\left(\alpha - \theta\right) \tag{5}$$

It is plotted in Figure 3 (top – dashed line).

The base moment – rotation relationship is given by equation (6)

$$M_{base} = mgR\sin a\cos\theta \tag{6}$$

and is plotted in Figure 3 (bottom – dashed line).

It is evident that the block has negative post-uplift stiffness while the base moment stays almost constant. An extensive discussion on the significance of the negative post-uplift stiffness is offered in Makris and Vassiliou [47] and Vassiliou and Makris [58]

3 ROLLING AND ROCKING RESPONSE OF A BLOCK ON A BASE WITH CURVED ENDS

This section presents the model of a rigid block rocking and rolling on an extended curved base [65] (Figure 3) and briefly discusses its properties. An extended presentation of the above model and the numerical study of tis properties under seismic excitation is a subject of ongoing research and lies beyond the scope of this paper.

The geometric properties of the block are shown on Figure 1. The added wedges are characterized by their radius of curvature r and by their angle β. The curved wedges are assumed to be massless. When a horizontal force is applied to the center of mass of the block, the block stays initially at rest until the load reaches the critical value of $mg\tan(\alpha)$. Next, the block rolls on the curved surface (Phase I) until the tilt angle reaches the value β. Phase II follows where the block rocks, i.e. rotates around the edge of the curved base. The force deformation relationships for the different cases are given in equations (7) and (8) (for positive θ):

Phase I – Rolling:

$$F = mg\frac{\sin\left(\alpha-\theta\right)+2\rho\cos\alpha\sin\theta}{\cos\left(\alpha-\theta\right)+2\rho\cos\alpha\left(1-\cos\theta\right)}, \quad \theta<\beta \tag{7}$$

Phase II – Rocking:

$$F = mg\frac{\sin\left(\alpha-\theta\right)+2\rho\cos\alpha\left(\sin\left(\beta-\theta\right)+\sin\theta\right)}{\cos\left(\alpha-\theta\right)+2\rho\cos\alpha\left(\cos\left(\beta-\theta\right)-\cos\theta\right)}, \quad \theta>\beta \tag{8}$$

where ρ is the normalized wedge radius of curvature:

$$\rho = \frac{r}{2H} \tag{9}$$

Linearization of the above equations gives:

Phase I – Rolling:

$$F = mg\left(\alpha+\left(2\rho-1\right)\theta\right), \quad \theta<\beta \tag{10}$$

Phase II – Rocking:

$$F = mg\left(\alpha+2\rho\beta-\theta\right), \quad \theta>\beta \tag{11}$$

Therefore, the post-uplift stiffness of the rolling phase is positive, if $\rho > 0.5$, and negative, if $\rho<0.5$.

The base moment is equal to

Phase I – Rolling:

$$\frac{M_{base}}{mgR\sin\alpha} = \cos\theta + 2\rho\cot\alpha\sin\theta, \quad \theta < \beta \tag{12}$$

Phase II – Rocking:

$$\frac{M_{base}}{mgR\sin\alpha} = \cos\theta + 2\rho\cot\alpha\left(\sin\left(\beta-\theta\right)+\sin\theta\right), \quad \theta > \beta \tag{13}$$

Linearization of the above equations gives:

Phase I – Rolling:

$$M_{base} = mg\left(B + r\theta\right), \quad \theta < \beta \tag{14}$$

Phase II – Rocking:

$$M_{base} = mg\left(B + B_{curved}\right), \quad \theta > \beta \tag{15}$$

The F-θ and the M_{base}-θ pushover response curves are shown in Figure 3. The post-uplift stiffness in Phase I depends on the curvature of the curved part of the base and can lie anywhere from negative to positive, resembling the behavior of the restrained rocking column presented in [58]. Overturning can occur either in the rocking phase, or in the rolling phase (when the wedge curvature is relatively large, e.g. case ρ=0.25 in Figure 3).

The equation of motion for the Phase I is:

$$\ddot{\theta} = \frac{\left(\begin{array}{l} -\frac{3}{2}\rho\cos\alpha\dot{\theta}^2\left(\sin\left(\pm a-\theta\right)+2\rho\cos\alpha\sin\theta\right)- \\ \qquad -p^2\left(\sin\left(\pm\alpha-\theta\right)+2\rho\cos\alpha\sin\theta+\frac{\ddot{u}_g}{g}\left(\cos\left(\pm\alpha-\theta\right)+2\rho\cos\alpha\left(1-\cos\theta\right)\right)\right) \end{array}\right)}{\left(\frac{3}{4}+\frac{I_c}{\frac{4}{3}m_cR^2}+6\rho^2\cos^2\alpha\left(1-\cos\theta\right)+3\rho\cos\alpha\left(\cos\left(\pm\alpha-\theta\right)-\cos\alpha\right)\right)} \tag{16}$$

and for the phase II it is:

$$\ddot{\theta} = -p^2\left(\frac{\left(\begin{array}{l} \sin\left(\pm\alpha-\theta\right)+2\rho\cos\alpha\left(\sin\left(\pm\beta-\theta\right)+\sin\theta\right)+ \\ \qquad +\frac{\ddot{u}_g}{g}\left(\cos\left(\pm\alpha-\theta\right)+2\rho\cos\alpha\left(\cos\left(\pm\beta-\theta\right)-\cos\theta\right)\right) \end{array}\right)}{\left(\frac{3}{4}+\frac{I_c}{\frac{4}{3}m_cR^2}+6\rho^2\cos^2\alpha\left(1-\cos\beta\right)+3\rho\cos\alpha\left(\cos\left(\alpha-\beta\right)-\cos\alpha\right)\right)}\right) \tag{17}$$

where p is defined as in the case of a rectangular rocking block:

$$p = \sqrt{\frac{3g}{4R}} \tag{18}$$

ρ is the normalized radius of curvature:

$$\rho = \frac{r}{2H} \tag{19}$$

I_c is the moment of inertia of the system around its center of mass. In order to take into account the mass of the wedges, they need to be accounted for in the computation of I_c.

Following Housner, it is assumed that at each impact is instantaeous and that all the impact forces are concentrated at the new pivot point (i.e. at a distance B from the axis of symmetry), the coefficient of restitution is:

$$\varepsilon = \frac{\dot{\theta}_{post-impact}}{\dot{\theta}_{pre-impact}} = 1 - \frac{2mR^2}{mR^2 + I_c}\sin^2 a \tag{20}$$

If the wedges are assumed massless the coefficient of restutition is given by the well known Housner coefficient:

$$\varepsilon = \frac{\dot{\theta}_{post-impact}}{\dot{\theta}_{pre-impact}} = 1 - \frac{3}{2}\sin^2 a \tag{21}$$

It is evident that according to the above assumptions the coefficient of restitution, and hence the damping, are controlled only by the slederness ratio, α, and are not influenced by the wedges.

4 FREE VIBRATION TESTS OF A RIGID COLUMN WITH CURVED WEDGES

4.1 Specimens and test setup

A specimen consists of two columns (C), two link plates (L) and four changeable feet (F), all made of aluminium (Figures 4, 5 and 6). Two linked columns (instead of one) were used to avoid out-of-plane motion. The top feet were used because the specimens will be used in the future to test the response of a rocking frame on columns with curved end. For the tests presented herein, the top feet are obsolete and only result to the center of gravity being at column mid-height.

The total height of all the specimens is 2H = 500mm. The horizontal projection of the curved feet ($2 \times (B_{\text{curved}} + B)$) is identical in all specimens and equal to 150mm, giving $\tan(\alpha') = 150/500 = 0.3$. Two groups of specimens are examined: One with a flat base equal to 2B = 50mm ($\tan(\alpha) = 0.1$) and one with a flat base equal to 2B = 75mm ($\tan(\alpha) = 0.15$). In each group, 4 different curvatures of the curved part are tested: *flat*, r = {500mm, 250mm, 125mm}. For the curved specimens $\rho = r/2H = \{1, 0.5, 0.25\}$. These curvatures correspond to a positive, zero and negative post-uplift stiffness. These geometrical properties of the specimens are sketched in Figure 7 and are summarized (together with the specimen masses) in Table 1.

Figure 4. Sketch of a specimen and ist components

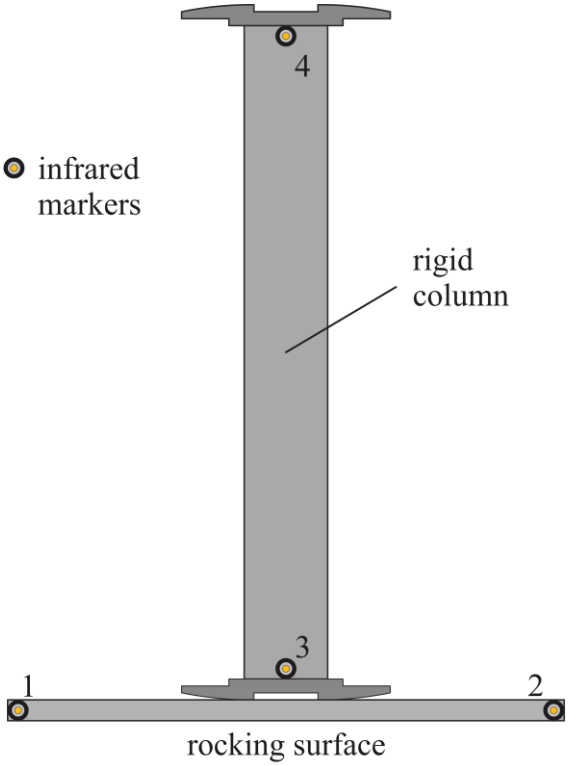

Figure 5. Position of infrared markers

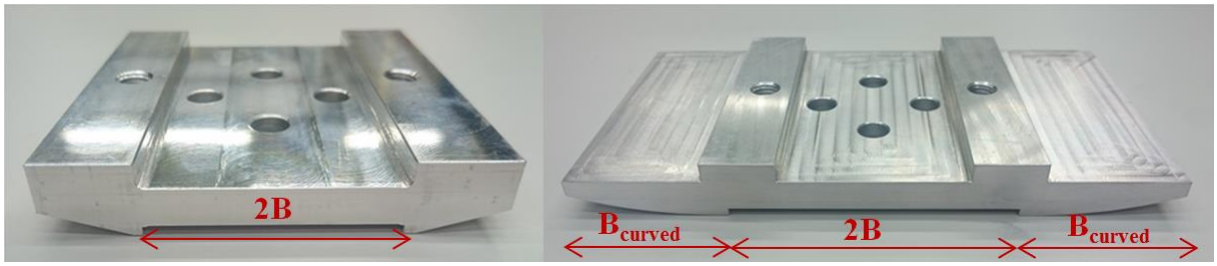

Figure 6. Flat foot (left) and curved foot (right)

	$2H$ [mm]	$2B+2B_{curved}$ [mm]	$2B$ [mm]	B_{curved} [mm]	tanα' [-]	tanα [-]	r [mm]	ρ [-]	β [-]	m_c [kg]	I_c [kg mm^2]
1	500	150	50	–	0.3	0.1	–	–	–	5.717	229‘662
2	500	150	50	50	0.3	0.1	500	1	0.100	6.331	266‘897
3	500	150	50	50	0.3	0.1	250	0.5	0.201	6.255	262‘445
4	500	150	50	50	0.3	0.1	125	0.25	0.412	6.391	270‘442
5	500	150	75	–	0.3	0.15	–	–	–	5.737	230‘171
6	500	150	75	37.5	0.3	0.15	500	1	0.075	6.328	267‘254
7	500	150	75	37.5	0.3	0.15	250	0.5	0.151	6.287	265‘393
8	500	150	75	37.5	0.3	0.15	125	0.25	0.305	5.717	261‘459

Table 1: Geometric characteristics of the specimens

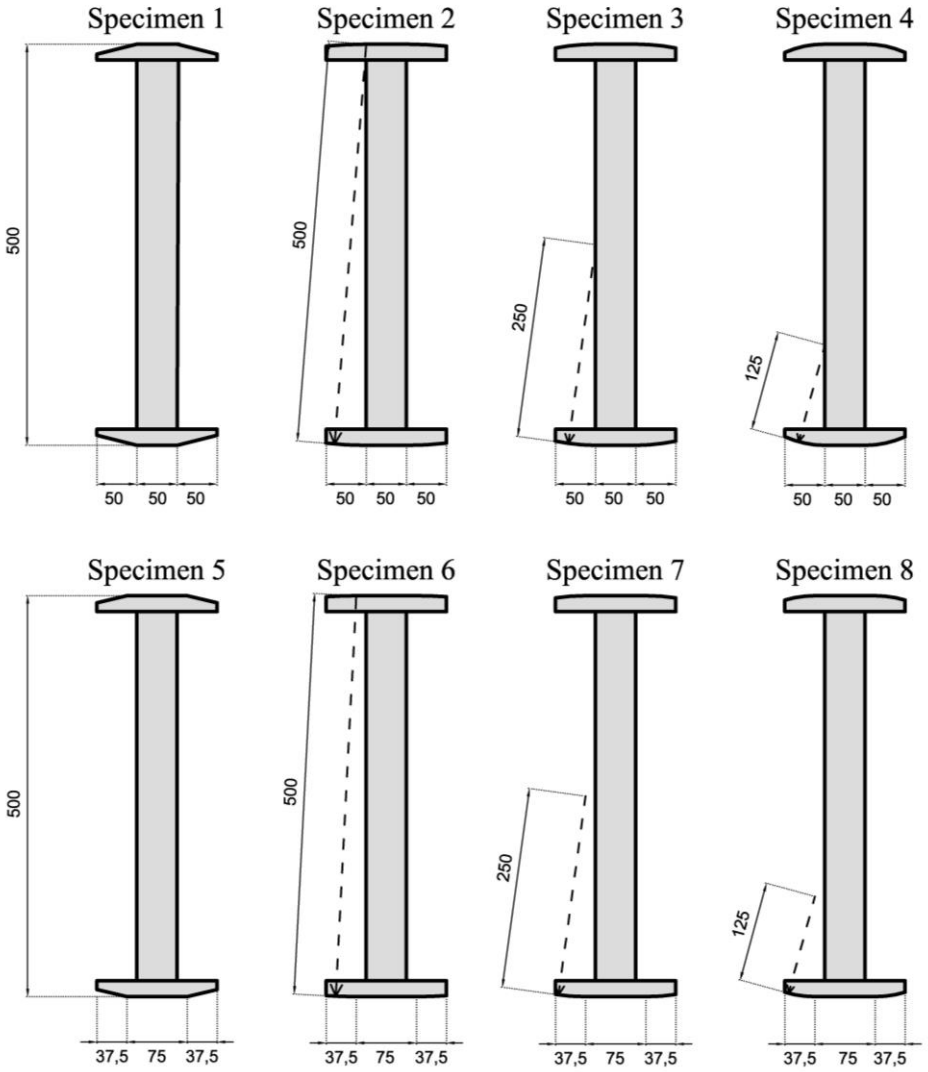

Figure 7. Geometric characteristics of the specimens.

4.2 Test Method

The specimens were tested on a flat, horizontal aluminium plate. They were tilted to an initial tilting angle and were let to move freely. The entire response time history was recorded, but in order to avoid experimental error due to potential unintended initial velocity, the time history was post processed and only the part after the maximum following the first impact was kept and later compared with the numerical solution.

4.3 Data Acquisition System

An Optotrak Certus System, manufactured by Northern Digital Inc., was used to track the position of the specimens during the tests. This system uses active infrared-emitting diodes as markers and a trinocular camera system to determine the position of the markers. In order to measure the tilt angle $\theta(t)$ and a potential slip on impact, four light-emitting diodes (LED) were used: two of them were placed on the rigid plate the structure was rocking on, a third one is positioned at the base, and the fourth one on top of the column (Figure 5). The NDI camera was able to compute the 3D angle between the LED 1-2 line and the LED 3-4 line as

well as the relative displacement between LED 1 and 3. The experimental design is shown in Figure 8.

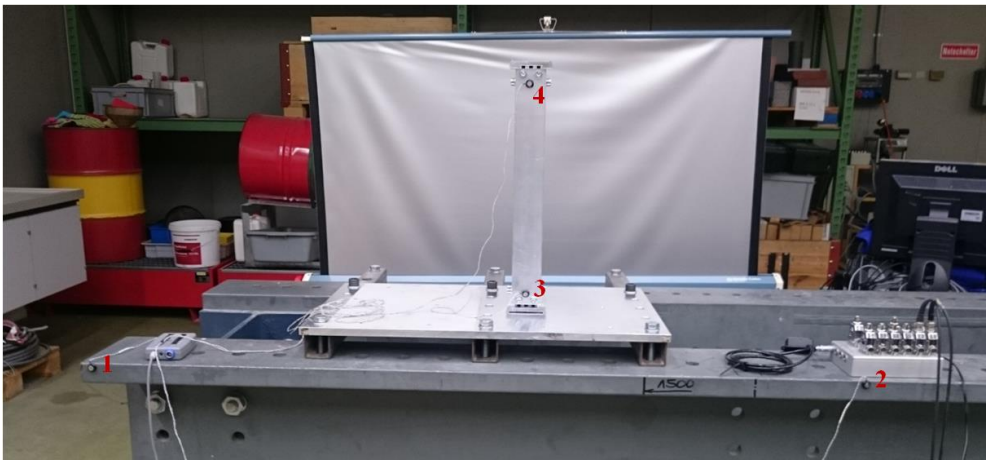

Figure 8. Experimental design

The accuracy of the system was determined by measuring the position of a marker at rest over a long period of time. In the x- and y-directions in the plane where rocking motion takes place, the accuracy was about 0.02 mm. In the z-direction, perpendicular to the plane of motion, the accuracy was about 0.10 mm. The position sampling frequency was 500 Hz.

4.4 Results and comparison with numerical solution

The objective of the experimental campaign was to validate the analytical model presented in the previous section. Each specimen was tested three times: 24 tests were performed. Figures 9-16 plot the time histories of the normalized tilt angle, θ/α. Three time histories are ploted in each plot: (a) the experiment results, (b) the numerical solution with the theoretical (Housner) coefficient of restitution, and (c) the numerical solution with an empirical coefficient of restitution. The empirical coefficient of restitution was obtained from the first 10 motion cycles assuming that energy dissipation takes place only at impact.

One can observe:

1) Hounser assumptions give a good estimate of the coefficient of restitution. For example, in Setup 1 the experimental value is ε_{emp}=0.990 while Housner assumptions would give ε_{th}=0.988. In terms of normalized energy loss per impact, the empirical coefficient would give $1-\varepsilon_{emp}^2 = 1.99\%$ while Housner would give $1-\varepsilon_{th}^2 = 2.39\%$. Considering the complicated nature of impact and damping, an accuracy of 20% is a good approximation.

2) Hounser-like coefficients of restitution slightly overestimate energy dissipation for the specimens without curved wedges (Specimens 1 and 5). In an effort to explore the source of this deviation, one has to explore Housner assumptions: (a) the impact is instantaneous, and (b) all the impact forces are concentrated on the new pivot point. Assumption (a) allows for the typical assumption that the non-impact forces (in this case the weight) can be neglected during the application of the impulse-momentum theorem. Assumption (b) leads to the Conservation of Angular Momentum Theorem (CAMT) applied about the new pivot point. Else, the CAMT should be applied about the point where the resultant of the impact forces is acting. Since

the bodies are rigid, the impact is expected to be instantaneous (and the weight is expected to be much smaller than the impact forces), at least for relatively large velocity impacts. On the other hand back-calculations for Specimen 1 show that the slight difference between the experimentally observed and the Hounser coefficient of restitution means that the point of action of the force should be 0.2mm away from the new pivot point. Missing the point of application of the resultant of the impact forces by only 0.2mm (which corresponds to 0.4% of the base) shows that Housner assumptions are valid and reasonable.

3) The addition of the curved wedges reverses the situation: Hounser assumptions underestimate the energy loss consistently (with the exception of Specimen 6). It seems that the addition of the wedges shifts the point of action of the impact forces away from the axis of symmetry, hence increasing the energy dissipation. However, apart from stating that qualitative result, it is impossible to quantify the increase.

4) In general, the coefficient of restitution decreases (implying a larger damping ratio) for low velocity impacts. This explains why a rocking block does not need infinite number of impacts to stop, as Hounser assumptions would predict [66] and is consistent with the results presented in [23]. Evidently, for smaller velocity impacts, the weight of the specimen is not negligible when compared to the impact forces and Hounser assumption (a) does not hold: The weight contributes to the impulse-momentum equation and slows down the motion.

5) Even though the coefficient of restitution is predicted relatively well, in many cases the numerical solutions diverge from the experiment data (e.g. become out of phase with the experiment data). Unlike elastic viscously-damped systems (where the period and the damping are only loosely related – $\omega_d = \omega_n \sqrt{1-\zeta^2}$) the „period“ or a rocking column (i.e. twice the time interval between two impacts) strongly depends on damping. This is attributed to the dependence of the period on the amplitude of vibration (hence on the coefficient of restitution). The above observation explains the difficulties in predicting the seismic response of a rigid block to a specific time history [56] and urges for a stochastic treatment of the rocking problem. It is evident that if deviations of 0.2mm in the prediction of the location of the impact point lead to different time history results, an error or 0.4% of the flat part of the foundation, then the deterministic treatment of the rocking problem is impossible.

5 CONCLUSIONS

Curved wedges are added to the flat base of a rocking rigid column in order to increase its overturning stability without significantly increasing the base moment. The equations of motion were derived and validated against free-vibration tests. It is shown that the theoretical values for the coefficient of restitution are numerically close to the experimentally obtained values. However, the response of the block is so sensitive to the exact coefficient of restitution value that a deterministic calculation of the response to a ground motion becomes practically impossible.

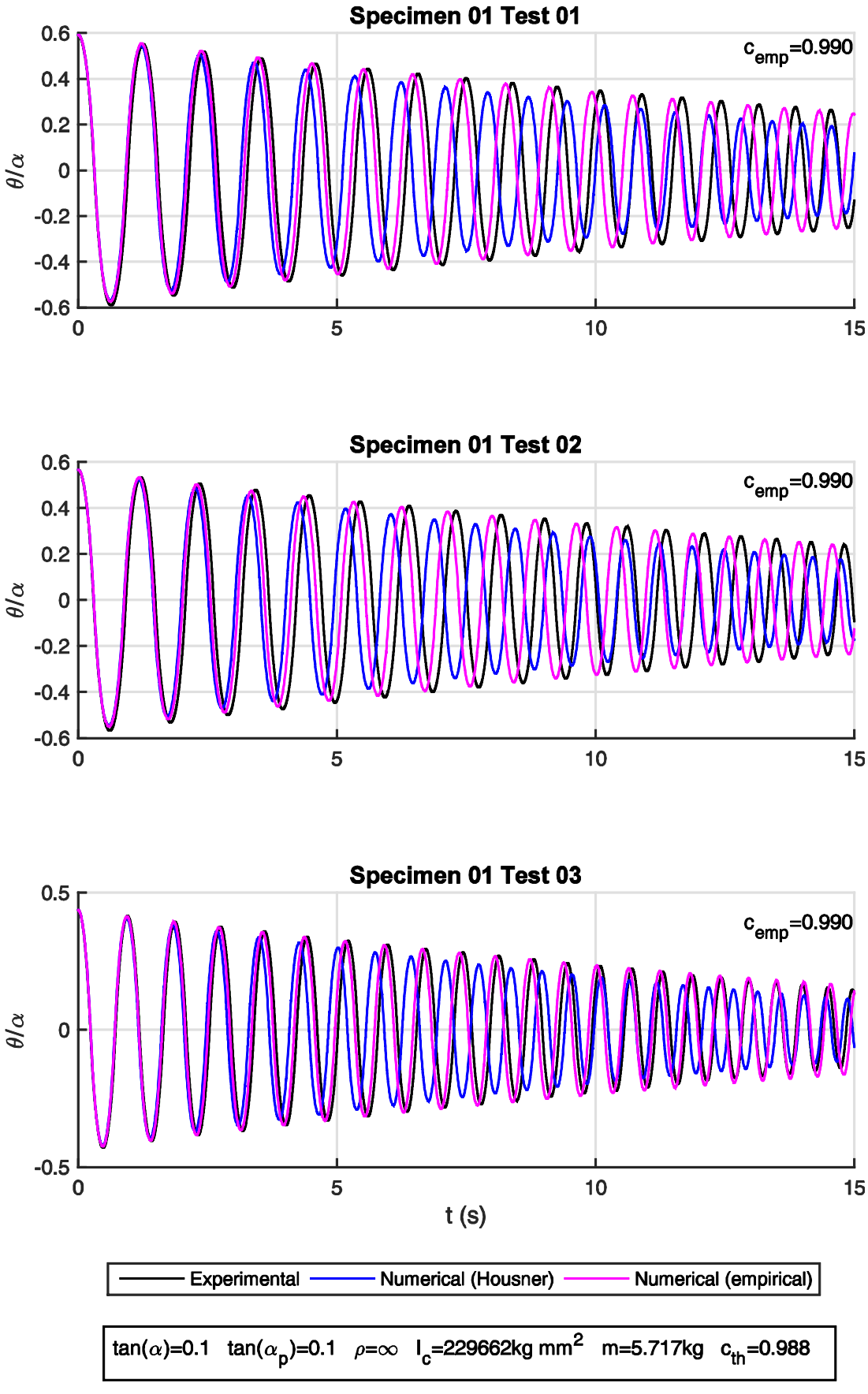

Figure 9. Normalized tilt angle, θ/α, time history for Specimen 1

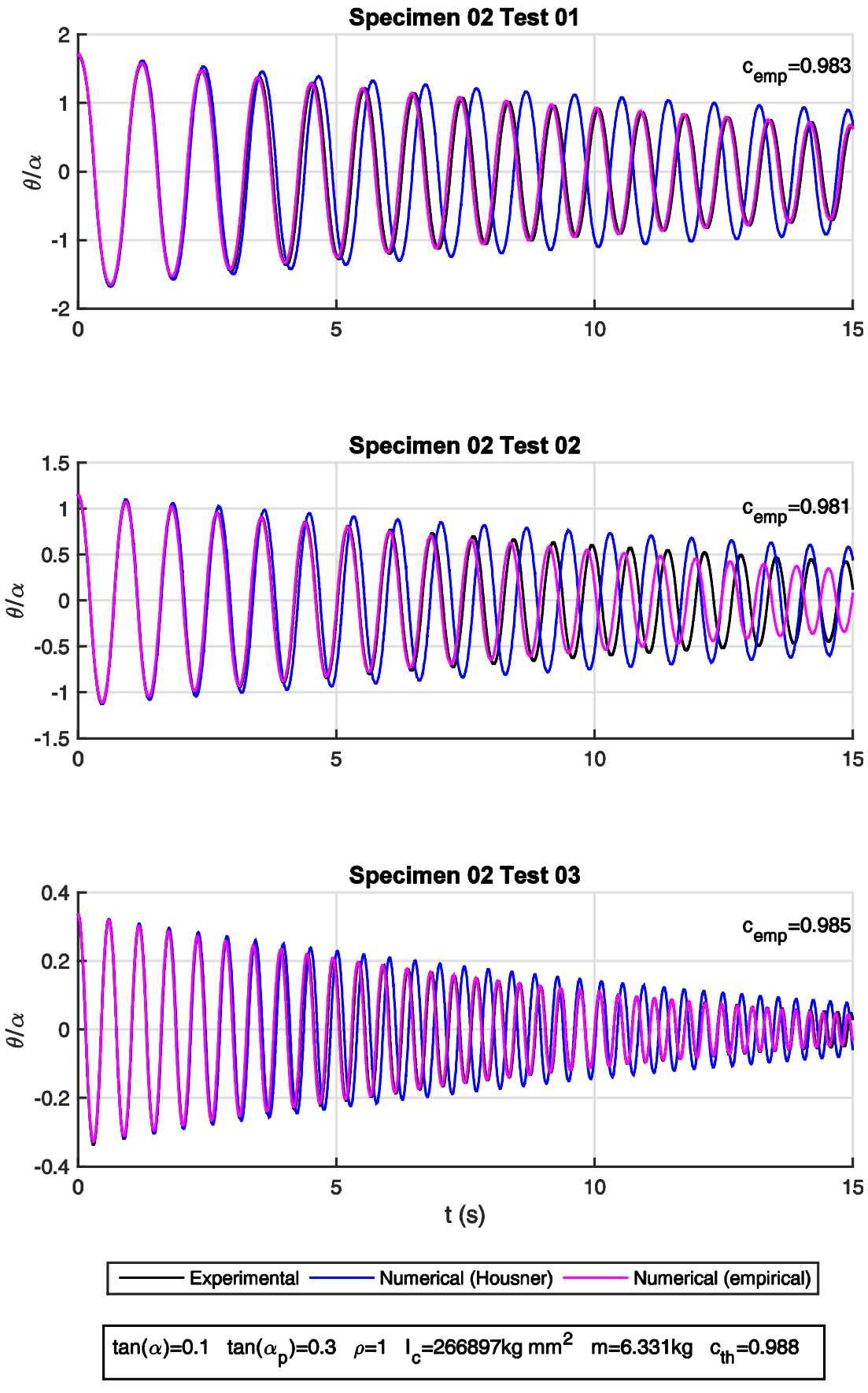

Figure 10. Normalized tilt angle, θ/α, time history for Specimen 2

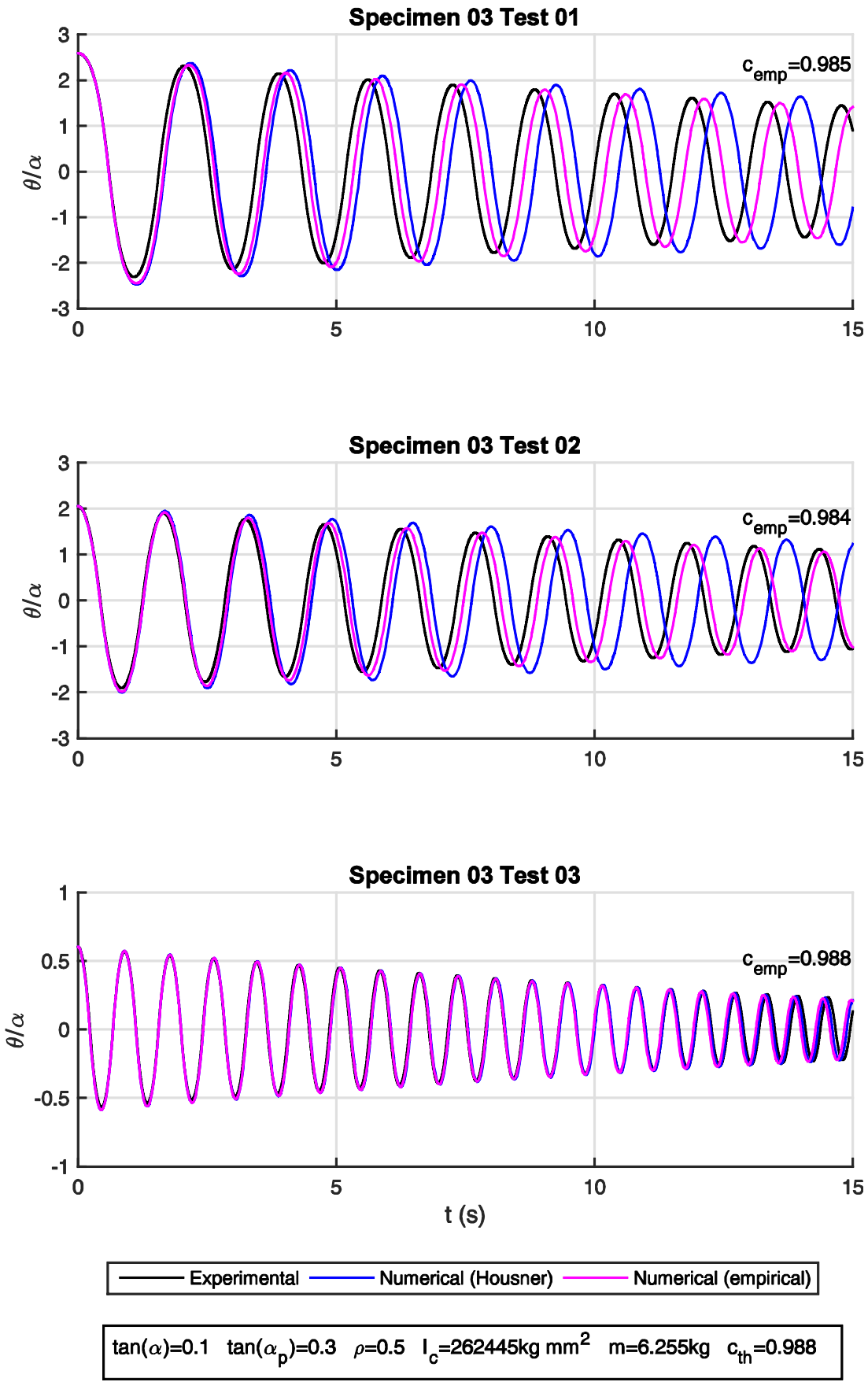

Figure 11. Normalized tilt angle, θ/α, time history for Specimen 3

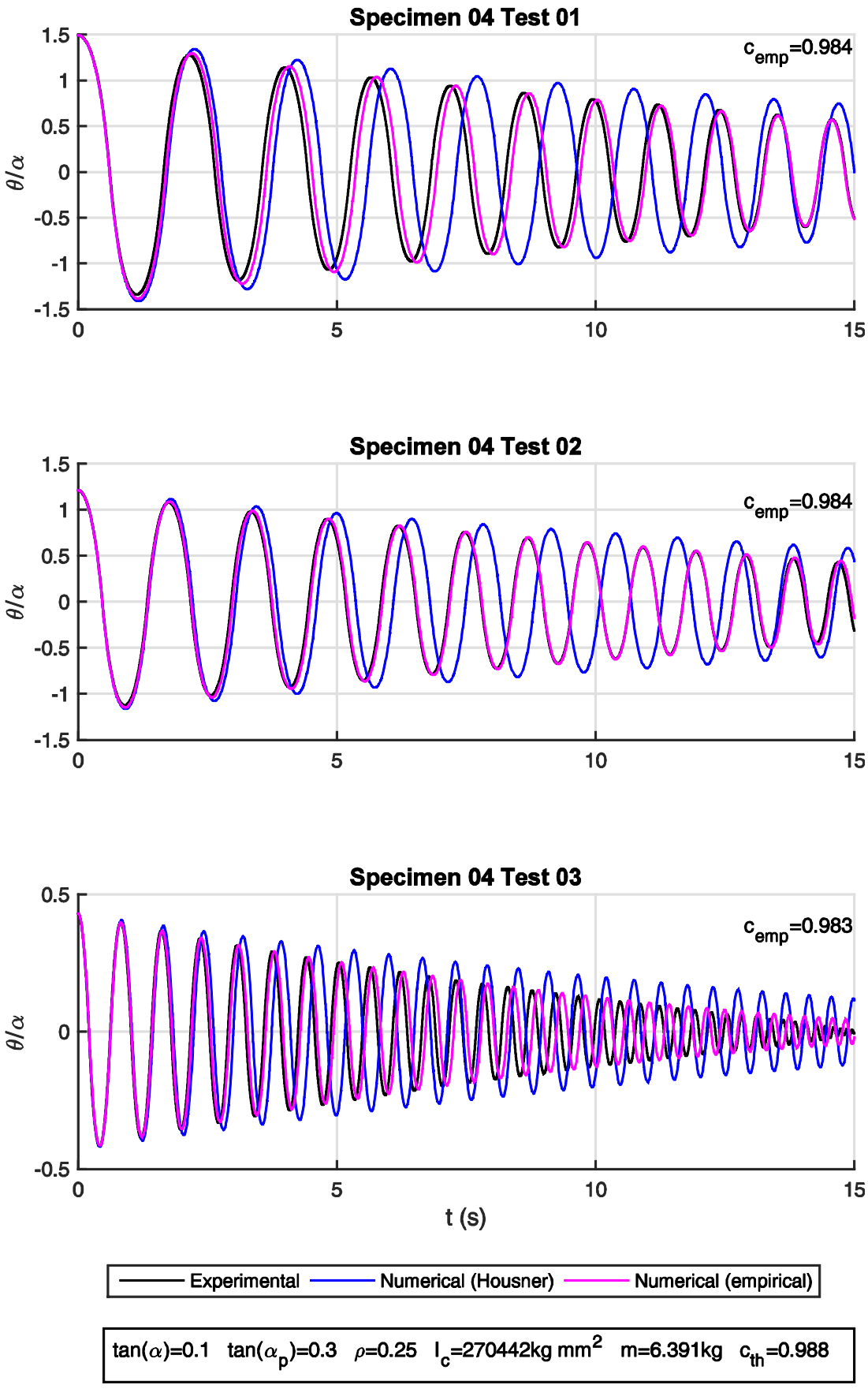

Figure 12. Normalized tilt angle, θ/α, time history for Specimen 4

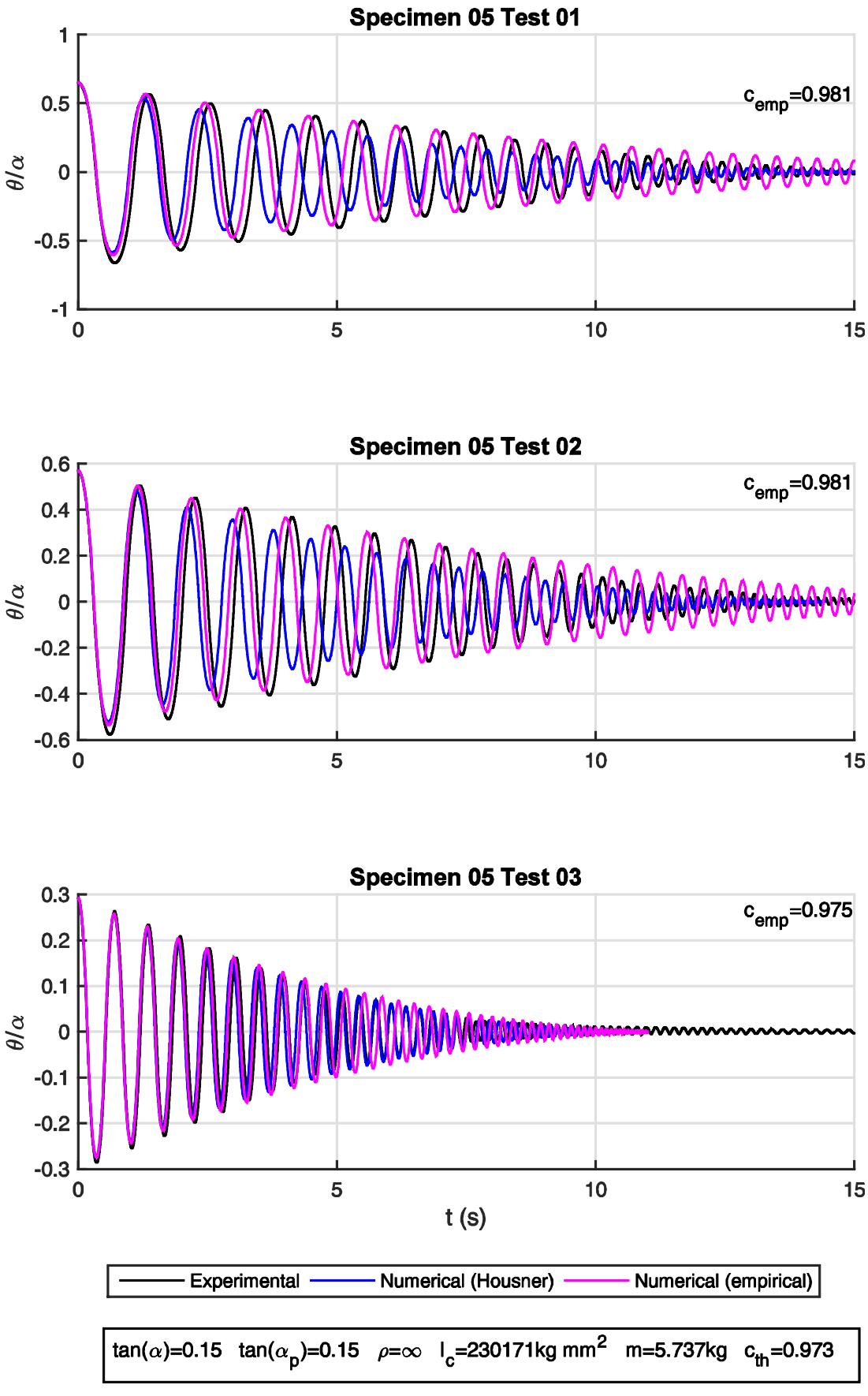

Figure 13. Normalized tilt angle, θ/α, time history for Specimen 5

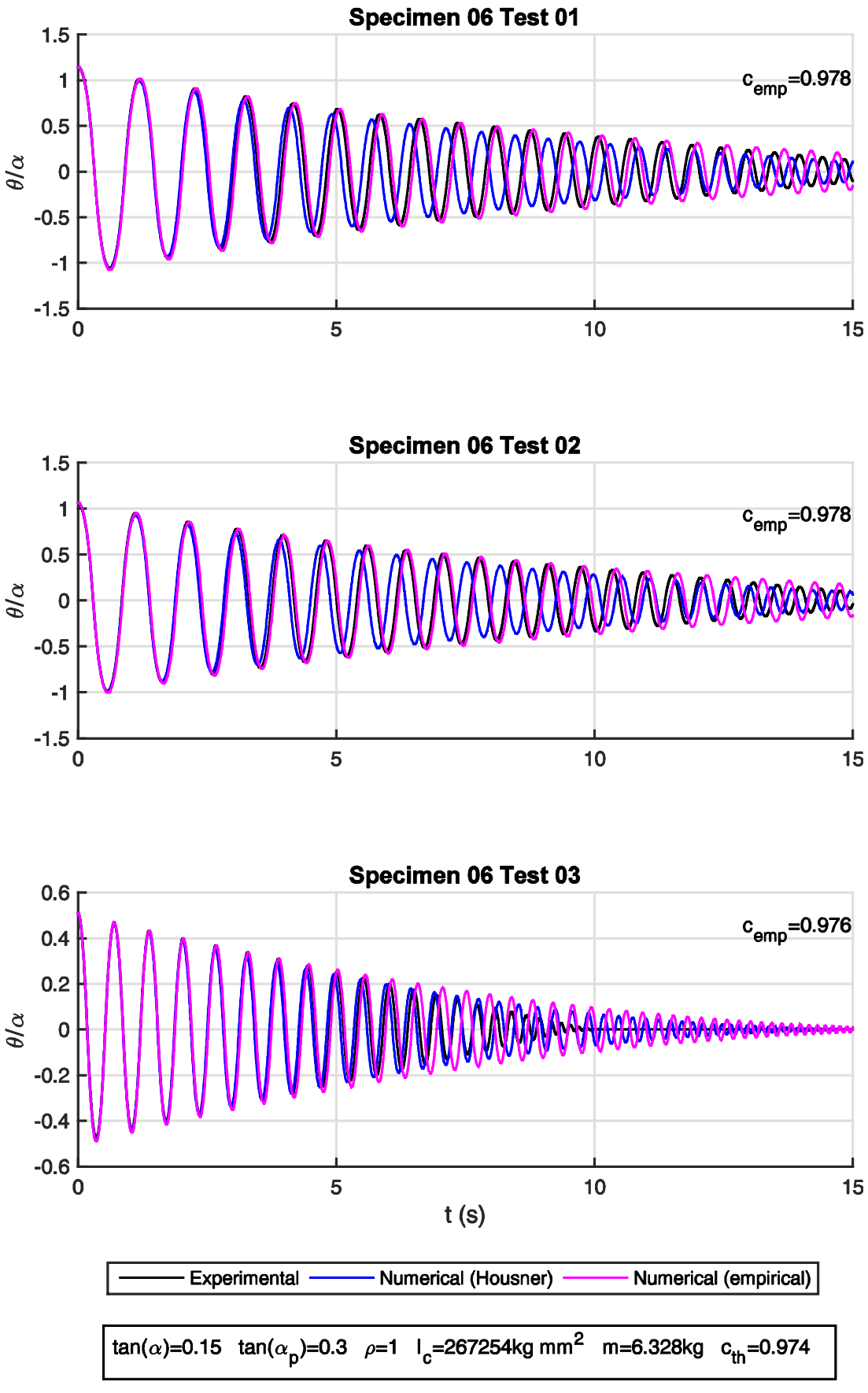

Figure 14. Normalized tilt angle, θ/α, time history for Specimen 6

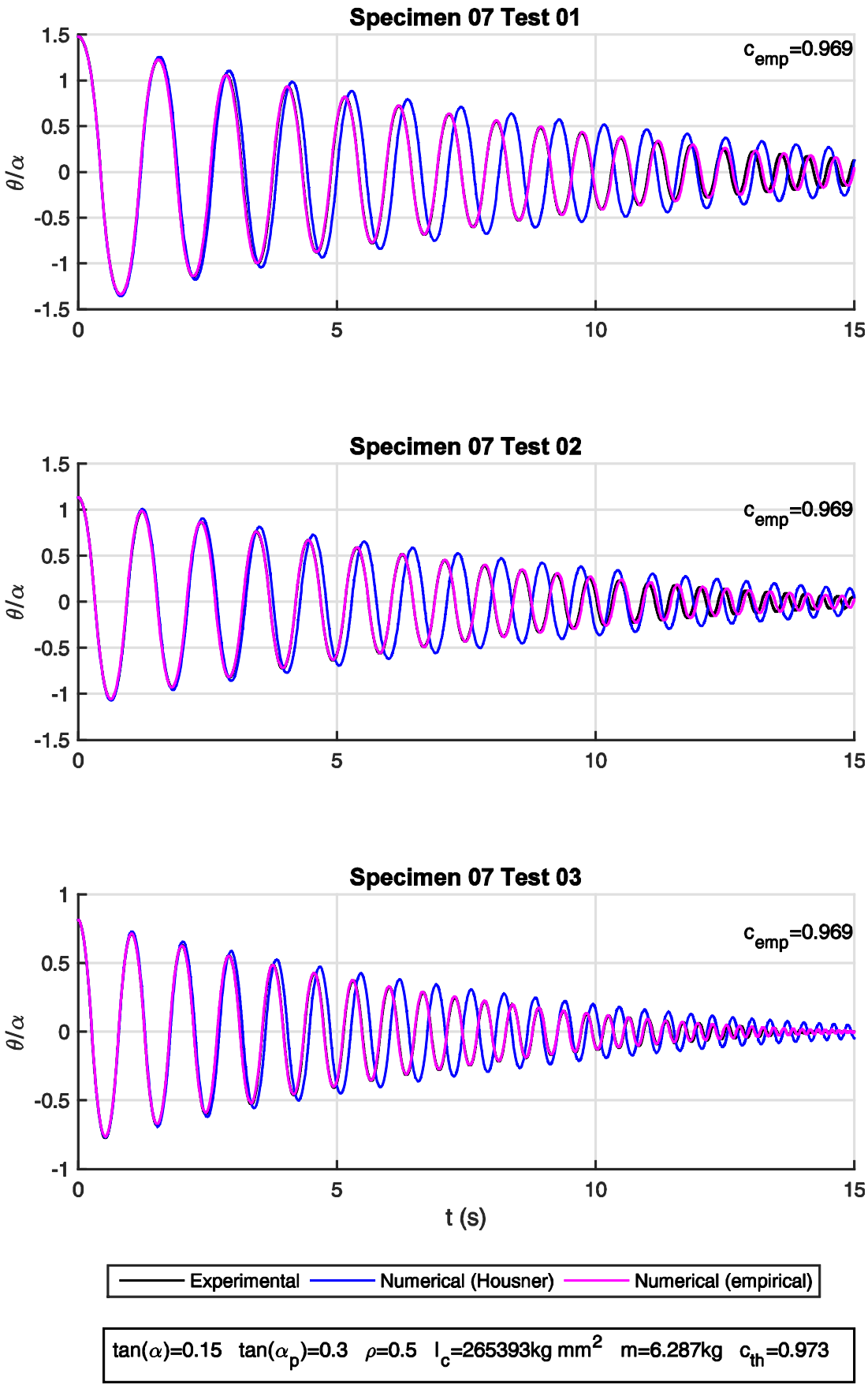

Figure 15. Normalized tilt angle, θ/α, time history for Specimen 7

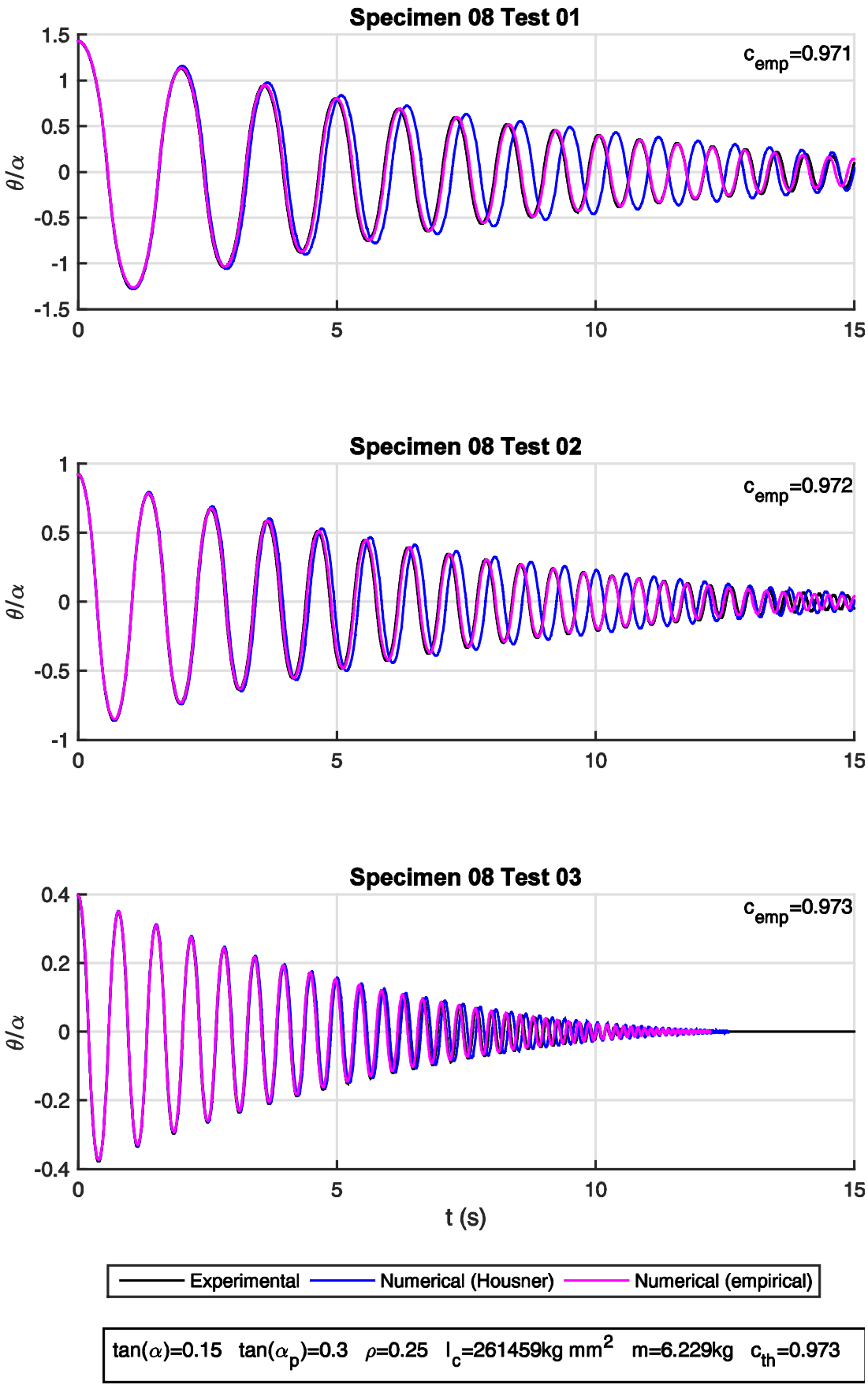

Figure 16. Normalized tilt angle, θ/α, time history for Specimen 8

REFERENCES

[1] Housner, G. W. (1963). The behavior of inverted pendulum structures during earthquakes. Bulletin of the seismological society of America, 53(2), 403-417.

[2] Beck, J. L. and Skinner, R. I. (1973), The seismic response of a reinforced concrete bridge pier designed to step. *Earthquake Engng. Struct. Dyn*., 2: 343–358.

[3] Yim, C. S., Chopra, A. K., & Penzien, J. (1980). Rocking response of rigid blocks to earthquakes. Earthquake Engineering & Structural Dynamics, 8(6), 565-587.

[4] Psycharis, I. N. and Jennings, P. C. (1983), Rocking of slender rigid bodies allowed to uplift. *Earthquake Engineering & Structural Dynamics*, 11: 57–76.

[5] Sharpe RD, Skinner RI, (1983) The seismic design of an industrial chimney with rocking base, *Bulletin of the New Zealand National Society for Earthquake Engineering* 16(2):98-106

[6] Chopra, A. K., & Yim, S. C. S. (1985). Simplified earthquake analysis of structures with foundation uplift. Journal of Structural Engineering, 111(4), 906-930.

[7] Hogan, S. J. (1990). The many steady state responses of a rigid block under harmonic forcing. Earthquake Engineering & Structural Dynamics, 19(7), 1057-1071.

[8] Psycharis, I. N. (1991). Effect of base uplift on dynamic response of SDOF structures. *Journal of Structural Engineering*, 117(3), 733-754.

[9] Makris, N., and Y. Roussos (1998*). Rocking response and overturning of equipment under horizontal pulse-type motions*, Rept. No. PEER-98/05, Pacific Earthquake Engineering Research Center, University of California, Berkeley, California.

[10] Zhang J, Makris N. (2001) Rocking response of free-standing blocks under cycloidal pulses. *Journal of Engineering Mechanics*, ASCE; 127(5):473–483.

[11] Makris, N. and Konstantinidis, D. (2003), The rocking spectrum and the limitations of practical design methodologies. *Earthquake Engineering & Structural Dynamics*, 32, 265–289.

[12] Oliveto, G., Caliò, I. and Greco, A. (2003), Large displacement behaviour of a structural model with foundation uplift under impulsive and earthquake excitations. *Earthquake Engng. Struct. Dyn*., 32: 369–393.

[13] Prieto, F., Lourenço, P. B., & Oliveira, C. S. (2004). Impulsive Dirac-delta forces in the rocking motion. Earthquake engineering & structural dynamics, 33(7), 839-857.

[14] Konstantinidis, D., & Makris, N. (2005). Seismic response analysis of multidrum classical columns. *Earthquake engineering & structural dynamics*,*34*(10), 1243-1270.

[15] Apostolou M, Gazetas G, Garini E. (2007) Seismic response of slender rigid structures with foundation uplifting, *Soil Dynamics and Earthquake Engineering*, 27(7), 642-654

[16] Konstantinidis, D., & Makris, N. (2007). The dynamics of a rocking block in three dimensions. In *8th Hellenic Society for Theoretical and Applied Mechanics International Congress on Mechanics*.

[17] Peña, F., Prieto, F., Lourenço, P. B., Campos Costa, A., & Lemos, J. V. (2007). On the dynamics of rocking motion of single rigid-block structures. *Earthquake Engineering & Structural Dynamics*, 36(15), 2383-2399.

[18] Ma, Q. T., & Khan, M. H. (2008). Free vibration tests of a scale model of the South Rangitikei Railway Bridge. In Proceedings of the New Zealand Society for Earthquake Engineering Annual Conference, Engineering an Earthquake Resilient NZ.

[19] Contento, A., & Di Egidio, A. (2009). Investigations into the benefits of base isolation for non-symmetric rigid blocks. Earthquake Engineering & Structural Dynamics, 38(7), 849-866.

[20] Konstantinidis, D., & Makris, N. (2009). Experimental and analytical studies on the response of freestanding laboratory equipment to earthquake shaking.*Earthquake Engineering & Structural Dynamics*, *38*(6), 827-848.

[21] Papaloizou, L., & Komodromos, P. (2009). Planar investigation of the seismic response of ancient columns and colonnades with epistyles using a custom-made software. *Soil Dynamics and Earthquake Engineering*, *29*(11), 1437-1454.

[22] Konstantinidis, D., & Makris, N. (2010). Experimental and analytical studies on the response of 1/4-scale models of freestanding laboratory equipment subjected to strong earthquake shaking. *Bulletin of earthquake engineering*,*8*(6), 1457-1477.

[23] Ma, Q. T. M. (2010). The mechanics of rocking structures subjected to ground motion (Doctoral dissertation, ResearchSpace@ Auckland).

[24] Vassiliou, M. F. (2010). *Analytical investigation of the dynamic response of a pair of columns capped with a rigid beam and of the effect of seismic isolation on rocking structures* (Doctoral dissertation, Doctoral dissertation, Dept. of Civil Engineering, Univ. of Patras, Greece (in Greek)).

[25] ElGawady, M. A., Ma, Q., Butterworth, J. W., & Ingham, J. (2011). Effects of interface material on the performance of free rocking blocks. Earthquake Engineering & Structural Dynamics, 40(4), 375-392.

[26] Acikgoz, S., & DeJong, M. J. (2012). The interaction of elasticity and rocking in flexible structures allowed to uplift. Earthquake Engineering & Structural Dynamics, 41(15), 2177-2194.

[27] Dimitrakopoulos, E. G., & DeJong, M. J. (2012). Revisiting the rocking block: closed-form solutions and similarity laws. Proceedings of the Royal Society A: Mathematical, Physical and Engineering Science, 468(2144), 2294-2318.

[28] Dimitrakopoulos, E. G., & DeJong, M. J. (2012). Overturning of retrofitted rocking structures under pulse-type excitations. *Journal of engineering mechanics*, *138*(8), 963-972.

[29] Gelagoti, F., Kourkoulis, R., Anastasopoulos, I. and Gazetas, G. (2012), Rocking isolation of low-rise frame structures founded on isolated footings. *Earthquake Engng. Struct. Dyn.*, 41: 1177–1197.

[30] Kourkoulis, R., Anastasopoulos, I., Gelagoti, F., & Kokkali, P. (2012). Dimensional analysis of SDOF systems rocking on inelastic soil. *Journal of Earthquake Engineering*, *16*(7), 995-1022.

[31] Makris, N., & Vassiliou, M. F. (2012). Sizing the slenderness of free-standing rocking columns to withstand earthquake shaking. *Archive of Applied Mechanics*, 82(10-11), 1497-1511.

[32] Vassiliou, M. F., & Makris, N. (2012). Analysis of the rocking response of rigid blocks standing free on a seismically isolated base. Earthquake Engineering & Structural Dynamics, 41(2), 177-196.

[33] Zulli, D., Contento, A., & Di Egidio, A. (2012). 3D model of rigid block with a rectangular base subject to pulse-type excitation. *International Journal of Non-Linear Mechanics*, *47*(6), 679-687.

[34] Acikgoz, S., & DeJong, M. J. (2013), Analytical and experimental observations on vibration modes of flexible rocking structures, SECED - Society for Earthquake and Civil Engineering *Dynamics Young Engineers Conference*, July 4th, 2013.

[35] Acikgoz, S., & DeJong, M. J. (2013). Linearization and Modal Analysis of Flexible Rocking Structures. In *Proceedings of NZSEE Conference*.

[36] Antonellis, G., & Panagiotou, M. (2013). Seismic Response of Bridges with Rocking Foundations Compared to Fixed-Base Bridges at a Near-Fault Site.*Journal of Bridge Engineering*, *19*(5).

[37] Dimitrakopoulos, E. G., & De Jong, M. J. (2013). Seismic overturning of rocking structures with external viscous dampers. In *Computational methods in earthquake engineering* (pp. 243-258). Springer Netherlands.

[38] Makris N. and Vassiliou M.F. (2013), Planar rocking response and stability analysis of an array of free standing columns capped with a freely supported rigid beam *Earthquake Engng. Struct. Dyn*, *42*(3), 431-449.

[39] Sextos, A., Nalmpantis, S., Faraonis, P., Skiada, D., & Stylianidis, K. (2013). Probabilistic seismic hazard assessment through geometrically non-linear back-analysis of byzantine and roman monuments. *10th HSTAM International Congress on Mechanics. Chania, Greece*.

[40] Vassiliou, M. F., Mackie, K. R., & Stojadinović, B. (2013). Rocking response of slender, flexible columns under pulse excitation. In Proceedings of the 4th ECCOMAS Thematic Conference on Computational Methods in Structural Dynamics and Earthquake Engineering, Kos Island, Greece (pp. 12-14).

[41] Zhang, H., Brogliato, B., & Liu, C. (2013). Dynamics of planar rocking-blocks with Coulomb friction and unilateral constraints: comparisons between experimental and numerical data. Multibody System Dynamics, 1-25.

[42] Acikgoz, S., & DeJong, M. J. (2014). The rocking response of large flexible structures to earthquakes. *Bulletin of earthquake engineering*, *12*(2), 875-908.

[43] DeJong, M. J., & Dimitrakopoulos, E. G. (2014). Dynamically equivalent rocking structures. *Earthquake engineering & structural dynamics*, *43*(10), 1543-1563.

[44] Drosos, V., & Anastasopoulos, I. (2014). Shaking table testing of multidrum columns and portals. *Earthquake Engineering & Structural Dynamics*, *43*(11), 1703-1723.

[45] Makris, N. (2014). The Role of the Rotational Inertia on the Seismic Resistance of Free-Standing Rocking Columns and Articulated Frames. *Bulletin of the Seismological Society of America*.

[46] Makris, N., & Vassiliou, M. F. (2014). Are Some Top-Heavy Structures More Stable?. *Journal of Structural Engineering*, 140(5).

[47] Makris, N., & Vassiliou, M. F. (2014). Dynamics of the rocking frame with vertical restrainers. Journal of Structural Engineering, 141(10), 04014245.

[48] Truniger, R., Vassiliou, M. F., & Stojadinovic, B. (2014). Experimental study on the interaction between elasticity and rocking. In *Proceedings of the 10th national conference in earthquake engineering, Earthquake Engineering Research Institute, Anchorage, AK*.

[49] Vassiliou, M. F., Mackie, K. R., & Stojadinović, B. (2014). Dynamic response analysis of solitary flexible rocking bodies: modeling and behavior under pulse-like ground excitation. *Earthquake Engineering & Structural Dynamics* 43: 1463–1481

[50] Zhang, H., Brogliato, B., & Liu, C. (2014). Dynamics of planar rocking-blocks with Coulomb friction and unilateral constraints: comparisons between experimental and numerical data. *Multibody System Dynamics*, *32*(1), 1-25.

[51] Dimitrakopoulos, E. G., & Giouvanidis, A. I. (2015). Seismic Response Analysis of the Planar Rocking Frame. *Journal of Engineering Mechanics,141*(7), 04015003.

[52] Dimitrakopoulos, E. G., & Paraskeva, T. S. (2015). Dimensionless fragility curves for rocking response to near-fault excitations. *Earthquake Engineering & Structural Dynamics*, *44*(12).

[53] Makris, N. "A Half-Century of Rocking Isolation" (2105) *Earthquakes and Structures*, Vol. 7, No 2, 2015

[54] Makris, N., & Vassiliou, M. F. (2015). The dynamics of the rocking frame. In *Seismic Assessment, Behavior and Retrofit of Heritage Buildings and Monuments* (pp. 37-59). Springer International Publishing.

[55] Makris, N., & Vassiliou, M. F. (2015). Seismic Response and Stability of the Rocking Frame. In *Computational Methods, Seismic Protection, Hybrid Testing and Resilience in Earthquake Engineering* (pp. 249-273). Springer International Publishing.

[56] Truniger, R., Vassiliou, M. F., & Stojadinović, B. (2015). An analytical model of a deformable cantilever structure rocking on a rigid surface: experimental validation. Earthquake Engineering & Structural Dynamics, 44(15), 2795-2815.

[57] Vassiliou, M. F., Mackie, K. R., & Stojadinović, B. (2015) Earthquake response of deformable rocking frames Engineering Mechanics Institute Conference, Stanford, June 2015.

[58] Vassiliou, M. F., & Makris, N. (2015). Dynamics of the Vertically Restrained Rocking Column. *Journal of Engineering Mechanics*, 141(12), 04015049.

[59] Vassiliou, M. F., Truniger, R., & Stojadinović, B. (2015). An analytical model of a deformable cantilever structure rocking on a rigid surface: development and verification. *Earthquake Engineering & Structural Dynamics*, 44(15), 2775-2794.

[60] Makris, N., & Kampas, G. (2016). Size Versus Slenderness: Two Competing Parameters in the Seismic Stability of Free-Standing Rocking Columns. Bulletin of the Seismological Society of America.

[61] Bakhtiary, E., & Gardoni, P. (2016). Probabilistic seismic demand model and fragility estimates for rocking symmetric blocks. Engineering Structures, 114, 25-34.

[62] Pappas, A., da Porto, F., & Modena, C. (2016). Seismic vulnerability assessment form for free-standing columns based on a simplified numerical analysis. International Journal of Architectural Heritage, (just-accepted).

[63] Eisenberg, J. M., & Smirnov, V. I. Development of Earthquake Protection Structural Systems Based on Response Control. *Proceedings of the 15th World Conference on Earthquake Engineering*. Lisbon, Portugal.

[64] Papadopoulos C, DOMOS Engineers, Athens, Greece, personal communication, September 19, 2014

[65] Bachmann J., Vassiliou MF & Stojadinovic B, (2015) Rocking of a rigid block on a curved foundation, Engineering Mechanics Institute Conference, Stanford, June 2015.

[66] Barthes, C. B. (2012). Design of Earthquake Resistant Bridges Using Rocking Columns. PhD Thesis, UC Berkeley, USA

ECCOMAS Congress 2016
VII European Congress on Computational Methods in Applied Sciences and Engineering
M. Papadrakakis, V. Papadopoulos, G. Stefanou, V. Plevris (eds.)
Crete Island, Greece, 5–10 June 2016

SEISMIC ASSESSMENT OF MASONRY ROCKING COLUMNS AND FRAMES UNDER GROUND MOTION EXCITATIONS

Ioannis E. Kavvadias[1], **Lazaros K. Vasiliadis**[1]

[1] Democritus University of Thrace, Dept. of Civil Engineering
Vas. Sofias 12, 67100 Xanthi, Greece
e-mail: {ikavvadi, lvasilia}@civil.duth.gr

Keywords: Ancient Columns, Rocking Columns; Rocking Frames, Ground Motion Intensity Measures, Fragility Curves, Earthquake Engineering.

Abstract. *In this study the seismic response of free standing, rocking columns and frames is investigated taking into account different intensity measures (IMs) of the seismic excitations. The seismic vulnerability of the examined structural systems is based on the probabilistic seismic demand model (PSDM), in which the degree of uncertainty is depended on the IM used. Thus 23 different IMs are evaluated in order to extract the most optimal one. A performance based analysis is performed and fragility curves are generated conditional on uni-variable and bi-variable IMs considering the maximum rotation normalized to the slenderness as engineering demand parameter (EDP). The seismic assessment of these structures is evaluated using three limit states. Nevertheless, in this study, the effect of the beams' mass on the seismic rocking behavior of the frames is also examined. Finite element analysis models are used for the simulation of the structural members as deformable bodies while rigid contact elements are employed for the interfaces. Time domain analyses are performed using a set of 30 natural ground motions. Results in terms of correlation coefficients and dispersion values are first presented, indicated that the length scale of the excitation (Lm) and the vector value IM, PGV-Tm are the most optimal uni-variable and bi-variable IMs, for describing the rocking response. Further results in terms of peak rocking rotations and fragility curves shown that free standing frames are less vulnerable than the single columns. Moreover, as the beam mass increases, the developed rocking rotation of the frame tends to be reduced.*

1 INTRODUCTION

The investigation of the seismic response of ancient structural systems such as ancient columns and colonnades has received increasing attention during the last decades. These structural systems comprise the construction technique of Archaic, Classical, and Roman temples. Different types of columns with numerous variations in their geometrical characteristics can be found mainly in the Eastern Mediterranean region. In general, ancient columns are earthquake resistant, as proven from the fact that many monuments like these have survived many strong earthquakes over the centuries. This notable stability is displayed mainly due to the design method of these structures which is based on articulated mechanisms that demonstrate rocking behavior. Usually these are constructed of limestone or marble blocks (drums), which are placed on top of each other, without connecting mortar between them. These rigid-body assemblies display a very different dynamic response compared to modern structures. Their main difference as shown in Figure 1 is that the rocking behavior exhibits negative stiffness and low damping that occur only at the instant of impact in contrast with the modern design philosophy which is based on the positive stiffness of the structure and the ductility of the structural members [1]. Their response is composed primarily of rocking and sliding among the individual blocks of the structure and the ground. This behavior can be characterized as highly nonlinear due to the continuous changing of geometry and boundary conditions of the structural system during a strong earthquake.

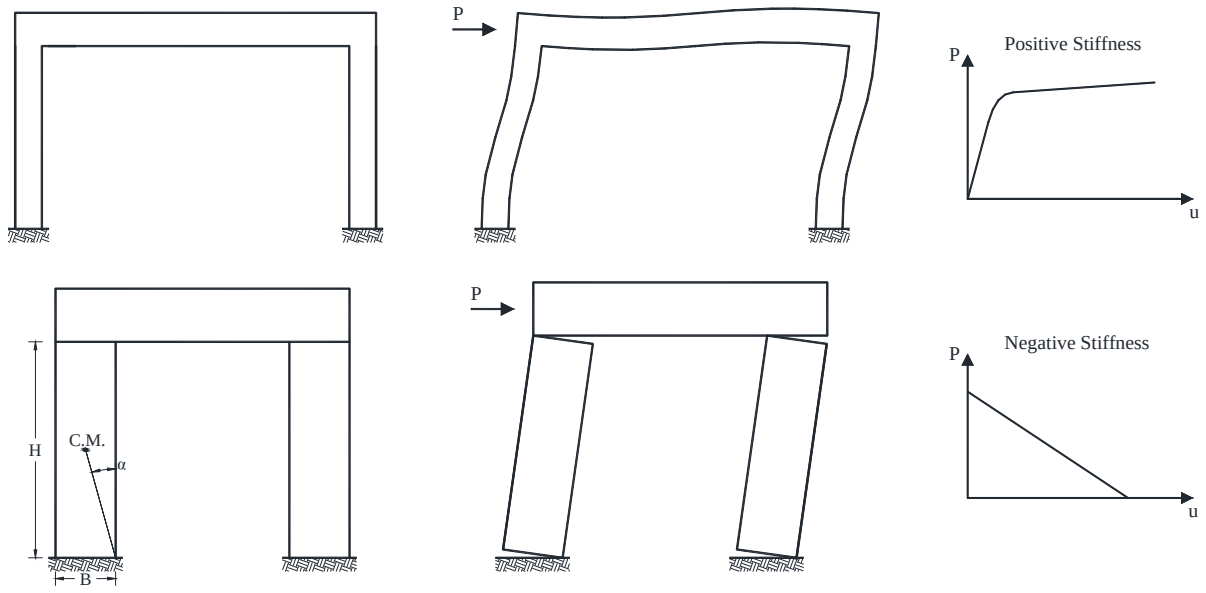

Figure 1: Response of a moment resistance frame versus a rocking frame.

Early work on the dynamics of the rocking column started analytically by Milne (1885) [2] while, Omori (1990) [3] was one of the first who performed experimental research on the seismic response of rectangular rocking columns. Subsequently, Kirkpatrick (1927) [4] presented a novel paper in which he relates the column size and the period of the excitation with the rocking response. It was Housner's (1963) [5] study that offers a solution for the dynamic behavior of a single block under pulse excitation, through the formulation of the inverted pendulum. Housner revealed both the size effect, which means that the larger block between two with the same aspect ratio exhibits greater stability under horizontal excitation, and the frequency effect which indicates that the frequency content of the excitation substantially affects

the rocking response, with long period excitations being more likely in causing overturning than the short period ones. His pioneer work constitutes the basis of the rocking analysis theory. After these studies several followed as researchers were motivated by the need to understand the rocking response, and they extended our previous knowledge, by revealing hidden aspects of rocking response [6-13].

Multi block rocking response has also been under investigation [14-18]. Sinopoli's work [14] has examined the impact problem between rigid bodies through a kinematic approach. Meanwhile, Psycharis [15] and subsequently Spanos et al. [16] proposed analytical solutions for the rocking response of two stacked rigid blocks assuming no sliding between them. Furthermore, Makris and Vassiliou [17] present the equivalence between a rocking frame and singular rocking blocks whereas, DeJong and Dimitrakopoulos [18] generalized it also for asymmetric rocking frames.

Extensive numerical investigation specifically on the response of ancient structural systems such as free standing single monolithic and multi-drum columns or columns connected to each other at the top level by architraves, which are usually consist the peristyles of ancient temples, has been presented by several researchers [19-25]. The numerical modeling of all these studies has been conducted using the Discrete Element Method (DEM). Using planar numerical modeling Psycharis et al. [19] investigated the seismic response of ancient columns. Moreover, Konstantinidis and Makris [20] also using a two dimension modeling, examined the effect of wooden poles installed in ancient times, but also of titanium poles which were installed during the restoration process, on the dynamic response of multidrum columns. Additionally, studies are presented on the seismic response of ancient columns and colonnades with epistyles using a custom-made software based on the DEM [23], [24]. On the other hand, Papantonopoulos et al. [21] and Psycharis et al. [22] performed numerical analyses in three dimensions. It was noticed that 2D analyses are capable of capturing the rocking phenomenon but without computing the out of plane oscillation, which makes the problem more complex. Thus is slightly underestimate the overall response. Experimental studies were also performed by Mouzakis et al. [26] Pena et al. [27] and Drosos and Anastopoulos [28] and confirmed the conclusion obtained from the numerical studies.

Due to the sensitivity of rocking response even to trivial changes of the ground motion characteristics or of the geometry of the model, Spanos and Koh [29] were the first to study the rocking response via a probabilistic framework. Afterwards, seismic vulnerability assessment of rocking columns and frames were presented by Psycharis et al. [30] and Dimitrakopoulos and Paraskeva [31].

In this paper, we present a numerical investigation of the seismic response of free standing columns and colonnades. Time domain analyses are performed with the use of 30 natural records. The scope of this study is to assess the seismic vulnerability of the examined rocking structures resulting in the most optimal intensity measures (IMs) [32] used for generating the probabilistic seismic demand model [33]. In addition, the difference of the colonnade with epistyle behavior against the single column response is studied while, the influence of the beams' mass on the rocking response is also examined.

2 NUMERICAL MODELING

For the purpose of this study, finite element models are utilized for the in space simulation of the members, in which the blocks are simulated as deformable elements and the ground as a rigid surface. Despite the structural members being modeled as 3D members, planar analyses were performed. Explicit dynamic analyses were employed as it is computationally efficient for discontinuous events like impact problems, using the central difference algorithm. Of particular significance for the simulation are the appropriate modeling of the contact between

the blocks and the base, and in the case of multi block models the contact between each block. Rigid contact is used to model the interfaces while a Mohr-Coulomb model is adopted to describe the mechanical behavior of the joints. For both normal and tangential direction of the contact element, the stiffness is assumed as infinite. In the normal direction no tensile strength is considered while the shear strength is governed by the Coulomb friction coefficient without considering cohesion. As mentioned by a thorough investigation made by Papantonopoulos et al. [21], damping affects the amplitude of the intense rocking response and thus, zero value of damping gives better results during the strong motion part of the excitation. Consequently both the mass proportional damping and the stiffness proportional damping coefficients are set zero for the analyses. The mechanical properties of the block material as well as the interface properties listed in Table 1 are assumed as typical values for marble blocks.

Material Properties	Density (kg/m^3)	2750
	Young's modulus (Gpa/m)	84.5
	Poison ratio	0.23
Interface Properties	Friction coefficient	0.70
	Cohesion (MPa)	0
	Tensile strength (MPa)	0

Table 1: Material and interface mechanical properties.

Column with 8m height and slenderness α=0.165rad is studied. The selection of the dimension was made to be in accordance with the size and the slenderness of recorded ancient columns. Specifically the columns of the Temple of Olympic Zeus and the Temple of Apollo in Syracuse have 8 m height. Additionally the Parthenon Pronaos columns have a slenderness of 0.16rad. Concerning the effect of the architrave existence, two varying geometry architraves are examined. The values of the beam (architrave) mass (m_b) are defined as a ratio over the columns mass (m_c), taking values $m_b/2m_c$=0.25, 0.5. The axial distance between the columns is 3m and is spanned with a single block architrave. Figure 2 shows the dimensions in meters of the examined rocking column and frames.

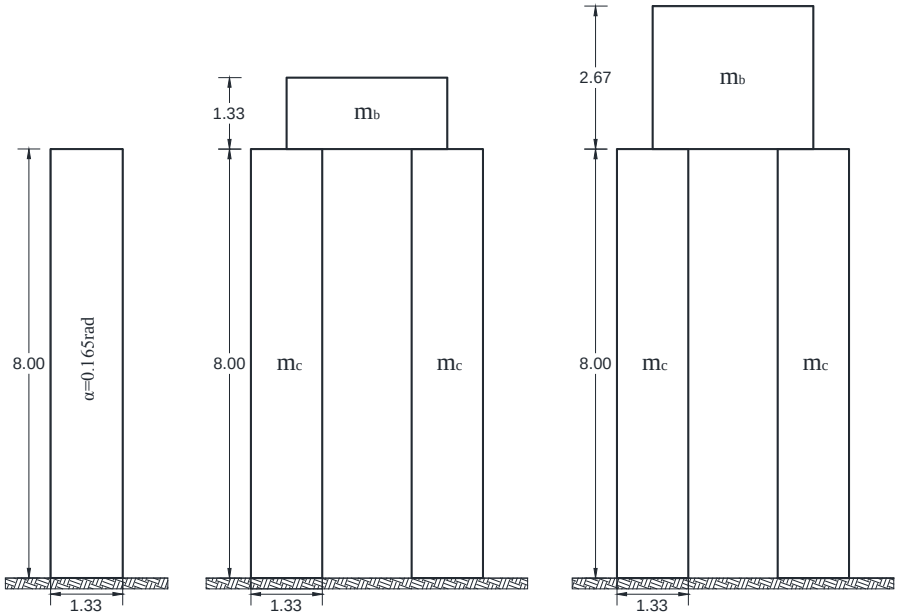

Figure 2: Examined cases of free standing column and free standing frames.

3 SELECTION OF NATURAL GROUND MOTIONS AND INTENSITY MEASURES (IMS)

3.1 Ground Motions

A set of 30 ground motion time histories is used as input ground motion for the analyses. What proved to be useful, for the selection was an extensive review of ground motion selection methods for dynamic analysis of structural systems presented by Katsanos et al. [34]. The events were chosen from worldwide well-known sites with strong seismic activity. Excitations generated from different types of fault types, with earthquake magnitudes (M_s) between 5.3 and 7.6, including both near fault and far fault records as the closest distance to fault rapture (R) varying from 0.6 to 115 km is employed in order to present a wide range of intensities and frequency contents. A further aspect which has been taken into consideration is the expected damage potential of the seismic excitation on the structure. Seismic excitations which provide a wide spectrum of structural damage, from negligible to severe, are taken into account. Based on the above assumption, a rigorous selection of ground motions carried out from the PEER [35] and the European [36] strong motion databases in order to use original records without any scaling. The complete list of the natural ground motions used for the analyses is shown in Table 2.

Earthquake	Record	Date	M_s	R (km)
Aigion	AIGA	25/06/1995	6.4	21.5
Athens	ATH4	07/09/1999	5.90	16.62
Bucharest	Bucharest	04/03/1977	7.50	115.0
Chi-Chi	CHY035	20/09/1999	7.62	12.56
Chi-Chi	TCU88	20/09/1999	7.62	18.16
Chuetsuoki	Nakanoshima Nagaoka	16/07/2007	6.8	19.89
Coalinga	Fault Zone 14	02/05/1983	6.36	29.48
Corinth	Corinth	24/02/1981	6.60	10.28
Darfield	Papanui High School	04/09/2010	7	26.76
Duzce	Lamont 531	12/11/1999	7.14	8.03
Erzincan	Erzincan	19/03/1992	6.69	4.38
Friuli	Tolmezo	06/05/1976	6.50	15.82
Gazli	Karakyr	17/05/1976	6.80	5.46
Imperial Valley	El Centro Array #9	19/05/1940	6.95	6.09
Imperial Valley	El Centro Array #7	15/02/1979	6.53	0.56
Imperial Valley	El Centro Array #8	15/02/1979	6.53	3.86
Irpinia	Sturno	23/11/1980	6.9	10.84
Iwake	Ichinoseki Maikawa	14/07/2008	6.9	23.02
Kalamata	Kalamata	13/09/1986	6.20	10.00
Kobe	Nishi -Akashi	16/01/1995	6.90	7.08
Kobe	Takatori	16/01/1995	6.90	1.47
Landers	Joshua Tree	28/06/1992	7.28	11.03
Loma Prietta	Los Gatos - Lexington Dam	17/11/1986	6.93	5.02
Northridge	Paicoma Dam	17/01/1994	6.69	7.01
Parkfield	Cholame #2	28/06/1966	6.20	17.64
San Fernando	Paicoma Dam	09/02/1970	6.61	1.81
Taiwan SMART1(40)	Smart1 M02	15/111986	6.32	60.89
Superstition Hill	Mtn Camera	24/11/1987	6.54	5.61
Tabas	Dayhook	16/09/1978	7.35	13.94
Whittier	LA - Obregon Park	01/10/1987	5.27	13.62

Table 2: List of the ground motions used in this study.

3.2 Intensity measures (IMs)

In order to designate the optimal earthquake intensity measures (IMs) for rocking response, a large number of seismic parameters is considered in the present study. Specifically 25 IMs were taken into account which can be classified into time history, energy, spectral, and frequency parameters. The definition of all the examined IMs is presented by Kramer [37]. Regarding the time history parameters, peak ground acceleration (PGA), peak ground velocity (PGV), peak ground displacement (PGD), sustain maximum acceleration (SMA), sustain maximum acceleration (SMV), and effective design acceleration (EDA) are taken under consideration. Additionally, with regard to the energy parameters the following were considered, root mean square of acceleration (A_{rms}), of velocity (V_{rms}), and of displacement (D_{rms}), characteristic intensity (I_c), Arias intensity (I_α), cumulative absolute velocity (CAV), specific energy density (SED), strong motion duration (T_D) and Fajfar index (I_F). The examined rocking structures do not possess natural modes in the classical sense [21] and so we do not use as intensity measures, spectral acceleration or velocity values for a certain period, although we consider the acceleration spectrum intensity (ASI), the velocity spectrum intensity (VSI) and the Housner Intensity (SI_H).

According to the frequency parameters, the period corresponding to the peak acceleration ($T_{p,A}$) and to the peak velocity ($T_{p,V}$) of the elastic response spectrum, are of the most extensively used frequency parameters in earthquake engineering. Nevertheless, none of these parameters represent the frequency content of a signal, except for the second one which seems to be a good approach to it. Mean period (T_m) [38] which is calculated by the Fourier spectra seems to be the best frequency parameter for excitations with arbitrary time-history shape. Moreover, the ratio PGV/PGA is related to the frequency content of the excitation, as for a harmonic motion this ratio is equal to $PGV/PGA=T/2\pi$. Finally, the characteristic length scale $L_p=v_p \cdot T_p$, which is introduced by Makris and Black [39] for pulse-type excitations and extended for non-distinct pulses by Dimitrakopoulos et al. [40], is considered too.

4 FRAGILITY ANALYSIS

4.1 Probabilistic seismic demand model

The vulnerability is assessed by estimating the conditional probability P where the seismic demand D measured to a specific engineering demand parameter (EDP), is higher than its capacity C, for a given value of a ground motion IM.

$$Fragility = P[D \geq C \,|\, IM] \tag{1}$$

The capacity is estimated by the proposed limit states while the demand is estimated using the relationship between the median structural demand Sd and each IM [33]:

$$S_d = aIM^b \tag{2}$$

where α and b are the linear regression coefficients for the logarithmic expression of the assumed scale law.

Assuming lognormal distribution for both the demand and the capacity of the structure and considering only demand uncertainties ($\beta_{D|IM}$), equation (1) can be rewritten in the following form:

$$P[D \geq C \,|\, IM] = \Phi\left(\frac{\ln(S_d / S_c)}{\sqrt{\beta_{D|IM}{}^2}}\right) \tag{3}$$

where Φ is the standard normal cumulative distribution function, Sc is the median value of the capacity which is estimated through the adopted limit states and $\beta_{D|IM}$ is the dispersion or logarithmic standard deviation for the demand conditioned the IM. For the calculation of the conditional standard deviation of the regression which is used to estimate the desperation, the following equation is utilized, where di is the i-th realization of the demands from the time history analyses.

$$\beta_{D|IM} \cong \sqrt{\frac{\sum(\ln(d_i) - \ln(aIM^b))^2}{N-2}} \tag{4}$$

In order to conclude in an intensity measure that could reduce even more the demand uncertainty ($\beta_{D|IM}$), also is examined vector IMs (couple of IMs) [41] to express the median demand as defined in the follow equation:

$$S_d = aIM_1^{b_1} IM_2^{b_2} \tag{5}$$

4.2 Definition of the engineering demand parameter

The introduced engineering demand parameter (EDP) has to get a clear physical meaning. Being aware of this principal, for the examined free standing structures, the best EDP that can be used has to be based on the rocking rotation as rocking is the dominant response of this structure. The absolute maximum developed rotation $|\theta_{max}|$ divided to the critical overturning rotation which is equal to the slenderness of the column α, was selected.

$$EDP = \frac{|\theta_{max}|}{\alpha} \tag{6}$$

4.3 Definition of the proposed limit states

Performance Based Earthquake Engineering has introduced the concept of acceptable performance levels. In vulnerability assessment analysis, capacity limit states (LS) are required to be defined, since the objective of the fragility analysis is to obtain the probability of exceedance the stated performance criteria. The capacity should be measured with the metrics of the EDP. Three performance levels, as presented in Table 3 are proposed for the current study. The first limit state (LS_I) corresponds to slight rocking of the structure, the second (LS_{II}) to moderate rocking which may cause local damage (imperfections) due to the impact and finally the third (LS_{III}) that corresponds to collapse due to rocking overturn.

Limit State	$\|\theta_{max}\|/\alpha$	Performance Level	Description
LS_I	0.20	Damage limitation	Lightly damaged structure.
LS_{II}	0.40	Moderate Damage	High likelihood of local damage due to impact.
LS_{III}	1.00	Near collapse	Rocking overturn of the structure.

Table 3: Proposed performance criteria.

5 RESULTS

5.1 Correlation analysis

To estimate the grade of interdependency between the intensity measures and the rocking response, the correlation coefficient according to Pearson is calculated. Pearson correlation coefficient shows how well the data fit to a linear relationship. The variables relationship is

based on the scale law of Equation (2). Figure 3 presents the correlation coefficient between the IMs and the EDP for the cases of a the free standing column and the free standing frame with masses ratio $m_b/2m_c=1/4$.

Examining Spearman's rank correlation coefficient of Figure 3, the maximum correlation of the adopted EDP with all the velocity based ground motion parameters is easily reconcilable. Specifically PGV and I_F is the IMs that has the strongest correlation with the EDP followed by the response spectrum IM SI_H. In addition, it is noted that the developed rocking rotation is influenced by the frequency parameters. The mean period of the excitation (T_m) and the ratio PGV/PGA exhibit the highest grade of interdependency, whereas between the predominant periods of the acceleration and the velocity elastic response spectrum, the second one has a higher value of correlation with the EDP. Finally the characteristic length scale of the excitation (L_m) displayed the strongest correlation among all the IMs.

On the other hand, the acceleration based parameters present the lowest grade of interrelationship with the rocking behavior. Additionally, the displacement based as the duration IMs show very low correlation levels with the EDP. Among the IMs which least affects the rocking behavior are the PGA the SMA and the TD.

From the results of the correlation analysis it can be concluded that the IMs associated with the velocity and the frequency content of the ground motion exhibit a far better correlation with the examined EDP. On the contrary, the IMs associated with the acceleration, the displacement and the duration of the excitation exhibit the lowest interdependency with the rocking rotation.

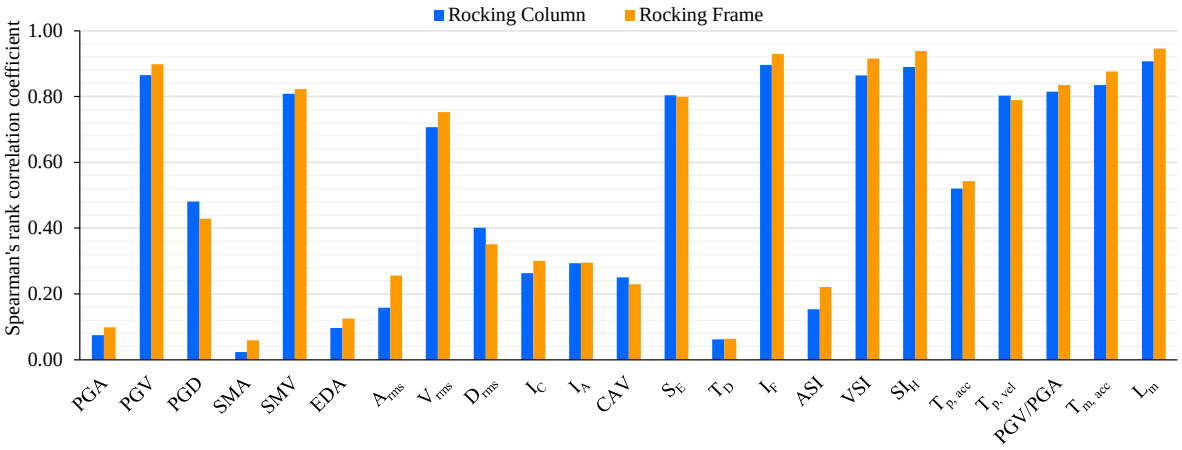

Figure 3: Correlation coefficients between the intensity measures and the engineering demand parameter.

5.2 Median seismic demand

The median demand models are generated from the linear regression analyses. Table 4 summarizes the expression of the median, the regression coefficient R^2 and the dispersion $\beta_{D|IM}$ of the seismic demand conditioned on a certain IM, for the cases of the free standing column. One of the main objectives of this paper is to estimate the most appropriate IM that reduces the uncertainty in the seismic demand model of rocking structures. The most efficient IMs are those that decrease the amount of the variation in the estimated median demand which means reduced uncertainty.

IM	PSDM	R^2	$\beta_{D\|IM}$
PGA	ln(0.202) + 0.256ln(IM)	0.01	1.31
PGV	ln(2E-4) + 1.729ln(IM)	**0.75**	**0.66**
PGD	ln(0.035) + 0.538ln(IM)	0.23	1.15
SMA	ln(0.172) + 0.072ln(IM)	0.01	1.31
SMV	ln(0.001) + 1.633ln(IM)	0.65	0.77
EDA	ln(0.219) + 0.331ln(IM)	0.01	1.30
A_{rms}	ln(0.803) + 0541ln(IM)	0.03	1.29
V_{rms}	ln(0.015) + 1.264ln(IM)	0.50	0.93
D_{rms}	ln(0.090) + 0.389ln(IM)	0.16	1.20
I_c	ln(1.010) + 0.68l3n(IM)	0.07	1.26
I_A	ln(0.133) + 0.549ln(IM)	0.09	1.25
CAV	ln(0.002) + 0.651ln(IM)	0.06	1.27
S_E	ln(0.001) + 0.755ln(IM)	0.65	0.78
T_D	ln(0.117) + 0.124ln(IM)	0.01	1.31
I_F	ln(8E-05) + 1.820ln(IM)	**0.80**	**0.58**
ASI	ln(0.289) + 0.475ln(IM)	0.02	1.30
VSI	ln(3E-05) + 1.761ln(IM)	0.75	0.66
SI_H	ln(1E-04) + 1.541ln(IM)	0.79	0.60
$T_{p,\,acc}$	ln(0.383) + 0.896ln(IM)	0.27	1.12
$T_{p,\,vel}$	ln(0.209) + 1.388ln(IM)	0.65	0.78
PGV/PGA	ln(5.759) + 1.619ln(IM)	0.67	0.76
$T_{m,\,acc}$	ln(0.419) + 1.688ln(IM)	**0.70**	**0.72**
$L_{m,\,acc}$	ln(0.008) + 0.984ln(IM)	**0.82**	**0.55**

Table 4: Seismic demands model for the examined IMs.

It is noted that as the coefficient of determination R2 reaches higher values, the dispersion $\beta_{D|IM}$ gets less. Indicated also from the correlation analysis the IMs that minimize the variation of the data in the median demand model, being in general, the velocity and the frequency based ground motion parameters. Specifically, as the performance of the IMs is evaluated regarding the reduction of the dispersion, the most efficient IMs are the PGV, the I_F, the T_m, and the Lm with dispersion values 0.66, 0.58, 0.72 and 0.55 respectively.

In order to achieve an even better intensity measure from the perspective of efficiency, we lead to examine also vector valued IMs. In this case a multilinear regression analysis was carried out (Equation (5)) in order to minimize the dispersion on the median demand model. Among all the probable IMs combinations, the couple PGV-T_m tends to be the best vector valued IM. The specific IM is generated from the combination of two individual IMs that are not directly interrelated, as the first one is an amplitude parameter and the second one a frequency ground motion parameter. The regression coefficients took values α=0.01, β_1=1.10 and β_2=0.85, the determination coefficient R^2=0.83 and the dispersion $\beta_{D|IM}$=0.54. In comparison with all the single IM models, the standard deviation has been reduced to the bi-variable one. Thus, the efficacy of the multivariable IM is shown in terms of uncertainty reduction.

5.3 Fragility curves

Fragility curves demonstrate the probability that the structure exceeds a certain capacity limit state, given a ground motion intensity level. The fragility curves of the rocking column resulting from the three most optimal IMs are presented in Figure 4.

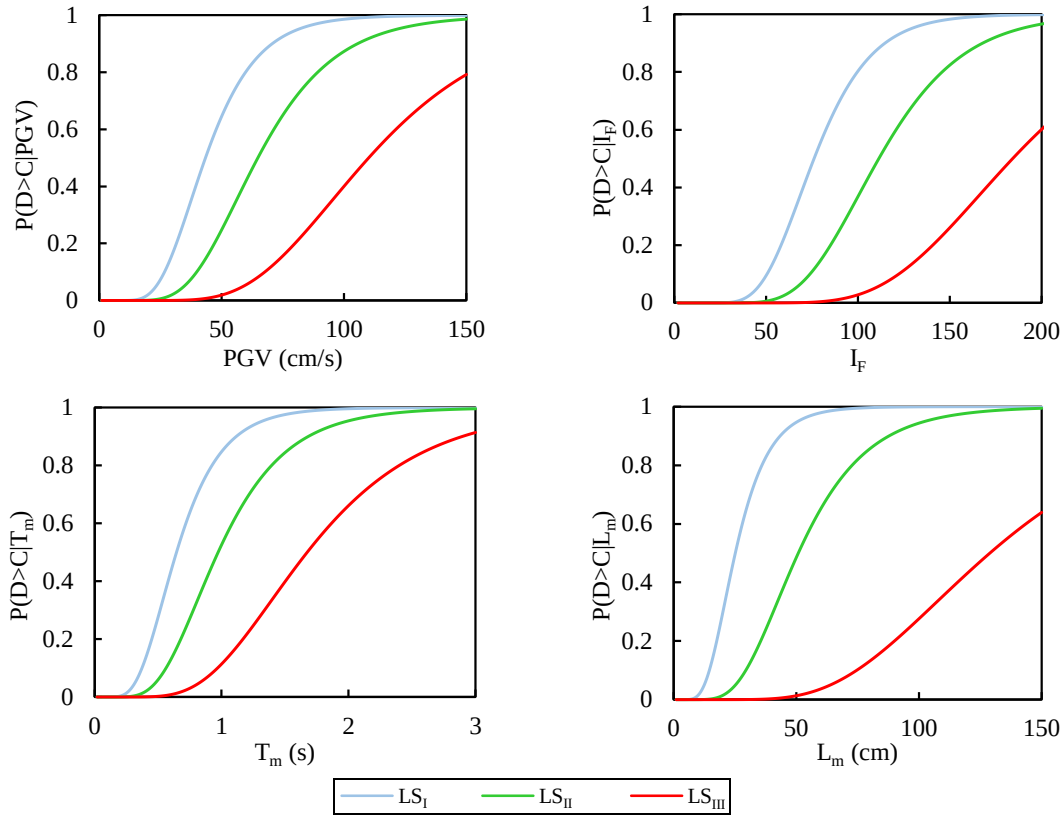

Figure 4: Fragility curves for the three most optimal IMs

The median values of the fragility curves using the PGV for the LS_I, LS_{II}, and LS_{III} are 43, 65 and 110 cm/s respectively whilst, for Farjfar index are 76, 112 and 184 cm/($s^{0.75}$). Using the T_m are 0.64, 0.98 and 1.68 s for the three limit states, and finally using the L_m as intensity measure, the median values of the fragility curves are 25, 51 and 129 cm for each limit state.

It is known that rocking structures exhibit an increased stability. This can also be observed from the fragility curves where the probability of exceeding the LS_{III} which corresponds to collapse by rocking overturn, are limited for intensity measure values that correspond to the majority of the ground motions. However, these structures which constitute some of the world's cultural heritage, have to be preserved undamaged throughout the years. Thus, if needed, we have to propose protection methods for these structures, in order to be preserved from seismic excitations of any magnitude.

Regarding the vector value IM, Figure 5 (a) depicts the surface fragility for all the limit states whilst, Figure 5 (b) shows the fragility curves of exceeding the LS_{II}, for the PGV and for the vector-valued IM which is the couple PGV-T_m. Comparing the single-variable with the bi-variable fragility curves for given Tm values, it is easily observed that as the mean period gets larger values, the vulnerability increases. In addition Table 5 lists the probability of exceedance the stated capacity for various pairs of the 2 IMs and for each IM individually. It is obvious that the bi-variable IM provided a more accurate approach on the definition of the structures' fragility as it can be shifted for even every simultaneous change of each of the two examined IMs. Comparing the probability values of Table 5, it can be seen that fragility curves generated using as uni-variable IM the mean period T_m seem to underestimate the probability of exceedance every stated performance level, especially when the mean period take low values.

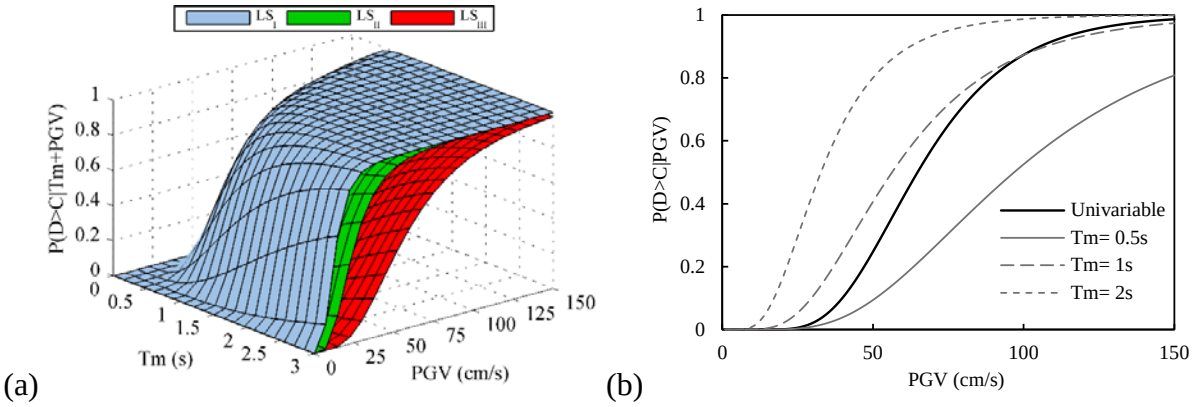

Figure 5: (a) Fragility surfaces using vector-value IM (T_m-PGV), (b) Compative results of univariable with bivariable fragility curves for given values of T_m.

Limit States	Velocity (cm/s)	Mean Period (s)			
		0.5	1	2	univariable
LS1	50	0.48	0.85	0.98	0.65
	100	0.91	0.99	1.00	0.99
	150	0.98	1.00	1.00	1.00
	univariable	0.22	0.85	0.99	-
LS2	50	0.09	0.44	0.80	0.25
	100	0.52	0.87	0.99	0.87
	150	0.81	0.97	1.00	0.98
	univariable	0.06	0.53	0.95	-
LS3	50	0.00	0.28	0.20	0.02
	100	0.05	0.30	0.71	0.40
	150	0.21	0.61	0.91	0.79
	univariable	0.00	0.11	0.66	-

Table 5. Probability values of exceeding the stated performance levels for both univariate and bivariate IMs.

5.4 Mass effect on the rocking response

In this section, the beams' mass effect on the rocking response is examined. The results in terms of peak developed rotation versus the most optimal uni-variable IM, which is the length scale of the excitation (L_m), are presented and compared between the different cases. Subsequently, to obtain results through a vulnerability perspective the fragility curves of exceeding the LS_{II} are displayed (Figure 6).

There are two rocking frames considered with differences of the ratio of the beam mass to the columns masses (Figure 2). From Figure 6 it can be noticed that the single free standing column presents larger values of rocking rotation in contrast with the rocking frames regardless of the rise of the gravity center of the cap beam. Moreover, comparing the seismic response of the frames, the one with the heavier beam exhibits increased stability. Both observations came into agreement with Papaloizou and Komodromos [23] and Makris and Vassiliou [17] conclusions. These remarks can easily be seen from the rotation versus the excitation length scale plot but also from the respective fragility curves.

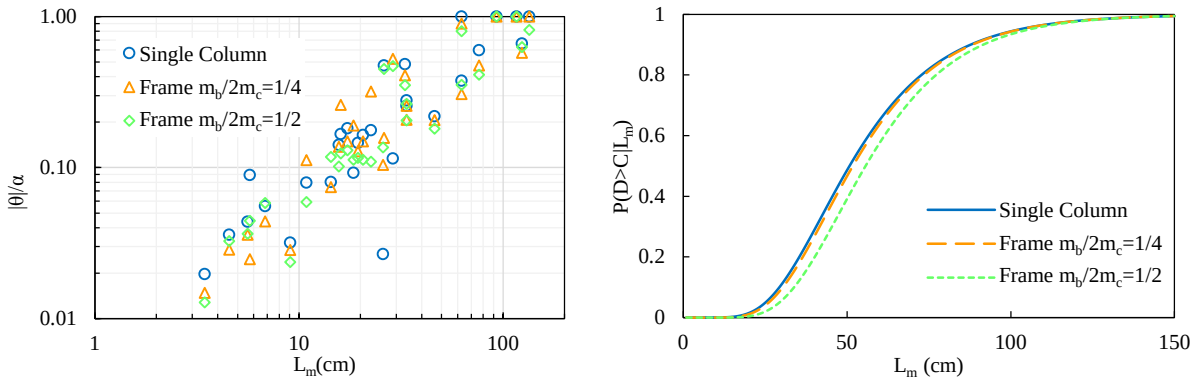

Figure 6: Comparative results of the maximum developed rocking rotation and the fragility curves of exceeding LS_{II}, between a single column and rocking frames with defferent beam masses.

6 CONCLUSIONS

The effect of the seismic excitations parameters on the rocking response of free standing columns and frames is numerically investigated in this paper, in order to conclude in an optimal uni-variable or bi-variable IM that reduces the uncertainties associated with the PSDM. Moreover, the influence of the size and the construction on the response of the structural systems is examined. The conclusion indicated by this study can be summarized as follows:

- Rocking behavior is primarily affected by the velocity based and the frequency content parameters of the ground motion. Specifically, the peak ground velocity (PGV), the Fajfar index (I_F), the mean period (Tm) and the length scale (Lm) of the excitation are the most optimal IMs.
- Vector valued IMs provided better approach on the determination of the fragility curves, than the uni-variable IMs. In addition, between the bi-variables IMs the couple PGV-Tm is the most efficient one.
- Rocking structures exhibit notable stability that can be seen also from the fragility curves in which the probability of overturning due to rocking is limited for IM values, which correspond to the majority of the ground motions.
- Free standing frames are less vulnerable than the single columns. Moreover, as the beam mass increases, the developed rocking rotation of the frame tends to be reduced.

REFERENCES

[1] N. Makris, M. F. Vassiliou, Seismic Response and Stability of the Rocking Frame. *Computational Methods, Seismic Protection, Hybrid Testing and Resilience in Earthquake Engineering*, 249-273, 2015.

[2] J. Milne, Seismic experiments. *Trans. Seismol. Soc. Jpn.*, **8**, 1-82, 1885.

[3] F. Omori, Seismic experiments on the fracturing and overturning of columns. *Publications of the Earthquake Investigation Committee in Foreign Language*, **4**, 69–141, 1900.

[4] P. Kirkpatrick, Seismic measurements by the overthrow of columns. *Bull. Seismol. Soc. Am.*, **17**, 95-109, 1927.

[5] G.W. Housner, The behavior of inverted pendulum structures during earthquakes. *Bulletin of the Seismological Society of America*, **53**, 403-417, 1963.

[6] C. S. Yim, A.K. Chopra, J. Penzien, Rocking response of rigid blocks to earthquakes. *Earthquake Engineering & Structural Dynamics*, **8**(6), 565–587, 1980.

[7] P. D. Spanos, A.S. Koh, Rocking of rigid blocks due to harmonic shaking. *J. Eng. Mech. (ASCE)*, **110**, 1627-1642, 1984.

[8] I. N. Psycharis, P.C. Jennings, Rocking of slender rigid bodies allowed to uplift. *Earthq. Eng. Struct. Dynam.*, **11**, 57-76, 1983.

[9] S.J. Hogan, The many steady state responses of a rigid block under harmonic forcing. *Earthq. Eng. Struct. Dyn.*, **19**, 1057-1071, 1990.

[10] H.W. Shenton, Criteria for initiation of slide, rock, and slide-rock rigid-body modes. J. Eng. Mech. (ASCE), **122**, 690-693, 1996.

[11] N. Makris, Y. Roussos, Rocking response and overturning of equipment under horizontal pulse type motions. *Rep. No. PEER-98/05, Pacific Earthquake Eng. Res. Ctr*. University of California, Berkeley, California, 1998.

[12] A. Pompei, A. Scalia, M.A. Sumbatyan, Dynamics of rigid block due to horizontal ground motion. *J. Eng. Mech. (ASCE)*, **124**, 713-717, 1998.

[13] J. Zhang, N. Makris, Rocking response of free-standing blocks under cycloidal pulses. *Journal of Engineering Mechanics*, **127(**5), 473-483, 2001.

[14] A. Sinopoli, Dynamic analysis of a stone column excited by a sine wave ground motion. *Applied Mechanics Reviews*, **44**(11), 246-255, 1989.

[15] I.N. Psycharis, Dynamic behaviour of rocking two-block assemblies. *Earthq. Eng. Struct. Dynam.*, **19**, 555-575, 1990.

[16] P.D. Spanos, P.C. Roussis, N.P. Politis, Dynamic analysis of stacked rigid blocks. *Soil Dyn. Earthq. Eng.*, **21**, 559-578, 2001.

[17] N. Makris, M.F. Vassiliou, Planar rocking response and stability analysis of an array of free - standing columns capped with a freely supported rigid beam. *Earthquake Engineering & Structural Dynamics*, **42**(3), 431-449, 2013.

[18] M.J. DeJong, E.G. Dimitrakopoulos, Dynamically equivalent rocking structures. *Earthquake Engineering & Structural Dynamics*, **43**, 1543-1563, 2014.

[19] I.N. Psycharis, D.Y. Papastamatiou, A.P. Alexandris, Parametric investigation of the stability of classical columns under harmonic and earthquake excitations. *Earthquake Engineering and Structural Dynamics*, **29**(8), 1093-1109, 2000.

[20] D. Konstantinidis, N. Makris, Seismic response analysis of multidrum classical columns. *Earthquake Engineering and Structural Dynamics*, **34**, 1243-1270. 2005.

[21] C. Papantonopoulos, I.N. Psycharis, D.Y. Papastamatiou, J.V. Lemos, H. Mouzakis, Numerical prediction of the earthquake response of classical columns using the distinct element method. *Earthquake Engineering and Structural Dynamics*, **31**(9), 1699-1717, 2002.

[22] I.N. Psycharis, J.V. Lemos, D.Y. Papastamatiou, C. Zambas, Numerical study of the seismic behaviour or a part of the Parthenon Pronaos. *Earthquake Engineering and Structural Dynamics*, **32**(13), 2063-2084, 2003.

[23] L. Papaloizou, P. Komodromos, Planar investigation of the seismic response of ancient columns and colonnades with epistyles using a custom-made software. *Soil Dynamics and Earthquake Engineering,* **29**, 1437-1454, 2009.

[24] P. Komodromos, L. Papaloizou, P. Polycarpou, Simulation of the response of ancient columns under harmonic and earthquake excitations. *Engineering Structures*, **30**(8), 2154-2164, 2008.

[25] R. Dimitri, L. De Lorenzis, G. Zavarise, Numerical study on the dynamic behavior of masonry columns and arches on buttresses with the discrete element method. *Engineering Structures*, **33**, 3172-3188, 2011.

[26] H.P. Mouzakis, I.N. Psycharis, D.Y. Papastamatiou, P.G. Carydis, C. Papantonopoulos, C. Zambas, Experimental investigation of the earthquake response of a model of a marble classical column. *Earthquake Engineering and Structural Dynamics*, **31**, 1681-1698, 2002.

[27] F. Peña, P.B. Lourenço, A. Campos-Costa, Experimental dynamic behavior of free-standing multi-block structures under seismic loadings. *J. Earthq. Eng.,* **12,** 953-979, 2008.

[28] V.A. Drosos, I. Anastasopoulos, Experimental investigation of the seismic response of classical temple columns. *Bulletin of Earthquake Engineering*, **13**(1), 299-310, 2015.

[29] P.D. Spanos, A.S. Koh, Analysis of block random rocking. *Soil Dynamics and Earthquake Engineering*, **5**(3), 178-183, 1986.

[30] I.N. Psycharis, M. Fragiadakis, I. Stefanou, Seismic reliability assessment of classical columns subjected to near‐fault ground motions. *Earthquake Engineering & Structural Dynamics,* **42**(14), 2061-2079, 2013.

[31] E.G. Dimitrakopoulos, T.S. Paraskeva, Dimensionless fragility curves for rocking response to near‐fault excitations. *Earthquake Engineering & Structural Dynamics,* **44**(12), 2015-2033, 2015.

[32] J.E. Padgett, B.G. Nielson, R. DesRoches, Selection of optimal intensity measures in probabilistic seismic demand models of highway bridge portfolios. *Earthquake Engineering & Structural Dynamics*, **37**(5), 711-725, 2008.

[33] C.A. Cornell, F. Jalayer, R.O. Hamburger, D.A. Foutch, Probabilistic basis for 2000 SAC federal emergency management agency steel moment frame guidelines. *Journal of Structural Engineering,* **128**(4), 526-533, 2002.

[34] E.I. Katsanos, A.G. Sextos, G.D. Manolis, Selection of earthquake ground motion records: A state-of-the-art review from a structural engineering perspective. *Soil Dynamics and Earthquake Engineering,* **30**(4), 157-169, 2010.

[35] Pacific Earthquake Engineering Research Centre (PEER). Strong motion database http://ngawest2.berkeley.edu/; 2013.

[36] European Strong-Motion Database. http://www.isesd.hi.is/ESD_Local/frameset.htm; 2008.

[37] S.L. Kramer, *Geotechnical earthquake engineering.* Prentice-Hall, 1996.

[38] E.M. Rathje, N.A. Abrahamson, J.D. Bray, Simplified frequency content estimates of earthquake ground motions. *Journal of Geotechnical and Geoenviromental Engineering,* **124**(2), 150-159, 1998.

[39] N. Makris, C.J. Black, Dimensional analysis of rigid-plastic and elastoplastic structures under pulse-type excitations. J. Eng. Mech. (ASCE), **130**, 1006-1018, 2004.

[40] E. Dimitrakopoulos, A.J. Kappos, N. Makris, Dimensional analysis of yielding and pounding structures for records without distinct pulses. *Soil Dynamics and Earthquake Engineering,* **29**(7), 1170-1180, 2009.

[41] P. Gehl, D.M. Seyedi, J. Douglas, Vector-valued fragility functions for seismic risk evaluation. *Bulletin of Earthquake Engineering,* **11**(2), 365-384, 2013.

ECCOMAS Congress 2016
VII European Congress on Computational Methods in Applied Sciences and Engineering
M. Papadrakakis, V. Papadopoulos, G. Stefanou, V. Plevris (eds.)
Crete Island, Greece, 5–10 June 2016

PARAMETRIC INVESTIGATION OF THE DYNAMIC RESPONSE OF RIGID BLOCKS SUBJECTED TO SYNTHETIC NEAR-SOURCE GROUND MOTION RECORDS

Michalis Fragiadakis[1], Ioannis Psycharis[1], Yenan Cao[2] and George P. Mavroeidis[2]

[1] School of Civil Engineering,
National Technical University of Athens,
5 Iroon Polytechniou 15773, Zografou Campus, Athens, Greece
e-mail: {mfrag,ipsych}@central.ntua.gr

[2] Department of Civil and Environmental Engineering and Earth Sciences,
University of Notre Dame,
Notre Dame, IN 46556, USA
e-mail: {ycao2,g.mavroeidis}@nd.edu

Keywords: rocking block; near source; synthetic ground motion; overturning.

Abstract. *We study the seismic response of rigid block structures against synthetic pulse-like ground motion records. A large number of synthetic ground motion records are systematically produced for various magnitude-distance scenarios. More specifically, we generate pulse-like ground motions for a grid of 56 receiver stations assuming a vertical strike-slip fault. The site conditions simulate a NEHRP Class D site, while for every combination of hypocenter, magnitude and receiver location, we generate 100 realizations consisting of low- and high-frequency components. The low-frequency component is based on a four-parameter wavelet, while the specific barrier model is used for the high-frequency component. The synthetic ground motions are used to study the seismic overturning of rigid blocks of various dimensions. The low-frequency pulse is described by four-parameters which refer to the amplitude, the prevailing frequency, the phase angle and the oscillatory character of the record, on top of which the high-frequency component is added. This description allows to parametrize the seismic response and thus improve our understanding on the effect of base motion characteristics on the overturning of rigid blocks.*

1 INTRODUCTION

Following the pioneering work of Housner (1963), the problem of rocking response and overturning of free-standing blocks to earthquakes, and especially to harmonic ground motion pulses, has been the subject of intense analytical and experimental research. Despite its apparent simplicity, the problem has proven to be a difficult task due to the nonlinear behavior introduced by the impact of the block with the base and the sensitivity of the response to even trivial changes of the problem parameters. Previous studies (e.g. Muto *et al.* 1960; Yim *et al*. 1980; Ishiyama 1982; Psycharis & Jennings 1983 & 1985; Priestley *et al*. 1983; Spanos & Koh 1984; Tso & Wong 1989; Cai *et al*. 1995; Anooshehpoor *et al*. 1999; Zhang & Makris 2001; Prieto *et al*. 2004; Peña *et al*. 2007; Purvance *et al.* 2008; Kounadis 2010 & 2013; Dimitrakopoulos & DeJong 2012, among others) have revealed the complex response, including certain counterintuitive trends such as: the stability of a block subjected to a particular ground motion does not depend monotonically on the size or the slenderness of the block; overturning of a block under a certain ground motion does not necessarily imply overturning for an increase in base excitation amplitude; the amplitude of the response does not always decrease with reduction in the value of the restitution coefficient.

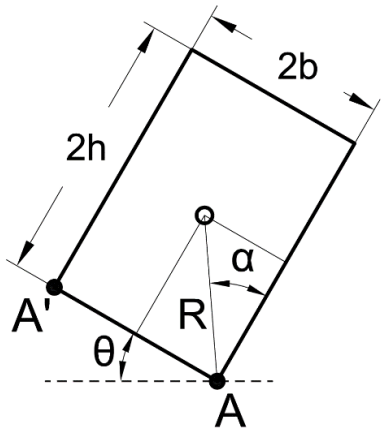

Figure 1. Rocking block geometry

In this paper, we investigate the seismic response of rigid blocks subjected to synthetic pulse-like ground motions. We consider rigid blocks of various dimensions which are subjected to pulse-like ground motions recorded at different locations with respect to the causative fault. The synthetic records consist of a low-frequency pulse, with known properties, and a high-frequency component. Following a systematic workflow, we investigate the sensitivity of the response of rigid blocks, and especially the overturning risk, to different problem parameters, such as the magnitude of the event, the distance, block dimensions and slenderness and other ground motion properties.

2 THE RIGID BLOCK PROBLEM

A rigid block of dimensions $2b \times 2h$ (Figure 1) oscillates about point A (or A'), provided that the coefficient of friction is large enough to prevent sliding. The block has weight W and moment of inertia I_0 about point A (Figure 1). Assuming that the block is homogeneous and thus

the center of gravity is located at height *h*, the block will start rocking only if the incipient ground acceleration exceeds the value of $(b/h)\cdot g$ or $g\cdot\tan(\alpha)$, where $\alpha = \text{atan}(b/h)$ is the block slenderness. Note that α together with the block size parameter $R = \sqrt{h^2 + b^2}$ fully define the geometry of the block. The equation of motion of the block (Housner 1963) thus becomes:

$$I_o\ddot{\theta}(t) + mgR\sin\left[\alpha\text{sgn}\theta(t) - \theta(t)\right] = -mg\ddot{u}_g(t)R\cos\left[\alpha\text{sgn}\theta(t) - \theta(t)\right] \quad (1)$$

where the angle of rotation θ is the only degree of freedom. The sign function is used to define the pivot point (A or A'), which depends on the sign of θ. Therefore, when A' is the pivot point, θ receives a negative value as implied by the sign function. For rectangular blocks, the moment of inertia becomes $I_0 = (4/3)mR^2$, while for small rotations θ, Equation (1) can be linearized:

$$\ddot{\theta}(t) = p^2\left[\text{-}\alpha\,\text{sgn}\left(\theta(t)\right) + \theta(t) - \ddot{u}_g(t)/g\right] \quad (2)$$

where *p* denotes the characteristic frequency of the rocking block and is defined as:

$$p = \sqrt{\frac{WR}{I_0}} = \sqrt{\frac{3g}{4R}} \quad (3)$$

Dimitrakopoulos and DeJong (2012) have shown that the frequency parameter *p* is equal to the oscillating frequency of the block if it is viewed as a pendulum with the rocking rotation point (A or A') being the pivot point. Damping is event-based, meaning that energy is lost only when the angle of rotation reverses and impact with the base occurs. The conservation of angular momentum just before and right after impact gives the coefficient of restitution η. This coefficient typically receives values between 0.6-0.9 and its theoretical value (Housner 1963) is:

$$\eta = \left[1 - \frac{3}{2}\sin^2\alpha\right]^2 \quad (4)$$

The equation of motion is solved numerically, while closed-form expressions for harmonic ground motions have been proposed by Dimitrakopoulos and DeJong (2012).

3 GENERATION OF BROADBAND SYNTHETIC GROUND MOTIONS

The hybrid method proposed by Mavroeidis and Papageorgiou (2003) is used to simulate broadband near-fault pulse-like ground motions. The incoherent (high-frequency) seismic radiation is synthesized using the specific barrier model (SBM) (Papageorgiou and Aki 1983). In the context of the SBM, the fault is visualized as an ensemble of non-overlapping circular subevents of equal diameter $2\rho_0$ that cover a rectangular fault with length *L* and width *W*. As the rupture front sweeps the fault plane with a rupture velocity *V*, a local stress drop $\Delta\sigma_L$ occurs on each subevent. The subevent rupture starts from its center and spreads radially outward with a constant spreading velocity until it is arrested by the barriers. The SBM has been calibrated to shallow crustal earthquakes of various tectonic regions (Halldorsson and Papageorgiou 2005). Given an earthquake magnitude and the tectonic region, the interdepend-

ence of other source parameters on the local stress drop $\Delta\sigma_L$ and the barrier interval $2\rho_0$ allows the causative earthquake fault to be constructed. Since the site of interest is considered to be in the "near field" of the ruptured fault, it is necessary to simulate time histories for each individual subevent of the SBM, rather than for the entire seismic event as an aggregate of subevents. The subevent time histories are subsequently summed up at the site with appropriate consideration of time delays.

On the other hand, the coherent (long-period) ground motion component is simulated using the mathematical model proposed by Mavroeidis and Papageorgiou (2003). The mathematical formulation for the representation of the near-fault velocity pulses is:

$$V(t) = 0.5A_p\left[1+\cos\left(\frac{2\pi f_p}{\gamma_p}(t-t_0)\right)\right]\cos\left[2\pi f_p(t-t_0)+\nu_p\right], \quad t\in\left[t_0-\frac{\gamma_p}{2f_p}, t_0+\frac{\gamma_p}{2f_p}\right] \tag{5}$$

where A_p controls the amplitude of the signal, f_p is the prevailing frequency of the signal, ν is the phase of the amplitude-modulated harmonic, γ_p is a parameter that defines the oscillatory character of the signal, and t_0 specifies the epoch of the envelope's peak. In addition, the pulse period T_p is defined as the inverse of the prevailing frequency f_p.

In what follows, we consider a vertical strike-slip fault in an interplate region and five scenarios with a distinct moment magnitude (M_w 5.5, 6.0, 6.5, 7.0, 7.5). The diameters of the subevents $2\rho_0$ are 2.9, 5.2, 9.2, 16.4 and 29.2 km for M_w 5.5, 6.0, 6.5, 7.0 and 7.5, respectively. According to the calibration of the SBM for interplate regimes (Halldorsson and Papageorgiou 2005), the total number of subevents that make up the SBM is typically 15. Consistent with realistic values of fault dimensions, the 15 subevents are arranged in a 5×3 pattern for events M_w 5.5, 6.0 and 6.5 (as illustrated in Figure 2), whereas for M_w 7.0 and 7.5 the subevents are placed in two rows with the upper and lower rows consisting of 8 and 7 subevents, respectively. The top edge of the fault is 0.1 km deep. The hypocenter is placed at $L/2$ along strike and $0.7W$ down dip whereas the rupture velocity is assumed to be 2.4 km/s.

The high-frequency ground motions are generated at a grid of 56 stations (Figure 2) at distances normal to the fault equal to 0.2, 1, 5, 10, 15, 20, 25 km. The spacing of the stations in the fault-parallel direction is: $-L/5$, 0, $L/5$, $2L/5$, $3L/5$, $4L/5$, $5L/5$, $6L/5$, where L is the fault length which is function of the moment magnitude M_w. The site characterization is assumed to be NEHRP site class D for all stations. We vary the seed number within the SBM so that 100 realizations are obtained for every combination of magnitude and receiver location. The long-period ground motion pulses are generated using the model input parameters as suggested by Mavroeidis and Papageorgiou (2003) and Halldorsson *et al.* (2011). The amplitude A_p is computed as A_p = 0.9 PGV, where the logarithm of PGV follows a normal distribution with the mean value provided by:

$$\log \mathrm{PGV} = 2.040 - 0.032 r_{rup} \tag{6}$$

and a standard derivation of 0.187. The distance measure r_{rup} is defined as the closest fault-to-station distance. The pulse period T_p scales self-similarly with earthquake magnitude, and the logarithm of T_p follows a normal distribution with the mean value determined by:

$$\log T_p = -2.9 + 0.5 M_W \quad (7)$$

and a standard deviation of 0.143. In addition, parameter γ_p follows a normal distribution with a mean value of 1.93 and a standard deviation of 0.47. This distribution is left-truncated to one to ensure that all γ_p values are greater than one. Finally, the phase angle follows a normal distribution with mean 1.83 and standard deviation of 0.98. Note that for every combination of magnitude and receiver location, 100 samples for each model parameter (e.g. A_p, f_p, ν_p and γ_p) are generated using Monte Carlo sampling. Finally, the long-period components of ground motion are superimposed on the high-frequency ground motions, with the initiation of the pulses aligned with time incident corresponding to 1% of the Arias intensity of the high-frequency motions.

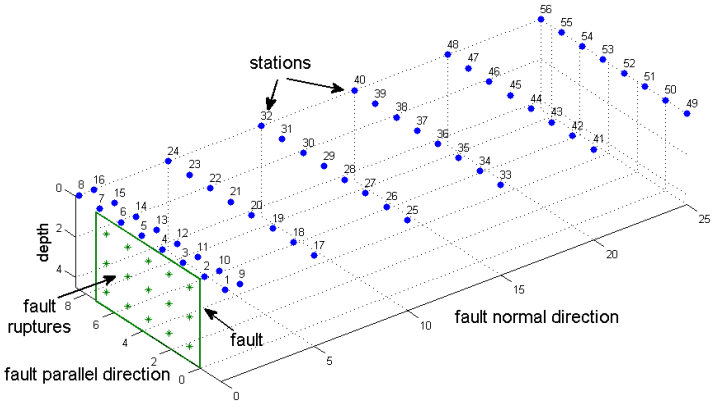

Figure 2 Fault geometry and grid of receivers (stations).

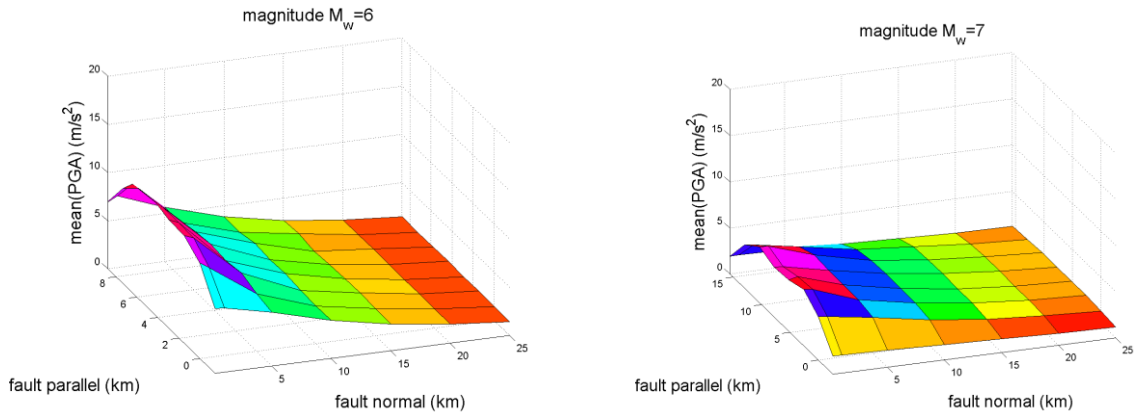

(a) (b)

Figure 3 Mean *PGA* values of the synthetic ground motion records for: (a) M_w = 6.0, (b) M_w = 7.0. Smaller M_w events produce larger PGA values.

Figure 3 shows the spatial distribution of the mean peak ground acceleration (*PGA*) of the synthetic broadband near-fault ground motions. For both M_w cases shown, larger mean *PGA* values are produced in the center of the fault-parallel direction that is closer to the epicenter, while the mean *PGA* attenuates as the distance in the fault-normal direction increases. Furthermore, the mean *PGA* values are larger for events of smaller magnitude (Figure 3). This

was first observed empirically by Somerville (2000), while Mavroeidis and Papageorgiou (2003) and Mavroeidis *et al.* (2004) discussed and explained mathematically that acceleration pulses generated by smaller earthquakes are typically stronger i.e., they have higher amplitude but shorter duration than acceleration pulses of larger earthquakes. However, once the high-frequency component is added to the pulse-type motions, this trend may be reversed.

4 PRELIMINARY RESULTS

4.1 Magnitude-distance plots

We consider twelve rigid block configurations with aspect ratio $\lambda = h/b$ equal to 2, 3, 5, 10 and characteristic frequencies p = 1.5, 2.5, 5.0. The grid consists of 56 receiver stations and, for every station and block configuration, we perform block response history analysis using 100 forward-directivity synthetic ground motions. Thus for every station, we perform 12000 rigid block response history analyses. Unless otherwise specified, all analyses refer to a fixed value of the coefficient of restitution η = 0.9.

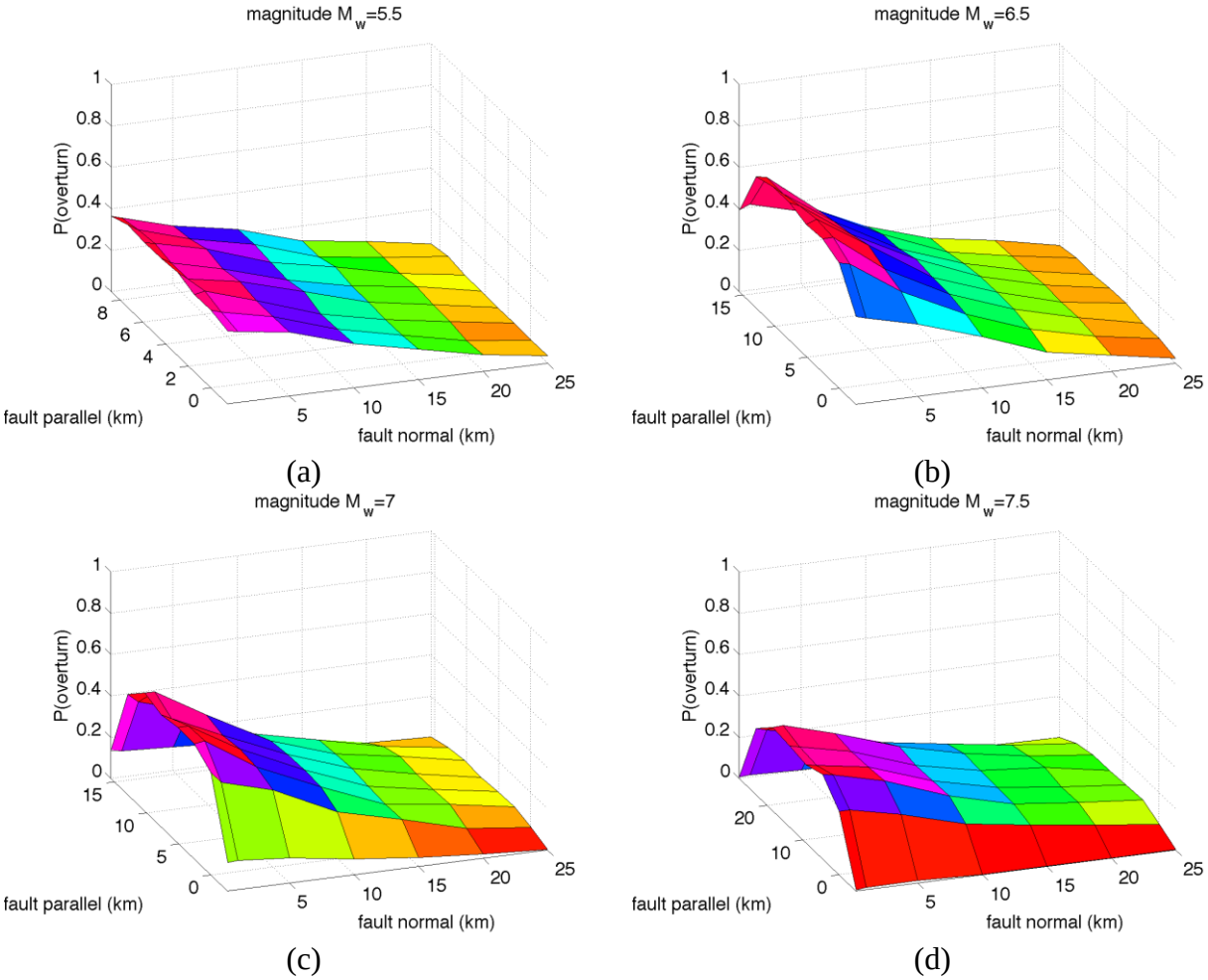

Figure 4 Probability of block overturning: (a) M_w = 5.5, (b) M_w = 6.5, (c) M_w = 7.0, (d) M_w = 7.5.

Figure 4 presents contour plots of the probability of block overturning. Four M_w scenarios, M_w = 5.5, 6.5, 7.0 and 7.5 are shown. The highest probabilities are observed for the M_w = 6.5 case,

while smaller probabilities were obtained for the M_w = 5.5 and M_w = 7.5 ground motions. Compared to the PGA plots of Figure 3, the spatial distribution is the same, but the overturning probabilities decrease for large magnitudes. This is due to the fact that large magnitude events produce weaker and longer pulses although they have a longer duration and a stronger high-frequency component.

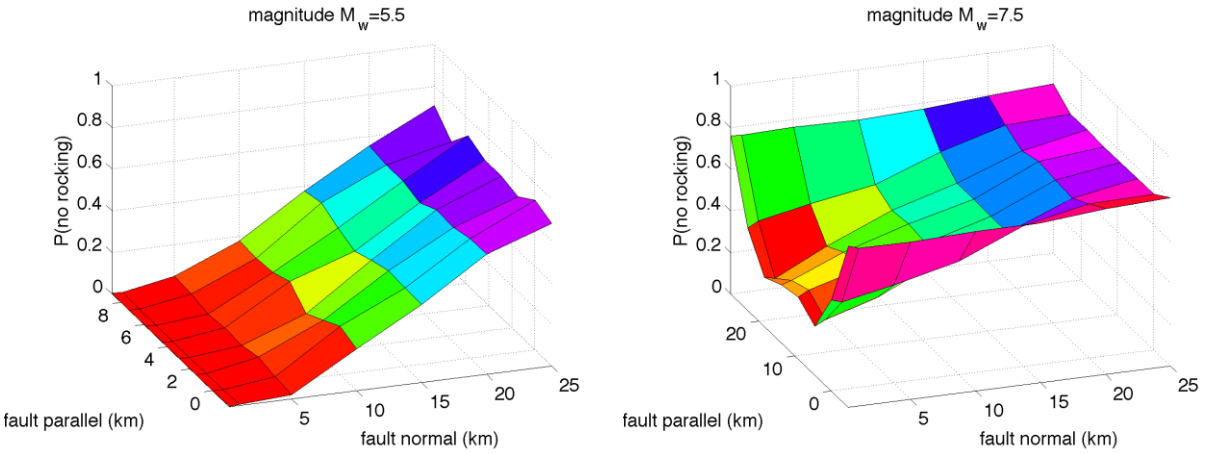

(a) (b)

Figure 5 Probability of not initiating rocking for the grid of stations: (a) M_w = 5.5, (c) M_w = 7.5.

Figure 5 shows the empirical probability that the ground motion is not strong enough to initiate rocking. It is reminded that a block starts rocking only if the *PGA* of the incipient ground motion exceeds $g \cdot \tan(\alpha)$. For the M_w = 5.5 case, practically all ground motions trigger rocking for small distances from the fault, while for stations far from the fault the probability that rocking is not initiated becomes very high. On the other hand, for the M_w = 7.5 case, the probability that no rocking is initiated is quite high even at sites very close to the fault (Figure 5b).

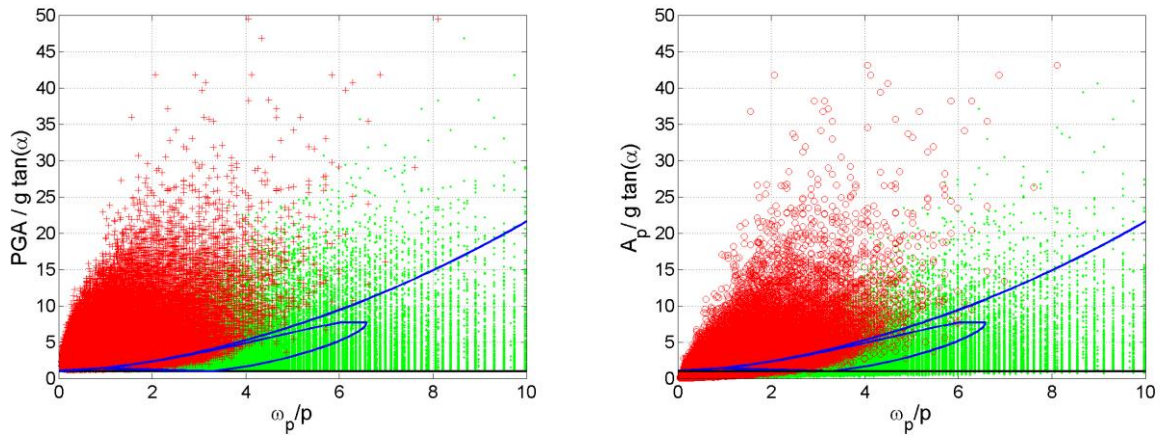

(a) (b)

Figure 6 PGA vs Ap. The blue lines refer to the closed-form expression of stable-unstable threshold for sine excitation according to Dimitrakopoulos and DeJong (2012).

4.2 Overturning spectra

The results are grouped in Figure 6 in stable-unstable plots in the acceleration-frequency domain. In Figure 6a, the normalized *PGA* with respect to the critical acceleration for the initia-

tion of rocking, $g \cdot \tan\alpha$, is plotted versus the normalized pulse period, ω_p/p, while in Figure 6b the normalized pulse acceleration, A_p, is plotted versus ω_p/p. Red points correspond to blocks that overturned and green points to blocks that did not overturn. Blocks that were not set to rocking motion are not shown; thus, $PGA/(g \cdot \tan\alpha)$ is larger than one for all points shown in Figure 6a. However, $A_p/(g \cdot \tan\alpha)$ can be smaller than one, as shown in Figure 6b.

These plots are referred as "overturning spectra", since the horizontal axis of Figure 6 measures frequency, while the vertical axis measures the intensity of the ground motion. Angle α controls the slenderness of the block (Figure 1), while parameter p accounts for the size of the block.

The two plots of Figure 6, which look similar, define the region in which the block might overturn. In both plots we also show, for comparison, with solid blue lines the closed-form solution of Dimitrakopoulos and DeJong (2012) that define the safe-unsafe threshold for a full sine pulse with amplitude equal to the PGA or the pulse amplitude A_p of our synthetic records and frequency ω_p equal to that of the low-frequency pulse. The sinusoidal ground motions are assumed symmetric (i.e. $v = 0$). The following observations can be made looking at Figure 6:

- $PGA/(g \cdot \tan\alpha)$ is preferable over $A_p/(g \cdot \tan\alpha)$, since it is easier to calculate and respects the condition that rocking will immense only if $PGA/(g \cdot \tan\alpha) \geq 1$.
- The use of a sinusoidal pulse is overall more conservative.
- As we move to the right side of each plot of Figure 6, the points shown refer to blocks that are either large (large R and small p) or are subjected to high frequency ground motions (large ω_p values). Therefore, these results show that overturning is rather improbable to occur in such cases. This seems to be true for ω_p/p larger than 8, independently of the amplitude of the normalized acceleration.
- On the left edge of the plots, specifically for values of ω_p/p smaller than about 2, corresponding to ground motions containing long-period pulses (small ω_p values) or to small-size blocks (large p values), overturning occurs for all ground motions capable to initiate rocking.
- The apparent limit between the safe and the unsafe region implies only that the blocks on the safe side do not overturn. In other words, there are many blocks on the "unsafe" region that did not overturn. In this sense, the threshold between the safe-unsafe regions corresponds to the minimum normalized ground acceleration $PGA/(g \cdot \tan\alpha)$ for each value of ω_p/p that could topple the block, without meaning that all excitations with larger values of $PGA/(g \cdot \tan\alpha)$ will cause overturning.
- Compared to our results, the sinusoidal ground motions are more conservative for ω_p/p values that exceed 6. Beyond this limit, our broadband simulations yield that the blocks do not overturn, as opposed to the case of sinusoidal pulse where the blocks are safe or their response does not depend on the $PGA/g \cdot \tan(\alpha)$ parameter.

5 SENSITIVITY ANALYSIS

5.1 Effect of distance and magnitude

In Figure 7, the probability of block overturning versus the magnitude of the event is shown for several distances. The black solid line denotes the average trend. It is evident that the probability of block overturning is affected by both magnitude and distance. Concerning the effect of distance, small distances result to higher probabilities of block overturning, as expected. However, concerning the effect of magnitude, it is seen that the overturning probability does not monotonically increase with magnitude as one would expect, since, for events of magnitude larger than $M_w = 6.5$, the overturning probability reduces as the magnitude increases. This counter-intuitive response is attributed to the saturation of the *PGV* for earthquakes with magnitude larger than 6.5 while the period of the pulse is increasing exponentially with the magnitude (Eq. (7)). As a result, the directivity pulse has small acceleration amplitude for large magnitudes, which is not capable to produce intense rocking.

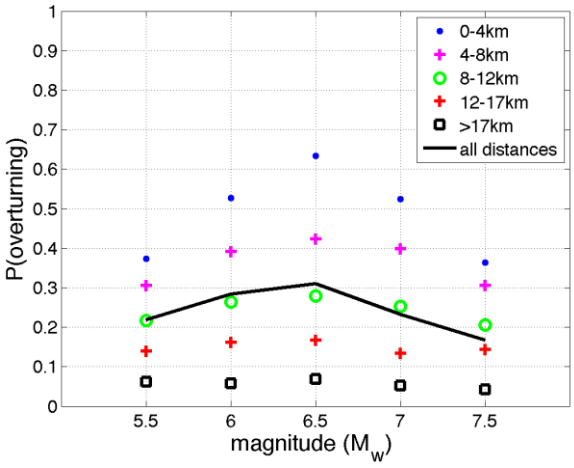

Figure 7 Variation of the probability of block overturning with magnitude and rupture distance. The black solid line denotes the average trend.

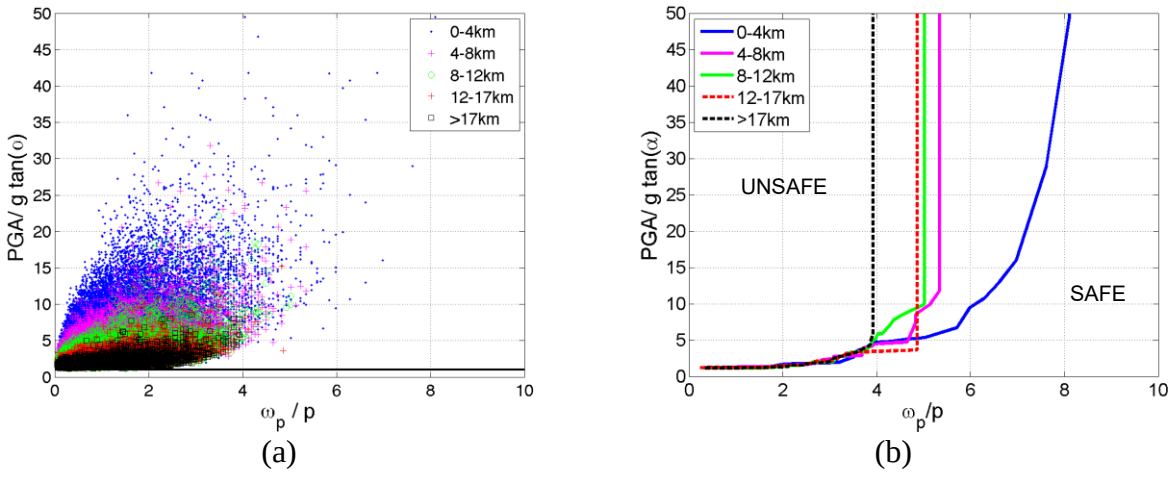

Figure 8 Clustering of the ground motions that caused block overturning with respect to the rupture distance: (a) all simulations; (b) envelope curves indicating the threshold between safe and unsafe regions.

Further insight on the dependence of the block overturning probability with distance and magnitude is offered by Figure 8 and Figure 9, respectively. Figure 8 shows the effect of distance on the block overturning spectra. The left plot (Figure 8a) clusters the data depending on the distance, while Figure 8b shows the threshold curves that define the safe and the unsafe regions, allowing a better comparison. The number of blocks that overturn decrease with distance as also indicated by the overturning probabilities of Figure 7, which is attributed to the fact that the *PGA*s decrease at large-distances (Figure 3). However, as evident from Fig. 8b, the distance does not affect the safe-unsafe threshold for small values of ω_p/p, but only for blocks with $\omega_p/p \geq 4$, for which the unsafe region expands to the right for small-distant events.

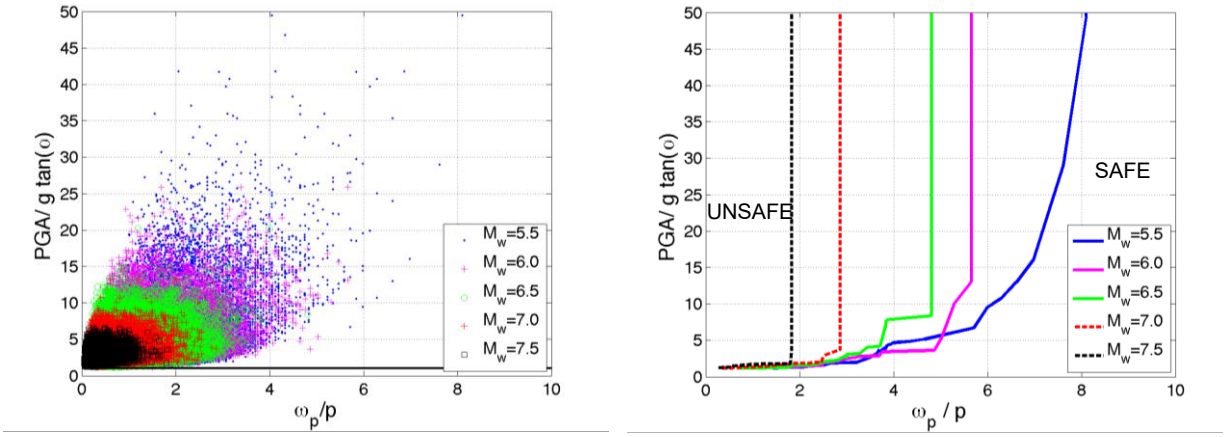

(a) (b)

Figure 9 Clustering of the ground motions that caused block overturning with respect to moment magnitude Mw: (a) all simulations; (b) envelope curves indicating the threshold between safe and unsafe regions.

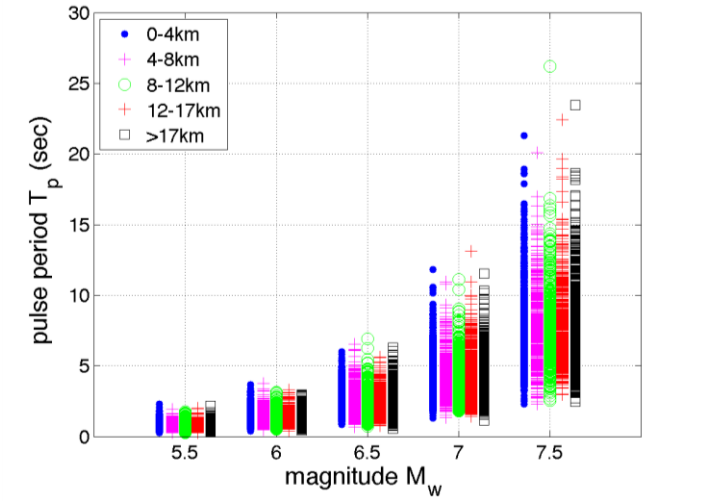

Figure 10 Relationship of the period T_p of the directivity pulse with moment magnitude M_w and distance. As M_w increases longer period values are obtained, while there is no dependence with respect to the distance.

Figure 9 shows the effect of moment magnitude M_w on the block overturning. The effect of M_w is strong, since the different magnitudes have distinct threshold curves (Figure 9b). This is due to the fact that both *PGA* and ω_p depend on the magnitude. As shown in Figure 3, events of small M_w (e.g. M_w=5.5) produce larger PGA values than larger magnitudes (e.g. M_w=6.5),

although the failure probabilities do not follow this trend (Figure 7). On the other hand, ω_p decreases quickly with amplitude due to the exponential increase of the pulse period T_p (Figure 10), which means that only small values of ω_p/p can be attained for large-magnitude events. In this sense, for a given block (given p), the normalized frequency ω_p/p decreases abruptly as M_w increases and, therefore, the safe-unsafe threshold moves to the left for the range of the block dimensions examined (block size is measured by parameter p).

Another interesting conclusion that can be drawn from Figure 9b is that, for values of $\omega_p/p < 3$ the minimum *PGA* required to overturn a block is almost equal or slightly larger to the one needed to set it on rocking motion, since $PGA/(g\cdot\tan\alpha)$ is close to unity. For events with large magnitude M_w (larger than 7.0), this means that, if the ground excitation is strong enough to trigger rocking, it will most probably cause overturning too. However, for events of smaller M_w, for which values of $\omega_p/p > 3$ can be attained, the minimum *PGA* required to overturn a block is significantly larger than the one needed to initiate rocking (equal to $g\cdot\tan\alpha$).

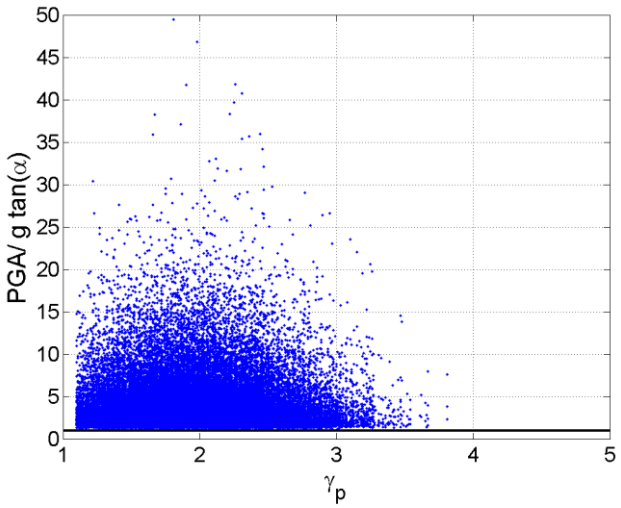

Figure 11 Distribution of the normalized PGA of the ground motions that caused overturning with the γp parameter that controls the oscillatory character of the ground motion.

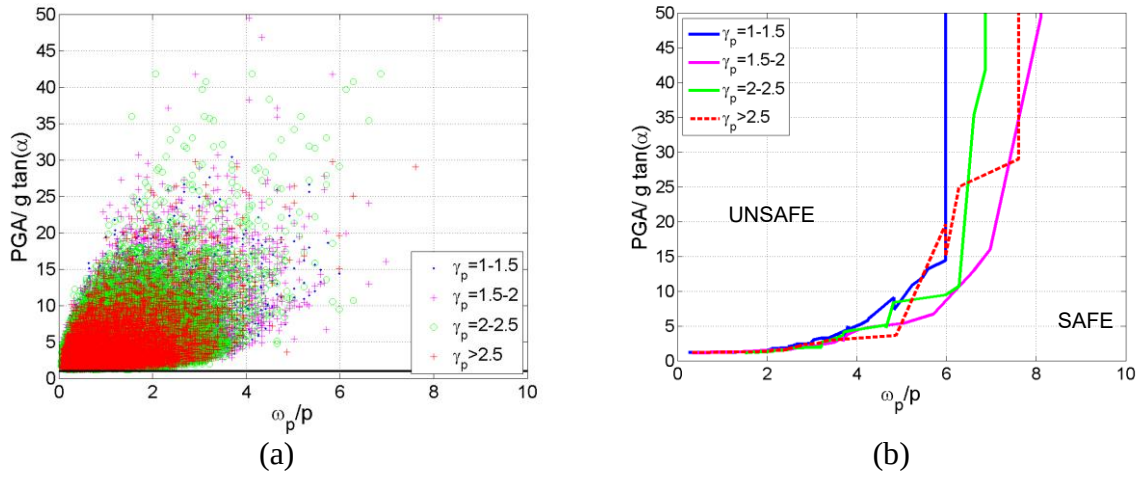

Figure 12 Clustering of the data with respect to γ_p: (a) all simulations that cause block overturning, (b) envelope curves indicating the threshold between safe and unsafe regions.

5.2 Effect of the oscillatory character of the directivity pulse (γ_p parameter)

The γ_p parameter is a constant of the wavelet proposed by Mavroeides and Papageorgiou (2003) that defines the oscillatory character (i.e. zero crossings) of the signal. This parameter was assumed normally distributed when the synthetic records were generated. Figure 11 shows the analyses that overturned the blocks as function of γ_p versus the normalized $PGA/(g \cdot \tan\alpha)$ intensity. The distribution of the analyses with respect to the values of γ_p resembles that of a normal distribution. Furthermore, Figure 12 shows the overturning spectra when the results are clustered with respect to γ_p. Both the cloud plots of Figure 12a and the threshold lines of Figure 12b indicate that γ_p has a small effect on the overturning of the blocks.

5.3 Effect of block properties

5.3.1. Sensitivity to the coefficient of restitution η

The coefficient of restitution η controls the damping of the rocking motion. Figure 13b shows the threshold curves of the overturning spectra (e.g. Figure 6a) for different values of the coefficient of restitution η, namely η = 0.7, 0.8 and 0.9. Practically there is no difference between η = 0.8 and 0.9, while η = 0.7 shifts the threshold curves slightly to smaller ω_p/p values. Therefore, the effect of η, in general, is small, although there are cases where this parameter may alter the results. This conclusion is compatible with the results of past studies based on pulse-like ground motions, as the ones shown in Figure 13b obtained with the aid of the closed-form relationships of Dimitrakopoulos and DeJong (2012). In this case, the coefficient of restitution affects only the closed-loop curves, which refer to block overturning after one impact, while the monotonically increasing upper curve, which corresponds to the threshold of overturning without impact, is independent of the coefficient of restitution.

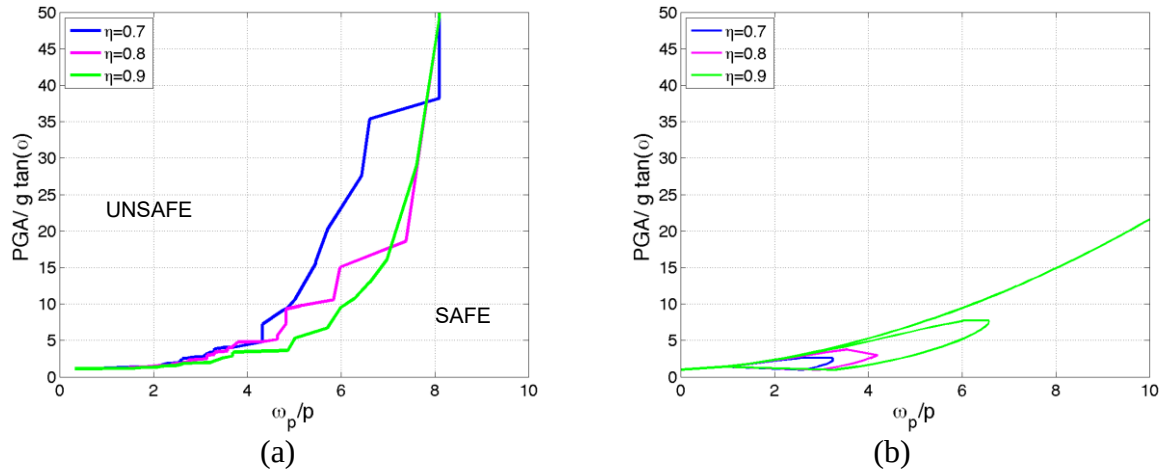

Figure 13 Effect of the coefficient of restitution η on overturning spectra: (a) this study; (b) obtained using sinusoidal pulses (Dimitrakopoulos & DeJong 2012).

5.3.2. Effect of block slenderness

Figure 14 shows the effect of the block slenderness ratio $\lambda = h/b$, i.e. the aspect ratio of the block. The h/b values considered are: 2, 3, 5 and 10, corresponding to slenderness angles α equal to 26.5, 18.4, 11.3 and 5.7 degrees, respectively. As expected, slender blocks are more

likely to overturn, as shown in Figure 14a, since they set to rocking motion for records with small enough *PGA*. Furthermore, slender blocks topple for significantly smaller angle of rotation than stocky ones, therefore, they are more vulnerable to small-period ground motions. This is the reason that the threshold curves of the overturning spectra move towards larger ω_p/p values as λ increases (Figure 14b).

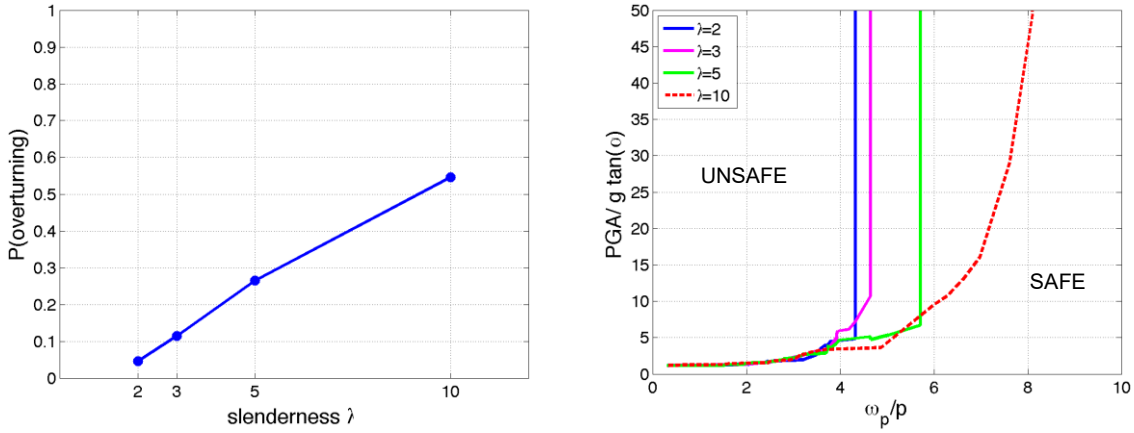

Figure 14 Overturning spectra for different values of the slenderness ratio λ of the blocks: (a) overturning probability versus λ; (b) overturning spectra.

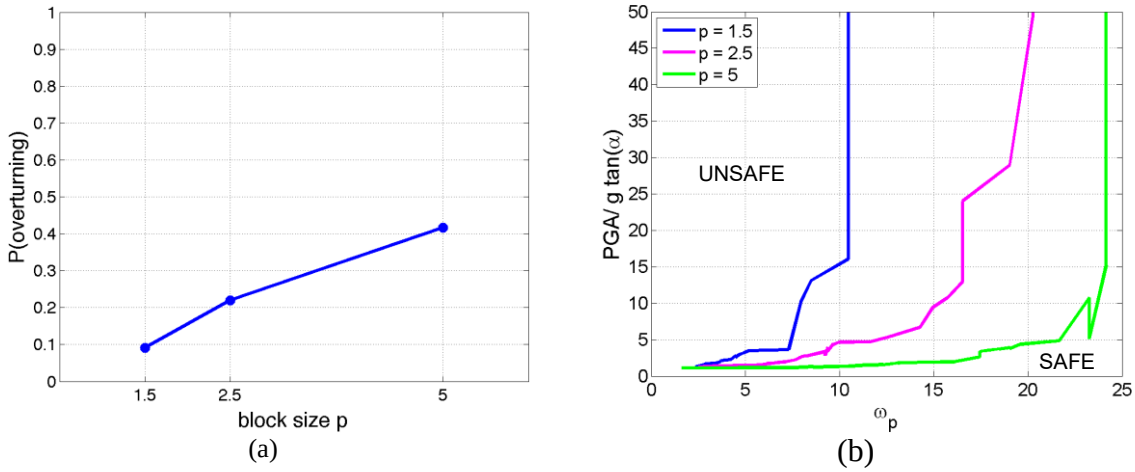

Figure 15 Effect of the frequency parameter p on the response of the block: (a) overturning probability versus p; (b) overturning spectra (note that the horizontal axis is not divided with p).

5.3.3. Effect of block size

In Figure 15, we examine the effect of the frequency parameter p which is used to measure the size of the block according to Eq. (3). We examine blocks with p = 1.5, 2.5 and 5, which correspond to blocks with half diameter R = 3.3 m, 1.18 m and 0.30 m, respectively. Figure 15a shows the scale effect on the probability of overturning, which was first observed by Housner (1963), with smaller blocks (larger p) been more vulnerable than larger ones (smaller p) of the same aspect ratio. This is also shown in Figure 15b, in which the safe-unsafe thresholds of the overturning spectra are shown w.r.t. the pulse frequency ω_p. It is evident that small blocks overturn even for high-frequency ground motions, for which large blocks of the same

aspect ratio are safe.

6 CONCLUSIONS

There are several parameters that control the seismic response of rigid block structures when subjected to pulse-like ground motion records. This paper offers a systematic investigation on the impact of several critical parameters through generating a large number of synthetic ground motion records and considering receiver locations at different places with respect to the fault. The response is post-processed in the form of overturning spectra, i.e. plots of the peak ground acceleration normalized by the critical acceleration required to trigger rocking ($PGA/g{\cdot}\tan\alpha$) versus the pulse frequency normalized by the characteristic frequency of the block (ω_p/p), from which the effect of various parameters on the threshold between the safe (no overturning) and unsafe (overturning) regions is investigated. The results show that the moment magnitude M_w is important, as it affects the pulse period T_p, while the effect of the distance is of lesser importance. Concerning the parameters of the directivity pulse, the oscillatory character of it (γ_p parameter) and the position of the hypocenter along the fault do not affect the results significantly. The same holds for the coefficient of restitution η, in contrast to the slenderness and the size of the block, which play an important role to the probability of overturning.

REFERENCES

[1] Anooshehpoor A, Heaton TH, Shi B & Brune JN. Estimates of the ground accelerations at Point Reyes station during the 1906 San Francisco earthquake. *Bulletin of the Seismological Society of America*, **89**(4), 845-853, 1999.

[2] Atkinson GW & Silva W. Stochastic modeling of California ground motions. *Bulletin of Seismological Society of America*, **90**, 255-274, 2000.

[3] Cai GQ, Yu JS & Lin YK. Toppling of rigid block under evolutionary random base excitations. *Journal of Engineering Mechanics - ASCE*, **121**(8), 924-929, 1995.

[4] DeJong MJ & Dimitrakopoulos EG. Dynamically equivalent rocking structures. *Earthquake Engineering and Structural Dynamics*, **43**(10), 1543-1563, 2014.

[5] Dimitrakopoulos EG & DeJong MJ. Revisiting the rocking block: Closed-form solutions and similarity laws. *Proceedings of the Royal Society A: Mathematical, Physical and Engineering Sciences*, **468** (2144), 2294-2318, 2012.

[6] Dimitrakopoulos EG & Paraskeva TS. Dimensionless fragility curves for rocking response to near-fault excitations. *Earthquake Engineering and Structural Dynamics*, **44**(12), 2015-2033, 2015.

[7] Halldorsson B & Papageorgiou AS (2005). Calibration of the specific barrier model to earthquakes of different tectonic regions, *Bulletin of the Seismological Society of America* **95**, 1276–1300.

[8] Halldorsson B, Mavroeidis GP & Papageorgiou AS (2011). Near-fault and far-field strong ground-motion simulation for earthquake engineering applications using the specific barrier model, *Journal of Structural Engineering-ASCE* **137**, 433-444.

[9] Housner GW. The behavior of inverted pendulum structures during earthquakes. *Bulletin of Seismological Society of America*, **53**, 403-417, 1963.

[10] Ishiyama Y. Motion of rigid bodies and criteria for overturning by earthquake excitations. *Earthquake Engineering and Structural Dynamics*, **10**, 635-650, 1982.

[11] Kounadis AN. On the dynamic overturning instability of a rectangular rigid block under ground excitation. *Open Mechanics Journal*, **4**, 43-57, 2010.

[12] Kounadis AN. Parametric study in rocking instability of a rigid block under harmonic ground pulse: A unified approach. *Soil Dynamics and Earthquake Engineering*, **45**, 125-143, 2013.

[13] Mavroeidis GP & Papageorgiou AS. A mathematical representation of near-fault ground motions. *Bulletin of Seismological Society of America*, **93**, 1099-1131, 2003.

[14] Mavroeidis, GP, Dong G. & Papageorgiou AS Near-fault ground motions, and the response of elastic and inelastic single-degree-of-freedom (SDOF) systems, *Earthquake Engineering and Structural Dynamics*, **33** (9), 1023-1049, 2004.

[15] Muto K, Umemura H & Sonobe Y. Study of overturning vibration of slender structures. *Proc. 2nd World Conference on Earthquake Engineering*, Tokyo, Japan, 1960.

[16] Papageorgiou AS & Aki K (1983). A specific barrier model for the quantitative description of inhomogeneous faulting and the prediction of strong ground motion. I. Description of the model, *Bulletin of the Seismological Society of America* **73**, 693-722.

[17] Peña F, Prieto F, Lourenço PB, Campos Costa A & Lemos JV. On the dynamics of rocking motion of single rigid-block structures. *Earthquake Engineering and Structural Dynamics*, **36**, 2383-2399, 2007.

[18] Priestley MJN, Evision RJ & Carr AJ. Seismic response of structures free to rock on their foundations. *Bulletin of the New Zealand National Society of Earthquake Engineering*, **11**, 141-150, 1983.

[19] Prieto F, Lourenço PB & Oliveira CS. Impulsive Dirac-delta forces in the rocking motion. *Earthquake Engineering and Structural Dynamics*, **33**(7), 839-857, 2004.

[20] Psycharis IN & Jennings PC. Rocking of slender bodies allowed to uplift. *Earthquake Engineering and Structural Dynamics*, **11**, 57-76, 1983.

[21] Psycharis IN & Jennings PC. Upthrow of objects due to horizontal impulse excitation. *Bulletin of the Seismological Society of America*, **75(**2), 543-561, 1985.

[22] Purvance MD, Anooshehpoor A & Brune JN. Freestanding block overturning fragilities: Numerical simulation and experimental validation. *Earthquake Engineering and Structural Dynamics*, **37**, 791-808, 2008.

[23] Somerville P. New developments in seismic hazard estimation, in Proc. of the Sixth Int. Conf. on Seismic Zonation, Palm Springs, California, 12–15 November 2000.

[24] Spanos PD & Koh AS. Rocking of rigid bodies due to harmonic shaking. *Journal of Engineering Mechanics - ASCE*, **110**(11), 1627-1642, 1984.

[25] Tso WK & Wong CM. Steady state rocking response of rigid block. Part I: Analysis. *Earthquake Engineering and Structural Dynamics*, **18**, 89-106, 1989.

[26] Yim CS, Chopra AK & Penzien J. Rocking response of rigid bodies to earthquakes. *Earthquake Engineering and Structural Dynamics*, **8**, 565-587, 1980.

[27] Zhang J & Makris N. Rocking response of free-standing blocks under cycloidal pulses. *Journal of Engineering Mechanics - ASCE*, **127**, 473-483, 2001.

ECCOMAS Congress 2016
VII European Congress on Computational Methods in Applied Sciences and Engineering
M. Papadrakakis, V. Papadopoulos, G. Stefanou, V. Plevris (eds.)
Crete Island, Greece, 5–10 June 2016

A MACRO-ELEMENT FORMULATION FOR ROCKING FLEXIBLE BODIES WITH A DEFORMABLE BASE

Evangelos Avgenakis and Ioannis N. Psycharis

School of Civil Engineering
National Technical University of Athens, Greece
Polytechnic Campus, Heroon Polytechniou 9, 15780 Zografou
e-mail: vavgen@outlook.com, ipsych@central.ntua.gr

Keywords: Rocking, Macro-element, Non-linear analysis

Abstract. *In recent years, an increased interest in the use of rocking members for the design of earthquake resistant structures is observed. As described in the literature, the use of rocking members leads to more resilient structural systems, since, in contrast to conventional members which develop damage and residual deformations, rocking members have the ability to re-center without significant damage, leading to increased structural safety and lower repair costs after a seismic event, while their yield-like response restrains the seismic forces acting on the structure.*

Although much research has been conducted on the response of rocking members, mainly regarding analytical solutions for free-standing rocking bodies with rigid bases and simplified guidelines for the design of structural rocking members, it is believed that there is a need for simple computational models, which can describe the response of rocking flexible members in structural systems more realistically.

In this paper, a new approach that is able to take into account the deformation along the height of the body and along the contact areas, especially required for cases of constrained structural members, is applied for the development of a generalized macro-element, which can be used in the context of a finite element program. The theoretical formulation of the problem is based on the solution of the normalized semi-infinite strip problem with random loads on its free side. The new macro-element is demonstrated using typical example problems and the results are compared with corresponding results obtained with Abaqus, showing excellent agreement. Concerning the required runtimes, the macro-element runs significantly faster compared to conventional finite element codes.

1 INTRODUCTION

The complex mechanics of the rocking motion of rocking bodies and structural members have attracted attention from the scientific community in recent years, although the phenomenon is known from ancient times, as many ancient monuments were built with members allowed to rock.

The rocking motion occurs when a member is unrestrained or at least partially restrained at its base, so that tensile stresses cannot be transmitted, as considered in classical structural mechanics. Given that the imposed forces are large enough, the rocking body detaches from the ground and rotates about one of its corners. The vertical force acts as the restoring force that tends to bring the body back to its original equilibrium position.

The inclusion of rocking members in real structures is considered a promising solution to the design of resilient structures. Conventional structural elements are designed to gradually yield and develop damage and residual deformations during an earthquake. Such an approach means that, after a seismic event, costly and time-consuming repairs of the building may be necessary. In contrast, the motion of rocking members is a yield-like response, able to limit the forces transmitted to the structure during an earthquake, without however developing significant damage, while the residual deformations are virtually non-existent. As as result, fewer repairs are needed after a seismic event in comparison to the conventional design.

Up to date, rocking members have been applied in case of bridge piers (e.g. the Rangitikei Railway Bridge [1]), while extensive analytical and experimental work has been performed on rocking shear walls in precast structures (e.g. [2], [3], [4]). Guidelines addressing this alternative seismic design have been published by several organizations ([5], [6], [7]), while in Eurocode 8 (EN 1998-1) [8], rocking is anticipated for large lightly reinforced walls during strong earthquakes.

Although various analytic solutions exist regarding the motion of the rigid rocking block (e.g. [9], [10], [11], [12]), as well as approximate formulas for the design of controlled rocking systems, few models exist for modeling the response of deformable rocking bodies (e.g. [13], [14], [15], [16]). These studies, however, consider only the deformability of the rocking member along its height, while the lower face, along which the contact with the base takes place, is considered rigid. As a result, rocking occurs around the corners of the bottom side. The main attempts that have been presented including the flexibility of the base concern the rocking of rigid bodies on a flexible foundation (e.g. [17], [18], [19], [20], [21], [22], among others). Computational approaches taking into account the deformability of the base of rocking members include [23], [24], [25], [26], [27].

In this paper, a new macro-element formulation is proposed, able to take into account both the deformability of the rocking member along its height and along the contact area with the base mat. The main idea behind the proposed approach is to assume a stress distribution acting on the section of the rocking interface, depending on the resultant forces on this interface, and try to predict the displacements of the rocking element due to this partial loading. To this end, the similarity between the original problem of the flexible rocking body and that of a cantilever, partially loaded on its free side with normal and shear stresses that model the ones acting on the contact region of the body while rocking (Fig. 1) is used. More information on the applied technique can be found in [28].

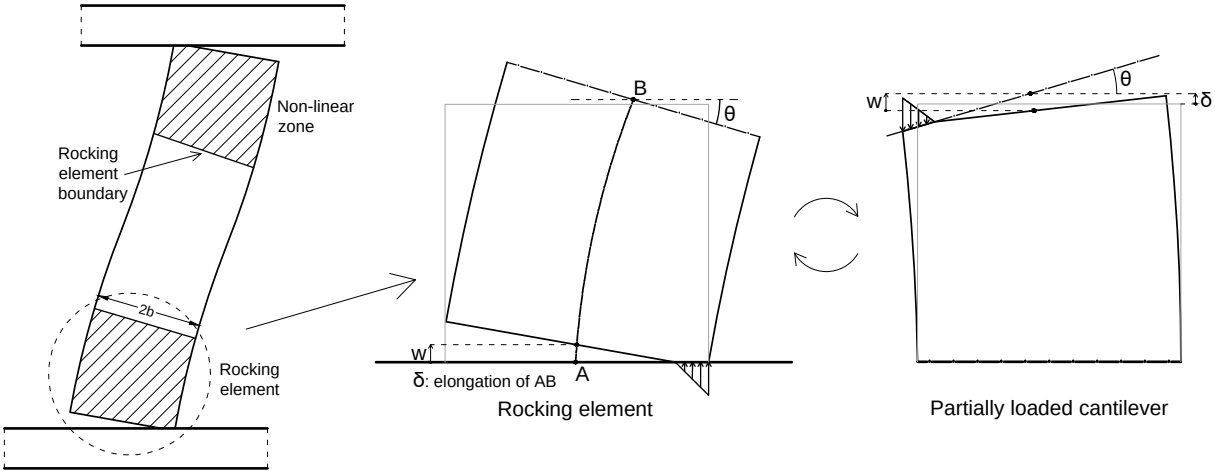

Figure 1: Rocking body and partially loaded cantilever analogy

2 NORMALIZED SEMI-INFINITE STRIP PROBLEM

In order to calculate the displacements of a cantilever due to partial loading on its free side, the spatial stress distribution near the loaded region has to be derived. From this stress distribution, an elongation profile across the member section can be found, from which the relative deformations of the element can be calculated.

The normal and shear stress distributions applied on the free side are separated into: *(i)* stresses produced by the resultant forces (axial force, shear force and moment); and *(ii)* self-equilibrating stresses. For the latter, since the effect of the self-equilibrating stresses is expected to vanish along the cantilever (rightmost diagram in Fig. 1), as the Saint-Venant assumption suggests, the easier semi-infinite strip problem is used instead. The stress distributions of the resultant forces are calculated according to the technical theory, so the use of a cantilever model is not necessary.

The general self-equilibrating stress problem for a semi-infinite strip of width $B = 2b$ is solved by first examining the normalized problem, which refers to a semi-infinite strip of $b = 1$ (Fig. 2).

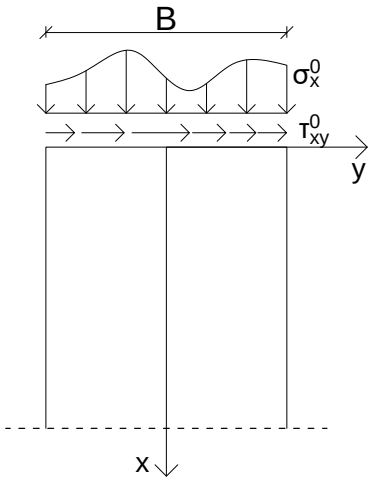

Figure 2: Semi-infinite strip normalized problem

The self-equilibrating stress distribution problem of the normalized semi-infinite strip is cal-

culated with the method developed in [29], using stress functions of certain form. The problem considered is that of a semi-infinite strip $x \geq 0$, $-1 \leq y \leq 1$ with generalized stress distributions on the free side, $x = 0$ (Fig. 2).

In the proposed macro-element, the results produced for specific load distributions of interest are approximated by polynomial expressions, which are easier and faster to implement.

The free surface of the semi-infinite strip is assumed to be loaded in the interval $[-1, p-1]$, representing a contact region of length p of the corresponding rocking body (Fig. 3). The self-equilibrating stress distributions assumed for the free surface of the semi-infinite strip originate from the following stress distributions, similar to the contact stresses at the interface between the rocking body and the base, after the removal of resultant forces:

Normal stresses which have a triangular distribution. The maximum value is s at the edge, $y = -1$, while it becomes zero after length p, that is at $y = p - 1$.

Shear stresses which are assumed to have a parabolic distribution. Its values are zero at $y = -1$ and $y = p - 1$, while its maximum value t occurs at $y = 0.5p - 1$

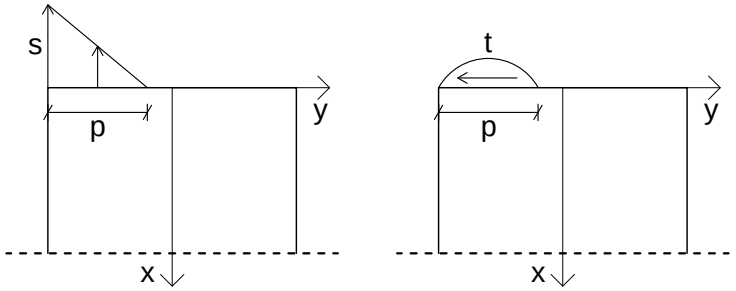

Figure 3: Semi-infinite strip normal (s) and shear (t) load distributions, for loaded region of length p

For the real problem, the interface between the body and the base mat remains flat. However, for the corresponding cantilever problem, the loaded region of the strip, although it remains close to flat, is not exactly flat. This causes problems when the elongation and the corresponding slope of a specific point on the loaded edge are used for the prediction of the axial elongation and the rotation of the body. For this reason, the elongation profile $u(y)$ of the fibers across the loaded region $[-1, -1 + p]$ is interpolated by a linear function $g(y) = \delta + \theta y$ (Fig. 1), in which δ and θ are the predicted axial elongation and the top rotation of the normalized problem, respectively, taking into account the gap existing between the loaded and non-loaded surfaces (Fig. 1).

It can be shown that for the stress distributions examined, the displacement vector $\boldsymbol{U} = [\delta, \theta]^T$ can be very well approximated by the following expressions:

$$\boldsymbol{U} = \begin{Bmatrix} \frac{1}{E} \left(s\boldsymbol{V}_s^T + t\boldsymbol{V}_t^T \right) \boldsymbol{P}_6 \\ \frac{1}{E} \left(s\boldsymbol{R}_s^T + t\boldsymbol{R}_t^T \right) \boldsymbol{P}_6 \end{Bmatrix} \tag{1}$$

where

$$\boldsymbol{P}_6 = [p^6 \quad p^5 \quad p^4 \quad p^3 \quad p^2 \quad p \quad 1]^T \tag{2}$$

$$\boldsymbol{V}_t = \boldsymbol{V}_{t0} + \nu \boldsymbol{V}_{td} \tag{3}$$

$$\boldsymbol{R}_t = \boldsymbol{R}_{t0} + \nu \boldsymbol{R}_{td} \tag{4}$$

Table 1: Polynomial approximation constant term vectors

$\boldsymbol{V}_s$	$\boldsymbol{V}_{t0}$	$\boldsymbol{V}_{td}$	$\boldsymbol{R}_s$	$\boldsymbol{R}_{t0}$	$\boldsymbol{R}_{td}$
-0.1403784	0.14011296	-0.2542931	0.00789778	0.09467081	-0.1525667
1.07433528	-1.0383282	1.50541409	-0.0232445	-0.5696705	0.90318304
-3.2789455	3.14664208	-3.3275039	0.01957306	1.40705090	-2.0163212
5.21236206	-5.1023030	3.28205442	-0.0568735	-1.7749925	1.95898891
-5.0376812	5.24787880	-1.2327789	-0.2965314	1.46712898	-0.5395043
3.53446524	-4.2918559	0.41774356	1.58546025	-2.1973954	0.21059712
-1.5484860	2.32362124	-0.8192345	-1.6046083	2.38392244	-0.8115360

E and ν being Young's modulus and the Poisson ratio, respectively, and the polynomial constant term $\boldsymbol{V}_s$ and $\boldsymbol{R}_s$ (for the normal stress contribution) and $\boldsymbol{V}_{t0}, \boldsymbol{V}_{td}, \boldsymbol{R}_{t0}, \boldsymbol{R}_{td}$ (for the shear stress contribution) vectors given in Table 1.

Also, the flexibility matrix of the normalized problem $\boldsymbol{F_t} = \partial \boldsymbol{U}/\partial \boldsymbol{R}$, with $\boldsymbol{R} = [p, s, t]^T$, is calculated by the following expression:

$$\boldsymbol{F_t} = \frac{\partial \boldsymbol{U}}{\partial \boldsymbol{R}} = \begin{bmatrix} \frac{1}{E}\left(s\boldsymbol{V}_s^T + t\boldsymbol{V}_t^T\right)\boldsymbol{dP}_6 & \frac{1}{E}\boldsymbol{V}_s^T\boldsymbol{P}_6 & \frac{1}{E}\boldsymbol{V}_t^T\boldsymbol{P}_6 \\ \frac{1}{E}\left(s\boldsymbol{R}_s^T + t\boldsymbol{R}_t^T\right)\boldsymbol{dP}_6 & \frac{1}{E}\boldsymbol{R}_s^T\boldsymbol{P}_6 & \frac{1}{E}\boldsymbol{R}_t^T\boldsymbol{P}_6 \end{bmatrix} \tag{5}$$

where

$$\boldsymbol{dP}_6 = [6p^5 \quad 5p^4 \quad 4p^3 \quad 3p^2 \quad 2p \quad 1 \quad 0]^T \tag{6}$$

The predicted displacements derived from the semi-infinite strip problem were compared against results obtained with Abaqus. Two cases for various cantilever heights were considered, with constant width $B = 2$: in the first one, the rocking member was loaded on its top with a concentrated moment, while in the second one it was loaded with a concentrated horizontal force. Figures (4) and (5) present the comparison results in relation to the different contact lengths, p, which show that, generally, there is very good agreement between the results of the two methods, especially for more slender members.

3 A MACRO-ELEMENT FORMULATION

By combining the self equilibrating stresses and the resultant force contributions (Fig. 6), a macro-element algorithm is developed which accounts for the total response of the rocking member.

For the rocking macro-element formulation, the concept of the simply supported beam natural system will be used, which is based on the geometrically non-linear force-based beam-column element formulation proposed by Neuenhofer and Filippou [30]. This coordinate system without rigid body modes demands only relative displacement values and not absolute ones, thus enabling the use of relative displacements presented previously for the self-equilibrating stresses contribution. The equations for the transformation of the displacements and forces to and from the simply supported beam natural coordinate system can be found in [30].

For the normalized semi-infinite strip problem discussed in section 2, given the load parameter vector $\boldsymbol{R} = [p, s, t]^T$, the displacements $\boldsymbol{U}$ and the flexibility matrix $\dfrac{\partial \boldsymbol{U}}{\partial \boldsymbol{R}}$ can be evaluated, which refer to the cantilever-like reference system of the semi-infinite strip. However, in order to combine these results with the resultant force ones, these quantities have to be converted from and to a reference system of a simply supported beam.

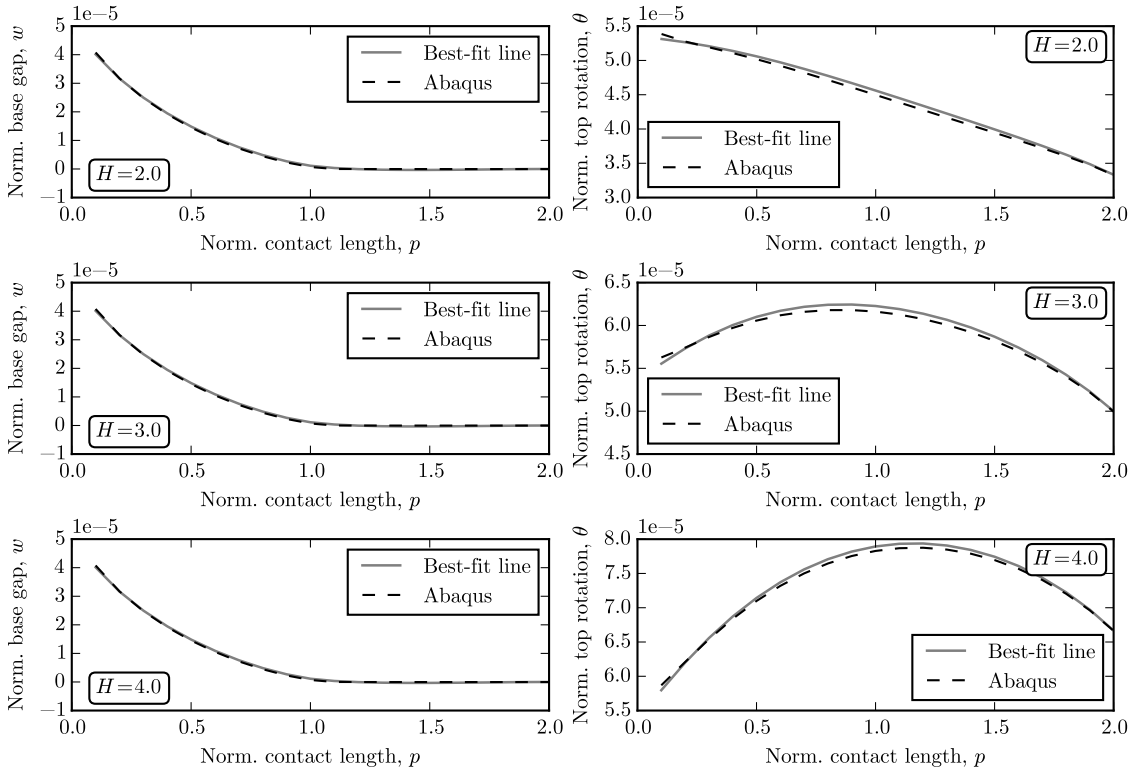

Figure 4: Rocking members with different heights loaded with a concentrated moment on their top: Central gap and top rotation versus the contact length at the bottom, p, and for $s = -1000, E = 30000000, \nu = 0.2$

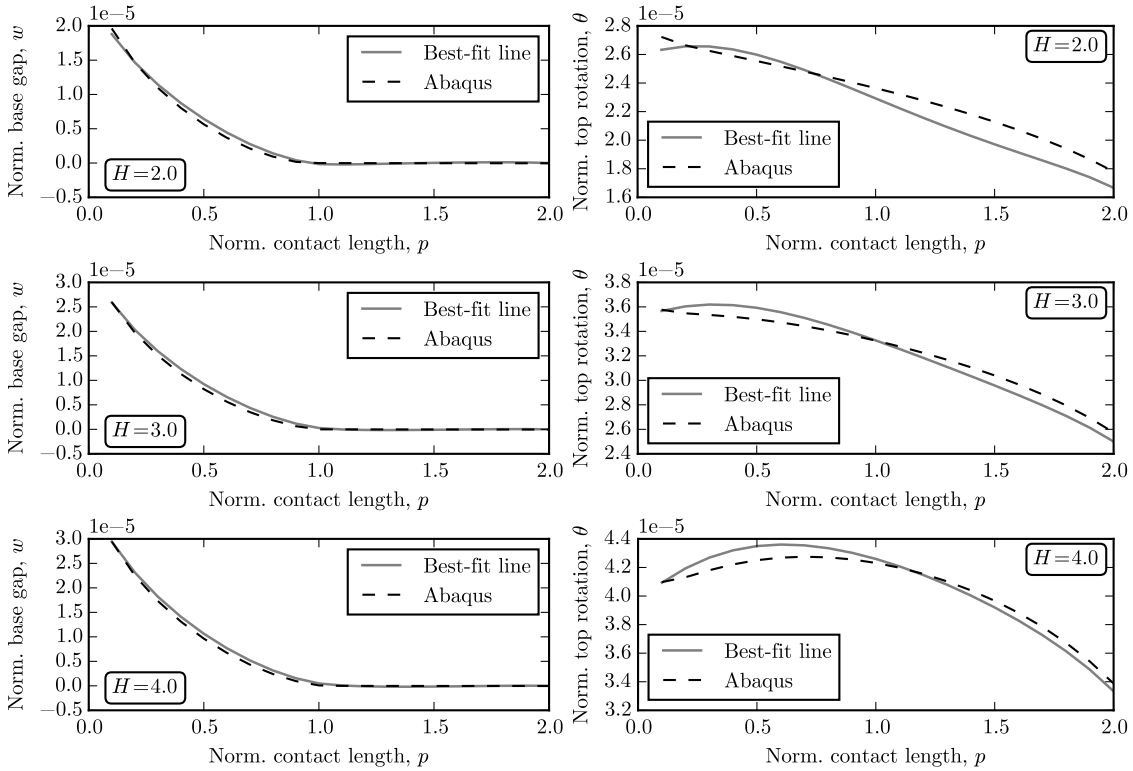

Figure 5: Rocking members with different heights loaded with a concentrated horizontal force on their top: Central gap and top rotation versus the contact length at the bottom, p, and for $s = -1000, E = 30000000, \nu = 0.2$

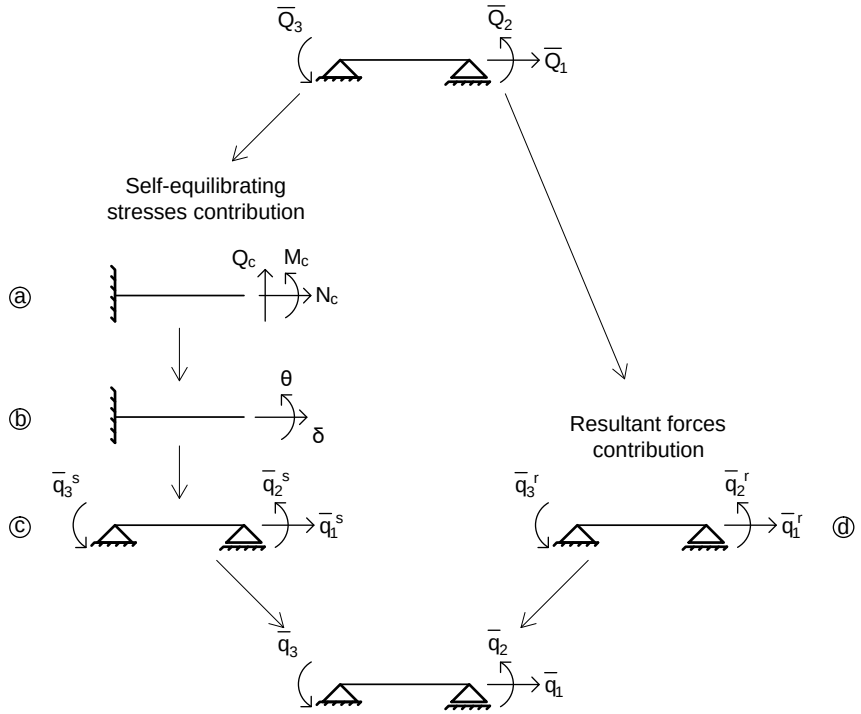

Figure 6: Schematic procedure used to calculate the combined displacements $\bar{\boldsymbol{q}}$ from the forces $\bar{\boldsymbol{Q}}$

Additionally, the problem that was formulated in section 2 referred to a semi-infinite strip of normalized semi-width $b = 1$, thickness $W = 1$ and stress distributions defined in the range $[-1, p-1]$. So, this problem has to be generalized to cover random width B, thickness W and load direction cases.

The conversion of the simply supported beam forces, $\bar{\boldsymbol{Q}} = [\bar{Q}_1, \bar{Q}_2, \bar{Q}_3]^T$, to the normalized problem cantilever ones, $\bar{\boldsymbol{Q}}_{\boldsymbol{c}} = [N_c, M_c, Q_c]^T$ (Fig. 6a), to the corresponding stress load parameters, $\boldsymbol{R}_{\boldsymbol{c}} = [c, s, t']^T$, and finally to normalized problem stress load parameters, $\boldsymbol{R} = [p, s, t]^T$, is described by the following equations:

$$\bar{\boldsymbol{Q}}_{\boldsymbol{c}} = \boldsymbol{S_1}\bar{\boldsymbol{Q}} \tag{7}$$

$$\boldsymbol{R}_{\boldsymbol{c}} = \begin{Bmatrix} 3\left(b + \dfrac{|M_c|}{N_c}\right) \\ \dfrac{2}{3}\dfrac{N_c}{b + \frac{|M_c|}{N_c}} \\ \dfrac{1}{2}\dfrac{Q_c}{b + \frac{|M_c|}{N_c}} \end{Bmatrix} \text{ with } N_c < 0 \tag{8}$$

$$\boldsymbol{R} = \boldsymbol{S_2}\boldsymbol{R}_{\boldsymbol{c}} \tag{9}$$

where

$$\boldsymbol{S_1} = \frac{1}{W}\begin{bmatrix} 1 & 0 & 0 \\ 0 & 1 & 0 \\ 0 & -\dfrac{1}{L} & -\dfrac{1}{L} \end{bmatrix} \quad \boldsymbol{S_2} = \begin{bmatrix} \dfrac{1}{b} & 0 & 0 \\ 0 & 1 & 0 \\ 0 & 0 & \rho \end{bmatrix} \text{ and } \rho = \text{sign}(M_c) \tag{10}$$

Similarly, after the calculation of the displacements $\boldsymbol{U} = [\delta, \theta]^T$ of the normalized problem (Fig. 6b), the conversion to the ones of the general simply supported beam problem, $\bar{\boldsymbol{q}} =$

$[\bar{q}_1, \bar{q}_2, \bar{q}_3]^T$ (Fig. 6c), is described by the equation:

$$\bar{\boldsymbol{q}} = \boldsymbol{S_3 U} \tag{11}$$

where

$$\boldsymbol{S_3} = \begin{bmatrix} b & 0 \\ 0 & \rho \\ 0 & 0 \end{bmatrix} \tag{12}$$

The self-equilibrating part of the rocking element is active only if a portion of the section supported on the ground is active, that is, only if

$$c < B \Rightarrow \left| \frac{M_c}{N_c} \right| > \frac{b}{3} \tag{13}$$

which means that the resultant normal force must be located outside the kern of the section.

Also, given the flexibility matrix of the normalized semi-infinite strip problem $\boldsymbol{F_t} = \dfrac{\partial \boldsymbol{U}}{\partial \boldsymbol{R}}$, the flexibility matrix in the simply supported beam coordinate system $\dfrac{\partial \bar{\boldsymbol{q}}}{\partial \bar{\boldsymbol{Q}}}$ is evaluated as follows:

$$\frac{\partial \bar{\boldsymbol{q}}}{\partial \bar{\boldsymbol{Q}}} = \frac{\partial \bar{\boldsymbol{q}}}{\partial \boldsymbol{U}} \frac{\partial \boldsymbol{U}}{\partial \boldsymbol{R}} \frac{\partial \boldsymbol{R}}{\partial \boldsymbol{R_c}} \frac{\partial \boldsymbol{R_c}}{\partial \bar{\boldsymbol{Q}}_{\boldsymbol{c}}} \frac{\partial \bar{\boldsymbol{Q}}_{\boldsymbol{c}}}{\partial \bar{\boldsymbol{Q}}} = \boldsymbol{S_3\ F_t\ S_2\ S_4\ S_1} \tag{14}$$

with

$$\boldsymbol{S_4} = \frac{\partial \boldsymbol{R_c}}{\partial \bar{\boldsymbol{Q}}_{\boldsymbol{c}}} = \begin{bmatrix} -3\dfrac{|M_c|}{N_c^2} & 3\dfrac{\rho}{N_c} & 0 \\ \dfrac{2}{3}\dfrac{b + 2\frac{|M_c|}{N_c}}{\left(b + \frac{|M_c|}{N_c}\right)^2} & -\dfrac{2}{3}\dfrac{\rho}{\left(b + \frac{|M_c|}{N_c}\right)^2} & 0 \\ \dfrac{1}{2}\dfrac{|M_c| Q_c}{(N_c b + |M_c|)^2} & -\dfrac{1}{2}\dfrac{\rho N_c Q_c}{(N_c b + |M_c|)^2} & \dfrac{1}{2}\dfrac{1}{b + \frac{|M_c|}{N_c}} \end{bmatrix} = \begin{bmatrix} -3\dfrac{|M_c|}{N_c^2} & 3\dfrac{\rho}{N_c} & 0 \\ \dfrac{4}{c} - \dfrac{6b}{c^2} & -6\dfrac{\rho}{c^2} & 0 \\ \dfrac{9}{2}\dfrac{|M_c| Q_c}{N_c^2 c^2} & -\dfrac{9}{2}\dfrac{\rho Q_c}{N_c c^2} & \dfrac{3}{2c} \end{bmatrix} \tag{15}$$

The contribution of the resultant forces can be calculated as usual. The flexibility matrix of the elastic simply supported beam, taking into account shear deformation effects, is (e.g. [31]):

$$\boldsymbol{F_r} = \begin{bmatrix} \dfrac{L}{EA} & 0 & 0 \\ 0 & \dfrac{L}{3EI} + \dfrac{\alpha}{GAL} & -\dfrac{L}{6EI} + \dfrac{\alpha}{GAL} \\ 0 & -\dfrac{L}{6EI} + \dfrac{\alpha}{GAL} & \dfrac{L}{3EI} + \dfrac{\alpha}{GAL} \end{bmatrix} \tag{16}$$

where α is the shear shape factor with $\alpha \approx 1.2$ for rectangular cross sections (shear deformations contribution can be neglected by setting $\alpha = 0.0$). So, the displacements at the nodes originating from the resultant forces (Fig. 6d) are given by

$$\bar{\boldsymbol{q}}_{\boldsymbol{r}} = \boldsymbol{F_r} \bar{\boldsymbol{Q}} \tag{17}$$

The general algorithm for the macro-element which combines these two contributions, based on the algorithm in [30], is presented in table 2, where index r refers to the resultant force problem and s refers to the self-equilibrating stress problem (extended semi-infinite strip algorithm).

Table 2: Rocking macro-element algorithm

1. Elimination of rigid body modes	$\bar{\boldsymbol{q}}_i = \boldsymbol{T}_i \boldsymbol{q}_i$ $\Delta\bar{\boldsymbol{q}}_i = \boldsymbol{T}_i \Delta\boldsymbol{q}_i$
2. Nodal force increments	$\Delta\bar{\boldsymbol{Q}}_i = \boldsymbol{F}_{i-1}^{-1} \Delta\bar{\boldsymbol{q}}_i$
3. Nodal forces	$\bar{\boldsymbol{Q}}_i = \bar{\boldsymbol{Q}}_{i-1} + \Delta\bar{\boldsymbol{Q}}_i$
4. Flexibility matrix and Nodal displacements for the resultant force problem	$\bar{\boldsymbol{q}}_{\boldsymbol{r}}^{*} = \boldsymbol{F_r} \bar{\boldsymbol{Q}}_i$
5. Check whether there is rocking or not. If not, ignore steps (6)-(10) and set $\bar{\boldsymbol{q}}_{\boldsymbol{s}}^{*}$ and $\boldsymbol{F_s}$ to the zero matrices	$\left\lvert \frac{\bar{Q}_2}{\bar{Q}_1} \right\rvert > \frac{b}{3} \rightarrow$ Rocking
6. Force parameters for the self-equilibrating stresses problem	$\bar{\boldsymbol{Q}}_{\boldsymbol{c}} = \boldsymbol{S_1} \bar{\boldsymbol{Q}}_i$ $\boldsymbol{R_c} = \boldsymbol{R_c}(\bar{\boldsymbol{Q}}_{\boldsymbol{c}})$ $\boldsymbol{R} = \boldsymbol{S_2} \boldsymbol{R_c}$
7. Displacements of the normalized problem	$\boldsymbol{U} = \boldsymbol{G}\ \boldsymbol{L}$
8. Displacements in the simply-supported beam natural system	$\bar{\boldsymbol{q}}_{\boldsymbol{s}}^{*} = \boldsymbol{S_3}\ \boldsymbol{U}$
9. Flexibility matrix of the normalized problem	$\boldsymbol{F_t} = \frac{\partial \boldsymbol{U}}{\partial \boldsymbol{R}}$
10. Flexibility matrix in the simply-supported beam natural system	$\boldsymbol{F_s} = \boldsymbol{S_3}\ \boldsymbol{F_t}\ \boldsymbol{S_2}\ \boldsymbol{S_4}\ \boldsymbol{S_1}$
11. Combined displacements	$\bar{\boldsymbol{q}}_i^{*} = \bar{\boldsymbol{q}}_{\boldsymbol{r}}^{*} + \bar{\boldsymbol{q}}_{\boldsymbol{s}}^{*}$
12. Displacement residuals	$\boldsymbol{r}_i = \bar{\boldsymbol{q}}_i - \bar{\boldsymbol{q}}_i^{*}$
13. Combined flexibility matrix	$\boldsymbol{F}_i = \boldsymbol{F_r} + \boldsymbol{F_s}$
14. Extra nodal forces	$\bar{\boldsymbol{Q}}_i^{*} = \boldsymbol{F}_i^{-1} \boldsymbol{r}_i$
15. Updated nodal forces	$\bar{\boldsymbol{Q}}_i = \bar{\boldsymbol{Q}}_i + \bar{\boldsymbol{Q}}_i^{*}$
16. *(Optional)* Check convergence	$\frac{\lvert \bar{\boldsymbol{Q}}_i^{*} \rvert}{\lvert \bar{\boldsymbol{Q}}_i^{old} \rvert} >$ error $\Rightarrow$ return to step 4
17. Inclusion of rigid body modes	$\boldsymbol{Q}_i = \boldsymbol{T}^{*} \bar{\boldsymbol{Q}}_i$ $\boldsymbol{K}_i = \boldsymbol{T}_{1i} + \boldsymbol{T_i^{*}} \boldsymbol{F}_i^{-1} \boldsymbol{T_i^{*T}}$

4 EXAMPLES

As a first example, the response of a simple cantilever model is calculated using the proposed macro-element. The results are compared with the results of the corresponding Abaqus model, consisting of 2D plane stress elements with contact properties at the base which allow only compressive stresses to develop.

In Fig. 7, a cantilever with height $H = 2$ m, width $B = 1$ m and thickness $W = 0.2$ m is examined, which is loaded with a vertical force $N = -400$ kN. In Fig. 7a, the pushover curves of such cantilevers with various E values and $\nu = 0.2$ are shown together with the theoretical rigid block case. It can be seen that, due to the non-linearity of the response, the maximum strength achieved decreases with decreasing E values.

In Fig. 7b, the response of the body with $E = 30$ GPa case is examined more thoroughly: apart from a magnification of the pushover curve in the initial region, the top rotation and the vertical displacement at the center of the body with and without shear deformation effects are presented. Comparison of the results with the ones of the corresponding Abaqus model shows

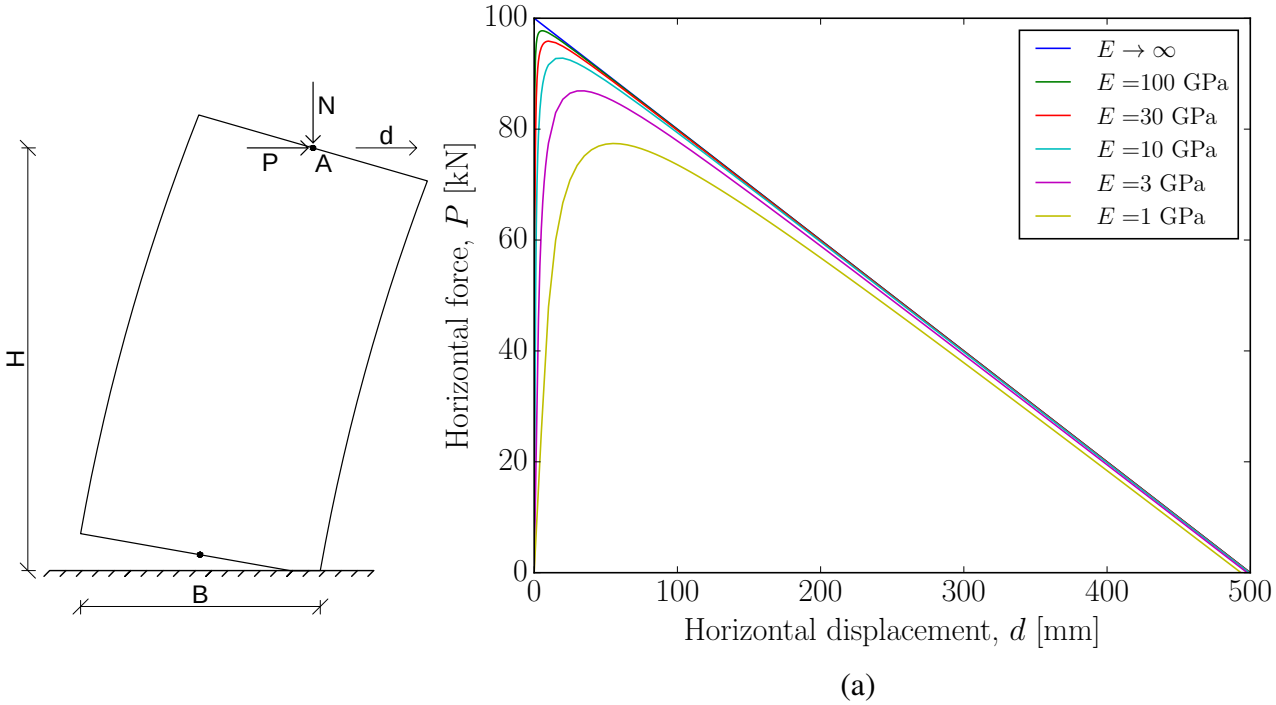

(a)

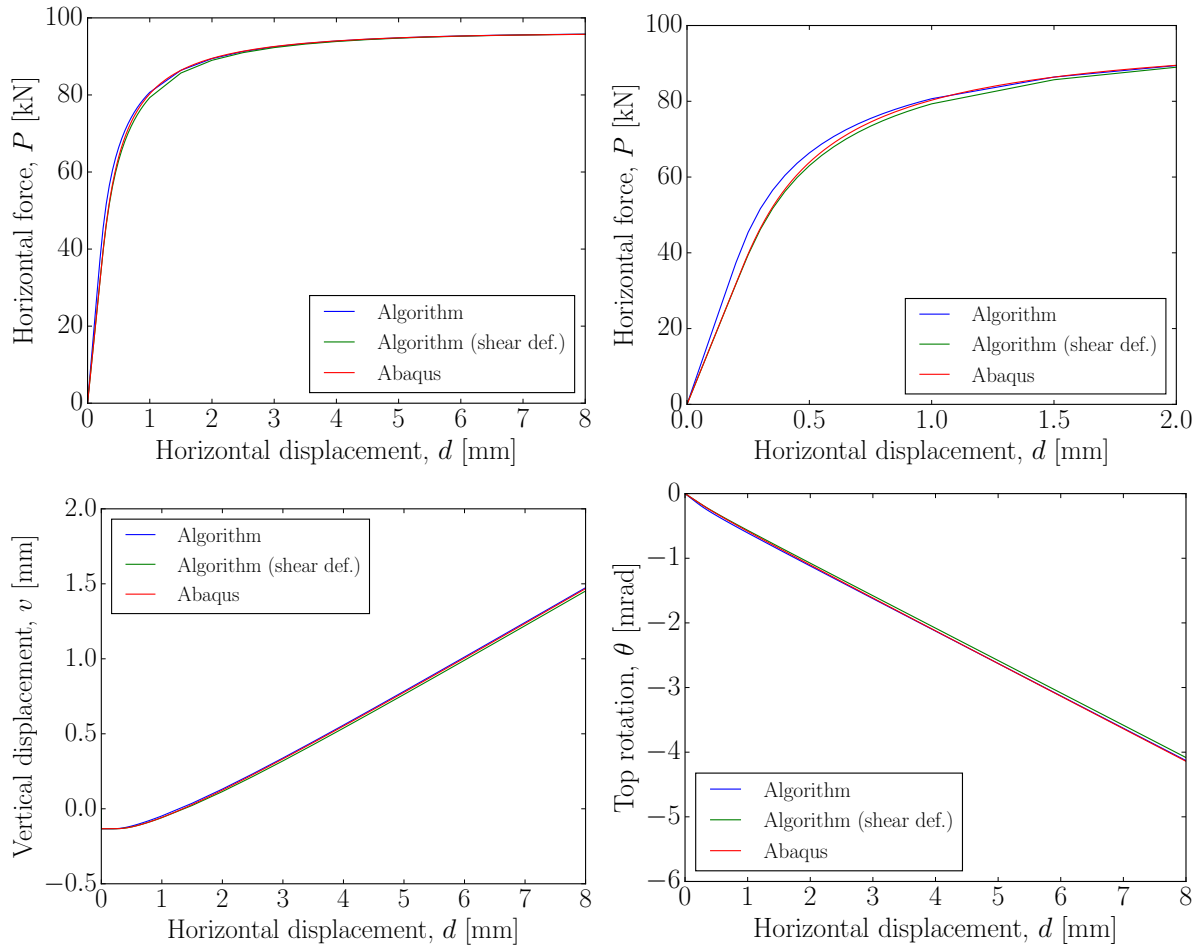

(b)

Figure 7: Example 1, $H = 2$ m panel loaded with vertical force $N = -400$ kN and horizontal force P at its top: (a) Pushover curves for different E values; (b) Pushover curves, top rotation and vertical displacement for the $E = 30$ GPa case, which is also compared with the corresponding Abaqus model

that, generally, the proposed macro-element can predict the response very accurately, especially if shear deformations are considered.

As a second example, the rocking body is examined with an elastic tendon with Young's modulus E_t and section area A_t installed along its center-line, imposing a prestress force with initial value $P_{t0} = 400$ kN. In this way, the vertical displacements are restrained after the onset of rocking, while the axial force originating from the tendon increases as its elongation increases.

The results are shown in Fig. 8 for typical values of tendon coefficients $E_t A_t$. It can be seen that the prestressing tendons force the pushover curve to be ascending instead of descending, offering stability to the system.

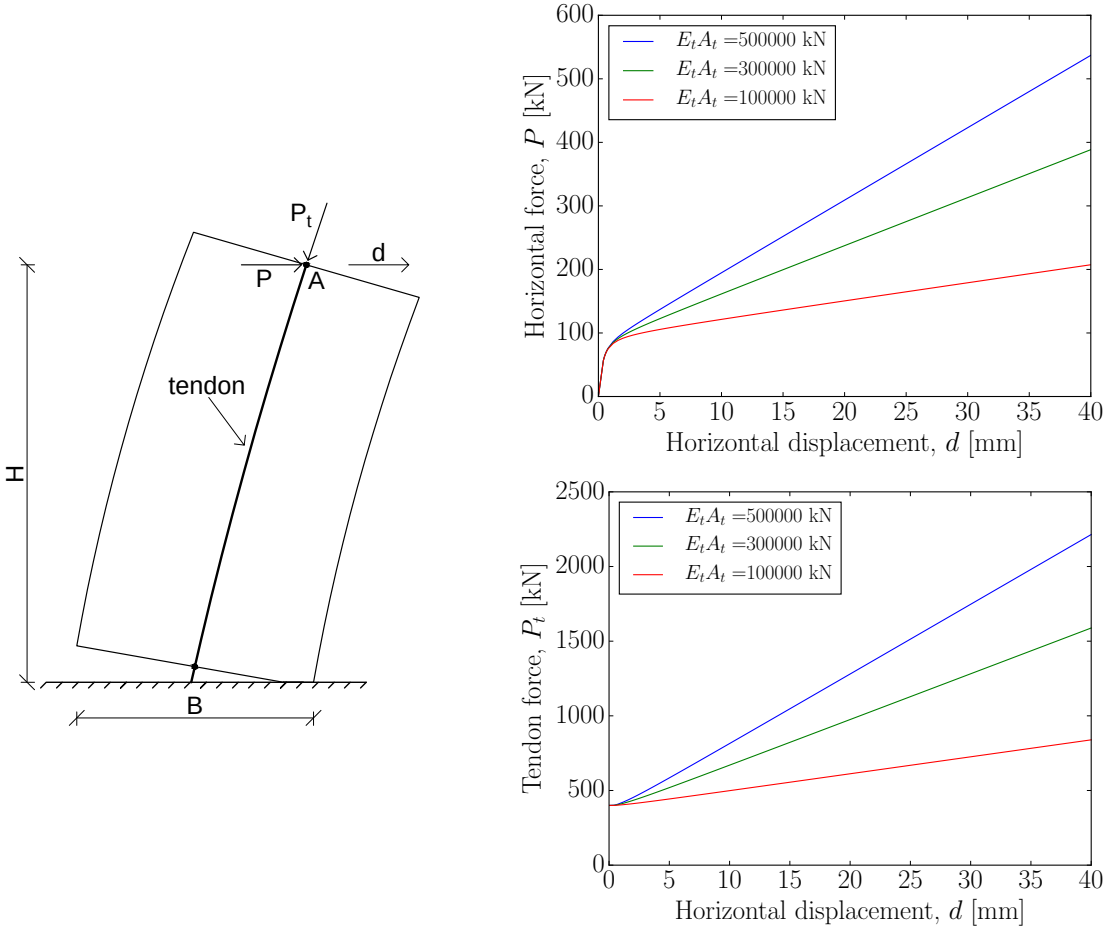

Figure 8: Example 2, $H = 2$ m panel with a horizontal force P at its top, constrained with a tendon with Young's modulus E_t, section area A_t and prestress force $P_{t0} = 400kN$: Pushover curve and tendon force

5 CONCLUSIONS

In this paper, a new macro-element algorithm is proposed, which can be used for the calculation of the rocking response of flexible bodies, also accounting for the deformability of their base. This is crucial in case of restrained rocking, when considerable axial forces develop. The formulation of the element is based upon the solution of the normalized semi-infinite strip problem, in order to account for the partial loading imposed on the rocking interface.

Two example problems are presented, showing typical cases where the proposed element can be used. Comparison of the results with ones obtained using equivalent Abaqus models

shows very good agreement between the two methods, while the proposed algorithm requires extremely low runtimes compared to conventional finite element codes.

ACKNOWLEDGEMENTS

The first author would like to thank the Greek State Scholarships Foundation for its financial support through the "IKY Fellowships of Excellence for Postgraduate studies in Greece - Siemens program".

REFERENCES

[1] R. Skinner, R. Tyler, A. Heine, and W. Robinson, "Hysteretic dampers for the protection of structures from earthquakes," *Bulletin of the New Zealand National Society for Earthquake Engineering*, vol. 13, no. 1, pp. 22–36, 1980.

[2] N. M. Priestley, "Overview of PRESSS research program," *PCI journal*, vol. 36, no. 4, 1991.

[3] S. Sritharan, S. Aaleti, and D. J. Thomas, "Seismic analysis and design of precast concrete jointed wall systems," *ISU-ERI-Ames Report ERI-07404, Submitted to the Precast/Prestressed Concrete Institute*, 2007.

[4] W. Y. Kam, S. Pampanin, A. Palermo, and A. J. Carr, "Self-centering structural systems with combination of hysteretic and viscous energy dissipations," *Earthquake Engineering & Structural Dynamics*, vol. 39, no. 10, pp. 1083–1108, 2010.

[5] ACI Innovation Task Group 1, "Special Hybrid Moment Frames Composed of Discretely Jointed Precast and Post-Tensioned Concrete Members (ACI T1.2-03) and Commentary (ACI T1.2R-03)," American Concrete Institute (ACI), 2003.

[6] "Seismic design of precast concrete building structures," *fib Bulletin no. 27*, International Federation for Structural Concrete (fib), 2003.

[7] "Special provisions for the seismic design of ductile jointed precast concrete structural systems," *NZS3101: 2006, Concrete Standards, Appendix B*, New Zealand Standards, 2006.

[8] "Eurocode 8: Design of structures for earthquake resistance Part 1: General rules, seismic actions and rules for buildings," *European Standard EN 1998-1:2004*, European Committee for Standardization, 2004.

[9] G. W. Housner, "The behavior of inverted pendulum structures during earthquakes," *Bulletin of the seismological society of America*, vol. 53, no. 2, pp. 403–417, 1963.

[10] C.-S. Yim, A. K. Chopra, and J. Penzien, "Rocking response of rigid blocks to earthquakes," *Earthquake Engineering and Structural Dynamics*, vol. 8, no. 6, pp. 565–587, 1980.

[11] J. Zhang and N. Makris, "Rocking response of free-standing blocks under cycloidal pulses," *Journal of Engineering Mechanics*, vol. 127, no. 5, pp. 473–483, 2001.

[12] E. G. Dimitrakopoulos and M. J. DeJong, "Revisiting the rocking block: closed-form solutions and similarity laws," in *Proceedings of the Royal Society of London A: Mathematical, Physical and Engineering Sciences*, vol. 468, pp. 2294–2318, The Royal Society, 2012.

[13] S. Acikgoz and M. J. DeJong, "The interaction of elasticity and rocking in flexible structures allowed to uplift," *Earthquake Engineering & Structural Dynamics*, vol. 41, no. 15, pp. 2177–2194, 2012.

[14] C. B. Barthes, *Design of Earthquake Resistant Bridges Using Rocking Columns*. PhD thesis, University of California, Berkeley, 2012.

[15] M. F. Vassiliou, K. R. Mackie, and B. Stojadinović, "Dynamic response analysis of solitary flexible rocking bodies: modeling and behavior under pulse-like ground excitation," *Earthquake Engineering & Structural Dynamics*, vol. 43, no. 10, pp. 1463–1481, 2014.

[16] M. F. Vassiliou, R. Truniger, and B. Stojadinović, "An analytical model of a deformable cantilever structure rocking on a rigid surface: development and verification," *Earthquake Engineering & Structural Dynamics*, 2015.

[17] I. N. Psycharis and P. C. Jennings, "Rocking of slender rigid bodies allowed to uplift," *Earthquake Engineering & Structural Dynamics*, vol. 11, no. 1, pp. 57–76, 1983.

[18] I. N. Psycharis, "Dynamics of flexible systems with partial lift-off," *Earthquake Engineering & Structural Dynamics*, vol. 11, no. 4, pp. 501–521, 1983.

[19] A. K. Chopra and S. C.-S. Yim, "Simplified earthquake analysis of structures with foundation uplift," *Journal of Structural Engineering*, vol. 111, no. 4, pp. 906–930, 1985.

[20] I. N. Psycharis, "Effect of base uplift on dynamic response of sdof structures," *Journal of Structural Engineering*, vol. 117, no. 3, pp. 733–754, 1991.

[21] A. Palmeri and N. Makris, "Response analysis of rigid structures rocking on viscoelastic foundation," *Earthquake Engineering & Structural Dynamics*, vol. 37, no. 7, pp. 1039–1063, 2008.

[22] A. Palmeri and N. Makris, "Linearization and first-order expansion of the rocking motion of rigid blocks stepping on viscoelastic foundation," *Earthquake Engineering & Structural Dynamics*, vol. 37, no. 7, pp. 1065–1080, 2008.

[23] H. Roh and A. M. Reinhorn, "Analytical modeling of rocking elements," *Engineering Structures*, vol. 31, no. 5, pp. 1179–1189, 2009.

[24] H. Roh and A. M. Reinhorn, "Nonlinear static analysis of structures with rocking columns," *Journal of structural engineering*, vol. 136, no. 5, pp. 532–542, 2009.

[25] H. Roh and A. M. Reinhorn, "Modeling and seismic response of structures with concrete rocking columns and viscous dampers," *Engineering Structures*, vol. 32, no. 8, pp. 2096–2107, 2010.

[26] A. Belleri, M. Torquati, and P. Riva, "Finite element modeling of rocking walls," in *4th ECCOMAS Them. Conf. on COMPDYN*, 2013.

[27] A. Penna, S. Lagomarsino, and A. Galasco, "A nonlinear macroelement model for the seismic analysis of masonry buildings," *Earthquake Engineering & Structural Dynamics*, vol. 43, no. 2, pp. 159–179, 2014.

[28] E. Avgenakis, "Modeling of rocking flexible bodies considering the deformability of their base," Master's thesis, National Technical University of Athens, 2015.

[29] F. Gaydon and W. Shepherd, "Generalized plane stress in a semi-infinite strip under arbitrary end-load," in *Proceedings of the Royal Society of London A: Mathematical, Physical and Engineering Sciences*, vol. 281, pp. 184–206, The Royal Society, 1964.

[30] A. Neuenhofer and F. C. Filippou, "Geometrically nonlinear flexibility-based frame finite element," *Journal of Structural Engineering*, vol. 124, no. 6, pp. 704–711, 1998.

[31] J. S. Przemieniecki, *Theory of matrix structural analysis*. Courier Corporation, 1985.

ECCOMAS Congress 2016
VII European Congress on Computational Methods in Applied Sciences and Engineering
M. Papadrakakis, V. Papadopoulos, G. Stefanou, V. Plevris (eds.)
Crete Island, Greece, 5–10 June 2016

NONLINEAR ANALYSIS AND EXPERIMENTAL BEHAVIOUR OF AN INNOVATIVE STEEL FRAME WITH REINFORCED CONCRETE INFILL WALLS

A. Dall'Asta[1], G. Leoni[1], F. Morelli[2], W. Salvatore[2], A. Zona[1]

[1] University of Camerino, School of Architecture and Design
Viale della Rimembranza, 63100 Ascoli Piceno, Italy
{andrea.dallasta, graziano.leoni, alessandro.zona}@unicam.it

[2] University of Pisa, Department of Civil and Industrial Engineering
Largo Lucio Lazzarino 1, 56122 Pisa, Italy
{francesco.morelli, walter}@ing.unipi.it

Keywords: concrete infill walls, ductile design, experimental tests, shear studs, steel structures, steel and concrete hybrid systems.

Abstract. *Steel frames with reinforced concrete infill wall (SRCW) are characterized by an high stiffness that minimize the inter-storey drift and the associated damage to non-structural elements. They are however characterized by critical drawbacks, that limit their use, such as the low dissipative capacity of the concrete wall that causes high seismic force and high overturning moment at the wall base foundation. Within the present study, an innovative steel frame with reinforced concrete infill shear wall system is proposed. It consists of a reinforced concrete infill walls surrounded by a steel frame which contains energy dissipation replaceable elements within the columns. In this way the force transmitted to the other structural elements, and in particular to the foundations, are limited and an important portion of the seismic energy dissipated through plastic deformation. Within this paper the behaviour of the proposed system is investigated through nonlinear analyses based on advanced models supported by the experimental results on real scale specimens, highlighting advantages and drawbacks of the system.*

1 INTRODUCTION

Steel frames with Reinforced Concrete infill Walls (SRCWs) are structural systems that offer many advantages such as their high initial stiffness, able to reduce the building damage under low-intensity earthquakes, and potentially easy repairs after moderate damage through the use of epoxy resins on the cracked wall [1]. In this way, SRCW systems provide a promising structural solution potentially able to reduce the seismic risk in all its aspects, i.e., economic loss and fatalities, as for example contemplated in recent studies [2][3] following the 2012 Emilia earthquakes in Italy and highlighting the necessity of an adequate structural behaviour also for low-to-moderate seismic events [4].

In SRCWs three different resisting mechanisms to horizontal actions can be identified as depicted in Figure 1: 1) flexural behaviour of the steel frame; 2) direct interactions between the steel frame and the compression strut in the reinforced concrete (RC) infill walls; 3) interactions between steel frames and the RC infill walls through friction and shear connectors. The ratio of horizontal forces resisted by each of the load transferring paths depends on the mechanical properties and geometrical configuration of the considered system.

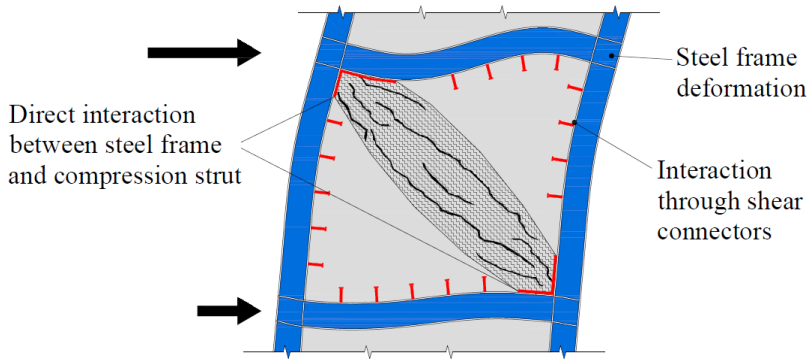

Figure 1: SRCWs resisting mechanisms to horizontal actions.

Despite all the available research studies carried out in the last decades, it is not easy to design a SRCW system in seismic areas due to the lack of specific capacity design rules that allow controlling the formation of a proper dissipating mechanism. Refined numerical analyses previously carried out on SRCW systems [5] designed according to the Eurocodes, in fact, pointed out an unsatisfactory fragile behaviour due to the severe damage occurring to concrete long before yielding of the ductile elements. The failure mechanism is generally characterised by yielding of the steel frame concentrated mainly in the elements near the bottom of the wall (more specifically at the connections of the horizontal to the vertical parts). The plastic deformation on the concrete infill walls concentrates in a diagonal path clearly highlighted by the distribution of cracking. In addition, localized plastic deformations are also present near the corners of the infill walls due to the local action of the first studs of the horizontal and vertical elements (Figure 2a). In order to overcome the observed critical aspects possibly affecting the considered structural system, an innovative approach for ductile design of SRCWs, recently studied during a European research project [5] that also involved innovative steel and concrete hybrid coupled walls [6], is presented in this work leading to the solution depicted in Figure 2b. The RC infill walls are not connected to the vertical elements where the energy dissipation is expected. The system is conceived to control the formation of diagonal struts in the infill walls and behaves as a latticed brace instead of a shear wall. The energy dissipation is expected to take place only in the vertical elements of the steel frame subjected mainly to axial forces without involving the reinforcements of the infill walls.

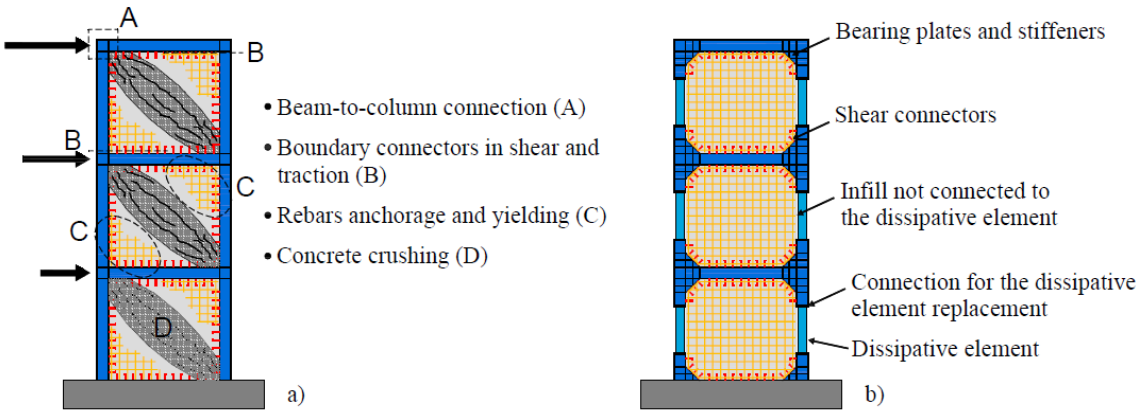

Figure 2: a) critical aspects in the behaviour of conventional SRCW systems; b) innovative SRCW system.

Detailing of the connection of the dissipating elements should allow their replacement and the presence of the infill wall limits the axial force in the compressed dissipative element avoiding its buckling. The formation of the diagonal strut is ensured by joint stiffeners and bearing plates. The joint may be welded in shops allowing speeding up the erection phases. The stud connectors are not required to transfer shear forces but they are mainly used to connect the infill and the frame together during the seismic shakings. A capacity design procedure, able to assure the desiderate energy dissipation mechanism, is proposed consistently with the Eurocode 8 [7] framework and explained in details. Sophisticated and simplified numerical models are then adopted to better understand the global behaviour of the system and to check the validity of the design procedure proposed. Finally, the results of an experimental campaign on two different 2/3 downscaled one-storey specimens are illustrated to validate the design procedure and to provide insight into the influence of the shear studs distribution on the behaviour of the proposed SRCW system.

2 DUCTILE DESIGN OF SRCW SYSTEMS

The proposed innovative SRCW is composed by elements with specific tasks according to the proposed capacity design. The design procedure consists of 9 steps, it is force-based and is applied by considering the simple statically determined scheme representing the limit behaviour of the SRCW depicted in Figure 3. The procedure is described hereafter.

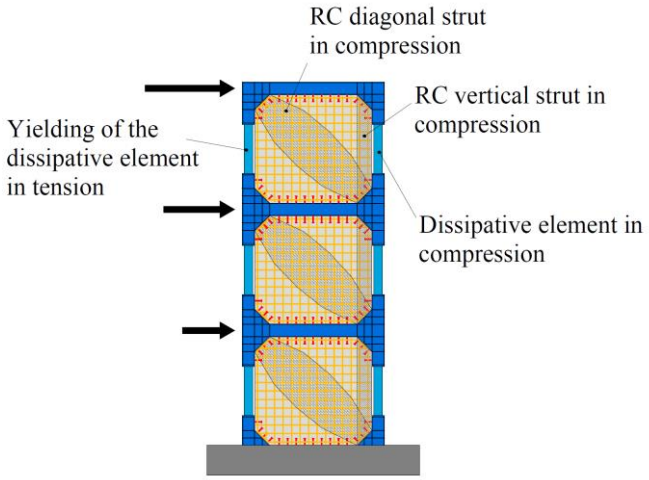

Figure 3: Limit behaviour under seismic action of the innovative SRCW system.

Step 1: definition of the static equivalent lateral loads and calculation of the truss actions.

A design spectrum reduced by a suitable behaviour factor is considered; the definition of the behaviour factor is rather delicate because the limit structural scheme adopted may not represent the behaviour of the system especially in the linear range for moderate earthquakes.

Step 2: design of the cross sections of the ductile boundary elements in traction.

These elements are subjected also to compression under the reversed loadings but they are not expected to yield in compression. Even if in principle no specific provisions are necessary, it is better to assure the element cross section being compact, e.g. at least class 2 according to Eurocode 3 [8].

Step 3: capacity design of the connection of the ductile elements and of the adjacent elements.

The design of the connection of the ductile elements and of the adjacent elements is performed with the formula

$$R_d \geq 1.1\gamma_{ov} R_{fy} \tag{1}$$

where γ_{ov} is the over-strength coefficient of the element with plastic resistance R_{fy} of the connected dissipative member based on the design yield stress of the material. The connection should be designed to resist the force in the linear range in order to reduce damage in the non-ductile elements and to permit the possibility to replace the ductile element after seismic damage. End-plates connections should be preferred to other types with the ductile element connected to the split plate by means of full penetration welding. The adjacent vertical elements to which the ductile elements are connected should be over-strengthened; this can be assured by using a different steel grade or by suitably enlarging the resisting cross section that should have width equal or greater than the infill wall thickness.

Step 4: calculation of geometric over-strength factors.

These factors are calculated as usual for steel structures by the ratio of the real plastic resistance of the ductile element and the relevant design force

$$\Omega = min\left\{\Omega_i = \frac{N_{pl,Rd,i}}{N_{Ed,i}}\right\} \tag{2}$$

To guarantee yielding of the edge steel elements at the different levels, and to avoid formation of soft storeys, the maximum over-strength Ω_i should not differ from the minimum value by more than 25%. At the higher levels, this condition may difficultly be satisfied. In such a case, the yielding takes place only at a limited number of storeys and the ductile elements should be designed to guarantee the global ductility, e.g. [9][10][11].

Step 5: calculation of axial forces in non-ductile elements by combining the effects of gravity loads with those of the seismic action suitably magnified.

These forces are calculated by suitably magnifying the seismic design component accounting for the material and geometric over-strength of the ductile elements with the usual formula

$$N_{Ed} = N_{Ed,G} + 1.1\gamma_{ov}\Omega N_{Ed,E} \tag{3}$$

Step 6: capacity design of the reinforced concrete infill against concrete crushing (definition of wall thickness t_w and width of the bearing plate l_b).

This step is crucial as it assures the good performance of the system that should not be affected by the wall failure (concrete crushing). As previously described, bearing plates are placed at the beam-to-column nodes to control the formation of the diagonal strut within the wall (Figure 4a).

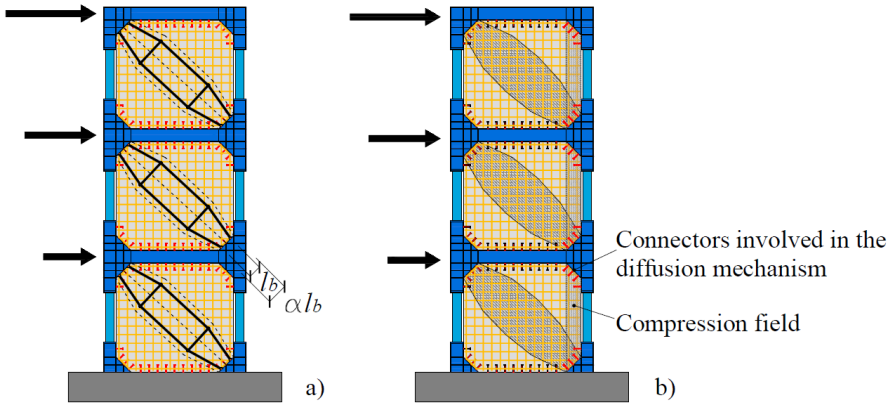

Figure 4: (a) diagonal struts within the infill walls; (b) compression fields involved to resist the axial force in the case lateral elements failed due to instability.

A fan-shaped stress field is expected at the bearing plate; the effective width of the wall should be equal to the bearing plate width l_b at the diagonal ends whereas the effective width is imposed by a coefficient $\alpha > 1$ at mid diagonal. The design formula

$$\left\{0.85\frac{f_{ck}}{\gamma_c}t_w l_b;\ 0.85\frac{f_{ck}}{\gamma_c}\nu\left(1-\frac{f_{ck}}{250}\right)\left(\alpha t_w l_b\right)\right\} \geq N_{Ed,G} + 1.1\gamma_{ov}\Omega N_{Ed,E} \tag{4}$$

is derived from Eurocode 2 (paragraph 6.5) [12]; the second value of the strut strength takes into consideration the transverse tension ($\upsilon = 0.6$ may be assumed) whereas the first value considers a simple compression field. The two design parameters l_b and coefficient α can be determined with a trial procedure or by imposing a tentative value for α. The bearing plate should be then proportioned and stiffened to avoid stress localization in the concrete.

The wall reinforcements should be checked to guarantee the diffusive mechanism that depends on the choice of the parameter α; for this purpose rules for partial discontinuity regions suggested in Eurocode 2 (paragraph 6.5.2) [12] are considered. In this case, tractions to be resisted by reinforcements is evaluated by means of the formula

$$T = \frac{1}{4}\left(1-\frac{1}{\alpha}\right)N_R \tag{5}$$

Two different reinforcement layouts may be adopted (Figure 5), the former is constituted by two sets of orthogonal reinforcements whereas the latter is constituted by a set of specific transverse (with respect to the strut direction) reinforcements. In the first case, vertical and horizontal reinforcements should fulfil the conditions

$$\frac{T^2}{f_{yd}^2} = A_{sl}^{v\,2} + A_{sl}^{h\,2} \qquad \frac{A_{sl}^h}{A_{sl}^v} = \frac{L}{h} \tag{6}$$

It is worth noting that the first reinforcement layout is simpler but possibly less stiff than the second, which instead requires a third order of reinforcements that can be placed only in the case of sufficiently thick walls.

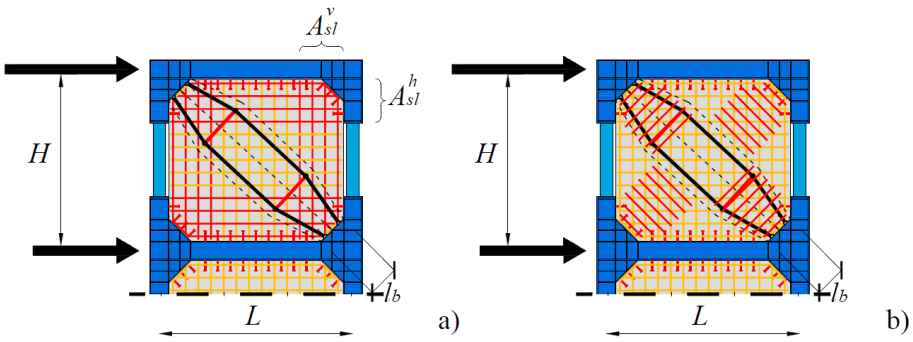

Figure 5: (a) reinforcements constituted by orthogonal rebar layout; (b) reinforcements constituted by additional stirrups.

Step 7: design of the beams in traction.

These elements are designed to resist magnified axial forces. To improve the system feasibility, it is better that their width is compliant with the wall thickness.

Step 8: check and possible re-design of the compressed edge elements.

The ductile elements are checked for instability by using the formula

$$\frac{Af_y\chi}{\gamma_{M1}} \geq N_{Ed,G} + 1.1\gamma_{ov}\Omega N_{Ed,E} \tag{7}$$

The effective length of the element can be selected to be equal to the distance between beam-to-column intersection nodes taking into account the real dimension of the enlarged zone necessary for realizing the bearing plate. In the case the verification is not satisfied, it is expected that the adjacent strip of the concrete wall collaborates to bear the compression force (Figure 4b); in such a case, the following points (8-1 and 8-2) have to be carried out.

Step 8-1: design of the shear connection between the wall and the frame.

The shear connection is designed to transmit to the adjacent RC wall the force in excess with respect to the bearing capacity of the ductile element given by

$$\upsilon_{Rd} \geq N_{Ed,G} + 1.1\gamma_{ov}\Omega N_{Ed,E} - \frac{Af_y\chi}{\gamma_{M1}} \tag{8}$$

In this case, shear connection has to be placed at the vertical elements. It has to be designed by taking into account that possible splitting failure mechanisms of the wall may occur instead of the usual failures due to concrete crushing and yielding. For this purposes, rules suggested by Eurocode 4 Part 2 (paragraph 6.6.4 and Annex C) [13] may be considered.

Step 8-2: check of the vertical strut developing in the wall.

This element withstands the same force calculated with equation (8) and has to be suitably reinforced with confinement stirrups. The same detailing rules suggested in Eurocode 8 (paragraph 5.4.3.4.2) [7] for RC walls may be adopted.

Step 9: calculation of the length of the dissipative element, in order to ensure the compliance between local and global ductility.

For this purpose, formulas derived by considering simplified mechanisms (Figure 6) can be adopted. To a first approximation, the following formula may be used:

$$H' = \frac{(\mu_s - 1)}{(\mu_m - 1)} \frac{\delta_{el} L}{\varepsilon_y \sum_{i=1}^{N} (z_N - z_{i-1})} \tag{9}$$

where μ_s and μ_m are the ductility of the structure and of the material of the dissipative element respectively; the summation is extended only to the N elements that fall in the $\Omega \div 1.25\ \Omega$ range, δ_{el} is the structure elastic displacement evaluated for the static equivalent loading inducing the first yielding; δ_{pl} is the structure plastic displacement evaluated considering only the elements expected to yield.

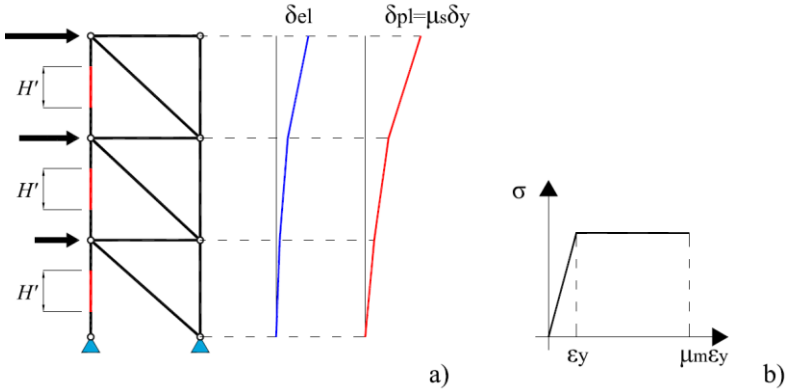

Figure 6: a) Elastic and plastic deformations of the SRCW; b) material stress-strain relationship.

3 NONLINEAR ANALYSIS OF THE INNOVATIVE SRCW SYSTEM

3.1 Finite element model

High fidelity finite element models are developed with the computer program ABAQUS for a preliminary analysis of the behaviour of the presented design approach for SRCW systems. A 4-storey system is considered and designed according to the procedure previously described. Details on the design parameters (i.e. geometry, vertical and horizontal loads, material properties) are reported in [5]. The geometry of the system is closely reproduced by using shell finite elements both for the steel frame and for the concrete infill walls (Figure 7); these are assumed to be connected to the frame only at the inclined bearing plates where stud connectors are placed. In particular, 4-node linear shell elements with 5 degrees of freedom per node (reduced integration, small membrane strains) are used. Wall reinforcements are considered by introducing two layers of reinforcements according to the construction drawings. A coarse mesh (mean size of 0.5 m) is adopted for the concrete walls to avoid numerical convergence problems, whereas a more refined mesh (mean size of 0.1 m) is adopted for steel members.

The behaviour of the concrete is described adopting a smeared cracking model with full shear retention. The concrete behaviour is assumed to follow Mander's law in compression and a linear elastic law in tension up to cracking, followed by a softening tract as later illustrated. Cracking is assumed to occur when the stress reaches a failure surface defined by a linear relationship between the equivalent pressure stress and the Mises equivalent deviatoric stress. When a crack is detected, its orientation is stored for subsequent calculations. Subsequent cracking at the same point is restricted to being orthogonal to this direction because stress components associated with an open crack are not included in the definition of the failure surface used for detecting the additional cracks. The behaviour of cracked concrete is modelled with a strain-softening branch that allows to simulate the interaction between rein-

forcements and concrete (tension stiffening); in particular, it is assumed a linear strain softening with zero stress at a total strain of about 10 times the strain at tensile failure. Elastoplastic-hardening models are considered for the reinforcements and the steel frame. The yielding point, the material plastic hardening and the ultimate stress for each steel grade considered are defined according to the mechanical characteristics of materials adopted in the design.

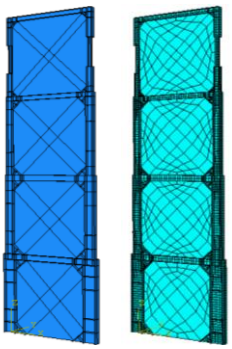

Figure 7: SRCW finite element model.

3.2 Results

Figure 8a; shows the yielding pattern of the steel frame for three displacement levels measured at the top level. It is observed that plastic strains are attained only at the ductile elements consistently with the dissipating mechanism assumed in the proposed design procedure. The resisting mechanism adopted in the design is also corroborated by the stress field in the wall (Figure 8b) that clearly depicts the formation of the diagonal struts in the concrete panels. The values of the principal stresses do not increase with the overall displacement demonstrating that the wall is protected against crushing due to yielding of the side fuses.

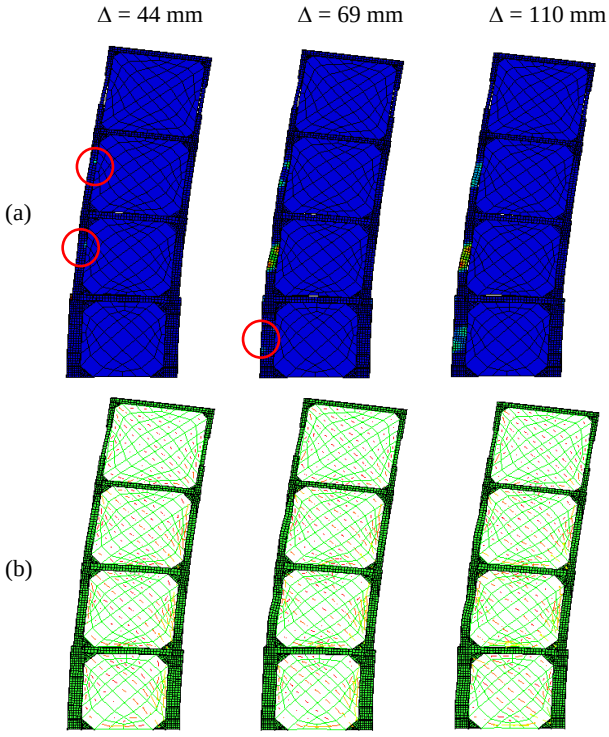

Figure 8: Results of finite element analysis: a) yielding pattern in the steel frame; b) stress field in the wall.

4 EXPERIMENTAL BEHAVIOUR OF THE INNOVATIVE SRCW SYSTEM

4.1 Introduction

An experimental campaign was carried out on two two-third downscaled specimens in order to validate the predicted behaviour of the proposed SRCW, evaluate possible problems related to the realization of such system, and highlight the influence of different shear stud distributions along the steel frame perimeter. The specimens, respectively named S1 and S2 are shown in Figure 9. S1 is characterized by the presence of shear studs only in the steel frame corner zones while S2 has shear studs distributed all along the steel frame perimeter (excluded the dissipative zones). In both cases the RC wall is 12 cm thick.

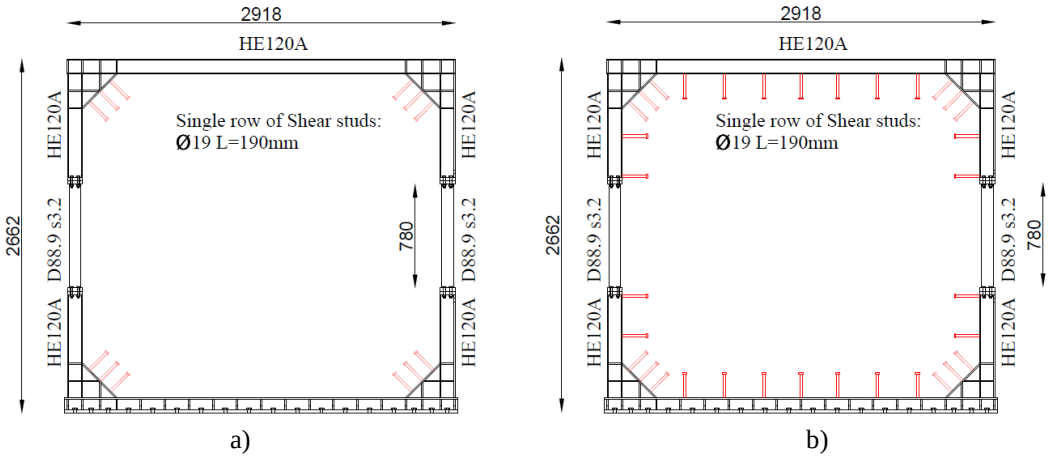

Figure 9: SRCW Steel frame specimens: a) Specimen S1 with shear studs only in the corner; b) Specimen S2 with shear studs all along the perimeter (excluded the dissipative zones).

4.2 Test setup

The SRCW specimen is bolted to a steel base firmly connected to the strong floor by means of an anchoring system and horizontal reaction system (Figure 10), while a lateral stabilizing system avoids transversal displacements of the wall.

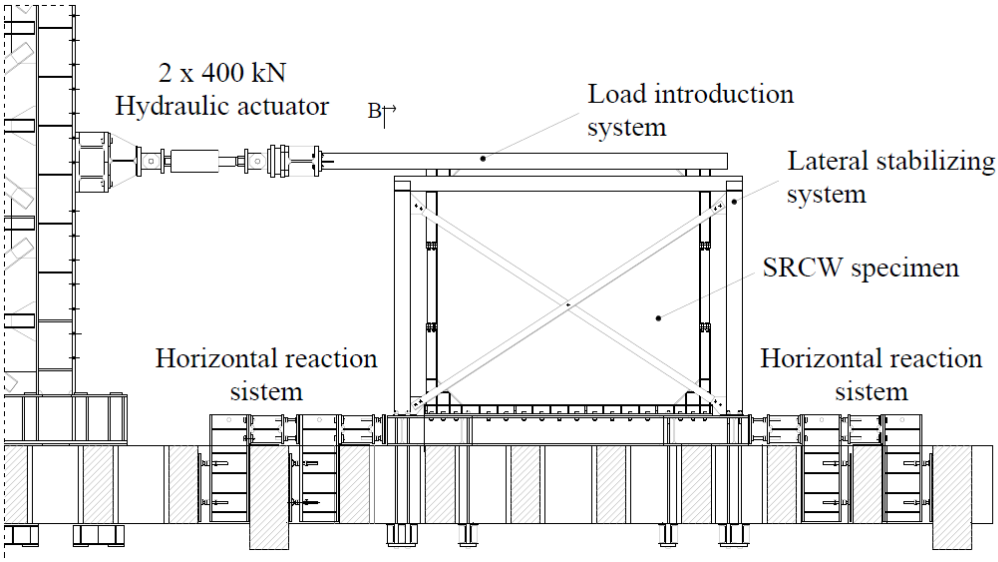

Figure 10: Global test setup.

The system is connected to the wall specimen by ten friction connections and it is independent from the lateral supporting system, allowing so the free tensile deformation of the dissipative elements. The displacements of the wall, the force applied, the deformation of dissipative elements and of the load introduction system are recorded by several sensors placed as shown in Figure 11.

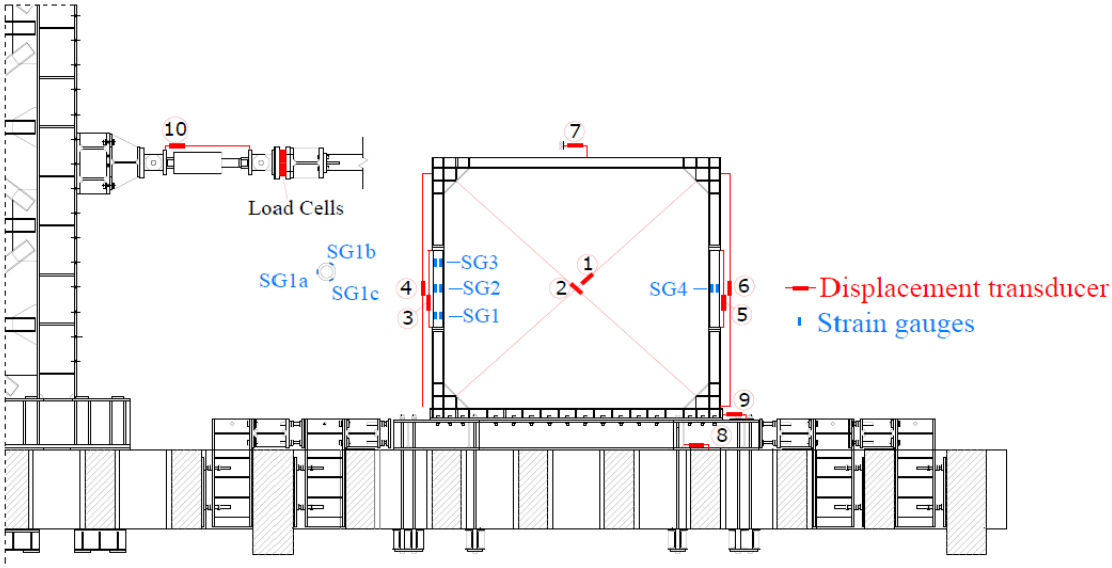

Figure 11: Sensors position.

The tests are carried out in displacement control and the displacement history imposed to the jacks end is reported, for both tests, in Figure 12. An initial maximum displacement equal to 20 mm is imposed cyclically in order to assess a displacement ductility equal at least to 3 (during the test a yield displacement equal to about 6 mm is observed). The imposed maximum displacement is then raised to about 30 mm.

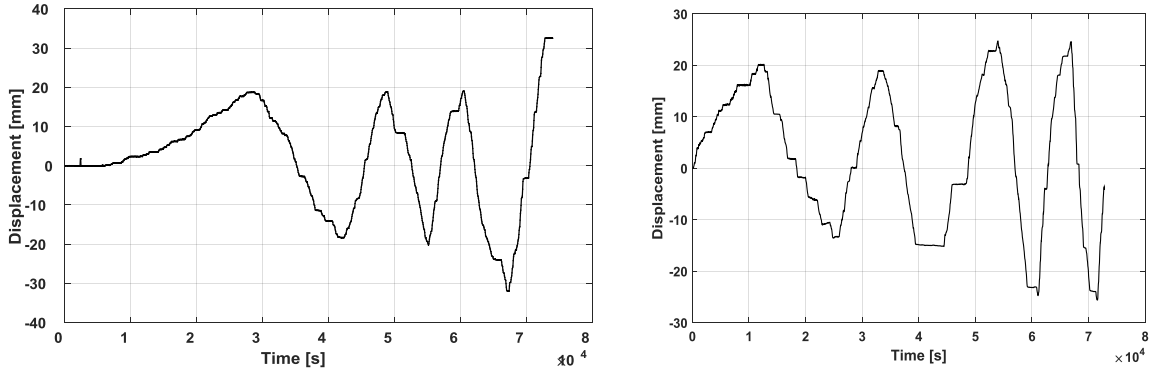

a) b)

Figure 12: Loading history of tests on a) specimen S1 and b) specimen S2.

4.3 Experimental results

In Figure 13 the experimental cyclic behaviour of specimen S1 is shown. The first loading cycle highlights a relatively "fat" hysteretic behaviour, while pinching phenomena, with the maximum resistance that remains practically constant, is exhibited during the subsequent cycles. The first semi-cycle shows that the system is characterized by a behaviour very close to an ideal elastoplastic one with a displacement ductility equal, at least, to 3.

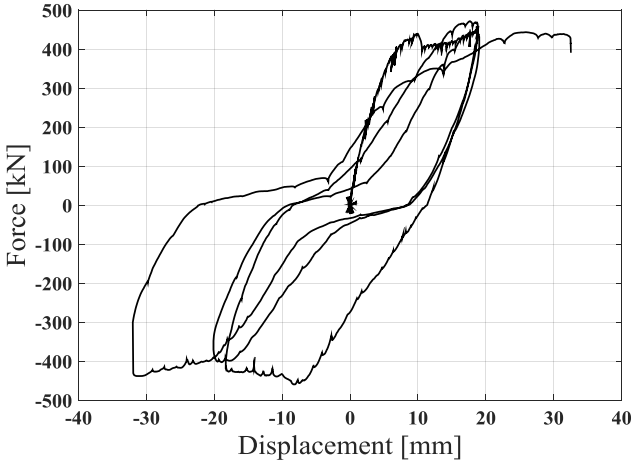

Figure 13: Specimen S1: cyclic force-displacement curve.

At the end of the first unloading phase, the concrete wall exhibits practically no damage, exception made for a little detachment from the lateral steel boundary elements. It can be inferred that, mainly due to the low number of shear studs connecting the RC wall to the steel boundary elements, the wall behaves as a rigid body within the steel frame, avoiding any damage, except for the corner zones. Due to the continuous accumulation, cycle after cycle, of the vertical displacements in the lower edge, the force application point of the compressed concrete diagonal strut changes and causes the failure of the specimen due to an excessive shear deformation of the non-dissipative vertical steel element (Figure 14a). At the same time, the spalling of the concrete on the opposite lower corner of the infill wall and the complete detachment of the infill wall from the steel frame occurs (Figure 14b). Practically no other damages are visible within the RC wall.

a) b)

Figure 14: Lower corners of S1 after failure: a) shear failure of the non-dissipative zone and b) spalling of the concrete and complete detachment by the steel frame.

Specimen S2 shows a behaviour similar to the one of specimen S1 as can be seen in Figure 15, with evident pinching phenomena but with an higher resistance. The diffused presence of the shear studs all along the perimeter of the steel frame allows the transmission of horizontal forces also through shear mechanism, as testified by the diffused diagonal cracking observed

within the wall. The more efficient connection between the wall and the boundary steel elements causes the propagation of a main crack from the base of the dissipative element in tension, as illustrated in Figure 16, avoiding any detachment phenomena between the RC wall and the steel frame. Due to the displacement accumulation, the vertical and horizontal reinforcing bars crossing the main crack break (Figure 16), causing the loss of some horizontal forces carrying capacity.

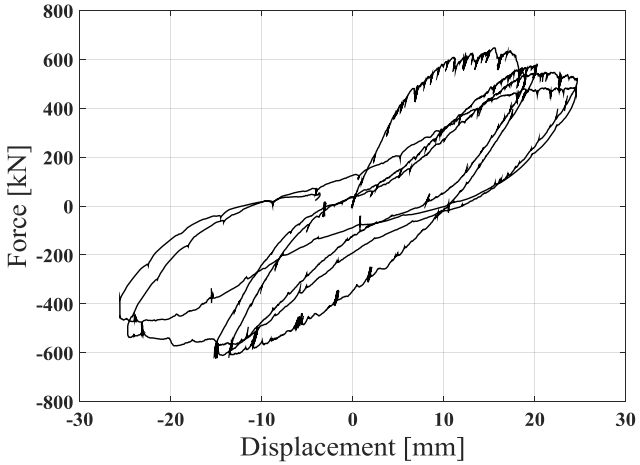

a) b)

Figure 15. Specimen 2: a) cyclic force-displacement curve; b) first loading and unloading phase

a) b)

Figure 16. Specimen S2 at the end of the test: a) global view; b) failure of the steel reinforcements in tension crossing the main crack.

5 CONCLUSIONS

A new steel frame with reinforced concrete infill wall (SRCW) is proposed and its actual behaviour assessed through experimental tests. The system is characterized by the presence of a dissipative element within the boundary steel columns that allows the activation of a proper dissipative mechanism. Consequently, the force transmitted to the other structural elements, and in particular to the foundations, are limited and an important portion of the seismic energy dissipated through plastic deformation. To allow the activation of the dissipative mechanism and in order to optimize the design of non-dissipative elements, a force-based capacity design method, applied by considering the simple statically determined scheme representing the lim-

it behaviour of the SRCW, is proposed. Rules and indications are supplied for the design of each element composing the system, selecting and adapting the design philosophy and the indications of the Eurocodes. The real behaviour of the proposed system is then studied through an experimental campaign on two 2/3 downscaled specimens, characterized by a different shear stud distribution. Both specimens results highlighted a good monotonic displacement ductility and cyclic pinching phenomena, a practically constant maximum resistance and a tendency to accumulate tensile plastic deformation on the dissipative elements. The specimen with shear studs only on the corners failed due to excessive shear damage to the non-dissipative zone of the column and the spalling of the concrete on the opposite lower corner of the infill wall. The failure was probably caused primary by the uplifting of the concrete infill wall and the consequent uplifting of the contact point between the concrete strut and the steel frame. The other specimen, with shear studs distributed all along the non-dissipative steel boundary elements, failed due to the tensile failure of concrete wall reinforcements. It showed the same tendency to accumulate vertical displacement, but the accumulation took place on the main crack formed on the RC wall, while no detachment was observed between the wall and the steel frame. While the first specimen exhibited a latticed structural behaviour, the second specimen highlighted also a shear resistance mechanism of the shear wall, with a consequent initial lateral resistance higher than the one of first specimen. Further researches are however needed for better understanding of the shear studs distribution influence and to study the effects on the failure mechanism of the vertical forces transmitted by the dead and live load to the SRCW systems. The presence of the vertical loads could, in fact, modify the effective failure mechanism, avoiding the accumulation of the vertical displacements. In this way, the re-centring capability, today accepted as one of the most important features for limiting the structural damage due to the earthquake actions [14][15], would be demonstrated also for SRCW systems.

6 ACKNOWLEDGMENTS

The research leading to these results has received funding from the European Union's Research Fund for Coal and Steel (RFCS) research programme under grant agreement n° [RFSR-CT-2010-00025] and from the Italian Department of Civil Protection within the Italian Research Project RELUIS-DPC 2014-2018.

REFERENCES

[1] J.F. Hajjar. Composite steel and concrete structural systems for seismic engineering, *Journal of Constructional Steel Research*, **58**, 703-723, 2002.

[2] F. Braga, R. Gigliotti, G. Monti, F. Morelli, C. Nuti, I. Vanzi, W. Salvatore, Post-seismic assessment of existing constructions: evaluation of the shakemaps for identifying exclusion zones in Emilia. *Earthquakes and Structures*, **8**, 37-56, 2014.

[3] F. Braga, R. Gigliotti, G. Monti, F. Morelli, C. Nuti, I. Vanzi, W. Salvatore, Speedup of post earthquake community recovery. The case of precast industrial buildings after the Emilia 2012 earthquake. *Bulletin of Earthquake Engineering*,**12**, 2405-2418, 2014.

[4] F. Braga, F. Morelli, W. Salvatore, A macroseismic approach for the evaluation of seismic risk, J. Kruis, Y. Tsompanakis, B.H.V. Topping eds, *Fifteenth International Conference on Civil, Structural and Environmental Engineering Computing*, Prague, Czech Republic, September 1-4, 2015

[5] A. Dall'Asta et al. *Innovative hybrid and composite steel-concrete structural solutions for building in seismic area*, Final Report, EUR 26932 EN, European Commission, 2015. DOI:10.2777/85404.

[6] A. Zona, H. Degeé, G. Leoni, A. Dall'Asta, Ductile design of innovative steel and concrete hybrid cou-

pled walls. *Journal of Constructional Steel Research*, **117**, 204-213, 2016.

[7] European Committee for Standardization, *Eurocode 8: Design of structures for earthquake resistance - Part 1: General rules, seismic actions and rules for buildings*. EN 1998-1, December 2004.

[8] European Committee for Standardization. *Eurocode 3: Design of steel structures - Part 1-1: General rules and rules for buildings*. En1993-1-1, August 2005.

[9] L. Ragni, A. Zona, A. Dall'Asta. Analytical expressions for preliminary design of dissipative bracing systems in steel frames. *Journal of Constructional Steel Research*, **67**, 102-113, 2011.

[10] A. Zona, L. Ragni, A. Dall'Asta. Sensitivity-based study of the influence of brace over-strength distributions on the seismic response of steel frames with BRBs. *Engineering Structures*, **37**, 179-192, 2012.

[11] Q. Gu, A. Zona, Y. Peng, A. Dall'Asta. Effect of buckling-restrained brace model parameters on seismic structural response. *Journal of Constructional Steel Research*, **98**, 100-113, 2014.

[12] European Committee for Standardization, *Eurocode 2 - Design of concrete structures - Part 1-1: General rules and rules for buildings*. EN 1992-1-1, November 2005.

[13] European Committee for Standardization, *Eurocode 4 - Design of composite steel and concrete structures - Part 2: General rules and rules for bridges*. EN 1994-1, January 2006.

[14] A. Braconi, F. Morelli, W. Salvatore, Development, design and experimental validation of a steel self-centering device (SSCD) for seismic protection of buildings, *Bulletin of Earthquake Engineering*, **10**, 1915-1941, 2012.

[15] A. Ioan, A. Stratan, D. Dubină, M. Poljanšek, F.J. Molina, F. Taucer, P. Pegon, G. Sabău, Experimental validation of re-centring capability of eccentrically braced frames with removable links, *Engineering Structures*, **113**, 335-346, 2016.

ECCOMAS Congress 2016
VII European Congress on Computational Methods in Applied Sciences and Engineering
M. Papadrakakis, V. Papadopoulos, G. Stefanou, V. Plevris (eds.)
Crete Island, Greece, 5–10 June 2016

MODAL PROPERTIES AND SEISMIC RESPONSE OF EXISTING BUILDING RETROFITTED BY EXTERNAL BRACINGS WITH VISCOUS DAMPERS

Laura Gioiella[1], Enrico Tubaldi[2], Fabrizio Gara[1] and Andrea Dall'Asta[3]

[1] DICEA – Università Politecnica delle Marche
via Brecce Bianche, 60121 Ancona, Italy
l.gioiella,f.gara@univpm.it

[2] Department of Civil Engineering – Imperial College
Skempton Building, South Kensington Campus, Imperial College London, SW7 2AZ, UK
etubaldi@ic.ac.uk

[3] Scuola di Architettura e Design – Università di Camerino
Viale delle Rimembranze, 63100 Ascoli Piceno, Italy
andrea.dallasta@unicam.it

Keywords: Passive Seismic Protection, Linear Viscous Dampers, External Seismic Retrofit, Dissipative Towers.

Abstract. *This paper deals with the seismic protection of existing buildings using external viscous damper systems to increase the energy dissipation capacity. Dampers and bracings can be arranged in very different configurations and the possible solutions can be grouped into different categories, depending on the specific kinematic behavior. The study analyzes a recent solution called "dissipative tower", which, for the dampers activation, exploits the rocking motion of a stiff steel truss hinged at the foundation level. A state space formulation of the dynamic problem is presented in general terms and some issues concerning the influence of the bracing properties on the behavior of a case study consisting of a building coupled with a dissipative tower are investigated. The results presented concern both the influence of the external dissipative bracings on the most important modal properties of the system, and the global effect on the seismic response, evaluated via the modal decomposition method. It is shown that the addition of the towers yields a regularization of the drift demand along the building height, but it can also induce significant changes in the distribution of internal actions in the existing frame. Moreover, the contribution of higher order modes can be important for the internal actions evaluation, while it is negligible for the displacement estimation. The results obtained by considering the coupled system are compared with the corresponding results obtained by considering two limit cases: the bare frame, and the frame equipped with an infinitely stiff dissipative tower.*

1 INTRODUCTION

Passive control systems have proven to be very efficient solutions for new constructions and for seismic retrofitting of existing structures [1-4]. Viscous dampers are traditionally installed within a building frame in either diagonal or chevron brace configurations connecting adjacent storeys and there are many studies concerning both the dynamic properties of the damped system and the methods for the design [*e.g.*, 5-10]. However, this type of damping system may present some disadvantages, particularly when employed for retrofitting existing buildings. Usually, the addition of dissipative diagonal in existing frames provides an increment of axial forces in the columns and this may lead to premature local failures [11]. Furthermore, there may be some feasibility limits on the strengthening of the existing foundations at the base of the bracing system. Also, the indirect costs related to the interruption of the building utilization during execution of the retrofit can be very demanding, in particular for strategic buildings, such as hospitals or schools.

These problems can be efficiently resolved by considering external damper configurations, i.e., by placing the dissipative bracings and the relevant foundations outside the building frame. External dampers and bracing components can be arranged in very different configurations and the possible solutions can be grouped into three main categories, characterized by substantially different kinematic behaviors, but all permitting the control of both the total amount of the dissipated energy and the frame deformation at the various storeys. A possible solution can be obtained by placing the dampers horizontally at the storey level, between the frame and an external stiff structure [12]. This way, the links are activated by the floor absolute displacements. A similar configuration can be obtained by placing the dampers between adjacent buildings, though this solution is efficient if the two buildings have strongly different dynamic properties [13-16]. An alternative solution can be obtained by coupling the frame with an external shear deformable bracing structure. The new and existing structures are connected at the storey level and the dissipative devices are activated by the relative displacements between adjacent floors, as in the more traditional case of bracings placed within the existing structure [3].

Recently, some applications have been developed by proposing a new configuration exploiting the rocking motion of a stiff brace hinged at the foundation level [17, 18]. In this configuration, known as "dissipative tower" (Figure 1) [19], the dampers are activated by the base rotation of the tower.

This work focuses on the coupling between an existing frame and a rocking dissipative configuration shown in Figure 1; the purpose is the investigation of the modal properties and the seismic response of the coupled system by means of a problem formulation presented in general terms. The dynamic behavior and seismic performance of the system is compared against that of two other limit cases, the first one being the bare building, the second the building coupled with an infinitely stiff dissipative tower.

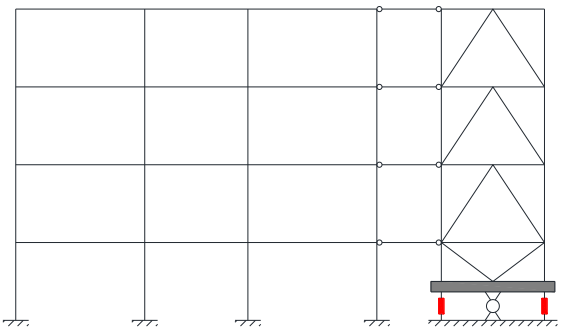

Figure 1: Dissipative Tower.

2 PROBLEM FORMULATION

In the first part of this section, the equation of motion and the state variables of the considered problem are presented by assuming that both the building and the external damping system exhibit a linear response. The limit case of stiff tower is also presented and the balance equations of the reduced single-degree-of-freedom (SDOF) system are obtained by introducing a constraint in the structure motion.

2.1 Equation of motion

The equations of motion for the system can be expressed as follows:

$$\mathbf{M}\,\ddot{\mathbf{u}}(t) + \mathbf{C}\,\dot{\mathbf{u}}(t) + \mathbf{K}\mathbf{u}(t) = \mathbf{M}\mathbf{p}\,a_g(t) \tag{1}$$

where $\mathbf{u}(t) \in R^l$, is the vector of nodal displacements, the dot (·) denotes time-derivative; $\mathbf{p} \in R^l$ is the load distribution vector, l denotes the total number of degrees-of-freedom, and $a_g(t)$ is the external scalar loading function describing the seismic base acceleration. The time invariant matrices $\mathbf{M}$, $\mathbf{K}$, $\mathbf{C}$ describe the mass, stiffness and damping operators $R^l \to R^l$; they result from the sum of the contribution due to the existing frame and the one coming from the external dissipative bracing system. The damping contribution of the frame and of the dissipative system are denoted respectively as $\mathbf{C}_F$ and $\mathbf{C}_D$. Generally, the external bracing system notably influences the stiffness and damping operators while it contributes only marginally to the mass operator. The displacement vector $\mathbf{u}(t)$ collects both the displacements required for the description of the frame response and the displacements involved in the bracing deformations.

In order to study the dynamic response of the system it is useful to separate the displacements associated with the masses, and thus involving inertial forces, from the displacements describing the internal degrees of freedom, related to stiffness and damping forces only. Accordingly, the total displacement vector $\mathbf{u}(t)$ can be split into the active components collected in the vector $\mathbf{x}(t) \in R^m$ and the other components $\mathbf{y}(t) \in R^n$ ($l = m + n$). The matrices describing the linear operators and the distribution vector can be consequently partitioned as follows

$$\begin{vmatrix} \mathbf{M}_{xx} & 0 \\ 0 & 0 \end{vmatrix} \begin{vmatrix} \ddot{\mathbf{x}} \\ \ddot{\mathbf{y}} \end{vmatrix} + \begin{vmatrix} \mathbf{C}_{xx} & \mathbf{C}_{xy} \\ \mathbf{C}_{yx} & \mathbf{C}_{yy} \end{vmatrix} \begin{vmatrix} \dot{\mathbf{x}} \\ \dot{\mathbf{y}} \end{vmatrix} + \begin{vmatrix} \mathbf{K}_{xx} & \mathbf{K}_{xy} \\ \mathbf{K}_{yx} & \mathbf{K}_{yy} \end{vmatrix} \begin{vmatrix} \mathbf{x} \\ \mathbf{y} \end{vmatrix} = \begin{vmatrix} \mathbf{M}_{xx} & 0 \\ 0 & 0 \end{vmatrix} \begin{vmatrix} \mathbf{p}_x \\ 0 \end{vmatrix} a_g \tag{2}$$

As usual, only the masses related to the horizontal floor displacements are considered in order to reduce the dimension of the dynamic problem and to simplify the interpretation of the results.

The distribution of the damping in the structure and, in particular, the location of the concentrated dampers of the external bracings, leads to a non-classically damped system. For its solution it is convenient to formulate the problem by introducing the vector $\mathbf{v}(t) = \dot{\mathbf{x}}(t)$ and the state vector $\mathbf{z}(t)$ collecting the displacements and the velocities of the active displacements and the displacements of the internal nodes:

$$\mathbf{z}(t) = \begin{vmatrix} \mathbf{x}(t) \\ \mathbf{v}(t) \\ \mathbf{y}(t) \end{vmatrix} \tag{3}$$

Eqn. (1) can be reduced to a first-order state space form:

$$\dot{\mathbf{z}}(t) = \mathbf{A}\mathbf{z}(t) + \tilde{\mathbf{p}}\, a_g(t) \tag{4}$$

where:

$$\mathbf{A} = \begin{vmatrix} \mathbf{0} & \mathbf{I} & \mathbf{0} \\ -\mathbf{M}_{xx}^{-1}\left(\mathbf{K}_{xx} - \mathbf{C}_{xy}\mathbf{C}_{yy}^{-1}\mathbf{K}_{yx}\right) & -\mathbf{M}_{xx}^{-1}\left(\mathbf{C}_{xx} - \mathbf{C}_{xy}\mathbf{C}_{yy}^{-1}\mathbf{C}_{yx}\right) & -\mathbf{M}_{xx}^{-1}\left(\mathbf{K}_{xy} - \mathbf{C}_{xy}\mathbf{C}_{yy}^{-1}\mathbf{K}_{yy}\right) \\ -\mathbf{C}_{yy}^{-1}\mathbf{K}_{yx} & -\mathbf{C}_{yy}^{-1}\mathbf{C}_{yx} & -\mathbf{C}_{yy}^{-1}\mathbf{K}_{yy} \end{vmatrix} \tag{5}$$

Vector $\tilde{\mathbf{p}}$ is defined as:

$$\tilde{\mathbf{p}} = \begin{vmatrix} 0 \\ \mathbf{M}_{xx}^{-1}\mathbf{p} \\ 0 \end{vmatrix} \tag{6}$$

2.2 Free vibrations and modal properties

The free vibration problem can be solved by assuming a solution of the form $\mathbf{z}(t) = \boldsymbol{\varphi} e^{\lambda t}$, where $\lambda, \boldsymbol{\varphi}$ are a eigenvalue-eigenvector pair of $\mathbf{A}$, such that:

$$\mathbf{A}\boldsymbol{\varphi} = \lambda\boldsymbol{\varphi} \tag{7}$$

Complex eigenvalue has the following form:

$$\lambda_i = -\xi_i\omega_{0i} + i\omega_{0i}\sqrt{1-\xi_i^2} \tag{8}$$

and contains information regarding both the damping ratio ξ_i and the corresponding undamped circular frequency ω_{0i} of the *i*-th mode. These information can be extrapolated as follows:

$$\begin{aligned} \omega_{0i} &= |\lambda_i| \\ \xi_i &= -\mathrm{Re}(\lambda_i)/|\lambda_i| \end{aligned} \tag{9}$$

Known the modal properties, the problem solution can be obtained as a linear combination of the single mode contributions. Let $\boldsymbol{\Lambda}$ be the diagonal matrix containing the complex eigenvalues and $\boldsymbol{\Phi} = |\boldsymbol{\varphi}_1, \boldsymbol{\varphi}_2, ..., \boldsymbol{\varphi}_{2m+n}|$ the complex eigenmatrix containing the eigenvectors, such that the orthogonality property $\boldsymbol{\Lambda} = \boldsymbol{\Phi}^{-1}\mathbf{A}\boldsymbol{\Phi}$ holds.

2.3 Seismic response via modal decomposition method

The motion can be obtained as a linear combination of modes:

$$\mathbf{z}(t) = \boldsymbol{\Phi}\mathbf{q}(t) \tag{10}$$

where $\mathbf{q}(t)$ is a vector collecting the modal coordinates. The orthogonality property leads to the diagonal problem:

$$\dot{\mathbf{q}}(t) = \boldsymbol{\Lambda}\mathbf{q}(t) + \boldsymbol{\gamma}\, a_g(t) \tag{11}$$

where $\gamma_i = \left[\boldsymbol{\Phi}^{-1}\tilde{\mathbf{p}}\right]_i$ is the *i*-th (complex-valued) modal participation factor.

Introducing the normalized complex modal response vector $\mathbf{s}(t)$ such that: $q_i(t) = \Gamma_i s_i(t)$, the problem can be written in a normalized form:

$$\dot{\mathbf{s}}(t) = \mathbf{\Lambda s}(t) + \mathbf{I}a_g(t) \tag{12}$$

Assuming that the system is initially at rest, the solution can be obtained by the Duhamel integral:

$$\mathbf{s}(t) = \int_0^t \mathbf{h}(t-\tau)a_g(\tau)d\tau \tag{13}$$

where the components $h_i(t) = e^{\lambda_i t}$ are the solutions related to an impulsive unitary input.

2.4 Generalized SDOF system approximation

The dissipative tower consists of an external bracings system that activates the dampers located at its base through its rocking motion. In the case of an infinitely stiff tower all the degrees of freedom of the system (active displacements of the frame and displacements involved in the bracing deformations) are governed by the base rotation φ. This means that the displacement vector $\mathbf{u}(t)$, shown in eqn. 1, can be expressed as

$$\mathbf{u}(t) = \mathbf{L}\varphi \tag{14}$$

in which **L** is a vector collecting the heights of the frame. The D'Alembert Principle for the problem at hand can be expressed by introducing a virtual velocity field $\hat{\eta} = \mathbf{L}\hat{\varphi}$, in which $\hat{\varphi}$ is an arbitrary base rotation. Eqn. 1 can be rewritten for any time instant *t* as

$$\mathbf{M}_b\ddot{\mathbf{u}} \cdot \hat{\eta} + \mathbf{C}_F\dot{\mathbf{u}} \cdot \hat{\eta} + \mathbf{C}_D\dot{\mathbf{u}} \cdot \hat{\eta} + \mathbf{K} \cdot \hat{\eta} = \mathbf{M}_b\mathbf{p} \cdot \hat{\eta}a_g \qquad \forall t \tag{15}$$

where the matrices $\mathbf{M}_b$, $\mathbf{K}_b, \mathbf{C}_F$ describe the mass, stiffness and damping of the frame and where $\mathbf{C}_D$ is the dissipative contribution of the dampers located at the tower base. This way, the tower influences only the damping operator and the shape of the virtual displacement field. Eqn. 15 can be rewritten as

$$\tilde{m}\ddot{\varphi} + (\tilde{c}_F + \tilde{c}_D)\dot{\varphi} + \tilde{k}\varphi = m^* a_g \tag{16}$$

where $\tilde{m} = \mathbf{M}_b\mathbf{L} \cdot \mathbf{L}$, $\tilde{c}_F = \mathbf{C}_F\mathbf{L} \cdot \mathbf{L}$, $\tilde{c}_D = \mathbf{C}_D\mathbf{L} \cdot \mathbf{L}$, $\tilde{k} = \mathbf{K}_b\mathbf{L} \cdot \mathbf{L}$, $m^* = \mathbf{M}_b\mathbf{p} \cdot \mathbf{L}$ are the scalar parameters describing the properties of the system reduced to a SDOF, and $\cdot$ denotes the scalar product. By solving Eqn. 15, the time-history of the base rotation is known, and the vector of nodal displacements of the MDOF system is determined by considering Eqn. (14).

3 CASE STUDY

3.1 Case study description

The application of the proposed approach is illustrated by considering a r.c. frame structure, with limited ductility, typical of many buildings designed during the 80s in Italy without any specific seismic detailing. Along the longitudinal direction, the structure consists of two external frames with 6 spans and a central one with 7 spans (Figure 2). The building has 5 storeys plus the roof.

The presented results concern three configurations, the bare existing frame (*As is*), the r,c, frame coupled with dissipative tower hinged at the foundation level and equipped with linear viscous dampers located at the base (*Retrofit*), and the r.c. frame coupled with an infinitely stiff dissipative tower (*Stiff*).

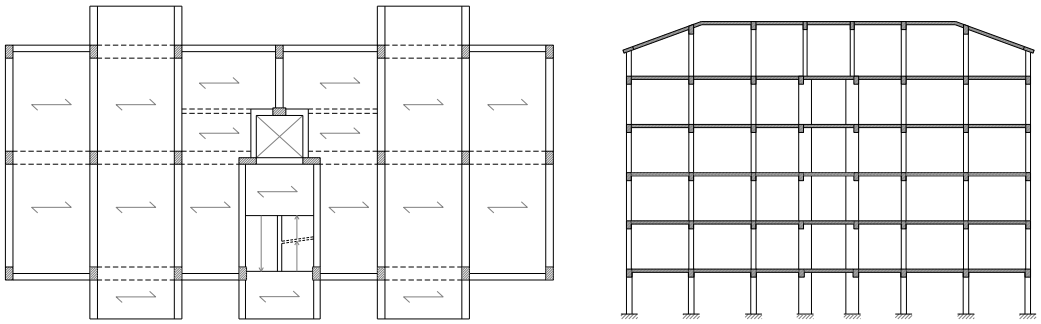

Figure 2: Planar view and longitudinal section of the bare building.

First, the previously described formulation is employed to investigate the influence of the external bracing properties on the overall dynamic properties of the coupled system, such as the modal displacement profile, the relevant internal action distribution and the modal damping ratios. Successively, the global effect of the retrofit on the seismic response is evaluated by solving the seismic problem with the modal decomposition method for the first two configurations (*As is* and *Retrofit*) and with a direct integration method for the last one (*Stiff*).

The dynamic system is described by considering only the motion along the longitudinal direction. The floors are assumed to be rigid in the horizontal plane and the masses are concentrated at the storey levels so that the vector of active degrees of freedom $\mathbf{x}$ collects the five storey motions only.

3.2 Modal properties of the undamped system

The bracing system influences both the stiffness and the damping properties of the coupled system, while its contribution to the masses is negligible. It is useful to separately analyze the variations on stiffness and damping and, for this purpose, the case of the added tower without dampers is considered separately from the case of the tower with dampers.

Table 1 reports, for the five modes of the bare building (*As is*), the vibration periods, the undamped natural frequencies and the participant mass ratios, defined as $M_i^* = (\mathbf{M}\mathbf{p} \cdot \boldsymbol{\psi}_i)^2 / \mathbf{M}\boldsymbol{\psi}_i \cdot \boldsymbol{\psi}_i$ where $\boldsymbol{\psi}_i$ are the eigenvectors of the undamped system.

T_i [s]	ω_0^2	M_i^*	ΣM_i^*
1.021	6.18	0.787	0.787
0.300	21.03	0.117	0.904
0.153	41.26	0.052	0.956
0.097	65.51	0.03	0.985
0.074	86.05	0.015	1

Table 1: Modal analysis results - *As is* configuration.

The modal analysis results of the coupled system in the *Retrofit* configuration are summarized in Table 2, where it can be observed that the first two vibration modes involve the 95% of the total mass and the second period reduces to about half the value obtained with the *As is* configuration. The third case, i.e. the existing frame coupled with an infinitely stiff tower (*Stiff*), is characterized by one vibration mode only (T=0.925 s) as it behaves like a SDOF system governed by the tower rocking motion.

T_i [s]	ω_0^2	M_i^*	ΣM_i^*
0.964	6.52	0.806	0.806
0.147	42.84	0.138	0.945
0.073	86.24	0.035	0.980
0.051	124.17	0.015	0.995
0.041	151.63	0.005	1

Table 2: Modal analysis results – *Retrofit* configuration.

Figure 3 reports and compares the values of the interstorey drifts along the building height corresponding to the first three modes of vibration for the *As is* and the *Retrofit* configurations. It can be observed that the addition of the towers yields a regularization of the drift demands along the building height, even though a higher value of the drift is required at the first level.

Figure 4 reports the distributions of the total shear forces in the *As is* and *Retrofit* cases for the first three modes, whereas Figure 5 shows, for the *Retrofit* configuration only, the storey shear demand for the building and the tower. It is worth to note that the shear contributions of the existing frame and the towers could have different signs at some levels and, for the considered case, the first mode shear forces acting on the existing frame is higher than the total shear force at the first level.

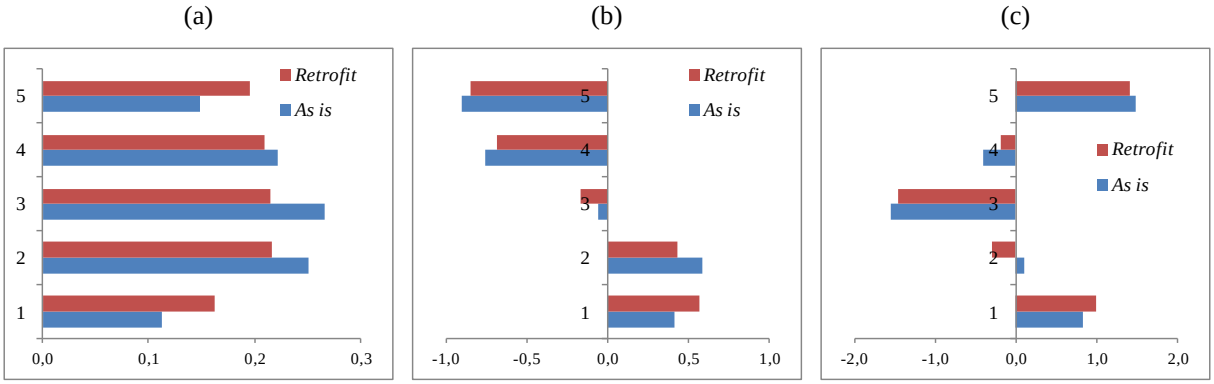

Figure 3: Interstorey drifts along the building height for mode 1 (a), mode 2 (b) and 3 (c).

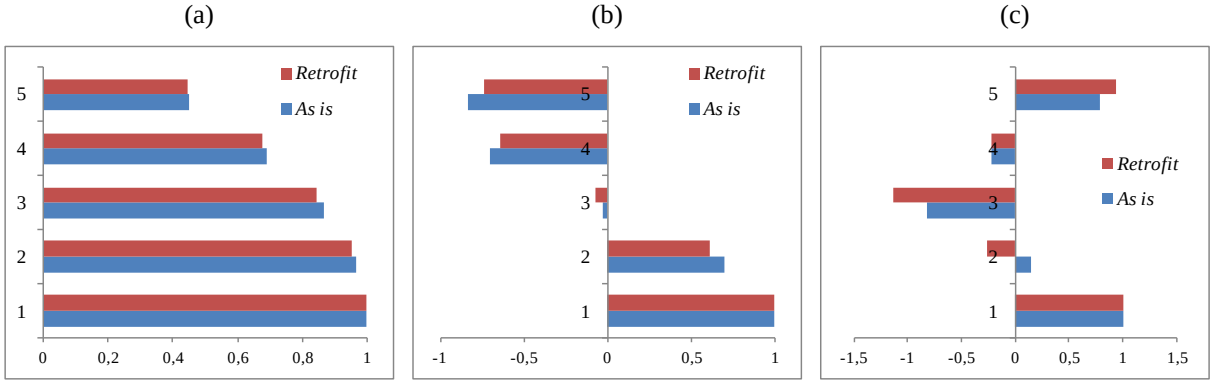

Figure 4: Total shear force comparison for mode 1 (a), mode 2 (b) and 3 (c).

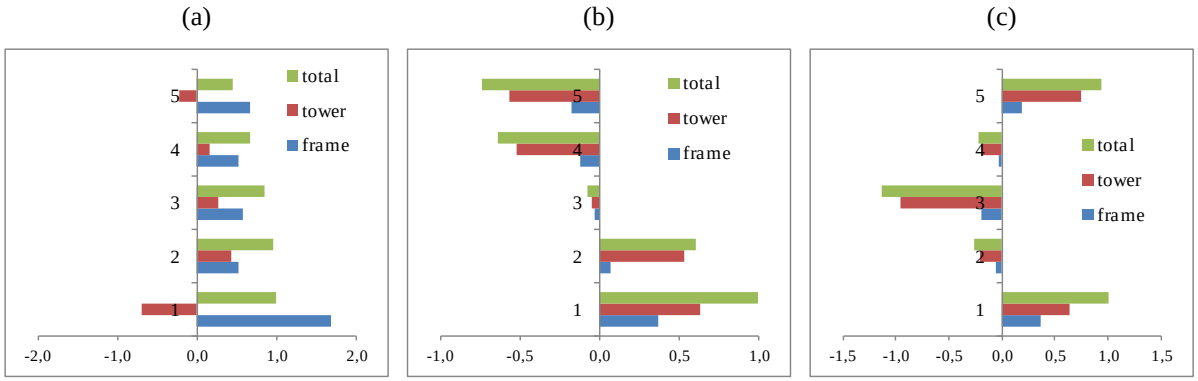

Figure 5: Shear force distribution for mode 1 (a), mode 2 (b) and 3 (c) – *Retrofit* configuration.

3.3 Modal properties of the damped system

The damping of the system is the sum of two contributions $\mathbf{C} = \mathbf{C}_F + \mathbf{C}_D$, the former is described by a Rayleigh damping matrix $\mathbf{C}_F = \alpha \mathbf{M} + \beta \mathbf{K}$, related to the existing frame, providing a inherent damping ξ=0.05 at the first two vibration modes. The latter contribution is due to the dampers and it is directly related to their displacements produced by the rocking motion.

A reference value of the damper dimensions is obtained by fixing a target total amount of the effective damping ratio β_{eff} =0.25 (0.05 due to the building and 0.20 due to the dampers), and by using the expression reported in ASCE/SEI 41-13 (2013)

$$\beta_{eff} = \beta + \frac{\sum_j W_j}{4\pi W_k} \tag{17}$$

where β is the damping in the structural frame (0.05), W_j the work done by j-th device in one complete vibration cycle and W_k is the maximum strain energy in the frame.

The retrofit configuration consists of two dampers placed as in Figure 1, whose viscous constant values are designed by employing eqn. (17) assuming that the system deforms according to its first undamped vibration mode. The total amount of added damping is measured by C_0=135020 kNs/m, which is the sum of the viscous damping constant of the two devices.

By means of the complex modal analysis it is possible to identify the damping ratio ξ_i corresponding to each one of the vibration modes, as shown in eqn. (9); moreover, by introducing a damper multiplier c for the total added damping C_0, it is possible to evaluate the variation of the modal properties at different damping levels, defined by the parameter c.

Figure 6(a) shows the influence of c on the vibration periods of the first three modes. The first three natural periods of the undamped system (dashed line in Figure 6) are 0.964 s the first period (blue line), 0.147 s the second (red line), and 0.073 s the third period (green line). The vibration periods of the coupled system decreases for increasing damping. For c=3.0, the first period attains the value 0.595 s, the second 0.141 s and the third 0.072 s. Thus, the amount of damping introduced influences significantly only the first vibration period of the system. Figure 6(b) shows the variation, with the total added damping c, of the damping ratio of the first, second and third vibration modes, ξ_1, ξ_2 and ξ_3. It also reports the variation of the estimate of the damping ratio β_{eff}, obtained by employing the approximate formula of Eqn.(17), for increasing values of c.

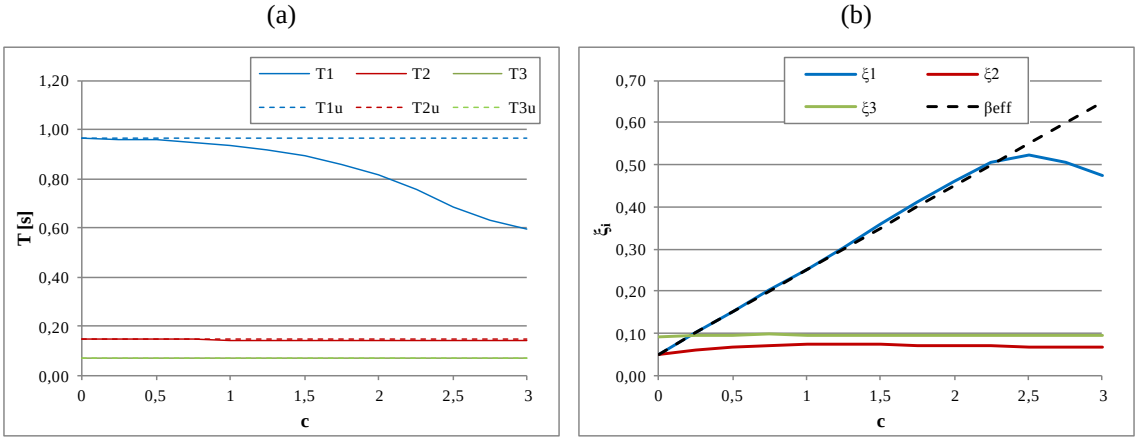

Figure 6: First three period trends (a) and first three modes damping trends (b) for increasing damping levels.

The first modal damping ratio ξ_1 is well approximated by the design formula of Eqn. (17) for ξ values up to 0.50 (c=2.25); for increasing values beyond this limit the amount of the effective damping decreases. As already observed for the periods, the influence of the damper dimensions on the second and third mode is negligible; the damping ratio varies in the range 0.050-0.067 with a maximum 0.074 when c=1.25 for the second mode, while for the third mode the range is 0.091-0.094 with a maximum value of 0.097 when c=0.75.

Due to the fact that all the dampers are concentrated at the tower base the system is notably non-classical damped and the extent of non-classical damping is synthetically quantified by the coupling index ρ (Claret e Venancio-Filho 1991), expressed as:

$$\rho = \max \left| \frac{\Xi_{ij}^{2}}{\Xi_{ii}\,\Xi_{jj}} \right| \quad (i,j=1,2,\ldots,m)\ i \neq j \tag{18}$$

where $\Xi_{ij} = \mathbf{C}_{xx}\boldsymbol{\psi}_i \cdot \boldsymbol{\psi}_j$ is the modal damping matrix component, $\mathbf{C}_{xx}$ and m are defined in section 2.1 and $\boldsymbol{\psi}_i$ are the eigenvectors of the undamped system. The index assumes the value 0 for classical damped systems and it spans the range [0,1] in the case of non-classical damping. Figure 7(a) shows the coupling index trend for increasing damping levels, while Figure 7(b) shows the values of ρ obtained for the damping target value c=1. In the latter case the maximum value of ρ is equal to 0.35 and corresponds to the coupling among the first and the second mode.

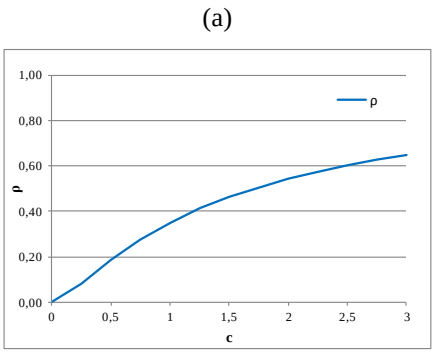

(b)

5	0.01	0	0	0	1
4	0.02	0.01	0	1	0
3	0.14	0.08	1	0	0
2	0.35	1	0.08	0.01	0
1	1	0.35	0.14	0.02	0.01
	1	2	3	4	5

Figure 7: ρ-index: (a) trend for increasing damping levels; (b) values for the fifth modes of the system (c=1).

3.4 Seismic response

This section reports some results concerning the response of the three system configurations to a seismic input. The seismic action is determined by assuming the building located in Camerino (MC, Italy), with soil category C and topographical one T1, according to Italian code [20]. Seven artificial earthquakes, generated in accordance with Italian Standards, are considered. The results reported concern the most interesting parameters, i.e., the displacements, interstorey drifts, shear action distribution and the absolute accelerations; the values of these parameters reported below are the mean of the maximum values obtained for each of the seven time-histories analyses. The results related to the coupled systems (*Retrofit* and *Stiff* configurations) correspond to a total added damping multiplier c =1.

Table 3 reports the floor displacements and the interstorey drifts for the three configurations analyzed. The maximum top displacement, normalized with respect to that of the bare frame, is 54% for the *Retrofit* case and 58% for the *Stiff case*. Figure 8(a) and (b) show the distribution along the height of the building displacements x_i and interstorey drifts θ_i, for i=1,2,..,5. The reported values are normalized by dividing them by the corresponding values obtained at the 5th level in the *Stiff* configuration.

level	*As is*		*Retrofit*		*Stiff*	
	x_i [m]	θ_i [m]	x_i [m]	θ_i [m]	x_i [m]	θ_i [m]
1	0.013	0.013	0.008	0.008	0.009	0.009
2	0.040	0.028	0.019	0.011	0.018	0.009
3	0.068	0.029	0.029	0.011	0.027	0.009
4	0.092	0.026	0.040	0.011	0.036	0.009
5	0.109	0.019	0.050	0.010	0.046	0.009

Table 3: Floor displacements and drifts results

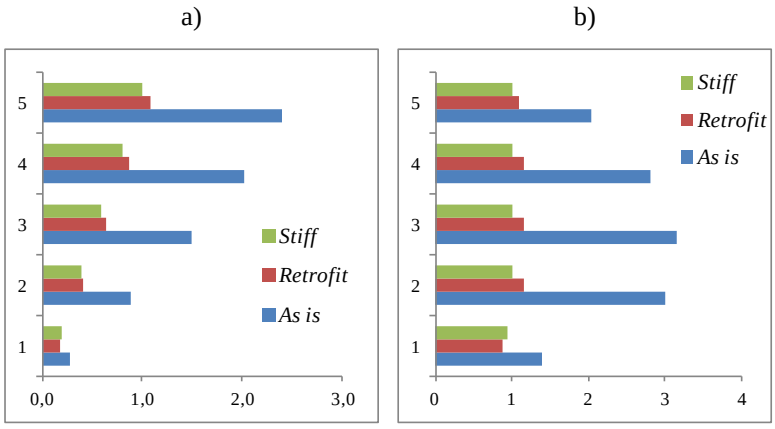

Figure 8: Displacements (a) and interstorey drifts (b) distributions for the three configurations.

It is noteworthy that the coupling with an infinitely stiff tower leads to a linear distribution of the displacements along the height. Moreover, the displacement demand at the first level is higher in the *Stiff* case than in the *Retrofit* case, while an opposite trend is observed at the top. This means that the regularization of the frame displacement distribution is achieved with the tower interacting with opposite forces at the base and at the top of the frame.

Having employed the complex mode superposition approach to solve the seismic problem, the contribution of the higher vibration modes to the response can be estimated by comparing the full response accounting for all the modes to the response obtained by considering the contribution of the first mode only. Table 4 reports the displacement response for the *As is* and the *Retrofit* case. Figure 9 comparises the displacement responses of the *As is* and *Retrofit* cases. In both the cases, the first mode contribution nearly controls the total response, while the effect of higher order modes is negligible.

level	*As is*		*Retrofit*	
	x_{full} [m]	x_1 [m]	x_{full} [m]	x_1 [m]
1	0.0129	0.0121	0.0080	0.0080
2	0.0405	0.0392	0.0188	0.0187
3	0.0684	0.0680	0.0295	0.0294
4	0.0918	0.0920	0.0399	0.0399
5	0.1092	0.1081	0.0497	0.0496

Table 4: Floor displacements and drifts results.

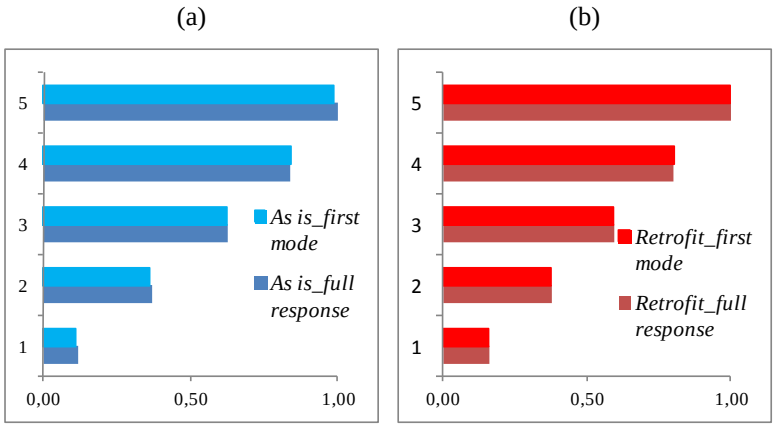

Figure 9: Contribution of the first mode to the full response of the (a) *As is* and (b) *Retrofit* cases.

Table 5 reports the shear actions resisted by the frame in the three configurations; for the *Retrofit* case the shear actions resisted by the tower and the total shear actions are also reported. It is noteworthy that the maximum shear for the tower and the frame may not occur at the same instant of time for all the records considered. As already discussed for the displacements, also the global shear demand decreases, but in a less significant way. The relative reduction of the maximum base shear acting on the frame, with respect to the bare frame, is nearly 19% for the *Retrofit* case and 6% for the *Stiff* one.

Figure 10(a) shows the shear actions distribution along the height of the frame, normalized after dividing them by the value of the base shear in the *Retrofit* configuration. Figure 10(b) shows the shear forces in the frame and the tower for the *Retrofit* case; the values are normalized with respect to the total base shear, obtained as the sum of the building plus the tower one.

level	*As is*	*Retrofit*			*Stiff*
	$V_{i,\text{frame}}$ [kN]	$V_{i,\text{frame}}$ [kN]	$V_{i,\text{tower}}$ [kN]	$V_{i,\text{total}}$ [kN]	$V_{i,\text{frame}}$ [kN]
1	5215.67	4232.33	2661.26	3544.64	4877.47
2	4789.76	1348.32	1915.45	3060.02	831.69
3	4197.01	1455.88	1292.91	2543.55	1290.06
4	3686.99	1366.94	1169.54	2336.51	1095.12
5	2755.01	1740.77	1020.58	1819.51	1643.12

Table 5: Shear actions results.

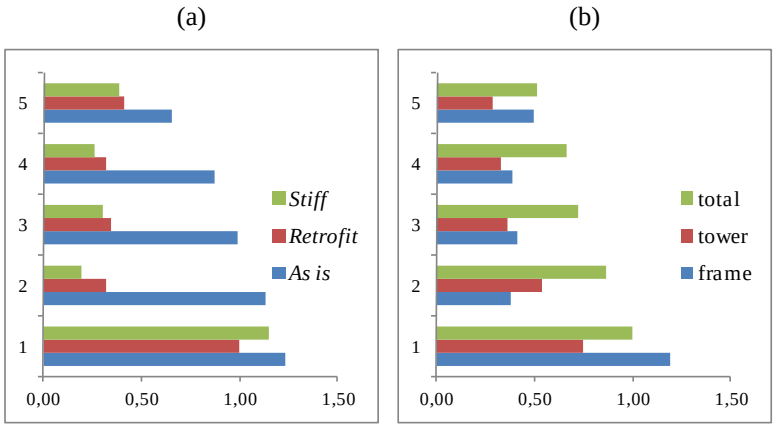

Figure 10: (a) Shear actions resisted by the frame in the three configurations and (b) shear actions resisted by the tower, the building and the frame compared to the total shear in the *Retrofit* case.

The complex mode superposition is also employed to estimate the contribution of the higher order modes of vibration on the shear actions before and after the retrofit. Table 6 reports the shear actions distribution resisted by the frame in the *As is* case and the contributions of both the frame and the tower in the *Retrofit* one, due to the full response and the first mode. Differently from the case of the displacements, the contribution of higher order modes is important as the values of both the total shear response and the tower shear response are higher than the corresponding values obtained by considering the first mode only. However, the building response appears to be still dominated by the first mode of the coupled system. These observations, together with the fact that the increase of damping ratio after the retrofit is lower for the higher modes than for the first mode, could explain why the reduction of the displacement demand is higher than that of the base shear.

level	*As is*		*Retrofit*					
	V_{full} [kN]	V_1 [kN]	$V_{\text{frame_full}}$ [kN]	V_{frame1} [kN]	$V_{\text{tower_full}}$ [kN]	V_{tower1} [kN]	$V_{\text{total_full}}$ [kN]	V_{total1} [kN]
1	5215.7	4751.3	4232.3	4202.4	2661.3	2204.3	3544.6	2963.0
2	4789.8	4600.0	1348.3	1329.6	1915.4	1734.4	3060.0	2825.4
3	4197.0	4116.0	1455.9	1440.3	1292.9	1344.5	2543.5	2507.4
4	3687.0	3276.9	1366.9	1316.7	1169.5	958.4	2336.5	2007.0
5	2755.0	2142.6	1740.8	1665.6	1020.6	687.9	1819.5	1328.4

Table 6: Higher order modes influence on the shear actions.

Figure 11(a) depicts the first mode contribution to the full shear response of the frame in the *As is* case, normalized by the value of the total base shear. Figure 11(b) shows the same comparison for the *Retrofit* configuration. Figure 12 a) and b) depicts the first mode contribution to the full shear response of the tower and of total system for the *Retrofit* case.

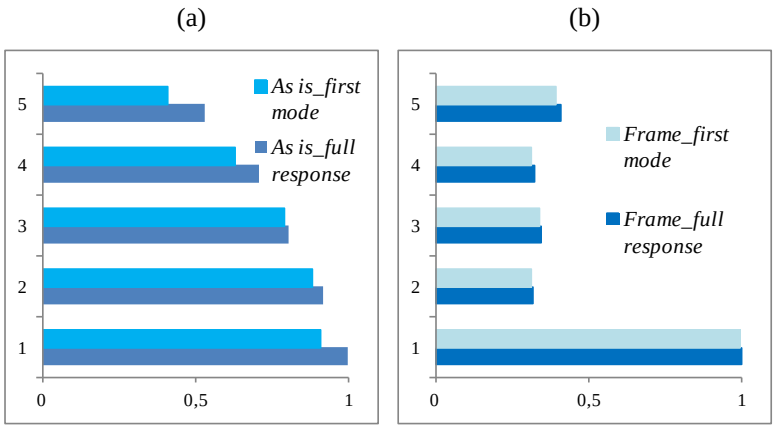

Figure 11: First mode contribution on the total shear response of the frame in the (a) *As is* case and (b) *Retrofit* configuration.

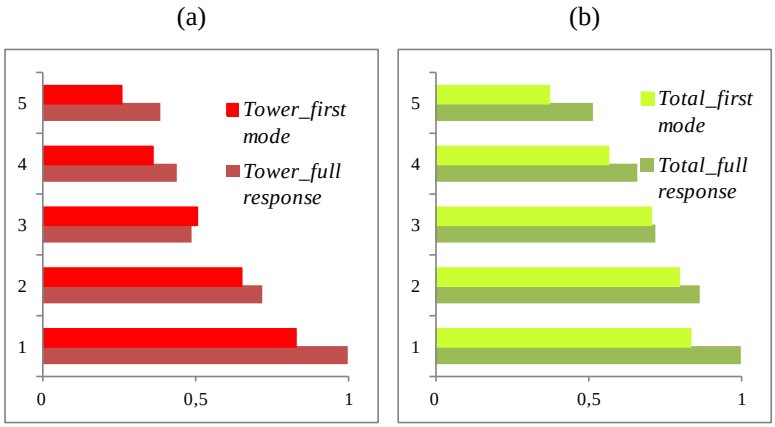

Figure 12: First mode contribution in the *Retrofit* case (a) on the total shear response of the tower and (b) on the overall response.

Table 7 contains the absolute acceleration values observed at the various levels of the building for the configurations investigated..

level	*As is* $\ddot{x}_i$ [m/s^2]	*Retrofit* $\ddot{x}_i$ [m/s^2]	*Stiff* $\ddot{x}_i$ [m/s^2]
1	2.98	2.77	2.10
2	3.86	3.36	1.80
3	4.58	3.02	1.70
4	4.14	2.34	1.97
5	5.27	3.49	2.69

Table 7: Absolute accelerations.

The coupling of the building with the external dissipative system induces a relative reduction of the maximum absolute acceleration values with respect to the values observed in the *As is* case. This result is noteworthy especially for all the non structural elements (e.g. medical devices) that could be hosted in a structure. Figure 13 shows the values of the absolute acceleration distribution along the height of the normalized by the value at the 5th floor observed for the *Stiff* case. The relative reduction of acceleration is nearly 34% for the *Retrofit* case and 48% for the *Stiff* case

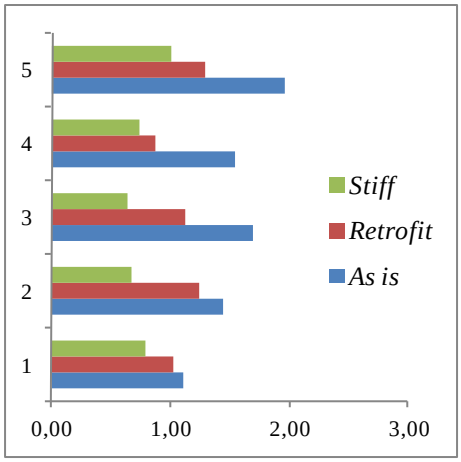

Figure 13: Absolute acceleration distribution along the height.

4 CONCLUSIONS AND FURTHER STUDIES

This paper presents and analyzes three alternative categories of external viscous dampers retrofitting system which exhibit a different kinematic behavior. Among them, the dissipative tower configuration is deeply investigated, in terms of modal properties and seismic response of the coupled system.

A problem formulation concerning the dynamic behavior of the coupled system is presented in general terms. The results include also two limit configurations, the bare building and the coupling with an infinitely stiff dissipative tower.

The case study results reveal that the addition of the towers leads to a regularization of the drift demand along the building height. After the retrofit, the shear force distribution in the existing frame could significantly change and the system is notably non-classical damped due to the fact that all the dampers are concentrated at the base of the tower. Moreover, from the dynamic response it appears that higher order vibration modes have a notable influence on the internal actions demand, while are almost negligible for the displacement response.

The *Stiff* configuration highlights the benefits and drawbacks of the dissipative system. This limit configuration provides the best distribution of the inter-storey drifts but provides high shear forces in the frame, which are larger than the forces observed in the *Retrofit* case and similar to the forces observed in the *As is* case.

A deeper and wider investigation is still necessary for a full comprehension of the problem, and should be oriented to understand the optimal stiffness range of the dissipative tower.

REFERENCES

[1] T.T. Soong, G.F. Dargush, *Passive Energy Dissipation Systems in Structural Engineering*. Wiley: New York, 1997.

[2] T.T. Soong, B.F. Spencer ,Supplemental energy dissipation: state-of-the art and state-of-the practice. *Engineering Structure*, **24**, 243–259, 2002.

[3] C. Christopoulos, A. Filiatrault, *Principles of Passive Supplemental Damping and Seismic Isolation*. IUSS Press: Pavia, Italy 2006.

[4] L. Ragni, L. Dezi, A. Dall'Asta, G. Leoni, HDR devices for the seismic protection of frame structures: Experimental results and numerical simulation. *Earthquake Engineering and Structural Dynamics*, DOI:10.1002/eqe891Vol. **38**(10), 1199-1217 (ISSN: 0098-8847, eISSN: 1096-9845), 2009.

[5] J.K. Whittle, , M.S. Williams, , T.L. Karavasilis, , A. Blakeborough, ,. Comparison of Viscous Damper Placement Methods for Improving Seismic Building Design. *Journal of Earthquake Engineering*, **16**(4), 540-560, 2012.

[6] J.S. Hwang, W.C. Lin, N.J. Wu, Comparison of distribution methods for viscous damping coefficients to buildings. *Structure and Infrastructure Engineering: Maintenance, Management, Life-Cycle Design and Performance*, **9**(1):28-41, 2013.

[7] O. Lavan , M. Avishur, . Seismic behaviour of viscously damped yielding frames under structural and damping uncertainties. *Bulletin of Earthquake Engineering*, **11**(6), 2309-2332, 2013.

[8] E. Tubaldi, L. Ragni, A. Dall'Asta, Probabilistic seismic response assessment of linear systems equipped with nonlinear viscous dampers. *Earthquake Engineering and Structural Dynamics*, DOI: 10.1002/eqe.2462, 2014.

[9] E. Tubaldi, M. Barbato, A. Dall'Asta, Efficient approach for the reliability-based design of linear damping devices for seismic protection of buildings. *ASCE-ASME Journal of Risk and Uncertainty if Engineering Systems, Part A: Civil Engineering, special issue on Stochastic Dynamics and Reliability Analysis of Structural and Mechanical Systems Subject to Environmental Excitations*. DOI: 10.1061/AJRUA6.0000858, 2015.

[10] A. Dall'Asta, E. Tubaldi, L. Ragni, Influence of the nonlinear behaviour of viscous dampers on the seismic demand hazard of building frames. *Earthquake Engineering and Structural Dynamics*, **45**(1), 149-169, 2016.

[11] F. Freddi, E. Tubaldi, L. Ragni, A. Dall'Asta, 2012. Probabilistic performance assessment of low-ductility reinforced concrete frames retrofitted with dissipative braces. *Earthquake Engineering and Structural Dynamics*, **42(7)**, 993-1011.

[12] T. Trombetti, , S. Silvestri, , Novel Schemes for Inserting Seismic Dampers in Shear-Type Systems Based Upon the Mass Proportional Component of the Rayleigh Damping Matrix. *Journal of Sounds and Vibrations*, **302**, 486-526, 2007.

[13] V. Gattulli, , F. Potenza, , M. Lepidi, Damping performance of two simple oscillators coupled by a dissipative connection. *Journal of Sound and Vibration*, **332**(26), 6934-6948, 2013.

[14] E. Tubaldi, M.Barbato, A. Dall'Asta, , Performance-based seismic risk assessment for buildings equipped with linear and nonlinear viscous dampers. *Engineering Structures*, **78**, 90-99, 2014.

[15] E. Tubaldi, Dynamic behavior of adjacent buildings connected by linear viscous/viscoelastic dampers. *Structural Control and Health Monitoring*, **22**(8), 1086-1102, 2015.

[16] C. Passoni, A. Belleri, A. Marini, P. Riva, Existing structures connected with dampers: state of the art and future developments, *2nd European Conference on Earthquake Engineering and Seismology*, Istanbul, Turkey, August 25-29, 2014,.

[17] D. Roia, F. Gara, A. Balducci, L.Dezi, , Dynamic tests on an existing r.c. school building retrofitted with "dissipative towers", *11th International Conference on Vibration Problems*, Lisbon, Portugal, September 9-12, 2013.

[18] D. Roia, F. Gara, A. Balducci, , L. Dezi, , Ambient vibration tests on a reinforced concrete school building before and after retrofitting works with external steel" dissipative towers", *Proceedings of the 9th International Conference on Structural Dynamics, EURODYN 2014*, Porto, Portugal, June 30-July 2, , 2014.

[19] A. Balducci, Dissipative Towers. Application n. EP2010074723820100831, WO2010EP62748 20100831, International and European classification E04H9/02 – Italian concession n 0001395591, 2005.

[20] Nuove Norme Tecniche per le Costruzioni, D.M. Infrastrutture 14 gennaio 2008, Circolare 02 febbraio 2009 n. 617/C.S.LL.PP. 2009 (in Italian).

ECCOMAS Congress 2016
VII European Congress on Computational Methods in Applied Sciences and Engineering
M. Papadrakakis, V. Papadopoulos, G. Stefanou, V. Plevris (eds.)
Crete Island, Greece, 5–10 June 2016

SIMPLE CLOSED FORM HOMOGENIZATION MODEL FOR THE NON LINEAR STATIC AND DYNAMIC ANALYSIS OF RUNNING BOND MASONRY WALLS IN AND OUT OF PLANE LOADED

Elisa Bertolesi, Gabriele Milani*

Department ABC
Technical University of Milan
Piazza Leonardo da Vinci 32, Milan, Italy
{gabriele.milani,elisa.bertolesi}@polimi.

Keywords: masonry; holonomic model; closed form solution; non-linear static analysis; non-linear dynamic analysis.

Abstract. *A simple total displacement homogenization model suitable for the non-linear analysis of in and out of plane loaded masonry walls is presented. In the model, a running bond rectangular elementary cell is discretized into few triangular elastic constant stress elements representing bricks and non-linear holonomic with softening mortar joints reduced to interfaces. The unrefined discretization adopted allows dealing with a homogenization problem ruled by few displacement variables, where homogenized stress-strain relationships can be found in semi-analytical form.*

The approach proposed is validated at a cell level in both the elastic and inelastic range, exhibiting excellent numerical stability and accuracy.

It finally allows a straightforward implementation at a structural level on a commercial code, where entire walls are modelled by means of rigid elements and non-linear homogenized interfaces. Some example of technical relevance are analyzed in both the non-linear static and dynamic range and compared with those achieved using alternative numerical procedures. To this aim a first set of simulation is performed on a deep beam tested by Page while the second series of analyses are conducted on a church façade subjected to dynamic excitation.

1 INTRODUCTION

Masonry is a traditional composite material obtained by the assemblage of bricks and mortar. The elastic behavior is quite limited because masonry is typically characterized by a reduced, almost vanishing tensile strength and either macro- or micro-modeling strategies are adopted over elasticity.

Macro-modeling [1]-[3] substitutes bricks and mortar with a homogeneous, sometimes orthotropic material with softening. It allows studying even large scale structures without the need of meshing separately bricks and mortar. It is therefore very convenient where efficient computations on engineering structures are needed. Nevertheless, the calibration of model parameters is typically done by means of comprehensive experimental campaigns. Theoretically, such approaches may be capable of adequately estimate the non-linear masonry behavior along any load combination, even if some meaningful limitations occur in specific cases but in practice the needed experimental data fitting would require –at least in principle- new calibrations case by case.

The alternative micro-modeling is simply characterized by a distinct modelling of mortar joints and blocks at a structural level. The reduction of joints to interfaces [4][5] helps in limiting variables, especially in the non-linear range, but the approach still remains computationally very demanding, because bricks and mortar are meshed separately. In order to obtain sufficiently reliable solutions in terms of displacements and stresses, constituent materials should be meshed with more than one element, with the consequent grow of the number of non-linear equations to deal with, even for small masonry panels. Furthermore, the preprocessing phase regarding the model generation is not straightforward. Partitioning methods have been recently proposed to overcome such computational limitations and speed up structural analyses.

For the previous reasons, it can be affirmed that macro-scale computations with FEs still remain preferable when non-linear analyses for engineering structures are needed.

In this framework, homogenization [5]-[16] is for sure much more suitable than both micro- and macro-modelling, because it allows in principle to perform non-linear analyses of engineering interest without a distinct representation of bricks and mortar, but still considering their mechanical properties and the actual pattern at a cell level.

Homogenization is roughly an averaging procedure performed at a meso-scale on a representative element of volume (REV), which generates the masonry pattern under consideration by repetition. A Boundary Value Problem BVP is formulated, allowing an estimation of the expected average masonry behavior to be used at structural level. As a matter of fact, the resultant material obtained from meso-scale homogenization turns out to be orthotropic, with softening in both tension and compression.

Instead of using refined FE discretization within the REV, in this paper a simplified homogenization two-step model is proposed for the non-linear structural analysis of masonry walls in- and out-of-plane loaded. The first step is applied at the meso-scale, where the assemblage of bricks and mortar in the REV is substituted with a macroscopic equivalent material through a so called compatible identification. The unit cell is meshed by means of 24 triangular constant stress (CST) plane stress elements (bricks) and interfaces for mortar joints. Triangular elements are assumed linear elastic, whereas the mechanical response of the interface elements is holonomic and non-linear, including two dominant deformation modes, namely peel (mode I) and shear (mode II) or a combination of two (mixed mode). Both a piecewise linear and an exponential law formally identical to an improved version of the Xu-Needleman law and proposed in another context [17]-[19] are implemented.

The second step, performed at a structural level, relies into the implementation of the homogenized stress-strain relationships into a rigid element approach (RBSM) where contiguous rigid elements are connected by shear and normal non-linear homogenized springs. The extension of the model to the out-of-plane mechanisms has been achieved by on-thickness integration of the homogenized stress-strain relationships obtained in the first step, thus adopting suitable out-of-plane interface laws at a structural level, whose behavior is formulated in order to describe flexural and torsional failures.

The procedure is quite efficient and reliable because it is not necessary to discretize with refined meshes the elementary cell (only three kinematic variables are needed at the meso-scale) and hence it is possible to drastically speed up computations. In addition, the holonomic laws assumed for mortar allow for a total displacement formulation of the model, where the only variables entering into the homogenization problem are represented by displacements.

The model is benchmarked at a structural level both in the non-linear static and dynamic range on a masonry deep-beam [20][21] in-plane loaded up to collapse and on a masonry church façade [22][23] loaded by a real accelerogram and collapsed during the 1976 Friuli (Italy) seismic sequence [24].

2 THE HOMOGENIZATION MODEL

2.1 The simplified compatible homogenization model

Homogenization relies in the determination of averaged quantities representing the macroscopic strain and stress tensors [1][6] on a REV (Y), i.e. $\mathbf{E} = <\boldsymbol{\varepsilon}> = \frac{1}{A}\int_Y \boldsymbol{\varepsilon}(\mathbf{u})dY$ and $\boldsymbol{\Sigma} = <\boldsymbol{\sigma}> = \frac{1}{A}\int_Y \boldsymbol{\sigma} dY$, where A stands for the area of the elementary cell, $\boldsymbol{\varepsilon}$ and $\boldsymbol{\sigma}$ stand for the local quantities (strains and stresses respectively) and <*> is the averaging operator.

Anti-periodicity conditions are imposed on the stress field and periodicity on the displacement field **u**, given by:

$$\begin{cases} \mathbf{u} = \mathbf{E}\mathbf{y} + \mathbf{u}^{\text{per}} & \mathbf{u}^{\text{per}} \text{ on } \partial Y \\ \boldsymbol{\sigma}\mathbf{n} & \text{anti-periodic on } \partial Y \end{cases} \tag{1}$$

Where **u** is the total displacement field, $\mathbf{u}^{\text{per}}$ stands for a periodic displacement field, $\widetilde{x} = \{x \quad y \quad z\}$ is the local frame of reference (see Figure 2), **E** is the homogenized strain tensor and **n** is the outward versor of the ∂Y surface.

In this work, a simple compatible homogenization model suitable for the analyses of masonry in and out of plane loaded is proposed. The method herein discussed allows to use a coarse discretization, where only ¼ of the REV is meshed with 6 constant stress triangles (see Figure 1). Bricks are supposed to behave elastically while mortar joints are reduced to non-linear zero thickness interfaces. Two interface relationships are considered: a piece-wise linear law and an improved version of the Xu-Needleman exponential law, accounting for, respectively, a decoupled and fully coupled approach.

The homogenization procedure is subdivided in two steps: in the first one the homogenization model is implemented in a Matlab environment, while in the second one a series of non-linear analyses on masonry panels are discussed.

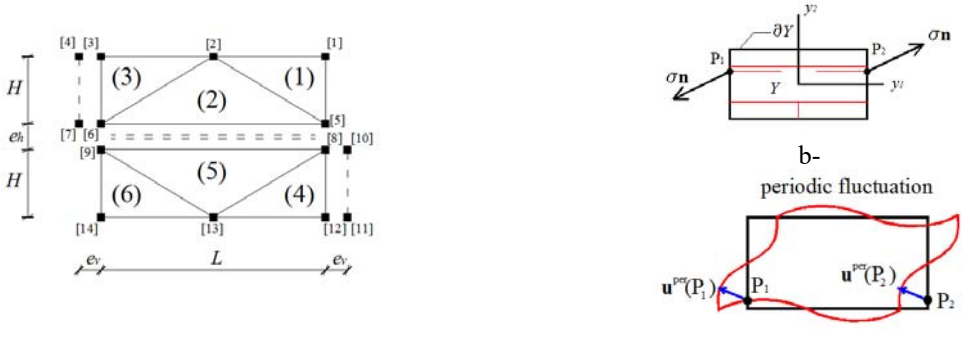

Figure 1. Micro-mechanical model proposed: a- Geometric properties of the elementary cell, b- Anti-periodicity of the micro-stress field and c- periodic displacement field.

Indicating with $\circ^{(n)}$ a stress component belonging to the n-th element, the plane stress Cauchy stress tensor inside the n-th CST element $\boldsymbol{\sigma}^{(n)}$ is constituted by the components $\sigma_{xx}^{(n)}$ (horizontal stress), $\sigma_{yy}^{(n)}$ (vertical stress) and $\tau^{(n)}$ (shear stress). When dealing with static quantities, equilibrium inside each element is a-priori satisfied, $div\boldsymbol{\sigma}=0$, whereas two equality constraints involving Cauchy stress tensor components of triangles have to be imposed for each internal interface between adjoining elements.
Assuming that the triangular elements are linear elastic, the following relationship between strains and stresses can be written:

$$\begin{bmatrix}\varepsilon_{xx}\\ \varepsilon_{yy}\\ \gamma_{xy}\end{bmatrix}=\begin{bmatrix}\dfrac{\sigma_{xx}}{E_b}-\dfrac{\nu_b\sigma_{yy}}{E_b}\\ -\dfrac{\nu_b\sigma_{xx}}{E_b}+\dfrac{\sigma_{yy}}{E_b}\\ \dfrac{\tau}{G_b}\end{bmatrix} \qquad (2)$$

Where E_b, ν_b and G_b are the brick elastic modulus, Poisson's ratio and shear modulus, respectively. The simplified compatible identification procedure allows separating the analyses of the biaxial macroscopic strain state from the pure shear deformation one. In the following sections both deformation states are discussed and the results obtained using both the non-linear interface laws are critically compared.

2.2 Elastic case, biaxial strain state

Let us consider a biaxial macroscopic strain state characterized by the following independent displacement variables: $\xi=\bar{U}_x^0-U_x^9$ and $\eta=U_y^{[5]}+U_y^{[6]}$. The evaluation of the aforementioned variables allows the determination of the kinematic and static unknowns governing the problem. The solution, fully explained in [9], can be obtained graphically plotting the two following curves:

$$\eta=\bar{U}_y^0+\frac{2H}{\nu_b L}\left[\bar{U}_x^0-\xi-L\frac{1-\nu_b^2}{E_b}f_n^I(\xi)-\frac{L^2}{2H}\frac{1-\nu_b^2}{E_b}f_t^{II}(\xi)\right] \qquad (3)$$

$$\xi = \bar{U}_x^0 + \frac{L}{2\nu_b H}\left[\bar{U}_y^0 - \eta - 2\frac{1-\nu_b^2}{E_b} H f_n^{II}(\eta)\right] \tag{4}$$

Where f_n^I and f_t^{II} are the non-linear laws of the interfaces I and II under normal (n) and shear (t) stresses. $\overline{U}_{x,y}^0$ are the applied displacements on the boundary of the REV mimicking a macroscopic homogeneous biaxial strain state, in agreement with the compatible identification procedure proposed.

2.3 Shear deformation

In case of a pure shear deformation, the deformation independent variables are ξ^t, η^t and κ, where:

$$\xi^t = 2\bar{U}_x^t - \frac{H}{G_b}\left[-\frac{\bar{U}_y^t - \eta^t}{L/2} G_b + 2 f_t^I\left(\eta^t\right) - \frac{4H}{L} f_n^{II}\left(\eta^t - \kappa\right) + 2\frac{\kappa}{L} G_b\right] \tag{5}$$

$$\eta^t = \bar{U}_y^t - \frac{L}{2G_b}\left[2 f_t^{II}\left(\xi^t - \bar{U}_x^t\right) - \frac{2\bar{U}_x^t - \xi^t}{H} G_b + 2\frac{\kappa}{L} G_b\right] \tag{6}$$

$$\kappa = \frac{e_v}{G_b}\left[2 f_t^{II}\left(\xi^t - \bar{U}_x^t\right) - f_t^I\left(\eta^t\right)\right] \tag{7}$$

$\overline{U}_{x,y}^t$ are the applied displacements on the boundary of the REV mimicking a macroscopic shear, in agreement with the compatible identification procedure proposed. The numerical approach used to solve the previous problem is discussed in [9], where the reader is referred for further details.

2.4 Holonomic relationship for non-linear interfaces

In the present work, mortar joint interfaces are assumed to behave in agreement with two interface relationships: (a) a multi-linear relationship, hereafter labeled as "PL", with normal and tangential decoupled responses, i.e. $\sigma(\Delta_n)$ and $\tau(\Delta_t)$; an improved version of the Xu–Needleman exponential law, hereafter labeled as "XN". In the latter case, the stress vector **T** at the interface is given by the following closed-form expression:

$$\begin{aligned}\sigma &= \frac{\phi_n}{\delta_n}\left(\frac{\Delta_n}{\delta_n}\right) e^{-\left(\frac{\Delta_t}{\delta_t}\right)^2} e^{-\frac{\Delta_n}{\delta_n}} \\ \tau &= 2\frac{\phi_t}{\delta_t}\left(\frac{\Delta_t}{\delta_t}\right)\left(1+\frac{\Delta_n}{\delta_n}\right) e^{-\left(\frac{\Delta_t}{\delta_t}\right)^2} e^{-\frac{\Delta_n}{\delta_n}}\end{aligned} \tag{8}$$

Symbols ϕ_n and ϕ_t denote the work of separation under pure Mode I and Mode II, respectively, while δ_n and δ_t indicate the relevant characteristic lengths [17][19].

2.5 Non-linear behavior

In the present section the results obtained with the proposed model are discussed with reference to two masonry patterns commonly used.
Two different textures are studied: the first one (Type A) is a running bond masonry with bricks having dimensions equal to 122x37x54 mm^3 and mortar joints of thickness 5 mm (see

Figure 2). The second one (Type B) is a header bond with blocks of dimensions 250x55x120 mm^3 and mortar joints 10 mm thick.

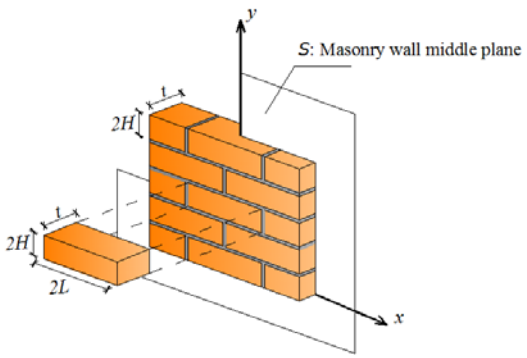

Figure 2. Running bond texture.

The elastic and inelastic mechanical properties of the considered masonry patterns are summarized in Table 1-Table 2.

Table 1. Mechanical properties assumed for the running bond texture.

Stretcher bond	*Mortar joints*	*Bricks*
Young Modulus	E_m=1250 MPa	E_m=7000 MPa
Poisson's ratio	-	ν=0.2
Shear Modulus	G_m=0.4* E MPa	G_b
Peak tensile stress	f_t= 0.29 MPa	-
Cohesion	c=1.4* f_t MPa	-

Table 2. Mechanical properties assumed for the running bond texture.

Stretcher bond	*Mortar joints*	*Bricks*
Young Modulus	E_m=1500 MPa	E_m=8000 MPa
Poisson's ratio	-	ν=0.2
Shear Modulus	G_m=0.4* E MPa	G_b
Peak tensile stress	f_t= 0.1 MPa	-
Cohesion	c= 0.1 MPa	-

Both a PL and XN holonomic law (for the sake of brevity only Type A masonry interfaces are depicted in Figure 3) has been adopted for mortar joints.

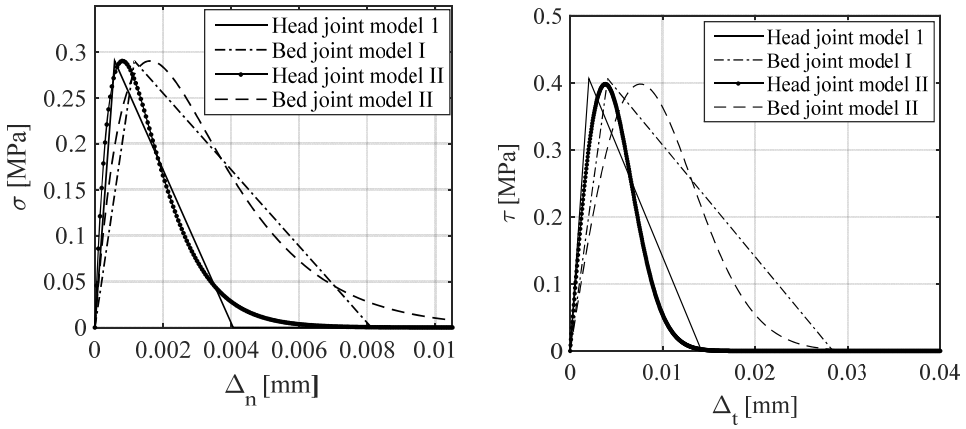

a- b-

Figure 3. Running bond model (Type A): Normal (a-) and tangential (b-) behavior.

3 INELASTIC CASE, BIAXIAL AND SHEAR DEFORMATIONS

3.1 Biaxial strain state

The homogenization approach discussed in the previous sections is herein adopted to perform a series of analyses at a cell level taking into account the non-linear behaviour of the mortar joint interfaces. Let us consider the strain E_{nn} defined as $E_{nn} = \sqrt{E_{xx}^2 + E_{yy}^2}$. In Figure 4, the homogenized stress-strain relationship obtained using the proposed model and assuming an $E_{xx} \neq 0$ and $E_{yy} = 0$ strain state applied up to failure of the REV is depicted. In Figure 4 the deformed shapes of the elementary cell at three different steps of the analysis (A elastic, B peak and C failure) are also represented (Type A and Type B).

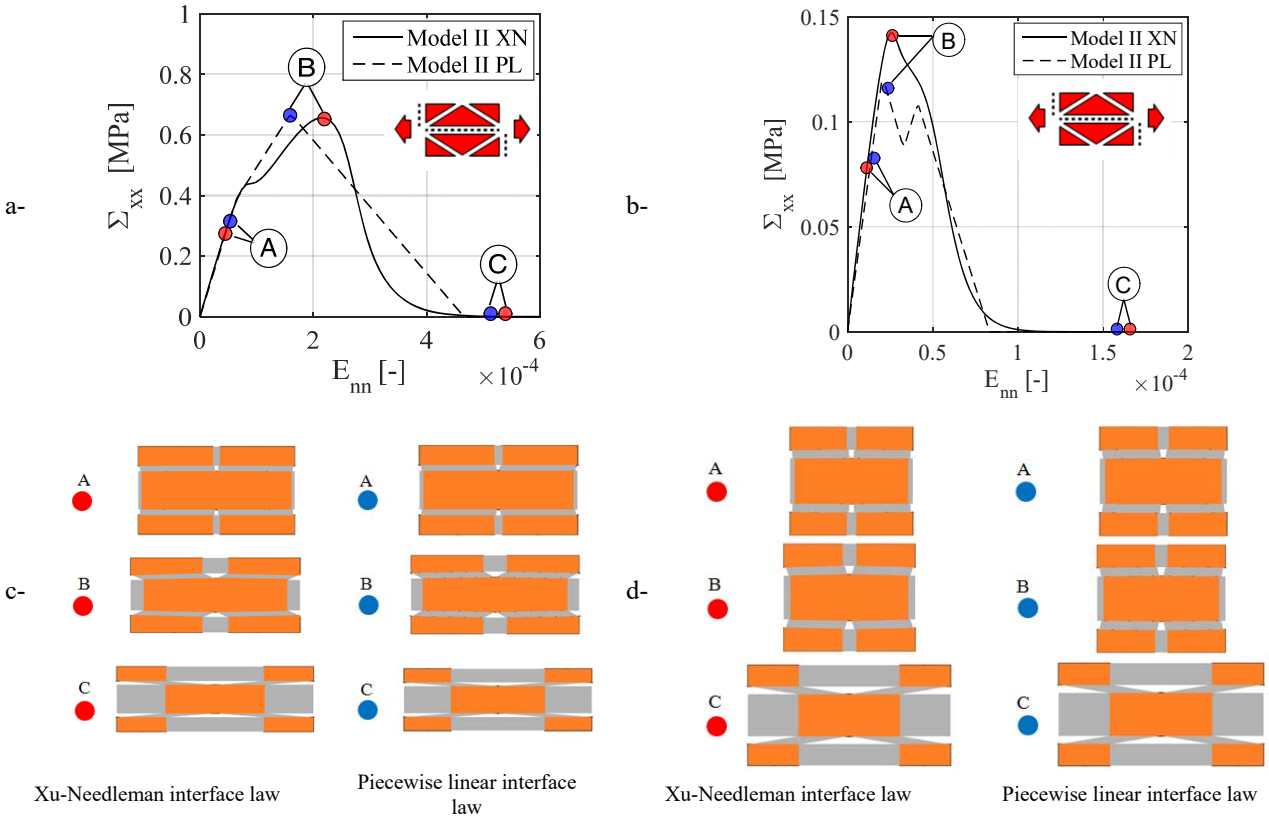

Figure 4. Homogenized stress-strain curves (Type A texture) (a-) and (Type B texture) (b-), deformed shapes of the homogenized cell at different steps for horizontal stretching, Type A texture c- and Type B texture d-.

The same results in case of application of $E_{yy} \neq 0$ and $E_{xx} = 0$ are summarized in Figure 5 (Type A) and (Type B). The reader is referred to [16] for further details.

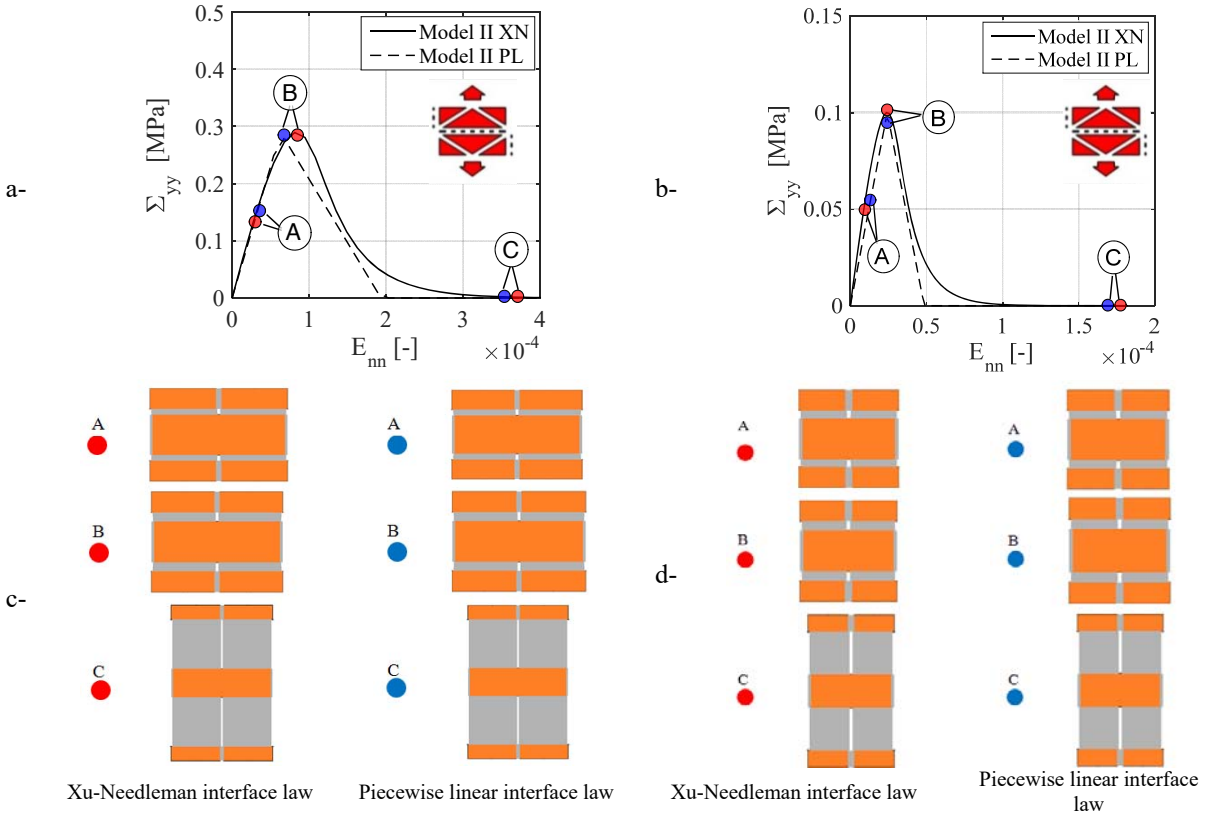

Figure 5. Homogenized stress-strain curves (Type A texture) (a-) and (Type B texture) (b-), deformed shapes of the homogenized cell at different steps for vertical stretching, Type A texture c- and Type B texture d-.

From an analysis of the results, the following considerations can be done:
- When dealing with a biaxial strain state both interface models furnish comparable outputs. Some differences can be found due to the coupling between normal and transversal response in the XN law.
- Under horizontal stretching (see Figure 4), a not-negligible shear stress is detected. The failure mechanism of the REV is characterized by bed joint cracking under tangential stresses while head joints fail under normal tensile stresses.
-For vertical stretching (see Figure 5) the failure experienced is always on the bed joint and strongly influenced by the value of the ultimate tensile strength adopted for mortar.

3.2 Shear deformation state

The results obtained applying a pure shear deformation state on the elementary cell are depicted in Figure 6 for Type A and Type B masonries. As expected in both cases both head and bed joint exhibit inelastic deformation that contributes to the overall strength and post peak behavior of the elementary cell.

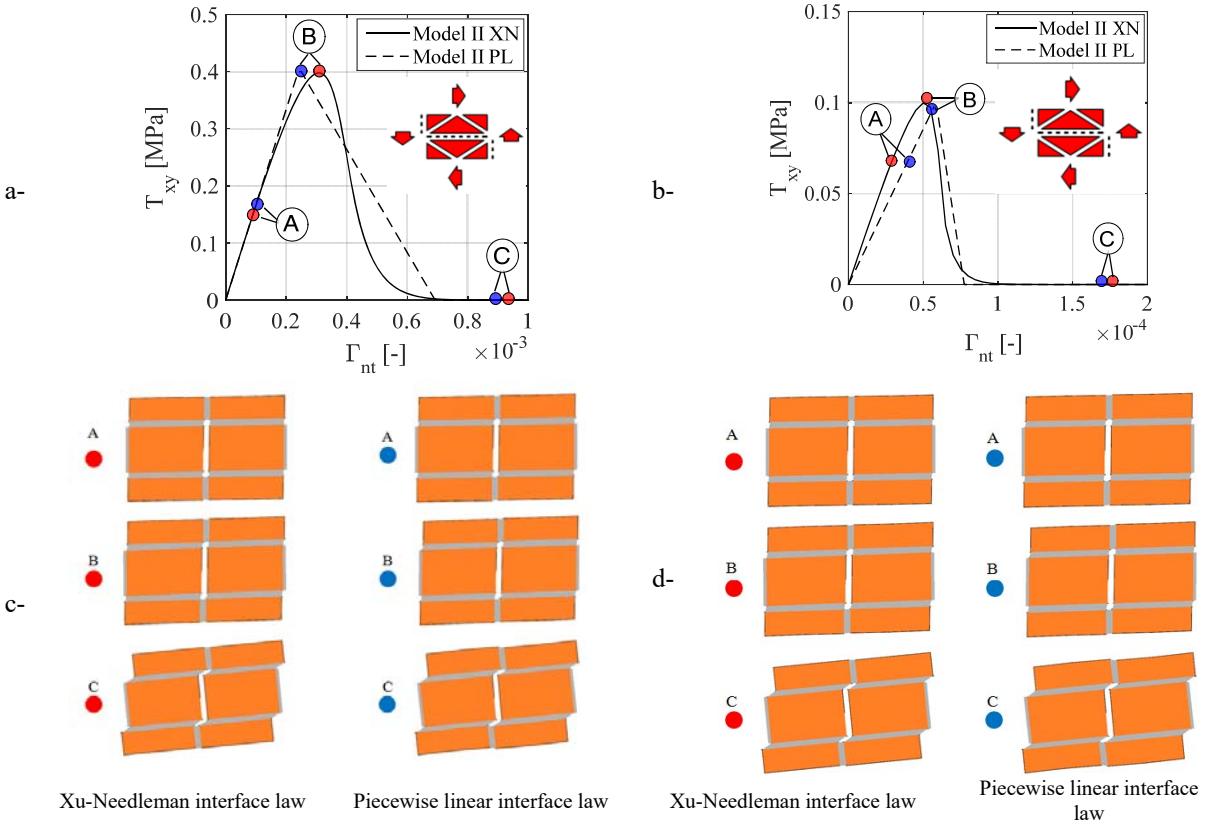

Figure 6. Shear deformation state (Type A texture) (a- c-) and (Type B texture) (b- d-).

4 STRUCTURAL IMPLEMENTATION

4.1 Rigid body and spring model

The present section is devoted to the discussion of a series of non-linear analyses performed in order to show the capability of the proposed model for the simulation of large scale panels subjected to different load conditions. All the analyses performed are conducted through the commercial software Abaqus, were the homogenized mechanical properties are implemented. The panels simulated are discretized by means of rigid quadrilateral elements connected with non-linear interfaces exhibiting an orthotropic behaviour. The interfaces are assumed to obey stress-strain curves with softening directly deduced by an energy equivalence criterion with the homogenized material. The method adopted for the spring identification will be briefly recalled in the following, but the reader is referred to [16] for further details.
In order to perform the identification of the springs two adjoining rigid elements connected through non-linear interfaces with dimensions showed in Figure 7 were considered.

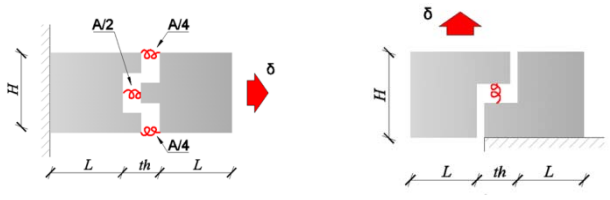

Figure 7. Spring model: a- Axial spring, b- Shear spring.

Equating the volumetric strain energy of the rigid-spring model and the one related with the continuum, the following expressions can be deduced for the identified elastic moduli:

$$E_{nxx} = \frac{th/2 \cdot E_{xx}}{2L + th} \tag{8}$$

$$E_{nyy} = \frac{th/2 \cdot E_{yy}}{H + th} \tag{9}$$

$$G_{nxy} = G_{xy} \cdot \frac{H^2/4}{th \cdot (2L + th)} \tag{10}$$

Where H and L are respectively the height and the length of the rigid elements and "t" is the out of plane thickness. The non-linear interfaces have thickness equal to "th". E_{xx}, E_{yy} and G_{xy} are the elastic properties of the homogenized orthotropic continuum model.
The procedure previously recalled is adopted even for the definition of the elastic properties of out of plane interfaces. The extension of the model to the out-of-plane mechanisms has been achieved adopting suitable interfaces, whose behaviors have been formulated in order to describe flexural and torsional failures. To this aim the following expressions can be obtained. Where "t" refers to the thickness of the rigid quadrilateral elements, while "E_{bxx}", "E_{byy}" and "G_{bxy}" refer respectively to the elastic properties of the flexural and torsional interfaces.

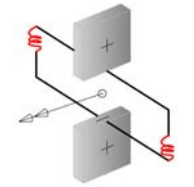

$$E_{bxx} = \frac{E_{xx}}{(1-\upsilon^2)} \cdot \frac{t \cdot th \cdot L}{12 \cdot 2 \cdot A_b \cdot (H + th)} \tag{11}$$

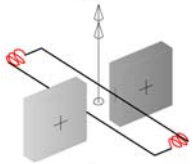

$$E_{byy} = \frac{E_{yy}}{(1-\upsilon^2)} \cdot \frac{t \cdot th \cdot L}{12 \cdot 2 \cdot A_b \cdot (H + th)} \tag{12}$$

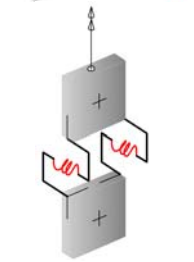

$$G_{bxy} = \frac{2G_{xy} \cdot t^4}{3th \cdot L^3} \tag{13}$$

4.2 Deep beam test

The previously discussed procedure is used to simulate a deep beam panel tested up to failure by Page [20]. The wall, with dimensions of 757x457 mm^2, was subjected to a uniform pressure applied by a stiff steel beam placed on the central upper part of the panel.
A running bond texture (Type A) was adopted to build the panel, using half scale bricks with dimensions equal to 122x37x54 mm^3 and 5 mm thick mortar joints.
The springs identification discussed in the previous section, led to use the following moduli for the springs: E_{nxx}= 360 MPa, E_{nyy}= 280 MPa and G_{nxy}= 2840 MPa.

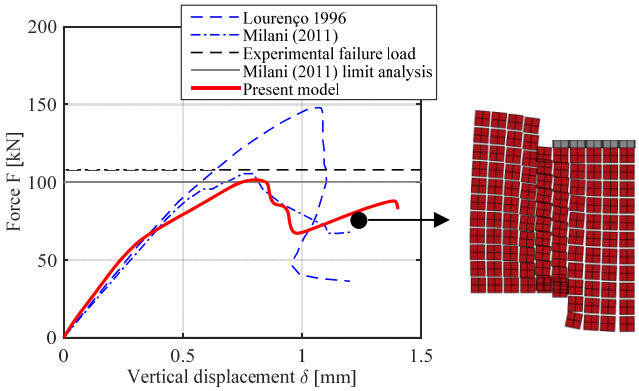

Figure 8. Deep beam. Numerical and experimental results.

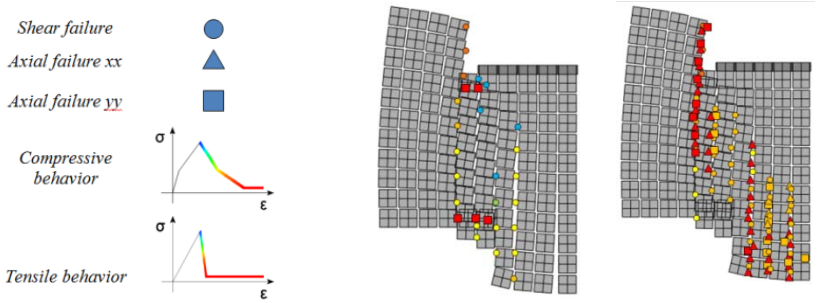

a- b-

Figure 9. Deep beam. Damage maps in compression (-a) and in tension (-b).

Despite the exiguous number of information reported by Page, in the recent past several researchers have tried to simulate the aforementioned deep beam test using different numerical approaches. A comparison between the results (force displacement curves) obtained using the present model and those found numerically by Lourenço [21] and Milani [13] is shown in Figure 8.

As can be noted, a satisfactory agreement is found, in terms of both elastic and post peak phase. The collapse load obtained numerically is very close to the value found experimentally by Page. In Figure 9 the damage maps obtained numerically at the end of the simulation are shown, in compression, tension and shear.

As can be noted, the collapse mechanism is clearly formed by a compressive strut departing from the steel beam and ending on the support, with shear cracks appearing on a vertical line (orange circles, Figure 9-a) and compressive damages near the toe (red squares, Figure 9-a). Tensile damages are mainly concentrated in the central part of the panel along vertical interfaces and near the steel beam. This latter finding can be explained with the high level of stress concentrations reached in that zone.

4.3 Transfiguration church non-linear static and dynamic analyses

A second series of simulations is performed with reference to 3D masonry structures subjected to both static and dynamic excitations, under in- and out-of-plane loads. As confirmed in the literature, some classes of buildings are particularly prone to experience severe damages during seismic events, among them masonry churches can be mentioned. In order to show how accurate results can be obtained using the proposed model even in presence of out of plane failure mechanisms, the authors chose to analyze the façade of the Transfiguration Church, collapsed during the 1976 Friuli, Italy seismic sequence. The church under considera-

tion was located in Moggio Udinese, in the North-East of Italy, in a region (called Friuli) characterized by a high seismicity level. On Thursday, 6 May 1976, a devastating 6.4 Richter magnitude earthquake took place there, killing 989 people. The church reported severe damage after the first main shock, and later collapsed as a consequence of the second seismic sequence that occurred during September of the same year. After the first main earthquake, a survey of the geometry and masonry walls was conducted by Doglioni et al. in [24], which is our main source of information for the problem at hand. The geometry of the façade, along with the discretization adopted for the present structural analyses are sketched in Figure 10. It is interesting to notice that a small portion of the unique nave perpendicular walls is modeled in order (a) to properly account for the actual lateral interlocking of the vertical edges and (b) to favor the reproduction of the 3D behavior, which includes a predominant two-way flexural deformation and a possible detachment for overturning in case of insufficient interlocking between façade and nave walls.

The façade of the Church is modeled using 354 rigid quadrilateral elements, which appears a fair compromise between numerical efficiency paramount for non-linear dynamic computations and refinement needed to properly reproduce actual crack patterns.

The church can be considered an example of Romanesque architecture quite frequent in the small towns of Italy, like those located in Friuli, and therefore it appears an interesting benchmark for the proposed models at the macro-scale. Approximately, the façade has a width of 16.30 meters, with a maximum height (tympanum top) of 18.05 meters and small openings in correspondence of the symmetry axis, see Figure 10. The façade has therefore global dimensions equal to 16.30x18.05 m, with walls 55 cm thick. Mechanical properties of the constituent materials are assumed in agreement with those available in the literature [22][23] and are not reported here for the sake of conciseness. Homogenized moment-curvature diagrams obtained with the model proposed and used at a structural level are depicted in Figure 11, under three levels of vertical pre-compression roughly indicating what occurs on the tympanum (almost zero vertical in-plane load), middle height and base of the façade. The utilization of different moment-curvature relationships as a function of vertical membrane load is paramount for masonry buildings, since it has been proved that vertical compression plays a key role in the increase of both ductility and out-of-plane strength.

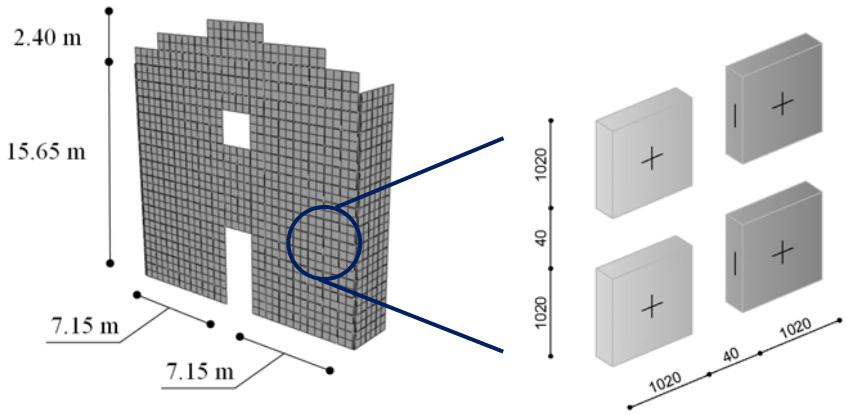

-a -b

Figure 10. Non-linear static and dynamic analysis of a church façade in Moggio Udinese (Transfiguration Church). –a: Geometric description of the case study. –b: FE discretization.

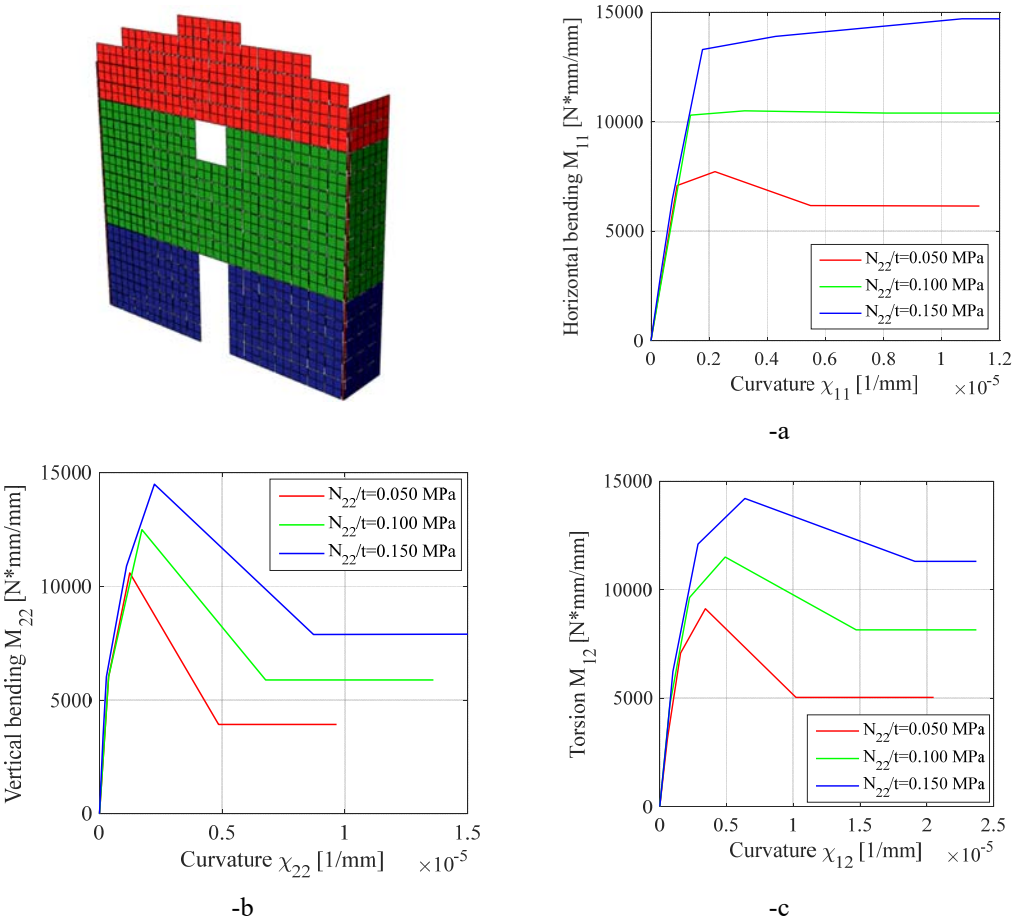

Figure 11. Moment curvature diagrams used at a structural level, Transfiguration Church. Diagrams are plotted at different levels of vertical pre-compression.

Two sets of simulations are performed in order to show the reliability of the proposed model for the seismic analyses of 3D masonry structures. First of all, the façade is analyzed using a non-linear static (pushover) approach and taking into account two distributions of forces in agreement with Italian code, one constant and the other reverse-linear along the height of the façade. Hereafter such distributions are called Mode 0 and Mode I respectively, but it is worth mentioning that in the Italian code they are labeled as G2 and G1 distributions. The results obtained using the proposed model are compared to those provided by Casolo and co-workers [22][23] in Figure 12. The control point for the displacement evaluation is placed in the upper part of the façade (tympanum center). As can be noted, there is satisfactory agreement with previously presented results, meaning that the proposed homogenization approach is able to accurately describe the elastic and inelastic behavior of real scale structures starting exclusively from the knowledge of the constituent materials mechanical properties.

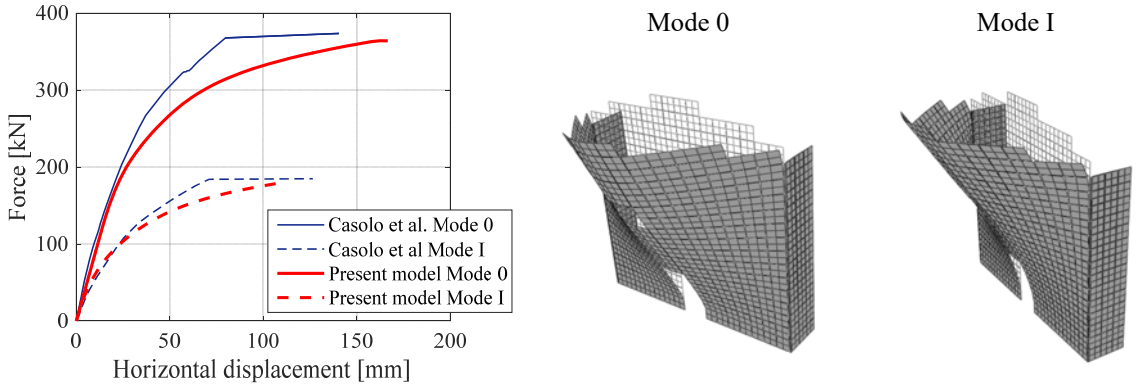

Figure 12. Pushover curves obtained (left) and corresponding deformed shapes (right)

A non-linear dynamic analysis is then performed in order to deepen the seismic behavior of the facade when subjected to natural accelerograms. The results obtained applying to the structure the Fogaria (Friuli 1976) accelerogram are summarized in Figure 13 and Figure 14.
In particular, in Figure 13 a comparison between a previous model [22][23] and present numerical results at different heights of the control point is provided, whereas Figure 14 shows the façade deformed shape and crack patterns numerically obtained at the end of the simulations(A: deformed shape. B1: vertical bending. B2: horizontal bending. B3: torsion).
As can be noted, good agreement is found between the results obtained using the proposed approach and those achieved by Casolo and co-workers [22][23], in terms of both time-displacements history and damage patterns found at the end of the simulations.
As highlighted by the residual displacement found at the end of the application of the accelerogram (Figure 13-b), the façade exhibits a collapse mechanism that mainly involves the upper part, with the resultant overturning of the tympanum. This finding suggests the activation of a slightly different failure mechanism with respect to that found in [22][23] where again the upper part is the most vulnerable, but with the formation of two inclined yield lines spreading from the upper corners down to the central rose window. Present results appear more in agreement with the expected behavior of masonry church façades. Damage patterns at the end of the simulation are depicted in Figure 14, separately for flexion and torsion as it usually occurs in RBSM models. As confirmed by the deformed shape of the façade in Figure 14-a, which clearly shows the overturning of the tympanum, high levels of damage are reached in correspondence of the horizontal line where the out-of-plane mechanism of the tympanum takes place. It is worth noting that severe damages are visible also in correspondence of the vertical edges and near the central opening, in quite reasonable agreement with the results found by Casolo and co-workers [22][23].

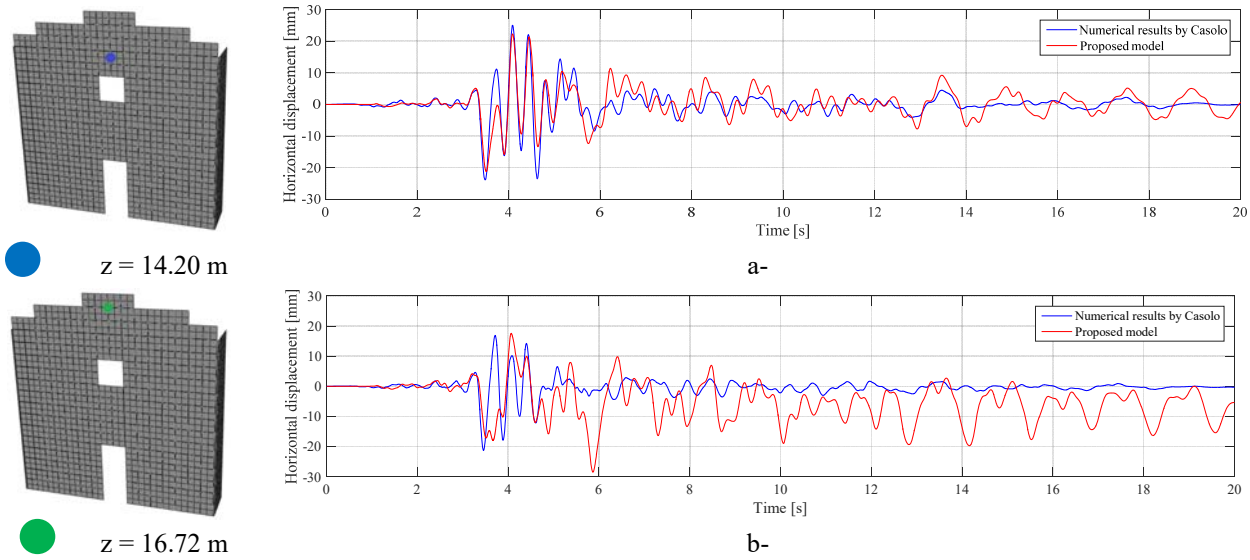

Figure 13. Comparison between previous models and present numerical results for the Transfiguration Church at different heights of the control point.

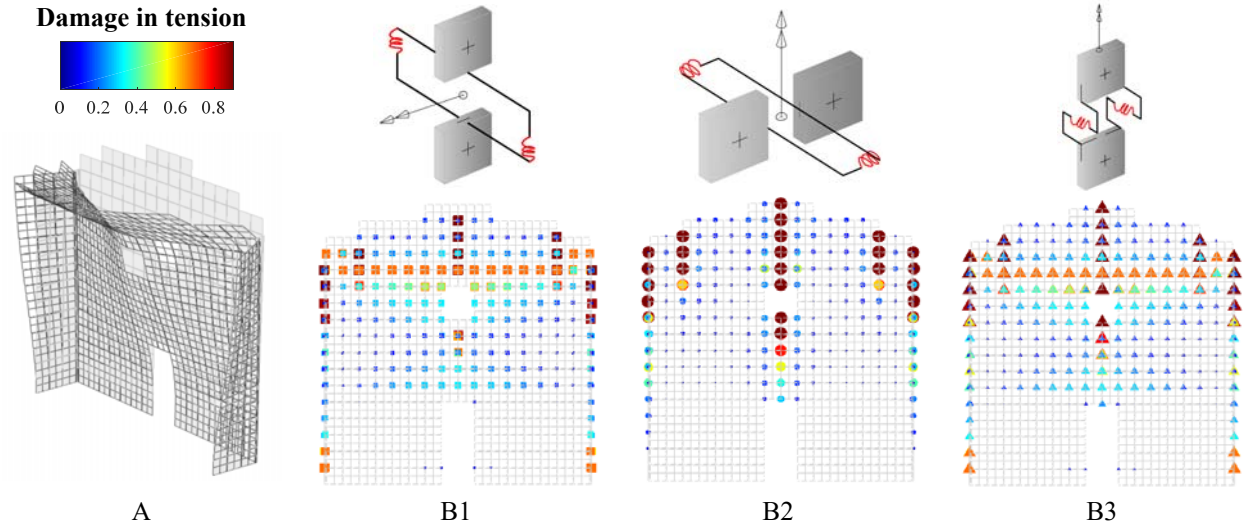

Figure 14. Deformed shape and crack patterns numerically obtained at the end of the application of the Fogaria accelerogram. A: deformed shape. B1: vertical bending. B2: horizontal bending. B3: torsion.

5 CONCLUSIONS

A simple compatible homogenization model for the non-linear static and dynamic analysis of masonry structures in- and out-of-plane loaded has been presented. The approach consists in a two-step procedure suitable for the analysis of masonry panels subjected to a variety of loads. First of all, the REV is discretized by means of triangular elastic FEs and joints are reduced to non-linear holonomic interfaces. In order to obtain quickly homogenized properties of the continuum, a pseudo analytical approach has been proposed. A series of structural analyses have been finally performed on two cases of technical relevance, namely a deep beam loaded in-plane up to collapse and a church façade subjected to equivalent static (push-over) and non-linear dynamic out-of-plane analyses. The structures have been discretized using a rigid body and spring model RBSM strategy. The springs identification has been carried

out using an energy equivalence on the stress-strain homogenized relationships deduced at the meso scale. The homogenized RBSM have been implemented into the commercial software Abaqus, where all the discussed analyses have been performed. The procedure is efficient and reliable because: (1) the homogenized mechanical properties can be directly implemented at structural level with a very limited computational effort; (2) it is not necessary to discretize with refined meshes the elementary cell; and (3) the holonomic laws assumed for mortar joints allow for a total displacement formulation of the model, where the only variables entering into the homogenization problem are represented by displacements.

REFERENCES

[1] S. Di Pasquale, New trends in the analysis of masonry structures, *Meccanica*, **27**, 173-184, 1992.

[2] P.B. Lourenço, R. de Borst, J.G. Rots, A plane stress softening plasticity model for orthotropic materials, *International Journal for Numerical Methods in Engineering*, **40**, 4033-4057, 1997.

[3] P.B. Lourenço, J. Rots, A multi-surface interface model for the analysis of masonry structures, *Journal of Engineering Mechanics ASCE*, **123** (7), 660-668, 1997.

[4] D.J. Sutcliffe, H.S. Yu, A.W. Page, Lower bound limit analysis of unreinforced masonry shear walls, *Computers & Structures*, **79**, 1295-1312, 2001.

[5] P. de Buhan, G. de Felice, A homogenization approach to the ultimate strength of brick masonry, *Journal of the Mechanics and Physics of Solids*, **45** (7), 1085-1104, 1997.

[6] P. Suquet, Analyse limite et et homogeneisation, *Comptes Rendus de l'Academie des Sciences - Series IIB – Mechanics*, **296**, 1355-1358, 1983.

[7] T. Massart, R.H.J. Peerlings, M.G.D. Geers, Mesoscopic modeling of failure and damage-induced anisotropy in brick masonry, *Eur J Mech A/Solids*, **23**, 719–35, 2004.

[8] P. Pegon, A. Anthoine, Numerical strategies for solving continuum damage problems with softening: application to the homogenization of masonry, *Computers & Structures*, **64** (1-4), 623-642, 1997.

[9] G. Milani, E. Bertolesi, Holonomic homogenized approach for the non-linear analysis of in-plane loaded masonry panels. Under review.

[10] G. Milani, P.B. Lourenço, A. Tralli, Homogenised limit analysis of masonry walls, Part I: failure surfaces, *Computers and Structures*, **84**(3-4), 166-180, 2006.

[11] G. Milani, P.B. Lourenço, A. Tralli, Homogenised limit analysis of masonry walls, Part II: structural examples, *Computers and Structures*, **84**(3-4), 181-195, 2006.

[12] G. Milani, P.B. Lourenço, A. Tralli, Homogenization approach for the limit analysis of out-of-plane loaded masonry walls, *Journal of Structural Engineering ASCE*, **132**(10), 1650-1663, 2006.

[13] G. Milani, Simple homogenization model for the non-linear analysis of in-plane loaded masonry walls, *Computers and Structures*, **89**, 1586-1601, 2011.

[14] G. Milani, Simple lower bound limit analysis homogenization model for in- and out-of-plane loaded masonry walls. *Construction & Building Materials*, **25**, 4426–4443, 2011.

[15] G. Milani, A. Tralli A, A simple meso-macro model based on SQP for the non-linear analysis of masonry double curvature structures, *International Journal of Solids and Structures*, **49**(5), 808-834, 2012.

[16] E. Bertolesi, P.B. Lourenço, G. Milani, Implementation and validation of a total displacement non-linear homogenization approach for in-plane loaded masonry. Under review.

[17] X.P. Xu, A. Needleman, Void nucleation by inclusion debonding in a crystal matrix, *Modell. Simulation Mater. Sci. Eng.*, **2**, 417-418, 1993.

[18] P. McGarry, É.Ó. Máirtín, G. Parry, G.E. Beltz, Potential-based and non-potential-based cohesive zone formulations under mixed-mode separation and over-closure. Part I: Theoretical analysis, *Journal of the Mechanics and Physics of Solids*, **63**, 336-362, 2014.

[19] E. Bertolesi, G. Milani, R. Fedele, Fast and reliable non-linear heterogeneous FE approach for the analysis of FRP-reinforced masonry arches. *Composites Part B: Engineering*, **80**, 189-200, 2016.

[20] A.W. Page, Finite element model for masonry, *J Struct Div ASCE*; **104**(8), 1267-85, 1978.

[21] P.B. Lourenço, Computational strategies for masonry structures, *PhD Thesis*, TU Delft, The Netherlands, 1996.

[22] S. Casolo, G. Uva, Nonlinear analysis of out-of-plane masonry façades: Full dynamic versus pushover methods by rigid body and spring model, *Earthquake Engineering and Structural Dynamics*, **42**(4), 499-521, 2013.

[23] S. Casolo, G. Milani, Simplified out-of-plane modeling of three-leaf masonry walls accounting for the material texture, *Construction & Building Materials*, **40**, 330–351, 2013.

[24] F. Doglioni, V. Petrini V, A. Moretti (Eds). Le chiese e il terremoto [Churches and earthquake]. LINT press, Trieste, Italy, 1994.

ECCOMAS Congress 2016
VII European Congress on Computational Methods in Applied Sciences and Engineering
M. Papadrakakis, V. Papadopoulos, G. Stefanou, V. Plevris (eds.)
Crete Island, Greece, 5–10 June 2016

CONSTRUCTION PHASES ANALYSIS OF UNREINFORCED MASONRY BUILDINGS THROUGH EQUIVALENT FRAME MODEL

Francesco Pugi[1], **Alessio Francioso**[2*] **and Giacomo Sevieri**[3]

[1] Aedes Software
56028 San Miniato Basso, Pisa, Italy
info@aedes.it

[2] National Technical University of Athens
15780 Zografou, Athens, Greece
alessiofrancioso@gmail.com

[3] University of Pisa, DESTEC
56100 Pisa, Italy
giacomo.sevieri@unifi.it

Keywords: masonry structures, equivalent frame model, construction phases analysis, construction stages.

Abstract. *Structural analysis of masonry buildings is affected by many uncertainties and characterized by issues related to the very nature of the material. In this scenario, refined analysis methodologies are confined to the research environment, while professional applications need simpler methodologies, which allow for a better understanding of the analysis results: the equivalent frame model is one of these methodologies. However, the method is affected by some issues, which, if not adequately addressed, may lead to unrealistic stress distributions. In this work, we propose a procedure that increases the reliability of the analysis results. It consists in the modification of the model depending on the nature of the acting loads in relation to the different construction phases of the structure. In addition, an extension of the method for the analysis of buildings constructed in different periods is introduced. Finally, the results of the analysis performed for a case study are presented in order to validate the proposed methods.*

1 INTRODUCTION

Among the various methods available for structural analysis of masonry buildings, the "equivalent frame model" is the most widely used in the professional field, thanks to the simplicity of one-dimensional finite elements and the good capacity to assess the real behavior of the structure.

More accurate finite element models, which make use of shell or solid elements, are mainly employed in the research field. They require a rather high computational effort for being used in engineering practice and are still affected by uncertainties related to various parameters (in particular, the constitutive laws of the materials).

Furthermore, dealing with existing buildings it should be pointed out that the fundamental method of analysis is the kinematic analysis of the collapse mechanisms, which assesses the stability of the structure.

Static and dynamic, linear and nonlinear analyses performed on elastic models are meaningful only if the local collapse mechanisms have been prevented. They assess the resistance of the building, which is generally secondary to its stability. Therefore, elastic modelling should be kept simple avoiding excessive complexity. This is the reason why many national and international Standards [1] including Eurocodes [2] indicate the equivalent frame model as the reference methodology.

On the other hand, modelling of a spatial structure through one-dimensional finite elements implies some critical issues, most of them related to the fact that one single model is used for the analysis under different load actions with the same mechanical parameters, internal and external constraints. Adjacent walls significantly different in dimensions correspond to a local inhomogeneity in the stiffness distribution. In fact, the stresses migrate towards the most stiff elements, with consequent unrealistic stress distribution even if the sole self-weight of the walls is applied. Moreover, under the action of vertical loads, significant shear and bending moment acting on masonry piers and spandrels appear quite unrealistic, as well as tensile stress, which may occur in masonry piers usually due to big stiffness discrepancy at the various stories or differential displacements in the foundations.

These issues are not caused by the equivalent frame method, but by the way it is normally applied. In compliance with this modelling technique, a methodology that allows a more realistic stress distribution can be applied.

The methodology illustrated in the following paragraphs stems from the will to overcome the difficulties described above through a generalized algorithm valid for any masonry structure and automatically executable by software. This procedure is based on the diversification of the characteristics of the model (mechanical parameters of the materials, internal and external constraints) depending on the type of load action. Although the methodology is calibrated on the equivalent frame model, it introduces concepts related to the construction phases, which are valid regardless of the modelling technique applied.

2 CONSTRUCTION PHASES ANALYSIS

Analysis of the construction phases has long been used in structural engineering for specific structural typologies, such as bridges. In general, before a construction is completed, the static scheme of the structure evolves. The mechanical characteristics and the restraint conditions can be considered variable during the different construction phases, which are characterized by loads of different nature.

Normally, dealing with buildings, all the loads, whether they are vertical or horizontal, permanent or variable (including wind, seismic action) are applied to the same structural model,

and the results of the analyses performed for the different load actions are then combined together. In frame structures, sufficiently regular in terms of geometry and stiffness, such as steel or reinforced concrete frame structures, this methodology leads to acceptable approximations. In masonry structures, instead, issues related to the stress distribution among the resistant elements may arise.

The proposed approach differentiates the structural scheme depending on the different load actions, which occur at different times during the life of the structure. While the structure is being built, it cannot be assumed that it behaves as a frame under the action of the self-weight; the frame will appear only once the construction is complete. The structure shows a frame behavior only under the actions that occur at the end of the construction: variable loads, wind and earthquake. Therefore, three construction phases have been defined and referred to as Phase 0, Phase 1 and Phase 2.

In Phase 0, the permanent loads, both structural (G1) and non-structural (G2), are applied on a static scheme, which leads to a stress distribution consistent with the influence area of each element. In Phase 1, the vertical variable loads (Q) are applied on a static scheme, which allows occurrence of in-plane and out-of-the plane stresses in masonry piers, while spandrels remain unstressed. Finally, in Phase 2 horizontal variable loads, wind and seismic action, are applied to the structure: in this last phase, the equivalent frame is considered totally reacting.

2.1 Phase 0

While the structure is being built, it settles under its own weight; this leads each pier to be mainly subjected to axial force with a value close to the one calculated with the classic method of the influence areas. Bending or shear stress may occur in the elements in case of walls which are offset at the different stories or in case of vaults and arches, whose thrust stresses the adjacent piers in-plane and out-of-plane.

In Phase 0, only permanent loads, both structural and non-structural, are applied. In order to achieve the previously described behaviour, the piers are assumed fixed at the base and with an in-plane hinge at the top, while the spandrels are considered hinged in their plane, taking into account the arch-behaviour, that is, the presence of an ideal arch which transform the distributed load acting on the spandrel as point loads at its two ends. Therefore, the spandrels are unstressed under vertical actions, since they develop an “arch behaviour” instead of a “beam behaviour”.

However, these hypotheses alone are not enough to ensure the desired behaviour. In fact, there remains the issue of stress migration due to large stiffness variation between adjacent elements. In addition, unrealistic moments may occur within irregular frames where piers are not continuous form foundations to top and lability may arise in the wall plane due to the applied releases.

The following modifications have been introduced in order to overcome these issues:

- Migration of stress due to sharp stiffness variation. Besides the pier restraints mentioned above (fixed end at the base and in-plane hinge at the top), the values of modulus of elasticity E and shear modulus G are amplified in order to obtain very stiff elements. In this way, the effects of stress redistribution due to different pier sections vanish, since the stresses are distributed within a rigid system. Furthermore, vertical translation is released in the rigid links between orthogonal walls, in this way a more realistic distribution of the slab loads is achieved, avoiding stress migration among transversal walls.
- Occurrence of local lability due to the applied releases. The figure below highlights the mechanism that may occur in the wall plane: the hinges introduced at the top of the piers and

at the two ends of the spandrels are aligned, thus the system is labile. To overcome this issue the joint X and Y rotations are restrained at the top of the piers and, as a result, the system assumes a "shear-type" behaviour.

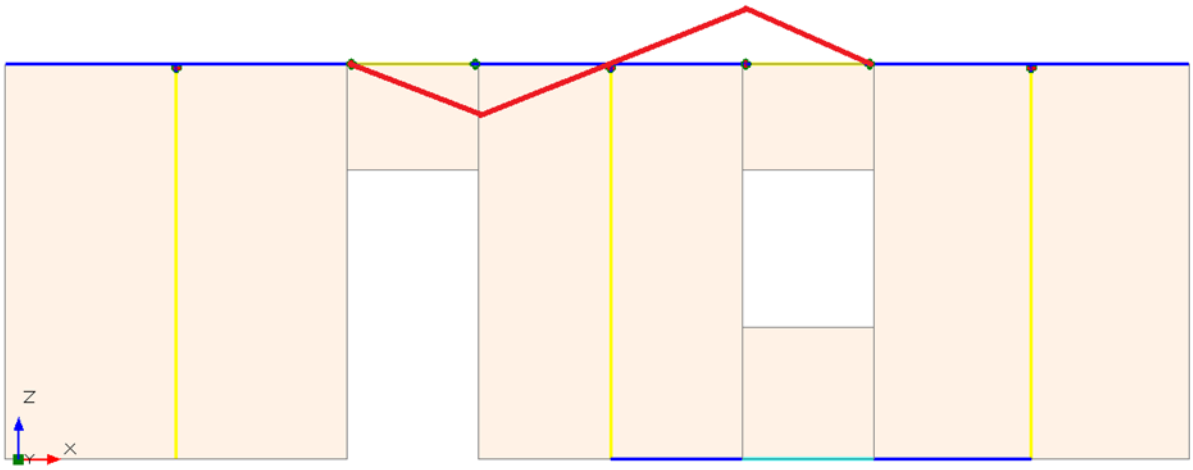

Figure 1. Possible lability in the wall plane.

In order not to create rigid relations among the joints, which may affect the distribution of the vertical loads, the hypothesis of rigid level and rigid slabs are ignored.

As regards the foundations, it should be pointed out that in masonry structures they are usually very stiff, they do not deflect and during the construction they settle under the weight of the structure. Therefore, in this phase it can be assumed that the stress are transferred to the ground through a rigid body and that differential settings capable to create stress states in the superstructure will occur in a later phase when the structure behaves as a spatial frame. In order to achieve the goal, first, the foundation joints at the base of the walls are fixed allowing evaluating the resultant of the action in terms of vertical load and bending moment. Then, the stress in the ground is determined using the formula for compression and flexure applied to the section defined by the foundation plan:

$$\sigma(\xi,\eta) = N/A + N \cdot \eta_N \cdot \eta/J_\xi + N \cdot \xi_N \cdot \xi/J_\eta$$

where: ξ and η are the coordinates of the vertex of each foundation frame in the global reference, N is the resultant vertical force, ξ_N and η_N are the eccentricity of N with respect to centroid of the section, A is the total area of the foundation plan, J_ξ and J_η are the second moment of inertia about the axes ξ and η.

To sum up, the hypothesis introduced in Phase 0 are the following:

- Piers fixed at the base and with in-plane hinge at the top.
- Spandrels hinged in their plane at the two ends with arch-behavior.
- Amplified modulus of elasticity for masonry elements.
- Shear-type behavior for joints at the top of masonry piers.
- Vertical translation released for rigid links between orthogonal walls.
- Rigid levels (master-slave relations) and slab stiffness are ignored.

- Rigid foundations and determination of soil stresses through the formula of compression and flexure applied to the section defined by the foundation plan.

2.2 Phase 1

In Phase 1, the vertical variable loads are applied to the equivalent frame. These loads occur once the structure is completely built, so it cannot be assumed that the structure settles under their action. Therefore, moments and shear force in masonry piers are considered plausible. However, since the vertical load acting in this phase are still static, the spandrels are modelled so as not to be subjected to bending moment and shear.

As regards the foundations, in this phase they can be modelled as beams on elastic soil according to Winkler theory, allowing for the occurrence of differential settlements.

To sum up, the described behavior is achieved through the following modification of the standard frame: spandrels are hinged in their plane with arch-behavior; rigid levels and slab stiffness are ignored.

2.3 Phase 2

In Phase 2, the horizontal loads (wind and seismic action) are applied to the completely reacting frame. Bending moments and shear forces are accepted in all the elements including spandrels. This is the last phase where the equivalent frames method is applied with the original formulation without modification of the elements.

2.4 Combination of the results

Construction phases analysis is performed by means of three different structural models, one for each phase. The final stress and strain state of each element is given from the combination of the results obtained for each phase, of course taking into account the combination coefficients.

However, modal analysis is carried out on the standard equivalent frame model (Phase 2), since it is representative of the dynamic behavior of the structure. In seismic analysis, the static effects obtained from Phase 0 and Phase 1 are combined with the seismic effects obtained from Phase 2.

3 ANALYSIS OF THE CONSTRUCTION STAGES

The study of the construction phases analysis provided the basis for developing a more accurate analysis procedure when dealing with buildings which have undergone modification in later construction stages. In particular, the study considers buildings that have been enlarged with the integration of new volumes, rather than those which have undergone a demolition. This case occurs frequently in the engineering practice, since interventions aimed to extend or raise an existing building are very common.

Looking at the very nature of the intervention, it is evident that it represent an extension of the construction phases methodology outlined in the previous paragraphs. Even in this case, the building can be analyzed considering three different construction phases, but it should be taken into account that when the enlargement has been built the original part of the structure was already consolidated.

For the purposes of the analysis the original structure is referred to as Structure A while the enlargement is referred to as Structure B. The construction phases analysis is performed through the analysis of the following models:

- *Model 0-A.* This model consists only of the original structure modelled according to the hypothesis of Phase 0. The analysis is performed for the corresponding permanent loads.
- *Model 0-B.* The enlargement is modelled according to Phase 0 while the original structure is modelled according to Phase 1. The analysis is performed for the permanent loads related to the enlargement.
- *Model 1.* Both original structure and enlargement are modelled according to Phase 1. The analysis is performed for vertical variable loads.
- *Model 2.* Both original structure and enlargement are modelled according to hypothesis of Phase 2. The analysis is performed for horizontal variable loads (wind, seismic action).

Once all the analysis have been performed on the four models, the results are combined taking into account the combination coefficients provided by the Standards for each different load action.

4 CASE STUDY

The proposed methodology has been applied to the case of a three-story building located in Fivizzano, Tuscany [5]. The construction dates back to 1918. In 1967, the building has undergone renovations that led to the enlargement of ground floor and first floor. The layout of the structure, although rather simple, shows all the critical aspects related to the equivalent frame modelling and allows focusing the attention on the effects of the construction phases analysis.

Figure 2. View of the building

The different typologies of masonry and slabs confirm that the structure was built in two different periods. The walls of the structure dating back to 1918 are made of irregular stone masonry, while the walls built in the later stage are made of brick masonry with regular pattern. The following figures show an elevation and two floor plan of the building, the different colors highlight the different construction stages.

Figure 3. South-East Elevation

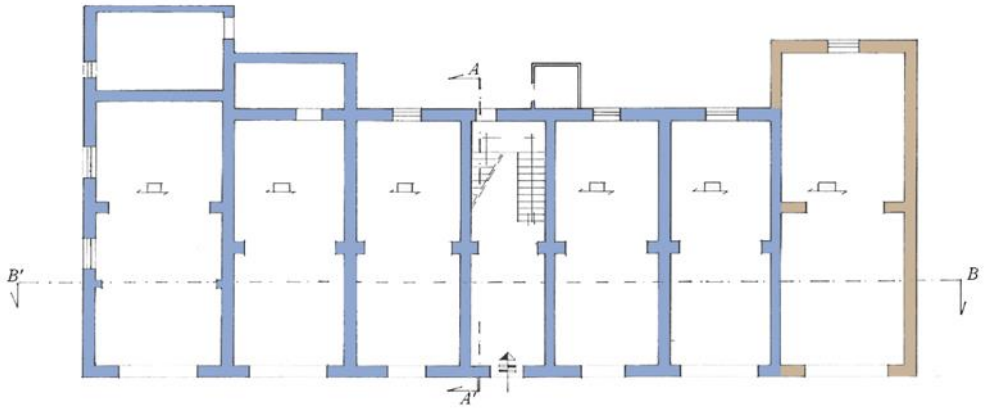

Figure 4. Plan of the Ground Floor.

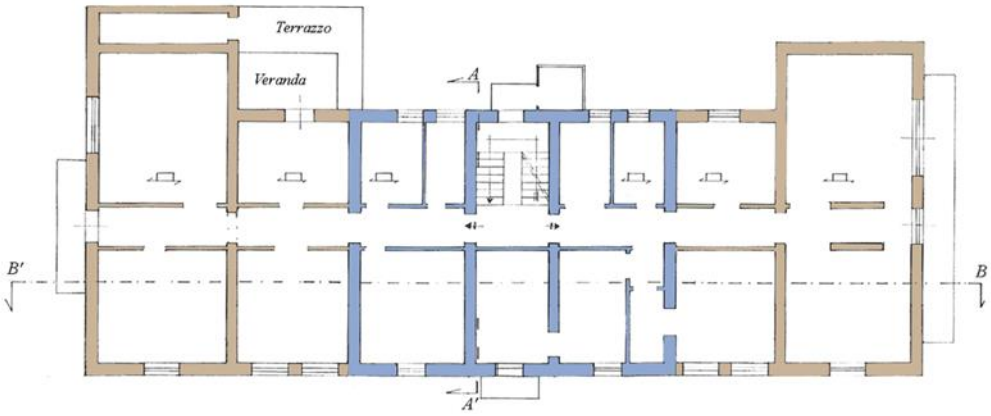

Figure 5. Plan of the First Floor

The analysis of the building was carried out according to three different approaches: (i) standard approach; (ii) construction phases analysis; (iii) analysis of the construction stages. The differences between the three methodologies are highlighted in terms of stress state resulting from linear static analysis.

4.1 Standard approach

The following figures show the modelling of the building through the standard equivalent frame method.

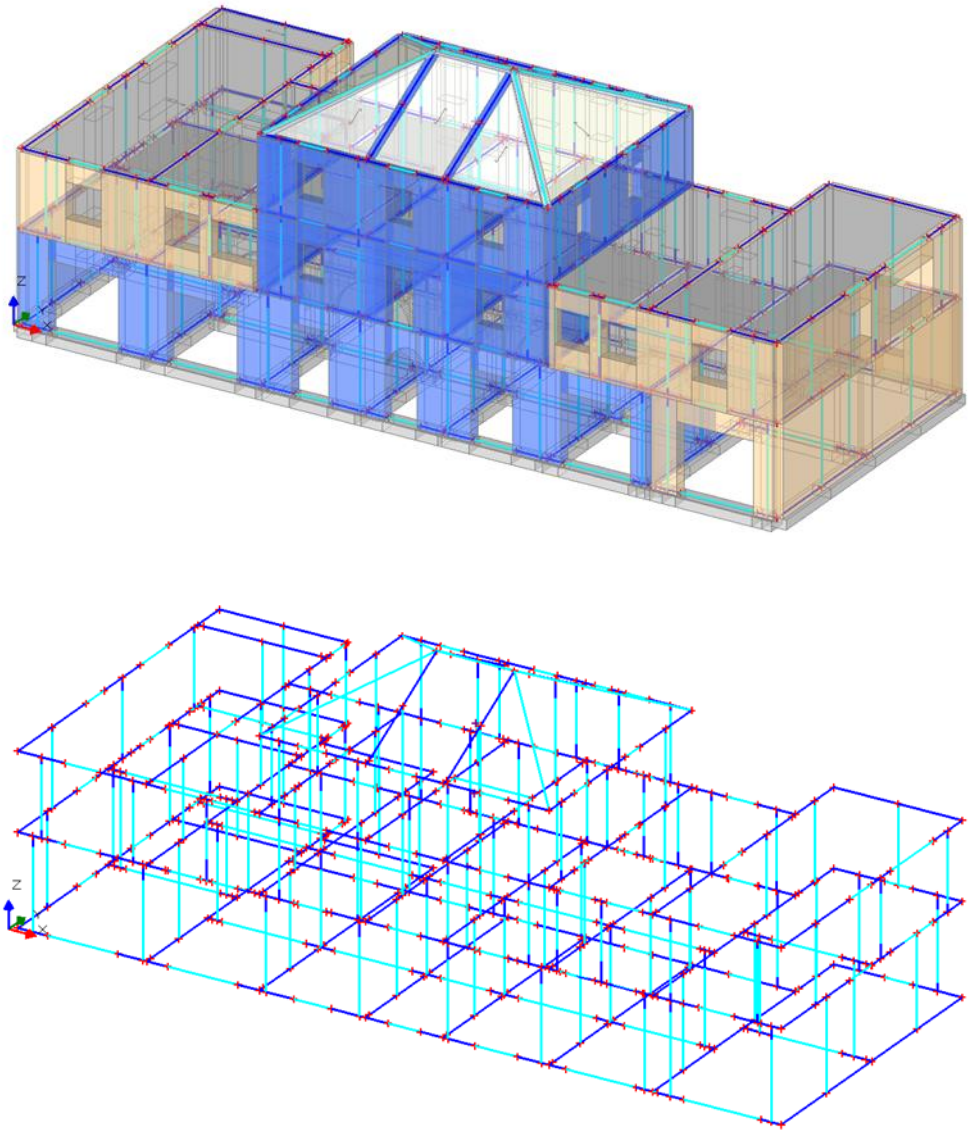

Figure 6. Standard equivalent frame model.

Masonry piers and spandrels are modelled through frame elements. Rigid links connect the spandrels to the adjacent piers and provide the connection between transversal walls. As a result each slab boundary is a closed polyline made of frame elements (spandrels and rigid links). The slabs in the original part of the building are considered deformable, while the ones made of concrete in the enlargement part are considered infinitely rigid. The spandrels are modelled assuming the arch-behavior [6 - 8]. As regards the foundations, they are modelled as beams on elastic soil with Winkler modulus $K = 0.05\ N/mm^3$. The following table gives the mechanical properties of the masonry materials.

		Stone masonry	Brick masonry	
Modulus of elasticity	E	1600	5000	N/mm^2
Shear modulus	G	240	500	N/mm^2
Weight per unit volume	w	23.50	18.00	kN/m^3

Table 1. Mechanical properties of masonry materials

Static linear analysis was performed with the aid of the software Aedes.PCM [9]. The results shown below refer to a load combination that includes only vertical loads with all the combination coefficients equal to 1. Such combination, although not required by the Standards, is useful to simplify the comparison of the results. In fact, the scope of this first analysis is to highlight the critical aspects of the equivalent frame model. The following figure shows the axial force diagram.

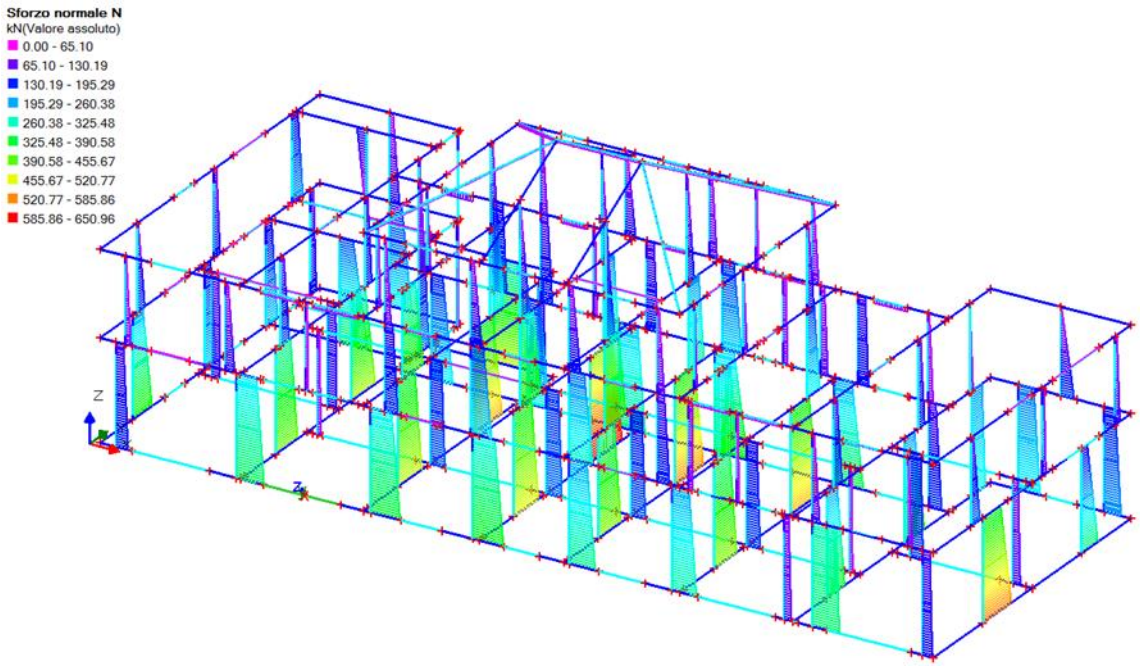

Figure 7. Static analysis. Axial force diagrams

Several issues affect the resulting stress distribution: masonry piers in tension, stress migration among adjacent elements, spandrels subjected to high bending moments and shear force. Let us focus our attention on the frontal alignment (Figure 8), evaluating the differences between the analysis results and a manual calculation of the stress state.

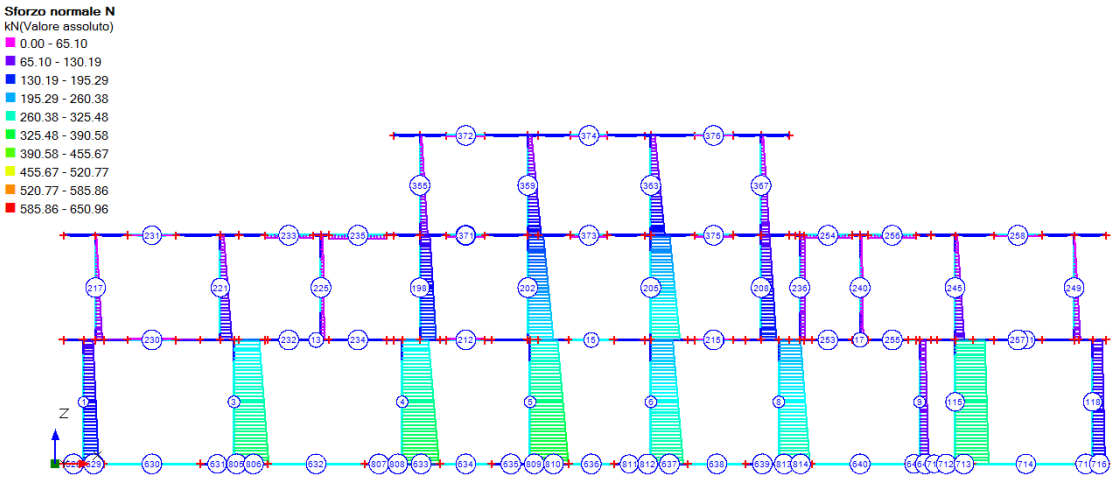

Figure 8. Axial force diagrams. Frontal alignment

Piers 6 and 205 are perfectly aligned and definitely affected by an issue: looking at the axial force diagram we notice an unnatural decrease at the interface between the two elements.

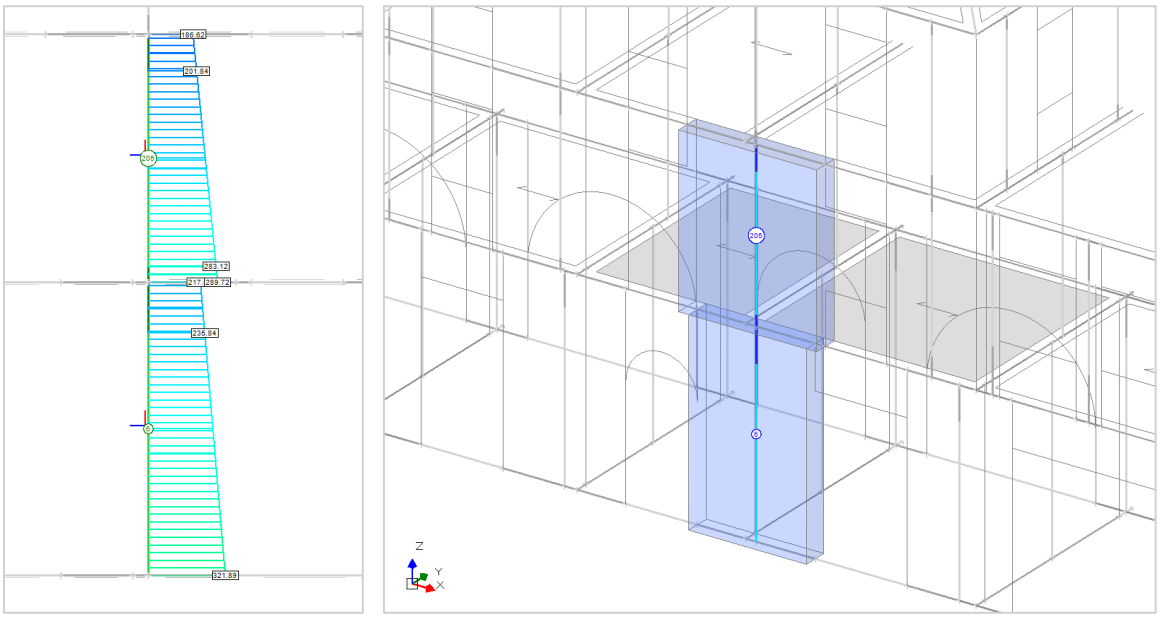

Figure 9. Axial force diagrams. Piers 6 and 205

This issue is caused by stress migration towards other elements. The amount of the decrease in axial force is at least equal to

$$N_{205} - N_6 = 289.72 - 217.84 = 71.88\ kN$$

Considering that the total weight of Pier 205 is equal to 103 kN, the error is rather large. In fact, about 70% of the weight of Pier 205 is not transferred to pier 6 but migrates to other elements.

Another important aspect is the stress state in the spandrels. Despite they were modelled with the arch-behaviour, the spandrels are subject to shear and bending moments under the action of the sole vertical loads. The following table shows the characteristics of the stress state resulting in Spandrel 14.

	Joint i	Joint j	
N	7.47	7.47	kN
V_y	0.78	0.78	kN
V_z	-8.92	8.92	kN
M_x	-0.08	-0.08	kNm
M_y	3.41	-10.85	kNm
M_z	0.65	-0.59	kNm

Table 2. Stress state in Spandrel 14

As highlighted before, these issues are caused by the way the equivalent frame method is applied and construction phases analysis is able to overcome them. The results of the analysis performed with the proposed approaches are given in the following paragraphs.

4.2 Construction Phases Analysis

The building is now analyzed with the construction phases approach described in §2. The following figures show the results of static linear analysis in terms of axial force diagram. Let us focus on the frontal alignment.

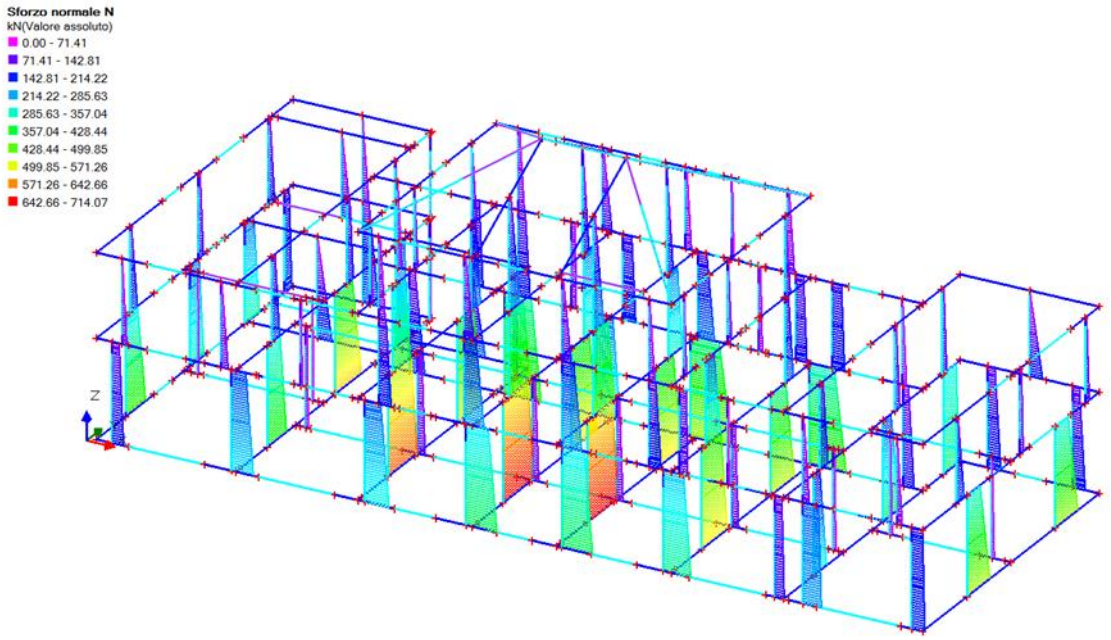

Figure 10. Static analysis results. Axial force diagrams

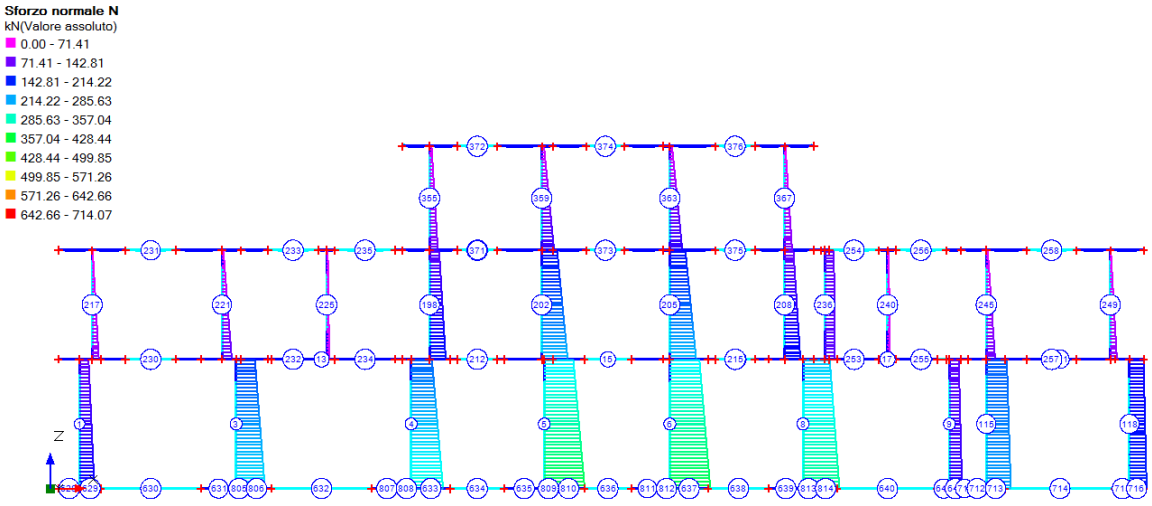

Figure 11. Axial force diagrams. Frontal alignment

The results of the analysis show no elements in tension. Comparing Figure 8 with Figure 11, we can notice in the latter a more rational stress distribution: there are no unnatural variation of axial force in continuous elements. Moreover, in-plane and out-of-plane bending moments are considerably reduced since now they are caused by the sole variable loads acting in Phase 1.

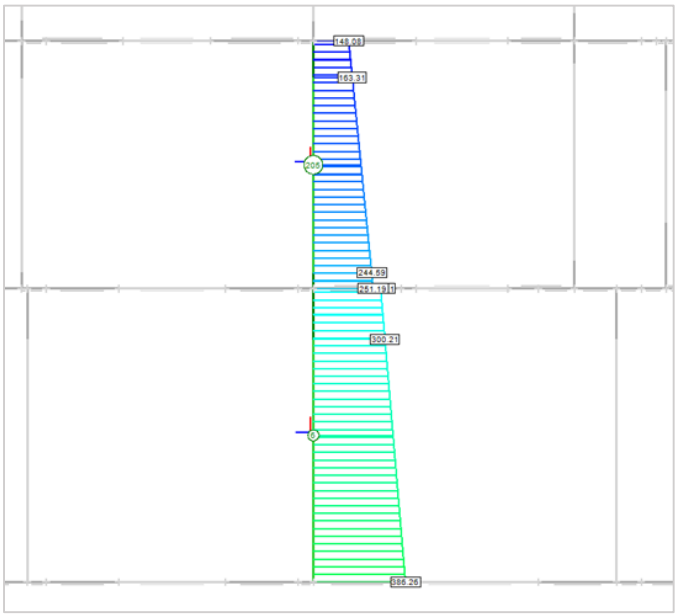

Figure 12. Axial force diagrams. Piers 6 and 205

Looking at Piers 6 and 205, we still notice a step in the axial force diagram, but this time it is the natural increment due to the weight of the spandrels:

$$N_6 - N_{205} = 282.21 - 251.19 = 31.02\ kN$$

The following table show the characteristics of the stress state in Spandrel 14. We notice a significant reduction of the stress, consistent with the hypothesis of arch-behaviour.

	Joint i	Joint j	
N	0.00	0.00	kN
V_y	-0.05	-0.05	kN
V_z	0.00	0.00	kN
M_x	0.00	0.00	kNm
M_y	0.00	0.00	kNm
M_z	-0.04	0.04	kNm

Table 3. Stress state in Spandrel 14

4.3 Analysis of the construction stages

The third approach refers to the analysis of the construction stages described in §3. As shown in Figure 6, part of the structure was built in 1918, while the rest was constructed in 1967 as part of the renovation interventions.

This approach is based on the hypotheses of the construction phases analysis, thus the results are similar to those obtained with the previous approach given in §4.2. The only difference is the influence that the structure built in a later stage exerts on the original structure. This aspect is properly addressed only in the current approach, where the analysis under the action of the permanent loads is carried out by means of two models (0-A and 0-B).

Similarly to the previous approaches, we discuss the results of static linear analysis with a load combination that includes the sole vertical loads, focusing on the frontal alignment of the building (Figure 13, 14). The axial force distribution is regular, without piers in tension or particular stress migration.

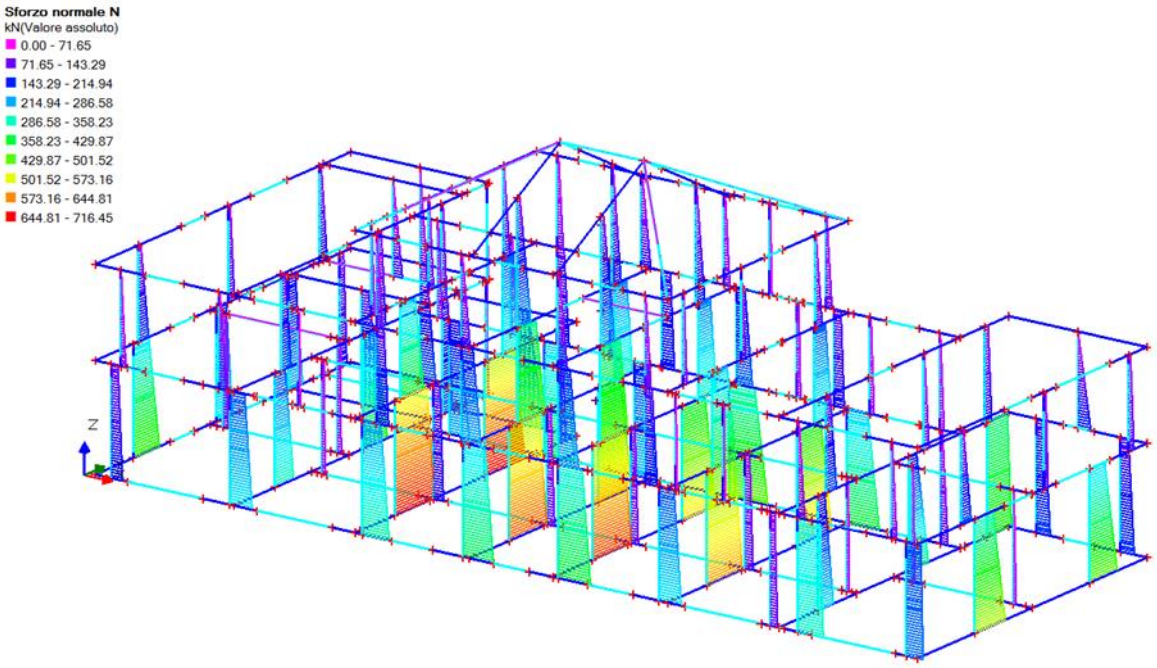

Figure 13. Static analysis results. Axial force diagrams

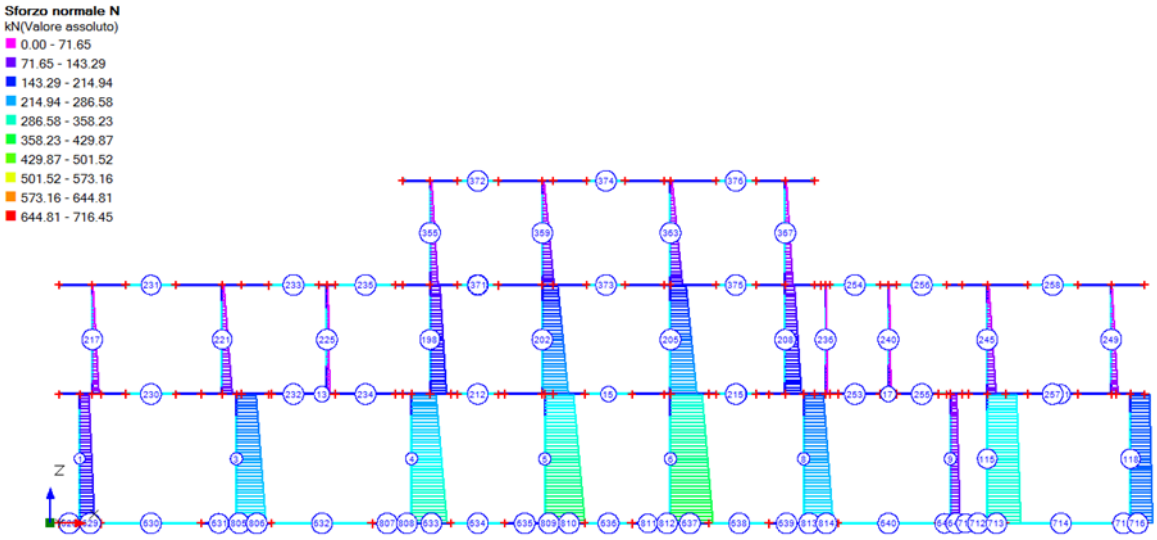

Figure 14. Axial force diagrams. Frontal alignment

As expected, the results are very similar to those obtained with the construction phases approach, although they are obtained through different models. This confirms the feasibility and the accuracy of the proposed methodology.

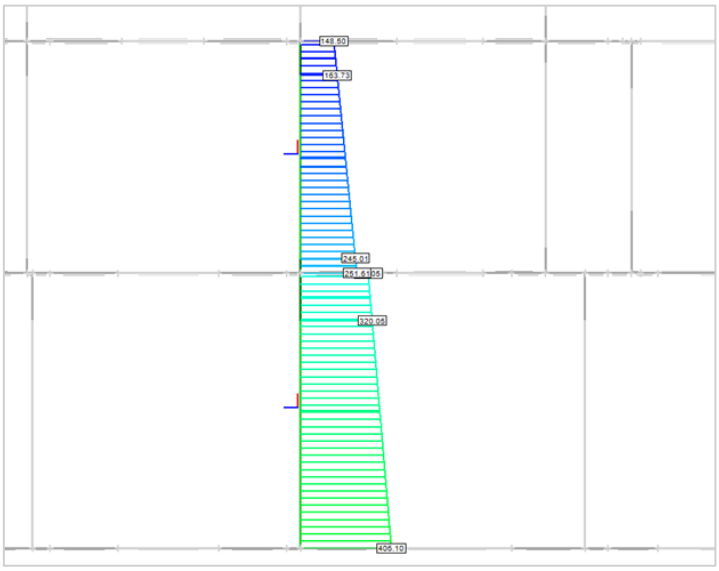

Figure 15. Axial force diagrams. Piers 6 and 205

Focusing on Piers 6 and 205 in Figure 15, we notice a larger value of the axial force with respect to the previous approach (Figure 12). The difference is more evident in Pier 6 at the ground floor, which is affected by the weight of the most recent part of structure. In this case the variation of axial force at the interface of the two piers is:

$$N_6 - N_{205} = 302.05 - 251.61 = 50.44\ kN$$

Shear forces and bending moments in masonry piers are considerably reduced with respect to the standard approach, except for the original elements, which are also influenced by the permanent loads acting on the structure built in a later stage.

Again, the following table reports the stress state in Spandrel 14.

	Joint i	Joint j	
N	0.00	0.00	kN
V_y	0.27	0.27	kN
V_z	0.00	0.00	kN
M_x	0.00	0.00	kNm
M_y	0.00	0.00	kNm
M_z	0.22	-0.20	kNm

Table 4. Stress state in Spandrel 14

The stress is slightly larger than the previous approach since the spandrel belongs to the original structure and is affected by the most recent part of the building. Nevertheless, the stress state remains acceptable and consistent with the physical problem and the hypothesis of the proposed approach.

4.4 Manual Calculation

In order to verify the accuracy of the results let us perform a manual calculation of the axial force diagram. The model considered here includes Piers 6 and 205 as well as the pier above them and all the adjacent spandrels. The piers are considered as cantilever, while the spandrels are considered hinged at the two ends in their plane with arch-behavior. Therefore, under the action of vertical loads, the spandrel are unstressed and the piers are simply in compression.

As shown in Figure 16, each pier is subjected to the self-weight and to additional forces, which account for the vertical loads acting on the spandrels and the slab loads at roof level. The values of these forces are:

$$N_3 = 20.00\ kN$$

$$N_2 = 24.16\ kN$$

$$N_1 = 25.10\ kN$$

The following Table provides the dimension of each pier together with the specific weight and allows the calculation of the self-weight.

	Pier 363 Second floor	Pier 205 First floor	Pier 6 Ground floor	
Thickness	0.50	0.50	0.50	m
Width	2.70	2.70	2.30	m
Height	3.10	3.25	3.85	m
Specific weight	23.50	23.50	23.50	kN/m^3
Self-weight	98.35	103.10	104.05	kN

Table 5. Calculation of self-weight

Given these data, the axial force acting on each pier can be calculated and the results may be represented in a diagram. The following Figure is a comparison of the axial force diagram obtained through analysis of the construction stages and the one calculated manually. We notice that the maximum deviation between the two diagrams, at the base of the wall, is equal to 11.49 kN, about 3% of the axial force in the corresponding section. Therefore, the analysis of the construction stages is very accurate especially if compared with the results of the standard approach, which show a much larger discrepancy with the manual calculation.

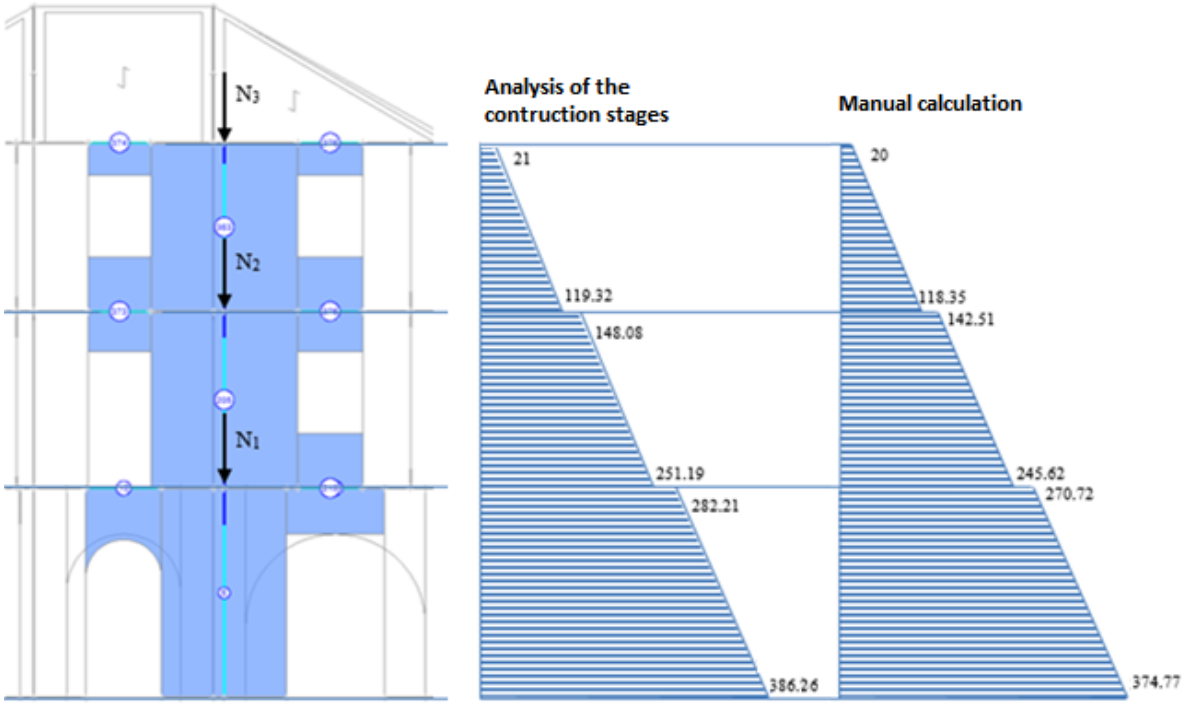

Figure 16. Comparison of axial force diagrams from analysis of the construction stages and manual calculation

5 CONCLUSION

In this paper, a methodology aimed to improve the application of the equivalent frame model, through a more realistic stress distribution, was introduced. The approach, based on the construction phases analysis, consists in the use of different structural models for the analysis of the different load actions. The models vary in terms of mechanical characteristics of the materials, internal releases of the frames, joint restraints and load distribution. This allows to obtain a more accurate stress state of the elements and to overcome the typical issues related to the equivalent frame method when applied according to the standard approach.

Three phases have been defined. Phase 0, where the sole permanent loads are applied, aims to catch the ability of the structure to settle under its own weight during the construction. Therefore, in this phase the equivalent frame is not completely established and the stress is distributed consistently with the influence areas of each element. Moreover, the spandrels are modelled with arch-behavior and remain unstressed under the action of vertical loads.

In Phase 1, only vertical variable loads are applied to the equivalent frame model. Besides axial force, piers may now be subjected to shear force and bending moments, while the spandrels still behave as arches.

In the third and last phase, Phase 2, horizontal variable loads (wind, seismic action) are applied. The hypothesis are the one of the standard equivalent frame model with no modifications.

Once the analyses are performed for each load action through the corresponding phase and model, the results are combined according to the relevant load combinations.

Furthermore, a procedure for the analysis of structures built in two different periods has been described. The analysis of the construction stages is based on the construction phases analysis but this time the original part of the structure and the one built in a later construction stage are treated differently. The application of the construction phases analysis in this case requires to split Phase 0 into two more Phases (0-A and 0-B). This allow to properly assess the influence of the most recent structure on the original one.

The case study of a building rather regular in plan and in elevation was presented. The structure, built in two different periods, was analyzed according to three approaches: standard approach, construction phases analysis and analysis of the construction stages. The typical issues related to the standard application of the equivalent frame model were highlighted; especially with respect to the stress distribution, which in many case is affected by unrealistic stress migration. A comparison of the results obtained with the proposed approaches confirmed that they are more realistic and consistent with the real physical problem. The accuracy of the results has been proven through comparison with the stress state obtained through a simple manual calculation.

The building was analyzed though static linear analysis since the proposed methodologies mainly influence the structural behavior under the action of vertical loads. In a later work, the results of seismic analyses performed through the construction phases approach will be presented. The advantages of the proposed methodologies are evident in pushover analysis where the capacity curve of the structure is more realistic than the one obtained with the standard approach.

Finally, the proposed procedures represent an improvement of the equivalent frame method, leading to more accurate results with a slightly higher computational effort. This is particularly important, considering that the equivalent frame method is widely used in the engineering practice. However, the concepts of construction phases analysis could be applied even to more refined finite element models, since they are based on the differentiation of the structural model depending on the nature of the load actions.

REFERENCES

[1] Ministero delle Infrastrutture e dei Trasporti. *Decreto 14 gennaio 2008. Approvazione delle nuove norme tecniche per le costruzioni*, §8.7.1. Gazzetta Ufficiale della Repubblica Italiana n. 29 del 4 febbraio 2008, Supplemento ordinario n.29. (in Italian)

[2] Ministero delle Infrastrutture e dei Trasporti. *Circolare. n. 617 del 02 febbraio 2009. Istruzioni per l'applicazione delle Nuove Norme Tecniche per le costruzioni*, §C8A.4. Gazzetta Ufficiale della Repubblica Italiana n. 47 del 26 febbraio 2009, Supplemento ordinario n.27. (in Italian)

[3] Eurocode 6: Design of masonry structures - Part 1-1: General rules for reinforced and unreinforced masonry structures, EN 1996-1-1, 2005.

[4] Eurocode 8: Design of structures for earthquake resistance - Part 1: General rules, seismic action and rules for buildings, EN 1998-1, 2005.

[5] AA.VV, *Manuale delle Murature Storiche: Analisi e conoscenza del costruito storico in muratura*, Direttore Scientifico A. Borri, a cura di C. Donà. DEI Tipografia del Genio Civile, Roma, 2011. Appendice §A.2.7. (in Italian)

[6] M. Ludovico, R. Fico, E.A. Cordasco, A. Prota, G.M. Verderame, G. Manfredi, *Alcune considerazioni sull'utilizzo del software tecnico nella Ricostruzione dell'Abruzzo*, a cura dell'Università di Napoli Federico II e del Consorzio RELUIS. (in Italian)

[7] B. Calderoni, E.A. Cardasco, P. Lenza, G. Pacella, Structural behaviour of masonry spandrels: experimental evaluation and reinforcing, *Proceedings of Prohitec Conference*, Rome, June 2009, Taylor & Francis Group, London, pag. 1591-1596.

[8] B. Calderoni, E.A. Cardasco, P. Lenza, G. Pacella, Analisi numerica su base sperimentale del comportamento strutturale delle fasce murarie di piano, *Atti del XIII Convegno Nazionale ANIDIS "L'Ingegneria Sismica in Italia"*, Bologna, June-July 2009, ed. PATRON. (in Italian)

[9] Aedes Software, *Aedes.PCM: Progettazione di Costruzioni in Muratura*, Version 2015, www.aedes.it

ECCOMAS Congress 2016
VII European Congress on Computational Methods in Applied Sciences and Engineering
M. Papadrakakis, V. Papadopoulos, G. Stefanou, V. Plevris (eds.)
Crete Island, Greece, 5–10 June 2016

A COMBINED EXPERIMENTAL AND NUMERICAL STUDY OF THE PULL-OUT MECHANISM OF THREADED TITANIUM BARS EMBEDDED IN MARBLE BLOCKS

S. K. Kourkoulis[1], A. Marinelli[2] and I. Dakanali[1]

[1] Laboratory of Testing and Materials, Department of Mechanics, School of Applied Mathematical and Physical Sciences, National Technical University of Athens, Zografou Campus, 157 73 Athens, Greece

[2] School of Engineering and the Built Environment, Edinburgh Napier University
10, Colinton Road, EH10 5DT, Edinburgh, UK
e-mail: A.Marinelli@napier.ac.uk

Keywords: monuments, marble, pullout phenomenon, restoration, contact interfaces.

Abstract. *The present study describes the first stage of an ongoing research project aiming to investigate the failure mechanisms activated when reinforcing bars are pulled-out from the body of the reinforced element. Attention is given to the progressive failure of the interfaces between the constituent elements of the marble-cement paste-titanium (MCT) complex, which appears in case marble structural members of classic stone monuments are restored according to the pioneering technique used on the Acropolis of Athens worksite. Experience from already implemented projects indicates that, when restored structural members are subjected to tension or bending, the failure of these interfaces leads to debonding and finally to catastrophic pull-out of the reinforcing bar from the body of the marble volume.*

In this direction, a series of pull-out experiments were implemented, with specimens made of Dionysos marble, in the form of prisms of various dimensions with threaded titanium bars inserted into predrilled holes which were then filled with suitable cement paste. The results obtained from these experiments, by employing both conventional and innovative sensing techniques, were used for the calibration of a Finite Element model, which will be used for the thorough investigation of the parameters affecting the overall response of the restored element.

The commercial package ABAQUS was used for the implementation of the numerical analysis. The surface contact features of the package were properly exploited in the direction of comparatively exploring and evaluating of possible modeling approaches for simulating the actual interfaces of the marble-cement-titanium complex. A reliable performance law, allowing for the incorporation of damage initiation and evolution criteria, was determined permitting satisfactory modeling of the pull-out behavior at the interface between marble and cement paste. Critical parameters, material properties and modeling choices that have a significant impact on the final outcome were considered. The numerical model finally designed approaches in a very satisfactory manner the experimentally obtained load-displacement curve, providing an easy-to-use, flexible and reliable tool for further study of the pull-out phenomenon.

1 INTRODUCTION

The pioneering technique that is nowadays adopted for the restoration of fractured structural members of classic marble monuments of Greek architecture is based on the insertion of threaded titanium bars into pre-drilled holes, while filling the intermediate gap with a suitable cementitious paste (Fig. 1) [1]. The number and the diameter of the bars are chosen in such a way that the restored epistyle sustains its self-weight and the weight of the structural elements that are planned to be superimposed on the structure in the future. Furthermore, attention is paid for the extent of interventions to the authentic marble to be the minimum possible. The basic principle that governs this kind of restorations is the reversibility of the interventions. This means that if needed, the monument can be restored to its condition prior to the intervention.

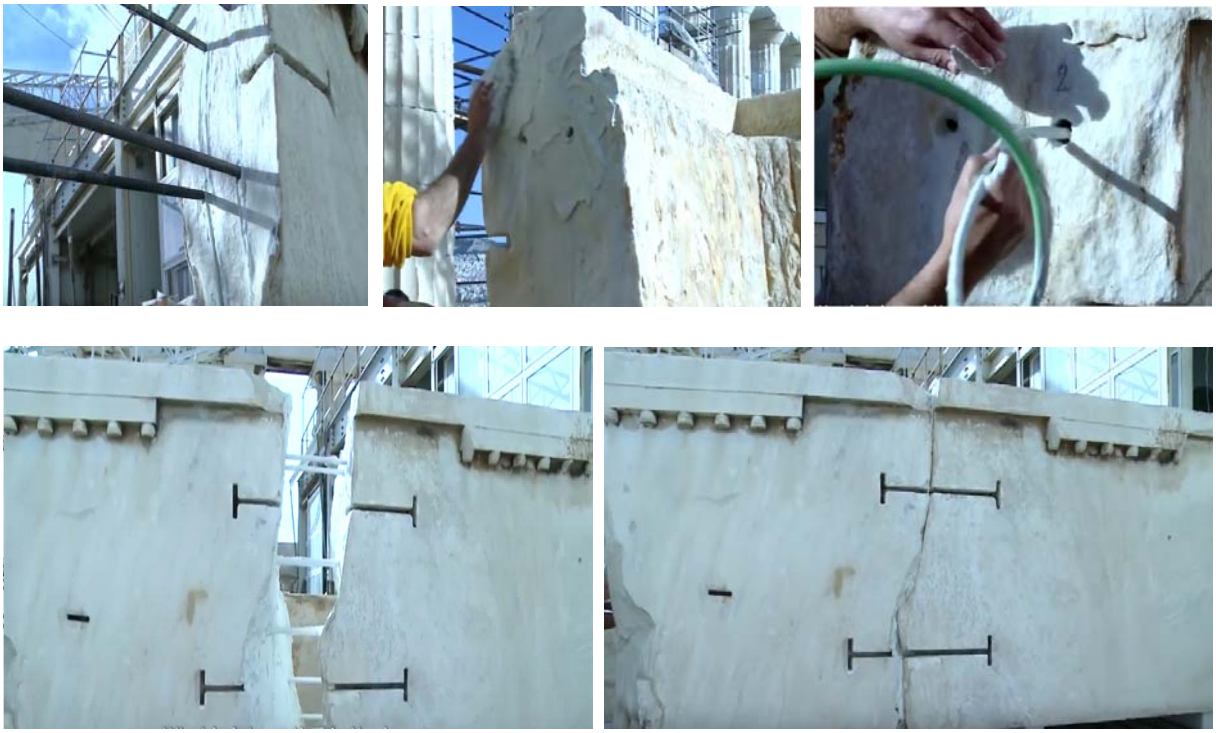

Figure 1: The main steps for the restoration of a marble epistyle [2].

Experience gathered by the scientists working for the restoration project of the Acropolis monuments has shown that the integrity of the structure after restoration strongly depends on quite a few details of the aforementioned technique. Several experimental and numerical studies have been conducted, investigating the parameters that influence the mechanical response of the specific joint [3]. It has been definitely proven that the weakest link of the three materials (MCT) chain lies within the layer of the cementitious material [3, 4]. The failure mode most commonly observed, is the relative slip of the bar-mortar block with respect to the marble volume (without fracture of neither the marble nor the bar) which is known as pull-out.

This work focuses on the development of a reliable numerical model that, hopefully, could effectively describe the behavior of a thin layer between the cement paste and the marble body while being effective concerning the computational time. Critical parameters influencing the effectiveness of the model in terms of time requirement are considered to be the model's meshing, the analysis of time-increment and the choice regarding two or three-dimensional modeling. The models developed are calibrated taking advantage of the data for the load-displacement curve of a series of pull-out experiments which were implemented at the Laboratory of Testing and Materials of the National Technical University of Athens.

2 EXPERIMENTAL PROCEDURE

2.1 Specimens

The specimens tested were orthogonal prisms cut from Dionysos marble blocks. Their dimensions were equal to 10x10x15 cm^3. A central through hole, of diameter equal to d_{hole}=14 mm, was drilled normally to the upper face of the prisms. The hole was then filled with liquid cementitious material and a threaded titanium bar, of outer diameter equal to d_{bar}=11.0 mm, was driven in the hole and kept normal to the upper face of the cube until setting of the cement paste. All specimens have the same dimensions, anchoring length (7.5 cm) and thread's geometry and were cured for 28 days (Fig. 2). Attention was paid for the prisms to be cut normally to the material layers of the blocks in order to reduce scattering due to marble's anisotropy.

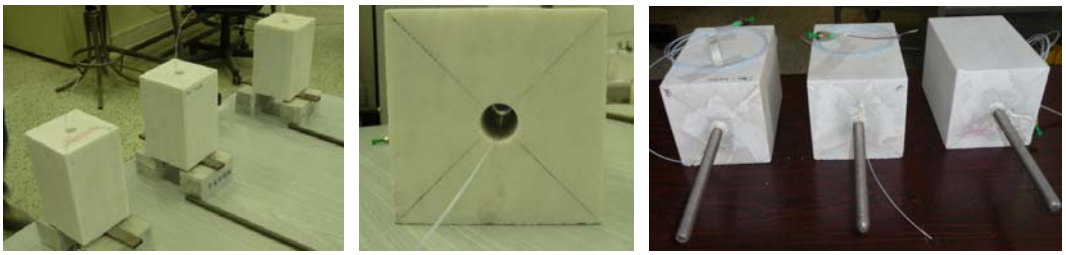

Figure 2: Preparation of the specimens.

2.2 Experimental procedure

For the experimental procedure, a stiff servo-hydraulic INSTRON loading frame of capacity 250 kN (Model 1126) was used. All tests were carried out under quasi-static displacement-control mode at a rate equal to 0.2 mm/min, with the titanium bar gripped by the frame's upper jaw. The marble cube was constrained by a rigid metallic plate with a hole of diameter equal to 50 mm in its center. The plate was supported by four stiff threaded bars (Fig. 3 (a), (b)). For the direct measurement of the axial strain developed along the titanium bar an Instron-Dynamic Extensometer of gauge length equal to 12.5mm was used (Fig. 3 (c)).

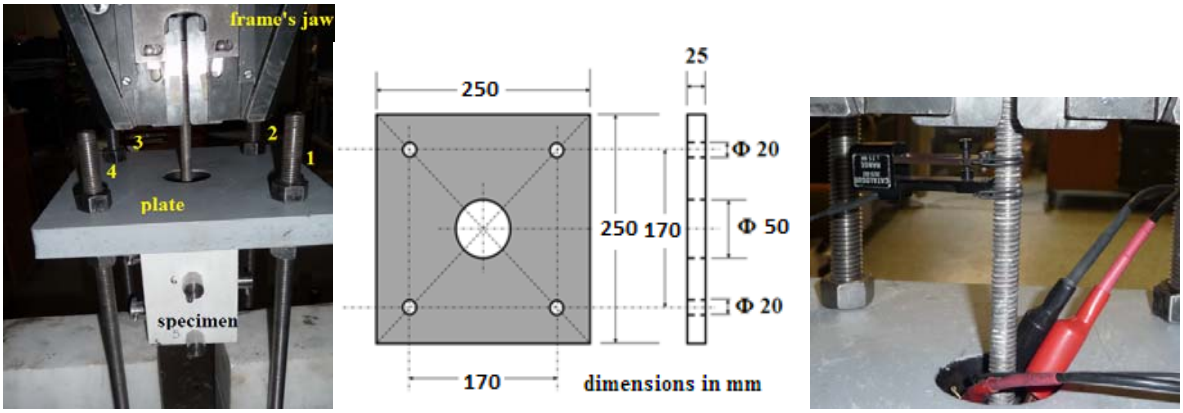

Figure 3: (a) The experiment set up, (b) The configuration of the metallic plate (c) The Dynamic Extensometer used in the experiments

During the tests, the relative displacement of the bar with respect to the marble prism was measured and recorded using a calibrated LVDT (Linear Variable Differential Transformer) touching the bar's lowest end through the cube's bottom face (Fig. 4 (a), (b)). Furthermore, in order to monitor the whole system's deformation and determine the actual movement of the bar, three additional LVDTs were placed at the bottom of the rigid plate (Fig. 4 (c)).

Figure 4: (a) The LVDT's position schematically (b) The lowest end of the cube (c) The LVDTs' positions under the rigid metallic plate.

In the experimental procedure, two innovative sensing techniques were employed, namely the Acoustic Emission (AE) and the Pressure Stimulated Currents (PSC) ones. So far, it is proven that these two techniques, when applied to brittle materials, can successfully detect cracks and damages at the material's interior while providing consistent pre-failure indicators [5, 6].

AE is based on the detection and record of transient elastic waves which are produced when the stress field developed exceeds (either locally or globally) the material's critical limits resulting to damage. The sudden release of energy accompanying damage produces waves which propagate spherically outwards until they are captured by a number of acoustic sensors, properly mounted on the specimen's surface [7]. In the present experimental protocol, eight acoustic sensors were attached on the marble surface, as close as possible to the area where the acoustic signals were expected to be produced, permitting 3D detection (Fig. 5(a)).

On the other hand, the PSC technique is based on the detection of weak electrical signals produced during the formation and growth of micro-cracks inside rock-like materials [5, 6]. For the PSC recordings two electrical contacts were placed in the specimens. The first one was embedded in the cement paste before its curing while the second one was inserted in a short predrilled hole (of depth equal to 1cm) on the marble (Fig. 5(b), (c)). The main goal is the accurate recording of electrical signals produced on the marble-cement paste interface.

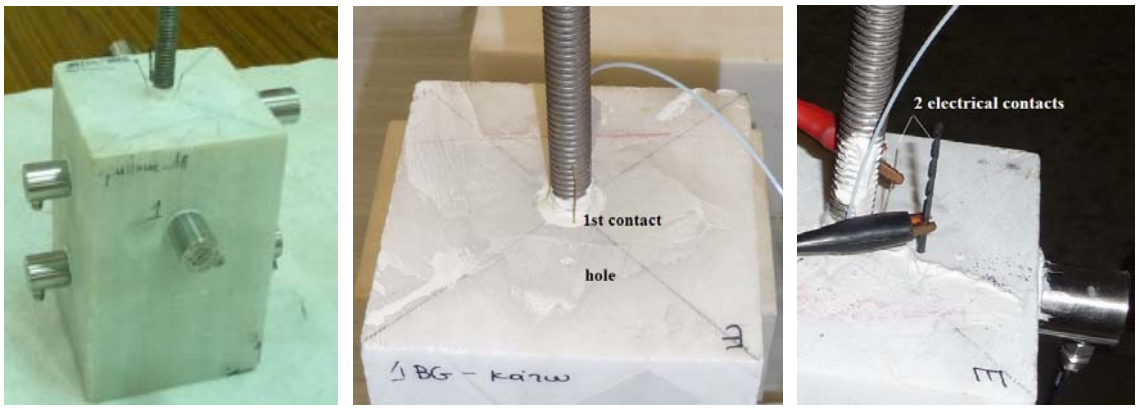

Figure 5: (a) The acoustic sensors on the marble surface (AE) (b), (c) The electrical contacts (PSC).

Observing macroscopically the fractured specimens, three main failure modes were distinguished, depending on the composition of the cementitious paste: pull-out of the titanium bar, fracture of the marble prism and failure (fracture or yield) of the titanium bar (Fig. 6 (a), (b), (c)). Taking into account the aim of the present study, attention is restricted from this point on to the tests for which the marble cube and titanium bar remained intact while the bar was pulled out.

Figure 6: (a) Pullout of the bar (b) Marble's fracture (c) Bar's failure.

2.3 Results

Typical results from experiments in which pure pull-out was observed are presented in Fig. 7(a), where the variation of the load is plotted versus the bar's axial strain. The differences observed, concerning the maximum load attained are significant and could be well attributed to uncontrollable parameters related to the inhomogeneity and anisotropy of Dionysos marble [8, 9], which dictate marble's response. On the contrary, the differences observed for the overall stiffness of the system (namely the slope of the load - axial strain curve) are rather negligible.

The pull-out phenomenon is typically described by the load-bar's displacement curve. Such a typical curve is shown in Fig.7b. It consists of an almost linear initial portion (until slightly before the maximum load) followed by a well distinguishable non-linear portion till the maximum load. A decreasing branch follows the peak force, the slope of which decreases gradually.

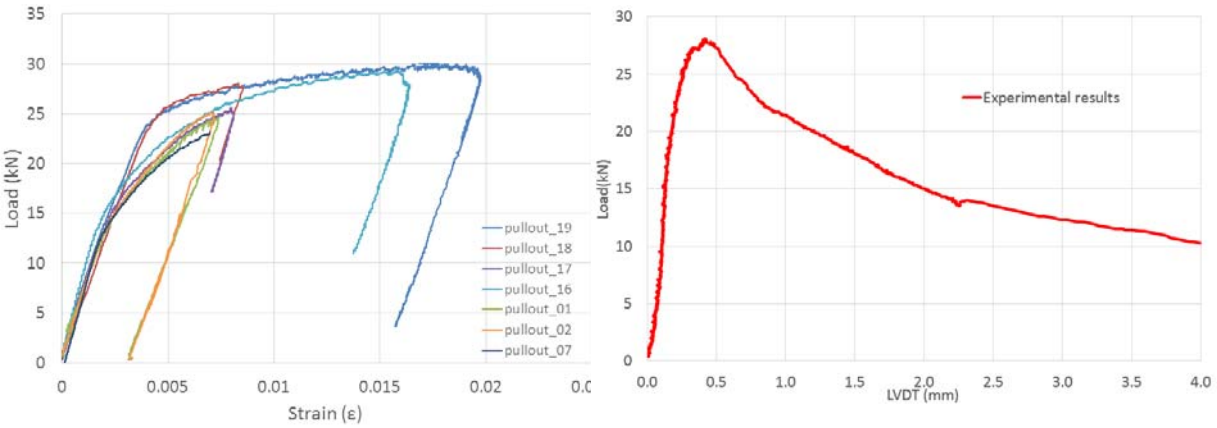

Figure 7: (a) Load vs bar's strain (b) load vs bar's displacement.

3 NUMERICAL ANALYSIS

The numerical model designed to simulate the pullout experiments was developed using the commercially available finite element software ABAQUS [14]. The specimens and the experimental procedure were simulated in every detail, to achieve optimum reproduction of the tests.

3.1 Model's geometry and materials' properties

The models consist of three bodies, i.e. the threaded titanium bar, the cement paste and the marble prism. The dimensions of the prism are the same as those of the tested specimens (Fig. 8 (a)). The geometrical characteristics of the threaded titanium bar are shown in Fig. 8 (b).

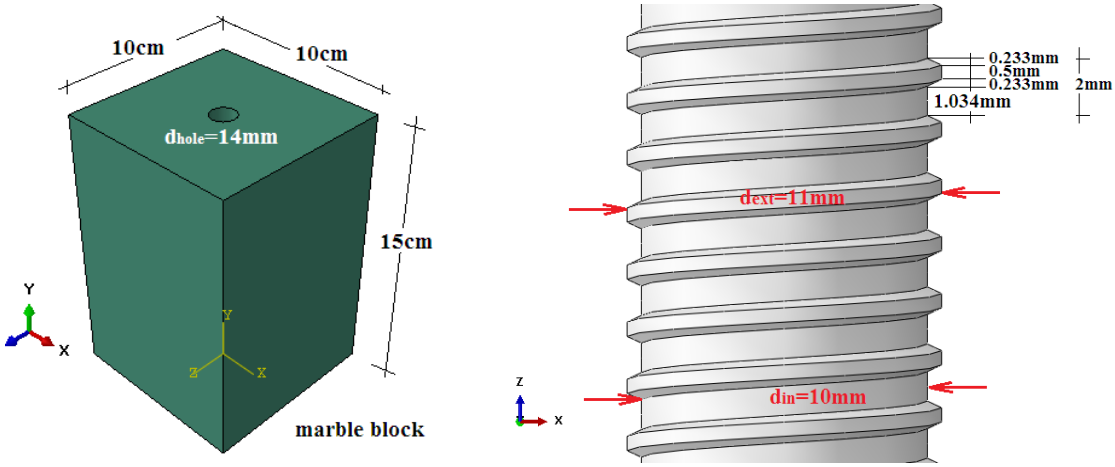

Figure 8: (a) Dimensions of the Marble block (b) Thread characteristics.

The second step of the numerical analysis is the identification of the mechanical properties of the three materials. For the Acropolis monuments, Dionysos marble is almost exclusively used since it is considered the material most compatible to the authentic building stone (i.e. Pentelic marble). It is characterized by two principal anisotropy directions (parallel to the material layers and normal to them) thus appearing to be transversely isotropic. Moreover, it is slightly non-linear and bimodular, i.e. its elastic modulus in compression exceeds slightly that in tension [8-10]. For the sake of simplicity, these features were here ignored and Dionysos marble was simulated as linearly elastic and isotropic. Its modulus of elasticity was set equal to E_m=84.5 GPa, its Poisson's ratio equal to v_m=0.26 and its density equal to 2.78 gr/cm^3.

Titanium was modeled also as linearly elastic (given that the loads to be imposed produce stresses well below its linearity limit) and isotropic material. Its modulus of elasticity was set equal to E_t=105 GPa, its Poisson's ratio equal to v_t= 0.32 and its density equal to 4.51 gr/cm^3.

Finally, with regard to the cementitious paste interposed between marble and titanium, it was considered, also, as linearly elastic and isotropic material with modulus of elasticity equal to E_p=15.4 GPa, Poisson's ratio equal to v_p=0.26 and density equal to 1.70 gr/cm^3 [11-13].

3.2 Contact properties

As already mentioned, previously reported experimental data, have definitely indicated that the most common failure mode in pullout tests was the debonding at the paste-marble interface [9, 10]. For this reason, the metallic bar in the model was considered perfectly bonded to the cementitious paste (obviously the threaded geometry of the bar is considered to play a significant role in this direction). Consequently, the overall behavior of the MTC complex is here dictated by the failure of the intermediate interface, i.e. that between marble and paste.

In ABAQUS practice, in case of bonded interfaces the thickness of which is negligibly small, the response of the cohesive layer is defined directly in terms of traction versus separation [10]. The available traction-separation model assumes an initially linear elastic behavior, which is followed by the initiation and evolution of damage. When the damage initiation criterion is met, the resultant behavior of the interface follows a damage evolution law. There are two alternative choices available for this law in the traction - seperation space, i.e. linearly or exponentialy decreasing. The respective curve is schematically shown in Fig. 9.

Concerning the initiation of damage the ABAQUS software provides four main criteria: The maximum nominal stress, the maximum nominal strain, the quadratic nominal stress and the quadratic strain [14]. Regardless of the criterion that is adopted in modeling, the results obtained are the same assuming of course that reasonable compatibility laws are applied for the transition between the various options.

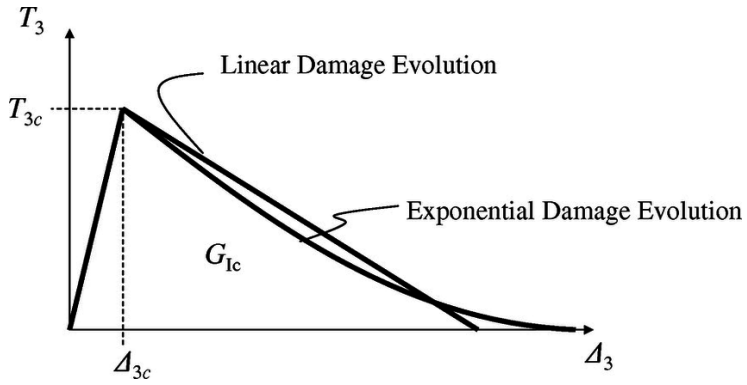

Figure 9: Schematical representation of traction-separation response [14].

4 THE NUMERICAL MODEL

4.1 Mesh density

In computational solutions, meshing is among the most significant parameters that can determine the reliability of the results. Improved mesh quality provides more accurate solutions. Unfortunately, the meshing quality is strongly related to another parameter that has to be considered, i.e. the CPU time or in other words how time-consuming the analysis is. It is generally accepted that finer meshing is related to increased computational time demands.

In this direction (and taking into account the increased number of parameters that will be investigated using the present model) the relation between the mesh quality and the CPU time was thoroughly considered. The validation of the model was achieved taking advantage of a typical experimental pull-out curve (Fig.7b). Models of different mesh densities are compared with reference to the CPU time. Four different models were constructed, for which tetrahedral elements were used for the mortar-bar complex and hexahedral elements for the marble body. The number of tetrahedral and hexahedral elements, the approximate ratio of their size and the respective CPU time for each model are recapitulated in Table 1. The mesh for the first testing case (model 01) is shown in Fig.10. The overall results of this step of the analysis are presented comparatively in Fig. 11, in juxtaposition to the respective experimental data.

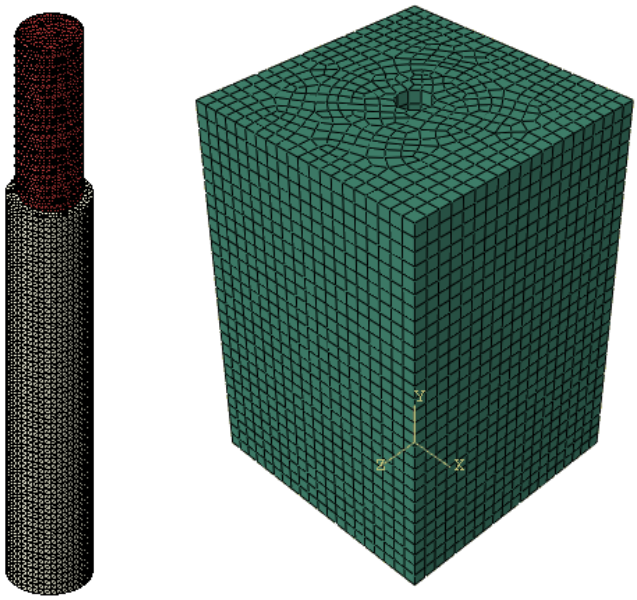

Figure 10: Mesh geometry of (a) bar-paste complex (b) marble block (model 01).

Title	CPU time (sec)	Number of tetrahedral elements	Number of hexahedral elements	Approximate size of tetrahedral /hexahedral element
Model 01	4878,8	152532	15150	1:5
Model 02	52853	352358	72350	~ 1:4
Model 03	65400	92620	93728	~ 1:2
Model 04	278673	42840	215625	1:1

Table 1: CPU time with the respective model's total number of elements.

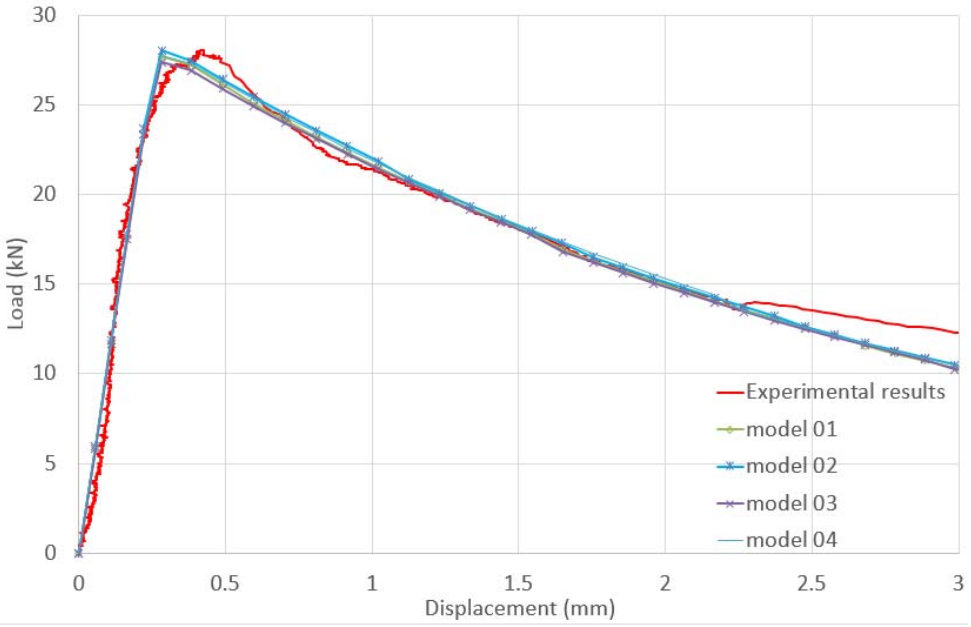

Figure 11: Load versus bar's displacement (experimental results/analyses of different mesh density).

It is definitely concluded from Fig.11 that all four numerically obtained curves are very close to each other. Moreover, their deviation from the experimental data is relatively small, despite the quite significant differences recorder for the respective CPU times (shown in Table 1).

4.2 Time increment analysis

In ABAQUS Standard, the overall convergence rate and the robustness of the progressive failure simulation of composite structures is significantly affected by the time increment of the analysis: Low time increment may give more precise results but it increases the CPU time.

For the model that was considered as the optimum one according to the results of Section 4.1 (i.e. model 01), three different time increments were considered in this step (Table2).

Title	CPU time (sec)	Time increment
Model_01	42584	0,001
Model_02	4878,8	0,01
Model_03	1508,8	0,1

Table 2: CPU time with the respective time increment.

The results of the analyses are given in Fig. 12. The larger time increment (blue curve), characterized by fewer integration points, results to deviations from the experimental data around the peak force, which may be proven critical. The medium (model_02-black curve) and fine time increments (model_01-yellow curve) provide identical curves but they differ significantly in their CPU time (Table 2). The model with finer time increments is almost 10 times more time-consuming compared to the one with medium time increments. Taking all these into account it can be concluded that the model with medium time increment is the optimum choice.

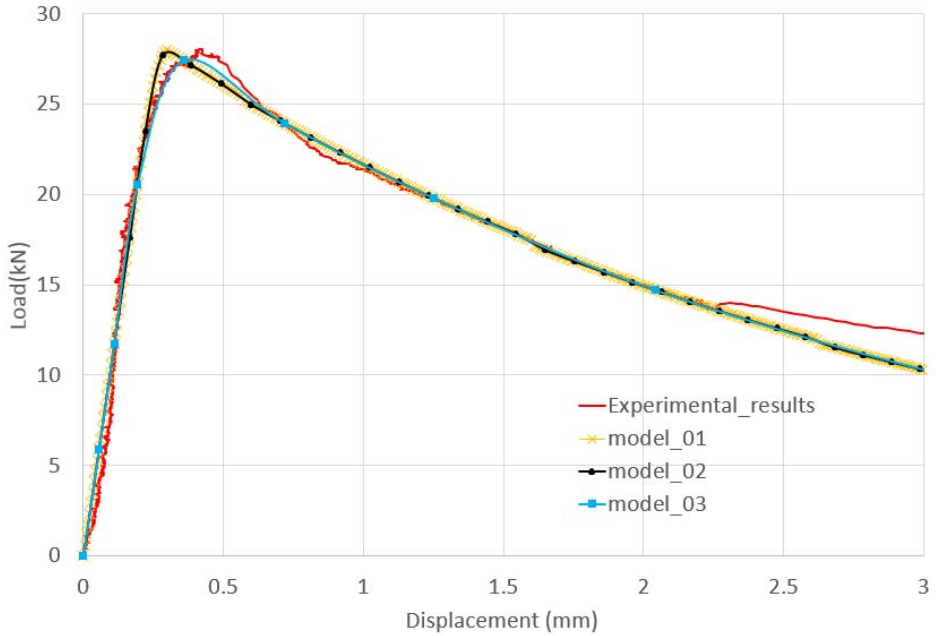

Figure 12: Load versus bar's displacement (experimental results/analyses of different time increment).

4.3 2D versus 3D models

In numerical simulations, it is important to achieve the required accuracy in the minimum possible computational time. The symmetry characterizing the specimens of the present experimental protocol permits the design of simplified numerical models, significantly decreasing the CPU time. In this direction, an axisymmetric model (with respect to the central symmetry axis of the configuration) was designed, as it is shown in Fig. 13. It is worth noticing that the computational time of the axisymmetric model is almost 10 times less than the computational time of the respective 3D one while the results seem to be well comparable (Fig. 14).

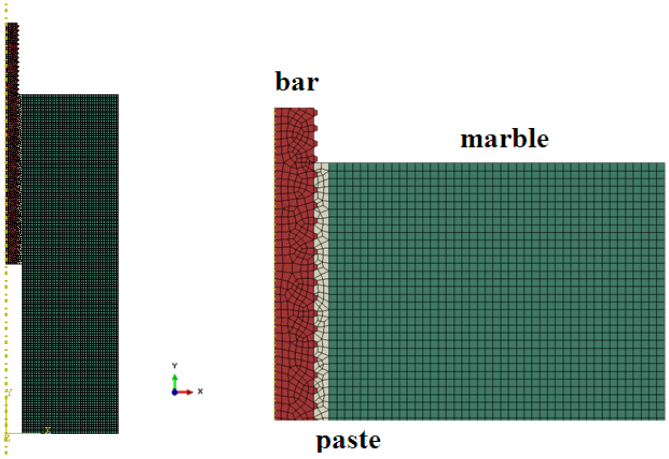

Figure 13: Axisymmetric model of pullout test

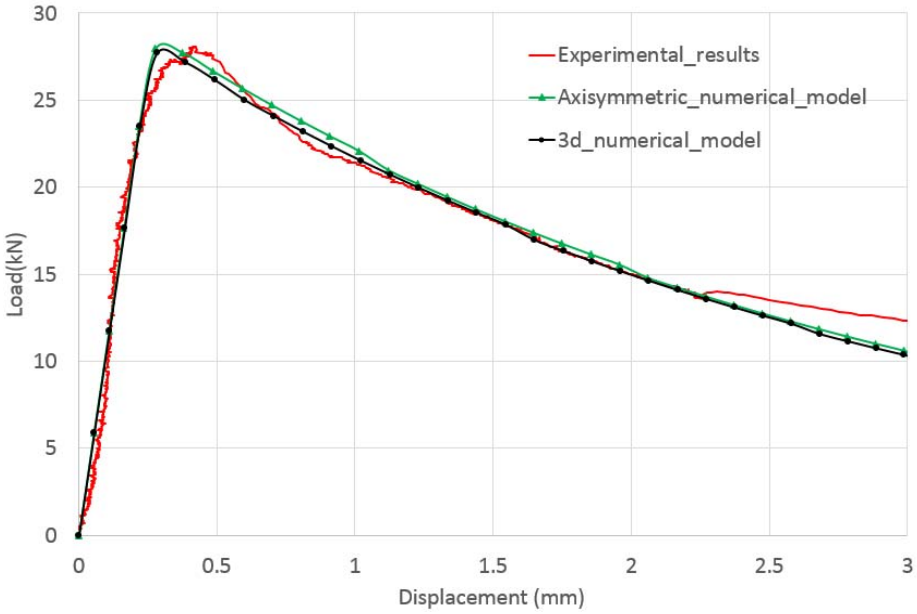

Figure 14: Load versus bar's displacement of axisymmetric and 3d pullout model.

5 DISCUSSION AND CONCLUSIONS

A finite element model was designed that will be used for the parametric study of the pull-out phenomenon observed in restored marble structural members. The model was calibrated according to the data gathered from a specially designed non-standardized experimental protocol. At this point the question could arise related to the accuracy and reliability of the experimental data themselves. In an attempt to eliminate such doubts the data of a typical test, as they were gathered by three different sensing techniques, are plotted in Fig. 15. More specifically the relative displacement of the bar with respect to the marble prism (as recorded by the respective LVDT) is plotted against the load level in conjunction to the cumulative electric load Q (as determined using the PSC technique) and the cumulative energy of the acoustic events (as determined by the AE technique). It is very intersting to observe that the data gathered by all three techniques are in excellent mutual qualitative agreement. In depth analysis of these data has proven that they are also in very good quantitative agreement [15], enhancing confidence to the reliability of the experimental results used to validate the numerical model.

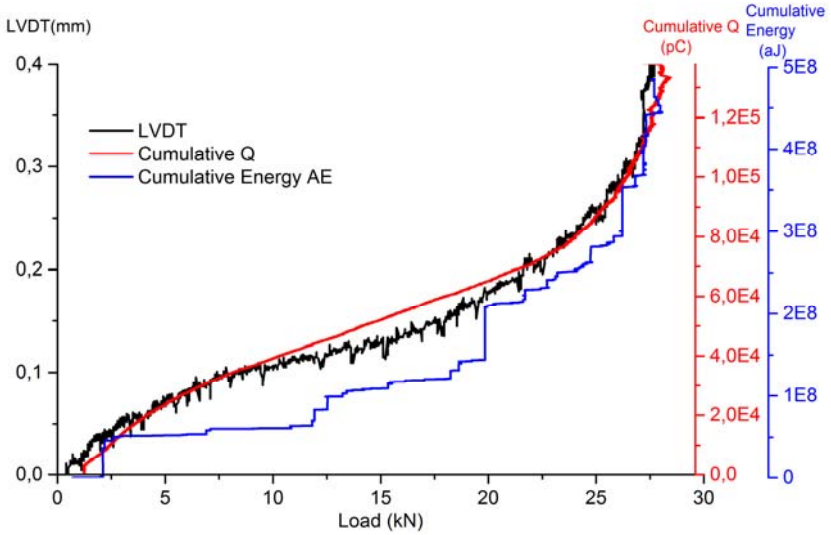

Figure 15: Comparative representation of the data gathered by the LVDT, the PSC- and AE-techniques.

The model designed was optimized in relation to two crucial aspects, i.e. meshing and time increment of the analysis. A satisfactory compomise between accurracy and CPU time consumption was achieved. Morever the model's effectiveness was assessed in case a simplified axisymmetric design is chosen against the "heavier" three dimensional version. It was concluded that the diffrences are rather negligible and, at least for this specific application, no reason exists to use three dimensional analysis.

REFERENCES

[1] M. Korres, N. Toganides, C. Zambas, Th. Skoulikidis, Study for the restoration of the Parthenon, Vol.2a, Athens: *Ministry of Culture, Committee for the Preservation of the Acropolis Monuments* (in Greek) 1989.

[2] Restoration works on the Parthenon-https://www.youtube.com/watch?v=uFJz2odV9jU, March 09, 2016.

[3] I. Vayas I., A. Merinelli, S. Kourkoulis, S. Papanicolopoulos, The pull-out problem in restoring marble fragments, *PROHITECH 09 Conference*, Rome, Italy, June 21-24, 2009.

[4] S.K Kourkoulis, S.-A. Papanicolopulos, A. Marinelli, I. Vayas, Restoration of antique temples: Experimental investigations on the pull-out behaviour of anchors in marble. *Bautechnik*, Vol. 85, No. 2, 109-119, 2008.

[5] D. Triantis et al., Innovative experimental techniques in the service of restoration of stone monuments - Part II: Marble epistyles under shear, *Procedia Engineering*, 109, 276-284, 2015.

[6] D. Triantis, I. Stavrakas, A. Kyriazopoulos, G. Hloupis, Z. Agioutantis, Pressure stimulated electrical emissions from cement mortar used as failure predictors, *International Journal of Fracture*, 175, 53-61, 2012.

[7] C. U. Grosse, M. Ohtsu, *Acoustic Emission Testing, Basics for Research-Applications in Civil Engineering*, Springer-Verlag Berlin Heidelberg, 2008.

[8] G.E. Exadaktylos, I. Vardoulakis and S.K. Kourkoulis, Influence of nonlinearity and double elasticity on flexure of rock beams – I. Technical theory, *International Journal of Solids and Structures*, 38(22-23), 4091-4117, 2001.

[9] G.E. Exadaktylos, I. Vardoulakis and S.K. Kourkoulis, Influence of nonlinearity and double elasticity on flexure of rock beams – II. Characterization of Dionysos marble, *International Journal of Solids and Structures*, 38(22-23), 4119-4145, 2001.

[10] S.K. Kourkoulis, E. Ganniari-Papageorgiou and M. Mentzini, Dionysos marble under bending: A contribution towards understanding the fracture of the Parthenon architraves, *Engineering Geology*, 115 (3-4), 246-256, 2010.

[11] S. K. Kourkoulis, E. Ganniari-Papageorgiou, Restoring fragmented marble epistyles: Some critical points, *Journal of Cultural heritage*, 11, 420-429, 2010.

[12] S. K. Kourkoulis, E. Ganniari-Papageorgiou, Bending of Fragmented Architraves Restored With Bolted Titanium Bars: a Numerical Analysis, *Engineering Transactions*, Vol. 56, No 2, 159–180, 2008.

[13] A. Marinelli, S.-A. Papanicolopulos, S.K. Kourkoulis, I. Vayas, The Pull-Out Problem in Restoring Marble Fragments: A Design Criterion Based on Experimental Results, *Strain*, Vol. 45, No 5, 433-444, 2009.

[14] *ABAQUS Analysis User's manual, v.6.10,* Hibbitt, Karlsson, and Sorensen, Inc., *2010.*

[15] I. Dakanali, I. Stavrakas, D. Triantis, S. K. Kourkoulis, Pull-out of threaded reinforcing bars from marble blocks, *21st European Conference on Fracture (ECF21)*, Catania, Italy, June 20-24, 2016.

ECCOMAS Congress 2016
VII European Congress on Computational Methods in Applied Sciences and Engineering
M. Papadrakakis, V. Papadopoulos, G. Stefanou, V. Plevris (eds.)
Crete Island, Greece, 5–10 June 2016

FINITE-DISCRETE ELEMENT MODELLING OF MASONRY INFILL WALLS SUBJECTED TO OUT-OF-PLANE LOADS

Laura Liberatore[1], Marta Bruno[1], Omar AlShawa[1], Monica Pasca[1] and Luigi Sorrentino[1]

[1] Department of Structural and Geotechnical Engineering, Sapienza University of Rome
Via Gramsci 53, 00197 Rome, Italy
e-mail: {laura.liberatore, marta.bruno, omar.alshawa, monica.pasca, luigi.sorrentino}@uniroma1.it

Keywords: Masonry Infills, Out-Of-Plane Loads, Finite-Element Modelling, Discrete-Element Modelling, Non-Linear Analyses.

Abstract. *In this paper, the out-of-plane response of infill walls is investigated by means of non-linear monotonic (push-over) analyses through a combined finite and discrete modelling approach. The model accounts for material deformability, crack formation, sliding, separation and formation of new contacts. Masonry units are modelled as finite elements, and different material models are assumed for the masonry. Contact between masonry units, and between masonry and frame elements is modelled by means of interfaces, which permit tangential motion with frictional sliding. Frame elements are modelled by means of a linear-elastic material. The results of the numerical analyses are compared with those of experimental tests available in the literature. The advantages and disadvantages of the adopted modelling strategy are investigated.*

1 INTRODUCTION

Masonry walls are widely used as infills in steel and reinforced-concrete (RC) frame structures. The failure of infills, which may develop both in- and/or out-of-plane, may cause casualties and heavy socio-economic consequences.

Recent earthquakes have shown that the out-of-plane failure of infills can occur even for moderate intensity of the ground motion [1, 2, 3]. For this reason, the interest in the out-of-plane behaviour of infill walls has been growing in the last years. A number of experimental tests have been performed by different investigators to assess strength and ductility of infill masonry walls loaded in the out-of-plane direction [4]. Moreover, several analytical models have been developed for the assessment of the out-of-plane response of masonry infills [5]. Most of them are based on rigid body mechanisms [6], either with or without the description of the arching behaviour.

More complex modelling is performed when numerical solution methods are adopted. These approaches involve either a smeared-crack or a discrete-crack modelling. The former is usually adopted to model the global behaviour of a structural system, while the latter is used to model the actual interaction between adjacent elements. The discrete-crack modelling can realistically predict the structural response when the crack pattern follows the locations of mortar joints [7].

The finite Element (FE) method has been applied more extensively to predict the in-plane behaviour for infills with [8] or without [9] openings. Some numerical studies are performed through the software DIANA [9, 10]. ANSYS software has been used by several researchers as well [11]; Mohyeddin et al. [12] have developed a three-dimensional FE model of infilled RC frames at a micro-level, showing that the model can be employed to interpret the response of the infilled frame under in- or out-of-plane loading over a wide range of drifts, allowing a parametric/sensitivity analysis [13].

Two classes of models can be identified [14]: discrete-crack modelling, including unit and joint model, with detailed micro modelling, where the material properties for the different components are generally taken from experiments [13, 14]; smeared-crack models, either weak or strong, for which a Total Strain Cracking Model is used to represent the material behaviour of the masonry [10] or macro-modelling of the masonry based on concrete smeared cracking and damaged plastic material (Concrete Damaged Plasticity model in Abaqus) [15].

A FE model is used to evaluate the out-of-plane capacity of an infill wall surrounded by a RC frame [10] with 3D curved-shell elements for both frame (8-node) and interface between infill and frame (6-node); mortar and unit-mortar interface are smeared out in the continuum. For the compressive and tensile behaviour of masonry the concrete material in the FE software DIANA is used. Two models are considered, depending on the boundary conditions of the infill wall, the first one representing two-way arching action, whereas the second represents one-way action.

FE modelling has been used also for the analysis of retrofitted infill masonry under out-of-plane loads [16], with simplified micro-modelling, where units are represented by continuum elements, mortar joints by interface elements, and reinforcing bars by truss elements; a more simplified FE model with equivalent vertical bars have been studied as well, in order to evaluate the sensitivity to modelling parameters. In this case the presence of the retrofitting reduces the sensitivity to variations of the material constants, which is usually rather high.

In this paper, the out-of-plane response of infill walls is investigated by means of non-linear analyses through a combined finite and discrete modelling approach. The results of the numerical analyses are compared with those of experimental tests available in the literature.

2 MODELLING ASPECTS

In order to reproduce the main characteristics of the response of different specimens of infill walls tested in the out-of-plane direction, several models are implemented using the LS-DYNA software package [17], which is a finite-discrete element code capable of simulating three-dimensional problems. This code is used here, within an ANSYS environment, to numerically reproduce the results of experimental tests.

A combined finite and discrete modelling approach is used. Units are modelled as linear elastic 8-node solid elements with a single integration point. The major disadvantage of one-point integration is the need to control the zero-energy modes that arise, called hourglassing modes, which might enlarge and destroy the solution. A Flanagan-Belytschko stiffness-type stabilisation is used here [18].

Mortar is not explicitly considered in the model; instead contact interfaces are used. Contact interfaces allow the transmission of both compressive and tensile forces, moreover a tangential motion with friction sliding is permitted. Frictional sliding occurs when the frictional stress limit is reached. In tension, the contact interface failure criteria is based on the normal tensile stress limit. In compression, to avoid the penetration between nodes and contact surface, the standard penalty method is used. The method consists in placing normal springs between all penetrating nodes and the contact surface. The interface stiffness depends on the stiffness of the materials that are in contact and on a scale factor, named penalty factor.

With the aim of comparison, FE models resorting to a smeared-crack approach are also implemented. In these cases, the contact surfaces are used only at the interface between the masonry panel and the surrounding structure.

Vertical loads are first applied to the system. Static or quasi-static processes can be simulated resorting to dynamic relaxation or to mass damping to eliminate dynamic oscillations. Preliminary analysis have shown that, for the cases at hand, the two methods give equivalent results. To avoid high frequency oscillations during the application of the gravity loads, these are applied slowly from zero to gravity acceleration. Afterward, horizontal displacements are applied in the out-of-plane direction.

2.1 Material modelling

Different types of material have been initially examined for modelling units: linear elastic (MAT_001), Winfrith smeared-crack concrete model (MAT_084/085), smooth-surface cap model (MAT_159), damage-plastic concrete model (MAT_273).

The linear elastic material (MAT_001) is particularly suitable when no damage is expected in the units, both in tension and compression, i.e. when the cracks pattern follows the joints. The use of this material requires the definition of a very limited number of parameters and allows to reduce the computational effort. However, given that the out of plane failure of infills may occur due to excessive compression in the units, a non linear material is more adequate to represent the actual behaviour.

The Winfrith material model (MAT_084-085) is a smeared-crack model developed in [19, 20]. The mechanical parameters that have to be defined are initial tangent modulus, Poisson's ratio, uniaxial compressive and tensile strengths. Moreover, a volumetric strain versus volumetric pressure curve is required. If the curve is omitted, a default pressure versus volumetric strain curve is automatically used. The Winfrith material includes also the option of considering reinforcement in a smeared fashion.

Material type 159 (MAT_159), which is available for solid elements, is a smooth-surface cap model, i.e. with a smooth intersection between the shear surface and the hardening cap [21]. This material has been created to reproduce accurately the response of concrete subject

to impact loads. Many parameters, such as moduli, strengths, hardening, softening, and rate effects parameters, must be supplied, otherwise default values are provided. Default parameters are fit for unconfined compression strengths between about 20 and 58 MPa and aggregate sizes between 8 and 32 mm and, therefore, are not suitable for the modelling of masonry. Given the difficulties in calibrating the parameters (more than thirty) with the experimental tests available for masonry materials, this material type was not used.

The damage-plastic concrete model (MAT_273) is based on the studies in [22][23], and is aimed to simulate the failure of concrete structures subjected to dynamic loads. The model is based on effective stress plasticity, with damage based on both plastic and elastic strain measures. The definition of the model requires a large number of parameters, but several of them are directly related to one another by explicit expressions. Other parameters can be determined from certain assumptions, or taken by their recommended default values [22], so that a limited number of material properties must be specified.

With the aim of highlighting the differences between these materials, a simple two-blocks model has been tested under compression (Figure 1). Input data are reported in Table 1. As already noted, values of the compression strength lower than 20 MPa are incompatible with the material MAT_159. In this case the analysis runs out immediately. For the other material types, the vertical resultant force and the minimum principal stress are reported in Figure 2. The use of MAT_273 leads to a larger stiffness of the model and the analysis stops before the attainment of the material compressive strength, hence this material is not used in the following analyses. The Elastic (MAT_001) and Winfrith (MAT_084-085) materials give the same results in the elastic range, the latter presents a stiffness reduction when the displacements increase.

Material	RO (kg/m^3)	E MPa	ν	A_s mm	f_c MPa	f_t MPa
MAT_001	2200	2.8E+3	0.2	-	-	-
MAT_084-085	2200	2.8E+3	0.2	1	2.84	-
MAT_159	2200	-	-	1	2.84	5.69E-1
MAT_273*	2200	2.8E+3	0.2	-	2.84	5.69E-1

RO = density; E = Elastic modulus; ν = Poisson's ratio; and A_s = Aggregate size; f_c = compressive strength; f_t = tensile strength.

Table 1: Input values for different material types.

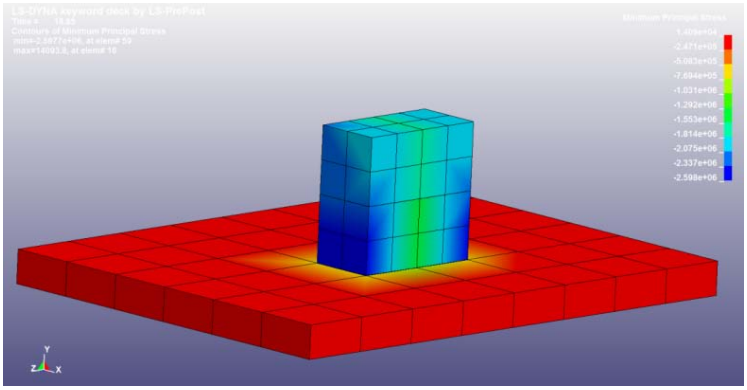

Figure 1: Two-blocks model: minimum principal stress.

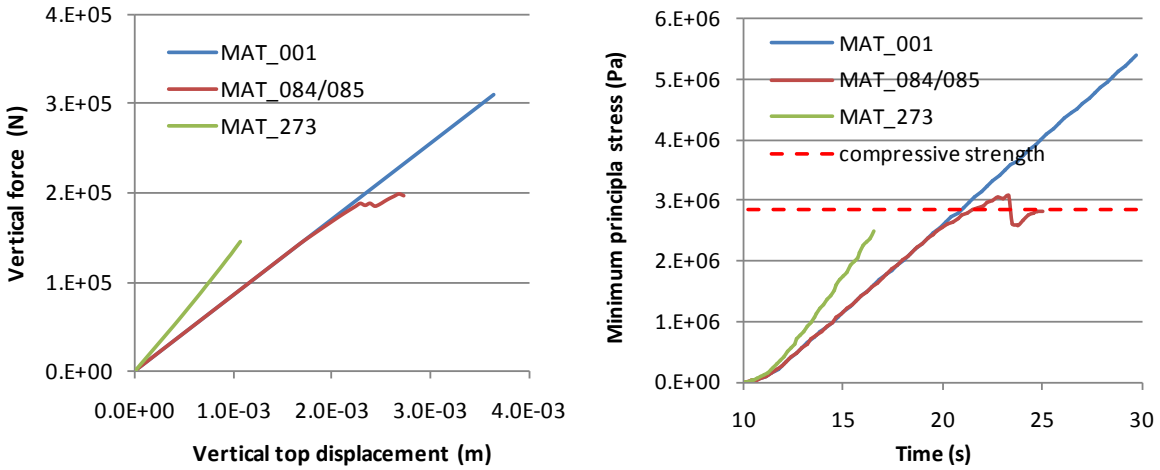

Figure 2: a) Force-displacement (a), and minimum principal stress-time plots (b).

3 CASE STUDY

Different models have been selected and analysed, in order to replicate the tests by Modena and da Porto [24]. This experimental investigation concerns nine hollow-block masonry panels (976×2520×291 mm^3, $b \times h \times t$) loaded at mid-height by means of a horizontal rigid beam. At the top and the bottom the panels are mortared to rigid RC supports, whereas vertical edges are not restrained. Six specimens were constructed with horizontal-hole blocks, the other three specimens were constructed with vertical-hole blocks, thus achieving the masonry compressive strength necessary for arching behaviour. Consequently, out-of-plane strength of vertical-hole blockwork is almost thrice that of horizontal-hole one and is noticeably underestimated by available equations [5]. One of the vertical-hole specimens, FVC1, is considered in the following analyses.

In the numerical simulations have been used both the Elastic and the Winfrith materials, whose main mechanical characteristics are reported in Table 2. For the finite-discrete models, the mechanical characteristics of the units have been adopted, the tensile strength has been increased so that the tensile failure occurs in the contact interfaces. For the smeared-crack model, the masonry elastic modulus has been used and tensile strength is assumed equal to 20% of compressive strength. As far as the contact interfaces is concerned, the parameters that affect the global response are: the normal failure stress (in tension), the frictional stress limit, the coefficient of friction and the scale factor on default penalty stiffness (penalty factor). As observed in Section 2, the penalty factor is used to calculate the interface stiffness. For this parameter, a default value of 0.1 is recommended in the case of contact between similarly refined meshes of comparably stiff materials. However, according to [7] a value of 0.05 is expected to give reasonable results for masonry walls. To investigate the influence of this factor, three values of the penalty factor are used herein, i.e. 0.02, 0.05, and 0.10. It is noted that this values are the product of two input parameters: SFS (or SFM), which is the scale factor included in the contact card, and SLSFAC, which is the scale factor for sliding interface penalties included in the control card.

The model geometry and the adopted mesh are shown in Figure 3. With the aim of capturing the stress field across the wall thickness, four finite elements are present in the transversal direction. Top and bottom supports are modelled as rigid bodies, so as the loading central beam. Prescribed horizontal displacements are assigned monotonically to the rigid beam up to 10 mm.

	Units properties					Contact properties		
Model ID	Material	E	ν	f_c	f_t	NFLS	SFLS	Penalty factor
		MPa		MPa	MPa	MPa	MPa	
M01	Elastic	20.83E+3	0.15	-	-	0.78	0.78	0.02
M02	Elastic	20.83E+3	0.15	-	-	0.78	0.78	0.05
M03	Elastic	20.83E+3	0.15	-	-	0.78	0.78	0.10
M04	Winfrith	20.83E+3	0.15	20.83	5.22	0.78	0.78	0.02
M05	Winfrith	20.83E+3	0.15	20.83	5.22	0.78	0.78	0.05
M06	Winfrith	20.83E+3	0.15	20.83	5.22	0.78	0.78	0.10
M07(1)	Winfrith	5.22E+3	0.15	5.22	1.04	-	-	-
M08(1)	Winfrith	5.22E+3	0.15	5.22	1.04	-	-	-

E = Elastic Modulus; ν = Poisson's ratio; f_c = masonry compressive strength; f_t = masonry tensile strength; NFLS = contact normal failure stress; SFLS = contact frictional stress limit.
(1) Smeared-crack modelling: elastic modulus is that of the masonry.

Table 2: Masonry and contact mechanical properties.

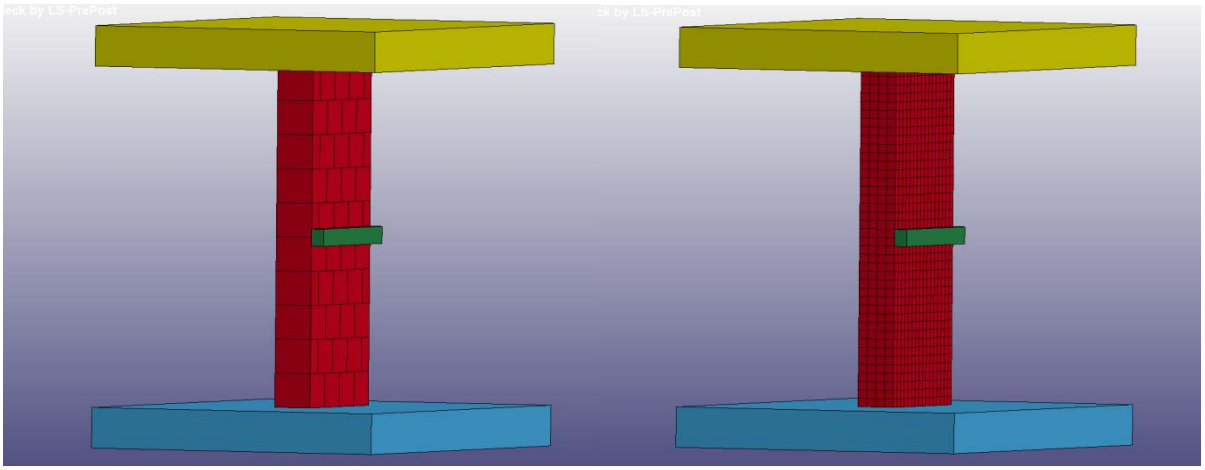

(a) (b)

Figure 3: Model: a) geometry; b) mesh.

3.1 Results

Horizontal force resultant versus prescribed displacements are reported in Figure 4 for the numerical models and for the specimen. The models with the Elastic material (M01, M02 and M03) are less stiff compared to the experimental results. A moderate stiffness increase can be obtained increasing the compressive stiffness of the contact interface, i.e. with an increase of the penalty factor (Figure 4a). However, an increase of the penalty factor leads to deformations that are inconsistent with the experimental ones. The deformed shape and the principal compression stress for models M02 and M03 are reported in Figure 5. The model M02 present an horizontal crack at mid-height, in agreement with experimental results, while, in the model M03, a sliding occurs at the second course. As shown in Figure 6, the sliding starts abruptly at about 52 s, when the displacement at mid-height of the wall is about 4.5 mm.

(a)

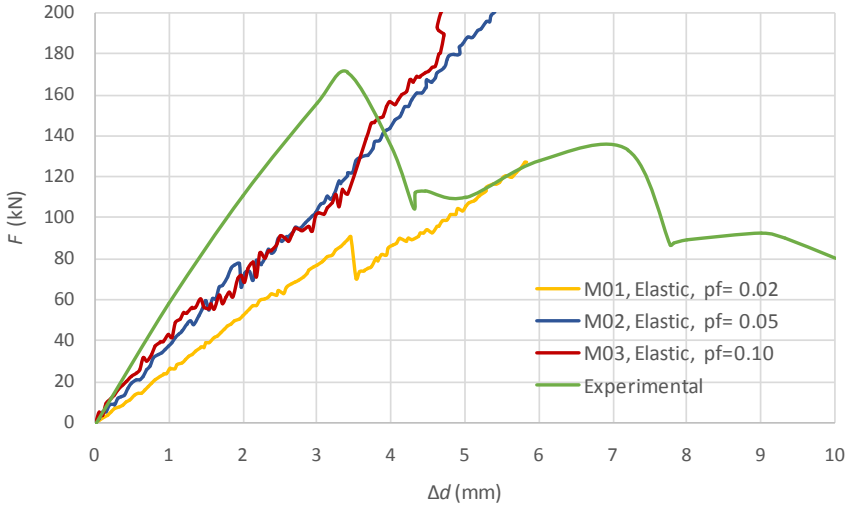

(b)

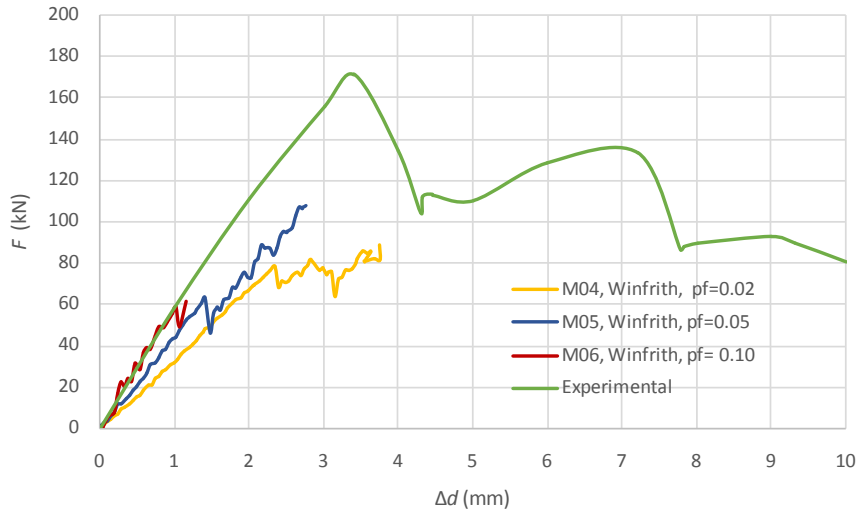

(c)

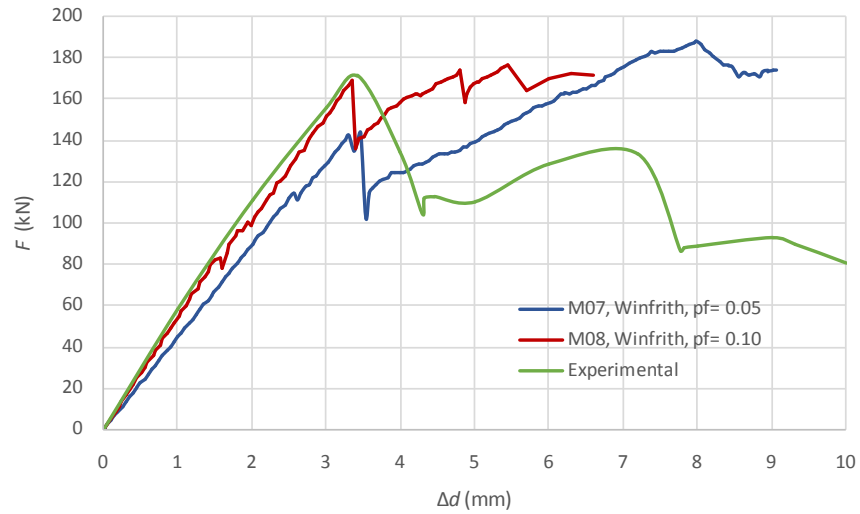

Figure 4: Horizontal force resultant versus prescribed mid-height displacements, experimental and numerical models: a) discrete-crack Elastic material; b) discrete-crack Winfrith material; c) smeared-crack Winfrith material.

In the case of the Winfrith material the increase of the penalty factor produces local stress increments and the earlier termination of the analysis. In fact, models M04, M05 and M06 do not terminate the analysis (Figure 4b) due to sudden increment of the principal compression stress, as shown in Figure 7. When the Winfrith material is used in a smeared-crack approach to model the blockwork, but interfaces are still present between masonry and RC frame, these local phenomena are avoided and the global response represents better the actual behaviour (Figure 4c). The stress distribution along the height of the walls is consistent with an arching behaviour (Figure 5c).

As observed, the finite-discrete models with higher penalty factors are not able to provide the maximum strength when the Winfrith material is adopted, whereas the smeared-crack models approximate better the experimental curve.

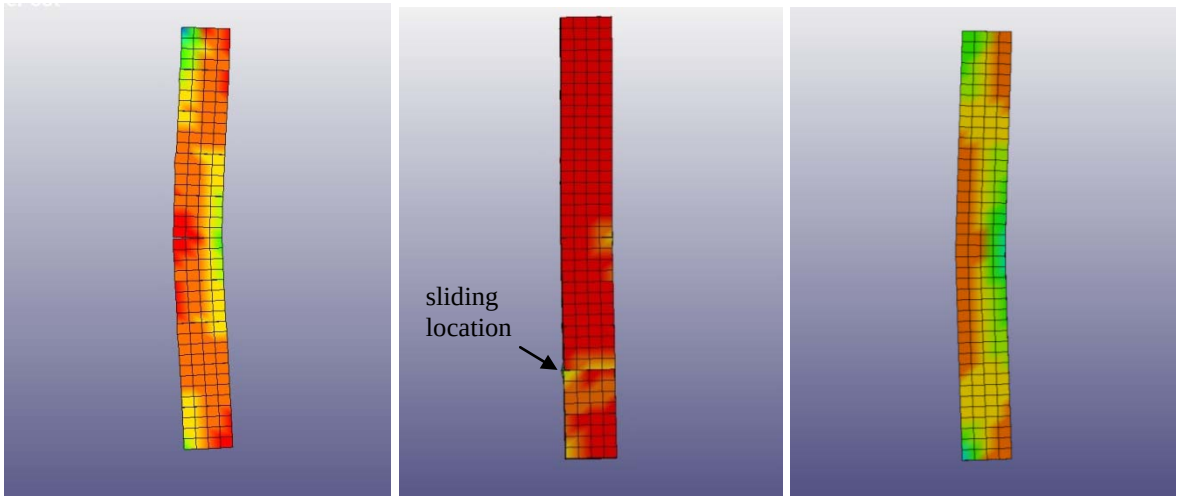

Figure 5: Deformed shape and principal compression stresses for models: a) M02; b) M03; c) M07. Displacement are not to scale.

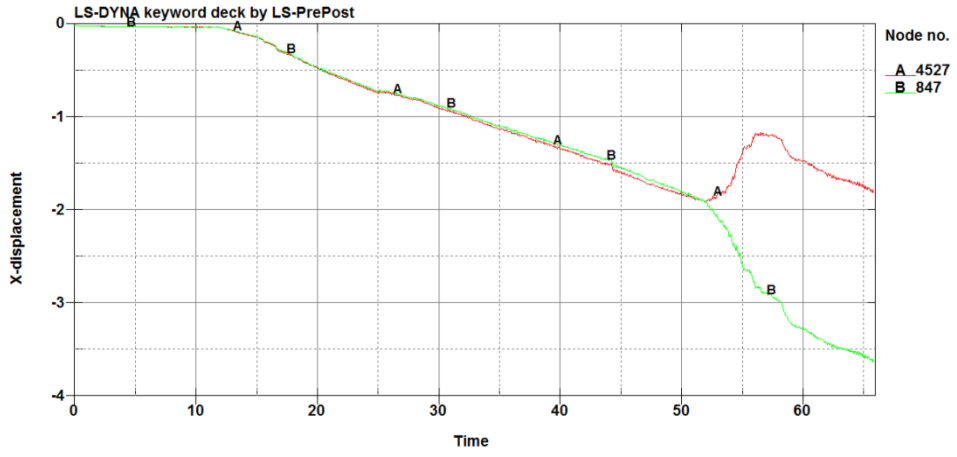

Figure 6: Model M03, horizontal displacement (mm) time history (s) at second course (see Figure 5b). Red line: displacement of the upper surface; green line: displacement of the bottom surface.

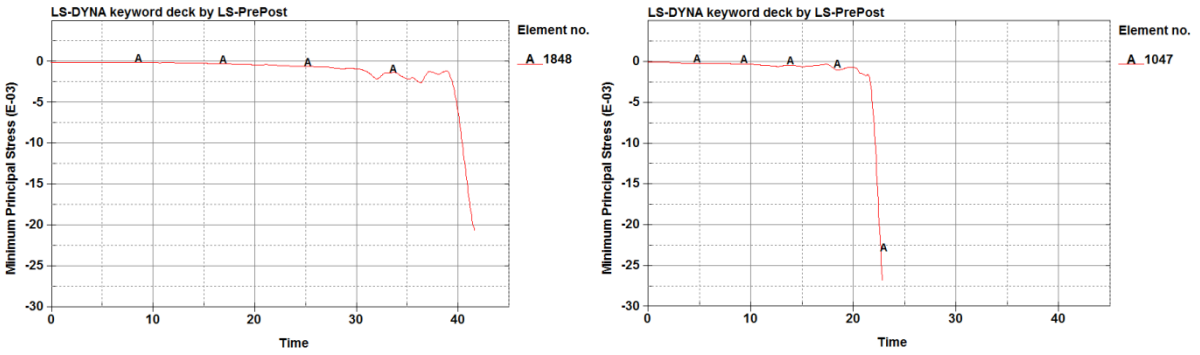

(a) (b)

Figure 7: Minimum principal stress (kN/mm^2) time history (s) in the most compressed elements for models: a) M04; b) M05.

4 CONCLUSIONS

In this paper the out-of-plane response of infill masonry panels is modelled through a discrete-finite element approach. Interfaces are present between masonry units, as well as between blockwork and reinforced-concrete frame. For the sake of comparison a smeared-crack approach has been also used to model masonry.

It is concluded that, when using a finite-discrete method, the stiffness of the contact interfaces is one of the most important parameters affecting the solution, because modifies the global stiffness of the model, if an elastic material is used for the blocks. When a non-linear material is used, in addition to the modification of the model stiffness, a local increment of stress occurs, leading to the earlier termination of the analysis. These shortcomings are avoided in a smeared-crack approach, reproducing better the experimental results, while still resorting to contact surfaces at the interface between masonry panel and surrounding structure.

ACKNOWLEDGEMENT

The financial support of the Ministry of the Instruction, University and Research of Italy (MIUR) is gratefully acknowledged. This work has been partially carried out under the programs “Dipartimento della Protezione Civile – Consorzio RELUIS”, signed on 2015-12-31, Masonry Constructions, General and Territorial Topics. The opinions expressed in this publication are those of the authors and are not necessarily endorsed by the Dipartimento della Protezione Civile.

REFERENCES

[1] L.D. Decanini, A. De Sortis, L. Liberatore, F. Mollaioli, Estimation of near-source ground motion and seismic behaviour of RC framed structures damaged by the 1999 Athens earthquake. *Journal of Earthquake Engineering*, **9(5)**, 609-635, 2005.

[2] L.D. Decanini, L. Liberatore, F. Mollaioli, Damage potential of the 2009 L’Aquila, Italy, earthquake. *Journal of Earthquake and Tsunami*, **6**(**3**), 1250032:1-32, 2012.

[3] L. Hermanns, A. Fraile, E. Alarcón, R. Álvarez, Performance of buildings with masonry infill walls during the 2011 Lorca earthquake. *Bulletin of Earthquake Engineering*, **12**, 1977-1997, 2014.

[4] L. Liberatore, M. Pasca, Out-of-plane response of infill masonry walls. *9th International Masonry Conference (IMC)*, Guimarães, Portugal, July 7-9, 2014.

[5] L. Liberatore, M. Pasca, Assessment of the Out-of-plane Resistance of Masonry Infill Walls. *15th International Conference on Civil, Structural and Environmental Engineering Computing (CIVIL-COMP)*, Prague, Czech Republic, September 1-4, 2015.

[6] L. Sorrentino, R. Masiani, M.C. Griffith, The vertical spanning strip wall as a coupled rocking rigid body assembly. *Structural Engineering and Mechanics*, **29(4)**, 433-453, 2008.

[7] S. Burnett, M. Gilbert, T. Molyneaux, G. Beattie, B. Hobbs, The performance of unreinforced masonry walls subjected to low-velocity impacts: Finite element analysis. *International Journal of Impact Engineering*, **34**, 1433-1450, 2007.

[8] X. Chen, Y. Liu, Numerical study of in-plane behaviour and strength of concrete masonry infills with openings. *Engineering Structures*, **82**, 226-235, 2015.

[9] V.G. Haach, G. Vasconcelos, P.B. Lourenço, Parametrical study of masonry walls subjected to in-plane loading through numerical modeling. *Engineering Structures*, **33**, 1377-1389, 2011.

[10] A.A. Tasnimi, E. Zomorodi, The Effect of Onplane Behavior on Inplane Interaction of URM Infilled RC Frame Under Lateral Loads. *14th European Conference on Earthquake Engineering*, Ohrid, Macedonia, August 30 – September 3, 2010.

[11] R Kanıt, M.S. Döndüren, Investigation of using ansys software in the determination of stress behaviours of masonry walls under out of plane cycling load. *International Journal of the Physical Sciences.* **5(2)**, 97-108, 2010.

[12] A. Mohyeddin, H.M. Goldsworthy, E.F. Gad, Sensitivity analysis of nonlinear behaviour of infill-frames under in-plane and out-of-plane loading. *Advances in Structural Engineering.* **16(10)**, 2013.

[13] A. Mohyeddin, H.M. Goldsworthy, E.F. Gad, FE modelling of RC frames with masonry infill panels under in-plane and out-of-plane loading. *Engineering Structures*. **51**, 73-87, 2013.

[14] J.R. Van Noort, Computational modelling of masonry structures, Master Thesis, *Delft University of Technology*, August 23, 2012.

[15] P. Agnihotri, V. Singhal, D.C. Rai, Effect of in-plane damage on out-of-plane strength of unreinforced masonry walls. *Engineering Structures*, **57**, 1-11, 2013.

[16] A.C. Shrestha, T. Nagae, Y. Araki, Finite element modeling of cyclic out-of-plane response of masonry walls retrofitted by inserting inclined stainless steel bars. *Journal of Disaster Research*. **6(1)**, 36-43, 2011.

[17] LSTC 2013. *LS-DYNA Keyword User's Manual*. Livermore: Livermore Software Technology Corporation.

[18] J.O. Hallquist, *LS-DYNA Theory Manual*. Livermore: Livermore Software Technology Corporation, 2006.

[19] B.J. Broadhouse, A.J. Neilson, *Modelling Reinforced Concrete Structures in DYNA3D*. Report: AEEW-M 2465, Safety and Engineering Science Division, United Kingdom Atomic Energy Authority. Winfrith Technology Center. Dorchester, UK October-1987.

[20] B.J. Broadhouse, *The Winfrith Concrete Model in LS-DYNA3D*. Report: SPDID(95)363, Structural Performance Department, Atomic Energy Authority Technology. Winfrith Technology Center. Dorchester, UK February-1995

[21] Y.D. Murray, A Abu-Odeh, R. Bligh, *Evaluation of LS-DYNA Concrete Material Model 159*. US Department of Transportation, Federal Highway Administration, Report FHWA-HRT-05-063, 2007.

[22] P. Grassl, M. Jirásek, Damage-plastic model for concrete failure. *International Journal of Solids and Structures*, **43**, 7166-7196, 2006.

[23] P. Grassl, U. Nyström, R. Rempling, K. Gylltoft, A damage-plasticity model for the dynamic failure of concrete. *Eurodyn 2011, 8th International Conference on Structural Dynamics*, Leuven, Belgium, 2011.

[24] C. Modena, F. da Porto, Experimental investigation on the out-of-plane seismic behaviour of masonry infills. Research Report, Draft 1, Department of Constructions and Transportations, University of Padua, Italy, 2005. (In Italian).

ECCOMAS Congress 2016
VII European Congress on Computational Methods in Applied Sciences and Engineering
M. Papadrakakis, V. Papadopoulos, G. Stefanou, V. Plevris (eds.)
Crete Island, Greece, 5–10 June 2016

PALAZZO LA SAPIENZA IN PISA: STRUCTURAL ASSESSMENT AND RETROFIT OF AN HISTORICAL MASONRY BUILDING IN ITALY

S. Caprili[1], F. Mangini[1], N. Mussini[1] and W. Salvatore[2]

[1] Department of Civil and Industrial Engineering, University of Pisa
Largo L. Lazzarino 1, 56122 Pisa
silvia.caprili@ing.unipi.it, f.mangini@ing.unipi.it, nicola.mussini@ing.unipi.it, walter@ing.unipi.it

Keywords: Instructions, ECCOMAS Congress, Computational Methods, Engineering Sciences, Proceedings.

Abstract. *Palazzo La Sapienza, historical seat of the University of Pisa since the XVI century, represents one of the most important examples of the Tuscany cultural heritage, nowadays not in use due to several problems related to maintenance and structural deficiencies. The building, in its current form, is the result of several modifications, enlargements, elevations, connection with adjacent parts, resulting finally more similar to a "structural aggregate" - made up of single units connected together without specific scheme and organization - than to a single unitary building. After the earthquake of May 2012, the Palace was temporarily closed in relation to the ordinance issued by the Major's Office and then subjected to wide in situ investigations aiming at analyzing in a very detailed manner all the criticisms related to structural, nonstructural, geotechnical and maintenance problems; the deep in situ survey campaigns allowed to reach a very deep knowledge of the building, of its progressive morphological evolution and of its actual condition, including problems not directly related to the structural condition but, as an example, to the instability and heterogeneity of the ground soil and of the foundation system. All the information so obtained allowed the execution of static and seismic vulnerability assessment – according to the actual prescriptions of Italian Standard for Constructions (D.M. 14/01/2008) – through the elaboration of complex global and local models and the final elaboration of an executive retrofit design comprehensive of local interventions on significant structural elements or sub-portions of the building. In the present paper, after a short description of the knowledge analysis of the building and of its safety verification, the retrofit executed to obtain a satisfying level of safety is presented.*

1 INTRODUCTION

Recent seismic events (i.e., Umbria - Marche 1997, Aquila 2009, Emilia-Romagna 2012) evidenced the high vulnerability of existing masonry cultural heritage and the need to define operational strategies for modifying, improving or locally retrofitting structures (or portions thereof) without altering their original characteristics and ensuring a sufficient margin of structural safety. Such buildings, during the centuries, underwent changes, expansions and reconstructions transforming them from 'single buildings' into 'structural aggregates', often in a significant state of decay caused by insufficient maintenance, earthquakes, collapses, cracking scenarios and so on, consequently evidencing the need to perform extensive static and seismic safety checks to plan suitable retrofit operations.

Several methodologies exist for the execution of seismic vulnerability analysis of monumental buildings. Some of such methods [1, 2] classify the buildings basing on a wide-scale damage analysis together with macroseismic intensity maps, defining vulnerability curves and identifying those structures for which retrofit shall be immediately organized.

Current standards for constructions [3, 4, 5] foresees the determination of the "*Knowledge Level*" (KL) – achieved through historical analysis, structural and geometrical surveys, geological and geotechnical investigations and mechanical characterization of materials – intended as the degree of uncertainty to be adopted when the safety checks and retrofit are performed.

Several applications aiming at evaluating the seismic behaviour of monumental buildings can be found in the current scientific literature, adopting detailed three-dimensional finite-element models elaborated basing on the results of laser-scanner surveys and in-situ deep investigations [6, 7] analyzing the local behaviour of significant portions of the buildings accounting for the damage scenario revealed [8] or proposing a displacement-based approach considering the ability of historical buildings to sustain earthquakes as long as they have sufficient capacity to move without collapse, so determining different limit states [9, 10, 11]. The problems regarding the numerically modelling of complex structures were widely discussed by [12], finally suggesting the execution of experimental dynamic analyses and investigations of both the whole aggregate and of portions thereof to characterize the structural behaviour of existing buildings.

D.M. 14.01.2008 [3] and the Guidelines of the Ministry for Cultural Heritage [13] prescribe global checks and evaluations of the local collapse mechanisms of significant structural units, identified through the mapping of the critical points from the surveys and the results of the global checks. The assessment of the structural safety of the building shall be executed with reference to different levels of analysis, ranging from large-scale evaluations to the local macro-element models representing independent portions of the whole building. The assessment of existing complex structural aggregates cannot then follow the usual approaches included in modern standards: complex models and cumbersome numerical analyses are not always able to represent masonry structural aggregates; many of the structural and maintenance diseases can be fully understood only through detailed surveys and the correlation between the morphological evolution of the building, its modifications throughout the centuries and its current condition.

A proper methodology, accounting for its intrinsic structural, architectural, geotechnical and functional complexities and their mutual interrelationships, shall be adopted for the safety assessment of a structural aggregate. A deep, extensive and multi-disciplinary approach, combining critical historical studies of the building's evolution, morphological/structural surveys, geotechnical investigations, mechanical characterization of materials and structural/geotechnical monitoring is necessary.

The present study deals with the assessment of structural safety and seismic vulnerability of the "Palazzo La Sapienza", in Pisa, Italy. The building, site of the University since the 14th century, is currently not in use due to the pending ordinance by the Mayor's Office of May 2012 because of ensuing surveys conducted by Pisa Fire Department. The Palace is a "structural aggregate" made up of interconnected units joined together during more than eight centuries [14, 15, 16]. The building's peculiarity and its importance to the urban setting was a unique occasion for the development and adoption of the multidisciplinary approach above mentioned. Accurate critical historical studies, including reconstruction of the building's evolution over time and detailed architectural surveys through both direct and indirect techniques, allowed identifying the structural units making up the aggregate. Each unit was subjected to accurate studies aiming at determining its structural system, the constituent materials and any critical detail revealed by geometrical and historical investigations, with the following organization of suitable monitoring systems able to identify causes of local (substructures, structural elements and units) and global (structural aggregate) problems. The proper combination of local and global numerical models, used and applied critically because of building complexity, allowed an accurate interpretation of the structural problems recognized by aforementioned multidisciplinary analysis, becoming the real "core" of the assessment procedure (rather than cumbersome, complex and often not representative global, linear and nonlinear, numerical analyses) and of the retrofit interventions, planned to preserve the original nature of the Palace giving a sufficient margin of safety.

2 STRUCTURAL ASSESSMENT

2.1 General presentation of the building

The building presents a trapezoidal plan (about 80.0 m x 53.7 m) with three floors above the ground and a gable roof accessible only for maintenance. The central courtyard, surrounded by a ground-level colonnade and a first-floor arcade running roughly parallel to the ground floor sides, has maximum dimensions of 35.5 m by 21.2 m. Due to the presence of different types vaulted surfaces and storey slabs, the height of the ground floor varies between 4.30 m and 5.50 m; similar situations can be found at the first and second floors, with maximum heights respectively equal to 5.60 m and 5.20 m.

The ground floor of the building houses staff rooms, university classrooms, university department offices and the historical Aula Magna. The 1st floor, besides department offices and the double volume of the Aula Magna Nuova, houses the University Library, covering about two sides of the building (along Piazza Dante square and Vicolo dell'Ulivo at 1st floor and Via della Sapienza and Vicolo dell'Ulivo at the 2nd floor), with mezzanines and loft structures to hold the books. Figure 1 shows the plan of all floors with indication of the use destinations foreseen just before the closure of the Palace.

2.2 Analysis of the state of art of the Palace

The analysis of the morphological evolution of the Palace [17] enabled to identify a series of critical structural issues, due to the modifications, heightening, enlargements and loading changes made over the centuries, currently evidenced by the widespread cracking scenario visible in various portions of the building, to be analyzed based on in-depth knowledge of the structure. The structural complexity of the building was confirmed through the extensive campaign of in situ studies, designed on the base of the results of the historical/evolutionary analysis and aiming to reconstruct the current structural condition of the building.

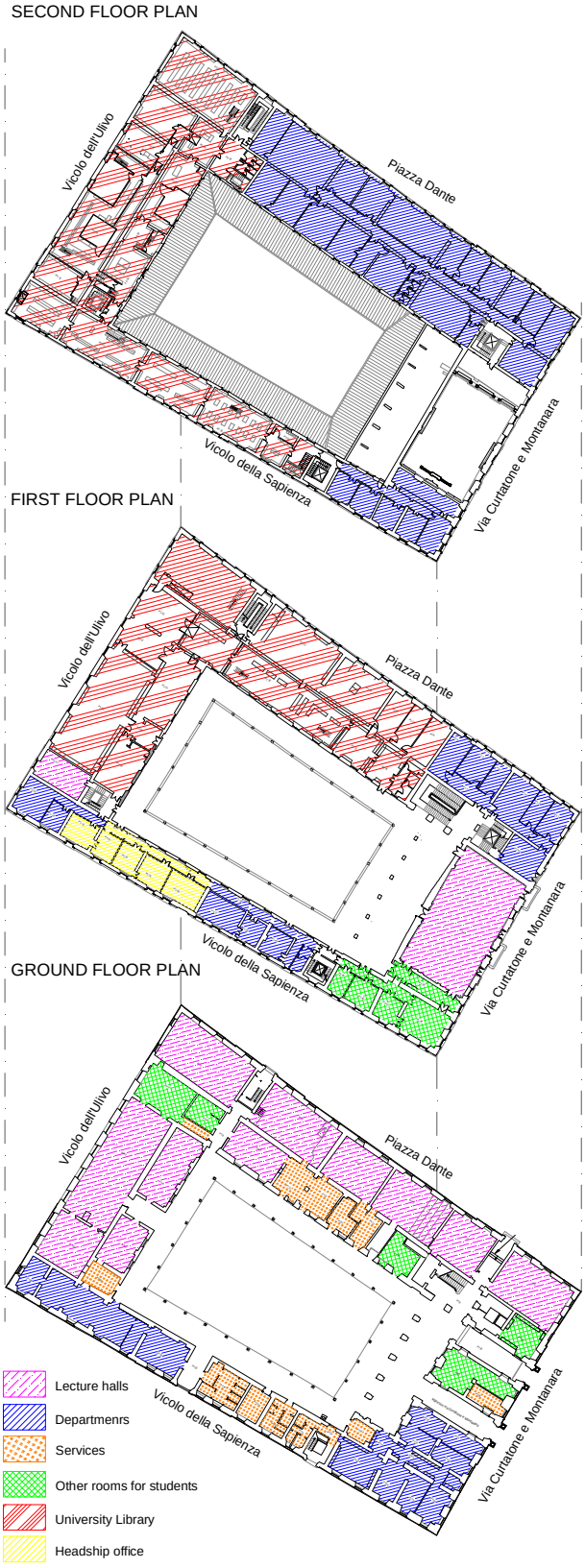

Figure 1: Plan overview of the different levels of the building and use destinations for the different rooms.

The masonry typologies of vertical walls were determined by removing the plaster on 50x50 cm portions with following endoscopic examination to check the presence of cavities or adjacent facings of different thickness and type. Figure 2 shows the periods of realization of vertical walls of the ground floor and the corresponding variability of revealed masonry typologies: six different patterns and the absence of suitable connections between perpendicular walls were determined.

Different types of horizontal structures are present in the building: the ground floor (Figure 3) shows cross or cloister vaults with solid-brick masonry, mainly located in correspondence of the ancient and not modified areas of the Palace – such as in the rooms around the internal courtyard parallel to Piazza Dante and Via dell'Ulivo. The double-height Aula Magna is topped by a masonry/r.c. vault. Floor slabs made of steel and brick blocks in single or double bonds - mainly located in correspondence of Piazza Dante at the ground floor and, in general, at 1st and 2nd floor, portions of the building that suffered for progressive modifications, enlargements and transformation due to use requirements – were also deeply surveyed to obtain information regarding structural profiles and weight of the upper filling layers.

The roofing structure, consisting of trusses of different types and materials is the result of the modifications undergone by the building over the years. On the Piazza Dante side, steel Polonceau trusses (similar to those over the double-height of the new Aula Magna, dated back to the early 20th century) are located; the other sides of the building present wooden trusses of different sizes and shapes, with various degrees of deterioration due to the poor maintenance, bad connections among elements, presence of small solid-brick walls to support the bearing elements, accumulations of debris etc., resulting from operations aiming at compensating for local deficiencies but losing sight of the building and its overall structure.

The cracking scenario present in several portions of the building (with different concentration and entity) is the result of the modifications undergone by the Palace during the centuries, with increasing acting load due to the library, to the activities developed inside the building and to the differential subsidence related to the heterogeneity of soil and foundation structure (Figure 3). The progressive growth of the cracks, especially in proximity of the separations of the structural units, is still quite evident in the building's vertical and horizontal surfaces: as an example, a wide cracking scenario was revealed in the corner between Via Curtatone e Montanara and Via della Sapienza, born by the incorporation of ancient tower houses into the current structure, and in correspondence of the vaulted surfaces of colonnade and internal arcade, characterized by the presence of different foundation settlements and by structural problems yet identified during the 18th and 19th centuries (Figure 3). Two monitoring systems (one periodic with fixed steel reference gauges and one continuous with electronic transducers) were set up in order to determine the possible evolution of the ongoing subsidence and damages (Figure 3). Analysis of the monitoring results enabled the identification of differential displacements, highlighting problems and evolution of structural cracking mainly in correspondence of the vaults of the ground floor colonnade and 1st floor arcade.

The inhomogeneous and inadequacy of the foundation structure to sustain the increasing loads due to the enlargements of the building in relation to the hosted activities was evident by the early 1900s. A deep in situ investigation of foundations was executed through micro-core samplings at different angles in the proximity of the masonry walls, at locations planned according to the evolutionary reconstruction of the building: different types of foundations (for both size and depth) were determined (Figure 3). The investigations performed in correspondence to the interior colonnade revealed the absence of connections between single columns, with an isolated square footing placed at -1.90 m from ground level, below the foundation of the portico pillars, laid at -1.75 m.

Figure 2: Hypothesis of the evolutive development of the building and plan of ground floor with indications of the various types of masonry.

Figure 3: Distribution of the floor slabs and types on the building's ground floor, Foundation plan, different typologies evidenced and ground floor plan with indication of monitoring points.

The foundation of the portico interior walls reaches different depths (between -1.0 m and -1.5 m), with width varying between 1.50 and 2.40 m. The two investigations performed along Vicolo dell'Ulivo provided similar results, with foundation depths of 2.75 and 2.10 m, and

widths of 1.75 and 1.60 m, respectively. The Piazza Dante side foundation reaches a depth of about -1.50 m below with a width of 0.90 m.

Deep investigations were executed to determine the geotechnical parameters and properties characterizing the foundation soil. Several experimental tests, including continuous core drillings, static penetration tests, tests with seismic dilatometer and dynamic penetration tests were executed. The obtained information allowed determining the local seismic response spectrum: a preliminary one-dimensional analysis under free-field conditions was performed. The procedure used for the local response seismic analysis is deeply presented in [15].

3 DISAGGREGATION AND ANALYSIS OF STRUCTURAL UNITS

3.1 Recognition of structural units

Critical issues of the structural aggregate were identified with reference to the single structural units recognized as constitutive parts of the building. The Palace was considered as composed by a suitable number of units connected by horizontal structures (foundations, floors and vaults, roof) influencing the mutual interactions among portions, preventing or activating local mechanisms. Structural units were identified in relation to the morphological/structural evolution of the Palace [17], to the modifications undergone during the centuries, to the presence/absence of connections among vertical and horizontal elements and to the interpretation of the cracking scenario. The behaviour of such units was investigated firstly separately and then the framework of the aggregate itself.

A diffused lack of connection between masonry walls was evidenced (Figure 4a) and different masonry typologies were revealed even in the same element: Figure 4b and Figure 4c, for example, show the presence of masonry arches of ancient openings nowadays closed due to the modified functional needs. The heterogeneity of masonry walls is higher at the ground and first floors (i.e. corner Via Curtatone e Montanara / Via della Sapienza, Figure 2) respect to the second level, realized at the beginning of the 19th century.

Horizontal floors and roofing systems can allow the connection among masonry walls, preventing the activation of local mechanisms; the horizontal systems of Palazzo La Sapienza are characterized by the presence of vaulted surfaces (mainly at the ground floor where no significant changes took place) and more recent floors with steel profiles (Figure 3). If vaulted structures can constitute a rather significant restraint for vertical structural elements, horizontal steel slabs cannot be considered a “rigid” diaphragm. A considerable geometric heterogeneity of foundations, influencing the mechanical response of the building and its bearing capacity in relation to the variable stiffness of the soil, was also evidenced.

Such more or less rigid systems connect several different structural units resulting from modifications executed during the centuries; according to the results of structural/architectural/geotechnical surveys, the following systems can be identified as “independent structural units inside the aggregate”, as simply summarized in Figure 5:

1. Corner between Via Curtatone e Montanara and Via della Sapienza.
2. Open gallery and arcade at the ground floor and colonnade at the first floor.
3. Aula Magna and adjacent rooms at ground floor.
4. Double volume of the Aula Magna Nuova at the first/second floor.
5. Portion of the building facing Piazza Dante.
6. Portion parallel to Piazza Dante facing the internal courtyard (ground and first floors).
7. Second floor of the Palace.

1. *Corner between Via Curtatone e Montanara and Via della Sapienza*. As visible from Figure 2, pillars characterized by the presence of full bricks and squared stones demonstrate the pre-existence of ancient tower houses incorporated and connected to adjacent masonry structures during the centuries. The discontinuity and heterogeneity of masonry belonging to different constructive typologies, realized in different periods and not connected to one another yielded, during the years, to the development and to the progressive spreading of a diffused cracking scenario visible both in vertical elements and in horizontal structures, allowing the clear identification of this structural unit.

2. *Open gallery and arcade at the ground floor and colonnade at the first floor*. The internal arcade and the open gallery facing the entrance along Via Curtatone e Montanara at ground floor are characterized by the presence of vaulted cross surfaces with different geometries and heights. The damages present in correspondence of the extrados of the vaults are the result of relative differential subsidence of foundations characterized by different width and depth (Figure 3), already demonstrated by past damages [17]. The absence of horizontal connection between the pillars of the internal arcade make the columns behave "separately" from one another, with relative displacements and rotations. Relative displacements between the wooden roof of the colonnade and the masonry walls are also clearly visible.

3. *Aula Magna and adjacent rooms at ground floor*. The portion of the building at the ground floor facing Via dell'Ulivo houses the historical Aula Magna and additional rooms once used for teaching activities. The Aula Magna and the adjacent room, actually characterized by the presence of a partition wall, present the same vaulted surface on which the masonry wall at the first floor directly loads [17]. The two teaching rooms facing the courtyard are the result of the closure of the original lodge that, on the western part of the Palace, exactly reproduced the opposite situation of the arcade, as justified by ancient plans and through the analysis of the cracking scenario and from the observation of the masonry pillars of the original colonnade (Figure 2).

4. *Double volume of the Aula Magna Nuova at the first/second floor*. The double volume of the Aula Magna Nuova, generated at the end of the 19th century in relation to the modifications of the building necessary to overcome the new use requirements, has an internal open space not provided by transversal retaining walls (demolished in 1905) and characterized by the lack of horizontal restraints between the two opposite facades. The roofing system presents brick truss with r.c. elements and masonry lightening blocks (thickness 3.0 cm) not able to constitute a rigid diaphragm.

5. Portion of the building facing Piazza Dante. The block constituted by the rooms facing Piazza Dante can be considered a separate structural unit, generated in a more recent period [17], modified at the beginning of the 20th century and clearly distinguishable from the rest of the building due to the presence of horizontal steel storey slabs and of masonry walls not connected to the pre-existences. This situation is clearly visible both at the ground and the first floor.

6. Portion parallel to Piazza Dante facing the internal courtyard. The architectural and structural surveys of the building evidenced the absence of perpendicular walls in correspondence of the first floor of the building in the portion facing the internal courtyard and parallel to Piazza Dante: the increasing need of place for the library and the new activities developed in the building leaded to the demolition of the walls perpendicular to the internal main façade, generating the activation of overturning mechanisms due to the absence of transversal restraints.

7. *Second floor of the Palace*. The 2nd floor of the building, according to the morphological and structural analyses of the Palace, can be considered a "separate" structural unit [17], characterized by a more recent edification and a more homogeneity for what concerns materials, masonry organization and floor typologies.

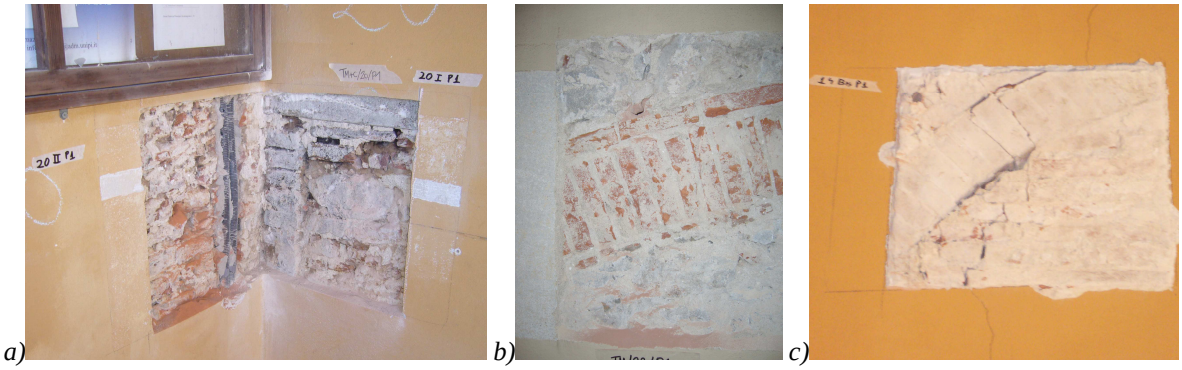

Figure 4: Discontinuities of vertical masonry walls: a) absence of connection between perpendicular walls, b-c) arches identified in correspondence of the first floor level, probably old windows currently closed.

3.2 Analysis of structural units of the building

The structural behaviour of the significant portions of the building (Figure 5) was analyzed through the adoption of local models able to reproduce their main features on the base of the knowledge obtained from in situ and experimental investigations. With reference to the list already elaborated for structural units, the following Limit States (LS) and vulnerabilities (V) can be determined.

1. *Corner between Via Curtatone e Montanara and Via della Sapienza*

A diffused cracking scenario is visible in correspondence of this area, directly related to the differential subsidence of foundations, with relative displacements that strongly affects the overall structural aggregate, and to the intrinsic nature of the masonry of vertical walls. The widespread discontinuities in the structure's geometry, materials and constraints, the presence of voids, air spaces and facings, together with the dubious degree of collaboration, lead to local stress concentrations confirmed by the results of the experimental flat jack tests and by the extensive cracking phenomena.

2. *Open gallery and internal arcade at the ground floor and colonnade at the 1st floor*

The relative displacements evidenced in correspondence of the wooden elements of the colonnade at the 1st floor and the masonry walls, as well as the diffused cracking scenario revealed in the crossed vaulted surfaces of the ground floor are the direct consequence of the differential subsidence due to the different typologies of foundations (Figure 3). The foundations of columns of the internal arcade are not connected to one another and lay at different levels respect to the masonry walls facing the courtyard: these differences result in relative subsidence evidencing the non uniformity of the overall mechanical response of the foundation system, the variability of soil stiffness and of ultimate loads. The structural analysis of foundations considering actual loads (permanent, live and seismic action) allowed the determination of the unit load-subsidence diagrams of the foundation-ground assemblage of the various analyzed sections (Figure 6a): the difference between the building's perimeter and its interior (i.e. colonnade and pillars of the interior courtyard) can expose the whole structure to considerable damages in those areas where significant differences in stiffness and loads were measured (Figure 6b).

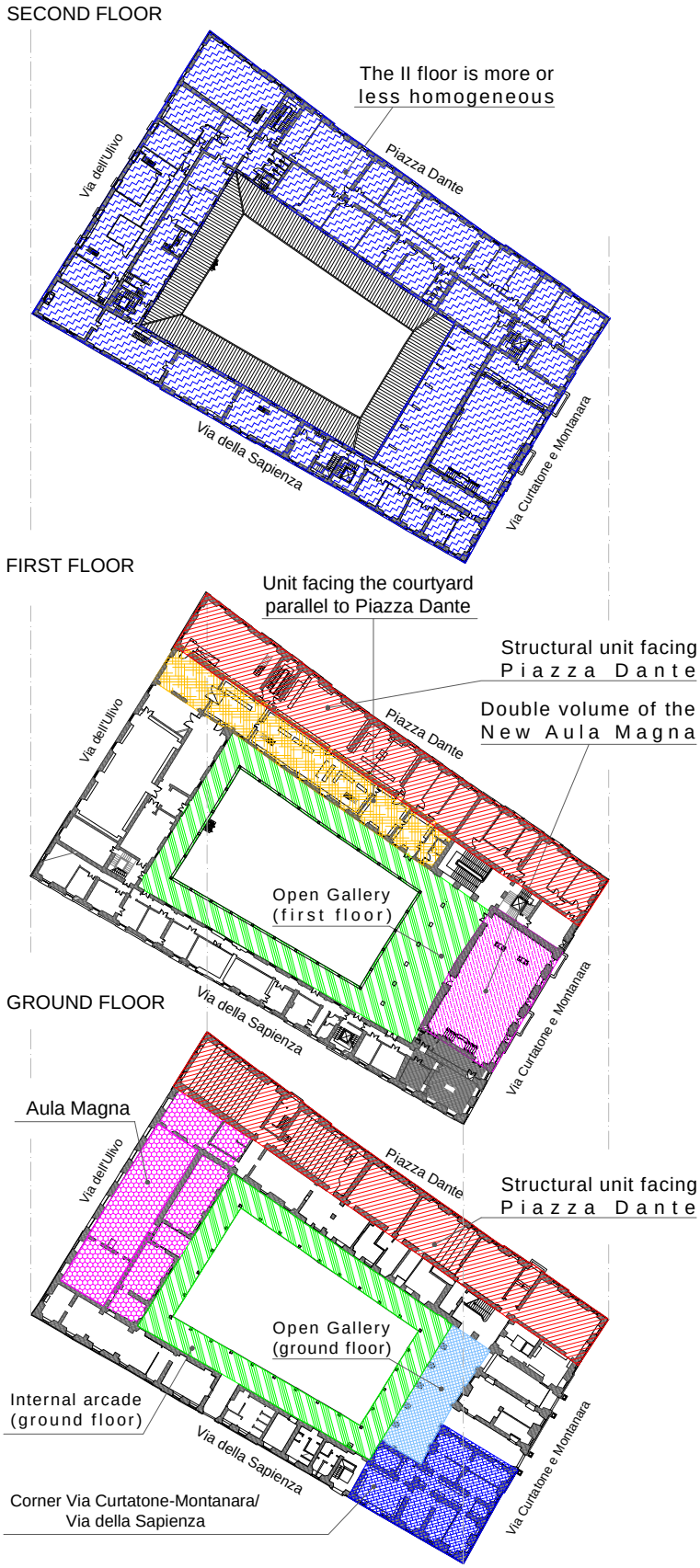

Figure 5: Structural units that can be determined as independent parts of the aggregate.

3. Aula Magna and adjacent rooms

The progressive enlargement of the building at the 1st floor necessary to house the library lead to the introduction of a solid brick curtain wall in order to separate the library rooms and those used for teaching activities. The masonry wall – with thickness equal to 17 cm, height equal to two floors – according to Figure 4 was already present at the end of the 16th century and nowadays represents the effective separation between the portion of the building belonging to the University of Pisa and the University Library. The wall directly rests upon the vaulted surface of the room adjacent to the Aula Magna, generating a critical situation especially in presence of seismic action. Moreover, the analysis of the cracking scenario affecting the Aula Magna at the ground floor, the adjacent rooms and the other areas facing the internal courtyard (Figure 5) is strictly related to the progressive modifications executed during the centuries. Severe damages can be observed in correspondence of the vertical masonry walls and in the vaulted surfaces of the two rooms facing the internal court: at the origin of the Palace, this portion was directly part of the colonnade (Figure 2) and the closure of the area was dated around the end of the XVI century; the relative displacements between the colonnade and the vertical masonry walls of the building – as well as proved by the analysis of the monitoring data – are directly connected to the evidenced cracking scenario.

4. Aula Magna Nuova: double volume at first and second floor

The analysis of the double volume (1st and 2nd floor) of the New Aula Magna evidenced cracks in the vertical masonry walls (not perfectly visible due to presence of ancient paintings) and on the vaulted surface. A deep in situ investigation allowed the determination of the effective structure of the roofing system: steel Polonceau trusses – dating back to the early 20th century – are present sustaining the roof, while the vaulted surface is made up of thin brick elements (3.0 cm) positioned between main r.c./masonry truss with a typical shape used not to transfer horizontal thrusts to the masonry walls. Cracks visible in correspondence of the vaulted surface are, mostly, due to the "geometrical" distance of light brick elements; the support of those elements in correspondence of the main bearing truss is equal, at maximum, to 3.0 cm, generating the possible detachment with the following risk to people and to the structure itself. The overturning phenomena of external and internal walls was analyzed following the linear kinematic approach: the PGA activating the mechanism was equal to 0.112g respect the design value of 0.118g.

5. Portion parallel to Piazza Dante facing the internal courtyard

The progressive increase of space due to the need to house the libraries during the last centuries – executed through the demolishing of internal walls and the introduction of mezzanines at the 1st and 2nd floors – leaded to overload the bearing structures, significantly altering their original local response towards dynamic loads and exposing the building to out-of-plane instability in correspondence of the walls to which the mezzanines' cantilever beams are anchored, characterized by the lack of adequate restraints between perpendicular walls. The out-of-plane problems were evident in correspondence of the sub-unit facing the internal courtyard and parallel to Piazza Dante (1st and 2nd floors), resulting from progressive modifications and demolitions of masonry walls as widely evidenced by the historical analysis). Since typical mechanisms were recognized (i.e., the overturning of masonry vertical walls), linear kinematic analysis was adopted for the determination of the value of horizontal peak ground acceleration (PGA) activating the mechanism. The internal masonry wall is not provided by perpendicular retains, resulting in the possibility to activate the global overturning of the wall both at first and second level: the PGA leading to the activation of the

collapse overturning mechanism were respectively equal to 0.060g and 0.079 g for the 1st and the 2nd floor, towards a foreseen design PGA equal, for the considered site, to 0.118g.

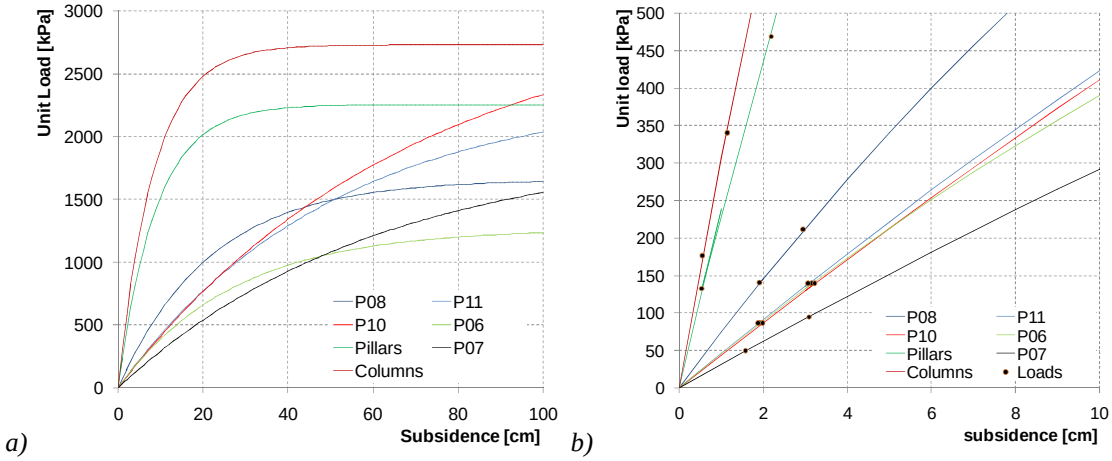

Figure 6: a) Unit load-subsidence curves for the different sections investigated, b) estimates of the subsidence of different building zones as a function of the applied loads.

3.3 Structural behaviour of the aggregate

Even if not strictly necessary for the understanding of the behaviour of a structural aggregate, in Italy the elaboration of a global three-dimensional model is nowadays required [3]) for the execution of safety checks on masonry vertical walls (i.e. shear, flexure in and out of the plane); the global model represents an improved condition respect to the effective situation of the Palace.

A simplified FEM model of the building was realized using SAP 2000, with two-dimensional elements for masonry walls and vaulted surfaces modelled as equivalent plane elements and one-dimensional elements for the steel profiles of the floor slabs, the roofing and the university library mezzanines. The soil-structure interaction was represented through the Winkler model, with elastic three-directional springs calibrated according to the results of the geotechnical investigations and in relation of foundations' shape and size. Cracking phenomena of masonry were considered by reducing the stiffness to values equal to 80% and 60% of the undamaged conditions respectively on the ground and the first and second floors [18]. Linear dynamic analysis with response spectrum was performed; a behaviour factor equal to 2.25 was adopted, conservative in comparison to the values contained in the 2010 Guidelines [13]. Global vibration modes were determined for both flexural behaviour in x and y directions; the significant periods ranged between 0.89 s (global flexural mode in y direction) and 0.59 s.

The described model it is not clearly able to include the extreme variability and strong nonlinear behaviour of constituent materials as well as complex behaviour of internal and external restraints among single structural elements and structural units, anyway can provide useful information when a critical analysis of results is executed basing on the multidisciplinary studies conducted on the building and on the results obtained on single structural units.

The safety checks were performed in agreement with D.M.14/01/2008 [3]. The most evident criticisms were revealed in correspondence of the portions of the building characterized by high heterogeneity of materials and structural typologies and in those areas that underwent the most significant changes and modifications during the centuries, confirming the considerations coming from the analysis of the structural behaviour of single

portions or units determined inside the aggregate (Figure 5), such as in correspondence of the corner Via Curtatone e Montanara/Via della Sapienza (i.e. heterogeneity of materials), of the historical Aula Magna (i.e. closure of the colonnade), of the New Aula Magna (i.e. modifications and enlargements up to the double volume).

4 RETROFIT OF THE STRUCTURAL AGGREGATE

The traditional global approach proposed by current standards for retrofit, foreseeing the possibilities of global/partial and local strengthening of the whole building or of several structural elements cannot be easily applied to historical buildings. The retrofit of cultural heritage shall pursue the preservation of the original nature of the building, maintaining its historical aspects and providing a considerable increase of the margin of structural safety. The retrofit can be considered, then, the final amount of many local interventions: local retrofit operations regarding single structural units globally cooperate to provide the aggregate with a higher level of structural safety. Many structural interventions were then planned for Palazzo La Sapienza to solve the problems evidenced through the structural analysis, related to the different structural units constituting the Palace. Some of them are briefly summarized in the following pages.

Open gallery at ground floor and colonnade at the first floor

The retrofit of the vaulted surfaces consisted in the removal of the filling material on the extrados of the vaulted surfaces – with the following decrease of the dead load – and in the restoration of cracks using specific materials for historical masonry buildings (Figure 7a); a similar retrofit procedure was also adopted for cracks present at the intrados of the vaults. A thin shaving layer of 2-3 cm of thickness with welded steel mesh (ϕ 3 mm and spacing 50x50 mm) was also foreseen provide a global behaviour without altering the structural feature of the aggregate. Some problems were revealed also in correspondence of the 1st floor colonnade, with relative displacement between the wooden secondary elements of the roof and the masonry wall, with support length equal, in some cases, only to few centimeters; in order to prevent the pull out of such elements, an additional steel profile was positioned in correspondence of the whole perimeter of the colonnade (Figure 7b), providing a final support length of about 10 cm. Several additional retrofit interventions were designed for damaged elements of the roofing system.

Aula Magna and adjacent rooms

To solve the problem of the masonry infill wall directly bearing on the vaulted surface close to the Aula Magna at the ground floor, the introduction of a steel HEA profile able to directly sustain the masonry wall and the rest of the superstructure - including the vault at 1st floor and the corresponding masonry wall at the 2nd floor - was accurately designed. The design of the bearing profile took into account both strength and stiffness aspects – this last to avoid the vertical deflection of the masonry wall – and, moreover, the analysis of the assembly procedure (Figure 8). A temporary bearing structure made up of two twin truss beams with transversal support steel beams with spacing equal to 50-70 cm was adopted, allowing safety conditions during the phases of cutting of the masonry wall and introduction of the HEA bearing beam.

Vertical masonry walls

Diffused interventions were executed on vertical masonry walls in order to solve the problems related to the diffused cracking scenario revealed and, in some cases, monitored at the different floors of the Palace, such as for example in correspondence of the corner

between Via Curtatone e Montanara, in which cracks appear mostly in relation to the progressive modifications and changes executed during the centuries as a consequence of functional requirements. Different typologies of interventions were foreseen in relation to the entity of revealed cracks.

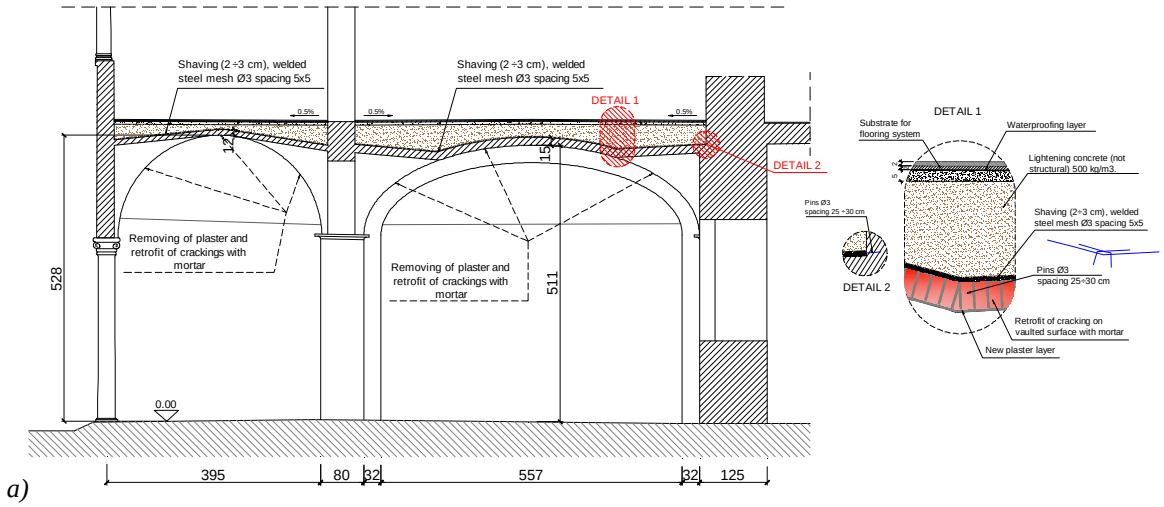

a)

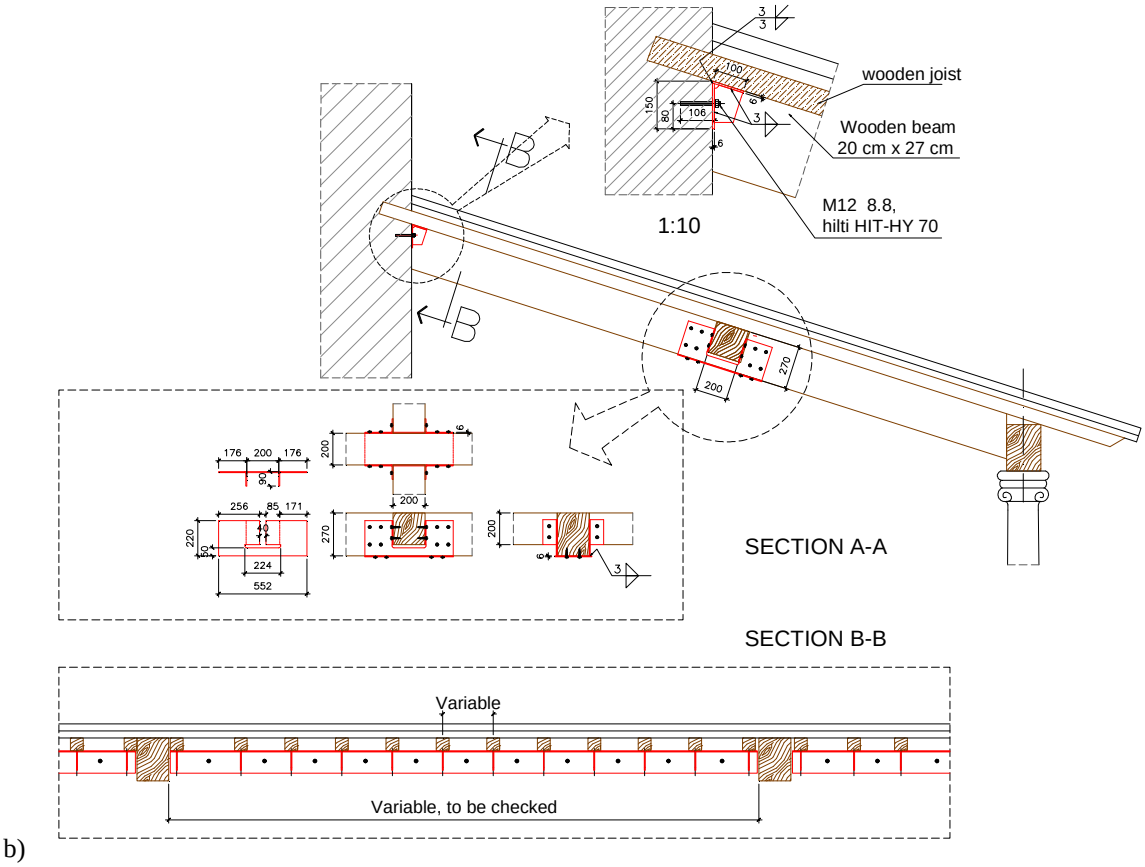

b)

Figure 7: a) Example of the intervention foreseen for the retrofit of the vaulted surfaces of the ground floor arcade; b) retrofit intervention foreseen to provide adequate support to the wooden elements of the first floor colonnade.

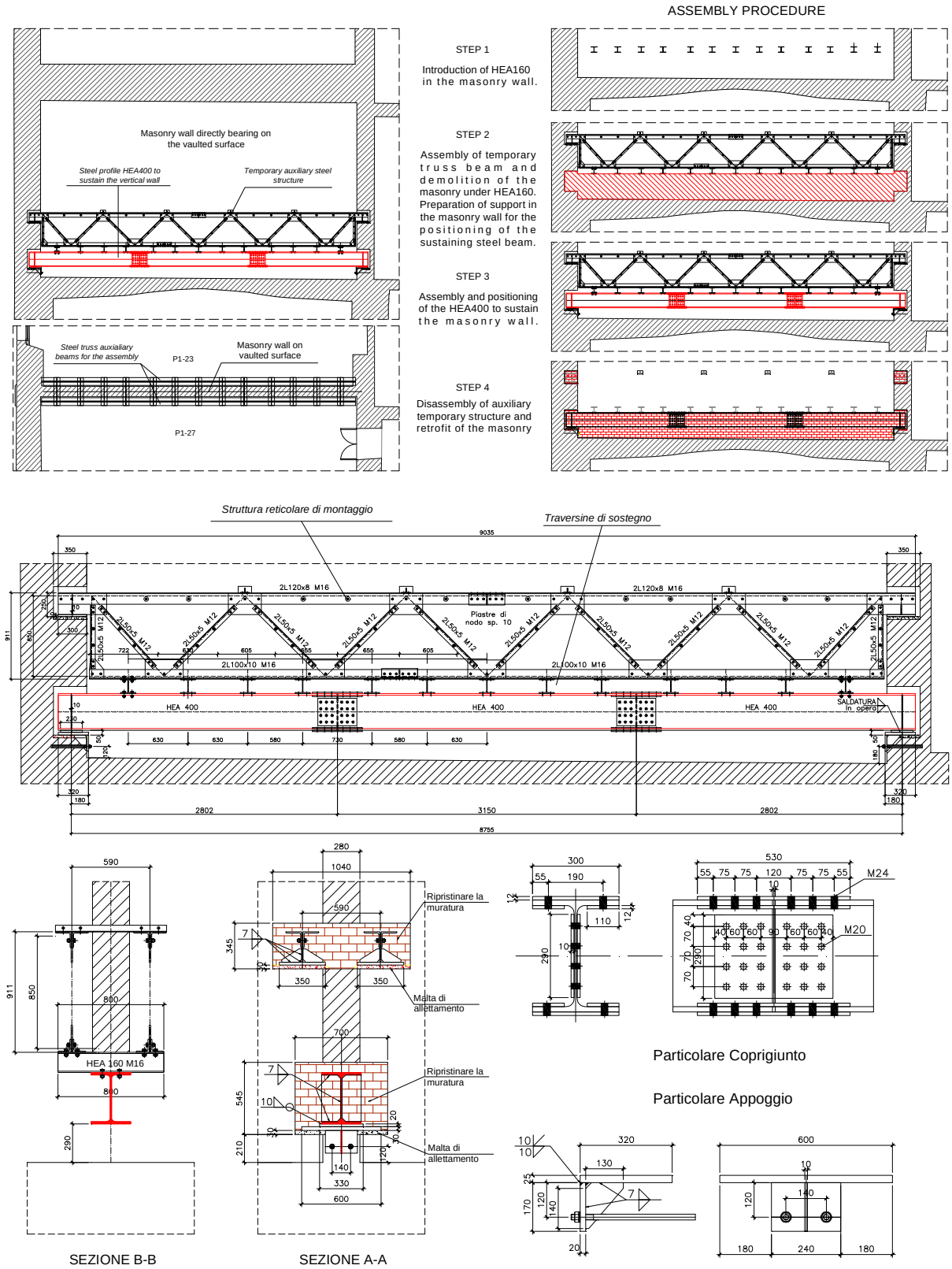

Figure 8: Introduction of stele profile and assembly procedure to avoid the load directly upon the vaulted surface near the Aula Magna.

5 CONCLUSIONS

The deep analysis of the current condition of such complex building as Palazzo La Sapienza in Pisa, including the historical and morphological investigation of its modifications and extensions during the centuries, the in situ survey of materials, walls, horizontal storeys and vaulted surfaces, the analysis cracking scenario, of foundations and roofing system, the geological and geotechnical characterization of the soil highlighted the need to consider the building not as a single structural unit, but rather as an aggregate made up of several units connected to each other and built using different techniques.

The combined analysis of the historical evolution of the Palace and of the structural survey of its current condition – especially for what concerns the cracking scenario and its main causes - allowed the determination of structural units, whose behaviour shall be deeply analyzed on the base of the progressive modifications of bearing elements, acting loads, connections and mutual influence. If, according to current standards for existing constructions a global analysis of the building is necessary for the execution of safety checks, in the present work the need of a "double" analysis including the interpretation of the structural behaviour of sub-units, their mutual interrelationships and the possible activation of significant partial/local mechanisms, and a simplified global analysis providing indications regarding static condition and relative information about the most critical and stressed portion of the building itself, is highlighted.

A critical evaluation of the building's safety, together with a clear, deep understanding and knowledge of the structure itself, constitute the basis to define the objective of any structural interventions, carefully designed to achieve appropriate safety levels, durability of relevant portions of the building and, at the same time, produce the least impact possible on this important living example of Italy's historical heritage.

REFERENCES

[1] S. Lagomarsino. On the vulnerability assessment of monumental buildings. *Bulletin of Earthquake Engineering*, **4**, 445-463, 2006.

[2] A. Bernardini, S. Lagomarsino. The seismic vulnerability of architectural heritage. In *Proceedings of the Institution of Civil Engineers – Structures & Buildings*, 161 (SB4): 171–181, 2008.

[3] D. M. Infrastrutture Trasporti 14 gennaio 2008, Norme Tecniche per le Costruzioni.

[4] CEN (2005). European standard EN1998-3. Eurocode 8: design provisions for earthquake resistance of structures - Part 3: assessment and retrofitting of buildings. European Committee for Standardisation, Brussels.

[5] FEMA 547. Techniques for the Seismic Rehabilitation of Existing Buildings. Federal Emergency Management Agency, Washington DC, 2006.

[6] G. Barbieri, L. Biolzi, M. Bocciarelli, L. Fregonese, A. Frigeri, Assessing the seismic vulnerability of a historical building. *Engineering Structures*, **57**, 523–535, 2013.

[7] G. Chellini, L. Nardini, B. Pucci, W. Salvatore, R. Tognaccini, Evaluation of seismic vulnerability of Santa Maria del Mar in Barcelona by an integrated approach based on terrestrial laser scanner and finite element modelling. *International Journal of Architectural Heritage*, **8**(6), 795-819, 2014.

[8] V. Mallardo, R. Malvezzi, E. Milani, G. Milani, Seismic vulnerability of historical masonry buildings: a case study in Ferrara. *Engineering Structures*, **30**, 2223–2241, 2008.

[9] S. Lagomarsino, S. Cattari, PERPETUATE guidelines for seismic performance-based assessment of cultural heritage masonry structures. *Bulletin of Earthquake Engineering*, **13**, 13-47, 2015.

[10] D. D'Ayala, S. Lagomarsino, Performance-based assessment of cultural heritage assets: outcomes of the European FP7 PERPETUATE project. *Bulletin of Earthquake Engineering*, **13**, 5-12, 2015.

[11] M. Kržan, S. Gostîc, S. Cattari, V. Bosiljkov, Acquiring reference parameters of masonry for the structural performance analysis of historical buildings. *Bulletin of Earthquake Engineering*, **13**, 206-236, 2015.

[12] C.S. Oliveira, Seismic Vulnerability of Historical Constructions: A Contribution. *Bulletin of Earthquake Engineering*, **1**: 37-82, 2003.

[13] Linee Guida per la valutazione e riduzione del rischio sismico del patrimonio culturale allineate alle nuove Norme Tecniche per le Costruzioni (D.M. 14/01/2008), 2010.

[14] S. Capril**i,** F. Mangini, W. Salvatore. Numerical modelling, analysis and retrofit of the historical masonry building La Sapienza. *COMPDYN 2015, 5th ECCOMAS Thematic Conference on Computational Methods in Structural Dynamics and Earthquake Engineering*, Crete Island, Greece, 25–27 May, 2015.

[15] S. Caprili, F. Mangini, W. Salvatore, G. Scarpelli, N. Squeglia. Influence of soil-foundation-structure interaction on overall behaviour and diseases of a medieval building in Pisa. *STREMAH 2015, 14th International Conference on Studies, Repairs and Maintenance of Heritage Architecture*, La Coruna, Spain, July 13-15, 2015.

[16] S. Caprili**,** F. Mangini, W. Salvatore, Evaluation of structural safety and seismic vulnerability of historical masonry buildings: studies and applications in Tuscany Region. *STREMAH 2015, 14th International Conference on Studies, Repairs and Maintenance of Heritage Architecture*, La Coruna, Spain, July 13-15, 2015.

[17] E. Karwacka Codini, Analisi storico-critica dell'edificio della Sapienza, Regesto documentario, in Verifica della sicurezza statica ed analisi della vulnerabilità sismica dell'edificio La Sapienza di Pisa, coordinatori scientifici Walter Salvatore, Università di Pisa, e Paolo Iannelli , Ministero dei Beni e delle Attività Culturali e del Turismo, Pisa 2014, pp. 21-85.

[18] T. Paulay, M.J.N. Priestley, *Seismic design of reinforced concrete and masonry buildings*. John Wiley and sons, INC. New York, U.S.A, 1991.

ECCOMAS Congress 2016
VII European Congress on Computational Methods in Applied Sciences and Engineering
M. Papadrakakis, V. Papadopoulos, G. Stefanou, V. Plevris (eds.)
Crete Island, Greece, 5–10 June 2016

THREE-DIMENSIONAL NONLINEAR BEHAVIOUR OF MASONRY WALLS MODELLED WITH DISCRETE ELEMENTS

D. Baraldi[1] **and A. Cecchi**[2]

Department of Architecture, Construction and Conservation, Università IUAV di Venezia
Dorsoduro 2206, 30123, Venezia, Italy

[1]e-mail: danielebaraldi@iuav.it

[2]e-mail: cecchi@iuav.it

Keywords: Masonry walls, discrete element model, 3D model, frictional contact, Mohr-Coulomb yield criterion.

Abstract. *The analysis of masonry structures is of particular interest in the civil engineering and architecture community due to the large amount of historical masonry constructions in Europe and in Italy in particular. Masonry is a heterogeneous material obtained by composition of blocks connected by dry or mortar joints. The use of refined models for investigating the in and out of plane nonlinear behaviour of masonry is an active field of research. Considering historical masonry, the mechanical properties of joints are usually lower than those of blocks, allowing to assume that damage occurs more frequently along joints. For this reason, discrete element models (DEMs) may be frequently adopted for representing masonry behaviour, assuming blocks as rigid bodies and joints as interfaces, with a small number of degrees of freedom and parameters involved in the analysis. As well known, masonry walls may be considered as the most important category of load-bearing elements in masonry structures and they are subject to vertical and horizontal actions generated by gravitational loads and seismic actions, respectively. Horizontal loads may act in plane or out of plane, causing two different collapse mechanisms for a masonry wall. In this work a simple and effective discrete element model, already developed in linear field for in and out of plane analysis and already extended in nonlinear field but only for in plane analysis, is here extended to the three dimensional nonlinear analysis of masonry walls. A Mohr-Coulomb yield criterion is adopted for modelling interface behaviour. A numerical experimentation is carried on in order to determine the limit load multiplier, together with the collapse behaviour, of several masonry walls. Moreover, existing results are taken in consideration in order to calibrate the proposed model and to evaluate its effectiveness.*

1 INTRODUCTION

Masonry is a heterogeneous material composed by natural or artificial blocks connected by dry or mortar joints. Masonry was the main building material for many centuries; earthquake actions are one of the main causes of collapse and the assessment of seismic performance of masonry structures remains a challenging task in the structural analysis field of research.
The strength of masonry structures is affected by geometrical configuration and constructive details. As well known, such details have effects on the two main different seismic induced damages and collapse modes of masonry walls: in-plane and out-of-plane collapse mechanisms. The former are responsible for extended shear deformations and cracks, while the latter may cause the tilting of entire wall portions, leading eventually to the partial or total collapse of the construction. These collapse mechanisms were observed in past earthquakes and adequate descriptions by means of numerical and analytical models were done and are still being developed [1,2].
Several types of numerical models may be adopted for studying masonry behaviour such as heterogeneous or homogenized Finite Element Models (FEMs) or Discrete Element Models (DEMs); moreover, several analysis types may be performed such as limit analysis or incremental analysis. For instance, an overview of the methods for modelling masonry structures may be found in the work of Smoljanović et al. [3] and a deep literature review of out of plane behaviour and models for masonry has been recently done by Ferreira et al. [4].
A DE Model, based on the assumptions of rigid blocks and joints modelled as interfaces, may be suitable for investigating masonry behaviour due to the small number of degrees of freedom (DOFs) needed for performing a numerical analysis of block assemblages. These assumptions may be suitable for historical masonry, in which block stiffness is larger than joint stiffness, allowing to assume blocks as rigid bodies; moreover joint thickness is negligible if compared with block size, especially in case of dry joints, allowing to model joints as interfaces. Discrete models were adopted in the past by many authors for studying masonry out of plane behaviour in linear and nonlinear fields [5-10]. In particular, Cecchi and Sab [7] defined a simple and effective DEM for studying the three-dimensional behaviour of masonry panels with a small computational effort due to the small number of degrees of freedom involved.
In this contribution, the original three-dimensional discrete element model (3D DEM) introduced by Cecchi and Sab [7] in the linear elastic field, is extended to the field of collapse analysis by assuming a Mohr-Coulomb yield criterion for restraining interface actions. With this aim, a nonlinear -elastic perfectly plastic- interface behaviour is considered by assuming action restraints as elastic limits. The theoretical work of Orduña and Lourenço [8] is taken as reference for defining restraint conditions relative to interface shear force, torsion and their combination. Moreover, a static solution approach characterized by the determination of the stiffness matrix of the masonry assemblage is adopted, following and extending the procedure already adopted by authors for the nonlinear incremental analysis of masonry walls in plane loaded [11] and for the in and out of plane modal analysis of masonry walls [12,13]. Several numerical experiments are carried on in order to validate the proposed nonlinear DEM with respect to existing numerical and laboratory results. For first, numeric out of plane tests performed by Orduña and Lourenço [9] are reproduced, then, the experimental campaign on scaled masonry-like specimens performed by Restrepo Vélez et al. [14] is taken in consideration and several cases are reproduced with the proposed nonlinear DEM. In general, the proposed numerical solution method turns out to be effective for the determination of limit loads and out of plane collapse mechanisms of the masonry walls considered.

2 THREE DIMENSIONAL DISCRETE MODEL

A regular masonry with standard running bond periodic pattern is considered; the generic block $B_{i,j}$ is in contact with six neighbours by means of six interfaces or joints S_{k_1,k_2}, with k_1, $k_2 = \pm 1$ for horizontal interfaces and $k_1 = \pm 2$, $k_2 = 0$, for vertical interfaces (Figure 1). Block dimensions are: *a* (height), *b* (width) and *s* (thickness).

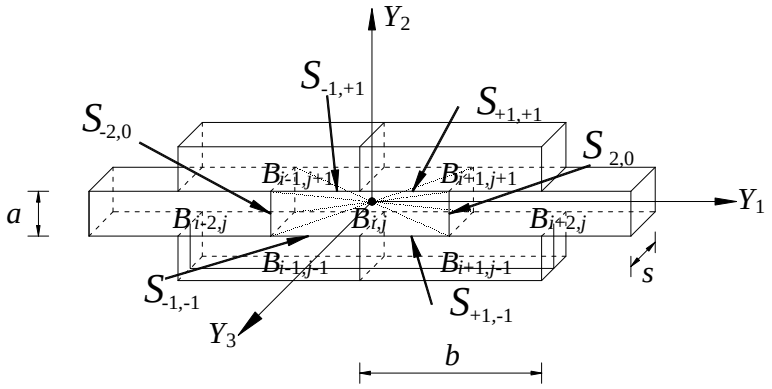

Figure 1. Discrete model, running bond Representative Elementary Volume (REV).

Assuming rigid block hypothesis, the displacement of a generic block is represented by a rigid body motion referred to the motion of its centre and the rotation with respect to its centre:

$$\mathbf{u}^{i,j}(\mathbf{y}) = \mathbf{u}^{i,j} + \mathbf{\Omega}^{i,j}(\mathbf{y} - \mathbf{y}^{i,j}). \tag{1}$$

Where $\mathbf{y}^{i,j}$ is the position of block centre in the Euclidean space: $\mathbf{y}^{i,j} = i(b/2)\mathbf{e}_1 + j\,a\,\mathbf{e}_2$; considering the three dimensional case $\mathbf{u}^{i,j} = \{u_1^{i,j}\ u_2^{i,j}\ u_3^{i,j}\}^T$ is the translation vector of $B_{i,j}$ and $\mathbf{\Omega}^{i,j}$ is the rotation skew tensor collecting block rotations with respect to coordinate axes:

$$\mathbf{\Omega}^{i,j} = \begin{bmatrix} 0 & -\omega_3^{i,j} & \omega_2^{i,j} \\ \omega_3^{j,j} & 0 & -\omega_1^{i,j} \\ -\omega_2^{i,j} & \omega_1^{i,j} & 0 \end{bmatrix} \tag{2}$$

In and out of plane block translations and rotations may be collected in $\mathbf{q}^{i,j} = \{u_1^{i,j}\ u_2^{i,j}\ u_3^{i,j}\ \omega_1^{i,j}\ \omega_2^{i,j}\ \omega_3^{i,j}\}^T$. Following the procedure described in [7], the interactions between two adjacent blocks $B_{i,j}$ and $B_{i+k_1,j+k_2}$ through a generic interface S_{k_1,k_2} are represented by interface tensions $\mathbf{\sigma}$ that are related to the relative displacement and rotations between adjacent blocks by means of a constitutive relation $\mathbf{\sigma n} = \mathbf{K}\,\mathbf{d}$, neglecting for simplicity apex k_1,k_2. Here $\mathbf{\sigma}$ is the stress tensor, $\mathbf{n}$ is the normal vector to the generic interface, $\mathbf{K}$ is the interface stiffness matrix and $\mathbf{d}$ is the vector that collects interface relative translations:

$$\begin{aligned} d_1^{k_1,k_2} &= u_1^{i+k_1,j+k_2} - u_1^{i,j} + k_2 a(\omega_3^{i+k_1,j+k_2} + \omega_3^{i,j})/2, \\ d_3^{k_1,k_2} &= u_3^{i+k_1,j+k_2} - u_3^{i,j} - k_1(b/2)(\omega_3^{i+k_1,j+k_2} + \omega_3^{i,j})/2, \\ d_3^{k_1,k_2} &= u_3^{i+k_1,j+k_2} - u_3^{i,j} + k_1(b/2)(\omega_2^{i+k_1,j+k_2} + \omega_2^{i,j})/2 - k_2 a(\omega_1^{i+k_1,j+k_2} + \omega_1^{i,j})/2, \end{aligned} \tag{3}$$

and relative rotations:

$$\begin{aligned}\delta_1^{k_1,k_2} &= \omega_1^{i+k_1,j+k_2} - \omega_1^{i,j},\\ \delta_2^{k_1,k_2} &= \omega_2^{i+k_1,j+k_2} - \omega_2^{i,j},\\ \delta_3^{k_1,k_2} &= \omega_3^{i+k_1,j+k_2} - \omega_3^{i,j}.\end{aligned} \tag{4}$$

and that may be written as $\mathbf{d}^{k_1,k_2} = \{d_1^{k_1,k_2}\ d_2^{k_1,k_2}\ d_3^{k_1,k_2}\ \delta_1^{k_1,k_2}\ \delta_2^{k_1,k_2}\ \delta_3^{k_1,k_2}\}^T$. It is worth noting that in order to better highlight the relation between relative displacements and global block translations and rotations, the above expressions may be written in matrix form as $\mathbf{d}^{k_1,k_2} = \mathbf{H}^{k_1,k_2}\mathbf{q}^{k_1,k_2}$, where $\mathbf{q}^{k_1,k_2}$ collects translations and rotations of two adjacent blocks and $\mathbf{H}^{k_1,k_2}$ may be defined as interface 'compatibility' matrix [15] that collects, following Equations (3)-(4), the relative distances between the centres of the blocks considered.

Assuming initially the hypothesis of elastic interface behaviour, the interface stiffness matrix $\mathbf{K}$ may be detailed for horizontal and vertical case: $\mathbf{K}_h^{k_1,k_2} = \mathrm{diag}\{K_t\ K_n\ K_t\ K_r\ K_t\ K_r\}$ and $\mathbf{K}_v^{k_1,k_2} = \mathrm{diag}\{K_n\ K_t\ K_t\ K_t\ K_r\ K_r\}$, collecting tangential (K_t), normal (K_n) and rotational (K_r) stiffness of the interface. It is worth noting that rotational stiffness assumes the same value of normal stiffness ($K_r = K_n$), but it is defined by a different variable given that in the following description of interface nonlinear behaviour it will be necessary to distinguish between nonlinear behaviour of normal forces with respect to that of bending moments. Assuming mortar joints with an isotropic and elastic behaviour, interfacial stiffness values are function of mortar elastic modulus E^m and Poisson ratio ν^m [7].

The elastic energy of the interface is determined by defining the product of interface stresses and interface relative displacements:

$$\Pi_{k_1,k_2} = \frac{1}{2}\int_{S_{k_1,k_2}} \boldsymbol{\sigma}^T\mathbf{d}\,dS = \frac{1}{2}\int_{S_{k_1,k_2}} \mathbf{d}^T\mathbf{K}\,\mathbf{d}\,dS = \frac{1}{2}\mathbf{d}^T(\mathbf{K}\mathbf{A})\,\mathbf{d} = \frac{1}{2}\mathbf{d}^T\bar{\mathbf{K}}\,\mathbf{d}, \tag{5}$$

where apex k_1,k_2 for vectors and matrices is omitted for simplicity, $\mathbf{A}$ is the generic (diagonal) matrix of area and inertias of the interface, that may be detailed for horizontal and vertical cases: $\mathbf{A}_h = \mathrm{diag}\{S_h\ S_h\ S_h\ I_{h1}\ (I_{h1}+I_{h3})\ I_{h3}\}$, $\mathbf{A}_v = \mathrm{diag}\{S_v\ S_v\ S_v\ (I_{v2}+I_{v3})\ I_{v2}\ I_{v3}\}$, with

$$\begin{aligned}&S_h = b\,s/2, \quad I_{h1} = b\,s^3/24, \quad I_{h3} = b^3 s/96,\\ &S_v = a\,s, \quad I_{v2} = a\,s^3/12, \quad I_{v3} = a^3 s/12.\end{aligned} \tag{6}$$

Interface forces and moments may be obtained by differentiating the expression of interface elastic energy in Equation (5) with respect to each block displacement component. Such unknown forces $f_1^{k_1,k_2}$, $f_2^{k_1,k_2}$, $f_3^{k_1,k_2}$ and moments $m_1^{k_1,k_2}, m_2^{k_1,k_2}, m_3^{k_1,k_2}$ may be collected in $\mathbf{f}^{k_1,k_2} = \{f_1^{k_1,k_2}\ f_2^{k_1,k_2}\ f_3^{k_1,k_2}\ m_1^{k_1,k_2}\ m_2^{k_1,k_2}\ m_3^{k_1,k_2}\}^T$ and it can be easily demonstrated that $\mathbf{f}^{k_1,k_2} = \bar{\mathbf{K}}^{k_1,k_2}\mathbf{d}^{k_1,k_2}$.

Extending Equation (5) to the entire masonry assemblage (i.e. masonry panel), the total elastic energy Π is obtained and the subsequent equilibrium equation for the assemblage subject to generic in and out of plane actions $\mathbf{F}^{ext}$ is:

$$\mathbf{F}^{ext} = \partial\Pi/\partial\mathbf{q} = \mathbf{K}^{panel}\mathbf{q}, \tag{7}$$

where $\mathbf{q}$ collects block displacements and rotations of the entire panel. Equation (7) may be solved by adopting a molecular dynamics algorithm [7] or directly by explicitly defining the stiffness matrix of the entire assemblage $\mathbf{K}^{panel}$, joining together the procedures already proposed by authors [11-13] for the in and out of plane cases, respectively, and used separately in

the field of in and out of plane modal analysis of masonry panels and in the field of nonlinear analysis of masonry panels in plane loaded. In particular, the determination of panel stiffness matrix is based on the definition of a 'compatibility' matrix [15] $\mathbf{H}^{panel}$ obtained by assembling matrices $\mathbf{H}^{k_1,k_2}$ over the panel and that relates relative displacements of the entire panel $\mathbf{d}^{panel}$ with block displacements and rotations: $\mathbf{d}^{panel} = \mathbf{H}^{panel}\mathbf{q}$. Then, panel stiffness matrix may be calculated as: $\mathbf{K}^{panel} = (\mathbf{H}^{panel})^T \bar{\mathbf{K}}^{panel} \mathbf{H}^{panel}$, where $\bar{\mathbf{K}}^{panel}$ is a diagonal matrix collecting interface stiffness values of the entire panel.

2.1 Yield criterion for interface

The nonlinear behaviour of interfaces is governed by a Mohr-Coulomb yield criterion, characterized by a cohesion c and a friction ratio $\mu = \tan\varphi$. For instance, dry interfaces cannot support tension and have a negligible cohesion, whereas mortar joints are characterized by a tensile strength σ_t and a cohesion value that may be determined by means of experimental tests (for instance EN 1052-3:2002). However, both interface types are characterized by a frictional behaviour and an unlimited compressive strength is assumed.
Considering a generic interface and assuming a local coordinate system $y_1y_2y_3$, with plane y_1y_2 coincident with interface mid-plane and y_3 orthogonal to it. Forces and moments exerted by two adjacent blocks at the interface centre are (Figure 2): normal force $f_3\mathbf{e}_3 = f_n\mathbf{e}_3$, shear forces $f_1\mathbf{e}_1$, $f_2\mathbf{e}_2$, bending moments $m_1\mathbf{e}_1$, $m_2\mathbf{e}_2$ and torsion $m_3\mathbf{e}_3$.

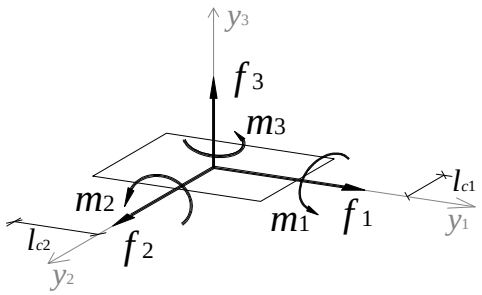

Figure 2: Generic interface with local coordinate system and interface forces and moments.

2.1.1 Normal and flexural interface strength

Considering for first interface normal force and bending moments, the nonlinear behaviour is governed by tensile strength and a simple elastic-plastic relation between actions and relative displacements is adopted. Normal force and bending moments must satisfy the following conditions:

$$\begin{aligned} & f_n = f_3 \le f_t, \\ & |m_1| \le (f_t - f_n)\, l_{c1}, \\ & |m_2| \le (f_t - f_n)\, l_{c2}. \end{aligned} \tag{8}$$

Where f_t represents the tensile strength of the interface, defined as the product of joint tensile strength σ_t and area of the interface (S_v or S_h) and l_{ci} with $i = 1,2$ is the characteristic length of the interface with respect to interface plane directions, namely the maximum eccentricity of normal force with respect to block centre that may be supported by the interface. Each value

is equal to $l_{c1} = s/2, l_{c2} = b/4$ for a horizontal interface and to $l_{c1} = a/2, l_{c2} = s/2$ for a vertical one.
First and second conditions in Equation (8) have been already adopted by authors for the in plane case [11] and they turn out to be coincident to those adopted by Trovalusci and Masiani [16]. In particular, the first condition may be defined as 'detachment' condition, whereas the second and third ones may be defined as 'rotation' conditions with respect to y_1 and y_2 axis.
The relationship between interface normal force and relative normal displacement and the relationships between interface bending moments and relative rotations follow an elastic-perfectly plastic behaviour. In particular, if the interface is subject to excessive moment, only its rotational stiffness is set equal to zero, whereas if the interface is subject to detachment, all interface stiffness values are set equal to zero:

$$\begin{aligned} &f_n > f_t \rightarrow K_n = K_t = K_r = 0, \\ &|m_i| > (f_t - f_n) l_{ci} \rightarrow K_r = 0 \quad i = 1,2. \end{aligned} \tag{9}$$

2.1.2 Shear and torsion interface strength

Differently than the in plane case, characterized by interface shear force acting together with a normal force and a bending moment, in the three dimensional case shear stresses are generated by two components of shear force f_1 and f_2 and by a torsion m_3 and such stresses act together with normal stresses generated by normal force and bending moments. Limit conditions for shear forces and torsion adopted here follow the expressions introduced by Orduña and Lourenco [8]. In particular, if torsion is not present, uniform shear stresses are assumed over the interface and the well-known Mohr-Coulomb yield criterion is applied to the resultant of interface shear forces as follows:

$$|f_s| = \sqrt{f_1^2 + f_2^2} \leq (f_t - f_n)\tan\varphi \quad \text{if} \quad m_3 = 0. \tag{10}$$

The condition above may be defined as 'sliding' condition and the quantity $[(f_t - f_n)\tan\varphi]$ represents the shear strength of the interface. It is worth noting that in this case the cohesion of the interface is represented by the shear strength in absence of a normal action, hence it can be assumed that such strength is equal to $[c\,S_h = f_t \tan\varphi]$ for a horizontal interface and to $[c\,S_v = f_t \tan\varphi]$ for a vertical one.
If shear forces over the interface are equal to zero, the torsion generates shear stresses depending on relative rotation and on the distance from interface centre, that represents the twisting centre. Torsion over the interface must be less than the torsion strength as follows:

$$|m_3| \leq C_t (f_t - f_n)\tan\varphi \quad \text{if} \quad f_s = 0, \tag{11}$$

where C_t is the torsion constant defined in [8], that is based on an interface subdivision into eight rectangular triangles. If shear forces and torsion act together over the interface, the twisting centre moves away from interface centre and the shear-torsion interaction may be defined analytically by integrating shear stresses over the interface. The simplified shear-torsion interaction curve defined by Orduña and Lourenço [8] is adopted. An elastic-plastic behaviour is assumed also in this case and if restraint conditions for shear force and torsion are not respected, the interface tangential stiffness K_t is set equal to zero, whereas normal and flexural stiffness values are not modified.
In order to appreciate the correct adoption of shear and torsion nonlinear behaviour in the proposed DEM, a simple specimen of two blocks connected by an interface modelled with DEM is tested by applying to the interface an increasing torsion with several fixed values of

shear force and by applying an increasing shear force with several fixed values of torsion. Friction ratio μ = 0.7 is assumed and a normal force f_n = 240 N is applied over the interface. Interface size are 0.2 m × 0.3 m. The following Figure 3 shows separately the torsion-relative rotation incremental curves for varying shear force and the shear force-relative displacement incremental curves for varying torsion. As expected, torsion strength decreases for increasing the applied shear force and similarly shear strength decreases for increasing the applied torsion. Both groups of incremental curves allow to obtain the simplified shear-torsion domain proposed by Orduña and Lourenço [8].

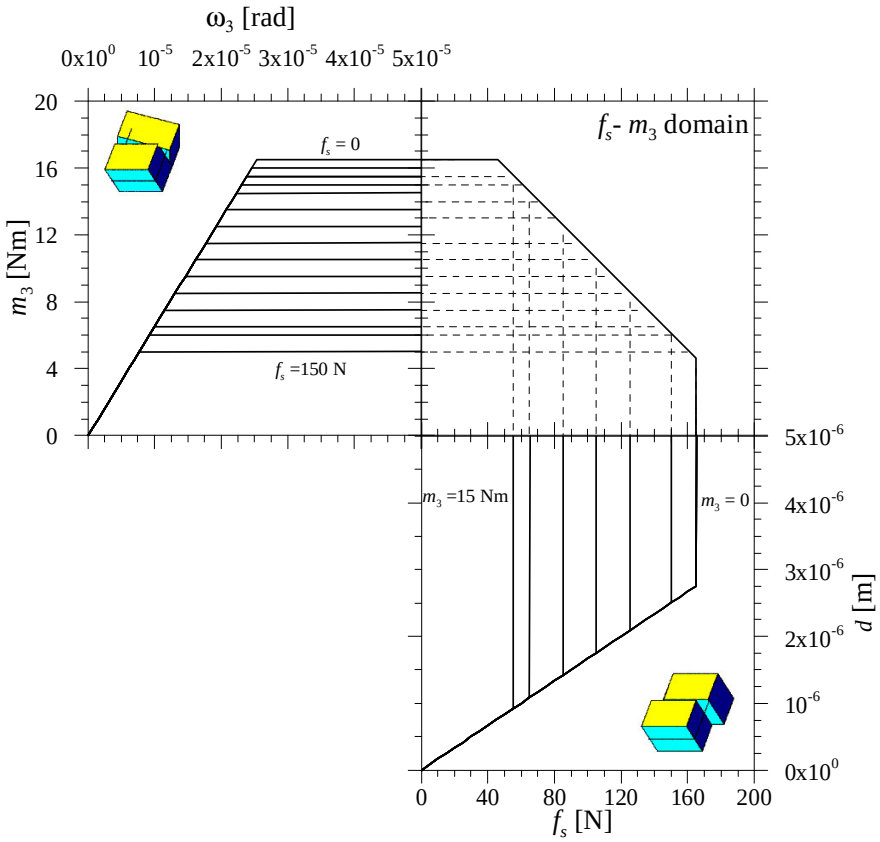

Figure 3: Incremental analyses of a simple specimen subject to increasing torsion with several values of fixed shear force and subject to increasing shear force with several values of torsion.

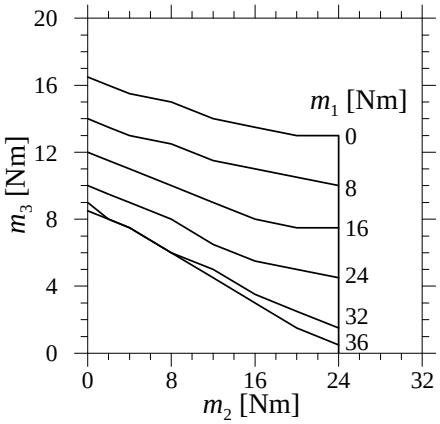

Figure 4: Torsion strength-bending moment interaction curves.

Finally, if bending moments act over the interface together with shear force and torsion, the effective area of the interface is reduced taking into account eccentricity values $e_1 = m_2/f_n$ and $e_2 = m_1/f_n$, then the torsion constant C_t gets smaller, leading to a smaller torsion strength with respect to the case without bending moments. Considering again a simple specimen made of two blocks connected by an interface and varying both values of bending moments over the interface, Figure 4 shows the corresponding torsion strength values and the curves obtained numerically are in excellent agreement with those obtained analytically by Orduña and Lourenço [8].

2.2 Nonlinear DEM

As previously stated, restraint conditions for interface forces and moments allow to define the elastic limits of force-relative displacement and moment-relative rotation constitutive laws, that are assumed to be elastic-perfectly plastic. Then, incremental analyses may be performed by applying incremental load steps to the discrete model and updating the stiffness matrix accounting for local interface nonlinear behaviour. For instance, the stiffness matrix at a generic load step, needed for the evaluation of the corresponding increment of displacements $\delta\mathbf{q}_i$ and internal forces $\mathbf{F}_i^{int}$, is based on interface damage at the previous step as follows: $\delta\mathbf{q}_i = (\mathbf{K}^{panel}_{(\mathbf{q}_{i-1})})^{-1}\delta\mathbf{F}^{ext}$ and $\mathbf{F}_i^{int} = \mathbf{F}_{i-1}^{int} + \mathbf{K}^{panel}_{(\mathbf{q}_{i-1})}\delta\mathbf{q}_i$. Then, internal forces are corrected accounting for the yield criterion adopted and residual forces $\mathbf{R}_i = \mathbf{F}_i^{int} - \mathbf{F}^{ext}$ are determined as a starting point of an iterative process of residuals minimization.
In the following paragraphs, numerical tests are performed considering masonry panels subject to self-weight and increasing lateral loads (in or out of plane). Such loads are proportional to the weight ($P = \gamma a b s$, where γ is block volumetric weight) and are identified by the load multiplier λ; then, the vector collecting the total forces applied at block centres may be defined as $\mathbf{F}^{ext} = \mathbf{F}_D + \lambda\mathbf{F}_L$, where $\mathbf{F}_D$ represents dead loads, collecting block weight P and $\lambda\mathbf{F}_L$ represents unknown horizontal live loads (in or out of plane).

3 IN PLANE NUMERICAL EXPERIMENTS

In order to appreciate the effectiveness of the proposed nonlinear DEM, several numerical experiments of masonry panels in plane loaded by self weight and increasing lateral loads are performed. For instance, the numerical tests originally performed by Baggio and Trovalusci [17] and already studied by authors [11] are reproduced, obtaining the same results of previous in plane analyses (Figure 5).

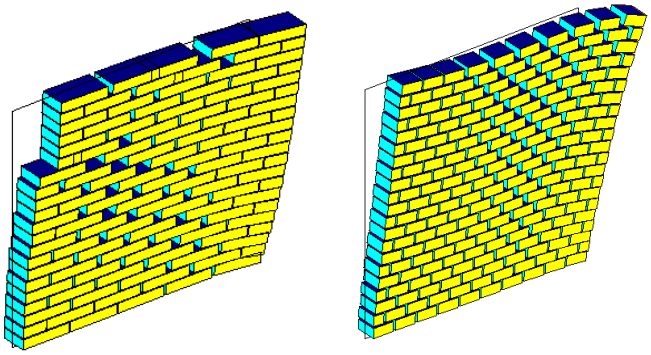

$\lambda^{DEM} = 0.49$; $\lambda^{REF\ [17]} = 0.50$ $\lambda^{DEM} = 0.36$; $\lambda^{REF\ [17]} = 0.34$

Figure 5: Failure mechanisms for masonry panels subject to self weight and increasing in plane lateral loads.

4 OUT OF PLANE NUMERICAL EXPERIMENTS

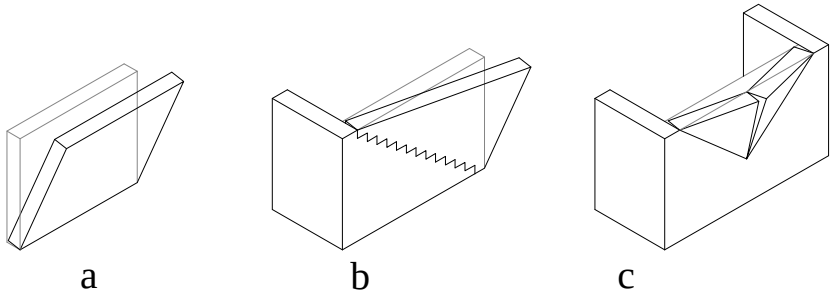

Figure 6: Typical out of plane collapse mechanisms for a masonry wall [18].

In this paragraph, several numerical experiments are carried on in order to evaluate the effectiveness of the proposed nonlinear DEM in the determination of out of plane collapse mechanisms and limit loads of masonry panels. In particular, the typical mechanisms described by Rondelet [18] are going to be reproduced numerically and several existing results, both numerical and experimental, are taken as reference. In particular, the first mechanism type defined by Rondelet is the typical out of plane rigid rotation of a free masonry wall with respect to its base (Fig. 6a), whereas the second mechanism regards a masonry wall restrained along a vertical edge by an orthogonal wall, leading to the formation of a diagonal crack and to a roto-translation of a triangular portion of the wall (Fig. 6b). This mechanism is characterized by a larger ultimate load with respect to the previous case. Finally the third mechanism regards a masonry wall restrained by two orthogonal walls at both vertical edges; in this case a vertical crack along panel axis of symmetry forms together with two diagonal cracks starting from panel upper corners (Fig. 6c), leading to two triangular portions that rotate with respect to diagonal cracks. In this last case, the ultimate load is larger than those of the previous mechanisms.

4.1 Case studies proposed by Orduña and Lourenço

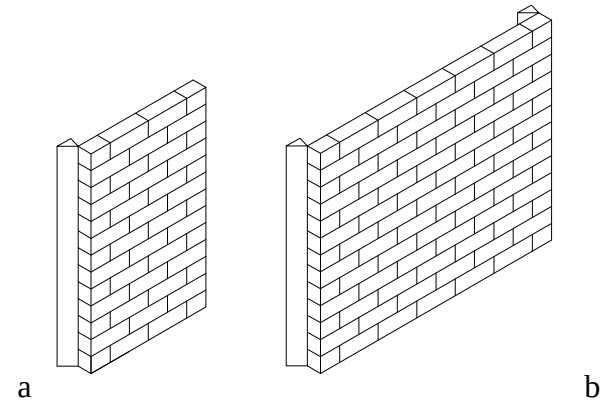

Figure 7: Case studies considered originally by Orduña and Lourenço [9].

Two simple examples of masonry panels out of plane loaded are taken into account for first, by assuming as reference the numerical tests performed by Orduña and Lourenço [9]. In both cases masonry panels are made of blocks assembled following a running bond pattern and having dimensions a = 0.081 m, b = 0.210 m, s = 0.07 m and volumetric weight equal to 20 kN/m^3. Contacts between blocks are dry, with μ = 0.7 and null cohesion. In the first example, panel overall dimensions are: length L = 0.630 m, height H = 1.053 m and thickness s =

0.07 m, obtained by assembling 3 blocks along panel length and 13 blocks along its height; moreover block translations are fixed along panel left column (Figure 7a). In the second example panel dimensions are: L = 1.260 m, H = 1.053 m and s = 0.07 m, obtained with 6 blocks along panel length and 13 blocks along its height. In this case, block translations are fixed along external columns (Figure 7b).
Figure 8a shows a collapse mechanism characterized by a diagonal crack starting from the right side of the panel after the 2nd row of blocks. Such mechanism is in quite good agreement with the one showed in the original analysis and the limit load obtained with the proposed nonlinear DEM is included between FEM and limit analysis performed by Orduña and Lourenço (Table 1). Figure 8b shows a collapse mechanism characterized by a symmetric flexural deformation with large displacements along vertical axis of symmetry. Similarly to the previous case, collapse mechanism and limit load (Table 1) are in quite good agreement with reference solutions.

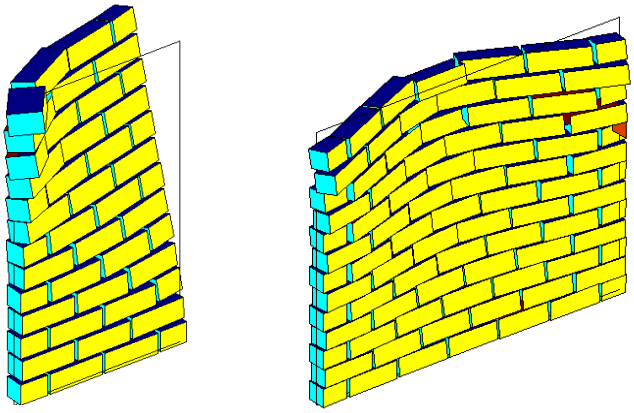

a b

Figure 8: Failure mechanisms for the masonry panels studied by Orduña and Lourenço [9] modelled with DEM.

	case 1	case 2
λ^{DEM}	0.175	0.215
$\lambda^{REF,FEM}$	0.210	0.260
$\lambda^{REF,lim}$	0.127	0.193

Table 1: Limit loads obtained with DEM and reference results of the masonry panels studied by Orduña and Lourenço [9].

4.2 Restrepo Vélez, Magenes and Griffith experiments

In this paragraph, several experimental tests performed by Restrepo Vélez et al. [14] are taken as reference. Original tests were performed on scaled masonry-like specimens with dry joints, subject to self-weight and increasing out of plane loads by means of an inclined plane machine, in order to obtain out of plane failure mechanisms. Block dimensions are a = 28.24 mm, b = 79.78 mm and s = 39.68 mm and block volumetric weight is 26.8 kN/m^3. Dry joints are characterized by friction ratio μ = 0.7 and null cohesion. All cases are characterized by 21 block courses along panel height and varying number n of blocks along panel length (from 4 to 14, for instance). Panel restraints at one or both lateral edges were obtained with one or two orthogonal walls (Figure 9a and b, respectively); for this reason, several mechanisms turned out to involve also blocks in orthogonal walls. In the present campaign, the effect of orthogo-

nal walls is simply modelled by restraining block translations and rotations along one or both lateral columns (Figure 9d and e, respectively). Then, the present model will not be able to represent complex collapse mechanisms involving orthogonal walls, leading to small differences between proposed numerical results and experimental tests. Moreover, an additional specimen type considered a panel without orthogonal walls simply supported at the base and loaded by several wooden beams (Figure 9c).

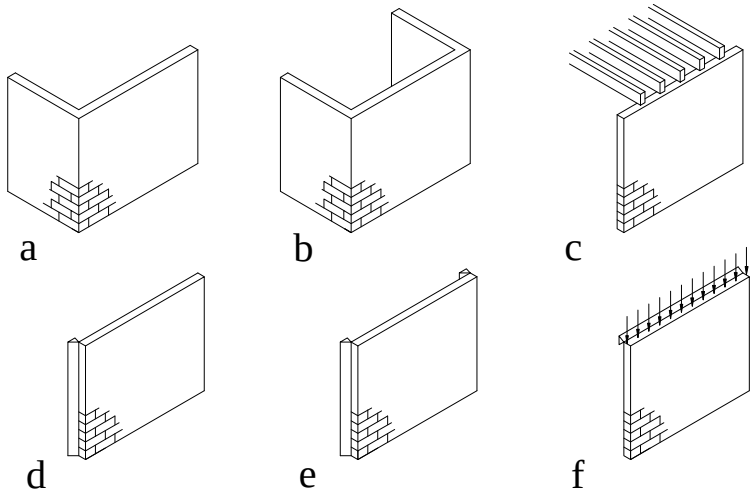

Figure 9: Masonry specimen types considered in the experimental campaign by Restrepo Vélez et al [14] (a-c); corresponding specimens modelled with DEM in present analysis (d-f).

Figure 10 shows failure mechanisms of several panels restrained along left column, varying the number of blocks along panel length (for further details about block number see the first row of Table 2). Mechanisms are characterized by a diagonal crack starting from lower-right panel corner, directed towards the upper-left panel corner and a triangular/trapezoidal portion of panel is subject to a roto-translation with respect to such diagonal crack. These mechanism types are in quite good agreement with experimental tests, moreover numerical results obtained with the proposed nonlinear DEM are in quite good agreement with experimental results (Table 2), especially for specimens S11, S12 and S13, thanks to the large number of blocks of the models, whereas for specimen S15, characterized by a small number of blocks along panel length, limit load obtained with DEM is quite far from experimental result with respect to other cases.
Figure 11 shows failure mechanisms of several panels restrained along both lateral vertical edges. Such mechanisms are characterized by a vertical crack along the axis of symmetry of the panel and diagonal cracks starting from lateral edges and moving down to panel axis of symmetry. Mechanisms are similar but not coincident with respect to those obtained experimentally, due to the real restraint adopted for masonry specimens; however limit loads obtained numerically with nonlinear DEM are still in quite good agreement with experimental results.
Finally figure 12 shows the failure mechanism of a simply supported panel loaded by eleven wooden beams (16.46 N transmitted by each beam) and subject to increasing out of plane loads (see Figure 9c for the corresponding specimen type and Figure 9f for the corresponding DEM representation). The mechanism is characterized by a horizontal hinge in the upper portion of the panel, along the joints between the 15^{th} and 16^{th} block courses and it is almost coincident with the real mechanism obtained during laboratory tests; similarly, the collapse load is close to the one evaluated experimentally.

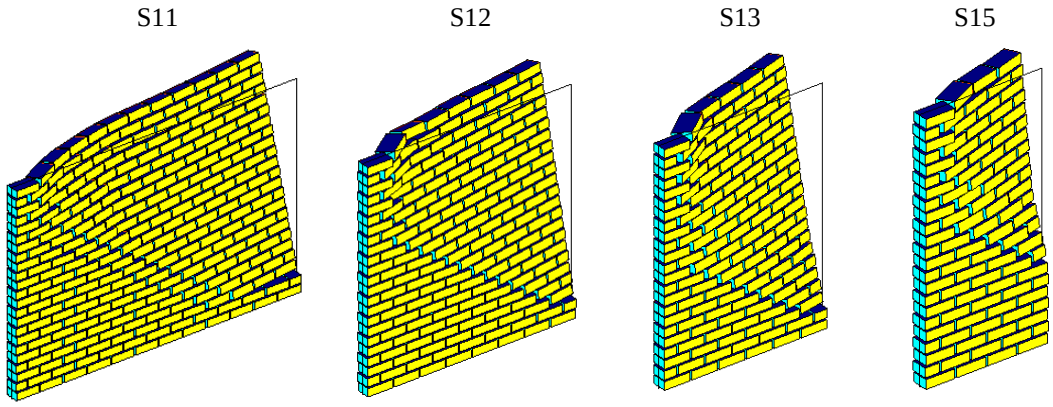

Figure 10: Failure mechanisms for several masonry panels restrained along left column considered by Restrepo Vélez et al. [14] modelled with DEM.

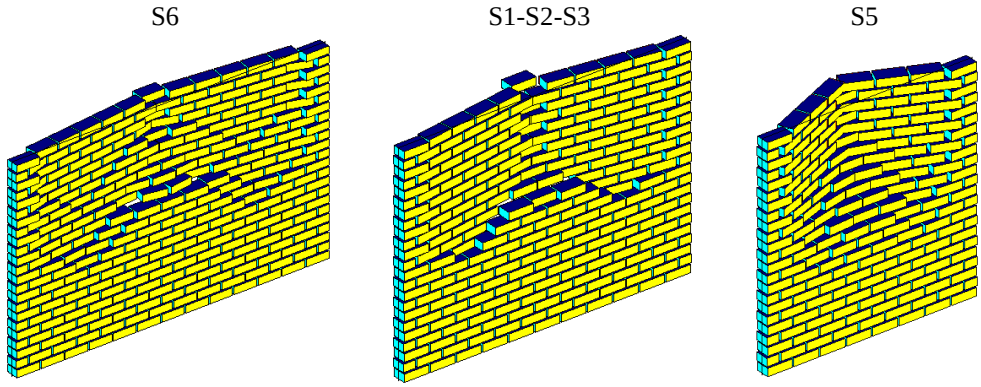

Figure 11: Failure mechanisms for several masonry panels restrained along lateral columns considered by Restrepo Vélez et al. [14] modelled with DEM.

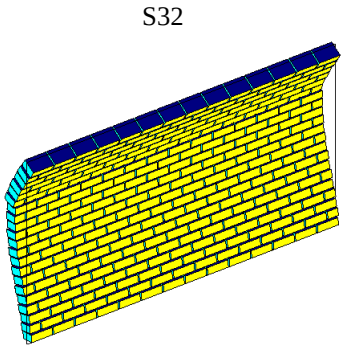

Figure 12: Failure mechanisms for the masonry panel loaded by a set of wooden beams and simply supported at its base considered by Restrepo Vélez et al. [14] modelled with DEM.

	S11	S12	S13	S15	S6	S1-S2-S3	S5	S32
n	12	8	6	4	13	11	8	14
λ^{DEM}	0.100	0.125	0.165	0.250	0.160	0.225	0.350	0.305
λ^{REF}	0.097	0.129	0.181	0.199	0.208	0.208	0.349	0.293

Table 2: Limit loads obtained with DEM and reference results of the masonry specimens considered by Restrepo Vélez et al. [14].

5 CONCLUSIONS

- In this contribution, the three-dimensional DEM introduced by Cecchi and Sab [7] for modelling regular masonry in the linear elastic field has been extended to the collapse analysis field by adopting a Mohr-Coulomb yield criterion and following the work of Orduña and Lourenço [8] for defining the interaction between interface shear forces, torsion and bending moments.
- The proposed nonlinear DEM for three-dimensional analysis turned out to be simple and effective in the determination of limit loads and collapse mechanisms of masonry panels having regular texture and dry joints, subject to self weight and out of plane loads.
- Several numerical tests reproduced the laboratory campaign carried out by Restrepo Vélez et al. [14], in this case the nonlinear DEM simulated correctly limit loads of the specimens taken into account. Moreover, considering collapse mechanisms, the ones relative to panels restrained by a lateral orthogonal wall have been reproduced correctly by the DEM, whereas small differences have been found in collapse mechanisms relative to panels restrained by orthogonal walls along panel lateral edges.
- Further developments of the model will regard the assessment of nonlinear analysis of more complex masonry specimens, characterized for example by blocks arranged irregularly, openings, lintels and also by real orthogonal walls and roofs.

REFERENCES

[1] G. de Felice, R. Giannini, Out of plane seismic resistance of masonry walls. *Journal of Earthquake Engineering*, **5** (2), 253-271, 2001.

[2] D. D'Ayala, E. Speranza, Definition of collapse mechanisms and seismic vulnerability of masonry structures. *Earthquake Spectra*, **19** (3), 479-509, 2003.

[3] H. Smoljanović, N. Živaljić, Ž. Nikolić, Overview of the methods for the modeling of historical masonry structures. *Gradevinar*, **65** (7), 607-618, 2013-

[4] T.M. Ferreira, A.A: Costa, A. Costa, Analysis of the Out-Of-Plane Seismic Behavior of Unreinforced Masonry: A Literature Review. *International Journal of Architectural Heritage: Conservation, Analysis, and Restoration*, **9** (8), 949-972, 2015.

[5] C. Baggio, P. Trovalusci, Limit analysis for no-tension and frictional three-dimensional discrete systems. *Mechanics of Structures and Machines*, **26** (3), 287-304, 1998.

[6] S. Casolo, Modelling the out-of-plane seismic behaviour of masonry walls by rigid elements. *Earthquake Engineering and Structural Dynamics*, **29**, 1797-1813, 2000.

[7] A. Cecchi, K. Sab, A comparison between a 3D discrete model and two homogenised plate models for periodic elastic brickwork. *International Journal of Solids and Structures*, **41** (9-10), 2259-2276, 2004.

[8] A. Orduña, P.B. Lourenço, Three-dimensional limit analysis of rigid blocks assemblages. Part I: Torsion failure on frictional interfaces and limit analysis formulation. *International Journal of Solids and Structures*, **42** (18-19), 5140-5160, 2005.

[9] A. Orduña, P.B. Lourenço, Three-dimensional limit analysis of rigid blocks assemblages. Part II: Load-path following solution procedure and validation. *International Journal of Solids and Structures*, **42** (18-19), 5161-5180, 2005.

[10] I. Stefanou, J. Sulem, I. Vardoulakis, Three-dimensional Cosserat homogenization of masonry structures: elasticity. *Acta Geotechnica*, **3**, 71-83, 2008.

[11] D. Baraldi, A. Cecchi, Discrete approaches for the nonlinear analysis of in plane loaded masonry walls: Molecular dynamic and static algorithm solutions. *European Journal of Mechanics A/Solids*, **57**, 165-177, 2016.
[12] D. Baraldi, A. Cecchi, A. Tralli, Discrete and Continuous Models for Out-of-Plane Loaded Masonry Like Structures: A Multiscale Comparative Study. J. Kruis, Y. Tsompanakis, B.H.V. Topping, (Editors), *Proceedings of the Fifteenth International Conference on Civil, Structural and Environmental Engineering Computing, Civil-Comp Press, Stirlingshire, UK, Paper 207*, Prague, Czech Republic, September 1-4, 2015.
[13] D. Baraldi, S. Bullo, A. Cecchi, Continuous and discrete strategies for the modal analysis of regular masonry. *International Journal of Solids and Structures*, **84**, 82-98, 2016.
[14] L.F. Restrepo Vélez, G. Magenes, M.C. Griffith, Dry stone masonry walls in bending – Part I: static tests, *International Journal of Architectural Heritage*, **8**, 1-28, 2014.
[15] M.C. Ferris, F. Tin-Loi, Limit analysis of frictional block assemblies as a mathematical program with complementarity constraints. *International Journal of Mechanical Sciences*, **43**, 209-224, 2001.
[16] P. Trovalusci, R. Masiani, Non-linear micropolar and classical continua for anisotropic discontinuous materials. *International Journal of Solids and Structures*, **40**, 1281-1297, 2003.
[17] C. Baggio, P. Trovalusci, Discrete models for jointed block masonry walls. *The Sixth North American Masonry Conference*, Philadelphia, Pennsylvania, June 6-9, 1993.
[18] J.B. Rondelet, *Traité théorique et pratique de l'art de bâtir*. Paris, France, 1802.

ECCOMAS Congress 2016
VII European Congress on Computational Methods in Applied Sciences and Engineering
M. Papadrakakis, V. Papadopoulos, G. Stefanou, V. Plevris (eds.)
Crete Island, Greece, 5–10 June 2016

NUMERICAL VALIDATION OF EQUIVALENT-FRAME MODELS FOR URM WALLS

R. Siano[1], G. Camata[1], V. Sepe[1], E. Spacone[1], P. Roca[2], L. Pelà[2]

[1] Department of Engineering and Geology, University "G. D'Annunzio" of Chieti-Pescara
Viale Pindaro 42, Pescara, Italy
e-mail: {rossella.siano, g.camata, v.sepe, e.spacone}@unich.it

[2] Department of Civil and Enviromental Engineering, Universitat Politècnica de Catalunya, UPC BarcelonaTech
Jordi Girona 1-3, Barcelona, Spain
{pere.roca.fabregat, luca.pela}@upc.edu

Keywords: Masonry, URM walls, Equivalent-Frame models, seismic vulnerability.

Abstract. *In the last decades increasing attention has been devoted to masonry structures both from researchers and professionals. This is due to the awareness of the great importance of these structures in the historical urban context, together with the great risk that they suffer in seismic areas.*

Growing success has been obtained by a simplified approach that models masonry walls through "equivalent" plane frames, with concepts and procedures drawn from the study of reinforced concrete and steel frames. In this approach, known as Equivalent Frame Method (EFM), each masonry resisting wall is modelled as a system of linear (frame) elements representative of the behaviour of finite portions of the wall (pier and spandrel panels).

Up to now EFM has proven to be effective in the case of new buildings characterized by regular geometrical configurations and with openings' dimensions for which the frame-like assumption is suitable. Critical issues emerge from existing buildings in European historical centres, where irregularities are almost always present and geometrical anomalies can be detected even in the case of regular walls.

For the specific case of geometrically regular URM walls, this paper presents sample cases tested with linear and non-linear analyses, with the aim to explore the applicability of EF procedures and to identify its limits. A comparison between an EFM procedure with a fiber approach and a more detailed FEM method with plane elements, is adopted as a validation tool, to evaluate the accuracy of the results provided by the EFM for walls characterized by different geometrical configurations.

1 INTRODUCTION

Unreinforced masonry (URM) structures are a worldwide recurring element in the huge variety of building local traditions. Associated to different construction techniques and structural materials, URM buildings make up a large part of the built heritage, having at the same time an enormous cultural and historical value but also a high seismic vulnerability. In general, masonry structures were not designed for seismic resistance. Moreover, they may have had over the time modifications altering their structural performance and increasing their vulnerability.

With the aim to provide effective tools for the modelling of this heterogeneous set of existing structures, researchers and professionals have dedicated significant efforts to investigate the behaviour of masonry structures [1]. Among the various methods, the Equivalent Frame Method (EFM) has become one of the more successful ones due to its compromise between accuracy and efficacy [2-4].

EFM is a simplified modelling procedure based on the assimilation of masonry walls in-plane behaviour to a plane frame structure. In this approach, each resistant masonry wall is discretized in finite portions whose structural behaviour is simulated by means of one-dimensional beam elements connected to each other by fully rigid nodes.

The EFM has been employed till now both in the case of new and existing buildings. In the first case, the structure is characterized by regular geometrical configurations and by openings' dimensions such that the *frame-like* assumption is suitable for modelling the resisting walls. On the other hand, in the case of existing constructions, the structure may show significant irregularities making the *frame-like* assumption hard to be accepted. In addition to these geometrical aspects, the application of the EFM to existing masonry constructions faces critical points related to the quality of masonry materials, the presence of deformable diaphragms and the interaction with other structures in aggregate configurations.

Considering the great popularity of EFM in professional practice, there is the need to validate the EF approach by means of a numerical comparison with the more detailed FEM approach. In this paper the attention is focused on the regular geometrical configurations. For these types of walls the EF discretization is generally considered reliable and suitable. However, as discussed here, also in the case of regular URM walls it is possible to identify some limit cases that cannot be readily represented by the frame-like scheme.

2 EQUIVALENT-FRAME MODELS FOR URM WALLS

EFM is currently one of the most popular tools adopted for structural modelling of masonry structures in professional practice, due to its remarkable simplicity of application and interpretation of the results.

As it is well known, EFM is based on the discretization of each masonry wall in macro-elements, namely masonry panels distinguishable for mechanical and geometrical properties and modelled as beam-column elements connected by rigid nodes. The wall is studied as a plane frame, with a consequent remarkable reduction of the number of degrees of freedom and hence of the computational effort, with respect to more detailed and accurate methods, such as FEM.

The macro-elements discretization of masonry walls on which the EFM procedures is based is compatible with the observed damages suffered by masonry structures under seismic catastrophic events. It is in fact recurrent the concentration of damages in such parts of the wall modelled as deformable mono-dimensional elements (piers and spandrels). Only minor damage is usually observed in correspondence of the connection area between piers and spandrels (node panels), suggesting the idea of a greater strength and stiffness for these elements.

The accuracy of the EFM procedures is strictly connected to the capability to correctly simulate all the failure mechanisms and the damaging phenomena that can affect a masonry wall subject to in-plane actions, namely flexural and shear failure mechanisms.

However, and generally speaking, the EFM can be considered suitable and realistic only in the case of masonry walls characterized by a regular distribution of openings with "standard" dimensions. In these cases, the identification of the structural elements composing the ideal frame is straightforward, while in the case of walls characterized by an irregular arrangement of openings (irregular walls) or by very small windows, the definition of the frame configuration is more uncertain and problematic.

2.1 Discretization of walls in macro-elements and definition of their characteristic dimensions

In the EF idealization, masonry walls are considered as an assemblage of mono-dimensional structural components that can be geometrically identified by extending the contours of openings. In this way, it is possible to identify the following macro-elements (Figure 1):

- **Pier panels**: vertical structural panels whose function is to carry the gravitational and seismic actions and to transfer them to the foundation system;
- **Spandrel panels**: horizontal panels whose function is to transfer the floors' loads to the piers and to connect piers;
- **Node panels**, connecting spandrels and piers, modelled as fully rigid nodes.

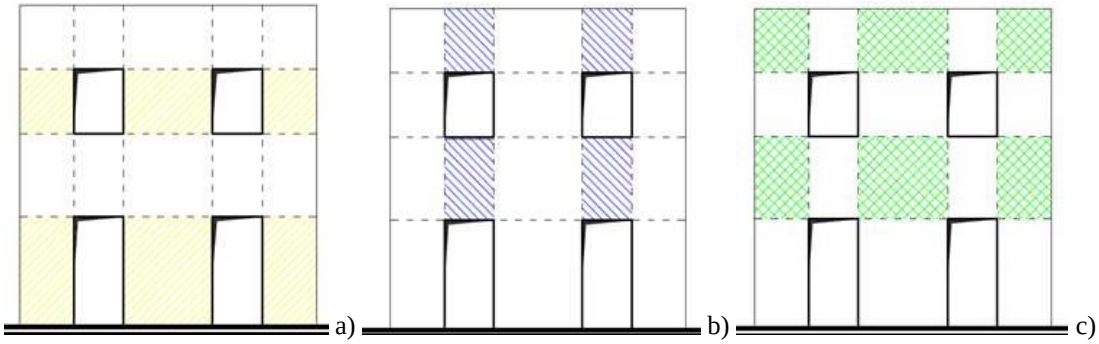

Figure 1: Identification of macro-elements in a masonry façade: piers (a), spandrels (b) and node panels (c).

Looking to the ideal frame configuration proposed in the EF approach, an important role in the walls' structural behaviour is played by spandrels. Such elements represent the horizontal resisting elements of the ideal frame configuration and can give an important contribution to the seismic performance of the wall by behaving as coupling elements and/or restraints for pier panels. The strength and stiffness of the spandrels, in fact, influence the mechanical behaviour of the adjacent piers, which can be modelled with static schemes ranging between the two extreme conditions of cantilever and double-fixed member. The activation of damaging mechanisms in the spandrels can also dissipate energy.

For what concerns the geometrical definition of spandrels, their characteristic width is usually assumed as equivalent to the average width of the openings that include it.

A more important role is played by pier panels, whose stiffness deeply influences the total stiffness and the global seismic behaviour of the wall. The definition of the effective height of the pier was actually one of the first important problems addressed in structural modelling of masonry buildings by the EFM.

The POR method [5] represents one of the first modelling procedures proposed for URM structures anticipating the EF approach, in which only the shear failure of piers is taken into account, with a simplified constitutive shear-deformation law. No clear rules are provided by the POR method about the piers' effective height, even though it strongly affects both their stiffness and shear strength.

A geometrical criterion was introduced by Dolce [2], taking into account the boundary conditions of each piers. The pier's behaviour and stiffness are in fact influenced by the mutual interaction with the surrounding spandrels and by their deformability.

Starting from these consideration and from a previous theoretical study carried out for coupling beams in reinforced concrete structures [6], Dolce proposed an empirical formula for the definition of the piers' effective height as a function of a geometrical parameter (*h'* in Figure 2a). This parameter is defined as the distance between the midpoints of the line connecting the vertices of two consecutive openings, fixing a limit value for the inclination of these lines equal to 30° [2]. The criterion proposed by Dolce was validated by numerical FEM simulation on different pier-spandrel systems. The formula provided by Dolce represents, with some simplifications, the main reference adopted in the most common EF methods actually available for structural modelling of URM structures [3, 4].

Recovering and updating the assumption of "strong spandrel and weak piers" contained in FEMA 356 [7], a different proposal was provided by Augenti [8] by assuming the piers' effective height equal to the height of the openings computed from the side of the earthquake loading. This assumption leads to the need for considering two different models for asymmetric walls, taking into account both the possible horizontal directions of the earthquake, as shown in Figure 2.

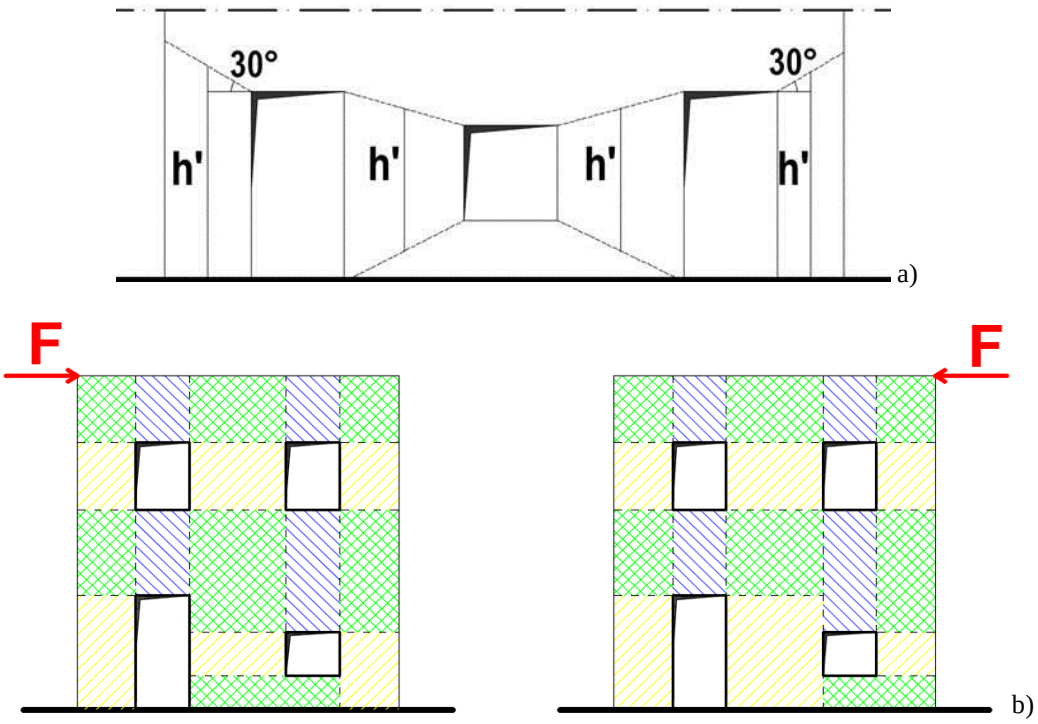

Figure 2: Proposals for piers' effective height by Dolce [2] (a) and by Augenti (b), as a function of the horizontal forces direction [8].

Augenti's proposal is based essentially on direct observation of recurrent damages and failure mechanisms caused by past earthquakes to ordinary masonry buildings. In most of the

cases it is usually possible to observe diagonal shear cracks starting from the corners of the openings, which suggest the idea of different structural responses depending on the direction of the seismic actions. This proposal was validated by experimental tests carried out on masonry building prototypes, whose damage patterns appeared in good agreement with Augenti's assumptions [9].

A comparative analysis between the two proposals for piers effective height has been recently presented by Marques and Lourenço [10]. They have compared the well-known EF methods and then tested on simple regular URM structures. In particular, non-linear static analyses have been carried out by the authors on a two-storey masonry wall by using several EFMs (SAM [4], 3MURI [3] and RAN [11]) related to Dolce's and Augenti's assumptions for piers' effective height and with different boundary conditions (double-fixed and cantilever schemes). The results of the analysis were compared in terms of capacity curves. The comparison showed an important aspect that has been confirmed in the present work. Augenti's assumption presents a better accuracy in evaluating the base shear capacity and the forces distribution among the vertical elements, while the global stiffness of the wall was is strongly overestimated. On the other hand, Dolce's approach obtaines better results for stiffness approximation, while base shear capacity is underestimated.

Due to the fundamental importance of the definition of piers' effective height for structural modelling of URM buildings, the assumptions provided by Dolce and Augenti have been taken into account in the present work and assumed as alternative criteria for the implementation of EF models. The aim of the present work is the evaluation of the accuracy of the EFM in simulating the structural behavior of regular masonry walls. For this purpose, some sample cases of regular masonry walls have been tested in linear and non-linear field. The models studied with EF approach have been modelled considering both the assumptions for piers' effective height formulated by Dolce and Augenti. The results have been compared with reference to corresponding FE models. This comparison gives the possibility to evaluate the effect of different geometric modellings of the piers on the results of the EF models.

2.2 Equivalent-Frame model with fiber approach

In the present work the EFM approach is implemented with a recent formulation for the mechanical characterization of walls' structural components, namely a fiber model initially implemented for reinforced concrete structures [12] and then extended also to URM structures [13]. Fiber approach represents in fact a good compromise between the accuracy of a tridimensional FE procedure and the computational convenience of a simplified uni-dimensional modelling approach.

Differently from other currently available EFM procedures, the use of the fiber approach allows the implementation of the non-linear behavior with a spread plasticity model.

The fiber model is based on the discretization of the beam elements' cross-section into longitudinal fibers, which allows the simulation of the flexural behaviour of the structural element by means of *ad hoc* non-linear constitutive $\sigma-\varepsilon$ laws. The fiber is assumed as having only axial deformation and, for this reason, with this model it is not possible to simulate the flexural and the shear behaviour at the same time. Given the importance of the shear failure mechanisms in masonry structures, the model has been therefore completed by introducing a non-linear spring with shear constitutive law into the fiber discretization [13].

The resulting model is composed therefore of three springs working in series. The central one is a non-linear spring calibrated according to a multi-linear V-γ law, to simulate the possible shear mechanisms than can affect masonry panels, i.e. diagonal cracking and shear sliding. The two extreme springs are defined by fiber discretization, so by means of a spread

plasticity model. For what concerns the simulation of the flexural behaviour, the uniaxial constitutive law provided by Kent and Park [14] has been adopted.

The models adopted in the present work for non-linear simulations have been implemented in the software Midas GEN © [15], where it is possible to combine the fiber discretization of beam elements with non-linear springs simulating shear constitutive laws.

3 REGULAR AND FRAME-LIKE MASONRY WALLS

The concept of structural regularity is usually referred to the global configuration of the structures. Making reference to the prescriptions provided by the Italian technical code [16], a generic construction can be defined regular if it fulfils requirements based on the stiffness, geometrical and inertial properties of the whole structural system.

In the case of URM buildings, namely structural systems composed by the intersection of vertical load-bearing walls and horizontal slab diaphragms, the global seismic performance is strongly dependent on the in-plane response of the single load-bearing walls, once ensured a low probability of activation of out-of-plane failure mechanisms. In this case, the global seismic vulnerability of a URM building is due to the in-plane performances of its load-bearing walls, each of them working for the horizontal forces transferred by the slab diaphragms. As a consequence, it is important to extend the concept of regularity to the single load-bearing wall and in particular to such structural features that can affect its in-plane response. The definition of regularity adopted in this work is therefore a purely geometrical concept referred to the configurations of single masonry walls. The arrangement of the openings in a URM wall is strictly connected to the definition of regularity. A URM wall can be defined regular if its openings are perfectly aligned in both vertical and horizontal directions [17], as for the sample schemes of Figure 3.

As already explained in section 2, the EFM is essentially based on the identification between a single load-bearing wall and an ideal plane frame. In this sense, it is possible to distinguish between configurations that appear clearly consistent with the frame idealization, here denoted as “frame-like”, and configurations for which the affinity with a frame system may be questionable, namely “non-frame-like” ones.

Two schemes are reported in Figure 3 to clarify the distinction between *frame-like* and *non-frame-like* walls, with reference to a two-story masonry wall. Both the sample schemes fulfill the definition of regular wall. However, only the scheme of Figure 3a is characterized by piers and spandrels having geometrical properties compatible with the assumption of mono-dimensional elements. For this scheme a good degree of affinity with a plane frame can be recognized, so the definition of *frame-like* is suitable to describe its configuration.

On the contrary, the extremely small dimensions of the windows in the scheme of Figure 3b induce anomalies in the geometrical properties of piers and spandrels. This scheme appears strongly in contrast with the frame idealization and hence with the previous definition of *frame-like* masonry walls.

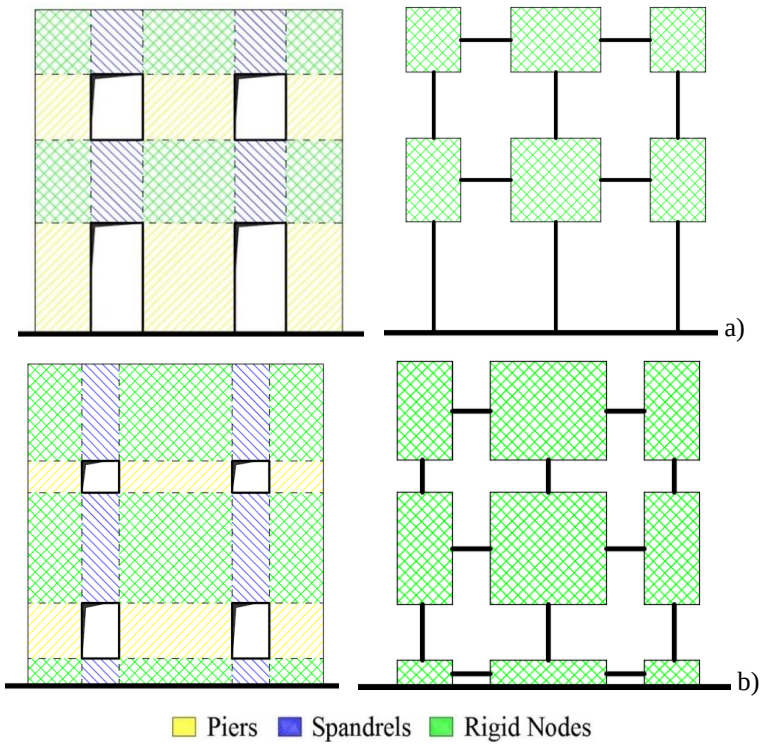

Figure 3: Identification of the equivalent-frame model for *frame-like* (a) and *non-frame-like* (b) URM walls.

4 NUMERICAL VALIDATION OF EQUIVALENT-FRAME METHOD FOR URM WALLS

This section discusses the accuracy of EFM for regular URM walls depending on their geometry. The study is part of a wider research on regular and irregular walls characterized by an increasing level of complexity [18]. The first results are discussed here with reference to the models introduced in Figure 4. Both the walls have been submitted to a linear static analysis under the same loading, mechanical and boundary conditions. A distribution of horizontal loads proportional to the first mode of vibration has been computed and distributed over the nodes of the wall in order to avoid any stress concentration.

The EF models have been built using the two aforementioned approaches for piers' effective height, i.e. the modelling scheme by Dolce [2] and the scheme of "strong spandrel and weak piers" by Augenti and co-workers [11].

The results given by the EF and FE models have been compared in terms of forces and displacements. The base shear reactions and the absolute horizontal displacements have been assumed for comparisons because of their importance in the evaluation of the wall's structural performance. The percentage difference between the predictions provided by EF models and by FE models, in terms of reactions and displacements, has been assumed as a measure of the accuracy of EFM in simulating the actual structural behaviour of URM walls.

Figure 4 shows the percentage differences between EF and FE results for the two sample schemes with regards to the base shear and the top displacement of one of the external piers of the wall.

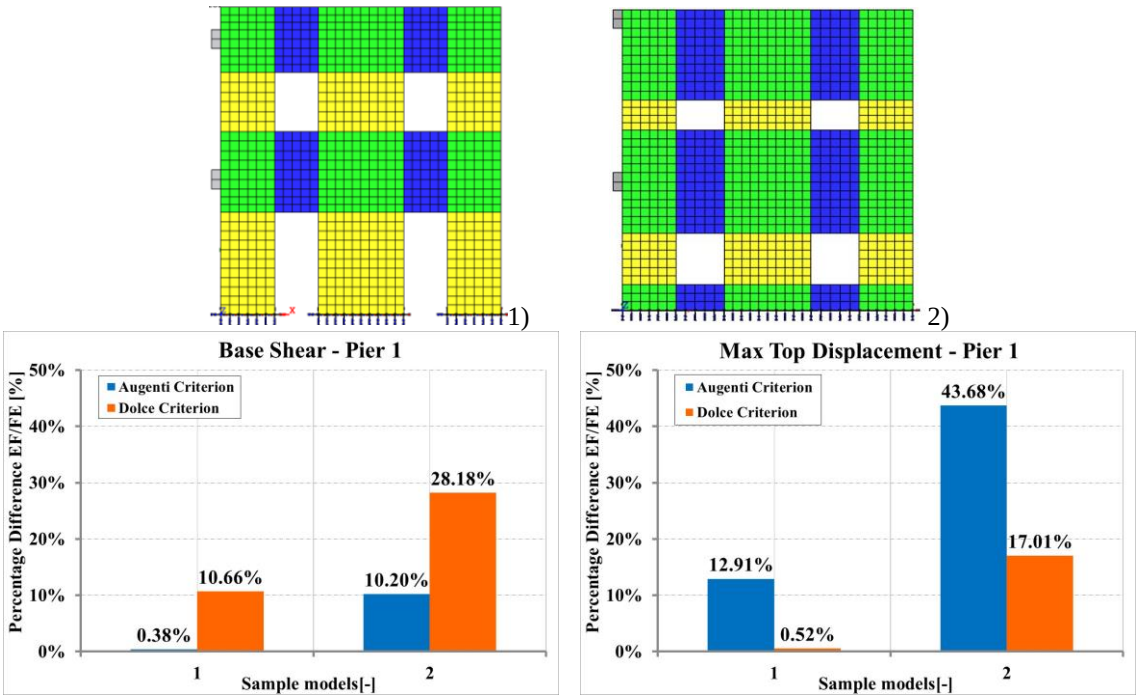

Figure 4: Percentage difference between EF and FE predictions of Base Shear and top Displacement for a frame-like (1) and a non-frame-like (2) URM wall.

Given the strong non-linearity of masonry structures, the validation of a numerical approach for the structural modelling of such structures cannot be limited only to the linear field. Masonry structures show in fact a non-linear behaviour also under low states of stress. Although the study of linear models can be helpful to check the capability of a numerical simulation to predict the elastic stiffness and the distribution of internal forces induced by gravitational loads, it is necessary to extend the study also to the non-linear field in order to have a complete overview of the critical points affecting the modelling method under consideration. For this reason, a non-linear analysis of the same regular schemes has also been performed. The results provided by FE models have been assumed as reference for the evaluation of the EFM accuracy. The FE models have been defined as two-dimensional systems composed by plane-stress rectangular elements implemented in MIDAS FEA © [15].

For what concerns the mechanical characterization of masonry non-linear behaviour, in the EF approach a fiber discretization has been adopted to simulate the flexural behaviour of the uni-dimensional beam elements (piers and spandrels). A non-linear element, located in the midsection of each structural element, has been also added to simulate the two possible shear mechanisms than can affect the masonry panels, i.e. diagonal cracking and shear sliding [13].

The definition of loading conditions has been made by steps, separating the application of gravitational and horizontal loads in both the modelling procedures adopted. An initial loading step has been defined to apply gravitational loads, that have been introduced by assuming a unit weight equal to γ =18.0 kN/m^3 and a slab load equal to 15.90 kN/m for both the levels. A second loading step has been defined to apply horizontal actions directly on the deformed shape obtained at the end of the first loading step. A monotonic incremental time function has been used to apply a distribution of horizontal forces proportional to seismic masses. Finally, a displacement controlled procedure has been adopted to carry out the non-linear static analysis by assigning the value of the horizontal displacement for a control node located at the second floor level of the wall. The iterative solution procedure applied is based on the "initial stiffness" method.

Figure 5 shows the comparison of the capacity curves obtained by the EFM and FEM approaches for the two sample schemes under consideration.

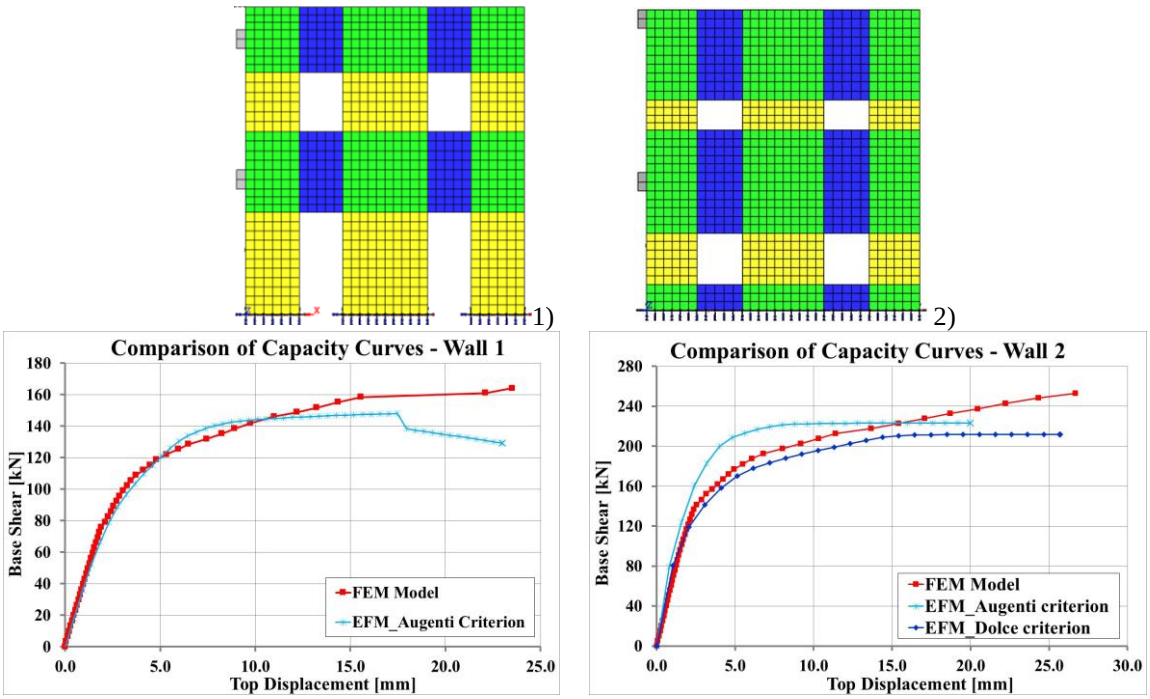

Figure 5: Comparison of the capacity curves obtained with EF and FE models for a frame-like (1) and a non-frame-like (2) URM walls.

4.1 Discussion of results

The two sample schemes analysed in this work show different levels of similarity with the ideal configuration of a frame structure. In particular, the analogy with a frame seems hardly applicable in the case of the second scheme. According to the distinction between *frame-like* and *non-frame-like* walls introduced in Section 3, the results obtained in both the linear and non-linear fields confirm that a regular geometry is not sufficient to justify the assumption of the EF discretization in the modelling of URM walls. As expected, the percentage differences associated to EF models predictions, with respect to FEM results, tends to increase for the second wall.

Figure 4 shows the different level of accuracy that characterizes the two assumptions for the piers' effective height in the EF models, namely the Dolce's and the Augenti's criteria (Section 2.1). As already observed by Marques and Lourenço [10], the criterion adopted by Augenti estimates better the actual distribution of forces among piers than the criterion provided by Dolce. As for the prediction of the base shear, the models defined according to Augenti's criterion provide percentage differences up to 10% with respect to the corresponding FEM results. An opposite trend is shown by the models defined according to Dolce's criterion. For such models a negligible error can be recognized with respect to FE models in the horizontal displacements predictions, while the difference increases significantly for what concerns the forces distributions among the piers.

Such observations about the prediction of shear distributions and horizontal displacements are confirmed by the theoretical bases of the two criteria. The rule provided by Dolce [2] to define the effective piers' height, in fact, is derived by equivalent stiffness considerations among EF and FE models. The effective height of masonry piers was defined following a principle of statistic equivalence between the elastic stiffness expressed by EF and FE models

for several examples of pier-spandrel modules. On the other hand, Augenti's criterion is tailored on observed damage and therefore provides better results for the evaluation of the strength.

The observations made in linear field have been generally confirmed also by the non-linear analyses, although the differences between the results provided by EF models and the FE ones are smaller in the non-linear cases. The higher accuracy shown by the EF approach in the non-linear field demonstrates a better performance of the approach in reproducing the redistribution of forces among the structural elements as a consequence of incremental damaging conditions.

5 CONCLUSIONS

This work presents a comparison between Equivalent Frame Method (EFM) and FEM in the simulation of URM existing buildings. The accuracy of EFM is treated as a function of the degree of similarity between the effective masonry wall's geometry and an ideal frame configuration. A distinction between *frame-like* and *non-frame-like* configurations is introduced with the aim to delimit the set of URM walls' configurations for which EFM approach can be applied.

Two sample URM walls are considered, in order to provide a measure of the EFM applicability. For both walls the definition of regular configuration can be assumed, i.e. a configuration characterized by openings aligned in both horizontal and vertical direction, but they differ in terms of "frame-like" or "non-frame-like" geometry. A comparison is discussed between EFM and FEM results for both models, with the purpose of measuring the applicability of EFM with respect to the predictions provided by the more detailed FE models.

The models are investigated using both linear and non-linear static analyses. The results of these analyses, expressed in terms of shear distributions and displacements, are compared with predictions provided by FE models. The study shows that the differences in results by EF and by FE models increase as the URM walls and the frame schemes are unlike.

The effects of different assumptions for the definition of the piers' effective height are also evaluated following the procedures proposed by Dolce [2] and Augenti [11]. Augenti's criterion shows a greater accuracy in predicting the distributions of shear forces among the piers. On the other hand, Dolce's criterion yields more accurate predictions of the horizontal displacements.

The models presented in this work are part of a broader research [18] aimed at exploring the range of applicability of EF procedures in the case of regular and irregular URM walls. In particular, it is aimed at further verifying the capability of EFM to simulate the main irregularities that can affect the in-plane structural behaviour of existing URM walls, such as those caused by misalignments of the openings or anomalies in their dimensions.

ACKNOWLEDGEMENTS

CSP Fea is deeply acknowledged for providing the software MIDAS Gen© and MIDAS Fea© [16] used in this work for the implementation of the numerical models.

The financial support of University "G. D'Annunzio" of Chieti-Pescara (MIUR ex 60% funds) is acknowledged by the authors. Partial support by the ReLUIS program 2014-2016 is also acknowledged by the authors.

REFERENCES

[1] Roca P., Cervera M., Gariup G., Pelà L., Structural analysis of masonry historical constructions. Classical and advanced approaches, *Archives of Computational Methods in Engineering*, **17**, 299–325, 2010.

[2] M. Dolce, Schematizzazione e modellazione degli edifici in muratura soggetti ad azioni sismiche, *L'Industria delle Costruzioni*, **25**, 44-57, 1991 [in Italian].

[3] A. Brencich, S. Lagomarsino, A macro-element dynamic model for masonry shear walls, *G.N. Pande & J. Middleton - Computer methods in structural masonry*, Proc. Intern. Symp., Pratolino (FI), 3-5 september 1997, Swansea.

[4] G. Magenes, A. Della Fontana, Simplified Non-linear Seismic Analysis of Masonry Buildings, *Proc. of the British Masonry Society*, London, 1998.

[5] M. Tomaževič, *The Computer Program POR*, Report ZRMK, Institute for Testing and Research in Materials and Structures, Ljubljana, Slovenia, 1978 [in Slovenian].

[6] D. Michael, *The effect of local wall deformations on the elastic interaction of cross-walls coupled by beams*, Tall Building Symposium, 1967.

[7] ATC, Applied Technology Council, (2000), *Prestandard and Commentary for the Seismic Rehabilitation of Buildings*, FEMA 356, Federal Emergency Management Agency, Washington D. C., USA.

[8] N. Augenti, Seismic behaviour of irregular masonry walls, *Proceedings of the 1st European Conference on Earthquake Engineering and Seismology*, Geneva, paper **86**, 2006.

[9] F.L. Moon, T. Yi, R.T. Leon, L.F. Kahn, Recommendations for seismic evaluation and retrofit of low-rise URM structures, *Journal of Structural Engineering*, **132**(5): 663-672, 2006.

[10] R. Marques, P. B. Lourenço, Possibilities and comparison of structural component models for the seismic assessment of modern unreinforced masonry buildings, *Computers and Structures*, **89**: 2079-2091, 2011.

[11] N. Augenti, *Il calcolo sismico degli edifici in muratura*, UTET Libreria, Torino, Italy [in Italian], 2004.

[12] E. Spacone, F.C. Filippou, F.F. Taucer, Fiber beam-column model for nonlinear analysis of R.C. frames. Part I: Formulation, *Earthquake Engineering and Structural Dynamics*, **25**(7): 711-742, 1996.

[13] E. Raka, E. Spacone, V. Sepe, G. Camata, Advanced frame element for seismic analysis of masonry structures: Model formulation and validation, *Earthquake Engineering and Structural Dynamics*, **44(**14), 2015.

[14] D.C. Kent, R. Park, Flexural members with confined concrete, *Journal of the structural division ASCE*, **97**(7): 1969-1990, 1971.

[15] MIDAS Gen© and MIDAS Fea©, MIDAS Information Technology Co., http://www.cspfea.net/

[16] IBC (Italian Building Code)- D.M. 14.01.2008, *Norme Tecniche per le Costruzioni*, Italian Ministry of Infrastructures and Transportation, Rome, Italy (in Italian).

[17] F. Parisi, N. Augenti, *Non-linear seismic behaviour of irregular URM walls with openings*, Proceedings XIV Conference of Italian Association for Earthquake Engineering ANIDIS, Bari, Italy, 2011.

[18] R. Siano, *On the Equivalent-Frame method for irregular masonry walls*, PhD Dissertation, University "G. D'Annunzio" of Chieti-Pescara, Pescara, Italy, 2016.

ECCOMAS Congress 2016
VII European Congress on Computational Methods in Applied Sciences and Engineering
M. Papadrakakis, V. Papadopoulos, G. Stefanou, V. Plevris (eds.)
Crete Island, Greece, 5–10 June 2016

SEISMIC ASSESSMENT OF HISTORICAL MASONRY TOWERS IN THE NORTH-EAST REGION OF ITALY

Marco Valente[1], **Gabriele Milani**[1]

[1] Department of Architecture, Built Environment and Construction Engineering (A.B.C.)
Technical University of Milan,
Via Ponzio 31, I-20133, Milan, Italy
e-mail: {marco.valente, gabriele.milani}@polimi.it

Keywords: Masonry towers, FE model, non-linear dynamic analysis, pushover analysis.

Abstract. *In the present paper a comprehensive seismic vulnerability assessment of several historical masonry towers, mainly built during the medieval age and located in the North-East region of Italy, is carried out by means of simplified and advanced FE approaches. Three-dimensional finite element models of the masonry towers are created on the basis of geometrical data deduced from both existing available documentation and in-situ surveys. Nonlinear static (pushover) and dynamic full 3D analyses are carried out to investigate the seismic performance of the towers. A comparison between non-linear dynamic analyses and non-linear static procedures, even at a global level, can provide useful information about the seismic vulnerability of such type of structures. Numerical results provide an accurate understanding of the behavior of the towers under horizontal loads and highlight the effects of some geometrical features, such as slenderness, thickness of the perimeter walls, presence of perforations, internal vaults, irregularities and inclination.*

1 INTRODUCTION

The protection of historical masonry constructions against seismic actions is of strategic importance in many European countries, especially in Italy, which are prone to earthquakes. Ancient masonry towers are widely disseminated in Italy and represent one of the main elements of the local cultural heritage. In ancient times these structures were usually conceived mainly to resist vertical loads and are particularly vulnerable to earthquakes because of the limited ductility of masonry combined with the slenderness of the towers that are sometimes characterized by complex geometry and irregularities. The axial stresses due to gravity loads could be of the same order of magnitude as the compression strength of the old masonry and, when combined with the dynamic loads induced by earthquakes, can produce heavy damage and even local collapse. The prediction of the seismic response of historical masonry buildings represents a crucial issue and a challenging research item. An effective seismic vulnerability assessment of such structures can be obtained through non-linear dynamic and static analyses by means of suitable finite element (FE) models. In recent times, national and international codes have imposed the evaluation of the structural performance under horizontal loads, encouraging the use of sophisticated non-linear methods of analysis.

The paper, which can be considered as a thoughtful collection of case studies useful to infer general considerations, presents a comprehensive numerical study on the seismic performance assessment of eight historical masonry towers located in the North-East region of Italy. The towers exhibit different geometrical characteristics in terms of slenderness, cross-section area, openings, wall thickness and internal irregularities, but they are built with similar technologies and masonries presenting similar mechanical properties. Their structural behavior under horizontal loads may be therefore thought to be influenced mainly by geometrical issues.

Detailed three-dimensional finite element (FE) numerical models are created through the software package Abaqus to represent the geometry of the towers. The main geometrical features of the towers are deduced from both existing available documentation and in-situ surveys. The evaluation of the seismic response of the historical masonry towers is carried out through non-linear dynamic analyses. A damage plasticity material model, exhibiting softening in both tension and compression, already available in the commercial code Abaqus, is used for masonry. The seismic performance assessment of the towers is carried out in terms of displacement time-history and tensile damage distribution. The effects of different geometrical characteristics and local irregularities on the seismic response of the towers are investigated.

A non-linear static procedure based on pushover analysis is also used for the seismic vulnerability assessment of the masonry towers. The results obtained by the two methods are compared in order to verify whether the simplified approach may represent the seismic behavior of the towers. A comparison between non-linear dynamic analyses and non-linear static procedures, even at a global level, can provide useful information about the seismic vulnerability of the towers.

2 TOWERS UNDER STUDY AND FE MODELS

This section provides a concise overview of the main geometrical features of the towers under study, along with some rough details on the FE discretization adopted. The elevation views and the FE models of the eight towers are presented in Figure 1 and Figure 2. The FE models of the eight towers (bell, clock or battle towers) are created directly in the commercial code Abaqus. Three-dimensional elements are used to model masonry, with different material properties where necessary, to suitably take into account the presence of infill over the vaults

or the possible central layer in multi-leaf walls. The choice of the element size is done in order to share the advantages of sufficiently reliable results and numerical efficiency during the non-linear dynamic analyses that usually needed very long time to be performed, even in workstations with large RAM. A preliminary size equal to 0.4-0.5 m is chosen for the sides of the 3D elements, with local or global refinements, depending on the specificity of the structure. Still, reasonable values of the mesh distortion are obtained, with a worst aspect ratio ranging between 2 and 3.

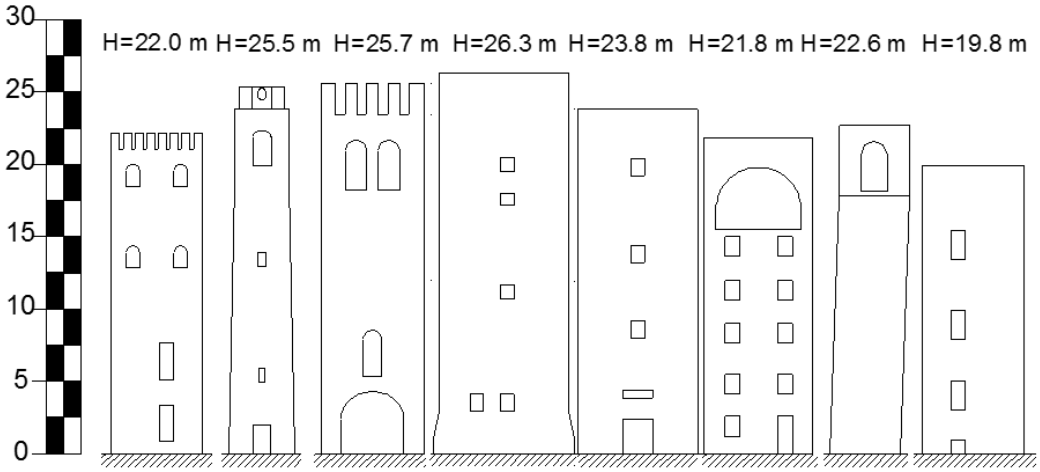

Figure 1: Schematic elevation views of the towers under study and indication of the height.

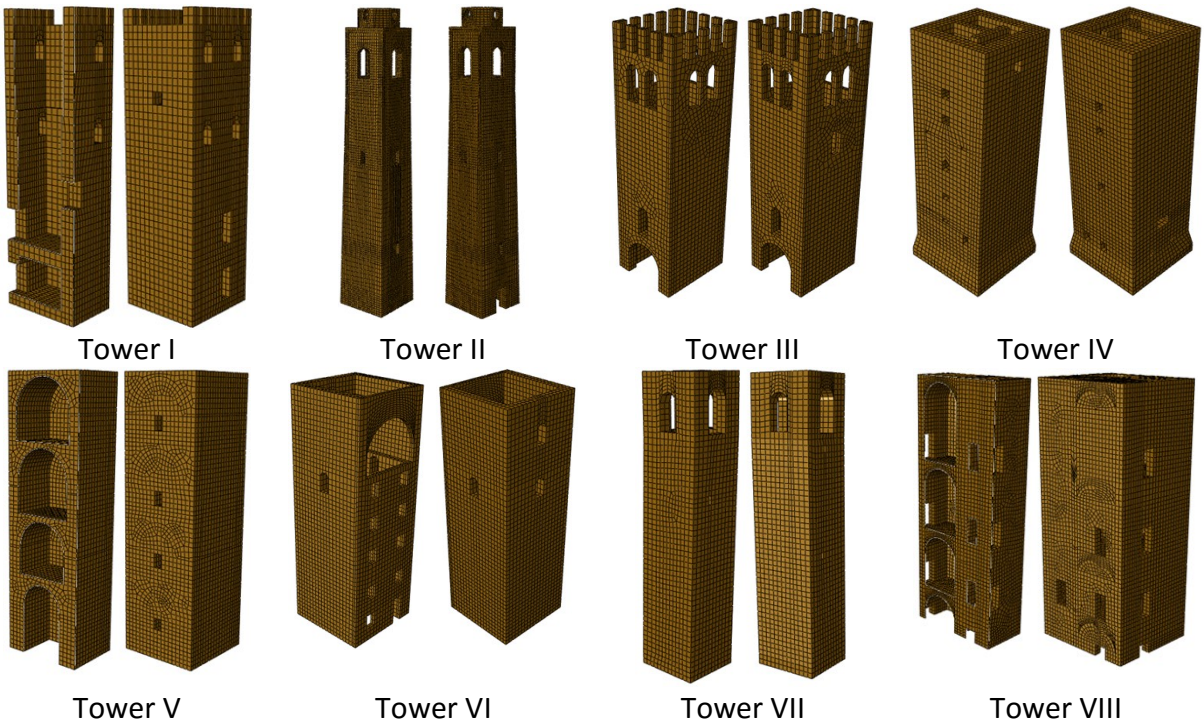

Figure 2: Finite element model of the towers under study

3 MATERIAL MODEL

The 3D FE models of the towers are implemented into Abaqus taking into consideration geometrical (large displacement effects) and material non-linearity by means of the Concrete Damage Plasticity (CDP) model, fully available in the standard package.
Concrete Damage Plasticity model is based on the assumption of a scalar isotropic damage with distinct damage parameters in tension and in compression. It is particularly suitable for applications in which the material exhibits damage, especially under loading-unloading conditions, and therefore for seismic analyses. A different inelastic behavior in tension and compression is then introduced.
To describe the multi-dimensional behavior in the inelastic range, masonry is assumed to obey a Drucker-Prager strength criterion with non-associated flow rule. The strength domain is a standard Drucker–Prager surface modified by means of the so-called K parameter, representing the ratio between the second stress invariant on the tensile meridian and that on the compressive meridian. This parameter is set equal to 0.666 in the numerical simulations.
A value equal to 10° is adopted for the dilatation angle, which seems reasonable for masonry subjected to a moderate-to-low level of vertical compression. This value is in agreement with experimental evidences available in the literature. To avoid numerical convergence issues, the tip of the conical Drucker-Prager strength domain is smoothed using a hyperbola. Abaqus code allows for smoothing the strength domain by means of the so-called eccentricity parameter, which represents the distance between the points of intersection with the p-axis of the cone and the hyperbola in the p-q plane, where p is the hydrostatic pressure stress and q is the Mises equivalent stress. A value equal to 0.1 is adopted for the eccentricity parameter in the numerical simulations.
The available experimental results on regular masonry wallets show a moderate orthotropy ratio (around 1.2) under biaxial stress states in the compression-compression region. Obviously, such feature cannot be taken into account when an isotropic model, like the present one, is utilized. However, it is commonly accepted in the literature the utilization of isotropic models (like concrete smeared crack approach available in both Ansys and Adina) after an adaptation of the parameters to fit an average behavior between vertical and horizontal compression. A suitable model should also take into account the ratio between the ultimate compression strength in biaxial stress states and in uniaxial conditions. Such a ratio, which exhibits similar values for concrete and masonry, is reasonably set equal to 1.16.
The final stress–strain relationship in tension adopted for the dynamic analyses follows a linear-elastic branch up to the peak stress σ_{t0}. Then, micro-cracks start to propagate within the material, leading to a macroscopic softening. In compression, the response is linear up to the yield stress σ_{c0}. Then, a linear hardening is assumed up to the crushing stress σ_{cu}, followed by a linear softening branch.
The damage variables in tension d_t and compression d_c are defined by means of the following standard relationships:

$$\begin{aligned} \sigma_t &= (1-d_t)E_0\left(\varepsilon_t - \varepsilon_t^{pl}\right) \\ \sigma_c &= (1-d_c)E_0\left(\varepsilon_c - \varepsilon_c^{pl}\right) \end{aligned} \quad (1)$$

where $\sigma_t(\sigma_c)$ is the uniaxial tensile (compressive) stress, E_0 is the initial elastic modulus, ε_t (ε_c) is the uniaxial total strain in tension (compression), $\varepsilon_t^{pl}(\varepsilon_c^{pl})$ is the equivalent plastic strain in tension (compression). In the present study, only tension damage is assumed to be active, because the adopted tensile strength of the material is significantly lower than the compressive strength. When the strain reaches a critical value, the material starts to degrade

showing, in the unloading phase, a modulus equal to $E < E_0$. In particular, in the numerical simulations conducted in this study a reduction equal to 5% of the Young modulus with respect to the initial value is assumed for a plastic deformation equal to 0.003.

.

4 ANALYSES PERFORMED

Two different numerical approaches, namely non-linear static procedure based on pushover analyses and non-linear dynamic analyses, are carried out in this study, with a level of numerical complexity that can be considered ranging from moderately high to high in common design practice.

4.1 Non-linear dynamic analyses

The real accelerogram registered in Mirandola on the 20th of May 2012 during the Emilia-Romagna seismic event is used to investigate the seismic response of the towers under study. The accelerogram is appropriately scaled in order to obtain two acceleration time histories with different values (0.1g and 0.2g) of the peak ground acceleration (PGA). Figure 3 shows the acceleration time history with PGA=0.1g along with some meaningful instants identified with different letters and colors.

The dynamic analyses are performed applying the accelerogram, separately, along the two principal (X and Y) directions of each tower. The horizontal displacement time histories of some control points, normally the nodes at the top of the towers, along with the damage state at the end of the simulations, are used to qualitatively determine if the structure is in a state of incipient collapse or not.

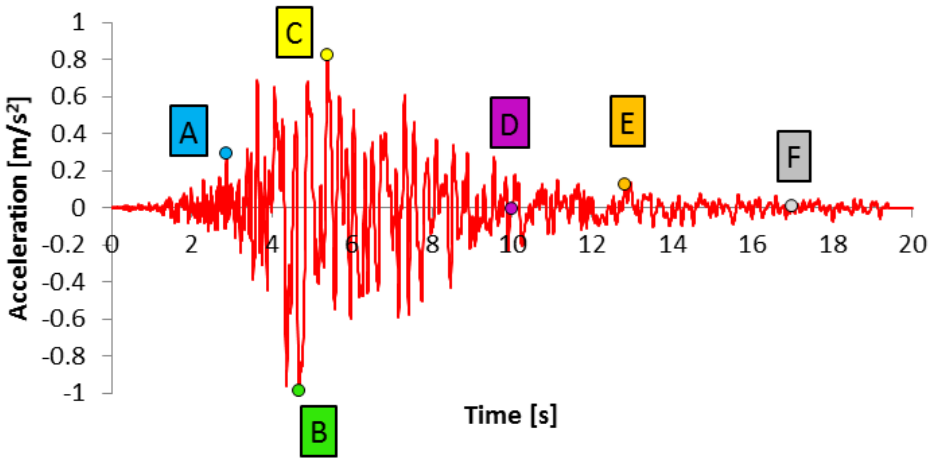

Figure 3: Scaled real accelerogram used in the non-linear dynamic analyses and meaningful points used to evaluate the state of damage of the towers under study.

4.2 Simplified procedure based on pushover analysis

A simplified assessment procedure is also adopted for the seismic verification of the global structural behavior of the towers under study. The procedure was developed at the University of Ljubljana by Fajfar and is based on pushover analyses and on inelastic demand spectrum. This simplified method of analysis is an effective technique for the seismic assessment of existing structures and combines pushover analysis of a multi-degree-of-freedom (MDOF)

model with the response spectrum analysis of an equivalent single-degree-of-freedom (SDOF) model. The method is formulated in the acceleration-displacement (AD) format, which enables the visual interpretation of the results. By means of a graphical procedure, the capacity of a structure is compared with the demand of an earthquake ground motion on the same structure, Figure 4.

The capacity of the structure is represented by a force-displacement curve obtained by non-linear static analysis. The capacity curve of the structure is transformed into the capacity curve of an equivalent SDOF system by means of the transformation factor $\Gamma = \sum m_i \phi_i / \sum m_i \phi_i^2$, where ϕ_i is the i^{th} component of the eigenvector $\mathbf{\Phi}$ deduced from modal analysis and m_i is the mass of the node i. The capacity curve of the equivalent SDOF system is then reduced to a bilinear elastic-perfectly plastic force-displacement diagram on the basis of the equal energy concept (the areas underneath the actual and bilinear curves are approximately the same, within the range of interest).

The displacement capacity corresponds to the end point of the bilinear curve. The inelastic demand in terms of accelerations and displacements is provided by the intersection point of the capacity curve with the demand spectrum corresponding to the ductility demand μ, as schematically shown in Figure 4. In this study, the seismic demand is computed with reference to the Eurocode 8 response spectrum (soil type C). The theoretical predictions are performed for Sa_g levels equal to 0.1g and 0.2g. The displacement demands refer to the equivalent SDOF system. The displacement demands of the structure are obtained by multiplying the displacement demands of the SDOF system by the transformation factor Γ. Seismic assessment is performed by comparing displacement capacity and demand. The main results of the non-linear static procedure are reported for a direct comparison with the results of the non-linear dynamic analyses.

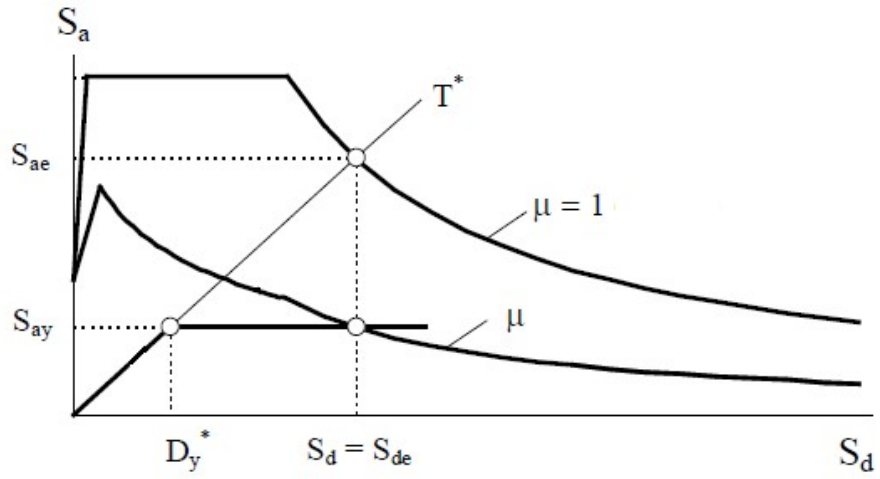

Figure 4. Elastic and inelastic demand spectra versus capacity diagram in acceleration-displacement (AD) format.

5 RESULTS OF NON-LINEAR DYNAMIC ANALYSES

It can be roughly stated that if a residual deformation, defined as the ratio between the horizontal inelastic residual displacement and the height of the tower, ranging between 0.4% and 0.8% is reached, the structure may be reasonably considered in incipient state of collapse. Values of 0.4% and 0.8 % of residual deformation are taken with reference to masonry piers behavior at failure under in-plane bending and shear, respectively, in agreement with Italian

code specifics. While such a choice is rather debatable, because masonry towers can be hardly thought to behave as single piers, it is probably the only quantitative indication that can be attempted in this case.

The inelastic residual deformations obtained for all the cases investigated are synoptically shown in Figure 5, where threshold values of 0.4% and 0.8% are also indicated. The maximum values of the top displacements normalized to the height of the towers are summarized in Figure 6.

From an overall analysis of the results of the dynamic simulations with two different PGAs, the following remarks may be drawn.

Under seismic excitation with PGA=0.1g, it can be noted that Tower I, Tower II, Tower III, Tower IV and Tower VIII exhibit values of residual deformations smaller than 0.4% of the height. It can be observed that the values of residual deformation are critical (within 0.4%-0.8%) for Tower VI and Tower VII; Tower V can be considered as prone to collapse. These results are confirmed in terms of non-dimensional top displacements.

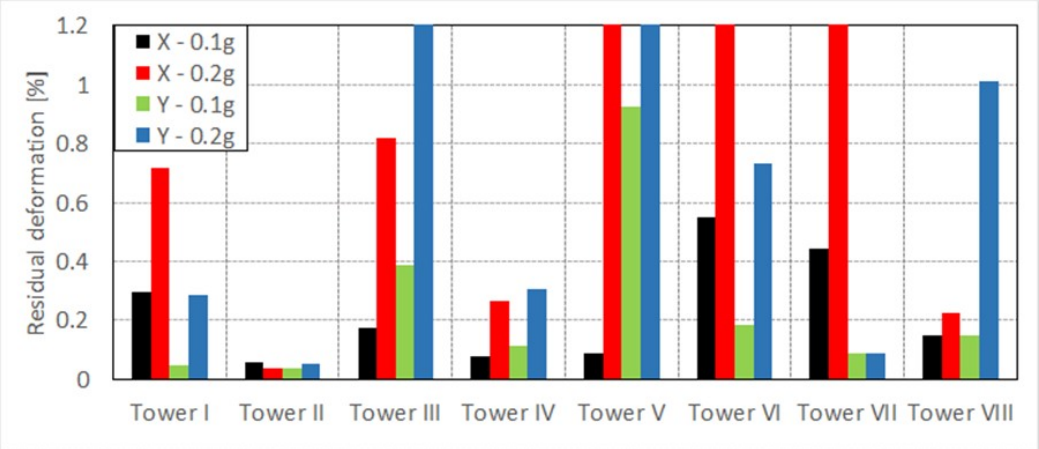

Figure 5: Non-linear dynamic analyses: residual deformations at PGA=0.1g and PGA=0.2g in the X and Y directions for the different towers.

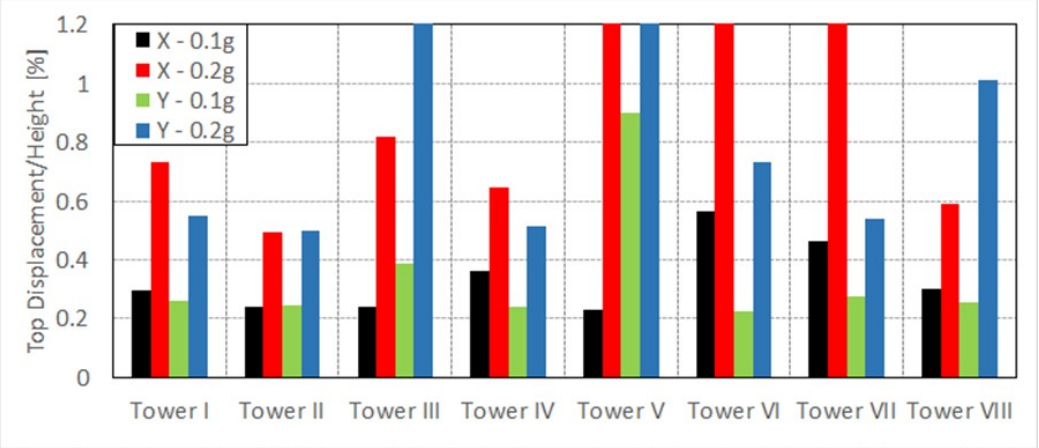

Figure 6: Non-linear dynamic analyses: maximum normalized top displacement (top displacement/height) at PGA=0.1g and PGA=0.2g in the X and Y directions for the different towers (values of normalized top displacements are interrupted at 1.2%).

Under seismic excitation with PGA=0.2g, basing on the criterion of inelastic residual deformations, a collapse mechanism is activated for Tower III, Tower V, Tower VI, Tower VII and Tower VIII. The values of residual deformations are critical (within 0.4%-0.8%) for

Tower I; Tower II and Tower IV exhibit acceptable residual deformations (smaller than 0.4% of the height). These results are confirmed in terms of normalized top displacement, but also Tower II and Tower IV present non-dimensional top displacement within 0.4%-0.8%.

6 SIMPLIFIED PROCEDURE BASED ON NON-LINEAR STATIC ANALYSES

The results of the non-linear static procedure in the acceleration-displacement response spectrum plane are illustrated in Figure 7. The capacity curve of the equivalent SDOF system, transformed in a bilinear curve, is reported and the seismic demand corresponds to two values of the effective peak ground accelerations equal to Sa_g=0.1 and Sa_g=0.2g; for the sake of clarity, only the elastic demand spectrum is shown. The seismic vulnerability is evaluated by comparing the displacement demand and the displacement capacity obtained through the pushover analyses. The displacement capacity and demand in the X and Y directions are then summarized for the towers under study in Figure 8 and Figure 9 for two different seismic intensity levels.

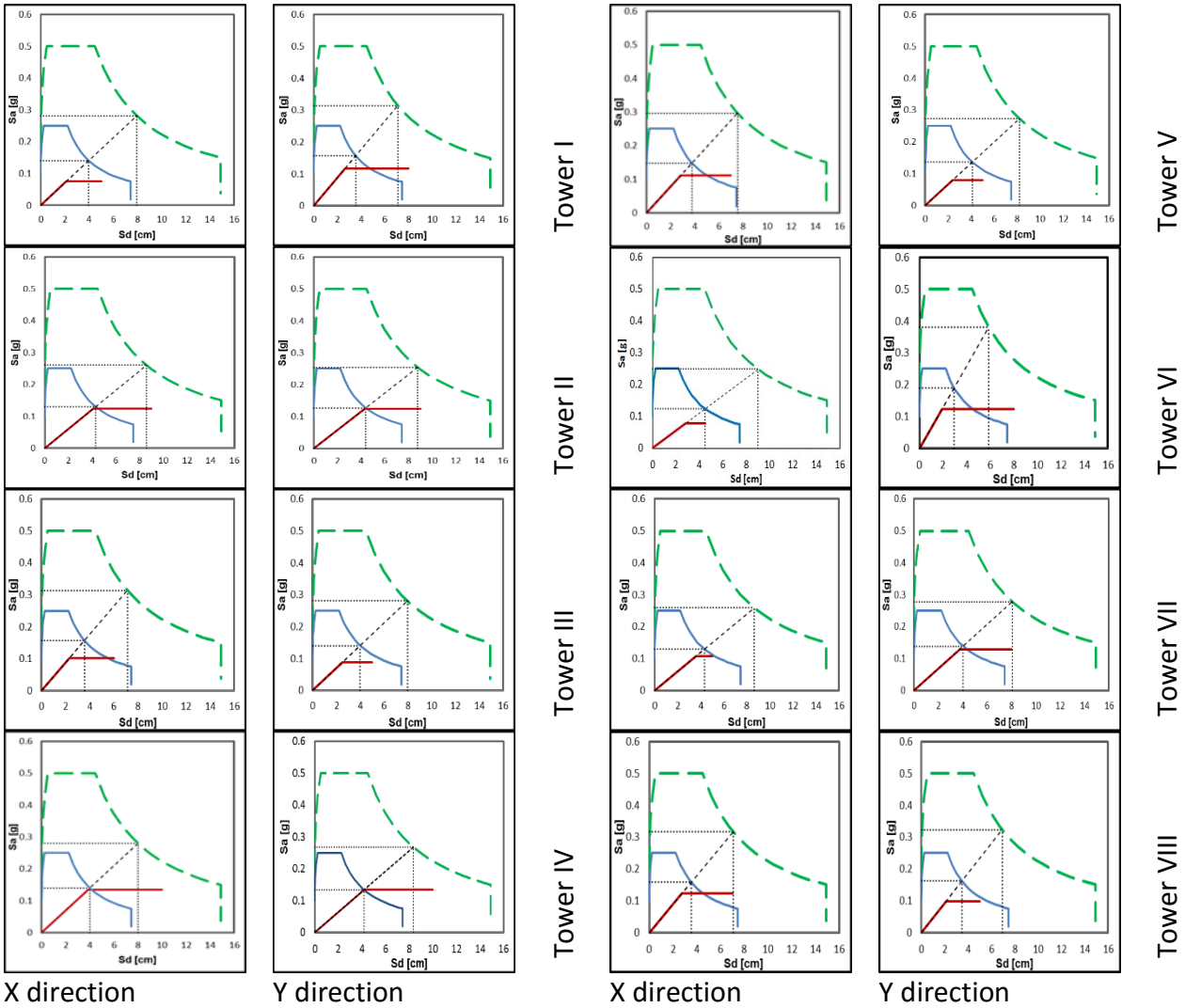

Figure 7: Non-linear static procedure in the acceleration-displacement response spectrum plane (X and Y directions) for different seismic intensity levels: Sa_g=0.1g (continuous blue line) and Sa_g=0.2g (dashed green line).

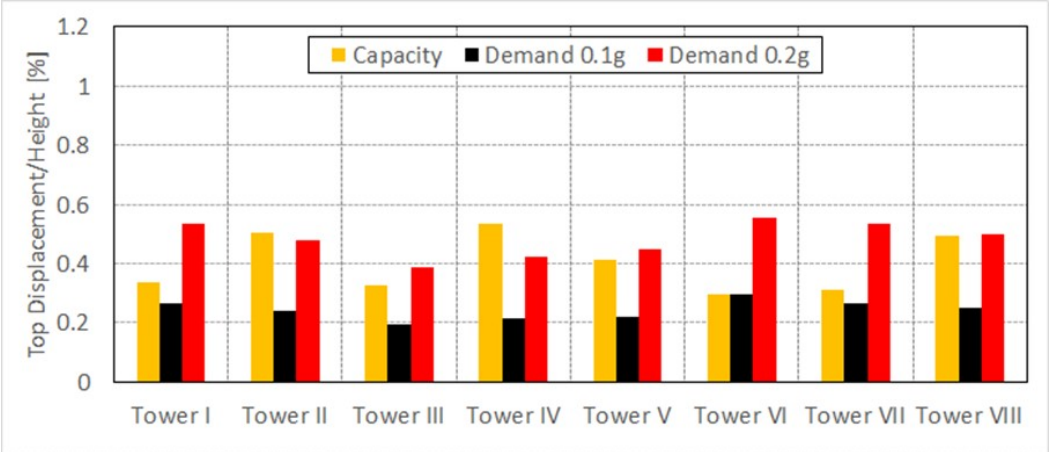

Figure 8: Non-linear static procedure, X direction: displacement capacity and displacement demand at different seismic intensity levels for the different towers.

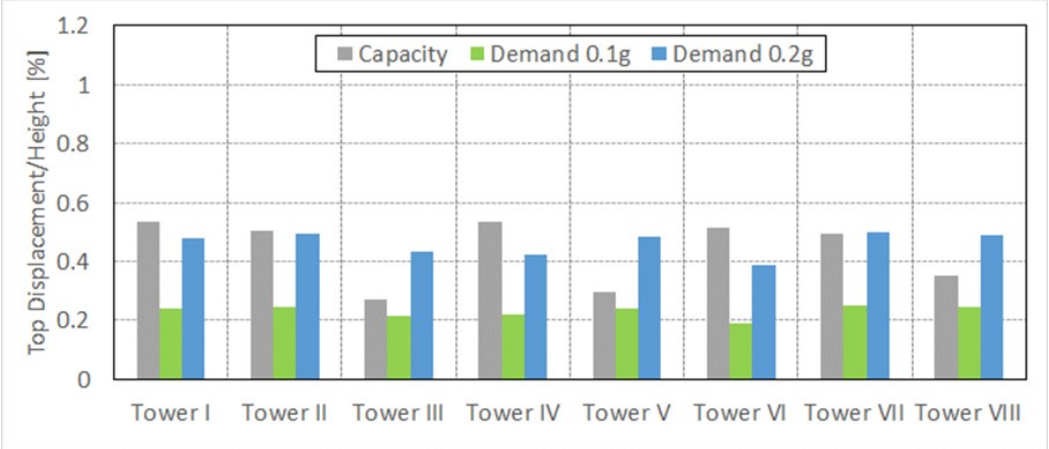

Figure 9: Non-linear static procedure, Y direction: displacement capacity and displacement demand at different seismic intensity levels for the different towers.

The results obtained from the non-linear static procedure are also synoptically summarized in Table 1 for a direct comparison with the outcomes of the non-linear dynamic analyses. As can be noted, the seismic safety assessment provided by the two methods is very similar for almost all the towers, in some cases with a very satisfactory agreement. The non-linear static procedure may provide reasonable synthetic predictions of the seismic vulnerability of the towers. A slightly more conservative trend for the non-linear dynamic simulations can be noticed after a detailed analysis of individual cases. The non-linear static procedure provides smaller values of displacement demand than those resulting from the non-linear dynamic analyses. The simplified static approach is not able to capture the inertial effects associated with seismic excitation that can lead to heavy damage and premature collapse of the structure.

7 DISCUSSION OF RESULTS

7.1 Comparison between the procedures

The displacement demands obtained by the non-linear static procedure are in a good agreement with those obtained by the non-linear dynamic analyses when the check of the structural safety is verified. When the check is not satisfied according to the non-linear static procedure, the seismic demand is smaller than the maximum value of the top displacement

experienced by the structure during the non-linear dynamic analyses. In the majority of cases this result can be explained by the large increase of the displacements registered in the non-linear dynamic analyses when a collapse mechanism occurs. From an overall analysis of the results, it can be noted that the non-linear static procedure generally gives reliable results in terms of displacements. Large differences are observed in the cases of Tower V and Tower VI, where local collapse mechanisms are registered during the non-linear dynamic analyses and for this reason the displacement distribution differs significantly. In the case study of Tower V, the non-linear static procedure does not catch the collapse of the upper vaults, which is registered at the end of the non-linear dynamic analyses. In the case study of Tower VI, a local collapse of the upper part of the thin wall is clearly observed during the non-linear dynamic analysis: moreover the presence of this type of irregularity triggers non-uniform displacement demands at the top of the structure. Non-linear dynamic analyses are able to account for higher mode effects that may be introduced by local irregularities.

Table 1. Comparison on the collapse state of the towers evaluated through the non-linear static procedure and the non-linear dynamic analyses: X and Y directions, PGA=0.1g and PGA=0.2g.

	X direction				***Y direction***			
Collapse √ YES × NO √/× Borderline	Non-linear static procedure		Non-linear dynamic analysis		Non-linear static procedure		Non-linear dynamic analysis	
Tower	PGA 0.1g	PGA 0.2g	PGA 0.1g	PGA 0.2g	PGA 0.1g	PGA 0.2g	PGA 0.1g	PGA 0.2g
I	×	√	×/√	√	×	×	×	×/√
II	×	×	×	×	×	×/√	×	×
III	×	√	×	√	×	√	×/√	√
IV	×	×	×	×/√	×	×	×	×/√
V	×	√	×	√	×	√	√	√
VI	×/√	√	√	√	×	×	×	√
VII	×	√	×/√	√	×	×/√	×	×
VIII	×	×/√	×/√	×/√	×	√	×	√

The tensile damage distribution corresponding to the displacement demand is generally similar to the damage pattern observed at the end of the non-linear dynamic analyses, but the numerical values of damage are always smaller. The only exception is the severe damage observed at the base of the towers during the pushover analyses: it is less evident at the end of the non-linear dynamic analyses. However, the damage pattern detected by the pushover analysis can represent a good indicator of the vulnerable parts of the structure.

The choice of the control point, representative of the global behavior of the structure, is a fundamental issue for the application of the non-linear static procedure. The results of the procedure significantly depend on the selection of the control point and, in some cases, show quite large variations. Therefore, the results obtained by the non-linear static procedure should be evaluated with caution in function of the control point chosen for the procedure. This result is proven by the study of the Tower VI, where torsional effects are evident. It is shown that the results obtained with a control point which is not part of the local collapse overestimate the capacity of the structure. On the contrary, if a point belonging to the vulnerable part of the structure is chosen as a control point, the results underestimate the capacity of the structure.

The non-linear static procedure can give a satisfactory representation of the seismic behavior of the towers in terms of structural safety verification and displacement demands when significant irregularities are not present. In slender towers with presence of irregularities the contribution of higher modes to the global response may be considerable. Structures with higher mode effects exhibit a complex dynamic response that necessitates the use of more sophisticated methods of analyses.

7.2 Seismic safety assessment and failure modes of the towers

The check of the seismic safety of the analyzed towers is satisfied according to the non-linear static procedure under Sa_g=0.1g, with the exception of Tower VI that is a borderline case. Similar results are obtained through the non-linear dynamic analyses. Only Tower V and Tower VI present large residual deformations, indicating the activation of local failure mechanisms, mainly due to the geometrical irregularities, even for peak ground acceleration equal to 0.1g.

According to the non-linear static procedure, the analysed towers are not able to accommodate the seismic demand under Sa_g=0.2g, with the exception of Tower IV and Tower II. These results are supported by the outcomes of the non-linear dynamic analyses.

The peculiar geometrical characteristics and configurations are the main reasons of the larger seismic resistance of these two towers than the one of the other towers. In the case of Tower IV, the thickness of the four perimeter walls is larger than the one of the other towers and it remains constant along the height of the structure. In addition, at the top of the tower there are no large openings, which can represent a vulnerable upper part, when compared to the majority of the other towers. Tower II is symmetrical both in plan and in elevation and presents a regular internal distribution. The tower has a square plan and its weight is much smaller than the one of the other towers, leading to a great reduction of the seismic forces.

For the other towers under study, different failure modes can be observed. The role played by both the geometrical characteristics and the presence of irregularities on the possible collapse mechanisms is highlighted by the results of the analyses. Problems relative to the structural configuration, especially asymmetry and inadequate arrangement of openings, can affect the level of damage in the towers.

A non-uniform stiffness and strength distribution, in plan and elevation, and torsional effects can be some of the main causes for a widespread damage and even collapse of the towers. Tower VI is characterized by a wall with small thickness and a large opening at the top. A failure mechanism involving the detachment of the wall is registered.

For Tower V and Tower VIII, the role played by the internal vaults in modifying the load path for gravity and earthquake loads is evident and unexpected stress concentrations may arise. Localized and severe damage as a result of a redistribution of internal actions transferred by the vaults is highlighted by the analyses. Moreover, Tower V exhibits sudden variations of the walls thickness along the height and Tower VIII presents some irregularities within the perimeter walls.

The quite marked inclination, the high slenderness and the plan asymmetry are the main causes for the widespread damage of Tower VII.

A significant reduction of stiffness and strength of a wall is observed when multiple openings are present, like in the cases of Tower I and Tower III. Tower I has several openings on two parallel walls and Tower III presents large openings both at the base and at the top. A damage concentration with cracks propagating vertically is observed near the openings.

8 CONCLUSIONS

A comprehensive numerical study conducted by means of advanced FE simulations (non-linear dynamic and static analyses) on eight historical masonry towers located in the North-East region of Italy is presented. From an overall analysis of the results obtained in this study, the following conclusions may be drawn.

-The results of the non-linear dynamic simulations show the high vulnerability of historical masonry towers under horizontal loads. It can be roughly stated that if a residual deformation ranging between 0.4% and 0.8% is reached, the structure may be reasonably considered near collapse.

-Some geometrical characteristics, such as plan and elevation irregularities, presence of belfry, large openings, sudden variation of cross-section, internal vaults and tower inclination, play a crucial role on the seismic performance of the towers. The correlation between local geometrical issues and possible failure modes of the towers is clearly highlighted by the numerical analyses.

-The seismic demands obtained by the non-linear static procedure are generally in a good agreement with those obtained by the non-linear dynamic analyses, above all when the check of the structural safety is verified according to the non-linear static procedure. When the check is not satisfied according to the non-linear static procedure, the seismic demand is smaller than the maximum value of the top displacement experienced by the tower during the dynamic simulations. The simplified static approach is not able to capture the inertial effects associated with seismic excitation that can lead to heavy damage and premature collapse of the structure.

-The non-linear static procedure may provide reasonable synthetic predictions of the seismic vulnerability of the towers. The two approaches provide similar results in terms of seismic safety assessment, with slightly less conservative predictions for the non-linear static procedure. A comparison between the results obtained by the two approaches shows that the non-linear static procedure is able to assess the structural safety only when local collapse failures are not involved.

REFERENCES

[1] DPCM 9/2/2011. Italian Guidelines for the evaluation and the reduction of the seismic risk for the built heritage, with reference to the Italian norm of constructions. Rome, Italy, 2011.

[2] DM 14/01/2008. New technical norms on constructions. Rome, Italy, 2008.

[3] Circolare n° 617 del 2 febbraio 2009. Instructions for the application of the new technical norms on constructions. Rome, Italy, 2009.

[4] Abaqus, Theory manual, version 6.14.

[5] Fajfar P.A. (2000). A nonlinear analysis method for performance-based seismic design. Earthquake Spectra, 16(3): 573-592.

[6] Valente M., Milani G. (2016). Seismic assessment of historical masonry towers by means of simplified approaches and standard FEM. *Construction and Building Materials*, 108, pp. 74-104.

[7] Valente M., Milani G. (2016). Non-linear dynamic and static analyses on eight historical masonry towers in the North-East of Italy. *Engineering Structures*, 114, 241-270.

[8] Milani G., Valente M. (2015). Numerical insight into the seismic behavior of eight masonry towers in Northern Italy: FE pushover vs non-linear dynamic analyses. 11th International Conference of computational methods in sciences and engineering, 20-23 March, Athens, Greece. *AIP Conference Proceedings*, 1702.

[9] Milani G., Valente M. (2015). Comparative pushover and limit analyses on seven masonry churches damaged by the 2012 Emilia-Romagna (Italy) seismic events: possibilities of non-linear Finite Elements compared with pre-assigned failure mechanisms. *Engineering Failure Analysis*, 47, pp. 129-161

[10] Milani G., Valente M. (2015). Failure analysis of seven masonry churches severely damaged during the 2012 Emilia-Romagna (Italy) earthquake: Non-linear dynamic analyses vs conventional static approaches. *Engineering Failure Analysis*, 54, pp. 13-56.

[11] Milani G., Valente M. (2014). Safety assessment of historical masonry churches based on pre-assigned kinematic limit analysis, FE limit and pushover analyses. 10th International Conference of Computational Methods in Sciences and Engineering, 4-7 April, Athens, Greece. *AIP Conference Proceedings*, 1618.

ECCOMAS Congress 2016
VII European Congress on Computational Methods in Applied Sciences and Engineering
M. Papadrakakis, V. Papadopoulos, G. Stefanou, V. Plevris (eds.)
Crete Island, Greece, 5–10 June 2016

NATIVITY CHURCH IN BETHLEHEM: FULL 3D NON-LINEAR FE APPROACH FOR STRUCTURAL DAMAGE PREDICTION

Gabriele Milani[1], **Marco Valente**[1], **Claudio Alessandri**[2]

[1] Department of Architecture, Built Environment and Construction Engineering (A.B.C.)
Technical University of Milan,
Via Ponzio 31, I-20133, Milan, Italy
e-mail: {gabriele.milani, marco.valente}@polimi.it

[2] Department of Engineering, University of Ferrara
Via Saragat 1, I-44122, Ferrara, Italy
e-mail: claudio.alessandri@unife.it

Keywords: Nativity Church, narthex, vault system, FE model, non-linear dynamic analyses.

Abstract. *This study presents some results of advanced numerical investigations carried out on the Nativity Church in Bethlehem in order to study the seismic response of the structure and identify possible causes of damage. Detailed three-dimensional finite element models of the church are developed and a damage plasticity material model, exhibiting softening in both tension and compression, is used for masonry. Non-linear bidirectional dynamic analyses are first performed on the model of the entire church in the actual configuration. From an overall analysis of the numerical results, it is possible to observe damage in the vault system, in the semi-domes and near the interlocking of the orthogonal walls. Then, the narthex is separated from the church and is analyzed under seismic excitation applied only in the longitudinal direction. The numerical simulations carried out provide some results that fit reasonably with the actual deformed configuration and can be considered as a useful tool for future rehabilitation interventions.*

1 INTRODUCTION

Very little is known about the history of the transformations of the narthex of the Nativity Church since its construction. The narthex that we see now, or at least the narthex that we can imagine on the basis of the current volumes or of the traces of some ancient and still visible openings on the walls, replaced in the second half of the VI century AD a larger cloister belonging to the previous Church, wanted by Queen Helena, mother of Emperor Constantine, in the IV century. From the outcomes of some archaeological excavations made in the thirties of the last century by R.W. Hamilton and from the results of the studies that have followed, it was possible to go back to the original form of the narthex that, unlike as it is now, was composed of a single volume, had a bigger central door flanked by two smaller side doors in both longer walls and two windows placed symmetrically with respect to the front door, Figure 1.

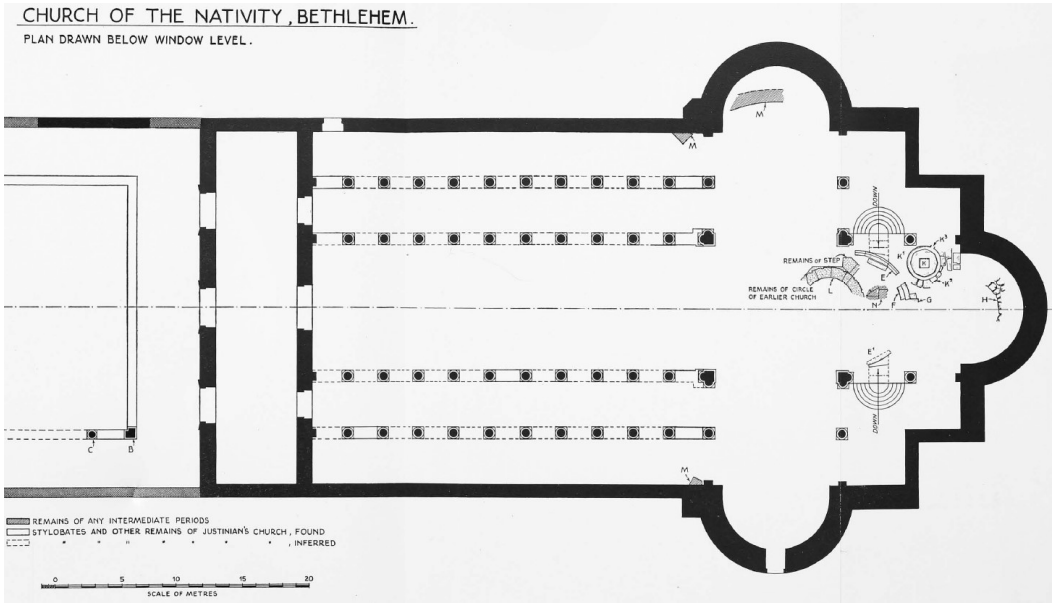

Figure 1: Original narthex of the Church of the Nativity.

From some traces found in the walls during the restoration works still in progress, it was possible to deduce that the original roof of the narthex was made of timber, with a single pitch, as in almost all early Christian and Byzantine basilicas with narthex. The typology of this wooden roof is still unclear, although the traces left on the walls suggest that it consisted of a series of simply supported beams arranged according to the slope of the roof. Anyhow it was a light roof. Over the centuries, especially during the Middle Ages, the Church increasingly took on the appearance of a fortress equipping itself with walls and towers for defense. Some traces of these additions are visible today even in the narthex, in particular in a small protective parapet above the façade and in two thick interior walls, perpendicular to the façade, probably the base of two outer towers, Figure 2 and Figure 3. Maybe, in order to allow these transformations for protective purposes, or in consequence of some destructive earthquakes, the original timber roof was replaced by a system of masonry cross vaults and some openings were infilled or reduced in size. The two internal walls are made of masonry of poor quality, or at least lower than that of the external walls, and they are simply adhering to the façade walls of the narthex and Church without any effective connection.

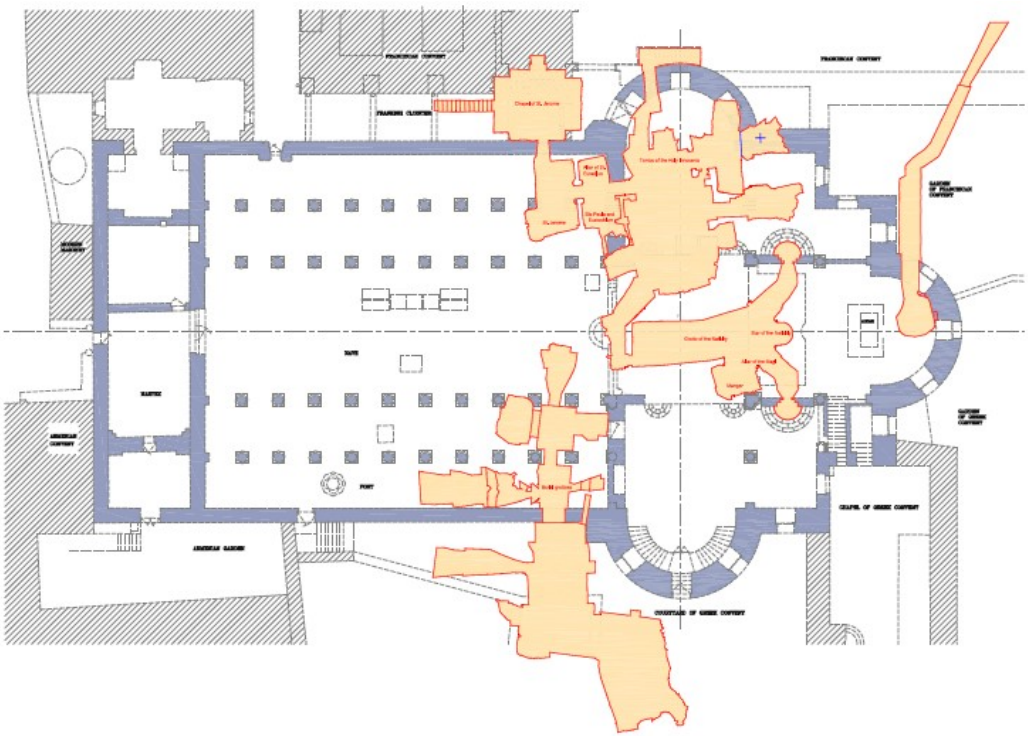

Figure 2: Plan of the Church with the current narthex.

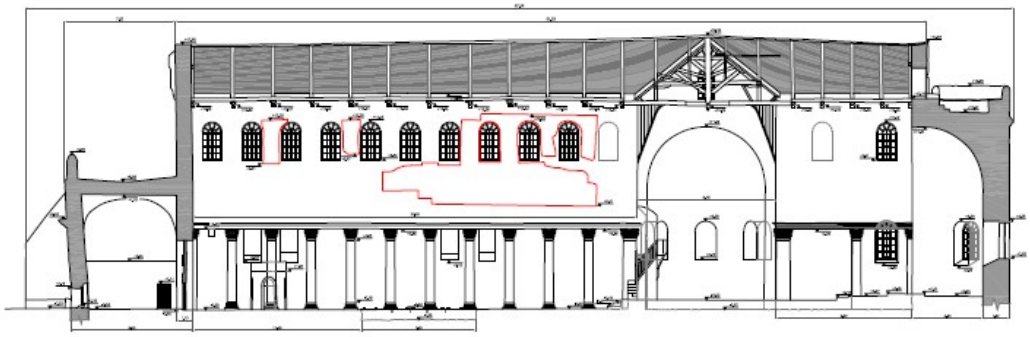

Figure 3: Longitudinal section of the Church

Also the vaults, made of irregular and roughly cut stones, are connected to the façade walls of both narthex and Church only in correspondence of the corbels at the base of the arches and for a height of about 1,10 – 1,30 m. Instead, such vaults are well connected with each other in the direction East-West (the longitudinal direction of the Church) by means of arches, orthogonal to the façade and built with greater and more regular stones; such stones have two different lengths, which alternate to allow for a greater connection between arches and vaults. Even the diagonal arches of the vaults are made with more regular stones, although not as the ones of the arches mentioned before. The thickness of the vaults is not constant everywhere and it varies between 35 – 40 cm. Before starting the restoration the space between the external paving and the extrados of the vaults was filled with sand and remains of a medieval paving. Some inspections made on site have shown that the walls of the narthex continue downwards with a constant thickness up to a depth of 94 cm from the floor; then they have an enlargement of 20 cm on each side up to a depth of 141 cm and continue with a compact layer of stones and mortar for other 150-165 cm before reaching the bedrock. The two side walls of the narthex are 1,00 m thick and have an inner core of undefined thickness; the façade wall,

like the façade of the Church, is 1,15 thick, made of regular stones and with limited or null inner core. The narthex is now connected with the monasteries of the Franciscans Friars (North) and of the Armenian religious community (South), Fig. 2, who, together with the Greek-Orthodox one, manage the activities in the Church according to the current *status quo*. On the external front, towards the square, there is a big buttress probably built after the XVI century: in fact some drawings by Fr. Bernardino Amico, dating back to 1609, show the façade of the narthex still without the buttress, Figure 4.

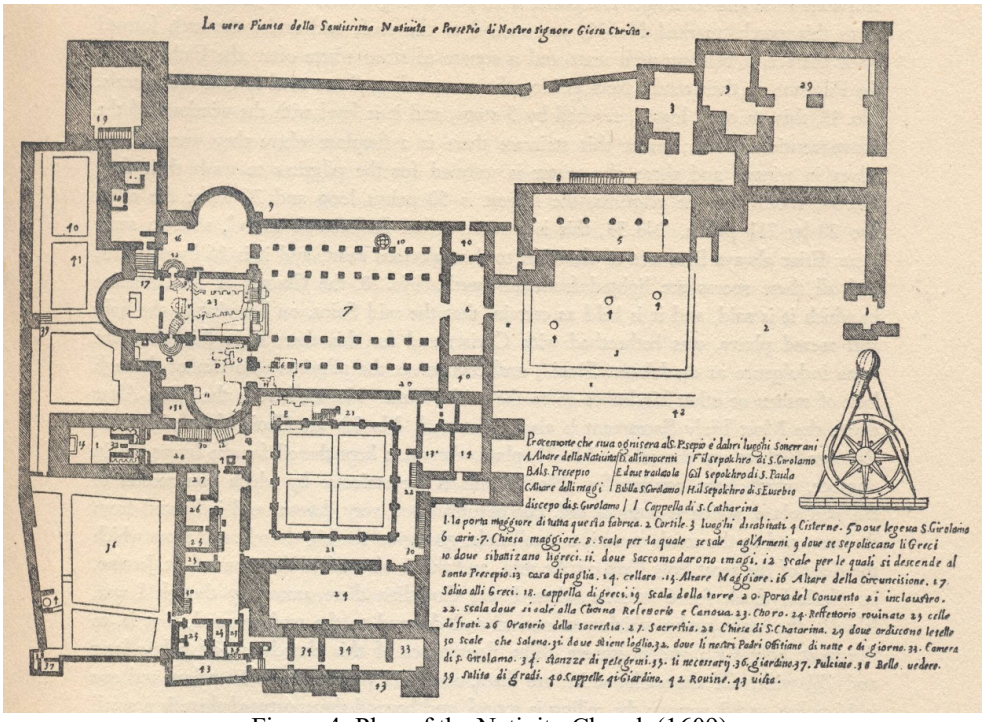

Figure 4: Plan of the Nativity Church (1609).

2 STATE OF STRUCTURAL DAMAGE AND CAUSES

The structure of the narthex is today strongly deformed. The façade wall exhibits a rotation towards the square more pronounced in the middle of its length and starting approximately from the architrave of the Humility door, about one meter above the ground. In consequence of this rotation, the façade wall has undergone a maximum horizontal displacement at the top, approximately in the middle of the wall, of about 40 - 42 cm measured from the base of the parapet. It is a very high value when compared with the height of the wall, about 8.70 meters. If some fractures have occurred in the past, these are now closed due to local interventions of cleaning and consolidation made over the centuries, which shows that the damage evolution is now over and that it was probably over even when the external buttress, still perfectly vertical, was added. The façade of the Church, opposite to the one of the narthex, exhibits a light out-of-plane deformation which starts from the roof of the narthex and achieves 10 cm at the top of the tympanum. In consequence of the rotation of the façade of the narthex the three central vaults, and in particular the one in the middle, underwent vertical displacements downwards in the central zones, detachments from the façade walls and cracks both at the extrados and the intrados. Especially the central vault, propped since the thirties of the last century, exhibits detachments 17-19 cm wide from the narthex façade and 10-11 cm wide from the Church façade Figure 5. Moreover big cracks, parallel to the façades, are visible at the extrados Figure 6.

Figure 5: Detachments from the wall.

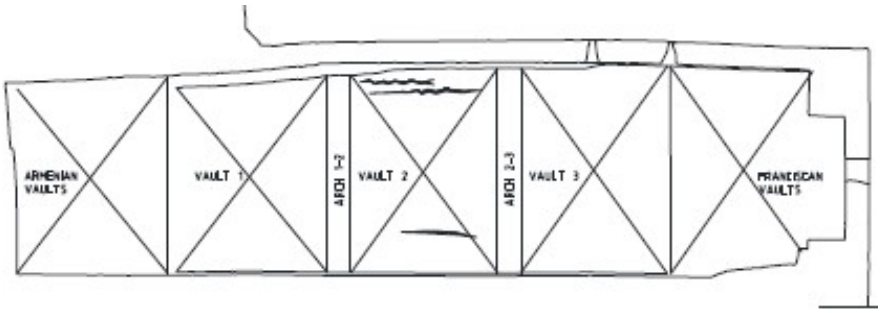

Figure 6: Cracks at the extrados of the central vault.

The arches connecting the vaults to each other (in the East – West direction) and also the ones along the diagonal planes of the vaults are strongly deformed. The causes of these damages have never been clarified. The replacement of the original wooden roof with a set of thrusting masonry vaults probably gave a significant contribution to the rotation of the façade towards the square. It is believed, however, that such thrusts alone cannot have been able to cause maximum horizontal displacements as large as those measured. Therefore, since Bethlehem is in a seismic area which over the centuries underwent several earthquakes, some of them even severe, it is very probable that a seismic event, occurred before the construction of the buttress, was one of the main causes of damage. The external buttress, added in the last centuries, as mentioned above, shows no sign of rotation and no differential vertical displacement.
The aim of this work is to identify, through a proper numerical simulation, the seismic event that, together with the thrust of the vaults, might have caused damage in the vault system and the present out-of-plane deformation of the narthex façade and of the tympanum of the main entrance. To this purpose, a 3D finite element model of the entire Church was built and analyzed by using the commercial software ABAQUS. The model reproduces the actual configuration of the church, but without the external buttress and without connections with the monasteries of the Franciscans Friars and of the Armenian religious community. The vaults at both ends of the narthex (North and South) were not modelled because their survey had not been yet carried out at the time of the present analysis. The presence of the three internal walls was taken into account. It is worth noting that a three-dimensional structural analysis of the entire Church is significant when a good level of interlocking among the structural elements is guaranteed. If such connections are not reliable, as in the case of the Church of the Nativity, it is, on the other hand, advisable to perform numerical analyses on smaller portions that may be affected by local collapse mechanisms.
A detailed finite element model of the narthex was then created by using a finer discretization. The model reproduces, with some approximations and simplifications, the structure of the narthex as depicted by Fra Bernardino Amico at the beginning of the XVII century, without the external buttress, with a unique access door (the Humility door) and only two small

windows on the façade, with masonry cross vaults instead of the original wooden roof. The side walls of the narthex are supposed clamped to the Church, the height and thickness of the vaults have values computed as an average of the real ones and the vaults are connected to the façade walls of both narthex and Church. Moreover they are connected to each other in the East - West direction (longitudinal direction of the Church) by means of arches similar to the real ones, Figure 6, and clamped to the façades of the narthex and Church. The façade of the Church is supposed to be clamped at the intersection with the orthogonal walls of the nave and the aisles. Figure 7 shows a view of the system of masonry cross vaults in the model of the narthex.

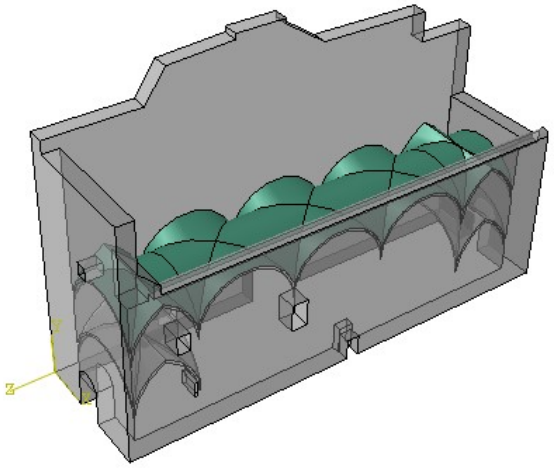

Figure 7: The system of masonry cross vaults in the model of the narthex.

3 FINITE ELEMENT NUMERICAL MODELS

With the aim of reproducing the actual state of damage on the narthex it is chosen to study the effects of a possible earthquake by non-linear dynamic analyses by applying spectrum compatible acceleration time-histories at the base of the structure. Such a method of analysis is very time consuming, but it is much more accurate and reliable than other approaches for its capability to identify in- and out-of-plane, as well as local and global failure mechanisms. Different three-dimensional finite element models of the church and the narthex are implemented in Abaqus, taking into consideration geometrical (large displacement effects) and material non-linearity (elastic-plastic with damaging behavior of the masonry material). Despite the general drawbacks regarding non-linear dynamic analyses, the use of sophisticated 3D models requires a relatively reasonable computational effort on sufficiently powerful workstations, if the discretizations are not excessively refined and the material models do not exhibit strong softening.

On the other hand, Italian Guidelines for the built heritage specify that such analyses can be conducted using finite element models and considering suitable constitutive models. Such models should be capable of reproducing the typical strength and stiffness degradation exhibited by the masonry material in the inelastic range. Italian Code on Constructions NTC 2008 and subsequent explicative notes underline that the aim of dynamic analyses would be the evaluation of the structure in the non-linear range under an expected accelerogram, allowing for a comparison between required and available ductility. Also, it is possible to verify the integrity of the structural elements which can potentially show brittle behavior.

When dealing with material properties assumed and available in Abaqus software code, the so-called “Concrete Damage Plasticity” model was adopted. Such a model is based on the assumption of a scalar isotropic damage with distinct damage parameters in tension and

compression. It is particularly suitable for applications in which the material exhibits damage, especially under load-unload conditions and hence for dynamic analyses. An elastic-plastic behavior in both tension and compression can be also taken into account.
To describe the multi-dimensional behavior in the inelastic range, masonry is assumed obeying a Drucker-Prager strength criterion with non-associated flow rule. A value equal to 10° is adopted for the dilatation angle, which seems reasonable for a masonry material subjected to moderate-low levels of vertical compression, also in agreement with experimental evidences available in the literature. To avoid numerical convergence issues, the tip of the conical domain of the Drucker-Prager strength domain is smoothed with a function having hyperbolic shape. Abaqus code allows ruling smoothing by means of the so-called eccentricity parameter, which represents the length of the segment between the points of intersection of the cone and of the hyperbola with the p axis in the p-q space. A value equal to 0.1 is adopted for the eccentricity parameter.
Experimental results reported by Page on regular masonry wallets and successive numerical models show that such a material exhibits a moderate orthotropy ratio (around 1.2) under biaxial stress states in the compression-compression region. Obviously, such feature cannot be taken into account when an isotropic model, like the present one, is used. However, the use of isotropic models (like concrete smeared crack approach available in both Ansys and Adina) is commonly accepted in the literature after adapting the parameters to fit and average behavior between vertical and horizontal compression. A suitable model should also take into account the ratio between the ultimate compression strength in biaxial stress states and in uniaxial conditions. Such a ratio, which exhibits some similarities between concrete and masonry, is reasonably set equal to 1.16.
In tension the stress-strain response follows a linear-elastic relationship until the peak stress σ_{t0} is reached. Then, micro-cracks start to propagate in the material, a phenomenon which is macroscopically represented by softening in the stress-strain relationship. Under axial compression, the response is linear up to the value of the yield stress σ_{c0}. After the yield stress, the response is typically characterized by hardening, which anticipates compression crushing, represented by a softening branch beyond the peak stress σ_{cu}.
Damage variables in tension and compression are defined by means of the following standard relationships:

$$\sigma_t = (1-d_t)E_0\left(\varepsilon_t - \varepsilon_t^{pl}\right)$$
$$\sigma_c = (1-d_c)E_0\left(\varepsilon_c - \varepsilon_c^{pl}\right) \quad (1)$$

where σ_t (σ_c) is the mono-axial tensile (compressive) stress, E_0 is the initial elastic modulus, ε_t (ε_c) is the total strain in tension (compression), ε_t^{pl} (ε_c^{pl}) is the equivalent plastic strain in tension (compression). When strain reaches a critical value, the material elastic modulus degrades in the unloading phase to $E < E_0$. In particular, within the simulations, a reduction equal to 5% of the Young modulus with respect to the initial value is assumed for a plastic deformation equal to 0.003.
The issue of mechanical properties to adopt for the constituent materials results particularly difficult, especially in the absence of ad hoc experimental campaigns and specific indications by local building codes. It is common opinion, however, that the major damages registered in historical churches are a consequence of very poor mechanical properties of joints, whereas clay bricks exhibit a quite high strength. In the absence of specific indications, it was chosen to refer to what stated by Italian Code for existing masonry buildings.

As a matter of fact, masonry is a material which exhibits distinct directional properties due to the mortar joints, acting as planes of weakness.

Considering the well-known limitation of use of both micro-modelling and homogenization at large scale, isotropic macro-models are adopted for masonry. The reason for adopting an isotropic material stands in the impossibility to evaluate many parameters

necessary for anisotropic materials in the inelastic range, in the absence of ad-hoc experimental characterizations. Finally, it is worth noting that commercial codes rarely make available to users anisotropic mechanical models suitable to describe masonry with regular texture in the non-linear range.

According to Italian Code NTC 2008 and subsequent Explicative Notes, the mechanical properties assumed for masonry material depend on the so-called knowledge level LC, which is related to the so-called Confidence Factor FC. There are three LCs, labeled from 1 to 3, related to the knowledge level about the mechanical and geometrical properties of the structure. The knowledge level LC3 is the maximum, whereas LC1 is the minimum. For the cases at hand, a LC1 level is assumed in the absence of specific in-situ test results.

Confidence Factor FC summarizes the knowledge level regarding the structure and the foundation system from a geometric and mechanical point of view. It can be determined defining different partial confidence factors FCk (k=1,4), on the basis of some numerical coefficients present in Italian Code (Table 4.1 Italian Guidelines). Due to the limited knowledge level achieved in this case, the highest confidence factor (FC = 1.35) was used.

The values adopted for cohesion and masonry elastic moduli are taken in agreement with Table C8A.2.1 of the Explicative Notes, assuming a masonry typology with very poor mechanical properties of the joint and quite regular courses. With the lowest knowledge level LC (confidence factor FC=1.35), Italian Code requires to select, in Table C8A.2.1, the lower bound values for strength and the average values between lower and upper bound for elastic moduli.

The application of the acceleration time-history occurs at the second step, where the structure is unrestrained using trailers, thus allowing it to move along the direction of the seismic action. The numerical analyses are carried out by means of a dynamic approach with implicit integration in the time domain, using a time step equal to 0.005 s, which corresponds to the accelerogram registration time interval. The results of the analyses conducted in this study are reported in the following sections.

4 NON-LINEAR DYNAMIC ANALYSES OF THE CHURCH

A detailed three-dimensional finite element model of the entire Church was developed by means of ABAQUS code, Figure 8, with the aim of investigating the seismic behavior of the structure through non-linear dynamic analyses. A finite element discretization, based on four nodes tetrahedral elements presenting an average size of 0.40 m, was adopted. The total number of elements of the model was equal to 131551. In particular, the mesh was refined near the regions where the main failure mechanisms were likely to start. Since not negligible out of plane displacement may occur during a seismic event, large displacement effects were considered. Perfect connection was assumed between perpendicular walls.

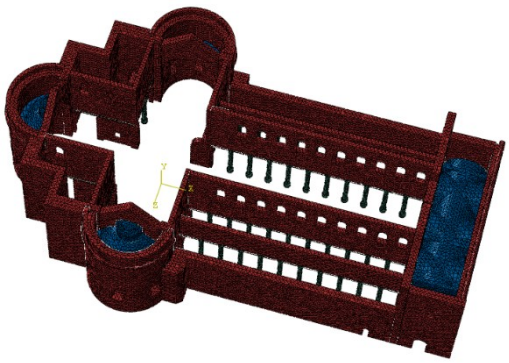

Figure 8: Finite element model of the entire Church of the Nativity.

The bidirectional non-linear dynamic analyses were performed by using artificial accelerograms generated by means of the software code SIMQKE. In this study the Church was subjected to spectrum compatible accelerograms corresponding to a peak ground acceleration equal to 0.15g according to Eurocode 8. The area where the Church is located is a medium-intensity seismic area with a_g = 0.15g, where a_g is the maximum horizontal acceleration occurring in the area, with a 10% of probability of exceeding this value over 50 years. Due to the complexity of the model and the high computing time of this type of analysis, the duration of the accelerograms was set equal to 10 s. In Figure 9 the contour plots of tension damage (red color is associated to full (1) damage and blue color to zero (0) damage), are shown from different points of view at the end of the numerical simulation. From an overall analysis of the numerical results, it is possible to notice that the Church exhibits significant damage under the expected earthquake excitation. It is evident that the damage spreads very quickly in the vault system, in the semi-domes and near the interlockings of the orthogonal walls. The damage in the vaults starts in the lateral right corner and then propagates towards the middle.

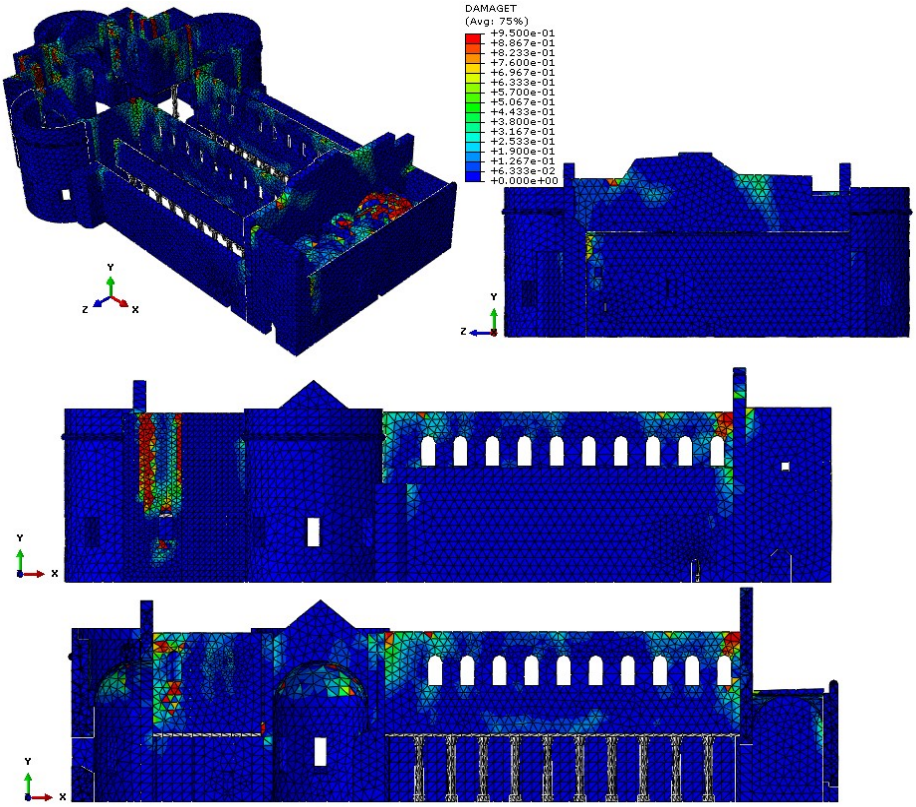

Figure 9: Contour plots of tension damage at the end of the non-linear dynamic analysis (red, 1: full damage; blue, 0: no damage).

Figure 10 shows the horizontal displacement time history for various control nodes of the Church along both the longitudinal and transversal directions. The main control nodes of the Church model monitored during the numerical simulations are shown in the same figure. In the longitudinal direction a maximum top displacement equal to 6 cm was computed for the top of the tympanum (control node P1) after about 7 s from the beginning of the ground motion. The stiffening presence of the internal walls of the narthex have the effect of reducing the out-of-plane rocking of the narthex façade during the application of the accelerograms. The maximum top displacement measured on the top of the narthex façade is about 5.5 cm.

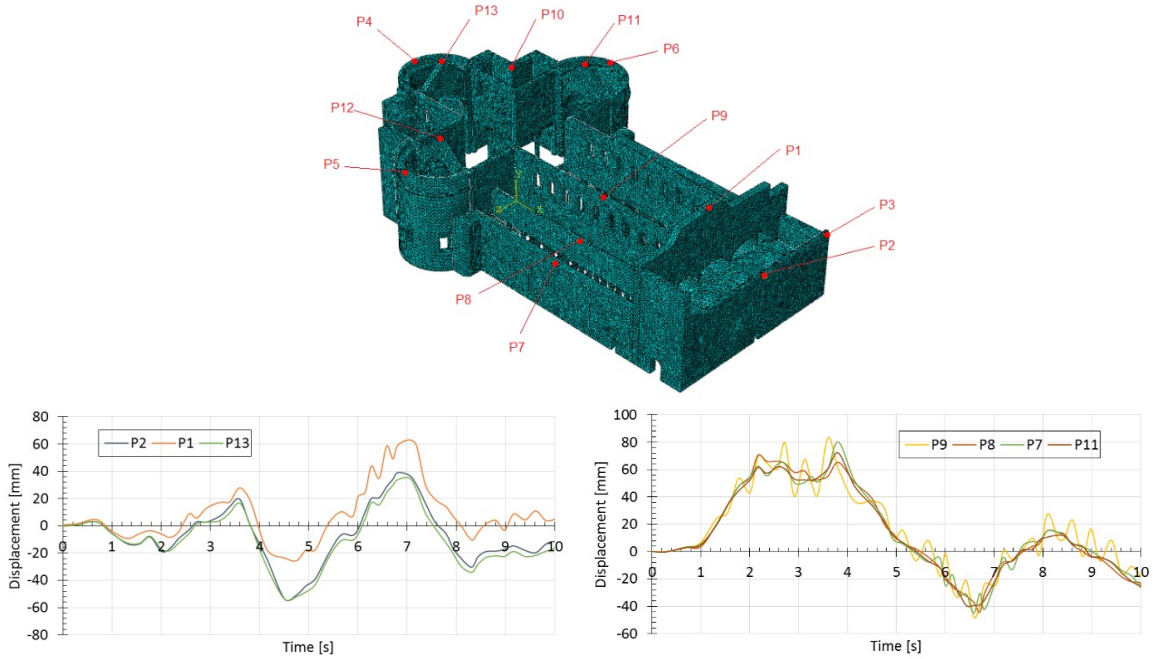

Figure 10: Displacement time history of some control nodes along the longitudinal and transversal directions during non-linear dynamic analyses.

5 NON-LINEAR DYNAMIC ANALYSES OF THE NARTHEX

The results of the non-linear dynamic analyses performed on the model of the whole Church showed the vulnerability of the structure under horizontal loads pointing out some critical regions. It is worth noting that the use of sophisticated three-dimensional finite element models requires a large computational effort and the model of the entire Church proved to be very-time consuming under bidirectional non-linear dynamic analyses. A finite element model of the narthex only was created in order to perform different non-linear dynamic analyses with various peak ground accelerations.

Then, the seismic performance of the narthex was assessed through non-linear dynamic analyses with response spectrum-compatible artificial accelerograms. A finer mesh, consisting of about 85000 tetrahedron elements and depicted in Figure 11, could be used for the narthex in this model. The internal walls were not modelled in order to reproduce the original configuration of the narthex and to neglect the stiffening effect provided by these elements.

The evaluation of the seismic response of the narthex was carried out using an artificial accelerogram, with duration equal to 20 s. For sake of simplicity, numerical analyses were carried out only in the longitudinal direction. The accelerogram used was generated by means of the software code SIMQKE in order to match the Eurocode 8 response spectrum. Different peak ground accelerations ranging between 0.15g and 0.25g were considered for the analyses.

This finite element model was used to identify the possible different collapse mechanism that can occur in the narthex. A ground motion applied in the longitudinal direction can determine the detachment of the narthex façade from the façade of the church, creating tensile stresses in the vault system. The vault system represents a critical element for the narthex and it is expected to undergo significant damage at the beginning of the numerical simulation.

Figure 11 describes the tensile and compression damage evolution, respectively, during the non-linear dynamic analysis. The results are reported at the end of the analysis (20 s). It can be noted that damage concentrates mainly in the cross vault system and, to a small extent, on

both the façades. In particular, the tensile damage starts at the base of the vault system and then propagates to the middle part involving the whole system of vaults.

On the contrary, the compression damage starts at the top of the vault system and then propagates to the base. It can be noted that the interlocking of the longitudinal walls with the western façade of the Church tends to experience considerable damage.

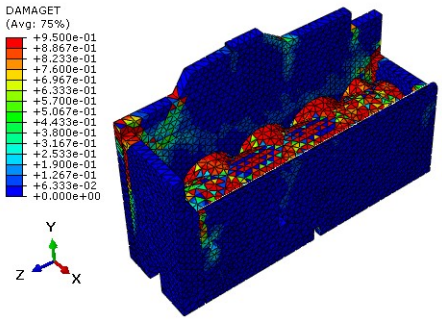

Figure 11: Contour plots of the tensile damage in the narthex at the end of the numerical simulation (red, 1: full damage; blue, 0: no damage).

The horizontal and vertical displacement time histories for some control nodes are reported in Figure 12. All the control nodes of the narthex model monitored during the numerical simulations are shown in the same figure. The horizontal displacements of three meaningful control nodes are measured during the numerical simulations: they are located on the top of the narthex façade, of the tympanum and of the central cross vault. The maximum horizontal displacement (about 10 cm) is observed for the control node N14 at the top of the tympanum of the main entrance. The narthex façade exhibits a peak horizontal displacement equal to about 6 cm. As regards the vertical displacement, the maximum value, equal to 9 cm, is registered for the central vault.

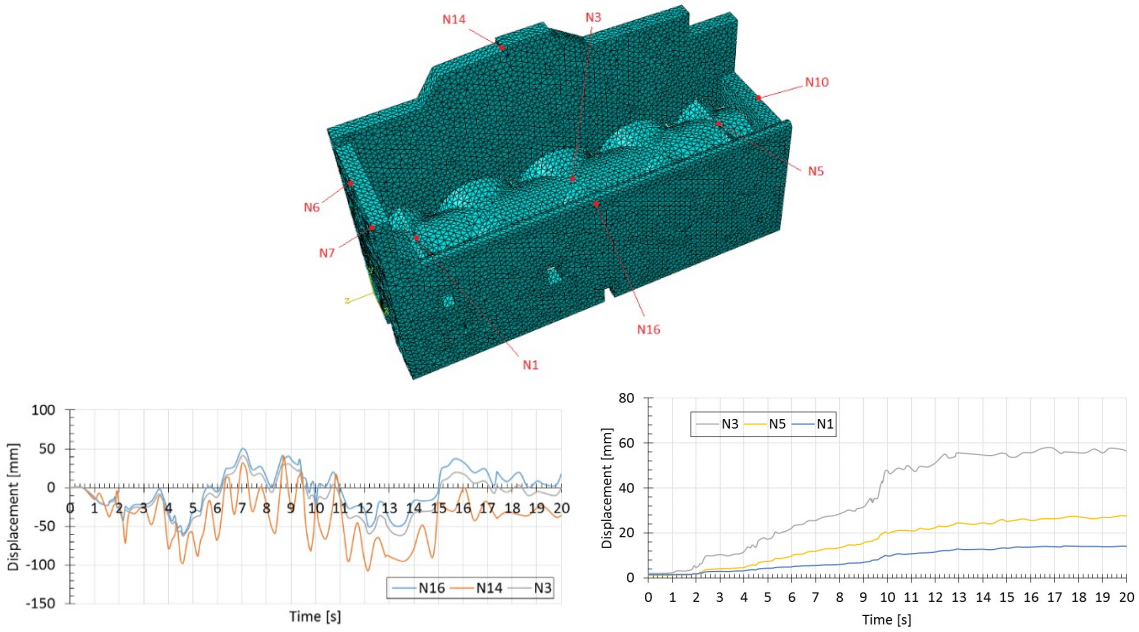

Figure 12: Horizontal and vertical displacement time-history of some control nodes during non-linear dynamic analyses.

The maximum values of the vertical displacements of the control nodes of the cross vaults are shown in Figure 13 for different peak ground accelerations. As can be noted, the maximum vertical displacements of the central vault is always larger than the other vaults. For higher values of seismic intensity levels (a_g=0.25g), the central vault presents a maximum value of vertical displacement equal to 15 cm.
The maximum values of the horizontal displacement of three meaningful control nodes are shown in Figure 14 for different peak ground accelerations. It can be noted that the peak values of the horizontal displacement of the narthex façade are always smaller than the top of the tympanum of the western façade. Under a seismic intensity level of 0.25g the tympanum exhibits peak displacements equal to about 35 cm, whereas the maximum displacement registered for the narthex façade is about 20 cm.

Non-linear dynamic analyses are able to provide, among other information, residual displacements of the control nodes. The maximum values of the residual displacements (35 cm) are registered for the western façade of the Church when subjected to seismic excitation with a_g=0.25g. As can be observed, the residual displacement found for the façade of the narthex is about 20 cm, still lower than the real ones, but indicating that a seismic event may be the cause of the present state of degradation. Probably larger residual displacements might be achieved by simulating the occurrence of a sequence of ground motions, as confirmed by the chronicles of the earthquakes in the area.

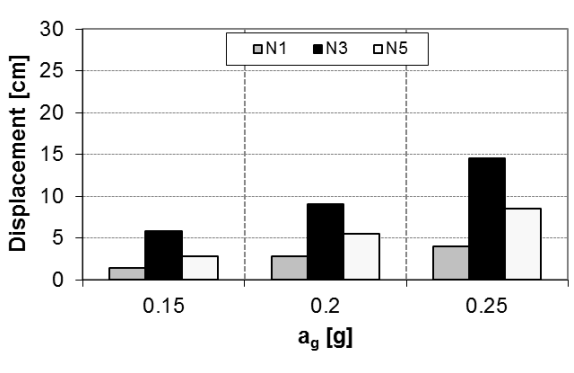

Figure 13: Maximum values of vertical displacement of some control nodes for different peak ground accelerations.

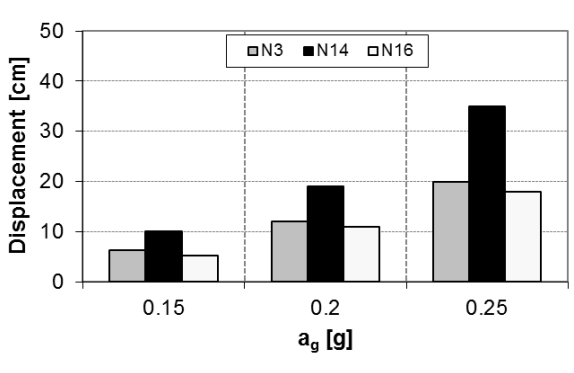

Figure 14: Maximum values of horizontal displacement of some control nodes for different peak ground accelerations.

6 CONCLUSIONS

This study summarizes the numerical investigations carried out on the narthex of the Nativity Church in Bethlehem. Advanced finite element numerical models accounting for

masonry damage and softening have been used within demanding non-linear dynamic simulations in order to identify the possible causes of damage in the narthex.
Non-linear bidirectional dynamic analyses were first performed on the model of the entire Church in the actual configuration. From an overall analysis of the numerical results, it is possible to notice that the Church exhibits damage for the expected earthquake excitation. It is evident that damage spreads very quickly in the vault system, in the semi-domes and near the interlocking of the orthogonal walls. The damage in the vaults starts in the lateral right corner and then propagates towards the middle.

Then, the narthex was separated from the Church and was analyzed under seismic excitation applied only in the longitudinal direction. Numerical results show the behavior of the narthex is considerably affected by the presence of the vaults that act as connecting element between the western façade of the Church and the façade of the narthex. During a moderate intensity earthquake, the vault system is subjected to significant stresses and consequently to severe damage. The second critical element of the narthex is the western façade that tends to show a local overturning mechanism due to the gradual accumulation of damage near the base of the vault system. Moreover, the façade of the narthex can reach significant displacements under seismic actions with a_g=0.25g. The results seem to indicate that the rotation of the narthex façade, with a consequent maximum out-of-plane displacement of 40 cm approximately, is probably due to a seismic event of great intensity or to several seismic events occurred in sequence over time. Certainly, results closer to the measured data can be obtained by introducing proper unilateral contact conditions at the interface between vaults and façade walls or between longitudinal walls and façade walls.

REFERENCES

[1] DPCM 9/2/2011. Italian Guidelines for the evaluation and the reduction of the seismic risk for the built heritage, with reference to the Italian norm of constructions. Rome, Italy, 2011.

[2] DM 14/01/2008. New technical norms on constructions. Rome, Italy, 2008.

[3] Circolare n° 617 del 2 febbraio 2009. Instructions for the application of the new technical norms on constructions. Rome, Italy, 2009.

[4] Hamilton R.W. (1934). Excavations in the Atrium of the Church of the Nativity, Q Depart Antiq Palestine; 3: 1–8.

[5] Harvey W. (1938). Recent Discoveries at the Church of the Nativity, Bethlehem, Archaeologia; 87: 7–17.

[6] Fra Bernardino Amico (1609). Trattato delle piante et imagini dei sacri edificii di Terra Santa, Franciscan Press, Jerusalem 1953.

[7] Bacci M., Bianchi G., Campana S., Fichera G. (2012). Historical and archaeological analysis of the Church of the Nativity, *Journal of Cultural Heritage*, 13: 5–26.

[8] Alessandri C., Mallardo V. (2012). Structural assessments of the Church of the Nativity in Bethlehem. *Journal of Cultural Heritage*, 13: 61–69.

[9] Abaqus, Theory manual, version 6.14.

[10] Milani G., Valente M. (2015). Comparative pushover and limit analyses on seven masonry churches damaged by the 2012 Emilia-Romagna (Italy) seismic events: possibili-

ties of non-linear Finite Elements compared with pre-assigned failure mechanisms. *Engineering Failure Analysis*, 47, pp. 129-161

[11] Milani G., Valente M. (2015). Failure analysis of seven masonry churches severely damaged during the 2012 Emilia-Romagna (Italy) earthquake: Non-linear dynamic analyses vs conventional static approaches. *Engineering Failure Analysis*, 54, pp. 13-56.

[12] Milani G., Valente M. (2014). Safety assessment of historical masonry churches based on pre-assigned kinematic limit analysis, FE limit and pushover analyses. 10th International Conference of Computational Methods in Sciences and Engineering, 4-7 April, Athens, Greece. *AIP Conference Proceedings*, 1618.

[13] Valente M., Milani G. (2016). Seismic assessment of historical masonry towers by means of simplified approaches and standard FEM. *Construction and Building Materials*, 108, pp. 74-104.

[14] Valente M., Milani G. (2016). Non-linear dynamic and static analyses on eight historical masonry towers in the North-East of Italy. *Engineering Structures*, 114, 241-270.

[15] Milani G., Valente M. (2015). Numerical insight into the seismic behavior of eight masonry towers in Northern Italy: FE pushover vs non-linear dynamic analyses. 11th International Conference of computational methods in sciences and engineering, 20-23 March, Athens, Greece. *AIP Conference Proceedings*, 1702.

ECCOMAS Congress 2016
VII European Congress on Computational Methods in Applied Sciences and Engineering
M. Papadrakakis, V. Papadopoulos, G. Stefanou, V. Plevris (eds.)
Crete Island, Greece, 5–10 June 2016

DYNAMIC BEHAVIOUR AND EARTHQUAKE PERFORMANCE OF GREEK BASILICA CHURCHES WITH FOUNDATION DEFORMABILITY

George C. Manos[1], **Evaggelos Kozokipoulos**[1], **and Lambros Kotoulas**[1]

[1] Laboratory of Strength of Materials and Structures, Aristotle University of Thessaloniki, Greece, gcmanos@civil.auth.gr

Keywords: Greek Basilicas, Dynamic Behaviour, Earthquake Performance, Stone Masonry, Soil Foundation Deformability.

Abstract. *This paper attempts to address the earthquake performance of Basilica churches in parts of Greece during the last 30 years. Towards this objective use is made of in-situ observations together with relatively simple numerical tools. The numerical study includes soil-foundation deformability. The earthquake performance of three specific stone masonry Basilica churches is investigated. The second and third of these churches are simply covered by a wooden roof whereas the first has also a stone masonry vaulted superstructure under its wooden roof. All three churches developed significant structural damage typical of churches of this Basilica typology as was observed in Greece during the last 30 years. It has been observed that such churches develop structural damage to the masonry walls and vaults, in certain cases quite serious, that is believed to arise from the amplitude of the gravitational and seismic actions combined with the deformability of the foundation which is included in the current investigation. The numerical models simulating the main structural system of these churches are supplemented at the foundation level with flexible springs in an effort to capture the influence of such soil-foundation deformability. Simple numerical analysis results together with assumed strength values are utilized to predict the behaviour of the various masonry parts that belong to the longitudinal and transverse peripheral wall in in-plane shear and normal stress as well as out-of-plane flexure. The recorded ground acceleration during the Kozani 1995 earthquake for the first two churches and the 1978 Thessaloniki earthquake for the third church, as it was recorded at a relatively close distance, is used in this numerical investigation. Towards this end, the dynamic characteristics in terms of eigen-modes and eigen-frequencies of the examined structural systems are also utilized.*

1 INTRODUCTION

During the last thirty years various parts of Greece have been subjected to a number of damaging earthquakes ranging from Ms=5.2 to Ms=7.2 on the Richter scale [1]. One of the most demanding tasks for counteracting the consequences of all these seismic events was the effort to ensure the structural integrity of old churches that were built in periods ranging from 400 A.D. up to today; in many cases they sustained considerable damage ([1], [2], [3], [4], [5]). The earthquake behaviour of churches belonging to the so-called Post-Byzantine period (16th to 19th century A.D.) has been studied numerically in some detail ([2], [3], [4], [5], [6]) In all these cases the foundation was considered to be non-deformable. However, this is a gross approximation as in most cases these churches are founded on deformable soil. In some instances, the deformability of the soil caused considerable damage as is the case of the church of The Assumption of the Virgin Mary at Dilofo-Voio-Kozani, as will be presented in section 2 ([7], [8]). In some other cases the main cause of recent damage is the earthquake activity that is accentuated by the deformability of the soil ([9], [10], [11], [12]). This is presented in the section 3, where the damage of the church of Agia Triada at Vithos-Kozani and of Profitis Elias at Siatista-Kozani is also included, as well as in section 4 where the earthquake performance of the old Byzantine church of Achiropoiitos in Thesalloniki is examined. It must be noted that all these churches were built in a number of phases on old existing sacred sites. During the Turkish occupation the most prominent Christian churches were transform to mosques or prohibitions were imposed forbidding the construction of new churches but allowing the maintenance of existing ones, after special permit [13]. In what follows an overview of three specific cases of Greek Byzantine churches where the foundation deformability influenced the dynamic and earthquake behaviour is presented and discussed.

Figure 1. Damage to the South-East corner

Figure 2. Partial collapse of the central dome

2 THE CHURCH OF THE ASSUMPTION OF THE VIRGIN MARY AT DILOFO

The West part of this church is founded on hard soil (weathered flysch layers) whereas the East part is founded on relatively soft soil that was deposited on top of the layers to compensate for the natural slope at this location ([7], [8]). The unequal settlement of the foundation of the stone masonry walls as well as of the internal columns that supported the vaulting system, which covered this church, caused considerable damage. A very wide crack initiates at the top of the East peripheral wall near the apse and propagates towards the bottom of this wall being inclined to the South-East corner (figure 1). Furthermore, a similarly wide crack propagates through the North peripheral wall from top to bottom. It must be noted that

the thickness of these masonry walls varies from 750mm to 800mm. From this extensive peripheral wall damage, the vaulting system that is supported by these peripheral walls also suffered extensive cracking that eventually caused the partial collapse of a part of the central dome, as shown in figure 2.

Initially, the 3-D numerical simulation of this church, including the peripheral walls, the vaulting system of the superstructure and the wooden roof, assumed that the foundation was non-deformable. The results of the modal analysis for the church supported on the non-deformable foundation are shown in a summary form in figures 3a and 3b. In these figures the most significant eigen-modes are depicted together with the corresponding values of the eigen-periods as well as the modal mass participation ratios either in the x-x direction (Ux) or in the y-y direction (Uy). As can be seen the longest eigen-period is, as expected, for the fundamental x-x direction translational mode, with a value equal to 0.228seconds that mobilizes 72.48% of the total mass. The next longest eigen-period is for the fundamental y-y direction translational mode, with a value equal to 0.132seconds that mobilizes 59.37% of the total mass.

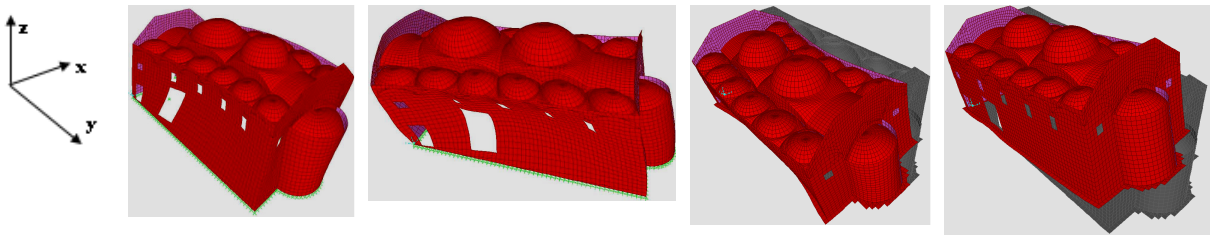

Figure 3. Eigen-modes

a) Mode 1, T1=0.228sec Ux=72.48%

b) Mode 2, T2=0.132sec Uy=59.37%

c) Mode 1, T1=0.391sec Ux=83.48%

d) Mode 2, T2=0.276sec Uy=78.37%

Next, layers of deformable soil were introduced beneath the foundation of all the peripheral walls and internal colonnades. The stiffness of these soil layers was varied with the depth as well as in plan in order to simulate the relatively hard soil at the West part of the church and the relatively soft soil at the North-East part of the church. The results of the modal analysis for the church (low-stiffness soil layers) supported on the deformable foundation are shown in a summary form in figures 3c and 3d. In these figures the most significant eigen-modes are depicted together with the corresponding values of the eigen-periods as well as the modal mass participation ratios either in the x-x direction (Ux) or in the y-y direction (Uy). As can be seen the longest eigen-period is, as expected, for the fundamental x-x direction translational mode, with a value equal to 0.391 seconds that mobilizes 83.48% of the total mass. The next longest eigen-period is for the fundamental y-y direction translational mode, with a value equal to 0.276seconds that mobilizes 78.37% of the total mass. As can be seen, apart from the lengthening of the fundamental eigen-period values, the deformable foundation resulted in a larger portion of the mass being mobilized for the first two translational eigen-modes in the x-x and y-y direction than for the case of non-deformable foundation.

The 3-D numerical representation of the church, including the peripheral walls, the vaulting system of the superstructure and the wooden roof were subjected to load combinations of either 0.9G±1.4Ex or 0.9G±1.4Ey, where G is the gravitational loads and Ex, Ey the earthquake forces along the x-x axis (longitudinal East-West direction) or the y-y axis (transverse North-South direction, respectively.

This was done for both the non-deformable and the deformable foundation. Selected results of the obtained maximum stress response are shown in figures 4a to 4d. More results

are given by Manos et al. ([7], [8]). The following summarize the most significant observations of this numerical study:

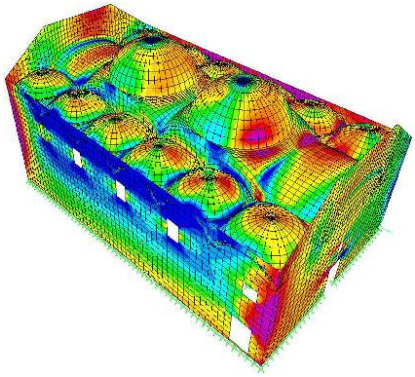

4a) **Non-deformable foundation**, $\boldsymbol{\sigma_{11}}$ top face, max $\boldsymbol{\sigma_{11}}$ = 0.38 MPa (NW view) 0.9G+1.4(+Ex)

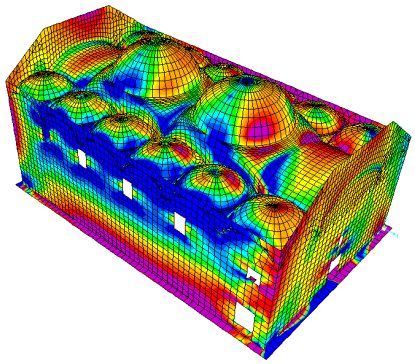

4b) **Deformable Foundation,** $\boldsymbol{\sigma_{11}}$ top face, max σ_{11} = 0.53 MPa (NW view) 0.9G+1.4(+Ex)

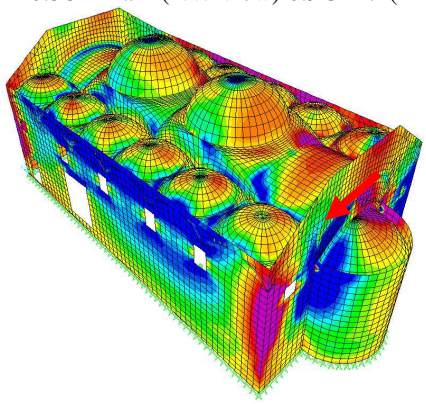

4c) **Non-deformable foundation,** σ_{11} bottom face, max $\boldsymbol{\sigma_{11}}$ = 0.46 MPa (SE view)) 0.9G+1.4(-Ex)

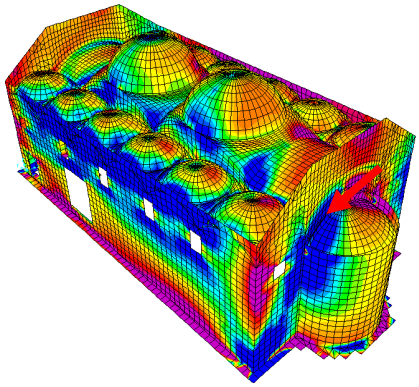

4d) **Deformable Foundation,** σ_{11} bottom face, max $\boldsymbol{\sigma_{11}}$ = 0.64 MPa (SE view) 0.9G+1.4(-Ex)

- The foundation deformability due to layers of soft-soil deposits at the North-Eastern part of the foundation, as was approximated numerically, increased both the fundamental translational modes eigen-periods and the corresponding modal mass participation factors.
- This foundation deformability, as was approximated numerically, also increased the maximum predicted vertical and horizontal displacement values. This increase was threefold for the horizontal displacements and ten-fold for the vertical displacements.
- This foundation deformability, as was approximated numerically, also increased the maximum predicted axial stress values parallel to the bed-joint. This increase was of the order of 20% up to 40%.
- Due to this increase of the predicted maximum axial stress values parallel to the bed-joint, arising from the foundation deformability, the assumed corresponding tensile strength is exceeded in all the locations where actual damage was observed.
- Despite the simplicity of the adopted numerical modeling as well as of the assumed failure criteria in the direction parallel to the bed-joint, this simple failure criterion and the predicted relevant maximum stress values can explain the observed damaged in all the locations.
- Further research is necessary in order to establish stone masonry strength values and failure criteria that are based on tests representative of the stone masonry that is investigated.
- The capabilities of more refined numerical modeling should also be investigated.

3 THE CHURCH OF PROFITIS ILIAS AT SIATISTA – KOZANI.

This is also a Post-Byzantine three nave Basilica built in 1701 A.D. on the top of a hill in the town of Siatista of the prefecture of Kozani. It also has a wooden roof without the vaulting system of the Basilica church described in section 2. The horizontal dimensions of this church are 23.25m in length and 16.60m in width. The top of the roof lies at 7.1m from the floor level of the interior of this church. The naves are formed by 4-column colonnades built with stone masonry. The lower part of the key of each arch of these colonnades lies at 5.25m from the floor level of the interior of this church. All the exterior walls are made of stone masonry. Apart from the main church a narthex was built at the North side at a later stage; this is of a relatively lower height than the main church. The West part of the church is allocated to the women's quarters that is separated from the rest of the interior by a mid-transverse wall. The South longitudinal wall is supported by a system of wooden beams. These were installed after the Kozani-1995 earthquake sequence. Additional wooden supports are also placed at the mid-transverse wall as well as at the mid-span of a longitudinal beam that spans the women's quarters from East to West. According to past records, the structural system of this church showed signs of distress from soil-settlement sometime before the occurrence of this particular earthquake sequence. The records do not give information of any countermeasures being taken in the past up to the point of the earthquake occurrence. The main structural damage, as recorded after this earthquake sequence, is described below. Inclination of the South longitudinal wall outwards that is accompanied by extensive cracking at its joints with the East and West exterior masonry walls as well as with the mid-transverse wall. Cracking is evident at the arches of the colonnades. Recently, almost 20 years after this earthquake damage, a number of counter measures were introduced towards repairing the masonry walls as well as introducing a relatively shallow reinforced concrete beam at the foundation level from the exterior of the West, South and East peripheral walls.

The numerical investigation of this church included the following ([9], [10], 11]):

a) Simulation of the behaviour assuming non-deformable supports at the foundation level.
b) Simulation of the behaviour assuming deformable supports at the foundation level, introducing at this level elastic springs with properties reflecting the actual soil deformability that was found from in-situ sampling.

The soil consists of clay in its upper layers. For quantifying the stiffness of these soil layers use was made of the data from three bore-holes drilled in the vicinity of the church relevant to the constitution of the soil deposits at a depth up to 15m. All the numerical simulations assumed elastic behaviour with relatively low-values of the modulus of elasticity for the stone masonry equal to E=1660MPa. In the case of Basilica churches damaged in Kefalonia Greece by the 2014 earthquake sequence in-situ measurements of the dynamic response of a bell-tower were utilized in order to define indirectly the soil-foundation deformability ([12], 14]). The system of the wooden roof was modeled as well as all the wooden elements that connect the longitudinal and transverse walls with the interior colonnades and the mid-transverse wall. A small number of mortar samples were taken from the church. The natural stone used in the masonry elements is a type of slate with a compressive strength equal to 24MPa, as given in the literature survey.

Next, the procedure outlined by Manos et al. ([9], [10], [11], [12]) was followed for evaluating the performance of this church. This is based:

a) On the numerical predictions of the state of stress of the masonry walls as obtained from the dynamic analysis of this elastic numerical simulation being subjected to a combination of dead load and seismic forces and
b) On the values of the strength over demand ratios at the most critical locations of the masonry walls and vaults. In doing so, strength values were assumed for in-plane shear and flexure as well as out-of-plane flexure for relatively weak unreinforced stone masonry ([9], [10], [11], [12]).

The ratio of the in-plane shear or tensile strength value over the corresponding demand is signified by $\boldsymbol{R\sigma}$ or $R\tau$ whereas $\boldsymbol{R_M}$ denotes the ratio of the out-of-plane tensile strength value over the corresponding demand. Ratio values smaller than one ($\boldsymbol{R\sigma}$, $\boldsymbol{R\tau}$,$\boldsymbol{R_M}$ <1) predict a corresponding limit state condition ([9], [10, [11], [12], [15]).

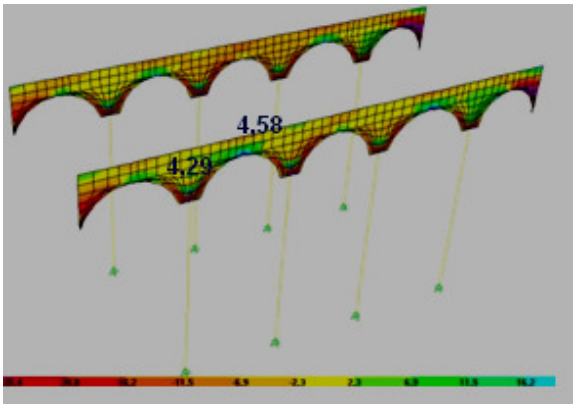

Figure 5a. G+0.3Q. Non-Deformable soil $\boldsymbol{R_\sigma}$ Ratio of in-plane strength / demand **F11** parallel to bed joint

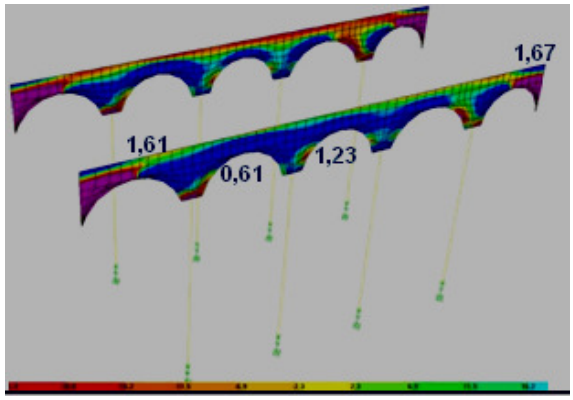

Figure 5b. G+0.3Q. Deformable soil $\boldsymbol{R_\sigma}$ Ratio of in-plane strength / demand **F11** parallel to bed joint

Figures 5a and 5b depict $\boldsymbol{R\sigma}$ ratio values for the masonry arches above the internal colonnades. These $\boldsymbol{R\sigma}$ ratio values of in-plane strength / demand were found by applying the limit tensile strength scenario parallel to bed-joint (F11). The demands in these figures were obtained for the load combination G+0.3Q. As can be seen from the above figures, the $\boldsymbol{R\sigma}$ ratio values are smaller for the deformable than the non-deformable foundation, which demonstrates the detrimental effect of the foundation deformability for this church even only for the gravitational forces. For the load combination 1.3G+1.5Q, that dictates the design for the gravitational forces under current code provisions, the above ratio values will become even smaller, which signifies that the colonnades cannot withstand the maximum gravitational forces. This is verified by the observed damage which is quite evident for these structural elements in this church having been supported for quite sometime after the earthquake event of 1995 by temporary wooden shoring internally as well as externally.

From the evaluation of the demands obtained from this numerical simulation as compared with the limit strength values adopted for the stone masonry of this church it can be concluded that the deformability of the foundation results in strength / demand ratio values smaller than the corresponding ratio values for the non-deformable foundation. This signifies critical regions of the masonry structural elements that cannot withstand the forces, as prescribed by the current code provisions. Moreover, such an evaluation can also explain, up to a point, the development of the existing current state of structural damage. Gaining such confidence in the employed methodology the designer gains also the advantage in evaluating with the same methodology the effectiveness of a potential retrofitting scheme.

In order for such a retrofitting scheme to be effective the resulting strength / demand ratios should attain values larger than the corresponding values without this retrofitting scheme and, if possible, larger than 1 (10], [11], [15]). Such an evaluation has been performed for the most vulnerable structural elements of this church; that is the internal colonnades, the South peripheral wall and the East peripheral wall with the apses. The existing or potential damage is predicted by the numerical analysis results when the strength / demand ratio values are well below 1. This is shown in figure 6 for the internal colonnade. In almost all structural elements the out-of-plane tensile behaviour results in strength / demand ratios with values well below one ($\boldsymbol{R_M}$ <1). The internal colonnade has visible signs of out-of-plane displacements and extensive cracking that are in agreement with the distress predicted by the followed methodology.

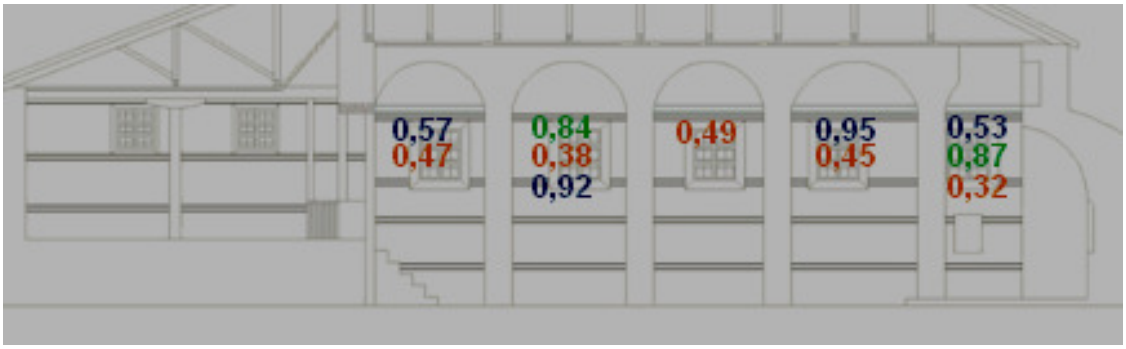

Figure 6. Internal colonnade. Regions with small values of the strength / demand $\mathbf{R_M}$ out-of-plane tensile behaviour (orange color), $\mathbf{R_\tau}$ in-plane shear behaviour (green color), $\mathbf{R_\sigma}$ in-plane tensile behaviour (blue color)

4 THE CHURCH OF ACHIROPOIITOS, AT THESSALONIKI

This church is a three nave Basilica located at the center of Thessaloniki, Greece. It is one of the oldest Greek Christian churches dating from the middle of the 5th century A.D. The interior is shaped by the peripheral (longitudinal and transverse) masonry walls and two series of colonnades formed by twelve columns each. The masonry is built with the old Christian construction technique whereby horizontal zones of brick masonry are succeeded by horizontal zones of stone masonry along the height of the peripheral walls.

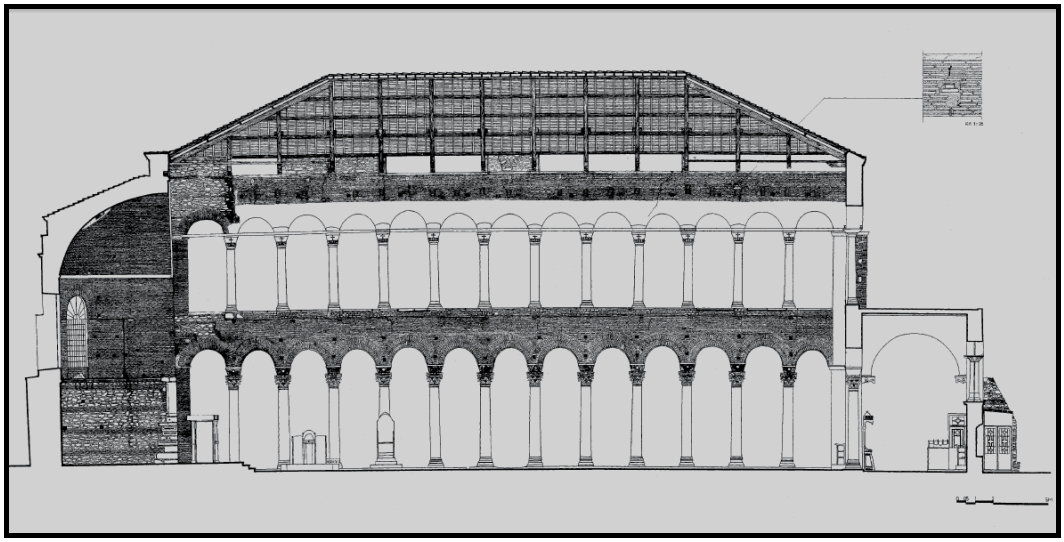

Figure 7. Longitudinal (East-West) cross section of the church of Achiropoiitos

The overall external dimensions are 51.9m in the longitudinal East-West direction and 30.80m in the transverse North-South direction and a height of 14.0m for the peripheral masonry walls. The clear width of the central nave is 14.20m whereas the North and South nave width is 6.20m and 6.30m, respectively. At the East end the central nave extends further than the North and South naves by an extension that is partly formed with an apse. The whole structure is covered by a wooden roof that rises from the ground level 22.0m at the central longitudinal axis. Initially the church was larger than the one which survives today.

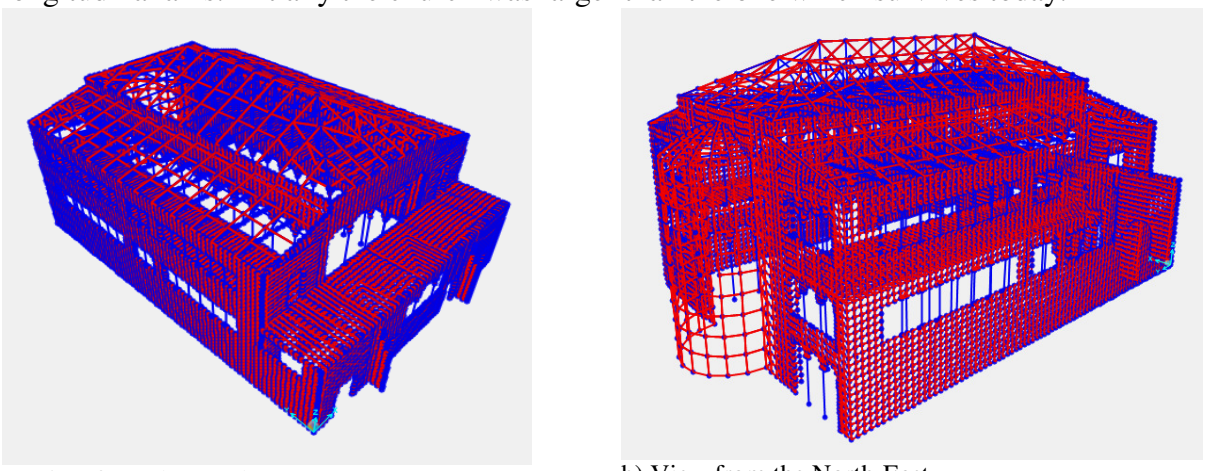

a) View from the North-West b) View from the North-East

Figure 8. Numerical simulation of the church of Achiropoiitos

Figure 7 depicts a longitudinal East-West cross section whereas figures 8a and 8b depict the numerical simulation of this church. As was done for the churches of the Assumption of Virgin Mary and for Profitis Ilias the foundation deformability was also examined for this church. This was done by assuming a) rigid soil-foundation conditions (pinned), b) deformable rather stiff soil-foundation and c) deformable rather flexible foundation condition. The soil-foundation deformability was introduced in the numerical simulation with a series of link elements at the soil-foundation interface.

Cumulative Modal participation mass ratios						
Eigen-Modes	Rigid Foundation (Pinned)		Stiff - Deformable Foundation		Flexible Deformable Foundation	
	$SumU_X$	$SumU_Y$	$SumU_X$	$SumU_Y$	$SumU_X$	$SumU_Y$
1st main translational transverse x-x (North-South, Transverse)	**30.5%**	0 %	**51. %1**	0 %	**68.8%**	0.1%
2nd	30.7%	0.6%	51.2%	1.7%	68.9%	16.7%
3rd	67.9%	0.7%	67.9%	14.1%	68.9%	70.6%
4th main translational longitudinal y-y (West – East, Longitudinal)	68.0%	**70.2%**	72.1%	**72.6%**	73.2%	**71.5%**
5th	70.2%	70.5%	73.8%	72.6%	73.3%	71.8%

Table 1. Cumulative Modal participation mass ratios of the church of Achiropoiitos

Table 1 lists the values of the cumulative mass participation ratios of the most significant eigen-modes (1st to 5th), whereas in table 2 the values of the corresponding eigen-periods are listed. As can be seen from table 1 the most significant eigen-modes are the 1st x-x translational eigen-mode in the transverse (North-South) direction and the 4th y-y translational longitudinal (East-West) direction. As can be seen in table 1, the increase in the flexibility of the soil-foundation results in a 1st x-x translational eigen-mode that mobilizes a larger modal

mass than for the case of the rigid foundation. Moreover, this increase in the flexibility of the foundation results, as expected, in the lengthening of the corresponding eigen-period values, as was also discussed for the previously examined churches of the Assumption of the Virgin Mary and for Profitis Ilias.

Eigen-period values (sec)			
Eigen-Modes	Rigid Foundation (Pinned)	Stiff - Deformable Foundation	Flexible Deformable Foundation
1st main translational transverse x-x (North-South, Transverse)	**0.5877**	**0.6111**	**0.6704**
2nd	0.5724	0.5740	0.5781
3rd	0.4974	0.5241	0.5617
4th main translational longitudinal y-y (West – East, Longitudinal)	**0.4734**	**0.5189**	**0.5439**
5th	0.3663	0.3688	0.3801

Table 2. Eigen-period values (sec) of the church of Achiropoiitos

As was done before, the loading conditions examined were a) G+E_x, b) G-E_x, c) G+E_y, and d) G-E_y, where G is the gravitational loads and Ex, Ey the earthquake forces ([1], [16], [17], [18]) along the x-x axis (transverse North-South direction) or the y-y axis (longitudinal East-West direction), respectively. The amplitude of these earthquake forces was obtained by utilizing the recorded ground acceleration during 1978 Thessaloniki earthquake at a close distance from the site of this church. In figures 9a to 9d the values of the ratio of shear strength value over the corresponding shear demand signified $R\tau$ is plotted for the case of rigid foundation and for the case of flexible foundation. In figures 9a and 9b this is done for the North peripheral wall and for the load combination G+Ey for the case of rigid and flexible foundation, respectively. In figures 9c and 9d this is done for the West peripheral wall and for the load combination G+Ex for the case of rigid and flexible foundation, respectively.

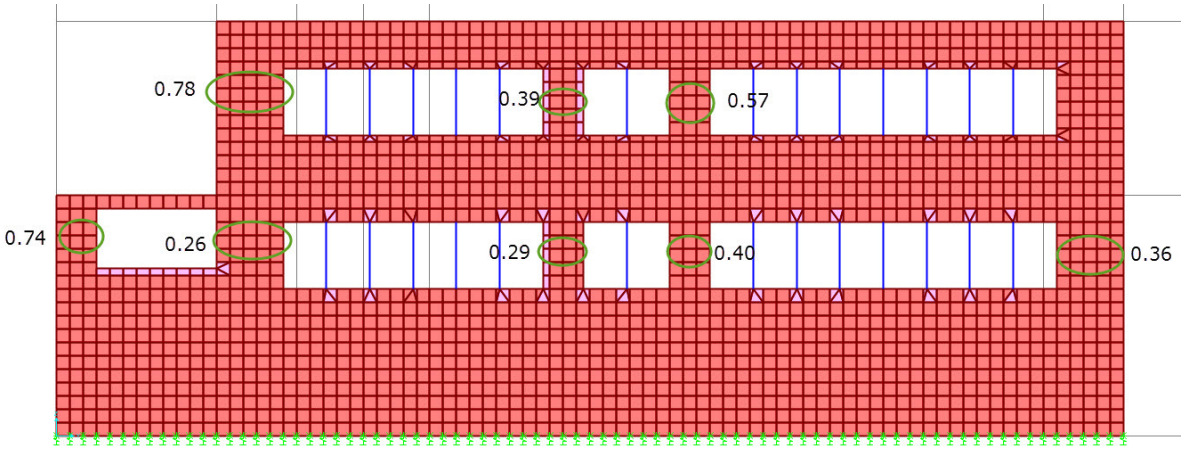

Figure 9a. Values of the ratio **Rτ** towards assessing the performance of the North peripheral wall against in-plane shear for load condition G+Ey . Case of rigid foundation

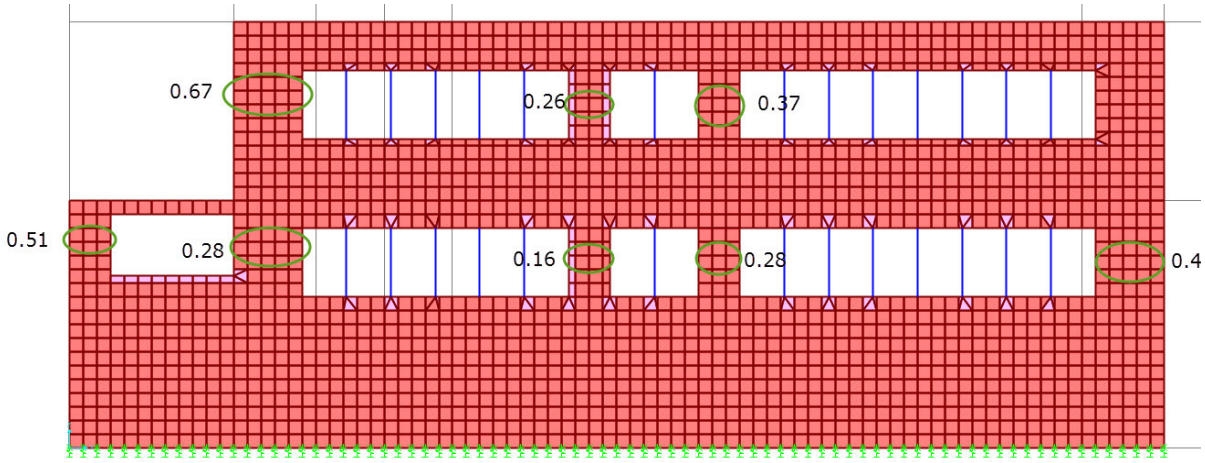

Figure 9b. Values of the ratio **Rτ** towards assessing the performance of the North peripheral wall against in-plane shear for load condition G+Ey . Case of flexible foundation

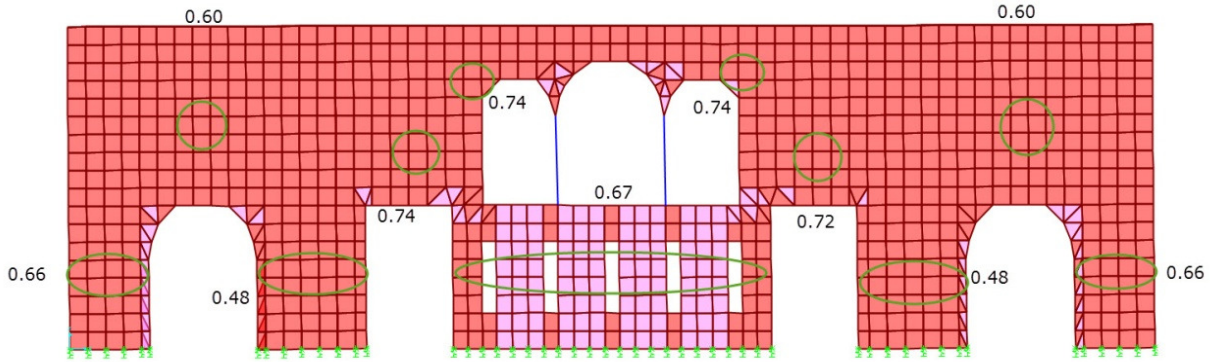

Figure 9c. Values of the ratio **Rτ** towards assessing the performance of the West peripheral wall against in-plane shear for load condition G+Ex . Case of rigid foundation

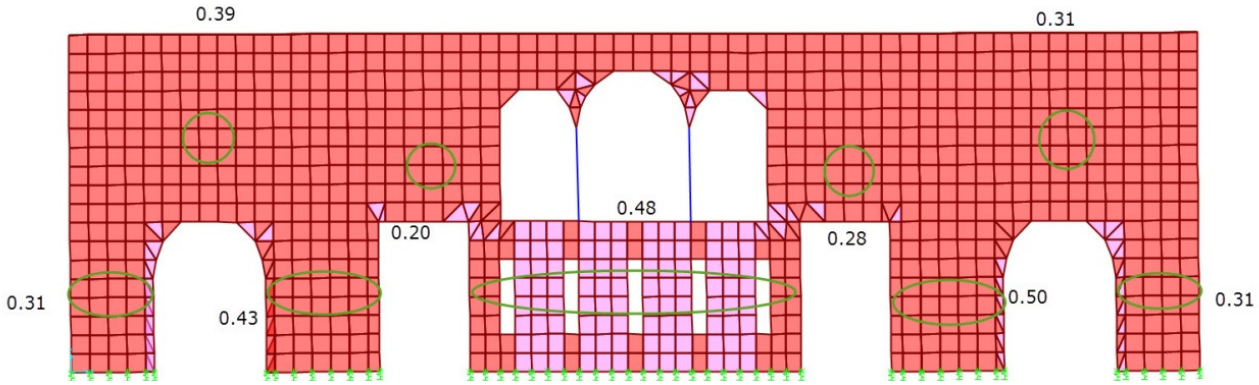

Figure 9d. Values of the ratio **Rτ** towards assessing the performance of the West peripheral wall against in-plane shear for load condition G+Ex . Case of flexible foundation

As can be seen in these figures 9a to 9d there are many locations in both the North and the West peripheral walls where these shear strength over shear demand ratio values are smaller

than 1, which signifies the appearance of shear mode of failure. This observation is in line with the damage that the masonry walls of this church sustained during the 1978 Thessaloniki earthquake sequence. Moreover, as can be seen by comparing the shear strength over shear demand $R\tau$ ratio values for the same location of these two peripheral walls (North wall, figures 9a and 9b or West wall, figures 9c and 9d) between the two cases of rigid and flexible foundation it can be seen that the flexibility of the foundation results in $R\tau$ values noticeably smaller than the case of flexible foundation. This observation supports the partial conclusion that the soil-foundation flexibility was an additional factor contributing to the observed earthquake damage.

5 CONCLUSIONS

- 1. The dynamic behaviour and earthquake performance of churches is a very wide subject. This paper attempts to address the earthquake performance of Basilica churches in parts of Greece during the last 30 years. Towards this objective use is made of in-situ observations together with relatively simple numerical tools. The numerical study includes soil-foundation deformability. The earthquake performance of three specific stone masonry Basilica churches is investigated. The second and third of these churches are simply covered by a wooden roof whereas the first has also a stone masonry vaulted superstructure under its wooden roof. All three churches developed significant structural damage typical of churches of this Basilica typology as was observed in Greece during the last 30 years.
- 2. The eigen-periods, eigen-modes and the deformation patterns to horizontal earthquake actions of the examined churches were predicted numerically. These numerical simulations resulted in large out-of-plane displacements at the top of the longitudinal peripheral walls for all examined churches. The presence of stone masonry vaulting systems increases the stiffening effect at the top of the peripheral wall level; however, such vaulting systems also add considerable masses at a high level that generate large seismic forces.
- 3. The predicted regions most vulnerable to damage are near the door and window openings for the in-plane behaviour; this agrees reasonably well qualitatively with observed damage, although the numerical simulation is based on elastic behaviour. For a superstructure consisting of vaults and domes, large seismic forces are generated leading to stress concentration at the bases of the domes and vaults and at the keys of the arches. Further investigation is needed to establish appropriate limit-state criteria for these stone masonry elements.
- 4. The foundation deformability was investigated introducing linear deformable springs at the foundation level. The results of such a numerical approximation combined with the followed methodology of limit state criteria of strength / demands ratio values ($R\tau$, $R\sigma$, R_M) demonstrate in all the examined cases that the foundation deformability, when combined with the gravitational forces and seismic actions, leads to $R\tau$, $R\sigma$, *and* R_M ratio values that are considerably smaller than for the case of non-deformable foundation thus verifying the detrimental effect of the foundation deformability in all the examined cases.

- 5. Retrofitting counter measures that aim at improving the earthquake performance of such structures must employ comprehensive means for improving the soil-foundation deformability and the interaction with the masonry walls resting on such foundation. This problem is also amplified by the presence of underground water pressures during certain time of the year with substantial rain fall or snow melting. Unfortunately, in many cases these counter measures of improving the soil-foundation-structure interaction are rather superficial.

REFERENCES

[1] Manos G.C., 2011. "Consequences on the urban environment in Greece related to the recent intense earthquake activity", Int. Journal of Civil Engineering and Architecture, Dec. 2011, Volume 5, No. 12 (Serial No. 49), pp. 1065–1090.

[2] Manos G.C., Soulis V.J, Karamitsios N., Felekidou O., 2009. "Numerical Simulation of the Dynamic and Earthquake Behaviour of Greek Post-Byzantine Churches with and without Base Isolation", PROHITECH 2009, 21 to 24 June 2009, Rome, Italy.

[3] Manos G.C., Soulis V., Felekidou O., 2010a. "Numerical Study of the Dynamic and Earthquake Behaviour of Byzantine and Post-Byzantine Basilicas", 8th International Masonry Conference, 2010, Dresden, Germany.

[4] Manos G.C., Soulis V., Felekidou O., Matsou V. 2010b. "A Numerical Investigation of the Dynamic and Earthquake Behaviour of Byzantine and Post-Byzantine Basilicas", 9th U.S. National and 10th Canadian Earthquake Engineering Conference, 2010, Toronto, Canada.

[5] Manos G.C., Soulis V. J & Karamitsios N., 2012. "The Performance of Post-Byzantine churches during the Kozani-1995 Earthquake – Numerical Investigation of their Dynamic and Earthquake Behaviour", 15WCEE, (2012) Portugal.

[6] Manos G.C., Soulis V., Diagouma A. (2008) "Numerical Investigation of the behaviour of the church of Agia Triada, Drakotrypa, Greece", Journal in Advances in Engineering Software 39, 284-300.

[7] G.C. Manos and L. Kotoulas "Dynamic and Earthquake Performance of Greek Post-Byzantine Churches made of stone masonry accounting for Foundation Deformability", Proc. 9th Int. Masonry Conference, July, 2014.

[8] George C. Manos and Lampros Kotoulas (2014) "Earthquake Performance of Greek Post-Byzantine Churches with Foundation Deformability " Proc. 2nd Int. Conf. on Protection of Historical Constructions, pp. 297-303, 2014, ISBN 978-975-518-361-9.

[9] G. C. Manos, L. Kotoulas, V. Matsou, (2013a) "Numerical Investigation of the influence of Earthquake Forces and Foundation Settlement on the Performance of Post-Byzantine Churches", STREMAH-2013, Southampton, England, June 2013.

[10] Manos G.C., Kotoulas L., Matsou V., Felekidou O., (2013b). "Dynamic behaviour of Greek Post-Byzantine churches with foundation deformability and evaluation of their earthquake performance", 4th ECOMASS Thematic Conference on Computational Methods in Structural Dynamics and Earthquake Engineering – CompDyn 2013, 12-14 June 2013, Kos Island, Greece.

[11] Manos G.C., Kotoulas L., Matsou V., Felekidou O., (2015) "Dynamic and Earthquake Behaviour of Greek Post-Byzantine Churches with Foundation Defornability – Experimental Investigation of Stone Masonry Materials Properties", Springer Publishing, I. N. Psycharis (seds.), I.N. Psycharis et al. (eds.), Seismic Assessment, Behavior and Retrofit of Heritage Buildings and Monuments, Computational Methods in Applied Sciences 37, DOI 10.1007/978-3-319-16130-3_9.

[12] Manos G.C. & Kozikopoulos E., 2015b. "The Dynamic and Earthquake Response of Basilica Churches in Kefalonia-Greece including Soil-Foundation Deformability and Wall Detachment", CompDyn 2015, Crete, Greece.

[13] Dimitriadis V. "An ordinance for the erection of the first church in Gianitsa", Mekedonika, Vol. 9, Society for Mecedonian Studies, Thessaloniki 1969.

[14] Manos G.C. & Kozikopoulos E., 2015a. "In-situ measured dynamic response of the bell tower of Agios Gerasimos in Lixouri-Kefalonia, Greece and its utilization in the numerical predictions of its earthquake response", CompDyn 2015, Crete, Greece.

[15] Manos G.C. & Karamitsios N., 2013a. "Numerical simulation of the dynamic and earthquake beheaviour of Greek post-Byzantine churches with and without base isolation", Earthquake Engineering Retrofitting of Heritage Structures, Design and evaluation of strengthening techniques, pp. 171-186, Edited By: S. Syngellakis, Wessex Institute of Technology, UK, ISBN: 978-1-84564-754-4, eISBN: 978-1-84564-755-1, 2013.

[16] Manos G.C., 1994. "Seismic Code of Greece, Chapter 17, International Handbook of Earthquake Engineering: "Codes, Programs and Examples", edited by Mario Paz, by Chap-man and Hall, ISBN 0-412-98211-0.

[17] Euro-Code 6 part 1 2003: Design of structures for earthquake resistance - Part 1: General rules, seismic actions and rules for buildings, FINAL DRAFT prEN 1998-1, Dec. 2003.

[18] Euro-Code 8 2003: Design of structures for earthquake resistance - Part 1: General rules, seismic actions and rules for buildings, FINAL DRAFT prEN 1998-1, Dec. 2003.

[19] Greek Seismic Code Provisions 2000, EPPO, Earthquake Planning and Protection Organization Athens, Greece, December 1999.

ECCOMAS Congress 2016
VII European Congress on Computational Methods in Applied Sciences and Engineering
M. Papadrakakis, V. Papadopoulos, G. Stefanou, V. Plevris (eds.)
Crete Island, Greece, 5–10 June 2016

PROBLEMS RELATED TO THE USE OF FIBER REINFORCED CEMENTITIOUS MATERIALS AS STRENGTHENING OF MASONRY MEMBERS

D. Sinicropi[1], A. Borri[2], M. Corradi[2,3] and M. Paradiso[1]

[1] University of Florence, Dept. of Architecture
Piazza Brunelleschi 6, 50121 Florence Italy
e-mail: sinicropi.daniela@gmail.com, michele.paradiso@unifi.it

[2] University of Perugia, Dept. of Engineering
Via Duranti 92, 05100, Perugia Italy
e-mail: antonio.borri@unipg.it

[3] Northumbria University, Dept. of Mechanical & Construction Engineering
Wynne-Jones Building, NE1 8ST Newcastle Upon Tyne, United Kingdom
e-mail: marco.corradi@northumbria.ac.uk

Keywords: Historic masonry, Mechanical testing, Steel fibers, GFRP grids, Confinement.

Abstract. *This paper gives the results of a series of tests carried out on brick columns and panels reinforced with Fibre Reinforced Cementitious Materials. Steel and glass fibres were used, and cement and lime mortars were employed as the matrices. The issue of durability of reinforced masonry structures, that is the transformation from sole masonry structures to hybrid ones, was investigated. Six brickwork columns (three unreinforced and three reinforced) and eighteen solid brick panels were built and tested (two unreinforced, 16 reinforced with steel cords or glass fibre). Tests were carried out in laboratory, and the results enabled the determination of the compression strength of the masonry before and after the application of the reinforcement, and before and after environmental effects. The main goal of the durability testing was to verify whether the artificial ageing process hinders the resistance. At the end of the cycles, a first visual observation was performed in order to evaluate if superficial alterations took place, such as efflorescence or micro cracking due to the immersion in the sodium chloride (NaCl) solution. The aged reinforced specimens appear to have a losses that range from 4% to 25% of the ultimate load, depending on the type of reinforcement and mortar used, although scattering of results confirm the need of more extensive testing.*

1 INTRODUCTION

Structural enhancement of masonry elements, built with natural stones or clay bricks, is frequently necessary; in particular, compressed members, as columns, are prone to brittle failure under seismic forces or static overloads. Recent earthquakes in Molise (2002), Umbria

(2009), Abruzzo (2009) and Emilia-Romagna (2012) have shown that masonry structures are extremely susceptible to the forces imposed during such events [1-2]. Thus, there is an urgent need to upgrade these deficient masonry elements to meet the current design standards in seismic regions. Steel jacketing and reinforced concrete (RC) have been extensively used in Europe, particularly Italy, to retrofit masonry columns and have proved to be effective, but have some drawbacks [3-4]. Such techniques are in fact often non-reversible, expensive and add mass to the structure. Such issues have led researchers to investigate new retrofit solutions using innovative materials such as Fibre Reinforced Polymers (FRP) [5-9] or Steel fibre-Reinforced Polymers (SRP) [10-12] composites in the form of bonded surface reinforcements. Wrapping with FRP or SRP reinforcement offers the designer an outstanding combination of properties, including ease of handling, speed of installation and high strength-to-weight ratio [13-15].

On the other hand, some considerations advise against the use of such techniques. In fact, frequently natural masonry blocks are subjected to moisture entrapment from the ground, released through the external surface during their service life; for that reason it is not always recommendable to apply continuous epoxy-bonded jacketing, inhibiting the material transpiration. As a result of such considerations, beside the "traditional" FRP/SRP wrapping this paper presents the results of a second experimental investigation in a series dealing with the possibility of application of Fibre Reinforced Cementitious Matrices (FRCM). This gives a promising technique that may represent a new opportunity in the field of restoration, since it is reversible, aimed at integrating the masonry rather than transforming it and compatible with the preservation of the building materials.

In this paper, the structural validity of FRCM materials has been analysed by doing compression tests on FRCM-confined columns. Subsequent experimental work focused on the durability of FRCM reinforced elements. After an initial period of durability testing solely on the fibres, with and without their polymeric matrix, attention turned to research that would prove whether the degradation of the FRP system when applied to structural support would increase damage or simply result in not providing the structural reinforcement it had been designed to give. There were cases in which the degradation which started in the FRP system caused mould or other aggressive attacks to the underlying structural system, provoking more damage than if the FRP had not been present [16]. From the data analysed in previous experimental campaigns [17], the more aggressive durability testing performed on FRCM specimens consisted in wet/dry cycles in a 5% sodium chloride solution. Therefore this type of cycle was chosen for the durability on an FRCM reinforced structural element, in the attempt to verify whether the artificial ageing registered in the second experimental campaign described above had the same detrimental effects when the FRCM system was applied to masonry structures. Different schemes of reinforcement were here investigated, the difference consisting in the type of fibres, glass or steel, and the type of matrix, cement mortar or lime mortar.

2 MATERIALS

Small brick columns and panels were assembled, subjected to both compression loads and wet/dry durability cycles and tested in laboratory.

Compression tests were first conducted on FRCM reinforced columns. The results of compression tests show an interesting increase of load bearing capacity with respect to unreinforced columns and give useful indications on the correct application of the reinforcement. The columns were built using solid bricks and reinforced with different types of steel wires. The brick columns were 50 cm in height, were made of 8 courses of bricks and had two different cross sections: octagonal and square.

For wet/dry durability cycles, each panel was composed of five bricks (dimensions: 200x100x50 mm). Total panel's dimensions were 290x100x200 mm (Fig. 1). The test matrix is reported in Table 1.

Number of Specimens	Type of cementitious matrix for Reinforcement	Type of Reinforcement	N° of wet/dry cycles	
8	Lime	Steel (4)	0 (2)	75 (2)
		Glass (4)	0 (2)	75 (2)
8	Cement	Steel (4)	0 (2)	75 (2)
		Glass (4)	0 (2)	75 (2)
2	None	Unreinforced (2)	0 (2)	

Table 1: Test matrix. In parenthesis the number of specimens per type.

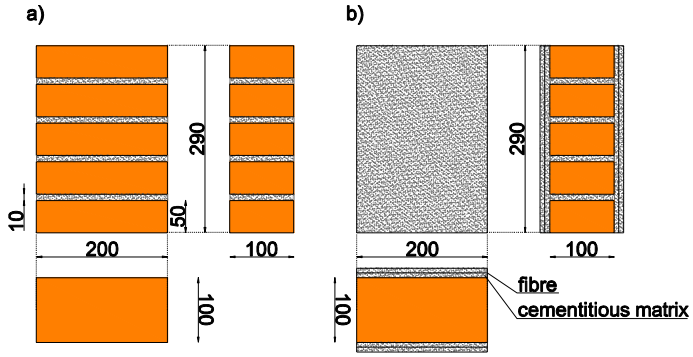

Figure 1: Graphic scheme (dimensions in mm) of the brick masonry panels, plan and elevation, a) unreinforced panel, b) reinforced panel.

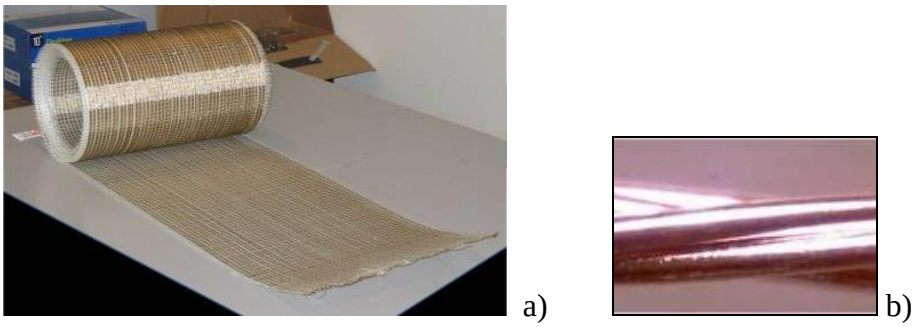

Figure 2: UHTSS steel fibres: a) the coil, b) detail of a single cord.

Two panels from a total of 18 remained unreinforced, as control specimens. All other panels, 16 in total, were reinforced though steel or glass fibres placed on the wide faces of the panels (200x290 mm) with either lime or cement-based mortar, in the manner of reinforced plaster. The mechanical properties of the steel and glass fibres used in the investigation are illustrated in Table 2.

The steel fibres are made of UHTSS (Ultra High Tensile Strength Steel) cords, which are provided from coils available on the market (with the commercial denomination 3X2), pro-

duced by Hardwire llc. They are either brass coated or galvanized with zinc, for increased protection against corrosion. When lime-based mortar is utilized for repointing, it is best to use cords protected by zinc galvanizing The coils used for the steel cords are about 30 cm wide and variable in length, and consist of a series of cords laid out parallel to each other and held together by a polyester mesh (Fig. 2). The most interesting property of the cords used in the proposed system consists in the high bonding and compatibility between the cords and the mortar surrounding them, due to their small size (their average diameter is 1 mm) and shape. In fact, the cords are made by twisting five individual filaments together (three straight filaments wrapped by two filaments at a high twist angle). The specifications of the single cord are shown in Table 2. The mechanical properties of the metal cords were verified by tensile tests carried out on 8 samples. The results substantially confirmed the values given by the manufacturer on the technical sheet, with small variations of the failure load (1539 N) and of the deformation at failure (2.1%) .

Cord diameter (mm)	0.89
Sample size	10
Tensile failure load (N)	1539
Cross section area (mm^2)	0.62
Young's modulus (GPa)	206.8 (16.4)
Tensile strength (MPa)	2479 (127)
Strain to failure (%)	2.1

Table 2: Mechanical properties of the steel fibres. Standard deviation in ( ).

Nominal dry section (mm^2)	3.8
Sample size	7
Tensile failure load (kN)	3.679
Tensile strength (MPa)	968.2 (85.93)
Young's modulus (GPa)	74.2 (3.4)
Strain to failure (%)	1.3

Table 3: Mechanical properties of the GFRP grid. Standard deviation in ( ).

The fiberglass grid (Glass Fiber Reinforced Polymer: GFRP) used in this research program was manufactured using AR-glass (Alkali-Resistant) fibers and a polyester resin. Specimens extracted from the composite mesh have been measured with a tensile modulus ranging from 71.1 to 79.8 GPa. The mesh has a nominal cross section dry fibre-area of 3.8 mm^2 both in the vertical (weft) and horizontal (warp) direction and has an opening of 66 mm in both directions (Fig. 3). The main mechanical characteristics of GFRP material measured via tensile tests, are shown in Table 3.

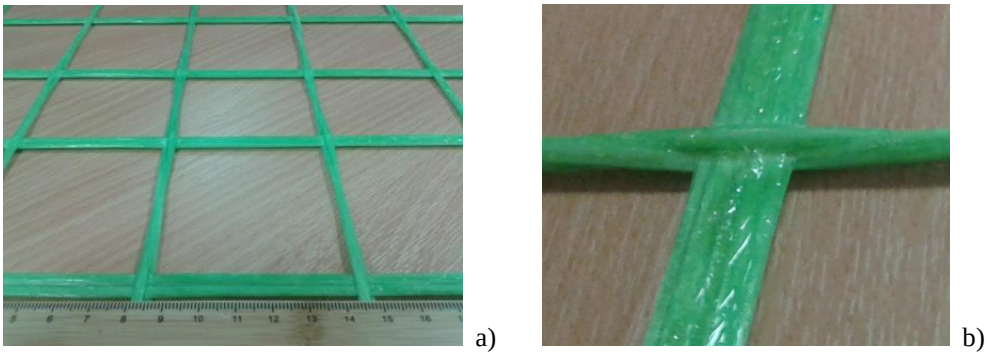

a) b)

Figure 3: GFRP grid: a) the grid, b) detail of the joint.

The lime and cement mortar used as cementitious matrices for the FRCM system are described in Table 4. The mortar used in the assembly of the panels was a cement mortar, hand

mixed (lime, cement 32.5 MPa, sand) with proportions in weight 1:1:6 (PCement, Tab. 4). This mortar was used solely in the building of the panels, and not in their reinforcement. Small cubic specimens of bricks, 5.5x5.5x5.5 cm in size, were tested in compression (Tab. 5).

Once the panels were assembled with the cement mortar described above, they were left to cure for 60 days in a humidity free environment at room temperature (circa 19°). Once curing was completed, the panels were reinforced, in number and type of reinforcement as described in Table 1. A layer of cementitious matrix was applied to the surface of the panel, covering the entire façade evenly. The reinforcement was then applied and pressed to ensure attachment to the applied layer of mortar. A second layer of mortar was applied, thus covering the fibre. The reinforced panels were left to cure again for another 60 days and in order to ensure complete curing, in order to avoid that this process could occur during the artificial ageing cycles.

Mortar Type	Average Flexural Strength (MPa)	Average Compressive Strength (MPa)
Lime	0.17	0.52
Cement	0.42	4.05
PCement	0.25	0.62

Table 4: Average values of flexural and compression strength obtained through testing on mortar specimens.

	Average maximum compression load (kN)	Average compressive strength (MPa)
Clay bricks	142.15	47.04

Table 5: Average compressive strength found for solid clay bricks used to build the panels.

3 ARTIFICIAL AGEING METHOD

Once curing was complete, wet/dry cycles on eight reinforced panels commenced. The cycles consisted in a wet period, during which the specimens were immersed in a solution of sodium chloride (NaCl) at 5%, followed by a dry period, during which the specimens were placed in a ventilated oven at 35°C. These specimens required a period of 45 minutes for complete sorption to occur. This amount of time was determined through weighing the specimens dry, and then after having been immersed in the NaCl solution at intervals of 5 minutes. Once the registered weight was stable, thus indicating that sorption was at maximum values, the time elapsed was considered to be the necessary amount for a complete wet cycle. The panels were immerged with the 5% NaCl solution at a level which covered the specimens for at least 2.5 cm and then placed in the oven and left to dry for 24 hours. One cycle duration of 75 days was chosen for all aged specimens.

4 TEST METHOD

4.1 Columns

For compression testing, six brick columns were subjected to axial compression tests in order to determine the efficacy of the confinement with steel fibres in terms of load bearing increase, ductility and axial stiffness. Testing was conducted through an oil-hydraulic Metrocom type press with a 3000 kN load cell with load increases of 5-7 kN/sec. Figure 4 shows the two types of columns tested while Figure 5 gives the cross-section dimension. The steel cords were glued by using a cement-based mortar. Reinforcement was executed in the following

steps: a) cleaning of the column surfaces of all inconsistent material to improve the adhesion between mortar and masonry; b) application of a first layer of mortar; c) application of a unidirectional FRCM sheet; d) application of a second layer of cementitious mortar. All specimens were wrapped with orientation perpendicular to their axis.

a)

b)

Figure 4: Brick columns: a) octagonal cross section, b) square cross section.

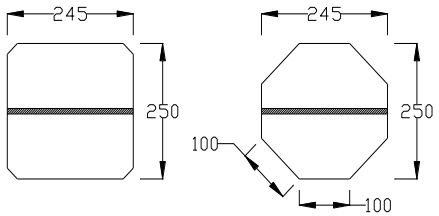

Figure 5: Column cross section (dimensions in mm).

4.2 Panels

Testing was carried out through eccentric compression loading. One of the objectives of this campaign was to study the behaviour of the fibres and the bonding, in an aged condition. By comparing the position of the central core of inertia with the compressive load, it was possible to verify that the compressive and tensile stresses were actively being applied to the brick panels. Loading was applied through a load cell (TCLP–10B Tokyo Sokki Kenkyujo Co, Ltd.) with a maximum capacity of 100 kN applying pressure on a steel cylinder positioned at 50 mm to the right of the central axis of the panel.

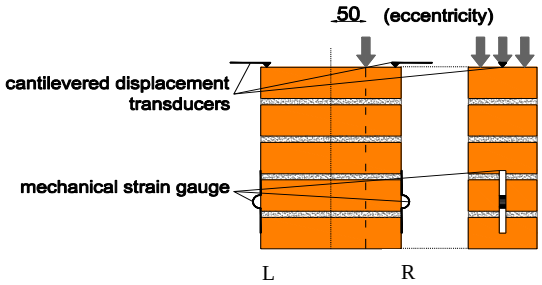

Figure 6: Graphic scheme of the positions of the mechanical strain gauges and transducers during testing (mm), with Left Hand (L) and Right Hand (R) sides indicated (dimension in mm).

Figure 7: Mechanical Strain Gauge.

The steel cylinder is the same width of the panel, ensuring that the load is applied only on the masonry structure and not on the FRCM reinforcement. Deformations were recorded through two mechanical strain gauges on the short sides of the panels and two cantilevered displacement transducers (CE-10 Tokyo Sokki Kenkyujo, Fig. 6). The two displacement transducers attached to the upper face of the panels measured the vertical displacement of the panel during loading. The second typology was applied for recording relative movements between the two extremities of the gauges. Omega-shaped (Fig. 7), the ends of these strain gauges are attached to the specimens and their hemispherical central part allows these ends to follow the displacements of the specimen.

5 RESULTS

5.1 Compression tests on columns

The specimens were subjected to axial monotonic load until failure occurs. The first three tests were conducted on unreinforced columns in order to obtain the average compressive strength of the columns, which resulted in 719 kN. Considering the area of the octagonal transversal section of the columns, 512 cm^2, the compressive strength is approx. 14 MPa. A similar value was measured for square cross section (14.8 MPa).

For octagonal cross-section columns confined by steel composites, the FRCM reinforcement (specimens 2&3) requires the application of a significant thickness of cementitious mortar, up to 5cm, which in some cases may be incompatible with the requirement of an unvaried transversal section. The compression testing on the reinforced columns show an increase of maximum load of 28% compared with unreinforced columns (Tab. 6).

Sample	Cross Section	Rinf.	Compression strength (MPa)	Failure load (kN)	Axial stiffness (MPa)
1	octagonal	no	14.0	719	2034
2	octagonal	steel	21.3	1089.8	2306
3	octagonal	steel	14.7	755.9	1462
4	square	steel	16.9	1020	2033
17	square	no	15.6	945	1745
18	square	no	14.0	847	2576

Table 6: Results of compression tests.

Figure 8: Compression test (reinforced column).

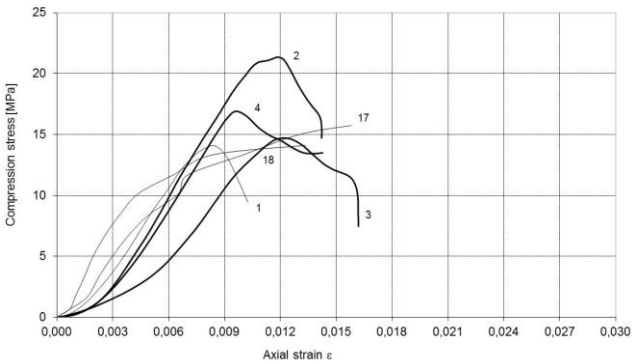

Figure 9: Stress vs. axial strain response.

For columns with a square cross-section, the effectiveness of the reinforcement is smaller (13.8%). This is mainly due to the stress-concertation near the columns corners. The flexural stiffness of the steel cords also prevent an adequate bonding of the fibres to the masonry surface and this partially compromises the confinement effect of the FRCM reinforcement.

The collapse mode of reinforced columns (Fig. 8) includes the cracking of the masonry underneath the fibres and the subsequent bulging of the columns around the midpoint. Total collapse of the columns occurs for the rupture of the fibres once the masonry is completely cracked internally. Significantly, the rupture of the FRCM reinforcement does not occur at the corners of the columns, a typical collapse mode in FRP reinforced columns, but at the midpoint of the specimens once the tensile strength of the fibres has been exceeded. Figure 9 shows the compression stress vs. axial strain response of reinforced and unreinforced columns.

5.2 Compression tests on small panels

Values for both reinforced and unreinforced specimens remain within values that range from 35 to 50 kN (Fig. 10). The small variation between reinforced and unreinforced specimens may be due to the fact that the FRCM system is simply bonded to the façades of the panels without mechanical anchoring systems. While the ultimate loads values do not vary greatly, the collapse mechanisms are different.

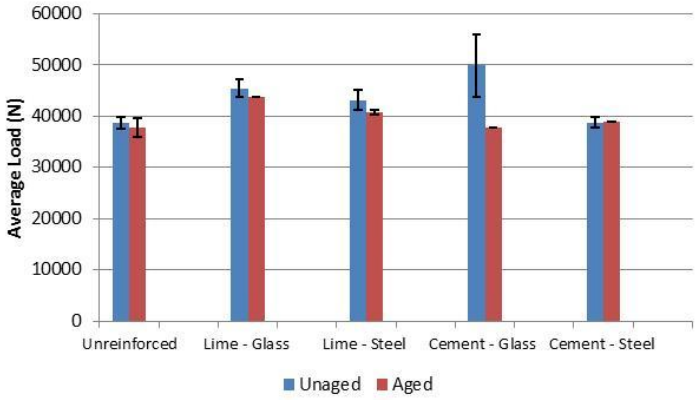

Figure 10: Average maximum loads for unaged and aged panels.

Unreinforced specimens fractured gradually. The average failure load of unaged specimen was 38.71 kN. The ageing process caused a negligible decrease of the panels' capacity of 2.3%. Cracks at first appear immediately below the point of load application, given by excessive compressive stress for a load of approx. 30 kN. At this point there is a drop in the load (Figs. 11-13). A secondary crack then appears at the bottom of the column opposite the loading point (Fig. 11a). This mechanism is not visible in the FRCM reinforced panels until the fibres detach completely from the side they are attached to, and even when detachment occurs it does not crack due to tensile strength; the rupture in reinforced specimens is abrupt and due to excessive compressive force as opposed to the gradual collapse verified in unreinforced specimens. The FRCM system does not prevent the masonry panel from cracking. The lateral shorter sides of the panels are free from reinforcement. Therefore when cracking of the bricks occurs, there may be a rotation of the elements shortly after the detachment of the fibres commences. This is the consequence of the eccentric compression, when the loads are outside the central core of inertia of the panel. The fact that the slate of FRCM detaches either completely or only partially makes little difference to the resistance of the panel; in fact, once the FRCM begins to detach, it is as if the fibre reinforcement is virtually non-existent.

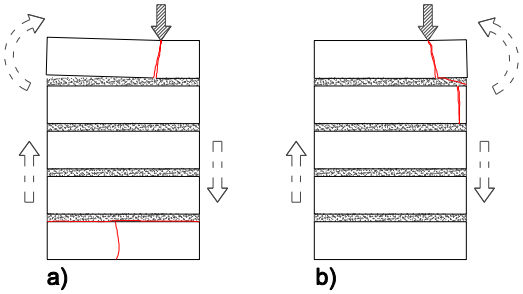

Figure 11: Graphic description of the cracks that occurred in unreinforced specimens; a) Specimen 1UR and b) Specimen 2UR.

It is possible that strain gauges and transducers register concurrently opposing displacements. Due to the position of the instruments separated by two bricks which may rotate and move in directions other than those of the two bricks the gauges are glued to (Fig. 14), displacements may have opposing sign when referring to one side of the specimen. In the testing condition, the larger displacement has been recorded under the loading point. After collapse, vertical cracks appeared with elongations of the right side (Fig. 15).

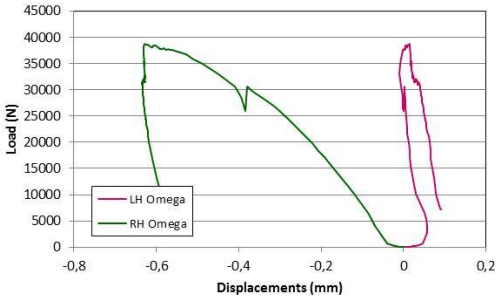

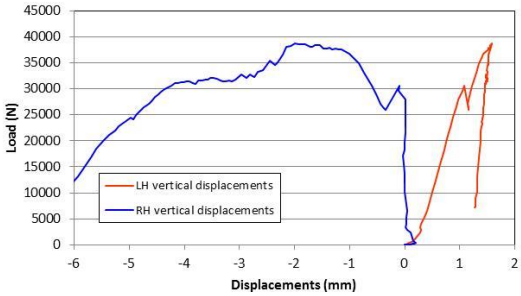

Figures 12 and 13: Load - displacement diagrams for Unreinforced Specimen 1; values given by cantilevered vertical displacement transducers and Omega transducers.

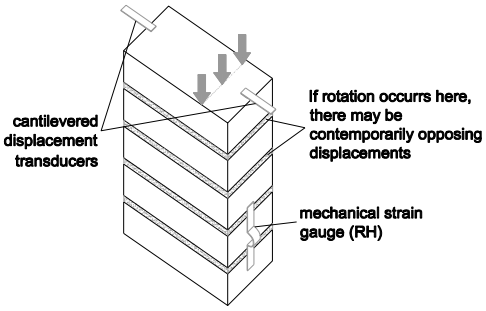

Figure 14: Axonometry of panels with strain gauges and displacement transducers. The mortar layers where possible rotations may lead to discording diagrams are highlighted.

The application of the FRCM reinforcement always caused an increase in the panel capacity. The application of the reinforcement is moderately able to absorb the tensile stresses and to partially prevent brickwork from cracking near the bed joints. The use of a cementitious mortar to bond the GFRP reinforcement increased the panel capacity of 29% compared to unreinforced specimens. The use of a lime-based mortar for both GFRP and steel reinforcements caused a limited increase of the panel capacity between 11.5 and 17%: this is probably due to the small tensile and shear strength of this mortar.

As for the differences in behaviour between aged and unaged specimens, none of the values of the aged specimens differed greatly from those of their unaged control specimens, as is clearly shown in Figure 10. However the ageing process caused a significant reduction of the panel capacity.

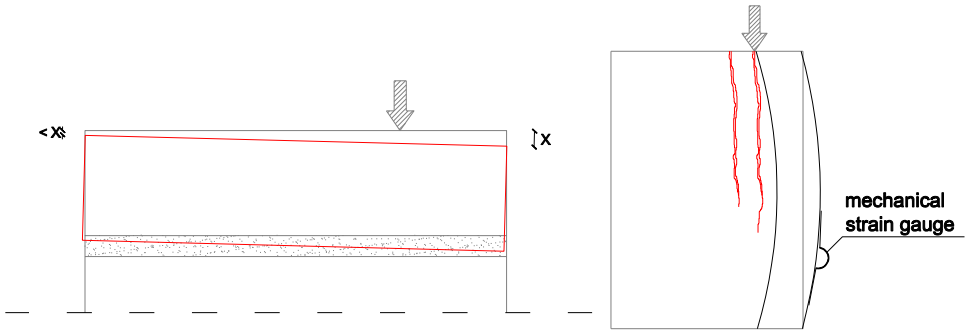

Figure 15: The upper section of the panel, showing larger displacements on the right side of the panels, and a graphic scheme of elongations that might occur in the right side of specimens.

Again, the ageing process on panels reinforced using a lime-based mortar caused a limited decrease of the panel capacity (approx. 5%) and this demonstrated that both the steel and GFRP reinforcement can be used to reinforce wall panels without significant ageing problems. However the oxidation of the steel fibers is another aspect to consider, when steel fibre - Cement matrix are used to reinforce masonry members. However since the number of specimens tested was limited, results should be confirmed by a larger experimental programme. However, the emerging line seems quite correct. As may be inferred by the following graphs, all of the reinforced panels reach their ultimate load abruptly (Figs. 16-17), with no substantial differences between aged and unaged specimens.

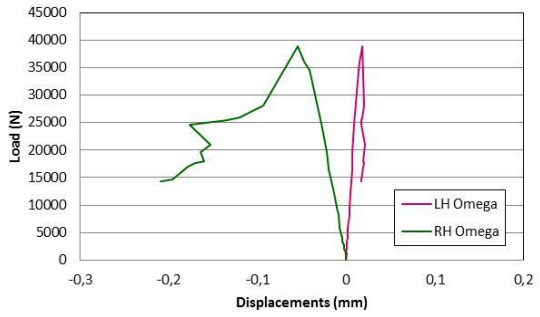

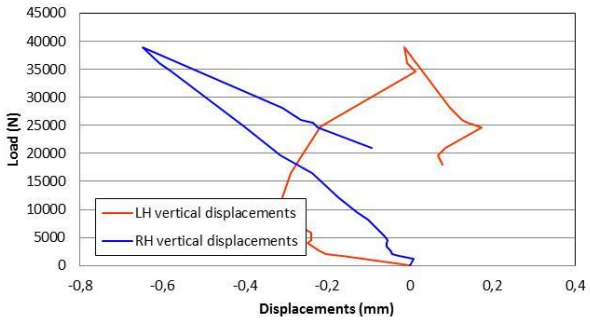

Figures 16 and 17: Load - displacement diagrams for Steel Fibre - Cement Matrix Specimen 4 after 75 wet/dry cycles; values given by cantilevered vertical displacement transducers and Omega transducers.

Some other considerations can be made from the observation of the photographic survey conducted during testing which seem to be relevant to all unaged specimens. From physical observations of the aged specimens, the most evident effects of the ageing cycles is in the efflorescence of the saline solution on the surface of both the brick structure, visible at the sides of the panels, and the cementitious matrix covered faces of the panels. The glass fibres did not show any signs of degradation after the artificial ageing cycles were complete, while the steel fibre reinforced specimens began to show rust on the surface of the matrix used to cover them as soon as the 5th cycle. By the end of the 75 wet/dry cycles, the rust was heavily distributed throughout the matrix surface. However, rust was not detected on the surface of the masonry

once the reinforcement detached after testing, and no other kinds of spots or smears were detected; the formation of mould, which could eventually cause the fibre reinforcements to detach from their structural supports, did not appear in the aged specimens.

6 CONCLUSIONS

The main inquiry of the present experimental campaign was aimed towards determining whether FRCM reinforced masonry panels are severely affected by artificial ageing, achieved in this particular case through wet/dry cycles in a 5% NaCl solution.

Sheet of steel or glass fibres (GFRP) can be easily applied as masonry strengthening. Preliminary compression tests demonstrated that it is possible to increase the compression capacity of brickwork columns by wrapping with FRCM systems using steel fibres. Increase in capacity up to 30% have been measured compared to unreinforced columns. However the shape of the cross-section could influence the effectiveness of the FRCM reinforcement.

It may be also noted that the FRCM system does not appear to be affected by the wet/dry cycles. While no substantial differences were found between the two types of specimens, due to the lack of anchorage of the reinforcement to the masonry substrate, the reinforced ones presented abrupt ruptures due to detachment of reinforcement, while the unreinforced ones collapsed in a more gradual manner. The degradation caused by the 5% NaCl solution appears only in saline efflorescence in all aged specimens, while in the steel fibre reinforced specimens rust was apparent from as soon as the 5th wet cycle. When the FRCM system was removed from the surface of the masonry panels after testing, no mould formations were detected. Regarding the resistance of the FRCM system to the tensile strength to which the panels were subjected as a consequence of eccentric compression, cracks caused by tensile stress did not appear in reinforced specimens, leading to the conclusion that the fibres successfully absorbed such stresses.

From the results of testing in the present campaign and the observations conducted throughout the cycles, it can be stated that FRCM reinforced panels are not affected by wet/dry cycles as regards the ultimate load carrying capacity. However, the superficial degradation of the specimens, in particular of those reinforced with steel fibre, must be addressed in order to avoid the detachment of the FRCM.

7 ACKNOWLEDGEMENTS

This project was sponsored by the Italian Ministry of Education [ReLUIS (2014) Linea di ricerca WP1 e WP2]. The authors acknowledge Fidia and Fibre Net for providing the composite materials.

REFERENCES

[1] M.R. Valluzzi, G. Cardani, L. Binda, C. Modena, Seismic vulnerability methods for masonry buildings in historical centers: validation and application for prediction analyses and intervention proposals, *13th World Conference on Earthquake Engineering (13WCEE)*, Vancouver, Canada, August 1-6, 2004.

[2] A. Borri, G. Castori, M. Corradi, R. Sisti, Masonry wall panels with GFRP and steel-cord strengthening subjected to cyclic shear: An experimental study, *Construction and Building Materials*, **56**, 63–73, 2014.

[3] M. El Gawady, P. Lestuzzi, M. Badoux, A review of conventional seismic retrofitting techniques for URM, *13th International Brick and Block Masonry Conference*. Amsterdam, Holland, July 4-7, 2004.

[4] M. Ilyas, S.H. Farooq, A.U. Qazi, R. Umair, Masonry confinement using steel strips. *Pakistan Journal of Engineering and Applied Sciences*, **5**,1-9, 2009.

[5] C. Bieker, W. Seim, J. Stürz, Post-strengthening of masonry columns by use of fiber-reinforced polymers, *3rd International Conference of Composites in Infrastructure (ICCI'02),* San Francisco, CA, June 10-12, 2002.

[6] C. Faella, E. Martinelli, S. Paciello, E. Nigro, Experimental tests and theoretical models on tuff masonry bricks and columns confined with C-FRP sheets, *International Conference on Innovative Materials for Construction and Restoration (IMTCR04)*, Lecce, Italy. June 6-9, 2004.

[7] T.D. Krevaikas, T.C. Triantafillou, Masonry confinement with fiber-reinforced polymers, *Journal of Composites for Construction*, **9**, 128-135, 2005.

[8] M.A. Aiello, F. Micelli, L. Valente, Structural upgrading of masonry columns by using composite reinforcements, *Journal of Composites for Construction*, **11**, 650-658, 2007.

[9] F. Micelli, A. La Tegola, Structural strengthening of masonry columns: a comparison between steel strands and FRP composites, *4th International Conference on Conceptual Approach to Structural Design CDS-07*, Venice, Italy, June 27-29, 2007.

[10] M. Di Ludovico, C. D'Ambra, A. Prota, G. Manfredi, FRP confinement of tuff and clay brick columns: Experimental study and assessment of analytical models, *Journal of Composites for Construction*, **14**, 583-596, 2010.

[11] C. Faella, E. Martinelli, S. Paciello, S. Camorani, M.A. Aiello, F. Micelli, E. Nigro, Masonry columns confined by composite materials: Experimental investigation, *Composites: Part B*, **42**, 692-704, 2011.

[12] A. Borri, G. Castori, M. Corradi, Masonry confinement using steel cords, *Journal of Materials in Civil Engineering*, **25**, 1910-1919, 2013.

[13] A. Borri, G. Castori, M. Corradi, Strengthening of fair face masonry columns with steel hooping, *Materials and Structures*, **47**, 2117–2130, 2014.

[14] L. Jurina, Tecniche di cerchiatura di colonne in muratura, *Structural*, 164, 38-49, 2010.

[15] C.N.R., Guide for the design and construction of externally bonded FRP systems for strengthening of existing structures, Technical Document No. 200/2004, Italian National Research Council, Rome, Italy, 2004.

[16] L. Binda, C. Tedeschi, M.R. Valluzzi, E. Garbin, M. Panizza, Salt crystallization tests on brick masonry reinforced by CFRP textiles. *12th International Conference on Durability of Building Materials and Components*, Porto, Portugal, April 12-15, 2011.

[17] M. Paradiso, A. Borri, D. Sinicropi, S. Galassi, E. Perria, An Experimental Study on Wet/Dry Effects on FRCM Reinforced Masonry. *Congreso Internacional Conservar Rehabilitar Innovar: Jornadas Internacionales Conmemorativas del 80° Aniversario del IETcc*, Madrid, Spain, November 12-14, 2014.

ECCOMAS Congress 2016
VII European Congress on Computational Methods in Applied Sciences and Engineering
M. Papadrakakis, V. Papadopoulos, G. Stefanou, V. Plevris (eds.)
Crete Island, Greece, 5–10 June 2016

FAST KINEMATIC LIMIT ANALYSIS OF FRP REINFORCED MASONRY VAULTS THROUGH A NEW GENETIC ALGORITHM NURBS-BASED APPROACH

Andrea Chiozzi[1], **Gabriele Milani**[2], **and Antonio Tralli**[1]

[1] Department of Engineering, University of Ferrara
1, Via Saragat, I-44122, Ferrara, Italy
e-mail: {andrea.chiozzi, tra}@unife.it

[2] Department of Architecture, Built Environment and Construction Engineering (A.B.C.)
Technical University of Milan,
31, Via Ponzio, I-20133, Milan, Italy
e-mail: gabriele.milani@polimi.it

Keywords: Masonry vaults, Limit analysis, NURBS, Genetic Algorithm.

Abstract. *In the present contribution, a novel Genetic Algorithm NURBS-based approach for the limit analysis of FRP reinforced masonry vaults based on an upper bound formulation is developed.Vaults geometry can be described by a NURBS representation of their mid-surface, which can be generated within any commercial free form modeler, together with information about the local thickness at each point of the surface. By exploiting the properties of NURBS functions, a mesh of the given surface, which still provides an accurate representation of the vaulted surface, can be obtained. Each element of the mesh is a NURBS surface itself and is idealized as a rigid body. Starting from the obtained rigid bodies assembly, an upper bound limit analysis problem with very few optimization variables can be devised and in which dissipation is allowed along element edges only. A possible dissipation at the interfaces between FRP and masonry is also considered in order to take into account, in an approximate but effective way, the possible delamination of the strips from the supports. Due to the very limited number of rigid elements used, the quality of the collapse load so found depends on the shape and position of the interfaces, where dissipation is allowed. Mesh adjustments are therefore needed which is carried out by adopting a simple meta-heuristic (like a standard Genetic Algorithm GA) approach of mesh adjustment. The strength of the proposed GA-NURBS method lies in the fact that even by using a mesh made of very few elements (which therefore require a negligible computational time to have an estimate of collapse loads), it is possible to obtain accurate load multipliers and failure mechanisms, thus exhibiting an edge over existing methods for the collapse analysis of masonry vaults in terms of computational efficiency.*

1 INTRODUCTION

Masonry vaults represent one of the most widespread structural typologies in the historical buildings of both Eastern and Western architecture. Therefore, the interest for their preservation is growing over time along with the need for developing new efficient tools to analyze and evaluate their load-bearing capacity.

As pointed out in [1, 2], it can be affirmed that the modern theory of limit analysis of masonry structures, which has been developed mainly by Heyman [3], is the most reliable tool to assess the ultimate load bearing capacity of masonry vaults. According to Heyman [3], limit theorems of plasticity, i.e. static (lower bound) theorem and kinematic (upper bound) theorem, can be applied to masonry structures provided that the following conditions are verified: i) the compressive strength of the material is infinite; ii) sliding between parts is prevented; iii) tensile strength of masonry is negligible.

Let us observe that for structures made of clay bricks and mortar, collapse generally occurs at small overall displacements. Moreover, in some cases sliding is possible though with a relatively high friction coefficient [4] and shear failure at the joints can be treated within the framework of non-associate plasticity [5]. Finally, although clay bricks masonry exhibits an almost zero tensile strength and a good compressive strength, the infinite compressive strength hypothesis is questionable and, as shown in [3], it is possible to include finite compressive strength within a limit analysis formulation. Nevertheless, material crushing play a minor role in the collapse behavior of masonry structures, except for very shallow segmental arches, pillars, towers and massive vertical structures.

Limit analysis can be also extended to the case of FRP (fibro-reinforced polymers) reinforced masonry structures [6].

Other essential aspects concerning actual masonry vaults should be considered, such as the effects due to material heterogeneity, the importance of the overall geometry for achieving the equilibrium, the importance of properly taking into account the infill and the presence of existing cracks [7].

The recently developed computational methods for masonry vaults, simple or reinforced, can be classified into two broad categories: the Finite Element methods developed both for nonlinear incremental analysis [8] and for limit analysis [9], and the thrust network methods [10-11] directly based on a lower bound formulation [12]. Practical application of these methods requires skilled users and, in the case of thrust network methods, the definition of an equilibrium surface for the vault, which is a priori unknown.

The present paper proposes a new NURBS-based approach [13] for the limit analysis of masonry vaults based on an upper bound formulation also allowing for the presence of FRP reinforcements, developing an idea proposed in [14] for masonry arches. NURBS (i.e. Non-Rational Uniform Bi-Spline) are special approximating base functions widely used in the field of 3D modeling [15]. A given masonry vault geometry can be represented by a NURBS parametric surface, which can be generated within any commercial free form modeler. By exploiting the properties of NURBS functions, a mesh of the given surface, which still provides an exact representation of the vaulted surface, can be obtained. Each element of the mesh is a NURBS surface itself and can be idealized as a rigid body.

Starting from the obtained rigid bodies assembly, an upper bound limit analysis formulation can be devised, which takes into account the main aspects of masonry material (i.e. negligible tensile strength and good compressive strength) and in which dissipation is allowed along element edges only. Furthermore, a meta-heuristic approach based on the implementation of a Genetic Algorithm allows adjusting the initial NURBS mesh until a good estimate of the collapse load multiplier is obtained. This happens when element edges describes the actual

failure mechanism. The strength of the proposed method lies in the fact that even by using a mesh made of very few elements, it is possible to obtain an accurate estimate of the load multiplier, thus exhibiting an edge over existing methods for the collapse analysis of masonry vaults in terms of computational efficiency,

The paper is organized as follows: in Section 2 a synthetic survey is given about how the geometric shape of a masonry vault can be described by a NURBS surface representation and a NURBS mesh can be defined on it. In Section 3, an upper bound limit analysis formulation is proposed, based on the NURBS geometric representation of the masonry vault, which allows to compute the collapse load for a set of given failure mechanisms. Section 4 outlines a Genetic Algorithm, which is capable of selecting the correct failure mechanism, by adequately adjusting the initial mesh. Finally, Section 5 is devoted to presenting several simple numerical results obtained by the proposed procedure.

2 NURBS GEOMETRIC DESCRIPTION

Description and computation of geometries in commercial CAD packages are based on B-Splines and NURBS approximating functions. More precisely, NURBS basis functions are built on B-splines basis functions, which are piecewise polynomial functions defined by a sequence of coordinates $\Xi = \{\xi_1, \xi_2, ..., \xi_{n+p+1}\}$, also known as the knot vector, where the so-called knots, $\xi_i \in [0,1]$, are points in a parametric domain, in which *p* and *n* denote the polynomial order and the total number of basis functions, respectively. Once the order of the basis function and the knot vector are known, the *i*-th B-spline basis function, $N_{i,p}$, can be computed by means of the Cox-de Boor recursion formula [15]. Given a set of weights, $w_i \in \mathbb{R}$, the NURBS basis functions, $R_{i,p}$, read

$$R_{i,p}(\xi) = \frac{N_{i,p}(\xi) w_i}{\sum_{i=1}^{n} N_{i,p}(\xi) w_i}. \tag{1}$$

NURBS share many properties with B-spline basis functions [13]. Among these, they are all nonnegative, they have a compact support, and build a partition of unity (PoU), that is

$$\sum_{i=1}^{n} N_{i,p}(\xi) = \sum_{i=1}^{n} R_{i,p}(\xi) = 1 \tag{2}$$

for each $\xi \in [0,1]$ [13]. Hence, according to Eqs. (1) and (2) B-spline basis functions can be thought of as NURBS basis functions when all weights w_i are equal to one. However, NURBS basis functions have the great advantage of representing exactly the geometry of a wide set of curves such as circles, ellipses, and parabolas [15], and of the surfaces that can be generated by these curves. Geometries that can be generated with B-spline and NURBS are obtained as linear combinations of basis functions [13]. If one considers a set of NURBS basis functions $R_{i,p}$, a NURBS curve of degree *p* is a parametric curve in the three-dimensional Euclidean space defined as

$$\mathbf{C}(u) = \sum_{i=1}^{n} R_{i,p}(\xi) \mathbf{B}_i \tag{3}$$

where coefficients $\mathbf{B}_i \in \mathbb{R}^3$ are known as control points. Unlike standard Lagrange and Hermite approximations, NURBS geometries do not usually interpolate these points. The conti-

nuity of the curve follows from that of the adopted basis functions [15], which is generally C^{p-1} throughout the domain. However, if a knot has multiplicity, *m*, the continuity decreases *m* times at that point [15]. Analogously, a NURBS surface of degree *p* in the *u*-direction and *q* in the *v*-direction is a parametric surface in the three-dimensional Euclidean space defined as

$$\mathbf{S}(u,v)=\sum_{i=0}^{n}\sum_{j=0}^{m}R_{i,j}(u,v)\mathbf{B}_{i,j} \tag{4}$$

where $\{\mathbf{B}_{ij}\}$ form a bidirectional net of control points. A set of weights $\{w_{i,j}\}$ and two separate knot vectors in both *u* and *v* directions must be defined. Given a NURBS surface $\mathbf{S}(u,v)$, isoparametric curves on the surface can be defined by fixing one parameter in the parameter space and letting the other vary. By fixing $u=u_0$ the isoparametric curve $\mathbf{S}(u_0,v)$ is defined on the surface $\mathbf{S}$, whereas by fixing $v=v_0$ the isoparametric curve $\mathbf{S}(u,v_0)$ is obtained.

Many commercial free form surface modelers, such as Rhinoceros® [16], utilize NURBS representation and its properties to generate and manipulate surfaces in the three-dimensional space. In what follows, simple vault geometries have been generated within Rhinoceros and the resulting NURBS structure have been imported within a MATLAB® environment through the IGES (Initial Graphics Exchange Specification) standard [17]. Once the NURBS structure has been transferred to the MATLAB® environment, it is possible to manipulate it by exploiting NURBS properties in order to define a NURBS mesh on the given surface, i.e. a mesh in which each element is a NURBS surface itself. When working with simple surfaces like the one considered in the present contribution, the easiest way to generate a NURBS mesh on the given surface is to define a subdivision of the two-dimensional parameters space *u*-*v*, which follows from subdividing the knot vectors in both *u* and *v* directions into equal intervals. The resulting mesh is formed by isoparametric curves on the surface in the three-dimensional Euclidean space. Each element is a NURBS surface and its edges are branches of isoparametric curves belonging to the initial surface. More precisely, the counter-image of each element of the mesh is a rectangle $S_{ij}=[u_i,u_{i+1}]\times[v_j,v_{j+1}]\in\mathbb{R}^2$ defined in the parameters space. For each element (which can be denoted by E_{ij}), the area of the surface can be computed through the following relation:

$$A_{ij}=\int_{S_{ij}}dS=\int_{u_i}^{u_{i+1}}\int_{v_j}^{v_{j+1}}\left\|\mathbf{S}_u\times\mathbf{S}_v\right\|du\,dv \tag{5}$$

where $\mathbf{S}_u$ and $\mathbf{S}_v$ are partial derivatives of the parametric surface $\mathbf{S}(u,v)$ in the *u* and *v* directions. Analogously, the center of mass of each element may be computed with the following relation:

$$\mathbf{c}=\frac{1}{A_{ij}}\int_{S_{ij}}\mathbf{x}\,dS=\frac{1}{A_{ij}}\int_{u_i}^{u_{i+1}}\int_{v_j}^{v_{j+1}}\mathbf{S}(u,v)\left\|\mathbf{S}_u\times\mathbf{S}_v\right\|du\,dv \tag{6}$$

Computations can be numerically carried out using a standard Gauss quadrature method.

3 KINEMATIC LIMIT ANALYSIS

Limit analysis is a powerful tool to assess the structural safety level of a masonry construction. As already discussed, given the NURBS geometric representation of the vaulted surface, a NURBS mesh can be defined on the same surface. Each element of the mesh, which is a NURBS surface itself, can be regarded as a rigid body. Starting from the geometrical proper-

ties of each element, an upper bound formulation can be outlined and implemented through a linear programming algorithm in order to assess the ultimate load bearing capacity of a given masonry vault. This paragraph summarizes the proposed upper bound formulation.

Be N_E the number of elements composing the NURBS mesh, which geometrically represents the vaulted surface. Each element is considered as a rigid element. Thus, the kinematics of each element is determined by the six (three translational and three rotational) generalized velocity components $\{u_x^i, u_y^i, u_z^i, \Phi_x^i, \Phi_y^i, \Phi_z^i\}$ of its center of mass G_i, expressed in a global reference system $Oxyz$. On the structure, dead loads $\mathbf{F}_0$ and live loads $\mathbf{\Gamma}$ are acting. Internal dissipation is assumed to occur only along element interfaces. Indicating by N_I the number of interfaces, total internal dissipation power D_{int} is equal to the sum of the power dissipated along each interface P_{int}^i, which is defined in Section . Furthermore, total internal dissipation power D_{int} is equal to the sum of the powers of live ($\mathbf{1} \cdot \Gamma$) and dead ($\mathbf{F_0}$) loads, indicated as $P_{\mathbf{\Gamma}}$ and $P_{\mathbf{F_0}}$ respectively:

$$D_{\text{int}} = \sum_{i=1}^{N_I} P_{\text{int}}^i = P_{\mathbf{\Gamma}} + P_{\mathbf{F_0}} \tag{7}$$

Γ is a load multiplier. The linear programming problem related to the kinematic formulation of limit analysis consists in an appropriate minimization of the load multiplier Γ under the action of suitable constraints, which are described in the following Subsections. The vector of unknowns of the linear programming problem, $\mathbf{X}$, contains the six generalized velocity components for each element and a number of plastic multipliers along each interface which will be defined in Subsection 3.2.

3.1 Geometric constraints

Vertex belonging to element free edges, which do not constitute an element interface, can be subjected to external kinematic constraints, by imposing an assigned value for translational and/or rotational velocities at these points. For each of such vertex V_j, kinematic constraints can be expressed in terms of generalized velocities of the center of mass of the *i*-th element they belong. For example, in case only translational velocities of a given vertex V_j, belonging to element *i*, are constrained to zero, the following relation holds as a geometric constraint:

$$\mathbf{u}_{V_j} = \mathbf{u}^i + \mathbf{R}\left[\mathbf{x}_{V_j} - \mathbf{x}_{G_i}\right] = \mathbf{0} \tag{8}$$

where $\mathbf{u}_{V_j} = [u_x^{V_j}, u_y^{V_j}, u_z^{V_j}]^T$ are the three translational velocity components of the vertex V_j, $\mathbf{u}^i = [u_x^i, u_y^i, u_z^i]^T$ are the three (unknown) translational velocity components of the center of mass of element *i* to whom vertex V_j belongs, and $\mathbf{R}$ is a rotation matrix whose elements are the (unknown) generalized rotational velocities of the center of mass of element *i*. In general, all linear geometric constraints can be re-written in the following standard form:

$$\mathbf{A}_{eq,geom}\mathbf{X} = \mathbf{b}_{eq,geom} \tag{9}$$

where $\mathbf{A}_{eq,geom}$ is the matrix of geometric constraints and $\mathbf{b}_{eq,geom}$ the corresponding vector of coefficients.

3.2 Compatibility constraints

In order to enforce plastic compatibility along interfaces and correctly evaluate dissipation power, intrados and extrados edges of each interface have been subdivided into an assigned number $(N_{sd}+1)$ of points P_i. On each point P_i, a local reference system $(\mathbf{n},\mathbf{s},\mathbf{t})$ have been defined, where $\mathbf{n}$ is the unit vector normal to the interface, $\mathbf{s}$ is the tangential unit vector in the longitudinal direction and $\mathbf{t}$ is the tangential unit vector in the transversal direction.

On each point P_i of each interface, which separates the two elements E' and E'', the following compatibility equation must hold:

$$\Delta\tilde{\mathbf{u}} = \dot{\boldsymbol{\lambda}}\frac{\partial f}{\partial \boldsymbol{\sigma}} \tag{10}$$

where $\boldsymbol{\sigma}=[\sigma_{nn},\sigma_{ns},\sigma_{nt}]$ is the stress vector acting on P_i in the three local reference directions, $f(\boldsymbol{\sigma})$ is a suitable yield function and $\dot{\boldsymbol{\lambda}}$ is an unknown plastic multiplier vector. In Eq. (10), $\Delta\tilde{\mathbf{u}}$ is the representation in the local reference system of the quantity $\Delta\mathbf{u}$ in the global reference system which is defined as:

$$\Delta\mathbf{u} = \mathbf{u}'_{P_i} - \mathbf{u}''_{P_i} \tag{11}$$

where $\mathbf{u}'_{P_i}$ is the vector composed by the three translational velocity components of the point P_i seen as belonging to element E' and $\mathbf{u}''_{P_i}$. $\Delta\mathbf{u}$ is related to $\Delta\tilde{\mathbf{u}}$ through the following relation:

$$\Delta\tilde{\mathbf{u}} = \tilde{\mathbf{R}}\Delta\mathbf{u} \tag{12}$$

where $\tilde{\mathbf{R}}$ is a suitable 3×3 rotation matrix whose rows are respectively the components of the three local vectors $(\mathbf{n},\mathbf{s},\mathbf{t})$ expressed in the global reference system.

For the sake of simplicity, the yield surface $f(\boldsymbol{\sigma})$ have been defined in the stress-space as the parallelepiped defined by the inequalities $-f_c \le \sigma_{nn} \le f_t$, $-\tau_{0,ns} \le \sigma_{ns} \le \tau_{0,ns}$, $-\tau_{0,nt} \le \sigma_{nt} \le \tau_{0,nt}$ where f_c, f_t, $\tau_{0,ns}$, $\tau_{0,nt}$ are material parameters corresponding respectively to compression strength, tensile strength, shear strength in the direction tangential to the interface midline and shear strength in the direction orthogonal to the interface midline. If the interface is reinforced by FRP strips at intrados or extrados f_t is replaced by the delamination stress f_d computed according to [18] in order to take into account dissipation due to FRP delamination.

With the assigned yield surface, Eq. (10) simplifies and must hold for each point P_i of each interface. On each point P_i, six unknown plastic multipliers $\dot{\lambda}^+_{nn},\dot{\lambda}^-_{nn},\dot{\lambda}^+_{ns},\dot{\lambda}^-_{ns},\dot{\lambda}^+_{nt},\dot{\lambda}^-_{nt}$ are defined. Therefore, the total number of unknown plastic multipliers is equal to $6\cdot(N_{sd}+1)\cdot 2N_I$.

3.3 Non-negativity of plastic multipliers

An additional constraint which must be included into the linear programming problem is the non-negativity of each plastic multiplier:

$$\dot{\lambda}_{ij} \geq 0. \tag{13}$$

3.4 Normality condition

The last condition to be applied is the so-called normality condition which requires that the external power dissipated by the live load $\mathbf{1} \cdot \Gamma$ set equal to one, is itself equal to one, i.e.:

$$P_{\Gamma=1} = 1 \tag{14}$$

This condition allows to rewrite Eq. (7) in the following way:

$$\Gamma = \sum_{i=1}^{N_I} P_{\text{int}}^i - P_{F_0} \tag{15}$$

3.5 Internal dissipated power and linear programming problem

On each interface i, covering the surface S_i, the internal dissipated power is defined as the integral:

$$P_{\text{int}}^i = \int_{S_i} \boldsymbol{\sigma} \cdot \Delta\tilde{\mathbf{u}} \, dS \tag{16}$$

in the local reference system, where both $\boldsymbol{\sigma}$ and $\Delta\tilde{\mathbf{u}}$ have been defined in Subsection 3.2. Therefore, remembering Eq. (15) and following the kinematic theorem of limit analysis, the related linear programming problem can be stated as follows:

$$\min \left\{ \sum_{i=1}^{N_I} P_{\text{int}}^i - P_{\mathbf{F_0}} \right\} \tag{17}$$

under geometric constraints (9), compatibility constraints (10), non-negativity of plastic multipliers constraints (13) and the normality condition (14). The unknowns of the linear programming problem are the $6 \cdot N_E$ generalized velocity components of the center of mass of each element and the $6 \cdot (N_{sd} + 1) \cdot 2N_I$ plastic multipliers at each point of each interface.

4 GENETIC ALGORITHM

A genetic algorithm is used to progressively modify the mesh in order to find the minimum collapse multiplier among all possible configurations and therefore to determine the actual collapse mechanism. A genetic algorithm is a method for solving both constrained and unconstrained optimization problems based on a natural selection process that mimics biological evolution. The algorithm repeatedly modifies a population of individual solutions. At each step, the genetic algorithm randomly selects individuals from the current population and uses them as parents to produce the children for the next generation. Over successive generations, the population "evolves" toward an optimal solution.

A NURBS mesh of a vaulted surface, is determined by a given number N_{par} of real parameters $p_1, p_2, ..., p_{Npar}$, that depend on the type of collapse mechanism which must be detected. A given NURBS mesh is regarded as an individual and each individual (or chromosome), is written as an array with $1 \times N_{par}$ elements:

$$individual = [p_1, p_2, ..., p_{Npar}] \tag{18}$$

Each individual has a cost, found by evaluating the cost function *f* at the parameters $p_1, p_2, ..., p_{Npar}$. The cost function *f* is defined as a function which outputs the collapse load multiplier λ_c for every assigned individual (i.e. an assigned mesh on the surface) through the implementation of the limit analysis procedure described in Section 3:

$$\lambda_c = f(individual) = f(p_1, p_2, ..., p_{Npar}) \tag{19}$$

To begin the genetic algorithm, we define an initial population of N_{ipop} individuals. A matrix represents the population with each row in the matrix being a $1 \times N_{par}$ array (individual) of continuous parameters values. Given an initial population of N_{ipop} individuals, the full matrix of $N_{ipop} \times N_{par}$ random values is generated by

$$IPOP = (hi - lo) \times \mathbf{random}\{N_{ipop}, N_{par}\} + lo \tag{20}$$

where $\mathbf{random}\{N_{ipop}, N_{par}\}$ is a function that generates an $N_{ipop} \times N_{par}$ matrix of uniform random numbers, *hi* and *lo* are the highest and lowest number in the parameter range.

Individuals are not all "create equal": each one's worth is assessed by the cost function. In order to decide which chromosomes in the initial population of individuals are fit enough to survive and reproduce offspring in the next generation the N_{ipop} costs and associated individuals are ranked from lowest cost to highest cost. We retain the best N_{pop} members of the population for the next iteration of the algorithm and the rest die off. This process is called natural selection and from this point on, the size of the population at each generation is N_{pop}. An equal number of mothers and fathers is selected within the N_{pop} individuals, which pair in some random fashion. There are various reasonable ways to pair individuals [19]. In this paper, a weighted cost selection with assigned probabilities is used [19]. Each pair produces two offspring that contain traits from each parent. Mating is carried out by choosing one or more points in the chromosome to mark as the crossover points and the, parameters between these points are merely swapped between the two parents.

Finally, if care is not taken, the genetic algorithm converges too quickly into one region of the cost surface and this may be not good if the problem we are modeling has several local minima, in which the solution may get trapped. To avoid this problem of overly fast convergence, we force the routine to explore other areas of the cost surface by randomly introducing changes, or mutations, in some of the parameters. A mutation rate of 15% is chosen.

5 NUMERICAL EXAMPLES

In this Section, two numerical examples of NURBS based kinematic limit analyses of both reinforced and unreinforced masonry vaults are synthetically described. For each example, the mid-surface of the vault have been modeled with the 3D free form modeler Rhinoceros® and the corresponding NURBS structure have been imported within a MATLAB® environment using the IGES protocol. The limit analysis procedure described in Section 3 have been implemented and the collapse mechanism is determined by suitably adjusting the mesh through the genetic algorithm described in Section 4.

5.1 Unreinforced skew barrel vault

The proposed GA-NURBS approach is applied to the skew circular arch experimentally tested in [20]. The arch, named *Skew 2* in [20], has a clear square span of 3000 mm, a rise of 750 mm and a skew of 45 degrees. The width of the barrel was approximately 670 mm and the average thickness 215 mm. The arch was constructed using Class A engineering bricks were on two reinforced concrete abutments representing rigid supports. The geometry of the arch is reported in Fig. In the test, a concentrated load *P* was applied under force control at the three quarter span mid-width of the arch barrel. The load was monotonically increased up to 17.4kN when collapse occurred because of the formation of cracks extending in the mortar joints through the whole width of the arch, giving rise to a 3D failure mode typical of skewed masonry arches. An average brickwork compression strength f_c of 2.4 MPa and a tensile strength f_t of 0.2 MPa were measured, whereas a shear strength τ of 0.1 MPa is assumed. Average specific weight of brickwork is $22\,kN/m^3$. The initial NURBS mesh of the vaulted surface is formed by three quadrangular elements. A single centered vertical live load of $\lambda \cdot 1kN$ is applied at 1/4L.

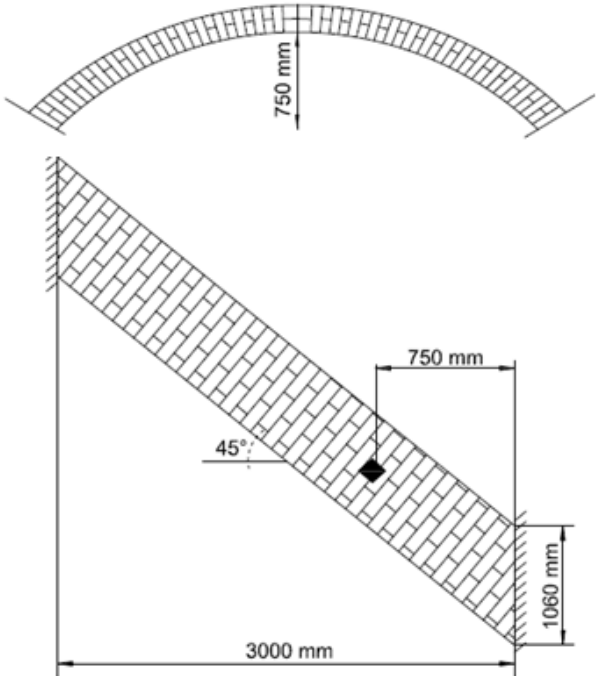

Figure 1: Skew arch geometry in the test configuration described in [20].

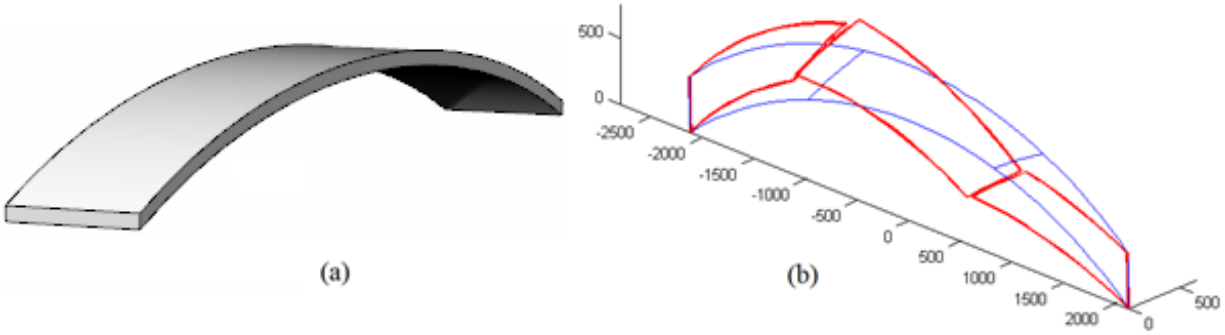

Figure 2: (a) 3D NURBS model of the skew arch experimentally tested in [20] generated with Rhinoceros®. (b) Three-element NURBS mesh (blue) and collapse mechanism from kinematic limit analysis (red).

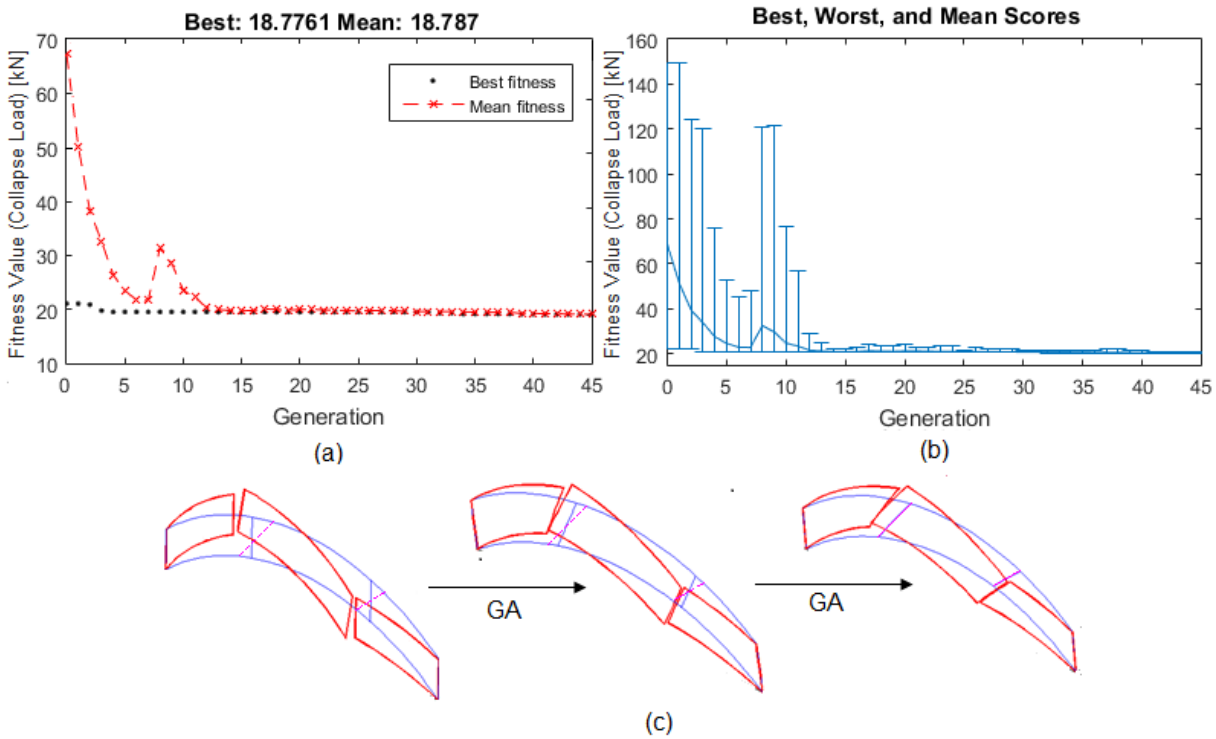

Figure 3: Skew arch: convergence of the genetic algorithm towards the optimal solution in terms of best fitness and mean value (a) and in terms of best, worst and mean scores (b) at each generation; evolution of the free interfaces towards the optimal solution (c).

The genetic algorithm allows evaluating the optimal position of the two active interfaces, in order to minimize the collapse load multiplier and therefore obtaining the actual collapse mechanism. Due to the point load presence, the position of the active interfaces is governed by three parameters: two parameters fix the extremes of the unloaded interface, whereas a third parameter fixes the position of the loaded interface (since this interface is bound to pass though the load application point). In the genetic algorithm an initial population of 40 individuals have been chosen, each individual being a 1x3 vector.

A collapse load multiplier $\lambda = 18.78$ have been obtained. Fig.2(a) shows the 3D NURBS model of the vault generated within Rhinoceros® and Fig.2(b) depicts the computed collapse mechanism, which proves to be equal to the one observed in [20].

As shown in Fig. 3(a-b), the algorithm presents a fast convergence towards the optimal solution and the final best fitness value is obtained after the first four generations. Fig. 3(c) represents the evolution of the mesh towards the optimal solution.

5.2 FRP reinforced square barrel vault

At first, a comparison with the experimental tests presented in [21] and later analyzed in [9, 14] for the unreinforced square barrel vault is carried out. In [21] the ultimate strength of a segmental masonry arch was tested, with a clear span of 3 m, an inner radius of 2.5 m and a sagitta of 0.5 m. The arch is a one-head brick structure with depth equal to 0.10 m and width equal to 1.25 m. The test-arch had 51 layers and was built with Rijswaard soft mud bricks and 1:2:9 mortar. Brick compressive strength was 27 MPa and mortar compressive strength was 2.5 MPa. The test-arch was loaded with four concentrated loads, applied by four hydraulic jacks 600 mm centre to centre. In Fig. 5a the geometry of the test-arch and its loading conditions are reported. Only the second concentrated load from the left was increased until failure, whereas the remaining loads were maintained constant at the values of 5.9, 9.1 and 9.1 kN

respectively. At failure, a four hinges collapse mechanism was observed in [21], which is depicted in Fig. 6a and measured a collapse load equal to 40.7 kN at the second jack. An average brickwork compression strength f_c of 2.4 MPa, a tensile strength f_t of 0.1 MPa and a shear strength τ of 0.1 MPa are assumed. Average specific weight of brickwork is $20\,kN/m^3$.

The described test-arch has been modeled within Rhino and its 3D model is reported in Fig. 5b. The initial NURBS mesh of the vaulted surface is formed by four quadrangular elements.

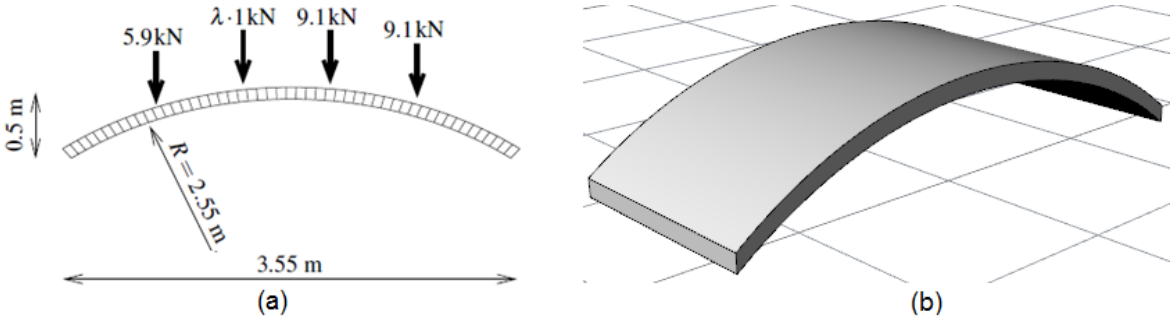

Figure 5: (a) Schematic representation of the segmental masonry test-arch used in [21]: geometry and loading conditions. (b) 3D NURBS model of the arch experimentally tested in [21] generated with Rhinoceros®.

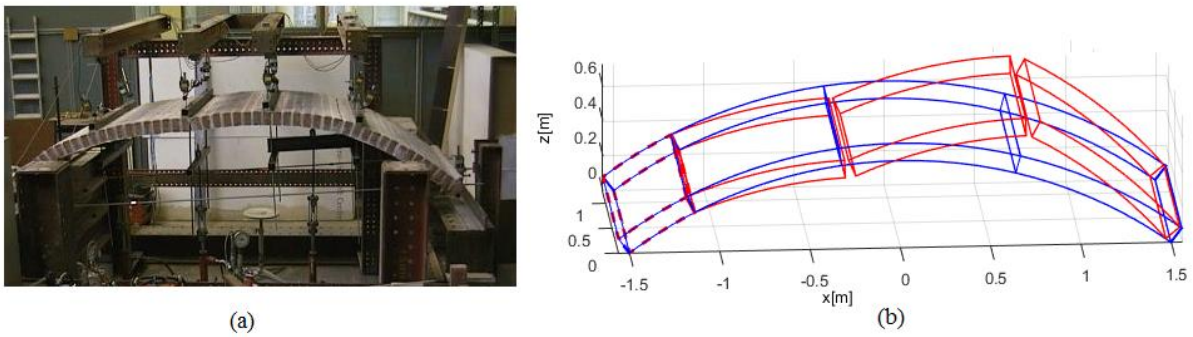

Figure 6: (a) Experimental failure mechanism obtained in [21]. (b) Failure mechanism computed through the GA-NURBS approach.

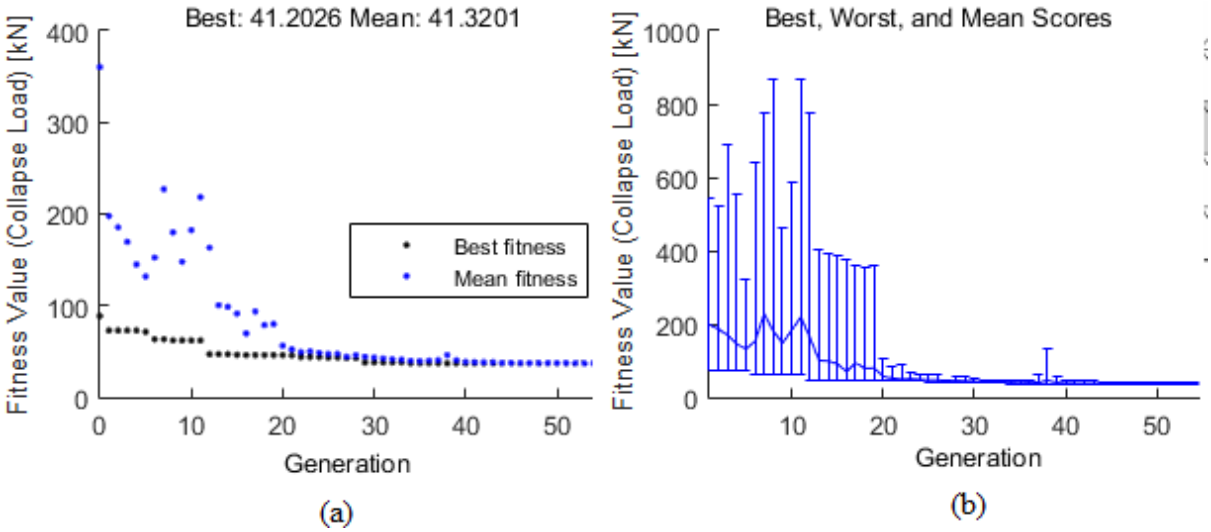

Figure 7: Square barrel vault: convergence of the genetic algorithm towards the optimal solution in terms of best fitness and mean value (a) and in terms of best, worst and mean scores (b) at each generation.

The genetic algorithm allows evaluating the optimal position of the active interfaces, in order to minimize the collapse load multiplier and therefore obtain the actual collapse mechanism. Only the second point load from the left have been marked as a live load. Collapse will occur after formation of four plastic hinges. Thus, the position of the active interfaces is governed by four parameters. In the genetic algorithm an initial population of 20 individuals have been chosen, each individual being a 1x4 vector. A collapse load multiplier $\lambda = 41.2$ have been obtained. Fig.6(b) depicts the computed collapse mechanism, which proves to be equal to the one observed in [21] and depicted in Fig. 6(a). As shown in Fig. 7, the algorithm presents a fast convergence towards the optimal solution.

Finally, the same vault was analyzed by assuming FRP reinforcement set on the extrados (Fig. 8). In order to prevent the formation of the plastic hinges indicated in Fig. 6(b), we suppose to strengthen the arch by means of two sets of FRP strips (width 100mm). The first set of strips is disposed at the extrados of the arch, whereas the second is applied at the intrados. The reinforcement tissue has thickness of 0.2 mm, Young's elastic modulus is assumed equal to 164 GPa (for tensile stress only) and an ultimate strain of 2% is adopted. FRP delamination stress f_d has been calculated by following the Italian FRP Design Guidelines [18]. Masonry strength parameters have been assumed the same of the unreinforced arch. The NURBS model is kept unchanged and so is the number of parameters governing the problem.

Again, the genetic algorithm allows evaluating the optimal position of the active interfaces, in order to minimize the collapse load multiplier and therefore obtaining the actual collapse mechanism.

The GA-NURBS approach allows to compute a collapse load multiplier $\lambda = 86.3$ of the FRP reinforced arch, which is in agreement with the results presented in [6].

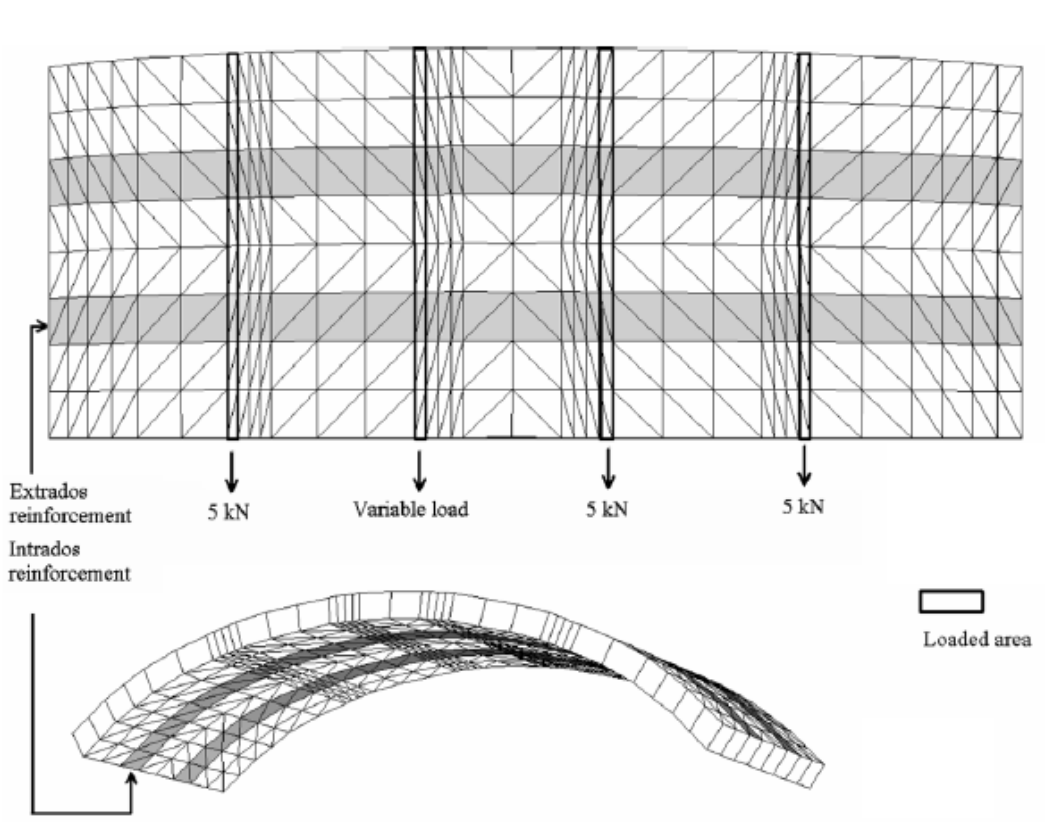

Figure 8: Reinforced parabolic arch. FRP strips dimensions and disposition.

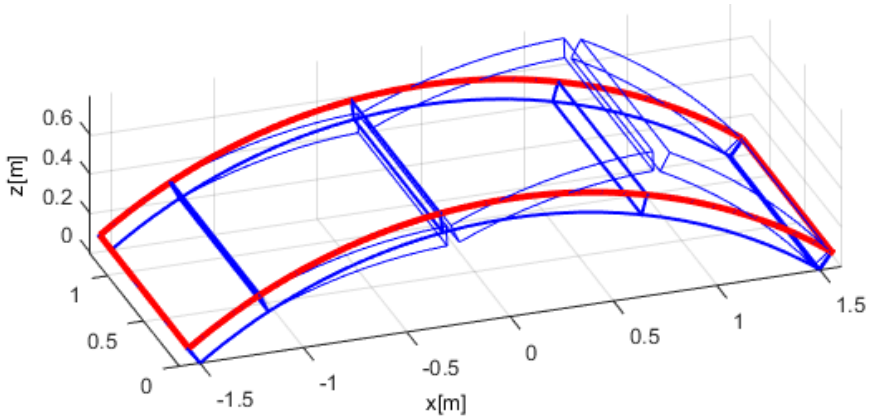

Figure 9: Square barrel vault: convergence of the genetic algorithm towards the optimal solution in terms of best fitness and mean value (a) and in terms of best, worst and mean scores (b).

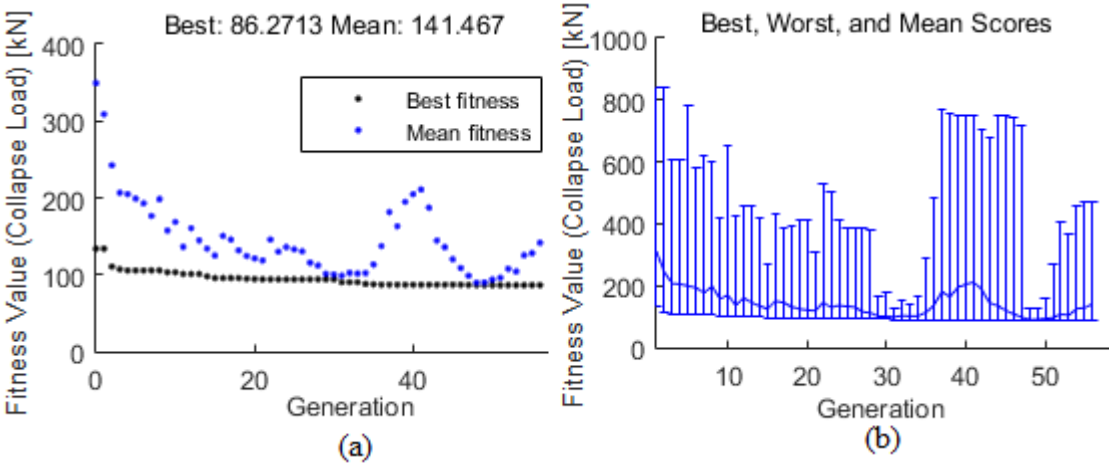

Figure 10: Square barrel vault: convergence of the genetic algorithm towards the optimal solution in terms of best fitness and mean value (a) and in terms of best, worst and mean scores (b).

In Figure 9 the four hinges collapse mechanism is shown: in this case the mechanism develops only after FRP delamination has occurred at the extrados hinges. The thick red line represents the outline of the FRP reinforcement.

As shown in Fig. 10, the algorithm presents a fast convergence towards the optimal solution and the final best fitness value is obtained after few generations.

REFERENCES

[1] M. Como, *Statics of historic masonry constructions*, Springer-Verlag, Berlin, 2013.

[2] S. Huerta, The analysis of masonry architecture: a historical approach. *Architectural Science Review*, **51**, 297-328, 2008.

[3] J. Heyman, *The stone skeleton: structural engineering of masonry architecture*, Cambridge University Press, UK, 1995.

[4] G. Vasconcelos, P.B. Lourenco, Assessment of the In-plane shear strength of stone masonry walls by simplified models. In *Proc. 5th International Conference of Structural Analysis of Historical Construction*, New Delhi, India, 2006.

[5] M. Gilbert, C. Casapulla, H.M. Ahmed, Limit analysis of masonry block structures with

non-associative frictional joints using linear programming. *Computers and Structures*, **84**, 873-887, (2006).

[6] G. Milani, E. Milani, A. Tralli, Upper bound limit analysis model for FRP–reinforced masonry curved structures. Part II: Structural analyses. *Computers and Structures*, **87**, 1534-1558, 2009.

[7] A. Tralli, C. Alessandri, G. Milani, Computational methods for masonry vaults: a review of recent results. *The Open Civil Engineering Journal*, **8**, 272-287, 2014.

[8] G. Milani, A. Tralli, A simple meso-macro model based on SQP for the non-linear analysis of masonry double curvature structures. *International Journal of Solids and Structures*, **49**, 808-834, 2012.

[9] G. Milani, E. Milani, A. Tralli, Limit analysis of masonry vaults by means of curved shell finite elements and homogenization. *International Journal of Solids and Structures*, **45**, 5258-5288, 2008.

[10] P. Block, T. Ciblac, J.A. Ochsendorf, Real-time limit analysis of vaulted masonry buildings. *Computers and Structures*, **84**, 1841-1852, 2006.

[11] P. Block, L. Lachauer, Three-dimensional (3D) equilibrium analysis of Gothic masonry vaults. *International Journal of Architectural Heritage*, **8**, 312-335, 2014.

[12] M. Angelillo, E. Babilio, A. Fortunato, Singular stress-fields for masonry-like vaults. *Continuum Mechanics and Thermodynamics*, **25**, 423-441, 2013.

[13] L. Piegl, W. Tiller, *The NURBS Book*, Springer, 1995.

[14] A. Chiozzi, M. Malagù, A. Tralli, A. Cazzani, ArchNURBS: NURBS-Based Tool for the Structural Safety Assessment of Masonry Arches in MATLAB. *ASCE Journal of Computing in Civil Engineering*, **30**, 2016.

[15] J. A. Cottrell, T.J.R. Hughes, Y. Bazilevs, *Isogeometric analysis: toward integration of CAD and FEA*, John Wiley & Sons, 2009.

[16] R. McNeel and Associates, *Rhinoceros, modeling tools for designers*, 5.0, www.rhino3D.com, 2015.

[17] US Product Data Association, *IGES 5.3 (ANSI-1996)*, 1996.

[18] National Research Council, *Instructions for the design, building and control of static retrofitting interventions through FRP composites*, DT200-2013, 2013.

[19] R.L. Haupt, S.E. Haupt, *Practical Genetic Algorithms*, John Wiley & Sons, 1998.

[20] J. Wang, C. Melbourne, The 3-Dimensional Behaviour of Skew Masonry Arches. *The British Masonry Society*, London, UK (1996).

[21] A. Vermeltfoort, Analysis and experiments of masonry arches. In: *Proceedings of Historical Constructions*, R.B. Lourenço and P. Roca Eds., Guimaraes, Portugal, (2001).

ECCOMAS Congress 2016
VII European Congress on Computational Methods in Applied Sciences and Engineering
M. Papadrakakis, V. Papadopoulos, G. Stefanou, V. Plevris (eds.)
Crete Island, Greece, 5–10 June 2016

THE ROLE OF RESTORATION MORTARS IN THE EARTHQUAKE PROTECTION OF THE KAISARIANI MONASTERY

A.Moropoulou[1]*, M.Apostolopoulou[1], P.Moundoulas†[1], E.Aggelakopoulou[1], L.Siouta[1], A.Bakolas[1], Maria Douvika[2], Panagiotis Karakitsios[3], Panagiotis G. Asteris[2]

[1] Laboratory of Materials Science and Engineering, School of Chemical Engineering, National Technical University of Athens, Athens, Greece
* Corresponding author, e-mail: amoropul@central.ntua.gr

[2] Computational Mechanics Laboratory, School of Pedagogical and Technological Education, Athens, Greece

[3] Department of Civil Engineering, National Technical University of Athens, Athens, Greece

Keywords: *mortar compatibility, mortar serviceability, restoration mortars, historical structures, fragility curves, masonry retrofitting*

Abstract. *Monuments and historical buildings are degraded as time passes due to natural ageing, environmental factors, as well as natural phenomena such as earthquakes. Their conservation and restoration thus becomes crucial in order to preserve our cultural heritage. Repointing of monuments and historical buildings is perhaps the most usual conservation action, as it restores and ensures masonry continuity in a reversible manner. However, this is accomplished only if the restoration mortar applied fulfills compatibility and serviceability criteria. In the current study, the characterization of the historical mortars of the Kaisariani monastery was undertaken and six restoration mortars were selected from literature and examined in order to assess their compatibility with the historical structure of the Kaisariani Monastery in Greece. The restoration mortars were assessed regarding their compatibility with the structural materials of the Kaisariani Monastery, as well as their impact on the earthquake resistance of the structure. A new stochastic computational framework for earthquake resistant design of masonry structural systems, based on fragility analysis and artificial neural networks was applied for the assessment of the seismic vulnerability of the Kaisariani Monastery, for three different repairing scenarios, utilizing the results of the examined restoration mortars. The results showed that a variety of restoration mortar characteristics can be achieved, an important feature, which coupled with the results of the fragility analysis for the repairing scenarios, can be utilized for the selection of the optimum restoration mortar in terms of compatibility and serviceability.*

1. INTRODUCTION

Monuments and historical buildings are degraded as time passes due to natural ageing, environmental factors, as well as natural phenomena such as earthquakes [1]. Their conservation and restoration thus becomes crucial in order to preserve our cultural heritage. **Repointing** of monuments and historical buildings is perhaps the most usual conservation action, as it restores and ensures masonry continuity in a reversible manner. However, this is accomplished only if the restoration mortar applied fulfills **compatibility** and **serviceability** criteria.

The need for knowledge of the traditional mortars has recently arisen from an increased interest in the techniques and materials used in the past. Negative results in recently restored buildings due to the use of improper materials have created a growing demand for research into the field of the traditional ones. Traditional building materials, such as joint mortars, plasters, waterproofing mortars etc., have exhibited remarkable longevity throughout time, however their production technology has been lost, as traditional materials have been replaced due to the extensive use of common contemporary materials, like cement and polymers, materials highly incompatible with the authentic building materials, resulting in extensive and irreversible damage to many cultural heritage monuments [2, 3, 4].

A methodology which has proved helpful in this procedure is reverse engineering [1, 5, 6]. Thus, by discovering the ancient technology employed for the production of the original mortars, new, compatible restoration mortars can be designed. The researcher however cannot rely solely on the results of the analysis of the historical mortar; one must examine the other building materials as well, such as stones and bricks, in order to assess whether the new restoration mortar is compatible with these materials as well. Furthermore, one must always take into consideration the specific environment of the monument, as environmental factors, such as excessive humidity or atmosphere pollution also affect the longevity of the materials [7, 8]. The most important steps that must be followed, are i) sampling of representative mortar samples, selecting the mortars that exhibit the least possible decay (environmental, physical, mechanical), ii) characterization of the historical mortar through various techniques, classification in order to determine the range of acceptability values, as well as analysis of specific considerations, deriving from the in situ analysis of the structure, the restrictions accompanying the other building materials and the study of the materials decay and iii) production of proper restoration mortars or selection of restoration mortars available in literature and compatibility and serviceability assessment [6].

In the current study a number of historical samples deriving from the Kaisariani monastery masonries were studied through *Fiber Optic Microscopy (FOM), Sieve analysis, Differential Thermal and Thermo-Gravimetric Analysis (DTA-TG), Mercury Intrusion Porosimetry (MIP)* and *Total Soluble Salts Measurements.* Several compatibility and serveacability criteria were set during this process, in order to then evaluate the selected restoration mortars and concretes. Six restoration mortars were selected from existing literature and the results of their analysis were examined in order to assess their compatibility with the historical structure of the Kaisariani Monastery in Greece. The restoration mortars examined were two lime-metakaolin mortars and one hydraulic lime mortar, and two lime-metakaolin concretes and one hydraulic lime concrete (thick joint mortars) [9, 10]. The concretes were designed with the addition of crushed bricks, in order to simulate historical mortars of byzantine monuments that have shown excellent performance in earthquakes [11]. The restoration mortars were examined by DTA/TG, in order to assess their

physicochemical characteristics and MIP in order to study their microstructural characteristics. These results were crucial in the assessment of compatibility. Finally, the mechanical strength of the restoration mortars was examined. Thus, the restoration mortars were assessed regarding their compatibility with the structural materials of the Kaisariani Monastery, as well as their impact on the earthquake resistance of the structure through the use of fragility analysis for different repairing scenarios, thus accomplishing the selection of the optimum restoration mortar in terms of compatibility and serviceability.

The Catholicon of the Kaisariani Monastery is a typical mid-byzantine Athenian church structure (11th or 12th century), its main building elements consisting of carved stones, bricks and mortars. The monastery has a rich history, and subsequently many construction phases throughout the centuries. The original building was a complex cross-in-square four-column domed church, without a narthex; the domed narthex was added to the west of the original structure in the early 17th century, and the barrel-vaulted chapel dedicated to Aghios Antonios positioned at the southwest of the Catholicon was added in the late 17th century (Fig. 1), thus comprising the present structure. The monastery complex has undergone many conservation treatments, which are not fully documented; however two important reconstruction projects took place in the complex in the beginning and the middle of the 20th century [12-14].

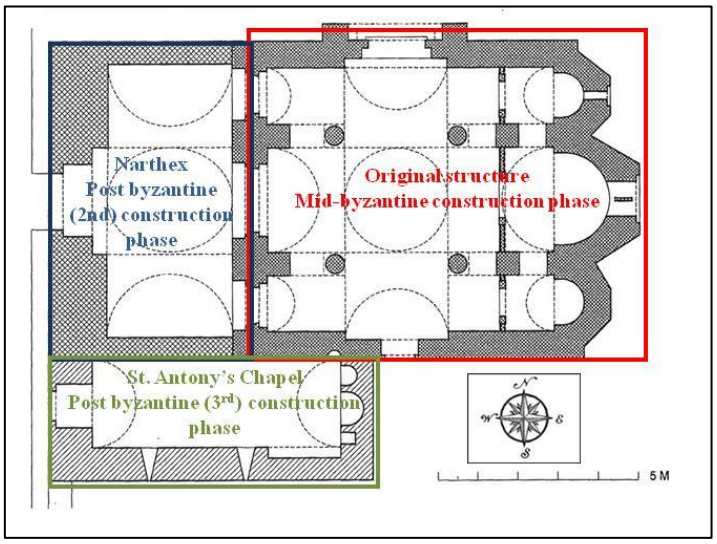

Figure 1: Ground plan of the church [15], with probable construction phases

2. SAMPLING

A number of historical mortar samples deriving from the historic masonry of the original Catholicon structure were examined (Table 1, Figure 2), as well as two brick samples. The samples were obtained internally and externally of the main temple, from different sides and depths of the walls.

Sample Code	Sampling Location	Sample Description
MK1	East wall of the Catholicon, in depth of the exterior masonry leaf. Position from ground level 1.4 m	Whitish mortar with the addition of straw, aggregates not discernible
MK2	East wall of the Catholicon, in depth of the exterior masonry leaf. Position from ground level 1.4 m	Mortar with evident lime lumps and the addition of straw, presence of dark-colored aggregates

MK2b	East wall of the Catholicon, exterior. Position from ground level 1.4 m	Whitish joint mortar, deriving from the joint of the cloisonné, presence of straw in matrix. Very low cohesion between mortar constituents
BR3a	East wall of the Catholicon, exterior. Position from ground level 0.4 m	Detached ceramic, evident biodegradation
BR3b	East wall of the Catholicon, exterior. Position from ground level 0.4 m	Whole piece of ceramic brick deriving from the cloisonné masonry. Mortar with straw adhered on the surface
MK4	North wall of the Catholicon, masonry left of the entrance, in depth of the exterior masonry leaf. Position from ground level 3.1 m	Whitish mortar straw additives, presence of dark-colored aggregates
MK5	North wall of the Catholicon, masonry right of the entrance, exterior. Position from ground level 3.5 m	Mortar, deriving from the joint of the cloisonné. Two layers visible: Exterior layer is pink hued and appears as 1mm thick (MK5a). Interior layer is (MK5b).
MK6	North wall of the Catholicon, masonry left of the entrance, in depth of the interior masonry leaf. Position from ground level 3 m	Whitish mortar with the presence of discernible dark-colored and light grey colored aggregates
MK7	Interior west wall of the Catholicon, joining with the Narthex Position from ground level 2.1 m	Whitish mortar. Presence of lime lumps. Presence of dark-grey colored aggregates, presenting a wide grain size distribution.
MK8	South wall of the Catholicon, in depth of the exterior masonry leaf. Position from ground level 3.6 m	Whitish mortar with dark-colored aggregates.

Table 1 Description of samples

3. METHODS AND TECHNIQUES

Various lab techniques were applied in order to characterize and study the samples taken from the Catholicon. *Fiber Optic Microscopy (FOM)* was employed in order to examine the samples microscopically, using a PICO SCOPEMAN-MORITEX and x50 magnification. *Sieve analysis* was performed according to Normal 27/88 [16] in order to analyze the mortar aggregates grain size distribution and to calculate the binder aggregate ratio. The sieves used were according to ISO 565. *Differential Thermal and Thermo-Gravimetric Analysis (DTA-TG)* provides qualitative and quantitative information regarding the composition of the samples (Mettler Toledo 651e). The temperature range applied was 25-1000^{o}C and the heating rate was selected at 10^{o}C/min [17]. X-ray diffraction (XRD) provides information regarding the mineralogical composition of the materials (Advance D8 Diffractometer of Bruker Corporation) [16-18]. The microstructural characteristics of the samples were studied through the use of *Mercury Intrusion Porosimetry (MIP)* with the use of a Pascal 400 Thermo-Electronics-Corporation [16, 19]. Taking into consideration the high water content of the masonries as well as the efflorescence of salts on the interior walls of the church [20], *Total Soluble Salts Measurements* were conducted, in accordance to the guidelines of Normal 13/83 [21], as well as spot tests in order to identify the salts present [22]. Finally, Water Absorption by Capillarity test was conducted in accordance to Normal 11/85, in order to estimate the capillarity absorption coefficient of the brick sample [23].

The restoration mortars were selected through extensive research of available literature [9, 10]. The selected mortars were all designed for use in historical buildings through the reverse engineering methodology. Furthermore, it was a prerequisite that the restoration mortars were examined with the same techniques as the historical samples, in order to assist the examination of their compatibility. The compatibility of the selected mortars was examined through the evaluation of their physicochemical and mechanical characteristics in relation to the historic mortars of the original structure, as well as the criteria arising from the study of the materials decay and the environmental factors affecting the monument. Finally, the use of the restoration mortars is evaluated as far as serviceability through the use of fragility curves.

4. RESULTS AND DISCUSSION

4.1 Characterization and classification of historical mortars

Fiber Optic Microscopy (FOM) results indicated that all samples are in a bad state of preservation, presenting low adhesion between binder and aggregates. Lime lumps are present in all samples, except for MK5a (the final mortar layer of the cloisonné). The presence of straw additives is detected in samples MK1, MK2, MK2b and MK4, whereas no straw is detected in samples MK5b, MK6, MK7, MK8. Furthermore, extensive biodeterioration is evident on the surface of brick sample BR3a (Fig. 2).

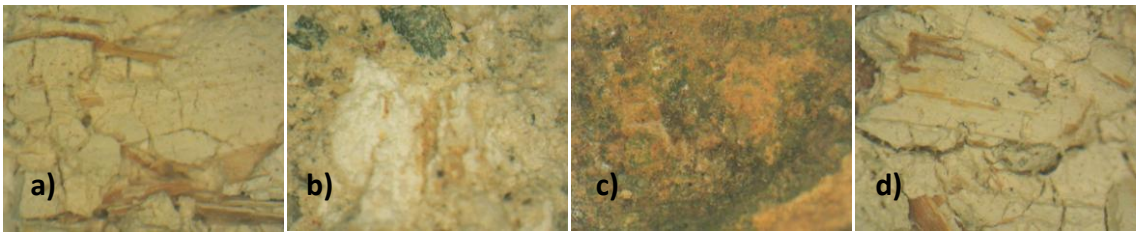

Figure 2: Selected FOM images of samples, a) MK2 – evident straw addition, b) MK2b – evident lime lumps, c) BR3a – Evident bio deterioration, d) Mortar attached on BR3b – evident straw hay addition

The grain size distribution analysis showed a good sorting of aggregates. MK1 and MK4, deriving from the exterior wall of the Catholicon present a greater similarity in comparison to sample MK7, the mortar of the interior wall joining the main temple and the Narthex (Fig. 3). The binder to aggregate ratio differs between samples.

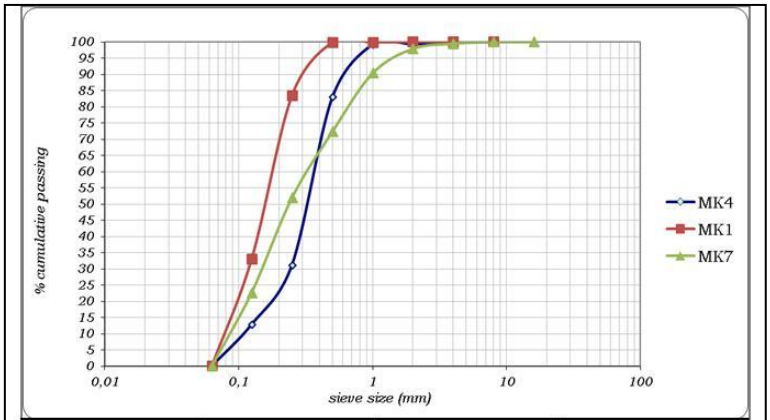

Sample Code	MK1	MK4	MK7
B/A ratio	0,41	0,65	0,22

Figure 3: Grain size distribution analysis results

The results from the historical mortar sieve analysis act as a guide for the selection of the aggregates for the restoration mortar. Taking into consideration that the gradation curves of the historical mortars are only indicative of the original aggregates' gradation curve, as after many centuries the material has deteriorated and altered, the gradation curve of the restoration mortar aggregates must be as close as possible to that of the historical mortars, thus fulfilling compatibility criteria, but at the same time it must present a normal distribution, in order to fulfill serviceability criteria.

Thermal analysis was conducted on all mortar samples, as well as on the binder parts of the mortars separated through sieve analysis. The results show two types of mortars. The first type (samples MK1, MK2, MK2b, MK6) presents a curve as seen in Figure 4a, and the second type (samples MK4, MK5a, MK5b, MK7 and MK8), which presents an exothermal peak at 420-480^{o}C, corresponds to a curve as seen in Fig. 4b. The values of physically bound water, which is connected to weight loss observed in the temperature range <120 ^{o}C, are very low, corresponding to lime mortars [1]. In the temperature 120-200 ^{o}C weight loss is attributed to the dehydration of hydrated salts. The weight loss in the temperature range 200-600^{o}C is attributed to the dehydration of water chemically bound to hydraulic compounds, however in the case of samples MK4, MK5a, MK5b, MK7 and MK8 the exact amount cannot be calculated, as an exothermal peak connected to the presence of organic matter, probably due to the addition of plant-based natural fibers, is also observed within this range (420-480^{o}C). Therefore the reversed hydraulicity index cannot be calculated for the aforementioned samples. The endothermal peak at 580^{o} C, not accompanied by any mass loss, is attributed to the transition of quartz-a to quartz-b. The high values of CO_2 loss (>600 ^{o}C), corresponding to the decomposition of calcium carbonate, in combination to the high reverse hydraulicity index calculated in the cases where no decomposition of organic matter was noticed, further confirms the classification of the mortars as lime mortars (Table 2, Fig.5) [24]. Furthermore, the mortar aggregates are solely calcitic in the case of samples MK1, MK2,MK2b, MK4, whereas in the rest of the samples, aggregates are a mix of calcitic and silicate nature. Thermal analysis results can be utilized to correlate physicochemical values to mortar tensile strength (Fig.6) [1].

Sample	**Mass loss for each temperature range (%)**				**$CO_2/H_2O_{ch.b}$**	**$CaCO_3$**
	<120	**120-200**	**200-600**	**>600**		
	$H_2O_{ph.b}$	**H_2O_{salts}**	**$H_2O_{ch.b.}$**	**CO_2**		
MK1	1,06	1,83	2,14	39,30	18,36	89,21
$MK1_{binder}$	0,85	2,02	2,33	39,22	16,83	89,03
MK2	1,21	2,34	2,03	31,43	15,48	71,35
MK2b	0,42	0,50	3,6	28,39	9,28	64,44
MK4	0,50	0,52	5,12**	39,25	7,67**	89,10
$MK4_{binder}$	0,52	0,45	3,82	40,00	10,47	90,80
MK5a	0,95	2,05	7,36**	27,50	3,74**	62,42
MK5b	0,68	0,90	6,05**	24,55	4,06**	55,73
MK6	0,38	0,54	2,76	20,35	7,37	46,19
MK7	0,50	0,57	5,93**	29,87	5,04**	67,80
$MK7_{binder}$	1,09	0,20	3,14	36,80	11,71	83,54
MK8	0,69	0,96	7,7**	26,48	3,44**	60,11

* $H_2O_{ph.b}$*: physically bound water,* $H_2O_{ch.b.}$*: chemically bound water*

***Samples with the presence of organic matter – the exact amount attributed to chemically bound water cannot be calculated and therefore the reverse hydraulicity index calculated is not indicative*

Table 2: Thermal Analysis Results

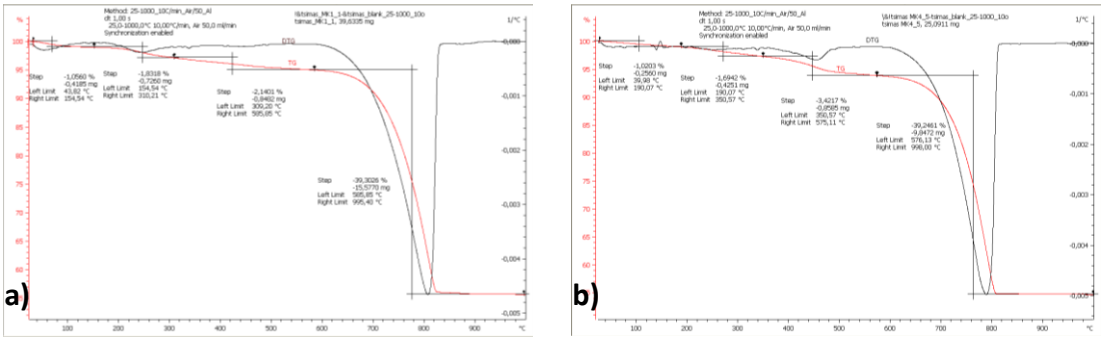

Figure 4: Selected thermal analysis diagrams a)MK1 – mortar with the addition of straw, b)MK4 – mortar with the addition of organic additive

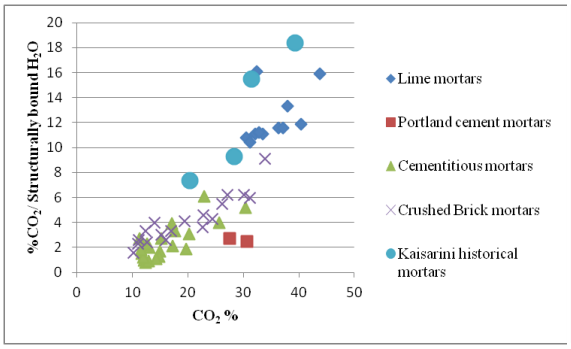

Figure 5: Grouping of the Kaisariani mortars according to thermal analysis results

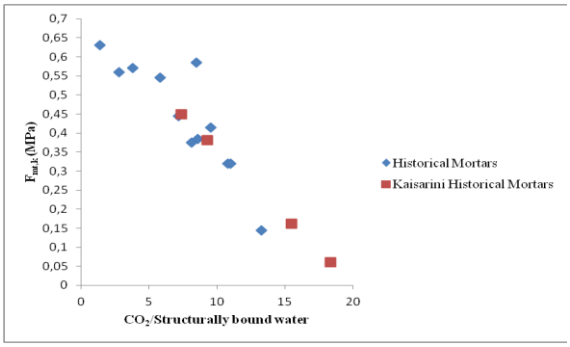

Figure 6: Correlation of tensile strength and inverse hydraulicity index

Thermal analysis results can be further utilized in the selection of the proper restoration mortars, as the restoration mortar selected must be compatible with the historical mortars, regarding its physicochemical characteristics, and in particular in terms of reverse hydraulicity index and CO_2 % loss.

X-ray diffraction analysis of mortar samples, showed the mineralogical compositions (Table 3 and Fig. 7). The principal mineralogical phase of all examined mortars is calcite. Quartz is detected in all samples, muscovite is detected in almost all samples.

X-ray diffraction results	
Sample	**Mineralogical Composition**
MK1	Calcite, quartz
MK2	Calcite, muscovite, quartz, albite, chlinochlore
MK2b	Calcite, quartz, muscovite, chlinochlore
MK4	Calcite, quartz
MK5a	Calcite, quartz, muscovite, hornblende, chlinochlore
MK5b	Calcite, muscovite, quartz
MK6	Calcite, quartz, muscovite, albite, chlinochlore, vaterite
MK7	Calcite, quartz, muscovite, chlinochlore, albite
MK8	Calcite, quartz, muscovite, albite, chlinochlore

Table 3: X-ray diffraction results

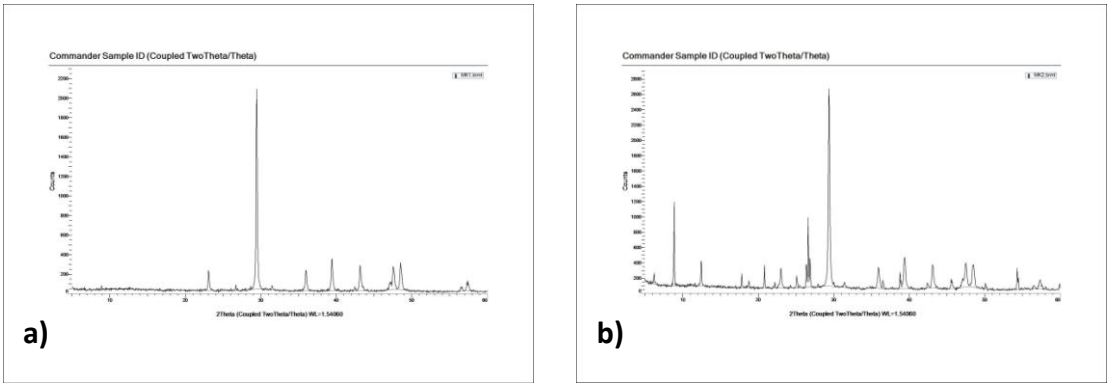

Figure 7: Selected X-ray diffraction diagrams, a)MK1, b)MK2

The microstructural characteristics of selected samples were examined through mercury intrusion porosimetry (Table 4, Fig.8). The brick samples present characteristics similar to handmade byzantine bricks, as found in literature [25, 26]. The mortars examined through MIP were MK6 deriving from the north wall and selected from the interior, MK7, from the interior west wall of the Catholicon, in joint with the Narthex wall and MK8, selected from the South Wall of the Catholicon. All samples present relatively high total cumulative volume values (MK7 total cumulative value is much higher than the other two). MK7 also presents a very low bulk density value, whereas MK6 and MK8 present similar values. MK6 and MK8 present similar average pore radius, total porosity and specific surface area values, whereas MK7 presents a much higher total porosity, as well as a lower average pore radius and higher specific area. The examination of the mortars microstructure confirms them as lime mortars [27].

Sample	***Total Cumulative Volume (mm^3/g)***	***Bulk Density (g/cm^3)***	***Total Porosity(%)***	***Average pore radius (μm)***	***Specific Surface Area (m^2/g)***
BR3a	131,24	1,89	24,85	0,81	5,82
BR3b	167,68	1,82	30,54	0,85	1,03
MK6	233,75	1,61	37,70	0,44	3,27
MK7	337,86	1,37	46,47	0,33	5,64
MK8	255,81	1,62	36,55	0,47	3,40

Table 4: Mercury Intrusion Porosimetry results

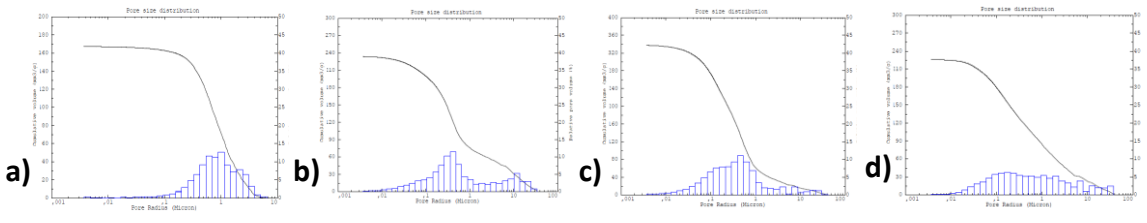

Figure 8: Pore size distribution for a)BR3b, b)MK6, c)MK7, d)MK8

The microstructural characteristics of the historical mortars, serve as a tool in the selection of the optimum restoration mortar, as it must present compatibility regarding microstructural characteristics. A study by Moropoulou & Bakolas 1998 assists in this task as it states the acceptability limits for restoration mortars for different mortar categories [27].

The presence of soluble salts in the church masonries was then assessed through the examination of the samples with Total Soluble Salts Measurements. The percentage of soluble salts is calculated through the following equation:

$$SST\% = (C \times 6{,}88) / M, \quad (1)$$

where C is the measured conductivity in μS and M is the mass of the sample undergoing the measurement. Following the Total Soluble Salts Measurements, the results of which are presented below, spot tests were conducted in order to identify the salts present. The detection of chloride (Cl^-), sulphate (SO_4^{-2}) and nitrate (NO_2^{--}) salts was possible through the use of $AgNO_3$, $BaCI_2$ and diphenylamine respectively.

Sample	Conductivity	TSS	Cl^-	SO_4^{3-}	NO^{2--}
MK1	72,2	4,84	-	-	+
MK2	83,3	5,54	-	-	+
MK2b	65,7	4,38	-	+	-
BR3b	53,8	3,57	-	-	-
MK4	97,1	6,53	+	-	++
MK5	122,1	8,28	-	-	+++
MK6	48,3	3,2	-	-	-
MK7	61,4	4,09	+	-	-
MK8	87,7	5,91	-	-	+

*Very high content (+++++), high content (++++), medium content (+++), low content (++), extremely low content (+), traces (tr).

Table 5: Total Soluble Salts measurements results and spot test results

All examined samples present high soluble salts contents, above the limit of 3%. A very high content of nitrates was detected in the mortar samples of the North wall, attributed to the more intense biodeterioration on this side, the transportation of fertilizers through rising damp into the masonries, as well as the presence of an underground ossuary at close proximity to the north wall of the church. The high amount of soluble salts must be taken into account when selecting the proper restoration mortars, as the presence of salts, as well as the movement of salts through water transportation phenomena, creates various problems to masonries.

Finally, the capillary rise coefficient of the brick sample (BR3b) was estimated through the Water Absorption by Capillarity test. The experiment was conducted at 15 ^oC and 70% RH. The capillary rise coefficient (C.R.C.) is calculated as:

$$C.R.C. = \Delta B/(S*t^{1/2}) \quad (2)$$

Where, S is the surface of the sample in contact with the water and ΔB is the amount of water absorbed at a chosen time t(s). The above results where then designed in the following diagram, selecting the experimental results up to the time of $\sqrt{t}$ = 30 which corresponds to the linear part of the experimental curve, in order to estimate the trend line, and calculate the coefficient which is equal to the trend line slope. The trend line shows a very good R-squared value of 0.9948. The capillary rise coefficient value was thus calculated as $C.R.C._{MK3b}$=16.5 mg/($cm^2 \cdot s^{1/2}$) (Fig.9). The restoration mortars must present a capillary rise coefficient equal or higher than this value in order to avoid moisture concentration in the brick elements.

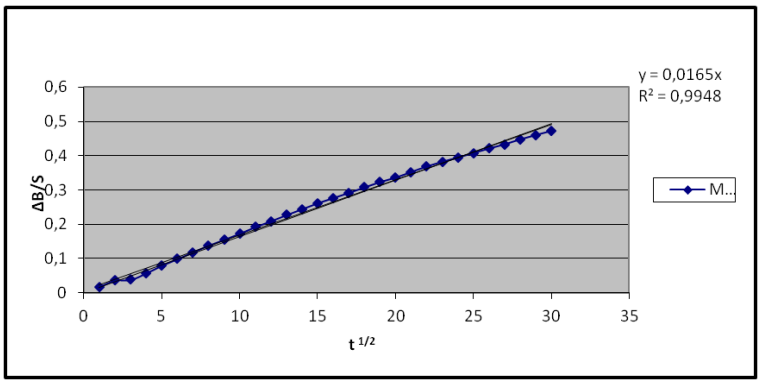

Figure 9: Plot of selected water absorption by capillary test results in order to estimate the capillary rise coefficient

4.2 Determination of decay factors, restriction arising from other building materials and earthquake behavior

An important degradation factor of the structure is the high water content of the structure, as revealed by non-destructive techniques in a previous study [20]. The high humidity content of the structural materials is attributed to rising damp, low sun radiation on all sides except for the south, as well as intense vegetation at a close proximity to the masonries of the structure and is further aggravated by problems in the roof system. The restoration mortars must be hydraulic in order to harden in high humidity conditions, as well as to serve adequately in this environment.

Furthermore, the detection of soluble salts above the acceptable limit of 3% for building materials dictates the use of a hydraulic mortar, either lime-pozzolan, either natural hydraulic lime, either a lime crushed brick restoration mortar, as these mortars exhibit a better behavior in the presence of soluble salts [8].

Although no stone samples were permitted, a previous study managed to categorize the building stones of the historical masonries of the Kaisariani Monastery and to estimate the compressive strength of the most common stone (fossiliferous) appearing in the structure. The compressive strength of the fossiliferous stone was estimated through a Schmidt hammer rebound test and the average value was estimated at 8.2 MPa with a standard deviation of 1.72 [20]. As the fossiliferous stone is the weakest building stone in the masonry, this values must act as a limit as far as the restoration mortar compressive strength is concerned, in order to avoid compatibility problems.

As the region of Greece is in constant danger from a potential earthquake, it is important to examine the structural system in earthquake stresses. Due to the thickness of the joint mortar in the Catholicon masonries, the restoration mortar is an important element contributing to the mechanical properties of the structure; the restoration mortar will inevitably affect the behavior of the structure to earthquake stresses. Therefore an important serviceability criterion must be the results of the fragility analysis for different repairing scenarios; the fragility analysis results can be utilized for the selection of the optimum restoration mortar.

Another important factor is the use of the monument; if a monument is in use or even only accessible to visitors as a cultural site, it is important that the restoration mortars used present high values of early strength. Therefore another serviceability criteria arises, namely the restoration mortar must present adequate early strength values.

4.3 Evaluation of selected restoration mortars

The goal in selecting the optimum restoration mortar is the compromise between all compatibility and serviceability requirements. The restoration mortars selected exhibit adequate hydraulicity, so as to ensure hardening in high humidity conditions and resilience in the presence of salts. Specifically, two lime-metakaolin and one hydraulic lime mortar, and two lime-metakaolin and one hydraulic lime concrete were selected (Table 6). The concretes were designed with the addition of crushed bricks, in order to simulate historical mortars of byzantine monuments that have shown excellent performance in earthquakes [11]. The raw materials used fulfilled all criteria in order to be acceptable for use in a historical masonry [6]. The selected aggregates presented a good agreement with the historical mortars' gradation curve, as well as a good sorting and normal distribution.

Sample Code	Lime powder	Meta kaolin	NHL3,5	Silicate Sand (0-2 mm)	Silicate Sand (0-6 mm)	Crushed brick (0-16 mm)
LM_1	27,5	2,5	-	70	-	-
LM_5	25	5	-	70	-	-
NHL	-	-	25	-	75	-
$LM_{C5.}$	27,5	2,5	-	-	35	35
NHL_{C10}	-	-	30	-	35	35
LM_{C15}	20	10	-	-	35	35

Table 6: Synthesis of selected restoration mortars [9, 10]

The thermal analysis results are stated for all selected restoration mortars (Table 7, 8). Furthermore, the resulting data is compared with the historical mortars thermal analysis results in order to assess compatibility (Fig.10); it is clear that they fulfill compatibility requirements, especially the lime-metakaolin mortars.

Restoration mortar	Curing time (months)	$(H)_{t.ch.b.}$	H-CH	CH	$(CH)_{react.}$ (%)	CO_2	$CaCO_3$	$CO_2/(H)_{t.ch.b.}$
LM_1	**0**	0,16	4,73	19,44	0	1,40	3,18	8,75
	1	2,44	3,06	12,58	35	3,91	8,88	1,60
	3	2,44	2,22	9,12	53	6,90	15,68	2,83
	6	2,20	1,30	5,34	73	8,50	19,31	3,86
	12	1,91	0,00	0,00	100	12,38	28,13	6,48
LM_5	**0**	0,23	4,70	19,33	0	1,85	4,21	8,04
	1	6,85	2,80	11,51	40	2,81	6,38	0,41
	3	3,24	2,50	10,28	47	2,88	6,54	0,89
	6	3,67	2,19	9,00	53	7,67	17,43	2,09
	12	3,60	0,00	0,00	100	10,70	24,31	2,97
NHL	**0**	0,00	0,83	3,41	0,00	9,82	22,30	9820
	1	1,15	0,18	0,74	10,84	17,43	39,57	15.16
	3	1,88	0,12	0,49	40,96	13,38	30,37	7.12
	6	1,83	0,00	0,00	100	12,40	28,15	6.78
	9	1,90	0,00	0,00	100	16,47	37,39	8.67

**$(H)_{t.ch.b.}$: total chemically bound water, H-CH: water chemically bound to $Ca(OH)_2$, CH: $Ca(OH)_2$, $(CH)_{react.}$(%): percentage of consumed CH*

Table 7 Mass loss percentages for restoration mortars in relation to curing time [9, 10]

Sample Code	CH (%) in relation to curing time				
	0 months	1 month	3 months	6 months	12 months
LM_{C5}	23,5	18,3	16,4	10,2	3,8
NHL_{C10}	12,5	12,1	14,1	11,7	4,1
LM_{C15}	16,5	3,2	0,0	0,0	0,0

**CH(%): percentage of $Ca(OH)_2$ not yet consumed at testing date*

Table 8 Mass loss percentages for restoration mortars in relation to curing time [9]

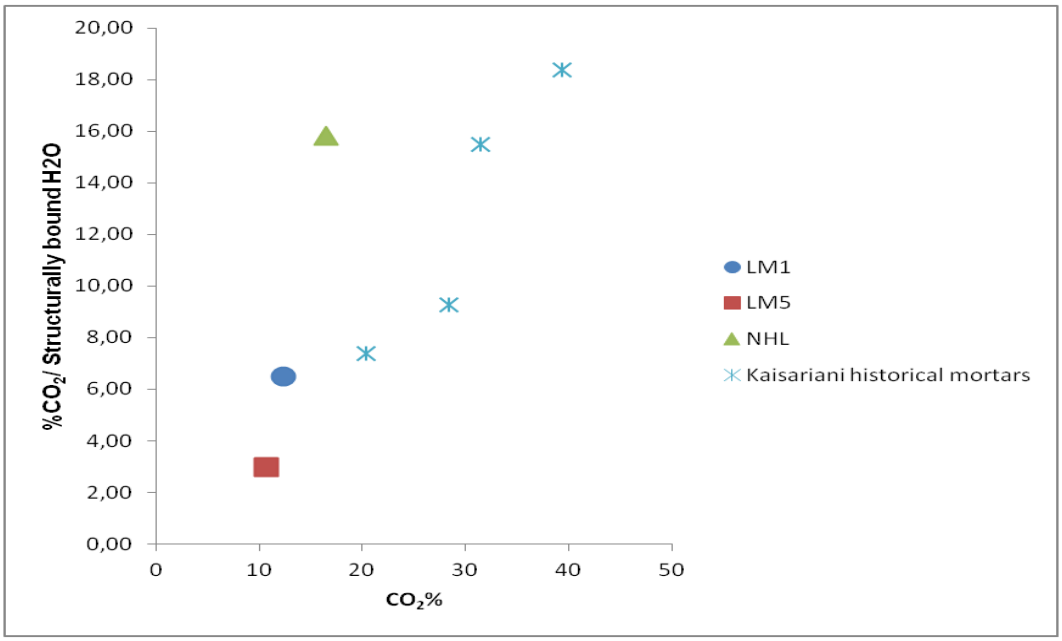

Figure 10: Correlation of $\%CO_2$ loss with inverse hydraulicity index

The microstructural characteristics of the selected mortars are presented in the following table. The concretes, due to the large size of the aggregates were only analyzed regarding their apparent density.

Sample code	T.C.V. (mm^3/g)	S.S.A. (m^2/g)	Por. Rad. Av. (μm)	d_{bulk} (g/cm^3)	$d_{corr.}$ (g/cm^3)	Total Porosity (%)
LM_1	198,78	4,15	0,32	1,73	2,63	34,30
LM_5	191,63	5,56	0,29	1,75	2,64	33,57
NHL	151,1	4,24	0,28	1,90	2,67	28,7
LM_{C5}	-	-	-	1,62	-	-
NHL_{C10}	-	-	-	1,85	-	-
LM_{C15}	-	-	-	1,69	-	-

**T.C.V.: Total Cumulative Volume, S.S.A.: Specific Surface Area, Por.Rad.Av.: Average Pore Radius, d_{bulk}: apparent density, $d_{corr.}$: corrected density, Total Porosity (%)*

Table 9 MIP results – Hardened restoration mortar characteristics [9, 10]

Regarding the thermal analysis results, at the end of twelve months the entire $Ca(OH)_2$ has reacted, except for concretes LM_{C5} and NHL_{C10}, where a very small amount remains. Regarding the microstructural characteristics of the selected mortars, all lime-metakaolin mortars, as well as the lime-metakaolin concretes, are within the range of acceptability limits [27]. Therefore, regarding physicochemical and microstructure compatibility, LM_1, LM_5, LM_{C5} and LM_{C15} are all deemed as acceptable and exhibit adequate hydraulicity, thus fulfilling serviceability criteria.

The average values of flexural and compressive strength measured for the examined mortars is listed in Table 10. The flexural strength values result as the average of the value measured for three different prismatic samples for each mortar mix, while the compressive strength values result as the average of the value measured for six different cubic samples for each mortar mix.

Sample Code	Curing time	F_f (MPa)	St.Dev.	F_c (MPa)	St.Dev.	Ed (MPa)
LM_1	**12 months**	1,59	0,34	3,92	1,40	6532
LM_5	**12 months**	1,51	0,46	5,88	0,88	6641
NHL	**12 months**	1,00	-	4,50	-	-
LM_{C5}	**12 months**	1,50	0,25	8,4	0,36	6981
NHL_{C10}	**12 months**	2,22	0,27	18,7	0,50	18547
LM_{C15}	**12 months**	2,40	0,35	21,4	1,26	13334

**Ff: Flexural strength (MPa), Fc: Compressive strength (MPa), St.Dev.: standard deviation, Ed:Dynamic elasticity modulus*

Table 10 Flexural and Compressive strength values for examined mortar and concrete mixes – Dynamic elasticity modulus [9, 10]

In the case of the lime-metakaolin mortar mixes, LM_1 και LM_5, it is concluded that the early acquirement in compressive strength noticed is enhanced due to the use of metakaolin (Fig.11). Furthermore, the results show that by increasing the percentage of metakaolin in relation to the lime powder, the compressive strength also increases. Regarding the gain in flexural strength with hardening, it is concluded that both lime-metakaolin mortar mixes present similar final values, however not the same trend in the progression of hardening in time. In the case of the hydraulic lime mortar, the highest compressive strength value is measured at 6 months of curing, while it has already acquired 66% of its final mechanical strength values already from the first month of hardening. The final compressive strength value measured for the hydraulic lime mortar is between the compressive strength values of LM_1 and LM_5. The flexural strength of the hydraulic mortar is relatively lower than the lime-metakaolin mortar mixes. The concretes examined present a large range of compressive and flexural strength values (Table 10). As expected the concretes mixes examined presented much higher modulus of elasticity values in comparison to the mortar mixes. Amongst the concretes, the lowest values of dynamic elasticity modulus are exhibited by concrete LM_{C5}, which also presented the lowest values of flexural and compressive strength; the highest dynamic modulus of elasticity values by far is exhibited by the hydraulic lime concrete, although it exhibited lower compressive and flexural strength values than LM_{C15}. The mortar containing the highest amount of metakaolin p.w., presented the highest compressive strength values, and also the highest modulus of elasticity value, however near the value exhibited by LM_1.

In Fig.11 compressive strength values are presented in relation to curing time. The results show that a large range of mechanical properties can be achieved with small variations to the mortar mixes and furthermore the use of the selected mortars fulfills the serviceability criteria set, namely the early acquirement of compressive strength.

The optimum selection in order to ensure a good behavior under seismic action is the compromise of a high compressive strength and low dynamic elasticity modulus. In Fig.12 these values are correlated for the selected restoration syntheses.

The selected lime-metakaolin mortars present C.R.C. values between 17-25 $mm^3/g.s^{1/2}$, and are therefore compatible with the original brisk elements of the historical masonry [9].

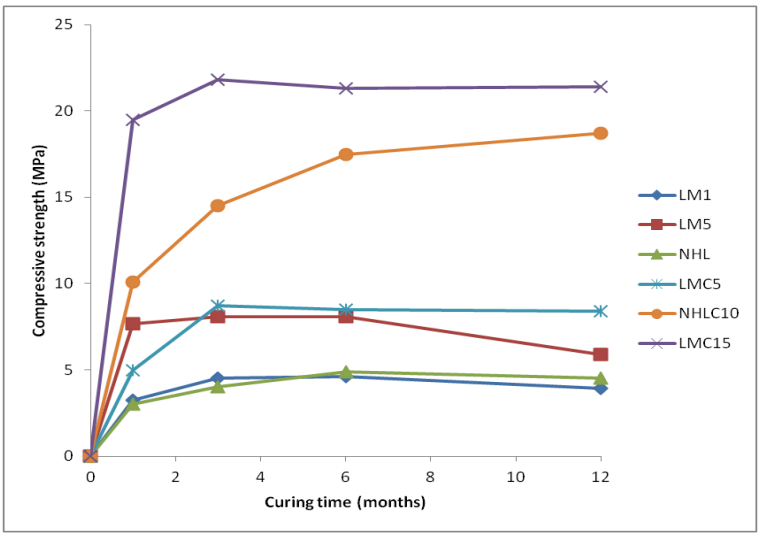

Figure 11: Compressive strength values (MPa) in relation to curing time (months)

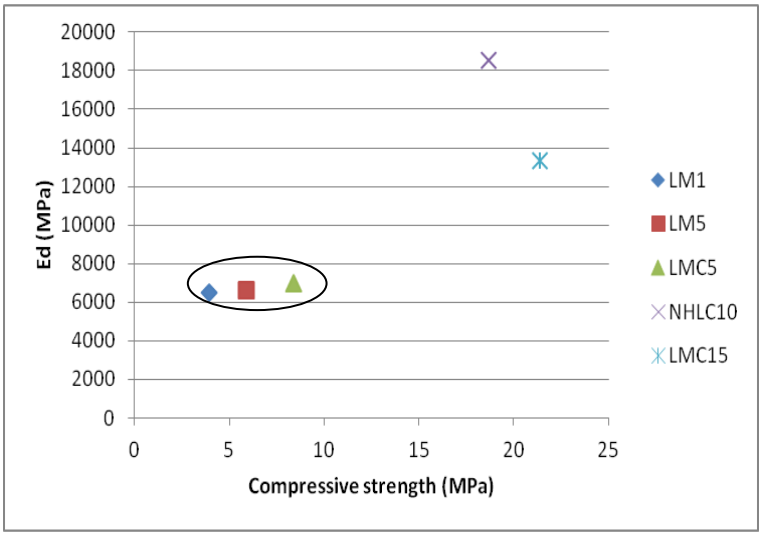

Figure 12: Correlation of compressive strength and dynamic elasticity modulus for selected restoration mortars and concretes

Fragility analysis was conducted for the case of the Catholicon of the Kaisariani monastery, for different repairing scenarios, in accordance to the analysis of the selected restoration mortars [28-36]. The entry values selected for the original materials was an average values of 12 MPa compressive strength for the building stones, taking available literature into account, and 1 MPa for the original mortars, as correlated through the analysis of the physic-chemical properties [20]. Specifically, the probability of damage occurring under the effect of different ground accelerations was estimated for a) the original structural materials, b) repointing of joints with restoration mortar exhibiting 5 MPa compressive strength, c) repointing of joints with restoration mortar exhibiting 10 MPa compressive strength. The fragility analysis concerned the probability of appearance of insignificant, moderate and heavy damage (Fig.13-15) for the different repairing scenarios.

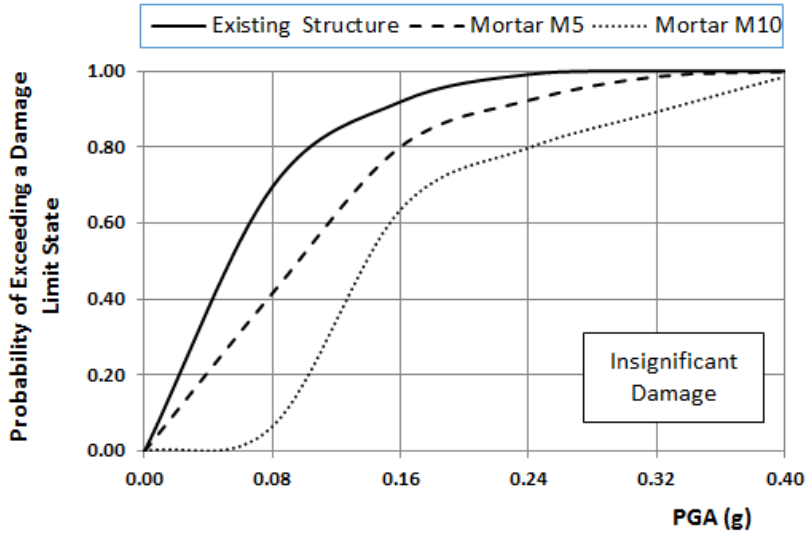

Figure 13: Probability of insignificant damages occurring for different ground accelerations

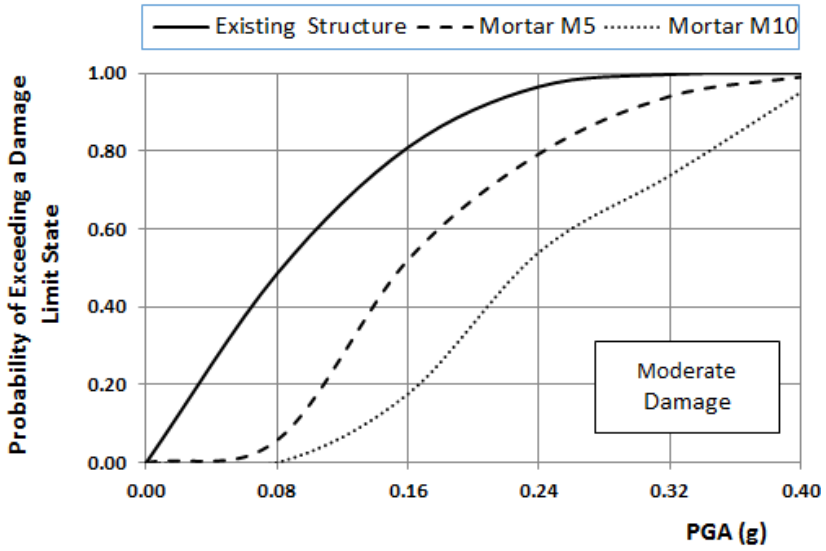

Figure 14: Probability of moderate damages occurring for different ground accelerations

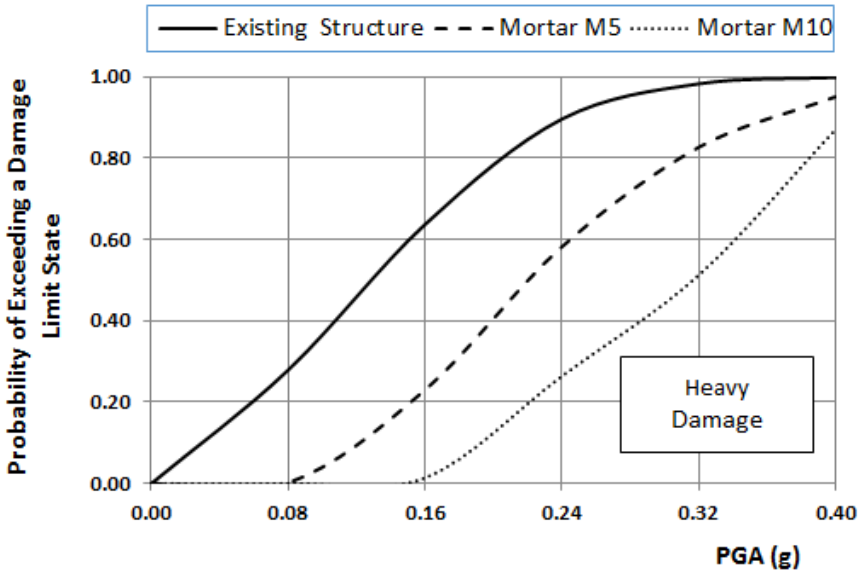

Figure 15: Probability of heavy damages occurring for different ground accelerations

The results show that even the use of a restoration mortar exhibiting compressive strength 5 MPa, can achieve an improvement in terms of damage in the case of an earthquake; the improvement is greater as the damage severity increases. At this point, the restriction deriving from the low compressive strength of the fossiliferous stone must be taken into consideration; NHL_{C10} and LM_{C15} are therefore rejected as possible restoration mortars, in order to ensure compatibility with the original structural materials. Thus, restoration mortar LM_5 and LM_{C5} can be selected in order to use according to the joint thickness, as these restoration mortars exhibit compatibility with the original structure and serviceability in the environment of the Kaisariani monastery, at the same time contributing to the mechanical performance of the structure under earthquake stresses.

5. CONCLUSIONS

- The mortars of the Kaisariani Monastery Catholicon are typical lime mortars mixed with calcite and aluminosilicate aggregates, with high porosity values and occasionally the addition of straw or fiber admixtures
- Tensile strength can be estimated for historical mortars, through correlation with physicochemical properties; this is only an estimation, but can be indicative and assist in the assessment of the seismic behavior of the masonry
- The microstructural characteristics of the examined bricks are typical for handmade bricks of the byzantine period
- By setting requirements during the characterization of the historical materials and the in situ investigation of the monument, the selection of the optimum mortar, complying with the set compatibility and serviceability requirements can be accomplished
- Lime-metakaolin mortars present similar physicochemical and microstructural characteristics with the examined historical mortars, at the same time contributing in a decisive manner to the behavior of the masonry under earthquake stress
- The role of restoration mortars is crucial in the earthquake protection of thick joint masonries
- Fragility analysis is a valuable tool that can be utilized for the selection of the optimum restoration mortar in terms of compatibility and serviceability amongst different repairing scenarios

ACKNOWLEDGEMENTS

Part of this investigation was performed within the research project “Seismic Protection of Monuments and Historic Structures - SEISMO” which is co-financed by the Greek Ministry of Education and Religions and the European Union under the action “Thales” within the context of the Operational Programme - Education and Lifelong Learning, NSRF 2007-2013. The authors would like to thank the employees of the 1st Ephorate of Byzantine Antiquities for their cooperation.

REFERENCES

[1] Moropoulou, A., Bakolas, A., Anagnostopoulou, S., “Composite materials in ancient structures”, Cement and Concrete Composites, 27 (2005) 295-300

[2] Moropoulou, A., Triantafyllopoulou, P., Aggelakopoulou, E., “Decision making methodology for strategical planning of compatible conservation interventions

through GIS management of structural materials and environmental impact data – Application in the case of Tobacco Factory in Heraklion, Crete", PACT, J. European Study Group on Physical, Chemical, Biological and Mathematical Techniques Applied to Archaeology, 59 (2000) pp. 239-251

[3] Moropoulou, A., Maravelaki-Kalaitzaki, P., Borboudakis, M., Bakolas, A., Michailidis, P., Chronopoulos, M., "Historic mortars technologies in Crete and guidelines for compatible restoration mortars", *PACT, J. European Study Group on Physical, Chemical, Biological and Mathematical Techniques Applied to Archaeology*, 55 (1998) pp. 55-72

[4] Moropoulou, A., Polikreti, K., Ruf, V., Deodatis G., "San Francisco Monastery, Quito, Equador: characterisation of building materials, damage assessment and conservation considerations", *Journal of Cultural Heritage*, 4 (2003) pp. 101-108

[5] Moropoulou, A., Bakolas, A., Moundoulas, P., Aggelakopoulou, E., "Reverse engineering: A proper methodology for compatible restoration of mortars", Int. Workshop on Repair Mortars for Historic Masonries, RILEM Technical Committee, Delft University of Technology, the Netherlands (2005)

[6] Moropoulou, A., "Reverse engineering to discover traditional technologies: A proper approach for compatible restoration mortars", PACT, J. European Study Group on Physical, Chemical, Biological and Mathematical Techniques Applied to Archaeology, 58 (2000) pp. 81-107

[7] Maravelaki-Kalaitzaki, P., Bakolas, A., Moropoulou, A., "Physico-chemical study of Cretan ancient mortars", Cement & Concrete Research, 33 5 (2003) p. 651-661

[8] Maravelaki-Kalaitzaki, P., Bakolas, A., Karatasios, I., Kilikoglou, V., "Hydraulic lime mortars for the restoration of historic masonry in Crete", Cement and Concrete Research 35 (2005) 1577– 1586

[9] Aggelakopoulou E., «Criteria and methodology for the evaluation of physico - chemical and mechanical characteristics of restoration mortars adressed to historic masonries restoration interventions», PhD thesis, School of Chemical Engineering, NTUA (2006)

[10] Moundoulas P., "Design and evaluation methodology of compatible restoration mortars for historic monuments according to their mineralogic - physicochemical and physicomechanical characteristics" PhD thesis, School of Chemical Engineering, NTUA (2004)

[11] Moropoulou, A., Aggelakopoulou, E., Bakolas, A., "Earthquakes and monuments – The role of materials in the earthquake protection of monuments", V Int. Conf. on Structural Analysis of Historical Constructions, eds Lourenço P.B., Roca P., Modena C., Agrawal S., N.Delhi, India (2006) Vol. 3, p. 1625-1631

[12] Nikolaos Charkiolakis, "The monasteries of mount Hymettus", 7days Kathimerini newspaper, 28/9/1997

[13] Charalambos Bouras – Laskarina Boura, "Greek religious architecture in the 12th centrury" Commersial Bank of Greece, 2002

[14] Giorgos Pallis, "Topography of the Athenian field during the post-Byzantine period", Post-Byzantine Mon-ments I, Thessalonica 2009

[15] Charalambos Bouras, "Byzantine Athens: 10th-12th c.", Benaki Museum 6th Supplement, Athens 2010

[16] Normal 27/88 : Caratterizzazione di una malta Roma CNR ICR, 1988

[17] Moropoulou, A., Bakolas, A., Bisbikou, K., "Characterization of ancient, byzantine and later historic mortars by thermal analysis and X-ray diffraction techniques", Thermochimica Acta, 269/270 (1995) pp. 779-795

[18] Normal 34/91: Analysis of Clay Materials by XRD Rome 1991

[19] Normal 4/80: Distribution of pore volume as a Function of Pore Diameter C.N.R.-I.C.R. Rome 1980

[20] Moropoulou A., Apostolopoulou M., Moundoulas P., Karoglou M., Delegou E., Lampropoulos K., Gritsopoulou M., Bakolas A.,*"The combination of NDTS for the diagnostic study of historical buildings: The case study of Kaisariani Monastery",* COMPDYN 2015 5th ECCOMAS Thematic Conference on Computational Methods in Structural Dynamics and Earthquake Engineering Crete Island, Greece, 25–27 May 2015, p. 2321-2336

[21] Normal 13/83: Dosage of Soluble Salts Rome 1983

[22] Pamela K. Walker and Philip J. Rodacy, «Field Test Kit for Gunshot Residue Detection», (2002)

[23] Normal 11/85 water absorption by capillarity-coefficient of capillarity absorption Rome 1985

[24] Moropoulou, A., Polikreti, K., Bakolas, A., Michailidis, "Correlation of physico-chemical and mechanical properties of historical mortars and classification by multivariate statistics", *Cement and Concrete Research*, 33 [6] (2003) pp. 891-898

[25] Moropoulou A.,Polikreti K., «Principal Component Analysis in monument conservation: Three application examples» Journal of Cultural Heritage 10 (2009) 73e81

[26] Francisco M. Fernandes, Paulo B. Lourenço and Fernando Castro Chapter 3 «*Ancient Clay Bricks: Manufacture and Properties»* ISISE, Civil Engineering Department Campus de Azuré

[27] Moropoulou, A., Bakolas, A., "Range of acceptability limits of physical, chemical and mechanical characteristics deriving from the evaluation of historic mortars", PACT, J. European Study Group on Physical, Chemical, Biological and Mathematical Techniques Applied to Archaeology, 56 (1998) pp. 165-178

[28] Asteris, P.G., Chronopoulos, M.P., Chrysostomou, C.Z., Varum, H., Plevris, V., Kyriakides, N., Silva, V. (2014). *«Seismic Vulnerability Assessment of Historical Masonry Structural Systems*», Engineering Structures, Volume 62-63, pp. 118-134.

[29] Syrmakezis, C.A., Asteris, P.G. (2001). *«Masonry Failure Criterion Under Biaxial Stress»* State Journal of Materials in Civil Engineering; American Society of Civil Engineers (ASCE), Vol. 13, Issue 1, pp. 58-64.

[30] Asteris, P.G., Tzamtzis, A.D., Vouthouni, P.P., Sophianopoulos, D.S. (2005). «*Earthquake Resistant Design and Rehabilitation of Masonry Historical*

Structures, Practice Periodical on Structural Design and Construction», American Society of Civil Engineers (ASCE), Vol. 10, Issue 1, pp. 49-55.

[31] Asteris, P.G. (2008). *«On the Structural Analysis and Seismic Protection of Historical Masonry Structures»*, The Open Construction and Building Technology Journal, vol. 2, pp.124-133.

[32] Asteris, P.G. (2010). *«A simple heuristic algorithm to determine the set of closed surfaces of the cubic tensor polynomial»*, The Open Applied Mathematics Journal, vol. 4, pp.1-5.

[33] Asteris, P.G. (2013). *«Unified Yield Surface for the Nonlinear Analysis of Brittle Anisotropic Materials*», Nonlinear Sci. Lett. A, Vol.4, No.2, 46-56, 2013.

[34] Plevris, V., Asteris, P.G. (2014). *«Masonry Failure Surface under Biaxial Compressive Stress using Neural Networks»,* Construction and Building Materials, Volume 55, Pages 447-461.

[35] Asteris, P.G., Plevris, V. (2016). *«Anisotropic Masonry Failure Criterion Using Artificial NeuralNetworks»*, Neural Computing and Applications (NCAA), DOI 10.1007/s00521-016-2181-3.

[36] Asteris, P.G., Douvika, M., Karakitsios, P., Moundoulas, P. Apostolopoulou, M., Moropoulou, A. (2016). *«*A Stochastic Computational Framework for the Seismic Assessment of Monumental Masonry Structures*»*, 5th International Conference on Integrity, Reliability and Failure, Porto, Portugal, 24–28 July, PAPER REF: 6316.

ECCOMAS Congress 2016
VII European Congress on Computational Methods in Applied Sciences and Engineering
M. Papadrakakis, V. Papadopoulos, G. Stefanou, V. Plevris (eds.)
Crete Island, Greece, 5–10 June 2016

FIRST RESULTS OF THE VIBRATION-BASED STRUCTURAL HEALTH MONITORING OF A MASONRY DOME

N.Cavalagli[1], G. Comanducci[2], M Gioffrè[1], V. Gusella[1] and F. Ubertini[1]

Department of Civil and Environmental Engineering, University of Perugia
via G. Duranti 93, 06125, Perugia, Italy

[1]e-mail: {nicola.cavalagli,massimiliano.gioffre,vittorio.gusella,filippo.ubertini}@unipg.it

[2]e-mail: comanducci@strutture.unipg.it

Keywords: Masonry dome, Historical construction, Structural health monitoring, FE model

Abstract. *This paper newly proposes the use of ambient vibration testing, vibration-based continuous dynamic monitoring and automated modal identification for structural assessment of monumental masonry domes. The final purpose of this research is the development of a general methodology for online structural health monitoring of large domes, enabling early detection of damages caused by low return period earthquakes, in a general framework of preventive conservation and heritage resilience. The case study considered here is the dome of the Basilica of Santa Maria degli Angeli in Assisi, recently added to the World Heritage List of Unesco. The basilica is located in the center of Italy and it was built between 1569 and 1679 on the design of the architect Galeazzo Alessi. It consists of a latin cross plan, with 126 m and 65 m dimensions, with a nave, two aisles and a semicircular apse. At the intersection between the transept and nave the building hosts the Porziuncola, a little ancient chapel, symbol of Franciscan spirituality and pilgrims destination since the construction of the basilica.*

In order to preliminary assess the structural behavior of the dome, several dynamic experimental investigations have been carried out and ended with the installation of a simple vibration-based monitoring system, based on the use of a few high sensitivity accelerometers, placed at the top and the base of the drum, as well as temperature and humidity sensors. This paper presents and discusses the first results of the vibration-based monitoring of the drum-dome system, demonstrating the potential for using similar approaches for the preservation of this special kind of historic structures.

Figure 1: Basilica of Santa Maria degli Angeli in Assisi.

1 INTRODUCTION

Monitoring the structural integrity of historical constructions is an important topic for the conservation of the architectural heritage [1], that has received a considerable interest both from researchers and practitioners in the last decades [2, 3, 4, 5, 6, 7]. Within this context, vibration-based dynamic monitoring can be considered as a quite novel approach, if applied to cultural heritage. In particular, while the use of Operational Modal Analysis (OMA) techniques is well-established for performing dynamic structural investigations and/or implementing continuous monitoring of relatively new slender structures [8, 9], their application in the context of heritage monumental buildings is far less common. A few documented applications of vibration-based monitoring to monumental buildings are however available, whereby some literature studies have proposed the use of OMA techniques for the dynamic identification of masonry civil and bell towers [10, 11, 12]. On the contrary, applications to different kinds of historic structures are quite rare and only a few studies have proposed to use OMA techniques in the context of continuous dynamic monitoring systems [13, 14]. This is mainly due to the low levels of vibration typically exhibited by massive masonry buildings, as well as to their complex structural behavior, that makes the development of vibration-based continuous monitoring systems for cultural heritage preservation a new and worthwhile scientific and technical challenge.

In this paper, the results of ambient vibration tests carried out on a masonry dome, which lead to the installation of a permanent dynamic monitoring system, are presented. The case study considered here is the dome of the Basilica of Santa Maria degli Angeli in Assisi, recently added to Unesco's World Heritage List, which represents one of the most important focal points of the franciscan spirituality (Figure 1). Field measurements of the dynamic response of the structure have been carried out by installing high sensitivity accelerometers both at the top and at the base of the drum. Data are first processed to preliminary assess the structural behavior and to attain a proper configuration of the sensors layout for the monitoring system. The same

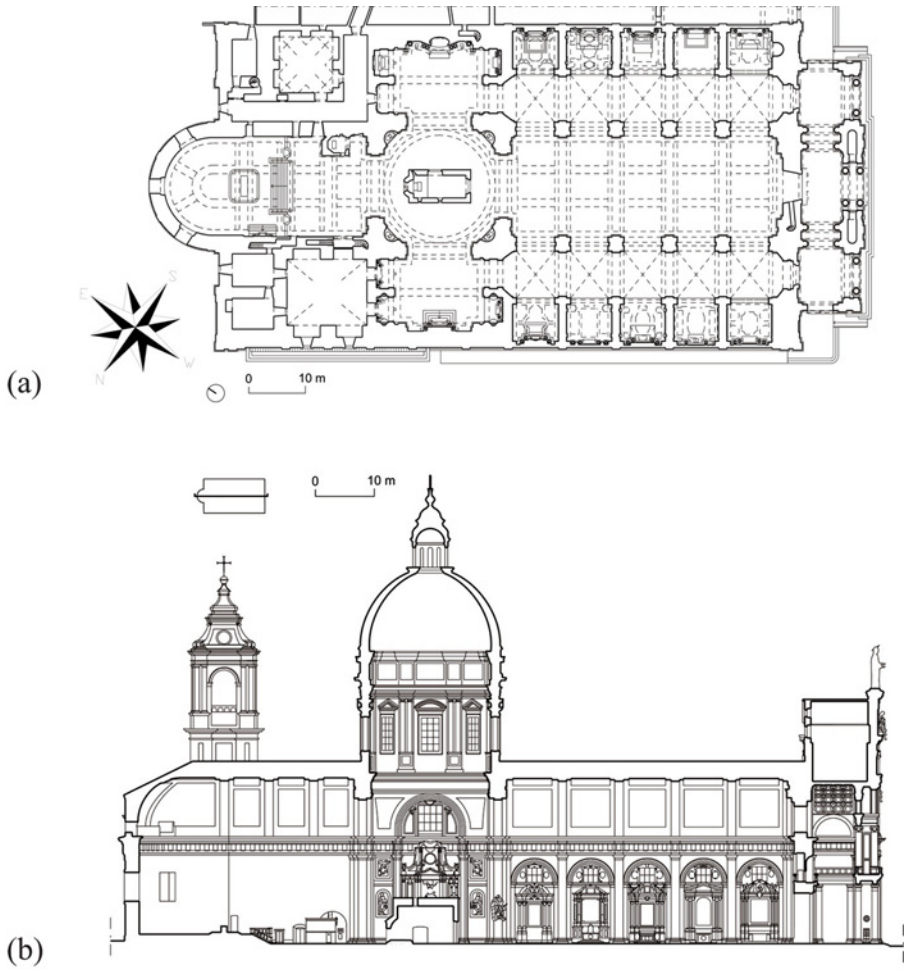

Figure 2: Basilica of Santa Maria degli Angeli in Assisi: (a) plan; (b) longitudinal section [15].

data are then continuously processed by using both classical Frequency Domain Decomposition (FDD) and Stochastic Subspace Identification (SSI) techniques. The results of the first months of monitoring are presented, providing an overall demonstration of the potential of this kind of measurements in the context of heritage preservation.

2 THE DOME OF THE BASILICA OF SANTA MARIA DEGLI ANGELI IN ASSISI

2.1 The architecture

The Basilica of Santa Maria degli Angeli in Assisi was built between the 16-th and the 17-th centuries, on the design of the architect Galeazzo Alessi. It consists of a latin cross plan, with 126 m and 65 m dimensions, with a nave, two aisles and a semicircular apse. The Basilica contains the Porziuncola, a little ancient chapel representing a symbol of Franciscan spirituality and an important pilgrims destination. This chapel is located at the intersection between the transept and nave. Figures 2(a) and 2(b) show the plan and the longitudinal section of the Basilica carried out after a recent architectural survey [15].

The presence of the Porziuncola inside the basilica, as well as the need to provide a visible sign for pilgrims coming from all over the world, have induced the architect to design an uncommonly high drum-dome system. In this way, the dome appears majestic and impressive owing to the singular slenderness and lightness of the drum. It is characterized by a single shell

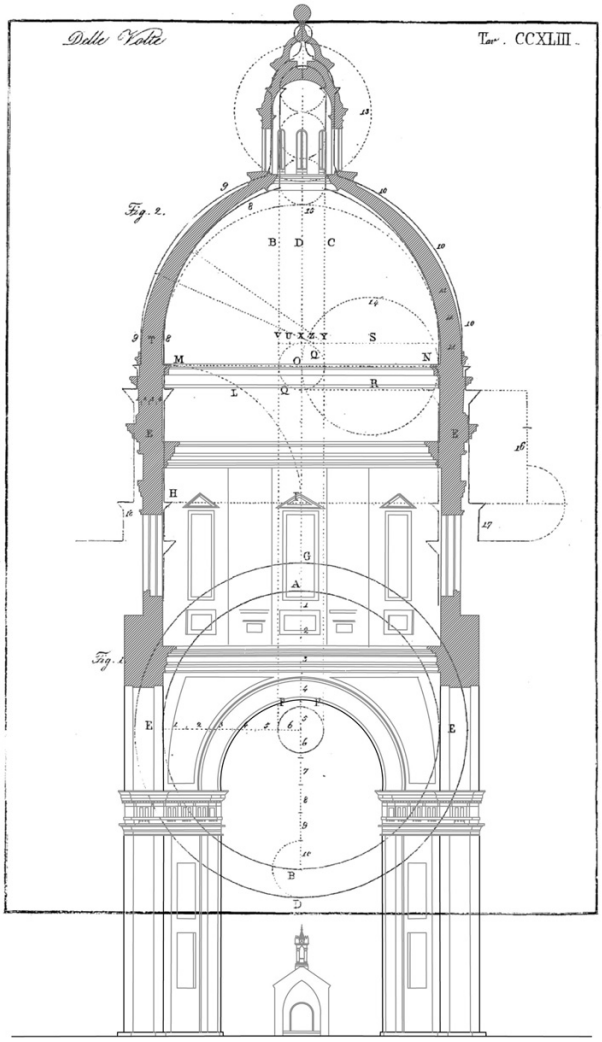

Figure 3: Superposition between Fontana's drawing and the dome section of the Basilica of Santa Maria degli Angeli [17].

and provided with an external staircase to climb up to the lantern. The inner diameter is of approximately 20 m and the variable thickness of the unique shell ranges from 1.80 m at the bottom, up to 0.90 m at the top. The inner perimeter of the drum is circular, while the outer one is octagonal; the coupled pilasters at the angles of the octagon become stiffening ribs over the dome's extrados, joining at the oculus, the base of the lantern, that gives to the architectural complex an overall height of approximately 75 m.

It should be noted that, if compared with the rules of construction illustrated in the most important architectural treatises, e.g. the work of Carlo Fontana [16], the drum appears to be very high. In particular, its height is more than twice the height that would correspond to the prescriptions proposed by Fontana, conferring to the structure a really unusual slenderness and unique architectural feature. This aspect is emphasized in Figure 3, where the section of the drum-dome system is superimposed to a drawing explaining the geometrical rules proposed by Fontana.

It is worth recalling that Fontana's graphical rules were developed for the design of some structural parts of the Vatican Temple, which made his treatise a fundamental reference for

Figure 4: Lineengraving of the basilica damage state after the 1832 earthquake. *Prospetto delle ruine del famoso Tempio di Santa Maria degli Angioli di Asisi*, by Cilleni Nepis.

architects of those times [19]. Nonetheless, the dome of the basilica of Santa Maria degli Angeli was a notable exception to those rules and differed from all other contemporary designs. This significant slenderness motivated the authors towards the implementation of a vibration-based monitoring system for the dome.

2.2 Evolution of the structural system

Throughout its history, the Basilica of Santa Maria degli Angeli was subjected to significant seismic events. The most important one was certainly the earthquake of 1832, which caused the collapse of the nave and of a portion of the left aisle (Figure 4). The drum-dome system was severely damaged, but did not collapse, conceivably because of its high flexibility and low natural periods of vibration. The strengthening of the drum with three orders of steel rings dates from this period. In the reconstruction phase, a particular attention was devoted to the cross section of the central vault and to the timber truss system of the roof designed by Poletti, in order to reduce the horizontal thrust acting on the lateral walls [20]. After the Umbria-Marche earthquake of 1997, the basilica was subjected to other phases of strengthening and restoration [21]. However, a pattern of cracks and micro-cracks, that can be attributed to seismic and static actions, is still evident both in the drum and the dome. The most significant through-wall cracks are located above the north-east side, for the presence of internal staircases and tunnels, and the west side of the drum.

3 ANALYSIS PROCEDURES AND MONITORING SYSTEM

3.1 Data processing

Field recorded vibration data have been processed using two different techniques. The first considered approach is the classic Frequency Domain Decomposition (FDD) based on the evaluation of the spectral matrix $\mathbf{G}(f)$ (i.e. the matrix of cross-spectral densities) of recorded accelerations, whose diagonal terms are the auto-spectral densities (ASD), while the out of diagonal are the cross-spectral densities (CSD). The time series are first resampled in order to estimate $\mathbf{G}(f)$ with a frequency resolution of 0.01 Hz. Subsequently, the contour plot of the first singu-

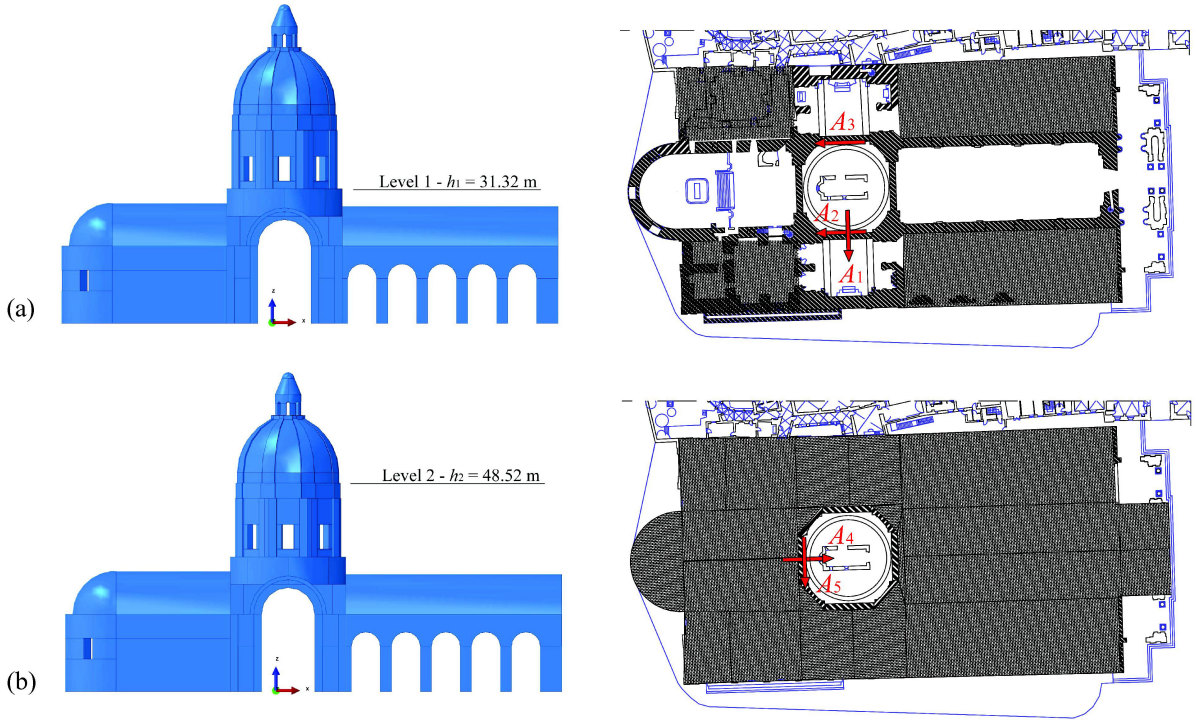

Figure 5: Structural monitoring system installed in the dome of the basilica.

lar value (SV) of the spectral matrix $\mathbf{G}(f)$ estimated in consecutive data sets has been obtained. This plot is commonly known as frequency spectrogram, which highlights resonant frequencies and their variation in time as local maxima of the SV contour plot and, consequently, of the energy content of the data, in the time-frequency domain.

The second considered approach is based on the Stochastic Subspace Identification (SSI) technique. This method has been used to identify the natural frequencies of the structure by a fully automated for step procedure [22, 23]: (i) run of SSI-data analysis, using the classic Canonical Variate Analysis (CVA) formulation, for different values of the order of the model and of the number of output block rows adopted to construct the block Hankel matrix of the data; (ii) elimination of noise modes on the basis of similarity checks between modal parameters estimates; (iii) clustering of remaining modes; (iv) extraction of mean values of modal parameters estimates with 95% confidence intervals, under variation of model's order and number of block rows of block Hankel matrix. Using the SSI technique to consecutive data sets it is possible to obtain a frequency time series of the lower structural natural modes.

3.2 Dynamic monitoring system

The monitoring system installed in the drum and the dome consists of five high-sensitivity (10V/g) uni-axial accelerometers placed at the base of the drum and at the base of the dome, as described in Figure 5. In particular, three accelerometers have been fixed on the easily accessible external side of the drum base (sensors A_1, A_2 and A_3 in Figures 6(a) and 6(b))). The sensors A_4 and A_5 have been placed in the only accessible part with highest location inside the dome shell (Figure 6(c)), at the top of the internal staircases which allow the access to the dome extrados. The data have been recorded by using a multi-channel system, carrier model cDAQ-9188 with NI 9234 data acquisition modules (24-bit resolution, 102 dB dynamic range and anti-aliasing filters), down-sampled at 100 Hz for storage purpose and stored in 30-minutes long

Figure 6: Images of the accelerometers installed at the base of the drum (a) and (b), and of the dome (c).

	ρ [t/m^3]	μ_E [MPa]	$\sigma_{ln,E}$	μ_G [MPa]	$\sigma_{ln,G}$
Brick	1.8	1500	0.2	500	0.2
Stone	2.2	2800	-	860	-

Table 1: Mechanical material properties: mass density (ρ); mean value (μ_E) and standard deviation of the logarithm ($\sigma_{ln,E}$) for the elastic modulus; mean value (μ_G) and standard deviation of the logarithm ($\sigma_{ln,G}$) for the shear modulus

time histories, representing the data sets. The monitoring system also includes humidity and temperature sensors, as well as displacement transducers monitoring the evolution of existing cracks. The related information is however not illustrated in this work and, therefore, these additional sensors are not considered.

4 ANALYSIS OF RESULTS

4.1 Preliminary numerical model

The Basilica of Santa Maria degli Angeli has been investigated focusing on both historical and structural aspects [17, 18]. As far as the structural analysis is concerned, a preliminary Finite Element numerical model has been developed in order to investigate the static and dynamic behavior of the structure, with a focus on the drum-dome system. The model details the central core of the basilica, i.e. the triumphal arches, the drum and the dome, while the remaining parts of the basilica are considered as lateral restraints. In this way, it has been sufficient to include a rough model of the nave, the transepts and the apse to reproduce a consistent lateral stiffness.

A peculiarity of the developed numerical model is the probabilistic approach for the estimation of the eigenfrequencies and eigenmodes starting from a stochastic model for the elastic moduli of the materials. The main constituent material is brickwork everywhere, except for the stone pillars of the nave. An homogeneous material with orthotropic elastic behaviour has been considered, in which the values of stiffness have been selected from the recent instructions proposed by the Italian National Research Council [24], with their lognormal distribution parameters (Table 1).

A set of 1000 samples have been generated for both the Young's modulus (E) and shear modulus (G) of the brickwork (Figure 7), and then multiplied by a coefficient $\alpha = 1.5$ which takes into account the good condition of the mortar.

Figure 8 shows the eigenproblem solutions of the first modes. For each mode the distribution of the corresponding frequencies for the 1000 samples of the elastic parameters is reported. It should be noted that all considered modes are flexural in x and y directions, with the only

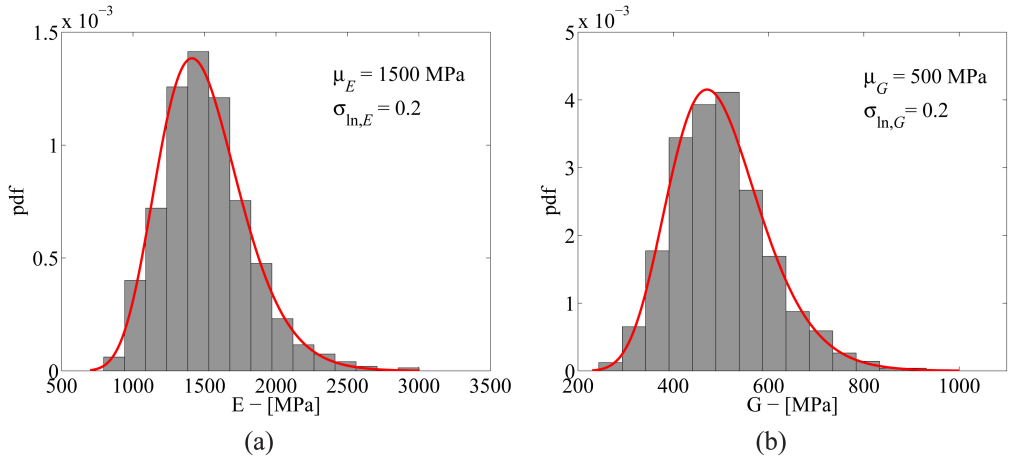

Figure 7: Generated values of Young's modulus (a) and shear modulus (b) from the statistical moments of the related distributions.

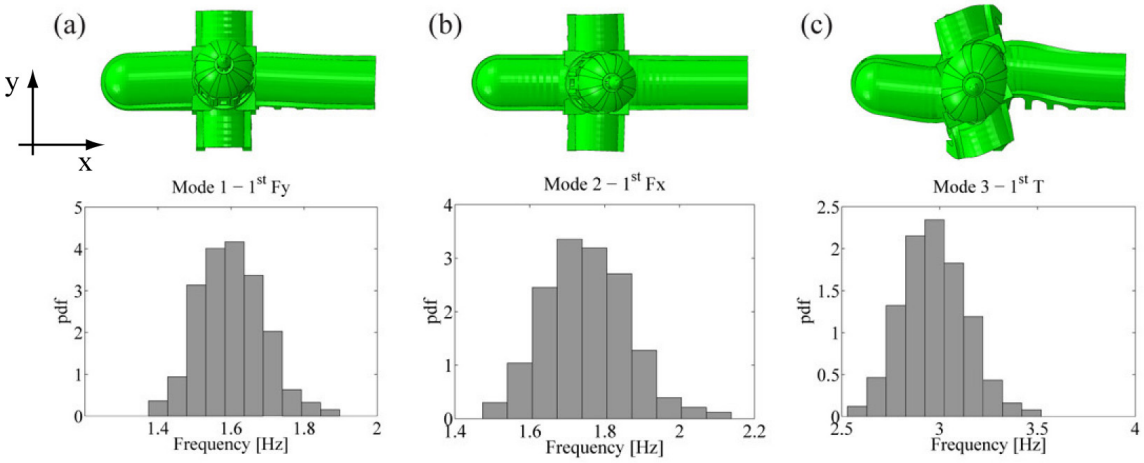

Figure 8: Modal shape and distribution of the related frequencies of the first seven modes derived by FE model by varying material stiffness [25].

exception of the third mode, which is a torsional mode. The x and y directions are defined according to the reference system of the numerical model (Figure 8).

4.2 Dynamic identification of the modal parameters and frequency tracking

The dynamic monitoring system has been started on October 16-th 2015. Figure 9 shows an example of acceleration time histories of a sample 30-minute data set, with excitation mainly given by micro-tremors due to road traffic around the Basilica and by wind loading. The very low levels of vibration in operational conditions are especially noteworthy, whereby peak accelerations are of the order of 0.2-0.3 mm/s^2. The different levels of noise in the signals can be conceivably due to the length of the cables connecting the sensors to the data acquisition unit.

The modal parameters of the structure have been estimated by means of the aforementioned SSI technique. In particular, the analysis has allowed to clearly identify the first five natural modes, where the first two modes are flexural in the y (Fy1) and x (Fx1) directions, respectively, the third mode is torsional (T1), and the last two modes are, again, flexural in the y (Fy2) and x (Fx2) directions, respectively. Figure 10 and Table 2 summarize the results of the modal parameters with their mean values and standard deviations identified from October 16th 2015

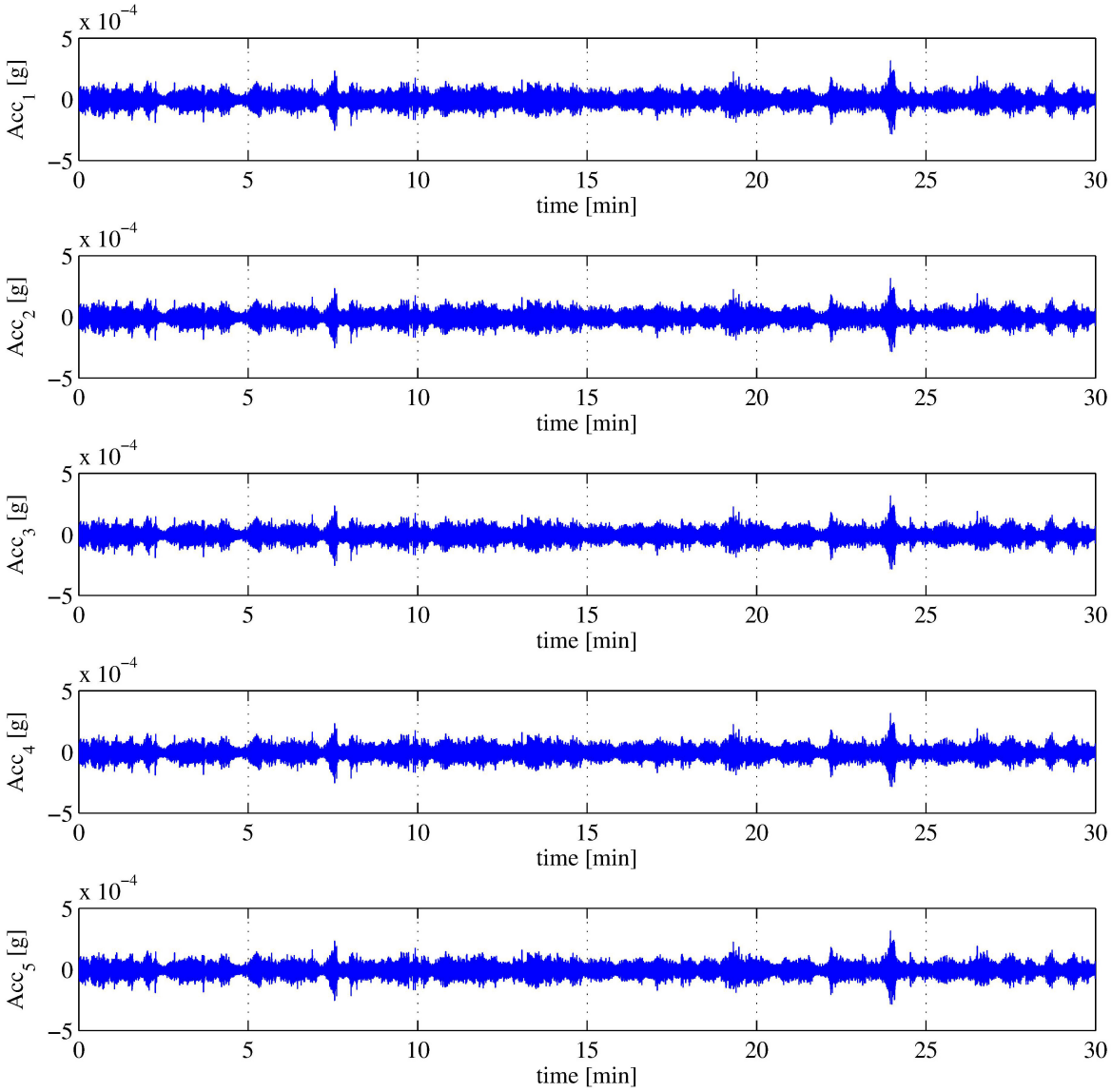

Figure 9: Sample of a 30-minutes recorded data.

Mode	Type	Frequency [Hz]	
		μ_f	σ_f
1	Fy1	1.77	9.25e-3
2	Fx1	1.81	1.10e-2
3	T1	3.08	1.01e-1
4	Fy2	3.51	4.78e-2
5	Fx2	4.40	5.57e-2

Table 2: Identified modal frequencies of the drum-dome system: mean values μ_f and standard deviations σ_f.

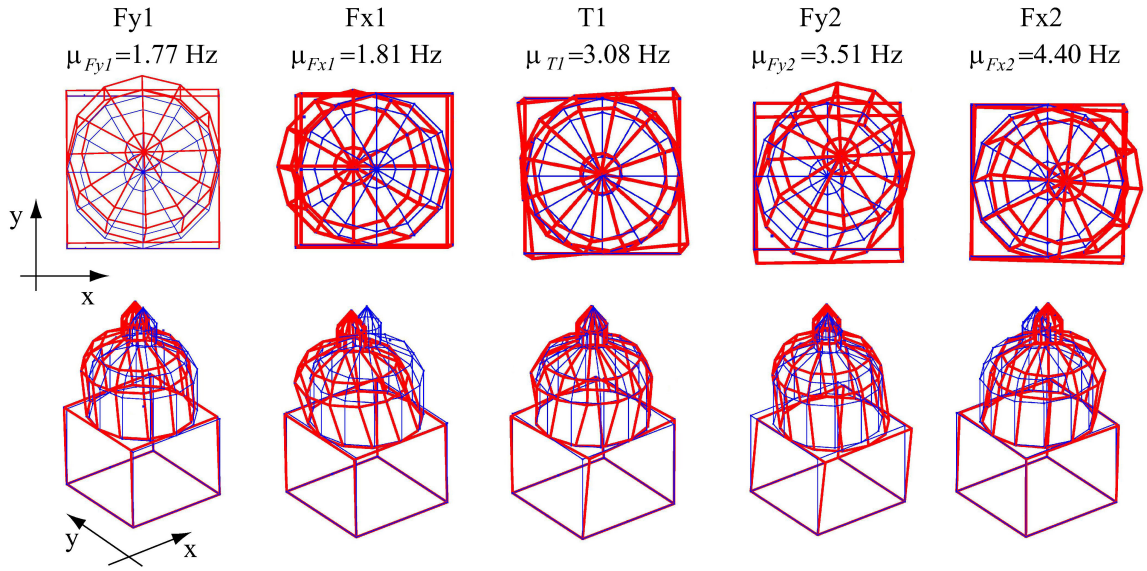

Figure 10: Representation of the identified modal shapes.

to January 4th 2016.

The application of the FDD technique has allowed to extract the first resonant frequencies through the peak-peking method. As an illustrative example, Figure 11(a) is a plot of the singular values of the power spectral density matrix of recorded accelerations as a function of frequency, for the sample data set in Figure 9. The first five resonant frequencies identified by SSI analysis can be clearly detected in the plot of Figure 11(a). Peaks associated to higher frequencies are also visible in this plot, which might conceivably correspond to higher order modes. A final decision about the nature of these peaks goes however beyond the purposes of the present investigation.

Figure 11(b) shows the spectrogram of the first singular value of the PSD matrix of the five acceleration records over the monitoring period. The traces of the first five modal frequencies are clearly visible in this plot and are indicated through dashed lines. By a closer inspection of the analysis results, it could be verified that these modes corresponds to those identified by FDD in a single data set, as discussed above. Another remark on the plot of figure Figure 11(b), is the presence of daily vertical lines that are associated with an increase in vibration energy during day-time and a decrease during night-time. This periodicity is conceivably associated to the periodicity of traffic intensity around the basilica.

Figure 12 shows the identified natural frequencies versus time, as obtained by the application of the aforementioned fully automated SSI technique on the data sets recorded over the monitoring period. The presented results are in perfect agreement with those obtained by spectral analysis of accelerations, as presented above. In particular, a quite clear tracking of the frequencies of the first five modes is achieved. Daily and long-term fluctuations of such frequencies are also clearly visible in this plot and conceivably attributable to changing environmental conditions, primarily ambient temperature. Also, natural frequencies are almost systematically identified during the day-time, while some frequencies are missing during night-time, due to a comparatively lower level of excitation.

From the results presented above, some comments on the agreement between experimentally identified and numerically predicted natural frequencies are mandatory. This comparison reveals that the frequencies of the second and the third numerical modes are in a good agreement

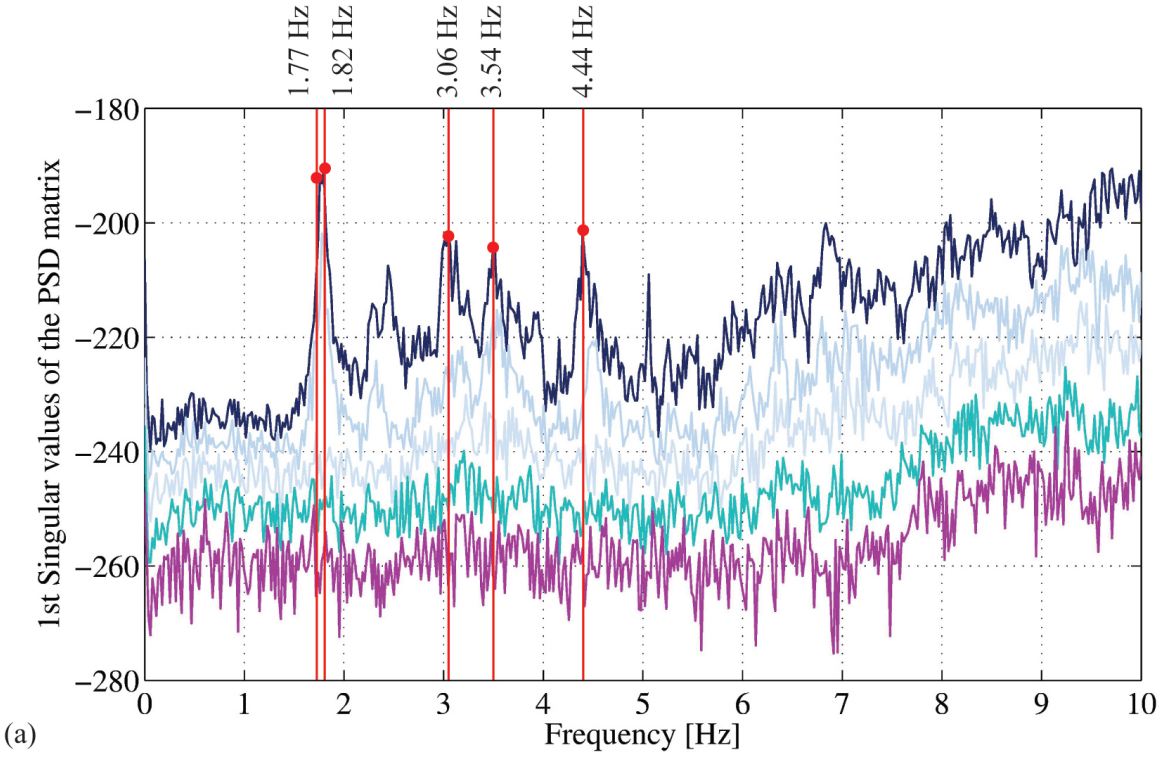

(a)

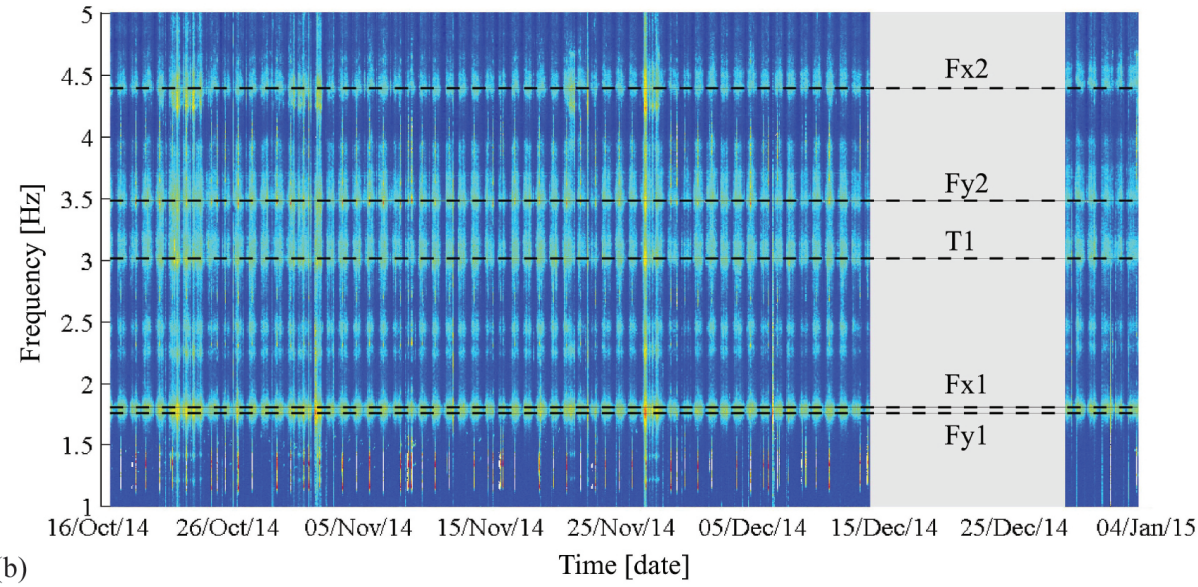

(b)

Figure 11: (a) Singular values of the power spectral density matrix and identification of the first resonant frequencies. (b) Spectrogram of the natural frequencies obtained by the FDD technique.

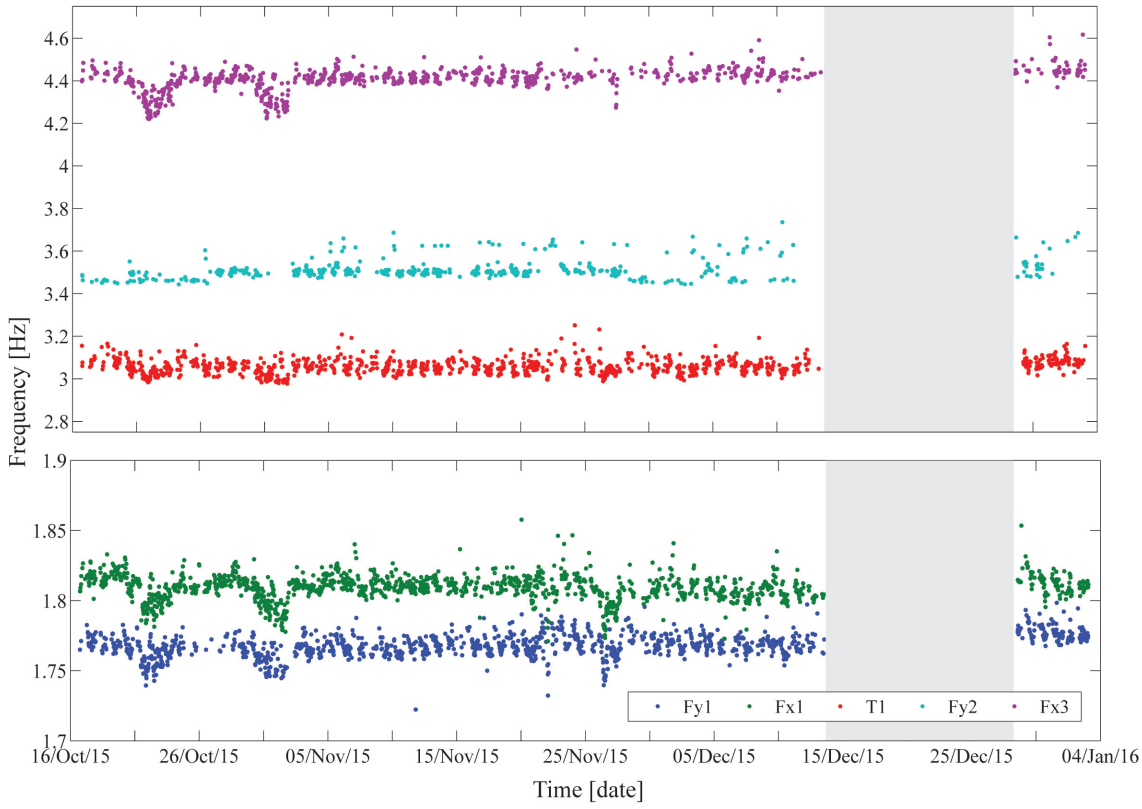

Figure 12: Frequency tracking of drum-dome system obtained by SSI technique.

with experimental results. The comparison with the higher modes requires further investigations which have not been carried out in this work. A final remark concerns some resonant frequencies in the range around $2.3 \div 2.5$ Hz which are often observed (e.g. Figure 11(a)). These phenomena are probably to be ascribed to the lateral restraint effect of the surrounding basilica. The numerical model is not able to describe these effects since, at this preliminary stage, the lateral structural elements are not fully reproduced. However, it can be concluded that the agreement between the preliminary developed finite element model and the identified natural frequencies is acceptable.

5 CONCLUSIONS

In this paper the first results obtained by a vibration-based monitoring system installed in the dome of the Basilica of Santa Maria degli Angeli in Assisi have been presented. The structural modal parameters and, in particular, the natural frequencies of the lower order modes, have been estimated over time in a continuous fashion using classic spectral analysis and a more advanced automated SSI technique. These natural frequencies have been also compared with those obtained by a FEM model developed in a previous study. In general, a good agreement between numerically predicted and experimentally identified modal parameters has been observed, both for natural frequencies and mode shapes.

Overall, the results presented in the paper represent a first attempt to monitor the behavior of large domes using vibration measurements and automated operational modal analysis. The presented results are promising towards the implementation of a vibration-based SHM procedure aimed at the early detection of damages in the structure caused by low return period earthquakes or other types of dynamic loads.

ACKNOWLEDGEMENTS

The Authors gratefully acknowledge the financial support of the "Cassa di Risparmio di Perugia" Foundation that funded this study through the project "Structural Monitoring for the protection of the Cultural Heritage: the bell-tower of the Basilica of San Pietro in Perugia and the dome of the Basilica of Santa Maria degli Angeli in Assisi" (Project Code 2014.0266.021).

The authors are also grateful to the Seraphic Province of St. Francis of Umbria, for the availability and the interest demonstrated to the research, and to the Master student Mr. Luca Botticelli for his cooperation in carrying out the experimental investigations.

REFERENCES

[1] M. Fanelli, Importance of Monitoring, Behavior Analysis, and Diagnostic Techniques for Preservation of Great Historical Structures. *International Journal of Architectural Heritage*, **9**(1), 2–6, 2015.

[2] G. Bartoli, A. Chiarugi, V. Gusella, Monitoring systems on historic buildings: the Brunelleschi Dome. *Journal of Structural Engineering, ASCE*, **122**(6), 663–673, 1996.

[3] M. Gioffrè, V. Gusella, F. Cluni, Performance evaluation of monumental bridges: testing and monitoring 'Ponte delle Torri' in Spoleto. *Structure and Infrastructure Engineering: Maintenance, Management, Life-Cycle Design and Performance*, **4**(2), 95–106, 2008.

[4] F. Ottoni, C. Blasi, Results of a 60-Year Monitoring System for Santa Maria del Fiore Dome in Florence. *International Journal of Architectural Heritage*, **9**(1), 7–24, 2015.

[5] N. Squeglia, G. Bentivoglio, Role of Monitoring in Historical Building Restoration: The Case of Leaning Tower of Pisa. *International Journal of Architectural Heritage*, **9**(1), 38–47, 2015.

[6] E. Coïsson, C. Blasi, Monitoring the French Panthéon: From Rondelet's Historical Surveys to the Modern Automatic System. *International Journal of Architectural Heritage*, **9**(1), 48–57, 2015.

[7] P.P. Rossi, C. Rossi, Monitoring of Two Great Venetian Cathedrals: San Marco and Santa Maria Gloriosa Dei Frari. *International Journal of Architectural Heritage*, **9**(1), 58–81, 2015.

[8] J. Ko, Y. Ni, Technology developments in structural health monitoring of large-scale bridges. *Engineering Structures*, **27**(12), 1715-1725, 2005.

[9] F. Magalhães, A. Cunha, E. Caetano. Vibration based structural health monitoring of an arch bridge: From automated OMA to damage detection. *Mech Syst Signal Proc*, **28**, 212-228, 2012.

[10] S. Bennati, L. Nardini, W. Salvatore, Dynamic behaviour of a medieval masonry bell tower. II. measurement and modelling of the tower motion. *J Struct Eng*, **131**, 1656-1664, 2005.

[11] S. Ivorra, F.J. Pallars. Dynamic investigations on a masonry bell tower. *Eng Struct*, **28**(5), 660-667, 2006.

[12] C. Gentile, A. Saisi, A. Cabboi. Structural identification of a masonry tower based on operational modal analysis. *Int J Archit Herit*, **9**(2), 98-110, 2015.

[13] A. Saisi, C. Gentile, M. Guidobaldi. Post-earthquake continuous dynamic monitoring of the Gabbia Tower in Mantua, Italy. *Constr Build Mater*, **81**, 101-112, 2015.

[14] F. Ubertini, N. Cavalagli, G. Comanducci, Sensing hardware optimization and automated condition assessment of a monumental masonry bell-tower. *Proceedings of the 1st International Conference on Uncertainty Quantification in Computational Sciences and Engineering, UNCECOMP 2015*, Crete Island, Greece, 25–27 May, 2015.

[15] L. Martini, *Alessi disegnato. Rilievo architettonico delle opere unbre di Galeazzo Alessi*. University of Perugia, PhD Thesis. Perugia, Italy, 2012.

[16] C. Fontana, *Il Tempio Vaticano e sua Origine*. Rome, Italy: nella Stamparia di Gio: Francesco Buagni, 1694.

[17] N. Cavalagli, V. Gusella, Dome of the Basilica of Santa Maria degli Angeli in Assisi: Static and Dynamic Assessment. *International Journal of Architectural Heritage*, **9**(2), 157–175, 2015.

[18] N. Cavalagli, V. Gusella, On the graphic statics for the analysis of masonry domes. *Proceedings in Applied Mathematics and Mechanics*, **15**(1), 701–702, 2015.

[19] N. Cavalagli, V. Gusella, Structural Investigation of 18th-Century Ogival Masonry Domes: From Carlo Fontana to Bernardo Vittone. *International Journal of Architectural Heritage*, **9**(3), 265–276, 2015.

[20] L. Sorrentino, D. Bruccoleri, M. Antonini, Structural interpretation of post-earthquake (19th century) retrofitting on the Santa Maria degli Angeli basilica, Assisi, Italy. *Proceedings of the 6th Intern. Conf. on Structural Analysis of Historic Construction* 1, 217-226, 2008.

[21] P. Capaldini, D. Ripa di Meana, B. Salvatici, Basilica patriarcale della Porziuncola: progetto di ripristino statico e funzionale a seguito degli eventi sismici del 26.09.1997 e successivi. *Ingegneria Sismica*, **2**, 5–16, 1999.

[22] A.L. Hong, F. Ubertini, R. Betti, New stochastic subspace approach for system identification and its application to long-span bridges. *J Eng Mech-ASCE*, **139**, 724-736, 2013.

[23] F. Ubertini, C. Gentile, A. Materazzi, Automated modal identification in operational conditions and its application to bridges. *Eng Struct*, **46**, 264-278, 2013.

[24] Consiglio Nazionale delle Ricerche, CNR-DT 212/2013. Istruzioni per la Valutazione Affidabilistica della Sicurezza Sismica di Edifici Esistenti. CNR, Rome, Italy, 2013.

[25] N. Cavalagli, M. Gioffrè, V. Gusella, Structural monitoring of monumental buildings: the Basilica of Santa Maria degli Angeli in Assisi (Italy). *Proceedings of the 5th International Conference on Computational Methods in Structural Dynamics and Earthquake Engineering, COMPDYN 2015*, Crete Island, Greece, 25–27 May, 2015.

ECCOMAS Congress 2016
VII European Congress on Computational Methods in Applied Sciences and Engineering
M. Papadrakakis, V. Papadopoulos, G. Stefanou, V. Plevris (eds.)
Crete Island, Greece, 5–10 June 2016

BEHAVIOR OF SINGLE STORY BEARING WALL MASONRY STRUCTURES IN VARIOUS CONDITIONS

A.T. Kassem

Department of Civil Engineering, Beni-Suef University
Beni-Suef Egypt
e-mail: abdelraouf_kassem@yahoo.com

Keywords: Bearing walls, Masonry, Bricks, Boulders, principle stresses, Cracks.

Abstract. As a part of a governmental action for studying the structural condition of public schools across Egypt, there was an awesome opportunity to perform such a research, using a valuable amount of available data for typical school models built in different environments and subjected to various loading and environmental conditions. A field study has been performed on fourteen, geometrically typical, single story schools to study effects of permanent gravitational loads, differential settlement and lateral pressure on the structural response of concrete and masonry. Structures under investigation were built by bricks or boulders and covered with an inclined reinforced concrete deck or steel or timber cladding. Finite element analyses have been performed to allocate regions and directions of principles stresses, expect failure pattern and compare with real structures. Modelling was capable to take into account various material and geometric parameters. Outcomes related to significance of various design parameters, loading and environmental conditions have been extracted. In addition response of various construction materials to the loading environment.

1 INTRODUCTION

Even bearing walls system is an ancient system for building lightly loaded structures, it is still the most used system worldwide, especially for single and double floor buildings. This extensive use of that system imposes a supporting research work studying structural properties, behavior, and response towards various loading conditions. This research was based on the opportunity arising from a governmental project of studying structural safety of school buildings all over EGYPT. The study has been performed on a typical single story bearing wall system used for educational purposes. Field investigation and measurements have been performed, in addition parametric and structural analyses have been established. All buildings studied in that paper have been built about twenty years ago and did not show seismic failure patterns since they did not face any significant seismic motion, in addition low rise restrained bearing walls behave well in moderate seismic actions[1&2]. Two main types of bearing walls materials were adopted in this research. The first is boulders and the second is bricks. The first type is known for its cracking resistance due to having irregular mortar interfaces[3]. Foundations of all the investigated models were of the same configuration and sub-base, resulting in the same stiffness[5].

2 FIELD INVESTIGATION

A typical building model, as shown in figure 1, has been considered for both investigation and analysis. The building is composed of a single compartment with a 15^{o} inclined ceiling.

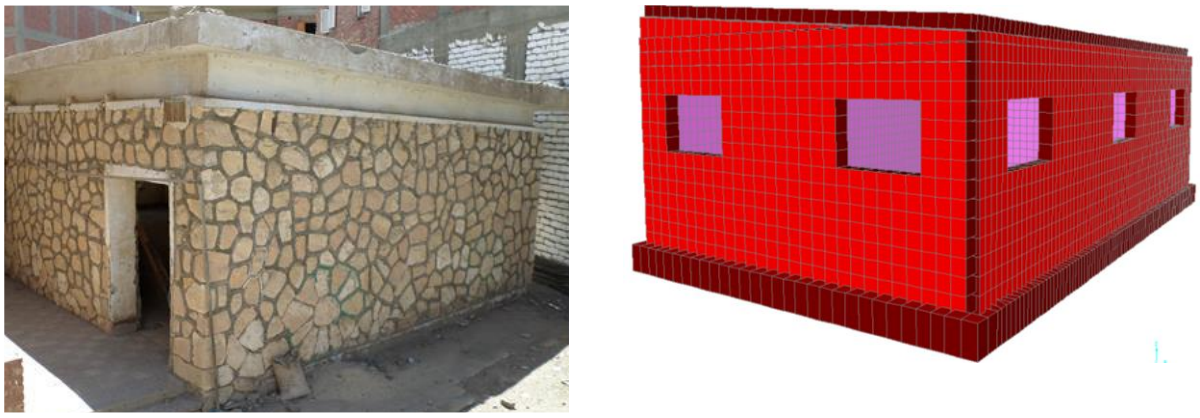

a) investigation model b) analysis model

Figure 1: Building typical model

Openings for the door and windows are shown in figure 2. Bearing walls are 25 cm thick with a typical strip footing as shown in figure 3. Building geometry and life time were not studied parameters (constants), while construction material for walls and ceiling, soil pattern, natural ground level inclination, presence of neighboring structures, and interference with ground water table were considered as studied parameters.

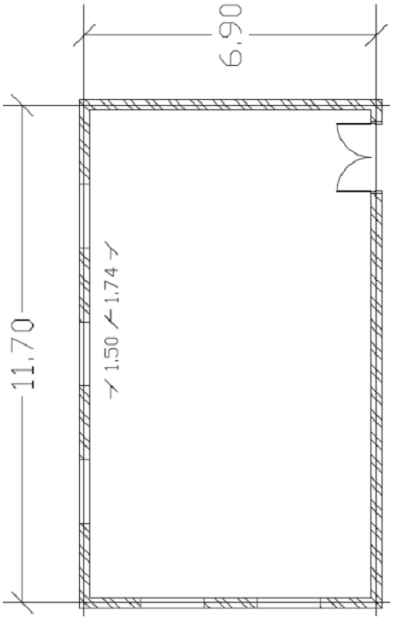

Figure 2: Building typical plan (Dim. in meters)

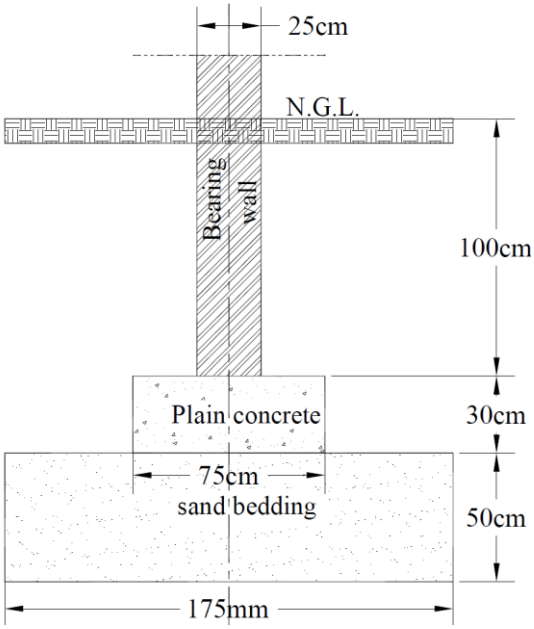

Figure 3: Typical wall x-section

3 FINITE ELEMENT MODEL

A finite element model has been developed to study stress distribution within the bearing walls body considering various loading conditions arising from field investigation. Shell elements were chosen to model walls and ceiling, as shown in figure 4. Specific releases were assigned at ceiling-walls interface to account for the difference in material and absence of rotational constraints. Springs have been used to model foundation elasticity, since foundation and subgrade properties were identical. Concrete slabs and bearing walls material non-linearities have been considered.

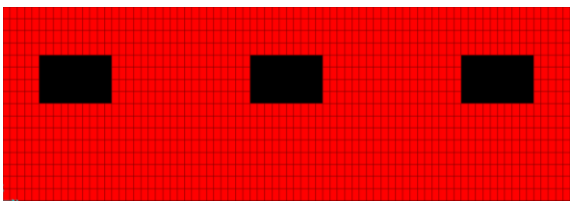

a) First side

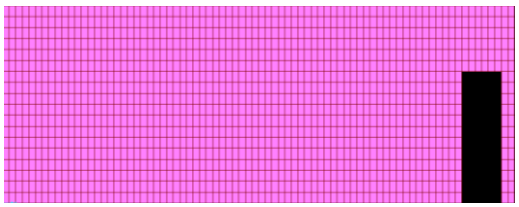

b) Second side

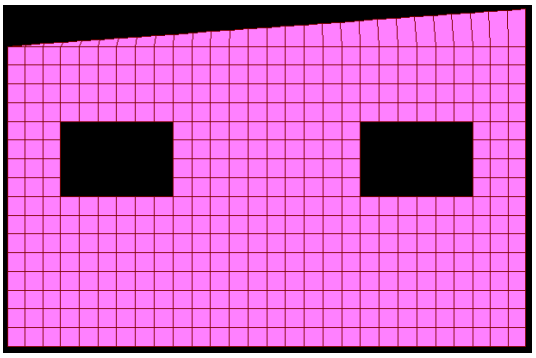

c) Third side

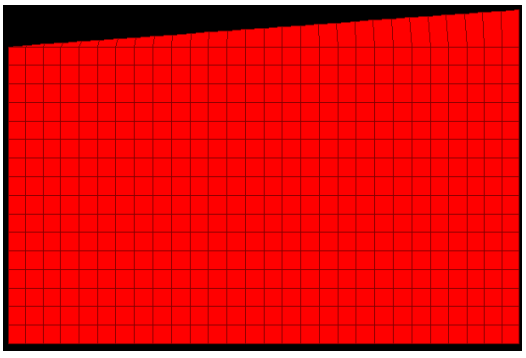

d) Fourth side

Figure 4: Finite element model

4 RESULTS AND DISCUSSION

Outputs of the study have been divided into two categories. The first is field investigation and measurements. Investigations considered loading conditions clarifying the structure's status, concentrating on the proposed most significant parameters as building material, ceiling type, soil type, natural ground level profile, presence of close neighboring structures, and interference with ground water level; in addition to crack pattern. While measurements concentrated on major crack width. Special conditions, as the presence of side embankment were found in a single building; so it was not considered as a studying parameter, but a load case. Table 1. Summarizes conditions of each building concerning studied parameters and noticed patterns of failure (major crack pattern and width).

Table 1: Brief Description of buildings condition

	walls		Ceiling			Soil			N.G.L.		Neigh.		G.W.T.		Crack Pattern				Crack width		
Building Id	Brick	Boulders	Concrete	Steel	Timber	Sandy	Clayey	Silty	Horizontal	Inclined	Close	Far	High	Low	Vertical	Inclined	Horizontal	None	x<5	5≤x≤10	x>10
1		■		■			■		■		■		■					■			
2		■		■			■		■		■		■					■			
3		■		■			■		■		■		■					■			
4		■	■				■	■	■		■		■					■			
5		■	■					■	■			■		■				■			
6	■		■				■			■	■		■			■				■	
7	■		■				■		■			■	■			■	■			■	
8	■				■			■	■		■		■					■			
9	■				■			■	■			■	■					■			
10	■		■					■	■			■	■		■				■		
11	■		■				■			■	■			■		■	■			■	
12	■		■			■			■			■		■	■	■					■
13	■		■					■		■		■	■			■	■				■
14	■		■				■	■	■		■		■			■			■		

The second output pattern is the finite element modeling. Two main finite element models have been established. The first reflects normal gravitational loads, while the second reflects the case of side embankment resulting in lateral loads. Figures 5, 6, and 7 represent horizontal normal stress (S11), vertical normal stress (S22), and maximum tensile stresses (Smax) in (kN/m^2).

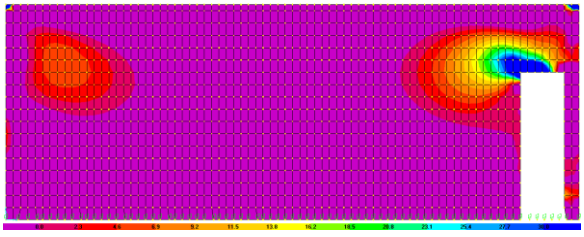

Figure 5a: S11 (gravitational loads)

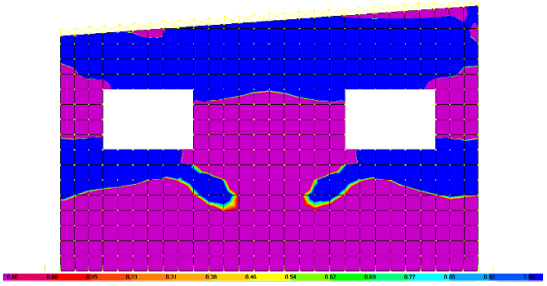

Figure 5b: S11 (gravitational loads)

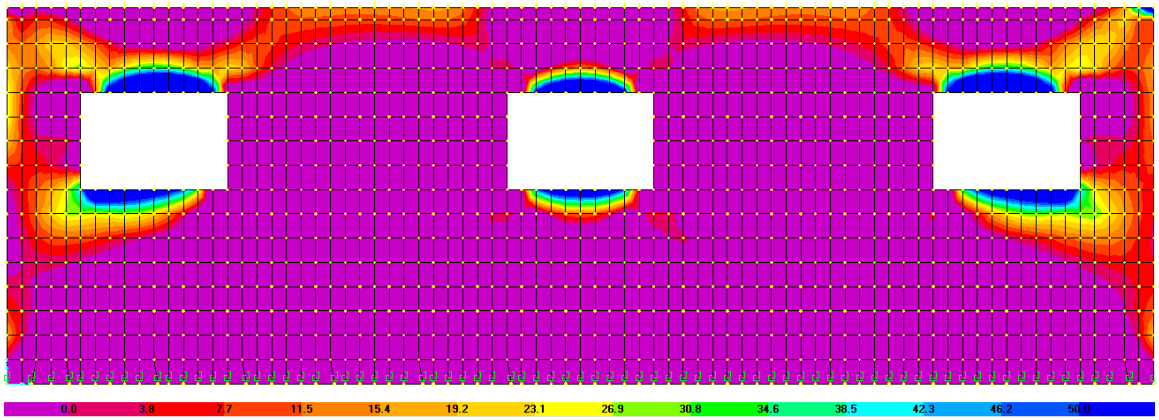

Figure 5c: S11 (gravitational loads)

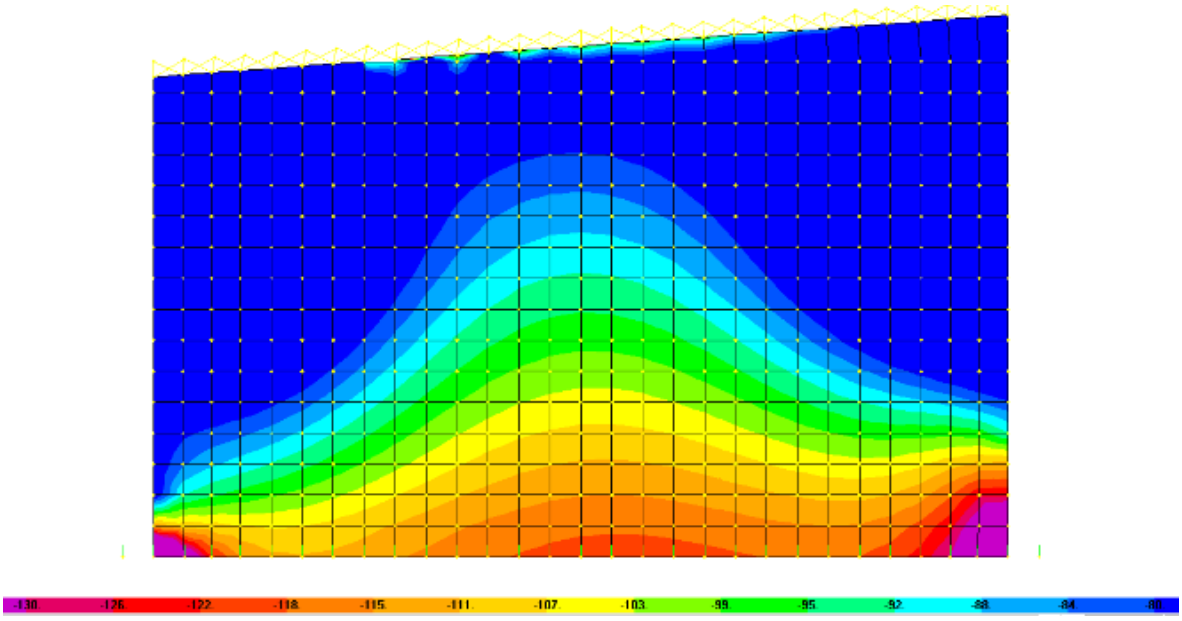

Figure 6a: S22 (gravitational loads)

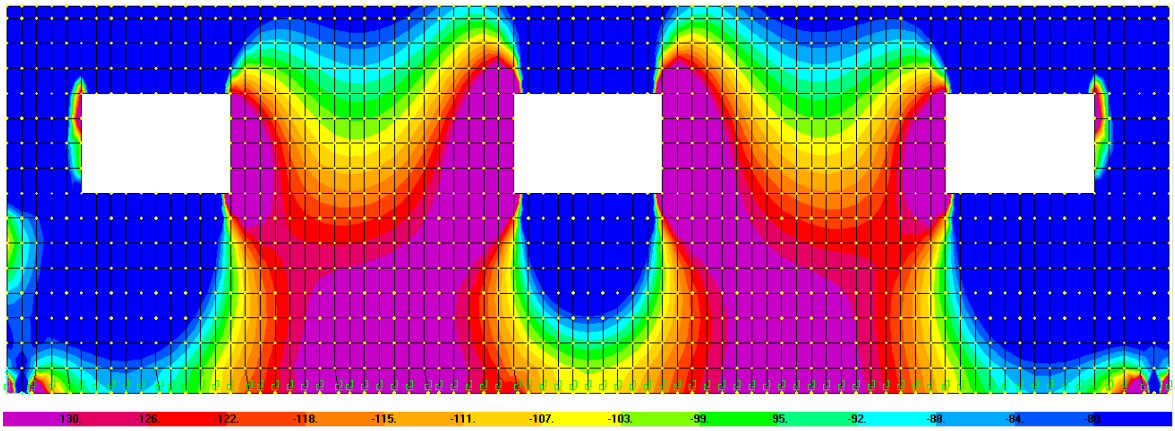

Figure 6b: S22 (gravitational loads)

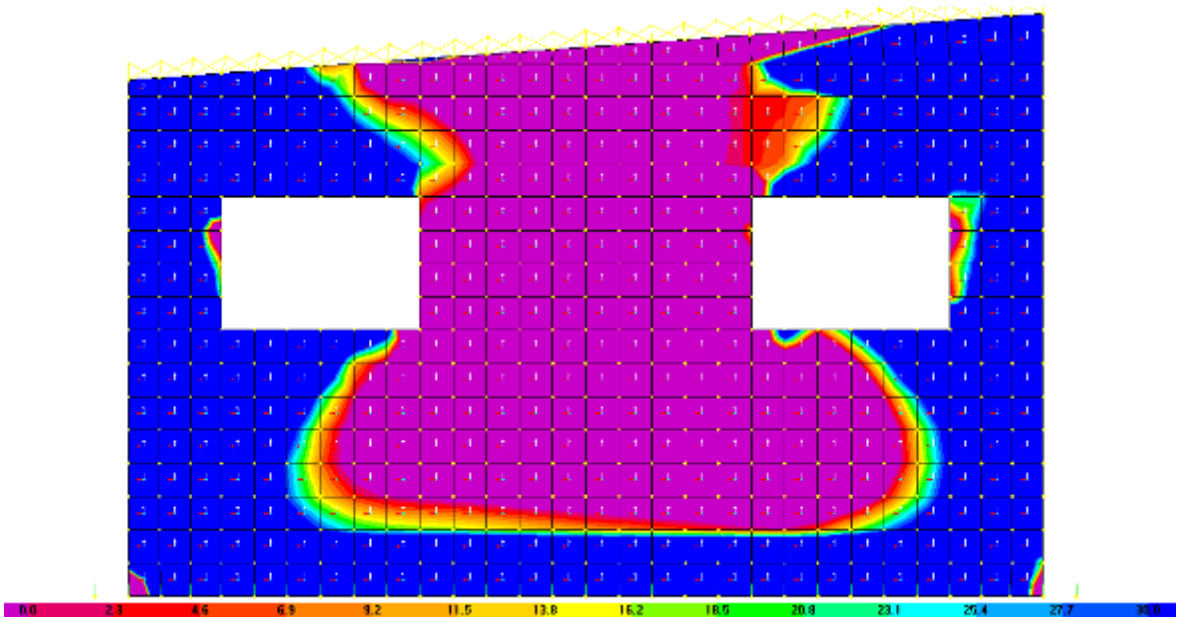

Figure 7a: Smax (lateral loads)

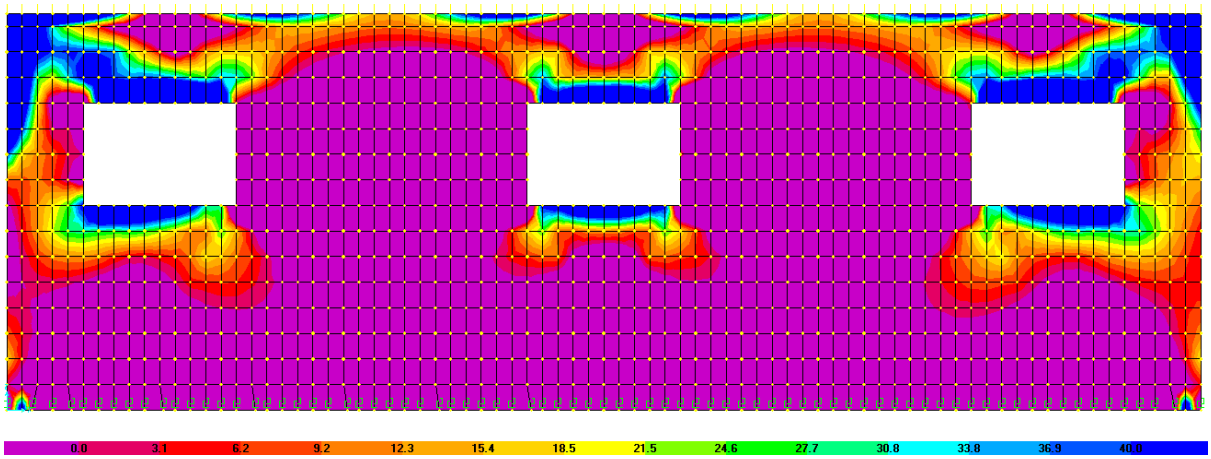

Figure 7b: Smax (lateral loads)

Reviewing field study outputs and analysis outputs showed an accepted level of compatibility between both of them. Consequently both of them have been considered to perform a parametric analysis to study parameters significance. Outputs of the parametric study could be summarized as follows. The most significant parameter concerning cracking is the use of boulders, where 35% of the investigated buildings were constructed by boulders and they all showed a high level of resistance towards cracking, this could be attributed to two factors, the first is the higher strength of boulders relative to bricks, while the second could be due to the irregularity if boulders interfaces that make crack propagation difficult. The second significant parameter is the natural ground level profile, where 21% of the investigated buildings were built on a sloping ground or at the edge of a slope. All these buildings suffered inclined cracking exceeding 5 mm width. The third significant parameter is soil formation, where 57% of structural failure took place in clayey soils, putting into consideration that clayey soils represent 57% of the investigated buildings sub-base. The forth significant parameter is applied loads, where lightly loaded buildings (steel or timber ceilings) did not show any failure patterns. Other parameters as interference with ground water table and the presence of adjacent structures seems to be insignificant.

A comparison has been conducted between field study and structural analyses. This comparison concentrated on location of relatively high tensile stresses, resulting from structural analysis and cracking, noticed in field investigation. Figure 8 shows door cracking at location of maximum tensile force due to gravitational loads, which is compatible with figure 5a. Figure 9. Shows windows cracking at the location of maximum tensile stresses, which is compatible with figure 5b. Figure 10 shows lateral earth pressure resulting from natural embankment reaching windows. This earth pressure resulted in tensile stresses shown in figures 7a and 7b and appeared in the form of cracking shown in figure 11

Figure 8: Door cracking (gravitational loads)

Figure 9: Window cracking (gravitational loads)

Figure 10: Windows Earth pressure loads

Figure 11: Window cracking due to earth pressure loads

5 CONCLUSIONS

Field and analytical studies resulted, concurrently, in the following conclusions:

- Bearing walls, built by boulders showed much more durability than those by bricks.
- Natural ground inclination has a highly passive influence on bearing walls failure.
- Lightly loaded ceilings (timber or corrugated sheets), results in no structural cracking, in case of proper foundations.
- Foundation submergence in ground water table does not influence bearing wall failure significantly.
- Most long-term cracking takes place in non-granular soils

6 REFERENCES

[1] Can C. SIMSIR, Mark A. ASCHHEIM and Daniel P. ABRAMS, "Out-Of-Plane Dynamic Response Of Unreinforced Masonry Bearing Walls Attached To Flexible Diaphragms", 13th World Conference on Earthquake Engineering Vancouver, B.C., Canada August 1-6, 2004 Paper No. 2045

[2] Kaspar Peter and Marc Badoux, "Application of The Capacity Spectrum Method to R.C. Buildings With Bearing Walls", 12th world conference on earthquake engineering.

[3] L. Gambarotta and S. Lagomarsino "Damage Models For the Seismic Response of Brick Masonry Shear Walls. Part I: The Mortar Joint Model and Its Applications", Earthquake Engineering And Structural Dynamics, Vol. 26, 423ð439 (1997).

[4] Alexandre A Costa, Andrea Penna, António Arêde, and Aníbal Costa, "Simulation of masonry out-of-plane failure modes by multi-body dynamics", Earthquake Engng. Struct. Dyn. (2015) DOI: 10.1002/eqe

[5] Erunt Mohsin "Support Stiffness Effect on Tall Load Bearing Masonry Walls" University of Alberta, Ph.D. thesis Spring 2005

[6] Mahdi Montazerolghaem and Wolfram Jäger "Characterization of uncertainty probabilistic models in verification of unreinforced masonry shear wall", Ernst & Sohn Verlag für Architektur und technische Wissenschaften GmbH & Co. KG, Berlin Mauerwerk 19 (2015), Heft 4 DOI: 10.1002/dama.201500665

[7] Ulf Schmidt, Wolfram Jager, Wolfgang Brameshuber, Tammam Bakeer "The bending strength of masonry", Ernst & Sohn Verlag für Architektur und technische Wissenschaften GmbH & Co. KG, Berlin · Mauerwerk 19 (2015), Heft 1V.

[8] Michael Schuller1, Wayne Ruth2, Celina Yan3, Shan Wo4, "Evaluation and Repair of Masonry Construction", journal of masonry international January 2011.

[9] A. Brencich, E. Sterpi "Compressive strength of solid clay brick masonry: calibration of experimental tests and theoretical issues" Structural Analysis of Historical Constructions, New Delhi 2006 ISBN 972-8692-27-7

[10] Michael Dominelli "An Analysis of the Load Carrying Capacity of an Existing Bearing Wall Building" Albert Neiken School of Engineering, M.Sc. thesis 2000

[11] Alok Madan "NON-LINEAR MODELING OF MASONRY WALLS FOR PLANAR ANALYSIS OF BUILDING STUCTURES" Faculty o f the Graduate School of the State University o f New York, Ph.D. thesis, 1996

[12] Tunde M. Olatunj" Behavi or and Strength of Masonry Wall/ Slab Joints" The University of Alberta, Ph.D. thesis, spring 1986.

[13] Taohida Parvin Akhi" Experimental investigation of effective modulus of elasticity and shear modulus of brick masonry wall under lateral load" The University of Manitoba, M.Sc. 2012

ECCOMAS Congress 2016
VII European Congress on Computational Methods in Applied Sciences and Engineering
M. Papadrakakis, V. Papadopoulos, G. Stefanou, V. Plevris (eds.)
Crete Island, Greece, 5–10 June 2016

SEISMIC PROTECTION OF MONUMENTS AND HISTORIC STRUCTURES – THE SEISMO RESEARCH PROJECT

Constantine C. Spyrakos and Charilaos A. Maniatakis

Laboratory for Earthquake Engineering, National Technical University of Athens
Heroon Polytechniou 9, 15780 Zografou, Athens, Greece
{cspyrakos@central.ntua.gr; chamaniatakis@gmail.com}

Keywords: SEISMO Research Project, Historic Structures, Seismic Response, Numerical Modeling and Analysis, Documentation, In-situ and laboratory surveying.

Abstract. *The research has developed an integrated, interdisciplinary and innovative methodology to evaluate the seismic behaviour of monuments and historic structures. This methodology enables condition assessment of monuments, in a way that allows selection of effective preservation intervention techniques using appropriate materials. It also yields useful recommendations for engineers and authorities responsible for the procurement, realization and approval of studies and their subsequent applications to protect monuments and historic structures. Given the importance and complexity of historic structures in terms of design, construction techniques and materials, advanced computational tools and methods were utilized to meet the needs of the proposed research. In particular, implementation of the proposed methodology on selected case-study historic structures included: (a) documentation of the existing state through surveys and architectural studies; (b) recording of damage; (c) identification of the construction materials; and (d) monitoring of the monument and the evaluation of parameters, such as regional seismicity and soil conditions, that affect their seismic response. Static tests on wall specimens as well as shaking table tests were conducted, producing valuable data related to the true seismic behaviour of structures. Two well known monuments have been selected as case studies in order to be analysed using several types of analysis and failure criteria. Moreover, methodologies established for the study of monuments and historic structures were assessed in terms of their reliability, accuracy and effectiveness by comparing analytical results with experimental data.*

1 INTRODUCTION

The interest of the scientific community involved in the protection of cultural heritage was rekindled at the end of the Second World War when many monuments across Europe showed irreparable damage [1-3]. This interest focused on the condition assessment of monuments, methods for more efficient maintenance, and development of simulation techniques to model their behaviour, facilitated by the evolution of computational tools and the parallel progress made in many scientific fields.

The study of the behaviour of a monument or a historic building is particularly difficult because of the complexity of the structure, construction method, age, and of course because of its historic significance [4]. These parameters limit the choice of means and methods of monitoring and intervention for these types of structures. Detailed data collection, use of advanced computational methods and development of complex models is usually required [5-7]. Assessing the status of a historic building becomes even more difficult when the structure is prone to seismic activities [8]. In this case the risk of partial or total collapse should be studied [7, 9]. Furthermore, the existence of seismic activity in the vicinity of an aging monument usually suggests that the structure has already suffered damage, which must be considered in the study, and in addition, any proposed interventions should be targeted to protect the structure from future earthquakes [10-13].

Therefore, it is evident that the seismic protection of monuments involves a great number of parameters that should be investigated thoroughly and systematically. Although the surveying of a historic structure is a prerequisite for its study and protection against seismic actions, current practice has demonstrated deficiencies, as demonstrated by several current examples of failures reported in the literature, such as the Tower in Pavia, Italy, an important monument that collapsed without any indication of damage. A similar case- study is a Cathedral in the south of Sicily that was partially propped after an earthquake in 1990, and then collapsed in the 1996 without another seismic event. Use of suitable investigation methods and testing would have allowed an accurate assessment of the status of the above monuments and early detection of damage.

This research develops a methodology for thorough documentation of the geometry, assessment of structural condition and calculation of seismic response through experimental and analytical methods, as well as application or enhancement of innovative preservation techniques to monuments and historic structures.

(a) (b)

Figure 1: The temple of Hephaestus in the Ancient Agora, Athens: (a) western façade; (b) southern view.

(a) (b)

Figure 2: The Catholikon of Kaisariani Monastery, Hymettus Athens: (a) western façade; (b) southern view.

Two monuments of major importance were selected, representing the classical and the byzantine era: (a) the Temple of Hephasteus in the ancient Agora in Athens; (b) the Catholicon of the Kaisariani Monastery. The temple of Hephaestus was probably erected between 460 and 420 BC by a yet unknown architect on top of Agoraios Kolonos hill, which is delimiting the Ancient Agora of Athens to the west. It is one of the best preserved ancient temples, partly because it was transformed into a Christian church. The central church (Catholicon) of the Monastery of Kaisariani is located on a hillside at the foot of Mount Hymettus on the east of Athens, Greece. The Catholicon is a Byzantine crossed-dome church constructed during the 11th/12th centuries. The two monuments are shown in Figures 1 and 2.

2 CONDUCTED RESEARCH

The geometric survey of monuments is a sophisticated and demanding process, as regards to the use of suitable equipment (simple tools, photogrammetry or laser scanners surveys), software, expertise, time and effort. The importance of accuracy in monument surveying is obvious. The need for a detailed record of the architectural elements of the bearing structure, deformation and damage is often a catalyst for the choice of retrofitting methods. A full documentation of the main structure, including the main horizontal, vertical and inclined structural elements that transfer the imposed stresses and strains at the foundation elements, has been performed for the two monuments. In Figure 3 the final 3D model for the temple of Hephaestus derived with the use of a Leica ScanStation 2 laser scanner is shown [14].

Figure 3: Documentation of temple of Hephaestus with laser scanner: View of the 3D model from the northeast corner [14].

Local soil conditions have a profound influence on the structural response. In this context, site surveying includes the study of local topography (i.e., slopes, valleys), nature of the bedrock and nature and geometry of the deposited soils. These factors may contribute to the qualitative interpretation of the observed damage. The role of soil behaviour and site characteristics on the seismic response is now internationally recognized. A Geophysical investigation has been performed for the Kaisariani Monastery to evaluate the velocities for P and S waves along depth, as depicted in Figure 4a. Based on the geological and geotechnical data available at the positions of the two monuments, the soil profiles have been derived and analysis of soil response has been conducted to estimate maximum acceleration, maximum velocity and design spectra at the top of the soil. An indicative elastic acceleration spectrum at the ground surface is shown in Fig. 4(b) [15].

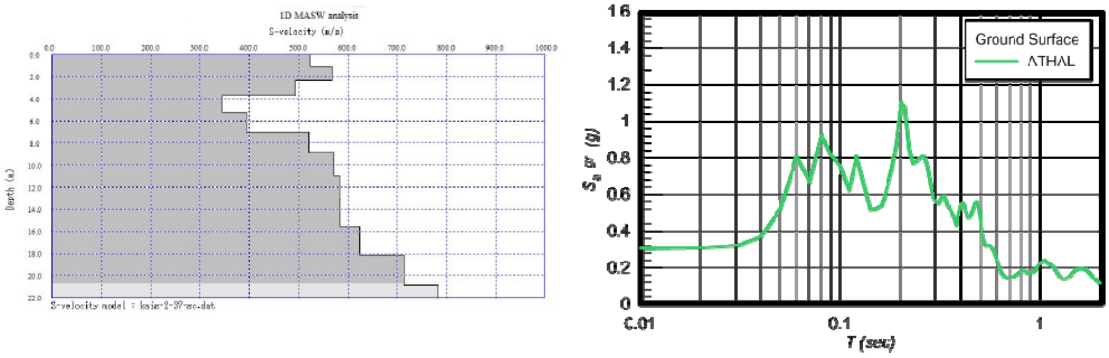

(a) (b)

Figure 4: Soil investigation: (a) determination of S-waves velocity in Kaisariani Monastery; (b) elastic spectral acceleration at ground surface in Hephaestus temple [15].

A detailed study of seismic hazard is also completed, that is, assessment and evaluation of seismic loads resulting from the seismicity of the area in which the monument is located, considering possible nearby active faults and near-fault phenomena. The significance of the monuments requires the probabilistic assessment of seismic risk, which is based on regional seismicity including historic earthquakes and the establishment of the probability distribution of occurrence for seismic events. The combination of the regional seismicity and attenuation relationships of ground motion result in the formation of seismic hazard curves that provide the expected ground acceleration, depending on soil type, for different annual frequencies of exceedance and return periods. Based on typical values of acceleration, appropriate pairs of earthquake magnitude and distance were determined, and used for seismic analysis. In Figure 5 the annual frequency of exceedance of peak ground acceleration for stiff soil conditions is depicted [16].

Another important parameter, necessary for the complete documentation of the structure and for understanding its behaviour, is the identification of material properties, which may have different characteristics depending on construction phases of the structure. Beyond identifying these components, namely the structure and the mechanical properties of the materials, the scientific community interest focuses on the modeling approach of historic mortars, since application of inappropriate mortars for the preservation of monuments in the past resulted in devastating effects, i.e., cracks, failure of the original materials, surface staining or spalling. A thorough and organized survey of the two monuments has been conducted including the implementation of various non-destructive techniques (NDTs) [17-19]. In the case of Kaisariani monastery, after a thorough in-situ macroscopic investigation, a variety of NDTs where ap-

plied: Ground-penetrating Radar (GRP), Infrared Thermography (IR), Fiber Optics Microscopy (FOM) and Schmidt rebound hammer.

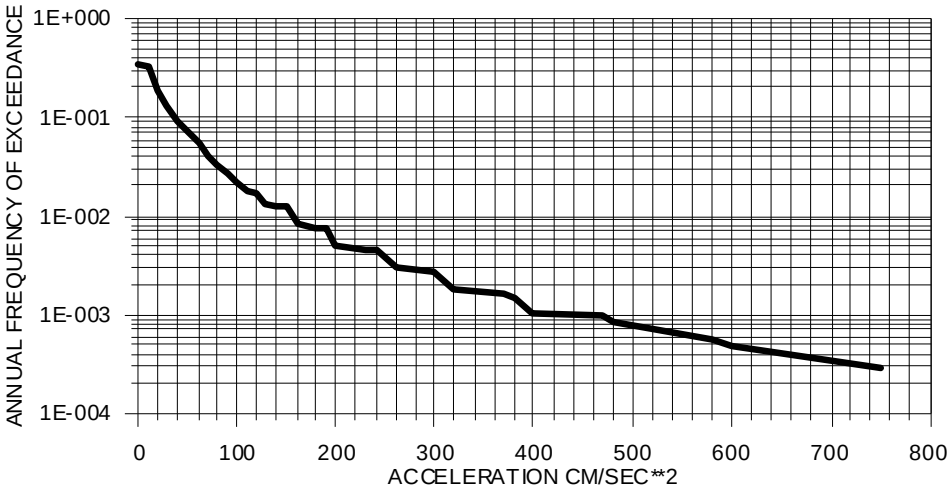

Figure 5: Seismic hazard curve [16].

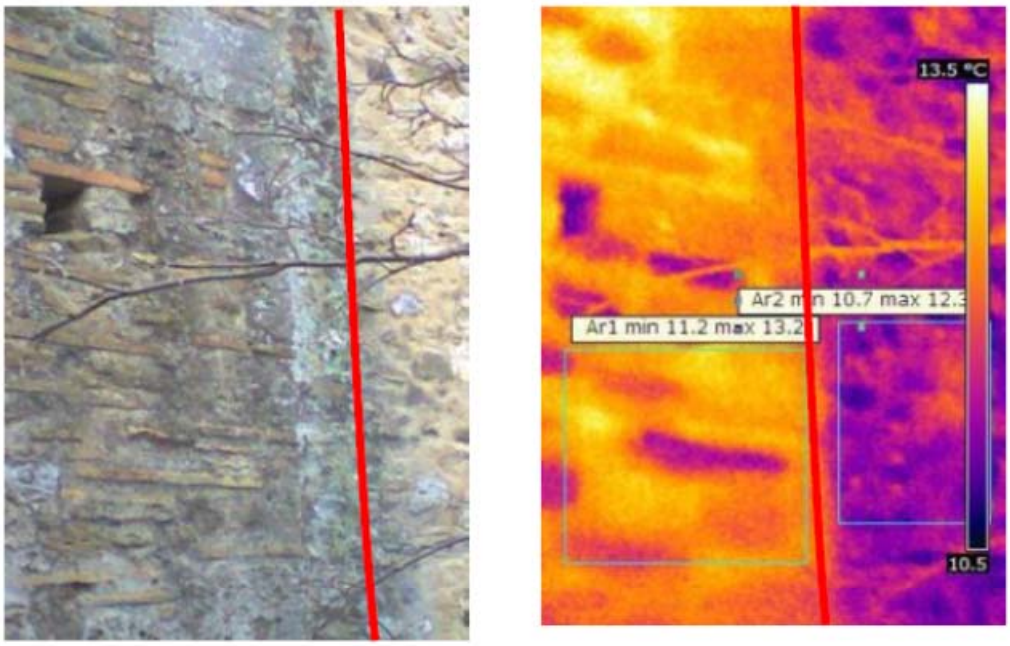

Figure 6: Results of Infrared Thermography at the Catholikon. Detection of different structural phases [17].

The results were analyzed and combined in order to extract information regarding the original building materials, the type of masonry construction, as well as information regarding non-documented different construction phases and problematic areas. In Figure 6 indicative results of infrared thermography are shown regarding the Catholikon. A series of NDT tests have been conducted also at the Hephaestus temple including the use of ground penetrating radar, endoscopy and rebound hammer testing. In Figure 7 the results of radar are shown regarding a wall of the south façade.

Monumental and historic buildings are generally constructed with masonry walls. These construction materials present significant variances of the mechanical and dynamic characteristics, which are very difficult to identify. The identification of these variances is required in

order to perform the analysis of the monument and assess its behaviour. The large dispersion of these characteristics is mainly attributed to the fact that the monument during its life has been strained by several actions, including subsidence, temperature changes, environmental vibration and seismic loads. The impact of these actions is partly depicted in the form of cracks. The existence of severe cracking could result in separating the monument in different parts; thus, increasing the difficulty to assess its behaviour under seismic excitations.

For these reasons, a thorough understanding of the behaviour of the monument is achieved through structural monitoring under small-intensity earthquakes in order to assess the effects of cracking on the behaviour of individual parts. The information from structural monitoring can be a basis for developing numerical and analytical models that will be validated according to the results of a monitoring program in order to approximate the real behaviour of the structure with acceptable accuracy. In Figure 8 the positions for the placement of six triaxial accelerometers are depicted for the Catholikon. The accelerometers are connected with a central data acquisition system.

Another important source of information is through testing of models. These experiments allow simulation of the seismic action by selecting the intensity, frequency spectrum and most parameters that characterize an earthquake motion. The specimens are constructed to satisfy, in as much as possible, the actual construction and to facilitate the study of specific parameters. However, there are few experiments in the literature related to historic structures because of the many implementation difficulties. A number of masonry specimens have been constructed at the Laboratory for Earthquake Engineering of the National Technical University of Athens, LEE-NTUA, to be tested under compression as shown in Figure 9.

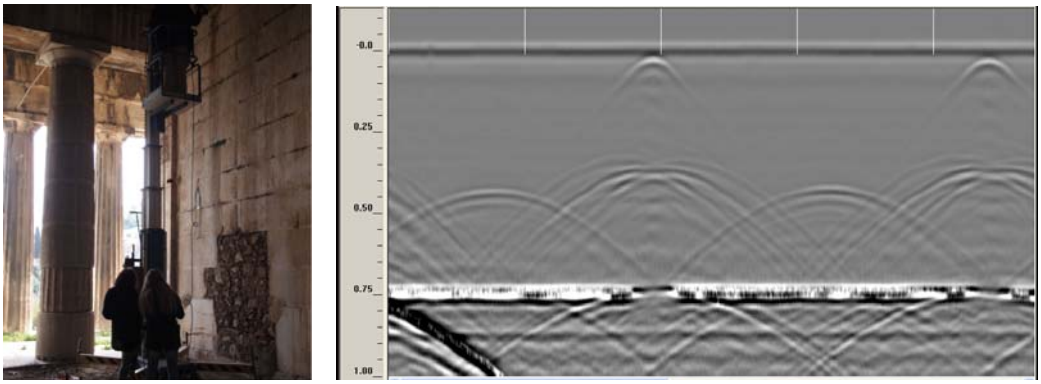

Figure 7: Results of ground penetration radar testing at the Hephaestus temple [19].

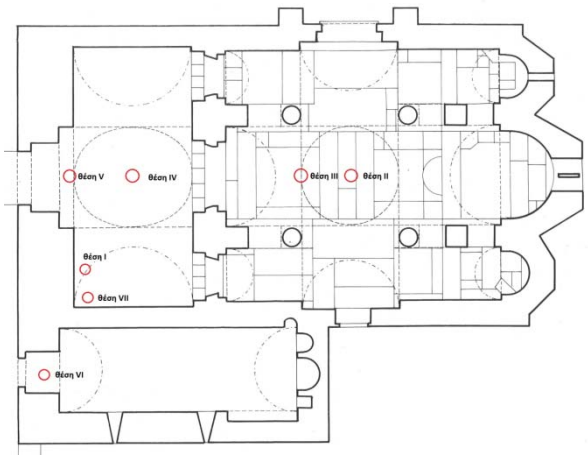

Figure 8: Monitoring scheme for the Kaisariani monastery. Placement of recording devices.

Identifying potential failure modes of a monument or a historic building requires understanding of its structural behaviour. This can be aided by examining the response of pertinent subsets of the structure based on the method of macroelements, or the finite-element method, using linear or non-linear analysis [20, 21]. Development of reliable macroelement and finite element models is necessary to perform elaborate analyses, including nonlinear static and dynamic time-history analysis. In Figure 10(a) and 10(b) the finite element models of the Hephaestus temple and the Catholikon are depicted, respectively [22]. In Figure 11(a) the central apse of the Catholicon is selected as a macroelements in order to study a local mechanism of failure governed by overturning. The transversal behaviour is assessed by means of a macroelement that isolates three arches and the supporting pillars of the central nave as shown in Figure 11(b) [9].

Common practice in describing failure is the application of criteria based on stress distribution. Successful use of an analytical mathematical model that incorporates the particular geometric, mechanical and structural features of a historic structure can provide information on the type, extent and location of damage. The results from such an analysis can be used in a deterministic way or alternatively, following a probabilistic approach with which parametric analyses are performed for a range of values of a critical parameter. The statistical evaluation of the results has led to the development of fragility curves that correlate the estimated damage to the seismic intensity based on a given type of probability. Indicative fragility curves for the Kaisariani monastery are shown in Figure 12b referring to the failure criterion depicted in Figure 12a [18, 23].

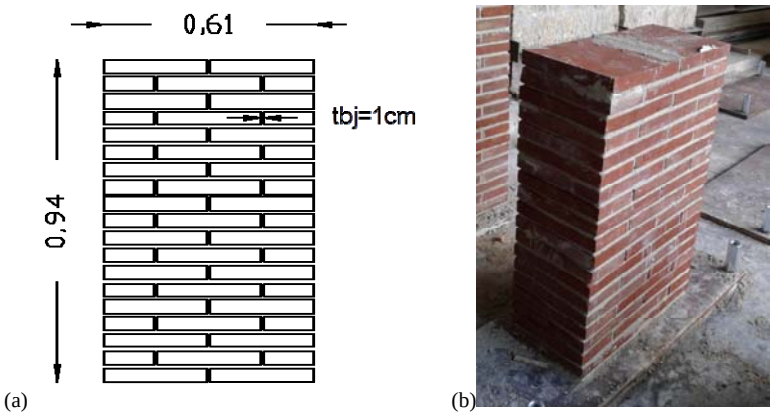

Figure 9: Masonry specimens to be tested for compression: (a) drawing; (b) as build.

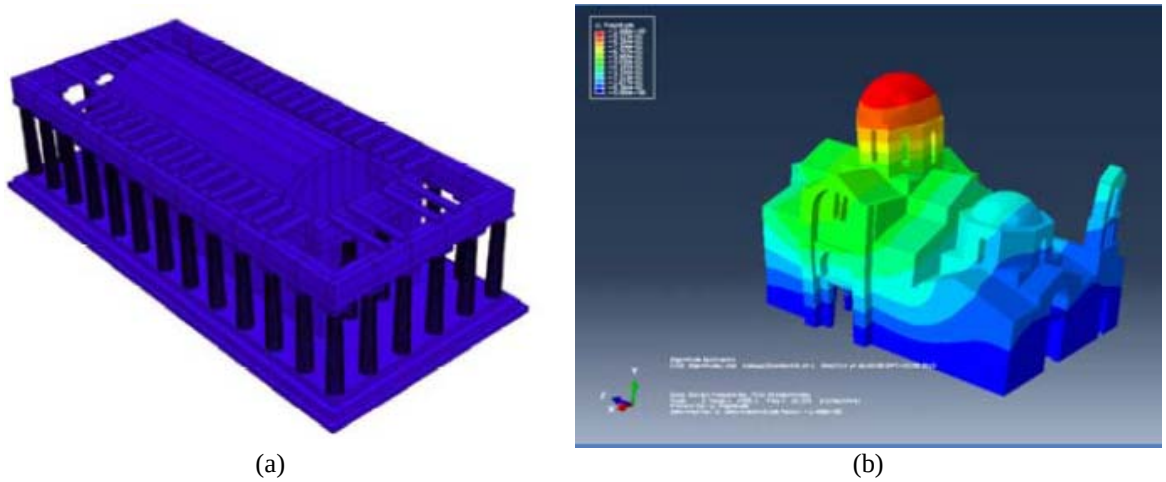

Figure 10: Finite element models: (a) Hephaestus temple; (b) Catholikon [9, 22].

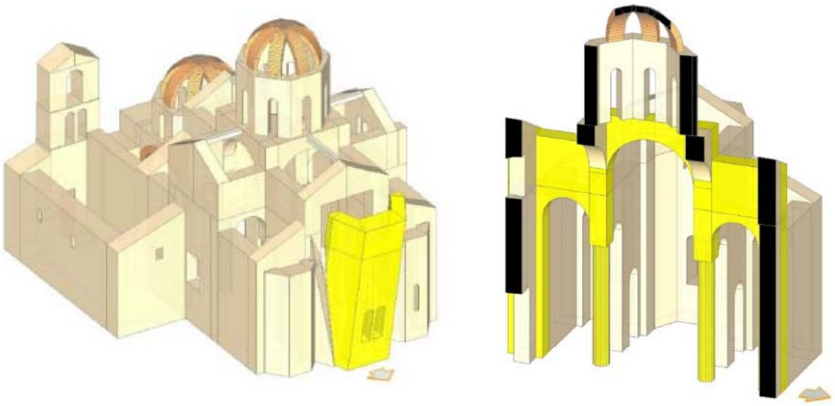

(a) (b)

Figure 11: Macroelement analysis for the Kaisariani monastery: (a) Overturning of the central apse; (b) Transversal behavior.

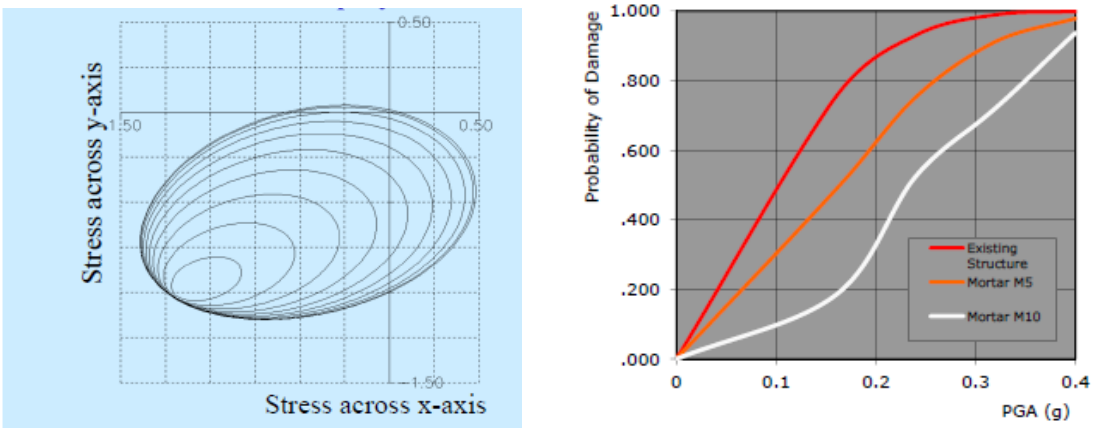

(a) (b)

Figure 12: Vulnerability the Kaisariani monastery: (a) development of failure criterion; (b) fragility curves for moderate damage [23].

The main purpose of the analysis of a monument or a historic building is to assess its seismic risk in order to propose specific intervention measures for an effective seismic upgrade and protection of such structures. In addition to conventional treatments, application of seismic base-isolation is an efficient engineering methodology designed to reduce or even eliminate damage caused by dynamic excitations. In fact, seismic isolation is a type of support that separates the structure from the soil response and results in a reduction of seismic energy input rather than enhancement of structural resistance. The application of this technology leads to structures that continue to behave elastically even during major seismic events [24]. The effectiveness of using base isolation is also studied at LEE-NTUA with the aid of a masonry specimen depicted in the drawing of Figure 13 [25-26].

3 MANAGEMENT STRUCTURE AND PROJECT TEAMS

The conducted research was organized in thirteen Work Packages (WP):

WP 1: Coordination of the project including synchronization of the research groups and financial management;

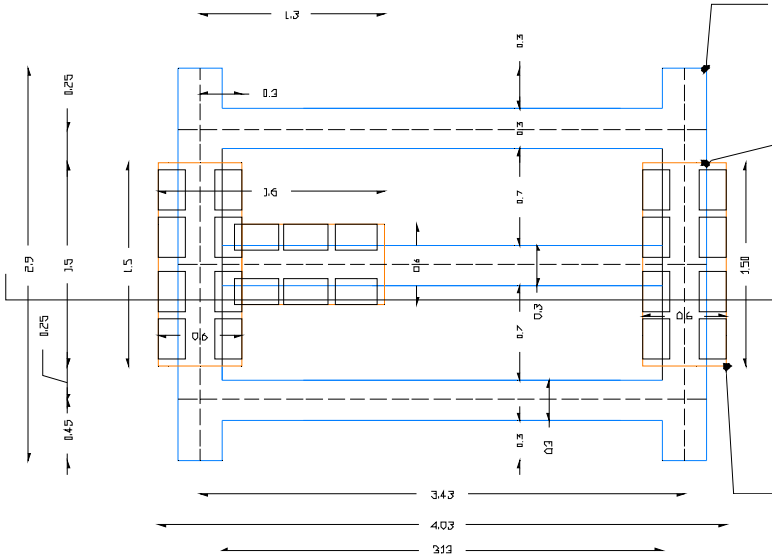

Figure 13: Masonry specimen for the study of base-isolation application in historic structures.

WP 2: Development and implementation of the methodology including development and documentation of the methodology and derivation of instructions for proper application;

WP 3: Geometrical documentation including surveying of the case-study structures, geometrical and damage documentation;

WP 4: Seismic hazard assessment including study of historic seismicity, derivation of Guttenberg-Richter curve, investigation of near-fault phenomena and development of seismic hazard curve;

WP 5: Assessment of the soil influence on seismic response including literature review, geological mapping and geotechnical investigation, seismic response analyses and soil failure analyses;

WP 6: Selection of proper monitoring system including assessment of the effectiveness of the system and installation on a case-study structure;

WP 7: In-situ surveying of materials and characterization of mechanical properties in the laboratory including application of non-destructive techniques, sampling and mapping of materials, damage and mechanical resistances, characterization of structural materials applying laboratory tests, correlation of in-situ results with laboratory results, design and construction of compatible mortars;

WP 8: Experimental evaluation of masonry characteristics including construction and testing of representative masonry wallets and assessment of their behaviour under static and seismic loading;

WP 9: Testing on the shaking table of LEE including construction of specimens, installation of base isolation and testing on shaking table until failure and comparison with the non-isolated behaviour to assess the effectiveness of base-isolation;

WP 10: Development of probabilistic models, fragility curves, evaluation of the results and preparation of recommendations/ instructions;

WP 11: Implementation of probabilistic methodology including application of the methodology on selected monumental and historic structures, correlation of analytical with experimental results and implementation of failure criteria for masonry;

WP 12: Numerical modeling and application of methodologies to determine the seismic response including correlation of the experimental results with analytical linear and non-linear deterministic methodologies and implementation on case-study structures;

WP 13: Application of seismic isolation including dynamic analysis of shaking table tested structures with and without base isolation, correlation with experimental results, analysis of case-study structure with and without base-isolation and preparation of recommendations/ instructions for seismic isolation.

Dr. Constantine Spyrakos, Professor NTU Athens, is the Project Coordinator responsible for the completion of the several stages of the work within the submitted timetable, as well as for the financial management of the project. The First Research Team coordinated by Dr. E. Vintzileou, Professor NTUA, has been responsible for the methodological development that determined the priorities of other groups and provided the theoretical framework of the activities. It has provided data to the other two research teams, through either field measurements or experimental results. The Second Research Team coordinated by Dr. A. Moropoulou, Professor NTUA has been responsible for the study and evaluation of critical parameters affecting the determination of the seismic response of monuments and historic structures. The results of the second group were essential for the continuity and reliability of the other research teams, since they were used by the first group during the experiments and by the third group as input data to complete their work packages. The Third Research Team coordinated by Dr. I. Psycharis, Professor NTUA has been responsible for the evaluation of experimental results from the shake table testing at LEE-NTUA, the development and validation of analytical models that simulated the seismic behaviour of the monuments as well as the evaluation of various methods that calculate the seismic response and estimate structural damage. Substantially, the third team was the receiver of information that was produced by the first and second teams aiming at the formulation of conclusions regarding the seismic behaviour of monuments and historic structures.

4 LEE INFRASTRUCTURE

In LEE an Earthquake Simulator with six degrees-of-freedom has been installed and used in this program. The equipment was initially calibrated and started its operation at the beginning of 1986 and has been operating ever since. The shaking table consists of a rigid steel platform with dimensions 4x4x0.6 (m) and 100 kN weight. It is capable of simultaneous vibration in all six degrees-of-freedom (6 DOFs), with vertical load capacity of 640kN and a horizontal reference at 320 kN. The maximum acceleration in both horizontal directions that can develop is 2g, while in the vertical direction is 4g. The operating frequency rate of the simulator ranges from 0.1 up to 50 Hz. The generation and processing of seismic excitations and analysis of the experimental results is performed by special signal processing programs available in the library of LEE.

An independent reaction wall is also available at the laboratory. Its capacity is 10 MNm, is 6m in height and consists of two sections each 4 and 5 m long, 1.1 m width. Several jacks are installed and may function with independent control. The jacks have capacities of 500 kN, 300 kN, 200kN and 100kN. A mobile data multi-channels acquisition system is supporting this facility. An innovative testing apparatus is also functioning at the laboratory in order to test specimens under recyclic loads horizontally applied, such as walls with up to 1.5 m height, 1.0 m long and 0.5 m thickness. The vertically applied load may be up to 1000 kN and can be kept constant without any variation throughout the tests. Innovative testing apparatus are also

functioning at the Laboratory in order to measure mechanical characteristics (compression strength, modulus of elasticity, Poisson's ratio, stress-strain curve) of masonry specimens.

Diverse instrumentation is also available for in-situ testing such as flat jacks, ambient testing, displacement strain measurements, pull-out tests, etc.

In 2000 the LEE-NTUA was certified by TUV CERT (TUV Austria Hellas), for Dynamic and Seismic Tests using the earthquake simulator, according to ISO 9002/1994. Starting on 12/1/2007, it implemented a Quality Management System for DYNAMIC SEISMIC TESTS certified by TUV Austria (the Austrian Organization of Inspection and Certification). The current relevant certification of the LEE by this organization is according to standard EN ISO 9001:2008.

In addition, LEE-NTUA has a highly experienced staff in preparing, testing and analyzing of the experimental results. The staff has over twenty five years of experience and participation in the successful completion of a multitude of national and international research programs. A representative number of international projects relevant to the proposed research are listed:

- New Integrated Knowledge based approaches to the protection of cultural heritage from Earthquake-induced Risk – NIKER (DCT - Università degli Studi di Padova).
- Seismic Engineering Research Infrastructures for European Synergies – SERIES (University of Patras/ European Commission/ Framework Programme 7).
- Performance of Innovative Mechanical Connections in Precast Building Structures under Seismic
- Conditions – SAFECAST (FP7-SME-2007-2).
- Seismic Resistance of new Reinforced or Isolated Perforated- Brick Masonry Housing Construction in Low
- Seismic Region (ECOLEADER Access to Research Infrastructures).
- Seismic Behaviour of Capacity designed masonry Walls in low Seismicity regions (ECOLEADER Access to Research Infrastructures).
- Experimental evaluation of technical interventions for reduced seismic vulnerability of old existing buildings.
- Experimental evaluation of technical interventions to reduce seismic vulnerability of masonry buildings.

ACKNOWLEDGEMENTS

The financial assistance of the research project "SEISMO" [27], that made this work possible, is gratefully acknowledged.

REFERENCES

[1] The Athens Charter for the Restoration of Historic Monuments. First International Congress of Architects and Technicians of Historic Monuments, Athens, 1931.

[2] International Council on Monuments and Sites – ICOMOS. International Charter for the Conservation and Restoration of Monuments and Sites (The Venice Charter 1964). Second International Congress of Architects and Technicians of Historic Monuments, Venice, 1964.

[3] Congress on the European Architectural Heritage, 21 - 25 October 1975: The Declaration of Amsterdam.

[4] C.C. Spyrakos, Seismic Risk of Historic Structures and Monuments: A Need for a Unified Policy. *5th ECCOMAS Thematic Conference on Computational Methods in Structural Dynamics and Earthquake Engineering (COMPDYN 2015)*, Crete Island, Greece, May 25-27, 2015.

[5] C.C. Spyrakos, P. Touliatos, D. Patsilivas, G. Pelekis, A. Xampesis, C.A. Maniatakis, Seismic analysis and retrofit of a historic masonry building, *In S. Syngellakis Editor, Retrofitting of Heritage Structures - Design and evaluation of strengthening techniques* (pp. 65-74). Southampton, UK: Wessex Institute of Technology Press, 2013.

[6] C.C. Spyrakos, P.D. Kiriakopoulos, E. Smyrou, Seismic Strengthening of the Historic Church of Sts Helen and Constantine in Piraeus. In Proceedings of the 3rd International Conference on Computational Methods in Structural Dynamics and Earthquake Engineering COMPDYN 2011. Corfu, Greece; ECCOMAS. M. Papadrakakis, M. Fragiadakis, V. Plevris eds. COMPDYN 2011, *3rd ECCOMAS Thematic Conference on Computational Methods in Structural Dynamics and Earthquake Engineering 2011*, Corfu, Greece, 25-28 May, 2011; 2401-2413.

[7] C.C. Spyrakos, A. Francioso, P.D. Kiriakopoulos, S. Papoutsellis, Seismic evaluation of the historic church of St. Nicholas in Piraeus before and after interventions. M. Papadrakakis, V. Papadopoulos, V. Plevris eds. COMPDYN 2013, *4th ECCOMAS Thematic Conference on Computational Methods in Structural Dynamics and Earthquake Engineering 2013*, Kos Island, Greece, 12–14 June 2013; 3015-3029.

[8] C.C. Spyrakos, Modern Approaches for the Earthquake Protection of Cultural Heritage Structures - Review and Proposal. *4th National Conference in Restoration*, Society for Research and Promotion of Scientific Restoration of Monuments (ETEPAM), Thessaloniki, Greece, November 26-28, 2015.

[9] C.C. Spyrakos, F. Pugi, C.A. Maniatakis, A. Franchioso, Evaluation of the dynamic response for a historic byzantine crossed-dome church through block-joint and kinematic analysis. *5th ECCOMAS Thematic Conference on Computational Methods in Structural Dynamics and Earthquake Engineering (COMPDYN 2015)*, Crete Island, Greece, May 25-27, 2015.

[10] C.C. Spyrakos, C.A. Maniatakis, P. Kiriakopoulos, A. Francioso, I.M. Taflampas, Performance of a post-Byzantine triple-domed basilica under near and far fault seismic loads: Analysis and intervention. In Asteris P.G. and Plevris V. eds. *Handbook of Research on Seismic Assessment and Rehabilitation of Historic Structures.* IGI Global Editions, 2015; Vol. II: 831-867.

[11] C.C. Spyrakos, C.A. Maniatakis, J. Taflambas, Evaluation of near source seismic records based on damage potential parameters: Case study: Greece. *Soil Dynamics and Earthquake Engineering*, **28**, 738-753, 2008.

[12] C.C. Spyrakos, C.A. Maniatakis, J. Taflambas, Critical evaluation of near field seismic records in Greece. In Syngellakis S. eds. *Earthquake Ground Motion - Input Definition for Aseismic Design*. Southampton, UK: Wessex Institute of Technology Press; 2015 (pp. 1-10).

[13] C.C. Spyrakos, *Strengthening of Structures for Seismic Loads*. Technical Chamber of Greece, 2004. (in Greek)

[14] C. Ioannidis, N. Kaskampas, F. Bourexis, Modern techniques for the three-dimensional geometric documentation of historical buildings: Implementation in the Hephaestus temple in Athens, Greece. SEISMO Research Project, 2015.

[15] G. Tsiambaos, H. Saroglou, A. Antoniou, Engineering geological and geotechnical investigation for seismic protection of monuments. *5th ECCOMAS Thematic Conference on Computational Methods in Structural Dynamics and Earthquake Engineering (COMPDYN 2015)*, Crete Island, Greece, May 25-27, 2015.

[16] I.M. Taflampas, WP4: Seismic Hazard Assessment, SEISMO Research Project, 2015.

[17] A. Moropoulou, M. Apostolopoulou, P. Moundoulas, M. Karoglou, E. Delegou, K. Lampropoulos, M. Gritsopoulou, A. Bakolas, The combination of NDTS for the diagnostic study of historical buildings: the case of Kaisariani Monastery. *5th ECCOMAS Thematic Conference on Computational Methods in Structural Dynamics and Earthquake Engineering (COMPDYN 2015)*, Crete Island, Greece, May 25-27, 2015.

[18] A. Moropoulou, M. Apostolopoulou, P. Moundoulas, E. Aggelakopoulou, L. Siouta, A. Bakolas, M. Douvika, P. Karakitsios, P. G. Asteris, The role of restoration mortars in the earthquake protection of the Kaisariani monastery. VII European Congress on Computational Methods in Applied Sciences and Engineering (ECCOMAS Congress 2016) Crete Island, Greece, June 5–10, 2016.

[19] E. Vintzileou, V. Palieraki, V. Nikolopoulou, Work Package 2: Development and implementation methodology. Deliverable: P.2.2.1: Report on implementation of the methodology in selected historical buildings or monuments and text specifications for the application of the methodology. SEISMO Research Project, 2015.

[20] C.C. Spyrakos, *Finite Element Modeling in Engineering Practice*. Pittsburg, PA, USA: Algor Publishing Division, 1995.

[21] C.C. Spyrakos, J. Raftoyiannis, *Linear and Nonlinear Finite Element Analysis*. Pittsburg, PA, USA: Algor Publishing Division, 1997.

[22] M.-E. Dasiou, I.N. Psycharis, Numerical investigation of the seismic response of Hephaestus temple in Athens, Greece. *5th ECCOMAS Thematic Conference on Computational Methods in Structural Dynamics and Earthquake Engineering (COMPDYN 2015)*, Crete Island, Greece, May 25-27, 2015.

[23] P.G. Asteris, G. Giannopoulos, P. Karakitsios, WP 11: Implementation of probabilistic methodology. Deliverable: P.11.1.1: Implementation of the methodology in particular historical buildings. SEISMO Research Project, 2015.

[24] A.A. Markou, Base isolated residential buildings: Field tests, laboratory experiments, numerical simulations. Doctoral Thesis, Institute of Statics and Dynamics, Department of Civil Engineering, Aristotle University of Thessaloniki, Greece, 2015.

[25] G.D. Manolis, A.A. Markou, A. Nikolakopoulos, G. Stefanou, WP 13: Design of Seismic Isolation. Deliverable: P.13.1.1: Description of the methodology. SEISMO Research Project, 2015.

[26] G.D. Manolis, A.A. Markou, A. Nikolakopoulos, G. Stefanou, WP 13: Design of Seismic Isolation. Deliverable: P.13.1.2: Application Examples. SEISMO Research Project, 2015.

[27] SEISMO - Seismic Protection of Monuments and Historic Structures. Thales Context - Greek Ministry of Education and Religions - The European Union, Operational Programme - Education and Lifelong Learning, NSRF 2007-2013. (webpage: http://excellence.minedu.gov.gr/thales/en/thalesprojects/380152)

ECCOMAS Congress 2016
VII European Congress on Computational Methods in Applied Sciences and Engineering
M. Papadrakakis, V. Papadopoulos, G. Stefanou, V. Plevris (eds.)
Crete Island, Greece, 5–10 June 2016

FORCED RESPONSE OF SHROUDED BLADES WITH VARIABLE OPERATING POINTS

Ferhat Kaptan[1], Lars Panning-von Scheidt[2], Jörg Wallaschek[3], Victor Salit[4]

[1,2,3]Institute of Dynamics and Vibration Research, Leibniz Universität Hannover
Appelstraße 11, 30167 Hannover, Germany
[1] kaptan@ids.uni-hannover.de
[2] panning@ids.uni-hannover.de
[3] wallaschek@ids.uni-hannover.de

[4]MAN Diesel & Turbo SE
Steinbrinkstraße 1, 46145 Oberhausen, Germany
[4] victor.salit@man.eu

Keywords: shrouded blades, nonlinear vibration, friction.

Abstract. *The variable operation of turbomachinery components turns out as a special challenge in the design process. Changing the turbines rotational speed leads to entirely new load conditions and, thus, to a range of different operating points. Beside structural mechanical dependencies (i.e. stiffening effects), the shroud contact situation is very sensitive to the systems rotational speed. In this paper a model of a real low pressure steam turbine blade is investigated numerically and experimentally. For the calculation, a three dimensional structural mechanical model including a spatial contact model is considered. The steady-state vibration response is calculated by the multi-harmonic balance method (MHBM) and an alternating frequency-time scheme (AFT). The test rig consists of a single blade clamped with two dummies at the shroud. The vibration response of the blade is measured by laser-doppler-vibrometry for various excitation levels and pressure distributions in the shroud contact. The comparison between measured and computed frequency response function (FRF) of the first edgewise bending mode (1E) shows a very good agreement. Both the frequency shift, as well as the reduction of the amplitude were detected by the MHBM and successfully verified experimentally. The obtained results of the single blade system are transferred to a rotating bladed disk assembly.*

1 INTRODUCTION

One of the main challenges in the mechanical design of turbine blades is the prevention of high cycle fatigue (HCF) failures. Successful blade design must account for both high static, caused for example by centrifugal forces, and high dynamic loads, caused, among others, by oscillating forces of the working fluid. These loads, even the static ones, depend on the turbines operating condition. However, not only the loading, but also material parameters, like the elastic modulus, and structural mechanical properties, like the damping ratio, and stiffening or softening of the blade, depend on the turbines operating condition. Indeed, material properties are temperature dependent, the tangent stiffness is stress dependent and the overall damping depends on many factors simultaneously - stress, temperature, contact pressure at the joints. Friction in the joints like the blade root or the blade tip shrouds can be used to dissipate the vibrational energy and, thus, the amplitude of the blade vibrations. However, the nonlinear dependence of the relative displacements on the contact pressure and thus on the operational condition, makes the design for friction a very challenging task.
Nonlinear steady-state forced response analysis, which can aid in such a design, has been a subject of active research for the last three decades [1–5]. However, a forced response analysis under variable operating conditions remained largely unstudied.
In this study, we analyze two different operating points with respect to the turbines rotational speed. The investigation is performed both experimentally and numerically. The experimental setup consists of a single model blade, fixed at its root, with variable contact pressure applied at the shroud through two dummies, mounted on air bearing. The blade is excited by shaker and the frequency response function (FRF) was measured using laser-doppler-vibrometry for various excitation and contact pressure levels. These results were used to verify the numerical approach, based on the multi-harmonic balance method (MHBM), described in [6] and [7], in which the nonlinear forces are computed by the means of an alternating frequency-time (AFT) scheme [8].

2 FORCED RESPONSE CALCULATION

2.1 Computation of the steady state solution by the multi-harmonic balance method

The dynamical behavior of a nonlinear mechanical system can be described by the following equation of motion in the time domain:

$$\mathbf{M}\ddot{\mathbf{u}}(t) + \mathbf{D}\dot{\mathbf{u}}(t) + \mathbf{K}\mathbf{u}(t) + \mathbf{f}_{\mathrm{nl}}(\dot{\mathbf{u}}(t), \mathbf{u}(t)) = \mathbf{f}_{\mathrm{e}}(t) \tag{1}$$

where $\mathbf{M}$, $\mathbf{D}$, $\mathbf{K}$ are the mass, viscous damping and stiffness matrices. The external force is denoted by $\mathbf{f}_{\mathrm{e}}$ and the nonlinear force by $\mathbf{f}_{\mathrm{nl}}$. For a forced response analysis, the external force $\mathbf{f}_{\mathrm{e}}$ is assumed to be a harmonic function

$$\mathbf{f}_{\mathrm{e}}(t) = \Re\left\{\hat{\mathbf{f}}_{\mathrm{e}} \mathrm{e}^{\mathrm{i}\Omega t}\right\}. \tag{2}$$

In the linear case, i.e. $\mathbf{f}_{\mathrm{nl}} = 0$, the resulting displacements, $\mathbf{u}(t)$, are harmonic functions with frequency Ω. In the presence of nonlinearities, e.g. contact forces, the response function $\mathbf{u}(t)$ is no longer harmonic, but nevertheless assumed to be periodic. This assumption allows the approximation of the displacments' vector $\mathbf{u}$, as well as the nonlinear forces $\mathbf{f}_{\mathrm{nl}}$, by a truncated Fourier series. This so-called multi-harmonic balance method (MHBM) is widely used to compute the nonlinear forces in conjunction with an alternating frequency-time scheme (AFT) [8].

Applying Galerkin's procedure the nonlinear equations of motion (1) can be rewritten in the frequency domain with the complex displacements

$$\mathbf{u}(t) = \Re\left\{\sum_{n=0}^{n_\mathrm{h}} \hat{\mathbf{u}}_n \mathrm{e}^{\mathrm{i}n\Omega t}\right\} \tag{3}$$

and the complex nonlinear forces

$$\mathbf{f}_\mathrm{nl}(t) = \Re\left\{\sum_{n=0}^{n_\mathrm{h}} \hat{\mathbf{f}}_{\mathrm{nl},n} \mathrm{e}^{\mathrm{i}n\Omega t}\right\} \tag{4}$$

as

$$\hat{\mathbf{S}}_n \hat{\mathbf{u}}_n + \hat{\mathbf{f}}_{\mathrm{nl},n} - \hat{\mathbf{f}}_{\mathrm{e},n} = \mathbf{R}_n. \tag{5}$$

Here, $\hat{\mathbf{S}}_n$ is the dynamic stiffness matrix

$$\hat{\mathbf{S}}_n = -(\Omega n)^2 \mathbf{M} + \mathrm{i}\Omega n \mathbf{D} + \mathbf{K} \tag{6}$$

and $\mathbf{R}_n$ denotes the residual vector. The set of nonlinear equations (5) constitutes a minimization problem, which has to be solved iterative by means of a Newton-Raphson algorithm. To reduce the computational effort, a model reduction of the dynamic system is performed by the well-known Craig-Bampton reduction technique [10].

2.2 Contact Model

In this study, an elastic point contact model is used to compute the nonlinear contact forces, see Fig. 1, a widely used model in dynamical systems with frictional contacts [6, 7, 11]. For the calculation of a three-dimensional spatial contact, it is assumed that the tangential components are independent of each other, a common assumption in forced response calculations with frictional contacts [7].

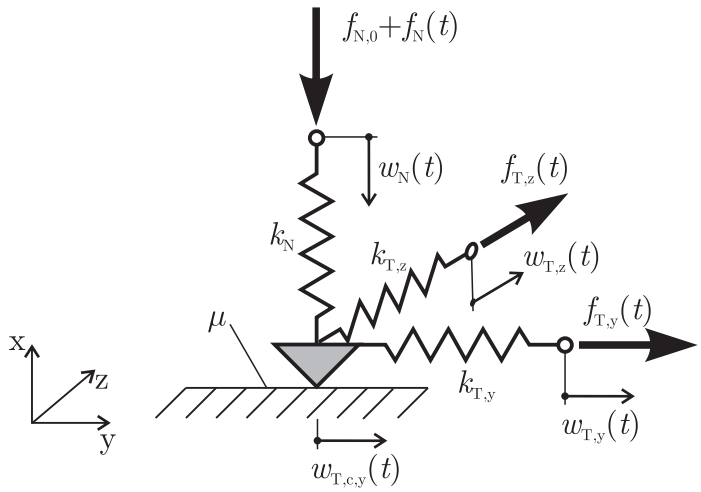

Figure 1: Unilateral elastic contact model

The normal force $f_\mathrm{N}(t)$ is given by the normal relative displacement $w_\mathrm{N}(t)$ and the contact stiffness k_N. The contact state ratio, closed or separated, depends on the static preload $f_{\mathrm{N},0}$ and

determined by the unilateral contact law

$$f_{\mathrm{N}}(t) = \max\left(f_{\mathrm{N},0} + k_{\mathrm{N}} w_{\mathrm{N}}(t), 0\right). \tag{7}$$

A negative preload value of $f_{\mathrm{N},0}$ is equivalent to a gap between the contact nodes and is defined as $g_{\mathrm{N},0} = -f_{\mathrm{N},0}/k_{\mathrm{N}}$. The contact force along the tangential directions y and z is given by the contact stiffness $k_{\mathrm{T},j}$ and the tangential relative displacement $w_{\mathrm{T},j}(t)$, for $j = y, z$. The Coulomb friction law is applied to determine the state ratio in tangential direction by

$$f_{\mathrm{T}}(t) = \begin{cases} k_{\mathrm{T},j}(w_{\mathrm{T},j}(t) - w_{\mathrm{T,c},j}(t)) & \text{sticking contact,} \\ \mu f_{\mathrm{N}}(t)\mathrm{sgn}(w_{\mathrm{T,c},j}(t)) & \text{sliding contact,} \\ 0 & \text{separation.} \end{cases} \tag{8}$$

3 APPLICATION TO SHROUDED TURBINE BLADES

3.1 Mechanical model of a single turbine blade

A model of a single low pressure shrouded turbine blade is investigated, see Fig. 2a. For convenience, the root of the blade is modeled as a rectangular block and the angular pitch is set to zero. The neighbored blades are simplified as dummies with high masses mounted by frictionless supports, see Fig. 2b. Thus, the normal load on the shroud can be stated as $f_{\mathrm{N}} = f_{\mathrm{L}} \sin\alpha$. Compared to a fully assembled bladed disk, changing the loading f_{L} is representing a

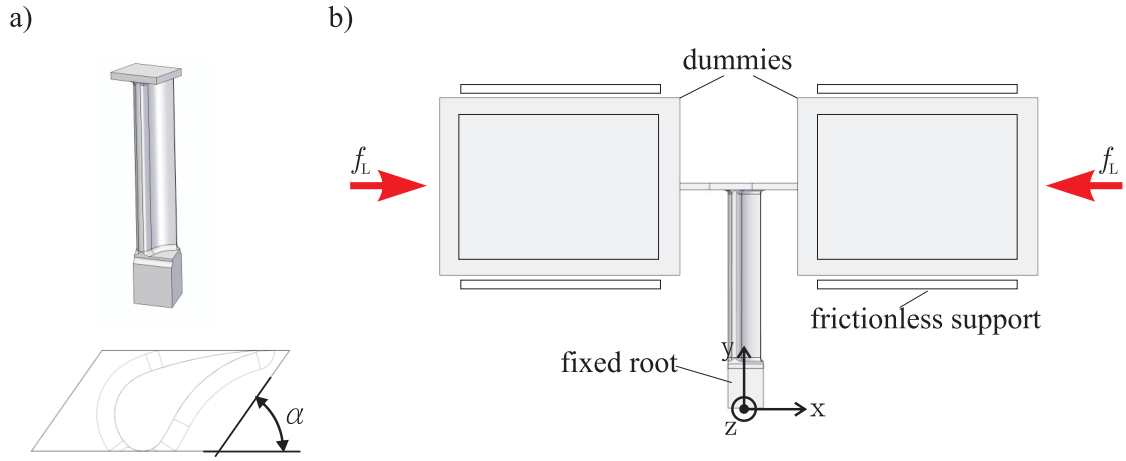

Figure 2: a) Single shrouded turbine blade, b) experimental setup.

variation of the turbine's operating point. Nevertheless, a change of the operating point of the real turbine influences in addition the pressure distribution at the shroud contact or the structural mechanical properties due to centrifugal stiffening. Since the main objective of the presented experimental setup is the correlation between excitation load f_{e}, preload f_{L} and the response of the system, here, the variation of the pressure distribution as the centrifugal stiffening is neglected.

Finite element analysis is used to discretize the shown model with a total number of 16755 elements and 28112 nodes. The shroud contact area is discretized with 30 contact nodes. The

structural mechanical matrices $\mathbf{M}$ and $\mathbf{K}$ of the whole system read:

$$\mathbf{M} = \begin{bmatrix} \mathbf{M}_{\mathrm{Blade}} & \mathbf{0} & \mathbf{0} \\ \mathbf{0} & \mathbf{M}_{\mathrm{Dummy,L}} & \mathbf{0} \\ \mathbf{0} & \mathbf{0} & \mathbf{M}_{\mathrm{Dummy,R}} \end{bmatrix}, \mathbf{K} = \begin{bmatrix} \mathbf{K}_{\mathrm{Blade}} & \mathbf{0} & \mathbf{0} \\ \mathbf{0} & \mathbf{K}_{\mathrm{Dummy,L}} & \mathbf{0} \\ \mathbf{0} & \mathbf{0} & \mathbf{K}_{\mathrm{Dummy,R},} \end{bmatrix}. \quad (9)$$

In the first instance, there are uncoupled submatrices in (9). The coupling of the substructures takes place in the nonlinear calculation by contact forces.
In this work the first flapwise bending mode (1F) and the first edgewise bending mode (1E) of the coupled system is investigated. The mode shapes of the coupled and the free standing blade are showed in Fig. 3. Note that the mode shapes are calculated assuming a rigid coupling of the linear system in the case of Fig. 3b. It should be emphasized here that a full separating of the contact is leading to a completely different dynamical system behavior. For the nonlinear forced response, contact parameters must be specified, i.e. contact stiffnesses, friction coefficient and pressure distribution. The contact stiffnesses are defined by a magnitude of 10^9 $\mathrm{N/m}$ and the friction coefficient is set for all simulations to $\mu = 0.3$. The pressure distribution is calculated by a quasi-static nonlinear FE-analysis.

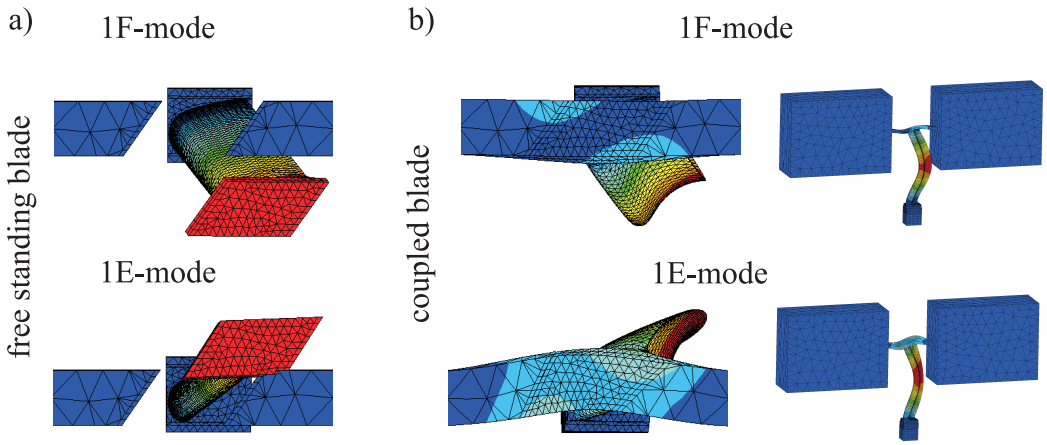

Figure 3: First two mode shapes of: a) the free standing, b) coupled blade.

3.2 Experimental Setup

The test rig in Fig. 4 is used to measure the forced response of the coupled structure. A shaker is set up for the force excitation and the vibration amplitudes are measured by laser-doppler-vibrometry. Due to the strong nonlinearities a controlled force amplitude is necessary. Hence, the excitation force is measured by a piezoelectric force sensor and controlled to the desired excitation level. Weights are applied by rope pulleys to impress the normal loading. The frequency response function is measured for various excitation levels and normal loadings. It is important to note that the measurements are based on the fundamental harmonic.

4 Results

4.1 Comparison of experiment and simulation

The experimental results show that the resonance frequencies of both modes are sensitive to a variation of the normal load f_{L}, see Fig. 5a and b. The reason for this effect depends on

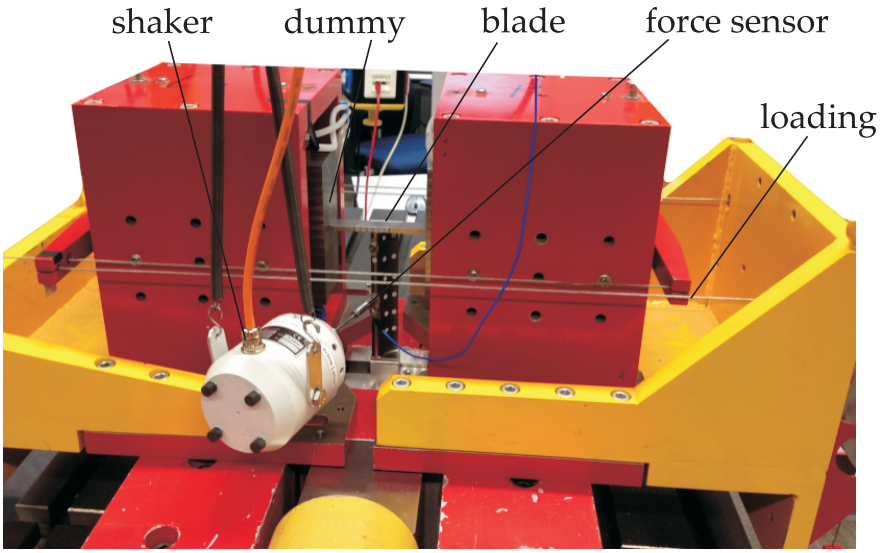

Figure 4: Test rig.

the mode shape and the contact kinematics. In Fig. 5b the maximum amplitude of the 1E-mode decreases for increasing excitation level f_{e} or decreasing normal load f_{L}, a well-known phenomenon of underplatform damper mechanics, see [9]. Due to high relative displacements in tangential direction of the shroud area sliding friction forces are leading to energy dissipation and, thus, to lower amplitudes. Besides, the resonance frequency significantly decrease due to microslip phenomena in the contact area. The 1F-mode shows a quiet different vibrational behavior. The mode shape depends highly on the contact situation and pressure distribution. Separation of the contact results to a shift of the nodal point of the mode shape and much higher amplitudes at the tip of the blade. Nevertheless, friction damping still occurs at the shroud area that is more dominant for lower normal loads, see Fig. 5a. A comparison to the simulation results shows a good agreement. The amplitudes are in the same order of magnitude and, in particular, a relative error of the resonance frequencies of $\frac{\Delta f}{f_0} < 1\%$ is remarkable. In addition, the amplitude reduction caused by friction of the 1E-mode correlates well to the experiment, see Fig. 5b. Note that the amplitude reduction depends on the friction coefficient, which is set to $\mu = 0.3$. The reduction of the resonance frequency due to microslip can also be shown by the simulation model. The simulation results of the 1F-mode show the same dynamical behavior as the experiment, see Fig. 5a. According to Eq. (7) either low normal preloads or high relative displacements lead to separation and at the same time to a loss of contact stiffness. Consequently the FRFs tend to tilt to the left side. However, the increase of the amplitude caused by a change of the mode shape can not be shown by the simulation model. This is motivated by the underlying Craig-Bampton reduction technique [10]. Here, the constraint interfaces are defined by the contact areas and, thus, the fixed interface modes are based on the coupled system.

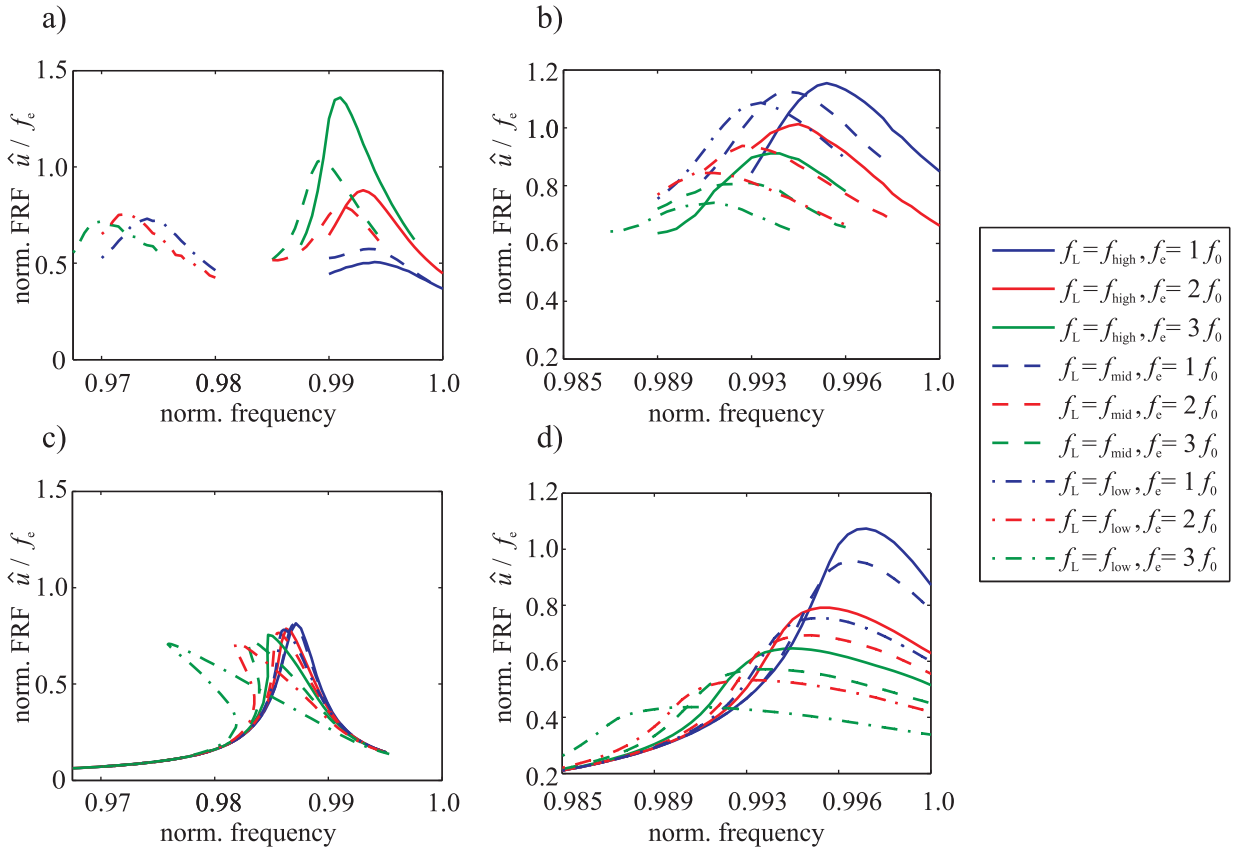

Figure 5: Forced response functions of the experiment a), b) and the simulation c), d) for various excitation levels and preloads.

4.2 Computation of a tuned bladed disk assembly

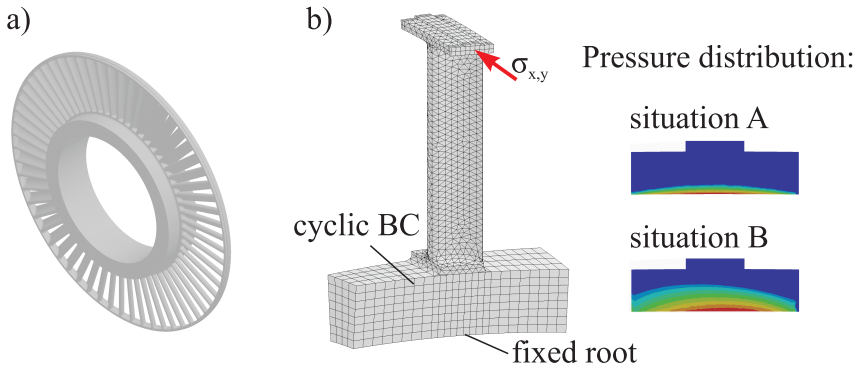

Figure 6: a) Bladed disk assembly, b) FE-model of a cyclic sector and calculated pressure distribution.

In this section a bladed disk with $N_{\mathrm{Seg}} = 60$ blades is analyzed, see Fig. 6a. All blades are assumed to be perfectly tuned and, thus, cyclic symmetry can be used to reduce the computational effort. Two different operating points with respect to the pressure distribution at the shroud contact are investigated, see Fig. 6b. For the forced response analysis Eq. 1 is set up for

one cyclic segment. The displacement vector for any segment k is

$$^{(k)}\mathbf{u}(t) = \mathrm{e}^{-\mathrm{i}(k-1)\Delta\varphi\ (1)}\mathbf{u}(t) \tag{10}$$

where $k = 1(1)N_{\mathrm{Seg}}$ and $\Delta\varphi = 2\pi/N_{\mathrm{Seg}}$ denotes the phase angle [12].
The results of the bladed disk assembly show similar characteristics as the single blade system, see Fig. 7. For pressure distribution A only the lower edge of the shrouds is in contact and the total preload is concentrated on the edge. The FRFs of the 1F-mode show strong nonlinear characteristics, see Fig. 7a. Due to the high normal relative displacement the contact closes and the stiffness of the dynamical system increases strongly. Increasing the excitation force or decreasing the preload is leading to lower maximum amplitudes due to frictional energy dissipation. Changing the pressure distribution, the FRF of the 1F-mode seems to be strongly influenced, see Fig. 7b. Again, an increase of the excitation level leads to lower amplitudes and a shift of the frequency at maximum amplitude. But, at a low preload value local separation of the contact appears and the FRF is tending to lower frequencies. The occurrence of a closing and a separating contact at once have a high impact on the convergence behavior. Care must be taken when choosing numerical parameters. The 1E-mode of the cyclic system is rarely influenced by the variable pressure distribution, see Fig. 7b and d. Both cases show the same behavior as the single blade system in Fig. 5d. The slight increase of the resonance frequencies at pressure distribution B is caused by increased initial contact area and, thus, by higher stiffness.

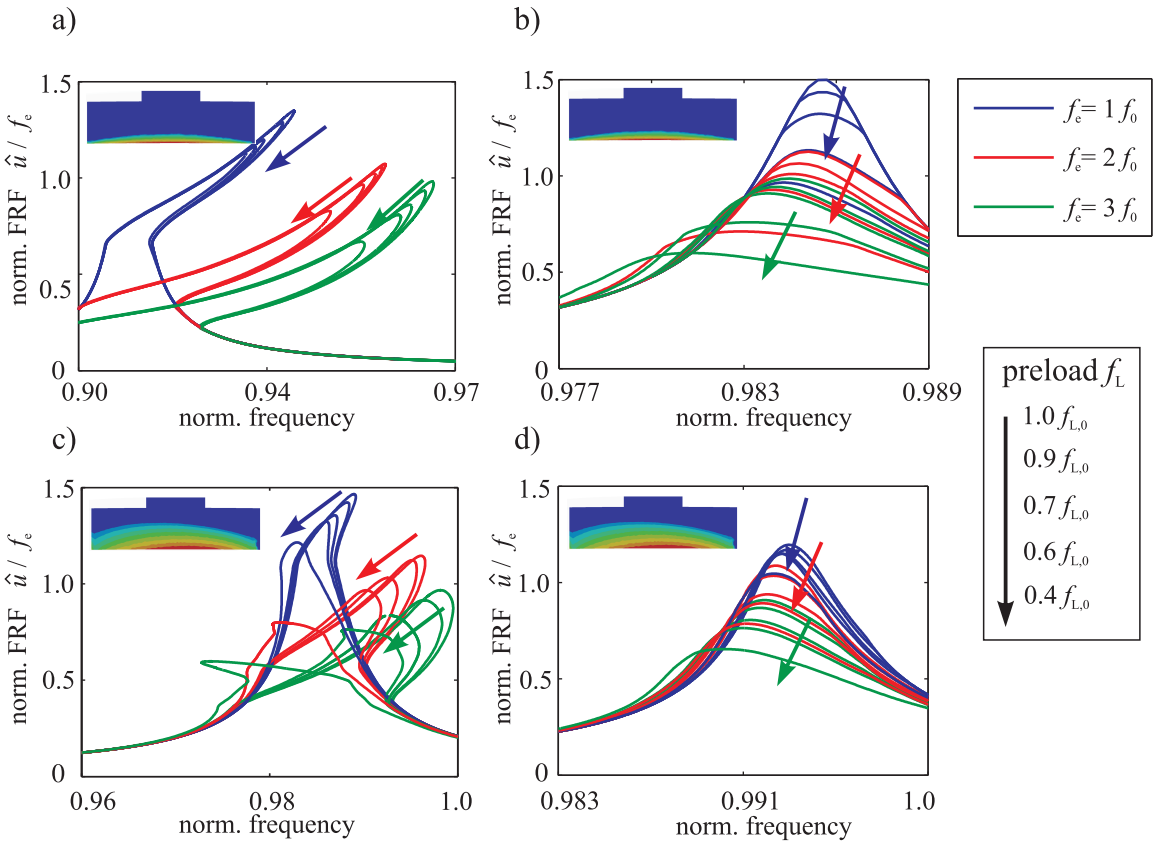

Figure 7: FRF of the 1F- and 1E-mode of the cyclic system (nodal diameter=25) for various preloads and excitation levels: a), b) pressure distribution A, c), d) pressure distribution B.

5 Conclusion and outlook

In this paper the dynamical behavior of a turbine blade model is analyzed numerically and experimentally. A comparison shows a very good agreement, qualitatively as well as quantitatively. The results are transferred to a rotating bladed disk. Two different operating points with respect to the pressure distribution are investigated showing similar phenomena as the single blade system. Regarding variable operating points turns out as a special challenge due to a high sensitivity by minor changes in the shroud contact. In particular, large relative displacements in normal direction may affect the convergence. The outlook of the work is the experimental investigation of a rotating bladed disk assembly for various operating points, i.e. rotational speed.

Acknowledgements. The investigations were conducted as part of the joint research programme COOREFlex-turbo in the frame of AG Turbo. The work was supported by the Bundesministerium für Wirtschaft und Technologie (BMWi) as per resolution of the German Federal Parliament under grant number 03ET7020K. The authors gratefully acknowledge AG Turbo and MAN Diesel & Turbo SE for their support and permission to publish this paper. The responsibility for the content lies solely with its authors.

REFERENCES

[1] Menq, C.-H., Griffin, J. H., Bielak, J.: *The forced response of shrouded fan stages.* Journal of Vibration and Acoustics 108.1: 50-55, 1986.

[2] Yang, B. D., Menq, C.-H.: *Modeling of friction contact and its application to the design of shroud contact.* Journal of Engineering for Gas Turbines and Power (Trans. ASME), Vol. 119, no. 4, pp. 958-963, 1997.

[3] Sextro, W.: *The calculation of the forced response of shrouded blades with friction contacts and its experimental verification.* ASME-Paper 2000-GT-540, Proceedings of the ASME Turbo Expo 2000, Munich (Germany), 2000.

[4] Szwedowicz, J., Sextro, W., Visser, R., Masserey, P. A.: *On forced vibration of shrouded turbine blades.* ASME-Paper GT2005-69062, Proceedings of the ASME Turbo Expo 2003, Atlanta (USA), 2003.

[5] Krack, M., Herzog, A., Panning-von Scheidt, L., Wallaschek, J., Siewert, C., and Hartung, A.: *Multiharmonic Analysis and Design of Shroud Friction Joints of Bladed Disks Subject to Microslip.* ASME 2012 International Design Engineering Technical Conferences and Computers and Information in Engineering Conference. American Society of Mechanical Engineers, 2012.

[6] Petrov, E. P., Ewins, D. J.: *Analytical Formulation of Friction Interface Elements for Analysis on Nonlinear Multi-Harmonic Vibrations of Bladed Discs Discs.* ASME-Paper GT-2002-30325, Proceedings of the ASME Turbo Expo 2002, Amsterdam, Netherlands, 2002.

[7] Siewert, C., Panning-von Scheidt, L., Wallaschek, J., Richter, C.: *Multiharmonic forced response analysis of a turbine blading coupled by nonlinear contact forces.* Paper GT2009-59201, Proc. of ASME Turbo Expo 2009: Power for Land, Sea and Air, GT2009, June 8-12, Orlando, Florida, USA, 2009.

[8] Cameron, T. M., Griffin, J. H.: *An Alternating Frequency/Time Domain Method for Calculating the Steady-State Response of Nonlinear Dynamic Systems.* Journal of Applied Mechanics, Vol. 56, pp. 149-154, 1989.

[9] Panning, L.: *Auslegung von Reibelementen zur Schwingungsdämpfung von Turbinenschaufeln.* Fortschrittberichte VDI, Reihe 11: Schwingungstechnik, Nr. 328,VDI-Verlag, Düsseldorf, 2005

[10] Craig, R. R., Bampton, M. C. C.: *Coupling of Substructures for Dynamic Analyses.* AIAA Journal, 6(7), pp. 13131319, 1968.

[11] Cigeroglu, E., An, N., Menq, C. H.: *A Microslip Friction Model with Normal Load Variation induced by Normal Motion.* Nonlinear Dynamics, Vol. 50(3), pp. 609-626, 2007.

[12] Thomas, D. L.: *Dynamics of Rotationally Periodic Structures.* International Journal for Numerical Methods in Engineering, Vol. 14, pp. 81-102, 1979.

ECCOMAS Congress 2016
VII European Congress on Computational Methods in Applied Sciences and Engineering
M. Papadrakakis, V. Papadopoulos, G. Stefanou, V. Plevris (eds.)
Crete Island, Greece, 5–10 June 2016

GEOMETRY EFFECTS ON THE NONLINEAR OSCILLATIONS OF VISCOELASTIC CYLINDRICAL SHELLS

Zenon J. G. N. del Prado[1], Marco Amabili[2], Paulo B. Gonçalves[3] and Frederico Da Silva[1]

[1] Escola de Engenharia Civil, Universidade Federal de Goiás, UFG
Av. Universitária, s/n, Setor Universitário, 74605-200, Goiânia, GO, Brazil
e-mail: {zenon, silvafma}@ufg.br

[2] Department of Mechanical Engineering, McGill University
817 Sherbrooke Street West, H3A 0C3, Montreal, Canada
e-mail: marco.amabili@mcgill.ca

[3] Catholic University of Rio de Janeiro, Department of Civil Engineering
Rua Marquês de São Vicente, 225, Gávea, 22453-900, Rio de Janeiro, RJ, Brazil
e-mail: paulo@puc-rio.br

Keywords: Cylindrical shells, viscoelastic material, Kelvin-Voigt model, lateral loads, non-linear vibrations.

Abstract. *In this work the influence of geometry, load and material properties on the non-linear vibrations of a simply supported viscoelastic circular cylindrical shell subjected to lateral harmonic load is studied. Donnell's non-linear shallow shell theory is used to model the shell, assumed to be made of a Kelvin-Voigt material type, and a modal solution with six degrees of freedom is used to describe the lateral displacements. The Galerkin method is applied to derive a set of coupled non-linear ordinary differential equations of motion. Obtained results show that the viscoelastic dissipation parameter has significant influence on the instability loads and resonance curves.*

1 INTRODUCTION

Circular cylindrical shells have been extensively used in modern industrial applications and have made their analysis an important research area in applied mechanics and biomechanics. Viscoelastic materials are frequently used in sandwich structures such as beams, plates and shells where damping is desired for a wide range of frequencies. However, in spite of a large number of studies on cylindrical shell dynamics, just a small number of these works is related to the analysis of viscoelastic shells.

An approximate theory for the linear dynamic response of viscoelastic cylindrical shells and cylindrical laminated composites with viscoelastic layers was proposed [1]. Also, ed the finite element method was applied to study the vibration of damped viscoelastic shells based on a first-order shear deformation theory including rotation around the normal [2]. A finite element formulation was developed to study the damping effects due to a constrained viscoelastic layer on the natural frequencies and loss factors of empty and fluid filled cylindrical shells [3].

Later, the dynamic behavior of viscoelastic cylindrical shells subjected to axial loads using the Von Kármán-Donnell non-linear shell theory, together with the Boltzmann laws to model the linear viscoelastic material was studied and observing the complex non-linear responses of the shell such as hyperchaos, chaos, strange attractors, and limit cycles [4]. The post buckling behavior of imperfect cylindrical panels considering a non-linear Schapery viscoelastic material was considered. It was possible to observe that, if linear viscoelastic and non-linear viscoelastic models are compared, the non-linear viscoelastic constitutive model predicts higher deflections than the linear viscoelastic ones [5].

After, a general methodology looking to describe the non-linear vibrations of viscoelastic shell structures, considering periodic or damped responses through the coupling of the harmonic balance method with one mode Galerkin discretization was considered [6]. The radial motions of compressible non-linearly viscoelastic cylindrical and spherical shells under lateral time-dependent pressures [7]. Considering temperature effects, the thermal post-buckled characteristics of cylindrical composite shells with viscoelastic layers by applying the finite element method considering transversal shear deformation and variable in-plane displacements through the thickness of the shell [8].

The problem of dynamic stability of viscoelastic, extremely shallow, circular cylindrical shells considering any viscoelastic functions as well as the inclusion of time-dependence of Poisson's ratio was also considered [9]. Forced vibrations of elastic and viscoelastic arches, panels and cylindrical shells using an asymptotic numerical method was studied in [10]. In the analysis, a mathematical formulation was developed in order to take into account various viscoelastic models in the frequency domain.

In a series of papers [11, 12, 13, 14, 15, 16] the vibrations and dynamic stability of viscoelastic cylindrical shells and cylindrical panels, with and without concentrated masses, using the Kirchhoff-Love hypothesis and Timoshenko theories and taking into account shear deformation and rotary inertia were considered.

Based on the profile of displacement fields of the core layer in static deformation, a new higher-order expansion of transverse and in-plane displacement fields in the thickness direction of the core layer was developped [17].

Recently, a detailed literature review of current studies on non-linear vibrations of shells where, a reduced number of studies dedicated to the analysis of viscoelastic cylindrical shells can be confirmed [18].

In the present paper, the influence of geometric relations, load and material properties on the non-linear vibrations and dynamic instability of a simply supported viscoelastic circular

cylindrical shells subjected to lateral harmonic load is studied. Donnell's non-linear shallow shell theory is used to model the shell, which is assumed to be made of a Kelvin-Voigt material type, and a modal solution with six degrees of freedom. The Galerkin method is applied to derive a set of coupled non-linear ordinary differential equations of motion that are, in turn, solved by the Runge-Kutta method. Results show that the viscoelastic dissipation parameter has a very significant influence on the instability loads and resonance curves.

2 MATHEMATICAL FORMULATION

Consider a perfect thin-walled simply supported circular cylindrical shell of radius *R*, length *L* and thickness *h*. The axial, circumferential and radial coordinates are denoted by x, $y = R\theta$ and *z*, respectively, and the corresponding displacements of the shell middle surface are denoted by *u*, *v* and *w*, as shown in Figure 1. The shell is assumed to be made of a Kelvin-Voigt viscoelastic material with initial Young's modulus *E*, Poisson ratio ν, and density ρ.

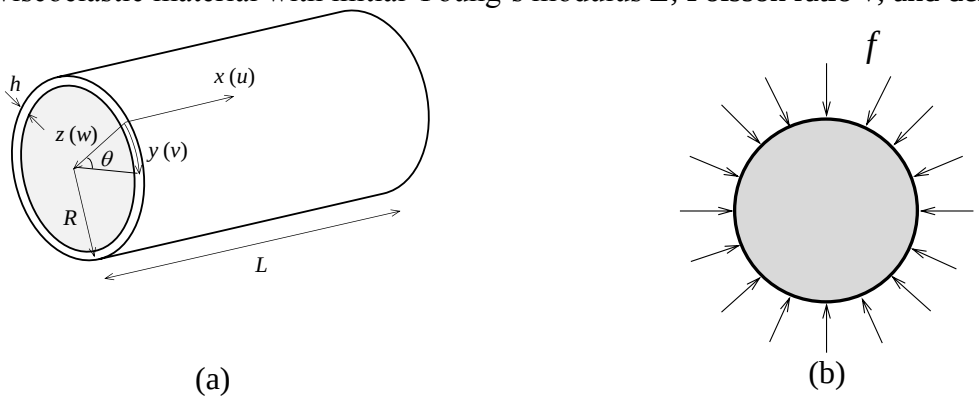

Figure 1: Shell characteristics. (a) Shell geometry; (b) Harmonic lateral pressure f.

The shell is subjected to the following harmonic lateral pressure:

$$f = F_L h^2 \rho \omega_o^2 \sin\left(\frac{m\pi x}{L}\right)\cos(n\theta)\cos(\omega_L t) \tag{1}$$

where F_L is the nondimensional coefficient of the amplitude of the load, ω_o is the natural frequency of the shell, *m* ,the number of axial half-waves, *n*, the circumferential wave number, ω_L , the frequency of the load and t the time.

Based on Donnell shallow-shell theory, the middle surface kinematic relations are given, in terms of the three displacement components, by:

$$\varepsilon_{x,0} = u_{,x} + \frac{1}{2}w_{,x}^2, \qquad \varepsilon_{\theta,0} = \frac{v_{,\theta}}{R} - \frac{w}{R} + \frac{1}{2}\frac{w_{,\theta}^2}{R^2}, \qquad \gamma_{x\theta,0} = \frac{u_{,\theta}}{R} + v_{,x} + w_{,x}\frac{w_{,\theta}}{R},$$
$$\chi_{xx} = -w_{,xx}, \qquad \chi_{\theta\theta} = -\frac{w_{,\theta\theta}}{R^2}, \qquad \chi_{x\theta} = -\frac{w_{,x\theta}}{R}, \tag{2}$$

where $\varepsilon_{x,0}$ and $\varepsilon_{\theta,0}$ are the strains in the axial and circumferential directions, $\gamma_{x\theta,0}$ is the shearing strain component at a point on the shell middle surface, χ_{xx} and $\chi_{\theta\theta}$ are the curvature changes and $\chi_{x\theta}$ is the twist.

The strain components ε_{xx}, $\varepsilon_{\theta\theta}$ and $\gamma_{x\theta}$ at an arbitrary point of the shell are related to the middle surface strains $\varepsilon_{x,0}$, $\varepsilon_{\theta,0}$ and $\gamma_{x\theta,0}$ and to the changes in the curvature by the following relations:

$$\varepsilon_{xx} = \varepsilon_{x,0} + z\chi_{xx}, \qquad \varepsilon_{\theta\theta} = \varepsilon_{\theta,0} + z\chi_{\theta\theta}, \qquad \gamma_{x\theta} = \gamma_{x\theta,0} + z\chi_{x\theta}. \tag{3}$$

In this analysis, the viscoelastic behavior of the material is modeled in the base of the Kelvin-Voigt viscoelastic theory. This viscoelastic model can be represented by a viscous damper element and an elastic spring element connected in parallel as illustrated in Fig. 2.

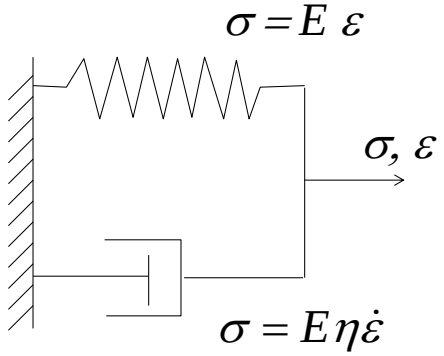

Figure 2. Kelvin – Voigt viscoelastic model

Considering the plane stress problem and the Kelvin-Voigt constitutive model of a viscoelastic material, the stress-strain relations can be written as [19]:

$$\sigma_{xx} = \frac{E}{1-\nu^2}\left[\varepsilon_{xx} + \nu\,\varepsilon_{\theta\theta} + \eta\frac{d}{dt}\left(\varepsilon_{xx} + \nu\,\varepsilon_{\theta\theta}\right)\right] \tag{4}$$

$$\sigma_{\theta\theta} = \frac{E}{1-\nu^2}\left[\varepsilon_{\theta\theta} + \nu\,\varepsilon_{xx} + \eta\frac{d}{dt}\left(\varepsilon_{\theta\theta} + \nu\,\varepsilon_{xx}\right)\right] \tag{5}$$

$$\sigma_{x\theta} = \frac{E}{2(1+\nu)}\left[\gamma_{x\theta} + \eta\frac{d}{dt}\left(\gamma_{x\theta}\right)\right] \tag{6}$$

where E is the Young's modulus , ν is the Poisson coefficient, t is the time and η is the coefficient of the viscoelastic dissipation parameter, also named retardation time, and it is measured in seconds.

Using the stress function F, the forces in the axial, circumferential and tangential directions are

$$N_x = \frac{1}{R^2}\frac{\partial^2 F}{\partial\theta^2}, \qquad N_\theta = \frac{\partial^2 F}{\partial x^2}, \qquad N_{x\theta} = -\frac{1}{R}\frac{\partial^2 F}{\partial x\,\partial\theta} \tag{7}$$

The non-linear equation of motion, based on the Donnell shallow shell theory, in terms of a stress function F, the lateral displacement w is given by:

$$\begin{aligned}&\frac{Eh^3}{12(1-\nu^2)}\left[\frac{\partial^4 w}{\partial x^4} + \frac{2}{R^2}\frac{\partial^4 w}{\partial x^2\,\partial\theta^2} + \frac{1}{R^4}\frac{\partial^4 w}{\partial\theta^4}\right] + \frac{Eh^3}{12(1-\nu^2)}\eta\frac{\partial}{\partial t}\left[\frac{\partial^4 w}{\partial x^4} + \frac{2}{R^2}\frac{\partial^4 w}{\partial x^2\,\partial\theta^2} + \frac{1}{R^4}\frac{\partial^4 w}{\partial\theta^4}\right]\\ &+ c\,h\frac{\partial w}{\partial t} + \rho\,h\frac{\partial^2 w}{\partial t^2} = f + \frac{1}{R^2}\frac{\partial^2 F}{\partial\theta^2}\frac{\partial^2 w}{\partial x^2} - 2\frac{1}{R^2}\frac{\partial^2 F}{\partial x\,\partial\theta}\frac{\partial^2 w}{\partial x\,\partial\theta} + \frac{\partial^2 F}{\partial x^2}\left(\frac{\partial^2 w}{R^2\,\partial\theta^2} + \frac{1}{R}\right)\end{aligned} \tag{8}$$

where $c = 2\zeta\rho\omega_o$ (kg/m^3 s) is the viscous damping coefficient, ζ is the viscous damping ratio of the shell and f is the radial pressure applied to the surface of the shell due to external

force. In equation (8) a global viscous damping has been introduced in addition to the viscoelasticity of the shell material.

The compatibility equation is given by

$$\frac{\partial^4 F}{\partial x^4}+\frac{2}{R^2}\frac{\partial^4 F}{\partial x^2\partial\theta^2}+\frac{1}{R^4}\frac{\partial^4 F}{\partial\theta^4}=E\,h\left[-\frac{1}{R}\frac{\partial^2 w}{\partial x^2}+\frac{1}{R^2}\left(\frac{\partial^2 w}{\partial x\partial\theta}\right)^2-\frac{1}{R^2}\frac{\partial^2 w}{\partial x^2}\frac{\partial^2 w}{\partial\theta^2}+\right.$$
$$\left.\eta\left(-\frac{1}{R^2}\frac{\partial^3 w}{\partial x^2\partial t}\frac{\partial^2 w}{\partial\theta^2}-\frac{1}{R^2}\frac{\partial^2 w}{\partial x^2}\frac{\partial^3 w}{\partial\theta^2\partial t}-\frac{1}{R}\frac{\partial^3 w}{\partial x^2\partial t}+\frac{2}{R^2}\frac{\partial^3 w}{\partial x\partial\theta\partial t}\frac{\partial^2 w}{\partial x\partial\theta}\right)\right]. \tag{9}$$

The simply supported out-of-plane (Eq. 10) and the in-plane (Eq. 11) boundary conditions are respectively given by:

$$w=0,\qquad M_x=0\qquad \text{at } x=0,L \tag{10}$$

$$N_x=0,\qquad v=0\qquad \text{at } x=0,L \tag{11}$$

For a formulation based on a stress function, the in-plane boundary conditions are satisfied on the average by introducing the following conditions, as justified, for example, in [20, 21, 22, 23, 24]

$$\int_0^{2\pi} N_x R\,d\theta=0\qquad \text{at } x=0,L \tag{12}$$

$$\int_0^{2\pi}\int_0^{L} N_{x\theta} R\,d\theta=0\qquad \text{at } x=0,L \tag{13}$$

Equation (12) assures a zero axial force *Nx* on the average, while Eq. (13) is satisfied when *u* and *w* are continuous in θ on average, and *v* = 0 on average at both ends.

In this work, the following modal expansion for the lateral displacements $w(x,\theta,t)$ in terms of the circumferential and axial variables is adopted:

$$w(x,\theta,t)=\xi_1(t)h\sin\left(\frac{m\pi x}{L}\right)\cos(n\theta)+\xi_2(t)h\sin\left(\frac{m\pi x}{L}\right)\sin(n\theta)+$$
$$\xi_3(t)h\sin\left(\frac{m\pi x}{L}\right)+\xi_4(t)h\sin\left(\frac{3m\pi x}{L}\right)+\xi_5(t)h\sin\left(\frac{5m\pi x}{L}\right)+ \tag{14}$$
$$\xi_6(t)h\sin\left(\frac{7m\pi x}{L}\right)$$

where $\xi_1(t)$, $\xi_2(t)$, $\xi_3(t)$, $\xi_4(t)$, $\xi_5(t)$ and $\xi_6(t)$ are the time-dependent non-dimensional modal amplitudes, where the shell thickness *h* has been used as non-dimensionalization parameter. This leads to a six-degrees-of-freedom reduced order model. This modal expansion satisfies the out-of-plane boundary conditions (10) and includes the basic vibration mode, the companion mode and four axi-symmetric modes and has been thoroughly tested in [20, 21, 24].

The solution for the stress function may be written as $F = F_h + F_p$, where F_h is the homogeneous solution and F_p, the particular solution. The particular solution F_p is obtained analytically by substituting the assumed form of the lateral displacement, Eq. (14), on the right-hand side of the compatibility equation, Eq. (9), and by solving the resulting partial differential equation together with the relevant boundary and continuity conditions.

The homogeneous part of the stress function can be written as (Amabili et al, 1999):

$$F_h = \frac{1}{2}\tilde{N}_x R^2 \theta^2 + \frac{1}{2}x^2\left\{\tilde{N}_\theta - \frac{1}{2\pi R L}\int_0^L\int_0^{2\pi}\frac{\partial^2 F_p}{\partial x^2} R\, d\theta\, dx\right\} - \tilde{N}_{x\theta} xR\theta \tag{15}$$

where $\tilde{N}_x$, $\tilde{N}_\theta$ and $\tilde{N}_{x\theta}$ are the in-plane restrain stresses at the ends of the shell.

Upon substituting the modal expressions for F and $w(x, \theta, t)$ into the equation of motion, Eq. (8), and applying the Galerkin method, a set of six non-linear ordinary differential equations is obtained in terms of the time-dependent modal amplitudes, $\xi_i(t)$.

In analysis, the following non-dimensional parameters are used for time and shell frequency:

$$\tau = \omega_o t; \qquad \Omega = \omega_L / \omega_o \tag{16}$$

3 NUMERICAL RESULTS

Consider a simply supported viscoelastic cylindrical shell with the following physical and geometrical properties: R = 0.2 m, L = 0.4 m, ρ = 1340.0 kg/m^3, ν = 0.195, E = 45.5e9 N/m^2 [25], ζ = 0.001.

To study the influence of geometry on nonlinear dynamic behavior of the orthotropic shells, Table 1 displays the selected L/R ratio, R/h ratios, associated longitudinal and circumferential wavenumber and natural frequencies which will be used on the foregoing analysis.

L/R	R/h	(m,n)	ω_o (rad/sec)
2,0	100	(1,5)	3447.29
	300	(1,7)	2007.06
	600	(1,8)	1427.86

Table 1: Selected shell geometries

To try to understand the influence of both the viscoelastic dissipation parameter and the lateral load on the non-linear dynamic behavior of the shell, several resonance curves and time responses have been computed. The bifurcation diagrams were obtained using Poncaré mapping and considering the excitation frequency as control parameter. The nondimensional coefficient of the amplitude of the lateral load F_L was assumed as 0.2; for the coefficient of the viscoelastic dissipation parameter of the Kelvin-Voigt model η, the following values were assumed: 0.0, 1.0e-5, 2.0e-5 and 3.0e-5 and 1.0e-4 s.

Figure 3 displays the resonance curves of driven mode for F_L = 0.2; L/R = 2.0; R/h=100 and increasing values of the dissipation parameter. As it can be observed in Fig. 3(a), for a shell without viscoelasticity (η = 0.0), as the frequency parameter Ω is increased the shell displays small amplitude period oscillations (1T). At excitation frequency near Ω = 0.90 the shell displays a jump from small to large amplitude oscillations displaying softening behavior. As the value of Ω is increased, the shell shows a reduction of the amplitude of oscillations.

Now, when the viscoelastic dissipation parameter is considered ($\eta \neq 0$), the non-linear behavior of the shell is strongly influenced. Figure 3(b) shows the resonance curve for η = 1.0e-5 s and as the frequency parameter Ω is increased, the shell displays small amplitude 1T period oscillations. Again at a value close to Ω = 0.90, the shell displays a jump to large amplitude oscillations with strong softening behavior. Then, for Ω between 0.72 and 0.77, the shell displays three different stable equilibrium points, which means that there will be three stable

attractors. At large amplitude a folding of the backbone curve (turning point) associated with large bending effects occurs.

When η is increased to 2.0e-5 s as shown if Fig. 3(c), the resonance curve is again affected and it shows softening behavior but with smaller vibration amplitudes than for the previous case. Also, in Figs. 3(b) and 3(c) for Ω=1.0 the shell displays a bifurcation point where the unstable path is linked to the large vibrations amplitudes path. Now, in Fig. 3(d) for n = 3.0e-5 s, the shells displays only small amplitude vibrations without any jump.

Figure 4 displays the resonance curves for F_L = 0.2; L/R = 2.0; R/h=300 and increasing values of the dissipation parameter. Now, in Fig. 4(a) for η = 0.0, as the frequency parameter Ω is increased the shell displays small amplitude period oscillations (1T). At excitation frequency near Ω = 0.92 the shell displays a jump from small to large amplitude oscillations displaying softening behavior, as can be observed, the vibrations amplitudes for this case are higher than those of Fig. 3(a) showing the great influence of geometric relations on the non-linear oscillations of the shell. For this case, it is also possible to observe a bifurcation point near to Ω = 1.00 where stable solutions coexist.

Now, if dissipation parameter is considered ($\eta \neq 0.0$), Fig. 4(b) the shells depicts the resonance curve for η = 1.0e-5s, as can be observed, there is softening behavior with large amplitude 1T oscillations with similar behavior as Fig. 4(a). Now, if dissipation parameter is increased to η = 2.0e-5s as displayed on Fig. 4(c), the non-linear response of the shell is affected and the shell displays softening behavior with smaller amplitude oscillations and the coexistence of stable and chaotic vibrations. When dissipation parameter is increased up to η = 3.0e-5s as shown in Fig. 4(d), the system displays a jump with softening behavior but again with smaller vibration amplitudes that in previous cases.

Finally, Fig. 5 depicts the resonance curves considering F_L = 0.2; L/R = 2.0; R/h=300. In Fig. 5(a) the dissipation parameter is not considered (η = 0.0) and, as observed, the shell displays softening behavior with very large amplitude if compared with previous cases. In Fig. 5(b), Fig. 5(c) and Fig. 5(d) the shell always shows softening behavior but only with 1T stable oscillations. For η = 3.0e-5s as seen in Fig. 5(d), the amplitude of oscillations are smaller than in Fig. 5(b) or Fig. 5(c).

From these diagrams, it is possible to see the strong influence that geometry ratios and dissipation parameter have on the non-linear dynamic response of the shell. For a shell with low R/h ratio the shell displays smaller vibration amplitudes than a shell with high R/h ratio. When dissipation parameter is considered, for low values the amplitude of oscillations of the shell are increased even knowing that this parameter is a dissipation, for higher values of the parameter the vibration amplitudes of the shell will be reduced.

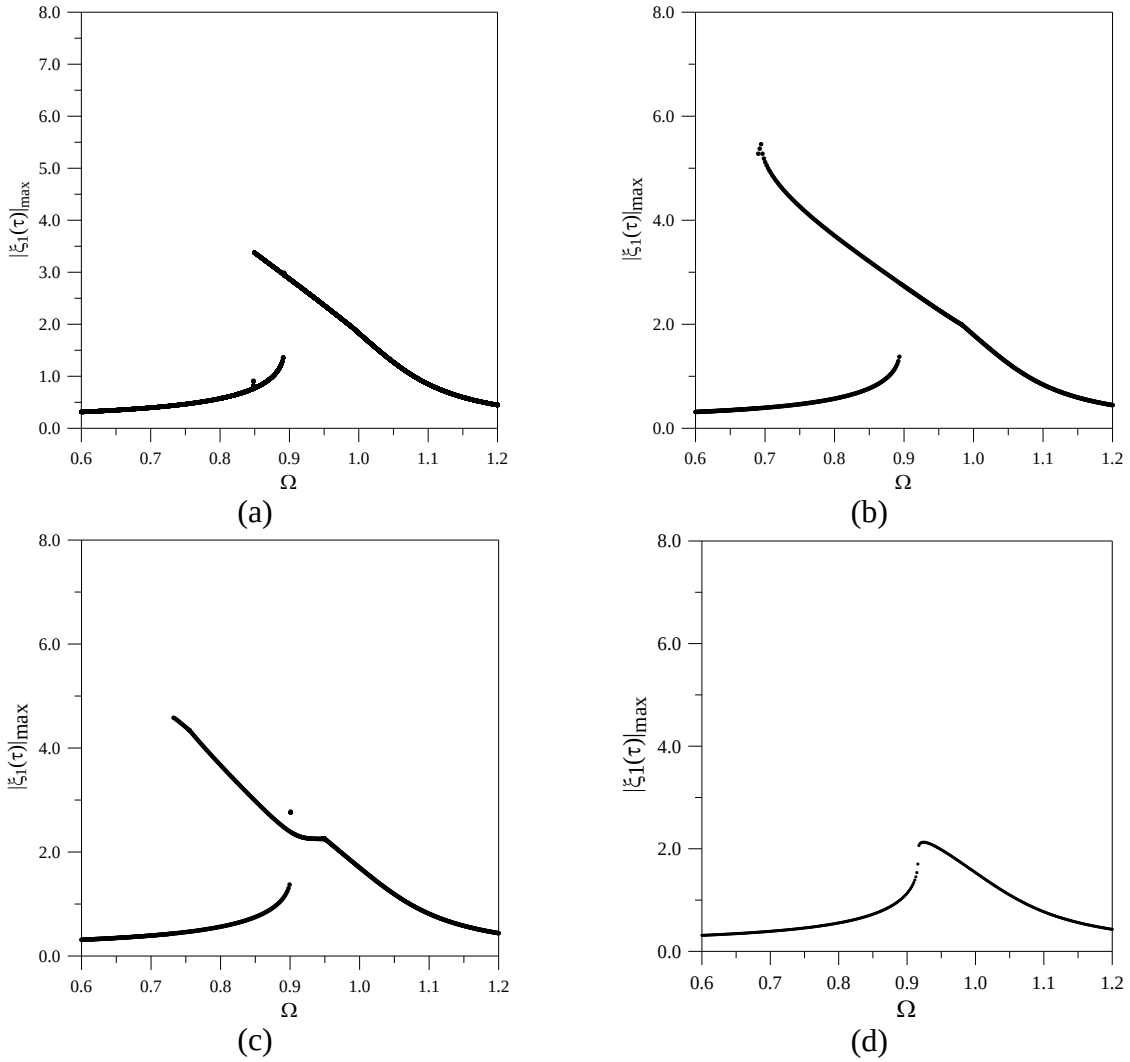

Figure 3. Ressonance curves for L/R = 2,0 and R/h = 100. (a) η = 0.0; (b) η = 1.0e-5s; (c) η = 2.0e-5s; (d) η = 3.0e-5s.

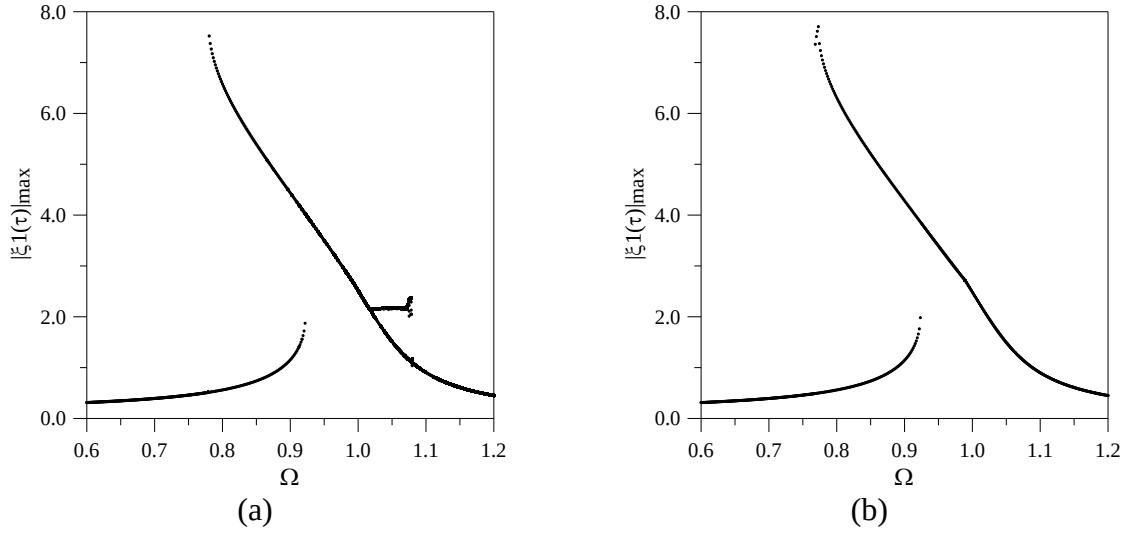

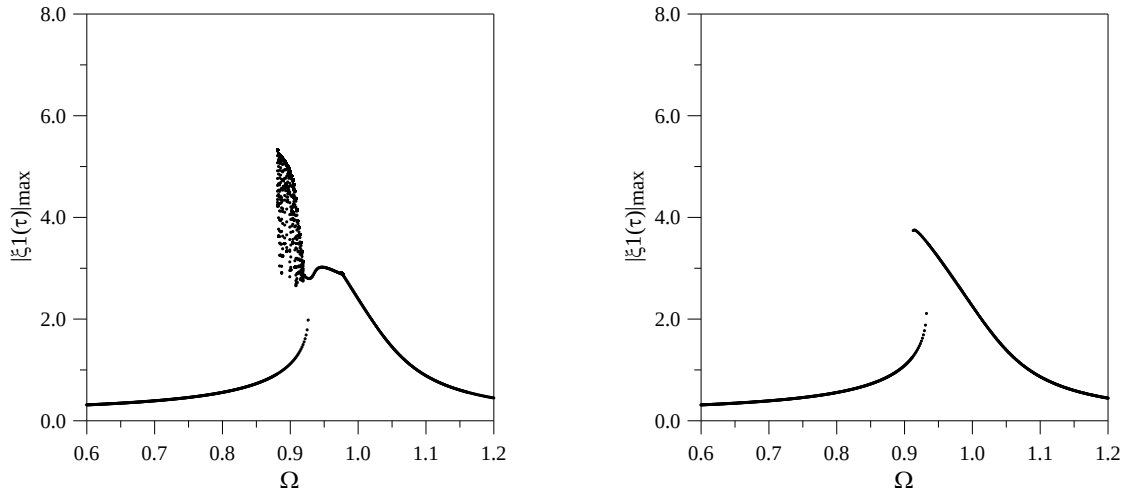

Figure 4. Ressonance curves for L/R = 2.0 and R/h = 300. (a) η = 0.0; (b) η = 1.0e-5s; (c) η = 2.0e-5s; (d) η = 3.0e-5s.

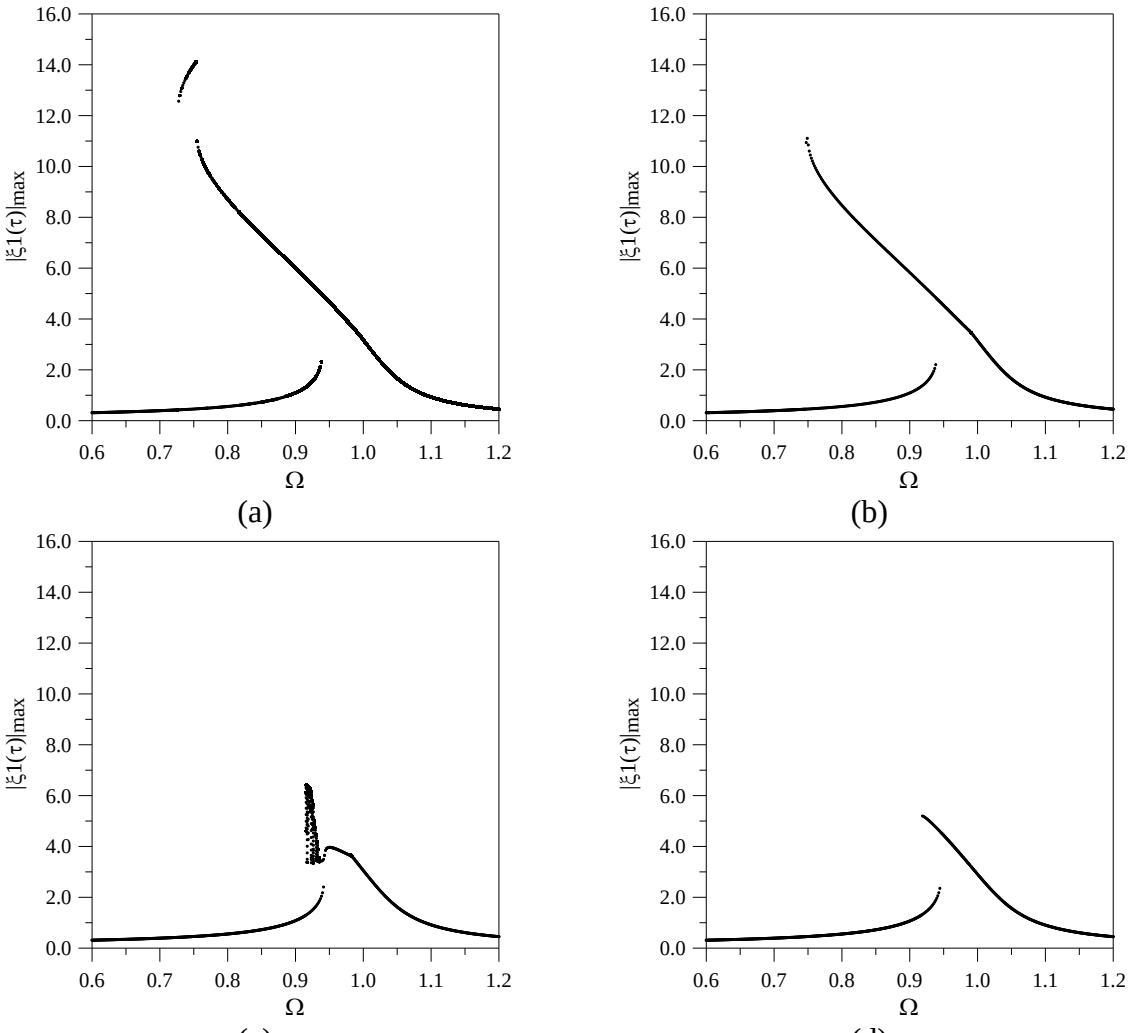

Figure 5. Ressonance curves for L/R = 2.0 and R/h = 600. (a) η = 0.0; (b) η = 1.0e-5s; (c) η = 2.0e-5s; (d) η = 3.0e-5s.

4 CONCLUSIONS

In this work, the non-linear vibrations analysis of a viscoelastic Kelvin-Voigt simply supported cylindrical shell subjected to lateral time dependent loads is analyzed. To model the shell, the Donnell's non-linear shallow shell theory is applied and an expansion with 6 degrees of freedom is used to describe the lateral displacements. Results show that the inclusion of the viscoelastic dissipation parameter η of the Kelvin-Voigt material affects strongly the non-linear response of the shell.

It is observed that the complexity of the non-linear response and consequently the number of bifurcations, non-linear paths and coexisting solutions depends on the value of the viscoelastic dissipation parameter.

For higher values of the dissipation parameter, the shell only displays small amplitude vibrations without jumps, hysteresis and multiple solutions. This illustrates the beneficial effect of viscoelasticity in reducing large amplitude unwanted vibrations. The amplitudes of vibrations obtained in the numerical results calls to the necessity to use a more refined shell theory to describe the non-linear dynamic behavior with good accuracy.

ACKNOWLEDGMENTS

This work was made possible by the support of the Brazilian Ministry of Education – CNPq and FAPERJ-CNE and NSERC Discovery Grant, Discovery Accelerator Supplement and Canada Research Chair.

REFERENCES

[1] Mengi Y, Birlik GA. A refined dynamic theory for viscoelastic cylindrical shells and cylindrical laminated composites, Part 1: General Theory. *Journal of Sound and Vibration*, **103**, 55-67, 1989.

[2] Rikards R, Chate A. Vibration and damping analysis of laminated composite and sandwich shells. *Mechanics of Composite Materials and Structures*, **4**, 209-232, 1997.

[3] Ramasamy R, Ganesan N. Vibration and damping analysis of fluid-filled orthotropic cylindrical shells with constrained viscoelastic damping. *Computers and Structures*, **70**, 363-376, 1999.

[4] Cheng C, Zhang N. Dynamic behavior of viscoelastic cylindrical shells under axial pressure, *Applied Mathematics and Mechanics*, **22**, 1-9, 2001.

[5] Cederbaum G, Touati D. Postbuckling analysis of imperfect non-linear viscoelastic cylindrical panels. *International Journal of Non-Linear Mechanics*, **37**, 757–762, 2002.

[6] Boutyour E H, Daya EM, Michel P. A harmonic balance method for the non-linear vibration of viscoelastic shells. *C. R. Mecanique*, **334**, 68–73, 2006.

[7] Antman SS, Lacarbonara W. Forced Radial Motions of Nonlinearly Viscoelastic Shells. *Journal of Elasticity*, **96**, 155–190, 2009.

[8] Shina W, Leeb S, Ohc I, Lee I. Thermal post-buckled behaviors of cylindrical composite shells with viscoelastic damping treatments. *Journal of Sound and Vibration*, **323**, 93–111, 2009.

[9] Ilyasov MH. Parametric vibrations and stability of viscoelastic shells. *Mechanics of Time-Dependent Materials*, **14**, 153–171, 2010.

[10] Abdoun F, Azrar L, Daya EM. Damping and Forced Vibration Analyses of Viscoelastic Shells, International *Journal for Computational Methods in Engineering Science and Mechanics*, **11**, 109-122, 2010.

[11] Eshmatov BK, Khodjaev DA. Non-linear vibration and dynamic stability of a viscoelastic cylindrical panel with concentrated mass. *Acta Mechanica*, **190**, 165–183, 2007a.

[12] Eshmatov BK. Nonlinear vibrations of viscoelastic cylindrical shells taking into account shear deformation and rotatory inertia. *Nonlinear Dynamics*, **50**, 353–361, 2007b.

[13] Eshmatov BK. Dynamic stability of viscoelastic circular cylindrical shells taking into account shear deformation and rotatory inertia. *Applied Mathematics and Mechanics*, **28**, 1319–1330, 2007c.

[14] Eshmatov BK, Khodzhaev DA. Non-linear vibration and dynamic stability of a viscoelastic cylindrical panel with concentrated mass. *Acta Mechanica*, **190**, 165–183, 2007d.

[15] Eshmatov BK, Khodzhaev DA. Dynamic stability of a viscoelastic cylindrical panel with concentrated masses. *Strength of Materials*, **40**, 491–502, 2008.

[16] Eshmatov BK. Nonlinear vibrations and dynamic stability of a viscoelastic circular cylindrical shell with shear strain and inertia of rotation taken into account. *Mechanics of Solids*, **44**, 421–434, 2009.

[17] Mohammadi F, Sedaghati R. Vibration analysis and design optimization of viscoelastic sandwich cylindrical shell. *Journal of Sound and Vibration*, **331**, 2729–2752, 2012.

[18] Alijani F, Amabili M. Non-linear vibrations of shells: A literature review from 2003 to 2013. *International Journal of Non-Linear Mechanics*, **58**, 233–257, 2013.

[19] Esmailzade E, Jalali MA. Nonlinear Oscillations of Viscoelastic Rectangular Plates. *Nonlinear Dynamics*, **18**, 311–319, 1999.

[20] Amabili M. *Nonlinear Vibrations and Stability of Shells and Plates. 1st Editon.* Cambridge University Press, 2008.

[21] Amabili M, Pellicano F, Païdoussis MP. Non-linear dynamics and stability of circular cylindrical shells containing flowing fluid. Part I: Stability. *Journal of Sound and Vibration*, **225**, 655-699, 1999.

[22] Stavridis L, Armenàkas A. Analysis of Shallow Shells with Rectangular Projection: Theory. *ASCE Journal of Engineering Mechanics*, **114**, 923–942, 1988.

[23] Breslavsky ID, Avramov KV. Effect of boundary condition nonlinearities on free large-amplitude vibrations of rectangular plates. *Nonlinear Dynamics*, **74**, 615-627, 2013.

[24] Del Prado Z, Argenta AL, Da Silva F, Gonçalves PB. The effect of material and geometry on the non-linear vibrations of orthotropic circular cylindrical shells. *International Journal of Non-Linear Mechanics*, **66**, 75–86, 2014.

[25] Balkan D, Mecitoglu Z. Nonlinear dynamic behavior of viscoelastic sandwich composite plates under non-uniform blast load: *Theory and experiment. International Journal of Impact Engineering*, **72**, 85-104, 2014.

ECCOMAS Congress 2016
VII European Congress on Computational Methods in Applied Sciences and Engineering
M. Papadrakakis, V. Papadopoulos, G. Stefanou, V. Plevris (eds.)
Crete Island, Greece, 5–10 June 2016

REDUCED ORDER MODELS FOR DYNAMIC BEHAVIOR OF PRESTRESSED ELASTOMER DAMPING DEVICES

A. Legay[1], J.-F. Deü[2] and B. Morin[3]

Structural Mechanics and Coupled Systems Laboratory
Conservatoire National des Arts et Métiers
292 rue Saint-Martin, 75141 Paris Cédex 03, France
[1]e-mail: antoine.legay@lecnam.net
[2]e-mail: jean-francois.deu@lecnam.net
[3]e-mail: benjamin.morin@lecnam.net

Keywords: anti-vibration junctions, elastomer material, reduced order model

Abstract. *Due to their damping properties, elastomer materials are commonly used in the industry to achieve anti-vibration junctions between mechanical subsystems. These links are usually made of various materials (metallic, composites and elastomers) and have complex geometries based on the targeted application. In order to predict the dynamic behavior of these junctions in their environment, efficient numerical dynamic models have to be developed. They should take into account the viscoelastic behavior of the elastomer and the material and geometric nonlinearity. The objective of this work is thus to develop effective models of flexible damping devices made of elastomer for the prediction of the dynamic behavior of complex systems.*

Firstly, a three-dimensional finite element nonlinear code using hyper-viscoelasticity constitutive relations is developed for the numerical modeling of the elastomer junctions. Secondly, the parameters of the viscoelastic law are identified in the frequency domain from experimental tests using DMA (Dynamic Mechanical Analysis). Thirdly, a reduced order model is developed. It is based on a component mode synthesis approach adapted to highly damped structures. We also propose in this study to construct models based on input-output laws connecting the generalized quantities of the faces of the junction in contact with substructures. In other words, the model links displacements and rotations of the faces to forces and torques applied to these faces.

1 INTRODUCTION

Due to their capacities to dissipate energy, elastomers are highly used in damping devices like silent blocs or joints. A typical example of this use is found in the spatial industry: during take off and flight, launchers are subject to a significant amount of vibrations from either the propulsion engine or the acoustical environment. Shocks may also occur during the pyrotechnic separation of the different floors of the launcher. All these vibration sources may damage the satellite or any other sensitive equipments on-board, and a common solution is to use viscoelastic damping devices to dissipate a part of the mechanical energy. The design and optimization of theses damping devices are usually done by using finite element codes. The computational cost of the associated models may become prohibitive. Many solutions already exist to reduce the numerical model of linear undamped structures, but only a few give access to reduced models with damping behavior, especially when it comes from viscoelasticity which may be seen as a strong form of damping. Two types of solutions for the reduction of viscoelastic models can be found in the literature. The first one is based on the theory of triboelasticity [6] and consists in the replacement of the damping device model by an equivalent rheological model which can be identified through a series of experimental measurements on the damper [7]. The main problem with this type of approach is that the behavior of the rheological model may not fit the real behavior of the damper in all directions, and more importantly it can't be used for a design purpose due to the non predictive aspect of the rheological model that is done for a specific geometry and material [8]. The second way of reducing a viscoelastic model is to extend the classical modal projection methods to the frequency dependent case and a review of the most common methods can be found in [2]. The chosen method in this work to achieve the reduction of the damper model is a modified Craig-Bampton method, based upon the work of Balmès [3] and Rouleau [2]. The original Craig-Bampton method [4] uses a combination of static and dynamic modes to reduce the finite element model of a sub-structure to a smaller finite element model called super-element. The super-element is first obtained by using a kinematical constraint to enforce rigid body motion of the sub-structure interfaces. Then, to further reduce the finite element model, the reduced finite element matrices are condensed onto the previously kinematically constrained interfaces. The combination of all these techniques leads to a twelve dofs super element replacing the initial full model.

2 STUDIED CASE AND MATERIAL MODELS

The complete model is composed of a support structure mounted on four hourglass shaped dampers, as seen on figure (1). The support structure is made of aluminum and the dampers are made of two aluminum thin interface plates and an elastomer core. Two different material models are used: a classic linear elastic Hooke's model is chosen for the aluminum, and a viscoelastic fractional Zener model for the elastomer. This fractional model is defined by its complex frequency dependent modulus $\mathrm{G}^*(\omega)$:

$$\mathrm{G}^*(\omega) = \frac{\mathrm{G}_0 + \mathrm{G}_\infty(\mathrm{i}\omega\tau)^\alpha}{1 + (\mathrm{i}\omega\tau)^\alpha} \tag{1}$$

where G_0 and G_∞ are two asymptotic values: the static modulus $\mathrm{G}_0 = \mathrm{G}^*(\omega \to 0)$ and the high frequency limit of the dynamic modulus $\mathrm{G}_\infty = \mathrm{G}^*(\omega \to \infty)$. Also, τ is the relaxation time and α is the order of the fractional derivative. More information about this model, its identification and its finite element implementation in time domain can be found in [5]. The adimensional viscoelastic modulus $\mathrm{G}^*(\omega)/\mathrm{G}_0$ is then used in the dynamic equation to take into account the

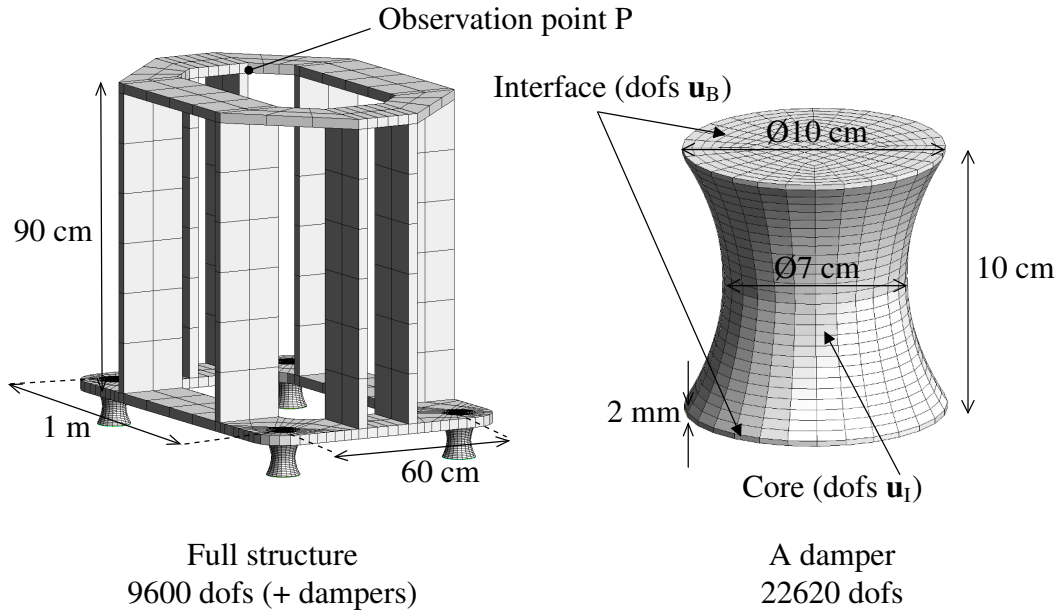

Figure 1: The complete structure mounted on four dampers, and details of a damper

viscoelastic behavior of the elastomer:

$$\left(\mathbf{K}^{\mathrm{e}} + \mathbf{K}^{\mathrm{v}}_{\mathrm{sph}} + \frac{\mathrm{G}^*(\omega)}{\mathrm{G}_0}\mathbf{K}^{\mathrm{v}}_{\mathrm{dev}} - \omega^2\mathbf{M}\right)\mathbf{u} = \mathbf{f} \tag{2}$$

where $\mathbf{M}$ is the mass matrix, $\mathbf{K}^{\mathrm{e}}$ is the purely elastic part of the stiffness matrix which is assembled on the aluminum interfaces dofs and $\mathbf{K}^{\mathrm{v}}$ is the viscoelastic part of the stiffness matrix which is assembled on the elastomer core dofs. The viscoleastic stiffness matrix is also separated into a spheric part $\mathbf{K}^{\mathrm{v}}_{\mathrm{sph}}$ and a deviatoric part $\mathbf{K}^{\mathrm{v}}_{\mathrm{dev}}$. This separation is used due to the fact that the viscoelastic behavior of elastomer is mainly caused by distorsional strain (not by volume change). This deviatoric stiffness matrix is the only matrix subjected to the complex modulus $G^*(\omega)$. The dynamic equation can also be expressed in terms of a static stiffness matrix $\mathbf{K}^0$ and a frequency dependent stiffness matrix $\mathbf{K}^\omega$:

$$\left(\mathbf{K}^0 + i\omega \mathrm{h}^*(\omega)\mathbf{K}^\omega - \omega^2\mathbf{M}\right)\mathbf{u} = \mathbf{f} \tag{3}$$

where $\mathbf{K}^0 = \mathbf{K}^{\mathrm{e}} + \mathbf{K}^{\mathrm{v}}_{\mathrm{sph}} + \mathbf{K}^{\mathrm{v}}_{\mathrm{dev}}$ and $\mathbf{K}^\omega = \left(\mathrm{G}_\infty/\mathrm{G}_0 - 1\right)\mathbf{K}^{\mathrm{v}}_{\mathrm{dev}}$ and where $\mathrm{h}^*(\omega)$ is a dimensionless frequency dependent modulus:

$$\mathrm{h}^*(\omega) = \frac{\tau^\alpha (i\omega)^{\alpha-1}}{1 + (i\omega\tau)^\alpha} \tag{4}$$

The material parameters used to build the mass and stiffness matrices are given in table 1 for the aluminum and table 2 for the elastomer. The materials parameters in table 2 comes from [1]. The structure is composed of 7540 nodes for each rubber damper, which is enough to get converged results in the frequency range of interest, and 3200 nodes for the upper aluminum structure. Only the computational cost of the dampers model is studied and reduced here, so the mesh of the upper structure is kept small for convenient computation time. Each damper represents 22620 dofs. The total number of dofs in the complete structure is about 10^5, including more than 90% for the dampers only, thus underlining the need for an efficient reduction

Table 1: Material parameters of the aluminum.

Parameters	Values
E	70 GPa
ν	0.3
ρ	2700 kg·m^{-3}

Table 2: Material parameters of the elastomer.

Parameters	Values
E	0.947 MPa
ν	0.45
ρ	1000 kg·m^{-3}
G_0	0.327 MPa
G_∞	0.126 GPa
α	0.3
τ	0.52 μ s

method. The finite element code for this study is an in house program developed in both Python and Fortran. The finite elements are 8 nodes hexahedra anywhere in the structure. Rubber dampers are connected to the aluminum structure through their upper interface.

3 MODEL REDUCTION OF THE DAMPERS

3.1 Rigid interfaces assumption

Due to the difference between the aluminum and the elastomer stiffness, the aluminum interfaces may be considered to be rigid compared to the rubber core. A kinematical constraint is used to enforce the rigid body motion of the interfaces. The velocity of any point A of an interface can be written in terms of the velocity of the center C of the same interface and the cross-product of the distance between point A and point C and the rotation Ω of the interface. This relationship can be extended to the displacement within the context of small displacement, namely:

$$\overrightarrow{u}_A = \overrightarrow{u}_C + \overrightarrow{AC} \times \overrightarrow{\Omega} \tag{5}$$

In matrix form, the same constraint is written by:

$$\begin{bmatrix} u_A \\ v_A \\ w_A \end{bmatrix} = \begin{bmatrix} 1 & 0 & 0 & 0 & (z_A - z_C) & (y_C - y_A) \\ 0 & 1 & 0 & (z_C - z_A) & 0 & (x_A - x_C) \\ 0 & 0 & 1 & (y_A - y_C) & (x_C - x_A) & 0 \end{bmatrix} \begin{bmatrix} u_C \\ v_C \\ w_C \\ \Omega_x \\ \Omega_y \\ \Omega_z \end{bmatrix} \tag{6}$$

where x, y and z are coordinates in the 3D space, u_X, v_X and w_X are the displacements of a point X following axes $\vec{x}$, $\vec{y}$ and $\vec{z}$, and Ω_x, Ω_y and Ω_z are the interface rotation around the same axes. Following this approach, all interfaces dofs are eliminated from the global finite element model dofs list, thus reducing the computational cost of the structure model. In place of those eliminated dofs, each damper face is now represented by 6 dofs: 3 translational dofs and 3 rotational dofs.

3.2 Model reduction of the core of the dampers

The method used here to reduce the damper finite element model combine a Craig-Bampton method [4] and a multi-model approach [2] [3]. In the case of a structure made of elastic and viscoelastic materials, the dynamic equation is given by equation (3). Following the Craig-Bampton method, boundary and internal dofs are separated. Here, the boundary dofs are the 12 dofs of the rigid interfaces noted $\mathbf{u}_{\mathrm{B}}$ and the internal dofs are the remaining dofs of the dampers noted $\mathbf{u}_{\mathrm{I}}$. This leads to write equation (3) as:

$$\left(\begin{bmatrix} \mathbf{K}^0_{\mathrm{BB}} & \mathbf{K}^0_{\mathrm{BI}} \\ \mathbf{K}^0_{\mathrm{IB}} & \mathbf{K}^0_{\mathrm{II}} \end{bmatrix} + i\omega \mathrm{h}^*(\omega) \begin{bmatrix} \mathbf{K}^\omega_{\mathrm{BB}} & \mathbf{K}^\omega_{\mathrm{BI}} \\ \mathbf{K}^\omega_{\mathrm{IB}} & \mathbf{K}^\omega_{\mathrm{II}} \end{bmatrix} - \omega^2 \begin{bmatrix} \mathbf{M}_{\mathrm{BB}} & \mathbf{M}_{\mathrm{BI}} \\ \mathbf{M}_{\mathrm{IB}} & \mathbf{M}_{\mathrm{II}} \end{bmatrix} \right) \begin{bmatrix} \mathbf{u}_{\mathrm{B}} \\ \mathbf{u}_{\mathrm{I}} \end{bmatrix} = \begin{bmatrix} \mathbf{f}_{\mathrm{B}} \\ \mathbf{0} \end{bmatrix} \tag{7}$$

where the right-hand side is only composed of reaction forces $\mathbf{f}_{\mathrm{B}}$ at the interfaces.

The first part of the reduced basis is composed of the static modes $\mathbf{\Psi}_{\mathrm{IB}}$ which are defined by:

$$\mathbf{\Psi}_{\mathrm{IB}} = -(\mathbf{K}^0_{\mathrm{II}})^{-1} \mathbf{K}^0_{\mathrm{IB}} \tag{8}$$

The number of static modes is equal to the number of interfaces dofs, 12 in the present case.

The second part of the reduced basis is composed of the eigenmodes of the fixed interface problem solutions of the following generalised :

$$\left(\mathbf{K}^0_{\mathrm{II}} + i\omega \mathrm{h}^*(\omega) \mathbf{K}^\omega_{\mathrm{II}} - \omega^2 \mathbf{M}_{\mathrm{II}} \right) \mathbf{u}_{\mathrm{I}} = \mathbf{0} \tag{9}$$

Solving equation (9) would lead to the vibration modes of the structure but due to the frequency dependence of the the term $i\omega \mathrm{h}^*(\omega)$, this eigenproblem is non-linear in frequency and can not be solved directly. The proposed solution is to use a multi-model approach which is inspired by the Takagi-Sugeno fuzzy model. It has been often used to represent non-linear dynamic systems by interpolating locally linear models obtained from the sampling of the non-linear system [9]. It has been applied by Balmès [3] and Rouleau [2] to build a projection basis representative of the complex non-linear eigenvalue of equation (9). The multi-model basis is here built by the combination of many smaller basis $\mathbf{\Phi}_{\omega_j}$ and each of these basis is computed by solving the pseudo-eigenvalue problem (10) where only the real part of the equation is kept:

$$\left(\mathbf{K}^0_{\mathrm{II}} + \Re\left(i\omega_j \mathrm{h}^*(\omega_j) \right) \mathbf{K}^\omega_{\mathrm{II}} - \omega_k^2 \mathbf{M}_{\mathrm{II}} \right) \mathbf{\Phi}_{\omega_j,k} = \mathbf{0} \tag{10}$$

where ω_j values are chosen to sample the whole frequency range of interest. In any basis $\mathbf{\Phi}_{\omega_j}$ the modes are independent but the modes from two different basis may be co-linear so a Gramm-Schmidt orthonormalisation algorithm may be necessary. In the literature, two modal basis evaluated at the minimum and the maximum frequency of the range of interest combined with a static correction lead to a good approximation of the dynamic response of highly damped structures. In this study, the static correction is already taken into account by the static modes of the static response, so only the modal basis at the minimum and maximum frequency need to be computed. Solving equation (10) for $\omega = \omega_{\min}$ and $\omega = \omega_{\max}$ lead to the two basis $\mathbf{\Phi}_{\min}$ and $\mathbf{\Phi}_{\max}$ which both respect the orthogonality conditions:

$$\mathbf{\Phi}^{\mathrm{T}}_{\bar{\omega}} \Re\left(\mathbf{K}^*_{\mathrm{II}}(\bar{\omega}) \right) \mathbf{\Phi}_{\bar{\omega}} = \mathrm{diag}\left(\omega_1^2, ..., \omega_{\mathrm{I}}^2 \right) \tag{11}$$

$$\mathbf{\Phi}^{\mathrm{T}}_{\bar{\omega}} \mathbf{M}_{\mathrm{II}} \mathbf{\Phi}_{\bar{\omega}} = \mathbf{1}_{\mathrm{I}} \tag{12}$$

where $\bar{\omega}$ stands for $\omega_{\min}$ or $\omega_{\max}$ and where:

$$\mathbf{K}^*_{\mathrm{II}}(\bar{\omega}) = \mathbf{K}^0_{\mathrm{II}} + i\bar{\omega} \mathrm{h}^*(\bar{\omega}) \mathbf{K}^\omega_{\mathrm{II}} \tag{13}$$

Both $\mathbf{\Phi}_{\text{min}}$ and $\mathbf{\Phi}_{\text{max}}$ diagonalize the $\Re\left(\mathbf{K}^*_{\text{II}}(\bar{\omega})\right)$ matrix but they don't diagonalize $\mathbf{K}^0$ or $\mathbf{K}^\omega$ and this will have an impact on the further condensation step. The dynamic of the system is then reduced by truncating the basis $\mathbf{\Phi}_{\text{min}}$ into $\mathbf{\Phi}_{\text{I}p}$ and the basis $\mathbf{\Phi}_{\text{max}}$ into $\mathbf{\Phi}_{\text{I}q}$ with $p < \text{I}$ and $q < \text{I}$. The complete dynamic response is then obtained by combining the two truncated modal basis $\mathbf{\Phi}_{\text{I}p}$ and $\mathbf{\Phi}_{\text{I}q}$ into matrix $\mathbf{\Phi}_{\text{I}m}$, with $m = p + q < \text{I}$.

By combining the static response coming from the behavior of structures connected to the damper's interfaces, and the dynamic response from the core of the damper, a complete reduced basis can be assembled in the form:

$$\begin{bmatrix}\mathbf{u}_{\text{B}}\\ \mathbf{u}_{\text{I}}\end{bmatrix} = \begin{bmatrix}\mathbf{I}_{\text{BB}} & \mathbf{0}_{\text{B}m}\\ \mathbf{\Psi}_{\text{IB}} & \mathbf{\Phi}_{\text{I}m}\end{bmatrix}\begin{bmatrix}\mathbf{u}_{\text{B}}\\ \mathbf{q}_m\end{bmatrix} \tag{14}$$

The projection of equation (7) onto this reduced basis gives the following reduced system:

$$\left(\begin{bmatrix}\bar{\mathbf{K}}^0_{\text{BB}} & \mathbf{0}_{\text{B}m}\\ \mathbf{0}_{m\text{B}} & \bar{\mathbf{K}}^0_{mm}\end{bmatrix} + i\omega\text{h}^*(\omega)\begin{bmatrix}\bar{\mathbf{K}}^\omega_{\text{BB}} & \bar{\mathbf{K}}^\omega_{\text{B}m}\\ \bar{\mathbf{K}}^\omega_{m\text{B}} & \bar{\mathbf{K}}^\omega_{mm}\end{bmatrix} - \omega^2\begin{bmatrix}\bar{\mathbf{M}}_{\text{BB}} & \bar{\mathbf{M}}_{\text{B}m}\\ \bar{\mathbf{M}}_{m\text{B}} & \bar{\mathbf{M}}_{mm}\end{bmatrix}\right)\begin{bmatrix}\mathbf{u}_{\text{B}}\\ \mathbf{q}_m\end{bmatrix} = \begin{bmatrix}\mathbf{f}_{\text{B}}\\ \mathbf{0}\end{bmatrix} \tag{15}$$

where $\bar{\mathbf{K}}^\omega_{m\text{B}} = \left(\bar{\mathbf{K}}^\omega_{\text{B}m}\right)^{\text{T}}$ and $\bar{\mathbf{M}}_{m\text{B}} = \left(\bar{\mathbf{M}}_{\text{B}m}\right)^{\text{T}}$. The details of the different terms of these reduced matrices are given by:

$$\bar{\mathbf{K}}^0_{\text{BB}} = \mathbf{K}^0_{\text{BB}} + \mathbf{K}^0_{\text{BI}}\mathbf{\Psi}_{\text{IB}} \tag{16}$$
$$\bar{\mathbf{K}}^0_{mm} = \mathbf{\Phi}^{\text{T}}_{\text{I}m}\mathbf{K}^0_{\text{II}}\mathbf{\Phi}_{\text{I}m} \tag{17}$$

$$\bar{\mathbf{K}}^\omega_{\text{BB}} = \mathbf{K}^\omega_{\text{BB}} + \mathbf{K}^\omega_{\text{BI}}\mathbf{\Psi}_{\text{IB}} + \mathbf{\Psi}^{\text{T}}_{\text{IB}}\mathbf{K}^\omega_{\text{IB}} + \mathbf{\Psi}^{\text{T}}_{\text{IB}}\mathbf{K}^\omega_{\text{II}}\mathbf{\Psi}_{\text{IB}} \tag{18}$$
$$\bar{\mathbf{K}}^\omega_{m\text{B}} = \mathbf{\Phi}^{\text{T}}_{\text{I}m}\left(\mathbf{K}^\omega_{\text{IB}} + \mathbf{K}^\omega_{\text{II}}\mathbf{\Psi}_{\text{IB}}\right) \tag{19}$$
$$\bar{\mathbf{K}}^\omega_{mm} = \mathbf{\Phi}^{\text{T}}_{\text{I}m}\mathbf{K}^\omega_{\text{II}}\mathbf{\Phi}_{\text{I}m} \tag{20}$$

$$\bar{\mathbf{M}}_{\text{BB}} = \mathbf{M}_{\text{BB}} + \mathbf{M}_{\text{BI}}\mathbf{\Psi}_{\text{IB}} + \mathbf{\Psi}^{\text{T}}_{\text{IB}}\mathbf{M}_{\text{IB}} + \mathbf{\Psi}^{\text{T}}_{\text{IB}}\mathbf{M}_{\text{II}}\mathbf{\Psi}_{\text{IB}} \tag{21}$$
$$\bar{\mathbf{M}}_{m\text{B}} = \mathbf{\Phi}^{\text{T}}_{\text{I}m}\left(\mathbf{M}_{\text{IB}} + \mathbf{M}_{\text{II}}\mathbf{\Psi}_{\text{IB}}\right) \tag{22}$$
$$\bar{\mathbf{M}}_{mm} = \mathbf{\Phi}^{\text{T}}_{\text{I}m}\mathbf{M}_{\text{II}}\mathbf{\Phi}_{\text{I}m} \tag{23}$$

It is also important to note that due to the multi-model approach used in the computation of the dynamic response, a major difference arises between the method presented here and the usual Craig-Bampton: the classic method would results in null matrix in place of $\bar{\mathbf{K}}^\omega_{m\text{B}}$ and the blocks $\bar{\mathbf{K}}_{mm}$ and $\bar{\mathbf{M}}_{mm}$ would be diagonals which is not the case here.

3.3 Condensing the system on interfaces dofs

In order to further reduce the size of the system, it is proposed to condense the generalized unknowns $\mathbf{q}_m$ on the boundary dofs. The second line of system (15) gives the following relation between the generalized coordinates $\mathbf{q}_m$ and the interfaces displacements $\mathbf{u}_{\text{B}}$:

$$\mathbf{q}_m = -\left(\bar{\mathbf{K}}^0_{mm} + i\omega\text{h}^*(\omega)\bar{\mathbf{K}}^\omega_{mm} - \omega^2\bar{\mathbf{M}}_{mm}\right)^{-1}\left(\bar{\mathbf{K}}^0_{m\text{B}} + i\omega\text{h}^*(\omega)\bar{\mathbf{K}}^\omega_{m\text{B}} - \omega^2\bar{\mathbf{M}}_{m\text{B}}\right)\mathbf{u}_B \tag{24}$$

For the undamped case, the terms in the first parentheses are diagonal so the inversion is instantaneous, but in the damped case these terms are non-diagonal and the inversion adds some

computation time. In order to limit this cost, it is possible to exploit the fact that the non-diagonal matrices are sparse. Replacing equation (24) into equation (15) leads to a condensed system on the interfaces which is equivalent to a super-element where its dimension is equal to the number of interface dofs (12 here):

$$\left(\mathbf{K}_{\text{super}}(\omega) - \omega^2 \mathbf{M}_{\text{super}}(\omega)\right) \mathbf{u}_{\text{B}} = \mathbf{f}_{\text{B}} \tag{25}$$

where the super-element mass and stiffness matrices are given by:

$$\mathbf{K}_{\text{super}}(\omega) = \bar{\mathbf{K}}^0_{\text{BB}} + i\omega \text{h}^*(\omega)\bar{\mathbf{K}}^\omega_{\text{BB}} - \left(\bar{\mathbf{K}}^0_{\text{B}m} + i\omega \text{h}^*(\omega)\bar{\mathbf{K}}^\omega_{\text{B}m}\right)\left(\bar{\mathbf{K}}^0_{mm} + i\omega \text{h}^*(\omega)\bar{\mathbf{K}}^\omega_{mm} - \omega^2\bar{\mathbf{M}}_{mm}\right)^{-1} \left(\bar{\mathbf{K}}^0_{m\text{B}} + i\omega \text{h}^*(\omega)\bar{\mathbf{K}}^\omega_{m\text{B}} - \omega^2\bar{\mathbf{M}}_{m\text{B}}\right) \tag{26}$$

$$\mathbf{M}_{\text{super}}(\omega) = \bar{\mathbf{M}}_{\text{BB}} - \bar{\mathbf{M}}_{\text{B}m}\left(\bar{\mathbf{K}}^0_{mm} + i\omega \text{h}^*(\omega)\bar{\mathbf{K}}^\omega_{mm} - \omega^2\bar{\mathbf{M}}_{mm}\right)^{-1} \left(\bar{\mathbf{K}}^0_{m\text{B}} + i\omega \text{h}^*(\omega)\bar{\mathbf{K}}^\omega_{m\text{B}} - \omega^2\bar{\mathbf{M}}_{m\text{B}}\right) \tag{27}$$

4 APPLICATION TO THE SUPPORT STRUCTURE MOUNTED ON 4 DAMPERS

A comparison between the reference full finite element model and the proposed super-element is made. An harmonic displacement is imposed on the structure lower interfaces, in a direction that is parallel to these interfaces: the dampers are not moving up and down but rather in a left-forward/right-backward kind of motion. The frequency range is chosen from 0 Hz to 500 Hz and the resulting displacements at observation point P (see figure (1)), for both the full reference model and the super-element, are plotted on figure (2). The displacement of point P for the full model without damping is also plotted to show that the chosen viscoelastics parameters lead to a well damped structure. In the same time, the error in displacement is plotted on figure (4). Two types of modes (damper only or full structure) are shown in figure (3) and their frequencies are plotted in vertical line on figure (2)

One hundred modes are taken in the dynamic modal basis at null frequency in the multi-model approach. The high number of modes needed here is due to the same stiffness difference that is exploited for the kinematical constraint of the dampers interfaces: the stiffness of the elastomer core is so low that around a hundred modes are found in the frequency range 0-500 Hz. The frequency limit chosen for the calculation of this modal basis is 512 Hz, which is roughly equal to the max frequency of the frequency range, so the method is accurate.

For the second basis of the multi-model, the one that contains the pseudo-normal modes at the max frequency, only ten modes are needed to give a good approximation. This is due to the fact that pseudo-normal modes are computed from the real part of the complex stiffness matrix at a given frequency. The real part of the complex modulus is greater than one thus adding stiffness to the system so a lower number of modes is present in the frequency range of interest. The frequency limit chosen for the calculation of this second modal basis is 582 Hz, which again is roughly equal to the max frequency of the frequency range.

As it can be seen on figure (2) and (4), the super-element matches the results of the reference model with a maximal error in displacement around 0.016%, thus validating the modified Craig-Bampton proposed in this work. The different computational times from both the FRF calculation of the reference model and the super-element are given in table 3. The same computer is used to do both of them. The assembly of the super-element is done once for all, before

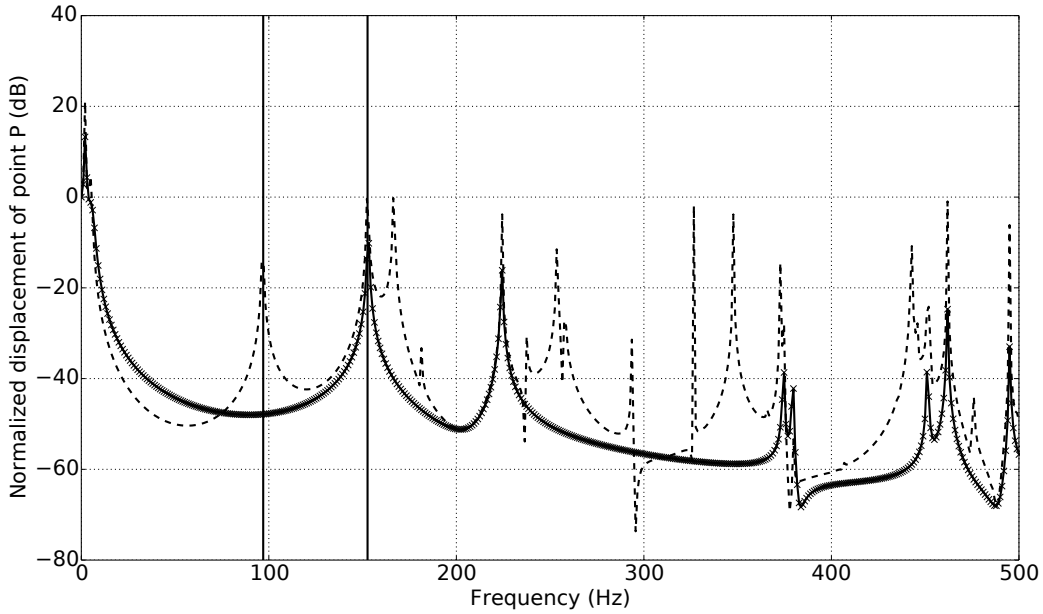

Figure 2: Normalized displacement of point P (see figure (1)) for the reference undamped model (dotted line), the reference damped (full line) and for the reduced model (cross-dotted line)

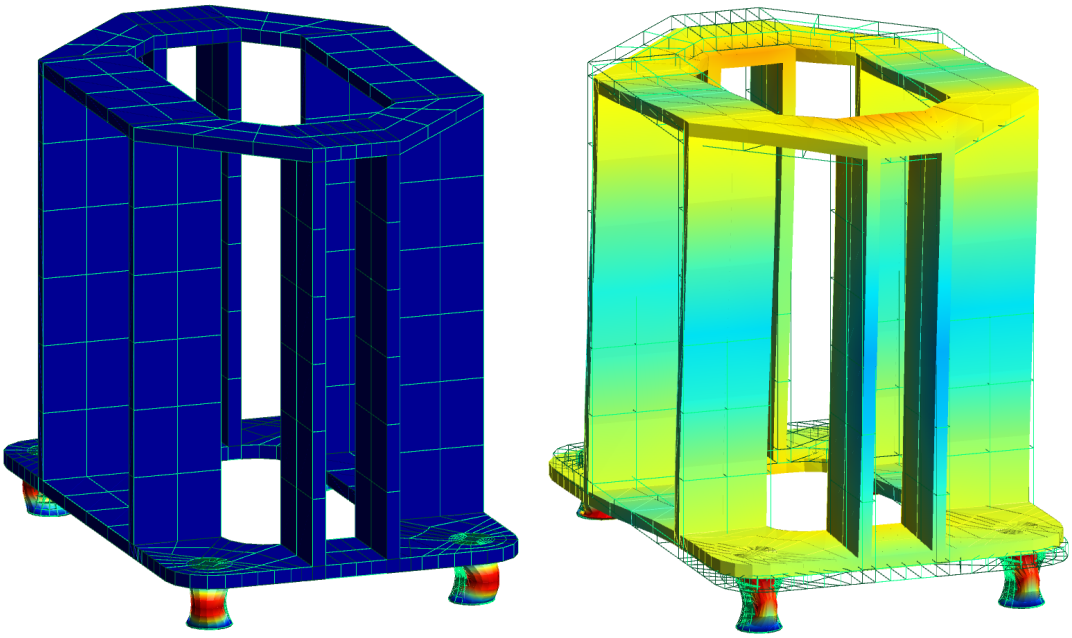

Figure 3: Modes of the undamped full structure at 98.23 Hz and 152.64 Hz (see the two vertical lines on figure 2)

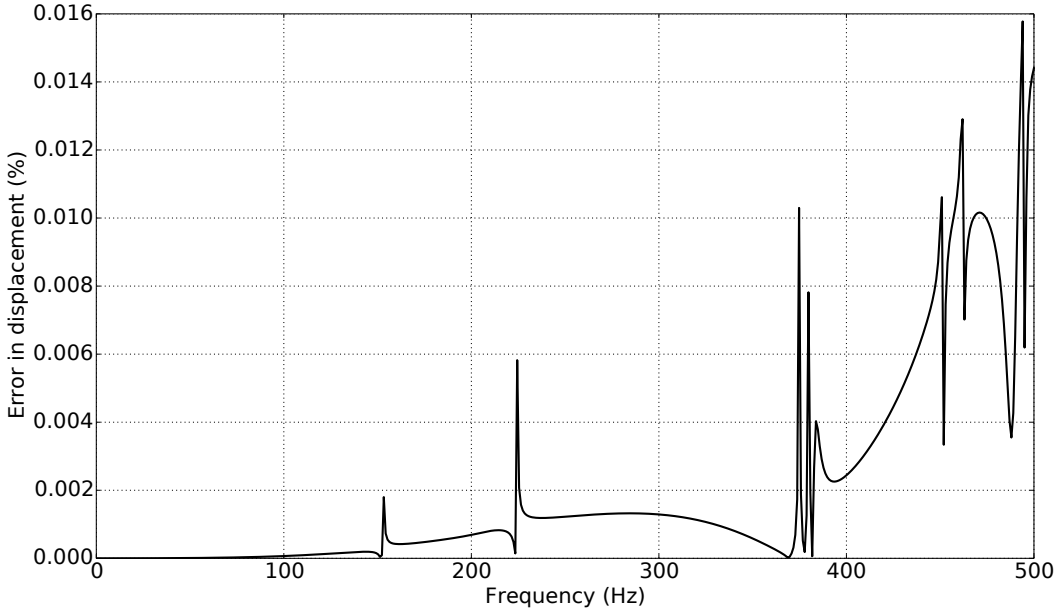

Figure 4: Error (norm 2) in displacement of the reduced model compared to the reference model

the FRF calculation, and the corresponding computational times is given under the name of Pre CPU time in table 3.

The sum of both the super-element assembly time and the FRF computational time of the modified Craig-Bampton is more than 10 times lower than the computational time of the reference model, thus further validating the present super-element approach.

Table 3: Computational time of both the reference and super-element models.

	Reference model	Super-element
Pre CPU time	-	23 min
FRF CPU time	14 h 40 min	51 min
total CPU time	14 h 40 min	1 h 14 min

5 Conclusion

The aim of the presented method is to reduce the finite element model of a damper made of elastomer and aluminium to a 12 dofs super-element. This super-element is built through the combination of a kinematical constraint to enforce rigid body motion at the damper interface and a Craig-Bampton to reduce and condense the finite element model on it's interfaces dofs. A multi-model approach is used to keep the frequency dependence of the finite element model during the Craig-Bampton reduction process. The result is a 12 dofs super-element that replace the more than 2.10^5 dofs finite element model. This super-element can be connected to any other finite element model through its interfaces nodes, each of them having three translational dofs and three rotational dofs. To test this method, the case of an aluminium structure supported on four dampers is studied. A reference model, consisting in the structure and four non-reduced

dampers, and a reduced model, made of the same structure with four super-elements, are compared. Displacements of one of the structure point are computed for both the reference and reduced models and are shown to be very close, and the error in displacement roughly stays under 0.016% on the whole frequency range thus validating the proposed method. The computational times of both models are also investigated and show that the reduced model is more than 10 times faster to compute than the reference model. A library of super-elements corresponding to different damper geometries and materials can be built off-line through this approach and then be used for design and optimization purposes in a full model.

REFERENCES

[1] L. Rouleau. Modlisation vibro-acoustique de structures sandwich munies de matriaux visco-lastiques. *PhD Thesis*. Cnam, 2013.

[2] L. Rouleau, J.-F. Deü and A. Legay. Review of reduction methods based on modal projection for highly damped structures. *Proc. 11th Wor. Cong. on Comp. Mech.* 2014.

[3] A.S. Plouin and E. Balmès. Pseudo-modal representations of large models with viscoelastic behavior. *Proc. Int. Modal Analysis Conf.* 1998.

[4] R.R. Craig and M.C.C. Bampton. Coupling of substructures for dynamic analysis. *A.I.A.A.* vol 6, no 7, 1968.

[5] A.C. Galucio, J.-F. Deü and R. Ohayon. Finite element formulation of viscoelastic sandwich beams using fractional derivative operators. *Comp. Mech.* vol 33, issue 4, pp 282-291, 2004.

[6] D.M. Turner. A triboelastic model for the mechanical behavior of rubber. *Plast and Rubber, Process. and Appl.* vol 9, no 4, pp. 197-201, 1988.

[7] V.A Coveney, S. Jamil, D.E Johnson, and M.A Keavey. Implementation in finite element analysis of a triboelastic law for dynamic behaviour of filled elastomers. *Finite Element Analysis of Elastomers*. 1999.

[8] V.A Coveney, D.E Johnson, S. Jamil, and M.A Keavey. Rate dependent triboelastic and other models for elastomers and prospects for implementation in finite element analysis. *Finite Element Analysis of Elastomers*. 1999.

[9] T. Takagi and M. Sugeno. Fuzzy identification of systems and its applications to modeling and control. *IEEE Transactions on Systems, Man and Cybernetics*. No 1, pp 116-132, 1985.

ECCOMAS Congress 2016
VII European Congress on Computational Methods in Applied Sciences and Engineering
M. Papadrakakis, V. Papadopoulos, G. Stefanou, V. Plevris (eds.)
Crete Island, Greece, 5–10 June 2016

LOCALIZATION OF VIBRATORY ENERGY OF A LINEAR SYSTEM IN A CHAIN OF FOUR NONLINEAR OSCILLATORS

Simon Charlemagne[1], **Claude-Henri Lamarque**[1] **and Alireza Ture Savadkoohi**[1]

[1]Univ Lyon, ENTPE, LTDS UMR CNRS 5513
Rue Maurice Audin, F-69518, Vaulx-en-Velin Cedex, France
{simon.charlemagne,claude.lamarque,alireza.turesavadkoohi}@entpe.fr

Keywords: Nonlinear oscillators, vibratory energy, multi-scales method, passive control

Abstract. *In this paper, dynamics of a five degree-of-freedom system formed by a main linear oscillator coupled to four light nonlinear systems in series is studied. The aim is to control and/or to harvest the energy of the main structure under harmonic excitations around its resonance. A multiple scales method is used to derive the behavior of the system at different time scales. At fast time scale, detected slow invariant manifold gives an overall comprehension of the possible behaviors that the system can undergo. At slow time scale, the modulated behavior of the system around its invariant is described by traced equilibrium and singular points. The former predict periodic regimes, while the latter hint at strongly modulated responses characterized by persisting bifurcations of the system around its unstable zones. All analytical results are validated by numerical simulations.*

1 INTRODUCTION

Nonlinear oscillators are known to be efficient to passively attenuate vibratory energy of mechanical systems. Several works in the literature deal with two degree-of-freedom (dof) systems. Gendelman [1] studies energy pumping by means of energy transfer to a nonlinear mode of a system consisting of a linear and a nonlinear coupled oscillators. Kerschen et al. [2] make experimental investigations on energy transfer from a linear oscillator to a cubic nonlinear one. Passive control of nonlinear systems have also been studied. Dahl type and piece-wise linear systems coupled to a piece-wise linear oscillator are examined by Ture Savadkoohi and Lamarque [3] and Lamarque et al. [4], respectively. The present work aims to study passive control of a linear system by four nonlinear oscillators in series. This represents a step towards investigation of system with higher dof, i.e. a main system coupled to a chain of oscillators. It is organized as it follows: model of the system and methodology of treatment are given in Sect. 2. Study of the system behavior at fast and slow time scale, leading to detection of slow invariant manifold and equilibrium and singular points, respectively, is led in Sect. 3. Analytical predictions are compared to numerical results in Sect. 4. Finally, concluding remarks are summarized in Sect. 5.

2 MODEL DESCRIPTION AND SYSTEM EQUATIONS

The five dof system described in Fig. 1 is studied. A linear structure under external excitation $F(t)$ which has a mass M, a stiffness K and a damping $\hat{a}$ is coupled to four nonlinear oscillators in series via a linear spring ρ and a damper $\tilde{a}$. The nonlinear oscillators have a mass m, a damping $\tilde{a}$ and a nonlinear potential $\tilde{V}$. Their masses is very small compared to the main system one's ($m = \epsilon M$, $0 < \epsilon \ll 1$).

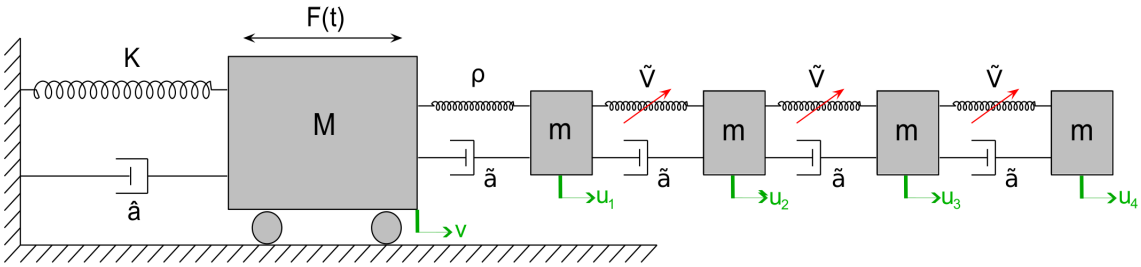

Figure 1: Five dof model studied consisting of a forced linear structure coupled to four nonlinear oscillators ($m = \epsilon M$, $0 < \epsilon \ll 1$)

Displacements of the main system and the nonlinear oscillators are called as v and u_j, $j = 1, \ldots, 4$, respectively. Let us introduce w_l as new variables of the system:

$$\begin{aligned} w_1 &= u_1 - v \\ w_l &= u_l - u_{l-1} \quad l = 2, 3, 4 \end{aligned} \tag{1}$$

Besides, new parameters are defined as followed: $\frac{K}{M} = \omega_0^2$, $\frac{\rho}{M} = \epsilon r$, $\frac{\tilde{V(z)}}{M} = \epsilon(Bz + Dz^3)$, $\frac{\hat{a}}{M} = \epsilon a$, $\frac{\tilde{a}}{M} = \epsilon a_1$ and $\frac{F(t)}{M} = \epsilon f(t)$. External forcing is assumed to be sinusoidal, oscillating at the angular frequency ω: $f(t) = f^0 \sin(\omega t)$. We study the system around resonance of the main structure: $\omega^2 = \omega_0^2(1 + \sigma\epsilon)$. Finally, a multiple scale method [5] is used by embedding

time to different scales, i.e. fast time scale $\tau_0 = t$ and slow time scales $\tau_j = \epsilon^j t,\ \ j = 1, 2 \ldots$ Governing equations of the system read:

$$\ddot{\mathbf{y}} + (\mathbf{C}_0 + \epsilon\mathbf{C}_1)\dot{\mathbf{y}} + (\mathbf{A}_0 + \epsilon\mathbf{A}_1)\mathbf{y} + \mathcal{N}(\mathbf{y}) = \epsilon\mathcal{F}(t) \tag{2}$$

where

$$\mathbf{A}_0 = \begin{pmatrix} \omega_0^2 & 0 & 0 & 0 & 0 \\ -\omega_0^2 & r & -B & 0 & 0 \\ 0 & -r & 2B & -B & 0 \\ 0 & 0 & -B & 2B & -B \\ 0 & 0 & 0 & -B & 2B \end{pmatrix} \quad \mathbf{A}_1 = \begin{pmatrix} 0 & -r & 0 & 0 & 0 \\ 0 & r & 0 & 0 & 0 \\ 0 & 0 & 0 & 0 & 0 \\ 0 & 0 & 0 & 0 & 0 \\ 0 & 0 & 0 & 0 & 0 \end{pmatrix}$$

$$\mathbf{C}_0 = \begin{pmatrix} 0 & 0 & 0 & 0 & 0 \\ 0 & a_1 & -a_1 & 0 & 0 \\ 0 & -a_1 & 2a_1 & -a_1 & 0 \\ 0 & 0 & -a_1 & 2a_1 & -a_1 \\ 0 & 0 & 0 & -a_1 & 2a_1 \end{pmatrix} \quad \mathbf{C}_1 = \begin{pmatrix} a & -a_1 & 0 & 0 & 0 \\ -a & a_1 & 0 & 0 & 0 \\ 0 & 0 & 0 & 0 & 0 \\ 0 & 0 & 0 & 0 & 0 \\ 0 & 0 & 0 & 0 & 0 \end{pmatrix} \tag{3}$$

$$\mathcal{N}(\mathbf{y}) = D \begin{pmatrix} 0 \\ -w_2^3 \\ 2w_2^3 - w_3^3 \\ -w_2^3 + 2w_3^3 - w_4^3 \\ -w_3^3 + 2w_4^3 \end{pmatrix} \quad \mathbf{y} = \begin{pmatrix} v \\ w_1 \\ w_2 \\ w_3 \\ w_4 \end{pmatrix} \quad \mathcal{F}(t) = \begin{pmatrix} f^0 \sin(\omega t) \\ 0 \\ 0 \\ 0 \\ 0 \end{pmatrix}$$

As $\mathbf{A}_0$ is diagonalizable, there exists a matrix $\mathbf{P}_0$ such as $\mathbf{P}_0^{-1}\mathbf{A}_0\mathbf{P}_0 = \mathbf{\Lambda}_0^2$, i.e. $\mathbf{A}_0$ and $\mathbf{\Lambda}_0^2$ are similar matrices. Furthermore, we assume that $\mathbf{\Lambda}_0^2 = \omega^2\mathbf{Id}_5 + \tilde{\mathbf{\Lambda}}_0^2$, where $\mathbf{Id}_5$ is the 5×5 identity matrix. System (2) can be rewritten:

$$\ddot{\mathbf{y}} + \omega^2\mathbf{y} + (\mathbf{C}_0 + \epsilon\mathbf{C}_1)\dot{\mathbf{y}} + \mathbf{P}_0\tilde{\mathbf{\Lambda}}_0^2\mathbf{P}_0^{-1}\mathbf{y} + \epsilon\mathbf{A}_1\mathbf{y} + \mathcal{N}(\mathbf{y}) = \epsilon\mathcal{F}(t) \tag{4}$$

Following complex variables of Manevitch [6] are introduced to the system (4):

$$\mathbf{\Phi}e^{i\omega t} = \dot{\mathbf{y}} + i\omega\mathbf{y} \quad \text{with} \quad \mathbf{\Phi} = \begin{pmatrix} \varphi_1 \\ \varphi_2 \\ \varphi_3 \\ \varphi_4 \\ \varphi_5 \end{pmatrix} \tag{5}$$

In order to keep only first harmonics and to truncate higher order ones, a Galerkin method is used by applying following formula on each equations $s_j,\ j = 1, \ldots, 5$ of system (4):

$$S_j = \frac{\omega}{2\pi}\int_0^{\frac{2\pi}{\omega}} s_j(\tau_0)e^{-i\omega\tau_0}d\tau_0 \tag{6}$$

Φ is supposed to be independent of τ_0, which will be eventually verified at least for an asymptotic state. Finally, system (4) reads:

$$\dot{\mathbf{\Phi}} + \frac{1}{2}(\mathbf{C}_0 + \epsilon\mathbf{C}_1)\mathbf{\Phi} + \frac{1}{2i\omega}(\mathbf{P}_0\tilde{\mathbf{\Lambda}}_0^2\mathbf{P}_0^{-1} + \epsilon\mathbf{A}_1)\mathbf{\Phi} - \frac{3iD}{8\omega^3}\mathcal{N}_m(\mathbf{y}) = \epsilon\mathcal{F}_m(t) \tag{7}$$

$$\mathcal{N}_m(\mathbf{y}) = \begin{pmatrix} 0 \\ -|\varphi_2|^2\varphi_2 \\ 2|\varphi_2|^2\varphi_2 - |\varphi_3|^2\varphi_3 \\ -|\varphi_2|^2\varphi_2 + 2|\varphi_3|^2\varphi_3 - |\varphi_4|^2\varphi_4 \\ -|\varphi_3|^2\varphi_3 + 2|\varphi_4|^2\varphi_4 \end{pmatrix} \quad \mathcal{F}_m(t) = \begin{pmatrix} \frac{f^0}{2i} \\ 0 \\ 0 \\ 0 \\ 0 \end{pmatrix} \tag{8}$$

3 SYSTEM BEHAVIOR AT DIFFERENT TIME SCALES

3.1 Fast time scale τ_0

The system behavior at fast time scale is described by system (7) derived at ϵ^0 order:

$$\begin{gathered} \frac{\partial \mathbf{\Phi}}{\partial \tau_0} + \frac{1}{2}\mathbf{C}_0\mathbf{\Phi} + \frac{1}{2i\omega_0}\mathbf{P}_0\tilde{\mathbf{\Lambda}}_0^2\mathbf{P}_0^{-1}\mathbf{\Phi} - i\mathcal{D}\mathcal{N}_m(\mathbf{y}) = 0 \\ \Leftrightarrow \frac{\partial \mathbf{\Phi}}{\partial \tau_0} + \begin{pmatrix} 0 \\ \mathcal{H}_2(\mathbf{\Phi}) \\ \mathcal{H}_3(\mathbf{\Phi}) \\ \mathcal{H}_4(\mathbf{\Phi}) \\ \mathcal{H}_5(\mathbf{\Phi}) \end{pmatrix} = 0 \end{gathered} \tag{9}$$

where $\mathcal{D} = \dfrac{3D}{8\omega_0^3}$.

Fix points of system (9) verify $\lim\limits_{\tau_0 \to +\infty} \dfrac{\partial \tilde{\mathbf{\Phi}}}{\partial \tau_0} = 0$ where $\tilde{\mathbf{\Phi}} = (\ \phi_1 \quad \phi_2 \quad \phi_3 \quad \phi_4 \quad \phi_5\ )^T$. They define the slow invariant manifold (SIM) of the system:

$$\mathcal{H} = \begin{pmatrix} \mathcal{H}_2(\tilde{\mathbf{\Phi}}) \\ \mathcal{H}_3(\tilde{\mathbf{\Phi}}) \\ \mathcal{H}_4(\tilde{\mathbf{\Phi}}) \\ \mathcal{H}_5(\tilde{\mathbf{\Phi}}) \end{pmatrix} = 0 \tag{10}$$

Introducing polar coordinates as $\phi_j = N_j e^{i\delta_j}$, $j = 1, \ldots, 5$, SIM can be written after some cumbersome algebra:

$$\begin{pmatrix} \phi_2 \\ \phi_3 \\ \phi_4 \\ \phi_5 \end{pmatrix} = \frac{\phi_1}{g(N_3^2, N_4^2, N_5^2)} \begin{pmatrix} h_2(N_3^2, N_4^2, N_5^2) \\ h_3(N_3^2, N_4^2, N_5^2) \\ h_4(N_3^2, N_4^2, N_5^2) \\ h_5(N_3^2, N_4^2, N_5^2) \end{pmatrix} \tag{11}$$

$h_j(N_3^2, N_4^2, N_5^2)$ and $g(N_3^2, N_4^2, N_5^2)$ are complex functions. From system (11), SIM can be plotted in the $(N_1, N_2, N_3, N_4, N_5)$ space. This manifold houses all possible asymptotic states of the system.

Stability of the SIM can be computed by introducing an infinitesimal perturbation of $\mathbf{\Phi}$ in system (9) around the SIM as:

$$\mathbf{\Phi} \to \tilde{\mathbf{\Phi}} + \mathbf{\Delta}\tilde{\mathbf{\Phi}} \quad , \quad \mathbf{\Delta}\tilde{\mathbf{\Phi}} = \big(\ 0 \quad \Delta\phi_2 \quad \Delta\phi_3 \quad \Delta\phi_4 \quad \Delta\phi_5\ \big)^T \tag{12}$$

Linearizing the obtained system leads to the following matrix system:

$$\begin{pmatrix} \dfrac{\partial \boldsymbol{\Delta}\tilde{\boldsymbol{\Phi}}}{\partial \tau_0} \\ \\ \dfrac{\partial \boldsymbol{\Delta}\tilde{\boldsymbol{\Phi}}^*}{\partial \tau_0} \end{pmatrix} = \boldsymbol{\Sigma} \begin{pmatrix} \boldsymbol{\Delta}\tilde{\boldsymbol{\Phi}} \\ \\ \boldsymbol{\Delta}\tilde{\boldsymbol{\Phi}}^* \end{pmatrix} \tag{13}$$

where $\boldsymbol{\Sigma}$ is an 10×10 matrix. Points where real parts of the eigenvalues of $\boldsymbol{\Sigma}$ are negative determine unstable zones of the SIM.

3.2 Slow time scale τ_1

Let us consider first equation of system (7) derived at ϵ^1 order:

$$\frac{\partial \varphi_1}{\partial \tau_1} + \left(\frac{i\sigma\omega_0}{2} + \frac{a}{2}\right)\varphi_1 + \left(\frac{ir}{2\omega_0} - \frac{a_1}{2}\right)\varphi_2 + \frac{if^0}{2} = 0 \tag{14}$$

This equation provide necessary additional information to detect equilibrium and singular points at slow time scale. Equilibrium points predict periodic regimes whereas singular points are hints of strongly modulated response (SMR) [7] which is characterized by persistent bifurcations of the system around its unstable zones. Separating its real and imaginary parts and using system (11), Eq. (14) becomes:

$$\begin{aligned} &\frac{\partial \varphi_1}{\partial \tau_1} + \underbrace{\left(\frac{i\sigma\omega_0}{2} + \frac{a}{2} + \frac{h_2}{g}\left(\frac{ir}{2\omega_0} - \frac{a_1}{2}\right)\right)}_{\alpha}\varphi_1 + \frac{if^0}{2} = 0 \\ &\Leftrightarrow \begin{cases} \dfrac{\partial N_1}{\partial \tau_1} = -\alpha_r N_1 - \dfrac{f^0}{2}\sin(\delta_1) = E_1 \\ \dfrac{\partial \delta_1}{\partial \tau_1} = -\alpha_i - \dfrac{f^0}{2N_1}\cos(\delta_1) = E_2 \end{cases} \end{aligned} \tag{15}$$

where $._r$ and $._i$ stand for real and imaginary parts, respectively. Moreover, from systems (10) and (15), one can obtain:

$$\begin{aligned} &\frac{\partial \mathcal{H}}{\partial \tau_1} = 0 \\ &\Rightarrow \det(\mathbf{S}_2)\mathbf{Id}_8 \begin{pmatrix} \dfrac{\partial N_2}{\partial \tau_1} \\ \vdots \\ \dfrac{\partial N_5}{\partial \tau_1} \\ \\ \dfrac{\partial \delta_2}{\partial \tau_1} \\ \vdots \\ \dfrac{\partial \delta_5}{\partial \tau_1} \end{pmatrix} = \underbrace{-\mathrm{adj}(\mathbf{S}_2)\mathbf{S}_1 \begin{pmatrix} E_1 \\ \\ E_2 \end{pmatrix}}_{\mathcal{G}} \end{aligned} \tag{16}$$

where $\mathrm{adj}(.)$ stands for the adjugate matrix and:

$$\mathcal{G} = \begin{pmatrix} \mathcal{G}_1 \\ \vdots \\ \mathcal{G}_8 \end{pmatrix} \mathbf{S}_1 = \begin{pmatrix} \frac{\partial \mathcal{H}_{2r}}{\partial N_1} & \frac{\partial \mathcal{H}_{2r}}{\partial \delta_1} \\ \frac{\partial \mathcal{H}_{2i}}{\partial N_1} & \frac{\partial \mathcal{H}_{2i}}{\partial \delta_1} \\ \vdots & \vdots \\ \frac{\partial \mathcal{H}_{5r}}{\partial N_1} & \frac{\partial \mathcal{H}_{5r}}{\partial \delta_1} \\ \frac{\partial \mathcal{H}_{5i}}{\partial N_1} & \frac{\partial \mathcal{H}_{5i}}{\partial \delta_1} \end{pmatrix} \quad \mathbf{S}_2 = \begin{pmatrix} \frac{\partial \mathcal{H}_{2r}}{\partial N_2} & \cdots & \frac{\partial \mathcal{H}_{2r}}{\partial N_5} & \frac{\partial \mathcal{H}_{2r}}{\partial \delta_2} & \cdots & \frac{\partial \mathcal{H}_{2r}}{\partial \delta_5} \\ \frac{\partial \mathcal{H}_{2i}}{\partial N_2} & \cdots & \frac{\partial \mathcal{H}_{2i}}{\partial N_5} & \frac{\partial \mathcal{H}_{2i}}{\partial \delta_2} & \cdots & \frac{\partial \mathcal{H}_{2i}}{\partial \delta_5} \\ \vdots & & \vdots & \vdots & & \vdots \\ \frac{\partial \mathcal{H}_{5r}}{\partial N_2} & \cdots & \frac{\partial \mathcal{H}_{5r}}{\partial N_5} & \frac{\partial \mathcal{H}_{5r}}{\partial \delta_2} & \cdots & \frac{\partial \mathcal{H}_{5r}}{\partial \delta_5} \\ \frac{\partial \mathcal{H}_{5i}}{\partial N_2} & \cdots & \frac{\partial \mathcal{H}_{5i}}{\partial N_5} & \frac{\partial \mathcal{H}_{5i}}{\partial \delta_2} & \cdots & \frac{\partial \mathcal{H}_{5i}}{\partial \delta_5} \end{pmatrix} \tag{17}$$

Equilibrium points verify:

$$\begin{cases} \det(\mathbf{S}_2) \neq 0 \\ E_1 = E_2 = 0 \end{cases} \Leftrightarrow \begin{cases} \det(\mathbf{S}_2) \neq 0 \\ \mathcal{G}_1 = \ldots = \mathcal{G}_8 = 0 \end{cases} \tag{18}$$

Singular points verify:

$$\begin{cases} \det(\mathbf{S}_2) = 0 \\ \mathcal{G}_1 = \ldots = \mathcal{G}_8 = 0 \end{cases} \tag{19}$$

4 NUMERICAL RESULTS

Analytical developments are compared in this section with numerical simulations obtained for direct integration of system (2). This task has been carried out thanks to function *ode45* of Matlab. Following parameters are fixed all along this section: $\omega_0 = 1$, $a = 0.2$, $\epsilon = 0.001$, $B = 0.2$, $r = 0.5$, $a_1 = 0.2$ and $D = 10$. Assumed initial conditions are: $v = 1$ and $\dot{v} = u_1 = \dot{u}_1 = u_2 = \ldots = \dot{u}_4 = 0$.

4.1 SIM

SIM of the system is illustrated in Fig. 2. Figures 2(a)-(d) represent N_1 versus N_2, N_3, N_4 and N_5, respectively. Unstable zones are plotted in dotted red line. The SIM presents two local extrema for N_1 which delimit an unstable zone. Furthermore, one can see what appears to be a double point in Fig. 2(a). This is an effect of the projection in the plane (N_1, N_2), as shown by the three-dimensional flow of the SIM in the (N_1, N_2, N_3)-space in Fig. 2(e).

4.2 $\mathbf{f^0 = 0.2}$ and $\sigma = 0$ (exact resonance)

Position of equilibrium and singular points are given in Fig. 3. The system possesses one stable equilibrium point (no. 1). SIM of the system and corresponding numerical results are given in Figs. 4(a) and (b). We picked two representations, N_1 versus N_2 and N_1 versus N_5, among four possible. Corresponding time series are given in Figs. 4(c),(d) and (e), where amplitudes of predicted equilibrium point no. 1 (see Fig. 3) are depicted by a blue dashed line. Besides, the amplitude that the main system would have without additional nonlinear oscillators is plotted in solid black line in Fig. 4(c). One can see that numerical results match analytical predictions, as the system behavior is instantaneously attracted to the SIM and stabilizes around the above-cited equilibrium point. Moreover, vibratory energy has been localized in the nonlinear oscillators, as the main system's amplitude equates to around 27% of the amplitude it would have on its own.

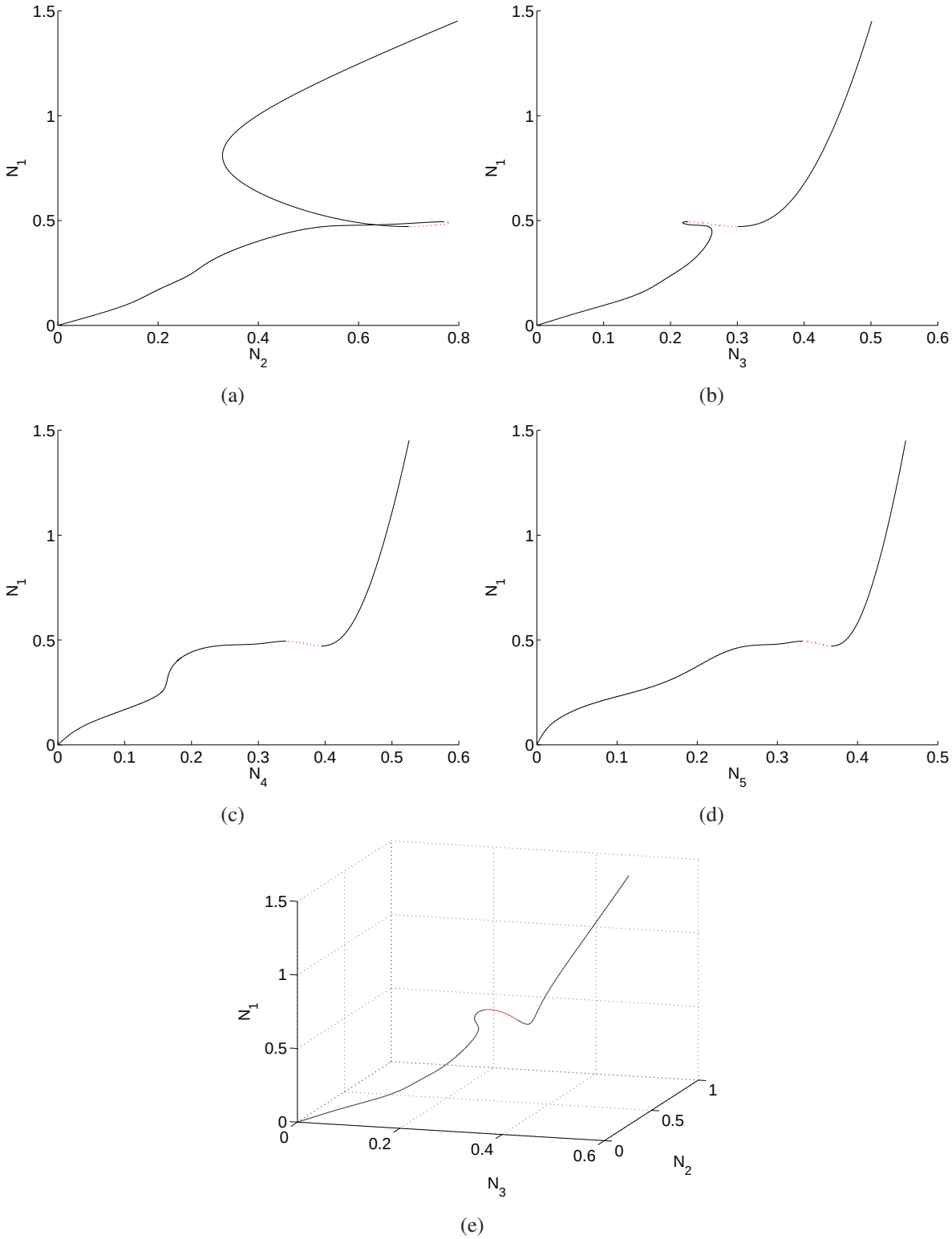

Figure 2: SIM of the system. (a) N_1 versus N_2, (b) N_1 versus N_3, (c) N_1 versus N_4, (d) N_1 versus N_5 and (e) Three-dimensional flow of the SIM in the (N_1, N_2, N_3)-space. Stable and unstable zones of the SIM are plotted in black solid line and dotted red line, respectively

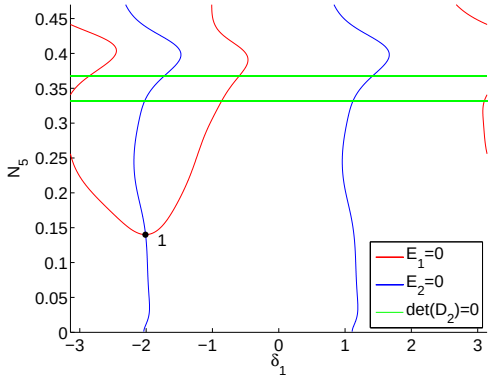

Figure 3: Position of equilibrium and singular points of the system with $f^0 = 0.2$ and $\sigma = 0$. The system possesses one equilibrium point (no. 1). Black points represent points where $\mathcal{G}_1 = \ldots = \mathcal{G}_8 = 0$ (see Sect. 3.2)

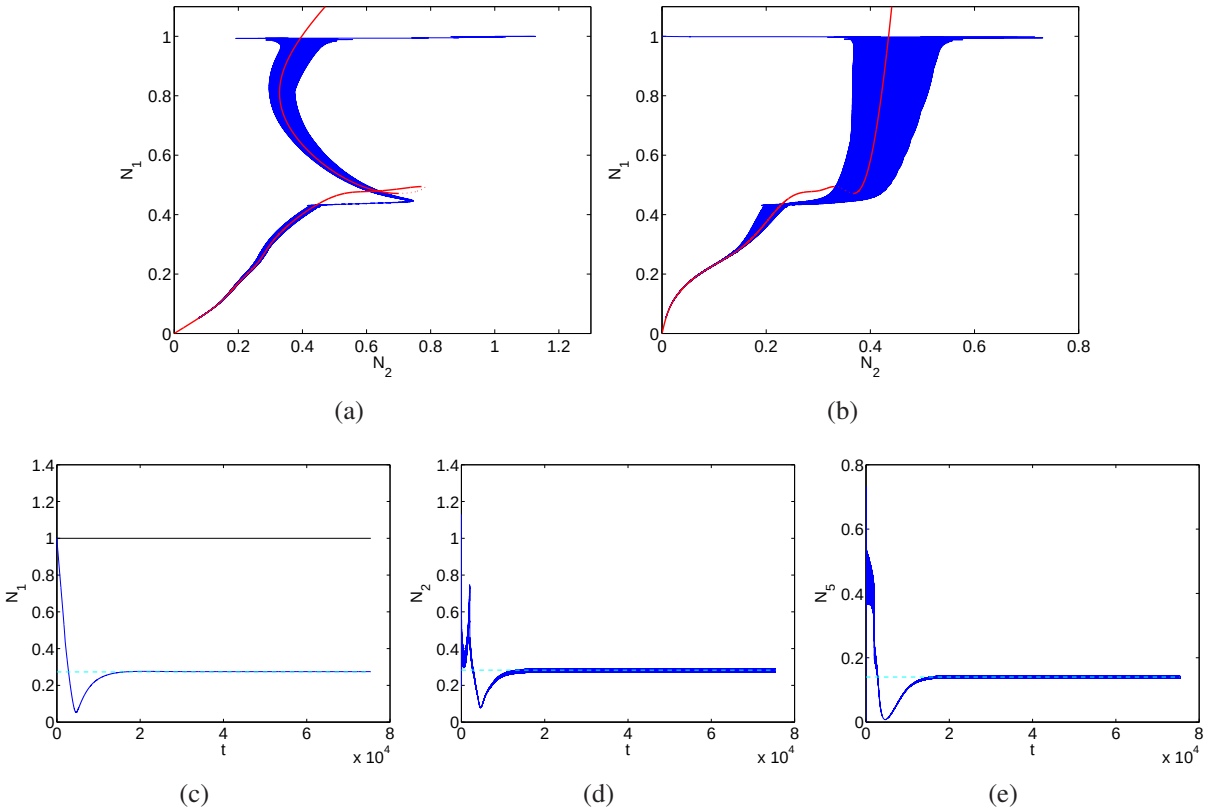

Figure 4: $f^0 = 0.2$ and $\sigma = 0$. (a) SIM of the system in red and corresponding numerical results in blue: N_1 versus N_2, (b) SIM of the system in red and corresponding numerical results in blue: N_1 versus N_5, (c) N_1 versus time, (d) N_2 versus time and (e) N_5 versus time. Amplitude of predicted equilibrium point no. 1 (see Fig. 3) is depicted by a blue dashed line. Amplitude that the main system would have without nonlinear oscillators is plotted in black

4.3 $f^0 = 0.5$ and $\sigma = 0.6$

Position of equilibrium and singular points are given in Fig. 5. The system possesses one unstable equilibrium point (no. 1) and four singular points (no. 2, no. 3, no. 4 and no. 5). Consequently, SMR is expected. Figures 6(a)-(e) depict SIM of the system, corresponding

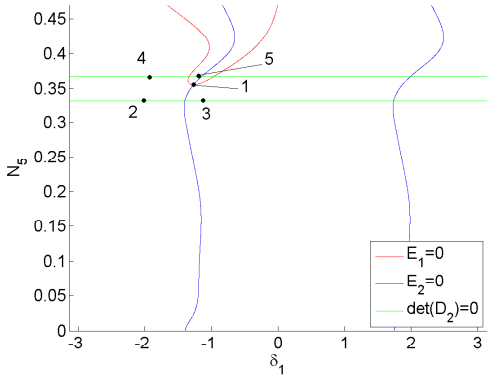

Figure 5: Position of equilibrium and singular points of the system with $f^0 = 0.5$ and $\sigma = 0.6$. The system possesses one equilibrium point (no. 1) and four singular points (no. 2, no. 3, no. 4 and no. 5). Black points represent points where $\mathcal{G}_1 = \ldots = \mathcal{G}_8 = 0$ (see Sect. 3.2)

numerical results and evolution versus time of the same variables as in the previous section. This time, the system faces repeated bifurcations around its unstable zone, i.e. it undergoes SMR. The system behavior during SMR is plotted in green in Figs. 6(a)-(b). Again, passive control has been operated on the main system as shown by the difference of its amplitude with nonlinear oscillators and without (marked by a solid black line in Fig. 6(c)).

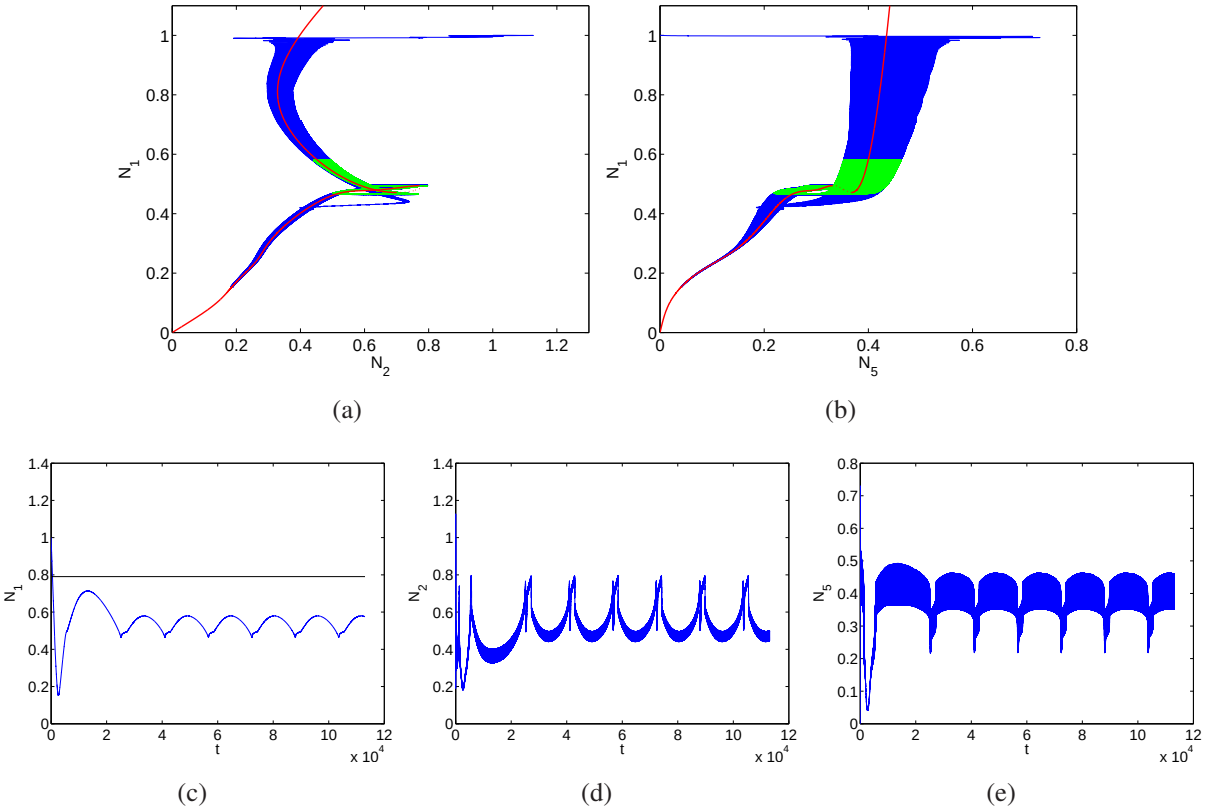

Figure 6: $f^0 = 0.2$ and $\sigma = 0$. (a) SIM of the system in red and corresponding numerical results in blue: N_1 versus N_2, (b) SIM of the system in red and corresponding numerical results in blue: N_1 versus N_5, (c) N_1 versus time, (d) N_2 versus time and (e) N_5 versus time. Amplitude that the main system would have without nonlinear oscillators is plotted in black

5 CONCLUSION

A five degree-of-freedom system consisting of a linear system coupled to four nonlinear oscillators is studied. Theoretical approaches such as implementation of Galerkin technique, complexification and time multi-scale methods are endowed for detection of fast and slow dynamics of the system. Numerical simulations and analytical predictions are in good agreement and provide evidence of passive control of the main system. In prospect, a similar method will be applied on a system with higher degree-of-freedom, in order to compare efficiency of passive control according to the number of nonlinear oscillators. Moreover, it will be interesting to study the behavior of the chain (propagation of a wave, localization in a few degrees of freedom, etc.) and to compare the results obtained with different approaches such as the search of nonlinear modes.

REFERENCES

[1] O.V. Gendelman, Transition of Energy to a Nonlinear Localized Mode in a Highly Asymmetric System of Two Oscillators. *Nonlinear Dynamics*, **25**, 237–253, 2001.

[2] G. Kerschen, D.M. McFarland, J.J. Kowtko, Y.S. Lee, L.A. Bergman, A.F. Vakakis, Experimental demonstration of transient resonance capture in a system of two coupled oscillators with essential stiffness nonlinearity. *Journal of Sound and Vibration*, **299**, 822–838, 2007.

[3] A. Ture Savadkoohi, C.-H. Lamarque, Dynamics of coupled Dahl type and nonsmooth systems at different scales of time. *International Journal of Bifurcation and Chaos*, **7**, 1350114 (14 p.), 2013.

[4] C.-H. Lamarque, A. Ture Savadkoohi, E. Etcheverria, Multi-scales dynamics of two coupled nonsmooth systems. *International Journal of Bifurcation and Chaos*, **22**, 1250295 (18 p.), 2012.

[5] A.H. Nayfeh, D.T. Mook, *Nonlinear oscillations*. John Wiley and Sons, 1979.

[6] L.I. Manevitch, The description of localized normal modes in a chain of nonlinear coupled oscillators using complex variables. *Nonlinear Dynamics*, **25**, 95–109, 2001.

[7] Y. Starosvetsky, O.V. Gendelman, Strongly modulated response in forced 2dof oscillatory system with essential mass and potential asymmetry. *Physica D*, **324**, 916–939, 2008.

ECCOMAS Congress 2016
VII European Congress on Computational Methods in Applied Sciences and Engineering
M. Papadrakakis, V. Papadopoulos, G. Stefanou, V. Plevris (eds.)
Crete Island, Greece, 5–10 June 2016

CONTINUATION OF QUASI-PERIODIC SOLUTIONS WITH TWO-FREQUENCY HARMONIC BALANCE METHOD

Louis Guillot[1], **Pierre Vigue**[1], **Christophe Vergez**[1] **and Bruno Cochelin**[1]

[1]Laboratoire de Mecanique et d'Acoustique
CNRS UPR 7051
4 impasse Nikola Tesla, CS 40006, F-13453 Marseille Cedex 13 - France
e-mail : vigue,vergez,cochelin@lma.cnrs-mrs.fr

Keywords: Quasi-periodic, Harmonic Balance Method.

Abstract. *Nonlinear systems can have periodic solutions evolving with the parameters of the system. Studying this evolution (numerical continuation of solutions) uncovers sought-after regimes in musical acoustics : many musical instruments rely on auto-oscillation, that is, the excitation of a nonlinear system coupled with a linear resonator, where some parameters may be adjusted by the player. Periodic solutions can be approximated as truncated Fourier series (Harmonic Balance Method) ; the period is one of the unknowns. Several stable or unstable solutions can be found for the same playing parameters thanks to continuation.*
An important challenge is the continuation of quasi-periodic solutions, also called multiphonic sounds by musicians. Depending on the context, these oscillation regimes are considered pleasant (jazz or contemporary music for instance) or unpleasant (classical music). We developed a method based on double Fourier series, coupled with a continuation technique. The two base frequencies are unknowns and incommensurable. The system is reformulated as quadratic in order to allow straight interface with previous work on periodic harmonic balance.
This method is illustrated on simple models relevant to musical acoustics, though the method can be applied to many nonlinear problems, without a priori knowledge of the solutions.

1 INTRODUCTION

Nonlinear systems can have periodic solutions evolving with the parameters of the system. Studying this evolution (numerical continuation of solutions) uncovers sought-after regimes in musical acoustics : many musical instruments rely on auto-oscillation, that is, the excitation of a nonlinear system coupled with a linear resonator, where some parameters may be adjusted by the player. Periodic solutions can be approximated as truncated Fourier series (Harmonic Balance Method) ; the period is one of the unknowns. Then, using a continuation technique, solutions can be continued ; they can be either stable or unstable, and different solutions may occur for the same playing parameters.

However, other solutions can arise, namely quasi-periodic solutions. They are well-known by musicians, who may call them multiphonics. These solutions can be undesirable : for instance, the wolf note on bowed string instruments is a rough, beating sound, and it is an example of a quasi-periodic regime of an autonomous system. These solutions can also be produced voluntarily, using a forced system: singing at a frequency f_1 while playing at a frequency f_2 on a brass instrument can create stunning effects.

Our aim is the continuation of two-frequencies, quasi-periodic solutions. It is important to notice that even the direct computation of quasi-periodic solutions can be difficult. Because of dependence on initial conditions, some solutions may be overlooked when using numerical integration. Moreover, compared to the periodic case, it is not relevant anymore to perform integration on long intervals to get rid of transient solutions : one cannot determine easily if the steady-state solution is reached. These drawbacks have lead to specific algorithms to compute quasi-periodic solutions, first as a response to a quasi-periodic drive [1]. More recently, the computation of quasi-periodic solutions for forced or autonomous systems, based on the Alternating Frequency/Time Domain Method (AFT [2]), was performed with good qualitative agreement on a disc brake model [3]. Peletan *et al.* [4] designed a continuation method, coupling AFT with pseudo-arclength continuation, and applied it to a Jeffcott rotor. For this system, one of the two frequencies is known ; and an harmonic selection procedure improves the efficiency of computations.

For periodic solutions, Cochelin and Vergez [5] showed that given a quadratic reformulation, a coupling of the Harmonic Balance Method and the Asymptotic Numerical Method was straightforward and allowed computations with high number of harmonics. The method developed here is an extension of this idea with double Fourier series. The two base frequencies are unknowns and incommensurable. The system is reformulated as quadratic in order to allow straight interface with previous work on periodic harmonic balance.

This method is illustrated on simple models, with a forced system and an autonomous one. System parameters could be chosen to present results more closely related to musical acoustics. However, simple values underline that the method can be applied to many nonlinear problems, without *a priori* knowledge of the solutions.

2 TWO-FREQUENCY HARMONIC BALANCE METHOD

2.1 Principle : quadratic formulation

Instead of one Fourier series, a variable x is sought after in the form

$$x(t) = \sum_{k_1=-H}^{H} \sum_{k_2=-H}^{H} x_{k_1,k_2} e^{i(k_1\omega_1 + k_2\omega_2)t} \tag{1}$$

where ω_1 and ω_2 are the two unknown pulsations. Adding auxiliary variables, a smooth nonlinear differential system can be transformed into a first-order differential system, with nonlinearities being only products, either of two variables, or a variable and the continuation parameter λ. Let U denote the vector of variables in the time domain, the following system is called quadratic formulation :

$$mU' = c_0 + \lambda c_1 + l_0 U + \lambda l_1 U + q(U,U) \tag{2}$$

where c_0, c_1 are constant vectors, m, l_0 and l_1 are constant linear operators, and q is a constant quadratic operator. Like in the periodic case [5], since eq. (2) is quadratic, and due to the decomposition of variables assumed in eq. (1), substituting this double series in eq. (2) leads to a (larger) quadratical system where the unknowns are Fourier coefficients plus the two pulsations ω_1, ω_2. Note that in the case of a forced system one of these pulsations is the forcing pulsation (see section 2.2). This larger system reads as a quadratical residual function R :

$$R : \mathbf{R}^{N+1} \longrightarrow \mathbf{R}^N, \quad (X,\lambda) \mapsto C_0 + \lambda C_1 + L_0(X) + \lambda L_1(X) + Q(X,X) \tag{3}$$

where X contains Fourier coefficients of U, ω_1 and ω_2. The solution branch $R(X,\lambda) = 0$ can then be followed thanks to the Asymptotic Numerical Method.

2.2 Forced system

An example of a forced system that exhibits a quasi-periodic behaviour is a forced Van der Pol oscillator :

$$x'' - \mu_1 x' + \mu_2 x x' + \mu_3 x^2 x' + a_1 x = \cos(\lambda t) \tag{4}$$

with $\mu_1 = \mu_2 = 0.1$, $\mu_3 = a_1 = 1$. A Neimark-Sacker bifurcation occurs at $\lambda \simeq 1.79$ [6], and the periodic solution at pulsation $\omega = \lambda$ becomes unstable. A quadratic formulation, emphasizing constant, linear and quadratic parts in the right-hand side, is

$$x' = 0 + y + 0 \tag{5}$$

$$y' = \cos(\lambda t) + \mu_1 y - a_1 x - \mu_2 xy - \mu_3 yz \tag{6}$$

$$\underbrace{0}_{mU'} = \underbrace{0}_{c_0} \underbrace{+ z}_{l_0 U} \underbrace{- x^2}_{q(U,U)} \tag{7}$$

The forcing term $\cos(\lambda t)$ is placed in the constant operator, similarly to the periodic version of the method (see [5], example 4).

The continuation of the quasi-periodic solution branch can be performed efficiently and precisely : in this example, Fourier series were truncated with $H = 5$. A plot of L^2 norm of x is shown in figure 2.2. Dots indicate the beginning of each continuation step : the ANM provides smooth continuation with an automatic step size determination. The solution obtained through this quasi-periodic Harmonic Balance is qualitatively good with $H = 2$ (figure 2.2, left) : peak-to-peak amplitude and general shape of the curve in the phase space are reached. But areas left blank are not actually correct, while with $H = 5$ (right), its pointwise agreement with a time integration scheme [7] is excellent.

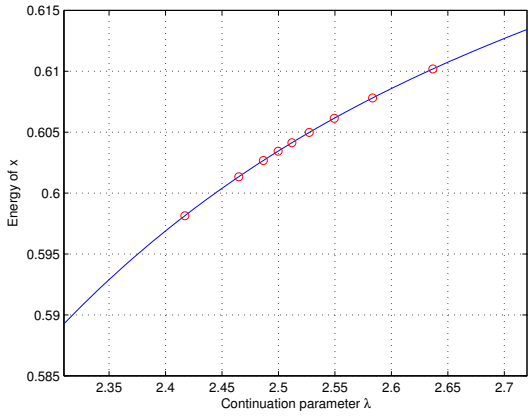

Figure 1: Energy (L^2 norm) of x with respect to the continuation parameter λ. Red dots indicate the beginning of each continuation step.

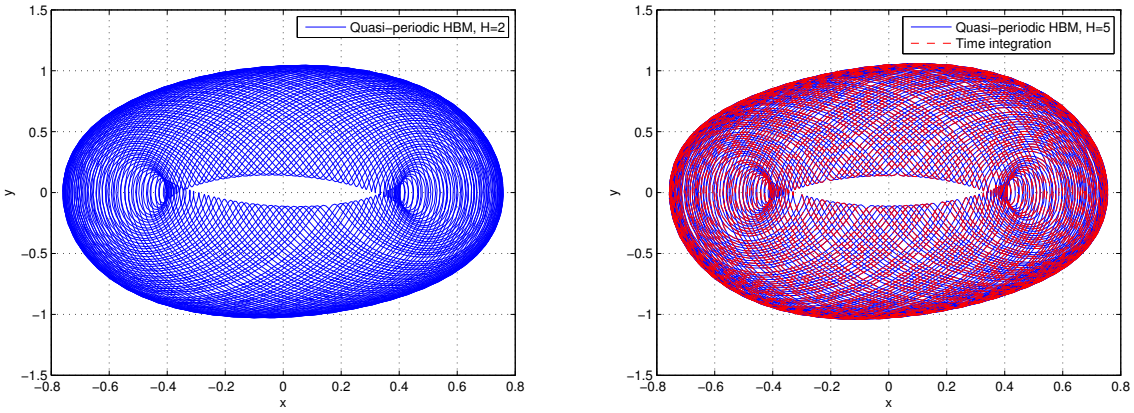

Figure 2: Phase diagrams (x, y), for $\lambda = 2.58$. Left : quasi-periodic Harmonic Balance, $H = 2$. Right : comparison of quasi-periodic Harmonic Balance ($H = 5$, blue solid line) and time integration (red dashed line).

2.3 Autonomous system

The equations used for two coupled Van der Pol oscillators are :

$$x_1'' + a_1 x_1' + \Omega_1^2 x_1 = a_2\lambda(x_1' + x_2') - a_3\lambda(x_1' + x_2')(x_1 + x_2) - a_4\lambda(x_1' + x_2')(x_1 + x_2)^2 \quad (8)$$

$$x_2'' + b_1 x_2' + \Omega_2^2 x_2 = b_2\lambda(x_1' + x_2') - b_3\lambda(x_1' + x_2')(x_1 + x_2) - b_4\lambda(x_1' + x_2')(x_1 + x_2)^2 \quad (9)$$

and the quadratic formulation is :

$$
\begin{aligned}
x_1' &= y_1 + 0 && + 0 && (10)\\
y_1' &= 0 \ - a_1 y_1 - \Omega_1^2 x_1 + \lambda\left(a_2(y_1+y_2) - a_3 v - a_4 w\right) && + 0 && (11)\\
x_2' &= y_2 + 0 && + 0 && (12)\\
y_2' &= 0 \ - b_1 y_2 - \Omega_2^2 x_2 + \lambda\left(b_2(y_1+y_2) - b_3 v - b_4 w\right) && + 0 && (13)\\
0 &= 0 \ + r && - (x_1+x_2)^2 && (14)\\
0 &= 0 \ + v && - (x_1+x_2)(y_1+y_2) && (15)\\
0 &= 0 \ + w && - r(y_1+y_2) && (16)
\end{aligned}
$$

Parameters values are chosen as : $\Omega_1 = 1$, $a_1 = 0.01$, $a_2 = 0.5$, $a_3 = a_4 = 2$; $\Omega_2 = 2.5$, $b_1 = 0.025$, $b_2 = 1$, $b_3 = b_4 = 4$. For these equations, the quasi-periodic solution branch requires higher orders of truncation of Fourier series H than the forced Van der Pol above. For example, around $\lambda = 0.36$, a good agreement with time integration is achieved with $H = 10$ (figure 2.3), and some differences are noticeable if H is too low (areas left empty are not correct with $H = 4$). For this system the continuation process takes roughly 6 seconds per step for $H = 4$, 43 seconds for $H = 6$, 220 seconds for $H = 8$.

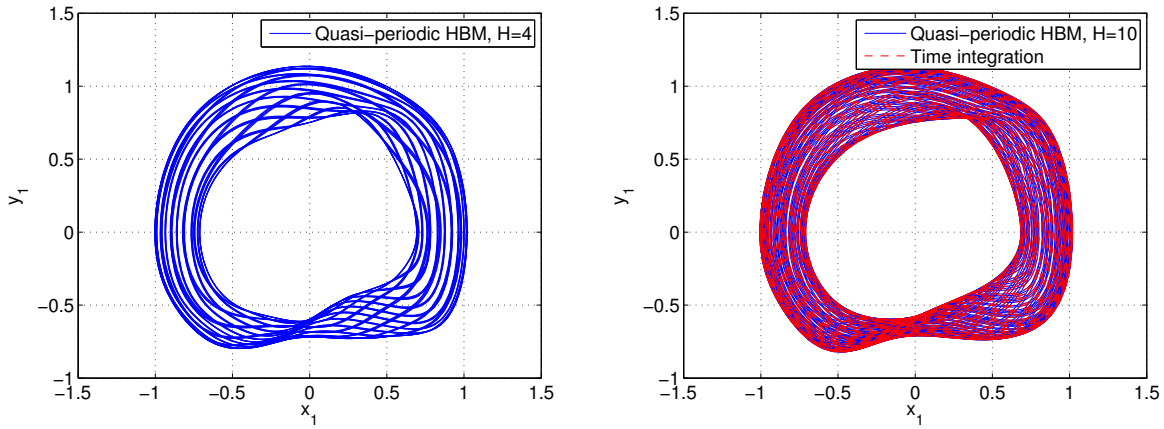

Figure 3: Phase diagrams (x_1, y_1), for $\lambda = 0.36$. Left : quasi-periodic Harmonic Balance, $H = 4$. Right : comparison of quasi-periodic Harmonic Balance ($H = 10$, blue solid line) and time integration (red dashed line).

3 CONCLUSION

The coupling of two-frequencies harmonic balance with the Asymptotic Numerical Method, a robust continuation technique, is performed automatically thanks to the quadratic framework. It proves very efficient to continue quasi-periodic solutions, without any *a priori* knowledge nor optimization. As one could expect, better accuracy is obtained using more Fourier coefficients, and comparison with time integration is successful. Future works will focus on musical examples, though this method is relevant for many nonlinear systems.

Acknowledgements

This work has been carried out in the framework of the Labex MEC (ANR-10-LABX-0092) and of the A*MIDEX project (ANR-11-IDEX-0001-02), funded by the *Investissements d'Avenir* French Government program managed by the French National Research Agency (ANR).

REFERENCES

[1] L. O. Chua, A. Ushida, Algorithms for computing almost periodic steady-state response of nonlinear systems to multiple input frequencies. *IEEE Transactions on Circuits and Systems,* **10**, 953-971, vol. CAS-28, 1981.

[2] T. M. Cameron, J. H. Griffin, An Alternating Frequency/Time Domain Method for Calculating the Steady-State Response of Nonlinear Dynamic Systems. *Journal of Applied Mechanics*, **56**, 149-154, 1989.

[3] N. Coudeyras, S. Nacivet, J.-J. Sinou, Periodic and quasi-periodic solutions for multi-instabilities involved in brake squeal. *Journal of Sound and Vibration*, **328**, 520540, 2009.

[4] L. Peletan, S. Baguet, M. Torkhani, G. Jacquet-Richardet, Quasi-periodic harmonic balance method for rubbing self-induced vibrations in rotorstator dynamics. *Nonlinear Dynamics*, **78(4)**, 2501-2515, 2014.

[5] B. Cochelin, C. Vergez, A high order purely frequency-based harmonic balance formulation for continuation of periodic solutions. *Journal of Sound and Vibration*, **324(1)**, 243-262, 2009.

[6] A. Lazarus, O. Thomas, A harmonic-based method for computing the stability of periodic solutions of dynamical systems. *Comptes Rendus Mecanique*, **338**, 510-517, 2010.

[7] L.F. Shampine, M.W. Reichelt, The Matlab ODE suite. *SIAM Journal on Scientific Computing*, **18**, 1-22, 1997.

ECCOMAS Congress 2016
VII European Congress on Computational Methods in Applied Sciences and Engineering
M. Papadrakakis, V. Papadopoulos, G. Stefanou, V. Plevris (eds.)
Crete Island, Greece, 5–10 June 2016

ASYMPTOTIC ANALYSIS OF DEFORMATIONS OF THE SLIGHTLY ORTHOTROPIC SPHERICAL LAYER UNDER NORMAL PRESSURE

Andrei L. Smirnov, Svetlana M. Bauer, Liudmila A. Venatovskaia and Eva B. Voronkova

St. Petersburg State Univessity
7/9 Universitetskaya nab., St. Petersburg, 199034, Russia
e-mail: {a.l.smirnov, s.bauer, l.venatovskaya, e.voronkova}@spbu.ru

Keywords: Lame problem, orthotropic spherical layer, asymptotic analysis

Abstract. *The deformation of the orthotropic spherical layer under normal pressure applied on the outer and inner surfaces is analyzed. The layer is assumed to be slightly orthotropic, it permits to apply asymptotic methods. The equations of zeroth and first approximations are derived. For the shell, which is much softer in the transverse direction than in the tangential plane, one gets singularly perturbed boundary value problem. Solving this problem in the zeroth approximation the asymptotic formula for the change of the relative layer thickness under normal pressure is obtained. Also the effect of Poisson ratio and the layer thickness on the deformation is studied. For the cases of the thick and thin layers the last formula may be simplified. The asymptotic results well agree with the exact solution. The developed formulas are used in analysis of the scleral shell under intraocular pressure and may also be used in solution of the inverse problem, i.e. in analysis of the stress-strain state of a human eye under injection. The solution of the problem helps to estimate the mechanical parameters of the sclera, i.e. to find the ratio of the tangential and transversal Young moduli using clinical data for the sclera thickness change.*

1 INTRODUCTION

The 3D problem for deformation of orthotropic spherical layer under normal pressure is considered. Such model may be used, for example, to describe the changes of the stress strain state of the external human eye shell under intraocular injections. For isotropic spherical layer this problem, known as Lame problem, is discussed, for example, in [1]. For transverse isotropic spherical layer the analytical solution has been obtained in [2, 3] and asymptotic solution in [4]. The stress-strain state of a two-layered transversely isotropic spherical shell is discussed in [5].

2 PROBLEM STATEMENT

2.1 Equilibrium equations in displacements

Consider orthotropic spherical layer with the internal radius R_1, external radius R_2 and thickness $h = R_2 - R_1$ (see Fig. 1).

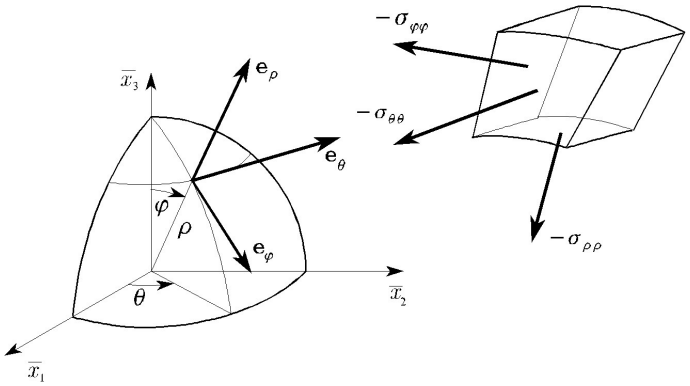

Figure 1: Orthotropic spherical layer

The position of the point of the spherical layer in given by spherical coordinates: ρ — radial coordinate, φ — meridional coordinate, θ — circumferential coordinate. Equilibrium equations for the spherical layer have the form [1]

$$\begin{aligned}
\frac{\partial\sigma_{\rho\rho}}{\partial\rho}+\frac{1}{\rho}\frac{\partial\sigma_{\rho\varphi}}{\partial\varphi}+\frac{1}{\rho\sin\varphi}\frac{\partial\sigma_{\rho\theta}}{\partial\theta}+\frac{\cos\varphi}{\rho\sin\varphi}\sigma_{\rho\varphi}+\frac{1}{\rho}(2\sigma_{\rho\rho}-\sigma_{\varphi\varphi}-\sigma_{\theta\theta})+f_\rho &= 0,\\
\frac{\partial\sigma_{\varphi\rho}}{\partial\rho}+\frac{1}{\rho}\frac{\partial\sigma_{\varphi\varphi}}{\partial\varphi}+\frac{1}{\rho\sin\varphi}\frac{\partial\sigma_{\varphi\theta}}{\partial\theta}+\frac{3}{\rho}\sigma_{\varphi\rho}+\frac{\cos\varphi}{\rho\sin\varphi}(\sigma_{\varphi\varphi}-\sigma_{\theta\theta})+f_\varphi &= 0,\\
\frac{\partial\sigma_{\theta\rho}}{\partial\rho}+\frac{1}{\rho}\frac{\partial\sigma_{\theta\varphi}}{\partial\varphi}+\frac{1}{\rho\sin\varphi}\frac{\partial\sigma_{\theta\theta}}{\partial\theta}+\frac{3}{\rho}\sigma_{\theta\rho}+\frac{2\cos\varphi}{\rho\sin\varphi}\sigma_{\theta\varphi}+f_\theta &= 0,
\end{aligned}$$

here $\sigma_{\rho\rho}$, $\sigma_{\varphi\varphi}$ and $\sigma_{\theta\theta}$ — normal stress, $\sigma_{\rho\varphi}$, $\sigma_{\rho\theta}$, $\sigma_{\varphi\theta}$ — tangential stress, f_ρ, f_φ, f_θ — projections of the external forces in corresponding directions.

We consider axisymmetric problem without external forces. In this case the displacements do not depend on angle θ, and tangential stresses $\sigma_{\rho\theta}$, $\sigma_{\varphi\theta}$ and deformations $\varepsilon_{\varphi\theta}$, $\varepsilon_{\rho\theta}$ are equal to zero.

Thus, system of equations becomes

$$\begin{aligned}
\frac{\partial\sigma_{\rho\rho}}{\partial\rho}+\frac{1}{\rho}\frac{\partial\sigma_{\rho\varphi}}{\partial\varphi}+\frac{\cos\varphi}{\rho\sin\varphi}\sigma_{\rho\varphi}+\frac{1}{\rho}(2\sigma_{\rho\rho}-\sigma_{\varphi\varphi}-\sigma_{\theta\theta}) &= 0,\\
\frac{\partial\sigma_{\rho\varphi}}{\partial\rho}+\frac{1}{\rho}\frac{\partial\sigma_{\varphi\varphi}}{\partial\varphi}+\frac{3}{\rho}\sigma_{\rho\varphi}+\frac{\cos\varphi}{\rho\sin\varphi}(\sigma_{\varphi\varphi}-\sigma_{\theta\theta}) &= 0.
\end{aligned} \tag{1}$$

The displacements of the spherical layer are given with projections of the displacement vector $(w,\, u,\, v)$ in directions ρ, φ and θ correspondingly. For axisymmetrilc problem $v = 0$. The relations for deformations and displacements of the spherical layer are the following [1]

$$\varepsilon_{\rho\rho} = \frac{\partial w}{\partial \rho},\;\; \varepsilon_{\varphi\varphi} = \frac{1}{\rho}\frac{\partial u}{\partial \varphi} + \frac{w}{\rho},\;\; \varepsilon_{\theta\theta} = \cot\varphi\frac{u}{\rho} + \frac{w}{\rho},\;\; \varepsilon_{\rho\varphi} = \frac{1}{2}\left(\frac{1}{\rho}\frac{\partial w}{\partial \varphi} - \frac{u}{\rho} + \frac{\partial u}{\partial \rho}\right). \tag{2}$$

Next consider constitutive relations for stresses and deformations. For the orthotropic media they contain 9 independent elastic moduli: E_ρ, E_φ, E_θ — Young moduli, $\nu_{\varphi\rho}$, $\nu_{\theta\rho}$, $\nu_{\theta\varphi}$, — Poisson ratios, $G_{\rho\varphi}$, $G_{\varphi\theta}$, $G_{\rho\theta}$ — shear moduli [6]

$$\begin{aligned}
\varepsilon_{\rho\rho} &= \frac{1}{E_\rho}\sigma_{\rho\rho} - \frac{\nu_{\rho\varphi}}{E_\varphi}\sigma_{\varphi\varphi} - \frac{\nu_{\rho\theta}}{E_\theta}\sigma_{\theta\theta}, \qquad \varepsilon_{\rho\theta} = \sigma_{\rho\theta}/G_{\rho\theta},\\
\varepsilon_{\varphi\varphi} &= -\frac{\nu_{\varphi\rho}}{E_\rho}\sigma_{\rho\rho} + \frac{1}{E_\varphi}\sigma_{\varphi\varphi} - \frac{\nu_{\varphi\theta}}{E_\theta}\sigma_{\theta\theta}, \quad \varepsilon_{\varphi\theta} = \sigma_{\varphi\theta}/G_{\rho\theta},\\
\varepsilon_{\theta\theta} &= -\frac{\nu_{\theta\rho}}{E_\rho}\sigma_{\rho\rho} - \frac{\nu_{\theta\varphi}}{E_\varphi}\sigma_{\varphi\varphi} + \frac{1}{E_\theta}\sigma_{\theta\theta}, \quad \varepsilon_{\rho\varphi} = \sigma_{\rho\varphi}/G_{\rho\varphi}.
\end{aligned} \tag{3}$$

Due to symmetry of relations (3) the following equalities are valid

$$E_\varphi\nu_{\varphi\rho} = E_\rho\nu_{\rho\varphi}, \quad E_\varphi\nu_{\varphi\theta} = E_\theta\nu_{\theta\varphi}, \quad E_\theta\nu_{\theta\rho} = E_\rho\nu_{\rho\theta}. \tag{4}$$

Introduce new constants [6]

$$\begin{gathered}
\nu^*_{\varphi\theta} = \frac{\nu_{\varphi\theta} + \nu_{\varphi\rho}\nu_{\rho\theta}}{1 - \nu_{\theta\rho}\nu_{\rho\theta}}, \quad \nu^*_{\varphi\rho} = \frac{\nu_{\varphi\rho} + \nu_{\varphi\theta}\nu_{\theta\rho}}{1 - \nu_{\theta\rho}\nu_{\rho\theta}}, \quad \nu^*_{\theta\varphi} = \frac{\nu_{\theta\varphi} + \nu_{\theta\rho}\nu_{\rho\varphi}}{1 - \nu_{\varphi\rho}\nu_{\rho\varphi}},\\
\nu^*_{\theta\rho} = \frac{\nu_{\theta\rho} + \nu_{\theta\varphi}\nu_{\varphi\rho}}{1 - \nu_{\varphi\rho}\nu_{\rho\varphi}}, \quad \nu^*_{\rho\varphi} = \frac{\nu_{\rho\varphi} + \nu_{\theta\varphi}\nu_{\rho\theta}}{1 - \nu_{\varphi\theta}\nu_{\theta\varphi}}, \nu^*_{\rho\theta} = \frac{\nu_{\rho\theta} + \nu_{\varphi\theta}\nu_{\rho\varphi}}{1 - \nu_{\varphi\theta}\nu_{\theta\varphi}},
\end{gathered} \tag{5}$$

$$\begin{gathered}
E^*_\varphi = E_\varphi/\left(1 - \nu^*_{\varphi\theta}\nu_{\theta\varphi} - \nu^*_{\varphi\rho}\nu_{\rho\varphi}\right), \qquad E^*_\theta = E_\theta/\left(1 - \nu^*_{\theta\varphi}\nu_{\varphi\theta} - \nu^*_{\theta\rho}\nu_{\rho\theta}\right),\\
E^*_\rho = E_\rho/\left(1 - \nu^*_{\rho\theta}\nu_{\theta\rho} - \nu^*_{\rho\varphi}\nu_{\varphi\rho}\right),
\end{gathered} \tag{6}$$

where

$$E^*_\rho\nu^*_{\rho\varphi} = E^*_\varphi\nu^*_{\varphi\rho}, \quad E^*_\varphi\nu^*_{\varphi\theta} = E^*_\theta\nu^*_{\theta\varphi}, \quad E^*_\theta\nu^*_{\theta\rho} = E^*_\rho\nu^*_{\rho\theta}. \tag{7}$$

Substituting (3) and (2) into (1) and taking into account (5)–(7) we get equilibrium equations in displacements as

$$\begin{aligned}
c_0\frac{\partial^2 w}{\partial\rho^2} + c_1\frac{\partial w}{\partial\rho} + c_2\frac{\partial^2 w}{\partial\varphi^2} + c_3\frac{\partial w}{\partial\varphi} + c_4 w + c_5\frac{\partial^2 u}{\partial\rho\,\partial\varphi} + c_6\frac{\partial u}{\partial\rho} + c_7\frac{\partial u}{\partial\varphi} + c_8 u &= 0,\\
d_0\frac{\partial^2 u}{\partial\rho^2} + d_1\frac{\partial u}{\partial\rho} + d_2\frac{\partial^2 u}{\partial\varphi^2} + d_3\frac{\partial u}{\partial\varphi} + d_4 u + d_5\frac{\partial^2 w}{\partial\rho\,\partial\varphi} + d_6\frac{\partial w}{\partial\rho} + d_7\frac{\partial w}{\partial\varphi} + d_8 w &= 0,
\end{aligned} \tag{8}$$

where expressions for c_i and d_i are listed in Appendix.

2.2 Boundary conditions

We consider the quarter of the spherical layer, i.e. domain $0 \leqslant \varphi \leqslant \dfrac{\pi}{2}$ and $R_1 \leqslant \rho \leqslant R_2$.

On the boundary $\varphi = 0$ and $\varphi = \dfrac{\pi}{2}$ we assume

$$u(\rho,0) = u\left(\rho,\frac{\pi}{2}\right) = 0, \quad \frac{\partial u}{\partial \varphi}(\rho,0) = \frac{\partial u}{\partial \varphi}\left(\rho,\frac{\pi}{2}\right) = 0, \quad \frac{\partial w}{\partial \varphi}(\rho,0) = \frac{\partial w}{\partial \varphi}\left(\rho,\frac{\pi}{2}\right) = 0. \quad (9)$$

On the boundary $\rho = R_1$ and $\rho = R_2$ we suppose that the normal pressure $P_1,\ P_2$ is given

$$\sigma_{\rho\rho}(R_1,\varphi) = -P_1, \qquad \sigma_{\rho\rho}(R_2,\varphi) = -P_2 \quad (10)$$

where

$$\sigma_{\rho\rho} = E^*_\rho \left(\frac{\partial w}{\partial \rho} + \frac{\nu^*_{\rho\varphi} + \nu^*_{\rho\theta}}{\rho} w + \frac{\nu^*_{\rho\varphi}}{\rho}\frac{\partial u}{\partial \varphi} + \frac{\nu^*_{\rho\theta}\cot(\varphi)}{\rho} u \right).$$

Equations (8) and boundary conditions (9)–(10) provide the boundary value problem.

2.3 Restrictions on elastic constants

As we mention above the descriptions of the orthotropic material requires 9 independent elastic moduli. However, due to the positive definiteness of the elastic potential its coefficient must satisfy Sylvester criterion, from which the following inequalities may be found [6]

$$\begin{aligned} &\nu_{\rho\varphi} < \sqrt{E_\varphi/E_\rho}, \qquad \nu_{\rho\theta} < \sqrt{E_\theta/E_\rho}, \qquad \nu_{\varphi\theta} < \sqrt{E_\theta/E_\varphi}, \\ &\nu_{\rho\varphi}\nu_{\varphi\theta}\nu_{\theta\rho} < 1/2\left(1 - \nu^2_{\rho\varphi}E_\rho/E_\varphi - \nu^2_{\varphi\theta}E_\varphi/E_\theta - \nu^2_{\theta\rho}E_\theta/E_\rho\right). \end{aligned} \quad (11)$$

3 SLIGHTLY ORTHOTROPIC MATERIAL. PERTURBATION METHOD

Consider that the elastic modulus in the circumferential direction is little different from the modulus in the meridional direction. We assume that the following relations for the material elastic constants are valid

$$\begin{aligned} &E_\rho = E_1,\ E_\varphi = E,\ E_\theta = E(1+\mu),\ \nu_{\theta\varphi} = \nu,\ \nu_{\varphi\rho} = \nu_{\theta\rho} = \nu_1. \\ &G_{\varphi\theta} = G + \mu G' = \frac{E}{2(1+\nu)} + \mu G',\ G_{\rho\varphi} = G_1,\ G_{\rho\theta} = G_1 + \mu G'', \end{aligned}$$

where $\mu \ll 1$. For $\mu = 0$ the material becomes transverse isotropic.

In this case the limitations on elastic modulii (11) are

$$\nu < \frac{1}{1+\mu}, \qquad \nu_1 < \sqrt{\frac{E_1}{E}} \cdot \min\left(1, \sqrt{\frac{1}{1+\mu}}, \sqrt{\frac{1+\mu-\nu^2}{(1+\mu)(2+\mu+2\nu)}}\right). \quad (12)$$

The domain of the material parameters (μ, ν, ν_1) is plotted in Fig. 2

Solution of equation (8) we seek in the form

$$w(\rho,\varphi) = w_0(\rho) + \mu w_1(\rho,\varphi) + O(\mu^2), \qquad u(\rho,\varphi) = \mu u_1(\rho,\varphi) + O(\mu^2).$$

Equation of zeroth approximation for function $w_0(\rho)$ have been considered in [4]. This is equation for the transversely isotropic layer. We report shortly the results of [4] in next section.

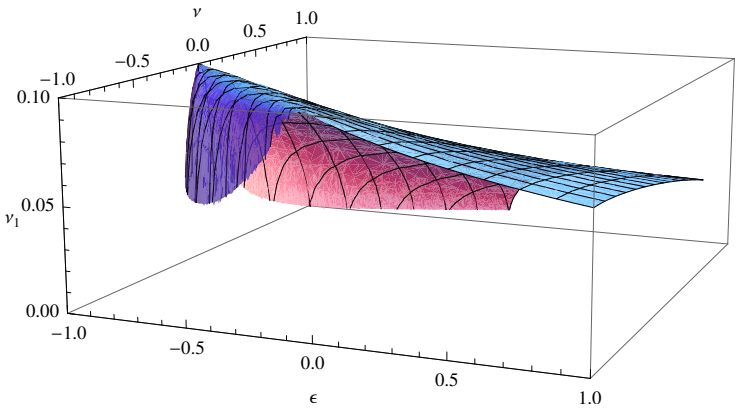

Figure 2: The domain of the elastic moduli (μ, ν, ν_1) for $E/E_1 = 0.01$.

4 EQUATION OF ZEROTH APPROXIMATION

For zeroth approximation the equilibrium equations for the normal displacement may be reduced to a single equation in the form

$$w_0''(\rho) + \frac{2}{\rho} w_0'(\rho) - 2\frac{E(1-\nu_1)}{E_1(1-\nu)\rho^2} w_0(\rho) = 0, \tag{13}$$

and boundary conditions are

$$2EE_1\nu_1 w(R_i) + E_1^2(1-\nu)w'(R_i)R_i = -P_i R_i \left(E_1(1-\nu) - 2E\nu_1^2\right), \qquad i = 1, 2.$$

The restrictions on elastic constants becomes

$$\nu < 1, \qquad \nu_1 < \sqrt{\frac{E_1}{E}} \cdot \min\left(1, \sqrt{\frac{1-\nu}{2}}\right),$$

and since for all known materials $\nu > -1$ then $\sqrt{\dfrac{1-\nu}{2}} < 1$. This problem has an exact analytical solution obtained in [2, 3], but formulas for the displacement w and stress functions are rather complicated. That is why it is more convenient to use an asymptotic approach to analyze the effect of the parameters of the spherical layer on the stress-strain state of the layer.

4.1 Asymptotic analysis

For the layer, which is much softer in the transverse direction than in the tangential surface we assume $E_1 = \varepsilon^2 E$. $\nu_1 = \varepsilon^\alpha \nu_1^*$, where $\varepsilon \ll 1$, $\nu_1^* \approx 1$, $\alpha \geq 1$. In the further analysis $\alpha = 1$. The equation for the normal displacement becomes

$$\varepsilon^2 w_0''(\rho)\rho^2 + 2\varepsilon^2 \rho w_0'(\rho) - (a + b\varepsilon) w_0(\rho) = 0, \tag{14}$$

where $a = \dfrac{2}{1-\nu}$; and $b = -\dfrac{2\nu_1^*}{1-\nu}$, and the boundary conditions are

$$\varepsilon f w(R_i) + \varepsilon^2 g w'(R_i) R_i = -c p_i R_i, \qquad i = 1, 2. \tag{15}$$

Here $p_i = P_i/E$, $c = (1 - \nu - 2\nu_1^{*2})$, $f = 2\nu_1^*$, $g = 1 - \nu$. To solve singularly perturbed equation (14) we follow [7] and seek a solution in the form

$$w(\rho) = e^{\frac{1}{\varepsilon}\int_0^\rho \lambda(t)dt}(w_0(\rho) + \varepsilon w_1(\rho) + \cdots). \tag{16}$$

After substitution in (14) and equating the coefficients at ε^k to zero we obtain a system of equations for the unknowns $\lambda(\rho), w_0(\rho), w_1(\rho), \ldots$

$$\begin{aligned} &w_0(\rho)(-a+\rho^2\lambda^2(\rho))=0,\\ &2\rho^2 w_0'(\rho)\lambda'(\rho)+w_0(\rho)(-b+2\rho\lambda'(\rho)-\rho^2\lambda''(\rho))=0,\\ &\ldots \end{aligned} \tag{17}$$

The solution of the first equation gives $\lambda(\rho)=\pm\dfrac{\sqrt{a}}{\rho}$ and the solution of the second equation is

$$w_0(\rho)=\rho^\beta, \qquad \beta=\frac{1}{2}\left(\pm\frac{b}{\sqrt{a}}-1\right).$$

So, for the first approximation we get

$$w(\rho)=A\rho^{\gamma_1}+B\rho^{\gamma_2}, \tag{18}$$

where $\gamma_{1,2}=\pm\dfrac{\sqrt{a}}{\varepsilon}+\dfrac{1}{2}\left(\pm\dfrac{b}{\sqrt{a}}-1\right)$. Constants A and B may be found from the boundary conditions

$$A=-\frac{c}{\varepsilon}\frac{R_1G_1p_1-R_2G_2p_2}{F^+(G_1^2-G_2^2)}, \qquad B=-\frac{c}{\varepsilon}\frac{G_1G_2(R_2G_1p_2-R_2G_2p_1)}{F^-(G_1^2-G_2^2)}$$

where $F^\pm=\sqrt{a}g\pm f$ and $G_i=R_i^{\sqrt{a}/\varepsilon}$. The change of the layer thickness is obtained using formula for the normal displacement

$$\Delta h=\frac{w(R_2)-w(R_1)}{R_2-R_1}$$

or

$$\Delta h=-\frac{c}{\varepsilon}\frac{p_1R_1(F^+G_2-F^-G_1)+p_2R_2(F^-G_2-F^+G_1)}{(F^-F^+(G_1+G_2))(R_2-R_1)} \tag{19}$$

4.2 Examples and applications

Further simplification of the formula for the change of the layer thickness is based on the assumptions on ratio of the values R_1 and R_2. For example, for the thick layer $R_1 \ll R_2$, then $\xi=R_1/R_2 \ll 1$ ($\xi \ll 1$) and $G_1 \ll G_2$. In this case the first approximation for Δh has the form

$$\Delta h=-\frac{c}{\varepsilon}\frac{p_1\xi F^+ + p_2F^-}{(F^+F^-)(1-\xi)}. \tag{20}$$

For the thin layer $R_1 \approx R_2$. In this case

$$\Delta h=-\frac{c}{\varepsilon\eta}\frac{p_1(1-\eta)(F^+-F^-(1-\eta)^\varkappa)+p_2(F^--F^+(1-\eta)^\varkappa)}{F^-F^+(1+(1-\eta)^\varkappa)},$$

where $R_1=(1-\eta)R_2$ ($\eta=1-\xi \ll 1$), $\varkappa=\sqrt{a}/\varepsilon$.

Let consider as an example the scleral shell with parameters [8] $\nu=0.48$, $P_1=p\times 133.3$ Pa, $P_2=0$ Pa, $E=14$ MPa, $\nu_1^*=0.5$, Here $p=20$ is the intraocular pressure in mm Hg. The change of the layer thickness as a function of ε is represented in Fig. 3 for thick layer ($\eta=0.7$) (left) and for thin layer ($\eta=0.04$) (right).

The change of the layer thickness as a function of ε and $\xi=R_1/R_2$ is represented in Fig. 4

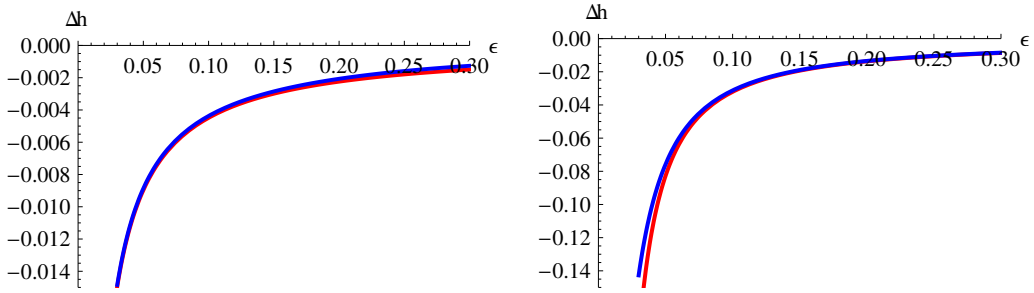

Figure 3: The change of the layer thickness vs. ε (the exact solution (blue line), the asymptotic solution (red line)).

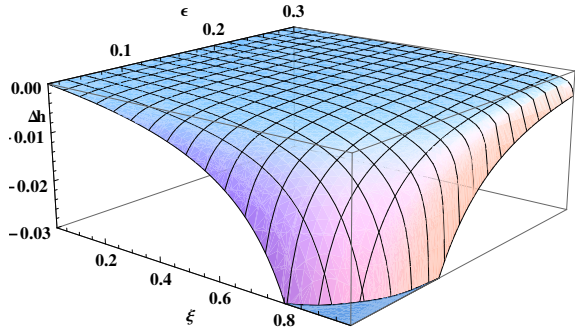

Figure 4: The change of the layer thickness as a function of ε and $\xi = R_1/R_2$.

.

5 EQUATIONS OF FIRST APPROXIMATION

For the first approximation we get equations

$$m_0\frac{\partial^2 w_1}{\partial\rho^2}+m_1\frac{\partial w_1}{\partial\rho}+m_2\frac{\partial^2 w_1}{\partial\varphi^2}+m_3\frac{\partial w_1}{\partial\varphi}+m_4 w_1+m_5\frac{\partial^2 u_1}{\partial\rho\,\partial\varphi}+m_6\frac{\partial u_1}{\partial\rho}+$$
$$+m_7\frac{\partial u_1}{\partial\varphi}+m_8 u_1+m_9 w_0=0, \qquad (21)$$
$$n_0\frac{\partial^2 u_1}{\partial\rho^2}+n_1\frac{\partial u_1}{\partial\rho}+n_2\frac{\partial^2 u_1}{\partial\varphi^2}+n_3\frac{\partial u_1}{\partial\varphi}+n_4 u_1+n_5\frac{\partial^2 w_1}{\partial\rho\,\partial\varphi}+n_6\frac{\partial w_1}{\partial\varphi}+$$
$$+n_7\frac{\partial w_0}{\partial\rho}+n_8 w_0=0,$$

where expressions for m_i and n_i are listed in Appendix and boundary conditions

$$u_1\big|_{\varphi=0}=u_1\big|_{\varphi=\pi/2}=0,\quad \frac{\partial u_1}{\partial\varphi}\Big|_{\varphi=0}=\frac{\partial u_1}{\partial\varphi}\Big|_{\varphi=\pi/2}=0,\quad \frac{\partial w_1}{\partial\varphi}\Big|_{\varphi=0}=\frac{\partial w_1}{\partial\varphi}\Big|_{\varphi=\pi/2}=0, \qquad (22)$$

and

$$\sigma^1_{\rho\rho}(R_1,\varphi)=\sigma^1_{\rho\rho}(R_2,\varphi)=0, \qquad (23)$$

where

$$\sigma^1_{\rho\rho}=l_0\frac{\partial w_1}{\partial\rho}+l_1 w_1+l_2\frac{\partial w_0}{\partial\rho}+l_3 w_0+l_4\frac{\partial u_1}{\partial\varphi}+l_5 u_1,$$

and

$$l_0 = 1, \quad l_1 = \frac{2}{\rho}\frac{E\nu_1}{E_1(1-\nu)}, \quad l_2 = \frac{E\nu_1^2}{(1-\nu)(E_1(1-\nu)-2E\nu_1^2)}, \tag{24}$$
$$l_3 = \frac{l_2}{\nu_1\rho}, \quad l_4 = \frac{E\nu_1}{E_1(1-\nu)\rho}, \quad l_5 = l_4\cot(\varphi).$$

So, the boundary value problem for the first approximation consists of equations (21) and boundary conditions (22)–(23). We note, that the change of the shear moduli (G',G'') do not effect equations and boundary conditions of the first approximation.

Figure 5 depicts deformed orthotropic layer for two different ratio of E_θ/E_φ. The layer parameters are taken as follows $R_2 = 12$ mm, $R_1 = 0.9R_2$, $E_\varphi = E = 14$ MPa, $E_\rho = E_1 = 1.26$ MPa, $\nu = 0.48$, $\nu_1 = 0.03$. The inner boundary $\rho = R_1$ is subjected to normal pressure $P_1 = 20 \times 133.3$ Pa.

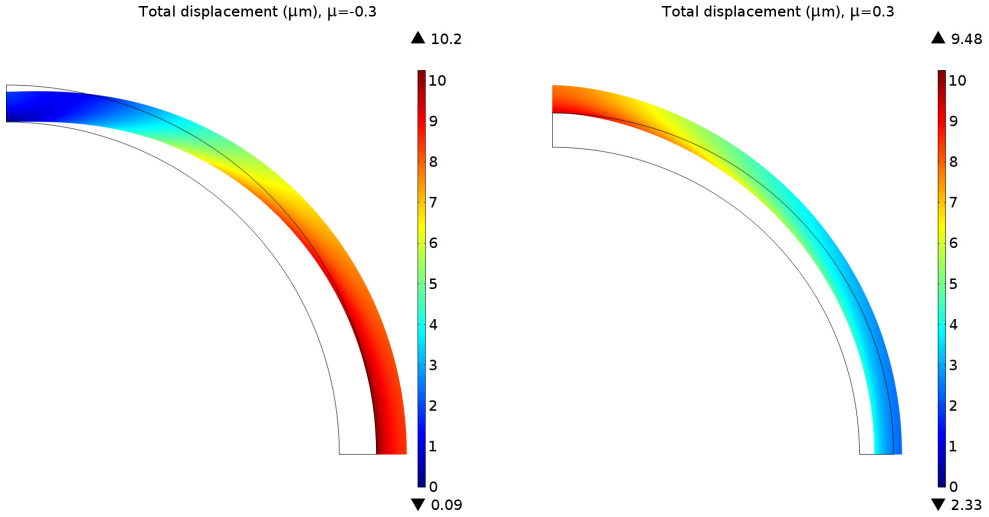

Figure 5: Deformed orthotropic layer with $E_\theta/E_\varphi = 0.7\,(\mu = -0.3)$ and $E_\theta/E_\varphi = 1.3\,(\mu = 0.3)$.

6 CONCLUSIONS

1. For transversely isotropic material the asymptotic formula describing the change of the layer thickness under normal pressure is obtained. Asymptotic relations show that for deformation of the spherical layer under the inner pressure the relative thickness varies more for the layer with smaller thickness.

2. The change of the scleral thickness under intraocular pressure (IOP) well agree with clinical data on decrease of scleral thickness in primary open-angle glaucoma (POAG) [8]. POAG is an eye disease, which is generally accompanied by the IOP increase.

ACKNOWLEDGEMENTS

This work was financially supported by the Russian Foundation for Basic Research, grants # 15-01-06311-a and 16-01-00580-a and was performed at the Observatory of Environmental Safety Center of Research park of St. Petersburg State University.

APPENDIX

$$
\begin{aligned}
&c_0 = 1, \;\; c_1 = \frac{2}{\rho}, \quad c_2 = \frac{1}{2\rho^2}\frac{G_{\rho\varphi}}{E^*_\rho}, \quad c_3 = c_2\cot(\varphi),\\
&c_4 = \frac{1}{\rho^2}\left(\nu^*_{\rho\varphi} + \nu^*_{\rho\theta} - \frac{E^*_\varphi + 2\,\nu^*_{\varphi\theta}E^*_\varphi + E^*_\theta}{E^*_\rho}\right),\\
&c_5 = \frac{1}{\rho}\left(\nu^*_{\rho\varphi} + \frac{G_{\rho\varphi}}{2E^*_\rho}\right), \quad c_6 = \frac{\cot(\varphi)}{\rho}\left(\nu^*_{\rho\theta} + \frac{G_{\rho\varphi}}{2E^*_\rho}\right),\\
&c_7 = \frac{1}{\rho^2}\left(\nu^*_{\rho\varphi} - \frac{E^*_\varphi}{E^*_\rho}(1+\nu^*_{\phi\theta}) - \frac{G_{\rho\varphi}}{2E^*_\rho}\right),\\
&c_8 = \frac{\cot(\varphi)}{\rho^2}\left(\nu^*_{\rho\theta} - \frac{E^*_\varphi\nu^*_{\varphi\theta} + E^*_\theta}{E^*_\rho} - \frac{G_{\rho\varphi}}{2E^*_\rho}\right)
\end{aligned}
\tag{25}
$$

$$
\begin{aligned}
&d_0 = 1, \;\; d_1 = \frac{2}{\rho}, \quad d_2 = \frac{2}{\rho^2}\frac{E^*_\varphi}{G_{\rho\varphi}}, \quad d_3 = d_2\cot(\varphi),\\
&d_4 = -\frac{2}{\rho^2}\left(1 + \frac{E^*_\varphi\nu^*_{\varphi\theta}}{G_{\rho\varphi}} + \frac{E^*_\theta}{G_{\rho\varphi}}\cot^2(\varphi)\right),\\
&d_5 = \frac{1}{\rho}\left(1 + 2\frac{E^*_\rho\nu^*_{\rho\varphi}}{G_{\rho\varphi}}\right), \quad d_6 = \frac{2\cot(\varphi)}{\rho}\frac{E^*_\rho}{G_{\rho\varphi}}(\nu^*_{\rho\varphi} - \nu^*_{\rho\theta}),\\
&d_7 = \frac{2}{\rho^2}\left(1 + \frac{E^*_\varphi}{G_{\rho\varphi}}(1+\nu^*_{\varphi\theta})\right), \quad d_8 = \frac{2\cot(\varphi)}{\rho^2}\frac{E^*_\varphi - E^*_\theta}{G_{\rho\varphi}},
\end{aligned}
\tag{26}
$$

$$
\begin{aligned}
&m_0 = 1, \;\; m_1 = \frac{2}{\rho}, \quad m_2 = \frac{G_{\rho\varphi}}{2\rho^2 E^*_{\rho_0}}, \quad m_3 = m_2\cot(\varphi),\\
&m_4 = -\frac{2}{\rho^2}\frac{E(1-\nu_1)}{E_1(1-\nu)}, \quad m_5 = \frac{1}{\rho}\left(\frac{G_{\rho\varphi}}{2E^*_{\rho_0}} + \frac{E\nu_1}{E_1(1-\nu)}\right),\\
&m_6 = m_5\cot(\varphi), \quad m_7 = -\frac{1}{\rho^2}\left(\frac{E(1-\nu_1)}{E_1(1-\nu)} + \frac{G_{\rho\varphi}}{2E^*_{\rho_0}}\right),\\
&m_8 = m_7\cot(\varphi), \quad m_9 = -\frac{1}{\rho^2}\frac{E(1-\nu_1)}{E_1(1-\nu)^2},\\
&E^*_{\rho_0} = \frac{E_1^2(1-\nu)}{E_1(1-\nu) - 2E\nu_1^2}.
\end{aligned}
\tag{27}
$$

$$
\begin{aligned}
&n_0 = 1, \;\; n_1 = \frac{2}{\rho}, \quad n_2 = \frac{2E^*_{\varphi_0}}{G_{\rho\varphi}\rho^2}, \quad n_3 = n_2\cot(\varphi),\\
&n_4 = -\frac{2}{\rho^2}\left(1 + \frac{E^*_{\varphi\theta_0}}{G_{\rho\varphi}} + \frac{E^*_{\varphi_0}}{G_{\rho\varphi}}\cot^2(\varphi)\right), \quad n_5 = \frac{1}{\rho}\left(1 + \frac{2E^*_{\rho\varphi_0}}{G_{\rho\varphi}}\right)\\
&n_6 = \frac{2}{\rho^2}\left(1 + \frac{2E^*_{\rho\varphi_0}}{G_{\rho\varphi}\nu_1}\right), \quad n_7 = -\frac{2\cot(\varphi)}{\rho}\frac{E^*_{\rho\varphi_0}}{G_{\rho\varphi}(1+\nu)}, \quad n_8 = \frac{n_7}{\nu_1\rho},\\
&E^*_{\varphi_0} = \frac{E(E_1 - E\nu_1^2)}{(1+\nu)(E_1(1-\nu) - 2E\nu_1^2)}, \quad E^*_{\rho\varphi_0} = \frac{EE_1\nu_1}{E_1(1-\nu) - 2E\nu_1^2},\\
&E^*_{\varphi\theta_0} = \frac{E(E_1\nu + E\nu_1^2)}{(1+\nu)(E_1(1-\nu) - 2E\nu_1^2)}.
\end{aligned}
\tag{28}
$$

REFERENCES

[1] T.M. Atanackovic, A. Guran, *Theory of Elasticity for Scientists and Engineers*. Birkhäuser, 2000.

[2] S.M. Bauer, L.A. Zamuraev, K.E. Kotliar, Model of the transversally isotropic spherical layer for estimation of intraocular pressure changes after intravitreal injections. *Russian Journal of Biomechanics*, **10**, 41-47, 2006.

[3] S.M. Bauer, E.B. Voronkova, Nonclassical shell theories in ocular biomechanics. *Advanced Structured Materials*. **45**, 81-97, 2015.

[4] S.M. Bauer, A.L. Smirnov, Axisymmetric Deformations of the Orthotropic Spherical Layer under Normal Pressure. *Vestnik St. Petersburg University. Mathematics,* **48**, 35-40, 2015.

[5] L.A. Karamshina, On deformation of transversally isotropic two-layered spherical shell, *Vestnik Sankt-Peterburgskogo Universiteta. Seriya 1: Matematika. Mekhanika. Astronomiya,* **2**, 133-138, 2011.

[6] V.A. Rodionova, V.F. Titaev, and K.F. Chernykh, *Applied Theory of Anisotropic Plates and Shells*. SPbU, 1996. (in Russian).

[7] S.M. Bauer, S.B. Filippov, A.L. Smirnov, P.E. Tovstik, R. Vaillancourt, *Asymptotic Methods in Mechanics of Solids*. Springer, 2015.

[8] K. Kotliar, M. Maier, S. Bauer, N. Feucht, C. Lohmann and I. Lanzl, Effect of intravitreal injections and volume changes on intraocular pressure: clinical results and biomechanical model. *Acta Ophthalmologica Scandinavica*, **85**, 777-781, 2007.

ECCOMAS Congress 2016
VII European Congress on Computational Methods in Applied Sciences and Engineering
M. Filippoupolitis, C. Hopkins, SK. Au
Crete Island, Greece, 5–10 June 2016

EXPERIMENTAL VALIDATION OF FINITE ELEMENT MODELS FOR REINFORCED CONCRETE BEAMS WITH AND WITHOUT DISCONTINUITES

Marios Filippoupolitis[1], Carl Hopkins[2] and Siu-Kui Au[3]

[1] Institute for Risk and Uncertainty, University of Liverpool
Liverpool, L69 7ZF, UK
e-mail: m.filippoupolitis@liverpool.ac.uk

[2] Acoustics Research Unit, School of Architecture, University of Liverpool
Liverpool, L69 7ZN, UK
e-mail: carl.hopkins@liverpool.ac.uk

[3] Centre of Engineering Dynamics, School of Engineering, University of Liverpool
Liverpool, L69 3GH, UK
e-mail: siukuiau@liverpool.ac.uk

Keywords: Reinforced Concrete Beams, Discontinuities, Finite Element Analysis, Experimental Modal Analysis, Eigenfrequencies, Validation.

Abstract. *The aim of this paper is to assess the degree of accuracy in modelling the dynamic behaviour of reinforced concrete beams with and without discontinuities. Finite element models of three damaged and undamaged reinforced concrete beams were developed in Abaqus combining solid and beam elements and experimentally validated using experimental modal analysis. For the undamaged beams the agreement between the lowest 24 eigenfrequencies from the models and the measurements were within ≈3 %. For the damaged beams, the agreement was within 4 % above the lowest axial mode, whereas the errors were up to 10 % below the lowest axial mode. The validated finite element models will be used for further studies on the dynamic behaviour of collapsed reinforced concrete buildings.*

1 INTRODUCTION

Every few years an earthquake of high magnitude occurs around the globe leading in collapsed structures with people trapped inside them. When victims are trapped inside a collapsed building, the challenge is to detect and locate survivors within a period of time that will allow them to be rescued. The majority of documented live rescues are accomplished within the first 5 to 6 days [1]. However, important variables affect the survivability including the structure type and void space formation, the cause of the structural collapse, the survival location in the building and the speed and sophistication of available search and rescue capabilities [2].

Airborne sound from survivors tends to be highly attenuated by layers of rubble and requires the existence of air paths for propagation to the surface. For this reason there is greater potential to detect physical movement or signals by measuring vibration due to structure – borne sound (i.e. seismic research method). In a seismic search, a small number of seismic sensors are moved over a regular grid so that the operators can be certain they have searched the entire site. The placement and positioning of these sensors is critical for the successful detection of the survivors. However, grid spacing and sensor placement are often decided simply by checking whether it is possible to detect transients generated by the operators in an adjacent grid area on the surface in places where the structure is safe to walk [3]. This can be misleading because horizontal propagation of vibration across the surface of a collapsed structure is only vaguely indicative of propagation into the depths of a collapsed structure.

This research forms part of a PhD project which is funded by the EPSRC and concerns an approach to search for human survivors using structure-borne sound propagation in collapsed and fragmented structures through the development, validation and use of theoretical models. The aim in this paper is to assess the degree of accuracy in modelling the dynamic behaviour of damaged and undamaged one-dimensional reinforced concrete building elements. Experimental modal analysis is carried out on three reinforced concrete beams with and without discontinuities and the results are used for the validation of finite element models.

2 METHODS

2.1 Test specimens

The experimental samples consist of three reinforced concrete beams (C25/30, S500) with the same dimensions (2.4 m length, 0.2 m width and 0.3 m depth). The beams are reinforced with four longitudinal steel bars of 16 mm diameter and transverse reinforcement consisting of 8 mm diameter stirrups placed at 200 mm centres along the beams (see Figure 1). Three beams were measured: Beam 1 - an undamaged beam, Beam 2 - a beam with a 100 mm discontinuity in one position and Beam 3 - a beam with two 100 mm discontinuities in two positions. Figure 1 shows the structural details of the three reinforced concrete beams.

The discontinuities on beams 2 and 3 were formed by using a diamond saw to cut out the concrete. This also introduced cuts into some of the longitudinal steel bars which randomly reduced their cross-sectional area by 15 to 60%. These cuts into the steel bars are located at the beginning and end of each discontinuity zone (see Figure 2) and increased the uncertainty in the Abaqus models.

Table 1 gives the weight of each reinforced concrete beam that was measured using a crane scale.

Beam	Weight [Kg]
1	352.0
2	330.8
3	322.6

Table 1. Beam weights.

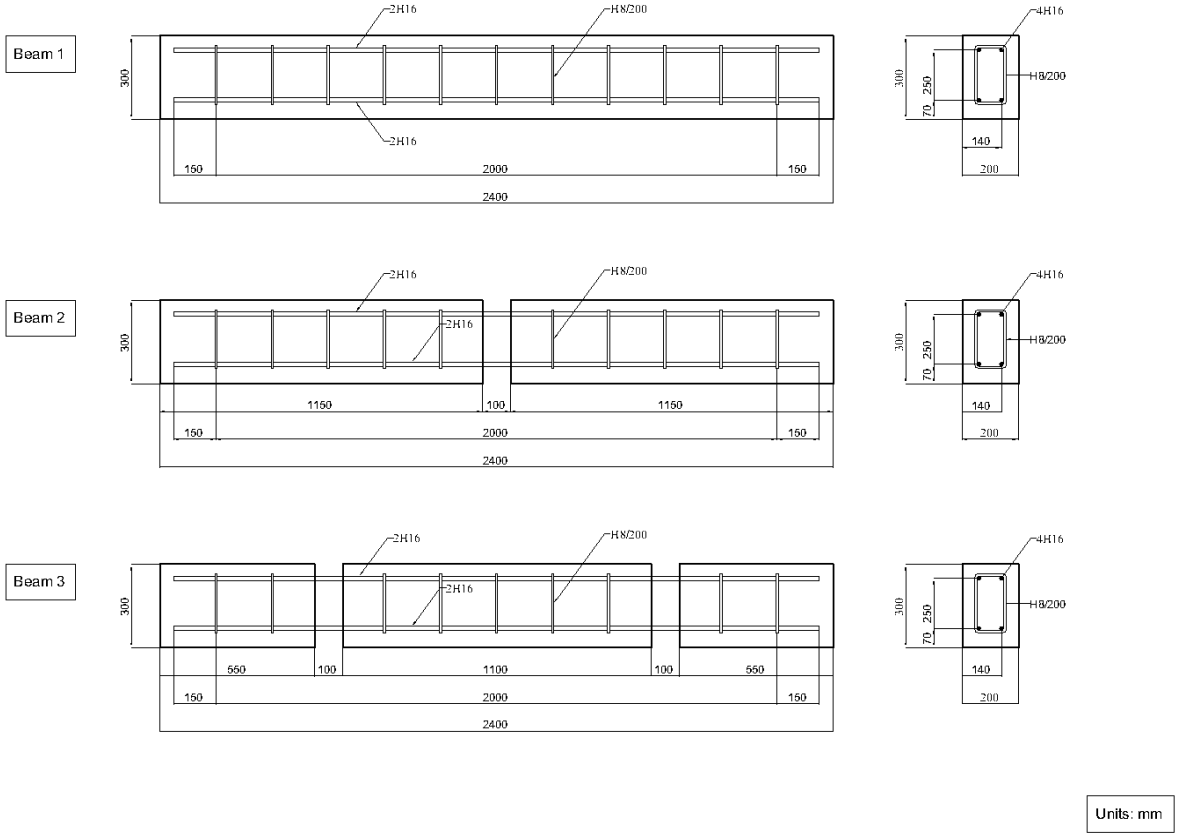

Figure 1. Structural details of the reinforced concrete beams.

Figure 2. Example of the reduction in the cross-section of a steel bar caused by a diamond saw cut

.

2.2 Experimental work

Experimental modal analysis was carried out on the three reinforced concrete beams in order to identify their dynamic characteristics (i.e. eigenfrequencies and modeshapes). The beams were suspended using polyester slings from an overhead crane in order to approximate a beam with free – free boundary conditions as the sling was assumed to have negligible effect on the dynamic response (Figure 3).

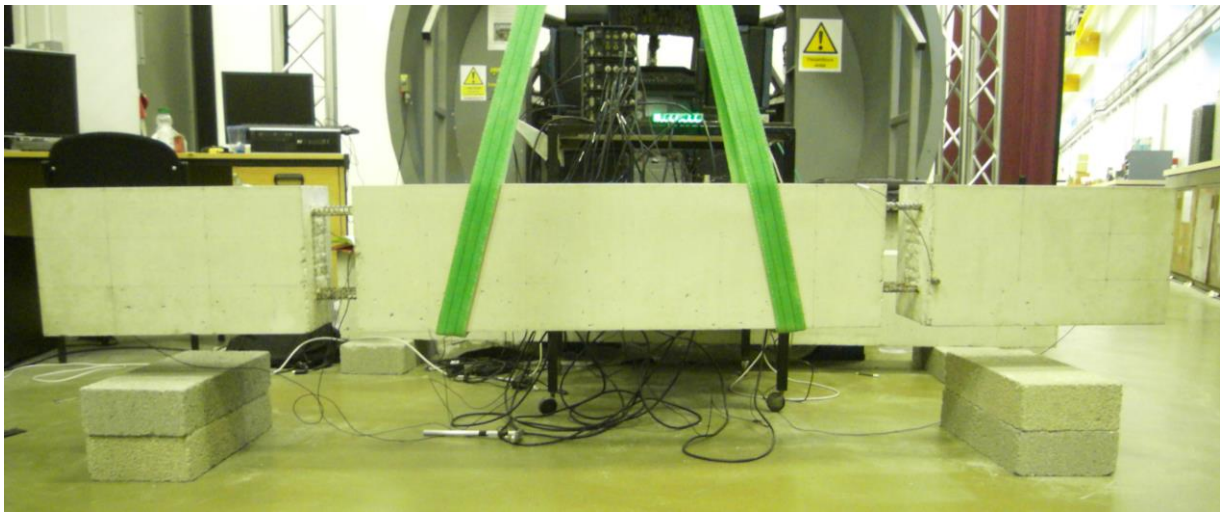

Figure 3 Test setup showing the test equipment and the polyester slings that approximate the free-free boundary condition for Beam 3

The beams were excited using a Brüel & Kjær Type 8200 impact hammer and the response on beams 1, 2 and 3 was measured using three, six and nine Brüel & Kjær Type 4371 accelerometers respectively. The transducers were connected to a Brüel & Kjær Type 3050-A-060 FFT analyser via a Type 2692 Nexus Conditioning Amplifier. The commercial software Brüel & Kjær Pulse Reflex was used for signal processing and the modal analysis. The accelerometers remained at fixed positions whilst the impact hammer was moved along a mesh of excitation points with spacing of 0.15m or 0.2m along the length and 0.1m in the other two directions. It is noted that only the concrete parts of the beams were excited. The total number of excited degrees of freedom was 206, 244 and 282 for beams 1, 2 and 3 respectively.

2.3 Finite element modelling

Finite element models of the three reinforced concrete beams were developed in Abaqus [4] and eigenfrequency analysis was carried out to define their dynamic characteristics (eigenfrequencies and modeshapes).

The solid element C3D20R (20 nodes) and the beam element B32 (3 nodes) were selected from the element library of Abaqus to model the concrete and the steel bars respectively. Both elements were selected to have interpolation functions of the same order (quadratic) to avoid accuracy issues [5]. This technique of combining three–dimensional (solid) with one dimensional (truss or beam) elements for modelling reinforced concrete members is well-established in the finite element analysis literature [6, 7]. A finite element mesh with dimensions of 25 mm in the longitudinal and 20 mm in the other two directions resulted in 27 elements per wavelength for the concrete and 8 elements per wavelength for the steel bars, at 3200 Hz.

This mesh density fulfils the requirement for at least 6 quadratic elements per wavelength in structural and vibroacoustic problems [8].

For the models of Beams 2 and 3 the discontinuities were formed by removing the appropriate number of solid and beam elements in each discontinuity zone (Figure 4). This approach was an efficient way of creating discontinuities in different positions of the beams without re-meshing.

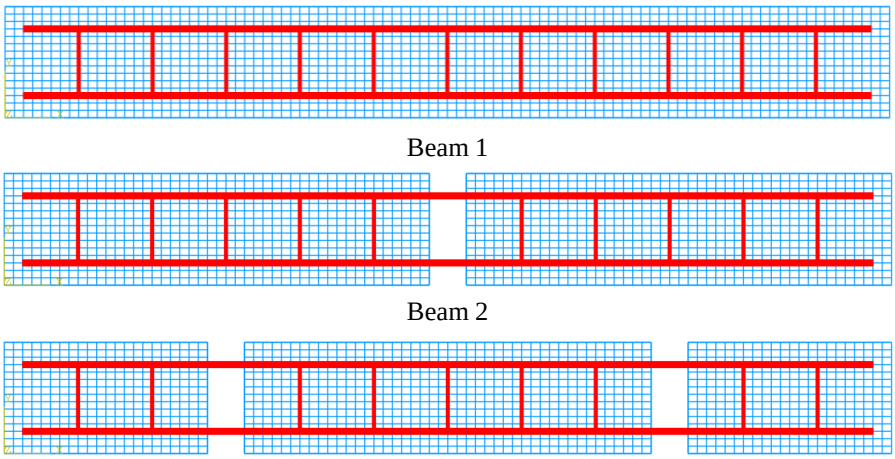

Figure 4. Finite element modeling of the reinforced concrete beams using solid and beam elements.

In order to investigate the influence of the steel cuts in the dynamic behavior of beams 2 and 3, local sectional area reduction zones of 2 mm length were modelled in Abaqus where generalized sections were used to approximate the profile properties.

Table 2 shows the physical and mechanical properties of the materials used in the models. The material properties of the steel and Poisson's ratio of the concrete were taken from the literature [9, 10]. The density of the concrete for each beam was defined by dividing the weight of the beams by their volume after extracting the weight of the steel reinforcement.

The Young's modulus of the concrete, E_c was estimated after model updating against the experimental results. Numerical trials with different Young's modulus, E_c were carried out for beam 1 up to the stage where the first numerical eigenmode had 0% difference against the first experimental eigenmode in terms of eigenfrequencies. The estimated value of the Young's modulus is relatively high but it is inside the range that is proposed in the literature for C25/30 concrete [11].

Material	Density, ρ [Kg/m^3]		Young's modulus, E [N/m^2]	Poisson's ratio, v
Concrete	Beam 1	2328.7	36875E06	0.2
	Beam 2	2277.8		
	Beam 3	2320.8		
Steel	7800		200E09	0.3

Table 2. Material properties.

3 RESULTS

In this section the mode pairs are characterized according to their mode shape as being either bending (B), torsional (T) or axial (A) modes. Table 3 compares the results of the finite element analysis against the experimental results for Beam 1 in terms of eigenfrequencies.

Mode type	Mode pair	Experimental modal analysis [Hz]	FEM [Hz]	Difference [%]
B	1	138.19	138.19	0.00
B	2	209.57	205.59	1.90
B	3	366.30	365.72	0.16
T	4	447.96	446.14	0.41
B	5	529.20	521.30	1.49
B	6	684.87	680.10	0.70
A	7	861.64	838.87	2.64
T	8	896.33	892.54	0.42
B	9	944.14	927.07	1.81
B	10	1069.14	1057.70	1.07
T	11	1343.43	1339.40	0.30
B	12	1408.26	1382.50	1.83
B	13	1499.09	1480.10	1.27
A	14	1721.10	1675.70	2.64
T	15	1799.68	1787.00	0.70
B	16	1902.95	1864.40	2.03
B	17	1961.47	1933.30	1.44
T	18	2253.04	2235.30	0.79
B	19	2410.26	2358.00	2.17
B	20	2451.17	2407.00	1.80
A	21	2577.19	2507.70	2.70
T	22	2709.78	2684.40	0.94
B	23	2920.24	2853.10	2.30
B	24	2948.11	2893.70	1.85

Table 3. Comparison between experimental modal analysis and FEM in terms of eigenfrequencies – Type A1 beam. (B, T and A correspond to bending, torsional and axial modes respectively).

Figure 5 and Figure 6 show the percentage difference between experimental and FEM eigenfrequencies for the 26 and 28 mode pairs of beams 2 and 3 respectively.

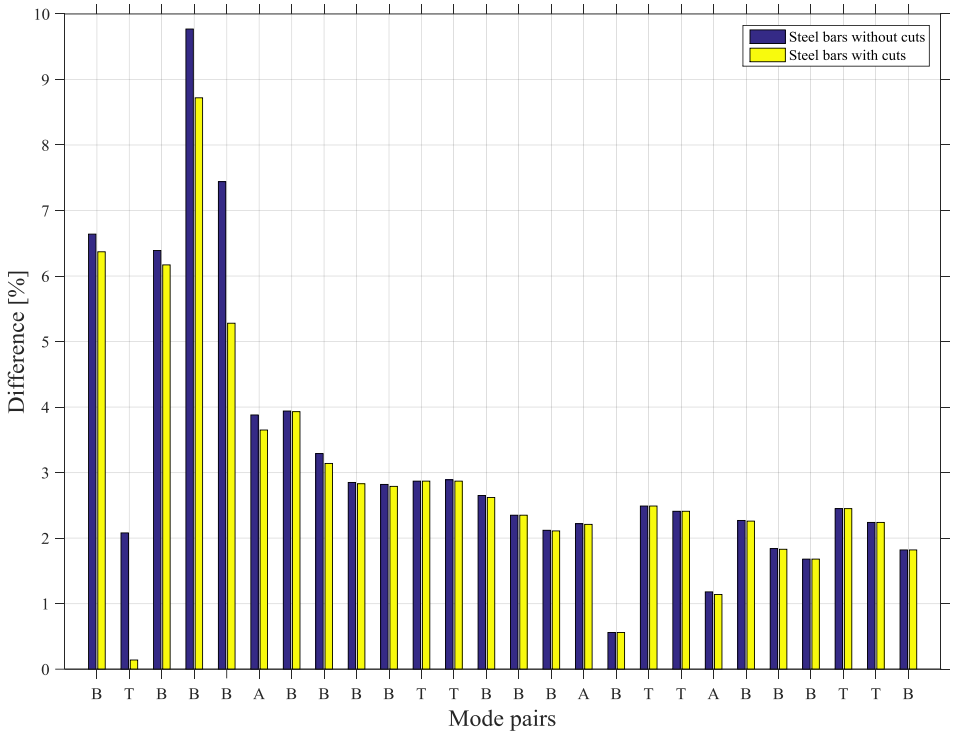

Figure 5. Percentage difference between FEM and experimental eigenfrequencies for beam 2 (B, T and A correspond to bending, torsional and axial modes respectively). Modes are ordered from the lowest to the highest eigenfrequency from left to right.

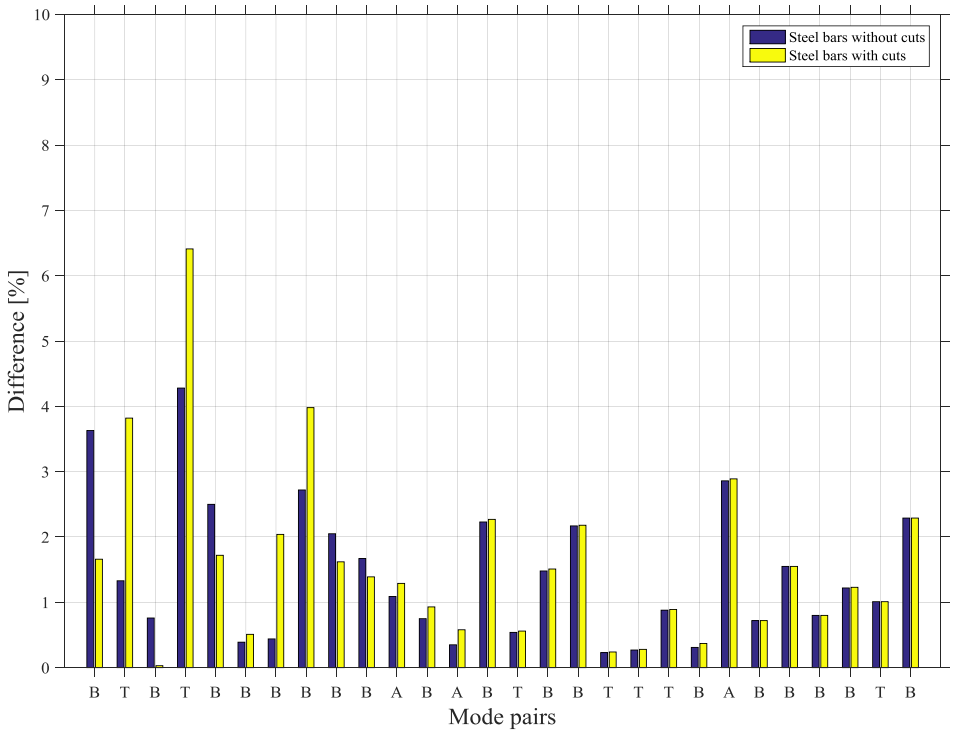

Figure 6. Percentage difference between FEM and experimental eigenfrequencies for beam 3 (B, T and A correspond to bending, torsional and axial modes respectively). Modes are ordered from the lowest to the highest eigenfrequency from left to right.

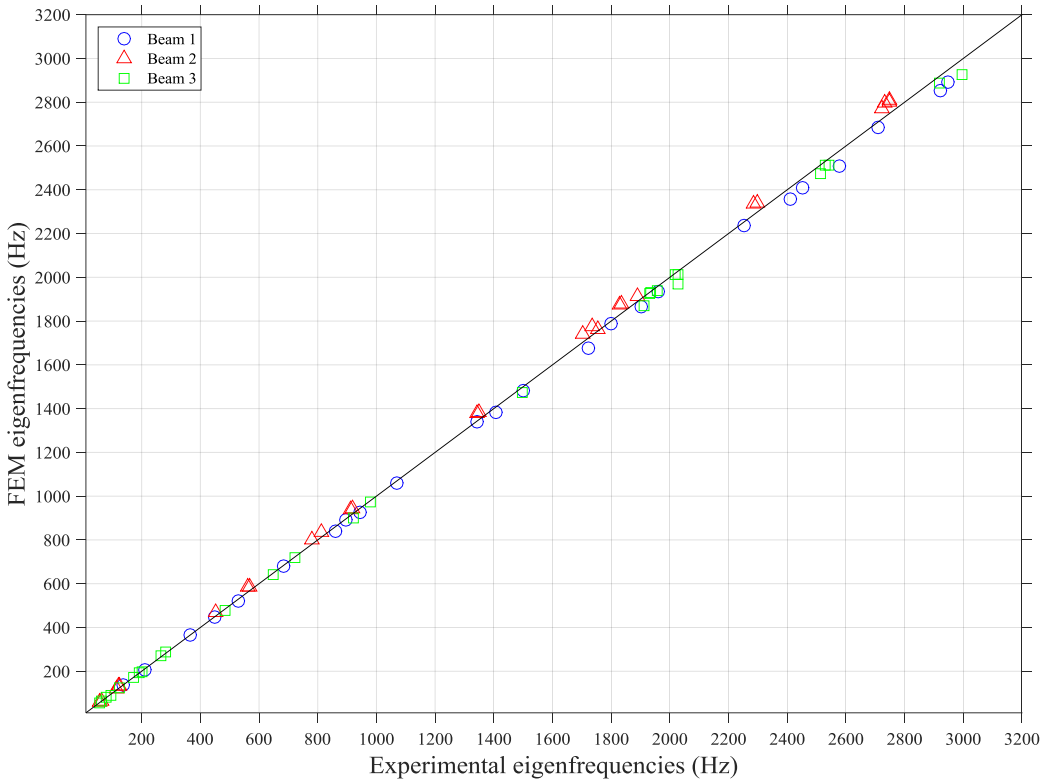

Figure 7. Comparison between experimental and FEM eigenfrequencies for beams 1, 2 and 3.

4 ANALYSIS AND DISCUSSION

In general, close agreement was achieved between FEM and experimental eigenfrequencies for all three reinforced concrete beams as indicated in Figure 7. Therefore the number of discontinuities did not significantly affect the accuracy of the finite element models in terms of their eigenfrequencies.

For beam 1, close agreement was achieved between FEM and experimental results (see Table 3). All the mode pairs in the frequency range from 1 to 3200 Hz had differences less than 3 % in terms of eigenfrequencies.

For beam 2, all the 21 mode pairs above the first axial mode (450.9 Hz) and mode pair 2, showed close agreement between FEM and the experimental results with differences in the eigenfrequencies of less than 4.0 % (see Figure 5). Higher differences occurred with mode pairs 1, 3, 4 and 5 with differences between 6 and 10 %.

For beam 3, close agreement was achieved between FEM and experimental results for all the mode pairs in the frequency range from 1 to 3200 Hz with differences less than 5 % (see Figure 6). Apart from mode pairs 1 and 4 the other pairs all showed differences below 3 %.

The effect of including the diamond saw cuts to the reinforcement bars in the FEM model of beams 2 and 3 was negligible above the first axial mode. Figure 5 and Figure 6 show that in the models with the discontinuities, the steel cuts mainly affect the modes before the first axial mode. Modelling the steel cuts improved the agreement between FEM and experimental results for beam 2 while it is not clear that including the steel cuts had a significant effect for beam 3.

5 CONCLUSIONS

Experimental work has quantified the material properties and the dynamic behavior of three reinforced concrete beams with and without discontinuities. These represent undamaged and damaged beams as might occur in a building after an earthquake.

Finite element models have been successfully validated against experimental modal analysis for these three beams. It was shown that the number of discontinuities did not significantly affect the accuracy of the predicted eigenfrequencies. For the undamaged beams the agreement between the lowest 24 eigenfrequencies from the models and the measurements were within ≈3 %. For the damaged beams, the agreement was within 4 % above the lowest axial mode, whereas the errors were up to 10 % below the lowest axial mode.

An efficient and accurate method of creating discontinuities was experimentally validated. This will inform later stages of the work where numerical experiments will be carried out to assess the influence that various patterns of discontinuities have in the dynamic behavior of one dimensional reinforced concrete members. This will allow Monte Carlo simulations to incorporate aspects of uncertainty that would exist in real fragmented buildings.

ACKNOWLEDGMENT

The authors are grateful for the funding provided by the EPSRC and ESRC Centre for Doctoral Training in Quantification Management of Risk & Uncertainty in Complex Systems and Environments at the University of Liverpool.

REFERENCES

[1] A. G. Macintyre, J. A. Barbera and E. R. Smith, "Surviving Collapsed Structure Entrapment after Earthquakes: A "Time-to-Rescue" Analysis," *Prehospital and Disaster Medicine,* vol. 21, no. 1, pp. 4-19, 2006.

[2] A. G. Macintyre, J. A. Barbera and B. P. Petinaux, "Survival Interval in Earthquake Entrapments: Research Findings Reinforced During the 2010 Haiti Earthquake Response," *Disaster Medicine and Public Health Preparedness,* vol. 5, no. 1, pp. 13-22, 2011.

[3] C.-J. Bäckström and N. Christofferson, "Urban search and rescue - an evaluation of technical search equipment and methods," Lund University, Lund, 2006.

[4] D. Hibbitt, B. Karlsson and P. Sorensen, Abaqus 6.12 Documentation and User Manual., Providence, Rhode Island, USA: Dessault Systemes Simulia Corp, 2012.

[5] D. V. Hutton, Fundamentals of Finite Element Analysis, New York: McGraw-Hill, 2004.

[6] G. C. Lykidis and K. V. Spiliopoulos, "3D Solid Finite Element Analysis of Cyclically Loaded RC Structures Allowing Embedded Reinforcement Slippage," *Journal of Structural Engineering,* vol. 134, no. 4, pp. 629 - 638, 2008.

[7] T. Potisuk, C. C. Higgins, T. H. Miller and S. C. Yim, "Finite Element Analysis of Reinforced Concrete Beams with Corrosion Subjected to Shear," *Advances in Civil Engineering,* vol. 2011, p. 14, 2011.

[8] N. Atalla and F. Sgard, Finite Element and Boundary Methods on Structural Acoustics and Vibration, Boca Raton: CRC Press, Taylor & Francis Group, 2015.

[9] C. Hopkins, Sound Insulation, 1st ed., Amsterdam: Elsevier/Butterworth-Heinemann, 2007.

[10] B. Mosley, J. Bungey and R. Hulse, Reinforced Concrete Design to Eurocode 2, New York: Palgrave Macmillan, 2012.

[11] P. Bamforth, D. Chisholm, J. Gibbs and T. Harrison, "Properties of Concrete for use in Eurocode 2," The Concrete Centre, Surrey, 2008.

ECCOMAS Congress 2016
VII European Congress on Computational Methods in Applied Sciences and Engineering
M. Papadrakakis, V. Papadopoulos, G. Stefanou, V. Plevris (eds.)
Crete Island, Greece, 5–10 June 2016

SEISMIC BEHAVIOR INDICES OF OLD TYPE REINFORCED CONCRETE MEMBERS

Anthos I. Ioannou [1], Stavroula J.Pantazopoulou

[1] University of Cyprus Department of Civil and Environmental Engineering P.O. Box 20537, 1687 Nicosia, Cyprus
e-mail: ioannou.anthos@ucy.ac.cy

Keywords: shear-strength models, shear failure, axial load, drift ratio models.

Abstract. *The study reviews the existing methods for estimation of the peak and residual shear strength of columns and the main parameters that affect their shear drift capacity. Shear force effects on the behavior of the columns seem to be significant as shear influences the flexural behavior of columns and encourages failure mechanisms that are more brittle, especially for columns which are shear critical (columns over-reinforced in flexure, short columns). The methods that have been developed up until now for the estimation of shear strength vary, but in all cases contributions from separate mechanisms of resistance, namely the contribution of concrete, web reinforcement and axial load are recognized. In establishing the degradation of shear strength under seismic load reversals the decomposition of concrete cover, the diagonal strut cracking of the element and the yielding or slip of the longitudinal reinforcement are determined. Another important parameter which must be taken into account in experimental results for the calibration of previous methods in establishing the rate of strength degradation as well as the residual strength is the contribution of axial load to the load-carrying capacity loss, with increasing displacement. This phenomenon is shown to be significant and for that reason separation from the other mechanisms of degradation will be essential in revision and refinement of design expressions for shear, necessary in assessment procedures. An analytical investigation of the relationship between shear drift capacity, transverse reinforcement, aspect ratio and axial load is presented in the paper.*

Introduction

Condition assessment of an existing reinforced concrete structure is the first step towards retrofit design and strengthening. Reinforced Concrete (R.C.) columns represent the most critical components in this assessment problem, as their possible failure can place at risk the integrity of the structure and its ability to support gravity loads. Thus, dependable assessment of columns is a prerequisite for the successful redesign of a structure, and requires a good understanding and interpretation of the current condition. A critical part of this procedure is the estimation of the degraded shear strength of reinforced concrete columns after inelastic reserved cyclic displacements such as those occurring during a severe earthquake. In the context of the following investigation, performance assessment makes direct reference to the state of damage attained

by the examined member. Damage is quantified in terms of lateral drift ratio. To facilitate calculations at distinct performance limits, drift capacity is estimated at the point of shear and axial failure on the experimental envelope curve. Current methods used in design codes to estimate the extent of degradation of shear strength with increasing displacement demand are built on previous researches by Aschheim(1992), Lynn(2001), Sezen(2002) and Elwood(2003). However, collective evaluation of the available data identify that certain parameters may have a great than what was thought before effect on the overall mechanism of shear strength degradation and on the deformation capacity of the member at performance limit states; such are, the aspect ratio, the second order effects generated by axial load, and the effect of transverse reinforcement ratio on the value of drift at failure. For this reason this problem is revisited aiming for a better understanding of the relationship between shear strength, P-Δ effects, and the drift ratios at shear and axial load failure.

In particular, evaluation of the residual shear strength of a member after degradation due to excessive displacement has set-in is a focal point of this study. While the displacement increases well beyond the peak point of the resistance curve of the member, the load-carrying capacity decreases owing to a variety of reasons, several of those reflecting implicit shear failure, such as diagonal tension cracking in the web of the member, yielding of longitudinal reinforcement, excessive compressive strains in the compression zone, loss of bond strength of the longitudinal reinforcement and disintegration of the web concrete due to diagonal compression. In some situations other effects may be responsible for what is often interpreted as damage-induced strength degradation – this refers to the influence of second order effects imparted by the axial load while the deformation increases. Especially this phenomenon seems to contribute dramatically to the macroscopically observed loss of lateral resistance, and the confusions caused thereof is occasionally passed-on into the calibrated expressions for shear-strength assessment of columns (the k(μ) factor, see ASCE/SEI 41, 2007). Linked with this is the value of drift at the onset of shear and axial failure. To address this problem from the beginning, a data base of 135 old type R/C columns has been created and an algorithm is followed taking into consideration the second order effects in correcting the experimental resistance envelope curves for some of the specimens. Comparison between the existing calibrated models for the evaluation of shear strength and the results illustrates the significance of second order effects on shear strength degradation. Experimental values of shear and axial drift ratios at the corresponding limit states are compared with values obtained from the proposed models. An investigation of how the values of aspect ratio, transverse reinforcement ratio and axial load influence the values of drift ratio at the reference limit states is also included in the discussion.

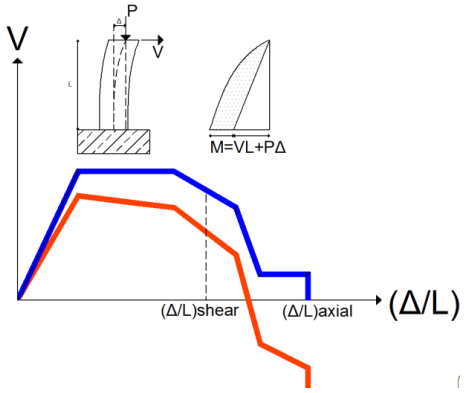

Figure 1 Schematic representation of the effects of P-Δ on the response curve of a member. Vertical axis represents the shear force required to produce a given drift magnitude (horizontal axis coordinate) if axial load is not considered (blue line) and after correction for the P- Δ effects (red line).

1 SHEAR STRENGTH

To investigate the behavior of columns under seismic shear, a data base of column tests was assembled. The data base contains columns of different cross sectional shapes, and tested under cyclic loading in single and double curvature simulating the action of earthquakes. Most of the specimens were observed to exhibit shear failure. Additionally, a small number of spiral columns were selected for study that failed in flexure. Important response parameters selected for the data base were the drift ratios at shear and axial failure, depicted in Fig. 1, and denoted as $(\Delta/L)_{shear}$ and $(\Delta/L)_{axial}$, respectively. According to the established practice in the field, the drift at shear failure is identified as the point where a 20% loss in lateral load carrying capacity is observed, whereas the drift at axial failure is associated with loss of axial load carrying capacity – i.e. collapse (this point sometimes may be identified as the final point of the envelope curve). Parameters used in the investigation were the following: the aspect ratio M/(Vd), the transverse reinforcement ratio ρ'', the average axial load ratio, $v_d=P/A_g f_c'$, the longitudinal reinforcement ratio and the material properties of the specimens. Values of the parameters for all assembled specimens are illustrated in the Table 4 in Appendix A . The specimens are categorized according to cross-section shape.

- Rectangular shaped columns
- Circular shaped columns
- L shaped columns.

The nominal shear strength of a reinforced concrete member, V_n , is estimated from the contribution of various strength components, namely, a contribution of the concrete web, V_C (comprising shear transfer over the compression zone, aggregate interlock and dowel action over the tension zone) and the contribution of transverse (web) reinforcement V_s as illustrated in Figure 3 (Elwood et al 2003). In most cases of design guidelines around the world the contribution of axial load, is either considered separately, or it is embedded in V_C.

$$V_n = V_C + V_s \tag{1}$$

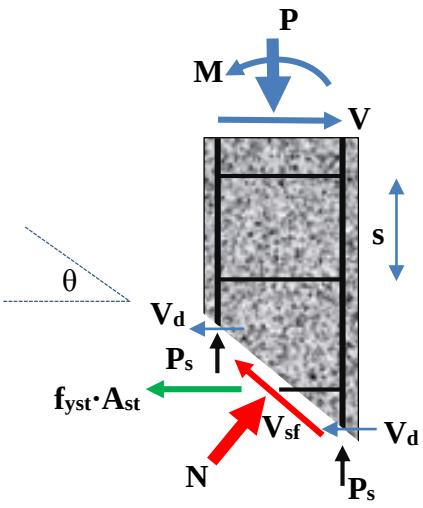

Figure 2 Components of shear force across a diagonal crack near failure (from Elwood 2003).

Because shear failure is a brittle mode of failure it is generally placed higher in the strength hierarchy scheme of capacity design, as compared to flexural failures; in the strength inequality flexural strength defines the demand for shear design of new, or the basis of assessment in existing members. As it is desirable to maintain shear demand below shear strength at least

within the range of design displacements (i.e. up to a displacement ductility of 5), strength is estimated by considering all possible forms of disintegration that may limit its magnitude. Strength reduction is effected by multiplying the nominal strength by a multiplier that accounts for the various effects that are responsible for shear strength loss, originally proposed by Aschheim and Moehle (1992) and later refined by several other researchers. Available proposals to date are listed in the table below:

Researcher	**Shear Strength Proposed Models**
Aschheim (1992), 45° truss angle corresponding to the approximate initial angle typically assumed by shear cracks	$V = V_C + V_s$; $V_C = a'(1+\frac{N_u}{2000A_g})\sqrt{f_c}bd \le 3.5\sqrt{f_c}bd$ For rectangular columns : $V_s = A_v f_{y,tr} d/s$ For spiral columns : $V_s = 2A_{sp} f_{y,tr}(0.8d_s)/s$
Lynn and Moehle (2001), 45° truss angle in this proposal. $\mu_\delta \le 1$ k=1 $1 \le \mu_\delta \le 6$ k varies from 1 and 0.7 $\mu_\delta \ge 6$ k=0.7	$V_n = kV_c + \frac{1}{2}V_c = k\frac{A_g 0.5\sqrt{f_c}}{\frac{a}{d}}\sqrt{1+\frac{P}{0.5A_g\sqrt{f_c}}} + \frac{1}{2}\frac{A_{s,tr} f_{y,tr} d}{s}$
Sezen and Moehle (2002), 45° truss (based on calibration of tests, the average truss angle is found near 55°). Parameter *k* ranges between 1.0 and 0.7 based on average shear crack angle for the test columns in the database (55°) and 45° crack angle, respectively.	$V_n = k(V_c + V_s) = k\frac{A_{s,tr} f_{y,tr} d}{s} + k\left(\frac{0.5\sqrt{f_c}}{\frac{a}{d}}\sqrt{1+\frac{P}{0.5A_g\sqrt{f_c}}}\right)0.80A_g$
Elwood and Moehle (2003), At shear failure (stirrup yielding) the truss angle is equal to **65°** or may be better approximated by $\theta = 55^o + 35^o \cdot (P/P_o)$	$V = \frac{A_{s,tr} f_{y,tr} d_c}{s}\tan\theta - P\left(\frac{25\frac{\Delta}{L}}{1+\tan^2 - \tan\theta\frac{\Delta}{L}}\right)$
Dionysis E. Biskinis, George K. Roupakias, and Michael N. Fardis(2004): from calibration of extensive database of tests. Mean values considered, $\gamma_V = 1$	$V_R = \gamma_V \cdot \left[\frac{b-c}{2L_s} min(N; 0.55A_c f_c) + (1-0.55, min(5; \mu_\Delta^{pl}))\right.$ $\left.\left[(0.16\, max(0.5; 100\rho_{tot})(1-0.16, min(5, \frac{L_s}{b}))\sqrt{f_c}A_c + V_s\right]\right]$
EC8 Part III: same as above, with $\gamma_V = 0.85$	
ASCE/SEI 41 k = 1 for $\mu \le 2$ k= 0.7 for $\mu \ge 6$ k varies linearly for $2 < \mu < 6$ λ= 0.75 for LWA concrete and 1.0 for NWA concrete.	$V_n = k\frac{A_v f_y d}{s} + \lambda k\left(\frac{0.5\sqrt{f_c}}{M/Vd}\sqrt{1+\left(\frac{N_u}{6\sqrt{f_c}A_g}\right)}\right)0.8A_g$

Table 1 Proposed Models for the evaluation of the degraded shear strength.

Notation: L=length of the column; b=column section width; h=column section height; d=depth to centerline of tension reinforcement; a= shear span; s=tie spacing; ρ_l=longitudinal reinforcement ratio ($A_{st}/(b_s)$), ρ''=transverse reinforcement ratio ($A_{st}/(bs)$); f_{yl}=longitudinal steel yield strength; f_{yt}=transverse steel yield strength ; f_c' =concrete strength; $P/(A_g * f_c')$= constant axial load; (M/(Vd))=aspect ratio; Δ/L=drift; c=neutral axis depth; A_c=web cross sectional area; μ_Δ^{pl}=plastic part of ductility demand; ρ_{tot}=total longitudinal reinforcement ratio; V_s=contribution of transverse steel; V_C=concrete web contribution

As is shown in Table 1, the shear strength models include coefficients that estimate the reduced shear strength. The strength reduction is attributed to the degradation of the concrete web which carries the shear through diagonal compressive struts. However, shear force measured in columns while conducting tests to lateral displacement (drift) history, undergoes an apparent loss of magnitude with increasing displacement, even if no web damage could be detected (e.g. in flexural response), and this is due to the second order effects of the column axial load as the longitudinal axis of the member is displaced from the reference point. This apparent reduction of column strength, *dV*, may calculated after consideration of the column in the deformed configuration. Thus, to maintain constant flexural moment at the column base, M_o, the shear force $V(\Delta)$ may be estimated from: $V(\Delta) = (M_o - P\cdot\Delta)/L = V_o - (P\cdot\Delta/L)$, thus $dV = -P\cdot\Delta/L$. Today with the vast number of available column experiments it appears that strength degradation may be overestimated, or may be insensitive to some important relevant parameters. Although behavioral factors such as diagonal cracking of concrete (flexural yielding, splicing of reinforcement in critical regions, compression buckling of longitudinal reinforcement) are the prime culprits, there is no question that second order effects consume a large fraction of the available strength giving the impression that strength loss takes place. It is actually a debated question whether the experiments used to calibrate the expressions for the degradation coefficient were corrected for *dV* before estimating the real strength loss with increasing displacement (Fardis et al.(2004), EC8, ASCE/SEI 41, Elwood and Moehle (2003), Sezen and Moehle (2002), Lynn and Moehle (2001) and Aschheim and Moehle (1992)).

In this paper this problem is revisited by studying strength loss only once after the data were systematically corrected in a uniform manner for the second order effects. The methodology followed in this process is described in detail: In order to understand the degree of influence of second order effects on shear strength, the experimental results will be compared with the results obtained from the proposed models as described in Table 1. As a first step the resistance curve was evaluated for each specimen contained in the database using established sectional analysis software (Response-2000). Next the analytical resistance envelope curve is analyzed and corrected accounting for second order effects; the corrected curve is subsequently compared with the experimental resistance envelope. Any residual difference observed between the experimental curve and the analytical curve after correction for P-Δ may be attributed to other sources of degradation such as compression softening of concrete and disintegration of the web of the member. See the figure below:

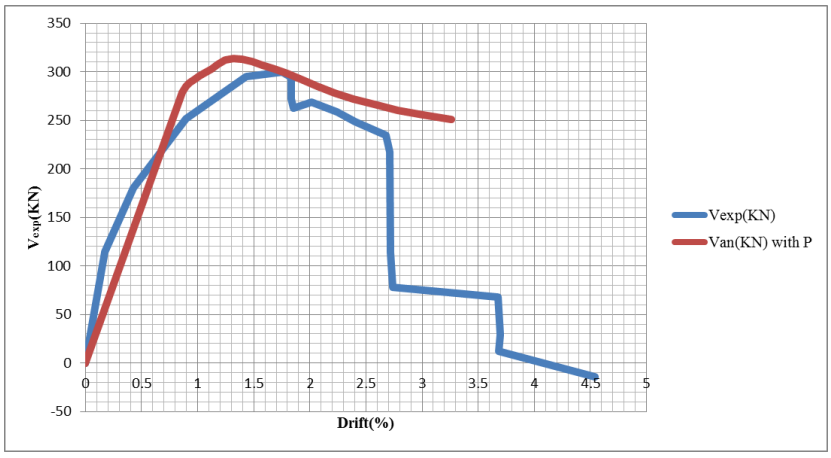

Figure 3 Comparison of the analytical envelope curve after considering the second order effects with the experimental envelope curve.

The background concept of this procedure is as follows: Ideally, a reinforced concrete member that undergoes flexural yielding without any shear degradation, would exhibit a response curve that is either elastoplastic or elastoplastic with hardening. Deviation from this ideal response may be owing to both, disintegration and P-Δ effects. Both of these components increase with deflection, however the latter of the two terms is easy to calculate given the lateral displacement of the column and the shear span length, L_s. The objective is therefore, to separate the contributions of these two sources of apparent strength loss by restructuring the total deviation of the actual response curve from its undegraded flexural response curve. Thus, the total lateral force reduction, ΔV comprises components as:

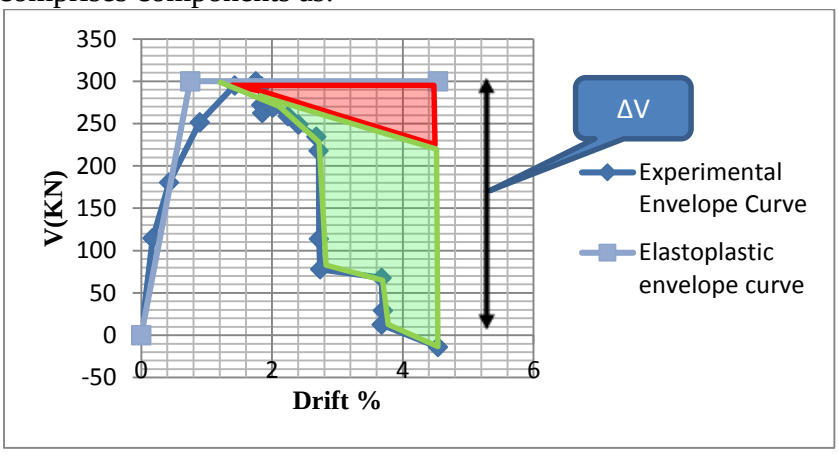

Figure 4 Difference between the elastoplastic and the experimental envelope curve. Red is the load carrying capacity occupied by P-Δ; Green is the load carrying capacity degraded (non-recoverable) due to damage.

$$\Delta V = \Delta V_{red} + \left(\frac{P\Delta}{L_s}\right) \Rightarrow \Delta V_{red} = \Delta V - \left(\frac{P\Delta}{L_s}\right) \quad (2)$$

ΔV= the difference between the elastoplastic and the experimental envelope curve
P= the axial load
Δ= the horizontal displacement
L_s = the span length of the column between the fixed support and the point of zero moment.

Therefore, a relationship is sought between the corrected shear strength degradation term, ΔV_{red}, and the drift ductility μ_θ. Figures 10 in Appendix B illustrates the graph obtained from the experimental results and the results exported from Equation 2. Figure 11 in Appendix B illustrates the comparison between $\Delta V_{red}/V_{max}$, $\Delta V/V_{max}$ with the results for normalized strength degradation as obtained from the available shear strength degradation models proposed by, Aschheim and Moehle (1992), Elwood and Moehle (2003), and Sezen and Moehle (2002). Calculation of ΔV estimated by each of the models was done according to the following procedure:

(1) Calculation of $V_{shear,max}$ for the minimum value of μ_n (ductility).
(2) For the minimum value of drift ductility μ_1 it turns out the following relationship : $V_1 = V_{max} \Rightarrow$ for μ_{v+1} is applicable $V_{n+1} \le V_{max}$
(3)Then $\Delta V = \left(\frac{V_{max} - V_{n+1}}{V_{max}}\right)$

2 SHEAR AND AXIAL DRIFT CAPACITY

Another aspect in the evaluation procedure is deformation capacity. It is established in the literature to refer to deformation capacity at the onset of shear and axial failure. Expressions have been proposed to that effect (Elwood and Moehle, 2003); these were used and the analytical results were compared with the experimental values. Expressions are obtained after empirical evaluation of the experimental database assembled by the investigators. Note that it is possible that this model may not be appropriate (applicable) for columns that were not included in the author's Database, as most of the specimens used to calibrate the expressions for the milestone drift capacities only come from a single research team. The aim of the present investigation is to calculate this shear drift capacity model for different types of columns and to observe the results.

The function used by Elwood and Moehle (2003) to estimate the drift ratio at shear failure of a column under lateral sway is as follows:

$$\left(\frac{\Delta_s}{L}\right) = \frac{3}{100} + 4\rho_t - \frac{1}{500}\frac{\nu}{\sqrt{f_c}} - \frac{1}{40}\frac{P}{A_g f_c} \geq \frac{1}{100} \quad \text{(in psi units)} \tag{3}$$

A comparison between the experimental and analytical results obtained for the shear drift capacity was conducted. The experimental shear force is compared with the value of shear force obtained from Response 2000 analysis taking into account the influence of second order effects and the aspect ratio of the member considered. A parametric investigation between transverse reinforcement ratio, axial load ratio, aspect ratio and experimental shear drift values was conducted.

Another concern is the estimation of the drift ratio at column axial failure. This is an extreme stage where the column is near imminent collapse. At this stage it is assumed that whatever residual shear strength is available to the column, this is owing to the frictional resistance that develops along the failure plane which is inclined at an angle θ from the member cross section (Fig. 2, see term V_{sf}). Based on this frictional concept,

$$V_{sf} = N\mu \tag{3}$$

The equations representing equilibrium of forces along *x* and *y* of the Free-Body Diagram of the column model depicted in Fig. 2 are as follows:

$$\Sigma F\chi \rightarrow \mathrm{N}\sin\theta + V = V_{sf}\cos\theta + \frac{\mathrm{A}_{st} f_{yt} d_c}{s}\tan\theta \tag{4}$$

$$\Sigma Fy \rightarrow P = N\cos\theta + V_{sf}\sin\theta + n_{bar}P_s \tag{5}$$

Since imminent collapse is considered, the external shear resisted, *V* is now taken equal to zero. Thus, Equation (3) will take the following form:

$$\Sigma F\chi \rightarrow N\sin\theta = N\cdot\mu\cos\theta + \frac{A_{st}f_{yt}d_c}{s}\tan\theta, \quad \text{and,} \quad \Sigma Fy \rightarrow P = N(\cos\theta + \mu\sin\theta) + n_{bar}A_b f_y \tag{6}$$

The coefficient of friction and the angle θ of the failure plane are required to perform a calculation; Elwood and Moehle (2003) using the results from their own database and using constant value of shear angle θ= 65^o calculated the coefficient of friction. As a result of this investigation proposed the following relationship between the effective coefficient of friction and the drift ratio at axial failure for the total capacity model.

$$\mu_t = \tan\theta - \frac{100}{3}\left(\frac{\Delta}{L}\right)_{axial} \geq 0 \tag{7}$$

Furthermore the coefficient of friction μ can be calculated from the following equation:

$$\mu = \frac{V}{N} \tag{8}$$

Calibration between the two equations, i.e., (7) and (8) is used to obtain the following expression for the drift at axial failure.

$$\left(\frac{\Delta_a}{L}\right) = \frac{0.5}{5 + \frac{Ps}{A_{tr}f_{yt}d_c}} \tag{9}$$

According to Elwood and Moehle (2003), the precision of such a model is comparable to that for the strength, since the longitudinal reinforcement capacity is not controlled when the drift ratios in the tests are recorded. The model requires information only about the transverse reinforcement and the axial load. In the present study a comparison is carried out between the results from Equation (9) and the independently assembled database of tests, presented herein. A next step investigating the performance of the proposed relationship for the axial drift ratio at failure is the parametric analysis of the effect of aspect ratio, taking into account the transverse reinforcement ratio and the axial load ratio considering collectively all the tests of the database.

4.0 DISCUSSION OF INVESTIGATION RESULTS

To investigate the influence of second order effects on shear strength degradation a bar chart was prepared to check the results for eight selected column specimens obtained from the data base. The specimens are shown in Table 2 and all the geometrical and mechanical properties can be found in Table 4 of Appendix A.The criterion of specimens selection was the same value of displacements ductility μ=4 due to the fact that for high values of displacements, the contribution to shear strength degradation is bigger.Figure 5 compares for a displacement ductility of μ=4 the ratios $\Delta V/V_{max}$, $\Delta V_{red}/V_{max}$ with the corresponding values which are obtained from the shear strength models of Table 1. According with the procedure described in section 2, and as shown in Figure 5, shear strength is decreased with increasing displacement ductility. More specifically, it may be seen in Fig. 8 which compares the ratios $\Delta V/V_{max}$ and $\Delta V_{red}/V_{max}$

for each specimen that a lower strength degradation occurs than previously thought, when the second order effects are accounted for; at the same time, the total strength loss expressed by the $\Delta V/V_{max}$ ratio is underestimated. The first of the models (Ashheim and Moehle 1992) is particularly unconservative. Overall, the model by Elwood and Moehle (2003) gives the closest approximation to the experimental results, although it appears that this too requires improvement (Fig. 8, Table 2) to better match the tests.

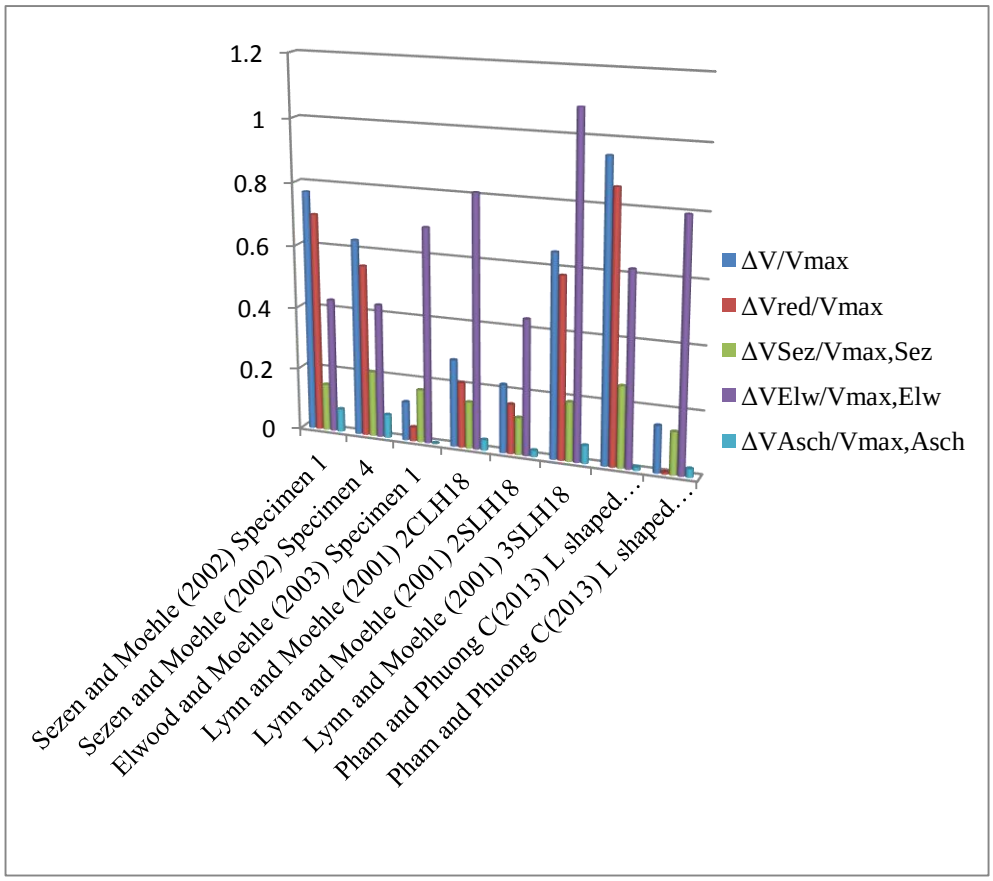

Figure 5 Distribution results for the calculations of ΔV,ΔV_{red},ΔV_{Sez},ΔV_{Elw} and ΔV_{Asch} for some of the specimens from the data base.

Specimens	$\frac{\Delta V}{V_{\max}}$	$\frac{\Delta V_{red}}{V_{\max}}$	$\frac{\Delta V_{Sez}}{V_{\max,Sez}}$	$\frac{\Delta V_{Elw}}{V_{\max,Elw}}$	$\frac{\Delta V_{Asch}}{V_{\max,Asch}}$
Sezen and Moehle (2002) Specimen 1	0.77	0.70	0.15	0.43	0.07
Sezen and Moehle (2002) Specimen 4	0.63	0.55	0.21	0.43	0.08
Elwood and Moehle (2003) Specimen 1	0.13	0.05	0.17	0.69	0.00
Lynn and Moehle (2001) Specimen 2CLH18	0.28	0.21	0.15	0.81	0.03
Lynn and Moehle (2001) Specimen 2SLH18	0.22	0.16	0.12	0.44	0.02
Lynn and Moehle (2001) Specimen 3SLH18	0.65	0.58	0.19	1.09	0.06
Pham and Phuong (2013) L shaped Columns-Specimen S1	0.95	0.86	0.26	0.62	0.01
Pham and Phuong (2013) L shaped Columns-Specimen S2	0.15	0.01	0.14	0.80	0.03

Table 2 Results from the calculations for μ=4, and $\frac{\Delta V}{V_{\max}}$, $\frac{\Delta V_{red}}{V_{\max}}$, $\frac{\Delta V_{Sez}}{V_{\max,Sez}}$, $\frac{\Delta V_{Elw}}{V_{\max,Elw}}$, $\frac{\Delta V_{Asch}}{V_{\max,Asch}}$.

Specimens	$\frac{\left(\frac{\Delta V_{red}}{V_{\max}}\right)}{\left(\frac{\Delta V}{V_{\max}}\right)}$	$\frac{\left(\frac{\Delta V_{Sez}}{V_{\max,Sez}}\right)}{\left(\frac{\Delta V}{V_{\max}}\right)}$	$\frac{\left(\frac{\Delta V_{Elw}}{V_{\max,Elw}}\right)}{\left(\frac{\Delta V}{V_{\max}}\right)}$	$\frac{\left(\frac{\Delta V_{Asch}}{V_{\max,Asch}}\right)}{\left(\frac{\Delta V}{V_{\max}}\right)}$
Sezen and Moehle (2002) Specimen 1	0.90	0.19	0.56	0.10
Sezen and Moehle (2002) Specimen 4	0.71	0.27	0.56	0.10
Elwood and Moehle (2003) Specimen 1	0.06	0.22	0.90	0.002
Lynn and Moehle (2001) Specimen 2CLH18	0.27	0.19	1.05	0.04
Lynn and Moehle (2001) Specimen 2SLH18	0.21	0.15	0.56	0.03
Lynn and Moehle (2001) Specimen 3SLH18	0.75	0.25	0.14	0.08
Pham and Phuong (2013) L shaped Columns- Specimen S1	1.12	0.34	0.80	0.01
Pham and Phuong (2013) L shaped Columns- Specimen S2	0.01	0.18	1.03	0.04

Table 3 Comparison of the proposed models results with the experimental results, for displacement ductility μ=4

In the following figures, the experimental results of the database specimens are plotted against the results of the models listed in Table 1.

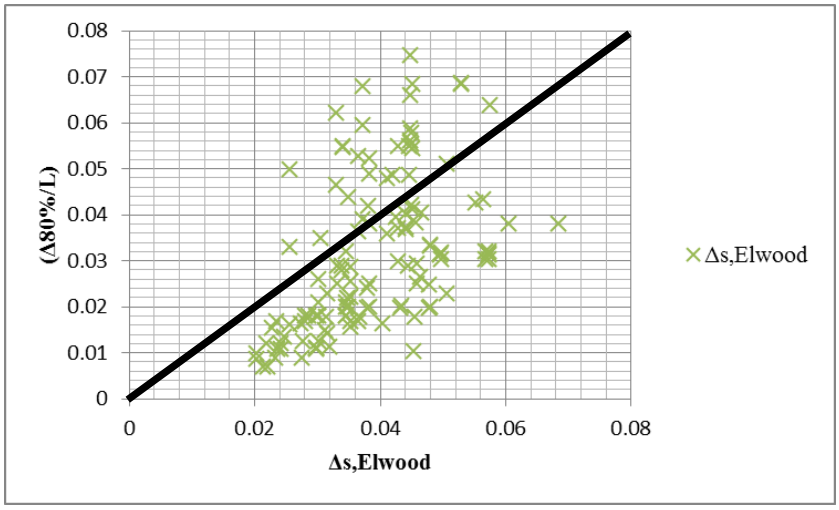

Figure 6 Comparisons between Elwood & Moehle (2003) proposed relationship for shear drift capacity of columns and the experimental values of the data base. The diagonal represents the equal value line.

Figure 7 compares experimental values of shear force with analytical peak lateral force values obtained after sectional analysis of the critical column cross section, using Response 2000 (2001) and considering second order effects; these values corresponding to the onset of shear failure (i.e., at Δ/L_s at a residual post peak strength of 80% of peak.)

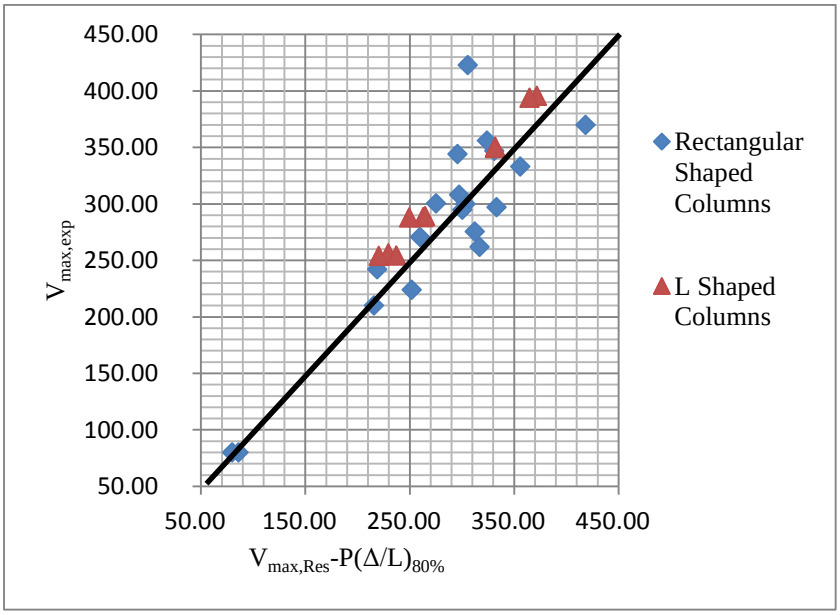

Figure 7 Correlation of $V_{max,exp}$ and $V_{max,Res}$- $P(\Delta/L)_{80\%}$

Results of a parametric investigation of the relationship between transverse reinforcement ratio, axial ratio, aspect ratio and experimental shear drift values are plotted in the following figures. Symbols used in Fig. 8 are color coded to represent the intensity of the axial load ratio (compressive) as follows:

$0 \leq \nu \leq 0.15$

$0.15 \leq \nu \leq 0.3$

$0.3 < \nu \leq 0.6$

Within each group, the rhomboid shape refers to low aspect ratio columns which are predisposed to shear failure; circles correspond to an aspect ratio between 2 and 4, whereas very slender members are plotted with triangles.

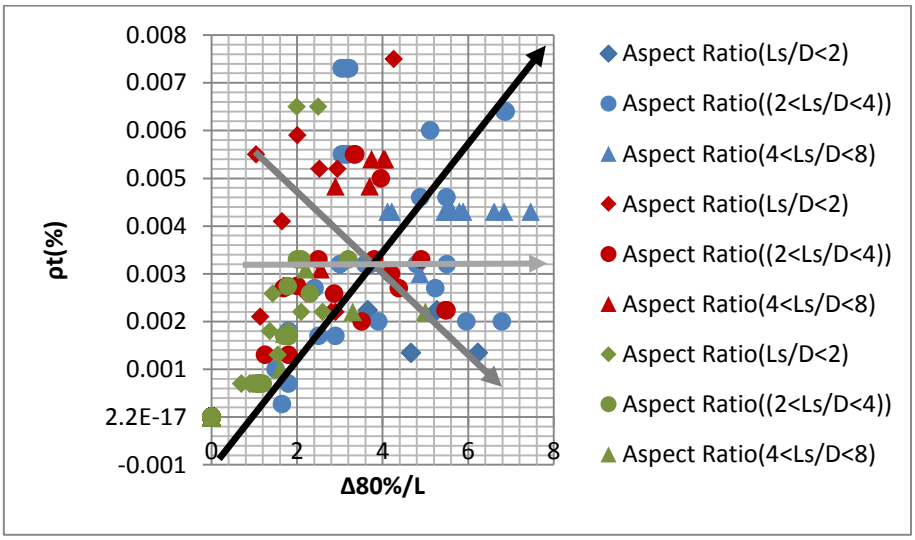

Figure 8 Influence of axial load ratio, transverse reinforcement ratio and aspect ratio, on drift ratio at shear failure.

From Figure 8 it is observed that several trends occur simultaneously: drift capacity at shear failure increases with the amount of transverse reinforcement, since better confinement and better shear reinforcement amounts postpone the occurrence of shear failure; green red and blue points are grouped sequentially in this order on the plot. Thus for the same amount of transverse reinforcement, specimens with higher axial load ratio correspond to lower values of lateral drift at shear failure. Higher drift values are possible as the axial load is reduced. Moreover for values of axial load in the range $0 \leq \nu \leq 0.15$ it may be seen that the drift capacity is proportional to transverse reinforcement ratio. Similar is the effect of the aspect ratio: higher aspect ratios lead to higher values of drift capacity at shear failure. This occurs whether as point of reference equal transverse reinforcement, or equal axial load ratio is considered.

Subsequently the value of drift at axial load failure as calculated by Eq. 9 is compared against its experimental counterpart in Figure 9; clearly the equation assesses the drift capacity at failure quire satisfactorily, however, the scatter is significant. It is possible that by accounting the other two important parameters, namely the aspect ratio and transverse reinforcement ratio the scatter may be reduced and correlation be improved.

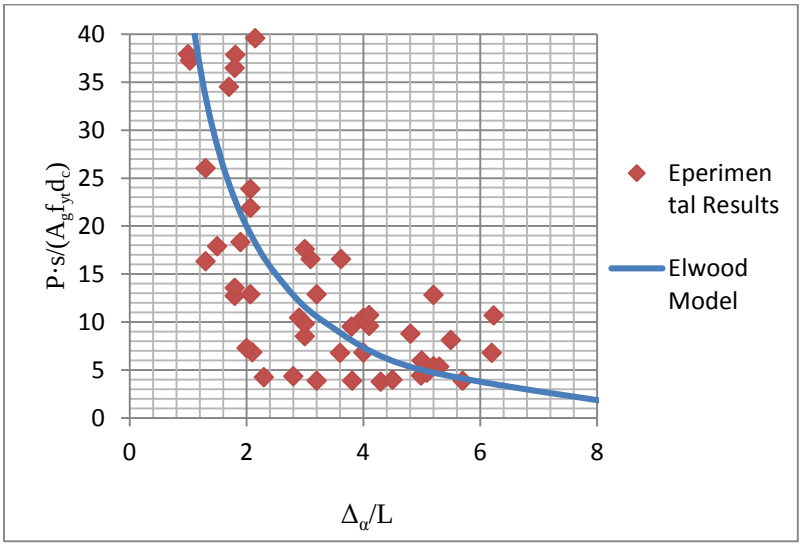

Figure 9 Comparison of experimental values of Δ_α with Elwood and Moehle (2003) proposed model.

6.0 CONCLUSIONS

- The current study aims to recapitulate the current knowledge concerning the estimation of the residual shear strength and pattern of strength degradation, taking into consideration the influence of axial load and the occurrence of second order effects during the lateral displacement history. Furthermore, drift capacities at the point associated with shear and axial load failures were also considered.
- Taking into account the contribution of axial load in estimating the remaining shear strength of a column with increasing displacement, it seems that a large fraction of the macroscopically observed lateral strength loss originally attributed to disintegration of the shear resistance mechanisms is really owing to the contribution of second order effects. This important response aspect accounts for a significant part of the lateral resistance of the column and therefore the coefficient of strength reduction with increasing ductility which has been introduced in assessment codes is found to overestimate the phenomena of strength degradation. Therefore, all the relevant assessment equations need to be reconsidered.
- Drift capacity at the onset of shear failure is defined at the point on the post peak branch associated with 80% residual member strength. After a parametric investigation, the results show that there is an agreement between the expressions by Elwood and Moehle (2003) and an independently assembled experimental database results in that the shear drift value increases almost proportionately with transverse reinforcement ratio, whereas it is inversely proportional to axial load ratio. Higher aspect ratio has the same effect; low shear drift values are observed in the case of shear critical columns.

6.0 REFERENCES

[1] Eurocode 8 (2005). Design of structures for earthquake resistance – Part.3: Assessment and retrofitting of buildings, European Committee for Standardization.

[2] Asadollah Esmaeily-Gh. and Yan Xiao, "Seismic Behavior of Bridge Columns Subjected to Various Loading Patterns", *PEER Report No 2002/15*. University of California, Berkeley , December 2002.

[3] Lynn, A. C., "Seismic Evaluation of Existing Reinforced Concrete Building Columns," *PhD dissertation*, Department of Civil and Environmental Engineering, University of California, Berkeley, Berkeley, Calif. 2001.

[4] Sezen, H., "Seismic Response and Modeling of Reinforced Concrete Building Columns," *PhD dissertation*, Department of Civil and Environmental Engineering, University of California, Berkeley, 2002.

[5] Chasioti G.S., K.G.Megalooikonomou & S.J. Pantazopoulou ," Shear Strength Assessment of Reinforced Concrete Columns", *CD ROM Proceedings*, Thematic Conference on Computational Methods in Structural Dynamic and Earthquake Egineering (COM-DYN 2013), Kos Island, Greece 12-14 June 2013.

[6] Curtis J.Holub., "Interaction of Variable Axial Load and Shear Effects in RC Bridges", *PhD dissertation*, Dep. Civil Engineering of University of Illionis at Urbana-Champaign, 2009.

[7] Sashi K.Kunnath, Ashraf El-Bahy & Andrew W.Taylor,W.C. Stone," Cumulative Seismic Damage of Reinforced Concrete Bridge Piers", *Report of Building and Fire Research Laboratory* NISTR 6075 ,NIST, Gaithersburg,MD 20899 October 1997.

[8] Kenneth J. Elwood & Jack P. Moehle, "Shake Table Tests and Analytical Studies on The Gravity Load Collapse of Reinforced Concrete Frames", *PEER Report No 2003/01*, University of California, Berkeley, November 2003.

[9] Evan C. Bentz, Frank J. Vecchio, and Michael P. Collins, "Simplified Modified Compression Field Theory For Calculating Shear Strength of Reinforced Concrete Elements", *ACI Structural J.* V103-No S65,July-August 2006.

[10] Cao Thanh Ngoc Tran & Bing Li ,"Ultimate Displaceent of Reinforced Concrete Columns with Light Transverse Reinforcement", *J. Earthquake Engineering*, V. 17:2 No 282-300, 08 Jan 2013.

[11] Lisa Matchulat, "Mitigation of Collapse Risk In Vulnerable Concrete Buildings", *M.Sc. Dissertation*, Department of Civil Engineering of Kansas University, 2008.

[12] Mark Aschheim & Jack P. Moehle, "Shear Strength and Deformability of RC Bridge Columns Subjected to Inelastic Cyclic Displacements", *Report No UCB/EERC-93/04*, March 1992.

[13] Pham, Thanh Phuong & Li, Binq, "Seismic Performance Assessment of L-Shaped Reinforced Concrete Columns", *ACI Structural J.* No S-2013-225.R3, August 2013.

[14] ASCE/SEI 41 (2007). Seismic Rehabilitation of Existing Buildings, American Society of Civil Engineers.

[15] Response – 2000, Reinforced Concrete Sectional Analysis using the Modified Compression Field Theory, E. Bentz and P.Collins, Version 1.0.5, 2000.

[16] Pham, Thanh Phuong & Li, Binq, "Seismic Performance of Reinforced Concrete Columns With Plain Longitudinal Reinforcing Bars ", *ACI Structural J.* No 111-S46, June2014.

[17] Yi-An Li, Yi-Tong Huang, and Shyh-Jiann Hwang, " Seismic Response of Rein-forced Concrete Short Columns Failed in Shear", *ACI Structural J.*, No 111-S80, August 2014.

[18] Y. Li, K.J. Elwood & S.-J. Hwang , " Assessment of ASCE/SEI 41 Concrete Column Provisions using Shaking Table Tests", ACI SP297-2, June 2014.

[19] M. Di Ludovico, G.M. Verderame, A. Prota, G. Manfredi, and E. Cosenza," Cyclic Behaviot Of Non-Conforming Full Scale RC Columns", J. of Structural Engineering, No. 10.1061/(ASCE)ST.1943-541X.0000891, June 2013.

[20] J.C.M. Ho and H.J. Pam, "Influence of Transverse Steel Configuration on Post-elastic Behaviour of High-strength Reinf. Concrete Columns", J. of HKIE TRANSACTIONS,Taylor & Francis, Apr 2013.

Appendix A

Specimens	B (mm)	D or h (mm)	L(mm)	fc'	a/D	ρl(%)	fyl(Mpa)	s(mm)	ρt(%)	fyt(Mpa)	P/Agfc'
Bechtoula,Kono,Arai and Watanade,2002,											
DIN 2002	250	250	625	37.60	2.5	0.02	461	40	0.01	485	0.30
Esaki ,1996											
H-2-1/3	200	200	400	23	2	0.03	363	40	0.01	363	0.33
H-2-1/5	200	200	400	23	2	0.03	363	50	0.01	364	0.20
HT-2-1/3	200	200	400	20	2	0.03	363	60	0.01	364	0.33
HT-2-1/5	200	200	400	20	2	0.03	363	75	0.01	364	0.20
Galeota et al 1996											
AB2	250	250	1,140	80	4.56	0.06	579	150	0.01	579	0.30
AB3	250	250	1,140	80	4.56	0.06	579	150	0.01	579	0.30
AB4	250	250	1,140	80	4.56	0.06	579	150	0.01	579	0.20
Nosho et al 1996											
AB2	279	279	2,134	40.6	7.64	0.01	407	229	0.001	351	0.34
Ohue et al. 1985											
2D16RS	200	200	400	32	2	0.02	369.00	50	0.005	316	0.14
4D13RS	200	299	400	30	2	0.03	370.00	50	0.005	316	0.15
Pujol 2002											
No.10-1-2.25N	152.4	304.8	686	36.5	2.25	0.02	453	57	0.01	411	0.08
No.10-1-2.25S	152.4	304.8	686	36.5	2.25	0.02	453	57	0.01	411	0.08
No.10-2-2.25N	152.4	304.8	686	34.9	2.25	0.02	453	57	0.01	411	0.08
No.10-2-2.25S	152.4	304.8	686	34.9	2.25	0.02	453	57	0.01	411	0.08
No.10-2-3N	152.4	304.8	686	33.7	2.25	0.02	453	76	0.01	411	0.09
No.10-2-3S	152.4	304.8	686	33.7	2.25	0.02	453	76	0.01	411	0.09
No.10-3-2.25N	152.4	304.8	686	27.4	2.25	0.02	453	57	0.01	411	0.10
No.10-3-2.25S	152.4	304.8	686	27.4	2.25	0.02	453	57	0.01	411	0.10
No.10-3-3N	152.4	304.8	686	29.9	2.25	0.02	453	76	0.01	411	0.10
No.10-3-3S	152.4	304.8	686	29.9	2.25	0.02	453	76	0.01	411	0.10
No.20-3-3N	152.4	304.8	686	36.4	2.25	0.02	453	76	0.01	411	0.16
No.20-3-3N	152.4	304.8	686	36.4	2.25	0.02	453	76	0.01	411	0.16
Ramirez and Jirsa , 1980											
00-U	305	305	458	34.5	1.5	0.02	374	65	0	455	-
Saatcioglu and Oscebe 1989											
U1	350	350	1,000	43.6	2.86	0.03	430	150	0.003	470	-
U2	350	350	1,000	30.2	2.86	0.03	453	150	0.003	470	0.16
U3	350	350	1,000	34.8	2.86	0.03	430	75	0.006	470	0.14
Soesianawati et al. 1986											
No.4	400	400	1,600	40	4	0.02	446	0.003	0.003	0.30	0.32
Takemura and Kawashima, 1997											

Test 1 (JSCE-4)	400	400	1,245	35.9	3.11	0.02	363	70	0.002	368	0.30
Test 2 (JSCE-4)	400	400	1,245	35.7	3.11	0.02	363	70	0.002	368	0.03
1997, Test 3 (JSCE-4)	400	400	1,245	34.3	3.11	0.02	363	70	0.002	368	0.03
1997, Test 4 (JSCE-4)	400	400	1,245	33.2	3.11	0.02	363	70	0.002	368	0.03
1997, Test 5 (JSCE-4)	400	400	1,245	36.8	3.11	0.02	363	70	0.002	368	0.03
Umehara and Jirsa 1982											
2CUS	230	410	455	42	1.11	0.03	441	89	0.01	414	0.27
Wehbe et al 1998											
A1	380	610	2,335	27.2	3.83	0.02	448	110	0.003	428	0.10
A2	380	610	2,335	27.2	3.83	0.02	448	110	0.003	428	0.24
Wight and Sozen 1973											
No.00.033(East)	152.4	304.8	876.0	32.0	2.88	0.02	496	127	0.003	345	-
No.00.033(West)	152.4	304.8	876.0	32.0	2.88	0.02	496	127	0.003	345	-
No.25.033(East)	152.4	304.8	876.0	33.6	2.88	0.02	496	127	0.003	345	0.07
No.25.033(West)	152.4	304.8	876.0	33.6	2.88	0.02	496	127	0.003	345	0.07
No.40.048(East)	152.4	304.8	876.0	26.1	2.88	0.02	496	89	0.005	345	0.15
No.40.048(West)	152.4	304.8	876.0	26.1	2.88	0.02	496	89	0.005	345	0.15
No.40.067(East)	152.4	304.8	876.0	33.4	2.88	0.02	496	64	0.01	345	0.11
No.40.067(West)	152.4	304.8	876.0	33.4	2.88	0.02	496	64	0.01	345	0.11
Xiao and Martyrossyan 1998											
HC4-8L16-T6-0.1P	254	254	508	86	2	0.02	510	51	0.01	449	0.10
HC4-8L16-T6-0.1P	254	254	508	86	2	0.02	510	51	0.01	449	0.19
Matchulat (2008)											
Specimen 1	457	457	2946.4	20.68	3.74	0.03	441.26	460	0.00	372.32	0.50
Specimen 2	457	457	2946.4	23.42	3.74	0.03	441.26	460	0.00	372.32	0.35
Elwood and Moehle (2003)											
Specimen 1	230	230	1470	25.55	3.69	0.03	689.48	150	0.02	689.48	0.10
Specimen 2	230	230	1470	23.92	3.69	0.03	689.48	150	0.02	689.48	0.24
Sezen and Moehle (2002)											
Specimen 1	457	457	2946.4	21.10	3.85	0.03	434.37	305	0.002	476	0.15
Specimen 2	457	457	2946.4	21.10	3.85	0.03	434.37	305	0.002	476	0.60
Specimen 4	457	457	2946.4	21.79	3.85	0.03	434.37	305	0.002	476	0.15
Lynn and Moehle (2001)											
Specimen 3CLH18	457	457	2946	25.58	3.66	0.03	330.95	460	0.001	400	0.12
Specimen 2CLH18	457	457	2946	33.09	3.63	0.02	330.95	460	0.001	400	0.12
Specimen 3SLH18	457	457	2946	25.58	3.66	0.03	330.95	460	0.001	400	0.12
Specimen 2SLH18	457	457	2946	33.09	3.63	0.02	330.95	460	0.001	400	0.12
Specimen 2CMH18	457	457	2946	25.51	3.63	0.02	330.95	460	0.001	400	0.35
Specimen 3CMH18	457	457	2946	27.58	3.66	0.03	330.95	460	0.001	400	0.35
Specimen 3CMD12	457	457	2946	27.58	3.66	0.03	330.95	460	0.002	400	0.35
Specimen 3SMD12	457	457	2946.4	25.51	3.63	0.03	330.95	460	0.002	400	0.35
Phuong and Li (2012)											

S-2.4-0.3	350	350	1700	49.3	2.77	0.03	409	130	0.001	393	0.30
SC-2.4-0.2	350	350	1700	22.6	2.75	0.02	409	130	0.001	393	0.20
SC-2.4-0.5	350	350	1700	24.2	2.75	0.02	409	130	0.001	393	0.50
SC-1.7-0.2	350	350	1200	27.5	1.94	0.02	409	130	0.001	393	0.20
SC-1.7-0.5	350	350	1200	26.4	1.94	0.02	409	130	0.001	393	0.50
M.D. Ludovico et al.(2013)											
S300D-C	300	300	1500	22.71	2.93	0.01	520	150	0.002	520	0.20
R300D-C	500	300	1500	22.71	1.64	0.01	520	150	0.001	520	0.10
R500D-C	300	500	900	22.71	1.76	0.01	520	150	0.002	520	0.10
S300P-C(plain re-bars)	300	300	1500	22.71	2.93	0.01	330	150	0.002	330	0.20
R300P-C(plain re-bars)	500	300	1500	22.71	1.64	0.01	330	150	0.001	330	0.10
R500P-C(plain re-bars)	300	500	900	22.71	1.76	0.01	330	150	0.002	330	0.10
Henkhaus, Pujol and Ramirez (2013)											
B1	457	457	1473	20.0	1.90	0.02	455	457	0.001	490	0.37
B2	457	457	1473	19.3	1.90	0.02	455	457	0.001	455	0.38
B3	457	457	1473	22.1	1.90	0.02	455	457	0.001	490	0.21
B4	457	457	1473	24.1	1.90	0.03	441	457	0.001	490	0.43
B5	457	457	746.5	23.4	1.90	0.03	441	457	0.001	490	0.46
B6	457	457	2947	27.6	3.70	0.03	490	305	0.002	469	0.11
B7	457	457	2947	28.3	3.70	0.03	490	305	0.002	469	0.11
B8	457	457	2947	29.0	3.70	0.03	490	305	0.001	490	0.11
Wood's (2010)											
Specimen 3	457	457	2946	17.31	3.72	0.03	441.26	457	0.0007	372.32	0.50
Specimen 4	457	457	2946	18.62	3.72	0.03	448.16	305	0.0003	372.32	0.15
Thanh Phuong Pham and Bing Li 2014 (smooth bars)											
SP1-1.7-0.2	350	350	1200	29.8	1.7	0.02	320	125	0.003	500	0.20
SP2-1.7-0.35	350	350	1200	29.2	1.7	0.02	320	125	0.003	500	0.35
SP3-2.4-0.2	350	350	1700	30.6	2.4	0.02	320	125	0.003	500	0.20
SP4-2.4-0.35	350	350	1700	28.7	2.4	0.02	320	125	0.003	500	0.35
SR1-1.7-0.35	250	490	1700	23.3	1.7	0.02	320	125	0.002	500	0.35
SR2-1.7-0.5	250	490	1700	22.5	1.7	0.02	320	125	0.002	500	0.50
J C M HO and H J PAM (2013)											
8S-60-06-61-S	325	325	1515	56.6	5.00	0.06	525	100	0.002	378	0.54
8S-60-06-61-C	325	325	1515	60.4	5.03	0.06	525	210	0.002	357	0.53
)8S-100-03-24-S	325	325	1515	95.1	4.93	0.02	522	100	0.003	357	0.28
8S-100-03-24-C	325	325	1515	109.5	4.93	0.02	522	150	0.003	357	0.31
NEW-60-06-61-S	325	325	1515	57.1	5.26	0.06	525	100	0.010	531	0.53
NEW-60-06-61-C	325	325	1515	62.4	5.26	0.06	525	210	0.002	531	0.53
NEW-l00-03-24-S	325	325	1515	96.5	5.26	0.02	522	70	0.009	531	0.28
NEW-l00-03-24-C	325	325	1515	108.4	5.26	0.02	522	90	0.012	531	0.30
8S'-100-02-15-900	325	325	1515	111.1	5.19	0.02	572	150	0.005	367	0.20
8S'-100-02-15-45°	325	325	1515	109.4	5.19	0.02	572	150	0.005	367	0.21

Specimens	D or h (mm)	L(mm)	fc'	a/D	ρl(%)	fyl(Mpa)	s(mm)	ρt(%)	fyt(Mpa)	P/Ag-fc'
Kunnath et al.1997										
A2	304.8	1372	29.041	5.6232	0.02	448.2	190.5	0.0043	430.491	0.0944
A3	304.8	1372	29.041	5.622	0.02	448.2	190.5	0.0043	430.491	0.0944

A4	304.8	1372	35.517	5.622	0.02	448.2	190.5	0.0043	430.491	0.0856
A5	304.8	1372	35.52	5.622	0.02	448.2	190.5	0.0043	430.491	0.0856
A6	304.8	1372	35.52	5.622	0.02	448.2	190.5	0.0043	430.491	0.0856
A7	304.8	1372	32.816	5.6232	0.02	448.2	190.5	0.0043	430.491	0.0926
A8	304.8	1372	32.82	5.6232	0.02	448.2	190.5	0.0043	430.491	0.0926
A9	304.8	1372	32.516	5.6232	0.02	448.2	190.5	0.0043	430.491	0.0935
A10	304.8	1372	27.0135	5.6232	0.02	448.2	190.5	0.0043	430.491	0.101
A11	304.8	1372	27.01	5.6232	0.02	448.2	190.5	0.0043	430.491	0.101
A12	304.8	1372	27.01	5.6232	0.02	448.2	190.5	0.0043	430.491	0.101
Arakawa et al. 1987										
UNIT1	275.08	600	28.81	1.36	0.04	366.2	100	0.002	368.18	0
UNIT2	275.08	600	29.31	1.36	0.04	366.2	50	0.004	368.18	0
UNIT 4	275.08	600	29.81	1.36	0.04	366.2	100	0.002	368.18	0.12
UNIT 6	275.08	600	28.61	1.36	0.04	366.2	50	0.004	368.18	0.12
UNIT 8	275.08	600	31.41	1.36	0.04	366.2	35	0.005	368.18	0.12
UNIT 9	275.08	600	30.51	1.36	0.05	366.2	50	0.004	368.18	0.12
UNIT 12	275.08	600	27.81	1.36	0.04	366.2	100	0.002	368.18	0.26
UNIT 13	275.08	600	30.51	1.36	0.04	366.2	50	0.004	368.18	0.24
UNIT 14	275.08	600	31.31	1.36	0.04	366.2	35	0.005	368.18	0.23
UNIT 17	275.08	600	31.31	1.36	0.04	363.2	75	0.003	381.19	0.12
UNIT 19	275.08	900	31.31	2.04	0.04	363.2	75	0.003	381.19	0.12
UNIT 22	275.08	900	20.51	2.04	0.04	363.2	75	0.003	381.19	0.18
UNIT 24	275.08	600	31.11	1.36	0.04	363.2	75	0.003	381.19	0.23
UNIT 25	275.08	900	29.71	2.04	0.04	363.2	75	0.003	381.19	0.24
UNIT 27	275.08	900	18.90	2.04	0.04	363.2	75	0.003	381.19	0.38
UNIT 28	275.08	900	41.32	2.04	0.04	363.2	75	0.003	381.19	0.18

Pham and Phuong 2013												
Speci-mens	b(mm)	h(mm)	h'(mm)	Ls(mm)	fc' (Mpa)	a/D	ρl(%)	fyl(Mpa)	s(mm)	ρt(%)	fyt(Mpa)	P/Ag-fc'
S1	170	430	414	1700	29.8	2.05	0.02	465	100	0.003	467	0.2
S2	170	430	414	1700	29.2	2.05	0.02	465	100	0.003	467	0.35
S3	170	430	414	1700	29.2	2.05	0.02	465	100	0.003	467	0.2
S4	170	430	414	1700	29.4	2.05	0.02	465	100	0.003	467	0.35
S5	170	430	414	1700	29.1	2.05	0.02	465	100	0.003	467	0.2
S6	170	430	414	1700	29.1	2.05	0.02	465	100	0.003	467	0.35
S13	170	430	414	1200	27	1.45	0.02	465	150	0.002	467	0.2
S14	170	430	414	1200	27.4	1.45	0.02	465	150	0.002	467	0.35
S15	170	430	414	1200	26.8	1.45	0.02	465	150	0.002	467	0.2
S16	170	430	414	1200	27.2	1.45	0.02	465	150	0.002	467	0.35

Table 4 : Data Base

Appendix B

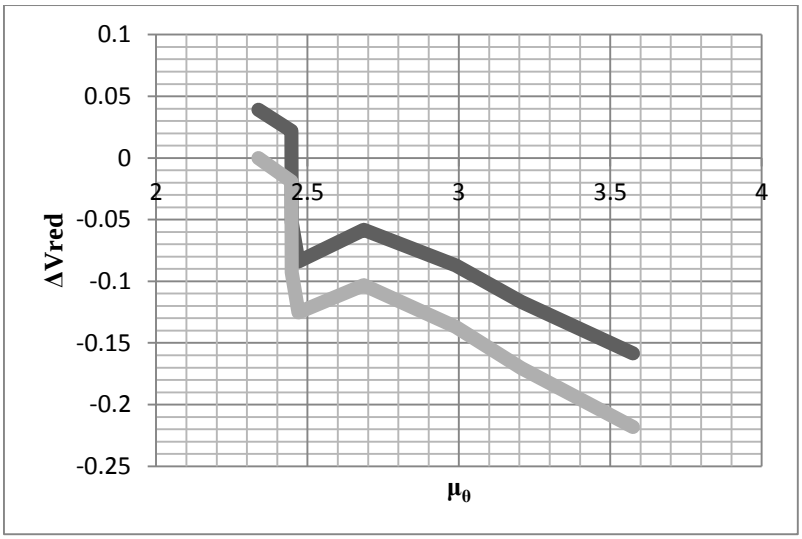

Figure 10 Difference between the experimental and the corrected shear strength degradation with increasing μ_θ

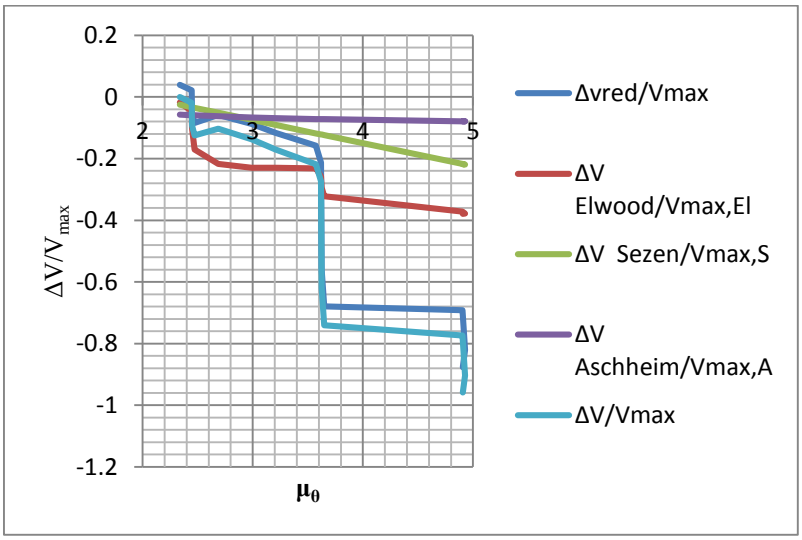

Figure 11 Comparisons between ΔV_{red} ,ΔV from the experimental data base with ΔV according with the models by Sezen and Moehle (2002), Aschheim and Moehle (1992) and Elwood and Moehle (2003) .

ECCOMAS Congress 2016
VII European Congress on Computational Methods in Applied Sciences and Engineering
M. Papadrakakis, V. Papadopoulos, G. Stefanou, V. Plevris (eds.)
Crete Island, Greece, 5–10 June 2016

EFFECT OF SOIL SPATIAL VARIABILITY ON THE DYNAMIC BEHAVIOR OF A SLOPE

Michael Michael[1], Tamara Al-Bittar[2], and Abdul Hamid Soubra[3]

[1] PhD student, University of Nantes, GeM, UMR CNRS 6183
Bd. de l'université, BP 152, 44603 Saint-Nazaire cedex, France
e-mail: Michael.Michael@etu.univ-nantes.fr

[2] Associate professor, Lebanese University, Faculty of Engineering
Tripoli, Al Kobeh, Liban
e-mail: Tamara.albittar@gmail.com

[3]Professor, University of Nantes, GeM, UMR CNRS 6183
Bd. de l'université, BP 152, 44603 Saint-Nazaire cedex, France
e-mail: Abed.Soubra@univ-nantes.fr.

Keywords: dynamic analysis, slope, spatial variability, kriging, Monte Carlo simulation, probability of failure.

Abstract. *The analysis of earth slopes situated in seismic areas has been extensively investigated in literature using deterministic approaches where average values of the soil properties were used. In this paper, a probabilistic dynamic approach is presented for the slope stability analysis. In this approach, the effect of the soil spatial variability on the dynamic responses was investigated. The soil shear modulus G was modeled as an anisotropic non-Gaussian random field. The deterministic model was based on numerical simulations using the dynamic option of the finite difference code FLAC^{2D}. Notice that when dealing with dynamic problems, the deterministic model becomes very time-consuming. For this reason, one needs to keep to a minimum the number of calls to the deterministic model when performing the probabilistic analyses, the probabilistic method generally employed when considering spatially varying soil properties being the Monte Carlo Simulation (MCS) methodology. This method is known to be not suitable for the computation of the small failure probabilities encountered in practice because it becomes very time-expensive in such cases due to the large number of simulations required. In order to overcome the shortcoming related to the excessive number of calls of the deterministic model when performing Monte Carlo simulations, Echard et al. (2011) proposed an Active learning reliability method (called AK-MCS) combining Kriging and Monte Carlo Simulation. The method was shown to be very efficient as the obtained probability of failure is very accurate needing only a small number of calls to the deterministic model. The probabilistic dynamic analyses presented in this paper were performed using AK-MCS methodology by Echard et al. (2011). The failure probability was computed for the point located on the toe of the slope. For a given realization of the random field, failure is considered to be achieved at the toe if the maximal acceleration A_{max} at this point, as computed bu FLAC^{2D} software, exceeds a prescribed threshold value. Some probabilistic results corresponding to different values of the maximum threshold value are presented and discussed.*

1 INTRODUCTION

The response of a geotechnical structure subjected to a seismic loading has been extensively investigated in literature using deterministic approaches where average values of the soil properties (shear modulus, angle of internal friction, cohesion, etc.) were used. Notice however that the spatial variability of the soil properties may affect the behavior of geotechnical structures. Consequently, reliable responses of a geotechnical system cannot be predicted using a deterministic approach; a probabilistic technique seems to be necessary.

The probabilistic techniques enable the rigorous propagation of the different uncertainties from the input parameters to the system responses. It should be emphasized here that few authors have worked on the analysis of the seismic responses using probabilistic approaches [1-5]. This is because of the significant computation time required per simulation especially when using finite element/finite difference dynamic models.

In this paper, the effect of the soil spatial variability on the seismic response of a geotechnical structure is investigated. The case of an elastic slope subjected to a seismic loading was considered. The effect of the soil spatial variability on the maximal acceleration at the top and/or at the toe of the slope was considered. The objective is the computation of the probability P_f of exceeding a tolerable maximum acceleration A_{max}. The soil shear modulus was considered as a two-dimensional lognormally distributed random field where it is assumed to vary in both vertical and horizontal directions. The deterministic model was based on numerical simulations using the dynamic option of the FLAC^{2D} software. Notice that when dealing with numerical dynamic problems, the deterministic model becomes very time-consuming. For this reason, one needs to keep to a minimum the number of calls to the deterministic model when performing the probabilistic analyses, the probabilistic method generally employed when considering spatially varying soil properties being the Monte Carlo Simulation (MCS) methodology. This method is known to be not suitable for the computation of the small failure probabilities encountered in practice because it becomes very time-expensive in such cases due to the large number of simulations required.

In order to overcome the shortcoming related to the excessive number of calls of the deterministic model when performing Monte Carlo simulations, [6] proposed an Active learning reliability method (called AK-MCS) combining Kriging and Monte Carlo Simulation. The method was shown to be very efficient as the obtained probability of failure is very accurate needing only a small number of calls to the deterministic model. The basic idea of the present approach is to construct a kriging metamodel which is a surrogate (or a substitute) of the real numerical model based only on a few realizations and then, to obtain an estimation of the failure probability and the corresponding coefficient of variation based on this metamodel. The choice of the realizations used in the construction of the metamodel is made in such a manner to focus on the configurations that are close to the limit state surface and that have sufficiently high density of probability so that their contribution on the failure probability is significant. This leads to an accurate value of the failure probability.

The paper is organized as follows: one first presents the deterministic numerical modeling of the dynamic problem and the corresponding results. Then, the probabilistic analyses and the corresponding probabilistic results are presented and discussed. The paper ends by a conclusion of the main findings.

2 DETERMINISTIC ANALYSIS

In this section, the deterministic numerical model is firstly presented. It is followed by the corresponding deterministic results.

2.1 Numerical modeling

The deterministic model is based on numerical simulations using the dynamic option of the finite difference code FLAC^{2D}. The input seismic signal used in this work is the synthetic signal of Nice for which the corresponding accelerogram is presented in Figure 1(a). This signal is used because it is representative of the French design spectrum [7]. It has a maximum acceleration equal to 0.33g. Its corresponding Fourier amplitude spectrum is shown in Figure 1(b).

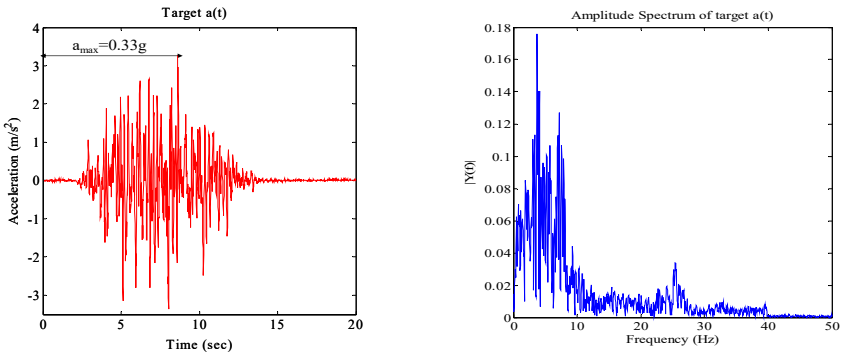

(a) (b)

Figure 1. (a) Accelerogram of the synthetic signal of Nice and (b) the corresponding Fourier amplitude spectrum

In the finite difference dynamic analysis by FLAC^{2D}, numerical distortions may occur during the propagation of the seismic waves if the elements size of the mesh is not convenient. The size Δl of an element of the mesh should respect the following condition [8]:

$$\Delta l \leq \frac{V_s}{10 * f_{\max}} \tag{1}$$

where V_s is the shear wave velocity, and f_{max} is the maximum frequency of the incident seismic signal [9]. The shear wave velocity V_s in Equation (1) can be calculated using the values of the soil shear modulus G and the soil density ρ as follows:

$$V_s = \sqrt{\frac{G}{\rho}} \tag{2}$$

Even though an elasto-plastic model would be more realistic to model the soil behavior especially for the cases of medium and high earthquake ground motions GMs, an elastic model was used in this work. The aim is to investigate the effect of the soil spatial variability using a simple model with a reasonable computation time. Concerning the boundary conditions, FLAC^{2D} offers the option of applying absorbing boundary conditions of type "quiet boundaries" or "free field". These boundary conditions absorb the energy of the wave approaching these limits and thus avoid the reflection of these waves. In this paper, the boundary conditions applied to the vertical boundaries are of type "free field". This type of boundary conditions is suitable for vertical surfaces, the boundary conditions of type "quiet boundaries" being generally convenient in the case of horizontal surfaces. Finally, it should be mentioned that in the natural dynamic systems, the internal friction may lead to partial dissipation of the energy of vibration. The software FLAC^{2D} provides a damping of type "Rayleigh damping"

(among other types of damping) which is based on two parameters (i) the natural frequency of the system and (ii) the damping ratio (defined as a percentage of the critical damping).

2.2 Deterministic results

For the dynamic analyses, the values of the shear modulus, bulk modulus and density of the soil were as follows: G=100MPa, K=250MPa and ρ=1800 kg/m^3. In order to avoid the numerical distortion that may occur during the propagation of the seismic waves in the model, the elements size must satisfy Equation (1). By using Equation (2), the shear wave velocity was found to be equal to 235.7m/s. From Figure 1(b), one can see that the maximal frequency f_{max} is equal to 40Hz. Thus, the maximum size of the different elements must be less than or equal to 0.59m. In the studied model, the size Δl of the different elements was taken equal to 0.5m. Concerning the boundary conditions, boundary conditions of type "free field" were applied along the vertical boundaries of the model. The lower horizontal boundary was subjected to the seismic load (i.e. the synthetic accelerogram of Nice). Concerning the damping effect, an undamped system was considered to reduce the number of involved parameters. The effect of damping will be the subject of future work.

The slope geometry considered in the analysis is 10m in height and 45° in inclination angle (see Figure 2). In order to obtain accurate results of the maximum acceleration at the top and at the toe of the slope, one need to position correctly the vertical boundary conditions. For this purpose, the width of the slope L was initially considered to be equal to 60m and was successively increased by 20m (i.e. 10m from each side) until one obtains convergence of the maximum acceleration for the profile presented in figure 2 in red color. Figure 3 presents the maximum acceleration profiles for L=60m, 80m, 100m, 120m, 140m and 160m. From this figure, one can deduce that for L $\geq$ 140m, all the presented profiles coincide. For this reason, a width L=140m was selected for the probabilistic analysis. The corresponding computation time is equal to 50 minutes.

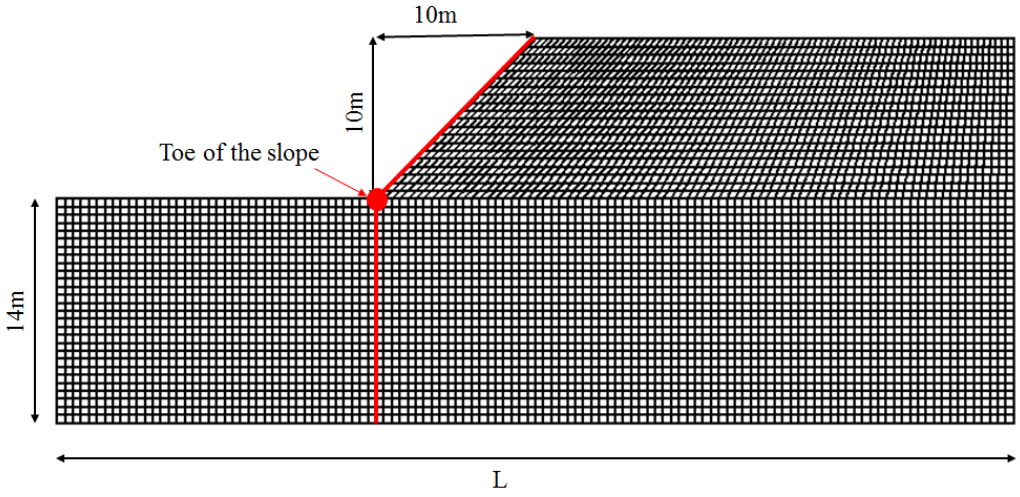

Figure 2. Slope geometry

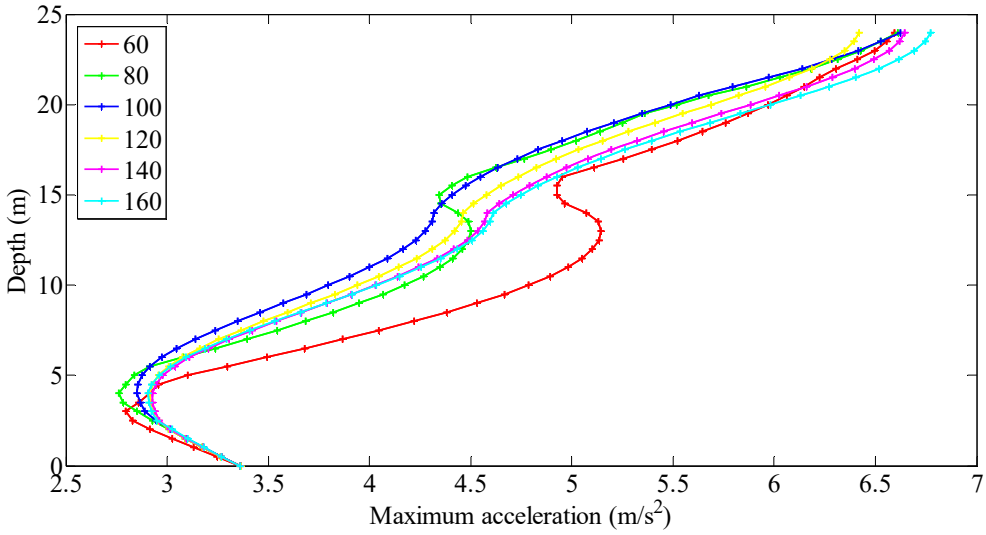

Figure 3. Maximum acceleration profiles for L= 60m, 80m, 100m, 120m, 140m and 160m

3 PROBABILISTIC ANALYSIS

The aim of this section is to present the probabilistic dynamic analysis. The impact of the soil spatial variability on the dynamic response was investigated. It should be noted here that the dynamic system response considered in this section involves the maximum acceleration (A_{max}) at the toe of the slope. The objective of the probabilistic analysis is the computation of the probability P_f of exceeding a tolerable maximum acceleration A_{max}. The soil shear modulus G was modeled as a two-dimensional log-normal random field. The EOLE methodology [10] was used to discretize the shear modulus random field (i.e. to obtain realizations of the soil shear modulus that respect the correlation structure of this field). For the two-dimensional random field used in this paper, the shear modulus was allowed to vary in both the horizontal and vertical directions. The deterministic model was based on numerical simulations using the finite difference code FLAC^{2D}. As for the probabilistic method used in this paper, the active learning reliability method combining kriging and Monte Carlo Simulation (i.e. AK-MCS) was employed. This method combines both the classical crude Monte Carlo Simulation (MCS) methodology and the Kriging meta-model technique. The performance function used to calculate the probability P_f of exceeding a tolerable maximum acceleration A_{max} was defined as follow:

$$\Gamma = \frac{A_{\max}}{A_{\max}\left(toe\right)} - 1 \tag{3}$$

where A_{max} is a prescribed tolerable maximum acceleration and A_{max}(toe) is the maximum acceleration at the toe of the slope as computed by FLAC^{2D} software due to the applied seismic loading.

In this section, the EOLE method of discretization of random fields is firstly presented. It is followed by a brief presentation of the crude Monte Carlo method, the kriging metamodeling technique and the combined use of the kriging and the Monte Carlo Simulation methodology (called AK-MCS) used for the probabilistic analysis.

3.1 Discretization of a non-isotropic log-normal random field

Consider a 2D non-isotropic log-normal random field Z^{LN} described by: (i) a log-normal marginal cumulative distribution function F_G, and (ii) a square exponential autocorrelation function ρ_Z^{LN} [(x, y), (x', y')] which gives the values of the correlation between two arbitrary points (x, y) and (x', y'). Notice that this function is given as follows:

$$\rho_z^{LN}[(x,\ y),\ (x\ ',\ y\ ')] = \exp\left(-\left(\frac{|x - x\ '|}{a_x} \right)^2 - \left(\frac{|y - y\ '|}{a_y} \right)^2 \right) \tag{4}$$

where a_x and a_y are the autocorrelation distances along x and y respectively. The EOLE method proposed by [10] to discretize a random field is used herein. In this method, one should first define a stochastic grid composed of s grid points (or nodes) and determine the log-normal autocorrelation matrix $\Sigma_{\chi;\chi}^{LN}$ which gives the correlation between each grid point of the stochastic mesh and the other grid points of this mesh using Equation (4). The number of grid points within the stochastic mesh is determined in such a manner that in each direction (x or y), there are five grid points within each autocorraltion distance. The log-normal autocorrelation matrix $\Sigma_{\chi;\chi}^{LN}$ should then be transformed into the Gaussian space using the Nataf transformation [11]. As a result, one obtains a Gaussian autocorrelation matrix $\Sigma_{\chi;\chi}^{G}$ that can be used to discretize the Gaussian random field Z as follows:

$$\tilde{Z}(x\ ,\ y\ ) \cong \mu_{\ln Z} + \sigma_{\ln Z} \sum_{j=1}^{N} \frac{\xi_j}{\sqrt{\lambda_j}} .\phi_j .\Sigma_{Z(x\ ,y\ );\chi} \tag{5}$$

where μ_{lnZ} and σ_{lnZ} are the mean and standard deviation values of the underlying normal distribution (i.e. ln(Z)); (λ_j ,ϕ_j) are the eigenvalues and eigenvectors of the Gaussian autocorrelation matrix $\Sigma_{\chi;\chi}^{G}$; $\Sigma_{Z(x\ ,y\ );\chi}$ is the correlation vector between the value of the field at an arbitrary point (x, y) and its values at the different grid points; ξ_j (j=1, ..., N) is a vector of standard normal random variables; and N is the number of terms (expansion order) retained in EOLE method. This number N is obtained (i) by sorting the eigenvalues λ_j (j=1, …, s) in a descending order and (ii) by choosing the number N of eigenmodes that leads to a variance of the error which is smaller than a prescribed tolerance ε ($\varepsilon \approx 10\%$ in this paper). Notice that the variance of the error for EOLE is given by [10] as follows:

$$Var\left[\ Z(x,\ y) - \tilde{Z}(x,\ y)\ \right] = \sigma_{\ln Z}^2 \left\{ 1 - \sum_{j=1}^{N} \frac{1}{\lambda_j} \left(\left(\phi_j \right)^T \Sigma_{Z(x,y);\chi} \right)^2 \right\} \tag{6}$$

where $Z(x\ ,\ y\ )$ and $\tilde{Z}(x\ ,\ y\ )$ are respectively the exact and the approximate values of the random field at a given point (x, y) and $\left(\phi_j \right)^T$ is the transpose of the eigenvector ϕ_j **.** Once the Gaussian random field is obtained, it should be transformed into the log-normal space by exponentiating the approximated Gaussian random field $\tilde{Z}(x\ ,\ y\ )$ given by Equation (5). Notice finally that Eq. (5) or rather its equivalence for the log-normal random field will be used in this paper to compute the value of the random field at the center of the different elements of the numerical dynamic model to assign values of G to the different elements of this numerical model.

3.2 Monte Carlo method

The Monte Carlo simulation method consists in generating K samples which respect the joint probability density function $f_X(X)$ of the M random variables ($X_1, \ldots, X_M$) gathered in a vector X. For each sample, the system response is calculated. Thus; for the K samples, one obtains K values of the system response gathered in a vector $\Gamma = \left\{\Gamma\left(X^{(1)}\right),\ldots,\Gamma\left(X^{(K)}\right)\right\}$ which may be used to determine the failure probability for a prescribed threshold of this system response. A very large number of samples (i.e. realizations) is required to obtain a rigorous value of the failure probability especially when computing small failure probabilities. It should be noted herein that the random variables considered in the present paper are the standard normal variables ξ_j ($j=1, \ldots, N$) that appear in Eq. (5) for the computation of a given realization of the shear modulus random field.

3.3 Kriging metamodeling technique

The metamodeling technique aims at replacing the response (or the performance function in this paper) of a computationally-expensive mechanical model by a metamodel (i.e. a simple analytical equation). The Kriging metamodeling technique is based on the idea that the performance function $\Gamma(\mathbf{x})$ is seen as a realization of a stochastic field $\delta(\mathbf{x})$ [12]. The first step of kriging consists of defining this stochastic field with its parameters according to an Experimental Design (ED) of length k. This stochastic field is given by:

$$\delta(\mathbf{x}) = F(\mathbf{x},\beta) + Z(\mathbf{x}) \tag{7}$$

Where:

- $F(\mathbf{x},\beta)$ is the deterministic part which gives an approximation of the mean value of the performance function. It corresponds to a regression model that can be written as:

$$F(\mathbf{x},\beta) = \sum_{j=1}^{p} \beta_j f_j(\mathbf{x}^{(i)}) \qquad i=1,\ldots,k \tag{8}$$

  Where $\beta^T = (\beta_j, j = 1, \ldots, p)$ is the vector of coefficients to be determined, $f^T = (f_j, j = 1, \ldots, p)$ is a collection of regression functions (or regressors) and k is the number of observations. The number p of regression functions is assumed to be less than or equal to the number k of observations so that the problem is not underdetermined (i.e. it does not lack equations to compute the unknowns). In this paper, ordinary kriging is selected which means that $F(\mathbf{x},\beta)$ is a scalar to be determined (i.e. $F(\mathbf{x},\beta) = \beta$).

- $Z(\mathbf{x})$ represents the fluctuation around the mean value. It is given by a Gaussian random process (or a random field) with zero mean and covariance between two points of space $\mathbf{x}$ and $\mathbf{x}'$ defined by:

$$COV\left(Z(\mathbf{x}), Z(\mathbf{x}')\right) = \sigma_Z^2 \rho_\theta(\mathbf{x},\mathbf{x}') \tag{9}$$

  Where σ_Z^2 is the process variance and ρ_θ the correlation function defined by its set of parameters θ. Several models exist to define the correlation function. However, in this paper, the anisotropic squared-exponential function is selected. It is given by:

$$\rho_\theta(\mathbf{x},\mathbf{x}') = \prod_{i=1}^{N} exp\left(-\left(\theta_i\left(x_i - x_i'\right)\right)^2\right) \tag{10}$$

Where N is the number of random variables, x_i and x_i' are the i[th] coordinates of the points $\mathbf{x}$ and $\mathbf{x}'$ and θ_i is a scalar which is equal to the inverse of the correlation length in the i[th] direction.

As mentioned above, in order to completely define the kriging model, one has to compute the following parameters: β, σ_Z and the correlation function parameters θ_i. Given an initial Experimental Design (ED) with k samples, $\mathbf{x} = \left\{\mathbf{x}^{(1)},...,\mathbf{x}^{(k)}\right\}$, for which the response values have been computed and stored in $\mathbf{\Gamma} = \left\{\Gamma\left(\mathbf{x}^{(1)}\right),...,\Gamma\left(\mathbf{x}^{(k)}\right)\right\}$, the scalars β and σ_Z^2 are estimated according to [12] by:

$$\hat{\beta} = (\mathbf{1}^T \Sigma_{\Gamma;\Gamma}^{-1} \mathbf{1})^{-1} \mathbf{1}^T \Sigma_{\Gamma;\Gamma}^{-1} \mathbf{\Gamma} \tag{11}$$

$$\hat{\sigma}_Z^2 = \frac{1}{k}(\mathbf{\Gamma} - \hat{\beta}\mathbf{1})^T \Sigma_{\Gamma;\Gamma}^{-1} (\mathbf{\Gamma} - \hat{\beta}\mathbf{1}) \tag{12}$$

Where $\mathbf{1}$ is the vector of length k filled with $\mathbf{1}$, $\Sigma_{\Gamma;\Gamma}^{-1}$ is the inverse of the correlation matrix $\Sigma_{\Gamma;\Gamma}$. It should be mentioned that a row i of the correlation matrix gives the values of the correlation between the value of the response at the sampled point $\Gamma\left(\mathbf{x}^{(i)}\right)$ and all the values of the response at the sampled points $\mathbf{\Gamma} = \left\{\Gamma\left(\mathbf{x}^{(1)}\right),...,\Gamma\left(\mathbf{x}^{(k)}\right)\right\}$ as follows:

$$\left(\Sigma_{\Gamma;\Gamma}\right)_{i,j} = \rho_\theta\left(\mathbf{x}_i, \mathbf{x}_j\right) \qquad i=1,...,k \text{ and } j=1,...,k \tag{13}$$

However, as $\hat{\beta}$ and $\hat{\sigma}_\Gamma^2$ in Eqs. (11) and (12) depend on the correlation parameters θ_i through the matrix $\Sigma_{\Gamma;\Gamma}$, it is first required to obtain them using maximum likelihood estimation:

$$\theta = \arg\min_\theta \left(\det \Sigma_{\Gamma;\Gamma}\right)^{\frac{1}{k}} \hat{\sigma}_Z^2 \tag{14}$$

The next step consists of predicting the response of $\Gamma(\mathbf{x})$ in a given unknown point $\mathbf{x}$. At such a point, the Best Linear Unbiased Predictor (BLUP) $\hat{\Gamma}(\mathbf{x})$ of $\delta(\mathbf{x})$ is computed as [12]:

$$\hat{\Gamma}(\mathbf{x}) = \beta + \sum_{\Gamma(\mathbf{x});\Gamma} \sum_{\Gamma;\Gamma}^{-1} (\mathbf{\Gamma} - \beta\mathbf{1}) \tag{15}$$

Where $\Sigma_{\Gamma(\mathbf{x});\Gamma}$ is the correlation vector whose elements provide the correlation between the value of the response at the unsampled point $\Gamma(\mathbf{x})$ and the values of the response at the sampled points gathered in the vector $\mathbf{\Gamma} = \left\{\Gamma\left(\mathbf{x}^{(1)}\right),...,\Gamma\left(\mathbf{x}^{(k)}\right)\right\}$ as follows:

$$\left(\Sigma_{\Gamma(\mathbf{x});\Gamma}\right)_i = \rho_\theta\left(\mathbf{x}_i, \mathbf{x}\right) \qquad i=1,...,k \tag{16}$$

The kriging variance is defined as the minimum of the mean squared error between $\Gamma(\mathbf{x})$ and $\hat{\Gamma}(\mathbf{x})$. It can be expressed as the following analytical function:

$$\sigma_{\hat{\Gamma}}^2(\mathbf{x}) = \sigma_Z^2\left(\mathbf{1} + u(\mathbf{x})^t \left(\mathbf{1}^t \Sigma_{\Gamma;\Gamma}^{-1} \mathbf{1}\right) u(\mathbf{x}) - \Sigma_{\Gamma(\mathbf{x});\Gamma}^T \Sigma_{\Gamma;\Gamma}^{-1} \Sigma_{\Gamma(\mathbf{x});\Gamma}\right) \tag{17}$$

Where:

$$u\left(\mathbf{x}\right)=\mathbf{1}^{t}\Sigma_{\Gamma;\Gamma}^{-1}\Sigma_{\Gamma(\mathbf{x});\Gamma}-\mathbf{1} \tag{18}$$

Kriging is an exact interpolation method. The prediction of $\hat{\Gamma}\left(\mathbf{x}^{(i)}\right)$ in a point $\mathbf{x}^{(i)}$ of the design of experiments is exact (i.e. $\hat{\Gamma}\left(\mathbf{x}^{(i)}\right)=\Gamma\left(\mathbf{x}^{(i)}\right)$). Therefore, the kriging variance is null in these points and it becomes important in unexplored areas. These properties are interesting in reliability studies and metamodels as the Kriging variance represents a good index to improve a design of experiments.

3.4 AK-MCS methodology

The active learning reliability method called AK-MCS combines both the Kriging metamodeling technique and Monte Carlo Simulation. The iterative procedure suggested by [6] for computing the probability of failure P_f using this approach can be described as follows:

1. Generate a population S of n_{MC} (say 1,000,000) realizations of the spatially varying soil shear modulus using Monte Carlo Simulation. It should be emphasized here that the computation of the performance function for these realizations (as defined in equation 3 based on the computationally-expensive FLAC^{2D} model) is not required at this stage.
2. Randomly select from the S population a small number of realizations (called initial Design of Experiments DoE) containing N_1 realizations (say 20). For those N_1 realizations, one should evaluate the performance function given by equation (3) based on the computationally-expensive FLAC^{2D} model. The required initial DoE may be greater than 20 for a great number of random variables (i.e. for a spatially varying soil property with small values of the autocorrelation distances). This is because for high dimensional problems (i.e. when a large number of random variables is needed to discretize the shear modulus random field), the kriging model needs more points (i.e. realizations) in order to compute correlation parameters θ_i given by equation (15).
3. Compute the kriging model according to the small initial DoE containing the N_1 realizations. This kriging model is given by equation (16). It should be mentioned here that this stage was performed using the Matlab toolbox DACE [7]. In this paper, ordinary kriging model was used (i.e. the regression model is considered to be constant) and a square exponential correlation function was adopted in the analysis.
4. By using DACE toolbox, compute (for the whole population S containing the n_{MC} realizations of the random field) both the kriging predictor values $\hat{\Gamma}$ of the performance function (based on equation 16) and their corresponding kriging variance values $\sigma_{\hat{\Gamma}}^2$ (based on equation 18). From the obtained values of the kriging predictors $\hat{\Gamma}$, obtain an estimation of the probability of failure $\hat{P}_f$ by counting the number of negative predictors $N_{\hat{\Gamma}\leq 0}$ and dividing it by the total number of samples in S as follows:

$$\hat{P}_f=\frac{N_{\hat{\Gamma}\leq 0}}{n_{MC}} \tag{19}$$

Also compute the coefficient of variation of $\hat{P}_f$ as follows:

$$C\hat{O}V(\hat{P}_f)=\sqrt{\frac{1-\hat{P}_f}{\hat{P}_f n_{MC}}} \tag{20}$$

5. Identify the best next realization in S for which one will compute the performance function using FLAC^{2D}. This is performed by evaluating a learning function U for each realization in S. The learning function U is given by:

$$U\left(\mathbf{x}^{(i)}\right)=\frac{\left|\hat{\Gamma}\left(\mathbf{x}^{(i)}\right)\right|}{\sigma_{\hat{\Gamma}}\left(\mathbf{x}^{(i)}\right)} \qquad i=1,...,n_{MC} \tag{21}$$

The best next candidate realization is the one with minimum value of U. If this minimum value of U is smaller than 2, the performance function based on FLAC^{2D} is evaluated for the best candidate and the initial DoE is updated. Thus one should go back to step 3 and evaluate a new kriging model based on the updated DoE. Steps 3, 4 and 5 are repeated until the minimum value of U become larger than 2. At this stage the learning stops and the metamodel is considered accurate enough based on the n_{MC} realizations.

6. When the learning stops, one must compute the estimated values of both the probability of failure $\hat{P}_f$ and the coefficient of variation $C\hat{O}V\left(\hat{P}_f\right)$. The obtained value of $\hat{P}_f$ is considered to be accurate if $C\hat{O}V\left(\hat{P}_f\right)\leq 5\%$. If the estimated coefficient of variation is larger than 5%, one must increase the population S in step 1 and repeat the procedure.

It should be emphasized herein that a small initial DoE is chosen within the present approach (see step 2) in order to keep to a minimum the number of calls to the deterministic model. This initial DoE is successively increased by a single realization at each time (see step 5). The chosen realization is the one that is improving the most the metamodel because equation (22) searches for the realization that has a small kriging predictor (i.e. a realization that is close to the limit state surface) and/or a high kriging variance (i.e. a high uncertainty in the sign of its performance function value). Notice that the realizations with high uncertainties in the sign of their performance function values (positive or negative) are those that are close to the limit state surface. Finally, notice that the stopping criterion min(U)>2 corresponds to a maximal probability of making a mistake on the sign of the performance function of $\Phi(-2)=0.023$. This means that the stopping criterion is relevant making use of the realizations with a small uncertainty in making a mistake in their performance functions' signs, the probability of making a mistake in the signs of their performance function values being negligible.

3.5 Probabilistic dynamic results

The aim of this section is to present the probabilistic dynamic results of a soil slope exhibiting a spatially varying shear modulus. The objective is the computation of the probability P_f of exceeding a tolerable maximum acceleration A_{max}. The shear modulus G was modeled by a random field and it was assumed to follow a log-normal probability density function. The mean value and the coefficient of variation of G were respectively μ_G=100MPa and COV_G=25%. A square exponential autocorrelation function was used in this study to represent the correlation structure of the random field. The random field was discretized using EOLE method. Although an isotropic random field is often assumed in literature [13, 14], the vertical autocorrelation length tends to be shorter than the horizontal one due to the geological soil formation process for most natural soil deposits [15]. A common ratio of about 1 to 10 for these autocorrelation lengths can be used [16]. Notice that in this paper, only one configuration of the autocorrelation distances (a_x=50m and a_y=5m) was considered. An extension to this work may consider other configurations of a_x and a_y. The present study was performed in order to explore some interesting features related to the values of P_f for different values of the tolerable maximum acceleration A_{max}.

3.6 AK-MCS results for different values of the tolerable acceleration

In this section, the results obtained based on AK-MCS methodology are presented and discussed for the case where a_x=50m and a_y=5m. It should be mentioned here that a population S containing a total number of simulations n_{MC} equal to one million was selected. Then, a small initial design of experiment (DoE) of N_1=20 realizations among the whole population S was randomly selected. The performance function given by equation (3) was evaluated for this DoE. Thus, the computationally-expensive dynamic model based on finite difference code FLAC^{2D} was only called 20 times before evaluating the kriging model. The Kriging model was thus built based on this DoE. A simple analytical equation is then obtained and the performance function can be evaluated for the whole population S with no time: Both the kriging predictor and the kriging variance for the whole S population were evaluated based on equations (15) and (17) of the kriging model using the DACE Matlab toolbox [17]. The probability of failure $\hat{P}_f$ and the corresponding coefficient of variation $C\hat{O}V(\hat{P}_f)$ were computed using equations (19) and (20). Notice finally that several points (realizations) were added based on the evaluation of the learning function U given by equation (21) until reaching convergence.

Table 1 present the evolution of $\hat{P}_f$ and $C\hat{O}V(\hat{P}_f)$ as a function of the number of added points (realizations) for four different values of the tolerable maximum acceleration A_{max} (A_{max}=15, 25, 30 and 35m/s^2). From this table, one may conclude that for small value of A_{max} (A_{max}=15m/s^2) one obtains a large value of $\hat{P}_f$. Figure 4 presents the variation of $\hat{P}_f$ and $C\hat{O}V(\hat{P}_f)$ as function of the number of added points using the AK-MCS algorithm. This figure shows that the values of $\hat{P}_f$ and $C\hat{O}V(\hat{P}_f)$ stabilized when the algorithm has added 100 extra points to the initial DoE containing 20 points. In the present paper extra points were added to show the efficiently of the algorithm and to demonstrate that no further modifications on the obtained values of $\hat{P}_f$ and $C\hat{O}V(\hat{P}_f)$ may occur.

A_{max}(m/s^2)	$\hat{P}_f$	$C\hat{O}V(\hat{P}_f)$ (%)	Number of added points
15	170 x10^{-3}	0.21%	248
25	50 x10^{-3}	0.41%	185
30	12 x10^{-3}	0.1%	270
35	2.5x10^{-3}	0.1%	248

Table 1: Variation of $\hat{P}_f$ and $C\hat{O}V(\hat{P}_f)$ together with the number of added points for different values of A_{max}.

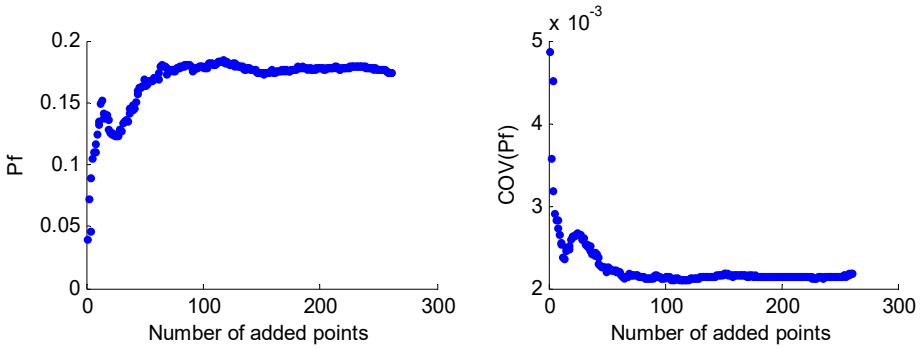

Figure 4. Variation of $\hat{P}_f$ and $C\hat{O}V(\hat{P}_f)$ as function of the number of added points for A_{max} =15m/s^2

4 CONCLUSION

The probabilistic dynamic analyses presented in this paper were performed using AK-MCS methodology. In a first stage (step 1), a significant number of realizations (about 1 million) of the spatially varying soil medium were generated by MCS using EOLE method. In a second stage (step 2), an initial design of experiments (DoE) based on a random selection of some realizations among the MCS population was determined and employed to compute the Kriging model. In a third stage (steps 3-5), a kriging model is constructed and a learning function U was employed to choose the best next realization to be used for the computation of the system response from the original deterministic model and to update the kriging model with this new response value. Notice that steps 3-5 were repeated several times until reaching the adopted stopping condition. At the end, the surrogate kriging model was considered to be enough accurate for the estimation of the failure probability and the corresponding value of the coefficient of variation, for the prescribed number of simulations (step 6). The probabilistic results have shown that for small value of the tolerable maximum acceleration A_{max} one obtains a large value of $\widehat{P}_f$. One the other hand, one can notice that number of realizations required by the AK-MCS algorithm (to obtain accurate values of $\hat{P}_f$ and $\widehat{COV}(\hat{P}_f)$) is relatively small. This is very interesting for computationally expensive dynamic problems.

REFERENCES

[1] Koutsourelakis, S., Prevost, J.H., and Deodatis, G. Risk assessement of an interacting structure-soil system due to liquefaction. *Earthquake Engineering and Structural Dynamic*, 31: 851-879, 2002.

[2] Nour, A., Slimania, A., Laouamia, N., and Afraa, H. Finite element model for the probabilistic seismic response of heterogeneous soil profile. *Soil Dynamics and Earthquake Engineering*, 23: 331-348, 2003.

[3] Popescu, R., Prevost, J.H., and Deodatis, G. 3D effects in seismic liquefaction of stochastically variable soil deposits. *Géotechnique*, 55(1): 21-31, 2005.

[4] Lopez-Caballero, F., and Modaressi Farahmand-Razavi,A. Assessment of variability and uncertainties effects on the seismic response of a liquefiable soil profile. *Soil Dynamics and Earthquake Engineering*, 30(7): 600-613, 2010.

[5] Al-bittar (2015)

[6] Echard B, Gayton N, Lemaire M. AK-MCS: an active learning reliability method combining Kriging and Monte Carlo simulation. Structural Safety 2011;33(2):145–54.

[7] Grange, S. Risque sismique: stratégie de modélisation pour simuler la réponse des structures en béton et leurs interactions avec le sol. *Ph.D thesis*, INPG, 2008.

[8] Itasca. FLAC 4.0 Manuals. – Minnesota, ITASCA Consulting Group, Inc 2000.

[9] Kuhlemeyer, R. L., and Lysmer, J. Finite element method accuracy for wave propagation problems. *Journal of Soil Mechanics & Foundations*, 99: 421-427, 1973.

[10] Li, C.C., and Der Kiureghian, A. Optimal discretization of random fields. *Journal of Engineering Mechanics*, 119(6): 1136-1154, 1993.

[11] Nataf, A. Détermination des distributions de probabilités dont les marges sont données. *CR Acad Sci*, 225: 42-3, 1962.

[12] Echard phd

[13] Fenton, G.A., and Griffiths, D.V. (2005). "Three-dimensional probabilistic foundation settlement." Journal of Geotechnical and Geoenvironmental Engineering, ASCE, 131(2): 232-239.

[14] Fenton, G.A., Zhou, H., Jaksa, M.B., and Griffiths, D.V. (2003). "Reliability analysis of a strip footing designed against settlement." Applications of statistics and probability in civil engineering, Der Kiureghian, Madanat & Pestana (eds) © 2003 Millpress, Rotterdam.

[15] Cho, S.E., and Park, H.C. (2010). "Effect of spatial variability of cross-correlated soil properties on bearing capacity of strip footing." *International Journal for Numerical and Analytical Methods in Geomechanics,* **34:** 1-26.

[16] Baecher, G.B., and Christian, J.T. (2003). "Reliability and statistics in geotechnical engineering." *John Wiley & Sons Ltd, The Atrium, Southern Gate, Chichewter, West Sussex PO19 8SQ, England,* 205-242.

[17] Lophaven SN, Nielsen HB, Sondergaard J. DACE, a matlab Kriging toolbox, version 2.0. Tech. Rep. IMM-TR-2002-12; Technical University of Denmark; 2002a. <http://www2.imm.dtu.dk/hbn/dace/>.

ECCOMAS Congress 2016
VII European Congress on Computational Methods in Applied Sciences and Engineering
M. Papadrakakis, V. Papadopoulos, G. Stefanou, V. Plevris (eds.)
Crete Island, Greece, 5–10 June 2016

ENERGY-MOMENTUM METHOD FOR NONLINEAR DYNAMIC OF 2D COROTATIONAL BEAMS

Sophy Chhang[1,2], Mohammed Hjiaj[1], Jean-Marc Battini[2] and Carlo Sansour[3]

[1]Structural Engineering Research Group /LGCGM , INSA de Rennes, Université Bretagne Loire, 20 Avenue des Buttes de Coësmes, 35708 Rennes Cédex 7, France
e-mail: Sophy.Chhang@insa-rennes.fr, Mohammed.Hjiaj@insa-rennes.fr

[2]Department of Civil and Architectural Engineering, KTH, Royal Institute of Technology, SE-10044 Stockholm, Sweden
e-mail: Jean-Marc.Battini@byv.kth.se

[3]Faculty of Engineering, University of Nottingham, Nottingham, UK
e-mail: Carlo.Sansour@nottingham.ac.uk

Keywords: Corotational formulation; energy-momentum method; conserving energy; nonlinear dynamic; 2D Beam

Abstract. *This paper presents an energy-momentum method for nonlinear dynamics of 2D Bernoulli corotational beams. It is shown that the time stepping algorithm conserves energy, linear momentum and angular momentum. To be consistent in the corotational approach, cubic interpolations of Bernoulli element are employed to derive both inertia and elastic terms. The shallow arch strain definition is used to get an element which produce accurate results for less number of elements. To avoid membrane locking, we use a constant and average value of the axial strains. In addition, the energy-momentum method is used to preserve the conserving properties, which is able to maintain the stability and accuracy in a non-dissipative system for a long period. The midpoint velocities of kinematic fields and strains are used to tackle any non-linear form of strain displacement relations. Finally, two examples including large overall displacement are presented to illustrate the stability and efficiency of the proposed algorithms.*

1 INTRODUCTION

The corotational method is an attractive approach to derive non-linear finite beam elements [1, 2, 3, 4, 5, 6, 7, 8] . The idea is to decompose the large motion of the element into rigid body and pure deformational parts through the use of a local system which continuously rotates and translates with the element. The deformational response is captured at the level of the local reference frame, whereas the geometric non-linearity induced by the large rigid-body motion, is incorporated in the transformation matrices relating local and global quantities. The main interest is that the pure deformation part can be assumed as small and can be represented by a linear or a low order non-linear theory.

Regarding corotational dynamic formulations, constant Timoshenko mass matrices [1, 2, 5] are often used to express the dynamic terms. However, such an approach assumes that the in-plane local displacements are zero, which is not accurate. For this reason, Le et al. [3] used the Interpolation Interdependent Element formulation [9], and hence cubic functions, to derive both the elastic and inertia terms. They show that this formulation is more efficient than using constant mass matrices.

Implicit time stepping methods are often used together with non-linear finite elements to study dynamic problems. The Newmark family of algorithms [10] is one of the most commonly employed. However, these methods present instabilities in non-linear analyses [4, 5]. To avoid these instabilities, Geradin and Cardona [11] introduced numerical dissipations (Alpha method [12]) in order to damp the high frequencies. However, by doing that, the energy in the system is not conserved [13, 14].

A different integration scheme, called Energy-Momentum Method, was developed from the standard midpoint rule. Simo and Tarnow [14] were the first authors to use this method that is unconditional stable in non-linear dynamics of three-dimensional elastic bodies. However, their formulation was only valid for quadratic-nonlinearities in the displacement field. In the corotational context, Crisfield and Shi [4] used a mid-point configuration combined to average strains in order to conserve the energy. Galvanetto and Crisfield [5] developed an energy-conserving time-integration procedure for implicit non-linear dynamic analysis of planar beam structures. They used the constant Timoshenko mass matrix for the inertia term.

In this paper, an energy-momentum method for corotational 2D Bernoulli beam elements is proposed. The main advantage of this scheme is that it preserves the total energy and the linear and angular momenta. Besides, this scheme maintains stability and accuracy in long term analyses. Regarding the element, Hermitian shape functions are used to derive both the inertia and elastic terms. A shallow arch strain definition is used for the local formulation. The element formulation is obtained by applying midpoint velocities to both the kinematic quantities and the strains.

2 BEAM KINEMATICS AND STRAIN

2.1 Beam kinematics

The kinematic of the beam and all the notations used in this section are shown in Figure 1. The vector of global displacements is defined by

$$\boldsymbol{q} = \left[\begin{array}{cccccc} u_1 & w_1 & \theta_1 & u_2 & w_2 & \theta_2 \end{array} \right]^{\mathrm{T}} \tag{1}$$

The vector of local displacements is defined by

$$\bar{\boldsymbol{q}} = \left[\begin{array}{ccc} \bar{u} & \bar{\theta}_1 & \bar{\theta}_2 \end{array} \right]^{\mathrm{T}} \tag{2}$$

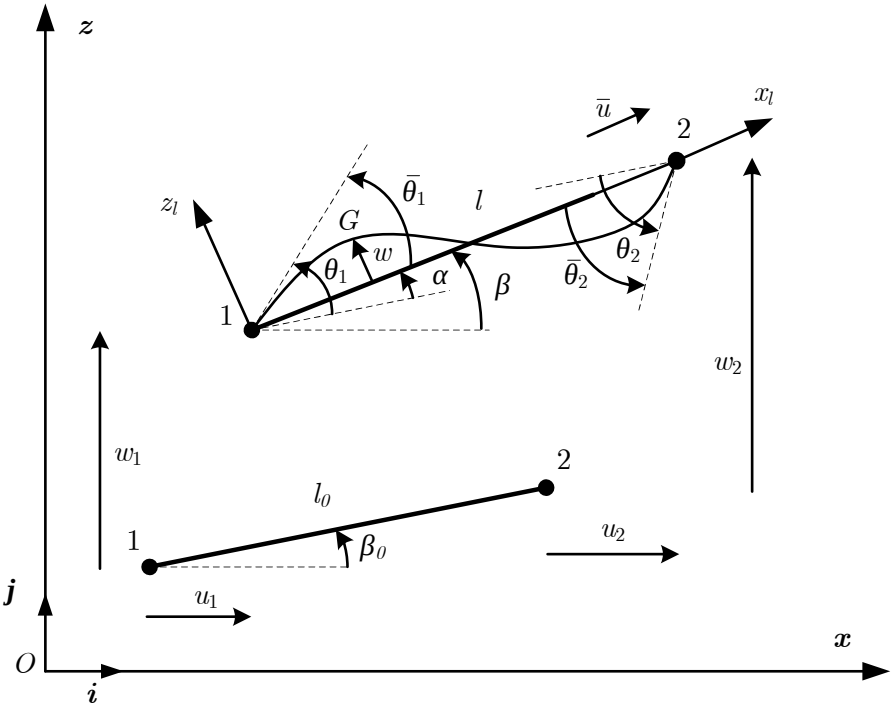

Figure 1: Beam kinematics.

The components of $\bar{\boldsymbol{q}}$ are computed according to

$$\bar{u} = l - l_0 \tag{3}$$
$$\bar{\theta}_1 = \theta_1 - \alpha \tag{4}$$
$$\bar{\theta}_2 = \theta_2 - \alpha \tag{5}$$

where l_0 and l denote the initial and current lengths of the element. The current angle of the local system with respect to the global system is denoted as β and is given by

$$c = \cos\beta = \frac{1}{l}(x_2 + u_2 - x_1 - u_1) \tag{6}$$
$$s = \sin\beta = \frac{1}{l}(z_2 + w_2 - z_1 - w_1) \tag{7}$$

The global position of the centroid G of the cross-section is given by

$$\boldsymbol{OG} = (x_1 + u_1)\,\mathbf{i} + (z_1 + w_1)\,\mathbf{j} + \frac{l_n}{l_0} x\,\boldsymbol{a} + w\,\boldsymbol{b} \tag{8}$$

with

$$\boldsymbol{a} = \cos\beta\,\mathbf{i} + \sin\beta\,\mathbf{j} \tag{9}$$
$$\boldsymbol{b} = -\sin\beta\,\mathbf{i} + \cos\beta\,\mathbf{j} \tag{10}$$

and w is the local transversal displacement of G. By using Eqs.(6) and (7), the components of the global displacements are obtained as

$$u_G = N_1(x_1 + u_1) + N_2(x_2 + u_2) - w\sin\beta \tag{11}$$
$$w_G = N_1(z_1 + w_1) + N_2(z_2 + w_2) + w\cos\beta \tag{12}$$

with

$$N_1 = 1 - \frac{x}{l_0} \tag{13}$$

$$N_2 = \frac{x}{l_0} \tag{14}$$

The global rotation of the cross-section is given by

$$\theta_G = \vartheta + \alpha \tag{15}$$

where ϑ is the local rotation of the cross-section.

2.2 Strain

The Bernoulli assumption is adopted for the local formulation. Hence, a linear interpolation is taken for the axial displacement u and a cubic one for the vertical displacement w.

The local strain is given by

$$\varepsilon_{11} = \varepsilon - \kappa\, z \tag{16}$$

in which the axial strain ε and the curvature κ are defined by

$$\varepsilon = \frac{1}{l_0}\int_{l_0}\left[\frac{\partial u}{\partial x} + \frac{1}{2}\left(\frac{\partial w}{\partial x}\right)^2\right]\mathrm{d}x \tag{17}$$

$$\kappa = \frac{\partial^2 w}{\partial x^2} \tag{18}$$

In Eq.(17), a shallow arch strain definition is taken. The purpose of introducing a low order of geometrical non-linearity in the local formulation is to obtain a more efficient formulation compared to a linear strain definition. The same level of accuracy is obtained with fewer elements. Besides, an average axial strain is taken in order to avoid membrane locking.

3 HAMILTON'S PRINCIPLE AND ENERGY-MOMENTUM METHOD

3.1 Hamilton's principle

Hamilton's principle states that the time integral of the Lagrangian at two specified states between two specified times t_1 and t_2 of a conservative mechanical system is stationary

$$\delta\int_{t_1}^{t_2}\mathcal{L}\,\mathrm{d}t = 0 \tag{19}$$

The integrand $\mathcal{L}$ is called Lagrange function

$$\mathcal{L} = \mathcal{K} - \mathcal{U}_{int} - \mathcal{U}_{ext} \tag{20}$$

$\mathcal{K}$ is the kinetic energy. $\mathcal{U}_{int}$ and $\mathcal{U}_{ext}$ are respectively the internal and the external potential energies. The body is non-conducting linear elastic solid and thermodynamic effects are not included in the system. The kinetic energy is the sum of the translational and rotational kinetic energies:

$$\mathcal{K} = \frac{1}{2}\int_{l_0}\rho A\,\dot{u}_G^2\,\mathrm{d}x + \frac{1}{2}\int_{l_0}\rho A\,\dot{w}_G^2\,\mathrm{d}x + \frac{1}{2}\int_{l_0}\rho I\,\dot{\theta}_G^2\,\mathrm{d}x \tag{21}$$

The elastic potential energy is defined as

$$\mathcal{U}_{int} = \frac{1}{2}\int_{l_0} EA\,\varepsilon^2 \mathrm{d}x + \frac{1}{2}\int_{l_0} EI\,\kappa^2 \mathrm{d}x \tag{22}$$

The external potential energy is defined as

$$\mathcal{U}_{ext} = -\int_{l_0} p_u\,u_G\,\mathrm{d}x - \int_{l_0} p_w\,w_G\,\mathrm{d}x - \int_{l_0} p_\theta\,\theta_G\,\mathrm{d}x - \sum_{i=1}^{6} P_i\,q_i \tag{23}$$

E is Young's modulus of the material, A is the area of the cross-section, I is the inertia moment of the cross-section, p_u and p_w are the distributed horizontal and the vertical loads, p_θ is the distributed external moment, P_i is the vector of concentrated forces and moments at the nodes.

By introducing Eqs.(21) to (23), the variation of Eq.(19) can be written as

$$\begin{aligned}
&\int_{t_1}^{t_2}\left(\int_{l_0}\rho A\,\ddot{u}_G\,\delta u_G\,\mathrm{d}x + \int_{l_0}\rho A\,\ddot{w}_G\,\delta w_G\,\mathrm{d}x + \int_{l_0}\rho I\,\ddot{\theta}_G\,\delta\theta_G\,\mathrm{d}x\right)\mathrm{d}t\\
-\;&\int_{t_1}^{t_2}\left(\int_{l_0} EA\,\varepsilon\,\delta\varepsilon\,\mathrm{d}x + \int_{l_0} EI\,\kappa\,\delta\kappa\,\mathrm{d}x - \int_{l_0} p_u\,\delta u_G\,\mathrm{d}x - \int_{l_0} p_w\,\delta w_G\,\mathrm{d}x\right)\mathrm{d}t\\
+\;&\int_{t_1}^{t_2}\left(\int_{l_0} p_\theta\,\delta\theta_G\,\mathrm{d}x + \sum_{i=1}^{6} P_i\,\delta q_i\right)\mathrm{d}t = 0
\end{aligned} \tag{24}$$

By using part integration for the first three terms of (24), the previous equation can be reformulated

$$\begin{aligned}
&\int_{t_1}^{t_2}\left(\int_{l_0}\rho A\,\ddot{u}_G\,\delta u_G\,\mathrm{d}x + \int_{l_0}\rho A\,\ddot{w}_G\,\delta w_G\,\mathrm{d}x + \int_{l_0}\rho I\,\ddot{\theta}_G\,\delta\theta_G\,\mathrm{d}x\right)\mathrm{d}t\\
+\;&\int_{t_1}^{t_2}\left(\int_{l_0} EA\,\varepsilon\,\delta\varepsilon\,\mathrm{d}x + \int_{l_0} EI\,\kappa\,\delta\kappa\,\mathrm{d}x - \int_{l_0} p_u\,\delta u_G\,\mathrm{d}x - \int_{l_0} p_w\,\delta w_G\,\mathrm{d}x\right)\mathrm{d}t\\
+\;&\int_{t_1}^{t_2}\left(-\int_{l_0} p_\theta\,\delta\theta_G\,\mathrm{d}x - \sum_{i=1}^{6} P_i\,\delta q_i\right)\mathrm{d}t = 0
\end{aligned} \tag{25}$$

3.2 Energy-momentum integration scheme

The classical midpoint time integration scheme is defined by the following equations:

$$\boldsymbol{q}_{n+\frac{1}{2}} = \frac{\boldsymbol{q}_{n+1}+\boldsymbol{q}_n}{2} = \boldsymbol{q}_n + \frac{1}{2}\Delta\boldsymbol{q} \tag{26}$$

$$\dot{\boldsymbol{q}}_{n+\frac{1}{2}} = \frac{\dot{\boldsymbol{q}}_{n+1}+\dot{\boldsymbol{q}}_n}{2} = \frac{\boldsymbol{q}_{n+1}-\boldsymbol{q}_n}{\Delta t} = \frac{\Delta\boldsymbol{q}}{\Delta t} \tag{27}$$

$$\ddot{\boldsymbol{q}}_{n+\frac{1}{2}} = \frac{\ddot{\boldsymbol{q}}_{n+1}+\ddot{\boldsymbol{q}}_n}{2} = \frac{\dot{\boldsymbol{q}}_{n+1}-\dot{\boldsymbol{q}}_n}{\Delta t} = \frac{2}{\Delta t^2}\Delta\boldsymbol{q} - \frac{2}{\Delta t}\dot{\boldsymbol{q}}_n \tag{28}$$

By extension of the classical midpoint rule, the average midpoint strains are developed in the context of energy-momentum method. This idea has been introduced in [16, 17]. The midpoint velocities are applied to both the kinematic fields and the strains because the nonlinear terms arise from both fields. This gives:

$$\int_{t_n}^{t_{n+1}} f(t)dt = f(t_{n+\frac{1}{2}})\Delta t = f_{n+\frac{1}{2}}\Delta t \tag{29}$$

$$f_{n+\frac{1}{2}} = f_n + \frac{\Delta t}{2}\dot{f}_{n+\frac{1}{2}} \tag{30}$$

where the function f can represent both the kinematic (u_G, w_G, θ_G) and deformational quantities (ε, κ).

The application of the midpoint rule (29) to the Hamilton's principle (25) gives

$$\begin{aligned}\Delta t \quad & \Big(\int_{l_0} \rho A\, \ddot{u}_{G,n+\frac{1}{2}}\, \delta u_{G,n+\frac{1}{2}}\, \mathrm{d}x + \int_{l_0} \rho A\, \ddot{w}_{G,n+\frac{1}{2}}\, \delta w_{G,n+\frac{1}{2}}\, \mathrm{d}x + \int_{l_0} \rho I\, \ddot{\theta}_{G,n+\frac{1}{2}}\, \delta \theta_{G,n+\frac{1}{2}}\, \mathrm{d}x \\ + \quad & \int_{l_0} EA\, \varepsilon_{n+\frac{1}{2}}\, \delta \varepsilon_{n+\frac{1}{2}}\, \mathrm{d}x + \int_{l_0} EI\, \kappa_{n+\frac{1}{2}}\, \delta \kappa_{n+\frac{1}{2}}\, \mathrm{d}x - \int_{l_0} p_{u,n+\frac{1}{2}}\, \delta u_{G,n+\frac{1}{2}}\, \mathrm{d}x \\ - \quad & \int_{l_0} p_{w,n+\frac{1}{2}}\, \delta w_{G,n+\frac{1}{2}}\, \mathrm{d}x - \int_{l_0} p_{\theta,n+\frac{1}{2}}\, \delta \theta_{G,n+\frac{1}{2}}\, \mathrm{d}x - \sum_{i=1}^{6} P_{i,n+\frac{1}{2}}\, \delta q_{i,n+\frac{1}{2}} \Big) = 0 \end{aligned} \tag{31}$$

As the variation $\delta \boldsymbol{q}$ is arbitrary, the dynamic equilibrium at time $n+\frac{1}{2}$ is obtained from the previous equation

$$\begin{aligned} & \int_{l_0} \rho A\, \ddot{u}_{G,n+\frac{1}{2}} \frac{\partial u_{G,n+\frac{1}{2}}}{\partial \boldsymbol{q}_{n+\frac{1}{2}}}\, \mathrm{d}x + \int_{l_0} \rho A\, \ddot{w}_{G,n+\frac{1}{2}} \frac{\partial w_{G,n+\frac{1}{2}}}{\partial \boldsymbol{q}_{n+\frac{1}{2}}}\, \mathrm{d}x + \int_{l_0} \rho I\, \ddot{\theta}_{G,n+\frac{1}{2}} \frac{\partial \theta_{G,n+\frac{1}{2}}}{\partial \boldsymbol{q}_{n+\frac{1}{2}}}\, \mathrm{d}x \\ + \quad & \int_{l_0} EA\, \varepsilon_{n+\frac{1}{2}} \frac{\partial \varepsilon_{n+\frac{1}{2}}}{\partial \boldsymbol{q}_{n+\frac{1}{2}}}\, \mathrm{d}x + \int_{l_0} EI\, \kappa_{n+\frac{1}{2}} \frac{\partial \kappa_{n+\frac{1}{2}}}{\partial \boldsymbol{q}_{n+\frac{1}{2}}}\, \mathrm{d}x - \int_{l_0} p_{u,n+\frac{1}{2}} \frac{\partial u_{G,n+\frac{1}{2}}}{\partial \boldsymbol{q}_{n+\frac{1}{2}}}\, \mathrm{d}x \\ - \quad & \int_{l_0} p_{w,n+\frac{1}{2}} \frac{\partial w_{G,n+\frac{1}{2}}}{\partial \boldsymbol{q}_{n+\frac{1}{2}}}\, \mathrm{d}x - \int_{l_0} p_{\theta,n+\frac{1}{2}} \frac{\partial \theta_{G,n+\frac{1}{2}}}{\partial \boldsymbol{q}_{n+\frac{1}{2}}}\, \mathrm{d}x - P_{i,n+\frac{1}{2}} = 0 \end{aligned} \tag{32}$$

4 NUMERICAL EXAMPLES

Two numerical applications are presented in this section. The first purpose of these examples is to verify numerically that the proposed energy-momentum algorithm conserves the total energy of the system and remains stable even if a very large number of time steps are applied. The second purpose is to show that in the absence of applied external loads, the proposed algorithm conserves the linear and angular momenta.

4.1 Cantilever beam

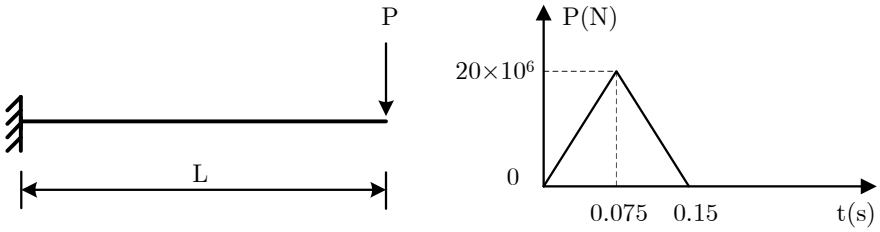

Figure 2: Geometry and load history.

The first example, see Figure 2, is a cantilever beam loaded by a triangular force at its end. The parameters of the problem are:

$$\begin{aligned} L &= 3\ m, A = 1000\ cm^2, I = 8330\ cm^4 \\ E &= 200\ GPa, \rho = 48831\ kg/m^3 \\ \Delta t &= 10^{-3}\ s, \text{Number of elements} = 4 \end{aligned}$$

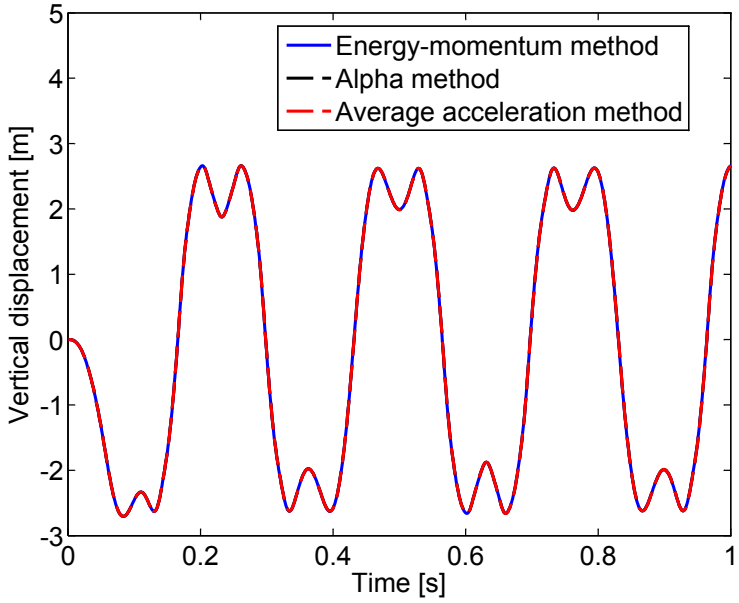

Figure 3: Comparison the displacements at the end of the tip.

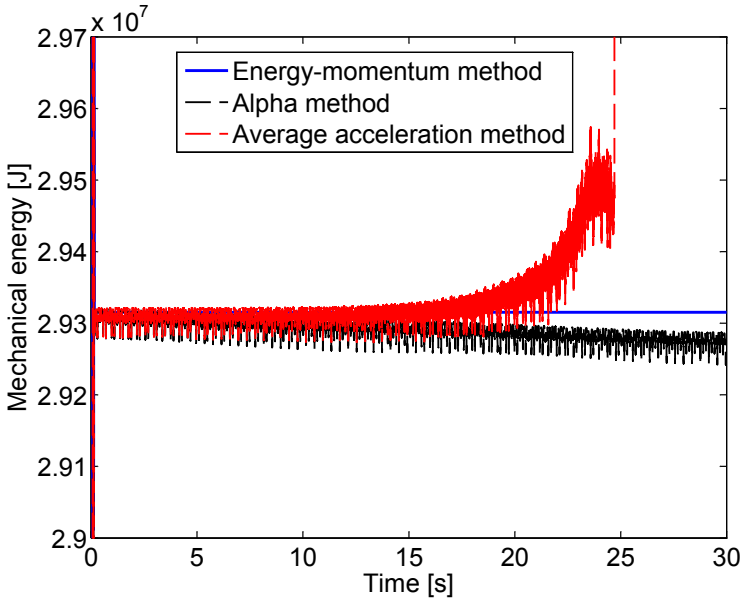

Figure 4: Comparison of mechanical energy from 0s to 30s.

The results obtained with the present energy-momentum formulation are compared to the ones obtained with the corotational formulation proposed by Le et al. [3]. In this previous formulation, the alpha method is used to solve the equations of motion. Two cases are considered here, $\alpha = 0$, which corresponds to the classical average acceleration method and $\alpha = -0.01$ which gives a small numerical damping that limits the influence of higher modes on the response.

The results presented in Figure 3 show that at the beginning the three approaches give exactly the same results. The results in Figures 4 and 5 show clearly that with the average acceleration

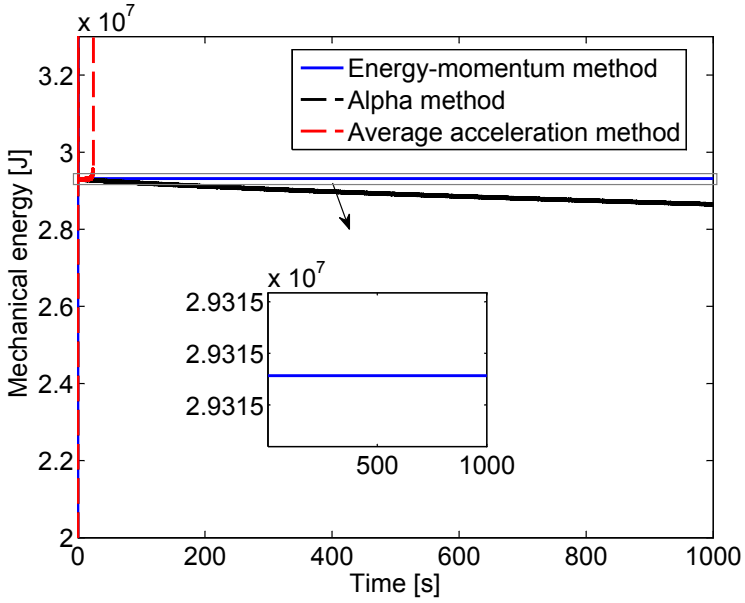

Figure 5: Comparison of mechanical energy from 0s to 1000s.

method, the mechanical energy (sum of kinetic energy and internal energy) blows up after about $24s$ and the solution diverges. With the alpha method, the solution does not diverge, but as expected, there is a loss of the mechanical energy due to the numerical damping. However, with the present energy-momentum approach, the mechanical energy is constant and the solution remains stable even if a very large number of steps (one million) is applied.

4.2 Free fly beam

The second example is a free flying beam, see Figure 6. The parameters of the problems are

$$\begin{aligned} L &= 3\ m, A = 200\ cm^2, I = 66.67\ cm^4 \\ E &= 200\ GPa, \rho = 48831\ kg/m^3 \\ \Delta t &= 10^{-4}\ s, \text{Number of elements} = 4 \end{aligned}$$

The interest of this problem is that after 0.4s, no forces and moments are applied to the beam. Consequently, this problem is suitable to study the conservation of the linear and angular momenta. Figures 7, 8 and 9 show the conservation of energy and momenta for one million time steps. The relative error is about 10^{-8} for the energy. We present here the two momenta on two different figures 8 and 9 with appropriate scale. The figures show that all the moments are constant.

5 CONCLUSION

This paper has presented an energy-momentum dynamic integration scheme in the context of corotational 2D beam elements. The main idea is to use the classical midpoint rules for both the kinematic and strain quantities. The advantage of the propose algorithm is that it conserves the total energy of the system and remains stable and accurate even if a very large number of time steps are applied. Besides, in the absence of applied external loads, the linear and angular momenta are constant. These characteristics have been proved numerically by using two numerical applications.

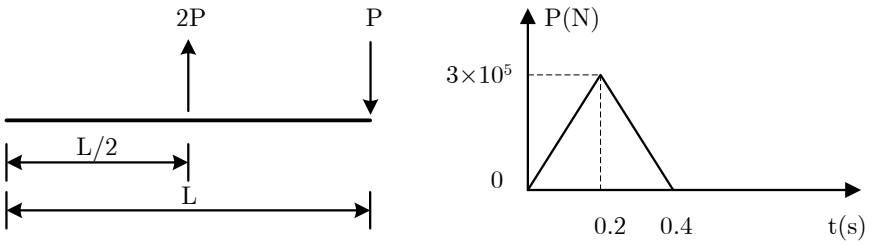

Figure 6: Geometry and load history of free fly beam.

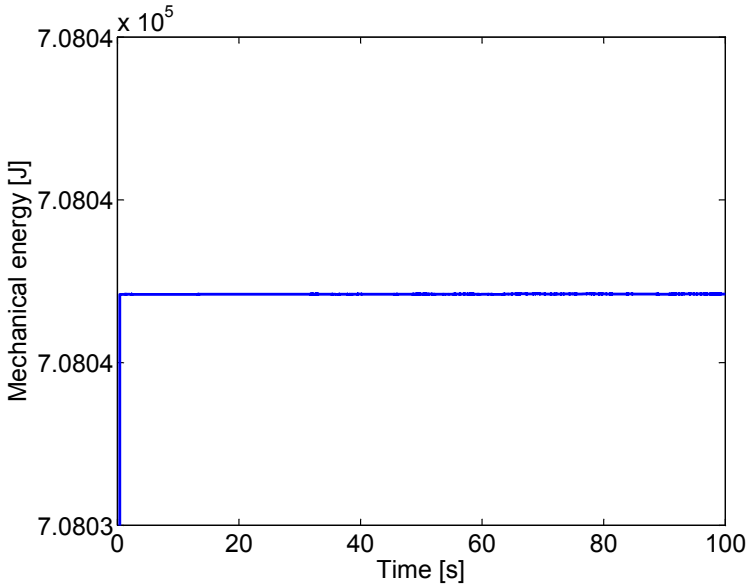

Figure 7: Mechanical energy.

REFERENCES

[1] M.A. Crisfield, U. Galvanetto, G. Jelenić, Dynamics of 3-D co-rotational beams. *Computational Mechanics*, **20**, 507–519, 1997.

[2] M. Iura , S.N. Atluri, Dynamic analysis of planar flexible beams with finite rotaions by using inertial and rotating frames. *Computers and Structures*, **55**, 453–462, 1995.

[3] T.-N. Le, J.-M. Battini, M. Hjiaj, Efficient formulation for dynamics of corotational 2D beams. *Computational Mechanics*, **48**, 153–161, 2011.

[4] M.A. Crisfield, J. Shi, An energy conserving co-rotational procedure for non-linear dynamcis with finite elements. *Nonlinear Dynamics* **9**, 37–52, 1996.

[5] U. Galvanetto, M.A. Crisfield, An energy-conserving co-rotational procedure for the dynamics of planar beam structures. *International Journal for Numerical Methods in Engineering*, **39**, 2265–2282, 1996.

[6] K.M. Hsiao, R.T. Yang, A co-rotational formulation for nonlinear dynamic analysis of curved Euler beam. *Computers and Structures*, **54**, 1091–1097, 1995.

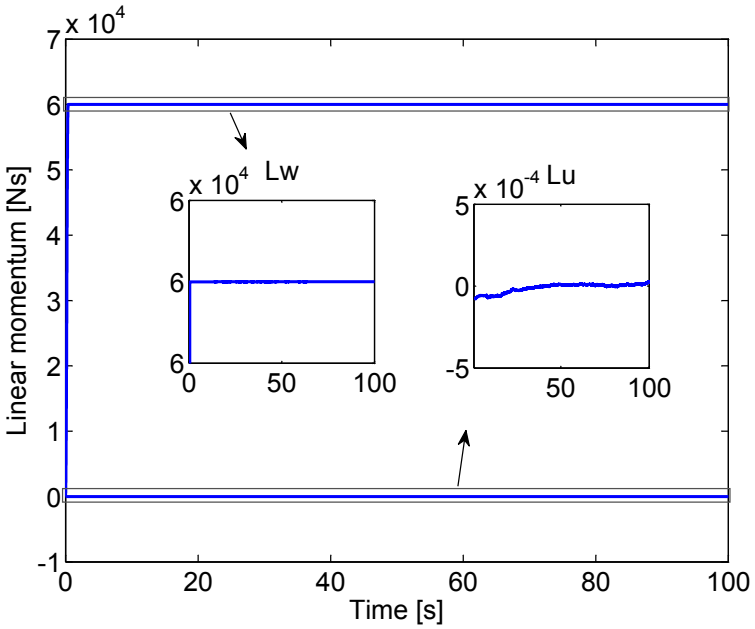

Figure 8: Linear momentum.

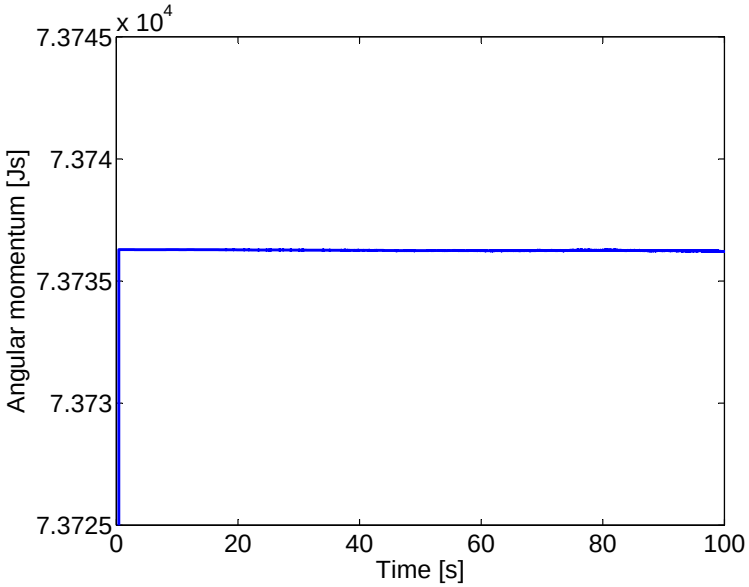

Figure 9: Linear momentum.

[7] K.M. Hsiao, J.Y. Lin, W.Y. Lin, A consisten co-rotational finite element formulation for geometrically nonlinear dynamic analysis of 3-D beams. *Computer Methods in Applied Mechanics and Engineering*, **169**, 1–18, 1999.

[8] Y. Urthaler, J.N. Reddy, A corotational finite element formulation for the analysis of planar beams. *Communications in Numerical Methods in Engineering*, **21**, 553–570, 2005.

[9] J.N. Reddy, On locking-free shear deformable beam finite elements. *Computer Methods in Applied Mechanics and Engineering*, **149**, 113–132, 1997.

[10] N.M. Newmark, A method of computation for structural dynamics. *Journal of the Enginneering Mechanics division ASCE*, **85**, 67–94, 1959.

[11] M. Geradin, A. Cardona, Time integration of the equations of motion in mechanism analysis. *Computers and Structures*, **33**, 801–820, 1989.

[12] H.M. Hilber, T.J.R. Hughes, R.L. Taylor, Improved numerical dissipation for time integration algorithms in structural dynamics. *Earthquake Engineering Strucuture Dynamic*, **5**, 282–292, 1977.

[13] M. Geradin, A. Cardona, *Flexible Multibody Dynamics. A Finite Element Approach*. John Wiley and Sons, 2001.

[14] J.C. Simo, N. Tarnow, The discrete energy-momentum method. Conserving algorithms for nonlinear elastodynamics. *Journal of Applied Mathematics and Physics*, **43**, 757–792, 1992.

[15] C. Sansour, T.-L. Nguyen, M. Hjiaj, An energy-momentum method for in-plane geometrically exact Euler-Bernoulli beam dynamcis. *International Journal for Numerical Methods in Engineering*, **102**, 99–134, 2015.

[16] C. Sansour, W. Wagner, P. Wriggers, J. Sansour, An energy momentum integration scheme and enhanced strain finite elements for the non-linear dynamics of shells. *International Journal of Non-linear Mechanics*, **37**, 951–966, 2002.

[17] C. Sansour, P. Wriggers, J. Sansour, Nonlinear dynamics of shells: theory finite element formulation, and integration schemes. *Nonlinear Dynamics*, **13**, 279–305, 1997.

ECCOMAS Congress 2016
VII European Congress on Computational Methods in Applied Sciences and Engineering
M. Papadrakakis, V. Papadopoulos, G. Stefanou, V. Plevris (eds.)
Crete Island, Greece, 5–10 June 2016

THE INFLUENCE OF UNCERTAINTY OF DESIGN PARAMETERS ON DYNAMIC CHARACTERISTICS OF STRUCTURE WITH DAMPERS

Magdalena Łasecka-Plura[1], **Roman Lewandowski**[2]

[1] Institute of Structural Engineering, Poznan University of Technology
Piotrowo 5, 60-965 Poznan, Poland
magdalena.lasecka-plura@put.poznan.pl

[2] Institute of Structural Engineering, Poznan University of Technology
Piotrowo 5, 60-965 Poznan, Poland
roman.lewandowski@put.poznan.pl

Keywords: Structures with dampers, fractional models of dampers, uncertainty of design parameters.

Abstract. *In this paper, the influence of the uncertainty of design parameters on the dynamic characteristics of structures with viscoelastic dampers mounted on them is considered. The fractional derivatives are used to describe the models of dampers. The uncertainty of their design parameters is introduced as an interval value. The lower and upper bounds of objective dynamic characteristics are obtained using the first- and second-order Taylor series expansion. Typical calculations are presented and compared with the results obtained using the vertex method.*

1 INTRODUCTION

In many practical situations, design parameters are uncertain. The uncertainty of parameters is caused by the inaccuracy of measurements, assembly errors, defect of material, temperature dependence, etc. The problem of uncertain parameters is widely described in numerous research papers. For issues with an unknown variability of the parameters, the interval analysis is often used. In this method, it suffices to know that the parameter values change within certain limits. Moore [1] did a pioneering work of interval analysis. In the last two decades, many methods which enable this theory to be used in engineering problems have been developed. In paper [2], the vertex method is presented. The method is based on the theorem of "inclusion monotonic". It assumes that the lower and upper bounds of the objective function should be calculated as the end-point combination of the design interval parameters. The method is also used in [3]. However, when the number of interval design parameters is large, the computational cost of the combination of all the parameters is very high. In this approach, the number of the required combinations equals 2^r, where r denotes the number of the interval parameters.

Alternative methods are required for non-monotonic problems. In papers [4,5], optimization-based interval analysis methods are presented. The lower and upper bounds of the objective function are obtained as the minimization and maximization of calculation using the interval parameters as constraints for the optimization problem.

For dynamic issues with uncertain design parameters, the lower and upper bounds of the objective function are often obtained using the Taylor series expansion. The method was extended in paper [6] and its application to optimization was shown. In [3, 7], the authors improved the method using the second-order Taylor series expansion. In [7], Fujita and Takewaki introduced an application of the method to the analysis of structures with passive dampers. A similar analysis of the structures with uncertain parameters was presented in [8] using the robustness analysis.

In this paper, the Taylor series expansion of the first- and second-order is used for determination of the lower and upper bounds of dynamic characteristics, such as natural frequencies, non-dimensional damping factors, and eigenvectors. The structure is modeled as a shear frame with dampers described by fractional derivatives. In the numerical example, the uncertainties of dampers' parameters are taken into consideration. The obtained results are compared with the vertex method of which the results are close to the exact solution. Such analysis is carried out for structures with dampers described by fractional derivatives for the first time.

2 DESCRIPTION OF STRUCTURES WITH DAMPERS

2.1 Models of dampers

Many rheological models of dampers have been proposed in the literature. The most frequently used models are the Kelvin and the Maxwell models. The first one consists of a spring and a dashpot connected in parallel whereas the second one is built of a serially connected spring and dashpot (Fig. 1).

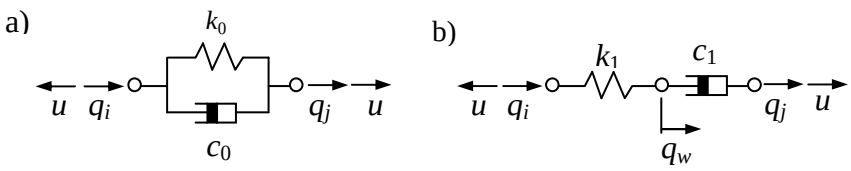

Figure 1. Classical models of dampers a) Kelvin model, b) Maxwell model.

In many instances, it is difficult to describe the rheological properties of viscoelastic dampers by basic classical models and it is necessary to use the generalized models which consist of numerous Kelvin or Maxwell elements. The number of parameters which are required for the description of the properties of dampers is rather high and sometimes it is more efficient to use the fractional models [9]. A damping element (called "a springpot element") is described by two constants, c and α, where α denotes the order of the fractional derivative. The fractional Kelvin and Maxwell models are shown in Fig. 2.

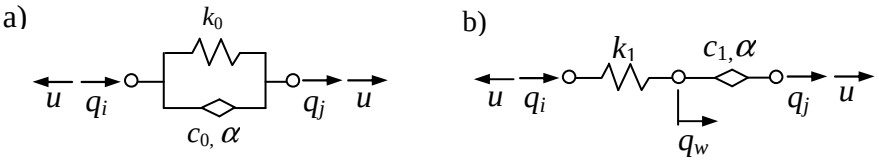

Figure 2. Fractional models of dampers a) Kelvin model, b) Maxwell model.

The equation of motion for the fractional Kelvin model can be written in the following way:

$$u(t) = k_0 \Delta q(t) + c_0 D_t^{\alpha} \Delta q(t) \tag{1}$$

and for the fractional Maxwell model, it could be described as follows:

$$u(t) + \frac{c_1}{k_1} D_t^{\alpha} u(t) = c_1 D_t^{\alpha} \Delta q(t) \tag{2}$$

where k_0 and k_1 denote stiffnesses, c_0 and c_1 denote damping factors, $\Delta q(t) = q_j(t) - q_i(t)$ is relative displacement of nodes of damper and the symbol D_t^{α} denotes the Riemann-Liouville fractional derivative of the order α with respect to time [10, 11].

After taking the Laplace transform, Equations (1) and (2) can be written in the forms:

$$\bar{u}(s) = k_0 \Delta \bar{q}(s) + c_0 s^{\alpha} \Delta \bar{q}(s) \tag{3}$$

$$\bar{u}(s) + \frac{c_1}{k_1} s^{\alpha} \bar{u}(s) = c_1 s^{\alpha} \Delta \bar{q}(s) \tag{4}$$

where: $\Delta \bar{q}(s) = L[\Delta q(t)]$, $\bar{u}(s) = L[u(t)]$, $s^{\alpha} \bar{u}(s) = L[D_t^{\alpha} u(t)]$, and s – Laplace variable. Finally, it is possible to write the general relationship:

$$\bar{u}(s) = G(s) \Delta \bar{q}(s) \tag{5}$$

where:

$$G(s) = k_0 + c_0 s^{\alpha} \tag{6}$$

for the fractional Kelvin model (see Fig. 2a) and

$$G(s) = k_1 \frac{c_1 s^{\alpha}}{k_1 + c_1 s^{\alpha}} \tag{7}$$

for the fractional Maxwell model (see Fig. 2b).

2.2 Equation of motion for structures with dampers

The equation of motion for structures with viscoelastic dampers can be written in the following form [12]:

$$\mathbf{M}_s\ddot{\mathbf{q}}(t)+\mathbf{C}_s\dot{\mathbf{q}}(t)+\mathbf{K}_s\mathbf{q}(t)=\mathbf{p}(t)+\mathbf{f}(t) \tag{8}$$

where: $\mathbf{M}_s$, $\mathbf{C}_s$ and $\mathbf{K}_s$ denote the mass, the damping and the stiffness matrix of structure, respectively. The structure is modeled as a shear frame with mass lumped at the storey level. $\mathbf{q}(t)=[q_1 \quad ... \quad q_n]^T$ is the vector of displacements of the structure, $\mathbf{p}(t)=[p_1 \quad ... \quad p_n]^T$ is the vector of excitation forces, $\mathbf{f}(t)=[f_1 \quad ... \quad f_n]^T$ is the vector of the interaction forces between the frame and the dampers (see Fig. 3) and *n* is the number of the degrees of freedom of the considered system.

Vector $\mathbf{f}(t)$ is a sum of the vectors $\mathbf{f}_k(t)$. Each of them is formed if damper *k* only is located on the frame, i.e.:

$$\mathbf{f}(t)=\sum_{k=1}^{m}\mathbf{f}_k(t)\,. \tag{9}$$

where *m* is the number of dampers.

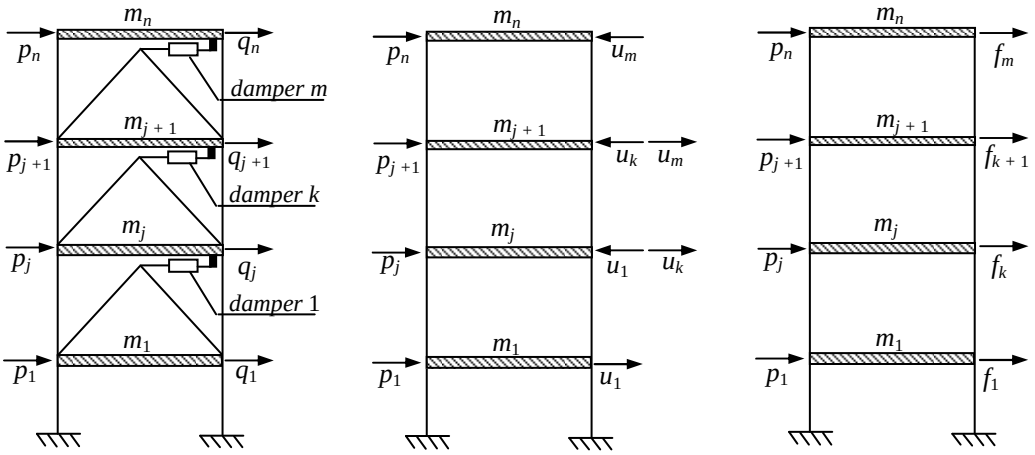

Figure 3. Diagram of frame with dampers.

For the damper located between the floors *j* and *j* + 1 (see Fig. 3), it is possible to write:

$$\mathbf{f}_k(t)=\mathbf{e}_k u_k(t), \qquad \mathbf{e}_k=[0 \quad ... \quad e_j=1 \quad e_{j+1}=-1 \quad ... \quad 0]^T\,. \tag{10}$$

After taking the Laplace transform, the equation of motion can be written as:

$$\left(s^2\mathbf{M}_s+s\mathbf{C}_s+\mathbf{K}_s\right)\bar{\mathbf{q}}(s)=\bar{\mathbf{p}}(s)+\bar{\mathbf{f}}(s) \tag{11}$$

where: $\bar{\mathbf{q}}(s)=L[\mathbf{q}(t)]$, $\bar{\mathbf{p}}(s)=L[\mathbf{p}(t)]$ and $\bar{\mathbf{f}}(s)=L[\mathbf{f}(t)]$.
The vector $\bar{\mathbf{f}}(s)$ is in the following form:

$$\bar{\mathbf{f}}(s)=\sum_{k=1}^{m}\bar{\mathbf{f}}_k(s)=\sum_{k=1}^{m}G_k(s)\mathbf{L}_k\bar{\mathbf{q}}(s) \tag{12}$$

and $\mathbf{L}_k=\mathbf{e}_k\mathbf{e}_k^{\mathrm{T}}$ is the matrix of the location of dampers.

After substituting Equation (12) to (11), the equation of the motion of structure with viscoelastic dampers is:

$$\mathbf{D}(s)\overline{\mathbf{q}}(s) = \overline{\mathbf{p}}(s) \tag{13}$$

where:

$$\mathbf{D}(s) = s^2\mathbf{M}_s + s\mathbf{C}_s + \mathbf{K}_s + \sum_{k=1}^{m}\mathbf{G}_k\,, \qquad \mathbf{G}_k(s) = G_k(s)\mathbf{L}_k\,. \tag{14}$$

If the vector of external forces equals zero ($\overline{\mathbf{p}}(s) = \mathbf{0}$), then Equation (13) leads to the following nonlinear eigenproblem:

$$\mathbf{D}(s)\,\overline{\mathbf{q}}(s) = \mathbf{0}\,. \tag{15}$$

Methods to solve a nonlinear eigenproblem for a structure with damping forces described using fractional derivatives were proposed in [13-15]. In this paper, the nonlinear eigenproblem was solved by the continuation method, described in detail in paper [15].

After determination of eigenvalues (s_i) and eigenvectors ($\mathbf{q}_i$), it is possible to calculate natural frequencies (ω_i) and non-dimensional damping factors (γ_i) according to the formulae:

$$\begin{aligned} \omega_i^2 &= \mu_i^2 + \eta_i^2 \\ \gamma_i &= -\mu_i / \omega_i \end{aligned} \tag{16}$$

where $\mu_i = \mathrm{Re}(s_i)$, $\eta_i = \mathrm{Im}(s_i)$.

3 UNCERTAIN PARAMETERS

3.1 Interval analysis - definition

Let us assume some design parameters have changed, though only within a specified range. These variations can be written as interval parameters in the form:

$$\mathbf{p}^I = \left[\mathbf{p}^c - \Delta\mathbf{p},\ \mathbf{p}^c + \Delta\mathbf{p}\right] \tag{17}$$

or as follows:

$$\mathbf{p}^I = \left[\underline{\mathbf{p}}, \overline{\mathbf{p}}\right] \tag{18}$$

where $\mathbf{p}^I = \left[p_1^I, p_2^I, ..., p_r^I\right]$ denotes the values of interval parameters, r denotes the number of interval design parameters, $\mathbf{p}^c$ denotes middle values of interval parameters:

$$\mathbf{p}^c = \frac{\overline{p} + \underline{p}}{2}\,, \tag{19}$$

$\Delta\mathbf{p}$ denotes half of the varied range of interval parameters (radius value):

$$\Delta\mathbf{p} = \frac{\overline{p} - \underline{p}}{2}\,, \tag{20}$$

$\underline{\mathbf{p}}$ and $\overline{\mathbf{p}}$ denote the lower and upper bounds of the interval parameters, respectively.

Let us consider an objective function $F(\mathbf{p})$ which depends on the design parameters. If the parameters' values change within a specified range, the considered function can be written in the form $F^I(\mathbf{p}^I)$. The interval analysis leads us to find the lower and upper bounds of the ob-

jective function in a feasible domain of the interval parameters $(-\Delta\mathbf{p}, \Delta\mathbf{p})$. The interval problem can be described as:

$$F^I(\mathbf{p}^I) = \left[\min_{\mathbf{p}\in\mathbf{p}^I} F(\mathbf{p}),\ \max_{\mathbf{p}\in\mathbf{p}^I} F(\mathbf{p})\right] \tag{21}$$

3.2 Interval analysis based on approximation of Taylor series expansion

An approximation of the objective function $\widetilde{F}(\mathbf{p})$ using the first-order Taylor series expansion around the middle values of parameters $\mathbf{p}^C$ is defined in the following form:

$$\widetilde{F}(\mathbf{p}) = F(\mathbf{p}^C) + \sum_{i=1}^{r} \frac{\partial F(\mathbf{p}^C)}{\partial p_i} \Delta p_i \tag{22}$$

where $\Delta p_i = p_i - p_i^C$ and $\partial F(\mathbf{p}^C)/\partial p_i$ denotes a first-order differentiation of the function $F(\mathbf{p}^C)$ at middle values of design parameters with respect to the changing parameter p_i.

From Equation (22), it is possible to write the increment of the objective function calculated using the first-order Taylor series expansion

$$\Delta F(\mathbf{p}) = \sum_{i=1}^{r} \frac{\partial F(\mathbf{p}^C)}{\partial p_i} \Delta p_i \tag{23}$$

as a sum of increments of the objective function for each one-dimensional perturbation. Hence, the increment of the objective function for the variation of parameter p_1 can be evaluated from:

$$\Delta F_1(p_1^I, p_2^C, ..., p_n^C) = \frac{\partial F(\mathbf{p}^C)}{\partial p_1}(p_1 - p_1^C). \tag{24}$$

According to an interval analysis, the following formula can be written:

$$\Delta F_1^I(p_1^I, p_2^C, ..., p_n^C) = \begin{bmatrix} \min\left[\Delta F_1(\underline{p}_1, p_2^C, ..., p_n^C), \Delta F_1(\overline{p}_1, p_2^C, ..., p_n^C)\right] \\ \max\left[\Delta F_1(\underline{p}_1, p_2^C, ..., p_n^C), \Delta F_1(\overline{p}_1, p_2^C, ..., p_n^C)\right] \end{bmatrix} \tag{25}$$

It is possible to write a similar relationship for each interval design parameter. Finally, substituting $\Delta F_i(p_i^I)$ to Equation (22) leads us to the equation:

$$F^I(\mathbf{p}^I) = \left[F(\mathbf{p}^C) + \sum_{i=1}^{r} \Delta\underline{F}_i(p_i^I),\ \ F(\mathbf{p}^C) + \sum_{i=1}^{r} \Delta\overline{F}_i(p_i^I)\right] \tag{26}$$

According to formula (26), the lower and upper bounds of the objective interval function, approximated using the first-order Taylor series expansion, can be written as:

$$\begin{aligned} \underline{F}(\mathbf{p}^I) &= F(\mathbf{p}^C) - \sum_{i=1}^{r} \left|\frac{\partial F(\mathbf{p}^C)}{\partial p_i} \Delta p_i\right| \\ \overline{F}(\mathbf{p}^I) &= F(\mathbf{p}^C) + \sum_{i=1}^{r} \left|\frac{\partial F(\mathbf{p}^C)}{\partial p_i} \Delta p_i\right| \end{aligned} \tag{27}$$

Some researchers [3,7] proposed an approximation of the objective function $\tilde{\tilde{F}}(\mathbf{p})$ using the second-order Taylor series expansion around the middle values of parameters $\mathbf{p}^C$:

$$\tilde{\tilde{F}}(\mathbf{p}) = F(\mathbf{p}^C) + \sum_{i=1}^{r} \frac{\partial F(\mathbf{p}^C)}{\partial p_i} \Delta p_i + \frac{1}{2} \sum_{i=1}^{r} \sum_{j=1}^{r} \frac{\partial^2 F(\mathbf{p}^C)}{\partial p_i \partial p_j} \Delta p_i \Delta p_j \tag{28}$$

where $\partial^2 F(\mathbf{p}^C) / (\partial p_i \partial p_j)$ build the Hessian matrix of the function $F(\mathbf{p}^C)$ with respect to the changing parameters p_i and p_j. The matrix consists of a second-order differentiation of the function $F(\mathbf{p}^C)$ at middle values of the design parameters. The increment of the objective function can be written in the following form:

$$\Delta F(\mathbf{p}) = \sum_{i=1}^{r} \frac{\partial F(\mathbf{p}^C)}{\partial p_i} \Delta p_i + \frac{1}{2} \sum_{i=1}^{r} \sum_{j=1}^{r} \frac{\partial^2 F(\mathbf{p}^C)}{\partial p_i \partial p_j} \Delta p_i \Delta p_j . \tag{29}$$

Based on inclusion monotonic, in order to find the lower and upper bounds of the objective function $\tilde{\tilde{F}}(\mathbf{p})$, it is necessary to calculate all end-point combinations of the interval parameters p_i and p_j. The number of combinations is the same as the number of combinations using the vertex method and it equals 2^r. The computational cost in this approach is very high, especially for high numbers of the interval parameters. Therefore, a simplification of the above method was proposed in [3]. In that paper, the non-diagonal elements of the Hessian matrix are neglected.

An approximation of the objective function $\tilde{\tilde{\tilde{F}}}(\mathbf{p})$ using the second-order Taylor series expansion with only the diagonal elements of the Hessian matrix is as follows:

$$\tilde{\tilde{\tilde{F}}}(\mathbf{p}) = F(\mathbf{p}^C) + \sum_{i=1}^{r} \left(\frac{\partial F(\mathbf{p}^C)}{\partial p_i} \Delta p_i + \frac{1}{2} \frac{\partial^2 F(\mathbf{p}^C)}{\partial p_i^2} \Delta p_i^2 \right). \tag{30}$$

The increment of the objective function can be written in the following form:

$$\Delta F(\mathbf{p}) = \sum_{i=1}^{r} \left(\frac{\partial F(\mathbf{p}^C)}{\partial p_i} \Delta p_i + \frac{1}{2} \frac{\partial^2 F(\mathbf{p}^C)}{\partial p_i^2} \Delta p_i^2 \right). \tag{31}$$

For variability of parameter p_1, Equation (31) is as follows:

$$\Delta F_1(\mathbf{p}) = \frac{\partial F(\mathbf{p}^C)}{\partial p_1} (p_1 - p^C) + \frac{1}{2} \frac{\partial^2 F(\mathbf{p}^C)}{\partial p_1^2} (p_1 - p^C)^2 . \tag{32}$$

It should be noted that, when using relationship (25) for calculating the lower and upper bounds of the objective function, the number of combinations is reduced to $2r$.

3.3 Dynamic characteristics of structures with uncertain design parameters

In this section, formulae describing the lower and upper bounds of the chosen dynamic characteristics are determined. The natural frequency (ω), non-dimensional damping factor (γ), and eigenvectors ($\mathbf{q}$) are taken into consideration. According the formula (26), it is possible to write:

$$\omega^I(\mathbf{p}^I)=\left[\omega(\mathbf{p}^C)+\sum_{i=1}^{r}\Delta\underline{\omega}_i(p_i^I),\quad \omega(\mathbf{p}^C)+\sum_{i=1}^{r}\Delta\overline{\omega}_i(p_i^I)\right] \tag{33}$$

for the natural frequency,

$$\gamma^I(\mathbf{p}^I)=\left[\gamma(\mathbf{p}^C)+\sum_{i=1}^{r}\Delta\underline{\gamma}_i(p_i^I),\quad \gamma(\mathbf{p}^C)+\sum_{i=1}^{r}\Delta\overline{\gamma}_i(p_i^I)\right] \tag{34}$$

for the non-dimensional damping factor and

$$\mathbf{q}^I(\mathbf{p}^I)=\left[\mathbf{q}(\mathbf{p}^C)+\sum_{i=1}^{r}\Delta\underline{\mathbf{q}}_i(p_i^I),\quad \mathbf{q}(\mathbf{p}^C)+\sum_{i=1}^{r}\Delta\overline{\mathbf{q}}_i(p_i^I)\right] \tag{35}$$

for the eigenvector.

When the objective function is approximated using the first-order Taylor series expansion, the increments can be written as:

$$\Delta\omega(\mathbf{p})=\sum_{i=1}^{r}\frac{\partial\omega(\mathbf{p}^C)}{\partial p_i}\Delta p_i\,, \tag{36}$$

$$\Delta\gamma(\mathbf{p})=\sum_{i=1}^{r}\frac{\partial\gamma(\mathbf{p}^C)}{\partial p_i}\Delta p_i\,, \tag{37}$$

$$\Delta\mathbf{q}(\mathbf{p})=\sum_{i=1}^{r}\frac{\partial\mathbf{q}(\mathbf{p}^C)}{\partial p_i}\Delta p_i\,. \tag{38}$$

When the objective function is approximated using the second-order Taylor series expansion, the increments are as follows:

$$\Delta\omega(\mathbf{p})=\sum_{i=1}^{r}\frac{\partial\omega(\mathbf{p}^C)}{\partial p_i}\Delta p_i+\frac{1}{2}\sum_{i=1}^{r}\sum_{j=1}^{r}\frac{\partial^2\omega(\mathbf{p}^C)}{\partial p_i\partial p_j}\Delta p_i\Delta p_j\,, \tag{39}$$

$$\Delta\gamma(\mathbf{p})=\sum_{i=1}^{r}\frac{\partial\gamma(\mathbf{p}^C)}{\partial p_i}\Delta p_i+\frac{1}{2}\sum_{i=1}^{r}\sum_{j=1}^{r}\frac{\partial^2\gamma(\mathbf{p}^C)}{\partial p_i\partial p_j}\Delta p_i\Delta p_j\,, \tag{40}$$

$$\Delta\mathbf{q}(\mathbf{p})=\sum_{i=1}^{r}\frac{\partial\mathbf{q}(\mathbf{p}^C)}{\partial p_i}\Delta p_i+\frac{1}{2}\sum_{i=1}^{r}\sum_{j=1}^{r}\frac{\partial^2\mathbf{q}(\mathbf{p}^C)}{\partial p_i\partial p_j}\Delta p_i\Delta p_j\,. \tag{41}$$

And when the objective function is approximated using the second-order Taylor series expansion with only the diagonal elements of the Hessian matrix, the increments are described as:

$$\Delta\omega(\mathbf{p})=\sum_{i=1}^{r}\left(\frac{\partial\omega(\mathbf{p}^C)}{\partial p_i}\Delta p_i+\frac{1}{2}\frac{\partial^2\omega(\mathbf{p}^C)}{\partial p_i^2}\Delta p_i^2\right), \tag{42}$$

$$\Delta\gamma(\mathbf{p})=\sum_{i=1}^{r}\left(\frac{\partial\gamma(\mathbf{p}^C)}{\partial p_i}\Delta p_i+\frac{1}{2}\frac{\partial^2\gamma(\mathbf{p}^C)}{\partial p_i^2}\Delta p_i^2\right), \tag{43}$$

$$\Delta\mathbf{q}(\mathbf{p})=\sum_{i=1}^{r}\left(\frac{\partial\mathbf{q}(\mathbf{p}^C)}{\partial p_i}\Delta p_i+\frac{1}{2}\frac{\partial^2\mathbf{q}(\mathbf{p}^C)}{\partial p_i^2}\Delta p_i^2\right). \tag{44}$$

The calculation of the lower and upper bounds of the dynamic characteristics requires the sensitivities of the first- and the second-order of the objective function $\left(\partial F\left(\mathbf{p}^C\right)/\partial p_i\,,\partial^2 F\left(\mathbf{p}^C\right)/\left(\partial p_i \partial p_j\right)\right)$ with respect to the design parameters. These sensitivities are obtained by the direct differentiation method, which is described in detail in [16]. The formulae for sensitivities with respect to the parameters of the Kelvin damper model are shown in Appendix A.

4 EXAMPLE

In the example, an eight-storey frame with three bays is considered (see Fig. 4). The frame is designed according to the EC8 Part 1. Construction data, with the exception of the unit mass of the floor, were adopted on the basis of [17]. The height of the columns is 3m and the span of the beams is 5m. Young's modulus (E) for concrete is 31GPa. Dimensions of columns and their replacement stiffnesses are shown in Table 1.

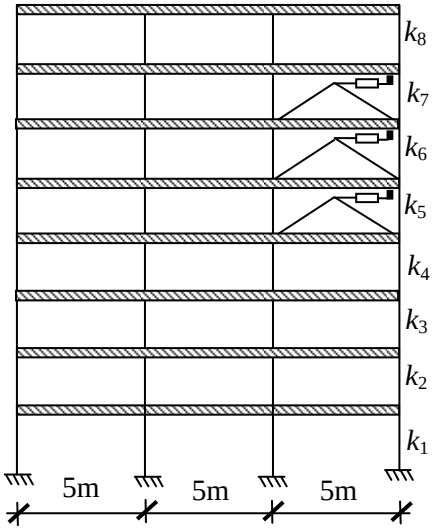

Figure 4. Diagram of the considered frame.

Storey level	Lateral column [cm]	Central column [cm]	Replacement stiffness [kN/m]
1,2	50x50	60x60	441119
3,4	45x45	53x53	275351
5,6	40x40	45x45	152948
7,8	35x35	40x40	93244

Table 1. Dimensions and replacement stiffness columns.

The mass per unit length of every floor equals 60000 kg/m. The dampers are attached on the fifth, sixth and seventh floors of the structure. Such locations were chosen according to paper [17]. A fractional Kelvin model of damper is taken into consideration (see Fig. 2a). The dampers‘ parameters were adopted in such a way that the first non-dimensional damping factor was $\gamma_1 \geq 0.04$. The following parameters are adopted for the dampers:

$k_0 = 20000\text{kN/m}$, $c_0 = 27000\text{kNs}^{\alpha}/\text{m}$ and $\alpha = 0.6$. The values of first natural frequencies ω_1 and the non-dimensional damping factor γ_1 for the structure without dampers and for the structure with the fractional Kelvin model are shown in Table 2. Damping in the structure is neglected.

The uncertainties of dampers' parameters are considered. They are shown in Table 3. The damper parameters are marked k_{0i} and c_{0i}, where i denotes the damper number. The order of the fractional derivative remains constant.

Structure without dampers	Structure with fractional dampers	
natural frequency ω_1 [rad/s]	natural frequency ω_1 [rad/s]	non-dimensional damping factor γ_1
3.10396	3.34162	0.04045

Table 2. First natural frequencies and non-dimensional damping factor without and with fractional dampers.

damper parameter	uncertainty [%]
c_{01}	10
c_{02}	15
c_{03}	15
k_{01}	15
k_{02}	20
k_{03}	15

Table 3. Uncertainties of damper parameters.

The parameters are assumed to vary independently. The interval parameters for dampers are listed in Tables 4-5.

bounded value	middle value	radius value
$c_{01}^I = [24300, 29700]$	$c_{01}^C = 27000$	$\Delta c_{01} = 2700$
$c_{02}^I = [22950, 31050]$	$c_{02}^C = 27000$	$\Delta c_{02} = 4050$
$c_{03}^I = [22950, 31050]$	$c_{03}^C = 27000$	$\Delta c_{03} = 4050$

Table 4. Interval parameters of damping factor [kNs$^{\alpha}$/m].

bounded value	middle value	radius value
$k_{01}^I = [17000, 2300]$	$k_{01}^C = 20000$	$\Delta k_{01} = 2000$
$k_{02}^I = [16000, 2400]$	$k_{02}^C = 20000$	$\Delta k_{02} = 1000$
$k_{03}^I = [17000, 2300]$	$k_{03}^C = 20000$	$\Delta k_{03} = 2000$

Table 5. Interval parameters of stiffness [kN/m].

The parameters' middle values are taken to find the solutions given in Table 2. In Table 6, the results of interval analysis are presented. The results obtained by the vertex method, first-order Taylor series expansion, second-order Taylor series expansion and second-order Taylor

series expansion with only the diagonal element of the Hessian matrix are compared. The critical combinations of the interval parameters are shown for each case. The solution of the vertex method is assumed as a comparative solution and the error is calculated in relation to that.

	lower $\underline{\omega}_1$			upper $\overline{\omega}_1$		
	value of $\underline{\omega}_1$ [rad/s]	error [%]	Combination of parameters	value of $\overline{\omega}_1$ [rad/s]	error [%]	Combination of parameters
Vertex method	3.31306	-	$\underline{c}_{01}, \underline{c}_{02}, \underline{c}_{03}$ $\underline{k}_{01}, \underline{k}_{02}, \underline{k}_{03}$	3.36841	-	$\overline{c}_{01}, \overline{c}_{02}, \overline{c}_{03}$ $\overline{k}_{01}, \overline{k}_{02}, \overline{k}_{03}$
First-order Taylor series expansion	3.31832	0.16	$\underline{c}_{01}, \underline{c}_{02}, \underline{c}_{03}$ $\underline{k}_{01}, \underline{k}_{02}, \underline{k}_{03}$	3.36493	0.10	$\overline{c}_{01}, \overline{c}_{02}, \overline{c}_{03}$ $\overline{k}_{01}, \overline{k}_{02}, \overline{k}_{03}$
Second-order Taylor series expansion	3.31780	0.14	$\underline{c}_{01}, \underline{c}_{02}, \underline{c}_{03}$ $\underline{k}_{01}, \underline{k}_{02}, \underline{k}_{03}$	3.36441	0.12	$\overline{c}_{01}, \overline{c}_{02}, \overline{c}_{03}$ $\overline{k}_{01}, \overline{k}_{02}, \overline{k}_{03}$
Simplified second-order Taylor series expansion	3.31801	0.15	$\underline{c}_{01}, \underline{c}_{02}, \underline{c}_{03}$ $\underline{k}_{01}, \underline{k}_{02}, \underline{k}_{03}$	3.36462	0.11	$\overline{c}_{01}, \overline{c}_{02}, \overline{c}_{03}$ $\overline{k}_{01}, \overline{k}_{02}, \overline{k}_{03}$

Table 6. Lower and upper bounds of ω_1.

	lower $\underline{\gamma}_1$			upper $\overline{\gamma}_1$		
	value of $\underline{\gamma}_1$	error [%]	Combination of parameters	value of $\overline{\gamma}_1$	error [%]	Combination of parameters
Vertex method	0.03587	-	$\underline{c}_{01}, \underline{c}_{02}, \underline{c}_{03}$ $\overline{k}_{01}, \overline{k}_{02}, \overline{k}_{03}$	0.04480	-	$\overline{c}_{01}, \overline{c}_{02}, \overline{c}_{03}$ $\underline{k}_{01}, \underline{k}_{02}, \underline{k}_{03}$
First-order Taylor series expansion	0.03656	1.92	$\underline{c}_{01}, \underline{c}_{02}, \underline{c}_{03}$ $\overline{k}_{01}, \overline{k}_{02}, \overline{k}_{03}$	0.04435	1.00	$\overline{c}_{01}, \overline{c}_{02}, \overline{c}_{03}$ $\underline{k}_{01}, \underline{k}_{02}, \underline{k}_{03}$
Second-order Taylor series expansion	0.03639	1.45	$\underline{c}_{01}, \underline{c}_{02}, \underline{c}_{03}$ $\overline{k}_{01}, \overline{k}_{02}, \overline{k}_{03}$	0.04417	1.41	$\overline{c}_{01}, \overline{c}_{02}, \overline{c}_{03}$ $\underline{k}_{01}, \underline{k}_{02}, \underline{k}_{03}$
Simplified second-order Taylor series expansion	0.03633	1.28	$\underline{c}_{01}, \underline{c}_{02}, \underline{c}_{03}$ $\overline{k}_{01}, \overline{k}_{02}, \overline{k}_{03}$	0.04412	1.52	$\overline{c}_{01}, \overline{c}_{02}, \overline{c}_{03}$ $\underline{k}_{01}, \underline{k}_{02}, \underline{k}_{03}$

Table 7. Lower and upper bounds of γ_1.

Based on the obtained results, it should be noted that the solutions using the first-order Taylor series expansion and the second-order Taylor series expansion are close to the solution

calculated with the use of the vertex method. In each of the four cases, the critical combination of the interval parameters is the same.

The lower and upper bounds of the first eigenvector are also calculated. The middle values of the eigenvector's elements are evaluated for the middle values of dampers' parameters. The lower and upper values of the eigenvector obtained by the vertex method $[\underline{\mathbf{q}}_1, \overline{\mathbf{q}}_1]$ are calculated for the relevant natural frequencies $[\underline{\omega}_1, \overline{\omega}_1]$ obtained by this method (solid lines). The obtained results are compared with the values calculated using the first-order Taylor series expansion (dashed line). The comparison is shown in Figures 6-7.

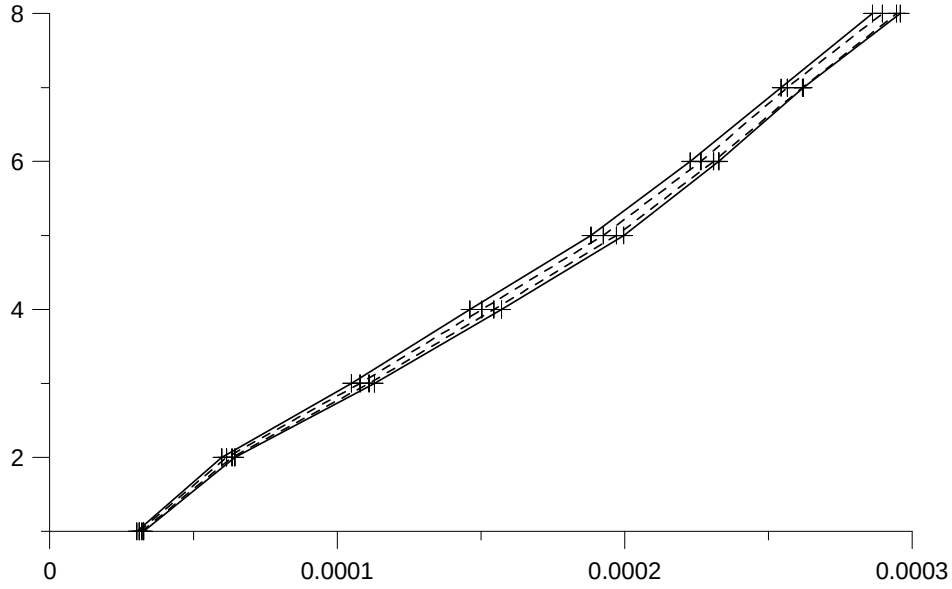

Figure 6. Lower and upper bounds of the real part of eigenvector $\mathbf{q}_1$.

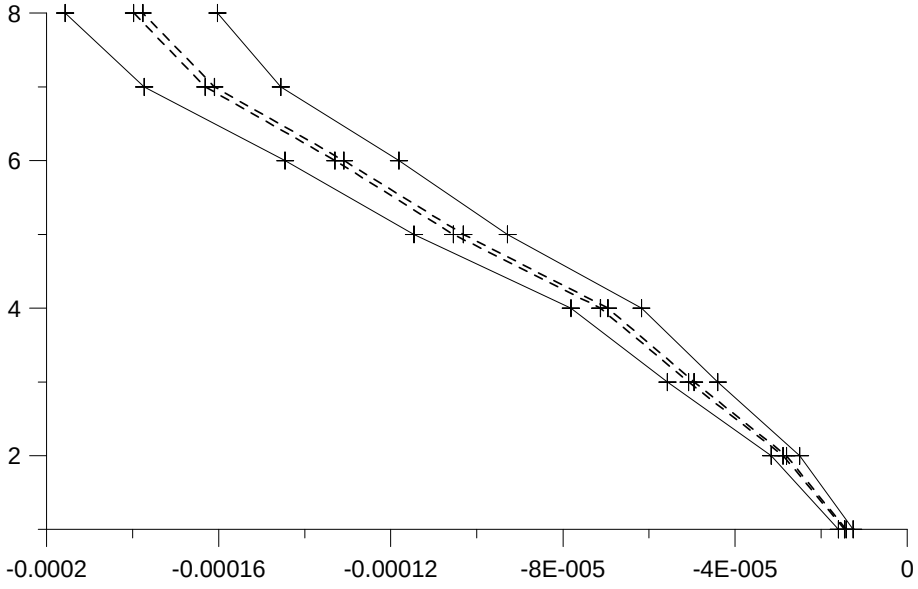

Figure 7. Lower and upper bounds of the imaginary part of eigenvector $\mathbf{q}_1$.

Evaluations of the lower and upper bounds of the eigenvector, carried out using the vertex method and the first-order Taylor series expansion differ by about 2-3% in the case of the real parts and 9-13% in the case of the imaginary parts.

5 CONCLUSIONS

The influence of uncertainties of the design parameters on the dynamic characteristics of structures with viscoelastic dampers are investigated. The presented formulae enable determination of the lower and upper bounds of the objective function. The different methods of evaluation of the lower and upper bounds are shown. The bounds are determined using the vertex method, first order Taylor series expansion, second-order Taylor series expansion and simplified second-order Taylor series expansion. The vertex method was chosen as a comparative solution but it should be noted that the exact solution in the form of a critical combination of the interval parameters can be obtained for values of parameters between the limit values. The methods based on the Taylor series expansion provide results which are close to those obtained by the vertex method. Errors of the calculations performed are similar in each of the three presented approximating functions but the second-order Taylor series expansion requires high computational costs, especially if all the elements of the Hessian matrix are taken into account.

REFERENCES

[1] R.E. Moore, *Interval analysis*, Englewood Cliffs, New York Prentice Hall, 1966.

[2] W. Dong, H. Shah, Vertex method for computing functions of fuzzy variables. *Fuzzy Sets and Systems*, **24** (1), 65-78, 1987.

[3] S.H. Chen, L. Ma, G.W. Meng, R. Guo, An efficient method for evaluating the natural frequency of structures with uncertain-but-bounded parameters, *Computers and Structures*, **87**, 582-590, 2009.

[4] S. Rao, L. Chen, Numerical solution of fuzzy linear equations in engineering analysis, *International Journal for Numerical Methods in Engineering*, **43**, 391-408, 1998.

[5] U. Akpan, T. Koko, I. Orisamolu, B. Gallant, Fuzzy finite element analysis of smart structures, *Smart Materials and Structures*, **10**, 273-284, 2001.

[6] S.H. Chen, J. Wu, Interval optimization of dynamic response for structures with interval parameters, *Computers and Structures*, **82**, 1-11, 2004.

[7] K. Fujita, I. Takewaki, An efficient methodology for robustness evaluation by advanced interval analysis using updated second-order Taylor series expansion, *Engineering Structures*, **33**, 3299-3310, 2011.

[8] K. Fujita, I. Takewaki, Robust passive damper design for building structures under uncertain structural parameter environments, *Earthquakes and Structures*, **3** (6), 805-820, 2012.

[9] N. Makris, M.C. Constantinou, fractional derivative Maxwell model for viscous damper, *ASCE Journal of Structural Engineering*, **117**, 2708-2724, 1991.

[10] I. Podlubny, *Fractional Differential Equations*, Academic Press, 1999.

[11] J.S. Leszczyński, *An introduction to fractional mechanics*, Czestochowa University of Technology, 2011.

[12] R. Lewandowski, Z. Pawlak, Dynamic analysis of frames with viscoelastic dampers modeled by rheological models with fractional derivatives, *Journal of Sound and Vibration*, 330, 923-936, 2011.

[13] A. Fenander, Modal synthesis when modeling damping by use of fractional derivatives, *AIAA Journal*, **34**, 1051-1058, 1996.

[14] F. Cortes, M.J. Elajabarrieta, Finite element formulations for transient dynamic analysis in structural systems with viscoelastic treatments containing fractional derivative models, *International Journal of Numerical Methods in Engineering*, **69**, 2173-2195, 2007.

[15] Z. Pawlak, R. Lewandowski, The continuation method for the eigenvalue problem of structures with viscoelastic dampers, *Computers and Structures*, **125**, 53-61, 2013.

[16] R. Lewandowski, M. Łasecka-Plura, Design sensitivity analysis of structures with viscoelastic dampers, *Computers and Structures*, **164**, 95-107, 2016.

[17] Y. Ribakov, G. Agranovich, A method for efficient placement of active dampers in seismically excited structures, *Structural Control and Health Monitoring*, **17**, 513-531, 2010.

ACKNOWLEDGMENTS

The study is supported by the National Science Centre, Poland, as part of Project No. DEC/2013/09/B/ST8/01733, carried out in the years 2014-2016. This support is gratefully acknowledged.

APPENDIX A

In order to calculate the sensitivities of dynamic characteristics with respect to the design parameter, the following sets of equations can be solved [16]:

$$\begin{bmatrix} \mathbf{D}(s) & \dfrac{\partial \mathbf{D}(s)}{\partial s}\overline{\mathbf{q}}(s) \\ \overline{\mathbf{q}}^T(s)\dfrac{\partial \mathbf{D}(s)}{\partial s} & \dfrac{1}{2}\overline{\mathbf{q}}^T(s)\dfrac{\partial^2 \mathbf{D}(s)}{\partial s^2}\overline{\mathbf{q}}(s) \end{bmatrix} \begin{Bmatrix} \dfrac{\partial \overline{\mathbf{q}}(s)}{\partial p_i} \\ \dfrac{\partial s}{\partial p_i} \end{Bmatrix} = \begin{Bmatrix} \mathbf{h}_1(s) \\ h_2(s) \end{Bmatrix} \tag{A.1}$$

for the first-order sensitivities and

$$\begin{bmatrix} \mathbf{D}(s) & \dfrac{\partial \mathbf{D}(s)}{\partial s}\overline{\mathbf{q}}(s) \\ \overline{\mathbf{q}}^T(s)\dfrac{\partial \mathbf{D}(s)}{\partial s} & \dfrac{1}{2}\overline{\mathbf{q}}^T(s)\dfrac{\partial^2 \mathbf{D}(s)}{\partial s^2}\overline{\mathbf{q}}(s) \end{bmatrix} \begin{Bmatrix} \dfrac{\partial^2 \overline{\mathbf{q}}(s)}{\partial p_i \partial p_j} \\ \dfrac{\partial^2 s}{\partial p_i \partial p_j} \end{Bmatrix} = \begin{Bmatrix} \mathbf{h}_3(s) \\ h_4(s) \end{Bmatrix} \tag{A.2}$$

for the second-order sensitivities.
The right-hand sides of the above equations are as follows:

$$\mathbf{h}_1(s) = -\mathbf{R}_1(s)\overline{\mathbf{q}}(s), \tag{A.3}$$

$$h_2(s) = -\frac{1}{2}\overline{\mathbf{q}}^T(s)\mathbf{R}_2(s)\overline{\mathbf{q}}(s), \tag{A.4}$$

$$\mathbf{h}_3(s) = -\left[\mathbf{R}_{31}(s)\overline{\mathbf{q}}(s) + \mathbf{R}_{32}(s)\frac{\partial \overline{\mathbf{q}}(s)}{\partial p_i} + \mathbf{R}_{33}(s)\frac{\partial \overline{\mathbf{q}}(s)}{\partial p_j}\right], \tag{A.5}$$

$$h_4(s)=-\left[\overline{\mathbf{q}}(s)^T\mathbf{R}_{41}(s)\overline{\mathbf{q}}(s)+\overline{\mathbf{q}}(s)^T\mathbf{R}_{42}(s)\frac{\partial\overline{\mathbf{q}}(s)}{\partial p_i}+\overline{\mathbf{q}}(s)^T\mathbf{R}_{43}(s)\frac{\partial\overline{\mathbf{q}}(s)}{\partial p_j}+\frac{\partial\overline{\mathbf{q}}(s)}{\partial p_i}^T\frac{\partial\mathbf{D}(s)}{\partial s}\frac{\partial\overline{\mathbf{q}}(s)}{\partial p_j}\right] \quad \text{(A.6)}$$

where:

$$\mathbf{R}_1(s)=\frac{\partial\mathbf{D}(s)}{\partial p_i},\qquad \mathbf{R}_2(s)=\frac{\partial^2\mathbf{D}(s)}{\partial p_i\partial s}, \quad \text{(A.7)}$$

$$\mathbf{R}_{31}(s)=\frac{\partial^2\mathbf{D}(s)}{\partial p_i\partial p_j}+\frac{\partial^2\mathbf{D}(s)}{\partial p_i\partial s}\frac{\partial s}{\partial p_j}+\frac{\partial^2\mathbf{D}(s)}{\partial p_j\partial s}\frac{\partial s}{\partial p_i}+\frac{\partial^2\mathbf{D}(s)}{\partial s^2}\frac{\partial s}{\partial p_i}\frac{\partial s}{\partial p_j}, \quad \text{(A.8)}$$

$$\mathbf{R}_{32}(s)=\frac{\partial\mathbf{D}(s)}{\partial p_j}+\frac{\partial\mathbf{D}(s)}{\partial s}\frac{\partial s}{\partial p_j},\qquad \mathbf{R}_{33}(s)=\frac{\partial\mathbf{D}(s)}{\partial p_i}+\frac{\partial\mathbf{D}(s)}{\partial s}\frac{\partial s}{\partial p_i} \quad \text{(A.9)}$$

$$\mathbf{R}_{41}(s)=\frac{1}{2}\left[\frac{\partial^3\mathbf{D}(s)}{\partial s^3}\frac{\partial s}{\partial p_i}\frac{\partial s}{\partial p_j}+\frac{\partial^3\mathbf{D}(s)}{\partial s^2\partial p_j}\frac{\partial s}{\partial p_i}+\frac{\partial^3\mathbf{D}(s)}{\partial s^2\partial p_i}\frac{\partial s}{\partial p_j}+\frac{\partial^3\mathbf{D}(s)}{\partial s\partial p_i\partial p_j}\right], \quad \text{(A.10)}$$

$$\mathbf{R}_{42}(s)=\frac{\partial^2\mathbf{D}(s)}{\partial s\partial p_j}+\frac{\partial^2\mathbf{D}(s)}{\partial s^2}\frac{\partial s}{\partial p_j},\qquad \mathbf{R}_{43}(s)=\frac{\partial^2\mathbf{D}(s)}{\partial s\partial p_i}+\frac{\partial^2\mathbf{D}(s)}{\partial s^2}\frac{\partial s}{\partial p_i}. \quad \text{(A.11)}$$

In the case of the Kelvin model of damper, the matrices $\mathbf{R}_1(s)$ and $\mathbf{R}_2(s)$ which are required for solving the first-order sensitivities, are as follows:

$$\mathbf{R}_1(s)=s^{\alpha_i}\mathbf{L}_i,\qquad \mathbf{R}_2(s)=\alpha_i s^{\alpha_i-1}\mathbf{L}_i \quad \text{(A.12)}$$

when the design parameter p_i is c_{0i} and

$$\mathbf{R}_1(s)=\mathbf{L}_i,\qquad \mathbf{R}_2(s)=\mathbf{0} \quad \text{(A.13)}$$

when the design parameter p_i is k_{0i}.

When the second-order sensitivities is of interest, the matrices $\mathbf{R}_{31}(s)$, $\mathbf{R}_{32}(s)$, $\mathbf{R}_{33}(s)$, $\mathbf{R}_{41}(s)$, $\mathbf{R}_{42}(s)$ and $\mathbf{R}_{43}(s)$ can be written as:

$$\mathbf{R}_{31}(s)=\frac{\partial^2\mathbf{D}}{\partial s^2}\frac{\partial s}{\partial c_{0i}}\frac{\partial s}{\partial c_{0j}}+\alpha_j s^{\alpha_j-1}\mathbf{L}_j\frac{\partial s}{\partial c_{0i}}+\alpha_i s^{\alpha_i-1}\mathbf{L}_i\frac{\partial s}{\partial c_{0j}}, \quad \text{(A.14)}$$

$$\mathbf{R}_{32}(s)=s^{\alpha_j}\mathbf{L}_j+\frac{\partial\mathbf{D}(s)}{\partial s}\frac{\partial s}{\partial c_{0j}},\qquad \mathbf{R}_{33}(s)=s^{\alpha_i}\mathbf{L}_i+\frac{\partial\mathbf{D}(s)}{\partial s}\frac{\partial s}{\partial c_{0i}}, \quad \text{(A.15)}$$

$$\mathbf{R}_{41}(s)=\frac{1}{2}\left[\alpha_j(\alpha_j-1)s^{\alpha_j-2}\mathbf{L}_j\frac{\partial s}{\partial c_{0i}}+\alpha_i(\alpha_i-1)s^{\alpha_i-2}\mathbf{L}_i\frac{\partial s}{\partial c_{0j}}+\frac{\partial^3\mathbf{D}}{\partial s^3}\frac{\partial s}{\partial c_{0i}}\frac{\partial s}{\partial c_{0j}}\right], \quad \text{(A.16)}$$

$$\mathbf{R}_{42}(s)=\alpha_j s^{\alpha_j-1}\mathbf{L}_j+\frac{\partial^2\mathbf{D}(s)}{\partial s^2}\frac{\partial s}{\partial c_{0j}},\qquad \mathbf{R}_{43}(s)=\alpha_i s^{\alpha_i-1}\mathbf{L}_i+\frac{\partial^2\mathbf{D}(s)}{\partial s^2}\frac{\partial s}{\partial c_{0i}} \quad \text{(A.17)}$$

when the design parameters p_i and p_j are c_{0i} and c_{0j}, respectively, and

$$\mathbf{R}_{31}(s)=\frac{\partial^2\mathbf{D}}{\partial s^2}\frac{\partial s}{\partial c_{0i}}\frac{\partial s}{\partial k_{0j}}+\alpha_i s^{\alpha_i-1}\mathbf{L}_i\frac{\partial s}{\partial k_{0j}}, \quad \text{(A.18)}$$

$$\mathbf{R}_{32}(s)=\mathbf{L}_j+\frac{\partial\mathbf{D}(s)}{\partial s}\frac{\partial s}{\partial k_{0j}},\qquad \mathbf{R}_{33}(s)=s^{\alpha_i}\mathbf{L}_i+\frac{\partial\mathbf{D}(s)}{\partial s}\frac{\partial s}{\partial c_{0i}}, \tag{A.19}$$

$$\mathbf{R}_{41}(s)=\frac{1}{2}\left[\alpha_i(\alpha_i-1)s^{\alpha_i-2}\mathbf{L}_i\frac{\partial s}{\partial k_{0j}}+\frac{\partial^3\mathbf{D}}{\partial s^3}\frac{\partial s}{\partial c_{0i}}\frac{\partial s}{\partial k_{0j}}\right], \tag{A.20}$$

$$\mathbf{R}_{42}(s)=\frac{\partial^2\mathbf{D}(s)}{\partial s^2}\frac{\partial s}{\partial k_{0j}},\qquad \mathbf{R}_{43}(s)=\alpha_i s^{\alpha_i-1}\mathbf{L}_i+\frac{\partial^2\mathbf{D}(s)}{\partial s^2}\frac{\partial s}{\partial c_{0i}} \tag{A.21}$$

when the design parameters p_i and p_j are c_{0i} and k_{0j}, respectively, and

$$\mathbf{R}_{31}(s)=\frac{\partial^2\mathbf{D}}{\partial s^2}\frac{\partial s}{\partial k_{0i}}\frac{\partial s}{\partial k_{0j}},\quad \mathbf{R}_{32}(s)=\mathbf{L}_j+\frac{\partial\mathbf{D}(s)}{\partial s}\frac{\partial s}{\partial k_{0j}},\quad \mathbf{R}_{33}(s)=\mathbf{L}_i+\frac{\partial\mathbf{D}(s)}{\partial s}\frac{\partial s}{\partial k_{0i}} \tag{A.22}$$

$$\mathbf{R}_{41}(s)=\frac{1}{2}\left[\frac{\partial^3\mathbf{D}}{\partial s^3}\frac{\partial s}{\partial k_{0i}}\frac{\partial s}{\partial k_{0j}}\right],\quad \mathbf{R}_{42}(s)=\frac{\partial^2\mathbf{D}(s)}{\partial s^2}\frac{\partial s}{\partial k_{0j}},\quad \mathbf{R}_{43}(s)=\frac{\partial^2\mathbf{D}(s)}{\partial s^2}\frac{\partial s}{\partial k_{0i}} \tag{A.23}$$

when the design parameters p_i and p_j are k_{0i} and k_{0j}, respectively.

The derivatives of matrix $\mathbf{D}(s)$ with respect to s in the case of the Kelvin model of damper are as follows:

$$\frac{\partial\mathbf{D}(s)}{\partial s}=2s\mathbf{M}+\mathbf{C}+\sum_{k=1}^{m}c_{0k}\alpha_k s^{\alpha_k-1}\mathbf{L}_k, \tag{A.24}$$

$$\frac{\partial^2\mathbf{D}(s)}{\partial s^2}=2\mathbf{M}+\sum_{k=1}^{m}c_{0k}\alpha_k(\alpha_k-1)s^{\alpha_k-2}\mathbf{L}_k, \tag{A.25}$$

$$\frac{\partial^3\mathbf{D}(s)}{\partial s^3}=\sum_{k=1}^{m}c_{0k}\alpha_k(\alpha_k-1)(\alpha_k-2)s^{\alpha_k-3}\mathbf{L}_k. \tag{A.26}$$

The derived formulae enable determination of all the elements of the Hessian matrix of dynamic characteristics with respect to the chosen design parameters.

ECCOMAS Congress 2016
VII European Congress on Computational Methods in Applied Sciences and Engineering
M. Papadrakakis, V. Papadopoulos, G. Stefanou, V. Plevris (eds.)
Crete Island, Greece, 5–10 June 2016

FINITE-DISCRETE NUMERICAL MODELLING OF REINFORCED CONCRETE STRUCTURES

N. Živaljić[1], Ž. Nikolić[1], H. Smoljanović[1] and I. Balić[1]

[1] University of Split, Faculty of Civil Engineering, Architecture and Geodesy
Matice Hrvatske 15, Split, Croatia
e-mail: nikolina.zivaljic@gradst.hr, zeljana.nikolic@gradst.hr, hrvoje.smoljanovic@gradst.hr, ivan.balic@gradst.hr

Keywords: Numerical Modelling, Reinforced Concrete Structures, Finite-Discrete Element Method, Static Load, Dynamic Load.

Abstract. *Crack opening is one of the dominant causes of nonlinearity in brittle and quasi-brittle structures which leads to localized failure and stands out as a serious challenge in numerical modelling. Therefore, a realistic modelling of crack initiation and propagation is one of the key factors that affect the reliability of the model for analysing the structures, especially those subjected to earthquakes. The largest number of structures in the world's most populated seismic areas is made of materials such as reinforced concrete, stone and masonry, in which localized failure dominantly influences the structural collapse. Sophisticated numerical models based on time dependent and incremental dynamic analysis can play an important role in simulating the behaviour of such structures. In this work 2D and 3D numerical modelling for analysis of reinforced concrete structures under static and dynamic load is presented. The model uses the finite-discrete element method; thus taking into account the discontinuous nature of the concrete at the failure stages. This approach considers the structure as a deformable continuum until the opening of the cracks. The transition from the continuum to the discontinuum is a result of the crack initiations which are modelled through the contact elements implemented between finite elements. The interaction between discrete elements is considered through the contact interaction algorithm based on the principle of potential contact forces which are computed using penalty function method and the Coulomb friction law. The non-linear behaviour of the concrete in tension and shear takes into account strain-hardening, strain-softening and cyclic behaviour during dynamic loading. The model for reinforcing bars is based on an approximation of the experimental curves for the bar strain in the crack. The developed numerical model includes interaction effects between reinforcement and concrete as well as cyclic behaviour of concrete and steel during dynamic loading. Thus, it is possible to describe the crack initiation and propagation, collapse mechanism, energy dissipation by non-linear effects, inertial effects and contact interaction which are very important in the analysis of RC structures, especially those subjected to seismic load.*

1 INTRODUCTION

The development of the numerical models for simulation of the response of reinforced concrete structures under static and dynamic load, taking into consideration non-linear behavior of the concrete and reinforcement, makes possible the results of high accuracy. One of the main causes of concrete non-linear behavior is cracking. A reliable model for simulation of the opening and closing the cracks is especially important in the structures under dynamic load. The most of the models described in literature is based on finite element method where the cracking is described with smeared crack models or with embedded models where the cracks are modelled as discontinuity within the elements by enriching interpolation function. In contrast to the finite elements, in discrete models cracks are simulated as discontinuities of displacement between two elements.

A numerical model for analysis of reinforced concrete structures under static and cyclic load developed in this work is based on combined finite-discrete element method [1]. Transition from continua to discontinua in this method occurs through fracture and fragmentation processes. A typical combined finite discrete element method based simulation may start with a few discrete elements and finished with very large number of discrete elements. Fracture occurs through alteration, damage, yielding or failure of micro structural elements of the material.

There has been a number of fracture models proposed in the context of both discrete element methods and combined finite discrete element method. Some of the models are based on a global approach applied to each individual body, while others used a local smeared crack approach or local single-crack approach. In this work a model for plane and spatial crack initiation and crack propagation in concrete is used [2]. The model combines standard finite element formulation for the hardening part of the constitutive law with the single-crack model for the softening part of stress-strain curve. Finite elements are used to model behavior of the material up to the ultimate tensile strength while a discrete crack model is used for modelling of the crack opening and separation along edges of finite elements.

In this work cracking of the concrete in plane and space are enabled by a combined single and smeared crack model. An embedded model of reinforcing bars [3, 4] is implemented in finite-discrete element code [1]. The concrete and reinforcing bars are analyzed separately, but they are connected by the relation between the size of the concrete crack and strain of the reinforcing bar [5, 6]. Cyclic behavior of the steel during the cyclic load is modelled with improved Kato's model [7].

2 MODELLING OF THE REINFORCED CONCRETE STRUCTURE

The concrete structure in plane is discretized on triangular finite elements, while in the space it is discretized by tetrahedron finite elements. Reinforcing bars are modelled with linear one-dimensional elements which can be placed in arbitrary position inside the concrete finite elements. The model of the reinforced concrete structure with the embedded reinforcing bars in 2D and 3D concrete structure is presented in Fig. 1.

The structure behaves as continuum until opening of the crack. The deformation of the finite triangular element influence to the deformation of the reinforcing bars. When the crack in concrete appears, joint element in concrete as well as joint element in reinforcing bars is occurred. The concrete and reinforcing bars are analyzed separately, but they are connected by the relationship between the size of the concrete crack and strain of the reinforcing bar.

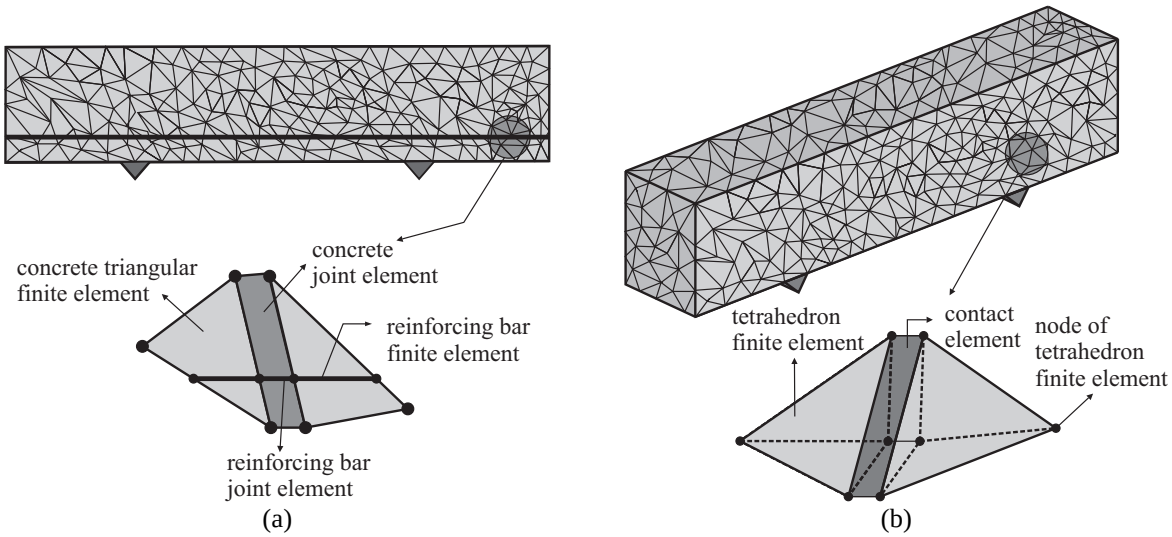

Figure 1: Discretization of reinforced concrete structure: (a) 2D model; (b) 3D model.

3 NON-LINEAR MATERIAL MODEL IN JOINT ELEMENTS

3.1 Concrete model in joint element

The concrete model is based on crack initiation and crack propagation in tension and shear [2]. It is developed on the basis of experimental stress-strain curves for concrete in tension.

The area under the stress-strain curve consists of two parts (Fig. 2), part for modelling of the concrete behavior up to the crack opening [2] and part which represents strain softening after the tensile strength is exceeded [8]. The assumption of the discrete crack model is that the cracks coincide with the finite element edges. The total number of nodes for each of the finite element meshes is doubled and the continuity between elements is realized through the penalty method [9]. Separation of the edges induces a bonding stress, which is a function of the size separation δ (Fig. 2).

The area under the stress-displacement curve represents the energy release rate $G_f = 2\gamma$, where γ is the surface energy, i.e. the energy needed to extend the crack surface by a unit area.

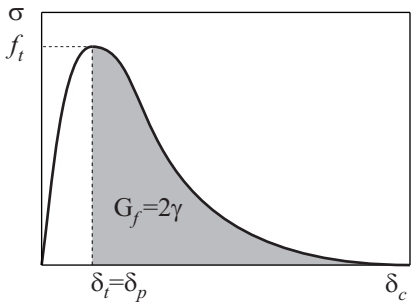

Figure 2: Strain softening stress-strain and stress-displacement curves.

No separation of the adjacent elements occurs before the tensile strength is reached, i.e. the edges of two adjacent elements are held together by normal and shear springs (Fig. 3). Procedure of the separation of the elements and complete relationship for the normal and shear bonding stress are given in [2].

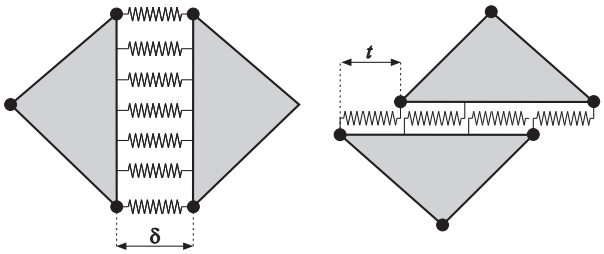

(a)

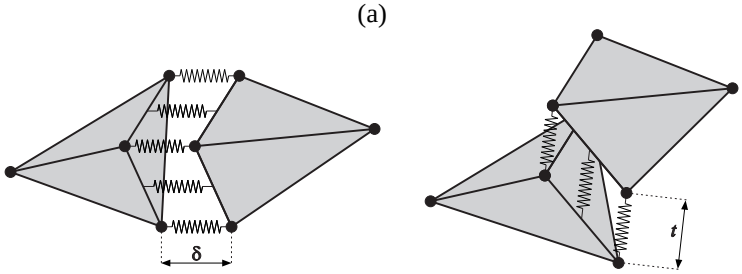

(b)

Figure 3: Normal and shear springs between the finite elements: (a) 2D model, (b) 3D model.

3.2 Steel material model in reinforcement joint element

In this work a model of the relationship between the concrete crack size and strain of the reinforcing bar developed by Shima [5] and Shin [6] is applied. The model is based on experimental strain-slip curves and represents well approximation of the behavior of reinforcing bar with the expressed plastic strain caused by cyclic loading.

The steel strain-slip relation before the yielding of reinforcing bar is given by expressions:

$$s = \varepsilon_s (6 + 3500\varepsilon_s) \tag{1}$$

$$s = \left(\frac{S}{D}\right) \cdot K_{fc}, \quad K_{fc} = \left(\frac{f_c'}{20}\right)^{2/3} \tag{2}$$

where $s = s(\varepsilon_s)$ is normalized steel slip, D is bar diameter and f_c' is concrete strength.

Normalized slip in the post-yield range is given by expression:

$$s = s_{pl} + s_e \tag{3}$$

where s_e is slip in the elastic region and s_{pl} is slip in the yield region. A strain distribution along the reinforcing bar in the post-yield region is shown in Fig. 4, where ε_{se} a strain at the yield boundary point on the elastic region is and ε_{sp} is a strain at the yield boundary point on the yield region.

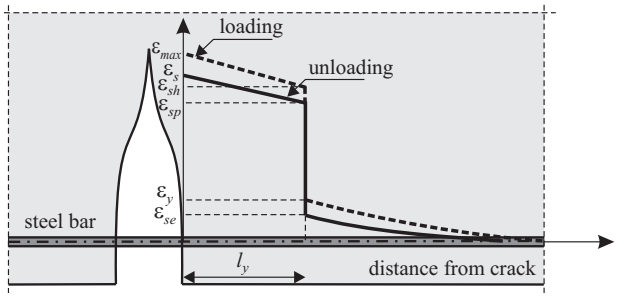

Figure 4: Strain distribution along the reinforcing bar in the post-yield range.

Normalized plastic steel slip in the yield region is given by an expression [5, 6]:

$$s_{pl} = \frac{(1+\beta)\varepsilon_s + \varepsilon_{sh} - \beta\varepsilon_{\max}}{\varepsilon_{\max} + \varepsilon_{sh}}(s_{\max} - s_y^*) \tag{4}$$

where $\beta = \sigma_{\max}/\sigma_y$ represents the gradient of the line shown in Figure 4, $\sigma_{\max}$ is the maximum stress in reinforcing bar under tensile loads, $s_{\max}$ is a function of $\varepsilon_{\max}$ and $s_y^* = \varepsilon_s(2+3500\varepsilon_s)$.

Non-linear material model for steel is based on experimental stress-strain curve and it is shown in Fig. 5a. Cyclic behavior of the steel during the cyclic load (Fig. 5b) is modelled with improved Kato's model [7].

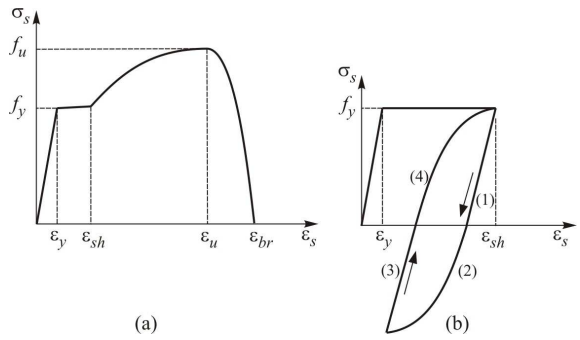

Figure 5: Material model for steel: (a) Stress-strain relation for steel, (b) Cyclic behavior of steel.

4 EXAMPLES

4.1 Sensitivity of the 3D model to the mesh refinement and penalty parameter

This example was chosen to analyse the sensitivity of the 3D numerical model to the mesh refinement and penalty parameter. Analysis was performed on concrete cantilever exposed to monotonic increasing tension load. Geometry and cross section of structure are shown in Fig. 6. Modulus of elasticity of concrete is E=30 GPa.

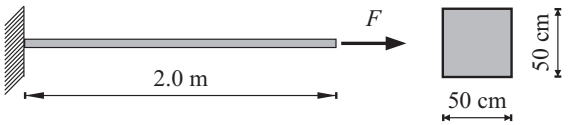

Figure 6: Geometry and load of structure.

The analyses were performed without and with contact elements using two different finite elements meshes refinement (mesh A, mesh B) as shown in Fig. 7.

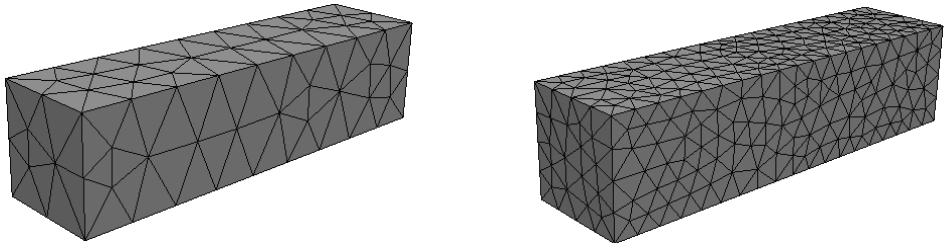

(a) (b)

Figure 7: Discretization of structure: (a) mesh A, (a) mesh B.

Mesh A was comprised of 320, while mesh B was comprised of 3102 finite elements. In analyses performed with contact elements, penalty term p was 20 times higher than E_c.

Fig. 8 shows the comparison of the analytical and numerical results obtained by the presented model. It can be seen that for homogeneous state of stress the numerical 3D model is not sensitive to the mesh refinement regardless of the presence of the contact elements. It can be also seen when analyses were performed without contact elements, the numerical results correspond to analytical solution while the introduction of contact elements leads to relative error of numerical results in comparison to analytical solution.

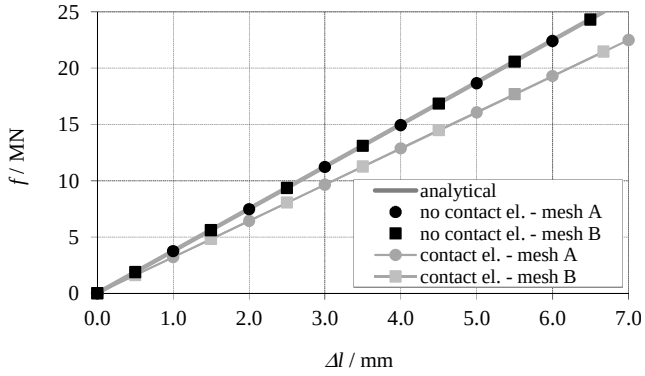

Figure 8: Force-displacement relations.

The sensitivity of the numerical model in linear elastic stage to the penalty parameter p was performed on concrete cantilever with finite element mesh shown in Fig. 7(a). The analyses were performed for three values of penalty parameter p. The comparison of the analytical and numerical results obtained by the presented model is shown in Fig. 9.

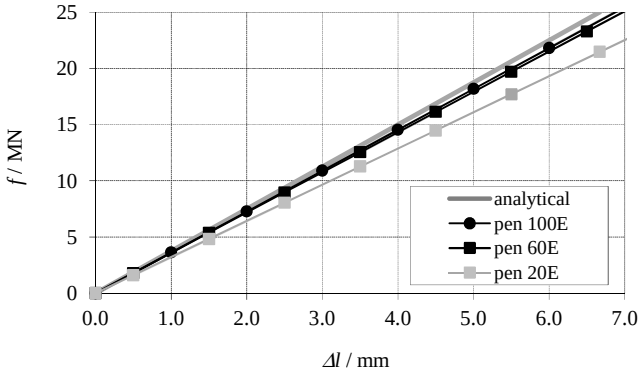

Figure 9: Force-displacement relations.

The influence of the penalty parameter p to the relative error is shown in table 1. It can be seen that for values of penalty term higher than $100E$ relative error is less than 2%. Similar conclusions have been obtained for 2D analysis [4].

Penalty parameter	Relative error
20Ec	14.1
60Ec	4.4
100Ec	1.9

Table 1: Influence of penalty parameter to the solution error.

4.2 Seismic analysis of coupled RC wall structure

The application of the presented finite-discrete numerical model of reinforced concrete structures was shown on five-storey reinforced concrete building with coupled wall system. The vertical load of the building consists of the own weight of structural elements, an additional dead load of 2.5 kN/m^2 and impose load of 4.0 kN/m^2 at floor slabs.

Material characteristics of concrete and steel used in a numerical analysis are shown in Table 1.

Concrete					
E_c / MPa	v	f_t / MPa	f_c / MPa	G_f/ N/m	ρ / kN/m^3
32800	0.2	3.80	38	150	25
Steel					
E_s / MPa	f_y / MPa	f_u / MPa	ε_{sh}	ε_u	
210000	500	600	0.02	0.1	

Table 2: Material characteristics of the RC wall.

The application of the presented model in incremental dynamic analysis [10] of RC structure was performed for the boundary coupled RC wall with geometry, reinforcement and discretisation shown in Fig. 10.

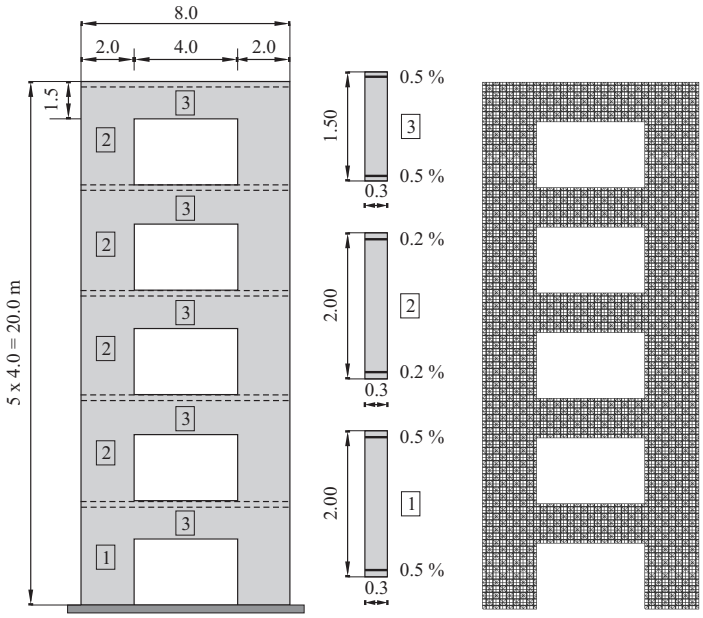

(a) (b)

Figure 10: Coupled RC wall: (a) Geometry and reinforcement of the cross-sections, (b) Discretisation.

Seismic loading is represented by a time function of the horizontal ground acceleration recorded during real earthquakes. The earthquake accelerograms were taken from the European Strong-Motion Database [11]. The selected earthquakes are Petrovac (Montenegro)-1979, South Iceland (Iceland)-2000 and Campano Lucano (Italy)-1980, as shown in Fig. 11.

The observed five-storey RC wall structure is exposed to the horizontal ground acceleration of selected three earthquakes. The amplitudes were gradually increased until the collapse of the structure. The relation between the ratio of peak ground acceleration and gravity con-

stant a and the ratio of maximum top displacement u and the height of structure H (u/H) obtained by incremental dynamic analysis is shown in Fig. 12.

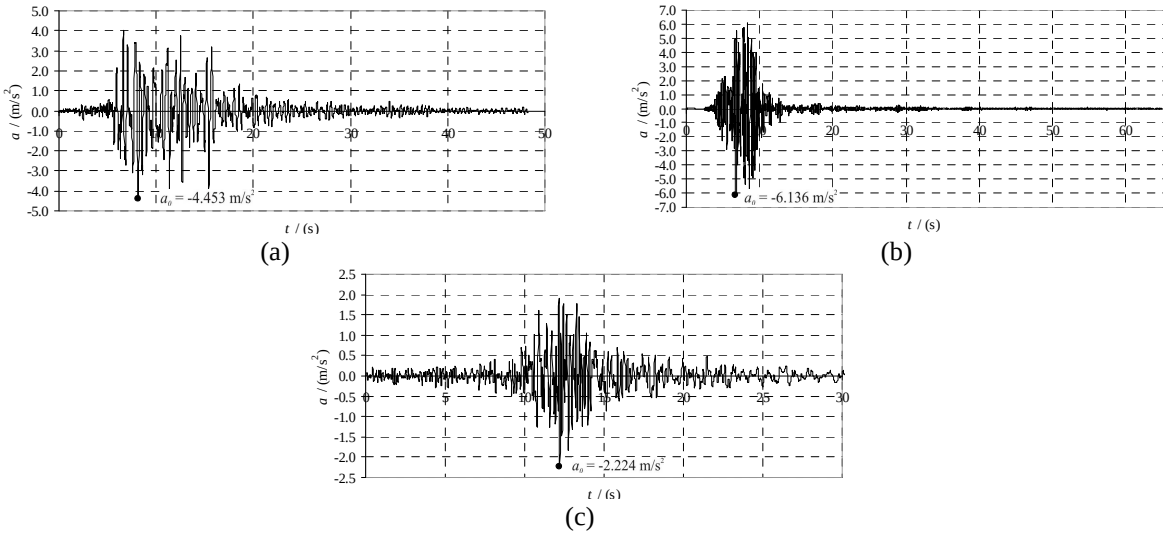

Figure 11: Accelerograms of three real earthquakes: (a) Petrovac (1979.), (b) South Iceland (2000.), (c) Campano Lucano (1980.)

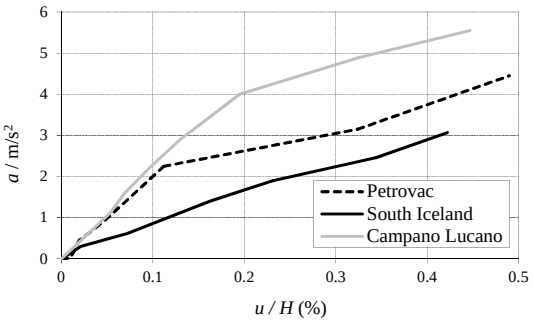

Figure 12: The ratio between the maximum roof displacement u and the height of structure H for coupled RC wall structure in dependence to the peak ground acceleration.

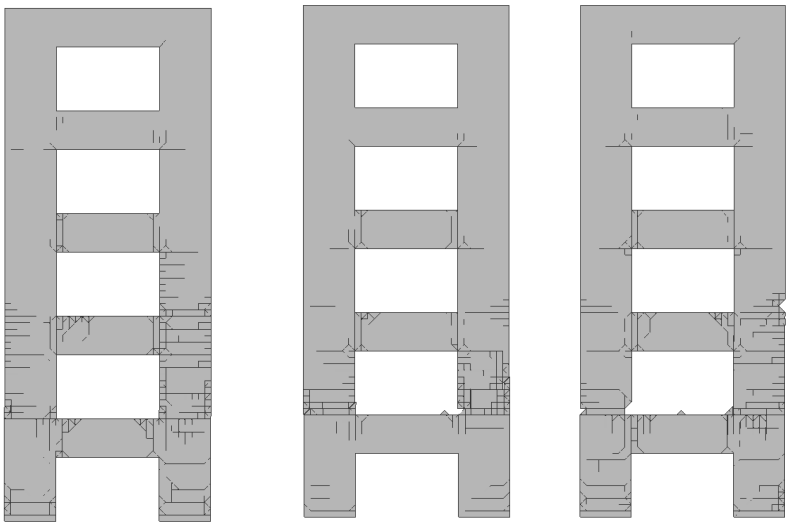

Figure 13: Crack pattern for the coupled RC wall structure exposed to the failure peak ground acceleration of earthquake: (a) Petrovac, (b) South Iceland, (c) Campano Lucano.

Finite-discrete numerical model based on discrete cracks presented in this paper can simulate opening and closing the cracks as well as realistic crack patterns for different intensity of accelerations. Crack pattern for the coupled RC wall structure exposed to the failure peak ground acceleration of three earthquakes is shown in Figure 13.

This example highlights the ability of the developed model based on discrete cracks for simulation of opening and closing the cracks during the earthquake loading as well as obtaining of the ultimate acceleration, which is very important in the estimation of the safety of RC structures under the seismic loading.

5 CONCLUSIONS

- This paper presents numerical model for analysis of reinforced concrete structures under static and dynamic load.
- Simple numerical model of reinforcement which is implemented in combined finite discrete element code is presented. Model based on approximation of the experimental curves for behaviour of the concrete and steel in crack, is primarily aimed for monitoring of the behaviour of reinforced concrete structure subjected to static and dynamic load up to failure.
- Cracking of the structure is enabled by discrete model of cracks where the cyclic behaviour of concrete and steel was successfully implemented.
- Interaction between reinforcement and concrete was not directly considered, but it was taken into consideration by defining the average spacing between the cracks.
- The model provides quite realistic description of cracking in the reinforced concrete structures under the seismic loading until the collapse.

REFERENCES

[1] A. Munjiza, *The combined finite-discrete element method*. John Wiley & Sons, 2004.

[2] A. Munjiza, K.R.F. Andrews, J.K. White, Combined single and smeared crack model in combined finite-discrete element analysis. *International Journal for Numerical Methods in Engineering*, **44** (1), 41-57, 1999.

[3] N. Živaljić, H. Smoljanović, Ž. Nikolić, A combined finite-discrete element model for RC structures under dynamic loading. *Engineering Computations*, **30** (7), 982-1010, 2013.

[4] N. Živaljić, Ž. Nikolić, H. Smoljanović, Computational aspects of the combined finite–discrete element method in modelling of plane reinforced concrete structures. *Engineering Fracture Mechanics*, **131**, 669-686, 2014.

[5] H. Shima, L. Chou, H. Okamura, Micro and macro model for bond in reinforced concrete. *Journal of the Faculty of Engineering, The University of Tokyo (B)*, **39** (2), 133-194, 1987.

[6] H. Shin, K. Maekawa, H. Okamura, Analytical approach of RC members subjected to reversed cyclic in-plane loading. *Proceeding of JCI Colloquium on Ductility of Concrete Structures and its Evaluation*, 245-256, March, 1988.

[7] B. Kato, Mechanical properties of steel under load cycles idealizing seismic action. *Bulletin D'Information CEB*, AICAP-CEB symposium, Rome, No. 131, 7-27, 1979.

[8] D.A. Hordijk, Tensile and tensile fatigue behaviour of concrete; experiments, modelling and analyses. *Heron*, **37** (1), 3-79, 1992.

[9] A. Munjiza, K.R.F. Andrews, J.K. White, Penalty function method for combined finite-discrete element system comprising large number of separate bodies. *International Journal for Numerical Methods in Engineering*, **49** (11), 1377-1396, 2000.

[10] D. Vamvatsikos, C.A. Cornell, Incremental Dynamic Analysis. *Earthquake Engineering and Structural Dynamics*, **31** (3), 491-514, 2002.

[11] European Strong-Motion Database, http://www.isesd.hi.is/ESD_Local/frameset.htm [Accessed 7 August 2015].

Acknowledgements

This work has been fully supported by Croatian Science Foundation under the project *Development of numerical models for reinforced-concrete and stone masonry structures under seismic loading based on discrete cracks* (IP-2014-09-2319).

ECCOMAS Congress 2016
VII European Congress on Computational Methods in Applied Sciences and Engineering
M. Papadrakakis, V. Papadopoulos, G. Stefanou, V. Plevris (eds.)
Crete Island, Greece, 5–10 June 2016

BEAM DYNAMIC STRESSES INCREMENTS AFTER PARTIAL DECONSTRUCTION OF FOUNDATION

Vladimir A. Gordon, Olga V. Pilipenko, Timur F. Gasimov

Oryol State University
address
e-mail: gordon1312@mail.ru

Keywords: Beam on elastic foundation, partial damage to the foundation, sudden structural changes, transient dynamic processes, the dynamic increments of strain and stress.

Abstract. *One of the major problems of modern structural mechanics is sensitivity analysis of actual and projected designs to various effects not provided for under normal operating conditions, arising in particular in emergency situations, as a result of wear and damage accumulation, etc. The paper presents a physical and mathematical model of the transient dynamical processes initiated in a beam on an elastic foundation with a sudden partial or fully destruction of the foundation. Mathematical models are the differential equations of the static bending of initial and damaged beam, equations of the free and forced vibrations of sections beams formed after damage foundation, with the initial and boundary conditions, conjugations conditions of the beam's parts, assumptions and limitations. Exact solution of the problem of forced vibrations loaded beam on an elastic foundation (partially or fully destroyed) was obtained, using the Fourier method of separation of variables, the expansion of dynamic movements on the modes of free vibrations of the damaged beams and Duhamel integral.*

1 INTRODUCTION

An important problem in structural mechanics is a sensitivity analysis of load-bearing systems in structural rearrangements under load such as a sudden turn off the links, cracks, partial damage, etc. Obtaining this information for real structures requires the development of special methods, because the problem can not be solved by universal methods. From the viewpoint of structural mechanics in these problems there is a need for calculating such systems as a constructively nonlinear with dynamic increments of strain and stress caused by sudden impacts beyond design basis. And if the design accidental situations are analyzed and regulated by the relevant documents, the situation is not beyond design basis and classified as responses to specific impacts on structural elements are insufficiently investigated. Engineering design and calculation methods that take into account the sudden restructuring and sudden damage to the structural systems, are few and far from being perfect. Absence and lack of knowledge about deformation and stress state of structural elements during dynamic processes initiated by a sudden damage, constrain the development of the theory and design techniques that take into account the possibility and potential consequences of beyond design impacts and ensure a high level of safety of their maintenance. As an example of work performed in the discussed direction, we note a number of publications [1-4] containing the results of the modeling of transient dynamic processes that occur in stressed beams at the sudden breakage of the support links, formation of transverse and longitudinal cracks, delamination and exfoliation, change conditions interfaces parts construction and others. All these works are made in relation to the free beams, that are not supported by solid foundations. It is of theoretical interest and practical importance of the spread of similar approaches to the beams on an elastic foundation.

Beams on elastic foundation, columns, piles, supported by length – widely used building blocks are long and detailed study of objects in many fields of mechanics and construction. However, despite the abundance of books, articles and reports related to the dynamic problems of structural elements resting on all sorts of grounds, in the scientific literature insufficiently investigated cases where structure simply supported partly initially or lost some (or all) of the foundation during exploitation. The problem of vibration of a homogeneous beam, partially supported by the Winkler foundation, first staged by Doyle and Pavlovic in [5], which investigated with two cases of symmetrical bearing beam ends: hinges and free ends. The authors identified three cases occurring in different ranges of values of the natural vibration frequencies, associated with the mechanical characteristics of the beam and foundation. Solutions are obtained analytically. Numerical results are presented for the first five modes of natural vibrations. Further development of the problem was in Eisenberger's at al work [6], in relation to arbitrary boundary conditions. The paper deduced the precise mass and stiffness matrix, developed by special finite elements, the displacement functions which are the solutions of the equations for the static beam on an elastic foundation. Dynamic solution produced a finite element procedure. These results take the form of generalized frequency dependency of rigidity generalized system of "beam-foundation" for the first four forms of eigenfunction. Later, the results of [5] extended to partially embedded piles [7]. The paper Kukla [8] investigated the free vibrations of a homogeneous beam, supported by the Winkler foundation with areas of piecewise constant stiffness which is given by the Heaviside function. The frequency equation was obtained by standard procedure satisfying the boundary conditions and the conditions of conjugation parts. As a special case, one of the numerical examples describes the vibration of a cantilever beam, consisting of two sections, one of which is not supported by the elastic foundation. It is shown an effect of the partial support on the first four natural frequencies. The paper Motaghian et al [9] provides a method for the analysis of natural vibra-

tions of the beam, in part supported by the Winkler foundation. The approach is to provide a foundation reactions as a some "external load", distributed along the length and depending on the desired deflection. Next eigenfunctions and "load" are expanded in Fourier series. The coefficients of the series are calculated by successive approximations by definite integrals, which bounds are the coordinates of the beginning and the end of the foundation part. The method is illustrated by calculations of natural frequencies of the beams with different boundary conditions, location and length of the supported part. In Cazzani work [10] studied in detail the natural vibrations of the beams, partially supported by an elastic foundation. Presents a number of exact solutions of the problem on the eigenvalues, in particular, the transcendental equations for the eigenfrequencies and their solutions. Analyzed three types of vibration modes, depending on the combination of the stiffness of the beam and the foundation. It is shown possibility of transfer of vibrations from one type to another with increasing number of forms of natural vibrations.

Thus, the vast majority of work on the dynamics of interaction between the beam and the grounds devoted to the analysis of natural vibrations. Forced vibrations caused by various external forces are considered in cases where the calculated scheme of the system "beam-foundation" in the process of loading is not changed.

In this paper, it is assumed that static load applied to the beam, fully supported by the elastic foundation, and only at some point part (or all) of the foundation suddenly collapses and the beam is set in motion, in which getting additional dynamic strain and stress. The aim of this study is to construct a mathematical model of transient dynamic processes in a loaded beam on an elastic foundation with the sudden occurrence of the defect foundation – total or partial destruction of it.

The structure of the paper is as follows: in the first part is given an analysis of the stress-strain state of the loaded beam with quasi-static fracture supporting its elastic foundation. Decisions of static problems are used in the second part to form the initial conditions of dynamic tasks and for comparison with the stress-strain state of the beam during the dynamic process initiated by the sudden damage to the foundation.

2 STATIC STRESS – STRAIN STATE OF THE BEAM SUPPORTED ON THE ELASTIC FOUNDATION

2.1 Beam fully supported on the elastic foundation

Consider the bending of the beam with stiffness *EI*, resting on the Winkler foundation with stiffness k, rigid clamped at both ends, under the action of uniformly distributed load of intensity q (Figure 1 *a*). The solution of the problem is carried out in Cartesian coordinates related to the beam axis. All movements and linear dimensions attributed to the length of the beam *L*. The deflection of the beam of the beam in the dimensionless variables and parameters described by the equation

$$\frac{d^4 w_{cm}}{d\xi^4} + 4\alpha^4 w_{cm} = \bar{q}, \tag{2.1}$$

where $\xi = \frac{x}{L}$, $w_{cm} = \frac{w}{L}$, $\alpha = \sqrt[4]{\frac{kL^4}{4EI}}$, $\bar{q} = \frac{qL^3}{EI}$.

The general solution of the inhomogeneous equation (2.1) in the case of clamped of the ends

$$w_{cm}(\xi)=\bar{q}\left\{\frac{1-R_4(\alpha\xi)}{4\alpha^4}+C_1(\alpha)R_2(\alpha\xi)+C_2(\alpha)R_1(\alpha\xi)\right\}, \tag{2.2}$$

where

$$C_1(\alpha)=\frac{(R_4(\alpha)-1)R_2(\alpha)+4\alpha^4R_1^2(\alpha)}{R_5(\alpha)},\quad C_2(\alpha)=\frac{(R_4(\alpha)-1)R_3(\alpha)+4\alpha^4R_1(\alpha)R_2(\alpha)}{R_5(\alpha)};$$

$$R_1(\alpha\xi)=\frac{\sin\alpha\xi ch\alpha\xi-\cos\alpha\xi sh\alpha\xi}{4\alpha^3},\quad R_2(\alpha\xi)=\frac{\sin\alpha\xi sh\alpha\xi}{2\alpha^2},$$

$$R_3(\alpha\xi)=\frac{\sin\alpha\xi ch\alpha\xi+\cos\alpha\xi sh\alpha\xi}{2\alpha},\quad R_4(\alpha\xi)=\cos\alpha\xi ch\alpha\xi,\quad R_5(\alpha\xi)=\frac{sh^2(\alpha\xi)-\sin^2(\alpha\xi)}{2}.$$

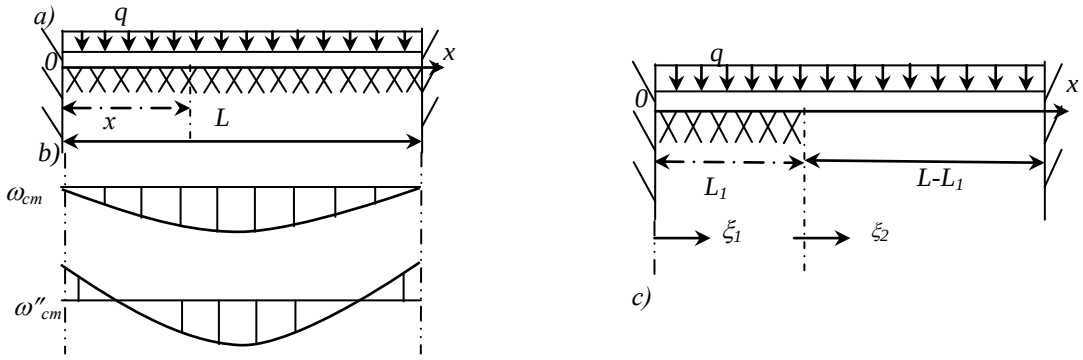

Figure 1: Beam on elastic foundation: *a)* completely simply supported on a foundation, *b)* diagrams of deflections and bending moments, *c)* simply supported on the part of foundation.

The function (2.2) is then used as the initial condition of the dynamic process resulting from the total or partial destruction of the foundation.

2.2 Beam partly supported on an elastic base

It is assumed that the formation of a defect – the removal a part of foundation of the loaded beams – was slowly (quasi-statically), i.e. without inertial forces. In this case, there is the problem of calculating the beam consisting of two coupled segments one of which is supported by an elastic foundation, the other – free (Figure 1 *c*).

Local coordinates are entered for each segment

$$\xi_1=\xi \quad \text{and} \quad \xi_2=\xi-v,\quad v=\frac{L_1}{L}.$$

Let us consider each segment bend sequence.

1) 1st segment bend described by the equation

$$\frac{d^4w_1}{d\xi_1^4}+4\alpha^4w_1=\bar{q},\qquad w_1=\frac{v_1}{L}, \tag{2.3}$$

the general solution (2.3) has the form

$$w_1(\xi_1)=\frac{\bar{q}}{4\alpha^4}(1-R_4(\alpha\xi_1))+w_{10}R_4(\alpha\xi_1)+w'_{10}R_3(\alpha\xi_1)+w''_{10}R_2(\alpha\xi_1)+w'''_{10}R_1(\alpha\xi_1), \tag{2.4}$$

where $w_{10}=w_1(0)$, $w'_{10}=w'_1(0)$, $w''_{10}=w''_1(0)$, $w'''_{10}=w'''_1(0)$ – the initial parameters.

We introduce:

– the vector of state of the 1st segment $\overline{W}_1(\xi_1)$

$$\overline{W_1}(\xi_1) = \{w_1(\xi_1) \quad w_1'(\xi_1) \quad w_1''(\xi_1) \quad w_1'''(\xi_1)\};$$

– the vector of initial parameters $\overline{W}_{10}$

$$\overline{W}_{10} = \{w_{10} \; w_{10}' \; w_{10}'' \; w_{10}'''\};$$

– functional matrix $V_1(\xi_1)$

$$\underset{4\times4}{V_1}(\xi_1) = \begin{pmatrix} R_4(\alpha\xi_1) & R_3(\alpha\xi_1) & R_2(\alpha\xi_1) & R_1(\alpha\xi_1) \\ -4\alpha^4 R_1(\alpha\xi_1) & R_4(\alpha\xi_1) & R_3(\alpha\xi_1) & R_2(\alpha\xi_1) \\ -4\alpha^4 R_2(\alpha\xi_1) & -4\alpha^4 R_1(\alpha\xi_1) & R_4(\alpha\xi_1) & R_3(\alpha\xi_1) \\ -4\alpha^4 R_3(\alpha\xi_1) & -4\alpha^4 R_2(\alpha\xi_1) & -4\alpha^4 R_1(\alpha\xi_1) & R_4(\alpha\xi_1) \end{pmatrix}$$

– load vector $\overline{\bar{q}V}_{1q}(\xi_1)$

$$\overline{\bar{q}V}_{1q}(\xi_1) = \bar{q}\left\{\frac{1-R_4(\alpha\xi_1)}{4\alpha^4} \; R_1(\alpha\xi_1) \; R_2(\alpha\xi_1) \; R_3(\alpha\xi_1)\right\}.$$

Then the state in an arbitrary section of the 1st segment describes the matrix equation

$$\overline{W}_1(\xi_1) = V_1(\xi_1)\overline{W}_{10} + \overline{\bar{q}V}_{1q}(\xi_1). \tag{2.5}$$

The state vector of the end 1st segment, with $\xi_1 = \nu$

$$\overline{W}_1(\nu) = V_1(\nu)\overline{W}_{10} + \overline{\bar{q}V}_{1q}(\nu). \tag{2.6}$$

2) 2nd segment bend described by the equation

$$\frac{d^4 w_2}{d\xi_2^4} = \bar{q}, \quad w_2 = \frac{v_2}{L}. \tag{2.7}$$

The general solution of equation (1.7) has the form

$$w_2(\xi_2) = w_{20}T_4(\xi_2) + w_{20}'T_3(\xi_2) + w_{20}''T_2(\xi_2) + w_{20}'''T_1(\xi_2) + \bar{q}_0 T_0(\xi_2), \tag{2.8}$$

where $T_0(\xi_2) = \frac{\xi_2^4}{24}$, $T_1(\xi_2) = \frac{\xi_2^3}{6}$, $T_2(\xi_2) = \frac{\xi_2^2}{2}$, $T_3(\xi_2) = \xi_2$, $T_4 = 1$; $w_{20} = w_1(\nu)$, $w_{20}' = w_1'(\nu)$, $w_{20}'' = w_1''(\nu)$, $w_{20}''' = w_1'''(\nu)$ – the initial parameters of the 2nd segment. These equations are also conditions of conjugation segments.

We introduce:

– the vector of state of the 2nd segment $\overline{W}_2(\xi_2)$

$$\overline{W_2}(\xi_2) = \{w_2(\xi_2) \quad w_2'(\xi_2) \quad w_2''(\xi_2) \quad w_2'''(\xi_2)\};$$

– the vector of initial parameters, the components of which are expressed through the components of the vector of initial parameters of the previous one, the 1st segment $\overline{W}_1(\nu)$

$$\overline{W}_{20} = \overline{W}_1(\nu) = V_1(\nu)\overline{W}_{10} + \overline{\bar{q}V}_{1q}(\nu). \tag{2.9}$$

– functional matrix $V_2(\xi_2)$

$$\underset{4\times4}{V_2(\xi_2)}=\begin{pmatrix}1 & T_3(\xi_2) & T_2(\xi_2) & T_1(\xi_2)\\ 0 & 1 & T_3(\xi_2) & T_2(\xi_2)\\ 0 & 0 & 1 & T_3(\xi_2)\\ 0 & 0 & 0 & 1\end{pmatrix};$$

– load vector $\bar{q}\overline{V}_{2q}(\xi_2)$

$$\bar{q}\overline{V}_{2q}(\xi_2)=\bar{q}\{T_0(\xi_2)\ T_1(\xi_2)\ T_2(\xi_2)\ T_3(\xi_2)\}.$$

Then the state of the 2nd segment described by the matrix equation

$$\overline{W}_2(\xi_2)=V_{21}(\xi_2,\nu)\overline{W}_{10}+\bar{q}(\overline{V}_{21}(\xi_2,\nu)+\overline{V}_{2q}(\xi_2)), \tag{2.10}$$

where the matrix $\underset{4\times4}{V_{21}(\xi_2,\nu)}=\underset{4\times4}{V_2(\xi_2)}\underset{4\times4}{V_1(\nu)}$ and vector $\underset{4\times1}{\overline{V}_{21}(\xi_2,\nu)}=\underset{4\times4}{V_2(\xi_2)}\underset{4\times1}{\overline{V}_{1q}(\nu)}$.

Thus, the state of the beam at both segment is expressed through the initial parameters of the 1st segment at $\xi_1=0$. In this case, two parameters known

$$w_{10}=w'_{10}=0.$$

The remaining two parameters w''_{10} and w'''_{10} are determined from boundary conditions at the end of $2^{\underline{\text{nd}}}$ segment with $\xi_2=1-\nu$. Denoted the elements of matrix $V_{21}(\xi_2,\nu)$ and vector $\bar{q}(\overline{V}_{21}(\xi_2,\nu)+\overline{V}_{2q}(\xi_2))$ as $a_{ij}(\xi_2,\nu)$ and $b_i(\xi_2,\nu)$ $(i,j=1\div4)$, respectively, and write the equation (2.10) in expanded form for $\xi_2=1-\nu$ taking into account the known boundary conditions

$$w_{10}=w'_{10}=w_2(1-\nu)=w'_2(1-\nu)=0$$

$$\begin{pmatrix}0\\0\\w''_2(1-\nu)\\w'''_2(1-\nu)\end{pmatrix}=\begin{pmatrix}a_{11}(1-\nu) & a_{12}(1-\nu) & a_{13}(1-\nu) & a_{14}(1-\nu)\\ a_{21}(1-\nu) & a_{22}(1-\nu) & a_{23}(1-\nu) & a_{24}(1-\nu)\\ a_{31}(1-\nu) & a_{32}(1-\nu) & a_{33}(1-\nu) & a_{34}(1-\nu)\\ a_{41}(1-\nu) & a_{42}(1-\nu) & a_{43}(1-\nu) & a_{44}(1-\nu)\end{pmatrix}\begin{pmatrix}0\\0\\w''_{10}\\w'''_{10}\end{pmatrix}+\bar{q}\begin{pmatrix}b_1(1-\nu)\\b_2(1-\nu)\\b_3(1-\nu)\\b_4(1-\nu)\end{pmatrix} \tag{2.11}$$

where, in particular

$$a_{13}(\xi_2,\nu)=R_2(\alpha\nu)+R_3(\alpha\nu)\xi_2+R_4(\alpha\nu)\frac{\xi_2^2}{2}-4\alpha^4R_1(\alpha\nu)\frac{\xi_2^3}{6};$$

$$a_{14}(\xi_2,\nu)=R_1(\alpha\nu)+R_2(\alpha\nu)\xi_2+R_3(\alpha\nu)\frac{\xi_2^2}{2}+R_4(\alpha\nu)\frac{\xi_2^3}{6};$$

$$a_{23}(\xi_2,\nu)=R_3(\alpha\nu)+R_4(\alpha\nu)\xi_2+4\alpha^4R_1(\alpha\nu)\frac{\xi_2^2}{2};$$

$$a_{24}(\xi_2,\nu)=R_2(\alpha\nu)+R_3(\alpha\nu)\xi_2+R_4(\alpha\nu)\frac{\xi_2^2}{2};$$

$$b_1(\xi_2,\nu)=\frac{1-R_4(\alpha\nu)}{4\alpha^4}+R_1(\alpha\nu)\xi_2+R_2(\alpha\nu)\frac{\xi_2^2}{2}+R_3(\alpha\nu)\frac{\xi_2^3}{6}+\frac{\xi_2^4}{24};$$

$$b_2(\xi_2,\nu)=R_1(\alpha\nu)+R_2(\alpha\nu)\xi_2+R_3(\alpha\nu)\frac{\xi_2^2}{2}+\frac{\xi_2^3}{6}.$$

From the matrix equation (2.11) we obtain a system of two algebraic equations for the un-

known w''_{10} and w'''_{10}

$$\begin{pmatrix} a_{13}(1-\nu) & a_{14}(1-\nu) \\ a_{23}(1-\nu) & a_{24}(1-\nu) \end{pmatrix} \begin{pmatrix} w''_{10} \\ w'''_{10} \end{pmatrix} + \bar{q} \begin{pmatrix} b_1(1-\nu) \\ b_2(1-\nu) \end{pmatrix} = 0,$$

where by Cramer method obtain

$$w''_{10} = \frac{\Delta_1}{\Delta}, \quad w'''_{10} = \frac{\Delta_2}{\Delta}, \tag{2.12}$$

where determinants Δ, Δ_1 and Δ_2 have the form

$$\Delta = \begin{vmatrix} a_{13}(1-\nu) & a_{14}(1-\nu) \\ a_{23}(1-\nu) & a_{24}(1-\nu) \end{vmatrix}, \quad \Delta_1 = \begin{vmatrix} -\bar{q}b_1(1-\nu) & a_{14}(1-\nu) \\ -\bar{q}b_2(1-\nu) & a_{24}(1-\nu) \end{vmatrix}, \quad \Delta_2 = \begin{vmatrix} a_{13}(1-\nu) & -\bar{q}b_1(1-\nu) \\ a_{23}(1-\nu) & -qb_2(1-\nu) \end{vmatrix}.$$

Now dimensionless deflections and bending moments on the areas determined by dependencies

$$w_1(\xi_1) = w''_{01}R_2(\alpha\xi_1) + w'''_{10}R_1(\alpha\xi_1) + \frac{\bar{q}}{4\alpha^4}(1 - R_4(\alpha\xi_1)), \quad 0 \le \xi_1 \le \nu$$

$$w''_1(\xi_1) = w''_{01}R_4(\alpha\xi_1) + w'''_{10}R_3(\alpha\xi_1) + \bar{q}R_2(\alpha\xi_1), \tag{2.13}$$

$$w_2(\xi_2) = w''_{10}a_{13}(\nu,\xi_2) + w'''_{10}a_{14}(\nu,\xi_2) + \bar{q}b_1(\nu,\xi_2), \quad 0 \le \xi_2 \le 1-\nu$$

$$w''_2(\xi_2) = w''_{10}a_{33}(\nu,\xi_2) + w'''_{10}a_{34}(\nu,\xi_2) + \bar{q}b_3(\nu,\xi_2).$$

Figure 2 shows the relationship (2.13), respectively, the largest deflection w_{max} and bending moments w''_{max} with the generalized parameter of rigidity of the system "beam-foundation" $\bar{\lambda} = 4\alpha^4 = \frac{KL^4}{EI}$ for a number of values of the parameter $\nu = 0; 0{,}25; 0{,}5; 0{,}75; 1$, characterizing the degree of damage to the foundation: $\nu = 1$ – fully justified, $\nu = 0$ – absence of a foundation. The calculations correspond to a single dimensionless load

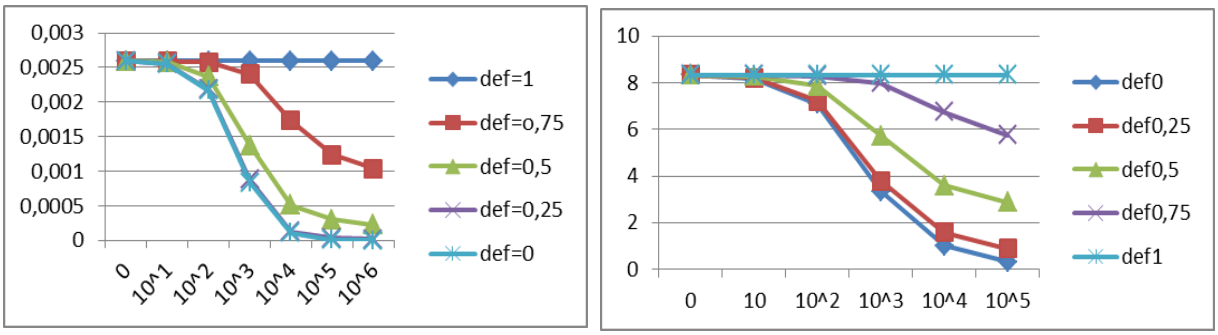

a) *b)*

Figure 2: The dependence:
a) the largest deflections; *b)* the largest bending moment in the right clamp – from length damage area.

Figure 3 shows the reduction (as a percentage of the free beam) the largest bending moment in the beam at the reinforcement of its foundation of varying length and relative stiffness.

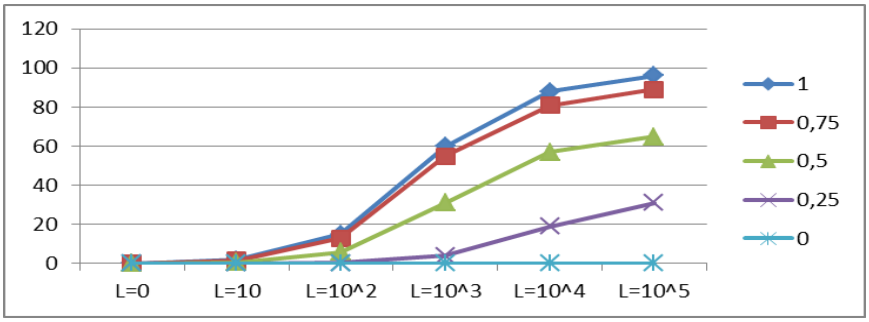

Figure 3: Effect of the length and rigidity to the foundation on value of the largest bending moment in the right clamp of beam.

3 FREE VIBRATION BEAM SUPPORTED ON AN ELASTIC FOUNDATION

To date, there are a number of works devoted to the study of dynamic processes caused by the sudden formation of defects in beams and plates. In particular, in papers [2-4] considers the transition dynamic process caused by the sudden formation of transverse cracks in a loaded beam. Beam modeled conjugation of two segments connected by a torsion spring whose stiffness is determined by the depth of cracks. One of the initial conditions is the static deflection of the intact beam. In [5-8] studied the dynamic process in the loaded component beams arising during sudden longitudinal stratification, caused break shift links in the seam. In [9-11] considered vibrations plates with a sudden change of support conditions, caused by partial separation of support links. In [12-14] solved the problem of the vibrations of the beam when it is sudden partial destruction. In [4, 6, 11, 16] studied transients dynamical process caused by sudden transformation of the internal structure of rod systems: coupling and bearing conditions their elements. In [17] is modeled by a sudden breaking of the reinforcing bar and the longitudinal vibrations caused by this defect. Note ,that in all these studies considered forced movement of the beam (plates) under the load ,produced by expansion into an infinite series of the initial state and the external load on the damaged natural vibration modes of the beam (the plate), and using the Duhamel integral.

It is practically important to develop methods of analysis of transient dynamic processes in the beams on an elastic foundation, initiated by the sudden operational damage of foundation: in the simplest case of total or partial destruction of it. Manifestations of structural nonlinearity, i.e. changes in the calculation scheme loaded beam on an elastic foundation, and the consequences of them – are not described in the prior literature.

In this part, an algorithm for determining the forms and frequencies of free vibrations of bending beams, in whole or in part simply supported on an elastic Winkler foundation. In its construction were used the approaches, the effectiveness of which is shown in the above-cited work: method of initial parameters, the vectors of state and the initial parameters, the matrix of influence of initial parameters and other. Eigenfunctions and eigenfrequencies of free vibrations are important dynamic characteristics of the "beam – foundation" system and used to solve inhomogeneous differential equations, describing forced vibrations.

3.1 Free vibration beam partially supported on the elastic foundation

Consider free transverse vibrations of a continuous beam (Figure 1 *c*) Deflections of the beams in the cross – sections denoted x_1 and x_2, respectively, v_1 and v_2. Without reducing the generality of the constructions it is supposed to be specific rigid clamping beam ends. Differential equations of natural vibrations of the beam segments are integrated separately, and in-

tegration constants are determined from the boundary conditions and the conditions of conjugation of segments.

3.1.1. Free transverse vibrations of the 1st segment

Natural vibrations of the beam in the area $0 \le \xi_1 \le \nu$ described by differential equations of the form [10]

$$\frac{\partial^4 w_1}{\partial \xi_1^4} + 4\alpha^4 w_1 + \frac{\partial^2 w_1}{\partial \tau^2} = 0, \tag{3.1}$$

where we have introduced the dimensionless variables and parameters

$$\xi_i = \frac{x_1}{L}; w_1 = \frac{v_1}{L}; \tau = \frac{t}{L^2}\sqrt{\frac{EI}{\rho A}}; A = bh; \alpha = \sqrt[4]{\frac{kL^4}{4EI}}; \nu = \frac{v_1}{L}.$$

Putting free harmonic vibrations, we divide the variables in the equation (3.1) the representation

$$w_1(\xi_1, \tau) = W_1(\xi_1)\sin\bar{\omega}\tau, \tag{3.2}$$

where $\bar{\omega} = \omega L^2\sqrt{\frac{\rho A}{EI}}$ – the dimensionless natural frequency of transverse vibration (natural frequency parameter); $\omega = \frac{\bar{\omega}}{L^2}\sqrt{\frac{EI}{\rho A}}$ – dimensional frequency.

Substituting (3.2) into (3.1) gives the equation forms its free vibrations of segment

$$W_1^{IV} + 4\alpha^4\left(1 - \left(\frac{\omega}{\omega_0}\right)^2\right)W_1 = 0, \tag{3.3}$$

where $\omega_0 = \sqrt{\frac{k}{\rho A}}$ – parameter having a dimension of frequency [1/*c*], and called "conventional", which compares the vibration frequency ω investigated beams.

We are looking for the solution of equation (3.3) Euler substitution

$$W_1 = Ce^{n\xi_1}, \tag{3.4}$$

where *C* and *n* – constants to be determined.

Substituting (3.4) into (3.3), we obtain the characteristic equation for the differential equation (3.3)

$$n^4 + 4\alpha^4\left(1 - \left(\frac{\omega}{\omega_0}\right)^2\right) = 0. \tag{3.5}$$

Multiplier in brackets depending on the value $\frac{\omega}{\omega_0}$ can be positive ($\frac{\omega}{\omega_0} < 1$), negative ($\frac{\omega}{\omega_0} > 1$) and zero ($\frac{\omega}{\omega_0} = 1$).

Let $\frac{\omega}{\omega_0} < 1$. Then the roots of the equation (3.5) can be represented in the form

$$n_j = (\pm i \pm 1)\beta_1, \quad (j=1,2,3,4),$$

where $\beta_1 = \alpha^4 \sqrt{1-\left(\frac{\omega}{\omega_0}\right)^2}$.

In this case, the natural vibration shape function defined by [10]

$$W_1(\xi_1) = w_{10}S_4(\xi_1) + w'_{10}S_3(\xi_1) + w''S_2(\xi_1) + w'''S_1(\xi_1), \tag{3.6}$$

where $w_{10} = w_1(0), w'_{10} = w'_1(0), w''_{10} = w''_1(0), w'''_{10} = w'''_1(0)$ – the initial parameters of the 1st segment.

$$S_1(\xi_1) = \frac{ch\beta_1\xi_1 \sin\beta_1\xi_1 - sh\beta_1\xi_1 \cos\beta_1\xi_1}{4\beta_1^3}; S_2(\xi_1) = \frac{sh\beta_1\xi_1 \sin\beta_1\xi_1}{2\beta_1^2};$$

$$S_3(\xi_1) = \frac{ch\beta_1\xi_1 \sin\beta_1\xi_1 + sh\beta_1\xi_1 \cos\beta_1\xi_1}{2\beta_1}; S_4(\xi_1) = ch\beta_1\xi_1 \cos\beta_1\xi_1 - \text{Krylov function.}$$

Note, that the $S'_1 = S_2, S'_2 = S_3, S'_3 = S_4, S'_4 = -4\beta_1^4 S_1$ и

$$S_1(0) = S_2(0) = S_3(0) = 0, S_4(0) = 1.$$

Let ω $\frac{\omega}{\omega_0} > 1$. Then the equation (3.5) in the form

$$W_1^{IV} - 4\alpha^4\left(\left(\frac{\omega}{\omega_0}\right)^2 - 1\right)W_1 = 0. \tag{3.7}$$

In this case, the roots of the characteristic equation

$$n^4 - 4\alpha^4\left(\left(\frac{\omega}{\omega_0}\right)^2 - 1\right) = 0, \tag{3.8}$$

take the form

$$n_{1,2} = \pm\lambda_1;\ n_{3,4} = \pm i\lambda_1;\ \lambda_1 = \lambda_1 = \sqrt{2}\alpha\sqrt{\left(\frac{\omega}{\omega_0}\right)^2 - 1} \tag{3.9}$$

and forms of natural vibrations determined by the function

$$W_1\xi_1 = w_{10}K_4(\lambda_1\xi_1) + w'_{10}K_3(\lambda_1\xi_1) + w''_{10}K_2(\lambda_1\xi_1) + w'''_{10}K_1(\lambda_1\xi_1), \tag{3.10}$$

where

$$K_1(\lambda_1\xi_1) = \frac{sh\lambda_1\xi_1 - \sin\lambda_1\xi_1}{2\lambda_1^3}; \qquad K_2(\lambda_1\xi_1) = \frac{ch\lambda_1\xi_1 - \cos\lambda_1\xi_1}{2\lambda_1^2}; \qquad K_3(\lambda_1\xi_1) = \frac{sh\lambda_1\xi_1 + \sin\lambda_1\xi_1}{2\lambda_1};$$

$K_4(\lambda_1\xi_1) = \frac{ch\lambda_1\xi_1 + cos\lambda_1\xi_1}{2}$ – another type of Krylov's functions.

Their properties

$$K_1' = K_2,\ K_2' = K_3,\ K_3' = K_4,\ K_4' = \lambda_1^4 K_1 \ \ and \ \ K_1(0) = K_2(0) = K_3(0) = 0,\ K_4(0) = 1.$$

Finally let $\frac{\omega}{\omega_0} = 1$. Then the equation (3.3) takes the form

$$W_1^{1V} = 0 \tag{3.11}$$

and deflection function $W_1(\xi_1)$ obtain the successive integration of the equation (3.11) using the initial parameters

$$W_1(\xi_1) = w_{10} + w_{10}'\xi_1 + w_{10}''\frac{\xi_1^2}{2} + w_{10}'''\frac{\xi_1^3}{6} \tag{3.12}$$

Further action on the first section we consider the case $\frac{\omega}{\omega_0} > 1$.

We introduce:

– the vector of state of the first segment: $\bar{W}_1(\xi_1)$:

$$\overline{W_1}(\xi_1) = \left\{ W_1(\xi_1)\ \ W_1'(\xi_1)\ \ W_1''(\xi_1)\ \ W_1'''(\xi_1) \right\},$$

where $W_1(\xi_1)$ – dimensionless deflection of the beam; W_1', W_1'', W_1''' – dimensionless cross-sectional angle of rotation, bending moment and shear force, respectively;

– the vector of initial parameters: $\overline{W}_{10}$

$$\overline{W}_{10} = \left\{ w_{10}\ \ w_{10}'\ \ w_{10}''\ \ w_{10}''' \right\}$$

– Influence function matrix: $V(\xi_1)$

$$V_{1\,(4\times4)}(\xi_1) = \begin{pmatrix} K_4(\lambda_1\xi_1) & K_3(\lambda_1\xi_1) & K_2(\lambda_1\xi_1) & K_1(\lambda_1\xi_1) \\ \lambda_1^4 K_1(\lambda_1\xi_1) & K_4(\lambda_1\xi_1) & K_3(\lambda_1\xi_1) & K_2(\lambda_1\xi_1) \\ \lambda_1^4 K_2(\lambda_1\xi_1) & \lambda_1^4 K_1(\lambda_1\xi_1) & K_4(\lambda_1\xi_1) & K_3(\lambda_1\xi_1) \\ \lambda_1^4 K_3(\lambda_1\xi_1) & K_2(\lambda_1\xi_1) & \lambda_1^4 K_1(\lambda_1\xi_1) & K_4(\lambda_1\xi_1) \end{pmatrix}.$$

Then the state of the first segment describes how the matrix equation

$$\bar{W}_1(\xi_1) = V(\xi_1)\bar{W}_{10}. \tag{3.13}$$

The vector of state $\bar{W}_1(\xi_1)$ at the end of the first segment

$$\bar{W}_1(\nu) = V(\nu)\bar{W}_{10}. \tag{3.14}$$

3.1.2 Free transverse vibrations of the 2nd segment.

Free transverse vibrations of the segment described by the equation [10]

$$\frac{\partial^4 w_2}{\partial \xi_2^4} + \frac{\partial^2 w_2}{\partial \tau^2} = 0. \tag{3.15}$$

Separating the variables, we obtain

$$w_2(\xi_2, \tau) = W_2(\xi_2)\sin\omega\tau, \tag{3.16}$$

$$W_2^{IV}(\xi_2) - \bar{\omega}^2 W_2(\xi_2) = 0, \quad W_2 = Ae^{r_2\xi_2}, \tag{3.17}$$

where $r_2^4 = \bar{\omega}^2$; $r_{21} = \lambda_2$; $r_{22} = -\lambda_2$; $r_{23} = i\lambda_2$; $r_{24} = -\lambda_2$; $\lambda_2 = \sqrt{\bar{\omega}}$.
The general solution of equation (2.17) has the form

$$W_2(\xi_2) = w_{20}K_4(\lambda_2\xi_2) + w'_{20}K_3(\lambda_2\xi_2) + w''_{20}K_2(\lambda_2\xi_2) + w'''_{20}K_1(\lambda_2\xi_2),$$

where $w_{20}, w'_{20}, w''_{20}, w'''_{20}$ – the initial parameters of the second segment.

We introduce:

– the vector of state of the second section: $\bar{W}_2(\xi_2)$

$$\bar{W}_2(\xi_2) = \{W_2(\xi_2)\ \ W_2'(\xi_2)\ \ W_2''(\xi_2)\ \ W_2'''(\xi_2)\};$$

– the vector of initial parameters: $\bar{W}_{20}$

$$\bar{W}_{20} = \{w_{20}\ \ w'_{20}\ \ w''_{20}\ \ w'''_{20}\};$$

– influence function matrix: $V_2(\xi_2)$

$$V_{2\,4\times4}(\xi_2) = \begin{pmatrix} K_4(\lambda_2\xi_2) & K_3(\lambda_2\xi_2) & K_2(\lambda_2\xi_2) & K_1(\lambda_2\xi_2) \\ \lambda_2^4K_1(\lambda_2\xi_2) & K_4(\lambda_2\xi_2) & K_3(\lambda_2\xi_2) & K_2(\lambda_2\xi_2) \\ \lambda_2^4K_2(\lambda_2\xi_2) & \lambda_2^4K_1(\lambda_2\xi_2) & K_4(\lambda_2\xi_2) & K_3(\lambda_2\xi_2) \\ \lambda_2^4K_3(\lambda_2\xi_2) & K_2(\lambda_2\xi_2) & \lambda_2^4K_1(\lambda_2\xi_2) & K_4(\lambda_2\xi_2) \end{pmatrix}.$$

Then the state of the second segment describes the matrix equation

$$\bar{W}_2(\xi_2) = V_2(\xi_2)\bar{W}_{20}. \tag{3.18}$$

From conditions of conjugation of segments areas has

$$\bar{W}_1(\nu) = \bar{W}_2(0) \ \text{ or } \ V_1(\nu)\bar{W}_{10} = V_2(0)\bar{W}_{20}.$$

Given that $V_2(0)$ – the identity matrix, we obtain $\bar{W}_{20} = V_1(\nu)\bar{W}_{10}$ and, consequently, from (3.18) we have $\bar{W}_2(\xi_2) = V_2(\xi_2)V_1(\nu)\bar{W}_{10}$.

Those: state at both segments is determined by the parameters of the first segments.

State at the end of the second segment when $\xi_2 = 1-\nu$ determined by the vector $\bar{W}_2(1-\nu)$

$$\bar{W}_2(1-\nu) = V_2(1-\nu)V_1(\nu)\bar{W}_{10} = V_{21}(1-\nu,\nu)\bar{W}_{10}. \tag{3.19}$$

Here the matrix of influence $V_{21}(1-\nu,\nu) = V_2(1-\nu)V_1(\nu)$.

Two initial parameter known $w_{10} = w'_{10} = 0$.

There are also known two components of the vector of state at the end of the second segment

$$W(1-\nu) = W_2'(1-\nu) = 0.$$

Substituting these values in the matrix equation (3.19), written in block form, we obtain

$$\begin{pmatrix} \begin{pmatrix} 0 \\ 0 \end{pmatrix} \\ \begin{pmatrix} W_2''(1-\nu) \\ W_2'''(1-\nu) \end{pmatrix} \end{pmatrix} = \begin{pmatrix} \begin{pmatrix} c_{11} & c_{12} \\ c_{21} & c_{22} \end{pmatrix} & \begin{pmatrix} c_{13} & c_{14} \\ c_{23} & c_{24} \end{pmatrix} \\ \begin{pmatrix} c_{31} & c_{32} \\ c_{41} & c_{42} \end{pmatrix} & \begin{pmatrix} c_{33} & c_{34} \\ c_{42} & c_{44} \end{pmatrix} \end{pmatrix} \begin{pmatrix} \begin{pmatrix} 0 \\ 0 \end{pmatrix} \\ \begin{pmatrix} w_{10}'' \\ w_{10}''' \end{pmatrix} \end{pmatrix}.$$

Whence

$$\begin{pmatrix} c_{13} & c_{14} \\ c_{23} & c_{24} \end{pmatrix} \begin{pmatrix} w_{10}'' \\ w_{10}''' \end{pmatrix} = 0. \tag{3.20}$$

The frequency equation is obtained by equating to zero the determinant

$$\begin{vmatrix} c_{13} & c_{14} \\ c_{23} & c_{24} \end{vmatrix} = 0, \tag{3.21}$$

where

$$C_{13} = K_4(\lambda_2(1-\nu))K_2(\lambda_1\nu) + K_3(\lambda_2(1-\nu))K_3(\lambda_1\nu) + K_2(\lambda_2(1-\nu))K_4(\lambda_1\nu) + \lambda_1^4 K_1(\lambda_2(1-\nu))K_1(\lambda_1\nu).$$

$$C_{14} = K_4(\lambda_2(1-\nu))K_1(\lambda_1\nu) + K_3(\lambda_2(1-\nu))K_2(\lambda_1\nu) + K_2(\lambda_2(1-\nu))K_3(\lambda_1\nu) + K_1(\lambda_2(1-\nu))K_4(\lambda_1\nu).$$

$$C_{23} = \lambda_2^4 K_1(\lambda_2(1-\nu))K_2(\lambda_1\nu) + K_4(\lambda_2(1-\nu))K_3(\lambda_1\nu) + K_3(\lambda_2(1-\nu))K_4(\lambda_1\nu) + \lambda_1^4 K_2(\lambda_2(1-\nu))K_1(\lambda_1\nu).$$

$$C_{24} = \lambda_2^4 K_1(\lambda_2(1-\nu))K_1(\lambda_1\nu) + K_4(\lambda_2(1-\nu))K_2(\lambda_1\nu) + K_3(\lambda_2(1-\nu))K_3(\lambda_1\nu) + K_2(\lambda_2(1-\nu))K_4(\lambda_1\nu).$$

Figure 4 shows the dependence of the two frequencies of the free vibrations of the beam from relative stiffness of grounds for different sizes of the damaged area of the foundation

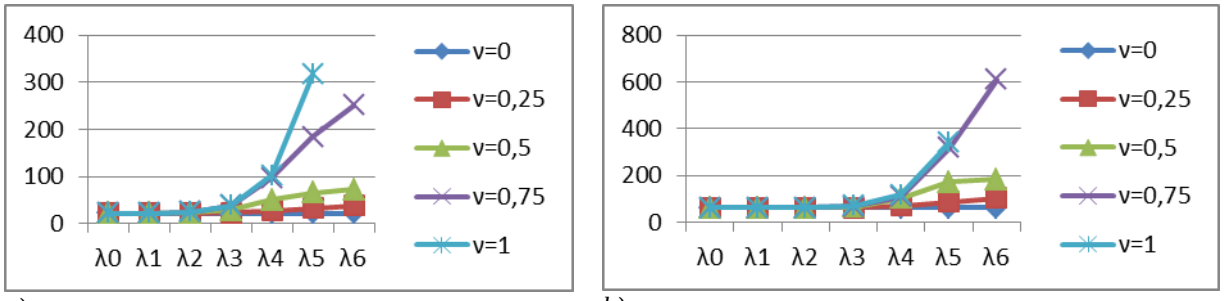

a) *b)*

Figure 4: The natural frequencies of flexural vibrations damaged beam: *a)* – first, *b)* – second.

4 FORCED VIBRATIONS BEAM PARTIALLY SUPPORTED ON THE ELASTIC FOUNDATION

Forced vibrations of the beam consisting of two segments, formed after the partial destruction of the foundation, described by corresponding non-homogeneous equation

$$\frac{\partial^4 w_1}{\partial \xi_1^4} + 4\alpha^4 w_1 + \frac{\partial^2 w_1}{\partial \tau^2} = q' \quad \text{and} \quad \frac{\partial^4 w_2}{\partial \xi_2^4} + \frac{\partial^2 w_2}{\partial \tau^2} = \bar{q} \tag{4.1}$$

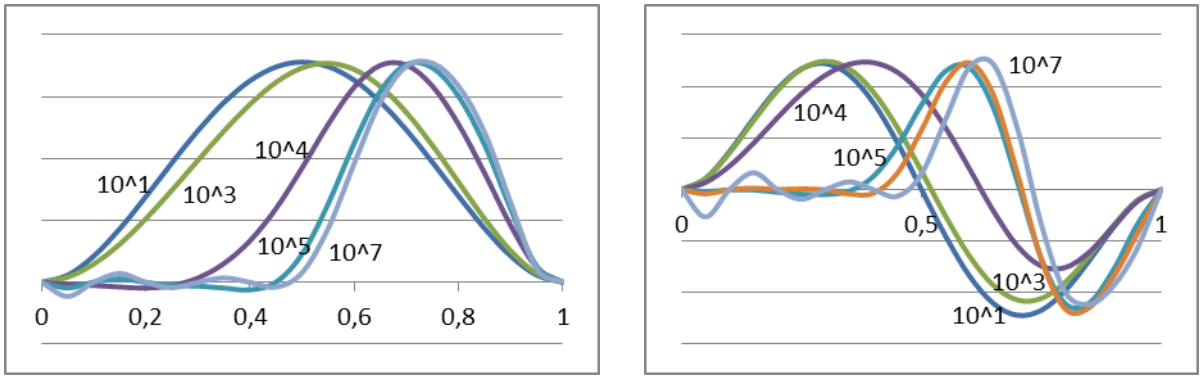

a) *b)*

Figure 5: Forms of free vibration of the beam: *a*) – first , *b*) – second.

Expending movement $w_i(\xi_i,\tau)$ (i = 1, 2) in the forms of natural vibrations (3.13) and (3.18), respectively, with coefficients in the form of well-known functions of time using orthogonal forms of natural vibrations, satisfying the initial conditions

$$w_i(\xi_i,0) = w_{cm}(\xi_i), \quad \left.\frac{\partial w_i}{\partial \tau}\right|_{\xi_i,0} = 0 \tag{4.2}$$

obtain function of deflection on segments [11]

$$w_i(\xi_i,\tau) = \sum_{n=1}^{\infty}\left[\frac{\int_0^{\nu_i} w_{cm}(\xi)W_{in}(\xi)d\xi}{\int_0^{\nu_i} W_{in}^2(\xi)d\xi}\cos\bar{\omega}_n\tau + \frac{2\bar{q}\int_0^{\nu_i}(\xi)W_{in}(\xi)d\xi}{\bar{\omega}_n^2\int_0^{\nu_i} W_{in}^2(\xi)d\xi}\sin^2\frac{\bar{\omega}_n\tau}{2}\right]W_{in}(\xi), \tag{4.3}$$

where $\nu_1 = \nu, \quad \nu_2 = 1-\nu.$

5 A NUMERICAL EXAMPLE

Reinforced concrete beam length L = 6,7 *m*, rectangular cross-section with sides of width b = 0,25 *m*, height h = 0,18 *m*, moment of inertia of the cross-section of the $I = 1{,}215\cdot10^{-4}\,m^4$, Young's modulus of the beam material $E = 3{,}05\cdot10^{10}\frac{N}{m^2}$. Material of foundation – a ballast layer of crushed stone with module $K_1 = 75\frac{MPa}{m}$. Coefficient of stiffness of foundation $K = K_i b = 18{,}75\cdot10^6\,Pa$. Parameter $\bar{\lambda} = \frac{KL^4}{EI} \approx 10^4$. Setting ends beams are clamped. The beam is loaded with a uniformly distributed load of intensity $q = 13{,}5\frac{kN}{m}$ (brick wall height of 3 *m*, a length of 6.7 *m*, a thickness of 0.25 *m*, the proportion of the material $18\frac{kN}{m^3}$).

In the initial (unstrained) state the maximum bending moment $\bar{M}_{\max 0} = 0{,}099\bar{q}$, $\bar{M} = \frac{ML}{EI}$, $\bar{q} = \frac{qL^3}{EI}$. Normal stress $\sigma = 39\frac{kg}{cm^2}$.

Table 1 contains the ratios $K_{quasi} = \frac{M_{quasi}}{M_{st.}}$ and $K_{dinam} = \frac{M_{dinam}}{M_{st.}}$ increasing the maximum bending moment in the beam at different degrees, respectively, quasi-static and sudden damage to the base

The degree of damage, $1-\nu$	1	0,75	0,5	0,25	0
Quasi-static, K_{quasi}	1	1,41	3,53	6,56	8,33
Sudden, K_{dinam}	1	1,57	4,52	11,29	14,53

Table 1: Splash of max bending moment at the foundation damage.

6 CONCLUSIONS

A mathematical model of free transverse vibrations of simply supported beam partially on an elastic Winkler foundation. The beam appears conjugation of two segments, one of which is fully supported by the foundation, the other is free. The spectrum of the natural frequencies of the beam on the foundation of partial damage frequency is determined by the equation obtained procedure similar to that used in the finite element method (FEM) in the construction of finite element stiffness matrix. We introduce four component vectors of the state – the dimensionless deflection, turn the cross-section, the bending moment and shear force. In matrix form obtained according to the state vectors in an arbitrary section of the vector of initial parameters. Vectors of state presented a set of blocks, including kinematic and power parameters. This matrix is the influence of the initial section of the cell becomes final, always 4×4. The frequency equation is obtained by equating the determinant of this matrix is zero. The use vectors of state, and the initial parameters of the procedure reduces the influence of the matrix to the fourth, with any number of mating parts of the beam, which significantly reduces the complexity of the calculations.

As a result, we obtained the relationship between the natural frequencies, the mechanical characteristics of the beam and the foundation and damage parameters: the length of the damaged portion of the foundation and its localization in the overall length of the beam.

REFERENCES

[1] V.A. Gordon, V.I. Brusova, E.A. Kravtsova, T.V. Poturaeva, Mathematical modeling of dynamic processes in the core system to the sudden changes in their structure, *Fundamental and applied problems of engineering and technology*, **5(283)**, 3-9, 2010.

[2] V.A. Gordon, V.I. Kolchunov, Y.S. Stepanov, Dynamical processes analysis in the load beams during partial destruction, *Proceedings of XVII International congress on sound and vibration*, Cairo, Egypt, July 18-22, 2010.

[3] V.A. Gordon, V.I. Kolchunov, Y.S. Stepanov, Dynamic loading of composite beam with the sudden longitudinal stratification, *Proceedings of XIX International congress on sound and vibration*, Vilnius, Lithuania, July 8-12, 2012.

[4] P.E. Doyle, M. Pavlovic, Vibration of beams on partial elastic foundation, *Earthquake Engineering and Structural Dynamics*, **10**, 663-674, 1982.

[5] M. Eisenberger, D.Z. Yankelensky, M.A. Adin, Vibration of beams fully or partially supported on elastic foundation, *Earthquake Engineering and Structural Dynamics*, **13**, 651-660, 1985.

[6] A. Valsangkar, R.Pradhanang, Vibrations of beam-columns on two-parameter elastic foundations *Earthquake Engineering and Structural Dynamics*, **16**, 217-225, 1988.

[7] S. Kukla, Free vibration of a beam supported on a stepped elastic foundation, *Journal of Sound and Vibration*, **149(2)**, 259-265, 1991.

[8] S.E. Motaghian, M. Mofid, P. Alanjari, Exact solution to free vibration of beams partially supported by an elastic foundation, *Scientia Iranica A,* **18(4)**, 861-866, 2011.

[9] A. Cazzani, On the dynamics of a beam partially supported by an elastic foundation: an exact solution-set, *International Journal of Structural Stability and Dynamics,***13**, 8, 1350045 (30 pages), 2013.

[10] V.A. Gordon, O.V. Pilipenko, Vibration of loaded beam initiated by fully or partially destruction of the elastic foundation, *Proceedings XVII International congress on sound and vibration*, Florence, Italy, July 12-16, 2015.

[11] V.A. Gordon, T.V. Poturaeva, G.A. Semenova, Stress-strain state of the beam, in part simply supported on an elastic foundation, *Fundamental and applied problems of engineering and technology*, **5-2**, 57-68, 2015.

[12] V.A . Gordon, T.V. Poturaeva, Frequencies free flexural vibrations of a freely supported beam with a crack, *Building mechanics and calculation of constructions*, **3**, 19-23, 2009.

[13] T.V. Poturaeva, V.A. Gordon, Dynamic loading freely supported beams initiated the formation of a crack , *Construction and reconstruction*, **4(24)**, 28-33, 2009.

[14] V.A. Gordon, E.A. Kravtsova, Effect of longitudinal stratification of the composite rod in the natural frequency of the flexural vibrations, *Building mechanics and calculation of constructions*, **1**, 19-24, 2011.

[15] V.A .Gordon, E.A .Kravtsova, Dynamic loading in the beam with multilevel longitudinal stratification, *Construction and reconstruction*, **6(44)**, 17-27, 2012.

[16] V.A. Gordon, E.A. Kravtsova, Methods of determining the spectrum of frequencies of flexural vibrations of the beam with multilevel longitudinal stratification, *Fundamental and applied problems of engineering and technology*, **2-5(292)**, 87-95, 2012.

[17] V.A. Gordon, T.A. Pavlova, Dynamic processes in the composite plate with a sudden longitudinal stratification, *Proceedings of the TulaSU. Series: Building materials, design and construction*, 40-49, 2006.

[18] V.A. Gordon, Y.S. Stepanov, P.N. Anokhin, Transitional processes in the constructions with the sudden structural reconstructions, *Proceedings XV International congress on sound and vibration*, Daejeon, Korea, July 6-10, 2008.

[19] V.A. Gordon, N.V. Klyueva, V.I. Brusova, Axisymmetric vibrations of circular plates with a sudden change of support conditions, *Building mechanics and calculation of constructions*, **1**, 41-43, 2009.

[20] V. A. Gordon, Y.S. Stepanov, V.S. Shorkin, Concepts for estimating of structural safety of bar system, *Proceedings XII International congress on sound and vibration*, Lisbon, Portugal, July 11-14, 2005.

[21] N.V. Klyueva, V.A. Gordon, Calculation of dynamic spatial loading in core system suddenly shuts down elements, *Building mechanics of engineering structures*, **6**, 72-79, 2008.

[22] V.A .Gordon, V.I. Brusova ,The transition process in the load beam at a detachment of the longitudinal layer ,*Construction and reconstruction*, **4(24)**, 8-10, 2009.

[23] T.V. Poturaeva, Transient dynamic process in the core design with a sudden change of support conditions, *Fundamental and applied problems of engineering and technology*, **4(272)**, 27-31, 2008.

[24] V.A. Gordon, T.V. Poturaeva, Evaluation of the dynamic effect of a sudden restructuring of the construction, *Fundamental and applied problems of engineering and technology*, **1**, 3-8, 2008.

[25] V.A. Gordon, A.G. Tamrazyan, T.V. Savostikova, Dynamic stress reinforcing bar with a sudden crack formation, *Herald SIC "Construction*", **2**, 167-176, 2010.

ECCOMAS Congress 2016
VII European Congress on Computational Methods in Applied Sciences and Engineering
M. Papadrakakis, V. Papadopoulos, G. Stefanou, V. Plevris (eds.)
Crete Island, Greece, 5–10 June 2016

RELIABILITY OF SYSTEMS EQUIPPED WITH VISCOUS DAMPERS WITH VARIABLE PROPERTIES

Andrea Dall'Asta[1], Laura Ragni[2], Fabrizio Scozzese[1*], Enrico Tubaldi[3]

[1] School of Architecture and Design, University of Camerino
Viale della Rimembranza, 63100 Ascoli Piceno (AP), Italy
{andrea.dallasta, fabrizio.scozzese}@unicam.it

[2] Department of Civil Engineering, Construction and Architecture, Polytechnic University of Marche
Via Brecce Bianche, 60131 Ancona (AN), Italy
laura.ragni@univpm.it

[2] Imperial College London
South Kensington Campus, London SW7 2AZ, UK
etubaldi@gmail.com

Keywords: Viscous damper, Reliability, Sensitivity, Subset Simulation.

Abstract. *Viscous dampers are energy dissipation devices widely employed for the seismic control of structures. The performance of systems equipped with viscous dampers has been extensively analyzed by employing deterministic approaches. However, these approaches neglect the response dispersion due to the uncertainties in the input as well as in the structural system properties. Some recent works highlighted the important role of these uncertainties in the seismic performance of systems with linear or nonlinear viscous dampers. The present study focuses on the uncertainty in the damper properties and it aims at evaluating its influence on the probabilistic response of the damped system. In particular, the variability of the damper properties is assumed to be constrained by the tolerances allowed in qualification and production control tests. A preliminary study on the damper response is carried out to relate the constitutive damper characteristics to the parameters controlled in the experimental tests and to evaluate the consequences of damper parameter variations on the dissipation properties of the device. In the subsequent part of the study, the response hazard curves, providing the relation between the values of the response parameters of interest and the relevant yearly exceedance probability, are evaluated. In the analyses, a simplified structural system is considered, and the Subset Simulation (SS) algorithm is employed together with the Markov Chain Monte Carlo method to achieve a good estimate of small probabilities of exceedance. A sensitivity analysis, considering the expected variations in the damper properties, is finally carried out by employing the Augmented SS method to study the influence of the device acceptance ranges on the hazard curves.*

1 INTRODUCTION

Supplemental energy dissipation systems are widely employed for the seismic control of new and existing structures. In particular, viscous dampers provide an efficient tool to dissipate the seismic input energy into heat, by reducing both the displacement and force demand in the structures [1, 2]. To date, the performance of systems equipped with viscous dampers has been extensively analyzed by employing deterministic approaches neglecting the response dispersion due to the uncertainties in the input as well as in the structural system properties.

However, these deterministic approaches provide only an approximate assessment of the seismic performance [3]. Some recent works have highlighted the important role of the uncertainties in the seismic performance of structures equipped with viscous dampers [4, 5, 6, 7] and the different propagation of ground motion uncertainties in systems equipped with linear or nonlinear viscous dampers [8, 9, 10]. The present study focuses on the influence of the uncertainties in the damper properties. In the approach suggested by codes and followed in practical design [11, 12, 13, 14], this uncertainty is bounded by the tolerances allowed in the qualification and production control tests. Consequently, design procedures usually involve a safety check based on the responses obtained by upper and lower bounds of the damper properties, chosen coherently with the test tolerances. However, the actual level of safety provided by the suggested design procedures is a problem requiring further investigation, as pointed out in [10], and the relevance of this topic is mainly due to the low robustness inherent to the structure-dampers system, where the unexpected dissipative device failure can lead to a progressive collapse of the potentially non-ductile structure.

The present paper aims at evaluating the influence of these allowed tolerances in the probabilistic performance of the system, by providing useful information on the exceedance probability of the response parameters of most interest for the performance assessment (as described by response hazard curves) and by using an approach to the problem that is more efficient and reliable with respect to those used in previous studies on the same topic.

A preliminary analysis of the damper response is developed to relate the damper constitutive characteristics to the parameters controlled in the experimental tests and to analyze the variation in the dissipation properties of the device.

In the subsequent part of the study, response hazard curves are developed by employing a simplified model of the structural system. These curves provide the relation between the values of the response parameters of interest and the relevant yearly probability of exceedance. A sensitivity analysis, considering the expected variations in the damper properties, is then carried out to assess the influence of the device acceptance ranges on the hazard curves. The response measures considered include the maximum values of the deformation, related to the damage of the structural system and the damper failure [15], and the maximum values of the relative velocity, related to the damper force. The model uncertainties considered in the applications concern the earthquake scenario parameters and the ground motion characteristics, while other uncertainties concerning the structure response are neglected [16, 17]. The numerical applications, involving both linear and nonlinear viscous dampers show that tolerances allowed in the tests provide notable differences among the observed values of the response parameters of interest.

It is noteworthy that the probabilistic response of the system was analyzed in the previous studies by employing approaches consistent with the PEER framework [18]. This latter is a widely employed framework that permits a separation of the tasks related to the seismic hazard, structural vulnerability and expected losses assessment. The application of the framework is usually based on a description of the seismic input in terms of a small set of real records.

This approach does not permit to achieve an accurate estimate of small failure probabilities. For this reasons, in this study the Subset Simulation algorithm with Markov Chain Monte Carlo method are employed to obtain a good estimate of small probabilities of exceedance [19]. Coherently with this approach, the Augmented SS method is used for the sensitivity analysis [20]. This simulation techniques require a seismological stochastic model and the one proposed in [21, 22] has been used for the analyses.

2 DAMPER RESPONSE SENSITIVITY

The response of viscous damper is usually described by an exponential constitutive law in the form [23, 24]

$$F_d = c|v|^{\alpha}\,\mathrm{sgn}(v) \tag{1}$$

where F_d is the measured force and c and α are two constitutive parameters: the former is a multiplicative factor while the latter describes the nonlinear behaviour ($\alpha = 1$ for the linear case).

In a sensitivity study aiming at evaluating the consequences of variations of the damper parameters on the system performance, these two parameters could be assumed to vary freely.

However, the experimental procedure for the production controls suggest a different approach to the sensitivity analysis, involving characteristic parameters directly linked to the experimental test results, as explained hereafter. In general, the design is based on a target value of the maximum velocity v_0 attained at a circular frequency $\omega_{0,test}$ relevant to the seismic response, and the production control tests are oriented to check the damper behavior at this design condition. More precisely, sinusoidal cycles simulating the design conditions, i.e., the displacement histories $u(t) = v_0 / \omega_{0,test} \sin(\omega_{0,test} t)$, are imposed to the damper and the corresponding maximum damper force $F_{d,test}$ is measured. Some tolerance is allowed in the force value and acceptance criteria usually requires that the difference between the measured value of the maximum force $F_{d,test}$ and the expected (design) value $F_{d0,test}$ is lower than +/- $pF_{d0,test}$ [11, 12, 13]. The safety check is coherently carried out by considering the worst conditions compatible with the acceptance criteria [11, 12, 13], by adopting a lower/upper bound approach.

In this context, rather than investigating the system response by considering a free variation of the constitutive parameters it is more useful to link the variability of the response to the outcomes of the acceptance tests. Thus, in this study the response is investigated by assuming p, describing the acceptance tolerance $pF_{d0,test}$, as a system parameter and by introducing a second parameter λ to identify the different pairs (c,α) providing the same force variation $pF_{d0,test}$. The pairs (c,α) satisfying the equality constraint lie on a curve, whose parametric expression is made explicit. Let c_0 and α_0 denote the reference values assumed in the structural design. A variation $(\hat{c},\hat{\alpha})$ of the constitutive parameters provides the following variation $\hat{F}_{d0,test}$ of the maximum force $F_{d0,test}$ expected in the sinusoidal test

$$\hat{F}_{d0,test} = F_{d,test} - F_{d0,test} = F_{d0,test}\left[\left(1+\frac{\hat{c}}{c_0}\right)\cdot(v_0)^{\hat{\alpha}} - 1\right] \tag{2}$$

The equation clearly shows that both $\hat{c}$ and $\hat{\alpha}$ contribute to this variation and the previous expression can be rewritten by introducing the tolerance parameter p as

$$p = \left(1 + \frac{\hat{c}}{c_0}\right) \cdot (v_0)^{\hat{\alpha}} - 1 \tag{3}$$

It is evident (Figure 1) that the same variation p can be obtained by different pairs $(\hat{c}, \hat{\alpha})$ and the constraint between these parameters can be described by introducing the parameter λ

$$\hat{c}(p, \lambda) = c_0 \frac{1+p}{(v_0)^{\lambda}} - 1 \tag{4}$$

$$\hat{\alpha}(p, \lambda) = \lambda \tag{5}$$

so that the pair (p, λ) provides a representation of the response variability that is alternative to the representation provided by $(\hat{c}, \hat{\alpha})$. The condition λ=0 coincides with a force variation due only to a variation of the response scale factor $\hat{c}$ =p, whereas the other values describe a force variation p involving a combination of $\hat{c}$ and $\hat{\alpha}$.

To complete the preliminary analysis of the damper variability effects, a linearized form of the previous relationship between the constitutive parameters is derived. This form can be of interest in the sensitivity analysis of problems where eqn(1) is the only source of nonlinear behaviour and the local response variation can be conveniently approximated by analytical linear operators [25, 26, 27]. The relationships corresponding to eqns(3-5) are

$$p = \frac{\hat{c}}{c_0} + \ln(v_0)\hat{\alpha} \tag{6}$$

$$\hat{c} = c_0[p - \lambda \ln(v_0)] \tag{7}$$

$$\hat{\alpha} = \lambda \tag{8}$$

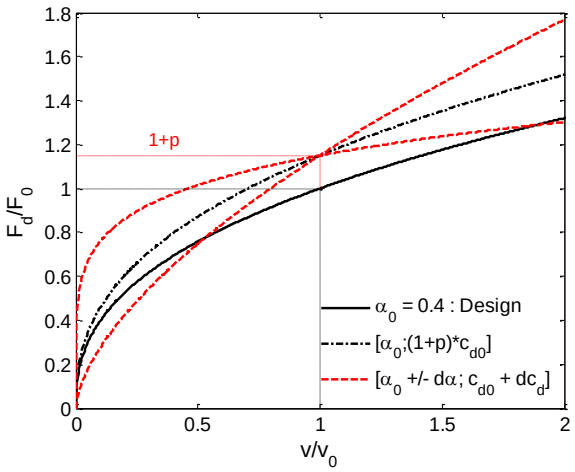

Figure 1: Variations allowed for the damper response.

Figure 2 shows the parametric curves containing the pairs $(\hat{c}, \hat{\alpha})$, evaluated for 3 values of the force variation factor p. The 3 cases reported correspond to p = - 0.3, p = 0.0, p = + 0.3.

These curves are obtained by intersecting the surfaces provided by eqn.(3) (nonlinear expression) and by eqn.(6) (linear approximation) with horizontal planes identifying the force variations. The results concerning the case of linear viscous damper (α =*1*) and nonlinear viscous damper with α =*0.2* are reported respectively in Figure 2a and Figure 2b. It can be ob-

served that the differences between the results obtained by using the nonlinear (exact) and the linear approximation become negligible in the case of the nonlinear damper. In this latter case, a notable percentage variation of α is linked to very small variation of c.

The energy dissipation properties are analyzed and reported in Figure 3. The energy dissipated in a cycle at the design conditions is denoted by W_{d0}. The corresponding energy dissipated in the same test by a damper with different properties depend on p and λ and it is denoted by W_d. Figure 3 shows the values of the ratio W_d / W_{d0} obtained by varying the parameters. The solid lines correspond to the results measured for fixed values of the force factor p. The cases $p = -0.30, -0.15, 0, 0.15, 0.30$ are reported and the points of these curves describe the variations relevant to different pairs $(\hat{c}, \hat{\alpha})$. Dashed lines connect the points with the same variation of c. Results of Figure 3a refer to a linear viscous damper and Figure 3b refers to a nonlinear viscous damper with $\alpha = 0.2$. Given a value of the force factor p, the energy dissipated changes significantly by varying the pair $(\hat{c}, \hat{\alpha})$. Higher values of $\lambda = \alpha$ result in a reduction of the dissipative properties and this trend is more evident in the linear case. The discussed trend of the dissipation properties are valid in the neighborhood of the design conditions and different trends are observed for cycles with larger (or smaller) amplitudes which can be representative of the response for seismic inputs with intensity levels higher (or lower) than the design one.

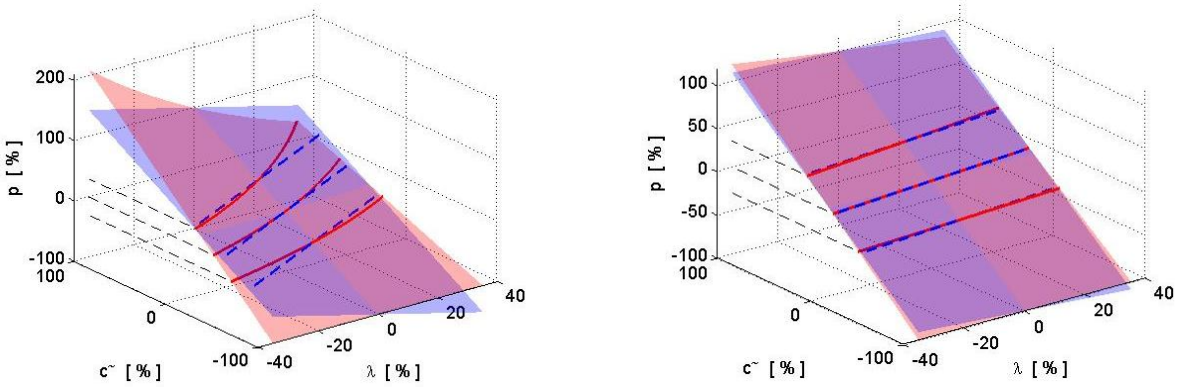

Figure 2: Linear/nonlinear p-α–c_d relationships for different p values (-30; 0; +30 %): a) α_0 = 1.0; b) α_0 = 0.2.

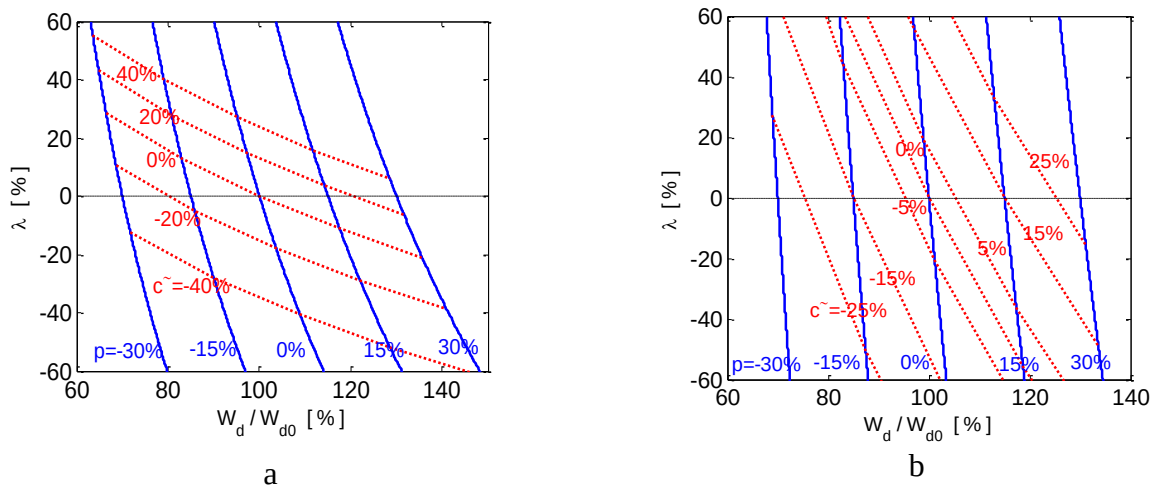

Figure 3. Dissipated energy variation in cyclic paths (amplitude 0.0454m, circular frequency 2π)

3 SEISMIC RESPONSE SENSITIVITY

3.1 Seismic performance

The seismic assessment and design of structures is usually carried out by evaluating via structural analysis the statistics of one (or more) response parameter of interest D and by ensuring that the $P[D > d^*]$ of exceedance of a fixed threshold d^* is lower than an acceptable value P^*. The random variable D can be expressed in terms of the ratio between a performance demand and the relevant capacity, so that a unitary threshold implies failure at ultimate condition. This way, D accounts for the uncertainties in the loading actions, in the model and the capacity. Typical response parameters employed in the context of the performance assessment of buildings with viscous dampers are: inter-storey drifts, absolute accelerations at storey, total base shear, forces on dampers, strokes on dampers.

Code design and assessment procedures aim at satisfying the reliability constraint in an indirect way, as they evaluate a conventional demand measure $d_0 < d^*$ which is obtained from loadings of intensity whose exceedance probability P_0 is lower than the acceptable probability P^* [3]. Amplification factors are usually considered to pass from d_0 *to* d^*.

In the specific case of the seismic analysis of buildings equipped with dampers, the design is carried out by evaluating the response for seismic events with a mean annual frequency of occurrence varying from $1 \cdot 10^{-2}$ (service limit state) to $2 \cdot 10^{-3}$ (ultimate limit state) [11, 28, 29] while the safety target requires that the probability of failure is lower than 10^{-5} -10^{-6} [11, 29].

In order to relate the design condition, described by the pairs (d_0, P_0), to the effective system reliability, described by the couple (d^*, P^*), it is useful to evaluate the response hazard function

$$G_d(d) = P[D > d] \tag{9}$$

associating a generic value of the response parameter threshold d to the corresponding probability of exceedance. The conventional design value d_0 can be linked to the response value associated to a given probability of exceedance by introducing the inverse function $G_D^{-1}(P)$ and defining the ratio

$$\gamma(P) = \frac{G_d^{-1}(P)}{d_0} \tag{10}$$

This ratio can be interpreted as the amplification factor for the design value d_0 providing the response parameter value corresponding to the desired probability of exceedance.

Design procedures generally do not involve a probabilistic analysis but aim at providing the value of d_0 by means of a deterministic analysis. For example, the seismic design is usually based on the description of the seismic input in terms of a pseudo-acceleration response spectrum and a reduced set of (artificial or natural) ground motions accounting for the record-to-record variability effects. The conventional design value of the response d_0 is obtained as the mean of the maximum response values. This design approach introduces further sources of approximation in the evaluation of the system reliability which are not addressed in this work.

3.2 Response hazard curve evaluation

Let X be the vector of the random variables of the system lying in the domain Ω, including both the variables describing the ground motion, for which a stochastic model is required,

and the structural system uncertainties. The system parameters are described by the vector $\vartheta \in \Gamma$, collecting the damper parameters p and λ, as discussed in the previous section.

The failure corresponds to the region of response events such that $G_d(d \mid \vartheta) = \{x : g_d(x \mid \vartheta) > d\}$, having denoted with $g_d(x \mid \vartheta)$ the response function providing the value of the parameter d, once the sample x and the parameters ϑ are assigned. The response hazard function can be obtained as

$$G_d(d \mid \vartheta) = \int_{\Omega} I_d(x \mid \vartheta) p_X(x) dx \tag{11}$$

where $p_X(x)$ if the probability density function (PDF) of the system variables and $I_d(x \mid \vartheta)$ is the indicator function, such that $I_d = 1$ if $x \in G_d(d|\vartheta)$ (equivalently $g_d(x|\vartheta) > d$), otherwise $I_d = 0$. In the following, it is assumed that the $p_X(x)$ is not influenced by the parameters ϑ, although the formulation can be extended to the general case $p_X(x|\vartheta)$ [20].

The sensitivity problem is approached by considering the augmented reliability problem proposed in [20], i.e., by considering ϑ as a fictitious random variable with arbitrary PDF $p_\Theta(\vartheta)$. By this approach, the response sensitivity can be estimated with the same simulations employed for estimating the reliability, thus significantly reducing the computational effort with respect to other approaches.

The response hazard function can be obtained through the Bayes' Theorem in the form

$$G_d(d \mid \vartheta) = \frac{p_\Theta(\vartheta \mid d)}{\Theta(\vartheta)} G_d(d) \tag{12}$$

where

$$G_d(d) = \int_{\Omega x \Gamma} I_d(x \mid \vartheta) p_X(x) p_\Theta(\vartheta) dx d\vartheta \tag{13}$$

and

$$p_\Theta(\vartheta \mid d) = \frac{\int_{\Omega x \Gamma} I_d(x \mid \vartheta) p_\Theta(\vartheta) d\vartheta}{G_d(d)} \tag{14}$$

In this formulation, both X and ϑ are random variables and the probability of exceeding the threshold d is a rare event that can be efficiently evaluated by the Subset Simulation-Markov chain method [19].

3.3 Uncertainties description

The seismic event is described by defining a seismic source characterized in terms of moment magnitude M and source-to-site (hypocentral) distance R. The description of the uncertainty associated with the seismic input is completed by the specification of a stochastic ground motion model, considering the properties of the construction site. The intensity of the seismic event is described by the moment magnitude M and its uncertainty is modeled by the Gutenberg-Richter law defined on the interval $[m_{\min}, m_{MAX}]$ and corresponding to the following PDF of M given an earthquake event [30]:

$$p_M(m) = \frac{\beta e^{-\beta m}}{\beta e^{-\beta m_{\min}} - \beta e^{-\beta m_{MAX}}} \quad m \in [m_{\min}, m_{MAX}] \tag{15}$$

where $\beta = \ln(10)b$ is a parameter related to the number of the expected earthquakes per annum with magnitude exceeding m. More precisely, it is assumed that the occurrence of an event with $M > m$ is a Poisson process with exceedance frequency $\lambda(m) = 10^{a-bm}$ and no event is expected for $M > m_{MAX}$. It is also assumed that no significant response is observed for $M < m_{\min}$, so the response hazard function, referred to a time interval one year long, can be obtained as $G_d(d) = \left(1 - e^{-\lambda(m_{\min})}\right) P[D > d \mid M > m_{\min}]$ by starting from the outcomes of the subset procedure $P[D > d \mid M > m_{\min}]$.

The ground motion is generated by starting from a white noise $w(t)$, described by the N-dimensional vector $\mathbf{w}$ of values w_i assumed at the instant $t_i = i\Delta t$, where Δt is the finite time interval assumed for the numerical integration.

Following the Atkinson-Silva model [21, 22], the ground motion is obtained by modulating in time the white noise by means of the function $e(t)$, which yields the time-function $z(t) = e(t)w(t)$. The amplitude and the frequency content are obtained by multiplying its Fourier transform $\bar{z}(f)$ (normalized to have a mean square amplitude of unity) by the radiation spectra $\varepsilon_{\text{mod}} A(f)$, where $A(f)$ is a deterministic function of the frequency f while ε_{mod} is a random scaling factor describing the amplitude variability [31]. The final ground motion acceleration $a(t)$ is obtained by the inverse Fourier transform of $\bar{z}(f) \& A(f)$. The time modulating function and the radiation spectra A depend on the moment magnitude, the distance and the local characteristic of soil. The scaling factor ε_{mod} is a random variable with lognormal distribution and unit median value. Further details on the ground motion model are reported in Appendix 1.

The set of random variables $x = [m, r, \varepsilon, \mathbf{w}]$ consists of the three scalar quantities m, r, ε and the vector-valued quantity $\mathbf{w}$ whose dimension N depends on the discretization of the time interval.

The uncertainties on the structural system are not considered in this work, given their generally low influence on the probabilistic response when also the seismic randomness is taken into account [16, 17].

4 STRUCTURAL RESPONSE

The structural system considered in the study consists of a linear S-DoF system with period $T = 1.0s$ and damping rate $\xi = 0.05$. Two added dissipative systems are analyzed, the former is a linear system with $\alpha_0 = 1.0$ and the latter is a nonlinear system with $\alpha_0 = 0.2$.

For what concerns the seismic scenario, the following values have been assumed for the seismic hazard parameters $a = 4.5$, $b = 1.0$, $m_{\min} = 5$, $m_{MAX} = 8$. An hypocentral distance $R = 20km$ is assumed and the soil conditions are described by Vs=310 m/s. For the time discretization, a time-interval $\Delta t = 0.02s$ is considered, corresponding to *N=3750.*

The linear system viscous constant c has been designed to add a damping ratio $\xi_d = 0.3$ whereas the nonlinear system viscous constant has been calibrated to provide similar performances at the design conditions. More precisely, the equivalence has been established by considering the value assumed by the maximum displacement mean hazard curve $G_U(u_0)$ at P_0 as performance indicator. The two systems are characterized by very close values of u_0 for the probability of exceedance $P_0 = G_U(u_0)$=0.0021 (10% within 50 years); this probability value is usually assumed for the seismic design at ultimate limit conditions [11, 28, 29].

Table 1 reports the viscous damper properties (α_0 and the c_0) and the performances for the linear and nonlinear damped system at the design conditions. The response parameters considered for the performance comparison are: the maximum relative displacement U (controlling the construction damage and the damper failure), the maximum relative velocity V and the maximum force on the damper F_d (controlling the damper failure), and the maximum absolute acceleration A (controlling the damage of acceleration sensitive facilities).

Viscous Properties	α_0		1.00	0.20
	c_0/m	[g-s$^\alpha$/m$^\alpha$]	3.77	0.94
Performances	u_0	[m]	0.037	0.037
	v_0	[m/s]	0.276	0.285
	F_{d0}	[N]	208	146
	a_0	[m/s^2]	1.799	1.896

Table 1: Properties of the damping systems and relevant response at the design conditions.

Subset simulation analyses are performed to estimate the reliability of the damped systems for both the linear and nonlinear viscous dampers case. The first part of the next section compares the reliabilities of the reference systems (corresponding to the nominal damper properties), whereas the second part shows the effects of the variability of the damper viscous properties on the reliability. The probabilistic description of the system response is given in terms of hazard curves (complementary cumulative distribution function CCDF), providing the annual probability of exceedance for each relevant response parameters.

4.1 Probabilistic response at the reference conditions

In evaluating the seismic reliability of the systems at the reference conditions ($p = 0, \lambda = 0$), the set of uncertain parameters consists of those characterizing the earthquake excitation, i.e., magnitude, white-noise components and the model parameter ε_{mod}. As stated before (in Section 3.0), structural system parameters are assumed to be deterministic.

In order to estimate exceedance probabilities up to 10^{-6}, subset simulations are carried out using 6 conditional levels (with threshold levels identified by a percentile equal to 10%) with 600 samples/level and a total number of samples equal to 540x5 + 600 = 3300. The averaged result of 10 independent simulations are presented.

Because of the adopted design criteria, the linearly and nonlinearly-damped systems show the same displacement u_0 at the probability of exceedance P_0 while the other response parameters exhibit different values. The ratios between the demand parameters and the reference values corresponding to the design conditions are reported in the Figure 4, so the unit values are located at the probability of exceedance P_0 and the values reported in the horizontal axis coincide with the ratio introduced in eqn.10. The maximum response parameters corresponding to the probability of exceedance 10^{-6} are highlighted in the figure by the coloured dashed lines, and relevant numerical values are collected in Table 2.

The linear and nonlinear damped systems exhibit different probabilistic responses within a range of exceedance probabilities up to 10^{-6}. In fact, the exceedance probabilities of the maximum displacements and velocities are higher for the linear system than for the linear system, for values below the design value, and lower for values higher than the design value. An opposite trend is observed for the damper force, with the linear system requiring an higher strength capacity than the nonlinear one for rare seismic events. The accelerations show also a

different trend and the performance required by the nonlinear system are generally higher than those required by the linear system both for frequent and rare events. Qualitative trends observed are in agreement with results presented in previous studies obtained by conditional based approaches (PEER framework) [8, 10].

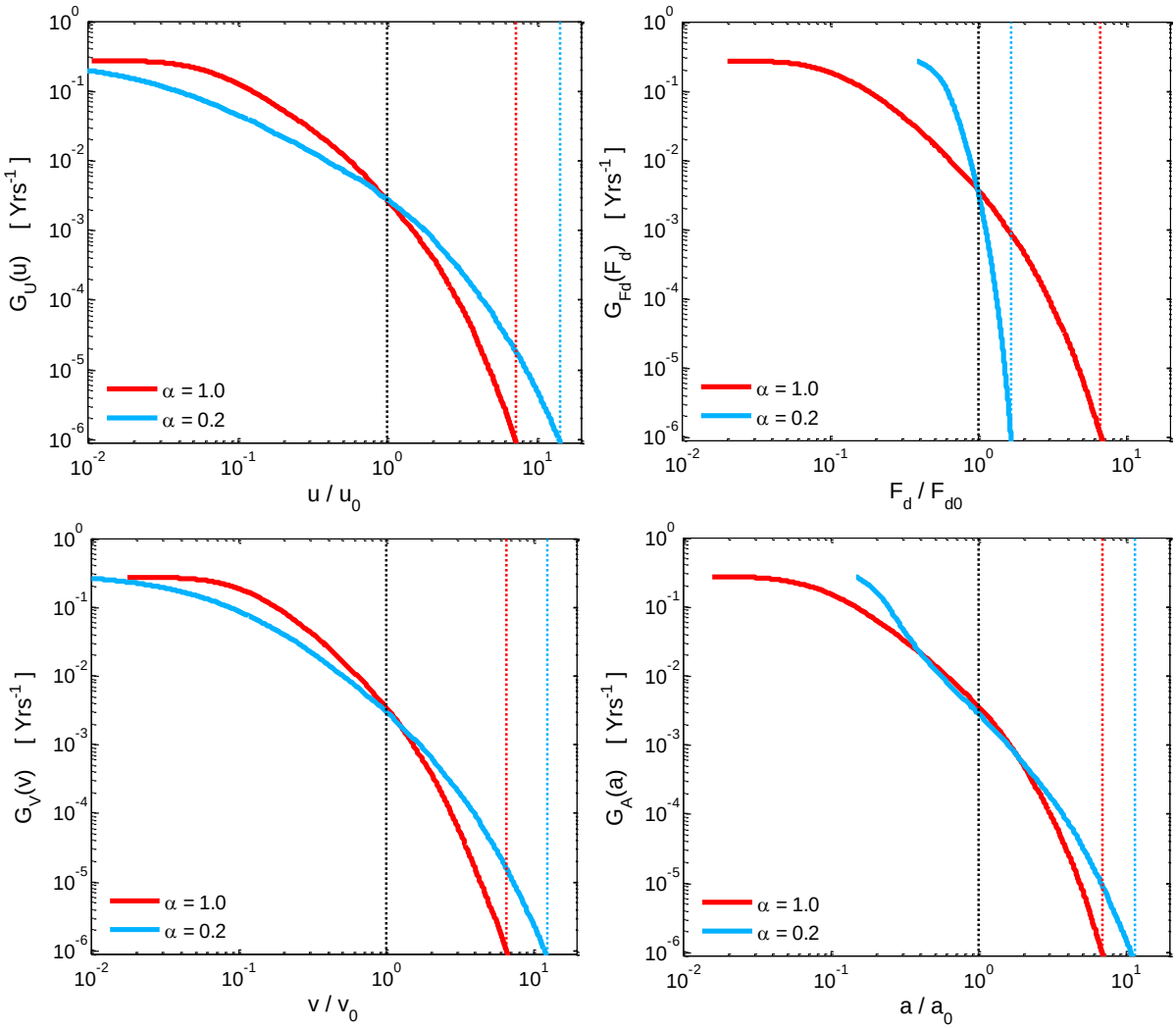

Figure 4. Normalized response hazard curves for linear (α=1.0) and nonlinear (α= 0.2) dampers.

α_0	1.00	0.20
$\gamma_U(P = 10^{-6})$	7.20	14.32
$\gamma_{Fd}(P = 10^{-6})$	6.93	1.65
$\gamma_V(P = 10^{-6})$	6.64	12.54
$\gamma_A(P = 10^{-6})$	6.86	11.39

Table 2: Numerical values of γ_d at $P = 10^{-6}$.

4.2 Effect of viscous damper properties variability

In this section, the influence of the variability of the viscous properties on the hazard curves is analyzed. The reference response evaluated in the previous section is compared with

the response obtained with the upper and lower bound of variations allowed in control production tests, as discussed in Section 2. The two limit values $p = \pm 0.15$ are assumed for the force $\hat{F}_{d0,test}$ measured in the test at the design conditions, according to the limits suggested in [13]. Once p is assigned, only the parameter λ varies and gives the possible pairs of constitutive parameter variations $\hat{\alpha}$ and $\hat{c}$ (see eqns. 4-5).

The system response sensitivity is carried out by considering an "augmented reliability problem" [20] in which the λ-variability is added to the seismic uncertainties previously introduced. In order to investigate a realistic field of variation in the damper response, a uniform distribution function on [-0.20,+0.20] is assumed for the system parameter, λ, in this case coinciding with the nonlinear exponent variation $\hat{\alpha}$. With the aim of increase the accuracy in the estimation of the exceedance probabilities a number of conditional samples greater than the number used in the previous section and equal to 1500 is used for each simulation level, for a total amount of samples equal to 1350x5 + 1500 = 8250. The range of the parameter variation has been discretized in 4 bins J_i (i=1,..,4), and the hazard curves of the two extreme bins, centered at $\lambda = \hat{\alpha} = \pm 0.15$ are reported in the following. An average of 50 independent simulations is used.

In Figures 5 the hazard curves of displacements, damper forces and absolute accelerations are plotted with a semi-logarithmic representation. Both the linear (left charts) and nonlinear (right charts) damped systems are considered, and the response parameters values are normalized by dividing them by the design value obtained in the reference design condition, as in the previous section. Each chart shows the reference curve (black solid line), a pair of blue dashed curves related to the upper bound $p = +0.15$ and describing the response variation for the two extreme bins of the parameter variation $\lambda = \pm 0.15$, a pair of red dashed curve related to the lower bound $p = -0.15$ and describing the response variation for the two extreme bins of the parameter variation $\lambda = \pm 0.15$

In the linear case, the perturbed condition with *p=-0.15* produces (moving towards the small probability range) an amplification on both the displacement and acceleration responses, while the opposite trend is observed for the damper force. The highest displacement variations occur when *p=-0.15* and λ is in the bin centred at the value λ*=-0.15*. This is a consequence of both the reduction of the damper force due to the negative value of *p* and the nonlinearity introduced by the negative variation of λ (α<1) in the system behaviour, which results in larger displacements for less probable events (see Figure 4 for *u* parameters). A different trend is observed for the forces, where the worst condition is represented by *p=+0.15*.

At the minimum probability of exceedance considered, the increment of the maximum displacement threshold is about 35% and the force threshold is about 20% while lower increments are observed for the absolute acceleration threshold.

Similar trends are shown in the nonlinear case where both the displacement and the acceleration demands grow for *p=-0.15*, while the damper forces increase when *p=+0.15*. However, in this case results are less sensitive to the parameter λ, expressing the percentile variation of the nonlinear exponent α.

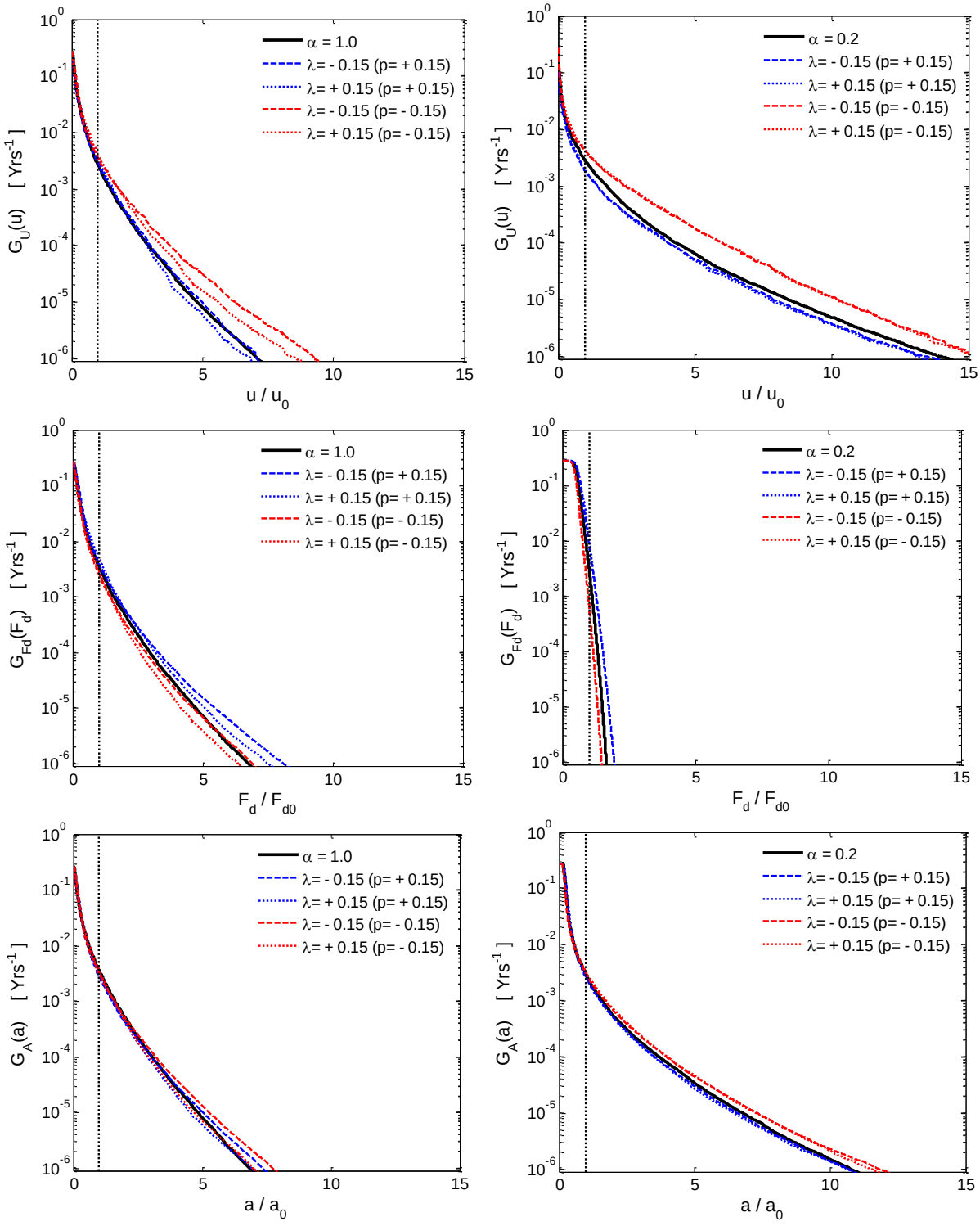

Figure 5. Effects on the response hazard curves due to the perturbation on the damper parameters.

5 CONCLUSIONS

The paper analyzes the influence of both the seismic uncertainties and the variability of the viscous damper behaviour on the probabilistic response of passively protected systems. The probabilistic response is evaluated by means of advanced statistical simulation methods (Subset simulation with Markov chains), able to furnish an accurate estimation of the demand hazard for low values of the exceedance probability.

The effects of the variability of the viscous damper properties coherent with the tolerance range allowed by the codes for device control tests is studied via reliability-sensitivity analysis. This analysis is performed by carrying Subset simulations on an "augmented reliability problem".

A comparison between the performances of two systems consisting of the same structure and of added linear (α=1) and nonlinear (α=0.2) viscous dampers is presented. The dampers are designed to achieve the same seismic performances (displacement response) at the usual design conditions suggested by codes of practice and corresponding to an annual probability of exceedance of 0.0021.

It is observed that the variability expected according to control production tests influences differently the response hazard curves for rare events. Considering probability of exceedance in the range 10^{-5}-10^{-6}, it is observed that some response parameters are more sensitive to the damper parameter variations than others. Liner and nonlinear cases exhibit similar trends of variation but the amount of the response variations are very different in the two cases.

Current design procedures are based on the estimation of the probabilistic response and relevant structural safety by means of amplification factors increasing conventional design values of the structural response. The results observed in this study provide a contribution towards a more reliable definition of these amplification factors.

6 ACKNOWLEDGEMENT

The study reported in this paper was sponsored by the Italian Department of Civil Protection within the Reluis-DPC Projects 2015. The authors gratefully acknowledge this financial support.

7 REFERENCES

[1] O. Lavan, G.F. Dargush, Multi-Objective Evolutionary Seismic Design with Passive Energy Dissipation Systems. *Journal of Earthquake Engineering*, **13**(6), 758-790, 2009.

[2] E. Pavlou, M.C. Constantinou, Response of Nonstructural Components in Structures with Damping Systems. *Journal of Structural Engineering*, **132**(7), 1108-1117, 2006.

[3] B.A. Bradley, A comparison of intensity-based demand distributions and the seismic demand hazard for seismic performance assessment. *Earthquake Engineering and Structural Dynamics*, **42**(15), 2235-2253, 2013.

[4] C.Y. Seo, T.L. Karavasilis, J.M. Ricles, R. Sause, Seismic performance and probabilistic collapse resistance assessment of steel moment resisting frames with fluid viscous dampers. *Earthquake Engineering and Structural Dynamics*, **43**(14), 2135-2154, 2014.

[5] I. Gidaris, A.A. Taflanidis, Performance assessment and optimization of fluid viscous dampers through life-cycle cost criteria and comparison to alternative design approaches. *Bulletin of Earthquake Engineering*, **13**, 1003-1028, 2015.

[6] E. Tubaldi, M. Barbato, A. Dall'Asta, Performance-based seismic risk assessment for buildings equipped with linear and nonlinear viscous dampers. *Engineering Structures*, **78**, 90-99, 2014.

[7] E. Tubaldi, M. Barbato, A. Dall'Asta, Efficient approach for the reliability-based design of linear damping devices for seismic protection of buildings. *ASCE-ASME Journal of Risk and Uncertainty if Engineering Systems, Part A: Civil Engineering, special issue on Stochastic Dynamics and Reliability Analysis of Structural and Mechanical Systems Subject to Environmental Excitations*. DOI: 10.1061/AJRUA6.0000858, 2015.

[8] E. Tubaldi, L. Ragni, A. Dall'Asta, Probabilistic seismic response assessment of linear systems equipped with nonlinear viscous dampers. *Earthquake Engineering and Structural Dynamics*, **44** (1), 101-120, 2014.

[9] E. Tubaldi, I.A. Kougioumtzoglou, Nonstationary stochastic response of structural systems equipped with nonlinear viscous dampers under seismic excitation. *Earthquake Engineering and Structural Dynamics* **44**(1), 121–138, 2015.

[10] A. Dall'Asta, E. Tubaldi, L. Ragni, Influence of the nonlinear behaviour of viscous dampers on the seismic demand hazard of building frames. *Earthquake Engineering and Structural Dynamics*, **45**(1), 149-169, 2016.

[11] ASCE/SEI 7-10. *Minimum Design Loads for Buildings and Other Structures*. American Society of Civil Engineers, Reston, Virginia, 2010.

[12] ASCE 41-13. *Seismic Evaluation and Retrofit of Existing Buildings*. American Society of Civil Engineers, Reston, Virginia, 2013.

[13] European Committee for Standardization. *EN 15129:2010 - Antiseismic devices*, Brussels, Belgium, 2010.

[14] European Committee for Standardization. *Eurocode 8-Design of Structures for Earthquake Resistance. Part 1: General Rules, Seismic Actions and Rules for Buildings*, Brussels, Belgium, 2004.

[15] H.K. Mijamoto, A.S.J Gilani, A. Wada, Viscous damper limit states and collapse analysis of steel frame buildings with dampers. *Proceedings of the 9th U.S. National and 10th Canadian Conference on Earthquake Engineering (EERI)*, Toronto, Ontario, Paper No 146, 2010.

[16] E. Tubaldi, M. Barbato, A. Dall'Asta, Influence of model parameter uncertainty on seismic transverse response and vulnerability of steel–concrete composite bridges with dual load path. *Journal of Structural Engineering*, **138**(3), 363-374, 2011.

[17] P.E Pinto, R. Giannini, P. Franchin, *Seismic Reliability Analysis of Structures, 1th Edition.* IUSS Press: Pavia, Italy, 2004.

[18] K.A. Porter, An overview of PEER's performance-based earthquake engineering methodology. *Proceedings of the 9th International Conference on Application of Statistics and Probability in Civil Engineering (ICASP9)*, San Francisco, California, 973-980, 2003.

[19] S.K. Au, J.L. Beck, Subset simulation and its applications to seismic risk based on dynamic analysis. *Journal of Engineering Mechanics (ASCE)*, **129**(8):901–917, 2003.

[20] S.K. Au, Reliability-based design sensitivity by efficient simulation. *Computer and Structure*, **83**(14) (2005) 1048–1061.

[21] G.M. Atkinson, W. Silva, Stochastic modeling of California ground motions. *Bulletin of the Seismological Society of America* **90**(2):255–274, 2000.

[22] D. M. Boore, Simulation of ground motion using the stochastic method. *Pure and Applied Geophysics*, **160**, 635–676, 2003.

[23] C. Christopoulos, A. Filiatrault, *Principles of Passive Supplemental Damping and Seismic Isolation*. IUSS Press: Pavia, Italy, 2006.

[24] M.G. Castellano, R. Borrella, S. Infanti, V. Gattulli, Experimental characterization of nonlinear fluid viscous dampers according to the New European Standard. *Proceedings of EACS 2012, 5th European Conference on Structural Control*. Genoa, Italy, June 18-20, 2012.

[25] A. Saltelli, K. Chan, E.M. Scott, *Sensitivity analysis. Wiley Series in Probability and Statistics*. Wiley, 2000.

[26] A. Zona, L. Ragni, A. Dall'Asta, Sensitivity-based study of the influence of brace over-strength distribution on the seismic response of steel frames with BRBs. *Engineering Structures*, **37**, 179-192, 2012.

[27] H.A. Jensen, F. Mayorga, M.A. Valdebenito, Reliability sensitivity estimation of nonlinear structural systems under stochastic excitation: A simulation-based approach. *Computer Methods in Applied Mechanics and Engineering*, **289**, 1–23, 2015.

[28] JCSS. *Probabilistic Model Code: Part 1: Basis of Design*. Joint Committee on Structural Safety, 2000.

[29] European Committee for Standardization. *Eurocode 0-Basis of structural design*. Brussels, Belgium, 2002.

[30] B. Gutenberg, C. Richter, Earthquake magnitude, intensity and acceleration. *Bulletin of the Seismological Society of America*, **62**(2), 105–145, 1958.

[31] F. Jalaye, J.L. Beck, Effects of two alternative representations of ground-motion uncertainty on probabilistic seismic demand assessment of structures. *Earthquake Engineering and Structural Dynamics* **37**(1):61–79, 2008.

[32] D. M. Boore, W.B. Joyner, Site amplifications for generic rock sites. *Bull. Seismol. Soc. Am.*, **87**(2), 327–341, 1997.

8 APPENDIX 1 - DETAILS OF ATKINSON-SILVA MODEL

The Atkinson-Silva ground motion model [21] used in this work is characterized by the radiation spectrum *A(f)* and the time modulating function *e(t).* The radiation spectrum gives a spectral representation of the ground motion at the construction site, accounting for several physical contributions influencing the wave propagation. Its analytical expression is

$$A(f) = \varepsilon_{\text{mod}} A_0(f) \cdot A_n(f) \cdot P_f(f) \cdot V(f) \tag{16}$$

The (two corner frequencies) point-source spectrum is represented by $A_0(f)$

$$A_0(f) = C \cdot M_0 \cdot (2\pi f)^2 \cdot \left((1-\varepsilon) \cdot \frac{1}{1+(f/f_a)^2} + \varepsilon \cdot \frac{1}{1+(f/f_b)^2} \right) \tag{17}$$

where, M_0 is the seismic moment (expressed in *dyne·cm*), related to the moment magnitude M by

$$M_0 = 10^{\frac{3}{2}(M+10.70)} \tag{18}$$

and C is a constant given by

$$C = 10^{-20} \cdot \frac{\hat{R} \cdot V \cdot F_s}{4\pi\rho\beta^3} \tag{19}$$

where $\hat{R}$, V, F_s are respectively the radiation pattern ($\hat{R} = 0.55$), a factor partitioning the total shear-wave energy into 2 horizontal components ($V = 0.71$) and the free-surface amplification factor ($F_s = 2.0$); ρ and β represent the soil density ($\rho = 2.8 t/m^3$) and wave velocity ($\beta = 3.5 km/s$) near the source; the multiplicative factor 10^{-20} is in order to obtain *cm* as unit dimension for the ground motion (*cm/s*^{2} for accelerations). The two corner frequencies f_a and f_b and the ε parameter are related to the magnitude by

$$\log(f_a) = 2.181 - 0.496 \cdot M \tag{20}$$

$$\log(f_b) = 1.380 - 0.227 \cdot M \tag{21}$$

$$\log(\varepsilon) = 3.223 - 0.670 \cdot M \tag{22}$$

The $A_n(f)$ function, characterizing the path effects of seismic waves, is given by

$$A_n(f) = \frac{1}{R} e^{\frac{-\pi f R}{Q(f)\beta}} \tag{23}$$

where the 1/R term represents the geometrical spreading effect. The effect of the waves-transmission is accounted by the *quality factor* $Q(f)$,, defined as

$$Q(f) = Q_0 f^n \tag{24}$$

whit $Q_0 = 180$ and $n = 0.45$ regional parameters. The $P_f(f)$ function accounts for the path-independent loss of high-frequency in the ground motion and it is defined by

$$P_f(f) = e^{(-\pi k f)} \left[1 + \left(\frac{f}{f_{\max}} \right)^8 \right]^{-0.5} \tag{25}$$

Whit k = 0.03 and f_{max} = 100 Hz. The soil amplification factor V(f) is taken according to [32] for generic soil ($V_{S,30}$ = 310 m/s). The model-error parameter ε_{mod} is the adding log-normal random variable ($\mu_{ln\varepsilon}$ = 0, $\sigma_{ln\varepsilon}$ = 0.5) , according to Jalayer and Beck [31], used for increasing the record-to-record variability. For which concerns the envelope function $e(t)$, it is given by

$$e(t) = a \cdot \left(\frac{t}{T_n} \right)^b \exp\left(-c \cdot \left(\frac{t}{T_n} \right) \right) \tag{26}$$

with parameters $b = -\varepsilon \cdot \frac{\ln(\eta)}{\left[1+\varepsilon\left(\ln(\varepsilon)-1\right)\right]}$, $c = \frac{b}{\varepsilon}$, $a = \left(\frac{\exp(1)}{\varepsilon}\right)^b$ and η=0.05, ε=0.2, as suggested in [22].

The ground-motion total duration is equal to $T_n = 2T_w$ with T_w defined as

$$T_w = 0.05 \cdot R + \frac{1}{2 f_a(M)} \tag{27}$$

The distance R from the earthquake source to the site can be defined as follow, in function of the epicentral distance r and the moment dependent nominal pseudo-depth h ($\log(h) = 0.15M - 0.05$)

$$R = \sqrt{r^2 + h^2} \tag{28}$$

ECCOMAS Congress 2016
VII European Congress on Computational Methods in Applied Sciences and Engineering
M. Papadrakakis, V. Papadopoulos, G. Stefanou, V. Plevris (eds.)
Crete Island, Greece, 5–10 June 2016

AN INVESTIGATION ON EFFECT OF SUBGRADE REACTION MODULUS OF SOIL ON NATURAL PERIOD OF LOW RISE BUILDINGS

Rafet Sisman[1] **and Abdurrahman Sahin**[2]

[1] Yildiz Technical University
Istanbul
e-mail: rafet@yildiz.edu.tr

[2] Yildiz Technical University
Istanbul
e-mail: abdsahin@yildiz.edu.tr

Keywords: Soil structure interaction, Natural period of low rise buildings, Seismic codes in the world, Subgrade reaction modulus of soil

Abstract. *Soil structure interaction (SSI) is an important topic when seismic performance of structures is investigated but rarely taken into account in seismic performance evaluation of low rise buildings. Seismic performance of structures is generally evaluated with three different approaches as equivalent linear earthquake method, modal superposition method and time history analysis method. Equivalent linear earthquake method is the most widespread analysis method for seismic performance evaluation of low rise buildings. Seismic codes in the world generally propose approximate natural period formulas to be used in equivalent linear earthquake analysis procedure. Despite that soil properties have a considerable effect on natural period of buildings; there is no soil related term in approximate natural period relations proposed in the seismic codes. This study aims to introduce the importance of subgrade reaction modulus of soil on natural period of buildings and produce a relation between these two phenomena. In accordance with this purpose, a number of relations being used over the world are examined. Consequently a number of novel approximations are introduced for use of design engineers.*

1 INTRODUCTION

During earthquakes buildings are exposed to base excitations and gives different responses to those excitations. Buildings responds to those excitations with three components: structure, foundation and soil underlying the foundation. As these components are combined with each other, structure, foundation and soil interacts with each other, this phenomenon is known as Soil Foundation Structure Interaction (SFSI) or simply Soil Structure Interaction (SSI) [1].

Soil Structure Interaction is rarely taken into account during dynamical analysis of low rise buildings. The simplifications and approximations made during dynamical analysis of low rise buildings, such as natural period approximations, neglects effect of SSI. ASCE 7 [2] and Eurocode 8 [3] are some of the important seismic codes in the world. The natural period approximations recommended in these seismic codes do not take SSI into account for low rise buildings.

There is not an exact definition for the terms high rise or low rise buildings, but it may be defined as buildings that have few number of storeys or height of the building is under a certain value. In ASCE 7 [2] the approximate natural period formula is recommended for buildings that have 12 or less number of storeys. In some seismically risky zones in Turkey, buildings are not allowed to have more than 3 or 4 storeys. Accordingly, in this study we examined a building with 3 storeys.

The examined building in this study is a typical low rise building with 3 storeys and is symmetric in both lateral directions. Also typical cross sections are defined for all beams, all columns and all slabs. Since we consider low rise buildings, building is modeled as a reinforced concrete structure. Floor plan of the examined generic building is shown in Figure 1.

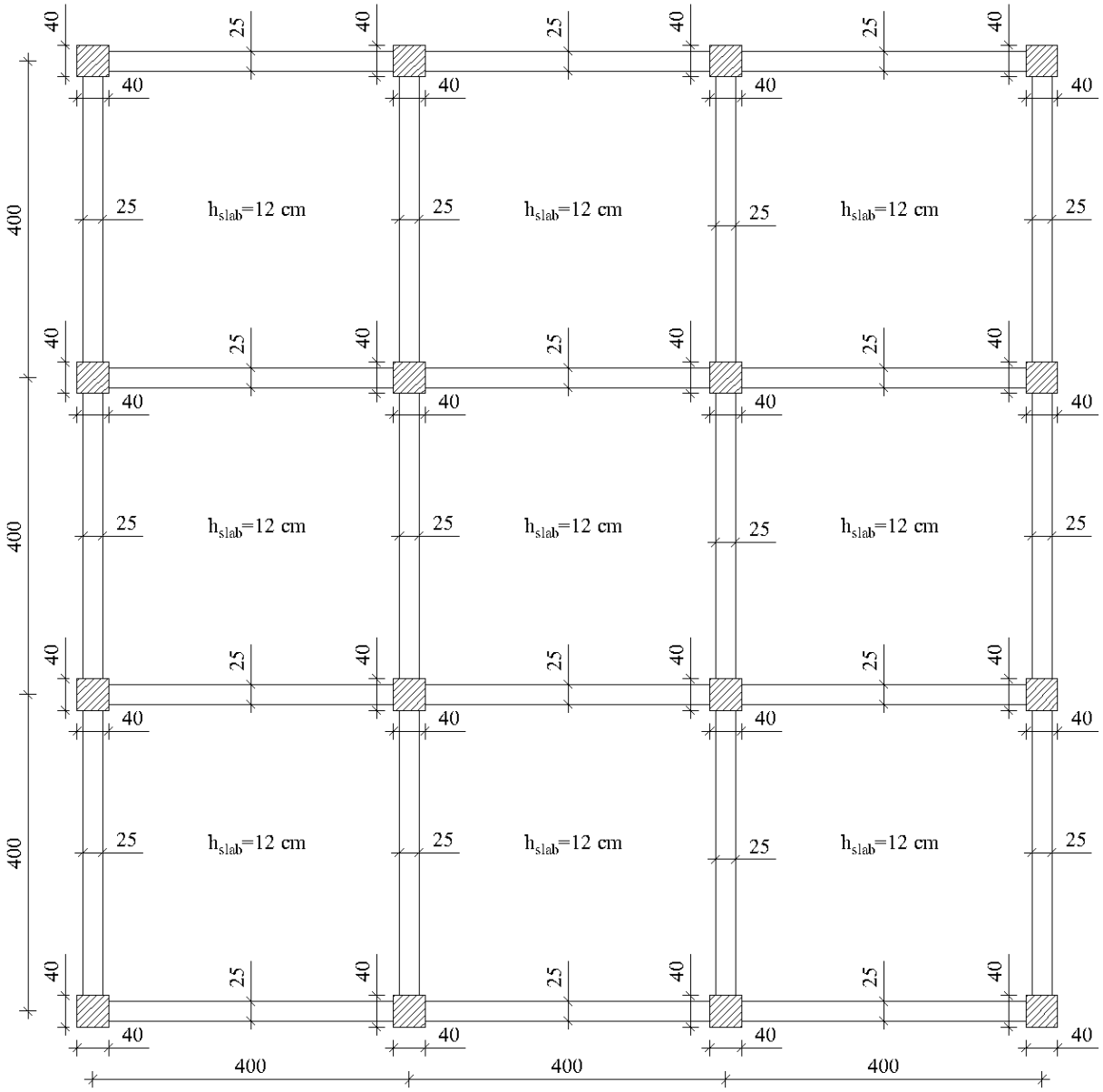

Figure 1 – Floor plan of the investigated building

The most widespread approach to consider SSI is the well-known Winkler Springs Method. In this approach, underlying soil layer is modeled as linear elastic springs in both lateral and vertical directions. Stiffness of those springs represents the subgrade reaction modulus of underlying soil layer.

In this study we aim to introduce novel approximations for natural period of low rise buildings which takes SSI into account. Accordingly a number of modal analysis are performed for a generic low rise building and we introduced a number of new approximations for first natural period of low rise buildings.

2 INVESTIGATION OF SUBGRADE MODULUS EFFECT

2.1 Properties of Investigated Building

As stated before, all columns and all beams are modeled with the same cross section. All beams are modeled as rectangular frame elements with dimensions of 50 cm depth and 25 cm width. All column elements are modeled as rectangular frame elements with $40\ \text{cm} \times 40\ \text{cm}$

dimensions. All slab elements are modelled as shell elements having a bending thickness of 12 cm. Also the foundation of the building is modeled as a shell element with a thickness of 100 cm.

All structural members are modelled with the same linear elastic material which represents reinforced concrete material. Young's modulus for this material is defined as $E = 3\times10^7$ kN/m^2 and Poisson's ratio is defined as $\upsilon = 0.2$. For this material mass per unit volume is defined as $\rho = 2.5$ kNs^2/m/m^3.

As shown in floor plan given in Figure 1, the investigated structure has 3 bays in X direction and Y direction. In both directions bay widths are equal to each other and 4 meters. This symmetric floor plan is adopted to simplify the problem and focus only on first natural period of the building which is equal to second natural period. As stated before the investigated building has 3 storeys and each storeys has the same height as 3 meters.

With those properties mentioned above, the investigated typical low rise building is defined and some modal analysis are performed.

2.2 SSI Procedure and Analysis

In this study Winkler springs method is employed to take SSI into account. In Winkler springs method, the underlying soil layer modeled as linear elastic springs and stiffness of these springs-spring constants- represents the subgrade reaction modulus of the soil layer. Lateral and vertical springs are modeled at column ends. Since the soil layer is continuous along the foundation or floor area, each spring set at each column end represents an area. Columns at inner points represents the area of a bay which can be calculated as $Area = 4\times4 = 16$ m^2 while columns at internal points on edges represents half of that area as $Area = 8$ m^2 and columns at corners represents quarter of that area as $Area = 4$ m^2. Spring constants calculated by using those areas and soil subgrade modulus.

$$K_s = k_s \times Area \tag{1}$$

To perform modal analysis OpenSees [4] software is utilized. Firstly, the investigated structure is modeled with a fixed base which means neglecting the SSI. Then, the modal analysis are performed considering SSI by using Winkler springs. At this step, subgrade reaction modulus of the soil layer is increased gradually and modal analysis performed repeatedly. To represent the subgrade reaction modulus values encountered generally, subgrade modulus values are increased gradually from 500 kN/m^3 to 10000 kN/m^3.

The calculated first natural periods are divided by the period value that neglects SSI to determine a simple ratio. As subgrade reaction modulus values increases, that ratio decreases exponentially. By using this relation two nonlinear regression coefficients are determined which relates period of SSI model to period of non-SSI model as a function of subgrade reaction modulus.

First natural period of the building with fixed base is determined as $T_{fix} = 0.2544$ sec. For subgrade reaction modulus values from 500 kN/m^3 to 10000 kN/m^3, first natural period of the building is determined as given in Table 1.

k_s (kN/m^3)	T (sec)	k_s (kN/m^3)	T (sec)
500	0,9751	5500	0,3535
1000	0,7014	6000	0,3447
1500	0,5829	6500	0,3372
2000	0,5140	7000	0,3308
2500	0,4683	7500	0,3253
3000	0,4356	8000	0,3204
3500	0,4110	8500	0,3161
4000	0,3918	9000	0,3123
4500	0,3764	9500	0,3089
5000	0,3639	10000	0,3059

Table 1 – First natural period and subgrade reaction modulus

Beside the first natural period values the ratio determined by dividing first natural period values of SSI models by first natural period of non-SSI model, can be plotted as shown in Figure 4.

$$\Gamma(k_s) = \frac{T_{SSI}}{T_{FIX}} \tag{2}$$

$$T_{SSI} = \Gamma(k_s).T_{FIX} \tag{3}$$

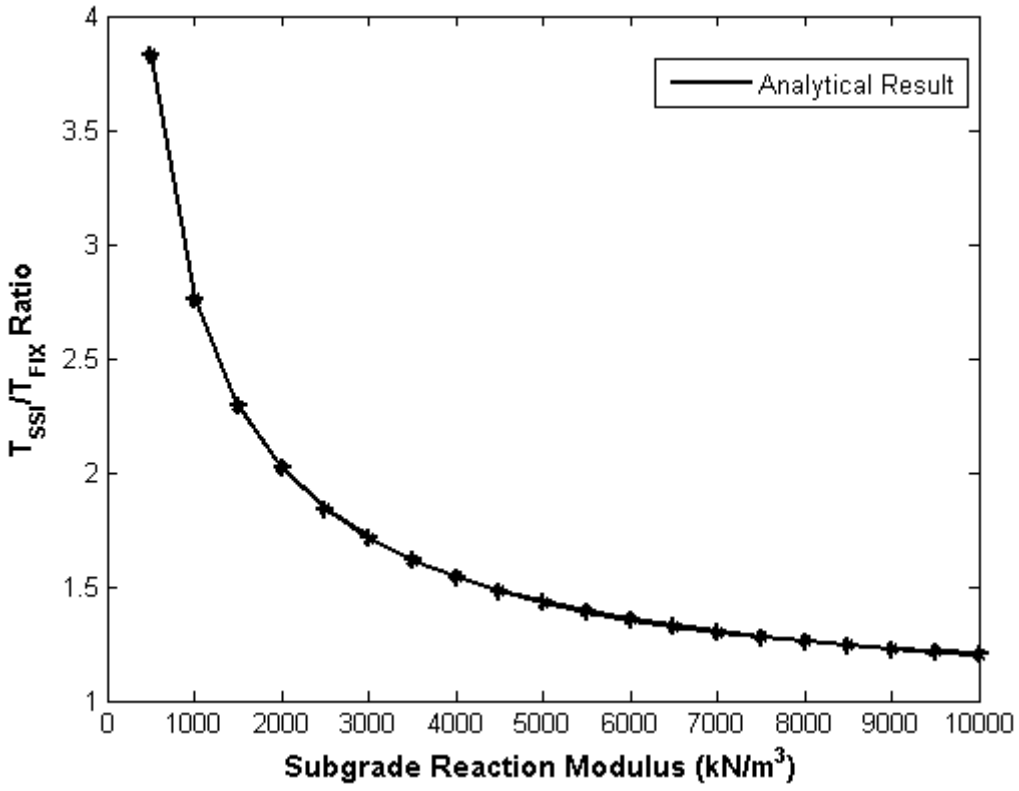

Figure 4 – First natural period ratio with respect to subgrade reaction modulus

In Figure 4 the graph shows the first natural period ratio determined by dividing period of SSI model by period of non-SSI model. As this plot is obtained by using analytical results, this curve is not an approximation. This curve represents the real relation between subgrade reaction modulus and $\Gamma(k_s)$.

The curve shown in Figure 4 can be represented by an inverse exponential function or inverse parabolic function. While using non-linear regression to determine an appropriate function to that curve, an inverse parabolic expression is recommended, regarding physical meaning of the problem.

The recommended relation is in the form shown below;

$$\Gamma\left(k_s\right)=1+\frac{\beta_1}{k_s}+\frac{\beta_2}{k_s^2} \tag{4}$$

Suitability of the recommended relation can be evaluated by considering that infinite subgrade reaction modulus yields 1, which corresponds to the fixed base condition. At the recommended expression, the third term is added to smoothen the expression.

The determined regression coefficients are as given below;

$$\begin{aligned}\beta_1 &= 2,2.10^3\\ \beta_2 &= -4.10^5\end{aligned} \tag{5}$$

Thus the recommended relation between the periods of SSI model and non-SSI model is determined as;

$$\Gamma\left(k_s\right)=1+\frac{2200}{k_s}-\frac{400000}{k_s^2} \tag{6}$$

In Figure 5 the graph shows the first natural period ratio determined by the recommended mathematical expression.

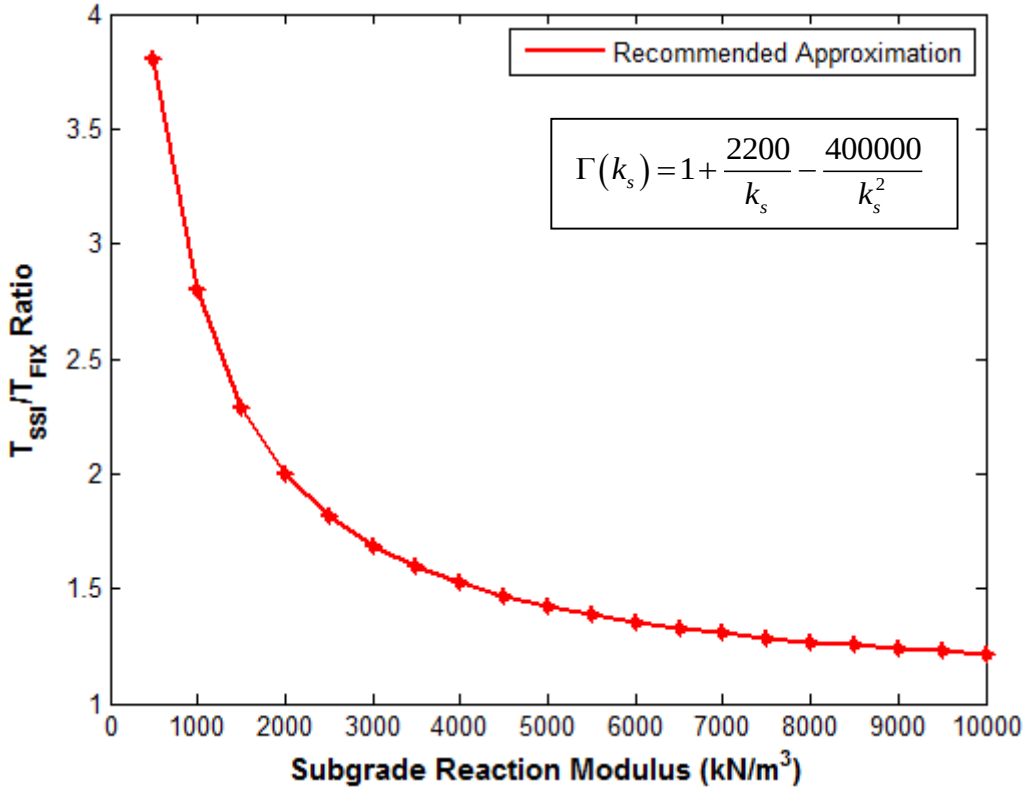

Figure 5 – Approximation for first natural period ratio with respect to subgrade reaction modulus

Thus the first natural period of structure while considering SSI, can be approximated by the relation given below.

$$T_{SSI} = \left(1 + \frac{2200}{k_s} - \frac{400000}{k_s^2}\right).T_{FIX} \tag{7}$$

3 CONCLUSION

In this study effect of subgrade reaction modulus on first natural period of low rise buildings is investigated. By utilizing nonlinear regression a novel approximation is introduced which relates first natural period of buildings determined by neglecting SSI to first natural period determined by not neglecting SSI. Then it can be said that the approximations recommended in prominent seismic codes to determine first natural period of low rise buildings can be modified. The introduced expression may be seen inconsistent since all analysis procedure considers a typical building with typical dimensions. However, the expression can give satisfactory results for low rise buildings, since aim of this study refers to low rise buildings. Nevertheless, further study is going on to introduce novel approximations for buildings with varying dimensions.

REFERENCES

[1] NEHRP Consultants Joint Venture, *Soil-Structure Interaction for Building Structures*, 2012.

[2] American Society of Civil Engineers, *ASCE 7-05 Minimum Design Loads for Buildings and Other Structures*, 2006.

[3] European Committee for Standardization (CEN), *Eurocode 8: Design of Structures for Earthquake Resistance – Part 1: General Rules, Seismic Actions and Rules for Buildings (Final Draft)*, 2003.12.

[4] McKenna, F., Fenves, G. L., Scott, M. H., and Jeremic, B., *Open System for Earthquake Engineering Simulation (OpenSees)*. Pacific Earthquake Engineering Research Center, University of California, Berkeley, CA, 2000.

ECCOMAS Congress 2016
VII European Congress on Computational Methods in Applied Sciences and Engineering
M. Papadrakakis, V. Papadopoulos, G. Stefanou, V. Plevris (eds.)
Crete Island, Greece, 5–10 June 2016

A PROBABILISTIC APPROACH TOWARDS AN EVALUATION OF EXISTING CODE PROVISIONS FOR SEISMICALLY ISOLATED STRUCTURES (ECCOMAS CONGRESS 2016)

Anastasios Tsiavos[1], **Bozidar Stojadinovic**[2]

[1] Doctoral Student, Institute of Structural Engineering, Swiss Federal Institute of Technology (ETH) Zürich, HIL E 12.1, Stefano-Franscini-Platz 5, 8093 Zürich, Switzerland
tsiavos@ibk.baug.ethz.ch

[2] Professor, Institute of Structural Engineering, Swiss Federal Institute of Technology (ETH) Zürich HIL E 14.1, Stefano-Franscini-Platz 5, 8093 Zurich, Switzerland
stojadinovic@ibk.baug.ethz.ch

Keywords: Seismic Isolation, Seismic probabilistic risk assessment, Performance-based design, Code provisions, Strength reduction factor

Abstract. *Following modern design codes, seismically isolated superstructures are designed to respond in the elastic response range or to exhibit limited inelastic behavior. However, the behavior of seismically isolated structures when the superstructure enters the inelastic response range has not been extensively investigated in the past. This paper aims at answering the following questions: What is the probability that a (code-compliant) seismically isolated structure will yield? Will it develop a ductility demand μ larger than that implied by its design strength reduction factor?*

The probabilistic investigation of such a behavior is important for two reasons: First, to estimate the conservativism implied by the existing code provisions for seismically isolated structures. Second, to account for the case in which the seismic forces acting on an existing seismically isolated structure could exceed the design forces due to a ground motion stronger than the design ground motion level. The investigation is conducted using a two-degree-of-freedom model of a seismically isolated structure. The hysteretic behavior of the seismic isolation devices and the isolated superstructure is simulated in Matlab and OpenSees using a bilinear elastic-plastic model. The results are obtained by analyzing the responses of the isolated structure to a large number of recorded ground motions.

Fragility curves to estimate the probability that the structure enters the inelastic range ($\mu>1$), if it is designed according to the existing American and European code provisions for seismically isolated structures are determined through probabilistic seismic demand analysis (PSDA). The influence of the isolated structure overstrength and the isolation system hardening is discussed. Additional fragility curves are provided for other values of the engineering demand parameter (EDP) that are not allowed in the existing code provisions (e.g. superstructure displacement ductility $\mu>2$). The effects of seismic isolation and superstructure design parameters on the fragility curves is quantified through parametric analysis.

1 INTRODUCTION

Base isolation is a seismic response modification technology developed in mid 1970's to control the extent of damage to structures subjected to strong ground motion excitation. However, the acceptance of the technology increased significantly after the observed response of seismically isolated structures in 3 earthquakes: The 1994 Northridge earthquake in the USA, the 1995 Hyogoken-Nanbu earthquake in Japan and the 1999 Chi-Chi earthquake in Taiwan. Over this period, the number of seismically isolated structures worldwide increased, and the building codes have been revised to include design requirements for seismically isolated structures [1].

The elastic design approach, which aims to avoid yielding of the isolated superstructure, is embedded in the design codes worldwide. Eurocode [2] allows a maximum behavior factor value of 1.5 for base-isolated buildings. US ASCE 7 [3] allows the strength reduction factor for a base-isolated superstructure to be 0.375 times the one for a corresponding fixed-base structure and no larger than 2. Given that the large majority of ASCE 7 overstrength factors are between 2 and 3, the superstructure is very likely to remain elastic for the design-level seismic hazard. However, it is still possible for these structures to enter the inelastic range due to an extreme seismic demand or unexpectedly low as-built overstrength.

Constantinou and Quarshie [4], Ordonez et al. [5], Kikuchi et al. [6], Thiravechyan et al. [7] and Cardone et al. [8] investigated the response of inelastic seismically isolated structures and agreed that allowing base-isolated superstructures to yield requires careful consideration because of possible occurrence of large ductility demands. Vassiliou et al. [9-11] concluded that designing typical seismically isolated structures to behave elastically, as prescribed by current seismic design codes, is not overly conservative but a necessity that emerges from the fundamental dynamics of such structures.

This study aims at quantifying the probability that an isolated superstructure designed according to the current design codes enters the inelastic behavior range. Additionally, incremental dynamic analysis [12] is performed to determine the behavior of the isolated structure for ground motions caused by events of higher seismic hazard than the design hazard level. Huang et al [13] have presented fragility curves for the estimation of the probability of failure of base-isolated nuclear power plants for a range of spectral acceleration values. Han et al [14] used the damped spectral acceleration at the effective period of the isolators $S_a\ (T_{eff})$ as an intensity measure to determine similar fragility curves for non-ductile reinforce concrete buildings.

Four assumptions are made in the study. First, the displacement and strength capacities of the isolators are assumed to be sufficient to meet any demands. Second, friction-pendulum bearings are assumed, unless explicitly stated otherwise. Third, the overstrength, i.e., the difference between the actual and the yield strength of the isolated superstructure, is not explicitly considered in the model. Fourth, the response of the dynamic model is computed in-plane to an earthquake excitation that has a single horizontal component, disregarding the coupled bi-directional horizontal and vertical response of the isolators as well as the effect of multi-directional excitation on the response of isolated superstructure.

2 DYNAMIC MODELLING

The dynamics of a base-isolated structure, following to the work of Naeim and Kelly [15], is investigated using a two-degree-of-freedom (2-DOF) in-plane model, presented in Fig. 1. The system consisting of the isolation bearings and the isolation base is defined as the isolation system. The structure above the isolation system is defined as the isolated superstructure.

Masses m_s *and* m_b represent the mass of the isolated superstructure and the mass of the base above the isolation system, respectively. The stiffness and damping are denoted as k_s, c_s, when referring to the superstructure and as k_b, c_b when referring to the base. The stiffness k_b is the post-yielding stiffness of the isolators [16], whereas the equivalent stiffness shown in Fig. 1 is the effective stiffness k_{eff} of the isolators.

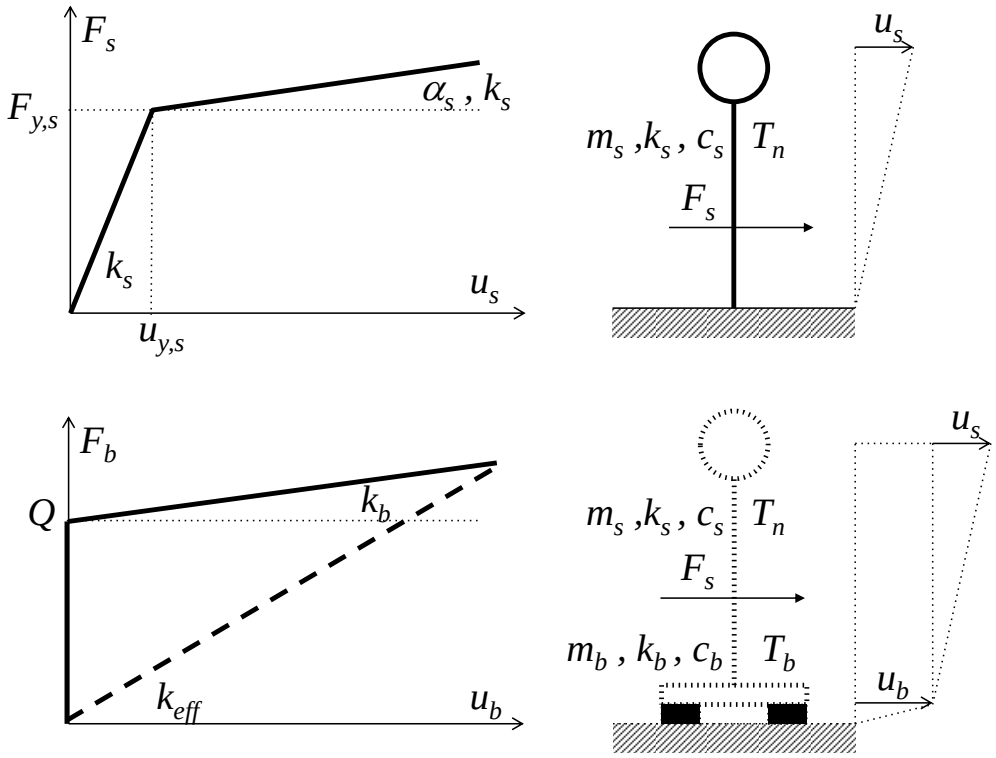

Figure 1: Parameters of the SDOF model of a fixed-base structure and of a 2-DOF model of a base-isolated structure.

Horizontal displacement u_s is the relative displacement of the superstructure with respect to the base and u_b is the horizontal displacement of the isolation bearings with respect to the ground. The ground displacement to which the system is subjected is denoted as u_g. The notation used to describe the inelastic response of fixed-base single-degree-of-freedom (SDOF) structures is adopted as follows. The vibration period of the SDOF system is T_n. The displacement ductility ratio μ is defined as:

$$\mu = \frac{u_m}{u_y} \tag{1}$$

where u_m and u_y denote the maximum inelastic displacement and the yield displacement of the SDOF system, respectively. The strength reduction factor R_y is the ratio of the minimum strength required to maintain the SDOF system response in the elastic range, $F_{el,s}$ to the SDOF system yield strength $F_{y,s}$:

$$R_y = \frac{F_{el,s}}{F_{y,s}} \tag{2}$$

The following quantities are defined for the 2-DOF model of the base-isolated structure:

1. Period and cyclic frequency of the isolated superstructure:

$$T_n = 2\pi\sqrt{\frac{m_s}{k_s}},\ \omega_n = \sqrt{\frac{k_s}{m_s}} \tag{3}$$

2a. Isolation period and cyclic frequency:

$$T_b = 2\pi\sqrt{\frac{m_s + m_b}{k_b}},\ \omega_b = \sqrt{\frac{k_b}{m_s + m_b}} \tag{4}$$

2b. Effective isolation period and cyclic frequency:

$$T_{eff} = 2\pi\sqrt{\frac{m_s + m_b}{k_{eff}}},\ \omega_{eff} = \sqrt{\frac{k_{eff}}{m_s + m_b}} \tag{5}$$

3. Non-hysteretic structural and isolation system damping ratios:

$$\xi_s = \frac{c_s}{2m_s\omega_s}, \qquad \xi_b = \frac{c_b}{2\left(m_s + m_b\right)\omega_b} \tag{6}$$

4. Mass ratio:

$$\gamma_m = \frac{m_s}{m_s + m_b} \tag{7}$$

The strength of the isolation system is defined as Q (force at zero displacement).

Dynamic equilibrium of the isolated superstructure and the base isolation system gives:

$$\left(m_s + m_b\right)\ddot{u}_b + m_s\ddot{u}_s + k_b u_b + Qz_b\left(t\right) + c_b\dot{u}_b\left(t\right) = -\left(m_s + m_b\right)\ddot{u}_g \tag{8}$$

Dynamic equilibrium of the isolated superstructure alone gives:

$$m_s\ddot{u}_s + m_s\ddot{u}_b + a_s k_s u_s(t) + (1-a_s)k_s u_{y,s} z_s(t) + c_s\dot{u}_s(t) = -m_s\ddot{u}_g \tag{9}$$

Consequently, Equations (8) and (9) become equations of motion of the combined structure-isolation system. Equations (10) and (11) are derived by dividing equations (8) and (9) by (m_s+m_b). The inelastic displacement demand for the isolation system and the isolated superstructure can be obtained by solving Equations (10) and (11) using Matlab [17].

$$\ddot{u}_b + \gamma_m\ddot{u}_s + \omega_b{}^2 u_b + \frac{Q}{m_s + m_b} z_b + 2\xi_b\omega_b\dot{u}_b = -\ddot{u}_g \tag{10}$$

$$\ddot{u}_s + \ddot{u}_b + 2\xi_s\omega_n\dot{u}_s(t) + a_s\omega_n^2 u_s(t) + (1-a_s)\omega_n^2 u_{y,s} z_s(t) = -\ddot{u}_g \tag{11}$$

An identical 2-DOF model was developed in OpenSees [18] to compute the inelastic displacement demand of both systems, using bilinear inelastic behavior models as the one shown in Fig. 1 for the superstructure and the isolators. This model gives identical results with the ones obtained using the Bouc-Wen models presented above in Matlab. The calculation process using Bouc-Wen models in Matlab was performed to quantify the fundamental parame-

ters of the problem. However, the results presented on this study are computed with bilinear models (Fig. 1) using OpenSees for reasons of computational efficiency.

3 CODE EVALUATION: DESIGN HAZARD LEVEL

Eurocode 8 [2] allows a maximum strength reduction factor value of 1.5 for base-isolated buildings, thus implying the development of limited inelastic behavior in the isolated superstructure for the design hazard level. A number of recorded ground motions were selected and scaled until its acceleration response spectrum matches the design spectrum, as defined in Eurocode 8 [2]. The 2-DOF structure of Fig. 1 was subjected to the scaled ground motion ensemble. Lognormal probability distributions were fit to the determined displacement ductility demand values of the structure for this ground motion ensemble. The probability that the structure enters the inelastic range, thus exceeding the values implied by the code, is determined through the statistical processing of the recorded ductility values.

3.1 Design of the isolated structure

The structure that has been investigated in this study is the National Opera of Greece, which belongs to the Stavros Niarchos Foundation (SNF) Cultural Center. This structure has been chosen as an example of inelastic design of base-isolated structures, as a strength reduction factor of 1.5 has been used for its seismic design [19]. The design spectrum for the structure (PGA=0.267g) was based on a microzonation study, conducted due to the importance of the project, and is shown in Fig. 2 below. The return period of this spectrum is 475 years, which corresponds to 10% probability of exceedance in any 50 year period.

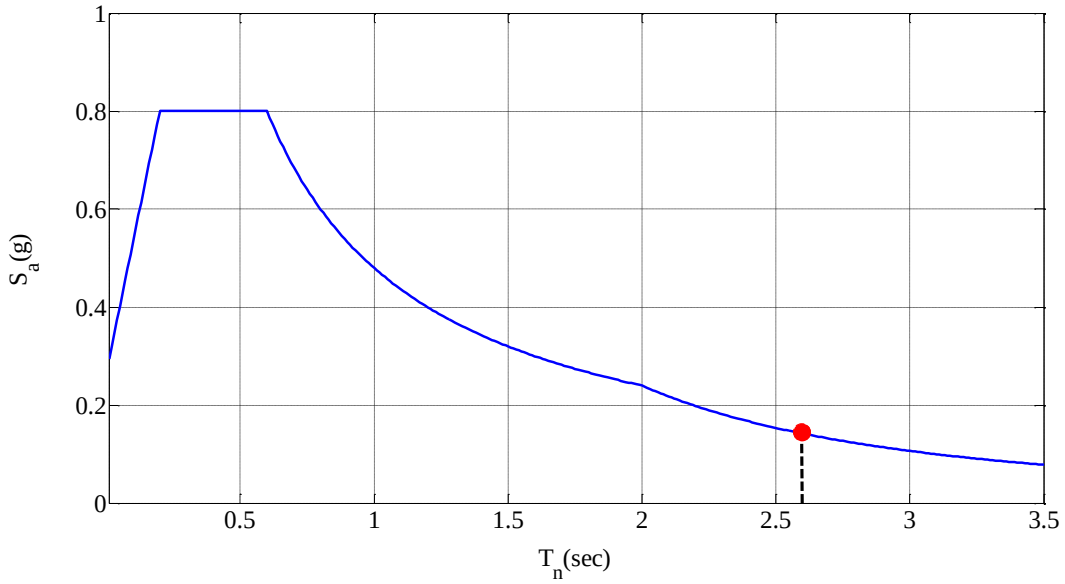

Figure 2: Elastic design acceleration spectrum [19]

The strength of the isolation system is determined using Equation (12) for friction-pendulum bearings with the coefficient of friction μ_f=0.05 (g the acceleration of gravity). The mass ratio is γ_m=0.9.

$$Q = \left(m_s + m_b\right)\mu_f\, g \tag{12}$$

Then, for m_s=120000 tons, Q=58860 kN. The effective period of the isolators is T_{eff}=2.6 sec. The design displacement for the isolators (ξ_{eff}=15%, S_e=0.141g) is D_d=235*1.5=351 mm. Then, the post-yielding stiffness of the isolators k_b=(k_{eff} D_d-Q)/D_d=303922 kN/m, which leads to a period T_b=4 sec. The yield strength of the structure for a behavior factor of q=1.5 is F_y=(m_s+m_b)S_a(T_{eff})/q=165536 kN.

3.2 Ground motion excitation

The ground motion ensemble used to excite the model of the isolated structure presented in Fig. 1 was taken from the strong motion database presented by Vassiliou and Makris [20]. From the 183 ground motions used that study, 20 motions were chosen for this study, using the minimization of the root-mean-squared error (*RMSE*) between the selected motions' acceleration response spectrum and the target design spectrum (Fig. 2), as performed by Carlson et al [21]. *RMSE* is defined as follows:

$$\mathrm{RMSE} = \sqrt{\frac{\sum_{i=1}^{n}\left[\ln\left(\mathrm{Sa}_{\mathrm{tar}}(\mathrm{T_i})\right) - \ln\left(\mathrm{Sa}_{\mathrm{rec}}(\mathrm{T_i})\right)\right]^2}{\mathrm{n}}} \tag{13}$$

where $Sa_{tar}(T_i)$ and $Sa_{rec}(T_i)$ represent the spectral acceleration at the ith period, T_i, for the target spectrum and recorded ground motion acceleration response spectrum, respectively, and n represents the number of spectral points. The median of the selected ground motion ensemble spectra and the target spectrum are shown in Fig. 3.

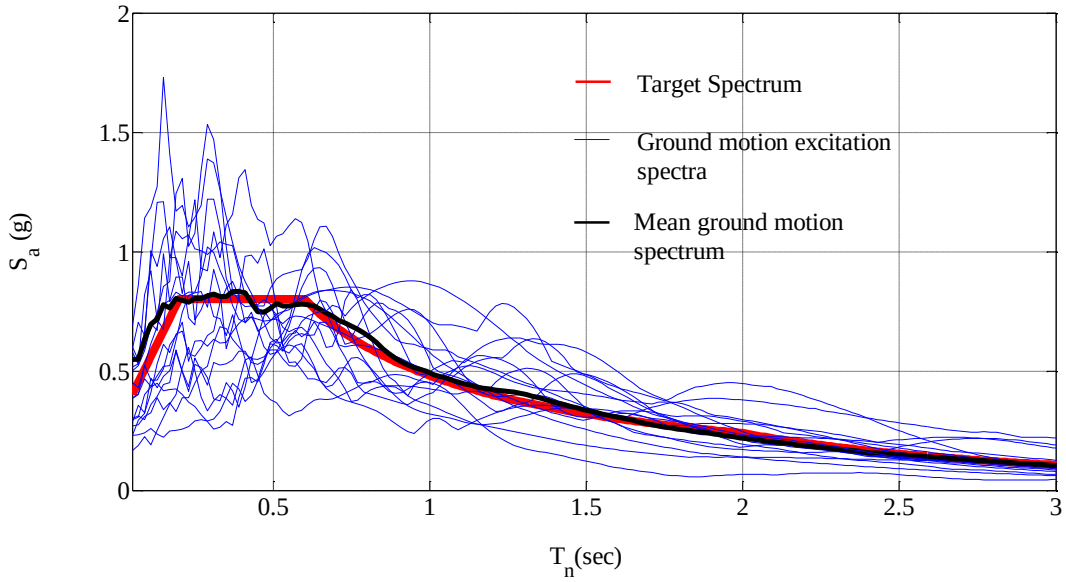

Figure 3: Elastic design acceleration spectrum (Eurocode 8) and median spectrum of the 20 ground motion excitation spectra selected based on their matching with the design spectrum (RMSE factor).

According to EC8, in the range of periods between $0.2T_1$ and $2T_1$, where T_1 is the fundamental period of the structure in the direction where the accelerogram is applied, no value of the mean 5%-damping elastic spectrum, calculated from all time histories, should be less than 90% of the corresponding value of the 5%-damping elastic response spectrum.

3.3 Probabilistic evaluation at the design hazard level

The structure presented at section 3.1 was excited by the ground motion excitation ensemble shown in Fig. 3. The displacement ductility demand developed in the superstructure was calculated for each ground motion excitation and it is shown in Fig. 4. A lognormal probability distribution was fit to the displacement ductility data and is presented in Fig. 4. The probability of exceedance of μ=1 for the given hazard level (Return period: 475 years, Probability of exceedance=10% in 50 years) is given by the PEER probabilistic PBEE evaluation methodology shown in Equation (14) [22, 23]:

$$G(EDP) = \int_0^\infty G(EDP \mid IM) f(IM) dIM \tag{14}$$

where *f(IM)* is the Probability Distribution Function (PDF) of the Intensity Measure *IM* and *G(EDP|IM)* is the Probability Distribution Function (PDF) of the Engineering Demand Parameter *EDP* given the Intensity Measure *IM*. The *EDP* chosen in this study is the displacement ductility μ and the IM is the 5% damped spectral acceleration at the effective period of the isolators S_a (T_{eff}) [14].

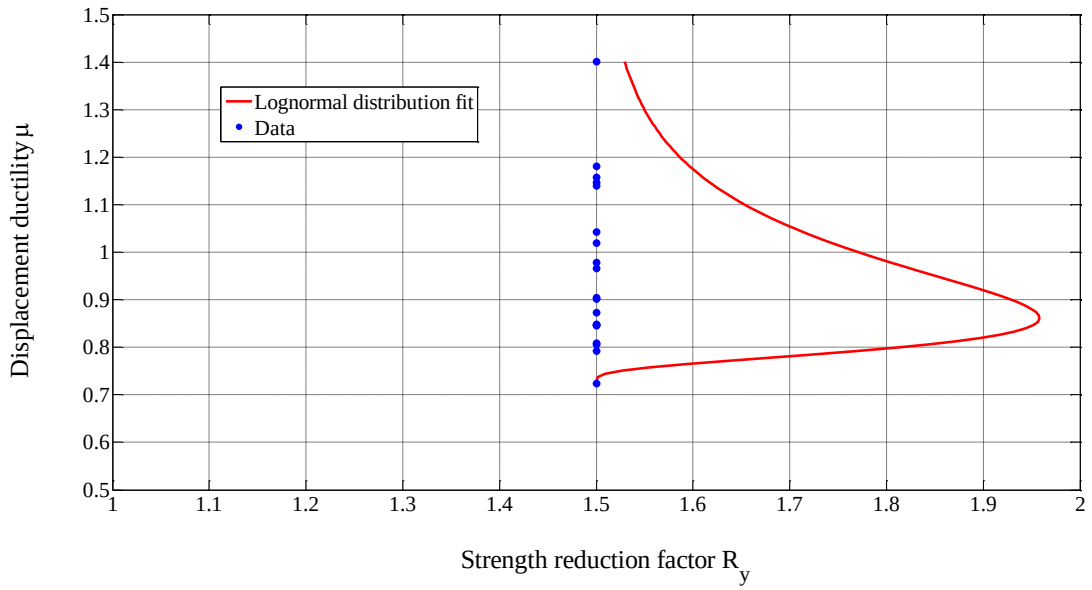

Figure 4: Displacement ductility values μ for Ry=1.5 and lognormal distribution fit

For this lognormal distribution (μ=0, σ=0.17), the probability of exceedance of μ=1 is 50% given the exceedance of the intensity measure S_a (2.59 sec)=0.141 g. The probability of the exceedance of the intensity measure S_a (2.59 sec)=0.141 g is 10% in 50 years, which corresponds to the design hazard return period of 475 years. Then, from Equation (14), the total probability that the displacement ductility μ exceeds 1 is 5%. This probability that is associated with damage in the superstructure is considered relatively high for the importance of this structure. Therefore, the choice of a strength reduction factor R_y=1.5 does not guarantee the quasi-elastic behavior implied by the code for this structure. However, the consideration of overstrength that has not been taken into account in this case study may change this conclusion, as it would reduce the probability of inelastic behavior in the superstructure.

4 CODE EVALUATION: BEYOND DESIGN HAZARD LEVEL

4.1 Incremental Dynamic Analysis

The evaluation of the existing code provisions for isolated structures for seismic hazard levels that are higher than the design hazard level requires the statistical processing of the dynamic response of the structure to a large number of strong ground motion excitations. This process can be effectively performed for the targeted hazard levels using Incremental Dynamic Analysis (IDA) [12]. The incremental analysis was performed for the fixed-base period of the isolated superstructure T_n=0.31 sec. The results of the analysis for a wide range of intensity measures S_a (T_{eff}) are shown in Fig. 5.

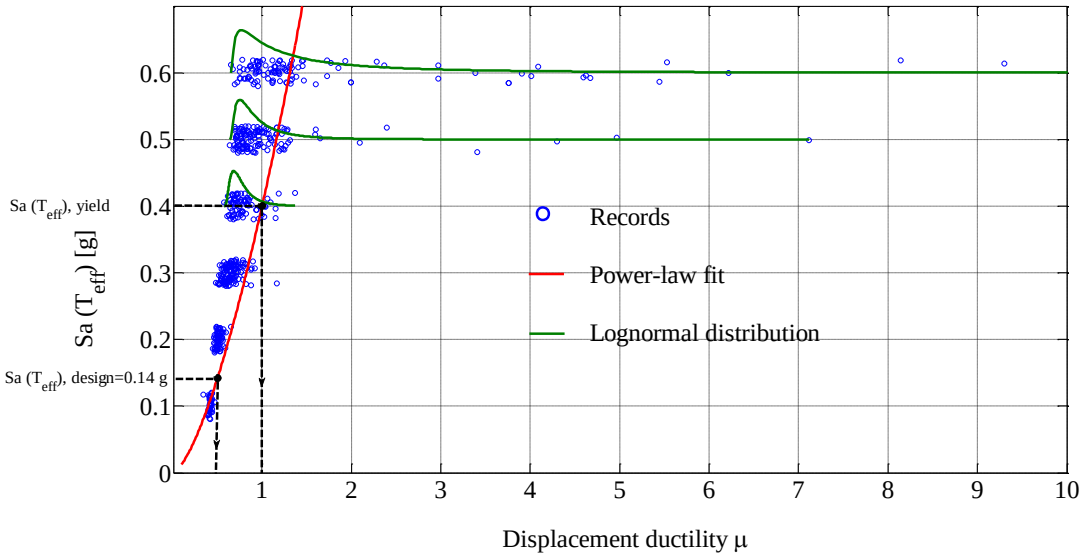

Figure 5: Displacement ductility values μ for different values of spectral acceleration $S_a(T_{eff})$, power-law fit to the presented displacement ductility values and lognormal distribution fit for each spectral acceleration $S_a(T_{eff})$

The $S_a(T_{eff})$ values presented are selected from the set {0.1g, 0.2g, 0.3g, 0.4g, 0.5g, 0.6g} within a 5% tolerance range. A power-law fit was performed to indicate the general trend of the displacement ductility μ results for varying $S_a(T_{eff})$ values. Lognormal probability distributions were fit to displacement ductility μ data for each spectral acceleration value $S_a(T_{eff})$ above the yield limit $S_a(T_{eff}),_{yield}$. According to the results of the power-law fit, the design acceleration of the structure corresponds to a displacement ductility μ=0.5. The yield spectral acceleration value, which corresponds to displacement ductility μ=1 is $S_a(T_{eff}),_{yield}$=0.4 g. This spectral acceleration, which can lead to damage in the superstructure, exceeds the design value by a factor of 3. If higher $S_a(T_{eff})$ values than this value are considered (e.g. $S_a(T_{eff})$=0.5 g or $S_a(T_{eff})$=0.6 g), extensive damage may occur in the superstructure, as the corresponding ductility demand values may exceed μ=7.

This exceedance of the design spectrum even by a factor as high as 3 over a large range of periods has been reported in numerous seismic events (Mexico City 1985, Kobe 1995, Nepal 2015) in the past. A large number of ground motions recorded on "soft" soils have produced response spectra of a sharp rather than flat shape, with well-defined peaks around the site fundamental period, as presented by Gazetas et al [24]. Thus, such high demands on isolated structures cannot be excluded from consideration.

5 CONCLUSIONS

- Two different ground motion selection procedures have been used in this study to evaluate the inelastic behavior of the National Opera of Greece for different seismic hazard levels.
- The results obtained through a spectral matching procedure based on the RMSE factor [21] indicate a 5% probability of inelastic behavior and associated damage in the superstructure for the design seismic hazard level (return period of 475 years).
- However, the results obtained through IDA [12] show that the design spectrum must be exceeded 3 times for a development of inelastic behavior in the superstructure. This scaling process was performed for selected values of spectral acceleration $S_a(T_{eff})$, which restricts the ground motion variability, compared to the spectral matching procedure that was used for the design hazard level evaluation.
- The overstrength of the superstructure was not considered in this study. The consideration of overstrength is expected to reduce the probability of inelastic behavior in the superstructure.

REFERENCES

[1] M. Higashino, S. Okamoto, Response Control and Seismic Isolation of Buildings. Taylor & Francis: London; 193–202, 2006

[2] CEN, Eurocode 8, Design of structures for earthquake Resistance—Part 1: general rules, seismic actions and rules for buildings. EN 1998-1:2004. Comité Européen de Normalisation,

[3] Structural Engineering Institute, Minimum design loads for buildings and other structures, ASCE; **7**(5), 2010

[4] M.C. Constantinou, J.K Quarshie, Response modification factors for seismically isolated bridges. *Report No. MCEER-98-0014, Multidisciplinary Center for Earthquake Engineering Research*, Buffalo, NY, 1998.

[5] D. Ordonez, D. Foti, L. Bozzo, Comparative study of the inelastic response of base isolated buildings. *Earthquake Engineering and Structural Dynamics*; **32**:151–164, 2003

[6] M. Kikuchi, C.J. Black, I.D. Aiken, On the response of yielding seismically isolated structures. *Earthquake Engineering and Structural Dynamics*; **37**(5):659–679, 2008

[7] P. Thiravechyan, K. Kasai, T.A. Morgan, The effects of superstructural yielding on the seismic response of base isolated structures., *Joint Conference proceedings, 9th International Conference on Urban Earthquake Engineering / 4th Asia Conference on Earthquake Engineering, Tokyo*, Japan; 1451-1458, 2012

[8] D. Cardone, A. Flora, G. Gesualdi, Inelastic response of RC frame buildings with seismic isolation. *Earthquake Engineering and Structural Dynamics*; **42**:871–889, 2013

[9] A. Tsiavos, M.F. Vassiliou, K.R Mackie and B. Stojadinovic, R-μ-T relationships for seismically isolated structures, *COMPDYN 2013, 4th International Conference on*

Computational Methods in Structural Dynamics and Earthquake Engineering, Kos Island, Greece, 12-14 June, 2013.

[10] A. Tsiavos, M.F Vassiliou, K.R Mackie and B. Stojadinovic, Comparison of the inelastic response of base-isolated structures to near-fault and far-fault ground motions, *VEESD 2013, Vienna Congress on Recent Advances in Earthquake Engineering and Structural Dynamics & D-A-CH Tagung*, Vienna, Austria, 28-30 August, 2013.

[11] M.F. Vassiliou, A. Tsiavos and B. Stojadinovic, Dynamics of Inelastic Base Isolated Structures Subjected to Analytical Pulse Ground Motions, *Earthquake Engineering and Structural Dynamics*, **42** (14), 2043-2060, 2013.

[12] J.D. Vamvatsikos, C.A. Cornell, Incremental Dynamic Analysis, *Earthquake Engineering and Structural Dynamics*, **31**(3): 491–514, 2002.

[13] Y-N. Huang, A.S. Whittaker, N. Luco, Seismic performance assessment of base-isolated safety-related nuclear structures, *Earthquake Engineering and Structural Dynamics*, **39**:1421–1442, 2010.

[14] R. Han, Y. Li, J.V.D. Lindt, Seismic risk of base isolated non-ductile reinforced concrete buildings considering uncertainties and mainshock–aftershock sequences. *Structural Safety*; **50**:39–56, 2014.

[15] F. Naeim, J.M. Kelly, Design of Seismic Isolated Structures: From Theory to Practice, Wiley, New York, 1999.

[16] N. Makris, G. Kampas, The engineering merit of the "effective period" of bilinear isolation systems. *Earthquakes and Structures*, **4** (4), 397-428, 2013.

[17] MATLAB and Statistics Toolbox Release 2012b, The Mathworks, Inc., Natick, Massachusetts, United States.

[18] OpenSees command language manual, S Mazzoni, F McKenna, MH Scott, GL Fenves, Pacific Earthquake Engineering Research (PEER) Center, 2006.

[19] C. Giarlelis, J. Keen, E. Lambrinou, V. Martin, G. Poulios, Dynamic behavior of the seismically isolated SNF Cultural Center in Athens, 14th World Conference on Seismic Isolation, Energy Dissipation and Active Vibration Control of San Diego, USA, 2015

[20] M.F. Vassiliou, N. Makris, Estimating Time Scales and Length Scales in Pulselike Earthquake Acceleration Records with Wavelet Analysis, *Bulletin of the Seismological Society of America*, vol. 101, no. 2, pp. 596-618, 2011

[21] C. Carlson, D. Zekkos, and A. Athanasopoulos-Zekkos, Predictive Equations to Quantify the Impact of Spectral Matching on Ground Motion Characteristics. *Earthquake Spectra*, 2015

[22] S. K. Kunnath, Application of the PEER PBEE Methodology to the I-880 Viaduct. *PEER Report 2006/10*. Pacific Earthquake Engineering Research Center, College of Engineering, University of California, Berkeley, February 2007

[23] K. R. Mackie, J. M. Wong, B. Stojadinovic, Integrated Probabilistic Performance-Based Evaluation of Benchmark Reinforced Concrete Bridges, *PEER Report 2007/09.* Pacific Earthquake Engineering Research Center, College of Engineering, University of California, Berkeley, January 2008

[24] G. Gazetas, A. Ziotopoulou, Bi-normalized Response Spectrum for a Rational Soil-Structure Interaction Analysis, Workshop on Soil Structure Interaction (SSI) Knowledge and Effect on the Seismic Assessment of NPPS Structures and Components, Otawa, Canada, 6-8, 2010

ECCOMAS Congress 2016
VII European Congress on Computational Methods in Applied Sciences and Engineering
M. Papadrakakis, V. Papadopoulos, G. Stefanou, V. Plevris (eds.)
Crete Island, Greece, 5–10 June 2016

EFFECT OF THE SEISMIC EXCITATION'S INCIDENCE ANGLE ON THE NONLINEAR BEHAVIOR OF BASE ISOLATED BUILDINGS CONSIDERING POUNDING TO ADJACENT MOAT WALLS

Eftychia A. Mavronicola[1*], Panayiotis C. Polycarpou[2], and Petros Komodromos[1]

[1,3] Department of Civil and Environmental Engineering, University of Cyprus
75 Kallipoleos Street, P.O. Box 20537, 1678 Nicosia, Cyprus
mavronicola.eftychia@ucy.ac.cy, *komodromos@ucy.ac.cy*

[2] Civil and Environmental Engineering Program, Department of Engineering, University of Nicosia
46 Makedonitissas Avenue, P.O. Box 24005 1700 Nicosia, Cyprus
polycarpou.p@unic.ac.cy

Keywords: pounding, non-linear analysis, three-dimensions, adjacent structures.

Abstract. *In the last decades, a number of reconnaissance reports have revealed that pounding between adjacent buildings, during strong earthquakes, may induce local and in some extreme cases severe structural damage. The problem of earthquake-induced pounding of adjacent buildings has been the subject of great scientific interest, while several recent numerical studies have quantified the effects of seismic pounding of buildings, with the majority of researchers simulating the problem in two dimensions (2D). The results from the various 2D parametric studies have demonstrated the potentially detrimental effects of pounding on the dynamic response of multistory buildings and revealed the importance of this problem regarding the safety and functionality of colliding structures. Furthermore, most of the numerical studies have been limited to the utilization of linear elastic structural models to simulate the adjacent buildings. The current study parametrically investigates the effect of pounding on the inelastic response of base isolated structures, which are simulated as non-linear 3D multi-degree of freedom systems subjected to bidirectional earthquake excitations. Specifically, the influence of certain parameters, such as the angle of the seismic incidence, the width of the seismic gap, characteristics of the isolation system and the configuration of the adjacent structures on the peak response, is parametrically examined, for various near-fault excitations. All numerical simulations are performed using a specially developed software that implements an innovative, simple and efficient approach to model impacts in 3D, taking into account the arbitrary location of contact points and the geometry at the vicinity of impact.*

1 INTRODUCTION

Frequently, neighboring buildings are constructed very close to each other, sometimes without any clearance between them. Hence, structural poundings may inadvertently occur between adjacent buildings, due to deformations of their stories, during strong seismic excitations. Consequences of such pounding incidences, ranging from local light damage to severe structural damage or even collapse, have been observed and reported after severe earthquakes. Poundings may also occur even in cases of seismically isolated buildings when the width of the available seismic gap around them is relatively limited, due to the large horizontal relative displacements that are expected at the isolation level, especially during near-fault, pulse-like ground motions.

Although several research studies have been conducted in order to investigate the problem of earthquake-induced poundings of adjacent structures and its consequences, most of them have been limited to simplified planar (2D) analyses [1–6], apparently due to the involved complexities and the consequently excessive computational cost. However, the effect of crucial factors, such as the consideration of both orthogonal seismic components, friction phenomena that occur during pounding, non eccentric impacts, irregularities, or asymmetries in the plan view of the colliding structures, which may excite the torsional vibration of a building and further increase the possibility of impacts during earthquakes, are essential parameters that can be taken into account only through three-dimensional (3D) simulations.

Recently, some researchers have shown great interest on the exploration of the effects of earthquake induced pounding of seismically isolated structures using 3D nonlinear dynamic analyses [7–12]. More specifically, Matsagar and Jangid, 2010 [7] investigated the seismic response of a single-story asymmetric structure supported on various base isolation systems during impact with adjacent structures. The effects of impact were found to be severe for systems with flexible superstructure, stiffer adjacent structures and increased eccentricities. Pant and Wijeyewickrema, 2014 [11] used a three-dimensional finite element model in order to investigate the seismic performance of a four-story building under bidirectional far-fault non-pulse-like and near-fault pulse-like ground motions scaled to represent two levels of shaking. Seismic pounding of the building with the retaining walls at its base was simulated using a specially developed purpose contact element that accounts for friction. Polycarpou *et al.*, 2015 [13] considered a new methodology for simulating earthquake induced pounding of seismically isolated buildings that are modeled as 3D multi-degree-of-freedom (MDOF) systems. An example of a 3-story seismically isolated building, pounding against the surrounding moat wall, has been presented to demonstrate the advantages of the proposed methodology.

The current study, utilizing the methodology described in [13, 14], aims to thoroughly investigate the circumstances under which spatial poundings may occur and assess the effect of some important parameters on the peak structural response considering pounding incidences. Nonlinear time-history analyses are carried out considering the arbitrary direction of the ground motion with respect to the structural axes of the simulated structures. The influence of the isolator's characteristics, the superstructure stiffness and the separation distance between the building and the retaining walls at its base is also investigated, while considering different geometrical arrangements for the moat walls.

2 MODEL FOR SIMULATION OF SEISMIC POUNDING

The numerical simulation of 3D pounding enables the investigation of certain parameters that are associated with the spatial movement of the seismically isolated building and cannot be explored through planar dynamic analyses. The effects of seismic pounding on the response of base-isolated reinforced concrete buildings under bidirectional excitations are

hereby investigated. A 3D model of a base isolated building is considered, where a recently proposed methodology [13, 14], which takes into account the arbitrary location of impacts and the geometry at the point of impact, is used. In particular, a new approach to the numerical problem of spatial impact modeling that does not require the a priori determination of the contact points was presented, taking also into account the geometries of the colliding structures at the vicinity of an impact.

More specifically, the simulated base isolated buildings are modeled as 3D-MDOF systems with shear-type behavior for their superstructures in the horizontal directions. The slab at each floor level of the superstructure is represented by a rigid diaphragm that is mathematically simulated as a convex polygon, while the masses are considered to be lumped at the floor levels, having three dynamic degrees of freedom (DOFs), i.e. two translational, parallel to the horizontal global axes, and one rotational along the vertical axis. Thus, considering ground excitations only in the horizontal directions, which is the most important case, no displacements occur in the vertical direction, since the translational dynamic DOFs of the structure refer only to horizontal planes. Consequently, it is assumed that the impact forces occur only in horizontal planes.

The time-history analysis involves the numerical integration of the differential equations of motion at each time step and the calculation of the resulting displacements, velocities and absolute accelerations at each DOF of each building. Based on the deformed position of each floor diaphragm in the 3D space, an automatic contact detection check is performed to identify potential contacts between structures, which are subsequently used for the computation of appropriate impact forces to be applied at the corresponding DOFs.

The majority of the force-based impact models that are available in the scientific literature calculate the impact force as a function of the interpenetration depth between the colliding bodies. However, the usage of the interpenetration depth as the key variable constitutes a significant drawback in the case of 3D impact modelling, as it cannot correctly assess the proper values of the impact forces. Therefore, in the proposed methodology, the area of the overlapping region, instead of the interpenetration depth, is used as the key variable in the calculation of the impact forces. Figure 1 describes, schematically, how the proposed impact model works. In particular, when two slabs, which are modelled as polygons, come in contact, they form an overlapping region that is either a triangle or a quadrilateral. The algorithm uses the geometry of the overlapping area at each time step in order to determine the location of the action point of the impact forces, as well as the direction and the magnitude of the impact forces. The Coulomb law of friction restricts the magnitude of the tangential impact force below a certain value.

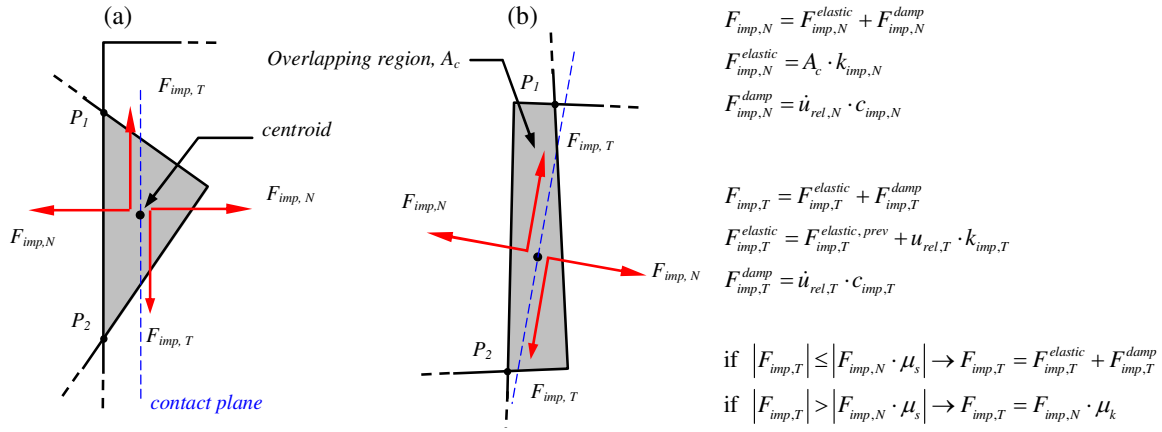

Figure 1: Schematic representation of the contact plane, based on the geometry of the indentation region, which can be either (a) a triangle, or (b) a quadrilateral.

3 DATA ANALYSIS

A three-storey (three-bay by three-bay), base-isolated reinforced concrete moment-frame building is chosen as a typical model structure (Figure 2). The building is symmetric with coinciding centers of mass and stiffness. The retaining walls extend from the ground level up to the base level of the building. All column sections of the simulated building have square dimensions of 45 x 45 cm^2. The bay width of the building in both directions is 5.5 m while each storey height is 3.2 m. The elastic modulus of concrete is assumed to be 30 GPa with a Poisson's ratio of 0.2. A uniformly distributed mass of 250 tons is considered for the roof mass, while a 340 tons floor mass is assumed at each other floor level, including the base of the building. For the determination of the Rayleigh damping matrix, the viscous damping ratios for the first and the fourth eigenfrequencies are taken as 0.05 and 0.02, respectively. Due to symmetry, the first two eigenmodes are translational along the two horizontal axes. The fundamental eigenperiods of the corresponding conventionally fixed-supported building are: $T_{x,fixed} = T_{y,fixed} = 0.311\sec$.

A coupled plasticity model is used for simulating the bidirectional lateral response of the seismic isolators. The aforementioned model is based on the hysteretic behavior proposed by Wen, 1976 [15] and Park *et al.*, 1986 [16] and recommended by Nagarajaiah *et al.*, 1991 [17]. Here, for each bearing element an isolation period based on the post-yield stiffness of 2.0 seconds, a yield displacement equal to 1.0 cm and a normalized characteristic strength $F_{xi}^{x}/W = F_{yi}^{y}/W$ equal to 0.05 or 0.10 are considered.

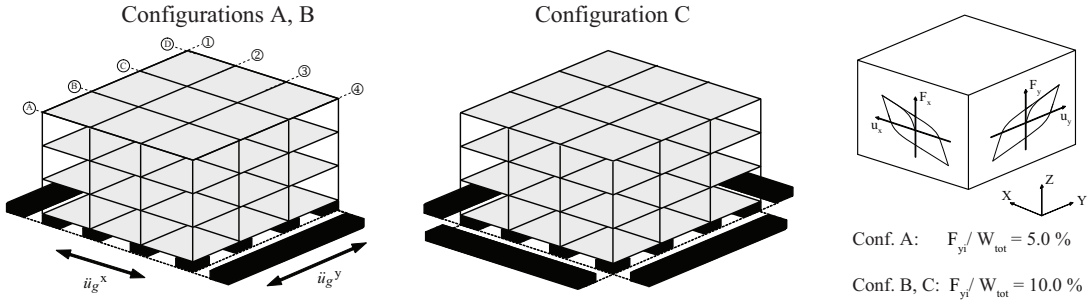

Figure 2: Configurations considered in the present study.

Impacts occur at the isolation level when the clearance from the surrounding moat wall, i.e. the seismic gap, is exceeded, during very strong seismic excitations. Nevertheless, the methodology provides the ability of considering impacts at all floor levels of the seismically isolated building in case of pounding with other adjacent buildings. The moat wall is modeled as a single-mass system, with three dynamic DOF, as in the case of a single-storey structure. The moat wall is taken to be 100 cm thick and 100 cm high, resulting in a substantially stiff barrier, while it's mass is assumed to be 5 tons/m, a number that takes into account the contribution of the backfill soil. The normal impact stiffness is $k_{imp,N}=2.58\times10^7$ kN/m^2, while the corresponding tangential impact stiffness is $k_{imp,T}=5.74\times10^6$ kN/m. The static and kinetic friction coefficients are taken as $\mu_s = 0.8$ and $\mu_k = 0.6$, respectively.

A set of earthquake ground motions has been selected from the Pacific Earthquake Engineering Research Center database. The selected seismic accelerograms (Table 1) are expected to induce large relative displacements to the seismically isolated building, since they are characterized by low-frequency contents, which is one of the most decisive factors for the occurrence of pounding in such structures. The response spectra of the five earthquakes' fault-

normal (FN) and fault-parallel (FP) components that have been used in this study are plotted in Figure 3.

NGA	Event	Year	Station	Mw	Comp	PGA (g)	PGV (cm/s)	PGD (cm)
#779	Loma Prieta	1989	LGPC	6.93	FN	0.94	97	62.5
					FP	0.54	72.1	30.5
#821	Erzican- Turkey	1992	Erzincan	6.69	FN	0.49	95.4	32.1
					FP	0.42	45.3	16.5
#828	Cape Mendocino	1992	Petrolia	7.01	FN	0.61	81.9	25.5
					FP	0.63	60.4	26
#1084	Northridge-01	1994	Sylmar – Converter Sta	6.69	FN	0.59	130.3	54
					FP	0.8	93.3	53.3
#2627	Chi-Chi- Taiwan-03	1999	TCU076	6.2	FN	0.52	59.3	9.6
					FP	0.16	19.5	3.6

Table 1: Summary of the main characteristics of the selected horizontal seismic excitations.

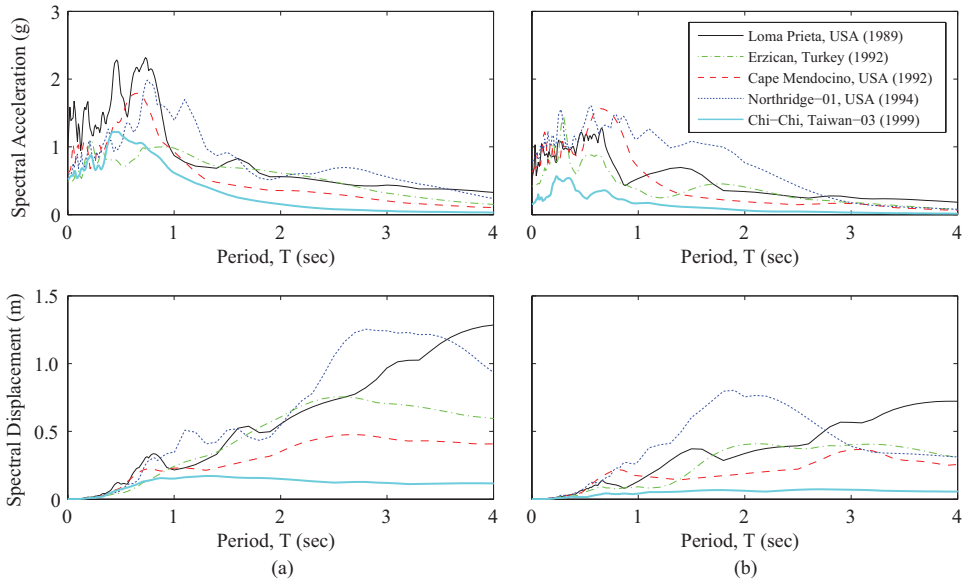

Figure 3: Acceleration and displacement response spectra of the (a) fault-normal, and (b) fault-parallel seismic components of the 5 earthquake records, considering a viscous damping ratio of 5 %.

4 INFLUENCING FACTORS IN 3D SIMULATIONS

The effect of the angle of incidence, on the peak structural response of the previously described 3-storey base isolated building, is presented in this section. The simulated structures are subjected, simultaneously, to two orthogonal, horizontal seismic excitations of their supporting ground. By rotating each of the 5 seismic record pairs, as presented in Table 1, from 0° to 180°, with respect to the system's principle axes of construction, with a 5° interval in the clockwise direction, one can consider 37 alternative excitation cases. In order to identify potential differences in the response of a 3-storey building due to the angle of incidence of the ground motion, the half polar plots of peak interstorey drifts are plotted in Figure 3, considering the Loma Prieta and the Northridge earthquakes. Specifically, the peak responses are presented for different characteristics of the seismic isolation system in Figure 4(a) and (b), for both seismic excitations. It is observed that the interstorey drifts tend to decrease with an increase in the normalized characteristic strength of the isolation system, Figure 4(b).

The simulation results indicate that the maximum responses occur at different angles. The critical angle in the longitudinal (*E-W* or *X*) direction is not always at 0 and 90 degrees, but occurs in incidental angles that are quite different for each excitation. In the case of seismically isolated buildings, the maximum relative displacements at the isolation level in the *X*-direction can vary by a factor of 3.9 and 1.4 over the possible angles of interest, for the Loma Prieta and the Northridge earthquakes, respectively. This is considered to be a significant variation. For both excitations, the critical excitation angle for the interstorey deflections is nearly common among all floors. The maximum floor relative displacement in the *X*- direction occurs at the complimentary angle of the maximum interstorey drift in the *Y*- direction. Although, the peak interstorey drifts in each direction depend highly on the incidence angle, the vector sum of the responses (i.e. the vectorial summation of the peak responses in the Cartesian Coordinates X and Y) slightly varies for different angles. As the peak responses of the X and Y components occur at different time intervals, although their vectorial summation does not have a physically meaning nevertheless it provides a conservative upper bound limit that can be used for design purposes.

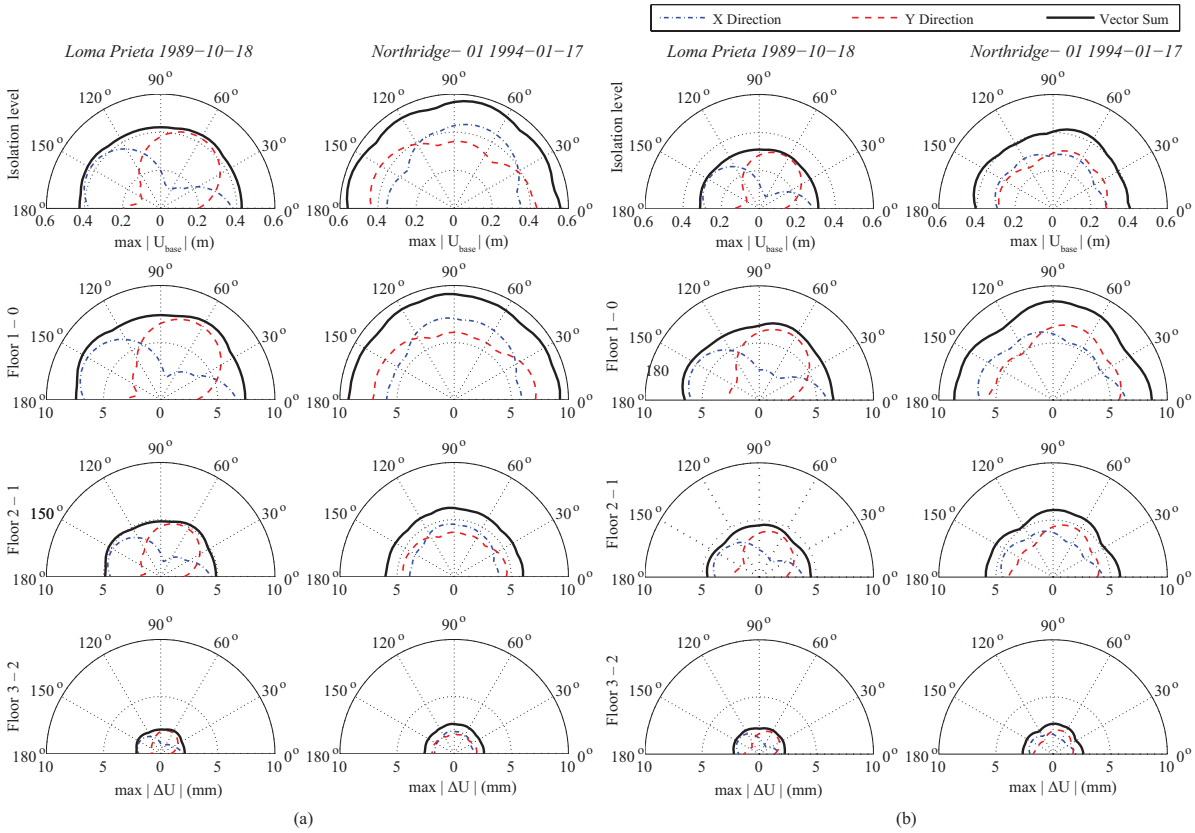

Figure 4: Peak responses of the buildings' corner column A_1 as a function of the angle of incidence considering the no pounding" case, for seismic isolation systems with T_b = 2.0 sec, u_y = 1.0 cm, F_{yi}/W_{tot} equal to (a) 0.05 and (b) 0.10; in both directions.

4.1 Isolator characteristics and configuration

Peak absolute values of the base drifts and the envelope of interstory deflections of the column A_1, are shown in Figures 5 and 6 for various angles of seismic incidence. For the analyses, both FN/FP components of the five selected near-fault ground motions are simultaneously used. The seismic gap is assumed to be 20 cm for the four of the selected exci-

tations and 10 cm for the remaining (Chi-Chi- Taiwan-03) ground motion. Three configurations are considered (Figure 2), as follow:

Conf. A: Base-isolated building with retaining walls in two sides (*E-W* direction)
LRBs: $T_b^x = T_b^y = 2.0$ sec, $u_y^x = u_y^y = 1.0$ cm, $F_{yi}^x / W = F_{yi}^y / W = 5.0\%$

Conf. B: Base-isolated building with retaining walls in two sides (*E-W* direction)
LRBs: $T_b^x = T_b^y = 2.0$ sec, $u_y^x = u_y^y = 1.0$ cm, $F_{yi}^x / W = F_{yi}^y / W = 10.0\%$

Conf. C: Base-isolated building with retaining walls in all four sides
LRBs: $T_b^x = T_b^y = 2.0$ sec, $u_y^x = u_y^y = 1.0$ cm, $F_{yi}^x / W = F_{yi}^y / W = 10.0\%$

In this section, the response of the base-isolated building in each configuration is discussed. The results for the "no pounding" case are presented in Figure 5, and, for comparison purposes, the restricted base drifts of the corner column are also plotted for each excitation in terms of the excitation angle. The variation of the unobstructed base drifts indicate that the value of the incidence angles depends on the characteristics of the earthquakes, in combination with the characteristics of the isolation system. The critical excitation angle of a certain response quantity differs among the various earthquakes.

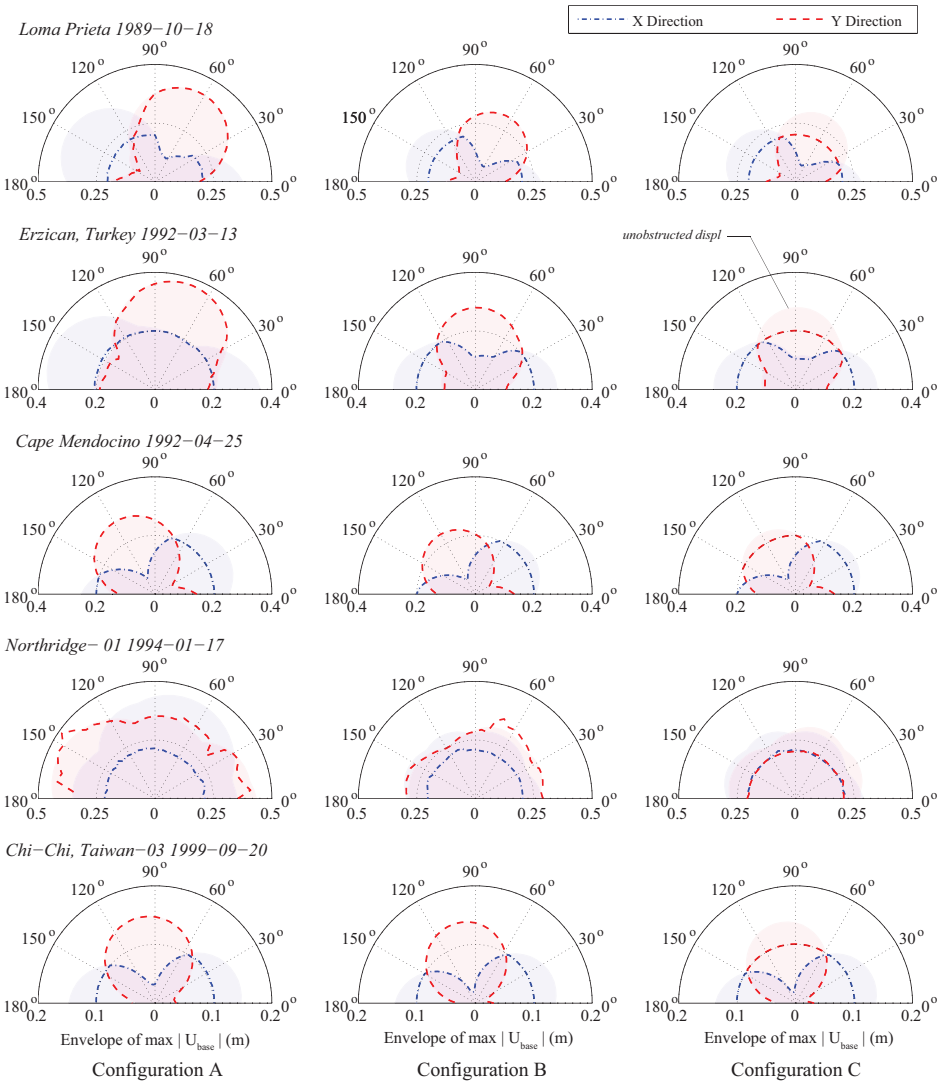

Figure 5: Half-polar plots of maximum unobstructed and restricted relative displacements at the isolation level of the buildings' corner columns in terms of the excitation angle for different configurations.

The peak responses of the superstructure of the base isolated building considering different configurations and the corresponding fixed-supported building without pounding are presented in Figure 6. It becomes evident from the computed results, that the direction of the seismic excitation affects substantially the maximum response of the seismically isolated building, especially during pounding with the surrounding moat walls. The increase in drift demands due to pounding in Configuration B is less compared to Configuration A for all examined ground motions (second and third columns of Figure 6). This is mainly because the available gap size is more restricted in the first case compared to the corresponding maximum unobstructed displacement of the base isolated building, as illustrated in the first two columns of Figure 5.

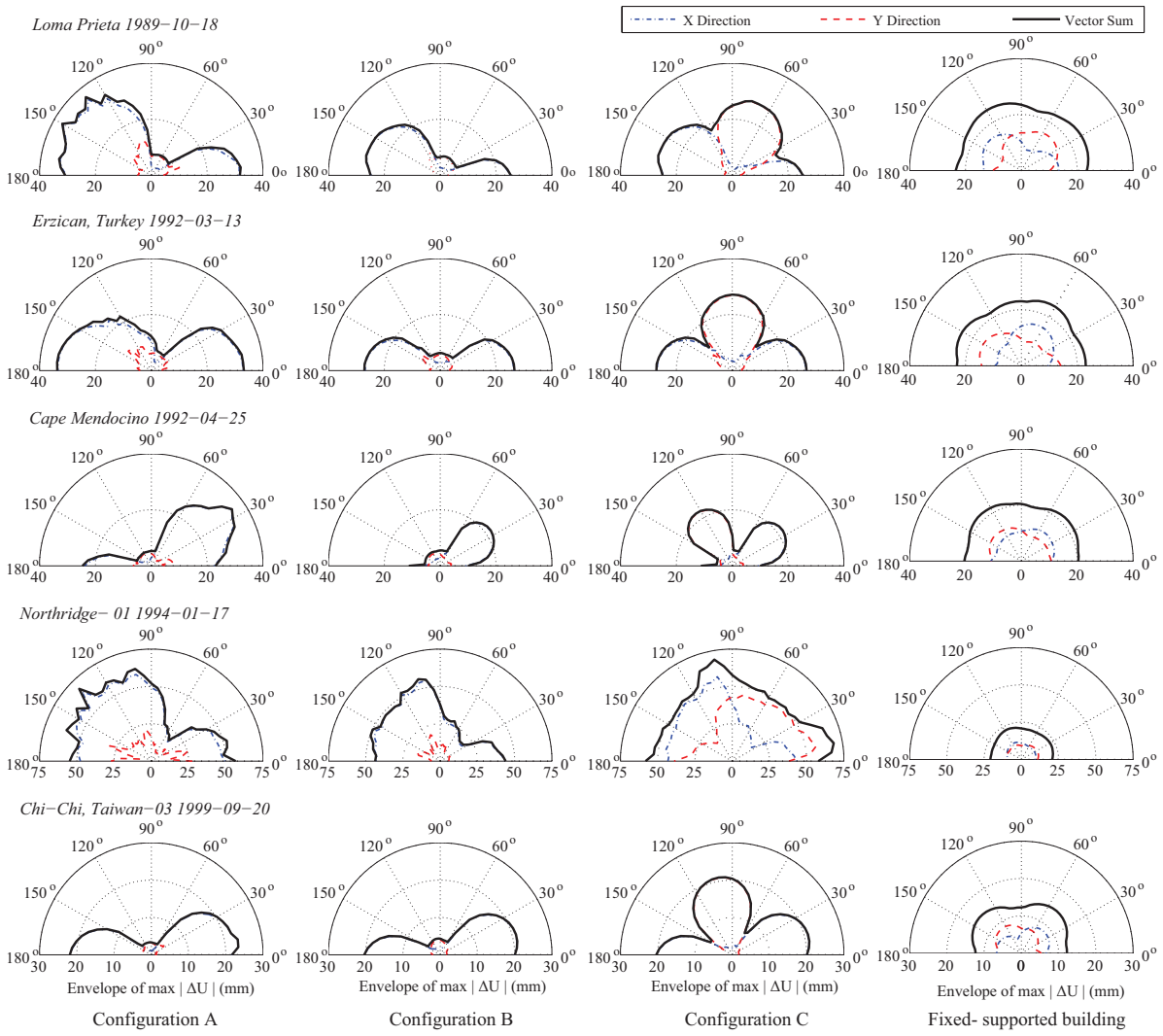

Figure 6: Envelope of peak interstorey drifts of the buildings' corner column A_1 in terms of the excitation angle, considering the pounding case with the moat wall for various configurations; under five near-fault ground motions, and the no pounding case of a conventionally fixed-supported building.

For the configurations A and B, due to poundings with the moat walls at the *X*-direction, if we consider 360°, due to the rotational symmetry of the 180° plots, the plots of the peak responses would resemble 8-shapes, exhibiting a pronounced dependence of the peak response on the incidence angle. Furthermore, the change in the response–angle relationship due to pounding is not so obvious in the *Y*-direction, since impacts occur only in the *X*-direction. For

the Configuration C, the peak response depends on the incidence angle, and the maximum interstorey drifts tend to exhibit two maxima in orthogonal directions. Furthermore, although the retaining walls are placed on each of the four sides of the building, four of the excitations resulted in one-direction impact for a range of excitation angles leading to a petal-like shape response, with two-orthogonal axes of symmetry. For example, for the Loma Prieta excitations, considering an incidence angle, $\theta \approx 30\text{-}100^\circ$, impacts occur only in the *Y*-direction.

The maximum interstorey drift over all examined orientations seems to be polarized in the direction in which the peak base displacement is observed; this polarization is almost perfect for this symmetric-plan building. The value of the maximum inter-storey drift ratio, due to the Northridge earthquake, indicates potential collapse of the first storey. Drift demands due to other earthquakes are significantly lower for all the cases that have been examined. As already discussed, the influence of poundings in the response of the base isolated building can be much less detrimental when isolators with normalized characteristic strength equal to 0.10 are incorporated, however the peak interstorey drifts due to impacts can become higher than those for the corresponding fixed-supported building (as shown in the last column of Figure 6).

4.2 Available gap size

In order to examine the effect of the seismic gap size on the response of the seismically isolated building during pounding with the moat wall, two of the aforementioned configurations are considered. The structural characteristics of the base isolated buildings, as well as the isolation characteristics are kept the same. The width of the seismic gap varies from 15 to 35 cm, with a step of 2.5 cm. Figures 7 (a) and (b) show the relationship among peak interstorey drifts of the 3-storey seismically building, the incidence angle and the width of the available seismic gap of the adjacent walls located in the *E-W* direction under the bidirectional excitation of the Loma Prieta and the Northridge earthquakes, respectively. Similarly organized results are presented in Figure 8, considering impacts with the surroundings walls located around all four sides of the simulated building.

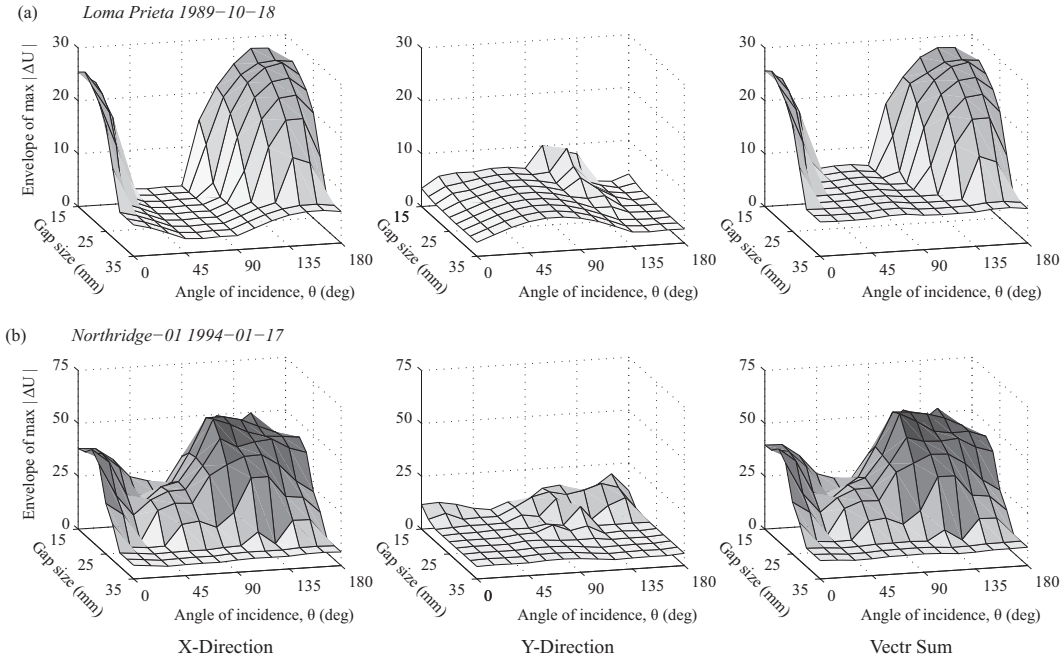

Figure 7: Envelope of the interstory deflections in the X and Y directions, as well as vector sum for different combinations of the excitation angle and the available gap size, considering adjacent walls in the two sides of the building (Conf. B) for (a) the Loma Prieta, and (b) the Northridge excitations.

It becomes evident from the plots, that the angle for which the maximum response is observed is not the same for the two earthquakes that are considered, while the degree by which pounding affects the peak response seems to depend on the ground motion characteristics and the available gap size. The influence of the excitation angle is more pronounced in the case of pounding in one direction, as shown in Figure 7. Furthermore, it is important to mention that although no pounding occurs in the *Y*-direction the deflections of the column A_1 in the Y direction are also considerably affected from pounding in cases with more restricted gap in the *E-W* direction. In general, the vector sum of the superstructure' drifts increases when the separation distance between structures decreases and, then, slightly decreases with further reduction in the separation. It is noteworthy that the interstorey drifts in the X and Y directions, as shown in the first two columns of Figure 8, respectively, present translational symmetry. Furthermore, translational symmetry seems to appear to the vector sum of interstorey drifts due to the bilateral symmetry of the building and the adjacent structures.

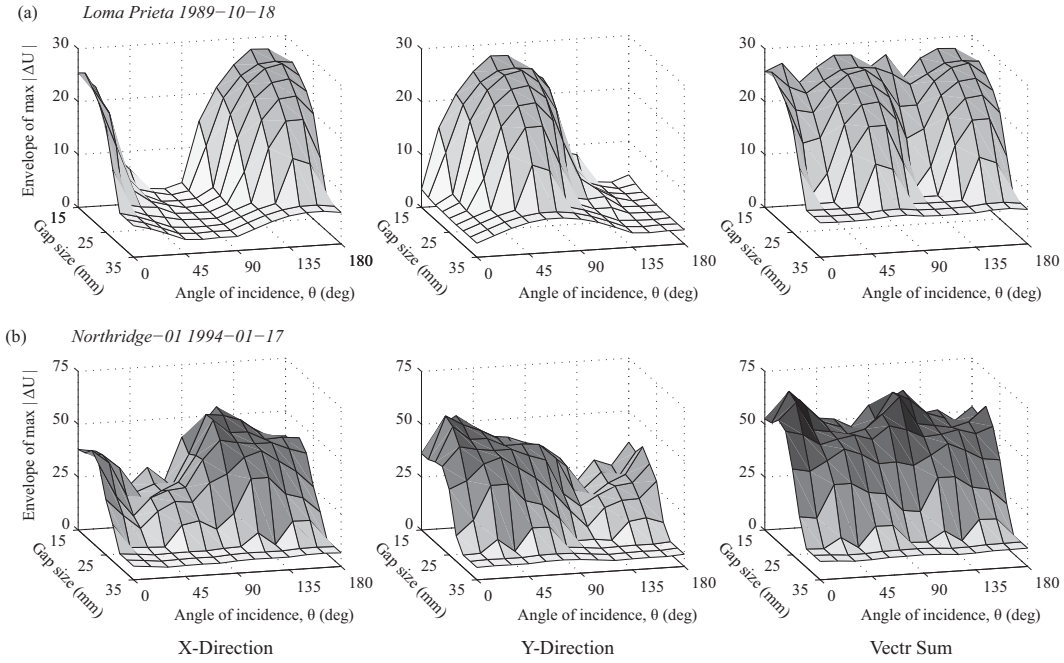

Figure 8: Envelope of the story drifts for various excitation angles and gap sizes for Configuration C under near fault ground motions.

4.3 Stiffness of the superstructure

In order to study the effects of the superstructure's flexibility on the overall dynamic response, the peak interstorey drifts are obtained for different fundamental eigenperiods of the superstructure of the examined three-storey isolated building with impact conditions under the Loma Prieta and Northridge earthquakes, as shown in Figure 9. Different superstructure's stiffnesses are obtained considering different cross sections of the columns. The isolation system considered consists of lead-rubber bearings (LRBs) with normalized characteristic strength $F_{yi}^{x}/W = F_{yi}^{y}/W$ of 0.10 in both directions, with isolation gap distances of 20 cm around all four sides of the structure. It should be noted that the results presented in Figure 9(b) refer to the peak response of the previous section described in Configuration C.

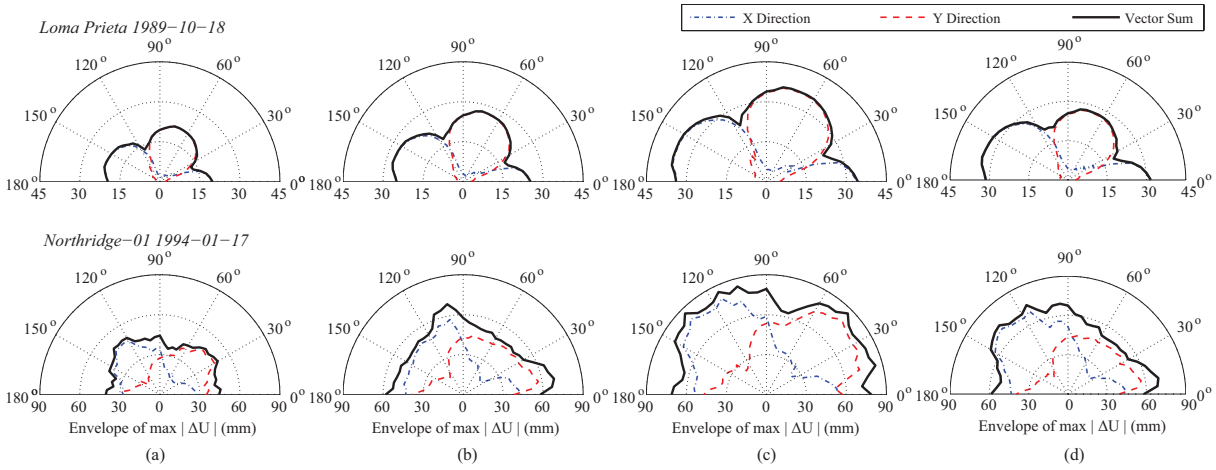

Figure 9: Envelope of peak interstorey deflections of the buildings corner columns in terms of the excitation angle considering superstructure stiffness: $T_{x,\,fixed} = T_{y,\,fixed}$ equal to (a) 0.25 sec, (b) 0.311 sec, (c) 0.394 sec, and (d) $T_{x,\,fixed} = 0.372$ sec, $T_{y,\,fixed} = 0.312$ sec.

These figures show that the superstructure's deflections undergo an increase when the fundamental eigenperiod of the corresponding superstructure increases. This implies that the behavior of the base isolated building during impact becomes adverse while increasing the flexibility of the superstructure. Furthermore, the stiffness of the superstructure does not seem to influence the excitation angle that dominates the response. It is possible to identify a clear pattern in the response of the structure. For structures with equal horizontal stiffness along the two axes of symmetry X and Y, where $T_{x,\,fixed} = T_{y,\,fixed}$, the response shows two separate peaks for the Loma Prieta excitation, one associated with $\theta = 75°$ and the second around $\theta = 165°$, leading to a petal-like shape with double symmetry. For the structures with unequal eigenperiod, instead, the peak tends to be in a single direction, and the plots assume a shape with unequal "petal" length. Furthermore, there is a similar response of the interstorey deflections in *Y*-direction in Figure 9(b) and (d), for both excitations, which relates to the almost identical superstructure stiffness in Y-direction.

5 CONCLUSIONS

The present study demonstrates the importance of implementing an efficient methodology with simple structural and impact modelling in three dimensions, in order to investigate the seismic pounding on the response of MDOF systems. Seismic response of a 3-storey base isolated building during impact with an adjacent moat wall is investigated. The comparative performance of different isolation systems during various impact conditions is studied under five near-fault ground motions. Parametric studies for simulating earthquake induced pounding of seismically isolated buildings are conducted in three-dimensions to observe the influence of the incidence angle, the width of the seismic gap and the flexibility of the superstructure on the peak response of the base isolated building. From the trend of the results presented hereby, the following conclusions are drawn:

- The deflection of the superstructure of a base-isolated building increases significantly when impact with a moat wall takes place during an earthquake. The bearing displacement is consequently reduced.
- The detrimental effects of pounding may become more severe for certain values of the excitation angle. The incidence angle, in which the amplification of the superstructure response due to pounding with the adjacent building obtains its maximum value, generally coincides with the angle in which the peak base displacement occurs.

- In general, the degree by which the incidence angle affects the interstory deflections seems to be significantly affected by the surrounding wall arrangement.
- The normalized characteristic strength of the isolators has significant influence on the peak response of a base-isolated structure during impact. This can be justified considering that with an increase of the F_{yi}/W_{tot} ratio, the relative displacements at the isolation level decrease substantially, in combination to the influence of the width of the available seismic gap compared to the corresponding maximum unobstructed displacements under those excitations.
- As the seismic gap between the base-isolated building and the adjacent wall decreases, there is an increase in the deflections of the superstructure up to a certain value of the gap distance and, then, onwards the deflections of superstructure decrease.
- Increased flexibility of the superstructure increases significantly the drifts of the superstructure during impact with the adjacent structure.

REFERENCES

[1] Matsagar, V. A.., Jangid, R. S., Seismic response of base-isolated structures during impact with adjacent structures. Eng. Struct. **25**(10), 1311–1323, 2003.

[2] Komodromos, P., Simulation of the earthquake-induced pounding of seismically isolated buildings. Comput. Struct. **86**(7-8), 618–626, 2008.

[3] Ye, K., Li, L.., Zhu, H., A modified Kelvin impact model for pounding simulation of base-isolated building with adjacent structures. Earthq. Eng. Eng. Vib. **8**(3), 433–446, 2009.

[4] Polycarpou, P. C.., Komodromos, P., On poundings of a seismically isolated building with adjacent structures during strong earthquakes. Earthq. Eng. Struct. Dyn. **39**(8), 933–940, 2010.

[5] Mavronicola, E., Polycarpou, P. C.., Komodromos, P., The effect of modified linear viscoelastic impact models in the pounding response of a base-isolated building with adjacent structures. *5th ECCOMAS Thematic Conference on Computational Methods in Structural Dynamics and Earthquake Engineering* (COMPDYN2015), Crete, 2015

[6] Jankowski, R.., Mahmoud, S., *Earthquake-Induced Structural Pounding,* Springer International Publishing, Cham, 2015.

[7] Matsagar, V. A.., Jangid, R. S., Impact Response of Torsionally Coupled Base-isolated Structures. J. Vib. Control **16**(11), 1623–1649, 2010.

[8] Sato, E., Furukawa, S., Kakehi, A.., Nakashima, M., Full-scale shaking table test for examination of safety and functionality of base-isolated medical facilities. Earthq. Eng. Struct. Dyn. **40**(13), 1435–1453, 2011.

[9] Jankowski, R., Non-linear FEM analysis of pounding-involved response of buildings under non-uniform earthquake excitation. Eng. Struct. **37**, 99–105, 2012.

[10] Varnava, V.., Komodromos, P., Assessing the effect of inherent nonlinearities in the analysis and design of a low-rise base isolated steel building. Earthq. Struct. **5**(5), 499–526, 2013.

[11] Pant, D. R.., Wijeyewickrema, A. C., Performance of base-isolated reinforced concrete buildings under bidirectional seismic excitation considering pounding with retaining walls including friction effects. Earthq. Eng. Struct. Dyn. **43**(10), 1521–1541, 2014.

[12] Moustafa, A.., Mahmoud, S., Damage assessment of adjacent buildings under earthquake loads. Eng. Struct. **61**(1), 153–165, 2014.

[13] Polycarpou, P. C., Mavronicola E., Komodromos, P., Planar and spatial numerical investigation of the effects of earthquake-induced pounding of base isolated buildings. *14th World Conference on Seismic Isolation, Energy Dissipation and Active Vibration Control of Structures* (14WCSI), San Diego, Ca USA, 2015.

[14] Polycarpou, P. C., Papaloizou, L.., Komodromos, P., An efficient methodology for simulating earthquake-induced 3D pounding of buildings. Earthq. Eng. Struct. Dyn. **43**(7), 985–1003, 2014.

[15] Wen, Y.-K., Method for random vibration of hysteretic systems. J. Eng. Mech. Div. **102**(2), 249–263, 1976.

[16] Park, Y. J., Wen, Y.-K.., Ang, A., Random vibration of hysteretic systems under bi-directional ground motions. Earthq. Eng. Struct. Dyn. **14**(4), 543–557, 1986.

[17] Nagarajaiah, S., Reinhorn, A. M.., Constantinou, M. C., Nonlinear Dynamic Analysis of 3D Base Isolated Structures. J. Struct. Eng. **117**(7), 2035–2054, 1991.

ECCOMAS Congress 2016
VII European Congress on Computational Methods in Applied Sciences and Engineering
M. Papadrakakis, V. Papadopoulos, G. Stefanou, V. Plevris (eds.)
Crete Island, Greece, 5–10 June 2016

NUMERICAL NON-LINEAR SIMULATION OF THE IN-PLANE BEHAVIOUR OF R/C FRAMES WITH MASONRY INFILLS UNDER SEISMIC-TYPE LOADING

George C. Manos [1], Vassilios J. Soulis [2]

[1] *Emeritus Professor, Department of Civil Engineering, Aristotle University of Thessaloniki, Thessaloniki, Greece*
gcmanos@civil.auth.gr

[2] *Lecturer Department of Civil Engineering, Technical Educational Institute of Piraeus, Piraeus, vassilios_soulis@yahoo.com*

Keywords: Numerical simulation, Masonry-infilled R/C frames, Shear failure of columns.

Abstract. *A non-linear 2-D numerical simulation is presented that can capture the in-plane hysteretic behaviour of reinforced concrete (R/C) frames with masonry infills when they are subjected to combined vertical and cyclic seismic type horizontal loads. The effectiveness of this simulation was validated extensively in the past by comparing numerical predictions with results from a series of pseudo-dynamic tests whereby a number of 1:3 scale, one-bay, one-storey R/C frame specimens, including relatively weak masonry infills, were subjected to combined vertical and cyclic horizontal seismic-type loads under controlled laboratory conditions. The numerical modelling of the surrounding R/C frame included its flexural non-linear behaviour by simulating the development of plastic hinges either at the two ends of the R/C beam and/or at the top and toe of the R/C columns. All geometric and mechanical characteristics of the concrete and the longitudinal reinforcement of the R/C cross-sections were considered in detail. Sufficient shear reinforcement was assumed for both R/C beam and columns capable of prohibiting shear mode of failure. However, observations of failure modes for R/C infilled frames with columns under-designed in shear have shown that, when subjected to earthquake loads, the development of shear failure for the columns is an additional realistic scenario. The first part of the work presented here is investigating such an interaction of masonry infill with the R/C frame simulating both flexural and shear modes of failure for the R/C columns. This numerical simulation retains the non-linear behaviour of the masonry infill itself as well as the non-linear behaviour at the contact area where the masonry-infill and the surrounding frame. The second part of the present work examines the influence of the foundation deformability for such multi-storey infilled frames having an increased in-plane stiffness due to the presence of the masonry infills.*

1 INTRODUCTION

An extensive experimental and numerical study ([3], [4], [5] ,[6], [7]) was carried out at the laboratory of Strength of Materials and Structures, Aristotle University, in order to examine the in-plane seismic behaviour of infilled R/C frames. This study as well as previous studies ([1], [2]) demonstrated that the stiffness and strength of the masonry infilled, single-storey, R/C frames can be affected by various non-linear mechanisms such as:

a) The non-linear behaviour of the R/C frame including flexural limit state (plastic hinges) and shear limit state.

b) The non-linear mechanisms that develop at the interface between the R/C frame and the masonry infill.

c) The level of non-linear deformations that develop within the masonry infill itself.

In all these cases it was reported that the frames developed plastic hinges at their R/C beam and columns. All these have been simulated successfully, as is shown in section 2. In addition, it is also demonstrated that through a certain modification to this numerical approach proposed by Soulis [1] the shear limit state of the R/C columns at predefined locations can also be simulated. In order to validate this proposed modification the experimental study conducted by Sariyiannis is utilized [8]. He subjected a number of one-storey one-bay 1/3 scaled infilled frames to axial forces at the columns as well as horizontal seismic type cyclic forces at the level of the beam. Nine repaired infilled frames and two repaired bare frames were examined in this study. These specimens were produced by repairing damaged 1/3 scaled R/C infilled frames tested previously by Stylianides [3]. These original virgin frames had a non-reinforced brick-masonry infill panel which was simply connected to the surrounding R/C frame by a continuous mortar joint. After this initial test sequence was completed the damaged frames were repaired in order to be tested again [8]. As expected, the type of failure of the columns depended on the type of failure of the masonry infills. In a number of specimens tested by Sariyiannis [8] shear sliding of the infill along a horizontal mid-height mortar joint or corner crushing of the masonry infill was accompanied by the shear failure of the R/C columns. Two of these masonry infilled frame specimens, namely F1NR and F8NR [8], failed as a result of corner crushing of the infill and shear failure of the column. The masonry infilled frame F8NR is employed in the current paper in an effort to validate the proposed modified numerical simulation of masonry infilled R/C frame that can also realistically simulate this shear type of failure.

Stavridis [9], also carried out an experimental program of quasi-static tests with single-bay, single-storey, masonry-infilled, non-ductile RC frames, which were scaled sub-assemblages of a prototype structure. These tested specimens were 2/3-scaled models of such frames in a prototype building with design details representative of those used in the construction practice in California during the 1920's [9]. Two of these specimens (referred to as CU1 and CU2) were single-storey, single bay masonry infilled frames that were tested with quasi-static cyclic loads [9]. A third specimen represented a three storey frame with two bays; this was tested on a shake table at UCSD [9]. After reaching the peak load, the specimen CU1 developed diagonal shear cracks in the concrete columns as an extension of the dominant cracks in the masonry infill. The same failure pattern was reported for the CU2 specimen with a window opening. Again, one of the columns in the CU2 specimen had a major shear crack which developed close to mid-height of the column. Koutromanos et al. [10], demonstrated the ability of a proposed nonlinear finite element model to capture the response of masonry-infilled reinforced concrete frames under cyclic loads. Diffused cracking and crushing in concrete and masonry are simulated by a smeared-crack continuum model, while dominant cracks as well as masonry mortar joints are modeled with a cohesive crack interface model.

The interface model adopts an elasto-plastic formulation to describe the mixed-mode fracture of concrete and masonry. This model accounts for cyclic crack opening and closing, reversible shear dilatation, and joint compaction due to damage. The constitutive models have been validated successfully with experimental data and applied to the dynamic analysis of a three-storey, two-bay, masonry-infilled, non-ductile, reinforced concrete frame, which was tested on a shake table [9]. The plane-stress smeared-crack model was used for the simulation of the continuum elements representing masonry units and concrete elements. The numerical simulation presented by Koutromanos et al. [12] can accurately reproduce the load–displacement response, crack patterns, and failure mechanisms of the infilled frames including the shear cracking of infill and the surrounding frame.

Valid numerical models of multi-storey infilled frames were investigated in the past by many researchers (see relevant review in [3] and [4]). The numerical simulation proposed by Soulis [1] was used to simulate the behaviour of three-storey structural formations including masonry infills; in particular a multi-storey planar R/C frame structure, which was constructed and tested at the University of California, Berkeley by Klingner and Bertero [11] was examined. Reasonably good agreement was observed between the numerical results and the experimental measurements regarding the hysteretic behaviour of the “bare”, and infilled three-storey specimens. In the second part of this paper the numerical simulation of the behaviour of a 6-storey masonry infilled R/C frame structure located at the Volvi-Greece European Test Site for Earthquake Engineering [12] is examined employing an elastic dynamic analysis and a non-linear “push over” analysis. Six basic structural configurations are studied including a "Bare" structure (only the R/C frames without any masonry infills) and various formations that resulted with the addition of masonry infills for this specimen of a simple R/C multi-storey building. These structural formations that were studied numerically correspond exactly to this 6-storey 1/3 scaled model building during a period of 10 years, from 1994 onwards. A large number of low-amplitude dynamic tests have been conducted in-situ over an extended period, mainly from 1995 till 2006. By combining this large volume of dynamic response measurement data from the various in-situ low-vibration sequences, the most important mode shapes and eigen-frequencies were identified. This six-storey masonry infilled structure is numerically simulated in section 3. Initially, its dynamic behaviour is predicted utilizing the same simulation technique adopted in section 2 assuming, however, linear material properties and different foundation conditions. Next, a non-linear “push over” numerical analysis is performed in order to identify numerically its bearing capacity and the sequential appearance of various failure modes as predicted by this numerical simulation. In this “push over” analysis the soil-foundation conditions of the six-storey masonry infilled R/C frame structure is examined assuming either rigid or relatively flexible contact interface.

Frame Code name	Vertical load on Columns (KN)	Technical description of masonry infill	Masonry Infill thickness (mm)	Technical description of the interface between frame and infill	Longitudinal reinforcement ratio (ρ)
F8NR **Repaired** [8]	80	Infill with mortar **O** reinforced with reinforced plaster, without transverse reinforcement	83	mortar **O** thickness **10mm** The reinforced plaster is in contact with the surrounding frame	1.01%
CU1[9]	156	Infill with mortar **N**	95	mortar **N** thickness **10mm**	1.00%
CU2[9]	156	Infill with mortar **N**	95	mortar **N** thickness **10mm**	1.00%

Table 1 Outline of all specimens for the 1st and 2nd group of specimen

2 THE NUMERICAL SIMULATION OF THE BEHAVIOUR OF SINGLE-STOREY SINGLE-BAY MASONRY-INFILLED R/C FRAMES

The present work studies the interaction of masonry infill with the R/C frame including in this numerical simulation the development of flexural (plastic hinge) and/or shear limit state for the surrounding R/C frame. Three scaled R/C infilled frame specimens, one of them, namely specimen F8NR, tested by Saryiannis [8] and two of them, namely CU1, CU2, tested by Stavridis[9], are utilized for the verification of the proposed numerical simulations. In all these cases the numerical response predictions are compared with the corresponding experimental results. Brief information on the selected masonry infilled R/C specimens is listed in table 1 and figures 1 and 2. The influence exerted by the interface mortar joint between the masonry infill and the surrounding frame was also examined here [3], [4], as was also done in both studies by Thauampteh [2] and by Soulis[1]. Tables 2, 3 and 4 list the mechanical properties of the materials used in the construction of the specimens.

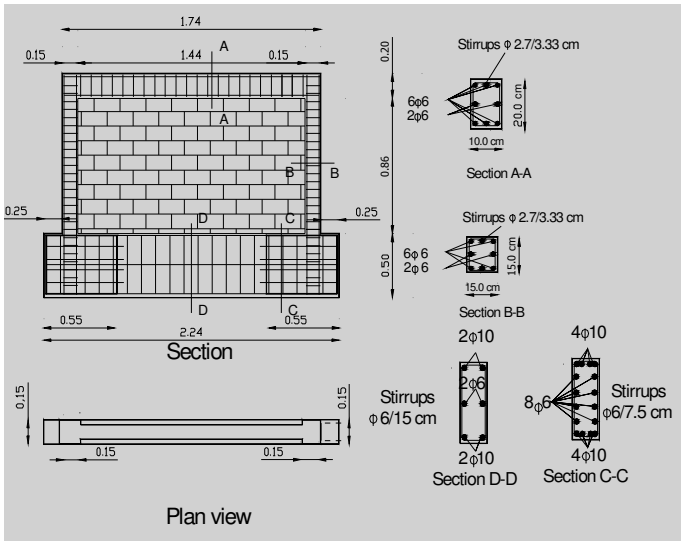

Figure 1. Masonry infilled R/C frame F8NR specimen and design details [8].

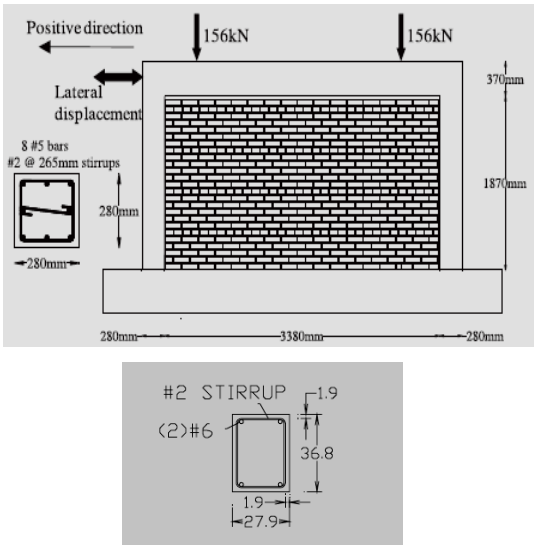

Figure 2. Masonry infilled R/C frame CU1 specimen and design details [9].

Masonry infill	Compressive strength of masonry (N/mm^2)	Shear strength of masonry diagonal compression (N/mm^2)	Compres. strength of masonry units (N/mm^2)	Compres. strength of concrete (N/mm^2)	Compres. strength of mortar cylinders (N/mm^2)	Compress. strength of cement plaster (N/mm^2)	Compres. strength of Injected Epoxy Resin (N/mm^2)
Reinforced infill F8NR [8]							
Infill with mortar **O**, reinforced with reinforced plaster without transverse reinforcement	2.12	0.64 (corner crushing)	5.50	25.9	2.7	11.3	94
Virgin infill CU1[9]							
Infill with mortar **N**	24.3		49	29,5	9.2		
Virgin infill CU2[9]							
Infill with mortar **N**	24.3		49	29,5	9.2		

Table 2**:** Strengths of masonry infills and concrete used in the specimens [8],[9]

A/α	Yield stress f_{sy} (N/mm^2)	Ultimate strength f_{su} (N/mm^2)	Strain at yield ε_{sy} (%)	Strain at ultimate stress ε_{su} (%)	Young Modulus (N/mm^2)
Reinforced infill F8NR [8]					
Φ5.5	348	457	0.174	18.0	2X10^5
Φ2.7stirrups	271	395	0.135	19.0	2X10^5
Virgin infill CU1[9]					
Φ#5 15.9mm	472	752	-	9.0	
Φ#2 6.4mm stirrups	431	472	-	13.0	

Table 3**:** Tensile strength of the reinforcement used in the specimens [8],[9]

A/a	Simulation of joint interface between frame and infill	**E** Young Modulus (N/mm^2)	**G** Shear Modulus (N/mm^2)	$\mathbf{f_k}$ Measured Compressive Strength of mortar (N/mm^2)	$\mathbf{f_{tn}}$ Assumed Tensile Strength of mortar (N/mm^2) (as % of f_c)	**τo** Local bond shear strength of mortar (N/mm^2)	**μ** friction coeffici ent
1	**O** mortar F8NR	540	234	2.70	0.27(10%)	0.31	0.58
2	**N** mortar CU1	1350	587	9,00	0.50		0.90
3	**N** mortar CU2	810	352		0,40		0.90

Table 4**:** Mechanical properties of the mortar joint located between the infill and the surrounding frame (mortar type H, N) [3], [4]

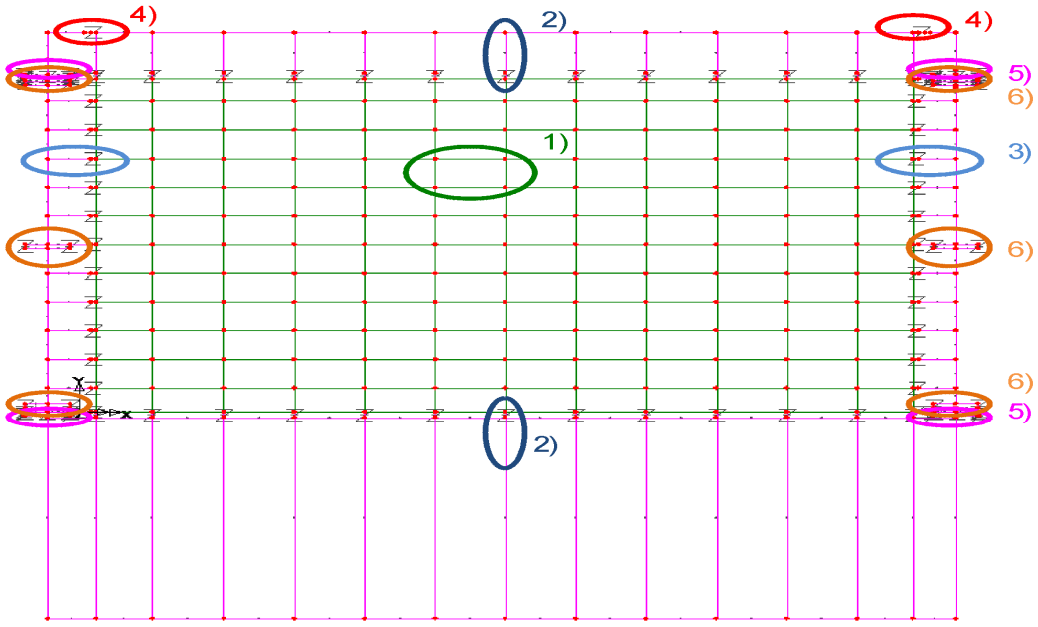

Figure 3. Features of the non-linear numerical simulation of a single-bay single-storey masonry infilled R/C frame

2.1 Simulation of the single storey masonry infilled R/C frame

An extensive study of various numerical simulations of the behaviour observed for masonry infilled R/C one-bay one-storey frame specimens tested by Thauampteh [2], by Stylianides [5], by Valiasis [6], and by Yasin [7] was included in the work by Soulis[1] together with an extensive validation process, utilizing the results of all these experimental studies ([2], [5], [6], [7]). Here a modified numerical model similar to the one presented before is examined that incorporates the simulation of the formation of shear limit state in predefined locations along the height of the two columns of such R/C specimens. The features of the numerical simulation are presented in figure 3 and in more detail in figures 4 and 5. These features are the same as the ones proposed by Manos, Soulis & Thauampteh before ([3], [4]) with the

addition of the possibility of shear limit state at predetermined locations along the height of the R/C columns of the single storey R/C frame. In figure 3 these non-linear mechanisms are denoted as: (1) corresponding to the non-linear behaviour of the masonry infill itself, (2) the infill-beam interaction at the contact region, (3) the infill-column interaction at the contact region (4) the formation of a plastic hinge at the end of a beam, (5) the formation of a plastic hinge at the top or bottom of a column and finally (6) the formation of a shear limit state along the height of a column. These non-linear mechanisms are also depicted in some detail in figure 4 (non-linear mechanisms (1), (2), (3) and (4) and in figure 5 (non-linear mechanisms (5) and (6)).

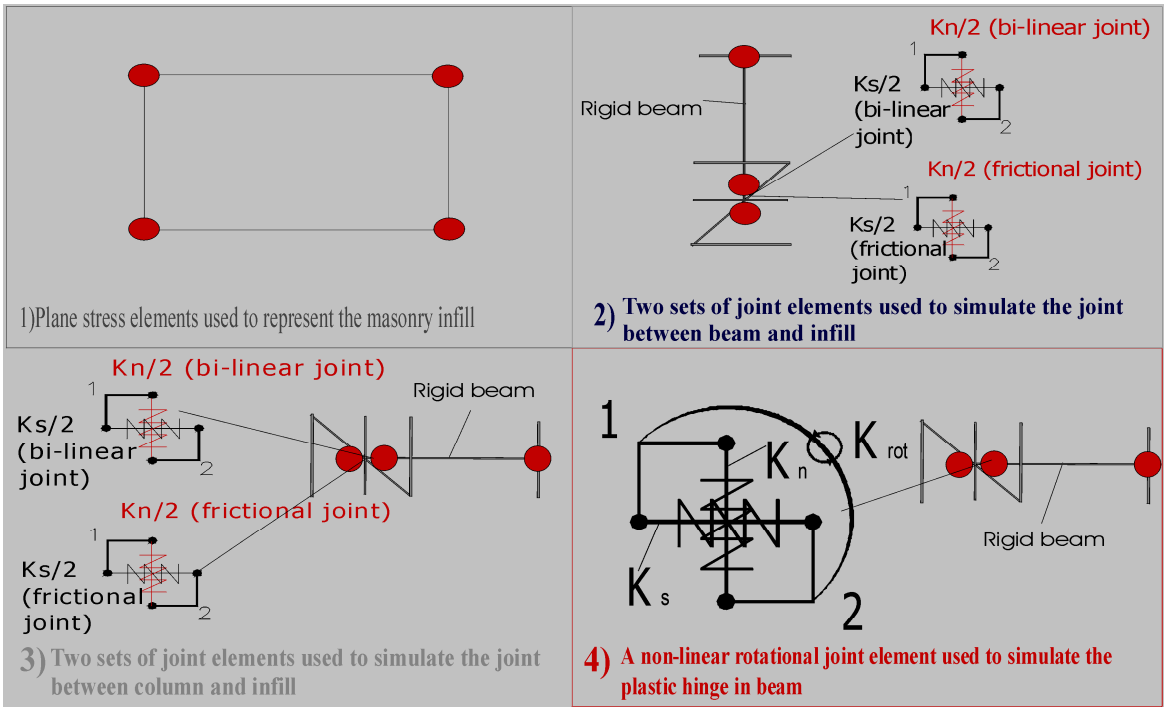

Figure 4. Details of the non-linear numerical simulation for the infill, the interface between infill and R/C frame and for the plastic hinge in the R/C beam.

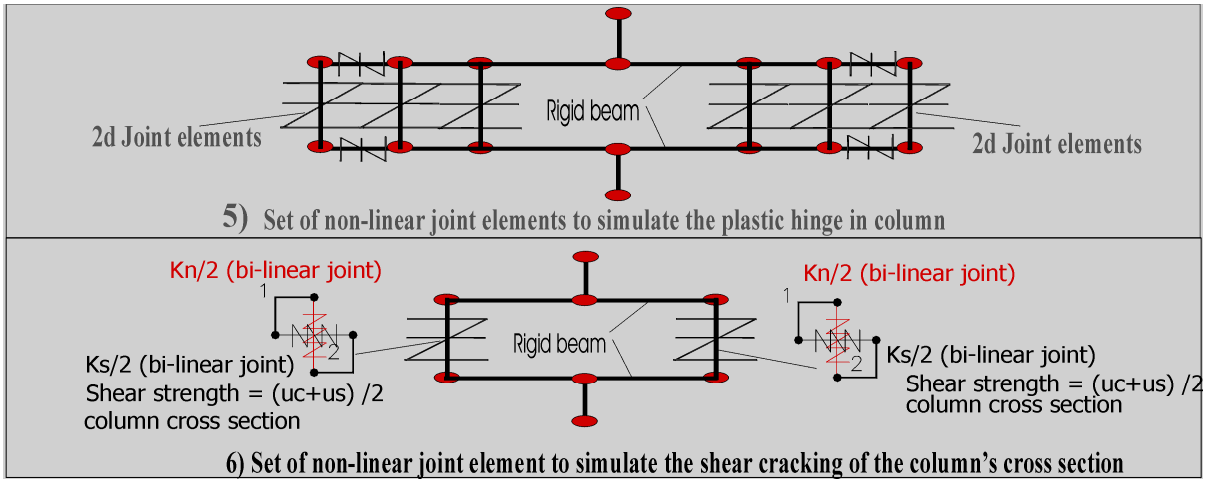

Figure 5. Details of the non-linear numerical simulation for the plastic hinge in the R/C column and for the shear limit state also at the column.

All these non-linear mechanisms are numerically simulated with a combination of rigid zones and non-linear joint elements (figures 4 and 5) with properties based on the geometric data, the material properties of the constituent materials (masonry, mortar, concrete, longitudinal steel) and the relevant structural detailing. Each one of the numerical simulations of the specific non-linear mechanisms (1) to (5) has been validated separately by Soulis [1] and Manos ([3], [4]) utilising relevant laboratory measurements obtained by Thauampteh [2]. Subsequently, this validation was also complemented by including all these non-linear mechanisms in the numerical simulation of a number of one-bay one-storey laboratory specimens by comparing the predicted cyclic behaviour for these specimens with observed performance ([1], [2], [3], [4], [5], [6], [7]). The additional shear limit state non-linear mechanism, represented by detail (6) in figure 5, is numerically approximated again by a combination of rigid zones and non-linear joint elements with properties based again on the geometric data of the column cross section, the material properties of the constituent materials (concrete, transverse steel), and the relevant structural detailing. The shear limit state was obtained by calculating the shear capacity for a column cross-section as specified by equations 1, 2 and 3. The location of these non-linear shear limit state zones is based on observed behaviour and accumulated experience for each given case. For the studied specimens three predefined locations along the height of each column were selected capable of developing this shear limit state. Two of these locations are at the ends (top and bottom) of each column in serial sequence with the non-linear mechanism simulating the flexural plastic hinges in these locations. An additional shear limit state mechanism was also placed at mid-height of each R/C column. Two elasto-plastic non-linear 2-D joint elements are used to simulate the shear post-elastic behaviour of a given R/C column cross section by considering also the corresponding column transverse reinforcement (figure 2 and detail No 6 in figures 3, 4 and 5). As per ACI 318:2008 [12] the total shear V_u resisted *(107KN)* by the column's cross section is carried by two parts; the shear resisted by the concrete and the shear resisted by the reinforcement. As already mentioned, the properties of these non-linear 2-D joint elements are specified utilizing the given structural details and equations 1 to 3. Independent numerical tests were carried out employing simple structural problems in order to verify that this way of simulating numerically the shear limit state mechanism responds in the expected way. Next, this numerical approach was applied to the infilled frame specimens included in table 2.

$$V_u = V_c + V_s \tag{1}$$

• Shear resisted by the concrete part of the cross section V_c

• Shear resisted by the transverse steel reinforcement V_s

For normal weight concrete,

$$V_c = \delta \times \left(0{,}17 \times \sqrt{f'_c}\right) \times b \times d \quad \left(where, \delta = 1 + \frac{P_u}{14A_g}\right) \tag{2}$$

$$V_s = \frac{A_{SV} \times f_{yh} \times d}{s_v} \qquad for\ transverese\ reinforcement \tag{3}$$

f_c =cylindrical compressive strength of concrete

b = width of member

P_u = axial force normal to cross section

A_g =gross cross sectional area of concrete

A_{sv} = area of transverse steel reinforcement expected to be effective in resisting the expected shear mode of failure

d = Effective depth of member

s_v = spacing of stirrups

f_{yh}= yield stress of stirrups

2.2 Validation of the proposed numerical simulation

Figures 6a, 6b and 6c depict a comparison between the predicted behaviour, in terms of envelope curves resulting from a monotonic type of loading on the adopted numerical simulation and the corresponding envelope curves resulting from the relevant experiments with the masonry infilled frame specimens F8NR and CU1, CU2.

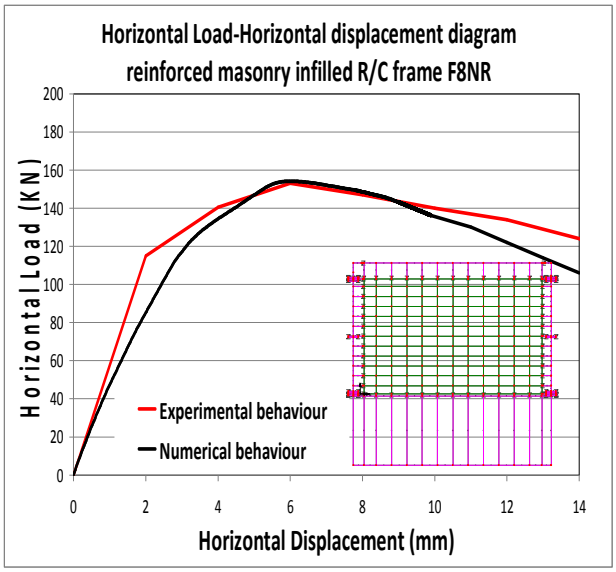

Figure 6a: Comparison of envelope curves for masonry infilled model frame F8NR

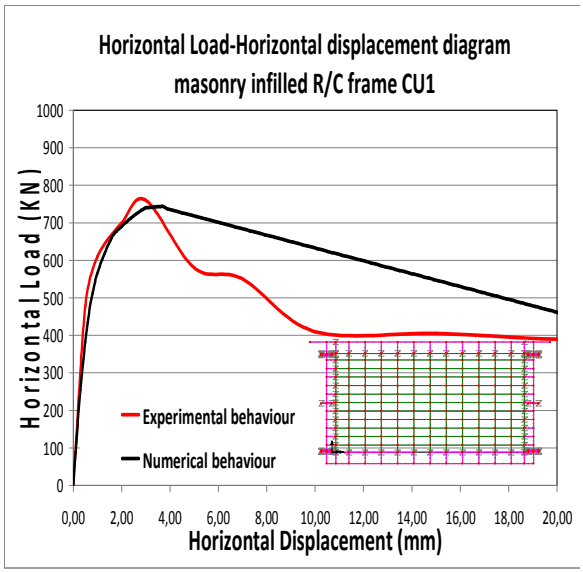

Figure 6b: Comparison of envelope curves for masonry infilled model frame CU1

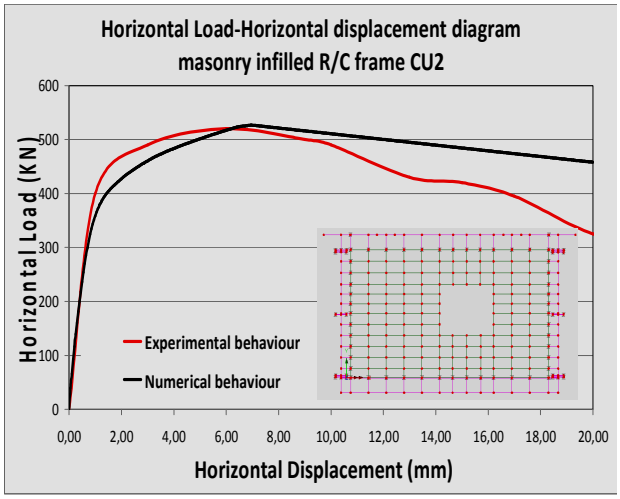

Figure 6c: Comparison of envelope curves for masonry infilled model frame CU2

The deformations to masonry infill observed during the tests and the numerically-predicted non-linear limit state is presented for frames F8NR (figures 7a and 7b), CU1 (figures 7c and 7d), CU2 (figures 7e and 7c). The observed damage patterns of the masonry infill were well approximated by the proposed numerical simulation. The damage pattern of F8NR masonry infilled R/C frame reported experimentally, consisted of corner crushing of the reinforced masonry infill corners in the R/C column and beam joint and a shear cracking in top right column(figure 7a).

Reasonably good agreement can be seen in the damage pattern predicted numerically except that shear limit state is observed both in the top left and the bottom right column (figure 7b). The damage pattern that was observed for masonry infilled frame CU1 includes diagonal/sliding cracks in the infill panels and shear cracks on the top left column and shear cracks in the bottom right column for the experimentally tested specimen (figure 7c). The same limit state pattern was predicted numerically as shown in figure 7d. For the masonry infilled panel with one opening in specimen CU2 the sequence of limit states included successively (figure 7e) a) Infill to frame separation b) diagonal cracks of the infill at the window corners c) shear crack in top left column , and d) diagonal crack in the right bottom

masonry pier and shear crack mid-height of the right column. The same limit state pattern was predicted numerically (figure 7f).

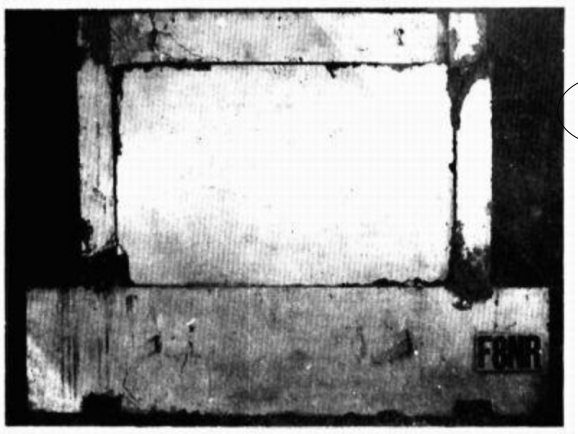

7a) Damage pattern [8]

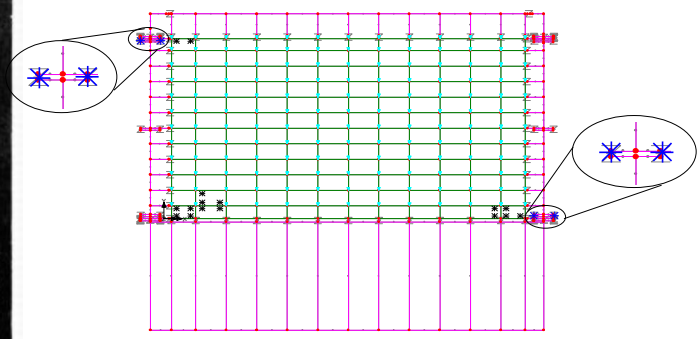

7b) Limit state numerical simulation (denored with *)

Figures 7a and 7b) Damage pattern of masonry infill observed experimentally for infilled frame F8NR, b) Damage pattern(x) predicted numerically

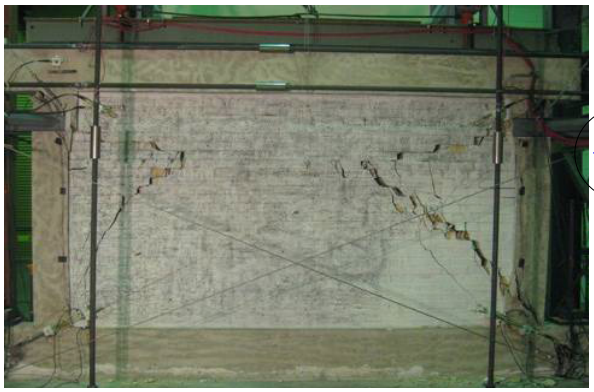

7c) Damage pattern [9]

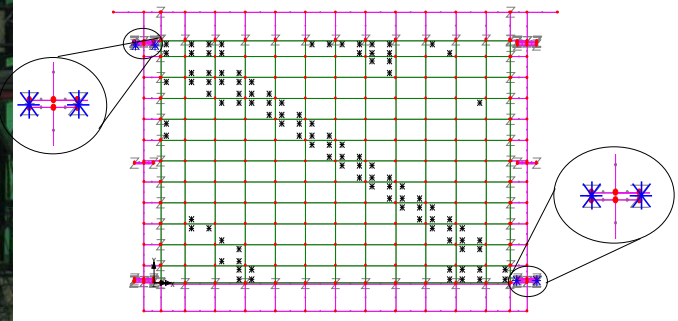

7d) Limit state numerical simulation (denored with *)

Figures 7c and 7d) Damage pattern of masonry infill observed experimentally for infilled frame CU1, b) Damage pattern(x) predicted numerically

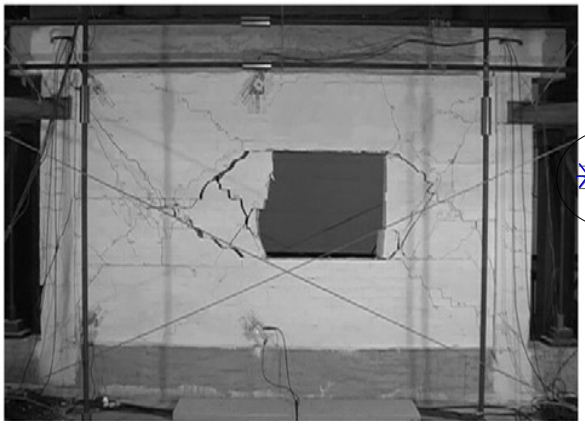

7e) Damage pattern [9]

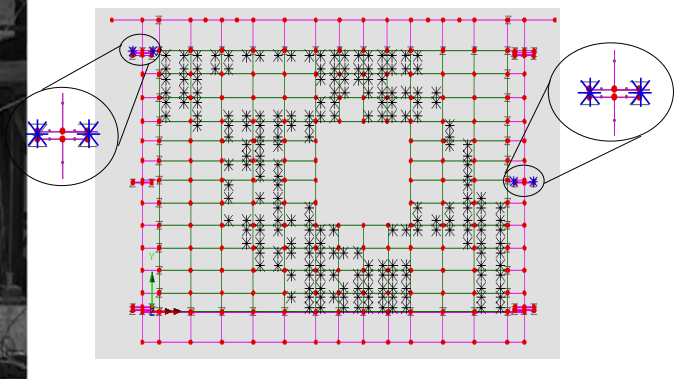

7f) Limit state numerical simulation (denored with *)

Figure 7e and 7f) Damage pattern of masonry infill observed experimentally for infilled frame CU2, b) Damage pattern(x) predicted numerically

3. VOLVI 6-STOREY MODEL STRUCTURE

The numerical investigation briefly reported in section 2 demonstrates that the proposed numerical model can successfully simulate a number of non-linear mechanisms that can be developed in a single storey masonry infilled frame. In this section it is shown that all these non-linear mechanisms (see introduction a, b and c) can be used to simulate the behaviour of a 6-storey masonry infilled R/C frame structure. This 6-storey masonry infilled R/C frame model structure was constructed and tested at the European Test Site at Volvi, by Manos et al [13], [14], [15]. This structure was utilized for the verification of the proposed numerical simulation.The investigation included two types of analyses; an initial linear dynamic analysis to predict numerically the recorded dynamic response of this structure followed by a non-linear "push over" step-by-step type of numerical analysis of the same infilled frame structure. It must be pointed out that both types of numerical simulations make use of only in-plane stiffness and strength behaviour of the masonry infills units whereas the out-of-plane behaviour and its possible effects, although important, are not addressed here.

3.1. Description of the model structure

This model building was constructed and instrumented at the European Test Site of Volvi in order to monitor its dynamic response under prototype earthquake conditions. An extensive sequence of low-amplitude dynamic tests has been performed. The model included one-bay in each direction, 6-storey, of 1/3-scale with overall external dimensions 1810mm (length) x 5000mm (height) in the weak direction and 1910mm(length) x 5000mm (height) in the strong direction. Its floor level had a height of 1000mm. The cross-section of the columns was 110mmx110mm and that of the beam 100mmx155mmm. In figures 8 a, b and c the masonry infilled, R/C , 6-storey structure is depicted. The basic properties for the concrete and the reinforcement have been monitored through samples taken during construction. Different structural configurations of the 6-storey structure have been tested at the European Test Site of Volvi, in the period of its existence (Manos at al [13], [14], [15]). The structural configuration that is utilized here includes apart from the existing added weight of 50KN, an extra weight of approximately 30KN on the top of a sixth floor specially constructed for this purpose (Masonry scheme 2b, September 1997 – January 2004).

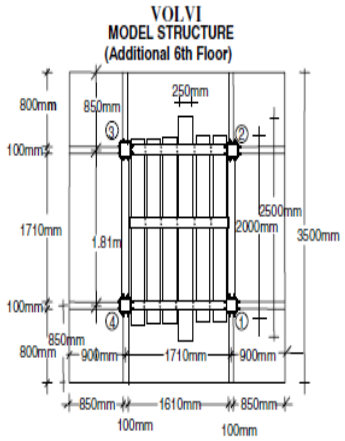

Figure 8 a)Plan view of 6-storey masonry infilled frame structure in European test site at Volvi

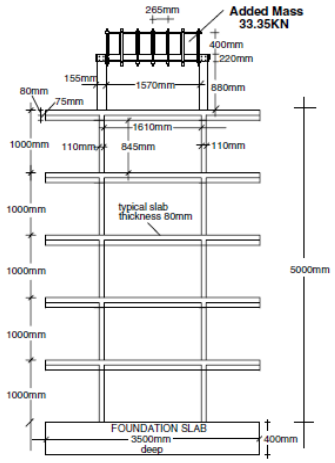

b)Side view of 6-storey "bare" frame structure in European test site at Volvi

c) Side view of 6-storey masonry infilled frame structure in European test site at Volvi

Brief information on the masonry infill used in this model building is listed in table 5. Relevant masonry properties and additional information are given by Thauampteh [2].

Description of the 6-storey structure masonry infill	Masonry Infill thickness (mm)	Technical description of the interface between frame and infill	Longitudinal reinforcement ratio (ρ)
Initial unreinforced Masonry with mortar type **V1**	58.5	mortar **V1** thickness **10mm** (without plaster)	1.01%

Table 5: Outline of all specimens for the 1st and 2nd groups of specimens

As already mentioned, the influence exerted by the interface between the masonry infill and the surrounding frame was also examined in both studies by Thauampteh [2] and by Soulis[1]. Tables 6, 7 and 8 list the mechanical properties of the materials used in the construction of the specimens. The masonry infill panel was connected to the surrounding frame with weak mortar (type V1) similar to the one used in the construction of F2N specimen Thauampteh [2]. In this numerical analysis the influence of this interface is examined together with three different cases of foundation-soil stiffness conditions.

Masonry infill	Masonry Infill thickness (mm)	Compres. strength of masonry (N/mm^2)	Shear strength of masonry diagonal compression (N/mm^2)	Compres. strength of masonry units (N/mm^2)	Compres. strength of concrete columns (N/mm^2)	Compres. strength of concrete slabs (N/mm^2)	Compres. strength of mortar cylinders (N/mm^2)
V1	58,5	2,765	0.180	6.50	26	15,6	1.125

Table 6**:** Strengths of masonry infills and concrete used in the specimens [10]

A/α	Yield stress f_{sy} (N/mm^2)	Ultimate strength f_{su} (N/mm^2)	Strain at yield ε_{sy} (%)	Strain at ultimate stress ε_{su} (%)	Young Modulus (N/mm^2)
Φ5.5	338	425	0.8	22.0	$6.5X10^4$
Φ5.5 stirrups	319	542	0.6	20.0	$6.5X10^4$

Table 7**:** Tensile strength of the reinforcement used in the specimens [10]

A/a	Simulation of joint interface between frame and infill	**E** Young Modulus (N/mm^2)	**G** Shear Modulus (N/mm^2)	$\mathbf{f_k}$ Measured Compressive Strength of mortar (N/mm^2)	$\mathbf{f_{tn}}$ Assumed Tensile Strength of mortar (N/mm^2) (as % of f_c)	**τo** Local bond shear strength of mortar (N/mm^2)	**μ** friction coefficient
1	**V1** mortar	150	65	1,20	0.12(10%)	0.157	0.20

Table 8**:** Mechanical properties of the mortar joint located between the infill and the surrounding frame (mortar type V1)

3.2. Three dimensional elastic numerical simulation of the dynamic response of the 6-storey model structure

Initially, the results from in-situ tests are presented here dealing with the dynamic response of a 6-storey reinforced concrete (R/C) frame structure with masonry infills, which was built for this purpose at the Volvi European Test site. Summary results from the measured main eigen-frequency values resulting from simple pull-out tests on the 6-storey specimen, with masonry infills in all stories, with steel diagonals and extra mass are included in Table 9. A numerical simulation of the 6-storey (R/C) frame structure with masonry infills utilizing the all the provisions considered in section 2 was built and a dynamic analysis was performed. The numerical simulation included a 3-D simulation of the foundation slab, of all the concrete

members (slabs, beams, columns), of the masonry infills, the interface between the masonry infill and the surrounding frame and finally the 6th storey extension. The simulation of the foundation flexibility was approximated by introducing linear springs at the foundation-soil interface. Three different numerical analyses were performed assuming three different levels of soil-foundation stiffness: a) Infinite stiffness (base fixity), b) Medium stiffness (flexible base with foundation-soil interface of E=200Mpa), c) Low stiffness (flexible base with foundation-soil interface of E=10Mpa). Table 9, includes the corresponding summary eigen-frequency results of the numerical simulation studies that were performed assuming these three different soil-foundation stiffness types.

Description of the Structural Configurations for the Volvi Model Structure	1st x-x (Hz) Translational Eigen-frequency	1st y-y (Hz) Translational Eigen-frequency	1st φ (Hz) Torsional	Measuring Procedure
Masonry scheme 2b, June 1998. 6th storey extension Infills in all 5 lower stories (with diagonals) . Measured values [14]	5.005*	4.761*		Permanent & Portable Instruments
Fixed base Values of eigen-frequencies numerically predicted	5.40**	5.31**	5.48**	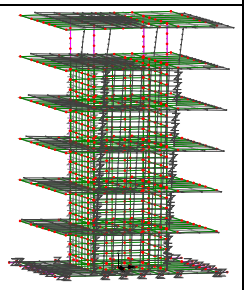 3-d Numerical simulation
Flexible base E=200Mpa Values of eigen-frequencies numerically predicted	4.75**	4.67**	5.12**	
Flexible base E=10Mpa Values of eigen-frequencies numerically predicted	2.58**	2.45**	2.69**	

* Experimental value., ** Numerical simulation results

Table 9: In-situ measured and numerically predicted vibration frequencies

3.3. Push over non-linear analysis of the masonry infilled 6-storey model structure

For this non-linear "pushover" analysis of the 6-storey structure, the maximum target displacement at the top was set equal to 61mm, with the displacement profile along the height of the structure assumed to be triangular. The in-plane displacements resulting in this way were imposed at each floor level in a gradual increasing step-by-step fashion. The numerical simulation discussed in section 2 for the R/C masonry infilled frames is applied this time for all the 16 masonry infilled bays that compose this 6-storey masonry infilled frame structure (figure 8c). The horizontal load-horizontal displacement "push-over" response curve resulting from this simulation, which as mentioned includes all non-linear mechanisms for the masonry infill, the surrounding R/C frame, the interface between the masonry infill and frame, is depicted in figure 9. The simulation of the masonry infill, was done utilizing non-linear thick shell finite elements. The isotropic nonlinear material law of Modified Von Mises was utilized for this purpose. The adopted mechanical properties of the initial and the strengthened masonry infill panel are listed in Table 10.

Young Modulus (N/mm^2)	1000
Poisson Ratio	0,20
Tensile strength (N/mm^2)	0,30
Compressive strength (N/mm^2)	1,2
Softening Modulus under compression (N/mm^2)	-10
Softening Modulus under tension(N/mm^2)	-10

Table 10: Mechanical properties used for the description of Von Mises failure criterion of the masonry infills

The numerical simulation of the interface between the prototype R/C frame and the masonry infill is done in the same way as described in section 2.1, utilizing non-linear joint elements in the axial and transverse direction. This interface is assumed to have been built with mortar type V1 (see Thauampteh 2] and Table 8). The simulation of the surrounding R/C frame was also performed utilizing the same simulation technique as described in section 2.1.

3.4 "Pushover" curves and Predicted damage for the numerical simulation of the 6-storey frame of Volvi

Figure 9 depicts the base shear – top horizontal displacement curve obtained for the fully non-linear "pushover" analysis for the 6-storey masonry infilled frame structure assuming base fixity. In the same figure the base shear – top horizontal displacement curve is also obtained assuming a flexible foundation with a foundation-soil interface of E=10Mpa. The target top displacement corresponds to approximately 1% angular deformation of the 6-storey masonry infilled frame structure. Figures 10a,b, and 11a,b depict in more detail the predicted damage pattern (shown with **x** signs) of the masonry infills of the 6-storey masonry infilled structural formation resulting from this "push over" type of analysis for two levels of angular deformation a) 0,41%, b)0,84%.

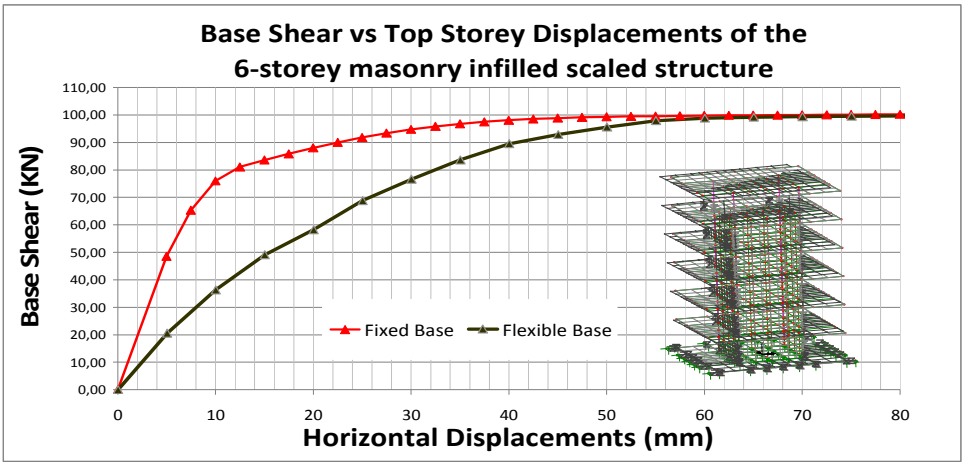

Figure 9: Comparison between push over curves obtained for different foundation conditions

γ=0,0042 ‰(dx=25mm)	γ=0,0084 ‰(dx=50mm)	γ=0,0042 ‰(dx=25mm)	γ=0,0084 ‰(dx=50mm)
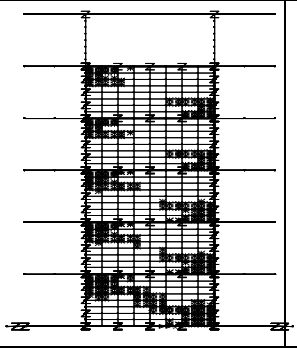	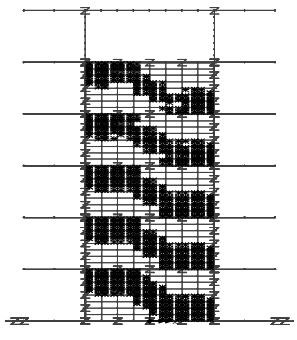	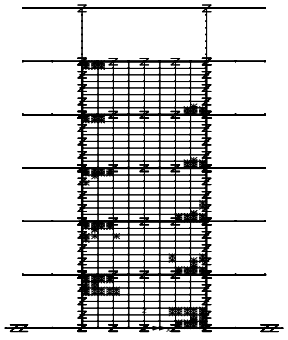	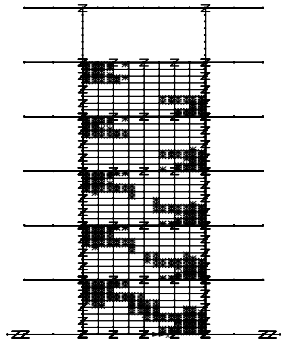
a) Fixed Foundation	b) Fixed Foundation	a) flexible foundation	b) flexible foundation

Figure 10: Masonry infill damage patterns, as predicted for top storey target displacement equal to a) 4,1‰, b)8,4‰ of the building height with fixed foundation

Figure 11: Detail of masonry infill damage patterns, as predicted for top storey target displacement equal to a)4,1‰, b)8,4‰ of the building height with flexible foundation

As can be seen in figure 9, the level of the soil-foundation stiffness influences significantly the non-linear "push-over" response of this 6-storey masonry infilled frame structure. The flexibility of the foundation decreases the shear deformation of the masonry infills and the predicted damage levels (figures 11a and 11b) more than for the case of rigid foundation (figures 10a and 10b). Instead, the predicted damage patterns of the masonry infills in this structure, assuming base fixity, develops as expected at a much lower amplitude of top horizontal displacement. The limit state pattern of the masonry infill predicted in this case is along its diagonal (figure 10b). In this sense the flexibility of the foundation acts as a protective mechanism, provided it is designed to be able to sustain such deformations without any side-effects. Moreover, as concluded by an additional experimental sequence conducted with another model structure at the Volvi European Test Site [15] soil-foundation-structure interaction could lead non-embedded foundations to non-linear behaviour resulting in uplift and/or soil plastification. Therefore, such non-linear foundation responses if controlled by design could be a beneficial source of energy absorption. Otherwise, they may lead to excessive displacements of the superstructure and to foundation failure.

4 CONCLUDING OBSERVATIONS

1. The strength and the monotonic load-displacement behaviour observed during the experiments of single-storey one-bay masonry-infilled R/C frames examined in this study is successfully predicted by the proposed numerical simulation.
2. The proposed numerical simulation represents in a reasonable way the most important influences that the interface between masonry infill and the surrounding frame could exert on the monotonic behaviour of such structural assemblies in terms of stiffness, strength, modes of failure, as demonstrated from the observed behaviour.
3. The development of a shear limit state at the predetermined positions of columns of the surrounding R/C frame observed during the experiments as well as the damage patterns for the masonry infill, in terms of crack propagation are also successfully predicted.
4. This numerical simulation was next validated by a 3-D numerical model for a multi-storey masonry infilled frame model structure located at the Volvi European Test Site. Good agreement could be seen between measured eigen-frequency values and predictions from linear dynamic analysis performed assuming different foundation conditions.
5. Finally, this numerical simulation was successfully applied to the same multi-storey masonry infilled frame model structure located at the Volvi European Test Site this time employing a non-linear "push over" type of analyses that included all the non-linear mechanism employed before. From the obtained results it can be demonstrated that the flexibility of the foundation decreases the shear deformation of the masonry infills and the predicted damage levels more than for the case of rigid foundation. In this sense the flexibility of the foundation acts as a protective mechanism, provided it is designed to be able to sustain such deformations without any side-effects.

REFERENCES

[1] Soulis V.J. "Investigation of the Numerical Simulation of Masonry Infilled R/C Frame Structures under Seismic-type Loading", Ph.D. Thesis, Department of Civil Engineering, Aristotle University of Thessaloniki, 2009.

[2] J. Thauampteh, "Experimental Investigation of the Behaviour of Single-storey R/C Frames with Masonry Infills, Virgin and Repaired, under Cyclic Horizontal Loading",

Ph.D. Thesis, Department of Civil Engineering, Aristotle University of Thessaloniki, 2009.

[3] G.C. Manos, V. J. Soulis and J. Thauampteh. "A Nonlinear Numerical Model and its Utilization in Simulating the In-Plane Behaviour of Multi-Storey R/C frames with Masonry Infills", *The Open Construction and Building Technology Journal,6,* (Suppl 1-M16) 254-277,2012.

[4] G.C. Manos, V.J. Soulis and J. Thauampteh, "The Behaviour of Masonry Assemblages and Masonry-infilled R/C Frames Subjected to Combined Vertical and Cyclic Horizontal Seismic-type Loading", Journal of Advances in Engineering Software, Vol. 45, pp. 213-231, 2011.

[5] K. Stylianides, "Experimental Investigation of the Behaviour of Single-storey Infilled R/C Frames under Cyclic Quasi-static Horizontal Loading (Parametric Analysis", Ph.D. Thesis, Department of Civil Engineering, Aristotle University of Thessaloniki, 1985.

[6] Th. Valiasis, "Experimental Investigation of the Behavior of R.C. Frames Filled with Masonry Panels and Subjected to Cyclic Horizontal Load - Analytical Modelling of the Masonry Panel", Ph.D. Thesis, Department of Civil Engineering, Aristotle University of Thessaloniki, 1989.

[7] B. Yasin, "Experimental Investigation of the Influence of Infills on the Dynamic Response of Building Structures Through the Study of Scaled Physical Models", Ph.D. Thesis, Department of Civil Engineering, Aristotle University of Thessaloniki, 1999.

[8] Sariyiannis D., "Experimental Investigation On The Behaviour Of R/C Infilled Frames Repaired With Various Infill Techniques Under Cyclic Horizontal Loading" , Ph.D. Thesis, Department of Civil Engineering, Aristotle University of Thessaloniki, 1989.

[9] Stavridis A., "Analytical and experimental study of seismic performance of reinforced concrete frames infilled with masonry walls". PhD thesis. San Diego: Department of Structural Engineering, University of California; 2010.

[10] I.Koutromanos , A. Stavridis, P. B. Shing, K. Willam, "Numerical modelling of masonry-infilled RC frames subjected to seismic loads" , Computers and Structures 89 (2011) ,pp 1026–1037

[11] R.E. Klingner and V.V. Bertero, "Infilled Frames in Earthquake - Resistant Construction", EERC, Report No. 76-32, University of California, Berkeley, California, USA, Dec. 1976.

[12] ACI 318:2008, Building Code Requirements for Reinforced Concrete, American Concrete Institute, Detroit, Michigan, 2002.

[13] G.C. Manos, M. Triamataki, J. Thauampteh, B. Yasin, P. ,Skalkos, M. Demosthenous, "The Dynamic Response of a 5-storey Structure at the European Test site at Volvi-Greece", 6th U.S. National Earthquake Engineering Conference, 1998.

[14] G.C. Manos, J. Thauampteh, M. Yasin, "Influence of Masonry Infills on the Earthquake Response of Multi-storey Reinforced Concrete Structures" presented at the 12th WCEE, Auckland, New Zealand, 2000.

[15] G. C. Manos , K.D. Pitilakis, A.G. Sextos, V. Kourtides, V. Soulis, J. Thauampteh, "Field experiments for monitoring the dynamic soil-structure-foundation response of model structures at a Test Site" Journal of Structural Engineering, American Society of Civil Engineers, Special Issue "Field Testing of Bridges and Buildings, D4014012, Vol. 141, Issue 1, January 2015.

ECCOMAS Congress 2016
VII European Congress on Computational Methods in Applied Sciences and Engineering
M. Papadrakakis, V. Papadopoulos, G. Stefanou, V. Plevris (eds.)
Crete Island, Greece, 5–10 June 2016

MODELING THE MECHANICAL RESPONSE OF A LEAD-CORE BEARING DEVICE: DAMAGE MECHANICS APPROACH

T. Zhelyazov[1], **R Rupakhety**[2], **and S. Ólafsson**[2]

[1] Technical University of Sofia, Sofia, Bulgaria
Sofia, 1000, 8 Kl. Ohridski Blvd
e-mail: todor.zhelyazov@tu-sofia.bg

[2] Earthquake Engineering Research Centre, University of Iceland
Austurvegur 2a, 800 Selfoss, Iceland
rajesh@hi.is
simon@hi.is

Keywords: Lead-core Bearing Device, Computational Methods, Damage Mechanics,

Abstract. This paper presents the results of a numerical study aimed at developing a rational approach to assess the degradation of mechanical properties of lead-core bearing devices used for passive seismic isolation. The lead-core rubber bearing is modeled as a multiple-component system. Appropriate constitutive laws and failure criteria are defined for each component of the system. Two alternative constitutive relations are defined for the lead core: bilinear material model by assuming isotropic hardening after yielding, and a model formulated in the framework of continuum damage mechanics. The numerical procedure used to simulate the mechanical response of the device allows the monitoring of accumulated mechanical damage throughout the loading history. Preliminary simulation results obtained by finite element analysis are reported. Specifically, these are shear force-displacement hysteresis loops under various loading conditions in a typical characterization test.

1 INTRODUCTION

The lead-core bearing device is modeled as a multiple-component system. It consists of the following components: lead core, rubber layers, steel shims and thick steel plates. For each material, lead, rubber and steel, an appropriate constitutive law is chosen. The constitutive laws are defined on the meso-scale. At this point, an analogy between the representative volume element in continuum damage mechanics and finite element is postulated. The stress and strain fields in the lead-core bearing device are obtained by finite element analysis on the basis of the postulated constitutive laws. Important macro-characteristics of the bearing can be evaluated throughout the loading history. Such macro-characteristics, if observable, can be employed to calibrate the model or to validate the results obtained by finite element analysis.

2 BEARING DEVICE: SPECIFICATIONS

The geometry of the bearing being modelled and analysed in this study is shown in Figure 1.

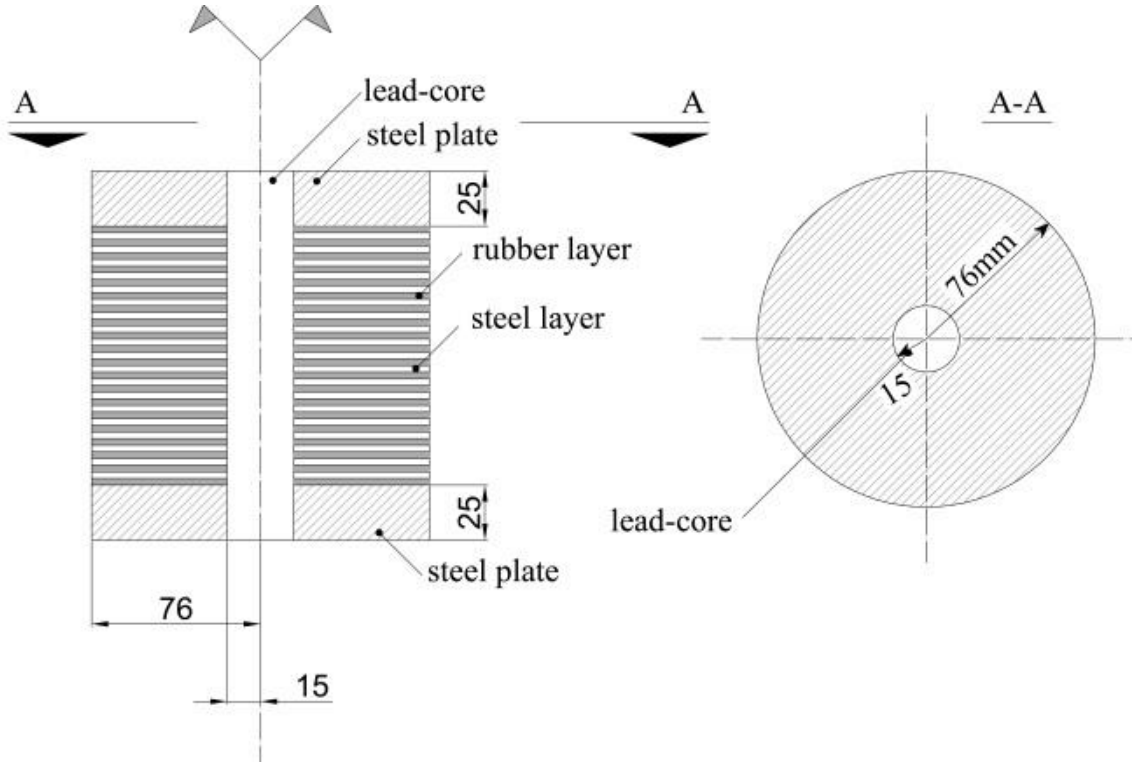

Figure 1: Geometry of the modelled bearing device

As it can be seen, the lead-core bearing device consists of two thick steel plates at the top and at the bottom, rubber layers separated by steel shims, and a lead-core. The thick steel plates are 182mm (2x76) in diameter and 25mm thick with a central cylindrical opening of 30mm diameter. Twenty rubber layers separated by 19 steel shims are stacked between the top and bottom steel plates. The rubber layers and the steel shims are both 182mm in diameter and 3mm thick. They also have a central opening of 30mm diameter along which a lead core of 30mm diameter is fitted.

3 CONSTITUTIVE LAWS

3.1 Steel

Steel is modelled as an isotropic and elastic material. This is justified because, in common usage conditions of the bearing devices, the steel layers and the top/bottom plates remain elastic while yielding occurs in the lead-core and rubber layers. Constitutive law for the steel layers and the top/bottom plates is thus completely defined by initial elastic modulus (Young's Modulus) and Poisson's ratio.

3.2 Lead-core

For the lead-core, a bi-linear stress-strain relationship [1][2][3] is assumed. It is assumed that the material obeys the von Mises yield criterion. An isotropic hardening rule is used to model the post-yielding behavior. As an alternative, a constitutive law based on continuum damage mechanics is formulated, specifically by coupling elasto-palsticity and damage [4]. In this formulation, material response is described by state variables. These variables can be derived form a dissipation potential P that can be written as:

$$P = f + P_X + P_D \tag{1}$$

where f is a function prescribing the yield criterion, P_X describes hardening and P_D represents damage potential [5]. The yield criterion has the following property.

$$\begin{aligned} f < 0 &\rightarrow elasticity \\ f = 0 &\rightarrow plasticity \end{aligned} \tag{2}$$

If both isotropic and kinematic hardening are considered the yield criterion is given by:

$$f = \left(\sigma_{ij} - X\right)_{eq} - R - \sigma_y \tag{3}$$

where

$$\left(\sigma_{ij} - X\right)_{eq} = \sqrt{\frac{3}{2}\left(\sigma_{ij}^D - X_{ij}^D\right)\left(\sigma_{ij}^D - X_{ij}^D\right)} = \left(\sigma_{ij}^D - X_{ij}^D\right)\sqrt{\frac{3}{2}} \tag{4}$$

In equation (4), T_{ij}^D denotes the deviatoric part of a symmetric second order tensor T_{ij}, σ_{ij} is the stress tensor and X is referred to as a back stress (Figure 2).

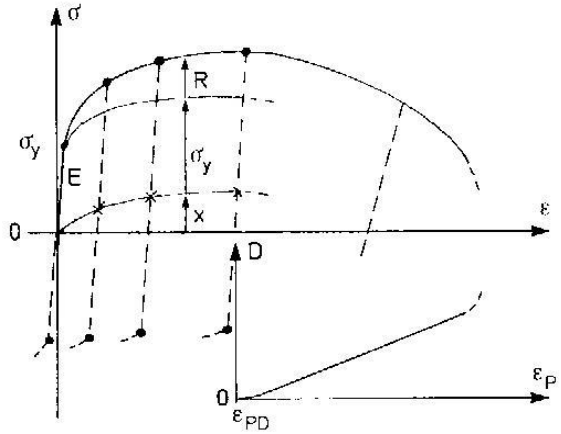

Figure 2: Kinematic back stress X and isotropic hardening stress R [6]

The kinematic back stress X is the locus of the elastic domain center in the stresses space and the isotropic hardening stress R measures the elastic domain increase:

$$R = \sigma - \sigma_y - X \tag{5}$$

The accumulated plastic strain rate is given by the following expression:

$$\dot{p}(t) = \sqrt{\frac{2}{3}\dot{\varepsilon}_{ij}^{p}\dot{\varepsilon}_{ij}^{p}} \tag{6}$$

In (6) $\dot{\varepsilon}_{ij}^{p}$ is the plastic strain rate, obtained after decomposition of the total strain into elastic and plastic part. It is assumed that damage begins when the plastic strain reaches the value corresponding to the ultimate stress (Figure 2) and its critical value is given by:

$$D_c = \left(\frac{\sigma_u^2}{2ES}\right)\left(\varepsilon_p - \varepsilon_{pD}\right) \tag{7}$$

where ε_p is the accumulated plastic strain and ε_{pD} is the plastic strain corresponding to the damage threshold. Damage is accumulated only if $\varepsilon_p > \varepsilon_{pD}$.

$$\begin{aligned} \varepsilon_p > \varepsilon_{pD} &\rightarrow \dot{D} \neq 0 \\ \varepsilon_p \leq \varepsilon_{pD} &\rightarrow \dot{D} = 0 \end{aligned} \tag{8}$$

3.3 Rubber

For rubber, a Neo-Hookean model is used. Strain energy potential is defined by using the following equation.

$$\mathrm{W} = \frac{\mu}{2}\left(\bar{\mathrm{I}}_1 - 3\right) + \frac{1}{\mathrm{d}}\left(\mathrm{J}-1\right)^2 \tag{9}$$

In Eq. (9) μ stands for the initial shear modulus of the material; d is the material incompressibility parameter, and $\bar{I}_1$ is the first invariant of the isochoric part of the right Cauchy-Green deformation tensor. According to [7] and [8], J is the ratio of the deformed elastic volume to the undeformed reference volume of the material. J can be evaluated by calculating the determinant of the Lagrangian strain tensor:

$$J = \det\left[F_{ij}\right] \tag{10}$$

In Eq. (10) F_{ij} denotes the components of the Lagrangian strain tensor. Furthermore, $\bar{I}_1$ can be obtained as

$$\bar{I}_1 = I_1 J^{-2/3} \tag{11}$$

where I_k is the k^{th} invariant of the right Cauchy-Green deformation tensor, and is given by

$$I_1 = \lambda_1^2 + \lambda_2^2 + \lambda_3^2 \tag{12}$$

where λ_i are the principal stretches. The material incompressibility parameter d is related to the material bulk modulus K as follows:

$$K = \frac{2}{d} \tag{13}$$

and the Young's modulus of the material is defined as:

$$E = 2\mu(1+\nu) \tag{14}$$

Based on experimental data, the following values are chosen for the material parameters μ and d [[1]]: μ=0.73MPa and d=0.001mm^2/N.

4 FINITE ELEMENT MODEL

A detailed 3-D finite element model is created. All elements of the bearing device are explicitly modeled in terms of geometry. Volumes are created for the rubber layers, steel shims, the lead-core and the thick top and bottom steel plates. Advantage is taken of the existing symmetries. Only half of the bearing device is modelled. Appropriate symmetry boundary conditions are defined on the plane of symmetry (Figure 3).

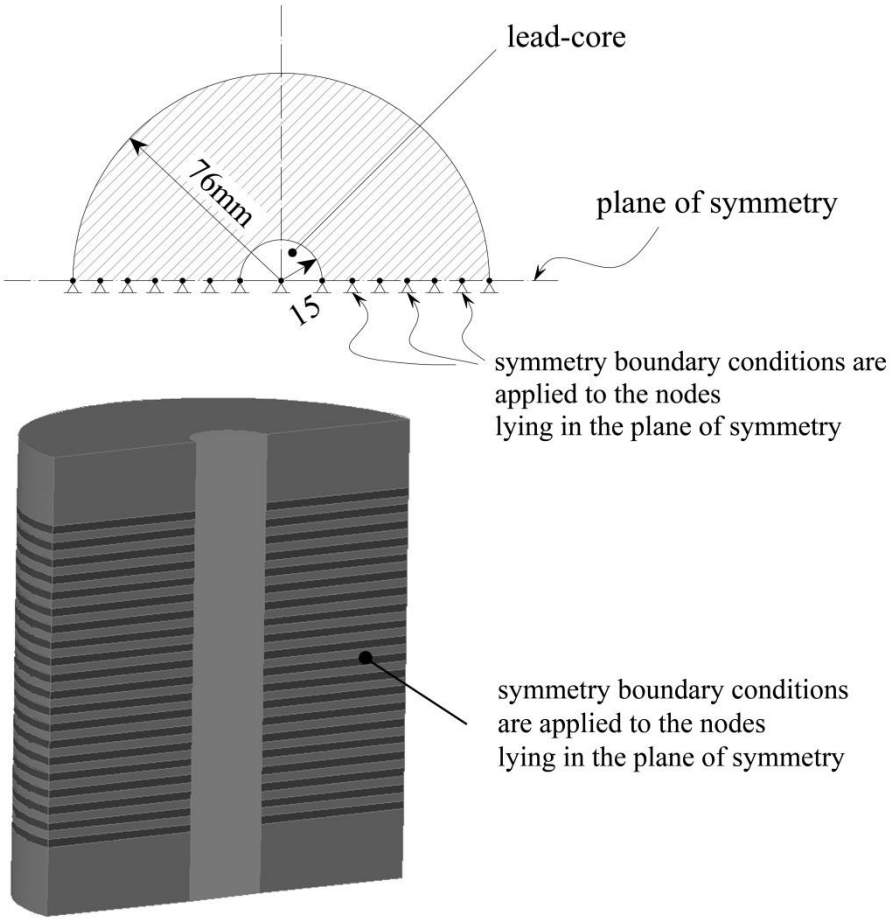

Figure 3: The half-space model and symmetry boundary conditions

For the finite element mesh 20-nodes 3-D structural solids are used (**Figure 4**). Components in steel are meshed with Solid 95 [9]. The lead-core and the rubber layers are meshed with Solid 185 [9]. Full integration option is used to avoid spurious stress hardening.

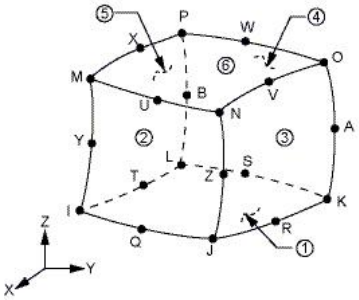

Figure 4: A 20-node 3-D structural finite element [9]

The finite element mesh is displayed in Figure 5. A total of 10290 Solid185 are employed to mesh the volumes of the lead-core, the thick steel plates, the rubber layers and the steel shims. All the interfaces are assumed to give have bonds.

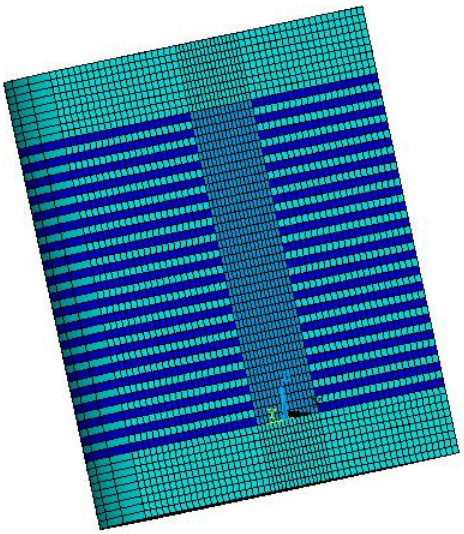

Figure 5: Half-space finite element model: finite element mesh

5 FINITE ELEMENT SIMULATION

The response of the lead-core bearing device is obtained by performing an explicit dynamic transient analysis. The equation of motion has the form:

$$[M]\{\ddot{u}\}+[D]\{\dot{u}\}+[K]\{u\}=\{F(t)\} \tag{15}$$

where [M] is the mass matrix; [D] is the damping matrix; [K] is the stiffness matrix; $\{\ddot{u}\}$ is the nodal acceleration vector; $\{\dot{u}\}$is the nodal velocity vector, and $\{u\}$ is the nodal displacement vector, and $\{F(t)\}$ is the time- dependent loading vector. All the nodes on the 'bottom' surface of the bearing device (Z = -25mm) are restrained against all possible displacements (nodal translations along X-, Y- and Z-axis). Both constant vertical loads and time-dependent horizontal loads are applied to the nodes on the 'top' surface of the bearing device (Z = 142mm). The vertical load is applied along the direction parallel to the global Z-axis in the model space. The time-dependent horizontal load is simulated by applying displacements to the top-surface-nodes in a direction parallel to the global X-axis. The boundary conditions defined for the simulation

of the characterization test are shown in Figure 6. In order to obtain the 'force-displacement' relationship, the evolution of the shear stresses in the lead-core along the global X-direction is monitored.

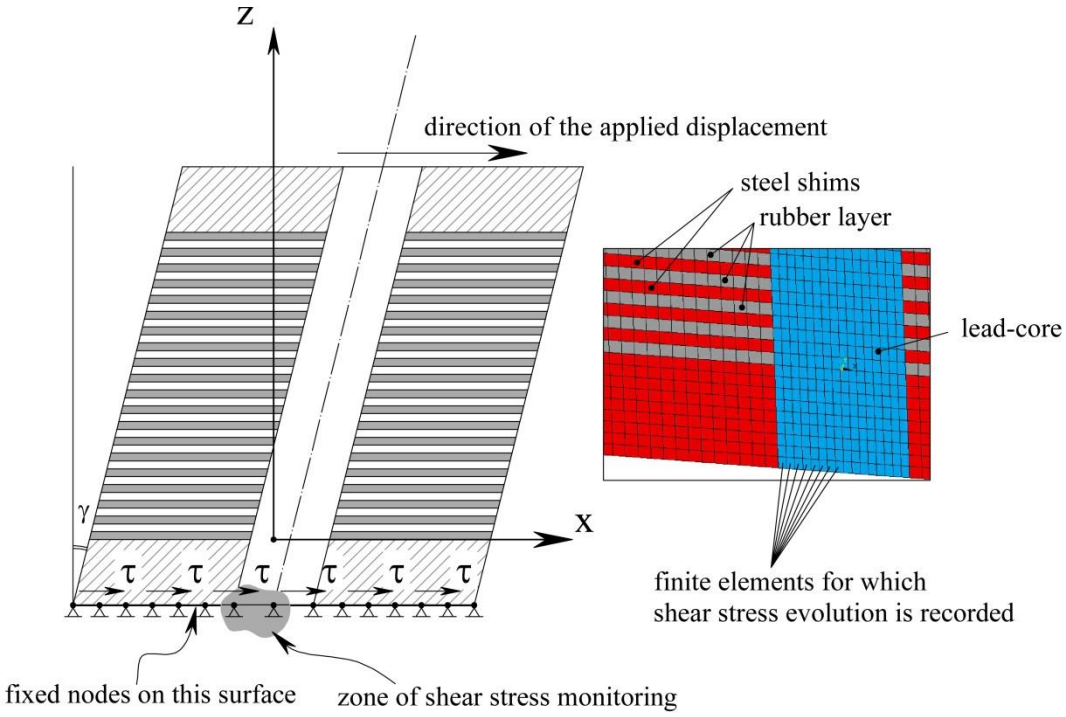

Figure 6: Schematization of the characterization test simulation

The shear strain γ in its turn is conventionally defined as the ratio between the relative horizontal displacement between the top and bottom surfaces of the bearing device- d_h and the total height of the rubber H_r (H_r =60 mm).

$$\gamma = \frac{d_h}{H_r} \tag{16}$$

One of the strain loading paths is visualized in Figure 7.

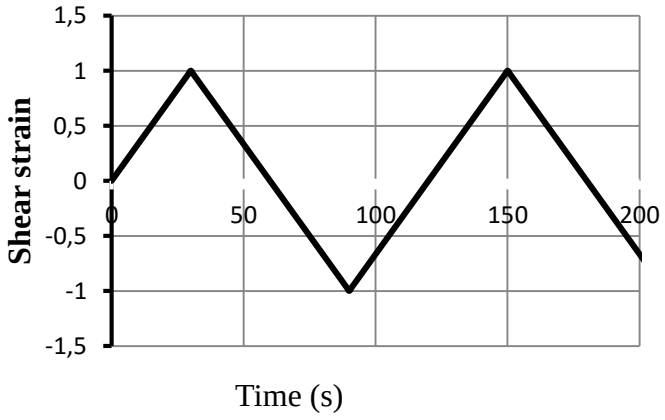

Figure 7: cyclic strain paths

6 RESULTS OBTAINED BY FINITE ELEMENT SIMULATION

In this section shear strain- displacement curves obtained for different shear strain amplitudes and shear strain rates are shown. The numerical procedure reproduces the typical hysteresis behavior exhibited by a bearing device in common identification test. All simulations contain three full hysteresis loops and the ascending branches of the fourth loop. It should be noted that these results should be further validated through comparison with experimental data.

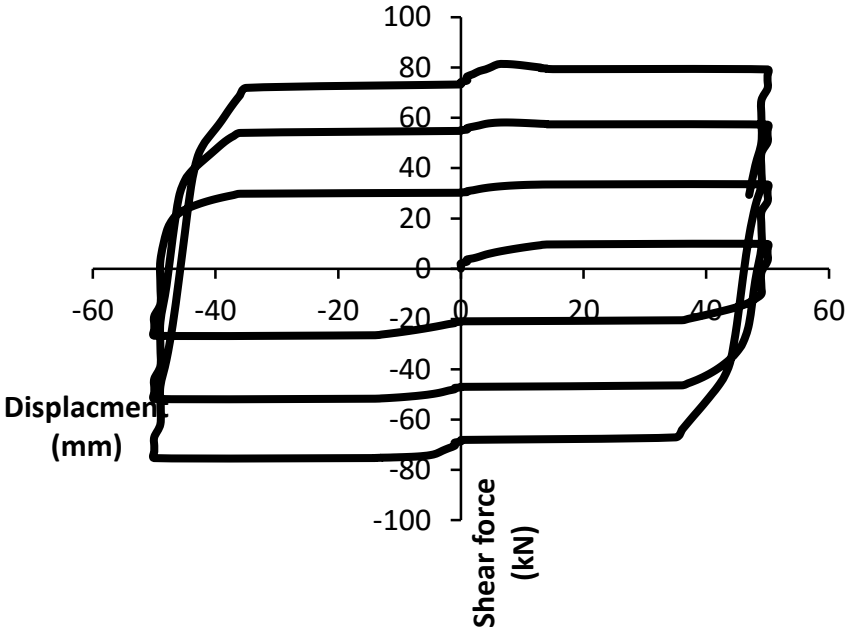

Figure 8: Shear force-displacement hysteresis loops for maximum shear strain γ=0.835 and shear strain rate $d\gamma/dt$=0.083

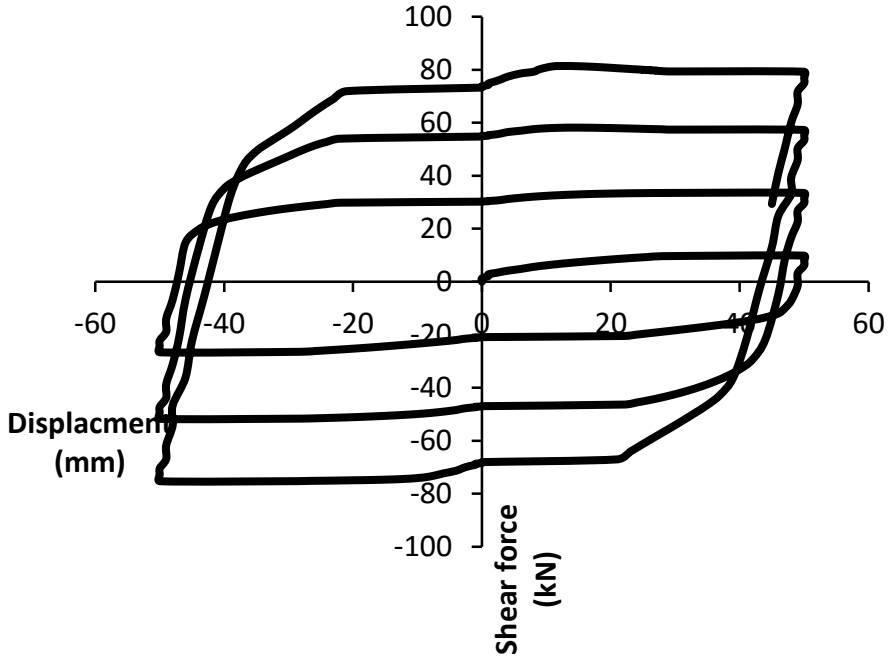

Figure 9: Shear force-displacement hysteresis loops for maximum shear strain γ=0.835 and shear strain rate $d\gamma/dt$=0.042

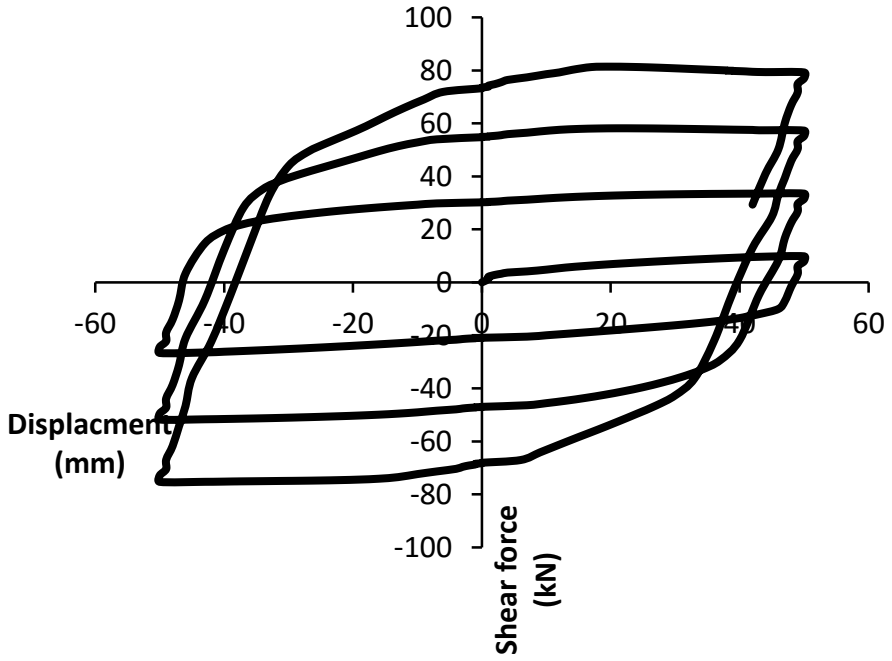

Figure 10: Shear force-displacement hysteresis loops for maximum shear strain γ=0.835 and shear strain rate dγ/dt=0.028

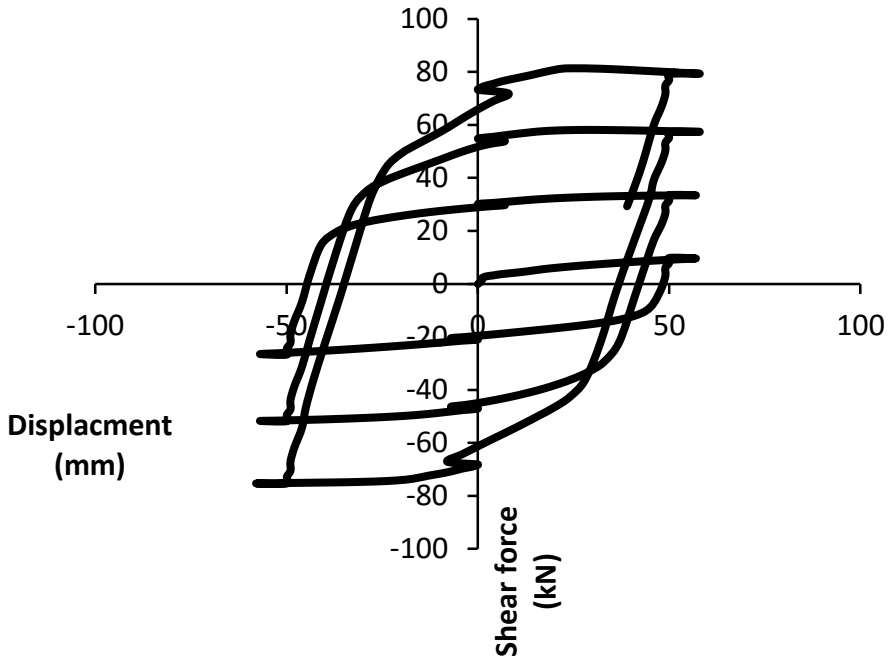

Figure 11: Shear force-displacement hysteresis loops for maximum shear strain γ=0.835 and shear strain rate dγ/dt=0.021

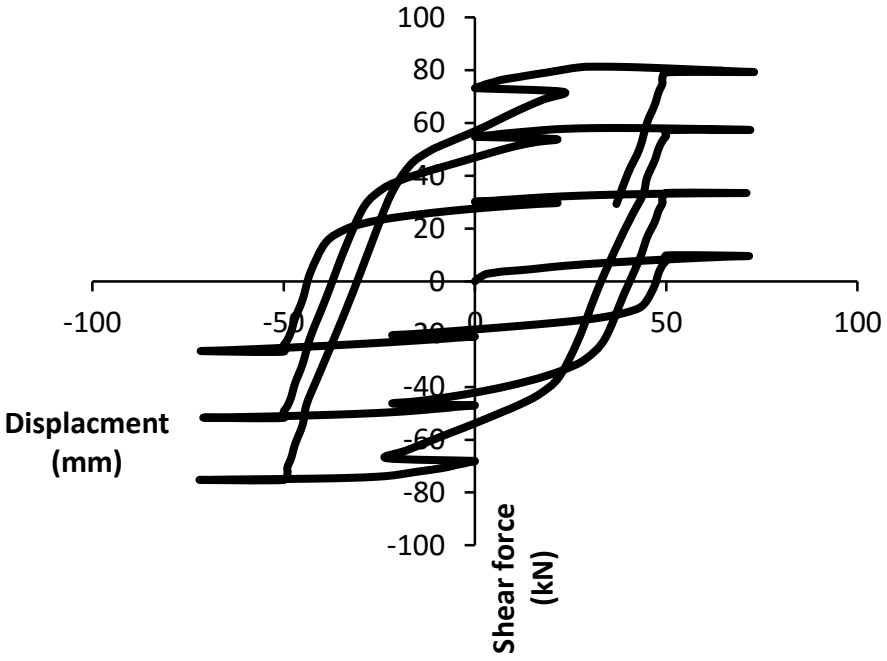

Figure 12: Shear force-displacement hysteresis loops for maximum shear strain γ=0.835 and shear strain rate $d\gamma/dt$=0.017

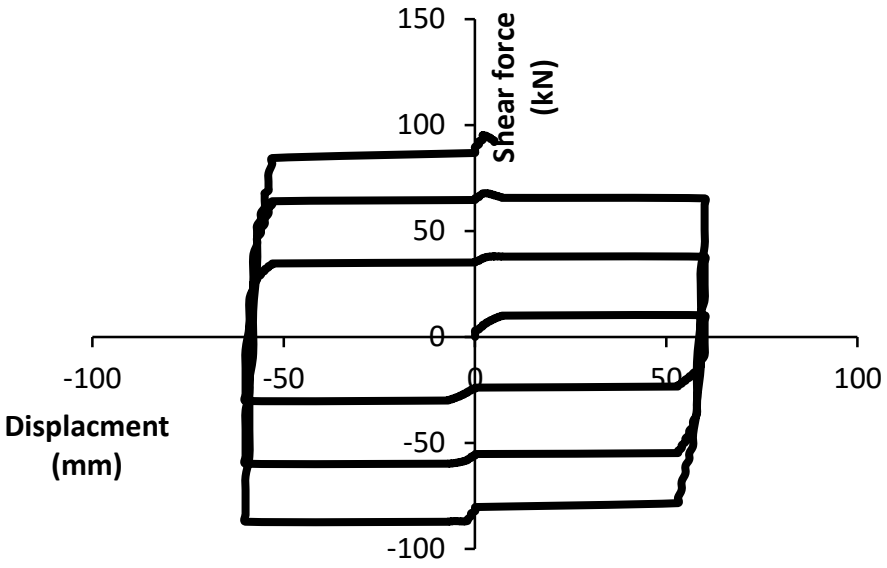

Figure 13: Shear force-displacement hysteresis loops for maximum shear strain γ=1.00 and shear strain rate $d\gamma/dt$=0.2

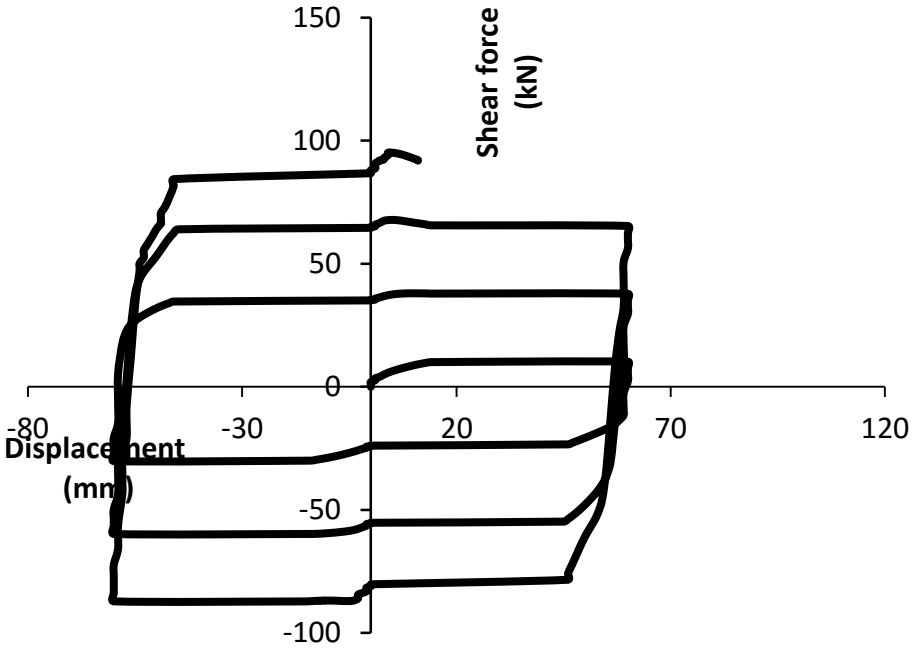

Figure 14: Shear force-displacement hysteresis loops for maximum shear strain γ=1.00 and shear strain rate $d\gamma/dt$=0.1

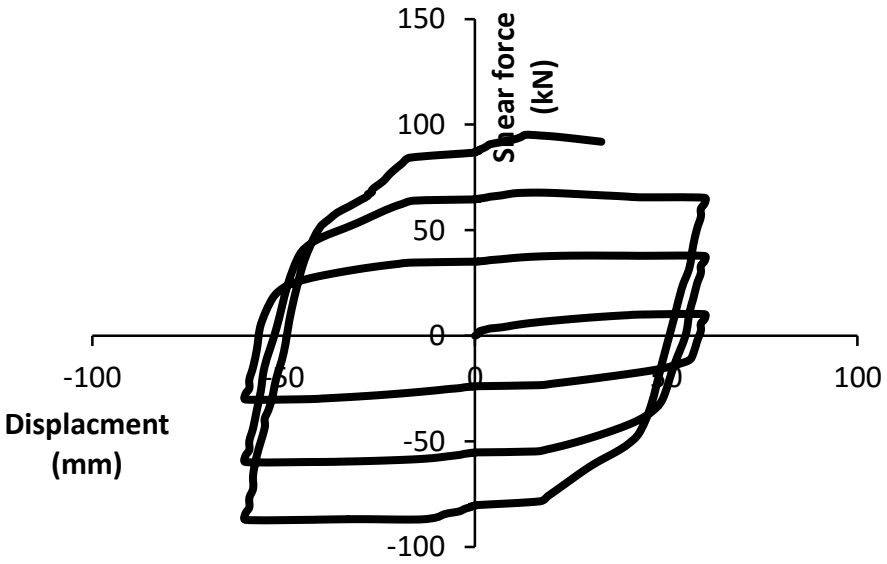

Figure 15: Shear force-displacement hysteresis loops for maximum shear strain γ=1.00 and shear strain rate $d\gamma/dt$=0.033

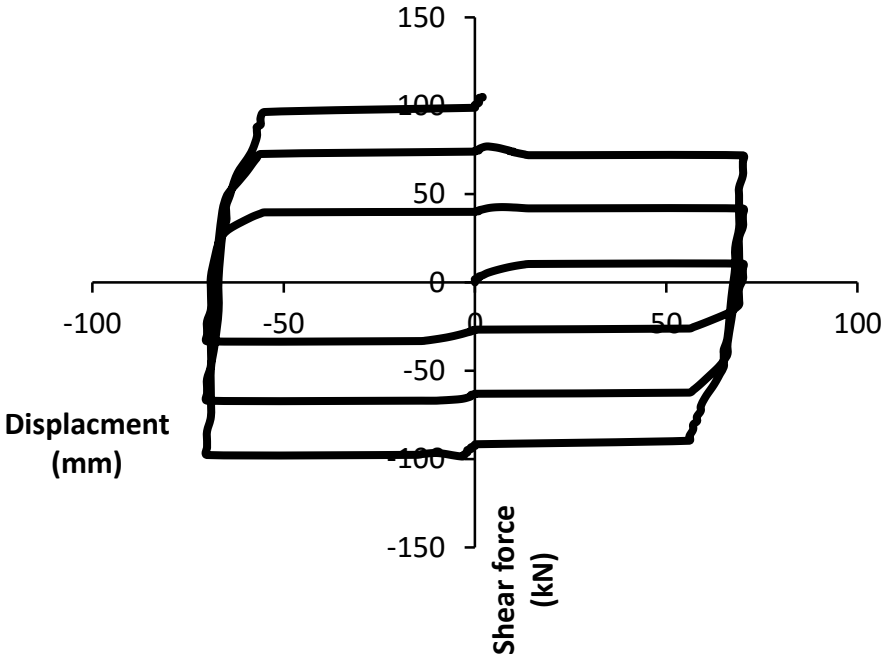

Figure 16: Shear force-displacement hysteresis loops for maximum shear strain γ=1.165 and shear strain rate $d\gamma/dt$=0.117

Qualitative comparison between different 'displacement-shear force' curves obtained by finite element analysis shows that the shear strain rate decrease results in hardening in the ascending branch of each hysteresis loop (compare Figure 8, Figure 9, Figure 10). For further decrease in shear strain rate this trend is conserved. Additionally a sharp discontinuity in the transition between ascending and descending branches as well as at the 'zero-shear strain point' can be observed (see Figure 11 and Figure 12). The latter observation should be addressed again when relevant experimental data is available.

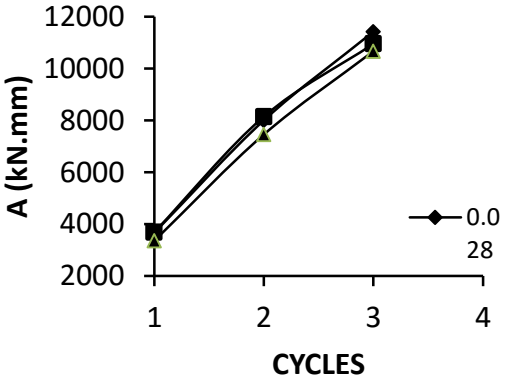

Figure 17: predicted dissipation capacity for different shear strain rates (0.028; 0.021; 0.017)

Furthermore, comparing numerical results obtained for various shear strain rates, it can be concluded that the model predicts a slight decrease in dissipation capacity with the strain rate decrease. This is visualized in Figure 17 which shows an estimate of the dissipation capacity based on results of three finite element simulations. For the three simulations the maximum imposed shear strain is the same whereas the shear strain rate differs.

7 CONCLUSIONS

- This paper presents preliminary results of the study of mechanical response of bearing devices used in passive seismic isolation carried out at the Earthquake Engineering Research Center of the University of Iceland. The study will be further extended by experimental investigation in order to furnish relevant data for model validation.
- Lead-core bearing is modelled as a multiple component system. Appropriate constitutive laws and failure criteria are defined for each material: lead, rubber and steel.
- An explicit and accurate finite element model of a lead-core bearing device is presented. Results obtained by finite element analysis reproduce the hysteresis response of a lead-core bearing device usually exhibited in a common identification test.
- Results obtained by finite element simulation can be further used as a basis for tuning of an analytical differential equation model (curve fitting) aiming a subsequent implementation of the calibrated single-degree-of freedom model into a numerical models of a damped large-scale structures.

REFERENCES

[1] G.P. Warn, K.L. Ryan, A Review of Seismic Isolation for Buildings: Historical Development and Research Needs, *Buildings*, **2(3),** 300-325, 2012.

[2] J. Weisman, G.P. Warn, Stability of Elastomeric and Lead-Rubber Seismic Isolation Bearings, *Journal of Structural Engineering*, 138(2), 215-233, 2012.

[3] G.P. Warn, A.S. Whittaker, A study of the coupled horizontal-vertical behaviour of elastomeric and lead-rubber seismic isolation bearings. *MCEER-06-0011, Multidisciplinary Center for Earthquake Engineering Research*, Buffalo, New York 2006.

[4] J. Lemaitre, Coupled Elasto-Plasticity and Damage Constitutive Equations, *Computer methods in Applied Mechanics and Engineering*, 51, 31-49, 1985

[5] J. Lemaitre, R. Desmorat, *Engineering damage mechanics*, Springer-Verlag Berlin Heidelberg, 2005.

[6] J. Lemaitre, *A Course on Damage mechanics*, Springer, Berlin Heidelberg, New York, 1996.

[7] R.W. Ogden, *Nonlinear Elastic Deformations*, Dover Publications, Inc., 1984.

[8] M.A. Crisfield, Non-linear Finite Element Analysis of Solids and Structures, Vol. 2, Advanced Topics, John Wiley & Sons, 1997.

[9] ANSYS Mechanical APDL Element Reference

[10] T. Zhelyazov, E.R. Thorhallsson, Simon Ólafsson, J.T. Snæbjörnsson, R. Sigbjörnsson, Seismic isolation: assessment of the damping capacity, *Second European Conference on Earthquake Engineering and Seismology*, Istanbul, August 25-29, 2014.

ECCOMAS Congress 2016
VII European Congress on Computational Methods in Applied Sciences and Engineering
M. Papadrakakis, V. Papadopoulos, G. Stefanou, V. Plevris (eds.)
Crete Island, Greece, 5–10 June 2016

INVESTIGATION OF THE PERFORMANCE OF VARIOUS MODAL CORRELATION CRITERIA IN STRUCTURAL DAMAGE IDENTIFICATION

Manolis Georgioudakis[1] **and Vagelis Plevris**[2]

[1] Institute of Structural Analysis & Antiseismic Research
School of Civil Engineering, National Technical University of Athens
Zografou Campus, Athens 15780
e-mail: geoem@mail.ntua.gr

[2] Department of Civil Engineering and Energy Technology
Oslo and Akershus University College of Applied Sciences
Pilestredet 35, Oslo 0166, Norway
email: vagelis.plevris@hioa.no

Keywords: Damage Identification, Differential Evolution, Modal Flexibility, Natural Frequencies, Optimization, Modal Correlation Criteria.

Abstract. *Structural damage identification is a scientific field that has attracted a lot of interest in the scientific community during the recent years. There have been many studies intending to find a reliable method to identify damage in structural elements both in location and extent. Most damage identification methods are based on the changes of dynamic characteristics and static responses, but the incompleteness of the test data is a great obstacle for both. In this paper, the performance of different modal correlation criteria in structural damage identification is investigated. The structural damage identification problem is treated as an optimization problem which is solved using the differential evolution search algorithm. The objective functions used in the optimization process are based on different modal correlation criteria, providing a measure of consistency and correlation between estimations of modal vectors. The performance of each of the objective functions is evaluated by a number of damage scenarios for a simply supported beam. Although the results of the various criteria on the different damage scenarios vary, it is clearly shown that some modal correlation criteria exhibit excellent performance in detecting the structural damage even in the case of strong incompleteness of the modal data.*

1. INTRODUCTION

Structural damage identification has drawn increasing academic literature, as witnessed by the number of relevant journal and conference papers, during the recent years. There have been many studies intending to find a reliable method to identify damage in structural elements both in location and extent [1]. Most damage identification techniques are based on the changes of dynamic characteristics and static responses, but the incompleteness of the test data is a great obstacle for both.

Generally speaking, the existing methods of damage identification techniques based on modal testing can be clarified into two major categories: direct and inverse methods. The direct methods utilize the change in modal measurement to instantly detect structural damage without the need of iterative computational procedures. In contrast, the second category of damage identification techniques poses the whole process as inverse problems [2-9], in which the structural damage is identified via optimizing the correlation between the theoretical and the experimental modal parametric change, respectively. In order to determine the level of correlation between the measured and the predicted natural frequencies or mode shapes modal correlation criteria are used as a simple mathematical tools, providing a measure of consistency and correlation between estimations of modal vectors.

In this paper, the performance of different modal correlation criteria in structural damage identification is investigated. The structural damage identification problem is treated as an optimization problem which is solved using the differential evolution optimization algorithm. The objective functions used in the optimization process are based on different modal correlation criteria to identify the location and the extent of structural damage. The performance of each of the objective functions is evaluated in a number of damage scenarios for a simply supported beam. It is shown that the results of the different modal correlation criteria vary, while certain criteria exhibit excellent performance in detecting the structural damage even in the case of strong incompleteness of the modal data.

2. STRUCTURAL DAMAGE IDENTIFICATION

The problem of damage identification is classified into four levels [10]: (A) detection, (B) localization, (C) quantification, and (D) prediction of future damage (damage prognosis). At the level of damage detection (Level A), the existence of damage can be detected, while its location and severity are unknown. Information about location of the damage can be provided by localization techniques at Level B. At the damage quantification level (Level C), both the location and severity of damage are estimated. Finally, at the prediction level (Level D), the remaining life of the structure is estimated based on the (identified) current damage state and future loads and damage propagation. This study reaches the third level of damage identification, which means it investigates the ability to detect, localize as well as estimate the severity of damage in structures.

It is proven that changes in the dynamic characteristics of a structure are related to damage occurrence. Specifically changes in the modal parameters, namely natural frequencies and mode shapes, can provide an accurate indication of damage in a structure. Since modal parameters are dependent on the physical properties of the structure, i.e. stiffness and mass, the FEM may be used as a tool for locating and quantifying damaged elements in a structure through the update of modal parameters, even in large-scale structures.

2.1. Damage identification model

If a structure is properly modeled using the FEM, structural damage mathematically affects its stiffness and physically its dynamic properties, such as natural frequencies and mode shapes [11]. It can be assumed that the global mass matrix remains the same in both the undamaged and the damaged structure. This assumption is considered quite accurate for the majority of real applications. The eigenvalue problem of a structure with n active degrees of freedom (DOFs) can be written as follows:

$$\left(\mathbf{K} - \omega_{(i)}^2 \mathbf{M}\right)\left\{\boldsymbol{\varphi}^{(i)}\right\} = 0, \quad i = \{1,\ 2, \ldots,\ m\} \tag{1}$$

where $\mathbf{K}$ is the global stiffness matrix of the structure ([$n \times n$]), $\mathbf{M}$ is the global mass matrix ([$n \times n$]), $\{\boldsymbol{\varphi}^{(i)}\}$ is the i-th natural mode vector of the structure ([$n \times 1$]) corresponding to the $\omega_{(i)}$ natural frequency and m is the total number of natural modes to be obtained ($m \leq n$).

Eq. (1) forms the basis of the damage identification method used in the present study. An inverse procedure is used, where the natural frequencies and natural modes of the damaged structure are measured and they are supposed to be known quantities (to a certain extent), while the damage of the structure is unknown and needs to be calculated through an optimization procedure.

2.2. Modal correlation criteria

We consider two structures A and B with n active degrees of freedom (DOFs) each, with eigenvalues $\lambda_{A(i)} = \omega_{A(i)}^2$ and $\lambda_{B(i)} = \omega_{B(i)}^2$, natural frequencies $\omega_{A(i)}$ and $\omega_{B(i)}$ ($i = 1, 2, \ldots, m$), where m is the total number of natural modes obtained ($m \leq n$). The corresponding mode shape vectors are $\{\boldsymbol{\varphi}^{(i)}\}$ and $\{\boldsymbol{\psi}^{(i)}\}$ ([$n \times 1$] each), for structures A and B, respectively.

In order to compare two sets of values for the two structures, the use of modal correlation criteria is imperative. The following criteria have been used in this study, as useful mathematical tools providing a measure of consistency and correlation between estimations of modal vectors:

1. The Modal Assurance Criterion (MAC)
2. The Modified Total Modal Assurance Criterion (MTMAC)
3. The Co-ordinate Modal Assurance Criterion (CoMAC)
4. The Modal Flexibility Assurance Criterion (MACFLEX)

An example of two structures

In the next sections we will show the mathematical formulation of each criterion and also provide numerical values for a given example of two structures, for better comprehension and in order to exhibit the different criteria used. We consider two example structures, A and B. Each structure has $n = 9$ active DOFs and up to $m = 4$ eigenvalues and eigenmodes are taken into consideration (are supposed to be known, for both structures A and B).

Structures A and B correspond to the example which is examined in the numerical results section of the present study. Specifically, Structure A is the structure of the example with no damage, while Structure B is the same structure but in a damaged state where the damage vector is [0.0, 0.0, 0.0, 0.2, 0.3, 0.4, 0.6, 0.6, 0.3, 0.0], i.e. damage 20%, 30%, 40%, 60%, 60%, 30% at the 4^{th}, 5^{th}, 6^{th}, 7^{th}, 8^{th}, 9^{th} element, respectively. The eigenproperties of structures A and B are shown in Table 1 and Table 2. Figure 1 shows the four eigenmodes of the two structures.

		1st Eigenmode	2nd Eigenmode	3rd Eigenmode	4th Eigenmode
	$\lambda = \omega^2$ (sec^{-2})	**3008.56**	**48108.77**	**243219.45**	**765859.94**
	Eigenperiod *T* (sec)	**0.1146**	**0.0286**	**0.0127**	**0.0072**
Nodal values	1st DOF	0.505	-0.960	-1.321	-1.553
	2nd DOF	0.960	-1.553	-1.553	-0.960
	3rd DOF	1.322	-1.553	-0.505	0.960
	4th DOF	1.553	-0.959	0.960	1.553
	5th DOF	1.633	0.001	1.633	0.000
	6th DOF	1.553	0.960	0.960	-1.553
	7th DOF	1.321	1.553	-0.505	-0.960
	8th DOF	0.959	1.553	-1.553	0.960
	9th DOF	0.504	0.960	-1.321	1.553

Table 1. Modal properties (eigenvalues and eigenvectors) of example structure A.

		1st Eigenmode	2nd Eigenmode	3rd Eigenmode	4th Eigenmode
	$\lambda = \omega^2$ (sec^{-2})	**1762.18**	**32163.04**	**174959.58**	**540463.95**
	Eigenperiod *T* (sec)	**0.1497**	**0.0350**	**0.0150**	**0.0085**
Nodal values	1st DOF	0.439	-0.854	-1.206	-1.438
	2nd DOF	0.849	-1.442	-1.552	-1.157
	3rd DOF	1.206	-1.585	-0.780	0.543
	4th DOF	1.476	-1.184	0.636	1.611
	5th DOF	1.627	-0.298	1.631	0.488
	6th DOF	1.629	0.787	1.269	-1.489
	7th DOF	1.441	1.576	-0.366	-1.164
	8th DOF	1.053	1.594	-1.582	1.035
	9th DOF	0.546	0.935	-1.245	1.468

Table 2. Modal properties (eigenvalues and eigenvectors) of example structure B.

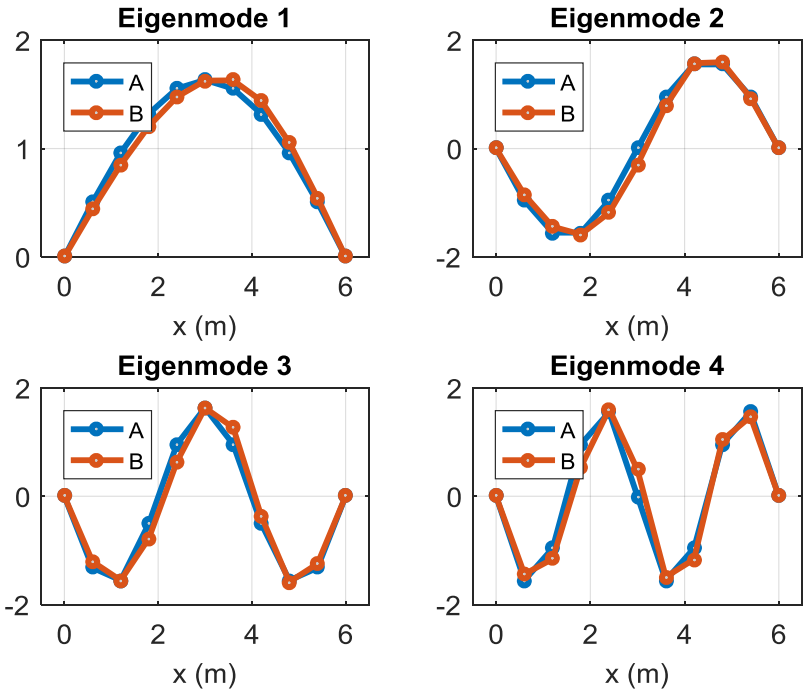

Figure 1. The four eigenmodes of the two example structures A and B.

2.2.1. The Modal Assurance Criterion (MAC)

The Modal Assurance Criterion (MAC) [12, 13] is one of the most popular tools for the quantitative comparison of modal vectors. The purpose of this criterion is to indicate the correlation between two sets of natural modes. Considering two mode shapes vectors $\{\boldsymbol{\varphi}^{(i)}\}$ ([n×1]) and $\{\boldsymbol{\psi}^{(j)}\}$ ([n×1]), for structures A and B, respectively, the term MAC_{ij} of the **MAC** matrix ([m×m]) is given by:

$$MAC_{ij} = \frac{\left(\{\varphi^{(i)}\}^T\{\psi^{(j)}\}\right)^2}{\left(\{\varphi^{(i)}\}^T\{\varphi^{(i)}\}\right)\left(\{\psi^{(j)}\}^T\{\psi^{(j)}\}\right)}, \quad i, j = \{1,\ 2,\ldots,\ m\} \tag{2}$$

or

$$MAC_{ij} = \frac{\left(\sum_{k=1}^{n}\varphi_k^{(i)}\psi_k^{(j)}\right)^2}{\sum_{k=1}^{n}\left[\left(\varphi_k^{(i)}\right)^2\right]\cdot\sum_{k=1}^{n}\left[\left(\psi_k^{(j)}\right)^2\right]}, \quad i, j = \{1,\ 2,\ldots,\ m\} \tag{3}$$

MAC_{ij} takes values from zero, representing no consistent correspondence, to one, representing a consistent correspondence between the two mode shapes vectors. In this manner, if the modal vectors under consideration, $\{\boldsymbol{\varphi}^{(i)}\}$ and $\{\boldsymbol{\psi}^{(j)}\}$, truly exhibit a consistent relationship, the modal assurance criterion element MAC_{ij} approaches unity. By calculating MAC_{ij} for all i, j = {1, 2,…, m} we obtain the **MAC** matrix. In our example, considering all four eigenmodes, we obtain:

$$\mathbf{MAC}(\mathrm{A},\mathrm{A}) = \mathbf{MAC}(\mathrm{B},\mathrm{B}) = \begin{bmatrix} 1 & 0 & 0 & 0 \\ 0 & 1 & 0 & 0 \\ 0 & 0 & 1 & 0 \\ 0 & 0 & 0 & 1 \end{bmatrix} \tag{4}$$

$$\mathbf{MAC}(\mathrm{A},\mathrm{B}) = \mathbf{MAC}(\mathrm{B},\mathrm{A})^T = \begin{bmatrix} 0.9950 & 0.0049 & 0.0001 & 0.0000 \\ 0.0049 & 0.9853 & 0.0077 & 0.0018 \\ 0.0000 & 0.0082 & 0.9765 & 0.0107 \\ 0.0001 & 0.0009 & 0.0121 & 0.9609 \end{bmatrix} \tag{5}$$

If we consider a lower number of eigenmodes *m*, then the size of the MAC matrix decreases accordingly but in any case, it corresponds to the upper left part of the above full matrix (which corresponds to 4 eigenmodes). In other words, the above matrix contains (as sub-matrices) the [1×1], [2×2], [3×3] **MAC** matrices that would have been calculated for a lower number of known eigenmodes (1, 2 or 3, respectively).

$\mathbf{\hat{MAC}}$ ([1×*m*]) is a vector holding the diagonal terms of **MAC** matrix and it can be easily calculated by setting $i = j$ in Eq. (2) or Eq. (3). $\mathbf{\hat{MAC}}$ is a vector with as many values as the number of known eigenmodes (*m*). In our example, considering all four eigenmodes, we obtain:

$$\mathbf{\hat{MAC}}(\mathrm{A},\mathrm{A}) = \mathbf{\hat{MAC}}(\mathrm{B},\mathrm{B}) = \begin{bmatrix} 1 & 1 & 1 & 1 \end{bmatrix} \tag{6}$$

$$\mathbf{\hat{MAC}}(\mathrm{A},\mathrm{B}) = \mathbf{\hat{MAC}}(\mathrm{B},\mathrm{A}) = \begin{bmatrix} 0.9950 & 0.9853 & 0.9765 & 0.9609 \end{bmatrix} \tag{7}$$

By multiplying the *m* individual values of the $\mathbf{\hat{MAC}}$ vector, we obtain the final *MAC* scalar value as follows:

$$MAC = \prod_{i=1}^{m} \hat{\mathrm{MAC}}_i \tag{8}$$

The table below shows the values of *MAC* for various values of the number of known eigenmodes, for our example.

No of known modes	**1**	**2**	**3**	**4**
MAC(A, B)	0.9950	0.9803	0.9573	0.9199

Table 3. *MAC* values for 1, 2, 3 or 4 known eigenmodes.

2.2.2. The modified total modal assurance criterion (MTMAC)

One limitation of the MAC criterion is that it does not take into account the eigenvalues of the different mode shapes of the structures. It takes into account only the eigenvectors, but not the eigenvalues. This means that in case of uniform damage, the MAC criterion will not be able to detect any change, as in this case, the structure becomes more flexible (the eigenperiod increases), but there is no difference in the eigenvectors which remain the same as before. The natural frequencies provide global information of the structure and they can be accurately identified through dynamic measurements.

Another criterion, the modified total modal assurance criterion (MTMAC) [14], is based on the MAC criterion but it takes also the eigenvalues into account. The MTMAC vector $\mathbf{MT\hat{M}AC}$ ([1×*m*]) is defined as follows:

$$\mathrm{MT\hat{M}AC}_i = \frac{\mathrm{M\hat{A}C}_i}{1+\left|\dfrac{\omega_{A(i)}^2 - \omega_{B(i)}^2}{\omega_{A(i)}^2 + \omega_{B(i)}^2}\right|}, \quad i = \{1,\ 2, \ldots,\ m\} \tag{9}$$

It should be noted that the MTMAC can be easily defined also as a matrix ([*m*×*m*]), whose diagonal is again the $\mathbf{MT\hat{M}AC}$ vector, as was the case with MAC. $\mathbf{MT\hat{M}AC}$ is a row vector with as many values as the number of natural modes considered (*m*). In our example, considering all four eigenmodes:

$$\mathbf{MT\hat{M}AC}(\mathrm{A,A}) = \mathbf{MT\hat{M}AC}(\mathrm{B,B}) = \begin{bmatrix} 1 & 1 & 1 & 1 \end{bmatrix} \tag{10}$$

$$\mathbf{MT\hat{M}AC}(\mathrm{A,B}) = \mathbf{MT\hat{M}AC}(\mathrm{B,A}) = \begin{bmatrix} 0.7889 & 0.8220 & 0.8395 & 0.8195 \end{bmatrix} \tag{11}$$

By multiplying the *m* individual values of the $\mathbf{MT\hat{M}AC}$ vector, we obtain the *MTMAC* scalar value as follows:

$$MTMAC = \prod_{i=1}^{m} \mathrm{MT\hat{M}AC}_i \tag{12}$$

The table below shows the values of *MTMAC* for various values of the number of known eigenmodes, for our example.

No of known modes	**1**	**2**	**3**	**4**
MTMAC(A, B)	0.7889	0.6484	0.5444	0.4461

Table 4. *MTMAC* values for 1, 2, 3 or 4 known eigenmodes.

2.2.3. The co-ordinate modal assurance criterion (CoMAC)

In the comparison of two sets of modal vectors, one of the issues of interest is the influence of individual DOFs on the vector resemblance. The spatial dependence of the MAC correlation criterion can be misleading. The co-ordinate modal assurance criterion (CoMAC) [15] is an extension of the modal assurance criterion which is used to detect differences between two modal vectors at the DOF level. It is basically a row-wise correlation of two sets of compatible vectors, while in MAC this is done column-wise.

Although we can also define a **COMAC** matrix ([*n*×*n*]), in the same way as we defined **MAC** earlier, this time we will go straight to the definition of the $\mathbf{CO\hat{M}AC}$ vector ([1×*n*]) which is most relevant and important. The off-diagonal terms of **MAC** were the ones giving the relationship between different mode shape vectors of the two structures, for example the element (2, 1) of **MAC** is the one which gives the relationship between the 2nd eigenmode of structure A and the 1st eigenmode of structure B. In the case of **COMAC**, in a similar manner, the off-diagonal terms are the ones giving the relationship between different DOFs of the two structures. For example the element (2, 1) of **COMAC** is the one which gives the relationship

between the 2nd DOF of structure A and the 1st DOF of structure B, for the various eigenvectors considered.

Hence, the $\mathbf{COM\hat{A}C}$ for the k-th DOF of the structure (k = 1, 2,…, n) is defined as follows:

$$\mathrm{COM\hat{A}C}_k = \frac{\left(\sum_{i=1}^{m}\left|\varphi_k^{(i)}\psi_k^{(i)}\right|\right)^2}{\sum_{i=1}^{m}\left[\left(\varphi_k^{(i)}\right)^2\right]\cdot\sum_{i=1}^{m}\left[\left(\psi_k^{(i)}\right)^2\right]}, \quad k=\{1,\ 2,\ldots,\ n\} \tag{13}$$

Unlike the MAC, the COMAC can compare modes that are close in frequency by detecting local differences between two sets of modal vectors. It does not identify modeling errors, because their location can be different from the areas where their consequences are felt. Another limitation is the fact that COMAC weights all DOFs equally, irrespective of their magnitude in the modal vector.

By calculating $\mathrm{COM\hat{A}C}_k$ for all k = {1, 2,…, n} we obtain the $\mathbf{COM\hat{A}C}$ vector ([1×n]). In case of full consistency between $\{\boldsymbol{\varphi}^{(i)}\}$ and $\{\boldsymbol{\psi}^{(i)}\}$ ($\{\boldsymbol{\varphi}^{(i)}\}=\{\boldsymbol{\psi}^{(i)}\}$ for all i = {1, 2,…, m}), all elements of the $\mathbf{COM\hat{A}C}$ vector will be equal to 1. By multiplying the n individual values of the $\mathbf{COM\hat{A}C}$ vector, we obtain the *COMAC* scalar value as follows:

$$COMAC = \prod_{i=1}^{n}\mathrm{COM\hat{A}C}_i \tag{14}$$

In our example:

$$\mathbf{COM\hat{A}C}(\mathrm{A},\mathrm{A}) = \mathbf{COM\hat{A}C}(\mathrm{B},\mathrm{B}) = \begin{bmatrix}1 & 1 & 1 & 1 & 1 & 1 & 1 & 1 & 1\end{bmatrix}^T \tag{15}$$

The table below shows the values of the various elements of $\mathbf{COM\hat{A}C}$ vector together with the corresponding values of *COMAC* scalar, for various values of the number of known eigenmodes, for our example.

No of known modes	**1**	**2**	**3**	**4**
1st DOF	1.0000	0.9999	0.9997	0.9997
2nd DOF	1.0000	0.9995	0.9979	0.9905
3rd DOF	1.0000	0.9970	0.9804	0.9509
4th DOF	1.0000	0.9850	0.9623	0.9754
5th DOF	1.0000	0.9678	0.9837	0.9421
6th DOF	1.0000	0.9892	0.9760	0.9814
7th DOF	1.0000	0.9987	0.9934	0.9906
8th DOF	1.0000	0.9991	0.9993	0.9992
9th DOF	1.0000	0.9980	0.9983	0.9990
COMAC	**1.0000**	**0.9356**	**0.8955**	**0.8395**

Table 5. $\mathbf{COM\hat{A}C}$ (A, B) and corresponding *COMAC* scalar value for 1, 2, 3 or 4 known eigenmodes.

2.2.4. The modal flexibility assurance criterion (MACFLEX)

It is well known that damage affects the stiffness matrix of the structure and more specifically it reduces the stiffness of the individual damaged elements. A reduction in stiffness is equivalent to an increase in the structural flexibility.

Flexibility matrix

In structural health monitoring it is advantageous to use changes in flexibility as an indicator of damage rather than using stiffness perturbations. This is due to the following reasons [16]:

1. The flexibility matrix is dominated by the lower modes and so good approximations can be obtained even when only a few lower modes are employed.
2. The flexibility matrices are directly attainable through the modes and mode shapes, determined by the system identification process.
3. Iterative algorithms usually converge the fastest to high eigenvalues.
4. In flexibility-based methods, these eigenvalues correspond to the dominant low-frequency components in structural vibrations.

Therefore, the dynamically measured flexibility matrix which is calculated from the identified modal parameters, can be used as a damage identification measure [7]. The flexibility matrix $\mathbf{F}_A$ ([$n \times n$]) for structure A is given by

$$\mathbf{F}_A = \mathbf{\Phi} \cdot \mathbf{\Lambda}_A^{-1} \cdot \mathbf{\Phi}^T \tag{16}$$

where $\mathbf{\Phi}$ is a matrix ([$n \times m$]) containing all the m mode shape vectors $\{\boldsymbol{\varphi}^{(i)}\}$ ([$n \times 1$] each) and $\mathbf{\Lambda}_A$ is a diagonal matrix ([$m \times m$]) which holds the eigenvalues $\lambda_{A(i)} = \omega_{A(i)}^2$ (i = 1, 2,…, m) on its diagonal. The individual elements of matrix $\mathbf{F}_A$ can also be obtained separately using the following formula:

$$F_{A,ij} = \sum_{k=1}^{m} \frac{1}{\omega_{(k)}^2} \varphi_k^{(i)} \varphi_k^{(j)} \tag{17}$$

The two figures below, show graphical representations of the flexibility matrices $\mathbf{F}_A$ and $\mathbf{F}_B$ of the two structures of our example, for 1 and for 4 known eigenmodes, respectively.

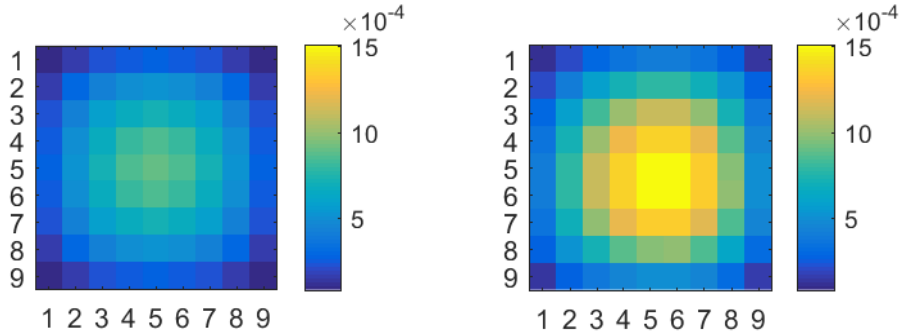

Figure 2. Flexibility matrices for structure A (left) and B (right), for one known eigenmode.

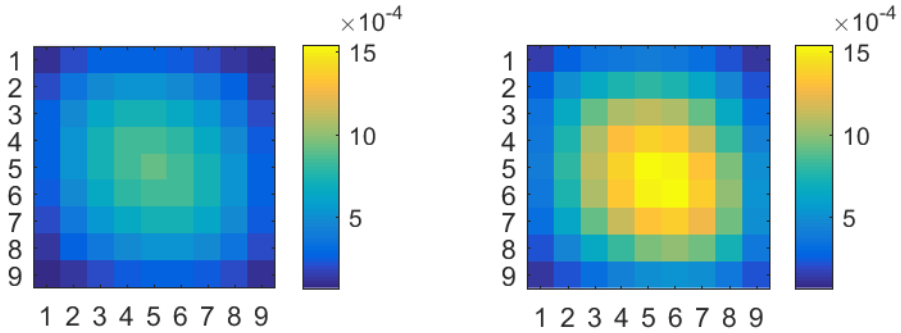

Figure 3. Flexibility matrices for structure A (left) and B (right), for 4 known eigenmodes.

Each column of the flexibility matrix represents the displacement pattern of a structure associated with a unit force applied to the associated degree of freedom. As shown in Eq. (17), as the value of frequency decreases (i.e. the eigenperiod increases) the modal contribution to the flexibility matrix increases also. As a result, a good estimate of the flexibility matrix can be calculated with a small number of the first low-frequency modes, which is also evidenced in the two figures above.

The MACFLEX criterion definition

In order to compare the values of the flexibility matrix of the two structures A and B, the modal flexibility assurance criterion (MACFLEX) is applied. The individual elements of the $\mathbf{MAC\hat{F}LEX}$ vector ([1×n]) can be calculated as follows:

$$\mathrm{MAC\hat{F}LEX}_i = \frac{\left(\hat{\mathbf{F}}_{\mathrm{A}}^{(i)T}\hat{\mathbf{F}}_{\mathrm{B}}^{(i)}\right)^2}{\left(\hat{\mathbf{F}}_{\mathrm{A}}^{(i)T}\hat{\mathbf{F}}_{\mathrm{A}}^{(i)}\right)\left(\hat{\mathbf{F}}_{\mathrm{B}}^{(i)T}\hat{\mathbf{F}}_{\mathrm{B}}^{(i)}\right)} \tag{18}$$

where $\hat{\mathbf{F}}_{\mathrm{A}}^{(i)}$ and $\hat{\mathbf{F}}_{\mathrm{B}}^{(i)}$ are the i-th column vectors ([n×1]) of the flexibility matrices $\mathbf{F}_{\mathrm{A}}$ and $\mathbf{F}_{\mathrm{B}}$, for structures A and B, respectively. $\mathbf{MAC\hat{F}LEX}$ is a vector with as many values as the number of columns in the flexibility matrices. Again, we could consider a full **MACFLEX** matrix by taking different vectors into account, instead of the i-th vector for both structures, but there is no point in that as again the diagonal terms of the **MACFLEX** matrix are the important ones.

By multiplying the n individual values of the $\mathbf{MAC\hat{F}LEX}$ vector, we obtain the *MACFLEX* scalar value as follows:

$$MACFLEX = \prod_{i=1}^{n} \mathbf{MAC\hat{F}LEX}_i \tag{19}$$

In our example, for any number of known modes (1, 2, 3 or 4), it is:

$$\mathbf{MAC\hat{F}LEX}(\mathrm{A},\mathrm{A}) = \mathbf{MAC\hat{F}LEX}(\mathrm{B},\mathrm{B}) = \begin{bmatrix}1 & 1 & 1 & 1 & 1 & 1 & 1 & 1 & 1\end{bmatrix} \tag{20}$$

However, the $\mathbf{MAC\hat{F}LEX}(\mathrm{A},\mathrm{B})$ = $\mathbf{MAC\hat{F}LEX}(\mathrm{B},\mathrm{A})$ vector changes depending on the number of the known eigenmodes, as shown in the table below (shown as the transpose, in column format).

No of known modes	1	2	3	4
1st DOF	0.9950	0.9929	0.9932	0.9933
2nd DOF	0.9950	0.9936	0.9939	0.9939
3rd DOF	0.9950	0.9947	0.9948	0.9948
4th DOF	0.9950	0.9957	0.9956	0.9956
5th DOF	0.9950	0.9963	0.9962	0.9962
6th DOF	0.9950	0.9965	0.9965	0.9965
7th DOF	0.9950	0.9967	0.9967	0.9967
8th DOF	0.9950	0.9972	0.9973	0.9973
9th DOF	0.9950	0.9978	0.9980	0.9979
MACFLEX	**0.9557**	**0.9621**	**0.9628**	**0.9629**

Table 6. $\mathbf{MAC\hat{F}LEX}(\mathrm{A},\mathrm{B})^T$ and corresponding *MACFLEX* scalar value for 1, 2, 3 or 4 known eigenmodes, for our example.

Figure 4 shows the values of MTMAC and MACFLEX criteria for different number of known eigenmodes (1, 2, 3 or 4), for our example.

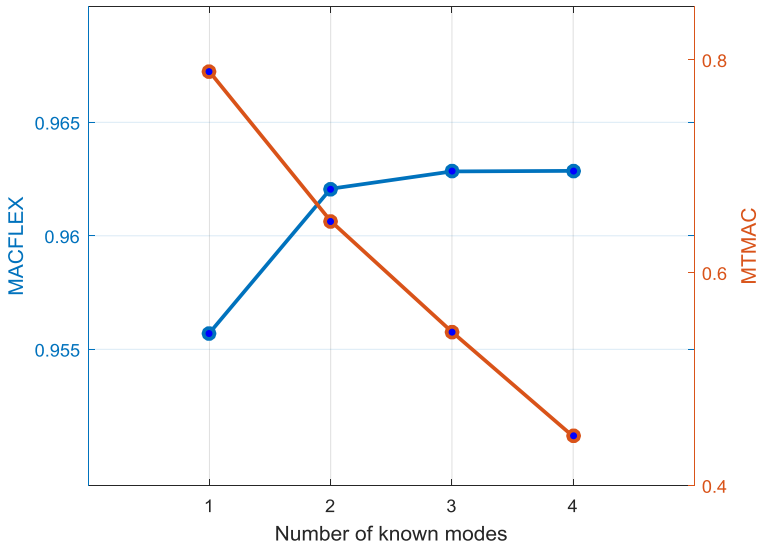

Figure 4. Comparison of *MACFLEX* and *MTMAC* scalar values for 1, 2, 3, and 4 known eigenmodes.

3. DAMAGE IDENTIFICATION AS AN OPTIMIZATION PROBLEM

3.1. Problem formulation

Setting-up an objective function, selecting the updating parameters and using robust optimization algorithms are three crucial steps in structural identification. They require deep physical insight and usually trial-and-error procedures have to be used. In our case, the damage identification problem is considered as an unconstrained optimization problem where the design variables denote the extent of damage of every single element of the structure. In this sense, the number of design variables is equal to the number of elements in the structure. Single beam elements are used to represent the structure of the numerical example. It has been assumed that no alteration occurs before and after damage related to the mass, which is acceptable in most real applications. Therefore, the parameterization of the damage has been represented by a reduction factor or damage index of the element bending stiffness. This damage index, d_e, for a damaged element e represents the relative variation of the damaged element bending stiffness, $(EI)_{e,d}$ to the initial (undamaged) bending stiffness $(EI)_e$, as follows:

$$d_e = 1 - \frac{(EI)_{e,d}}{(EI)_e} \tag{21}$$

This definition of a damage index for each element of the structure allows estimating not only the damage extent but also the damage location since the damage identification is carried out at the element level. The damage index can take values between 0 (no damage) and 1 (100% damage, no stiffness), although for numerical stability purposes, the maximum damage has to be limited to a value slightly below 1 (i.e. 0.999) or the structure can become a mechanism that cannot be analyzed and numerical instabilities will occur.

The objective function has to reflect the deviation between the numerical prediction and the real behavior of the structure. For this reason, an objective function may be formulated in terms of the discrepancy between FE and experimental quantities. The following four objective functions have been considered in this study, corresponding to the four different modal correlation criteria (MAC, MTMAC, CoMAC and MACFLEX respectively) between the real damage (according to each examined damage scenario) and the damage which is estimated by the finite element model:

- $F_1 = 1 - \text{MAC}$
- $F_2 = 1 - \text{MTMAC}$
- $F_3 = 1 - \text{COMAC}$
- $F_4 = 1 - \text{MACFLEX}$

The minimum value (target value) for each objective function is zero. At this point it has to be noted that in real life, the dynamics properties (eigenvalues and eigenmodes) of the real damaged structure would have to be determined (measured) by experiment. In our case, these properties are also calculated numerically using a FE "real damage" model, which is perfectly acceptable for the purposes of the present study and does not cause any problems or limitations to the procedure.

3.2. The differential evolution algorithm

Choosing the proper search algorithm for solving an optimization problem is not a straightforward procedure. In the past a number of studies have been published where structural optimization are solved using the metaheuristic search algorithms and especially those based on

adopting Darwinian principles of evolutionary process. These algorithms achieve efficient performance for a wide range of combinatorial optimization problems. Among the plethora of such algorithms, the differential evolution (DE) algorithm is adopted in this study to solve the optimization problem of Section 3.1.

Differential evolution (DE) is a stochastic population-based evolutionary algorithm for global optimization, introduced by Storn & Price [17]. It follows the standard evolutionary algorithm flow with some significant differences in mutation and selection process. The simplicity of DE algorithm is based on only three tunable parameters, the mutation factor $F \in [0,2]$, the crossover probability $CR \in [0,1]$ and the total number or particles (population size) *NP*. The fundamental idea behind DE is the use of vector differences by choosing randomly selected vectors, and then taking their difference as a means to perturb the parent vector with a special kind operator and probe the search space. Several variants of DE have been proposed so far [18], but this study is focused on the nominal approach (DE/rand/1/bin). According to this, each of the members of the population undergoes mutation and crossover. Once crossover occurs, the offspring is compared to the parent, and whichever fitness is better moves to the next generation (selection process). In more detail:

We consider an optimization problem with *D* dimensions. First, all individuals $\boldsymbol{x}$ are initialized at random positions in the search-space. After initialization each member of the population $\boldsymbol{x}$ undergoes mutation and a donor vector $\boldsymbol{v}$ is generated such as:

$$\boldsymbol{v} = \boldsymbol{a} + F \cdot (\boldsymbol{b} - \boldsymbol{c}) \tag{22}$$

where $\boldsymbol{a}$, $\boldsymbol{b}$ and $\boldsymbol{c}$ are three individuals from the population at random, which must be distinct from each other as well as from individual $\boldsymbol{x}$ ($\boldsymbol{x} \neq \boldsymbol{a} \neq \boldsymbol{b} \neq \boldsymbol{c}$).

In the next step the crossover operator is applied by generating the trial vector $\boldsymbol{u}$ which is defined either from the *i*-th component (v_i) of $\boldsymbol{v}$ or the *i*-th component (x_i) of $\boldsymbol{x}$, with probability *CR* as follows:

$$u_i = \begin{cases} v_i & \text{if } r_i \leq CR \text{ or } i = R \\ x_i & \text{otherwise} \end{cases} \qquad i = \{1, 2, ..., D\} \tag{23}$$

where r_i is a random number with uniform distribution, $r_i \in U[0,1]$, and *R* is a random integer in [1, 2, …, *D*] which ensures that in any case, after the crossover operation it is $\boldsymbol{u} \neq \boldsymbol{x}$. The last step of the generation procedure is the implementation of the selection operator where the target vector $\boldsymbol{x}$ is compared to the trial vector $\boldsymbol{u}$. If the trial vector $\boldsymbol{u}$ has a better fitness value, then the individual $\boldsymbol{x}$ is replaced in the population with the trial vector $\boldsymbol{u}$ as follows:

$$\boldsymbol{x}' = \begin{cases} \boldsymbol{u} & \text{if } f(\boldsymbol{u}) < f(\boldsymbol{x}) \\ \boldsymbol{x} & \text{otherwise} \end{cases} \tag{24}$$

where *f* is the objective function to be minimized and $\boldsymbol{x}'$ is the new design vector for the next generation. The optimization procedure finished when the maximum number of generations has been reached.

4. NUMERICAL EXAMPLES

A simply supported beam [19] is analyzed in this section to illustrate the performance of the proposed methodology and the different criteria. The geometry, boundary conditions and finite element mesh of the beam are shown in Figure 5. The beam has a total length of 6 m and it is discretized by 10 equal length beam elements of rectangular cross section b (width) x h (height)

= 0.25 m × 0.20 m. The beam is considered to have a Young's modulus E equal to 30 GPa and a density ρ equal to 2500 kg/m^3.

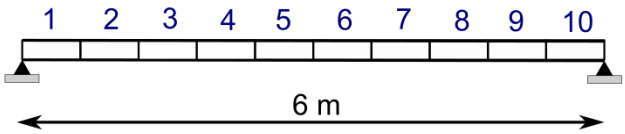

Figure 5. The beam structure under investigation.

The parameters of the DE optimization problem are the following:

- D = 10 (dimension of the problem)
- NP = 40 (population size)
- F = 0.6 (mutation factor)
- CR = 0.9 (crossover probability)
- MAXGEN = 3000 (maximum numbers of generations)

Four different damage scenarios are considered: (1) A single-element damage scenario (Figure 6a); (2) a two-element damage case (Figure 6b); (3) a three-element damage case (Figure 6c); and (4) a uniform damage case (Figure 6d). The finite element model of the beam is based on Euler–Bernoulli assumption of the planar elements with two degrees of freedom per node (the axial deformation is ignored).

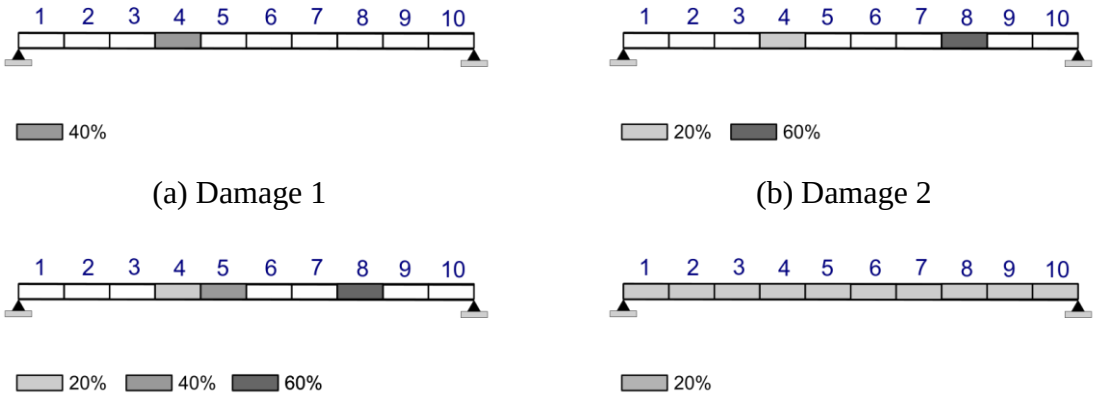

(a) Damage 1 (b) Damage 2

(c) Damage 3 (d) Damage 4

Figure 6. The four different damage scenarios.

4.1. Results

The same optimization algorithm has been applied to all damage scenarios. For each damage scenario, the four different modal correlation criteria have been used for the formulation of the objective function. For each criterion, the number of known eigenmodes varies from 1 to 4. The results are presented in bar charts, where the target damage (real damage) is always denoted in red color and the other colored bars denoted the damage estimation by the optimization procedure.

4.1.1. Damage 1 scenario (single-element damage)

Figure 7 shows the performance of the four different criteria for the first damage scenario. We see that the MTMAC criterion shows very good performance, since it manages to identify the damage almost 100% in the cases where 3 or 4 eigenmodes are known, while a good performance is also recorded for the difficult cases of 2 or even only 1 known eigenmode. The MAC criterion shows also good performance, but again it cannot be compared to the performance of the MTMAC criterion.

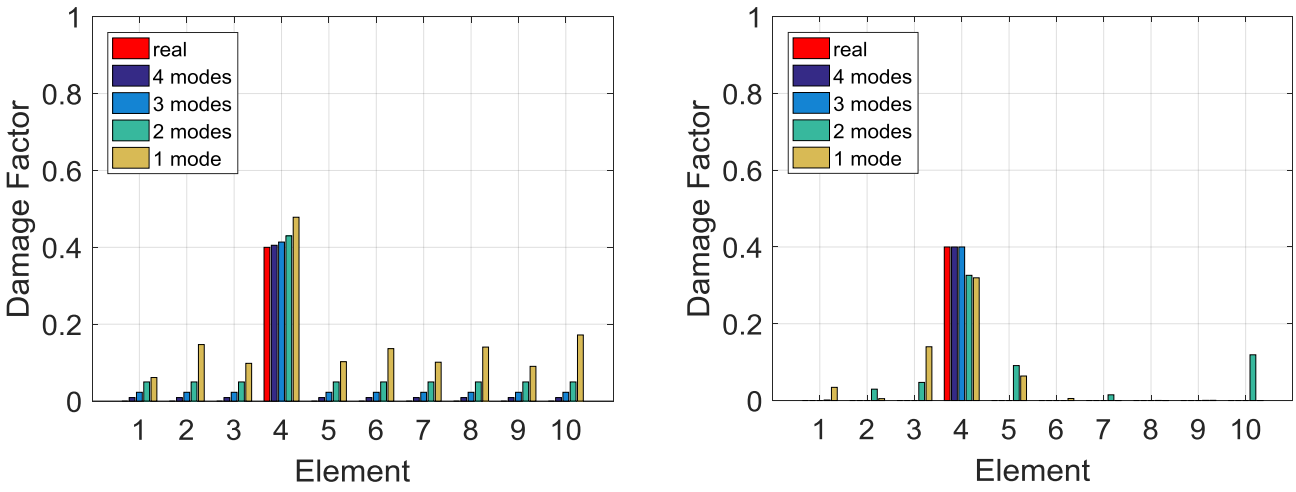

(a) MAC (b) MTMAC

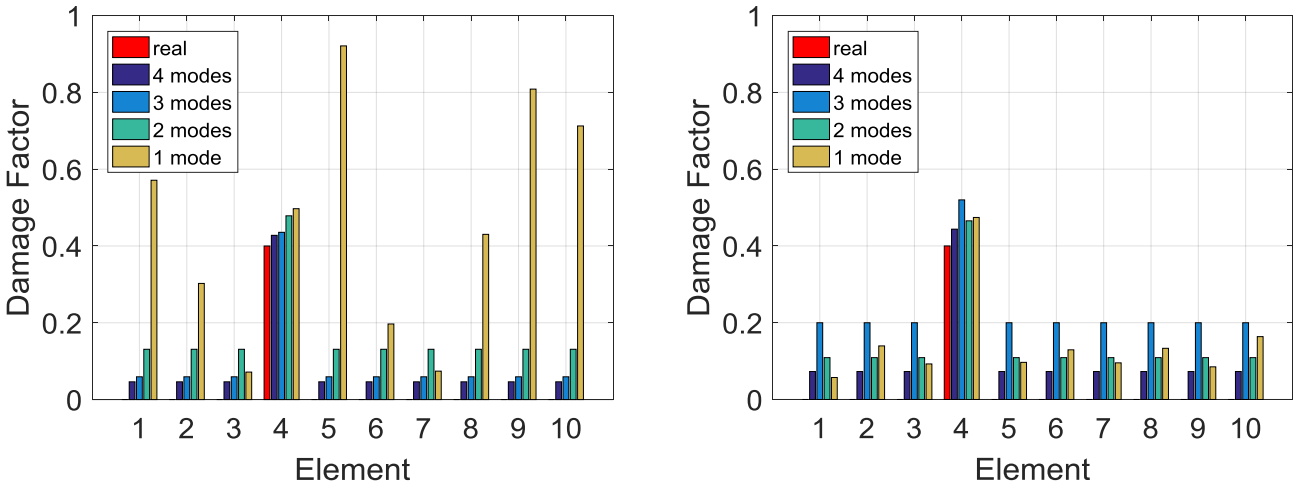

(c) CoMAC (d) MACFLEX

Figure 7. Performance of the four different criteria for the single-element damage scenario (Damage 1).

4.1.2. Damage 2 scenario (two-element damage)

Figure 8 shows the performance of the four different criteria for the second damage scenario. This damage scenario appears to be more difficult than the first one. Again, we see that the MTMAC criterion shows exceptional performance in the cases where 3 or 4 eigenmodes are known. The other criteria appear not to exhibit a very good performance, even in the cases where 4 eigenmodes are known.

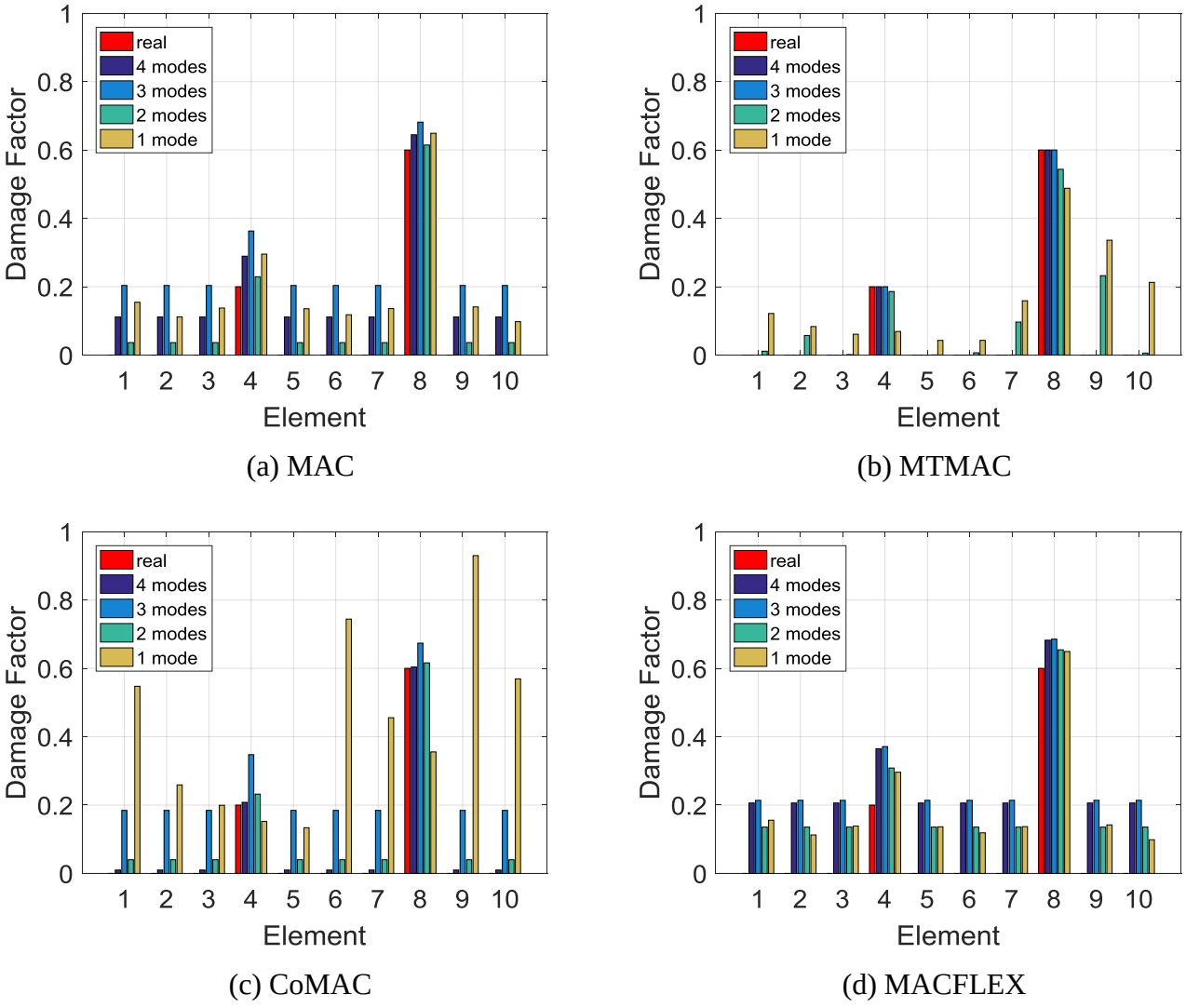

(a) MAC (b) MTMAC

(c) CoMAC (d) MACFLEX

Figure 8. Performance of the four different criteria for the two-element damage scenario (Damage 2).

4.1.3. Damage 3 scenario (three-element damage)

Figure 9 shows the performance of the four different criteria for the third damage scenario. Again the trend is the same. Only the MTMAC shows excellent performance, especially in the cases of 3 or 4 known eigenmodes, while the other criteria fail to identify the location and extent of damage adequately, even in the cases where 4 eigenmodes are known.

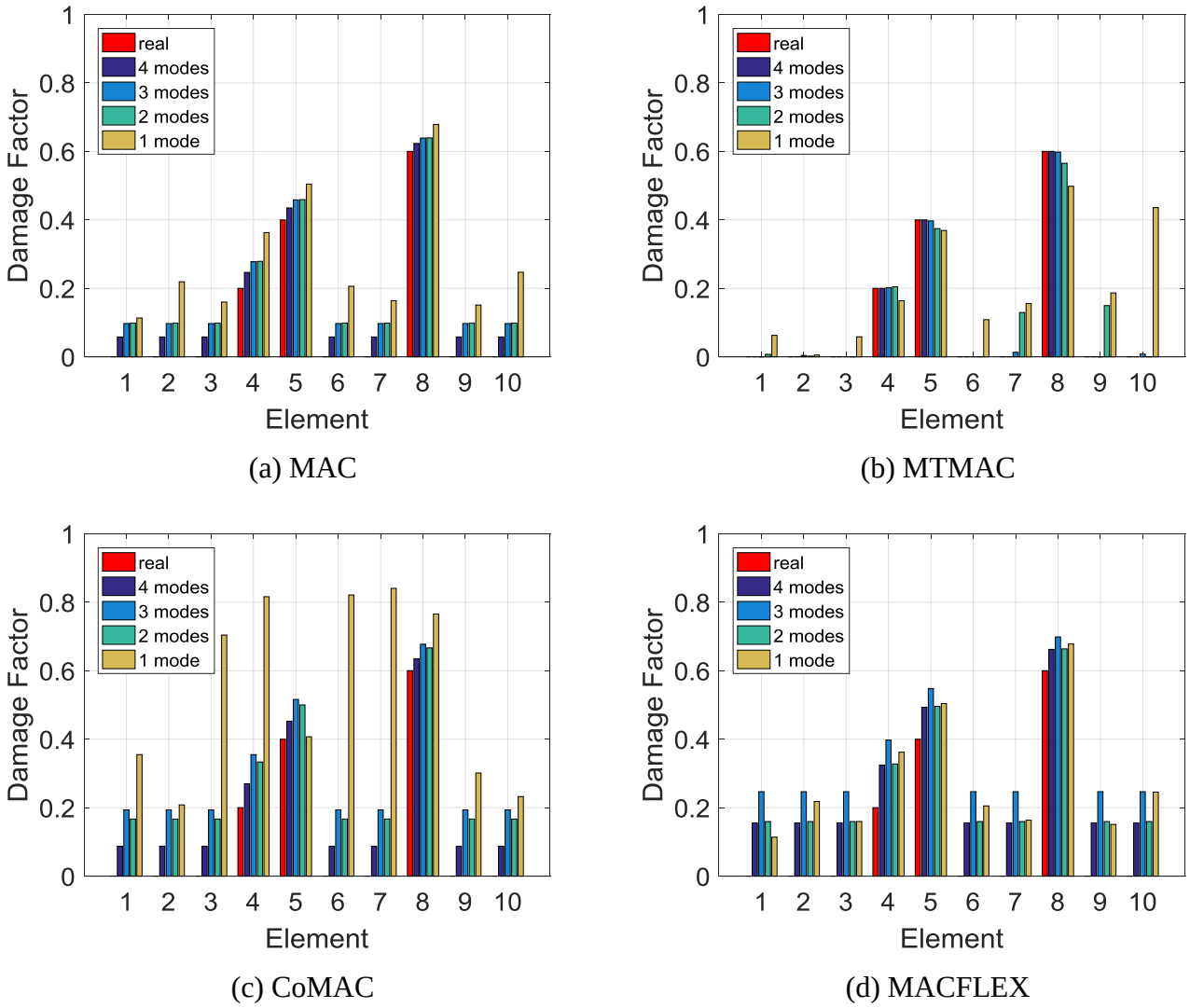

(a) MAC (b) MTMAC

(c) CoMAC (d) MACFLEX

Figure 9. Performance of the four different criteria for the three-element damage scenario (Damage 3).

4.1.4. Damage 4 scenario (uniform damage)

Figure 10 shows the performance of the four different criteria for the last damage scenario. The uniform damage appears to be the most difficult scenario. With the exception of MTMAC, the three other criteria completely fail to identify the location or extent of damage and they seem to just not be working at all. On the other hand, MTMAC shows very good performance when 4 eigenmodes are known, while its performance in the case where 3 eigenmodes are known can be still considered as acceptable. The overall performance of MTMAC is good but it is not as good as in the three other damage scenarios.

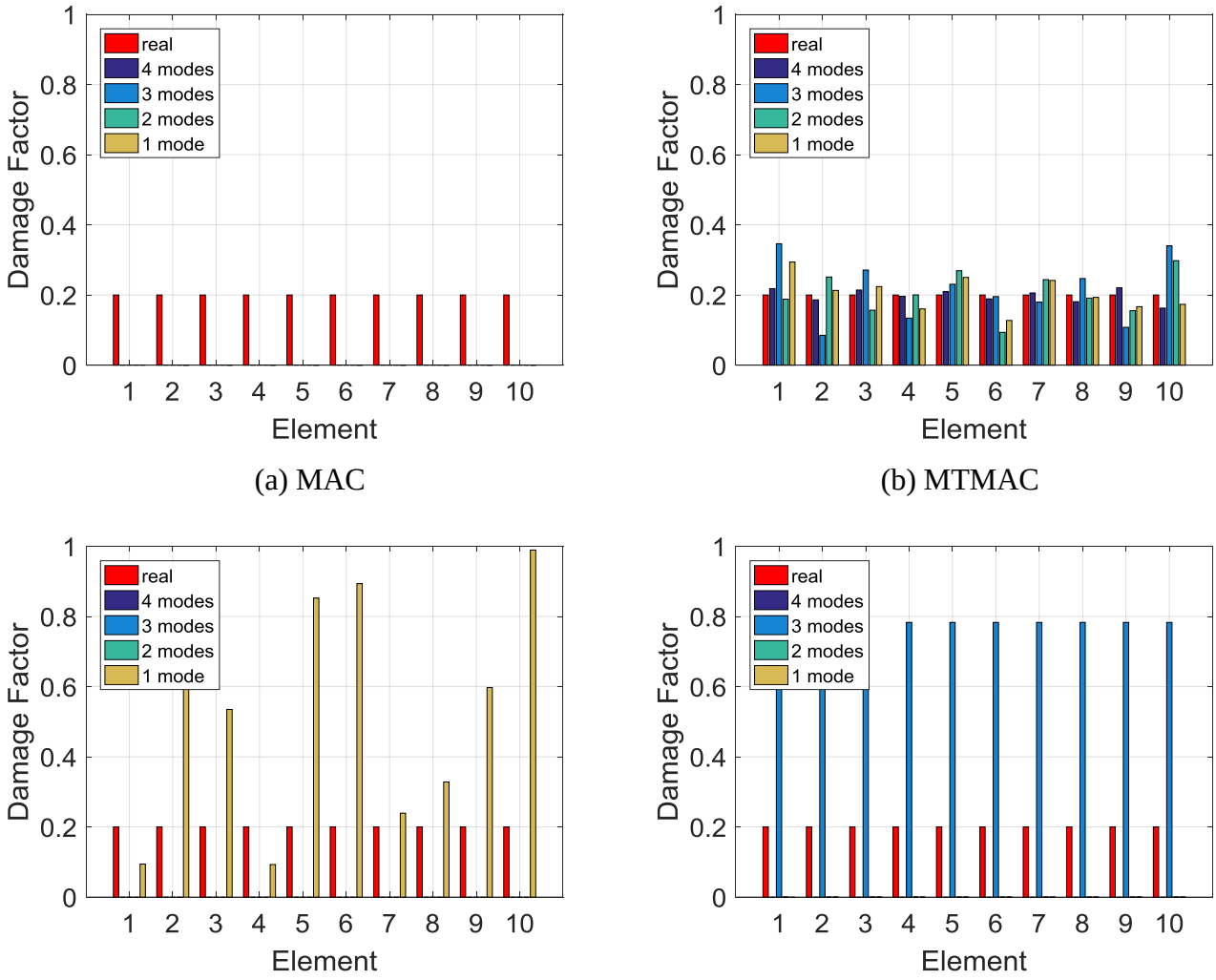

(a) MAC (b) MTMAC

(c) CoMAC (d) MACFLEX

Figure 10. Performance of the four different criteria for the uniform damage scenario (Damage 4).

The reason that the other three criteria (MAC, CoMAC and MACFLEX) fail completely is that only the MTMAC criterion contains also information about the eigenvalues (or eigenperiods) of the structure. The other criteria take into account only information about the eigenmodes. It is known that in the special case of uniform damage, the eigenmodes of the structure themselves do not change and the only property that changes is the eigenperiod which becomes larger (the structure becomes more flexible). As a result, only the MTMAC criterion manages to identify this special kind of damage and can be trustworthy for such damage cases.

5. CONCLUSIONS

- In this paper, the performance of different modal correlation criteria in structural damage identification was investigated. The structural damage identification problem was treated as an optimization problem which was solved using the differential evolution optimization algorithm.
- The DE algorithm proved to be very efficient and robust in all cases, while the four correlation criteria exhibited different performances for each damage case.
- In general, the MTMAC criterion showed excellent performance, managing to identify almost 100% the location and extent of damage for all damage cases, when 3 or 4 eigenmodes were known. In the cases were limited data were available (1 or 2 known eigenmodes), this criterion showed also an acceptable performance which was the best among the different criteria.
- The other criteria showed good performance only in some individual damage cases, but their general performance was not reliable, especially when a smaller number of eigenmodes were considered (1, 2 or 3).
- Some damage scenarios were more difficult than others. The most difficult was the uniform damage (4^{th}) scenario. Only the MTMAC criterion managed to give a good estimation for this damage case and again, the quality of the solution was not perfect, even in the case of 4 known eigenmodes.

REFERENCES

[1] Wang, X., C.-C. Chang, and L. Fan, *Nondestructive damage detection of bridges: A status review.* Advances in Structural Engineering, 2001. **4**(2): p. 75-91.

[2] Chou, J.-H. and J. Ghaboussi, *Genetic algorithm in structural damage detection.* Computers & Structures, 2001. **79**(14): p. 1335-1353.

[3] Koh, C.G. and M.J. Perry, *Structural Identification and Damage Detection using Genetic Algorithms*. Structures and Infrastructures. Vol. 6. 2009: CRC Press. 140.

[4] Levin, R.I. and N.A.J. Lieven, *Dynamic Finite Element Model Updating Using Simulated Annealing And Genetic Algorithms.* Mechanical Systems and Signal Processing, 1998. **12**(1): p. 91-120.

[5] Marwala, T., *Finite Element Model Updating Using Computational Intelligence Techniques: Applications to Structural Dynamics*. 2010: Springer Science & Business Media.

[6] Nobahari, M. and S.M. Seyedpoor, *Structural damage detection using an efficient correlation-based index and a modified genetic algorithm.* Mathematical and Computer Modelling, 2011. **53**(9–10): p. 1798-1809.

[7] Perera, R., A. Ruiz, and C. Manzano, *An evolutionary multiobjective framework for structural damage localization and quantification.* Engineering Structures, 2007. **29**(10): p. 2540-2550.

[8] Friswell, M.I. and J. Mottershead, *Finite Element Model Updating in Structural Dynamics*. 1995: Springer, Netherlands.

[9] Mottershead, J.E. and M.I. Friswell, *Model Updating In Structural Dynamics: A Survey.* Journal of Sound and Vibration, 1993. **167**(2): p. 347-375.

[10] Rytter, A., *Vibrational Based Inspection of Civil Engineering Structures*. 1993, Aalborg University, Denmark.

[11] Yu, L. and X. Chen. *Bridge damage identification by combining modal flexibility and PSO methods*. in *2010 Prognostics and System Health Management Conference*. 2010.
[12] Allemang, R.J., *The Modal Assurance Criterion – Twenty Years of Use and Abuse.* Sound and Vibration, 2003: p. 7.
[13] Pastor, M., M. Binda, and T. Harčarik, *Modal Assurance Criterion.* Procedia Engineering, 2012. **48**: p. 543-548.
[14] Perera, R. and R. Torres, *Structural damage detection via modal data with genetic algorithms.* Journal of Structural Engineering (ASCE), 2006. **132**(9): p. 1491-1501.
[15] Rades, M., *Mechanical Vibrations II: Structural Dynamic Modeling*. 2010: Printech.
[16] Bernal, D., *Extracting flexibility matrices from state-space realizations*, in *Proceedings of the European COST F3 Conference on System Identification and Structural Health Monitoring*. 2000. p. 127-135.
[17] Storn, R. and K. Price, *Differential Evolution – A Simple and Efficient Heuristic for global Optimization over Continuous Spaces.* Journal of Global Optimization, 1997. **11**(4): p. 341-359.
[18] Das, S. and P. Suganthan, *Differential evolution: A survey of the state-of-the-art.* IEEE Transactions on Evolutionary Computation, 2011. **15**(1): p. 4-31.
[19] Perera, R., R. Marin, and A. Ruiz, *Static–dynamic multi-scale structural damage identification in a multi-objective framework.* Journal of Sound and Vibration, 2013. **332**(6): p. 1484-1500.

ECCOMAS Congress 2016
VII European Congress on Computational Methods in Applied Sciences and Engineering
M. Papadrakakis, V. Papadopoulos, G. Stefanou, V. Plevris (eds.)
Crete Island, Greece, 5–10 June 2016

EXPLOITING MULTIPLE REFERENCE MODELS FOR ADAPTIVE CONTROL OF FLEXIBLE STRUCTURES

Ilaria Venanzi, Laura Ierimonti

Department of Civil and Environmental Engineering, University of Perugia
via G. Duranti 93, 06125 Perugia, Italy
e-mail: ilaria.venanzi@unipg.it
e-mail: ierimonti@strutture.unipg.it

Keywords: Active Control, Model-Reference Adaptive Control, Multiple Hazards, Multiple Reference Model, Control force.

Abstract. *Flexible structures like tall buildings are often equipped with active control systems which allow the reduction of structural vibration induced by wind and earthquakes. Wind gusts and earthquakes are different in terms of intensity level, frequency and duration of the excitation. In particular, wind induced vibrations are usually moderate and require a continuously operating control system whose main goal is to provide occupants' comfort in serviceability conditions. Conversely, earthquakes of significant intensity are rarely experienced by the structure and may produce structural damage that leads to deterioration in structural stiffness.*
The use of Model-Reference Adaptive Control (MRAC) has recently been considered for structural applications for its capability of dealing with systems's uncertainties and time dependence of parameters. The adaptive controller has two loops: the inner loop consists of an ordinary feedback control process while the outer loop adjusts the controller parameters through an adaptation rule in order to minimize the difference between measured output and model output. In this paper the use of MRAC in conjunction with a Lyapunov-based adaptation rule is investigated for the response mitigation of a tall building equipped on top with an active device and subjected to both wind and seismic hazards. Since the required structural performances in case of wind and earthquake-excited vibrations are different, in order to optimize the control effectiveness, a modified MRAC algorithm based on multiple reference models (M-MRAC) is proposed in which the switch between the targets is performed based on the measured feedback information. The main advantage of the proposed methods is its capability of providing power saving and limitation of the peak control force. Parametric analyses allow to identify proper threshold levels for the switching condition and optimal reference models providing a compromise between safety and economy. Results of the numerical analyses on a benchmark tall building show the effectiveness of the control strategy for several loading conditions.

1 INTRODUCTION

Active control is an appealing technique, already adopted in many tall buildings for mitigation of wind- and earthquake-induced vibrations. The effectiveness of active control is closely linked to the selected control algorithm. The most widespread strategies are those based on linear optimal control or robust control [1, 2] but they can not fully manage uncertainties in modal parameters evaluation, loads variability, system's non-linearities and physical limits of actuators [3]. For these reasons adaptive control strategies recently have started to be used for structural control.

Model Reference Adaptive Control is an adaptive algorithm which updates the parameters of the controller for tracking the response of a reference model. The actual system's response is compared to the target response and the control parameters are modified as a function of the error. While many applications of MRAC are available in the mechanical and aeronautical fields, still a few studies exist for civil structures [4, 5, 6].

Tall buildings can experience different vibration levels when subjected to earthquake and wind hazards. Consequently, active control has to allow satisfaction of serviceability requirements under wind load and to avoid occurrence of severe damage under seismic load.

In this paper a modified MRAC algorithm based on multiple reference models (M-MRAC) is proposed, capable of switching between targets depending on the measured feedback information. The idea of switching between different models has recently been proposed in literature [7] but never exploited for civil engineering applications. A preliminary parametric analysis on a tall building equipped with an AMD on top and subjected to both seismic and wind loads allows to define the characteristics of multiple reference models. Analysis results demonstrate the effectiveness of the method in optimizing the control performance and in reducing the required control force.

2 ADAPTIVE CONTROL WITH MRAC

2.1 Dynamics of the structure and the reference model

The considered structure is a tall building modeled as a multi-degrees of freedom dynamic system, subjected to external excitation $\mathbf{f}$ and to a control force $\mathbf{u}$. The equation of motion is:

$$\mathbf{M}_s\ddot{\mathbf{z}}_s + \mathbf{C}_s\dot{\mathbf{z}}_s + \mathbf{K}_s\mathbf{z}_s = \bar{\mathbf{E}}_s\mathbf{f} + \bar{\mathbf{B}}_s\mathbf{u} \tag{1}$$

where $\mathbf{M}_s$, $\mathbf{C}_s$ and $\mathbf{K}_s$ are the mass, damping and stiffness matrices of the building, $\bar{\mathbf{E}}_s$ and $\bar{\mathbf{B}}_s$ are the location matrices of the external excitation and the control force, respectively. In MRAC, a reference model is defined that is subjected to the same external disturbance $\mathbf{f}$ whose dynamic behavior is the target. The equation of motion of the reference system is:

$$\mathbf{M}_r\ddot{\mathbf{z}}_r + \mathbf{C}_r\dot{\mathbf{z}}_r + \mathbf{K}_r\mathbf{z}_r = \bar{\mathbf{E}}_r\mathbf{f} \tag{2}$$

where $\mathbf{M}_r$, $\mathbf{C}_r$ and $\mathbf{K}_r$ are the mass, damping and stiffness matrices of the reference model, $\bar{\mathbf{E}}_r$ is the location matrix of the external excitation.

In state-space formulation, the equations of motion become:

$$\dot{\mathbf{x}}_s = \mathbf{A}_s\mathbf{x}_s + \mathbf{E}_s\mathbf{f} + \mathbf{B}_s\mathbf{u} \tag{3}$$

$$\dot{\mathbf{x}}_r = \mathbf{A}_r\mathbf{x}_r + \mathbf{E}_r\mathbf{f} \tag{4}$$

where

$$\mathbf{x}_s = [\mathbf{z}_s, \dot{\mathbf{z}}_s]^T \tag{5}$$

$$\mathbf{x}_r = [\mathbf{z}_r, \dot{\mathbf{z}}_r]^T \tag{6}$$

$\mathbf{A}_s$, $\mathbf{A}_r$ are the system matrices of the structure and the reference model respectively, $\mathbf{E}_s$, $\mathbf{E}_r$ and $\mathbf{B}_s$ are the location matrices.

A linear feedback control law is adopted for computing the control force:

$$\mathbf{u} = \mathbf{K}\mathbf{x}_s \tag{7}$$

where $\mathbf{K}$ is the vector collecting the states' gains.

2.2 Adaptation law

In MRAC control scheme both the structure and the reference model are subjected to the same external excitation $\mathbf{f}$ which is supposed to be measured. To derive the adaptation law, the error vector $\mathbf{e}$ is computed as follows:

$$\mathbf{e} = \mathbf{x}_s - \mathbf{x}_r \tag{8}$$

The knowledge of the states of the structure is considered available and the target response is computed through the reference model.

A stable adaptation law used to adjust the controller's parameters is computed based on the definition of a Lyapunov function as follows:

$$V = \mathbf{e}^T\mathbf{P}\mathbf{e} + \boldsymbol{\phi}^T\boldsymbol{\Gamma}^{-1}\boldsymbol{\phi} \tag{9}$$

where $\boldsymbol{\phi}$ is the parameter error vector, $\mathbf{P}$ is a positive definite symmetric matrix, $\boldsymbol{\Gamma}$ is the positive definite adaptation gain matrix. In order to obtain an asymptotically stable adaptive system, the time derivative of the Lyapunov function $\dot{V}$, must be negative definite. Differentiating V yields:

$$\dot{V} = \mathbf{e}^T(\mathbf{A}_r^T\mathbf{P} + \mathbf{P}\mathbf{A}_r)\mathbf{e} + 2\mathbf{e}^T\mathbf{P}\mathbf{b}_I\boldsymbol{\phi}^T\mathbf{x}_s + 2\boldsymbol{\phi}^T\boldsymbol{\Gamma}^{-1}\boldsymbol{\phi}\mathbf{P}\mathbf{e} + \boldsymbol{\phi}^T\boldsymbol{\Gamma}^{-1}\boldsymbol{\phi} \tag{10}$$

By applying the Lyapunov's equation ($\mathbf{A}_r^T\mathbf{P}+\mathbf{P}\mathbf{A}_r = -\mathbf{Q}$), positive definite symmetric matrices $\mathbf{P}$ and $\mathbf{Q}$ can be found such that the first part of Equation 10 is negative definite. By putting the last two terms of Equation 10 to zero, the adaptive law is obtained:

$$\dot{\boldsymbol{\phi}} = -\boldsymbol{\Gamma}\mathbf{e}^T\mathbf{P}\mathbf{b}_I\mathbf{x}_s \tag{11}$$

$$\dot{\mathbf{K}} = \dot{\boldsymbol{\phi}}\mathbf{M}_s^{-1} \tag{12}$$

The adaptive control gain vector $\mathbf{K}$ is obtained by time integration.

3 MULTIPLE-MODEL REFERENCE ADAPTIVE CONTROL (M-MRAC)

Structures subjected to multiple hazards with different levels of excitation exhibit different performance. In order to guarantee the respect of various limit states under multiple hazard, it is convenient to define multiple reference models providing different target performance. The choice of the reference models is important for the determination of the best compromise between structural performance and power saving.

The reference model is a dynamic system described by the following equation:

$$\dot{\mathbf{x}}_r = \mathbf{A}_r(\sigma)\mathbf{x}_r + \mathbf{E}_r\mathbf{f} \tag{13}$$

where the state matrix $\mathbf{A}_{r\sigma}$ is a piecewise continuous function of time depending on the parameter characterizing switching conditions $\sigma(t)$. The multiple reference models' state matrix is defined as follows:

$$\mathbf{A}_r(\sigma) = \begin{cases} \mathbf{A}_{r,0} & \text{for } \sigma(t) < \sigma_1 \\ \mathbf{A}_{r,1} & \text{for } \sigma_1 \leq \sigma(t) < \sigma_2 \\ \dots & \\ \mathbf{A}_{r,n} & \text{for } \sigma(t) \geq \sigma_n \end{cases} \tag{14}$$

where $\sigma_1, ..., \sigma_n$ are switching thresholds. The parameter σ can be a measured state of the system or a generic response parameter.

In the simplified case of two reference models, the switching rule becomes:

$$\mathbf{A}_{r,\sigma} = \begin{cases} \mathbf{A}_{r,0} & \text{for } \sigma(t) < \bar{\sigma} \\ \mathbf{A}_{r,1} & \text{for } \sigma(t) \geq \bar{\sigma} \end{cases} \tag{15}$$

where $\bar{\sigma}$ is the switching threshold.

In order to obtain good performance of the control system, the switching rule must be properly selected. Repeated switching may potentially lead to optimized performance but a too high commutation frequency can lead to improper system's behavior [8]. Nevertheless, due to the high natural periods of structures under investigation the critical dwell time is usually reasonably well below the switching time intervals.

4 THE CASE STUDY

4.1 Description of the tall building

The structure chosen as case study is the 76-story building, 306 meters high, proposed as a benchmark problem for response control under wind load [9]. It is a reinforced concrete building consisting of a concrete core, designed to resist lateral loads and concrete frames mainly devoted to support gravity loads. The building has a square cross section with chamfer at two corners, constant along the height. A simplified dynamic model of the building with 1DOF for each floor is considered in the analyses. Damping ratio for all modes is 1% and the first natural frequency is 0.16 Hz. Figure 1 shows the plan and elevation views of the structure.

4.2 Wind and seismic loads modeling

Wind loads adopted for the analyses were obtained by tests performed in the boundary layer wind tunnel facility at the Department of Civil Engineering at University of Sidney, Australia [10]. The rigid model of the building had a length scale of 1:400. Wind pressures were recorded for 27 seconds, corresponding to about 1 hour in prototype scale. Pressure coefficients were integrated and converted into across-wind forces at each story. The mean wind velocity at the top of the building was 47.25 m/s corresponding to a reference wind velocity $V_{ref} = 13.5$ m/s at 10 m above ground, representing serviceability conditions at which occupant's comfort and motion perception are important design criteria.

In order to consider uncertainties on measurement variability and to characterize statistically the wind load, 7 sets of time histories each one having a duration of 10 minutes are extracted from the measured time histories of the lateral wind forces and used to compute the structural response.

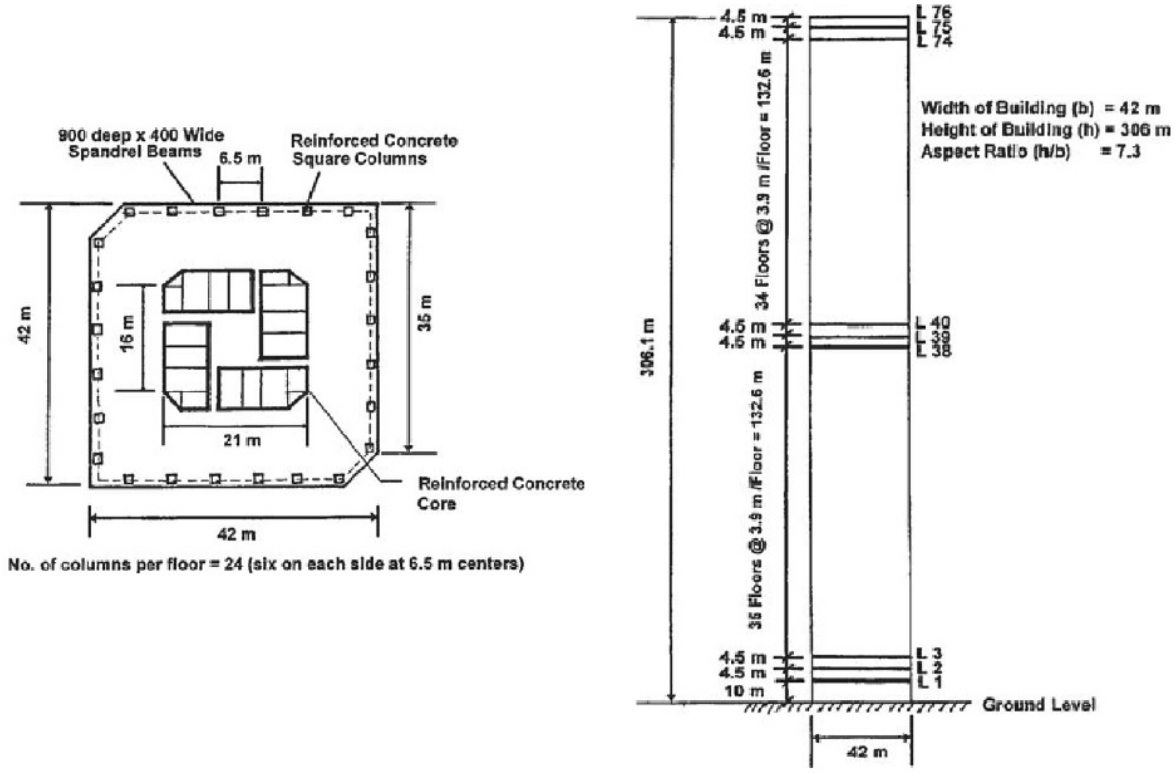

Figure 1: Plan and elevation views of the building [9].

To characterize the seismic load, 7 accelerograms relative to the Los Angeles area, with a 10% probability of exceedance in 50 years, are taken from the PEER-NISEE online library [12]. The accelerograms are preliminary scaled to have the same reference value of peak ground acceleration PGA_{ref}, which is the mean value (among the 7 accelerograms) of the PGA.

5 NUMERICAL RESULTS

5.1 Sensitivity analysis on the choice of the reference models

Tall buildings must satisfy different performance requirements under wind and earthquake. Therefore control systems have the dual purpose of guaranteeing occupants' comfort under ordinary wind conditions and limiting damage under extreme seismic events. The possibility of adopting multiple reference models is exploited with the aim of reducing costs associated with elevated power supply.

In order to characterize reference models, a parametric analysis by varying the target system damping is carried out. Without loss of generality, the investigated reference dynamic systems have mass and stiffness matrices equal to the corresponding nominal matrices of the real structure and damping ratio of all modes varying from 1% to 15%.

Proper performance indices are defined in order to have quantitative comparison between the

results:

$$J_1(\%) = \frac{\max|\text{IDR}|_r}{\max|\text{IDR}|_{lim}} \tag{16}$$

$$J_2(\%) = \frac{\max|\ddot{\mathbf{z}}|_r}{\max|\ddot{\mathbf{z}}|_{lim}} \tag{17}$$

$$J_3(\%) = \frac{\max|\text{M}_b|_r}{\max|\text{M}_b|_{lim}} \tag{18}$$

where IDR is the interstory drift ratio, $\ddot{\mathbf{z}}$ is the structural acceleration, M_b is the bending moment at the base of the building. Subscript r refers to the reference model and subscript lim refers to the acceptable threshold levels.

The most important response components to limit in order to ensure comfort and avoid damage to non-structural components are interstory drifts and accelerations. For serviceability, according to [13], 1/400 of the story height can be set as the limit state threshold for maximum interstory drift. For the motion perception acceleration threshold, the following relation can be adopted [14]:

$$\ddot{\mathbf{z}}_{lim} = \frac{a_0}{{f_0}^{0.56}} \tag{19}$$

where f_0 is the dominant natural frequency, $a_0 = 6$ cm/s^2, for office buildings.

Regarding the strength limit state, the threshold value of maximum bending moments at the base of the internal core is obtained as follows:

$$\text{M}_{b,lim} = \varphi_{lim} EI \tag{20}$$

where EI is the flexural stiffness and φ_{lim} is the curvature at the elastic limit of the reinforced concrete central core. Since the control system is supposed to maintain the central core below its yielding limit, the hypothesis of linear elastic behavior is justified and the structural response is computed by linear analysis with time domain integration.

Table 1 shows mean values and standard deviations of the peak response components. Results are obtained for damping ratio equal to the 1% (the nominal value for the building), under wind and seismic loads. Results show that interstory drifts and base bending moments due to wind load are one order of magnitude smaller than those due to seismic load. Moreover, earthquake-induced accelerations are much higher than wind-induced ones. This results is in keeping with full scale observations. High accelerations in tall buildings were observed in response to the 2011 Tohoku earthquake, and shown to be due to higher mode effects [15].

	Wind		Earthquake	
	Mean value	Standard deviation	Mean value	Standard deviation
IDR_{max} (m)	1.70e-3	0.61e-3	1.72e-2	1.12e-2
$\ddot{\mathbf{z}}_{max}$ (m/s^2)	0.25	0.02	26.19	7.45
$\text{M}_{b,max}$ (Nm)	5.39e6	1.85e6	6.06e7	3.39e7

Table 1: Mean values and standard deviations of peak response components for damping ratio of 1%.

Figure 2 reports the mean values of performance indices (computed adopting the 7 accelerograms and the 7 wind load time histories) for different values of damping ratio (1%, 5%, 10%,

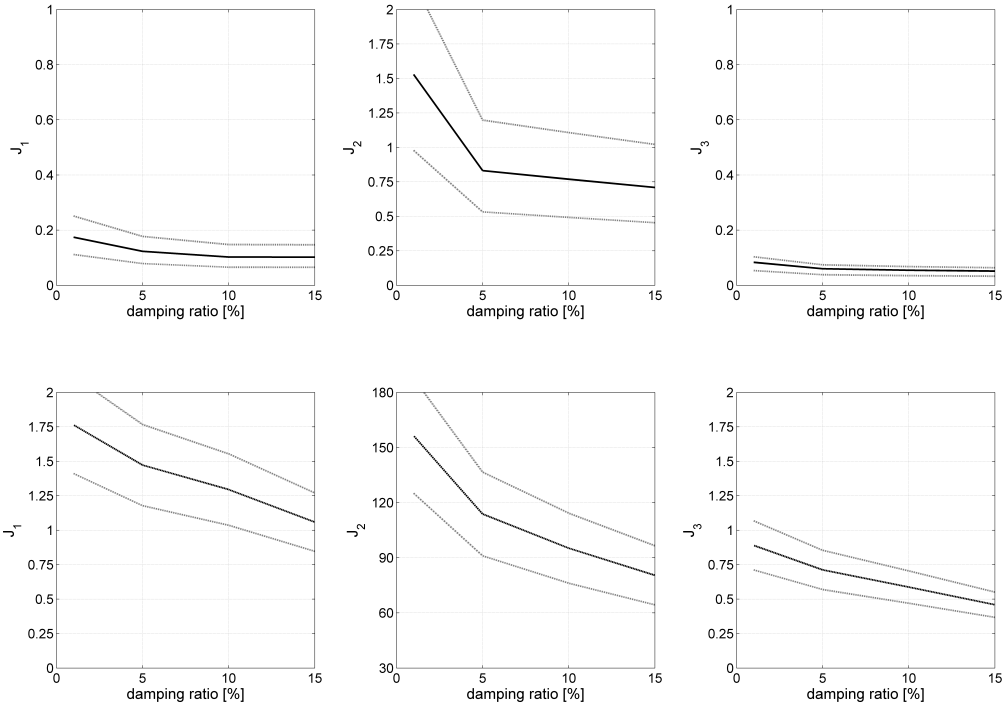

Figure 2: Performance indices as a function of damping ratio computed using wind load (top) and seismic load (bottom)

and 15%). The three top diagrams show response under wind load and the bottom ones show response obtained using the set of earthquakes. The grey dotted lines represent the performance indices obtained by varying PGA_{ref} and V_{ref} by the 40% ($\pm 20\%$) to account for randomness of the seismic intensity and the reference wind speed. Values of performance indices larger than unity indicate limit state crossing. Results show that index J_1 on interstory drifts ratio is smaller that unity for wind load and higher than unity for earthquake, unless damping ratios higher than 15% are adopted. Index J_2 on peak accelerations is significantly higher than unity for earthquake load, meaning that in seismic conditions limit state on motion perception is always exceeded and occupants comfort condition cannot be satisfied. In case of wind load, index J_2 can be reduced below unity for values of damping ratio higher than about 5%. Index J_3 related to yielding of the central core is smaller than unity for both wind and seismic load.

In order to ensure occupants' comfort, a reference model with 5% damping ratio can be used but to the extent of reducing drift-dependent damage to non-structural elements a reference model with 15% damping ratio must be adopted. Although the choice of reference models' damping con not be generalized (as it depends on the building's dynamic characteristics and the specific site's conditions), the sensitivity analyses demonstrate that the optimal target damping is not unique for different limit states.

5.2 Analysis with M-MRAC

In order to evaluate the effectiveness of the modified MRAC procedure (M-MRAC), several analysis are carried out on a simplified 1 degree of freedom model having mass equal to the first

modal mass and natural period equal to the one of the selected tall building.

The two reference models are chosen on the basis of the preliminary analyses presented in Section 5.1. In particular, in order to ensure occupants' comfort in serviceability conditions, an uncontrolled target system with 5% damping ratio is adopted. In order to avoid damage to drift-sensitive non-structural elements, an uncontrolled target system with 15% damping ratio is selected.

The response component $\sigma(t)$ which determines the switching condition is the building's peak displacement that is related to drift dependent damage. In the present analyses, without loss of generality, the switch between different models is activated when the structural displacement is $\bar{\sigma} = 0.5$ m.

Figure 3(a) shows the response of the uncontrolled system (U), the reference model (R) and the controlled system with M-MRAC to a step loading with a short ramp. The reference model has no control system and a damping of 15%. In this case the applied load does not activate the switching condition. Structural responses and load are normalized with respect to their maximum absolute values. Results show very good matching between the target model and the real system. Figures 3(b) and (c) show the states errors and control force, normalized with respect to their maximum absolute values, which tend to zero with time. Figure 4 shows

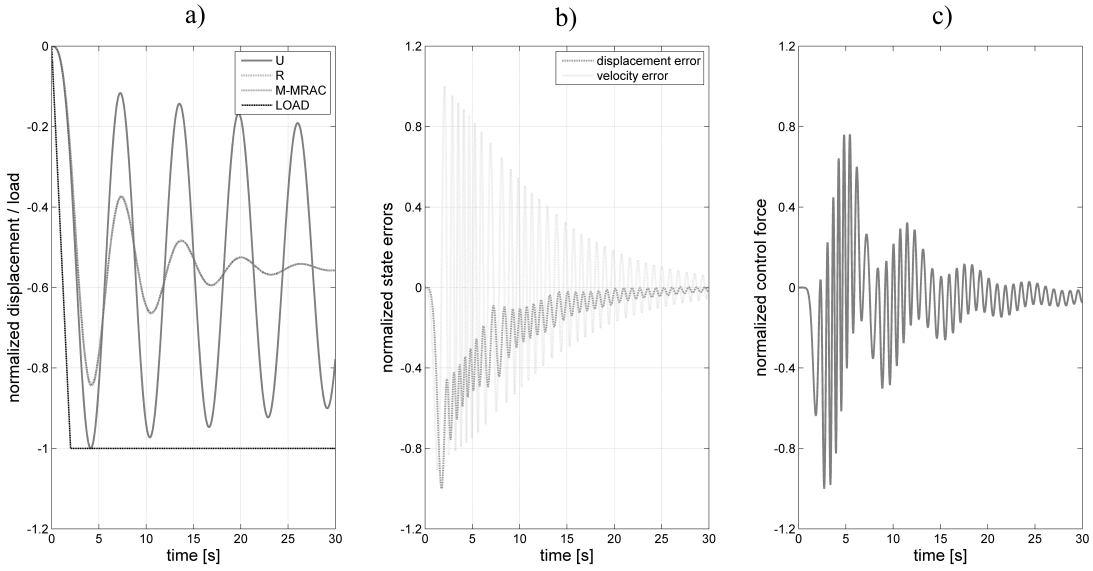

Figure 3: Controlled response obtained with M-MRAC to a step loading if reference model switching is not activated.

the performance of M-MRAC to a sinusoidal loading with natural frequency of 0.4 Hz and amplitude which increases up to its maximum value and after a slight impulsive variation is kept constant. Figure 4a shows the uncontrolled response (U), the response of the reference model (R) and the controlled response obtained with M-MRAC. Displacements are normalized with respect to $\bar{\sigma}$, showing that reference model switching is activated repeatedly. It can be observed that there is a very good matching between responses of the reference model and the controlled structure and that the system properly reduces peak displacements with respect to the uncontrolled case. Figure 4(b) compares normalized displacements obtained with the proposed M-MRAC and traditional MRAC. In this latter case, the reference model that the

system has to track is unique and has a damping ratio equal to 15%, corresponding to the damping required in case of seismic events. Figures 4(c) and (d) show the displacement error and control forces, normalized with respect to their maximum absolute values. It is possible to observe that state errors are kept limited and have the tendency to decrease with time. The control force required by M-MRAC is smaller than the one required by traditional MRAC, demonstrating the advantage of adopting multiple reference models.

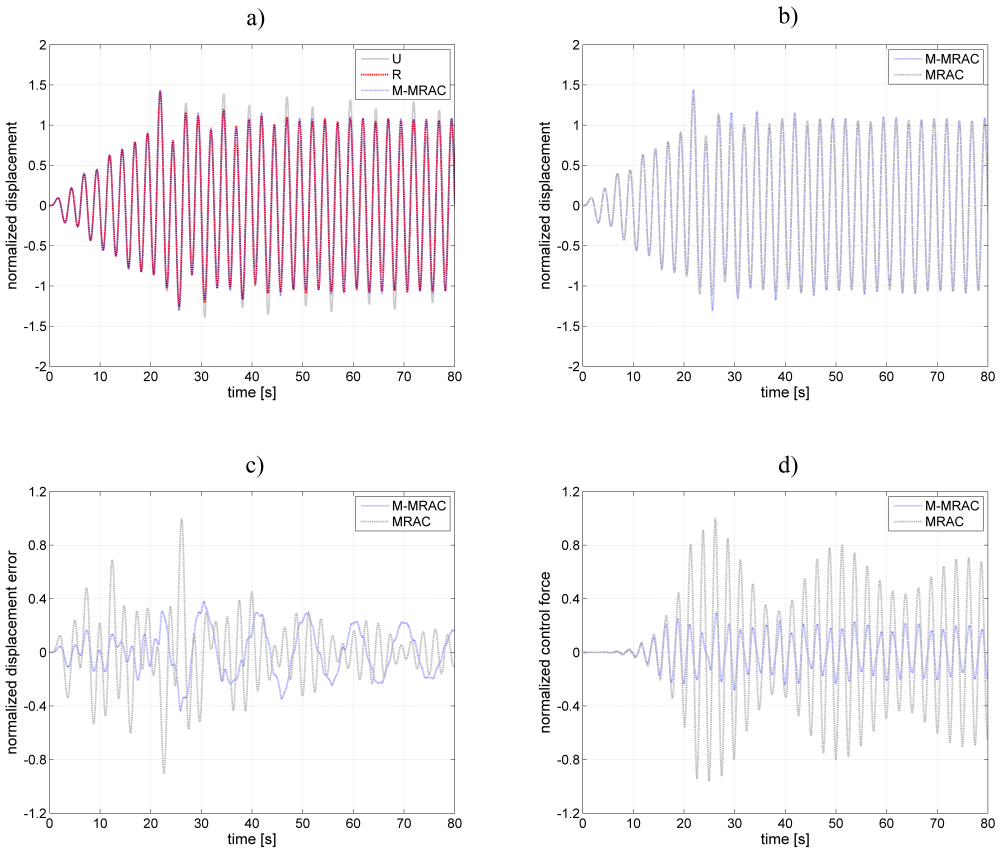

Figure 4: Performance of M-MRAC under sinusoidal loading.

In order to investigate the M-MRAC performance to real loading conditions, an erthquake capable of activating switching condition for several cycles is applied to the structure. Figure 5 shows the performance of M-MRAC to a base seismic accelerogram (represented in Figure 5(a)). Figure 5(b) shows the uncontrolled response and the response of the controlled systems with the proposed M-MRAC and traditional MRAC. Figures 5(c) and (d) show the displacement error and control forces, normalized with respect to their maximum absolute values. Also in case of extreme seismic loading, state errors tend to decrease with time and the control force required by M-MRAC is smaller than the one required by MRAC.

The effect of excitation frequency on M-MRAC performance is investigated by computing systems' responses to harmonic loads with frequency varying between 0.05 Hz and 1.00 Hz. As system's maximum response depends on frequency, the displacement threshold establishing switching condition is set equal to the 80% of the peak uncontrolled value. Figure 6(a) shows

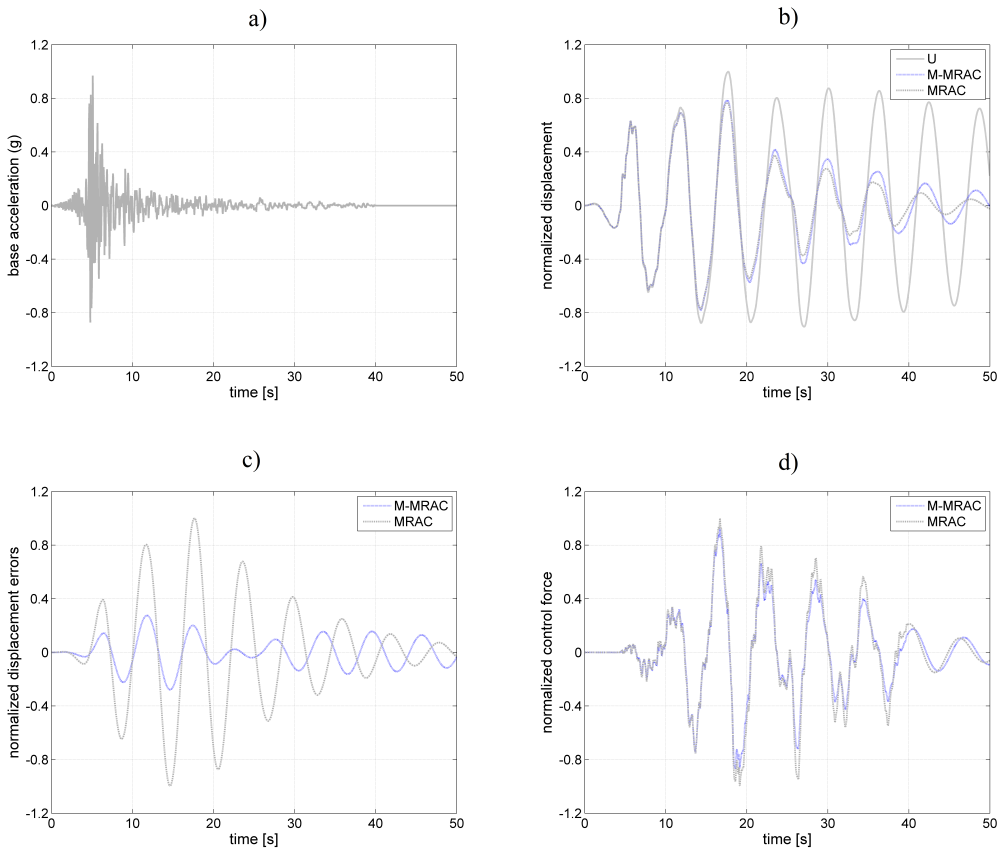

Figure 5: Performance of M-MRAC under seismic loading.

the peak displacements of the uncontrolled system and the controlled systems with M-MRAC and MRAC, normalized with respect to the maximum uncontrolled peak response. Figure 6(b) shows the peak control forces required by M-MRAC and MRAC normalized with respect to maximum peak control force. Results show that M-MRAC provides a significant reduction of the maximum required control force at the expense of an increase in structural response. This limited growth in structural response, which is less important in case of non-harmonic excitation (Figure 5), can be partially compensated by properly varying the gap between reference models' dampings.

6 CONCLUSIONS

The paper exploits the possibility of adopting multiple reference models for adaptive control of tall buildings subjected to multiple hazards. With this aim, the standard Model Reference Adaptive Control algorithm is modified through the adoption of multiple reference models. The motivation of the proposed algorithm enhancement is that flexible buildings require various damping levels to avoid the occurrence of different limit states. This problem is also more important when the tall building is subjected to multiple hazards, like wind and earthquake, having different characteristics in terms of frequency, amplitude and duration of load.

A benchmark tall building is chosen as case study to examine the effectiveness of the pro-

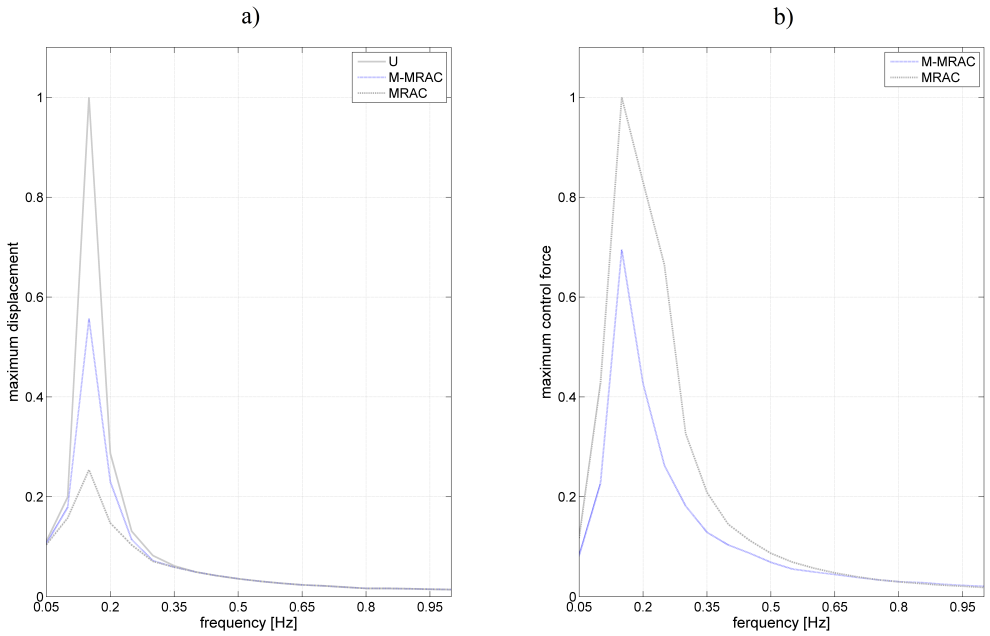

Figure 6: Peak displacements and control forces as a function of the harmonic excitation frequency.

posed control strategy. After preliminary parametric analyses for choosing the optimal reference systems, several investigations on the performance of M-MRAC are carried out. Results show the capacity of M-MRAC in tracking the target system and in reducing the structural response. Comparison between results obtained with traditional MRAC demonstrates that the main advantage of M-MRAC is the reduction of the required control force, at the expense of a slight reduction of control effectiveness.

Future developments of the work will deepen the effects of dwell time, reference models' characteristics, system's uncertainties and non-linearities.

ACKNOWLEDGEMENTS

The authors gratefully acknowledge Prof. Oren Lavan, from Technion, Israel Institute of Technology, for suggestions on seismic response of tall buildings and Prof. Mario Luca Fravolini, from University of Perugia for advice on adaptive control methods.

REFERENCES

[1] V. Gattulli, M. Lepidi, F. Potenza, Seismic protection of frame structures via semi-active control: Modeling and implementation issues. *Earthquake Engineering and Engineering Vibration*, **8**(4), 627–645, 2010.

[2] I. Venanzi, A.L. Materazzi, Robust optimization of a hybrid control system for wind-exposed tall buildings with uncertain mass distribution. *Smart Structures and Systems*, **12**(6), 641–659, 2013.

[3] I. Venanzi, L. Ierimonti, F. Ubertini, An enhanced nonlinear damping approach accounting for system constraints in active mass dampers. *Journal of Sound and Vibration*, **357**, 2–15, 2015.

[4] K. Baba, D. Yamamoto, M. Akagi, Model reference adaptive control systems with state estimators to mitigate seismic responses of structures. *Theoretical and Applied Mechanics Japan*, **51**, 123–132, 2002.

[5] S.-Y. Chu, S.-C. Lo, M.-C. Chang, Real-time control performance of a model-reference adaptive structural control system under earthquake excitation. *Structural Control and Health Monitoring*, **17**(2), 198–217, 2010.

[6] J. Tu, X. Lin, B. Tu, J. Xu, D. Tan, Simulation and experimental tests on active mass damper control system based on Model Reference Adaptive Control algorithm. *Journal of Sound and Vibration*, **333**, 4826–4842, 2014.

[7] N. A. Sofianos, Y. S. Boutalis Robust adaptive multiple models based fuzzy control of nonlinear system. *Neurocomputing*, **173**, 1733–1742, 2016.

[8] J. Xie, J. Zhao Model reference adaptive control for nonlinear switched systems under asynchronous switching. *International Journal of Adaptive Control and Signal Processing*, in press, 2016.

[9] J.N. Yang, A.K. Agrawal, B. Samali, J.C. Wu, Benchmark problem for response control of wind-excited tall building. *Journal of Engineering Mechanics*, **130**(4), 437–446, 2004.

[10] B. Samali, K.C.S. Kwok, G.S. Wood, J.N. Yang, Wind tunnel tests for wind-excited benchmark building. *Journal of Engineering Mechanics*, **130**(4), 447–450, 2004.

[11] Americal Society for Civil Engineers *ASCE7-Minimum Design Loads for Buildings and Other Structures*, 2003.

[12] PEER-NISEE *Suites of Earthquake Ground Motions for Analysis of Steel Moment Frame Structures*. http://nisee.berkeley.edu/data/strongmotion/sacsteel/groundmotions.html, 2012.

[13] L.G. Griffis, Serviceability limit states under wind load. *American Institute of Steel Construction*, 2003.

[14] CNR-DT 207/2008, *Instructions to evaluate wind actions and effects on structures (in italian)*, 2008.

[15] W. Pu, K. Kasai, T. Kashima, Response of conventional seismic-resistant tall buildings in Tokyo during 2011 great East Japan earthquake. *Proceedings of the 15th World Conference on Earthquake Engineering*, Lisbon, Portugal.

ECCOMAS Congress 2016
VII European Congress on Computational Methods in Applied Sciences and Engineering
M. Papadrakakis, V. Papadopoulos, G. Stefanou, V. Plevris (eds.)
Crete Island, Greece, 5–10 June 2016

PASSIVE CONTROL OF WAVE PROPAGATION IN PERIODIC ANTI-TETRACHIRAL META-MATERIALS

Marco Lepidi[1], **Andrea Bacigalupo**[2]

[1]DICCA Department of Civil, Chemical and Environmental Engineering, University of Genova
Via Montallegro, 1 - 16145 Genova (Italy)
e-mail: marco.lepidi@unige.it

[2] IMT School for Advanced Studies Lucca
Piazza S. Francesco, 19 - 55100 Lucca (Italy)
e-mail: andrea.bacigalupo@imtlucca.it

Keywords: Auxetic materials, Wave propagation, Resonators, Meta-materials, Passive control

Abstract. *Periodic anti-tetrachiral materials are strongly characterized by a marked auxeticity, the unusual and fascinating mechanical property mathematically expressed by negative values of the Poisson's ratio. The auxetic behavior is primarily provided by pervasive rolling-up mechanisms developed by the doubly-symmetric micro-structure of the periodic cell, composed by a regular pattern of rigid rings connected by tangent flexible ligaments. Adopting a beam-lattice model to describe the linear free dynamics of the elementary cell, the planar wave propagation along the bi-dimensional material domain can be studied according to the Floquet-Bloch theory. Parametric analyses of the dispersion curves, carried out with numerical or asymptotic tools, typically reveal a highly-dense spectrum, with persistent absence of total band-gaps in the low-frequency range. The paper analyses the wave propagation in the meta-material developed by introducing rigid massive inserts, locally housed by all the rings and working as undamped linear oscillators with assigned inertia and/or stiffness properties. The elastic coupling between the cell microstructure and the oscillators, if properly tuned (inertial resonators), is found to significantly modify the Floquet-Bloch spectrum of the material. The effects of the resonator parameters (tuning frequency and mass ratio) on the low-frequency band structure of the meta-material are discussed, with focus on the valuable possibility to (i) open total band gaps, by either the widening of an existing partial band gap or the avoidance of a crossing point between adjacent dispersion curves, (ii) finely control the total band-gap amplification, in order to assess the maximum achievable performance of the meta-material against the vibration propagation.*

1 INTRODUCTION

Auxetic materials are characterized by the unconventional and fascinating ability to develop transversal expansions in response to a longitudinal stretching. This physical peculiarity, which is described by negative Poisson's ratios in solid mechanics, is rarely observable in nature, but can be smoothly obtained by artificial synthesis [1–3]. The recent and increasing interest in auxetic materials is being strongly catalyzed by the compelling demand for advanced applications in aerospace, chemical, naval, nuclear, biomedical, sport engineering fields. Indeed, auxetic sheets and solids are potentially featured by a variety of functional super-capacities, including higher fracture toughness and indentation resistance, as well as augmented properties of acoustic damping and energy absorption, with respect to their conventional counterparts [4–6].

Artificial realizations of auxetic materials include polymeric or metallic foams and laminates, on the one hand, and micro-structured composites, which typically possess periodic cellular geometries (namely reticular networks, chiral lattices, re-entrant honeycombs and origami folds), on the other hand [8–10]. Leveraging their intrinsic periodicity, obeying to the well-established Floquet-Bloch theory, a promising theoretical and technological research challenge concerns the employment of chiral auxetic media as versatile elastic guides for planar optical and acoustic waves. Indeed, a proper tuning of their mechanical properties may allow the effective design of such materials as tailor-made signal propagators or – especially – selective passive filters for noise reduction and vibration mitigation [11–14]. In this respect, the high performance and versatility ensured by tunable arrays of light and flexible resonant subsystems is a promising trend coming from a multi-disciplinary cross-fertilization [15–21].

Among different chiral topologies, the anti-tetrachiral material is gaining major attention, due to its strong auxeticity, accompanied by a marked anisotropy [9, 14, 22–24]. Employing a linear beam-lattice model of the cell microstructure, the wave propagation properties of this material have been studied by means of both numerical and asymptotic tools [30]. Parametric analyses of the dispersion curves typically reveal a highly-dense spectrum, with persistent absence of band-gaps in the low-frequency range. Such shortcomings, confirmed also by continuum models and in presence of soft matrices [14] may actually limit the practical efficiency of the anti-tetrachiral materials as adjustable passive controllers against the free propagation of vibration waves with target frequencies, wavenumbers, or polarization modes.

The paper explores the possibility to develop a meta-material by introducing rigid massive inserts, locally housed by all the rings and working as undamped linear oscillators with assigned inertia and/or stiffness properties. The elastic coupling between the cell microstructure and the oscillators, if properly tuned (inertial resonators), has the potential to significantly modify the Floquet-Bloch spectrum of the material [25–28]. A suited design of this purely-mechanical behavior opens the valuable perspective to passively control the wave propagation by, first, artificially regulating the tailored opening or closure of one or more frequency band-gaps, and, second, maximizing their respective amplitudes according to optimal criteria [29].

According to this leading idea, the beam-lattice model of the anti-tetrachiral material is enriched by coupling the global dynamics of the periodic cell with the local dynamics of the resonators (Section 2). Then the coupled eigenproblem governing the wave propagation in the meta-material is formulated (Section 2.2). The effects of the resonator key-parameters (mass ratio and frequency tuning) on the dispersion curves and frequency band gaps are discussed (Section 3). These parametric studies pave the way for the analytical, although approximate, description of the enriched Floquet-Bloch spectrum by means of asymptotic perturbation techniques, suited to carry out explicit design criteria. Concluding remarks are finally drawn.

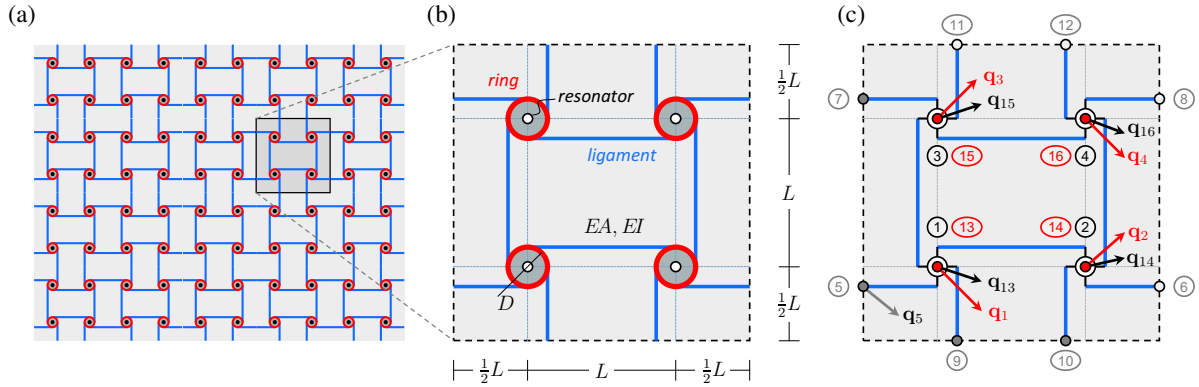

Figure 1: Anti-tetrachiral cellular meta-material: (a) pattern, (b) periodic cell, (c) beam lattice model.

2 BEAM LATTICE MODEL

Focusing on the microscopic scale, a cellular meta-material characterized by a square periodic cell, fully tiling a two-dimensional infinite domain, is considered (Figure 1a). A beam lattice model is formulated to describe the linear elasto-dynamic response of the unit cell, featured by a double geometric symmetry which realizes an anti-tetrachiral topology (Figure 1b). The internal structure, or *microstructure*, of the elementary cell is composed by four circular rings connected by twelve tangent ligaments. The *rolling-up* mechanism, responsible for the auxetic behavior, consists in the opposite-sign, iso-amplitude rotations developed by any pair of adjacent disks in-a-row (or column), when the cell is stretched along one of the symmetry axes.

A rigid body model is assumed for the massive and highly-stiff rings, possessing identical mean diameter D. The ring centers are located at the four corners of an ideal internal square, concentric with the external cell boundary. The ring small width S is considered a free parameter, allowing the independent assignment of the rigid body mass M and moment of inertia J. A linear, extensible, unshearable model of massless beam is employed for all the identical light and flexible ligaments, in the small-deformation range. As long as the beam-ring connections nominally realize perfectly-rigid joints, the natural length L of the *inner* horizontal and vertical ligaments coincide with half the side of the square cell. By virtue of the periodicity, the cell boundary crosses the midspan – and halves the natural length – of all the *outer* ligaments. Assuming the same linear elastic material (with Young's modulus E) and cross-section shape (with area A and second area moment I) for each ligament, all the beams have identical extensional EA and flexural rigidity EI. The effects of a homogeneous soft matrix, which may likely embed the microstructure [14], are neglected as first approximation.

Moving from this structural layout, a novel meta-material can be realized by supplying each ring with a light soft annular filler, hosting a central heavy circular inclusion, serving as inertial resonator with adjustable mechanical properties. All the identical inclusions are modelled as rigid disks, co-centered with the respective housing rings, with body mass M_r and moment of inertia J_r. As long as the internal coupling provided by the filler can be assumed linearly elastic, the ring-resonator differential displacements are affected by equivalent translational and rotational stiffnesses [28]. Therefore, the local (translational and rotational) motion of each resonator is essentially characterized by two natural frequencies Ω_r and Ω_θ.

Introducing a certain circular frequency Ω_c of the cellular solid as known dimensional reference, a suited minimal set of independent nondimensional parameters, sufficient to describe the inertial, elastic and geometric properties of the square periodic cell, is

$$\delta = \frac{D}{L}, \qquad \varrho^2 = \frac{I}{AL^2}, \qquad \omega_c^2 = \frac{EA}{M\Omega_c^2 L}, \qquad \chi^2 = \frac{J}{ML^2} \tag{1}$$

where ω_c stands for a frequency characterizing the beam lattice. The geometric parameter δ roughly expresses the material compositeness, measured as the linear density of the circular rings. The nondimensional form ϱ of the gyration radius of inertia accounts for the (inverse) slenderness of the ligaments. Finally, χ^2 is the rotational-to-translational mass ratio of the disks.

Together with the microstructural parameters, the meta-material is further characterized by additional nondimensional parameters, describing the properties of the local resonators

$$\gamma = \frac{\Omega_r}{\omega_c\,\Omega_c}, \qquad \alpha = \frac{M_r}{M}, \qquad \gamma_\theta = \frac{\Omega_\theta}{\omega_c\,\Omega_c}, \qquad \chi_r^2 = \frac{J_r}{M_r L^2}$$

where γ and γ_θ can be recognized as *tuning* parameters for the two resonator frequencies, α accounts for the resonator-to-ring mass ratio and χ_r^2 is the rotational-to-translational mass ratio of the resonator.

2.1 Equations of motion

According to the mechanical assumptions, the linear dynamics of the unit cell is governed by a multi-degrees-of-freedom discrete model, referred to a full set of 16 configurational nodes, located by the position vectors $\mathbf{x}_i$ (with $i = 1, ..., 16$) in the natural configuration. The actual configuration of the i-th node is described by three time-dependent components of motion, corresponding to the horizontal displacement $U_i(t)$, the vertical displacement $V_i(t)$ and the in-plane rotation $\phi_i(t)$. The nondimensional variables can be introduced

$$u_i = \frac{U_i}{L_r}, \qquad v_i = \frac{V_i}{L_r}, \qquad \tau = \Omega_r t \tag{2}$$

where L_r stands for a reference length L_r which preserves the smallness of the displacements. All the nondimensional configuration variables can be collected in the 48-by-one displacement column-vector $\mathbf{q} = (\mathbf{q}_1, ..., \mathbf{q}_i, ..., \mathbf{q}_{16})$, where the i-th nodal subvector $\mathbf{q}_i = (u_i, v_i, \phi_i)$.

Depending on the position of the lumped masses in the discrete model and with reference to the labels in Figure 1c, the model nodes can conveniently be distinguished into three subsets

i. four *internal* nodes located at the ring centroids (red nodes ①...④), whose 12 *active* displacements can be collected in the subvector $\mathbf{q}_a = (\mathbf{q}_1, \mathbf{q}_4)$

ii. eight *external* nodes located at the outer ligament midspans (gray nodes ⑤...⑫), whose 24 *passive* displacements can be cast in the subvector $\mathbf{q}_p = (\mathbf{q}_5, \mathbf{q}_{12})$

iii. four *inner* nodes located at the disk centroids (black nodes ⑬...⑯), whose 12 *resonant* displacements can be collected in the subvector $\mathbf{q}_r = (\mathbf{q}_{13}, \mathbf{q}_{16})$

The distinction remarks that the internal and inner nodes develop both nondimensional elastic $(\boldsymbol{\sigma}_a, \boldsymbol{\sigma}_r)$ *and* inertial forces $(\mathbf{f}_a, \mathbf{f}_r)$, which actively participate in the dynamic cell equilibrium. On the contrary, the external nodes can develop only elastic forces $\boldsymbol{\sigma}_p$, which partially depend on the stiffness coupling with the internal nodes, and quasi-statically balance the reactive forces $\mathbf{f}_p$ transferred by the adjacent cells. Due to the geometric assumptions, the positions of the *internal* and *inner* node sets (nodes ①...④ and ⑬...⑯) coincide in the undeformed configuration.

According to displacement/force decomposition, the nondimensional equilibrium equation governing the undamped free oscillations of the discrete model has the matrix form

$$\begin{pmatrix} \mathbf{f}_r \\ \mathbf{f}_a \\ \mathbf{0} \end{pmatrix} + \begin{pmatrix} \boldsymbol{\sigma}_r \\ \boldsymbol{\sigma}_a \\ \boldsymbol{\sigma}_p \end{pmatrix} = \begin{pmatrix} \mathbf{0} \\ \mathbf{0} \\ \mathbf{f}_p \end{pmatrix} \tag{3}$$

or, making explicit the force dependence on the nodal acceleration or displacements

$$\begin{bmatrix} \mathbf{M}_r & \mathbf{O} & \mathbf{O} \\ \mathbf{O} & \mathbf{M}_a & \mathbf{O} \\ \mathbf{O} & \mathbf{O} & \mathbf{O} \end{bmatrix} \begin{pmatrix} \ddot{\mathbf{q}}_r \\ \ddot{\mathbf{q}}_a \\ \ddot{\mathbf{q}}_p \end{pmatrix} + \begin{bmatrix} \mathbf{K}_r & -\mathbf{K}_r & \mathbf{O} \\ -\mathbf{K}_r & \mathbf{K}_{aa}+\mathbf{K}_r & \mathbf{K}_{ap} \\ \mathbf{O} & \mathbf{K}_{pa} & \mathbf{K}_{pp} \end{bmatrix} \begin{pmatrix} \mathbf{q}_r \\ \mathbf{q}_a \\ \mathbf{q}_p \end{pmatrix} = \begin{pmatrix} \mathbf{0} \\ \mathbf{0} \\ \mathbf{f}_p \end{pmatrix} \tag{4}$$

where dot indicates differentiation with respect to the τ-time and $\mathbf{O}$ stands for empty matrices.

Focusing on the micro-structural matrices, the *global* mass submatrix $\mathbf{M}_a$ is diagonal, as far as a lumped mass description is assumed. The symmetric submatrices $\mathbf{K}_{aa}$ and $\mathbf{K}_{pp}$ account for the *global* stiffness of the internal and external nodes, respectively. The rectangular submatrix $\mathbf{K}_{ap} = \mathbf{K}_{pa}^{\top}$ expresses the elastic *global* coupling among the internal and external nodes. A parametric expression of these matrices can be found in [30]. Focusing on the resonators, both the *local* mass and stiffness submatrices $\mathbf{M}_r$ and $\mathbf{K}_r$ are diagonal. The submatrix $\mathbf{K}_r$ accounts also for the *global-local* coupling between the inner and internal nodes.

2.2 Free wave propagation

The free wave propagation along the bi-dimensional cell domain can be studied according to the Floquet-Bloch theory [31–33]. Moving in the $\mathbf{k}$-transformed space the active ($j = 1...4, 13...16$) and passive displacements and passive force vectors assume the representations

$$\mathbf{q}_j = \tilde{\mathbf{q}}_j \, \mathrm{e}^{\mathrm{i}\,\mathbf{k}\cdot\mathbf{x}_j}, \qquad \mathbf{q}_p = \mathbf{F}_p \tilde{\mathbf{q}}_p, \qquad \mathbf{f}_p = \mathbf{F}_p \tilde{\mathbf{f}}_p \tag{5}$$

where i denotes the imaginary unit, $\mathbf{k} = (k_1, k_2)$ is the (dimensional) wavevector and the block diagonal matrix $\mathbf{F}_p = \mathrm{diag}[\,\mathbf{I}\,\mathrm{e}^{\mathrm{i}\,\mathbf{k}\cdot\mathbf{x}_5}, ..., \mathbf{I}\,\mathrm{e}^{\mathrm{i}\,\mathbf{k}\cdot\mathbf{x}_{12}}\,]$ with $\mathbf{I}$ being the three-by-three unit matrix.

The passive displacement and force vector can be ordered and partitioned as $\mathbf{q}_p = (\mathbf{q}_p^-, \mathbf{q}_p^+)$, $\mathbf{f}_p = (\mathbf{f}_p^-, \mathbf{f}_p^+)$ to separate the variable pairs $(\mathbf{q}_p^-, \mathbf{f}_p^-)$ belonging to the left/bottom cell boundary (composed by the external nodes ⑤,⑦,⑨,⑩) from the variable pairs $(\mathbf{q}_p^+, \mathbf{f}_p^+)$ belonging to the right/top boundary (composed by the external nodes ⑥,⑧,⑪,⑫). Extending the same partition to the respective transformed variables, the equation (5) can be written

$$\mathbf{q}_p^- = \mathbf{F}_p^- \tilde{\mathbf{q}}_p^-, \qquad \mathbf{q}_p^+ = \mathbf{F}_p^+ \tilde{\mathbf{q}}_p^+, \qquad \mathbf{f}_p^- = \mathbf{F}_p^- \tilde{\mathbf{f}}_p^-, \qquad \mathbf{f}_p^+ = \mathbf{F}_p^+ \tilde{\mathbf{f}}_p^+, \tag{6}$$

where, based on the decomposition, the matrices $\mathbf{F}_p^- = \mathrm{diag}[\,\mathbf{I}\,\mathrm{e}^{\mathrm{i}\,\mathbf{k}\cdot\mathbf{x}_5}, \mathbf{I}\,\mathrm{e}^{\mathrm{i}\,\mathbf{k}\cdot\mathbf{x}_7}, \mathbf{I}\,\mathrm{e}^{\mathrm{i}\,\mathbf{k}\cdot\mathbf{x}_9}, \mathbf{I}\,\mathrm{e}^{\mathrm{i}\,\mathbf{k}\cdot\mathbf{x}_{10}}]$ and $\mathbf{F}_p^+ = \mathrm{diag}[\,\mathbf{I}\,\mathrm{e}^{\mathrm{i}\,\mathbf{k}\cdot\mathbf{x}_6}, \mathbf{I}\,\mathrm{e}^{\mathrm{i}\,\mathbf{k}\cdot\mathbf{x}_8}, \mathbf{I}\,\mathrm{e}^{\mathrm{i}\,\mathbf{k}\cdot\mathbf{x}_{11}}, \mathbf{I}\,\mathrm{e}^{\mathrm{i}\,\mathbf{k}\cdot\mathbf{x}_{12}}\,]$.

Imposing the periodicity conditions on the transformed variables ($\tilde{\mathbf{q}}_p^+ = \tilde{\mathbf{q}}_p^-$ and $\tilde{\mathbf{f}}_p^+ = -\tilde{\mathbf{f}}_p^-$), the free wave propagation throughout the cell domain between the two complementary boundaries is governed by the quasi-periodicity conditions on the anti-transformed variables

$$\mathbf{q}_p^+ = \mathbf{L}\mathbf{q}_p^-, \qquad \mathbf{f}_p^+ = -\mathbf{L}\mathbf{f}_p^- \tag{7}$$

where, following from the equations (6), the block diagonal transfer matrix reads

$$\mathbf{L} = \mathrm{diag}\left[\mathrm{e}^{\mathrm{i}\,\mathbf{k}\cdot\mathbf{d}_{56}}\,\mathbf{I}, \mathrm{e}^{\mathrm{i}\,\mathbf{k}\cdot\mathbf{d}_{78}}\,\mathbf{I}, \mathrm{e}^{\mathrm{i}\,\mathbf{k}\cdot\mathbf{d}_{911}}\,\mathbf{I}, \mathrm{e}^{\mathrm{i}\,\mathbf{k}\cdot\mathbf{d}_{1012}}\,\mathbf{I}\right] \tag{8}$$

and $\mathbf{d}_{ij} = \mathbf{x}_j - \mathbf{x}_i$ represents the vector connecting the i-th and the j-th external nodes.

Consistently with the passive displacement and force decomposition, and imposing the quasi-periodicity conditions (8), the lower (quasi-static) part of equation (4) reads

$$\begin{bmatrix} \mathbf{K}_{pa}^{-} \\ \mathbf{K}_{pa}^{+} \end{bmatrix} \mathbf{q}_a + \begin{bmatrix} \mathbf{K}_{pp}^{=} & \mathbf{K}_{pp}^{\mp} \\ \mathbf{K}_{pp}^{\pm} & \mathbf{K}_{pp}^{\#} \end{bmatrix} \begin{bmatrix} \mathbf{I} \\ \mathbf{L} \end{bmatrix} \mathbf{q}_p^{-} = \begin{bmatrix} \mathbf{I} \\ -\mathbf{L} \end{bmatrix} \mathbf{f}_p^{-} \tag{9}$$

with $\mathbf{I}$ being now the twelve-by-twelve unit matrix. This equation can be solved to express the passive variables as slave functions of the master active displacements, yielding

$$\mathbf{q}_p^{-} = \mathbf{R}\big(\mathbf{K}_{pa}^{+} + \mathbf{L}\mathbf{K}_{pa}^{-}\big)\mathbf{q}_a, \qquad \mathbf{f}_p^{-} = \big(\mathbf{K}_{pa}^{-} + \big(\mathbf{K}_{pp}^{=} + \mathbf{K}_{pp}^{\mp}\mathbf{L}\big)\mathbf{R}\big(\mathbf{K}_{pa}^{+} + \mathbf{L}\mathbf{K}_{pa}^{-}\big)\big)\mathbf{q}_a \tag{10}$$

where the $\mathbf{k}$-dependent matrix $\mathbf{R} = -\big(\mathbf{L}\mathbf{K}_{pp}^{\mp}\mathbf{L} + \mathbf{L}\mathbf{K}_{pp}^{=} + \mathbf{K}_{pp}^{\#}\mathbf{L} + \mathbf{K}_{pp}^{\pm}\big)^{-1}$ is diagonal.

Similarly, the imposition of the quasi-periodicity conditions to the upper (dynamic) part of the equation (4) leads to a coupled equation which, after *condensation* of the passive variables by virtue of the enslaving relations (11), depends on the active variables only

$$\begin{bmatrix} \mathbf{M}_r & \mathbf{O} \\ \mathbf{O} & \mathbf{M}_a \end{bmatrix} \begin{pmatrix} \ddot{\mathbf{q}}_r \\ \ddot{\mathbf{q}}_a \end{pmatrix} + \begin{bmatrix} \mathbf{K}_r & -\mathbf{K}_r \\ -\mathbf{K}_r & \mathbf{K}_r + \mathbf{K}_a \end{bmatrix} \begin{pmatrix} \mathbf{q}_r \\ \mathbf{q}_a \end{pmatrix} = \begin{pmatrix} \mathbf{0} \\ \mathbf{0} \end{pmatrix} \tag{11}$$

where the condensed stiffness matrix $\mathbf{K}_a = \mathbf{K}_{aa} + (\mathbf{K}_{ap}^{-} + \mathbf{K}_{ap}^{+}\mathbf{L})\mathbf{R}(\mathbf{K}_{pa}^{+} + \mathbf{L}\mathbf{K}_{pa}^{-})$, with the symmetries $\mathbf{K}_{ap}^{-} = (\mathbf{K}_{pa}^{-})^{\top}$ and $\mathbf{K}_{ap}^{+} = (\mathbf{K}_{pa}^{+})^{\top}$ is known to be Hermitian and is derived in [30].

As brief discussion, the upper part of equation (11) can still be recognized to govern the local resonator dynamics, whereas the lower part governs the global dynamics of the cell microstructure. It is worth noting that the passive variable condensation, including the enforcement of the quasi-periodicity, is not mathematically affected by the resonator presence. Indeed, the condensed *global* stiffness matrix $\mathbf{K}_g = (\mathbf{K}_r + \mathbf{K}_a)$ of the meta-material is not formally different from the matrix $\mathbf{K}_a$ governing the wave propagation in the resonator-free material, apart for the mere addiction of the *local* stiffness term $\mathbf{K}_r$. Conversely, the uncoupled global dynamics the resonator-free material can be restored by simply zeroing the local matrices $\mathbf{M}_r$ and $\mathbf{K}_r$. Physically, this remark can immediately be justified by the absence of any internal coupling between the resonant active variables $\mathbf{q}_r$ and the condensed passive variables $\mathbf{q}_p$.

Denoting ω the unknown nondimensional frequency, the harmonic monofrequent solution $\mathbf{q}_a = \mathbf{F}_a\boldsymbol{\psi}_a\,\mathrm{e}^{\mathrm{i}\,\omega\tau}$ and $\mathbf{q}_r = \mathbf{F}_r\boldsymbol{\psi}_r\,\mathrm{e}^{\mathrm{i}\,\omega\tau}$ can be imposed in the equation (11). Eliminating the dependence on time, an eigenproblem in the unknown eigenvalues $\lambda = \omega^2/\omega_c^2$ and eigenvectors $\boldsymbol{\psi} = (\boldsymbol{\psi}_r, \boldsymbol{\psi}_a)$ can be stated in the non-standard form $(\mathbf{K} - \lambda\mathbf{M})\,\mathbf{F}\boldsymbol{\psi} = \mathbf{0}$, or more explicitly

$$\left(\begin{bmatrix} \mathbf{K}_r & -\mathbf{K}_r \\ -\mathbf{K}_r & \mathbf{K}_a \end{bmatrix} - \lambda \begin{bmatrix} \mathbf{M}_r & \mathbf{O} \\ \mathbf{O} & \mathbf{M}_a \end{bmatrix}\right) \begin{bmatrix} \mathbf{F}_r \\ \mathbf{F}_a \end{bmatrix} \boldsymbol{\psi} = \begin{pmatrix} \mathbf{0} \\ \mathbf{0} \end{pmatrix} \tag{12}$$

where the diagonal block matrices $\mathbf{F}_r = \mathbf{F}_a = \mathrm{diag}[\,\mathbf{I}\,\mathrm{e}^{\mathrm{i}\,\mathbf{k}\cdot\mathbf{x}_1}, ..., \mathbf{I}\,\mathrm{e}^{\mathrm{i}\,\mathbf{k}\cdot\mathbf{x}_4}\,]$.

The eigenproblem solution gives twenty-four real-valued eigenvalues λ_i (or frequencies ω_i), sorted in ascending order. It is worth remarking that, owing to the Hermitian property, the $\mathbf{K}$-matrix is certainly non-defective, that is, possesses a complete eigenspace spanned by twenty-four proper eigenvectors. Therefore, each eigenvalue λ_i has coincident algebraic and geometric multiplicity m_i and corresponds to a complex-valued eigenvector $\boldsymbol{\psi}_i$, collecting the non-passive eigencomponents $\boldsymbol{\psi}_{ri}$ and $\boldsymbol{\psi}_{ai}$ only. The passive eigencomponents depend on the active eigencomponents through the quasi-static relations $\boldsymbol{\psi}_{pi}^{-} = \mathbf{R}\big(\mathbf{K}_{pa}^{+} + \mathbf{L}\mathbf{K}_{pa}^{-}\big)\boldsymbol{\psi}_{ai}$ and $\boldsymbol{\psi}_{pi}^{+} = \mathbf{L}\boldsymbol{\psi}_{pi}^{-}$.

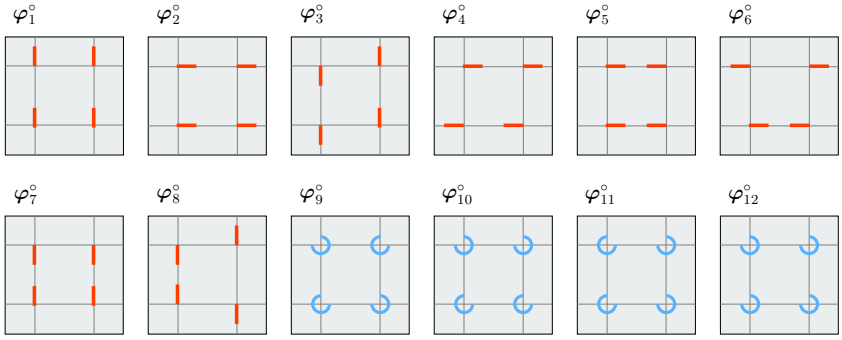

Figure 2: Stationary translational (red) or rotational (blue) modes $\boldsymbol{\psi}_{ai}$ of the anti-tetrachiral material (a omitted).

3 FLOQUET-BLOCH SPECTRUM

Fixed certain parameter values for the beam-lattice model and the resonators, the twenty-four eigenvalues (or frequencies) and the corresponding eigenvectors can be determined under variation of the nondimensional wavevector $\mathbf{b} = (\beta_1, \beta_2)$, composed of the wavenumbers

$$\beta_1 = \mathbf{k} \cdot \mathbf{d}_{56} = \mathbf{k} \cdot \mathbf{d}_{78}, \qquad \beta_2 = \mathbf{k} \cdot \mathbf{d}_{911} = \mathbf{k} \cdot \mathbf{d}_{1012} \tag{13}$$

in the square Brillouin domain $\mathcal{D} = [-\pi, \pi] \times [-\pi, \pi]$. According to the Floquet-Bloch theory [31–33], this investigation can be focused on the two edges

$$\mathcal{B}_1 = \{\beta_1 \in [0, \pi], \beta_2 = 0\}, \qquad \mathcal{B}_{12} = \{\beta_1 = \beta_2 \in [0, \pi]\} \tag{14}$$

which bound the irreducible triangular zone of the $\mathcal{D}$-domain and are spanned by the abscissae β_1 and $\beta_{12} = (\beta_1^2 + \beta_2^2)^{1/2}$, respectively. The corresponding ω-frequent vibration waves propagate through the periodic material along the horizontal direction (with β_1-wavenumber ranging in $[0, \pi]$) and diagonal direction (with β_{12}-wavenumber ranging in $[0, \sqrt{2}\pi]$).

The frequency loci versus the variable wavenumber constitute the Floquet-Bloch spectrum, composed of twenty-four dispersion curves for the meta-material or twelve dispersion curves for the resonator-free material (as can be carried out by setting $\mathbf{M}_r = \mathbf{K}_r = \mathbf{O}$). The curve *roots*, located at the $\mathcal{D}$-origin ($\beta_1 = \beta_2 = 0$), correspond to the quasi-periodicity conditions (7) degenerating into conditions of standard periodicity. Therefore, the corresponding eigenpairs $(\lambda^\circ, \boldsymbol{\varphi}^\circ)$ can be interpreted as the natural frequencies, possibly null, and (real-valued) vibration modes of the single elementary cell in the free stationary harmonic oscillation of the periodic system. In the absence of resonators, these modes are participated only by an homogeneous subset of active displacements (Figure 2). so that they can be classified as *translational modes*, if contributed by the four horizontal or the four vertical components, or *rotational modes*, if contributed by the four rotation components. With minor abuse of nomenclature, the same classification can be extended to the $\mathbf{b}$-dependent eigenvectors, which can be interpreted as polarization modes of the propagating wave, characterized by a certain (not null) wavenumber.

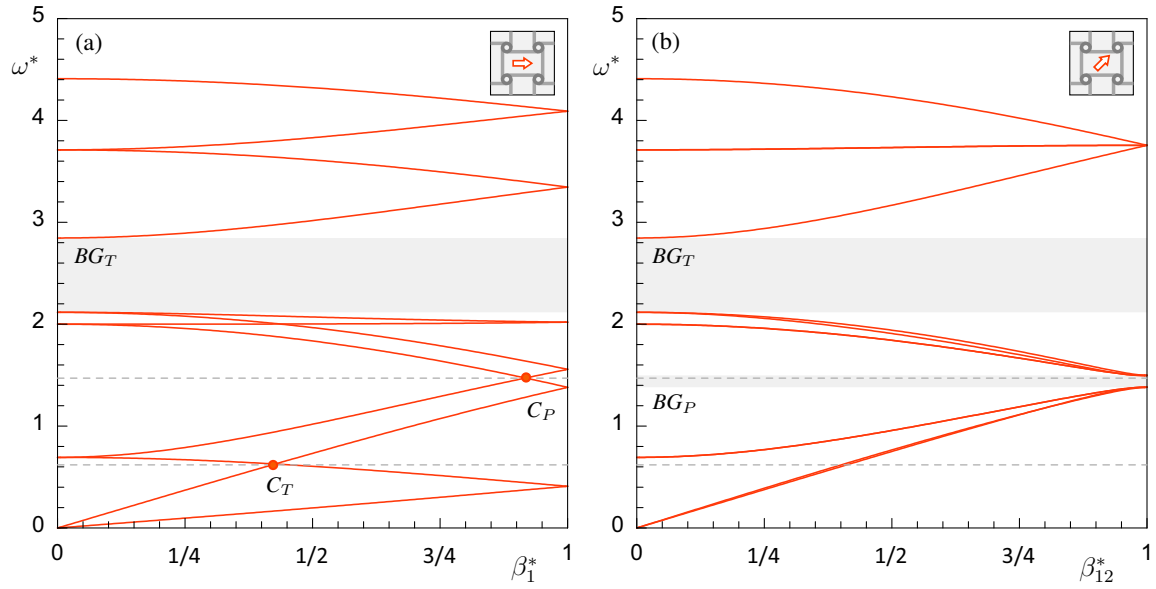

Figure 3: Floquet-Bloch spectrum ($\omega* = \omega/\omega_c$) of the anti-tetrachiral material (without resonators): (a) horizontal and (b) diagonal direction of wave propagation ($\beta_1^* = \beta_1/\pi$, $\beta_{12}^* = \beta_{12}/(\sqrt{2}\pi)$).

3.1 Parametric analysis

In the absence of resonators, the Floquet-Bloch spectrum is presented in Figure 3 for a set of parameter values ($\chi^2 = 1/81, \delta = 1/10, \varrho^2 = 1/100$). For both the propagation directions, the low-frequency (namely ω_1-ω_8) and high-frequency (namely ω_9-ω_{12}) ranges are separated from each other by the total band gap BG_T, and the respective polarizations are systematically dominated by translational and rotational modes, respectively. Some parametric analyses show that, as long as the two frequency ranges remains well-separated, the translational frequency curves (rigorously, the curves related to the frequencies of translational modes) undergo only minor qualitative and quantitative changes for slight variations of the parameter set $(\varrho^2, \chi^2, \delta)$. On the contrary, the rotational frequencies (rigorously, the curves related to the frequencies of rotational modes) strongly depend on the δ and χ parameters, with an approximately linear law of direct and inverse proportionality, respectively. Physically, this remark states that the amplitude of the total band gap BG_T can be amplified/reduced by modifying the ring density (higher/lower δ-values) or their rotational-to-translational mass ratio (lower/higher χ^2-values). For instance, the band gap can be verified to close (null amplitude) for $\chi^2 \geq 1/36$.

As major remark, the material does not present low-frequency total band gaps, neither they can be obtained for a different, generic parameter set. This persistent scenario is a direct consequence of the high spectral density characterizing the translational frequencies, together with the large number of crossing points between their dispersion curves. Looking at waves propagating along the diagonal direction (Figure 3b), the small-amplitude partial band-gap BG_P can be found at low-frequencies, ranging between two translational-translation curves. It can be verified that this gap occurs in the direction of minimum auxeticity of the material, consistently with the findings of [14]. Fixed the other parameter, the gap amplitude A_{12} can be moderately increased by an increment of the δ-parameter, up to $A_{12} \simeq 0.250$.

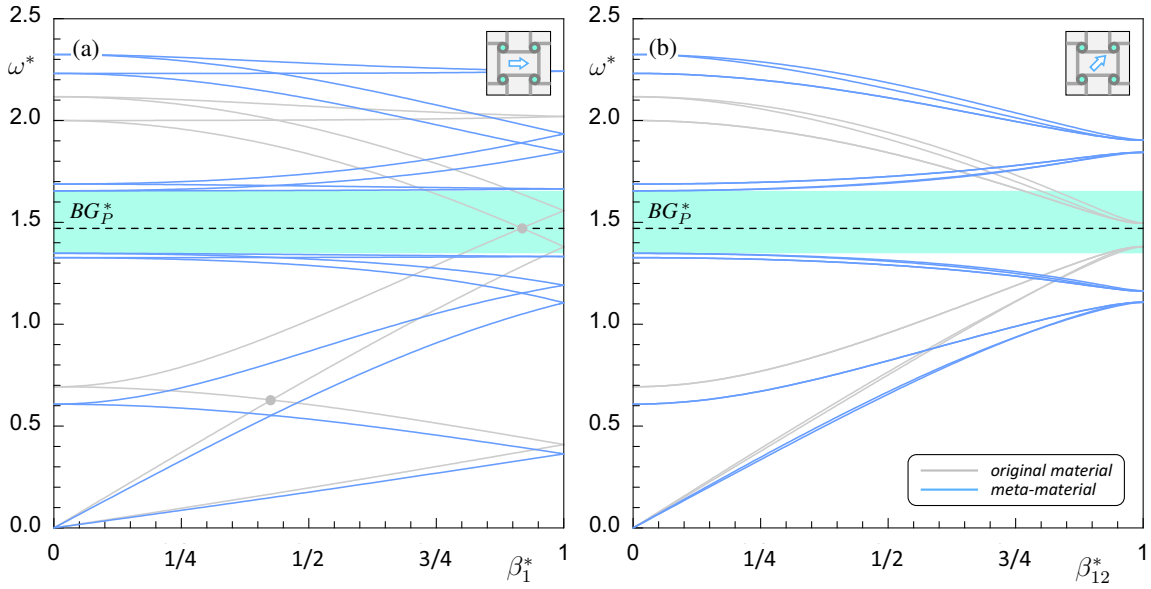

Figure 4: Low-frequency Floquet-Bloch spectrum ($\omega* = \omega/\omega_c$) of the meta-material ($\gamma = 148/100$): (a) horizontal and (b) diagonal direction of wave propagation ($\beta_1^* = \beta_1/\pi$, $\beta_{12}^* = \beta_{12}/(\sqrt{2}\pi)$).

3.2 Effects of the local resonators

The strong potential recognized to micro-oscillator arrays in preventing the wave propagation through periodic lattices can be explained by the effective negative values of mass density achievable in the equivalent elastic continua [25, 26]. Inter-oscillator distances lower than the typical wavelengths let the meta-material internally resonate in the low-frequency range, where band gaps may open in the Floquet-Bloch spectrum, in correspondence with the tunable natural frequencies of the oscillators (resonators). The present study is focused on two different tasks

i. check whether a proper tuning of the meta-material resonators (through the γ-parameter) allow the opening of total band gaps, by either the widening of an existing partial band gap or the transformation of a crossing point into a veering between adjacent curves,

ii. verify the possibility to finely control (through the α-parameter) the total band-gap amplification/deamplification, in order to quantitatively evaluate the meta-material potential in terms of achievable performance range against undesired wave propagation.

To the former task, the oscillator-to-ring mass can be tentatively assigned to the reference value $\alpha = 1/2$, which optimizes the resonator performance in similar chiral meta-materials [29]. First, the partial-to-total widening of the low-frequency band gap BG_P is challenged. The crossing C_P between the forth and fifth dispersion curves, which closes the band gap in the horizontal propagation direction, is pointed as target frequency by tuning $\gamma = 148/100$ (corresponding to the upper dashed line in Figure 3). The efficiency of the resonator action is confirmed by the low-frequency Floquet-Bloch spectrum of the meta-material (Figure 4). Indeed, a new total band BG_P^*, with almost $\mathbf{b}$-independent amplitude $A_1 = A_{12} \simeq 0.300$, rises up and lies just across the tuned frequency. The original crossing point is removed by a strong softening/hardening effect, consisting in the downward/upward frequency shifting of the previously intersecting curves (gray lines). The band gap opening is not compromised by the local densification of the spectrum owing to the doubled dimension of the meta-material model.

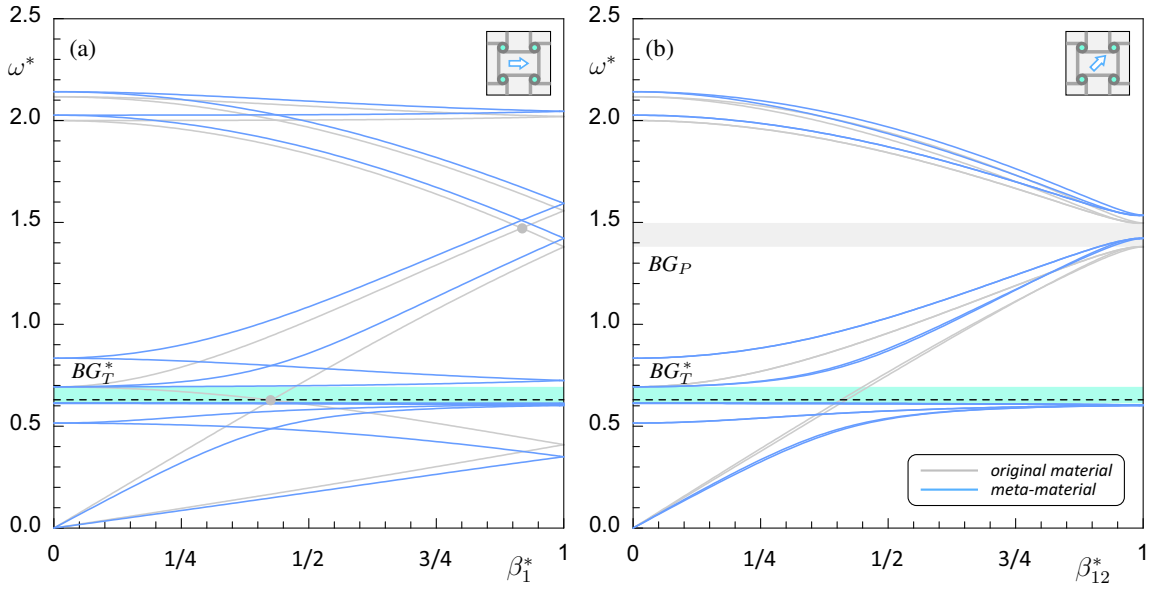

Figure 5: Low-frequency Floquet-Bloch spectrum of the anti-tetrachiral meta-material ($\gamma = 62/100$): (a) horizontal and (b) diagonal direction of wave propagation ($\beta_1^* = \beta_1/\pi$, $\beta_{12}^* = \beta_{12}/(\sqrt{2}\pi)$).

Second, the crossing C_T between the second and third dispersion curves, which characterizes the horizontal propagation direction, is pointed as target frequency by tuning $\gamma = 62/100$ (corresponding to the lower dashed line in Figure 3). Again, the resonator action successes in opening a low-frequency total band BG_P^*, with almost $\mathbf{b}$-independent amplitude $A_1 = A_{12} \simeq 0.037$, lying across the tuned frequency (Figure 5). The band gap is provided by a strong linear interaction among the new spectrum curves and the previously intersecting curves (gray lines), which are forced to veer away form their original crossing point.

To the latter task, a few parametric analyses have been carried out under variation of the resonator-to-ring mass, without changes in the tuning parameters (Table 1). The results tend to confirm that the total band gap amplitudes are $\mathbf{b}$-independent ($A_1 = A_{12}$) and that – fixed the resonator mass – larger band gap are achievable at higher tuning frequencies. Finally, the band gap amplitudes are found to grow up with the increments of the resonator mass. In this respect, the trend of the mass-to-amplitude ratios suggests an underlying quadratic relationship which could be investigated by means of local analyses based on perturbation methods.

Table 1: Amplitudes of the low-frequency band-gaps obtainable in the anti-tetrachiral meta-material.

	PERIODIC MATERIAL ($\omega^* \simeq 148/100$)			PERIODIC MATERIAL ($\omega^* \simeq 62/100$)		
	A_1	A_{12}	Description	A_1	A_{12}	Description
	–	0.114	Partial	–	–	Absent
	META-MATERIAL ($\gamma = 148/100$)			META-MATERIAL ($\gamma = 62/100$)		
α	A_1	A_{12}	Description	A_1	A_{12}	Description
1/4	0.086	0.086	Total	0.021	0.021	Total
1/3	0.148	0.148	Total	0.037	0.037	Total
1/2	0.307	0.307	Total	0.080	0.080	Total
2/3	0.501	0.501	Total	0.138	0.138	Total

4 CONCLUSIONS

A parametric beam-lattice model has been formulated to describe the linear planar dynamics of the unit cell which characterizes the periodic microstructure of the auxetic anti-tetrachiral material. The persistent absence of low-frequency band gaps in the Floquet-Bloch spectrum has been verified. This lack limits the smart functionalities of passive noise suppression and vibration filtering of the material, when it is used as elastic waveguide. The transformation into a meta-material, by introducing local undamped resonators with flexible properties of tunable *frequency* and selectable *mass* ratio, has demonstrated its potential in strongly modifying the original low-frequency band structure. In particular, a tailor-made design of the resonator parameters has allowed the widening of an existing partial band gap, as well as the opening of a new band gap across the tuned frequency, with adjustable amplitude depending on the selected mass.

References

[1] R. Lakes, Deformation mechanisms in negative Poisson's ratio materials: structural aspects. *Journal of Materials Science* **26**(9) 2287–2292, 1991.

[2] A. Alderson, K. Alderson, Auxetic materials. *Proceedings of the Institution of Mechanical Engineers, Part G: Journal of Aerospace Engineering* **221**(4) 565–575, 2007.

[3] Y. Prawoto, Seeing auxetic materials from the mechanics point of view: a structural review on the negative Poisson's ratio. *Computational Materials Science* **58** 140–153, 2012.

[4] D. Prall, R. Lakes, Properties of a chiral honeycomb with a Poisson's ratio of-1. *International Journal of Mechanical Sciences* **39**(3) 305–314, 1997.

[5] J. Dirrenberger, S. Forest, D. Jeulin, Effective elastic properties of auxetic microstructures: anisotropy and structural applications. *International Journal of Mechanics and Materials in Design* **9**(1) 21–33,2013.

[6] A. Bacigalupo, L. Gambarotta, Homogenization of periodic hexa-and tetrachiral cellular solids. *Composite Structures* **116** 461–476, 2014.

[7] J.E. Cadman, S. Zhou, Y. Chen, Q. Li, On design of multi-functional microstructural materials. *Journal of Materials Science* **48**(1) 51–66, 2013.

[8] O. Sigmund, S. Torquato, I. Aksay, On the design of 1-3 piezocomposites using topology optimization. *Journal of Materials Research* **13**(4) 1038–1048, 1998.

[9] A. Alderson, K. Alderson, D. Attard, K. Evans, R. Gatt, J. Grima, W. Miller, N. Ravirala, C. Smith, K. Zied, Elastic constants of 3-, 4- and 6-connected chiral and anti-chiral honeycombs subject to uniaxial in-plane loading. *Composites Science and Technology* **70**(7) 1042–1048, 2010.

[10] L. Yang, O. Harrysson, H. West, D. Cormier, Mechanical properties of 3d re-entrant honeycomb auxetic structures realized via additive manufacturing. *International Journal of Solids and Structures* **69-70** 475–490, 2015.

[11] M. Ruzzene, F. Scarpa, Directional and band-gap behavior of periodic auxetic lattices. *Physica Status Solidi (b)* **242**(3) 665–680, 2005.

[12] A. Spadoni, M. Ruzzene, S. Gonella, F. Scarpa, Phononic properties of hexagonal chiral lattices. *Wave Motion* **46**(7) 435–450, 2009.

[13] K. Tee, A. Spadoni, F. Scarpa, M. Ruzzene, Wave propagation in auxetic tetrachiral honeycombs. *Journal of Vibration and Acoustics* **132**(3) 031007, 2010.

[14] A. Bacigalupo, M.L. De Bellis, Auxetic anti-tetrachiral materials: equivalent elastic properties and frequency band-gaps. *Composite Structures* **131** 530–544, 2015.

[15] V. Gattulli, F. Potenza, M. Lepidi, Damping performance of two simple oscillators coupled by a visco-elastic connection. *Journal of Sound and Vibration* **332**(26) 6934–6948, 2013.

[16] I. Venanzi, F. Ubertini, A.L Materazzi, Optimal design of an array of active tuned mass dampers for wind-exposed high-rise buildings. *Structural Control and Health Monitoring* **20**(6) 903–917, 2013.

[17] M. Lepidi, Multi-parameter perturbation methods for the eigensolution sensitivity analysis of nearly-resonant non-defective multi-degree-of-freedom systems. *Journal of Sound and Vibration* **332**(4) 1011–1032, 2013.

[18] A. Casalotti, A. Arena, W. Lacarbonara, Mitigation of post-flutter oscillations in suspension bridges by hysteretic tuned mass dampers. *Engineering Structures* **69** 62–71, 2014.

[19] I. Venanzi, Robust optimal design of tuned mass dampers for tall buildings with uncertain parameters. *Structural and Multidisciplinary Optimization* **51**(1) 239–250, 2015.

[20] M. Lepidi, G. Piccardo, Aeroelastic stability of a symmetric multi-body section model. *Meccanica* **50**(3) 731–749, 2015.

[21] F. Tubino, G. Piccardo, Tuned Mass Damper optimization for the mitigation of human-induced vibrations of pedestrian bridges. *Meccanica* **50**(3) 809–824,2015.

[22] J.N. Grima, R. Gatt, P.-S. Farrugia, On the properties of auxetic meta-tetrachiral structures. *Physica Status Solidi (b)* **245**(3) 511–520, 2008.

[23] Y. Chen, F. Scarpa, Y. Liu, J. Leng, Elasticity of anti-tetrachiral anisotropic lattices. *International Journal of Solids and Structures* **50**(6) 996–1004, 2013.

[24] R. Gatt, D. Attard, P.-S. Farrugia, K.M. Azzopardi, L. Mizzi, J.-P. Brincat, J.N. Grima, A realistic generic model for anti-tetrachiral systems. *Physica Status Solidi (b)* **250**(10) 2012–2019, 2013.

[25] H. Huang, C. Sun, G. Huang, On the negative effective mass density in acoustic metamaterials. *International Journal of Engineering Science* **47**(4) 610–617, 2009.

[26] H. Huang, C. Sun, Wave attenuation mechanism in an acoustic metamaterial with negative effective mass density. *New Journal of Physics* **11**(1) 013003, 2009.

[27] D. Bigoni, S. Guenneau, A.B. Movchan, M. Brun, Elastic metamaterials with inertial locally resonant structures: Application to lensing and localization. *Physical Review B* **87**(17), 174303, 2013.

[28] A. Bacigalupo, L. Gambarotta, Simplified modelling of chiral lattice materials with local resonators. *International Journal of Solids and Structures* **83** 126–141, 2016.

[29] A. Bacigalupo, M. Lepidi, G. Gnecco, L. Gambarotta, Optimal design of auxetic hexachiral metamaterials with local resonators. *Smart Materials and Structures*, **25**(5), 054009, 2016.

[30] A. Bacigalupo, M. Lepidi, High-frequency parametric approximation of the Floquet-Bloch spectrum for anti-tetrachiral materials. *International Journal of Solids and Structures*, under review 2016.

[31] L. Brillouin, Wave propagation in periodic structures: electric filters and crystal lattices. *Courier Corporation*, 2003.

[32] I.V. Andrianov, V.I. Bolshakov, V.V. Danishevs'kyy, D. Weichert, Higher order asymptotic homogenization and wave propagation in periodic composite materials. *Proc. Royal Society A: Mathematical, Physical and Engineering Sciences* **464**(2093) 1181–1201, 2008.

[33] A. Bacigalupo, L Gambarotta, Second-gradient homogenized model for wave propagation in heterogeneous periodic media. *International Journal of Solids and Structures* **51**(5) 1052–1065, 2014.

ECCOMAS Congress 2016
VII European Congress on Computational Methods in Applied Sciences and Engineering
M. Papadrakakis, V. Papadopoulos, G. Stefanou, V. Plevris (eds.)
Crete Island, Greece, 5–10 June 2016

FLEXIBLE COMPLEX SYSTEM OF A DOUBLE-STRING UNDER EXTREME MOVING LOADS

J. Rusin[1]

[1] University of Zielona Góra, Faculty of Civil Engineering,
Architecture and Environmental Engineering
prof. Z. Szafrana 1, 65-516 Zielona Góra, POLAND
e-mail: J.Rusin@ib.uz.zgora.pl

Keywords: flexible model, vibration complex system, extreme moving load, closed-form solution.

Abstract. *In this paper the dynamic response of a complex double-string system traversed by extreme moving load is considered. The paper includes the study of a dynamic behavior of a finite, simply supported double-string flexible complex system subject to moving forces with a constant velocity on the top string. The strings are identical, parallel one upon the other and continuously coupled by a linear Winkler elastic element. The moving loads are around an extreme position of the shear wave velocity of the strings. The classical solution of the response of complex systems subjected to forces moving with a constant velocity has a form of an infinite series. But also it is possible to show that in the considered case part of the solution can be presented in a closed, analytical form instead of an infinite series. The presented method to search for a solution in a closed, analytical form is based on the observation that the solution of the system of partial differential equations in the form of an infinite series is also a solution of an appropriate system of ordinary differential equations. The closed solutions take different forms depending if the velocity of a moving force is smaller, equal or larger than the shear wave velocity of the strings. This follows from the fact that in string wave phenomena may occur. The solution for the dynamic response of the composite strings under moving force is important because it can be used also in order to find the solution for other types of moving loads. The double string connected in parallel by linear elastic elements can be studied as a theoretical model of composite system or prestressed structure in which coupling effects and transverse wave effects are taken into account.*

1 INTRODUCTION

Flexible complex systems have a wide range of applications to civil, military, mechanical, transport, naval, aeronautical and aircraft as structural members with high strength to weight ratios. One of the most important issues in the dynamics of structures is moving load problems witch have been studied by many authors for many years [2-22]. Modeling of movement is very difficult in its complications and generates many mathematical problems [1,3,7,21]. Even simply models give very complex and unpredicted solutions of structural in dynamical and stability meaning. Thusly different types of structures and girders like beams, plates, shells, and frames also membranes, strings and cables have been considered. As well different models of moving loads have been assumed [3]. The paper includes the study of a dynamic behavior of a finite, simply supported double-string flexible complex system subject to moving force with a constant velocity on the top string. The strings are identical, parallel one upon the other and continuously coupled by a linear Winkler elastic element. The most critical situation is when moving loads are around an extreme position of the shear wave velocity of the strings. Responses of structures to extreme speed of load are often complex and difficult to understand, especially because of the complex nature of vibration repeatedly complicated systems. For instance, it is possible to observe some anomalies while the aircraft reaching speed of sound. The Prandtl–Glauert singularity [Fig.1] is the prediction by the Prandtl–Glauert transformation that infinite pressures would be experienced by an aircraft as it approaches the speed of sound. A certain similarity can be expected in the solid body, which can be proved by a closed-form solution of a string with a load moving at the speed of the transverse wave propagating in the string.

Figure 1: A F/A-18 Hornet during transonic flight, a Prandtl–Glauert singularity [NASA].

A string as a simple model of a one-dimensional continuous system resistant to tension but not to bending is often used in analysis of numerous engineering structures and has been a subject of great scientific interest for a considerable time. This follows from the fact that the vibrations of a string are described by the wave differential equation. This allows one to see the wave effect in a string, contrary to many more complex systems for example structural elements where it might be either not present or not clearly visible. The analogies between a string and the beams have been considered in papers [5,6,11]. Various aspects of the dynamics response of a string under a moving load have been considered, among others, in the papers [2,4,8,10,12-15,18-20,22]. The classical solution of the response of complex systems subjected to forces moving with a constant velocity has a form of an infinite series. But also it

is possible to show that in the considered case part of the solution can be presented in a closed, analytical form instead of an infinite series. Using the method, of superposed deflections Kączkowski [9] has shown for a simply supported Euler-Bernoulli beam that, in the case of undamped vibration, the aperiodic part of the solution can be presented in a closed-form. Next, Reipert obtained a closed form solutions for a beam with arbitrary boundary conditions [16] and for a frame [17]. In this paper, we use a different method to obtain the solutions in a closed form. The presented method to search for a solution in a closed, analytical form is based on the observation that the solution of the system of partial differential equations in the form of an infinite series is also a solution of an appropriate system of ordinary differential equations. The closed solutions take different forms depending if the velocity of a moving force is smaller, equal or larger than the shear wave velocity of the strings. This follows from the fact that in string wave phenomena may occur. The presented solutions can be also used in axial and torsional vibration of the rod. Using this method, the closed solutions for undamped vibration of string and beam due to moving force have been obtained in the papers [18-21]. The solution for the dynamic response of the composite strings under moving force is important because it can be used also in order to find the solution for other types of moving loads. The double string connected in parallel by linear elastic elements can be studied as a theoretical model of composite system or prestressed structure in which coupling effects and transverse wave effects are taken into account.

2 MATHEMATICAL MODEL AND GOVERNING EQUATION

Consider the problem of a dynamic behavior of flexible complex system consist of a finite, simply supported double-string. The strings are identical, parallel one upon the other and continuously interfaced by a linear Winkler elastic element with *k* coefficient. The strings are under axial compression *N* and the system are excited by a load *p(x,t)* moving with a constant velocity *v* on a top string as on Fig.2.

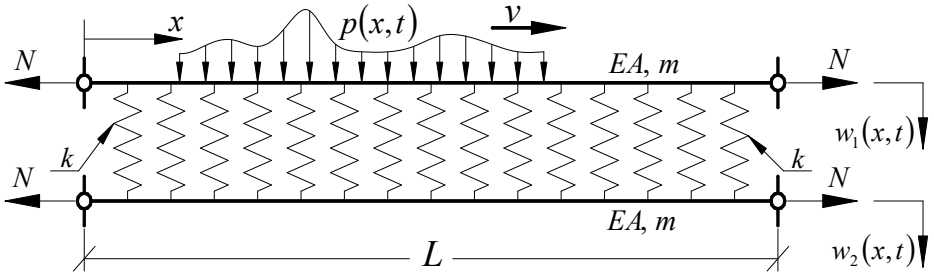

Figure 2: Double-string system under a moving force.

Vibrations describe functions $w_1(x,t)$ and $w_2(x,t)$ which solution in the classical-forms and closed-form is investigated. Hence an equation of motion of double-string system is governed by two conjugate partial differential equations:

$$-N\frac{\partial^2 w_1(x,t)}{\partial x^2}+m\frac{\partial^2 w_1(x,t)}{\partial t^2}+k\left[w_1(x,t)-w_2(x,t)\right]=p(x,t), \tag{1}$$

$$-N\frac{\partial^2 w_2(x,t)}{\partial x^2}+m\frac{\partial^2 w_2(x,t)}{\partial t^2}+k\left[w_2(x,t)-w_1(x,t)\right]=0, \tag{2}$$

where *m* is the mass per unit length ρA of each string, *k* denotes the stiffness modulus of a springs system, and furthermore, *EA* is the axial rigidity of the strings, *E* denotes Young's

modulus of elasticity and A is the area of the cross-section of the strings. The load function in expression (1) and from figure 2 has a form:

$$p(x,t) = P\,\delta(x - vt), \tag{3}$$

where P is the intensity value of the load and $\delta(.)$ denotes Dirac delta. After introducing the dimensionless variables:

$$\xi = x/L, \quad T = vt/L, \quad \xi \in [0,1], \quad T \in [0,1], \tag{4}$$

the differential equations of motion of the string-string system have the form:

$$-\frac{\partial^2 w_1(\xi,T)}{\partial \xi^2} + \eta^2 \frac{\partial^2 w_1(\xi,T)}{\partial T^2} + k_o\left[w_1(\xi,T) - w_2(\xi,T)\right] = P_o\,\delta(\xi - T), \tag{5}$$

$$-\frac{\partial^2 w_2(\xi,T)}{\partial \xi^2} + \eta^2 \frac{\partial^2 w_2(\xi,T)}{\partial T^2} + k_o\left[w_2(\xi,T) - w_1(\xi,T)\right] = 0. \tag{6}$$

The parameters from equations (5) and (6) have the following designations:

$$v_s = \sqrt{N/m}, \qquad \eta = v/v_s, \qquad k_o = k\,L^2/N, \qquad P_o = P\,L/N. \tag{7}$$

The quantity v_s represents velocity of the transverse wave in the system of double-string. On the other hand the boundary conditions for both Eq. (5) and Eq. (6) take the form:

$$w_j(0,T) = 0, \qquad w_j(1,T) = 0, \qquad j = \{1,\ 2\} \tag{8}$$

whereas the initial conditions are the following:

$$w_j(\xi,0) = 0, \qquad \left.\frac{\partial w_j(\xi,T)}{\partial T}\right|_{T=0} = 0, \qquad j = \{1,\ 2\}. \tag{9}$$

It is easy to see that if you add together the equations (5) and (6) and introduce a new function as $w_I(\xi,T)$ we get:

$$-\frac{\partial^2 w_I(\xi,T)}{\partial^2 \xi} + \eta^2 \frac{\partial^2 w_I(\xi,T)}{\partial^2 T} = P_o\,\delta(\xi - T), \tag{10}$$

which describes vibrations of a single string. But then again, when we take the difference of these equations and differences of deflection functions take as a new function $w_{II}(\xi,T)$, that can be saved:

$$-\frac{\partial^2 w_{II}(\xi,T)}{\partial^2 \xi} + \eta^2 \frac{\partial^2 w_{II}(\xi,T)}{\partial^2 T} + 2k_o\,w_{II}(\xi,T) = P_o\,\delta(\xi - T). \tag{11}$$

In turn, this one describes vibrations of a single string resting on an elastic Winkler support with double parameter k ($2k_o$). So the solution (10) and (11) is also a solution of expressions (5) and (6), after appropriate transformation function $w_I(\xi,T)$ and $w_{II}(\xi,T)$ into $w_1(\xi,T)$ and $w_2(\xi,T)$. In addition, the solutions of equations (5), (6), (10) and (11) for boundary conditions (8) and initial conditions (9) are assumed to be in the form of sine series:

$$w_k(\xi,T) = \sum_{n=1}^{\infty} y_{kn} \sin n\pi\xi, \qquad k = \{1,\ 2, I, II\}. \tag{12}$$

By substituting expression (10) into equations (5), (6), (10) or (11) and using the orthogonalization method one obtains set of uncoupled ordinary differential equations. Eventually, the solution of the above differential equations are sums of the particular integrals $w_k^A(\xi,T)$ and general integrals $w_k^S(\xi,T)$. We know that the angle of inclination of the tangent to the deflection function $w_k(\xi,T)$ can be presented:

$$\varphi_k(\xi,T)=\frac{\partial w_k(x,t)}{\partial x}=\frac{1}{L}\frac{\partial w_k(\xi,T)}{\partial \xi}, \tag{13}$$

additionally the dynamic component of the tension in the strings is given by:

$$N_k(\xi,T)=EA\frac{\partial w_k(x,t)}{\partial x}=\frac{EA}{L}\frac{\partial w_k(\xi,T)}{\partial \xi}. \tag{14}$$

3 THE CLASSICAL SOLUTIONS

The classical solution has a form of an infinite series, so classical part of the particular and general solution of the first string presents itself as:

$$w_1(\xi,T)=w_1^A(\xi,T)+w_1^S(\xi,T)=\frac{P_o}{1-\eta^2}\left\{\sum_{n=1}^{\infty}\frac{\left[2\,(n\pi)^2\,(1-\eta^2)+k_o\right]\,\sin n\pi T}{(n\pi)^4\,(1-\eta^2)+(n\pi)^2 k_o}\sin n\pi\xi+\right.$$
$$\left.-\sum_{n=1}^{\infty}\frac{\left[\frac{(n\pi)^3}{(1-\eta^2)^{-1}}\sin\left[\frac{\sqrt{(n\pi)^2+k_o}}{\eta}T\right]+\sqrt{(n\pi)^2+k_o}\left[\frac{(n\pi)^2}{(1-\eta^2)^{-1}}+k_o\right]\sin\frac{n\pi}{\eta}T\right]}{\eta^{-1}\,(n\pi)^2\sqrt{(n\pi)^2+k_o}\left[(n\pi)^2(1-\eta^2)+k_o\right]}\sin n\pi\xi\right\}, \tag{15}$$

and the second string:

$$w_2(\xi,T)=w_2^A(\xi,T)+w_2^S(\xi,T)=\frac{P_o}{1-\eta^2}\left\{\sum_{n=1}^{\infty}\frac{k_o\,\sin n\pi T}{(n\pi)^4\,(1-\eta^2)+(n\pi)^2 k_o}\sin n\pi\xi+\right.$$
$$\left.-\sum_{n=1}^{\infty}\frac{\left[\frac{(n\pi)^3}{(1-\eta^2)^{-1}}\sin\left[\frac{\sqrt{(n\pi)^2+k_o}}{\eta}T\right]-\sqrt{(n\pi)^2+k_o}\left[\frac{(n\pi)^2}{(1-\eta^2)^{-1}}+k_o\right]\sin\frac{n\pi}{\eta}T\right]}{\eta^{-1}\,(n\pi)^2\sqrt{(n\pi)^2+k_o}\left[(n\pi)^2(1-\eta^2)+k_o\right]}\sin n\pi\xi\right\}. \tag{16}$$

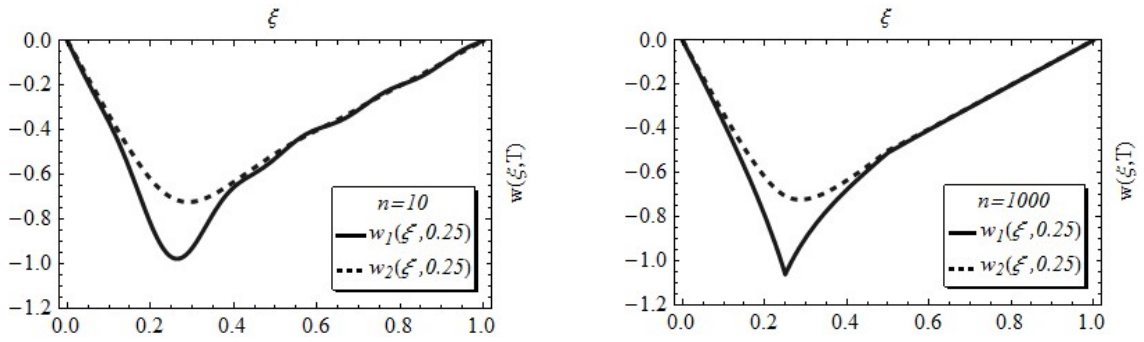

Figure 3: Deflection of the strings system depending on the number of approximation functions.

Analysis of functions (15) and (16) at the critical speed is difficult, even impossible, for example when $v = v_s$ ($\eta = 1$). On the one hand, the accuracy of the solution depends on respectively large number of approximation functions.

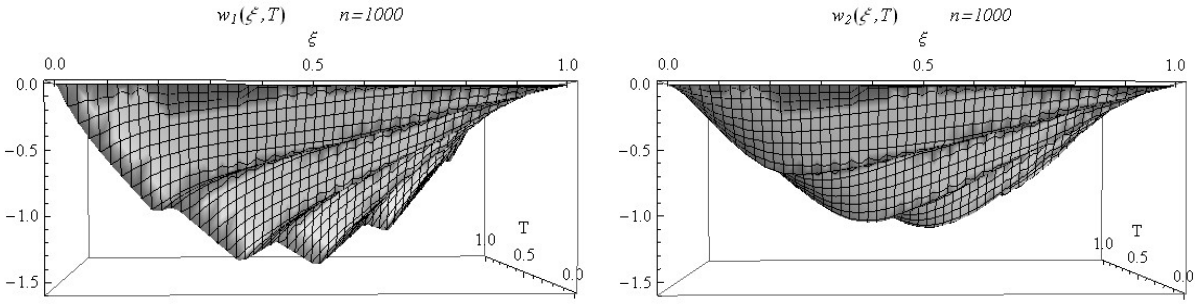

Figure 4: Overlap transverse waves in time of the double-string system under a moving force.

4 THE CLOSED-FORM SOLUTIONS

The classical solution of the response of complex systems subjected to forces moving with a constant velocity has a form of an infinite series, expressions (15) and (16). But also it is possible to show that in the considered case part of the solution can be presented in a closed, analytical form instead of an infinite series. The presented method to search for a solution in a closed, analytical form is based on the observation that the solution of the system of partial differential equations in the form of an infinite series is also a solution of an appropriate system of ordinary differential equations. For instance, let's take into consideration the particular solution Eq. (10) in the form of a series that is:

$$w_I^A(\xi,T)=\frac{2P_o}{1-\eta^2}\sum_{n=1}^{\infty}\frac{\sin n\pi T\sin n\pi\xi}{(n\pi)^2}. \tag{17}$$

It can be proved that the expression (17) is also integral ordinary differential equation:

$$-\frac{d^2w_I^A(\xi,T)}{d\xi^2}=\frac{2P_o}{1-\eta^2}\delta(\xi-T), \tag{18}$$

where T is only a parameter of time. Solving formula (18), by a finite Fourier sine transform, we get:

$$(n\pi)^2\,\overline{w}_I^A(n,T)=\frac{P_o}{1-\eta^2}\sin n\pi T, \tag{19}$$

where

$$\overline{w}_I^A(n,T)=\int_0^1 w_I^A(\xi,T)\sin n\pi\xi\;d\xi, \tag{20}$$

and thus we return to the expression (17), which proves our assumption. Therefore if the function (17) satisfies the equation (18), it can be represented as closed-solution:

$$w_I^A(\xi,T)=\frac{P_o}{1-\eta^2}\left[(1-T)\xi-(\xi-T)H(\xi-T)\right], \tag{21}$$

where $H(.)$ denotes the Heaviside step function, or the unit step function.

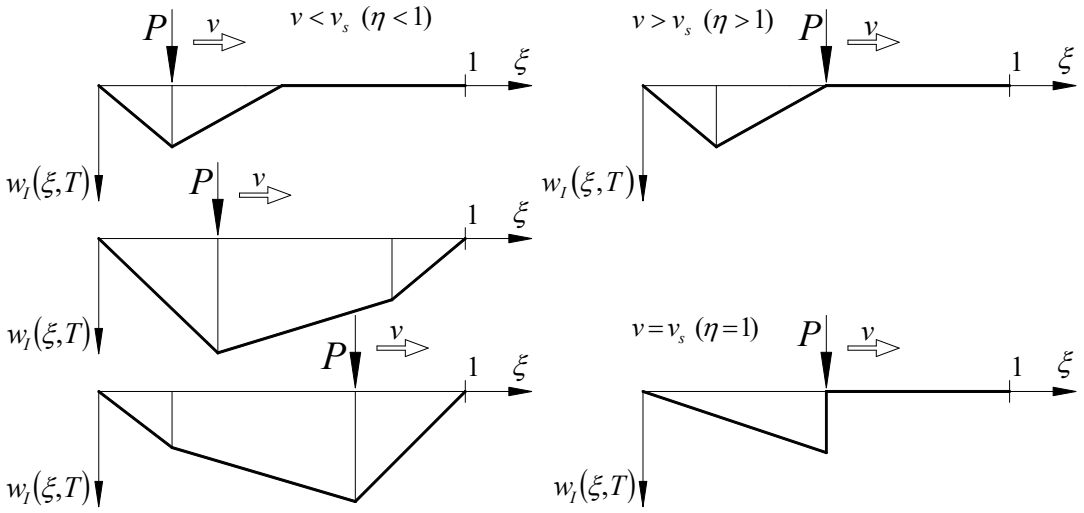

Figure 5: Deflection of string depending on velocity of moving force v and velocity of propagation transverse wave in string v_s.

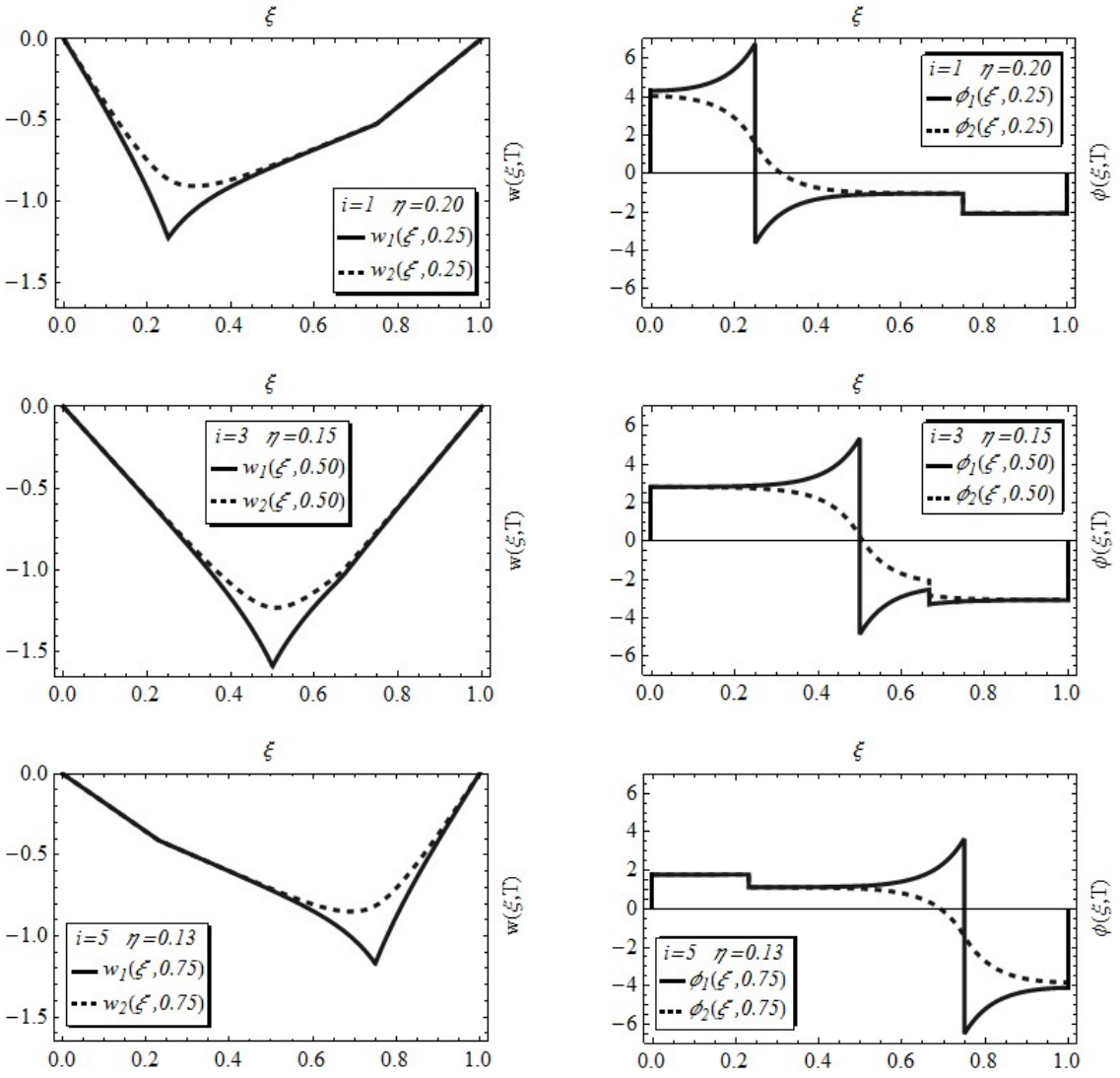

Figure 6: Deflection $w_i(\xi,T)$ and rotation $\varphi_i(\xi,T)$ of double-string system under a moving force.

The general integral $w_I^S(\xi,T)$ can be represented as closed-form solution, too. In a period of time $i\,\eta \le T \le (i+1)\,\eta \le 1$, where $i = 0, 2, 4,\ldots, 2n$, it satisfies the differential relationship:

$$\frac{d^2 w_I^S(\xi,T)}{d\xi^2} = \frac{P_o\,\eta}{1-\eta^2}\,\delta\left[\xi - \left(\frac{T}{\eta} - i\right)\right], \tag{22}$$

with the closed-form solution:

$$w_I^S(\xi,T) = \begin{cases} -\dfrac{P_o}{1-\eta^2}\,\xi\,\left[(i+1)\eta - T\right] & \text{for} \quad \xi \le \dfrac{T}{\eta} - i, \\ -\dfrac{P_o}{1-\eta^2}\,(1-\xi)(i\,\eta - T) & \text{for} \quad \xi \ge \dfrac{T}{\eta} - i. \end{cases} \tag{23}$$

For example, assuming $i = 0$ and consider the cases when the velocity of a moving force is smaller, equal or larger than the shear wave velocity of the strings. In a situation where $\eta < 1$ ($v < v_s$) and $\eta > 1$ ($v > v_s$) we get the formulas:

$$\eta < 1 \qquad w_I^S(\xi,T) = \begin{cases} \dfrac{P_o}{1+\eta}\,\xi & \text{for } \xi \le T, \\ \dfrac{P_o}{1-\eta^2}\,(T - \eta\,\xi) & \text{for } T \le \xi \le \dfrac{T}{\eta}, \\ 0 & \text{for } \dfrac{T}{\eta} \le \xi \le 1, \end{cases} \qquad \eta > 1 \qquad w_I^S(\xi,T) = \begin{cases} \dfrac{P_o}{1+\eta}\,\xi & \text{for } \xi \le \dfrac{T}{\eta}, \\ \dfrac{P_o}{1-\eta^2}\,(\xi - T) & \text{for } \dfrac{T}{\eta} \le \xi \le T, \\ 0 & \text{for } \xi \ge T. \end{cases} \tag{24}$$

Whereas when $\eta = 1$ ($v = v_s$):

$$w_I^S(\xi,T) = \begin{cases} \dfrac{P_o}{2}\,\xi & \text{for} \quad \xi < T, \\ 0 & \text{for} \quad \xi \ge T. \end{cases} \tag{25}$$

The closed-form solutions take different forms depending on the velocity of a moving force in relation to shear wave velocity of the strings. The graphic interpretation of this relationship is shown in Figure 5. And Figure 6 shows graphs in a period of time $i\,\eta \le T \le (i+1)\,\eta \le 1$, where $i = 1, 3, 5,\ldots, 2n-1$. More examples of closed-form solutions can be found [8,18-21].

5 SOME NUMERICAL RESULTS

In Figures 3-6, we presented deflections $w_k(\xi,T)$ and rotations $\varphi_k(\xi,T)$ of double-string complex system under the concentrated moving force. And the following dimensionless values of the parameters are used in the numerical calculations: $n = \{10, 1000\}$, $P_o = 10$, $k_o = 200$, $i = \{1, 3, 5\}$, $\eta = \{0.10, 0.13, 0.15, 0.20, 1.00\}$ and $T = \{0.25, 0.50, 0.75\}$. The results for different location of the moving force are presented in graphical form in Figs. 3-6. The continuous line represents the functions of the loaded string. The dashed line shows the functions of the second string for which the load is transferred with the coupling.

6 CONCLUSIONS

- The solution of the response of string-string complex systems subjected to forces moving with a constant velocity has a form of an infinite series, but also it is possible to show that in the considered case part of the solution can be presented in a closed, analytical form.

- A system of partial differential equations with solution in the form of an infinite series can be also a solution of an appropriate system of ordinary differential equations where a variable of time becomes only a parameter of time.
- The closed solutions take different forms depending if the velocity of a moving force is smaller, equal or larger than the shear wave velocity of the strings.
- The wave phenomena may occur in a complex system of double-string under moving forces.
- It is predicted a nonlinear solution in solid under load moving at a speed of transverse wave propagating in a solid.
- It is easier to observe the wave effect in a string, contrary to many more complex systems where it might be either not present or not clearly visible.
- The accuracy of solution gives the locate position of a transverse wave's front and a soliton which is a self-reinforcing solitary wave that maintains its shape while it propagates at a constant velocity.
- The double string connected in parallel by linear elastic elements can be studied as a theoretical model of composite system or prestressed structure in which coupling effects and transverse wave effects are taken into account.

REFERENCES

[1] J.W. Brown, R.V. Churchill, *Complex Variables and Applications, 7th Edition*. McGraw-Hill Higher Education, Boston, 2004.

[2] H.A. Dieterman, A.V. Kononov, Uniform motion of a constant load along a string on an elastically supported membrane. *Journal of Sound and Vibration*, **208**, 575-586, 1997.

[3] L. Frýba, *Vibration of Solids and Structures under Moving Load, 3rd Edition*. Thomas Telford Ltd., London, UK, 1999.

[4] S. Gavrilov, Non-stationary problems in dynamics of a string on an elastic foundation subjected to a moving load, *Journal of Sound and Vibration*, **222**(3), 345–361, 1999.

[5] J. B. Gunda, R. K. Gupta, R. Ganguli, Hybrid stiff-string polynomial basis functions for vibration analysis of high speed rotating beams, *Computers & Structures*, **87**(3-4), 254-265, 2009.

[6] J. B. Gunda, R. Ganguli, Stiff-string basis functions for vibration analysis of high speed rotating beams. *Journal of Applied Mechanics, Transactions ASME,* **75**(2), 0245021-0245025, 2008.

[7] D.H. Hodges, G.A. Pierce, *Introduction to Structural Dynamics and Aeroelasticity*, Cambridge University Press, UK, 2002.

[8] R. Idzikowski, M. Mazij, P. Śniady, P. Śniady, Vibrations of String due to a Uniform Partially Distributed Moving Load: Closed Solutions. *Mathematical Problems in Engineering*, vol. 2013, ID 163970, 8 pp, 2013.

[9] Z. Kączkowski, Vibration of a beam under a moving load. *Proceedings of Vibration Problems*, **4** (4), 357-373, 1963.

[10] H. Kruse, K. Popp, A.V. Metrikine, Eigenfrequencies of a two-mass oscillator uniformly moving along a string on a viscoelastic foundation. *Journal of Sound and Vibration*, **218**, 103-116, 1998.

[11] A. V. Kumar, R. Ganguli, Analogy between rotating Euler-Bernoulli and Timoshenko beams and stiff strings, *Computer Modeling in Engineering & Science*, **88**, 443–474, 2012.

[12] Z. Oniszczuk, Transverse vibrations of elastically connected double-strings complex system, Part I: free vibrations. *Journal of Sound and Vibration*, **232**(2), 355-366, 2000.

[13] Z. Oniszczuk, Transverse vibrations of elastically connected double-strings complex system, Part II: forced vibrations. *Journal of Sound and Vibration*, **232**(2), 367-386, 2000.

[14] Z. Oniszczuk, Damped vibration analysis of an elastically connected complex double-string system. *Journal of Sound and Vibration*, **264**, 253-271, 2003.

[15] A. Phylactopoulos, G. G. Adams, The response of a non-uniformly tensioned circular string to a moving load. *Journal of Sound and Vibration*, **182**, 415-426, 1995.

[16] Z. Reipert, Vibration of a beam arbitrarily supported on its edges under moving load. *Proceedings of Vibration Problems*, **2**(10), 249-260, 1969.

[17] Z. Reipert, Vibration of frames under moving load, *Archiwum Inżynierii Lądowej*, **16**(3), 419–447, 1970.

[18] J. Rusin, P. Śniady, Vibration of a Complex Strings System under a Moving Force. *Proceedings in Applied Mathematics and Mechanics*, **6**(1), 839-840, 2006.

[19] J. Rusin, P. Śniady, P. Śniady, Vibrations of double-string complex system under moving forces. Closed solutions. *Journal of Sound and Vibration*, **330**, 404-415, 2011.

[20] J. Rusin, Vibrations of a double-string complex system subjected to uniformly distributed moving forces. J. Awerejcewicz, M. Kaźmierczak, J. Mrozowski, P. Olejnik eds. *Dynamical Systems. Mechatronics and Life Sciences*. Department of Automation, Biomechanics and Mechatronics, 443-452, Poland, Łódź, 2015.

[21] J. Rusin, Vibrations of a double-beam complex system subjected to a moving force. M. Kleiber, T. Burczyński, K. Wilde, J. Gorski, K. Winkelmann, Ł. Smakosz eds. *Advances in Mechanics: Theoretical, Computational and Interdisciplinary Issues Proceedings of the 3rd Polish Congress of Mechanics (PCM) and 21st International Conference on Computer Methods in Mechanics (CMM)*, Poland, Gdańsk, 8-11 September 2015, CRC Press Taylor & Francis, 2016.

[22] C. S. Smith, Motions of a stretched string carrying a moving mass particle. *Journal of Applied Mechanics*, Transactions of the ASME, **31**, 29-37, 1964.

ECCOMAS Congress 2016
VII European Congress on Computational Methods in Applied Sciences and Engineering
M. Papadrakakis, V. Papadopoulos, G. Stefanou, V. Plevris (eds.)
Crete Island, Greece, 5–10 June 2016

ON THE MODELING OF SELF-DAMPING IN STRANDED CABLES

Francesco Foti[1], **Luca Martinelli**[1] **and Federico Perotti**[1]

[1] Politecnico di Milano, Dep. of Civil and Environmental Engineering
P.zza L. Da Vinci 32, 20133, Milano, Italy
e-mail: francesco.foti@polimi.it
luca.martinelli@polimi.it
federico.perotti@polimi.it

Keywords: Self damping, cable dynamics, hysteretic bending, friction.

Abstract. *A new formulation is presented to model the hysteretic bending behaviour of metallic strands. The interaction between the wires of the strand is modeled through a frictional contact model based on the Amontons-Coulomb law and accounts for the effects of the tangential compliance mechanism. The new model is presented with reference to a single-layered mono-metallic strand and is applied to the study of the energy dissipation in cyclic bending.*

1 INTRODUCTION

Overhead electrical lines and, more in general, suspended cable structures subjected to wind forces are typically subjected to aeolian vibration, due to the alternate shedding of Von Karman's vortices. These vibrations can strongly affect the service life of cable structures, by inducing alternate bending stresses leading to wear damage and fretting fatigue of the strands and of the connected support equipment [3]. The assessment of the aeolian vibration level, therefore, is a crucial issue in the design and maintenance of cable supported structural systems.

During aeolian vibration, a relevant fraction of the power transmitted by the wind to the structure is dissipated through frictional dissipation phenomena, which occur within the vibrating cable (also referred to as *cable self-damping*) [3]. Stranded cables, in fact, are made of wires, which tend to slip relatively one to each other during the bending of the element.

An upper bound of the aeolian vibration amplitude can be found by imposing the balance between the input power, provided by the wind, and the total dissipation in the cable structure (Energy Balance Principle, see e.g. [1, 3]). Within this context, the most common approach to estimate the self-damping of the cables is based on experimental measurements on indoor laboratory test spans [4] and empirical or semi-empirical (e.g. [13]) expressions.

Focusing on overhead electrical lines, the following power law is commonly adopted to evaluate the power per unit-length, P_d, dissipated when the conductor vibrates according to a flexural natural mode with amplitude A [m] (single-peak antinode vibration amplitude) and frequency f [Hz]:

$$P_d = k \frac{A^l f^m}{T^n} \tag{1}$$

where: T [kN] is the axial load of the cable (assumed constant over the span) and k is a proportionality factor, depending in general on the mechanical and geometrical properties of the strand (see e.g. [2, 3]). The exponents (l, m, n) of the power law are determined by fitting the experimental data from laboratory forced vibration tests.

The approach based on the empirical power law (1) for the definition of the cable self-damping has two major drawbacks: (a) firstly, it relies on expensive and time consuming laboratory tests, and (b) secondly, it is subjected to quite relevant uncertainties since even small variations in the values of the exponents (l, m, n) can lead to a large scatter in the results of equation (1) (see e.g. [1]).

On the other hand, mechanical models starting from a description of the cable internal structure and of the interaction between wires to determine cable self-damping, up to date are still at the research stage (see e.g. the recent review by Spak et al. [14]).

Recently, the authors proposed a new approach to define the self damping of metallic cables [11], starting from the description of the hysteretic bending behaviour of metallic strands provided in [5, 8, 9]. The relative sliding between wires of a strand is first studied, by modeling each wire as a curved thin rod, according to the classic Kirchhoff-Clebsh-Love structural theory. A kinematic model is defined to relate the generalized strains of the wires to those of the strand and the internal contact conditions are analyzed by neglecting the deformation of the contact surfaces and assuming the classic Amontons-Coulomb friction law. The cross sectional response of the strand under cyclic bending is then studied, to obtain a closed-form expression for the dissipated energy per cycle. The latter turns out to be a non-linear function of the maximum bending curvature reached during the cycle. Furthermore, the dissipated energy depends also on the axial load of the strand and on the friction coefficient of the internal contact surfaces. Finally, once the cross sectional hysteretic bending behaviour is fully character-

ized, the cable self-damping can be easily evaluated through a straightforward analytical procedure.

The application of this new approach to overhead electrical lines has shown (see [11] for details) that it allows to recover the same structure of the empirical power law introduced in equation (1), while providing a full mechanical interpretation of the exponents (l, m, n) and of the proportionality factor k. The proposed approach has been successfully compared with experimental data from vibration tests on 20-60 m length laboratory test spans. Within this context, it has been shown that the proposed model delivers an upper-bound estimate of the cable self-damping. The latter finding has been recognized as a consequence of the assumption of non-deformable contact surfaces adopted to describe the hysteretic cross sectional behaviour of the strand. Neglecting the tangential compliance of the internal contact surfaces, indeed, can lead to an overestimate both of the dissipated energy per cycle as well as of the maximum bending stiffness of the strand cross section.

The aim of the present paper is to investigate the effect of the tangential compliance mechanism of the internal contact surfaces on the hysteretic bending behaviour of metallic strands. Accordingly, the mechanical model of the strand originally proposed in [5] is extended to account for the effects of the internal relative displacements due to the tangential contact compliance (see also [6]) and applied to evaluate the energy dissipated under cyclic bending loading.

The new mechanical model is presented in this paper with reference to the special case of a single-layered mono-metallic strand, in order to avoid cumbersome calculations stemming from a more complex internal geometry.

2 INTERNAL STRUCTURE OF THE STRAND

A typical structural steel strand is considered in this work. The strand is made of six circular round wires (diameter d_1) wrapped around a straight round core wire (diameter d_0), as it is sketched in Figure 1.

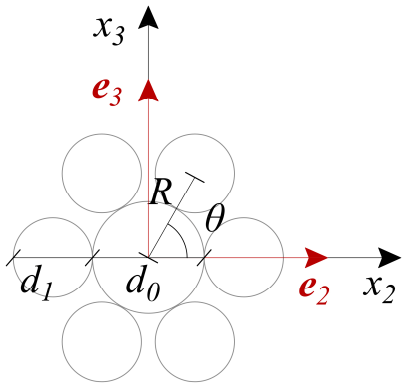

Figure 1: Cross section of the strand.

The external wires are in contact with the core, but not among them. Their centerline can be described as a circular helix in a reference system attached to the strand centerline, with axes $\{x_i\}$ (i=1, 2, 3). The axes x_2 and x_3 are defined on the cross section of the strand, as it is shown in Figure 1, while x_1 identifies the strand centerline. By denoting $\{\mathbf{e}_i\}$ the unit vectors of the axes $\{x_i\}$, the position vector of generic wire centerline can be defined as:

$$\mathbf{x}(\theta) = \frac{R}{\tan(\alpha)}(\theta - \theta_0)\mathbf{e}_1 + R\cos(\theta)\mathbf{e}_2 + R\sin(\theta)\mathbf{e}_3 \tag{2}$$

where: R is the *helix radius*, which can be simply evaluated as R=0.5(d_0+d_1), α is the lay angle, i.e. the constant angle which the tangent vector to the helix defines with the strand centerline (axis x_1), θ is the *swept angle* defined in Figure 1, and θ_0 denotes the value of the swept angle on the strand cross section identified by the coordinate: x_1=0.

3 MODELING OF THE HYSTERETIC BENDING BEHAVIOUR OF THE STRAND

The cross-sectional behaviour of a strand subjected to a combination of axial load F_s and bending moment M_s (herein assumed acting in the plane (x_1, x_3), without loss of generality) can be described through the following constitutive equations (see [5, 6, 8, 9] for details):

$$\begin{cases} F_s = EA_s\varepsilon_s \\ M_s = EI_{\min}\chi_s + M_s^{add}(\varepsilon_s, \chi_s) \end{cases} \tag{3a, b}$$

where ε_s and χ_s are the axial strain and bending curvature of the strand, respectively.

The axial behaviour of the strand (equation (3a)) is linear and independent of the bending curvature. By denoting as EA_0 and EA_1 the axial stiffness of the core and of the external wires, the axial stiffness EA_s can be evaluated (see also [6]) as:

$$EA_s = EA_0 + 6EA_1\cos^3(\alpha) \tag{4}$$

On the other hand, two contributions can be recognized in the expression of the bending moment M_s (equation (3b)). The first one is linear, independent on the axial strain of the strand and accounts for the individual bending of the wires with respect to a diameter parallel to the axis x_2 (see e.g. [8] for details). This term can be evaluated by assuming that the strand behaves as a bundle of individually bent elastic curved thin rods, i.e. by neglecting interaction between the wires of the strand. Under this limit kinematic assumption, the cross sectional bending stiffness attains its minimum value [8]:

$$EI_{\min} = EI_0 + 6\cos^3(\alpha)EI_1 \tag{5}$$

where EI_0 and EI_1 are the bending stiffness of the core and of the external wires, respectively.

The additional term M_s^{add} in equation (3b), instead, is non-linear and accounts for the contribution to the total bending moment of the cross section due to the axial force acting in the individual wires: F_{w1}. The latter, can be decomposed (see also [6]) into a first contribution, $F_{w1,a}$, due to the axial load F_s, and a second one, $F_{w1,b}$, due to the bending of the strand, i.e.: $F_{w1} = F_{w1,a} + F_{w1,b}$. Due to the axial symmetry of the strand, the term $F_{w1,a}$ doesn't depend on the swept angle θ and the additional bending moment in (3b) can be expressed as a function of the components $F_{w1,b}$. The following expression can be easily obtained through equilibrium:

$$M_s^{add} = \sum_{i=1}^{6} R\cos(\alpha)F_{w1,b}(\theta_i)\sin(\theta_i) \tag{6}$$

As long as the friction forces on the internal contact surfaces are large enough to prevent relative displacements (*gross-sliding*) between the wires and the core, i.e. in the *no-sliding* regime, the force $F_{w1,b}$ can be evaluated as:

$$F_{w1,b}^{no-sliding}(\theta) = \frac{\cos^2(\alpha) R\, EA_1\, \chi_s}{1 + \dfrac{C_{Ti}(P)\, EA_1 \sin^2(\alpha)}{R^2}} \sin(\theta) \tag{7}$$

The above expression accounts for the effect of the internal relative displacements due to the tangential contact compliance mechanism and has been first derived by one of the authors in [6] by extending the mechanical model previously developed in [5] under the assumption of non-deformable contact surfaces.

The variable C_{Ti} in equation (7) is the initial value of the tangential compliance between the external wires and the core, evaluated in the straight configuration of the strand (i.e. for χ_s=0), which depends on the normal force per unit length P exerted from the external wires on the core. The latter, in turn, depends on the axial force acting on the strand and introduces a coupling between the axial problem and the bending of the strand, as already highlighted in equation (3b). Closed-form expressions for the normal contact force P and for the tangential compliance C_{Ti}, here omitted for the sake of conciseness, can be found in [6].

The gradient of the wire axial force $F_{w1,b}$, which can be easily derived from (7), gives the wires the trend to slip with respect to the underlying core. The gross-sliding of the wires, however, is contrasted by the tangential contact forces which act on the internal contact surfaces and are bounded by the Amontons-Coulomb friction law. To study the non-linear transition between the no-sliding and gross-sliding regime, a numerical strategy has been developed by the authors (see e.g.: [5, 9]) and is adopted also in this work. The numerical procedure is based on a classic *Return-Map algorithm*, based on a *no-sliding* prediction and a *gross-sliding* correction. The algorithm delivers the value of the gradient of the wire axial force which satisfies the Amontons-Coulomb friction law, over a discrete set of control points defined along the pitch of the wire. Then, the wire axial force $F_{w1,b}$ is obtained through numerical integration along the wire length.

Once the axial force $F_{w1,b}$ is known, the additional bending moment M_s^{add} can be evaluated from equation (6). Finally, by assuming that the strand is subjected to a bending curvature χ_s cyclically variable in the range $\pm \chi_{\max}$, the dissipated energy per cycle can be simply evaluated as the area A_c enclosed in the hysteretic moment-curvature diagrams, i.e.:

$$A_c = \oint_{\pm\chi_{\max}} M_s(\chi_s)\, d\chi_s \tag{7}$$

A more detailed discussion on the cross sectional model can be found e.g. in [6] where the results of the implementation into a corotational beam finite element [7, 10] are also presented. The relation between A_c and the dissipated power P_d per unit length of the cable (self-damping), instead, is extensively discussed in [11].

4 NUMERICAL APPLICATION

The proposed model is applied to study the cross sectional hysteretic behaviour of a well-documented steel strand (see e.g. [12, 15]), already studied by the authors under the action of axial load and planar bending in [6, 9]. The geometric and material properties of the element are listed in Table 1.

d_0 (mm)	d_1 (mm)	α (deg)	E (GPa)	ν (-)
3.94	3.73	11.8	188	0.3

Table 1: Geometric and material parameters from [12].

The results obtained with the new formulation proposed in this paper are systematically compared with the predictions of the previous authors' model [5], which neglects the effect of the tangential compliance mechanism (i.e. C_{Ti}=0 in equation (7)). The initial behaviour of the latter model, will be referred to, in the following, as the *full-stick initial behaviour*, to emphasize the fact that in this case the cross section of the strand is initially considered to behave as an ideal rigid body.

Figures 2(a, b, c) show the cross sectional hysteresis loops evaluated for several values of the maximum curvature χ_{max}. The results have been evaluated for different values of the interwire friction coefficient μ and of the non-dimensional axial load parameter η, defined as the ratio between the axial force F_s and the Rated Tensile Strength of the strand (here 137 kN – see [15]).

From Figures 2(a) and 2(b), it can be easily appreciated that by increasing the strand axial load, the area of the hysteresis loop can be remarkably enlarged. A similar effect is obtained by increasing the value of the friction coefficient (see Figures 2(a) and 2(c)).

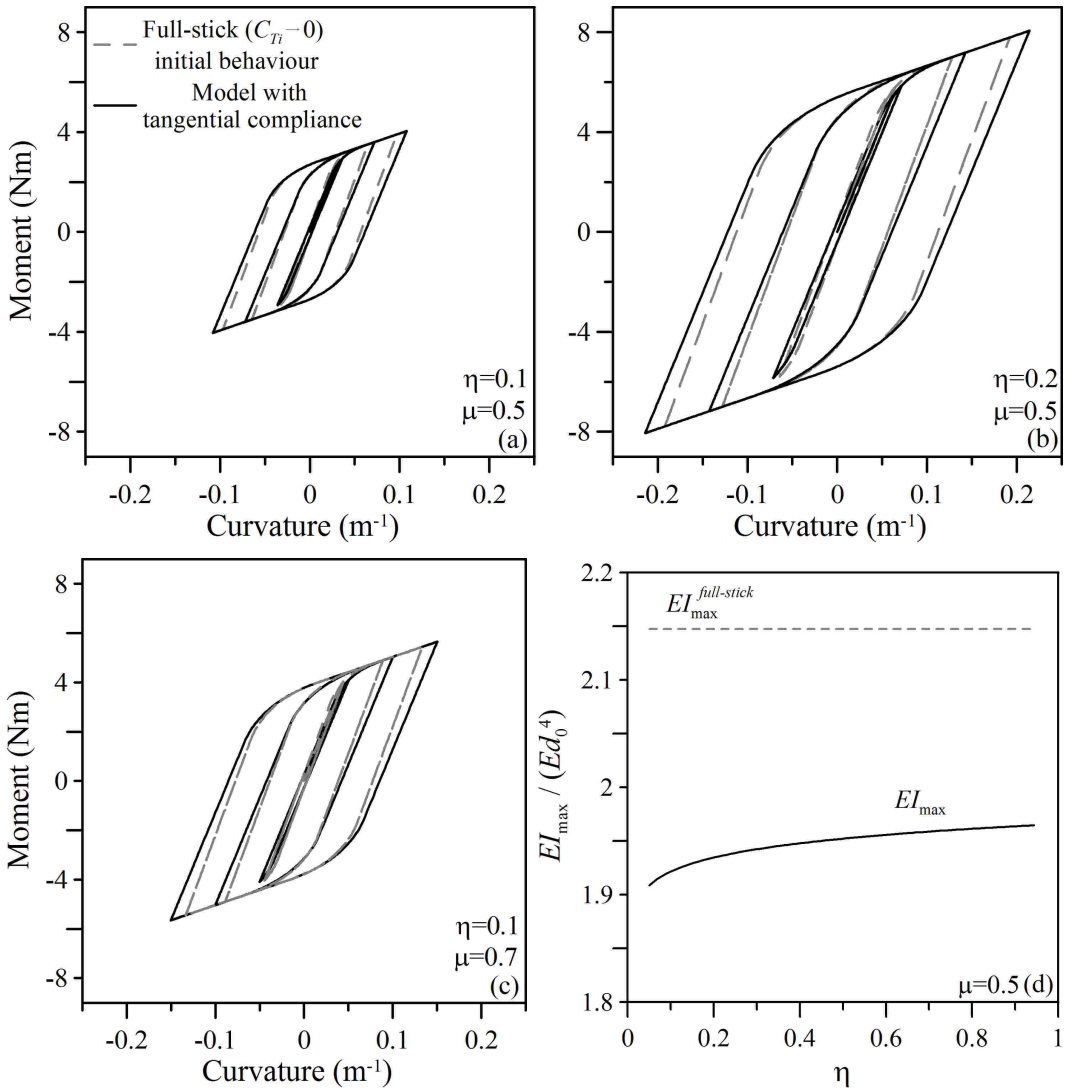

Figure 2: Cross sectional hysteretic behaviour. Hysteresis loops evaluated for: (a) η=0.1 and μ=0.5, (b) η=0.2 and μ=0.5, (c) η=0.1 and μ=0.7. Figure 2(d) shows the non-dimensional initial bending stiffness vs. the axial loading parameter η.

The results of the two models are very similar, for the special case considered in this application. As a matter of fact, the main effect of the tangential compliance mechanism can be recognized in a reduction of about 10% of the value of the initial stiffness of the moment-curvature relation (i.e. the maximum bending stiffness of the strand section: $EI_{\max}$). This effect can be clearly appreciated from Figure 2(d), where the non-dimensional initial bending stiffness $EI_{\max}/(Ed_0^4)$ is plotted against the loading parameter η. As a reference, the corresponding constant value evaluated under the full-stick assumption is also plotted with a grey dashed line.

On the other hand, both the area as well as the shape of the hysteresis loops are very slightly affected by the presence of the tangential compliance mechanism. The latter findings can be further appreciated from Figures (3) and (4), where the secant stiffness of the hysteresis loops and the dissipated energy per cycle (see equation (7)), respectively, are plotted against the maximum curvature of the cycles. It's worth noting that, as expected, the dissipated energy per cycle predicted by the new model is always slightly lower than the one evaluated by neglecting the tangential compliance between the external wires and the core.

5 CONCLUSIONS

A new formulation to model the hysteretic bending behaviour of metallic strands has been developed and presented for the special case of single-layered mono-metallic elements. Each wire of the strand is individually modeled as an elastic curved thin rod, in linear contact with the underlying core. A contact model is then introduced to describe the interaction among the external wires and the core. Friction is modeled through the Amontons-Coulomb law and the effects of the tangential contact compliance are accounted for, aiming at extending a previous authors' model taking into account the gross sliding only.

The proposed model, then, has been applied to study the energy dissipation of a steel strand subjected to cyclic bending loading. For the particular strand considered in this work, it is found that the tangential contact compliance mainly influence the initial bending stiffness of the strand, while it has only a small effect on the secant stiffness and area of the hysteresis loops. Ongoing research is devoted to the extension of the proposed formulation to other strand geometries, including the case of multi-layer elements, for which the effects of the tangential compliance are expected to be more pronounced.

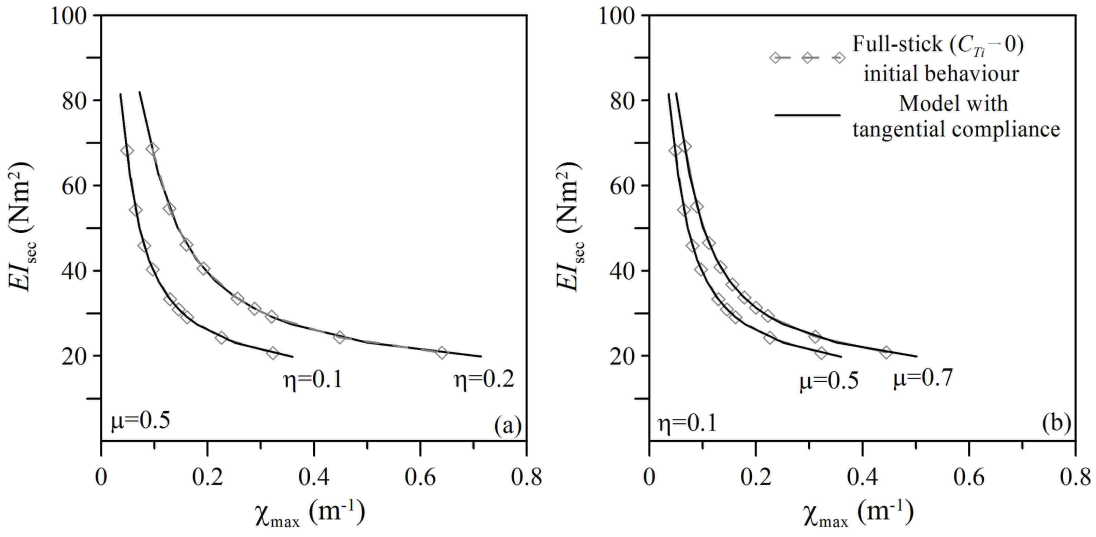

Figure 3: Secant stiffness EI_{sec} of the hysteresis loops vs. the maximum curvature of the cycles χ_{max}. (a) Friction coefficient μ=0.5, different values of η. (b) Axial loading parameter η=0.1, different values of μ.

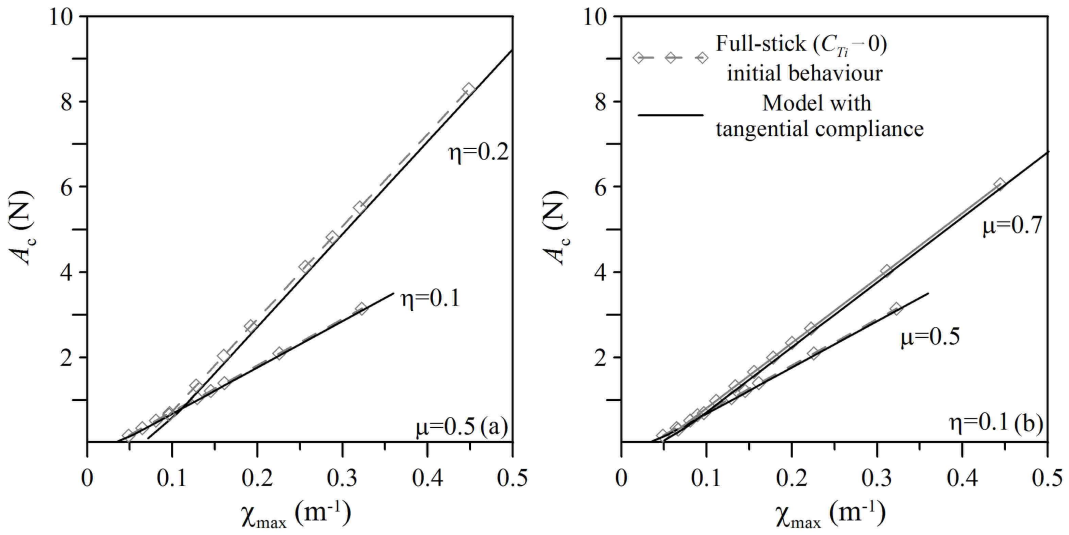

Figure 4: Dissipated energy per cycle A_c vs. the maximum curvature of the cycles χ_{max}. (a) Friction coefficient μ=0.5, different values of η. (b) Axial loading parameter η=0.1, different values of μ.

REFERENCES

[1] CIGRE SC22 WG11 TF 1. Modelling of Aeolian Vibrations of Single Conductors: Assessment of the Technology. *Electra*, **198**, 53-69, 1998.

[2] EPRI, Electric Power Research Institute, Palo Alto CA. *Transmission line reference book- Wind Induced Conductor Motion*, 1979.

[3] EPRI, Electric Power Research Institute, Palo Alto CA. *Transmission line reference book- Wind Induced Conductor Motion*, 2006.

[4] IEEE Power Engineering Society. *IEEE Std. 563.Guide on Conductor Self-Damping Measurements*, 1978.

[5] F. Foti, *A corotational beam element and a refined mechanical model for the nonlinear dynamic analysis of cables*, Doctoral Dissertation, Politecnico di Milano, Milan (Italy), 2013.

[6] F. Foti, A corotational finite element to model bending vibrations of metallic strands. M Papadrakis et al. eds. *Proceedings of the 7th European Congress on Computational Methods in Applied Sciences and Engineering (ECCOMAS)*, Crete Island (Grece), 2016.

[7] F. Foti, L. Martinelli, Dynamics of co-rotational beam elements – some aspects on the kinetic energy and the integration of the equations of motion. J. Eberhardsteiner et.al. eds. *Proceedings of the 6th European Congress on Computational Methods in Applied Sciences and Engineering (ECCOMAS)*, Vienna (Austria), (ISBN:978-3-9502481-9-7) 2012.

[8] F. Foti, L. Martinelli, An analytical approach to model the hysteretic bending behavior of spiral strands, *Applied Mathematical Modelling*. in press (http: //dx.doi.org/ 10.1016/j.apm.2016.01.063), 2016.

[9] F. Foti, L. Martinelli, Mechanical modeling of metallic strands subjected to tension, torsion and bending, Submitted to: *International Journal of Solids and Structures*, 2016.

[10] F. Foti, L. Martinelli, F. Perotti, Numerical integration of the equations of motion of structural systems undergoing large 3D rotations: dynamics of corotational slender beam elements, *Meccanica*, **50**, 751-765, 2015.

[11] F. Foti, L. Martinelli, F. Perotti (2016) A new approach to the definition of self-damping for stranded cables. Submitted to *Meccanica*.

[12] W.G. Jiang, M.S. Yao, J.M. Walton, A concise finite element model for simple straight wire rope strand, *International Journal of Mechanical Sciences*, **41**, 143-161, 1999.

[13] D.U. Noiseux, Similarity laws of the internal damping of stranded cables in transverse vibrations, *IEEE Transactions on Power Delivery*, **7**, 1574-1581, 1992.

[14] K. Spak, G. Agnes, D. Inman, Cable modeling and internal damping developments, *Applied Mechanics Reviews*, **65**, 010801, 2013.

[15] W.S. Utting, N. Jones, The response wire rope strands to axial tensile loads – Part I. Experimental results and theoretical predictions, *International Journal of Mechanical Sciences*, **29**, 605-619, 1987.

ECCOMAS Congress 2016
VII European Congress on Computational Methods in Applied Sciences and Engineering
M. Papadrakakis, V. Papadopoulos, G. Stefanou, V. Plevris (eds.)
Crete Island, Greece, 5–10 June 2016

COMPUTATIONAL EFFECTIVENESS OF LMI DESIGN STRATEGIES FOR VIBRATION CONTROL OF LARGE STRUCTURES

Francisco Palacios-Quiñonero[1], Josep Rubió-Massegú[1], Josep M. Rossell[1] and Hamid Reza Karimi[2]

[1]CoDAlab, Department of Mathematics, Universitat Politècnica de Catalunya (UPC)
Av. Bases de Manresa 61–73, 08242 Manresa, Barcelona, Spain
e-mail: {francisco.palacios, josep.rubio, josep.maria.rossell}@upc.edu

[2]Politecnico di Milano, Department of Mechanical Engineering, via La Masa 1, 20156 Milan, Italy
e-mail: hamidreza.karimi@polimi.it

Keywords: Computational Effectiveness, Structural Vibration Control, Seismic Protection, Linear Matrix Inequalities.

Abstract. *Distributed control systems for vibration control of large structures involve a large number of actuation devices and sensors that work coordinately to produce the desired control actions. Design strategies based on linear matrix inequality (LMI) formulations allow obtaining controllers for these complex control problems, which are characterized by large dimensionality, high computational cost and severe information constraints. In this paper, we conduct a comparative study of the computational effectiveness of three different LMI-based controller design strategies: H_∞, energy-to-peak and energy-to-componentwise-peak. The H_∞ approach is a well-known design methodology and has been widely used in the literature. The energy-to-peak approach is a particular case of generalized H_2 design that is gaining a growing relevance in structural vibration control. Finally, the energy-to-componentwise-peak approach is a less common case of generalized H_2 design that produces promising results among the three considered approaches. These controller design strategies are applied to synthesize active state-feedback controllers for the seismic protection of a five-story building and a twenty-story building both equipped with complete systems of interstory actuation devices. To evaluate the computational effectiveness of the proposed LMI design methodologies, the corresponding computation times are compared and a suitable set of numerical simulations is carried out to assess the performance of the obtained controllers. As positive results, two main facts can be highlighted: the computational effectiveness of the energy-to-peak control design strategy and the particularly well-balanced behavior exhibited by the energy-to-componentwise-peak controllers. On the negative side, it has to be mentioned the computational inefficiency of the considered LMI design methodologies to properly deal with very-large-scale control problems.*

1 INTRODUCTION

Over the last years, controller design strategies based on linear matrix inequality (LMI) formulations have been attracting increasing interest [1]. In the field of vibration control of large structures, these design strategies allow obtaining optimal controllers for complex control problems that involve a large number of actuation devices and sensors, and are typically characterized by large dimensionality, high computational cost and severe information constraints [2–7].

An important family of controller design methodologies for linear systems is based on the idea of minimizing the worst-case gain from the disturbance-input $w(t)$ to the closed-loop controlled-output $z(t)$, which can be modeled as the value

$$\sup_{\|w\|_{\mathrm{w}}\neq 0} \frac{\|z\|_{\mathrm{z}}}{\|w\|_{\mathrm{w}}}, \tag{1}$$

where $\|\cdot\|_{\mathrm{z}}$ and $\|\cdot\|_{\mathrm{w}}$ denote particular signal norms defined on the controlled-output and disturbance-input sets, respectively. Broadly speaking, an optimal controller is computed by minimizing the worst-case gain and, simultaneously, demanding asymptotic stability of the closed-loop system. From a computational point of view, an important fact is that some of these optimization problems can be formulated in terms of LMIs and solved using the existing LMI solvers [8]. Following this approach, different control design strategies can be obtained by selecting different signal norms in the controlled-output and disturbance-input spaces. In the present work, three different signal norms are considered: (i) the continuous 2-norm

$$\|f\|_2 = \left[\int_0^\infty f^T(t) f(t) dt\right]^{1/2}, \tag{2}$$

which is commonly understood as the signal energy content, (ii) the usual continuous peak-norm

$$\|f\|_\infty = \sup_{0\leq t<+\infty} \left[f^T(t) f(t)\right]^{1/2} \tag{3}$$

and (iii) the componentwise-peak-norm

$$\|f\|_{\infty,\mathrm{cw}} = \sup_{0\leq t<+\infty} \max_i |f_i(t)| = \max_i \sup_{0\leq t<+\infty} |f_i(t)|, \tag{4}$$

where $f(t) = [f_1(t), \ldots, f_n(t)]^T$ is a real vector of dimension n. The objective of the paper is to conduct a comparative study of the computational effectiveness of three different LMI-based controller design strategies: H_∞, energy-to-peak and energy-to-componentwise-peak. The H_∞ approach is a well-known design methodology that uses the 2-norm to measure both the controlled-output and the disturbance-input [9–15]. The energy-to-peak approach is a particular case of generalized H_2 design [16] that is gaining a growing relevance in structural vibration control [17–20]. This second case uses the 2-norm for the disturbance-input and the peak-norm for the controlled-output. Finally, the energy-to-componentwise-peak approach is a less common case of generalized H_2 design, which uses the 2-norm for the disturbance input and the componentwise-peak-norm for the controlled-output [21]. These three controller design strategies are applied to synthesize active state-feedback controllers for the seismic protection of a five-story building and a twenty-story building equipped with complete systems of inter-story actuation devices. To assess the performance of the obtained controllers, a proper set of numerical simulations is conducted and the computational effectiveness of the proposed LMI design methodologies is evaluated by comparing the corresponding computation times.

The rest of the paper is organized as follows: In Section 2, a brief summary of the LMI formulations corresponding to the H_∞, energy-to-peak and energy-to-componentwise-peak controller design strategies is presented. In Section 3, a mathematical model for a n-story building is provided. In Section 4, the controllers corresponding to the three proposed design strategies are computed, the computation times are compared and the results of the numerical simulations are discussed. Finally, some conclusions are presented in Section 5.

2 LMI CONTROLLER DESIGN STRATEGIES

Let us consider the system

$$\begin{cases} \dot{x}(t) = Ax(t) + Bu(t) + Ew(t) \\ z(t) = Cx(t) + Du(t) \end{cases} \tag{5}$$

where $x(t) \in \mathbb{R}^{n_x}$ is the state, $u(t) \in \mathbb{R}^{n_u}$ is the control input, $w(t) \in \mathbb{R}^{n_w}$ is the disturbance input, $z(t) \in \mathbb{R}^{n_z}$ is the controlled output and A, B, E, C, D are constant real matrices with appropriate dimensions. Given a state-feedback controller

$$u(t) = Gx(t), \tag{6}$$

with state gain matrix $G \in \mathbb{R}^{n_u \times n_x}$, we obtain the closed-loop system

$$\begin{cases} \dot{x}(t) = A_G x(t) + Ew(t) \\ z(t) = C_G x(t) \end{cases} \tag{7}$$

where

$$A_G = A + BG, \quad C_G = C + DG. \tag{8}$$

The worst-case gain from the disturbance-input to the closed-loop controlled-output associated to the control gain matrix G can be modeled by the system norm

$$\gamma(G) = \sup_{\|w\|_{\mathrm{w}} \neq 0} \frac{\|z\|_{\mathrm{z}}}{\|w\|_{\mathrm{w}}}, \tag{9}$$

where $\|\cdot\|_{\mathrm{z}}$ and $\|\cdot\|_{\mathrm{w}}$ denote particular signal norms defined on the controlled-output and disturbance-input spaces, respectively. An optimal state-feedback controller

$$u(t) = \widetilde{G}x(t) \tag{10}$$

can then be obtained by solving the following optimization problem:

$$\min_G \{\gamma(G) : A_G \text{ asymptotically stable}\}. \tag{11}$$

The H_∞ controller design considers the system norm

$$\gamma_\infty(G) = \sup_{\|w\|_2 \neq 0} \frac{\|z\|_2}{\|w\|_2}, \tag{12}$$

where $\|\cdot\|_2$ is the continuous 2-norm in (2). The optimization problem (11) corresponding to this case can be formulated as the following LMI optimization problem [1]:

$$\mathcal{P}_\infty : \begin{cases} \text{maximize } \eta \\ \text{subject to } X > 0,\ \eta > 0 \text{ and the LMI in (14)} \end{cases} \tag{13}$$

$$\begin{bmatrix} AX + XA^T + BY + Y^T B^T + \eta EE^T & (CX + DY)^T \\ CX + DY & -I_{n_z} \end{bmatrix} < 0, \tag{14}$$

where $X = X^T \in \mathbb{R}^{n_x \times n_x}$ and $Y \in \mathbb{R}^{n_u \times n_x}$ are the optimization variables and I_n is the identity matrix of order n . If an optimal value $\widetilde{\eta}_\infty$ is attained in $\mathcal{P}_\infty$ for the pair $\big(\widetilde{X}_\infty, \widetilde{Y}_\infty\big)$, then the state gain matrix

$$\widetilde{G}_\infty = \widetilde{Y}_\infty \widetilde{X}_\infty^{-1} \tag{15}$$

is an optimal solution to the H_∞ controller synthesis problem and the corresponding γ-value can be computed as

$$\widetilde{\gamma}_\infty = \gamma_\infty\big(\widetilde{G}_\infty\big) = \big(\widetilde{\eta}_\infty\big)^{-1/2}. \tag{16}$$

The energy-to-peak controller design uses the system norm

$$\gamma_{\mathrm{p}}(G) = \sup_{\|w\|_2 \neq 0} \frac{\|z\|_\infty}{\|w\|_2}, \tag{17}$$

where $\|\cdot\|_2$ is the 2-norm in (2) and $\|\cdot\|_\infty$ is the peak-norm given in (3). The optimization problem (11) associated to this second case admits the following LMI formulation [16]:

$$\mathcal{P}_{\mathrm{p}} : \begin{cases} \text{minimize } \eta \\ \text{subject to the LMIs in } (19) \text{ and } (20) \end{cases} \tag{18}$$

$$AX + XA^T + BY + Y^T B^T + EE^T < 0, \tag{19}$$

$$\begin{bmatrix} X & (CX + DY)^T \\ CX + DY & \eta I_{n_z} \end{bmatrix} > 0, \tag{20}$$

with LMI variables $X = X^T \in \mathbb{R}^{n_x \times n_x}$, $Y \in \mathbb{R}^{n_u \times n_x}$. If an optimal value $\widetilde{\eta}_{\mathrm{p}}$ is attained in $\mathcal{P}_{\mathrm{p}}$ for the pair $\big(\widetilde{X}_{\mathrm{p}}, \widetilde{Y}_{\mathrm{p}}\big)$, then the state gain matrix

$$\widetilde{G}_{\mathrm{p}} = \widetilde{Y}_{\mathrm{p}} \widetilde{X}_{\mathrm{p}}^{-1} \tag{21}$$

is an optimal solution to the energy-to-peak controller synthesis problem with an associated γ-value

$$\widetilde{\gamma}_{\mathrm{p}} = \gamma_{\mathrm{p}}\big(\widetilde{G}_{\mathrm{p}}\big) = \big(\widetilde{\eta}_{\mathrm{p}}\big)^{1/2}. \tag{22}$$

Finally, the energy-to-componentwise-peak controller design considers the system norm

$$\gamma_{\mathrm{cwp}}(G) = \sup_{\|w\|_2 \neq 0} \frac{\|z\|_{\infty,\mathrm{cw}}}{\|w\|_2}, \tag{23}$$

where $\|\cdot\|_2$ is the usual 2-norm and $\|\cdot\|_{\infty,\mathrm{cw}}$ is the componentwise-peak-norm defined in (4). The optimization problem corresponding to this third case

$$\min_G \{\gamma_{\mathrm{cwp}}(G) : A_G \text{ asymptotically stable}\} \tag{24}$$

can be formulated as follows [16]:

$$\mathcal{P}_{\mathrm{cwp}} : \begin{cases} \text{minimize } \ \eta \\ \text{subject to the LMIs in } (26) \text{ and } (27) \end{cases} \tag{25}$$

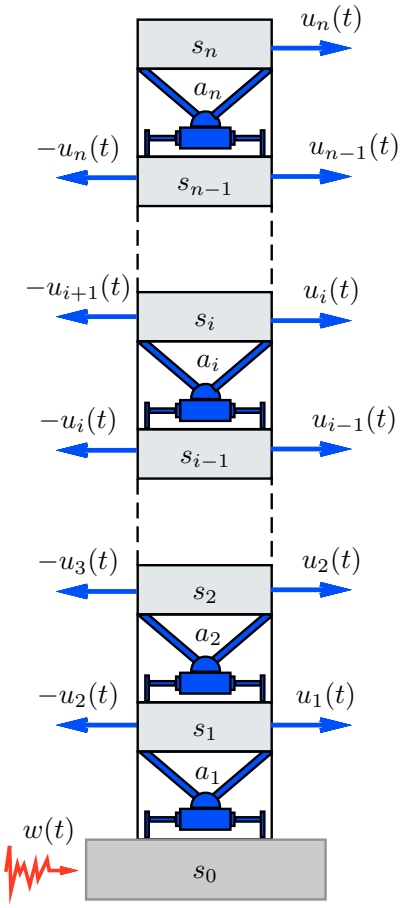

Figure 1: Building structure equipped with interstory actuation devices.

$$AX + XA^T + BY + Y^T B^T + EE^T < 0, \tag{26}$$

$$\begin{bmatrix} X & (C_i X + D_i Y)^T \\ C_i X + D_i Y & \eta \end{bmatrix} > 0, \quad \text{for } 1 \leq i \leq n_z, \tag{27}$$

where C_i and D_i denote the ith row of the matrices C and D, respectively, and $X = X^T \in \mathbb{R}^{n_x \times n_x}$, $Y \in \mathbb{R}^{n_u \times n_x}$ are the LMI variables. As it happened in the previous designs, if an optimal value $\widetilde{\eta}_{\text{cwp}}$ is attained in $\mathcal{P}_{\text{cwp}}$ for the pair $\left(\widetilde{X}_{\text{cwp}}, \widetilde{Y}_{\text{cwp}}\right)$, then the state gain matrix

$$\widetilde{G}_{\text{cwp}} = \widetilde{Y}_{\text{cwp}} \widetilde{X}_{\text{cwp}}^{-1} \tag{28}$$

is an optimal solution to the energy-to-componentwise-peak controller synthesis problem with an associated γ-value

$$\widetilde{\gamma}_{\text{cwp}} = \left(\widetilde{\eta}_{\text{cwp}}\right)^{1/2}. \tag{29}$$

3 BUILDING MODEL

Let us consider the n-story building structure schematically depicted in Figure 1, where a_i, $i = 1, \ldots, n$, represents an interstory actuation device implemented between the stories s_{i-1} and s_i, $w(t)$ denotes the seismic ground acceleration and $u_i(t)$ is the control action exerted by

the actuator a_i, which produces a pair of opposite structural forces as indicated in the figure. By considering the vector of displacements

$$q(t) = \left[q_1(t), \ldots, q_n(t)\right]^T, \tag{30}$$

where $q_i(t)$ is the lateral displacement of the story s_i with respect to the ground level s_0, the lateral motion of the structure can be described by the differential equation

$$M\,\ddot{q}(t) + C_d\,\dot{q}(t) + K\,q(t) = T_u u(t) + T_w w(t), \tag{31}$$

where

$$u(t) = \left[u_1(t), \ldots, u_n(t)\right]^T \tag{32}$$

is the vector of control actions, M, C_d and K are the mass, damping and stiffness matrices, respectively, T_u is the control location matrix and T_w is the excitation input matrix. The mass matrix is a diagonal matrix

$$M = \begin{bmatrix} m_1 & & & \\ & \cdots & & \\ & & \cdots & \\ & & & m_n \end{bmatrix} \tag{33}$$

and the stiffness matrix has the following tridiagonal structure:

$$K = \begin{bmatrix} k_1 + k_2 & -k_2 & & & & & \\ -k_2 & k_2 + k_3 & -k_3 & & & & \\ & \cdots & \cdots & \cdots & & & \\ & & \cdots & \cdots & \cdots & & \\ & & & -k_{n-1} & k_{n-1} + k_n & -k_n & \\ & & & & -k_n & k_n \end{bmatrix}, \tag{34}$$

where m_i and k_i, $i = 1, \ldots, n$ denote the mass and stiffness coefficients of the i-th story, respectively. The damping matrix C_d can be computed from M and K by setting a proper damping ratio on the building modes [22], the control location matrix is a square matrix of size n with the following upper-diagonal band form:

$$T_u = \begin{bmatrix} 1 & -1 & & & & \\ & 1 & -1 & & & \\ & & \cdots & \cdots & & \\ & & & \cdots & \cdots & \\ & & & & 1 & -1 \\ & & & & & 1 \end{bmatrix}, \tag{35}$$

and the excitation input matrix has the form

$$T_w = -M[1]_{n\times 1}, \tag{36}$$

where $[1]_{n\times 1}$ denotes a vector of dimension n with all its entries equal to 1. By introducing the interstory drifts

$$\begin{cases} r_1(t) = q_1(t) \\ r_i(t) = q_i(t) - q_{i-1}(t) \quad \text{for } \; i = 2, \ldots, n, \end{cases} \tag{37}$$

story	1	2	3	4	5
mass ($\times 10^5$ Kg)	2.152	2.092	2.070	2.048	2.661
stiffness ($\times 10^8$ N/m)	1.470	1.130	0.990	0.890	0.840
relative damping	5%				

Table 1: Parameter values corresponding to the five-story building model.

and the augmented state vector

$$x(t) = \begin{bmatrix} r(t) \\ \dot{r}(t) \end{bmatrix}, \tag{38}$$

we obtain the following first-order state-space model:

$$\dot{x}(t) = A\,x(t) + B\,u(t) + E\,w(t), \tag{39}$$

with

$$A = P\,\widehat{A}\,P^{-1}, \quad B = P\,\widehat{B}, \quad E = P\,\widehat{E}, \tag{40}$$

$$\widehat{A} = \begin{bmatrix} [0]_{n\times n} & I_n \\ -M^{-1}K & -M^{-1}C_d \end{bmatrix}, \quad \widehat{B} = \begin{bmatrix} [0]_{n\times n} \\ M^{-1}T_u \end{bmatrix}, \quad \widehat{E} = \begin{bmatrix} [0]_{n\times 1} \\ -[1]_{n\times 1} \end{bmatrix}, \tag{41}$$

where $[0]_{n\times m}$ represents a zero-matrix of the indicated dimensions and P is the change-of-basis matrix corresponding to the state transformation

$$\begin{bmatrix} r(t) \\ \dot{r}(t) \end{bmatrix} = P \begin{bmatrix} q(t) \\ \dot{q}(t) \end{bmatrix}. \tag{42}$$

Assuming that the control objective is to reduce the interstory drift values in the seismically excited building by means of moderate control actions, we also consider the controlled-output vector

$$z(t) = Cx(t) + Du(t), \tag{43}$$

defined by the matrices

$$C = \begin{bmatrix} I_n & [0]_{n\times n} \\ [0]_{n\times n} & [0]_{n\times n} \end{bmatrix}, \quad D = \alpha \begin{bmatrix} [0]_{n\times n} \\ I_n \end{bmatrix}, \tag{44}$$

where α is a scaling factor that compensates the different magnitude of interstory drifts and control forces.

4 NUMERICAL RESULTS

Let us consider the particular five-story building model [23] corresponding to the mass, stiffness and damping parameters presented in Table 1. For this small-building problem, we first solve the LMI optimization problem $\mathcal{P}_\infty$ in (13) with the matrices A, B and E in (40) and the controlled-output matrices in (44) with $n = 5$ and the scaling factor $\alpha = 10^{-7.3}$, obtaining the H_∞ control gain matrix

$$\widetilde{G}_\infty = 10^6 \times \begin{bmatrix} -1.7423 & 0.8569 & -0.2631 & -0.1886 & -0.1406 & -1.6424 & -1.4244 & -1.1155 & -0.7819 & -0.4437 \\ -0.2858 & -2.3937 & 1.0316 & -0.2427 & -0.1045 & -1.8366 & -1.7286 & -1.4129 & -1.0100 & -0.5778 \\ 0.9696 & -0.7657 & -2.7917 & 0.9250 & -0.1450 & -1.6440 & -1.6154 & -1.4853 & -1.1130 & -0.6484 \\ 0.6555 & 0.7633 & -0.7879 & -3.2342 & 0.5932 & -1.2969 & -1.2853 & -1.2396 & -1.0883 & -0.6678 \\ 0.4777 & 0.3678 & 0.4047 & -0.6065 & -3.5459 & -0.7887 & -0.7835 & -0.7630 & -0.7086 & -0.5564 \end{bmatrix}. \tag{45}$$

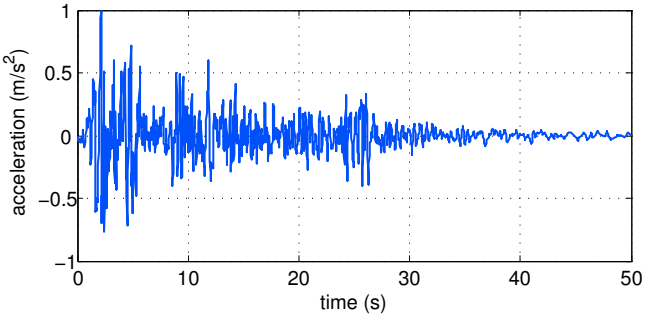

Figure 2: North-South El Centro 1940 seismic record scaled to 1m/s^2.

controller	H_∞	ETP	ETCWP
computation time (s)	0.6724	0.2105	0.3209

Table 2: Computation time (in seconds) corresponding to the H_∞, energy-to-peak (ETP) and energy-to-componentwise-peak (ETCWP) control gain matrices obtained for the five-story building.

Next, we solve the optimization problem $\mathcal{P}_{\rm p}$ in (18) with the same matrices A, B, E , and C used in the previous design, and the matrix D corresponding to the values $n=5$ and $\alpha=10^{-7.55}$. As a result, we obtain the following energy-to-peak control gain matrix:

$$\widetilde{G}_{\rm p}=10^7\times\begin{bmatrix} 2.0601 & -0.0664 & -0.6853 & -0.9248 & -0.6478 & -0.2957 & -0.1719 & -0.1008 & -0.0544 & -0.0253\\ 1.5023 & -0.1639 & -0.4423 & -0.6833 & -0.4994 & -0.1944 & -0.2417 & -0.1429 & -0.0877 & -0.0453\\ -0.5285 & 0.2894 & -0.2447 & 0.2835 & 0.1484 & -0.1126 & -0.1279 & -0.1886 & -0.0995 & -0.0532\\ -1.8625 & 0.0735 & 0.8007 & 0.3661 & 0.6780 & -0.0563 & -0.0626 & -0.0846 & -0.1506 & -0.0606\\ -1.7561 & -0.0616 & 0.7355 & 0.9459 & 0.0174 & -0.0237 & -0.0239 & -0.0341 & -0.0533 & -0.1178 \end{bmatrix}. \tag{46}$$

Finally, by solving the optimization problem $\mathcal{P}_{\rm cwp}$ in (25) with the same matrices A, B, E , C and D used in the energy-to-peak design, we obtain the energy-to-componentwise-peak control gain matrix

$$\widetilde{G}_{\rm cwp}=10^6\times\begin{bmatrix} -3.2275 & 4.1177 & -0.9820 & -0.7206 & -0.6506 & -2.2112 & -1.3045 & -0.9855 & -0.7097 & -0.3988\\ -6.1129 & -9.5642 & -2.3243 & -1.1240 & -0.3647 & -1.1163 & -1.5038 & -0.9947 & -0.6253 & -0.3360\\ 1.7722 & 0.1933 & -7.6837 & -5.2039 & -0.9188 & -1.3303 & -1.3716 & -1.5983 & -1.0710 & -0.5912\\ 1.7341 & 2.9811 & 5.6210 & -4.0119 & -6.3957 & -1.3482 & -1.2888 & -1.3998 & -1.5583 & -0.9837\\ 2.0888 & 1.3659 & 1.4997 & 8.0527 & 1.5823 & -0.9926 & -1.0051 & -1.0788 & -1.2018 & -1.0811 \end{bmatrix}. \tag{47}$$

All the controllers in this section have been computed with the LMI solver included in the MATLAB Robust Control Toolbox [8] and using a personal computer with a two-core Intel i5 processor. The computation times corresponding to the control gain matrices $\widetilde{G}_\infty$, $\widetilde{G}_{\rm p}$ and $\widetilde{G}_{\rm cwp}$ are collected in Table 2.

To demonstrate the performance of the proposed controllers, a suitable set of numerical simulations has been carried out using the scaled North-South El Centro 1940 seismic record as a ground acceleration input (see Figure 2). The obtained absolute interstory-drift peak-values are displayed in Figure 3(a), where the black line with squares represents the uncontrolled response, the blue line with circles corresponds to the H_∞ controller $u(t)=\widetilde{G}_\infty\,x(t)$, the green line with triangles presents the response of the energy-to-peak controller $u(t)=\widetilde{G}_{\rm p}\,x(t)$ and the red line with asterisks describes the energy-to-componentwise-peak controller $u(t)=\widetilde{G}_{\rm cwp}\,x(t)$. The corresponding absolute control-effort peak-values are displayed in Figure 3(b) using the

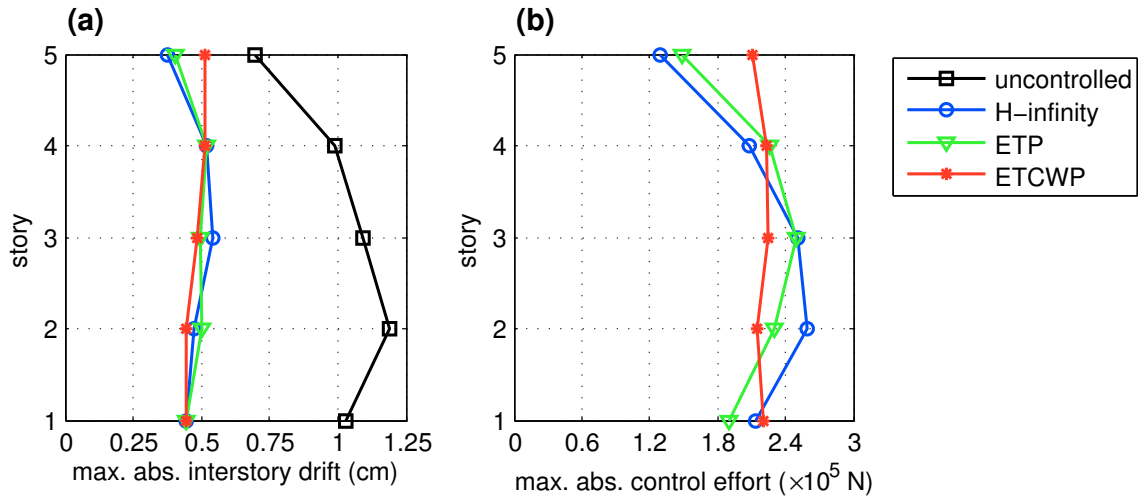

Figure 3: Response of the five-story building model corresponding to the scaled North-South El Centro 1940 seismic record for the uncontrolled configuration (black line with squares), the H_∞ controller (blue line with circles), the energy-to-peak controller (green line with triangles) and the energy-to-componentwise-peak controller (red line with asterisks). (a) Maximum absolute interstory drifts. (b) Maximum absolute control efforts.

story	1–5	6–11	12–14	15–17	18–19	20
mass ($\times 10^6$ Kg)	1.10	1.10	1.10	1.10	1.10	1.10
stiffness ($\times 10^8$ N/m)	8.62	5.54	4.54	2.91	2.56	1.72
relative damping	5%					

Table 3: Parameter values corresponding to the twenty-story building model.

same colors and symbols.

Looking at the matrices in (45), (46) and (47) it can be appreciated that the proposed design methods certainly produce different results. A quick inspection of the plots in Figure 3 reveals two clear facts: (i) the three controllers provide a good level of seismic protection with similar levels of control effort and (ii) the energy-to-componentwise-peak controller exhibits a particularly well-balanced behavior. The computation times in Table 2 also indicate two facts: (i) all the proposed design strategies demand very small computation times and, consequently, are suitable for control problems involving small-size building models and (ii) the shortest computation time is attained by the energy-to-peak controller.

Now we consider the twenty-story building model [10] corresponding to the mass, stiffness and damping parameters presented in Table 3. For this large-building problem, we compute an H_∞ controller by solving the LMI optimization problem $\mathcal{P}_\infty$ in (13) with the matrices A, B and E corresponding to the values in Table 3 and the controlled-output matrices in (44) with $n=20$ and the scaling factor $\alpha=10^{-8.0}$. We also design an energy-to-peak controller and an energy-to-componentwise-peak controller by solving the optimization problems $\mathcal{P}_{\rm p}$ in (18) and $\mathcal{P}_{\rm cwp}$ in (25), respectively, with the same matrices A, B, E and C used in the H_∞ design and the matrix D defined by $n=20$ and the scaling factor $\alpha=10^{-8.2}$. The computation times corresponding to this second set of controllers are collected in Table 4. To illustrate the seismic performance of the proposed design strategies in this harder control problem, the twenty-story building vibration response has been numerically simulated using also the scaled North-South El Centro 1940

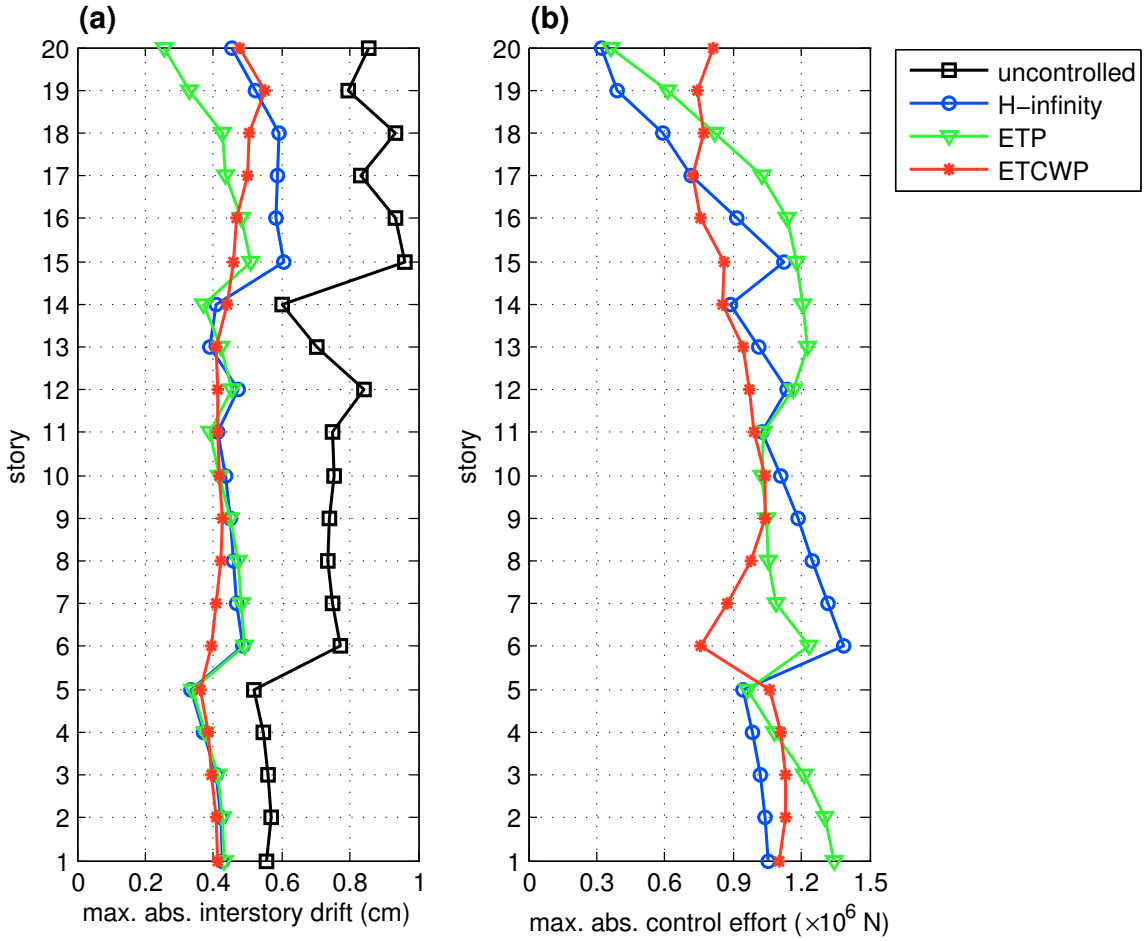

Figure 4: Response of the twenty-story building model corresponding to the scaled North-South El Centro 1940 seismic record for the uncontrolled configuration (black line with squares), the H_∞ controller (blue line with circles), the energy-to-peak controller (green line with triangles) and the energy-to-componentwise-peak controller (red line with asterisks). (a) Maximum absolute interstory drifts. (b) Maximum absolute control efforts.

controller	H_∞	ETP	ETCWP
computation time (s)	169.25	60.63	458.24

Table 4: Computation time (in seconds) corresponding to the H_∞, energy-to-peak (ETP) and energy-to-componentwise-peak (ETCWP) controllers designed for the twenty-story building model.

seismic record as ground acceleration input. The corresponding absolute interstory-drift and absolute control-effort peak-values are displayed in Figure 4(a) and Figure 4(b), respectively, using the same colors and symbols: black line with squares for the uncontrolled response, blue line with circles for the H_∞ controller, green line with triangles for the energy-to-peak controller and red line with asterisks for the energy-to-componentwise-peak controller.

The inspection of the plots in Figure 4 indicates that the same two facts observed in the five-story building problem still hold in the present case: (i) the three controllers provide a good level of seismic protection with similar levels of control effort and (ii) a particularly well-balanced behavior is exhibited by the energy-to-componentwise-peak controller. Looking at the

computation times in Table 4 and comparing with the data in Table 2, three main facts can be appreciated: (i) the best results are still attained by the energy-to-peak controller, (ii) all computation times are significantly larger and, (iii) a particularly larger computation time is required by the energy-to-componentwise-peak controller. The good computational performance of the energy-to-peak design strategy is a remarkable fact that converts this design methodology in an interesting option for vibration control of large structures. The observed increment of the computation times can be partially explained by the increase in the number of LMI variables. It should be observed that, in the general case of a n-story building with n actuation devices, the dimensions of the LMI variable matrices X and Y are $2n \times 2n$ and $n \times 2n$, respectively, and the total number of variables in the considered LMI optimization problems is $4n^2 + n$. This means that a controller design for a five-story building involves 105 LMI variables while a twenty-story building design requires 1620 LMI variables. Additionally, the larger computation time required by the energy-to-componentwise-peak design in the twenty-story building problem is consistent with the higher complexity of the corresponding LMI formulation.

5 CONCLUSIONS

In this paper, we have conducted a comparative study of three LMI-based controller design strategies for structural vibration control, paying special attention to the computational effectiveness in large-dimension problems. Together with the well-known H_∞ approach, the study includes the energy-to-peak and energy-to-componentwise-peak methodologies, which are particular cases of generalized H_2 designs. These three controller design strategies have been applied to synthesize active state-feedback controllers for the seismic protection of a five-story building and a twenty-story building, both equipped with a complete system of interstory actuation devices. The corresponding computation times have been considered to evaluate the computational effectiveness of the proposed design strategies and a proper set of numerical simulations has been carried out to assess the performance of the obtained controllers. In the five-story building problem, all the proposed design strategies have demanded computation times inferior to one second and the obtained controllers provide a good level of seismic protection with similar levels of control effort. In the twenty-story building problem, a good level of performance is also attained by all the controllers but an important increment of the computation times has been observed and significant differences can be appreciated in the computational effectiveness of the different design strategies. Overall, the following three main facts can be highlighted: (i) significantly shorter computation times are required by the synthesis of energy-to-peak controllers, (ii) a particularly well-balanced behavior is exhibited by the energy-to-componentwise-peak controllers and (iii) important computational difficulties should be expected when applying the considered controller design strategies to very-large-scale control problems.

ACKNOWLEDGMENTS

This work was partially supported by the Spanish Ministry of Economy and Competitiveness under Grant DPI2015-64170-R.

REFERENCES

[1] S. Boyd, L. El Ghaoui, E. Feron, and V. Balakrishnan. *Linear Matrix Inequalities in System and Control Theory*. SIAM, Philadelphia, USA, 1994.

[2] G.W. Housner, L.A. Bergman, T.K. Caughey et al. Structural control: Past, present, and future. *Journal of Engineering Mechanics*, 123(9):897–971, 1997.

[3] B.F. Spencer and S. Nagarajaiah. State of the art of structural control. *Journal of Structural Engineering*, 129(7):845–856, July 2003.

[4] S.Y. Chu, T.T. Soong, and A.M. Reinhorn. *Active, Hybrid and Semi-Active Structural Control*. Wiley, 2005.

[5] Y. Ikeda. Active and semi-active vibration control of buildings in Japan - Practical applications and verification. *Structural Control and Health Monotoring*, 16(7–8):703–723, 2009.

[6] H. Li and L. Huo. Advances in structural control in civil engineering in China. *Mathematical Problems in Engineering*, pages 1–23, 2010.

[7] A. Zečević and D.D. Šiljak. *Control of Complex Systems. Structural Constraints and Uncertainty*. Springer, 2010.

[8] G.J. Balas, R.Y. Chiang, A.K. Packard, and M.G. Safonov. *MATLAB^{TM} Robust Control Toolbox 3. User's Guide, Version 4.2*. The MathWorks, Inc., 3 Apple Hill Drive. Natick, MA 01760–20, USA, 2012.

[9] H. Du, J. Lam, and K.Y. Sze. Non-fragile H_∞ vibration control for uncertain structural systems. *Journal of Sound and Vibration*, 273(4–5):1031–1045, 2004.

[10] Y. Wang, J.P. Lynch, and K.H. Law. Decentralized H_∞ controller design for large-scale civil structures. *Earthquake Engineering and Structural Dynamics*, 38(3):377–401, 2009.

[11] J.M. Rossell, F. Palacios-Quiñonero, and J. Rodellar. Semi-decentralized output feedback H_∞ control strategy for large building structures. In *Proceedings of the 5th World Conference on Structural Control and Monitoring (5WCSCM)*, Shinjuku, Japan, July 2010.

[12] Y. Wang. Time-delayed dynamic output feedback H_∞ controller design for civil structures: A decentralized approach through homotopic transformation. *Structural Control and Health Monotoring*, 18(2):121–139, 2011.

[13] F. Palacios-Quiñonero, J. Rubió-Massegú, J.M. Rossell, and H.R. Karimi. Discrete-time static output-feedback semi-decentralized H_∞ controller design: an application to structural vibration control. In *Proceedings of the 2012 American Control Conference*, pages 6126–6131, Montréal, Canada, 2012.

[14] J. Rubió-Massegú, F. Palacios-Quiñonero, and J.M. Rossell. Decentralized static output-feedback H_∞ controller design for buildings under seismic excitation. *Earthquake Engineering and Structural Dynamics*, 41(7):1199–1205, 2012.

[15] F. Palacios-Quiñonero, J. Rubió-Massegú, J.M. Rossell, and H.R. Karimi. Feasibility issues in static output-feedback controller design with application to structural vibration control. *Journal of the Franklin Institute*, 351(1):139–155, 2014.

[16] M.A. Rotea. The generalized H_2 control problem. *Automatica*, 29(2):373–385, 1993.

[17] H. Du and J. Lam. Energy-to-peak performance controller design for building via static output feedback under consideration of actuator saturation. *Computers and Structures*, 84(31–32):2277–2290, 2006.

[18] W. Zhang, Y. Chen, and H. Gao. Energy-to-peak control for seismic-excited buildings with actuator faults and parameter uncertainties. *Journal of Sound and Vibration*, 330(4):581–602, 2011.

[19] F. Palacios-Quiñonero, J. Rubió-Massegú, J.M. Rossell, and H.R. Karimi. Vibration control for adjacent structures using local state information. *Mechatronics*, 24(4):336–344, 2014.

[20] F. Palacios-Quiñonero, J. Rubió-Massegú, J.M. Rossell, and H.R. Karimi. Optimal design of complex passive-damping systems for vibration control of large structures: an energy-to-peak approach. *Abstract and Applied Analysis*, pages 1–9, 2014.

[21] J.N. Yang, S. Lin, and F. Jabbari. Linear multi-objective control strategies for wind-excited buildings. *Journal of Engineering Mechanics*, 130(4):471–477, 2004.

[22] A.K. Chopra. *Dynamics of Structures. Theory and Applications to Earthquake Engineering*. Prentice Hall, Upper Saddle River, New Jersey, USA, 3rd edition, 2007.

[23] N. Kurata, T. Kobori, M. Takahashi, N. Niwa, and H. Midorikawa. Actual seismic response controlled building with semi-active damper system. *Earthquake Engineering and Structural Dynamics*, 28(11):1427–1447, 1999.

ECCOMAS Congress 2016
VII European Congress on Computational Methods in Applied Sciences and Engineering
M. Papadrakakis, V. Papadopoulos, G. Stefanou, V. Plevris (eds.)
Crete Island, Greece, 5–10 June 2016

A SMART BASE RESTRAINT FOR WIND TURBINES TO MITIGATE UNDESIRED EFFECTS DUE TO STRUCTURAL VIBRATIONS

N. Caterino[1], **C.T. Georgakis** [2], **M. Spizzuoco** [3] **and A. Occhiuzzi**[4]

[1] Department of Civil Engineering, University of Naples "Parthenope"
Centro Direzionale di Napoli, Isola C4, 80143, Naples, Italy
nicola.caterino@uniparthenope.it

[2] Department of Civil Engineering, Technical University of Denmark (DTU)
Building 118, 2800 Kgs. Lyngby, Denmark
cg@byg.dtu.dk

[3] Department of Structures for Engineering and Architecture, University of Naples Federico II
Via Claudio 21, 80125, Naples, Italy
spizzuoc@unina.it

[4] Construction Technologies Institute, National Research Council (CNR)
Viale Lombardia, 49, 20098, San Giuliano Milanese (MI), Italy
occhiuzzi@itc.cnr.it

Keywords: Semi-Active Control, Wind Turbine, Magnetorheological Damper.

Abstract. *Concerns in the last decades of the negative impact of the use of fossil fuels on the environment has lead to a boom in the production of wind turbines. To take advantage of the smoother stronger winds at height, wind turbine heights are progressively increasing. This has led to an increased demand to control tower forces. The application of a semi-active (SA) control system is herein proposed and discussed. Its aim is to limit bending moment demand at the base of a wind turbine by relaxing the base restraint of the turbine's tower, without increasing the top displacement. This is done thanks to the sharp increase of the dissipated energy in selected intervals of time and an adaptive change in tower dynamic properties. This SA control system reproduces a variable restraint at the base that changes in real time its mechanical properties according to the instantaneous response of the turbine's tower. This smart restraint is made of a central smooth hinge, elastic springs and SA magnetorheological dampers driven by a control algorithm properly designed for the specific application. A commercial 105 m tall wind turbine has been assumed as a case study. Several numerical simulations have been performed with reference to an extreme load, aimed at establishing a procedure for the optimal calibration of the control algorithm according to the specific case, finally proving the actual potential of the proposed control technique in reducing the structural demand with respect to the "fixed base" structure.*

1 INTRODUCTION

Wind turbine manufacturers have become ever more interested in methods for reducing or limiting tower base moments for turbines of increasing height. There are two main reasons for this. First, the tower diameters at the base are increasing beyond the point where they can be fabricated off-site and shipped to the location of installation. This significantly increases construction costs and complexity. Second, the tower diameters and associated base moments of newer wind turbines far exceed those of existing wind turbines that the newer ones hope to replace. Therefore, existing foundations cannot be utilized and new or strengthened foundations need to be constructed.

The maximum base moments of a wind-turbine are generated by few very specific, and in some cases improbable, load cases. These include the load cases which involve extreme gusts of wind combined with emergency shut-down procedures and extreme wind loading in a parked configuration. All of the extreme load cases generate maximum expected tower base moments via short duration impulse loading – something which cannot be combated using traditional damping devices. Damping is generally considered ineffective for impact type loading. Instead, a variable tower stiffness and damping approach needs to be followed. Therefore, in this paper, the concept of an adaptive wind turbine tower is examined, where the adaptation is realized through the implementation of a semi-active (SA) control system.

Chen and Georgakis [1] performed an experimental analysis of a 1/20-scale wind tower model equipped with a passive rolling-ball damper to reduce vibrations. Such damper consists of a glass container placed at the top of the model and having one or more steel balls inside. Different configurations have been tested, changing the geometry of the container (one or two layers) and the number of balls (one to six) placed inside, showing a significant reduction of the peak value and standard deviation of top displacement and base bending moment. The same authors [2] tested the same model using water rather than steel balls inside the glass container, i.e. realizing a spherical tuned liquid damper. The optimal degree of filling with water (1-2% of the total generalized mass of the system) has been found as leading to the maximum reduction of structural demand.

About active/semi-active control strategies from literature related to wind turbines, Karimi et al. [3] and Luo et al. [4] propose a SA control technique for floating wind turbines with TLCD. This device, generally used as a passive damper, turns into a SA device using a controllable valve. The orifice opening is real time adapted according to the structure response and loading conditions, with a control logic based on a H_∞ feedback methodology. Lackner and Rotea [5] investigate the effectiveness of an optimal passive TMD and of a hybrid mass damper (HMD, i.e. a TMD improved with the addition of a controlled force actuator) in reducing fatigue loads due to bending moment at the base of the tower, showing a percentage reduction of about 10% and 30% respectively due to each of the two proposed systems. Kirkegaard et al. [6] have been the first to explore the use of magnetorheological (MR) dampers to control a wind turbine, assuming such type of smart device to be installed, in a vertical position, between the base and the top of the tower. Even hard to be implemented in a real case, the numerical simulations show good results. Experimental results are also made available by the authors, unfortunately referred to the passive use (constant voltage fed to the MR damper) of the device only.

The authors recently proposed a SA control system based on the application of MR devices to realize a time-variant base restraint whose 'stiffness' can be driven in real time by a properly written control logic [7]. The high promptness of response of the SA control chain based on the use of MR dampers and of an appropriate electronic and power equipment has been experimentally demonstrated [8], showing that unavoidable delays however are always less than 10

ms, thus negligible compared to the long period of the flexible structures under examination. This is one of the aspects strongly encourage the use of such technology for the application in question. The controller has to be programmed to instantaneously calibrate the MR devices installed at the base of the tower in order to reduce the base bending moment, relaxing in selected intervals of time the base restraint. Again, the control logic has to hold the top displacement within acceptable values so as to avoid significant, detrimental second order effects. At the laboratory of the Denmark Technical University (DTU) in Copenaghen, some shaking table tests of a wind turbine tower model semi-actively controlled as above has been recently performed by the authors. After the formulation of the above idea, a finite element model of the structure has been calibrated so as to develop several numerical simulations addressed to optimally calibrate the control logic properly designed for such kind of applications.

2 A VARIABLE BASE RESTRAINT FOR WIND TURBINE TOWERS: CONTROL ALGORITHM

A smart restraint at the base of high-rise wind turbine towers is proposed with the aim of reducing wind induced structural demand by exploiting magnetorheological devices. This is schematically shown in Figure 1, where the uncontrolled wind turbine, fully restrained at the base, is modeled as a single degree of freedom dynamic system (Figure 1(a)), having top mass m, stiffness k_T and inherent damping c_T. In order to control the structural demand, the authors proposed to replace the perfectly rigid base restraint with a controllable one that is able to instantaneously become more or less "stiff", during the motion. Figure 1(b) just sketches the materialization of this idea by a smooth hinge, with a rotational spring (of stiffness k_ϕ) and a rotational variable damper whose damping constant c_ϕ can be driven in real time by a control algorithm. The same result can be obtained in practice by mounting two vertical linear springs (k_s) placed at a certain distance (l_s) from the hinge and two vertical SA dampers (c_d) at a distance l_d from the central hinge (Figure 1(c)).

SA MR dampers were considered as smart devices within the proposed control system: when a low value is imposed to the base damping, the base restraint is less 'stiff', so that the structure's restraint is able to relax by converting its potential energy into kinetic energy, and the bending moment at the base is reduced. A direct consequence of controlling the demand of base bending stress could be an increase of top displacement demand; therefore, the SA base control system was thought to reduce base stress, by restraining the increase of top displacements within certain limits to control second order effects. A specific bang-bang control algorithm has been formulated by the authors [7] to instantaneously decide the system's base configuration: it switches back and forth from an "OFF" state (intensity of current $i = i_{\min}$, i.e. the minimum current set to be given to the dampers) to an "ON" state ($i = i_{\max}$, i.e. the maximum assumed value for the current) according to a logic aiming to control both the base stress and the top displacement. Therefore, the control algorithm was so formulated:

$$\begin{aligned}
&1)\ \text{if } |\pm(t)| < \pm_{\lim} && && && \rightarrow i(t) = i_{\max}\\
&2)\ \text{if } |\pm(t)| \geq \pm_{\lim} && \text{and } |x(t)| < x_{\lim} && && \rightarrow i(t) = 0\\
&3)\ \text{if } |\pm(t)| \geq \pm_{\lim} && \text{and } |x(t)| \geq x_{\lim} && \text{and } x(t)\cdot\dot{x}(t) > 0 && \rightarrow i(t) = i_{\max}\\
&4)\ \text{if } |\pm(t)| \geq \pm_{\lim} && \text{and } |x(t)| \geq x_{\lim} && \text{and } x(t)\cdot\dot{x}(t) \leq 0 && \rightarrow i(t) = 0
\end{aligned} \tag{1}$$

where $\sigma(t)$, $x(t)$ and $\dot{x}(t)$ are respectively the value of stress at the base, top displacement and top velocity at the instant of time t. In other words, the controller keeps 'stiffer' the base restraint until the stress exceeds the limit value σ_{lim} (expression 1) of Eq. (1)), whereas 'relaxes' it ("OFF" state of the dampers) when this limit is overpassed and the displacement falls within

the limit of acceptability x_{lim} (expression 2) of Eq. (1)). When both stress and displacement are beyond the respective threshold values, the controller switches "ON" the dampers if the displacement is going towards a larger value (so trying to damp or invert the displacement's trend; expression 3) of Eq. (1)), otherwise it switches "OFF" the MR devices to make them collaborating to both stress and displacement reduction. Figure 2 schematically describes the above defined logic: the decision of the controller (switch "ON" or switch "OFF") depends on the occurrence of each of the four possible combinations regarding the value of base stress and top displacement. The application of the proposed control algorithm requires the definition of rational criteria to optimally calibrate the parameters involved in ($i_{\min}$, $i_{\max}$, σ_{lim} and x_{lim}). A large numerical campaign has been performed with reference to a case study structure, aiming to investigate the role each parameter has regarding the structural response, and to learn a possible procedure to calibrate them aiming at achieving the maximum reduction of stresses and displacements.

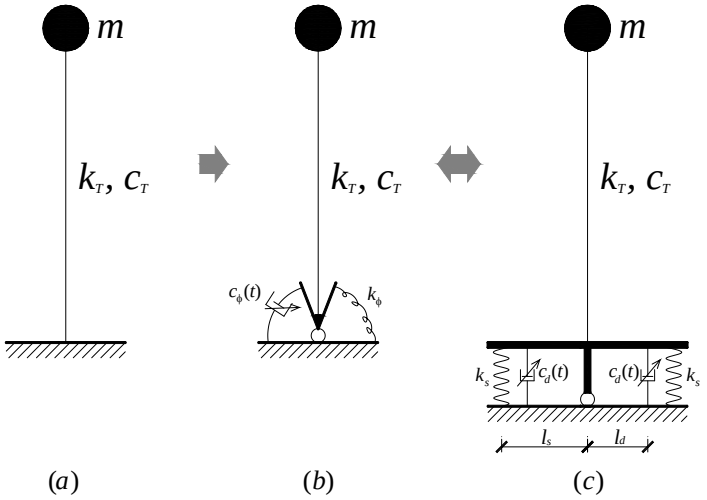

Figure 1: Basic idea of SA control of a wind turbine via MR dampers.

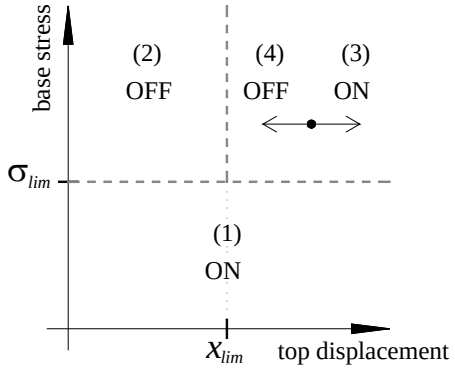

Figure 2: The logic behind the controller (symbols refer to Eq. (1)).

3 CALIBRATION OF THE SA CONTROLLER: A CASE STUDY

A possible calibration procedure is herein proposed to provide the optimal choice of values to be assigned to the parameters involved in the control algorithm. The first step is generating a finite element model of the structure to be examined, able to reproduce both fixed base (FB) and SA controlled configurations. With reference to a given wind load, the structural response in the FB case has to be determined. Then a wide number of SA numerical simulations has to

be designed and performed. Analyzing the results using a constrained optimization approach allows to single out the optimal configuration of the controller able to achieve the maximum reduction of base stress while not causing increasing of top displacement in respect to the FB case. This procedure is practically applied in the following with reference to a specific case study.

3.1 Case Study

The case study structure is a 1/20-scale structural model of a prototype real wind turbine. The reference real structure is a 3 MW wind turbine with horizontal power transmission axle, 102.4 m tall, with a variable hollow circular cross section whose external diameter is variable from 2.30 m (top) to 4.15 m (bottom). Chen and Georgakis [1] demonstrated its dynamic equivalence (in terms of equivalent flexural stiffness) with a single degree of freedom (SDOF) structural system made up of a tapered tubular cantilever beam with a concentrated mass at the top. The scaled mock-up structure is characterized by a 5.12 m high vertical tube with uniform cross section Φ133/4 (133 mm is the external diameter, 4 mm the thickness), and a lumped mass of 280 kg placed at the top (Figure 3).

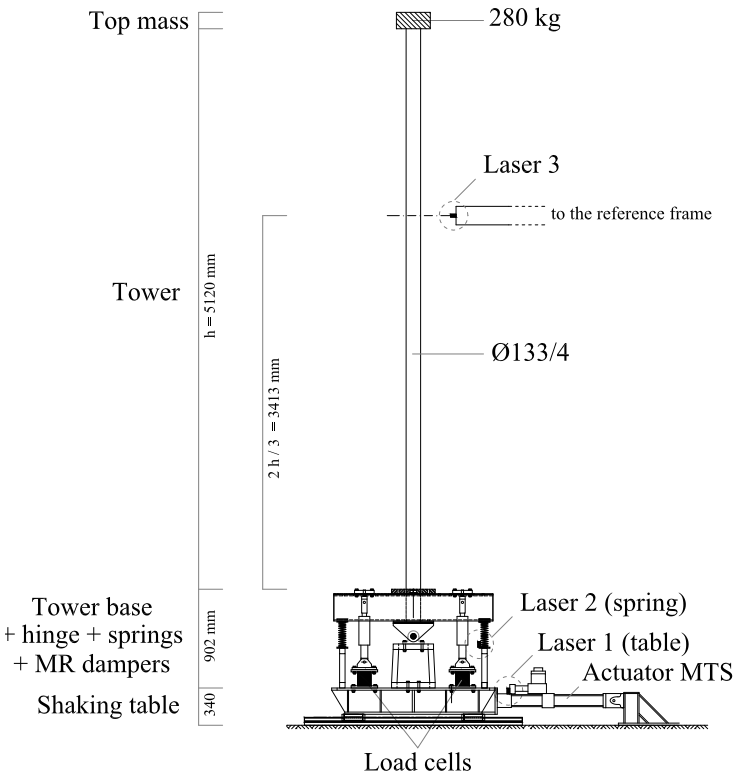

Figure 3: Case study model and experimental setup at the DTU laboratory.

The base of the model is highly stiff and is supported in the middle by a cylindrical steel hinge. On both sides of the base, one cylindrical spring (89 kN/m stiff) and one MR damper are installed. The assembly “elastic springs + SA MR dampers”, placed in parallel at the base of the tower, just represents the smart base restraint herein proposed to control the dynamic behavior of the structure. An extreme operating gust loading has been considered in the following as reference wind action: a sharp increase, then decrease in wind speed within a short period of time. Chen and Georgakis [1] defined an equivalent base acceleration time history

(Figure 4), that is the base input that would provide the same top mass response of the real fixed base structure subjected to the wind action.

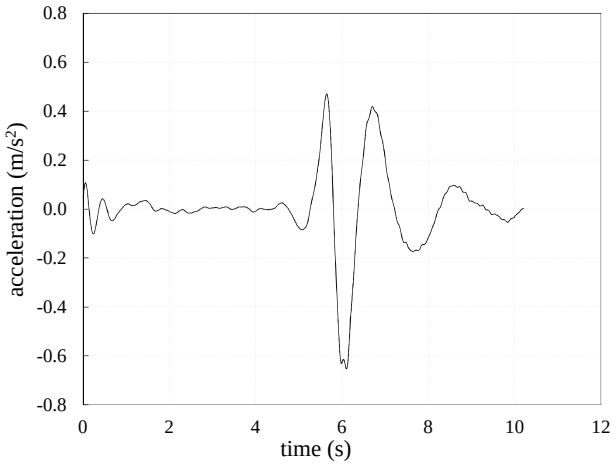

Figure 4: Equivalent base acceleration time history for the wind load case.

3.2 Numerical model

A finite element model has been generated in Matlab environment to simulate the dynamic behavior of the case study structure. It consists in 37 elements: 36 elements simulate the tower with uniform diameter (133 mm) and thickness (4 mm) along the height, while the last element (37^{th}) is more rigid and represents the connection of the top of the tower to the barycenter of the nacelle. The rotor and the aerodynamics have not been included in the model due to its complexity, and the nacelle and its internal components are represented by a concentrated mass at the top of the structure, with no dynamic interaction considered. Such mass is added in the global mass matrix at the translational degree of freedom at the top of the tower.

The base support has been modeled as in Figure 5, that is by a rotational spring k_{spring} and a Maxwell element (representing the MR dampers) working in parallel. The value for k_{spring} (7.5e4 Nm/rad) has been easily derived known the stiffness of the two linear springs and their distance from the center of rotation (hinge).

The Maxwell element, as known, consists of a spring $k_{Maxwell}$ and a linear viscous damper $c_{Maxwell}$ in series. The controllable part of this device is represented by the constant $c_{Maxwell}$, while $k_{Maxwell}$ has been simply assumed high enough (1.5e6 Nm/rad) so as to behave like a rigid link. Two different values of $c_{Maxwell}$ (c_{on}, c_{off}) have been determined so as to reproduce the dissipative capability of MR dampers respectively in the "ON" and "OFF" states. These two opposite configurations of the MR dampers are assumed to be those of the experimental campaign cited above, respectively corresponding to $i=i_{min}=0$ A and $i=i_{max}=1$ A. The MR dampers considered to calibrate the Maxwell device properties are those adopted for the test at DTU also [9]. Suitable numerical models for such devices are described in [10]. The values of c_{on}, c_{off} have been experimentally calibrated and resulted to be c_{on}=1e7 Nms/rad and c_{off}=2e3 Nms/rad.

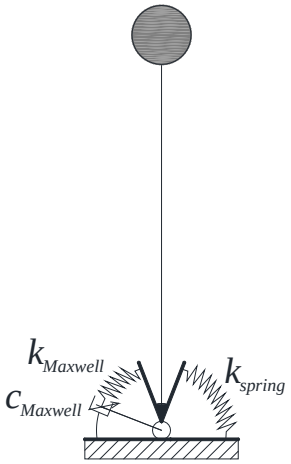

Figure 5: Representation of the base restraint within the FE model of the SA controlled structure.

3.3 Numerical simulations

A number of 100 numerical tests have been performed with reference to the above FEM model in SA configuration. This is the total number of different combinations of stress (σ_{lim}) and displacement (x_{lim}) limits that have been tested, chosen within the ranges [5, 50] MPa and [5, 50] mm with a step of 5 MPa and 5 mm, respectively. Performance indices have been assumed to quantitatively summarize the structural response in the examined cases.

These allow to compare the effectiveness of the SA control strategy for each of the above settings for the controller, then to select the optimal calibration of the latter. They are:

- ratio of maximum bending stress σ_{max} to limit value σ_{lim} assumed to calibrate the controller (σ_{max} / σ_{lim});
- ratio of maximum bending stress in SA to fixed base (FB) conditions (σ_{max} / $\sigma_{max,FB}$);
- ratio of maximum top displacement in SA to FB conditions (x_{max} / $x_{max,FB}$).

Moreover, to better interpret the results, the following two additional information have been gathered from each simulation performed:

- total amount of time in which the MR damper has been switched off by the controller (t_{off});
- total number of switches (on→off and vice versa) commanded to the variable device (n_{sw}).

The ratio σ_{max} / σ_{lim} is assumed so as to check if and how the controller has been able to limit the bending stress to the desired value σ_{lim}, while the ratio x_{max} / x_{lim} has not been assumed as parameter for comparison because it is not significant to the same extent given that x_{lim} has a reduced impact on the controller operation. The indices σ_{max} / $\sigma_{max,FB}$ and x_{max} / $x_{max,FB}$ express the effectiveness of the controller in reducing the structural response with respect to the FB conditions. Values less than one are desired, in fact they reflect the main purpose of the control strategy. The indices t_{off} and n_{sw} give a quantitative idea about the activity of the MR damper during each test. When the smart device is set to "ON", it is not very far from acting as a rigid link. Therefore, the above t_{off} gives also a measure of the overall duration of the dissipation phase.

4 DISCUSSION ABOUT RESULTS AND CONCLUSIONS

The constrained optimization of the controller is performed according to the condition:

$$\min\left(\sigma_{max} / \sigma_{max,FB}\right) \quad \text{subject to} \quad x_{max} / x_{max,FB} \leq 1 \tag{2}$$

that is, aiming to achieve the greatest reduction of the base stress (objective function) and, at the same time, a top displacement (constraint function) no higher than that in uncontrolled FB conditions.

Analyzing diagrams (a) in Figure 6, it emerges that the SA control of the case study wind turbine is always beneficial in terms of reduction of base stress with respect to the fixed base scheme. Considered the whole set of examined cases, the maximum base stress reduction results to be around 80%, and corresponds to the case (σ_{lim}, x_{lim})=(5 MPa, 25 mm). The maximum top displacement reduction is about 35%, for (σ_{lim}, x_{lim})=(10 MPa, 15 mm). The worst case, i.e. that corresponding to the maximum amplification of x (+40%) with respect to the FB case is (σ_{lim}, x_{lim})=(35 MPa, 50 mm).

Higher operation of the SA controller for smaller value of σ_{lim}, as expected, can be deduced from Figure 6(d). Figure 6(c) instead highlights that response values in terms of maximum base stress σ_{max} are practically always included in the interval [σ_{lim}, $2\sigma_{lim}$], with the exception of those cases where both very small values are fixed both for σ_{lim} and x_{lim}.

Actually, about half (53%) of the examined configurations of the controller leaded to undesired response in top displacement, i.e. values of x_{max} larger than $x_{max,FB}$. Figure 7 helps to understand better which are the combinations of limit values σ_{lim} and x_{lim} that give undesired response in displacement. It results that, when values of σ_{lim} greater than 30 MPa are adopted (i.e. roughly greater than half of the $\sigma_{max,FB}$ value), there is no chance to reduce displacements in respect to the FB case. The reason is related to the fact that in such cases the SA operations are really limited, as from Figure 6(d) clearly emerges. Therefore, the dissipation phases are concentrated in much small intervals of time, not effective in reducing significantly the response in displacement. Vice versa, when smaller values of σ_{lim} are used (i.e. less than 30 MPa), the reduction or amplification of x_{max} in respect to $x_{max,FB}$ also depends on the assumed value for x_{lim}. Also in this case, it seems that selecting values for x_{lim} less than $0.5x_{max,FB}$ leads always to good results in terms of displacement response.

According to the criterion defined in the condition above, the optimal configuration of the control algorithm corresponds to the case (σ_{lim}, x_{lim})=(5 MPa, 25 mm) since it leads to the maximum response reduction (about 80%) in base stress, and also to a reduction (about 30%) of displacement in respect to the FB case.

Therefore, preliminary conclusions about a possible way to optimally calibrate the controller could be drawn suggesting to assume, for σ_{lim} and x_{lim}, values respectively around $0.1\sigma_{max,FB}$ and $0.5x_{max,FB}$. Moderately low values of σ_{lim} (25-50% of $\sigma_{max,FB}$) leaded to increased top displacements, even higher than the reference value $x_{max,FB}$. A trend reversal for values of σ_{lim} even more smaller (10-20% of $\sigma_{max,FB}$) has been registered, leading them to significant reduction of both base stress and top displacement, as said above, due to the higher operation of the controller and, consequently, to the sharp increase of dissipated energy due to the larger rocking of the base.

The above results cannot be directly generalized, since clearly dependent on the specific wind load case and turbine model assumed for the analyses. On the contrary, the conceptual findings they allowed to gather are always valid and will be exploited by the authors to program further investigations aimed at consolidating those outcomes and to finally determine the practical implications they could have. Future further research about this topic will have to consider a larger set of wind load cases, different for magnitude, duration and frequency content, to understand if and how the optimal calibration of the control algorithm depends on the characteristics of the external action.

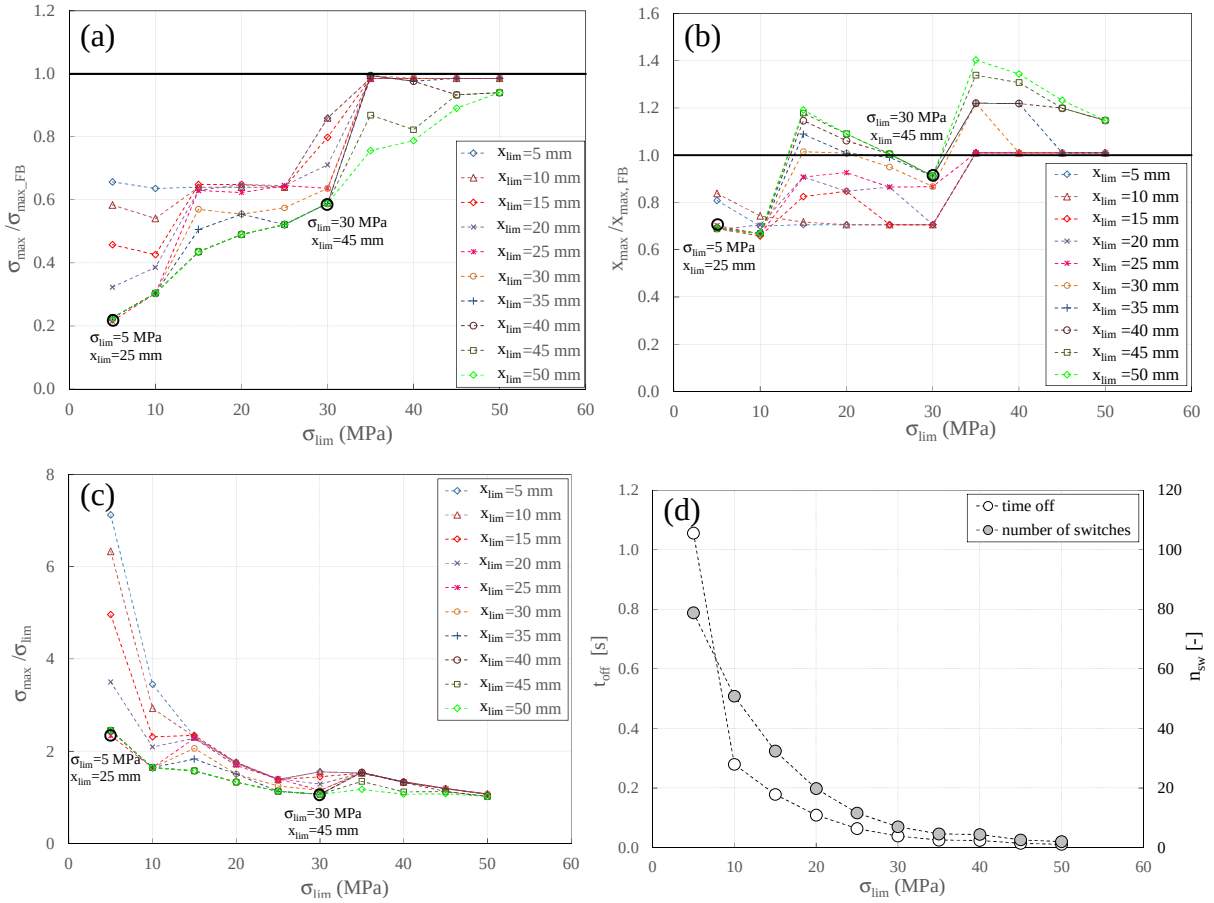

Figure 6: Performance indices for the 100 configurations of the SA controller.

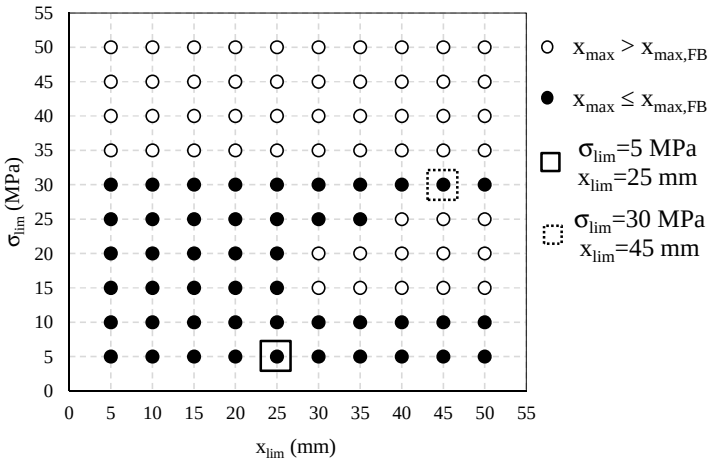

Figure 7: Configurations of the controller corresponding to acceptable (black filled circle) and excessive (empty circle) top displacement response.

ACKNOWLEDGEMENTS

The presented activity has been partially funded by the Italian consortium Reluis in the framework of the 2015 and 2016 research projects supported by the Italian Department for Civil Protection. This support is gratefully acknowledged.

REFERENCES

[1] J. Chen, C.T. Georgakis, Tuned rolling-ball dampers for vibration control in wind turbines. *Journal of Sound and Vibration*, **332**, 5271-5282, 2013, dx.doi.org/10.1016/j.jsv.2013.05.019.

[2] J. Chen, C.T. Georgakis, Spherical tuned liquid damper for vibration control in wind turbines. *Journal of Vibration and Control*, **21**(10), 1875-1885, 2015, doi: 10.1177/1077546313495911.

[3] H.R. Karimi, M. Zapateiro, N. Luo, Semiactive vibration control of offshore wind turbine towers with tuned liquid column dampers using H∞ output feedback control. *Proceedings of the IEEE International Conference on Control Applications*, Yokohama, Japan, 2010.

[4] N. Luo, C.L. Bottasso, H.R. Karimi, M. Zapateiro, Semiactive Control for floating offshore wind turbines subject to aero-hydro dynamic loads. *Proceedings of the International Conference on Renewable Energies and Power Quality*, Las Palmas de Gran Canaria, Spain, 2011.

[5] M. Lackner, M. Rotea, Structural control of floating wind turbines. *Mechatronics*, **21**, 704-719, 2011, doi:10.1016/j.mechatronics.2010.11.007.

[6] P.H. Kirkegaard, S.R.K. Nielsen, B.L. Poulsen, J. Andersen, L.H. Pedersen, B.J. Pedersen, *Semi-active vibration control of a wind turbine tower using an MR damper*. H. Grundmann, G.I. Schuëller, Rotterdam: Balkema Publishers, A.A. / Taylor & Francis The Netherlands, 1575-1580, 2002.

[7] N. Caterino, C.T. Georgakis, F. Trinchillo, A. Occhiuzzi, A semi-active control system for wind turbines. In: N. Luo, Y. Vidal, L. Acho, *Wind Turbine Control and Monitoring*, Springer International Publishing, 375-407, Advances in Industrial Control, 2014, doi: 10.1007/978-3-319-08413-8_13.

[8] N. Caterino, M. Spizzuoco, A. Occhiuzzi, Promptness and dissipative capacity of MR dampers: experimental investigations, *Structural Control and Health Monitoring*, 2013, 20(12), 1424–1440, doi: 10.1002/stc.1578.

[9] N. Caterino, Semi-active control of a wind turbine via magnetorheological dampers. *Journal of Sound and Vibration*, **345**, 1-17, 2015, doi:10.1016/j.jsv.2015.01.022.

[10] N. Caterino, M. Spizzuoco, A. Occhiuzzi, Understanding and modelling the physical behaviour of magnetorheological dampers for seismic structural control. *Smart Material and Structures*, **20**(6), 2011, doi:10.1088/0964-1726/20/6/065013.

ECCOMAS Congress 2016
VII European Congress on Computational Methods in Applied Sciences and Engineering
M. Papadrakakis, V. Papadopoulos, G. Stefanou, V. Plevris (eds.)
Crete Island, Greece, 5–10 June 2016

NONLINEAR DYNAMIC BEHAVIOUR OF BASE-ISOLATED BUILDINGS WITH THE FRICTION PENDULUM SYSTEM SUBJECTED TO NEAR-FAULT EARTHQUAKES

F. Mazza[1] **and S. Sisinno**[2]

[1]Dipartimento di Ingegneria Civile, Università della Calabria
Via P. Bucci, 87036 Rende (CS), Italy
fabio.mazza@unical.it

[2]Dipartimento di Ingegneria Civile, Università della Calabria
Via P. Bucci, 87036 Rende (CS), Italy
sandro_sisinno@libero.it

Keywords: R.c. base-isolated structures, Friction pendulum system, Torsional effect, Residual displacement, Uplift, Near-fault earthquakes, Nonlinear dynamic analysis.

Abstract. *In spite of the fact that avant-garde sliding bearings have been proposed, the application of the single friction pendulum (FP) bearing is increasing due to its conceptual simplicity; yet there are still important aspects of its behaviour that need further attention. More specifically, the FP system presents spatial variation of friction coefficient, depending on the sliding velocity of the FP bearings. Moreover, the frictional force and restoring stiffness during the sliding phase are proportional to the axial load. Long duration intense velocity pulses in the horizontal direction and high values of the ratio between vertical and horizontal peak ground acceleration are expected for near-fault earthquakes. Torsion with residual displacement and uplift of the FP system need to be better understood for base-isolated structures located in near-fault areas. To this end, a numerical investigation is carried out with reference to a six-storey reinforced concrete (r.c.) framed building, characterized by an L-shaped plan with wings of different length and setbacks at different heights along the main in-plan directions. Twelve base-isolated test structures are designed in line with the Italian seismic code, considering (besides the gravity loads) the horizontal seismic loads acting alone or in combination with the vertical ones. Three design values of the radius of curvature for the FP system and two in-plan distributions of dynamic-fast friction coefficient for the FP bearings, ranging from a constant value for all isolators to a different value for each, are assumed. A nonlinear force-displacement law of the FP bearings in the horizontal direction, depending on sliding velocity and axial load, is considered, while a gap model takes into account the vertical uplift of the FP bearings. The nonlinear seismic analysis is performed on two sets of seven near-fault earthquakes, both sets with significant horizontal or vertical components selected and normalized on the basis of the design hypotheses adopted for the test structure.*

1 INTRODUCTION

The friction pendulum (FP) system is one of the most in-demand techniques for the seismic isolation of buildings [1], where the geometry and gravity allow a minimization of torsion and a self-centring of the base-isolation FP system for a wide range of frequency inputs [2]. However, the (low) constant isolation frequency, proportional to the curvature of the sliding surface, may induce resonance of base-isolated structures if it is close to the predominant vibration period of near-fault ground motions [3]. Specifically, fling-step and forward-directivity in near-fault areas can produce long duration pulses of intense velocity in the horizontal direction [4, 5], amplifying the displacement and inducing torsional and re-centring problems [6, 7]. On the other hand, since the response of the FP system during the sliding phase is strongly influenced by the axial load, amplification of torsional demand and residual displacement and uplift of the FP bearings may also be induced by the high frequency vertical component of near-fault earthquakes [8-10]. This vertical motion is characterized by peak ground acceleration higher than the horizontal one and closer in time for decreasing values of distance from the fault [11, 12].

In order to verify the occurrence of torsion with residual displacement and uplift of the FP system for base-isolation of structures located in near-fault areas, this study aims to investigate the following two effects in FP bearings: friction variability, as a function sliding velocity; friction force and restoring stiffness during the sliding phase, proportional to the axial load variation. To this end, a six-storey reinforced concrete (r.c.) framed building, characterized by an L-shaped plan with wings of different length and setbacks at different heights along the in-plan X (i.e. one setback, at the third-storey) and Y (i.e. two setbacks, at the second- and fourth-storey) principal directions is considered. In detail, twelve base-isolated structures are designed in line with the Italian seismic code (NTC08, [13]), with the horizontal seismic loads acting alone or in combination with the vertical ones. Furthermore, two in-plan distributions of low-type friction properties, ranging from a constant value for all isolators to a different value for each, are designed for three low-to-medium design values of the radius of curvature of the FP bearings. Two sets of seven near-fault earthquakes, each with significant components in the horizontal or vertical direction, are selected from the *Pacific Earthquake Engineering Research center database* (PEER, [14]) and normalized with the design hypotheses adopted for the test structure (i.e. medium-risk seismic region and stiff site).

2 LAYOUT AND DESIGN OF THE BASE-ISOLATED BUILDINGS

A six-storey r.c. office building base-isolated with the FP system, characterized by an L-shaped plan with wings of different length (Figure 1a) and setbacks at different heights (Figure 1b), is considered as test structure. It is designed in line with NTC08 [13] and besides the gravity loads, the horizontal seismic loads are assumed to act alone or in combination with the vertical ones. The following design assumptions are considered: elastic response of the superstructure (i.e. behaviour factor for the horizontal seismic loads, q_H=1; behaviour factor for the vertical seismic loads, q_V=1); stiff site (i.e. subsoil class B); medium-risk seismic region (i.e. peak ground accelerations: $PGA_{H,LS}$=0.16gx1.2=0.19g and $PGA_{V,LS}$= 0.08g, at the life-safety limit state for the superstructure; $PGA_{H,CP}$=0.21gx1.2=0.25g and $PGA_{V,CP}$=0.13g, at the collapse prevention limit state for the base-isolation system). The gravity loads used in the design are represented by a dead load of 6.7 kN/m^2 and a live load of 2.0 kN/m^2, on all floors, and a perimeter masonry-infills of 2.7 kN/m^2, on the first five floors. A cylindrical compressive strength of 25 N/mm^2 for the concrete and a yield strength of 450 N/mm^2 for the steel are assumed for the r.c. frame members, whose cross sections are reported in Tables 1 and 2.

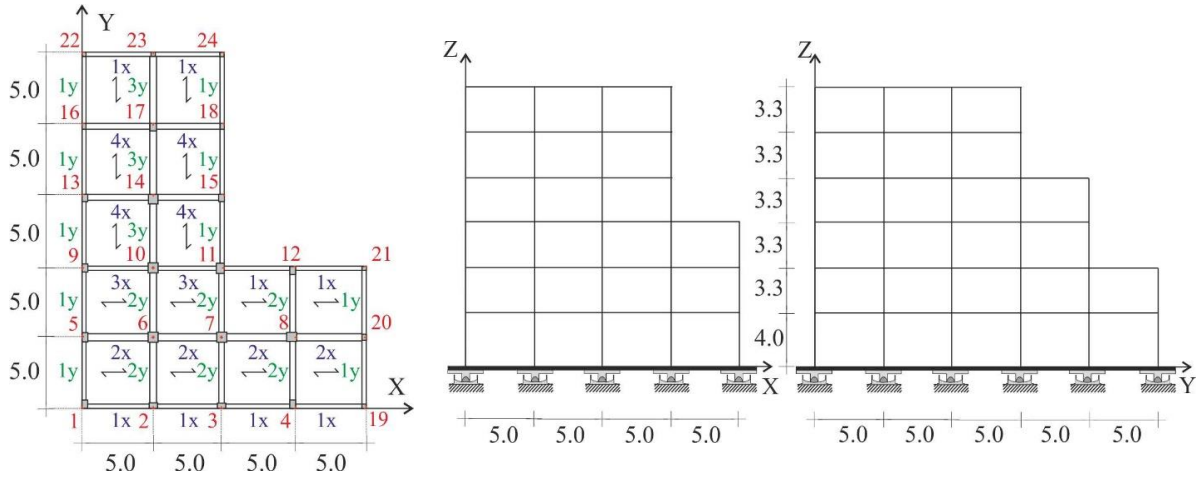

(a) Plan. (b) Elevations.

Figure 1: Base-isolated test structure (units in m).

	Floor level					
Beam	1	2	3	4	5	6
1x	30×60	30×60	30×60	30×60	30×60	30×60
2x	50×21	50×21	50×21	50×21	50×21	50×21
3x	30×55	30×55	30×55	30×55	30×55	30×55
4x	40×65	40×65	40×65	40×65	-	-
1y	30×60	30×60	30×60	30×60	30×60	30×60
2y	40×65	40×65	40×65	40×65	40×65	40×65
3y	50×21	50×21	50×21	50×21	50×21	50×21

Table 1: Cross-sections of r.c. beams (units in cm).

	Storey					
Column	1	2	3	4	5	6
1	40×60	35×55	30×50	30×45	30×40	30×35
2	60×40	50×35	50×30	40×30	30×30	30×30
3	60×40	50×35	50×30	40×30	30×30	30×30
4	40×60	35×55	30×50	30×45	30×40	30×35
5	40×60	35×50	35×40	30×40	30×30	30×30
6	70×70	65×65	60×60	50×50	40×40	30×30
7	70×70	65×65	60×60	50×50	40×40	30×30
8	60×60	55×55	50×50	45×40	40×30	35×30
9	40×60	35×50	30×50	30×40	30×30	30×30
10	70×70	65×65	60×60	50×50	40×40	30×30
11	55×70	50×65	45×60	40×50	35×40	30×30
12	40×60	35×55	30×50	30×45	30×40	30×35
13	40×50	35×50	30×40	30×35	30×30	30×30
14	65×65	60×60	50×50	45×45	35×40	30×35
15	40×50	35×45	30×40	30×35	30×30	30×30
16	30×40	30×35	30×30	30×30	-	-
17	50×50	45×45	35×40	30×35	-	-
18	30×40	30×35	30×30	30×30	-	-
19	30×30	30×30	30×30	-	-	-
20	30×40	30×35	30×30	-	-	-
21	30×30	30×30	30×30	-	-	-
22	30×30	30×30	-	-	-	-
23	35×30	30×30	-	-	-	-
24	30×30	30×30	-	-	-	-

Table 2: Cross-sections of r.c. columns (units in cm).

The FP system is designed at the CP limit state, requiring the fulfilment of the provisions imposed by NTC08: i.e. maximum compression axial load of the FP bearing less than its capacity; maximum horizontal displacements less than the spectral value; absence of tensile axial loads at the level of the FP system.

Three values of the effective fundamental vibration period of the isolation system

$$T_{e,I} = 2\pi \sqrt{\frac{1}{g\left(\frac{1}{R} + \frac{\mu_{fast}}{u_{H,d}}\right)}} \tag{1}$$

are considered (i.e.=2s, 2.5s and 3s), corresponding to the effective stiffness

$$K_e = N_{Sd}\left(\frac{1}{R} + \frac{\mu_{fast}}{u_{H,d}}\right) \tag{2}$$

and a value equal to 20% for the effective equivalent viscous damping

$$\xi_{e,I} = \frac{2}{\pi}\frac{1}{1+\frac{u_{H,d}}{\mu_{fast}R}} \tag{3}$$

The nonlinear system based on Equations (1) and (3) returns the values of the radius of curvature (R) and dynamic-fast friction coefficient (μ_{fast}) of the FP bearings, which correspond to the spectral displacement ($u_{H,d}$). Then, the maximum axial load capacity of the FP bearings (N_{Ed}) is evaluated by Equations (4a) and (4b), as function of the assigned value of the quasi-permanent gravity loads (N_{Sd}) transmitted from the superstructure [15]

$$\mu_{fast}(\%) = 17, \quad \left(\frac{N_{Sd}}{N_{Ed}}\right) \le 0.1 \tag{4a}$$

$$\mu_{fast}(\%) = 2.5\left(\frac{N_{Sd}}{N_{Ed}}\right)^{-0.834}, \quad \left(\frac{N_{Sd}}{N_{Ed}}\right) > 0.1 \tag{4b}$$

Moreover, two in-plan distributions of N_{Ed} are assumed for the FP bearings: case A in Figure 2a, with fifteen types of FP bearings (i.e. μ_{fast} equal for all isolators); case B in Figure 2b, with only three types of FP bearings (i.e. μ_{fast} different for each isolator), which are selected with reference to the maximum value of N_{Ed} from those of the isolators corresponding to three ranges of $\beta=N_{Sd}/N_{Sd,max}$ (i.e. $\beta\le0.4$; $0.4<\beta\le0.7$; $\beta>0.7$). It is worth noting that the final values of μ_{fast} take into account the fact that the FP bearings need the fulfilment of the CP limit state imposed by NTC08. For all the examined cases, design parameters of the FP systems are reported in Tables 3 and 4 where horizontal seismic loads act alone (i.e. H) or in combination with the vertical ones (i.e. HV), respectively.

	BI.AH1	BI.AH2	BI.AH3	BI.BH1	BI.BH2	BI.BH3
T_{eI} (s)	1.95	2.33	2.62	1.97	2.33	2.61
ξ_{eI} (%)	22.0	25.8	30.2	21.0	25.3	30.2
R (m)	1.45	2.26	3.26	1.45	2.26	3.26

Table 3: Dynamic and geometric parameters of Friction Pendulum (FP) systems designed for horizontal seismic loads.

	BI.AHV1	BI.AHV2	BI.AHV3	BI.BHV1	BI.BHV2	BI.BHV3
T_{eI} (s)	1.90	2.21	2.49	1.95	2.26	2.54
ξ_{eI} (%)	24.0	29.3	33.5	22.0	27.4	32.0
R (m)	1.45	2.26	3.26	1.45	2.26	3.26

Table 4: Dynamic and geometric parameters of Friction Pendulum (FP) systems designed for horizontal and vertical seismic loads.

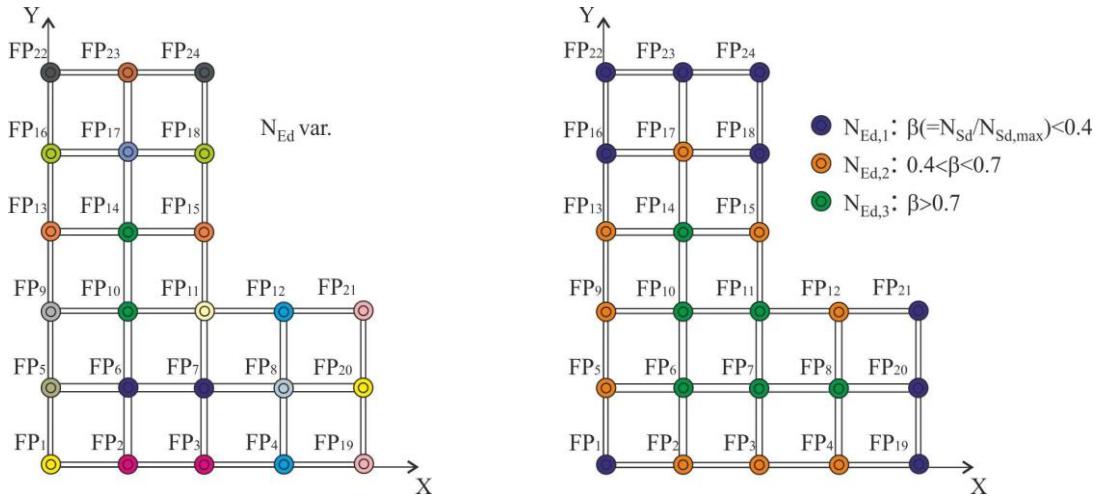

(a) BI.A structures: n.15 FP. (b) BI.B structures: n.3 FP.

Figure 2: In-plan distributions of axial load capacity for the Friction Pendulum (FP) bearings.

3 NONLINEAR MODELLING OF THE FP BEARINGS

The single FP bearing consists of a spherical concave sliding surface of polished stainless steel, with a radius of curvature R and a centre of curvature C, and an articulated slider coated with a layer of low friction composite material. The frictional force and stiffness during the sliding phase are proportional to the axial load. Moreover, an exponential analytical law can describe the velocity dependence of the dynamic friction coefficient [16]

$$\mu = \mu_{fast} - \left(\mu_{fast} - \mu_{slow}\right) e^{-\alpha \dot{u}_H} \tag{5}$$

where μ_{fast} and μ_{slow} are the friction coefficients at fast and slow sliding velocities $\dot{u}_H$, respectively, and α is a rate parameter which depends on the contact pressure and condition of the interface. The experimental results indicate that μ_{slow} can be assumed to be 2.5 times lower than μ_{fast} [17], while α can be considered approximately equal to 0.0055 s/mm [18].

The friction force for horizontal (bidirectional) motion is equal to [19]

$$\boldsymbol{F}_f = \begin{Bmatrix} F_{f,x} \\ F_{f,y} \end{Bmatrix} \cong \mu N \frac{1}{\|\dot{\boldsymbol{u}}_H\|} \begin{Bmatrix} \dot{u}_{H,x} \\ \dot{u}_{H,y} \end{Bmatrix} \tag{6}$$

where N is the axial load on the FP bearing. Finally, the restoring force can be evaluated as [20]

$$\boldsymbol{F}_H = \begin{Bmatrix} F_{H,x} \\ F_{H,y} \end{Bmatrix} \cong \frac{N}{R} \begin{Bmatrix} u_{H,x} \\ u_{H,y} \end{Bmatrix} + \begin{Bmatrix} F_{f,x} \\ F_{f,y} \end{Bmatrix} \tag{7}$$

containing a pendular component, directed toward the centre of the bearing, and a friction component, acting in the opposite direction to the velocity. For constant values of axial load and friction coefficient, the force-displacement behaviour of the FP bearing in the horizontal

direction (F_H-u_H) can be idealized by a bilinear law with lateral restoring stiffness

$$K_r = \frac{N}{R} \tag{8}$$

However, due to high values of vertical ground acceleration and global overturning moment produced by the horizontal seismic loads, the axial load variation on the FP bearing leads to changes in μ, F_f and K_r. In particular, at any given moment during an earthquake, the weight (W) of the superstructure acting on a FP bearing can be modified in accordance with the following expression [9]

$$N = W\left(1 - \frac{\ddot{u}_{g,V}}{g} + \frac{N_{OM}}{W}\right) \tag{9}$$

where $\ddot{u}_{g,V}$ is the vertical ground acceleration (positive when the direction is downwards) and N_{OM} is the additional axial load due to overturning (positive when compressive). It is worth noting that the fluctuation in the bearing axial load can be large enough to produce reversal of the axial load from compression to tension. A gap element is considered in the vertical direction, to take into account the fact that the FP bearing does not resist tensile axial loads and thus is free to uplift, assuming infinite rigidity in compression.

Maximum floor rotation at the level of the FP system, during the total duration (t_{tot}) of each ground motion, is evaluated as

$$\tan\vartheta_{max} = \max\left\{\left|u_{X,1}(t) - u_{X,22}(t)/L_Y\right| = \left|u_{Y,1}(t) - u_{Y,19}(t)/L_X\right|\right\},\ t\text{=0-}t_{tot} \tag{10}$$

referring to the horizontal displacement of three FP bearings at the corners of the building plan (i.e. FP_i, i=1, 19 and 22 in Figure 1a), being L_X=20m and L_Y=25m the maximum length along the X and Y directions. Moreover, the maximum residual displacement of the FP bearings is obtained as the vector sum of the residual displacement along the local axes

$$u_{res,max} = \max\left\{\sqrt{(u_{resx,i})^2 + (u_{resy,i})^2 + (u_{resz,i})^2}\right\},\ \text{i=1-24} \tag{11}$$

while the maximum vertical uplift

$$u_{up,max} = \max\left\{\left|u_{V,i}(t) - R\left[1 - cos\left(arcsin\frac{u_{H,i}(t)}{R}\right)\right]\right|\right\},\ \text{i=1-24} \tag{12}$$

is obtained as function of vertical and horizontal displacements on their spherical surface.

4 UNSCALED AND SCALED NEAR-FAULT GROUND MOTIONS

Ground motions recorded at near-fault sites may be characterized by strong long-duration velocity pulses in the horizontal direction, which may affect the friction coefficient of the FP bearings and their axial load variation due to overturning. To study torsional and re-centring problems of base-isolated structures with the FP system subjected to near-fault ground motions, seven recordings with significant horizontal components are selected from the *Pacific Earthquake Engineering Research center database* [14] on the basis of the design hypotheses adopted for the test structures. In Table 5a their main data are shown: i.e. year; recording station; closest distance from the fault (Δ); magnitude (M_w); peak ground acceleration for the two horizontal (i.e. PGA_{H1} and PGA_{H2}) and the vertical component (i.e. PGA_V); orientation of the strongest observed pulse (α_{sp}), clockwise from North [21].

Earthquake (EQ)	Station	Δ (km)	M_w	$PGA_{H,1}$	$PGA_{H,2}$	PGA_V	α_{sp}
Chi-Chi, 1999	TCU068	0.3	7.6	0.566g	0.462g	0.486g	144°
Imperial Valley, 1979	El Centro D.A.	5.1	6.5	0.353g	0.481g	0.770g	253°
Kobe, 1995	Takatori	1.5	6.9	0.618g	0.671g	0.284g	318°
Loma Prieta, 1989	Gilroy A#3	12.8	6.9	0.559g	0.368g	0.342g	277°
Northridge, 1994	Rinaldi R.S.	6.5	6.7	0.874g	0.472g	0.958g	209°
Parkfield, 2004	Fault Zone 1	2.5	6.0	0.605g	0.833g	0.255g	13°
Superstition Hills, 1987	Parachute T.S.	1.0	6.5	0.432g	0.384g	-	242°

Table 5a: Characteristics of the selected near-fault ground motions with significant horizontal components.

On the other hand, near-fault ground motions may be characterized by high values of the acceleration ratio $\alpha_{PGA}(=PGA_V/PGA_H)$, which may influence the friction force and lateral stiffness of the FP bearings during the sliding phase and produce uplift of the FP bearings. To study the nonlinear response of base-isolated structures with the FP system subjected to near-fault ground motions with significant vertical component, seven recordings are selected from the *PEER database*. Table 5b shows their main data: i.e. year; recording station; closest distance from the fault (Δ); magnitude (M_w); peak ground accelerations (i.e. PGA_{H1}, PGA_{H2} and PGA_V); maximum value of the acceleration ratio (i.e. $\alpha_{PGA,max}$).

Earthquake (EQ)	Station	Δ (km)	M_w	$PGA_{H,1}$	$PGA_{H,2}$	PGA_V	$\alpha_{PGA,max}$
Nahanni, 1985	Station I	6.0	6.76	1.108g	1.201g	2.281g	2.059
Imperial Valley, 1979	El Centro D.A.	5.1	6.50	0.353g	0.481g	0.770g	2.181
Imperial Valley, 1979	El Centro A#7	0.6	6.50	0.341g	0.469g	0.579g	1.698
Morgan Hill, 1984	Gilroy A#3	10.3	6.19	0.195g	0.201g	0.403g	2.067
Coyote Lake. 1979	Gilroy A#4	5.7	5.70	0.233g	0.252g	0.422g	1.811
Whittier Narrows, 1987	Arcadia Campus	17.4	5.9	0.293g	0.176g	0.223g	1.267
Westmorland, 1981	Westmorland F.S.	6.5	5.9	0.377g	0.498g	0.812g	2.154

Table 5b: Characteristics of the selected near-fault ground motions with significant vertical component.

To account for the potential structural damage of near-fault earthquakes, maximum value of spectral acceleration is assumed as a seismic intensity measure. In detail, horizontal components corresponding to the effective fundamental vibration period (i.e. T_{eI}) and equivalent viscous damping (i.e. ξ_{eI}) of the base-isolated structures reported in Tables 3 and 4 (i.e. $S^{(NF)}{}_{aH,1}$ and $S^{(NF)}{}_{aH,2}$) are considered. Then, the scale factor (*SF*), whereby the selected accelerograms are normalized with respect to the NTC08 spectrum, is evaluated as

$$SF = \frac{S_{aH}^{NTC08}\left(T_{eI},\xi_{eI}\right)}{\max\left\{S_{aH,1}^{NF}\left(T_{eI},\xi_{eI}\right),S_{aH,2}^{NF}\left(T_{eI},\xi_{eI}\right)\right\}} \tag{13}$$

Finally, normalization of the selected near-fault ground motions is carried out by scaling their *PGA* values with reference to *SF* values reported in Tables 6a and 6b.

	SF					
Earthquake (EQ)	BI.AH1	BI.AH2	BI.AH3	BI.BH1	BI.BH2	BI.BH3
Chi-Chi, 1999	0.28	0.25	0.21	0.28	0.25	0.21
Imperial Valley, 1979	0.64	0.52	0.47	0.64	0.52	0.47
Kobe, 1995	0.17	0.22	0.28	0.17	0.22	0.27
Loma Prieta, 1989	0.61	0.62	0.62	0.62	0.62	0.62
Northridge, 1994	0.27	0.32	0.32	0.27	0.32	0.32
Parkfield, 2004	0.59	0.75	0.82	0.60	0.75	0.82
Superstition Hills, 1987	0.21	0.23	0.22	0.21	0.23	0.22

Table 6a: Scale factors of the selected near-fault ground motions with significant horizontal components.

	SF					
Earthquake (EQ)	BI.AHV1	BI.AHV2	BI.AHV3	BI.BHV1	BI.BHV2	BI.BHV3
Nahanni, 1985	1.08	1.05	1.04	1.07	1.11	1.04
Imperial Valley, 1979	0.67	0.54	0.50	0.64	0.53	0.49
Imperial Valley, 1979	0.37	0.34	0.32	0.36	0.34	0.32
Morgan Hill, 1984	2.06	2.33	2.16	2.04	2.32	2.12
Coyote Lake. 1979	1.64	1.89	2.14	1.70	1.94	2.15
Whittier Narrows, 1987	3.08	3.24	3.30	3.22	3.26	3.27
Westmorland, 1981	0.69	0.89	1.00	0.71	0.94	1.02

Table 6b: Scale factors of the selected near-fault ground motions with significant vertical component.

5 NUMERICAL RESULTS

A numerical study is carried out to analyze torsional response, re-centring capability and uplift of base-isolated structures subjected to near-fault ground motions. In detail, maximum effects are evaluated for the orientation of the strongest pulse (i.e. $\alpha=\alpha_{sp}$) in the case of earthquakes with significant horizontal components, while accelerograms applied in line with the direction of the recording station (i.e. $\alpha=\alpha_{rs}$) are considered for earthquakes with significant vertical component. A computer code is adopted for the nonlinear dynamic analysis of the test structures [22-25], considering an elastic-linear behaviour of the superstructure and a nonlinear force-displacement law of the FP bearings in the horizontal direction depending on sliding velocity and axial load. A gap model is also assumed to capture the uplift of the FP bearings in the vertical direction. Moreover, a stiffness-proportional damping matrix of the superstructure is considered, by applying a viscous damping ratio ξ_S=1% to the fundamental vibration period of the base-isolated structures [26]. To take into account the uncertainty in the selection of the seismic intensity measure [27] and code-mandated damping modification factor [28] to be adopted for base-isolated structures subjected to near-fault earthquakes, two series of analyses are carried out on the selected ground motions applied with and without the scaling factor described in Section 4.

Firstly, maximum values of floor rotation ($tan\theta_{max}$) and residual displacement ($u_{res,max}$) at the level of the FP system are reported in Figures 3a-4a and 3b-4b, respectively, for base-isolated structures subjected to the unscaled Chi-Chi and Nahanni near-fault earthquakes (EQs). Two in-plan distributions of dynamic-fast friction coefficient for the FP system (i.e. BI.A and BI.B structures) are compared for three low-to-medium values of the radius of curvature for the FP bearings (i.e. R=1.45m, 2.26m and 3.26m).

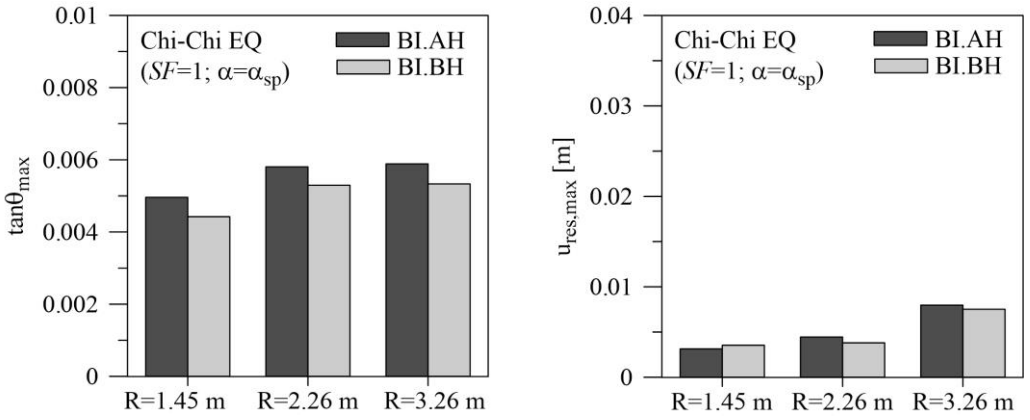

(a) Floor rotation. (b) Residual displacement.

Figure 3: Effects of the radius of curvature of the FP bearings on the nonlinear response of base-isolated structures subjected to the unscaled Chi-Chi EQ.

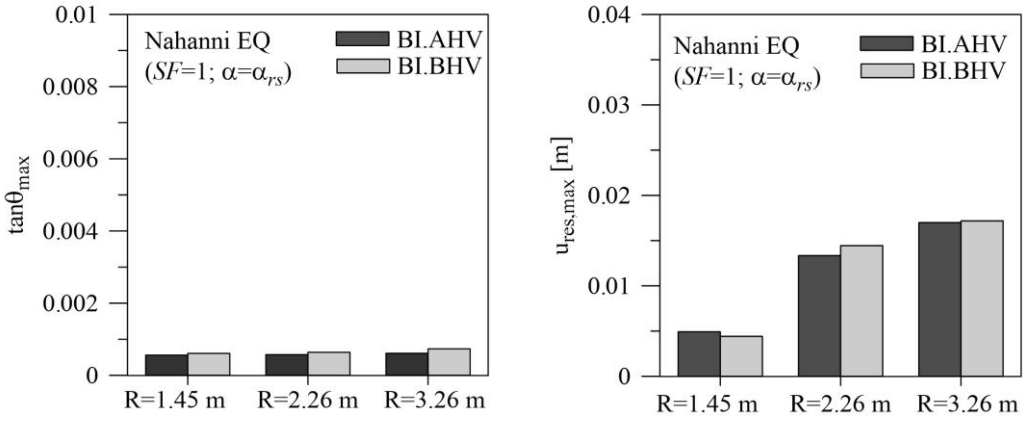

(a) Floor rotation. (b) Residual displacement.

Figure 4: Effects of the radius of curvature of the FP bearings on the nonlinear response of base-isolated structures subjected to the unscaled Nahanni EQ.

The BI.AH and BI.BH structures are designed considering the horizontal seismic loads acting alone and thus they are subjected to the Chi-Chi EQ (Figure 3), in which significant horizontal components are dominant; on the other hand, the Nahanni EQ (Figure 4), with a significant vertical component, is considered for the BI.AHV and BI.BHV structures designed also considering the vertical seismic loads. As can be noted, torsional effects are found to be important for the Chi-Chi EQ (Figure 3a), while in the case of the Nahanni EQ the effect is minor (Figure 4a). On the other hand, the residual displacement is generally more marked for the base-isolated structures subjected to the Nahanni EQ (Figure 4b) than the Chi-Chi EQ (Figure 3b). This behaviour can be interpreted by observing that higher spectral values of acceleration in the vertical direction are obtained for the Nahanni EQ, at least for rather low values of the vibration periods, thereby increasing the friction threshold of the FP bearings. As expected, the concave spherical surface of the FP bearing ensures a reduction of the residual displacement for decreasing values of the radius of curvature (Figures 3b and 4b). The BI.BH and BI.BHV structures respond in a similar way to the corresponding BI.AH and BI.AHV structures, but the former are less expensive because they require only three typologies of isolators in accordance with the maximum axial load capacity of the FP bearings.

Similar graphs in Figure 5 refer to minimum and maximum percentage of re-centring displacement ($u_{rec,\%}$) compared to maximum horizontal displacement.

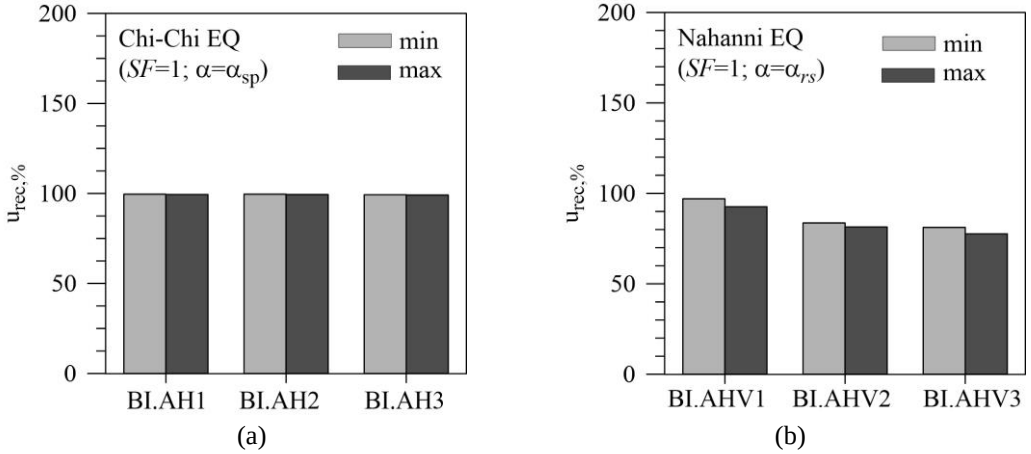

(a) (b)

Figure 5: Percentage of re-centring displacement for base-isolated structures subjected to the unscaled Chi-Chi and Nahanni EQs.

The BI.AHV structures subjected to the unscaled Nahanni EQ (Figure 5b) highlight values of $u_{rec,\%}$ lower than those obtained for the BI.AH structures under the Chi-Chi EQ (Figure 5a). Moreover, it is worth noting that the BI.AHV structures subjected to the Nahanni EQ exhibit different minimum and maximum values of $u_{rec,\%}$, highlighting the possibility of residual floor rotation at the level of the FP system.

Next, maximum values of uplift ($u_{up,max}$) for the BI.AHV and BI.BHV structures subjected to the unscaled Nahanni EQ are compared in Figure 6. More specifically, uplift of the six FP bearings at the corners of the building plan (i.e. FP_i, i=1, 11, 19, 21, 22 and 24 shown in Figure 1a) are reported. Note that uplift takes place in all the examined cases although the presence of tensile axial loads at the level of the FP system was prevented when designed for the horizontal seismic loads acting in combination with the vertical seismic ones. As can be observed, the variability of the in-plan distribution of friction coefficient and the choice of different radii of curvature for the FP bearings are not able to prevent uplift. Further results, omitted for brevity, confirm the absence of uplift due to overturning produced by the horizontal components of the unscaled Chi-Chi EQ.

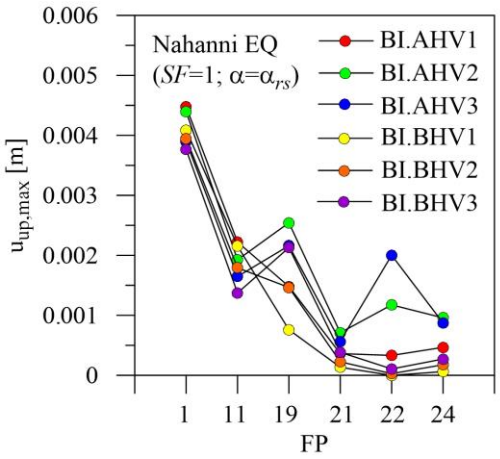

Figure 6: Effects of the radius of curvature of the FP bearings on the uplift of base-isolated structures subjected to the unscaled Nahanni EQ.

Afterwards, in order to evaluate the effects of the modelling assumptions related to velocity dependence of the friction coefficient of the FP bearings, maximum values of the floor rotation and residual displacement are reported in Figures 7 and 8.

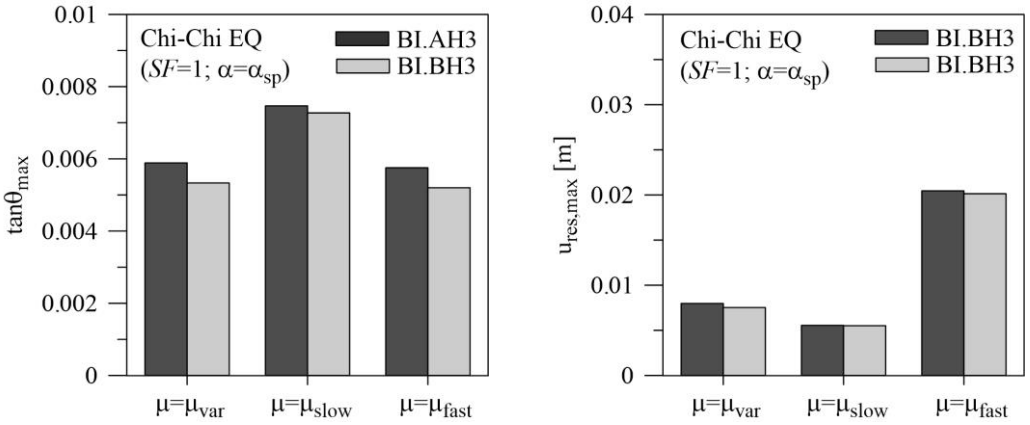

(a) Floor rotation. (b) Residual displacement.

Figure 7: Effects of modelling of the friction coefficient on the nonlinear response of base-isolated structures subjected to the unscaled Chi-Chi EQ.

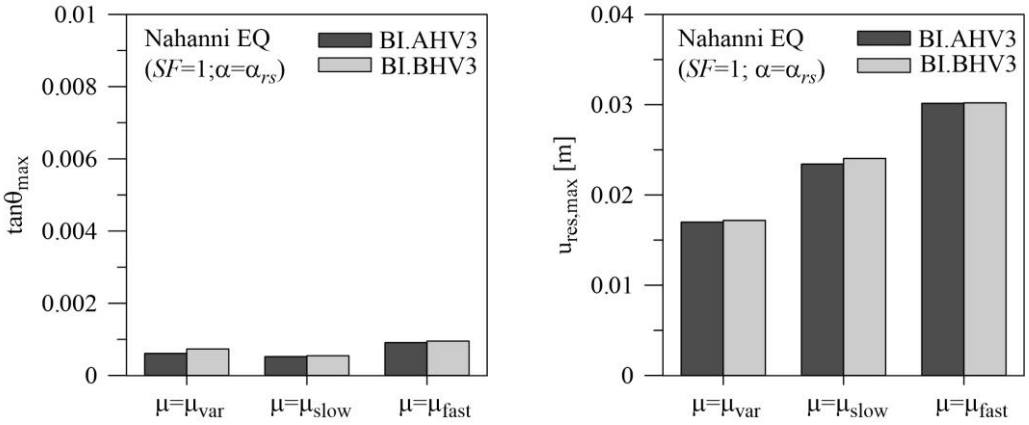

(a) Floor rotation. (b) Residual displacement.

Figure 8: Effects of modelling of the friction coefficient on the nonlinear response of base-isolated structures subjected to the unscaled Nahanni EQ.

Only results for base-isolated structures exhibiting maximum effects are examined for the unscaled Chi-Chi (i.e. BI.AH3 and BI.BH3 structures) and Nahanni (i.e. BI.AHV3 and BI.BHV3 structures) EQs. Three cases are compared: (a) friction coefficient variability as a function of the sliding velocity (i.e. $\mu=\mu_{var}$); (b) constant friction coefficient, at fast sliding velocity (i.e. $\mu=\mu_{fast}$); (c) constant friction coefficient, at slow sliding velocity (i.e. $\mu=\mu_{slow}$). As can be observed, maximum floor rotation is obtained for the BI.AH3 and BI.BH3 structures subjected to the Chi-Chi EQ (Figure 7a). This is evident when the minimum friction coefficient is assumed (i.e. μ_{slow}), while comparable results are found for the maximum (i.e. μ_{fast}) and variable (i.e. μ_{var}) friction coefficients. On the other hand, maximum values of residual displacement are obtained for the BI.AHV3 and BI.BHV3 structures under the Nahanni EQ (Figure 8b) and correspond to maximum friction coefficient (μ_{fast}); lower values are obtained for the minimum (μ_{slow}) and variable (μ_{var}) friction coefficients. In all the examined cases, comparable results are obtained for the base-isolated structures designed to consider the two in-plan distributions of the FP bearings (i.e. cases A and B shown in Figure 2).

Finally, maximum ($tan\theta_{max}$) and mean ($tan\theta_{mean}$) floor rotations along the building height are plotted for base-isolated structures subjected to two sets of seven scaled near-fault ground motions with significant horizontal (Figure 9) and vertical (Figure 10) components.

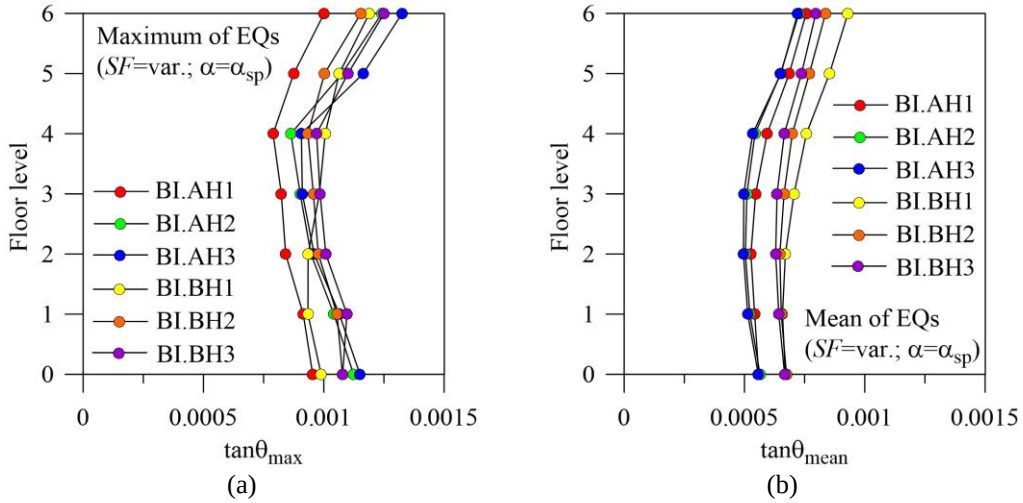

(a) (b)

Figure 9: Maximum and mean floor rotations of the superstructure for scaled near-fault EQs with significant horizontal components.

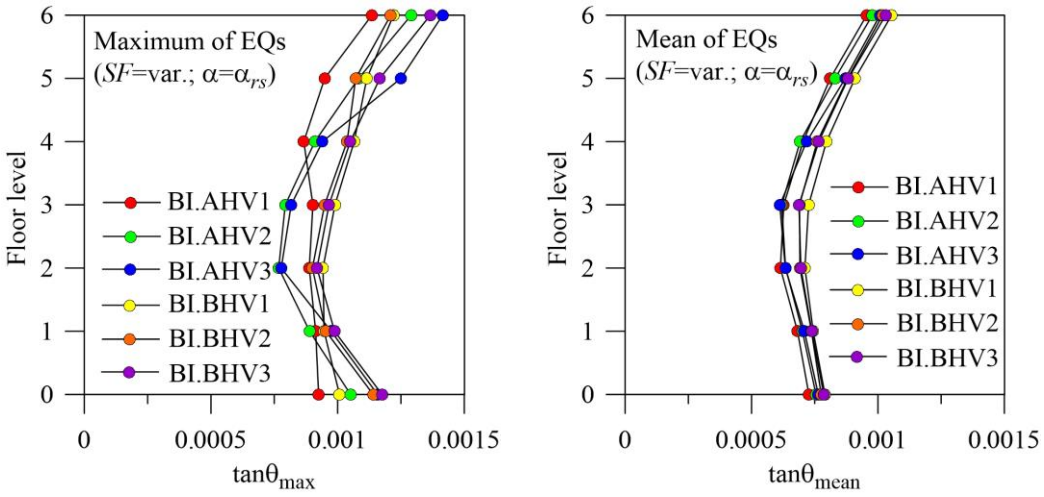

Figure 10: Maximum and mean floor rotations of the superstructure for scaled near-fault EQs with significant vertical component.

Note the highest values of floor rotation at the top level, with variability of torsional effects at the floor levels of the superstructure which are more evident in terms of $tan\theta_{max}$ (Figures 9a and 10a) than $tan\theta_{mean}$ (Figures 9b and 10b). However, limited torsional effects are highlighted for all the examined structures subjected to scaled near-fault EQs, which are normalized in accordance with a medium risk seismic region. Further results, omitted for the sake of brevity, highlight low values of maximum and mean residual displacement and uplift of the FP system.

6 CONCLUSIONS

The nonlinear seismic analysis of base-isolated structures with the FP system is carried out under near-fault ground motions, considering three low-to-medium design values of the radius of curvature of the FP bearings and two in-plan distributions of their dynamic-fast friction coefficient. Torsional effects are found to be more evident for unscaled earthquakes with significant horizontal components (e.g. the Chi-Chi EQ). On the other hand, residual displacement are generally more marked for base-isolated structures subjected to unscaled earthquakes with significant vertical component (e.g. the Nahanni EQ). Torsional and residual effects of the BI.BH and BI.BHV structures are similar to those of the corresponding BI.AH and BI.AHV structures, but the former are less expensive because they require only three typologies of isolators. As expected, a reduction of the residual displacement is obtained for decreasing values of the radius of curvature of the FP bearings. It is interesting to note that the BI.AHV structures subjected to the Nahanni EQ exhibit different minimum and maximum values of the percentage of re-centring displacement, highlighting the possibility of residual floor rotation at the level of the FP system. Moreover, the BI.AHV and BI.BHV structures exhibit uplift when subjected to the Nahanni EQ. The modelling of the friction coefficient highlights maximum floor rotation under the Chi-Chi EQ, when the minimum (constant) friction coefficient is assumed, while comparable results are found for maximum (constant) and variable friction coefficients. Maximum values of residual displacement are obtained under the Nahanni EQ, corresponding to maximum (constant) friction coefficient, while lower values are obtained for the minimum (constant) and variable friction coefficients. Finally, the highest values of mean floor rotation are found at the top level of the superstructure. However, torsional effect and residual displacement and uplift are less evident for scaled near-fault earthquakes, confirming the crucial importance of selecting suitable seismic intensity measure and code-mandated damping modification factor.

ACKNOWLEDGEMENTS

The present work was also financed by Re.L.U.I.S. (Italian network of university laboratories of earthquake engineering), in accordance with "Convenzione D.P.C.–Re.L.U.I.S. 2014–2016, WPI, Isolation and Dissipation".

REFERENCES

[1] L. Petti, F. Polichetti, B. Palazzo, Analysis of seismic performance of FPS base isolated structures subjected to near fault events. *International Journal of Engineering and Technology*, **5**(6), 5233-5240, 2014.

[2] V.A. Zayas, S.S. Low, S.A. Mahin, A simple pendulum technique for achieving seismic isolation. *Earthquake Spectra*, **6**, 317–333, 1990.

[3] R.S. Jangid, Optimum friction pendulum system for near-fault motions. Engineering Structures **27**(3), 349-359, 2005.

[4] J.D. Bray, A. Rodriguez-Marek, J.L. Gillie, Design ground motions near active faults. *Bulletin of the New Zealand Society for Earthquake Engineering*, **42**(1), 1-8, 2009.

[5] E. Chioccarelli, I. Iervolino, Near-source seismic demand and pulse-like records: A discussion for L'Aquila earthquake. *Earthquake Engineering and Structural Dynamics* **39**(9), 1039-1062, 2010.

[6] G.M. Calvi, P. Ceresa, C. Casarotti, D. Bolognini, F. Auricchio, Effects of axial force variation in the seismic response of bridges isolated with friction pendulum systems. *Journal of Earthquake Engineering*, **8**(1), 187-224, 2004.

[7] F. Mazza, A. Vulcano, M. Mazza, Nonlinear dynamic response of rc buildings with different base-isolation systems subjected to horizontal and vertical components of near-fault ground motions. *The Open Construction and Building Technology Journal*, **6**, 373-383, 2012.

[8] J.L. Almazan, J.C. De la Llera, J.A.Inaudi, Modelling aspects of structures isolated with the frictional pendulum system. *Earthquake Engineering and Structural Dynamics* **27**, 845-867, 1998.

[9] P.C Roussis, M.C. Constantinou, Uplift-restraining friction pendulum seismic isolation system. *Earthquake Engineering and Structural Dynamics*, **35**, 577–593, 2006.

[10] M, Rabiei, F. Khoshnoudian, Response of multistory friction pendulum base-isolated buildings including the vertical component of earthquakes. *Canadian Journal of Civil Engineering*, **38**, 1045-1059, 2011.

[11] A.J. Papazoglou, A.S. Elnashai, Analytical and field evidence of the damaging effect of vertical earthquake ground motion. *Earthquake Engineering and Structural Dynamics*, **25**, 1109-1137, 1996.

[12] P. Carydis, C.A. Castiglioni, E. Lekkas, I. Kostaki, N. Lebesis, A. Drei, The Emilia Romagna, May 2012 earthquake sequence: the influence of the vertical earthquake component and related geoscientific and engineering aspects. *Ingegneria Sismica*, **2-3**, 31-58, 2012.

[13] NTC08. Technical Regulations for the Constructions. Italian Ministry of the Infrastructures 2008.

[14] PEER, Pacific Earthquake Engineering Research center. Next Generation Attenuation (NGA) database 2008, http://peer.berkeley.edu/peer_ground_motion_database.

[15] FIP Industriale S.p.A. Catalogue S04: Curved Surface Sliders. Padova, 2013, http://www.fipindustriale.it.

[16] M.C. Constantinou, A. Mokha, A.M. Reinhorn, Teflon bearings in base isolation. II: modeling. *Journal of Structural Engineering*, **116**(2), 455–474, 1990.

[17] M. Dolce, D. Cardone, F. Croatto, Frictional behavior of steel-PTFE interfaces for seismic isolation. *Bulletin of Earthquake Engineering*, **3**, 75–99, 2005.

[18] D. Cardone, G. Gesualdi, P. Brancato, Restoring capability of friction pendulum seismic isolation systems. *Bulletin of Earthquake Engineering*, **13**(8), 2449-2480, 2015.

[19] K.L. Ryan, A.K. Chopra, Estimating the seismic displacement of friction pendulum isolators based on non-linear response history analysis. *Earthquake Engineering and Structural Dynamics*, **42**, 2321-2339, 2004.

[20] G. Mosqueda, A.S. Whittaker, G.L. Fenves, Characterization and modeling of friction pendulum bearings subjected to multiple components of excitation. *Journal of Structural Engineering*, **130**(3), 433-442, 2004.

[21] S. Shahi, J. Baker, Pulse Classifications from NGA West2 database, 2012, http://web.stanford.edu/~bakerjw/pulse_classification_v2/Pulse-like-records.html.

[22] F. Mazza, M. Mazza, Nonlinear modeling and analysis of R.C. framed buildings located in a near-fault area. *The Open Construction & Building Technology Journal*, **6**, 346-354, 2012.

[23] F. Mazza, Nonlinear incremental analysis of fire-damaged r.c. base-isolated structures subjected to near-fault ground motions. *Soil Dynamics and Earthquake Engineering*, **77**, 192-202, 2015.

[24] F. Mazza, Effects of near-fault vertical earthquakes on the nonlinear incremental response of r.c. base-isolated structures exposed to fire. *Bulletin of Earthquake Engineering*, **14**, 433–454, 2016.

[25] F. Mazza, F. Alesina, Effects of site condition in near-fault area on the nonlinear response of fire-damaged base-isolated structures. *Engineering* Structures, **111**, 297-311, 2016.

[26] D.R. Pant, A.C. Wijeyewickrema, M.A. ElGawady, Appropriate viscous damping for nonlinear time-history analysis of base-isolated reinforced concrete buildings. *Earthquake Engineering and Structural Dynamics*, **42**, 2321-2339, 2013.

[27] H. Ebrahimian, F. Jalayer, A. Lucchini, F. Mollaioli, G. Manfredi, Preliminary ranking of alternative scalar and vector intensity measures of ground shaking. *Bulletin of Earthquake Engineering*, **13**, 2805-2840, 2015.

[28] F. Mollaioli, L. Liberatore, A. Lucchini, Displacement damping modification factors for pulse-like and ordinary records. *Engineering Structures*, **78**, 17-27, 2014.

ECCOMAS Congress 2016
VII European Congress on Computational Methods in Applied Sciences and Engineering
M. Papadrakakis, V. Papadopoulos, G. Stefanou, V. Plevris (eds.)
Crete Island, Greece, 5–10 June 2016

ABSOLUTE FINITE ELEMENT COORDINATES IN THE DYNAMICS OF LARGE FLEXIBLE STRUCTURES

Evtim V. Zahariev

Institute of Mechanics, Bulgarian Academy of Sciences
Acad. G. Bonchev St., bl. 4, 1113 Sofia, Bulgaria
evtimvz@bas.bg

Keywords: Multibody Systems, Dynamics, Finite Elements, Absolute Coordinates, Seismic Excitations, Flexible Structures.

Abstract. *In the paper a novel method of finite elements in absolute coordinates is presented. The flexible elements and their node coordinate systems are considered free objects in space which motion is restricted by the elastic forces of the adjacent flexible elements. So, no kinematic restrictions, respectively algebraic equations, are imposed to the dynamic equations and the dynamic model is presented as Ordinary Differential Equations. Incremental approach for definition of system configuration during its global motion is applied, which avoids singularity of the large rotations. The proposed numerical procedure defines the element nodes as moving coordinate systems that makes possible their motion coordinates to be compared to rigid bodies and the large rotations to be taken into account. External excitations as wave propagation and earthquakes are subjects of the investigations.*

Generalized Newton – Euler dynamic equations for rigid and flexible bodies are applied for precise definition of the velocity dependent inertia forces in the dynamic equations. The seismic excitations are presented as reonomic constraints. Examples of large spatial flexible deflections of complex flexible structure verify the effectiveness of the method proposed.

1 INTRODUCTION

Multibody system methodology is a recently developing field in the theoretical and applied mechanics. Multibody dynamics as independent branch of mechanics was agreed to and established in 1977 at an IUTAM Symposium held in Munich, Germany and chaired by Magnus [1]. The first steps of the new discipline started with the dynamic analysis of rigid and flexible body systems striving to solve complicated nonlinear problems that the analytical methods cannon cover. In particular, elastic or flexible multibody systems, respectively, contact and impact problems where key issues for researchers worldwide. Multibody dynamics depends on computational dynamics and is closely related to control design and vibration theory.

Recently the multibody system methodology experienced huge progress including real time simulation, contact and impact problems, extension to electronics and mechatronics, dynamic strength analysis, optimization of design and control devices, integration codes in particular for differential algebraic systems, challenging applications in biomechanics, robotics and vehicle dynamics, manufacturing science and molecular dynamics and etc. Multibody dynamics is an excellent foundation for multivariable vibration analysis and sophisticated control design. The natural relations between the motion behavior of the mechanical systems with the sensors and the control devices make the mechatronic systems a basic subject for the Multibody system methodology. The precise analysis, simulation and planning of the system motion and design could be done deriving the dynamic equations including the control inputs and the information coming from the sensors. Obviously, the higher level of the mechatronic devices is the intelligent multibody systems which include all the characteristics of the mechatronics, as well as, the precise dynamics simulation and motion planning and control [2, 3].

Example of such mechatronic (intelligent) multibody systems are autonomous vehicles, space structures, structures imposed on external and seismic excitations, large flexible structures and wind generators. Solution of these tasks requires up-to-date methods for dynamics analysis and simulation, novel methods for numerical solution of ODE and DAE, real time simulation, passive, semi-passive and active control algorithms taking into account the control system and the feedback information.

The methods of the finite element theory (FET) [4] have been constantly developing to successfully solve the up-to-date tasks in structural statics. The problem of deriving the dynamics equations of flexible bodies using finite element discretization is really topical. Many books and papers [5, 6] discuss the problems that could arise using the finite element methodology and commercially available software (NASTRAN, ANSYS, ABAQUS) for simulation of nonlinear phenomena. It was pointed out that the FET approach cannot effectively simulate nonlinear effects of high velocity global motion in space and large flexible deformations.

The finite element theory proposed the theoretical basis for profound numerical analysis of complex flexible structures. The methodology for discretization of the continuum and the theory for polynomial approximation of the form of the deformations and on this basis computation and distribution of the mass and stiffness properties of the materials of flexible elements to discrete objects (nodes), actually, have been used afterward for development of various methods for static and dynamic analysis, even in the multibody system dynamics (MDS) simulation of rigid and flexible bodies. Attempts had been made for direct application of FET for dynamics simulation of systems that undergo global motion in space superimposed by large flexible deflections. In the recent decades the scientists successfully developed up-to-date methods for dynamics analysis of rigid and flexible mechanical systems setting the basis of multibody system methodology. Actually, the scientists use the theoretical rules of the FET for deriving the basic properties of the discretized elastic bodies but, on the other hand, they

strive to escape from the motion parameters of the FET in order to catch the nonlinear effects of the large displacements and deformations. It was proven [7 – 9] that using the FET approach the dynamic equations are free of centrifugal and Coriolis accelerations and the corresponding inertia forces.

Khan and Anderson [10] proposed the most recent classification of the methods for MBS dynamics. Tthey applied the Floating Frame of Reference (FFR) and Absolute Nodal Coordinate Formulation (ANCF) approaches for realization of their numerical procedure.

The FFR approach was developed [7, 11, 12] and has been successfully applied for dynamics simulation of large spatial motion and rotation of flexible multibody systems. This approach is also used for application of the modal coordinates and significant decreasing of the flexible coordinates.

Recently a novel method of ANCF has been developed [13, 14]. It is based on the theory of the curvilinear coordinates. The slopes of the nodes in the tangential line or plane of the space curve or shell are applied as coordinates. The method proposes important advantages mainly in large rotation simulation and mass matrices formulation. Review on the ANCF method for large deformation dynamics simulation of flexible multibody systems was presented by Gerstmayr et al. [15]. The paper provided a comprehensive review of the advantages and further developments of the ANCF method.

As it was said above the dynamic equations derived on basis of the FET do not include the Coriolis and the centrifugal accelerations. Shabana [16] and Meijard [17] derived generalized Newton – Euler dynamic equations for the case of FFR formulation. The equations represent the inertia forces as function of the velocities and accelerations of the global and flexible coordinates. Zahariev [18] derived generalized Newto-Euler dynamics equations for the rigid and flexible bodies for which the kinetic energy is quadratic form of the velocities. The equations are applicable for the flexible elements of the FET. The inertia forces are with respect to the quasi velocities and accelerations and are invariant to the kind of the coordinates.

In [19] a method of Finite Elements in Relative Coordinates (FERC) based on the FET was proposed for dynamic simulation of large flexible structures. Using the generalized Newton-Euler dynamic equations nonlinear effects and velocity dependent terms are successfully simulated. But using this approach for complex structures with many mutually connected adjacent flexible bodies one could experience a lot of difficulties that mainly consists in its program system realization and complex pre-processor procedures.

A method of Finite Elements in Absolute Coordinates (FEAC) is discussed in the paper. It was recently presented in [18] and further developed for different applications. FEAC are proposed here for simulation of structures subject to seismic excitations. Acceleration and force methods are used in practice for dynamics simulation of the earthquake structure response. Acceleration approach consists in registration of the motion of a structure foundation by accelerographs and normally consists in three orthogonal components of the ground acceleration. The velocity and displacement of the ground are obtained integrating the data of the accelerograms. The statistical data for the specific regions are than applied as input data for the dynamic simulation. In [20] the accelerations of the foundation are reonomic constraints for the dynamic equations which are transformed with respect to the parameters that consists of structure displacement and the forces, applied to the foundation.

Investigation of the forces loading the basement is a natural way for simulation of the structure response because of earthquakes [21]. This task is implemented analyzing the soil-structure interaction. Computation of the forces loading the foundation as a function of the relative motion ground – basement is the first stage for the numerical simulation process using the multibody system methodology.

The problems related to the subjects of the large scale flexible structures are discussed in [22]. Problem oriented articles devoted to the structures subject to seismic excitation were collected in [23]. The up-to-date methods and devices for prevention of structure damages and collapse are based manly of passive, semi-active and active structure basement suspension. Mainly spring, dampers and rubber isolators are used for passive suppression of the structure deflections. Shock absorbers or dampers are added to the structure to dissipate the seismic shocks. Active Tuned Mass Dampers use a computer controlled counter moving weight to actively move against the building sway. Active large scale springs and dampers together with computer controlled motion of large masses ensure calculated action against the building deflections. The article of Yao [24] seems to be the cornerstone in the structural control in civil engineering. An early review article of active control in structural engineering was published by Soong [25]. Latest surveys in 2003 [26] and another recent one in 2012 [27] emphasize on the semi-active and active control of structures subject to earthquake excitations and discuss theoretical backgrounds of different control schemes.

Dynamics simulation is extremely important for the design process of slender and large scale flexible systems as skyscrapers, bridges, wind power generators and many others. The devices for deviation suppression including passive, semi-active or active, although being designed on the basis of the eigenvalue analysis, should be simulated and analyzed for long time operational time and different kind of external excitations. This process includes development of reliable dynamic model and deriving precise dynamic equations. For efficient dynamic and motion simulation of complex structures that implement spatial motion and experience external excitations an important thing is to provide numerical procedure that ensures long lasting operational time of simulation and convergence of the numerical integration. Keeping in mind that such structures are with tremendously high nodes and degree of freedom with many complicated relations and geometrical constraints the following requirements to the program systems for dynamic simulation are stated:

a) Simple and straight forward algorithm for pre-processor development of the input data compliant with the dynamic model.

b) An approach to presentation of the rotational parameters keeping in mind that the systems could implement large rotations and translations.

c) Efficient dynamic model for simulation of rigid and flexible systems taking into account nonlinear effects as geometrical stiffening, velocity dependent terms and external excitations;

d) Reliable methods for node, respectively, degree of freedom reduction.

e) Efficient program procedures for numerical integration of Ordinary Differential Equations (ODE) and Differential Algebraic Equations with proven convergence.

The efficient simulation procedure based on a precise dynamic model and efficient numerical solution significantly improves the design process making him more reliable and inexpensive. In the paper the main attention is paid to first three items (a, b, c). The numerical procedure proposed here defines the element nodes as moving coordinate systems that makes possible their motion coordinates to be compared to rigid bodies, respectively, the large rotations to be taken into account. In the paper a novel method of finite elements in absolute coordinates of modified finite elements is presented. External excitations as wave propagation and earthquakes are subjects of the investigations. The flexible elements and their node coordinate systems are considered free objects in space which motion is restricted by the elastic forces of the adjacent flexible elements. So, no kinematic restrictions, respectively algebraic equations, are imposed to the dynamic equations and the dynamic model is presented as ODE. Incremental approach for definition of system configuration during its global motion is applied, which avoids singularity of the large rotations.

Generalized Newton – Euler dynamic equations for rigid and flexible bodies are applied for precise definition of the velocity dependent inertia forces. Wave propagations and seismic excitation are presented as reonomic constraints. Examples of large spatial and flexible deflections of complex rigid and flexible body structure verify the effectiveness of the method proposed.

2 KINEMATICS OF LARGE SPATIAL ROTATIONS OF FLEXIBLE ELEMENTS

2.1 Relative node position of a flexible element

To understand the difference between the classical FET and the method of the finite elements in absolute nodal coordinates using multibody system methodology some explanations about the kinematics of flexible nodes will be presented here. Since the basic relations and deductions as discretization of the flexible elements, the forms of the deformations, as well as, the methods for computation of the mass and stiffness matrices are well known for the readers [4, 28] no special attention will be paid to that procedures.

In Figure 1 a non-isoparametric space beam element (with index i) is presented. This finite element is relatively simple for explanation but, at the same time, presents the most common six degree of freedom (dof) space deflections of the nodes. In the figure the beam and small translations and rotations, respectively $\boldsymbol{\Delta}_{i,k} = \left[\Delta x_{i,k} \;\; \Delta y_{i,k} \;\; \Delta z_{i,k}\right]^{\backslash}$, $\boldsymbol{\theta}_{i,k} = \left[\theta x_{i,k} \;\; \theta y_{i,k} \;\; \theta z_{i,k}\right]^{\backslash}$, $i = 1,2$ of its nodes (indices i,1 and i,2 – the first and second nodes of element i) with respect to the initial not deformable element coordinate system $\underline{X}_i\underline{Y}_i\underline{Z}_i$ are depicted [4].

With the superscript "\" a matrix transpose is denoted. The underlined notations denote initial configurations. With bold characters matrices are pointed out. For scalars and objects, for example points, bodies, coordinate systems, italic notations are used.

It should be said that in FET these deflections are with respect to the element reference frame in its initial position (not deformed position) and no rotation of the element coordinate system is taken into account. Of course, coordinate system transformation with respect to the absolute reference frame $X_0Y_0Z_0$ of mass and stiffness matrices is considered but for the structure initial configuration only. As a result of the node deflections the element coordinate system $X_iY_iZ_i$, respectively the node i,1 coordinate system $X_{i,1}Y_{i,1}Z_{i,1}$, moves to a new position defined by the radius – vector $\boldsymbol{\rho}_{i,1}$ that could be easily estimated adding the initial

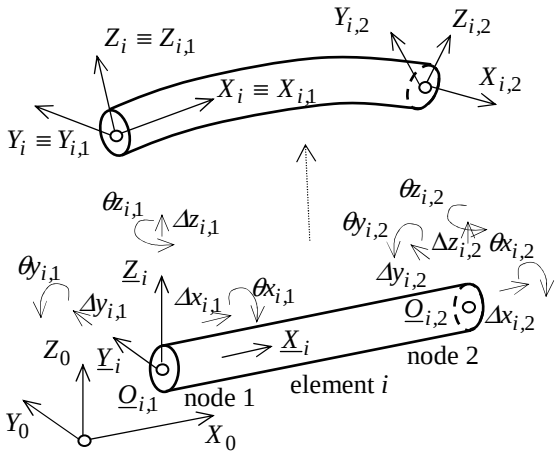

Figure 1: Small flexible node deflections of space non-isoparametric beam finite element

position of element coordinate system origin, radius – vector $\underline{\boldsymbol{\rho}}_i \equiv \underline{\boldsymbol{\rho}}_{i,1}$, and the node *i*,1 deflections $\boldsymbol{\Delta}_{i,1}$. The same holds for the radius –vector $\boldsymbol{\rho}_{i,2}$, taking into account the initial position of node *i*,2 coordinate system origin - radius – vector $\underline{\boldsymbol{\rho}}_{i,2}$, and the node *i*,2 deflections $\boldsymbol{\Delta}_{i,2}$. The node deflections of the i-*th* beam element are set in a 12×1 matrix – column $\boldsymbol{\Theta}_i = \left[\boldsymbol{\Theta}_{i,1}^{\backslash} \;\; \boldsymbol{\Theta}_{i,2}^{\backslash}\right]^{\backslash} = \left[\boldsymbol{\Delta}_{i,1}^{\backslash} \;\; \boldsymbol{\theta}_{i,1}^{\backslash} \;\; \boldsymbol{\Delta}_{i,2}^{\backslash} \;\; \boldsymbol{\theta}_{i,2}^{\backslash}\right]^{\backslash}$.

In Figure 2 the element *i* is not drawn but only the coordinate systems *i*,1 and *i*,2 of its nodes are shown in their initial and final configurations. The nodes are actually free objects, respectively coordinate systems that implement free motion in space restricted by the elastic forces only. Six possible deflections of the nodes are assumed (translations and rotations). The elastic forces $\mathbf{F}_{i,1}$ and torques $\mathbf{L}_{i,1}$ in the first node, as well as, $\mathbf{F}_{i,2}$, $\mathbf{L}_{i,2}$ in the second node, which are 3×1 matrix – vectors, are set in a 12×1 matrix – column $\boldsymbol{\Xi}_i = \left[\mathbf{F}_{i,1}^{\backslash} \;\; \mathbf{L}_{i,1}^{\backslash} \;\; \mathbf{F}_{i,2}^{\backslash} \;\; \mathbf{L}_{i,2}^{\backslash}\right]^{\backslash}$ arranged in the same order as the corresponding elements of $\boldsymbol{\Theta}_i$.

Actually, the position of the element coordinate system $X_i Y_i Z_i$ in the deformed configuration coincides with the coordinate system $X_{i,1} Y_{i,1} Z_{i,1}$ of node *i*,1. So, the deflections of the flexible element could be considered as free motion of the element coordinate system and the flexible deflections of the second node with respect to it. These are the flexible deflections relative to the element coordinate system.

In Figure 3 the beam element in the configuration as this of Figure 1 is depicted including the length L_i of the beam (along axis *X*) and the small deflections $\boldsymbol{\Delta}_{i,2\rangle i}$ of node *i*,2 relative to the beam coordinate system *i*. In the right subscript $\boldsymbol{\Delta}_{i,2\rangle i}$ the symbol "$\rangle$" serves as an arrow pointing out that the coordinate system with index *i*,2 is with respect to coordinate system *i*.

The right symbol of the subscript could be omitted if it points the absolute reference frame with index "0" – zero. Obviously, the beam configuration is quite the same and the fact that the flexible deflections are read relative to the moving element coordinate system does not change the regulations for FET discretization and for computation of the mass and stiffness matrices. The position of node *i*,2 coordinate system relative to the coordinate system of the moving beam is presented by 4×4 homogeneous transformation matrix $\mathbf{T}_{i,2\rangle i}$, i.e.:

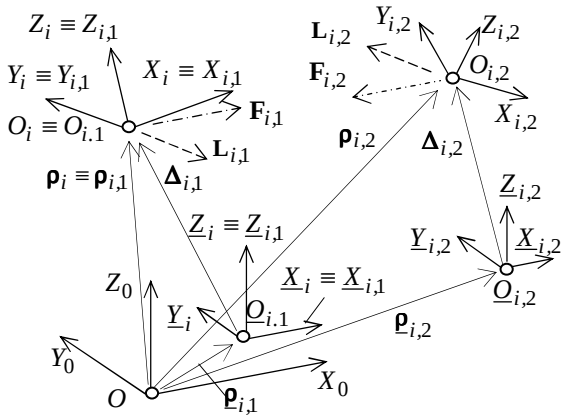

Figure 2: Presentation of the nodes as moving coordinate systems

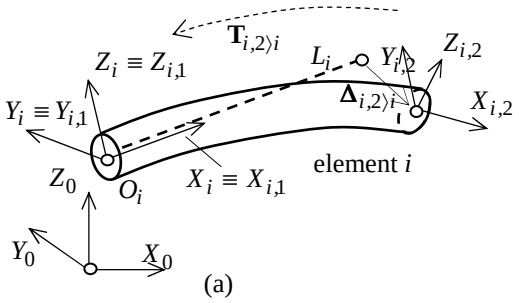

Figure 3: Finite beam element in relative coordinates

$$\mathbf{T}_{i,2\rangle i} = \begin{bmatrix} {}^{3.3}\boldsymbol{\tau}_{i,2\rangle i} & {}^{3,1}\boldsymbol{\rho}_{i,2\rangle i} \\ {}^{1,3}\mathbf{0} & 1 \end{bmatrix} =$$

$$= \begin{bmatrix} 0 & -\theta z_{i,2\rangle i} & \theta y_{i,2\rangle i} & L_i + \Delta x_{i,2\rangle i} \\ \theta z_{i,2\rangle i} & 0 & -\theta x_{i,2\rangle i} & \Delta y_{i,2\rangle i} \\ -\theta y_{i,2\rangle i} & \theta x_{i,2\rangle i} & 0 & z y_{i,2\rangle i} \\ 0 & 0 & 0 & 1 \end{bmatrix} = \begin{bmatrix} 0 & -q_{i_6} & q_{i_5} & L + q_{i_1} \\ q_{i_6} & 0 & -q_{i_4} & q_{i_2} \\ -q_{i_5} & q_{i_4} & 0 & q_{i_3} \\ 0 & 0 & 0 & 1 \end{bmatrix} \tag{1}$$

which for small rotational deflections does not include trigonometric functions. With this assumption that the homogeneous transformation matrix is linear for the relative coordinates $q_{i_j}, j = 1,2,...6$ of element i that include the small translational and rotational flexible deflections. ${}^{3,3}\boldsymbol{\tau}_{i,2\rangle i}$ is 3×3 rotational matrix; the left superscripts point out (used if needed) the matrix dimensions (rows, columns).

Since the beam coordinate system is moving the flexible deflections of node i,1 relative to the element coordinate system are zero and the matrix vector of the beam relative coordinates $\mathbf{q}_i$ is $\boldsymbol{\Theta}_{i\rangle i} = \begin{bmatrix} \boldsymbol{\Delta}_{i,2\rangle i}^{\backslash} & \boldsymbol{\theta}_{i,2\rangle i}^{\backslash} \end{bmatrix}^{\backslash} = \mathbf{q}_i = \begin{bmatrix} q_{i_1} & q_{i_2} & \dots & q_{i_6} \end{bmatrix}^{\backslash}$ (see Equation 1), as well as, the beam mass and stiffness matrices are constant.

2.2 Finite elements in absolute coordinates

In Figure 4 the coordinate systems of the beam element and its nodes are depicted without the beam shape and configuration. As we said above the beam coordinate system and that of node i,1 coincide and their relative position does not change during the beam motion. That is why we shall regard the motion of node coordinate systems taking into account which one is of the beam. Loading the nodes with the inertia, elastic and external forces, just like free rigid bodies they will implement, for a small increment of time, small increments of the motion parameters. Six are the minimal number of the coordinates that define the position as of a rigid body, so of a node. When a flexible element implements global motion in space overlapped by flexible deflections even small increments of the node coordinates with respect to their initial position do not present the real deformation of the flexible element.

The solution of the problem how to use the FET in case of global motion and large flexible deflections consists in:

a) definition of proper node reference frame coordinates for the case of small increments of time, respectively, for small increments of that coordinates;

b) estimation of the magnitudes of the elastic deformations.

The solution of problem (a) consists in selection of node reference frame coordinates compatible with the coordinates used in FET. The solution of problem (b) consists in separation of the flexible deflections from the global motion of the node coordinate systems.

In Figure 4, similar to Figure 2, the coordinate systems of nodes *i*,1 and *i*,2, $X_{i,k}Y_{i,k}Z_{i,k}$; $i=1,2$, are located in their final configuration. The initial positions of the node coordinate systems are presented by the same but underlined notations. FET claims for the small deflections to be read with respect to the system initial configuration.

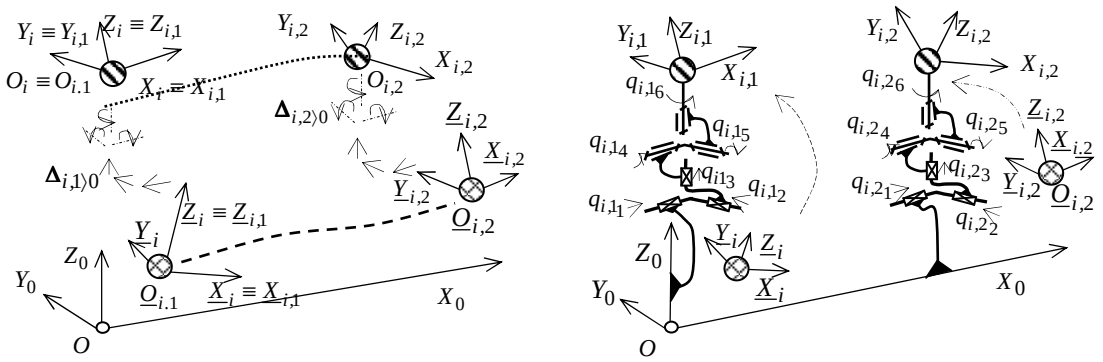

(a) possible small global deflections

(b) virtual joint presentation of the deflections

Figure 4: Nodes as free coordinate systems and corresponding motion coordinates

In Figure 4 (a) these deflections are presented by arrows and in Figure 4 (b) they are presented by virtual translational and rotational joints. These presentations are one and the same but give proper comparison to the free moving objects, constraint kinematics, joint coordinates, as well as, reveal the generality of the methodology proposed in the paper.

The homogeneous transformation matrices $\mathbf{T}_{i,1\rangle 0}$, $\mathbf{T}_{i,2\rangle 0}$ of the absolute position of the node coordinate systems *i*,1 and *i*,2, respectively, are expressed by the matrices $\underline{\mathbf{T}}_{i,1\rangle 0}$ and $\underline{\mathbf{T}}_{i,2\rangle 0}$ of their initial configuration and the transformation matrix because of the small node deflections.

$$\mathbf{T}_{i,k\rangle 0}=\left[\begin{array}{c|c}\boldsymbol{\tau\Delta}_{i,k\rangle 0}\cdot\underline{\boldsymbol{\tau}}_{i,k} & \underline{\boldsymbol{\rho}}_{i,k}+\boldsymbol{\Delta}_{i,k}\\ \hline \mathbf{0}_{1,3} & 1\end{array}\right]=\left[\begin{array}{ccc|c} & & & \underline{\rho x}_{i,k}+q_{i,k_1}\\ & \boldsymbol{\tau\Delta}_{i,k\rangle 0}\cdot\underline{\boldsymbol{\tau}}_{i,k} & & \underline{\rho y}_{i,k}+q_{i,k_2}\\ & & & \underline{\rho z}_{i,k}+q_{i,k_3}\\ \hline 0 & 0 & 0 & 1\end{array}\right];$$

$$\boldsymbol{\Delta}_{i,k\rangle 0}^{\backslash}=\left[q_{i,k_1}\;\; q_{i,k_{21}}\;\; q_{i,k_3}\right]^{\backslash}; \tag{2}$$

$$\boldsymbol{\tau\Delta}_{i,k\rangle 0}=\begin{bmatrix}0 & -\theta z_{i,k\rangle 0} & \theta y_{i,k\rangle 0}\\ \theta z_{i,k\rangle 0} & 0 & -\theta x_{i,k\rangle 0}\\ -\theta y_{i,k\rangle 0} & \theta x_{i,k\rangle 0} & 0\end{bmatrix}=\begin{bmatrix}0 & -q_{i,k_6} & q_{i,k_5}\\ q_{i,k_6} & 0 & -q_{i,k_4}\\ -q_{i,k_5} & q_{i,k_4} & 0\end{bmatrix}\quad k=1,2,$$

where $\mathbf{q}_{i,k}=\left[\boldsymbol{\Delta}_{i,k\rangle 0}^{\backslash}\quad \boldsymbol{\theta}_{i,k\rangle 0}^{\backslash}\right]^{\backslash}=\left[q_{i,k_1}\quad q_{i,k_2}\quad \ldots\quad q_{i,k_6}\right]^{\backslash}$, $k=1,2$ are the deflections of node *k* from element *i* with respect to the absolute reference frame (index 0), which are also the coordinates of the free moving nodes. To apply Equation (2) the deflections are to be small al-

though they do not present the flexible deformations only. The deflections q_{i,k_n}, $k=1,2; n=1,6$ include also the global motion of the nodes. To define the flexible deformations of the element i the relative position of node $i,2$ with respect to node $i,1$ that coincides with the element coordinate system i, should be defined, i.e.:

$$\begin{aligned}\mathbf{T}_{i,2\rangle i,1} = \mathbf{T}_{i,1\rangle 0}^{-1} \cdot \mathbf{T}_{i,2\rangle 0} = \left[\underline{\mathbf{T}}_{i,1\rangle 0} \cdot \mathbf{T}\boldsymbol{\Delta}_{i,1}\right]^{-1} \cdot \underline{\mathbf{T}}_{i,2\rangle 0} \cdot \mathbf{T}\boldsymbol{\Delta}_{i,2} = \\ = \mathbf{T}\boldsymbol{\Delta}_{i,1}^{-1} \underline{\mathbf{T}}_{i,1\rangle 0}^{-1} \cdot \underline{\mathbf{T}}_{i,2\rangle 0} \cdot \mathbf{T}\boldsymbol{\Delta}_{i,2}\end{aligned} \tag{3}$$

The matrix elements $\mathbf{T}_{i,2\rangle i,1} = \mathbf{T}_{i,2\rangle i}$ are actually the flexible deformations (rotations and translations) and, since they are to be small, the rotations could be presented without trigonometric functions, i.e.:

$$\mathbf{T}_{i,2\rangle i} = \begin{bmatrix} 0 & -\theta z_{i,2\rangle i} & \theta y_{i,2\rangle i} & L_i + \Delta x_{i,2\rangle i} \\ \theta z_{i,2\rangle i} & 0 & -\theta x_{i,2\rangle i} & \Delta y_{i,2\rangle i} \\ -\theta y_{i,2\rangle i} & \theta x_{i,2\rangle i} & 0 & z y_{i,2\rangle i} \\ 0 & 0 & 0 & 1 \end{bmatrix} \tag{4}$$

Taking into account that the relative deformations of node 1 are zero, the flexible deformations of the element i relative to its own reference frame are as follows $\boldsymbol{\Theta}_{i\rangle i} = \left[\boldsymbol{\Delta}_{i,2\rangle i}^{\backslash} \;\; \boldsymbol{\theta}_{i,2\rangle i}^{\backslash}\right]^{\backslash}$ and appear explicitly in matrix $\mathbf{T}_{i,2\rangle i}$ without trigonometric functions.

To realize the numerical algorithm with the proposed coordinates the integration process should be realized with small increments of time, respectively, with small increments of the nodal coordinates. For this purpose on every step of the time increment the new configuration of the system is the initial configuration for the next iteration and the absolute nodal coordinates start again with zero values. That process is not disadvantage since during the numerical integration of the dynamic equations the new positions of the coordinate systems are to be recalculated and the new mass and stiffness properties of the bodies are to be computed. Detailed statements of the procedures are presented in [29].

3 FORCES LOADING THE NODES OF FLEXIBLE ELEMENTS

The forces loading the nodes are internal elastic forces, external forces and, during the global motion, the inertia forces. Regarding static structures the internal elastic and external forces are in equilibrium. The external forces could be included in the dynamic equations using the principle of the virtual work and here we will not discuss this matter. The main subjects related to the dynamics in FET these are the internal elastic and inertia forces. The stiffness matrices play the major role in computation of the elastic forces, while the mass matrices are used for computation of the inertia force. Since the nodes of the flexible elements are considered coordinate systems implementing free motion in space they are kinematical independent, which means that the coordinates of a node do not depend on the coordinates of the adjacent ones. Unfortunately the static and dynamic equations cannot be solved separately for the nodes since deflections of a node give rise of elastic forces added to the adjacent nodes. The same holds for the velocities and accelerations and the resulting inertia forces.

3.1 Elastic and inertia forces of flexible elements

In the paper special attention is paid to the elastic and inertia forces loading the nodes of flexible elements. As it could be seen above the relative flexible deformations of nodes with respect to the element coordinate system, $\mathbf{\Theta}_{i\rangle i}$ play significant role for FEAC. The relative flexible deformations for the first node, in which the moving coordinate system of the element is located, are equal zero. The matrix-vector $\mathbf{\Theta}_{i\rangle i}$ is compiled without the deformations in the first node and is used for computation of the elastic forces loading both element nodes, i.e.:

$$\mathbf{\Xi}_{i\rangle i} = -\mathbf{K}_{i\rangle i} \cdot \mathbf{\Theta}_{i\rangle i}\,, \tag{5}$$

where for a beam element $\mathbf{K}_{i\rangle i}$ is 12×6 matrix compiled from the last six columns of the conventional FET stiff matrix of element *i* relative to its own beam coordinate system. The first six elements of $\mathbf{\Xi}_{i\rangle i}$ are the forces and torques loading the coordinate system of node *i*,1 and the last six elements are the forces and torques loading node *i*,2.

Taking into account that the nodes are coordinate systems and summarizing the results for FEAC methodologies one concludes that the dynamics analysis of multibody systems of rigid and flexible bodies could be analyzed by a common methodology. As it was discussed above one of the major problems for application of the FET in dynamics of rigid and flexible mutibody systems it is definition of the node accelerations, respectively, the inertia forces. In [18] generalized Newton-Euler dynamic equations for rigid and flexible bodies discretized using the FET are derived. The inertia forces in the nodes of the flexible elements are expressed with respect to the quasi velocities and accelerations and are independent of the kind of coordinates. The notations for the quasi-velocities and accelerations of node *i,k* are $\dot{\mathbf{\Theta}}_{i,k} = \left[\mathbf{v}_{i,k}^{\backslash} \;\; \boldsymbol{\omega}_{i,k}^{\backslash}\right]^{\backslash}$, $\ddot{\mathbf{\Theta}}_{i,k} = \left[\mathbf{a}_{i,k}^{\backslash} \;\; \boldsymbol{\varepsilon}_{i,k}^{\backslash}\right]^{\backslash}$ where $\mathbf{v}_{i,k}^{\backslash}$ and $\mathbf{a}_{i,k}^{\backslash}$, respectively, $\boldsymbol{\omega}_{i,k}^{\backslash}$ and $\boldsymbol{\varepsilon}_{i,k}^{\backslash}$, are the node linear and angular velocities. For a flexible element *i* with two nodes (indices 1 and 2), and 12×12 mass matrix **M** the inertia forces and torques, 12×1 matrix vector $\mathbf{F}_i = \left[\mathbf{P}_{i,1}^{\backslash} \;\; \mathbf{\Phi}_{i,1}^{\backslash} \;\; \mathbf{P}_{i,2}^{\backslash} \;\; \mathbf{\Phi}_{i,2}^{\backslash}\right]^{\backslash}$, is as follows:

$$\mathbf{F}_i = \mathbf{M}_i \cdot \begin{bmatrix} \ddot{\mathbf{\Theta}}_{i,1} \\ \ddot{\mathbf{\Theta}}_{i,2} \end{bmatrix} + \begin{bmatrix} \boldsymbol{\omega}_{i,1}^{\times} & {}^{3,3}\mathbf{0} & {}^{3,3}\mathbf{0} & {}^{3,3}\mathbf{0} \\ \mathbf{v}_{i,1}^{\times} & \boldsymbol{\omega}_{1}^{\times} & {}^{3,3}\mathbf{0} & {}^{3,3}\mathbf{0} \\ {}^{3,3}\mathbf{0} & {}^{3,3}\mathbf{0} & \boldsymbol{\omega}_{i,2}^{\times} & {}^{3,3}\mathbf{0} \\ {}^{3,3}\mathbf{0} & {}^{3,3}\mathbf{0} & \mathbf{v}_{i,2}^{\times} & \boldsymbol{\omega}_{i,2}^{\times} \end{bmatrix} \cdot \mathbf{M}_i \cdot \begin{bmatrix} \dot{\mathbf{\Theta}}_{i,1} \\ \dot{\mathbf{\Theta}}_{i,2} \end{bmatrix} - \mathbf{M}_i \cdot \begin{bmatrix} \boldsymbol{\omega}_{i,1}^{\times} \cdot \mathbf{v}_{i,1} \\ {}^{3,1}\mathbf{0} \\ \boldsymbol{\omega}_{i,2}^{\times} \cdot \mathbf{v}_{i,2} \\ {}^{3,1}\mathbf{0} \end{bmatrix}, \tag{6}$$

where the notation "×" means skew-symmetric matrix. In Equations (8) all vectors and matrices are to be with respect to one and the same coordinate system. For elements with more than two nodes, for examples plates and shells, their elements are to be arranged in a similar order. The forces of elements in the common nodes are to be summarized.

The general Newton – Euler dynamic equations are applicable as for rigid, so for flexible systems and provide the basis for effective general recursive algorithms and program systems for multibody system dynamics analysis. The elements of the homogeneous transformation matrices are explicitly defined with respect to the deflections and computational expenses are low. The numerical procedure uses constant relative mass and stiffness matrices for definition of the elastic and inertia forces. Here we do not discuss the methodology for application of the principle of virtual work for reduction of forces to the system coordinates and deriving the

dynamic equations since that is well known procedure. Possible kinematic constraints are to be expressed in the same way as in the case of rigid bodies.

4 DYNAMICS OF STRUCTURES SUBJECT TO SEISMIC EXCITATIONS

The methodology based on the FEAC has been successfully applied for large structures with many flexible elements and nodes that compose closed chains with many dependent coordinates. The approach is successfully applied for simulation of complex structures subject to external disturbances like seismic excitations.

Two methods are used for simulation of seismic excitation, ground – structure force interaction method and the basement acceleration method. The first one uses data from simulation of ground structure interaction and the output data so obtained, the forces loading the basement, are input data for the dynamics analysis of the structure. This approach is the easiest for dynamics simulation of the structures and is fully compatible with the methods discussed above.

The acceleration based approach uses statistical data for the accelerograms for specific regions and the motion characteristics of the basement are input data for the dynamics simulation process. Actually, the basement acceleration and the integrated velocities and displacements are reonomic constraints for the dynamic equations. Further down an approach for solution of the dynamic equations subject to reonomic constraints and on application of FEAC is presented.

Using the principle of the virtual work the forces are reduced to the system coordinates to derive the dynamic equations

$$\mathbf{M}\cdot\ddot{\mathbf{q}}+\mathbf{B}(\mathbf{q},\dot{\mathbf{q}})=\mathbf{S} \tag{7}$$

where $\mathbf{S}$ is $n\times 1$ matrix-vector of the generalized forces, $\mathbf{B}(\mathbf{q},\dot{\mathbf{q}})$ is velocity depend term.

Earthquake shaking affects forced motion of the structure basement. For a region using statistical data the accelerograms for the space displacements are as follows:

$$\ddot{q}_i=\ddot{q}_i(t), i=1,2,3 \tag{8}$$

These are reonomic constraints that depend on time. For a multibody system with dof n which motion is described by ODE, Equation (7), subject to m reonomic constraints, Equation (8), the dynamic equations are presented as follows:

$$\mathbf{M}\cdot\left[\ddot{q}_1\ \cdots\ \ddot{q}_{k+1}\ \cdots\ \ddot{q}_{k+m}\ \cdots\ \ddot{q}_n\right]^{\backslash}+\mathbf{B}(\mathbf{q},\dot{\mathbf{q}})=\left[S_1\ \cdots\ S_{k+1}\ \cdots\ S_{k+m}\ \cdots\ S_n\right]^{\backslash} \tag{9}$$

In Equation (9) the coordinates $\ddot{q}_i=\ddot{q}_i(t), i=k+1,k+2,..,k+m$ are known, while the generalized forces $S_i=S_i(t), i=k+1,k+2...,k+m$ are unknown. The dynamic equations, Equation (9), are transformed as follows:

$$\underline{\mathbf{M}}\cdot\left[\ddot{q}_1\ \cdots\ S_{k+1}\ \cdots\ S_{k+m}\ \cdots\ \ddot{q}_n\right]^{\backslash}+\mathbf{B}(\mathbf{q},\dot{\mathbf{q}})=-\underline{\underline{\mathbf{M}}}\cdot\left[\ddot{q}_{k+1}\ \cdots\ \ddot{q}_{k+m}\right]^{\backslash}+\underline{\mathbf{S}} \tag{10}$$

where the matrices $\underline{\mathbf{S}}$, $\underline{\underline{\mathbf{M}}}$, $\underline{\mathbf{M}}$ are compiled according to the indices of the coordinates.

The well know beam of Kane et al. [30] is an example of the dynamic analysis subject to a reonomic constraint. It is a horizontal cantilever beam that rotates around a vertical axis. The rotation is prescribed by its angular velocity and this example is a test for many researchers analyzing their methods. Here the same example is used to present FEAC method in case of reonomic constraints differentiating the velocity function to obtain the angular acceleration as inpt data. In Figure 5 the results of the simulation are presented. The angular velocity of the

beam input shaft (coordinate q_1) are presented in the Figure 5 (a). The mass and inertia characteristics of the beam are: (all measures are in SI UNIT): modulus of elasticity $E = 7 \cdot 10^{10}$; shear modulus $G = 2.8 \cdot 10^{10}$; length L=10.; density $\rho = 3000$; cross section area $S = 4 \cdot 10^{-4}$; cross-section moments of inertia $I_x = I_z = \frac{1}{2} I_c = 2.10^{-7}$. The beam discretization is of three elements. In Figure 5 (b) the experimental results are presented while in Figure 4 (c) the results of the simulation using FEAC are depicted.

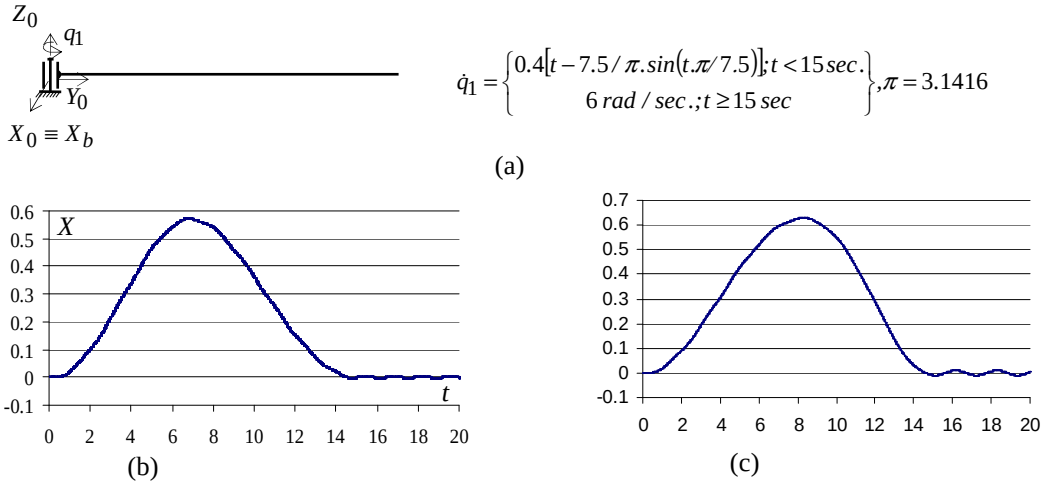

Figure 5: Kane's flexible beam [30]:
(a) the beam and driving motion; (b) experimental results; (c) results of the FEAC.

5 EXAMPLE

In Figure 6 an example of space flexible structure compiled of rigidly connected beams that build many closed contours is presented. The flexible beams are consequently numbered, as well as the nodes are also numbered by numbers in ellipses. The structure is mounted on a basement imposed on external excitation – one dimensional motion q_1 in the horizontal plane and rotational excitation q_2 along the vertical axes. Because of the external excitations the basement implements two dimensional motion which functions of the accelerations are also shown in the figure. In the function of $\ddot{q}_1$ **G** is the earth acceleration. The structure will be simulated using the method of FEAC proposed in the paper.

In Figure 7 the nodes of the beams are shown as a moving coordinate system. The nodes connected to the basement are assumed connected to a rigid body (the basement). The nodes are loaded by internal elastic forces $\mathbf{F}_i, 1,2,...,16$ and torques $\mathbf{L}_i, 1,2,...,16$ caused as a result of the flexible deflections. The nodes are loaded by inertia forces and torques (not shown on the figure) exaggerated because of forced motion of the basement and the resulting space motion of the whole structure. The nodes 1 – 4 are connected to the basement and are considered part of the basement as a rigid body, i.e.: their motion characteristics coincide with that of the basement q_1 and q_2.

The size, the mass and the stiffness properties of the vertical beams are the same as these of the beam of Figure 5. The lengths of the horizontal beams are 0.7 of the lengths of the vertical beams.

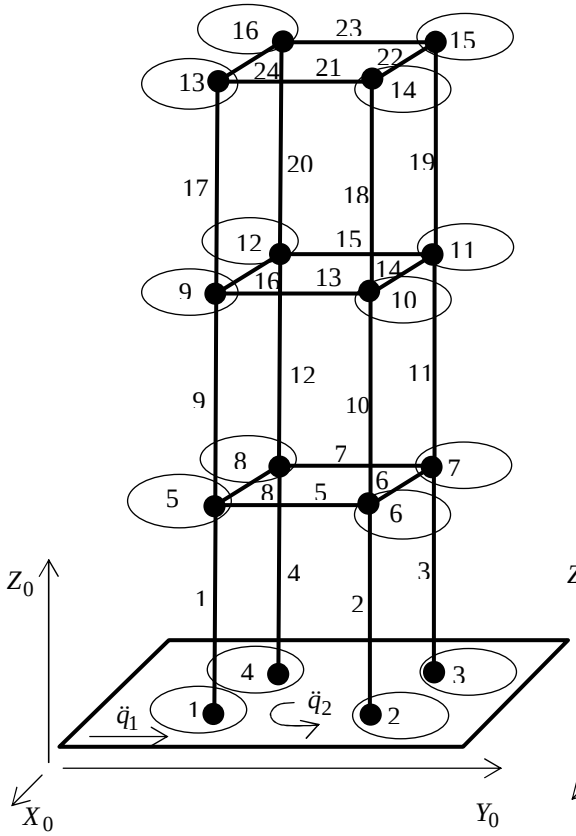

Figure 6: Flexible space beam structure. Elements and nodes

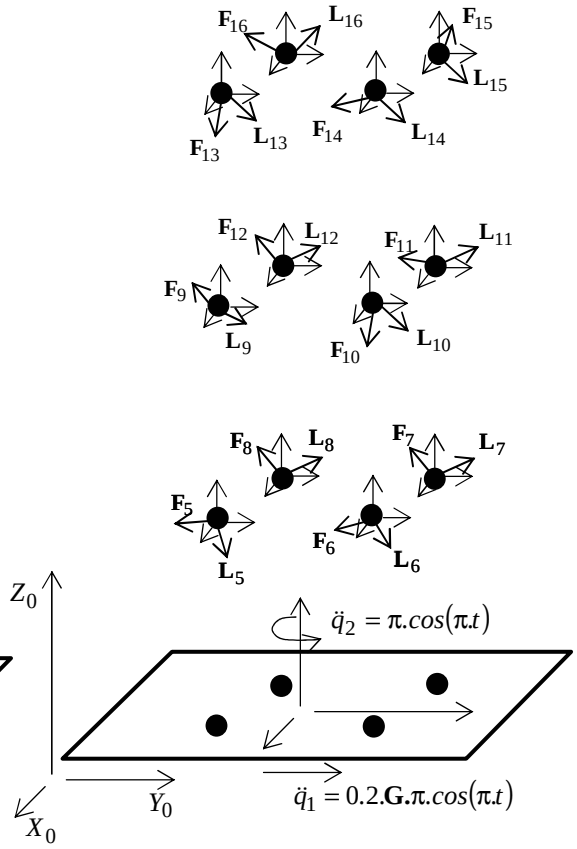

Figure 7: The dynamic model of the structure as free nodes – coordinate system

The dynamic model of Figure 7 is derived using the method proposed in the paper and the incremental approach for numerical integration of the dynamic equations [29, 31]. In Figure 8 the configuration of the structure for three instants of time are depicted.

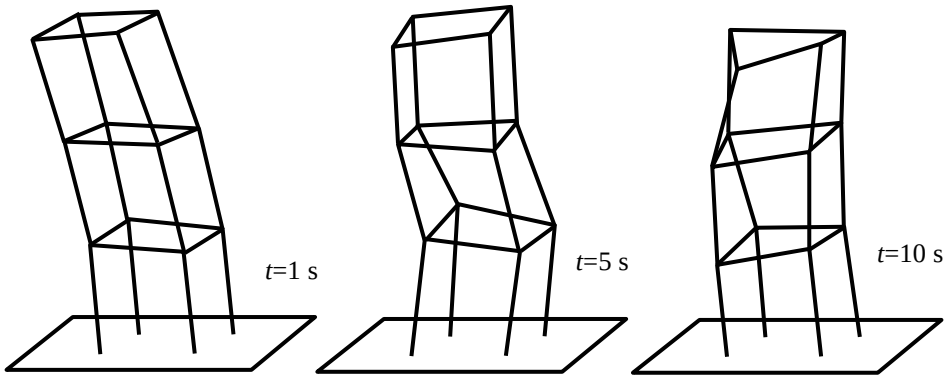

Figure 8: Configuration of the structure for three instants of time

6 CONCLUSIONS

- A method of Finite Elements in Absolute Coordinates is applied for dynamic simulation of large flexible structures subject to external excitations.
- The method is applicable for structures with many flexible elements and degrees of freedom. It is realized using simple and straight forward procedure with no kinematic constraints, as well as, algebraic constraint to the dynamic equations.
- Since the kinematic constraints are substituted by internal elastic forces of the elements large amplitudes of these forces are observed that could decrease the precision of the numerical algorithm and increase the time of simulation. This effect could be observed in the test example of Figure 5.
- The next step in application of the method will consist in development of a numerical procedure for solution of ordinary differential equations that truncate the high amplitudes of the elastic forces.

Aknovledgement: The author acknowledges the financial support of Ministry of Education and Science, contract No. DUNC 01/3 – 2009.

REFERENCES

[1] K. Magnus editor, *Dynamics of Multibody Systems*, Springer, Berlin, 1978.

[2] W. Schiehlen, Multibody System Dynamics: Roots and Perspectives, *Multibody System Dynamics*, **1** (2), 149-188, 1997.

[3] P. Eberhard, W. Schiehlen, Computational Dynamics of Multibody Systems: History, Formalisms, and Applications, *Journal of Computational and Nonlinear Dynamics*, **1** (1), 3-12, 2006.

[4] O.C. Zienkiewicz, R.L. Taylor, *Finite Element Method (5th Edition). Volume 1 - The Basis*, Elsevier, 2000.

[5] W. Pan, S. Mao, E. J. Haug, D. Solis, Efficient Modal Approach for Flexible Multibody Dynamic Simulation, *Mechanics Based Design of Structures and Machines*, **31**, 1 – 24, 2003.

[6] A. Shabana, Non-Linear Dynamics of Multibody Systems with Generalized and Non-Generalized Coordinates, *Virtual Nonlinear Multibody Systems*, W. Schiehlen and M. Valašek (eds.), NATO ASI Series, Kluwer Academic Publishers, Netherlands, **103**, 1 – 16, 2003.

[7] T. R. Kane, R. R. Ryan, A. R. Banerjee, Dynamics of a cantilever beam attached to a moving rigid base, *AIAA Journal of Guidance, Control and Dynamics*, **10**, 139 – 151, 1987.

[8] I. Sharf, Geometric stiffening in multibody dynamics formulations, *AIAA Journal of Guidance, Control, and Dynamics*, **18** (4), 882 – 890, 1995.

[9] J. M. Mayo, D. García-Vallejo, J. Domínguez, Study of the Geometric Stiffening Effect: Comparison of Different Formulations, *Multibody System Dynamics*, **11** (4), 321 – 341, 2004.

[10] I. M. Khan, K. S. Anderson, Large Deformation Formulation for the Flexible Divide-and-Conquer Algorithm, *Proc. of the ECCOMAS Thematic Conference Multibody Dynamics*, University of Zagreb, Croatia, 343 – 357, 2013.

[11] A. Shabana and R. Schwertassek. Equivalence of the floating frame of reference approach and finite element formulations. *International journal of non-linear mechanics*, Elsevier, **33**(3), 417–432, 1998.

[12] R. Schwertassek, Flexible bodies in multibody systems. In: J. Angeles, E. Zakhariev eds. *Computational Methods in Mechanical Systems. Mechanism Analysis, Synthesis, and Optimization*, *NATO ASI Series F 161*,. Berlin, Springer Verlag, 329–363, 1998.

[13] A. A. Shabana, An absolute nodal coordinate formulation for the large rotation and deformation analysis of flexible bodies. *Technical Report MBS96-1-UIC*, Dept of Mechanical Engineering, Univ of Illinois at Chicago, 1996.

[14] A. A. Shabana and A. P. Christensen, Three-dimensional absolute nodal co-ordinate formulation: plate problem, *International Journal for Numerical Methods in Engineering*, **40**(15), 2775–2790, 1997.

[15] J. Gerstmayr, H. Sugiyama, A. Mikkola, Review on the absolute nodal coordinate formulation for large deformation analysis of multibody systems, *ASME Journal of Computational and Nonlinear Dynamics*, **8**(3), 031016 (12 pages), 2013.

[16] A. Shabana, Dynamics of flexible bodies using generalized Newton-Euler equations, *ASME J. of Dynamic Systems, Measurement and Control*, **112**, 496-503, 1990.

[17] J. P. Meijard, Validation of flexible beam element in dynamics programs, *Nonlinear Dynamics*, Springer Verlag, **9**(1-2), 21-36, 1996.

[18] E. V. Zahariev, Generalized Finite Element Approach to Dynamics Modeling of Rigid and Flexible Systems, *Mechanics Based Design of Structures and Machines*, Taylor & Francis Group, **34**(1), 81 - 109, 2006.

[19] E.V. Zahariev, Relative Finite Element Coordinates in Multibody System Simulation, *Multibody System Dynamics*, Kluwer Academic Publishers, **7**(1), 51 – 77, 2002.

[20] E. Zahariev, Earthquake dynamic response of large flexible multibody systems, *Mechanical Science*, **4**, 131–137, 2013.

[21] G. Vasilev, S. Parvanova, P. Dineva, Fr. Wuttke, Soil-structure interaction using BEM–FEM coupling through ANSYS software package, *Soil Dynamics and Earthquake Engineering*, **70**, 104-117, 2014.

[22] M. Papadrakakis (Ed.), *Solving Large-Scale Problems in Mechanic*s, John Wiley & Sons, 1993.

[23] M. Papadrakakis, M. Fragiadakis, Nikos D. Lagaro eds., *Computational Methods in Earthquake Engineering*, Springer, 2011.

[24] J.T.P. Yao, Concept of structural control, Journal of the Structural Division, *ASCE* **98**(7), 1567–1574, 1972.

[25] T.T. Soong, Active structural control: Theory and practice, *Longman Scientific*, Essex, UK, 1990.

[26] T.K. Datta, A State-of-the-Art Review on Active Control of Structures, *ISET Journal of Earthquake Technology*, **40**(1), 1-17, 2003.

[27] Fabio Casciati, Jose´ Rodellar and Umut Yildirim, Active and semi-active control of structures – theory and applications: A review of recent advances, *Journal of Intelligent Material Systems and Structures*, **23**, 1181-1195, 2012.

[28] J. F. Doyle, Nonlinear Analysis of Thin – Walled Structures, *Springer-Verlag*, 2001.

[29] E. Zahariev, Numerical Multibody System Dynamics, Rigid and Flexible Systems, *Lambert Academic Publishing GmbH & Co. KG*, 2012.

[30] T. R. Kane, R. R. Ryan, A. R. Banerjee. Dynamics of a cantilever beam attached to a moving rigid base, *AIAA Journal of Guidance, Control and Dynamics*, **10**, 139 – 151, 1987.

[31] E. Zahariev, V. Jivkov, I. Danchev, Absolute Finite Element Nodal Coordinates in the Dynamics of Large Flexible Structures - an Incremental Approach, *International Journal of Mechanical Engineering and Automation*, **2** (10), 442-453, 2015.

ECCOMAS Congress 2016
VII European Congress on Computational Methods in Applied Sciences and Engineering
M. Papadrakakis, V. Papadopoulos, G. Stefanou, V. Plevris (eds.)
Crete Island, Greece, 5–10 June 2016

MODAL ANALYSIS OF A FRAME MODEL UNDER UNMEASURED SEISMIC INPUT

C. Valente[1], V. Sepe[1], M. Di Pilla[2], F. Iezzi[1], R. Siano[1], L. Zuccarino[1]

[1] Department of Engineering and Geology, University "G. d'Annunzio" of Chieti-Pescara
Viale Pindaro 42, 65127 Pescara, Italy
e-mail: {c.valente, v.sepe, fabrizio.iezzi, rossella.siano, l.zuccarino}@unich.it

[2] graduate in Building Engineering, University "G. d'Annunzio" of Chieti-Pescara

Keywords: Structural identification, modal analysis, civil engineering SHM applications, unknown seismic input.

Abstract.

The paper reports the first results of an experimental campaign aimed at the validation of a procedure, proposed in previous theoretical works by one of the writers, for the structural identification in frequency domain of linear structural systems subjected to base seismic excitation. Differently from the classical identification techniques based on the transfer-function processing, that require to measure the excitation (input-output problem), such procedure allows the solution of the identification problem also in case of unknown input (output-only problem) if the responses of at least three degrees-of-freedom are available for the system.

An experimental campaign has been carried out on a three storeys shear-type frame, carefully designed in order to minimize the uncertainties and errors.

After validating the model setup and the measuring chain by means of a classical input-output procedure, the paper discusses the first results of the output-only identification. The outcomes show a fair agreement with the results obtained by including the input knowledge.

1 INTRODUCTION

Modal identification of frame structures is a widely acknowledged and effective technique for the Structural Health Monitoring (SHM) and the calibration of retrofitting interventions on existing structures. However, in many cases the practical applications of classical input-output procedures are limited by the need of a complete knowledge of both the excitation and the structural response. This happens especially in the case of existing structures subjected to seismic motion; in fact, in this instance, the records of the input can be often unavailable or not sufficiently accurate.

A possible solution to these limitations has been already given, among the others, in a previous paper of one of the writers [1], where an extension of the classical structural identification procedure in frequency domain (e.g. Goyder [2]) has been provided in the case of spatial frames subjected to unknown (time contents and direction) seismic input. The identification procedure is based on the analysis of only the structural response at the floor levels. More specifically, the uniqueness of the solution is demonstrated in the case in which the structural response is known for at least three different floors of the framed structure.

The present study is part of a research, still in progress, aimed at providing a comprehensive experimental validation of the above procedure, following a previous pilot work [3] where the original procedure was improved through a more refined minimization algorithm in the complex field.

An experimental campaign was carried out on a three storeys shear-type frame model subjected to unmeasured base displacements, simulating the effect of seismic excitation. The accuracy of the algorithms for numerical data treatment was preliminarily checked and optimized in the classical case of measured non-stationary base motion.

2 DYNAMIC IDENTIFICATION IN FREQUENCY DOMAIN

Classically, dynamic identification is aimed at deriving the modal properties of structural systems, namely natural frequencies, modal damping and modal shapes, by means of the processing of time-histories describing both the excitation and the structural response.

For what regards the nature of the excitation, a distinction has to be made between stationary random processes, including ambient excitations such as wind, traffic and so on, and non-stationary processes, as in the case of earthquakes.

However, in many civil applications it can be not possible or really arduous the recording of the loading forces; the structural identification should be consequently carried out by processing only the structural response of the system.

Two cases can therefore be distinguished:

- *Input-output problem*, where measures of the structural response at different degrees-of-freedom (dofs) of the system (e.g. time-history of displacements, velocities or accelerations of the floors) and of the loading actions (e.g. time-history of the base acceleration) are simultaneously available;
- *Output-only problem*, where only measures of the structural response at different dofs of the system are available, without any data about the loading actions [4].

In this paper the attention is focused on the dynamic identification of linear structural systems submitted to non-stationary input, by means of a numerical formulation developed in the frequency domain by one of the writers [1] in case of unknown input. It is based on the independence by the input measure of the ratio between the Fourier transforms (FT) of the responses measured at different dofs of the structure. The procedure has been numerically validated in [1] and checked by the writers in a preliminary experimental campaign [3].

A short descriptions is provided in the following for both the input-output and the output-only problems, to give a general overview of the theoretical basis of the procedure.

2.1 Input-output problem

In the case of structures subjected to a base motion, the structural identification can be carried out in the frequency domain by using the inertance transfer function $H_i(\omega)$ [5], expressed as follows with reference to a N-dofs system

$$H_i(\omega) = \frac{Y_i(\omega)}{A(\omega)} \qquad i = 1, 2, ..., N \tag{1}$$

where $Y_i(\omega)$ is the Fourier Transform (FT) of the relative acceleration measured at i-th dof, while $A(\omega)$ is the FT of the imposed base acceleration.

The inertance $H_i(\omega)$ depends on the unknown modal parameters (natural frequencies, modal shapes and damping) of the system under consideration [5][6]:

$$H_i(\omega) = \sum_{k=1}^{N} \frac{\omega^2 \vartheta_{ik}}{\omega^2 - \left(\omega_k{}^2 + 2j\omega\omega_k\xi_k\right)} \tag{2}$$

where i denotes the degree of freedom, k is referred to the mode, j is the imaginary unit, ω_k and ξ_k are the frequency and the damping coefficients corresponding to the k-th mode of the structure, respectively, while ϑ_{ik} is the modal shape component for the k-th mode at the i-th degree of freedom of the structure.

The identification problem can be solved by searching those modal parameters that allow to minimize the error (in the least square sense) between the theoretical expression of the transfer functions and its measured counterpart.

2.2 Output only problem

In many civil applications it can be necessary or simply useful to solve the identification problem by only referring to the measured response. Accessibility limitations or other technical and economic obstacles can make not possible the complete definition of the spatial and time distribution of the external actions on the structure; also when the spatial distribution is known (e.g. seismic input simulated by a unidirectional base motion, as considered here), the time-history of the external action can be difficult to measure. In this case, however, the identification problem can be solved [1] by evaluating the ratio between the FT of the output measured at two degrees of freedom i and j of the structure, that does not depend on the input:

$$R_{ij}(\omega) = \frac{Y_i(\omega)}{Y_j(\omega)} = \frac{H_i(\omega)A(\omega)}{H_j(\omega)A(\omega)} = \frac{H_i(\omega)}{H_j(\omega)} \tag{3}$$

As well as the transfer function introduced by the equations (1) and (2), the ratio $R_{ij}(\omega)$ in equation (3) depends only on the unknown modal parameters of the system, but does not require any information about the input excitation. The identification problem can be therefore solved, by minimizing the error between the theoretical expression of $R_{ij}(\omega)$ and its measured counterpart, that only depends on the measured response. As already demonstrated in [1], the problem thus defined admits only one solution if the measures of the structural response in at least three different dofs are available.

2.3 Numerical procedure for the dynamic identification

In both cases of *input-output* and *output-only* problems, the unknown modal parameters are found by minimizing the least-square error $E(x)$ between the theoretical expressions governing each type of identification problem, i.e. the equation (2) for $H_i(\omega)$ in the *input-output* problem and the equation (3) for $R_{ij}(\omega)$ in the *output-only* problem, and their measured counterparts.

The solution of the identification problem will correspond to the minimum of the error function, i.e. to the set of modal parameters minimizing such function, defined by means of a non-linear curve fitting algorithm expressed as follows:

$$\min_x E(x) = \min_x \sum_i \left(F\left(x, xdata_i\right) - ydata_i\right)^2 \tag{4}$$

where x represents the vector collecting all the unknown modal parameters of the structure, $F(x, xdata)$ is the vector collecting the values obtained by the curve fitting procedure, while *ydata* represents the vector of the data ($H_i(\omega)$ or $R_{ij}(\omega)$) corresponding to a suitable range of the angular frequencies ω, collected in *xdata*.

With the aim to guarantee the convergence of the error minimization procedure, the real and the imaginary parts of both the analytical functions and the components of the solution vector have been treated separately. Once defined the problem by changing the variables from complex to real, lower and upper bounds can be fixed to the unknown parameters, based on reliable information about their range of variation. The introduction of physical bounds to the range of variation of the unknown parameters can help to find the solution of the identification problem and is of course possible only in case of real variables. On the other hand, the modification of the unknown parameters from complex to real values is not in contrast with their actual nature; the modal parameters are in fact real values from a physical point of view, but become complex for their inclusion in complex-valued functions. Details of the procedure can be found in [3].

3 EXPERIMENTAL TESTS

3.1 Model details

In order to validate the proposed procedure, dynamic tests have been carried out on an experimental prototype, properly designed to ensure a typical behavior of shear-type frame. A particular attention has been given to all the details necessary to guarantee the shear-type behavior. The rotation of beam-column joints has therefore been prevented and a rigid floor displacement has been obtained by means of a large out-of-plane stiffness of the floor diaphragms. The tested model is a spatial frame with three floors and one span; the columns have been made with a much higher stiffness in one direction than the other, so as to get a plane frame behavior.

Several preliminary solutions have been studied with respect to the selection of the materials, the beam-column connections, the possibility to modify the mass and stiffness of the model, the excitation system to simulate both an applied force and the effect of a seismic input.

Some sketches of the final solution are reported in Figure 1, while in Table 1 the geometrical properties are resumed.

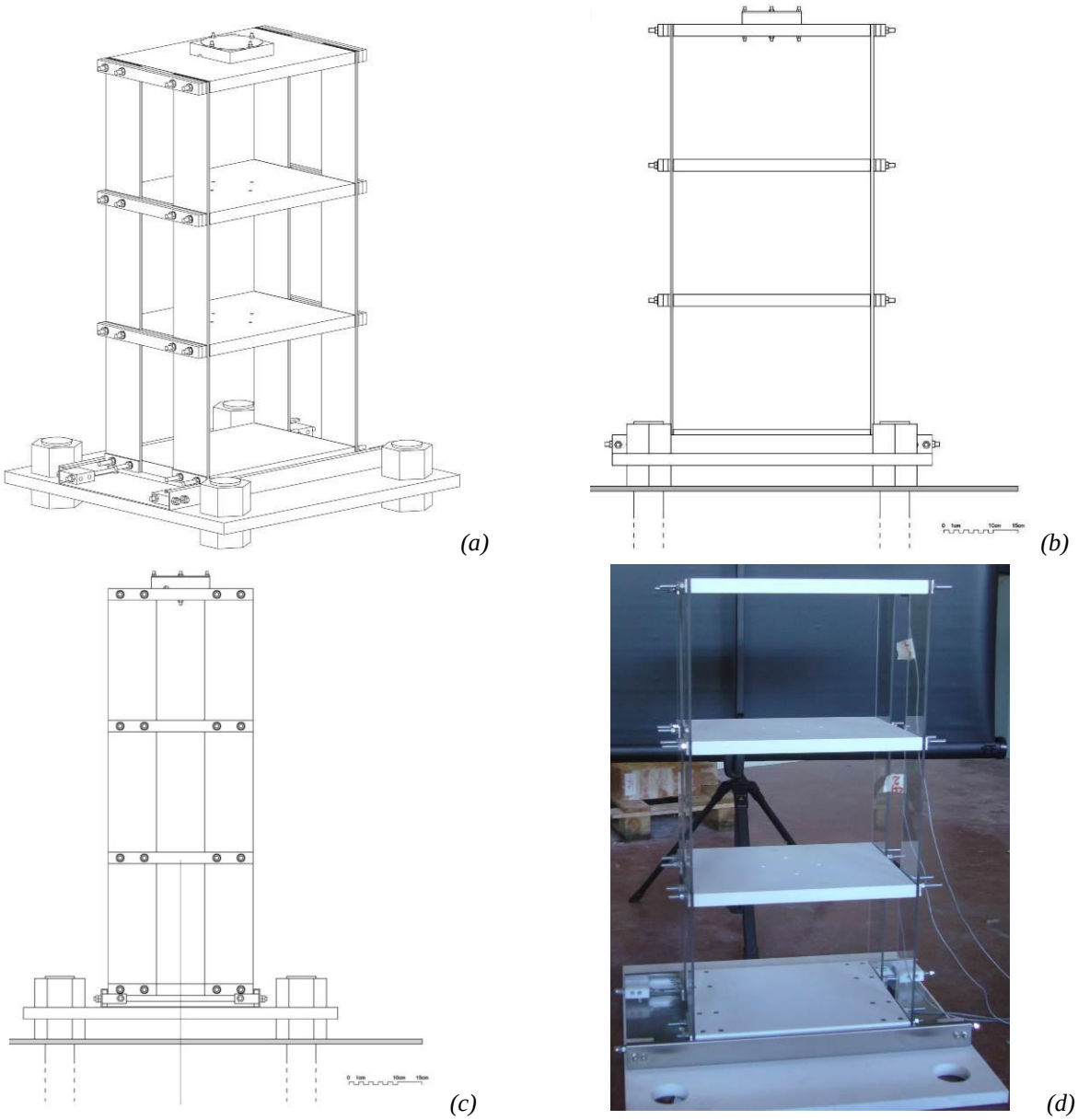

Figure 1: Details of the tested model: (a) axonometric, (b) front, (c) lateral view, (d) picture.

Element	Material	Width mm	Length mm	Thickness mm
Column	Polycarbonate	100	846	3 - 6
Floor	Corian®	300	400	24

Table 1: Geometrical characteristic of the tested 3 dofs shear-type model.

Polycarbonate and Corian® have been used for the model, both of them with high heat resistance, excellent workability and lightness.

The model is composed by four columns made of polycarbonate with cross-section 100 x 846 mm and a thickness variable from 3 to 6 mm. The inter-storey height is 250 mm.

To guarantee the out-of-plane floor stiffness, three rectangular decks made in Corian® have been used, having dimensions 300x400x24 mm. Each floor is anchored to the polycar-

bonate columns through a bolted system that allows to modify the mass and stiffness of the model.

A further panel of identical dimensions as decks has been used for the basement, that is anchored to a larger panel, also made in Corian®, with dimensions 650x650x24 mm, that can be fixed to the floor.

The base panel is equipped with two steel C-shaped profiles, which allow the sliding of the frame model through four nylon wheels with ball bearings. In this configuration the model can be excited by a time-varying base displacement, at the moment applied by hand, to simulate seismic actions. The sliding system can also be locked, obtaining in this way a fixed-base model to be used for free vibration tests or forcing time-histories at floor levels.

The mechanical properties of the materials used for the model are listed in Table 2.

Corian®			
Properties	Norm/Standard	Plate t= 6 mm	Unit
Density	DIN ISO 1183	1.73 - 1.76	[g/cm^3]
Flexural Modulus	DIN EN ISO 178	8920 - 9770	[MPa]
Flexural Strength	DIN EN ISO 178	49.1 - 76.4	[MPa]
Compressive Strength	EN ISO 604	178 - 179	[MPa]
Elongation	DIN EN ISO 178	0.58 - 0.94	[%]

Polycarbonate			
Properties	Norm/Standard	Typical Values	Unit
Density	ISO 1183	1.20	[g/cm^3]
Flexural Modulus	ISO 178	2300	[MPa]
Flexural Strength	ISO 178	90	[MPa]
Ultimate Tensile Strength	ISO 527	70	[MPa]
Ultimate Tensile Strain	ISO 527	120	[%]

Table 2: Mechanical properties of Corian® and Polycarbonate

3.2 Test Setup

In order to work with different values of mass and stiffness of the model, modifications to the initial configuration have been considered.

In the first case, the floor mass has been increased by adding steel plates at each deck level, paying specific attention to keep unchanged the centroid position. The Figure 2 shows the three mass configurations available:

- configuration m_0: mass of each floor = 5.78 kg;
- configuration m_1: two steel plates added at each floor, with mass 2x0.57 kg = 1.14 kg;
- configuration m_2: four steel plates added at each floor, with mass 4x0.57 kg = 2.28 kg.

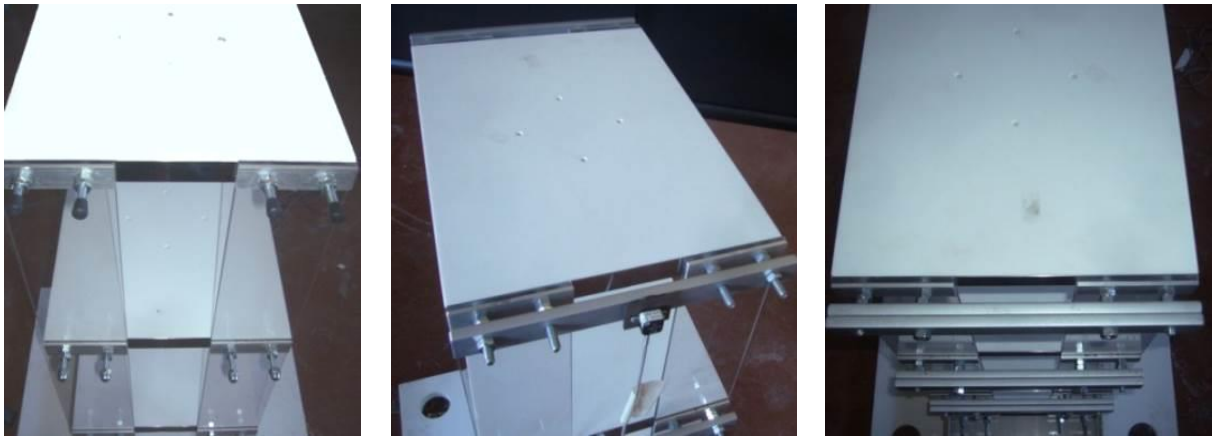

(a) configuration m_0 *(b) configuration m_1* *(c) configuration m_2*

Figure 2: Experimental model: (a) m_0=5.78 kg for each floor; (b) m_1=6.92 kg for each floor; (c) m_2=8.06 kg for each floor; mass of columns depending on their thickness.
Total mass of floors and columns is reported in Table 3 for each mass-thickness combination.

Also the stiffness of the columns has been changed. Four different values, i.e. 3, 4, 5 and 6 mm have been considered for the thickness of columns.

The natural frequencies for the different mass and stiffness combinations are shown in Table 3.

	m_0 *initial configuration*	**m_1** *3.42 kg added mass*	**m_2** *6.84 kg added mass*
	M_f^* = 17.34 kg	M_f^*= 20.76 kg	M_f^* = 24.18 kg
t_3 *t= 3 mm* M_c^{**} *= 1.22 kg*	f_1= 1.10 Hz f_2= 3.09 Hz f_3= 4.44 Hz	f_1= 1.01 Hz f_2= 2.82 Hz f_3= 4.07 Hz	f_1= 0.94 Hz f_2= 2.62 Hz f_3= 3.78 Hz
t_4 *t= 4 mm* M_c^{**}*= 1.63 kg*	f_1= 1.69 Hz f_2= 4.71 Hz f_3= 6.77 Hz	f_1= 1.54 Hz f_2= 4.32Hz f_3= 6.21 Hz	f_1= 1.43 Hz f_2= 4.01Hz f_3= 5.77 Hz
t_5 *t= 5 mm* M_c^{**}*= 2.03 kg*	f_1= 2.34 Hz f_2= 6.52 Hz f_3= 9.37 Hz	f_1= 2.14 Hz f_2= 5.99 Hz f_3= 8.61 Hz	f_1= 1.99 Hz f_2= 5.57 Hz f_3= 8.01 Hz
t_6 *t= 6 mm* M_c^{**}*= 2.44 kg*	f_1= 3.05 Hz f_2= 8.50 Hz f_3= 12.20 Hz	f_1= 2.80 Hz f_2= 7.82 Hz f_3= 11.22 Hz	f_1= 2.60 Hz f_2= 7.27 Hz f_3= 10.45 Hz

M_f^*= Total mass of the floors - M_c^{**} = Total mass of the columns

Table 3: Frequencies of the 3dofs model for the different configurations, as obtained by FE models.

3.3 Testing program

The experimental campaign has been carried out by submitting the model to three types of dynamic tests:

- free oscillations (FO);

- forced vibrations (FV) induced by a rotating eccentric mass driven by an electric equipment, allowing sinusoidal force (vibrodyne);
- base motion (BM) simulating the effect of seismic excitation.

Figure 3 shows the different experimental configurations available for the tested frame, i.e. fixed during a forced vibration (left) and allowed to slide (right) for time-varying base displacement.

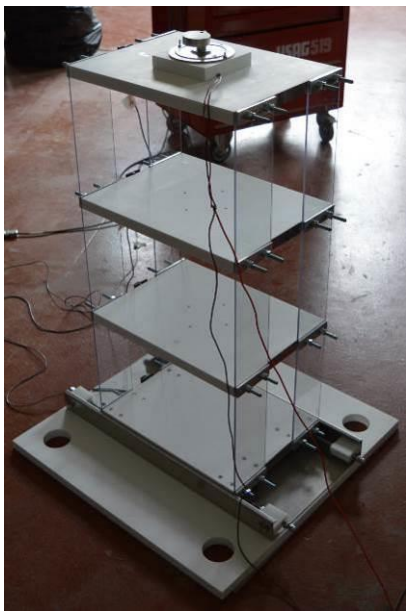

(a)

(b)

Figure 3: Experimental configuration of the tested frame: (a) fixed base; (b) sliding base

Each test has been performed and repeated several times, as reported in Table 4.

Test	Intensity or Type	Repetitions	Total No. Tests
free vibration	-	m_0, m_1, m_2	3
forced vibration	$1^{st} – 2^{nd} – 3^{rd}$ *	m_0, m_1, m_2	9
base motion	L – H – V **	m_0, m_1, m_2	9

** 1^{st} = at first floor, 2^{nd} = at second floor, 3^{rd} = at third floor*
*** L= low intensity, H = high intensity, V= variable intensity during the time-interval*

Table 4: Dynamic tests for thickness of columns t = 5 mm

3.4 Response measurement

The dynamic response has been recorded using four unidirectional piezoelectric accelerometers with a full scale, resolution and linearity range, equal to ± 2 g, 10 μg and 0.3-4000 Hz, respectively. The accelerometers have been installed at each floor to record the acceleration response in the horizontal direction. A fourth accelerometer has been fixed at the basement to record the imposed input in the BM cases. The tests were performed using a sampling rate of 250 Hz. The acquisition was provided by a multichannel analyzer equipped with 24-bit A/D card. The equipment used is shown in Figure 4.

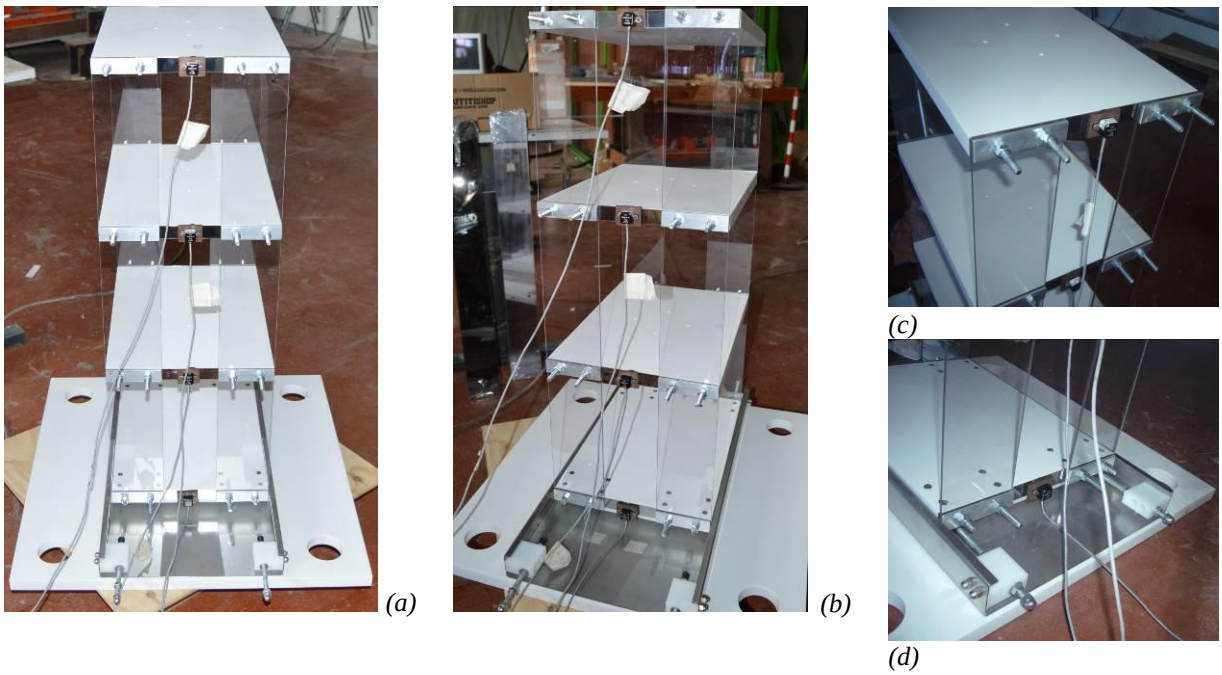

Figure 4: Experimental equipment: (a) – (b) measurement stations, (c) detail of the accelerometer at third floor, (d) detail of the accelerometer at the basement (sliding panel).

4 RESULTS AND DISCUSSION

In order to verify the effectiveness of the identification procedure described in Section 2, an experimental validation has been carried out by using the data obtained from the dynamic tests performed with the shear-type model of Section 3.

As already explained, the model can be excited by impressing, at the moment by hand, time-varying base displacements to the sliding-base configuration, to simulate the effects of seismic actions.

The data for the identification procedure are given by records of the absolute acceleration, reported in Figure 5 for a sample case (m_0t_5, in Table 3). .

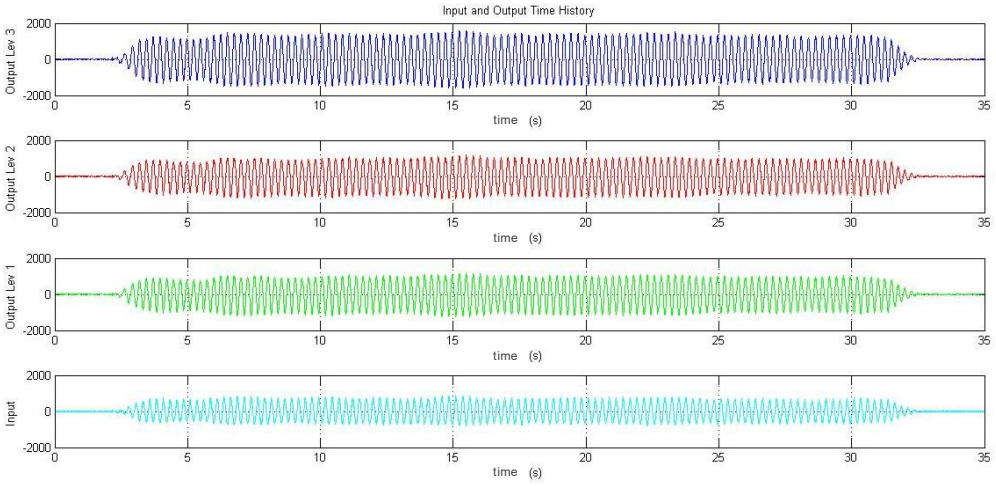

Figure 5: Input and output records of the 3 dofs frame model m_0t_5 of Table 3.

Table 5 lists the identified modal parameters obtained by means of the classical *input-output* Goyder procedure [2].

Mode	frequency Hz	damping ratio [%]	modal displacements		
			1st floor	2nd floor	3rd floor
1	2.63	1.61	-0.605	-0.880	-1.377
2	6.79	1.63	-0.285	-0.177	0.283
3	9.63	2.40	-0.088	0.139	-0.048

Table 5: Modal parameters identified by the Goyder procedure for the case m_0t_5 of Table 3.

Based on the same experimental data of case m_0t_5, Table 6 reports the modal parameters identified by means of the *output-only* procedure described in Section 2; as a starting point of the error minimization, natural frequencies, damping ratios and modal constants fairly distant from those identified with the *input-output* technique have been assumed (30 % difference), in order to test the robustness of the procedure; the *output-only* solution has been found with the minimization algorithm described in Section 2.3, within the boundaries ± 30 % with respect to the reference solution, i.e. the solution identified with the Goyder procedure.

As shown by comparison between modal parameters in Table 5 and Table 6, the *output-only* procedure, introduced in [1] and modified in [3] with an improved minimization algorithm, provides, for the sample case described here, a good agreement with the classical *input-output* procedure, as also shown by the comparison of modal shapes in Figure 6.

Mode	frequency [Hz]	damping ratio [%]	modal displacements		
			1st floor	2nd floor	3rd floor
1	2.64	1.57	-0.664	-0.956	-1.590
2	6.79	1.52	-0.306	-0.194	0.330
3	9.64	2.36	-0.078	0.157	-0.054

Table 6: Modal parameters identified by the output-only procedure for the case m_0t_5 of Table 3.

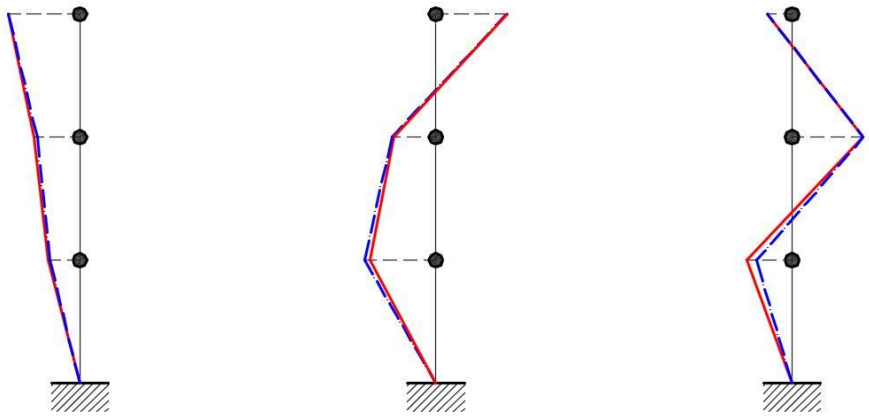

Figure 6: Comparison between modal shapes identified via the Goyder procedure (red line, values of Table 5) and via the output-only procedure (blue line, values of Table 6).

5 CONCLUSIONS

This paper describes the first results of an experimental campaign on a 3-dofs shear-type frame model, carried out to validate the *output-only* procedure proposed by one of the writers [1] to identify the modal parameters of a structure subjected to unmeasured base motion.

The modal parameters are identified by means of a minimisation algorithm, improved from the computational point of view as described in [3]. The error function to be minimised compares, in the least square sense, the analytical relationships of the dynamic response and their experimental counterparts.

As shown by the results reported, the *output-only* procedure provides a good agreement with a classical *input-output* procedure.

A larger experimental campaign is currently in progress for the validation of the procedure. A particular attention will be given to all the uncertainties emerged in the present work, as for example the dependence of the identified modal parameters on their initial estimate and the boundaries, and on the intensity and the time-length of the imposed base motion.

ACKNOWLEDGEMENTS

The financial support of University "G. d'Annunzio" of Chieti-Pescara (MIUR ex 60% funds) is acknowledged by the authors.

REFERENCES

[1] V. Sepe, D. Capecchi, M. De Angelis, Modal model identification of structures under unmeasured seismic excitations, *Earthquake Engineering and Structural Dynamics*, **34**: 807-824, 2005.

[2] H. D. G. Goyder, Methods and application of structural modelling from measured frequency response data, *Journal of Sound and Vibration*, **68**: 209-230, 1980.

[3] V. Sepe, F. Iezzi, R. Siano, C. Valente, Validation of a Modal Identification Procedure for Linear Frames under Unmeasured Seismic Input, *IEEE Workshop EESMS 2014*, September 12-17, Naples, Italy, 2014.

[4] Brinker R., L. Zhang, Andersen P., Modal identification of Output-only Systems Using Frequency Domain Decomposition, *Smart Materials and Structures*, **10** (3), 441-445, 2001.

[5] Ewins D.J., Modal testing: theory and practice, *Research Study Press –Wiley*: Chichester, 1996.

[6] M. De Angelis, V. Sepe, F. Vestroni, Identificazione dei parametri modali di una struttura eccitata alla base, *Ingegneria Sismica*, Anno XVIII n. 3, September – December 2001 (*in Italian*).

ECCOMAS Congress 2016
VII European Congress on Computational Methods in Applied Sciences and Engineering
M. Papadrakakis, V. Papadopoulos, G. Stefanou, V. Plevris (eds.)
Crete Island, Greece, 5–10 June 2016

EQUIVALENT UNIAXIAL ACCELEROGRAM FOR CSS-BASED ISOLATION SYSTEMS ASSESSMENT UNDER TWO-COMPONENTS SEISMIC EVENTS

M. Furinghetti[1], **A. Pavese**[2]

[1] EUCENTRE - Pavia
via Ferrata 1, 27100 Pavia - Italy
e-mail: marco.furinghetti@eucentre.it

[2] University of Pavia
via Ferrata 1, 27100 Pavia - Italy
a.pavese@unipv.it

Keywords: Concave Surface Slider, bi-axial interaction, frictional force, equivalent uniaxial accelerogram, bi-directional motion, base-isolation.

Abstract. *Concave Surface Slider (CSS) devices represent an effective solution for base-isolation design problems. In such isolators the energy dissipation capability is induced by the sliding motions which occur at one or more sliding interfaces. The spherical shape of the sliding surfaces provides a significant recentering behavior, by means of the stepwise projection of the applied vertical load with respect to both horizontal directions. One of the most important assumptions states that the lateral response of a CSS device can be considered as the direct summation of the recentering force and the frictional force. For two-components earthquake excitations, the recentering force is computed as a linear spring with respect to displacements along the main directions of motion; whereas, the frictional response is returned by the stepwise projection of the total frictional force, which is aligned with respect to the trajectory of the device: thus, a bi-axial interaction of the directions of motion has to be accounted for, when a friction-based device is modelled. However, available commercial software which can capture such a behavior are limited. In this work an analytical procedure is defined, for the computation of an "equivalent uniaxial accelerogram" for the seismic assessment of a base-isolated structure, subjected to a bi-directional earthquake. Thanks to the proposed theory, it is possible to compute a single ground acceleration time-history, related to a proper direction angle, which can reproduce the same effects of a two-components seismic event on a base-isolated structural system: the analogy between the equivalent uniaxial and the bi-directional events has been studied in terms of acceleration, velocity and displacement spectra respectively. Results for the base-isolated structure have been analyzed in terms of displacement, absolute acceleration and interstorey shear responses.*

1 INTRODUCTION

Concave Surface Slider (CSS) devices are widely used in real applications for seismic vulnerability mitigation all over the world. Thanks to the easy geometric and mechanical definition of such isolators, it is possible to achieve high values of dissipated energy and, consequently, lower internal forces are induced into the superstructure during the seismic event [10]. Nonetheless, a lot of research, both numerical and experimental, has been developed in last years, aiming at getting a better understanding of the lateral response characteristics of friction-based devices [3, 6]. One of the key points of the behavior of CSS isolators is represented by the frictional response under bi-directional seismic events [4, 6, 8]. Generally, the force response of a CSS device can be considered as the direct summation of a recentering force and a frictional force. The recentering contribution can be modelled as a linear spring with respect to displacements along both x and y directions, whereas the frictional force is a complicated function of vertical load, sliding velocity and cyclic effects, and it is parallel to the trajectory of the device [1]. Thus, the main frictional force has to be stepwise projected along the main directions of the reference system, and a bi-axial interaction has to be considered. This aspect has been noticed in experimental results as well as in analytical simulations [3, 5]. In Figure 1 the analytical hysteretic responses along x and y directions of a single device subjected to a cloverleaf displacement trajectory are shown (friction coefficient: 7% ; Equivalent radius of curvature: 3.1m).

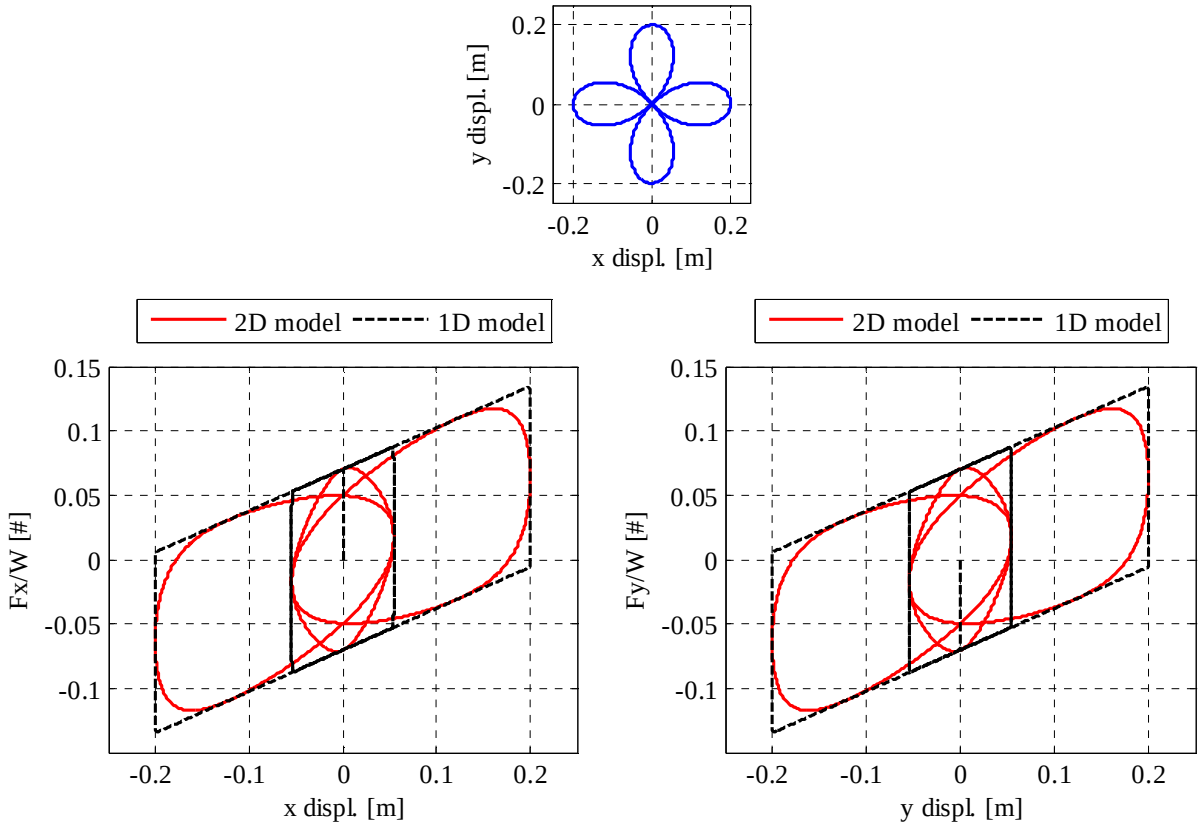

Figure 1: Analytical simulation the CSS hysteretic response under a cloverleaf trajectory.

It can be noted that by accounting for bi-axial interaction of the directions of motion, the maximum force value decreases along both x and y directions, due to the changing in orientation of the main frictional force during motion, in comparison to the unidirectional model, which considers the frictional force parallel to the recentering one at each time step. Hence,

the seismic response of a base-isolated structure can be strongly affected by the bi-axial interaction of the directions of motion. However, most of the design and verification procedures are based on simplified unidirectional approaches [9]; moreover, testing protocols for such a kind of devices mainly consist of unidirectional tests, according to UNI:EN15129 standard code [7], and bidirectional tests can be substituted by a unidirectional motion along an orthogonal direction. Furthermore, only recent versions of commercial softwares can model such behavior, and significantly high run times may be experienced.

In this work an analytical procedure is presented, which can return an equivalent uniaxial accelerogram representative of a bi-directional seismic event. Thanks to the present theory, it is possible to apply a uni-directional radial motion to the structure, for the evaluation of structural internal forces and displacements under a general bi-directional earthquake. Results of a base-isolated building structure have shown a good agreement of the response under the equivalent uniaxial event in comparison to the bi-axial one, in terms of displacement, absolute acceleration and interstorey shear values.

2 EQUIVALENT UNIAXIAL EVENT

In this section the presented procedure for the computation of the equivalent uniaxial event of a bidirectional earthquake is reported.

Generally, a bidirectional seismic event is represented by two individual ground acceleration time-series along x and y directions respectively, where x and y are plan orthogonal directions of the reference system of the analyzed structure. Since there are a lot of aspects which influence the propagation of seismic waves during an earthquake (such as rupture mechanism, soil mechanical characteristics, topographic and stratigraphic distributions, etc…), the resulting diagram which represents both the ground acceleration time series together, that is $\ddot{y}_g$ vs. $\ddot{x}_g$, consists of a scatter plot of acceleration points, and no preferential direction of motion can be immediately detected. In Figure 2 the ground acceleration diagram related to the Irpinia earthquake 1980 is reported.

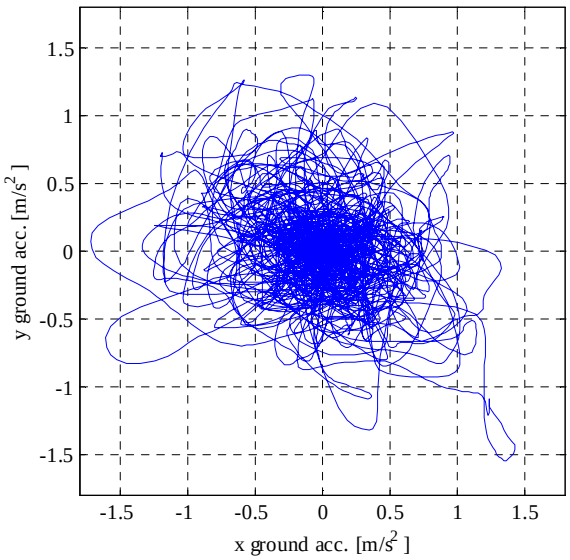

Figure 2: Irpinia earthquake 1980 – Ground acceleration diagram.

Thus, the response spectrum of the seismic event has to be considered. A response spectrum of the bi-directional event has been defined, by means of the direct integration of the

equations of motion along both x and y directions of a linear single oscillator with different values of structural periods T and for a given damping ratio ξ:

$$\begin{aligned} \ddot{x} + 2\xi\omega\dot{x} + \omega^2 x &= -\ddot{x}_g \\ \ddot{y} + 2\xi\omega\dot{y} + \omega^2 y &= -\ddot{y}_g \end{aligned} \tag{1}$$

Hence, the maximum vectorial displacement and absolute acceleration are detected.

$$\begin{aligned} S_d^{2D}(\xi, T) &= \max\left(\sqrt{x^2 + y^2}\right) \\ S_a^{2D}(\xi, T) &= \max\left(\sqrt{\left(\ddot{x} + \ddot{x}_g\right)^2 + \left(\ddot{y} + \ddot{y}_g\right)^2}\right) \end{aligned} \tag{2}$$

By considering several period values, the reference response spectrum related to the bidirectional earthquake is finally obtained. Therefore, for a given direction angle, the projection of each acceleration point shown in Figure 2 is obtained, in order to compute a single ground acceleration component along the considered direction. In Figure 3 the projection procedure is reported.

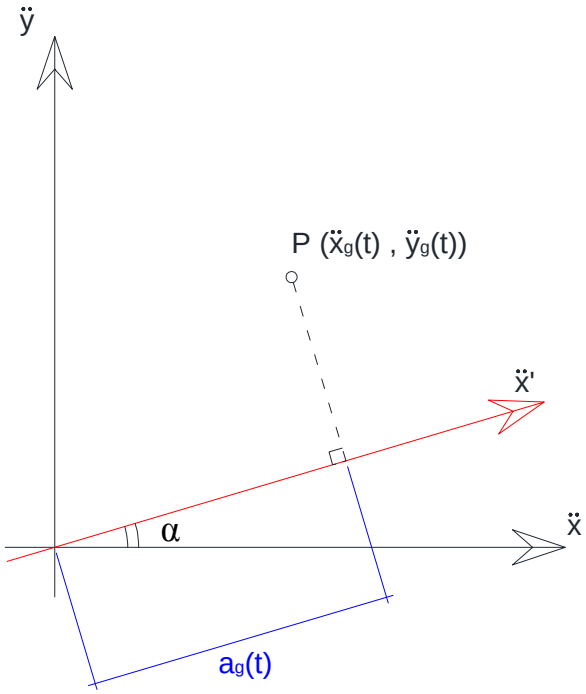

Figure 3: Equivalent uniaxial event – Projection procedure.

According to the aforementioned scheme, the uniaxial projection of the bidirectional earthquake $a_g(t)$ is defined for the given orientation α as follows:

$$a_g(t) = \ddot{x}_g(t)\cos(\alpha) + \ddot{y}_g(t)\sin(\alpha) \tag{3}$$

Consequently, the ordinary 1D acceleration and displacement response spectra associated to $a_g(t)$ can be obtained, by assuming the same damping ratio of the reference 2D response spectrum. Then, a parameter which describes the discrepancies between the reference 2D and the 1D response spectra is defined, by computing the square root of the Mean Squared Error:

such a parameter can be computed by considering either the acceleration or the displacement response spectrum; both the approaches have been evaluated for sake of comparison.

$$E^{S_d}(\xi,\alpha) = \sqrt{MSE^{S_d}} = \sqrt{\frac{1}{n_T}\sum_{i=1}^{n_T}\left(S_d^{2D}(\xi,T_i) - S_d^{1D}(\xi,\alpha,T_i)\right)^2}$$
$$E^{S_a}(\xi,\alpha) = \sqrt{MSE^{S_a}} = \sqrt{\frac{1}{n_T}\sum_{i=1}^{n_T}\left(S_a^{2D}(\xi,T_i) - S_a^{1D}(\xi,\alpha,T_i)\right)^2} \quad (4)$$

Where n_T is the total number of structural periods, considered for the computation of the response spectra. Finally, by considering the direction angle α within a range between 0° and 180°, the optimum direction angle which returns the minimum error parameter can be obtained. In Figure 4 and Figure 5 the aforementioned procedure has been applied to the Irpinia earthquake 1980, by considering a damping ratio equal to 5% and acceleration and displacement spectra respectively.

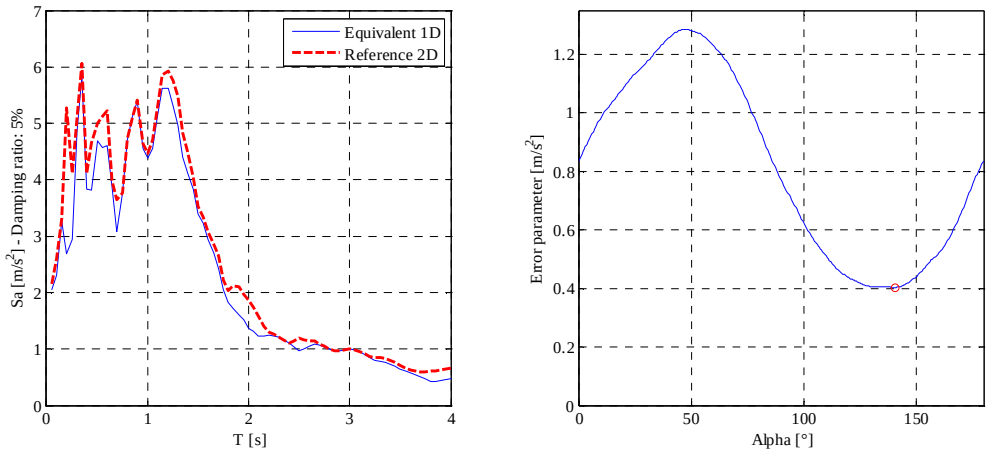

Figure 4: Equivalent uniaxial event – Irpinia earthquake – acceleration-based procedure.

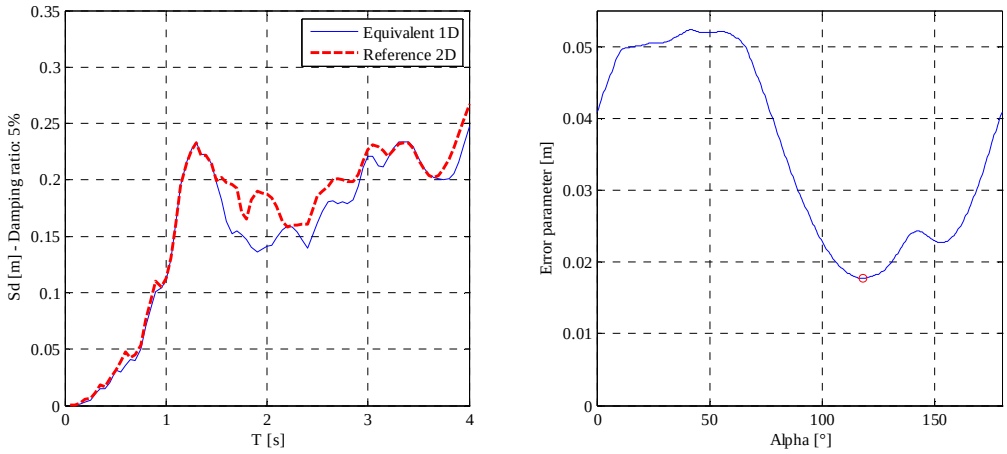

Figure 5: Equivalent uniaxial event – Irpinia earthquake – displacement-based procedure.

In what follows results for three different bidirectional earthquakes are reported, by varying the damping ratio; the analyzed seismic events are listed in Table 1.

Event #	Location	Year	Mw	PGA_x [m/s^2]	PGA_y [m/s^2]
1	Irpinia	1980	6.9	1.718	1.550
2	Emilia	2012	6.1	2.574	2.591
3	L'Aquila	2009	6.3	6.442	5.352

Table 1: Equivalent uniaxial event – seismic events characteristics.

Results are shown in terms of both optimum direction angle and error parameter values as a function of the damping ratio. In Figure 6 and Figure 7 results are shown, by considering acceleration and displacement error respectively.

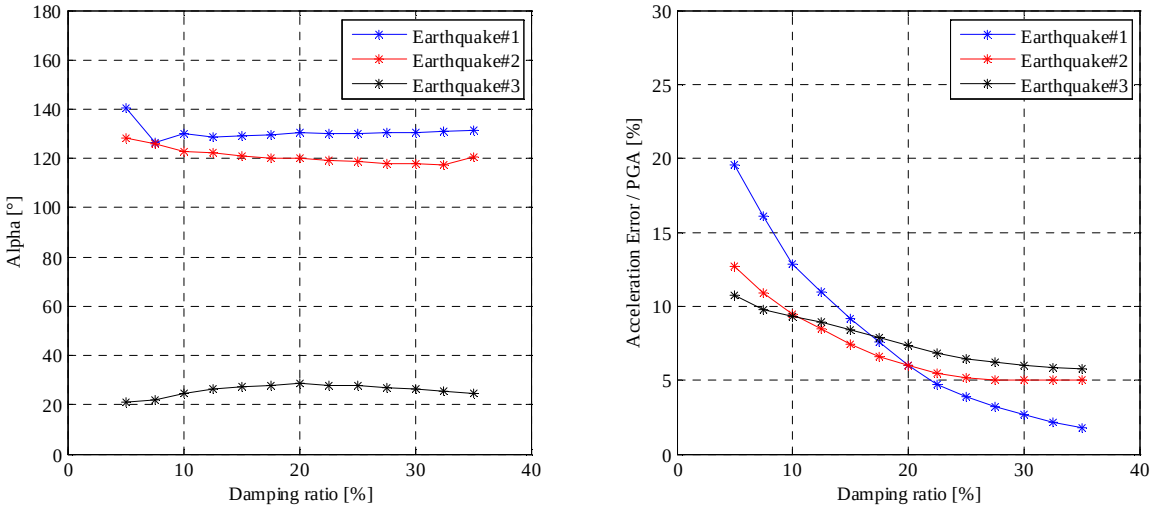

Figure 6: Equivalent uniaxial event – damping analysis – acceleration-based procedure.

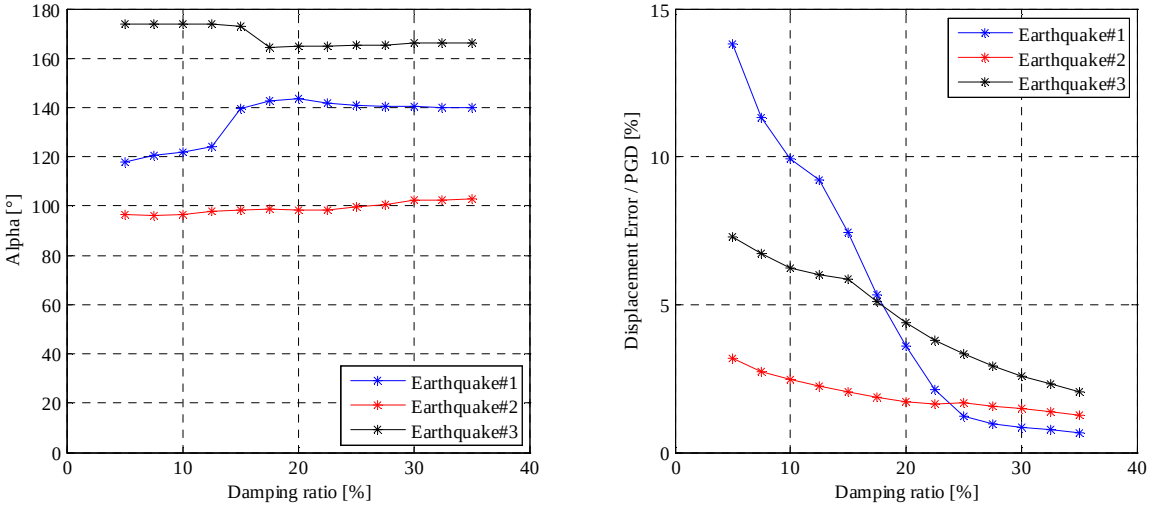

Figure 7: Equivalent uniaxial event – damping analysis – displacement-based procedure.

It can be noted that the acceleration spectrum approach leads to more stable results, in terms of optimum direction angle value, which can be considered approximately constant with respect to increasing values of damping ratio; in addition, as the damping ratio increases, the acceleration error parameter significantly decreases, and a similar decay trend of the acceleration error has been found among the considered earthquakes. On the other hand, the dis-

placement-based procedure returns more irregular results: the optimum variation angle value can be affected by the damping ratio and, decreasing trend of the displacement error parameter is found at high values of damping ratio as well as for the acceleration procedure.

3 ANALYTICAL MODEL DEFINITION

In this endeavor the structural model presented in Furinghetti and Pavese 2015 has been used [4], which consists of a Multi Degrees Of Freedom (MDOF) scheme, base-isolated by means of an equivalent CSS device, which is representative of the entire isolation system (Figure 8).

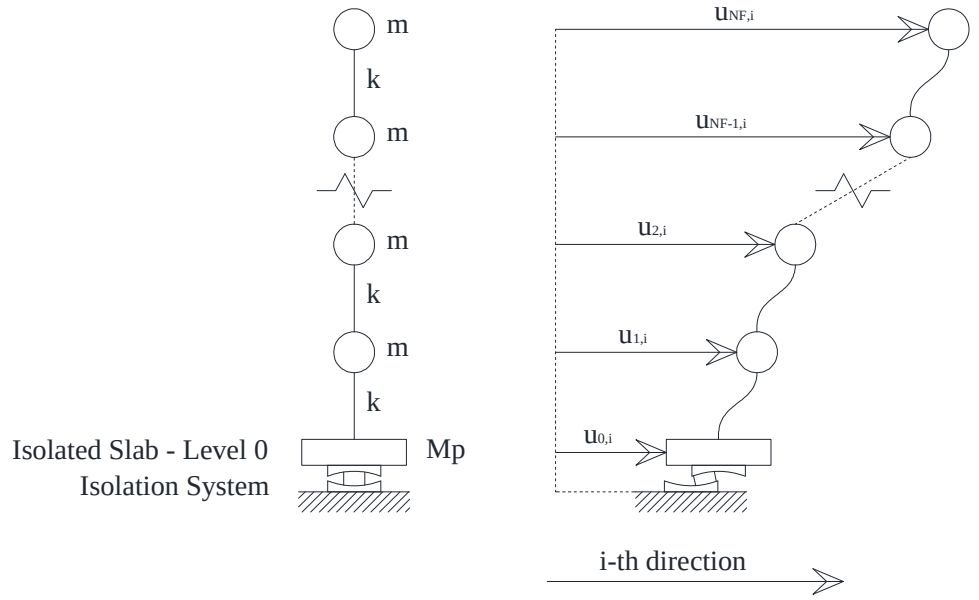

Figure 8: Dynamic model of the isolated structure.

This assumption can be adopted when a building with a large plan development is considered. Thus, all the isolators have averagely the same vertical load, directly equal to the total weight of the isolated structure divided by the number of devices. Hence, the horizontal force along both x and y directions of the isolation system can be computed as follows:

$$\frac{F_{is}}{m} = g \cdot N_F \cdot \left(1+\frac{1}{r}\right) \cdot \left\{ \frac{1}{R_{eq}} \begin{bmatrix} u_{0,x} \\ u_{0,y} \end{bmatrix} + \mu(W,v,E) \cdot \tanh\left(\frac{v}{v_s}\right) \cdot \begin{bmatrix} \dfrac{\dot{u}_{0,x}}{\sqrt{(\dot{u}_{0,x})^2+(\dot{u}_{0,y})^2}} \\ \dfrac{\dot{u}_{0,y}}{\sqrt{(\dot{u}_{0,x})^2+(\dot{u}_{0,y})^2}} \end{bmatrix} \right\}$$

being (5)

$$\frac{W_{tot}}{m} = \frac{g}{m} \cdot \left(M_B + M_P\right) = \frac{g}{m} \cdot M_B \cdot \left(1+\frac{M_P}{M_B}\right) = \frac{g}{m} \cdot M_B \cdot \left(1+\frac{1}{r}\right) = g \cdot N_F \cdot \left(1+\frac{1}{r}\right)$$

Where M_B is the total mass of the building, and M_P is the mass of the isolated plate. Finally, the normalized dynamic system of the isolated structure is consequently defined for direction

i = x, y. The contribution of the isolation system has to be added in the first equation only for both directions, which represents the translational dynamic equilibrium of the isolated slab.

$$\left[\frac{M_{tot}}{m}\right]\begin{pmatrix}\ddot{u}_{0,i}\\ \hline \ddot{u}_{1,i}\\ \ddot{u}_{2,i}\\ \vdots\\ \ddot{u}_{N_F,i}\end{pmatrix}+\left[\frac{C_{tot}}{m}\right]\begin{pmatrix}0\\ \hline \dot{u}_{1,i}-\dot{u}_{0,i}\\ \dot{u}_{2,i}-\dot{u}_{0,i}\\ \vdots\\ \dot{u}_{N_F,i}-\dot{u}_{0,i}\end{pmatrix}+\left[\frac{K_{tot}}{m}\right]\begin{pmatrix}u_{0,i}\\ \hline u_{1,i}\\ u_{2,i}\\ \vdots\\ u_{N_F,i}\end{pmatrix}+\frac{F_{is,i}}{m}\begin{pmatrix}1\\ 0\\ 0\\ \vdots\\ 0\end{pmatrix}=-\left[\frac{M_{tot}}{m}\right]\cdot\ddot{u}_{g,i} \qquad (6)$$

The damping matrix is obtained by accounting for Rayleigh damping, with a target damping ratio equal to 5% [11].

4 CASE STUDY STRUCTURE AND SEISMIC INPUT

The case study building consists of a three storey R.C. frame structure, with a total mass equal to 2048 tons [2], which is base-isolated by means of CSS devices, and a R.C. isolated slab with a thickness of 0.5m, as shown in Figure 9.

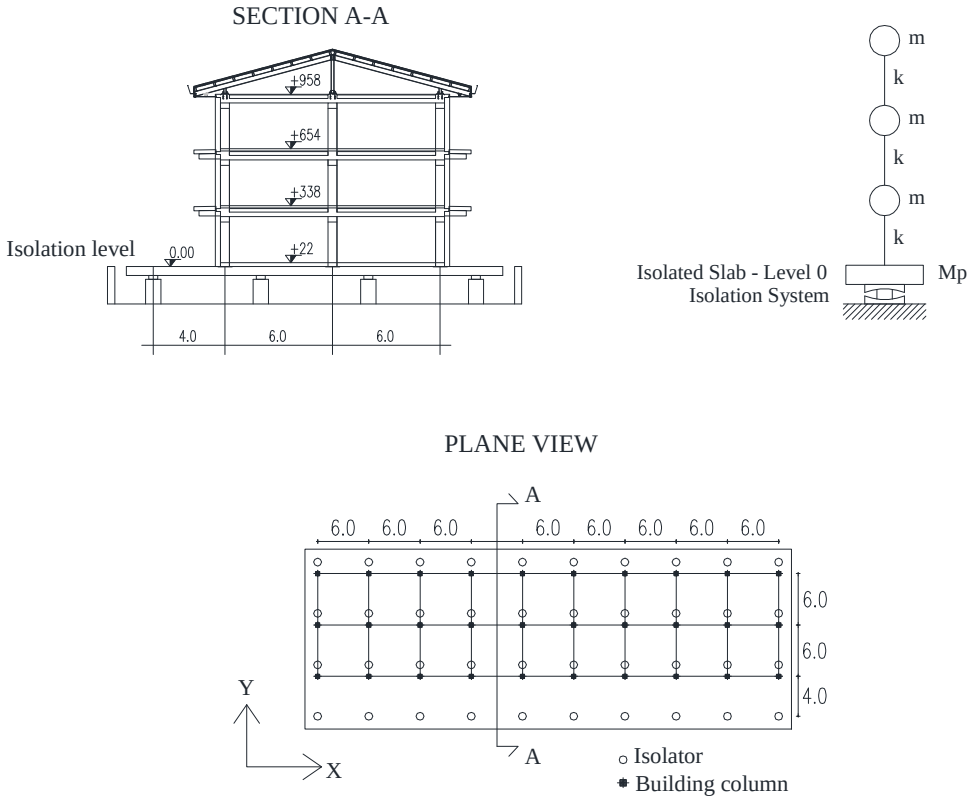

Figure 9: Case study structure.

The isolated plate has a total mass equal to 1496 tons: thus, according to the aforementioned analytical model, the ratio between the masses of the building and the isolated plate is equal to 1,37. The first mode period is equal to 0,48s and a target damping ratio of 5% has been set for all the modes. CSS devices have been modelled with a an equivalent radius of curvature equal to 3,1m; furthermore, in this work the friction coefficient has been considered

as a constant function of vertical load, sliding velocity and dissipated energy: the numerical value is equal to 7% [3, 4].

For what concerns the input signals, all the previously analyzed earthquakes have been applied to the case study structure. Since the displacement demand and the associated hysteretic damping ratio is not a priori known, for all the bi-directional earthquakes the optimum direction angle of the equivalent uniaxial event has been computed with a damping ratio equal to 5% and both acceleration and displacement approaches have been processed. In Table 2 the characteristics of the seismic events are listed.

Event #	Location	Scale factor	1D angle [°] acc. approach	1D angle [°] displ. approach
1	Irpinia	1.5	140.5	118.0
2	Emilia	1.5	128.0	94.5
3	L'Aquila	1.5	21.0	179.5

Table 2: Case study– seismic events characteristics.

A scale factor for both x and y components equal to 1.5 has been used for all the considered seismic events, in order to achieve a maximum displacement demand comparable to the design displacement capacity of the devices.

5 ANALYSES RESULTS

In the followings the results are shown in terms of displacement, absolute acceleration and interstorey shear profiles of the case study structure, subjected to the bidirectional event in comparison to the equivalent uniaxial cases.

In Figure 10 , Figure 11 and Figure 12 displacement results are reported for earthquake #1, #2 and #3 respectively, and by accounting for acceleration (left) rather than displacement (right) approach.

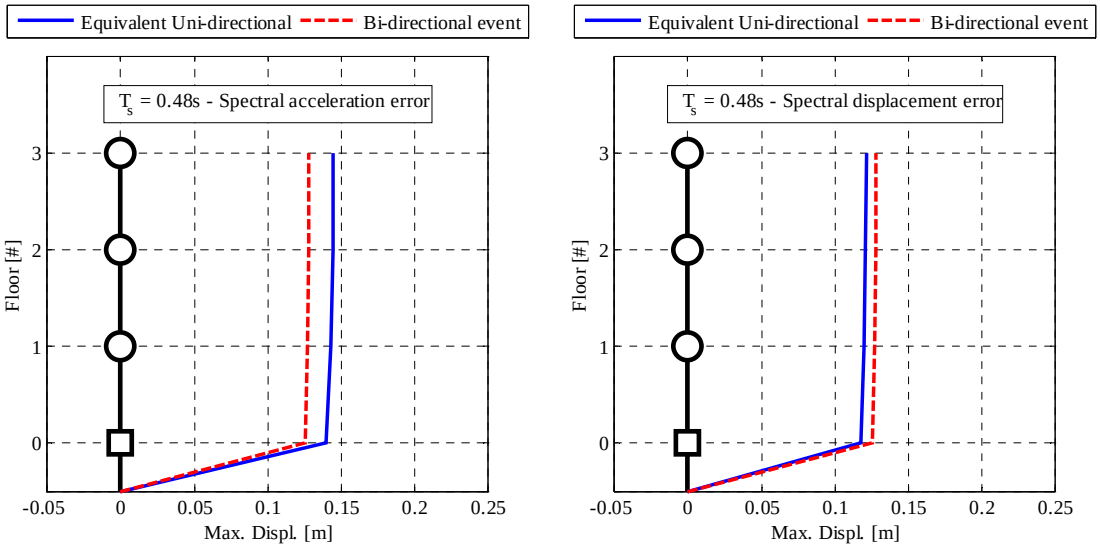

Figure 10: Results – Eqk#1 – displacement profiles.

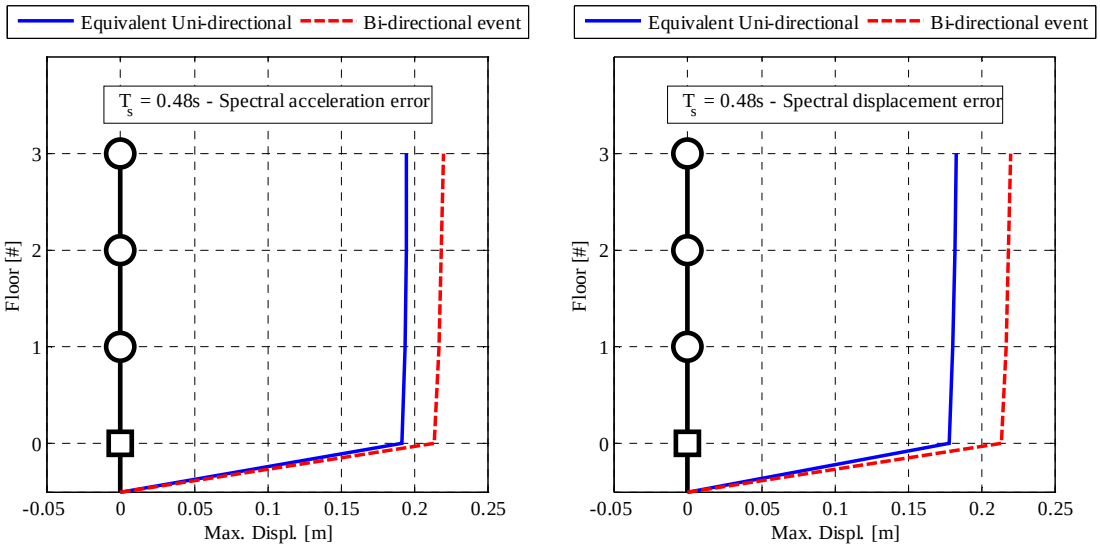

Figure 11: Results – Eqk#2 – displacement profiles.

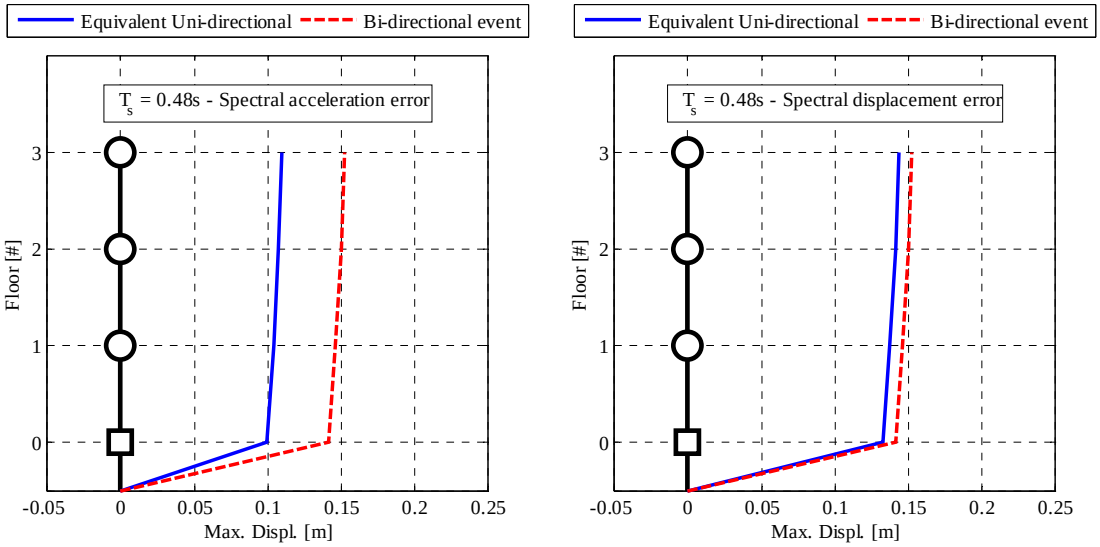

Figure 12: Results – Eqk#3 – displacement profiles.

In Table 3 the variation percentages at all levels of the displacement demand related to the equivalent uniaxial earthquake in comparison to the biaxial seismic event.

	Eqrthquake #1		Eqrthquake #2		Eqrthquake #3	
Level #	Acc. approach	Displ. approach	Acc. approach	Displ. approach	Acc. approach	Displ. approach
0	11.9%	-6.3%	-10.7%	-17.0%	-29.6%	-6.0%
1	12.4%	-5.8%	-10.8%	-16.8%	-28.7%	-5.8%
2	13.0%	-5.3%	-11.1%	-16.8%	-28.2%	-5.7%
3	13.3%	-5.0%	-11.4%	-16.8%	-28.1%	-5.6%

Table 3: Results – Variation percentages – displacement response.

As can be noted, for earthquake #1 and #3 the best agreement is achieved by using the displacement spectrum approach, whereas for the second earthquake the direction angle returned by the acceleration procedure leads to better results. Generally, the displacement demand decreases at all levels, if the equivalent uniaxial event is considered; only for earthquake #1 with acceleration approach opposite evidences have been found.

In Figure 13 , Figure 14 and Figure 15 absolute acceleration results are reported for earthquake #1, #2 and #3 respectively, and by accounting for acceleration (left) rather than displacement (right) approach.

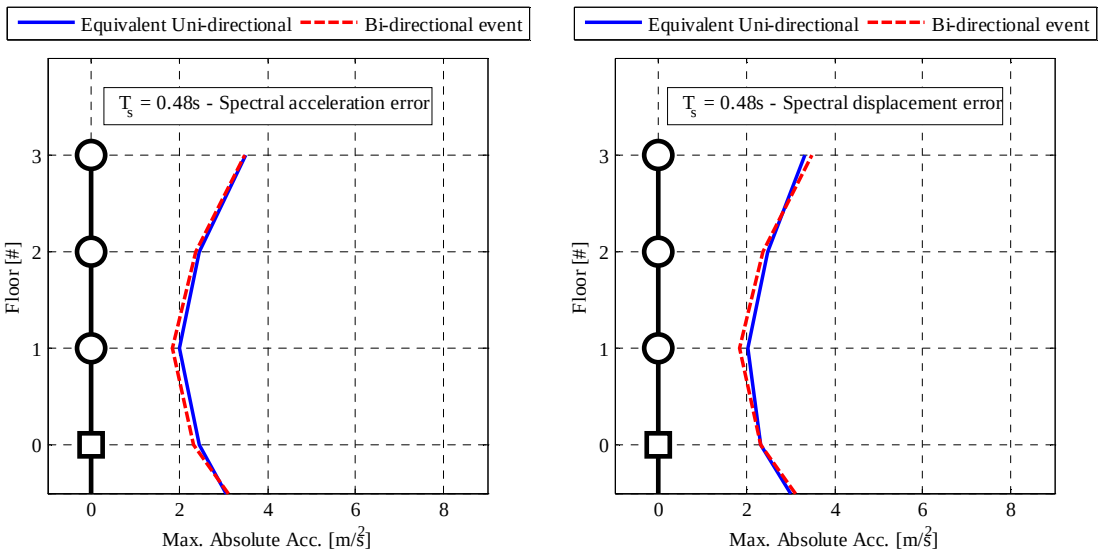

Figure 13: Results – Eqk#1 – absolute acceleration profiles.

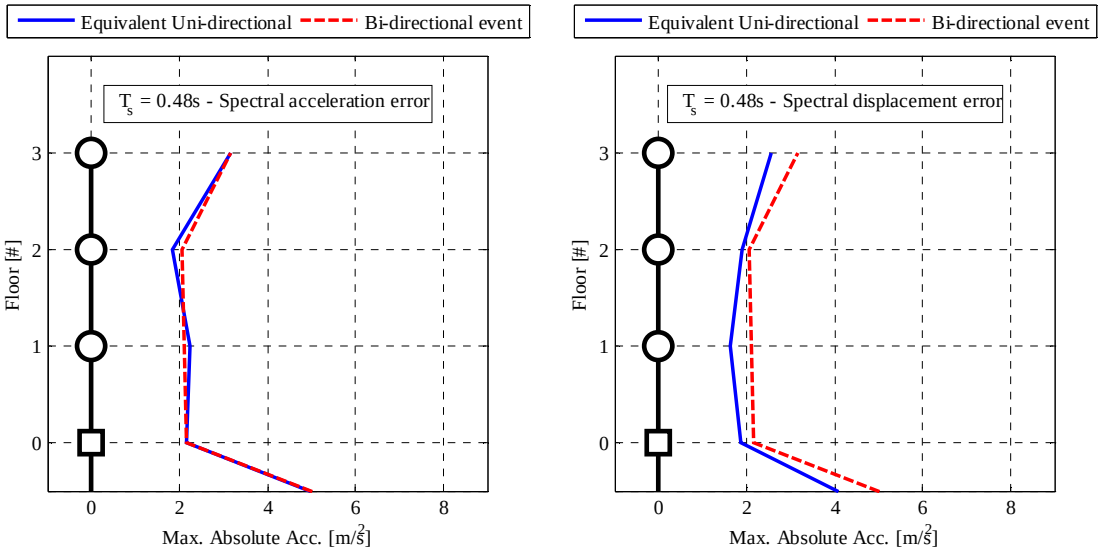

Figure 14: Results – Eqk#2 – absolute acceleration profiles.

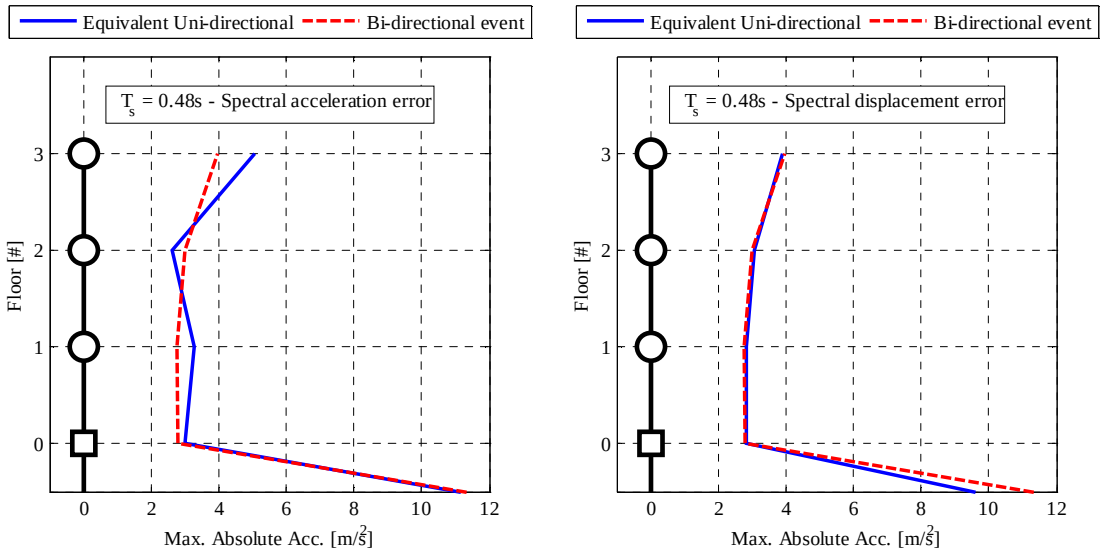

Figure 15: Results – Eqk#3 – absolute acceleration profiles.

In Table 4 the variation percentages at all levels of the absolute acceleration demand related to the equivalent uniaxial earthquake in comparison to the biaxial seismic event.

	Eqrthquake #1		Eqrthquake #2		Eqrthquake #3	
Level #	Acc. approach	Displ. approach	Acc. approach	Displ. approach	Acc. approach	Displ. approach
0	4.8%	0.0%	0.3%	-13.1%	7.5%	0.9%
1	7.9%	9.0%	6.0%	-22.5%	17.6%	2.3%
2	3.9%	4.3%	-10.1%	-7.9%	-12.2%	2.6%
3	0.7%	-4.8%	0.1%	-19.1%	28.2%	-1.4%

Table 4: Results – Variation percentages – absolute acceleration response.

In all cases acceleration profiles relative to the biaxial seismic event are almost overlapped to the ones associated to the equivalent uniaxial earthquake: thus, even though 5% damping is assumed for the computation of the optimum direction angle for both displacement and acceleration approaches, the acceleration response can be properly captured by applying an equivalent radial motion. For eqk#1 and #2 the best comparison is obtained by accounting for the acceleration procedure, whereas for eqk#3 the displacement approach provides a better estimates of the bidirectional acceleration profile.

In Figure 16 , Figure 17 and Figure 18 interstorey shear results are reported for earthquake #1, #2 and #3 respectively, and by accounting for acceleration (left) rather than displacement (right) approach.

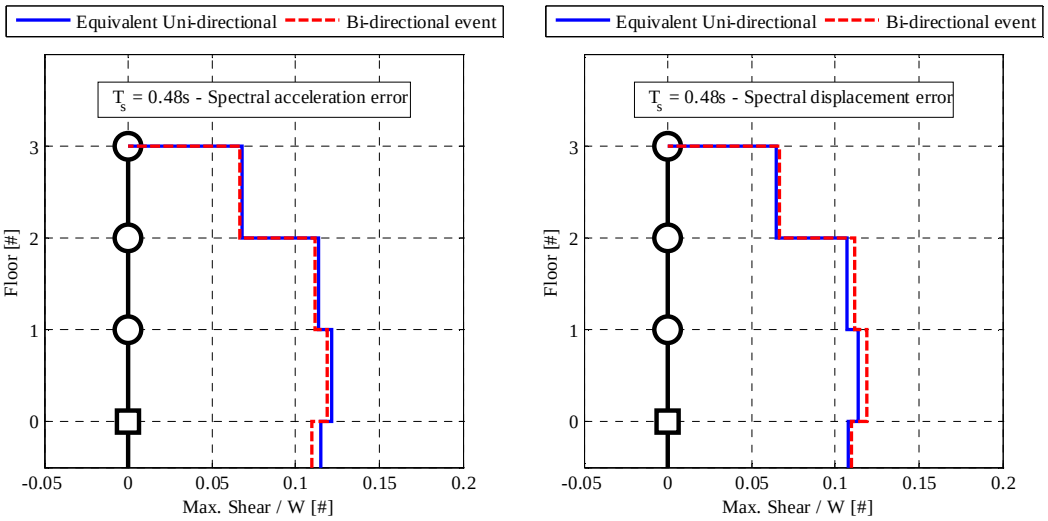

Figure 16: Results – Eqk#1 – interstorey shear profiles.

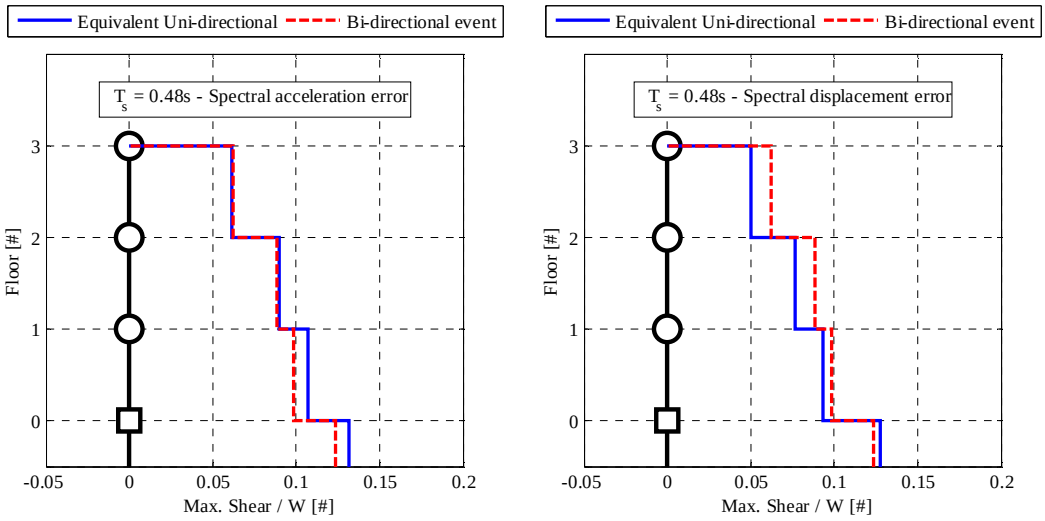

Figure 17: Results – Eqk#2 – interstorey shear profiles.

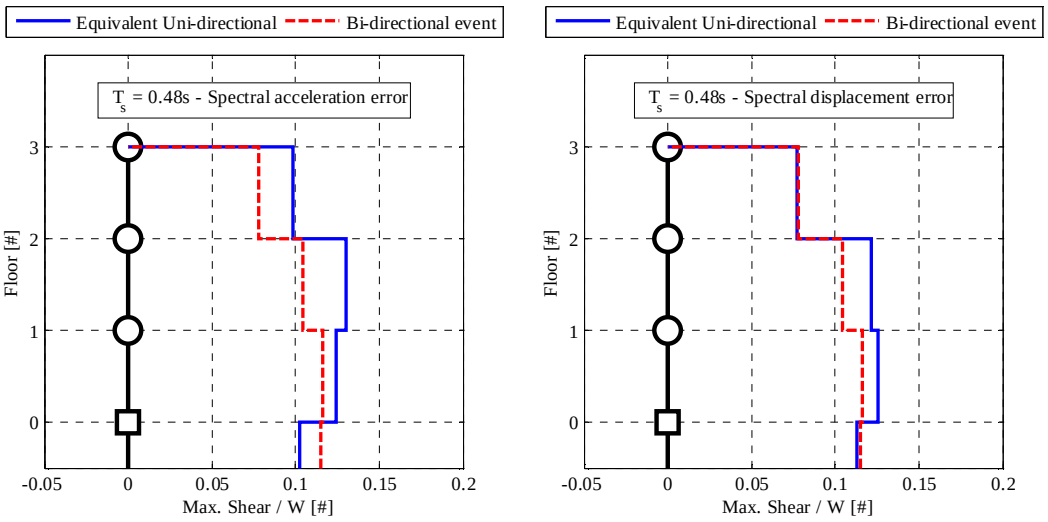

Figure 18: Results – Eqk#3 – interstorey shear profiles.

In Table 5 the variation percentages at all levels of the interstorey shear demand related to the equivalent uniaxial earthquake in comparison to the biaxial seismic event.

	Eqrthquake #1		Eqrthquake #2		Eqrthquake #3	
Level #	Acc. approach	Displ. approach	Acc. approach	Displ. approach	Acc. approach	Displ. approach
0	5.1%	-1.6%	6.8%	3.3%	-11.1%	-1.7%
1	2.2%	-4.3%	8.8%	-4.9%	6.5%	7.7%
2	2.1%	-4.1%	1.4%	-13.4%	25.0%	16.6%
3	1.9%	-2.9%	-1.1%	-19.2%	26.4%	-1.1%

Table 5: Results – Variation percentages – interstorey shear response.

Also concerning shear profiles, the equivalent unidirectional event provides a good estimate of the bidirectional response at all levels. Again, the acceleration procedure leads to better results for eqk#1 and #2.

6 CONCLUSIONS AND FUTURE DEVELOPMENTS

In this work an analytical procedure for the computation of an equivalent uniaxial seismic event for a bidirectional earthquake is presented. Such a procedure allows to compute the optimum direction angle of the equivalent radial motion, by projecting along several directions all the acceleration points of the bidirectional earthquake and evaluating the associated error parameter between the biaxial and the uniaxial response spectrum; both acceleration and displacement response spectra have been considered. Three different bidirectional seismic events have been studied and then applied to a case study base-isolated structure, in order to underline differences between the biaxial and the equivalent uniaxial responses, in terms of displacement, absolute acceleration and interstorey shear demands.

For the analyzed earthquakes it has been noticed that the optimum direction angle can be approximately considered constant with respect to the damping ratio and the error parameter significantly decreases with increasing values of damping ratio, if the acceleration spectrum approach is used; on the other hand the displacement approach leads to more irregular results.

Concerning structural responses, displacement demands at all levels are underestimated when the equivalent uniaxial earthquake is applied, exception made for earthquake #1, with acceleration approach. The best approximation is returned by the acceleration approach, which leads to variations in the range between 5% and 15%, whereas higher variations can be experienced with displacement approach. Regarding absolute acceleration responses, a good agreement between biaxial and equivalent uniaxial events is reached with both the approaches, even though in most of the cases the lowest variations can be found with the acceleration-based procedure (less than 10%). Similar conclusions can be drawn also for interstorey shear responses.

Future developments of the present work will consist of a wide numerical study on a real application, modelled with a commonly used commercial software, in order to underline influences in the main response parameters of the effective horizontal and vertical spatial distribution of the structural elements, by accounting for both biaxial and equivalent uniaxial earthquakes; furthermore, a wider set of seismic events will be analyzed, aiming at generalizing all the previously discussed aspects.

REFERENCES

[1] M. Furinghetti, C. Casarotti, A. Pavese, Effects of bi-directional motion on a structural system isolated with DCSS devices with laying defects. *15th WCEE, World Conference on Earthquake Engineering*, Lisbon, Portugal, September 24-28, 2012.

[2] C. Casarotti, M. Furinghetti, A. Pavese, Evaluation of response of an isolated system based on Double Curved Surface Slider. *Computational method in Earthquake Engineering*, **30**, pp 397-416, 2013.

[3] M. Furinghetti, C. Casarotti, A. Pavese, Bi-directional experimental response of full scale DCSS devices. *2ECEES, Second European Conference on Earthquake Engineering and Seismology*, Istanbul, Turkey, August 25-29, 2014.

[4] M. Furinghetti, A. Pavese, Numerical Assessment on the Seismic Response of a Base-Isolated Building under Bi-Directional Motion. *5th ECCOMAS Thematic Conference on Computational Methods in Structural Dynamics and Earthquake Engineering*, Crete Island, Greece, May 25-27, 2015.

[5] G. Lomiento, N. Bonessio, G. Benzoni, Concave sliding isolator's performance under multi-directional excitation. *Ingegneria Sismica*, **30:3**,17-32, 2013.

[6] G. Mosqueda, A.S. Whittaker, G.L. Fenves, Characterization and modeling of friction pendulum bearings subjected to multiple components of excitation. *Journal of Structural Engineering*, **130**, 433-442, 2004.

[7] CEN, Comité Européen de Normalisation TC 340, *European Code UNI EN 15129:2009 Anti-seismic devices*. Brussels, 2009.

[8] F. Khoshnoudian, V.R. Hagdoust, Response of pure-friction sliding structures to three components of earthquake excitation considering variations in the coefficient of friction. *Scientia Iranica*, **16**, 429-442, 2009.

[9] M. Dolce, D. Cardone, F. C. Ponzo, A. Di Cesare, *Progetto di edifici con isolamento sismico, Seconda Edizione*. IUSS Press, 2010.

[10] D. Fenz, M. C. Constantinou, Behaviour of the double concave friction pendulum bearing. *Earthquake Engineering And Structural Dynamics*, **35**,1403–1424, 2006.

[11] A. K. Chopra, *Dynamics of Structures Theory and Applications to Earthquake Engineering*. Prentice Hall, Upper Saddle River, NJ, 1995.

ECCOMAS Congress 2016
VII European Congress on Computational Methods in Applied Sciences and Engineering
M. Papadrakakis, V. Papadopoulos, G. Stefanou, V. Plevris (eds.)
Crete Island, Greece, 5–10 June 2016

MIXED SOLID MODELS IN NUMERICAL ANALYSIS OF SLENDER STRUCTURES

D. Magisano[1], **L. Leonetti**[1], **and G. Garcea**[1]

[1]Dipartimento di Infromatica, Modellistica, Elettronica e Sistemistica, Università della Calabria
87030 Rende (Cosenza), Italy
e-mail: domenico.magisano@hotmail.it, leonardo.leonetti@unical.it, giovanni.garcea@unical.it

Keywords: Slender beam and shell, mixed formulations, 3D solid element, Koiter analysis

Abstract. *The reasons of the better performances of mixed, stress–displacements, 3D solid finite elements in the analysis of slender elastic structures are explained. It will be shown that mixed or compatible description, also when derived from the same finite element and then completely equivalent from the discretization point of view, behave very differently when implemented in both asymptotic and path–following solution strategies due to the occurrence of a pathological locking phenomenon in the compatible formulation. The notable advantages of the used of a 3D mixed solid finite element in Koiter asymptotic analysis are also highlighted.*

1 INTRODUCTION

In recent years an increasing amount of research has aimed at developing new efficient solid finite elements [1] for the linear and nonlinear analysis of thin structures. This is due to the advantages of solid elements in comparison to classical shell elements. In particular in the elastic nonlinear analysis of slender structures they allow the use of the 3D continuum strain and stress measures employing translational degrees of freedom only [1, 2, 3, 4]. In this way it is possible to avoid the use of complicated and expensive rules for updating the rotations and, by using the Green-Lagrange strain measure, to coherently describe the structural behavior through a low order dependence on the displacement field. Moreover in this context, solid elements allow: a simpler expression of the strain energy and its variations with a gain in computational efficiency; the recovery of the complete 3D stress state and the application of nonlinear constitutive laws; simpler geometric and kinetic descriptions; the simple discretization of structures with both solid and shell-like regions. Furthermore the independence of the model from rigid body motion or change in the observer (objectivity) is automatically fulfilled without the need to employ complex, geometrically exact formulations, which are not always available or accurate [5, 6, 7].

However, formulating robust solid-shell elements is more demanding than shell elements. To maintain an acceptable number of degrees of freedom, the elements proposed are usually based on a low order displacement interpolation. Consequently they have the disadvantages of *interpolation lockings*: the shear and membrane locking also present in classical shell elements and trapezoidal and thickness locking, typical of low order solid-shell elements [8]. Interpolation lockings are usually sanitized by means of Assumed Natural Strain, Enhanced Assumed Strain [9, 10, 11, 12] and mixed (hybrid) formulations [1, 4, 13, 14]. In this way solid-shell elements have now reached a high level of efficiency and accuracy and have also been used to model composites or laminated beams [11, 15, 13, 16] and shell structures in both the linear [9, 3] and nonlinear [12, 2, 1] range. Among the most effective and interesting proposals we refer to are the mixed solid-shell elements of Sze and coauthors [1, 13, 17, 18, 19, 20, 21, 16, 22, 23] which extend the initial PT18β hybrid element of Pian and Tong to thin shell.

When comparing mixed and compatible finite elements many authors (see for example [1] and [2]) observe that the mixed ones are more robust and allow larger steps in path–following geometrically nonlinear analyses. However the reasons for these better performances are, in our opinion, not clear, as they are often wrongly attributed to the properties of the finite element interpolation. One of the goals of this paper is therefore to clarify the true reason and the origin of this phenomenon, extending the results presented some years ago [24, 25] in the context of path-following and Koiter [26, 27, 28] asymptotic analyses of 2D framed structures.

Mixed and compatible description, while completely equivalent at the continumm level, behave very differently when implemented in path-following and asymptotic solution strategies even when they are based on the same finite element interpolations, that is when they are equivalent also at the discrete level. This is an important, even if frequently misunderstood, point in developing numerical algorithms and it has been discussed in [24, 25, 29] to which we refer readers for more details. To represent the strain energy in a *smooth enough* way in order to make the truncation error of its Taylor expansion up to a given order as small as possible is crucial: in path-following analysis, this ensures a fast convergence of the Newton (Riks) iterative process; in asymptotic analysis, which is based on Taylor series the expansion of the strain energy [26, 28] implies an accurate recovery of the equilibrium path. Since the smoothness of a nonlinear function strictly depends on the set of variables used for its description, a key point to

be considered when approaching the solution of a nonlinear problem is the selection of the most appropriate set of variables. In fact mixed and compatible descriptions are characterized by a different smoothness of the strain energy and so they behave very differently when used within a numerical solution process. In particular representing the strain energy by using displacements only (compatible description) as variables has to be considered the least suitable choice as, in this case the truncation error of a Taylor expansion depends, pathologically, on the presence of directions with very different stiffness, while this is not the case in a mixed format. For shells or beams, in the presence of large displacements (rigid rotations) and high membranal/flexural stiffness ratios, the truncation error of the compatible description becomes large and causes a very slow convergence rate in path-following analysis and an unreliable estimate of the bifurcation point and of the post–critical coefficients in the asymptotic analysis. As will be shown, using solid elements means the mixed description is unaffected by this kind of locking, that we call *extrapolation locking*.

In this paper a mixed and a compatible description are derived for the same finite element, so obtaining two completely equivalent discrete problems, in order to show that their different behavior is not due to the interpolation fields and that the extrapolation locking occurs for any compatible finite element. This is an important aspect not taken into account by the scientific community because, usually, lockings are attributed to the interpolation only.

Moreover, note that the solid element based on the quadratic Green-Lagrange strain measure, minimizes the strain energy dependence on the finite element (FE) discrete variables: the fourth order dependence on displacement variables in the compatible formulation and the third order in stress and displacement variables in the mixed case. Although this does not produce any real important benefit with respect to the extrapolation locking it does however have a significant effect on the efficiency, robustness and coherence of the asymptotic analysis when the mixed description is used. It allows, in fact, the zeroing of all the strain energy variations of an order greater than the third and, consequently, permits light numerical formulations and an improvement in accuracy. In this way it is possible to develop new asymptotic algorithms well suited to the imperfection sensitivity analysis of structures presenting coincident or almost coincident buckling loads, which are more accurate and computationally efficient than those based on classical shell elements. This advantage holds in standard path-following analysis where however it only allows simpler expressions of the tangent stiffness matrix and the structural response.

Finally it is worth mentioning that the use of both displacement and stress variables increases the dimension of the problem, but generally the computational extra–cost, with respect to a compatible analysis, is very low. This is because the global operations involve displacement dofs by performing a static condensation of the stress variables, when locally defined at element level. This small computational extra-cost is largely compensated for: in path-following analysis by larger steps and fewer iterations with respect to the compatible case; in asymptotic analysis by the zeroing of the computationally expensive fourth order strain energy variations. We will also show how the small nonlinearity that the equilibrium path assumes when represented in mixed variables allows, in path following analyses, an efficient use of the modified Newton method with a further significant reduction in the computational cost.

2 MIXED AND COMPATIBLE DESCRIPTIONS

In this section, two equivalent descriptions, one in stresses and displacements called *mixed description* and another in displacement parameters only, called *compatible description*, are derived. We refer to [29, 28, 7, 6] for a description of the asymptotic method.

2.1 The discrete nonlinear equations

We consider a slender hyperelastic structure subject to conservative loads $p[\lambda]$ proportionally increasing with the amplifier factor λ. The equilibrium is expressed by the virtual work equation

$$\Phi[u]'\,\delta u - \lambda \hat{p}\,\delta u = 0 \quad , \quad u \in \mathcal{U}\ ,\ \delta u \in \mathcal{T} \tag{1}$$

where $u \in \mathcal{U}$ is the field of configuration variables, $\Phi[u]$ denotes the strain energy, $\mathcal{T}$ is the tangent space of $\mathcal{U}$ at u and a prime is used to express the Frechèt derivative with respect to u. We assume that $\mathcal{U}$ will be a linear manifold so that its tangent space $\mathcal{T}$ will be independent of u. When a mixed format is adopted the configuration variables u collect both displacement and stress fields.

The element strain energy can, as usual in a FE context, be expressed as a sum of element contributions that, using a mixed interpolation for the displacement and the stress field $\boldsymbol{\sigma}$ and letting with Ω_e the element domain, becomes

$$\begin{aligned}
\Phi[u] &\equiv \sum_e \Phi_e[u] = \sum_e \int_{\Omega_e} \left(\boldsymbol{\sigma}^T \boldsymbol{\varepsilon} - \frac{1}{2}\boldsymbol{\sigma}^T \mathbf{C}^{-1} \boldsymbol{\sigma} \right) dV_e \\
&= \boldsymbol{\beta}^T (\mathbf{L} + \frac{1}{2}\mathbf{Q}[\mathbf{d}])\mathbf{d} - \frac{1}{2}\boldsymbol{\beta}^T \mathbf{H} \boldsymbol{\beta} \\
\Phi_e[u] &= \boldsymbol{\beta}_e^T (\mathbf{L}_e + \frac{1}{2}\mathbf{Q}_e[\mathbf{d}_e])\mathbf{d}_e - \frac{1}{2}\boldsymbol{\beta}_e^T \mathbf{H}_e \boldsymbol{\beta}_e
\end{aligned} \tag{2}$$

where $\boldsymbol{\varepsilon}$ is the Green-Lagrange strain measure $\mathbf{L}$ and $\mathbf{Q}[\mathbf{d}]$ are the linear and quadratic discrete compatibility matrices, $\mathbf{d}$ is the vector collecting all the finite element displacement variables while $\boldsymbol{\beta}$ is the vector collecting all the stress parameters, $\mathbf{C}$ and $\mathbf{H}$ are the continuum and discrete elastic matrices and a subscript 'e' denotes the corresponding finite element quantities. It is worth to note as, by using the Green strain measure, the mixed strain energy (2) has a third order nonlinearity with respect to the configuration variable vector $\mathbf{u} = \{\boldsymbol{\beta}, \mathbf{d}\}$.

The element can also be described in a compatible format by requiring that the discrete form of the constitutive laws is "a priori" satisfied. As in the present FE model the stress variables are locally defined at the element level we have

$$\boldsymbol{\beta}_e[\mathbf{d}_e] = \mathbf{H}_e^{-1}(\mathbf{L}_e + \frac{1}{2}\mathbf{Q}_e[\mathbf{d}_e])\mathbf{d}_e \tag{3}$$

where, to highlight that in the compatible format the stresses are not independent variables, we explicitly report the dependence of $\mathbf{d}_e$.

Substituting Eq.(3) in Eq.(2) we obtain the *compatible description* of the element strain energy

$$\Phi_e = \frac{1}{2}\left\{ \mathbf{d}_e^T (\mathbf{L}_e + \frac{1}{2}\mathbf{Q}_e[\mathbf{d}_e])^T \mathbf{H}_e^{-1} (\mathbf{L}_e + \frac{1}{2}\mathbf{Q}_e[\mathbf{d}_e])\mathbf{d}_e \right\} \tag{4}$$

that has a 4th order dependence on the displacement variables only.

Similarly a fourth order dependence of the strain energy from the displacements parameters, is obtained with any compatible finite element interpolation when a 3D solid formulation is employed. In this paper we intentionally use the compatible description derived from the mixed finite element in order to have the same discrete approximation for both the description, i.e. the finite element is the same but the format of the problem changes. This allows us to focus of the way as the problem description affects its solution in large deformation problems (see

also [24, 25]) and then to show the reasons of the better performance of the use of a mixed description. The conclusions are general and hold for any other compatible or mixed finite element. In the numerical experiments the Pian and Tong PT18 element [50] will be used.

2.2 Tangent stiffness matrix for mixed and compatible descriptions

Eq.(2) allows the expression of the strain energy as an algebraic nonlinear function of the element vector

$$\mathbf{u}_e := \begin{bmatrix} \boldsymbol{\beta}_e \\ \mathbf{d}_e \end{bmatrix} \tag{5}$$

related to the vector $\mathbf{u}$, collecting all the parameters of the FE assemblage, through the relation

$$\mathbf{u}_e = \boldsymbol{\mathcal{A}}_e \mathbf{u} \tag{6}$$

where matrix $\boldsymbol{\mathcal{A}}_e$ contains the link between the elements. Furthermore we denote with $\delta\mathbf{u}_{ei} = \{\delta\boldsymbol{\beta}_{ei}, \delta\mathbf{d}_{ei}\}$ the element vector corresponding to the variation $\delta\mathbf{u}_i$.

Exploiting the linear dependence of $\mathbf{Q}_e[\mathbf{d}_e]$ from $\mathbf{d}_e$ and its symmetry we have

$$\begin{aligned} \mathbf{Q}_e[\mathbf{d}_{e1}]\mathbf{d}_{e2} &= \mathbf{Q}_e[\mathbf{d}_{e2}]\mathbf{d}_{e1}, \quad \forall \mathbf{d}_{e1}, \mathbf{d}_{e2} \\ \boldsymbol{\beta}_e^T \mathbf{Q}_e[\mathbf{d}_e]\mathbf{d}_e &= \mathbf{d}_e^T \boldsymbol{\Gamma}_e[\boldsymbol{\beta}_e]\mathbf{d}_e \end{aligned} \tag{7}$$

and the second strain energy variation on the mixed element is obtained as

$$\begin{aligned} \Phi_e'' \delta u_1 \delta u_2 &= \begin{bmatrix} \delta\boldsymbol{\beta}_{e1} \\ \delta\mathbf{d}_{e1} \end{bmatrix}^T \begin{bmatrix} -\mathbf{H}_e & \mathbf{B}_e[\mathbf{d}_e] \\ \mathbf{B}_e[\mathbf{d}_e]^T & \boldsymbol{\Gamma}_e[\boldsymbol{\beta}_e] \end{bmatrix} \begin{bmatrix} \delta\boldsymbol{\beta}_{e2} \\ \delta\mathbf{d}_{e2} \end{bmatrix} \\ &= \delta\mathbf{u}_{e1}^T (\mathbf{K}_{0e} + \mathbf{K}_{1e}[\mathbf{u}_e]) \delta\mathbf{u}_{e2} \end{aligned} \tag{8}$$

where δu_i are generic variations of the configuration field u and $\delta\mathbf{u}_i$ the corresponding FE vectors. Eq.(8) provides the element tangent stiffness matrix $\mathbf{K}_e[\mathbf{u}_e] = \mathbf{K}_{0e} + \mathbf{K}_{1e}[\mathbf{u}_e]$ as a sum of the linear elastic contribution $\mathbf{K}_{0e}$ and the geometric matrix $\mathbf{K}_{1e}[\mathbf{u}_e]$ implicitly defined in Eq.(8).

For the compatible description we have

$$\Phi_e'' \delta u_1 \delta u_2 = \delta\mathbf{d}_{e1}^T \left\{ \mathbf{B}_e^T[\mathbf{d}_e] \mathbf{H}_e^{-1} \mathbf{B}_e[\mathbf{d}_e] + \boldsymbol{\Gamma}[\boldsymbol{\beta}_e[\mathbf{d}_e]] \right\} \delta\mathbf{d}_{e2} \tag{9}$$

where the tangent stiffness matrix has a second order dependence on $\mathbf{d}_e$. To emphasize this we write

$$\mathbf{K}_e = \mathbf{K}_{0e} + \mathbf{K}_{1e}[\mathbf{d}_e] + \mathbf{K}_{2e}[\mathbf{d}_e, \mathbf{d}_e] \tag{10}$$

Finally the evaluation the whole matrix is obtained by standard asseblage as

$$\mathbf{K} = \sum_e \boldsymbol{\mathcal{A}}_e^T \mathbf{K}_e \boldsymbol{\mathcal{A}}_e. \tag{11}$$

2.3 Advantages of mixed solid finite elements in path-following and asymptotic analysis of slender structures

FE models directly derived from the 3D continuum using the Green strain measure have a low order dependence on the strain energy from the discrete FE parameters: $3rd$ and $4th$ order for mixed and compatible respectively. On the contrary geometrically exact shell and beam models [5, 6] or those based on corotational approaches [26, 47, 51], explicitly make use of

the rotation tensor and its highly nonlinear representation. This implies that the strain energy is infinitely differentiable with respect to its parameters and leads to very complex expressions for the energy variations with a high computational burden of path following and much more of asymptotic analyses. In this last case the high order strain energy variations become so complex that often "ad hoc" assumptions are required to make the solution process effective (see section 4.3 of [26]). The consequence is that the fewer global degrees of freedom that could be employed using a shell FE model do not necessarily imply a lesser computational cost as it depends, from the others, on the cost of evaluation of the strain energy variations. On the contrary for solid finite elements the strain energy, in both compatible and mixed form, has the lowest polynomial dependence on the corresponding discrete parameters and in particular in the mixed format of Eq.(2) has just one order more than in the linear elastic case. It implies the zeroing of all the fourth order strain energy variations required by the Koiter analysis with important advantages in terms of both computations and coherence of the method.

3 THE EXTRAPOLATION LOCKING AND ITS CURE USING MIXED SOLID ELEMENT

In this section the better performances of the mixed description in geometrically nonlinear analysis, in terms of robustness, efficiency and, relative to Koiter formulation, also in terms of accuracy, are shown and explained. In this context the compatible description of the problem, whatever the FE and the structural model used, is affected by a pathological *extrapolation locking* phenomenon investigated for the first time for 2D frames in [24, 25].

3.1 Mixed versus compatible description in path-following analysis

The convergence of the Riks scheme is as fast as the iteration stiffness matrix $\tilde{\mathbf{K}}$ is near to $\mathbf{K}_s$ and then, as slow $\mathbf{K}[\mathbf{u}]$ changes with $\mathbf{u}$. The similarity of the stiffness matrices in two different points $\mathbf{K}_j \equiv \mathbf{K}[\mathbf{u}_j]$ and $\mathbf{K}_{j+1} \equiv \mathbf{K}[\mathbf{u}_{j+1}]$ is evaluated by the difference (see [24])

$$\Delta k[\mathbf{u}] \equiv \mathbf{u}^T(\mathbf{K}_{j+1} - \mathbf{K}_j)\mathbf{u} = \Phi''_{j+1}u^2 - \Phi''_j u^2 \tag{12}$$

For the mixed description we have

$$\Delta k_M[\mathbf{u}] = \Phi'''_j(u_j - u_i)u^2 = \mathbf{d}^T\boldsymbol{\Gamma}[\boldsymbol{\beta}_{j+1} - \boldsymbol{\beta}_j]\mathbf{d} + 2\boldsymbol{\beta}^T\mathbf{Q}[\mathbf{d}](\mathbf{d}_{j+1} - \mathbf{d}_j) \tag{13}$$

while for the compatible description the same quantity becomes

$$\begin{aligned}\Delta k_C[\mathbf{u}] &= \Phi'''_j(u_j - u_i)u^2 + \frac{1}{2}\Phi''''_j(u_j - u_i)^2u^2 \\ &= \mathbf{q}_{j+1}^T\mathbf{H}^{-1}\mathbf{q}_{j+1} - \mathbf{q}_j^T\mathbf{H}^{-1}\mathbf{q}_j + \mathbf{d}^T(\boldsymbol{\Gamma}[\boldsymbol{\beta}[\mathbf{d}_{j+1}] - \boldsymbol{\beta}[\mathbf{d}_j]])\mathbf{d}\end{aligned} \tag{14}$$

where $\mathbf{q}_{j+1} = \mathbf{B}[\mathbf{d}_{j+1}]\mathbf{d}$ and $\mathbf{q}_j = \mathbf{B}[\mathbf{d}_j]\mathbf{d}$.

For slender structures it occurs that $\boldsymbol{\beta}_{j+1} \approx \boldsymbol{\beta}_j$ undergoing large rigid element deformations and very small stress and strain increments and then

$$\Delta k_M \approx 2\boldsymbol{\beta}^T(\mathbf{q}_{j+1} - \mathbf{q}_j) \tag{15}$$

and

$$\Delta k_C \approx f[\mathbf{q}_{j+1}] - f[\mathbf{q}_j] \quad \text{with} \quad f[\mathbf{q}] = \mathbf{q}^T\mathbf{H}^{-1}\mathbf{q} \tag{16}$$

When, as is usual for slender structures, the condition number of $\mathbf{H}$ is high due to very different stiffness ratios (i.e. membranal/flexural) the ellipsoids associated to $\mathbf{H}$

$$\mathcal{E} \equiv \{\mathbf{q} : \mathbf{q}^T\mathbf{H}\mathbf{q} = 1\}$$

are very stretched. As $f[\mathbf{q}]$ is related to the radius $r[\mathbf{q}]$ of $\mathcal{E}$ in the direction $\mathbf{q}$ by the following expression

$$f[\mathbf{q}] = r[\mathbf{q}]^2(\mathbf{q}^T\mathbf{q})$$

Δk_c becomes

$$\Delta k_C \approx r^2[\mathbf{q}_{j+1}]\mathbf{q}_{j+1}^T\mathbf{q}_{j+1} - r^2[\mathbf{q}_j]\mathbf{q}_j^T\mathbf{q}_j$$

In this case even small differences in the direction of $\mathbf{q}_{j+1}$ and $\mathbf{q}_j$ may produce a large Δk_C growing with the condition number of $\mathbf{H}$ even when the Euclidean norm of the two vectors is similar (see Fig.1). This produces, in path following analyses a pathological reduction in the

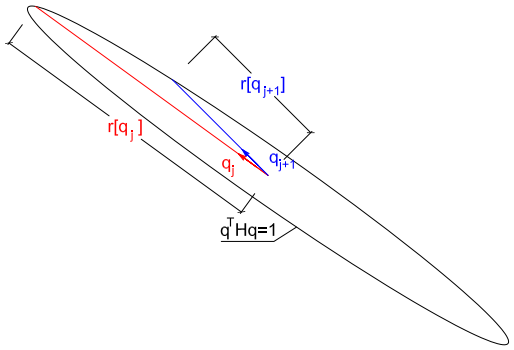

Figure 1: Graphical interpretation of Δk for the compatible description

step length, an increase in the total number of the iterations and, sometimes, the loss of convergence. This phenomenon is called *extrapolation locking* from which the mixed models are free because they are unaffected by the "hard terms" in $\mathbf{H}^{-1}$ and Δk_M is proportional to the difference $\mathbf{q}_{j+1} - \mathbf{q}_j$. As expressions like those in Eqs.(13) and (14) are obtainable using any mixed or compatible finite element the conclusions reported here can be generalized. In particular note that for any structural model the strain energy can be expressed as a quadratic function of the stress variables through the Hellinger-Reissner principle and so its higher order variations are not influenced by $\mathbf{H}$. On the contrary all the compatible strain energy variations always involve terms in $\mathbf{H}^{-1}$. This means that extrapolation locking heavily affects any compatible finite element/description while it does not occur in mixed formulation.

We show the occurrence of the locking in the simple case of the Euler beam, for which the geometry and load conditions are reported in fig. 2.

In tab.2 the number of steps and iterations (loops) to obtain the equilibrium path, directly related to the CPU time, are presented. The results of the mixed formulation, denoted by M, are unaffected by the coefficient $k = (t/\ell)^2$ while the compatible ones (C) pathologically depend on it.

Finally in Fig.3 we report the minimum ρ_{min} and maximum ρ_{max} absolute value of the eigenvalues of the matrix $\mathbf{K}_{n+1}\mathbf{K}_n^{-1}$ for both descriptions, where $n+1$ and n denote two equilibrium points. The set of points in which the ρs are evaluated belongs on the equilibrium path obtained by the mixed description. It is important to observe how the mixed description ρ_{max} is independent of k and has almost the optimal value 1.0 while for the compatible description it

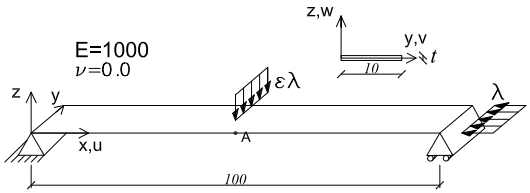

	Compatible				Mixed
k	10^4	10^5	10^6	10^7	(all k)
steps	38	43	67	failed	27
loops	133	166	328	failed	75

Figure 2: Eulero beam: analysis evolution for increasing k, mesh $1 \times 1 \times 40$

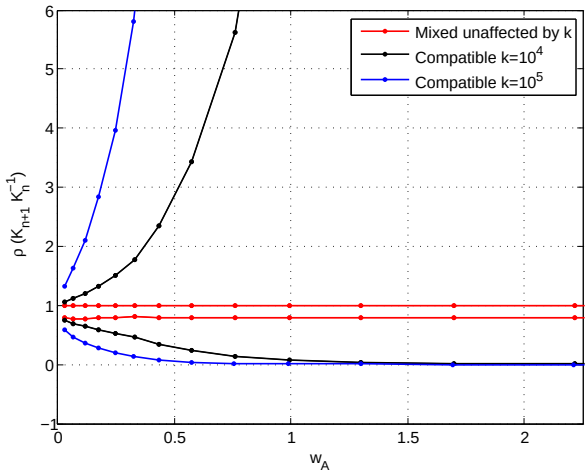

Figure 3: Minimum and maximum eigenvalues of matrix $\mathbf{K}_{n+1}\mathbf{K}_n^{-1}$ for the simple tests

increases with the step length. Also note that is the extrapolation locking that heavily affects also the convergence of the arc-length solution while the singular direction is filtered by the Riks constraint. We refer readers to [24, 25] for further details.

3.2 Mixed vs compatible description in Koiter analysis using 3D solid elements

As the Koiter method is based on Taylor expansion of the strain energy the use of a mixed description has a tremendous impact not only in terms of efficiency but also of accuracy. For any finite element (see [25, 35, 6]) the mixed description makes the truncation independent of $\mathbf{H}^{-1}$ and small with respect to the retained terms.

Using compatible format in Koiter analysis the locking already occurs in the evaluation of the buckling loads (see [25]). To avoid extrapolation locking usually the compatible bifurcation analysis is performed by zeroing the quadratic displacements terms into the tangent stiffness matrix (*direct extrapolation* hypothesis) or by evaluating the geometric terms using zeroed displacements (*frozen configuration* hypothesis). In both cases the bifurcation search reduces to a linear eigenvalue problem.

In Tab.1 the buckling loads obtained from the various descriptions and locking cures are presented for the Euler beam of Fig. 2 by changing both the aspect ratio k and the imperfection load amplitude ϵ. In particular we denote with (C) and (M) the results obtained respectively with the compatible and mixed description and by (F) and (D) those of the frozen configuration and direct extrapolation respectively. For this case which has small precritical nonlinearities it is worth noting that: i) the frozen configuration hyphothesis sanitizes the locking effect and fur-

Table 1: Bifurcation locking for the Euler beam/(exact value for the elastica)

k	$\epsilon = 0.01$		$\epsilon = 0.005$		$\epsilon = 0.001$		for all ϵ	
	C	D	C	D	C	D	F	M
10^4	failed	0.673	1.112	0.865	1.004	0.994	1.001	1.001
10^5	failed	0.309	failed	0.517	1.040	0.937	1.001	1.001
10^6	failed	0.111	failed	0.209	failed	0.673	1.001	1.001
10^7	failed	0.033	failed	0.071	failed	0.308	0.999	0.999

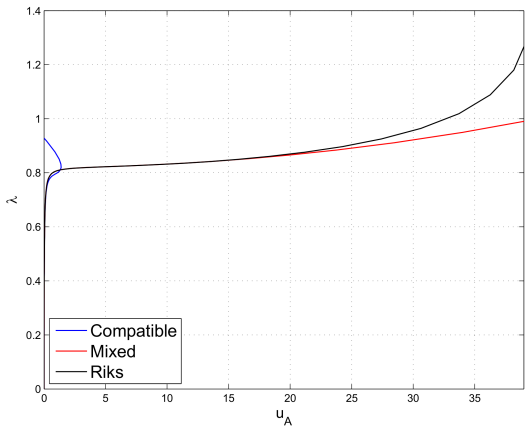

Figure 4: Equilibrium path for the Euler beam for $\epsilon = 0.001$ and $k = 10^4$

nishes accurate results; ii) the compatible description misses the bifurcation point and the direct extrapolation furnishes an inaccurate solution, getting worse with the precritical nonlinearity due to the transversal force. Inaccuracy on the bifurcation points obviously leads to completely wrong equilibrium path evaluation.

The zeroing of all the precritical displacements could, however, lead to inaccuracy when the precritical displacements are not negligible as in the shallow arc reported in Fig.5. In this case the frozen configuration is not capable of producing the correct bifurcation load and mode as reported in Tab.2. The buckling point is used to evaluate the energy terms also reported in Tab.2, so the equilibrium path obtained with the frozen configuration hyphothesis is very inaccurate. In Fig.6 the equilibrium path of the Koiter mixed formulation is presented and compared with the frozen one and path following solution.

However the great advantage in adopting mixed solid elements in Koiter analysis is in the evaluation of all the fourth order coefficients required by the formulation (see [29]) that, for mixed solid elements, requires only second variations for their evaluation since the usually very complex fourth order strain energy variations are automatically zero.

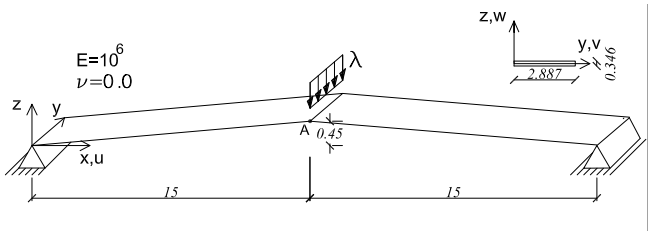

Figure 5: Geometry and material properties of the shallow arc

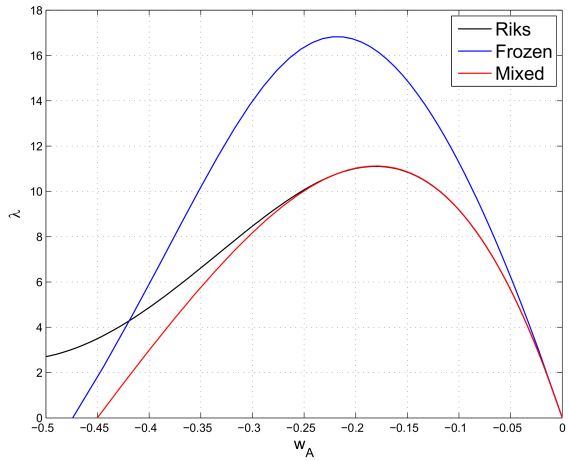

Figure 6: Equilibrium path for the shallow arc

	M	F
λ_1	22.0202	30.6526
λ_2	30.6671	47.0652
$\mathcal{A}_{001}$	0.0196	0.0190
$\mathcal{A}_{111}$	47.9305	182.3644
$\mathcal{B}_{0011}$	-6.32 10^{-4}	0
$\mathcal{B}_{1111}$	8.2117	207.3178

Table 2: Shallow arc: comparison of relevant energy asymptotic quantities

	Mixed	Frozen
λ_1	1266.8	1291.5
λ_2	1828.1	1719.0
λ_3	3092.3	2949.7
λ_4	3114.7	2970.6

Table 3: Channel section: first 4 buckling loads.

4 NUMERICAL RESULTS

In this section the effectiveness and reliability of both methods of analysis are tested in a series of benchmark problems. In particular for the path-following analysis the efficiency of the mixed description, which allows very large steps in comparison with the compatible one, is highlighted. For the asymptotic formulation we show the accuracy given by the mixed solid element.

For all the tests only one element in the thickness is used while the same convergence conditions and arc-length parameters are adopted for mixed and compatible path-following analyses. The label Riks denotes the equilibrium paths obtained by the arc-length scheme (the same for both the description), while labels Mixed and Frozen denote the asymptotic paths using mixed and compatible frozen descriptions.

4.1 Simply supported C-shaped beam

The first test, with geometry and material reported in figure 7, consists in a simply supported compressed beam with a C shaped section. It presents a nonlinear prebuckling behavior due to two forces (torsional imperfections) at the mid-span and coupled instability. For this reason it is a good benchmark to test the accuracy of the asymptotic analysis. A similar test was studied

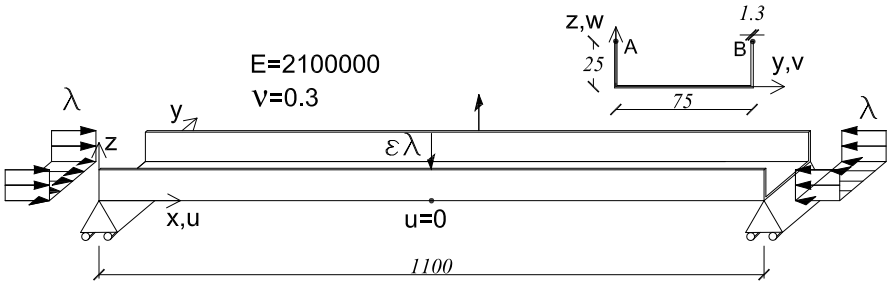

Figure 7: Channel section: geometry and loads.

in [35] using shell elements and in [52] using a generalized beam model. The buckling values, obtained by using a mesh of $(8+8+18)\times 50$ elements are reported in Table 3 and compared with those computed using the compatible description with the frozen configuration hyphothesis. The Koiter analysis uses the first four buckling modes plotted in Fig.8. It is possible to see how the first two modes are global, essentially flexural and torsional respectively, while the others are local modes.

The accuracy of the mixed asymptotic strategy in the evaluation of the limit load and of the initial postcritical behavior is shown in Fig.9. It is also possible to observe the poor accuracy of the frozen configuration analysis in estimating both the limit load and equilibrium path. In Fig.10 the equilibrium path of Koiter method, in terms of the modal contributions ξ_k, is plotted.

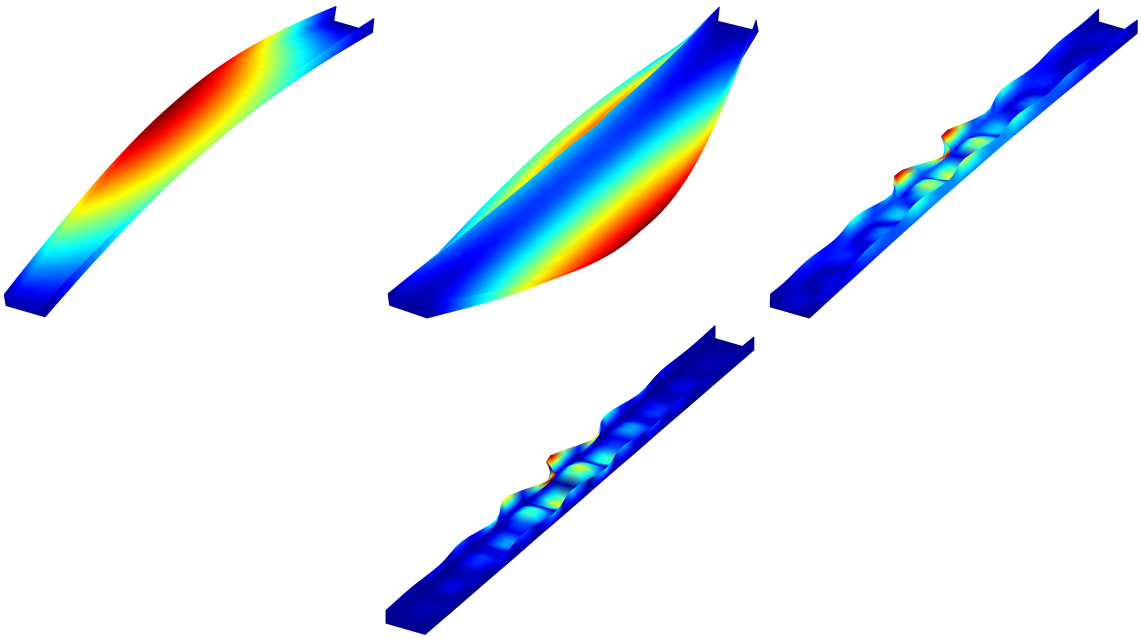

Figure 8: Channel section: Buckling modes

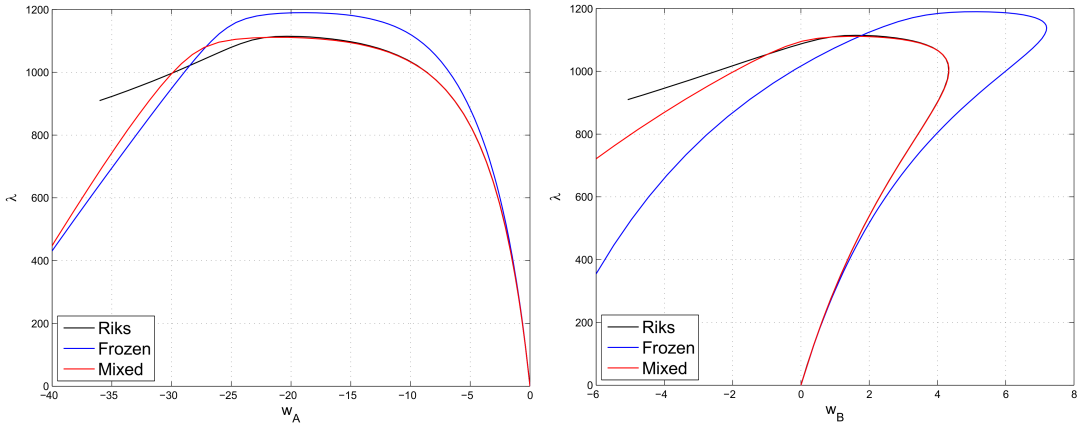

Figure 9: Channel section: Equilibrium paths $\lambda - w_A$, $\lambda - w_B$

	Mixed	Compatible	Mixed MN
steps	24	74	45
loops	73	175	233

Table 4: Channel section: steps and iterations for path–following analysis.

The strong effect of modal interaction between the third (local) mode and the first two flexural–torsional (global) modes is shown.

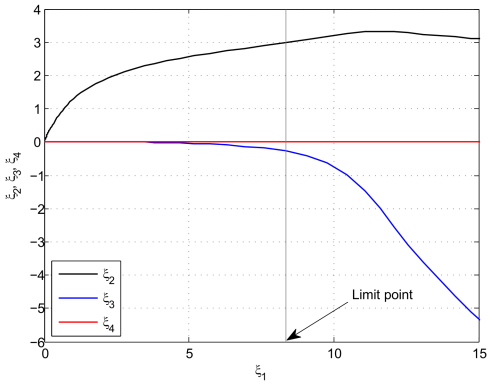

Figure 10: Channel section: Equilibrium paths in ξ_k space.

The results of the mixed asymptotic analysis are in good agreement with the path-following ones. In Tab.4 the steps and iterations of the mixed and compatible descriptions are compared. Obviously the equilibrium path is exactly the same but the better performances of the mixed description are evident even when a modified Newton-Raphson method (MN) is adopted.

4.2 A T beam

The second test regards the beam with data reported in Fig. 11. It consists in a simply supported beam with a T shaped section loaded by a shear force acting at the mid-span and by a small imperfection ($\epsilon = 1/1000$) load as reported in the same figure. The precritical behavior exhibits a strong nonlinearity and coupled bucklings are also present in this case. A mesh of $(9 + 9 + 18) \times 100$ elements has been used.

In Fig.12 the first 4 buckling modes, considered in the multimodal Koiter analysis, are plotted.

In Fig.13 the equilibrium paths recovered by using both asymptotic and path-following analysis are reported and compared. The solution is accurately recovered by the asymptotic strategy up to quite large displacements and the occurrence of a secondary bifurcation.

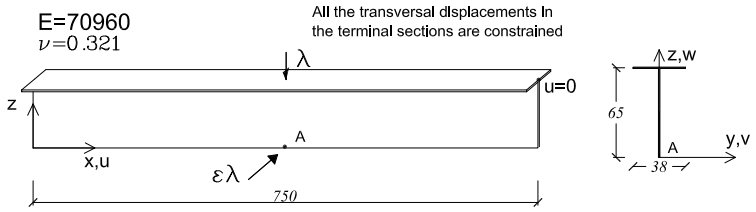

Figure 11: T section beam: geometry and loads

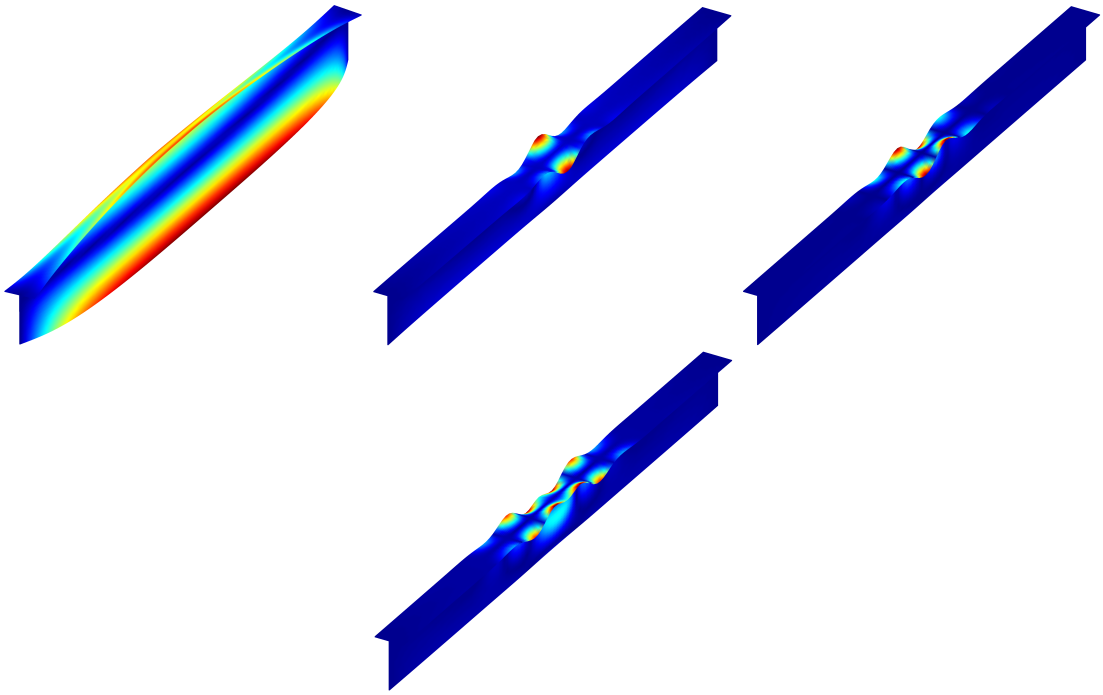

Figure 12: Channel section: First 4 Buckling modes

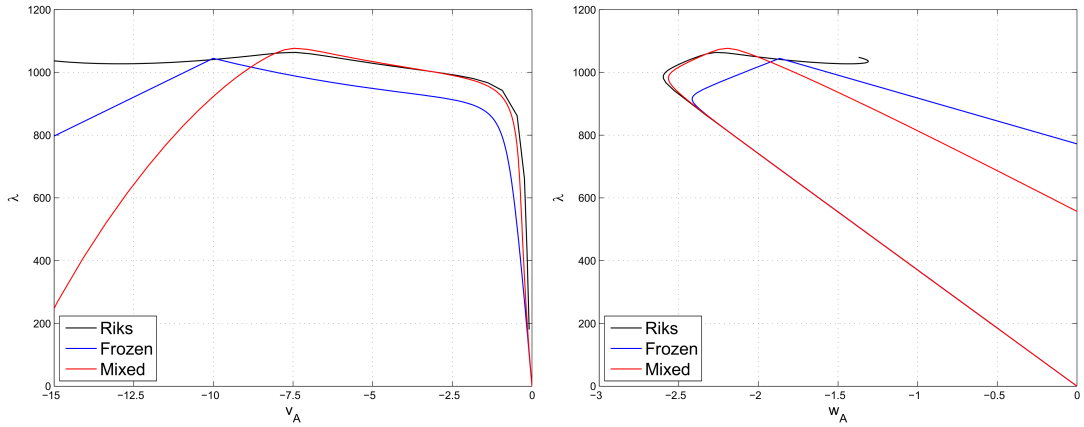

Figure 13: T section beam: Equilibrium paths $\lambda - w_A$, $\lambda - v_A$

	Mixed	Frozen
λ_1	1092.1	936.8
λ_2	1869.1	1860.4
λ_3	1993.5	1989.6
λ_4	2258.9	2252.1

Table 5: T section beam: first 4 buckling loads.

	Mixed	Compatible	Mixed MN
steps	20	42	55
loops	60	169	252

Table 6: T section beam: steps and iterations for path–following analysis.

Also in this case (see Fig.14) the equilibrium path is plotted in terms of the modes amplitudes ξ_k showing a strong interaction among modes 1, 2 and 4.

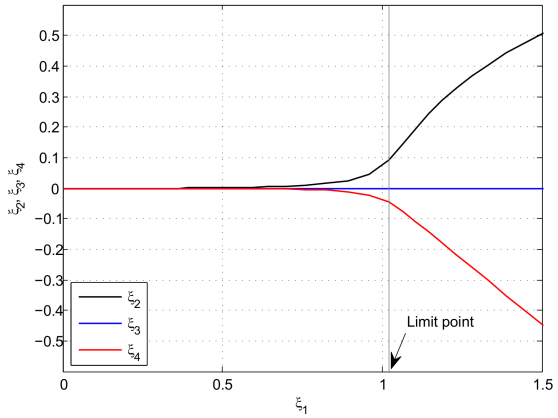

Figure 14: T section beam: Equilibrium paths in ξ_k space.

In Tab.6 the steps and iterations of the mixed, using both full o modified Newton (MN) methods, and compatible descriptions are compared. This example highlights the excellent performances of the mixed description even more than the previous test.

4.3 A simple frame

Finally Fig. 15 reports the geometry and the material properties of a simple portal frame, similar to that analyzed in [52]. It consists of two beams with a C shaped section loaded as depicted in the same figure. Coupled instability is present also in this case. Both the beams are discretized using a mesh of $(6+12+6)\times 40$ elements. The node discretization is automatically defined from those of the two beams.

In Fig.16 the first 3 buckling modes considered in the multimodal Koiter analysis are reported.

Also in this case the equilibrium paths recovered using both the asymptotic and path-following analysis are reported and compared in Fig.17. The frozen configuration asymptotic analysis furnishes a similar equilibrium path to the mixed one but an overestimate in the limit load. The mixed Koiter analysis accurately recovers the solution up to quite large displacements.

In Fig.18 the equilibrium path is plotted in terms of the modes amplitudes ξ_k showing a

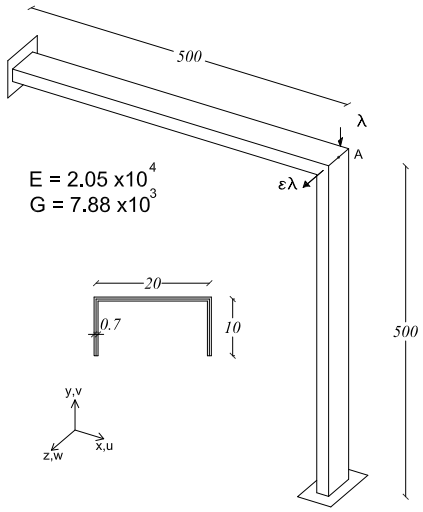

Figure 15: T section beam

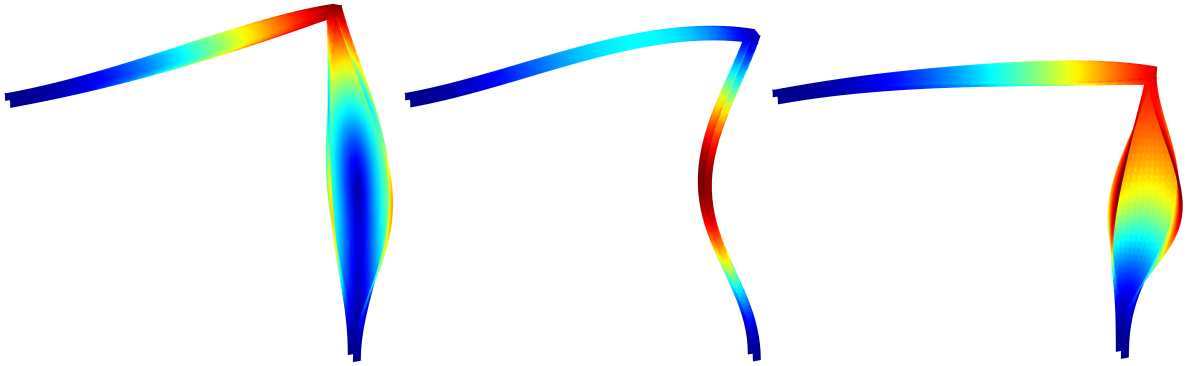

Figure 16: Simple frame: First 3 Buckling modes

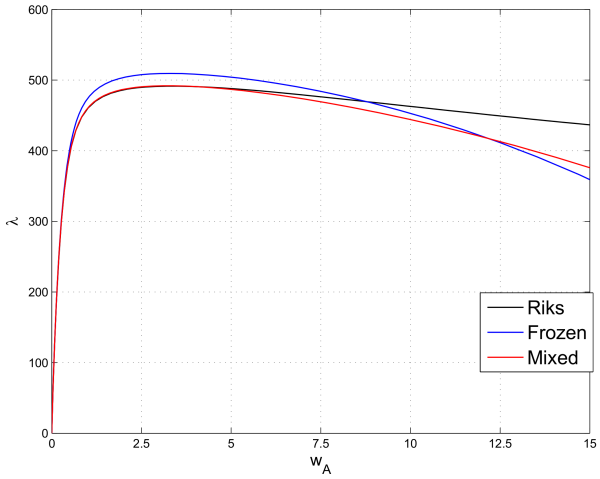

Figure 17: Simple frame: Equilibrium paths $\lambda - w_A$

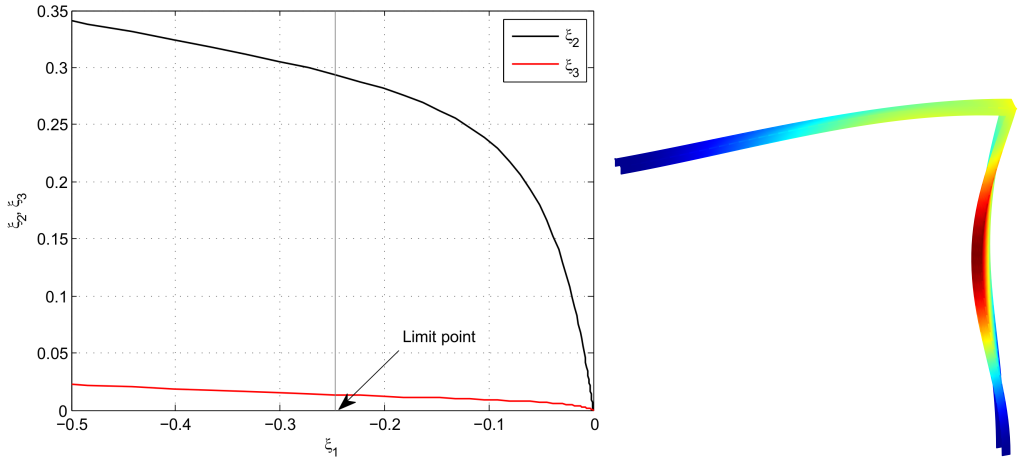

Figure 18: Simple frame: deformed shape at the limit point and equilibrium paths in ξ_k space

	Mixed	Frozen
λ_1	588.92	641.01
λ_2	683.50	684.59
λ_3	1025.90	993.66

Table 7: Simple frame: first 3 buckling loads.

strong interaction among modes 1, 2. In the same figure the deformed configuration at the limit point is also reported.

Finally in Tab.8 the steps and iterations required by the mixed, using full and modified Newton method, and compatible descriptions are compared.

5 Conclusions

In this paper the better performances of mixed elements in the nonlinear analysis of slender structures have been shown and explained. To focus on the origin of this behavior, which is independent of the finite element interpolation, a compatible description of a mixed 3D solid finite element has been derived. In this way it has been possible to show how the compatible description, and so any compatible finite element, is affected by an underhand and neglected extrapolation locking phenomenon that produces slow or lack of convergence for the path–following analyses and inaccurate solutions for the Koiter method. The occurence of the locking has been theoretically investigated and it has been indicated that it is due to the presence of directions with different stiffness as typically occurs for slender structures which are usually characterized by a high membranal/flexural stiffness ratio. These conclusions are general and hold for any nonlinear structural model and finite element.

Many advantages of solid elements in geometrically nonlinear analysis are already known in literature. In this paper we show further important properties of mixed solid FE within the Koiter asymptotic formulation. In fact, due to the simple 3rd order dependence of the strain energy on

	Mixed	Compatible	Mixed MN
steps	24	51	51
loops	73	196	198

Table 8: Simple Frame: steps and iterations for path–following analysis.

its FE parameters, all the higher order energy variations are null and so it is possible to have: i) an exact linear bifurcation analysis with improvements in its computational efficiency and accuracy for non near buckling loads; ii) simplification and greater accuracy in the evaluation of the energy variations required to recover the equilibrium path with a gain in terms of the computational cost; iii) a more simple and effective numerical method which is easy to include in FE packages.

REFERENCES

[1] Sze K, Chan W, Pian T. An eight-node hybrid-stress solid-shell element for geometric non-linear analysis of elastic shells. *International Journal for Numerical Methods in Engineering* 2002; **55**(7):853–878.

[2] Klinkel S, Gruttmann F, Wagner W. A robust non-linear solid shell element based on a mixed variational formulation. *Computer Methods in Applied Mechanics and Engineering* 2006; **195**(1-3):179–201.

[3] Vu-Quoc L, Tan XG. Optimal solid shells for non-linear analyses of multilayer composites. I Statics. *Computer Methods in Applied Mechanics and Engineering* 2003; **192**(9-10):975–1016.

[4] Li Q, Liu Y, Zhang Z, Zhong W. A new reduced integration solid-shell element based on EAS and ANS with hourglass stabilization. *International Journal for Numerical Methods in Engineering* 2015; 1885–1891.

[5] Garcea G, Madeo A, Casciaro R. The implicit corotational method and its use in the derivation of nonlinear structural models for beams and plates. *J. Mech. Mater. Struct.* 2012; **7**(6):509–539.

[6] Garcea G, Madeo A, Casciaro R. Nonlinear FEM analysis for beams and plate assemblages based on the implicit corotational method. *J. Mech. Mater. Struct.* 2012; **7**(6):539–574.

[7] Genoese A, Genoese A, Bilotta A, Garcea G. A geometrically exact beam model with non-uniform warping coherently derived from the saint venant rod. *Engineering Structures* 2014; **68**:33–46.

[8] Sze K. Three-dimensional continuum finite element models for plate/shell analysis. *Prog. Struct. Engng. Mater* 2002; **4**:400–407.

[9] Klinkel S, Gruttmann F, Wagner W. Continuum based three-dimensional shell element for laminated structures. *Computers and Structures* 1999; **71**(1):43–62.

[10] Reese S, Wriggers P, Reddy BD. New locking-free brick element technique for large deformation problems in elasticity. *Computers and Structures* 2000; **75**(3):291–304.

[11] Schwarze M, Reese S. A reduced integration solid-shell finite element based on the EAS and the ANS conceptGeometrically linear problems. *Computer Methods in Applied Mechanics and Engineering* 2009; (80):1322–1355.

[12] Schwarze M, Reese S. A reduced integration solid-shell finite element based on EAS and the ANS concept: Large deformation problems. *International Journal for Numerical Methods in Engineering* 2011; (85):289–329.

[13] Sze K, Ghali A. Hybrid hexahedral element for solids, plates, shells and beams by selective scaling. *International Journal for Numerical Methods in Engineering* 1993; **36**(9):1519–1540.

[14] Vu-Quoc L, Tan X. Efficient Hybrid-EAS solid element for accurate stress prediction in thick laminated beams, plates, and shells. *Computer Methods in Applied Mechanics and Engineering* 2013; **253**:337–355.

[15] Frischkorn J, Reese S. A solid-beam finite element and non-linear constitutive modelling. *Computer Methods in Applied Mechanics and Engineering* Oct 2013; **265**:195–212.

[16] Sze K, Liu X, Lo S. Hybrid-stress six-node prismatic elements. *International Journal for Numerical Methods in Engineering* 2004; **61**(9):1451–1470.

[17] Sze K, Zheng SJ. A stabilized hybrid-stress solid element for geometrically nonlinear homogeneous and laminated shell analyses. *Computer Methods in Applied Mechanics and Engineering* 2002; **191**(17-18):1945–1966.

[18] Sze K, Liu X, Lo S. Hybrid-stress six-node prismatic elements. *International Journal for Numerical Methods in Engineering* 2004; **61**(9):1451–1470.

[19] Sze K, Lo S, Yao LQ. Hybrid-stress solid elements for shell structures based upon a modified variational functional. *International Journal for Numerical Methods in Engineering* 2002; **53**(12):2617–2642.

[20] Sze K, Yao L. A hybrid stress ANS solid-shell element and its generalization for smart structure modelling. Part I - solid-shell element formulation. *International Journal for Numerical Methods in Engineering* 2000; **48**(4):545–564.

[21] Wu D, Lo S, Sheng N, Sze K. Universal three-dimensional connection hexahedral elements based on hybrid-stress theory for solid structures. *International Journal for Numerical Methods in Engineering* 2010; **81**(3):307–334.

[22] Sze K, Zheng SJ, Lo S. A stabilized eighteen-node solid element for hyperelastic analysis of shells. *Finite Elements in Analysis and Design* 2004; **40**(3):319–340.

[23] Sze K, Yao LQ, Pian T. An eighteen-node hybrid-stress solid-shell element for homogenous and laminated structures. *Finite Elements in Analysis and Design* 2002; **38**(4):353–374.

[24] Garcea G, Trunfio G, Casciaro R. Mixed formulation and locking in path-following nonlinear analysis. *Computer Methods in Applied Mechanics and Engineering* NOV 2 1998; **165**(1-4):247–272.

[25] Garcea G, Salerno G, Casciaro R. Extrapolation locking and its sanitization in Koiter's asymptotic analysis. *Computer Methods in Applied Mechanics and Engineering* 1999; **180**(1-2):137–167.

[26] Garcea G, Madeo A, Zagari G, Casciaro R. Asymptotic post-buckling FEM analysis using corotational formulation. *International Journal of Solids and Structures* 2009; **46**(2):377–397.

[27] Garcea G, Trunfio GA, Casciaro R. Path-following analysis of thin-walled structures and comparison with asymptotic post-critical solutions. *International Journal for Numerical Methods in Engineering* 2002; **55**(1):73–100.

[28] Garcea G, Bilotta A, Madeo A, Casciaro R. *Direct evaluation of the post-buckling behavior of slender structures through a numerical asymptotic formulation*. Springer Verlag, 2014.

[29] Casciaro R. Computational Asymptotic Post-Buckling Analysis of Slender Elastic Structures. *CISM Courses and Lectures NO. 470* 2005; :.

[30] Riks E. An incremental approach to the solution of snapping and buckling problems. *International Journal of Solids and Structures* 1979; **15**(7):529–551.

[31] Lacarbonara W. *Nonlinear Structural Mechanics*. Spinger Verlag: New-York, 2013.

[32] Lanzo AD, Garcea G, Casciaro R. Asymptotic post-buckling analysis of rectangular plates by hc finite elements. *International Journal for Numerical Methods in Engineering* 1995; **38**(14):2325–2345.

[33] Lanzo AD, Garcea G. Koiter's analysis of thin-walled structures by a finite element approach. *International Journal for Numerical Methods in Engineering* 1996; **39**(17):3007–3031.

[34] Casciaro R, Garcea G, Attanasio G, Giordano F. Perturbation approach to elastic post-buckling analysis. *Computers & Structures* 1998; **66**(5):585–595.

[35] Garcea G. Mixed formulation in Koiter analysis of thin-walled beams. *Computer Methods in Applied Mechanics and Engineering* 2001; **190**(26-27):3369–3399.

[36] Dubina D, Ungureanu V. Instability mode interaction: From van der neut model to ecbl approach. *Thin-Walled Structures* 2014; **81**:39–49.

[37] Rahman T, Jansen E. Finite element based coupled mode initial post-buckling analysis of a composite cylindrical shell. *Thin-Walled Structures* 2010; **48**(1):25–32.

[38] Flores F, Godoy L. Elastic post-buckling analysis via finite element and perturbation techniques. part 1: Formulation. *International Journal for Numerical Methods in Engineering* 1992; **33**(9):1775–1794.

[39] Barbero E, Raftoyiannis I, Godoy L. Finite elements for post-buckling analysis. ii-application to composite plate assemblies. *Computers and Structures* 1995; **56**(6):1019–1028.

[40] Boutyour E, Zahrouni H, Potier-Ferry M, Boudi M. Asymptotic-numerical method for buckling analysis of shell structures with large rotations. *Journal of Computational and Applied Mathematics* 2004; **168**(1-2):77–85.

[41] Silvestre N, Camotim D. Asymptotic-numerical method to analyze the postbuckling behavior, imperfection-sensitivity, and mode interaction in frames. *Journal of Engineering Mechanics* 2005; **131**(6):617–632.

[42] Schafer B, Graham-Brady L. Stochastic post-buckling of frames using koiter's method. *International Journal of Structural Stability and Dynamics* 2006; **6**(3):333–358.

[43] Chen H, Virgin L. Finite element analysis of post-buckling dynamics in plates-part i: An asymptotic approach. *International Journal of Solids and Structures* 2006; **43**(13):3983–4007.

[44] Rizzi NL, Varano V, Gabriele S. Initial postbuckling behavior of thin-walled frames under mode interaction. *Thin-Walled Structures* 2013; **68**:124 – 134.

[45] White S, Raju G, Weaver P. Initial post-buckling of variable-stiffness curved panels. *Journal of the Mechanics and Physics of Solids* 2014; **71**(1):132–155.

[46] Koiter W. On the stability of elastic equilibrium.

[47] Barbero E, Madeo A, Zagari G, Zinno R, Zucco G. Imperfection sensitivity analysis of laminated folded plates. *Thin-Walled Structures* 2015; **90**:128 – 139.

[48] Liang K, Ruess M, Abdalla M. The Koiter-Newton approach using von Karman kinematics for buckling analyses of imperfection sensitive structures. *Computer Methods in Applied Mechanics and Engineering* 2014; **279**:440–468.

[49] Liang K, Abdalla M, Grdal Z. A Koiter-Newton approach for nonlinear structural analysis. *International Journal for Numerical Methods in Engineering* 2013; **96**(12):763–786.

[50] Pian THH, Wu CC. *Hybrid and Incompatible Finite Element Methods*. Chapman & All, CRC: New-York, 1969.

[51] Zagari G, Madeo A, Casciaro R, De Miranda S, Ubertini F. Koiter analysis of folded structures using a corotational approach. *International Journal of Solids and Structures* 2013; **50**(5):755–765.

[52] Genoese A, Genoese A, Bilotta A, Garcea G. Buckling analysis through a generalized beam model including section distortions. *Thin-Walled Structures* 2014; **85**:125–141.

ECCOMAS Congress 2016
VII European Congress on Computational Methods in Applied Sciences and Engineering
M. Papadrakakis, V. Papadopoulos, G. Stefanou, V. Plevris (eds.)
Crete Island, Greece, 5–10 June 2016

COMPUTATIONAL ANALYSIS OF THE COLLAPSE BEHAVIOUR OF THIN-WALLED POLYGONAL STEEL BEAMS

Raffaele Ardito[1]

[1] Dept. of Civil and Environmental Engineering, Politecnico di Milano
Milan, Italy
e-mail: raffaele.ardito@polimi.it

Keywords: Local Buckling, Steel Structures, FE Analysis, Elastic-plastic Behavior, Thin-walled profiles, Imperfections

Abstract. *The present paper is focused on the development of an accurate computational method, based on the Finite Element (FE) approximation, for predicting the collapse behavior of thin-walled polygonal steel beams subject to bending. The numerical model has been created using the software ABAQUS, and has been validated with experimental data obtained from the literature, concerning rectangular hollow section (RHS) in the four-point-bending situation. The model has been improved by means of a thorough study of material hardening, imperfections and residual stresses. The computational results of the analyses have been compared with the design procedures provided by Eurocode 3 (effective cross-section method and reduced stress method), in order to check their suitability.*

1 INTRODUCTION

This paper describes the realization of a computational model for studying the flexural behaviour of polygonal, thin-walled sections at the ultimate limit state. This type of section is widely used as support of antennas in telecommunications, for lighting facilities and, in some cases, for small-scale wind turbines, see Figure 1.

(a)

(b)

Figure 1: Examples of application of beams with thin-walled polygonal cross-section: (a) lighting tower; (b) mast for small-scale wind turbines.

The main goal is to evaluate the flexural strength of the examined sections. Because of the high slenderness, these structures are subjected to local buckling phenomenon, which complicates the determination of the load-carrying capacity. After a literature survey, we realized that many Authors have considered the load-carrying capacity of polygonal section, even though in most cases the reference problem was represented by axial load only (see e.g. [1], [2], [3]). The basic formulation for local buckling due to bending can be retrieved in the classical textbook [4], which reports the stability assessment for elastic plates rigidly jointed along their edges, in order to obtain open and closed thin-walled profiles. An attempt for the numerical simulation of local buckling can be found in [5], which reports also some results of an experimental campaign. The load carrying capacity of such structures is widely influenced by the presence of imperfections: some relevant information on residual stresses and geometric information can be retrieved in [6], [7] and [8], whereas the effect of metalworking process has been considered in [9].

In this paper, a computational model has been devised and the results of the analyses are compared to the expeditious procedures provided by Eurocode 3 (effective cross-section method and reduced stress method), checking their suitability. The numerical model has been created using the software ABAQUS [10], and has been validated with experimental data obtained from the literature, concerning rectangular hollow section (RHS) [11]. The model was developed, improving on it with the addition of material hardening, imperfections and residual stresses. The relevant data have been taken from Eurocode 3, literature or by experimental tests. The critical comparison with respect to experimental data has been used in order to assess the validity of the model in terms of load-curvature response.

The analyses allowed us to understand the mechanisms by which the resistance develops in this type of sections. The comparison of the results of the numerical models with the Eurocode 3 ones has shown that often the legislation does not estimate accurately the resistance values. Moreover, in cases of tapered sections or lightened ones, the legislation proves to be deficient if not entirely inapplicable.

2 PROBLEM FORMULATION

The safety of slender steel beams can be endangered by the lack of stability in many different ways: global buckling refers to the overall collapse due to axial, bending, torsional or combined loads; distortional buckling is specially related to thin walled profiles, in terms of distortion of the cross-section with relative displacement of the nodes; local buckling, which is specifically treated in this paper, can be defined as the unstable behaviour of each single panel that constitute the cross-section, in the absence of global buckling and of relative displacement of the profile's nodes (which are basically fixed).

A simple treatment of local buckling is obtained by considering each panel as a plate subject to membrane loading and suitably constrained in order to account for the effect of adjacent plates. The axial compressive stress, which eventually lead to buckling, can be provided, for instance, by the overall bending moment, as shown in Figure 2.

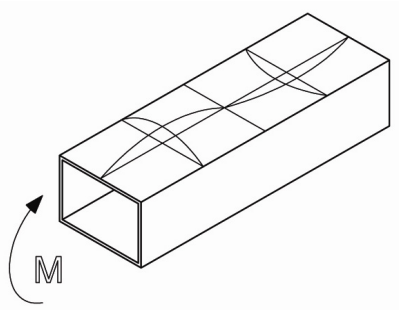

Figure 2: Local buckling of a thin-walled polygonal beam subject to bending moment M.

The simplistic approach is represented by the computation of the Eulerian critical load for elastic behaviour, in the case of simply supported rectangular plate (see [4]). In that way, one finds that the critical stress can be computed as:

$$\sigma_E = \frac{N_E}{t} = k_\sigma \frac{\pi^2 E}{12\left(1-\nu^2\right)}\left(\frac{t}{b}\right)^2 \tag{1}$$

where: b is the minimum width of the plate; t is its thickness; E and ν are the Young's modulus and the Poisson's ratio, respectively; k_σ is the load factor, which depends on the elastic distribution of axial stress. For instance, in the case of uniform compression (as it happens in the upper flange in Figure 2), one finds $k_\sigma = 4$; other values are reported in [4] for various non-uniform distributions.

A more reliable approach, which accounts for the post-critical behaviour, has been developed by Von Kármán on the basis of the concept of effective width [4]. Roughly speaking, the non-uniform stress distribution at plastic collapse is replaced by a piecewise constant distribution, with null value in the zone around the plate centre (which is assumed to be in the buckled configuration) whereas the lateral zones are subject to the yield stress for the given material. By enforcing the equivalence of the yield stress with the buckling tension of the effective zone, one finds:

$$\sigma_{cr}\left(b_{eff}\right)=f_y=k_\sigma\frac{\pi^2E}{12\left(1-\nu^2\right)}\left(\frac{t}{b_{eff}}\right)^2 \tag{2}$$

where b_{eff} is the sum of the length of the lateral zones subject to the yield stress.

This approach does not take into account the effect of imperfections, which play a paramount role in the evaluation of critical load. Imperfections in steel structures may have different nature but they can be divided into a couple of categories: mechanical imperfections and geometrical imperfections. The former include the presence of residual stresses, due to the specific metalworking procedure (e.g. hot rolling or cold forming), and the non-uniform distribution of pristine yield limit, due e.g. to the folding process. An example of this kind of imperfection, which is quite important for polygonal sections, is reported in Figure 3.

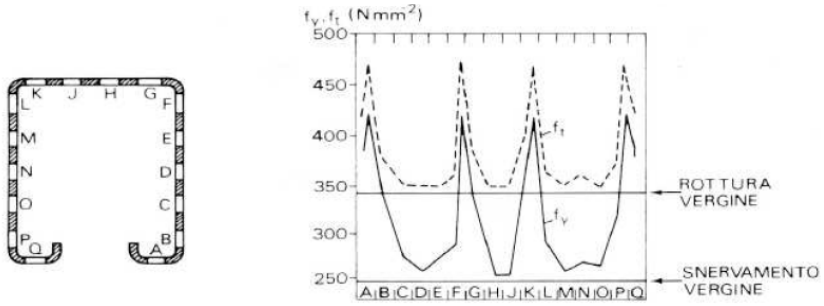

Figure 3: Typical distribution of the material properties on a cold-formed profile.

Geometric imperfections can be further divided into global defects (e.g. overall bow of the beam) and local defects (e.g. non-uniform thickness, lack of orthogonality, etc.). In the case of local buckling, the latter are by far more important. According to Eurocode 3 part 5, Annex C [12], the geometric imperfections can be modeled on the basis of the buckling modes (such as the one represented in Figure 2), with a recommended amplitude equal to 80% of the fabrication tolerances.

One theoretical approach, which accounts for the presence of imperfections, has been formulated by Winter [4]. The evaluation of the effective width is based on the dimensionless slenderness parameter λ_p:

$$\lambda_p=\sqrt{\frac{f_y}{\sigma_E}} \tag{3}$$

where the critical stress is referred to the whole width, see Equation (1). Winter proposed the following expression, which is assumed in the current code provisions [12]:

$$\frac{b_{eff}}{b}=\left(1-\frac{0.22}{\lambda_p}\right)\frac{1}{\lambda_p}\le 1 \tag{4}$$

A graphical comparison of the abovementioned approaches, in terms of the average collapse stress $\sigma_{L,}$ is reported in Figure 4.

In the present paper, a computational approach is preferred in order to capture the collapse load for the whole cross-section. A 3D Finite Element (FE) model has been devised, as better specified in the next section, and a set of non-linear static analyses have been carried out, encompassing the non-linear geometric effects and the elastic-plastic behaviour. In any case, a preliminary step has been represented by linear buckling analyses, in order to evaluate the

buckling modes which are used to model the geometric imperfections. The final load-curvature response has been obtained by applying an incremental (step-by-step) analysis with arc-length control. Such a provision is necessary in order to account for strongly unstable behaviour, such as snap-back or snap-through phenomena, that are likely to occur in the present structural case, dominated by imperfections. The analyses have been repeated for different width-to thickness ratios, with the purpose of evaluating the collapse behaviour in various cases. It is worth noting that the width-to-thickness ratio represent the basic parameter used to decide whether the considered section is prone to local buckling.

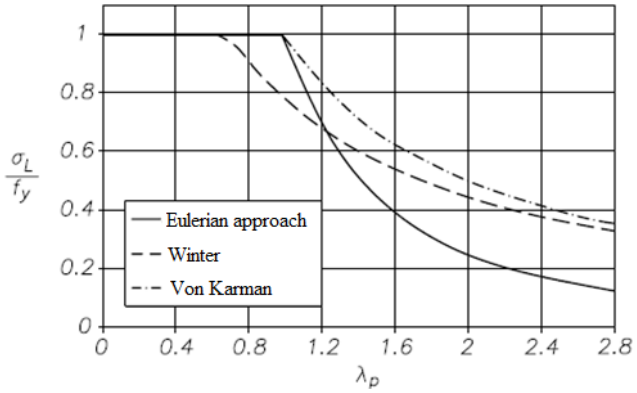

Figure 4: Stability curves for a simply supported plate (representative of a panel in thin-walled cross-sections) with reference to different theoretical approaches.

3 RESULTS

3.1 Finite Element model

The computational model has been tested with reference to experimental data, obtained at the University of Sidney, Australia, by Wilkinson and Hancock [11]. Those Authors have carried out a set of four-point bending tests on steel beams with rectangular hollow section (RHS). Several specimens with different thickness of the flanges have been tested, more specifically RHS 150x50x4, RHS 150x50x3 and RHS 150x50x2.3 (all the measurements are in millimeters); in that way, it was possible to evaluate the increasing sensitivity to imperfection for decreasing thickness. The scheme of the experiments is depicted in Figure 5a; conversely, Figure 5b shows a simplified model of a beam subject to pure bending. In the following, both models will be considered, since the *experiment model* (Figure 5a) was used for a direct comparison with the tests and the *simplified model* (Figure 5b) could be adopted for further generalization and application to cross-sections of different shapes. The main outcome of the experimental campaign was a set of moment-curvature plots, which are normalized with respect to the elastic limit moment (M_p, namely the moment that corresponds to the first attainment of yield stress in the worst point on the cross-section) and to the corresponding curvature (χ_p, given by the elastic limit moment M_p divided by the elastic stiffness EI).

The Finite Element model was represented by a fine discretization of the RHS beams, using quadrilateral shell elements. In view of the very small thickness of the flanges, we chose a formulation which is suitable for thin shells, thus neglecting the shear deformation. Linear, 4-node, elements have been used, with 5 degrees of freedom per node and reduced integration with hourglass mode control. The FE mesh has been chosen after the convergence analyses and is more refined in the central zone, as shown in Figure 6. The *experiment model* included also the discretization of the load posts and of the bearing devices.

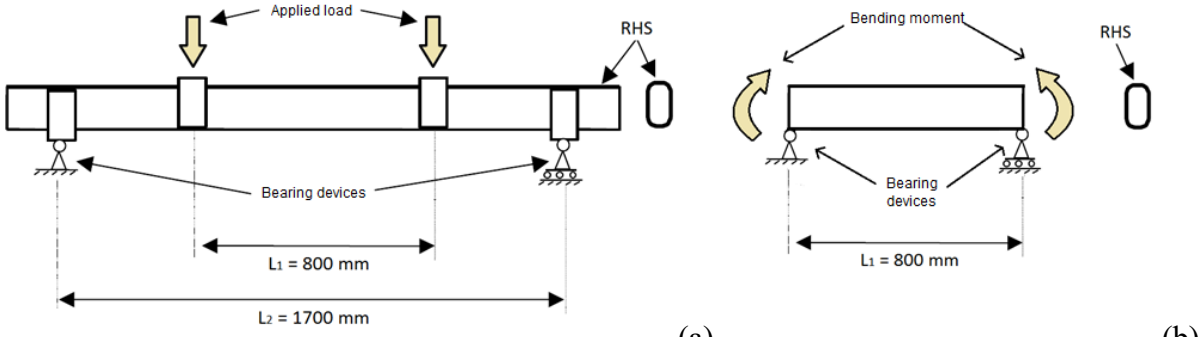

Figure 5: Scheme of the models considered in the computational analyses: (a) *experiment model*, which shares the geometric features with the tests in [11]; (b) *simplified model*, used for further generalization.

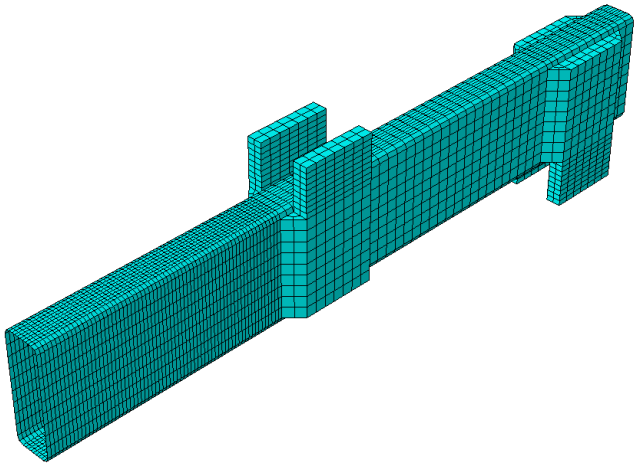

Figure 6: Typical FE model adopted in the non-linear analyses until collapse.

The preliminary step was represented by linear buckling analyses. In that way, it was possible to have an idea of the different buckling modes, shown in Figure 7: (a) local buckling due to compression on the upper flange; (b) local buckling due to bending on the vertical flanges; (c) local buckling due to shear on the lateral bays; (d) overall buckling. The knowledge of buckling modes was also necessary in order to include geometric imperfection in the subsequent non-linear analyses.

The collapse analyses, based on the arc-length method, included non-linearity from the geometric point of view and for material behavior. An elastic-plastic model, based on the Mises' yield function, has been adopted. Non-linear hardening was included, with the main purpose of simulating the actual behavior of steel specimens extracted from the tested structure [11]. It is worth noting that the material law was not uniform in space: indeed, due to fabrication process, the material close to the corners is more resistant and more brittle than the material in other locations. More specifically, three different zones have been considered: corners, horizontal flanges, vertical flanges (see Figure 8).

The optimal version of the FE model has been obtained after several parametric analyses. First, the effect of imperfections, both in terms of amplitude and in terms of shape, was considered. Nice results have been obtained by considering the imperfection as proportional to the first local buckling mode (see Figure 7a), with a typical amplitude equal to 1/250 ÷ 1/500 of the beam's height. The effect of residual stresses was included as well: we finally adopted the typical values proposed by [6] and [7] (ranging between 0.08 f_y and 0.17 f_y, in correspondence of the longitudinal weld and of other locations, respectively).

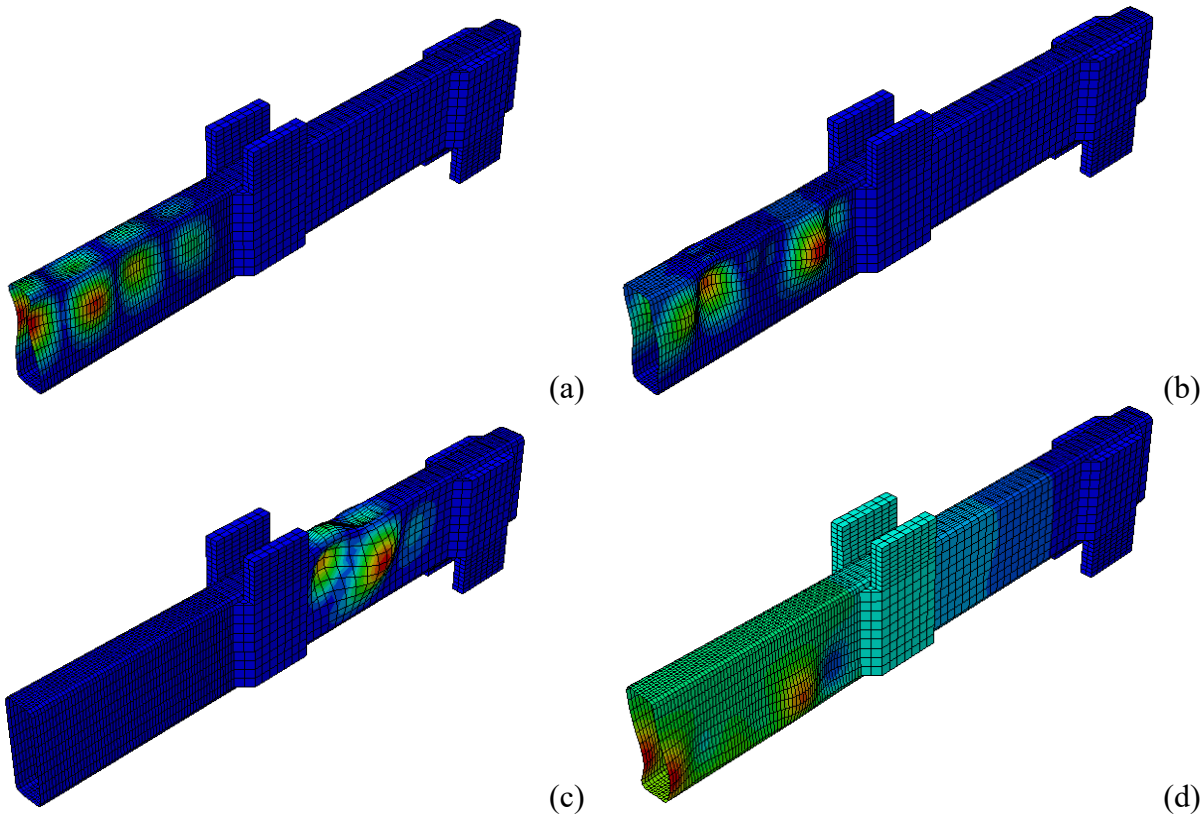

Figure 7: Results of the preliminary buckling analyses: (a), (b) local buckling for bending; (c) local buckling for shear; (d) overall buckling.

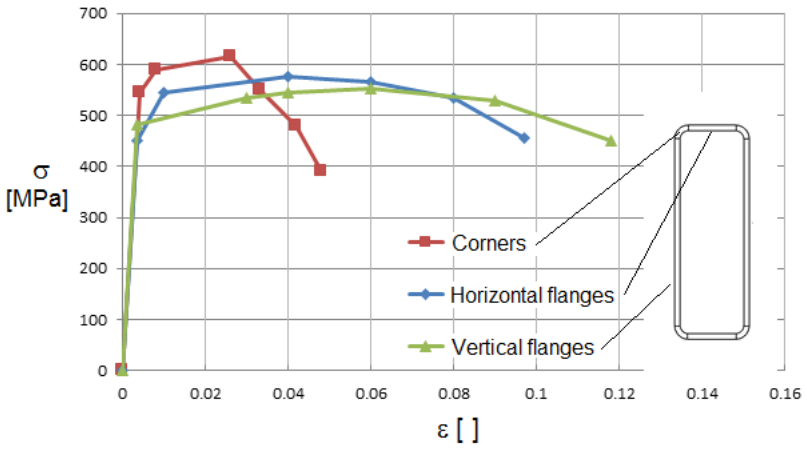

Figure 8: Uniaxial elastic-plastic material behavior for different zones of the RHS cross-sections.

3.2 Comparison of load-curvature responses

The optimal FE model, which did not include any fitting parameter, provided us the collapse load (see Figure 9 for the final deformed shape) and (after some post-processing) the load-curvature response (see Figure 10-12).

Generally speaking, satisfactory agreement between experimental and numerical data was obtained. The ultimate bending moment was captured with a reasonable relative error in all the considered cases; the ultimate curvature (as well as the initial stiffness) was very well simulated; also the deviation from linearity, owing to second-order geometric effects, was attained at the same load level with respect to the experimental outcomes.

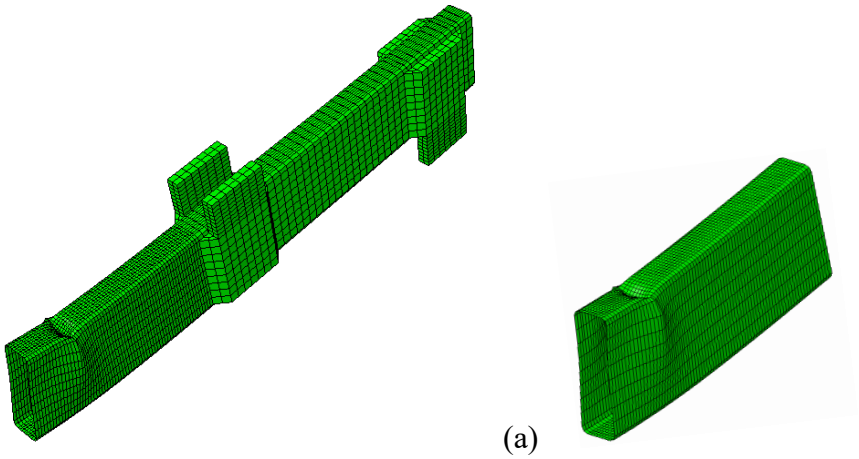

(a) (b)

Figure 9: Deformed shape at collapse: (a) *experiment model*; (b) *simplified model*.

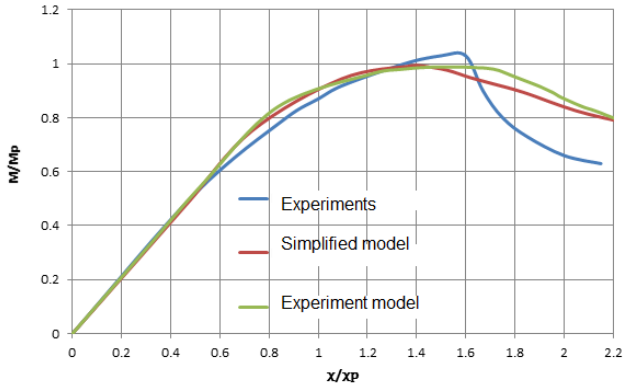

Figure 10: Load-curvature response for RHS 150x50x2.3.

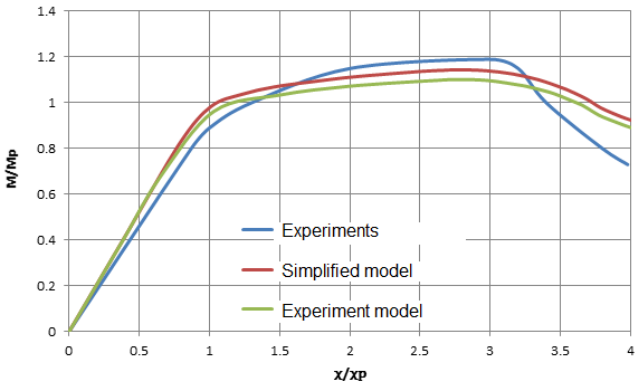

Figure 11: Load-curvature response for RHS 150x50x3.

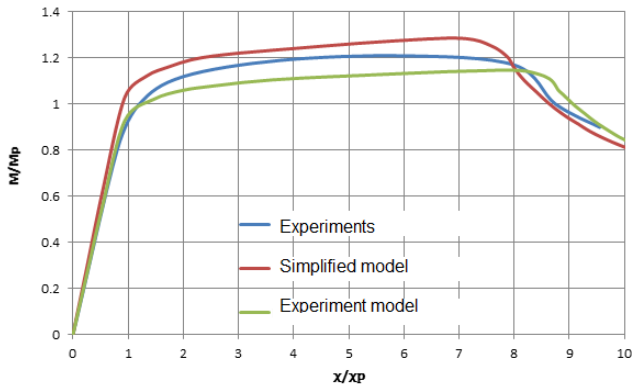

Figure 12: Load-curvature response for RHS 150x50x4.

Some differences between the curves could be due to the spatial discontinuities of the constitutive law. In the real case, the stress-strain model is smoothly changing between the various parts of the section highlighted in Figure 8, conversely the FE model includes piecewise constant material laws. Another cause of discrepancies could be represented by the stochastic nature of imperfections, which turned out to play a paramount role in the definition of the collapse load.

All the analyses have been repeated by adopting the *simplified model*: as a matter of fact, some differences arose with respect to the *experiment model*. Even though the curves shared the same shape, the simplified model involved slightly larger ultimate loads. The difference could be explained by considering the effect of the loading posts, which have been completely modeled in the experiment model and are totally absent in the simplified model. However, both model revealed to be adequate to catch, with sufficient accuracy, the experimental response. This provided a sound validation of the computational models.

4 CONCLUSIONS

An optimized FE model for the collapse analyses of polygonal steel beams has been proposed and validated against reliable experimental data. Satisfactory agreement between the computational outcomes and the experimental data has been achieved, so that the computational model is basically ready to be used in other cases. As an example, the case of hexagonal or octagonal profiles could be considered, in order to execute the safety assessment of structures with practical interest.

The presence of a computational tool for that kind of structures is specifically important, since the application of simplified formulas, which can be retrieved in the Eurocode (EC) [15], is rather questionable for polygonal cross-section with six sides or more. As an example, we considered the theoretical computation of ultimate moment for three cases of RHS: the results are summarized in Table 1. One can easily realize that the formula proposed by the EC, though very simple to be used, finally yields poorly approximate results, which are not on the safe side (the ultimate moment is overestimated by the EC procedure). Some current research, which will be reported in a forthcoming paper, shows that the inaccuracy of EC formulas is even larger for sections with six sides or more

Section	*Class*	M_u *(EC)* *[kN·m]*	M_u *(FE)* *[kN·m]*	*Δ* *[%]*
RHS 150x50x2	3	12.36	11.91	+ 3.73
RHS 150x50x3	1	23.05	20.51	+ 12.38
RHS 150x50x4	1	29.95	28.69	+ 4.38

Table 1: Comparison between the ultimate moment obtained via the numerical procedure (FE) and the formula proposed by the Eurocode (EC).

REFERENCES

[1] A. Godat, F. Legeron, D. Bazonga, "Stability investigation of local buckling behavior of tubular polygon columns under concentric compression," *Thin-walled Struct.*, vol. 53, pp. 131-140, 2012.

[2] K.H. Law, L. Gardner, "Buckling of elliptical hollow section members under combined compression and uniaxial bending", *J. of Constr. Steel Res.*, vol. 86, pp. 1-16,

2013.

[3] A. Rossi, Z. Fawaz, K. Behdinam , "Numerical simulation of the axial collapse of thin walled polygonal section tubes", *Thin-Walled Struct.*, vol. 43, pp. 1646-1661, 2005.

[4] T.V. Galambos, *Guide to stability design criteria for metal structures – 5th Edition*", John Wiley & Sons, New York, 1998.

[5] K.S. Wanniarachchi, M. Mahendran, "Design of rectangular hollow flange steel beams," *Proc. of the 8th International Conference on Steel, Space and Composite Structures*, Kuala Lumpur, Malaysia, pp. 393-400, 2006.

[6] B.W. Schafer, T. Pekoz, "Geometric imperfection and residual stresses for use in the analytical modeling of cold-formed steel members", *Thirteen International Specialty Conference of Cold-Formed Steel Structures*, Missouri U.S.A., 1996.

[7] B.W. Schafer, T. Pekoz, "Computational modeling of cold-formed steel: characterizing geometric imperfections and residual stresses", *J. of Constr. Steel Res.*, vol. 47, pp. 193-210, 1998.

[8] R.B. Cruise, L. Gardner, "Residual stress analysis of structural stainless steel sections", *J. of Constr. Steel Res.*, vol. 64, pp. 352-366, 2008.

[9] L. Gardner, N. Saari, F. Wang, "Comparative experimental study of hot rolled and cold formed rectangular hollow sections". *Thin-Walled Struct.*, vol. 48, pp. 495-507, 2010.

[10] Dassault Systémes Simulia, *Abaqus 6.10 Analysis User's Manual*. Providence, 2010.

[11] T. Wilkinson, G.J. Hancock, *Finite element analysis of plastic rectangular hollow sections beams*, Research report N° R792, Department of Civil Engineering, University of Sydney, Australia.

[12] EN 1993-1-5, *Eurocode 3 – Design of Steel Structures. Part 1-5: Plated Structural Elements*, 2007.

ECCOMAS Congress 2016
VII European Congress on Computational Methods in Applied Sciences and Engineering
M. Papadrakakis, V. Papadopoulos, G. Stefanou, V. Plevris (eds.)
Crete Island, Greece, 5–10 June 2016

INFLUENCE OF STRAIN DEFINITIONS ON TRUSSES CRITICAL LOADS

Reyolando M. Brasil[1] **and José M. Balthazar**[2]

[1] Federal University of ABC (UFABC)
Av. dos Estados, 5001, 09210-180, Santo André, SP, Brazil
e-mail: reyolando.brasil@ufabc.edu.br

[2] Aeronautics Technological Institute (ITA)
Pr. Mal. Eduardo Gomes, 50, 12.228-900, São José dos Campos, SP, Brazil
e-mail: jmbaltha@gmail.com

Keywords: geometric nonlinearity, material nonlinearity, elastic constitutive laws, trusses, structural stability.

Abstract. *In this paper, the influence of several elastic constitutive laws upon the stability analyses of plane trusses is discussed. The chosen laws are connected to the engineering strain, Green's strain and logarithmic strain concepts. A geometrically exact nonlinear formulation for a truss bar element is developed for each of them and the correspondent tangent stiffness matrices are obtained.*

The stability analyses of some sample plane trusses are performed by finding the conditions when the determinant of their respective global tangent stiffness matrices is found to be zero. The first example is a symmetric two-bar structure and both limit loads and buckling loads are plotted for the full range of possible initial inclination angles of the bars, for the three chosen constitutive laws. A similar truss with an extra vertical bar is studied to discuss possible material instability if Green's strain concept is adopted.

1 INTRODUCTION

The presented direct formulation of the geometrically exact nonlinear theory of elastic trusses is of great simplicity and elegance and has already been obtained, for plane trusses and adopting the engineering strain concept, in a pioneer paper by Turner et al (1960) [5].

The central idea of this approach can be abstracted as follows, following Levy and Spillers (1995) [2]. Let the equation of equilibrium of a system be written as

$$\mathbf{P} = \mathbf{C}\mathbf{N} \tag{1}$$

where **P** represents the applied loads, **N** the internal forcers or stresses and **C** an appropriate equilibrium operator. Under a load perturbation *d***P**, the system responds as

$$d\mathbf{P} = \mathbf{C}\, d\mathbf{N} + d\mathbf{C}\,\mathbf{N} \tag{2}$$

For discrete systems such as trussed structures it turns out to be relatively simple matter to convert this equation into the usual

$$d\mathbf{P} = \mathbf{K_T}\, d\mathbf{q} \tag{3}$$

where $d\mathbf{q}$ represents the system's incremental generalized displacements and $\mathbf{K_T}$ is the tangent stiffness matrix containing the usual elastic and geometric stiffness matrices. With this approach, which is followed throughout this paper, nonlinear structural analysis becomes simply an application of Newton-Raphson's method of nonlinear equations solution.

2 GENERAL THEORY

In the geometrically exact theory for trusses, no restrictions are made to the amplitude of angular deflections. Let us consider the plane truss bar of Fig. 1. Its initial length is *L*. The relationships between the vector of nodal displacements **q** of a plane truss bar and the values of θ and L' (the angle between the displaced position of the bar and its original position and the deformed length of the bar, respectively) are

$$L' - L = \mathbf{c}\,\mathbf{q} \tag{4}$$

where

$$\mathbf{c} = \begin{bmatrix} -\cos\theta & -\sin\theta & \cos\theta & \sin\theta \end{bmatrix} \tag{5}$$

$$\mathbf{q} = \begin{bmatrix} q_1 & q_2 & q_3 & q_4 \end{bmatrix}^t \tag{6}$$

To compute the strain ε_i (with *i*= 1 for engineering strain, *i* = 2 for Green's strain and *i* = 3 for logarithmic or natural strain) the following expressions are used, according to Argyris *et al* (1960) [1],

$$\varepsilon_1 = \lambda - 1 \tag{7}$$

$$\varepsilon_2 = \frac{\lambda^2 - 1}{2} \tag{8}$$

$$\varepsilon_1 = \ln\lambda \tag{9}$$

where $\lambda = L'/L$.

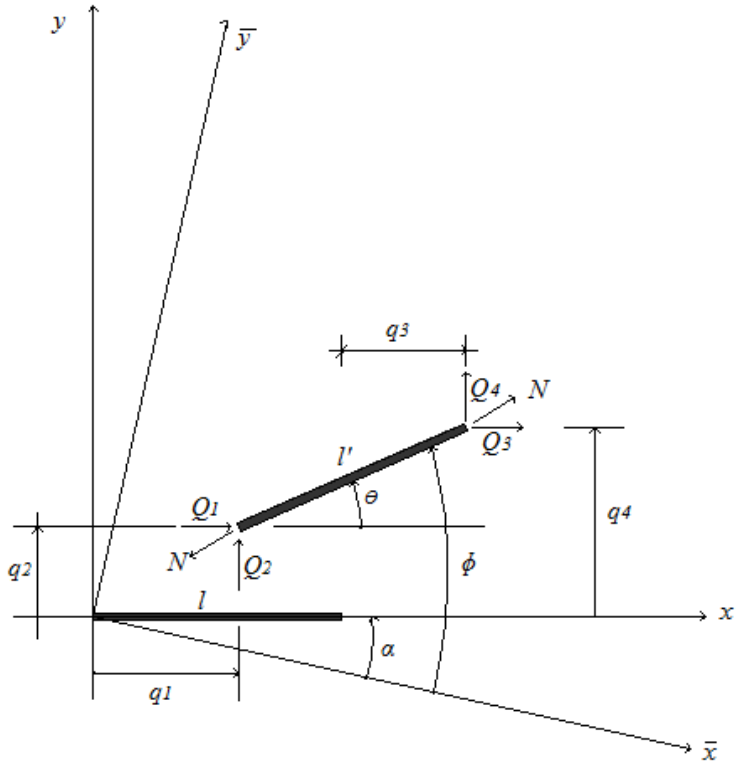

Figure 1: Reference and actual configuration of a truss element

The exact values of the components of nodal forces, as depicted in Fig. 1, are

$$\mathbf{Q} = N\,\mathbf{c}^t \tag{10}$$

where

$$\mathbf{Q} = \begin{bmatrix} Q_1 & Q_2 & Q_3 & Q_4 \end{bmatrix}^t \tag{11}$$

and N is the normal force in the bar. The constitutive laws render the actual normal stress σ_i by the following expressions

$$\sigma_1 = E_1 \varepsilon_1 \tag{12}$$

$$\sigma_2 = \lambda E_2 \varepsilon_2 \tag{13}$$

$$\sigma_3 = E_3 \frac{\varepsilon_3}{\lambda} \tag{14}$$

where E_i is the elastic modulus correspondent to the chosen strain concept.

Thus, the normal force is given, for each constitutive law, by

$$N_i = \sigma_i\, A \tag{15}$$

where A is the area of the cross section of the bar.

To obtain the expression of the tangent stiffness matrix $\mathbf{k_T}$, one must differentiate Eq. 10 to get

$$d\mathbf{Q} = \mathbf{c}^{\mathbf{t}}\, dN + N\,\mathbf{s}^{\mathbf{t}}\, d\theta \tag{16}$$

where

$$\mathbf{s} = \begin{bmatrix} \sin\theta & -\cos\theta & -\sin\theta & \cos\theta \end{bmatrix} \tag{17}$$

Next, one must establish relationships between the differentials $d\theta$ and dN and the displacement increments $d\mathbf{q}$. To that end, Eqs. 4 and 15 are used, to obtain

$$d\theta = \frac{1}{L}\mathbf{s}\, d\mathbf{q} \tag{18}$$

$$dN = \frac{1}{L} D_i\, A\mathbf{c}\, d\mathbf{q} \tag{19}$$

where

$$D_1 = E_1 \tag{20}$$

$$D_2 = \frac{E_2}{2}\left(3\lambda^2 - 1\right) \tag{21}$$

$$D_3 = \frac{E_3}{\lambda^2}\left(1 - \ln\lambda\right) \tag{22}$$

It is now necessary to introduce into Eq. 16 the values of $d\theta$ and dN given by Eqs. 18 and 19, to obtain

$$d\mathbf{Q} = \left(\frac{D_i A}{L}\mathbf{c}^{\mathrm{t}}\mathbf{c} + \frac{N_i}{L'}\mathbf{s}^{\mathrm{t}}\mathbf{s} \right) d\mathbf{q} \tag{23}$$

the equation that renders the tangent stiffness matrix of the exact theory for each of the elastic constitutive laws adopted:

$$\mathbf{k_T} = \frac{D_i A}{L}\mathbf{c}^{\mathrm{t}}\mathbf{c} + \frac{N_i}{L'}\mathbf{s}^{\mathrm{t}}\mathbf{s} \tag{24}$$

As in the usual matrix analysis of structures, once the tangent stiffness matrix of the bar in the local reference frame is known, its counterpart in the global one is easily obtained by the rotation formula, given, by example, by Meek (1991)[3],

$$\bar{\mathbf{k}}_{\mathbf{T}} = \mathbf{T}^{\mathrm{t}}\mathbf{k_T}\mathbf{T} \tag{25}$$

where

$$\mathbf{T} = \begin{bmatrix} \cos\alpha & \sin\alpha & 0 & 0 \\ -\sin\alpha & \cos\alpha & 0 & 0 \\ 0 & 0 & \cos\alpha & \sin\alpha \\ 0 & 0 & -\sin\alpha & \cos\alpha \end{bmatrix} \tag{26}$$

and α is the angle between the original direction of the bar and the $\bar{x}$ axis of the global reference frame, as shown in Fig. 1.

As a more practical alternative, one can introduce the new matrices

$$\bar{\mathbf{c}} = \begin{bmatrix} -\cos\phi & -\sin\phi & \cos\phi & \sin\phi \end{bmatrix} \tag{27}$$

$$\bar{\mathbf{s}} = \begin{bmatrix} \sin\phi & -\cos\phi & -\sin\phi & \cos\phi \end{bmatrix} \tag{28}$$

where $\phi = \theta + \alpha$, which are related to Eqs. 5 and 17 by

$$\bar{\mathbf{c}} = \mathbf{cT} \tag{29}$$

$$\bar{\mathbf{s}} = \mathbf{sT} \tag{30}$$

Thus, a new form of the tangent stiffness matrix of the truss member in the global reference frame is

$$\bar{\mathbf{k}}_{\mathbf{T}} = \frac{D_i A}{L}\bar{\mathbf{c}}^{\mathbf{t}}\bar{\mathbf{c}} + \frac{N_i}{L'}\bar{\mathbf{s}}^{\mathbf{t}}\bar{\mathbf{s}} \tag{31}$$

which is formally identical to Eq. 24.

To obtain the tangent stiffness matrix of the structure as a whole, the following summation process is extended to all members of the system

$$\mathbf{K}_{\mathbf{T}} = \sum \mathbf{A}^{\mathbf{t}}\bar{\mathbf{k}}_{\mathbf{T}}\mathbf{A} \tag{32}$$

where **A** is the usual incidence matrix of each bar.

3 THE FIRST EXAMPLE

The first chosen example is the classic two bars truss whose stability was studied by Ratzersdorfer (1936) [4], also known as von Mises truss, depicted in Fig. 2.

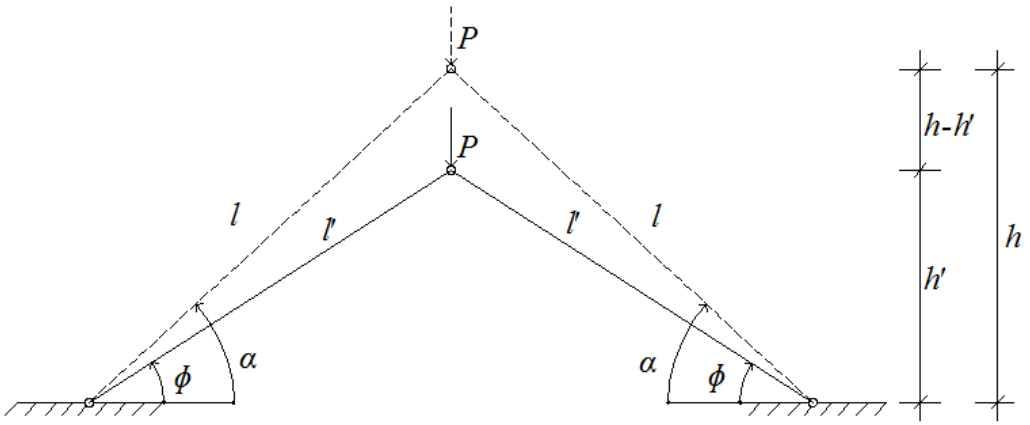

Figure 2. The first example

As it is well known, depending to the initial geometry, either bifurcation or limit point instabilities may happen. The original length of the bars is L and their original inclination α. After a vertical load P is applied to the central node the length of the bars becomes L' and their inclination ϕ.

If the exact theory is applied, the tangent stiffness matrix associated to the two degrees of freedom of the central node is

$$\mathbf{K}_{\mathbf{T}} = \frac{2D_i A}{L}\begin{bmatrix} \cos^2\phi & 0 \\ 0 & \sin^2\phi \end{bmatrix} + \frac{2N_i}{L'}\begin{bmatrix} \sin^2\phi & 0 \\ 0 & \cos^2\phi \end{bmatrix} \tag{33}$$

where the constant D_i and the normal force N_i depend on the particular constitutive law chosen.

The instability criterion is that the determinant of this matrix must be zero.

3.1 Engineering Stain

For the engineering strain constitutive law, the instability criterion is

$$\left(\sin^2\phi\cos\phi-\cos\alpha\right)\left(\cos^3\phi-\cos\alpha\right)=0 \tag{34}$$

The condition for lateral buckling of the structure is given by

$$\sin^2\phi\cos\phi=\cos\alpha \tag{35}$$

and the corresponding buckling load is

$$P_b=2E_1A\cos^2\phi\sin\phi \tag{36}$$

Limit point instability (snap-through) may be reached according to the condition

$$\cos^3\phi=\cos\alpha \tag{37}$$

and the corresponding buckling load is

$$P_l=2E_1A\sin^3\phi \tag{38}$$

In Fig. 3, both bucking and limit loads are plotted for the full range of possible initial inclination angles of the bars. One should note that for $\alpha > 68.898^o$ bifurcation instability (lateral buckling) will prevail with bucking loads given by the lower branch of the respective curve. For α bellow that value the structure may undergo snap through instability. It is important to see that this value, denoted as point A in the figure, is slightly different from that of the tangential point between the limit point and buckling curves, where $\phi = 45^o$ and $\alpha = 69.295^o$.

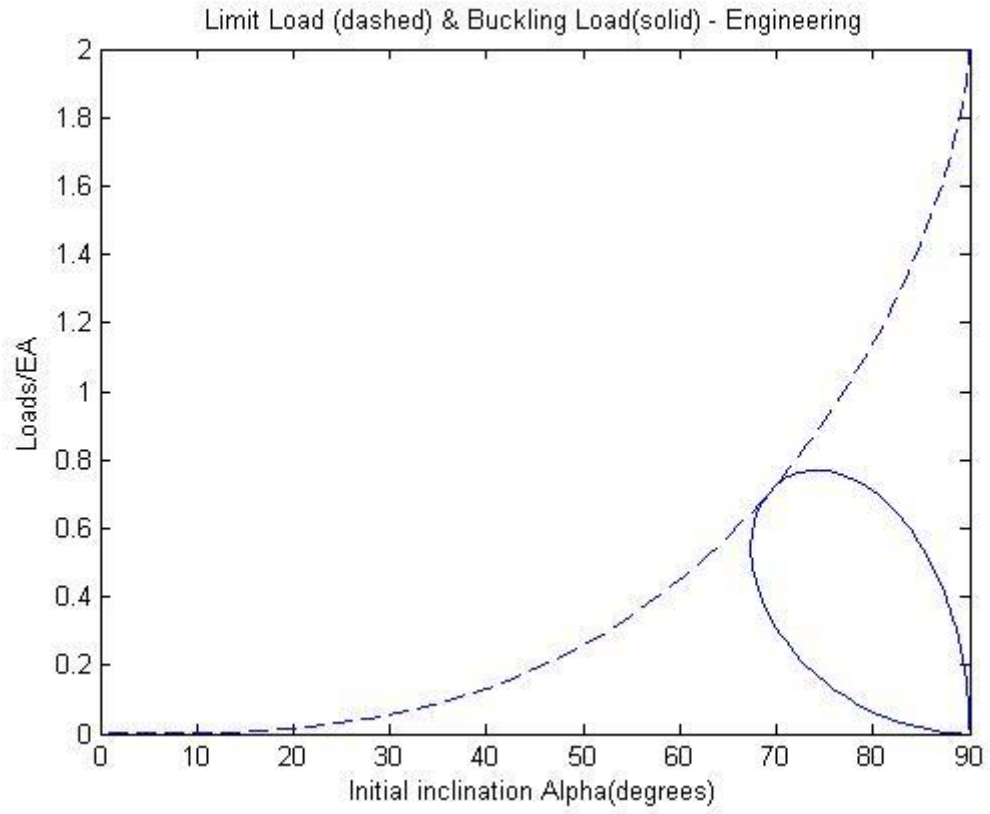

Figure 3: Instability loads, First Example, Engineering Strain

3.2 Green's Strain

For this strain definition, the condition for lateral buckling of the structure is given by

$$\tan^2 \phi = \tan^2 \alpha - 2 \tag{39}$$

and the corresponding buckling loads are

$$P_b = 2E_2 A \cos^3 \alpha \sqrt{\tan^2 \alpha - 2} \tag{40}$$

For Green's strain, limit point instability (snap-through) may be reached according to the condition

$$\tan \phi = \frac{\sqrt{3}}{3} \tan \alpha \tag{41}$$

and the limit load is

$$P_l = \frac{2\sqrt{3}}{9} E_2 A \sin^3 \alpha \tag{42}$$

In Fig. 4, both bucking and limit loads are plotted for the full range of possible initial inclination angles of the bars. One should note that for $\alpha > 60^o$ bifurcation instability (lateral buckling) will prevail with bucking loads given by the right branch of the respective curve. For α bellow that value the structure may undergo snap through instability. It is important to see that this value is exactly that of the tangential point between the limit point and buckling curves.

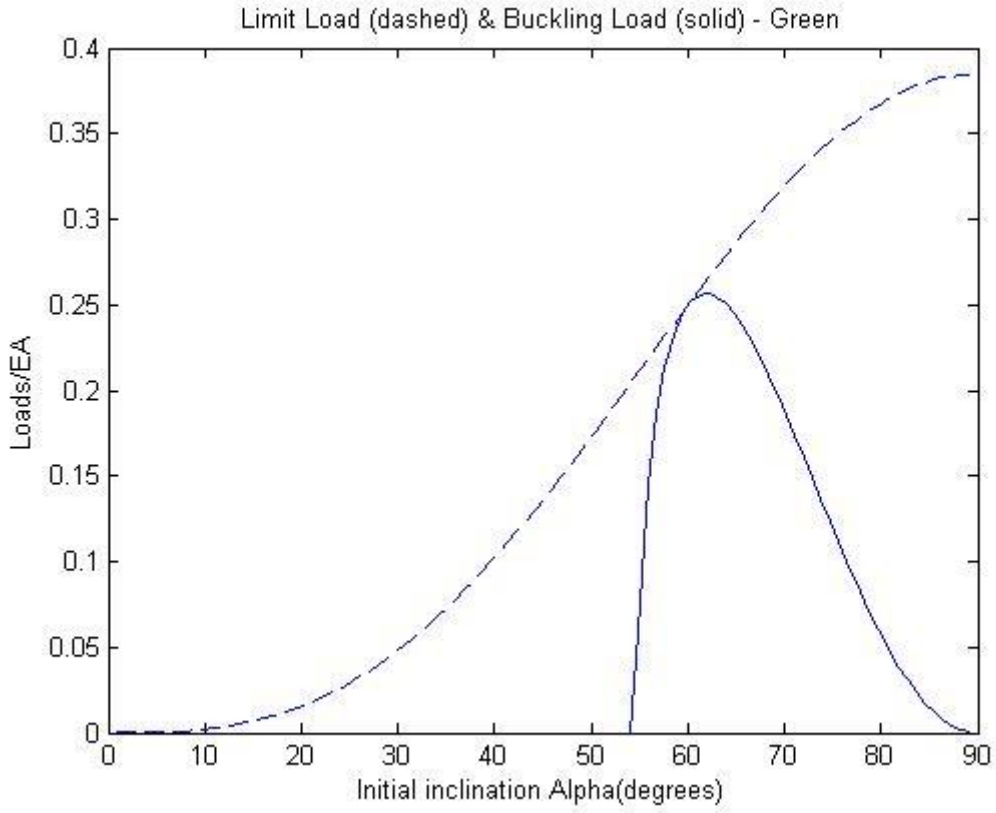

Figure 4: Instability loads, First Example, Green's Strain

3.3 Logarithmic Strain

For this strain definition, the condition for lateral buckling of the structure is given by

$$\lambda^2 \ln\lambda + (1-2\ln\lambda)\cos^2\alpha = 0 \tag{43}$$

For natural strain, limit point instability (snap-through) may be reached according to the condition

$$\lambda^2(1-\ln\lambda) - (1-2\ln\lambda)\cos^2\alpha = 0 \tag{44}$$

Instability loads for both cases are given by

$$P = -\frac{2E_3A}{\lambda^2}\ln\lambda\sqrt{\lambda^2-\cos^2\alpha}. \tag{45}$$

In Fig. 5, both bucking and limit loads are plotted for the full range of possible initial inclination angles of the bars. It is important to see that the two curves never touch each other and for α >71.278º bifurcation instability (lateral buckling) will prevail with bucking loads given by the lower branch of the respective curve. For α bellow that value the structure may undergo snap through instability.

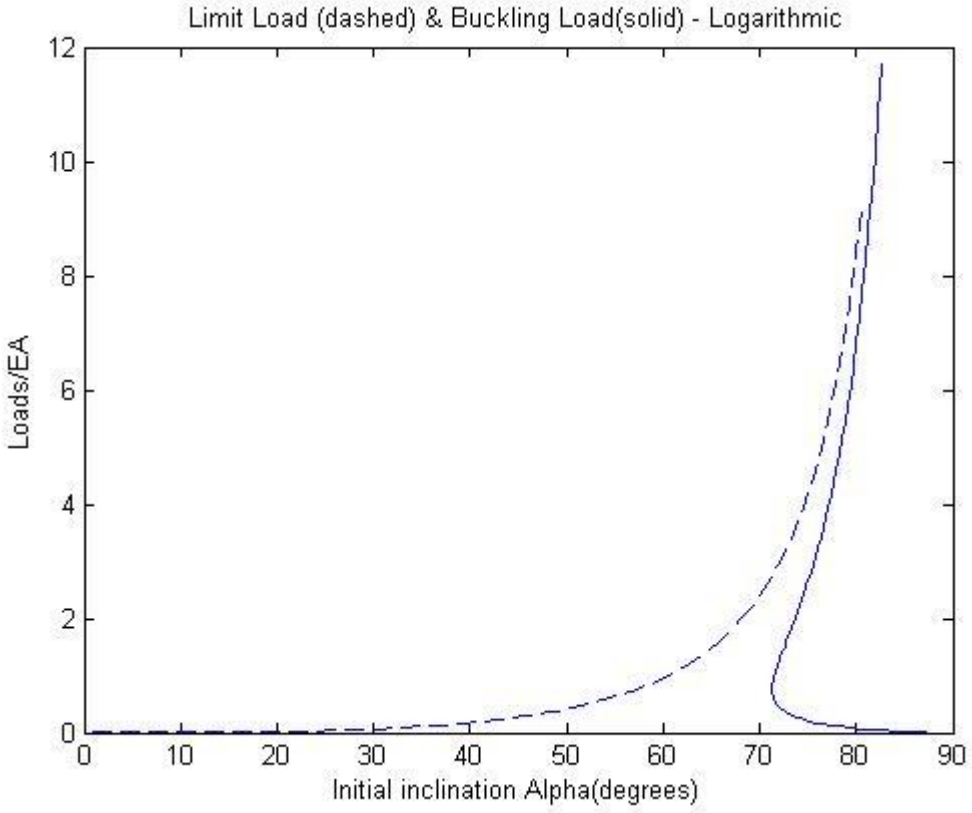

Figure 5: Instability loads, First Example, Natural or Logarithmic Strain

4 THE SECOND EXAMPLE

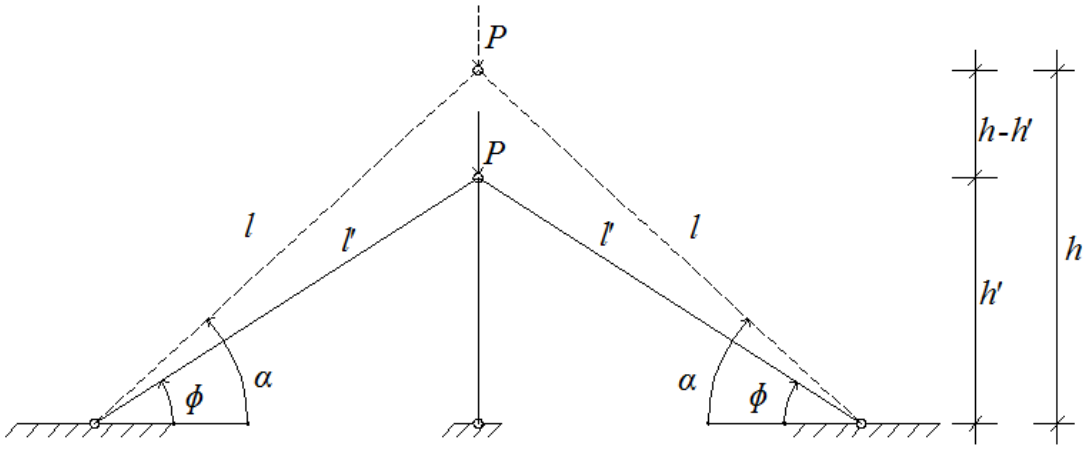

Figure 6: The Second Example

The structure of Fig. 6, similar to the first example except for an extra vertical bar under the upper node, is now analyzed using Green's strain constitutive law. The starting point is Eq. 32 which gives the contribution of the two inclined bars to the tangent stiffness matrix of the structure.

By adding to this equation the new term:

$$\mathbf{k_T} = \frac{E_2 A}{2h}\left(3\lambda_V^2 - 1\right)\begin{bmatrix} 0 & 0 \\ 0 & 1 \end{bmatrix} + \frac{V}{h'}\begin{bmatrix} 1 & 0 \\ 0 & 0 \end{bmatrix} \tag{46}$$

where

$$\lambda_V = \frac{h'}{h} = \frac{\tan\phi}{\tan\alpha} \tag{47}$$

is the stretching of the vertical bar, the complete $\mathbf{K_T}$ is found to be

$$\mathbf{K_T} = \frac{2D_2 A}{L}\lambda^2\begin{bmatrix} \cos^2\phi & 0 \\ 0 & \sin^2\phi\left(1+1/2\ \csc^3\alpha\right) \end{bmatrix} + \left(\frac{2N_i}{L'} + \frac{V}{L'}\csc\phi\right)\begin{bmatrix} 1 & 0 \\ 0 & 0 \end{bmatrix} \tag{48}$$

In Eq. 47,

$$N = \frac{E_2 A\lambda(\lambda^2 - 1)}{2} \tag{49}$$

and

$$V = \frac{E_2 A\lambda_V(\lambda_V{}^2 - 1)}{2} \tag{50}$$

according to the assumed constitutive law.

The instability criterion requires the determinant of this matrix to be zero. The first condition, corresponds to the lateral buckling of the structure and leads to the buckling load:

$$P_b = 2E_2 A \cos^3 \alpha \tan \phi \tag{51}$$

The second condition corresponds to a null value of the stiffness coefficient related to the vertical displacement of the upper node. However, this is not an indication of a genuine snap snap-through phenomenon, but is a consequence of the material instability inextricably present in the constitutive law.

This assertion can be easily proven from Eqs. 13 and 21 and:

$$\sigma_2 = \lambda E_2 \varepsilon_2 = \frac{E_2}{2} \lambda(\lambda^2 - 1) \tag{52}$$

The zero value of its derivative is

$$3\lambda^2 - 1 = 0 \tag{53}$$

which gives the limit value:

$$\lambda_l = \frac{\sqrt{3}}{3} \tag{54}$$

This is the very value that is obtained combining the definition of λ_V given by Eq. 46 with the condition of Eq. 53:

$$\lambda_V = \frac{\tan \phi}{\tan \alpha} = \frac{\sqrt{3}}{3} \tag{55}$$

In Fig. 7, both bucking and limit loads are plotted for the full range of possible initial inclination angles of the bars. It is important to see that limit point and buckling curves touch each other in two points. One should note that for $\alpha < 10^o$ bifurcation instability (lateral buckling) will prevail with bucking loads given by the left branch of the respective curve. For $10^o<\alpha<50^o$the structure may undergo snap through instability. For larger values of α the structure may experience bifurcation (lateral buckling) instability, with buckling loads given by the right branch of the respective curve.

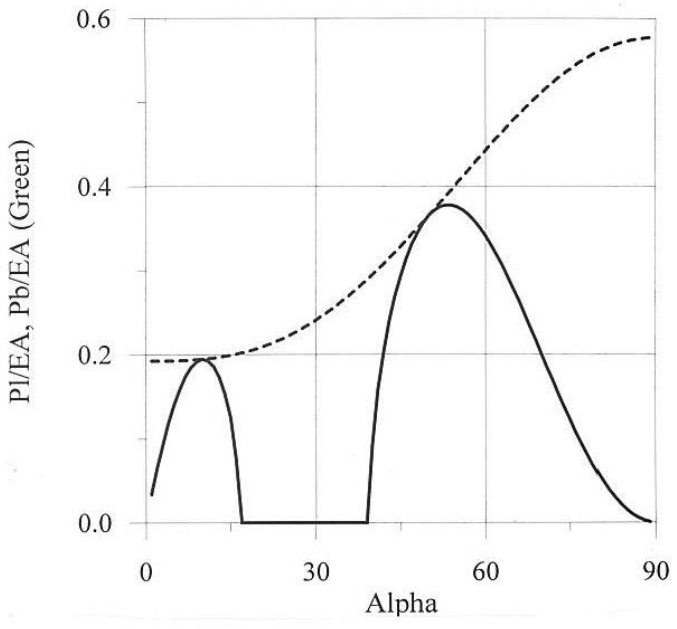

Figure 7: Instability loads, Second Example, Green's Strain

5 CONCLUSIONS

In this paper, the influence of several elastic constitutive laws upon the stability analyses of plane trusses is discussed. The chosen laws are connected to the engineering strain, Green's strain and logarithmic strain concepts. A geometrically exact nonlinear formulation for a truss bar element is developed for each of them and the correspondent tangent stiffness matrices are obtained.

The stability analyses of some sample plane trusses are performed by finding the conditions when the determinant of their respective global tangent stiffness matrices is found to be zero. The first example is a symmetric two-bar structure and both limit loads and buckling loads are plotted for the full range of possible initial inclination angles of the bars, for the three chosen constitutive laws. A similar truss with an extra vertical bar is studied to discuss possible material instability if Green's strain concept is adopted.

ACKNOWLEDGMENTS

The authors acknowledge support by FAPESP, CAPES and CNPq, all Brazilian research funding agencies.

REFERENCES

[1] Argyris, J.H. Matrix methods of structural analysis – a precís of recent developments. In: Matrix methods of Structural Analysis, Ed. B. Fraejs de Veubeke, Mac Millan, New York, 1964.

[2] J Levy, R., Spillers, W.R. Analysis of geometrically nonlinear structures, Chapman and Hall, New York, 1995.

[3] Meek, J.L. Computer methods of structural analysis, Chapoman and Hall, Melbourne, 1991.

[4] Ratzersdorfer, J. Die Knickfestigkeit von Staben and Stabwerken. Springer Verlag, Wien, 1936.

[5] Turner, M.J., Dill, E.H., Martin, H.C., Melosh, R.J. Large deflections of structures subjected to heating and external loads. Journal of Aerospace Sci., v.27, 1960.).

ECCOMAS Congress 2016
VII European Congress on Computational Methods in Applied Sciences and Engineering
M. Papadrakakis, V. Papadopoulos, G. Stefanou, V. Plevris (eds.)
Crete Island, Greece, 5–10 June 2016

ULTIMATE STRENGTH ANALYSIS OF STIFFENED PANELS OF SHIP STRUCTURES UNDER COMBINED LOAD

Li Hong[1], Meng Linghua[1], Qin Zhongwen[2], Zhang Enguo[3] and Li Li[4]

[1] College of Aerospace and Civil Engineering, Harbin Engineering University
Harbin, Heilongjiang,150001, China
e-mail: {lihong,menglinghua}@hrbeu.edu.cn

[2] Dalian Shipbuilding Industry Co.,Ltd.
Dalian, Liaoning,116000, China
e-mail: qinzhongwen@dsic.cn

[3] Dalian Shipbuilding Industry Co.,Ltd.
Dalian, Liaoning,116000, China
e-mail: zhang_enguo@dsic-design.cn

[4] College of Materials Science and Chemical Engineering, Harbin Engineering University
Harbin, Heilongjiang,150001, China
e-mail: lili_heu@hrbeu.edu.cn

Keywords: Stiffened panels, Ultimate strength, Combined load, Nonlinear.

Abstract. *Ultimate strength of stiffened panels of Ship Structures can evaluate the bearing capacity of stiffened plate structure more accurately, and it provides a way to evaluate the safety and reliability of the hull structure. A lot of studies on ultimate strength of the hull structure are basically focused on stiffened panels under uniaxial compression, without considering combined load acting on the hull structure.But in the voyage, the hull structure is subjected to combined effect involved with various type of external loads at the same time. These external loads will inevitably have some impact on the ultimate strength of the hull structure. So it is necessary to study the ultimate strength of the stiffened panels under combined load. The nonlinear finite element method was introduced based on the assessment requirements of buckling and ultimate strength of stiffened panels in IACS Common Structural Rules for Double Hull Oil Tankers. Some important factors of influence such as the structural dimensions, element size, boundary conditions, initial imperfections and loading types are studied. To check the accuracy of the analysis performed in this method.Numerical results were compared with data in the Background Document of buckling strength assessment in CSR and results calculated by empirical formulations performed by other researchers. This paper focuses on investigating the effect of combined load on the ultimate strength of stiffened plates by calculating the ultimate strength of stiffened plates under combined biaxial compression and lateral pressure loads, by means of the famous nonlinear finite element software Ansys. The different influence on the ultimate strength of the stiffened plates are analyzed.*

1 INTRODUCTION

The traditional checking method of ship structure strength checking based on linear elastic rationale. The impact of material nonlinearity and geometric nonlinearity caused by other factors not be considered,therefore it can not accurately assess the true strength reserve hull structure. "Common Structural Rules for Double Hull Oil Tankers" (herein after referred to as CSR-OT) introduced the concept of the ultimate strength of stiffened panels what can evaluate the bearing capacity of stiffened plate structure [1]. A lot of studies on ultimate strength of the hull structure are basically focused on stiffened panels under uniaxial compression, without considering combined load acting on the hull structure. But in the voyage, the hull structure is subjected to combined effect involved with various type of external loads at the same time. These external loads will inevitably have some impact on the ultimate strength of the hull structure. So it is necessary to study the ultimate strength of the stiffened panels under combined load. The nonlinear finite element method was introduced based on the assessment requirements of buckling and ultimate strength of stiffened panels in IACS Common Structural Rules for Double Hull Oil Tankers. This paper focuses on investigating the effect of combined load on the ultimate strength of stiffened plates by calculating the ultimate strength of stiffened plates under combined biaxial compression and lateral pressure loads.

2 NON-LINEAR FINITE ELEMENT ANALYSIS

Ultimate strength can be performed using the element analysis software ANSYS. The paper adopts ANSYS nonlinear finite element method for ultimate limit state assessment.

2.1 Geometric and Material Properties

For the current research a VLCC double hull oil tanker structure designed by CSR method is studied. The deck panel is chosen for the analysis purposes. Geometrical properties of the stiffened panel of the deck of the object ship are tabulated as follows:

The length of the panel is L=5640 mm. The longitudinal stiffener spacing is w=850 mm, because the number of longitudinal stiffeners with the type of Tee bar is 6. Therefore, the total breadth of the stiffened panel is W=5100mm.The plate thickness is t=21mm. The stiffener height (dw) is 393 mm and the stiffener webthickness (tw) is 13 mm. The stiffener flange breadth (df) is 172 mm and the stiffener flange thickness (tf) is 17mm. Young's modulus of the material is E=205.8 GPa, and Poisson's ratio is v=0.3. The yield stress is σy =315 MPa for both plating and stiffeners. A plastic tangent modulus of 1000MPa is acceptable for higher strength steel.

2.2 Structural Modeling.

The extent of the model used in the ultimate strength assessment is to be sufficient to account for the structure that is surrounding the panel of interest, and to reduce the uncertainties introduced through the boundary conditions.

In general, the model is to include more than one stiffener span in the stiffener direction and the portion between two primary support members in the direction normal to the stiffeners [2].

The structural model and assessment method applicable for deck is to be taken as:

(a) parallel to the stiffener direction: at least two frame bays, in order to model imperfections between adjacent panels.

(b) normal to the stiffener direction: between primary support members, but maybe limited to six stiffener spacings.

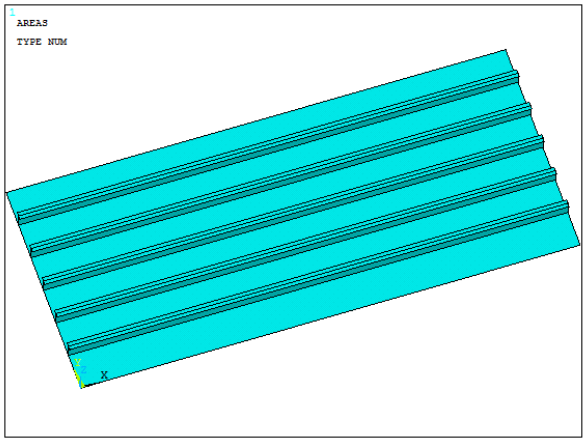

Figure 1: Stiffened plate geometry.

For the present nonlinear FEA, a half+one+half-bay model (1/2+1+1/2-bay model) in the length (x) direction is applied to accurately take into account the effect of rotational restraints along transverse floors, as described in Fig. 1. The meshing of the 3-D FE model of hull structure is to be carried out considering both calculation accuracy and computing time. The meshes are to be as square as possible.

The element type chosen for analysis is 'Shell181'. This element is most suitable for ultimate strength analysis [3]. Stiffened plate plate and stiffener (including panels and web) are modeled with 'Shell181'. The element size is to be small enough to describe the deflections accurately. A mesh size of 141 is chosen to mesh the area.

The coordinate system used within these Rules is shown in Figure 1. Motions and displacements are considered positive in the forward, up and to port direction. Angular motions are considered positive in the clockwise direction about the x, y or z axis.

2.3 Boundary Conditions

The boundary conditions are to represent the actual response of the stiffened panel. the simply supported boundary condition is often adopted in maritime industry . The edges of model may be taken as free to move in-plane, but forced to remain straight[4]. The panels can be taken as supported in the vertical direction at the primary support members. The stiffeners should be taken as horizontally supported at the crossing of primary support members. In this model, the transverse floor is not modeled. Instead appropriate boundary conditions are applied along the length of the transverse floor attached with plating and longitudinal stiffeners to account for the effects of the transverse floor [5]. The following are the boundary conditions of the nonlinear finite element model, namely

Longitudinal edges Y=0 and Y=W: UZ=0,ROTY=O,ROTZ=0.

At X=2L all nodes to have equal X-displacement.

At X=0 edge UX=0.

At Y=0 and Y=W: ROTY=0, ROTZ=0.

At Y=0 and Y=W all nodes to have equal y-displacement.

At transverse frame: All plate nodes UZ=0.

All stiffener web nodes all nodes to have equal Y displacement.

The boundary conditions for nonlinear analysis is shown in Figure 2.

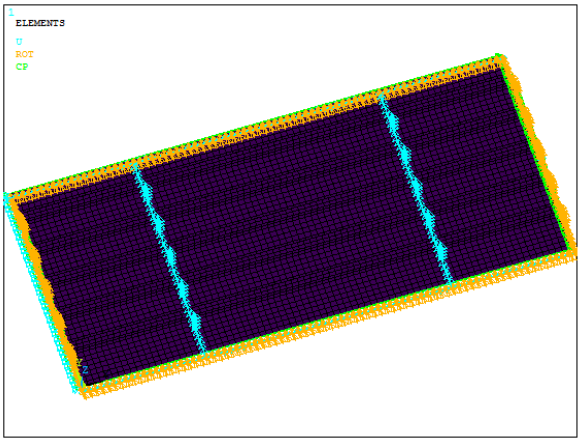

Figure 2: Boundary conditions of stiffened plate.

2.4 Initial Distortions

Initial distortions make significant impact on the result of the ultimate strength behavior of stiffened plate structures. Therefore, it is important to model the shape and magnitude of initial imperfections in a relevant way [6]. The imperfections may be divided into local imperfections (plate out-of-flatness and stiffener sideways out-of-straightness), and global imperfections of the stiffeners(stiffener lateral/vertical out-of-straightness). No residual stress is supposed to exist for this research study.

For performing a nonlinear finite element computations, the pattern of initial imperfections that are required to be generated for initiation of the buckling eigenvalue analysis is assumed to be the buckling mode of the structure that provides the minimum resistance against the actions.

2.5 Comparison of the Method.

To check the accuracy of the analysis performed in this method,Numerical results were compared with data in the Background Document of buckling strength assessment in CSR and results calculated by empirical formulations performed by other researchers.

In 2009, Shengming Zhang [7] calculated the ultimate strength of 132 Ship Common stiffened plate, and summed up the following empirical formula:

The following example is a single line equation:

$$\frac{\sigma_u}{\sigma_y} = \frac{1}{\beta^{0.28}} \frac{1}{\sqrt{1+\lambda^{5.2}}}, \text{take} \beta = 1, \text{if } \beta < 1 \tag{1}$$

The following example is a single line equation:

$$\beta = \frac{b}{t}\sqrt{\frac{\sigma_y}{E}} \tag{2}$$

The following example is a single line equation:

$$\lambda = \frac{a}{\pi r}\sqrt{\frac{\sigma_y}{E}} \tag{3}$$

Where B = (n + 1) b, n = the number of ribs, B = stiffened plate width, r = the radius of inertia ribs.

Background document lists the ultimate strength of stiffened plate[8], A quick comparison among the background document results, the non-linear FE results and empirical formula results for the six stiffened panels in Table 1 and 2 were carried out.

No.	L(mm)	w(mm)	t(mm)	d_w(mm)	t_w(mm)	d_f(mm)	t_f(mm)
T-1	6	850	15	613	10	200	13
T-2	4.5	850	25	613	10	200	13
T-3	6	850	20	613	10	200	13
T-4	4.5	850	20	613	10	200	13
T-5	5	850	19	462	9	150	12
T-6	3.5	850	19	462	9	150	12

Table 1: Basic characteristics of stiffened panels.

No.	background document results(Mpa)	empirical formula results(Mpa)	non-linear FE results(Mpa)
T-1	254	249.11	248.95
T-2	289	289.12	294.29
T-3	273	269.48	261.01
T-4	280	271.81	281.97
T-5	264	263.17	259.54
T-6	273	267.66	256.14

Table 2: Comparison of ultimate strength.

Contrast to results in this paper, the calculation method is right. The paper will analyze the ultimate strength of stiffened plates under combined loads using the above method.

3 ULTIMATE STRENGTH OF STIFFENED PANEL

3.1 Different Proportions of Axis Pressure

The ultimate strength of stiffened panels under different proportions of axis pressure is studied, include: σx: σy = 1.0: 0,0.79: 0.21,0.4: 0.6,0: 1.0, where σx: σy = 1.0: 0 the corresponding longitudinal uniaxial compression, σx: σy = 0: 1.0 corresponds to transverse uniaxial compression, the following table shows the strength of stiffened panels under different proportions of axis pressure.

σx:σy	σxu（MPa）	σyu（MPa）
1.0:0	246.38	-
0.79:0.21	236.37	62.83
0.4:0.6	63.31	94.96
0:1.0	-	96.89

Table 3: Ultimate strength of stiffened panels under different proportions of axis pressure.

3.2 Combined Biaxial Compression and Lateral Pressure Loads

The ultimate strength of stiffened plates under combined biaxial compression and lateral pressure loads is studied.All calculations lateral pressure is added in 2.1, and remains constant lateral pressure, namely p = 0.16MPa throughout the calculation process [9]. Before the finite element calculation process, the lateral pressure is applied on the stiffened plates, and obtain the the ultimate strength of stiffened plates. The following table shows the ultimate strength of stiffened plates under combined biaxial compression and lateral pressure loads.

σx:σy	σxu（MPa）	σyu（MPa）
1.1:0	209.40	-
0.79:0.21	210.91	56.06
0.4:0.6	64.90	97.35
0:1.0	-	98.19

Table 4: Ultimate strength of stiffened plates under combined biaxial compression and lateral pressure loads.

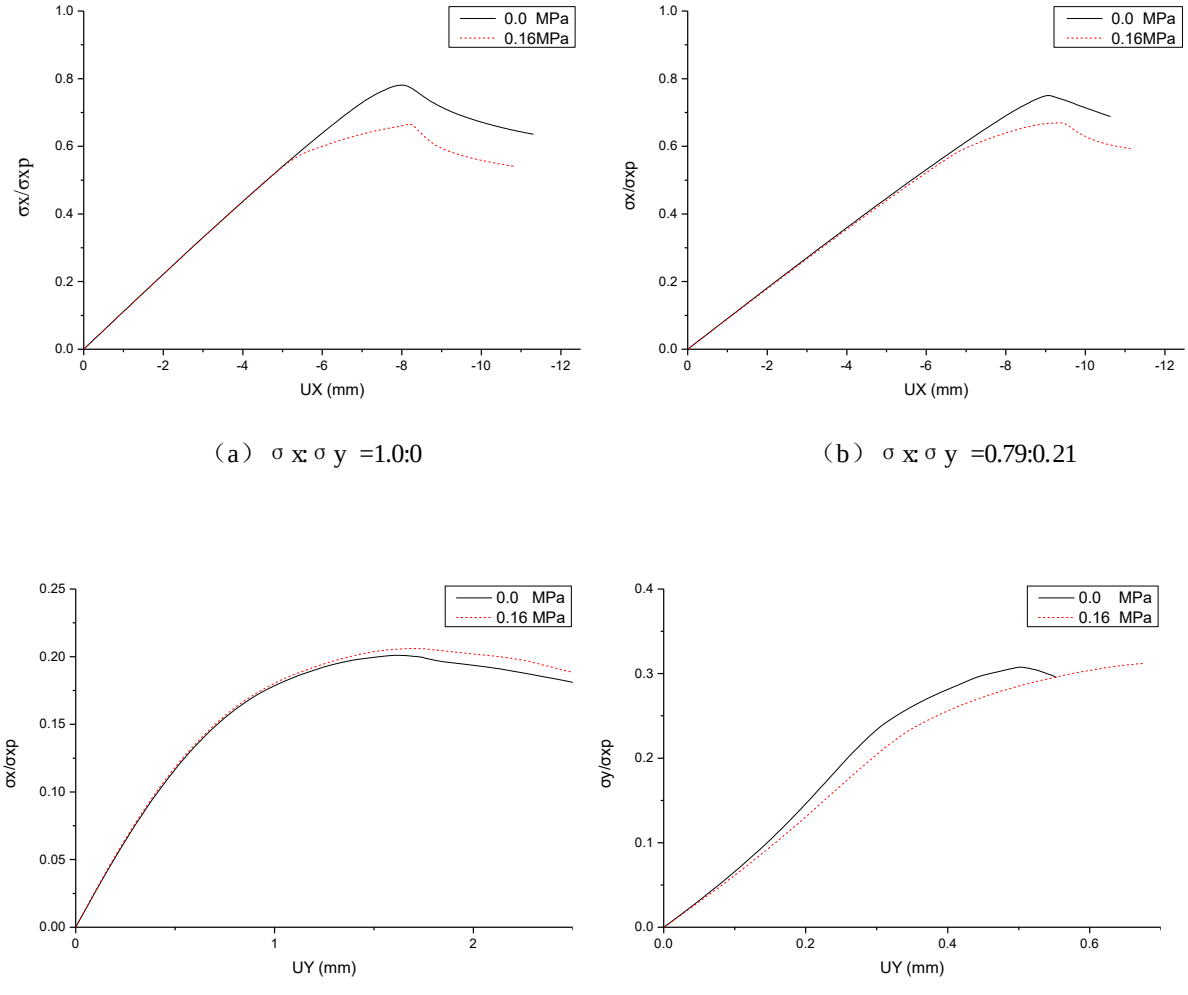

（a） σ x:σ y =1.0:0

（b） σ x:σ y =0.79:0.21

（c） σ x:σ y =0.4:0.6

（d） σ x:σ y =0:1.0\

Figure 3: stress-strain curves of stiffened plates under combined biaxial compression and lateral pressure loads.

4 CONCLUSIONS

- A FEA method of ultimate strength was put forward based on the analysis of the influence of different factors and the study on the CSR. Some important factors of influence such as the structural dimensions, element size, boundary conditions, initial imperfections and loading types are studied. A comparison among the background document results， the non-linear FE results and empirical formula results was provided to verify the method.
- By the calculation and analysis of stiffened plates under axial compression and lateral pressure, the results showed that lateral pressure make a negative impact on the ultimate strength of stiffened panels when t the proportion of Uni-axial compression in the direction of the stiffener is greater, and lateral pressure make a negligible impact on the ultimate strength of stiffened panels when the proportion of Uni-axial compression in the direction of the transverse is greater.

5 ACKNOWLEDGEMENTS

This paper is funded by the International Exchange Program of Harbin Engineering University for Innovation-oriented Talents Cultivation.

REFERENCES

[1] IACS. Common Structural Rules for Double Hull Oil Tankers , *International Association of Classification Societies*,2006.

[2] Paik J K，Seo J K. Nonlinear finite clement method models for ultimate strenth analysis of steel stiffened- plate structures under combined biaxial compression and lateral pressure actions-Part II:Stiffened panels,J, *Thin-walled Structures*, 2009(47):998-1017.

[3] ANSYS, Inc *ANSYS structural analysis guide. Release 12.0*,2009.

[4] IACS. Background Document Of Common Structural Rules for Double Hull Oil Tankers, *International Association of Classification Societies*,2012

[5] Ming Cai Xu , Daisuke Yanagihara , Masahiko Fujikubo,C. Guedes Soares, Influence of boundary conditions on the collapse behaviour of stiffened panels under combined loads, *Marine Structures*,34 (2013) 205–225.

[6] Gordo JM, Guedes Soares C. Compressive tests on stiffened panels of intermediate slenderness. *Thin-Walled Structres*, 2011(49):782–94.

[7] Zhang Jing, Shi Xinghual, Gu Xuekang,Ultimate Strength Study of Stiffened Plate under Complex Loading with Initial Imperfections， *Ship Building Of China*, 2013(201):60-70.

[8] Shengming Zhang, Imtaz Khan. Buckling and ultimate capability of plates and stffened panels in axial compression,*Marine Structural*，2009，22(4)：79l—808

[9] International Ship and Offshore Structures Congress (ISSC). *Report on ultimate strength. Southampton*, 2006.

ECCOMAS Congress 2016
VII European Congress on Computational Methods in Applied Sciences and Engineering
M. Papadrakakis, V. Papadopoulos, G. Stefanou, V. Plevris (eds.)
Crete Island, Greece, 5–10 June 2016

NUMERICAL ANALYSES OF THE INFLUENCE OF STRUCTURAL SLENDERNESS ON THE SEISMIC RESPONSE OF SINGLE AND CLUSTERED STRUTCURES

Gonzalo Barrios[1], Tam Larkin[2], and Nawawi Chouw[3]

The University of Auckland
Department of Civil and Environmental Engineering
Auckland Mail Centre, Private Bag 92019, Auckland, New Zealand
e-mail: [1]gbar737@aucklanduni.ac.nz, [2]t.larkin@auckland.ac.nz, [3]n.chouw@auckland.ac.nz

Keywords: Soil-foundation-structure interaction, slenderness, adjacent structures, numerical modelling, earthquake engineering

Abstract. *The seismic design of structures generally considers a fixed base assumption, thus neglecting interaction with the supporting soil. The main structural property considered is usually the fundamental period. However, when the influence of soil-foundation-structure interaction (SFSI) is taken into account, other parameters such as structural slenderness, may play an important role in the response. Current design codes, (e.g. FEMA-440 and FEMA-450), assume that SFSI always has beneficial effects in the form of a reduction in the fundamental period spectral acceleration or base shear. This assumption has been studied and discussed by several authors. Additionally, in major urban areas structures are generally closely adjacent, and this situation is more complex than that of a structure whose response may be considered independent of all others. This study sets-out to improve the understanding of the behaviour of a clustered structure-soil-structure system. A 2D numerical model is used to simulate the behaviour of single and multiple structures on sand considering a range of slenderness ratios. Linear single degree-of-freedom (SDOF) structures and nonlinear soil are considered. The role of key parameters, e.g. effective building period and slenderness ratio of the structure-foundation system, will be elucidated.*

1 INTRODUCTION

A common practice in structural design is to neglect the influence of foundation soil by assuming a fixed base condition. Also, the natural period of the fixed base structure, T, is usually considered as the main design parameter. Furthermore, when soil-foundation-structure interaction (SFSI) is considered, the possible effects are generally assumed beneficial (e.g. reducing the spectral acceleration or the base shear). The effects of SFSI have been discussed by e.g. Mylonakis and Gazetas [1] who presented a study showing an increase of seismic demand due to SFSI for certain soil conditions. The influence of structural slenderness has also been highlighted when SFSI is considered in the structural response [2]. Karaca and Turkeli [3] identified the relevance of the slenderness on the response of reinforced concrete chimneys. The increasing lack of space, especially in dense urban areas, has made the interaction between adjacent structures an active research field in the last decades. The concept of structure-soil-structure interaction (SSSI) was introduced e.g by Luco and Contesse [4] and Chouw and Schmid [5,6]. A literature review about SSSI was presented e.g by Lou, et al. [7]. However, most of the advances in SSSI are achieved with analytical solutions for simplified problems based on an assumption of linearity for the different components of the system (i.e. soil and structure). It is well known that an assumption of linear behaviour for soil is valid only for a very small range of deformation, which is clearly not the case in the seismic response..

The National Earthquake Hazards Reduction program (NEHRP) [8] developed guidelines to consider the influence of SFSI on structural design. This NEHRP publication highlights the limited application of SFSI and describes the effects in common engineering practice, while also summarising several methods presented in other codes and guidelines.

One of the methodologies is presented by FEMA-440 [9]. This guideline divides SFSI into the effects of the fundamental period ($\tilde{T}$) and the damping of the soil-structure system. Based on the foundation damping (β_f) a modified damping ratio (β_0) is proposed for the computation of the response spectrum. The design response spectrum is calculated with the damping ratio β_0. Other approach is presented by FEMA-450 [10]. This methodology considers a reduction of the base shear. The final outcome as to beneficial or detrimental effect of SFSI depends of the combined effect of the two factors: (1) increase in damping due to SFSI system and (2) period elongation of the SFSI system (Figure 1). It is possible for a structure with a fundamental fixed-base period on the ascending branch of the response spectrum to have an increase system spectral acceleration. This can be seen in the left most part of Figure 1. The opposite can be seen, an overall decrease of the spectral acceleration, for a structure with a fixed-base period on the descending branch.

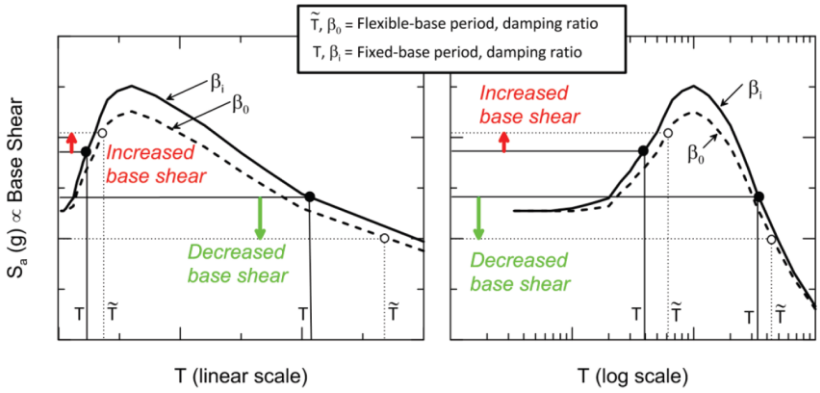

Figure 1: SFSI effects on spectral acceleration and base shear [5]

In previous studies the incorporation of the site-specific frequency content of the ground excitation, structural slenderness and the presence of the adjacent structures is hardly considered. This paper presents the results of the preliminary work to elucidate the consequence of structural slenderness λ and closely adjacent structures. λ is the ratio of the structural height (see Table 2) to the footing width of 6 m.

2 METHODOLOGY

2.1 FEM model

The finite element (FE) software GEFDyn [11,12] was used for all the studies performed. A 2D model and a plane-strain approach were utilised. A 30 m height soil profile was considered. Beneath the soil a 5 m thick layer of bedrock was assumed. Paraxial elements [13] were used at the lateral boundaries of each model. Those elements allow entry of the incident wave and, at the same time, satisfies radiation damping. The width of each model was selected to minimise the influence of the lateral boundaries. Figure 2 shows the FE model for 2 closely adjacent structures. When a single structure is considered it is located at the centre of the model to avoid asymmetry effects.

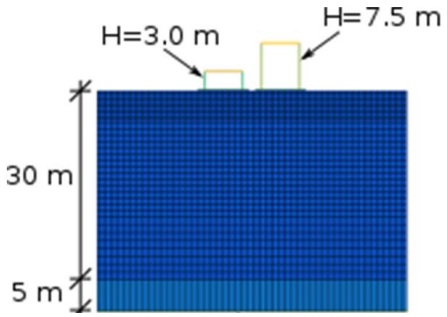

Figure 2: FE model considering adjacent structures

2.2 Soil parameters

The elasto-plastic multi-mechanism model developed at Ecole Centrale Paris (ECP) also known as Hujeux or ECP's model was used to represent the soil behaviour.

The following are the main hypotheses of the soil model:

- The model considers small deformations. The total deformation can be divided into elastic and plastic contributions.
- The formulation is based on the principle of effective stress.
- Isotropic behaviour is assumed for the elastic response.
- Shear behaviour is represented by three bi-dimensional mechanisms, each using a Mohr-Coulomb failure criterion.

Table 1shows some of the selected soil parameters. Refer to Aubry et al. [11] and Hujeux [12] for further information about the ECP's constitutive model.

Elasticity		**Critical state and plasticity**	
K_{ref} [MPa]	444	ϕ'_{pp} [°]	31
G_{ref} [MPa]	222	β [°]	43
n_e	0.40	d	3.5

		b	0.20
		p'_{co} [MPa]	-1.8
Flow rule and isotropic hardening		**Threshold domains**	
ψ [°]	31	r^{ela}	5.0×10^{-3}
a_{cyc}	1.0×10^{-4}	r^{ela}_{iso}	1.0×10^{-3}
a_m	4.0×10^{-3}	r^{hys}	3.0×10^{-2}
c	6.0×10^{-2}	r^{mob}	0.80
c_{cyc}	3.0×10^{-2}		
m	1.0		

Table 1: Soil parameters

The soil parameters utilised represent Toyoura sand with a relative density D_r = 37%.

A preliminary linear analysis was conducted for a soil column in the free field. A natural period of 0.46 s was obtained for the soil based on the ratio of the acceleration at the top to the acceleration at the base of the column in the frequency domain. A small amplitude input was used to guarantee linear behaviour of the soil. Considering the approximate expression presented in Equation (1) the shear wave velocity is $V_s = 260\ m/s$. Thus, the soil can be considered as medium-dense.

$$T_s \approx 4H/V_s \tag{1}$$

2.3 Structural models

The structures studied were single degree-of-freedom (SDOF) systems represented in 2D by elastic frame elements (2 m span) with two columns and a top beam. Three natural periods were selected. For each natural period a 3 m and 7.5 m high model was considered. All the seismic mass was concentrated in the top beam. To avoid differences in the confining stress in the foundation sand under the structure, the same mass (50 tonne) was considered for all models. The foundation was considered to be a massless beam of 6 m length. No uplift of the structural foundation was allowed at the soil-foundation interface. Table 2 shows some of the selected parameters for the SDOF structural models.

Structure	Height (m)	Columns (cm x cm)	Beam (cm x cm)	Natural period (s)
$T_{long} - L_1$	3.0	22×22	20×30	0.78
$T_{long} - L_2$	7.5	52×52	20×30	0.78
$T_{mid} - L_1$	3.0	28×28	30×45	0.44
$T_{mid} - L_2$	7.5	67×67	30×45	0.44
$T_{short} - L_1$	3.0	33×33	35×52.5	0.32
$T_{short} - L_2$	7.5	78×78	35×52.5	0.32

Table 2: Structural models parameters

2.4 Ground motion

Local site effects were directly included in the numerical model. The ground motion recorded on bedrock was used as the input motion. For all the analyses the strong motion recorded at the Gilroy station during the 1989 Loma Prieta Earthquake was utilised. A total duration of 10 s of the main shock was used (Figure 3).

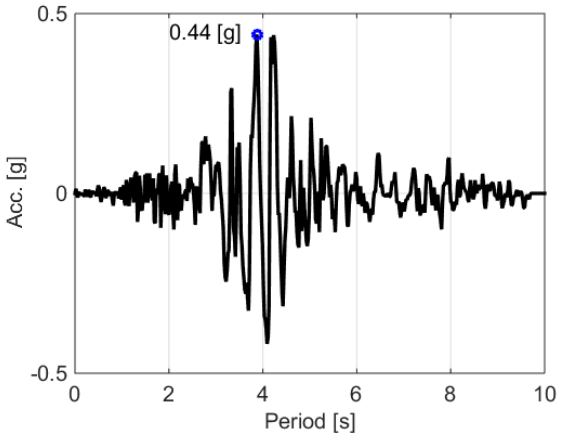

Figure 3: Ground motion (Loma Prieta, 1989)

3 RESULTS AND DISCUSSION

3.1 Stand-alone structures

The acceleration and displacement at the top of each model was calculated and the ratios of the maximum value to the maximum obtained for a free-field condition are presented for acceleration and displacement in Figure 4 and Figure 5, respectively as a function of the ratio of the natural period (T_{str}) of the SDOF to the natural period (T_{site}) of a 1D column of soil.

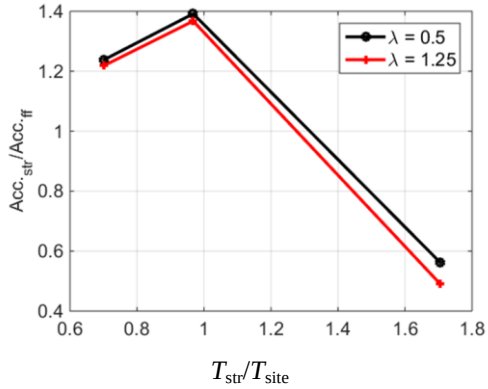

Figure 4: Ratio of maximum acceleration beneath the structure to the maximum on free-field

Regarding the maximum acceleration, the effect of slenderness is shown to be of minimal importance over the period range employed in this study. A higher slenderness ratio tends to give a marginally lower maximum acceleration for the same period.

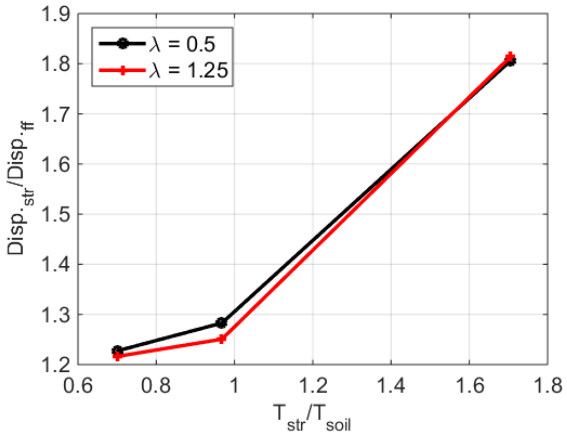

Figure 5: Ratio of maximum displacement beneath the structure to the maximum on free-field

The effects of slenderness on the maximum horizontal displacement are shown to be small for structures with a natural period close to the natural period of the site. Otherwise, slenderness has very little effect for the three structures considered.

The settlement beneath the structure was also studied. Figure 6 shows the results for the different single structures .

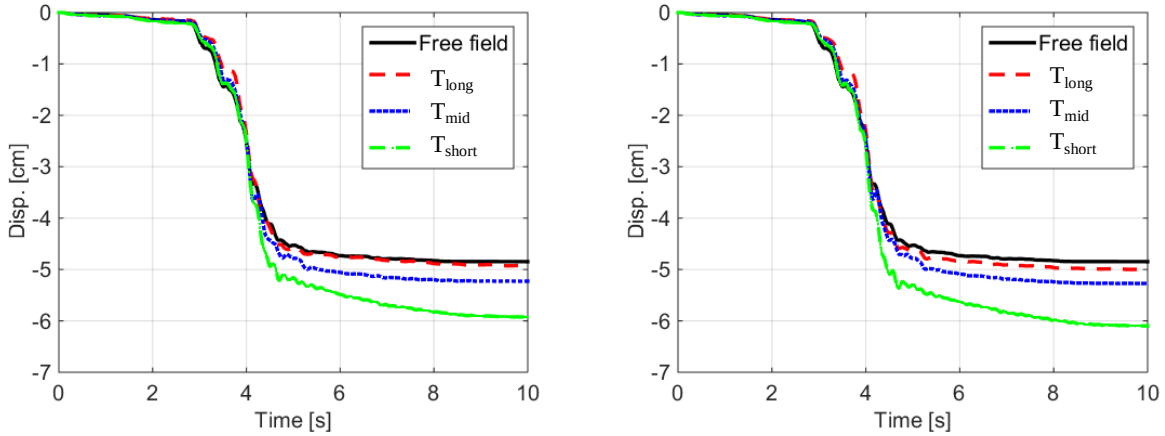

a. Lower slenderness models ($\lambda = 0.5$)

b. Higher slenderness models ($\lambda = 1.5$)

Figure 6: Settlement beneath the structure (alone on soil)

A similar trend is shown in Figure 6 for the settlement for both slenderness ratios. However, the lower period structures encountered higher settlement. The slenderness ratio has almost no effect. Thus, in the cases considered the natural period of the structure is more important than the slenderness ratio.

The influence of the structural slenderness and period on the response spectra of the acceleration beneath the structure are shown in Figure 7.

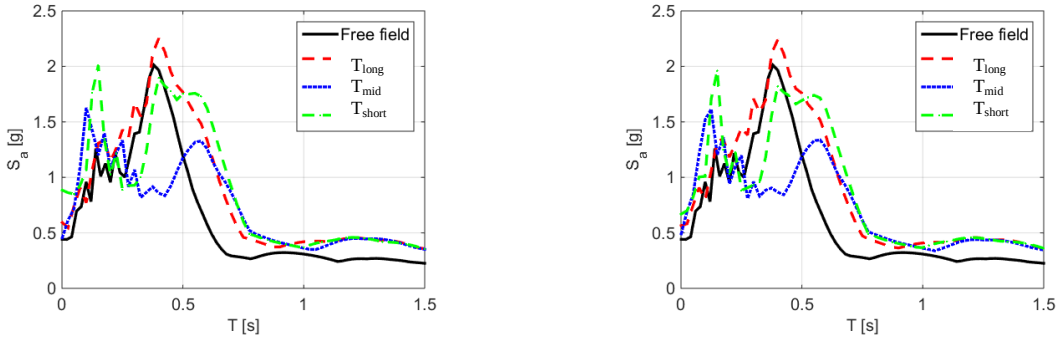

a. Lower slenderness models ($\lambda = 0.5$) b. Higher slenderness models ($\lambda = 1.5$)

Figure 7: Response spectra for acceleration beneath the structure

The obtained spectra were compared with the spectrum from free-field (black solid line). When stand-alone structures were tested the slenderness has very little influence.

3.2 Adjacent structures on soil

Each pair of structures with the same natural period but a different slenderness were tested with a one meter separation distance. In this case different response spectrum have been obtained beneath each structure (Figure 8). Again, the spectrum from free-field condition is also presented (black solid line).

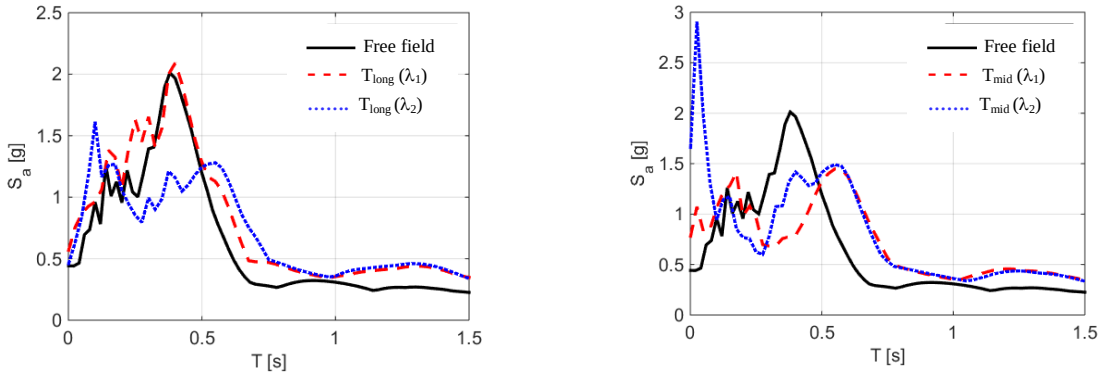

a. High period structure (T_{long}) b. Intermediate period structure (T_{mid})

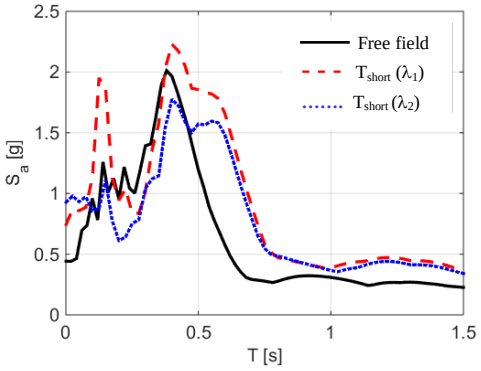

c. Low period structure (T_{short})

Figure 8: Effect of slenderness, structural period and an adjacent structure on the acceleration beneath the structure ($\lambda_1 = 0.5$ and $\lambda_2 = 1.5$)

Even though, no clear trends have been observed to define the influence of an adjacent structure there are significant differences between the spectra of the free field and the spectra beneath the structures. Differences can also be observed between the spectra of the soil beneath the two buildings. Further work is needed to clearify the observations.

4 CONCLUSIONS

FE models based on a 2D plain-strain approach were used to study the influence of slenderness on the structural response. The elasto-plastic multi-mechanism ECP constitutive model was used to represent the soil behaviour. Stand-alone structures and closely adjacent structures were considered. The influence of natural period, slenderness and an adjacent structure were studied.

In the cases considered the results for stand-alone structures show:

- The maximum displacement at the top of the structure increases with the natural period of the structure.
- Slenderness has marginal effect.
- Structures with the shortest period experienced the largest settlement. In contrast, for the highest slenderer ratio the permanent settlement was slightly bigger.

In the case of closely adjacent structures of equal period:

- Slenderness significantly effects the spectral acceleration for periods below 0.5 s.
- The natural period of the structures has a significant influence on SSSI.
- The free-field ground motions should not be used as a design structural excitation.

ACKNOWLEGEMENTS

The authors are grateful for the support of the Ministry of Business, Innovation and Employment through the Natural Hazards Research Platform under the Award 3708936.

REFERENCES

[1] G. Mylonakis and G. Gazetas, Seismic soil-structure interaction: beneficial or detrimental?, *Earthquake Engineering*, **4**(3), 277-301, 2000.

[2] Chouw, N. Unequal soil-structure interaction effect on seismic response of structures, *Proceedings of the 18th New Zealand Geotechnical Society Geotechnical Symposium on Soil-Structure Interaction –From rules of thumb to reality*, University of Auckland, 4-5 September, 214-219, 2008.

[3] Z. Karaca and E. Turkeli, The slenderness effect on wind response of industrial reinforced concrete chimneys, *Wind and Structures*, **18**(3), 281-294, 2014.

[4] J. E. Luco and L. Contesse, Dynamic structure-soil-structure interaction, *Bulletin of the Seismological Society of America*, **63**(4), 1289-1303, 1973.

[5] Chouw, N., Schmid, G. Influence of the geometrical effects of the soil on the structure-soil-structure interaction, In: *Structural Dynamics*, Vol. 2, (Eds.: Krätzig, W. B., et al.), A. A. Balkema, 795-802, 1991.

[6] Chouw, N., Schmid, G. Structure-soil-structure interaction considering local non-linearities, *Engineering Structures under Earthquake Loading*, Civil-Comp Press, Edinburgh, 61-66, 1997.

[7] M. Lou, H. Wang, X. Chen and Y. Zhai, Structure-soil-structure interaction: literature review, *Soil Dynamics and Earthquake Engineering*, **31**(12), 1724-1731, 2011.

[8] NEHRP Consultants Joint Venture, Soil-structure interaction for building structures, National Institute of Standards and Technology (NIST), 2012.

[9] Applied Technology Council (ATC), Improvement of nonlinear static seismic anlysis procedures (FEMA-440), Washington, D.C., 2005.

[10] Building Seismic Safety Council, NEHRP Recommended Provisions for Seismic Regulations for New Buildings and Other Structures (FEMA-450), Building Seismic Safety Council, National Institute of Building Sciences, 2004.

[11] D. Aubry and A. Modaressi, *GEFDYN Manuel Scientifique. Ecole Centrale Paris*, 1996.

[12] D. Aubry, D. Chouvet, A. Modaressi and H. Modaressi, GEFDYN: Logiciel d'analyse de comportement mécanique des sols par éléments finis avec prise en compte du couplage sol-eau-air, *Manuel scientifique, Ecole Centrale Paris, LMSS-Mat*, 1986.

[13] H. Modaressi and I. Benzenati, Paraxial approximation for poroelastic media, *Soil Dynamics and Earthquake Engineering*, **13**(2), 117-129, 1994.

ECCOMAS Congress 2016
VII European Congress on Computational Methods in Applied Sciences and Engineering
M. Papadrakakis, V. Papadopoulos, G. Stefanou, V. Plevris (eds.)
Crete Island, Greece, 5–10 June 2016

EFFECT OF HIGHER MODES ON STRUCTURAL RESPONSE WITH NONLINEAR SOIL-FOUNDATION-STRUCTURE INTERACTION

X. Qin[1], N. Chouw[2], and T. Larkin[3]

The University of Auckland
Dept. of Civil and Environmental Engineering
Auckland Mail Centre, Private Bag 92019, Auckland, New Zealand
e-mail: [1]xqin009@aucklanduni.ac.nz; [2]n.chouw@auckland.ac.nz; [3]t.larkin@auckland.ac.nz

Keywords: Nonlinear SFSI, higher modes, macro element, seismic response of structure.

Abstract. *To calculate the response of a multi-storey structure (MDOF model) with structure-foundation-soil interaction (SFSI), for simplicity the structure is often assumed as a SDOF model corresponding to the fundamental mode. However, depending on the distribution of mass and stiffness of the structure, the contribution of the fundamental mode may vary. The contribution of the higher modes to the response of the structure could become more significant. This study reveals the effect of higher modes on the response of structure including SFSI. The response of a multi-storey structure and the response associate with the fundamental mode of the structure are compared. To calculate the response of structures with SFSI, a macro element model is used to simulate the plastic soil deformation. The consequence of using a SDOF model for the structural response including nonlinear SFSI is discussed.*

1 INTRODUCTION

For structures with a shallow footing, seismic forces induced by a ground excitation may cause a moment at the footing to exceed the elastic limit of the foundation soil. Consequently, soil bearing failure may occur. It is commonly accepted that nonlinear soil behaviour should be avoided in seismic design by providing more than sufficient foundation bearing strength. However, it has been observed that although the footing has been properly designed, the structure can still experience plastic deformation of foundation soil during earthquake [1-6]. Examples can be found in almost all major earthquakes, e.g. Valdivia Earthquake 1960 [2], Michoacan Earthquake 1985 [3], Kobe Earthquake in 1995 [4], Izmit Earthquake 1999 [5, 6], and the 2010 Darfield and 2011 Christchurch earthquakes [7]. Study of the response of structure with nonlinear SFSI is thus relevant.

Observations of buildings following major earthquakes e.g. Housner [2] and Gazetas et al. [5] showed that structures experiencing minor nonlinear SFSI, in fact, performed better than expected. These observations triggered a number of analytical and numerical investigations. Yim and Chopra [8] developed one of the first SFSI models using a Winkler foundation. The flexibility and damping of the supporting soil were represented by independent spring-damper elements distributed over the width of the foundation. Psycharis and Jennings [9] extended the study by simplifying the Winkler foundation model using a two-spring foundation model. Psycharis [10] used the Winkler foundation model to conduct a parametric study. The influence of damping ratio, aspect ratio and stiffness ratio between the structure and the supporting spring on the structural response was investigated. Based on the results obtained from these analytical models [8-10], a series of response spectra were proposed to determine the seismic response of structures on flexible supporting ground. Recently, numerical methods were also developed to incorporate the nonlinearity of soil. The response of a structure with SFSI calculated using finite-element approach was discussed by Wolf [11]. Nova and Montrasio [12] proposed an equation to calculate the movement of the footing during soil plastic deformation. This equation was incorporated in a macro element model so that the response of structure with nonlinear SFSI can be calculated [13]. Chouw and Hao [14] also numerically studied and showed that SFSI can affect the pounding force between adjacent bridge structures.

For simplicity, most numerical studies of structures with SFSI use a single-degree-of-freedom (SDOF) system to represents the structure. The contribution of higher modes to the total response of the structure with SFSI was neglected. Depending on the distribution of mass and stiffness of the structure, the contribution of the higher modes to the response of the structure could be significant. This study reveals the effect of higher modes on the response of a structure with SFSI. The response of a two storey structure with SFSI was numerically calculated by representing the structure using a SDOF system and a 2-degree-of-freedom (2DOF) system. To include the effect of nonlinear SFSI, a macro element model is used.

2 NUMERICAL SIMULATION

2.1 Higher mode of structure

The structure used for this study was a two storey steel building. The structure had a storey height of 3 m and floor area of 25 m^2. For the 1st floor and the roof, the seismic mass was 42000 kg and 21000 kg, respectively. The columns of the structure were 250UC72.9 steel section. The footing mass (m_o) was 42000 kg. The beams and foundation were assumed rigid. The structure can be described using a 2DOF system. Each DOF represented the horizontal

movement at the floor level. The lateral bending stiffness of each floor can be calculated using the total bending stiffness of the columns.

The structure can also be represented using a SDOF system. An equivalent base shear method was used to obtained the effective mass (m^*) and height (h^*). The procedure is described e.g. by Chopra [15]. The effective mass and height of the SDOF system was determined to be 61000 kg and 4.3 m, respectively. The effective mass represented 96.8% of the total mass of the structure. The fundamental frequency of the SDOF system was defined to be the same as that of the two storey structure. Figure 1 shows the parameters of the 2DOF system and the SDOF system. The footing mass and size of the SDOF system were identical to that of the 2DOF system.

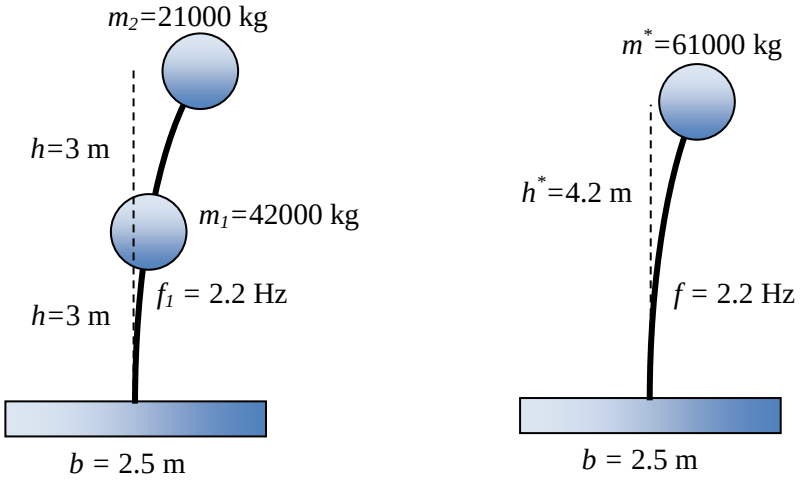

Figure 1: The 2DOF system and the equivalent SDOF system.

2.2 Macro element model

The response of a structure with nonlinear SFSI was calculated with the help of a macro element model. The concept of the model is to simplify the response of a foundation-soil system using three degrees of freedom. They are the vertical, horizontal displacements and rotation of the center of the foundation. With these additional DOFs at the footing location, the effect of footing response under the deformation of foundation soil can be included. Figure 2 shows the macro element model. The elastic stiffness of the 3DOF footing system can be calculated using the formulation described in Chouw and Hao [14].

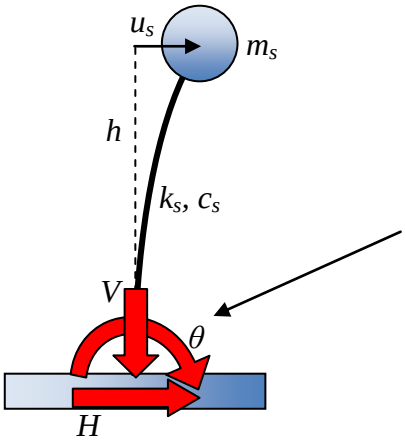

$$\mathbf{m_F} = \begin{bmatrix} m_s + m_o & m_s h & 0 \\ m_s h & m_s h^2 + J_o & 0 \\ 0 & 0 & m_s + m_o \end{bmatrix}$$

$$\mathbf{k_F} = \begin{bmatrix} k_H & & \\ & k_\theta & \\ & & k_V \end{bmatrix} \quad \mathbf{c_F} = \begin{bmatrix} c_H & & \\ & c_\theta & \\ & & c_V \end{bmatrix}$$

$$\mathrm{u_F} = \begin{bmatrix} H & \theta & V \end{bmatrix}^T$$

Figure 2: The macro element model.

2.3 Nonlinearity of the foundation system

The nonlinearity of the structure-foundation-soil system is described at the 3DOF of the foundation system. The nonlinearity will be initiated when a bearing failure of soil is intitiated. To determine the initiation of the bearing failure, a bearing strength surface was considered. Nova and Montrasio [12] have proposed an equation for determining the initiation of a bearing failure of a strip footing on sand (Eq. (2)). The equation was developed and improved though a number of experimental and numerical studies (e.g. [16]).

$$f(\mathbf{F}) = \left(\frac{H}{\mu V_{\max}}\right)^2 + \left(\frac{M}{\psi B V_{\max}}\right)^2 - \left(\frac{V}{V_{\max}}\right)^2 \left(1 - \frac{V}{V_{\max}}\right)^{2\xi} \tag{2}$$

where B is the width of the foundation; V_{max} is the ultimate bearing capacity of foundation soil under vertical centered load; ψ, μ and ξ are the parameters of the bearing strength surface and suggested to be 0.43, 0.9 and 0.95, respectively [16]; **F** is a vector which contains the horizontal, vertical actions and moment at the foundation (H, V and M in Figure 2).

With **F** calculated using the product of the stiffness matrix ($\mathbf{k_F}$) and the displacement vector ($\mathbf{u_F}$) of the foundation. Eq. (2) can be evaluated. If $f(\mathbf{F}) < 0$, the combined action of a shallow foundation is below the bearing capacity of foundation soil. Bearing failure of the foundation soil does not occur. In contrast, a value of $f(\mathbf{F}) = 0$ indicates that the foundation action will cause bearing failure. Theoretically, it is impossible to have a value of $f(\mathbf{F}) > 0$, since the soil cannot sustain any actions greater than the bearing capacity.

Once the indication of bearing failure was confirmed, a non-associated flow rule (Eq. (3)) was applied to calculate the unrecoverable displacement and rotation of the foundation due to soil plastic deformation.

$$g(F) = \lambda^2 \left(\frac{H}{\mu V_{\max}}\right)^2 + \chi^2 \left(\frac{M}{\psi B V_{\max}}\right)^2 + \left(\frac{V}{V_{\max}}\right)^2 - 1 \tag{3}$$

where B is the width of the foundation; λ and χ are two non-dimensional parameters, and V_{max} is the maximum bearing capacity of soil under vertical loading.

This flow rule was originally developed by conducting a large scale shake table test to quantify the non-dimensional parameters of Eq. (3) [13, 16 and 17]. For sand, the values of λ and χ were suggested to be 2.5 and 3, respectively. In this study, the supporting soil was defined to be sand and had a shear wave velocity of 400 m/s. The Poisson's ratio and density were assumed to be 0.33 and of 1560 kg/m^3, respectively. It is assumed that the structure behaves elastically during the earthquake loading.

2.4 Earthquake excitation

The ground excitation for the nonlinear time history analysis was simulated based on a Japanese design spectrum [18]. In this study, medium soil category was considered. This is because in general, loose soil is of no practical interest for shallow foundation design. An alternative foundation scheme, such as foundation through piles, is usually preferred. On the other hand with dense or very-dense soil condition significant settlements are not likely to occur [19]. The applied ground acceleration is shown in Figure 3.

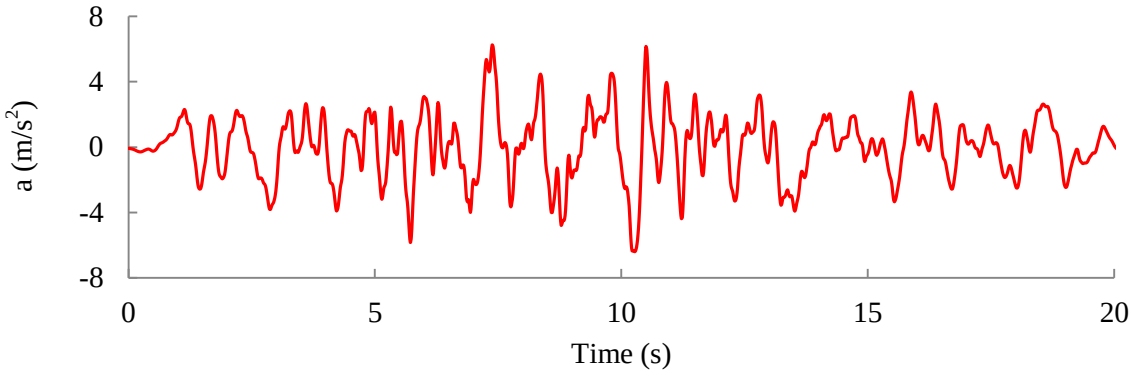

Figure 3: Ground acceleration.

3 RESPONSE OF STRUCTURE WITH SFSI

3.1 SFSI with elastic soil

Figure 4 shows the horizontal displacement (u) at the top of the structure relative to the ground. The structure was represented using the SDOF (dashed line) and 2DOF (solid line) system, respectively. Considering elastic soil, the horizontal displacement calculated using the SDOF system was larger than that using the 2DOF system. Using the SDOF system, the maximum top horizontal displacement was 66.4 mm. When considering the 2DOF system, the maximum top horizontal displacement was 59.1 mm. The maximum horizontal displacement of structure estimated using the SDOF system was 12.4% larger than that calculated using 2DOF system. It is shown that without considering the higher modes, horizontal displacement of structure can be overestimated.

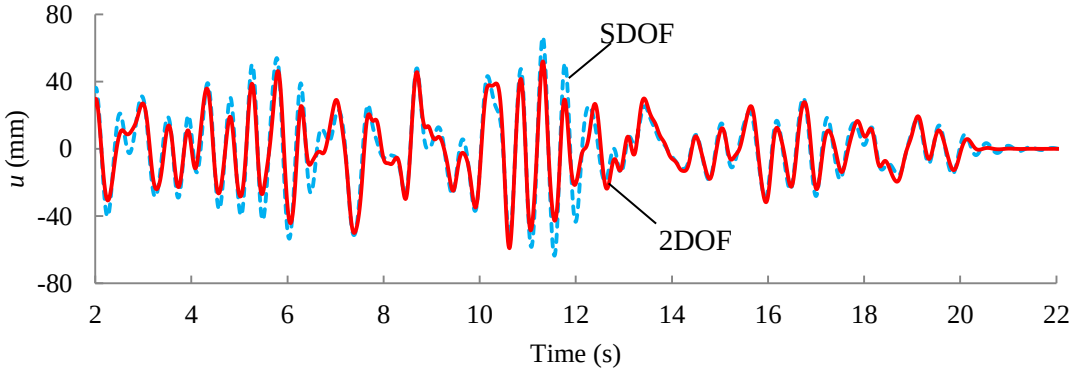

Figure 4: Influence of MDOF system on the structural response with linear SFSI

3.2 Response of structure with nonlinear SFSI

Figure 5 shows the horizontal relative displacement (u) at the top of the structure with non-linear SFSI. While the dashed line represents the result calculated using the SDOF, the solid line illustrates that obtained considering the 2DOF system. A residual horizontal displacement was found at the end of the excitation due to soil plastic deformation. When using the SDOF and 2DOF system, the residual horizontal displacement was 4.9 mm and 1.4 mm, respectively. Including the structural higher mode, the residual displacement of the structure was smaller. The maximum horizontal displacement at the top of the 2DOF system was also smaller than that of the SDOF system. The maximum horizontal relative displacement considering the SDOF and the 2DOF systems was 62.6 mm and 57.5 mm, respectively.

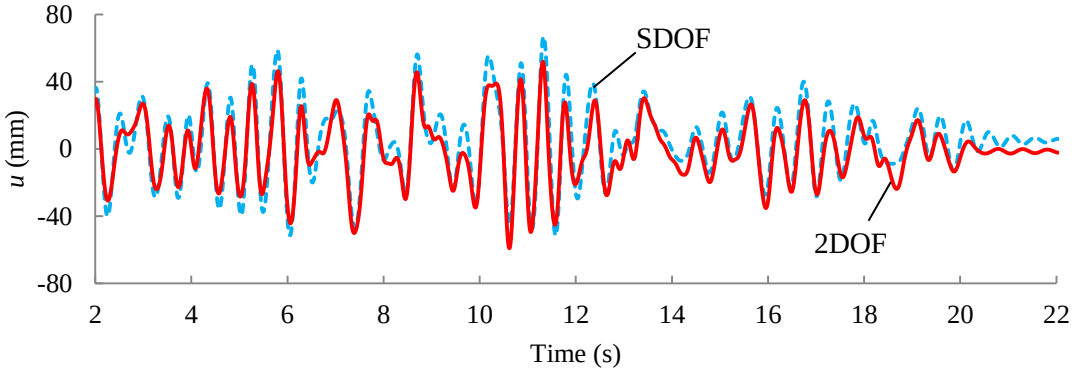

Figure 5: Influence of MDOF system on the structural response with nonlinear SFSI

Using the SDOF and 2DOF systems, the calculated footing rotation (θ) of the structure was also different. As shown in Figure 6, the maximum footing rotation calculated using the SDOF system was 0.17^o. Using the 2DOF system, the maximum footing rotation was -0.06^o. At the end of the excitation, the residual rotation of the footing was 0.06^o and -0.02^o for the case of the SDOF and 2DOF, respectively.

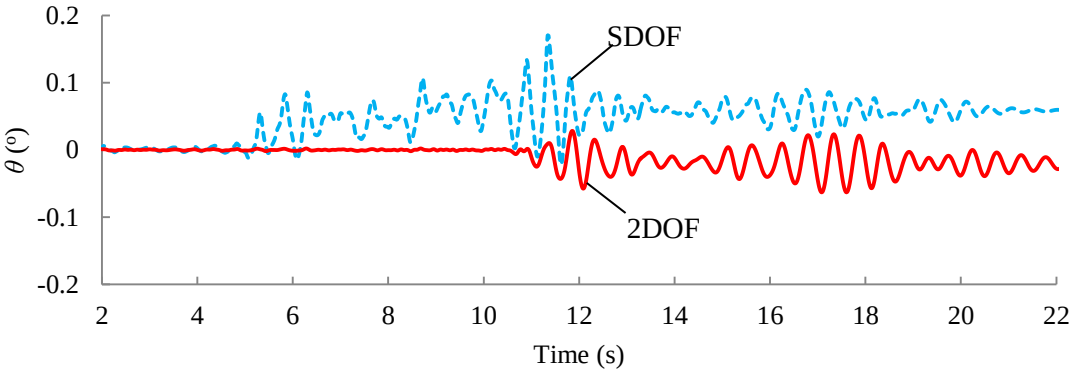

Figure 6: Effect of nonlinear SFSI and 2DOF system on footing rotation θ

4 CONCLUSIONS

This study focused on the effect of a higher mode on the response of a structure with SFSI. The response of a two storey structure was numerically calculated by representing the structure using a SDOF system and a 2DOF system. The effect of foundation soil deformation was included using a macro element model. Both elastic and nonlinear SFSI were considered. The mass of the SDOF system represented 96.8% of the total mass of the structure.

- Despite the mass of the SDOF system represents a large portion of the structural mass, the responses of the structure with SFSI calculated using the SDOF and the 2DOF system were different.
- With an elastic soil , the horizontal displacement of the structure calculated without including the higher mode was larger.
- Considering nonlinear soil, the maximum and residual horizontal displacement of the structure calculated using the SDOF system was also larger than the corresponding 2DOF system.
- Without considering the higher mode, the maximum and residual footing rotation of structures during earthquake can be overestimated.

ACKNOWLEDGEMENT

The authors are grateful for the support of the Ministry of Business, Innovation and Employment through the Natural Hazards Research Platform under the Award 3708936.

REFERENCES

[1] N. Chouw and H. Hao. Pounding damage to structures in the 2011 Christchurch earthquake. *International journal of Protective Structures,* **3**(2): 123-139. 2011.

[2] G.W. Housner. The behavior of inverted pendulum structures during earthquakes. *Bulletin of the Seismological Society of America*, **53**(2): 403-417. 1963.

[3] M. J. Mendoza and G. Auvinet. The Mexico earthquake of September 19, 1985 Behaviour of building foundations in Mexico City. *Earthquake Spectra,* **4**(4), 835-852, 1988.

[4] N. Chouw. Effect of the earthquake on 17th of January 1995 on Kobe, D-A-CH meeting of the German, Austrian and Swiss Society for Earthquake Engineering and Structural Dynamics, Technical University of Graz, Austria, 135-169

[5] R. Ulusay, O, Aydan and M. Hamasa. The behaviour of structures built on active fault zones: Example from the recent earthquakes of Turkey. *Structural Engineering and Earthquake Engineering,* **19**(2), 149-167, 2002.

[6] G. Gazetas, M. Apostolou and J. Anastasopoulos. Seismic uplifting of foundations on soft soil, with examples from Adapazari (Izmit 1999 earthquake), in *Foundations: Innovations, observations, design and practice*. London: Thomas Telford, 2003.

[7] L. Wotherspoon, A. Bradshaw, R. Green, C. Wood, A. Palermo, M. Cubrinovski and B. Bradley. Performance of bridges during the 2010 Darfield and 2011 Christchurch earthquakes. *Seismological Research Letters,* **82**(6), 950-964,2011.

[8] C. S. Yim and A. K. Chopra. Earthquake response of structures with partial uplift on winkler foundation. *Earthquake Engineering and Structural Dynamics*. **12**: 263-281. 1984.

[9] I. N. Psycharis and P. C. Jennings. Rocking of slender rigid bodies allowed to uplift. *Earthquake Engineering and Structural Dynamics*, **11**(1), 57-76, 1983.

[10] I. N. Psycharis. Effect of base uplift on dynamic response of SDOF structures. ASCE *Journal of Structural Engineering*, **117**(3), 733-754, 1991.

[11] J. P. Wolf. *Soil-Structure-Interaction Analysis in Time Domain*. Prentice Hall, Englewood Cliffs (NJ), 1988.

[12] R. Nova and L. Montrasio. Settlements of shallow foundations on sand. *Géotechnique*, **41**(2), 243-256, 1991.

[13] C. Cremer, A. Pecker and L. Davenne. Cyclic macro-element for soil-structure interaction: material and geometrical non-linearities. *International Journal for Numerical and Analytical Methods in Geomechanics*, **25**(13), 1257-1284,2001.

[14] N. Chouw and H. Hao. Significance of SSI and nonuniform near-fault ground motions in bridge response I: Effect on response with conventional expansion joint. *Engineering Structures*, **30**(1), 141-153, 2008.

[15] A. K. Chopra. *Dynamics of structures, 3rd Edition*. New Jersey: Prentice Hall, 2007.

[16] R. Paolucci, M. Shirato and M.T. Yilmaz. Seismic behaviour of shallow foundations: Shaking table experiments vs numerical modeling. *Earthquake Engineering and Structural Dynamics*, **37**(4), 577-595, 2008.

[17] P. Negro, R. Paolucci, S. Pedretti and E. Faccioli. Large-scale soil-structure interaction experiments on sand under cyclic loading. *Proceedings of the 12th World Conference on Earthquake Engineering*, Paper 1191, 2000.

[18] Japan Society of Civil Engineering (JSCE). *Earthquake resistant design code in Japan*, Tokyo, Maruzen, 2000.

[19] R. Paolucci. Simplified evaluation of earthquake-induced permanent displacements of shallow foundations. *Journal of Earthquake Engineering*, **1**(03), 563-579, 1997.

ECCOMAS Congress 2016
VII European Congress on Computational Methods in Applied Sciences and Engineering
M. Papadrakakis, V. Papadopoulos, G. Stefanou, V. Plevris (eds.)
Crete Island, Greece, 5–10 June 2016

SEISMIC RETROFIT OF AN INDUSTRIAL STRUCTURE THROUGH AN INNOVATIVE SELF-CENTERING HYSTERETIC DAMPER: MODELLING, ANALYSIS AND OPTIMIZATION

F. Morelli[1], **A. Piscini**[1], **W. Salvatore**[1]

[1] University of Pisa, Department of Civil and Industrial Engineering
Largo Lucio Lazzarino 1, 56122, Pisa, Italy
{francesco.morelli, andrea.piscini, walter}@ing.unipi.it

Keywords: seismic risk, industrial building, self-centering, seismic energy, energy dissipation.

Abstract. *Recent earthquakes, as the one that hit Fukushima in Japan in 2011 or the one that produced extensive damage in Turkish petrochemical facilities during the Kocaeli earthquake of 1999 or, more recently, the seismic events in May 2012 in Emilia (Italy), highlighted the increasing need of providing adequate protection to industrial installations. Industrial facilities often store a large amount of hazardous material and, in case of seismic event, there is a high probability that accidental scenarios as fire, explosion, toxic or radioactive dispersion may occur. In these cases, the ensuing disaster certainly harms the people working in the installation and it may endanger the population living in the neighborhood or in the urban area where the industrial installation is located. The consequences of such accidental scenarios can be disastrous in terms of casualties, economic losses and environmental damage. Within this work, the seismic behavior of an industrial structure is studied through several Incremental Dynamic Analyses, IDA, and particular attention is given to the selection of suitable performance criteria and the modelling of non linear phenomena (II order effects, buckling, mechanical non-linearity, etc.). The seismic behavior is then enhanced applying to the structure an innovative typology of self-centering hysteretic damper, whose mechanical characteristics are optimized through the execution of IDAs on the retrofitted structures. A final comparison between the seismic behavior of the original structure and of the retrofitted one highlights the advantages of the innovative self-centering hysteretic dampers.*

1 INTRODUCTION

Recent earthquakes, as the one that hit Fukushima in Japan in 2011, the one that produced extensive damage in Turkish petrochemical facilities during the Kocaeli earthquake of 1999 or, more recently, the seismic events in May 2012 in Emilia (Italy), highlighted the increasing need of providing adequate protection to industrial installations.

Industrial facilities often store a large amount of hazardous material and, in case of seismic event, there is a high probability that accidental scenarios as fire, explosion, toxic or radioactive dispersion may occur. In these cases, the ensuing disaster certainly harms the people working in the installation and it may endanger the population living in the neighbourhood or in the urban area where the industrial installation is located. The consequences of such accidental scenarios can be disastrous in terms of casualties, economic losses and environmental damage.

Even in the cases in which the content does not represent a direct threat to human lives or to the environment, damage to structural and/or non structural elements can result in huge indirect economic losses, as testified from the numerous studies [1] [2] devoted to the speedup of community recovery after the 2012 Emilia (Italy) earthquakes. From his point of view, for industrial buildings, it should be more appropriate to speak about "seismic resilience" than "seismic risk", that is more appropriate for civil building [3], meaning that it is necessary to take into account also the time necessary for the recovery of the production activities.

In this field, a parameter strictly correlated to the post-earthquake recovery is represented by the re-centering capability of the structure, defined as the capacity of minimizing the residual displacement after the end of the seismic action.

In this contest, a particular attention for the retrofit of existing industrial plants is given to the use of passive dissipation systems, such as Isolation Systems (IS) or Energy Dissipation Systems (EDS). The initial higher cost associate to a retrofit using an IS or EDS, comprised the ones consequent to the adaptation of the non-structural elements (e.g. pipelines), will be likely compensate by the avoided losses in case of moderate-to-strong earthquakes. This is especially true for industrial steel structures, where the substitution of the existing bracing elements with dissipative ones can be accomplished using simple operations. Modern codes [4] and guidelines [5] lists the recentering capability of the anti-seismic device as one of the fundamental capacities. In [5] it is evaluated, for linear analysis and seismically isolated structures, comparing the energy dissipated by the isolation device, E_H, with the reversibly stored (elastic strain and potential) energy, E_S :

$$E_S \geq 0.25 E_H \qquad (1)$$

Traditional hysteretic devices, however, does not provide a real "active" recentering force, resulting in the presence of residual forces within the devices at the end of the earthquake also in the case of negligible residual displacement and in the consequent complication of the substitution operations.

In order to mitigate such problems, re-centering devices have been the object of ever increasing research study ([6], [7], [8], [9], [10], [11], [12]). This type of dissipative device is characterized by the presence of a re-centering force that mitigates, and may even eliminate, the residual deformations in buildings and residual forces in the dissipative devices after earthquakes.

In the present paper, the influence, in terms of maximum displacement, interstorey drift, acceleration and dissipated energy, of the retrofit of an existing industrial steel building using the steel self-centering device (SSCD) developed in [13] is studied. The industrial building, selected within one of the most important Italian industrial plant, the ILVA S.p.A. plant, can

be considered as representative of the industrial structure sensitive to the seismic action, being characterized by an important mass placed at high altitude.

The case study building analysis is carried out indentifying, in the first phase, the structural and non-structural limit states, considering both the national and international standards and the peculiarity of the building itself. Given the need of simplifying, as much as possible, the structural scheme to obtain a reliable and time-saving nonlinear model, a preliminary comparison between a full-comprehensive linear model and the geometrically-simplified one is carried out, studying also the effect of the infill material modelling on the overall behavior. Several IDA are then carried out in order to identify the main seismic vulnerabilities, to define the seismic retrofit intervention and evaluate their effects on the structural behavior.

2 CASE STUDY DESCRIPTION: MODELLING, ANALYSIS AND SEISMIC VULNERABILITY

The selected case study, shown in Figure 1, has the function of filtering the gasses coming from the steelwork and can be schematized as made up of a supporting structure, the silos containing the filtering material and the roof.

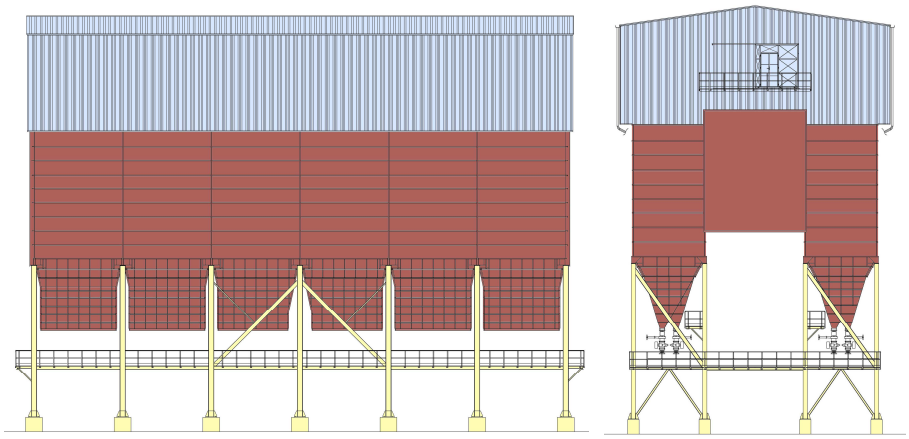

Figure 1. Front and lateral view of the Filter Building

The building has a regular plan, with overall dimensions 37.80 m x 16.94 m and total height 29.64m. The supporting structure, with a total height of about 10.80 m, has six bays in the longitudinal direction and three in the transversal one. Different horizontal resisting systems can be individuated such as moment resisting frames, inverted V bracings, diagonal bracings, as shown in Figure 2 .

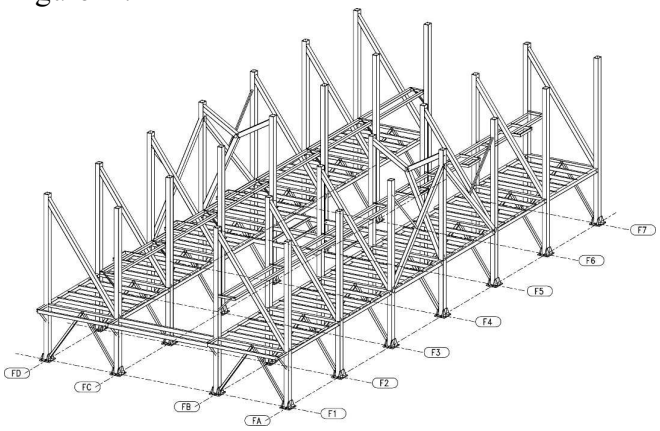

Figure 2. 3D view of the supporting system

The silos are realized with thin (4 mm) walls stiffened with a close series of horizontal UPN and vertical HEA profiles. The total mass of the silo (23700 kN), considering structural elements and infill material, represent the 86% of the total mass (27650 kN).

The roof is connected directly to the filter walls and its contribution is considered only in terms of vertical load and mass.

2.1 Linear and non linear modelling

To develop a suitable nonlinear model of the building for the execution of Incremental Dynamic Analyses, IDAs, in reasonable amount of time, it is necessary to simplify the structural scheme. In order to have, however, a model able to well represent the structural behavior, it is initially studied a "complete" linear model, see Figure 3a), in which the contribution of practically almost all the structural and non-structural elements is taken into account.

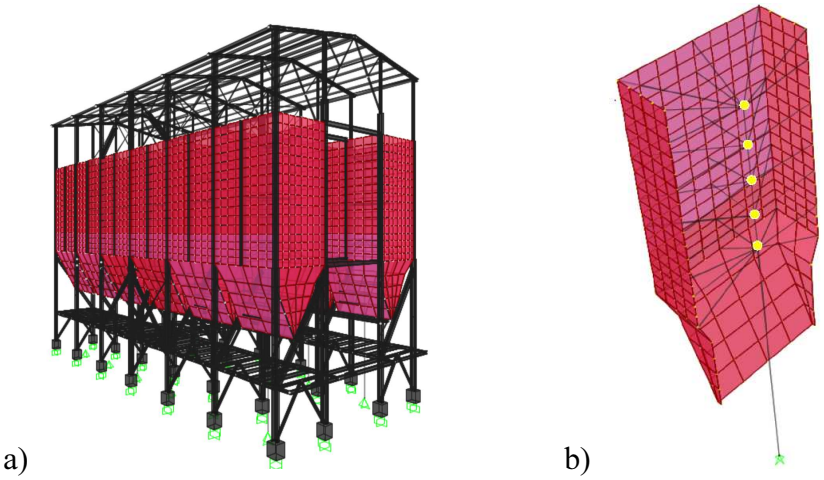

a) b)

Figure 3. "Complete" linear model: a) globall view; b) modelling of the infill-silo interaction.

The dynamic interaction between the silos wall-infill material can sensibly vary the global response of the building. Given the high level of uncertainty associated to the infill material behavior, similar to dust, a refined non-linear interaction model would lead to non-reliable results. For this reason, different infill material modelling solutions are studied and compared and a parametric study is carried out to study the sensitivity of the global behavior to the variation of the characteristics of the schematization assumed.

Three different types of modelling are compared: i) the attribution of the infill material mass directly to the silos walls; ii) the concentration of the infill material total mass of each silo in a single point placed in the baricenter of the silo and connected to the silos walls by linear springs; iii) subdivision of the infill material total mass in 5 points, see Figure 3b), each one of them connected to the silos walls by linear springs. Models i) and ii) highlighted several drawbacks, such as, for the former, the unrealistic high number of the silos walls local vibration modes and the problem of overestimating the rotational inertia, while, for the latter, the high force concentration on the silos wall. The model iii) is then assumed and a parametric analysis varying the spring stiffness is carried out and the results, in terms of period of vibration and participating mass is reported in Figure 4.

It can been noticed that for infill material edometric modulus higher than 25000 kN/m^2, the period and the participating mass associated to the first period can be considered practically constant. Given that the edometric modulus of the dust varies, approximately, between 30000 to 80000 kN/m^2, the response of the model can be assumed to be not influenced by the uncertainties related to the infill material mechanical behavior.

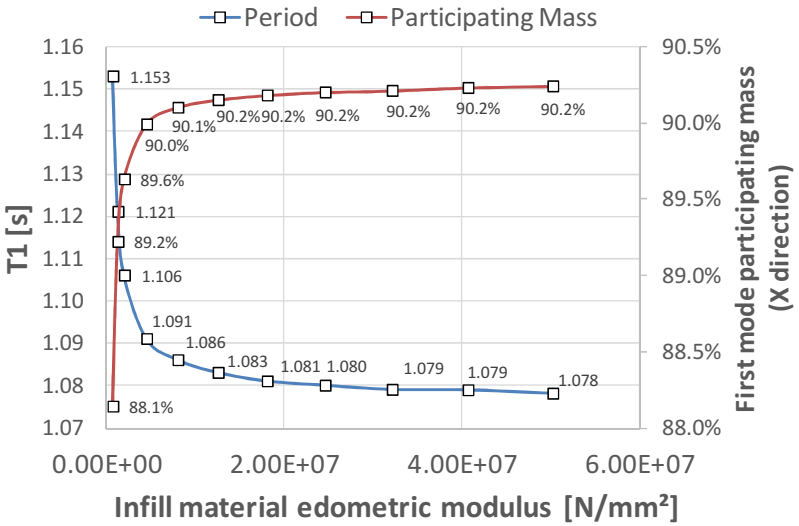

Figure 4. Period of vibration and participanting mass associate to the first vibration period varying the stiffness of the connecting spring in model iii)

The linear model described highlights a structural behavior similar to the one of a single degree of freedom (SDOF), where the great part of the displacement demand is located in the supporting structure. The silos and the roof behave such as a rigid body and the resultant stresses are far below the yielding or buckling threshold. For this reason the structural behavior can be represented by the simplified model shown in Figure 5, where the roof is considered simply as dead load and mass, while the silos are substituted by a trusses system, whose characteristics are evaluated to obtain the same first period and modal shape of the "complete" model.

The simplified model is used to perform the nonlinear IDAs. Each element is modelled using a fiber element and the material is assumed to be elasto-plastic. The global second-order effects are explicitly taken into account, while, in order to consider the post-critic behavior of the bracings in compression, they are modelled introducing the initial imperfection as foreseen by Eurocode 3 [14]. The viscous damping is taken into account introducing an damping ratio associated to the first and second vibrating modes equal to 2% and setting the damping matrix proportional to the mass and initial stiffness matrix.

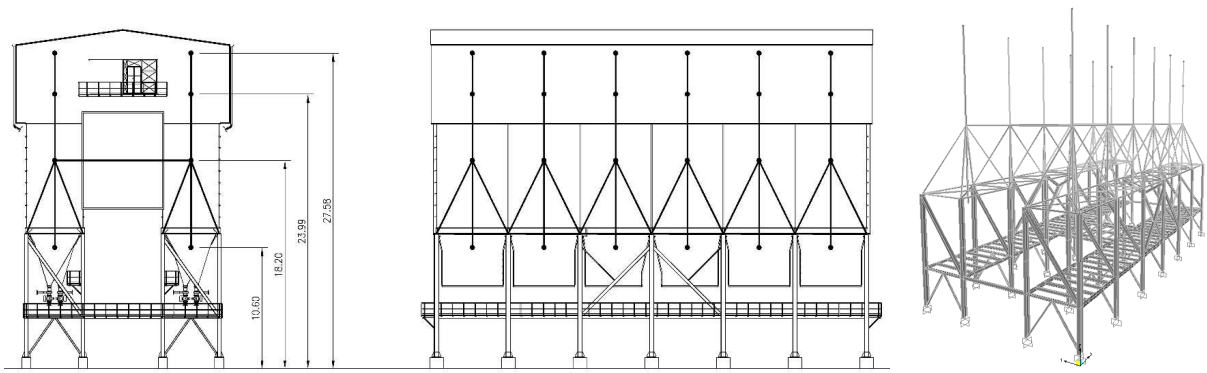

Figure 5. Case study building simplified model

2.2 Limit states and performance parameters

The Ultimate Limit State considered during the structural analysis are resumed, together with the reference standard, in following table .

ULTIMATE LIMIT STATE	ELEMENT	CHECK	STANDARD
Shear resistance	Column	$V_{Ed} / V_{pl,Rd} \leq 0.50$	EN 1998-1:2013 [15]
Plastic rotation capacity	Columns	$\phi < \phi_u$	EN 1998-3:2005
Plastic rotation capacity	Beams	$\phi < \phi_u$	EN 1998-3:2005
Axial deformation capacity in tension and compression	Dissipators/ Bracings	$\Delta L < \Delta Lc$ (compression/buckling) $\Delta L < \Delta Ly$ (tension)	EN 1998-3:2005
Check of sensibility coefficient Theta	Global	$\vartheta < 0.3$	EN 1998-1:2013 [15]
Maximum displacement	Global	dr < 0.50m Due to the interaction with non structural elements	--

Table 1. Main limit state considered

To evaluate the building performance, four different parameters are evaluated during the IDA analysis:

1. maximum displacement. Related to the non structural elements (such as external cladding) damage;
2. maximum acceleration. Related to the acceleration-sensitive systems damage;
3. residual deformation. Related to the structural damage and resilience;
4. seismic energy. The different components of the energy supply important information on the structural damage and on the retrofit choices.

In particular, four type of seismic energy are analyzed: input energy, defined as the energy transmitted by the ground movement to the structure; kinetic energy, related to the building movements; adsorbed (strain + dissipated) energy, related to the damaging of the structure; viscous energy.

2.3 Selection of ground motions

In order to achieve the worst damage scenarios with a robust and reliable procedure, an Uniform Hazard Spectrum -coherent method is adopted for the ground motions. The complete procedure, together with all the background and motivations, is described in the paper presented by Faggella et al. at the 2016 ECCOMAS conference "Performance-based Nonlinear Response History Analysis Framework for the “PROINDUSTRY” Project Case Studies".

A major drawback of using unscaled GMs is that a higher number of records need to be used. At least 7 GMs are needed but, considered their high variation, a higher number is preferred, at least equal to 11. The selected ground motions are listed in Table 2. The IDAs are executed applying simultaneously the three components (2 horizontal and 1 vertical) of each ground motion and using 9 scale factors, SFs, see Figure 6. A total of 198 nonlinear time-history analyses are carried out for the case study (11 GMs x 9 SFs x 2 directional combinations).

DB	ID	Earthquake Name	Mw	Fault Mec.	R(kM)	Site Class	Date
ED	6349	South Iceland	6,4	Strike slip	5	A	21/06/2000
ED	196	Montenegro	6,9	Thrust	25	B	14/04/1979
ED	535	Erzincan	6,6	Strike slip	13	B	13/03/1992
ED	74	Gazli	6,7	Thrust	11	D	17/05/1976
ED	1257	Izmit	7,6	Strike slip	20	C	17/08/1999
IN	113	South Iceland	6,5	Strike slip	5,25	A	17/06/2000
IN	466	Duzce	7,1	Strike slip	5,27	C	12/11/1999
IN	331	Darfield	7,1	Strike slip	17,82	C	03/09/2010
IN	445	Imperial Valley	6,5	Strike slip	27,03	C	15/10/1979
IN	451	Loma Prieta	6,9	Oblique	7,1	B	18/10/1989
IN	461	Northridge	6,7	Reverse	20,25	C	17/01/1994

Table 2. Ground motions selected for the execution of IDAs

REGGIO CALABRIA						
	Vr	P_{vr}	λ	Tr	ag	S.F.
	yrs	%	1/yrs	yrs	g	\
0	100	4%	0.0004	**2475**	0.512	1.43
1	100	**5%**	0.0005	1950	0.4687	1.307
2	100	**10%**	0.0011	949	0.3586	**1.000**
3	100	22%	0.0025	402	0.2502	0.698
4	100	30%	0.0036	280	0.2122	0.592
5	100	39%	0.0049	202	0.1829	0.510
6	100	50%	0.0069	144	0.1552	0.433
7	100	**63%**	0.0099	101	0.1292	0.360
8	100	**81%**	0.0166	60	0.0987	0.275

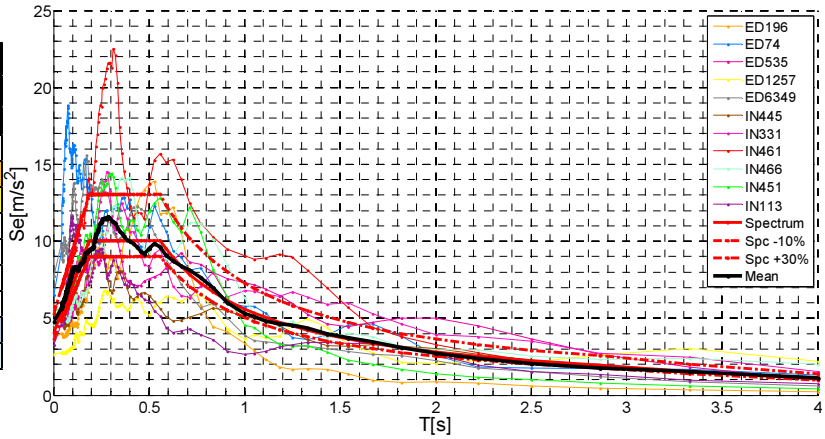

Figure 6. Selected ground motions response spectrum and Scale Factor, S.F., used

2.4 Seismic vulnerability of the case study current state

The seismic vulnerability of the case study is studied through the IDAs and represented through the IDA curves, in terms of maximum displacement, maximum acceleration, residual displacement and seismic energy (elastically stored or dissipated by the structure). All the parameters are registered at three different levels of the structure, see Figure 7.

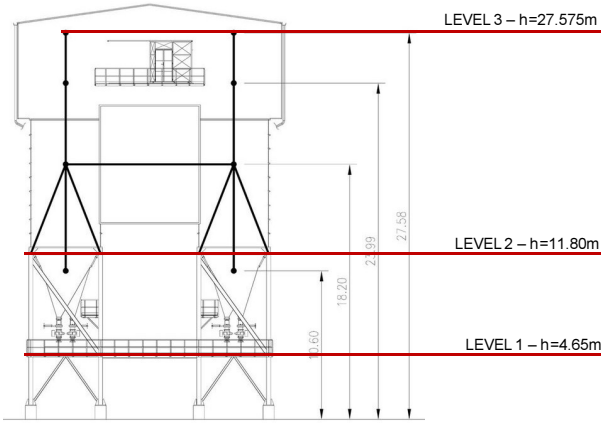

Figure 7. Individuation of recorded levels

In Figure 8 and Figure 9, the IDA curves more representative of the strucruarl behavior are shown, while in Figure 10 the maximum displacements versus the maximum shear force plotted.

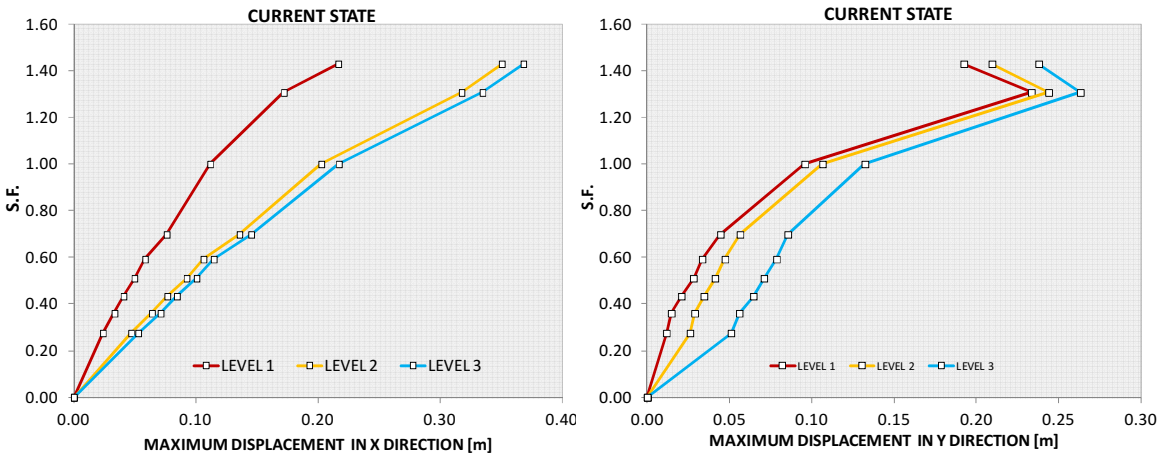

a) b)

Figure 8. Maximum displacements (mean values) at different level in the a) X and b) Y directions

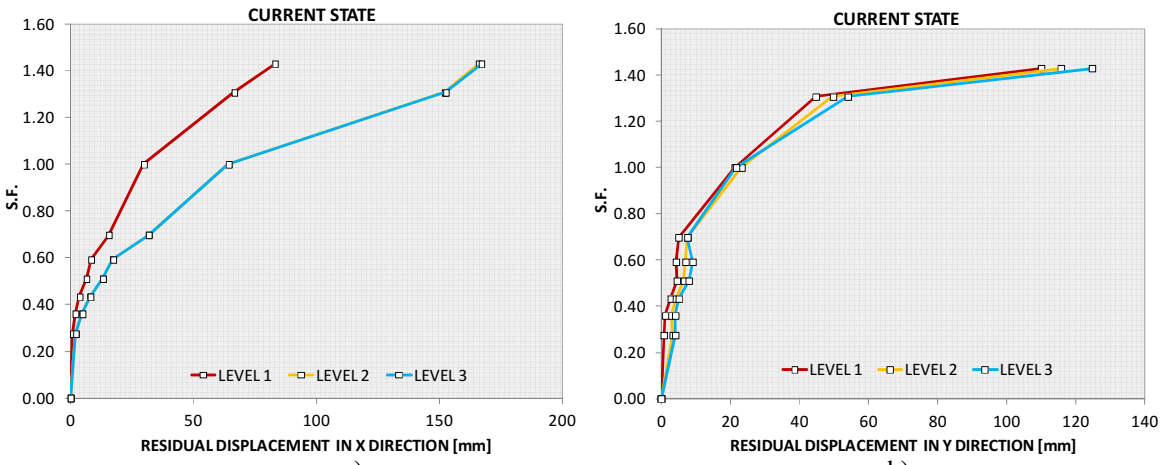

a) b)

Figure 9. Residual displacements (mean values) at different level in the a) X and b) Y directions

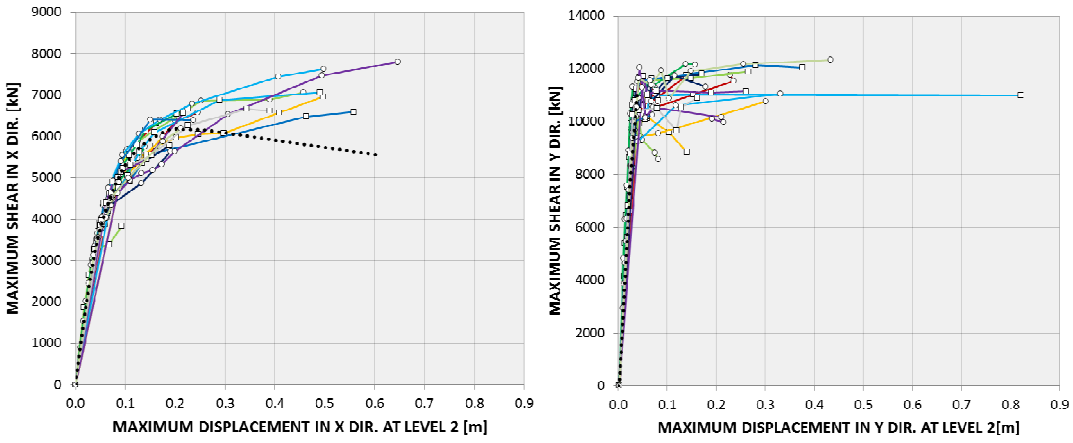

a) b)

Figure 10. Maximum base shear vs maximum displacement at level 2 graph in the a) X direction and b) Y direction

From the analysis of Figure 8 and Figure 9 it can be seen that, in the X direction the displacement demand is equally distributed between the ground and first floor. This is mainly due to the low number of bracing in the first floor. In the Y direction, the displacement demand is concentrated at the ground floor, highlighting an early plasticization of the inverted V bracings with respect to the first floor diagonal bracings. In both directions, important residual displacements are registered at the end of each time-history analysis. The presence of such residual displacements lower considerably the resilience of the building, given the great difficulties in repairing a deformed and unstable structure.

Interesting information on the building behavior, especially in view of the retrofitting study and optimization, are supplied by the analysis of the input seismic energy transmitted by the earthquake to the structure and the stored and/or dissipated one. In Figure 11 an example of the energy time-histories recorded for the ground motion IN113A (the final A means that the main horizontal component is applied in the X direction) are reported for two different scale factors. It can be observed that, for low SCs, the energy dissipation takes place mainly for viscous damping, while, increasing the seismic action, the energy adsorbed by the structure, strictly related to the structural damage, represent the main component of the input energy.

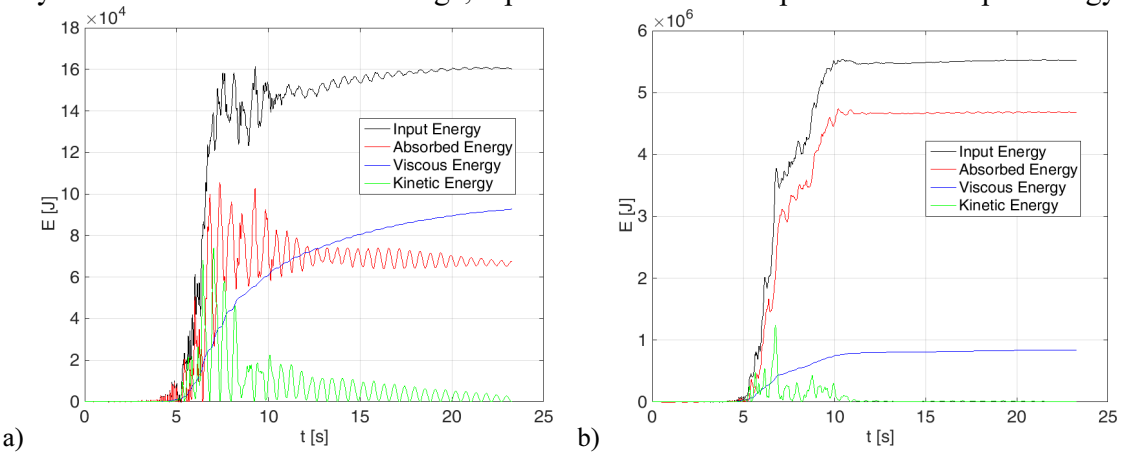

Figure 11. Energy time-histories for the IN113A GM recording: a) SF = 0.275; b) SF= 1.430.

Interesting results can be obtained comparing the ratio between the adsorbed or the viscous energy and the input one for all the GMs and SFs considered, as shown in Figure 12. It can be noticed, in fact, that for all the GMs the ratio with the input energy tends to a certain value, respectively equal to 0.83 for the adsorbed and 0.17 for the viscous energy. This means that, for SFs higher than 0.592 the structure develops the complete collapse mechanism.

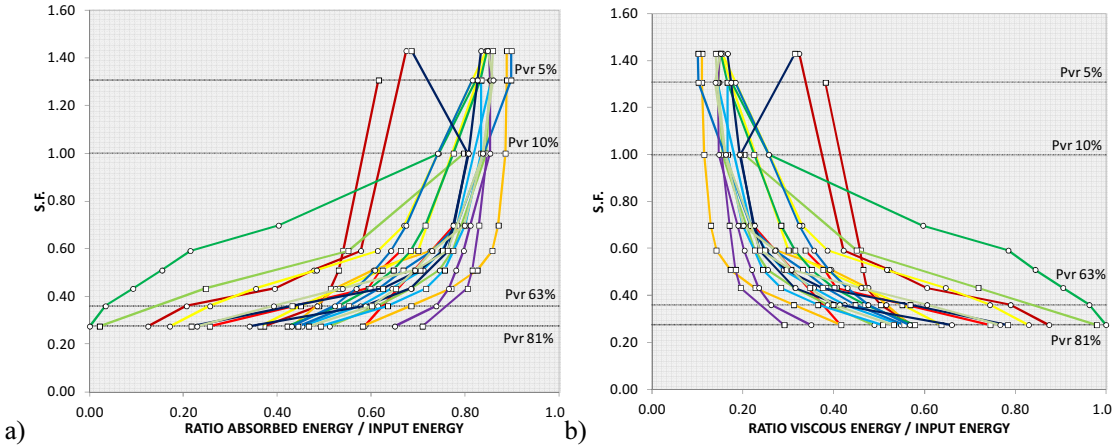

Figure 12. Ratios between: a) the adsorbed and input energies; b) viscous and input energies

3 SEISMIC RETROFIT

The IDAs on the current state evidenced several structural problems, such as:

- the building is characterized by a low stiffness in the X direction, both at ground and first floor. The seismic energy dissipation in this direction is mainly obtained through the formation of plastic hinges in the beams and columns;
- in the Y direction, the initial stiffness is sufficient to avoid excessive displacements, but the high slenderness of the bracings implies a insufficiently ductile dissipating mechanism;
- the eccentricity between the bracings and the column in the X direction causes excessive shear forces in the column;
- the structure is characterized by important residual displacements in both directions at the end of the earthquakes (mean values greater than 100 mm for the higher scale factor considered).

On the base of the aforementioned results, a seismic retrofit intervention, using the Steel Self-Centering Device described in [13] is proposed. In the following, after a short description of the device, the pre-sizing of the retrofit is described and its effectiveness is assessed through IDAs. Finally, the influence of the re-centering capability of the SSCD inserted within the structure is investigated trough a parametric analysis.

3.1 The steel self-centering device (SSCD)

The SSCD, a complete description of which is available in [13], is made up of three groups of elements, each with specific functions: the Skeleton, the Dissipative Elements and the Pretension Elements. The Skeleton serves to transmit and distribute any external forces between the Dissipative Elements and the Pretension Elements. Figure 13 shows the main Skeleton elements (External Carter, Internal Sliding Frame and Endplates), the Dissipative Elements and the Pretension Elements. The Internal Sliding Frame is positioned within the External Carter.

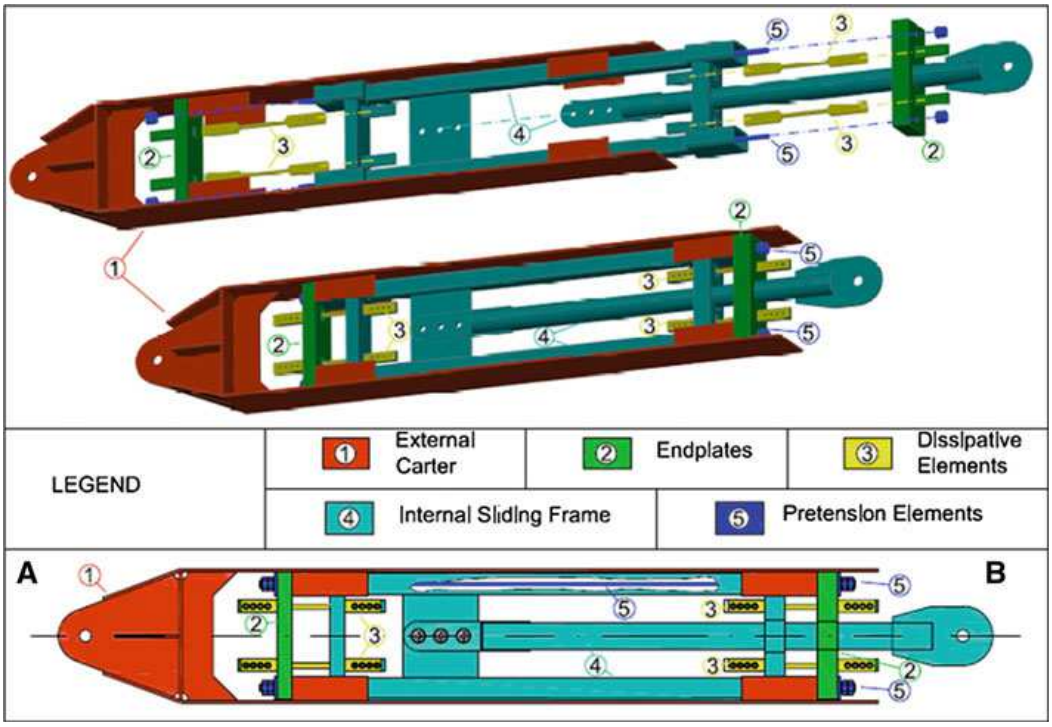

Figure 13. Main elements of the SSCD [13]

The Carter has guide elements that allow the Internal Sliding Frame to move only in the axial direction and, at the same time, serve as stops for the Endplates in the longitudinal direction. The endplates are located in correspondence to the ends of the Internal Sliding Frame. The Dissipative Elements, located within the skeleton, are made up of dog bone shaped steel elements linked to the Internal Carter and the Endplates. They are equipped with a lateral buckling restraining system. The Pretension Elements, made with Prestressing Cables, are located within the Skeleton and linked at both their extremities to the Endplates.

The elements are positioned and connected to each other in order to ensure the same global behavior of the SSCD device under both tension and compression external forces.

Thus, the cyclic behavior of the SSCD is characterized by a flag-shaped hysteretic curve with a residual displacement of zero.

The experimental results carried out in [13] showed the very good capacity of the system in minimizing the residual deformations when the external force drops to zero, see Figure 14.

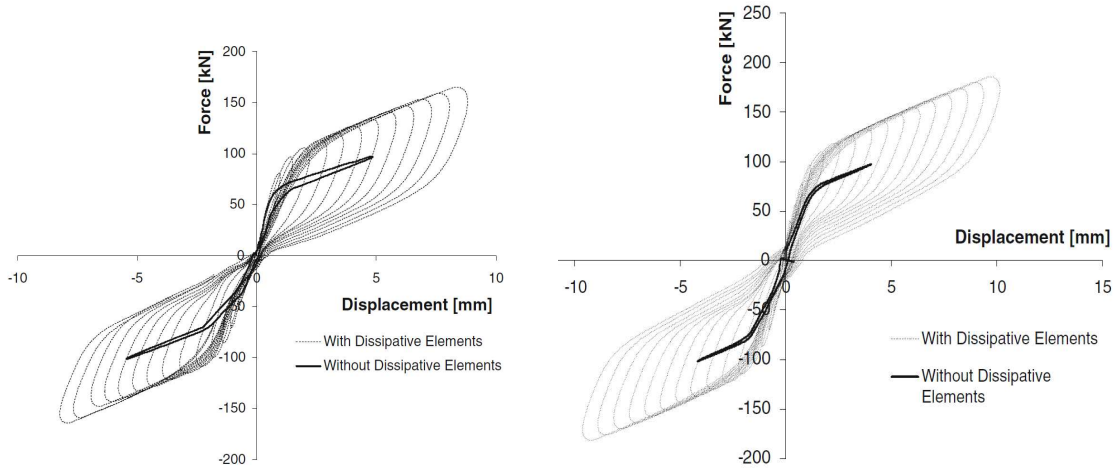

Figure 14. Force-displacement curve of the SSCD with dissipative elements, a) test 1 and b) test 2 [13]

Depending mainly on the value of the ratio between the initial pretension force and the yield strength of the Dissipative Elements, the hysteretic curve of the SSCD may present different shapes, each characterized by different values of the dissipated energy, residual displacement and residual re-centering force, as shown in Figure 15.

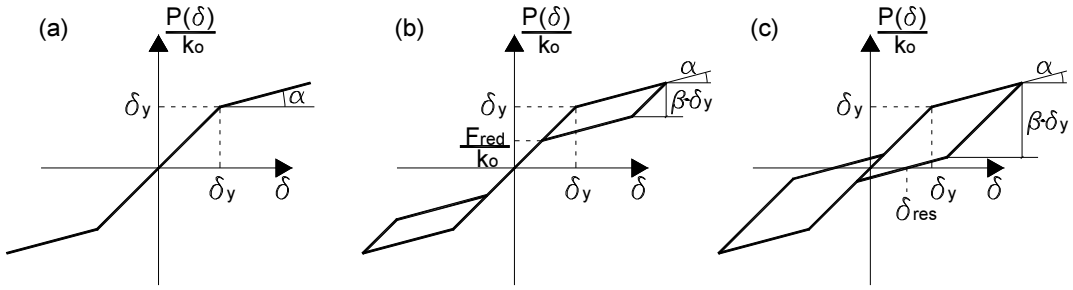

Figure 15. Idealized flag-shaped hysteretic curve normalized by the initial stiffness ko: a) $\beta = 0$, b) $0 < \beta < 1$ and c) $\beta > 1$

The shape of the hysteretic curve can be represented determined by two parameters, α and β, where α is the ratio between the hardening and the initial stiffness, while β reflects the energy dissipation and the system's re-centering capacity [9], which, as mentioned, can be assumed equal to the ratio between the yield strength of the Dissipative Elements and the initial pretension force. A hysteretic curve with $\beta = 0$ can be obtained by using the SSCD without

any Dissipative Element, in which case the device exhibits nonlinear elastic behavior with great re-centering capacity, but no energy dissipation. On the other hand, values of $\beta > 1$ lead to residual displacements (when the external force drops to zero) but also to an higher energy dissipation.

3.2 Pre-dimensioning of the SSCD bracings

The SSCD position is assumed limiting, as much as possible, the interferences with the functionality of the building. The SSCD are so introduced, substituting, in the Y direction and at the first floor of the X direction, the existing bracings. To protect also the ground floor elements in the X direction, supplemental SSCD bracings are introduced as schematically shown in Figure 16.

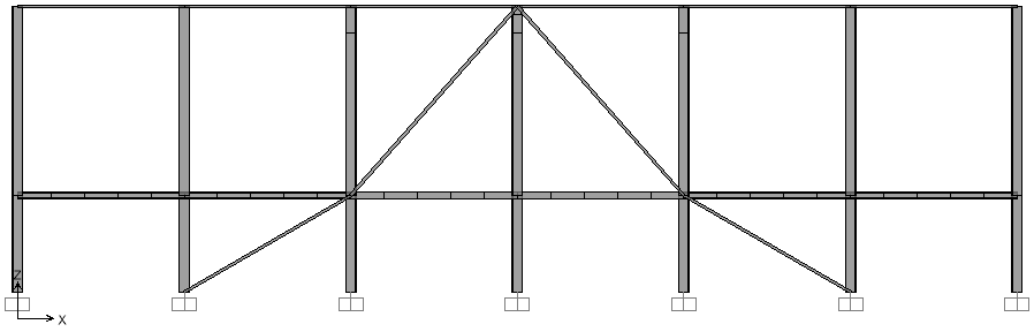

Figure 16. SSCD bracings disposition in the X direction

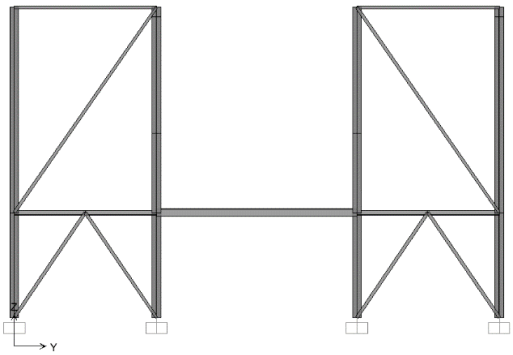

Figure 17. Figure 16. SSCD bracings disposition in the Y direction

The retrofit pre-design is carried out evaluating the characteristics of the SSCD bracings to limit the gravity structure (beams and columns) damage as much as possible. For this reason, the yielding force of the SSCDs are evaluated taking into account the elements resistance to which they are connected. The initial stiffness is estimated imposing a maximum displacement of the gravity structure equal to the one corresponding to the 0.2% of the residual displacement, see Figure 18. The mechanical characteristics of the resulting SSCD are resumed in Table 3.

Level - direction	Number of SSCD	k_o [kN/mm]	F_y [kN]	α	β
Ground floor - X	8	72	529	0.26	0.85
First floor - X	8	88	848	0.26	0.85
Ground floor - Y	28	112	332	0.16	0.85
First floor - Y	14	77	556	0.20	0.85

Table 3. Mechanical characteristics of the SSCDs

Figure 18. Evaluation of the gravity structure displacement corresponding to the 0.2% of residual displacement in the X direction

3.3 IDA results for the retrofitted case

With reference to the levels definition of Figure 7, in the following are reported the main results, in terms of IDA curves.

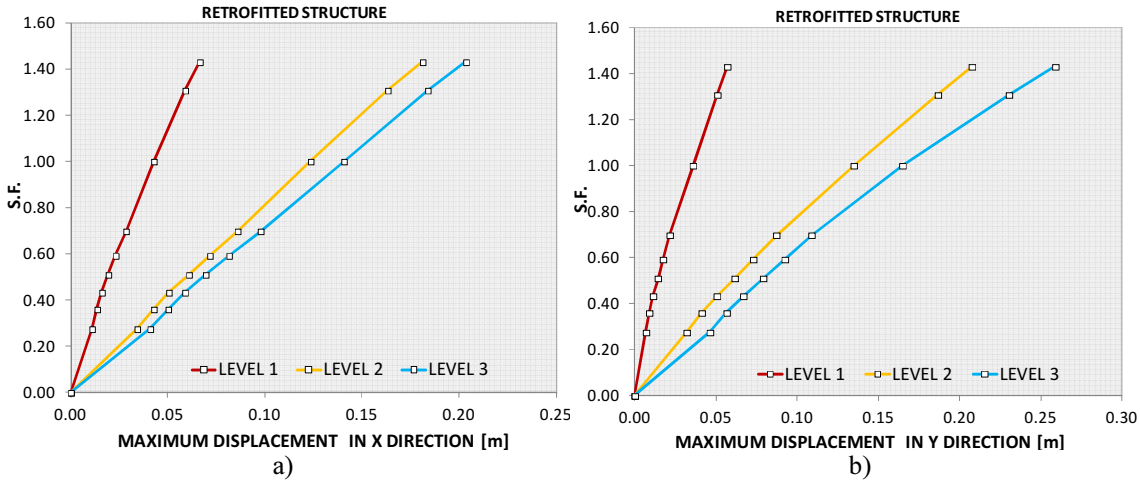

Figure 19. Maximum displacements (mean values) at different level in the a) X and b) Y directions

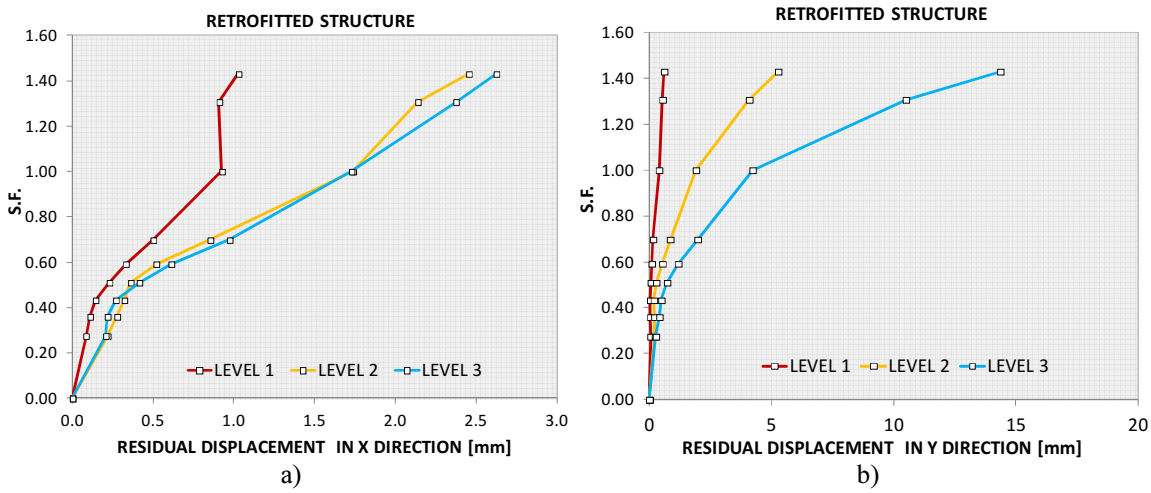

Figure 20. Residual displacements (mean values) at different level in the a) X and b) Y directions

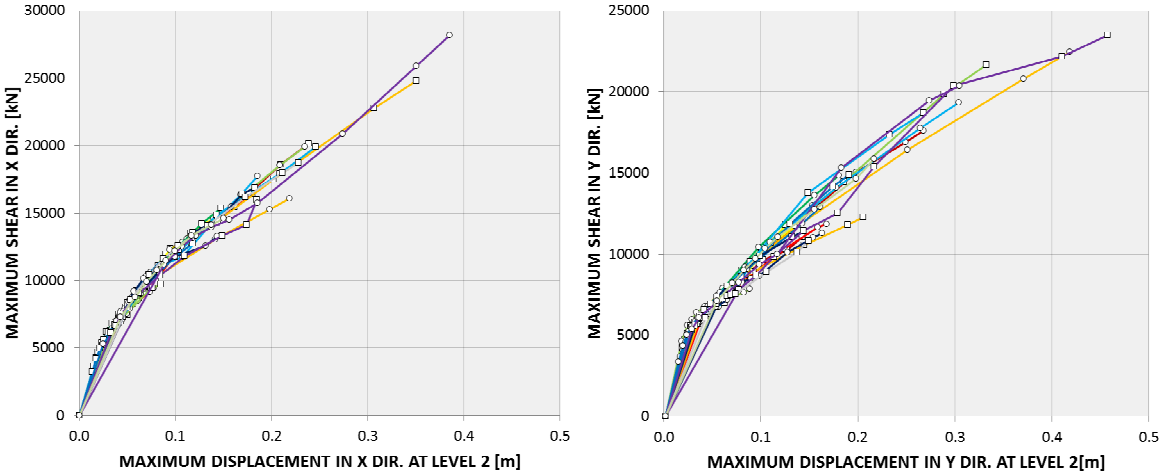

Figure 21. Maximum base shear vs maximum displacement at level 2 graph in the a) X direction and b) Y direction

From the analysis of Figure 19 it can be seen that, in both directions, the displacement demand is now equally distributed between the first and second floor. Figure 20 testifies the optimum re-centering capability of the retrofitting solutions: the residual displacements are lower than 3 mm in the X direction and 15 mm in the Y one. In Figure 22 the displacement time-histories for the Ground motion IN445A, SF=1.430, in both the main directions highlights, together with the global hysteretic curves, the differences in terms of maximum and residual displacements in the case of un-retrofitted and retrofitted structure.

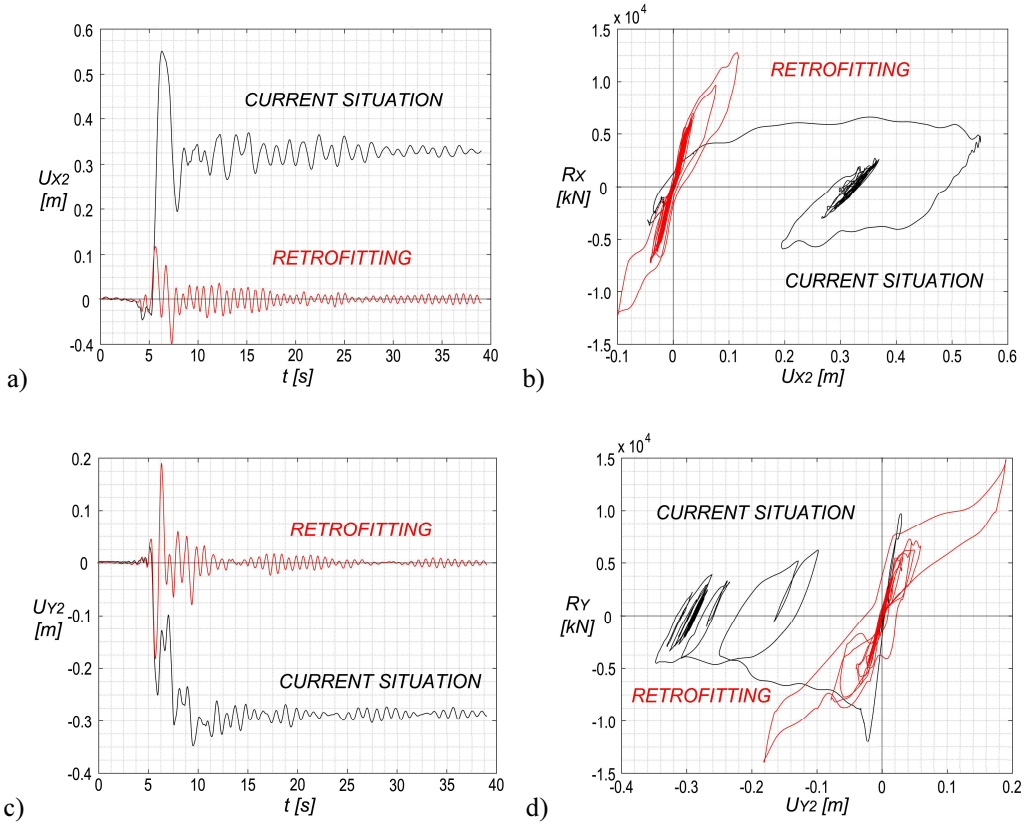

Figure 22. Ground motion IN445A, SF=1.430: level 2 mean displacement time history in a) X and c) Y directions; level 2 mean displacement vs total base shear in b) X and d) direction.

Figure 23 shows, for clarification purpose, the energy time-histories for the IN113A GM for the minimum and maximum scale factor adopted, respectively equal to 0.275 and 1.430. For low value of the seismic action, the gravity structure remains in the elastic field and the energy adsorbed by it is practically equal to zero and all the input energy is dissipated by viscous phenomena, contrarily to the case of the un-retrofitted structure, see Figure 11. When the seismic action and, consequently, the input energy increase, the ratio of energy dissipated by viscous phenomena decreases and the input energy is mainly dissipated by the SSCDs. A low ratio (about 1/5 with respect to the un-retrofitted case) is absorbed by the gravity frame, evidencing so a good level of structural protection.

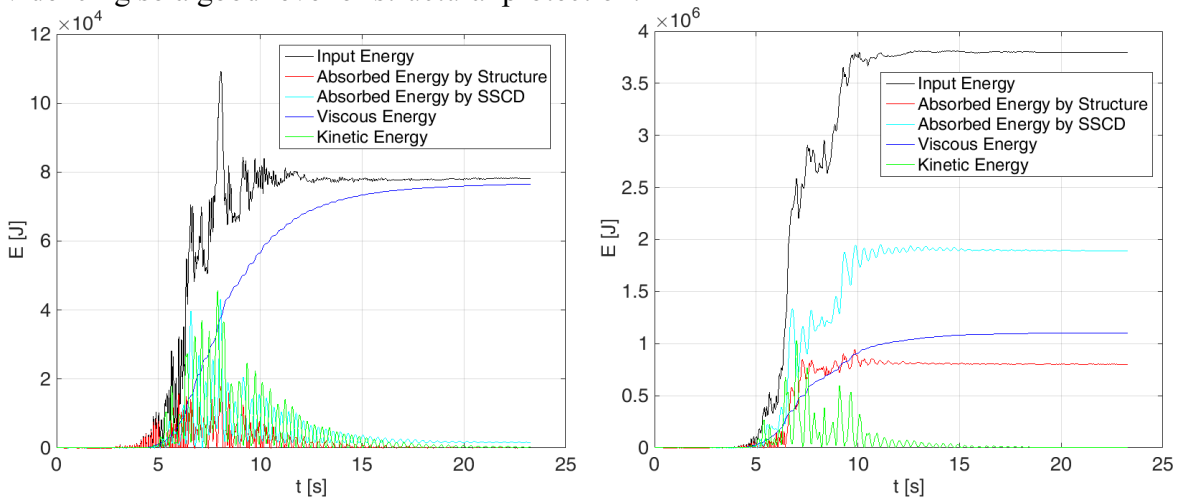

Figure 23. Energy time-histories for the IN113A GM recording: a) SF = 0.275 ; b) SF= 1.430.

The effectiveness of the retrofit can be appreciated analyzing Figure 24 where the energies adsorbed by the gravity structure, representative of the structural damage, and the one dissipated by the SSCDs, both normalized by the input energy, are represented. The structural protection is optimized for values equal to about 0.6, while, for higher values, also the gravity structure dissipates energy, accumulating so damages.

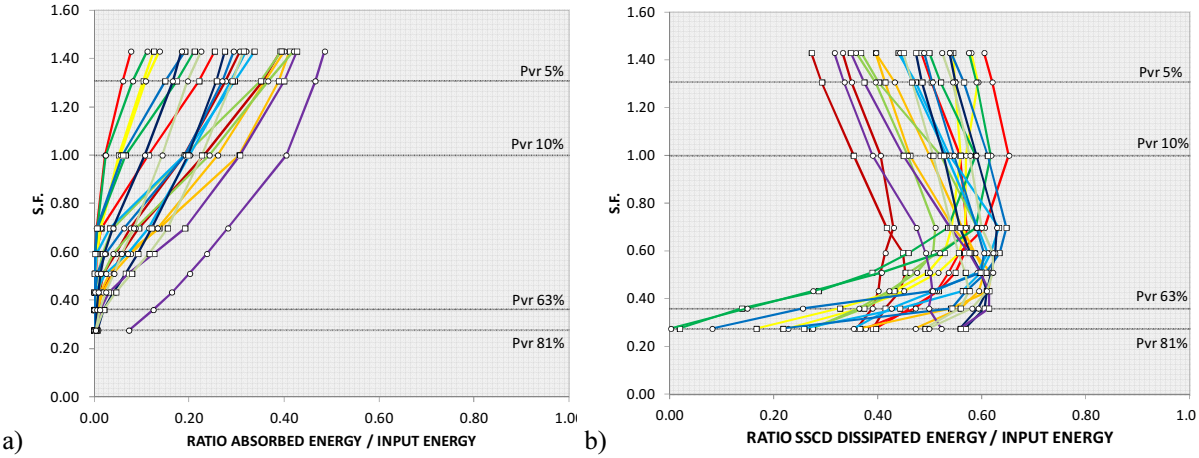

Figure 24. Ratios between: a) the energy adsorbed by the gravity structure and the input one; b) energy dissipated by the SSCDs and input one

4 CONCLUSIONS

In the present paper the seismic retrofit of an industrial structure through an innovative self-centering hysteretic dampers is proposed. The need of performing several Incremental Dynamic Analyses required a preliminary simplification phase of the nonlinear model. It resulted that, even for the linear model, the uncertainties related to the missing of a precise knowledge of the infill material mechanical characteristics, does not influence sensibly the dynamic behavior of the whole model. Moreover, for the specific case study analyzed, where the main structural problems are located in the supporting structure, the modelling of the supported silos as elements with equivalent stiffness and mass, provides results, in terms of dynamic responses, very close to one supplied by a refined model.

The execution of IDAs on the nonlinear model of the building in the current state, highlighted several structural problems, even for low value of the seismic action, especially in terms of excessive maximum displacements demand and of residual displacements.

To solve these problems, a retrofit solution using an innovative Steel Self-Centering Device (SSCD) is proposed. The execution of IDAs also in the retrofitted state, highlighted that:

- the dampers minimize, in a very effective way, both the maximum and residual displacements of the structure;
- the gravity structure is completely protected for low-to-mid value of the seismic action, as highlighted by the analysis of the seismic energy components;
- the proposed retrofit solution is optimized for a scale factor, associated to the design spectrum adopted, equal to 0.60. For higher values of scale factors, the building is however able to sustain the seismic action, but some damage is accumulated also in the gravity structure.

Supplemental studies are currently ongoing to evaluate the sensitivity of the building response to the SSCD mechanical characteristics and to compare the efficacy of the innovative damper adopted with respect to the one of a "classical" solution, such as a buckling restrained brace (BRB), not characterized by the presence of a re-centering force, but with an increased energy dissipation capacity [16] [17].

5 ACKNOWLEDGMENTS

The research leading to these results has received funding from the European Union's Research Fund for Coal and Steel (RFCS) research programme under grant agreement n° [RFSR-CT-2013-00019] and from the Italian Department of Civil Protection within the Italian Research Project RELUIS-DPC 2014-2018.

REFERENCES

[1] F. Braga, R. Gigliotti, G. Monti, F. Morelli, C. Nuti, I. Vanzi, W. Salvatore, Post-seismic assessment of existing constructions: evaluation of the shakemaps for identifying exclusion zones in Emilia. *Earthquakes and Structures*, **8**, 37-56, 2014.

[2] F. Braga, R. Gigliotti, G. Monti, F. Morelli, C. Nuti, I. Vanzi, W. Salvatore, Speedup of post earthquake community recovery. The case of precast industrial buildings after the Emilia 2012 earthquake. *Bulletin of Earthquake Engineering*,**12**, 2405-2418, 2014.

[3] F. Braga, F. Morelli, W. Salvatore, A macroseismic approach for the evaluation of seismic risk, J. Kruis, Y. Tsompanakis, B.H.V. Topping eds, *Fifteenth International*

Conference on Civil, Structural and Environmental Engineering Computing, Prague, Czech Republic, September 1-4, 2015.

[4] Ministero delle Infrastrutture, Norme Tecniche per le Costruzioni, D.Min. Inf. 14 gennaio 2008, Gazzetta Ufficiale n. 29 of february 4th 2008 - Suppl. Ordinario n. 30, 2008.

[5] European Committee for Standardization. Anti-seismic devices. EN 15129, November 2009.

[6] M. J. N. Priestley, S. Sritharan, J. R. Conley, S. Pampanin, Preliminary results and conclusions from the PRESSS five-storey precast concrete test building. *PCI Journal* **44**(6):42–47, 1999.

[7] C. Christopoulos, A. Filiatrault, B. Folz, C. M. Uang, Post-tensioned energy dissipating connections for moment-resisting steel frames. *ASCE Journal of Structural Engineering* **128**(9):1111–1120, 2002a.

[8] C. Christopoulos, A. Filiatrault, B. Folz, Seismic response of self-centering hysteretic SDOF systems. Earthquake Engineering and Structural Dynamic **31**(5):1131–1150, 2002b.

[9] C. Christopoulos, A. Filiatrault, *Principles of supplemental damping and seismic isolation*. IUSS Press, Pavia, 2006.

[10] C. Christopoulos, R. Tremblay, H. J. Kim, M. Lacerte, Self-centering energy dissipative bracing system for the seismic resistance of structures: development and validation. *Journal of Structural Engineering* **134**(1): 96–107, 2008a.

[11] C. Christopoulos, H. Choi, J. Eronchko, Comparison of the seismic response of steel buildings incorporating self-centering energy dissipative braces, buckling restrained braces and moment resisting frames. In: *Proceedings of the 14th world conference on earthquake engineering*, Beijing, China, 12–17, 2008b.

[12] X. Ma, H. Krawinkler, G. G. Deierlein, Seismic design, simulation and shake table testing of self-centering braced frame with controlled rocking and energy dissipating fuses. J.A. Blume Earthquake Engineering Center, TR 174, Stanford University, (2011).

[13] A. Braconi, F. Morelli, W. Salvatore, Development, design and experimental validation of a steel self-centering device (SSCD) for seismic protection of buildings, *Bulletin of Earthquake Engineering*, **10**, 1915-1941, 2012.

[14] European Committee for Standardization. Eurocode 3: Design of steel structures - Part 1-1: General rules and rules for buildings. En1993-1-1, August 2005.

[15] European Committee for Standardization, Eurocode 8: Design of structures for earthquake resistance - Part 1: General rules, seismic actions and rules for buildings. EN 1998-1, December 2004.

[16] A. Zona, A. Dall'Asta, Elastoplastic model for steel buckling-restrained braces. *Journal of Constructional Steel Research*, **68**(1)118-125, 2012. DOI: 10.1016/j.jcsr.2011.07.017

[17] A. Zona, L. Ragni, A. Dall'Asta, Sensitivity-based study of the influence of brace overstrength distributions on the seismic response of steel frames with BRBs. *Engineering Structures*, **37**(1) 179-192, 2012. DOI: 10.1016/j.engstruct.2011.12.026

ECCOMAS Congress 2016
VII European Congress on Computational Methods in Applied Sciences and Engineering
M. Papadrakakis, V. Papadopoulos, G. Stefanou, V. Plevris (eds.)
Crete Island, Greece, 5–10 June 2016

PERFORMANCE ASSESSMENT OF SEISMIC RETROFITTING MEASURES ON SILO STRUCTURES USING INNOVATIVE SEISMIC PROTECTION SYSTEMS

Marius Pinkawa[1], **Benno Hoffmeister**[1], **and Markus Feldmann**[1]

[1] Institute of Steel Construction
Mies-van-der-Rohe-Straße 1, 52074 Aachen, Germany
e-mail: m.pinkawa@stb.rwth-aachen.de

Keywords: Industrial Structures, Silo Structures, Seismic Retrofitting, Seismic Protection Devices, Model Simplification, Incremental Dynamic Analyses

Abstract. *This paper deals with a real-world silo structure and the assessment of its seismic performance and possible retrofitting measures by using seismic protection devices. Firstly, the silo structure is shortly described followed by a simplified numerical modelling approach with the aim to save computational effort as much as possible but still achieve a reliable response of demands and failure modes. A comparison between the complex and simplified model is done, showing a very good match in terms of its dynamic properties, which are Eigenfrequencies, modal shapes and effective modal masses. With this simplified model incremental dynamic analyses are conducted to assess the current performance of the structure as-built. Strengths and weaknesses are highlighted by the simulation outcomes. Following, two possible retrofitting strategies using torsion-based hysteretic dampers are discussed. Hereby it is shown, how the seismic device can be modelled in any finite element software by using rheological models. In one strategy of seismic retrofit an innovative torsional device is inserted at single bays of the structural frame. In the second strategy the steel torsional hysteretic damper is applied at the base of the steel columns, such that the structure is separated from the ground. The first retrofit approach proves to be effective in prohibiting a severe sides-way collapse which occurred for some earthquakes. The second shows to be greatly effective in preventing failure and also decreases deformation demands on the structure efficiently.*

1 INTRODUCTION

Seismic events may have disastrous effects on industrial sites; for example the Duzce earthquake in Turkey 1999, the L'Aquilla earthquake 2009 in Italy or the more recent Tohoku earthquake in Japan 2011 caused huge financial losses, as they all affected important industrial areas. One reason for the high losses are the high financial investment costs gathered on industrial sites which are at risk due to direct damage of industrial components and facilities. However, also more frequent smaller seismic events can lead to impairment of the functionality of key components and thus cause costly business interruptions. A further special characteristic of industrial facilities is the usual high risk potential of environmental damage as well as potentially threats to health and life of employees. For these reasons industrial structures are ideally suited for seismic design and retrofit by using special seismic protection systems.

The European project "PROINDUSTRY – Seismic PROtection of INDUSTRial plants by enhanced steel based sYstems" aims at developing such enhanced seismic protection devices applicable to new and already existing industrial structures. One of the several case studies investigated in the scope of the project is a large silo structure located in a steel plant. This silo is a very important member of the supply chain and its loss of functionality may lead to business disruption of the whole plant.

In this paper this realistic silo structure is firstly investigated as-built and further on different seismic retrofit strategies are applied. To assess on the effectiveness of the seismic retrofitting measure incremental dynamic analyses are the most detailed tools available. Due to the scatter in the characteristics of natural earthquakes a big amount of analyses needs to be conducted to obtain reliable results. As especially industrial facilities are often large and of complex nature, computational effort might be unmanageable. Therefore, usually a simplified model of the complex structure is sought after, which preserves characteristic dynamic behavior by being feasible to handle. Moreover, in order to obtain a reliable structural response not only the structure itself needs to be modelled realistically, also the applied seismic device needs to be represented appropriately. If the used finite element software does not provide special elements to model the behavior, which is often the case for new innovative seismic devices, it will be needed to use more or less complex rheological models or to implement ones own algorithm in the analysis core of the used software.

After a short description of the case study, a simplified modelling approach for the complex structure as well as the seismic device is presented. With these models first the as-built seismic performance is assessed and secondly two retrofitting strategies are investigated and its outcomes are compared to the initial stage.

2 SILO STRUCTURE CASE STUDY

2.1 Description of the case study

The case study investigated herein is an elevated silo structure with several rectangular silos constructed in the early 70s. The silo is part of a huge steel plant and stores iron ore, limestone and sinter. Thus, the structure has a key role in the storage and supply chain of the whole industrial facility. When the silo is out of function, this will lead to a costly downtime of several other operations within the industrial site. An assessment of the seismic performance and a potential seismic upgrade is therefore highly advantageous.

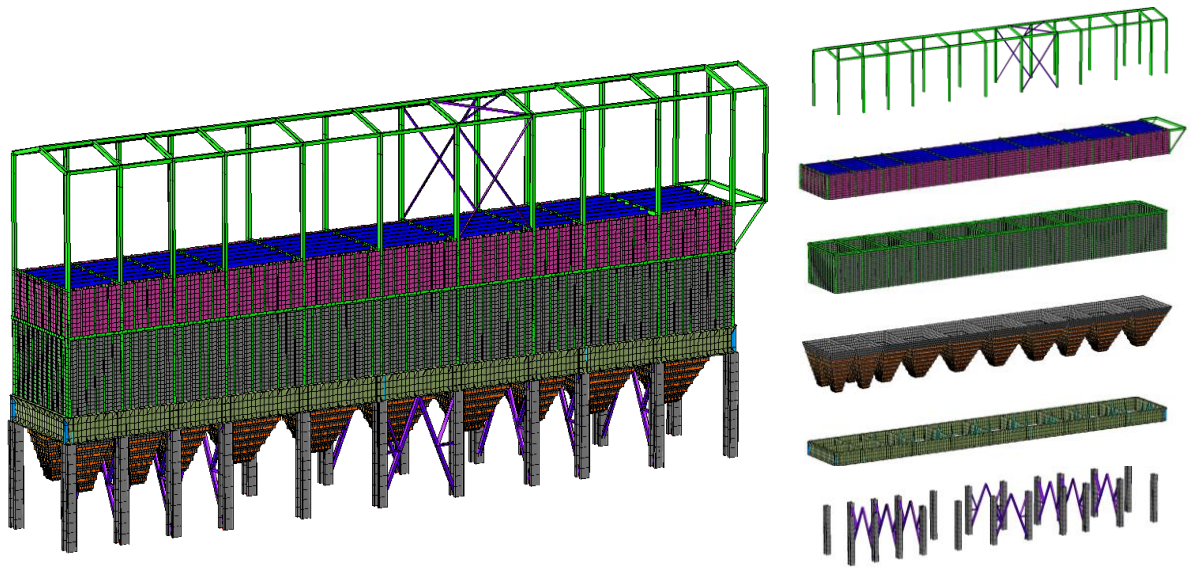

Figure 1: Silo steel structure. Complete model (left) and single subassemblies of silo structure (right).

The building has dimensions of W x H x D equal to 78 x 40 x 11 m. The structural layout and main characteristics can be seen in Figure 1. The most significant single subassemblies of the structure are shown on the right of Figure 1. The top is made of a roof beam structure, which is based on vertically stiffened shells and horizontal beams. The level below is formed by the silo shaft composed of shells with vertical stiffeners and an upper ring beam. Adjoining are the silo hopper shells stiffened by horizontal beams. Below is the hopper skirt support, which is also strengthened with vertical stiffener plates. Finally, at the lowest level the steel supporting structure is visible, which is made of heavy built-up columns and braced frames, whereby inverted V-bracings are used. It can be seen that 6 braces are built in the short Y-direction which will be named transversal direction in the following, and 2 braces in the long X-direction, labeled as longitudinal direction. Probably, the unbalanced number of braces in the two directions is attributed to the fact that wind forces were the essential considerations for the design of the bracing system, thus more braces are needed in transversal direction due to the big area where wind forces can act on. The calculated mass of stored material equals approximately 25,000 t and the self-weight of the steel structure equals to 2,400 t. The structure is made of S275 structural steel.

2.2 Description of the simplified model

The complete finite element model shown in Figure 1 is very complex and has a large number of degrees of freedom. The total number of dynamic simulations equals to 198, which results from two sets of ground motions (low-to-medium and high seismicity) with each eleven ground motion time histories times nine scaling factors. Taking into account that both the original and the retrofitted have to be simulated the number already rises to 396 dynamic time history simulations. Moreover this number is the absolute minimum. It does not consider repeated simulations due to different retrofitting strategies and varying parameters of the used seismic protection device and does not take into account several runs due to debugging . Thus, in total several hundred analyses will be needed to be conducted. Not only the computational time, but also the limited storage for simulation output may show up to be problematic. Therefore, due

to the huge amount of dynamic simulations which need to be conducted during the PROINDUSTRY project a computationally more efficient model was sought after.

The approach in simplifying the numerical model was to concentrate on the supporting structure and neglect the silo structure. This assumption was based on several reasons: Firstly, the silo shells are quite thick and massively stiffened, such that global failure of the structure is assumed to take place in the steel supporting structure rather than in the steel silos. Secondly, the dynamic modelling of the bulk material inside the silo would be needed to obtain reliably local failure of the silo shell. However, complex interaction models would be needed which further need several input parameters afflicted with a high level of uncertainties. Thus, on the one hand the reliability of the sophisticated approach would be still questionable and on the other hand the complexity excludes practically the simulation of several hundreds of analyses.

However, with the simplified approach just demands on the supporting structure and the mass points representing the silos are determined, without giving information about demands on the silo shells. However, peak forces and differential displacements obtained by the simplified model might be statically applied to the bottom or center of gravity of the silos bins. In a more complex approach, for bypassing this lack of information acceleration time history of the supporting structure may be applied to the bottom of the silo structure in a separate analysis, i.e. a cascaded approach similar to the floor response spectrum method used for SDOF systems. In this case the most detrimental excitation cases could be applied, to avoid extensive simulations but still to obtain reliable performance of the superstructure.

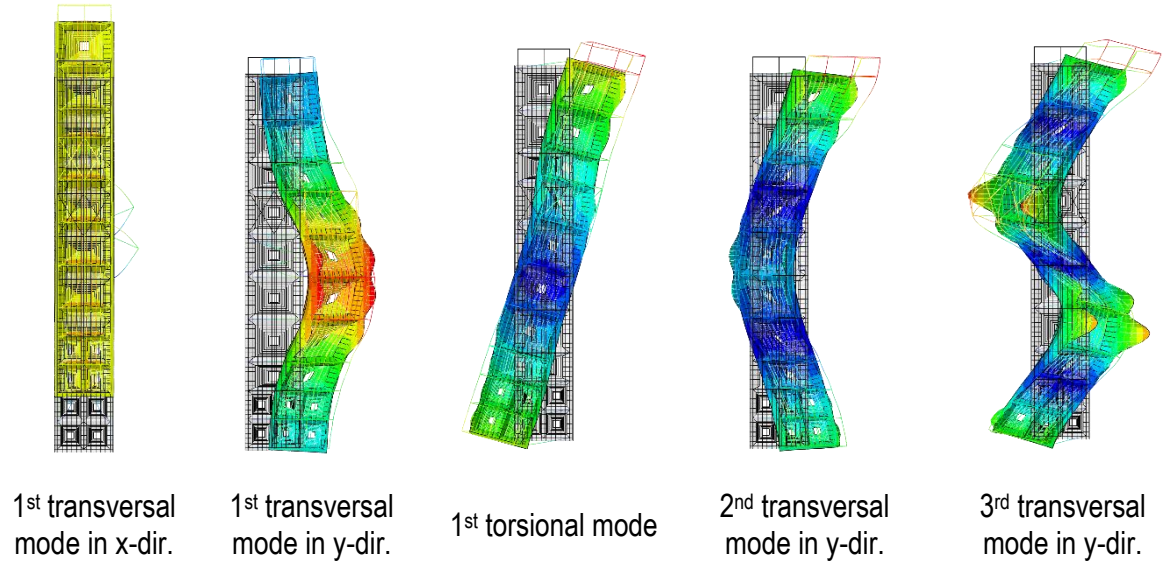

Figure 2: First five global mode shapes of complex structure.

Summarizing a simplified model is sought after, where the supporting structure is modelled explicitly by beam elements and the superstructure is taken into account by equivalent mass and stiffness properties applied to the supporting structure. Considering the Eigenmodes of the complex model shown in Figure 2, it is obvious that the superstructure cannot be modelled as rigid. Thus, a simplified model needs to capture the flexible behavior of the superstructure without explicitly modelling it. The flexibility needs to be modelled at the connection of the columns to the silos, representing the joint details shown in Figure 4 left. Finally, the simplified model shown in Figure 3 has been found to be appropriate. The silos are represented by mass points, which are located at the center of gravity of the full silo bins. A configuration of all silo bins totally filled has been investigated in this research work, which is in general the most critical

situation. Torsional response due to extreme misbalanced filling configurations might be also critical, however this issue was not investigated further herein. The silo mass points are connected to each other by several constraints. The cross sections are modelled as fibre elements, where the stress strain law is intergrated at every interpolation point. Conservatively, an almost elastic – ideal plastic stress strain curve with a yield point of 27.5 kN/cm² has been assumed. The connection of the silo mass assembly with the column tops was the key point and is discussed in the following.

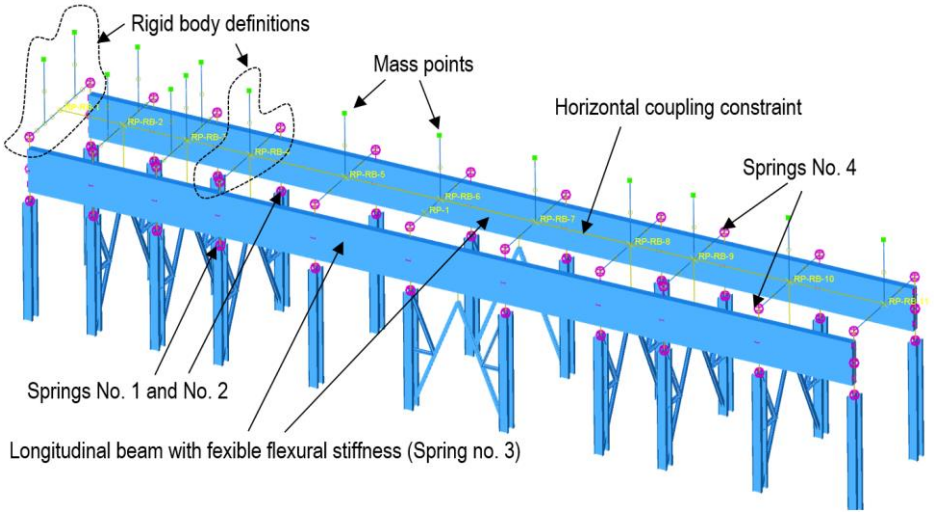

Figure 3: Simplified model with explicitly modelled supporting structure made of columns and frame braces with equivalent springs and couplings in order to take the flexible superstructure into account.

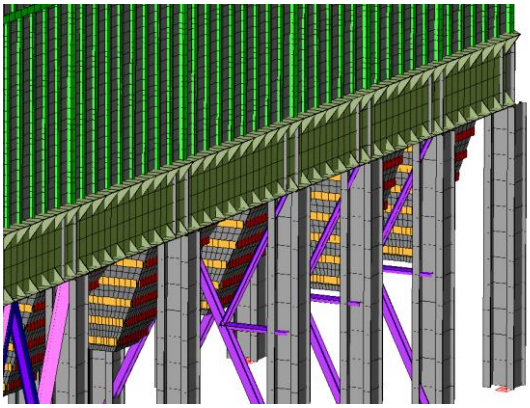

Figure 4: Connection detail between supporting and superstructure at columns.

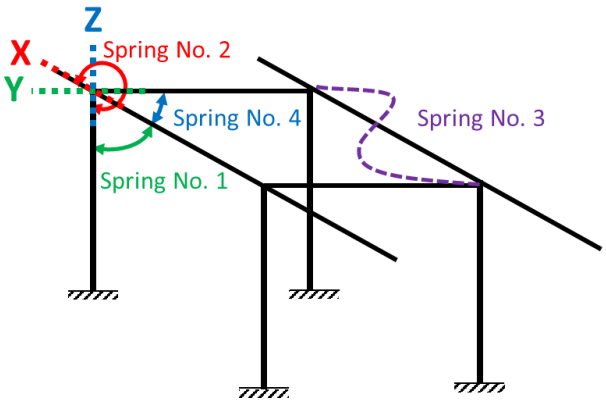

Figure 5: Schematical drawing of spring subassembly.

In order to obtain a reliable response of the simplified model, in total four spring or flexural stiffness properties respectively have been applied to the model. A schematical drawing of these springs can be found in Figure 5. A short description of each spring characteristic is given in the following Table 1.

The spring parameters were calibrated by a trial-and-error procedure until three aspects in the simplified model matched the complex model's ones for the relevant modes:

- Eigenfrequencies
- Modal shapes
- Effective modal masses

Spring No. 1

- *Rotational spring about global Y-axis*
- *Connecting column top nodes and node of longitudinal beam*
- *Dominant spring for fundamental mode, not affecting higher relevant modes*

Spring No. 2

- *Rotational spring about global X-axis*
- *Connecting column top nodes and node of longitudinal beam*
- *Influencing higher relevant modes*

Spring No. 3

- *Rather a smeared stiffness property than a spring*
- *Flexural stiffness about local z-Axis of longitudinal beams (i.e. also global Z-Axis)*
- *Influencing higher modes, is needed to achieve transversal flexible behavior*

Spring No. 4

- *Rotational spring about global Z-axis*
- *Connecting longitudinal beam and transversal rigid T-type beam nodes. Influencing higher modes, is needed for the transversal flexible behavior to distribute transversal deflection from the higher displacement value at the middle to both ends in the longitudinal dimension, or in other words to form a more smooth transition from the middle bulge to the outer frames (see e.g. Figure 2: 1st transversal mode in y-dir.)*

Table 1: Spring characteristics used in simplified beam model.

The final spring values which yielded the best match of the dynamic properties are given in Table 2. Whereby the rotational springs No. 1, 2 and 4 can be specified directly, the flexural stiffness of the longitudinal beams (spring No. 3) is achieved by defining a cross section with dimensions of 70 x 400 cm and an elastic modulus of 21000 kN/cm².

Spring No.	Label	Value	Units
1	$K_{1,\phi}$	610 000	kNm/rad
2	$K_{2,\phi}$	5 500	kNm/rad
3	$K_{3,EI}$	24 010 000	kNm²
4	$K_{4,\phi}$	10 000 000	kNm/rad

Table 2: Spring parameters used for the simplified model.

In the following the achieved match of dynamic properties between the simplified beam model and the full structure model is shown. Modal frequencies of the first five modes are shown in Table 3. Effective modal masses in both horiziontal directions are listed in Table 4. The total mass of the system is 27 400 t. Corresponding modal shapes of the simplified and the full complex model are shown in Figure 6 to Figure 10 for comparison. It can be stated that for the most relevant modes no. 1, 2 and 4, the dynamic properties of the complex model are well represented with the simplified beam model.

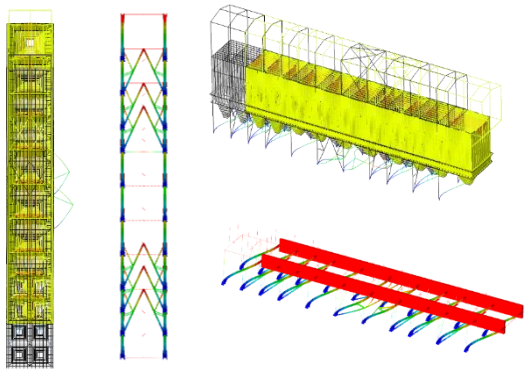

Figure 6: 1st global transversal mode (Mode 1).

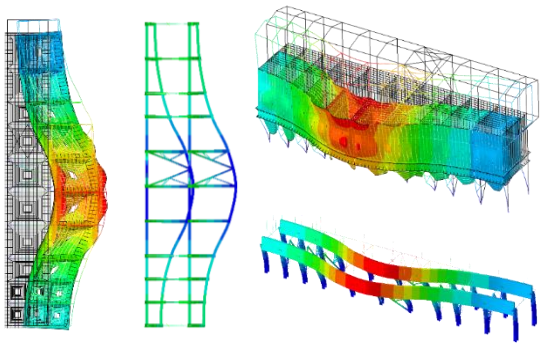

Figure 7: 1st global transversal mode (Mode 2).

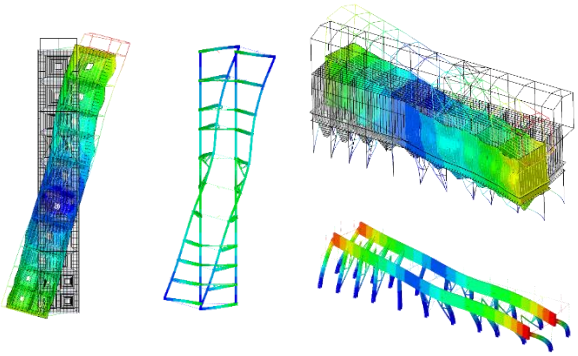

Figure 8: 1st global torsional mode (Mode 3).

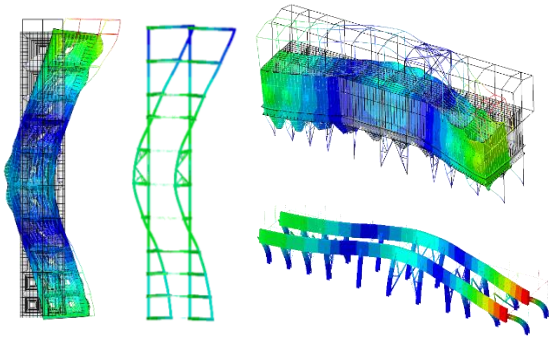

Figure 9: 2nd global transversal mode (Mode 4).

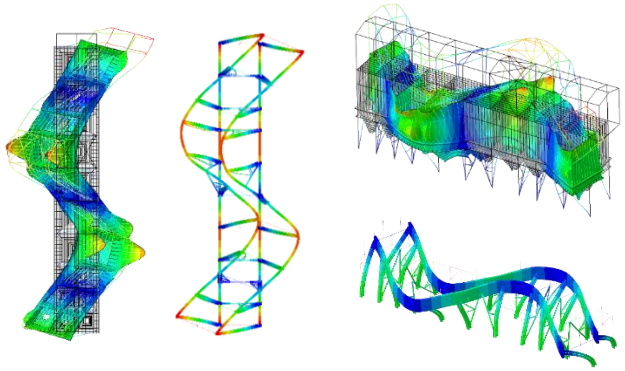

Figure 10: 3rd global transversal mode (Mode 5).

Mode No.	Modal period [s]		Ratio simplified / complex
	Complex model	Simplified model	
1	1.69	1.69	100%
2	1.24	1.24	100%
3	0.94	0.90	95%
4	0.76	0.72	95%
5	0.62	0.59	94%

Table 3: Comparison of modal periods of complex and simplified model.

Mode No.	Effective modal mass [t] Longitudinal direction		Ratio simpl. / complex	Mode No.	Effective modal mass [t] Transversal direction		Ratio simpl. / complex
	Complex model	Simplified model			Complex model	Simplified model	
1	27 299	27 285	100%	1	0	0	-
2	0	0	-	2	22 661	22 311	98%
3	0	0	-	3	3	4	133%
4	0	0	-	4	4 345	4 630	107%
5	0	0	-	5	72	185	257%

Table 4: Comparison of effective modal masses in longitudinal (left) and transversal (right) direction.

2.3 Seismic input

As input for the Incremental Dynamic Analyses recorded ground motion time histories have been used. A detailed description on the selection criteria and characteristics of the accelerograms can be found in [1]. Two sets with each eleven ground motions have been assembled: One set representative for low-medium seismicity regions and one representative for high seismicity regions (see Table 5 and 6 respectively). For the matching of the target spectrum the geometrical mean of both horizontal components has been used. Figure 1 and Figure 12 show the individual spectra of the selected accelerograms along with the mean and target spectrum. All three components – two horizontal and one vertical – were taken from the same recording. Also the vertical component has been applied in the simulations, because it might be critical due to the very high gravity loads present in the silo structures.

For the incremental dynamic analyses in total nine scale factors – different ones for the low-medium seismicity and high seismicity ground motion sets – have been used. The scale factors were chosen such that different return periods have been covered, starting from rather frequent earthquakes (return period of 60 years) to extreme rare earthquakes (return period of 2475 years).

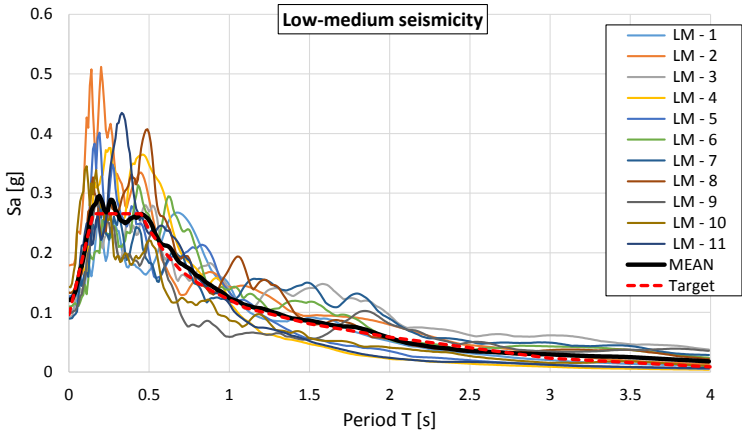

Figure 11: Low-medium seismicity acceleration spectra

Label	Event location	M_W	R [km]
LM - 1	Friuli	6	14
LM - 2	Friuli	6	9
LM - 3	Lazio Abruzzo	5.9	16
LM - 4	Umbria Marche	6	22
LM - 5	Tabas	7.3	68
LM - 6	Manjil	7.4	81
LM - 7	Komilion	5.4	15
LM - 8	Izmit	7.6	96
LM - 9	Izmit	5.8	25
LM - 10	Emilia	6	19
LM - 11	Christchurch	5.3	17

Table 5: Low-medium seismicity set

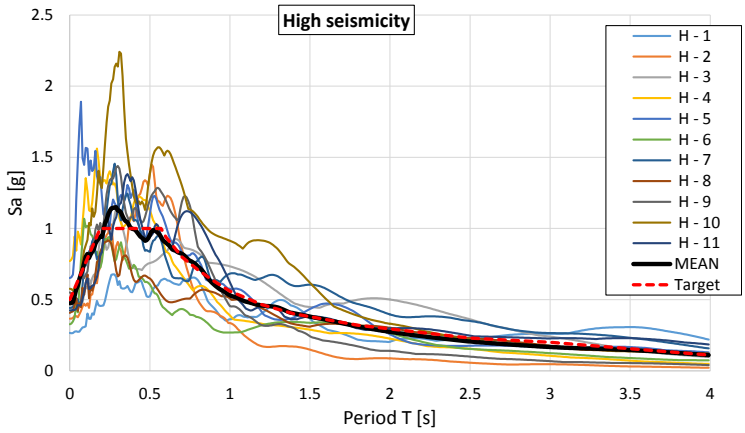

Figure 12: High seismicity acceleration spectra

Label	Event location	M_W	R [km]
H - 1	South Iceland	6.4	5
H - 2	Montenegro	6.9	25
H - 3	Erzincan	6.6	13
H - 4	Gazli	6.7	11
H - 5	Izmit	7.6	20
H - 6	South Iceland	6.5	5
H - 7	Duzce	7.1	5
H - 8	Darfield	7.1	18
H - 9	Imperial Valley	6.5	27
H - 10	Loma Prieta	6.9	7
H - 11	Northridge	6.7	20

Table 6: High seismicity set

3 SEISMIC PERFORMANCE OF AS-BUILT STRUCTURE

First the as-built structure has been subjected to all earthquake time histories and scale factors. The most important outcomes are discussed in the following sections separated for the low-medium and the high seismicity ground motion sets. In general all simulations have been conducted geometrically fully nonlinear (large displacement theory).

3.1 Low-medium seismicity ground motion set

The incremental dynamic analyses with the low-medium seismicity accelerograms showed no larger convergence problems. Figure 14 shows the displacement at the top of the supporting structure in longitudinal and transversal direction as function of peak ground acceleration PGA. At the lowest scale factors the structure behaved almost elastic. For lower scale factors braces buckled in compression and yielded in tension. For the highest scale factors strong yielding and buckling occurred in almost all braces. Also all columns yielded at their base. However, no failure of the structure occurred for all of the earthquakes even at the highest scale factor.

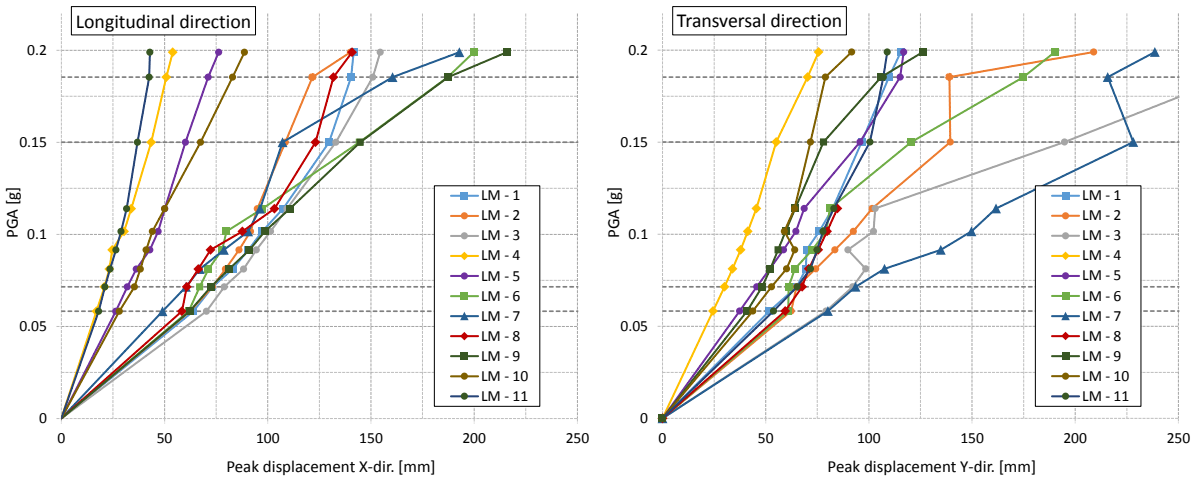

Figure 13: Low-medium seismicity IDA curves in longitudinal X- (left) and transversal Y-direction (right)

3.2 High seismicity ground motion set

As expected the high seismicity ground motion set provided much higher demands on the structure. Strong yielding patterns (yielding and buckling of braced frames, yielding of columns at base and top) occurred already for low scale factors. Figure 14 shows the corresponding IDA curves. At higher scale factors convergence difficulties occurred, thus, the IDA curves are not complete, as just fully completed simulations are shown in the diagram. The premature abortion of simulations mainly arrived due to collapse of the structure or excessive deformations of braces. The performance of the structure for each earthquake is summarized in Table 7.

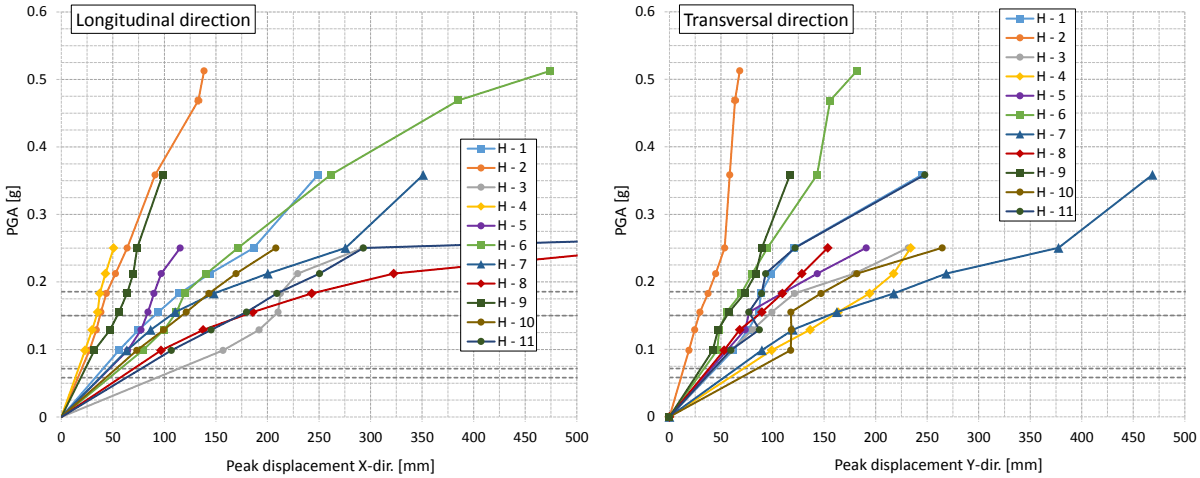

Figure 14: High seismicity IDA curves in longitudinal X- (left) and transversal Y-direction (right).

Ground motion	Comment
H – 1	Excessive deformation of one brace causes convergence problems
H – 2	Full range of scale factors finished
H – 3	Global sidesway collapse in longitudinal direction
H – 4	Five braces exhibit excessive deformations leading to abortion of the simulation
H – 5	Excessive deformation of one brace causes convergence problems
H – 6	Full range of scale factors finished
H – 7	Three braces deform extensively and cause abortion of the simulation
H – 8	Global sidesway collapse in longitudinal direction
H – 9	Five braces exhibit excessive deformations leading to abortion of the simulation
H – 10	Three braces deform extensively and cause abortion of the simulation
H – 11	Global sidesway collapse in longitudinal direction

Table 7: Comments on performance of IDA simulations.

Three of eleven earthquakes triggered a clear sides-way collapse in longitudinal direction. This highlights one of the weakness of the structural layout. Whereby in the transversal direction the structure is stiffened by in total 6 braced frames just two braced frames exist in the longitudinal direction. Obviously wind forces have governed the brace layout, where due to a much larger influence area the resulting lateral force is high in transversal direction and is relatively low in longitudinal direction. The evolution of the typical sides-way collapse is illustrated in Figure 15. Yielding at the bottom of columns is followed by yielding and buckling of the two frame braces and yielding of column tops and finally the structure collapses due to P-Delta-effects. In six of the eleven earthquakes the simulation aborted prematurely either due to torsional buckling of the columns, which was triggered by out of plane displacements of the bracing frames, or due to or excessive deformations of the braces. See Figure 16 for an impression. Two of the eleven earthquakes finished without signs of global collapse.

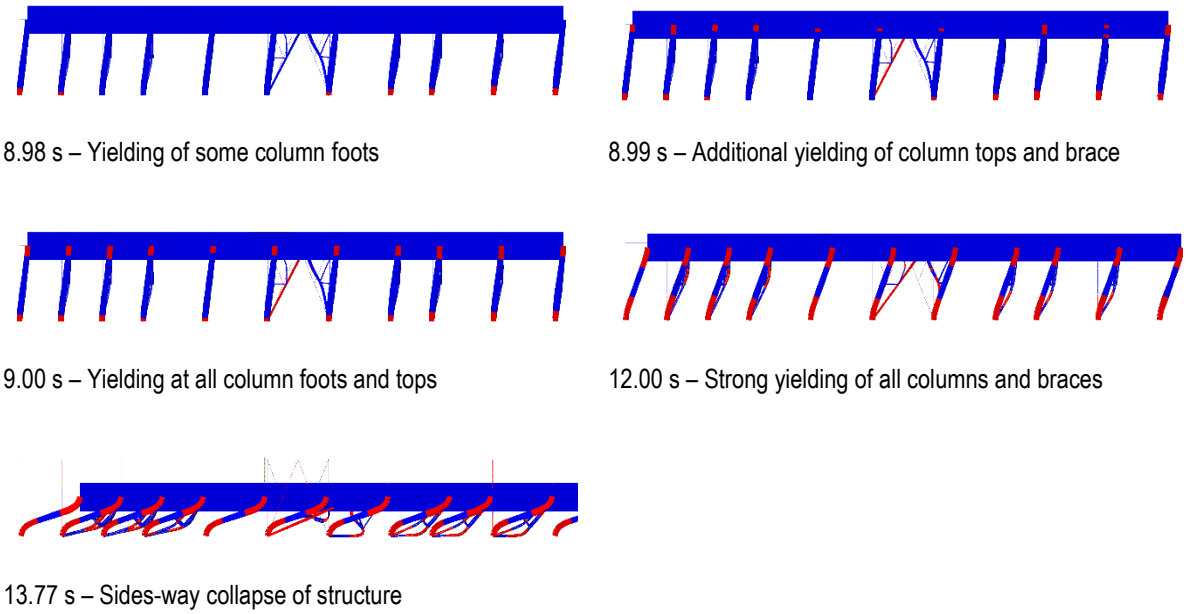

Figure 15: Chronological evolution of sides-way collapse which occurred for earthquakes no. 3, 8 and 11, deformation scale factor 1.

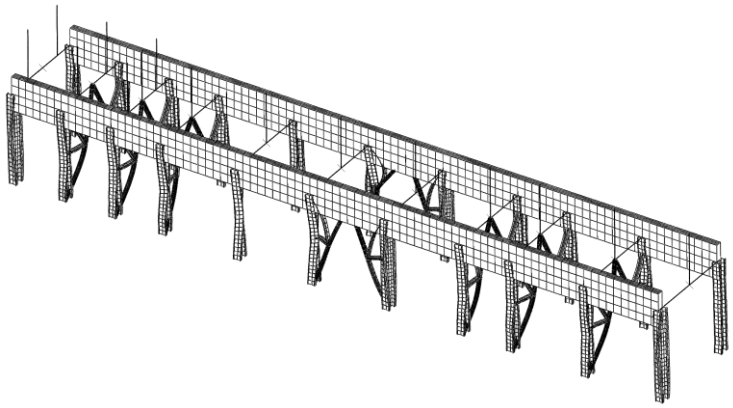

Figure 16: Failure mode torsional buckling of columns triggered by out of plane displacement of brace layer, deformation scale factor 1.

4 SEISMIC RETROFITTING STRATEGIES

The principle of torsional yielding of steel rods shall be used in the phenomenologically modelled applied seismic devices. Such devices exist for example as Multi-Directional Hysteretic Devices explained in [2]. After a short introduction into the hysteretic behavior of such devices two generic retrofitting strategies will be investigated: As first retrofitting strategy a torsional damping device is applied inside the braced frames and as second strategy it is used as base isolation layer inserted between ground and structure at each column base.

4.1 Torsional energy dissipation devices

The seismic device hysteresis loop is shown in Figure 17. The most important aspects are the beneficial stiffening effect for higher displacements and the isotropic hardening of the yield surface. The stiffening effect is accomplished by the kinematics of the system. Two numerical

models have been tested to simulate the hysteresis loop of the seismic device, which are schematically sketched in Figure 18. Basically a plastic spring is put in parallel with either contact elements which are themselves put in series with additional elastic springs or just one multilinear elastic spring. The plastic spring accounts for the yielding and the isotropic hardening effect, which is accomplished by choosing appropriate isotropic hardening parameters. The stiffening effect is modelled by the contact element and elastic spring series or the multilinear elastic spring. The more contact spring combinations or data points for the multilinear spring are used, the more smooth the post yielding curve will look like. Both systems are able to reproduce the same hysteresis curve shown in Figure 17. The fit between test and simulation seems to be acceptable taking into account the simplified modelling approach. Although both modelling approaches yield the same results, the second one proves to be more robust and computational efficient, mainly due to the lack of highly discontinuous contact elements. In general, no convergence issues could be observed for the second approach and runtime of simulations compared to the unretrofitted simulations just slightly increased.

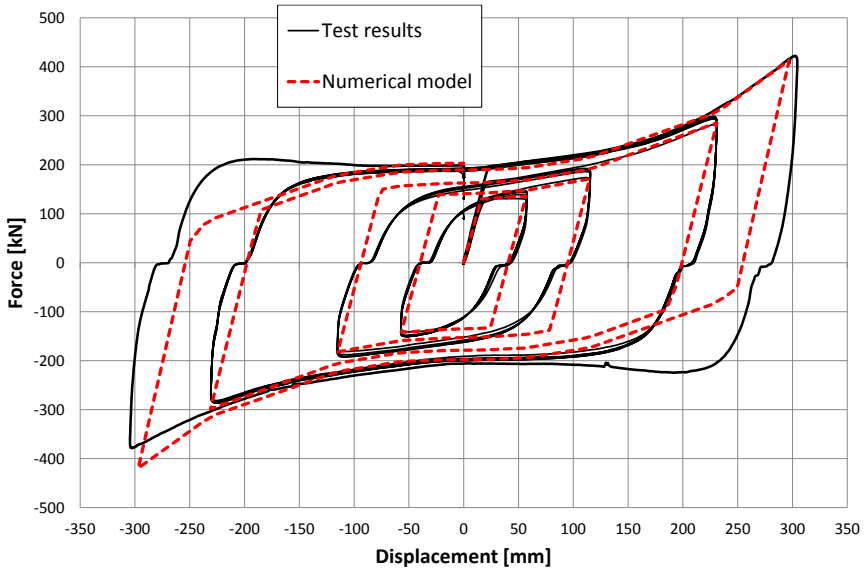

Figure 17: Typical force displacement hysteresis for torsional devices obtained by experimental tests (prototype with one default yielding core) [provided by MAURER SÖHNE] and results of numerical representation.

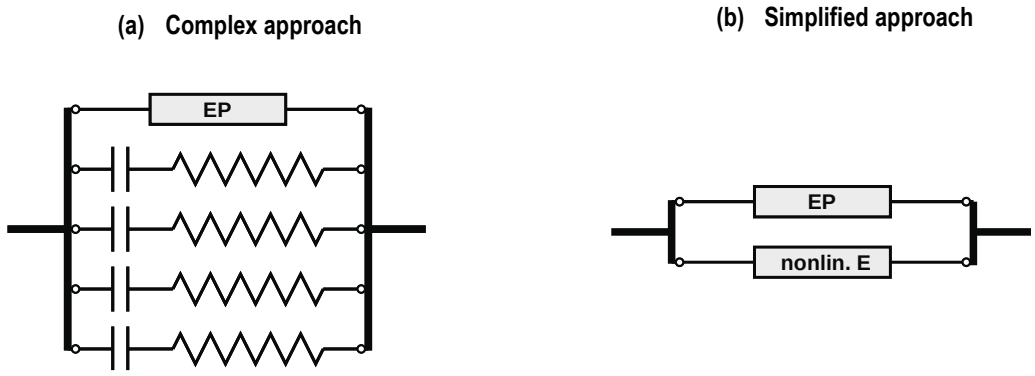

Figure 18: Rheological models to simulate the hysteresis of the torsional seismic device: approach with contact elements (a) and approach with multilinear elastic spring (b).

4.2 Retrofitting approach I: Energy dissipation in braced frames

The torsional hysteretic device inserted between an added V-brace and the bottom of the superstructure has been modelled phenomenologically by inserting the rheological model discussed aboved at this spot. Figure 19 ashows a schematical sketch of this approach. The diagonals in the V-brace need to act both in tension as well as in compression. In order to prevent buckling the braces need to be sufficiently squat. In the simulations the flexibility of the V-brace was assumed to be negligible compared to the flexibility of the device and thus was modelled as rigid.

The analysis conducted is considered as demand identification, i.e. how much torsional rods of the characteristic shown in Figure 17 are needed to improve the structural response significantly. The main purpose was to prevent the global sides-way collapse which happened in three of eleven earthquakes for the original structure. By an iterative procedure it was find out that in total 48 of torsional yield cores used for the whole structure would achieve this aim. Using thicker yielding cores the total amount would decrease accordingly. Number of cores per bay and number of bays need to be adapted to constructive and practicability boundary conditions. For example Figure 19 shows a device equipped with four yielding cores.

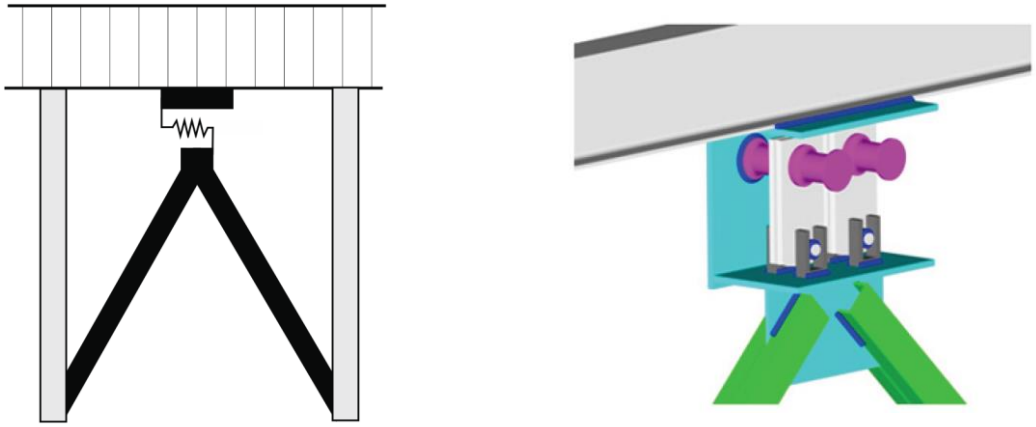

Figure 19: Schematical drawing of applied torsional hysteretic device into frame bay (left) and detail of prototype torsional device equipped with four yielding cores (right, [3]).

The applied retrofitting strategy adds additional amount of damping to the structure but also increases the stiffness of the longitudinal sway mode. Thus, this mode shifts to a higher acceleration value in the response spectrum which might cause an increase in demands. The modal periods of the structure after application of one of the discussed retrofitting strategies are listed in Table 8 while the mode numbering is in accordance to the mode shapes shown in Figure 6 to Figure 10.

	Modal period T [s]		
	As-built	Retrofit I	Retrofit II
Mode 1	1.69	1.18 (*70%*)	2.50 (*150%*)
Mode 2	1.24	1.24 (*100%*)	2.09 (*169%*)
Mode 3	0.90	0.89 (*100%*)	1.71 (*190%*)
Mode 4	0.72	0.72 (*100%*)	0.89 (*124%*)
Mode 5	0.59	0.59 (*100%*)	0.65 (*110%*)

Table 8: Modal periods after application of retrofitting.

A comparison between the as-built structural performance and the retrofitted structure shows that with the determined amount of steel cores the failure mode of sides-way collapse could be completely excluded. Figure 20 shows the corresponding IDA curves. Whereby for the H – 8 peak displacement are still high – but without collapse taking place – the peak displacement for the other two earthquakes H – 3 and H – 11 are siginificantly reduced. Figure 21 shows a comparison for the no failure earthquakes. In general peak displacements are in most cases equal or lower, especially at the highest peak ground acceleration yielding a reduction of at least 20% can be obtained. The same holds true for the other earthquakes. Due to the period shift in some cases peak displacements may also be higher. The ratio of peak displacements of as-built to retrofitted behaviour is shown in Figure 22. Otherwise than the sides-way collapse failure mode, the other premature abortion reasons due to excessive brace deformations still occur. The behavior in transversal direction was essential the same, because the braced bays act in general just in longitudinal direction.

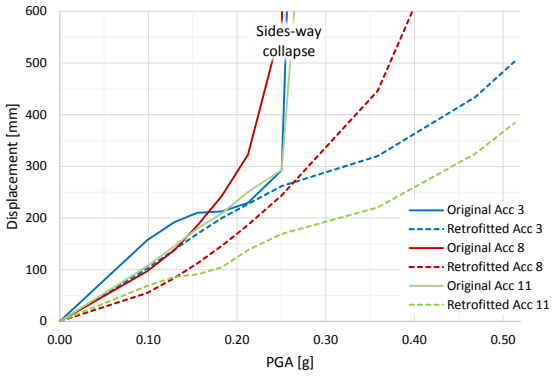

Figure 20: Comparison between as-built and retrofitted structure performance for sides-way collapse triggering earthquakes.

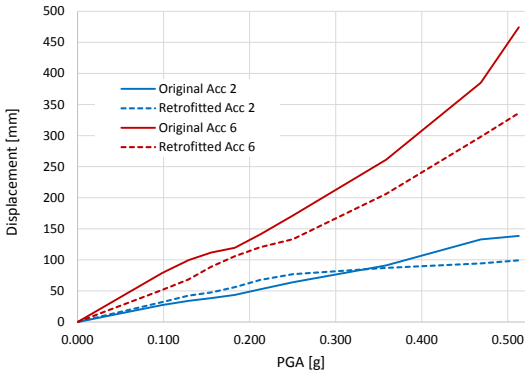

Figure 21: Comparison between as-built and retrofitted structure performance for no global failure earthquakes.

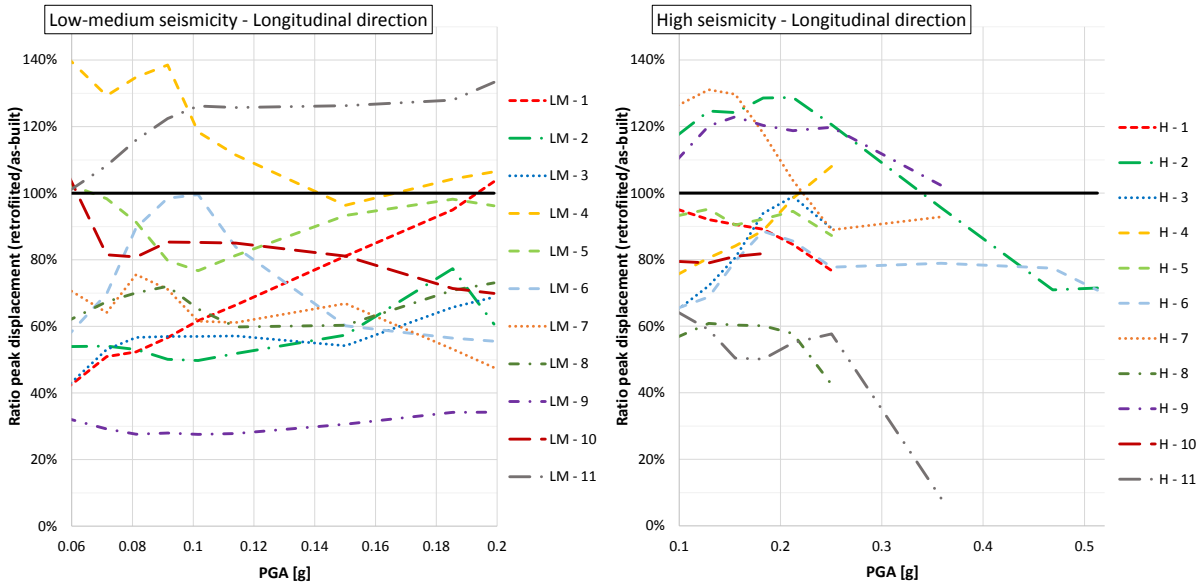

Figure 22: Ratio of as-built structure peak displacements in longitudinal X-direction to that ones of retrofitted structure for low to medium (left) and high (right) seismicity ground motion sets.

4.3 Retrofitting Approach II: Base isolation with torsional hysteretic dampers

For the base isolation retrofitting strategy every column base has been separated from ground in both horizontal directions and the numerical model of the seismic device has been applied in both orthogonal directions. The hysteretic curve looks similar as that one shown in Figure 17 with the modification that the initial stiffness has been tuned in such a way to yield an increase in the period in longitudinal direction of 50%, which yields a fundamental period of 2.5 seconds. The impact on the other modes is listed in Table 8.

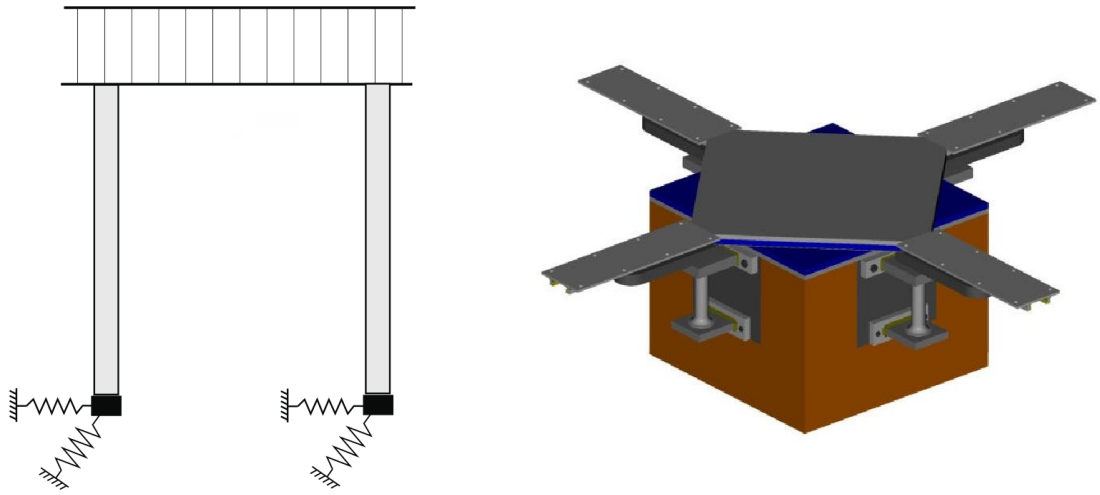

Figure 23: Schematical drawing of applied torsional hysteretic device as base isolation (left) and detail of multi-directional torsional hysteretic device (right, according to [4])

The retrofitted structure performed very well, as also for the high seismicity conditions no structural failure occurred. Figure 24 shows the relation between the peak displacements in the structure for both low to medium seismicity and high seismicity ground motions in longitudinal and transversal direction. For the retrofitted structure these are the displacements related to the top of the seismic device, which itself has to perform additional displacements. At higher peak ground accelerations for some high seismicity earthquakes the ratio was set to zero, in these cases when the as-built structure did not converge due to failure or excessive deformations. Otherwise the ratio is computed just for fully completed simulations. As can be seen for all of the ground motions deformation demand in the structure is efficiently decreased, for some even to 20% of its initial values.

The relative displacements inside the seismic device have been evaluated and are listed in Table 9. Demands have to be lower than capacity of the seismic device, otherwise the obtained results are not achievable in reality. For all of the low to medium seismicity earthquakes the displacements are well within the range of feasible displacements as can be compared to Figure 17. For some of the higher seismicity ground motions the demand on the seismic device is quite high for peak ground accelerations in the range of 0.25g to 0.5g. However, up to a peak ground acceleration of 0.2 g also for all of the high seismicity ground motions the peak relative displacement is below 400 mm, which is a well achievable capacity for this type of device.

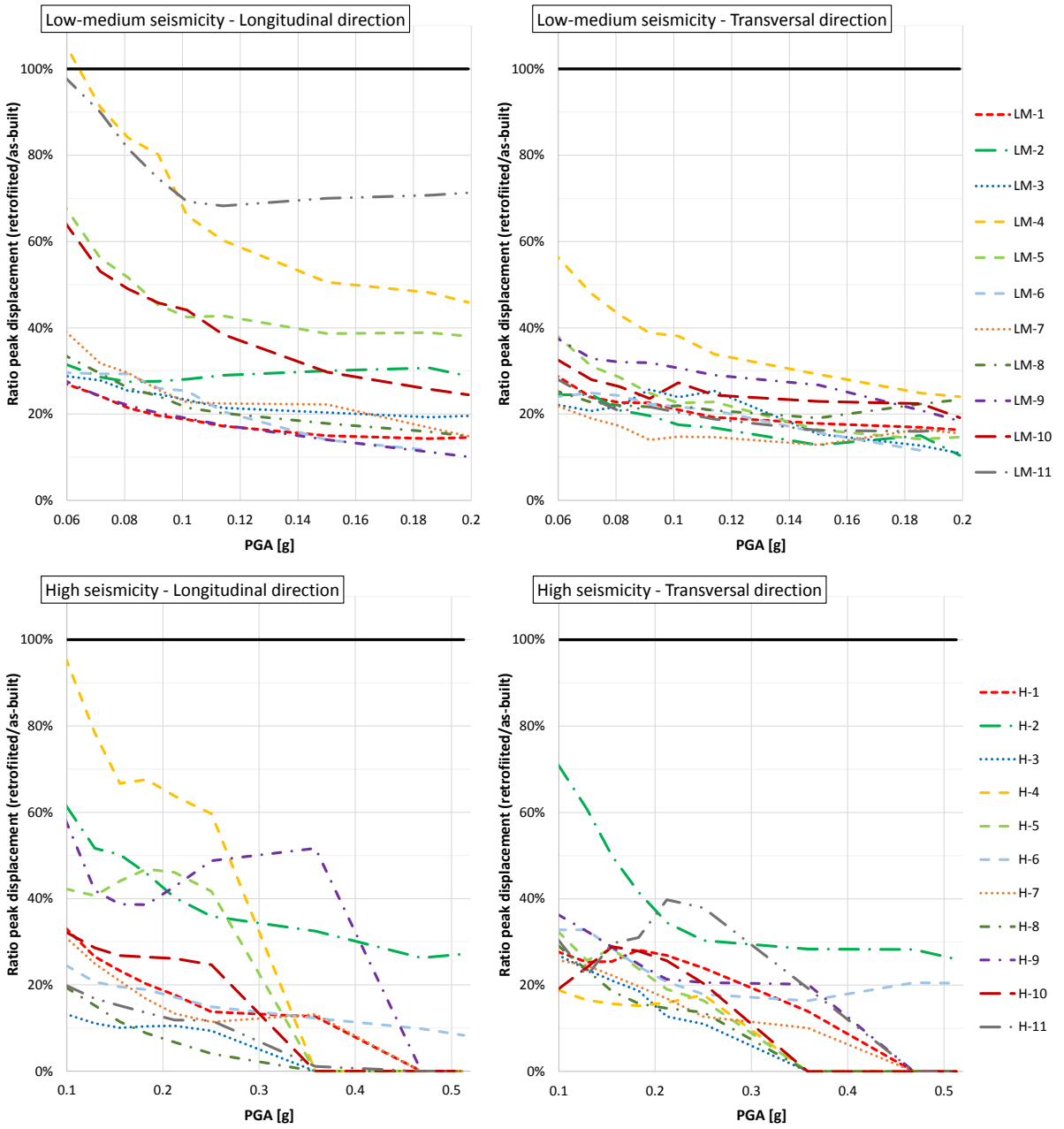

Figure 24: Ratio of structural relative displacements between as-built structure and retrofitted structure.

	Peak relative displacements in seismic device u_{rel} [mm]										
LM-	**1**	**2**	**3**	**4**	**5**	**6**	**7**	**8**	**9**	**10**	**11**
X	91	150	141	53	95	143	150	216	205	109	49
Y	122	163	240	55	53	91	263	156	138	97	85
H-	**1**	**2**	**3**	**4**	**5**	**6**	**7**	**8**	**9**	**10**	**11**
X	364	163	431	128	345	512	665	1212	258	320	1282
Y	375	50	346	589	659	605	966	347	257	812	1016

Table 9: Peak displacements in seismic device at highest scale factor for low to medium (LM) seismicity and high (H) seismicity ground motions in longitudinal (X-) and transversal (Y-) direction.

5 CONCLUSIONS

This paper has shown how a complex finite element model may be transferred into a simplified model to save computational effort and storage need by maintaining its most important dynamic properties. Such simplifications are needed to be able to handle the huge amount of seismic analyses which need to be conducted for the purpose of Incremental Dynamic Analyses.

With this simplified model Incremental Dynamic Analyses have been conducted to assess on the current performance. Further on, two retrofitting strategies have been applied in a generic way: Additional stiffness and energy dissipation with additional bracings equipped with seismic devices and a base isolation layer between column footings and ground. The simple modelling of the characteristic hysteresis by help of a rheological model has been discussed. While the first retrofitting strategy showed to be effective in preventing the global sides-way collapse failure mode, the second one moreover could drastically reduce displacement demands in all the earthquakes.

In these analyses the seismic devices have been applied in a generic way. In future the modelling strategies and used parameters for the seismic device will be investigated more deeply regarding practicability and economic issues. Moreover, further limit states have to be incorporated as solely the displacement or occurrence of global failure. The demand on the seismic device has to be compared in detail with its realistic capacity.

6 ACKNOWLEDGMENTS

The research leading to these results has received funding from the European Union's Research Fund for Coal and Steel (RFCS) research programme under grant agreement n° RFSR-CT-2013-00019, project "PROINDUSTRY – Seismic PROtection of INDUSTRial plants by enhanced steel based sYstems".

The test results of the prototype of the torsional seismic device have been provided by Maurer Söhne Engineering GmbH & Co. KG, which is greatly acknowledged.

REFERENCES

[1] PROINDUSTRY, Seismic PROtection of INDUSTRial plants by enhanced steel based sYstems, Mid-Term Report, Grant Agreement Number: RFSR-CT-2013-00019, 2015.

[2] A. Salem Milani, TORSIONAL HYSTERETIC DAMPER FOR SEISMIC PROTECTION OF STRUCTURES, PhD Dissertation, Middle East Technical University, Turkey, May 2014.

[3] MULTI-DIRECTIONAL TORSIONAL HYSTERETIC DAMPER WITH RECENTERING CAPABILITY (MRSD) – A New Anti-Seismic Device for seismic protection of buildings and bridges, http://www.metu.edu.tr/announcement/profdr-murat-diclelis-seismic-damper, 10/10/2013.

[4] M. Dicleli; A. Salem Milani, MARTI and MRSD: Newly Developed Isolation-Damping Devices with Adaptive Hardening for Seismic Protection of Structures, International Journal of Civil, Environmental, Structural, Construction and Architectural Engineering, Vol: 9, No: 6, 2015.

ECCOMAS Congress 2016
VII European Congress on Computational Methods in Applied Sciences and Engineering
M. Papadrakakis, V. Papadopoulos, G. Stefanou, V. Plevris (eds.)
Crete Island, Greece, 5–10 June 2016

SEISMIC RETROFIT OF INDUSTRIAL SILOS BY MEANS OF BASE ISOLATION DEVICES

Alper Kanyilmaz[1], **Carlo Andrea Castiglioni**[1, 2], **and Julia Georgi**[2]

[1]Politecnico di Milano

Department of Architecture, Built environment and Construction Engineering

Via Ponzio 31, Milano-Italy

alper.kanyilmaz@polimi.it, carlo.castiglioni@polimi.it

[2]Neapolis University in Cyprus

School of Architecture, Land & Environmental Sciences

Zdanaes Ave. Paphos 8042-Cyprus

j.georgi@nup.ac.cy

Keywords: Silos, seismic retrofit, seismic isolation, curved surface sliders

Abstract. *Silos are industrial facilities used for storing a huge range of different materials. In the last decades, many silos were damaged by natural events, among which the seismic events are the most significant. Indeed many plants are located in territories in which seismic risk is not negligible. Furthermore, most of these plants have been designed, and built before the latest updates of the seismic design codes took place, and most of them are prone to earthquakes. In this study, seismic behaviour of an existing industrial steel silo system in Italy has been investigated, and a retrofit solution has been proposed making use of seismic isolation technology. Curved surface single sliding pendulums have been designed as a base isolation retrofitting solution. Incremental dynamic analysis method has been used in order to evaluate the seismic performance of both the non-isolated and isolated cases. Structural benefits of the seismic isolation retrofitting solution has been quantified in terms of inelastic deformations, base shear, floor drifts, isolator displacements, and residual drifts, and comparisons between the original and retofitted solutions are presented. The impact of vertical ground accelerations on the global behaivour of seismic isolated silos has been highlighted, which showed that a fully elastic superstructure behaviour can be achieved only when the vertical component of earthquake is not significant. Uplift has been investigated and stated as a limiting parameter for the design of seismically isolated silos. The study has been realized thanks to EU-RFCS research fund for PROINDUSTRY project [1].*

1 SILOS CASE STUDY

The case study is composed of three silos, elevated on a steel structure, constructed next to another 2 elevated silos. It's a silo system from SOLVAY Italy (Figure 1).

Figure 1 Case study

Main characteristics of the system are the following:

Internal radius of silos:	1.75 m
Total height of silos:	13.356 m
Thickness of silo body:	Changes along height from 12 to 8 mm.
Steel:	Fe360b
Silo content:	Sodium percarbonate
E =	210000 MPa
ν =	0,3
ϒsteel =	7850 kg/m3
ϒcontent =	1200 kg/m3 (sodium percarbonate)

Layout of the system can be seen in Figure 2. The stairs and connection structure between three silos are neglected for simplicity, since the rigidity and the mass of the silos probably will lead the global behaviour, without an important effect of the connecting structures and stairs.

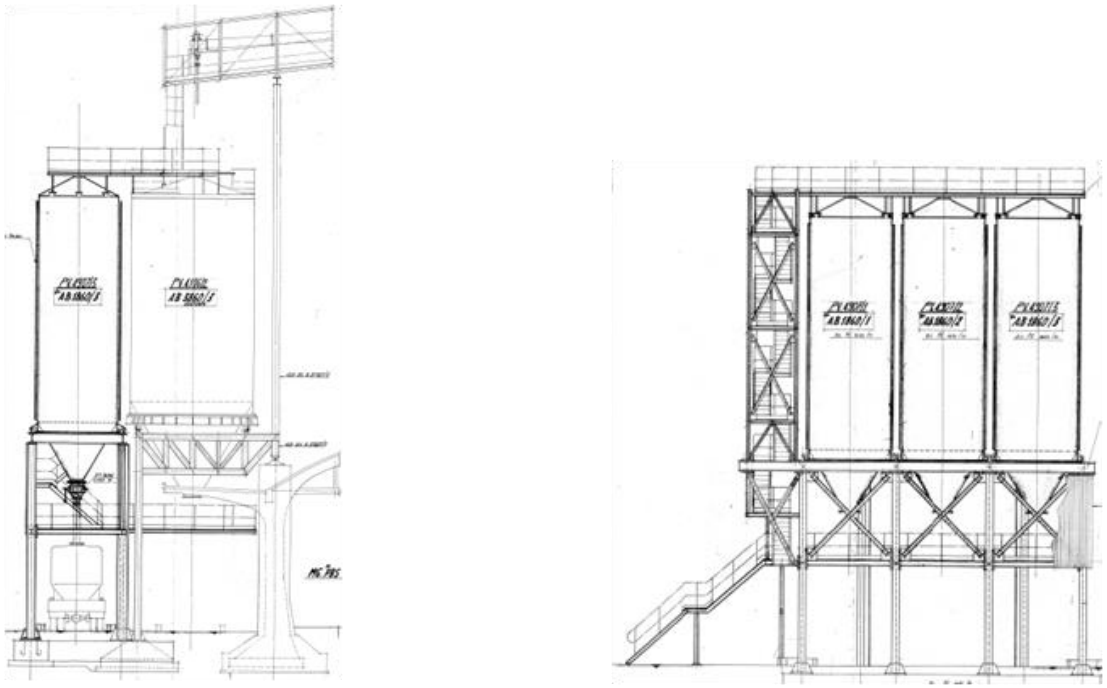

a. Transversal view b. Longitudinal view

Figure 2 System layout

The silos are connected to the support structure by means of stiffener plates (Figure 3). 24 stiffener plates are welded to the silo wall, equally spaced around its perimeter. These stiffener plates are then welded to the ring beam with 150x30 mm cross section. The ring beam is bolted to the support structure beams.

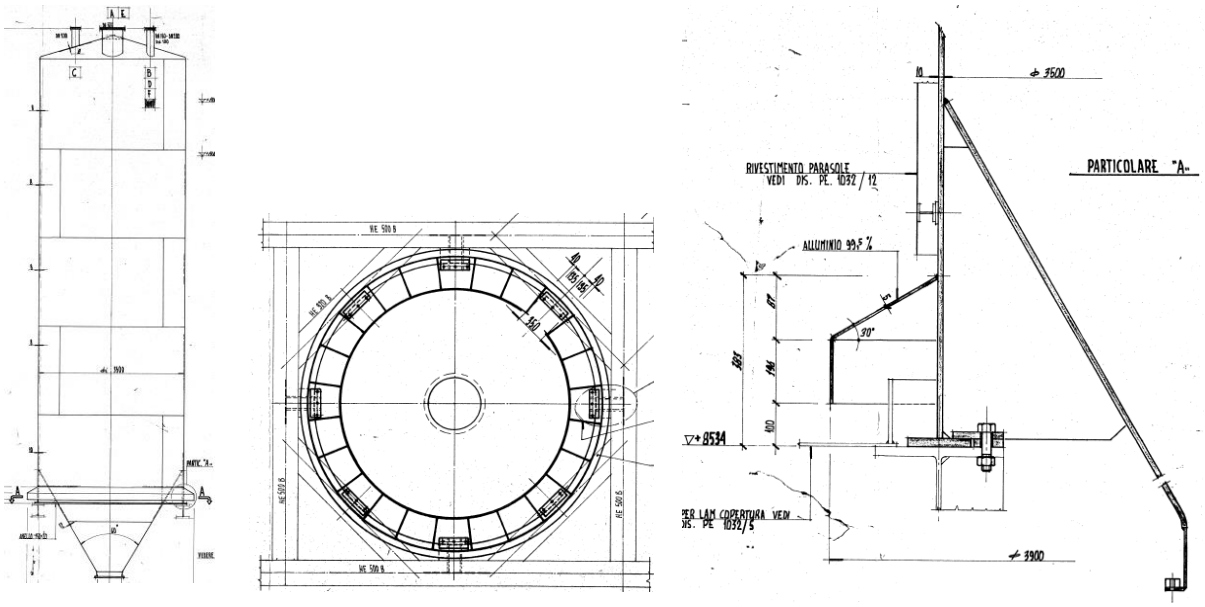

Figure 3 Ring beam-silo connection detail

Three main levels are considered in the numerical model:

Level +0 mm: The columns are fixed at this level, which corresponds to "-650.00 mm" level of the drawings (Figure 4.a)

Level +4850 mm: First beam level (Figure 4.c)

Level +8934 mm: Second beam level (Figure 4.d)

Level +20580 mm: Top point of silos (Figure 4.b)

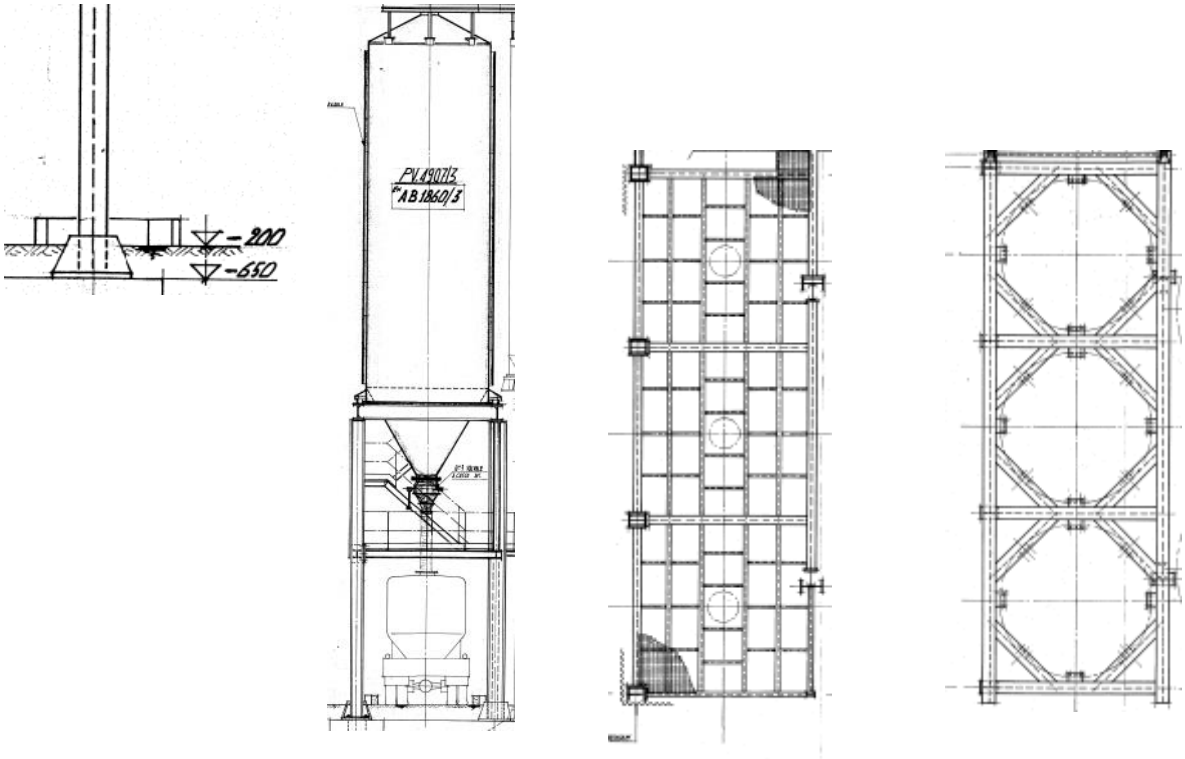

a. Ground level b. Section view c. +4850 mm plan view d. +8934 mm plan view

Figure 4 Different levels of the system

The supporting structure is an asymmetric steel frame braced only in longitudinal direction, with different bracing layouts in two sides (Figure 5).

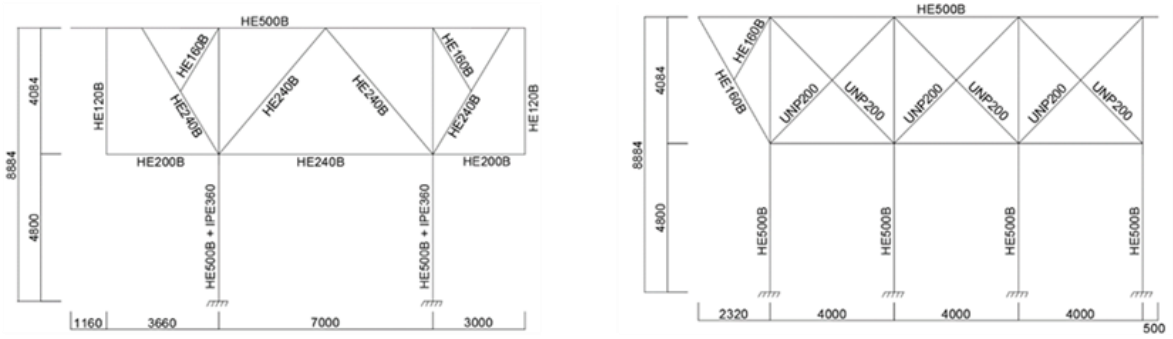

a. V-braced side b. X-braced side

Figure 5 Two sides of the structure

2 NUMERICAL MODEL

Numerical model is composed of silo bodies made of shell elements, steel structure made of beam elements formulated by fiber-based distributed plasticity approach [2], steel plate elements and rigid links that connect silo bodies and steel structure. Bracing elements are given initial imperfections according to EC3, as shown in Table 1.

S235 Steel	e_0 [mm]
HE240B [m]	35,9
HE160B [m]	15,9
HE240B [m]	16,0
UPN200 [m]	19,1

Table 1 Initial imperfections for bracing elements

The supporting structure has different bracing configurations in two sides of the frame (Figure 6.a.b). Lumped dynamic masses simulate the silo content, distributed at 7 levels inside silo, connected to silo walls by rigid links (Figure 6.c).

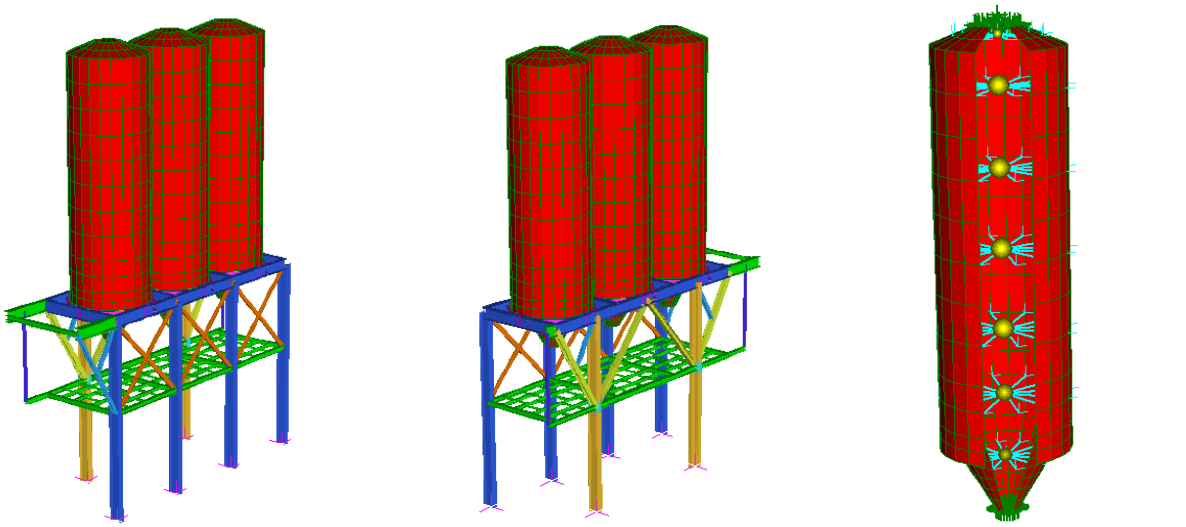

a. Model view 1 (X-braced side) b. Model view 2 (V-braced side) c. Lumped masses

Figure 6 Numerical model

The connection between HE500B longitudinal beams and silo are simulated with rigid links in the model. The connection between silo and ring beam is composed of 24 steel plates, which are simulated with shell elements in the model.

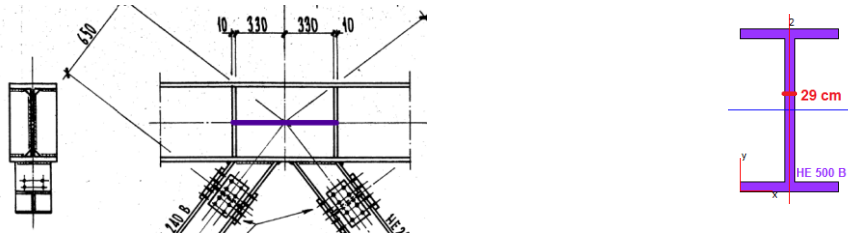

Figure 7 Reinforcement of the joints

As shown in Figure 7, the reinforcements of nodes are simulated by an ideal section with a doubled thickness of the core between the two reinforcement plates: stiffening the joint in this way, its behaviour is almost the same that the real one with the stiffening due only to the two reinforcement plates. The main areas where the joints are stiffened are contact points between the silos and the frame, and the joint between the two composite columns HE500B+IPE360 and the beams at the first floor.

Total mass of the system is 453,9 tons with following components:

Silo content: 391,1 tons

Silo body steel weight: 31,37 tons

Structural steel: 31,43 tons

Stress-strain relationship of the steel material has been defined with the following parameters:

Yield strength fy = 235 MPa
Ultimate strength fu = 360 MPa
Kinematic strain hardening: 1 %
Ultimate strain = 0.06

In Table 2 Modal analysis results, modal analysis results are reported. Mode shapes are shown in Figure 8 Mode shapes.

	Period	Mass participation
1st global mode in y direction (transversal)	1.2 sec	97.96%
2nd global mode in x direction (longitudinal)	1.05 sec	90.177%
3rd global mode in z direction (vertical)	0.13 sec	95.541%
1st global torsional mode	0.84 sec	9.4%

Table 2 Modal analysis results

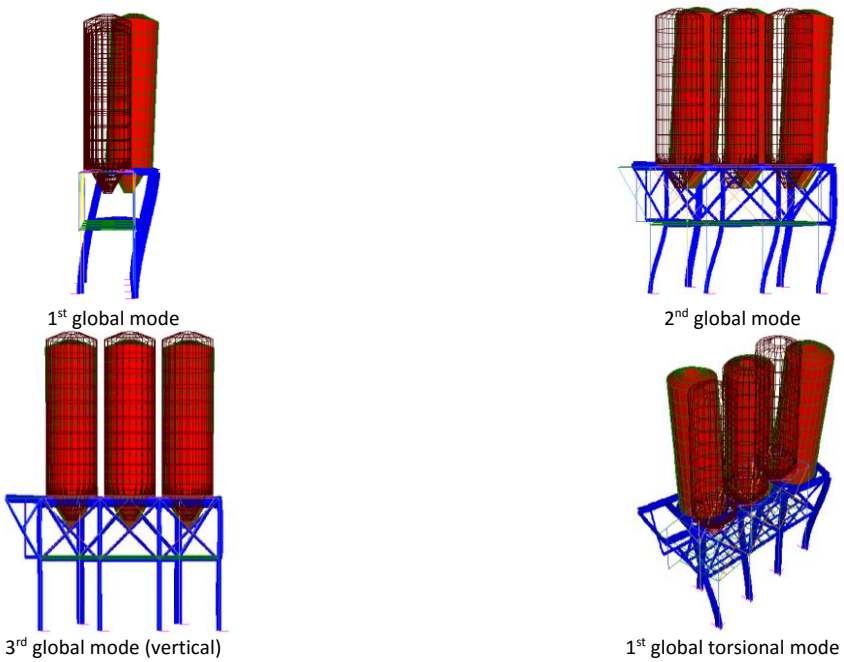

Figure 8 Mode shapes

3 FAILURE MECHANISMS OBSERVED IN THE ORIGINAL STRUCTURE

Results of Incremental Dynamic Analysis performed on the original structure have been presented in deliverable 2.3. In this report, only failure mechanisms of the original structure are presented, in order to provide the degree of improvement by means of seismic isolation devices.

In the original structure, yield takes places at column bases even in the analysis with low scale factors. Increasing the intensity, the plastic behaviour is redistributed to the column ends, bracings, and connections between silo and supporting structure (Figure 9).

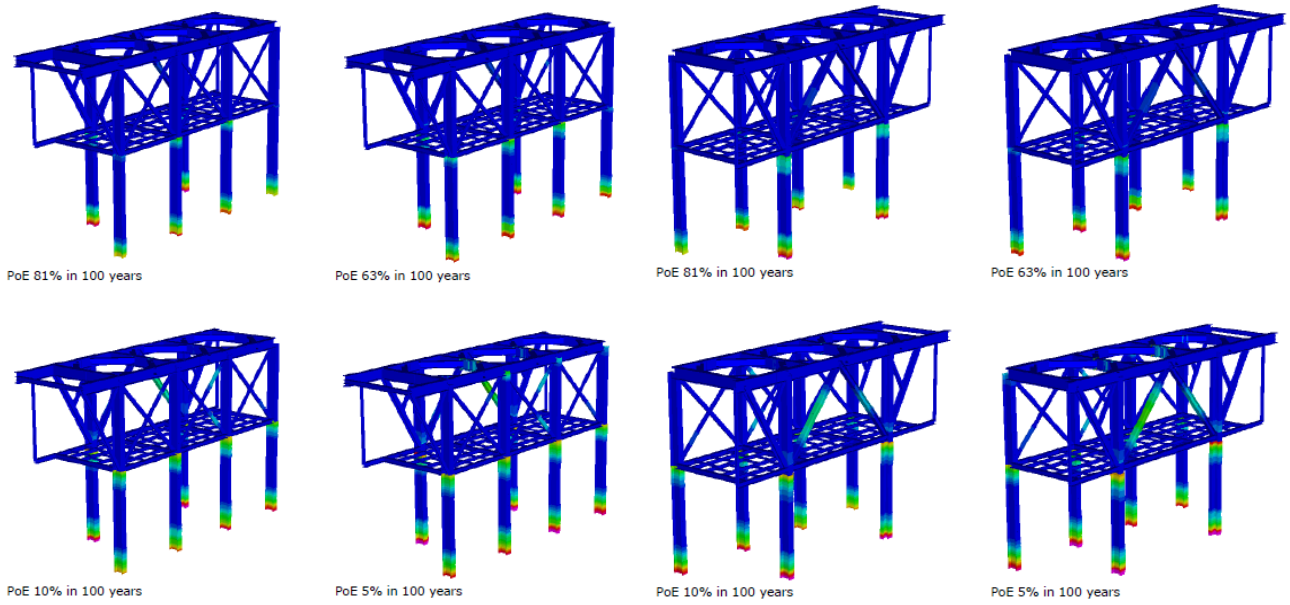

a. X-braced side b. V-braced side

Figure 9 Failure mechanisms of the original structure

Figure 10 shows that the numerically obtained failure mechanisms represent common structural damages that can be observed after strong earthquakes, such as Van Earthquake. Therefore, the seismic retrofitting solution should address these criticalities.

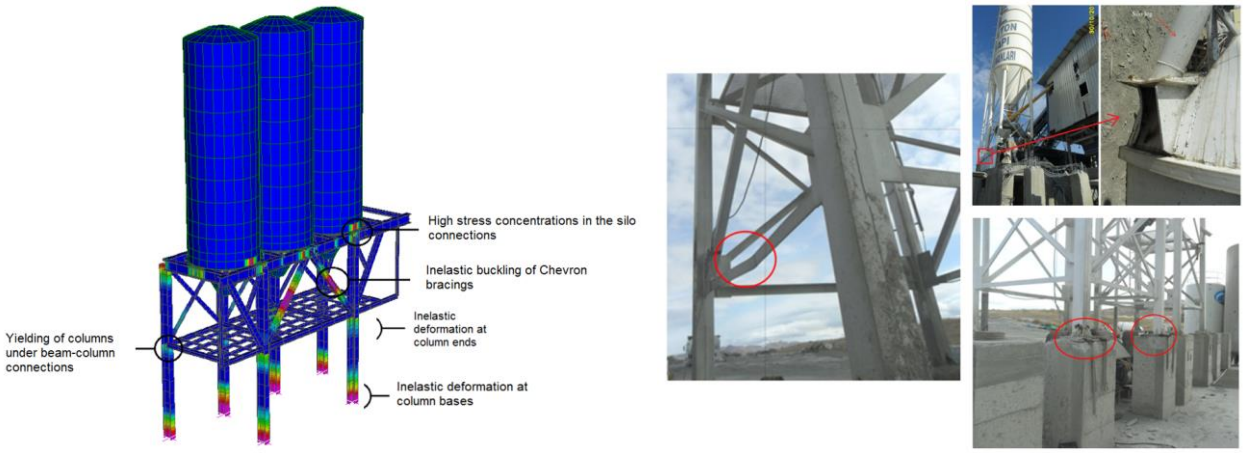

a. Failure mechanisms obtained from numerical analysis b. Damages observed on the support structure of elevated silos after Van Earthquake (2011)

Figure 10 Structural damages observed in Van Earthquake and numerically obtained failure mechanisms [3]

4 DESIGN OF SEISMIC ISOLATION SOLUTION

To retrofit the structure, a single sliding pendulum isolator has been designed in cooperation with project partner MAURER [4]. A static diagram of the forces acting in a sliding pendulum isolator used for the retrofitting is shown in Figure 11, while the force - displacement relationship is displayed in Figure 12.

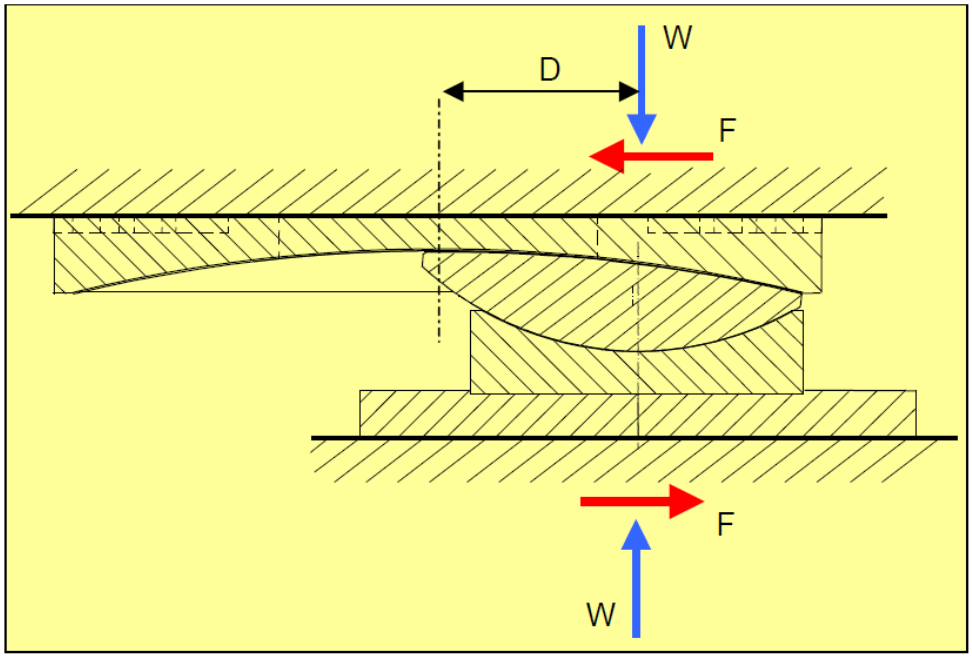

Figure 11 Forces acting in a sliding pendulum isolator

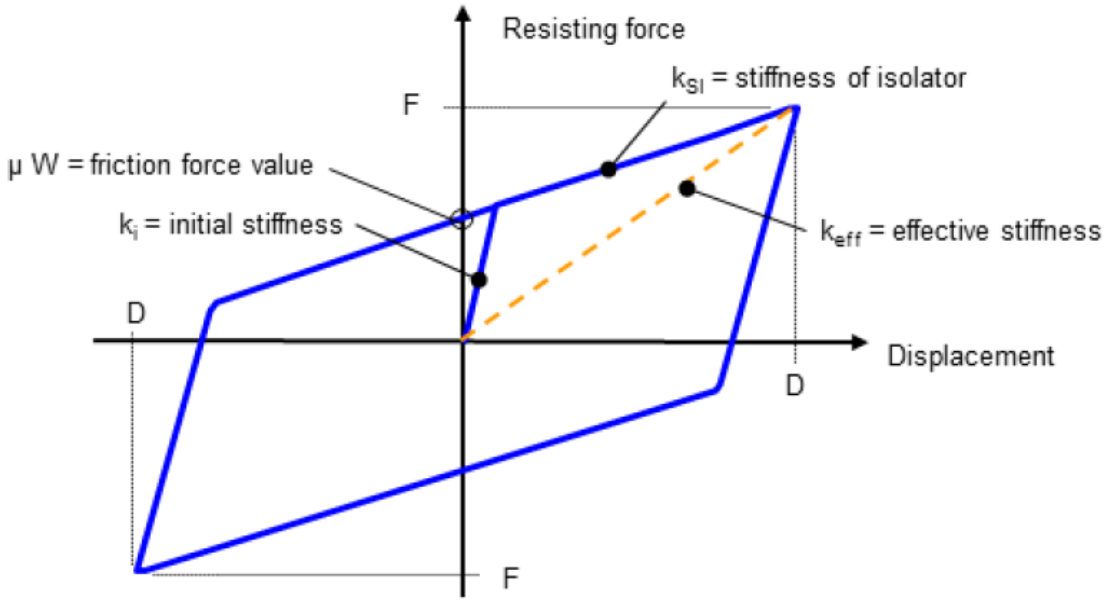

Figure 12 Force - displacement relationship in a sliding pendulum isolator

The equations governing the behaviour of a single isolators are the following:

Response period of the Isolator $$T = 2 \cdot \pi \cdot \sqrt{\frac{R}{g}} \cong 2 \cdot \sqrt{R}$$

Horizontal resisting force $$F = \frac{W}{R} \cdot d + \mu \cdot W \cdot sgn(d)$$

Horizontal stiffness due to the vertical load $$K_H = \frac{W}{R}$$

Effective stiffness $$K_{eff} = \frac{W}{R} + \frac{\mu \cdot W}{D}$$

Effective response period $$T_{eff} = 2 \cdot \pi \cdot \sqrt{\frac{R}{K_{eff} \cdot g}}$$

Damping due to friction $$\beta_{eff} = \frac{2}{\pi} \cdot \frac{\mu}{\frac{D}{R} + \mu}$$

Vertical displacement $$\delta_V \cong \frac{1}{2} \frac{D}{R^2}$$

Re-centering criterion $$\frac{D}{R} > \mu$$

Where W is the vertical load acting on the isolator agent, μ is the dynamic friction factor, d is the horizontal displacement, D is the horizontal speed and R is the radius of curvature. Note that the horizontal stiffness is linked to the load acting on the isolators: in an optimal design should therefore a different isolator should be adopted for each design vertical load.

In particular an isolator can be modelled by placing in parallel the two following elements, as shown in Figure 13.

1) Point Contact element: by means of an element of this type it is possible to define the friction factor and the vertical stiffness of the isolator. You can also define the yield surface of the isolator (rectangular or elliptical) and the friction model (elastic or plastic). Using an elliptical surface we ensure that the point at which the isolator begins to flow is the same in all directions, while the plastic friction model governs the hysteretic behaviour of the isolator.

2) Connection element: using an element of this type the stiffness of the isolator to sliding in horizontal directions can be defined.

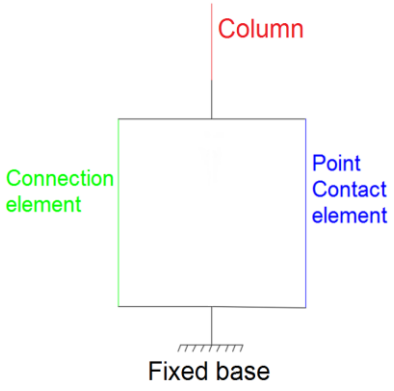

Figure 13 Modelling of the isolator in Straus7

It should be noticed that in Strand7 the length of the two elements of the isolator is not influencing the isolator behaviour, which is completely defined by the intrinsic properties of the

two elements. Assuming a fictitious length of the isolators equal to 500 mm, to each column of the previously modelled structure are added a Point Contact and a Connection element. The modelled isolators are shown by Strand7 as lines, whose lower point is stuck to the ground and whose upper end is connected to the column, as shown in Figure 14.

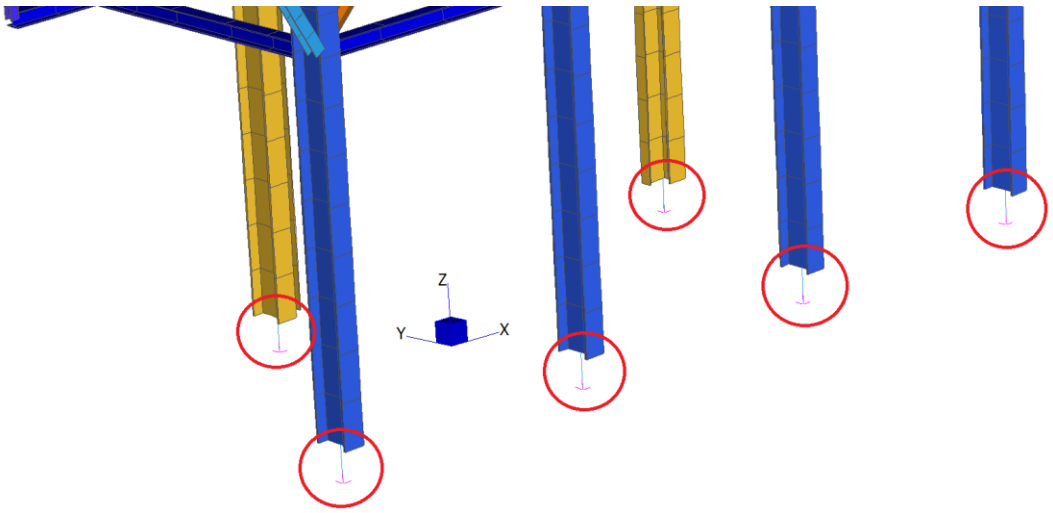

Figure 14 modelling the isolators in Straus7

To verify the correctness of the isolation system modelling, a non-linear static analysis was carried out, gradually applying a hypothetical design displacement of ± 300mm to the isolators as shown in Figure 15. A period of 4 seconds hence a sliding stiffness k_s equal to 0.187 kN / mm) and 4 % friction factor was assumed for all the isolators.

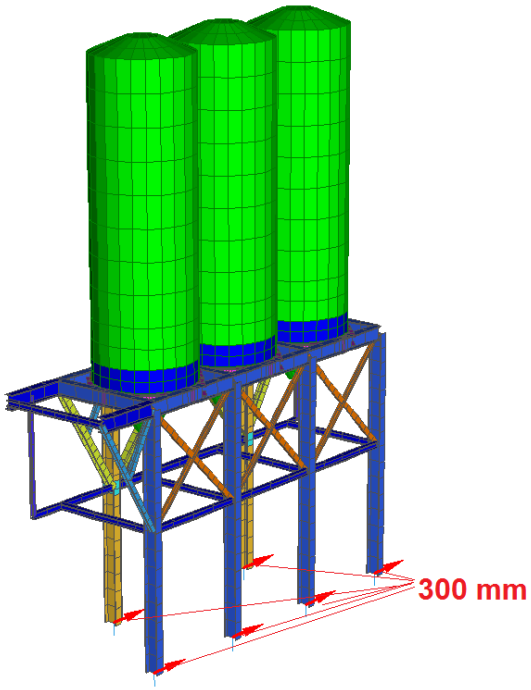

Figure 15 Displacements imposed to the isolators

With reference to the nodes numbering shown in Figure 3.50, let's consider, for example, the isolator in the node 5, on which acts a vertical load of 777.8 kN. The force-displacement response of the isolator in the node 5, obtained by the nonlinear static analysis is shown in Figure 16, where the displacements are dimensionless for a better understanding.

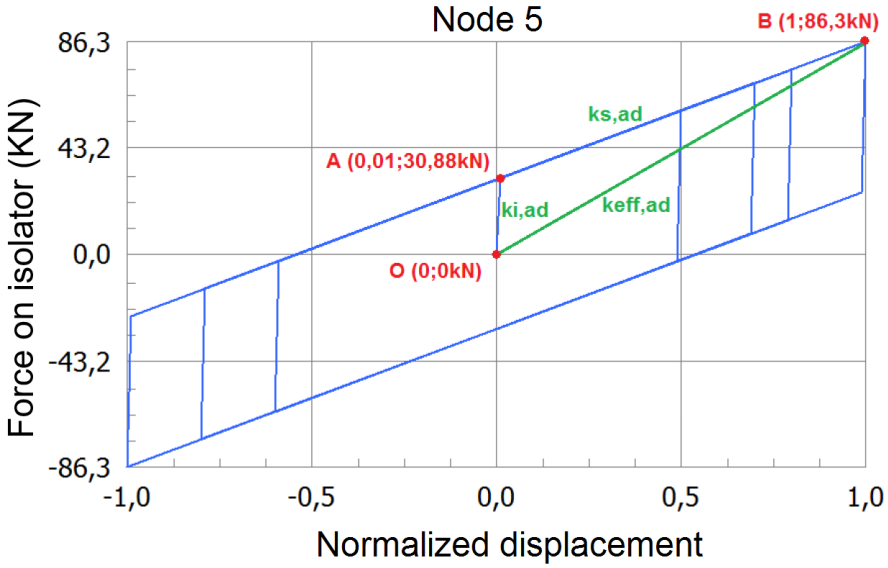

Figure 16 Constitutive law of the isolator in node 5 in terms force-displacement (period 4 seconds and friction factor 4%)

From the constitutive law obtained by the nonlinear static analysis, the initial stiffness k_i and the sliding stiffness k_s of the isolator are:

$$k_{i,ad} = \frac{y_A - y_O}{x_A - y_O} = \frac{30{,}88\ kN}{0{,}01} = 3088\ kN$$

$$k_{s,ad} = \frac{y_B - y_A}{x_B - y_A} = \frac{86{,}3\ kN - 30{,}88 kN}{1 - 0{,}01} = \frac{55{,}42\ kN}{0{,}99} = 55{,}98\ kN$$

As the constitutive law of the isolator has been plotted by normalizing the displacements, the stiffness must also be calculated scaled to the hypothetical design displacement for the isolators, assumed equal to 300 mm:

$$k_i = \frac{k_{i,ad}}{300\ mm} = \frac{3088\ kN}{300\ mm} = 10{,}293\ \frac{kN}{mm}$$

$$k_s = \frac{k_{s,ad}}{300\ mm} = \frac{55{,}98\ kN}{300\ mm} = 0{,}187\ \frac{kN}{mm}$$

It can be noticed that the sliding stiffness ks coincides with that initially assumed, that is:

$$k_{i,def} = \frac{\mu W}{D_y \cdot 300\ mm} = \frac{0{,}04 \cdot 777{,}8\ kN}{0{,}01 \cdot 300\ mm} = 10{,}37\ \frac{kN}{mm}$$

Where μ is the friction factor, D_y is conventionally assumed as 0.01 and W is the load applied on the isolator. It is observed that also in this case $k_{i,def}$, obtained by means of the theoretical definition , is approximated to k_i obtained from the actual constitutive law of the isolator. Finally, the effective stiffness related to the dimensionless displacement $K_{eff,ad}$ and to the design displacement K_{eff} are:

$$k_{eff,ad} = \frac{y_B - y_O}{x_B - y_O} = 86{,}3\ kN$$

$$k_{eff} = \frac{k_{eff,ad}}{300\ mm} = 0{,}288\ \frac{kN}{mm}$$

With reference to the definition of effective stiffness, it is:

$$k_{eff,def} = \frac{\mu W}{300\ mm} + W \cdot \frac{4 \cdot \pi^2}{g \cdot T^2} = \frac{777{,}8\ kN}{300\ mm} \cdot \left(0{,}04 + \frac{4 \cdot 3{,}14^2}{9810\ \frac{mm}{s^2} \cdot (4\ s)^2} \cdot 300\ mm \right)$$
$$= 0{,}299\ \frac{kN}{mm}$$

Also the effective stiffness obtained from the constitutive law reflects the one obtained with reference to the theoretical definition, unless of some negligible differences due to the approximation of the values assumed for the various parameters.

The numerical modelling is therefore correctly defined as the constitutive law in Figure 16 reflects the theoretical response of the isolators. To characterize an isolator, it is then necessary to identify optimal values for the friction factor and the horizontal stiffness.

As a starting hypothesis, it was assumed to have isolators of equal stiffness, assuming different values of the period of the isolation system and of the friction factor. The three most significant cases of this initial phase are reported in Table 3, in which the results in terms of displacement of the isolators have been obtained from the analyses carried out adopting the high seismic intensity accelerogram ED74.

Case	Modelling assumptions			Max displacements	
	Friction [%]	T_{is} [s]	k [kN/mm]	$\lvert s_{x,max} \rvert$ [cm]	$\lvert s_{y,max} \rvert$ [cm]
1	3	4	0,187	22,8	27,3
2	4	3	0,332	22	20,6
3	4	2,5	0,478	17,9	16,7

Table 3 First iterative phases

In general it can be observed that, by increasing the stiffness of the isolators and thus decreasing their period, the maximum displacements of the isolators in the two directions decrease.

One disadvantage when allowing high displacements in the devices is that this might easily result in increments of the displacements incompatible with the maximum allowable dis-

placements of the isolators. This is the most dangerous condition since exceeding the limit displacement might cause failure of the isolators and furthermore a sudden stop of the structure with high impact forces, a sort of hammering at the base of the structure.

On the other hand, limiting the displacements has the primary disadvantage that in this way smaller displacements are allowed. The dissipated seismic energy will also be lower and therefore the isolation system may not be sufficient to completely protect the structure. High stress concentrations might occur, although locally, which might lead to plasticization or extreme loading conditions in the connections.

Even considering an isolation system with period equal to 4 seconds, plasticisation of columns occurs in the first floor, as shown in Figure 17. For the cases 2 and 3, the stresses in the structure increase even more and not negligible plasticization occurs also in the top of the columns.

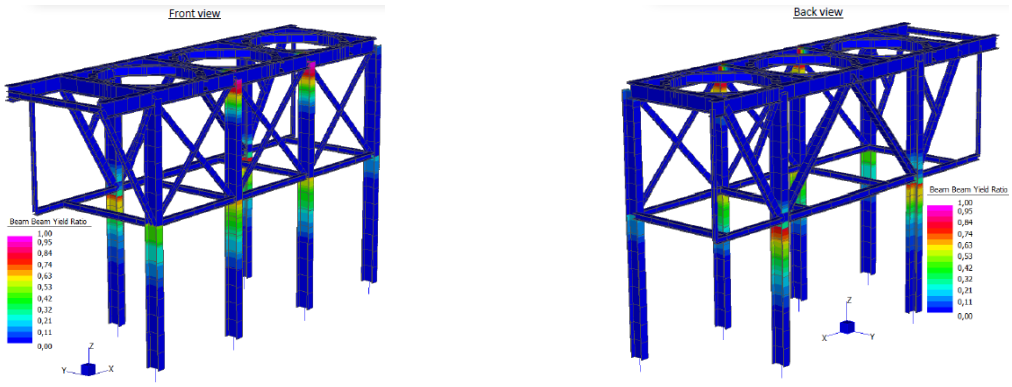

a. Case 1 – Side with X bracing

b. Case 1 – Side with chevron bracing

Figure 17 Inelastic behaviour observed with isolators placed at the column bases

This effect is due to additional torsional effects, caused by different displacement time histories experienced by the isolators, which cause rotations of the structure in the x - y plane (Figure 18).

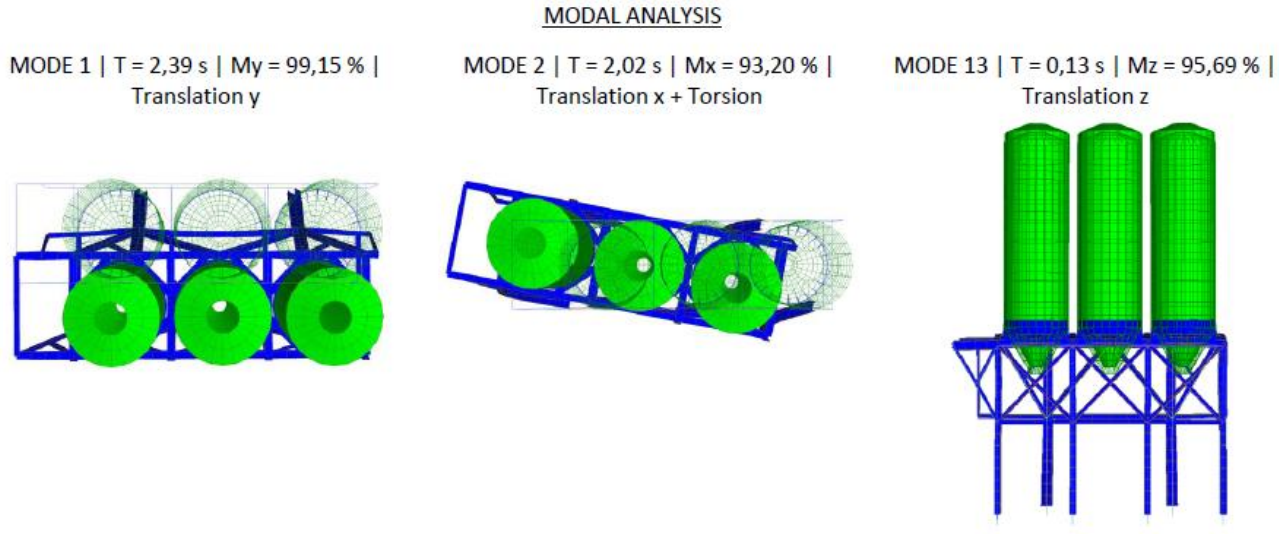

Figure 18 Torsional effects in the structure.

For example, in case 1 with isolators having a period of 4 seconds and a friction factor 3 %, it can be noticed that the isolator displacements in the x-direction (Figure 19) and in the y-direction (Figure 20) are not uniform, since the isolators are not connected with each other. Approximately after 12 seconds, the maximum difference between the displacement of the two isolators along x is approximately about 15 cm.

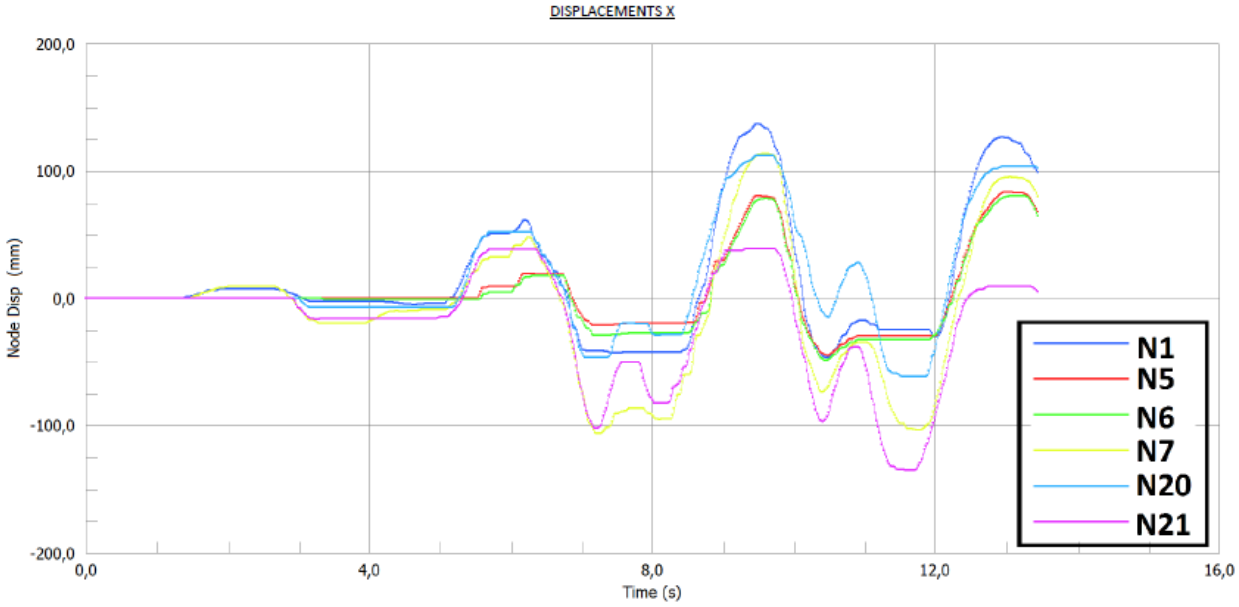

Figure 19 Isolator displacements along x-direction of the isolated structure for case 1

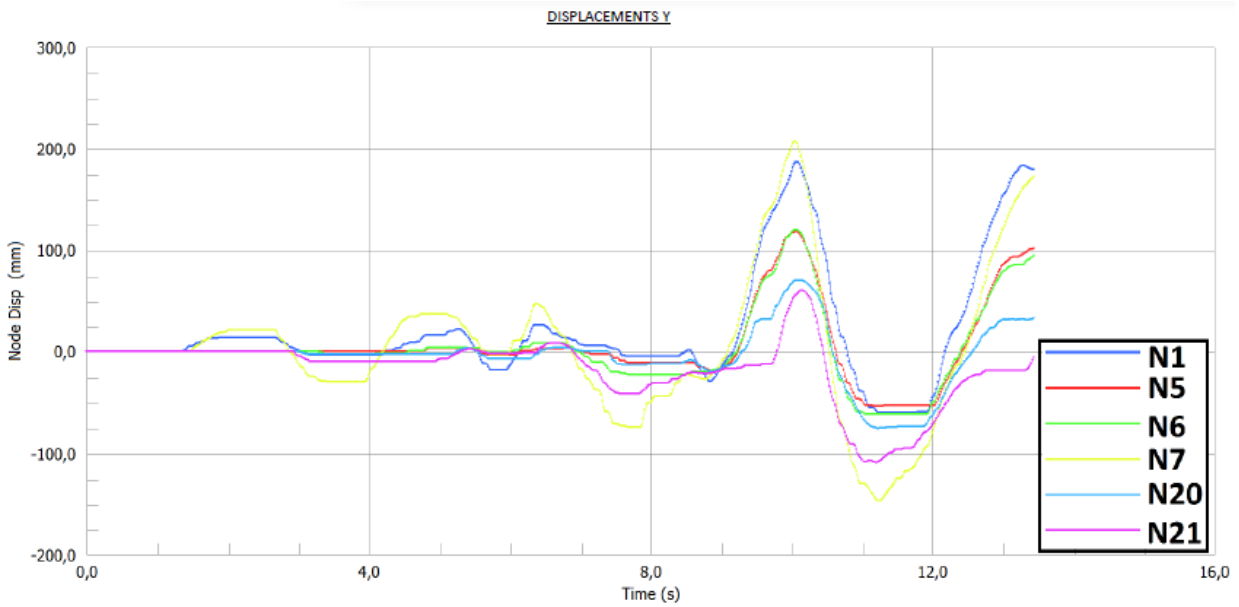

Figure 20 Isolator displacements along y-direction of the isolated structure for case 1

Such a solution is not optimal. To force the isolators to have the same displacement, and then get a translational motion in the x - y plane, different alternatives can be considered. Several solutions have been analysed to solve this asymmetry problem (Figure 21)

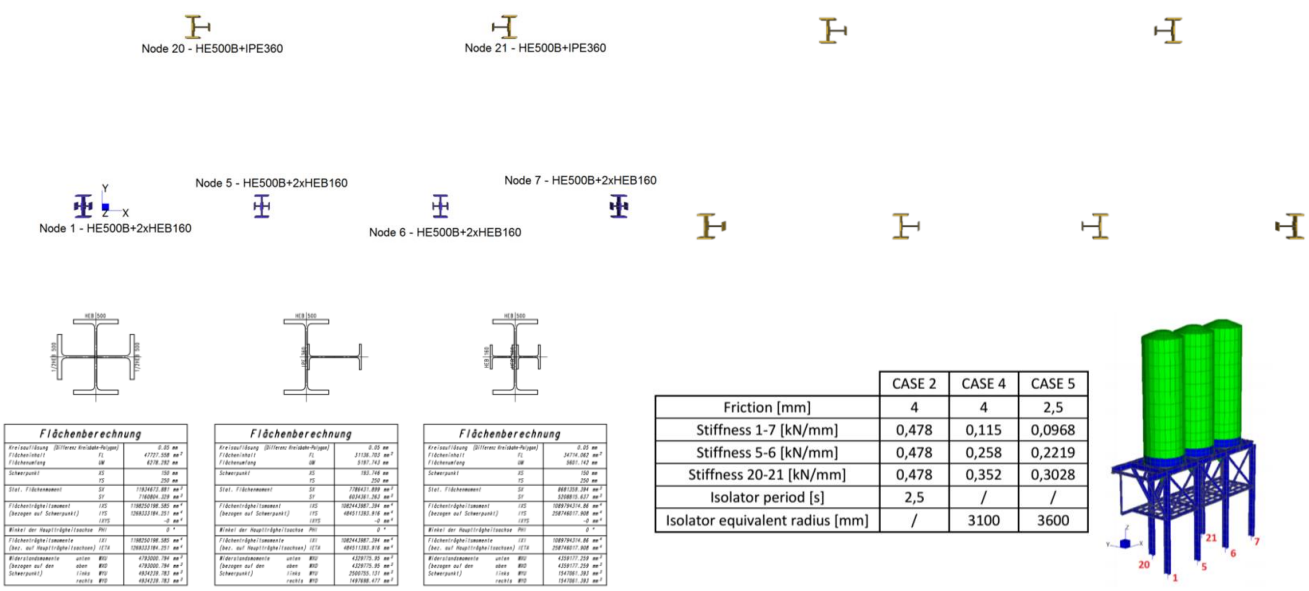

	CASE 2	CASE 4	CASE 5
Friction [mm]	4	4	2,5
Stiffness 1-7 [kN/mm]	0,478	0,115	0,0968
Stiffness 5-6 [kN/mm]	0,478	0,258	0,2219
Stiffness 20-21 [kN/mm]	0,478	0,352	0,3028
Isolator period [s]	2,5	/	/
Isolator equivalent radius [mm]	/	3100	3600

Figure 21 Different Retrofit strategies tried to solve asymmetry issue

After several iterations, the best solution has been obtained by using 6 seismic isolators connected by a rigid diaphragm made of as a horizontal steel frame with beams and horizontal bracing elements at ground level as shown in Figure 22. Solutions without a rigid diaphragm did not provide a feasible solution because of excessive global torsional behaviour.

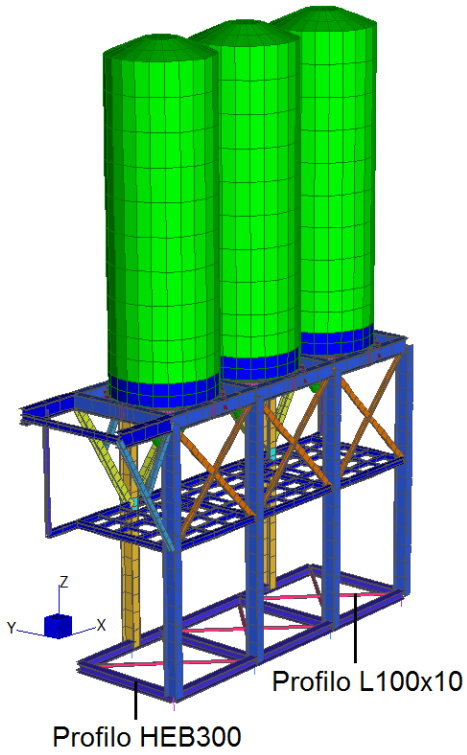

Figure 22 Retrofitted silo system

Horizontal stiffness and friction parameters have been iterated to find an optimal balance between best structural performance and acceptable maximum displacements. Inelastic deformations on the steel structure have been avoided (Figure 23).

Case	Modelling hypotheses					Max displacements	
	Friction coefficient [%]	T_{is} [s]	$k_{1,7}$ [kN/mm]	$k_{5,6}$ [kN/mm]	$k_{20,21}$ [kN/mm]	$\|s_{x,max}\|$ [cm]	$\|s_{y,max}\|$ [cm]
4	4	4	0,09	0,2	0,274	14,2	24,8
5	4	3,5	0,118	0,263	0,358	14,3	23,6
6	4	3	0,16	0,357	0,488	12,3	21,8
7	3	3	0,16	0,357	0,488	15,4	25,2
8	4	2,5	0,23	0,515	0,7	12,6	20,1
9	3	2,5	0,23	0,515	0,7	14,6	21,1

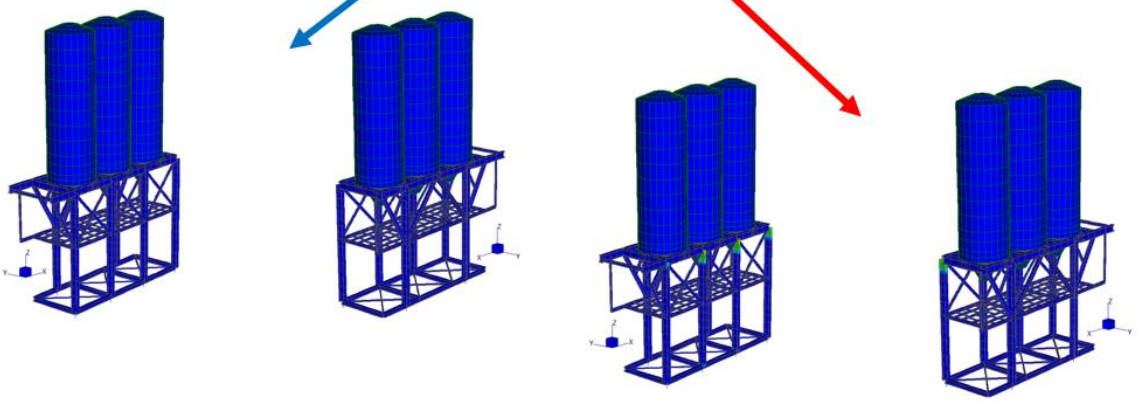

Figure 23 Comparison of retrofit solution 4 and 8: In case 4, full elastic behaviour can be obtained

Table 4 shows the most suitable isolator properties obtained after several iterations. Please note that different horizontal stiffness values have been used for different supports, which are calibrated according to the vertical reaction force under full-silo gravity loading condition.

Isolator properties	
Friction	4%
T_{is}	4 seconds
$k_{1,7}$	0,09 kN/mm
$k_{5,6}$	0,2 kN/mm
$k_{20,21}$	0,274 kN/mm
k_v	3000 kN/mm

a. Isolator properties

Nodo	F_z [kN]
1	358,3
5	777,8
6	798,8
7	340,2
20	1090,2
21	1080,7

b. Nodal reaction of structure supports

Table 4 Isolator properties and nodal reactions

Modal shapes and values are shown in Figure 24 and Table 5.

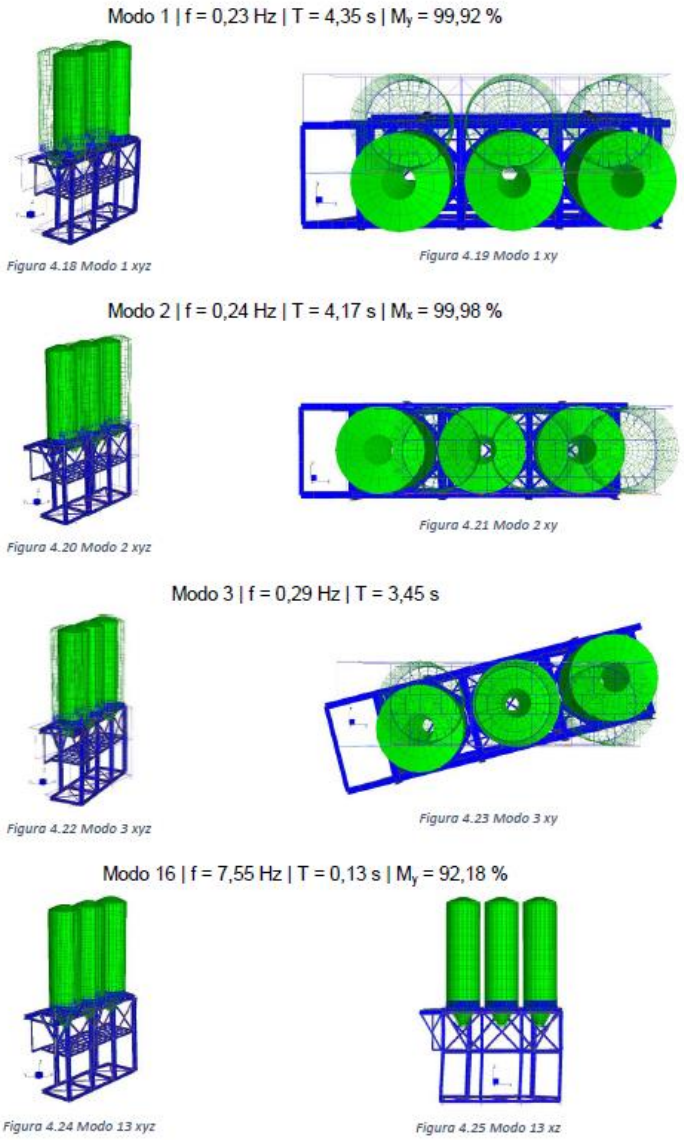

Figure 24 Modal shapes of retrofitted solution

Mod	T [s]	Direction
1	4,35	y (transversal)
2	4,17	x (longitudinal)
3	3,45	Torsional
16	0,13	z (vertical)

Table 5 Modal analysis results

To quantify the performance of the selected isolators, 7 nonlinear time history analysis have been performed. Max/min values of isolator displacements and residual displacements obtained from each accelerogram, and as an average of 7 accelerograms are shown in Table 6 and Figure 25.

Seismic Input	Max displacement of isolators [cm]		Max residual displacement of isolators [cm]	
	x	y	x	y
ED74	14,0	24,5	3,72	4,21
ED196	3,8	2,6	1,14	1,64
ED535	34,5	29,0	0,84	1,13
ED6349	5,6	29,0	1,43	1,45
IN113	21,2	11,9	3,23	2,21
IN331	29,3	41,2	1,58	2,31
IN461	21,3	33,9	0,79	2,06
Avg	**18,5**	**24,2**	**1,86**	**2,12**

Table 6 Max/Min displacements

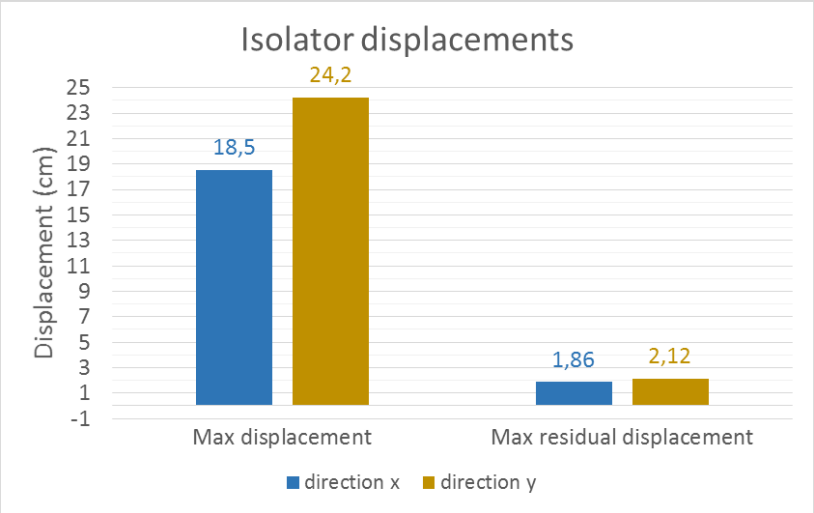

Figure 25 Max/Min displacements

Max/min values of base shear and relative displacements of the structure's mass center obtained from each accelegoram, and as an average of 7 accelerograms are shown in Table 7 and Figure 26.

Seismic Input	Base shear [kN]		Relative displacements of structure mass center [cm]	
	x	y	x	y
ED74	374,5	287,3	5,1	9,4
ED196	272,0	138,4	3,8	5,2
ED535	538,7	303,3	8,8	9,3
ED6349	165,1	419,0	2,2	11,1
IN113	487,1	167,4	7,1	5,8
IN331	607,8	513,3	11,6	17,4
IN461	480,1	448,2	7,4	14,4
Average	**417,9**	**325,3**	**6,6**	**10,4**

Table 7 Max/Min displacements and base shear

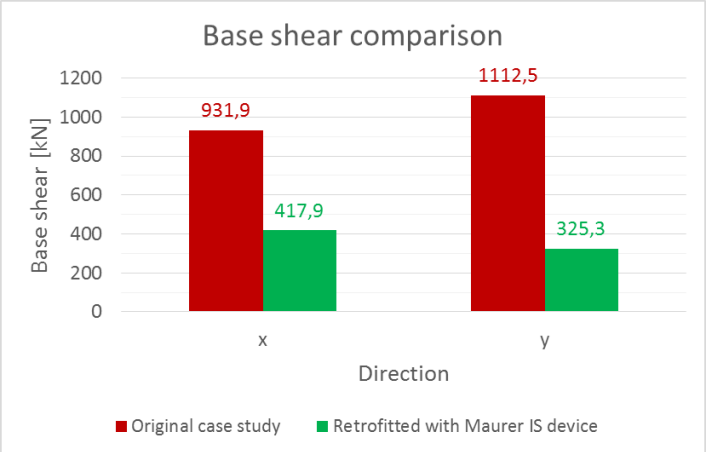

Figure 26 Max/Min base shear

Reductions in mean relative displacements of the two storeys are shown in Figure 27 for x and y directions.

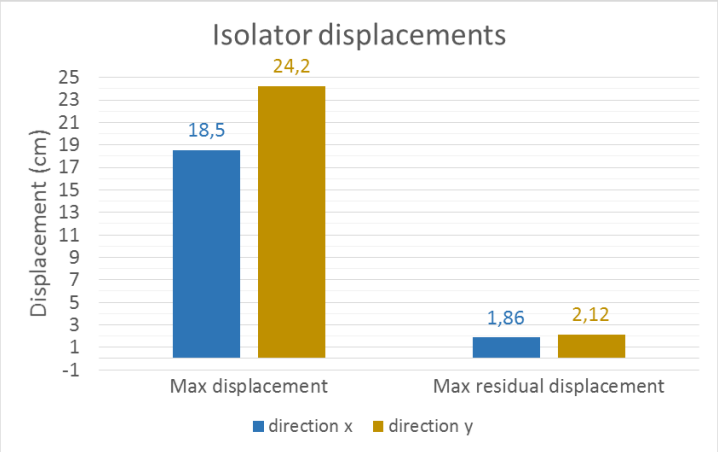

Figure 27 Reductions in mean relative displacements

Comparisons in terms of floor drifts are shown in Figure 28, Figure 29, and Table 8. The weak floor in the longitudinal direction of the structure is the first one, as the second floor is braced. The bracing was effective already in the case of a fixed base structure, wherein the average relative movement in the x direction of the second floor was equal to about 0.1%. In the isolated-base structure, the average relative movement of the second floor in the x direction is of 0.05% and is then maintained almost in the same order of magnitude as the previous case. In any case, the mean relative movement of the second plane in the direction x is negligible, and the reduction of 50% is relative and has just a minor impact on the structural response.

On the contrary, the first floor benefits from the isolation system. In particular in the x-direction (braced), in which the first floor is weak, the reduction is significant (approximately 64%) and the average relative displacement falls from a critical value equal to 3.49% in a fixed base structure to a value 1.24%.

In transverse y-direction (non-braced) a reduction of 35% for the first floor and 53% for the second floor can be observed. Also in this direction the structure takes advantage of the

isolation system, with limited mean relative displacements for both floors, unlike the fixed-base system in which values larger than 1.5% could be observed.

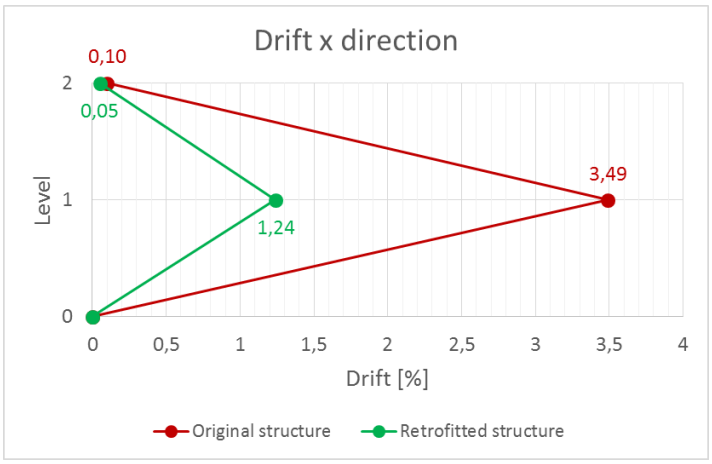

Figure 28 Drift comparison in x direction

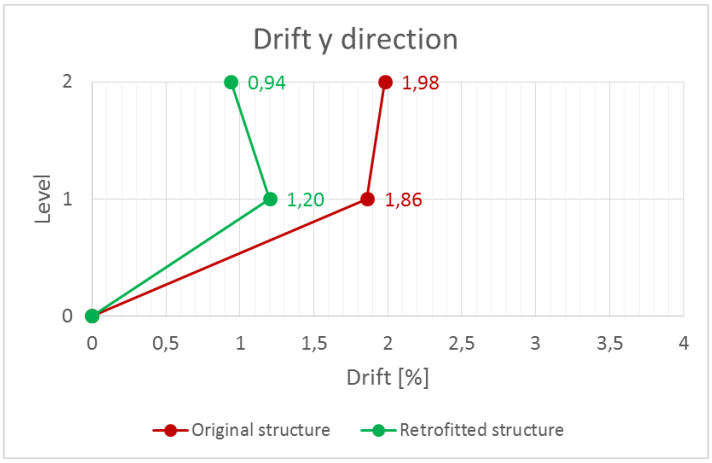

Figure 29 Drift comparison in y direction

Average interstorey drift				
Floor	Direction	Fixed-base structure	Isolated structure	Reduction
1	x	3,49 %	1,24 %	64 %
	y	1,86 %	1,20 %	35 %
2	x	0,10 %	0,05 %	50 %
	y	1,98 %	0,94 %	53 %

Table 8 Comparisons in terms of floor drifts

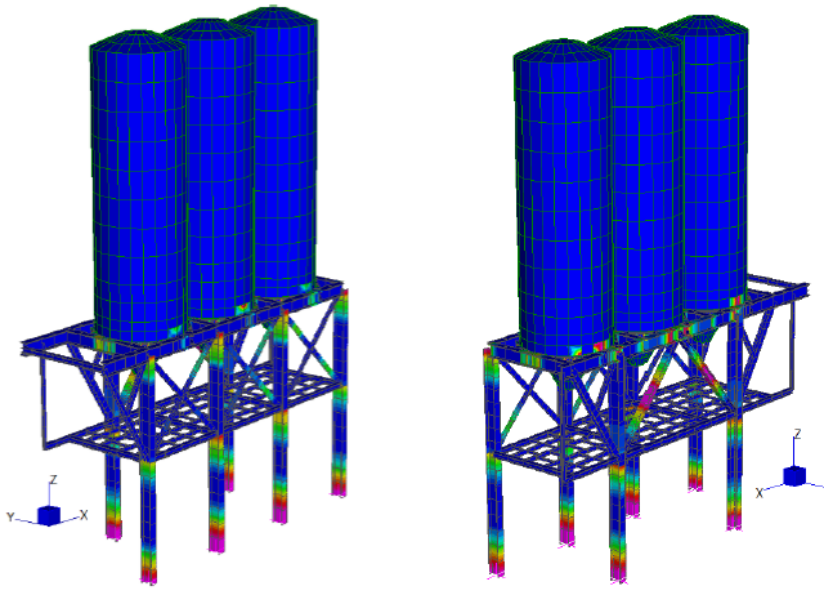

Figure 30 Yield index of the original structure

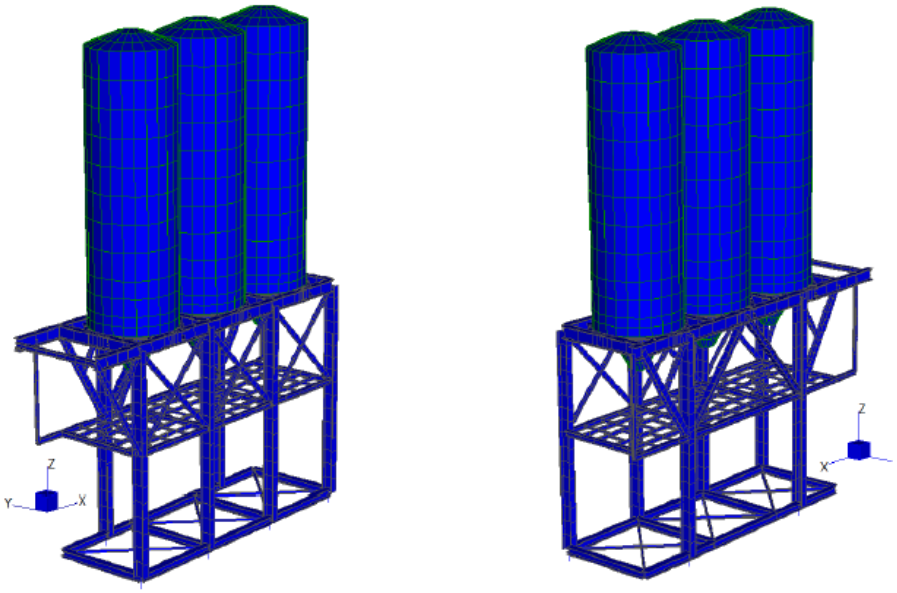

Figure 31 Yield index of the retrofitted structure

The yield index of the original and retrofitted structure can be compared from Figure 30 and Figure 31, with reference to the ED74 accelerogram. The retrofitted structure remains fully elastic.

5 IDA RESULTS IN HIGH SEISMICITY

Results of the IDA analysis based on high seismicity accelerograms are shown in terms of peak displacements and total base shear. For peak displacements, the control node is taken as the center of gravity of whole system. (x direction: longitudinal, y direction: transversal, z direction: vertical).

From Figure 32, it is seen that in general, retroffited structure responses in a linear manner to the increase in global base shear forces with increasing scale factors, while a global elasto-plastic behaviour is evident in case of the original structure.

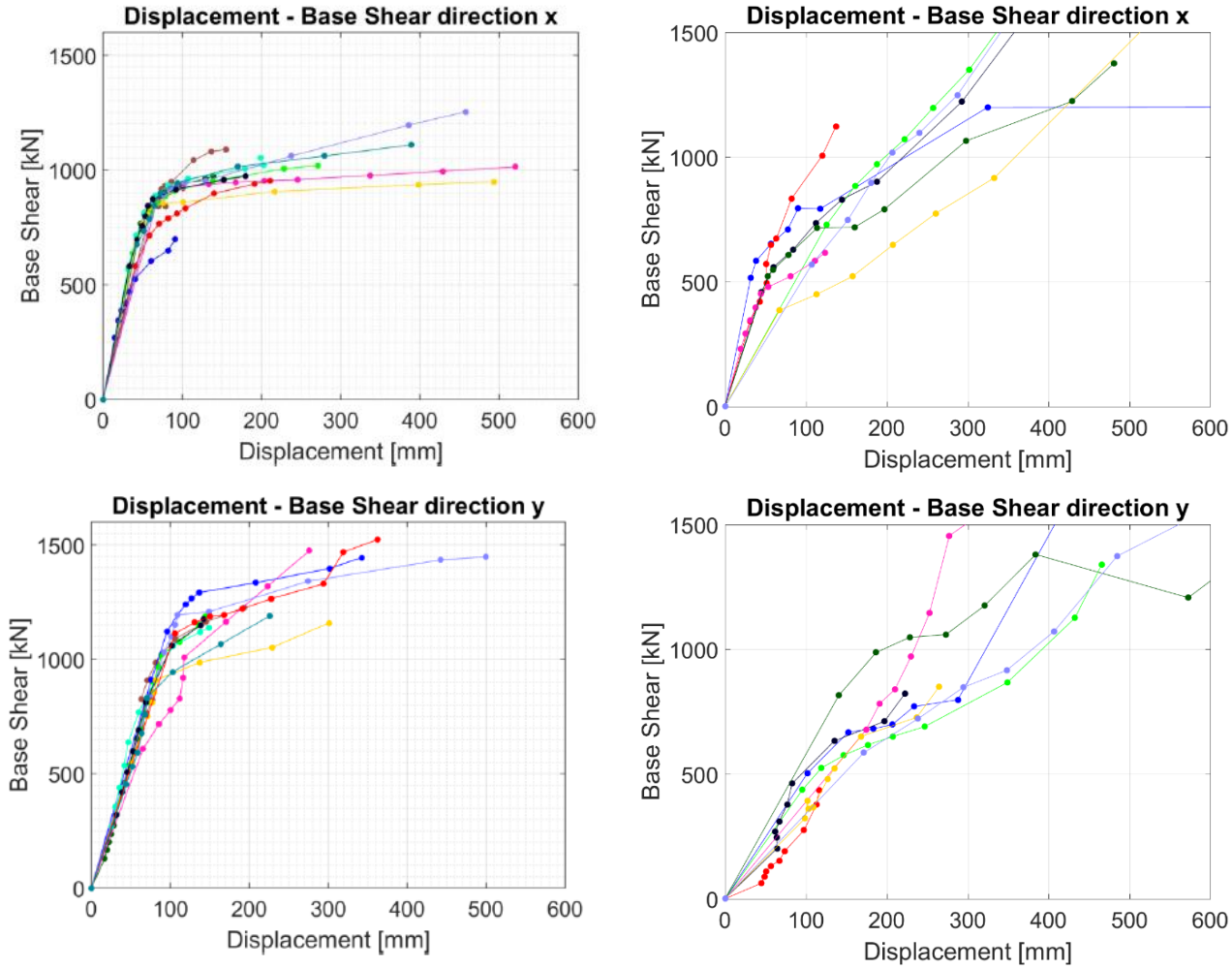

a. Original Structure b. Retrofitted structure

Figure 32 IDA results in terms of global displacement vs base shear

Figure 33 shows and Figure 34 show that drifts of both floors have been decreased significantly in case of retrofitted structure. Most importantly, the soft-storey behavior observed in the original structure has been eliminated thanks to the seismic retrofitting, as can be observed from the very low drift ratios of floor 1.

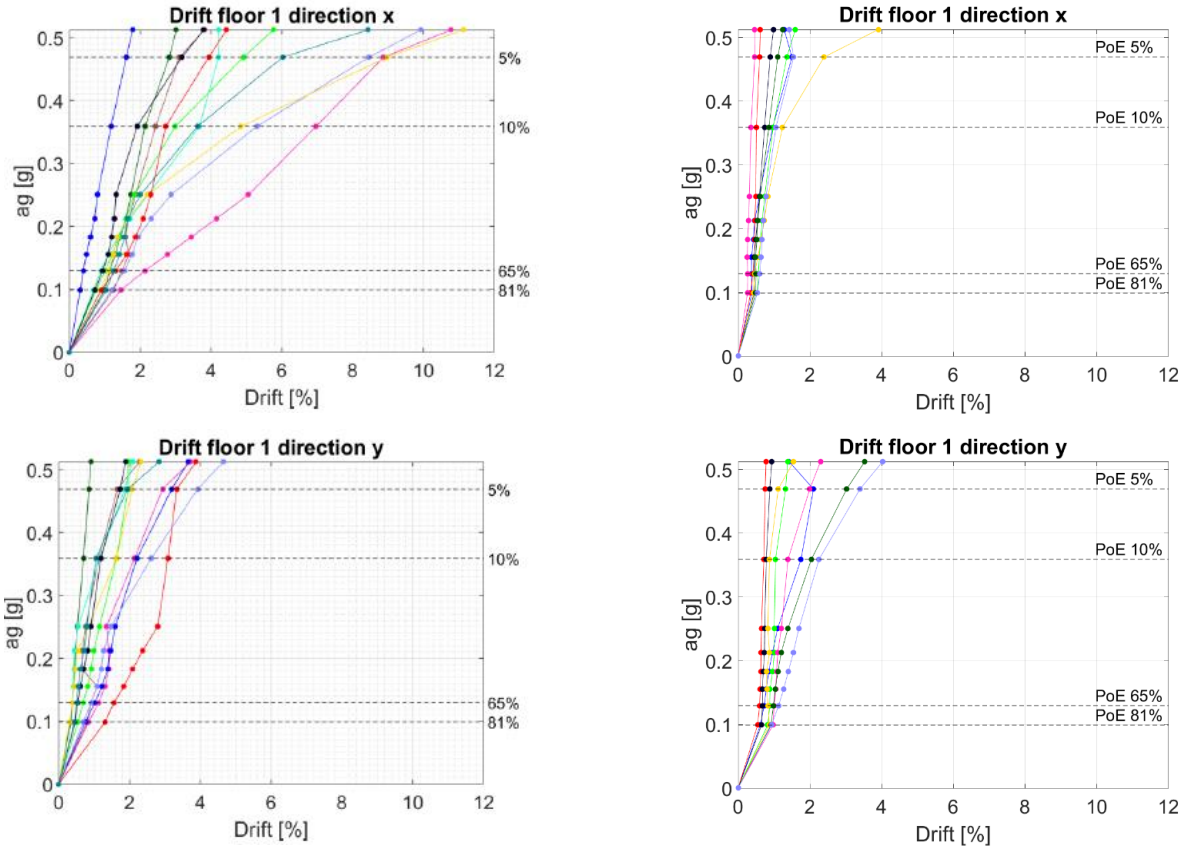

a. Original Structure

b. Retrofitted structure

Figure 33 IDA results in terms of drift 1st floor

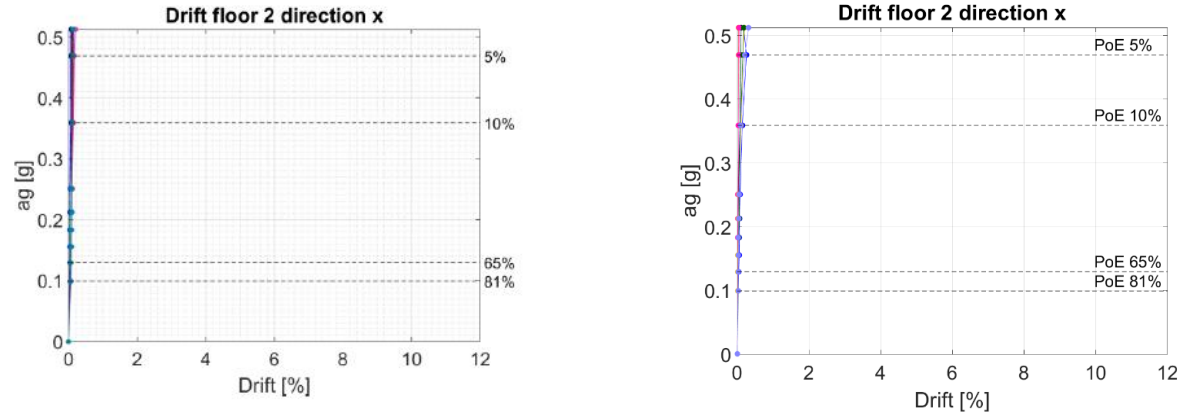

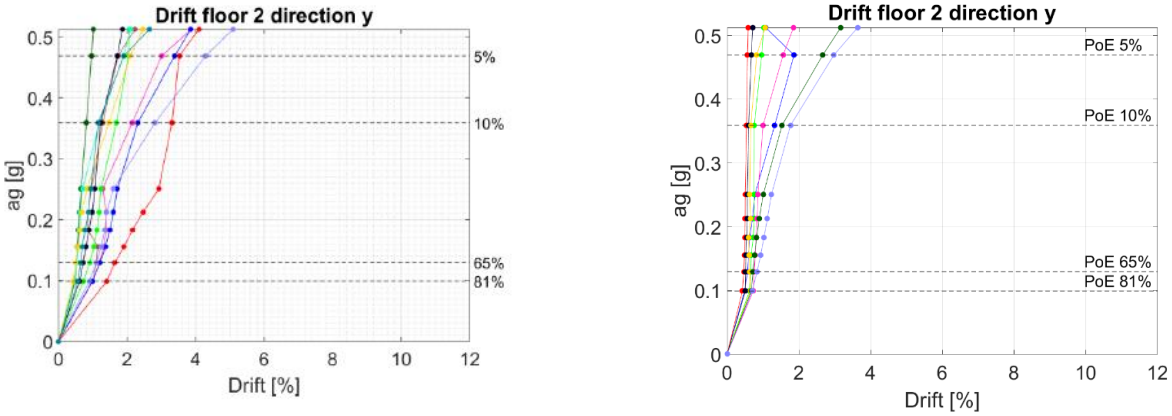

a. Original Structure b. Retrofitted structure

Figure 34 IDA results in terms of drift 2nd floor

Although the global behavior of the structure is very satisfactory, in some cases, especially with high vertical earthquake component, uplift occurs (Figure 35). It could be avoided either with the introduction of proper ropes that prevent the uplifting of the isolation devices.

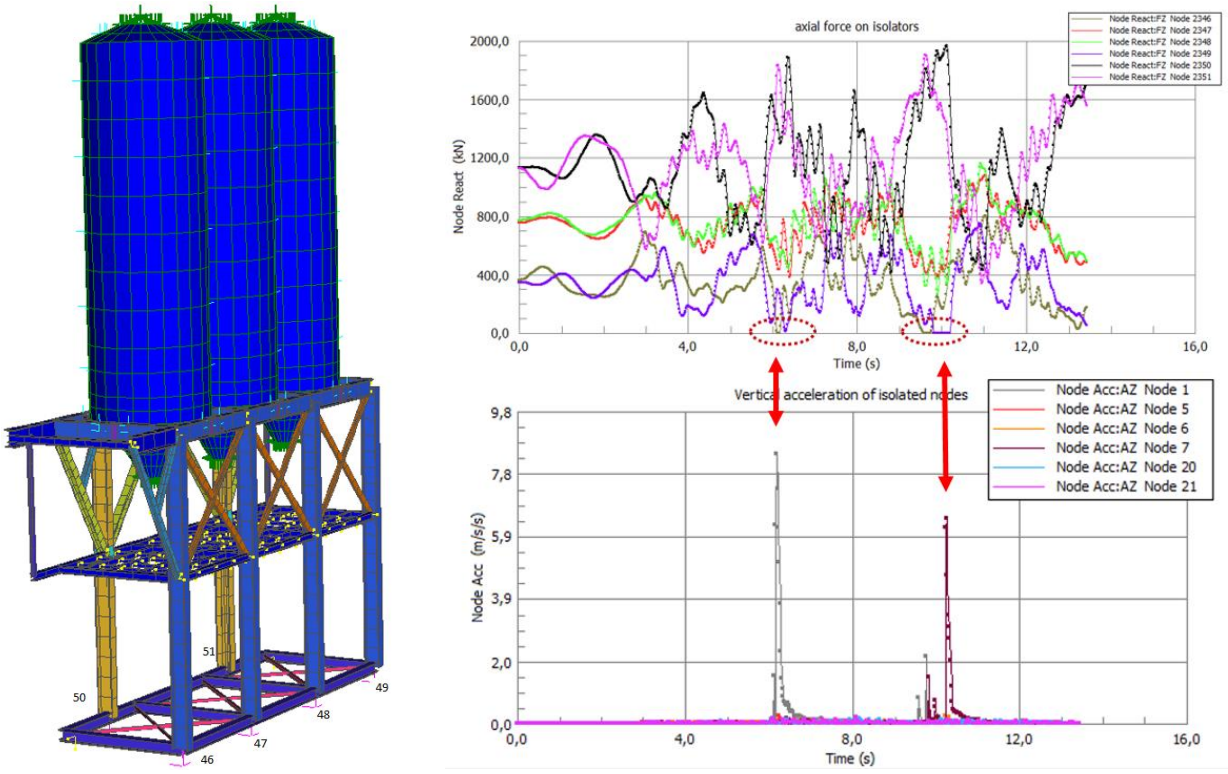

a. Retrofitted structure b. Uplift instants during ED74 time-history (without vertical accelerations)

Figure 35 Uplift problem

In the cases with high vertical acceleration content (Figure 36), uplift is inevitable with the seismic isolation solution.

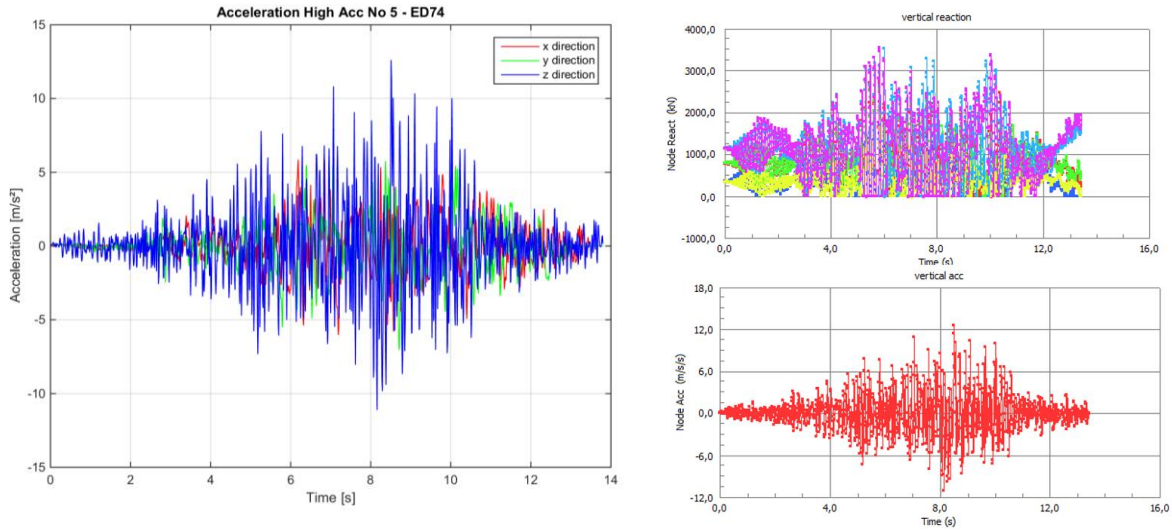

a. Three components of the ED74 time-acceleration history

b. Uplift instants during ED74 time-history (with vertical accelerations)

Figure 36 Uplift problem

To reduce the rocking effect and overturning moments which are the main causes of uplift, 2 other retrofitting strategies have been analysed:

i. Seismic isolators placed at the second floor level, under the silos

ii. Seismic isolators placed at the first floor level

The first approach resulted in global collapse of the system, causing high stresses in the beams which caused also a column loss and eventually the global collapse occurred (Figure 37). With the second approach, column bases suffer yielding due to second order effects caused by large displacements of isolated silos (Figure 38). Further analysis to investigate the performance of the structure with second retrofitting strategy is underway.

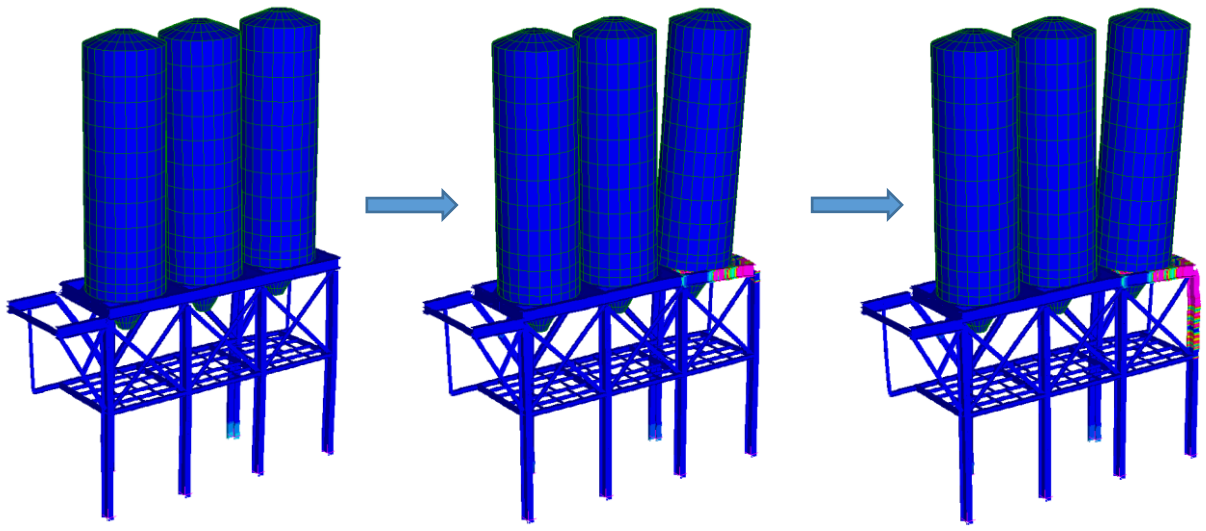

t= 6 sec t=8 sec (beam yielding starts) t=11 sec (column collapse)

Figure 37 Isolators placed at the second floor level, under the silos

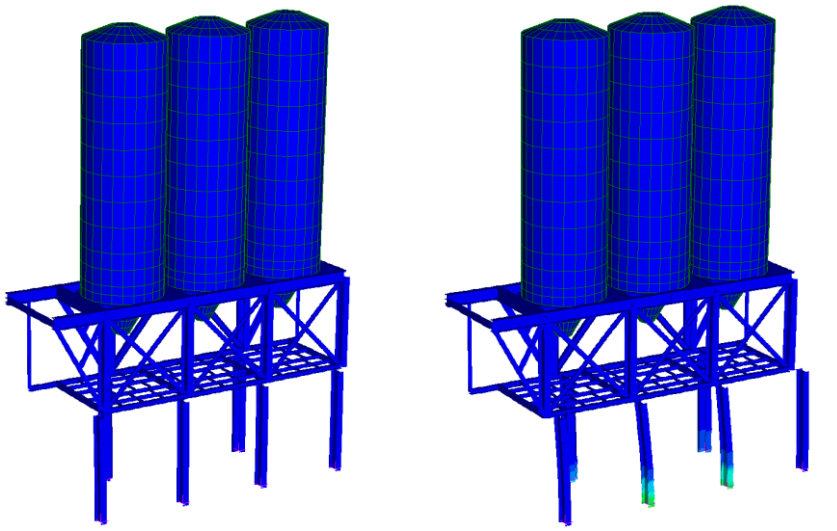

Figure 38 Isolators placed at the first floor level

It has also been noted that, vertical component of the earthquakes impact significantly the global behavior of the retrofitted structure. This can be seen from Figure 39, Figure 40, and Figure 41 where the red colored curves represents the global behavior with vertical component of the ED74 earthquake. When they are compared with the blue curves representing the global behavior without considering the vertical acceleration component, it is seen that achievement of the full elastic behavior will not be possible. In these cases, retrofitted solution can be seen as an improvement rather than a total rehabilitation solution.

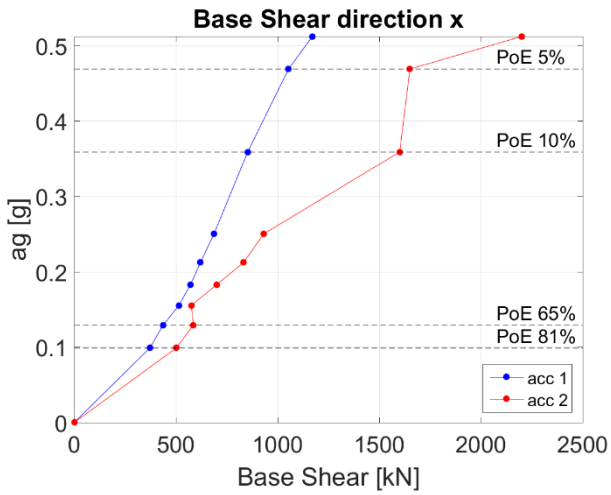

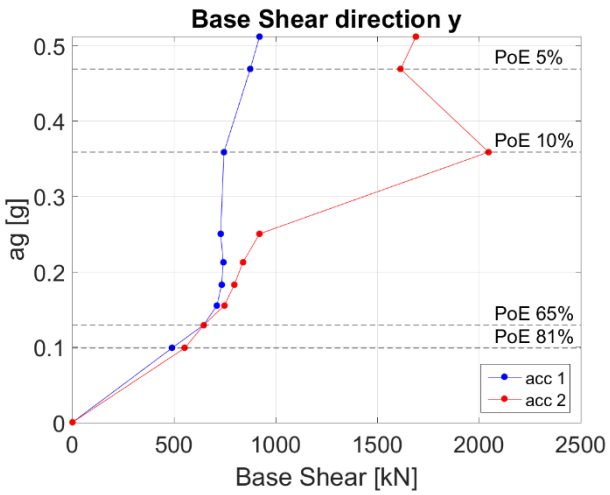

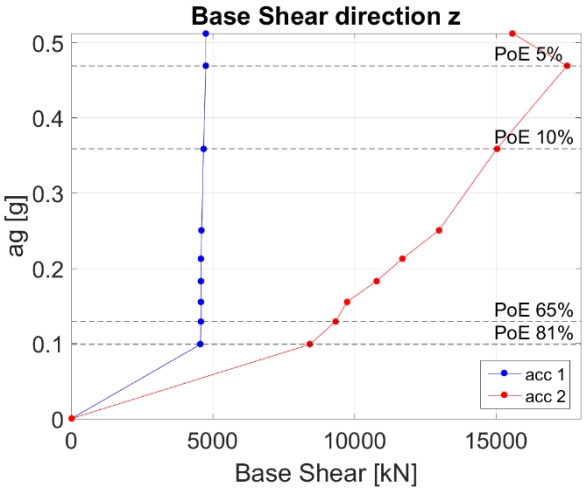

Figure 39 Impact of vertical component of ED74 earthquake in terms of base shear

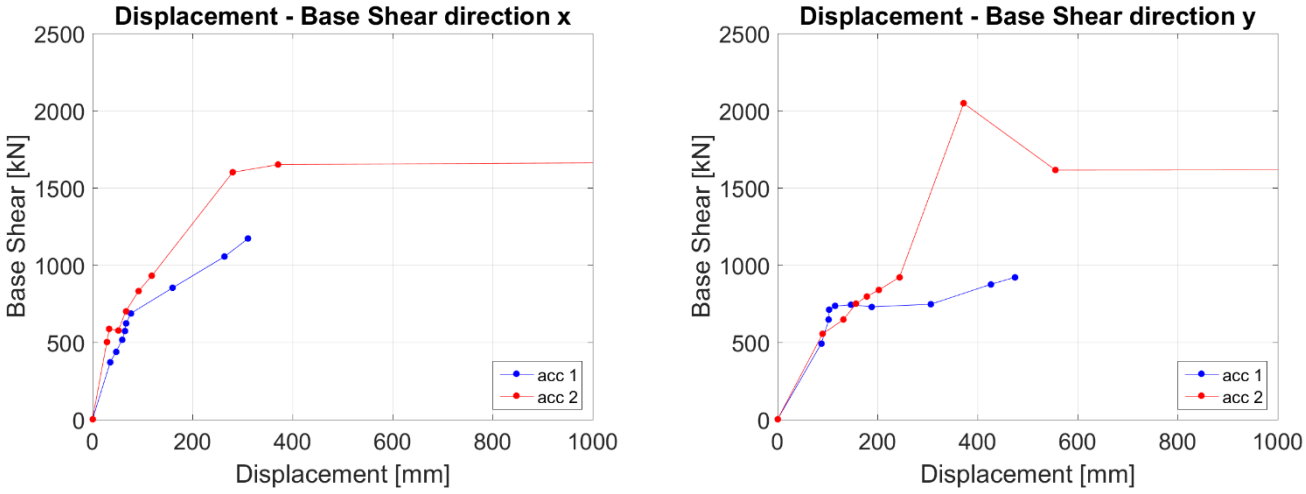

Figure 40 Impact of vertical component of ED74 earthquake in terms of displacement-base shear

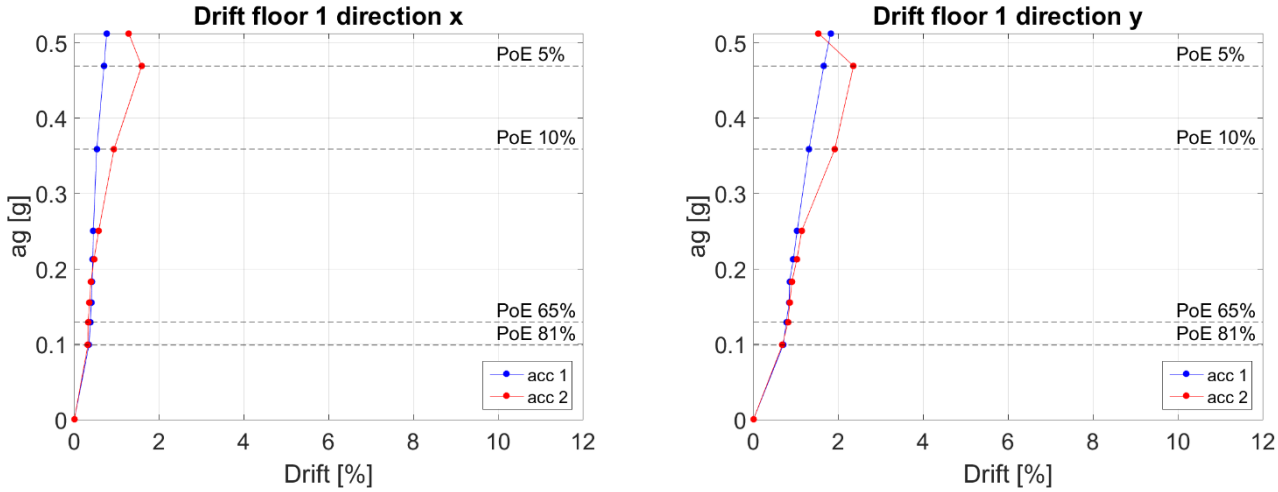

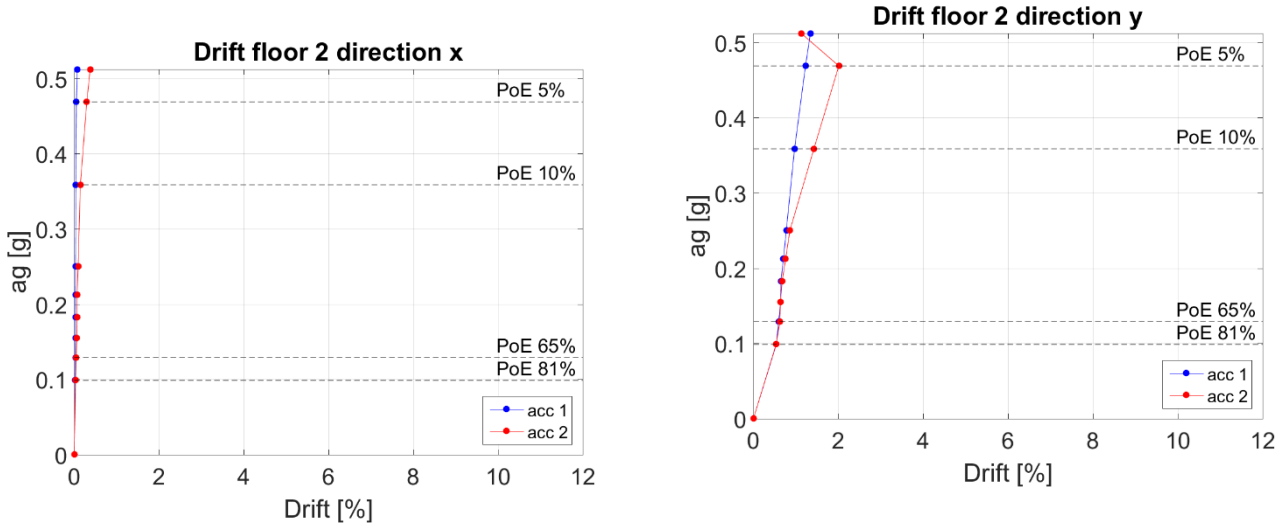

Figure 41 Impact of vertical component of ED74 earthquake in terms of floor drifts

6 CONCLUSIONS

The best seismic retrofit solution has been obtained by using 6 seismic isolators connected by a rigid diaphragm realized as a horizontal steel frame composed of beam and horizontal bracing elements at ground level. Global base shear values have been reduced significantly. Residual displacements of the retrofitted structure are very small, and much smaller than the residual displacements of the original structure. With the seismic retrofit, floor drifts are reduced, and the soft-storey behavior observed in the original structure has been eliminated. Vertical component of the earthquakes impact significantly the global behavior of the retrofitted structure. A fully elastic superstructure behaviour can be achieved only when the vertical component of earthquake is not significant. In summary, this retrofit solution improves significantly the seismic behaviour of the elevated silo system. In the final design of the isolators, uplift issue should be addressed.

REFERENCES

[1] 2nd Annual Report, EU-RFCS project PROINDUSTRY RFSR-CT-2013-00019

[2] A. Kanyilmaz, Inelastic Cyclic numerical analysis of steel struts using distributed plasticity approach, *COMPDYN 2015, 5th ECCOMAS Thematic Conference on Computational Methods in Structural Dynamics and Earthquake Engineering, Crete Island, Greece, 2015*

[3] E. Uckan, B. Akbas, J. Shen, R. Wen, K. Turandar, M. Erdik, Seismic performance of elevated steel silos during Van earthquake, October 23, 2011, *Natural Hazards*, January 2015, Volume 75, Issue 1, pp 265-287

[4] «MAURER Seismic Isolation with Sliding Isolation Devices for Bridge Structures,» Maurer Sohne, 2012.

ECCOMAS Congress 2016
VII European Congress on Computational Methods in Applied Sciences and Engineering
M. Papadrakakis, V. Papadopoulos, G. Stefanou, V. Plevris (eds.)
Crete Island, Greece, 5–10 June 2016

EFFICIENCY OF SEISMIC ISOLATION ON INDUSTRIAL PLANTS - CASE STUDY OF A GAS TANK

J. Henriques[1], F. Morelli[2], B. Vandoren[1], W. Salvtore[2] and H. Degée[1]

[1] Construction Engineering Research Group, Faculteit IIW, Universiteit Hasselt
e-mail: jose.gouveiahenriques@uhasselt.be; bram.vandoren@uhasselt.be; herve.degee@uhasselt.be

[2] Dipartimento di Ingegneria Civile ed Industriale, Universitá di Pisa
email: francesco.morelli@dic.unipi.it; walter@ing.unipi.it

Keywords: Industrial Plants, Seismic Protection, Ground Motion, Time-History Analysis, Numerical Simulation.

Abstract. *Recent earthquakes such as the one in Fukushima in Japan in 2011 highlighted the need of providing adequate protection to industrial installations. To answer this need, the ongoing RFCS research project PROINDUSTRY is addressing the question of the development of innovative seismic protection systems, both for the design of new industrial plants and for the retrofit of existing ones. This paper presents a specific aspect of the ongoing investigations within the referred project, namely a case study considering a Gas Tank. The protection systems under development contemplate both seismic isolation and energy dissipation techniques. For the presented case study, the base isolation system under development was finally chosen to improve the seismic performance of the Tank structure. In order to characterize the behavior of the Gas Tank structure, several numerical simulations were performed comprising modal analyses, push-over analyses and time-history nonlinear analyses. For the time-history nonlinear analysis ground motions were generated on the basis of available information on ground motion histories from national, European and Mediterranean Strong Motion Data-bases. Finally, the efficiency of the base isolation used in the Gas Tank structure is investigated by comparing the results of the time-history nonlinear analysis on the protected and the non-protected structure.*

1 INTRODUCTION

Recent earthquakes such as the one in Fukushima in Japan in 2011 highlighted the need of providing adequate protection to industrial installations storing a large amount of hazardous material. In the event of an earthquake, and following accidental scenario, the consequences may be severe for the neighborhood population, for the economy and for the environment [1]. In particular process plants, like process units, storage units and piping systems are characterized by high level of seismic risk [2]. The consequences of an earthquake may be the total collapse (Fig. 1-a) or a partial damage (Fig. 1-b) of the industrial unit. Consequently, providing adequate seismic protection to industrial installations is imperative to this construction sector.
In order to answer to this problematic, the on-going RFCS research project PROINDUSTRY [3] is addressing the question by developing innovative seismic protection systems, both for the design of new industrial plants and for the retrofit of existing ones. The seismic protection systems considered in the project programme are the Base Isolation (IS) and the Energy Dissipation (EDS) types. Emphasis is given to the self-centering capability of these systems, since it is an essential feature that allows the industrial facility not to discontinue its operations even after a strong earthquake and that makes eventual repair work easier. The work programme considers experimental tests on the developed devices, including application in substructures, and numerical modelling of real industrial structures used as study cases to investigate and calibrate the seismic protection systems developed. The cases studies of real industrial buildings consider process and storage units which the superstructure is made of steel [4].

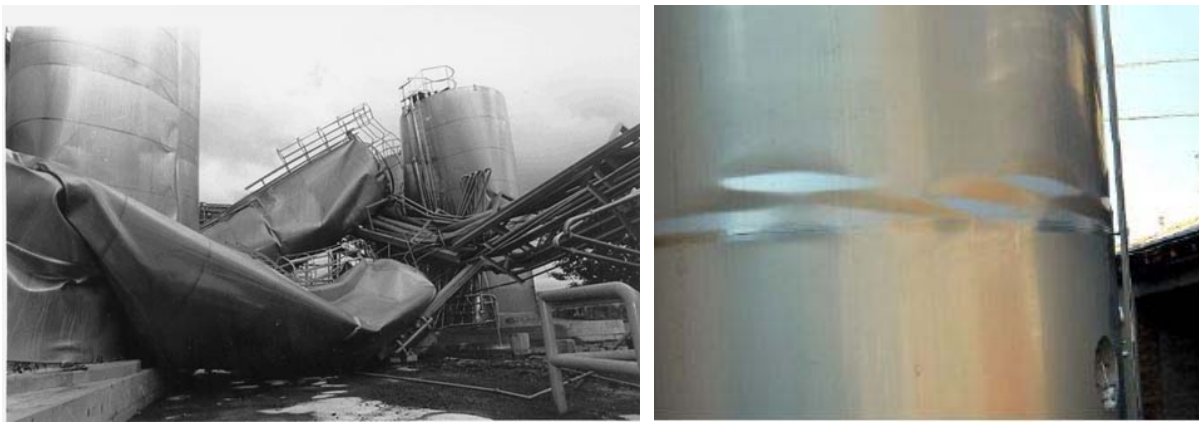

a) Tank collapse (Edgecumbe Earthquake, New Zeeland) b) Local shell buckling (Emilia earthquake, Italy)

Figure 1: Earthquake impact on industrial units

This paper presents a specific aspect of the on-going investigations within the referred project, namely a case study considering a gas tank. For this structure, a base isolation system was chosen to improve its seismic performance. In order to characterize the behavior of the Gas Tank structure, several numerical simulations were performed comprising modal, push-over and time-history nonlinear analysis. For the latter, the Ground Motions generated within the project tasks have been used. The calibration of the foreseen base isolation system is under investigation and the preliminary results of the time-history nonlinear analysis on the protected structure are compared with the response of the non-protected structure.

2 SEISMIC PROTECTION OF INDUSTRIAL PLANTS

2.1 General

In the case of seismic event, the prevention of the collapse of buildings may rely in two strategies: i) capacity design; ii) seismic isolation and/or energy dissipation (seismic protection). The PROINDUSTRY research project is focus on the latter. Accordingly, base isolation systems and energy dissipation systems are under development for the retrofit intervention of existing industrial structures or the design of new ones. In the case study presented in this paper, the base isolation system has been selected to improve the seismic performance of the structure under analysis. Herein, only a brief description of the base isolation system is given. More detailed information on the base isolation and on the dissipation devices subject of the PROINDUSTRY investigations may be found in [4].
The aim of the base isolation system is to mitigate the impact of seismic action on the structure by decoupling the structure from the shaking ground. The principle of seismic base isolation is to increase the fundamental period of the structure and modify the mode shape leading to smaller rigid mass displacements, and consequently reduce the loads due to inertia effects. An isolator shall provide a combination of vertical-load carrying capability with one or more of the following functions: i) lateral flexibility; ii) energy dissipation; iii) re-centering capability. The base isolation system implemented in the numerical simulation is the Curved Surface Slider (CSS) which may present different versions: single CSS, double CSS and triple CSS. Within the project, an innovative version of this device is under development [4].

2.2 Base Isolation System: Curved Surface Slider

The simple version of the CSS was proposed in [5] and consisted in a single curved surface slider (Figure 2-a). In concept, the single surface slider is derived from the regular spherical bearing in which the flat surface accommodating the translation movements is substituted by a curved concave surface (Figure 2-b). The spherical sliding isolators are consisting of three main steel parts with inner sliding surfaces. The shape of the internal part is always spherical and allowing rotation and horizontal sliding displacements. The device transmits vertical loads, provides horizontal flexibility and dissipates energy simultaneously. The concave surface introduces the re-centering capability into the isolator: the slide moves up the concave surface (under the seismic excitation), increasing the potential energy, inducing in the bearing a restoring force, as the building should return to its stable equilibrium point. The theoretical behavior of the device is characterized by hysteretic bilinear relationship between horizontal force – horizontal displacement (Figure 3). From the single CSS, a double and triple CSS were developed (Figure 2-c). These modified versions of the single CSS improve its capacity to accommodate substantially larger displacements and allows the adaptation of device to the earthquake intensity.

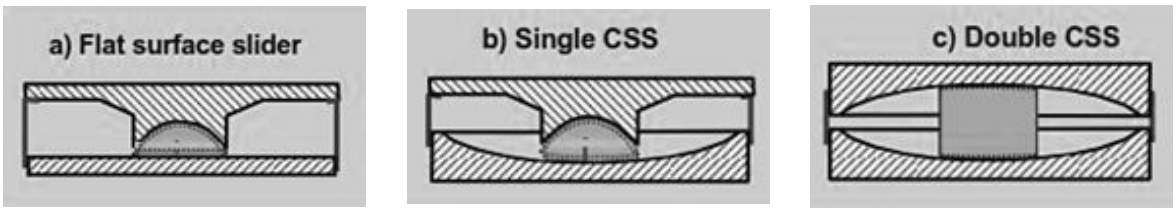

Figure 2: Flat and curved surface sliding isolators [4]

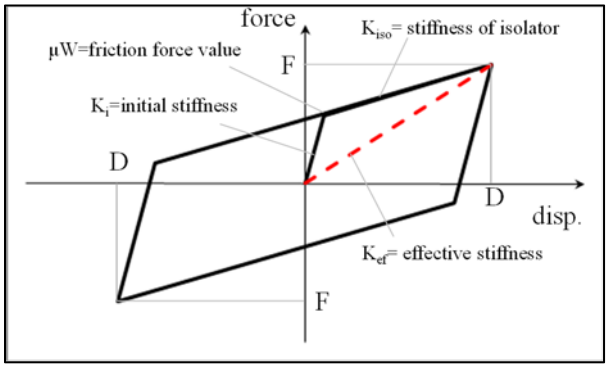

Figure 3: Hysteretic force – displacement relationship of the CSS [4]

3 CASE STUDY: GAS TANK

3.1 Geometric and mechanical properties

The present case study consists in a Gasometer which is used to store Gas AFO (Figure 4) and was constructed by Ilva s. p. a. in the early eighties. The gas tank is a steel cylinder where the walls are made with curved steel plates reinforced with circular steel rings (UNP 100) and with vertical steel columns (IPB 180). The roof is composed by a steel structure using a steel circular grid made of IPE, L and UNP steel profiles and steel plates. The tank works with a piston-fender system and a rubber sealing system which allows the variation of the sealed volume. In Table 1 the main geometric characteristics are summarized and in Table 2 are given the material properties of the main structural components. The self-weight of the different structural components is given in Table 3. Finally, the working pressure in this gas tank is 400mmH2O, and the volume between the roof and the sealed reservoir is full of air at atmospheric pressure. Detailed information on the tank properties is given in [4].

Figure 4: Gasometer

Table 1: Main Geometric Properties

Height	70m
Diameter	44m
Volume	75000m^3
Wall Shell Thickness	5mm
Roff Shell Thickness	3mm
Columns	IPB180
Ring Stiffeners	UNP 100

Table 2: Material Properties

Wall Shell	S275 JR
Roof Shell	S275 JR
Profiles	S235JR

Table 3: Structural Mass

Cylinder	519ton
Roof	153ton
Piston	712ton
Auxiliary Structure	43ton

3.2 Finite element model

The finite element (FE) numerical model developed considered some simplifications, as only the main structural components of the tank were modeled. These parts are: i) wall shell; ii) columns; iii) wall stiffening rings; iv) roof shell; v) roof structure. In Figure 5 is illustrated the FE model developed. According to the parts modeled, the following types of finite elements were used:

- Wall shell and roof shell: the element used is the S4R. This is a 4-node doubly curved thin or thick shell, reduced integration hourglass control, finite membrane strains. Five integration points through thickness.
- Columns, stiffening rings and roof structure: the element used is B31. This is a 2-node linear beam in space.

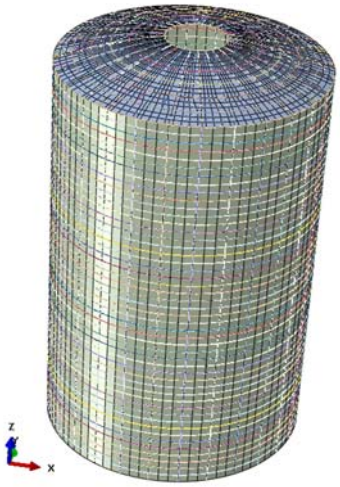

Figure 5: FE model developed

In order to consider the total mass of the tank, as the non-structural elements were neglected in the modelling, additional masses were introduced as non-structural masses. In Table 4 are described the additional masses considered. The total mass of the tank model, including structural and non-structural elements, is 1427ton. The connections between the different structural members have been considered continuous, even in the case of the wall shell-column. These two members are connected using rivets along the total height of the columns, as depicted in Figure 6. In what concerns to the supports, connection to the ground, the column base were modeled as pinned connections. For the material mechanical behavior, an elasto-plastic with hardening constitutive law was used. Finally, it should be noticed the following:

- In the non-linear analyses, both material and geometrical nonlinearities are considered.
- As the working pressure ($400mmH_2O \approx 0{,}039atm \approx 3{,}92kPa$) is relatively low; the mass of the gas was neglected.
- No geometrical imperfections and residual stresses were considered (analysis on perfect structure).

Table 4: List of non-structural masses considered in the FE model

Member	Additional Mass [ton]	Comments
Columns	0.25	Mass of the non-structural elements distributed along the total height of the columns.
	713.0	Piston mass applied at highest possible position. The mass is distributed amongst all columns and along ≈6m of the column length so that the resultant is at the highest working position.
Roof Structure	2.52	Additional mass due to non-structural elements and distributed along the total length of the roof structure members.

a) Connection detail

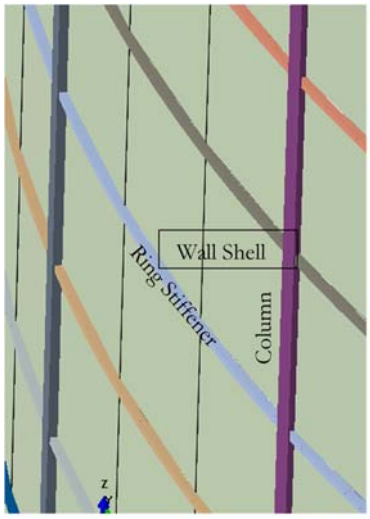

b) FE model detail

Figure 6: Connection between Column and Wall

3.3 FE model failure criteria

In order to identify a possible failure of the structure during the analysis, the failure criteria in Table 5 have been specified.

Table 5: List of failure criteria

Criterion	Description
1 – Limit of plastic strains	$\varepsilon_u = 0.2$
2 – Global or local instability	Global loss of stability of the structure or local instability of parts of the structure.
3 – Resistance of the column bases connection	Exceedance of the resistance of the column bases connection to uplift loads.

In order to avoid the complexities related to the modelling of the column bases connection, the third criterion is verified in the post-processing of the numerical results, comparing the uplift forces with the column base resistance. The resistance of the column bases was determined according to the design rules given in [6] and [7]. For the present case study, the resistance is 315kN.

In what concerns the wall shell of the gas tank, though at first one may regarded the tank structure as a shell structure reinforced by the columns (usually called stringers in shell structures), their resistance to buckling is barely inexistent. The resistance of the shell was estimated according to [8] and [9]. The tank structure stability is then guaranteed by a "classic" structure composed of columns and beams, being the main function of the wall and roof shells the resistance to the internal and external pressures, and consequently distribute these pressures to the main structural members. The second function of the wall shell is to contribute to the global lateral stiffness of the structure.

4 SEISMIC PERFOMANCE OF NON-ISOLATED STRUCTURE

4.1 General

In a first stage, the performance of the original gas tank structure to seismic actions was evaluated. Several numerical simulations were conducted in order to characterize the structure response to dynamic actions, developing inertia forces on the structure, and to evaluate the seismic performance of the non-isolated structure. The performed simulations considered the following types:

- Modal Analysis
- Push-over Analysis
- Time-History Nonlinear Analysis → Incremental Dynamic Analysis

For the Time-History Nonlinear Analysis, and Incremental Dynamic Analysis, and within the scope of the PROINDUSTRY project [4], two sets of 11 Ground Motions (GM) have been generated on the basis of available information on ground motion histories from national, European and Mediterranean Strong Motion Data-bases. One set is representative of areas with low-medium seismicity and another set is representative of areas with high seismicity. ground motions were

4.2 Modal analysis

In order to obtain the natural vibration modes, a modal analysis was executed. The procedure used consists in the Lanczos method. The range of frequencies in the calculation was limited to 20Hz. Within the range of frequencies between 0Hz and 20Hz, only two global modes were observed and these correspond to the same mode though, for each orthogonal direction. Many local modes (percentage of mass participation is almost zero) were obtained. The first natural frequency is 2,64Hz with a total mass participation of 88,65% in the main direction and nearly 0% in the other orthogonal direction. Figure 7-a) presents the shape of the 1st natural frequency. The local deformation at approximately 2/3 of the height is due to the consideration of the piston mass at this position (highest position possible). Figure 7-b) presents the first mode obtained in the calculations which represents a local mode.

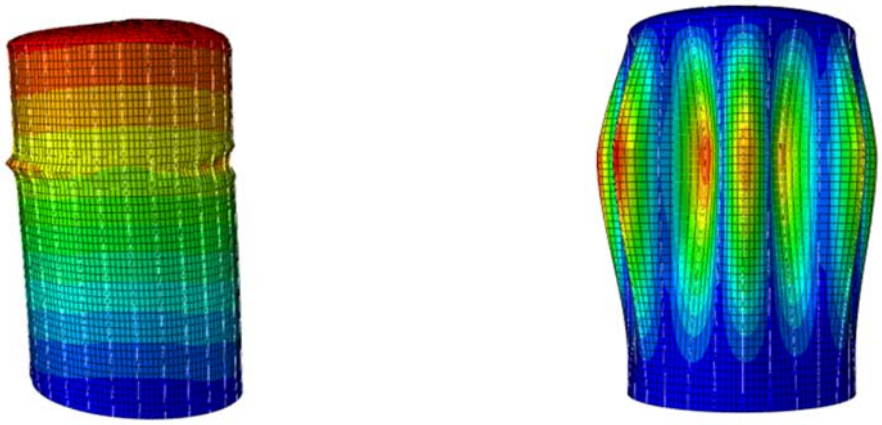

a) 1st global mode b) 1st local mode

Figure 7: Natural vibration modes of the gas tank structure

4.3 Push-over analysis

The push-over analysis consisted in applying a horizontal force at the center of mass of the tank. Given the magnitude of the piston mass, the position considered was the highest working height of the piston, approximately 2/3 of the gas tank height (see Figure 8). The load was applied directly to the columns, as these members are the vertical support of the piston. The load was distributed within a length which approximates the length of the piston structure inside the tank. The load was increased until one of the following failure criteria was achieved: i) plastic limit strain attained; ii) local or global instability detected by the numerical calculation. In this analysis the column bases connections resistance was disregarded.

In Figure 9 is presented the force-displacement curve obtained from the push-over analysis. The force corresponds to the base shear and the displacement is the displacement measure at the top of the gas tank structure (at the top of the columns). The maximum load is identified by a peak in the force-displacement curve. A sudden loss of resistance after this peak load is observed which is due to loss of stability of the gas tank structure. Then, there is an increase of resistance after equilibrium is recovered. The ultimate strain is attained in the tank structure members later for a significant lateral displacement.

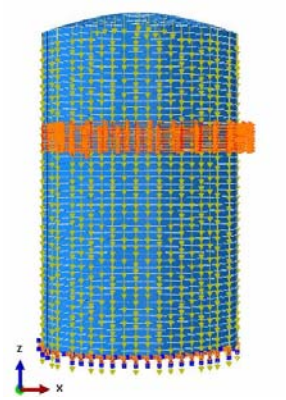

Figure 8: Location of the loading in the push-over analysis

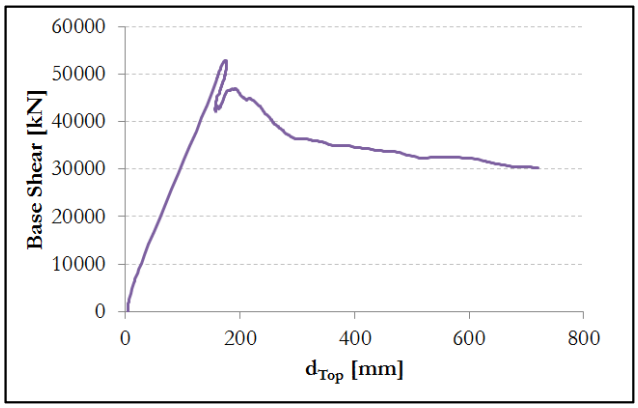

Figure 9: Force-displacement curve obtained from the push-over analysis

4.4 Incremental dynamic analysis

The nonlinear time-history analysis, basis of the incremental dynamic analysis (IDA), were performed using the general nonlinear dynamic analysis available using implicit time integration to calculate the transient dynamic or quasi-static response of a system.
The procedure used consisted in imposing base acceleration at the support nodes of the gas tanks structures. The base acceleration applied represent the ground motions generated within the project and referred above. These ground-motions are characterized by a time-history acceleration for each orthogonal direction (X, Y and Z). In the performed calculations, the ground motions (base accelerations) for each orthogonal direction were applied simultaneously. Two sets of ground motions were considered; one representative of low-medium seismicity areas, and one representative of high seismicity areas. In Table 6 are listed the spectral accelerations and the corresponding scale factors considered in IDA analyses.

Table 6: List of spectral accelerations used in the IDA

Low Seismicity Areas				High Seismicity Areas			
Pvr	Tr	ag	S. F.	Pvr	Tr	ag	S. F.
%	Yrs	g	\	%	Yrs	g	\
4	2475	0.199	2.78	4	2475	0.512	1.43
5	1950	0.1854	2.592	5	1950	0.4687	1.307
10	949	0.1501	2.098	10	949	0.3586	1.000
22	402	0.1140	1.593	22	402	0.2502	0.698
30	280	0.1016	1.420	30	280	0.2122	0.592
39	202	0.0916	1.280	39	202	0.1829	0.510
50	144	0.0812	1.135	50	144	0.1552	0.433
63	101	0.0715	1.0	63	101	0.1292	0.360

In all executed calculations, the time-history was completed. Consequently, the two first failure criteria specified in Table 5 were not violated. In order to evaluate the global deformation of the structure, the relative displacement of the roof was computed. In Figure 10 are presented the results for both sets of GMs, High and Low-Medium seismicity areas, and for one of the orthogonal directions in the ground plane. The values represent the maximum values obtained

through the time-history simulation. For almost all cases the structure is on the linear range. Local yielding is observed however; this is not reflected on the global response. The maximum value is 150mm. Taken into account the height of the gas tank and that in the vicinity, at least 2m separate this gas tank from other structure, the values is barely insignificant.

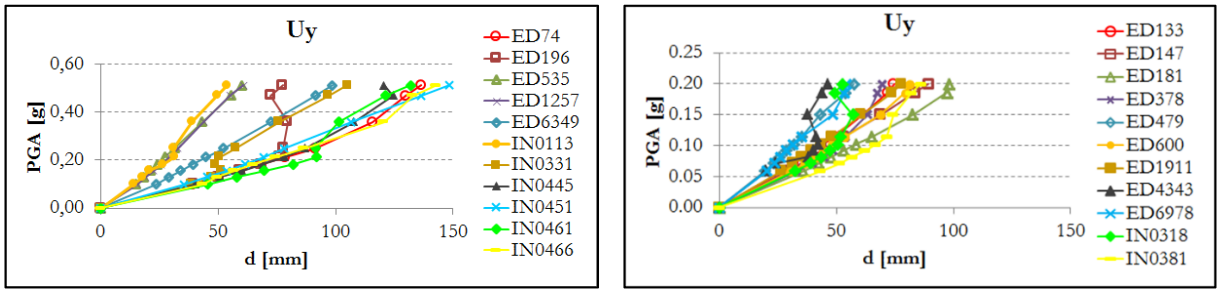

a) High seismicity areas b) Low seismicity areas

Figure 10: Gas tank roof relative displacements result of IDA calculations on non-isolated structure

In Figure 11 is plotted the parameter which expresses the plastic strains, the equivalent plastic strain (PEEQ). These plastic deformations are located in the members, mainly in columns and ring stiffeners, in the region of the piston mass and consequently, the region were the inertia forces are greater. In Figure 11 only the maximum values are shown, for each time-history simulation of the IDA analysis. Since for Low-Medium Seismicity GMs these are barely inexistent, only the values for the High Seismicity GMs are presented. In the chart is included the limit strain considered in the numerical models (0.2). It can be observed that not only this limit was not exceeded, but the maximum equivalent plastic strain is approximately half of this limit. Up to a scale factor of 1.0, an almost linear relation between the peak ground acceleration characterizing the GMs and this parameter is obtained. For higher scale factors, for some cases this linearity is lost. This may be due to the damping effects when the plasticity becomes higher. However, in general this is not significantly reflected in the global response, as discussed above.

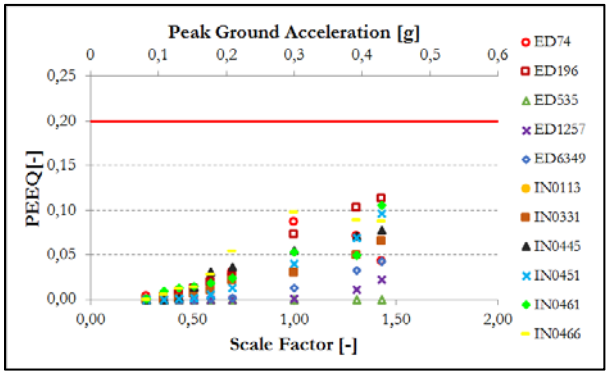

Figure 11: Maximum PEEQ result of IDA calculations on non-isolated structure (only High Seismicity areas GMs)

In order to verify the third failure criterion, the uplift forces on the column bases and the respective resistance were compared in Figure 12. These forces are due to the tank overturning and the vertical component of the seismic action. It can be seen that this is clearly a critical point of the structure. Only for few cases, amongst all GMs representing both seismicity's areas, and for the lowest scale factors, this resistance was not exceeded. In the case of the High Seismicity areas, the maximum values are considerably high, approximately 10 times greater, and

almost impossible to overcome with improvement of the connection and therefore, seismic protection is required.

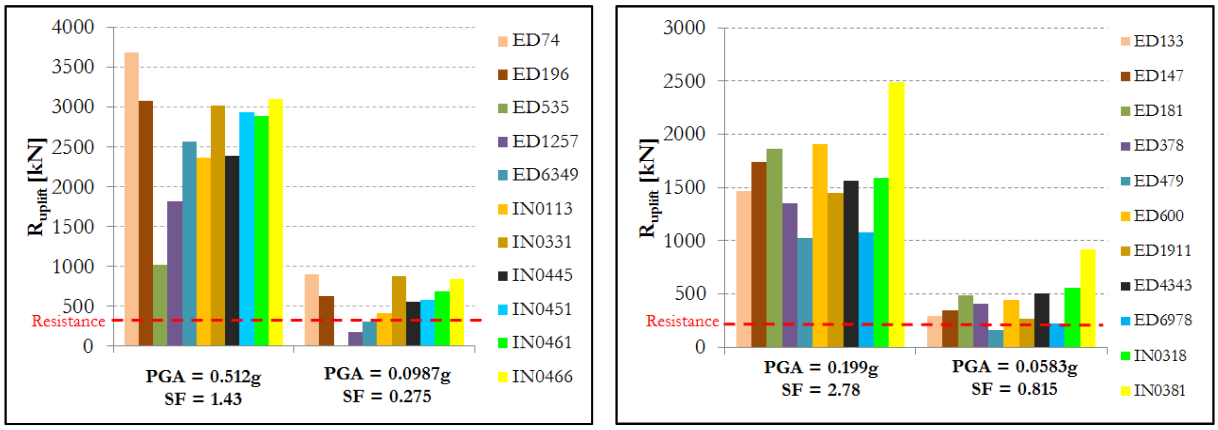

a) High seismicity areas b) Low seismicity areas

Figure 12: Column bases uplift forces results of IDA calculations on the non-isolated structure

5 EFFICIENCY OF THE SEISMIC PROTECTION SYSTEM: BASE ISOLATION SYSTEM

5.1 Model of the base isolation system

For the base isolation system of the gas tank structure 28 units (isolators), one under each column, are foreseen. Note, that this should be placed in the same vertical position of the columns, not directly under the columns, but between a "Support" slab and the foundation (isolation interface), as illustrated in Figure 13. The incorporation of the isolators on the FE model consisted in a system that combines a spring element and an elastio-plastic element (or friction element) working in parallel. The spring element has a pure elastic linear behavior which represents the isolator stiffness to slip (dynamic friction). The friction element, incorporates the friction force (static friction) developed between the slider and the concave surfaces. The friction force is proportional to the superstructure mass (M). It is usually assumed that the behavior of this element is rigid until the static friction is exceeded. Then, free deformation of this element is considered.

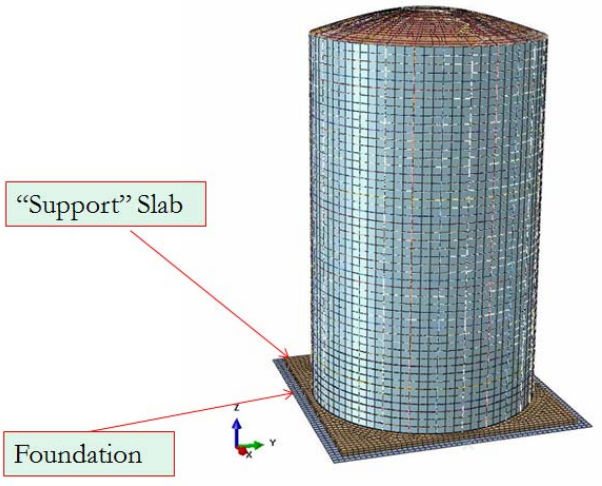

Figure 13: FE model of the base isolated gas tank structure

To model the behavior of the isolation system, the following parameters are determined:

- The total weight (W) and mass (M) of the superstructure and of the "Support" slab above the isolation system.
- The friction coefficient (μ) between the slider and the concave surfaces.
- The fundamental period of the device. This values are usually between 3,5s and 4s (T).
- The stiffness of the Isolator which may be approximated by the following equation:

$$k_{isol} = M\frac{4\pi^2}{T^2} \quad (1)$$

In Table 7 are presented the values of the parameters described above and assumed in the present case study. In Figure 14 is illustrated the force-displacement response of the isolation system.

Table 7: Properties of the base isolation system of gas tank structure

M [ton]	W [kN]	μ [-]	T [s]	$K_{iso,system}$ [kN/m]
1581.1	15495.3	0.3	3.5	5095.6

The determination of the properties of each isolator unit is obtained through "decomposition" of the equivalent isolation system properties described above. Remember, that in this case 28 individual isolators are considered. Given the symmetry of the structure, these 28 isolators have equal properties. Thus, the equivalent isolation system reproduces the behavior of 28 parallel isolators and accordingly the properties of each isolator unit are obtained: the elastic spring stiffness and friction element maximum force are divided by 28. In Figure 15, the properties of these two elements representing an isolator unit are shown.

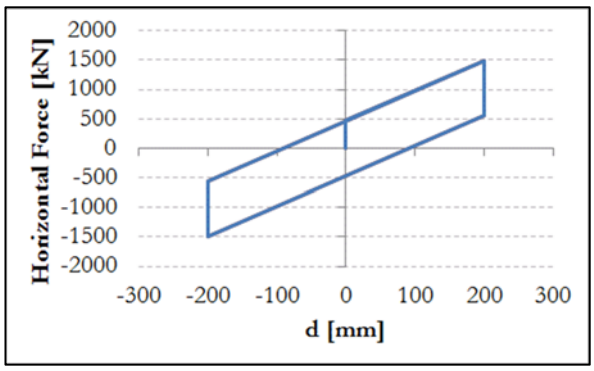

Figure 14: Force-displacement behavior of the base isolation system

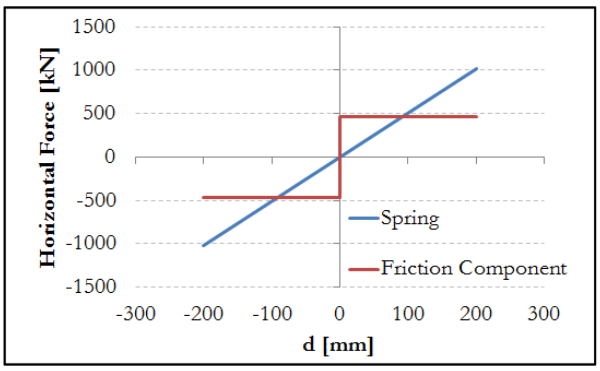

Figure 15: Behavior of the spring and friction element representing an isolator

5.2 Impact on the structure response

The purpose of the base isolation system is to reduce the horizontal (soil plane) base displacement of the superstructure. This is achieved through the seismic energy dissipated by the isolation system. At this stage, the isolators properties are in a process of calibration and therefore, only the time-history nonlinear analysis using the GMs, representing the high seismicity areas, were used. Furthermore, the simulations only considered the scale factor equal 1. In Figure 16 is shown the time-history tank roof relative displacement for one of the orthogonal direction on

the base (ground) plane for GM ED74. The chart includes the results for both cases, non-isolated and isolated structure. The impact of the base isolation system is evident. The tank roof relative displacement on the isolated structure is 26% of the value obtained in the non-isolated structure. In Figure 17 are presented the maximum tank roof relative displacement, for one of the orthogonal directions (ground plane) achieved during the time-history nonlinear simulation. The chart includes all GMs representative of the high seismicity areas. The reduction on the gas tank roof relative displacement is a constant for all GMs. The results of the different GMs show that the most demanding GM for the non-isolated structure do not correspond to those for the isolated structure. This is expected as the isolated structure has a different response due to the modification on the fundamental period, which corresponds to that of the isolation system.

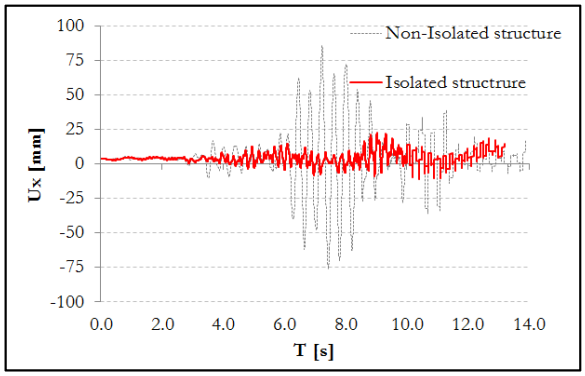

Figure 16: Time-history gas tank roof relative displacements comparing non-isolated and isolated structure

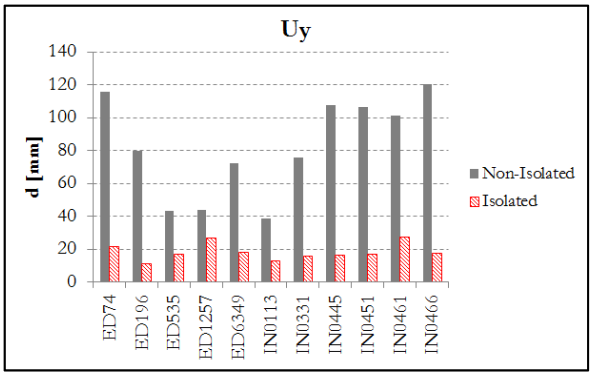

Figure 17: Maximum gas tank roof relative displacements comparing non-isolated and isolated structure (all GMs)

In Figure 18 are presented the results of the uplift forces on the columns. Remember that, according to the simulations on the non-isolated structure, column bases resistance to uplift forces are the critical parts of the present structure. A comparison with the results of the simulations on the non-isolated structure and the theoretical resistance of the column bases to uplift forces is included. Again, it is evident the impact of the base isolation system. It possible to see that for the isolated structure only GM ED74 exceeds the theoretical resistance of the column bases. In the case of the non-isolated structure, all GMs exceeded this value. Though, in the case of the GM ED74 the uplift forces, on the isolated structure, are greater than the column base resistance, the values are now closer (of the same order). Thus, an improvement of the column base may solve the problem. The values on the non-isolated structure were impossible to bear with reasonable modifications. As explained above, the uplift forces arise from two sources: the vertical component of the seismic action and the structure overturning due the inertia forces. The base isolation system is capable of mitigate the impact of the latter, but not of the first. In Figure 19 this is demonstrated. In one simulation, the vertical component of the seismic action was considered, and in the other neglected. The simulations were performed on the isolated structure. One can observe that when the vertical component of the seismic action is removed, the uplift loads are barely inexistent. It also clear that the base isolation system manages to eliminate almost 2000kN of uplift load showing clearly its efficiency. On the other hand, it must be noted that the vertical component of the seismic action is real and cannot be neglected. Therefore, together with the base isolation system, an auxiliary system has to be considered to transfer these forces.

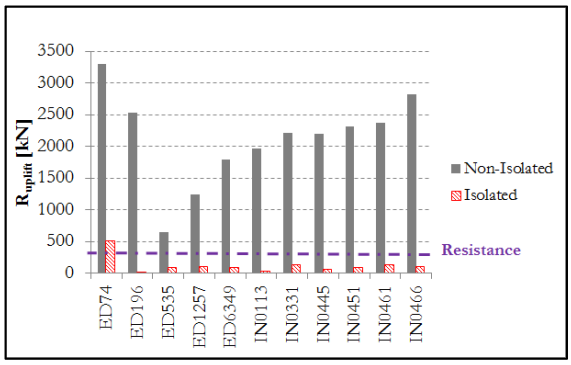

Figure 18: Maximum uplift loads on column bases (all GMs) and theoretical resistance

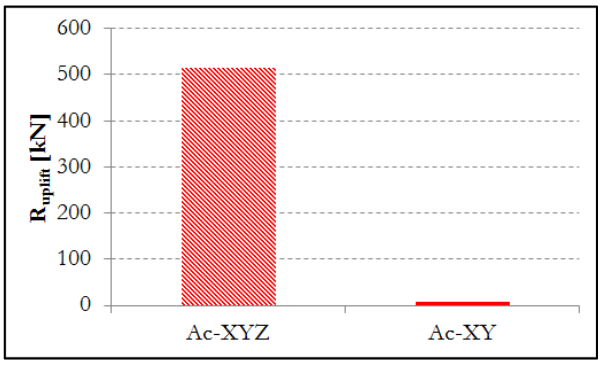

Figure 19: Effect of the vertical component of the seismic action (GM ED74)

5.3 Performance of the base isolation system

In order to evaluate the isolators performance demands, the results of the numerical simulations, on the elements of reproducing the devices behavior, are herein discussed. In Figure 20 are shown the force-deformation curves obtained for two GMs. Remember that the deformation represents the distance between the superstructure base and the foundation. This has to be accomplished through movement of the slider on bottom and upper sliding surfaces. The force represents the inertia forces developed in the superstructure which have to be transferred to the supports through the isolators. The two GMs shown represent the extreme cases: the one with smaller deformations and the one with higher deformations. The values measured are considerably different. In the case of GM ED196 the maximum deformation is approximately 125mm, while in the case of ED1257, the maximum is of approximately 1500mm. If in the first, the value is perfectly within the deformation capacity of the isolator, the second overcomes this limit excessively. The reason for such differences is on the fundamental period of the base isolation system and on the period at which the ground displacement spectrum attains its maximum. As it can be seen in Figure 21, the latter occurs at approximately 3,5s which corresponds to the fundamental period of the isolators. Thus, a calibration of the isolator properties is required in order to have an isolator that can also perform in the case of seismic actions as GM ED1257. This issue is under investigation at the current stage.

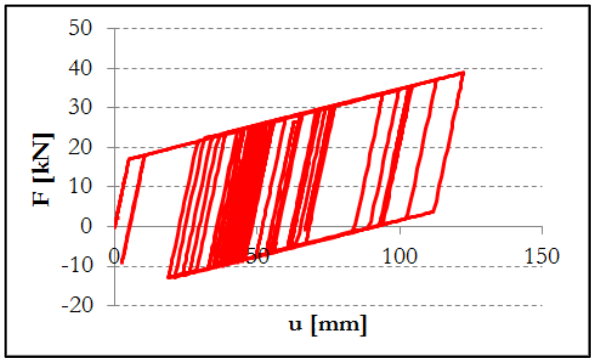

a) ED196

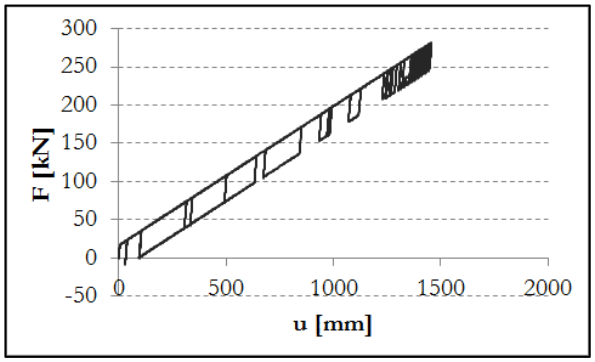

b) ED1257

Figure 20: Force-deformation curve on isolators

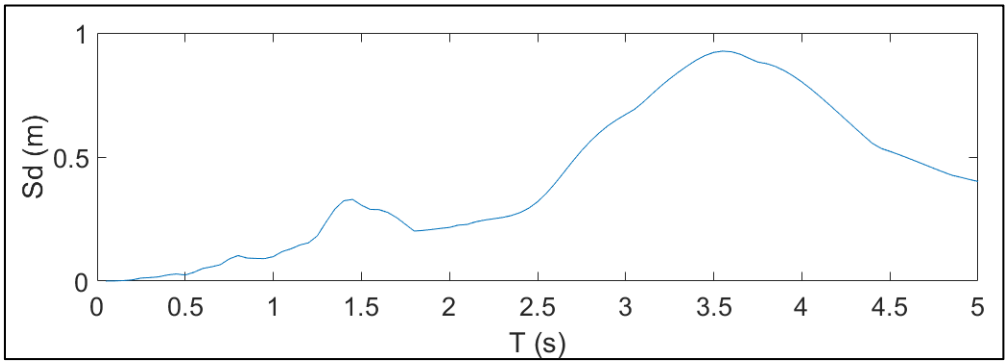

Figure 21: Ground displacement spectrum for GM ED1257 in the X direction (in soil plane)

Figure 20 shows that several cycles are accomplished. A quantification of the number was performed and is shown in Figure 22. The chart presents the number of cycles for different ranges of cycles amplitude. Intervals of 50mm of amplitude were defined. In the chart are included all GMs representative of the high seismicity areas. The following observations highlight from these results: i) the majority of the cycles have a small amplitude; ii) only for few GMs high amplitude of cycles occur; iii) the maximum amplitude of the cycles is smaller than the maximum displacement shown in Figure 20-b) for GM ED1257. The latter shows that cycles may occur with minimum deformations of the isolators greater than zero (considerably in some cases). In Figure 23 are quantified the total number of cycles the isolators undergo, independently of the cycles amplitude. The maximum number is 35 and this occurs for the GM ED1257. The minimum is 7 for ED6349.

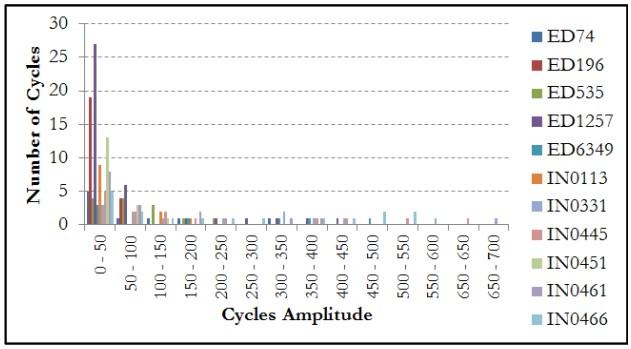

Figure 22: Isolator number of cycles for different cycles amplitude (all GMs)

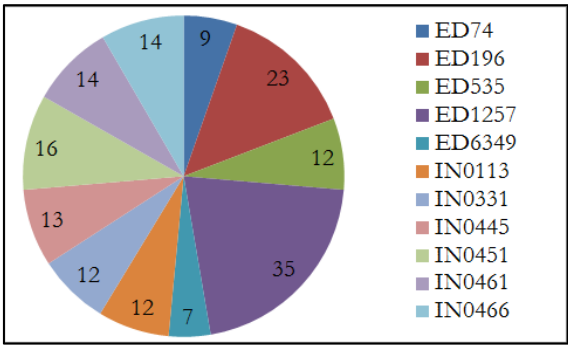

Figure 23: Total number of cycles on isolator (all GMs)

6 CONCLUSIONS

This paper presented the work in progress within the RFCS research project PROINDUSTRY dedicated to the seismic protection of industrial plants. In particular, a case study of a gas tank was discussed. The behavior of the tank structure was characterized based on several numerical simulations considering: modal, push-over and time-history nonlinear analysis (in an incremental dynamic analysis procedure). From the latter, the column bases resistance to uplift loads have been identified has the critical part of the structure. Subsequently, the investigation considered the implementation a base isolation system to provide seismic protection to the structure. The base isolation system considered is the double curved surface slider (CSS). From the numerical simulations, on the isolated structure, has been observed that the seismic impact on the structure is mitigated using this device. However, for some ground motions, the deformation

required on the isolation system, to dissipate the seismic energy, is excessive. This happens because, for some ground motions, the fundamental period of the seismic device is very close to the peak ground response spectrum. Consequently, a calibration of the base isolation system is under investigation.

ACKNOWLEDGEMENTS

The research leading to these results has received funding from the European Union's Research Fund for Coal and Steel (RFCS) research programme under grant agreement n° [RFSR-CT-2013-00019].

REFERENCES

[1] G. Antonioni, S. Bonvicini, G. Spadoni, V. Cozzani, *Development of a Frame-work for the Risk Assessment of Na-Tech Accidental Events*, Reliability Engineering & System Safety 94 (9), 1442-50, 2009.

[2] Minitère de l'écologie, du développement durable et de l'énergie, *Panorama Des Accidents Industriels Survenus Lors Du Grand Séisme et Tsunami Du Tohoku*, Minis-tère de l'écologie, du développement durable et de l'energie, 2013.

[3] W. Salvatore, E. De Pasquale, H. Degee, B. Hoffmeister, C. Castiglioni, F. Braga, C. Butz, *Seismic protection of industrial plants by enhanced steel based systems*, Annual Re-port - Technical report No 1, project Nº RFSR-CT-2013-00019, European commission, Brussels, 2013.

[4] W. Salvatore, E. De Pasquale, H. Degee, B. Hoffmeister, C. Castiglioni, F. Braga, C. Butz, *Seismic protection of industrial plants by enhanced steel based systems*, Mid-Term Report, project Nº RFSR-CT-2013-00019, European commission, Brussels, 2015.

[5] V.A. Zayas, S.A. Low, S.A. Mahin, *The FPS Earthquake Resisting System*, Experi-mental Report, Report UCB/EER 87/10, Earthquake Engineering Research Center, University of California, Berkeley, 1987.

[6] European Committee for Standardization, CEN, *EN 1993-1-8. Eurocode 3: Design of steel structures. Part 1-8: Design of joints*, Brussels, 2005.

[7] European Committee for Standardization, CEN, *CEN/TS 1992-4: Design of fastenings for use in concrete*, Brussels, 2009.

[8] European Committee for Standardization, CEN, *EN 1993-1-6. Eurocode 3: Design of steel structures. Part 1-6: Strength and stability of shell structures*, Brussels, 2007.

[9] European Convention for Constructional Steelwork, ECCS, *Buckling of steel shells European design recommendations*, Publication nº 125. John Michael Rotter and Hebert Schmidt (Eds), 5th Edition, September 2013.

ECCOMAS Congress 2016
VII European Congress on Computational Methods in Applied Sciences and Engineering
M. Papadrakakis, V. Papadopoulos, G. Stefanou, V. Plevris(eds.)
Crete Island, Greece, 5–10 June 2016

PERFORMANCE-BASED NONLINEAR RESPONSE HISTORY ANALYSIS FRAMEWORK FOR THE "PROINDUSTRY" PROJECT CASE STUDIES

Marco Faggella[1], Raffaele Laguardia[1], Rosario Gigliotti[1], Francesco Morelli[2], Franco Braga[1] and Walter Salvatore[2]

[1]Sapienza University of Rome
Via Eudossiana 18
{marco.faggella, raffaele.laguardia, rosario.gigliotti, franco.braga}@uniroma1.it

[2]University of Pisa
Largo Lucio Lazzarino 2, 56126 Pisa, Italy
{francesco.morelli@dic, walter@ing}.unipi.it

Keywords: Nonlinear Response History Analysis (NL RHA), Performance Based Earthquake Engineering (PBEE), Incremental Dynamic Analysis (IDA), Ground Motions (GM), Uniform Hazard Spectrum (UHS), Conditional Mean Spectrum (CMS).

Abstract.*Within the PROINDUSTRY project a Performance-based analysis framework is defined for seismic assessment of industrial structures, based on Nonlinear Response History Analysis (NL RHA) using in particular the Incremental Dynamic Analysis (IDA) method. This paper describes the choice of the PBEE and IDA analysis methods starting from an overview of state-of-the-art methods. The choice is analyzed in relation to: analysis goals for the selected case studies (design-based vs. risk-based), availability of databases/tools for hazard analysis and GMs selection, accuracy of criteria to scale and match GMs to a target spectrum (UHS, CMS, etc.) and treatment of record components. Three possible approaches of GMs selection are described and analyzed: (1) UHS-coherent Unscaled (Design), (2) UHS-coherent GMs scaled to Sa(T1) (Risk/Loss), (3) CMS-coherent GMs scaled to Sa(T1), (Risk/Loss). Within the scopes of PROINDUSTRY, the approach (1) is proposed, as a trade-off between simplicity of conventional PBEE design methods and probabilistic robustness for a heterogeneous portfolio of structures/facilities.*

1 INTRODUCTION

Recent seismic events in Europe have pointed out the importance of assessing, managing and mitigating the seismic risk of industrial plants [1], [2]. The"Seismic PROtection of INDUSTRial plants by enhanced steel based sYstems" (PROINDUSTRY) project aims at developing enhanced seismic protection systems for process plants, process units, storage units, pipeline and pipe systems, through innovative antiseismic techniques: seismic isolation and energy dissipation systems (such as the one described in [3]). The project includesthe definition of a framework for seismic assessment of industrial structures, based on Nonlinear Response History Analysis (NL RHA) using in particular the Incremental Dynamic Analysis (IDA) method. The framework shall be defined to allow not only the assessment of the current case studies seismic vulnerability, but also the comparison between the seismic behavior before and after the application of the anti-seismic systems.

Seismic design provisions for industrial plant structures can be found under the ASCE/SEI 7-10 provisions [1], particularly for the structure types of 'non-buildings similar to buildings', and 'non buildings not-similar to buildings'. Design codes classify structures types and behavior based on q, R factors for use in force-based linear analysis and design. Correspondence between US codes and Eurocode 8 [5] and capacity design rules are described in [6] and [7]. A comprehensive review of NL RHA code procedures for different types of structures is carried out in the NIST GCR 11-917-15 document 'Selecting and Scaling Earthquake Ground Motions for Performing Response-History Analyses', [8]. In general, the different seismic design codes prescribe a reference spectrum and indicate the number of Ground Motions (GMs) needed to perform NL RHA. The general requirement is to use 7 different GMs and process results in terms of best estimates, or use 3 different GMs and the max response values.

A review of current Performance-Based Earthquake Engineering (PBEE) code provisions for NL RHA in terms of their evolution and underlying vision is useful to analyze what is the most appropriate context, what are the objectives of the prescriptions, and what should be the expectations of a chosen protocol of analysis. Two main types of PBEE design and assessment are identified and discussed: (A) 1st Generation PBEE approach, described in the most commonly used codes of practice; and (B) a Next generation PBEE approach, with new performance metrics and a broader vision in terms of risk analysis.

1.1 First Generaton PBEE (Design-based)

1st Generation reference codes/guidelines for design/assessment prescribe force-based linear methods of analysis/design classifying structures based on type (new/existing buildings, bridges, seismically isolated structures, nuclear plants, liquefied natural gas tanks), and define structural performance matching limit states (identification of component damage level) with a probability of exceedance of the seismic intensity (FEMA356/ASCE41). These codes prescribe also methods of NL analysis, both static and dynamic, and rules for RHA and GM selection. The objective of these code provisions is the performance assessment at the component level, checking/comparing member demand with capacity. Assessment/design of industrial structures and their retrofit using innovative devices are covered by the following documents:

- **Eurocodes**:
  - UNI EN 1998-1 (New Buildings)
  - UNI EN 1998-3 (Assessment and retrofit of buildings)
  - UNI EN 1998-4 (Silos, tanks and pipelines)
  - UNI EN 1998-6 (Towers, piles and chimneys)

- **US codes and guidelines**:
  - New buildings, ASCE/SEI 7-05 (2005), ASCE/SEI 7-10 (2010)
  - Existing buildings, ASCE/SEI 41-06 (2007)
  - Isolated and conventional bridges (AASHTO, 2010 a, b)
  - Nuclearfacilities, ASCE/SEI 43-05, (2005)
  - Liquefied natural gas facilities (FERC, 2007)
  - Dams, FEMA 65, (2005)
  - Civil works, EC1110-2-600 (U.S. Army Corps of Engineers, 2009)
  - Department of Defense facilities, UFC 3-310-04, (Dept. of Def., 2004, 2007, and 2010)
  - Storage tanks, API Standard 650 (2007), API Standard 620 (2009)

Whether used with linear force-based analyses or nonlinear procedures, design methods of the first generation contain a number of limitations regarding in particular:

- *Discrete limit states*: the definition of performance, with respect tosingle components or to the structure as a whole, related to the achievement of a certain limit state is still coarse and often involves questionable margins of conservatism.
- *Accuracy and reliability of procedures.*
- *Performance measures:* Engineering parameters used for definition of performances, such as drift, accelerations, stresses, strains etc., are not understood by entrepreneurs, investors, lenders, and decision makers.
- *Deterministic approach:* the assessment of performance is purely deterministic, only the intensity of the seismic action is modeled in a probabilistic way.

Figure 1. PROINDUSTRY project: someof the industrial case study structures.

1.2 Next-Generation PBEE (Risk/loss-based)

To address these limitations the Pacific Earthquake Engineering Research center developed a Performance Based Earthquake Engineering methodology (PEER PBEE, [12]) and tested it on a number of benchmark structures. For building structures these efforts culminated in the release of the FEMA P-58guidelines, which is a fully probabilistic new paradigm for risk/loss based PBEE [13], [14], and of its companion tool for damage-based accumulation of monetary performance/loss at the global level (PACT tool, [15]). Uncertainties are explicitly considered in terms of: human losses (loss of lives, injuries, etc.), direct economic losses (cost of repairs, replacements, etc.), and indirect economic losses (downtimes, Unsafe placarding, etc.).

The methodology incorporates the components of the PEER PBEE approach, namely the Probabilistic Seismic Hazard Analysis (PSHA), the Structural Analysis, the Damage and Loss analyses. The seismic hazard is defined in terms of Uniform Hazard Spectrum (UHS), or alternatively in terms of Conditional Mean Spectrum (CMS) [16] and Conditional Spectrum (CS) [17]. Three main types of assessment are considered: a) Intensity-based, b) Scenario-based and c) Risk/Time-based. At the core of the methodology is the structural analysis module, based on NL RHA with sets of natural GMs.

Analysis of these documents is important to define a protocol for PROINDUSTRY, giving due consideration to the fact that the FEMA P-58 methodology is developed specifically for building structures, and there is no codified reference document on application of complete PBEE risk/loss framework for industrial structures in general. It is also very important to remark that a comprehensive risk-based approach is beyond the scopes of PROINDUSTRY, which foresees a 1st-gen design/assessment approach. Therefore an appropriate, sufficient, and closer reference document for the analysis approach to develop in WP2 is the NIST GCR 11-917-15. This document is intended for practicing engineers and structural analysts, and contains recommendations on NL RHA analysis protocols and ground motions selection/scaling/matching to target spectra.

An important aspect to consider is that the analysis protocol should be aimed at comparing the structural performance and behavior before and after retrofit with innovative protective devices. Since isolation and energy dissipation devices change drastically the structural system and properties, and in particular the parameter $S_a(T_1)$, and modify the system response as a whole as well as the nonlinear interaction with the superstructure [18], it is desirable that the analysis method and the inherent scaling criterion of the input GMs is as much as possible independent on the properties of the structure.

The FEMA P-58 and NIST guidelines would be easy to follow selecting GMs from the PEER NGA database [19], and scaling to the UHS or CMS provided by USGS, using the extensive database and interactive online tools. However this approach may not be consistent with this EU project. On the other hand some difficulties may arise using the currently available interactive tools (INGV-ESSE project, [20], [21], [22], [23], [24], [25]) or those under development [26] from the Italian/EU databases and PSHA. Some limitations may persist if the CMS is used as target spectrum, and if the GMs are to be scaled to this CMS, particularly due to the inherent type of the local seismicity, both related to the intensity and to the causative sources, [16].

2 OVERVIEW OF NL RHA AND IDA

A key component of modern codes for PBEE design and assessment is the simulation of the structural behavior through realistic nonlinear models, and appropriate analysis protocols. For few cases of very simple and regular structures (1st mode dominated response) the analysis protocol can be of the static type (NL Pushover). In all other cases a dynamic type (NL RHA) is needed to simulate the realistic response due to multi-mode contributions, velocity-dependent effects, randomness of the input, etc.Although many traditional performance-based codes and guidelines describe methods for performing RHA, it must be noted that most of these documents contain rules that were developed in the 80s and were intended for performing analyses of structures with nonlinearseismic isolation and energy dissipation devices [8], with less evidence from application to structures with NL behavior due to plastic hinging, buckling, or structural damage in general.

A crucial point for the selection of the method for NL RHA analysis is to identify the project's goals in terms of analysis, and the key Engineering Demand Parameters (EDP) representative of the structural response/behavior.

This choice is reflected in the two types of approaches that can be found in traditional and more recent PBEE codes/guidelines:

- DESIGN approach: the analysis goal is to compute mean values of response (few GMs are needed, codes prescribe 7 or 3 GMs).
- FRAGILITY/RISK approach: the analysis goal is to compute mean and distribution of response and evaluate collapse probabilities. (Many more GMs are needed, normally 30+, or 11 if conditioning to an IM, less if particular spectra are used).

The Incremental Dynamic Analyses (IDA is a parametric extension of the NL RHA used to estimate performance under seismic loads subjecting a structural model to one (or more) GM records [27]. It consists in a sequence of Monte Carlo analyses, and performs an intensity sweep for each GM by scaling the records to an increasing reference IM until collapse occurs.

IDA has been proposed as 1) a dynamic protocol capable of describing the structural behavior over a number of intensity/response levels and ranges, (to capture the changing in the dynamic structural behavior increasing the seismic intensity, conceptually similar to static pushover), and 2) a probabilistic analysis protocol that incorporates the randomness inherent to the detail of the GM input record, and the randomness in the seismic hazard intensity, through scaling/conditioning the GMs to an appropriate Intensity Measures (IM). Usual choices for IM have been the PGA and the spectral acceleration at the fundamental period $S_a(T_1)$.

IDA can be used for different types of assessment, depending on what kind of information is sought, whether the interest is on structural performance and component checks, or on fragility and decision-oriented information. It may be useful to note that in some cases, the inherent computational burden of performing a large number of Monte Carlo simulation runs, which can be typical of IDA, can be overcome by running parallel parametric probabilistic simulations of a same FEM model, [28]. This approach is feasible with FEM software with capabilities to run relatively simple models on parallel supercomputers [29].

2.1 GMs SELECTION

The first step to perform NL RHA or IDA is the selection of appropriate sets of GMs. The NIST guidelines [8] present a comprehensive overview of codes provisions for NL RHA and provide guidance on methods for selection/modification of input GMs.

2.2 ASCE/SEI 7-05

Rules for selecting and scaling GMs provided by ASCE/SEI 7-05(§16.1.3) [1] can be summarized as follows:

- A GM shall consist of a horizontal acceleration history, selected from an actual recorded event having magnitudes, fault distance, and source mechanisms that are consistent with those that control the maximum considered earthquake.
- The GMs shall be scaled such that the average value of the 5 percent damped response spectra for the suite of motions is not less than the design response spectrum for the site for periods ranging from 0.2T to 1.5T where T is the fundamental period of the structure in the fundamental mode for the direction of response being analyzed
- For 3D analysis GMs shall consist of pairs of appropriate horizontal ground motions components.

- For each pair of horizontal GM components, a square root of the sum of the squares (SRSS) spectrum shall be constructed by taking the SRSS of the 5% damped response spectra for the scaled components (where an identical scale factor is applied to both components of a pair). Each pair of motions shall bescaled such that for a period between 0.2T and 1.5T, the average of the SRSSspectra from all horizontal component pairs does not fall below 1.3 times thecorresponding ordinate of the design response spectrum by more than 10 percent.
- If 3sets (or more) of GMs are selected, the component checking must be done with the maximum values that come from the analysis.
- If 7 sets (or more) of GMs are selected, the component checking must be done using the average values that come from the analysis.

It must be noted that the SRSS method for spectrum matching has no solid technical basis, and the use of Geomean Spectrum is suggested by NIST for spectrum matching [8]. These guidelines point out clearly that the use of a certain number of sets of GMs (in this case 3 or seven are suggested) has no sound technical basis too. As mentioned above, these rules were developed mostly in the 80s in the context of NL RHA of structures with nonlinear base isolation and energy dissipation devices. The correct number of GMs needed depends on many factors such as the goodness of fit of the scaled motion to the target spectral shape, the expecteddispersion in the response, the required degree of confidence, and the required level of accuracy. Some formulations are available which permit to estimate the correct number of GMs needed independentonthe spectral shape [30]. In general more than seven GMs are needed to obtain a reliable and accurate evaluation of the mean response and, as a consequence many tens of GMs are needed to obtain correct evaluations of the dispersions.

2.3 ASCE/SEI 7-10

Rules defined in ASCE/SEI 7-10 [31] are similar to those defined in ASCE/SEI 7-05, the main difference being that the design spectrum definition is done using the maximum rotated component spectrum instead of the geomean spectrum, and so the SRSS method for spectrum matching of 3D components should be preferred to have more reliable results.

2.4 FERC 2007

The US Federal Energy Regulatory Commission drafted the Seismic Design Guidelines andData Submittal Requirements for LNG Facilities (FERC, [32]), whichidentify the performance criteria to be met for this type of structures and refer to ASCE/SEI 7-05 for the procedures for GMs selection.

2.5 Eurocode8 (buildings)

UNI EN 1998-1defines the methods for representing the seismic action through GMs in §3.2.3.1 and prescribes that:

- Recorded GMs may be used, provided that thesamples used are adequately qualified with regard to the seismogenic features of thesources and to the soil conditions appropriate to the site, and their values are scaled tothe value of a_g*S for the zone under consideration.
- A minimum of 3 GMs should be used.
- The mean of the zero period spectral response acceleration values (calculated from singleGMs) should not be smaller than the value of a_g*S for the site inquestion.
- In the range of periods between $0,2T_1$ and $2T_1$, where T_1 is the fundamental period of

the structure in the direction where the GM will be applied; no value of themean 5% damping elastic spectrum, calculated from all time histories, should be lessthan 90% of the corresponding value of the 5% damping elastic response spectrum.

In §4.3.3.4.3 EC8 defines the required number of GMs:

- If the response is obtained from at least 7 nonlinear time-history analyses with GMs in accordance with 3.2.3.1, the average of the response quantities fromall of these analyses should be used as the design value of the action effect E_d in therelevant verifications of 4.4.2.2. Otherwise, the most unfavorable value of the responsequantity among the analyses should be used as E_d.

2.6 Eurocode8 part 4 (silos, tanks, pipelines)

For the definition of the seismic action UNI EN 1998-4 refers to UNI EN 1998-1.

2.7 Eurocode8 part 6 (towers, pile, chimneys)

For the definition of the seismic action the UNI EN 1998-6 in §3.4 refers to UNI EN 1998-1 in general and allow the use of rotational components of ground motion. These provisions also suggest paying specific attention to the long period components of the time-histories which affect in a critical way the response of this type of structures.

2.8 FEMA P-58 (Next generation PBEE methodology. Buildings)

As noted above the prescriptions of FEMA P-58 could apply to industrial structures in those particular cases where the structural type is similar to buildings. The same hazard and analysis modules would apply in this case, however the exposure and loss modules would have to be made consistent to the particular case studies. We already discussed how exposure and risk/loss are beyond the scopes of PROINDUSTRY. As far as the NL RHA and IDA analysis module is concerned, the FEMA P-58 guidelines are in agreement with the NIST 2011 guidelines.

FEMA P-58 dedicates the entire third chapter to the definition of the seismic hazard, and to themethodsfor selection and scaling of GMs, with the following recommendations:

- Three different kind of spectrum are defined: UHS (Uniform Hazard spectrum), CMS (Conditional Mean Spectrum), and CS (Conditional Spectrum).
- Regardless of the type of selected spectrum, the selected ground motions must match (without specific limitation), on average, the selected spectrum over the period range T_{min} to T_{max}, where $T_{max}$is taken as twice the period of the fundamental translational mode (the larger of T_x, T_y if a 3D analysis is performed) and T_{min} is taken as 0.2 times the fundamental period (the smaller of T_x, T_y if a 3D analysis is performed).
- Selected records should have faulting mechanisms, earthquake magnitudes, site-to source distances, and local geology that are similar to those thatdominate the seismic hazard at the particular intensity level.
- At least 7 pairs of GMs should be used, but when fit with spectral shape is poor eleven or more pairs of motions are needed to correctly capture the median response.

3 POSSIBLE APPROACHES

Inthe scientific literature and in building codes it is difficult to identify a general ruleNL RHA and IDA method, and the protocols are strictly dependent upon what is the goal of the analysis, in terms of what is the type of assessment sought, and in terms ofwhat are the critical mechanisms and the relevant Engineering Demand Parameters (EDPs) and response indicators (drift-governed structural damage, force-controlled mechanisms, floor acceleration-

governed component vibrations, anticipated relevance of higher modes, etc.), and what is the level of confidence requested.

Based on the building codes and guidelinesalready described, three different approaches for selecting and scaling GMs are analyzed. For each approach advantages and disadvantage are discussed, with respect tothe specific goals and challenges of the PROINDUSTRY project, and of the specific case-study structures.

In general, the possible methods comprise the following steps:

1) Definition of facilities and locations;
2) Identification of the analysis needs;
3) Identification of the Ground Motions Intensity Measure (PGA or IM=$S_a(T^*)$, etc.) for a specific Hazard Level (HL);
4) Development of the Probabilistic Seismic Hazard Analysis (PSHA) in terms of IM, (Attention to how the local PSHA is derived, one horizontal component, maximum, or geomean, etc.);
5) Definition of the Target Spectrum (UHS, CMS, or CS);
6) *Selecting horizontal GMs for coherence/scaling to the target spectrum*;

The three approaches suggested herein differ in how point 6) is developed, based on which of different kinds of target spectra and on the use of scaled vs. unscaled GMs.

The criteria to perform the spectrum matching are similar in most guidelines/codes, and require that the average spectrum of the set does not differ from the reference spectrum with a tolerance of +30% / -10%. The period range where it is necessary to ensure this tolerance is between $0.2T^*$(to account for higher modes) and $2T^*$(to consider inelastic response with relative loss in stiffness and shift of period, as per UNI EN 1998-1). If the structurehas identifiablemodes associated with translational response along two orthogonal axes, X and Y, the corresponding fundamental translational periods associated witheach axis are denoted with T^*_X andT^*_Y, respectively. The reference period T^* to use for spectrum matching/anchoring can be the mean of the two periods T^*_X andT^*_Y. For the particular case of this project, and due to the difficulty of defining a reference period, it would be desirable to enlarge the period range used for coherence as much as possible.

Table 1. NL RHA and IDA GM selection/scaling approaches as per ASCE-7, NIST 2011, FEMA P-58.

APPROACH	Reference Spectrum	Scaling	Goal(s)	Coherence	GMs
1. UHS, Unscaled	Uniform Hazard Spectrum (UHS) Design Spectrum (DS)	Unscaled	Median	Y	**7+**
			Median and STD	Y	30+
2. UHS, Scaled	Uniform Hazard Spectrum (UHS) Design Spectrum (DS)	Scaled to IM=$S_a(T^*)$	Median and STD	Y	7+
				N	11+
3. CMS, Scaled	Conditional Mean Spectrum (CMS)	Scaled to IM=$S_a(T^*)$	Median	Y	7+
			Confidence on median	Y	<11

With reference to spectral matching and scaling, specific attention deserves the choice of the directional GM components. A common method suggested by several guidelines (FEMA P-58) performs the spectrum matching or in general the coherence assessment based on the geomean of the X and Y components. Other reference codes, in particular building codes provisions, may consider the two components separately, their maximum or a different combination, such as the SRSS. The consistency of the methods is strictly related to the hazard definition, whether the reference spectra and the underlying PSHA are derived based on the geomean, or on a single GM component. The consistency should be checked on a case-by-case basis, particularly for those case study structures where the directional effect can be significant due to different behavior in two orthogonal directions.The three candidate approaches for the WP2 of the PROINDUSTRY project are summarized in Table 1, in terms of number of GMs needed, of scaling/unscaling criterion, of spectral coherence, and goal in statistic confidence.

3.1 APPROACH 1 (UHS-coherent Unscaled GMs, Design).

IDA with unscaled GMs, consistent with a design spectrum (UHS), referred to PGA of HL.

The first approach is a 'design' approach, in line with 1st generation PBEE codes/guidelines. It is based on unscaled recorded GMs coherent with the UHS or with the Design Spectrum. In this method the PGA is used as reference IM, therefore the definition of the input is independent on the structure.

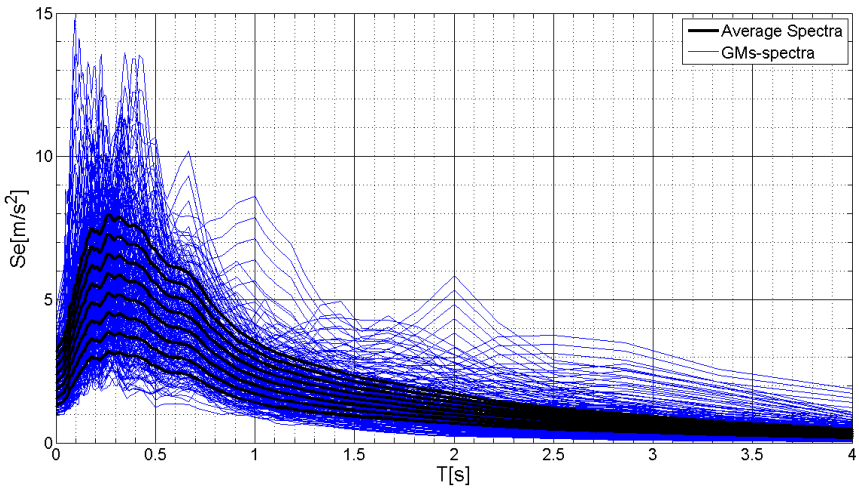

Figure 2.Example of relatively unscaledGMs sets, uniformintensity-scalingto different HLs based on PGA.

Unscaled natural GMs will have a fairly uniform dispersion of spectral ordinates over the range of periods of interest. This type of input is not specific to a particular structure or behavior and is intended to give the same importance to first mode, higher modes, and period-elongated/damaged fundamental modes. This will be reflected in the estimates of the different response parameters (drifts, accelerations, etc.). As a consequence of this dispersion, a greater number of GMs will be required to capture the median response and dispersion, normally 7+ GMs to capture the median, and 30+ GMs to capture a distribution. Given the design/check-oriented objectives of PROINDUSTRY, the suggested number of GMs is 11.

3.2 APPROACH 2 (UHS-coherent GMs scaled to $S_a(T_1)$).

IDA with scaled GMs conditioning/anchoring to Sa(T_1) of HL on the UHS.

This approach uses as reference IM the spectral acceleration at a defined conditioning period IM=$S_a(T^*)$. Usually, for structures that are 1st mode dominated $S_a(T_1)$ is a good predictor of the response, and is well correlated with nonlinear response at increasing intensity levels. However, in general T^* could differ from the 1st mode period and should be selected on a case-by-case basis as the period whose spectral ordinate more influences the EDP that governs the seismic behavior and the design/assessment process.

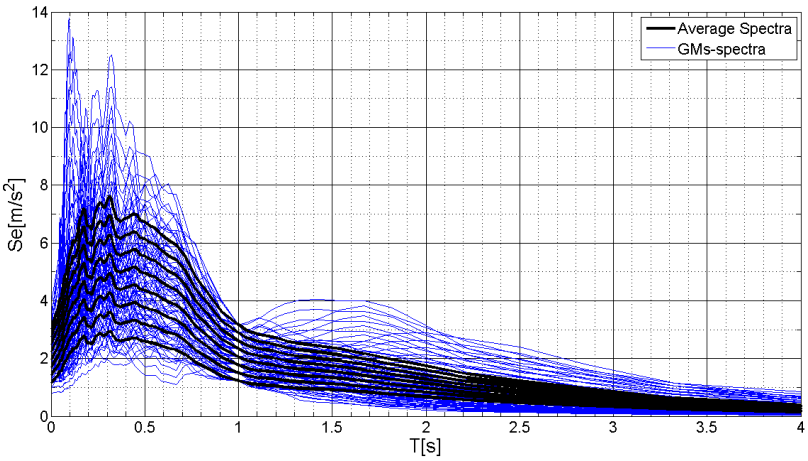

Figure 3. Example of GMs sets with different intensity, scaled to $S_a(T^*)$ values.

Scaling/anchoring the GMs to a given IM allows obtaining sets with less variability around the selected spectral ordinate, resulting in a reduced number of GMs needed to capture the distribution of the response. On the other hand, scaling to a specific IM can result in overly inflated ordinates and increased dispersion at other frequencies (Figure 3). For this reason this method could introduce inconsistencies if the analyzed structures and the selected response parameters are not well correlated to $S_a(T^*)$, since this IM can be not sufficient nor efficient [34] for many structures. For the PROINDUSTRY case studies, and in particular for those sensitive to acceleration spectra [35], [36], this method could result in too conservative and not realistic IDA estimates of forces as well as of displacements/damage.

3.3 APPROACH 3 (CMS-coherent GMs scaled to Sa(T1)).

IDA with scaled GMs conditioning/anchoring to $S_a(T_1)$ of HL on the CMS.

Recent studies proposed the so-called Conditional Mean Spectrum (CMS), [16], to overcome the limitationsof UHS.In a single event it is very unlikely that the spectral ordinates of the UHS are observed at all periods, especially for rare events and so coherence of GMs with UHS is not realistic. The CMS refers to a scenario event for a given HL and conditioning period T^* based on disaggregation data (M, R); the spectral ordinate at this period is maximized (through the parameter ε) and should reach the value given by the UHS for the HL selected. The spectral ordinates at other periods are then related to the $S_a(T^*)$ through conditional probability and correlation factors, and their values are less than those of the UHS. In this way it is possible to reduce the seismic demand for periods away from the conditioning period (reduc-

ing overestimates of high-mode response for example) while retaining consistency with the seismic hazard derivation in terms of a primary IM at a given HL.

The CMS provides the expected (mean) response spectrum, conditioned on occurrence of a target spectral acceleration value at the period of interest. This is a better tool for GMs selection because it is very unlikelyfor a single event to containall the spectral ordinates with the same probability of exceedance. It is more realistic to correlate the different spectral ordinates through conditional probability. The limitations of this method are similar to those of for the approach n.2, and are due to the definition of a specific spectral ordinate for scaling. In addition, computing the CMS could be difficult due to limited disaggregation data for Europe [37], and due to the multi-modal hazard scenarios in most cases, [16], particularly for the sites where the case-study facilities are located.

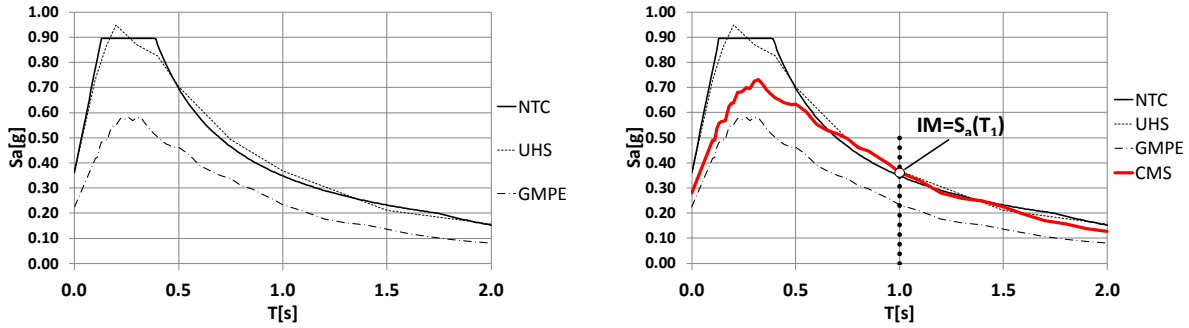

Figure 4.Reggio Calabria site, (a) determination of the median Spectrumusing M, R values, (b)determination of the CMS.

4 CONCLUSIONS AND RECOMMENDATIONS

The three methods illustrated herein can produce different results. It is therefore necessary to identify a reference method that would lead to consistent results for the different project case studies. It is also desirable to compare analysis results among partners working on different case studies. As requested by the project, in order to achieve the worst damage scenarios with a robust and reliable procedure, the first method suggested should be preferred.

The approach n.1 is based on unscaled GMs and is consistent with 1st gen. PBEE design/assessment. This would decouple the definition of the action from the evaluation of the response, and render the seismic input not strictly structure-specific. A major drawback of using unscaled GMs is that a higher number of records need to be used.The project focus is on the assessment of the structural behavior [38] and on proposing retrofit solutions [39], and the interest is on capturing the mean response. To achieve this goal at least 7 GMs are needed but, considered the high variation of the selected GMs (Approach n.1) a higher number of GMs is to be preferred, at least 11 GMs. The results will be processed in terms of best estimates and where necessary also in terms of distribution. This would allow, in a subsequent phase, to compare results and performance assessment based on 2nd gen. risk-based PBEE approaches, by introducing scaling criteria to key IMs, and perform more accurate probabilistic analyses, as well as loss-based comparisons of retrofit solutions [40], [41], 0.

ACKNOWLEDGEMENTS

The authors acknowledge the support of the European Union's Research Fund for Coal and Steel (RFCS) research programme through the project PROINDUSTRY, "Seismic PROtection of INDUSTRial plants by enhanced steel based sYstems", grant agreement n° [RFSR-

CT-2013-00019]. The content of this paper reflects the opinions of the authors and do not necessarily represent the opinions of the funding agency.

REFERENCES

[1] F. Braga, R. Gigliotti, G. Monti, F. Morelli, C. Nuti, W. Salvatore, I. Vanzi, Post-seismic assessment of existing constructions: evaluation of the shakemaps for identifying exclusion zones in Emilia. *Earthquakes and Structures*, 8(1), 37-56, 2015.

[2] F. Braga, R. Gigliotti, G. Monti, F. Morelli, C. Nuti, W. Salvatore, I. Vanzi, Speedup of post earthquake community recovery: the case of precast industrial buildings after the Emilia 2012 earthquake. *Bulletin of Earthquake Engineering*, 12(5), 2405-2418, 2014.

[3] A. Braconi, F. Morelli, W. Salvatore, Development, design and experimental validation of a steel self-centering device (SSCD) for seismic protection of buildings, Bulletin of Earthquake Engineering, Springer, vol. 10, pp. 1915–1941, DOI 10.1007/s10518-012-9380-9, 2012.

[4] ASCE/SEI 7-05, Minimum Design Loads for Buildings and Other Structures. American Society of Civil Engineers, Reston, 2006.

[5] EN 1998-4:2007-07. Design of structures for earthquake resistance – Part 4: Silos, tanks and pipelines. European Committee for Standardization, Brussels, 2007.

[6] M. Wieschollek, M. Kopp, B.Hoffmeister, M. Feldmann, Seismic Design of Spherical Liquid Storage Tanks. In *COMPDYN 2011, III ECCOMASThematic conference on computational methods in structural dynamics and earthquake engineering*, Corfu, Greece, 26–28 May, 2011.

[7] A. Braconi, S. Caprili, H. Degee, M. Guendel, M. Hjaij, B. Hoffmeister, S.A. Karamanos, V. Rinaldi, W. Salvatore, Efficiency of Eurocode 8 design rules for steel and steel-concrete composite structures. *Journal of Constructional Steel Research*, 2015.

[8] NIST, GCR 11-917-15, Selecting and Scaling Earthquake Ground Motions for Performing Response-History Analyses, 2011.

[9] D.M. 14/01/2008. Norme tecniche per le costruzioni, Gazzetta Ufficiale n.29, February 2008.

[10] API Standard 620, Design and Construction of Large, Welded, Low-pressure Storage Tanks, 11th Edition, American petroleum Institute, Washington D.C., 2009.

[11] API Standard 650: Welded Steel Tanks for Oil Storage", 11th Edition, American petrole-um Institute, Washington D.C., 2007.

[12] J. Moehle and G. Deierlein, A Framework Methodology for Performance-Based Earthquake Engineering, Proceedings, *13th World Conference on Earthquake Engineering*, Vancouver, British Columbia, Paper No. 679, 2004.

[13] R.O. Hamburger, C. Rojahn, J.A. Heintz, M.G. Mahoney, FEMA P58: Next-Generation Building Seismic Performance Assessment Methodology,*15th World Conference on Earthquake Engineering,*Lisbon, 2012.

[14] FEMA P-58-1. Seismic Performance Assessment of Buildings. Volume 1 – Methodology, 2013.

[15] FEMA P-58-2. Seismic Performance Assessment of Buildings, Volume 2 - Implementation Guide, 2013.

[16] J. Baker, Conditional Mean Spectrum: Tool for Ground-Motion Selection.*J. Struct. Eng. 137, SPECIAL ISSUE: Earthquake Ground Motion Selection and Modification for Nonlinear Dynamic Analysis of Structures*, 322–331, 2011.

[17] T. Lin, S.C.Harmsen, J. Baker, N.Luco, Conditional Spectrum Computation Incorporating Multiple Causal Earthquakes and Ground‐Motion Prediction Models. *Bulletin of the Seismological Society of America*, 103(2A), 1103-1116, 2013.

[18] F. Braga, M. Faggella, R. Gigliotti, M. Laterza, Nonlinear dynamic response of HDRB and hybrid HDRB-friction sliders base isolation systems. *Bulletin of Earthquake Engineering*, 3 (3), 333-353, 2005.

[19] PEER NGA, Technical Report for the PEER Ground Motion Database Web Application Beta Version – October 1, 2010.

[20] V. Montaldo, C. Meletti, F. Martinelli, M. Stucchi, M. Locati M, On-line seismic hazard data for the new italian building code. *J EarthqEng* 11(S1):119–132, 2007.

[21] C. Meletti, V. Montaldo, Stime di pericolosità sismica per diverse probabilità di superamento in 50 anni: valori di ag. Progetto DPC-INGV S1, Deliverable D2, http://esse1.mi.ingv.it/d2.html, 2007.

[22] D. Spallarossa, S. Barani, Disaggregazione della pericolosità sismica in termini di M-R.Progetto DPC-INGV S1, Deliverable D14, http://esse1.mi.ingv.it/d14.html, 2007.

[23] N. Ambraseys, P. Smith, J. Douglas, B. Margaris, R. Sigbjornsson, S. Olafsson, P. Suhadolc, G. Costa, Internet site for European strong-motion data, *Bollettino di GeofisicaTeoricaedApplicata*, 45(3), 2004.

[24] L. Luzi, S. Hailemikael, D. Bindi, F. Pacor, F. Mele, P. Sabetta, ITACA (ITalianACcelerometric Archive): a web portal for the dissemination of Italian strong-motion data, *Seismological Research Letters,* 79(5), 716-722, 2008.

[25] C. Smerzini, C. Galasso, I. Iervolino, R. Paolucci, Ground motion record selection based on broadband spectral compatibility, *Earthquake Spectra*, 30(4), 1427-1448, 2014

[26] EFEHR portal, European Facility for Earthquake Hazard & Risk. www.efehr.org.

[27] D. Vamvatsikos, C.A. Cornell, Incremental dynamic analysis. *Earthquake Engineering & Structural Dynamics*, 31(3), 491-514, 2002.

[28] M. Faggella, A.R. Barbosa, J.P. Conte, E. Spacone, J.I. Restrepo, Seismic Assessment of R/C Building Structure through Nonlinear Probabilistic Analysis with High-performance Computing. In *AIP Conference Proceedings*, (Vol. 1020, p. 930), 2008.

[29] F. McKenna, G. Fenves, Using the OpenSees interpreter on parallel computers.NEESit report no. TN-2007-16; NEES Cyberinfrastructure Center; La Jolla, CA, 2007.

[30] Y.-N.Huang, A.S.Whittaker, N.Luco, and R.O. Hamburger, Selection and scaling of earthquake ground motions in support of performance-based design. *Journal of Structural Engineering*, Vol. 137, No. 3, pp. 311-321, 2011.

[31] ASCE,Minimum Design Loads for Buildings and Other Structures. American Society of Civil Engineers, ASCE Standard No. ASCE/SEI 7-10, Reston, VA, 2010.

[32] R. Backman,D. Nyman,K.Bhushman,E.V.Leyendecker,L. Lister, Draft Seismic Design Guidelines and Data Submittal Requirements for LNG Facilities, prepared for the Federal Energy Regulatory Commission. (FERC), 2007.

[33] EN 1998-1:2010-12. Design of structures for earthquake resistance – Part 1: General rules, seismic actions and rules for buildings. European Committee for Standardization, Brussels, 2010.

[34] M. Faggella, A.R. Barbosa, J.P. Conte, E. Spacone, J.I. Restrepo, Probabilistic seismic response analysis of a 3-D reinforced concrete building. *Structural Safety* 44, 11-27, 2013.

[35] B. Hoffmeister, M. Gündel, M., Feldmann, Floor response spectra for dissipative steel supports of industrial equipment. In C*OMPDYN 2011, III ECCOMAS Thematic conference on computational methods in structural dynamics and earthquake engineering*, Corfu, Greece, 26–28 May, 2011.

[36] M. Pinkawa, B. Hoffmeister, M. Feldmann, Floor Response Spectra Considering Influence of Higher Modes and Dissipative Behaviour. In *Seismic Design of Industrial Facilities*, (pp. 235-246). Springer Fachmedien Wiesbaden, 2014.

[37] G.P. Cimellaro, Correlation in spectral accelerations for earthquakes in Europe. Earthquake Engineering & Structural Dynamics, 42 (September 2012), 623–633, 2013.

[38] E. Rossi, M. Ventrella, M. Faggella,R. Gigliotti, F. Braga, Seismic Performance of Industrial Storage Plants Retrofitted with Innovative Devices. In *ECCOMAS Congress 2016 VII European Congress on Computational Methods in Applied Sciences and Engineering*, Crete Island, Greece, 5–10 June, 2016. (Submitted).

[39] E. Rossi, M. Ventrella, M. Faggella,R. Gigliotti, F. Braga, Performance-based Earthquake Assessment of an Industrial Silos Structure and Retrofit with Sliding Isolators. In *ECCOMAS Congress 2016 VII European Congress on Computational Methods in Applied Sciences and Engineering*, Crete Island, Greece, 5–10 June, 2016. (Submitted).

[40] V. Terzic, S.K. Merrifield, S.A. Mahin, Lifecycle Cost Comparisons for Different Structural systems designed for the same location Systems Designed for the Same Location. *15th World Conference on Earthquake Engineering*, Lisbon, 2012.

[41] F. Romano, M. Faggella, R.Gigliotti, F. Braga, Seismic Loss Analysis of a Non-ductile RC Buildings with Masonry Infills. *SEMC 2016: The Sixth International Conference on Structural Engineering, Mechanics and Computation*. 5-7 September 2016 Cape Town, South Africa, 2016. (Submitted).

[42] F. Romano, M. Faggella, R. Gigliotti, F. Braga, Components Fragility Functions and Comparative Seismic Risk Analysis of an older R/C Building based on FEMA P-58, *XVI Convegno ANIDIS Ingegneria Sismica in Italia*, L'Aquila, Italy, September 13-17, 2015.

ECCOMAS Congress 2016
VII European Congress on Computational Methods in Applied Sciences and Engineering
M. Papadrakakis, V. Papadopoulos, G. Stefanou, V. Plevris (eds.)
Crete Island, Greece, 5–10 June 2016

PERFORMANCE BASED EARTHQUAKE ASSESSMENT OF AN INDUSTRIAL SILOS STRUCTURE AND RETROFIT WITH SLIDING ISOLATORS

Edoardo Rossi[1], **Michelangelo Ventrella**[1], **Marco Faggella**[1], **Rosario Gigliotti**[1], **Franco Braga**[1]

[1] Università degli studi "La Sapienza" di Roma
Via Eudossiana 18
e-mail: {edoardo.rossi, michelangelo.ventrella, marco.faggella, rosario.gigliotti, franco.braga}@uniroma1.it

Keywords: Industrial Plants, Performance based assessment, Incremental Dynamic Analyses, Retrofit, Friction Isolators.

Abstract. Recent seismic events pointed out the high vulnerability of existing industrial facilities, stressing on safety and high losses inherent to interruption of economic activities and release of environmentally hazardous materials. These structures often have irregular geometry and structural configuration, are subject to aging and corrosion, and are designed without specific performance-based or seismic design criteria. Due to these inherent complexities, retrofit using friction isolators can be a viable and practical solution for performance improvements. This work presents a case study of irregular industrial storage plant structure consisting of a group of six elevated silos resting on a steel frame on one side and connected to a vaulted RC structure on the other. A computational model is built incorporating nonlinearities from the components (braces, beams, columns, etc.) and from the mitigation devices. Retrofit using friction isolators is analyzed and evaluated through linear and nonlinear dynamic analyses under a set of natural ground motions. Results show the effectiveness of the mitigation strategy in terms of performance improvement.

1 INTRODUCTION

Recent seismic events (Bam 2003, Chile 2010, Fukushima 2011, Emilia 2012, etc.) [1–4] pointed out the high vulnerability of industrial plants both in life threatening, economical losses and environmental contamination terms. Damages were observed both in structural and non-structural components such as mechanical equipment, piping systems and storage racks. The consequences of such damages ranged from the complete collapse of the structure to interruption of the activities, including the triggering of fires and the release of hazardous content.
Within the framework of the Seismic PROtection of INDUSTRial plants by enhanced steel based sYstems (PROINDUSTRY) project, a group of case studies has been selected. Each case study is representative of a particular category of structures, depending on the geometry, the activity of the plant and the type of material processed. This paper presents a retrofit solution of a storage structure consisting of a group of elevated silos containing sodium percarbonate.
The main cause of damage observed on elevated steel silos during earthquakes lies in the failure of the support structure, which generally results in the collapse of the structure [6]. The shell structure of the silo can be considered safe since the acceleration needed to cause buckling phenomena of the wall is generally several times higher than the one causing damage to the substructure or the anchorage [6– 8].
The retrofit solution proposed for the structure object of this study focuses on the reduction of the action transmitted to the substructure.

2 CASE STUDY STRUCTURE

The case study industrial structure consists of a group of six elevated silos supported by a steel structure and connected on one side to a concrete vaulted industrial building. The silos, located approximately 7m above ground, have a cylindrical shape with a diameter of 3.1m, a height of 6.77m and a wall thickness of 5mm. The content is sodium percarbonate, a typical product used in the cleaning industry, characterized by a weight per unit volume of 1200kg/m^3. A single silo can contain up to 16.3m^3 of material. The silos rest on a steel structure composed of a deck and two slender columns. The two columns are HEA360 profiles with an S235 steel grade. The deck is composed a series of main beams realized through HSU profiles, several secondary beams (IPE profiles) with the function of transferring the weight of the silos to the main beams and two horizontal bracing systems, located at the top and at the bottom of the HSU profiles, mainly composed of L or double L profiles. The connection to the RC structure is made via two spherical hinges. The concrete structure is composed of four hollow pillars with a dimension of 1400x900mm and a central hole of 800x300mm and a 30mm thick vault anchored to the pillars at a height of 6m and with a maximum rise of 2.5m.

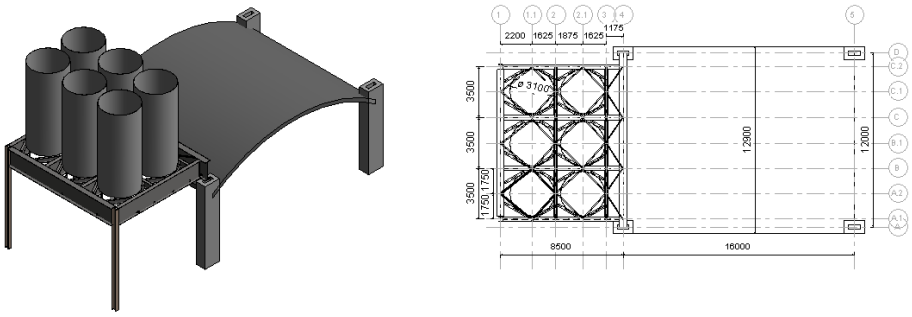

Figure 1: Case study silos structure 3D and plan view.

The actual performance was established through an assessment study of the structure. A preliminary analysis on the components has shown how a traditional or simplified model may lead

to large errors. In particular the attention was focused on the main beams, the silos and the RC vault. On the first two components the comparison has been carried out between a frame and a shell model. The last one was investigated in terms of actions transmitted to the steel structure and of stiffness. Comparisons are reported in Figure 2. The numerical model was built using SAP2000. The main beams have been modeled through linear elastic shell elements with connection only on the web. The secondary beams have been modeled as frame elements with fiber plastic hinges while the braces have been modeled using multi-linear plastic links incorporating a phenomenological model for their buckling hysteresis cycle. The steel columns are modeled with frame elements and fiber plastic hinges. The concrete structure is linear elastic; the pillars are modeled with frame elements while the vault is made with shell elements. The foundations blocks are modeled with rigid shell elements to simulate the soil-structure interaction with linear springs. The silos are modelled through elastic shell elements with distributed mass so to correctly account for their deformability.

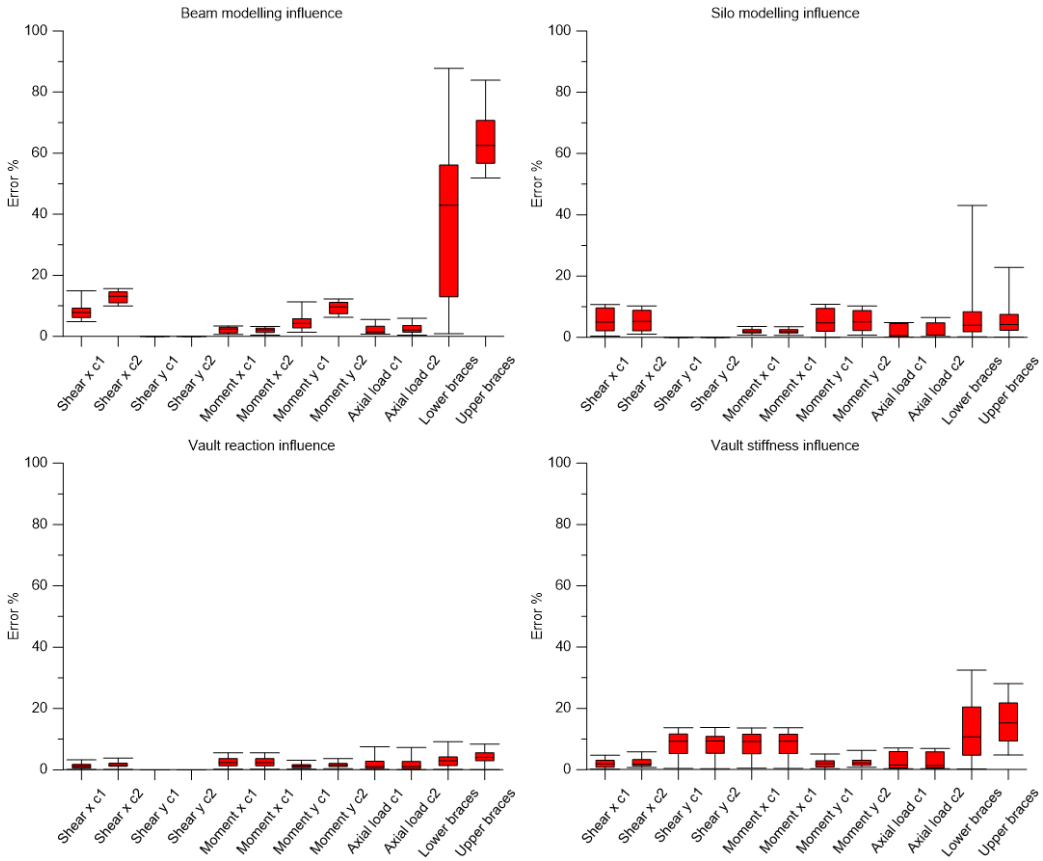

Figure 2: Influence of the different models in the numerical response of the structure.

Static and dynamic analyses, which considered the variability of the action through through a suite of earthquake records [9], were used to establish the main damage causes, which were due to a fragile failure of the steel columns, caused by buckling effects, resulting in a complete collapse of the system. The silos remained fully elastic, consistent with observation found in the literature [6–8]. The braces suffered extensive yielding without however triggering any brittle behavior. The consequences of the damage were mainly economic (collapse of part of the plant, interruption of activities, loss of content) and environmental (dispersion of polluting material). As a reference performance objective for the retrofit solution, prescription of the Eurocodes were adopted [10]. It is worth noting that different performances were evaluated using

nonlinear static and response spectrum dynamic analyses, as it is reported in Figure 3. Although the pushover curve shows a qualitative representation of the behavior under horizontal forces, it fails to correctly estimate the actual performance of the structure since it does not take into account the vertical component. Vertical actions in combination with relative high displacements due to a torsional behavior, produce a collapse mechanism governed by buckling in the column, which can correctly be detected only using nonlinear dynamic analysis.

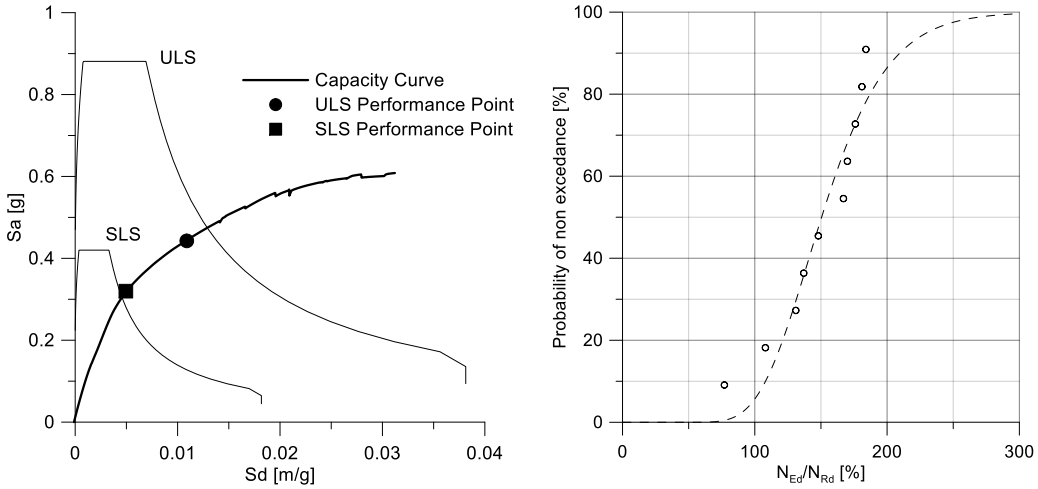

Figure 3: Structure assessment using nonlinear static analysis (left) and response spectrum dynamic analysis (right).

3 NONLINEAR ANALYSES AND RETROFIT

The retrofit solution chosen consists of isolation of the main mass (i.e. the silos) of the system. Curved surface sliders have been introduced between the vertical elements (pillars and columns) and the deck, thus limiting the horizontal action transmitted to the substructure and decoupling the behavior of the system. The steel columns have been connected to the pillars introducing three beams positioned below the isolation plane. The substructure in this configuration was, however, too flexible, thus reducing the effectiveness of the isolation solution (Figure 4). A vertical bracing has been introduced between the two steel columns in order to stiffen the substructure, which has been considered to remain elastic and thus has been modeled with linear elastic truss elements. The friction devices have been modeled with nonlinear link elements with parameters reported in Table 1.

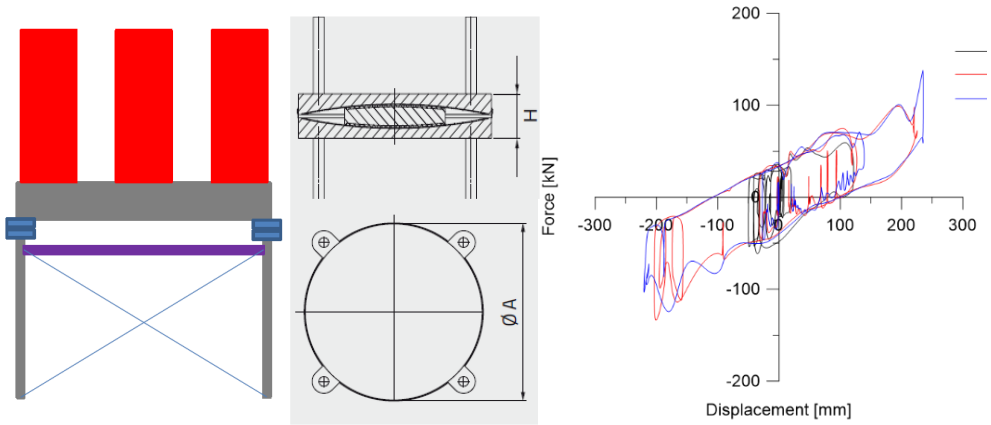

Figure 4: Retrofit scheme: Isolation and bracing of the substructure.

.

Parameter	Value
μ	3,6%
R	3000mm
d_{max}	350mm
N_{Ed}	1000kN
A	580mm
H	135mm

Table 1: Friction Isolator Device parameters.

The seismic action has been modeled with a set of unscaled Ground Motions (Figure 5) [9] and various scale factors calculated dividing the probabilistic hazard curve in regular steps. The hazard curve has been calculated from the hazard definition of the Italian Code NTC08 [11-12]. The resulting limit states however were different from Eurocodes prescriptions, for this reason other two scale factors were introduced: 0.86, corresponding to an Ultimate Limit State with an importance factor of 1.2, and 0.41, corresponding to a Serviceability Limit State with an importance factor of 1.2 (Figure 5) [10].

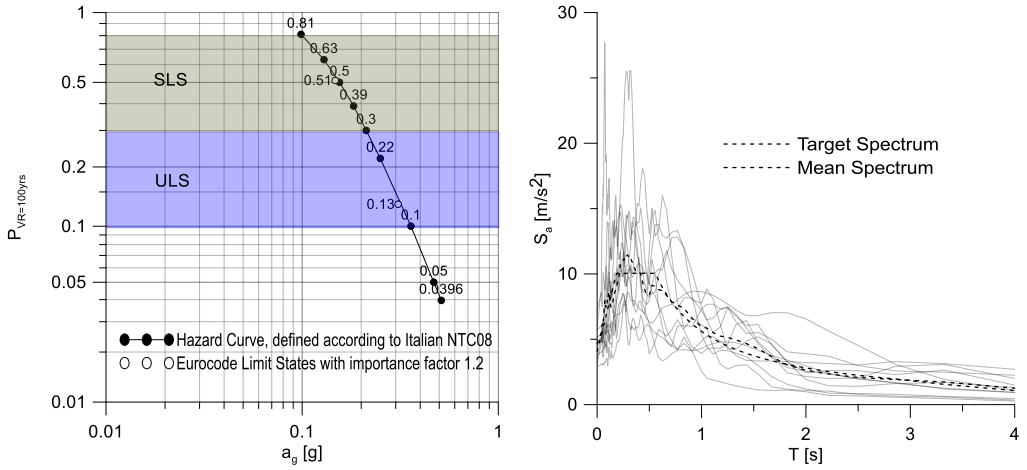

Figure 5: Action definition. Left: Probabilistic Hazard Curve. Right: Ground Motions spectra matching to the target spectrum.

The linear analyses were done using the response spectra of the set of selected ground motions. CQC was used as modal combination and CQC3 as directional combination.
Since the only source of nonlinearities, in the retrofitted structure, were the links used to model the isolation devices it has been possible to perform Fast Nonlinear which were more computationally efficient than Direct Integration method (D.I.) both in terms of time and accuracy of results, due to the issue of damping leakage [13]. Results of the modal analysis show how the introduction of the isolation devices just below the deck is effective in decoupling the structure response. Figure 6 clearly shows the differences in the modal response of the structure before and after the retrofit intervention and how the retrofit solution strongly reduces the torsional behavior of the structure. The increment in period can be found in Table 2

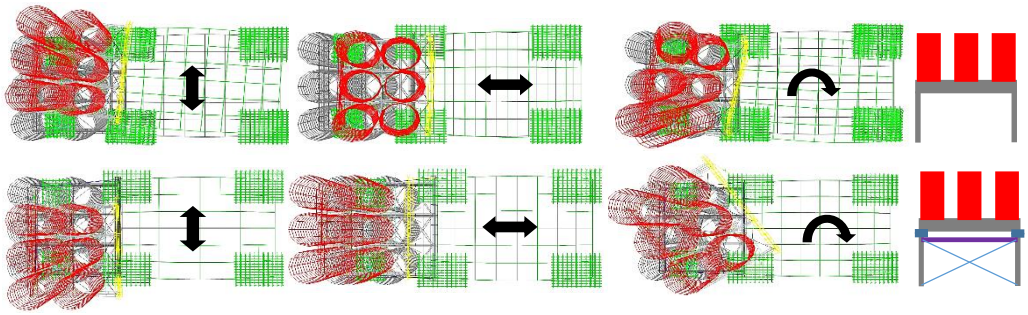

Figure 6: Comparison of the behavior of the structure at ULS.

Existing		Isolated	
Period [s]	Mass	Period [s]	Mass
0.87	74%	3.02	60%
0.65	81%	3.07	60%
0.37	35%	1.61	12%

Table 2: Modal Periods and Masses.

Results of the non-linear dynamic analyses presented in Figure 7 show the improvement of the structural behavior after the introduction of the isolation devices. In particular in the pre-retrofit situation, the structure exhibited a critical behavior, due to the collapse of the columns for buckling phenomena, triggering a complete collapse of the structure. The introduction of the isolation devices proves to be an effective strategy since, due to the reduction of the displacement of the substructure, the vulnerability of the steel columns is greatly reduced, both in terms of critical load and moment at the base, especially in the y direction.

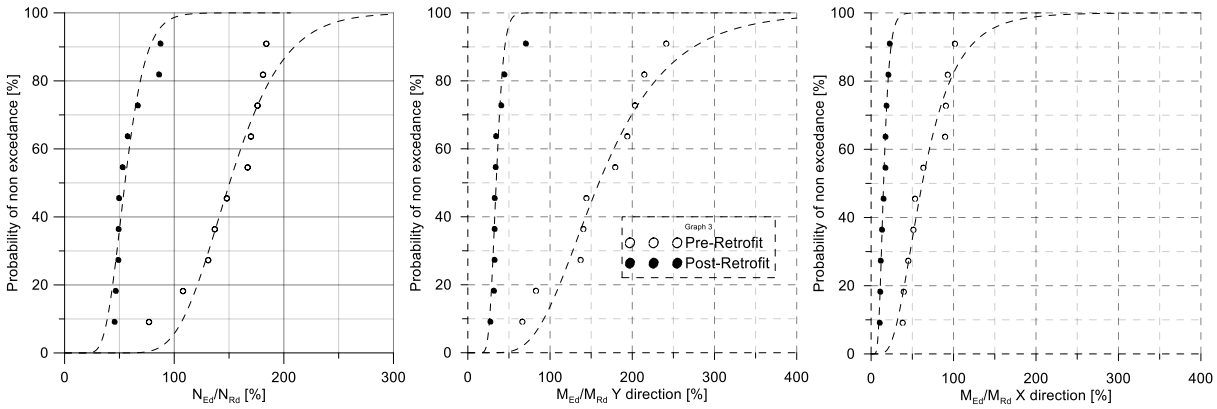

Figure 7: Comparison of the behavior of the structure at ULS.

4 CONCLUSIONS

Performance based assessment of an existing steel silo structure was carried out through linear, nonlinear static and incremental dynamic analyses, both in the existing and retrofit solution using sliding devices. Results have shown that:

- The complex geometry of most industrial structures needs a thorough study of the single components. Using traditional models may lead to important errors in describing correctly the behavior of the system;
- Static nonlinear analyses neglect the effect of the vertical component and may thus lead to inaccurate results;

- The use of isolation devices regularizes the structure behavior, eliminating the torsional effects;
- The use of Direct Integration nonlinear dynamic analyses on very deformable or isolated structures, due to damping leakage phenomena, can cause a strong reduction of the displacement, thus providing nonrealistic results as compared to Fast Nonlinear Analyses;
- Placing the isolation plane just below the stock units, and thus just below the main mass, can significantly increase the performance of the sub structure, both in terms of reduction of the horizontal component and in the protection against buckling phenomena induced by the vertical component;
- The strong reduction of the stiffness of the superstructure enables the designer to have a wider range of choices in terms of stiffening the substructure, being thus able to find an optimum solution, which can take into consideration the processing activities.

5 ACKNOWLEDGMENTS

The research leading to these results has received funding from the European Union's Research Fund for Coal and Steel (RFCS) research programme under grant agreement n° [RFSR-CT-2013-00019].

6 REFERENCES

[1] S. Eshghi and M. S. Razzaghi, Performance of Industrial Facilities in the 2003 Bam, Iran, Earthquake, *Earthquake Spectra*, **S1**, 395–410, 2005.

[2] S. Fujita, I. Nakamura, O. Furuya, T. Watanabe, et al., Seismic damage of mechanical structures by the 2011 Great East Japan Earthquake, in *15th World Conference on Earthquake Engineering*, Lisbon, Portugal, September 24-28, 2012.

[3] E. F. Cruz and D. Valdivia, Performance of industrial facilities in the Chilean earthquake of 27 February 2010, *The Structural Design of Tall and Special Buildings*, **20**, 83–101, 2010.

[4] F. Braga, R. Gigliotti, G. Monti, F. Morelli, et al., Speedup of post earthquake community recovery: the case of precast industrial buildings after the Emilia 2012 earthquake, *Bulletin of Earthquake Engineering*, **5**, 2405–2418, 2014.

[5] E. Uckan, B. Akbas, J. Shen, R. Wen, et al., Seismic performance of elevated steel silos during Van earthquake, October 23, 2011, *Natural Hazards*, **75**, 265–287, 2015.

[6] H. Moghaddam and S. Sangi, Elephant's Foot Buckling of Cylindrical Steel Storage Tanks Subjected to Earthquake Excitation, in *6th National Congress on Civil Engineering*, Semnan University, Semnan, Iran, April 26-27, 2011.

[7] R. J. Nielsen and A. S. Kiremidjian, Tall Column Reliability under Nonstationary Loads: Model Formulation, *Journal of Engineering Mechanics*, **7**, 1107–1128, 1988.

[8] F. Paolacci, H. N. Phan, D. Corritore, S. Alessandri, et al., Seismic fragility analysis of steel storage tanks, in *COMPDYN 2015 - 5th ECCOMAS Thematic Conference on Computational Methods in Structural Dynamics and Earthquake Engineering*, Crete Island, Greece, May 25–27, 2015.

[9] M. Faggella, R. Laguardia, R. Gigliotti, and F. Braga, et al., Performance-based Nonlinear Response History Analysis Framework for the PROINDUSTRY Project WP2 Case Studies, in *ECCOMAS Congress 2016 VII European Congress on Computational*

Methods in Applied Sciences and Engineering, Crete Island, Greece, June 5–10, 2016, (Submitted).

[10] European Committee for Standardisation, *Eurocode 8 Design of structures for earthquake resistance Part 4: Silos, tanks and pipelines*. 2000.

[11] Ministero delle Infrastrutture, *Istruzioni per l'applicazione delle Norme Tecniche delle costruzioni*, 2009.

[12] Ministero delle Infrastrutture, *DM 14 gennaio 2008, Norme Tecniche per le Costruzioni*, 2008.

[13] A. A. S. Sarlis and M. C. Constantinou, Modeling Triple Friction Pendulum Isolators in Program Sap2000. 1–55, 2010.

ECCOMAS Congress 2016
VII European Congress on Computational Methods in Applied Sciences and Engineering
M. Papadrakakis, V. Papadopoulos, G. Stefanou, V. Plevris (eds.)
Crete Island, Greece, 5–10 June 2016

A CRITICAL REVIEW OF FRAGILITY CURVES FOR EXISTING RC BUILDINGS

M. Mastroberti[1], **M. Vona**[2]

[1] School of Engineering – University of Basilicata
Potenza, Italy
monicamastroberti@hotmail.it

[2] School of Engineering – University of Basilicata
Potenza, Italy
marco.vona@unibas.it

Keywords: Seismic Risk Mitigation; Existing RC buildings; Fragility Curves; Structural Performance; Damage Levels.

Abstract. *In recent years, many studies were been carried out in order to understanding and later mitigate the seismic risk. Several important projects have been funded, different methodologies have been developed; in particular, for emergencies management several application have been carried out with good results. On the contrary, mitigation and prevention of seismic risk could be more efficient by setting a careful assessment, maintenance and retrofitting of the built. In this sense, it to be noted that the seismic capacities of existing RC buildings have shown a key role in recent seismic events (e.g. Southern Italy 1980, Turkey 1999, L'Aquila 2009, Lorca, 2011, Emilia plan 2012). In particular, old RC buildings have often shown a poor and brittle behavior. Moreover, the low seismic performances of these buildings are the main reason of significant earthquake losses (in terms of economic, social and political activities) that can been considered generally as a direct consequence of physical damages on the buildings. About these important topics, it is the opinion of the authors, that quantitative models of fragility, referring to the most common types of buildings, have a key role in the evaluation process of risk and should been continuously improved. Therefore, in the seismic risk studies, a fundamental step is the development and use of fragility curves representative of the behavior of existing RC buildings. A significant number of proposals are currently available in the scientific literature. In this study, a critical review of existing different procedures for RC with Moment Resisting Frames (MRF) has carried out in order to highlight advantages and weakness of each proposal. A great variability in terms of geometrical, mechanical and structural characterization, structural modeling, method of analysis, scale of damage, parameters of seismic intensity and statistical procedure has been highlighted, and finally an optimal procedure of fragility analysis has been outlined.*

1 INTRODUCTION

Recent European earthquakes have shown that the economic loss and urban resilience are closely related to the seismic performance of existing buildings, designed without seismic criteria or with old codes, that showed an unsatisfactory behavior [1]. For this reason, in order to mitigate the seismic risk and increase resilience in urban areas, reduction strategies risk should be developed.

In seismic risk mitigation polices, with regard to the most common types of existing buildings the quantitative fragility models have a key role. Exist different approaches for the construction of fragility models: analytical approaches, empirical approaches, approaches based on expert opinion and hybrid method. In this paper, only analytical methods have been considered; they are based on damage distributions simulated from the numerical analyses. Due to the importance of the topic, a significant number of studies were developed and published in the last years. In first part of the paper, a short critical review of different methods and procedures has been performed. In this way, the difference due to choices about analysis method, idealization, seismic hazard, and the damage model, have been highlighted. In particular, following a careful literature review, six studies have been selected, with the same analysis object and purpose. In fact, the selected seismic risk studies , have investigated the existing Reinforced Concrete (RC) with Moment Resisting Frame (MRF). These typologies represent the highest percentage of building stock in several European areas with high seismicity, and they have similar properties.

For each study the main advantages and weakness have been pointed out. Then, the paper focuses on the importance of an adequate damage model; damage model should be able to take in to account the different damage state, as structural and non structural damage. The main topics of different damage models considered have been highlighted.

2 CRITICAL REVIEW OF METHODS

A wide literature review have been carried and six studies have been selected; they are focused on the construction of fragility curves and resulting FCs have been defined for similar structural typologies of existing Reinforced Concrete with Moment Resisting Frame structures (RC-MRF).

The selected studies are following listed and in the following they will be called with relative acronym: Masi et Vona 2012 [2] (MV12), Vona 2014 [3] (V14), Kyriakides et al. 2015 [4] (K15), Polese et al. 2008 [5] (P08), Erberik 2008 [6] (E08) and Silva et al. 2014 [7] (S14). In this studies, different methodologies have been defined in order to obtain fragility curves. In table 1 are reported the main characteristics of each study.

Several main steps can be identified in all studies:

- Selection of the structural types most vulnerable and widespread in region under examination;
- Geometrical, structural and mechanical characterization of selected structural class;
- Generation of adequate sample of structural models able to represent the real geometrical, structural and mechanical variability;
- Selection of ground motion;
- Structural modeling and evaluation of the seismic response;
- Definition of damage model;
- Construction of fragility curves.

In each step, a probabilistic approach should be used, because a high degree of uncertainty involved each of them. The structural models for numerical simulation should be able to rep-

resent the real probabilistic variability (for example material and geometric-structural, properties of structural, ect).

In several cases, it is excessive consider probabilistic some topics, especially when their variation is negligible, and not affect substantially the structural behavior. Farther, a probabilistic approach requires an accurate and extensive investigation in order to obtain reliable probability distributions. Actually, the highest computational power and the available numerical method allow a significant diffusion of the probabilistic approaches.

	Framework	V14	K15	P08	E08	S14
Selection and characterization of reference structural class	Building type studied	RC-MRF				
	Area surveyed	Italy and Mediterranean countries	Limassol (Cyprus)	Arenella district Naples	Dŭzce (Turkey)	Marmara region (Turkey)
Approach used in geometrical-mechanical-structural characterization of sample RC-MRF D=Deterministic P=Probabilistic	Form in plan	D	D	D	D	D
	Dimension plan	D	D	P	D	D
	Interstorey height	D	D	D	D	P
	Number of storey	D	D	D	D	D
	Beam length	D	D	P	D	P
	Column depth	D	D	D	D	P
	Concrete strength	D	P	P	D	P
	Steel yield strength	D	P	P	D	P
Evaluation of seismic response	Analysis Method	NLDA	NLDA	NLSA	NLDA	NLSA and NLDA
	Structural modeling	2D lumped plasticity	2D fiber element	3D lumped plasticity	SDOF	2D fiber element
	Type of seismic action	natural accelerogram	accelerogram base on spectrum	accelerogram base on code spectrum	natural accelerogram	natural accelerogram
Construction of FC	Intensity parameter	I_H	S_d	S_d	PGV	S_a
	Probability distribution	lognormal	lognormal	lognormal	lognormal	lognormal

Table 1: Main characteristics of frameworks selected.

In any cases, the trivial uses of probabilistic approaches carry out to unnecessary or incorrect choice about structural models or unrepresentative characteristics (for example, for beam length and column depth). Therefore, several simplified approaches (for example MV12/V14/E08) that consider any probabilistic variables as deterministic are more reliable. In other words, RC-MRF structural models are able to reproduce the behavior of real buildings also choices several deterministic values. For example, in MV12, V14 and E08, the role of infill masonry walls have been considered; they have been investigated with deterministic approach.

Generally, reliable FCs should be defined on the based of more accurate NonLinear Dynamic Analyses result (as in MV12, V14, K15, S14). On the contrary, FCs based on NonLinear Static Analyses (P08/S14) could be less able to simulate the real behavior of buildings. In E08, FCs have been defined on NLDAs; nevertheless the global response of buildings have been investigated using SDOF equivalent analytical models that have been characterized from structural non linear static analysis.

The seismic input plays a key role in FS definition. In order to obtained a realistic evaluation of structural performance, the accelerograms recorded during real earthquakes should be considered further less appropriate synthetic events. In V14, S14, E08 natural accelerograms extracted from different data-base have been used; in K15, time-history have been derived from response spectrum; finally, in P08, EC8 [10] spectrum has been used.

Equally relevant, the seismic intensity should be able to represent the damage potential of ground motion. Integral seismic parameters, such as Arias Intensity I_A and Housner Intensity I_H seem more effective with regard to peak or spectral parameters [11].

2.1 Characterization of Damage Models

In FCs definition, the Damage Model plays a key role. Damage Model should be defined from limit states that define the thresholds between different damage conditions. The limit states should be able to take into account the structural e nonstructural damage and their evaluation. Further, for each limit state should be associate an analytical characterization using a Damage Measure.

The main distinction in terms of Damage Measure (DM) is local or global DM. The first is structural response parameters due to single structural members; the second is referred to whole structure. The choice of local or global DM is strongly linked with modeling and analysis methods choices. For example, if the equivalent SDOF are considered, the limit states cannot be defined in a detailed way (e.g. based on member behavior, local strains or hinge mechanisms, ecc). In these cases, the global DM will be defined in terms of simplified global parameters. In addition, for each limit state a qualitative description of non-structural e structural damage should be considered (for example, using a typical damage scale as EMS98 [8] or specific defined scale). In the tables 2-3-4, the damage models used in the investigated studies are reported.

Damage model (V14)			**Damage model (MV12)**
EMS98	**Damage Level**	**Limit condition**	**Limit condition**
0	SD=None; NSD=None	IDR ≤ 0,05%	IDR≤ 0,1%
1	SD=None; NSD=Weak	$R_y \leq 1$ and 0,05%<IDR≤0,1%	0,1% < IDR≤ 0,25%
2	SD=Low; NSD=Moderate	$0<R_p \leq 0,25$ or IDR>0,1% and $R_y \leq 1$	0,25% < IDR ≤ 0,5%
3	SD=Medium; NSD=Significant	$0,25< R_p \leq 0,75$	0,5% < IDR≤1%
4(5)	Near Collapse/Collapse	$0,75 < R_p \leq 1$	IDR>1%
SD=Structural Damage; NSD=NoStructural Damage $R_y=\phi/\phi_y$; $R_y=\phi-\phi_y/\phi_u-\phi_y$			

Table 2: Damage Model in V14 and MV12.

Damage model (E08)		**Damage model (S14)**	
Limit state	**Limit condition**	**Limit state**	**Limit condition**
Serviceability LS	S_I=0.2	Limit state 1	IDR(%)→Δ_{roof}→75% $V_{base,max}$
Damage Control LS	IDR(%)→$\Delta_{roof,DC}$=75% $\Delta_{roof,CP}$	Limit state 2	IDR(%)→Δ_{roof}→$V_{base,max}$
Collapse Prevention LS	IDR(%)→$\Delta_{roof,CP}$=75% $\Delta_{roof,max}$	Limit state 3	IDR(%)→Δ_{roof}→$V_{base,max}$ descrease of 20%
S_I=Softening index			

Table 3: Damage Model in E08 and S14.

Damage model (K15)	
Limit state	**Limit condition**
Damage Limitation	$\theta_{column} < \theta_y$
Significant Damage	$\theta_{column} < 3/4\theta_u$
Near Collapse	$\theta_{column} = \theta_u$ and $V=V_R$
Building Collapse	all columns of floor reach L.S.3 or IDR=4%

Table 4: Damage Model in K15.

Generally, the interstorey drift is considered as Damage Measure. The interstorey drift is a good damage index for RC-MRC structures but reliable specific values should be defined. In this way, some results could be used: real test building during several earthquakes; laboratory experimental dynamic and pseudo-dynamic tests on models in scale or in full-scale; virtual experimental tests using numerical simulation.

Experimental calibration and validation of interstory drift limit is an hard work [9]. Generally, specific values should be defined in each studies and projects. In S14 and E08 each limit state has been defined through specific interstorey drift value; these values are corresponding to limit state in terms of base shear and roof displacement.

In order to verify the representativeness of these condition, these values have been compared with the interstory drift as defined in V14. The interstory drift limit values for each classes in according to E08 and S14 are reported in Table 5 and Table 6.

DM S14	IDR%(BF 2storey Pre71)	IDR%(IF 2storey Pre71)	IDR%(PF 2storey Pre71)
LS1	0,48	0,07	0,32
LS2	0,80	0,33	0,71
	IDR%(BF 4storey Pre71)	IDR%(IF 4storey Pre71)	IDR%(PF 4storey Pre71)
LS1	0,66	0,08	0,26
LS2	0,89	0,41	0,58
	IDR%(BF 8storey Pre71)	IDR%(IF 8storey Pre71)	IDR%(PF 8storey Pre71)
LS1	0,32	0,11	0,11
LS2	0,83	0,49	0,52

Table 5: Inter-story drift values for LS1 and LS2 of DM S14.

E08	IDR% (BF 2storey Pre71)	IDR% (IF 2storey Pre71)	IDR% (PF 2storey Pre71)
Serviceability LS	0,32	0,20	0,44
Damage Control LS	0,84	0,50	0,74
Prevention Collapse LS	1,17	0,67	1,01
	IDR% (BF 4storey Pre71)	IDR% (IF 4storey Pre71)	IDR% (PF 4storey Pre71)
Serviceability LS	0,22	0,11	0,19
Damage Control LS	0,75	0,50	0,60
Prevention Collapse LS	0,94	0,67	0,77
	IDR% (BF 8storey Pre71)	IDR% (IF 8storey Pre71)	IDR% (PF 8storey Pre71)
Serviceability LS	0,53	0,15	0,22
Damage Control LS	1,19	0,70	0,66
Prevention Collapse LS	1,57	0,93	0,91

Table 6: Inter-story drift values for Limit States of DM E08

On the basis of the values reported in Table 5 and 6, it must highlighted that LS and LS2 is generally equal, except for structures high-rise types buildings. Generally, the limit LS3 is not able to represent the limit between extensive damage and structural collapse. The values reported in Table 5-6 have been compared with interstory drift (IDR) values defined from V14. In this work, the comparison between frameworks reported described in table 1 has been carried out in a graphic way (figures 1 - 6) for 2 storey Bare Frame Pre71 type buildings.

As main results, the global limit condition used by S14 and E08 are not consistent with local condition of V14; in particular, it to be highlighted that the base shear not are able to take into account the ductile capacity of the structures.

However, the Damage Model in E08 is able to bring into account the deformation capacity of structure; a better correspondence with the local limit condition (V14) is realizable considering the ultimate deformation, not the 75%.

The quantitative characterization of limit states must take into account of real capacities of structural class. In addition, if the definition of a single interstory drift value for each limit

states, of a certain sub-class, is reductive because an extreme variability was been found, and the probabilistic approach is more complex, an alternative is the approach used in V14.

In fact in V14 the Damage Model has been characterized for each limit states; on the basis on the NLDAs results, an accurate assessment of repair cost is possible.

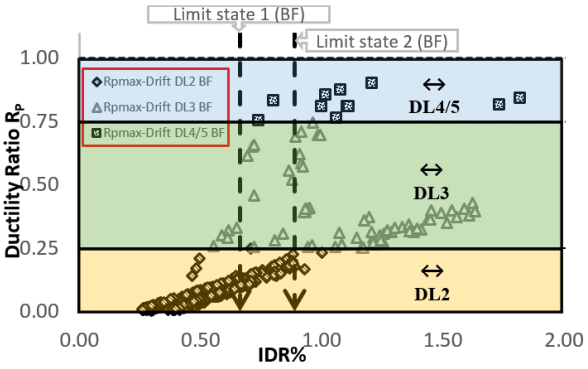

Figure 1: Comparison between the limit values IDR DL2-3-4 (V14) and LS1-LS2 (S14).

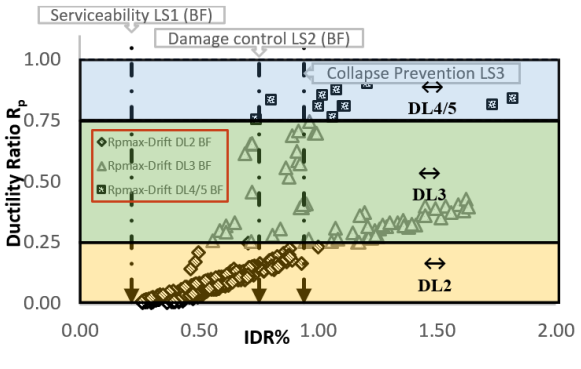

Figure 2: Comparison between the limit values IDR DL2-3-4 (V14) and LS1-LS2-LS3 (E08).

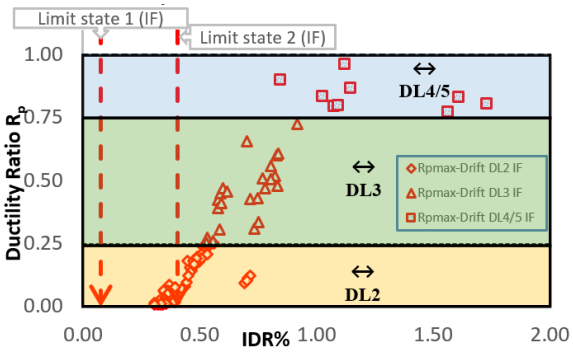

Figure 3: Comparison between the limit values IDR DL2-3-4 (V14) and LS1-LS2 (S14).

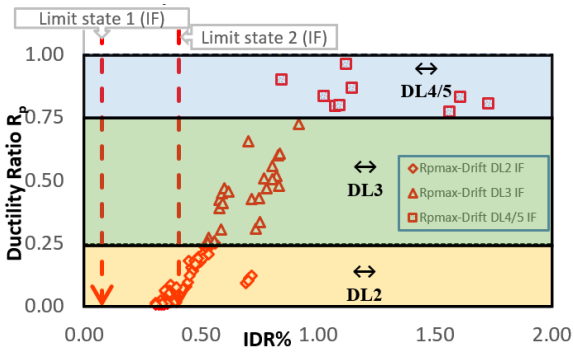

Figure 4: Comparison between the limit values IDR DL2-3-4 (V14) and LS1-LS2-LS3 (E08)

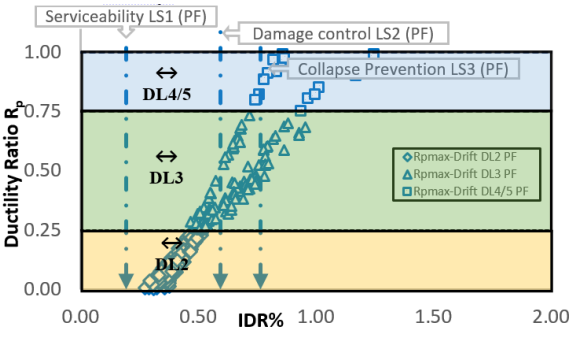

Figure 5: Comparison between the limit values IDR DL2-3-4 (V14) and LS1-LS2 (S14).

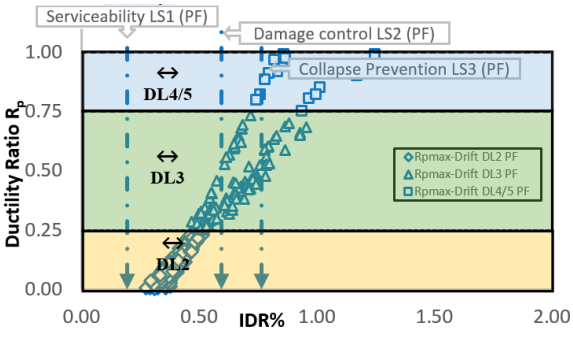

Figure 6: Comparison between the limit values IDR DL2-3-4 (V14) and LS1-LS2-LS3 (E08)

3 CONSIDERATION AND IMPROVEMENT ABOUT THE GENERATION A FRAGILITY MODEL

The accuracy of the FCs and consequent seismic risk studies (economic loss, cost-effectiveness of repairing damage and seismic retrofit) are mainly linked to structural modeling and analysis, structural performance and Damage Model. Therefore, a different efforts are need to define these topics.

The critical review of different procedures, models, choices in the construction process for fragility curves definition is carried out. A great variability in terms of geometrical, mechanical and structural characterization, structural modeling, method of analysis, scale of damage, parameters of seismic intensity and statistical procedure has been highlighted, and finally an optimal procedure of fragility analysis has been outlined.

An optimal procedure of FCs construction must be based on numerical simulations performed through NLDAs; the seismic action must been modeled by natural accelerograms. The Damage Model must been defined considering a representative limit states; they should be able to describe the different damage conditions. At each limit state must been associated a clear description of structural and nonstructural damage.

REFERENCES

[1] Vona M., Harabaglia P., Murgante B. (2015), *Thinking about resilient cities studying Italian earthquakes*, Urban Design and Plannig 1400007.

[2] Masi A. and Vona M., (2012), *Vulnerability assessment of gravity-load designer RC buildings: Evaluation of seismic capacity through non-linear dynamic analyses*, Engineering Structures **45** 257-269.

[3] Vona M. (2014), *Fragility Curves of Existing RC Buildings Based on Specific Structural Performance Levels*, Open Journal of Civil Engineering, **4** 120-134.

[4] Kyriakides N. C., Chrysostomou C. Z., Tantele E. A., Votsis R. A. (2015), *Framework for the derivation of analytical fragility curves and life cycle cost analysis for non-seismically designed buildings*, Soil Dynamics and Earthquake Engineering **78** 116-126.

[5] Polese M., Verderame G.M., Mariniello C., Iervolino I., Manfredi G. (2008) *Vulnerability Analysis for Gravity Load Designed EC Buildings in Naples-Italy* Journal of Earthquake Engineering 12:S2,234-245

[6] Erberik M.A. (2008) Fragility-based assessment of typical mid-rise and low-rise RC buildings in Turkey, Engineering Structures **30** 1360-1374.

[7] Silva V., Crowley H., Varum H., Pinho R. and Sousa R. (2014), *Evaluation of analytical mythologies used to derive vulnerability functions*, Earthquake engineering e Structural Dynamics **43** 181-204

[8] Grunthal G. (editor). *European Macroseismic Scale 1998 (EMS-98)*. European Seismological Commission, sub commission on Engineering Seismology, working Group Macroseismic Scales. Conseil de l'Europe, Cahiers du Centre Europeen de Geodynamique et de Seismologie, vol. 15. Luxembourg; 1998.

[9] Rossetto T., Elnashai A. (2003) *Derivation of vulnerability functions for European-type RC structures based on observational data*, Engineering Structures **25** 1241-1263

[10] CEN (2005) EN 1998-3-1-4 Eurocode 8, Design of Structures for Earthquake Resistance, Part 3, Assessment and Retrofitting of Buildings. European Committee for Standardization.

[11] Masi A., Vona M., Mucciarelli M., (2011). *Selection of natural and synthetic accelerograms for seismic vulnerability studies on RC frames*, Journal of Structural Engineering, **137** (3).

ECCOMAS Congress 2016
VII European Congress on Computational Methods in Applied Sciences and Engineering
M. Papadrakakis, V. Papadopoulos, G. Stefanou, V. Plevris (eds.)
Crete Island, Greece, 5–10 June 2016

DYNAMIC IDENTIFICATION AND MODELLING OF A RC HOSPITAL BUILDING

Giorgio Lacanna[1], Pauline Deguy[1], Maurizio Ripepe[1], Massimo Baglione[2], Marco Tanganelli[3], Stefania Viti[3], Mario De Stefano[3]

[1] Department of Earth Science (*DST*), University of Florence
Via G. La Pira 4, 50121 Firenze
e-mail: giorgio.lacanna@unifi.it, pauline.degui@unifi.it, maurizio.ripepe@unifi.it

[2] Tuscan Regional Government, Seismic Office
Via S. Gallo 34, 50121 Firenze
massimo.baglione@regione.toscana.it

[3] Department of Architecture (DiDA), University of Florence
Via della Mattonaia 14 , 50121 Firenze
mario.destefano@unifi.it, marco.tanganelli@unifi.it, stefania.viti@unifi.it

Keywords: Dynamic identification, ambient vibration test, modal analysis.

Abstract. *The conservation of structures mainly relies on our ability to monitor their aging and to promptly detect relevant damage. Dynamic characterization is considered a powerful technique for testing the conservation status of buildings as their natural frequencies, damping and modal shapes are directly related to their stiffness and structural integrity. In this work a dynamic monitoring based on ambient vibrations measurements has been performed on a case-study, i.e. a RC 4-storey Hospital building. An identification procedure based on the Enhanced Frequency Domain Decomposition has been performed to evaluate the modal parameters of the building. The dynamic information provided by the experimental analysis have been compared to the one found by performing the analytical modal analysis. To this purpose a structural model has been built, by representing all the major geometrical and mechanical properties of the building, through the Seismostruct software. The comparison has pointed out the role of the non-structural component and of the interaction between the monitored structure and the adjacent buildings on the dynamic response of the case-study.*

…

1 INTRODUCTION

The seismic assessment of existing buildings can be performed by different alternative procedures. In all cases the dynamic properties of the building, i.e. the vibrational periods, the amount of damping and the waves propagation within the building, play a crucial role in the evaluation of its seismic response. In these years, the improvement of data acquisition and processing capabilities, has increased the diffusion of experimental campaign based on the dynamic monitoring of the buildings [1, 2].

Dynamic characterization is considered a powerful technique for testing the conservation status of structures as their natural frequency, damping ratio and modal shapes are directly related to their stiffness and integrity [3]. The dynamic monitoring of a sample building requires a wave propagation motion, and, consequently, an accelerations source. The acceleration sources consist in forced vibrations, weak earthquakes and ambient vibrations. The ambient vibrations have been extensively used in these last years [4, 5, 6, 7], since they are always available without requiring any specific effort. They are characterized by low intensities, and therefore the dynamic response of the monitored building can be investigated in the elastic range only. Furthermore, for RC buildings, such response can be even more rigid than the theoretical elastic one, since the cracking limit is hardly achieved [8].

In this work the dynamic monitoring based on ambient vibrations has been applied to an Hospital building located in Sansepolcro (Italy), with a medium seismic hazard (PGA equal to 0.227g for the Severe Damage, *SD*, limit state), i.e. the highest seismicity in Tuscany [9]. The building has been built before the current seismic legislation, so requiring a special attention in terms of seismic reliability, and it has been object of careful investigations. The building, 4 storey height, has rectangular shape and a framed RC structure. Two stations at each level, one at the foundation, and further three ones at the top of the three adjacent buildings have been adopted in the analysis, for a global number of 9 stations. The location of the stations at each storey has been carefully evaluated, in order collect meaningful data, and to check the possible interaction between the examined structure and the next ones. The recording phase had a duration of about 20 hours; the long time recording interval has allowed to check the stability of the vibrations and to get robust average values of the frequency response. An automatic identification procedure via Enhanced Frequency Domain Decomposition (EFDD) [10, 11, 12] has been used to evaluate the modal parameters and to remove any user interaction.

The dynamic information provided by the experimental monitoring analysis have been compared to the one found by performing an analytical analysis. To this purpose a structural model has been built, by representing all the major geometrical and mechanical properties of the building, by using the Seismostruct [13] software. A modal analysis has been performed, and the elastic vibrational periods, together with the corresponding modal shapes, have been found.

The comparison between experimental and analytical data have evidenced some differences between the two analyses. The first one is about the stiffness found for the building: the experimental campaign provides a n higher estimation of the building stiffness, since it is based on a completely elastic response, due to the low intensity of the adopted acceleration source, and to the contribution of some non-structural components, like partitions, and architectural finishing, not included in the analytical model. The second difference is about some of the modal shapes, which are conditioned by the buildings adjacent to the checked one, which are not included in the analytical model.

2 THE CASE STUDY

The Hospital complex, shown in Fig. 1, is made by 18 independent buildings, differing for age, material and number of storeys. The buildings shown in Fig. 1 have been classified during the assessment analysis made in the jointed agreement between the University of Florence and the Regional Government [14]. The examined building, named 07 in Fig. 1b, adjoins three other ones, along three of its sides, as can be seen even by views shown in Fig. 2. It has a rectangular plan, of sides of 30.15 m and 18.90 m respectively. The RC structure is made by 10 transversal frames along the E-W direction, and by three RC frames along the N-S direction. Figs 3 and 4 show, respectively, the standard plan and two 3D views and cross sections of the building.

Figure 1: Hospital complex of Sansepolcro a) Air view b) General plan

Figure 2: The examined building.

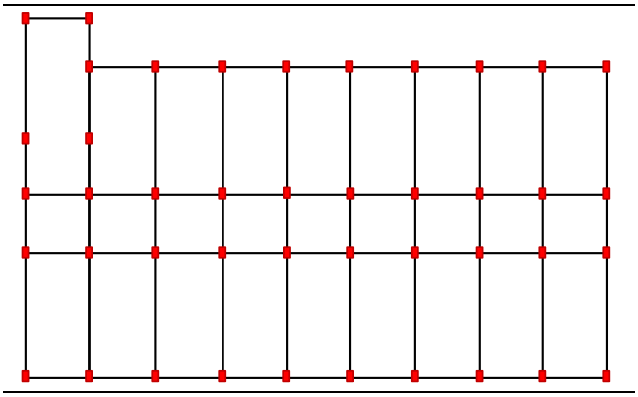

Figure 3: Plan of the building

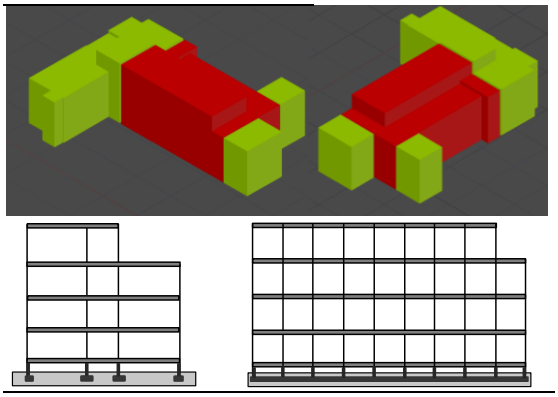

Figure 4: 3D views and sections of the building

The columns have different sections at each storey, ranging between 30x50 cm at the first level, and 30x35 cm at the top one. The transversal beams (EW direction), which sustain the floors, have a section of 30x60 cm, with the exception of some beams on the external wall, which have a special S shape to sustain the infill panels. The longitudinal beams (NS direction) have a lower depth at the first level, whilst they have the same dimensions of the transversal ones (30x60cm) at the upper storeys. The ceiling is made of two different floors, next each other, while the flat roofs includes 1m long cantilever along the entire perimeter. More details about the building can be found in [14].

3 THE DYNAMIC MONITORING

Ambient vibration measurements were performed for 20 hours from 23 to 24 April 2015 with 9 seismic stations (Fig. 5). Each seismic station was equipped with 3-component seismometers; more precisely, six stations were made by Lennartz 3D/5s (sensitivity 400 V/m/s and flat transfer function up to 5 s); one station by Guralp CMG-6T seismometer (sensitivity 2400 V/m/s and flat transfer function up to 10 s), one station by Guralp CMG-40T seismometer (sensitivity 800 V/m/s and flat transfer function up to 30 s) and one station by Trilium Compact 120s model (sensitivity 750 V/m/s and flat transfer function up to 120 s). All the seismometers were digitized by with a 24 bit Guralp CMG24 Digitizer at 100 Hz, and the time synchronization between stations was achieved using GPS.

The F01 station, located on the foundations of the building, has been used as reference station, while two stations were installed at each floor in the opposite corner (Fig. 5).

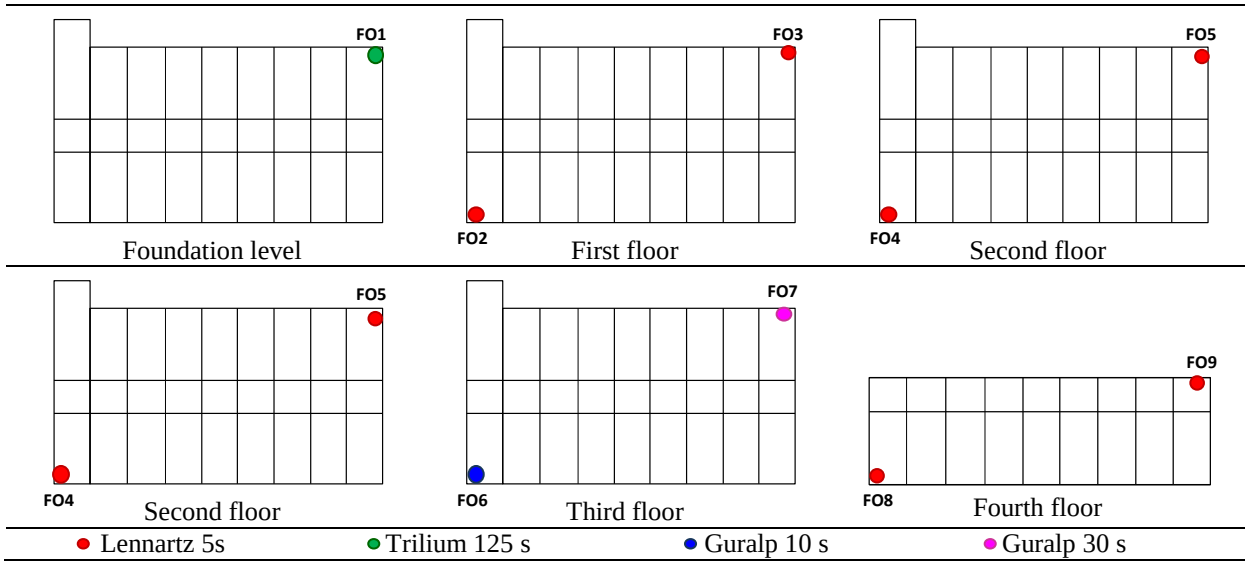

Figure 5: Position of the nine stations used to measure the effects of the ambient motion.

In order to apply the operational modal analysis, the 20 hours long record has been divided into times windows of 300 s and the data have been first deconvolved for the instrument response function and then filtered to frequencies above 0.1 Hz. The time window of 300 s is long enough with respect to the Brincker criterion [10], which requires time series ~1000 times longer than the fundamental oscillation period (~0.3 s in our case). An automatic identification procedure via Enhanced Frequency Domain Decomposition (EFDD) [15] has been used to calculate the modal parameters (frequency, damping and modal shape).

The EFDD is a frequency domain technique for operational modal analysis of structures, whose theoretical background is described in numerous papers [15, 16, 17]. The EFDD is an

extension of the Basic Frequency Domain technique (BFD), often called Peak-picking method, which is based on the Singular Value Decomposition (SVD) of the Power Spectral Density (PSD) matrix $G_{yy}(\omega)$, where ω_i are the single angular frequency. The modal shapes are automatically found within the modal domain (or modal bandwidth) using the modal coherence [14, 16, 12]. The latter is evaluated between each frequency line of two first singular vectors calculated for two consecutive records 300 s length.

The modal coherence is equal to 1 for stationary signals and allows to define the modal domain due to the structural modes. A *mean* value over 0.96 (Fig. 6a) and a *standard deviation* below 0.01 (Fig. 6b), calculated for a set of 10 consecutive modal coherences, are used to reduce the noise and to identify the modal domain. This procedure is repeated for the entire record every 300 s. Within each modal bandwidth, the maximum amplitude of the first singular value indicates the modal frequency. For such frequency peak, the corresponding first singular vector provides the modal shape every 300 s long data set. The application of the EFDD method has allowed to automatically identify the first five bandwidth modes of the checked building (Fig. 6c).

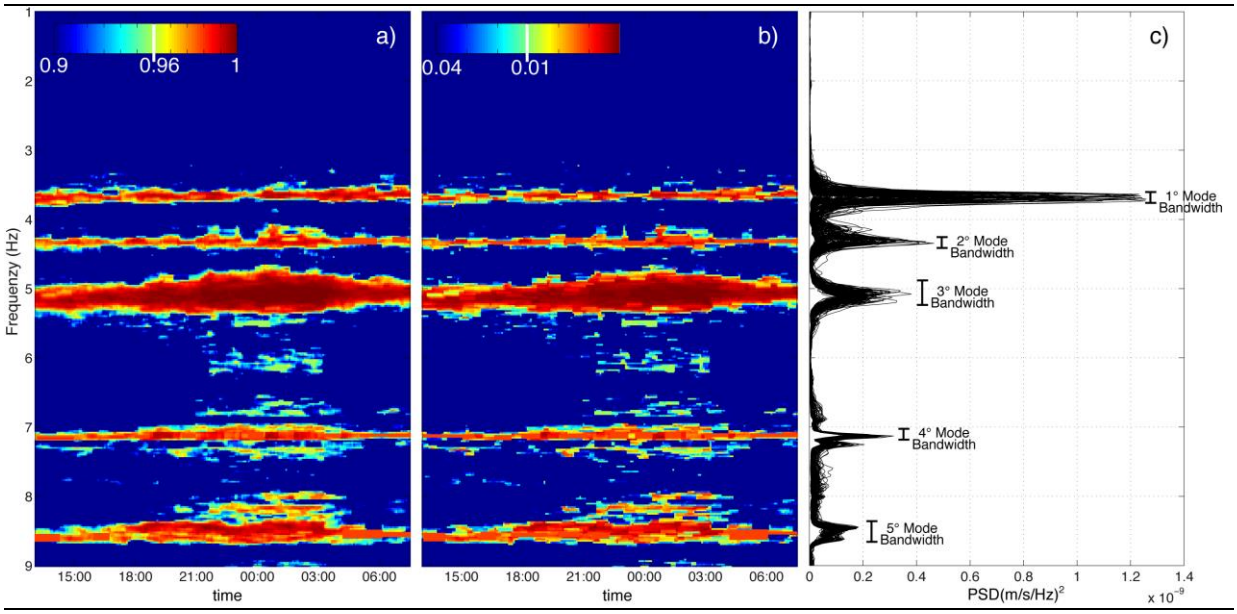

a) *mean* of modal coherence evaluated during the observation time on 10 consecutive records, the white line on the color bar indicates the threshold (>0.96) used for the identification of the mode bandwidth;
b) *standard deviation* of the modal coherence evaluated on 10 consecutive records, the white line on the color bar indicates the threshold (<0.01) used for identification of the mode bandwidth;
c) 240 first singular values calculated for all the observation time (20 hours).

Figure 6: Modal coherence found by the analysis.

An example of the five modal shapes calculated following the EFDD procedure during 300 s time window relative to the 15:00 to 15:05 interval is illustrated in Fig 7, which shows the first five modal shapes found from the analysis. As can be seen by the plots, the first mode is translational and occurs along the X direction (Fig. 7a), with a frequency of 3.71 Hz (T_1 = 0,27 s) and a damping ratio of 1.3 %, whereas the second mode shape is still translational, but along the Y direction (Fig. 7b) with a frequency of 4.32 Hz (T_2 = 0,23 s) and damping ration of 1.4 %. The third mode has a torsional modal shape with a frequency of 5.08 Hz (T_3 = 0,20 s) and damping ratio of 1.61%, while the fourth and fifth modes have a frequency of 7.12 Hz (T_4 = 0,14 s) and 8.54 Hz (T_4 = 0,12 s) and a damping ratios of 0.5% and 0.7% respectively.

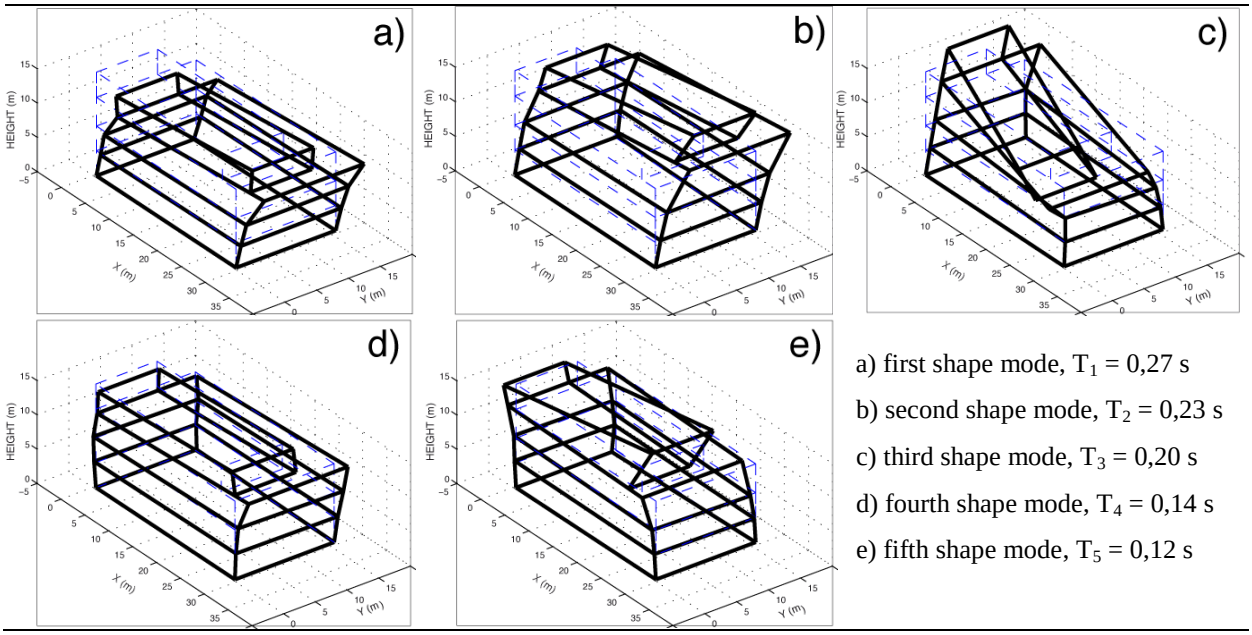

Figure 7: Tri-dimensional representation of the first five modes.

4 THE MODAL ANALYSIS

An analytical model has been made through the computer code Seismostruct [13] to achieve an analytical representation of the seismic response of the building. A detailed representation of the building geometry has been achieved, by tracing the original architectural and structural drawings. The mechanical properties of the materials have been carefully checked during the knowledge process, but in the current analysis only the concrete Young modulus is adopted, which is assumed to be equal to 27000 MPa.

A fiber model has been adopted to describe the cross sections; the Mander *et al*. model [18] has been assumed for the core concrete, a three-linear model has been assumed for the unconfined concrete, and a bilinear model has been assumed for the reinforcement steel. Contribution of floor slabs has been considered by introducing a rigid diaphragm. The model only represents the structural system of the building, neglecting the non-structural components, like the internal partitions and the architectural accessories. In the same way, in this first approach to the numerical representation of the seismic response of the building, the possible interaction with the adjacent buildings has been neglected. Fig. 8 shows two views of the model adopted in the analysis.

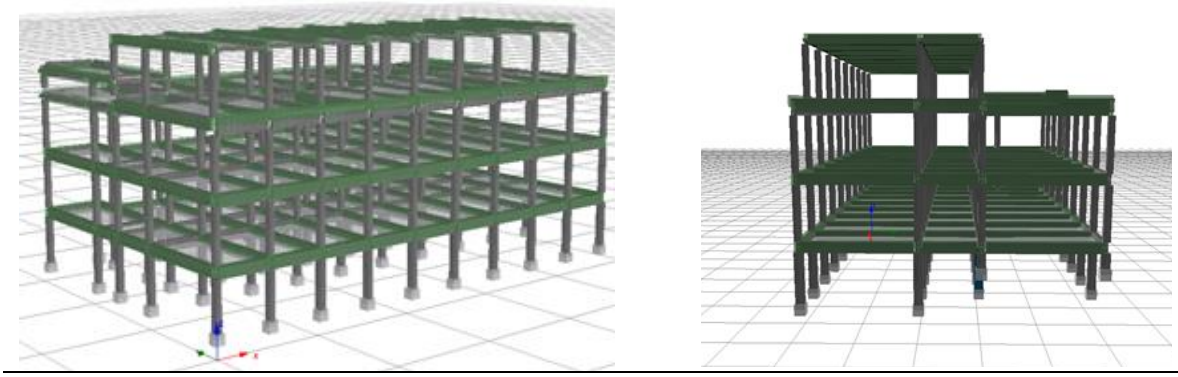

Figure 8. Views of the structural model.

The modal analysis has been performed by assuming an elastic behavior of the structure. Tab. 1 shows the main information (period and percentage of the total mass activate by each motion) of the first modal shapes, while Fig. 9 shows the corresponding modal shapes.

Table 1. Modal shapes found by the numerical analysis

Mode	Period (sec)	% of participation mass		
		Ux	Uy	Rz
1	0.462	80.23%	0.16%	2.30%
2	0.377	0.33%	78.14%	2.90%
3	0.333	1.94%	1.91%	73.07%
4	0.179	5.81%	0.00%	0.26%
5	0.128	0.51%	8.02%	0.03%

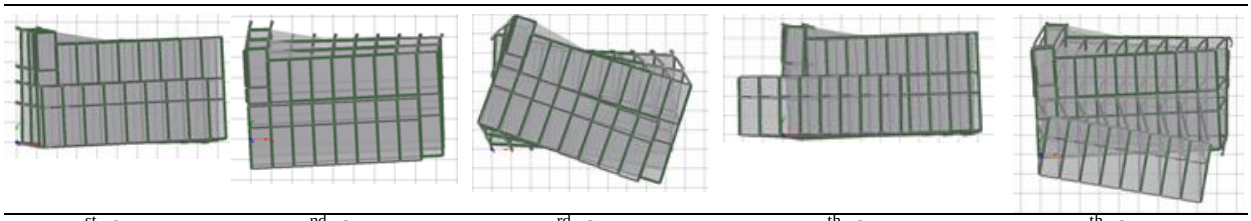

1st shape | 2nd shape | 3rd shape | 4th shape | 5th shape

Figure 9. Modal shape found through the modal analysis.

5 COMPARISON BETWEEN EXPERIMENTAL AND ANALYTICAL DYNAMICAL RESPONSE

Before proceeding to the comparison between the numerical results and those provided by the experimental campaign, some observations should be made. The dynamic response of buildings related to ambient vibrations is largely affected by all the non-structural components that, at the increasing of the dynamic intensity, lose their entirety, and, consequently, their influence on the building response. The checked building is separated by the adjacent ones through seismic joints: at the occurring of an earthquake, therefore, it should experience an independent dynamic response, resulting not affected by their behavior. Under ambient vibration, instead, the seismic joints have not lost their entirety, and therefore the dynamic response of the case- study found through the experimental test is affected by the dynamic properties of the next buildings. Moreover, the internal partition and the perimeter infill walls are known to largely affect the initial stiffness of the building, before they become ineffective due to the amount of the experienced stress.

The analytical model used in this work is very simple: it only considers the structural elements of the building and the mass distribution, and therefore it can be assumed to be a first attempt to represent the dynamic response of the case-study. The effects of the adjacent buildings is not taken into account, and the non-structural components have been neglected. Therefore, a more deformable system should be foreseen, and only the first shapes can be expected to be comparable, since the torsional behavior of the building is certainly affected by the contribution of the neglected aspects. In the following, therefore, only the first two modes, which represent the translational response of the building along the two main directions, have been discussed.

As regards the elastic periods of the first two modes, it should be noted that the numerical model provides values about 40% larger than the ones obtained by the experimental campaign. The amount of this increase is compatible to more general studies [19] referred to the contribution of the non-structural components on the dynamic response of RC structures.

Fig. 10 shows the comparison of the modal shape found for the first (translational) two modes through the two approaches. The shapes have been normalized to the maximum response along the main direction.

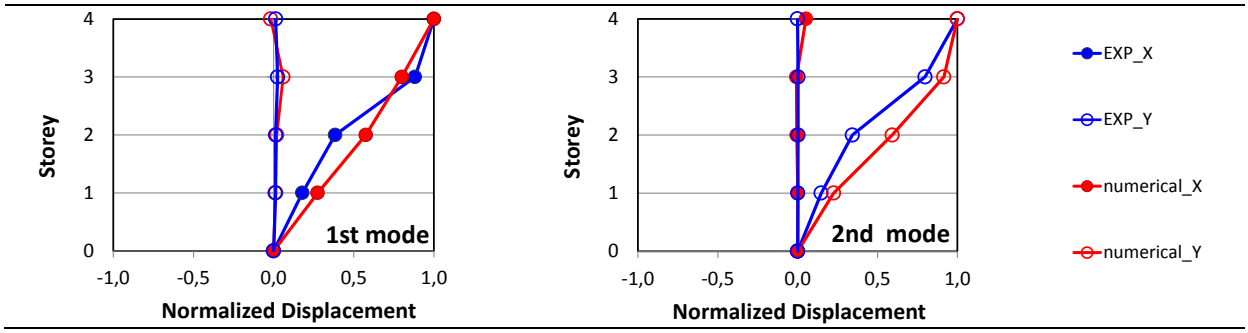

Figure 10: comparison between the first two modes of the dynamic response of the case-study.

6 CONCLUSIONS

In this work a dynamic monitoring based on ambient vibrations has been applied to an Hospital building located in Sansepolcro (Italy). Nine seismic stations, consisting in 3-component seismometers, have been placed in the building, checking every floor, included the foundation level. The recording phase had a duration of about 20 hours, and an automatic identification procedure via Enhanced Frequency Domain Decomposition (EFDD) has been performed on the obtained data to evaluate the modal parameters, i.e. frequency, damping and corresponding modal shape.

The dynamic response found through the experimental campaign has been numerically simulated by representing the building by means of a simplified model. The model represents a first attempt to describe the dynamic response of the building, since it does not take into account the non-structural components, or the possible interaction between the building itself and the adjacent structures. It has been prepared through the platform Seismostruct, and takes into account the effective geometry of the building, and its main dynamical properties, like the mass and the stiffness distribution.

The fundamental periods provided by the numerical model for the building are about 40% larger than the ones provided by the experimental campaign, whilst the two first (translational) modal shapes are very similar with each other. A more detailed model of the building should be made in order to check the effects related to the experimental campaign, like the continuity between the case-study and the adjacent buildings and the effects of the non-structural components.

ACKNOWLEDGMENTS

The financial support of the Government of Regione Toscana through the project “Valutazione del grado di operatività strutturale su una coppia di edifici strategici nell’ambito del programma VEL”, is gratefully acknowledged.

REFERENCES

[1] D. Bindi, B. Petrovic, S. Karapetrou, M. Manakou, T. Boxberger, D. Raptakis, K. D. Pitilakis, S. Parolai (2015). Seismic response of an 8-story RC-building from ambient vibration analysis. *Bull. Earth. Eng.*

[2] G. Fabbrocino, C. Rainieri, G. M. Verderame (2007). L'analisi dinamica sperimentale e il monitoraggio delle strutture esistenti. In: Controllo e monitoraggio di edifici in Calcestruzzo Armato: il caso-studio di Punta Perotti Giornata di Studio ENEA.

[3] C. Gentile, A. Saisi (2007). Ambient vibration testing of historic masonry towers for structural identification and damage assessment. *Construction and Building Materials* 21 (6) (2007) 1311–1321.

[4] J.M.W. Brownjohn (2003). Ambient vibration studies for system identification of tall buildings. *Earthq Eng Struct Dyn* 32:71–95

[5] C. Ventura, W-D. Liam Finn, J.F. Lord, N. Fujita (2003). Dynamic characteristics of a base isolated building from ambient vibration measurement and low level earthquake shaking. *Soil Dyn Earthq Eng* 23: 313-22

[6] A. D'Ambrisi, V. Mariani, M. Mezzi (2012). Seismic assessment of a historical masonry tower with nonlinear static and dynamic analyses tuned on ambient vibration tests. *Eng Struct* 36: 210–219.

[7] M. Ripepe, M. Coli, G. Lacanna, E. Marchetti, M.T. Cristofaro, M. De Stefano, V. Mariani,· M. Tanganelli, P. Bianchini (2015). Dynamic response of the Giotto'S Bell-Tower, Firenze, Italy. In Engineering Geology for Society and Territory Vol. 8 - Preservation of Cultural Heritage: 323-327

[8] P. Ricci, G.M. Verderame, G. Manfredi (2011). Analytical investigation of elastic period of infilled RC MRF buildings. *Engineering Structures*, 33(2): 308-319.

[9] M. Tanganelli, S. Viti, D. Forcellini, V. D'Intisonante, M. Baglione (2016). Effect of Soil Modeling on Site Response Analysis (SRA). Proc. SEMC 2016.

[10] R. Brincker, C. Ventura, P. Anderson (2003). Why output-only modal testing is a desirable tool for a wide range of practical applications: *Proc. 21st International Modal Analysis Conference IMAC XXI*, Kissimmee, Florida, February 3-6, 2003, pp. 265-272.

[11] C. Rainieri, G. Fabrocino (2010). Automated output-only indentification of civil engineering structures, *Mechanical Systems and Signal Processing* 24 678-695.

[12] G. Lacanna, M. Ripepe, E. Marchetti, M. Coli, C.A. Garzonio (2016). Dynamic response of the Baptistery of San Giovanni in Florence, Italy, based on ambient vibration test, Journal of Cultural Heritage, http://dx.doi.org/10.1016/j.culher.2016.02.007

[13] Seismosoft (2006). Seismostruct Version 5.2.2 - A computer program for static and dynamic nonlinear analysis of framed structures. Available online from URL: www.seismosoft.com.

[14] M. De Stefano (2013). Studio sulla caratterizzazione meccanica dei materiali e sulla stabilità statica del Presidio Ospedaliero di Sansepolcro. Firenze, 2013.

[15] R. Brincker, P. Andersen and N. J. Jacobsen (2007). Automated Frequency Domain Decomposition for Operational Modal Analysis. *Proc. of the 25th SEM International Modal Analysis Conference*, Orlando, Florida, USA, February 19-22 2007.

[16] P. Andersen, R. Brincker, M. Goursat, L. Mevel (2007). Automated Modal Parameter Estimation For Operational Modal Analysis of Large Systems: *Proceedings of the 2nd International Operational Modal Analysis Conference*, Copenhagen, Denmark, Vol. 1, , pp. 299-308.

[17] C.Rainieri; G. Fabbrocino (2010). On the relevance and methods for structural health monitoring in seismic areas: theory, implementation, applications. *5th European Workshop on Structural Health Monitoring* (EWSHM2010).

[18] J.B. Mander, M.J.N. Priestley, and R. Park (1988). Theoretical stress-strain model for confined concrete, *J. Struct. Div., ASCE,* 114: 1804-1826.

[19] A. Masi, M. Vona (2010). Experimental and numerical evaluation of the fundamental period of undamaged and damaged RC framed buildings. *Bulletin of Earthquake Engineering*, 8: 643-656.

ECCOMAS Congress 2016
VII European Congress on Computational Methods in Applied Sciences and Engineering
M. Papadrakakis, V. Papadopoulos, G. Stefanou, V. Plevris (eds.)
Crete Island, Greece, 5–10 June 2016

SEISMIC HAZARD OF URBAN AREAS: A CASE-STUDY

Giorgio Lacanna[1], Pauline Deguy[1], Maurizio Ripepe [1], Massimo Coli[1], Barbara Paoletti[2], Sara Barducci[2], Marco Tanganelli[2], Stefania Viti[2], Mario De Stefano[2]

[1] Department of Earth Science (DST), University of Florence
Via G. La Pira 4, 50121 Firenze
e-mail: giorgio.lacanna@unifi.it, pauline.deguy@unifi.it, maurizio.ripepe@unifi.it, coli@unifi.it

[2] Department of Architecture (DiDA), University of Florence
Via della Mattonaia 14, 50121 Firenze
sara.barducci@unifi.it, barbarapaolettiarch@gmail.com, mario.destefano@unifi.it, marco.tanganelli@unifi.it, stefania.viti@unifi.it

Keywords: urban seismic hazard, urban vulnerability, seismic assessment, vulnerability map, data collecting, data management.

Abstract. *This work deals with the evaluation of the seismic vulnerability of urban areas. The city of Florence has been selected to be the case-study of the analysis. The work is organized in two main parts. The first one consists of the representation of the area hazard. Starting from the PGA of the area, a map of the amplification factors and of the fundamental frequencies has been made, by performing an extensive experimental campaign. The second step is focused on the buildings properties, and on the increase in the seismic hazard – and the consequent vulnerability – due to the possible occurrence of resonance. A large data-bank of the buildings has been collected, and they have been classified after their structural material (masonry versus reinforced concrete) and height. As a result of the collected information, a map of the fundamental period of vibration of the buildings has been obtained, by adopting the expressions provided by the current International Codes. The comparison between the period of each building and the one of its foundation soil has provided the resonance index (RI), which can be considered as an hazard parameter related to each building.*

1 INTRODUCTION

The evaluation of the safety of urban areas is one of the most important challenges that the Community is facing in these decades. The increase of the scientific and technical knowledges, together with the outstanding development of the capacity to collect and to manage databases, let the territory protection more affordable than it never was in the past. Many different retrofitting techniques [1, 2, 3] have been developed, suitable to be applied to all types of existing buildings. Nevertheless, the achievement of a satisfactory safety level of the building population is totally impossible, at the current time. If the inadequacy of the economical sources is certainly the first reason of this impossibility, also the lack of an intervention plan plays an important role. In many Italian towns, in fact, the buildings population is made mostly by ancient or, anyway, pre-normative structures. If the historical buildings, made in the past centuries, have been made without any anti-seismic criteria, even the pre-normative ones present, in many cases, an unsatisfactory safety level. The Italian country, indeed, experienced an economic boom in the 1960s, which was characterized by a great expansion, and by the construction of many buildings. Many of them have been made with poor materials [4], which did not comply with the technical requirements of the time. As a consequence of these observations, the Italian towns are, in most cases, vulnerable, i.e. they have an unsatisfactory seismic capacity. In the last decades, many procedures have been developed to check the seismic vulnerability of urban areas [5, 6, 7, 8, 9], which can be divided into three main groups: the empiric, the analytical and the hybrid methods. The vulnerability analyses are focused on the reliability of the buildings with regard to the seismic actions expectable for the area.

The current work deals with the urban vulnerability of the city of Florence, (Italy), which is an example of complexity, both for the outstanding architectural heritage and the for multi-level dimensions. The work develops a previous research [10], aimed at evaluating the urban vulnerability of Florence through an empirical approach based on a simplified vulnerability index. The analysis was based on the database available at the time, consisting in the information collected by GIS, which was very basic, providing only the total height and the age of the building population.

This work is focused on the seismic hazard of the buildings located in the area of Florence. The maximum seismic acceleration expected for each point of the urban area has been defined by assuming a PGA equal to 0.13g over the entire urban area, according to the Code [11] classification, and determining the amplification factor map, which is a function of the specific geological features of each micro-zone of the area.

A further development has been achieved, by determining the maximum acceleration which each building of the Florence area can experience as an effect of the relationship between its own dynamical properties and the ones of the foundation soil. To obtain this information, the maps of the fundamental period both of the soil and of the buildings would be needed. The map of the fundamental period of the soil has been found after an extensive experimental campaign made on the Florence area. The map of the fundamental periods of the buildings, in turn, has been found by applying a simplified approach to the buildings population. To this purpose, further information has been achieved on the buildings population, like their structural system and material. As a consequence of the more detailed classification, a reliable evaluation of the main frequencies of the building population has been made. The comparison between the maps of the fundamental periods of the area and of the buildings pointed out the probability of the buildings to experience resonance phenomena during seismic events. A “resonance index” (*RI*) has been defined to measure the sensitiveness of the buildings to this phenomenon, and a *RI* map of the area has been consequently drawn.

2 THE CASE-STUDY: FLORENCE

Florence is a city of about 353,000 inhabitants, with a larger number of people (supposed to almost achieve 700,000 units), living in the whole urban area. This work is focused on the vulnerability of the buildings population of the urban area of Florence, made by about 55,000 units. The area has been historically subjected to earthquakes, with local magnitude ML until 5, and maximum intensity equal to VIII MCS (Mercalli-Cancani Sieberg scale).

Despite the high density of population and the not negligible seismicity, the buildings of the area do not present any anti-seismic criteria, since most of them are ancient or – anyway – built before the seismic regulations have been introduced.

In this study each building is ranked by the Florence municipality database through few main parameters, i.e. the total height and the range of the construction year. This research does not include the area of the historical center (UNESCO protected area), since it is object of another survey. The current investigation, therefore, has been applied over about 40,000 buildings. The town lies in a valley (about 50 m a.s.l.) crossed by Arno river and surrounded by hills. Many investigations [12, 13] have been made on the soil of the Florence area, providing a detailed knowledge of the lithostratigraphic subsurface, of the lithoid substrate profile and of the geotechnical properties of its soils. In these years all the available drilling data have been collected and implemented into a GIS. Each data has been expressed in terms of unconformable boundary stratigraphic units [14] and unified soil classification system (USCS), and then transcribed into a geodatabase (UBSU).

The Florence basin had been developing since late pliocene thanks to the role played by the Fiesole faults on its NE border; these faults have no any sign of tectonic activity in the last 200ky. This geological evolution led to the filling of the basin by plio-pleistocene palustrine and alluvial deposits, followed by two sedimentary cycles related to the paleo-Arno river and the holocene geomorphic evolution, respectively (Fig. 1).

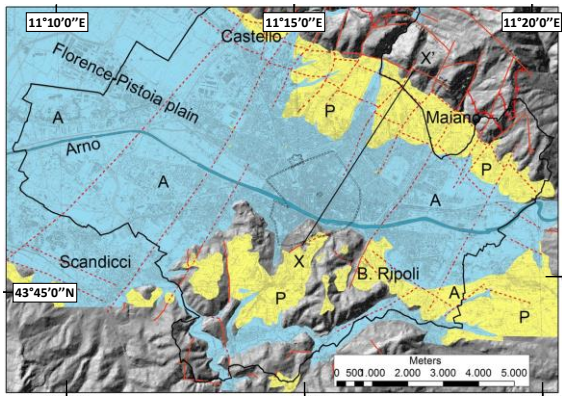

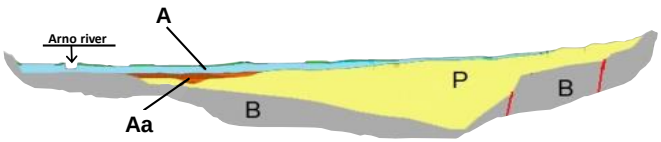

B (shadowed grey) = bedrock
P = Plio-Pleistocene palustrine and alluvial deposits
A = recent alluvial deposits of the Arno River and its tributaries
Aa = ancient channel deposits of the Arno River.

red lines (plain and dotted): faults.
blue line (dotted): 14th century city-walls ring
black line: Florence Municipality area

Figure 1: Geological sketch map and cross-section of the Florence area (from: [12]).

3 HAZARD MAPS OF THE SOIL

The seismic hazard of the area of Florence has been checked by performing an extensive experimental investigation [12], consisting in a 1,850 drillings, whose location has been shown in Figure 2, enhanced by 32 downhole proofs. For each test the maximum peak of the transfer function has been found, which has been combined with information provided by the downhole proofs about the stratigraphy of the area. A seismic-stratigraphic analysis has been performed, which provided the transfer function of the area. By integrating the transfer function found over a range of periods between 0,1s and 0,5s (the range of major interest as re-

gards the buildings interaction), the amplification factor of each test has been found. Figure 2 shows the map of the amplification factor obtained after the experimental investigation [12]. In the map the values below the unity have not be evidenced, while the red area represents the points with the highest amplification.

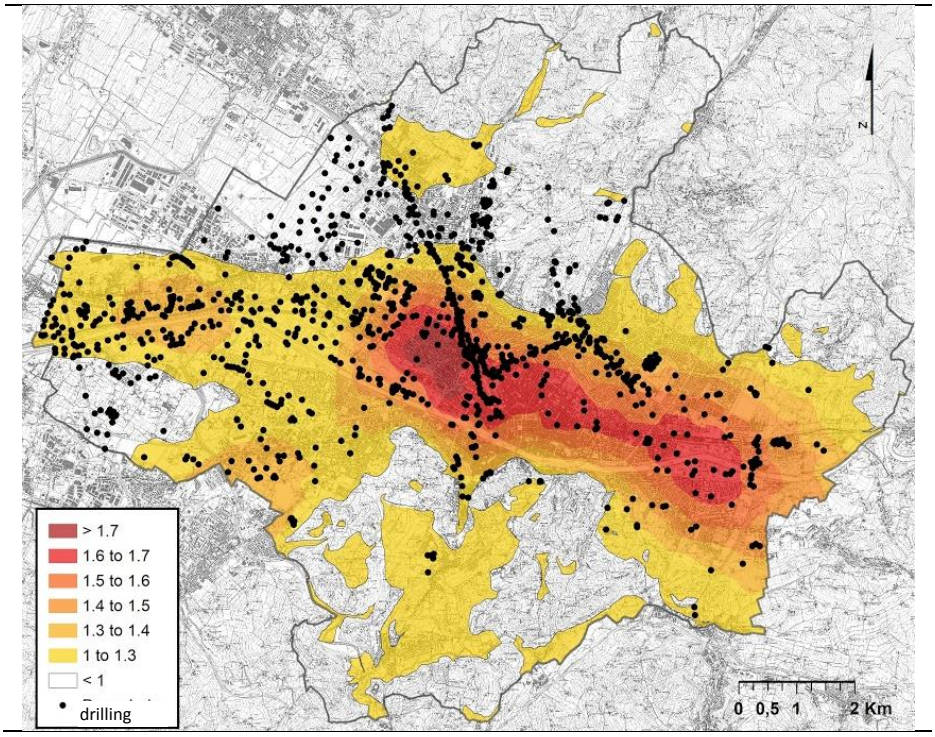

Figure 2: Map of the amplification factor (from: [10])

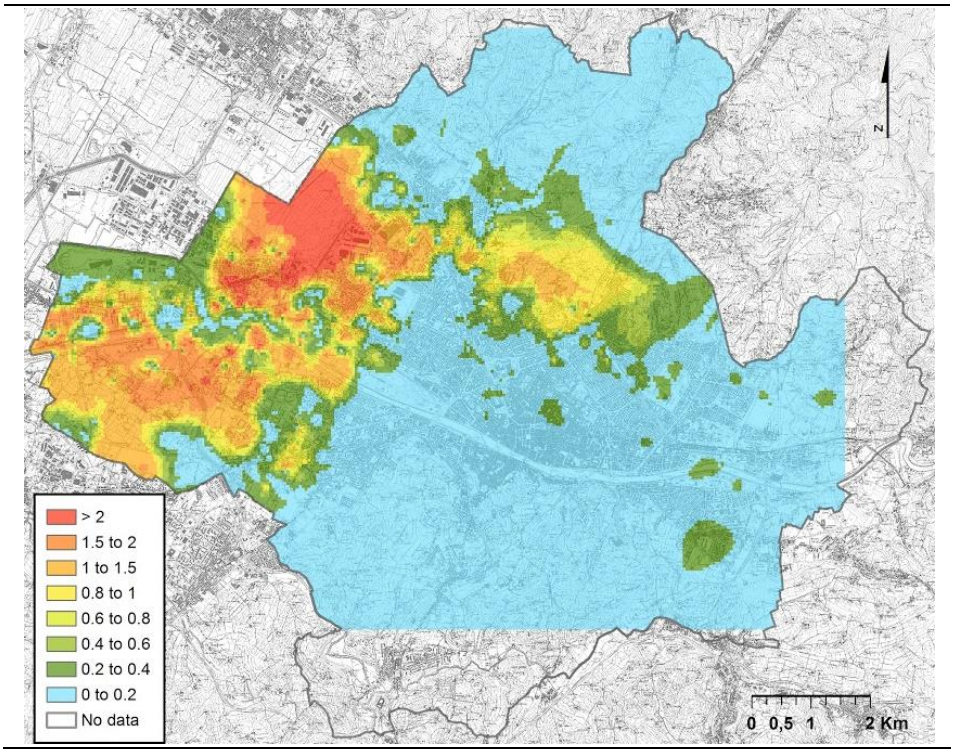

Figure 3: Map of the proper period (in seconds) of the soil.

The same experimental campaign has provided the map of the fundamental periods of the area, shown in Figure 3.

Even in this case the information provided by the two types of investigation have been integrated, i.e. the strathigraphies found through the drilling proofs have been represented by the mechanical properties and the shear velocity (v_s) values provided by the downhole investigations. For each drilling the filtering process through the soil columns has provided the fundamental frequency of the soil. The map of the fundamental periods of the soil cannot be considered as an hazard map; nevertheless it has a crucial role in the evaluation of the buildings vulnerability, since it affects the intensity of the seismic acceleration which each building will face at the occurring of an earthquake.

As can be observed in Fig. 3, only a relatively small area, represented in green, presents a period compatible to the buildings ones (0.20s - 0.60s). The amount of the seismic acceleration expectable by each building as an effect of its position can be related both to the relationship between the fundamental period of the building and the one of its foundation soil, and to the amplification factor. The maps shown in Figs 2 and 3, therefore, should be compared to the map of the fundamental period of the buildings, shown in the next section.

4 HAZARD MAPS OF THE BUILDINGS

4.1 The buildings population

The buildings population consists of about 55,000 unities. No distinctions are made about their use: residential, scholastic, commercial and industrial buildings have been considered as well. Each unity has been classified through an *ID*, and the parameters adopted in the database are the total height, the surface, the volume and the age range. Fig. 4 shows the classification of the buildings population of the entire city referred to the age of construction and to the total height.

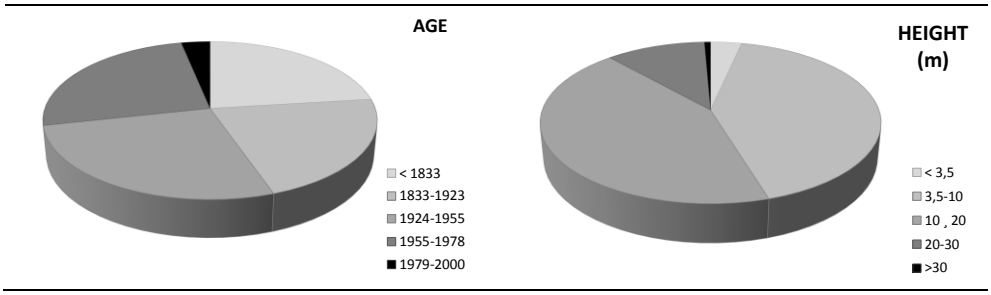

Figure 4: Database referred to the entire city of Florence.

In this work, a more detailed classification has been made on the residential buildings of the city, external to the most historical center - which is the object of another research - i.e. about 40000 buildings. In this database, the number of information has been upgraded, by the introduction of the type of structure. The buildings, indeed, have been classified after their main technology/material. The considered classes are: masonry (*M*), reinforced concrete (*RC*) and other structures (*OS*). The *OS* class comprehends buildings below 3.5m, and the structures not belonging to any of the previous classes. The buildings population of the area basically does not present any steel unities, which, anyway, would belong to the *NC* class. Fig. 5 shows the classification of this more specific database. The total height of the buildings, together with their material, leads to achieve an evaluation of their fundamental period of vibra-

tion. It should be noted that only few buildings exceed the height of 30 m. This evidence depends on an ancient law, passed in the XIII century, still in force, which topped the height of the civil buildings to 50 "florentine braccia" (about 30 m).

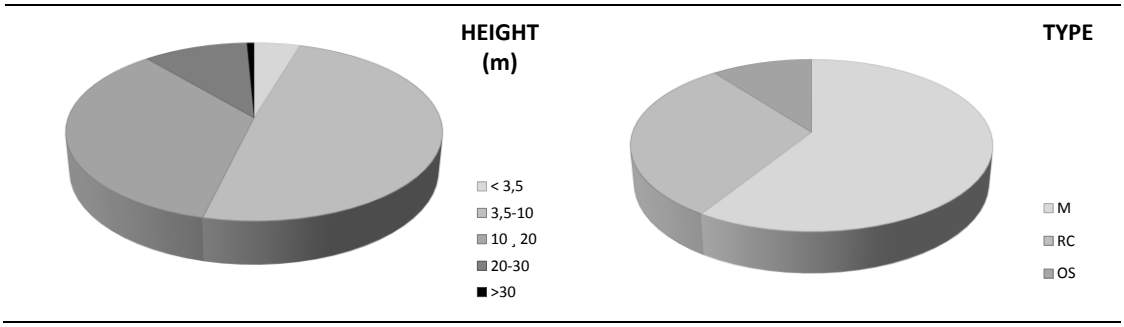

Figure 5: Upgraded database referred to the residential building of the city of Florence (with the exclusion of the historical center)

4.2 The dynamic characterization

The fundamental period (T_0) of the buildings population is a derivative information provided for the database, as a function of the total height of each building and its type class, as explained in the previous section. The vibrational properties of the buildings can be evaluated by performing an eigenvalue analysis on a mechanical model representing the structural behavior, or by calibrating approximate expressions, based on the observation of experimental data [15]. The empirical approach is the most largely adopted so far, and it is followed even by the main International Codes [16, 17, 18, 19]. In this work the simplified relationships proposed by the Italian [10] and European [20] technical Codes, which are identical each other, have been adopted:

masonry buildings: $$T_e = 0.050\, h^{0.75} \quad (1)$$

RC framed buildings: $$T_e = 0.075\, h^{0.75} \quad (2)$$

where h is the building eight (in meters). The provided period depends only on the total height of the building and on its constructive system (masonry vs framed structure). The reliability of (1) and (2) could be argued. It is well known, in fact, that the dynamic response of buildings depends on their stiffness, which experiences a considerable decrease during the seismic excitation; depending on the level of assumed damage, a different amount of stiffness - and consequently of the period - can be assumed [21]. In most cases, the period values provided by the most recent empirical expressions [15] [22] are larger than the ones found by following the Code approach. The most accurate expressions which evaluate the period of buildings, however, require a large number of information, like the amount of walls in the two main directions (wall systems), or the presence and quantity of infilled walls inside the structure (framed systems). Therefore, at the current time, the adopted Code expressions seem to be suitable to the work purpose, and compatible to the collected information.

The obtained T_0 values, however, should be considered as a lower limit for the buildings period. Fig. 6 shows the map of the Period found for the buildings population (the map has been slightly cut, to lead a larger size of the plot). In the same figure, the percentage of the period ranges of the database has been shown.

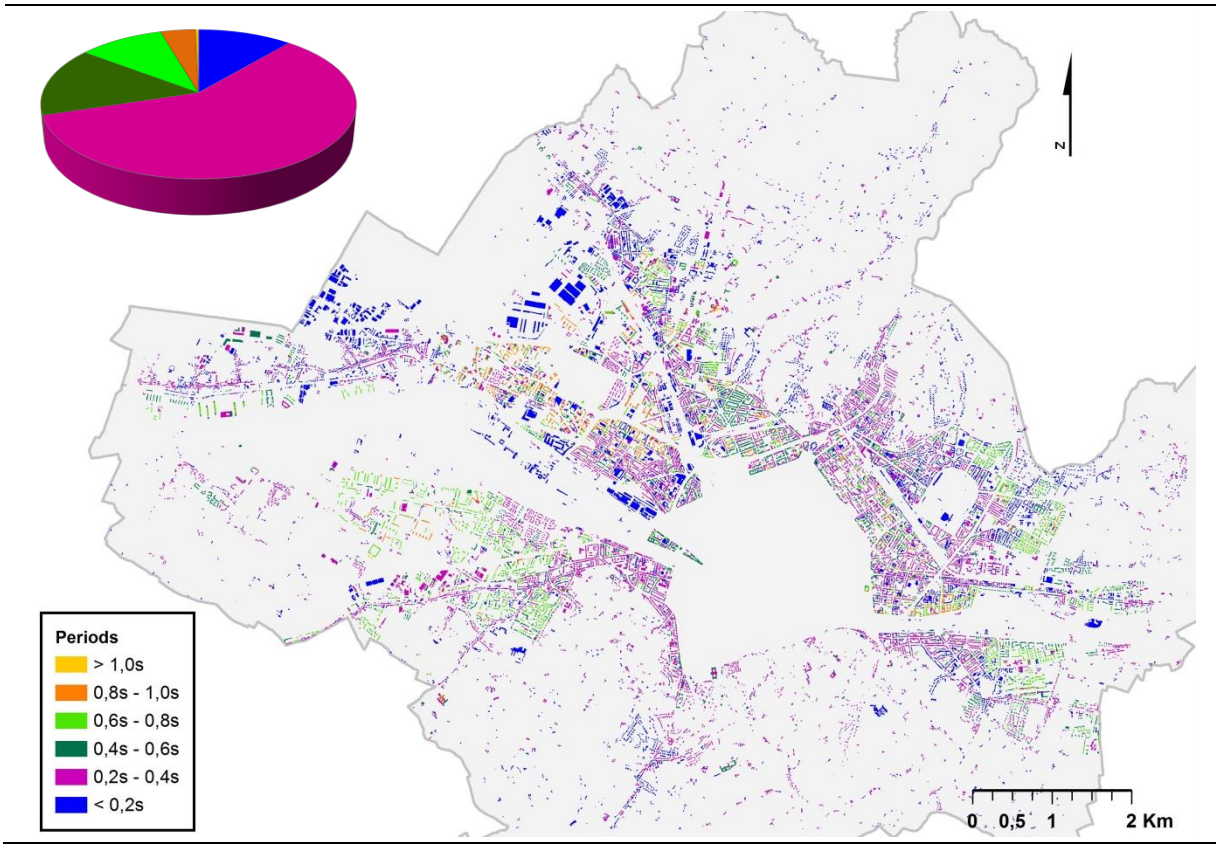

Figure 6. Map of the fundamental periods (T_0) of the buildings population.

4.3 The "resonance index" map

The maps representing the period distribution found for the buildings (Fig. 6) and for the soil (Fig. 3) have been compared, in order to find the "resonance map", which express how much the fundamental period of each building differs by the one of its foundation soil. The resonance index (*RI*) has been expressed as the ratio between the period of the building and the one of the soil (equation 3):

$$RI = T_{building} / T_{soil} \quad (3)$$

The obtained *RI* values have been classified in five different classes, listed in Table 1, which express the vulnerability of the buildings population regard the resonance phenomena. Since the periods found for the buildings can easily lengthen, due to the occurring of structural damage, the *RI* values over the unity are supposed to represent absence of resonance.

Table 1: Assumed ranges for the resonance index (RI)

RI range	Expected resonance phenomenon
0.0 - 0.3	No resonance
0.3 - 0.6	Low resonance probability
0.6 - 0.9	Possible resonance for moderate/strong earthquakes
0.9 – 1.1	Elastic resonance
> 1.1	No resonance

With reference to the introduced *RI* classification, the most "dangerous" ranges, i.e. the ones of the maximum resonance, are the one around the unity (0.9-1.1) and the one between 0.6 and 0.9, which represents the building with a fundamental period slightly lower than the one of their foundation soil. This last *RI* range can be dangerous at the occurring of moderate or strong earthquakes, which could induce a large increase of the elastic period of the buildings. The *RI* values below 0.3, instead, can be assumed to represent a low probability of resonance. The classification proposed in Tab. 1 should be assumed as a simplified instrument to evaluate the resonance problems; to achieve a more affordable classification, a more detailed description should be needed about the buildings, and more accurate expressions should be adopted to estimate the fundamental period of the buildings. Moreover, especially for isolated buildings, the two first periods, along the two main directions, should be considered, to avoid that the second vibrational mode could have resonance problems with the soil.

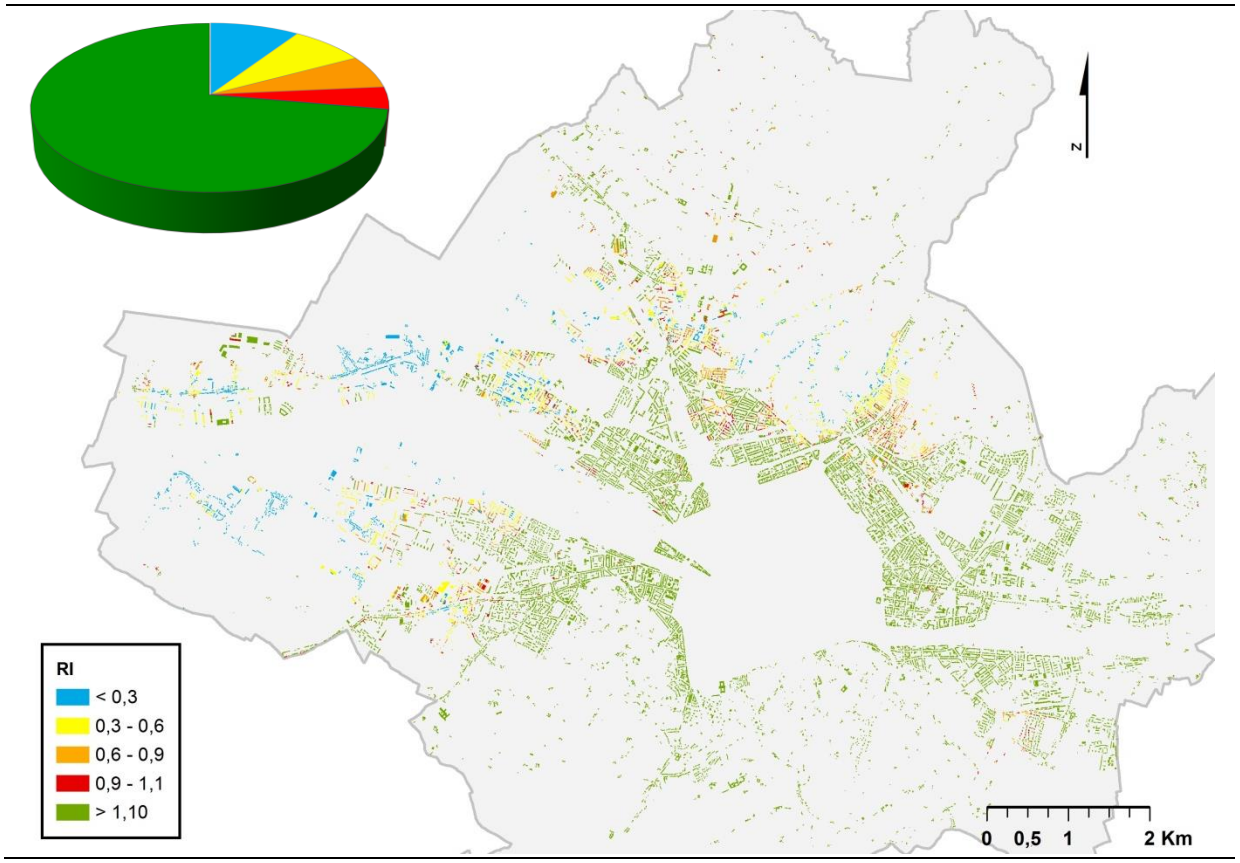

Figure 7. Resonance map.

5 CONCLUSIVE REMARKS

In this work an evaluation of the seismic vulnerability has been made on the area of Florence. To this purpose the dynamic properties both of the soil and of the buildings population of the urban area have been checked.

The hazard of the area has been achieved by performing an extensive experimental campaign over the area soil, consisting of 1,850 drillings and 32 downhole tests. The information provided by the two types of testing have been combined, returning a mapping of the funda-

mental frequency of the soil all over the Florence area. The same investigation has provided the distribution of the amplification factor over the selected area.

The existing database referred to the buildings population has been upgraded, by introducing further information about the constructive system and the materials of all buildings, and by determining their vibrational period by means of the conventional expressions provided by the Technical Codes. A vulnerability index, *RI*, has been introduced to express the probability of the buildings to experience resonance phenomena. *RI* has been defined as the ratio between the period of the buildings and the one of their foundation soil, and a classification has been introduced to evaluate the resonance probability of each building. A further map, expressing the *RI* classification, has been provided for the urban area of Florence.

The obtained *RI* map should be improved, by introducing further information about the buildings geometric and mechanical properties, and by evaluating the buildings fundamental periods through more accurate expressions.

ACKNOWLEDGMENTS

The financial support of the Cassa di Risparmio di Firenze through the project "SISMED - Modelli sperimentali di valutazione della vulnerabilità sismica di aree urbane complesse: il caso della città di Firenze" is gratefully acknowledged.

REFERENCES

[1] A. Anelli, M. De Luca Picione and M. Vona (2015). Selection of optimal seismic retrofitting strategy for existing RC building. COMPDYN 2015, Crete Island, Greece, 25–27 May 2015.

[2] A. Ilki, F. Karadogan, S. Pala, E. Yuksel (2009). Seismic Risk Assessment and Retrofitting: With Special Emphasis on Existing Low-Rise Structures. Springer.

[3] VM Vaghani, AS Vasanwala and AK Desai (2014). Advanced Retrofitting Techniques for RC Building: A State of an Art ReviewInternational Journal of Current Engineering and Technology, Vol.4, No.2 (April 2014)

[4] M. De Stefano, M. Tanganelli, S. Viti (2014). Variability in concrete mechanical properties as a source of in-plan irregularity for existing RC framed structures, Engineering Structures 59: 161-172

[5] G.M. Calvi, R. Pinho, G. Magenes, J.J. Bommer, L.F. Restrepo-Vélez and H. Crowley (2006). Development of seismic vulnerability assessment methodologies over the past 30 years. ISET Journal of Earthquake Technology, Paper No. 472, Vol. 43, No. 3, September 2006, pp. 75-104.

[6] S. Giovinazzi, S. Lagomarsino (2004). A macroseismic method for the vulnerability assessment of buildings. Proc. of 13th World Conference on Earthquake Engineering, Vancouver, Canada, Paper No. 896.

[7] Dolce, M., Masi, A., Marino, M. and Vona, M. (2003). Earthquake Damage Scenarios of the Building Stock of Potenza (Southern Italy) Including Site Effects, Bulletin of Earthquake Engineering, Vol. 1, No. 1, pp. 115-140.

[8] G. Di Pasquale, G. Orsini, and R.W. Romeo (2005). New Developments in Seismic Risk Assessment in Italy. Bulletin of Earthquake Engineering, Vol. 3, No. 1, pp. 101-128.

[9] M. Rota, A. Penna, C. Strobbia, G. Magenes (2008). Derivation of empirical fragility curves from Italian damage data. IUSS Press, Pavia, Italia

[10] NTC (2008). Nuove norme tecniche per le costruzioni. 2008 DM 14 Gennaio 2008, Gazzetta Ufficiale n. 29 del 04/02/2008 (in Italian).

[11] M. Ripepe, G. Lacanna, P. Deguy, M. De Stefano, V. Mariani and M. Tanganelli (2015). Large-scale seismic vulnerability assessment method for urban centres. An application to the city of Florence. Key Engineering Materials Vol 628 (2015) pp 49-54.

[12] M. Coli & P. Rubellini (2013). Geological anamnesis of the Florence area, Italy. Z. Dt. Ges. Geowiss. (German J. Geosci.), 164 (4), p. 581–589.

[13] M. Coli, L. Guerri & P. Rubellini (2015). Geotechnical characterization of the Florence (Italy) soils. Proc. 5th Asian Regional Conference on Soil Mechanics and Geotechnical Engineering, Fukuoka November 9-13, Japan.

[14] International Stratigraphic Guide (1994). A guide to stratigraphic classification, terminology, and procedure (A. Salvador, ed.) 2nd edition. *The International Union of Geological Sciences and The Geological Society of America*.

[15] P. Ricci, G.M. Verderame, G. Manfredi (2011) - Analytical investigation of elastic period of infilled RC MRF buildings. Engineering Structures, 33(2): 308-319.

[16] FEMA (2000). Prestandard and commentary for the seismic rehabilitation of buildings. FEMA 356. Federal Emergency Management Agency, Washington DC.

[17] BSSC (2001). NEHRP Recommended provisionsfor seismic regulations for new buildings and other structures. 2000 Edition. Part 1: Provisions (FEMA 368). Building Seismic Safety Council, Washington DC.

[18] UBC (1997). Uniform building code. International Conference of Building Officials, Whittier, California.

[19] NBCC (2005). National Building Code of Canada. Institute for Research in Construction (IRC), Canada.

[20] UNI EN 1998-1 (2005). Eurocodice 8: Progettazione delle strutture per la resistenza sismica. Parte 1: Regole generali, azioni sismiche e regole per gli edifici. Versione italiana del gennaio 2007, Ente Nazionale Italiano di Unificazione, Milano (in Italian).

[21] G.M. Verderame, I. Iervolin, G. Manfredi (2010). Elastic period of sub-standard reinforced concrete moment resisting frame buildings. Bulletin Earthquake Engineering, 8: 955-972

[22] A. Masi, M. Vona (2010) – Experimental and numerical evaluation of the fundamental period of undamaged and damaged RC framed buildings. Bulletin of Earthquake Engineering, 8: 643-656.

ECCOMAS Congress 2016
VII European Congress on Computational Methods in Applied Sciences and Engineering
M. Papadrakakis, V. Papadopoulos, G. Stefanou, V. Plevris (eds.)
Crete Island, Greece, 5–10 June 2016

SPO2FRAG V1.0: SOFTWARE FOR PUSHOVER-BASED DERIVATION OF SEISMIC FRAGILITY CURVES

Iunio Iervolino[1], Georgios Baltzopoulos[2], Dimitrios Vamvatsikos[3] and Roberto Baraschino[4]

[1] Università degli Studi di Napoli Federico II
Via Claudio 21, 80125 Naples, Italy
iunio.iervolino@unina.it

[2] Istituto per le Tecnologie della Costruzione ITC-CNR, URT Napoli c/o DiSt
Via Claudio 21, 80125 Naples, Italy
georgios.baltzopoulos@itc.cnr.it

[3] National Technical University of Athens
9 Heroon Politechneiou, 157 80 Athens, Greece
divamva@mail.ntua.gr

[4] AMRA s.c.a r.l.
Via Nuova Agnano 11, 80125 Naples, Italy
roberto.baraschino@gmail.com

Keywords: vulnerability, incremental dynamic analysis, seismic risk, loss assessment.

Abstract. *This article presents SPO2FRAG V1.0, the first (beta) version of the Static PushOver to FRAGility software. The SPO2FRAG software is an interactive and user-friendly tool that can be used for approximate, computer-aided calculation of building seismic fragility functions, based on static pushover analysis. It is coded in MATLAB® environment and is currently under development at the Department of Structures for Engineering and Architecture of the University of Naples Federico II. At the core of the SPO2FRAG tool lies the SPO2IDA algorithm, which permits analytical predictions for incremental dynamic analysis summary fractiles at the single-degree-of-freedom system level. By effectively interfacing SPO2IDA with a series of operations, intended to link the results of static pushover analysis with the variability that typically characterizes non-linear dynamic structural response, SPO2FRAG provides an expedient solution to the computationally demanding task of analytically evaluating seismic building fragility, which would otherwise require a large number of non-linear dynamic analyses.*

1 INTRODUCTION

Seismic risk and loss estimation studies performed within a probabilistic framework employ structural fragility (or vulnerability) functions, which provide the probability of exceeding some predefined performance limit state in a single seismic event, given a certain level of seismic intensity. In the case of structure-specific studies, the trend is to rely increasingly on analytical derivation for these fragility functions. State-of-the-art in analytical fragility estimation is the use of non-linear dynamic analyses – for example, incremental dynamic analysis (IDA, [1]), the cloud method [2] or multi-stripe analysis [3]. However, despite the advantages of the analytical approaches over the damage probability matrices and empirical fragility curves employed earlier, their chief disadvantage remains the computational burden involved [4], which may include the selection and manipulation of hazard-consistent ground motion records.[1]

In order to sidestep the computationally demanding methods of seismic structural assessment that involve non-linear dynamic analysis, engineers have long relied on approximate methods, such as static non-linear procedures, which estimate seismic demand of the structure by making recourse to an equivalent single-degree-of-freedom (SDOF) oscillator [6]. A simple and effective link between IDA and static non-linear analysis has been provided by the SPO2IDA algorithm [7], which acts as a predictive equation of the fractile IDA curves for SDOF systems with multi-linear pushover curves. The SPO2IDA algorithm forms the backbone around which the SPO2FRAG (Static Pushover to Fragility) tool, a MATLAB® coded software whose presentation is the objective of the present paper, is built. SPO2FRAG offers an expedient solution to the analytical derivation of seismic fragility for buildings and can provide support to previously developed seismic risk assessment software such as the one described in [8].

The remainder of this article is structured in the following manner: first a brief presentation of past research most relevant to the development of the SPO2FRAG tool is provided. This is followed by an operational description of the software itself, complete with a flowchart and graphical user interface (GUI) description. Subsequently, an example application is provided, accompanied by a comparison of the SPO2FRAG output with a set of fragility functions derived by means of IDA. Finally, some commentary and discussion on development concludes the article.

2 BACKGROUND

2.1 Static pushover to IDA

The most fundamental concept behind SPO2FRAG is the ability to predict efficiently IDA results of a given SDOF system without having to actually run any analysis, a prediction achieved thanks to SPO2IDA. On any monotonic static pushover curve (SPO), some characteristic regions can be typically identified: an elastic portion leading up to the yield point, a post-yield region characterized by positive stiffness (hardening) extending up to the capping point, a descending branch exhibiting negative stiffness (softening) and sometimes even a final residual strength segment (Fig. 1a). Based on the observation that the 16%, 50% and 84% fractile IDA curves of SDOF systems also exhibit distinctive characteristics within the ductility intervals that delimit these SPO segments, the SPO2IDA algorithm was developed. SPO2IDA comprises a set of equations that can directly predict the three summary fractile IDA curves for any

[1] It is appropriate to recall at this point that, in principle, fragility curves are site-specific. This is because the records employed to run non-linear dynamic analyses should be selected based on the joint and conditional distributions of hazard variables (e.g., magnitude, source-to-site distance, and accelerations) specific for the site. To overcome issues of this nature, the software discussed in the paper assumes conditional independence of first-mode spectral acceleration with respect to other hazard variables; see also [5].

SDOF system, with a given quadrilinear backbone geometry; this introduces an approximation but has the advantage of eschewing the need for laborious computations. An example of SPO2IDA-predicted fractile IDA curves is given in Fig. 1b, where the predictions are compared against the corresponding fractiles of explicitly calculated IDAs.

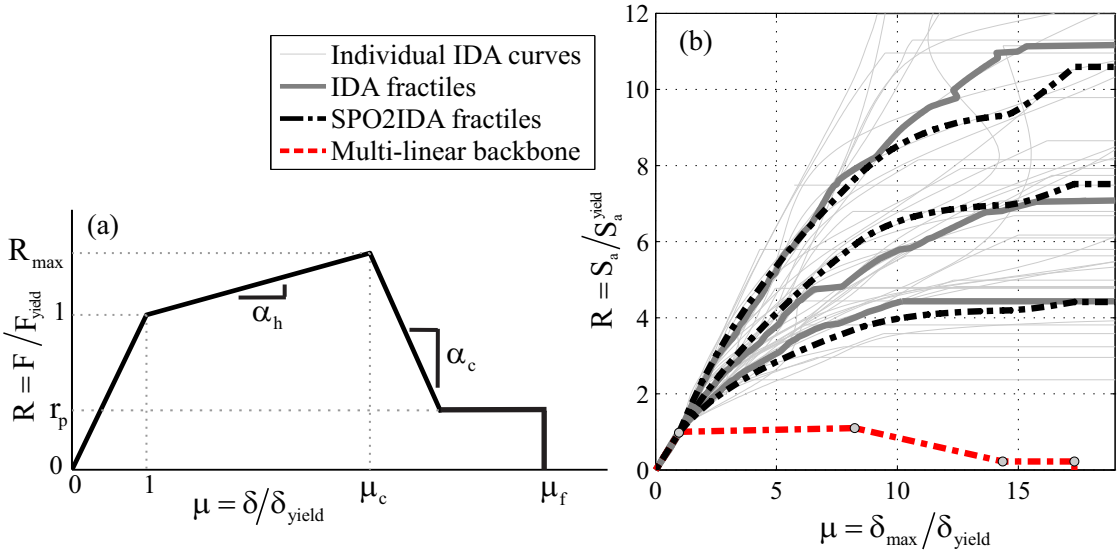

Figure 1: (a) Generic SDOF oscillator's quadri-linear backbone curve plotted in reduction factor (R, ratio of maximum to yield force) – ductility (μ, ratio of maximum to yield displacement) coordinates and (b) an example of SPO2IDA-predicted 16%, 50%, 84% fractile IDA curves, super-imposed over the fractile and individual IDAs calculated analytically for the same SDOF system using the FEMA P695 [9] far-field set of forty-four records. Backbone geometry is defined by the parameters α_h (post-yield to elastic stiffness ratio), μ_c (ductility at capping point marking the beginning of the descending branch), a_c (post-capping to elastic stiffness ratio) and μ_f (fracture ductility.)

2.2 Multi-linear fit of the monotonic backbone curve

Another important part of the SPO2FRAG algorithm is the automatization of obtaining a multi-linear backbone for the equivalent SDOF oscillator. As recently as – roughly – a decade ago, the norm for the implementation of static non-linear procedures (e.g., [10]) used to be a combination of simple elastic-perfectly-plastic or bi-linear hardening approximations of SPO backbones coupled with R-μ-T relationships (e.g., [11]) that only consider some central value of inelastic response. Under these circumstances, empirical "rules of thumb" for the multi-linear fit chosen for the SPO may have been good enough, but this may no longer be the case.

Advances in computing power and the sophistication of numerical modelling, for the non-linear aspects of structural behavior, have gradually led to SPO curves containing appreciable initial curvature (in cases where cracking is a factor) and descending post-peak-strength branches. In order to exploit the capabilities of more powerful R-μ-T relationships, such as SPO2IDA, there is a need for an efficient fully quadrilinear fitting scheme of such elaborate SPO backbones. A set of rules to that effect was proposed in [12], based on a study that employed IDA of SDOF systems with curvilinear and piece-wise-linear backbones.

2.3 SDOF to MDOF conversion of the fractile IDA curves

SPO2IDA can provide (an estimate of) the 16%, 50% and 84% fractile IDA curves of an equivalent SDOF system, processing a piecewise-linear backbone curve derived from the SPO of a given structure. The SDOF IDAs naturally come in reduction factor-ductility terms and therefore, in order to relate these IDA curves back to the original MDOF system, a series of

conversion operations are necessary (see Fig. 2). These conversions entail passage from non-dimensional coordinates R - μ to spectral acceleration – roof drift format, the possibility of adding the response variability at the nominal yield point that the MDOF system experiences due to the effect of higher modes (but is lost on its SDOF counterpart, [13]) and possibly a roof drift to inter-storey drift conversion, since the latter is oftentimes better suited for the definition of limit-state thresholds.

2.4 IM-based parametric fragility functions

The final output and stated objective of SPO2FRAG is the estimation of fragility functions for building-type structures. A fragility function provides the conditional probability that a structure will exceed a limit-state threshold ("fail") in a single seismic event, given a certain ground motion intensity measure (IM) level. If it is assumed that the level of seismic intensity causing failure (or, equivalently, the capacity of the structure per limit-state in IM terms, $IM_{C,LS}$) is a random variable that follows some specific model, for example the log-normal distribution, determining the fragility function boils down to estimating the mean-of-the-logarithm of capacity per limit-state, η , and the logarithmic standard deviation, β . This can be seen in Eq. 1, where $\Phi(\bullet)$ denotes the Gauss function.

$$P\left[IM_{C,LS} \le im\right] = \Phi\left(\frac{\ln im - \eta}{\beta}\right) \tag{1}$$

When the median and 16%, 84% fractile IDA curves are provided for the structure, one may estimate these two parameters by adopting a threshold engineering demand parameter (EDP) value (or probability distribution thereof) for each limit state – see for example Fig. 2c.

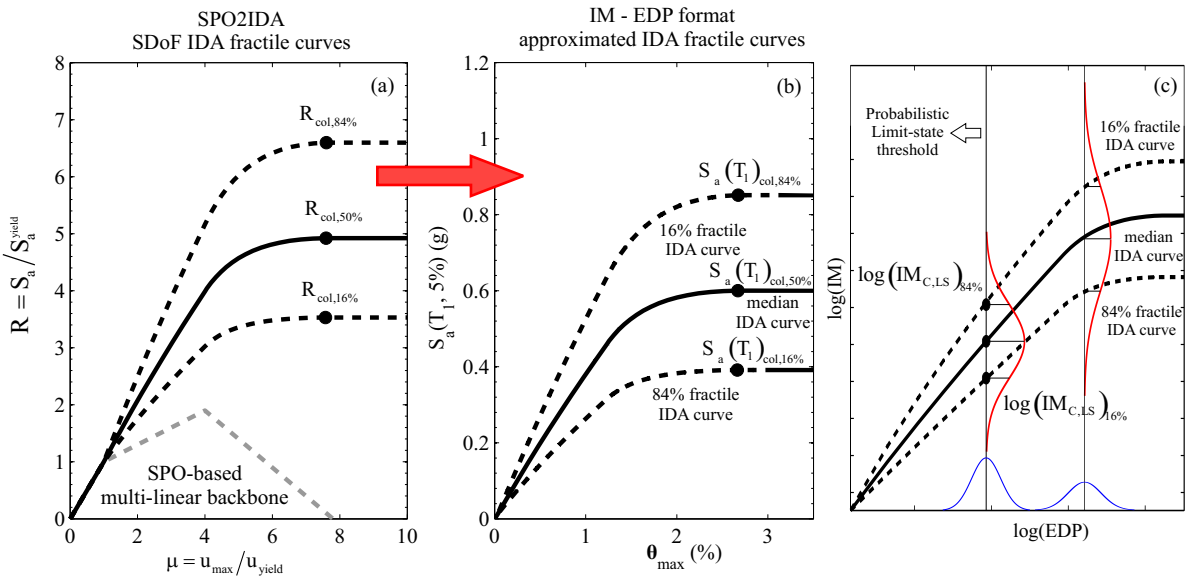

Figure 2: (a) Example of SPO2IDA-predicted 16%, 50% and 84% fractile SDOF IDA curves in terms of reduction factor – ductility, (b)conversion to first mode spectral acceleration – inter-storey drift ratio, (c) estimation of fragility function parameters assuming a log-normal distribution for the seismic intensity level causing exceedance of each limit-state threshold, $IM_{C,LS}$.

2.5 Model uncertainty in seismic structural response

SPO2FRAG simulates non-linear dynamic analysis via the SPO2IDA algorithm. Actual IDA, using a deterministic numerical model of the structure, can provide an estimate of record-to-record (aleatory) variability characterizing structural response. However, modelling parameters (such as material properties, member geometry, mass distribution, etc.) may also exhibit their own uncertainty, which will necessarily affect the distribution of $IM_{C,LS}$. Furthermore, some specific cases may violate some of the assumptions behind IDA to a certain extent, which can also result in additional uncertainty infiltrating the results. One, very simple, approach towards accounting for this additional uncertainty is to consider that the mean logarithmic capacity η is itself a random variable, assumed, for example, normally distributed with a standard deviation β_U (e.g., [14]). This additional parameter can be either obtained directly from relevant studies in the literature or estimated still via SPO2IDA [15].

3 SPO2FRAG, OPERATIONAL OUTLINE

3.1 Graphical user interface and flowchart

The SPO2FRAG software revolves around a GUI that allows the user prompt visualization of all intermediate results produced by the various modules and sub-routines. The individual modules that comprise the operational part of the software are the input interfaces, automatic multi-linearization module, dynamic characteristics toolbox, SPO2IDA module, interfaces for definition of limit states, their corresponding thresholds and any additional sources of uncertainty, the fragility function module and the output post-processing module. A flowchart of SPO2FRAG's operation is presented in Fig. 3 and a more detailed description of the same is given in the following paragraphs.

3.2 Data input, pre-processing and multi-linear fit

SPO2FRAG operates on the premise that the user performs the necessary SPO analysis using outside structural analysis code. Thus, the entry-level part of the tool is the data input interface, which reads SPO force-displacement results from either a text or a spreadsheet file. Preferentially, SPO displacements at all stories are requested; this lateral deformation profile can then be used by the program to internally calculate modal characteristics and convert maximum roof drift to maximum inter-storey drift. In cases where only roof displacement - base shear results are available in terms of SPO, the subsequent *Dynamic Characteristics Input* window will require vibration period, modal participation factor and participating mass ratio to be input by the user, along with floor masses and storey heights.

Subsequently, user input is subjected to some rudimentary checks for consistency and/or obvious errors and the roof displacement – base shear curve is then fed to the automated piecewise linear fitting algorithm. This algorithm allows for a full quadrilinear fit (elastic, hardening, softening and residual plateau segments) based on [12], but the user may also request bilinear or elastic-perfectly plastic fits (e.g., in cases where strength degradation was not included in the numerical model of the SPO). The GUI windows and dialogue boxes relevant to this input procedure can be seen in Figs. 4, 5.

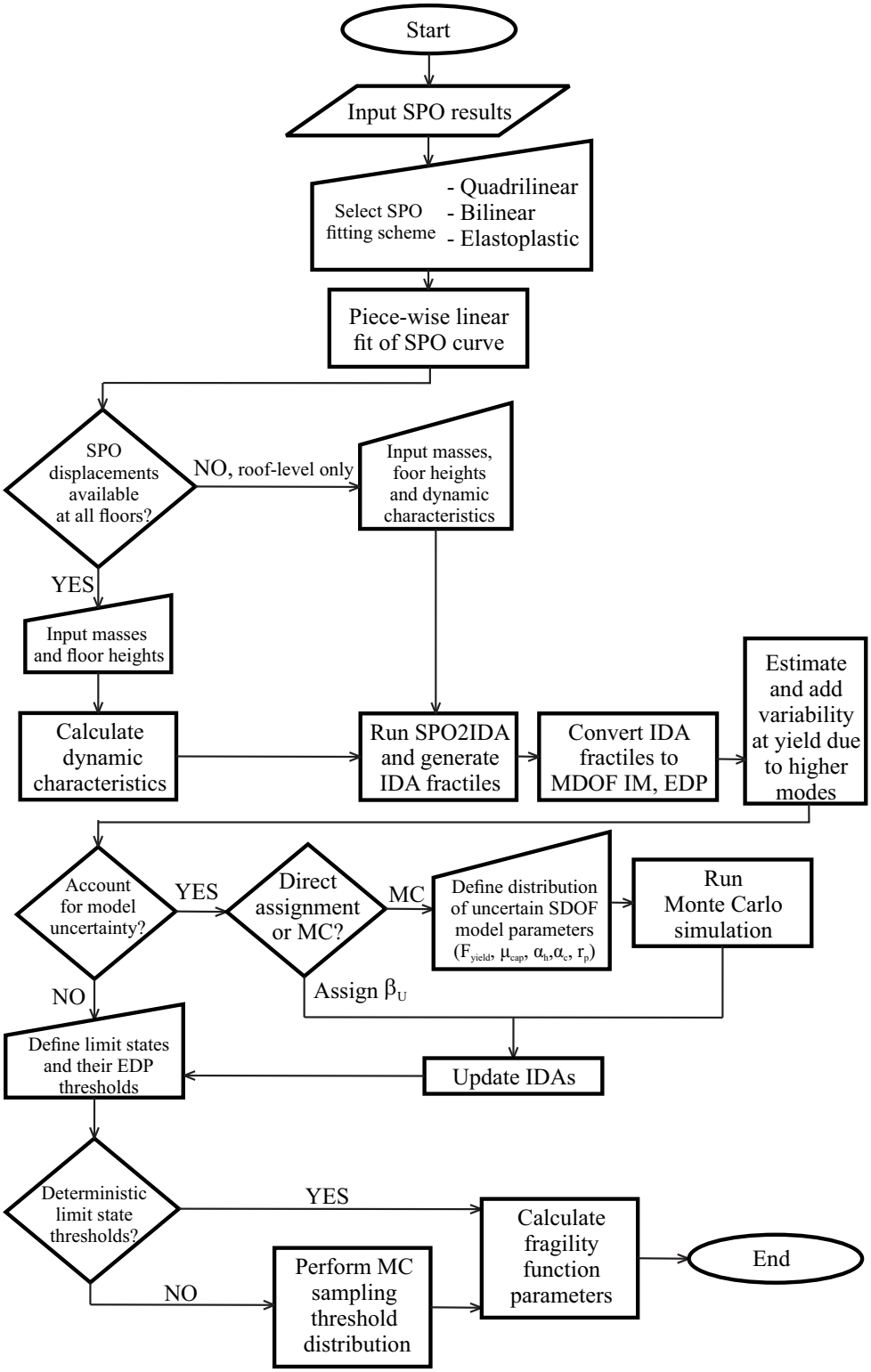

Figure 3: SPO2FRAG V1.0 flowchart.

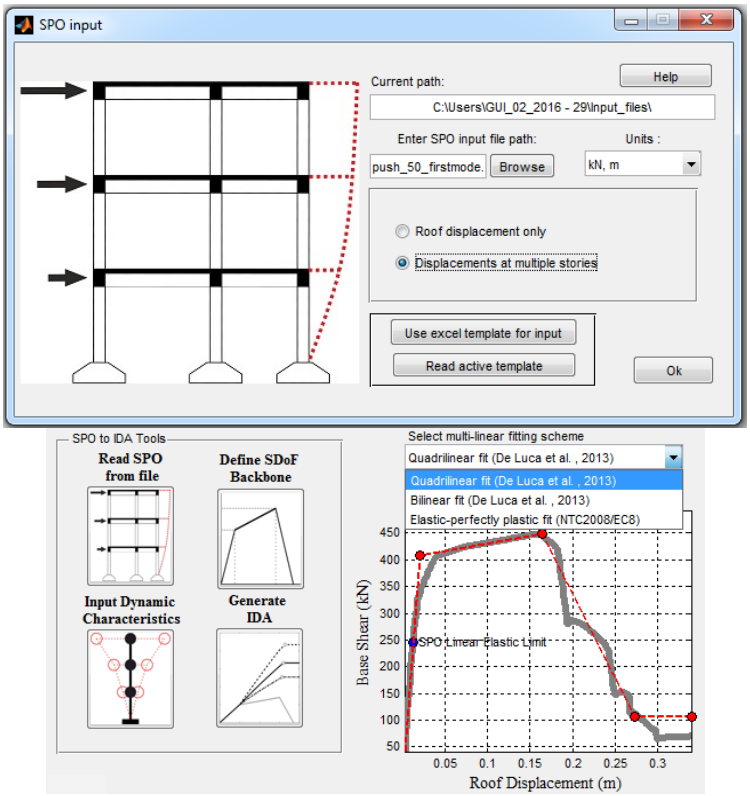

Figure 4: SPO data input from file window (upper panel) and GUI excerpt after piece-wise linear fit of the SPO curve (lower panel).

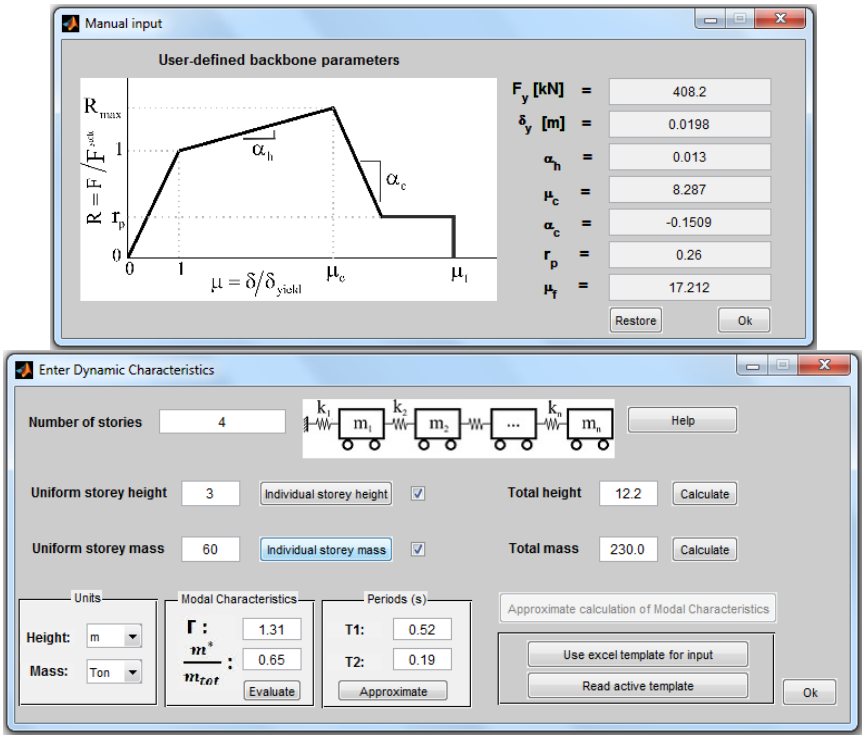

Figure 5: Dialogue box reporting the backbone parameters resulting from implementation of the multilinear fit algorithm (center) and input of dynamic characteristics window (lower part).

3.3 SPO2IDA and SDOF to MDOF conversions

Once data input is completed and a multi-linear fit of the SPO curve has been obtained, the SPO2IDA algorithm is launched, providing the 16%, 50% and 84% fractile SDOF IDA curve predictions in R-μ terms. The SPO2IDA output is automatically converted into spectral acceleration – drift format, using the dynamic characteristics of the structure. In cases where the SPO displacements at all storeys have been provided, the IDAs are converted in maximum interstorey drift ratio (IDR) terms by default; otherwise, EDP is set to roof drift. Even in the latter case, the user may still choose to convert to IDR, by selecting an appropriate approximation for the lateral post-yield deformation profile.

After this operation, an issue pertaining to the MDOF IDA curves that remains to be addressed is the fact that the MDOF system should exhibit greater record-to-record variability than its equivalent SDOF, due to the effect of higher modes of vibration. This additional variability is estimated by means of in-built empirical rules, injected at the nominal yield point and propagated along the IDA 16% and 84% fractiles.

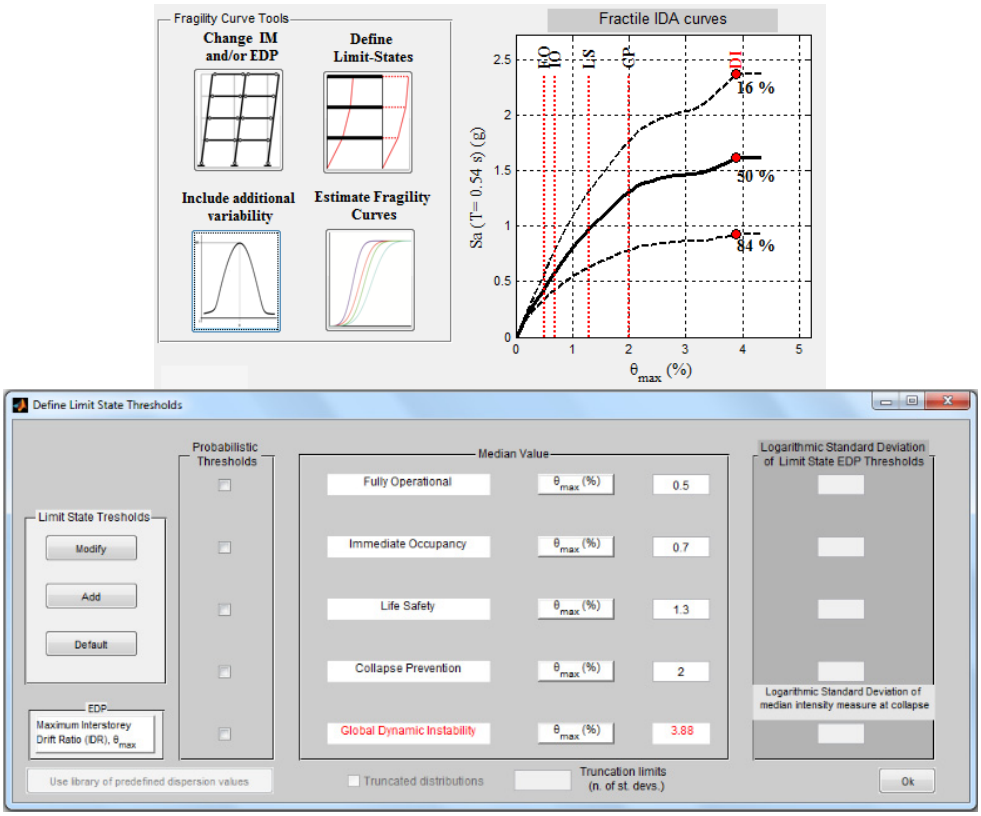

Figure 6. GUI excerpt showing the approximate (predicted) fractile IDA curves after completion of SDOF to MDOF conversion (upper panel) and window for the definition of limit states and limit-state-thresholds in terms of EDP (lower panel).

3.4 Limit-states and handling additional uncertainty

By default, the SPO2FRAG tool recognizes four limit states: *fully operational*, *immediate occupancy*, *life safety* and *collapse prevention* (see [16] for definitions). In cases where the SPO exhibits a negative-stiffness, softening branch a fifth limit state, *dynamic instability* will appear, corresponding to the IDA flat-lines. The user may also define more limit states via the GUI. In all cases, the user must define thresholds in terms of EDP, which determine exceedance of each limit state. Such thresholds need not be deterministic; the user has the option to treat them in a

probabilistic manner, by assuming that some thresholds follow a lognormal distribution, whereas the median and log-standard deviation of said distribution must be defined (Fig. 6).[2]

In cases where the user wishes to include (additional) modelling uncertainty into the calculation, two alternative options are available in the relevant GUI panel. First option is to define a logarithmic standard deviation β_U for mean logarithmic capacity η at one of the predefined limit states. This additional uncertainty is then propagated along the IDA curves. The second option is to consider some of the parameters that define the SDOF multi-linear backbone curve as random variables. In this second case, it is possible for the user to define the variance of the backbone parameters one wishes to treat probabilistically (log-normal distribution is assumed where the median is by default taken as the value initially provided by the automated fitting algorithm). Subsequently, Monte Carlo simulation is performed internally, where SPO2IDA realizations are created by sampling from within the user-defined parameter distributions and the IDA fractiles are updated accordingly.

3.5 Estimation of fragility curve parameters

Once the series of operations described above have been concluded, the fragility function parameters per limit state can be estimated based on the resulting approximated IDA curves of the structure. In the case of deterministic definition for the limit state EDP thresholds the logarithmic mean η is taken simply as the logarithm of the median IDA value at each threshold EDP level. The standard deviation β can be estimated as either the distance (in log-space) between the median and 84% fractile IDA or half the distance between the 16% and 84% fractile IDAs, at the discretion of the user (the latter being the default option, Eq. 2).

$$\begin{cases} \eta = \ln IM_{C,LS}^{50\%} \\ \beta = \ln\left[IM_{C,LS}^{50\%} \,/\, IM_{C,LS}^{16\%} \right] \text{, or alternatively} \\ \beta = 1/2 \cdot \ln\left[IM_{C,LS}^{84\%} \,/\, IM_{C,LS}^{16\%} \right] \end{cases} \tag{2}$$

In cases where the user has defined a probability distribution for the EDP threshold, rather than a deterministic value thereof, the parameter estimation procedure remains conceptually the same. The difference lies in the fact that Eq. 2 is applied for a number of EDP threshold realizations per limit state, sampled from the user-defined distribution and the final parameter estimates are provided by Monte Carlo simulation.

4 EXAMPLE APPLICATION

4.1 Four-storey “modern code” RC frame

In order to provide a fully-worked example of SPO2FRAG usage, a four-storey, bare, reinforced concrete (RC), plane frame was employed. This frame belongs to a symmetrical building designed under EN 1998-1 provisions in the context of a previous study (see [17] for more details) and was modelled numerically using the OpenSees open-code, structural analysis software [18]. Overall dimensions, member cross-sections, floor masses, shapes and periods of the first and second vibration modes and the SPO curve resulting from a first-mode-proportional

[2] Note that, for the sake of consistency limit state ranking (from milder to more severe) is adjusted automatically by the software, based on the corresponding user-defined (median or deterministic) thresholds.

lateral load profile are reported in Fig. 7. Inelasticity in the RC members was modelled following the concentrated plasticity approach, with plastic hinges at members' ends represented by rotational springs featuring trilinear backbones and hysteresis loops exhibiting mild pinching [19]. Concrete cracking was accounted for via the smeared crack approach of reducing the elastic pre-cracking stiffness of each member according to axial load [20].

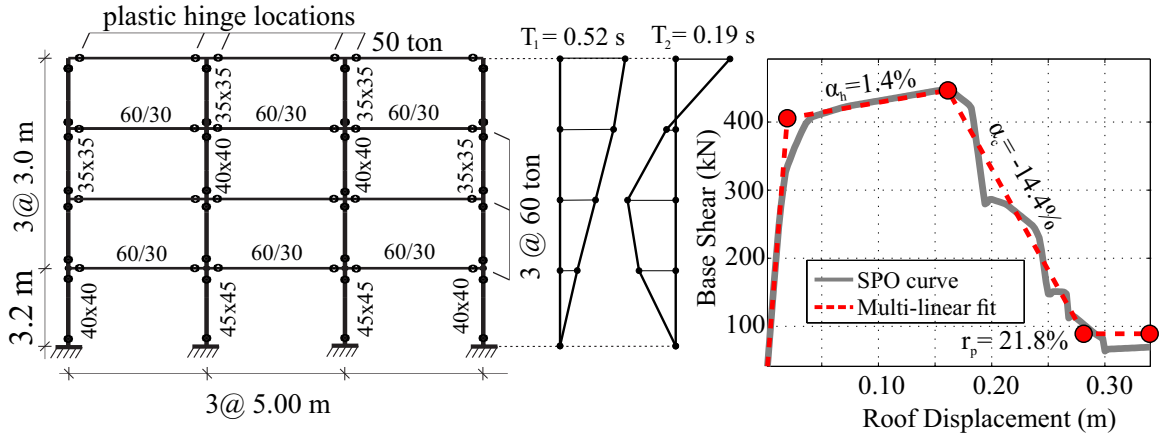

Figure 7: Dimensions, member cross-sections, floor masses, first two modes of natural vibration and first-mode SPO curve of the code-conforming four-storey RC frame used in the SPO2FRAG example application.

4.2 Example – fragility function calculation through SPO2FRAG

The SPO curve of the four-storey RC frame presented in the preceding paragraph is used as input for SPO2FRAG; displacements at all four diaphragms are provided via the input interface.

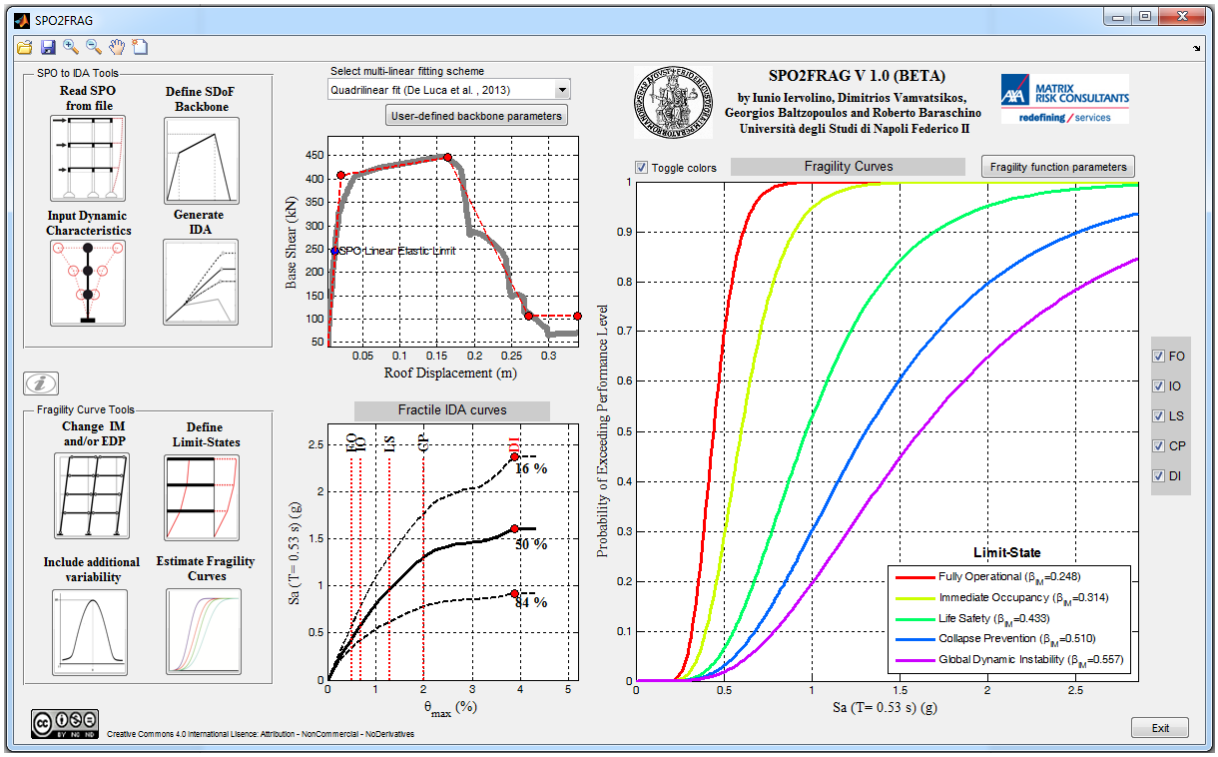

Figure 8: GUI view after implementation of the SPO2FRAG tool for an eight-storey "high-code" bare RC frame.

The roof displacement – base shear SPO is then subjected to a multilinear fit by the algorithm based on [12] (resulting fit is visible in Figs. 7, 8 and the corresponding backbone parameters in Fig. 4). Due to the availability of SPO results at all storeys, the only further input required, prior to obtaining the SPO2IDA approximate IDA fractiles, are the storey heights and masses (vibration period, modal participation factor and participating mass ratio are all calculated internally).

For this particular example, deterministic EDP thresholds (in terms of IDR) were assumed for the calculation. Indicative IDR thresholds for each limit state were calculated based on the *acceptance criteria* plastic rotation values for RC members found in [16]. A snapshot of the GUI display at the conclusion of this SPO2FRAG run can be seen in Fig. 8.

5 SPO2FRAG VS. IDA

It is only natural that the reference solution for the SPO2FRAG software should be the rigorous IDA procedure, i.e., the very same computational result that the tool is meant to emulate. Therefore, the same four-storey RC frame model that formed the basis of the preceding example application was also subjected to IDA using a set of forty-four records (far-field set in [9]; acceleration recordings from twenty-two stations, both horizontal components used separately). The resulting individual and fractile IDA curves can be seen in Fig. 9, in terms of both roof drift ratio (RDR) and IDR. The corresponding SPO2FRAG output is superimposed for comparison.

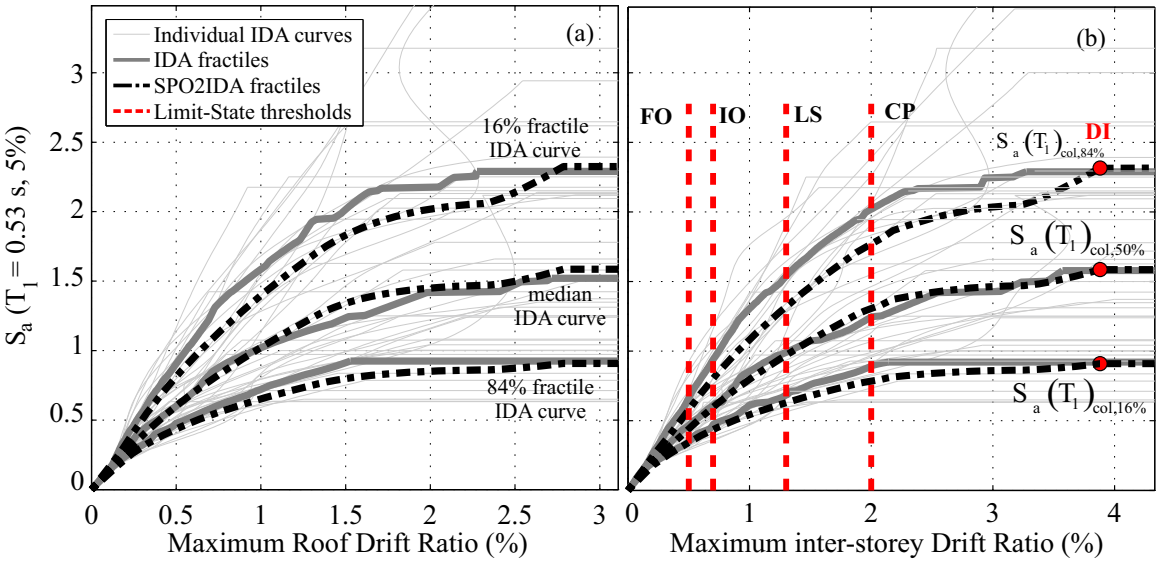

Figure 9: Comparison of SPO2FRAG approximated IDA fractiles with actual IDA results for a four-storey, high-code, bare RC frame using as EDP (a) roof drift ratio and (b) inter-storey drift ratio.

It can be observed that the adherence of the approximate SPO2FRAG result to its analytical counterpart is equally good for both cases of RDR and IDR, where the 50% and 84% fractile IDAs are concerned, but less so for the 16% curve. One of the reasons behind this is the fact that the shape of the SPO employed in this example (first-mode proportional lateral load profile) was able to capture one of the more unfavorable failure mechanisms (see also [13]). A comparison between the fragility functions resulting as SPO2FRAG output and those calculated by means of IDA can be found in Fig. 10.

Another meaningful comparison that can be made between the IDA and SPO2FRAG results, is between the annual rates of exceeding each limit state, λ_{LS}, as calculated by integrating the

fragility functions from the two procedures with the hazard curve for a given site, according to Eq. 3.

$$\lambda_{LS} = \int_{IM} P\left[IM_{C,LS} \le im\right] \cdot \left|d\lambda_{im}\right| \tag{3}$$

In Eq. 3 the notation λ_{im} is used to signify the rate of exceeding a given IM value while for the fragility function the notation introduced in Eq. 1 is followed. For this example in particular, the seismic hazard curve for the site of Caivano in southern Italy (in terms of 5% damped spectral acceleration at a period of 0.53s) was employed – Fig. 11. This hazard curve was calculated using the software REASSESS [21]. For this calculation the seismic source zones model of [22] was considered; Gutenberg-Richter [23] seismicity parameters for these zones were provided by [24], [25] and the ground motion prediction model used was that of [26].

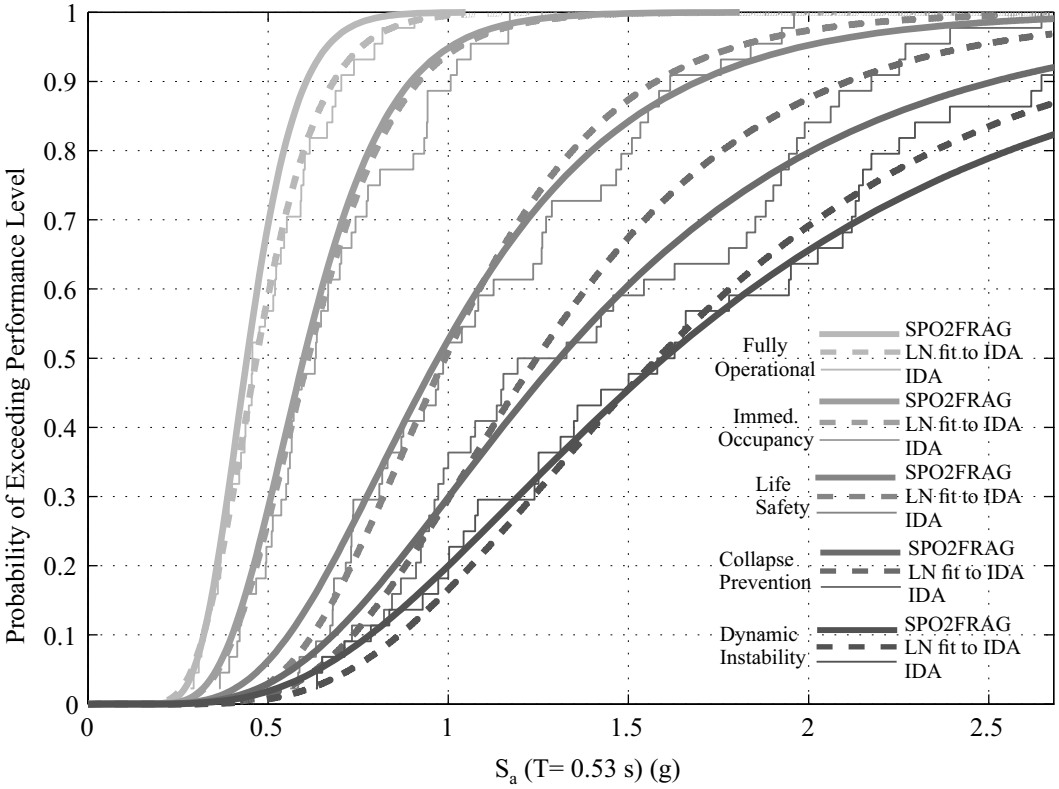

Figure 10: Comparison of fragility functions generated by SPO2FRAG and the same fragility functions estimated by means of IDA (see also Fig. 9). In both cases, the parameters of a log-normal (LN) distribution were estimated (see Table 1).

The results of these calculations can be found in Table 1, along with the estimators of the parameters corresponding to the curves appearing in Fig. 10. The estimators of the log-mean capacity per limit-state, η, correspond to taking the logarithm of the median IDA value for both of the IDA and SPO2FRAG cases. The estimator for the standard deviation of the logs, β, in the case of SPO2FRAG was the distance between the median and 16% fractile IM (see Eq. 2). In the case of IDA β was taken as the sample moment estimator of the standard deviation. It can be seen that the results display a reasonably good agreement between the approximate and rigorous procedure on all accounts.

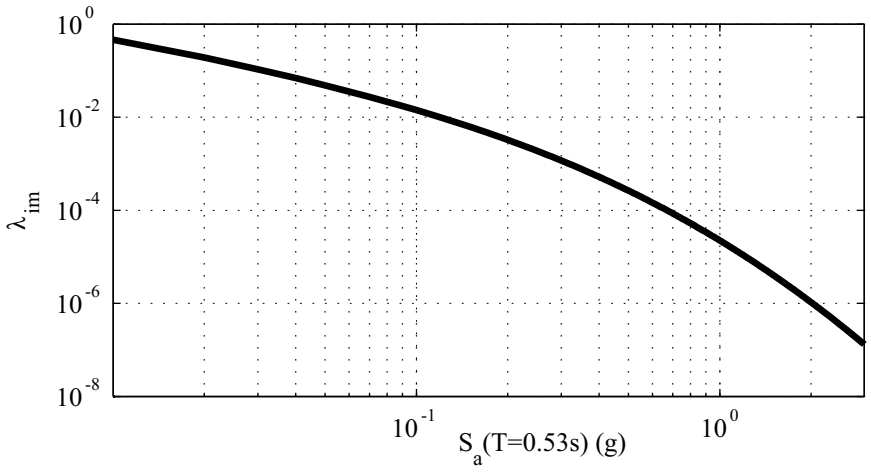

Figure 11: Hazard curve for an Italian site: annual rate of exceedance of 5% damped spectral acceleration at a period of 0.53s (period of equivalent SDOF of the four-storey frame in the example application).

Limit state	$\exp(\eta)$ (IDA)	$\exp(\eta)$ (SPO2FRAG)	β (IDA)	β (SPO2FRAG)	λ_{LS} (IDA)	λ_{LS} (SPO2FRAG)
Fully Operational	0.456 g	0.442 g	0.294	0.187	$4.9\cdot10^{-4}$	$4.5\cdot10^{-4}$
Immediate Occupancy	0.631 g	0.599 g	0.318	0.269	$2.0\cdot10^{-4}$	$2.1\cdot10^{-4}$
Life Safety	0.988 g	0.972 g	0.362	0.401	$5.3\cdot10^{-5}$	$6.6\cdot10^{-5}$
Collapse Prevention	1.260 g	1.308 g	0.410	0.484	$2.8\cdot10^{-5}$	$3.5\cdot10^{-5}$
Global Dynamic Instability	1.590 g	1.584 g	0.571	0.534	$1.7\cdot10^{-5}$	$2.4\cdot10^{-5}$

Table 1: Parameter estimators for the log-normal fragility functions of the illustrative example (see also Fig. 10) and corresponding calculated annual rates of exceeding each limit state at a site in Southern Italy.

6 CONCLUSIONS

This article dealt with the introduction of the SPO2FRAG V1.0 software. It is an interactive tool, coded in MATLAB® , that can be used for approximate, computer-aided calculation of building seismic fragility functions, based on static pushover analysis. It was shown that SPO2FRAG can provide a convenient and expeditious solution to the problem of analytical calculation of building fragility functions, at least in cases where the basic assumptions behind SPO analysis and IDA hold.

In a future, second version of the SPO2FRAG tool, whose development is currently underway, additional options are expected to be available. These additional features will include, among others the possibility to manage input consisting of more than one SPO curve per structure (corresponding to either loads applied in two principal directions of a three-dimensional structure, or different load patterns applied in the same direction – or both) and an in-built library of deformation limits per limit state from the literature.

ACKNOWLEDGEMENTS

The work presented in this paper was developed within the AXA-DiSt (*Dipartimento di Strutture per l'Ingegneria e l'Architettura, Università degli Studi di Napoli Federico II*) 2014-2017 research program, funded by AXA-Matrix Risk Consultants, Milan, Italy. The second author also wishes to acknowledge the support of the European Research Executive Agency via Marie Curie grant PCIG09-GA-2011-293855.

REFERENCES

[1] D. Vamvatsikos, C.A. Cornell. Incremental dynamic analysis. *Earthquake Engineering and Structural Dynamics*, **31**, 491-514, 2002.

[2] P. Bazzuro, C.A. Cornell, N. Shome, J.E. Carballo. Three proposals for characterizing MDOF non-linear seismic response. *Journal of Structural Engineering*, **124**, 1281-1289, 1998.

[3] N. Shome, C.A. Cornell, P. Bazzuro, J.E. Carballo. Earthquakes, records and non-linear responses. *Earthquake Spectra*, **14**(3), 469-500, 1998.

[4] G.M. Calvi,R. Pinho, G. Magenes, J.J. Bommer, L.F. Restrepo-Vélez, H. Crowley. Development of seismic vulnerability assessment methodologies over the past 30 years. *ISET Journal of Earthquake Technology*, **43**(3), 75-104, 2006.

[5] N. Luco, C.A. Cornell. Structure-Specific Scalar Intensity Measures for Near-Source and Ordinary Earthquake Ground Motions. *Earthquake Spectra*, 23(**2**), 357-392, 2007.

[6] M. Fragiadakis, D. Vamvatsikos, M. Ascheim. Application of nonlinear static procedures for seismic assessment of regular RC moment frame buildings. *Earthquake Spectra,* **30**(2), 767–794, 2014.

[7] D. Vamvatsikos, C.A. Cornell. Direct estimation of the seismic demand and capacity of oscillators with multi-linear static pushovers through IDA. *Earthquake Engineering and Structural Dynamics*, **35**, 1097–1117, 2006.

[8] F. Petruzzelli, I. Iervolino. FRAME V.1.0: A rapid fragility-based seismic risk assessment tool. *Proceedings of the Second European Conference on Earthquake Engineering and Seismology*, 2ECEES, Istanbul, Turkey, 24-29 August, 2014.

[9] FEMA P695. *Quantification of Building Seismic Performance Factors*. Federal Emergency Management Agency, Washington D.C., 2009.

[10] P. Fajfar. A nonlinear analysis method for performance based seismic design. *Earthquake Spectra*, **16**(3), 573-592, 2000.

[11] T. Vidic, P. Fajfar, M. Fischinger. Consistent inelastic design spectra: strength and displacement. *Earthquake Engineering and Structural Dynamics*, **23**, 507-521, 1994.

[12] F. De Luca, D. Vamvatsikos, I. Iervolino. Near-optimal piecewise linear fits of static pushover capacity curves for equivalent SDOF analysis. *Earthquake Engineering and Structural Dynamics*, **42**(4), 523-543, 2013.

[13] D. Vamvatsikos, C.A. Cornell. Direct estimation of seismic demand and capacity of multiple-degree-of-freedom systems through incremental dynamic analysis of single degree of freedom approximation. *Journal of Structural Engineering*, **131**, 589-599, 2005.

[14] C.A. Cornell, F. Jalayer, R.O. Hamburger, D.A. Foutch. The probabilistic basis for the SAC/FEMA steel moment frame guidelines. *Journal of Structural Engineering*, **128**, 526-533, 2002.

[15] M. Fragiadakis, D. Vamvatsikos. Fast performance uncertainty estimation via pushover and approximate IDA. *Earthquake Engineering and Structural Dynamics*, **39**(6), 683-703, 2010.

[16] FEMA 356. *Prestandard and commentary for the seismic rehabilitation of buildings*. Federal Emergency Management Agency, Washington D.C., 2000.

[17] G. Baltzopoulos, E. Chioccarelli, I. Iervolino. The displacement coefficient method in near-source conditions. *Earthquake Engineering and Structural Dynamics*, **44**(7), 1015-1033, 2015.

[18] F. McKenna, G.L. Fenves, M.H. Scott, B. Jeremic. *Open System for Earthquake Engineering Simulation (OpenSees)*. Pacific Earthquake Engineering Research Center, University of California, Berkeley, CA, 2000.

[19] L.F. Ibarra, R.A. Medina, H. Krawinkler. Hysteretic models that incorporate strength and stiffness deterioration. *Earthquake Engineering and Structural Dynamics*, **34**, 1489-1511, 2005.

[20] T.B. Panagiotakos, M. Fardis. Deformations of Reinforced Concrete Members at Yielding and Ultimate. *ACI Structural Journal*, 98(**2**), 135-148, 2001.

[21] I. Iervolino, E. Chioccarelli, P. Cito. REASSESS V1.0: A computationally efficient software for probabilistic seismic hazard analysis. Paper submitted to *ECCOMAS Congress 2016: VII European Congress on Computational Methods in Applied Sciences and Engineering.* M. Papadrakakis, V. Papadopoulos, G. Stefanou, V. Plevris (eds.), Crete Island, Greece, 5–10 June 2016.

[22] C. Meletti, F. Galadini, C. Valensise, M. Stucchi, R. Basili, S. Barba, G. Vannucci, E. Boschi. A seismic source zone model for the seismic hazard assessment of the Italian territory. *Tectonophysics*, **450**, 85-108, 2008.

[23] B. Gutenberg, C.F. Richter. Frequency of earthquakes in California. *Bulletin of the Seismological Society of America*, **34**, 185-188, 1944.

[24] S. Barani, D. Spallarossa, P. Bazzurro. Disaggregation of probabilistic ground-motion hazard in Italy. *Bulletin of the Seismological Society of America*, **99**, 2638-2661, 2009.

[25] S. Barani, D. Spallarossa, P. Bazzurro. Erratum to disaggregation of probabilistic ground-motion hazard in Italy. *Bulletin of the Seismological Society of America*, **100**, 3335-3336, 2010.

[26] N.N. Ambraseys, K.A. Simpson, J.J. Bommer. Prediction of horizontal response spectra in Europe. *Earthquake Engineering and Structural Dynamics,* **25**, 371-400, 1996.

ECCOMAS Congress 2016
VII European Congress on Computational Methods in Applied Sciences and Engineering
M. Papadrakakis, V. Papadopoulos, G. Stefanou, V. Plevris (eds.)
Crete Island, Greece, 5–10 June 2016

COMPUTER-AIDED RISK ASSESSMENT AT URBAN SCALE. MODEL DEFINITION AND VALIDATION ON A CASE STUDY.

A. Basaglia[1], A. Aprile[1], F. Pilla[2] and Enrico Spacone[3]

[1] Department of Engineering, University of Ferrara
Via Saragat 1, 44122 Ferrara, Italy
e-mail: {alberto.basaglia,alessandra.aprile}@unife.it

[2] Department of Civil, Structural and Environmental Engineering, Trinity College Dublin
College Green, Dublin 2, Ireland
e-mail: pillaf@tcd.ie

[3] Department of Engineering and Geology, University of Chieti - Pescara
Viale Pindaro 42, 65129 Pescara, Italy
e-mail: espacone@unich.it

Keywords: ECCOMAS Congress, Proceedings, Computational Methods, Earthquake Engineering, Risk Assessment, Urban Systems.

Abstract. *Disaster risk reduction has become a global urgent need. Similarly to other natural hazards, earthquakes may cause significant damages on a large scale. In Europe, seismic events mainly affect historical city centers, which are characterized by dense urban structure, usually constituted by ancient masonry and pre-code R.C. buildings, often in aggregate sequence. Historical city centers are very much part of the European cultural heritage and their preservation is considered a strategic issue for the EC due to their tangible and intangible values. Furthermore, it is an undisputable fact that natural disasters may have severe negative short-term economic impacts on the built environment and adverse longer-term consequences for economic growth and development. For this reason, the development of an efficient digital tool for urban seismic risk assessment and resilience enhancement becomes essential. With this aim, an original numerical procedure is proposed in this paper, based on multidisciplinary concepts combined in an innovative way. First of all, the concept of Limit States for the Minimum Urban Structure is introduced and described by means of simple mechanically based models. Then, elliptically distributed vulnerability indices are worked out by considering multidirectional seismic hazard, and 2D seismic risk assessment computation is performed. The results are implemented within the GIS software, where they are easily shown and discussed thanks to the graphical mapping tool. The proposed approach allows the definition and evaluation of a global intervention plan for resilience enhancement at the urban scale. Finally the proposed numerical procedure is applied for validation to the Italian city-center of Concordia Sulla Secchia (Italy), damaged by the 2012 Pianura Padana Earthquake (PPE). The predicted damage scenarios are compared with the actual post-seismic damage scenarios in order to evaluate the accuracy of the proposed evaluation procedure.*

1 INTRODUCTION

Disaster risk reduction is one of the biggest global challenge, as attested by the U.N. [1]. The first step to achieve disaster resilience enhancement is to propose unified guidelines for disaster management. Among all natural events, earthquakes produce most damage on a vast scale. They cause high number of casualties, severe economic damages and are a major threat for cultural heritage sites. In Europe, historical city centers represent an essential part of the cultural heritage. This immeasurable asset is a "strategic resource for a sustainable Europe" that need to be preserved [2]. Among all European countries, Italy holds the highest number of listed heritage sites as confirmed by UNESCO (*whc.ujnesco.org*). Seismic risk assessment and urban risk management improvement is the only way to avoid casualties, damages, and consequent settlements abandonment.

2 PROBLEM DEFINITION

Most authors express seismic risk, *R*, as the relationship between hazard, vulnerability and exposure, as reported in Eq. (1):

$$R_{ie|T} = |(H_i \otimes V_e) \otimes E|_T \tag{1}$$

where *H* is the hazard, i.e. the probability of exceedance of the seismic activity level of intensity *i*, during a specified recurrence period *T*; *V* is the vulnerability, i.e. the intrinsic predisposition of the *e-th* exposed element to suffer damage, resulting from a seismic event of intensity *i*; *E* is the exposure of all the *e-th* exposed elements. *H* and *E* are directly linked to the site geological properties and the social and economical value of buildings respectively. V, on the contrary can be determined with different methods [3]. Detailed approaches, highly efficient for individual buildings, become ineffective while moving to urban scale analysis. In fact, the use of less sophisticated but more practical methods is required by such complex task.

Currently, one of the main assessment methods used by researchers is the combined approach of the *Vulnerability Index* method [4, 5, 6] and the *Macroseismic* method [7, 8]. The first method determines the vulnerability of buildings as a weighted sum of 11 parameters, which represents the main features that influence the buildings' response to a seismic event. To determine the vulnerability index, a detailed inspection of buildings is required, regarding both geometrical and structural aspects. I_v, have always to fall within the range $0 \div 100$. The Macroseismic method derives from the definition of the European Macroseismic Scale, *EMS-98* [9] and related *mean damage grades*, $\mu_D \in [0 \div 5]$, and *Damage Probability Matrixes* (DPMs). Buildings are ranged into 6 vulnerability classes with an assigned *Vulnerability parameter*, V, which can be correlated with the I_v parameter of the aforementioned method, using Eq. (2). Then, using a probabilistic approach, it is possible to determine the damage level the constructions will undergo after an earthquake as well as the number of collapsed or unusable buildings and the seismic effect on the population.

$$V = 0.592 + 0.0057 \cdot I_V \tag{2}$$

This approach presents some main limitations:

a) it considers only masonry constructions;

b) it does not take into account the effects of buildings in aggregate sequence;

c) it considers the overall vulnerability as the simple sum of buildings' vulnerabilities.

Therefore, a complete methodology for seismic risk assessment and management at urban scale is still lacking.

3 MULTIDIRECTIONAL URBAN RELIABILITY ASSESSMENT (MURA-SH) METHOD

In this work, a new methodology is presented as "Multidirectional Urban Reliability Assessment - Seismic Hazard (MURA-SH)" method [10], based on the improvement of the previously described method.

3.1 Vulnerability index integration for masonry aggregates

A modified approach to the aggregate evaluation proposed by [11] is used: 5 additional parameters (see Tab. 1) are considered together with the 11 ones of the original Vulnerability Index Method [4, 5, 6]. The additional parameters take into account the building's behaviour when inserted into an aggregate sequence. It is important to remark that contiguity of buildings can either increase or reduce the seismic vulnerability within the range of ±30% of the detached building vulnerability.

Parameters		Class C_{vi}				Weight
		A	B	C	D	p_i
P12	Interactions in elevation	0	15	25	45	1.25
P13	Floor plans interactions	0	5	15	45	1.75
P14	Presence of offset ceilings	0	25	35	45	0.75
P15	Structural of typological heterogeneity	0	10	20	45	1.50
P16	Percentage difference within facade openings	0	15	35	45	1.25

Table 1: Vulnerability Index I_V additional parameters for masonry buildings in aggregate sequence

3.2 Proposed $I_V - V$ correlation for R.C. buildings

Historical city centers often present an heterogeneous mix of masonry and R.C. constructions. In this work, a mathematical correlation between the Vulnerability Index method and the Macroseismic approach for R.C. building is proposed, as reported by Eq. (3).

$$V = 0.8568 - 0.0083 \cdot I_V - 0.000039 \cdot I_V^2 \tag{3}$$

The proposed correlation is determined following the same analytical steps described in [3] but, unlike the linear correlation used for masonry buildings, a quadratic correlation is adopted for R.C. constructions.

3.3 Vulnerability ellipses for directional risk assessment

Buildings have usually a non regular plant shape and present different structural properties in each direction. Vulnerability is considered as the sum of isotropic and anisotropic factors [12]. The isotropic factor consists of all features not related to the input direction, like building's material quality and age. The anisotropic one includes all features dependant on the input direction, like the structural strength and stiffness as well as the boundary conditions. For this reason, each building vulnerability can be geometrically represented by an *ellipse*. Since buildings are arranged in a city according to different orientations, seismic events of similar intensities but different directions can produce different effects. In the current work, a directional risk assessment is proposed, following 3 subsequent steps:

a) Main directions *x* and *y* of the building under assessment are found out (Fig. 1a). Vulnerability indexes I_X and I_Y are then determined in both directions, by considering the different resistant areas in *x* and *y* direction. I_X and I_Y are now the semi-axes of the

vulnerability ellipses (Fig. 1b);

b) An external reference system is fixed (for example, in this case, cardinal axes E-N). The angle between the x main direction and the cardinal axes E is called θ, (Fig. 1c). By considering $I_X = a$ and $I_Y = b$, the vulnerability ellipse is determined through Eq. (4):

$$\frac{(x \cdot \cos\theta + y \cdot \sin\theta)^2}{a^2} + \frac{(y \cdot \cos\theta + x \cdot \sin\theta)^2}{b^2} = 1 \tag{4}$$

c) Given a possible earthquake direction, α, vulnerability ellipses return the corresponding vulnerability value I_α for each building.

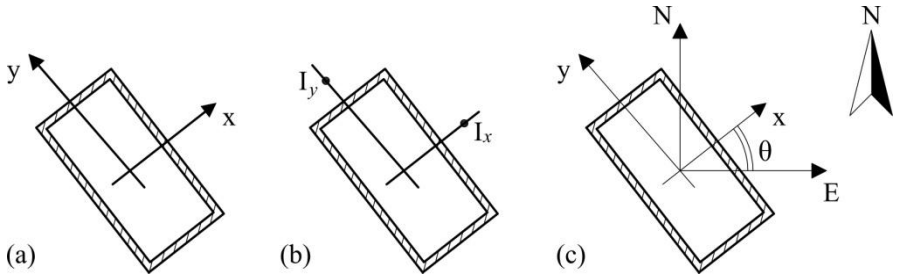

Figure 1: (a) Main directions of a building; (b) vulnerability indexes I_X and I_Y along main directions and (c) θ angle definition.

3.4 Definition of urban system reliability

The overall vulnerability of a city is not the simple sum of all buildings' vulnerability. Different constructions have different roles, which make them more or less relevant for the settlement, and their overall functioning is possible thanks to the accessibility of connection elements (routes, bridges, public open spaces, ecc). Furthermore, urban management policies must deal with the emergency phase after an earthquake, as well as with the *minimum urban structure* [13] preservation, in order to prevent the settlement abandonment. In this work, a performance-based approach for the urban system has been introduced, by adopting the definition of the *limit conditions for settlements* [14, 15]. Following this approach, the probability of the *e-th* building to undergo a certain damage level $P(D_k)|_e$, is accounted in a model that represents the overall city behavior with reference to the most significant limit conditions, expressed as CLE (emergency), CLV (life-saving) and CLD (damage).

- **CLE condition** - Only essential activities for the emergency phase are considered and the majority of the buildings can undertake even severe damages. The CLE is represented by a *series* of emergency sub-systems (see Fig. 2).

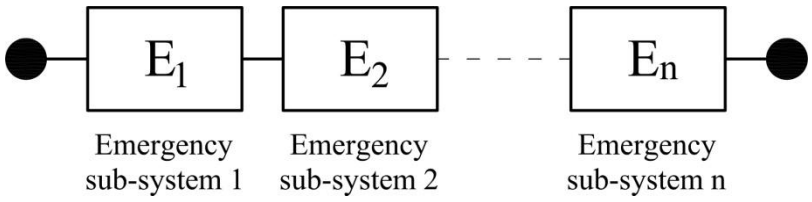

Figure 2: Urban system behaviour of the emergency limit condition (CLE)

Each *emergency sub-system* includes a strategic building, whose operation is essential in the emergency phase, and all "interfering" buildings related to it. An interfering building is an ordinary building that faces a strategic connection route (from/towards a strategic building or an emergency area). The CLE survival probability (*urban reliability*) is evaluated using Eq. (5).

$$P[\text{system survival}] = \prod_{i=1}^{n}(1 - P_i) \tag{5}$$

The component's failure probability P_i is defined according to the *importance class* c_u of buildings [16]. In particular, only the collapse, even partial, has to be prevented for interfering buildings (c_u= I, II), while any activity has to continue without interruption for strategic buildings (c_u= III, IV), see Eq. (6).

$$\begin{aligned} &c_u = \text{I, II (interfering)} \quad P_i = P(D4) + P(D5) \\ &c_u = \text{III, IV (strategic)} \quad P_i = P(D2) + P(D3) + P(D4) + P(D5) \end{aligned} \tag{6}$$

- **CLV condition** - The whole settlement is considered. The complete functionality of all strategic buildings is guaranteed, and only modest-to-long interruption of ordinary urban functions is accepted. The behaviour of the city is represented by a series-parallel combination of strategic and ordinary sub-systems (see Fig. 3). Each strategic sub-system includes an emergency system (see CLE) along with their "redundancy", i.e. other strategic systems of similar functions but not essential during the emergency phase. Ordinary sub-systems are considered in order to recover the settlement pre-seismic standard, including residential and economic activities. The CLV probability is evaluated using Eq. (7).

$$P[\text{system survival}] = \prod_{i=1}^{n}\left(\prod_{j=1}^{m} P_{ij}\right) \tag{7}$$

where P_{ij} accounts the interaction of the considered sub-systems and is defined by Eq. (6).

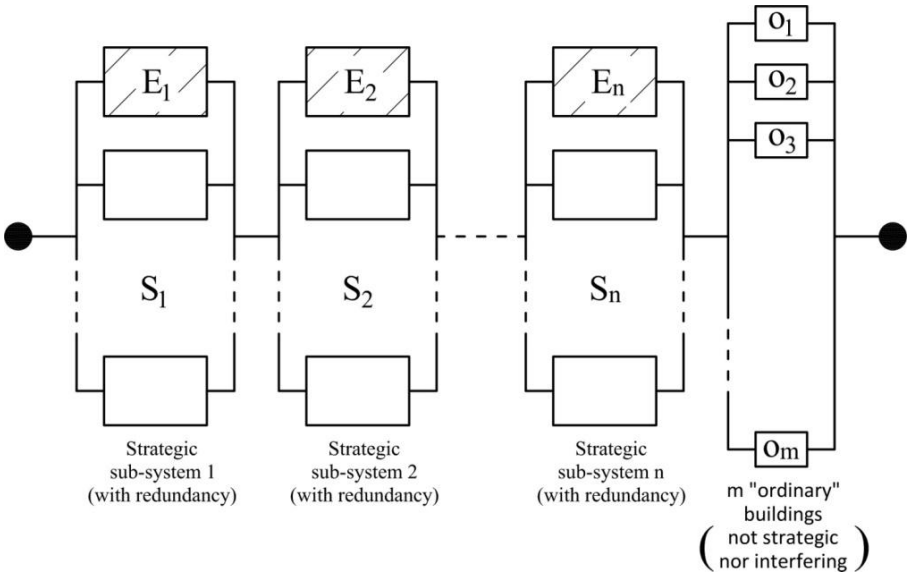

Figure 3: Urban system behaviour of the life-saving limit condition (CLV)

- **CLD condition** - Conceptually similar to the CLV, the only short-to-modest or partial interruption of ordinary urban functions is accepted. The behaviour of the city is still represented by a *series-parallel system* (see Fig. 3), and the urban reliability is evaluated using Eq. (7) where P_{ij} is defined by Eq. (8). The CLD represents the possibility for the settlement to undergo limited damage after an earthquake in order to guarantee the shorter recovery time targeted by the urban management policy.

$$c_u = \text{I, II (ordinary)} \qquad P_i = P(D3) + P(D4) + P(D5)$$

$$c_u = \text{III, IV (strategic)} \quad P_i = P(D2) + P(D3) + P(D4) + P(D5)$$

4 COMPUTER-AIDED RISK ASSESSMENT

The MURA-SH method application can be time-consuming even for small settlements, mainly due to the complexity of the urban system reliability model and the multi-directional damage scenarios evaluation. The development of a computer-aided procedure for the MURA-SH numerical implementation becomes highly efficient from the computational point of view by using the MATLAB® software. The proposed numerical procedure is presented in herein.

The preliminary phase of the procedure consist on the definition of a *.txt* input file listing all the required data of the MURA-SH method. The input files format holds seven columns and as many rows as the number of buildings under assessment. The columns data contain the following information:

- Vulnerability index along *x*-main direction, I_X;
- Vulnerability index along *y*-main direction, I_Y;
- θ angle, see Eq. (4);
- Structure Identifier (ID = 0 for masonry buildings, ID = 1 for R.C. buildings and ID = 2 for other structural types);
- Local soil amplification factor related to each building, F_a,
- Importance class, c_u [16];
- Occupants' number.

All data are loaded from the input file and vulnerability ellipses are created for every building using Eq. (4). Then, a coordinates transformation from the local to the global reference system is arranged. Finally, oriented vulnerability indexes I_α are evaluated.

Indexes I_α have to be converted into vulnerability values V_α using Eq. (2) and (3) depending on the structural type. Mean damage grades, μ_D, are evaluated for increasing intensities in the range $I_{EMS-98} = 5 \div 12$ with the equations of the Macroseismic method [8], but assuming the ductility factor, Q, equal to 2.1 for masonry buildings and 3 for other buildings. This assumption is introduced to consider that masonry structures can undergo local failure modes with limited ductility, when the global behavior is not guaranteed by the structural features.

Then, damage distributions histograms are defined making use of the $Beta$ probability density function (PDF), already included in the MATLAB® library as "betapdf". Numerical integration is made within defined intervals with the MATLAB® "trapz" function. Evaluated

damage probabilities are listed in matrixes for increasing intensities in the range $I_{EMS-98} = 5 \div 12$.

Total damage occurrence probability is used for losses evaluations, assessing the number of damaged or unusable buildings as well as the number of casualties and severed injured or homelessness. Equations to evaluate these data can be found in [3].

Finally, computed probabilities are combined to determine the reliability of the urban system, using equations introduced in §3.4, depending on the considered limit condition (CLE, CLV, CLD). The overall settlement reliability is evaluated for every direction α and for increasing intensities $I_{EMS-98} = 5 \div 12$. The proposed method application allows to easily predict which earthquake direction will cause the worst damage scenario, and the evolution of the settlement performance from moderate to strong earthquake intensity.

The overall MURA-SH numerical procedure is summarized in flowchart of Fig. 4.

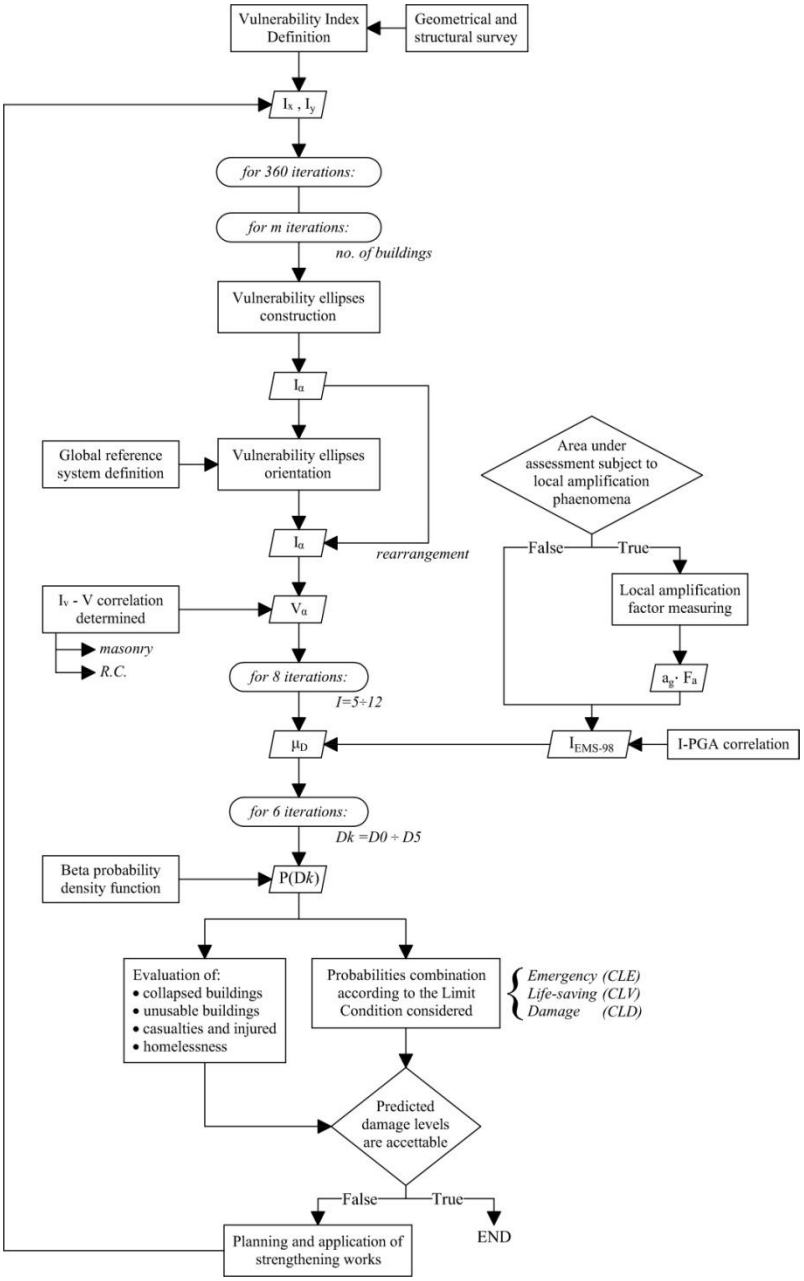

Figure 4: The MURA-SH method flowchart.

5 MODEL VALIDATION ON A CASE STUDY

Italy has recently experienced a seismic event (PPE, 2012). Among all the affected settlements, the city of Concordia sulla Secchia has a peculiar historical city center, constituted by an heterogeneous mix of masonry and R.C. constructions, built in different periods of time and mostly in aggregate sequence. The Municipal authorities of Concordia commissioned a post-earthquake survey, regarding its CLE sub-system, to the University of Ferrara, gathering geometrical and structural features of the majority of the buildings. Thanks to the available information, the MURA-SH method has been applied to the CLE sub-system of Concordia and μ_D values have been obtained for the PPE event. The PPE registered intensity that hit he city was within the range $I_{EMS-98} = 7 - 8$ (source: INGV) and the spatial distribution of seismic waves had the WNW-ESE predominant direction, i.e. 22° East (source: Italian Civil Protection).

Predicted damages were subsequently compared to the observed ones [10]. The comparison shows that, for $I_{EMS-98} = 7$, the predicted damage matches the observed damage on 15 of the 42 total number of buildings, with a positive feedback on the 36% of cases; for $I_{EMS-98} = 8$, the predicted damage matches the observed damage on 19 of the 42 total number of buildings, with a positive feedback on the 45% of cases. Maximum I_{EMS-98} registered during the PPE was equal to 8, and Concordia Sulla Secchia was the second most affected city. Therefore, it is reasonable to deduce that the actual intensity event that hit the settlement was closer to the upper bound of the measured range. The MURA-SH procedure needs to undergo more validations to improve the results accuracy. However, recognizing the task complexity, the obtained results are considered promising.

Some numerical results obtained with the MATLAB® procedure are shown in Fig. 5, where the collapse probability is represented along with the survival probability (*reliability*) of the CLE sub-system. Starting from intensity $I_{EMS-98} = 6$, the collapse probability assumes positive values and rapidly increases while the reliability drops to zero, accordingly with the CLE series system definition.

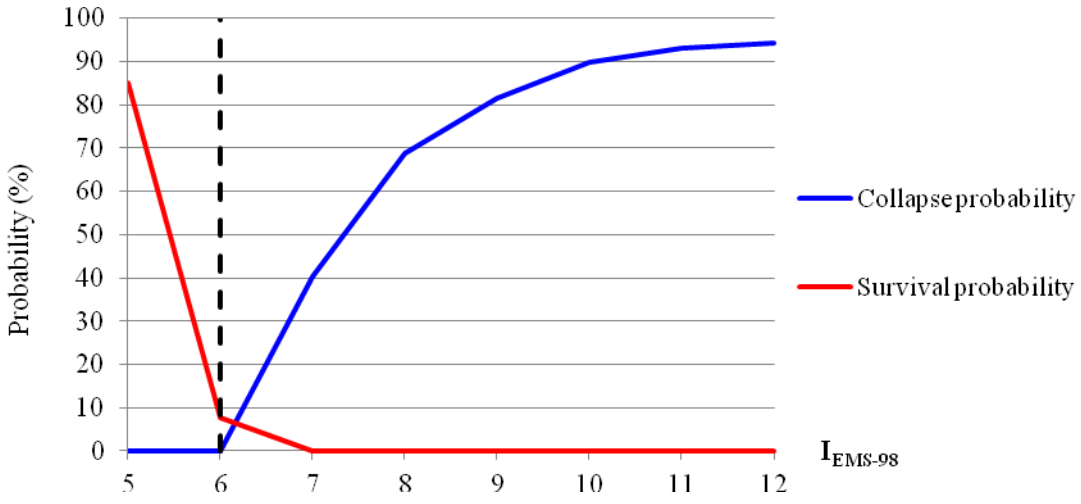

Figure 5: Collapse probability and survival probability of Concordia sulla Secchia CLE sub-system for increasing seismic intensities.

Furthermore, assessment output values can be reported directly on a city map (see Fig. 6), using the geospatial processing program ArcMap, of the Esri's ArcGIS suite (*http://desktop.arcgis.com/en/arcmap/*). With this representation it is possible to have an immediate overview of the earthquake effects for different directions and increasing seismic in-

tensities. A unique "feature identifier", also called FID, has to be assigned to every building in order to correctly refer corresponding output results. Assessment output values need to be previously organized in Excel files, using different sheets for increasing seismic intensities. Different colour maps can be used to represent the effects of increasing seismic intensities, and to identify most vulnerable areas.

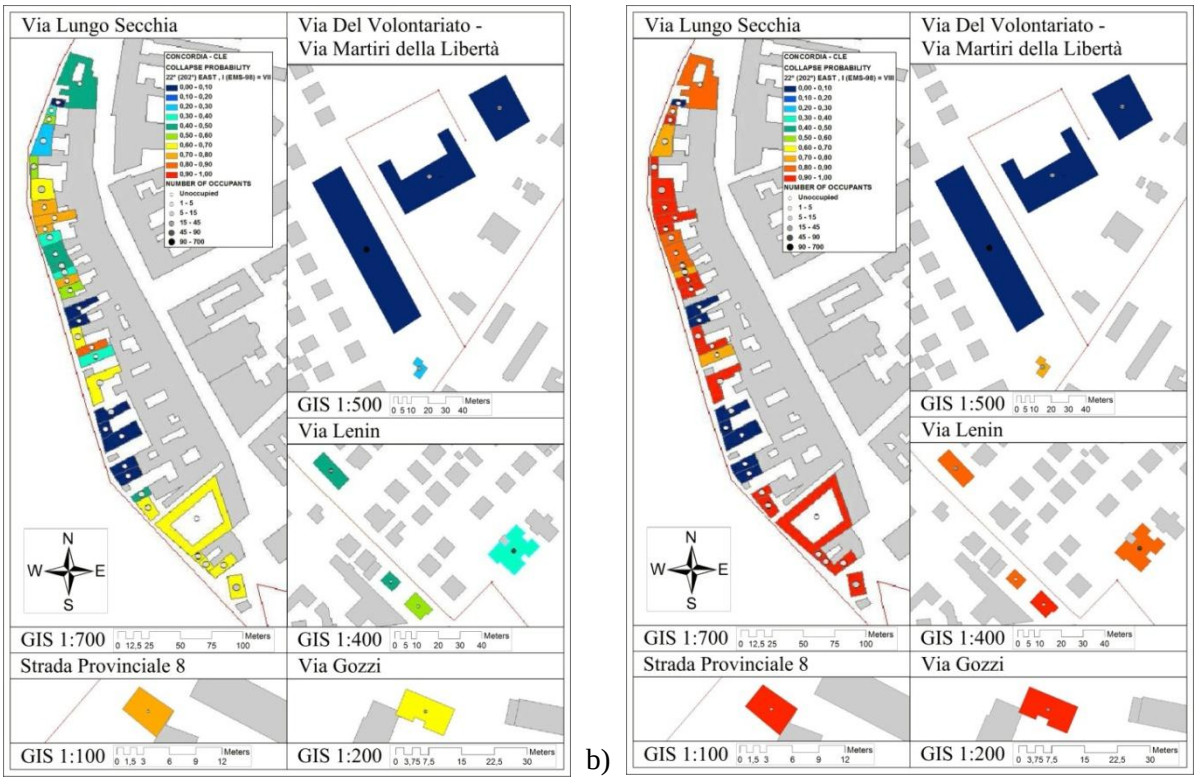

Figure 6: Mapping results of the collapse probability for the Concordia sulla Secchia CLE sub-system for (a) $I_{EMS-98} = 7$ and (b) $I_{EMS-98} = 8$.

6 CONCLUSIONS

In this work, a new methodology for the risk assessment at urban scale called MURA-SH method has been proposed. The MURA-SH method includes R.C. buildings in the evaluation, takes into account the effect of buildings aggregate sequence and performs multi-directional assessments, using the vulnerability ellipses. The MURA-SH method applies a performance-based approach to the settlement, with the definition of the urban system reliability. Thanks to its features, this method can predict whether the settlement will be able to withstand an earthquake, and what performance loss it will endure. The MURA-SH method has been implemented in a computer-aided procedure using the MATLAB® software. The obtained output results can be easily visualized with simple curves and GIS maps.

The proposed MURA-SH method has been applied on the case study of the historical city centre of Concordia sulla Secchia (Italy). The settlement experienced the PPE (2012) and a post-seismic survey of the CLE sub-system was carried out. The possibility to compare predicted damage scenarios to the observed ones has been extremely important to test the MURA-SH method accuracy. From the comparison, a matching rate of 45% ($I_{EMS-98} = 8$) was found. The procedure needs to undergo more validations to improve the results accuracy. However, recognizing the task complexity, the MURA-SH method results are considered promising.

REFERENCES

[1] Sendai Framework for Disaster Risk Reduction 2015-2030, *Third UN World Conference in Sendai*, Japan, March 18, 2015.

[2] Council conclusions on participatory governance of cultural heritage. Council of the European Union, Brussels, 13 November 2014

[3] R. Vicente, S. Parodi, S. Lagomarsino, H. Varum, J. A. R. Mendes Silva, Seismic vulnerability and risk assessment: case study of the historic city centre of Coimbra, Portugal. *Bull Earthquake Eng* (2011) 9:1067–1096, 2011.

[4] D. Benedetti, V. Petrini, On seismic vulnerability of masonry buildings: proposal of an evaluation procedure. *Ind. Constr.* 18:66–78, 1984.

[5] Gruppo Nazionale per la Difesa dai Terremoti – GNDT-SSN, Scheda di esposizione e vulnerabilità e di rilevamento danni di primo livello e secondo livello (muratura e cemento armato). *Gruppo Nazionale per la Difesa dai Terremoti: Roma*, 1994.

[6] M. Bezzazi, A. Khamlichi, J. R. A. González, Vulnérabilité sismique des constructions de type béton armé au Nord du Maroc. *Canadian Journal Of Civil Engineering* 35(6):600-608 · June, 2008.

[7] S. Giovinazzi, S. Lagomarsino, A macroseismic model for the vulnerability assessment of buildings. In: *Proceedings of 13th world conference on earthquake engineering*. Vancouver, Canada, 2004.

[8] A. Bernardini, S. Giovinazzi, S. Lagomarsino, S. Parodi, Matrici di probabilità di danno implicite nella scala EMS-98. *XII Convegno ANIDIS "L'ingegneria sismica in Italia"*, Pisa, 2007.

[9] G. Grünthal, European Macroseismic Scale 1998. *Cahiers du Centre Européen de Géodynamique et de Séismologie*, 15: p. 1-97, 1998.

[10] A. Basaglia, Seismic risk assessment and resilience enhancement at urban scale. The historical city center of Concordia sulla Secchia (MO) – Italy. *MSc Dissertation, University of Ferrara – Trinity College Dublin*, October 14, 2015.

[11] A. Formisano, F. M. Mazzolani, G. Florio, R. Landolfo, Un metodo per la valutazione su larga scala della vulnerabilità sismica degli aggregati storici. *STADATA*, 2011.

[12] S. Grimaz, Valutazione della vulnerabilità sismica di edifici in muratura appartenenti ad aggregate strutturali sulla base di analisi a posteriori. *Ingegneria sismica*, Anno X – N. 3 – Settembre-Dicembre, 1993

[13] W. Fabietti, Vulnerabilità e trasformazione dello spazio urbano. *Alinea*, Firenze, 1999.

[14] S. Staniscia, Definizione e valutazione di condizioni limite urbane a supporto della pianificazione urbanistica preventiva del rischio sismico. *PhD in Progettazione ed Ingegneria del Sottosuolo e dell'Ambiente Costruito, ciclo XXVI*. Università degli Studi "G. d'Annunzio", Chieti-Pescara, 2013.

[15] M. Olivieri, et al., Rischio sismico urbano: indicazioni di metodo e sperimentazioni per l'analisi della Condizione limite per l'emergenza e la Struttura urbana minima. *DGR n. 793 del 18/7/2011* – Determinazione dirigenziale n. 3928 23 Maggio, 2012.

[16] Eurocode 8: Design of structures for earthquake resistance. EN 1998-1 Part 1: General rules, seismic actions and rules for buildings. *CEN*, December, 2004.

ECCOMAS Congress 2016
VII European Congress on Computational Methods in Applied Sciences and Engineering
M. Papadrakakis, V. Papadopoulos, G. Stefanou, V. Plevris (eds.)
Crete Island, Greece, 5–10 June 2016

TOWARDS INTEGRATED SEISMIC RISK ASSESSMENT IN PALESTINE – APPLICATION TO THE CITY OF NABLUS

Ricardo Monteiro[1], Paola Ceresa[1], Vania Cerchiello[1], Jamal Dabeek[1], Antonella Di Meo[2] and Barbara Borzi[2]

[1] Institute for Advanced Study (IUSS) of Pavia
Piazza della Vittoria 15, Pavia, 27100, Italy
e-mail: name.surname@iusspavia.it

[2] European Centre for Training and Research in Earthquake Engineering (EUCENTRE)
Via Ferrata 1, Pavia, 27100, Italy
e-mail: name.surname@eucentre.it

Keywords: Seismic Risk, Hazard, Vulnerability, Exposure, Palestine.

Abstract. *Using large-scale seismic risk assessment studies for reduction of potential losses is becoming an evermore popular trend around the globe. Accordingly, a number of different models and techniques for the characterization of the different risk variables have proliferated in the recent years. Furthermore, the quality, or accuracy, of risk estimates will be certainly higher when a truly integrative model is employed, characterizing hazard, (physical and social) vulnerability and exposure in the most complete as possible manner. Regions with a large percentage of non-seismically designed buildings are particularly vulnerable to seismic events and are those that can benefit the most from risk assessment studies for decision making. As such, the main purpose of this study is to propose a framework for integrated seismic risk assessment in Palestine, where earthquake induced risk awareness is still at an early stage. A methodology to combine an existing state-of-the-art hazard model with new vulnerability and exposure models, specifically built upon local field surveys and national data collection, is proposed. The outcome of the study will enable the identification of the regions that are more vulnerable to earthquakes and future rapid loss assessment at regional scale.*

1 INTRODUCTION

The seismic activity in Palestine is not negligible and is largely affected and controlled by geodynamic processes acting along the Dead Sea Transform (DST). The DST is a north-south striking left-lateral shear zone extending from the incipient oceanic ridge (Red Sea) in the south to the Taurus plate collision in the north (Turkey). About 105-110 km of left-lateral displacement between the African and Arabian tectonic plates took place along this fault system during the last 15 million years. Historically, estimated events reached up to IX in the Modified Mercalli Scale in the Dead Sea region. In the same area, the determinable magnitudes of the recorded earthquakes range between 1.0 and 7.0 on the local magnitude Richter scale.

Together with observed seismicity, the Palestinian region faces important issues related to structural and societal factors. First, a high vulnerability, as a direct result of a high percentage of weak buildings not complying with seismic design requirements, thus with high potential for damage and losses. Secondly, measures of seismic risk mitigation are not enforced with national and public policies, which results in an absence of effective control of design and construction practice. The two aforementioned elements are exacerbated by the weakness in the general institutional capacity in disaster management, by insufficient professional capabilities of both engineers and decision makers and by a lack of awareness of citizens on seismic risk matters.

In the light of such facts, strategic directions were devised for the implementation of seismic disaster risk reduction. Recently, the population of Palestine has become more aware of the concept of seismic risk, significantly due to the results of the FP7-SASPARM (Support Action for Strengthening Palestinian-administrated Areas capabilities for Seismic Risk Mitigation) project, held during 2013 and 2014. SASPARM activities were focus on the strengthening of the research capabilities of An-Najah National University through the development of a comprehensive database of existing research data, the promotion of training for scientists and students in the field of seismic risk with the collaboration of European partners – EUCENTRE (European Centre for Training and Research in Earthquake Engineering) and IUSS (Institute for Advanced Study). Subsequently, new activities proposed within the DG-ECHO SASPARM 2.0 (2015-2016) project are further raising such awareness and strengthening their capabilities to cope with seismic risk. Engagement in training courses and workshops takes place not only at the local community level but also even Palestinian stakeholders, governmental (GO) and non-governmental (NGO) institutions, students and practitioners are effectively involved. One of the major goals of the SASPARM 2.0 initiative is the development of an integrated seismic risk model for Palestine, based on a state-of-the-art hazard model and in-field collected vulnerability and exposure data. The city of Nablus, the first Palestinian city to join the UNISDR's Making city resilient campaign, constitutes the case study area for the implementation and calibration of the model. In this paper, the framework for the achievement of the integrated model for the challenging Palestinian region is described, together with the main assumptions and assessment of options for the different risk components.

2 CONTEXT – THE SASPARM 2.0 PROJECT

The activities of SASPARM 2.0 (Support Action for Strengthening Palestine capabilities for seismic Risk Mitigation) are organised into eight main operative tasks, comprising the collection of vulnerability data and implementation of vulnerability models; training for targeted groups; development of self-assessment tools to understand potential unsafe situations and the related mitigation measures (retrofitting and insurance coverage). The project is managed by the same consortium of SASPARM and is creating a Web-Based Platform (WBP) for seismic

risk mitigation, which integrates a database of vulnerability data on buildings, collected on field.

The awareness of the community is a fundamental step in the resilience process, since the citizens have to monitor their individual properties and be able to understand, with and, when feasible, without the advice of an expert, if their house can withstand an earthquake or if retrofit is required, applying seismic standards. On the other hand, practitioners as well as governmental (GO) and non-governmental (NGO) stakeholders have to be made aware of the importance of the right application and implementation of the new Seismic Building Code. The outcomes and tools released during SASPARM 2.0 will put together all the available information on the different risk components for a better management and mitigation of seismic risk in Palestine. An overview of the framework defined for the development of an integrated risk model for Palestine, together with the description of choices and assumptions for the main risk components is given in the following sections.

3 SEISMIC HAZARD

The Eastern Mediterranean region, due to its geological structure that is characterized by the junction of major tectonic plates (African, Arabian and Eurasian) results in very high tectonic activity. Over the time, the region has indeed frequently witnessed natural hazard phenomena, resulting in great losses of life and property. Field studies and investigations indicate that large portions of the land surface, population and infrastructure of the region have been subjected to earthquakes in the past or will be subjected to earthquakes in the future [1].

Seismicity information including historic and prehistoric data indicates that major destructive earthquakes have occurred in the Jordan – Dead Sea region (Fig.1). The most recent earthquake (M_L 5.2) took place on February 11th, 2004 [2].

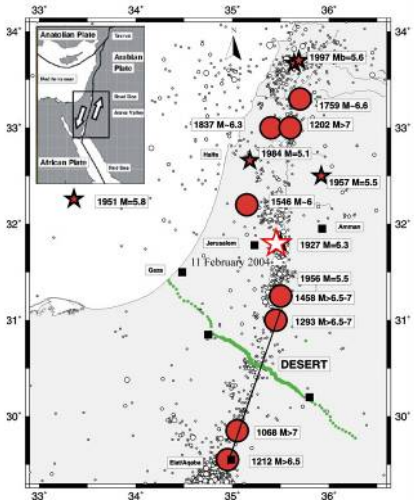

Figure 1. Seismic Activity in the Dead Sea Transform Region for the period 1000 - 2007.

Currently, in Palestine the in-use seismic hazard map dates back to 1997 [3]. It is defined in terms of peak ground acceleration, which is assessed for 10% of exceedance in 50 years for generic rock (Fig.2). Based on such hazard map, Palestine has been divided in four seismic zones: 1, 2A, 2B and 3. Adopting the American Uniform Building Code (UBC97), a seismic zone factor (Z) has been associated to each of them (Fig.3).

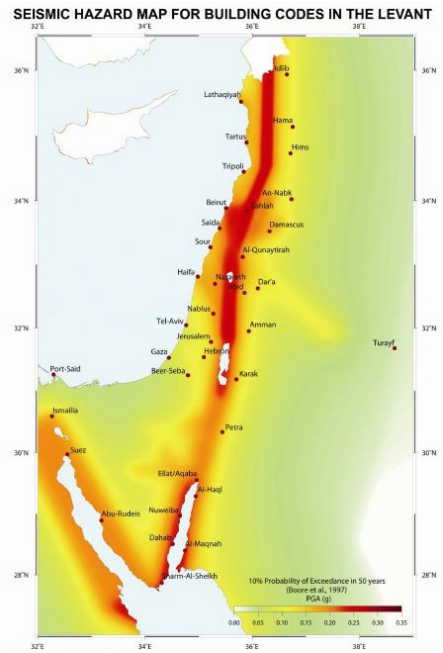

Figure 2. Hazard Map with 10% probability of exceedance in 50 years [2]

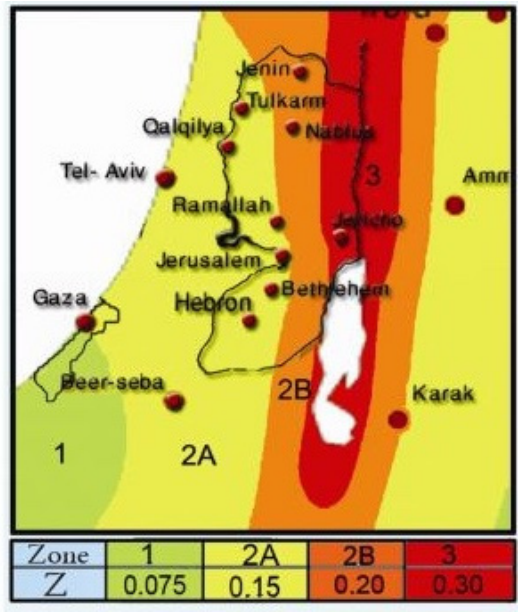

Figure 3. Seismic Zone Factors in Palestine according to Hazard Map and UBC 97.

Additional initiatives have been undertaken to improve such hazard map, aiming to improve the global and regional seismic hazard evaluation in the Eastern Mediterranean region. Specifically, three projects up to the early 2000s are worth mentioning:

i. GSHAP (Global Seismic Hazard Assessment);
ii. SESAME (Seismotectonic and Seismic Hazard Assessment of Mediterranean Basin); and
iii. ESC/WG-SHA (European Seismological Commission Working Group on Seismic Hazard Assessment).

The first regional seismic hazard map developed for the European – Mediterranean region in terms of peak ground acceleration was GSHAP (1992-1999) and was compiled based on the integration of independent hazard results of a number of different test areas and regional and national programs [4]. During the GSHAP project, no attempts were made to harmonize the individual regional or national seismogenic models in the Mediterranean.

For such reason, a further endeavour for the regional hazard assessment in the Mediterranean was carried out within SESAME (1996-2000). By considering a new geometry implementation to avoid the lack of data between different regional sources or gaps at border areas, SESAME succeeded in the final unified seismogenic source model for the Mediterranean region, which consists of 346 sources. Each source was characterized by the corresponding seismicity parameters in terms of minimum and maximum magnitude and earthquake occurrence rates, as illustrated in Fig. 4 [5].

The third project, ESC/WG-SHA, was completed in 2002, and resulted in a unified seismic hazard modelling for Europe and the Mediterranean, integrating the GSHAP Central Northern Europe results with those from SESAME for the Mediterranean (Fig. 5). This comprehensive model for seismic hazard assessment allows, for the first time, the generation of hazard maps, expressing ground motion in different parameters, for different soil conditions and probability levels [6].

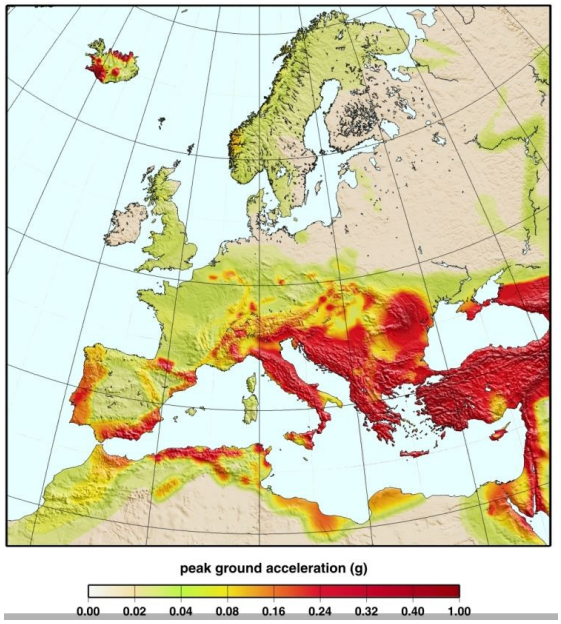

Figure 4. SESAME map with 10% probability of exceedance in 50 years for stiff soil condition [5]

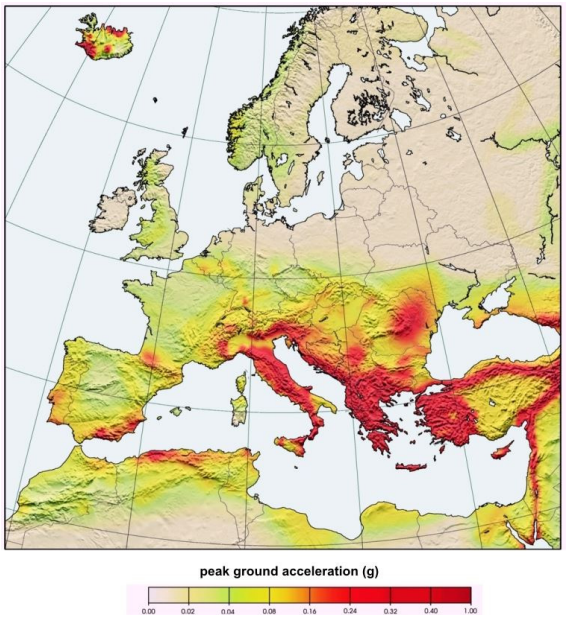

Figure 5. ESC/WG-SHA map with 10% probability of exceedance in 50 years for stiff soil condition [5]

For the development of the integrated risk model of the study herein presented, the use of a further updated hazard model is planned. The updated model is part of the outcomes of the EMME (Earthquake Model of the Middle East Region) project, which aimed at the assessment of seismic hazard, the associated risk in terms of structural damages, casualties and economic losses and also at the evaluation of the effects of relevant mitigation measures in the Middle East region. EMME was carried out between 2010 and 2013 and the final products have just been publicly released [7].

The model for Palestine will thus make use of the most up-to-date hazard data from the EMME initiative. The hazard model will be further employed to selection of real records for fragility analysis (input for Section 4 – Vulnerability), through disaggregation and PSHA calculations (using OpenQuake [8]) for the Nablus municipality.

4 VULNERABILITY

The vulnerability model will foresee two components: physical, calculated for a number of building classes that constitute the taxonomy for Nablus and social, taking into account the feedback provided by the population through specifically developed questionnaires.

4.1 Physical vulnerability

Physical vulnerability is a measure of how prone a building is to damage for a given severity of the ground shaking. The aim of most research works dedicated to this subject is to give a mathematical formulation to vulnerability. The two widely used formulations to describe the vulnerability are: damage probability matrices and fragility curves. The latter describe the conditional probability of exceeding a certain damage limit state in terms of the selected intensity measure of the ground motion. The same probability in discrete terms is a component of a damage probability matrix. In the technical literature, damage probability matrices have been produced when the vulnerability studies are based on observations: data from post-earthquake surveys are treated probabilistically to identify the conditional probability of damage and hence the terms of the damage probability matrices. On the other hand, fragility

curves are calculated when the vulnerability studies are mechanics-based, i.e. the seismic behaviour of structures is modelled. The model can be more or less simplified as a function of the level of knowledge of the building stock. The option of quantifying the vulnerability through damage probability matrices is not feasible in Palestine, since databases of damages occurred after past earthquakes are not available. Therefore, sets of fragility curves will be defined for the as built structural typologies identified in Nablus first and then in other Palestinian municipalities.

The case study of Nablus foresees a web database to gather physical vulnerability data on buildings. The definition of a catalogue of building typologies is the first step for large scale vulnerability assessment. Recognition of structural types in Nablus was undertaken by a selected group of practitioners already trained during SASPARM. As it will be described with more detail in [9], the as-built in Nablus can be classified according four main building types: reinforced concrete frame buildings; shear walls buildings; masonry buildings; buildings with soft storey **(**Fig. 7). Once the building types have been identified the seismic vulnerability of each type is assessed.

Citizens, practitioners and university students are the main groups involved in the in-situ collection of building data through specially designed forms. The collection forms, one detailed for practitioners and one more simple for citizens, aim to detect the structural characteristics of Palestinian buildings and it is a self-assessment tool to understand how their own buildings are made up of (Fig. 6). The forms allow a quick evaluation as a first cataloguing of the building stock, since they are made of typological and metrical data of the structures. The practitioners' form is composed of six sections, while the citizens' one of four. The sections of the forms are summarised in Table 1.

Section	Practitioners	Citizens
1	Identification of the Building	Identification of the Building
2	Description of the Building	Description of the Building
3	Structural Data	Main material of the Building's Vertical Structure
4	Regularity	Notes
5	Geomorphological Data	
6	Notes	

Table 1. Sections of the collection forms for practitioners and citizens.

Before collecting structural data, training activities were fundamental for the three main local stakeholders – university students, citizens, and practitioners. Both forms were introduced to the students of the An-Najah National University because their support to both the citizens in filling in the forms related to their properties and the practitioners during their field surveys is of fundamental importance. Then, practitioners were trained on the content of the forms and for increasing their knowledge on seismic design and seismic risk prevention. Then, citizens were trained in understanding the type of information required in the form. Practical examples were used for supporting the training. Direct engagement of GO and NGO stakeholders is carried out with the organisation of seminars, workshops, lectures in a collaborative effort between the partners of the Consortium.

Survey data will not just be stored in the on-line georeferenced platform and grouped according to their structural typology, but a specific vulnerability assessment will be performed. Sets of fragility curves will be identified according to their structural types, first in Nablus and, then, in other Palestinian municipalities, hence providing a collection of vulnerability functions that best fit the Palestinian region.

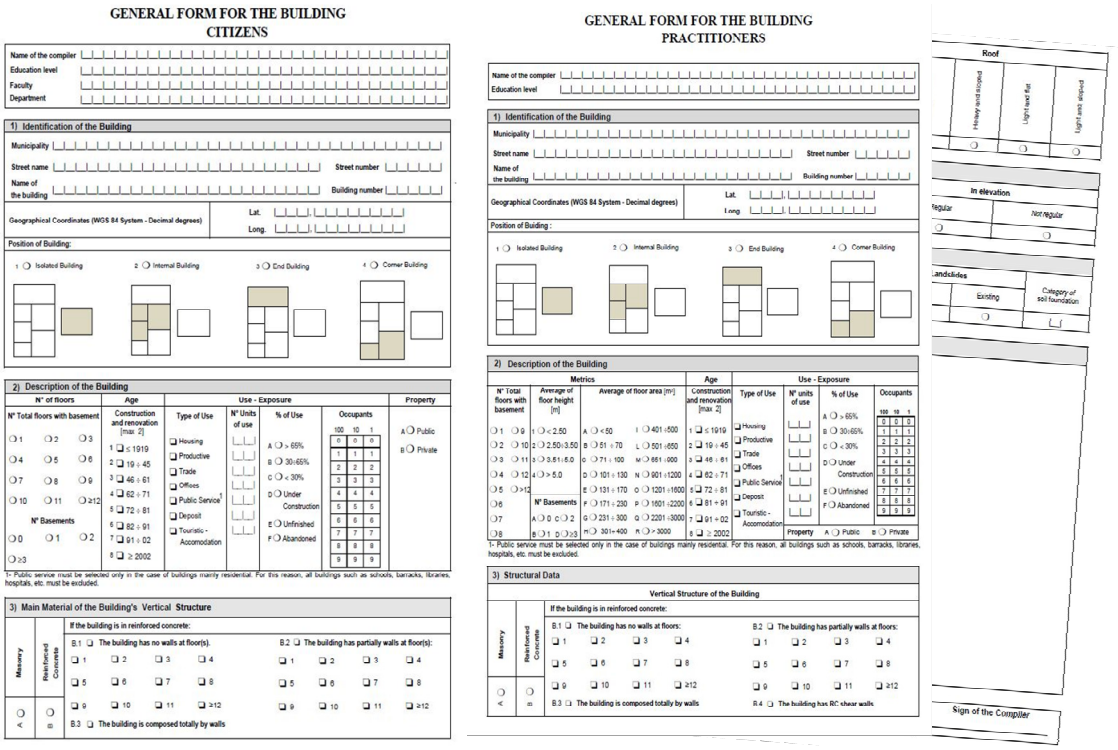

Figure 6. Collection Forms.

Nonlinear static analysis [10; 11] will be used for the estimation of the structural demand in the buildings, through a refinement of the SP-BELA (Simplified Pushover – Based Earthquake Loss Assessment) procedure [12; 13]. The method defines the nonlinear behaviour of a random population of buildings through a simplified pushover and displacement-based procedure. The application of the simplified pushover methodology leads to the assessment of a large number of buildings with reasonable computational effort [14; 15], as in the real case study.

Figure 7. RC Building, Building with Soft Storey failure mode, Shear Wall Building and Masonry Building (Clockwise Order).

With the aim of extending the applicability of SP-BELA to the Palestinian context, special attention has to be given to the structural typologies that mainly characterise the building taxonomy, such as frame systems with dominant torsional response and/or vertical/horizontal irregularities [16]. For this reason, SP-BELA procedure will take into consideration suitable correction factors derived from Incremental Dynamic Analysis of a selected groups of different irregular RC building typologies. Finally, the vulnerability curves will be generated comparing the displacement capacity limits identified on the pushover curve and the displacement demand, defined from a response spectrum, for each building in the random population.

4.2 Social vulnerability

Beside the assessment of fragility curves for physical assets, a non-negligible aspect in terms of vulnerability comes from society with its own knowledge, conditions and cultural context. In order to build indicators, able to capture the social characteristics, publically available databases (e.g. national census) are not satisfactory, and a specific tool needs to be defined, as the "Scorecard approach" based on a participatory assessment process [17].

In detail, this approach will measure the concept of city resilience to crisis and disasters. As established in the Hyogo Framework for Action (HFA) and more recently in the United Nations campaign for urban disaster reduction [18], the resilience is "the capacity of an individual, community, organization, city and nation to respond, cope and recover from disaster". Further, UN-ISDR established a set of indicators for measuring resiliency and these were implemented in six key areas in the Scorecard (Table 2).

Theme	General Question
Awareness and advocacy	What is the level of awareness and knowledge of earthquake disaster risk?
Social Capacity	What are the capacities of the population to efficiently prepare, respond and recover from a damaging earthquake?
Legal and institutional arrangements	How effective are mechanisms to advocate earthquake risk reduction in your quarter?
Planning, regulation and mainstreaming risk mitigation	What is the perceived level of commitment and mainstreaming of disaster risk reduction through regulatory planning tools?
Emergency preparedness, response and recovery	What is the level of effectiveness and competency of disaster management including mechanisms for response and recovery?
Critical services and public infrastructure resiliency	What is the level of resilience of critical services to disasters?

Table 2. Scorecard themes.

The Scorecard is built with specific questions and answer schemes for each key areas and has been adapted to Nablus background to meet peculiarities. To really measure resiliency, questionnaire will be spread among population and the municipal representatives and an evaluation of potential gaps will be assessed especially for critical areas where further analysis are needed.

5 EXPOSURE

The other relevant factor in the general risk assessment is exposure. The model would like to take into account people, property, systems and other elements present in the case-study area that are thereby subject to potential losses. It is developed to be comprehensive and in agreement with both vulnerability and hazard models, also considering the latest available area to produce up to date estimates.

Data used to build the exposure model can be prepared using two approaches:

i. Using data available to the general public and coming from an official source;
ii. Collecting data directly on the site through the forms already employed for the collection of fragility data. This is a more accurate version but is also strongly dependent on the effective participation of the involved citizens.

A hybrid approach will most likely be employed, in which the exposure model will be initially set up using census and/or national databases data. This version will then be updated and/or validated with real data collected in-situ.

As far as the first approach is concerned, the Palestinian Central Bureau of Statistics [19] has been used to collect databases, statistical data and key indicators (e.g. Housing condition, Population, Price Indices). Some difficulties arise due to the unavailability of some information at the same geographical level. For example, the distribution of the population is available at all levels from Country to Municipality but the number of house units is not. A possible solution to overcome this issue is to disaggregate the number of house units from the national level into the municipality level using the population as proxy. The proposed model takes into account indicators that best describe the exposed asset, such as relative percentages of buildings, floor area, building type and replacement cost. The final aim at this level is to come up with an updated model that could be applied at different levels of resolution.

5.1 Preliminary exposure data

Regarding the types of residential buildings, there are three main typologies: individual houses, apartments (multi-storey buildings) and villas. Respectively, the percentages of distribution of the typologies are 44%, 54% and 2%.

As far as the floor area is concerned, preliminary data for Nablus shows that most of the housing units, around 36%, have an average area of 139.5 m^2, followed by 25% with an average area of 100 m^2 (Fig. 8).

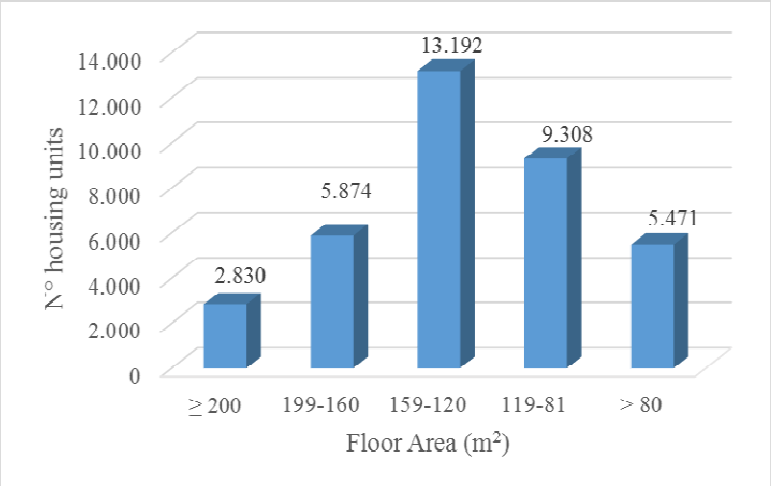

Figure 8. Distribution of housing units by floor area in Nablus.

Finally, with respect to the replacement cost, two methodologies were adopted to obtain the best results accounting for the wide variety in the region in terms of lack of homogeneity due to consecutive changes in the local law and variation in the construction materials and building techniques.

The first procedure takes into account data available on the governmental statistics website. The replacement cost is calculated by knowing the yearly expenditure on new buildings with specific materials (e.g. stone, masonry), adding the number of squares meter licensed in that specific year for that specific class. Table 3 illustrates an example of such data processing for stone buildings.

Year of survey	Construction material of external wall	Licensed area in 1,000 m^2	Expenditure in 1,000$
2014	Stone	2,719.9	249,897.3

Table 3. Example of calculation for replacement cost.

Taking into account the figures presented in Table 3, the final replacement cost comes as 91$/$m^2$.

On the other hand, the second procedure is based on expert opinion, using feedback from practitioners, engineers, engineering associations, etc. The replacement cost varies according to the building types: 550-600$/$m^2$ for apartments in multi-storey buildings, 750$/$m^2$ for individual houses and at least 900$/$m^2$ in case of villas. When comparing with the data from the official website, a large gap is observed with the reality of construction for the Nablus case study.

6 LEGAL AND REGULATORY FRAMEWORK

Finally, the development of an integrated risk model in Palestine will also enable the elaboration of guidelines and recommendations to promote local risk governance and management. Such task will include and redefine, if needed, the respective inputs of various GO and NGO Institutions by suggesting roles and possible forms of partnership between the three main stakeholders: government, private sector, including the (re)insurance and finance sectors, and the civil society (scientific/academic institutions, civil society organizations, media, the general public). Guidelines focusing on common procedural frameworks for encouraging and, whenever feasible, setting-up new partnerships and a set of methods and tools for cooperation between the different actors or stakeholders will be released at the end of the project. In this way, tailor-made recommendations will be available for the various institutional (policy, legislative and organizational) frameworks and cultures in Palestine. Therefore, the guidelines to be developed will be useful to quantify and assess physical, environmental and social resilience also from the risk governance point of view. In particular, to reach this aim, a questionnaire has been developed on the basis of the Self-Assessment Guiding Tool annexed to the G20/OECD Methodological Framework on Disaster Risk Assessment and Risk Financing (http://www.oecd.org/gov/risk). The questionnaire has been spread among the three main stakeholders in Palestine. The outcomes of the questionnaire will be processed suggesting roles and possible forms of partnership between the three main actors for a better management of seismic risk.

7 CONCLUSIONS

This paper intended to provide a general overview of the construction of a first-hand integrated seismic risk model for the Palestinian territory, using the municipality of Nablus as pilot study. A detailed framework including considerations around the different risk components – hazard, vulnerability and exposure – was presented.

The hazard model is established essentially on the basis of the recent EMME project that covered the entire Middle East region with significant detail and up-to-date tools (OpenQuake). The model will be further exploited to select real records to accurately develop a building fragility model.

The vulnerability model is largely comprehensive, as it includes both physical and social vulnerability components. Furthermore, both are modelled with different levels of detail, using census/database data and in-situ collected information. Indeed, the latter aspect, fulfilled through the use of specifically developed survey forms, constitutes one of the major novelties of this study. Fragility curves for a predefined building taxonomy are built using expedite nonlinear static analyses, adapted to the Palestinian in-built. On the other hand, social vulnerability indices are identified and established based on tailored questionnaires distributed to the general population and stakeholders in Nablus.

Finally, the exposure model builds upon extensive public data collection and feedback from several experts in the field. The entire model relies significantly on the cooperation with local bodies, entities and universities, yielding a double effect: sharing information and increasing awareness.

The general framework is seen as a pilot study, starting from the area of Nablus city, characterized by a difficult political context. Ultimately, the goal is to extend it to other regions in Palestine as well as to neighbour countries that features similar in-built environment. The achievements of risk assessment and loss estimation results in this case study, particularly the ones based on crowdsourcing data, also represent an enrichment for Europe.

ACKNOWLEDGMENTS

This research has been carried out under the project “ECHO/SUB/2014/694399 SASPARM 2.0 Support Action for Strengthening PAlestine capabilities for seismic Risk Mitigation”. Project Co-funded by ECHO – Humanitarian Aid and Civil Protection.

REFERENCES

[1] Final Report – XXXII UNESCO-RELEMR International Workshop – 13-16 February 2012 – Sliema, Malta.

[2] USAID MERC Project Team (M18-057), Earthquake Hazard Assessment and Building Code, Final report, Earth Sciences and Seismic Engineering Center at An Najah National University, 2004.

[3] D. M. Boore, W. B. Joyner, T. E. Fumal, Equations for Estimating Horizontal Response Spectra and Peak Acceleration from Western North American Earthquakes: A Summary of recent Work, *Seismological Research Letters*, **68**, N° 1, 128-153, 1997.

[4] D. Giardini, The Global Seismic Hazard Assessment Program (GSHAP) – 1992/1999, *Annali di Geofisica*, **42** (6), 957-974, 1999.

[5] M. J. Jimenez, D. Giardini, G. Grünthal, SESAME Working Group, Unified seismic hazard modelling throughout the Mediterranean region, *Bollettino di Geofisica Teorica ed Applicata*, **42**, 1-2, 3-18, 2001.

[6] M. J. Jimenez, D. Giardini, G. Grünthal, The ESC-SESAME Unified Hazard Model for the European-Mediterranean region. *EMSC/CSEM Newsletter*, **19**, 2-4, 2003.

[7] www.emme-gem.org

[8] http://www.globalquakemodel.org/openquake/about/

[9] I. Grigoratos, J. Dabeek, B. Borzi, V. Cerchiello, P. Ceresa, R. Monteiro, Development of a fragility and exposure model for Palestine – application to the city of Nablus, Procedia Engineering, 2016. (submitted)

[10] R. Monteiro, M. Marques, G. Adhikari, C. Casarotti, R. Pinho, Spectral reduction factors evaluation for seismic assessment of frame buildings, *Engineering Structures*, **77**, 129-142, 2014.

[11] R. Pinho, M. Marques, R. Monteiro, C. Casarotti, R. Delgado, Evaluation of nonlinear static procedures in the assessment of building frames, *Earthquake Spectra*, **29** (4). 1459-1476, 2013.

[12] I. Grigoratos, B. Borzi, A. Di Meo, R. Monteiro, P. Ceresa, Extending simplified pushover-based methods for vulnerability assessment of irregular RC buildings in Palestine, Proceedings of the 1st International Conference on Natural Hazards and Infrastructure: Protection, Design, Rehabilitation", Chania, 28-30 June, 2016. (submitted)

[13] B. Borzi, R. Pinho, H. Crowley, Simplified pushover-based vulnerability analysis for large-scale assessment, *Engineering Structures*, **30**(3), 804–820, 2007.

[14] B. Borzi, P. Ceresa, M. Faravelli, E. Fiorini, M. Onida, Definition of a prioritisation procedure for structural retrofitting of Italian school buildings, *ECCOMAS Thematic Conference - COMPDYN 2011 proceedings*, ISBN: 978-960-99994-0-3, Corfu, Greece, 26–28 May, 2011.

[15] B. Borzi, P. Ceresa, M. Faravelli, E. Fiorini, M. Onida, Seismic Risk Assessment of Italian School Buildings, *Computational Methods in Earthquake Engineering*, **2**, 317-344, ISBN: 978-94-007-6572-6, ISSN: 1871-3033, doi:10.1007/978-94-007-6573-3_15 C, 2013.

[16] B. Borzi, H. Crowley, R. Pinho, The influence of infill panels on vulnerability curves for RC buildings, *The 14th World Conference on Earthquake Engineering*, Beijing, China, October 12-17, 2008.

[17] J. Anhorn, C.G. Burton, B. Khazai, The risk and resilience scorecard: Benchmarking disaster resilience in cities. A monitoring & evaluation tool to engage local stakeholders, *ICLEI conference proceedings,* 2014.

[18] www.unisdr.org/campaign/resilientcities/toolkit/essentials

[19] www.pcbs.gov.ps/en

ECCOMAS Congress 2016
VII European Congress on Computational Methods in Applied Sciences and Engineering
M. Papadrakakis, V. Papadopoulos, G. Stefanou, V. Plevris (eds.)
Crete Island, Greece, 5–10 June 2016

REASSESS V1.0: A COMPUTATIONALLY-EFFICIENT SOFTWARE FOR PROBABILISTIC SEISMIC HAZARD ANALYSIS

Iunio Iervolino[1], **Eugenio Chioccarelli**[2], **and Pasquale Cito**[1]

[1] Università degli Studi di Napoli Federico II
Via Claudio 21, 80125 Naples, Italy
e-mail: {iunio.iervolino, pasquale.cito}@unina.it

[2] Istituto per le Tecnologie della Costruzione ITC-CNR, URT Napoli c/o DiSt
Via Claudio 21, 80125 Naples, Italy
e-mail: eugenio.chioccarelli@itc.cnr.it

Keywords: site-specific PSHA, logic tree, disaggregation, conditional hazard, conditional mean spectrum.

Abstract. *A stand-alone software for the probabilistic assessment of seismic hazard is developing. In its final version, it shall be structured in three modules for: (i) site-specific, (ii) scenario-based and (iii) multi-site (regional) analyses. This paper focuses on (i), which is devoted to single-site probabilistic seismic hazard analysis (PSHA).*
Seismic sources can be either zones or individual faults. The algorithm to compute PSHA is implemented assuming, classically, that the process of occurrence of earthquakes on each seismic source follows a homogeneous Poisson process; the processes for different sources are independent.
The required input data are: (1) the source(s) geometry and the annual rate(s) of occurrence of earthquakes in the magnitude interval of interest; (2) the distribution of magnitude given the occurrence of one earthquake; (3) the ground motion propagation model (GMPM); (4) the soil classification at the site for which hazard is evaluated. Regarding (1-3), the user is aided by some library implemented in the software.
REASSESS also is able to account for model uncertainty, in fact, logic trees can be built based on alternatives for the source's annual rate of earthquake occurrence, magnitude distribution and GMPM.
The strength of REASSESS, beyond the user-friendly interface, stays in the PSHA computation algorithms. These have been coded in MATLAB®, targeting accuracy and reduced computing time. Its potential for earthquake engineering and engineering seismology applications is illustrated by a few applications discussed in the paper.

1 INTRODUCTION

The case of probabilistic seismic hazard assessment for a specific site is consolidated [1, 2] and acknowledged by the most advanced national and international seismic codes (e.g., [3, 4]). Indeed, there are several computer programs for site-specific probabilistic seismic hazard analysis (PSHA) publicly available or produced as proprietary codes. On the other hand, the attention toward the seismic hazard assessment for multiple sites is growing recently (e.g., [5, 6, 7]) and the developed knowledge has not found yet its direct application in the engineering practice.

The aim of the work partially presented in this study is to develop a user-friendly software for both site-specific and multi-site PSHA. The name of the tool is *REgionAl, Site-SpEcific and Scenario-based Seismic hazard analysis* (REASSESS) and, as the name suggests, it will be divided in three modules. The one preliminarily presented in this contribution is about site-specific PSHA, while the others are under-development.

The flow chart in Figure 1 schematically summarizes the main features of the site-specific module. Input parameters, defined by the user or selected from embedded databases, are the geographical coordinates and soil condition of the site of interest, the seismic sources, the magnitude distributions and the annual rates of earthquake occurrence (within the magnitude limits of interest) for each source, and the models of ground motion propagation (parameters and GMPMs can be multiple if a logic tree is adopted [8]). The primary outputs are the hazard curves for the selected intensity measures, which, along fragility curves (e.g., [9]), can be the input for seismic risk assessment software (e.g., [10]). Additionally, the software is able to provide the disaggregation of seismic hazard [11] and, according to the latter, the distribution of conditional hazard [12] (i.e., the distribution of a secondary intensity measure conditional to the occurrence or exceedance of a primary one). Moreover, when spectral ordinates are chosen as intensity measures, REASSESS provides the uniform hazard spectrum (UHS) [2] for a given return period and the conditional mean spectrum (CMS) [13] (in which disaggregation is also involved).

Each of these issues is analyzed in the following sections providing the essential basics of PSHA and the details about the software implementation. In the final part, the main features of the graphical interface and some results of illustrative analyses are shown.

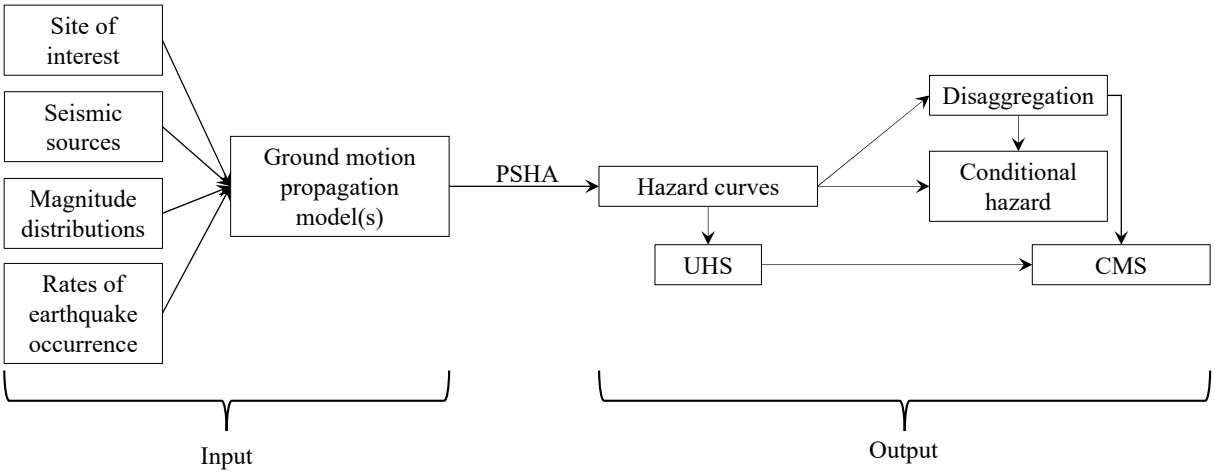

Figure 1. Flow chart of the first module of REASSESS

2 PROBABILISTIC SEISMIC HAZARD ANALYSIS

PSHA aims at computing the rate (λ_{im}) of seismic events exceeding a ground motion intensity measure (IM) threshold (im) at a specific site. When more than one seismic source affects the site, the rate is due to superposition of the contributions from each source, as illustrated in Equation 1 where n_s is the number of sources. In the equation, M is the event magnitude, R is the source-to-site distance, ν_i is the mean annual rate of earthquakes within a magnitude range of interest at source i, $f_{R,M,i}$ is the joint probability density function (pdf) of R and M for the i-th source. The exceedance probability of an intensity measure threshold, given a magnitude and distance pair, $P\left[IM > im \middle| r,m\right]$, is the complementary cumulative distribution function of the IM, which is provided by a ground motion propagation model.

$$\lambda_{im} = \sum_{i}^{n_s} \nu_i \cdot \int_r \int_m P\left[IM > im \middle| r,m\right] \cdot f_{R,M,i}(r,m) \cdot dr \cdot dm \tag{1}$$

Equation 1 accounts for the uncertainties related to seismic hazard. In some cases, however, the choice for models and distributions to be used in PSHA may not be straightforward. In these cases, the use of a logic tree, which is also implemented in REASSESS, allows to deal with model uncertainty [8]. Indeed, according to the logic tree, λ_{im} is computed as a weighted average of alternative models; the weight assigned to each model is the probability of that model being correct (see Section 2.4 for further details).

Plotting λ_{im} as a function of im provides the hazard curve. In the following section, it is described how computation of hazard curves has been coded in REASSESS, targeting accuracy and reduced computing time.

2.1 Calculation of PSHA via matrix algebra

The algorithms of REASSESS have been developed in MATLAB® [14] and the hazard integral is approximated by matrix operations, for which MATLAB® is especially effective [15]. Such operations are described in this section referring to the case of a single source, for the sake of simplicity. Moreover, it has to be clarified that in the algorithms of REASSESS the joint magnitude-distance distribution in Equation 1, is computed as the product of the distribution of distance conditional on magnitude and the marginal distribution of magnitude itself (Equation 2):

$$f_{R,M}(r,m) = f_{R|M}(r|m) \cdot f_M(m) \tag{2}$$

In the following, the discretized values of event magnitude and source-to-site distance involved in PSHA will be indicated as $\{M\} = \{m_1, m_2, \ldots, m_k\}$ and $\{R\} = \{r_1, r_2, \ldots, r_s\}$ of dimensions $1 \times k$ and $1 \times s$, respectively. The ground motion intensity measure at the site is discretized in the vector $\{IM\} = \{im_1, im_2, \ldots, im_q\}$ of dimension $1 \times q$.

The GMPM is accounted for via a $(k \cdot s) \times q$ matrix, $[A]$, in which each column represents the exceedance probability of a specific IM value conditional to magnitude and distance arranged in the form of Equation 3. Different columns of the matrix only differ by the IM threshold considered.

$$[A]=\begin{bmatrix} P[IM>im_1 \mid m_1,r_1] & \cdots & P[IM>im_q \mid m_1,r_1] \\ P[IM>im_1 \mid m_2,r_1] & \cdots & P[IM>im_q \mid m_2,r_1] \\ \vdots & \vdots & \vdots \\ P[IM>im_1 \mid m_k,r_1] & \cdots & P[IM>im_q \mid m_k,r_1] \\ \vdots & \vdots & \vdots \\ P[IM>im_1 \mid m_1,r_s] & \cdots & P[IM>im_q \mid m_1,r_s] \\ P[IM>im_1 \mid m_2,r_s] & \cdots & P[IM>im_q \mid m_2,r_s] \\ \vdots & \vdots & \vdots \\ P[IM>im_1 \mid m_k,r_s] & \cdots & P[IM>im_q \mid m_k,r_s] \end{bmatrix} \quad (3)$$

The pdf of magnitude, $f_M(m)$, is approximated by finite probabilities of event's magnitude belonging to *k* intervals; i.e., $\{P[m_1],P[m_2],\ldots,P[m_k]\}$. These probabilities, arranged in the form of a column vector, are the elements of the $[B]$ matrix in Equation 4. In fact, this matrix has *q* identical columns, each of which is made of the magnitude probability vector repeated *s*-times.

$$[B]=\begin{bmatrix} P[m_1] & \cdots & P[m_1] \\ P[m_2] & \cdots & P[m_2] \\ \vdots & \vdots & \vdots \\ P[m_k] & \cdots & P[m_k] \\ \vdots & \vdots & \vdots \\ P[m_1] & \cdots & P[m_1] \\ P[m_2] & \cdots & P[m_2] \\ \vdots & \vdots & \vdots \\ P[m_k] & \cdots & P[m_k] \end{bmatrix} \quad (4)$$

Similarly, the $[C]$ matrix is a row vector with $(k \cdot s)$ elements. The first *k* elements are the conditional probabilities of r_1 conditional to the *k* magnitude values. The elements from $k+1$ until $2k$ are the probabilities of r_2 conditional to the each of the magnitudes and so on, until r_s conditional to all magnitudes; i.e., Equation 5.

$$[C]=\begin{bmatrix} P[r_1|m_1] & P[r_1|m_2] & \cdots & P[r_1|m_k] & \cdots & P[r_s|m_1] & P[r_s|m_2] & \cdots & P[r_s|m_k] \end{bmatrix} \quad (5)$$

At this point, the operation of pointwise multiplication between two matrices of the same dimensions has to be recalled (i.e., the *Hadamard product* [16]). It is here indicated by the $\odot$ symbol and provides a resulting matrix of the dimensions of those multiplied. Its elements are the products of the corresponding elements in the original matrices. More specifically, $[D]=[A]\odot[B]$ implies that the resulting matrix has each element of the type: $d_{ij}=a_{ij}\cdot b_{ij}$.

Therefore, the unit-time rates of exceedance of the *im* values considered, $\{\lambda_{im_1},\lambda_{im_2},\ldots,\lambda_{im_q}\}$, can be obtained by the product in Equation 6, where the dot represent matrix multiplication.

$$[\lambda_{im}]=\begin{bmatrix} \lambda_{im_1} & \lambda_{im_2} & \cdots & \lambda_{im_q} \end{bmatrix}=\nu\cdot[C]\cdot([A]\odot[B]) \quad (6)$$

2.2 Soil effect

The GMPMs provide the (usually lognormal) cumulative density function of the IM at the site of interest given the magnitude of the earthquake, the source-to-site distance and some possible additional seismic parameters (e.g., soil site condition). In most cases, the different soil conditions at the site are considered in the GMPMs through modification factors that operate only on the mean of the (lognormal) distribution. When such kinds of GMPMs are chosen for PSHA, i.e. when the standard deviation of the residuals of the GMPM does not depend on the soil class, a deterministic relationship between the hazard curves for different soils exists [17]. This allows REASSES to provide hazard curves for any kind of soil conditions performing a single analysis.

In particular, it has been demonstrated that, if the soil in the GMPM only affects the mean given magnitude and distance, for example via addition of a coefficient θ_{soil}, as it often happens, then once the hazard curve is obtained for a reference condition (e.g., rock), the hazard curve for soil, $\lambda_{im_{soil}}$, is obtained by horizontally translating, in log scale of the abscissa, the original curve, $\lambda_{im_{rock}}$, by a factor equal to the soil coefficient in the GMPM (Equation 7).

$$if\ \log(im_{soil}) = \log(im_{rock}) + \theta_{soil} \Rightarrow \lambda_{im_{soil}} = \lambda_{im_{rock}} \tag{7}$$

2.3 Seismic sources and magnitude distributions

In REASSESS, seismogenic zones and/or finite tridimensional faults can both be inputs for PSHA. Seismogenic zones are geographic areas with homogeneous seismicity; i.e., each location has the same probability to be the location of the earthquake and the magnitudes of events in each location are independent and identically distributed random variables. For the characterization of seismogenic zones, the software requires the following input parameters: (i) the geographic coordinates of the vertexes of the source, (ii) the seismic parameters and (iii) the predominant faulting style, if known. Regarding (ii), it is assumed that the distribution of the magnitude of the earthquakes is described by a truncated exponential distribution consistent with the Gutenberg-Richter (GR) relationship [18]; hence, the seismic parameters of (ii) are the slope of such a relationship, together with minimum and maximum magnitude and the mean annual rate of earthquake occurrence in the seismic source zone. The pdf of the epicentral distance is derived from the uniform distribution of the epicenters within the fault. However, the GMPM may refer to one among a variety of distance metrics; e.g., the minimum distance from the horizontal projection of the rupture, known as Joiner and Boore distance (R_{jb}) [19]. In the V1.0 of REASSESS the epicentral distances are converted into R_{jb} according to [20].

The definition of the zones is not the only possibility in REASSESS. In the software, some known databases of seismogenic zones are already implemented. These are, referring to Italy, the seismogenic zones described in [21] with the seismic parameters taken from [22, 23]. At the European scale, the database of seismogenic zones provided by the SHARE research project (available at http://www.share-eu.org/, last accessed 22/02/2016) is embedded.

On the other hand, finite tridimensional faults can also be considered. The geometry and location of the single fault have to be known in this case. The required input parameters are the geographical coordinates of the vertexes of the fault and the *rake*, *strike* and *dip* angles (see [8] for example). A uniform probability distribution of the epicenter on the fault plane is assumed. Regarding the distribution of magnitude, apart from the GR, REASSESS V1.0 al-

lows the definition of a characteristic model [24] that may be more appropriate in the case of individual faults.

2.4 Logic tree and GMPMs

PSHA is often implemented considering a logic tree, which allows accounting for model uncertainty [2, 8]: indeed, it allows the use of alternative models, each of which is assigned a weighing factor that is interpreted as the probability of that model being correct. The sum of the weights of all the alternative models must be equal to one. When the logic tree is of concern, λ_{im}, is computed through Equation 8 in which p_j and $\lambda_{im,j}$ are the weight and the result of each branch of the logic tree, respectively; n_b is the total number of branches.

$$\lambda_{im} = \sum_{j=1}^{n_b} \lambda_{im,j} \cdot p_j \tag{8}$$

In REASSESS accepted models' heterogeneity refers to: (i) parameters of the magnitude distributions (i.e., magnitude range and *b*-value), (ii) mean annual frequency of earthquake occurrence on the sources and (iii) GMPMs. In particular, (i) and (ii) may be from direct input of the user, while GMPMs have to be chosen among a set of already implemented models. To guide the user, general indications about the tectonic regime each GMPM refers to [25] are provided.

An example of logic tree is shown in Figure 2 in which two alternatives for the total rates $\{\nu_1, \nu_2\}$, Gutenberg-Richter parameters (synthetically identified as GR_1 and GR_2) and propagation models ($GMPM_1$ and $GMPM_2$) are adopted. The relative likelihood of each alternative model is arbitrarily chosen and reported in parentheses.

REASSESS requires the user to provide the total weight of each branch skipping the implementation of a relative likelihood for each alternative model. Hence, the software automatically verifies that all the weights of the branches sum up to one.

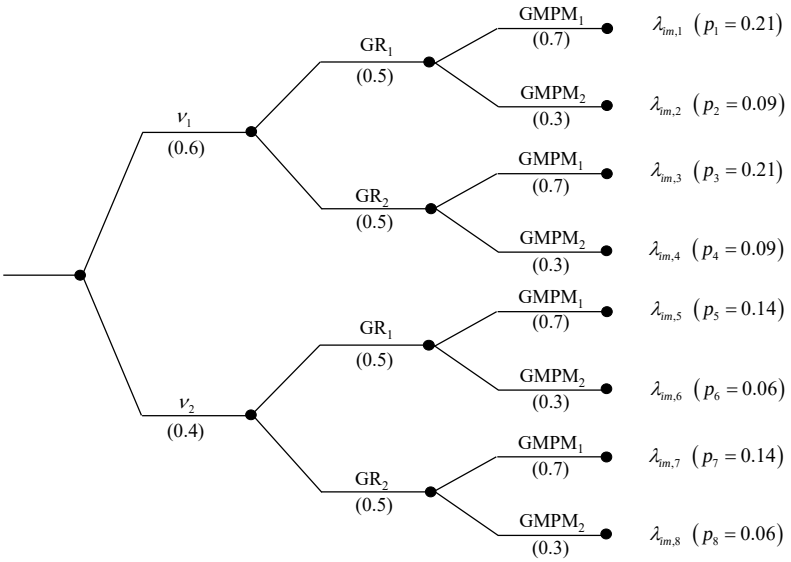

Figure 2. Example of logic tree.

3 DISAGGREGATION, CONDITIONAL HAZARD AND CONDITIONAL MEAN SPECTRA

Once hazard curves are ready, REASSESS also allows enhancing the characterization of the seismic threat for the site in three ways. The first is the disaggregation of the seismic hazard [11] that can be calculated for several exceedance rates; i.e., several values of the intensity threshold. Disaggregation is a procedure that allows the computation of the pdf of $\{M,R,\varepsilon\}$ given the exceedance, or occurrence, of a chosen hazard threshold, $f_{M,R,\varepsilon}\left(m,r,\varepsilon\middle|IM>im\right)$, being ε the number of standard deviations *im* is away from its median value estimated by the assumed GMPM. Analytically, such a distribution can be computed through Equation 9 that refers to the case of single seismic source and multiple-branches arranged in a logic tree. In the equation, in the case of disaggregation of the exceedance hazard, I is an indicator function equal to one if IM is larger than the threshold and zero otherwise. The subscript refers to the *j-th* branch of the logic tree.

$$f_{M,R,\varepsilon}\left(m,r,\varepsilon\middle|IM>im\right)=\frac{\sum_{j}^{n_b}\nu_j\cdot I\left(IM>im\middle|m,r,\varepsilon\right)\cdot f_{M,R,\varepsilon,j}\left(m,r,\varepsilon\right)\cdot p_j}{\lambda_{im}} \tag{9}$$

A discussion of the possible uses of disaggregation (e.g., [26]) is out of the scope of this paper however it is worth noting that, although disaggregation for the exceedance of the hazard threshold is a traditional choice, in the context of performance based earthquake engineering disaggregation for the occurrence of the IM may be more appropriate. REASSESS allows to compute disaggregation of both ground motion intensity exceedance and occurrence hazards.

The software also allows the computation of conditional hazard [12] and uniform hazard spectra and conditional mean spectra [13]. The former is the distribution of a secondary IM conditional on the exceedance (or occurrence) of a primary IM for which the hazard has been calculated. This allows assessing the hazard consistent distribution of more than one IM, which is equivalent to vector-valued PSHA [27]. In REASSESS, once the UHS for a fixed return period has been calculated, it is possible to choose a spectral period defining as primary parameter, IM_1, the corresponding pseudo-spectral acceleration and asking for the conditional distribution of the secondary intensity measure, IM_2, chosen among a few considered.

The distribution of conditional hazard, $f\left(\log IM_2\middle|\log IM_1\right)$, is computed under the assumption of joint lognormality of the two IMs conditional to the hazard variables and according to Equation 10 in which $f\left(\log IM_2\middle|\log IM_1,M,R,\varepsilon\right)$ depends on the GMPM of IM_2 and $f\left(M,R,\varepsilon\middle|\log IM_1\right)$ is the disaggregation of the seismic hazard (occurrence or exceedance) for IM_1.

$$f\left(\log IM_2\middle|\log IM_1\right)=\int_M\int_R\int_\varepsilon f\left(\log IM_2\middle|\log IM_1,M,R,\varepsilon\right)\cdot f\left(M,R,\varepsilon\middle|\log IM_1\right)\cdot dm\cdot dr\cdot d\varepsilon \tag{10}$$

Finally, the conditional mean spectrum can be computed. It is a target response spectrum able to account for the statistical correlation of residuals between different spectral ordinates of the same GMPM. This issue, which is disregarded in UHS, is believed helpful for hazard-compatible record selection [28].

The analytical definition of CMS is reported in Equation (11) in which $\mu_{\log Sa(T_2)}$ and $\sigma_{\log Sa(T_2)}$ are the mean and the standard deviation of the logarithm of the pseudo-spectral acceleration $(\log Sa)$ at the vibration period T_2 and depend on the selected GMPM; $\rho_{\log Sa(T_2)|\log Sa(T_1)}$ is the model of correlation between spectral ordinates at two different periods (the one implemented in REASSESS is [29]). The values of M, R and ε are taken from the disaggregation of $\log Sa(T_1)$. In fact, if M, R and ε are chosen to be representative of the whole disaggregation distribution (e.g., modal values). Equation 11 can also be the basis for marginalization with respect to M, R and ε, via $f\left(M,R,\varepsilon\middle|\log Sa(T_1)\right)$, to obtain $\mu_{\log Sa(T_2)|\log Sa(T_1)}$ (this is the case of the REASSESS).

$$\mu_{\log Sa(T_2)|\log Sa(T_1),M,R,\varepsilon} = \mu_{\log Sa(T_2)}(M,R) + \sigma_{\log Sa(T_2)}(M)\cdot\rho_{\log Sa(T_2)|\log Sa(T_1)}\cdot\varepsilon(T_1) \tag{11}$$

4 GRAPHIC USER INTERACE

The main features of the graphic user interface (GUI) of REASSESS are described in this section.[1] The GUI is conceptually divided in three sections identified in Figure 3 with the dotted red lines. The first section is dedicated to the definition of input parameters required for PSHA. The site is defined by the geographical coordinates and the soil class. The latter is provided through the Vs30 (expressed in m/s^2) that is, the shear wave velocity of the top 30 m of the subsurface profile (see Section 2.2).

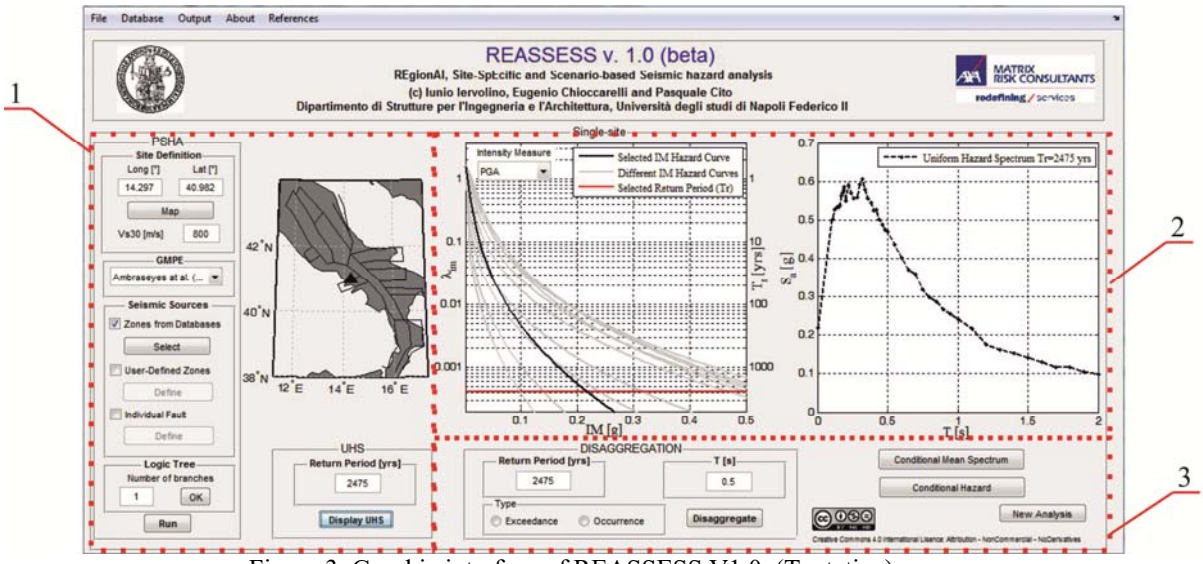

Figure 3. Graphic interface of REASSESS V1.0. (Tentative)

The GMPM is selected with a pull-down menu in which all the implemented GMPMs are reported (see Section 2.4). Then the seismic sources have to be characterized. The user is first required to choose between embedded databases of known seismogenic sources, user-defined seismogenic sources and individual faults. These three choices are not exclusive so it is possible, as an example, to integrate sources from databases with information derived from specific studies. For each seismic source, a separate window with all the required parameters (see Section 2.3) appears. Site and source locations are shown in a map. The user is also required to

[1] The development of the other two modules of the software may cause some modification to the GUI. However, the main features described in this section will be maintained.

choose between single- or multiple-branch of logic tree; the features of the different branches of the logic tree are specified in a separate window. A return period of interest is also required.

Hitting the *run* button, PSHA is performed and the hazard curves are plotted in the second section of the GUI. In the illustrative case of Figure 3, selected GMPM refers to pseudo-spectral accelerations. Hence, the UHS is computed for the selected return period $\left(T_r = 1/\lambda_{im}\right)$ and reported in same section.

Finally, the third section is for the analyses that can be performed after PSHA. These are disaggregation, conditional hazard and conditional mean spectra (see Section 3).

5 ILLUSTRATIVE EXAMPLES

In this section, how the site-specific module of REASSESS works is shown via some illustrative examples. A site (40.982N, 14.297E) close to Naples, in the Campania region (southern Italy), is selected and reported in Figure 4 with a star. Seismic sources are the seismogenic zones of [21]. The limiting magnitudes for each zone as well as the slope of the Gutenberg-Richter relationship and the mean annual rate of earthquake occurrence on the zones are those reported in [22, 23]. In the same papers, the prevalent faulting style for each zone is also reported. These are divided in four categories: normal (N), reverse (R), strike-slip (SS) and undetermined (U).

The selected GMPM is that of [30] that provides the distribution of peak ground acceleration (PGA) and pseudo-spectral accelerations for forty-six oscillation periods between 0.1 and 2.0s. The model is defined within the intervals of magnitude and distance equal to [4.0, 7.6] and [0km, 200km], respectively. In REASSESS, the GMPMs are always applied in their definition ranges. Hence, the seismogenic zones contributing to the hazard are those (or their portions) within 200km from the site. Moreover, although in the original paper [30], the attenuation model was independent on the rupture mechanism, the latter is considered via the modification factors provided by [31].

According to these criteria, the seismogenic zone within 200 km from the site are reported in Figure 4. Seismic parameters of these zones are summarized in Table 1.

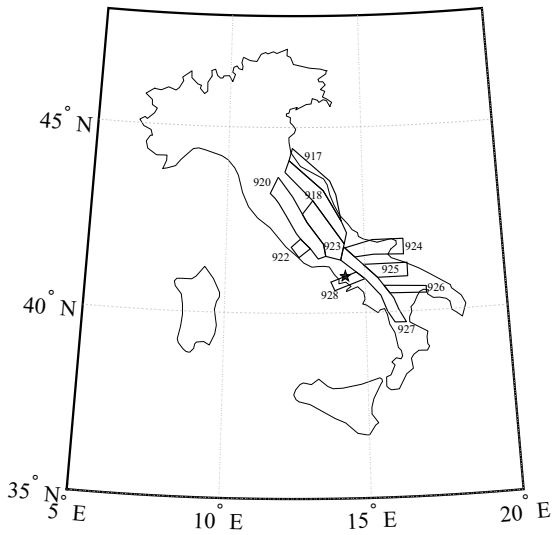

Figure 4. Selected site (star) and the seismogenic zones involved in the hazard analysis.

Zone	M_{min}	M_{max}	ν	b	RM
917	4.3	6.1	0.121	0.794	R
918	4.3	6.4	0.217	0.84	U
920	4.3	5.5	0.317	1.503	N
922	4.3	5.2	0.09	1.409	N
923	4.3	7.3	0.645	0.802	N
924	4.3	7	0.192	0.945	SS
925	4.3	7	0.071	0.508	SS
926	4.3	5.8	0.061	1.017	SS
927	4.3	7.3	0.362	0.557	N
928	4.3	5.8	0.054	1.056	N

Table 1. Parameters associated to each zone: minimum (M_{min}) and maximum magnitude (M_{max}), annual rate of earthquake occurrence (ν), negative slope of GR relationship (b) and rupture mechanism (RM).

For the selected site, the UHS are here derived. Referring to rock site, Figure 5a shows the UHS' for the annual exceedance probabilities equal to about 2%, 0.2% and 0.04%, corresponding to return periods of 50, 475 and 2475 years, respectively. On the other hand, the UHS' for T_r equal to 2475 years and the three different soil conditions provided by [30] are reported in Figure 5b: rock, stiff and soft soil.

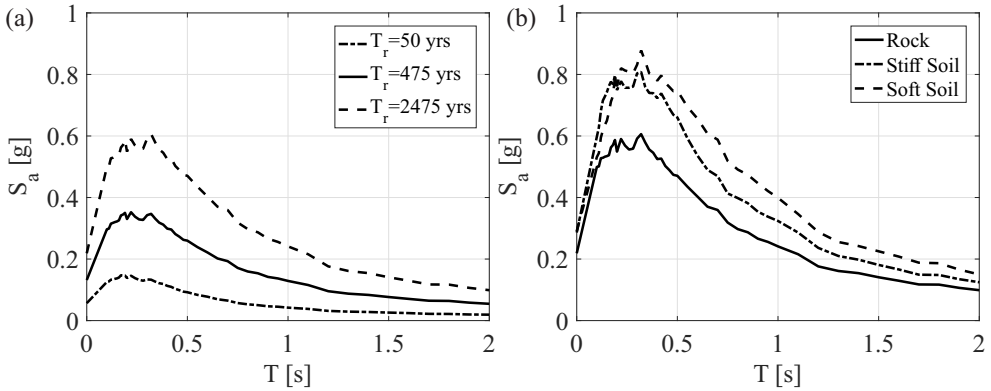

Figure 5. (a) UHS for different return periods on rock soil and (b) for a T_r = 2475 years and different soil conditions.

A simple case of logic tree is also discussed. Two GMPMs are selected: $GMPM_1$ [30] and $GMPM_2$ [32] (and [33]) with associated weights equal to 0.7 and 0.3 respectively. No other sources of model variability are considered. Hence, resulting logic tree is a simplified form of that reported in Figure 2 (Figure 6a). The UHS for $T_r = 2475$ years and rock soil condition are derived from the two alternative branches of the logic tree and shown in Figure 6b together with their weighted mean (note that the spectrum is computed only at the spectral periods common to both GMPMs).

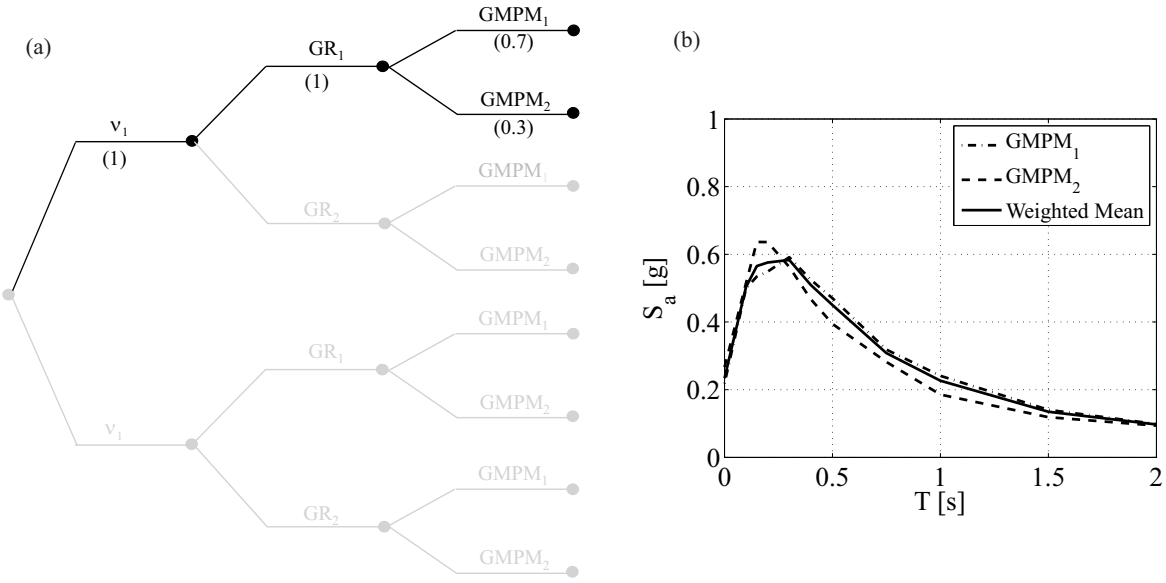

Figure 6. (a) Simplified adopted logic tree and (b) resulting UHS.

Referring to the case of single-branch (Figure 5), the occurrence disaggregations of the UHS for $T_r = 2475$ years, rock soil condition and three spectral periods equal to 0.2s, 0.5s and 1.0s are reported in Figure 7 (a, b, and c, respectively). According to these disaggregation distributions, the CMS' are computed and reported in Figure 7d together with the UHS.

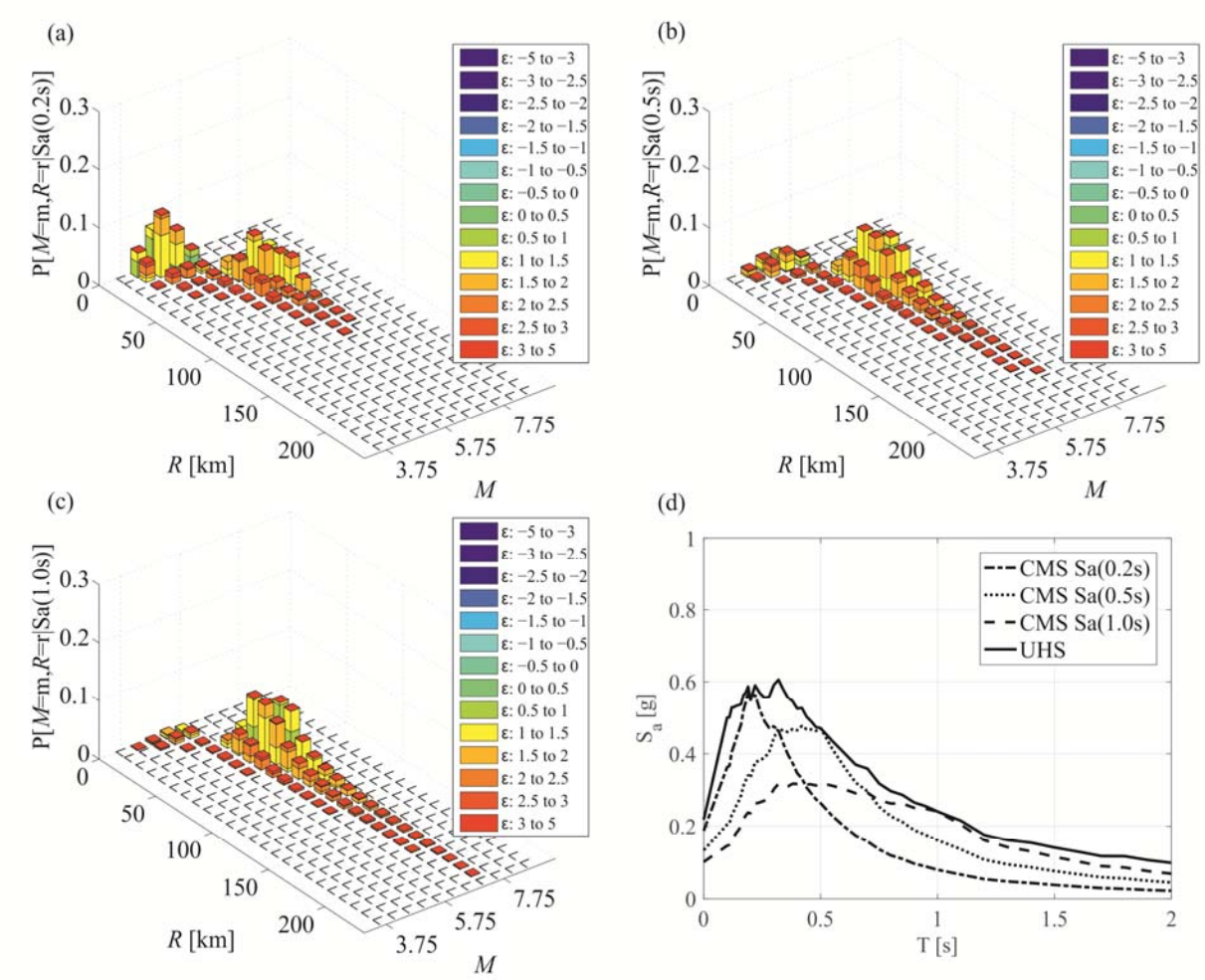

Figure 7. Disaggregation distributions for the occurrence at Tr = 2475: spectral period equal to (a) 0.2s, (b) 0.5s and (c) 1.0s. (d) Corresponding conditional mean spectra for rock and UHS.[2]

6 CONCLUSIONS

A stand-alone software for the probabilistic assessment of seismic hazard is developing. The first module is dedicated to site-specific probabilistic seismic hazard analysis (PSHA), and a preliminary description of it was provided with this paper.

PSHA is consolidated, but hazard assessment may still be demanding for earthquake engineering researchers and is very rare for practitioners. In this context, the REASSESS software is presented as a user-friendly and computationally-efficient option to tackle PSHA.

The present version of REASSESS is able to address the following issues:

- PSHA for several intensity measures accounting for model uncertainty;
- disaggregation for occurrence or exceedance hazard;
- conditional hazard for secondary intensity measures, when spectral acceleration is the primary one;

[2] As a general comment to Figure 7, it is to recall that the REXEL, a software for record selection [34], also provides disaggregation distributions for Italian sites [35]. Although REXEL relies on the same models used in these illustrative applications, the disaggregations of REASSESS are expected to present some differences with respect to those of REXEL. These are due to different computational choices between the two software, which, however, provide comparable outputs.

- uniform hazard and conditional mean spectra.

REASSESS, so far, only deals with site-specific PSHA; however, in some cases, the assessment of the seismic hazard requires considering multiple sites at once. This happens when the analysis of spatially distributed systems is of concern, or when aggregated losses for portfolio of structures and/or supply chains are of interest. The need to account for all the uncertainties and the statistical dependencies involved, make the seismic hazard for multiple sites a not straightforward task. It is a specific goal of the ongoing developments of REASSESS to address multi-site probabilistic hazard assessment, which will include, as special cases, scenario-based regional analyses.

ACKNOWLEDGMENTS

The work presented in this paper was developed within the AXA-DiSt (Dipartimento di Strutture per l'Ingegneria e l'Architettura, Università degli Studi di Napoli Federico II) 2014-2017 research program, funded by AXA-Matrix Risk Consultants, Milan, Italy.

REFERENCES

[1] C.A. Cornell, Engineering seismic risk analysis. *Bulletin of the Seismological Society of America*, **58**, 1583-1606, 1968.

[2] R.K. McGuire, *Seismic hazard and risk analysis, Report MNO-10*. Oakland, CA, USA. Earthquake Engineering Research Institute Publication, 2004.

[3] CEN, European Committee for Standardization TC250/SC8/(2003) Eurocode 8: Design provisions for earthquake resistance of structures, Part 1.1: general rules, seismic actions and rules for buildings, PrEN1998-1.

[4] CS.LL.PP. DM 14 gennaio 2008 Norme Tecniche per le Costruzioni. Gazzetta Ufficiale della Repubblica Italiana, **29**, 2008 [in Italian].

[5] R. Lee, A.S. Kiremidjian, Uncertainty and correlation for loss assessment of spatially distributed systems. *Earthquake Spectra,* **23**(4), 743–770, 2007.

[6] S. Esposito, I. Iervolino, A. d'Onofrio, A. Santo, P. Franchin, F. Cavalieri, Simulation-based seismic risk assessment of gas distribution networks. *Computer-Aided Civil and Infrastructure Engineering*, **30**(7), 508-523, 2015.

[7] M. Giorgio, I. Iervolino, On multi-site probabilistic seismic hazard analysis. *Bulletin of the Seismological Society of America*, 2016. (in press)

[8] S.L. Kramer, *Geotechnical earthquake engineering*, Prentice Hall, 1996.

[9] I. Iervolino, D. Vamvatsikos, G. Baltzopoulos, R. Baraschino, SPO2FRAG V1.0: software for pushover-based derivation of seismic fragility curves. Paper submitted to *ECCOMAS Congress 2016: VII European Congress on Computational Methods in Applied Sciences and Engineering.* M. Papadrakakis, V. Papadopoulos, G. Stefanou, V. Plevris (eds.), Crete Island, Greece, 5–10 June 2016.

[10] F. Petruzzelli, I. Iervolino. FRAME V.1.0: A rapid fragility-based seismic risk assessment tool. *Proceedings of the Second European Conference on Earthquake Engineering and Seismology*, 2ECEES, Istanbul, Turkey, 24-29 August, 2014.

[11] P. Bazzurro, C.A. Cornell, Disaggregation of seismic hazard. *Bulletin of the Seismological Society of America,* **89,** 501–520, 1999.

[12] I. Iervolino, M. Giorgio, C. Galasso, G. Manfredi, Conditional hazard maps for secondary intensity measures. *Bulletin of the Seismological Society of America,* **100**(6): 3312–3319, 2010.

[13] T. Lin, S.C. Harmsen, J.W. Baker, N. Luco, Conditional spectrum computation incorporating multiple casual earthquakes and ground motion prediction models. *Bulletin of the Seismological Society of America,* **103**(2A), 1103-1116, 2013.

[14] MATLAB Release 2015b, The MathWorks, Inc., Natick, Massachusetts, United States, 2000.

[15] G. Recktenwald, *Numerical methods with Matlab: implementation and applications*. Prentice Hall, 2000, ISBN 0201308606.

[16] G.H. Golub, C.F. Van Loan, *Matrix computations, 4th Edition.* The Johns Hopkins University Press, 2013.

[17] I. Iervolino, Soil invariance of site specific hazard and disaggregation, 2016. (under review)

[18] B. Gutenberg, C.F. Richter, Earthquake magnitude, intensity, energy, and acceleration. *Bulletin of the Seismological Society of America,* **32**, 163–191, 1942.

[19] W.B. Joyner, D.M. Boore, Peak horizontal acceleration and velocity from strong-motion records including records from the 1979 Imperial Valley, California, Earthquake. *Bulletin of the Seismological Society of America,* **71**, 2011–2038, 1981.

[20] V. Montaldo, E. Faccioli, G. Zonno, A. Akinci, L. Malagnini, Treatment of ground-motion predictive relationships for the reference seismic hazard map of Italy. *Journal of Seismology*, **9**(3), 295-316, 2005.

[21] C. Meletti, F. Galadini, G. Valensise, M. Stucchi, R. Basili, S. Barba et al., A seismic source zone model for the seismic hazard assessment of the Italian territory. *Tectonophysics,* **450**, 85-108, 2008.

[22] S. Barani, D. Spallarossa, P. Bazzurro, Disaggregation of probabilistic ground motion hazard in Italy. *Bulletin of the Seismological Society of America,* **99**, 2638–2661, 2009.

[23] S. Barani, D. Spallarossa, P. Bazzurro, Erratum to disaggregation of probabilistic ground-motion hazard in Italy. *Bulletin of the Seismological Society of America,* **100**, 3335–3336, 2010.

[24] V. Convertito, A. Emolo, A. Zollo, Seismic-hazard assessment for a characteristic earthquake scenario: an integrated probabilistic-deterministic method. *Bulletin of the Seismological Society of America,* **96**(2), 377-391, 2006.

[25] J.P. Stewart, J. Douglas, M. Javanbarg, Y. Bozorgnia, N.A. Abrahamsons, D.M. Boore et al., Selection of ground motion prediction equation for the global earthquake model. *Earthquake Spectra*, **31**(1), 19-45, 2015.

[26] I. Iervolino, E. Chioccarelli, C. Convertito, Engineering Design Earthquakes from Multimodal Hazard Disaggregation, *Soil Dynamics and Earthquake Engineering*, **31**(9), 1212-1231, 2011.

[27] J.W. Baker, Probabilistic structural response assessment using vector-valued intensity measures. *Earthquake Engineering and Structural Dynamics,* **36**, 1861–1883, 2007.

[28] J.W. Baker, C.A. Cornell, Spectral shape, epsilon and record selection. *Earthquake Engineering and Structural Dynamics*, **35**, 1077-1095, 2006.

[29] J.W. Baker, N. Jayaram, Correlation of spectral acceleration values from NGA ground motion models. *Earthquake Spectra*, **24**(1), 299-317, 2008.

[30] N.N. Ambraseys, K.A. Simpson, J.J. Bommer, Prediction of horizontal response spectra in Europe. *Earthquake Engineering and Structural Dynamics,* **25**, 371–400, 1996.

[31] J.J. Bommer, J. Douglas, F.O. Strasser, Style-of-faulting in ground-motion prediction equations. *Bulletin of Earthquake Engineering,* **1**, 171-203, 2003.

[32] S. Akkar, J.J. Bommer, Empirical equations for the prediction of PGA, PGV, spectral acceleration in Europe, the Mediterranean region, and the Middle East. *Seismological Research Letters* **81**(2), 195-206, 2010.

[33] J.J. Bommer, S. Akkar, S. Drouet, Extending ground-motion prediction equations for spectral accelerations to higher response frequencies. *Bulletin of Earthquake Engineering,* **10**, 379-399, 2012.

[34] I. Iervolino, C. Galasso, E. Cosenza, REXEL: computer aided record selection for code-based seismic structural analysis. *Bulletin of Earthquake Engineering,* **8**, 339-362, 2010.

[35] I. Iervolino, C. Galasso, E. Chioccarelli, REXEL 3.3: Closing the Loop of Computer Aided Record Selection. 15th World Conference on Earthquake Engineering (15WCEE 2012), Lisbon, Portugal, September 24-28, 2012.

ECCOMAS Congress 2016
VII European Congress on Computational Methods in Applied Sciences and Engineering
M. Papadrakakis, V. Papadopoulos, G. Stefanou, V. Plevris (eds.)
Crete Island, Greece, 5–10 June 2016

SIMPLIFIED PERIOD ESTIMATION OF ITALIAN RC BRIDGES FOR LARGE-SCALE SEISMIC ASSESSMENT

C. Zelaschi[1], R. Monteiro[1], and R. Pinho[2]

[1] Institute for Advanced Study of Pavia (IUSS)
Palazzo del Broletto, Piazza della Vittoria n.15, 27100 Pavia (Italy)
e-mail: {claudia.zelaschi,ricardo.monteiro} @iusspavia.it

[2] University of Pavia, Department of Civil Engineering and Architecture
Via Ferrata n. 1, 27100 Pavia (Italy)
e-mail: rui.pinho@unipv.it

Keywords: Seismic assessment, Latin Hypercube sampling, RC bridges, Period estimation

Abstract. *The nodes of a road transportation network of a certain region can represent a population of bridges. In view of a sound characterization of corresponding fragility or vulnerability functions, the knowledge of real data, such as geometrical and material properties available from a national bridge inventory database, is a crucial element. In fact, the outcome of damage seismic assessment can be strongly affected by the variability of such information. When only limited information for each node is known and the relevant structural behaviour needs to be assessed for e.g. loss estimation studies at macro-scale level, the use of statistical tools is of extreme importance. Accordingly, the present paper furnishes a double-fold contribution: (1) provide the systematic statistical characterization of geometrical and material properties of typical Italian reinforced concrete (RC) bridges and (2) simplified formulae for the quick evaluation of the fundamental elastic period of vibration of RC bridges. This allows the development of typological fragility curves for RC bridge classes, which might be chosen according to their fundamental period of vibration. As such, the bridges can be identified with a specific bridge class, characterized by a representative fragility curve, used for expedite large-scale seismic assessment.*

1 INTRODUCTION

Severe past earthquakes had a significant impact on road network systems as well as considerable catastrophic effects on human life, buildings and economy. Examples of such disastrous events are the San Fernando earthquake in 1971, Loma Prieta in 1989, Northridge in 1994 and more recent events such as Italian and New Zealand earthquakes in 2009 and 2011, respectively. It is due to such consequences that the management of the emergency phase in the immediate aftermath of an earthquake is significant. One way to efficiently tackle such an issue is to rapidly assess the status of the main network components, which may exhibit weak seismic response, which, in turn, may cause infrastructure or cascading system disruptions. The main components of a network can be point-site or distributed components [1]. Bridges belong to the former category and they play an important role to ensure the efficiency of the network system itself and the interconnection between cities' strategic facilities or of its surrounding area [2]. A number of past studies have addressed the seismic assessment of individual bridge structures through nonlinear static or dynamic analysis [3-7]. However, such research was built upon the knowledge and the applications initially developed for building structures [8-12] and it resulted in the proposal of fragility curves for individual structures [13-16].

The derivation of fragility curves from a number of relevant geometrical or structural parameters taken from real case studies is of utmost importance for the accuracy of loss assessment investigations as part of decision-making strategies [17-18]. In such way, civil protection or other expert bodies can rely on them during the management of post-extreme event emergency phases. Yet, especially when dealing with broad areas, the development of fragility curves for each individual bridge can be unfeasible, mainly for the computational onus that such approach requires. Therefore, a parametric statistical approach may be particularly advantageous to characterize the parameters that affect the existing RC bridges response [19]. Given such characterization, one can simulate reliable data to represent additional structural configurations to fully characterize a wide range of bridges.

With the above in mind, the present study uses statistical tools to characterize populations of Italian bridges, targeting a specific typology. The collected data includes construction year, pier heights, total bridge length, span length, number of spans, superstructure area, pier main section sizes, compressive strength, tensile strength, shear strength, Young modulus and shear modulus of materials. In particular, geometrical and material properties associated to a real bridge stock are presented in a statistically usable form. Specifically, in the initial phase, they are summarized in terms of average (mean values) and corresponding dispersion (standard deviation and coefficient of variation). Successively, statistical distributions are assigned to each parameter by means of goodness-of-fit tests for small and larger samples. Such summary statistics are then used as input for the generation of a population of a specific bridge typology, representing a typical class of Italian bridges, through standard or Latin Hypercube-based Monte Carlo sampling schemes [20] in order to obtain a wide variety of bridge configurations. Finally, the configurations are analysed in order to define a simplified relationship between the period of vibration and the bridge geometrical properties that can be easily obtained or estimated through field survey or other equivalent methods. This relationship is intended for use in risk and loss assessment models and constitutes a first step towards the assignment and/or the generation of analytical fragility and vulnerability functions for specific bridge categories. In spite of its drawbacks, the relationship can be used as a potential proxy for seismic structural demand estimate of well-defined bridge typologies. It would also enable the possibility of rapidly sub-dividing bridge populations in classes for the expedite application of recent record selection procedures (e.g. conditional spectrum method) or early loss assessment

approximations, through immediate assignment of a proper fragility curve for the assessment of damage level. Ultimately, this relationship may also be applied to estimate structural properties or damage levels when no detailed information on the bridge is available.

2 SEISMIC ASSESSMENT FRAMEWORK

The global framework involving the present study targets the development of typological fragility and vulnerability functions for specific bridge classes. The framework, illustrated in Figure 1, starts with the random generation of multiple bridge structural configurations, generated through summary statistics of geometrical and material properties, which can be typically drawn from national bridge inventories. The obtained bridge portfolio can then be characterized in terms of eigenvalue analyses output, which will be useful to either identify the fundamental period of vibration or define pushover curve loads for nonlinear seismic demand estimation methods. In fact, in the past, a large number of simplified equations to estimate the fundamental period of vibration have been proposed and are commonly used for buildings (e.g. [21, 22]) whereas the absence of similar equations for bridges is well known. This paper intends to contribute to fill such a gap by proposing simplified equations as function of one or more parameters strongly correlated to the fundamental period. The fundamental period of vibration becomes also handy to e.g. carry out proper selection of records according to recent methodologies, such as the conditional spectrum method [23], also successfully applied to bridges [24]. Such a selection guarantees reliable performance points for any employed nonlinear static procedure or seismic input for nonlinear dynamic analyses.

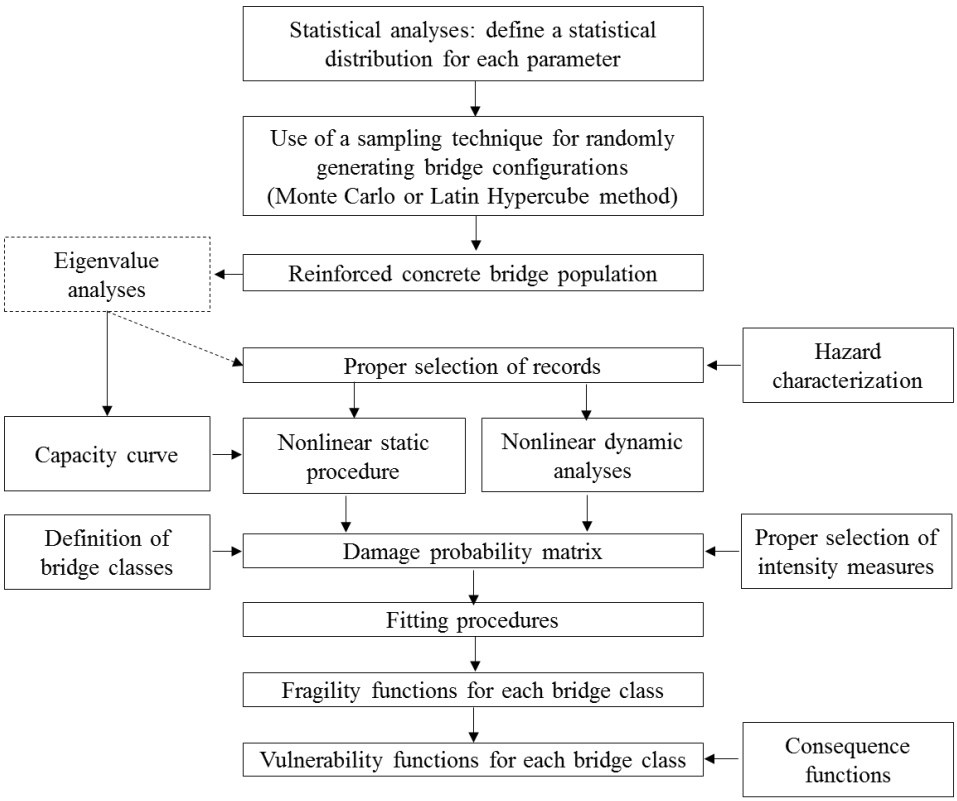

Figure 1. General framework

Once bridge classes are identified, a proper intensity measure and damage limit states are selected so that the damage probability matrix can be derived. This matrix becomes the input of a fitting procedure developed to identify the main fragility function parameters. Therefore,

the framework is very much dependent on randomly simulated bridges, featuring different geometrical configurations. Indeed, the randomness that characterizes the simulated population is exclusively related to the structural layout of the pier heights and deck spans, together with the variability associated to the material properties. With this portfolio it is possible to establish, through regression analysis, empirical equations that relate geometrical properties with corresponding structural response and, afterwards, fragility. Such equations may then find useful application in expedite risk assessment methodologies or national design codes.

3 STATISTICS AROUND BRIDGE PROPERTIES

In order to provide the input for numerical simulation of bridge populations, the available information of the bridge stock under investigation has been statistically characterized. Statistical distributions were assigned to each parameter deemed relevant to the behaviour of reinforced concrete bridges. For the selected geometrical and material properties, the main statistical quantities were evaluated from the sample. Chi-Square and/or Kolmogorov-Smirnov goodness-of-fit (GoF) tests were applied to assign normal, lognormal, gamma, exponential or Weibull distributions, according to typical alpha values (0.05, 0.10 and 0.20). At an initial stage, all the properties available from the source database were statistically characterized through GoF testing. Afterwards, bridge configuration sampling and empirical relationships were carried out only for the properties that were relevant for a common RC bridge configuration, as detailed in Section 4, namely piers height, total length of bridges, span length, section diameter, reinforcing bars' Young modulus, concrete compressive strength.

3.1 Chi-Square Goodness-of-Fit test

This test should be employed under specific conditions: it requires a sufficient sample size, only binned data are allowed and a minimum expected frequency is required. Given that the selection of the number of bins affects the value of the test, some rules (e.g. Sturge's rule, Normal reference rule and Scott's rule) suggest the most appropriate bin widths in order to minimize the squared error in the approximation of the Chi-Square test. The minimum expected frequency is unanimously established by literature equal to five, and if this minimum requirement is not reached, the combination of adjacent bins in the tails is applied. The subsequent overlapping of the theoretical probability density function of the assumed distribution on each histogram shows if there is probabilistic agreement; if there is not, the null hypothesis, which asserts that the data follows the pre-specified distribution, is most likely incorrect.

3.2 Kolmogorov-Smirnov Goodness-of-Fit test

The Kolmogorov-Smirnov GoF test belongs to the class of distance tests and is among the best distance tests for small samples, yet it is still reliable for large ones. The test is developed starting from the assumption of an empirical distribution, characterized by parameters estimated from the data set or from expert judgment. The comparison between theoretical and empirical CDFs follows. If the two CDF curves agree from the probabilistic point of view, the assumed distribution is accepted. Such comparison consists of defining the maximum vertical distance between the two curves and the p-value based on the maximum distance. The Kolmogorov-Smirnov test is widely used in practice and it works properly even if the sample size is small; hence it becomes particularly useful for the statistical characterization of geometrical and material properties of existing structures, such as the ones herein investigated.

3.3 Goodness-of-Fit testing with data truncation

A non negligible percentage of the data for the different variables was located at the tails of the corresponding distribution functions. The identification of outliers was therefore necessary. One way to recognize outliers is by using box plots, which synthetically represent all the data and group it in quartiles. The variability outside the upper and lower quartiles (respectively q3 and q1 in Figure 2) was assumed as 1.5 times the interquartile range (IQR) and is represented by whiskers. The data outside the whiskers length is identified as outliers. The range of data that excludes outliers is the so-called inner fence and it was used as input for the statistical tests [25].

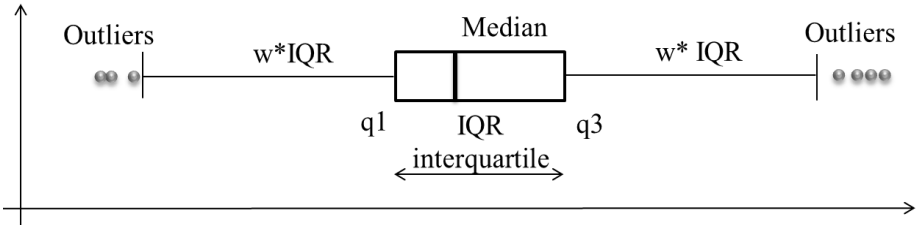

Figure 2. Typical box plot for identifying outliers

In the present work, the variables that did not satisfy goodness of fit tests were analysed through box plots and in some cases, to better fit the theoretical statistical distribution, a whisker length of 3.0 was allowed. All the distribution parameters were accordingly derived.

4 DEFINITION OF A TYPICAL BRIDGE STOCK

The statistical treatment of geometrical and material properties was conducted by selecting, among the available data, the most relevant parameters from the structural seismic response viewpoint. The main bridge typology considered corresponds to Italian reinforced concrete bridges built between the 1970s and 1990s, when the major development of the highway network took place. In most cases, such bridges are characterized by simply supported deck or monolithic connections (Figure 3). About 30% of the structures exhibit circular or rectangular pier cross sections, whereas 35% include several section shapes such as octagonal or composite sections. The pier-to-deck connection is typically of the concrete-concrete or elastomeric bearings or other devices type.

Figure 3. Typical Italian highway bridge. [26]

A case study made up of nearly five hundred Italian bridges (the exact number is 458), illustrated in Figure 4, was built up with a view to the simplified seismic vulnerability estimates for RC bridges by using parameterized structural behaviour relationships and future fragility curves.

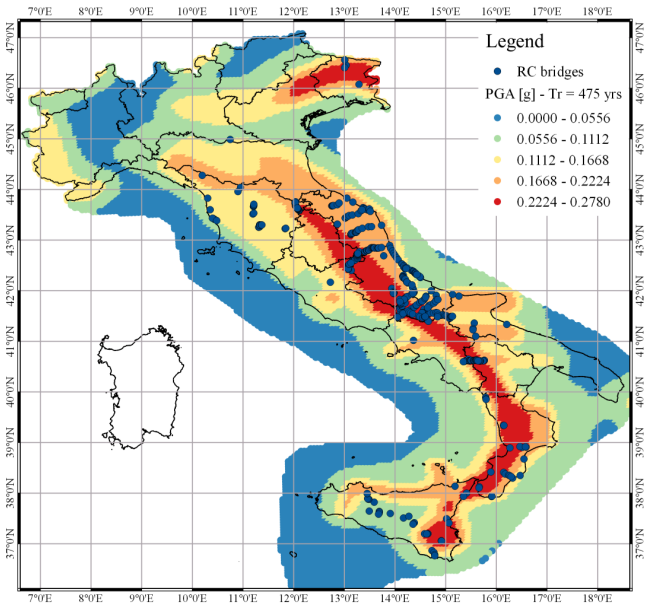

Figure 4. Case study: Italian reinforced concrete bridge population

Ideally, within a seismic risk assessment context, the definition of fragility curves of each bridge should be carried out. However, to avoid the considerable time demand of such an approach, the definition of bridge classes for a certain country would be reasonable if one assumes that the characteristics of bridges in a certain region are typically similar. Furthermore, the approach followed in the present section is based on general geometric and material information provided by a database, which is not enough to define an exhaustive characterization of different bridge classes.

At this point, the portfolio characterization in terms of random simulation of bridge properties can follow two macro strategies. The first is to consider specific geometric configurations with a specific layout (predefined number of piers, spans and regularity level) and then establish a distribution for every variable of the layout to perform simulations. The second, that is adopted here, considers the number of piers, spans and regularity level (pier heights) as random variables, defined statistically.

As such, the Italian bridges represented in Figure 4 were gathered in a single macro bridge category, corresponding to straight multi-span continuous reinforced concrete bridges. These bridges were modelled using the same deck and pier cross section type and featured no isolation at the pier-to-deck connection level. Abutments were considered as of very high stiffness hence nearly fully fixed. Furthermore, curved bridges were assumed as straight and were grouped in that same class, whilst arch bridges were considered as part of a different configuration type hence not included in the present study. The available geometrical parameters for each bridge, schematically depicted in Figure 5, were individually analysed and general inference on bridge class was made when the full set of bridge properties was not available.

Construction type, column height, span length, number of spans, superstructure area, radius of curvature in plan, main geometrical dimension of the column section, steel bars tensile strength, steel bars Young Modulus were the available parameters that provide insight to-

wards the typical geometric configuration and material properties of the selected bridges. No specific information related to the seismic design was available. A possible indicator to determine whether the bridges were seismically designed or not could be the year of construction. With respect to the bridges for which the construction year is known, 65% were built before 1970; 25% between 1970 and 1980, and 10% after 1980. Therefore, all the bridges were conservatively assumed as non seismically designed.

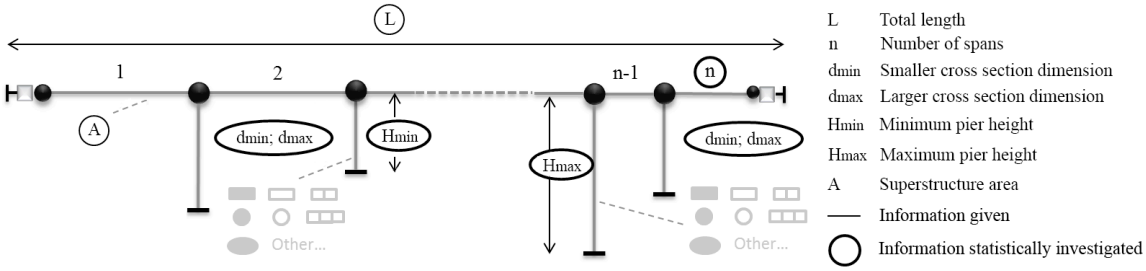

Figure 5. Available information on the case study bridges

For most of the properties, statistical details were investigated using the conventional statistical tools for distribution testing, described in Section 3, to define input for numerical simulation. Specific attention was paid to discrete data, for which different statistical treatment was required, particularly for the number of spans variable, which only admits integer values. In fact, even though the use of Poisson regression would be required, the resulting inappropriate short spans obtained with such an approach led the authors to consider instead the relationship between number of spans and total length, as given in Table 1.

Variable	**Distribution**	**Distr. parameters**	**Statistical tests**
Pier height [m]	Lognormal	Mean (log): 1.95 std: 0.8275	Chi-sq. not sat. K-S: **10%, sat.**
Total length [m]	Lognormal	Mean (log): 5.10 std: 1.145	Chi-sq. not sat. K-S not sat
Span length [m]	Normal	Mean: 31.18 std: 11.527	Chi-sq. not sat. K-S not sat.
Average span length [m]	Normal	Mean: 29.936 std: 12.174	Chi-sq. not sat. K-S not sat.
Number of spans	Regression	# spans=1.483+0.0273*Total length R^2=0.89	
Superstructure area [m^2]	Lognormal	Mean (log): 7.88 std: 0.9087	Chi-sq.: **5 %, sat.** K-S: **10%, sat.**

Table 1. Statistical distributions – geometrical layout properties

The superstructure width, required for structural modelling and not included in the set of available variables, was derived from the superstructure area, considering a trapezoidal widespread Italian deck cross section with the assumption of a solid cross section. The depth of the section was defined in line with real bridges, taking into account the average span length. In particular, for an average span length of 20m, a reasonable value of deck depth was registered to be 1.30m; whilst in the case of 40m, the deck depth assumed was 2.20m. In order to randomly generate superstructure widths, a linear trend was assumed and inference of data was then applied. The 458 observations for superstructure width were then derived from the corresponding superstructure area and total bridge length, whose fitting to the most common statis-

tical distributions were tested through Chi-squared and Kolmogorov-Smirnov GoF tests. Although the test was not satisfied at either 99%, at 90% or at 95% confidence levels, the best fit was observed to be obtained with a lognormal distribution, without truncation of data. The random data was generated between 4.7m and 34.7m, with a mean value of 12.5m and coefficient of variation of 29.1%.

The pier cross section characterization was carried out in terms of solid sections, particularly circular cross sections, which were used for the random simulation in Section 5. As for material properties, elevation compressive strength, bar tensile strength and reinforcing bars Young Modulus statistical distributions were available.

Finally, it is worth noting that when carrying out data truncation of the geometrical properties that exhibited a number of outliers, the distribution parameters sometimes significantly changed.

5 RANDOM SAMPLING: GENERATION OF BRIDGE POPULATIONS

Following the statistical characterization of the geometrical and material properties, the random generation of bridge populations can be carried out by simulating possible values from the probability distribution functions, adjusted to the different variables described in Section 4. To accomplish this, two random simulation schemes, sharing the same underlying concepts, were selected: standard and Latin Hypercube-based Monte Carlo. A sufficient number of iteration steps was ensured to guarantee that sampled parameters approximate the initially assumed probability distribution functions. Accurate results for output distributions depend on how complete the sampling from the input distributions is, thus more efficient methods are those that reach this objective with the lower number of iterations. The most popular sampling algorithm in engineering applications is standard Monte Carlo (MC), which generally requires a large number of iteration steps, whereas a more recent sampling strategy proposed is the Latin Hypercube Sampling-based Monte Carlo (LHS) that converges faster on the statistics of the input distribution. Needless to say, the selection of a proper sampling method is a crucial phase of nonlinear engineering data analysis applications, as it affects both computational onus and accurateness of results.

5.1 Sampling with standard Monte Carlo scheme

Monte Carlo is a widely spread technique applied to many problems that require the extraction of random or pseudo-random numbers to sample from a probability distribution. In its crude or standard version, the Monte Carlo sampling technique assumes that any given sample may fall anywhere within the range of the input distribution. Its main drawback is that when probability distributions are noticeably skewed, it can present outcomes of low probability, together with clustering. These limitations have incited researchers to develop new sampling schemes, such as the Latin Hypercube-based Monte Carlo, discussed ahead. In the study presented herein, Monte Carlo sampling was tested for the generation of a population set of 1000 bridges, assuming as variables the pier height (lognormal distribution), span length (normal distribution), total bridge length (lognormal distribution), section diameter (normal distribution), longitudinal reinforcement yield strength (normal distribution), transverse reinforcement yield strength (normal distribution) and steel Young Modulus (normal distribution).

5.2 Sampling with Latin Hypercube scheme

The Latin Hypercube sampling scheme is a particular case of the Monte Carlo method and consists of the stratification of the input cumulative distribution function (CDF). This CDF is

subdivided into equal intervals from which the samples are randomly drawn without replacement, retracing the input probability distribution [27]. The input parameters of each simulation constitute the rows of an NxK matrix (N is the number of the numerical simulations and K is the number of parameters), obtained according to the inverse target distribution of the parameter associated with the column involved [28].

Even though the LHS-based method exhibits the advantage of reducing computational time demand, it does not allow the specification of parameter lower and upper bounds nor generating a new single bridge configuration. To be consistent with the bounds specified in the standard Monte Carlo method, for each parameter, such a drawback was overcome by imposing a greater number of simulations and by eliminating the entire input rows associated to those out of range values. Moreover, in order to avoid unrealistic negative parameter values, the possible entire input rows of the aforementioned N by K matrix with negative values were removed. Very few simulations did not respect the imposed restrictions therefore the described assumptions were considered acceptable.

According to the aforementioned rationale, assumptions, steps, and available information (Figure 5), a sample of 100 bridge configurations was generated. This sampling size is in agreement with recent studies in the field [29], which focused on the employment of LH sampling to the probabilistic seismic assessment of RC bridges. The distributions of the fundamental period in the transverse direction of the bridge populations generated with standard and LH-based Monte Carlo sampling are shown in Figure 6.

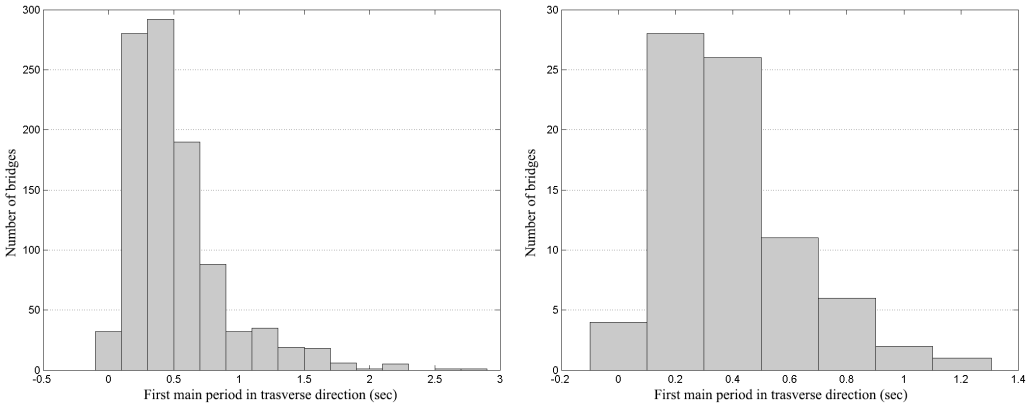

Figure 6. Fundamental transverse period of bridges randomly generated with (left) standard and (right) Latin Hypercube–based Monte Carlo sampling schemes.

6 PERIOD ESTIMATION – REGRESSION ANALYSIS

In seismic analysis, the knowledge related to the fundamental period of vibration is very important as it represents a parameter capable of providing relevant information related to the global demand on a structure under a given ground motion. Structural mass, stiffness and strength are the variables that primarily affect such a dynamic behaviour parameter. However, their knowledge is not always immediate, which renders many times useful a relationship between the period and easily obtainable properties, such as geometrical information. This relationship will in turn be useful to get an accurate estimate whenever detailed data for a certain bridge is missing. The lack of this sort of studies for bridges, as opposed to buildings, led to the identification of one or more parameters strongly correlated to the fundamental period of vibration, through an analytical procedure based on the numerical simulation of bridge portfolios. Single variable and multivariate regression analyses were carried out on the randomly generated bridge populations for the development of the period estimation relationship.

6.1 Existing bridge period relationships

Eurocode 8 proposes different formulae for the structural period of vibration based on stiffness and displacements, differentiated for the cases of rigid and flexible decks. A recent methodology [30] produced simplified capacity curves to be used for seismic loss assessment of bridges. A bridge population of twenty-one assets was considered as case study. It was characterized by two deck lengths (200m and 400m), three different types of abutments and different geometrical layouts, corresponding to different regularity classes: regular, semi-regular, and irregular. The initial period in the transverse direction, corresponding to the equivalent single-degree-of-freedom system's yielding point, resulted as a relevant parameter for characterizing simplified capacity curves, thus a preliminary trend line was drawn for defining its relationship with deck length. The number of bridges used was very limited hence the need for an improved relationship of that sort is evident. When detailed information of existing bridges is not readily available, the properties that can be easily obtained are of geometric nature. For such reason, at this initial stage, only their correlation with the fundamental period is considered.

6.2 Bridge modelling

Each case-study bridge was modelled in [31], which enabled the creation of an automatized procedure controlled by an external script [32], capable of generating and updating model files for each run. The deck was modelled as a continuous elastic element, located right at the pier top, with lumped masses and with geometrical properties referred to its centre of mass, connected through rigid link elements. Considered the bridge stock characteristics, circular solid sections were assigned to each pier. With respect to material modelling, Kent-Scott-Park model with zero tensile strength was assigned to represent concrete behaviour, accounting for confinement factor in case of concrete cores. The confinement level was evaluated for each bridge component through equations proposed by Mander, since neither Kent-Park's model nor its modified version provided information about the confining effects of spiral hoops. A bilinear model was assumed for steel, with no isotropic hardening. On the other hand, kinematic hardening was considered through the ratio between post-yield tangent and initial elastic tangent, i.e. strain-hardening ratio equal to 0.002. The connection between the piers and the deck was assured by shear keys that were modelled with rigid zero length elements and equal-degree-of-freedom connections. As far as abutments were concerned, a simplified model made up of very high stiffness springs with bilinear response along horizontal directions and fully restrained at the ground was employed.

6.3 Parametric study

Trying to fill the identified gap in the current state-of-the-art, a relationship between the fundamental period of the defined bridge class and relevant geometrical parameters was sought using eigenvalue analysis. Such approach made use of the randomly generated bridges, guaranteeing the consideration of a large breadth of different structural configurations. The representation of the fundamental period versus various geometrical parameters (tallest pier height, shortest pier height, average pier height, bridge length, average pier height) for 1000 bridges generated with standard Monte Carlo simulation was carried out in accordance with the statistical distributions proposed in Section 4. This did not evidence a clear nor satisfactory trend between fundamental period and each parameter considered individually. This is certainly due to the fact that several variables are being randomly considered and, as such, multivariate regression is envisaged with a view to an improvement in the strength of such a relationship. Nevertheless, pier height and average pier height parameters seemed to yield a

stronger correlation with the fundamental period, which preliminary indicates a possible influence by factors as regularity and bridge length.

With respect to the set of 100 bridges generated with LH–based Monte Carlo sampling, a screening of the different configurations was carried out to eliminate those including characteristics without physical meaning (e.g. negative pier heights). After such filtering, the remaining number of configurations was 78.

Considering multivariate regression, the analyses were carried out using the standard (1000) and LH–based Monte Carlo (78) sampling generated bridges. The corresponding equations and plots are presented, respectively, in Tables 2 and 3. The results denote a trend very similar to the standard Monte Carlo based results. Indeed, the comparison between the results obtained from multivariate regression analyses applied to the bridge populations associated with the two sampling procedures are summarized in Table 4. Such results demonstrate that the LH–based sampling scheme provides very close results, even slightly better, to those obtained with the standard Monte Carlo algorithm.

Period Total length Maximum pier height	Eq.1: $T=-5.5*10^{-5}Ltot+0.019Hmax+0.161$ **$R^2=0.233$**	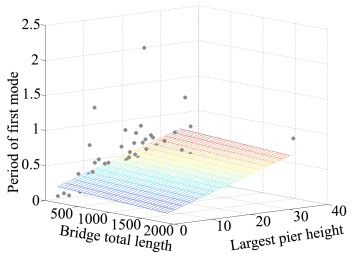
Period Maximum pier height Section diameter	Eq.1: $T=0.017Hmax-0.225Dsec+0.718$ **$R^2=0.594$**	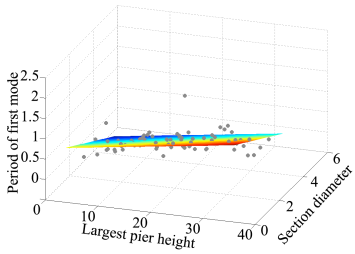
Period Average pier height Section diameter	Eq.1: $T=0.054Hav-0.215Dsec+0.523$ **$R^2=0.656$**	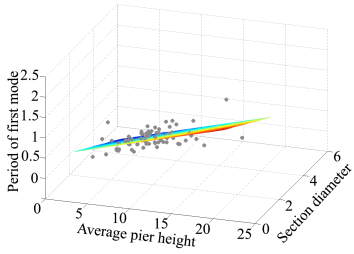

Table 2. Multivariate regression for 1000 bridges using standard Monte Carlo simulation

The final set of regression analysis tests considered the ratio between the two best performing variables (average pier height and section diameter), H_{av}/D_{sec}, which better fitted the results obtained with numerical simulation. Further improvement of the quality of the fitting was obtained by:

- carrying out robust regression, which assigns a different weight to each point while performing the regression;
- considering the semi-studentized residuals in order to identify the presence of outliers. According to a rough rule of thumb, suggested in [25], semi-studentized residuals with

absolute value of four or more are to be considered outliers hence they were not included when deriving regression equations.

Period Total length Maximum pier height	Eq.1: $T=-5.5*10^{-5}Ltot+0.019Hmax+0.161$ **$R^2=0.233$**	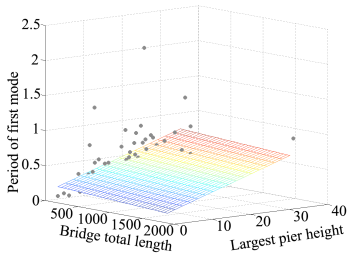
Period Maximum pier height Section diameter	Eq.1: $T=0.017Hmax-0.225Dsec+0.718$ **$R^2=0.594$**	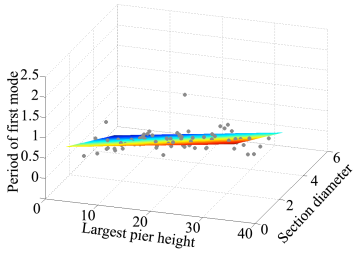
Period Average pier height Section diameter	Eq.1: $T=0.054Hav-0.215Dsec+0.523$ **$R^2=0.656$**	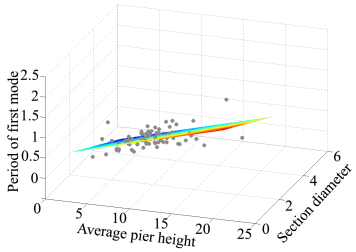

Table 3. Multivariate regression for 78 bridges using LH-based Monte Carlo sampling

Relationship	**Standard Monte Carlo (1000 simulations)**	**LHS-based Monte Carlo (78 simulations)**
Period Total length Maximum piers height	Eq.1: $T=2.0*10^{-4}Ltot+0.015Hmax+0.239$ **$R^2=0.163$**	Eq.1: $T=-5.5*10^{-5}Ltot+0.019Hmax+0.161$ **$R^2=0.233$**
Period Maximum piers height Section diameter	Eq.1: $T=0.016Hmax-0.229Dsec+0.977$ **$R^2=0.591$**	Eq.1: $T=0.017Hmax-0.225Dsec+0.718$ **$R^2=0.594$**
Period Average piers height Section diameter	Eq.1: $T=0.048Hav-0.303Dsec+0.777$ **$R^2=0.590$**	Eq.1: $T=0.054Hav-0.215Dsec+0.523$ **$R^2=0.656$**

Table 4. Comparison between multivariate regression results for the two sampling schemes

The plots and equations representing the improved relationship, associated with both Latin Hypercube and Monte Carlo sampling schemes, are illustrated in Table 5. When considering the ratio between average pier height and section diameter, the improvement in the period of vibration parametric characterization is notorious, whether standard or LH–based Monte Carlo sampling is employed. The quality and strength of the identified correlation is now at a level able to provide enough confidence in the use of the corresponding formulae. Indeed, a very quick estimate of the period of vibration of bridges with the characteristics used in this study can be taken as one tenth of the ratio between the average pier height and the pier cross section diameter.

Standard Monte Carlo sampling	**LH-based Monte Carlo sampling**
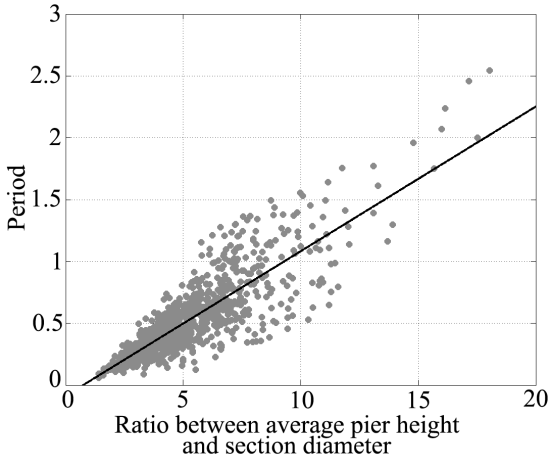	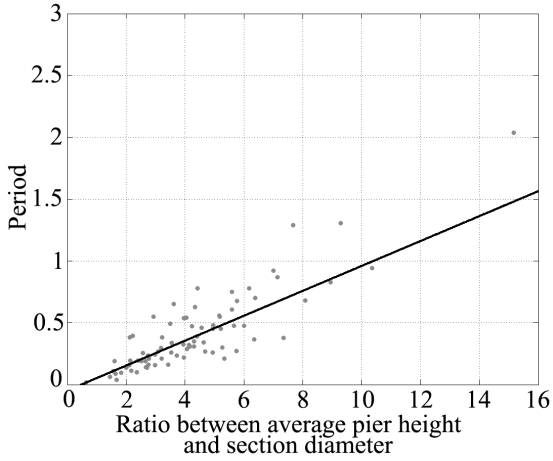
$T = \text{-}0.088 + 0.117\frac{H_{av}}{D_{sec}}$	$T = -0.048 + 0.101\frac{H_{av}}{D_{sec}}$
$R^2 = 0.830$	$R^2 = 0.805$

Table 5. Fundamental period versus ratio (average pier height / section diameter)

7 CONCLUSIONS

The study presented in this paper shows, as main contribution, a relationship to estimate the period of vibration of a typical class of Italian reinforced concrete bridges, based on easily measurable geometrical parameters. with a view to seismic assessment studies. Such bridge typology features simply supported continuous deck, nearly fixed abutments and piers with circular cross section. The geometrical variability was defined in terms of pier and span layout (number and, respectively, height or length) and material properties. The parametric characterization is useful to e.g. rapid loss assessment studies of bridge portfolios. In such a context, expedite estimates of structural characteristics are useful, especially when limited information is available. In specific, the period of vibration is intended to provide simplified seismic structural demand information, enabling also future development of fragility curves by classes.

The geometrical and material properties characterization related to existing bridges was successfully carried out through a thorough assignment of statistical distributions based on goodness-of-fit tests and outlier elimination techniques. Using such distributions, the random generation of a large number of bridges was then performed by applying two different sampling schemes: standard Monte Carlo, characterized by fully randomness, and Latin Hypercube–based Monte Carlo, based on stratified randomness. Both procedures proved to be effective in sampling bridge populations to obtain the desired parametric relationships through robust nonlinear regression analysis. For both sets of generated bridges, corresponding to the

different simulation techniques, the determination coefficients were similar and higher than 0.8, a fair result from an engineering viewpoint. Taking into account the reduced computational onus without loss of accuracy, the Latin Hypercube–based Monte Carlo sampling scheme revealed itself more advantageous and is therefore proposed as the preferable solution for numerical simulation in engineering applications of this sort.

For what concerns the specific relationship between the period of vibration and the geometrical parameters of the bridges, a simplified equation has been successfully proposed. From the authors perspective, it can be employed as a starting step for the expedite assessment of existing bridges of predefined bridge classes (with corresponding e.g. fragility curves). For the considered class, the period of vibration is seen as typically related to the ratio between the average pier height and the pier cross section diameter, properties that can be easily obtained through visual inspection or even remote techniques (e.g. GIS tools). It is believed that the work herein presented overcomes its inherent limitations when considering that current risk assessment studies, carried out in academic and industry, are based on fragility and exposure models built upon proxies with less technical content (e.g. census data). Future developments of the present work will indeed investigate the possibility to extend the proposed period equation to other branches of bridge taxonomy i.e. structural bridge classes. Important developments will also concern the consideration of code-prescribed levels of seismic design in terms of strength and ductility in the classification of bridges.

REFERENCES

[1] M.T. Bensi, *A Bayesian Network Methodology for Infrastructure Seismic Risk Assessment and Decision Support*, PhD thesis, 2010.

[2] A. Sextos, ICT applications for new generation seismic design, construction and assessment of bridges. *Structural Engineering International: Journal of the International Association for Bridge and Structural Engineering (IABSE)*, **24**(2), 173-183, 2014.

[3] C. Casarotti, R. Monteiro and R. Pinho, Verification of spectral reduction factors for seismic assessment of bridges. *Bulletin of the New Zealand Society for Earthquake Engineering*, **42**(2), 111, 2009.

[4] R. Pinho, R. Monteiro, C. Casarotti, R. Delgado, Assessment of continuous span bridges through nonlinear static procedures. *Earthquake Spectra*, **25**(1), 143-159, 2009.

[5] M. Kohrangi, R. Bento, M. Lopes, Seismic performance of irregular bridges–comparison of different nonlinear static procedures. *Structure and Infrastructure Engineering*, 1-19, 2014.

[6] R. Monteiro, R. Delgado, R. Pinho, Probabilistic seismic assessment of RC bridges: Part I - Uncertainty models. *Structures*, **5**, 258-273, 2016.

[7] R. Monteiro, R. Delgado, R. Pinho, Probabilistic seismic assessment of RC bridges: Part II – Nonlinear demand prediction. *Structures*, **5**, 274-283, 2016.

[8] M. Fragiadakis, D. Vamvatsikos, M. Aschheim, Application of Nonlinear Static Procedures for the Seismic Assessment of Regular RC Moment Frame Buildings. *Earthquake Spectra*, **30**(2), 767-794, 2014.

[9] R. Monteiro, M. Marques, G. Adhikari, C. Casarotti, R. Pinho, Spectral reduction factors evaluation for seismic assessment of frame buildings. *Engineering Structures*, **77**, 129-142, 2014.

[10] R. Pinho, M. Marques, R. Monteiro, C. Casarotti, R. Delgado, Evaluation of nonlinear static procedures in the assessment of building frames. *Earthquake Spectra*, **29**(4), 1459-1476, 2013.

[11] R. Monteiro, P. Ceresa, V. Cerchiello, J. Dabeek, A. Di Meo, B. Borzi, Towards integrated seismic risk assessment in Palestine – Application of the city of Nablus. M. Papadrakakis, V. Papadopoulos, G. Stefanou, V. Plevris eds. *VII European Congress on Computational Methods in Applied Sciences and Engineering (ECCOMAS Congress)*, Crete Island, Greece, 5–10 June, 2016.

[12] I. Grigoratos, J. Dabeek, M. Faravelli, A. Di Meo, V. Cerchiello, B. Borzi, R. Monteiro, P. Ceresa, Development of a fragility and exposure model for Palestine – Application to the city of Nablus. *Proceedings of the The World Multidisciplinary Civil Engineering-Architecture-Urban Planning Symposium*, Prague, 13-17 June, 2016.

[13] K. Mackie, B. Stojadinovic, Probabilistic Seismic Demand Model for California Bridges. *Journal of Bridge Engineering*, **6**(6), 468–480, 2001.

[14] E. Choi, R. DesRoches, B. Nielson, Seismic Fragility of Typical Bridges in Moderate Seismic Zones. *Engineering Structures*, **26**(2), 187–199, 2004.

[15] A.C. Cornell, F. Jalayer, R.O. Hamburger, Probabilistic Basis for 2000 SAC Federal Emergency Management Agency Steel Moment Frame Guidelines. *Journal of Structural Engineering*, **128**(4), 526–532, 2002.

[16] B. Nielson, R. DesRoches, Analytical seismic fragility curves for typical bridges in the central and southeastern United States. *Earthquake Spectra*, **23**(3), 615-633, 2007.

[17] C. Zelaschi, D. Forcellini, G. De Angelis, R. Monteiro, Performance based earthquake engineering approach applied to bridges in a road network. *Proceedings of the 5th ECCOMAS Thematic Conference on Computational Methods in Structural Dynamics and Earthquake Engineering (COMPDYN)*, Crete, Greece, May 25-27, 2015.

[18] M. Fragiadakis, D. Vamvatsikos, M. Karlaftis, N. Lagaros, M. Papadrakakis M, *Seismic assessment of structures and lifelines*. Journal of Sound and Vibration, **334**, 29-56, 2015.

[19] M.S. Saiidi, A. Arêde, D. Cardone, P. Delgado, M. Dolce, M. Fischinger, T. Isaković, S. Pantazopoulou, G. Pekcan, R. Pinho and A. Sextos, Modelling of bridges for inelastic analysis. *Geotechnical, Geological and Earthquake Engineering*, **21**, 5-84, 2012.

[20] R. Monteiro, Sampling based numerical seismic assessment of continuous span RC bridges. *Engineering Structures*, in-press, 2016.

[21] H. Crowley, R. Pinho, Period-height relationship for existing European reinforced concrete buildings. *Journal of Earthquake Engineering*, **8**(1), 93-119, 2004.

[22] R.K. Goel, A.K. Chopra, Period Formulas for Moment-Resisting Frame Buildings. *Journal of Structural Engineering*, **123**(11), 1454-1461, 1997.

[23] C. Bernier, R. Monteiro, P. Paultre, Using the Conditional Spectrum Method for Improved Fragility Assessment of Concrete Gravity Dams in Eastern Canada. *Earthquake Spectra*, In-Press, 2016.

[24] C. Zelaschi, R. Monteiro, R. Pinho, Improved fragility functions for RC bridge populations. M. Papadrakakis, V. Papadopoulos, V. Plevris eds. *5th ECCOMAS Thematic Conference on Computational Methods in Structural Dynamics and Earthquake Engineering (COMPDYN 2015)*, Crete Island, Greece, 25–27 May, 2015.

[25] M.H. Kutner, C. Nachtsheim, J. Neter, *Applied linear regression models*. McGraw-Hill, Irwin, 2004.

[26] Gruppo di Lavoro MPS, *Redazione della mappa di pericolosità sismica prevista dall'Ordinanza PCM 3274 del 20 marzo 2003*. Rapporto Conclusivo per il Dipartimento della Protezione Civile, INGV, Milano-Roma, 2004. (in Italian).

[27] R.L. Iman, J.M. Davenport, D.K. Zeigler, *Latin Hypercube Sampling (A Program User's Guide)*. Technical Report SAND79-1473, Sandia Laboratories, Albuquerque, 1980.

[28] A.M.J. Olsson, S.G. Sandberg, Latin hypercube sampling for stochastic finite element analysis. *Journal of Engineering Mechanics*, **128**(1), 121-125, 2002.

[29] R. Monteiro, R. Delgado, R., Pinho, Using different uncertainty models for seismic assessment of RC bridges. COMPDYN 2015 - *5th ECCOMAS Thematic Conference on Computational Methods in Structural Dynamics and Earthquake Engineering*, 887-899, Crete, May 25-27, 2015.

[30] S. Broglio, H. Crowley, R. Pinho, Structure-Dependent Displacement-Based Intensity Measure for Bridges. *Proceedings of 14th European Conference on Earthquake Engineering and Engineering Seismology*, Ohrid, Macedonia, 2010.

[31] OpenSees, *Open System for Earthquake Engineering simulation*. Pacific Earthquake Engineering Research Center, US, 2002. available from http://opensees.berkeley.edu/

[32] Matlab, version 7.1.0.246. Natick, Massachusetts: The MathWorks Inc., 2005.

ECCOMAS Congress 2016
VII European Congress on Computational Methods in Applied Sciences and Engineering
M. Papadrakakis, V. Papadopoulos, G. Stefanou, V. Plevris (eds.)
Crete Island, Greece, 5–10 June 2016

FLOW FIELD ESTIMATION IN OPEN CHANNEL BASED ON KALMAN FILTER FINITE ELEMENT METHOD

T. Yoshiara[1], T. Kurahashi[2], Y. Kobayashi[3], and T. Eto[4]

[1] Graduate school of Nagaoka University of Technology,
1603-1 Kamitomioka, Nagaoka, Niigata, 940-2188, Japan.
e-mail: s133085@stn.nagaokaut.ac.jp

[2] Department of Mechanical Engineering, Nagaoka University of Technology,
1603-1 Kamitomioka, Nagaoka, Niigata, 940-2188, Japan.
e-mail: kurahashi@mech.nagaokaut.ac.jp

[3] Department of Mechanical Engineering, Nagaoka University of Technology,
1603-1 Kamitomioka, Nagaoka, Niigata, 940-2188, Japan.
e-mail: kobayasi@mech.nagaokaut.ac.jp

[4] National Institute of Technology Nagaoka college,
888 Nishikatakai, Nagaoka, Niigata, 940-8532, Japan.
e-mail: eto@nagaoka-ct.ac.jp

Keywords: Finite element method, Kalman filter theory, Estimation of flow field

Abstract. *The Kalman filter developed by R. E. Kalman and R. S. Bucy is states estimation theory in the target domain and has been employed in various field of engineering. In general, observation data in any system include observation noise and the computational model includes system noise. The finite element equation is applied to derive the state transition matrix in the system equation of the Kalman filter. We can estimate state values after the time progress of spatial models. On the other hand, tidal power generation has the potential to contribute significantly as one of the clean energy. In tidal power generation, propellers of generator are rotated by tidal current and tidal power is converted to electric energy. Therefore, the generator should be placed in the fast point of tidal current to produce more electric energy. Thus, we focused on the flow field estimation using the observation data at limited observation points to find out the fast point of tidal current. As the fundamental study, the estimation of the flow field in open channel is carried out based on the finite element method and the Kalman filter theory. As the governing equation, the shallow water equations are employed, and the finite element and the selective lumping methods are applied to discretize the governing equations in space and time, respectively. The estimation of the distribution of the velocity vector and the water elevation is carried out by using the discretized equation. The open channel model is employed in the numerical experiment, and some examinations are carried out by changing the observation variables, number and position of observation points. In addition, numerical experiments using practical observed values are carried out.*

1 INTRODUCTION

In this study, the estimation of the flow field is carried out based on the finite element method and the Kalman filter theory in open channel. Figure 1 shows an example of open channel. As the governing equation, the shallow water equation is employed, and the finite element and the selective lumping methods are applied to discretize the governing equation in space and time, respectively. The estimation of the distribution of the velocity vector and the water elevation is carried out by using the discretized equation obtained by the Kalman filter theory. In the numerical experiments, the open channel flow is treated, and some examinations are carried out by changing the observation variables, number and position of observation points.

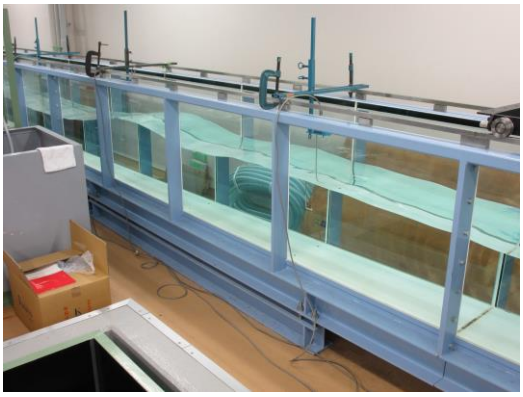

Figure 1: Open channel.

2 DISCRETIZATION OF GOVERNING EQUATIONS

The shallow water equations are used as a governing equations, which is represented as equation (1) and (2) in the two-dimensional plane.

$$\dot{u}_i + g\eta_{,i} = 0 \tag{1}$$

$$\dot{\eta} + hu_{,i} = 0 \tag{2}$$

where u, η, g, and h are flow velocity, water elevation, the gravitational acceleration and water depth. The Galerkin method and the selective lumping method are applied to discretize the governing equations in space and time, respectively. Consequently, the finite element equation can be written as equation (3). Equation (3) is represented by equation (4).

$$\begin{Bmatrix} \{u^{n+1}\} \\ \{v^{n+1}\} \\ \{\eta^{n+1}\} \end{Bmatrix} = \begin{bmatrix} [\overline{M}] & [0] & [0] \\ [0] & [\overline{M}] & [0] \\ [0] & [0] & [\overline{M}] \end{bmatrix}^{-1} \begin{bmatrix} [\tilde{M}] & [0] & -g\Delta t[S_x] \\ [0] & [\tilde{M}] & -g\Delta t[S_y] \\ -\overline{h}\Delta t[S_x] & -\overline{h}\Delta t[S_y] & [\tilde{M}] \end{bmatrix} \begin{Bmatrix} \{u^n\} \\ \{v^n\} \\ \{\eta^n\} \end{Bmatrix} \tag{3}$$

$$\{\hat{\phi}^{n+1}\} = [A]\{\hat{\phi}^n\} \tag{4}$$

where, Δt, $\overline{h}$, $[S_i]$, $[M]$ and $[\overline{M}]$ are time increment, mean water depth in the element, the matrix for the pressure, consistent mass matrix and diagonal mass matrix. $[\tilde{M}]$ is represented as equation (5) by ramping parameter $e(0 \le e \le 1)$. $\{\hat{\phi}\}$ indicates the true value.

$$\left[\tilde{M}\right] = (1-e)\left[\overline{M}\right] + e[M] \tag{5}$$

The system equation in the Kalman filter is obtained by adding the vector represented by the multiplication of the driving matrix $[\Gamma]$ and the system noise vector $\{q\}$, and is shown as Equation (6). Here, the vector $\{\phi\}$ indicates the estimation value in computation by the Kalman filter. In addition, the observation equation shown in Equation (7) is introduced. The vectors $\{z\}$ and $\{r\}$ and the matrix $[H]$ denote the observation value and the observation noise vectors and the observation matrix.

$$\left\{\phi^{n+1}\right\} = [A]\left\{\phi^{n}\right\} + [\Gamma]\left\{q^{n}\right\} \tag{6}$$

$$\left\{z^{n+1}\right\} = [H]\left\{\phi^{n+1}\right\} + \left\{r^{n+1}\right\} \tag{7}$$

3 COMPUTATIONAL ALGORITHM

It shows the numerical calculation algorithm by Kalman filter below.

1. Set input data : $[A]$, $\left[P_{(+)}^{0}\right]$, $\left\{\hat{\phi}_{(+)}^{0}\right\}$, $[\Gamma]$, $[Q]$, $[R]$, ε, $\left\{z^{n+1}\right\}$*(n = 0~imax)*
2. Calculation of estimated error covariance matrix: $\left[P_{(-)}\right] = [A]\left[P_{(+)}\right][A]^{T} + [\Gamma][Q][\Gamma]^{T}$
3. Calculation of Kalman gain matrix: $[K_1] = \left[P_{(-)}\right][H]^{T}\left([H]\left[P_{(+)}\right][H]^{T} + [R]\right)^{-1}$
4. Calculation of predicted error covariance matrix: $\left[P_{(+)}\right] = \left[P_{(-)}\right] - [K_1][H]\left[P_{(-)}\right]$
5. Check of convergence: if $\sqrt{tr\left(\left(\left[P_{(+)}^{k+1}\right] - \left[P_{(+)}^{k}\right]\right)\left(\left[P_{(+)}^{k+1}\right] - \left[P_{(+)}^{k}\right]\right)^{T}\right)} \le \varepsilon$ then go to 6, else go to 2.
6. Calculation of estimated value: $\left\{\hat{\phi}_{(-)}^{n+1}\right\} = [A]\left\{\hat{\phi}_{(+)}^{n}\right\}$
7. Calculation of optimal estimated value: $\left\{\hat{\phi}_{(+)}^{n+1}\right\} = \left\{\hat{\phi}_{(-)}^{n+1}\right\} + [K_1]\left(\left\{z^{n+1}\right\} - [H]\left\{\hat{\phi}_{(-)}^{n+1}\right\}\right)$

4 EXMINATION BY NUMERICAL EXPERIMENT

This examination is carried out by changing the observation variables, number and location of observation points. The computational conditions in this study is shown in Table 1. Computational model is shown in Figure 2.

Time increment Δt, s	0.001
Time steps	2000
Number of nodes	153
Number of elements	200
Gravitational acceleration g, m/s^2	9.8
Lumping parameter *e*	0.8
Initial of estimated error covariance $P_{(+)}^{0}$	1.0
Initial of estimated value $\hat{\phi}_{(+)}^{0}$	0
Convergence determination constant ε	0.01

Table 1: Computational conditions.

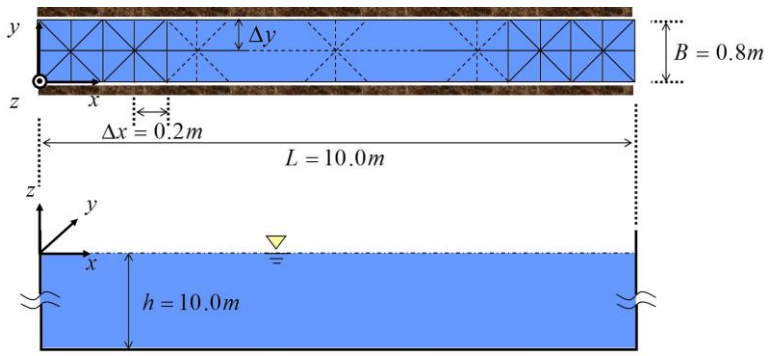

Figure 2: Computational model.

When the water elevation in amplitude 1.0m and period 2.0π s are given for the equation (5), the shallow water flow analysis is carried out. The results by this analysis are used as the artificial observation values. In this computation, the covariance for the system noise and observation noise is set 0.0001 and 0.1, respectively. The system noise covariance matrix $[Q]$ and observation noise covariance matrix $[R]$ are the diagonal matrix that diagonal component are 0.0001 and 0.100. In addition, case 'a' represents that observation variables are flow velocity for *x*-*y* direction u, v and water η and case 'b' of setting that observation variable is η only. These cases are distinguished by subscript 'a' or 'b', number of observation points and position of observation points are shown in Figure 3. Numerical results are shown in Figure 4 - 7.

	Observation variable	Position and number of observation points
Case1	Case 1a : x-y velocities and water elevation	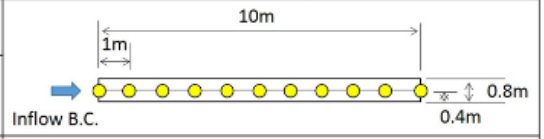
	Case 1b : only water elevation	
Case2	Case 2a : x-y velocities and water elevation	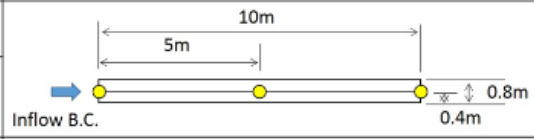
	Case 2b : only water elevation	
Case3	Case 3a : x-y velocities and water elevation	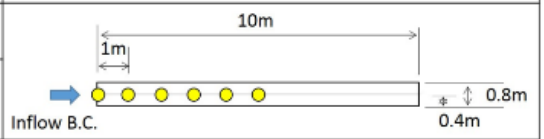
	Case 3b : only water elevation	
Case4	Case 4a : x-y velocities and water elevation	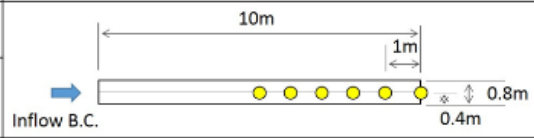
	Case 4b : only water elevation	
Case5	Case 5a : x-y velocities and water elevation	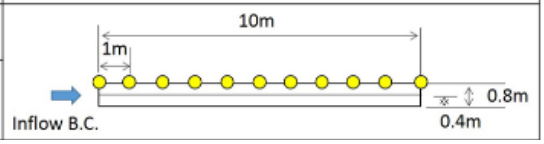
	Case 5b : only water elevation	

Figure 3: Numerical test conditions.

In Cases 1-4, the observation points are set on center line of the channel, and number and position of the observation points are changed. In Case 5, the observation points are set on one side of the wall boundary.

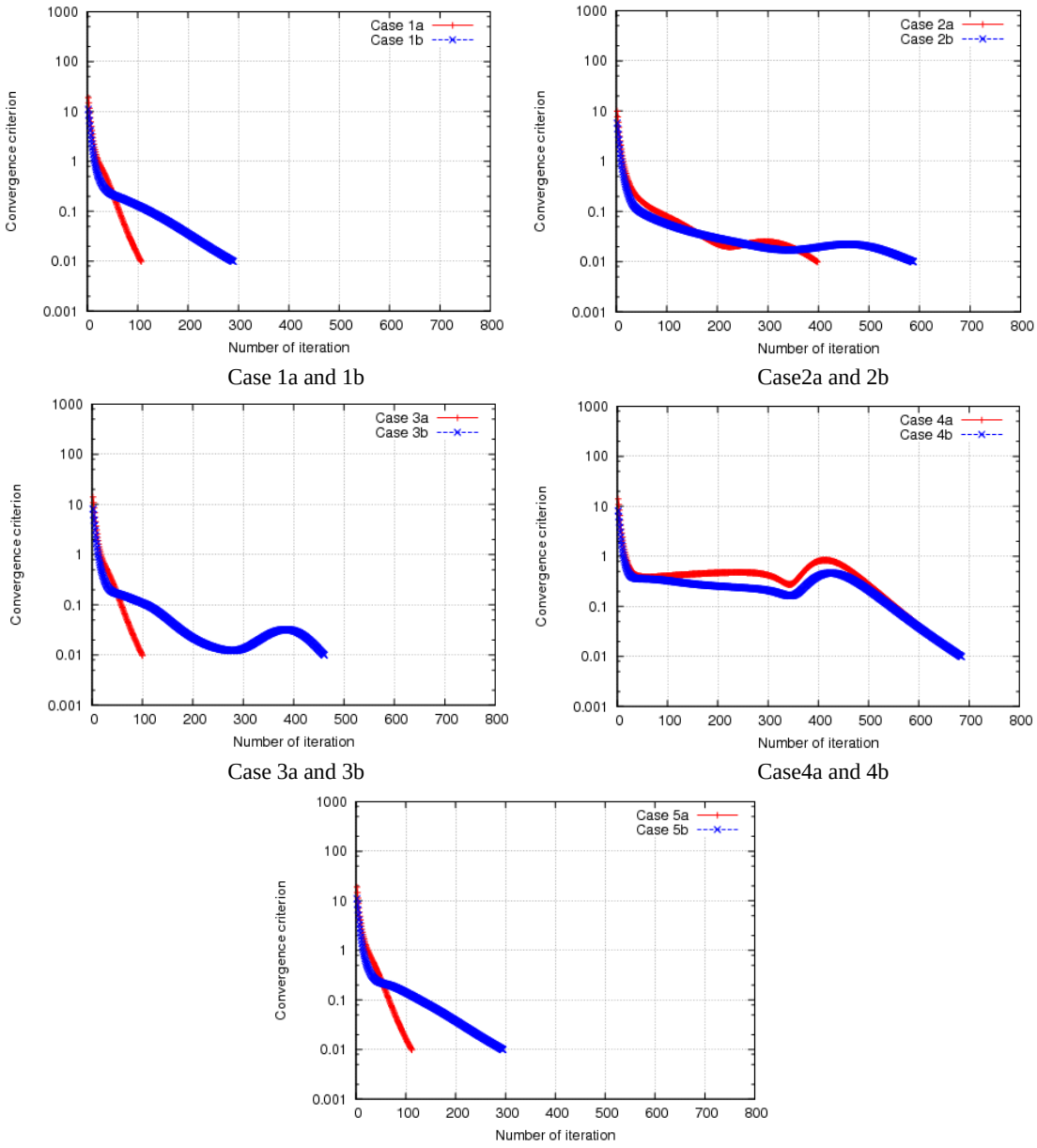

Figure 4: Comparison of variation of convergence criterion.

Figure 4 shows comparison of variation of convergence criterion expressed by the Frobenius norm. The equation of the Frobenius norm is shown in the flow chart of section 3.The convergence criterion ε is set 0.01. This convergence criterion follows to the reference by Heemink [3]. From this result, it was found that convergence rate in Case 'a' is faster than that in Case "b" in the iterative computation of the predicted error covariance matrix.

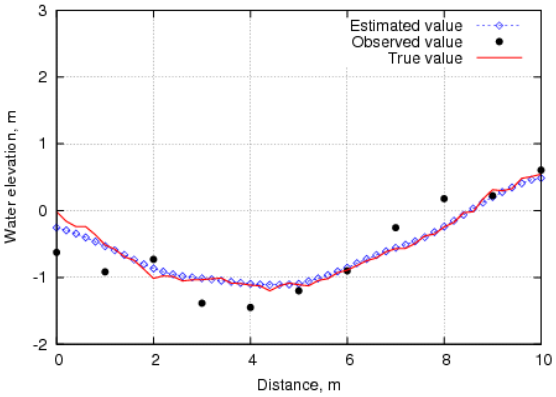

Case 1a

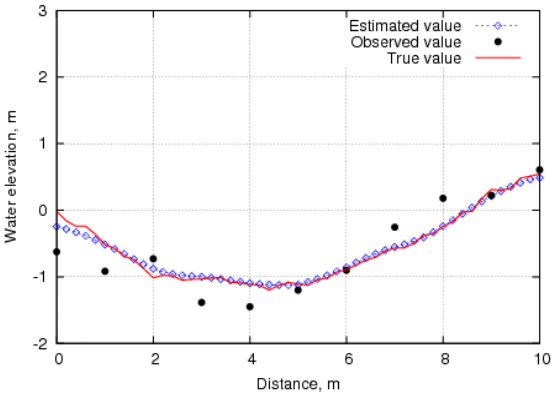

Case 1b

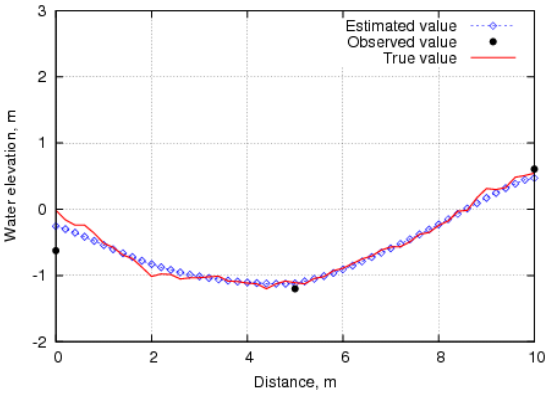

Case 2a

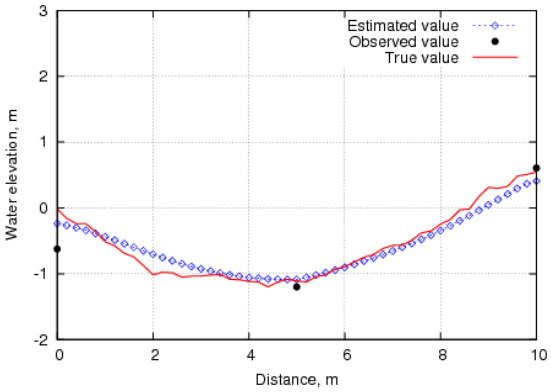

Case 2b

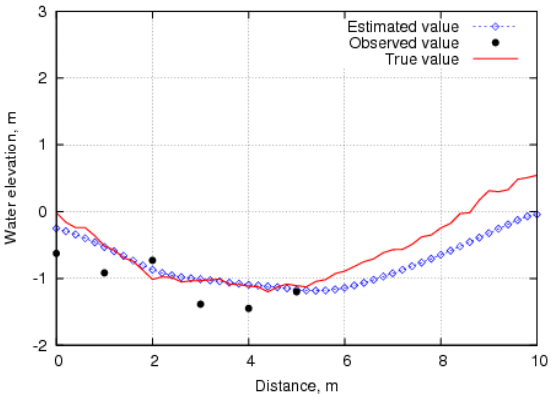

Case 3a

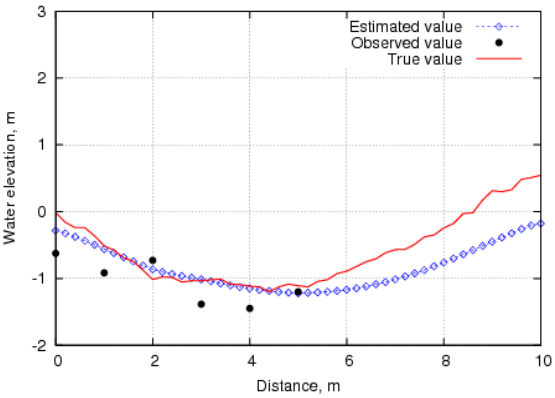

Case 3b

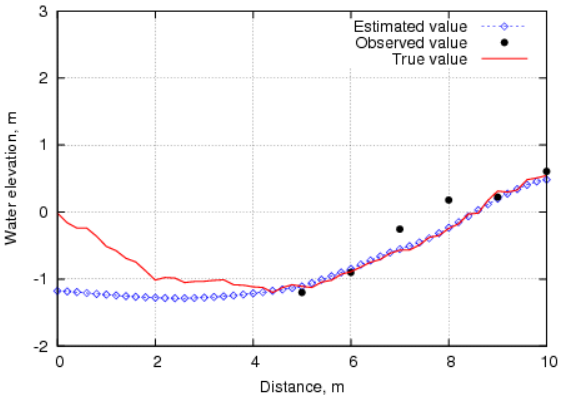

Case 4a

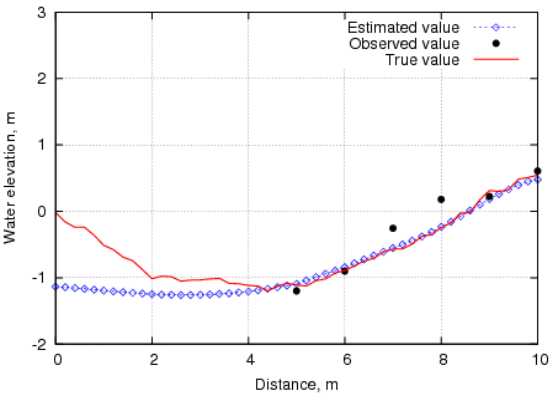

Case 4b

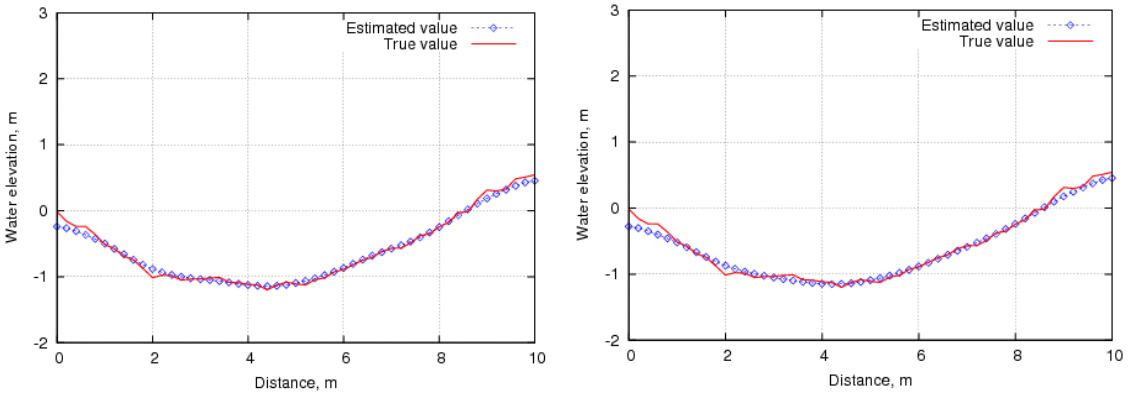

Case 5a Case 5b

Figure 5: Comparison of distribution of estimated water elevation at T =2.0s.

Figure 6 shows the distribution of estimated water elevation of the channel center line at T =2.0s. In Case 1 and Case 2, estimated values are good agreement with the true value. In Case 3, when the observation points are set on the inflow boundary side, the estimated value is good agreement with the true value in the outflow boundary side region, but, In Case 4, when the observation points are set on the outflow boundary side, it was found that it is difficult to estimate the distribution of the water elevation in inflow boundary side region. In Case 5, when the observation points are set on one side of the wall boundary, it was confirmed that the distribution of the water elevation is similar to that in Case 1.

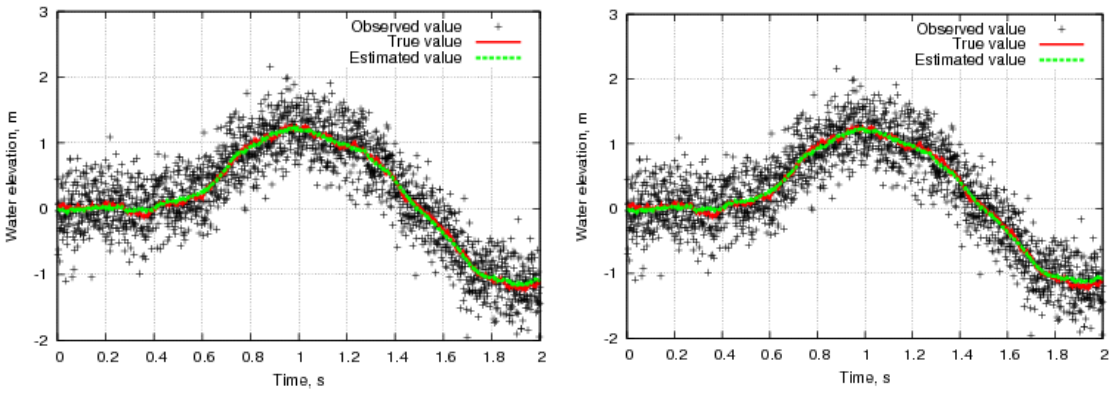

Case 1a Case 1b

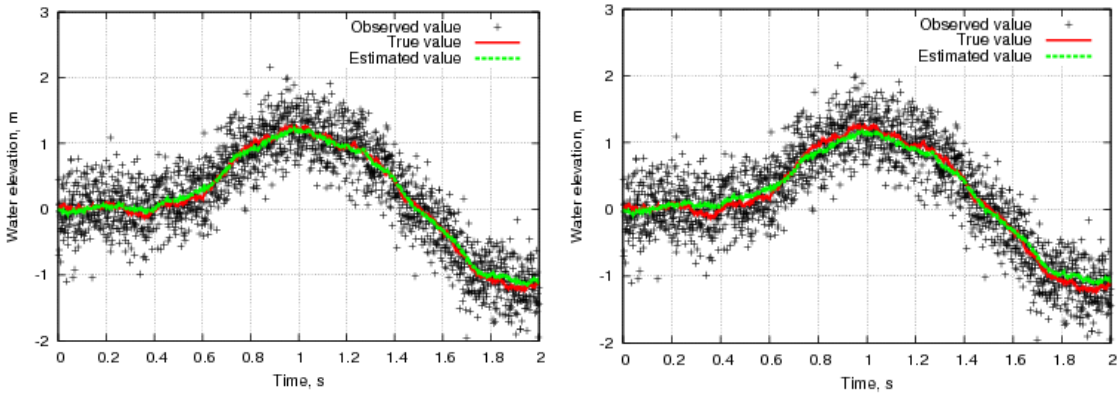

Case 2a Case 2b

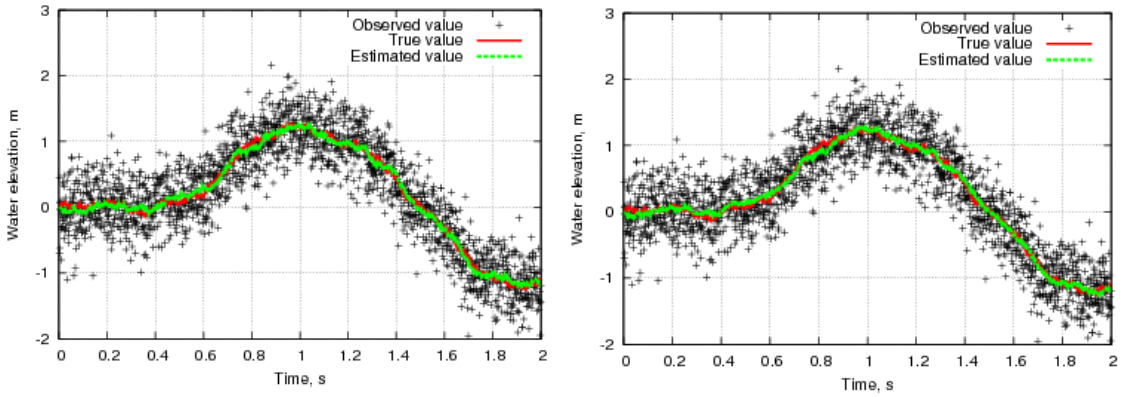

Case 3a Case 3b

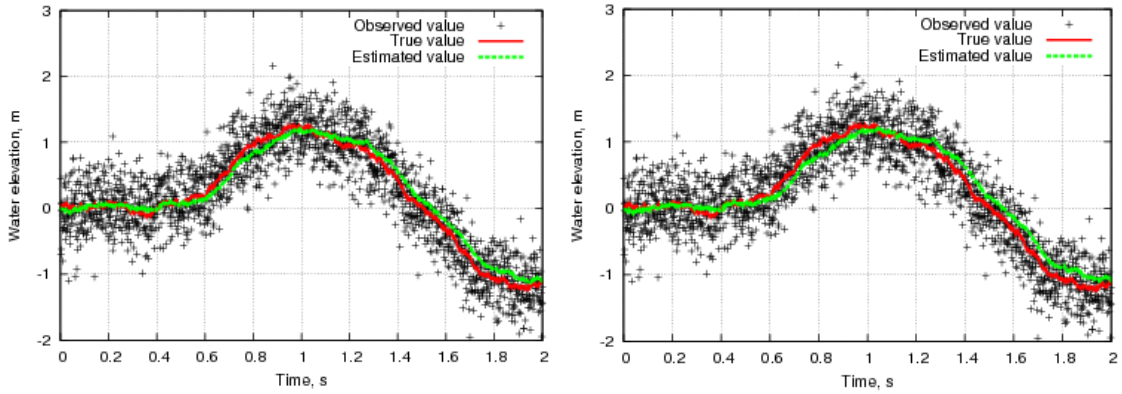

Case 4a Case 4b

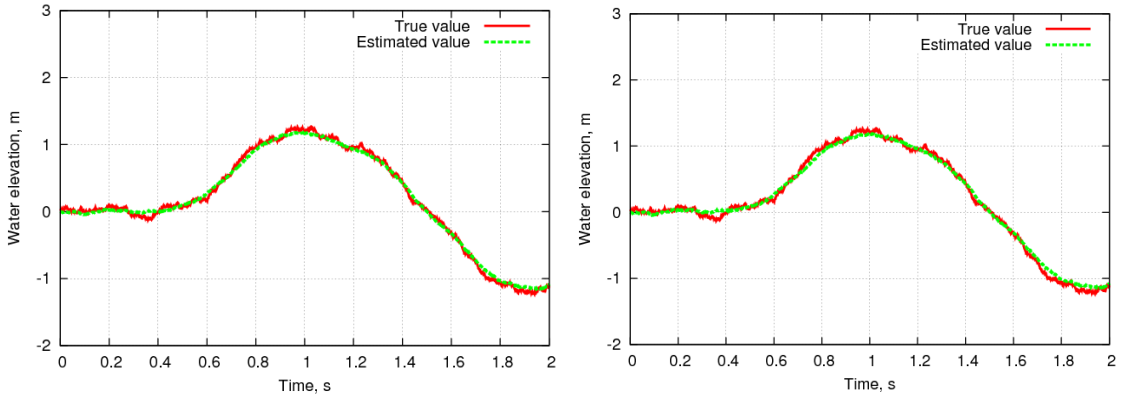

Case 5a Case 5b

Figure 7: Comparison of time history of estimated water elevation at center point of channel (x =5.0m, y =0.4m).

Figure 7 shows time history of estimated water elevation at center point of channel (x =5.0m, y =0.4m). In all cases, observation noise is removed from observed value, and estimated values are good agreement with the true value. Table 2 shows L^2 norm for difference of true and estimated values in Figure 7. In Case 3a and Case 3b, L^2 norm is approximately equivalent. In other cases, the value of L^2 norm in Case 'a' (the flow velocity for x and y directions and the water elevation are set as the observation variable) is less than that in Case 'b' (the water elevation is only set as the observation variable.). Therefore, it can be said that estimated values in Case 'a' are better agreement with the true value than estimated values in Case 'b'.

Case	L^2 norm for difference of true and estimated values
1a	1.899
1b	1.984
2a	2.339
2b	4.050
3a	2.531
3b	2.524
4a	4.161
4b	4.988
5a	2.126
5b	2.206

Table 2: Comparison of L^2 norm for difference of true and estimated values.

5 CONCLUSIONS

In this study, flow field estimation analysis in open channel was carried out based on the Kalman filter FEM. The linear shallow water equation is employed as the governing equation, the Galarkin and the selective lumping methods are used to discretize the governing equation in space and time, respectively. The conclusions in this study is shown as follows.

- It was seen that high accurate flow field estimation result is obtained in case that the observation points are set to the downstream side in the open channel in comparison with the case that the observation points are set to the upstream side in the open channel.
- It was found that if the flow velocities for x and y directions and the water elevation are set as the observation variable in the computation of the flow field estimation, high accurate estimation result is obtained comparing to the case that the water elevation is only set as the observation variable.

APPENDIX

An example of flow field estimation using the practical measurement water elevation is shown in the appendix. The position of observation points and the size of the channel is shown in Figure 8, and the finite element mesh is shown in Figure 9. In addition, Table 3 shows the computational conditions in the flow field estimation. The flow field estimation analysis is carried out using the observed data at only points No.1 and No.2. The comparison of the time history of water elevation in case of the observed and the estimated values at points No.1 – No.3 is shown in Figures 10-12. From this result, it is found that though the flow field estimation can be carried out, there is difference between the observed and the estimated water elevation at point No.3. Therefore, it can be said that there is a possibility that flow distribution can't be appropriately obtained, if a lot of observation points are not employed, and the period of the inflow wave is short. We suppose that this is one of the future work of this study.

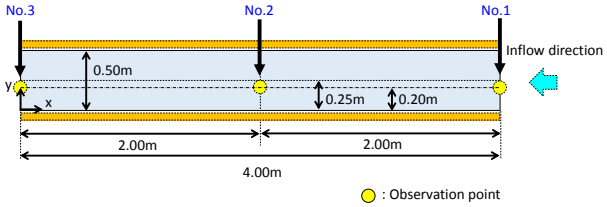

Figure 8: Size of target domain and location of observation points.

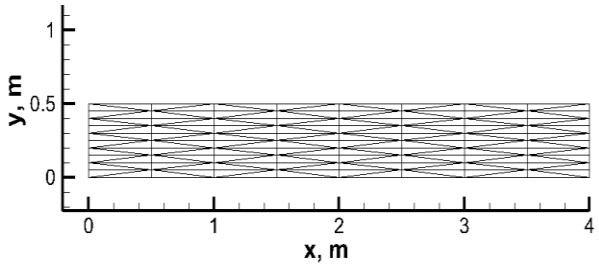

Figure 9: Finite element mesh.

Total number of nodes	99
Total number of elements	160
Time increment Δt , s	0.001
Number of time step	1000
Lumping parameter *e*	0.80
Gravitational acceleration g , m/s^2	9.8
Water depth h , m	0.46
Driving matrix $[\Gamma]$	Unit matrix
System error covariance matrix $[Q]$	$0.01\times$Unit matrix
Observation error covariance matrix $[R]$	$0.1\times$Unit matrix
Initial value of estimated error covariance matrix $[P_{(+)}^0]$	$1.0\times$Unit matrix
Initial value of state vector $\{\hat{\phi}_{(+)}^0\}$	Zero vector
Convergence criteria ε	10^{-4}

Table 3: Computational conditions.

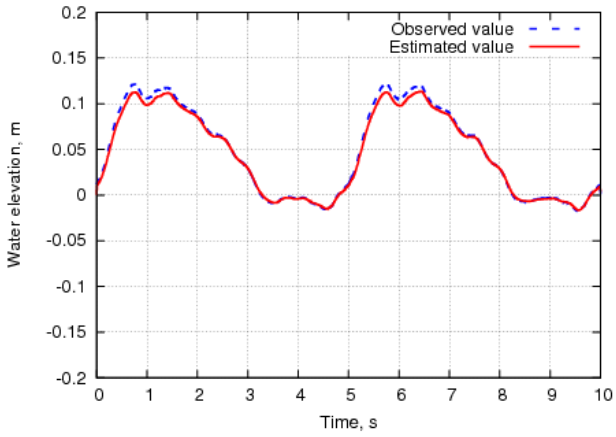

Figure 10: Comparison of water elevation at point No.1, $(x, y) = (4, 0.2)$.

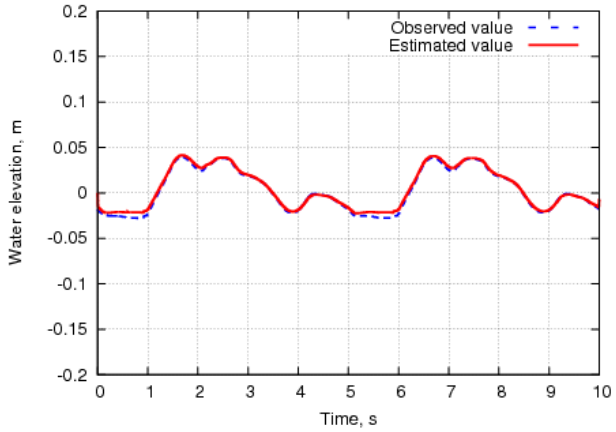

Figure 11: Comparison of water elevation at point No.2, $(x, y) = (2, 0.2)$.

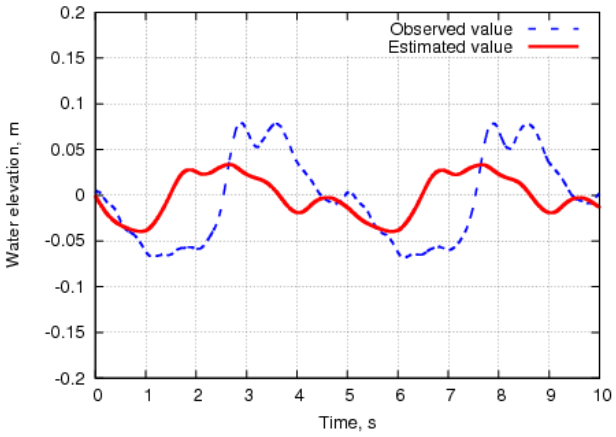

Figure 12: Comparison of water elevation at point No.3, $(x, y) = (0, 0.2)$.

ACKNOWLEDGEMENTS

This work was supported by Grants-in-Aid for scientific Research(C) Grant Number 15K05786.

REFERENCES

[1] R.E.Kalman, A New Approach to Linear Filtering and Prediction Problems, *Transactions of the ASME -Journal of Basic of Engineering*, Vol. 82，No. 1, (1960), pp.35-45.

[2] R.E.Kalman, R.S.Bucy, New Results in Linear Filtering and Prediction Theory, *Transactions of the ASME -Journal of Basic of Engineering*, Vol. 83，No. 1, (1961), pp.95-108.

[3] Heemink, A. W., Two-dimensional Shallow Water Flow Identification, Applied Mathematical Modelling, Vol. 12(1988), pp.109-118.

[4] Toshimitsu Takagi, Kosuke Inamoto, Yutaka Hayakawa, Mutsuto Kawahara, Flow estimation of shallow water by the Kalman filter finite element method, Coastal engineering proceedings，Vol. 43，(1996), pp.346-350.

ECCOMAS Congress 2016
VII European Congress on Computational Methods in Applied Sciences and Engineering
M. Papadrakakis, V. Papadopoulos, G. Stefanou, V. Plevris (eds.)
Crete Island, Greece, 5–10 June 2016

STOCHASTIC TECHNIQUES FOR THE NUMERICAL SOLUTION OF ENGINEERING BOUNDARY VALUE PROBLEMS.

V. Maceiras and M. Casteleiro

Group of Numerical Methods in Engineering
E.T.S. de Ingenieros de Caminos, Canales y Puertos
Universitity of Coruña, Spain
e-mail: victormaceiras@hotmail.com, casteleiro@udc.es

Keywords: Stochastic analysis, PDE solutions, Random walk, Itô's theorem.

Abstract. *This paper describes a family of stochastic methods based on Itô's theorem for the numerical solution of Dirichlet, Neumann and mixed boundary value problems. The major advantages of these techniques are:*

- *No mesh is needed. Only the geometry of the domain and the boundary conditions should be defined.*
- *The solution can be obtained at any point or at any part of the integration domain. It is not necessary to solve the whole domain, which can be of special interest in 3D applications.*
- *The error threshold can be controlled mainly with the step width of the random walk generation*
- *The algorithms can be easily parallelized.*
- *The same approach could be used to the numerical solution of stochastic partial differential equations.*

The theoretical approach is described, the corresponding algorithms are presented, and the general technique is applied to well-known engineering PDE equations of the elliptic and parabolic type.

1 INTRODUCTION

From the origin of calculus in the 17th century by Isaac Newton and Gottfried Leibniz partial differential equations have been used to generate mathematical models of natural, economic and social phenomena. In general, these equations cannot be solved by analytical methods and, from the beginning of the 20th century, different approaches generating several discretization approximations have been developed (i.e. Ritz methods [1]). Since then a number of numerical methods, as Finite Differences, Finite Element Method, Boundary Element Method, Finite Calculus Techniques and many others have proved to give accurate results for quite difficult problems, both linear and nonlinear, in one, two and three dimensions.

In general, all these techniques imply some type of domain decomposition or discretization, and the solution of the problem must be obtained in the whole integration domain. As a consequence of the discretization, a set of algebraic equations (linear or nonlinear) must be solved.

A different approach to the solution of PDE's is presented in this paper. Probabilistic methods that have been developed from 1940 [2] may be used to solve both deterministic and stochastic differential equation by means of simulation techniques.

One of these possible techniques, based in Brownian motion particle simulation will be shown to be applied to elliptic and parabolic partial differential equations.

The advantages of this technique are:

- No mesh is needed. Only the geometry of the domain and the boundary conditions should be defined. This implies that the time-consuming discretization process in unnecessary.
- As it is not necessary to get the solution at every point of the domain, no system of equations must be solved.
- The solution can be obtained at any point or at any part of the integration domain. It is not necessary to determine the solution at the whole domain, and therefore there is not system of equations to solve, which can be of special interest in 3D and nonlinear problems.
- The error threshold can be controlled mainly with the step width of the random walk generation
- The algorithms can be easily parallelized.
- The same approach could be used to the numerical solution of stochastic partial differential equations [3].

In this paper the general technique for elliptic and parabolic differential equations will be presented, and will be applied to benchmark problems whose analytical solution is known.

2 PREVIOUS DEFINITIONS

2.1 Wiener processes.

A real stochastic process $\{W_t, t \geq 0\}$ is called a Wiener process if all the following requirements are accomplished:

- $W_0 = 0$
- $W_t - W_s$ is a random normal variable $N(0, t-s)$ for every t and s such that $t > s \geq 0$
- For every set of arguments $0 < t_1 < t_2 < \cdots < t_n$, the set of random variables $W_{t_1}, W_{t_{12}} - W_{t_1}, \ldots . W_{t_n} - W_{t_{-1}}$ are independent.
- W_t has continuous paths for every t > 0.

2.2 Martigales

Consider a sequences of random variables $Z_1, Z_2 \ldots\ldots Z_n$ and the conditional expected value $E[Z_{n+1}|Z_1, Z_2 \ldots\ldots Z_n]$ for each n. The conditional expected value is the mean of Z_{n+1} if all values $Z_1, Z_2 \ldots\ldots Z_n$ are known. If $E[Z_{n+1}|Z_1, Z_2 \ldots\ldots Z_n] = Z_n$ the sequence, $Z_2 \ldots\ldots Z_n$ is a martingale.

The Wiener process is a Markov process as well as a martingale.

2.3 Itô's process

The stochastic process

$$dX = b(X(t), t)dt + \sigma(X(t), t)dB \tag{1}$$

in which dB is a standard Brownian motion (BM), is called an Itô's process and $b(X(t), t)$ and $\sigma(X(t), t)$ are functions both of time and the stochastic process $X(t)$. [4, 5]

2.4 Standard Brownian motion

A standard Brownian motion $B(t)$ is a Wiener process such that:

- $E[B(t)] = 0$
- $\Delta B = B(t + \Delta t) - B(t)$ has a probability distribution $N(0, s^2)$

Therefore $Var(\Delta B) = \Delta t = E(\Delta B^2) - \big(E(\Delta B)\big)^2 = E(\Delta B^2)$ and as the variance of ΔB is small it can be assumed that $\Delta t \approx \Delta B^2$. [6, 7]

2.5 Stochastic ordinary differential equations

An ordinary differential equation is only a rule which determines the change of a dependent variable which is a function of an independent variable expressed in terms of the function and its derivatives.

$$\boldsymbol{\frac{dX}{dt} = a(t, X)} \tag{2}$$

If non deterministic parameters appear in the differential system, the equation becomes a stochastic differential equation

$$\frac{dX}{dt} = a(t, X, Y) \tag{3}$$

where $Y(t)$ represents a stochastic process. It is obvious that in this case $X(t)$ is also a stochastic process and the solution will be the given by the probability distribution of $X(t)$.

2.6 Itô's integral

If one cannot integrate $a(t, X, Y)$ the stochastic ordinary differential equation can be rewritten as

$$\frac{dX}{dt} = b(X, t) + \sigma(X, t)\frac{dB(t)}{dt} \tag{4}$$

where $dB(t)$ is a standard brownian motion. The integral of the above equation is

$$X(t) = X_0 + \int_{t_0}^{t} b\big(s, X(s)\big)\, ds + \int_{t_0}^{t} \sigma\big(s, X(s)\big) dB(t) \tag{5}$$

This second integral $\int_{t_0}^{t} b\big(s, X(s)\big) dB(t)$ cannot be univocally defined, because W(s) variations are unbounded, given that $\sup \sum_{k=1}^{n-1} \left|B_{t_{k+1}} - B_{t_k}\right| = \infty$. The most correct definition

from a mathematical point of view was established by Itô in the forties and was the origin of the so called stochastic analysis [4, 5, 8, 9].

The most important property of Itô's integral is $E\left(\int_0^T GdB\right) = 0$ [10, 11].

2.7 Itô's formula

Let $u = u(t, \bar{x})$ be a continuous function defined over $[t_0, T] \times \mathbb{R}^d$ taking values in $\mathbb{R}^d$ and with continuous partial derivatives. We will use the following notation:

$$\begin{aligned} \frac{\partial}{\partial t}u(t,\bar{x}) &= u_t(t,\bar{x}) \\ \frac{\partial}{\partial x}u(t,\bar{x}) &= u_x(t,\bar{x}) \\ \frac{\partial^2}{\partial x^2}u(t,\bar{x}) &= u_{x^2}(t,\bar{x}) \end{aligned} \tag{6}$$

For $i, j = 1 \ldots . d$ let $\{X, t_0 \leq t \leq \mathrm{T}\}$ be a stochastic process in $\mathbb{R}^d$. This process is defined by the following stochastic differential (Itô's process)

$$dX = b(X(t), t)dt + \sigma(X(t), t)dB \tag{7}$$

where dB is a standard Brownian motion. Then, the process defined by

$$Y(t) = u\big(t, X(t)\big), \forall t \in [t_0, \mathrm{T}] \tag{8}$$

can be differentiated with respect the same Brownian motion

$$\begin{aligned} dY &= u_t(t, X_t)dt + u_x(t, X_t)dX + \frac{1}{2}u_{x^2}(t, X_t)\sigma^2 dt = \\ &= \left(u_t(t, X_t) + u_x(t, X_t)b(X(t), t) + \frac{1}{2}u_{x^2}(t, X_t)\sigma^2\right)dt + u_x(t, X_t)\,\sigma(X(t), t)dB \end{aligned} \tag{9}$$

To prove this result we apply Taylor's expansion to *u*,

$$du = \frac{\partial u}{\partial X}\Delta X + \frac{\partial u}{\partial t}\Delta t + \frac{1}{2}\frac{\partial^2 u}{\partial X^2}\Delta X^2 + \cdots \tag{10}$$

Itô's process can be rewritten as:

$$\begin{aligned} dX &= b(X(t), t)dt + \sigma(X(t), t)\sqrt{dt} \\ (dX)^2 &= (b(X(t), t))^2 dt^2 + (\sigma(X(t), t))^2 dt + 2b(X(t), t)dt\sigma(X(t), t)\sqrt{dt} \\ (dX)^2 &= (\sigma(X(t), t))^2 dt \end{aligned} \tag{11}$$

By replacing dX y $(dX)^2$ in the above Taylor expansion expression

$$\begin{aligned} du &= \frac{\partial u}{\partial X}(b(X(t), t)dt + \sigma(X(t), t)dB) + \frac{\partial u}{\partial t}\Delta t + \frac{1}{2}\frac{\partial^2 u}{\partial X^2}(\sigma(X(t), t))^2 dt \\ du &= \frac{\partial u}{\partial X}\sigma(X(t), t)dB + dt\left(b(X(t), t)\frac{\partial u}{\partial X} + \frac{\partial u}{\partial t} + \frac{1}{2}\frac{\partial^2 u}{\partial X^2}(\sigma(X(t), t))^2\right) \end{aligned} \tag{12}$$

Which is known as Itô's formula.

3 ELLIPTIC PROBLEM GENERAL APPROACH

Let be the following elliptic partial differential equation in one spatial dimension

$$\mathrm{L}u = -f(x) \tag{13}$$

with Dirichlet boundary condition

$$u(x) = g(x)\ si\ x \in \partial D \tag{14}$$

being ∂D the boundary of the integration domain D and L(.)

$$\mathrm{L}(.) = \sum b_i \frac{\partial(.)}{\partial x_i} + \frac{1}{2}\sum\sum \sigma_{ij} \frac{\partial^2}{\partial x_i \partial x_j} \tag{15}$$

that will be applied to a function $u(t, X(t))$. The *du* differential can be written as

$$du = \frac{\partial u}{\partial X}\sigma(X(t), t)dB + dt\left(b(X(t), t)\frac{\partial u}{\partial X} + \frac{\partial u}{\partial t} + \frac{1}{2}\frac{\partial^2 u}{\partial X^2}\big(\sigma(X(t), t)\big)^2\right) \tag{16}$$

As the problem is steady state by definition

$$\frac{\partial u}{\partial t} = 0 \tag{17}$$

and therefore

$$du = \frac{\partial u}{\partial X}\sigma(X(t), t)dB + dt(L(u)) \tag{18}$$

or

$$du = \frac{\partial u}{\partial X}\sigma(X(t), t)dB - \big(f(x)\big)dt \tag{19}$$

This equation can be integrated as

$$\int_0^{\tau_x} du = \int_0^{\tau_x} \frac{\partial u}{\partial X}\sigma(X(t), t)dB - \int_0^{\tau_x} \big(f(x)\big)dt \tag{20}$$

being τ_x the so called stopping time, which is defined as the shortest time in which the stochastic process X reaches the boundary ∂D,

$$\tau_x = \inf\left(\frac{t}{X} \in \partial D\right) \tag{21}$$

and consequently

$$u(X^{\tau_x}) - u(X^0) = \int_0^{\tau_x} \frac{\partial u}{\partial X}\sigma(X(t), t)dB - \int_0^{\tau_x} \big(f(x)\big)dt \tag{22}$$

The expected value of these expressions is

$$E\big(u(X^{\tau_x})\big) - E\big(u(X^0)\big) = E\left(\int_0^{\tau_x} \frac{\partial u}{\partial X}\sigma(X(t), t)dB\right) - E\left(\int_0^{\tau_x} \big(f(x)\big)dt\right) \tag{23}$$

As we have defined the stopping time τ_x as the shortest time in which the stochastic process X reaches the boundary ∂D, if $u(X^0)$ is the value of $u(x)$ to obtain inside the integration domain,

$$E\big(g(X^{\tau_x})\big) - u(x) = E\left(\int_0^{\tau_x} \frac{\partial u}{\partial X}\sigma(X(t), t)dB\right) - E\left(\int_0^{\tau_x} \big(f(x)\big)dt\right) \tag{24}$$

where $g(X^{\tau_x})$ is the boundary condition at the point in which the stochastic process X reaches the boundary ∂D. Remember that dB is a martingale and one of its properties is $E\left(\int_0^T GdB\right) = 0$.

Therefore

$$E\big(g(X^{\tau_x})\big) - u(x) = 0 - E\left(\int_0^{\tau_x} \big(f(x)\big)dt\right) \tag{25}$$

and the Itô's formula becomes

$$u(x) = E\big(g(X^{\tau_x})\big) + E\left(\int_0^{\tau_x} (f(x))dt\right) \tag{26}$$

3.1 Problem solution in several variables

In the case of more than one variable the elliptic problem can be stated as

$$\begin{gathered} \mathrm{L}u = -f(\bar{x}) \\ u(\bar{x}) = g(\bar{x})\ si\ \bar{x} \in \partial D \\ \mathrm{L}(.) = \sum b_i \frac{\partial(.)}{\partial x_i} + \frac{1}{2}\sum\sum \sigma_{ij} \frac{\partial^2}{\partial x_i \partial x_j} \end{gathered} \tag{27}$$

The corresponding stochastic process could be written as

$$d\bar{X} = \bar{b}(\bar{x}))dt + \bar{\bar{Z}}(\bar{x}))d\bar{B} \tag{28}$$

where b_i are the components of vector $\bar{b}(\bar{x}))$.

The matrix $\bar{\bar{Z}}(x)$ is defined as follows [12]

$$\bar{\bar{C}} = \bar{\bar{Z}} * \bar{\bar{Z}}^T \tag{29}$$

where σ_{ij} are the components of the $\bar{\bar{C}}$ matrix. This matrix $\bar{\bar{Z}}$ can be easily determined if $\bar{\bar{C}}$ is symmetric, by using, for example, the Cholesky factorization technique.

The b_i and σ_{ij} components are the parameters of the differential operator $\mathrm{L}(.)$.

3.2 Problems with Neumann boundary conditions

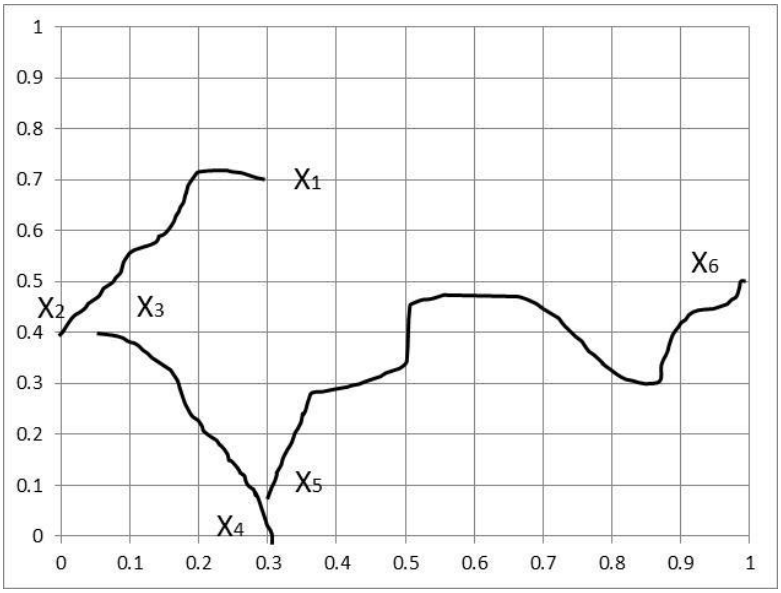

Figure 1 Particle random walk

It must be noted that every particle follows a random walk determined by the Itô's stochastic process (Figure 1).

But in this case there are some Neumann boundary conditions. We describe now the procedure to take into account these boundaries. [13].

In a general case with Neumann boundary conditions and at least a Dirichlet boundary condition the procedure will be as follows:

$$\begin{gathered} \mathrm{L}u = -f(\bar{x}) \\ u(\bar{x}) = g(\bar{x})\ si\ \bar{x} \in \partial D_d \\ \frac{\partial\big(u(\bar{x})\big)}{\partial n} = c(\bar{x})\ si\ \bar{x} \in \partial D_n \end{gathered} \tag{30}$$

where ∂D_d are the boundaries in which Dirichlet conditions hold and $\partial \mathrm{D_n}$ the boundaries in which Neumann conditions are defined.

One should determine X_1 when the particle reaches a Neumann boundary before getting to a Dirichlet boundary.

$$u(X_5) = E\big(g(X^{\tau_x})\big) + E\left(\int_0^{\tau_x}(f(x))dt\right) = E\big(g(X_6)\big) + E\left(\int_{\tau_{X_5}}^{\tau_{X_6}}(f(x))dt\right) \tag{31}$$

The integration limits $[\tau_{X_5}, \tau_{X_6}]$ correspond to the time the particle takes to move from X_5 to X_6

If the coordinates X_4 correspond to a point located in a boundary with Neumann condition, the value $u(X_4)$ may be determined by Taylor expansion as

$$u(X_4) = u(X_5) - \frac{\partial u}{\partial y}(X_4)h_y = u\ (X_5) - c(X_4)h_y \tag{32}$$

In this way, the Neumann condition in X_4 is transformed to a Dirichlet condition and therefore:

$$\begin{gathered} u(X_3) = E\big(g(X^{\tau_x})\big) + E\left(\int_0^{\tau_x}\big(f(x)\big)dt\right) = E\big(u(X_4)\big) + E\left(\int_{\tau_{X_4}}^{\tau_{X_5}}\big(f(x)\big)dt\right) = \\ = E\big(u(X_5)\big) - E\big(c(X_4)h_y\big) + E\left(\int_{\tau_{X_4}}^{\tau_{X_5}}\big(f(x)\big)dt\right) = \\ = E\big(g(X_6)\big) + E\left(\int_{\tau_{X_3}}^{\tau_{X_4}}\big(f(x)\big)dt\right) + E\left(\int_{\tau_{X_5}}^{\tau_{X_6}}(f(x))dt\right) - E\big(c(X_4)h_y\big) \end{gathered} \tag{33}$$

If this procedure is repeated with X_2 the solution at point X_1can be written

$$\begin{gathered} u(X_1) = E\big(g(X^{\tau_x})\big) + E\left(\int_0^{\tau_x}(f(x))dt\right) = E\big(u(X_2)\big) + E\left(\int_{\tau_{X_1}}^{\tau_{X_2}}(f(x))dt\right) = \\ = E\big(u(X_3)\big) - E(c(X_3)h_x) + E\left(\int_{\tau_{X_1}}^{\tau_{X_2}}(f(x))dt\right) = \\ = E\big(g(X_6)\big) + E\left(\int_{\tau_{X_1}}^{\tau_{X_2}}(f(x))dt\right) + E\left(\int_{\tau_{X_3}}^{\tau_{X_4}}\big(f(x)\big)dt\right) \\ +E\left(\int_{\tau_{X_5}}^{\tau_{X_6}}(f(x))dt\right) - E\big(c(X_4)h_y\big)\ - E(c(X_3)h_x) \end{gathered} \tag{34}$$

In a general case Itô's formula can be written as

$$u(\bar{x}) = E\big(g(X^{\tau_x})\big) + E\left(\int_0^{\tau_x}(f(x))dt\right) + E\left(-\sum_i \frac{\partial u}{\partial n}(X_i)h_n\right) \tag{35}$$

where

$E\big(g(X^{\tau_x})\big)$ is the contribution of Dirichlet boundary conditions

$E\big(\int_0^{\tau_x}(f(x))dt\big)$ is the contribution of the input function

$E\left(-\sum_i \frac{\partial u}{\partial n}(X_i)h_n\right)$ is the contribution of Neumann boundary conditions

In these expressions X_i are the points where the particle reaches a Dirichlet boundary and h_n is a small value such that Taylor's expansions are accurate enough.

It is clear that for a unique simulation Neumann boundaries can be reached several times.

To explain more clearly the general technique we propose the following academic example.

$$\frac{\partial^2 u}{\partial x^2} + 3\frac{\partial^2 u}{\partial y^2} = -16 \tag{36}$$

with a rectangular boundary $D = (0,1)x(0,1)$ and mixed boundary conditions.

$$\begin{aligned} &\frac{\partial u}{\partial x} = \beta(y) \quad x = 0 \\ &u = 0 \qquad\quad x = 1 \\ &\\ &\frac{\partial u}{\partial y} = \alpha(x) \quad y = 0 \\ &u = \gamma(x) \qquad y = 1 \end{aligned} \tag{37}$$

Itô's process is in this case:

$$d\bar{X} = \bar{b}(x)dt + \bar{\bar{Z}}(x)d\bar{B} \tag{38}$$

with $b_i = 0,\ \sigma_{11} = 2,\ \sigma_{12} = 0,\ \sigma_{21} = 0,\ \sigma_{22} = 6.$:

To determine the $\bar{\bar{Z}}$ matrix we use $\bar{\bar{C}} = \bar{\bar{Z}} * \bar{\bar{Z}}^T$, this is to say

$$\begin{pmatrix} 2 & 0 \\ 0 & 6 \end{pmatrix} = \begin{pmatrix} z_{11} & z_{12} \\ z_{21} & z_{22} \end{pmatrix}\begin{pmatrix} z_{11} & z_{12} \\ z_{21} & z_{22} \end{pmatrix}^T \tag{39}$$

and therefore

$$\bar{\bar{Z}} = \begin{pmatrix} \sqrt{2} & 0 \\ 0 & \sqrt{6} \end{pmatrix} \tag{40}$$

If we apply now Itô`s formula, the solution at point (x, y) is

$$u(\bar{x}) = E\big(g(X^{\tau_x})\big) + E\left(\int_0^{\tau_x}(f(x))dt\right) \tag{41}$$

In this example:

$$\begin{aligned} u(\bar{x}) = E\big(g(X^{\tau_x})\big) + E\left(\int_0^{\tau_x} 16\, dt\right) = E\big(g(X^{\tau_x})\big) + 16E\left(\int_0^{\tau_x} dt\right) = \\ = E\big(g(X^{\tau_x})\big) + 16E\,(T_x) \end{aligned} \tag{42}$$

where:

- $E\left(g(X^{\tau_x})\right)$ is the expected value of the particles positions when they reach for the first time a Dirichlet boundary condition.
- $E\ (T_x)$ is the expected value of the time the particles take to reach for the first time a Dirichlet boundary condition. In other words, the expected value of the particles stopping times.

Let a particle initially at position X_1 (see Figure 1). After a random walk as previously described the particle reaches the boundary at X_2 where a Neumann condition holds. Then the particle is reflected to X_3, and the process will be restarted at point $X_3 = X_2 + (h_x, 0)$. After the corresponding walk, the particle reaches the boundary at X_4 where again a Neumann condition holds. The particle is then reflected to $X_5 = X_4 + (0, h_y)$ and the process continues until the particle reaches a point in which a Dirichlet boundary condition holds (X_6). Then the process stops.

Let:

T_1 the time it takes the particle to go from X_1 to X_2
T_2 the time it takes the particle to go from X_3 to X_4
T_3 the time it takes the particle to go from X_5 to X_6

By using Itô's formula, the contribution of this particle to the solution is

$$u(X_1) = g(X_2) + 16(T_1) = u(X_2) + 16(T_1) \tag{43}$$

In this expression $u(X_2)$ can be expanded as $u(X_2) = u(X_3) - \frac{\partial u}{\partial x}(X_2)h_x$ and therefore

$$u = u(X_2) + 16(T_1) = u(X_3) - \frac{\partial u}{\partial x}(X_2)h_x + 16(T_1) \tag{44}$$

but

$$u(X_3) = g(X_4) + 16(T_2) = u(X_4) + 16(T_2) \tag{45}$$

and again

$$u(X_4) = u(X_5) - \frac{\partial u}{\partial y}(X_4)h_y \tag{46}$$

and the above expression (44) becomes

$$u = u(X_3) - \frac{\partial u}{\partial x}(X_2)h_x + 16(T_1) = u(X_5) - \frac{\partial u}{\partial y}(X_4)h_y - \frac{\partial u}{\partial x}(X_2)h_x + 16(T_1 + T_2) \tag{47}$$

Finally, as X_6 is a point in which a Dirichlet condition is stablished

$$u(X_5) = g(X_6) + 16(T_3) = 0 + 16(T_3) \tag{48}$$

and the contribution of this particles to the final solution is

$$u = 0 - \frac{\partial u}{\partial y}(X_4)h_y - \frac{\partial u}{\partial x}(X_2)h_x + 16(T_1 + T_2 + T_3) \tag{49}$$

3.3 Simulation procedures

The partial differential equation to solve is:

$$\mathrm{L}u = -f(x) \tag{50}$$

with the following boundary conditions:

$$u(x) = g(x)\ si\ x \in \partial D_d$$
$$\frac{\partial u(x)}{\partial n} = t(x)\ si\ x \in \partial D_n \tag{51}$$

with $\partial D_d \cup \partial D_n = \partial D$ and $D_d \cap \partial D_n = \emptyset$, being ∂D the boundary of the integration domain D and

$$\mathrm{L}(.) = \sum b_i \frac{\partial(.)}{\partial x_i} + \frac{1}{2}\sum\sum \sigma_{ij} \frac{\partial^2(.)}{\partial x_i \partial x_j} \tag{52}$$

As previously stated the solution is

$$u(\bar{x}) = E\big(g(X^{\tau_x})\big) + E\Big(\int_0^{\tau_x}(f(x))dt\Big) + E\left(-\sum_i \frac{\partial u}{\partial n}(X_i)h_n\right) \tag{53}$$

Then the simulation procedure is as follows:

3.3.1 Determine the Ito's process b_i y σ_{ij} coefficients:

$$d\bar{X} = \bar{b}(x)dt + \bar{\bar{Z}}(x)d\bar{B}$$
$$\begin{pmatrix} dx_1 \\ \vdots \\ dx_n \end{pmatrix} = \begin{pmatrix} b_1 \\ \vdots \\ b_n \end{pmatrix} dt + \begin{pmatrix} Z_{11} & \dots & Z_{1n} \\ \vdots & \ddots & \vdots \\ Z_{n1} & \dots & Z_{nn} \end{pmatrix} \begin{pmatrix} dB_1 \\ \vdots \\ dB_n \end{pmatrix} \tag{54}$$

$\bar{\bar{Z}}(x)$ is defined as the matrix calculated from the equation

$$\bar{\bar{C}} = \bar{\bar{Z}} * \bar{\bar{Z}}^T \tag{55}$$

where the parameters σ_{ij} are the elements of the $\bar{\bar{C}}$ matrix and the parameters b_i are the elements of the $\bar{b}(x)$ vector.

3.3.2 Set the s and h values, where s^2 is the variance of the Brownian motion process and h the increment to use in the Taylor series expansions.

The Brownian motion variance will determine the length of every leap of a particle for every time step.

The following figures show some examples of a Brownian motion process going on from the same point (x=0.6, y=2.7) with Dirichlet boundary condition at x=0 and Neumann condition at the reflecting border (Figures 2 and 3).

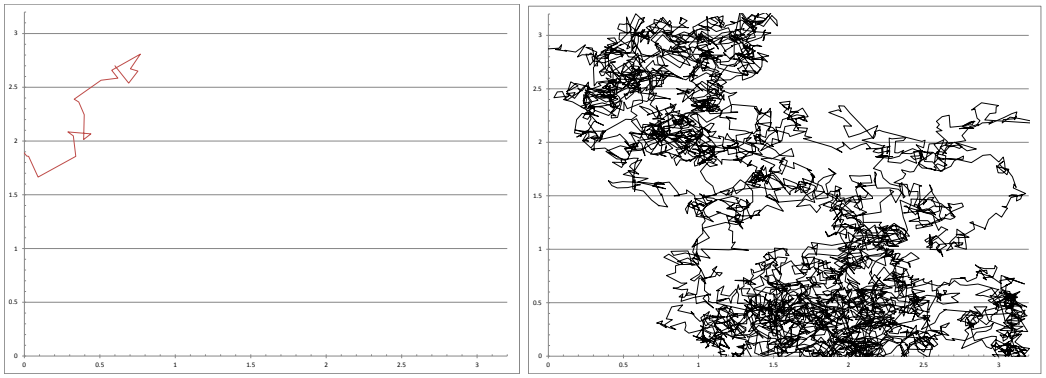

Standard deviation 0.1 Standard deviation 0.05

Figure 2. Examples of paths for different values of the BM standard deviation

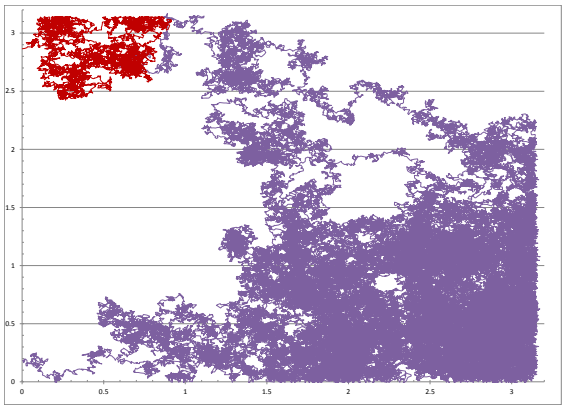

Figure 3. Two BM examples starting from the same point with the same standard deviation 0,01

A high value of the variance s^2 means a faster simulation process but it is generally less exact if the boundaries lie near the particle.

The h value has to be small enough to fulfill the Taylor expansion conditions but large enough to guarantee that the particle is always inside the domain of integration. In this paper a value of h five times the standard deviation of the Brownian motion process has been used, this is to say

$$h = 5\sqrt{\Delta t} = 5s$$

3.3.3 Obtain the solution in $\bar{x}$.

To obtain the problem solution we must calculate

$$u(\bar{x}) = E\big(g(X^{\tau_x})\big) + E\left(\int_0^{\tau_x}(f(x))dt\right) + E\left(-\sum_i \frac{\partial u}{\partial n}(X_i)h_n\right) \tag{56}$$

A possibility is to use Montecarlo method: we select a large number of particles for each point in which the solution must be evaluated.

From $\bar{x}$, every one of these particles performs, for each Δt, a random step defined by Itô's process, namely

$$d\bar{X} = \bar{b}(x)dt + \bar{\bar{Z}}(x)d\bar{B} \tag{57}$$

where dB is a standard Brownian motion with Gaussian distribution $N(0, s^2)$

Remember that the time spent for each particle to reach a boundary in which a Dirichlet condition holds, τ_x, is called stopping time.

The contribution of a particle to the solution is

$$u_j = \frac{\big(g(X^{\tau_x})\big) + \left(\int_0^{\tau_x}(f(x))dt\right) + \left(-\sum_i \frac{\partial u}{\partial n}(X_i)h_n\right)}{N} \tag{58}$$

where i is the number of times the particle reaches a boundary with Neumann condition, N the number of particles used in the simulation and τ_x the time spent for each particle to reach a boundary in which a Dirichlet condition holds (the so called stopping time). In equation (58):

- $g(X^{\tau_x})$ is the contribution of Dirichlet type boundary conditions. It is evaluated as the value of the boundary condition at the point first reached by the particle.
- $\int_0^{\tau_x}(f(x))dt$ is the contribution of the input function at the solution and must be evaluated until the stopping time.

- $-\sum_i \frac{\partial u}{\partial n}(X_i)h_n$ is the contribution of Neumann type boundary conditions. A particle may reach a Neumann type condition never, once or more times before reaching a point in which a Dirichlet boundary condition holds.

The final solution estimation is:

$$u = \sum_{j=1}^{N} u_j \tag{59}$$

3.4 Two dimensional examples

3.4.1 Let Ω be the unit circle defined as $x^2 + y^2 \leq 1$ in Cartesian coordinates. We state the following differential operator.

$$\Delta U = 0 \tag{60}$$

with boundary conditions

$$\begin{gathered} U(r,0) = U(r,2\pi) = 0 \\ U(1,\theta) = \sin\left(\frac{\theta}{2}\right), \;\; 0 < \theta < 2\pi \end{gathered} \tag{61}$$

The analytical solution of this problem is $U = sin\left(\frac{\theta}{2}\right)\sqrt{r}$ (See Figure 4)

The Itô's process governing the particles motion is

$$d\bar{X} = \bar{b}(x)dt + \bar{\bar{Z}}(x)d\bar{B} \tag{62}$$

In this case $b_i = 0$, $\sigma_{i,j} = 1 \;\; \forall \; i = j$ and $\sigma_{i,j} = 0 \; \forall \;\; i \neq j$. Therefore, as $\bar{\bar{C}} = \bar{\bar{Z}} * \bar{\bar{Z}}^T$ and $\bar{\bar{C}} = \begin{pmatrix} 1 & 0 \\ 0 & 1 \end{pmatrix}$, it results that $\bar{\bar{Z}} = \begin{pmatrix} 1 & 0 \\ 0 & 1 \end{pmatrix}$.

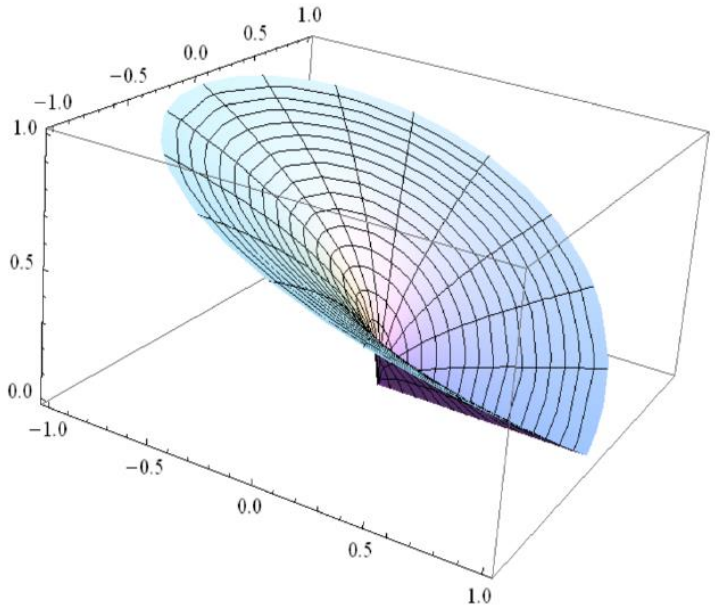

Figure 4. Analytical solution of the problem stated in section 3.4.1

It follows that $dx_1 = dB_1$ and $dx_2 = dB_2$

The numerical solution is:

$$u(\bar{x}) = E\big(g(X^{\tau_x})\big) + E\Big(\int_0^{\tau_x}(f(x))dt\Big) \tag{63}$$

because in this example there are not Neumann boundary conditions. In this case $f(x) = 0$, and therefore

$$u(\bar{x}) = E\big(g(X^{\tau_x})\big) \tag{64}$$

where τ_x is the stopping time of each particle.

Figure 5 shows the comparison between the exact (analytical) solution and the simulation for different points of the integration domain.

For radii in the [0.3 al 0.9] interval 5.000 particles have been generated with a process standard deviation of 0.01.

For 0.2 and 0.1 radii 15.000 particles have been generated with a process standard deviation of 0.001.

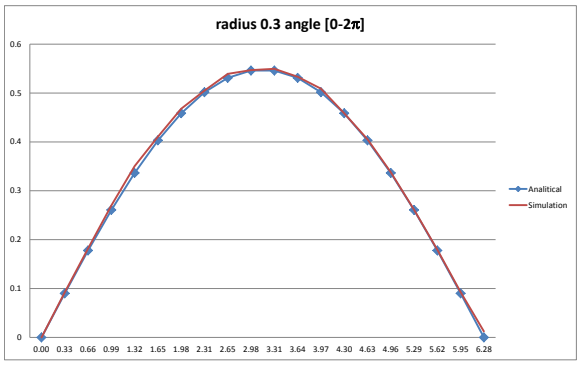

a) r = 0.3, θ in [0,2π]

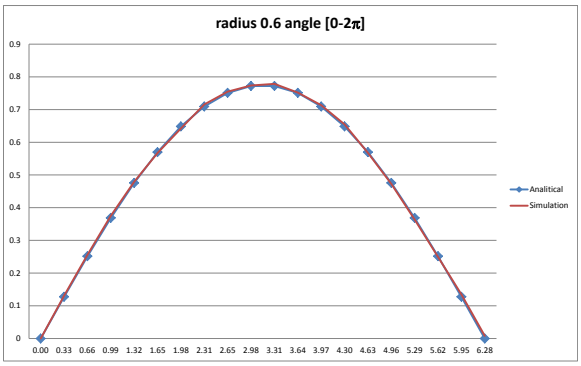

b) r = 0.6, θ in [0,2π]

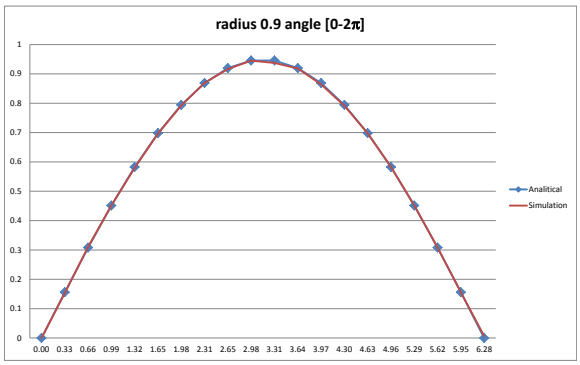

a) r = 0.9, θ in [0,2π]

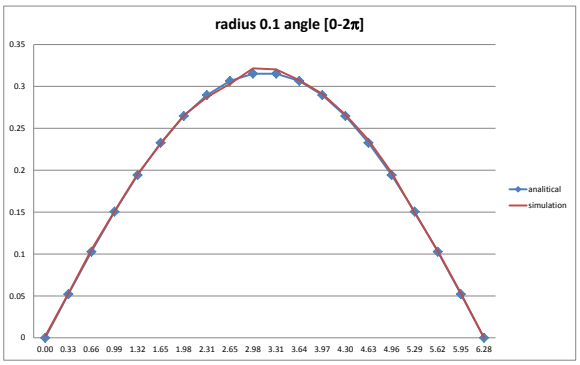

b) r = 0.1, θ in [0,2π]

Figure 5. Simulation vs. analytical solutions of problem 3.4.1 for different domain points

3.4.2 Consider the following problem, in which both Dirichlet and Neumann boundary conditions are defined:

$$\Delta U = 0, \quad 0 \le X \le \pi \quad 0 \le Y \le \pi \tag{65}$$

with boundary conditions

$$u(x=0,y) = -\frac{1}{\tanh(\pi)}[\cosh(y) - \tanh(\pi)\, senh(y)]$$
$$\left.\frac{\partial u}{\partial x}\right|_{(\pi,y)} = 0; \quad 0 \le y \le \pi$$
$$\left.\frac{\partial u}{\partial y}\right|_{(x,0)} = cos(x) \tag{66}$$
$$\left.\frac{\partial u}{\partial y}\right|_{(x,\pi)} = 0 \quad 0 \le x \le \pi$$

The analytical solution, shown in Figure 6, is:

$$\mathrm{u(x,y)} = -\frac{1}{\tanh(\pi)}[\cosh(y) - \tanh(\pi)\, senh(y)]\cos(x) \tag{67}$$

The Itô's process governing the particles motion is

$$d\bar{X} = \bar{b}(x)dt + \bar{\bar{Z}}(x)d\bar{B} \tag{68}$$

Therefore $dx_1 = dB_1$ and $dx_2 = dB_2$

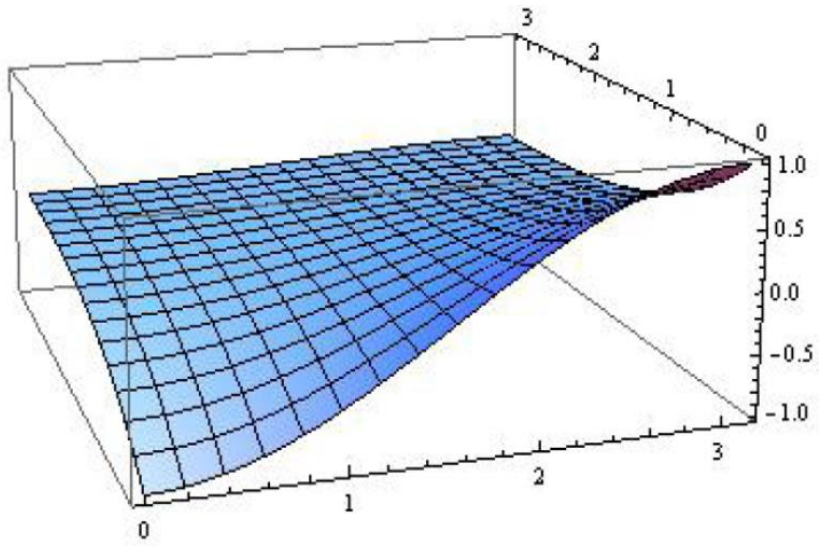

Figure 6. Analytical solution of problem stated in section 3.4.2

The simulation solution is

$$u(\bar{x}) = E\big(g(X^{\tau_x})\big) + E\left(\int_0^{\tau_x}(f(x))dt\right) + E\left(-\sum_i \frac{\partial u}{\partial n}(X_i)h_n\right) \tag{69}$$

because in this case $f(x) = 0$

15.000 particles have been generated for each point, the h value is 0.05 and the standard deviation of the Brownian motion is 0.01.

Figure 5 shows the comparison between the exact (analytical) solution and the simulation for different points of the integration domain.

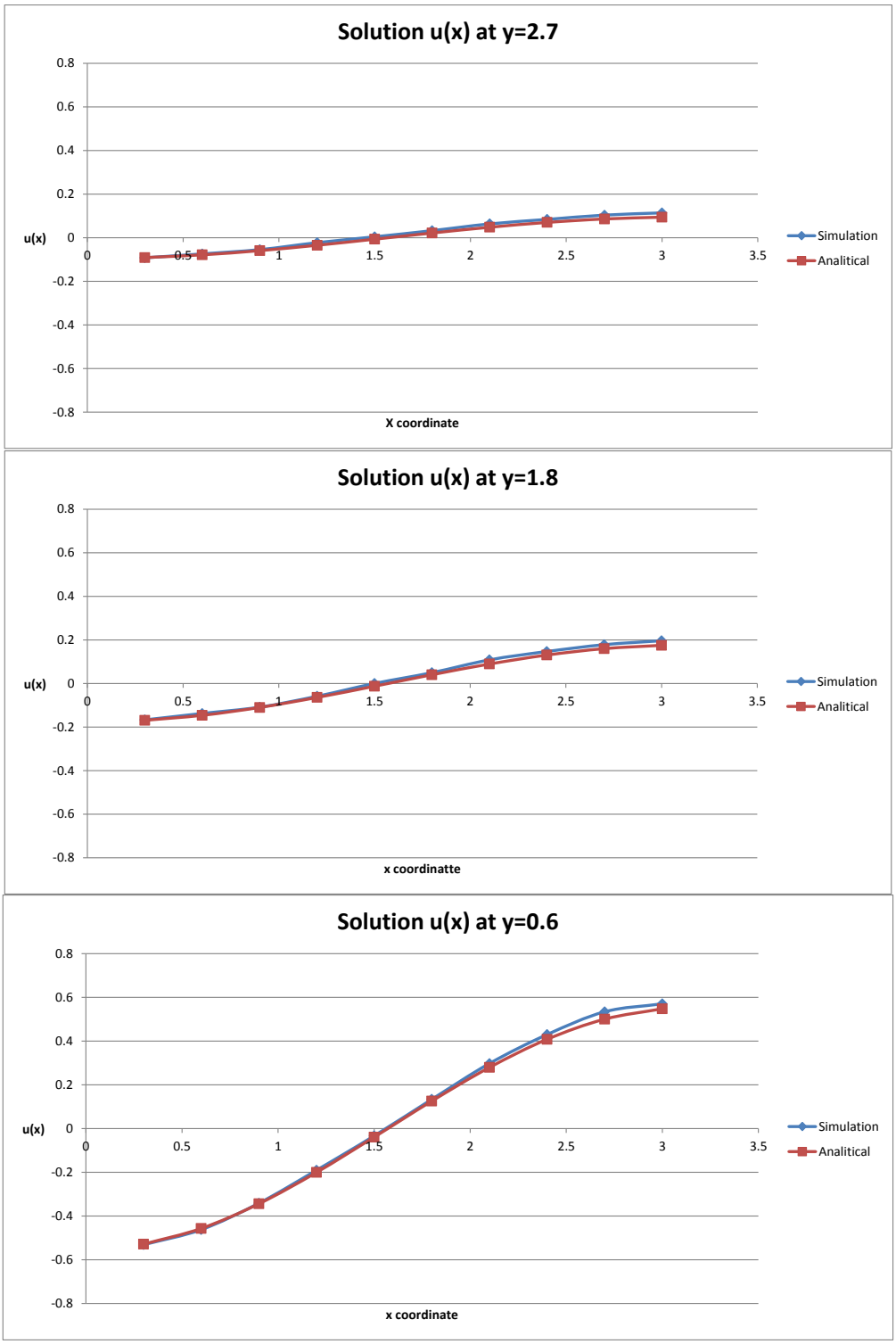

Figure 7. Simulation vs. analytical solutions of problem 3.4.2 for different domain points

4 PARABOLIC PROBLEM GENERAL APPROACH

Consider the following partial differential equation:

$$\mathrm{L}(u) = -f(\bar{x}, t) \tag{70}$$

with boundary and initial conditions:

$$u(\bar{x},t) = g(\bar{x},t)\ si\ \bar{x} \in \partial D_d$$

$$\frac{\partial u(\bar{x},t)}{\partial n} = c(\bar{x},t)\ if\ \bar{x} \in \partial D_n \tag{71}$$

$$u(\bar{x}) = l(\bar{x})\ if\ t = 0$$

with $t > 0$, $\bar{x} \in D$, $\partial D_d \cup \partial D_n = \partial D$ and $D_d \cap \partial D_n = \emptyset$, being ∂D the boundary of the integration domain D. The L(.) operator can be written as

$$\mathrm{L}(.) = -\frac{\partial(.)}{\partial t} + \sum b_i \frac{\partial(.)}{\partial x_i} + \frac{1}{2}\sum\sum \sigma_{ij} \frac{\partial^2}{\partial x_i \partial x_j} \tag{72}$$

where the time *t* may be considered as a new coordinate in the process.

In the n-dimensional case

$$d\bar{X} = \bar{b}(x)dt + \bar{\bar{Z}}(x)d\bar{B} \tag{73}$$

that can also be written as

$$\begin{pmatrix} dx_0 \\ dx_1 \\ \vdots \\ dx_n \end{pmatrix} = \begin{pmatrix} -1 \\ b_1 \\ \vdots \\ b_n \end{pmatrix} dt + \begin{pmatrix} 0 & \cdots & 0 \\ Z_{11} & \cdots & Z_{1n} \\ \vdots & \ddots & \vdots \\ Z_{n1} & \cdots & Z_{nn} \end{pmatrix} \begin{pmatrix} dB_0 \\ dB_1 \\ \vdots \\ dB_n \end{pmatrix} \tag{74}$$

where x_0 is the time coordinate and $x_{i,}$ $i \in (0,n)$ the spatial coordinates.

At every time interval dt, the particle moves randomly in the space (x_i) and goes back a fixed time increment dt.

If the particle reaches a Neumann boundary condition, the particle bounces back and continues the random motion inside the integration domain.

The initial condition $\mathrm{u}(\bar{\mathrm{x}}) = \mathrm{l}(\bar{\mathrm{x}})$ if $\mathrm{t} = 0$ is, in this process, considered as a Dirichlet boundary condition.

The particle random motion may stop because:

- Particle reaches a Dirichlet boundary in the space (x_i)
- Particle reaches time t=0, because, as it was stated before, this initial condition works as a Dirichlet Condition for this simulation process.

4.1 Two dimensional parabolic example

To explain more clearly the general technique we propose the following academic example:

The PDE to solve is:

$$\frac{\partial \mathrm{u}}{\partial \mathrm{t}} = \left(\frac{\partial^2 \mathrm{u}}{\partial \mathrm{x}^2} + \frac{\partial^2 \mathrm{u}}{\partial \mathrm{y}^2}\right) \tag{75}$$

with integration domain $0 \le x \le 2$,$0 \le y \le 4$,$t \ge 0$ (see Figure 8) and boundary conditions

$$\frac{\partial u(x=0,y,t)}{\partial x} = 0, \qquad u(x,y=0,t) = 0$$
$$\frac{\partial u(x=2,y,t)}{\partial x} = 0, \quad u(x,y=4,t) = 0 \tag{76}$$

and the inital condition

$$u(x, y, t = 0) = 7 \tag{77}$$

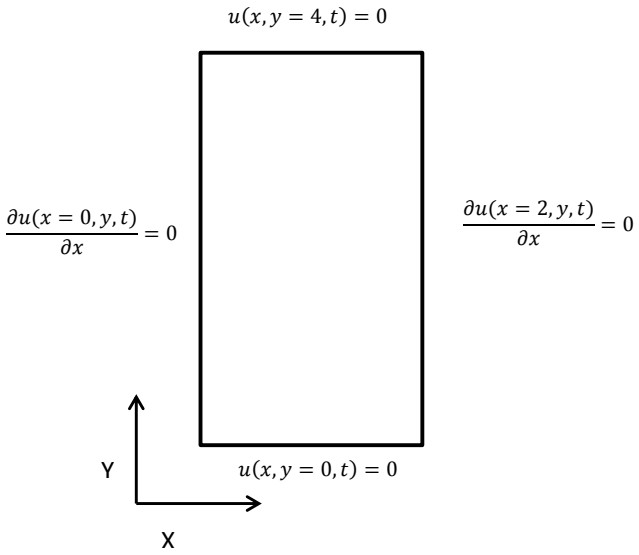

Figure 8. Integration domain for the problem presented in section 4.1

The analytical solution for this problem is:

$$u(x, y, t) = \frac{14}{\pi} \sum_{n=1}^{\infty} (1 - \cos(n\pi)) \left(\frac{1}{n}\right) e^{\left(\frac{-t\pi^2 n^2}{16}\right)} \sin\left(\frac{n\pi y}{4}\right) \tag{78}$$

The stochastic process approach is

$$\begin{gathered} \left(\frac{\partial^2 \mathrm{u}}{\partial \mathrm{x}^2} + \frac{\partial^2 \mathrm{u}}{\partial \mathrm{y}^2}\right) - \frac{\partial \mathrm{u}}{\partial \mathrm{t}} = 0 \\ L(.)u(x)) - f(x) \\ f(x) = 0 \\ L(.) = \sum_i b_i \frac{\partial .}{\partial x_i} + \frac{1}{2} \sum_{ij} \sigma_{ij} \frac{\partial^2}{\partial x_i \partial x_j} \end{gathered} \tag{79}$$

In this case $i = 0, 1, 2$ y $j = 0, 1, 2$.
The Itô process can be written as

$$d\bar{X} = \bar{b}(x)dt + \bar{\bar{Z}}(x)d\bar{B} \tag{80}$$

or

$$\begin{pmatrix} dx_0 \\ dx_1 \\ dx_2 \end{pmatrix} = \begin{pmatrix} -1 \\ 0 \\ 0 \end{pmatrix} dt + \begin{pmatrix} 0 & 0 & 0 \\ 0 & \sqrt{2} & 0 \\ 0 & 0 & \sqrt{2} \end{pmatrix} \begin{pmatrix} dB_0 \\ dB_1 \\ dB_2 \end{pmatrix} \tag{81}$$

with $dB = N(0, dt)$.

The estimate of the solution is

$$u(\bar{x}) = E\big(g(X^{\tau_x})\big) + E\left(\int_0^{\tau_x} (f(x))dt\right) + E\left(-\sum_i \frac{\partial u}{\partial n}(X_i)h_n\right) \tag{82}$$

The second and third addends are null because $f(x) = 0$ and all Neumann boundary conditions are also null.

Then

$$u(\bar{x}) = E\big(g(X^{\tau_x})\big) \tag{83}$$

where τ_x is the already defined stopping time.

Suppose we want to calculate the problem solution at a point with coordinates (x, y, t). As always, the simulation solution is to generate a number of particles at this point and apply the above described technique..

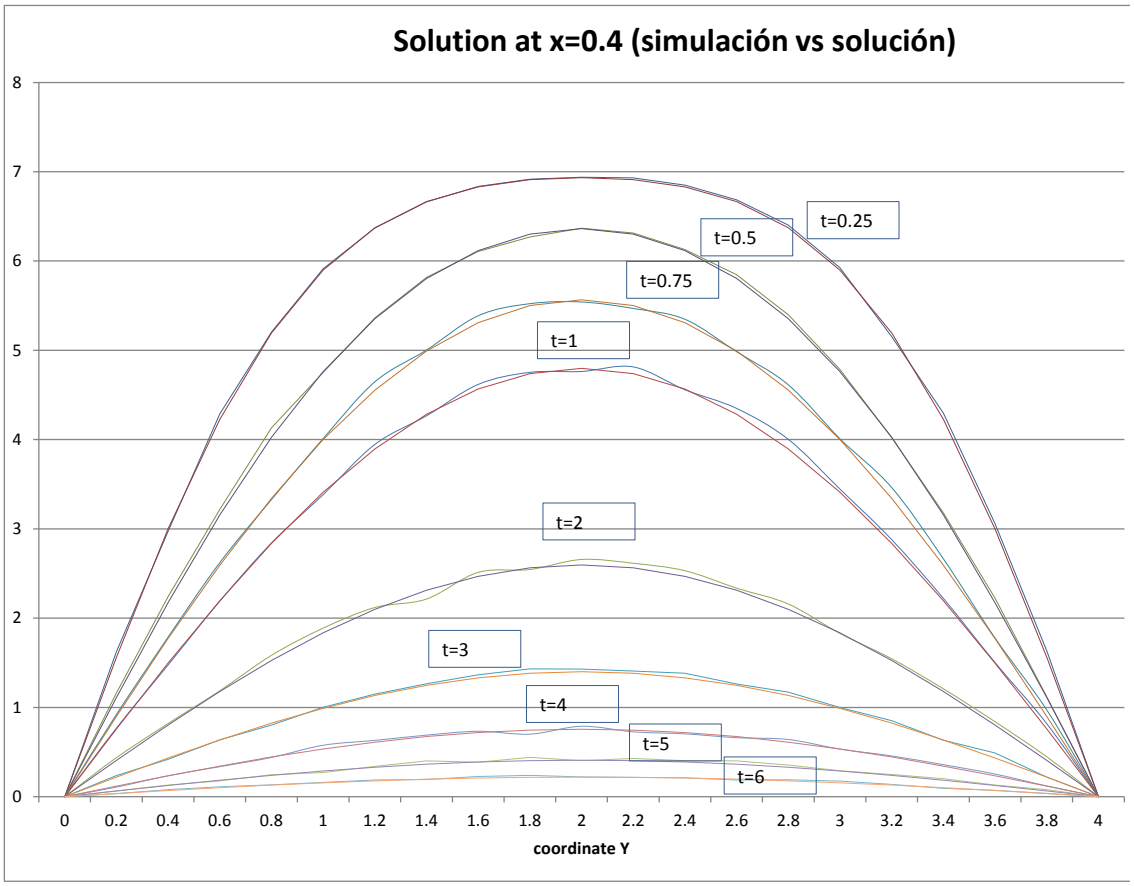

Figure 9. Solution of the problem proposed in section 4.1

5 CONCLUSIONS

A simulation stochastic method to solve partial differential equations (of elliptic and parabolic type) has been presented. The analysis of the specific boundary and (in the parabolic type) initial conditions has been carried out. A number of academic examples, with known analytical solutions, have been used as benchmarks, and the simulation solution has agreed very well with the exact solutions in all cases.

The main advantages of this technique are:

- No domain discretization is necessary.

- No need for a solver, because there are not systems of equations in the solution process
- It is not necessary to solve the PDE in the whole integration domain. The solution can be obtained only where it is needed (a point, several points, a particular area of the domain).
- In parabolic problems, to obtain the solution at time T_f it is not necessary to obtain it at intermediate times $(T_0; T_f)$.
- The approximation error is a function of the number of particles generated in the simulation, and decreases as the number of particles increases. This is so because the solution is an expected value, and because of the central limit theorem the variance will decrease as the number of elements (particles) increases.
- The speed of the process increases as the variance of the stochastic process (Itô's process) increases. However, near the boundaries, the variance should be kept small enough as the walk does not go outside the domain
- As the solution estimate is an expected value, parallel methods may be applied in a very easy way. For instance, the same accuracy will be obtained with a CPU generating a 10.000 particles simulation as with 100 CPU's generating a 100 particles simulation each. As the only process that can be considered time consuming is the particles generation and the corresponding random walk, the process time can be directly divided by the number of CPU's in the cluster.

6 AKNOWLEGMENTS

The authors acknowledge the financial support provided by Grant GRC2014/039, "Axudas para a consolidación e estruturación de unidades de investigación competitivas do Sistema Universitario de Galicia do 2014: Grupo de Referencia Competitiva" of the Xunta de Galicia (Spain) and by the Research Group of Numerical Methods in Engineering of the University of A Coruña.

7 REFERENCES

[1] Ritz, Walter, *Über eine neue Methode zur Lösung gewisser Variationsprobleme der mathematischen Physik*, Journal für die Reine und Angewandte Mathematik**, vol. 135**, pages 1–61, 1909.

[2] Øksendal, Bernt, *Stochastic Differential Equations. An Introduction with Applications*, 5th edition, corrected 2nd printing. Springer Verlag, 2000.

[3] Kloeden, P.E., Platen, E., *Numerical Solution of Stochastic Differential Equations*, Volume 23 of the series Applications of Mathematics pp 103-160, Springer Verlag, 1992

[4] Itô, Kiyosi, Stochastic Integrals. Proc. Imperial Acad. Tokyo, **20**, 519-524, 1944.

[5] Itô, Kiyosi, *On stochastic differential equations*. Memoirs, American Mathematical Society 4, 1–51, 1951.

[6] Carmona, Alexis, *Ecuaciones diferenciales estocásticas*. Thesis. Universidad de Buenos Aires, Argentina, 2009

[7] Karatzas, I., S. Steven, *Brownian Motion and Stochastic Calculus (2nd ed.)*, Springer Verlag, 1991

[8] Rincón, Luis, *Construyendo la integral estocástica de Itô*. Aportaciones Matemáticas, Series en Comunicaciones **35**, 265-283, 2005.

[9] Itô, Kiyosi, *On a formula concerning stochastic differentials*, Nagoya Mathema-tical Journal **3**: 55–65, 1951

[10] Chung, K.L., Williams, R.J., *Introduction to Stochastic Integration*, Springer Verlag, 2014

[11] Granero Belinchón, Rafael, *Sobre algunas relaciones entre la probabilidad y las ecuaciones diferenciales*, Thesis, Université Paris-Dauphine and Universidad Autónoma de Madrid, 2009

[12] Mascagni, Michael, *Monte Carlo Methods for Partial Differential Equations.* Florida State University, USA, 2011

[13] Grigoriu, Mircea, *Stochastic Calculus, Applications in science and engineering.* Birkhäuser, 2002

ECCOMAS Congress 2016
VII European Congress on Computational Methods in Applied Sciences and Engineering
M. Papadrakakis, V. Papadopoulos, G. Stefanou, V. Plevris (eds.)
Crete Island, Greece, 5–10 June 2016

THE BOOTSTRAP APPROACH TO THE STATISTICAL SIGNIFICANCE OF PARAMETERS IN THE FIXED EFFECTS MODEL

Jacek Pietraszek[1], **Renata Dwornicka**[1], **and Agnieszka Szczotok**[2]

[1] Department of Software Engineering and Applied Statistics
Faculty of Mechanical Engineering
Cracow University of Technology
37 Jana Pawla II, 31-864 Krakow, Poland
e-mail: {pmpietra, dwornick}@mech.pk.edu.pl

[2] Institite of Materials Science
Faculty of Materials Science and Metallurgy
Silesian University of Technology
8 Krasinskiego, 40-019 Katowice, Poland
e-mail: agnieszka.szczotok@polsl.pl

Keywords: Bootstrap, Statistical Significance, Fixed Effects Model, ANOVA, Materials Science, Surface Layers, Nanoparticles.

Abstract. Since R.A. Fisher introduced the analysis of variance (ANOVA), the classic design of experiments (DoE) utilizes factorial model of fixed effects. The typical procedure assumes the normal distribution of the noise and uses the least square method (LSQ) to identify effects of the model with a priori assumed structure of main effects and some interactions, usually up to the second order. The terms of model are repeatedly eliminated in the specific backward stepwise regression.

Methods of approximation and prediction rapidly evolved in recent years. Apart from this, the classic approach of the fixed effects model is still very useful and popular. In fact, this model is intrinsic to ANOVA however hidden. The significance analytical improvements have appeared in the background of fixed effects models in recent decades: statistics based on widespread strict requirements of the normal distribution have been replaced by so-called robust statistics based on the weak requirement of the continuous distribution or even on the statistics based on numerical simulation like e.g. bootstrap approach. Practically, in the case of small size datasets, the conformity with the normal distribution has very weak reliability and it leads to very uncertain assessment of parameters statistical significance. The bootstrap approach with simulation-based identification of parameters confidence intervals (CI) appears to be better solution than theoretically proved but only asymptotically equal t-distribution based evaluations.

1 INTRODUCTION

The research investigation in a materials science always leads to the datasets. The large (or even huge) datasets should be analyzed to obtain summary results expressed in qualitative or quantitative forms. Such conclusions should be semi-proved by a statistical analysis.

One of the typical methodology is to observe behavior of the phenomenon against different treatments of controlled factors being precisely defined in a matrix known as a design of experiment. The general term 'behavior' is narrowed to a quantitative variable called 'response' or 'output'. The experiment focuses on the 'effect': the difference of the output as a result of the difference of treatments. If only one controlled factor is changed at time, the experiment is named One-Factor-At-Time (OFAT) [1]. On the opposite side, the factorial experiment [2] may be found where all controlled factors are changed simultaneously in a specific manner. The factorial experiment is also known as ALLFAT (All-Factors-At-Time). This name is often used in an industrial environment and quality management procedures.

The sensitivity of the investigated phenomenon to changes of controlled factor decides on the statistical significance of such factor. However this definition is intuitively clear, it requires some quantitative measure and its evaluation. Typical procedure used to assessment of factors significance is the analysis of variance (ANOVA).

ANOVA [2] is a well-known procedure to identify an inequality of means evaluated for subsets selected from the general dataset by a chosen particular classification factor. The null hypothesis H_0 states that all means are mutually equal against the alternative hypothesis H_1 that not all means are equal. The ANOVA workflow leads from the general dataset through its decomposition to subsets. Mathematically, it is described as a decomposition of a variance, which finally leads to comparison of MS_{factor} (variance explained by classification factor) against MS_{error} (remained variance). Technically, it replaces the original null hypothesis to its equivalent: the ratio of MS_{factor} by MS_{error} is equal to zero. As was proved by Fisher, this ratio has F-distribution however it requires some additional assumptions about an independency of observations, a normality of residuals and a homoscedascity in subsets. These assumptions are often questionable, especially when the size of a dataset is small and the statistical inference is weak.

The proposed solution consists of two elements: (a) the replacement of the original null hypothesis with its equivalent related to parameters of an associated fixed effects model and (b) the replacement of the classic test of parameters significance with the bootstrap-based checking of zero existence inside the parameter confidence intervals. This solution is more practical for large datasets with the unknown distribution because it does not require to meet the ANOVA assumptions.

Authors have been tried [3] previously to combine a bootstrap approach with an artificial neural network approximator to analyze materials science data processed by image analysis however they have with many numerical artifacts. Such approach was more successfully for processing non-parametric statistical analysis for surface layer [4].

The bootstrap approach appears to be a promising solution for some aspects of fuzzy statistics which is developed mainly by Buckley [5, 6]. The general workflow for such implementations has been proposed by Grzegorzewski [7]. Some preliminary investigations in the field of a design of experiments (DoE) have been made by Pietraszek [8, 9].

2 COMPUTATIONAL METHODS

Two main methods were used: the fixed effects model [2] and the bootstrap method [10]. The fixed effects model is used to evaluate effects being deviations of particular means from the grand mean. The bootstrap method is used to evaluate confidence intervals for effects. Fi-

nally, the existence of zero inside the intervals is inspected. If any of intervals contains zero, the null hypothesis of ANOVA is rejected.

2.1 Fixed-effects model

The fixed-effects model [2]consist of three terms:

$$y_{ij} = \mu + \alpha_i + \varepsilon_{ij} \tag{1}$$

where:
μ – grand mean (average response),
α_i – an effect at *i*-th treatment,
ε_{ij} – an random error at *i*-th treatment and *j*-th replication,
y_{ij} – the observed response at *i*-th treatment and *j*-th replication.

The grand mean and effects are evaluated using the ordinary least squares (OLS) [2].

2.2 Bootstrap

The bootstrap approach [10] to fixed-effects model (Eq.1) is described by the following workflow. In the beginning, the parameters $\hat{\mu}, \hat{\alpha}_i$ of the model were identified from the dataset using the least squares criterion L

$$\min L(\mu, \alpha_i) = L(\hat{\mu}, \hat{\alpha}_i) \tag{2}$$

then fits $\hat{y}_i$ were evaluated

$$\hat{y}_i = \hat{\mu} + \hat{\alpha}_i \tag{3}$$

and at last residuals r_{ij} of the model

$$r_{ij} = y_{ij} - \hat{y}_i \ . \tag{4}$$

Then, iteratively, (a) the new dataset $\mathbf{R}_\mathrm{B}$ of the same size containing bootstrapped residuals $r_{\mathrm{b}|ij}$ was constructed by drawing with replacement from the set of residuals:

$$\mathbf{R}_B = \left\{ r_{b|ij} : (1 \le i \le n) \wedge (1 \le j \le r) \wedge (\forall i, j \, \exists k, l : r_{b|ij} = r_{kl}) \right\} \tag{5}$$

and (b) new bootstrapped residuals were added to the model fits creating new bootstrapped "observations":

$$y_{B|ij} = \hat{y}_i + r_{B|ij} \ . \tag{6}$$

That new observations were used (c) to identify bootstrapped parameters of the model.

$$\min L(\mu, \alpha_i) = L(\hat{\mu}_B, \hat{\alpha}_B) \tag{7}$$

The parameters were collected until large number of iterations will be reached. Finally, (d) the quantiles were evaluated (typically 2.5% and 97.5%) for datasets of parameters as a range of confidence intervals and at last (e) zero existence inside confidence intervals was checked.

3 MATERIALS AND DATASET

The data were obtained during investigation of the ceramic shell mould of the airfoil blade casting. The description below is a brief, while details can be found in article of Szczotok *et al.* [11].

Nickel-based superalloys are mainly used in aircraft and power-generation turbines. Creep-resistant polycrystalline turbine blades are typically produced by an investment casting process. It is especially useful for making castings of complex and near-net shape geometry, where machining may be impossible or too wasteful. Studies were performed on the IN 713C superalloy. The castings described in the work were produced by the Laboratory for Aerospace Materials at Rzeszow University of Technology in Poland. One casting called GK was selected for the microstructural and statistical analysis. Final castings were cut off. The cross-sections were included and prepared as metallographic samples from nickel-based superalloy. To reveal the microstructure of the investigated material the surfaces of the samples were etched. The microstructural investigations of the cross-sections of the GK casting were carried out by a scanning electron microscope. The recorded microphotographs were next subjected to a computer-aided image analysis program to estimate quantitatively the main parameters describing the (γ+γ') eutectic islands that occurred in the investigated superalloy.

The dataset was created by counting number and size of eutectic island detected at six different traces labelled from T1 to T6 (Table 1). The issue was to check the homogeneity of the eutectic phase i.e. statistical equivalence of observations at any trace.

Trace	No of islands	Mean Area	SE	Median	Quartiles	
					Q1	Q3
T1	31	34.5	7.8	12.0	3.8	53.6
T2	49	22.0	3.8	12.1	4.2	28.1
T3	80	24.0	3.4	10.8	4.0	32.2
T4	75	26.9	3.9	14.6	4.6	35.8
T5	64	25.1	4.2	11.3	3.9	35.1
T6	61	24.5	3.5	14.2	8.6	28.4

Table 1: Descriptive statistics of raw data (source [11])

4 ANALYSIS

The typical method for checking the homogeneity of quantitative data is ANOVA. Due to the fact that area measures are positive they need to be transformed by a specific transformation into the whole real space to avoid nonsense negative values [12]. The natural logarithm was selected as transformation mapping i.e.:

$$LnY = \ln(area)\,. \tag{8}$$

Such transformation guarantees that any value has physical sense after retransformation. Descriptive statistics of transformed data are presented in Table 2.

The ANOVA protocol leads to the classic ANOVA table which decomposes the total variation into part assigned to grouping factor and the remain assigned to all other factors grouped under name 'error' which should be treated rather as 'unexplained' than only 'random error'. For the mentioned data, the ANOVA table (Table 3) revealed that critical p-Value is equal to 0.841, much greater than significance level $\alpha = 0.05$, what means that homogeneity of traces was not rejected.

Trace	No of islands	Mean LnY	SE	Median	Quartiles	
					Q1	Q3
T1	31	2.63	0.28	2.49	1.34	3.98
T2	49	2.44	0.18	2.49	1.43	3.33
T3	80	2.43	0.15	2.38	1.40	3.47
T4	75	2.55	0.15	2.68	1.53	3.58
T5	64	2.45	0.17	2.42	1.36	3.56
T6	61	2.68	0.14	2.65	2.15	3.35

Table 2: Descriptive statistics of transformed data (source [11])

Effect	SS	df	MS	F	p
Trace	3.318	5	0.664	0.411	0.841
Error	572.019	354	1.616	–	–
Total	575.338	359	1.603	–	–

Table 3: ANOVA table for transformed data (source [11])

Simultaneously, the general linear model (GLM) (Eq.1) was introduced for 6 levels (T1…T6). The identification of the model resulted in a set of parameters (Table 4). Note that lack of the parameter for T6 is a typical presentation of results by statistical programs (here: StatSoft STATISTICA v12), because all effects from T1 to T6 should sum to 0 and T6 should be deducted from such condition.

Effect	Parameter	SE	t	p [1)]	-95 CI	+95 CI
const	2.527	0.070	35.88	0.000	2.389	2.666
T1	0.100	0.199	0.50	0.617	-0.292	0.492
T2	-0.091	0.164	-0.56	0.578	-0.414	0.232
T3	-0.099	0.136	-0.73	0.467	-0.366	0.168
T4	0.021	0.139	0.15	0.880	-0.252	0.294
T5	-0.082	0.148	-0.55	0.580	-0.372	0.208

Table 4: Parameters of fixed-effects model for transformed data
[1)] p-value evaluated from inverse cumulative distribution for t-Student at d.o.f. = 354

Trace	Fit	SE	-95 CI	+95 CI	N
T1	2.627	0.228	2.178	3.076	31
T2	2.436	0.182	2.079	2.793	49
T3	2.428	0.142	2.149	2.708	80
T4	2.548	0.147	2.260	2.837	75
T5	2.445	0.159	2.133	2.758	64
T6	2.678	0.163	2.358	2.999	61

Table 5: Model fits and their confidence intervals for transformed data

The model predictions and their confidence intervals are presented in Table 5. It should be noted that such results are still from classic ANOVA for further comparisons.

Now, the approach was switched to the bootstrap. The number of draw iterations was set to 10.000 to easy selection of quantiles from the bootstrapped dataset. After the full bootstrap procedure, the descriptive statistics were evaluated for model parameters (Table 6) and model predictions (Table 7), similarly to Table 4 and Table 5.

The bounds of the confidence intervals were easy identified due to the selected number of bootstrap iterations. They were values found at positions 250 and 9750 in the sorted bootstrapped results. Similarly, the bootstrapped p-Value was evaluated as relative position of sign switching inside the sorted bootstrapped results.

Effect	**Parameter mean**	**SE**	**p-Value$_{bootstrapped}$ [1] / p-Value$_{theoretical}$ [2]**	**-95 CI**	**+95 CI**
const	2.527	0.070	0.000 / 0.000	2.388	2.665
T1	0.101	0.196	0.614 / 0.607	-0.281	0.490
T2	-0.092	0.161	0.576 / 0.568	-0.407	0.224
T3	-0.099	0.135	0.468 / 0.464	-0.364	0.167
T4	0.021	0.137	0.869 / 0.878	-0.250	0.290
T5	-0.082	0.148	0.580 / 0.580	-0.367	0.206
T6	0.151	0.147	0.310 / 0.305	-0.136	0.435

Table 6: Parameters of fixed-effects model for transformed data

[1] bootstrapped p-Value was evaluated from relative position of sign switching inside a bootstrap table

[2] theoretical p-Value was evaluated from ratio (mean/SE) and t-Student distribution at d.o.f. = 354

Trace	**Fit**	**SE**	**-95 CI**	**+95 CI**
T1	2.628	0.225	2.189	3.073
T2	2.435	0.179	2.090	2.785
T3	2.428	0.141	2.153	2.703
T4	2.549	0.145	2.261	2.835
T5	2.445	0.159	2.136	2.754
T6	2.678	0.160	2.360	2.988

Table 7: Boostrap fits and their confidence intervals for transformed data

The analysis of confidence intervals bounds revealed that small asymmetric exists between left and right side relative to means (Table 8). The coefficients were evaluated as studentized i.e. a quotient of a deviation and standard error, where deviation was difference between confidence interval bound and respective mean:

$$cf = \frac{\pm 95CI - mean}{SE}. \tag{9}$$

Trace / Effect	Parameters intervals coefficients		Fits intervals coefficients	
	-95 CI	**+95 CI**	**-95 CI**	**+95 CI**
const	-1.986	1.971	–	–
T1	-1.949	1.985	-1.951	1.978
T2	-1.957	1.963	-1.927	1.955
T3	-1.963	1.970	-1.950	1.950
T4	-1.978	1.964	-1.986	1.972
T5	-1.926	1.946	-1.943	1.943
T6	-1.952	1.932	-1.988	1.938

Table 8: Studentized coefficients of confidence intervals for the bootstrap model and its fits

5 CONCLUSIONS

- Bootstrap approach appears to be effective computational method to identify parameters of fixed effects model and their statistical properties.
- Bootstrap approach does not require to make *a priori* inconvenient assumptions.
- Bootstrap approach is very convenient to automatize in computational workflow and further statistical postprocessing.

REFERENCES

[1] C. Daniel, One-at-a-Time Plans. *Journal of the American Statistical Association* **68**, 353-360, 1973.

[2] O. Kempthorne, K. Hinkelmann, *Design and analysis of experiments. Vol.1. Introduction to experimental design*. John Wiley & Sons, Hoboken, NJ, USA, 2007.

[3] J. Pietraszek, A. Gadek-Moszczak, The Smooth Bootstrap Approach to the Distribution of a Shape in the Ferritic Stainless Steel AISI 434L Powders. *Solid State Phenomena* **197**, 162-167, 2013.

[4] J. Pietraszek, N. Radek, K. Bartkowiak, Advanced Statistical Refinement of Surface Layer's Discretization in the Case of Electro-Spark Deposited Carbide-Ceramic Coatings Modified by a Laser Beam. *Solid State Phenomena* **197**, 198-202, 2013.

[5] J.J. Buckley, *Fuzzy probability and statistics*. Springer Verlag, Heidelberg, 2006.

[6] J.J. Buckley, Fuzzy statistics: hypothesis testing. *Soft Computing* **9**, 512-518, 2005.

[7] P. Grzegorzewski, *Decision support under uncertainty. Statistical methods for imprecise data.* EXIT, Warszawa, 2006.

[8] J. Pietraszek, Fuzzy Regression Compared to Classical Experimental Design in the Case of Flywheel Assembly. *Lecture Notes in Artificial Intelligence* **7267**, 310-317, 2012.

[9] J. Pietraszek, A. Gadek-Moszczak, T. Torunski, Modeling of Errors Counting System for PCB Soldered in the Wave Soldering Technology. *Advanced Materials Research* **874**, 139-143, 2014.

[10] J. Shao, D. Tu, *The Jackknife and Bootstrap*. Springer, New York, 1995.

[11] A. Szczotok, J. Nawrocki, A. Gądek-Moszczak, M. Kołomycki, The Bootstrap Analysis of One-Way ANOVA Stability in the Case of the Ceramic Shell Mould of Airfoil Blade Casting. *Solid State Phenomena* **235**, 24-30, 2015.

[12] J. Pietraszek, A. Goroshko, The Heuristic Approach to the Selection of Experimental Design, Model and Valid Pre-Processing Transformation of DoE Outcome. *Advanced Materials Research* **874**, 145-149, 2014.

ECCOMAS Congress 2016
VII European Congress on Computational Methods in Applied Sciences and Engineering
M. Papadrakakis, V. Papadopoulos, G. Stefanou, V. Plevris (eds.)
Crete Island, Greece, 5–10 June 2016

ON FULLY COUPLED THERMO-ELASTO-PLASTIC STOCHASTIC FINITE ELEMENT ANALYSIS OF STEEL STRUCTURES

Marcin Kamiński[1*], **Michał Strąkowski**[1]

[1] Lodz University of Technology
Department of Structural Mechanics
Al. Politechniki 6, 90-924 Lodz, Poland
Marcin.Kaminski@p.lodz.pl

Keywords: Stochastic Finite Element Method, Fire simulation, Fully coupled thermal-stress analysis.

Abstract. *This work demonstrates an application of the generalized stochastic perturbation technique and the corresponding Stochastic Finite Element Method in numerical analysis of the stresses for the steel structural element subjected to higher temperatures. This approach is based on higher order Taylor expansion of the input random parameters and of the resulting state functions and, independently, on the Least Squares Method determination of the structural responses to the input random parameters. An initial temperature equivalent to the fire exposure of the steel structure is taken as the input Gaussian random variable and uniquely defined by the constant mean value at outer surfaces of this element, where material parameters of the steel as Young modulus, yield strength, heat conductivity, capacity and thermal elongation are all considered as highly temperature-dependent. These functions are adopted according to the experimental evidence provided in the literature. We adopt various degree of polynomial functions to verify an influence of the response function choice upon the resulting probabilistic characteristics. This study is an example of a hybrid usage of the FEM system ABAQUS and the computer algebra system MAPLE in stochastic transient fully coupled thermo-mechanical analysis, where up to the fourth order probabilistic characteristics of the temperatures, displacements and stresses may be directly used in fire reliability analysis of the civil engineering structures with the temperature both independent and dependent material characteristics. The results obtained in this study may serve directly in the stochastic reliability analysis of the steel structures subjected to a fire according to both First and Second Order Reliability Methods (FORM and SORM).*

1 INTRODUCTION

Reliability of engineering structures under fire conditions remains always very challenging and practically important knowledge. It is possible to use it for an efficient prediction of the failure time for the structures to get specific information about their fire resistance and evacuation time. The well-known Monte-Carlo simulation needs huge computer time effort. In this case it is better to use higher order perturbation techniques implemented with the FEM originating from the Second Order Second Moment method [1] relevant to small initial random fluctuations. We compute probabilistic coefficients of up to the fourth order to gain more information about probability density function itself. The basic probabilistic moments as well as skewness and kurtosis are calculated by full symbolic expansion of integral definitions and partial differentiation of the nodal response functions with respect to given random input variable. In this case we consider strength test of elasto-plastic steel cylindrical specimen subjected to high temperatures. All physical and mechanical steel properties like Young modulus, yield strength, conductivity, heat capacity and thermal elongation are temperature-dependent.

2 THEORETICAL BACKGROUND

Let us introduce the random variable b and its probability density function as $p_b(x)$. Then, the first two probabilistic moments of this variable are defined as [2]

$$E[b] \equiv b^0 = \int_{-\infty}^{+\infty} b p_b(x) dx \,, \tag{1}$$

where b^0 means the average value of b itself and

$$Var[b] = \int_{-\infty}^{+\infty} [b - E(b)]^2 \, p_b(x) dx \,. \tag{2}$$

Higher probabilistic moments and related coefficients may be defined according to the classical definitions from the probability theory. The basic idea of the stochastic perturbation approach employed here is to expand all input random variables and all the resulting state functions of the given boundary initial problem via Taylor series about their spatial expectations using the perturbation parameter ε. The random function f with respect to its parameter b around its mean value is given as follows

$$f = f^0 + \sum_{n=10}^{1} \frac{\varepsilon^n}{n!} \frac{\partial^n f}{\partial b^n} \Delta b^n \,, \tag{3}$$

where

$$\varepsilon \Delta b = \varepsilon \left(b - b^0 \right) \tag{4}$$

is the first variation of variable b about its expected value and symbol $(.)^0$ represents the value of a function calculated at its mean. Let us analyse further the expected values of stress state function $\sigma(b)$ defined analogously to the Eqn. 3 by its expansion via Taylor series as follows

$$E[\sigma(b)] = \int_{-\infty}^{+\infty} \sigma(b) p_b(x) dx = \int_{-\infty}^{+\infty} \left(\sigma^0\left(b^0\right) + \sum_{n=10}^{1} \frac{\varepsilon^n}{n!} \frac{\partial^n \sigma(b)}{\partial b^n} \Delta b^n \right) p_b(x) dx \,. \tag{5}$$

We remind that this power expansion is valid only if the state function is analytic in ε and the series converge and, therefore, any criteria of convergence should include the magnitude of the perturbation parameter; perturbation parameter is taken as equal 1 in several practical computations and also here [3, 4]. It yields for the input random variable with symmetric probability density function in the second order perturbation approach

$$E\left[\sigma(b)\right]=\sigma^0\left(b^0\right)+\frac{1}{2!}\frac{\partial^2\sigma(b)}{\partial b^2}\mu_2(b)+\cdots+\frac{1}{10!}\frac{\partial^{10}\sigma(b)}{\partial b^{10}}\mu_{10}(b), \tag{6}$$

where $\mu_n(b)$ denotes nth order central probabilistic moment of the variable b. All the terms with odd orders are equal to 0 for the symmetric random variable and the orders higher than the 10th one are neglected additionally. Similar considerations leads to the expressions, like the variance, for instance

$$Var\left[\sigma(b)\right]=\mu_2(\sigma(b))=\int_{-\infty}^{+\infty}(\sigma(b)-E\left[\sigma(b)\right])^2\,p(b)db\,. \tag{7}$$

Quite similarly, it is possible to derive 3rd central probabilistic moments using also the 10th order approach as

$$\mu_3(\sigma(b))=\int_{-\infty}^{+\infty}(\sigma(b)-E\left[\sigma(b)\right])^3\,p(b)db\,, \tag{8}$$

and also the 4th order probabilistic moment may be recovered from this scheme as

$$\mu_4(\sigma(b))=\int_{-\infty}^{+\infty}(\sigma(b)-E\left[\sigma(b)\right])^4\,p(b)db\,. \tag{9}$$

Let us mention that it is necessary to multiply each of these equations by the relevant order probabilistic moments of the input random variable to get the algebraic form convenient for any symbolic computations. Based on the classical definition of the variance we can calculate the coefficient of variation as fallows

$$\alpha(\sigma(b))=\frac{\sqrt{\mu_2(\sigma(b))}}{E\left[\sigma(b)\right]}\,. \tag{10}$$

Higher order moments and characteristics are determined to recognize the type of probabilistic distribution od the state functions. We compute in turn the skewness coefficients as the ratio of the third central probabilistic moment and the third power of standard deviation as

$$S(\sigma(b))=\frac{\mu_3(\sigma(b))}{\left[\sqrt{\mu_2(\sigma(b))}\right]^3}\,, \tag{11}$$

and kurtosis as

$$\kappa(\sigma(b))=\frac{\mu_4(\sigma(b))}{\left[\sqrt{\mu_2(\sigma(b))}\right]^4}-3\,. \tag{12}$$

It should be mentioned that at this stage the proposed procedure is independent from a choice of the initial probability distribution function, however a satisfactory probabilistic conver-

gence of the final results may demand various lengths of the expansions for random variables with different distributions.

The method is based on the iterative coupled deterministic FEM [5] equations as follows

$$\begin{cases} \mathbf{C}^{(\alpha)}\dot{\boldsymbol{\theta}}^{(\alpha)} + \hat{\mathbf{K}}^{(\alpha)}\boldsymbol{\theta}^{(\alpha)} = \hat{\mathbf{R}}^{(\alpha)} \\ \mathbf{K}^{(\alpha)}(\boldsymbol{\theta})\mathbf{q}^{(\alpha)}(\boldsymbol{\theta}) = \mathbf{R}^{(\alpha)} \end{cases}, \tag{13}$$

where $\mathbf{C}$ is heat capacity matrix, $\boldsymbol{\theta}$ is nodal temperatures vector, $\hat{\mathbf{K}}$ is heat conductivity matric, $\mathbf{K}$ denotes stiffness matrix, $\mathbf{R}$ is matrix of nodal loads, $\hat{\mathbf{R}}$ is a matrix of thermal loads and $\mathbf{q}$ is the solution displacement vector and α indices the test number relevant to Response Function Method [6]. We solve Eq. (13) in ABAQUS system. Further determination of the probabilistic moments from Eqs. (5÷12) thanks to the symbolic derivation of all partial derivatives with respect to the given random variable b. We carry out all these calculations in computer algebra system MAPLE.

3 NUMERICAL EXAMPLE

Numerical example consist of the necking of an axi-symmetric steel specimen (Fig. 1). Its initial length is $2L_0$ and initial radius is R_0 and $L_0 / R_0 = 4$. We make small cut of its corner $\Delta R = 0{,}005R_0$ * 0.05 mm to ensure necking in the middle of it [7].

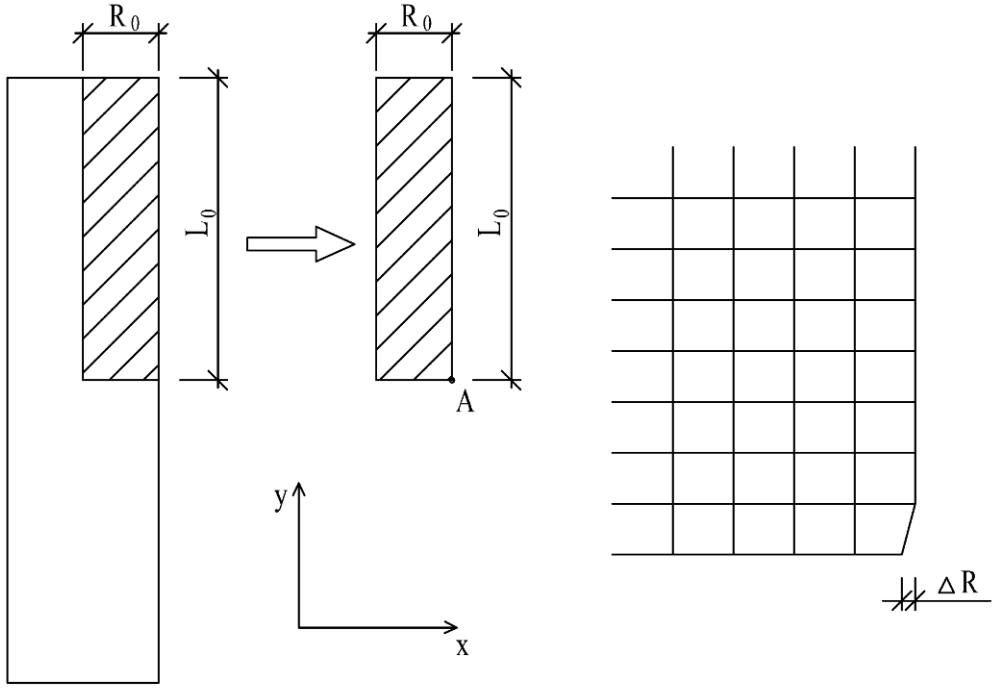

Figure 1: Geometry and imperfection of the specimen.

4-noded FEM elements [8] are used for discretization which divide the specimen into 1600 pieces called in ABAQUS system CAX4RT (Fig. 2a). Each node has 7 degree of freedom (6 mechanical and 1 thermal which is temperature). Mechanical boundary conditions are $u_x = 0$ on the left side, $u_y = 0$ on the bottom side and forced displacement $u_y = 0.125L_0$ applied to the top side (Fig. 2b).

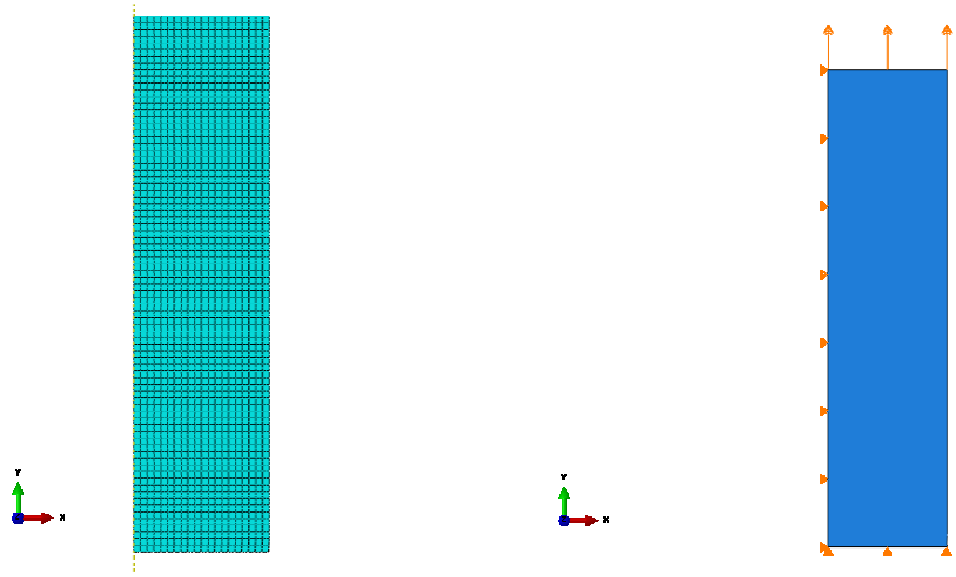

Figure 2: FEM model (a) and thermal boundary conditions (b).

Initial temperatures are set equal to $T_0 = 20\,°\mathrm{C}$ for all nodal points, while fire simulation is performed by setting surface temperatures equal to these calculated from the fire curve after ISO 834-1 statement (Fig. 3a). We set these temperature to the top and the right side of the specimen (Fig. 3b).

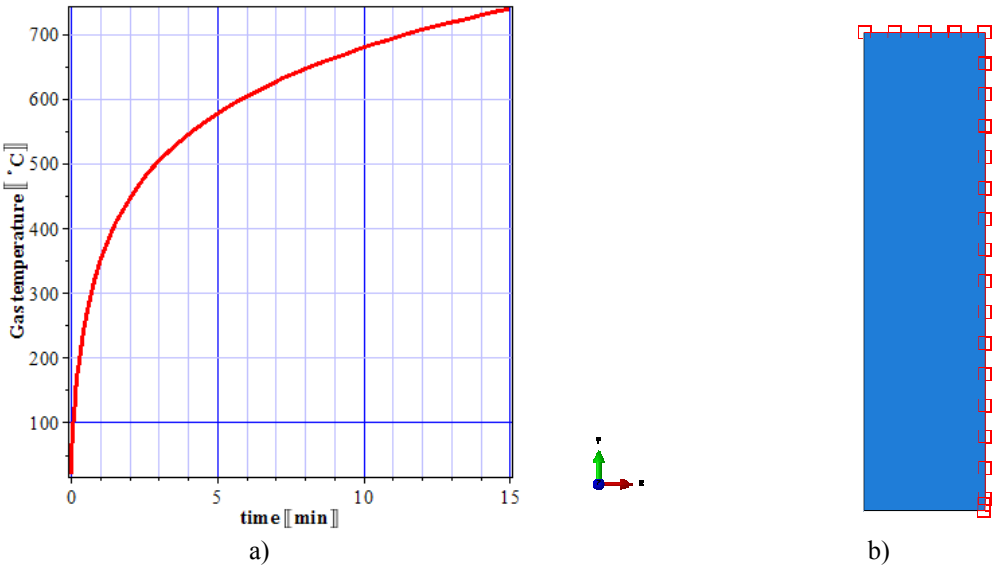

Figure 3: Time-temperature curve (a) and thermal boundary conditions (b).

Steel properties as Young modulus, yield strength, conductivity, specific heat and coefficient of thermal elongation are highly temperature-dependent according to EN 1993-1-2. Fully coupled thermal-stress analysis is used where element temperature affects stress and displacements values. 11 tests were carried out with time period equal to 15 minutes for 11 different values of random variable which was gas temperature $b \equiv T_s$ in this case. Figures 4÷6 show resulting Huber-Mises stress distribution on deformed specimen. As can be expected this distribution is not uniform. Moreover we can see precisely how necking rise.

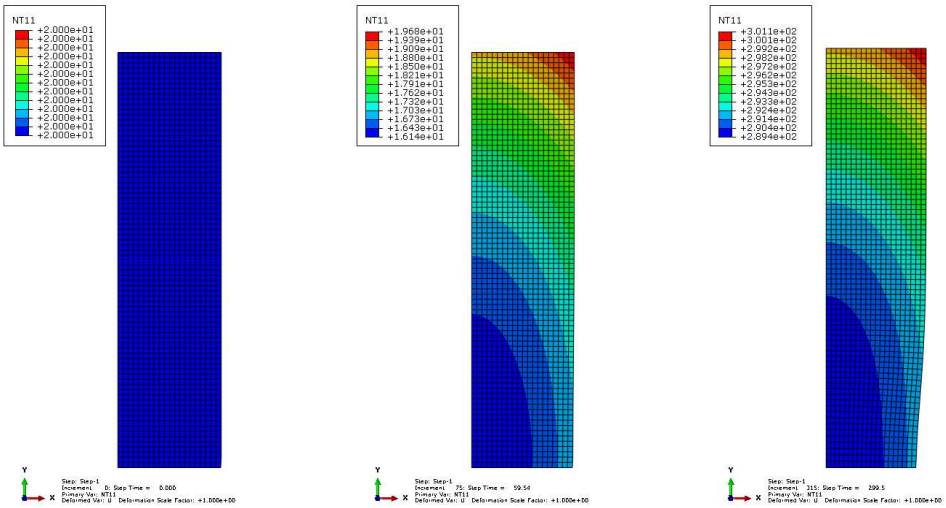

Figure 4: Stress distribution at t=0, 60, 300 s.

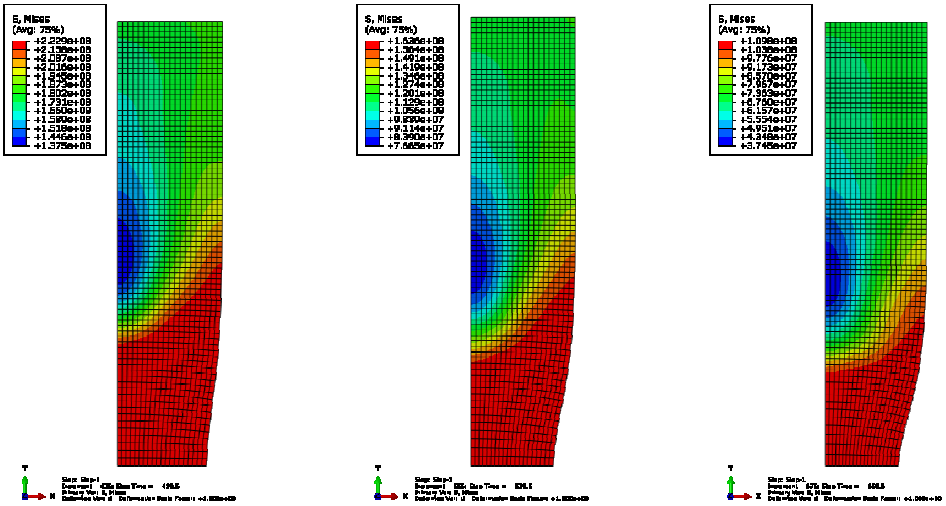

Figure 5: Stress distribution at t=420, 540, 660 s.

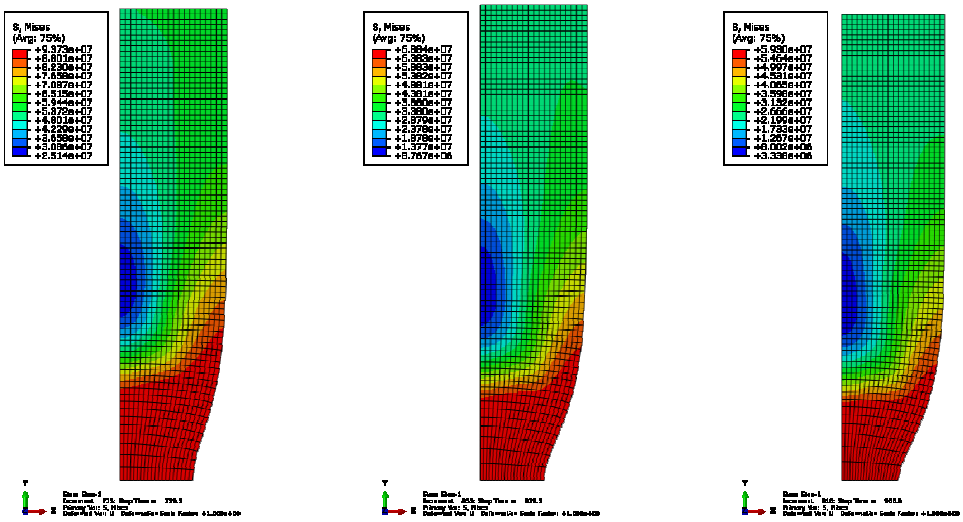

Figure 6: Stress distribution at t=720, 860, 900 s.

19 polynomial response functions were performed to describe the response of the structure (Fig. 7a). Based on resulting stress values taken from FEM analysis results at an interval of 60 seconds we made time-dependent Huber-Mises diagram (Fig. 7b).

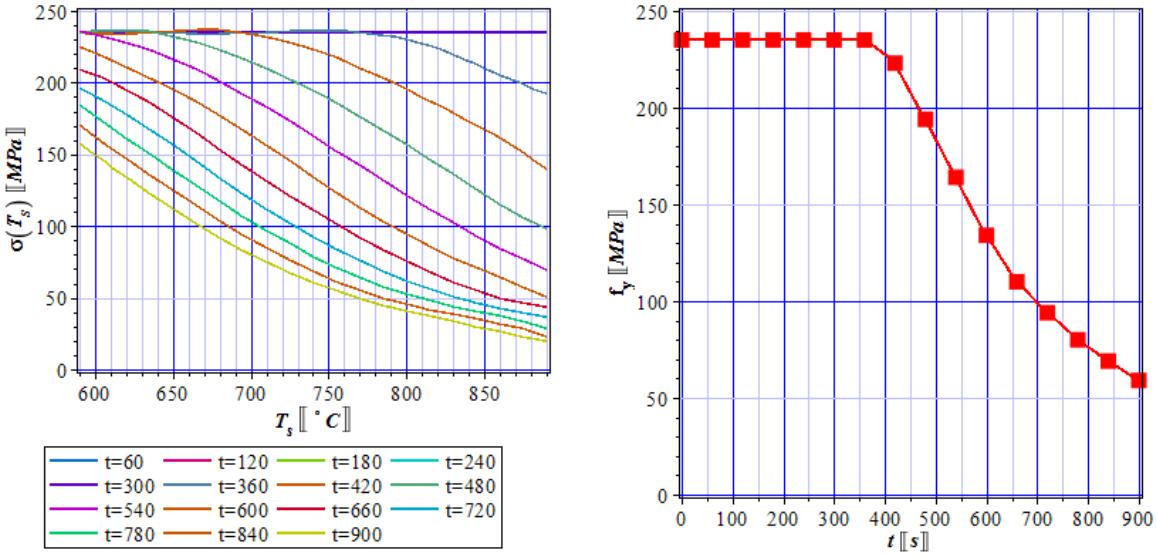

a) b)

Figure 7: Response functions (a) and resulting yield strength reductions (b).

Resulting gas temperature is also random variable in this case with its input coefficient of variation $\alpha(T_s)$ in the range of [0.0,0.2]. Figures 8÷9 show expectation, coefficient of variation, skewness and kurtosis for extreme Huber-Mises stress in the point A of the specimen (Fig. 1). The biggest fluctuations of expected values and coefficient of variation could be observed for $\alpha(T_s)=0.20$. Coefficients of variation are close to zero (small dispersion) for $\alpha(T_s)\leq 0.10$ and it means that values of stress are concentrated round its means.

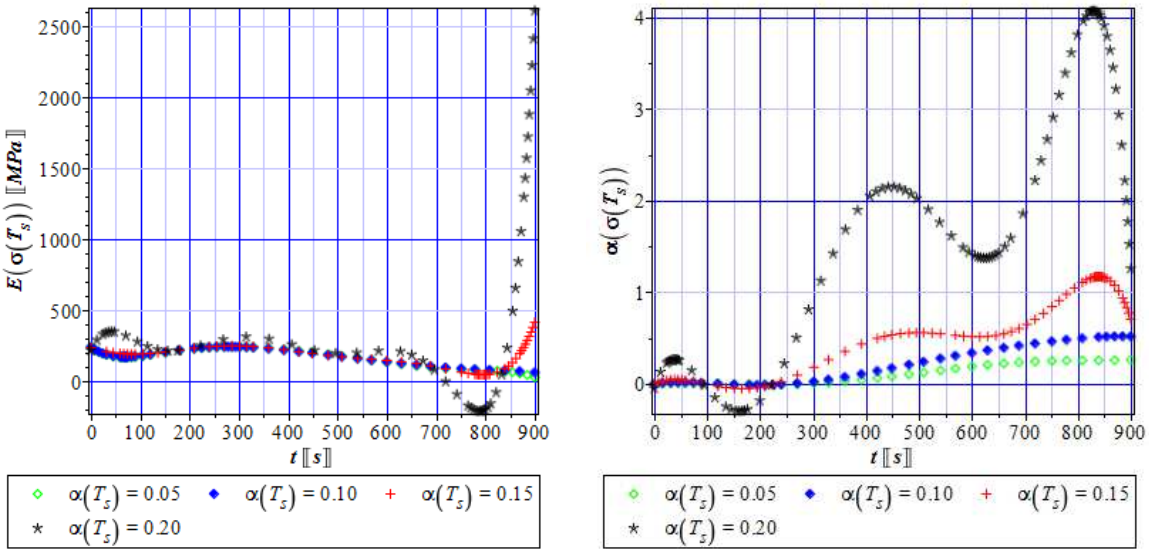

a) b)

Figure 8: Expectations (a) and coefficient of variation of stress (b).

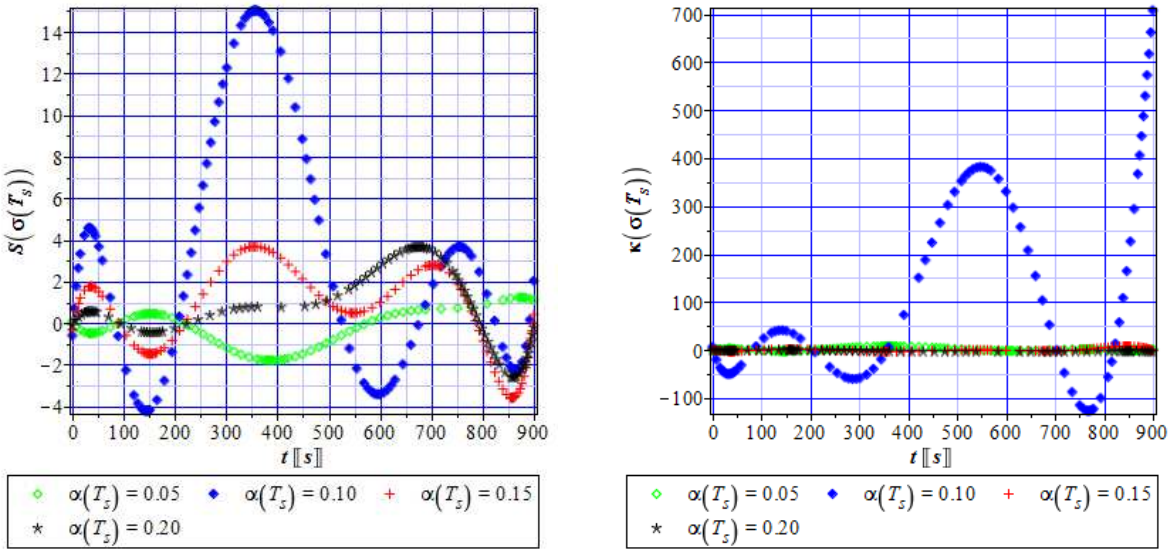

a) b)

Figure 9: Skewness (a) and kurtosis of stress (b).

Studying stress and kurtosis distributions we can see fluctuations for $\alpha(T_s) = 0.10$. According to this plots we can conclude that Huber-Mises stress distribution is Gaussian when $\alpha(T_s) \leq 0.05$ because in this range skewness and kurtosis are close to zero.

This computation example has been made to determine the probabilistic characteristics for stress distribution under fire condition which is very often taken as non-Gaussian. This test illustrates the strength test cylindrical steel rod at elevated temperatures, the results of which enable determination of the yield point of the curve changes as a function of time.

4 CONCLUSIONS

Based on this computation we can say that probability distribution of reduced stress under fire condition is Gaussian only if we narrow the range for input coefficient of variation to $\alpha(T_s) < 0.05$. Moreover we shown the common usage of FEM software ABAQUS and computer algebra system MAPLE which is crucial to use Stochastic Finite Element Method [9] (SFEM). We looked at the influence of polynomial degree [10] on the results of stochastic analysis. In such non-linear problems we have to use different functions to fit the response of the structure. The information about stress distribution obtained in this study can be use in the stochastic reliability analysis of the steel structures under fire according to both First and Second Reliability Method [3].

REFERENCES

[1] M. Kleiber, T.D. Hien, *The Stochastic Perturbation Method for Computational Mechnics*. Wiley, 1992.

[2] M. Kamiński, *The Stochastic Perturbation Method for Computational Mechanics*. Wiley, 2013.

[3] M. Kamiński, M. Strąkowski, On the least squares stochastic finite element analysis of the steel skeletal towers exposed to the fire. *Archives of Civil and Mechanical Engineering*, **13**, 242-253, 2013.

[4] M. Kamiński, P. Świta, Generalized stochastic finite element method in elastic stability problems. *Computers and Structures*, **89**, 1241-1252, 2011.

[5] R. Putanowicz, J. Jaśkowiec, P. Pluciński, A. Stankiewicz, Finite element implementation of nonlinear thermo-elasticity as typical coupling of diffusion and momentum balance. *Mechanics and Control*, **32**, 152-163, 2013.

[6] M. Kamiński, J. Szafran, Stochastic Analysis and reliability of the steel telecommunication towers. *CMES: Computer Modeling in Engineering and Science*, **83**, 143-168, 2012.

[7] N. Aravas, On the numerical integration of a class of pressure-dependent plasticity models. *International Journal for Numerical Methods in Engineering*, **24**, 1395-1416, 1987.

[8] O.C. Zienkiewicz, R.C. Taylor, *The finite element method, Vol. I, 4th Edition*. McGraw Hill, 1989.

[9] G. Stefanou, M. Papadrakakis, Stochastic finite element analysis of shells with combined random material and geometrical properties. *Computer Methods in Applied Mechanics and Engineering*, **193**, 139-160, 2004.

[10] A. Björck, Numerical Methods for Least Squares Problems. SIAM, 1996.

ECCOMAS Congress 2016
VII European Congress on Computational Methods in Applied Sciences and Engineering
M. Papadrakakis, V. Papadopoulos, G. Stefanou, V. Plevris (eds.)
Crete Island, Greece, 5–10 June 2016

AN INTRODUCTION TO STOCHASTIC FINITE ELEMENT METHOD ANALYSIS OF HYPERELASTIC STRUCTURES

Marcin M. Kamiński[1], **Damian K. Sokołowski**[1],

Lodz University of Technology, Department of Structural Mechanics
Al. Politechniki 6, 90-924 Łódź, Poland
e-mail: Marcin.Kaminski@poczta.p.lodz.pl, sokolowski.dmn@gmail.com

Keywords: Stochastic Finite Element Method, hyperelasticity, rubber-like materials.

Abstract. *The main idea of this work is to demonstrate an application of the generalized iterative stochastic perturbation technique to numerical analysis of the hyperelastic materials and structures with Gaussian random parameter, where the input random variable is a magnitude of the vertical uniformly distributed load. Theoretical apparatus is connected with the general order Taylor expansion of both input and state parameters with random coefficients and analytical derivation of their first four probabilistic moments and coefficients. Our computational implementation is released with the Response Function Method having polynomial basis of the order minimizing variance and maximizing correlation of the least squares fitting to the series of numerical experiments. Computational experiment concerns the hyperelastic rubber-like prismatic beam under three-point bending discretized in the FEM system ABAQUS with the use of various 3D brick finite elements. Large deformations in the vertical symmetry plane of this structure are analyzed in the stochastic context – by determination of their expectations, coefficients of variations, skewness and kurtosis for different increments of the external load. It enables also to recover the basic probabilistic characteristics of the stress-strain curve of such a material, whose further comparison with the experiments will allow a full validation of such a probabilistic model. The entire probabilistic algorithm together with statistically optimized Weighted Least Squares Method fitting are implemented in the symbolic algebra package MAPLE. The proposed scheme of the Stochastic Finite Element Method is contrasted with the crude Monte-Carlo scheme and also with the semi-analytical calculations of the same probabilistic characteristics by direct integration of the response functions.*

1 INTRODUCTION

Modern probabilistic computational mechanics focuses on a development of the new, still more efficient theoretical and numerical methods as well as on their applications in experimentally driven models or on these research problems where the input statistics are available. Statistical nature of structural properties obviously necessary for realistic durability analysis and property prediction of materials is almost perfectly known for the area of elastic homogeneous materials but still deserves some attention in hyperelastic, visco-elastic [1], elasto-plastic, elasto-visco-plastic and especially in thermo-elasto-visco-plastic models. Although some stochastic models are known in thermal transient processes for temperature independent and dependent cases [2], a full coupling in-between elastic and thermal analysis in terms of coupled problem is still to be performed also in terms of uncertainty in temperature affecting all material and physical characteristics in terms of coupled analyses. A little bit separate problem is an identification of all material characteristics for the hyperelastic solid that needs more material constants than their elastic counterpart; the statistical point of view seems to be quite natural in this context [3], even accounting for the neural networks employed to provide such an identification [4]. Deterministic constitutive models in the area of hyperelasticity relevant to the rubber-like materials are quite well known and systematically documented. They include the Neo-Hooekan [5], Mooney-Rivlin [6], Ogden [7], Yeoh [8], Gent [9], Arruda-Boyce [10] as well as the very recent so-called extended tube model [11] resulting from molecular statistical-mechanical approach for rubber networks provided by Henrich and Kaliske. They have some Finite Element Method implementations and applications [11] that concern only an entirely deterministic case; even for a composite made of particle-reinforced rubber [12]. Probabilistic counterparts of nonlinear material models [13] are definitely less known and not systematically worked out [14] (some exceptional Monte-Carlo simulations are available but they return only quantitative results), so that such a systematic extension would be necessary. The very important aspect is that the aforementioned theories of hyperelastic behavior contain various numbers of material parameters, so that their comparisons in terms of material uncertainty will not be so straightforward as in linear elastic case; such a study needs definitely more experimental work and theoretical assumptions than before.

The main objective of this work is application of the iterative generalized stochastic 10^{th} order perturbation technique [15] implemented together with the Finite Element Method [16, 17, 18] to calculate the first four probabilistic characteristics of the ultimate vertical displacement and the corresponding Huber-Mises stress for the three-point bended hyperelastic beam. This study is undertaken to analyze the hyperelastic material with Mullins effect subjected to large deformations in a large-strain non-linear analysis with a complex contact properties and stabilization of computation. This example is also focused on numerical error determination of the FEM solution for various 3D brick finite elements and an increasing discretization density; it is also concentrated on a sensitivity analysis of the ultimate vertical displacement and the corresponding Huber-Mises stress in addition to the magnitude of an external vertical load. Probabilistic considerations included in this work are based on the Weighted Least Squares Method (WLSM) with the polynomial basis, whose order is statistically optimized and relates the displacement and stress with the uncertain external load. These optimal polynomials are then used in the iterative perturbation-based SFEM, Monte-Carlo and semi-analytical integration technique in order to determine expectations, coefficients of variation, skewness and kurtoses of the vertical deflections and the corresponding stresses in the function of the input coefficient of variation. Such a study is carried out to determine accuracy of the iterative perturbation method in analyses of hyperelastic materials and to check the probabilistic properties of the output variables, i.e. the ultimate vertical deflec-

tions and the corresponding Huber-Mises stresses. Such iterative generalized Stochastic Perturbation (SPT) method is applied here since it yields more accurate results than the classical SPT, including the negative and mixed moment terms that are absent in the linearized version. The input random parameter is chosen here as an external load in a form of the uniform pressure, whose Probability Density Function (PDF) is Gaussian. Such a parameter has been chosen here, since it is one of the most unpredictable variables included in the model. It usually cannot be exactly calculated in real structures and it varies non-monotonously with large time variations and its underestimation may certainly cause an overall failure. This is the case of civil engineering structures, machinery, vehicles or aircrafts. This work serves as a preliminary study for further expansion towards experimentally-calibrated hyperelastic material model probabilistic analysis based on a crack initiation or rubber softening.

2 HYPERELASTIC MATERIAL MODEL

Let us consider the total strain energy U in some material, which is defined as

$$U = U_{dev}\left(\lambda_i\right) + U_{vol}\left(J^{el}\right), \tag{1}$$

where U_{dev} stands for the deviatioric part of the strain energy and U_{vol} for the volumetric part of this energy. The Yeoh material definition defines these variables in a following way

$$U_{dev}\left(\lambda_i\right) = C_{10}(\overline{I}_1 - 3) + C_{20}\left(\overline{I}_1 + 3\right)^2 + C_{30}\left(\overline{I}_1 - 3\right)^3 \tag{2}$$

and

$$U_{vol}\left(J^{el}\right) = \frac{1}{D_1}\left(J^{el} - 1\right)^2 + \frac{1}{D_2}\left(J^{el} - 1\right)^4 + \frac{1}{D_3}\left(J^{el} - 1\right)^6, \tag{3}$$

in which C_{io} and D_i are temperature-dependent material parameters, $\overline{I}_1$ stand for the first deviatioric strain invariant defined as $\overline{I}_1 = \overline{\lambda}_1^2 + \overline{\lambda}_2^2 + \overline{\lambda}_3^2$ and where the stretches $\overline{\lambda}_i$ are defined as $\overline{\lambda}_i = J^{-\frac{1}{3}}\lambda_i$. J stands here for the total volume ratio and λ_i are the principal stretches. The initial shear modulus and bulk modulus are given as $\mu_0 = 2C_{10}$, $K_0 = 2/D_1$. When a thermal dependence is taken into consideration, the elastic volume ratio J^{el} relates the total volume ratio J and the thermal volume ratio J^{th} in a following manner $J^{el} = J/J^{th}$, where $J^{th} = \left(1 + \varepsilon^{th}\right)^3$. ε^{th} stands for the linear thermal expansion strain obtained from the temperature and the isotropic thermal expansion coefficient; it is not considered here.

The augmented Mullins effect strain energy density function applied in this study is following

$$U = \eta U_{dev}\left(\lambda_i\right) + \Phi\left(\eta\right) + U_{vol}\left(J^{el}\right), \tag{4}$$

where the damage variable η is defined as

$$\eta = 1 - \frac{1}{r} erf\left(\frac{U_{dev}^m - U_{dev}}{m + \beta U_{dev}^m}\right) \tag{5}$$

and the damage function is adopted here as

$$\Phi(\eta) = \int_1^n f\left(\eta, U_{dev}^n\right) d\eta + (1-\eta) U_{dev}^m, \tag{6}$$

which on the primary path $\eta = 1$ and satisfying the requirement $\Phi(1) = 0$ can be expressed as

$$\Phi'(\eta) = \left(m + \beta U_{dev}^m\right) erf^{-1}\left(r(1-\eta)\right) - U_{dev}^m. \tag{7}$$

The variables r, β and m all denote the input material constants, the first two of which are dimensionless and the latter has dimensions of energy. The error function erf used in this definition is defined as $erf(x) = \frac{2}{\sqrt{\pi}} \int_o^x \exp\left(-w^2\right) dw$ and the function $f\left(\eta, U_{dev}^n\right)$ can be further expressed as $f\left(\eta, U_{dev}^m\right) = \Phi'(\eta) + U_{dev}^m = U_{dev}^m - U_{dev} = -\Phi'(1) - U_{dev}$. Fundamental properties of this damage function are that (a) when $U_{dev}^m = U_{dev}$, then it corresponds to a point on the primary curve and $\eta = 1.0$ (b) η attains its minimum value η_m upon complete removal of deformation, i.e. when $U_{dev} = 0$ and (c) in all other cases η varies monotonously from η_m to 1.0.

3 COMPUTATIONAL EXPERIMENTS AND DISCUSSION

3.1 Computational model

A computational model applied in this study consists of three elements, the 10 m long hyperelastic beam with section of 1.5 m x 1 m, the support cylinders with diameter of 1.2 m and a 0.3 m deep loading plate having section of 1 m x 1 m (Fig. 1). The beam is supported on the two cylinders placed on each side of the beam and loaded with various magnitude of pressure of $p = 1\ Pa$ mean value, which is applied on the upper surface of the centrally placed plate. The static scheme of three-point bending is applied here firstly because it is a usual scheme used in laboratory tests, secondly since such loading is common in various applications of cyclically loaded parts and finally as it creates regions dominated by bending and shear. Both, an upper loading plate and the cylinders are deformable and much stiffer than the beam with elastic parameters set as Young modulus $E = 10\,GPa$ and Poisson ratio $\nu = 0.3$. The hyperelastic beam has a complex material definition of the Yeoh model with the following parameters: $C_{10} = 1.326$, $C_{20} = -0.326$, $C_{30} = 0.1319$, $D_1 = 0.000725$, $D_2 = 0$, $D_3 = 0$, whose Mullins effect has the following parameters: $r = 1.1$, $m = 100$, $\beta = 0.1$. This ensures a hyperelastic behavior and cyclic softening of the beam. A connection between the elements is assured by a hard contact in the normal direction enforced by the penalty method and a penalty-driven tangential contact behavior with a friction coefficient of $\mu = 0.99$ for the cylinders- and of $\mu = 0.8$ for the plate-beam boundary; the slippage of the beam from the cylinders is prevented by tying its outer edges to the cylinder surface. A possibility of separation of the model elements after an initial and repeated contact is allowed here (surfaces are not tied after the contact). In order to keep the mechanical boundary conditions for a three-point loading, bases of the cylinders are fully restrained (no displacement or rotation allowed) and the loading plate has only the vertical displacement degree of freedom (dof) active; it further supports a sym-

metry of the loading. Additionally, the beam is divided into 8 cells to shorten the surface length of both contacts, which speeds up numerical analysis.

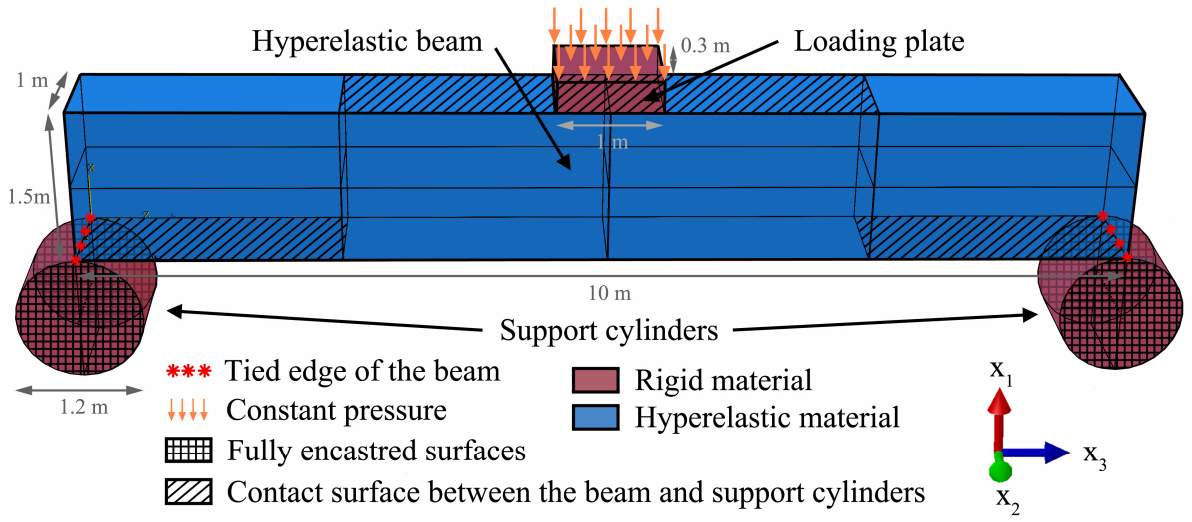

Figure 1: FEM model of the beam.

Computational model and numerical experiments are provided both in the FEM system ABAQUS with a series of beam loadings for the ultimate vertical displacement and the corresponding Huber-Mises stress of the beam. The elements are meshed with 104 397 reduced (stress) integration linear brick finite elements (C3D8R) giving a total of 418 602 independent variables (Fig. 2); the entire beam element additionally has a hybrid definition of elements of type C3D8HR, which deal with a full (or nearly full) incompressibility of this FEM domain. The type and amount of elements is selected to obtain the best possible quality of results for an acceptable computational effort via the error analysis of computational simulations presented in Fig. 4 and, separately, by a sensitivity analysis of the resulting displacements and the corresponding stress available in Fig. 5. Numerical computations include a material and contact non-linearity and are based on the non-linear theory of large strains. Completion of each simulation requires partitioning to 40-150 steps, each calculated on the basis of the result of the previous one (usually consisting of 2-16 iterations); this is a main reason for the lower amount of the Finite Elements (FEs) than in the single-step linear-elastic computations. Results of these analyses (in a form of the stress mapped on a deformed shape of the beam) show large symmetric deformations of a thick beam with also symmetric stress map – a typical work range of usual hyperelastic (rubber) materials. Predictably, the stress pattern is symmetric and the highest near the bottom of the beam; there also exist particular stress concentrations nearby the cylindrical supports and on each side of the loading plate. The stress concentrations on the support edges of the beam are disregarded in this study since they are rather enforced by the tied internal conditions and would differ for the exact type of the slippage-preventing support applied in the experiments.

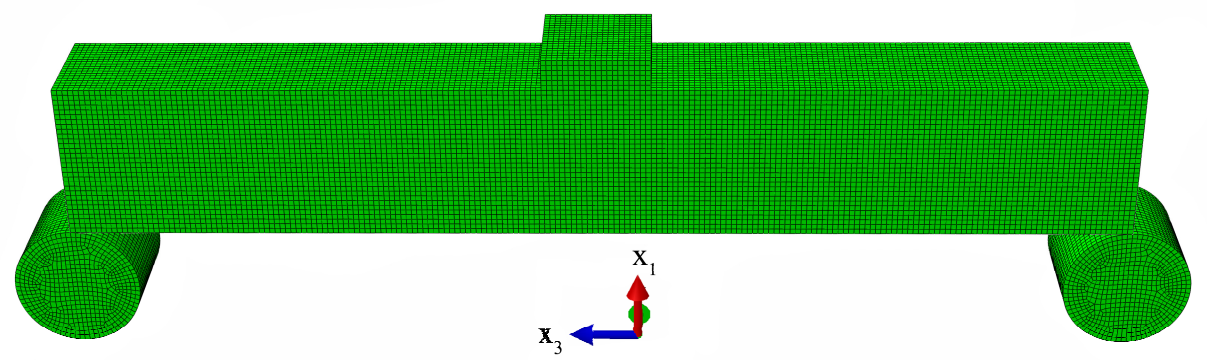

Figure 2: The finest mesh of the beam.

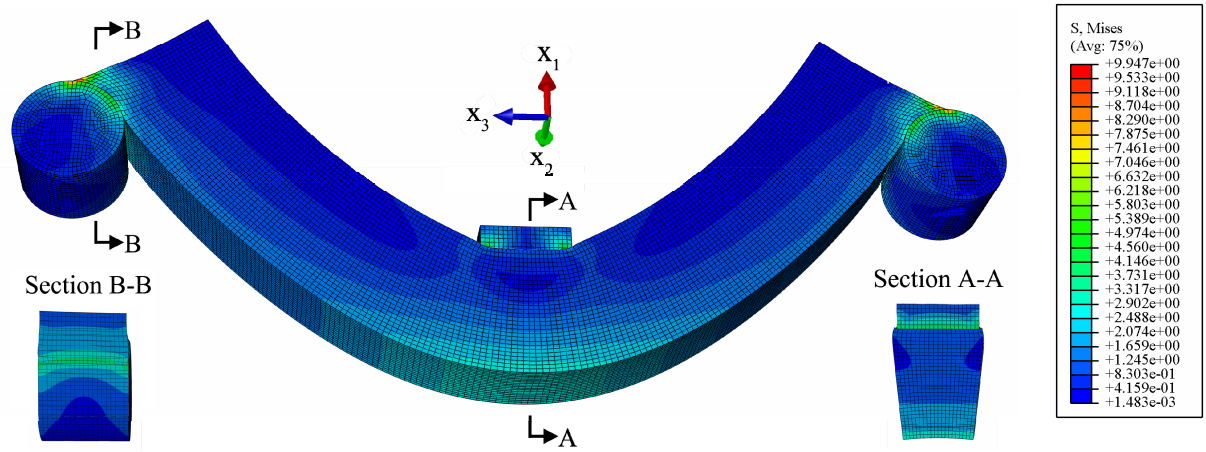

Figure 3: Map of the reduced stress plotted on deformed configuration of the beam under bending.

3.2 Computational error and sensitivity analysis

Within the error study, three types of FEs are used, i.e. the reduced integration linear brick C3D8R, the incompatible modes linear brick C3D8I and the reduced integration quadratic brick C3D20R; due to incompressibility of the material, the beam is discretized here always with the hybrid finite elements (C3D8RH, C3D8IH, C3D20RH). These particular types of elements are chosen after their best performance range, which for the linear reduced elements is large distortion in bending, for the incompatible modes – bending and for the second-order (quadratic) elements with reduced integrations - nonlinearity; all the above phenomena take place in this analysis and therefore such an error and performance study seems to be profitable here. An error graph presented in Fig. 4 firstly shows the very good convergence of results and a small error $E_r(n)$ for all the discretization densities applied, which never crosses 3% and is as small as 0.15% for the higher amount n of the FEs. The smoothness of convergence is not so evident, as in the linear analyses [20], but an overall reduction of the error together with an increase in the FEs amount is still clear. When an influence of material and contact non-linearities as well as occurrence of large strain theory is taken into consideration, this result is more than satisfactory. A secondary observable is, that in this particular case the computations of quadratic elements have a very low convergence and, additionally, that not all of the computations lead to the final result – some particular distributions of the elements are stuck in various points of the analysis. Basing on this (C3D8I brings no additional variation), the standard C3D8R elements are chosen for the further analysis. Please note, that the computational effort for the quadratic FEs is much higher than for the linear ones of the identical

amount and, therefore, Fig. 4 cannot serve for the final evaluation of time-performance of these methods.

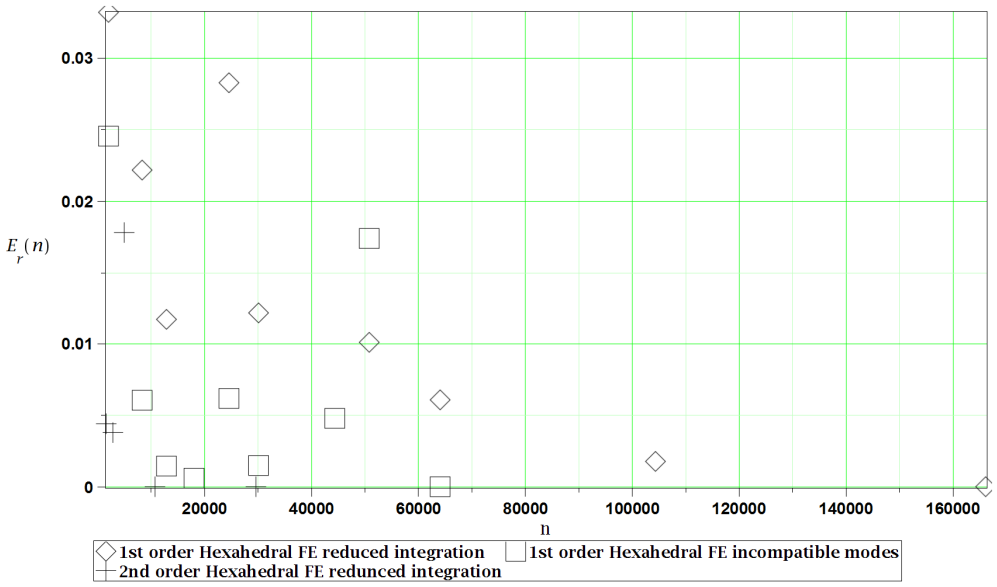

Figure 4: Computational error of the Finite Element Method results.

Sensitivity coefficients $S(p)$ of both ultimate vertical deformations and the corresponding stresses are computed by 11 separate simulations in 20% neighborhood of the mean external load, which ranges from 0.9 Pa till 1.1 Pa, via a direct algebraic differentiation based on the additional response functions (Fig. 5). These sensitivities are quite naturally all positive, since the increase of the external load should also increase both the ultimate vertical displacement and also its corresponding reduced stress. The Huber-Mises stress is much more sensitive to the fluctuations in an external load but has smaller curvature than the sensitivity of displacement in this particular load region.

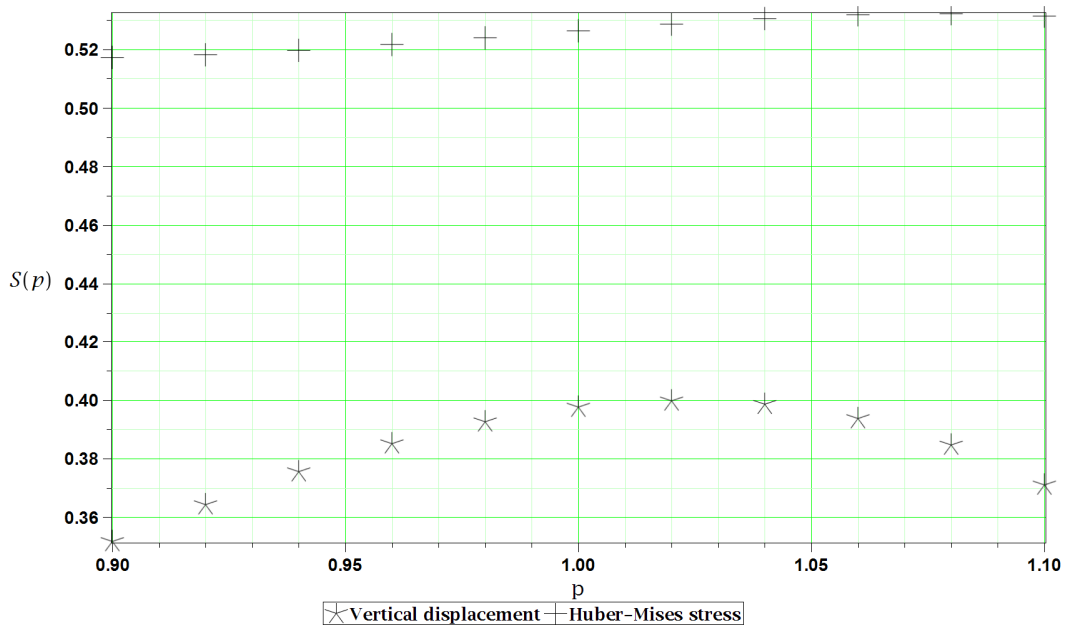

Figure 5: Sensitivity coefficients for the ultimate deformation and the corresponding von Mises stress.

3.3 Probabilistic analysis

The probabilistic computations are all carried out in the symbolic system MAPLE and are focused firstly on a determination of the optimum order of the response function of the WLSM (Tab. 1), which is then used in the main computation of the probabilistic characteristics based on the ultimate displacements and the corresponding Huber-Mises stresses. The procedure of calculation of these characteristics consists of (a) integration of the response function together with the Gaussian PDF in a semi-analytical method, (b) its insertion into the 2^{nd}, 4^{th} and 6^{th} (only for the stresses) order Taylor expansions in stochastic perturbation-based approach and (c) its sampling in a discrete Monte-Carlo analysis (with 500 000 random trials) for an increasing value of the input coefficient of variation $\alpha(p)$. The characteristics calculated in this manner include the expectation (Fig. 6), the coefficient of variation (Fig. 7), the skewness (Fig. 8) and the kurtosis (Fig. 9). The Least Squares Method is used here in its weighted form and non-linear version with a weighting scheme similar to the Dirac function – [1,1,1,1,1,10,1,1,1,1,1] – making the influence of the mean value equivalently important as the remaining test results. Maximization of the optimal polynomial order is done via simultaneous maximization of the correlation and minimization of the variance of the WLSM and the RMS error. The total number of WLSM increments equals 20 in this study and the chosen polynomial order is 4^{th} for the displacement and 5^{th} for the stress. The resulting parameters used in the optimization process are well illustrated in Tab. 1 and correlate the subsequent results with the polynomial order; all the beneath given probabilistic results (Figs 6-9) consecutively show the characteristics of the ultimate vertical displacements on the left and of the corresponding reduced (Huber-Mises) stresses on the right side. The input uncertain parameter – an external load p – varies in 20% neighborhood of the mean value of 1 Pa with 11 discrete values of $p \in [0.90, 0.92, \ldots, 1.00, \ldots, 1.10]$.

Variable		Vertical deformation			Huber-Mises stress		
Parameter		Correlation	Variance	RMS error	Correlation	Variance	RMS error
Polynomial order	10	0.986783	6.54E+04	3.87E+10	-0.988917	5.94E+04	2.73E+10
	9	0.99122	2.59E+03	5.39E+07	-0.985964	2.76E+02	3.88E+06
	8	-0.99389	6.80E+01	1.27E+04	-0.999826	1.78E+01	8.21E+03
	7	-0.964519	3.55E-01	2.04E+00	0.999923	1.21E-02	5.70E-03
	6	0.999816	1.11E-02	5.26E-04	0.999951	2.66E-03	3.64E-05
	5	0.999807	1.68E-03	1.02E-05	**0.999952**	**1.04E-03**	**1.34E-06**
	4	**0.999468**	**2.70E-03**	**7.94E-06**	0.999891	1.25E-03	1.70E-06
	3	0.999405	2.85E-03	8.94E-06	0.999884	1.30E-03	1.84E-06
	2	0.99539	8.00E-03	7.04E-05	0.998737	4.29E-03	2.03E-05
	1	0.999449	1.29E-01	1.83E-02	0.99989	7.63E-02	6.38E-03

Table 1: Weighted Least Squares Method optimization results for a Dirac type of weights.

The expectations of the output variables both are a little decreasing in a concave manner together with an increase of the uncertainty. Additionally, they both have a horizontal asymptote approached at the zero uncertainty, for which they obviously must return the exact results obtained in the computational FEM experiments. These output functions are continuous, smooth and with no local inflections or discontinuities. The 2^{nd} order (based on the first two Taylor expansions) perturbation-based approach returns here a little divergent results and is

valid only for $\alpha(p) \in [0.00,\ 0.05]$, but as long as the higher order is applied, all the three separate methods yield exactly the same output.

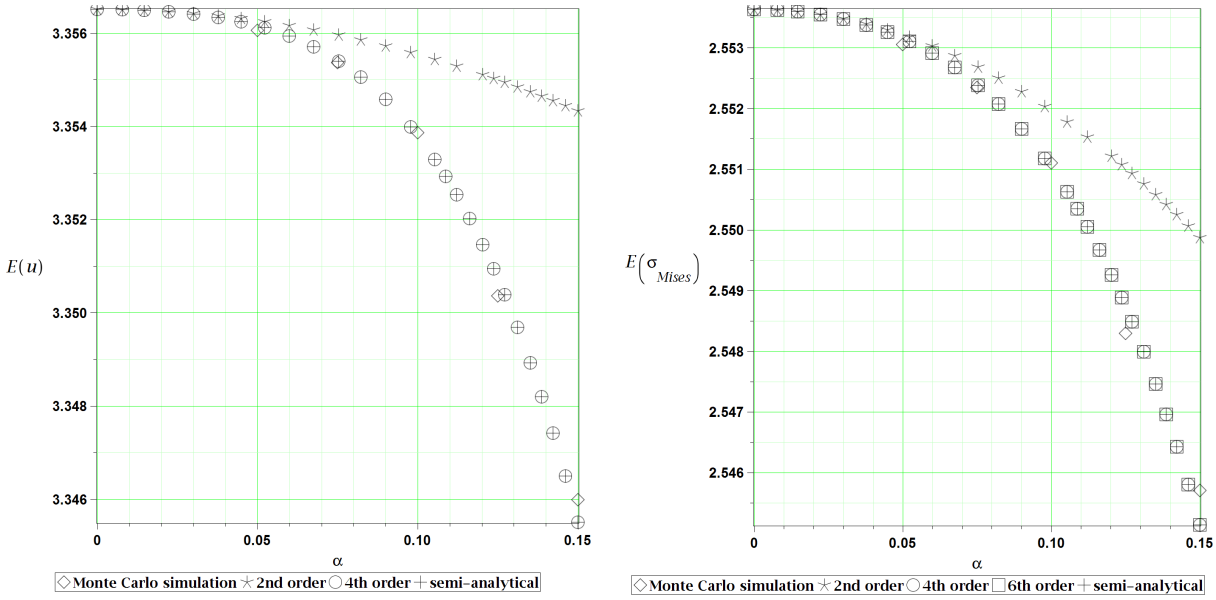

Figure 6: Expected values of
a) the ultimate deflection and b) the corresponding Huber-Mises stress
of the beam subjected to three-point bending with respect to the uncertainty in the external load.

The resulting coefficients of variation (Fig. 7) of both output variables are always increasing in the concave manner while staying lower than the input uncertainty. The differences come (a) in the curvature, which is much higher for the displacement than for the stress, (b) in the magnitude, a little smaller for the displacements, and (c) in the agreement of the probabilistic methods, being perfect for the case of the stress and not so ideal for the displacement based coefficient of variation. Predictably, the 4th order stochastic perturbation is much better correlating with the other results - up to $\alpha(p) = 0.12$, while the 2nd order – only to $\alpha(p) = 0.07$; the 6th order, available only for the stress-based characteristics, is precise for all the considered uncertainty range.

The higher order probabilistic characteristics (Figs 8-9) are generally less convergent than the previous ones. In this case not only the perturbation-based approach yields different results, but also correlation of the Monte-Carlo and semi-analytical outputs is not perfect, especially for the kurtosis based on the reduced stress. The 4th order perturbation-based approach quite early diverges – at $\alpha(p) \in [0.03,\ 0.06]$, the 6th order is much better here – it diverges only at $\alpha(p) \simeq 0.13$. Nevertheless, these higher characteristics are all smooth and without discontinuities. The 2nd order analysis disallows consideration of these higher order characteristics, since it simply vanishes. The Skewness is all negative with a rather concave manner and a small magnitude comparable for the both output characteristics. This means that both PDFs are increasingly leaning to the right side with an increase in uncertainty. Kurtoses are either only negative with an exponential manner (based on the displacement) or positive with a concave-convex curvature and an apparent inflection point at $\alpha(p) = 0.085$ (based on the stress). Since both, the kurtosis and skewness are quite close to zero, distributions of both output parameters have PDFs close, but still diverging from the normal (Gaussian) distribution for the entire uncertainty range considered here.

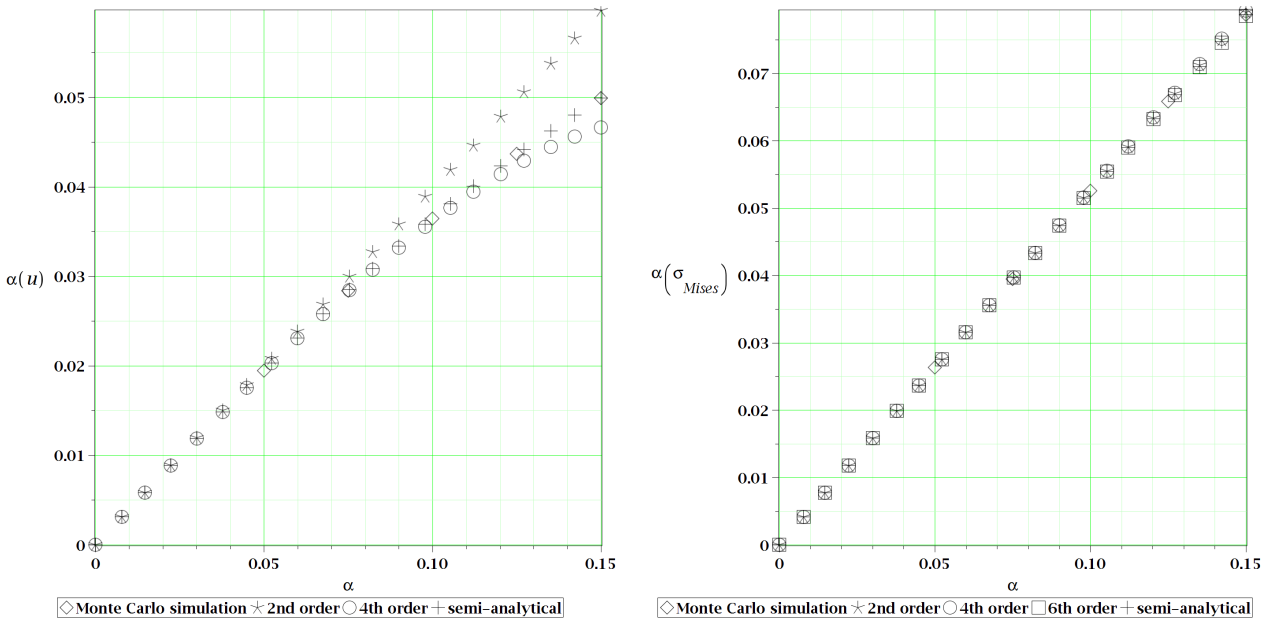

Figure 7: Coefficients of variation of
a) the ultimate deflection and b) the corresponding Huber-Mises stress
of the beam subjected to three-point bending with respect to the uncertainty in the external load.

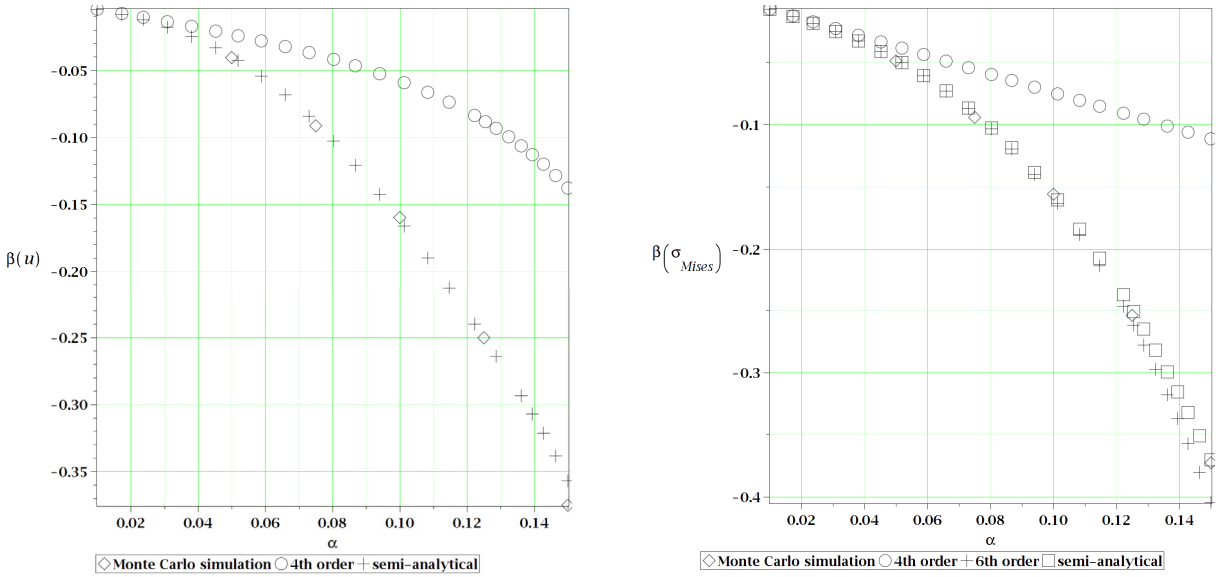

Figure 8: Skewness of
a) the ultimate deflection and b) the corresponding Huber-Mises stress
of the beam subjected to three-point bending with respect to the uncertainty in the external load.

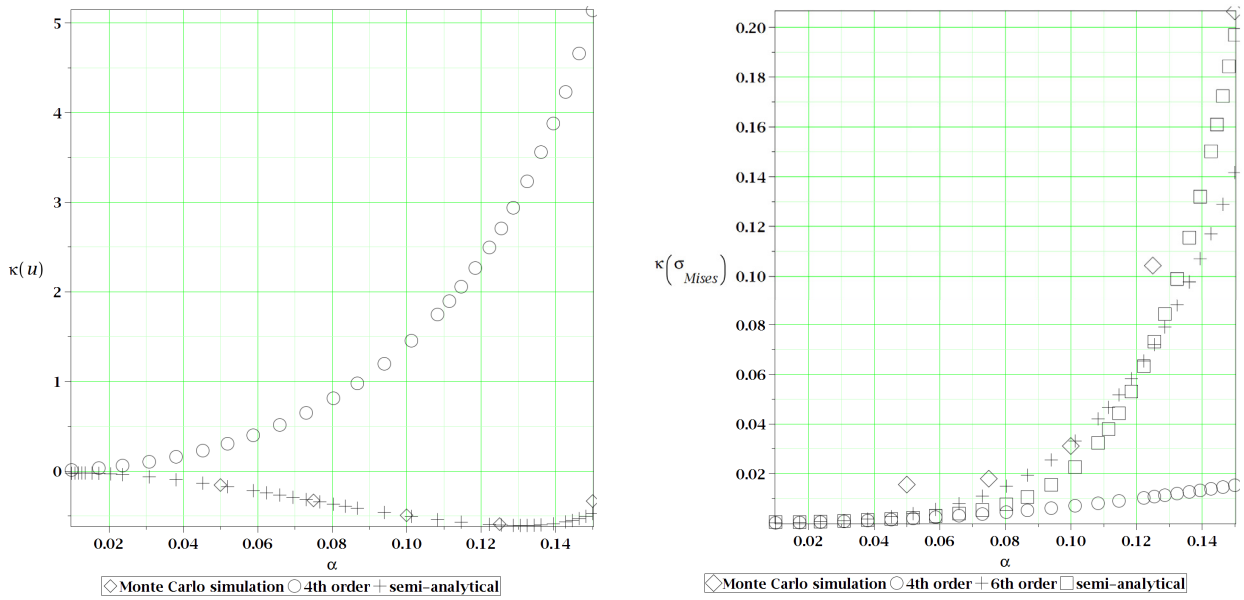

Figure 9: Kurtoses of
a) the ultimate deflection and b) the corresponding Huber-Mises stress
of the beam subjected to three-point bending with respect to the uncertainty in the external load.

4 CONCLUSIONS

This study reports calculation of the first four probabilistic characteristics of the ultimate displacements and the corresponding Huber-Mises stresses based on an input uncertain variable of the external load. The output variables are computed for the three-point bended hyperelastic beam with a Yeoh definition of material, additionally augmented by the Mullins effect. An analysis not only uses a novel iterative stochastic perturbation technique, but also connects it with a hyperelastic material in a large-strain non-linear numerical simulation. The nonlinearities come from the material, contact and constitutive relation. A further extension of this study may include (a) correlation of the material characteristics with experimental results, (b) incorporation of the fracture model in the hyperelastic material definition and (c) sequential or full coupling of this study with temperature analysis; such coupling is important here because the deformation process of elastomers is exothermic and their mechanical properties depend on temperature already in the typical environmental conditions.

Numerical analysis clearly shows that the computational error is quite small for the entire range of the FEs amount and that the preferable brick element type is C3D8R, which has a relatively high precision and provides the highest convergence for a moderate computational effort. The minimum amount of elements used in such study should generally exceed 60 000 elements, since the complex support and material definitions are susceptible to the discretization density. The resulting displacements range here from 3.22 m to 3.48 m and the Huber-Mises stresses - 2.42 Pa to 2.69 Pa for the external load in form of pressure of 0.9 Pa to 1.1 Pa. Both, the stress and the strain obtained here is much below the rupture limit for elastomers, but it certainly belongs to large deformations. Sensitivities of the displacement and Huber-Mises stress to the change in an external load are all positive and much higher for the reduced stress. Probabilistic considerations show a relatively good correspondence in-between different techniques and, predictably, an increasing correlation of the stochastic perturbation-based technique together with an increase of the length of the proposed Taylor expansion. The 6th order expansion is already almost perfectly agreeing with the remaining methods with an ex-

ception of the kurtoses higher than $\kappa(p) \simeq 0.12,$ where it slightly diverges. It should be, however, noted that this order of expansion is available only for the stresses, whose optimal response polynomial has a higher order than the one for the displacements. The probabilistic distributions of the state variables may generally be considered here as close to Gaussian, since both the Kurtosis and Skewness are quite close to zero. Nevertheless, such an assumption should rather be exceptional.

REFERENCES

[1] R. Christensen, *Theory of Viscoelasticity*. Dover Publ., Dover, 2010.

[2] T. Hien, M. Kleiber, On solving nonlinear transient heat transfer problems with random parameters, *Computer Methods in Applied Mechanics and Engineering*, **151**, 287-299, 1998.

[3] T. Harth, S. Schwan, J. Lehn, F. Kollmann, Identification of material parameters for inelastic constitutive models: statistical analysis and design of experiments. *International Journal of Plasticity*, **20**, 1403-1440, 2004.

[4] Y. Shen, K. Chandrashekhara, W.F. Breig, L.R. Oliver, Neural network based constitutive model for rubber material. *Rubber Chemistry and Technology*, **77**, 257-277, 2004.

[5] R.W. Ogden, *Non-linear Elastic Deformations*. Dover Publ., Dover, 1984.

[6] M. Mooney, A theory of large elastic deformation. *Journal of Applied Physics*, **11(9)**, 582-592, 1940.

[7] R. Ogden, D. Roxburgh, A pseudo-elastic model for the Mullins effect in filled rubber. *Proceedings of the Royal Society of London A*, **455**, 2861-2877, 1999.

[8] O. Yeoh, Some forms of the strain energy function for rubber. *Rubber Chemistry and Technology*, **66(5),** 754-771, 1993.

[9] A. Gent, A new constitutive relation for rubber. *Rubber Chemistry and Technology*, **69**, 59-61, 1996.

[10] E. Arruda, M. Boyce, A three-dimensional model for the large stretch behavior of rubber elastic materials. *Journal of the Mechanics and Physics of Solids*, **41(2)**, 389–412, 1993.

[11] M. Kaliske, G. Heinrich, An extended tube-model for rubber elasticity: statistical-mechanical theory and finite element implementation. *Rubber Chemistry and Technology*, **72**, 602-632, 2010.

[12] A. Dorfmann, R. Ogden, A constitutive model for the Mullins effect with permanent set in particlereinforced rubber. *International Journal of Solids and Structures*, **41**, 1855-1878, 2004.

[13] C. Truesdell, W. Noll, *The Non-Linear Field Theories of Mechanics. 3rd Edition*, Springer Verlag, Berlin-Heidelberg, 2004.

[14] M. Guedri, A. Lima, N. Bouhaddi, D. Rade, Robust design of viscoelastic structures based on stochastic finite element models. *Mechanical Systems and Signal Processing*, **24(1)**, 59-77, 2010.

[15] M. Kamiński *The Stochastic Perturbation Method for Computational Mechanics*, Chichester: Wiley; 2013.

[16] J.T. Oden, J.N. Reddy, *A Mathematical Theory of Finite Elements*. New York: Wiley-Intertscience; 1976.

[17] M. Kamiński, On the dual iterative stochastic perturbation-based finite element method in solid mechanics with Gaussian uncertainties. *International Journal of Numerical Methods in Engineering*, **104**, 1038-60, 2015.

[18] M. Kamiński, D. Sokołowski, Dual probabilistic homogenization of the rubber-based composite with random carbon black particle reinforcement. *Composite Structures*, **140**, 783-797, 2016.

ECCOMAS Congress 2016
VII European Congress on Computational Methods in Applied Sciences and Engineering
M. Papadrakakis, V. Papadopoulos, G. Stefanou, V. Plevris (eds.)
Crete Island, Greece, 5–10 June 2016

IDENTIFICATION OF INTERVAL FIELDS FOR SPATIAL UNCERTAINTY REPRESENTATION IN FINITE ELEMENT MODELS

Matthias Faes[1], Jasper Cerneels[1], Dirk Vandepitte[2], and David Moens[1]

[1]KU Leuven, Department of Mechanical Engineering, Technology Campus De Nayer
Jan De Nayerlaan 5, B-2860 St.-Katelijne-Waver
e-mail: {Matthias.Faes, Jasper.Cerneels, David.Moens}@kuleuven.be

[2] KU Leuven, Department of Mechanical Engineering, Campus Heverlee
Celestijnenlaan 300, B-3001 Leuven
e-mail: Dirk.Vandepitte@kuleuven.be

Keywords: Interval Fields, Uncertainty identification, Finite Element modelling, Spatial Uncertainty

Abstract. *In the context of integrating uncertainty and variability in Finite Element (FE) models, several advanced techniques for taking both inter- (between nominally identical parts) and intra-variability (spatial variability within one part) into account have recently been introduced. In the framework of non-probabilistic variability, especially the theory of Interval Fields (IF) has been proven to show promising results. Following this approach, variability in the input parameters of the FE model is introduced as the superposition of a number of base vectors scaled by interval factors. Application of the IF concept however requires identification of these parameters. Recent work has focused on the identification of interval uncertainty for the case of inter-variability. However, to the knowledge of the authors, no such techniques for identifying interval intra-variability are present in literature.*

This work focuses on finding a solution to the inverse problem, where the variability on the output side of the model is known from measurement data, but the spatial uncertainty on the input parameters is unknown. This paper proposes a methodology to solve this inverse problem. The uncertain simulation space, created by propagating an interval field throughout an FE model, is modelled using its convex hull. The same concept is used to model the uncertainty in the measurement space. A metric to describe the discrepancy between these convex hulls, based on the difference of their volumes and overlap, is defined and minimised in order to identify the spatial variability on the input side of the model. Validation of the methodology is performed using simulated measurement data. It is shown that numerically exact identification of a simulated measured IF is possible following the proposed methodology.

1 INTRODUCTION

During the last decades, the incorporation of non-determinism in Finite Element (FE) simulations received wide acceptance among academia and the industry for taking uncertainties that are omnipresent in our everyday life, already into account in an early design phase [1]. Especially for these design purposes, the study of inter-variability (variability between different nominal identical products) as well as intra-variability (variability of model properties within a single component, also referred to as 'spatial variability') proves to be extremely valuable. In this context, non-probabilistic approaches such as Interval Finite Elements (IFE) or Fuzzy Finite Elements (FFE) were introduced, where the uncertainty is depicted as an interval or fuzzy set and thus propagated. In the IFE concept, the uncertainty is modelled as two crisp bounds on the variable between which all possible values lie, and thus propagated. The FFE concept is an extension to this principle, where the membership of a variable to an interval is considered as a continuous function, ranging from 0 (the variable is certainly no part of the interval) to 1 (the variable lies for sure in the interval). [2–5].

In the specific case of spatial uncertainty for the description of intra-variability, two extreme methodologies for the representation of the spatial character of the uncertainty are usually adopted [6, 7]. The first method consists of defining a single interval to represent a spatial varying parameter for the entire model, assuming it is homogeneous throughout the modelled geometry. The second method considers one interval per individual element in the FE model, neglecting all possible dependency throughout the model. The former method poses a serious underestimation of the complexity of the spatial nature of the uncertainty; the latter gives rise to physically infeasible realizations of the uncertainty throughout the model. Moreover, by neglecting all possible dependency, the numerical cost of evaluating the model increases drastically due to the high dimensionality of the input space. As a solution to this, the framework of Interval Fields (IF) was recently introduced [6–8]. The Interval Field concept is based on the superposition of n_b base vectors ,$\boldsymbol{\psi}_i$, which represent a set of spatial uncertainty *patterns*, scaled by independent interval factors α_i^I, which cover the uncertainty.

Despite the current availability of these very advanced techniques for the uncertainty propagation, the use of representative measurement data to quantify the input uncertainty of FE analyses remains nowadays the major challenge. Especially for a designer who is facing a substantial (and often beforehand unknown) variability in the realisation of his design, this knowledge is indispensable when creating reliable products. In literature, some techniques are available to improve the quality of non-deterministic analyses (see e.g., [9–11]). Techniques for updating IFE and FFE models on experimental data were introduced only very recently, based on the minimization of the difference between the extreme boundaries on simulation and measurement data. **Haag et al.** introduced in this context an inverse methodology for the identification of the parameters of FFE models [12]. **Khodaparast et al.** employed a Kriging predictor as a meta-model for the updating of interval [13] and fuzzy [14] finite element models. **Erdogan and Bakir** used a hybrid combination of a Genetic Algorithm and Particle Swarm as updating scheme in the context of the identification of uncertainty in Fuzzy Finite Element models [15]. **Fedele et al.** used an adjoint-based optimisation technique to estimate the bounds of a model parameter, based on uncertain raw measurements [16]. They handled overestimation of the interval width using the inclusion isotonicity property of interval arithmetic. Finally, **Fang et al.** employed interval response surface models for the inverse propagation of the interval uncertainty [17]. The proposed techniques however are incapable of dealing with spatially varying uncertainty, due to the assumption of homogeneity of the uncertainty throughout the model.

It is clear that in order to be representative for the actual intra-variability present in the final components, the Interval Field concept needs an accurate quantification of the driving parameters: the base vectors and interval factors for IF. In the specific case of elastostatic mechanical properties, this quantification is impossible to attain following traditional experimental approaches such as uniaxial tensile tests. This paper therefore focuses on the identification of the spatial uncertainty on the input parameters of an FE model following an inverse approach. The variability in the measurement data is represented as the convex hull in q-dimensions of the complete set of measurement replica. Identification is performed, based on the minimisation of the variability in the simulation output and this convex hull following an Interior-point minimisation scheme. The concept is demonstrated for Interval FE models, but is easily extendable to Fuzzy FE models. Simulated measurement data are used for demonstrating the developed principles.

2 The Interval Finite Element method

The goal of an Interval FE calculation is to find the bounds on the uncertainty in a general multidimensional result $\mathbf{y}$ of an FE calculation $f()$, based on an interval description of the uncertainty in a number of physical properties $\boldsymbol{\gamma}^{\mathbf{I}}$, which are defined as parameters on the input side of the model. Formally, the uncertainty space $\tilde{\mathbf{y}}$ on the output side of an interval FE calculation is defined as:

$$\tilde{\mathbf{y}} = \left\{ \mathbf{y} | \mathbf{y} = f(\boldsymbol{\gamma}) \wedge \boldsymbol{\gamma} \in \boldsymbol{\gamma}^{\mathbf{I}} \right\} \tag{1}$$

By definition, an interval parameter x is indicated using superscript I: x^I. Vectors are expressed as lowercase boldface characters $\mathbf{x}$, whereas matrices are depicted as uppercase boldface characters $\mathbf{X}$. Usually, $\mathbf{y}^{\mathbf{I}}$ is calculated following an optimisation approach, where the extreme responses of each dimension $\underline{y}_i$ and $\overline{y}_i$ are determined by searching the domain, defined by $\boldsymbol{\gamma}^{\mathbf{I}}$ [3]:

$$\begin{aligned} \underline{y}_i &= \min_{\boldsymbol{\gamma} \in \boldsymbol{\gamma}^I} \quad f_i(\boldsymbol{\gamma}) \qquad i = 1, ..., d \\ \overline{y}_i &= \max_{\boldsymbol{\gamma} \in \boldsymbol{\gamma}^I} \quad f_i(\boldsymbol{\gamma}) \qquad i = 1, ..., d \end{aligned} \tag{2}$$

Herein, $y_i^I = [\underline{y}_i; \overline{y}_i]$ is the result interval scalar for the i^{th} node of the model. Solution of eq. (2) returns the smallest hypercubic approximation $\mathbf{y}^{\mathbf{I}}$ of the uncertainty in the solution set $\tilde{\mathbf{y}}$. For the remainder of the text, interval parameters are either represented using the bounds of the interval $x^I = \{\underline{x}, \overline{x}\}$ or the centerpoint $\hat{x} = \frac{\underline{x}+\overline{x}}{2}$ and interval radius $r_x = \frac{\overline{x}-\underline{x}}{2}$.

In the case of spatial interval uncertainty, the input of the IFE model is given as an Interval Field (IF) $\boldsymbol{\gamma}_{\mathbf{F}}^{\mathbf{I}}(\boldsymbol{r})$. The description of an IF is based on the superposition of n_b base vectors $\boldsymbol{\psi}_i$, which represent a set of spatial uncertainty patterns, scaled by independent interval scalars α_i^I, which cover the uncertainty. In this way the dependency between locally defined intervals is given by the base vectors, while the local intervals themselves remain independent. Moreover, the dimensionality of the input space is reduced drastically as compared to defining a local interval for each node of the model. This favours the numerical cost of an evaluation of the IF FE model. Formally, an interval field for the description of spatial uncertainty in the input parameters $\boldsymbol{\gamma}_{\mathbf{F}}^{\mathbf{I}}(\mathbf{r})$ is expressed in the explicit form as:

$$\boldsymbol{\gamma}_{\mathbf{F}}^{\mathbf{I}}(\mathbf{r}) = \sum_{i=1}^{n_b} \alpha_i^I \boldsymbol{\psi}_i(\mathbf{r}) \tag{3}$$

3 Identification of interval fields

The application of the interval field approach for the representation of spatial uncertainty requires the identification of its constituting parameters. The methodology starts from the expert knowledge of the analyst on the amount and shape of the base functions necessary to represent the interval field at the input side of the model and incorporates measurement data to identify the amount of uncertainty, which is captured by the interval vector $\boldsymbol{\alpha}^I$.

The propagation of the uncertainty in the physical parameters $\boldsymbol{\gamma}_{\mathbf{F}}^{\mathbf{I}}(\mathbf{r})$ of an FE model typically yields a d-dimensional uncertainty space $\tilde{\mathbf{y}}$, of which $\mathbf{Y}_s \in \mathbb{R}^{d \times q}$ is the matrix containing all q propagated realisations of $\boldsymbol{\gamma}_{\mathbf{F}}^{\mathbf{I}}(\mathbf{r})$. In the context of identifying the input interval field, a quantification of $\mathbf{Y}_s$ is necessary to steer the updating procedure. Therefore its convex hull $\mathbf{C}_s$ and corresponding volume V_s are calculated. In general, the convex hull of a finite set of vectors in Euclidean space is defined as the set of all convex combinations of these vectors. It may also be shown that the convex hull is the smallest possible convex set, encompassing the vectors in $\mathbf{Y}_s$. The uncertainty space, spanned by the computed realizations in $\mathbf{Y}_s$, may contain any combination of output quantities, ranging from nodal output quantities such as displacements, stresses or temperatures to global quantities such as eigenfrequencies and -modes.

The measurement data are obtained trough an experimental procedure where the model is physically tested in analogy to the FE model under consideration. The scattered measurement points, having the same dimensionality d as $\tilde{\mathbf{y}}$, are grouped in $\mathbf{Y}_m \in \mathbb{R}^{d \times t}$, with t the number of test replica. In general, the dimensionality of the experimental and simulation data is not identical. However, through the usage of data interpolation for the measurement data or model reduction techniques for the simulation model, this condition can be achieved. Analogous to the simulation data, the convex hull $\mathbf{C}_m$ and its corresponding volume V_m are calculated. The QHULL library is used to compute the convex hulls. This library makes use of the "Quickhull" algorithm, as developed by **Barber et. al** [18].

Identification of $\boldsymbol{\alpha}^I$ is made through the minimisation of a cost function $\delta(\boldsymbol{\alpha}^I)$, expressing the discrepancy between the output space of the IFE simulation $\mathbf{Y}_s$ and repeated measurement data $\mathbf{Y}_m$. $\delta(\boldsymbol{\alpha}^I)$ is calculated, based on the geometrical properties of the d-dimensional convex hulls $\mathbf{C}_m$ and $\mathbf{C}_s$. More specifically, the difference between the volumes V_m and V_s of the respective hulls and the volume V_o of the intersection $\mathbf{C}_o$ of $\mathbf{C}_m$ and $\mathbf{C}_s$ is taken into account. Due to the convexity of $\mathbf{C}_m$ and $\mathbf{C}_s$, $\mathbf{C}_o$ is also convex. When there is no overlap (i.e. $\mathbf{C}_o = \emptyset$) present between $\mathbf{C}_m$ and $\mathbf{C}_s$, a descent direction for the optimisation problem is ensured by incorporating the squared L_2 norm of the difference between the center of gravity of respectively $\mathbf{C}_m$ ($\mathbf{c}_m$) and $\mathbf{C}_s$ ($\mathbf{c}_s$). Formally, $\delta(\boldsymbol{\alpha}^I)$ is defined as:

$$\delta(\boldsymbol{\alpha}^I) = \left(\left(1 - \frac{V_s}{V_m}\right)^2 + \left(1 - \frac{V_o}{V_m}\right)^2 + \|\mathbf{c}_m - \mathbf{c}_s\|_2^2 \right)^{1/2} \tag{4}$$

The goal interval vector $\boldsymbol{\alpha}^{I,*}$ is finally identified according to:

$$\boldsymbol{\alpha}^{I,*} = argmin\ \delta(\boldsymbol{\alpha}^I) \tag{5}$$

4 VALIDATION

Validation the developed methodology is performed using a dynamic model of a 1-dimensional cantilever beam, shown in figure 1. A finite element model containing 10 quadratic shell elements with 4 nodes is constructed and evaluated for the first 10 eigenfrequencies f_e. Without

the loss of generality, it is assumed that the stiffness of the beam is subjected to spatial uncertainty, which is modelled using the Interval Field concept, with $\mathbf{r}_1 = 2$ and $\mathbf{r}_2 = 7$, with locally defined intervals $\boldsymbol{\alpha}_1^I$ and $\boldsymbol{\alpha}_2^I$ capturing the uncertainty. Hyperbolic base functions $\boldsymbol{\psi}_i(\mathbf{r})$ are assumed, which are known *a priori*. This leads to a simulation space $\mathbf{Y}_s \in \mathbb{R}^{q \times d}$, with $d = 10$. In this specific case, the Interval Field FE model is solved using the vertex method, leading to $q = 2^2 = 4$ realisations of the simulation space.

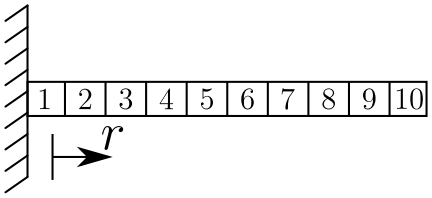

Figure 1: Illustration of the Finite-Element model of the cantilever beam on which the methodology is validated. $\mathbf{r}$ indicates the positive direction along the beam, the numbers in the finite elements indicate the element numbers.

For benchmarking purposes, measurement data is simulated using an *a priori* defined interval field, based on known local intervals $\boldsymbol{\alpha}^I \in \mathbb{IR}^2$, located at $\mathbf{r}_1$ and $\mathbf{r}_2$. Concretely, the goal local intervals are defined as $\alpha_1^I = [1.35e6; 1.55e6]$ and $\alpha_2^I = [1.65e6; 1.85e6]$.

The measurement space $\mathbf{Y}_m \in \mathbb{R}^{t \times d}$ is generated by performing $t = 500$ Monte Carlo simulations, while assuming a uniform distribution between the extreme boundaries of the local intervals $\boldsymbol{\alpha}^I$. Thus, 500 deterministic fields on the stiffness are solved for the first 10 f_e, in order to construct the 10-dimensional measurement space.

The results of the identification procedure are shown in table 1. It can be seen that the proposed methodology is capable of determining the goal interval field, with a local maximum error of 0.042%. This error could be improved by tightening the convergence criteria on the optimization process or propagating more Monte Carlo samples for the representation of the measurement data. However, because it is already negligible, it can be defined as *numerically exact*. The error listed in table 1 is defined as:

Table 1: Results of the identification procedure on an Interval Field capturing the spatial variability in the cantilever beam example.

	$\underline{\boldsymbol{\alpha}}_1^I\ [Pa]$	$\overline{\boldsymbol{\alpha}}_1^I\ [Pa]$	$\underline{\boldsymbol{\alpha}}_2^I\ [Pa]$	$\overline{\boldsymbol{\alpha}}_2^I\ [Pa]$
Goal	$1.35 \cdot 10^6$	$1.65 \cdot 10^6$	$1.55 \cdot 10^6$	$1.85 \cdot 10^6$
Initial	$1.00 \cdot 10^6$	$1.1 \cdot 10^6$	$1.81 \cdot 10^6$	$2.30 \cdot 10^6$
Initial error (%)	15.5%	35.5%	9.7%	24.3%
Result	$1.356 \cdot 10^6$	$1.652 \cdot 10^6$	$1.554 \cdot 10^6$	$1.849 \cdot 10^6$
Error (%)	0.042%	0.025%	0.001%	0.007%

Figure 2 shows the convergence plots. Absolute convergence is obtained after 37 iterations of the optimization process, whereas the locally defined input intervals do not change significantly after 22 iterations. The discrepancy metric δ, defined in equation 4 decreases over the optimization from 8.99 to 0.017.

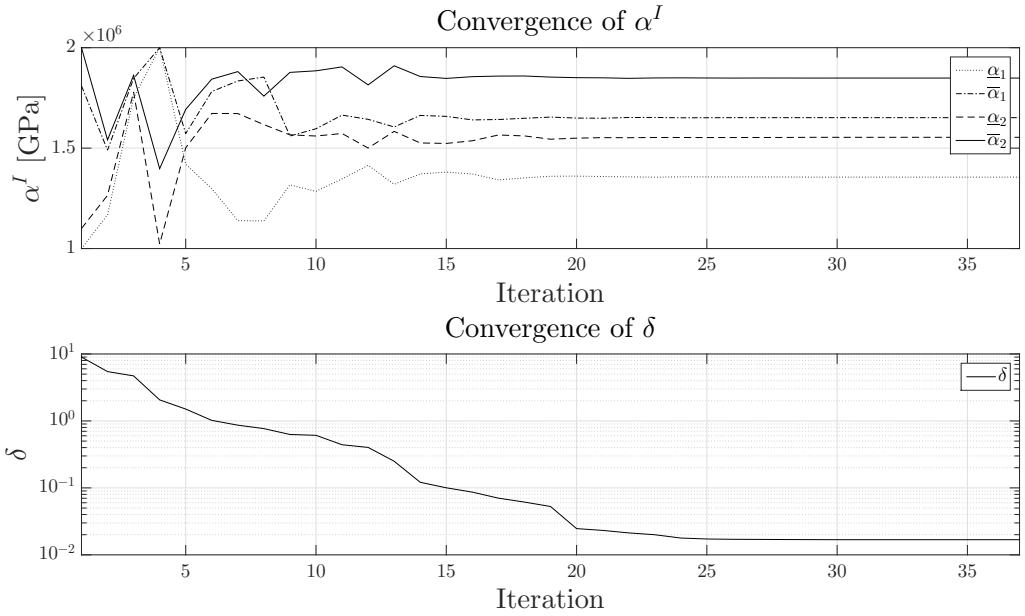

Figure 2: Convergence of the updating procedure. As can be noted, convergence is approximately obtained after 20 iterations. Absolute convergence is only obtained after 37 iterations.

Finally, figure 3 shows a selection of the convex hull over 4 sets of eigenfrequencies before and after the updating procedure. The accurate identification of the interval field encompassing the measurement data is also evident from these plots.

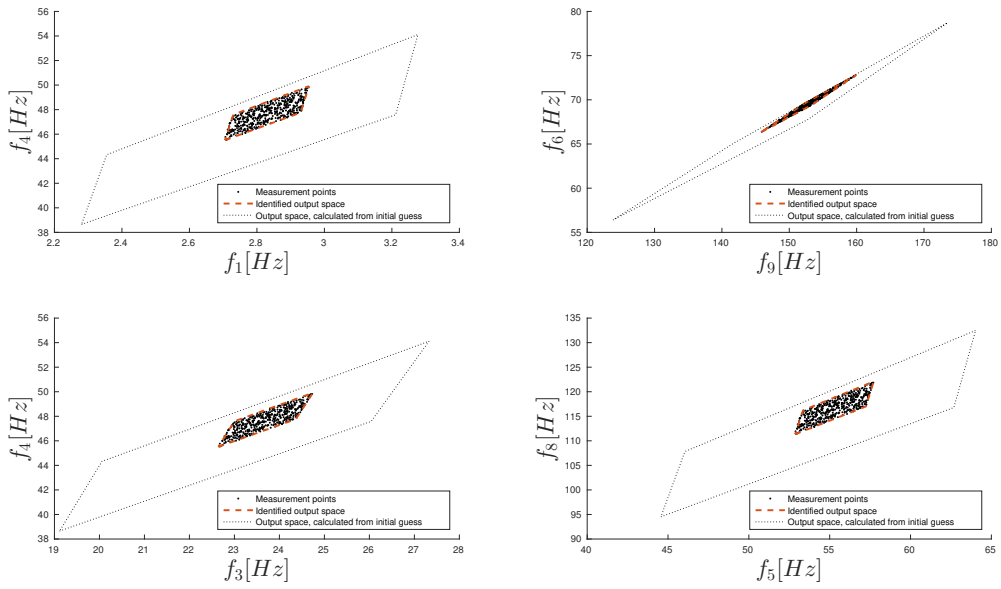

Figure 3: Illustration of the extreme realizations of the input field $\boldsymbol{\gamma}_F^I(\mathbf{r})$ before and after identification, as well as the *goal* input field as a function of the element number.

5 CONCLUSIONS AND FUTURE WORK

In order to represent spatial uncertainty in the physical model parameters constituting the input of a Finite Element (FE) model, the Interval Field theorem proves to deliver accurate results with a limited set of data. The use of this concept however, requires the identification of its driving parameters, the interval factor $\boldsymbol{\alpha}^I$ and a number n_b of base vectors $\boldsymbol{\psi}_i(\mathbf{r})$. A general methodology to identify $\boldsymbol{\alpha}^I$, based on the incorporation of measurement data was introduced. The concept of the identification is based on the convex properties of the uncertainty space, stemming from propagating the input interval field through the interval FE solver on the one hand, and the calculation of the convex hull of the measurement data on the other hand. A measure of discrepancy is defined, and identification is performed by minimising this measure.

The methodology was validated on an industrially sized case study of an axisymmetric model of a pressure vessel using simulated measurement data. It was found that $\boldsymbol{\alpha}^I$ could be identified up to *numerically exact*, using the proposed methodology, within a limited number of iterations.

Future work will be aimed at extending the developed methodology towards the identification of base vectors $\boldsymbol{\psi}_i(\mathbf{r})$ and dimensionality of input space n_b, based on the defined discrepancy measure. Also techniques for the reduction of the output dimensionality will be considered for speeding up the updating process. Finally, also the incorporation of real life measurement data, e.g. coming from full-field strain measurement techniques for elastostatic applications or eigenfrequencies for structural dynamic applications is foreseen in the near future.

REFERENCES

[1] D. Moens and D. Vandepitte, "Recent advances in non-probabilistic approaches for non-deterministic dynamic finite element analysis," *Archives of Computational Methods in Engineering*, vol. 13, no. 3, pp. 389–464, 2006.

[2] L. Farkas, D. Moens, D. Vandepitte, and W. Desmet, "Fuzzy finite element analysis based on reanalysis technique," *Structural Safety*, vol. 32, pp. 442–448, nov 2010.

[3] D. Moens and M. Hanss, "Non-probabilistic finite element analysis for parametric uncertainty treatment in applied mechanics: Recent advances," *Finite Elements in Analysis and Design*, vol. 47, no. 1, pp. 4–16, 2011.

[4] W. Desmet, D. Vandepitte, M. De Munck, W. Verhaeghe, and D. Moens, "Recent Advances in Interval and Fuzzy Finite Element," in *Proceedings of the 1st International Symposium on Uncertainty Quantification and Stochastic Modeling*, no. 2007, (Sao Sebastiao, Brazil), 2012.

[5] M. Hanss, "The transformation method for the simulation and analysis of systems with uncertain parameters," *Fuzzy Sets and Systems*, vol. 130, pp. 277–289, sep 2002.

[6] W. Verhaeghe, W. Desmet, D. Vandepitte, and D. Moens, "Random field expansion with interval correlation length using interval fields," in *Eurodyn 2011*, (Leuven), pp. 2662 – 2667, apr 2011.

[7] W. Verhaeghe, W. Desmet, D. Vandepitte, and D. Moens, "Interval fields to represent uncertainty on the output side of a static FE analysis," *Computer Methods in Applied Mechanics and Engineering*, vol. 260, no. 0, pp. 50–62, 2013.

[8] W. Verhaeghe, W. Desmet, D. Vandepitte, and D. Moens, "Interval fields: Capturing spatial uncertainty within a non-probabilistic Framework," in *Safety, Reliability, Risk and Life-Cycle Performance of Structures and Infrastructures - Proceedings of the 11th International Conference on Structural Safety and Reliability, ICOSSAR 2013*, no. 2, pp. 2963–2969, 2013.

[9] Q. Rui, H. Ouyang, and H. Y. Wang, "An efficient statistically equivalent reduced method on stochastic model updating," *Applied Mathematical Modelling*, vol. 37, pp. 6079–6096, apr 2013.

[10] D. Straub and I. Papaioannou, "Bayesian Updating with Structural Reliability Methods," *Journal of Engineering Mechanics, Trans. ASCE*, vol. 141, no. 3, pp. 1–34, 2015.

[11] I. Boulkaibet, L. Mthembu, T. Marwala, M. I. Friswell, and S. Adhikari, "Finite element model updating using the shadow hybrid Monte Carlo technique," *Mechanical Systems and Signal Processing*, vol. 52-53, no. 1, pp. 115–132, 2015.

[12] T. Haag, M. Hanss (sup.), D. Moens (cosup.), and L. Gaul (cosup.), *Forward and Inverse Fuzzy Arithmetic for Uncertainty Analysis with Applications to Structural Mechanics*. Phd thesis, Universität Stuttgart, 2012.

[13] H. H. Khodaparast, J. E. Mottershead, and K. J. Badcock, "Interval model updating with irreducible uncertainty using the Kriging predictor," *Mechanical Systems and Signal Processing*, vol. 25, pp. 1204–1206, may 2011.

[14] H. Haddad Khodaparast, Y. Govers, S. Adhikari, M. Link, M. I. Friswell, J. E. Mottershead, J. Sienz, and H. H. Khodaparast, "Fuzzy model updating and its application to the DLR AIRMOD test structure," in *Proceedings of the International Conference on Uncertainty in Structural Dynamics, USD 2014*, pp. 4509–4522, 2014.

[15] Y. Serhat Erdogan and P. Gundes Bakir, "Inverse propagation of uncertainties in finite element model updating through use of fuzzy arithmetic," *Engineering Applications of Artificial Intelligence*, vol. 26, no. 1, pp. 357–367, 2013.

[16] F. Fedele, R. L. Muhanna, N. Xiao, and R. L. Mullen, "Interval-Based Approach for Uncertainty Propagation in Inverse Problems," *Journal of Engineering Mechanics*, vol. 4, pp. 1–7, may 2014.

[17] S.-E. Fang, Q.-H. Zhang, and W.-X. Ren, "An interval model updating strategy using interval response surface models," *Mechanical Systems and Signal Processing*, vol. 60-61, pp. 909–927, 2015.

[18] C. B. Barber, D. P. Dobkin, and H. Huhdanpaa, "The quickhull algorithm for convex hulls," *ACM Transactions on Mathematical Software*, vol. 22, no. 4, pp. 469–483, 1996.

ECCOMAS Congress 2016
VII European Congress on Computational Methods in Applied Sciences and Engineering
M. Papadrakakis, V. Papadopoulos, G. Stefanou, V. Plevris (eds.)
Crete Island, Greece, 5–10 June 2016

INTRODUCTION OF BEADINGS INTO A CRASH TUBE USING A ROBUST OPTIMISATION APPROACH

Stefan Scheiblhofer[1]

[1] LKR Leichtmetallkompetenzzentrum Ranshofen GmbH
Austrian Institute of Technology
5282 Ranshofen, Austria
e-mail: stefan.scheiblhofer@ait.ac.at

Keywords: Robust Design Optimisation, crash tube, LS-OPT, response surface method, uncertainty

Abstract. *Deterministic optimisations result in optimum designs for the specified load case but in unstable designs when load cases change. Limitations or uncertainties have to be taken into account leading in design optimisations which will then be insensitive to small fluctuations of geometric or input parameters. Such a stochastic analysis is often referred to as robust design optimisation.*

This paper presents a Robust Design Optimisation for the illustrative example of a cylindrical metal crash tube. The goal of the optimisation is to attain a crash structure which is insensitive to small fluctuations in the magnitude of the crash load, the direction of the velocity, as well as the mass of the impactor. The tilting of the impactor is modelled with a stochastic approach. The geometry of the crash tube shall be insensitive to uncertainties by optimising the wall thickness and by introducing beadings into the tube. Robust design optimisation was conducted with LS-OPT, combining ALTAIR HYPERMORPH for small geometrical adaptions and LS-DYNA for finite element method simulations. To reduce the computational effort, the optimisation is based on metamodels as this allows for mathematical optimisation.

Robust design optimisation allows for results less sensitive to small system fluctuations and hence the geometric tube tolerances can be reduced or the field of application (e.g. vehicle class) can be increased.

For the presented crash tube this advantage results in more stable crash results for scenarios departing from the standard. This in turn leads to increased safety levels of life protection systems. The use of robust design optimisations on the presented crash tube leads to geometries being 6% heavier than the ideal optimum results, but being more robust towards geometric or load fluctuations.

1 INTRODUCTION

The safety level of automotive industry increases steadily in order to accomplish stringent regulations at reduced weight. To attain these targets crash structures have to be refined and optimised. These optimisations are mostly performed with deterministic approaches, assuming that the optimisation systems behave idealistically. But, as Weigert [1] illustrated (figure 1), the input as well as output parameters face fluctuations (blue and greens bars), which are neglected by a state-of-the-art deterministic analysis (red dots). Stochastic optimisations can be used considering statistical distributions of input and output parameters to improve the optimisation and its results.

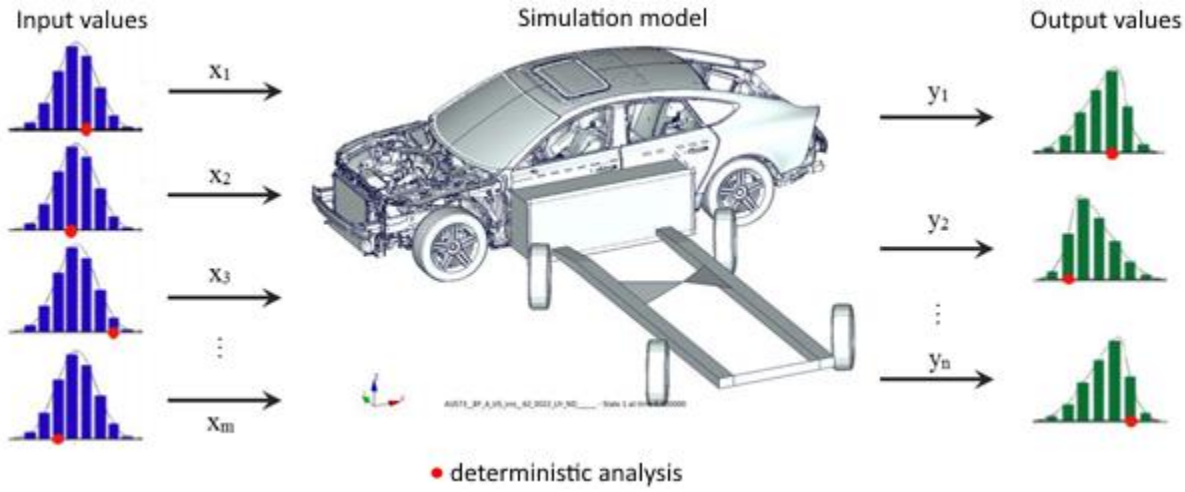

Figure 1: Illustration of a finite element simulation model and its fluctuations of the input values (blue bars) and the output values (green bars) which are neglected by a deterministic analysis (red dots) [1]

Robust Design Optimisation (RDO) is a stochastic optimisation method investigating the robustness of components or assemblies. A robust design is not susceptible to small fluctuations or uncertainties in the observed system. These uncertainties may occur through environment (e.g. ambient temperature), the Finite Element (FE) model (e.g. material parameters) or in the sensors and measurements (e.g. measuring errors) [2, 3]. RDO considers such uncertainties as noise variables with statistical measures as for example the normal distribution of the yield strength.

The aim of such an RDO is a design which is insensitive to these uncertainties and which is ideally leading to a fail-safe system. The influence of the noise variables shall be minimised by optimising the control parameters (e.g. the wall thickness, a parameter controllable by the design engineer).

A deterministic optimum is mostly located near the limit given by the constraints. As a consequence a deterministic design tends to failure, if small fluctuations occur in the system. Therefore a robust design is very important for safety of critical systems.

The following sections will focus on the process necessary to develop a robust design optimisation. Section two deals with the optimisation setup and its methodology. Section three presents the FE model, particularly its boundary conditions and loadings, while the forth section shows and discusses the results. The final section concludes the present paper.

2 OPTIMISATION SETUP AND METHODOLOGY

As the idea of the robust design originates in Taguchi [4], his methods are widely spread. Taguchi's idea was to reduce the impact of uncertainties in the system rather than to control them which is hardly possible. In order to reduce the computational effort the mean value and variance of the parameters are then combined into one variable. This simplification is not necessary for today's standards and does not meet the grown demands. Current optimisation programmes use the Dual Response Surface Methodology (DRSM) [5], as for example LS-OPT [6], which was applied in the course of this paper. DRSM uses a response surface for both the mean value and the variance. This simplifies the optimisation process and enables multi-criteria optimisation, in contrast to the Taguchi approach where detailed information of the variables is lost by combining them.

The robust parameter design method of LS-OPT is a metamodel-based optimisation [7]. A metamodel is a surface, describing the systems response. As the metamodel can be analysed by mathematical methods, the optimisation is very fast. This can be seen in the timing information shown in figure 2. The comparison of clock time shows that the completion of the FE simulations needs 75% of the total time, whereas the metamodeling (0.12%) and its optimisation (0.22%) needed together 0.34% of the total time.

```
================================================================================
RBDO ITERATIVE PROCESS DONE (10 iterations)
================================================================================

 T i m i n g   i n f o r m a t i o n
                          CPU(seconds)   %CPU     Clock(seconds)  %Clock
  ------------------------------------------------------------------------
  Initialization .......     5.0000e-02    0.00         1.0000e+00    0.01
  Sampling .............     3.6499e+03   92.25         3.6560e+03   22.57
  Simulation ...........     2.6030e+01    0.66         1.2255e+04   75.64
  Result extraction ....     2.2697e+02    5.74         2.3500e+02    1.45
  Metamodeling .........     1.7970e+01    0.45         1.9000e+01    0.12
  Optimization .........     3.5820e+01    0.91         3.6000e+01    0.22
  ------------------------------------------------------------------------
  T o t a l s               3.9568e+03  100.00         1.6202e+04  100.00
  ------------------------------------------------------------------------
```

Figure 2: Timing information for a robust design optimisation

In this paper robust optimisations are presented whose aim is to gain a better performance of a crash tube, insensitive to uncertainties in the loading and boundary conditions, through introducing beadings to the crash tube and optimising the wall thickness.

ALTAIR HYPERMORPH [8] was used to introduce beadings into the crash tube. This programme allows the morphing of an existing mesh hence enabling small changes of the geometry by displacement of nodes. Figure 3a shows the original mesh. The mesh is sectioned with morph volumes (green boxes). The red dots are handles which are used to change the position of the tube's nodes (see Figure 3b). The displacement of the tube's nodes can be parameterised. Due to a specific interface between HYPERMORPH and LS-OPT handle parameters can be changed by LS-OPT. This enables a fully automated optimisation of the mesh within the given boundaries.

The morphed mesh models are then transferred to the LS-DYNA solver and simulations are calculated. Again the input decks are parameterised for an automated optimisation. The setup for the FEM simulations will be discussed in the following section.

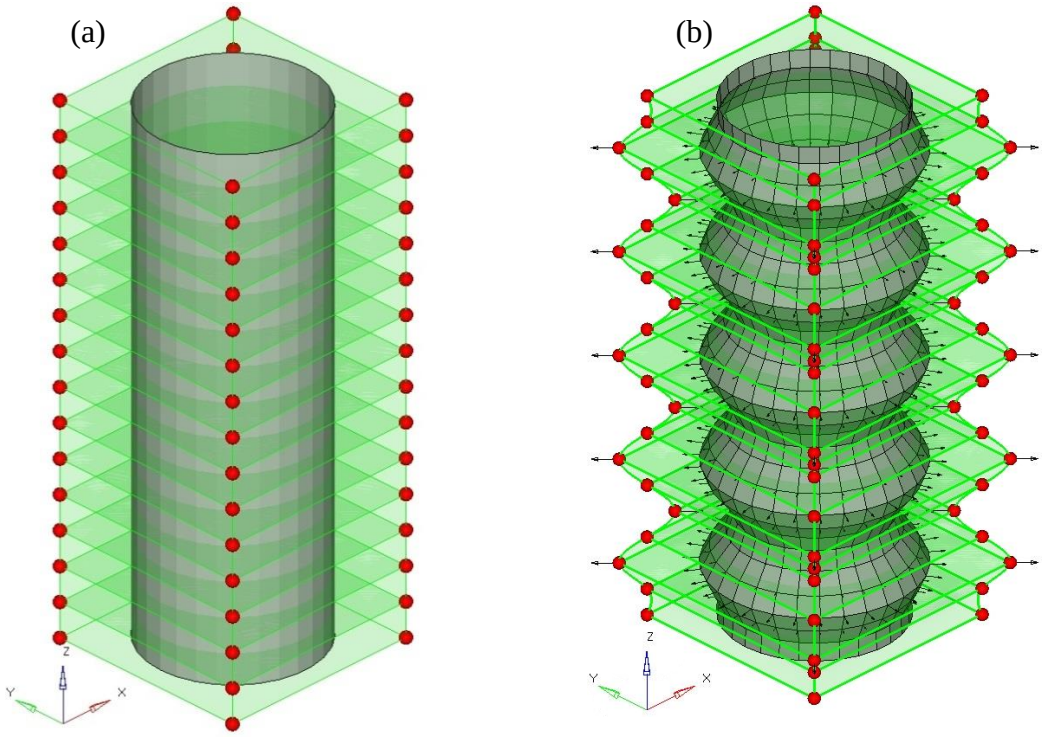

Figure 3: Illustration of the morphing with ALTAIR HYPERMORPH; (a) display of the morph volumes (green boxes) and the handles (red dots); (b) illustration of moved handles and morphed mesh

3 FINITE ELEMENT MODEL

The basic FE model (Figure 4a) describes a crash tube with a mid-section diameter of 100 mm, a height of 300 mm and a wall thickness of 3 mm. The mesh of the tube consists of quadratic shell elements with an edge length of 10 mm. The tube is fixed in space on a solid base plate with a groove to support the tube and prevent it from sideward sliding. The load is applied via a top rigid plate, which has an artificial mass of 1.5 tons and a velocity of about 30 km/h. The present FE model is a fictional example and not based on any standard crash procedure.

The crash tube is modelled as a steel component. The used material is a carbon steel A572 with a yield strength of 315 MPa and an ultimate strength of 683 MPa. The maximum elongation of this material is about 60%. The material data are taken from Varmint [9], due to the possibility to absorb the loads without material failure. It would be possible to consider material failure, but this would increase the simulation time enormously without further information concerning RDO. MAT_PIECEWISE_LINEAR_PLASTICITY was chosen to model this material in LS-DYNA. The impactor and the solid plate are modelled as rigid components with MAT_RIGID definition.

The FEM model is parameterised in the wall thickness. The wall thickness is controlled by separate parameters for each node over the height of the tube. The parameters for the wall thickness can be used to weaken or strengthen the tube through the introduction of beadings. The wall thickness and the beadings introduced by HYPERMORPH are the defined control parameters, which shall decrease the influence of the noise parameters.

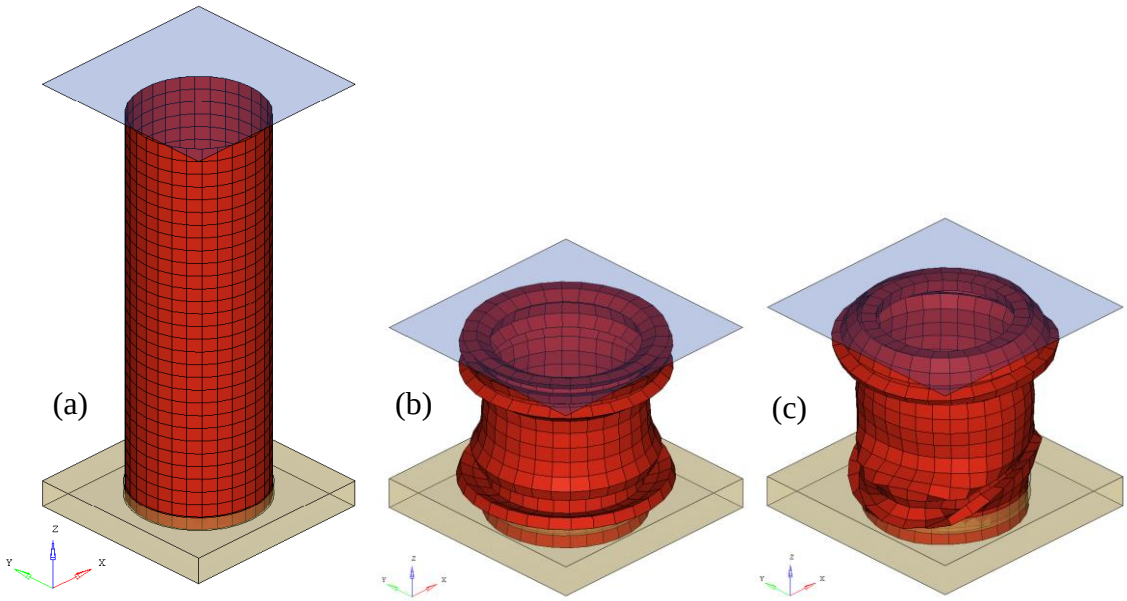

Figure 4: (a) FE model of crash tube and set up for a RDO (b) crash pattern of the original geometry and (c) crash pattern of the robust geometry

The noise parameters (=fluctuations) are the impactor mass, its velocity in terms of magnitude and direction, as well as a small tilting of the impactor. All of the noise parameters are described with a Gaussian distribution. The impactors mass has a mean value of 1.5 tons with a standard deviation of ±0.1 tons. The normal distribution of the magnitude of the velocity is described with a mean value of 8340 mm/s and a standard deviation of ±200 mm/s. The direction of the velocity is modified in a spherical coordinate system, where φ describes the angle between the x-axis and the projection of the vector on the x-y-plane and ϑ describes the angle between the vector and the z-axis. A mean value of 0^o and a standard deviation of $\pm 0.5^o$ build up the normal distribution of ϑ. The angle φ is described with a truncated normal distribution with a mean value of 0^o and a standard deviation of $\pm 0.5^o$.

4 RESULTS

Figure 5 illustrates the force displacements curves of the different optima (solid lines) as well as their mean values (dashed lines).The initial tube geometry (black line) has a maximum load capacity of 450 kN and an energy absorption of 38 kJ (at a deformation length of about 160 mm). The deterministic design optimisation (green lines) increases the maximum load capacity by 18% to 540 kN by varying the wall thickness and introducing beadings. In contrast, the robust design optimisation (blue lines) achieves an increase of 8% to 495 kN for the maximum load capacity. The energy absorption is increased by 21% for the deterministic design and by 13% for the robust design.

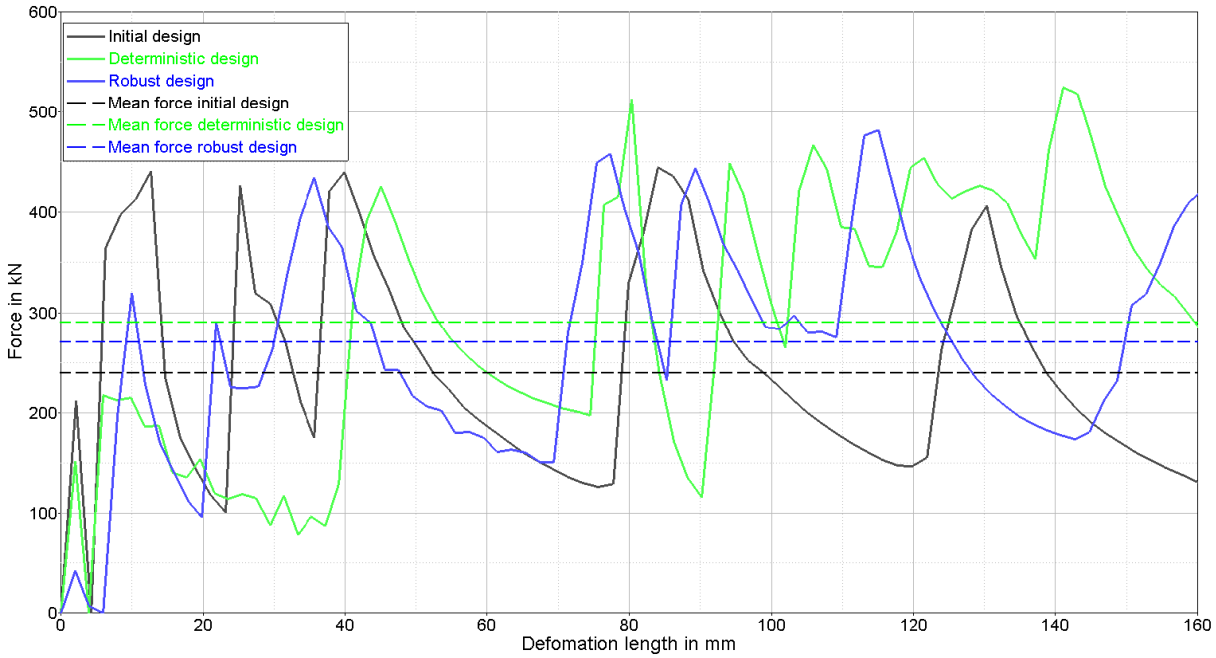

Figure 5: Force-displacement curves (solid lines) and corresponding mean force values (dashed lines)

Figure 6 shows the comparison of the beading depth of the robust and the deterministic optimum. The beading depth of the deterministic optimum is more pronounced compared to the robust optimum (with a difference of about 0.25 mm).

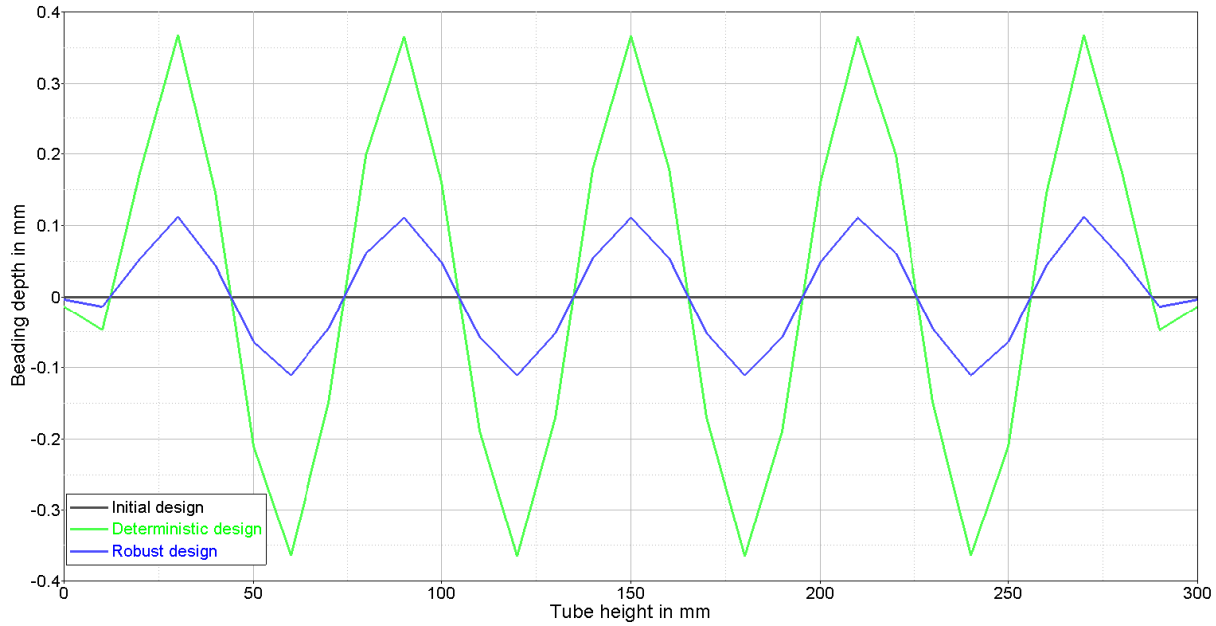

Figure 6: Illustration of the beading depth of the optimised designs compared to the initial design

Figure 7 compares the resulting wall thicknesses along the height of the tube. The curves of the deterministic and the robust design follow similar paths. Nevertheless the maximum wall thicknesses vary significantly from 1.2 mm to 4.8 mm in the case of the deterministic optimum but only from 1.5 to 4.7 mm in the robust optimum.

The robust optimum allows for a better resistance against non-standard loads, while the deterministic optimum optimises the folding behaviour for the ideal load scenario.

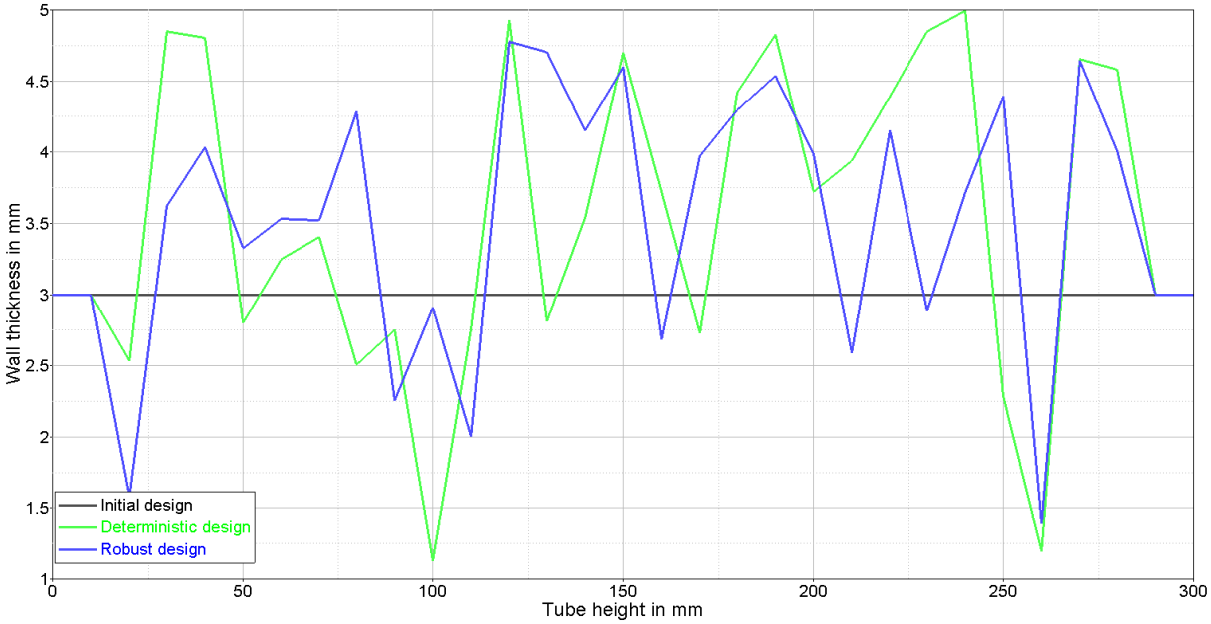

Figure 7: Illustration of the wall thickness along the height of the tube

5 CONCLUSION

Robust optimisation leads to an optimal design, which is better convertible to real life than deterministic designs as being robust against fluctuations. The present paper shows that the robust optimum design achieves increased maximum load capacity as well as a better overall energy absorption compared to the initial design. However, the optimal deterministic design achieves better results for the ideal load case. If there are deviations from the standard scenario, the deterministic optimum tends to failure. This happens, because a deterministic optimum is very often near the border of the constraints. Consequently a small modification of the optimised system may lead to constraint violation and therefore failure of the system.

Investigations show that the robust design optimisation does not necessarily result in the global optimum. It results in a local optimum, which is less sensitive to small system fluctuations. As a result the geometric tube tolerances (=process tolerances) can be reduced or the field of application (e.g. vehicle class) can be increased. For the presented crash tube, this advantage results in more stable crash results for scenarios departing from the standard. This in turn leads to increased safety levels of life protection systems.

ACKNOWLEDGEMENTS

The author would like to thank the Austrian Institute of Technology (AIT) for the financial support in this project.

REFERENCES

[1] D. Weigert, F. Duddeck, S. Brack, H. Schluder, and G. Geißler, “Anwendung stochastischer und geometrischer Analysen zur systematischen Robustheitsuntersuchung im Strukturcrash,” presented at the 11. LS-DYNA Forum, Ulm, 2012.

[2] H.-G. Beyer and B. Sendhoff, “Robust optimization - A comprehensive survey,” *Comput. Methods Appl. Mech. Eng.*, vol. 196, pp. 3190–3218, 2007.

[3] F. Jurecka, “Robust Design Optimization based on Metamodeling Techiques,” Technische Universität München, München, 2007.
[4] M. W. Trosset, “Taguchi and robust optimization.” 15-Mar-1997.
[5] N. Stander, W. Roux, A. Basudhar, T. Eggleston, T. Goel, and K. Craig, “LS-OPT User’s Manual - A design optimization and probabilistic analysis tool for the engineering analyst.” Jun-2014.
[6] LSTC, “LS-OPT,” *Livermore Software Technology Coproration - LS-OPT*. [Online]. Available: http://www.lstc.com/products/ls-opt. [Accessed: 14-Jan-2016].
[7] W. Roux, “Robust Parameter Design in LS-OPT,” presented at the 6th European LS-DYNA Users’ Conference, Gothenburg, 2007.
[8] Altair, “HyperMorph,” *Altair Hyperworks - HyperMesh > HyperMorph*. [Online]. Available: http://www.altairhyperworks.com/HWTemp3Product.aspx?product_id=7&item_name=HyperMorph%20About. [Accessed: 12-Jan-2016].
[9] A. Varmint, “Mats for Ls-Dyna,” *Varmint Al’s Engineering Page*, 19-Jul-2015. [Online]. Available: http://www.varmintal.com/aengr.htm#Mats-for-LS-DYNA. [Accessed: 24-Sep-2015].

ECCOMAS Congress 2016
VII European Congress on Computational Methods in Applied Sciences and Engineering
M. Papadrakakis, V. Papadopoulos, G. Stefanou, V. Plevris (eds.)
Crete Island, Greece, 5–10 June 2016

DYNAMICAL ANALYSIS OF PLATE MODELS WITH UNCERTAIN STRUCTURAL PROPERTIES USING THE INTERVAL FIELD METHOD

Maurice Imholz[1], **Dirk Vandepitte**[1], **and David Moens**[1]

[1]KU Leuven, Department. of Mechanical Engineering
Celestijnenlaan 300B, 3001 Heverlee, Belgium
e-mail: maurice.imholz@kuleuven.be - dirk.vandepitte@kuleuven.be - david.moens@kuleuven.be

Keywords: possiblistic analysis, interval analysis, interval fields, Finite Element analysis

Abstract. *In uncertainty quantification, interval arithmetic provides an appropriate procedure when little knowledge is available on the nature of the probability distribution of uncertain or imprecise quantities. This commonly occurs in engineering applications due to subjective knowledge or incomplete availability of test data. Intervals are by definition unable to take into account dependent input and output quantities, which forces the assumption of independency when applying them. This is a severe limitation on the accuracy of the analysis as dependency is always present to some extent. The concept of interval fields (IF) [1] provides a solution by defining non-deterministic fields using interval parameters. In its simplest form [2], the field is expressed as a weighted sum of basis functions, the weights being modelled using interval parameters. The dependency within the field is then captured by the basis functions, which describe the spatial nature of dependency, whereas the magnitude of uncertainty is captured by the weights. Field parameters are usually associated to geometric quantities (such as plate thickness), but they can be applied generally whenever multiple uncertain input or output quantities are involved. Both at the input and output side of a numerical analysis, IF can be used for a more realistic description of the estimated uncertainty. At the input side, taking into account dependency reduces overestimation on the output uncertainty bounds. At the output side, it is important that a realistic uncertain set of output quantities is represented as closely as possible without adding conservatism, as this corrupts the results of possible postprocessing or follow-up analysis. The application of IF here provides an important step towards achieving this goal.*

This paper aims to apply IF to analyse structural Finite Element models with uncertain structural properties. The property of interest in this paper will be the E-modulus. The concept of IF will be used to model spatial dependency within this parameter and will lead to a more accurate estimation of the output uncertainty.

1 INTRODUCTION

1.1 Possibilistic uncertainty analysis

In numerical modelling, Uncertainty Analysis (UA) concerns the identification and quantification of possible sources of uncertainty within a model, with the purpose of obtaining information on the uncertainty present in the model's relevant output. In this context, a non-deterministic approach of the modelling process is essential. Instead of the classical deterministic representation of model parameters, non-deterministic concepts are used to open up the possiblity of representing uncertainty on the parameters. These concepts can be divided in two groups. Firstly, *probabilistic analysis* uses probability distributions and stochastic parameters to assign a finite probability to a parameter having a certain value. Secondly, *possiblistic analysis* omits the concept of probability and only concerns the possiblity of a parameter having a certain value. Intervals, fuzzy numbers and convex regions are commonly used for this purpose. The choice of which approach to follow is usually based on the availability of knowledge on the uncertainty that is present. The definition of probability functions requires extensive knowledge on the uncertain parameter of interest. In practise, the Gaussian distribution is often assumed to estimate the stochastic moments, but the infinite base of this distribution poses a fundamental objection to this. Also, to accurately estimate stochastic parameters, a lot of experimental data is required. When experimental data is hard or expensive to obtain or their quality is questionnable, possibilistic analysis becomes an interesting alterative. The interval approach provides a much lower threshold to perform a non-determistic analysis than the stochastic approach. Also numerically, experiments can be expensive in terms of computational time, limiting the use of sample based stochastic techniques such as Monte Carlo Sampling. This paper will focus on the interval approach as basic tool for possibilistic analysis, and apply it in the context of a structural Finite Element (FE) model.

1.2 Modelling geometric uncertainty

Uncertain parameters in FE models typically have a spatial character: material properties such as density and Young's modulus or geometric properties such as plate thicknesses are geometrically oriented in space. In uncertain context, these parameters can show variability over the spatial domain, referred to as *geometric variability*. In FE-models, such a geometric parameter is discretised to the elements, leading to a set of discrete variables representing that variable in each element of the model. According to the possibility of geometric variability, the value in each element can vary separately, leading to different values in each element. However, some degree of dependency will usually be present and the value in different elements can not vary independently. Here the interval concept poses a problem. The uncertainty in each element could be captured by an interval parameter marking the bounds of the variation, but interval parameters are by definition incapable of incorporating the dependency present in the spatial domain. To mark the uncertainty present in such *field parameters* using a possiblistic technique, the *interval field* technique can be used as illustrated in equation 1. In its simplest form, an interval field consists of basis functions $\phi(\mathbf{r})$ representing the dependency and interval coefficients α^I representing the uncertainty.

$$y^I(\mathbf{r}) = \sum_{i=1}^{n} \alpha^I \phi_i(\mathbf{r}) \tag{1}$$

1.3 Dependency in a possibilistic context

For non-deterministic field parameters, a parameter needs to be defined that represents the level of dependency within the field. In stochastic FE context, as dictated by the theory of random fields (RF) [3], the correlation length is often used as measure for the dependency in the spatial domain. In this case, the correlation between values in different points is made a function of the distance between the points, with the correlation length $L_\rho$as governing parameter. The example of an exponential relationship is given in equation 2.

$$COV(x(\mathbf{r}_1), x(\mathbf{r}_2)) = \exp\left(\frac{\|\mathbf{r}_1 - \mathbf{r}_2\|}{L_\rho}\right) \tag{2}$$

As correlation is only defined in stochastic context, use of this parameter in possibilistic context is not straightforward. The authors proposed the use of the *maximum gradient* as parameter governing the dependency in the field, as this better fits the possiblistic approach than the correlation. The subject of this paper will be to apply this approach to identify the variability of the natural frequencies of a steel plate with geometrically varying Young's modulus.

2 MODELLING THE INPUT UNCERTAINTY: THE LOCAL INTERVAL FIELD DECOMPOSITION

2.1 General concept

Referring to [4], the Local Interval Field Decomposition (LIFD) was introduced to incorporate the maximum derivative constraint in a 1D non-deterministic field. This decomposition method puts a radial-based basis function and corresponding interval parameter in each element of the FE model. Therefore, *the dimensionality of the uncertainty is equal to the number of elements*. The reason for this approach is that, regardless of the level of dependency, each element can (at least partially) determine its own value and as a result, the dimensionality is equal to the number of elements. However, the issue of the dependency between the elements still stands. Through the LIFD, the initial interdependent interval set is transformed to an interval set of (at least) equal size that is *independent*, while still obeying the maximum derivative constraint. The following section considers the expansion of the LIFD to 2D non-deterministic fields.

2.2 Derivation of the LIFD in 2 dimensions

Suppose we have a field parameter $u(x, y)$ with x, y the spatial coordinates in a 2D-plane. We define the gradient $\nabla u(x, y)$ and its norm G as:

$$\nabla u(x, y) = \left(\frac{\partial u(x, y)}{\partial x}, \frac{\partial u(x, y)}{\partial y}\right) \tag{3}$$

$$G = \sqrt{\left(\frac{\partial u(x, y)}{\partial x}\right)^2 + \left(\frac{\partial u(x, y)}{\partial y}\right)^2} \tag{4}$$

For a certain realisation $\tilde{u}(x, y)$, the maximal and minimal value for that specific realisation are defined as $\max_{x,y} \tilde{u}(x, y) = \overline{u}$ and $\min_{x,y} \tilde{u}(x, y) = \underline{u}$. The LIFD in 2D will write the non-determistic field $u(x, y)$ as an interval field $u^I(x, y)$ in the form of equation 1 that obeys the following statements:

1. $\forall(\tilde{x}, \tilde{y}) \in \Omega : U_{min} \leq u(\tilde{x}, \tilde{y}) \leq U_{max}$

2. $\forall(x,y) \in \Omega : \sqrt{\left(\frac{\partial u(x,y)}{\partial x}\right)^2 + \left(\frac{\partial u(x,y)}{\partial y}\right)^2} \leq G_{max}$

3. $\forall \tilde{u}(x,y) : \overline{u} - \underline{u} \leq D_{max}$

The parameters G_{max}, U_{min}, U_{max} and D_{max} can be independently set. The first statement demands that the absolute bounds on the field parameter U_{min} and U_{max} are never exceeded. The second statement demands that the norm of the gradient never exceeds a preset value. This statement accounts for the dependency in the field. The third statement puts a bound on the difference between the maximal and minimal value of any realisation of the interval field. The objective of the LIFD is to obey the statements using the four governing uncertainty parameters mentioned above with an explicit interval field description with *independent* interval coefficients.

The only freedom we have is the shape of the basis functions. In the 2D-case, the basis functions have the following properties:

1. All ϕ_i are identically shaped radial basis functions.

2. A single ϕ_i is positioned at each element at location $\mathbf{r}_i$ of the FE mesh.

3. All ϕ_i are piecewise second order polynomial functions so the first derivatives are continuous.

figure 1 illustrates the shape of a basis function. For a basis function centered at element i with coordinates x_i and y_i, the mathematical definition is given by equation 5.

$$\phi_i(x,y) = \begin{cases} 0 & R < \sqrt{(x-x_i)^2 + (y-y_i)^2} \\ \frac{2(r-r_i+R)^2}{R^2} & \frac{R}{2} < \sqrt{(x-x_i)^2 + (y-y_i)^2} \leq R \\ 1 - \frac{2(r-r_i)^2}{R^2} & 0 \leq \sqrt{(x-x_i)^2 + (y-y_i)^2} \leq \frac{R}{2} \end{cases} \tag{5}$$

with $r = \sqrt{x^2+y^2}$ and $r_i = \sqrt{x_i^2+y_i^2}$. To comply with all demands, the following explicit field is proposed:

$$u^I(x,y) = C^I + \sum_{i=1}^{n} a \cdot 1_i^I \cdot \phi_i(x,y,R), \tag{6}$$

with $C^I = \left\langle \underline{C} | \overline{C} \right\rangle$ and $1_i^I = \langle 0|1 \rangle$ defined as the *unity* interval. The four controllable parameters are $\underline{C}$, $\overline{C}$, a and R. A unique mapping between these parameters and the four global uncertainty pararmeters is given by equation 7:

$$\begin{aligned} U_{max} &= \frac{7\pi \cdot a \cdot R^2}{24 \cdot dx \cdot dy} + \overline{C} \\ U_{min} &= \underline{C} \\ G_{max} &= \frac{a \cdot R}{dx \cdot dy} \\ D_{max} &= \frac{7\pi \cdot a \cdot R^2}{24 \cdot dx \cdot dy} \end{aligned} \tag{7}$$

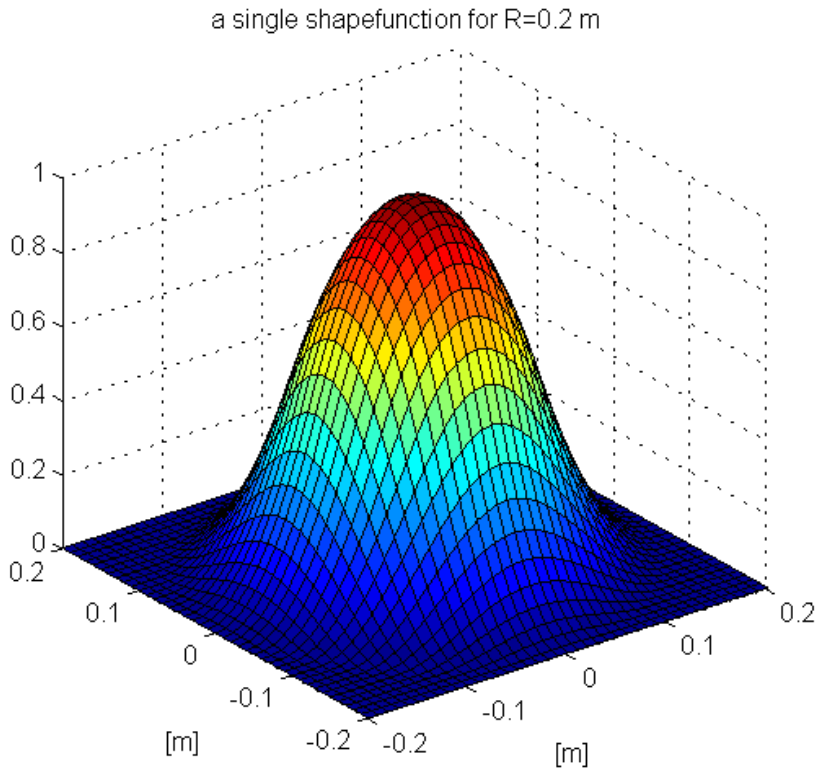

Figure 1: shape of a 2D radial basis function. Beyond a radius R from the center point, the basis function equals zero.

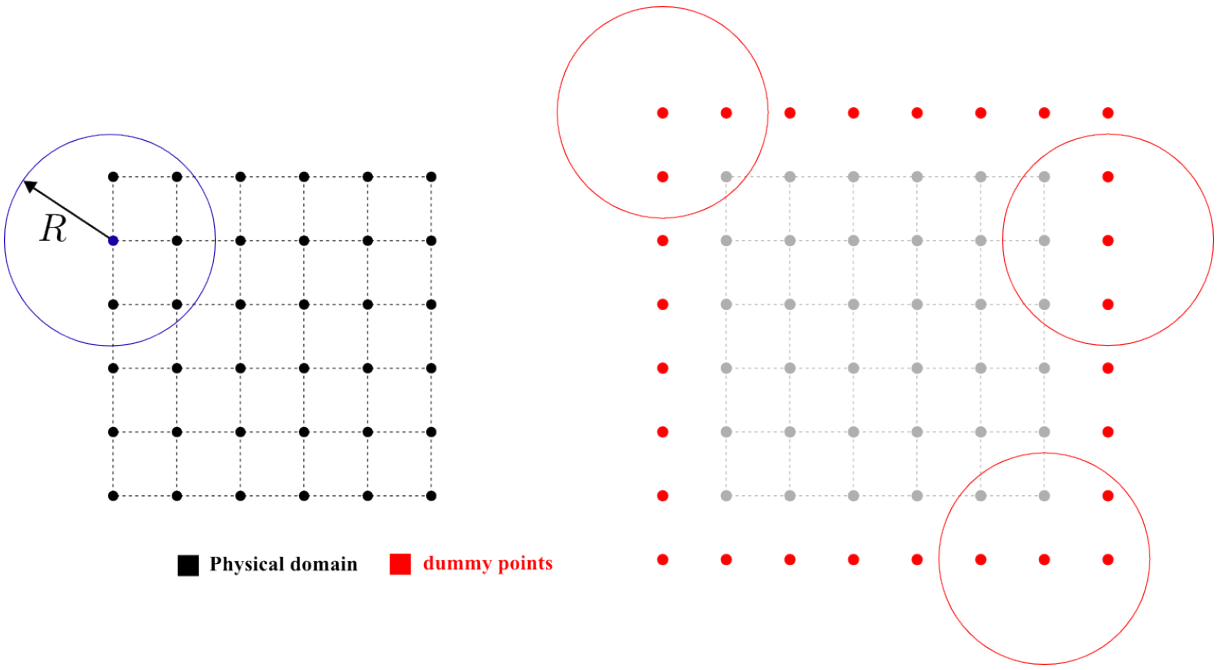

Figure 2: Illustration how dummy points are added beyond the physical domain to keep the maximum gradient constraint valid close to the edges.

With these relations, the four global uncertainty parameters can be independently set, leading to a unique field definition as in equation 6.

To ensure the maximum gradient constraint is kept over the entire domain, an adjustment is needed close to the edge of the domain. For points that lie within a distance R from a domain edge, the maximum constraint does not hold, because fewer basis functions have an effect in these points, leading to a smaller interval on the gradient in these points. To counter this, *dummy points* are added **beyond** the physical domain up to a distance R. The basis functions placed in these points lie partly in the physical domain and will ensure that the maximum gradient constraint is kept over the entire physical domain. Figure 2 shows the dummy points beyond the physical domain.

Figure 3 shows some realisations of a field within a rectangular plane for different values of R and a. One can clearly see how the combined choice of a and R produce more or less spatially dependent realisations.

3 PROPAGATING THE UNCERTAINTY: THE CONTINUOUS FIELD RESPONSE SURFACE

The analysis case in this paper will be the natural frequencies of a simple plate model with uncertain Young's modulus. The plate has a total of $20 \times 20 = 400$ elements, which leads to (at least) 400 interval parameters in the input field. To propagate this uncertain field to the output, a response surface will be defined. Assume we define a second order polynomial model on an output w within an input space $u_1, u_2, ..., u_n$ given by equation 8.

$$w = w_0 + \sum_{i=1}^{n} a_i u_i + \sum_{i=1}^{n} \sum_{j=1}^{n} b_{ij} u_i u_j \tag{8}$$

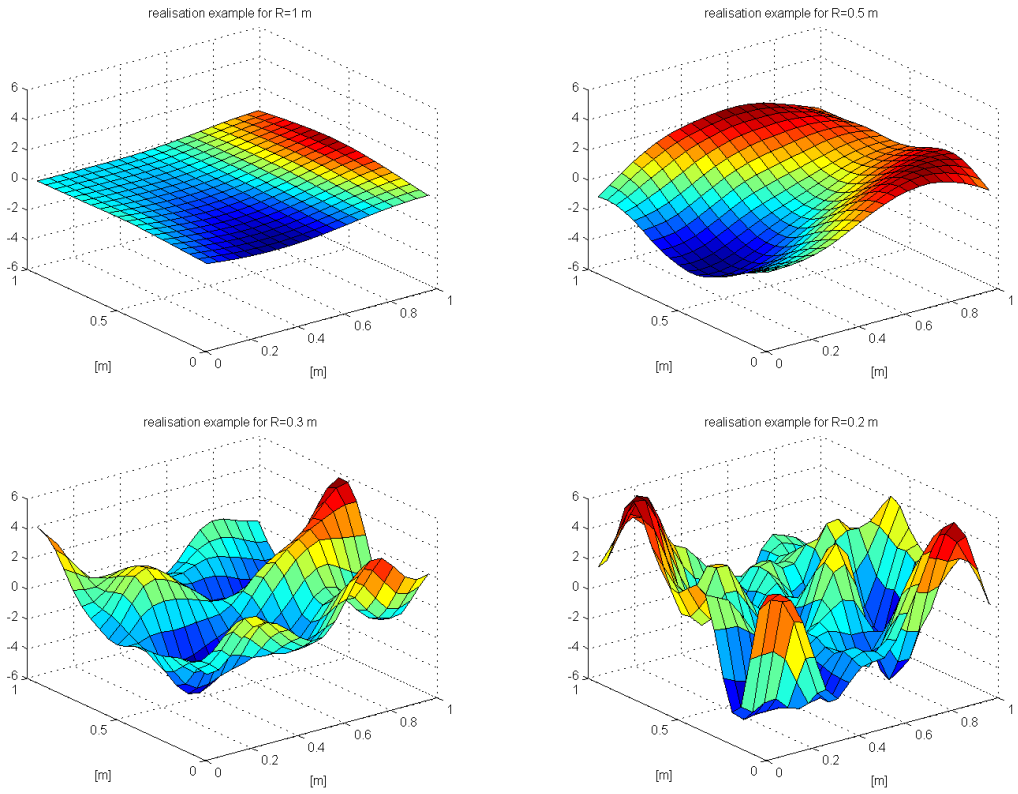

Figure 3: realisation examples for different values of R.

We assume n is a very large number, but all input parameters are instances of the same geometric parameter at different locations, e.g. the Young's modulus in each element of the FE-model. Obviously, determining the coefficients of such a high-dimensional model would require a very large amount of training samples, especially when the interaction terms are considered. To reduce the actual dimension of the response surface, we will take into account the high similarity of the input parameters. For example, the coefficients corresponding to the parameter value in adjacent elements have to be quite similar. The fact that the *coefficients are correlated in space* leads to a response surface description in terms of the spatial coordinates x and y, which the authors introduced earlier in [5], and is given by equation 9.

$$w = C + \iint_{x,y} a(x,y)u(x,y)dxdy + \iint_{x,y} b(x,y)u^2(x,y)dxdy + \iint_{x,y,\Delta x,\Delta y} q(x,y,\Delta x,\Delta y)u(x,y)u(x+\Delta x, y+\Delta y)dxdyd\Delta xd\Delta y \tag{9}$$

The discrete coefficients of the discrete model have been replaced by continuous *coefficient fields* that are defined over the spatial domain. The function also includes an interaction term which includes the product of the geometric parameter $u(x,y)$ at different elements in the model. Based on the first order approximation:

$$u(x_i + \Delta x, y_i + \Delta y) = u(x_i, y_i) + \Delta x \frac{\partial u(x,y)}{\partial x} + \Delta y \frac{\partial u(x,y)}{\partial y}, \tag{10}$$

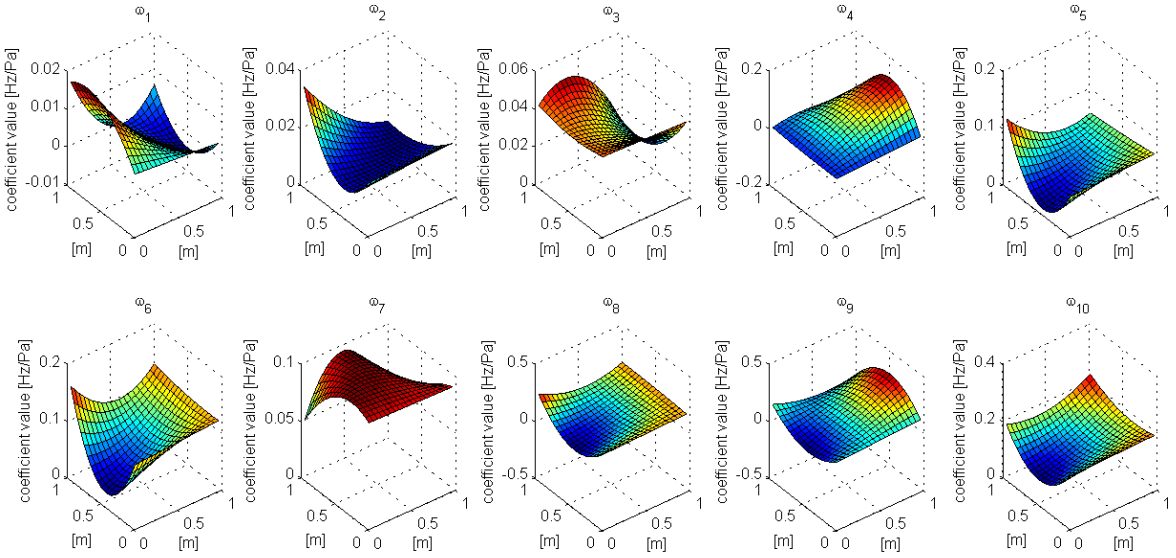

Figure 4: coefficient fields corresponding to each of the first 10 natural frequencies.

we replace this term by 2 terms including the product of the geometric parameter and its derivatives, leading to equation 11.

$$y = C + \iint_{x,y} a(x,y)u(x,y)dxdy + \iint_{x,y} b(x,y)u^2(x,y)dxdy + \iint_{x,y} q_x(x,y)u(x,y)\frac{\partial u(x,y)}{\partial x}dxdy) + \iint_{x,y} q_y(x,y)u(x,y)\frac{\partial u(x,y)}{\partial y}dxdy) \tag{11}$$

For the training process, we assume that the *coefficient fields* $a(x,y)$, $b(x,y)$ etc. are continuous functions in the spatial domain, thereby transforming the training process to a much lower actual dimension. For example, a coefficient field a(x,y) with 400 discrete locations can be written with a 2D polynomial as in equation 12.

$$a(x,y) = a_{00} + a_{10}x + a_{01}y + a_{11}xy + a_{20}x^2 + a_{02}y^2 \tag{12}$$

This representation only has 6 unknown coefficients, so instead of determining all 400 coefficients independently, redefining the problem reduces this number to only 6.

4 APPLICATION: STEEL PLATE WITH UNCERTAIN STIFFNESS PROPERTIES

4.1 Coefficient functions

We now continue towards applying this continuous model on our analysis case. The coefficient fields $a(x,y)$, $b(x,y)$, etc. are determined by using a linear least-squares based algorithm. For the specific case of the plate frequencies, first order polynomials lead to errors of only 1%. The coefficient function for each of the 10 first eigenfrequencies are given in figure 4.

4.2 Resulting output field

With the response surface defined, we can very easily make the step towards an output interval field description. The interval field can be written as

$$u^I(x,y) = u_0(x,y) + \sum_{i=1}^{N_{ext}} \cdot 1_i^I \cdot \phi_i(x,y) \tag{13}$$

with N_{ext} the total number of elements and dummy points (figure 2). If we put this in equation 9, we obtain the following description of the output field:

$$\boldsymbol{\omega}^I = \boldsymbol{\omega}_0 + \sum_{i=1}^{N_{ext}} a \cdot \boldsymbol{\xi}^{(i)} \cdot 1_i^I \tag{14}$$

with $\boldsymbol{\omega}^I$ an interval vector with the 10 first natural frequencies in it. $\boldsymbol{\xi}^{(i)}$ are vectors with elements:

$$\boldsymbol{\xi}_j^{(i)} = \iint_{x,y} a_i(x,y)\phi_j(x,y)dxdy \tag{15}$$

4.3 Identifying the uncertain region

The resulting interval field has a total of N_{ext} terms. For ease of calculation, the interval parameters are depicted by normalized intervals $1_i^I = \langle 0|1 \rangle$.

The interval field mentioned above corresponds to an uncertain region of frequency combinations. Because the example considers only the first 10 natural frequencies, this is a 10-dimensional region. If we look at 2D projections of this region on all possible (ω_i, ω_j)-subspaces, we observe 'shuttle'-shaped regions, an example of which is given in figure 5. This is due to the monotonous behaviour of natural frequency w.r.t increasing stiffness. Such a shuttle shape has two cornerpoints corresponding to the input points where al inputs are at their lowest or highest value respectively. Between these points, two curves bound the uncertain region, an *upper* and a *lower* curve.

From the fields $\boldsymbol{\xi^{(i)}}$ we can reconstruct the 2D projections of the uncertain region. For frequencies ω_p and ω_q, we define the vector $\boldsymbol{\rho^{(pq)}}$ with elements $\rho_i^{(pq)} = \frac{\xi_i^{(p)}}{\xi_i^{(q)}}$. Define $\overset{+}{\boldsymbol{\rho}}^{(pq)}$ as the vector with the elements of $\boldsymbol{\rho}^{(pq)}$ sorted in ascending order, and $\overset{-}{\boldsymbol{\rho}}^{(pq)}$ as the vector with the elements of $\boldsymbol{\rho}^{(pq)}$ sorted in descending order. Additionally, we rearrange $\boldsymbol{\xi^{(p)}}$ and $\boldsymbol{\xi^{(q)}}$ so that (equation 16)

$$\overset{+}{\rho}_i^{(pq)} = \frac{\overset{+}{\xi}_i^{(p)}}{\overset{+}{\xi}_i^{(q)}} \quad \text{and} \quad \overset{-}{\rho}_i^{(pq)} = \frac{\overset{-}{\xi}_i^{(p)}}{\overset{-}{\xi}_i^{(q)}}. \tag{16}$$

To each element in $\overset{+}{\boldsymbol{\rho}}^{(pq)}$ and $\overset{-}{\boldsymbol{\rho}}^{(pq)}$, we assign coordinates $\overset{+}{\phi}_i = \frac{\sum_{k=1}^{i} \overset{+}{\xi}_k^{(q)} - \overset{+}{\xi}_i^{(q)}/2}{\sum_{k=1}^{N_{ext}} \overset{+}{\xi}_k^{(q)}}$ and $\overset{-}{\phi}_i = \frac{\sum_{k=1}^{i} \overset{-}{\xi}_k^{(q)} - \overset{-}{\xi}_i^{(q)}/2}{\sum_{k=1}^{N_{ext}} \overset{-}{\xi}_k^{(q)}}$. Finally, we define the continuous functions $\overset{+}{h}\ (\overset{+}{\phi})$ and $\overset{-}{h}\ (\overset{-}{\phi})$ that interpolate

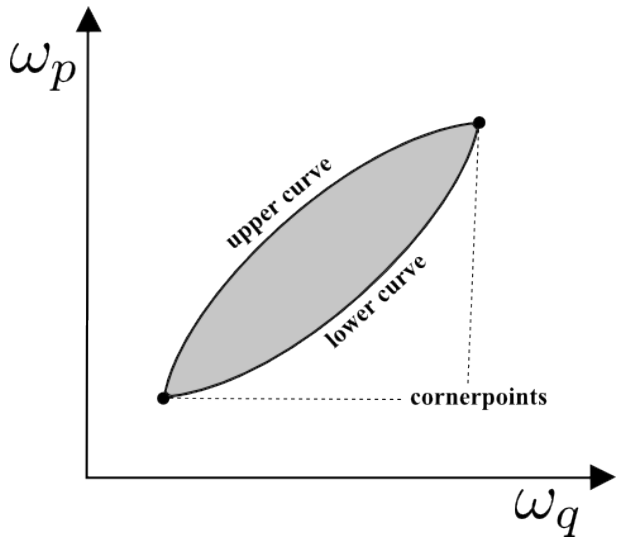

Figure 5: Example of a 'shuttle'-shaped uncertainty region.

the points $\left(\overset{+}{\rho}{}_i^{(pq)}, \overset{+}{\phi}_i\right)$ and $\left(\overset{-}{\rho}{}_i^{(pq)}, \overset{-}{\phi}_i\right)$. The lower and upper curve are then described by equation 17.

$$\begin{aligned} \text{lower curve}: \quad \overset{+}{c}\,(\overset{+}{\phi}) :\rightarrow & \begin{cases} \omega_p(t) = \int_{\overset{+}{\phi}=0}^{t} \overset{+}{h}\,(\overset{+}{\phi}) d\,\overset{+}{\phi} \\ \omega_q(t) = \int_{\overset{+}{\phi}=0}^{t} d\,\overset{+}{\phi} \end{cases} \\ \text{upper curve}: \quad \overset{-}{c}\,(\overset{-}{\phi}) :\rightarrow & \begin{cases} \omega_p(t) = \int_{\overset{-}{\phi}=0}^{t} \overset{-}{h}\,(\overset{-}{\phi}) d\,\overset{-}{\phi} \\ \omega_q(t) = \int_{\overset{-}{\phi}=0}^{t} d\,\overset{-}{\phi} \end{cases} \end{aligned} \tag{17}$$

Figure 6 illustrates the process described above.

4.4 Observations

In the 2D-projections of the uncertain region we can clearly see the effect of a varying Young's modulus. We examine 7 cases of increasing maximum gradient. The extreme values of the Young's modulus are 210 GPa and $1.2 \cdot 210 = 252$ GPa. From figures 7 to 10, that show some 2D projections for all 7 cases, a few observations can be made:

1. Increasing the maximum gradient does not change the cornerpoints, as these depend on the extreme values of the Young's modulus itself, but the uncertain region does change. The shuttle-shaped regions become wider, effectively decreasing the dependency between the frequencies as the gradient increases.

2. For lower frequencies, the effect of increasing the gradient on the uncertain region appears to saturate. This saturation effect is much less outspoken for higher frequencies.

3. Some frequencies, such as 5 and 8 (figure 9), appear to be much more interdependent than others, which can be seen from the relatively slim shuttle shape. The increased maximum gradient appears to have little effect on the dependency between these frequencies.

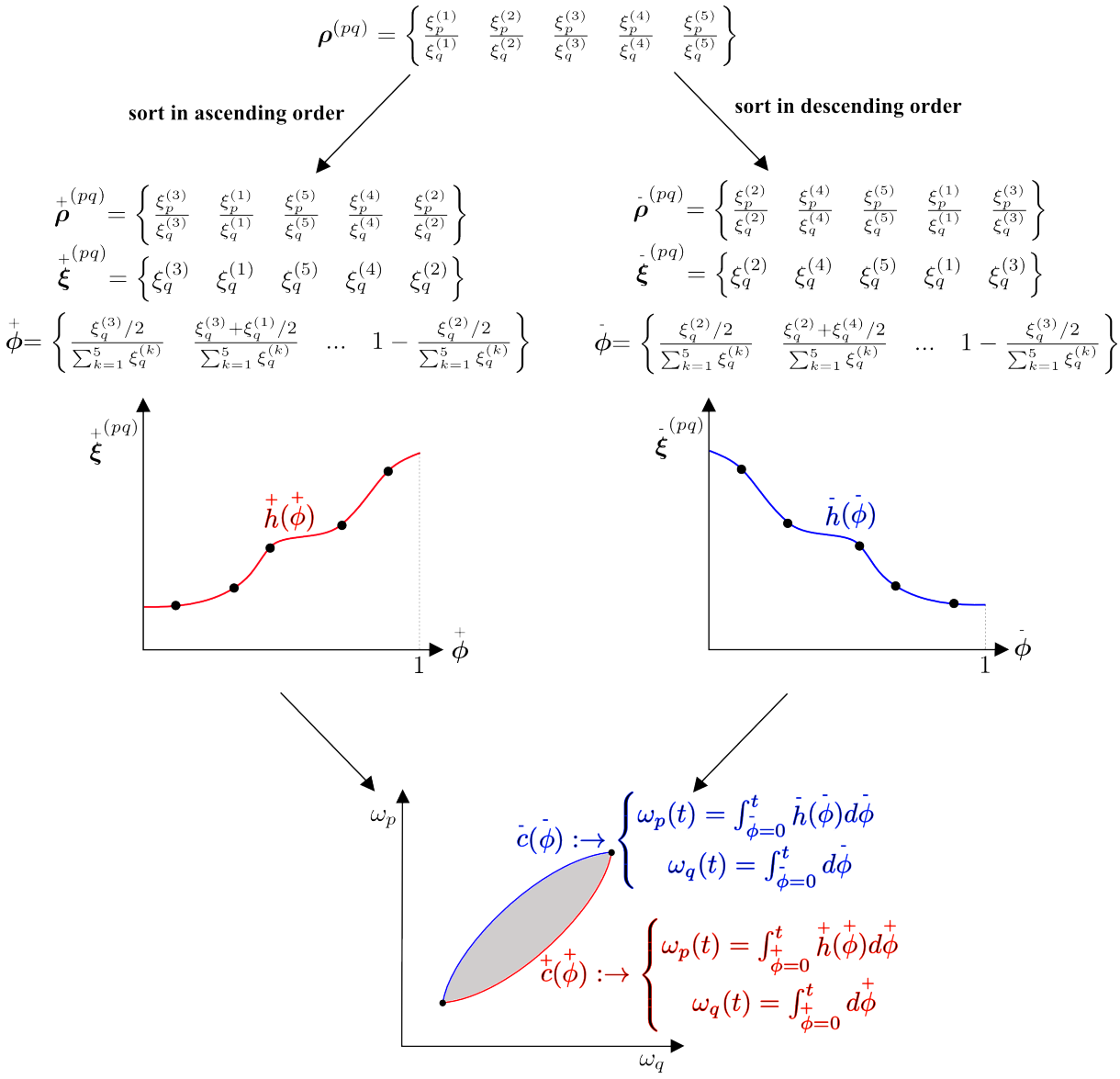

Figure 6: illustration of the process to determine the uncertain region, for the case of only 5 fields $\boldsymbol{\xi}^{(i)}$.

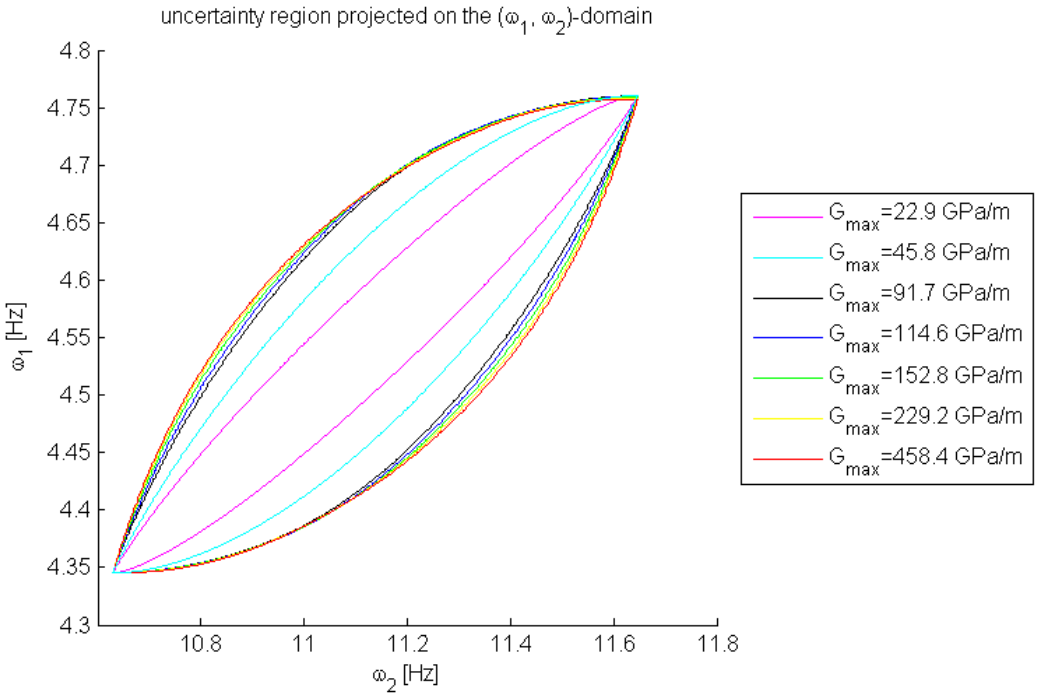

Figure 7: uncertainty region projected on the (ω_1, ω_2)-plane.

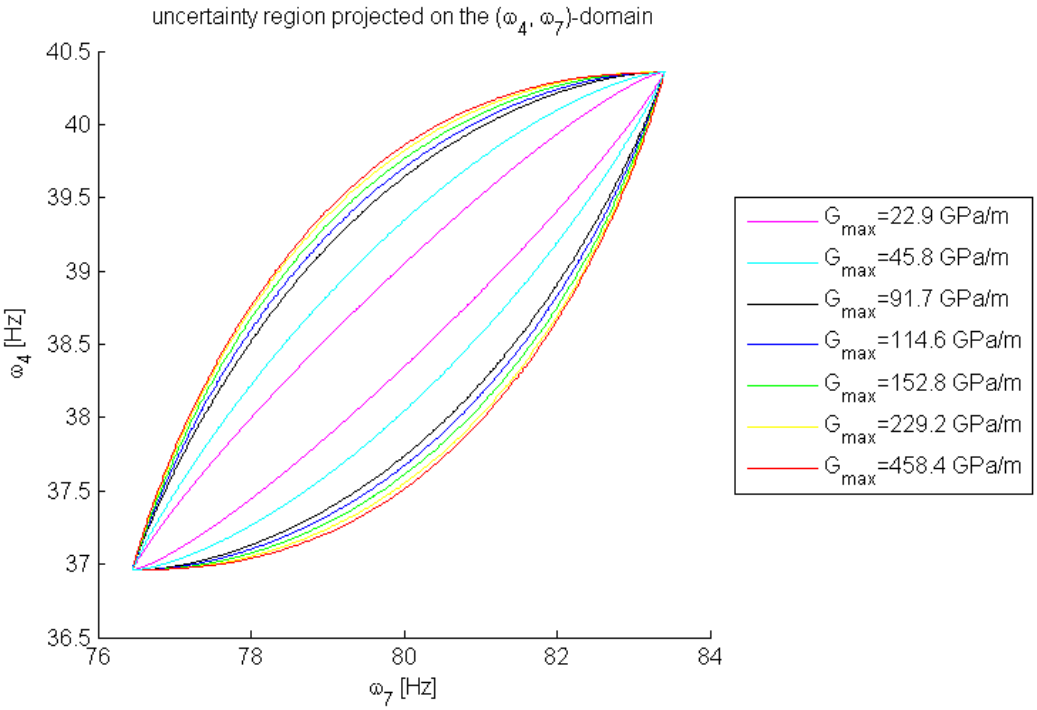

Figure 8: uncertainty region projected on the (ω_4, ω_7)-plane.

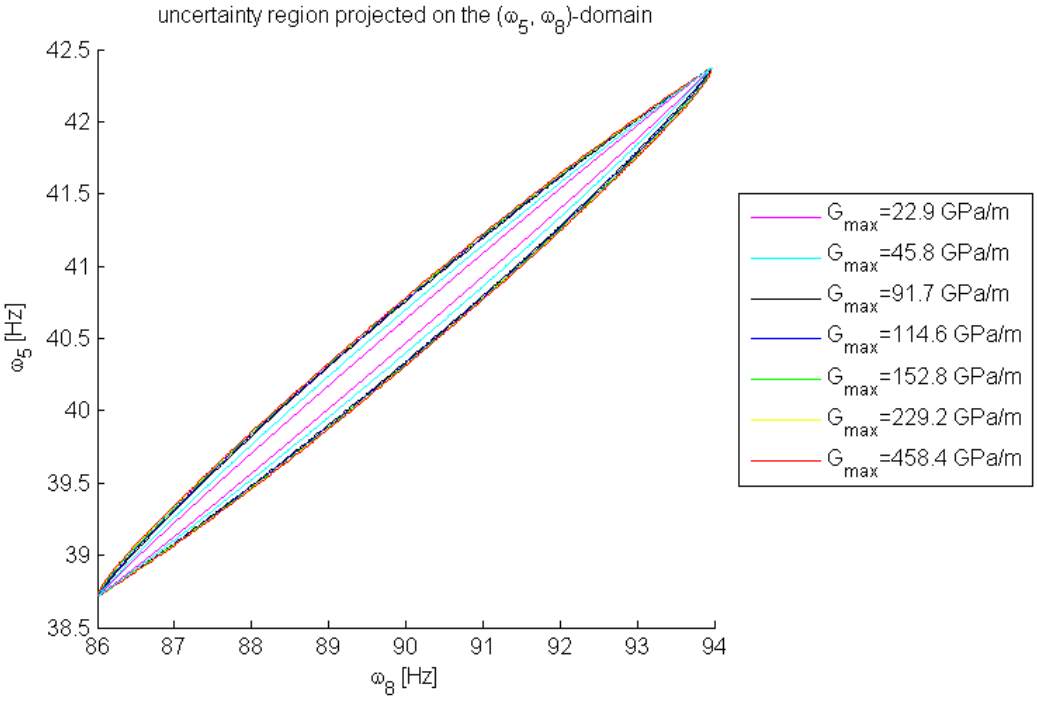

Figure 9: uncertainty region projected on the (ω_5, ω_8)-plane.

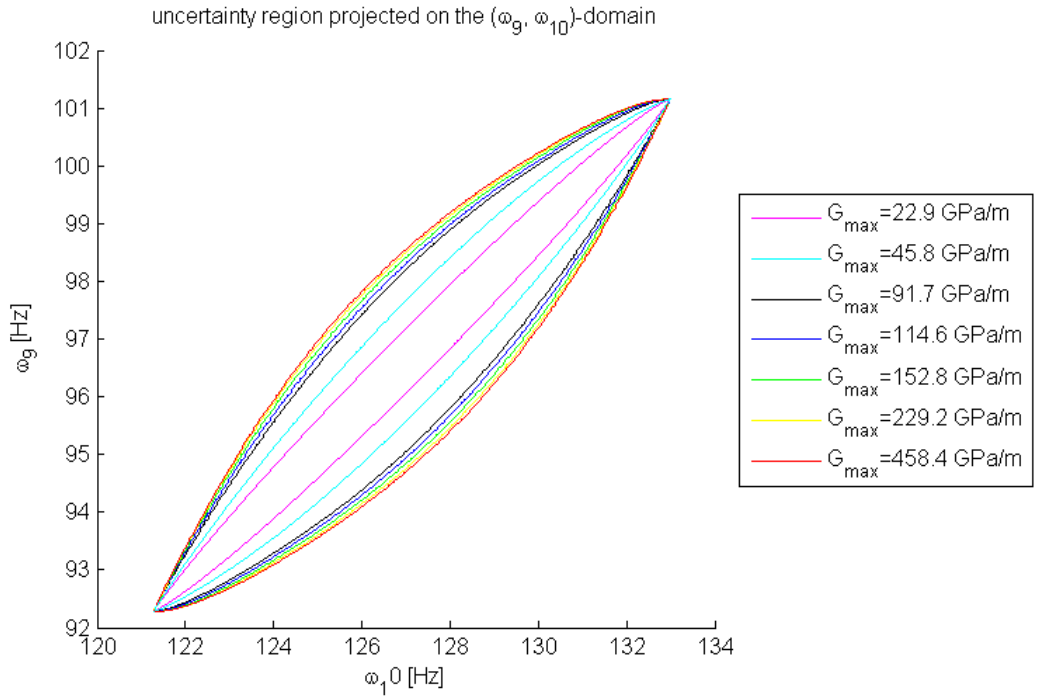

Figure 10: uncertainty region projected on the (ω_9, ω_{10})-plane.

5 CONCLUDING REMARKS & FUTURE RESEARCH TOPICS

In a possiblistic framework, the inability to use correlation forces us to look at dependency at a more general level. According to the authors, the shape of the uncertain region itself holds the most information not only on the degree of dependency between parameters, but also on the nature of it. In this paper, the interval concept is specifically designed towards the fast computation of these regions. For the purpose of monotonous and linear behaviours, which lead to so-called 'shuttle'-shaped uncertain regions, this paper introduced an easy way of computing them without the need of additional simulations. Further research will be done towards formulating relationships between interval field formulations and uncertain region shapes, for non-linear and also non-monotonous input-output relations.

REFERENCES

[1] D. Moens, M. De Munck, W. Desmet, D. Vandepitte, Numerical dynamic analysis of uncertain mechanical structures based on interval fields, IUTAM 2009, *IUTAM Symposium on the Vibration Analysis of Structures with Uncertainties* VOL. 27(2011) 71-83.

[2] W. Verhaeghe, W. Desmet, D. Vandepitte, D. Moens, Interval fields to represent uncertainty on the output side of a static Finite Element analysis, *Computational Methods in Applied Mechanical Engineering* 260(2013) 50-63.

[3] E.Vanmarcke, Random Fields: analysis and synthesis, MIT Press, Cambridge, 1993.

[4] M. Imholz, D. Vandepitte, D. Moens, Derivation of an input interval field decomposition based on expert knowledge using locally defined basis functions, UNCECOMP 2015, *proceedings of UNCECOMP 2015*, Hersonissos, Greece.

[5] M. Imholz, D. Vandepitte, D. Moens, Application of interval fields to geometric output quantities of Finite Element models, UNCERTAINTIES 2016, *proceedings of UNCERTAINTIES 2016*, Maresias, Brazil .

ECCOMAS Congress 2016
VII European Congress on Computational Methods in Applied Sciences and Engineering
M. Papadrakakis, V. Papadopoulos, G. Stefanou, V. Plevris (eds.)
Crete Island, Greece, 5–10 June 2016

POWER GRID ROBUSTNESS TO SERE FAILURES: TOPOLOGICAL AND FLOW BASED METRICS COMPARISON

Roberto Rocchetta[1]**,Edoardo Patelli**[1]

[1]Institute of Risk and Uncertainty, University of Liverpool
L69 7ZF, Liverpool, United Kingdom
e-mail: {Roberto.Rocchetta,Edoardo.Patelli}@liverpool.ac.uk

Keywords: Power Grid Robustness, Vulnerability Metrics, Spectral Graph Analysis, Cascading Failures, Uncertainty.

Abstract. *Power grids are generally regarded as very reliable systems, nevertheless outages and electricity shortfalls are common events and have the potential to produce significant social and economic consequences. It is important to reduce the likelihood of those severe accidents by assuring safe operations and robust topologies. The grid safety relies on accurate vulnerability measures, control schemes and good quality information. For instance, in power network operations, contingency analysis is used to constrain the network to secure operative states with respect to predefined failures (e.g. list of single component failures). An exhaustive failure list is often not treatable, therefore a selection or ranking is performed to help in the choice. In order to better understand the power network weakness and strengths a variety of robustness metrics have been introduced in literature, although many do not account or partially account for uncertainties which might affect the analysis. In this work power network vulnerability to failure events is analysed and single line outages (N-1 contingencies) have been ranked using different metrics (i.e. topology-based, flow-based and hybrid metrics). Sources of uncertainty such as power demand variability and lack of precise knowledge on the network parameters have been accounted for and its effect on the component ranking quantified. A modified version of the IEEE 118 bus power network has been selected as representative case study. The assumption underpinning the methodologies and the vulnerability results also accounting uncertainty are discussed.*

1 INTRODUCTION

Robustness of power grids is defined as the degree to witch the network is able to withstand an unexpected event without degradation in performance [1]. A closely related concept is the vulnerability, which is sometime regarded as lack of robustness. Robustness and vulnerability are nowadays major concerns for the future power networks. Historically, power networks were developed to distribute electricity from large size isolated power plants to the various end-user loads (e.g. industry or residences) by means of power transmission and distribution networks. Distribution grids topologies were usually designed in radial fashion to comply with the needs of a simple one-way flow of electricity, i.e. from the main grid to the local users.

In the last decades this traditional design has deeply changed, the allocation of renewable energy sources are making its behaviour less predictable and vulnerability assessments less reliable, mainly due to the considerable amount of uncertainty injected in the system [2]. Non-radial meshed topologies and not classical structures are likely to became more common in the future [3]. The presented scenario highlights the need of develop more reliable and robust frameworks for power grid vulnerability analysis (i.e. adopting sophisticated uncertainty quantification techniques), as well as the need of define enhanced metric for the assessment and identification of operational and structural risks. In order to improve robustness it is important to understand the role played by the variability the grid state variables (e.g. power produced, loads, voltage phases, magnitudes.) and by the imprecisely known network parameters (flow and voltage limits, topology, line resistances, etc.). Structural weaknesses have to be identified to design better topologies (e.g. by efficient ranking of components failures) and mitigate likelihood of unexpected hazardous situations .

In literature, a wide range of indexes have been proposed for vulnerability and robustness assessment, e.g. using realistic simulation of network response and power-flow solution ("power-flow-based metrics") or based on topological analysis of networks, using techniques founded on complex network theory [4]. The latter are computed using pure topological approaches (i.e. 'topology-based metrics') or enhanced by including electrical engineering concepts in the analysis (i.e. 'hybrid metrics'). Examples of recently applied metrics are the effective resistance ($R_{\mathcal{G}}$), network spectral radius ($\rho_{\mathcal{G}}$), algebraic connectivity ($\Lambda_{\mathcal{G}}$) and extended betweenness ($\mathcal{B}_e$) M. Ouyang et al. [6] analysed correlation of six topology-based vulnerability metrics respect to multiple components failure. E. Bompard et al. [5] compared two hybrid metrics (i.e. extended betweenness and net-ability) in their ability to rank components failures. Power-flow-based metric, such as system cascading index (CEI), has been applied to estimate likelihood and extent of cascading failures [7].

To the Authors knowledge, few among the reviewed works quantified the effect of uncertainty in the metrics and compared the different ranks of component failures. Hence, further comparison between different indices, with particular regard to the uncertainties affecting the different approaches seems to be needed. In this survey vulnerability metrics are compared, with particular regard to the line failures ranking. Power demand uncertainty and system parameters (line power flow limits) uncertainty are analysed and their effect quantified. In addition, different power-flow models (i.e. alternate current and direct current power-flows) have been compared in the results. The work aim is to better understand strength and limitations of the different metrics in ranking critical components and spot network weaknesses, also accounting

uncertainty.

The paper is structured as follows:
Power network modelling is introduced in Section 2. Contingency analysis and uncertainty modelling are described in in Section 3. In Section 4 robustness and vulnerability concepts are discussed and the metrics defined. A case study is defined in Section 5 and results displayed. Limitation faced and further discussions are presented in Section 6. Section 7 close the paper.

2 BACKGROUND AND POWER NETWORK MODELLING

A power network structure can be represented by an unweighed graph $\mathcal{G} = \{\mathcal{N}, \mathcal{L}\}$, where $\mathcal{N}$ is the set of network nodes (or busses) and $\mathcal{L}$ is the set of links (branches or feeders). The topology of the graph is identified by a squared symmetric matrix called adjacency matrix A, which elements $a_{i,j}$ are equal 1 if the node i is linked to the node j or 0 if no direct link exists. Links can be associated to some measure of interest (e.g. length, traffic, power flow, line resistance, etc.) and the adjacency matrix rewritten in its weighted form W, where the matrix elements $w_{i,j}$ are the weights of the links between nodes i and j and 0 if not linked.

Spectral graph theory can be used analyse spectral graph proprieties of networks such as its eigenvalues eigenvectors. Spectral proprieties of graph $\mathcal{G}$ bears valuable information about the network the graph represent and some eigenvalues can be associated to its robustness [8]. Further details are going to be discussed in Section 4.
The Laplacian L_A of the adjacency matrix A is defined as [9]:

$$L_A = D_A - A \tag{1}$$

where A is the adjacency matrix and D_A is the diagonal matrix of degrees for A. The matrix Laplacian can be computed using the weighed adjacency matrix W (i.e. including electrical concepts such as susceptances).

AC and DC Power Flow

Power flow methods are commonly used to solve problem in power grid analysis, as example the energy dispatch problem, i.e. optimal schedule of power production, or security constrained optimal power scheduling. The AC power flow is a non linear solver accounting both active and reactive power flows without neglecting loses. In the AC formulation the active and reactive nodal equations are as follow [10]:

$$P_k = \sum_{i}^{N} |V_i||V_k|[G_{i,k}cos(\theta_{i,k}) + B_{i,k}sin(\theta_{i,k})] \tag{2}$$

$$Q_k = \sum_{i}^{N} |V_i||V_k|[G_{i,k}sin(\theta_{i,k}) - B_{i,k}cos(\theta_{i,k})] \tag{3}$$

where P_k and Q_k are active and reactive power injected in the node k, respectively, $|V_i|$ is the voltage magnitude of node i and $\theta_{i,j}$ is the voltage angle difference between node i and k. The elements $G_{i,k}$ and $B_{i,k}$ are the conductance and susceptance of the link connecting node i and k, respectively.The Equations 2-3 are solved for each $k \in \mathcal{N}$ by some iterative techniques (e.g. Newton-Raphson method) although convergence is not always assured.

The DC power flow is a linear approximation of the AC power flow which account for just active power flows, neglecting power loses and reactive power management. It has been widely used to alleviate the computational cost of numerically intensive codes and it has always a feasible solution. The majority of works which aimed at including electrical engineering concepts in graph theoretical approaches made use of the DC assumption, e.g. in defining weighted adjacency matrix of the graph. The DC power flow formulation can be written as follows [10]:

$$P_k = \sum_{i}^{N} |V_i||V_k|B_{i,k}sin(\theta_{i,k}) \approx \sum_{i}^{N} B_{i,k}\theta_{i,k} \tag{4}$$

were the equation 4 is obtained under the following DC power flow assumptions:

- Flat voltage profile $|V_i| = 1$ per unit. $\forall\, i \in \mathcal{N}$
- Small voltage angle differences$sin(\theta_{i,k}) \approx \theta_{i,k}$;
- $R \ll X$ negligible resistance;

It is worth remarking that DC model although useful in reducing computational time, might result in a poor approximation [10]. In order to obtain good quality results, grid voltage profile should be as flat as possible and ratio X/R relatively high. This means that the quality of the DC solution is system dependent and operative state dependent, hence its validity should be carefully assessed before use. The vast majority of topology-based metrics when enhanced by using electrical concepts made use of the DC assumptions [4].

3 TREATMENT OF UNCERTAINTY

Generally speaking, uncertainty can be separated in two groups, the so called aleatory and epistemic uncertainties [11]. The aleatory is related to stochastic behaviours and randomness in events and variables. The epistemic is commonly related to lack of knowledge about a particular behaviour, imprecision in measurement and poorly designed models. Adequately model uncertainty is paramount to improve robustness of the analysis accounting for both lack of information and inherent randomness (e.g. environmental conditions, future power demand, power produced by renewable generators, etc.). In the power grid context well-recognized sources of uncertainty are electricity price volatility, load power demand and environmental variability, model assumption (e.g. DC or AC power flow, contingency selection). The sources of uncertainty investigated in this work are:

- Uncertainty in the line emergency rating (line power flow constrain) which might be due to, e.g. neglected effect of ambient wind and temperature. The lack of precise knowledge on the emergency ratings of network lines have been modelled using uniform distributions around a given design value [12]. The uniform distribution has been used consistently with the principle of maximum entropy.
- Load demand uncertainty and variability. The aggregated load connected to a node i ($P_{L,i}$) can be described by a Normal distribution [13].The parameter of the distribution can be estimated from historical records of load demand per node.

A Monte Carlo sampling procedure have been used to propagate uncertainty from the input to the output quantities of interest. Within each Monte Carlo run, sampling procedure (e.g. inverse transform sampling) is used to obtain a random realization for each uncertain parameter

(nodal loads and line loading limits). The samples are forwarded to the system for further vulnerability assessment and contingency ranking. The algorithm allows obtaining a probabilistic description of the outputs variability, i.e. the output probability distribution functions with respect to the input uncertainties and wider prospective on the result of the ranking.

A contingency in power networks is defined as the unexpected failure of one of its components (e.g. links, nodes, generators, transformers) [13]. Contingency analysis is commonly used to constrain the network to safe operational states if a contingency occurs. Generally speaking, even if the network has modest size (e.g. small distribution grid), a complete analysis of all possible failures is infeasible. An exhaustive contingency list will has to include $\sum_{k=1}^{N} N!/k!(N-k)!$ failures, where k is the number of failed components. In power grid reliability and risk assessment, common practice consists in selecting a subset of the more threatening contingencies based on expert opinion or by some identification procedure [15]. In this work, the $N-1$ single line trips are analysed and the most threatening failures ranked using different metrics.

4 ROBUSTNESS AND VULNERABILITY METRICS

Robustness in power grid is defined as the degree to witch the network is able to withstand an unexpected event without degradation in performance [6]. Vulnerability is used to score low reliability power grids by assessing drops in performance metrics. The network vulnerability $\mathcal{V}(C_i)$ after the contingency (C_i) occurs can be quantified as follows [4]:

$$\mathcal{V}(C_i) = \frac{\mathcal{M} - \mathcal{M}(C_i)}{\mathcal{M}} \tag{5}$$

where $\mathcal{M}(C_i)$ is the network vulnerability metric after contingency Ci and $\mathcal{M}$ is the metric value for the undamaged network.

Power flow-based metrics

Flow-based indexes can be obtained by simulating network in normal and damaged states and using power flow solvers (e.g. DC or AC). In this work a cascading metric ($CEI(C_i)$) is obtained simulating the outages by both AC power flow contingency analysis and its linear DC approximation. Generally speaking, a "cascading" is a sequential successions of dependent events [18].The metric adopted to assess the cascading overload vulnerability is defined as follows [18]:

$$CEI(C_i) = \sum_{l \in \mathcal{L}} \mathcal{P}(C_l|C_i) SevOL_l(C_i) \tag{6}$$

where $\mathcal{P}(C_l|C_i)$ is the probability of secondary trip of line l after line i contingency occurs and $SevOL_l(C_i)$ is the severity function for line l overload if failure C_i occurs. Severity functions are used to quantify the extent of the failure and different definitions are available [13]. The continuous severity function for overload is specifically defined for each link l (distribution lines and transformers) and it measures the extent of violation in terms of excessive power flow ratio PR_l. PR_l is the ratio between active power flowing in the line P_l and its emergency rating $P_{emerg,l}$. The expression for the continuous severity due to overload ($SevOL_l$) of a line l is findable in [13].

$$SevOL_l = d * PR_l + c \quad \textit{for} \quad PR_l \geq PR_l^{min} \tag{7}$$

where $SevOL_l$ is zero for values of the flow rating less than a safety limit PR_l^{min}=0.9. The deterministic limit for the violation of line l is PR_l=1, the near violation region is 0.9$\leq PR_l <$1, and the value PR_l under 0.9 is regarded as safe, d=10 and c=-9.

Continuous severity functions, if compared with discrete severity functions, have the advantage of providing non zero risk results for scenarios close to the performance limits, but not failure, which reflects the realistic sense that near violation scenarios have not null risk. The probability of cascading trip of line k after an initiating contingency i can be expressed as in [7]:

$$\mathcal{P}(C_j|C_i) = \frac{P_j(C_i,\zeta) - P_{0,j}(\zeta)}{P_{\textit{trip},j}(C_i,\zeta) - P_{0,j}(\zeta)} \tag{8}$$

where $P_j(C_i,\zeta)$ is the post-contingency flow on circuit j given contingency i and operative-environmental condition ζ, $P_{\textit{trip},j}(C_i,\zeta)$ is defined as the flow leading to a certain trip of the line j (assumed to be 125% of its maximum capacity) and $P_{0,j}(\zeta)$ is the pre-contingency flow in the line j if condition ζ holds. Equation 8 is related to the fact that higher load levels and larger transients increases the likelihood of cascading event on circuit k after initiating event on circuit i. The probability $\mathcal{P}(C_j|C_i)$ is zero for $P_j(C_i,\zeta) \geq 0.9P_{\textit{emerg},j}$.

Topology-based and hybrid metrics

Power network vulnerability can by pure topological analysis of the grid structure. These approach use unweighted adjacency matrix A, components are regarded as identical and no rough electrical concept is included in the analysis [4]. Similarly, hybrid metrics adopt complex network concepts often include concepts such as DC approximation and electrical concepts such as line emergency rating $P_{\textit{emerg},l}$ or link impedances. For these approaches the weighted adjacency matrix W is built using the matrix of susceptances $B_{i,k}$. The analysed metrics in this paper are: graph spectral radius, algebraic connectivity, effective graph resistance, graph global efficiency [22] and extended betweenness [5].

In spectral analysis of graphs, the largest eigenvalue of the adjacency matrix is known as graph spectral radius ($\rho_{\mathcal{G}}$). Few works attempted to relate spectral radius to the power grid vulnerability and relatively small values have been considered as indicator of robustness [8]. Another important metrics obtained through spectral analysis of the network graph is the second smallest eigenvalue of the Laplacian matrix L, also known as the algebraic connectivity ($\Lambda_{\mathcal{G}}$). The metric $\Lambda_{\mathcal{G}}$ is used as indicator of the level of connection between nodes in a graph,and is regarded as a basic indication of the network robustness level [16]. The effective graph resistance ($R_{\mathcal{G}}$) is an hybrid metric which have been sometimes related to the power grid vulnerability [8]. The effective resistance $R_{i,j}$ between a pair of nodes i and j is the potential difference between these nodes when a unit current is injected at node i and withdrawn at node j.$R_{\mathcal{G}}$ can be obtained as follows:

$$R_{\mathcal{G}} = \sum_{i=1}^{N-1} \frac{1}{\mu_i} \tag{9}$$

were μ_i are the eigenvalues of the L obtained from the weighted adjacency matrix of susceptances. Others vulnerability indicators commonly used in the power network topological analysis are global efficiency ($\mathcal{E}_\mathcal{G}$) and betweenness. The efficiency of a network is defined as the average of inverses of the distance for all nodes. For calculation of $\mathcal{E}_\mathcal{G}$ the reader is reminded to [22]. Betweenness has been recently used in [14] to identify most vulnerable lines in power systems. The extended betweenness ($T_e(l)$) has been introduced in [5] as fast metric to spot most critical lines in terms of system vulnerability. The metric $T_e(l)$ is based on both complex network and electrical concepts. For the line l is defined as:

$$T_e(l) = max(|\sum_{g \in G} \sum_{d \in Ld} C_g^d f_l^{gd}|) \; l \in \mathcal{L} \tag{10}$$

where Gn and Ld are set of generation nodes and load nodes, C_g^d is the power transmission capacity from generator g to load d and f_l^{gd} is the linearised power flow sensitivity in the line l with respect to an injection in generation node g and withdraw in the demand node d. C_g^d and df_l^{gd} are computed as described in [5].

5 CASE STUDY

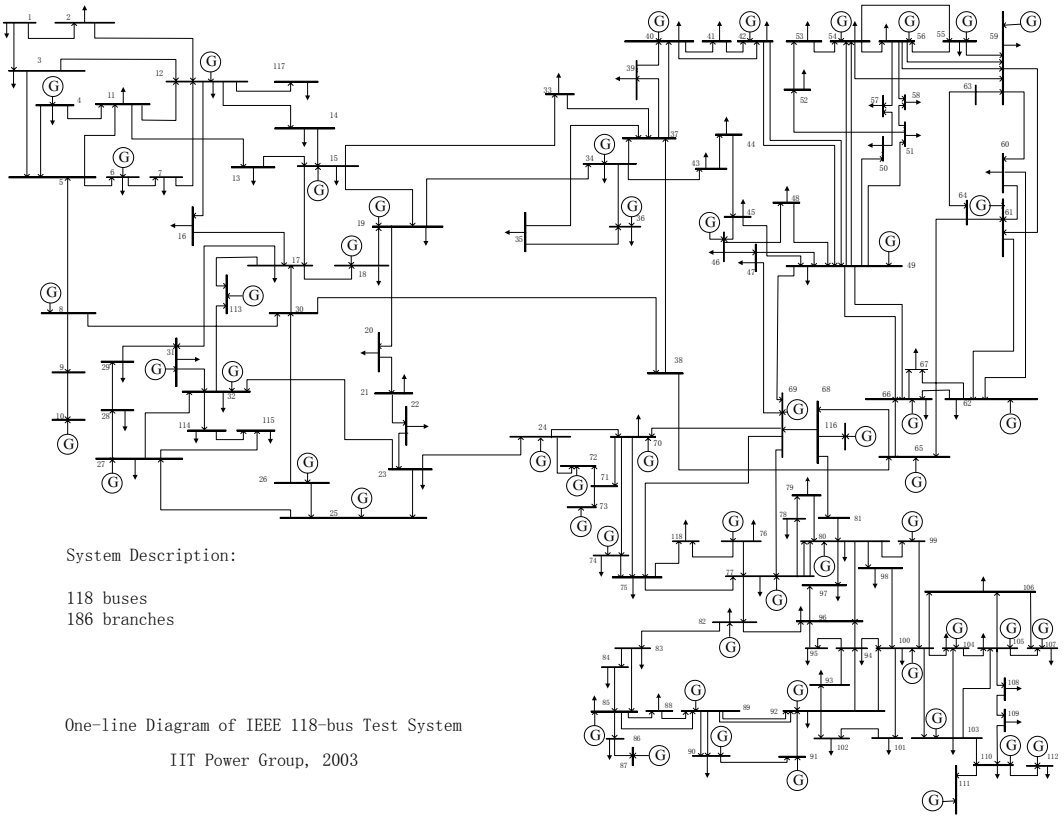

Figure 1: The IEEE 118 bus test system [21].

The selected case study is a modified version of the IEEE 118 nodes test system. The network counts 118 nodes, 186 lines and 54 generators which makes it fairly complex and suitable for the analysis. Within the gird there are 55 PV nodes (i.e. generators nodes g) and 64 PQ nodes

(i.e. load nodes d). The network model and load demand and lines emergency ratings data are available in [20]-[21]. Figure 1 displays the network structure and generators location. The original network data have been modified in order to simulate a condition of higher stress for the network. Increment in the load demand of 30 $\%$ and $P_{emerg,l}$ for all the lines l in the links set $\mathcal{L}$ reduced of 20$\%$.

Results power-flow-based metrics

The AC and its linearised version are used to simulate the network in normal and contingency states the cascading indices CEI computed and line outages ranked. The analysis is performed as follows:

- First, AC or DC approach is used to compute the optimal power production subject to line flow limits, generation constraints and load demanded.
- The contingency analysis is performed by removing one line at a time from the system. The AC or DC methods simulate the power flows redistribution in the branches given the optimal power scheduled.
- Finally, the $CEI(l)$ are computed for each contingency based on the equation 6. Line vulnerability are ranked and ordered based on the CEI values.

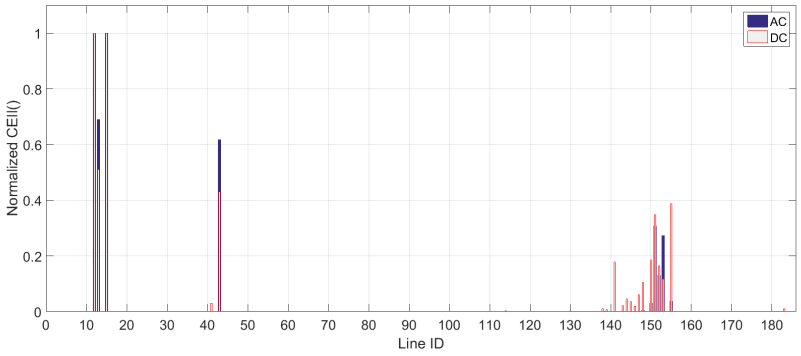

Figure 2: Normalized CEI results comparison between AC solution and and its DC approximation. On the X-axis the failed line (Line ID).

Figures 2 shows the optimal power production computed by means of the AC and DC method, respectively. The Y-axis shows the normalized CEI results and the X-axis the line identification number (ID). It can be noticed that DC power flow, when compared to AC power flow, overestimate the cascading indices for some of the contingency listed (e.g. lines ID 141-150) and underestimate them for others e.g line ID 13, 43, 153 (l_{8-5}, l_{26-30}, l_{89-92}). This is mainly due to the approximate percentage of rating PR_k obtained in the DC approach. Nevertheless, the results are in relatively good agreement, therefore it might be argued that DC solutions approximate AC solutions fairly well in both undamaged and damaged network conditions. Results are summarized in Table 5 which displays the 10 most vulnerable lines in the system, with respect to all the metrics analysed. In both AC and DC flow-based approaches the ranking results are fairly similar and similar to previous studies, see as example [19]. The most threatening lines result to be l_{9-10}, l_{8-9}, l_{8-5}, l_{26-30} for both cases.

Uncertainty Quantification for the AC and DC Solutions

The AC and DC cascading indexes have been obtained by propagation of the uncertainty in the load and in the emergency ratings. In accordance with previous studies, but with different aims, the load demand $P_{L,i}\ \forall i \in \mathcal{N}$ has been modelled as normal random variable distributed around mean μ_i and with σ_i equal to 10 $\%$ of μ_i. Uniform distributions are assumed to model lack of precision in the line maximum allowed flows. The upper and lower bounds have been set equal to 0.98 $\%$ and 1.02 $\%$ of the design values. A single loop Monte Carlo has been employed to sample input uncertainty and quantify its extent in the output. The number of MC samples for each uncertain variable have been set equal to 2x10^3, each run counts 64 samples of load demand $P_{L,d}$ and 185 samples of emergency rating $P_{emerg,l}$ one for each demand node and each line $\in \mathcal{G}$ in the network. Samples have been forwarded to the AC and DC system solver and $CEI(l)$ values obtained as described in the previous subsection. The contingencies have been ranked based on the expected value of the cascading metric and the 10 most vulnerable links have been selected. The ranking scores accounting uncertainty results slightly different compared to the deterministic case. Nevertheless, metrics drops are affected by uncertainty and some of the lines failures are more affected than others. The CEI variabilities boxes for the 10 most vulnerable lines are shown in figure 3. It can be noticed that for the DC approximation CEI for lines l_{9-10} and l_{8-9} (rank 1 and 2) bear less uncertainty if compared to the AC case. In Table 1 are displayed coefficients of variation (Cov) for the 5 most dangerous lines. Coefficient of variation is computed as ratio between standard deviation and expected value and it is a standardized measure of dispersion for the CEI distribution. The higher values confirm that AC solutions are more sensitive to the input uncertainty, which is probably due to the assumption made in order to apply the DC solver.

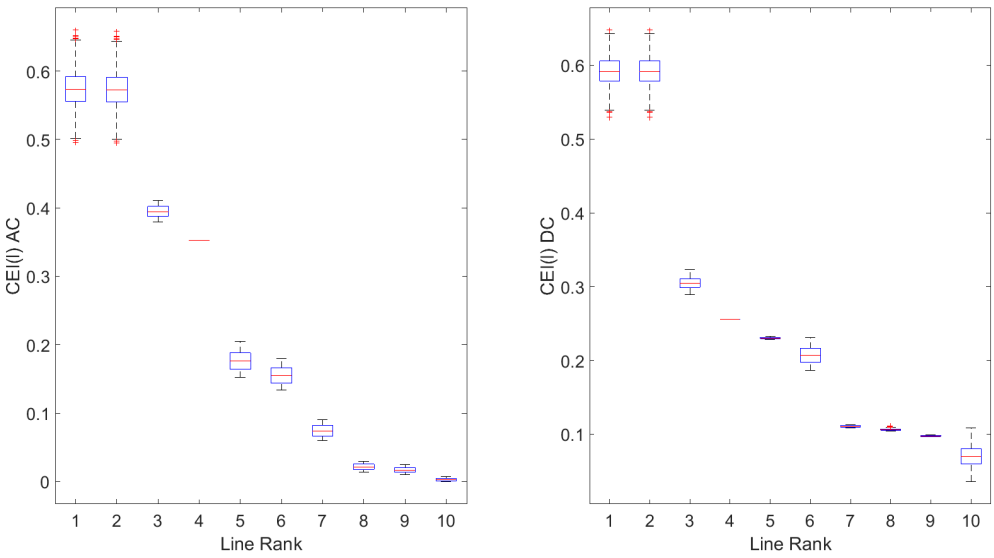

Figure 3: Variability in the normalized cascading index CEI for the 10 most vulnerable lines. Comparision between AC and DC power flow solutions.

rank	1	2	3	4	5	6	7	8	9	10
Cov_{AC}	4.5%	4.5%	2.2%	0.0%	8.0%	8.5%	11.8%	20.7%	23.6%	81.2%
Cov_{DC}	3.2%	3.2%	2.5%	0.0%	0.5%	5.4%	1.3%	1.%	0.9%	20.2%

Table 1: Variability box-plot for the ten most vulnerable lines in the IEEE 118 bus system. Coefficients of variations comparison when AC and DC power flows models are used.

Topology-based metrics and hybrid metrics results

Topology-based and extended hybrid metrics have been computed in both damaged and undamaged states. The analysis is carried as follows:

- First, adjacency matrix A and weighted adjacency matrix W are obtained for the undamaged network.
- The considered metrics $\mathcal{M}_A$ and $\mathcal{M}_W$ are computed for adjacency matrix A and W respectively, as described in section 4.
- The contingency analysis is performed by removing lines from the network. The matrix A and W corresponding to the graph of the damaged network are obtained and $\mathcal{M}(l)$ computed.
- Finally, vulnerabilities $\mathcal{V}(l)$ are computed as in equation 5 for each line failure. Topology-based and hybrid approach used A and W matrix respectively. The line failure are ranked based on normalized increment in the system vulnerability.

The topology-based metric which have been obtained in the approach are the graph global efficiency $\mathcal{E}_\mathcal{G}$, $\Lambda_\mathcal{G}(A)$ and $\rho_\mathcal{G}(A)$. These are computed using the unweighted adjacency matrix A in a purely topological way. Similarly, the extended hybrid metrics have been computed using the weighted adjacency matrix W built using susceptance matrix. These approaches account for both topology and electrical concepts. In this work $R_\mathcal{G}$, $\Lambda_\mathcal{G}(W)$ and $\rho_\mathcal{G}(W)$ are the hybrid metrics being analysed. Furthermore, normalized $T_e(l)$ have been computed fore each line as in equation 10, used as an additional metric for branch ranking. Table 5 shows metric values for the undamaged IEEE 118 power network.

$\mathcal{E}_\mathcal{G}(A)$	$\rho_\mathcal{G}(W)$	$\rho_\mathcal{G}(A)$	$\Lambda_\mathcal{G}(W)$	$\Lambda_\mathcal{G}(A)$	$R_\mathcal{G}(W)$
0.216	259.56	4.112	0.3	0.0274	1565.6

Table 2: Topology-based and hybrid metrics results for the undamaged original network.

Table 5 shows the 10 most relevant links with respect to $T_e(l)$ and the variation in the vulnerability. Although different vulnerability metrics produce different scores, the most vulnerable lines are successfully spotted. For instance, critical lines are l_{38-65}, l_{23-24}, l_{65-68}, l_{30-38} all ranked among the top 10 in 6 of the considered metrics. Similarly, lines l_{81-80} and l_{68-81} have been identified as critical by 5 metrics. This result suggest that for the components ranking purposes few differences can be found between hybrid and topology-based metrics.

Relative metrics drops and increments are displayed in figure 4, the results have been normalized for graphical reasons. It can be noticed that some of the lines failure cause a drop below

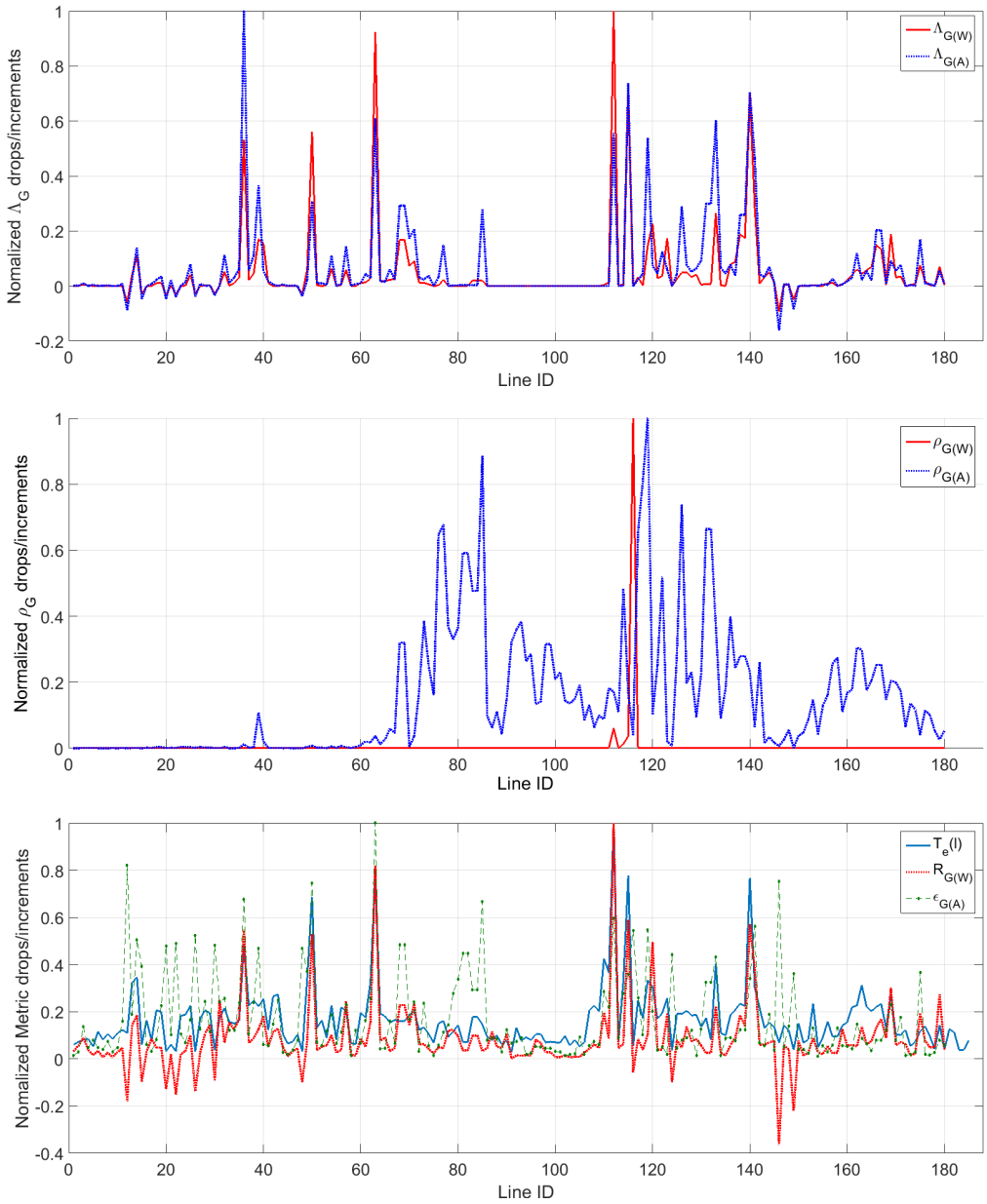

Figure 4: Comparison of relative drops and increment in vulnerability metrics, Y-axis, due to single line failures(X-axis).

Rank	$\mathcal{V}_{\mathcal{E}_\mathcal{G}(A)}$	$\mathcal{V}_{\rho_\mathcal{G}(W)}$	$\mathcal{V}_{\rho_\mathcal{G}(A)}$	$\mathcal{V}_{\Lambda_\mathcal{G}(W)}$	$\mathcal{V}_{\Lambda_\mathcal{G}(A)}$	$\mathcal{V}_{R_\mathcal{G}(W)}$	$T_e(l)$	CEI_{AC}	CEI_{DC}
1	l_{38-65}	l_{68-116}	l_{69-77}	l_{65-68}	l_{23-24}	l_{65-68}	l_{65-68}	l_{9-10}	l_{8-9}
2	l_{8-9}	l_{65-68}	l_{49-69}	l_{38-65}	l_{68-81}	l_{38-65}	l_{38-65}	l_{8-9}	l_{9-10}
3	l_{85-86}	l_{68-81}	l_{69-75}	l_{68-81}	l_{81-80}	l_{68-81}	l_{68-81}	l_{8-5}	l_{8-5}
4	l_{30-38}	l_{68-69}	l_{75-77}	l_{81-80}	l_{38-65}	l_{81-80}	l_{81-80}	l_{26-30}	l_{26-30}
5	l_{23-24}	l_{64-65}	l_{47-69}	l_{30-38}	l_{77-82}	l_{23-24}	l_{30-38}	l_{89-90}	l_{91-92}
6	l_{49-69}	l_{65-66}	l_{77-80}	l_{23-24}	l_{65-68}	l_{30-38}	l_{23-24}	l_{89-92}	l_{89-90}
7	l_{65-68}	l_{81-80}	l_{69-70}	l_{82-83}	l_{69-77}	l_{70-71}	l_{64-65}	l_{89-91}	l_{88-89}
8	l_{82-83}	l_{38-65}	l_{47-49}	l_{77-82}	l_{82-83}	l_{82-83}	l_{77-82}	l_{91-92}	l_{82-83}
9	l_{69-77}	l_{63-64}	l_{49-54}	l_{70-71}	l_{24-70}	$l_{100-103}$	l_{65-66}	l_{88-89}	l_{89-91}
10	l_{68-116}	l_{69-77}	l_{70-75}	l_{80-98}	l_{30-38}	$l_{105-108}$	l_{8-30}	l_{85-89}	l_{89-92}
Rank	$\mathcal{V}_{\mathcal{E}_\mathcal{G}(A)}$	$\mathcal{V}_{\rho_\mathcal{G}(W)}$	$\mathcal{V}_{\rho_\mathcal{G}(A)}$	$\mathcal{V}_{\Lambda_\mathcal{G}(W)}$	$\mathcal{V}_{\Lambda_\mathcal{G}(A)}$	$\mathcal{V}_{R_\mathcal{G}(W)}$	$T_e(l)$	CEI_{AC}	CEI_{DC}
1	0.031	0.4956	0.020	0.382	0.241	0.194	0.342	0.5931	0.57365
2	0.025	0.0299	0.017	0.352	0.178	0.159	0.267	0.5931	0.57246
3	0.023	0.0183	0.016	0.272	0.170	0.115	0.266	0.3028	0.39562
4	0.023	0.0062	0.014	0.266	0.147	0.111	0.263	0.2549	0.35366
5	0.021	0.0005	0.013	0.214	0.145	0.106	0.235	0.2297	0.17620
6	0.020	0.0004	0.013	0.203	0.134	0.103	0.165	0.2066	0.15594
7	0.018	0.0002	0.013	0.109	0.130	0.096	0.145	0.1099	0.07426
8	0.017	0.0000	0.013	0.102	0.113	0.074	0.138	0.1056	0.02133
9	0.017	0.0000	0.012	0.087	0.088	0.059	0.126	0.0973	0.01678
10	0.017	0.0000	0.010	0.072	0.074	0.053	0.119	0.0691	0.00246

Table 3: Ten most vulnerable lines for the IEEE 118 system. Ranking comparison with respect to different metrics and normalized drops in the vulnerability.

zero some of the normalized vulnerability index (e.g. algebraic connectivity). A drop below zero means an increment in the robustness of the grid which is caused by the lines removal (e.g. line ID 146). The capability of the metrics to spot components which have unexpected negative effects for the network robustness can have an interesting features of hybrid and topology based metrics, exploitable to improve network robustness and future topology design.

Uncertainty Quantification for Topology-based and hybrid vulnerability metrics

Single loop Monte Carlo sampling procedure has been adopted as in the previous analysis and uncertain input variable propagated and effects quantified in the output. The Monte Carlo simulation approach and input distributions used are the same as for the AC and DC power flow uncertainty quantification. The results obtained for the IEEE 118 power system shows that the rankings are the same as in the deterministic case. For sake of synthesis, only results for one of the metrics are displayed, the extended betweenness. Coefficient of variation for the $T_e(l)$ have been displayed in Table 4.

The results shows that considered sources of uncertainty affect less these approaches, i.e. the

Rank	1	2	3	4	5	6	7	8	9	10
$Cov\ T_e(l)$	0.5 %	0.3%	0.5%	0.5%	0.3%	0.3%	0.4%	0.5%	0.4%	0.3%

Table 4: Comparison of coefficients of variations for the ten most vulnerable lines ranked using extended betweenness $T_e(l)$.

maximum value for the Cov 0.5 $\%$ for the ten most vulnerable lines. This is a rather expected result if considered that the load demand variability do not influence any of the considered topology-based and hybrid metrics.

6 DISCUSSION AND LIMITATIONS

A modified version of the IEEE 118 nodes power network has been analysed and lines sorted with respect to their contribution to the grid vulnerability. The comparison between topology-based and hybrid approaches shows similarities in the ranking results. Spectral analysis of the network require higher computational cost for obtaining a full spectrum of eigenvalues and eigenvector for each damaged condition (and relative W, A and L).

Contingency analysis has been used to obtain a power flow-based cascading metrics, the CEI indices. Both AC and DC power flow solver have been adopted for the calculation and comparison between line ranking showing minor differences between the approaches. This has been regarded as a confirmation of well-founded DC hypothesis for the system in exam. The comparison of the CEI indices with topology-based and hybrid metrics suggest significant differences in the ranking. The differences can be explained by lack of considerations about nodal power injections and withdraw of some of the approaches. The considered topology-based metrics even if enhanced in hybrid metrics cannot capture in full the operational vulnerabilities in the network. On the other hand, power-flow-based approaches included power injection and demands magnitudes in the calculation and hence able to identify critical components accounting changes in the operational state. Nevertheless, many of the lines ranked using CEI index resulted in a null contribution to the system vulnerability (due to null post-failure overload severity). This might be seen as a limitation of the CEI metric which has not been able to capture all the relevant aspect and information enclosed in the line failures.

Uncertainty propagated through the AC and DC methods have been quantified in the $CEI(l)$ indexes. Ranking results show good agreement with the deterministic solution and between the different power flow solvers. The AC output seems to be more sensitive to the uncertainties in the input, which can be due to the less restrictive assumptions compared to the DC method. The largest majority of the hybrid approaches make use of the DC assumptions. Generally the goodness of DC approximation should be tested and model adopted carefully[10]. Especially in scenarios where grid stress is high, such as sudden component failures or attacks, the approximation might result poor and not represent adequately the reality. Comparisons between hybrid metrics and pure topological metrics show a good agreement in the line ranking although some of them, i.e. ranking based on drops in spectral radius, differs substantially. This might be due to limitation of the latter metric or computational inaccuracies.

7 CONCLUSIONS

The future electric power grid is a complex network which have to deal with uncertainty from different sources. The correct functioning of the system and components will strongly depend on the operational context. Therefore providing easy to follow guidances and robustness metrics is uttermost important point. The metrics have to be capable of capturing uncertainties and variability in the network dynamic and as well intrinsic topological weaknesses in a reliable way. In this paper different vulnerability metrics have been compared in their ability to spot system criticality and ranking important components.The effects of uncertainty have been

analysed and relative drops or increments in the metrics discuses and compared to the same approaches with no uncertainty accounted for. The IEEE 118 power grid has been used as case study. The AC and DC power flow cascading metrics showed higher uncertainty in the outputs if compared to topology based metrics. This is due to operational variability not fully accounted in the latter approaches and to the different assumptions. In conclusion, the selection of metrics for vulnerability assessment of power grids have o be selected carefully. The analyst should account both influence of the underling model assumptions and system variability. Wrong consideration of uncertainty can lead to imprecise considerations on the system vulnerability and in the worst case to misleading results on its robustness and reliability.

REFERENCES

[1] A. Kott, T. Adbelzaher, *Resiliency and Robustness of Complex Systems and Networks*. Adaptive Dynamic Resilient Systems,19, 1387-1401, 2004.

[2] E. Zio and T. Aven, *'Uncertainties in smart grids behavior and modeling: What are the risks and vulnerabilities? How to analyze them?'*. Energy Policy Volume 39, 6308-6320, 2011.

[3] G. A. Pagani, M. Aiello, *'From the grid to the smart grid, topologically'*. Physica A: Statistical Mechanics and its Applications, 2015.

[4] Cuadra, Lucas, Salcedo-Sanz, Sancho, Del Ser, Javier, Jimnez-Fernndez, Silvia, Geem, Zong Woo, *A Critical Review of Robustness in Power Grids Using Complex Networks Concepts*.Energies Volume 8, 9211-9265, 2015.

[5] E. Bompard, D. Wu, F. Xue, *'Structural vulnerability of power systems: A topological approach'*. Electric Power Systems Research, Volume 81, 1334-1340, 2011.

[6] Min Ouyang, Zhezhe Pan, Liu Hong, Lijing Zhao, *'Correlation analysis of different vulnerability metrics on power grids'*. Physica A: Statistical Mechanics and its Applications, Volume 396, 204 - 211, 2014.

[7] F. Xiao, McCalley, J.D. C., *'Power System Risk Assessment and Control in a Multiobjective Framework'*. Power Systems, IEEE Transactions on Volume 24, 78-85, 2009.

[8] . Koç, M. Warnier, P. Van Mieghem, R. E. Kooij, F. M.T. Brazier, *'A topological investigation of phase transitions of cascading failures in power grids'*. Physica A: Statistical Mechanics and its Applications Volume 415, 273-284,2014.

[9] P. Van Mieghen, *'Graph Spectra For Complex Networks'*. Cambridge University Press. 2011.

[10] Van Hertem, D., Verboomen, J., Purchala, K., Belmans, R., Kling, W.L.*'Usefulness of DC power flow for active power flow analysis with flow controlling devices'*. AC and DC Power Transmission, 58-62, 2006. ACDC 2006.

[11] R. Rocchetta, M. Broggi, E. Patelli, *'Efficient Epistemic-Aleatory Uncertainty Quantification: Application to the NAFEMS challenge problem'*. NAFEMS World Congress 2015, At San Diego, CA, 2015

[12] S.Zhang, I. Dobson, F.L. Alvarado, *'Quantifying transmission reliability margin'*. Electrical Power and Energy Systems 26, 697702, 2004.

[13] R. Rocchetta, Y.F. Li, E. Zio, *'Risk assessment and risk-cost optimization of distributed power generation systems considering extreme weather conditions'*. Reliability Engineering & System Safety, Volume 136, 4 -61, 2015.

[14] Dwivedi A., Xinghuo Y., Sokolowski P., *'Identifying vulnerable lines in a power network using complex network theory'*. Industrial Electronics, 2009. ISIE 2009. IEEE International Symposium on, 18-23, 2009.

[15] K.S. Turitsyn, P.A. Kaplunovich, *'Fast Algorithm for N-2 Contingency Problem'*. System Sciences (HICSS), 2013 46th Hawaii International Conference on.

[16] Jamakovic A., Uhlig S., *'On the relationship between the algebraic connectivity and graph's robustness to node and link failures'*. Next Generation Internet Networks, 3rd EuroNGI Conference on, 96-102, 2007.

[17] E.R. van Dam, R.E. Kooij, *'The minimal spectral radius of graphs with a given diameter'*. Linear Algebra and its Applications, Volume 423, 2-3, 2007.

[18] J. McCalley, M. Ni, V. Vittal, T. Tayyib, *'Online risk-based security assessment'*. IEEE Transactions on Power Systems Volume 18, 258-265, 2003.

[19] Greene S., Dobson I., Alvarado F.L.,*'Contingency ranking for voltage collapse via sensitivities from a single nose curve'*. Power Systems, IEEE Transactions on, Volume 14, 232-240, 1999.

[20] R. D. Zimmerman, C. E. Murillo-Snchez,, R. J. Thomas, *MATPOWER Steady-State Operations, Planning and Analysis Tools for Power Systems Research and Education*, Power Systems, IEEE Transactions on, Volume 26, no. 1, 12-19, Feb. 2011

[21] M. Shahidehpour, Y.Wang, *'Communication and Control in Electric Power Systems'*. IEEE Press Power Engineering Series, 477-48, 2003.

[22] Monfared, M. A. S., Jalili, M., Alipour, Z.*'Topology and vulnerability of the Iranian power grid'*. Physica A: Statistical Mechanics and its Applications, Volume 406, 24 - 33, 2014.

ECCOMAS Congress 2016
VII European Congress on Computational Methods in Applied Sciences and Engineering
M. Papadrakakis, V. Papadopoulos, G. Stefanou, V. Plevris (eds.)
Crete Island, Greece, 5–10 June 2016

MULTILEVEL STOCHASTIC REDUCED-ORDER MODEL IN LINEAR STRUCTURAL DYNAMICS FOR COMPLEX STRUCTURES

O. Ezvan[1], **A. Batou**[1], **and C. Soize**[1]

[1]Université Paris-Est, Laboratoire Modélisation et Simulation Multi-Echelle,
MSME UMR 8208 CNRS
5 bd Descartes, 77454 Marne-la-Vallée, France
e-mail: {olivier.ezvan, anas.batou, christian.soize}@univ-paris-est.fr

Keywords: Uncertainty quantification, Reduced-Order Model, Structural dynamics

Abstract. *We present the construction of a multilevel stochastic reduced-order model devoted to the robust prediction of frequency response functions of complex linear dynamical systems that are characterized by the presence of several structural scales in which there are local displacements in addition to the usual global displacements, and which are associated with the distinct low-, medium-, and high-frequency bands. As the levels of uncertainties are different in the three frequency bands, a multilevel stochastic reduced-order model using several orthogonal subspaces associated with the several types of displacements is developed. The objective of the paper is to demonstrate the capability of the multilevel stochastic reduced-order model to adapt the stochastic modeling of uncertainties to each one of the three frequency bands.*

1 Introduction

We present a new method for the robust prediction of frequency response functions (FRF) of complex linear dynamical structures exhibiting a high modal density. Commonly, the low-frequency range [1] is characterized by the presence of a few dozen isolated eigenfrequencies that are associated with global modes, in which case the modal analysis method [2, 3, 4] allows an effective and efficient small-dimension reduced-order model (ROM) to be obtained. In contrast, the complex structures we deal with can exhibit more than hundreds or thousands modes in low frequencies. This unusual feature is due to the presence of several structural scales within the complex geometry of the structure. Small flexible components attached to the stiff skeleton of the structure induce the presence of numerous local modes intertwined with the usual global modes of the stiff skeleton. For such complex structures, besides the absence of separation of scales, the global displacements (or global modes) cannot easily be identified because coupled with the large-amplitude local displacements (or local modes). For constructing an adapted reduced-order model of such complex structures, a first version of a two-levels reduced-order model has been proposed [5], and then has been extended and applied to complex mechanical systems [6, 7]. Then the methodology has been generalized [8] for constructing multilevel reduced-order models. This paper is mainly devoted to the stochastic aspects and their implementation in the multilevel reduced-order model.

First, the proposed method allows for constructing a ROM of smaller dimension, which is obtained by introducing a subspace of global displacements. The construction of the latter is based on the introduction of high-degree polynomial shape functions. The vector basis of the global-displacements subspace is constituted of the eigenmodes calculated using such an approximation for the kinetic energy. The choice of the polynomial degree allows for controlling the filtering between the so-called global and local displacements, as well as the resulting dimension and accuracy of the so-called global ROM. Furthermore, it is well known that local displacements are in general more sensitive to uncertainties than global displacements. The nonparametric probabilistic approach [9] allows all sources of uncertainty to be globally accounted for by randomizing each reduced matrix whose probability density function, constructed applying the maximum entropy principle [10, 11], is parameterized by a unique dispersion hyperparameter. In order to separately control the uncertainty level of the displacements of each of the scales, we propose to use a multilevel ROM, based on the introduction of orthogonal subspaces. The basis of each of these subspaces is constructed by using, notably, the aforementioned polynomial approximation for the kinetic energy, with an adapted polynomial degree. Each basis is constituted of displacements associated with a given structural scale. Then, the multilevel stochastic ROM is obtained by using the nonparametric probabilistic approach for each scale. This stochastic model is then controlled by some dispersion hyperparameters devoted to each scale. The method is applied to the complex computational model of a car. The objective of this work is to present a sensitivity analysis of the multilevel stochastic ROM with respect to the

dispersion hyperparameters in order to demonstrate the capability of the method proposed to adapt the stochastic modeling to the level of uncertainties as a function of the frequency bands.

2 Classical nominal reduced-order model

Let $[\mathbb{M}]$, $[\mathbb{D}]$, and $[\mathbb{K}]$ denote the $(m \times m)$ positive-definite real symmetric mass, damping and stiffness matrices of a m-dimensional finite element model of a linear damped structure with bounded domain, Ω. The m-dimensional complex vector $\mathbb{U}(\omega)$ of the displacements satisfies, for all ω in the frequency band $\mathcal{B}$, the matrix equation,

$$(-\omega^2[\mathbb{M}] + i\omega[\mathbb{D}] + [\mathbb{K}])\mathbb{U}(\omega) = \mathbb{F}(\omega)\,, \tag{1}$$

in which the m-dimensional complex vector $\mathbb{F}(\omega)$ represents the external forces. For $\alpha = 1, \ldots, m$, the elastic modes $\boldsymbol{\varphi}_\alpha$ are the eigenvectors of the following generalized eigenvalue problem associated with the conservative dynamical system,

$$[\mathbb{K}]\boldsymbol{\varphi}_\alpha = \lambda_\alpha[\mathbb{M}]\boldsymbol{\varphi}_\alpha\,, \tag{2}$$

in which λ_α is the eigenvalue associated with mode $\boldsymbol{\varphi}_\alpha$ such that $\lambda_\alpha = \omega_\alpha^2$ and $\omega_\alpha = 2\pi f_\alpha$, with f_α the associated eigenfrequency in Hz. The classical nominal reduced-order model (C-NROM) is obtained by projecting Eq. (1) onto the subspace, $\mathcal{S}_c \subset \mathbb{C}^m$, spanned by the first n elastic modes (associated with the n smallest eigenfrequencies). Normalizing the eigenmodes with respect to the mass matrix, the associated reduced-order basis (ROB) is given by $[\Phi] = [\boldsymbol{\varphi}_1 \ldots \boldsymbol{\varphi}_n]$ and verifies $[\Phi]^T[\mathbb{M}][\Phi] = [I_n]$ as well as $[\Phi]^T[\mathbb{K}][\Phi] = [\Lambda]$, with $[\Lambda]$ the matrix of the first n eigenvalues. In the rest of this paper, the eigenvectors of any eigenvalue problem such as in Eq. (2) will follow the same normalization. Introducing the generalized damping matrix $[\mathcal{D}] = [\Phi]^T[\mathbb{D}][\Phi]$ and the vector $\mathcal{F}(\omega) = [\Phi]^T\mathbb{F}(\omega)$ of the generalized forces, the vector $\mathbf{q}(\omega) = (q_1(\omega) \ldots q_n(\omega))$ of the generalized coordinates of the C-NROM is the solution of the reduced-matrix equation,

$$(-\omega^2[I_n] + i\omega[\mathcal{D}] + [\Lambda])\mathbf{q}(\omega) = \mathcal{F}(\omega)\,, \tag{3}$$

and allows displacements $\mathbb{U}(\omega)$ to be approximated by

$$\mathbb{U}(\omega) \simeq [\Phi]\mathbf{q}(\omega) = \sum_{\alpha=1}^{n} q_\alpha(\omega)\,\boldsymbol{\varphi}_\alpha\,. \tag{4}$$

In the rest of this paper, several ROMs will be constructed. For simplicity, the notations will be introduced only for the associated ROB, since any ROM is straightforwardly obtained, using its ROB, by projection of Eq. (1) and by recovering the physical degrees of freedom (DOF) $\mathbb{U}(\omega)$ such as in Eq. (4).

For the complex structures under consideration, due to the presence of numerous local displacements, dimension n of the C-NROM is quite large. We propose the

construction of a global-displacements ROB, from which local displacements are removed. Such filtering relies on the introduction of a reduced kinematics for the mass matrix.

3 Reduced-kinematics mass matrix

The proposed filtering of local displacements is based on the use of polynomial shape functions defined on domain Ω, the filtering being controlled by the degree, $\mathcal{D}$, of the polynomial approximation. The construction of the polynomial basis is detailed in [8]. Let $[B]$ denote the $(m \times N_p)$ real matrix constituted of the concatenation of the $N_p = (\mathcal{D}+1)(\mathcal{D}+2)(\mathcal{D}+3)/2$ polynomials, which are orthogonal such that

$$[B]^T[\mathbb{M}][B] = [I_{N_p}]\,. \tag{5}$$

The polynomials are only used for approximating the kinetic energy (the elastic energy remains exact). Let $\mathbb{V}(t)$ denote a time-dependent real vector of dimension m. The orthogonal projection $\mathbb{V}^r(t)$ of $\mathbb{V}(t)$ onto the subspace spanned by the polynomials basis is given by

$$\mathbb{V}^r(t) = [\mathbb{P}]\mathbb{V}(t)\,, \tag{6}$$

in which the projector $[\mathbb{P}]$ is a $(m \times m)$ real matrix which is written [8] as

$$[\mathbb{P}] = [B][B]^T[\mathbb{M}]. \tag{7}$$

Then, the kinetic energy $E_k(\mathbb{V}(t)) = \frac{1}{2}\mathbb{V}(t)^T[\mathbb{M}]\mathbb{V}(t)$ is replaced by the reduced kinetic energy $E_k^r(\mathbb{V}(t)) = \frac{1}{2}\mathbb{V}^r(t)^T[\mathbb{M}]\mathbb{V}^r(t) = \frac{1}{2}\mathbb{V}(t)^T[\mathbb{M}^r]\mathbb{V}(t)$ in which the $(m \times m)$ reduced-kinematics mass matrix $[\mathbb{M}^r]$ is positive-semidefinite symmetric real of rank N_p and such that

$$[\mathbb{M}^r] = [\mathbb{M}][B][B]^T[\mathbb{M}]\,. \tag{8}$$

For constructing the global-displacements ROB, matrix $[\mathbb{M}^r]$ is used instead of $[\mathbb{M}]$.

4 Global-displacements reduced-order basis

4.1 Definition

Let $\boldsymbol{\psi}_\alpha^g$ ($\alpha = 1, \ldots, N_p$) be the eigenvectors and let σ_α^g be the associated eigenvalues such that

$$[\mathbb{K}]\boldsymbol{\psi}_\alpha^g = \sigma_\alpha^g[\mathbb{M}^r]\boldsymbol{\psi}_\alpha^g\,, \tag{9}$$

for which the kinetic energy is subjected to the polynomial approximation and which allows the $(m \times \nu)$ real matrix $[\Psi^g] = [\boldsymbol{\psi}_1^g \ldots \boldsymbol{\psi}_\nu^g]$ to be constructed, with $\nu \leq N_p$. Then, the ROB associated with the global nominal reduced-order model (G-NROM) is

given by $[\Phi^g] = [\Psi^g][R]$, where $[R] = [\mathbf{r}_1 \dots \mathbf{r}_{n_g}]$ is constituted of the n_g eigenvectors $\mathbf{r}_\alpha$ of the small-dimension generalized eigenvalue problem

$$\left([\Psi^g]^T[\mathbb{K}][\Psi^g]\right)\mathbf{r}_\alpha = \lambda^g_\alpha \left([\Psi^g]^T[\mathbb{M}][\Psi^g]\right)\mathbf{r}_\alpha\,, \tag{10}$$

where dimension n_g of the G-NROM is chosen as minimum under the constraint $f^g_{n_g} \geq f^c$, with $f^g_\alpha = \sqrt{\lambda^g_\alpha}/2\pi$. Frequency f^c is related to the upper bound of frequency band of analysis $\mathcal{B}$. The global-displacements subspace, spanned by the n_g columns of $[\Phi^g]$, is denoted by $\mathcal{S}_g$. The matrix $[\Lambda^g]$ of the associated eigenvalues is such that $[\Lambda^g] = [\Phi^g]^T[\mathbb{K}][\Phi^g]$.

4.2 Numerical implementation

The proposed method is adapted so as to be non-intrusive with respect to commercial software for which extraction of mass and stiffness matrices can be difficult or even impossible. Given the considered approximation for constructing mass matrix $[\mathbb{M}^r]$, replacing consistent mass matrix $[\mathbb{M}]$ by a lumped approximation in order to construct $[\mathbb{M}^r]$ is legitimate. We then propose an indirect method for constructing the global-displacements ROB.

Let $\mathcal{S}_0$ be a subspace spanned by the n_0 columns of a ROB $[\Phi^0]$, which can, for instance, be constituted of elastic modes, available through commercial software. We suppose having $[\Phi^0]^T[\mathbb{M}][\Phi^0] = [I_{n_0}]$ and $[\Phi^0]^T[\mathbb{K}][\Phi^0] = [\Lambda^0]$ with $[\Lambda^0]$ a diagonal matrix with positive elements. Then, considering the approximation $\mathcal{S}_g \subseteq \mathcal{S}_0$ obtained writing $\boldsymbol{\psi}^g_\alpha = [\Phi^0]\mathbf{s}_\alpha$ for all $\alpha = 1, \dots, N_p$, Eq. (9) leads us to the reduced-order generalized eigenvalue problem

$$\left([\Phi^0]^T[\mathbb{K}][\Phi^0]\right)\mathbf{s}_\alpha = \sigma^g_\alpha \left([\Phi^0]^T[\mathbb{M}^r][\Phi^0]\right)\mathbf{s}_\alpha\,. \tag{11}$$

Since $[\Phi^0]^T[\mathbb{K}][\Phi^0] = [\Lambda^0]$, the latter eigenvalue problem does not require having $[\mathbb{K}]$ but $[\Lambda^0]$ instead. Moreover, denoting as $[\mathbb{M}^\ell]$ a lumped approximation of $[\mathbb{M}]$, the generalized mass matrix of Eq. (11) is approximated as

$$[\Phi^0]^T[\mathbb{M}^r][\Phi^0] \simeq [N^0][N^0]^T\,, \tag{12}$$

with $[N^0] = [\Phi^0]^T[\mathbb{M}^\ell][B^\ell]$, in which $[B^\ell]$ denotes the orthonormalization of $[B]$ with respect to $[\mathbb{M}^\ell]$. Matrix $[S] = [\mathbf{s}_1 \dots \mathbf{s}_\nu]$ is such that $[\Psi^g] = [\Phi^0][S]$ and we then have $[\Phi^g] = [\Phi^0][Q^g]$ with $[Q^g] = [S][R]$. Furthermore, reduced matrices involved in Eq. (10) are given by

$$[\Psi^g]^T[\mathbb{K}][\Psi^g] = [\Sigma^g]\,, \qquad [\Psi^g]^T[\mathbb{M}][\Psi^g] = [S]^T[S]\,, \tag{13}$$

with $[\Sigma^g]$ the matrix of the first ν eigenvalues σ^g_α.

4.3 Complementary local-displacements reduced-order basis

The complementary basis of local displacements belonging to subspace $\mathcal{S}_0$ spans a subspace $\mathcal{S}_\ell$ that is such that

$$\mathcal{S}_0 = \mathcal{S}_g \oplus \mathcal{S}_\ell \,, \tag{14}$$

which means that $\mathcal{S}_g$ and $\mathcal{S}_\ell$ are in direct sum. The construction of the associated ROB, $[\Phi^\ell]$, is proposed as follows. It verifies $[\Phi^g]^T[\mathbb{M}][\Phi^\ell] = [\,0\,]$ (orthogonality of the local basis vectors, $\boldsymbol{\varphi}^{\boldsymbol{\ell}}_{\boldsymbol{\alpha}}$, and the global basis vectors, $\boldsymbol{\varphi}^{\boldsymbol{g}}_{\boldsymbol{\alpha}}$, with respect to the mass matrix) as well as $[\Phi^\ell] = [\Phi^0][Q^\ell]$ (the local basis vectors belong to $\mathcal{S}_0$), with $[Q^\ell]$ a real matrix of generalized coordinates that is defined hereinafter. The orthogonality condition is written as $[C][Q^\ell] = [\,0\,]$, where matrix $[C]$ is given by $[C] = [\Phi^g]^T[\mathbb{M}][\Phi^0]$, and can be rewritten as

$$[C] = [Q^g]^T \,. \tag{15}$$

Let $[C] = [U_C][\Sigma_C][V_C]^T$ be the singular value decomposition (SVD) of $[C]$. Let $[Z]$ be the concatenation of the columns of $[V_C]$ associated with the zero singular values (zero diagonal elements of $[\Sigma_C]$). Then, the columns of $[Z]$ constitute a vector basis of the kernel of $[C]$ and matrix $[Z]$ verifies $[Z]^T[Z] = [I_{n_\ell}]$, where $n_\ell = n_0 - n_g$ is the dimension of the kernel of $[C]$. Orthogonality condition $[C][Q^\ell] = [\,0\,]$ leads us to $[Q^\ell] = [Z][U]$, with $[U]$ a matrix of generalized coordinates. The columns $\mathbf{u}_\alpha$ of $[U] = [\mathbf{u}_1 \ldots \mathbf{u}_{n_\ell}]$ are the solutions of the reduced-order generalized eigenvalue problem

$$\Big([Z]^T[\Phi^0]^T[\mathbb{K}][\Phi^0][Z]\Big)\,\mathbf{u}_\alpha = \lambda^\ell_\alpha \Big([Z]^T[\Phi^0]^T[\mathbb{M}][\Phi^0][Z]\Big)\,\mathbf{u}_\alpha \,, \tag{16}$$

which can be more simply rewritten as the eigenvalue problem

$$\Big([Z]^T[\Lambda^0][Z]\Big)\,\mathbf{u}_\alpha = \lambda^\ell_\alpha\,\mathbf{u}_\alpha \,. \tag{17}$$

5 Multilevel nominal and stochastic reduced-order models

To sum up, for a given polynomial degree $\mathcal{D}$ and a given truncation order ν for $[\Psi^g] = [\boldsymbol{\psi}^g_1 \ldots \boldsymbol{\psi}^g_\nu]$, global-displacements subspace $\mathcal{S}_g$ and local-displacements subspace $\mathcal{S}_\ell$ of any given space $\mathcal{S}_0$ can be constructed such that $\mathcal{S}_0 = \mathcal{S}_g \oplus \mathcal{S}_\ell$. Dimension $n_g \leq \nu$ of $\mathcal{S}_g$ also depends on cutting frequency f^c. Therefore, there is a function $\mathcal{G}$ such that

$$\mathcal{G} : (\mathcal{S}_0, \mathcal{D}, \nu, f^c) \longmapsto (\mathcal{S}_g, \mathcal{S}_\ell) \,, \tag{18}$$

which includes the described construction in a compact form.

5.1 Definition of the orthogonal subspaces

For the multilevel nominal reduced-order model (ML-NROM), three subspaces $\mathcal{S}_{\mathcal{L}}$, $\mathcal{S}_{\mathcal{M}}$, and $\mathcal{S}_{\mathcal{H}}$ associated with the low-, medium-, and high-frequency bands (LF, MF, and HF) are constructed. These subspaces are such that $\mathcal{S}_g = \mathcal{S}_{\mathcal{L}} \oplus \mathcal{S}_{\mathcal{M}} \oplus \mathcal{S}_{\mathcal{H}}$. Space $\mathcal{S}_g$ corresponds to a filtering of local displacements that allows the final dimension (and thus the computational cost) of the ML-NROM to be reduced. Subspaces $\mathcal{S}_g$ and $\mathcal{S}_\ell$ are given by

$$(\mathcal{S}_g, \mathcal{S}_\ell) = \mathcal{G}(\mathcal{S}_c, \mathcal{D}_g, \nu_g, f_g^c)\,, \tag{19}$$

where we recall space $\mathcal{S}_c$ to be spanned by the first n elastic modes that would be used in a classical modal analysis, with f_g^c a cutting frequency associated with the upper bound of frequency band of analysis $\mathcal{B}$, and where parameters $\mathcal{D}_g$ and ν_g allow the filtering to be controlled. It should be noted that, for constructing the ML-NROM, the construction of $\mathcal{S}_\ell$ that is such that $\mathcal{S}_c = \mathcal{S}_g \oplus \mathcal{S}_\ell$, is not needed.

We then introduce a second filtering, using $\mathcal{D}_{\mathcal{LM}} \leq \mathcal{D}_g$ and $\nu_{\mathcal{LM}} \leq n_g$ as well as a cutting frequency $f_{\mathcal{LM}}^c$ associated with the upper bound of the MF band. The associated global-displacements and local-displacements subspaces $\mathcal{S}_{\mathcal{LM}}$ and $\mathcal{S}_{\mathcal{H}}$ are given by

$$(\mathcal{S}_{\mathcal{LM}}, \mathcal{S}_{\mathcal{H}}) = \mathcal{G}(\mathcal{S}_g, \mathcal{D}_{\mathcal{LM}}, \nu_{\mathcal{LM}}, f_{\mathcal{LM}}^c)\,, \tag{20}$$

and satisfy $\mathcal{S}_g = \mathcal{S}_{\mathcal{LM}} \oplus \mathcal{S}_{\mathcal{H}}$.

For obtaining subspaces $\mathcal{S}_{\mathcal{L}}$ and $\mathcal{S}_{\mathcal{M}}$, a third filtering parameterized by $\mathcal{D}_{\mathcal{L}} \leq \mathcal{D}_{\mathcal{LM}}$ and $\nu_{\mathcal{L}} \leq \dim(\mathcal{S}_{\mathcal{LM}})$ as well as a cutting frequency $f_{\mathcal{L}}^c$ associated with the upper bound of the LF band is introduced. The associated global-displacements and local-displacements subspaces $\mathcal{S}_{\mathcal{L}}$ and $\mathcal{S}_{\mathcal{M}}$ are given by

$$(\mathcal{S}_{\mathcal{L}}, \mathcal{S}_{\mathcal{M}}) = \mathcal{G}(\mathcal{S}_{\mathcal{LM}}, \mathcal{D}_{\mathcal{L}}, \nu_{\mathcal{L}}, f_{\mathcal{L}}^c)\,. \tag{21}$$

Since $\mathcal{S}_{\mathcal{LM}} = \mathcal{S}_{\mathcal{L}} \oplus \mathcal{S}_{\mathcal{M}}$, we thus have $\mathcal{S}_g = \mathcal{S}_{\mathcal{L}} \oplus \mathcal{S}_{\mathcal{M}} \oplus \mathcal{S}_{\mathcal{H}}$.

5.2 Multilevel nominal reduced-order model

Due to the orthogonality property, it can be shown that the reduced mass matrix of the ML-NROM, $[M]$, is such that $[M] = [I_{n_g}]$. In contrast, the reduced stiffness matrix $[K]$ of the ML-NROM is a full matrix that is written as

$$[K] = \begin{bmatrix} [K^{\mathcal{LL}}] & [K^{\mathcal{LM}}] & [K^{\mathcal{LH}}] \\ [K^{\mathcal{ML}}] & [K^{\mathcal{MM}}] & [K^{\mathcal{MH}}] \\ [K^{\mathcal{HL}}] & [K^{\mathcal{HM}}] & [K^{\mathcal{HH}}] \end{bmatrix}\,, \tag{22}$$

in which, for $\mathcal{I}$ and $\mathcal{J}$ in $\{\mathcal{L}, \mathcal{M}, \mathcal{H}\}$, the matrix block $[K^{\mathcal{IJ}}]$ is given by $[K^{\mathcal{IJ}}] = [\Phi^{\mathcal{I}}]^T [\mathbb{K}]\, [\Phi^{\mathcal{J}}]$, with $[\Phi^{\mathcal{I}}]$ the ROB of $\mathcal{S}_{\mathcal{I}}$. The damping matrix $[D]$ of the ML-NROM is also a full matrix with the blocks $[D^{\mathcal{IJ}}] = [\Phi^{\mathcal{I}}]^T [\mathbb{D}] [\Phi^{\mathcal{J}}]$.

5.3 Multilevel stochastic reduced-order model

The construction of the multilevel stochastic reduced-order model (ML-SROM) is based on the nonparametric probabilistic approach of uncertainties. This approach consists in replacing any positive-definite symmetric real $(N \times N)$ matrix $[X]$ of a ROM by an associated random matrix $[\mathbf{X}]$ whose probability density function is obtained applying the maximum entropy principle under the constraints (available information)

- Matrix $[\mathbf{X}]$ is with values in the set of all the positive-definite symmetric real $(N \times N)$ matrices.
- $E\{[\mathbf{X}]\} = [X]$, where E is the mathematical expectation: the mean value is chosen as the value of the nominal model.
- $E\{||[\mathbf{X}]^{-1}||_F^2\} < +\infty$, with $||.||_F$ denoting the Frobenius norm.

Given the Cholesky factorization $[X] = [L_X]^T[L_X]$ with $[L_X]$ an upper triangular matrix, random matrix $[\mathbf{X}]$ is written as

$$[\mathbf{X}] = [L_X]^T[\mathbf{G}][L_X]\,, \tag{23}$$

in which the algebraic construction of the positive-definite symmetric real $(N \times N)$ random matrix $[\mathbf{G}]$ is given in [9] and only depends on a scalar (dispersion) hyperparameter, δ, verifying

$$\delta^2 = \frac{1}{N}\, E\{||[\mathbf{G}] - [I_N]||_F^2\}\,. \tag{24}$$

In general, the local displacements are more sensitive to uncertainties than the global displacements. The ML-SROM allows the variability of each type of displacements (belonging to either subspace $\mathcal{S}_\mathcal{L}$, subspace $\mathcal{S}_\mathcal{M}$, or subspace $\mathcal{S}_\mathcal{H}$) to be modeled separately. For each random matrix $[\mathbf{A}] = [\mathbf{M}], [\mathbf{D}], [\mathbf{K}]$ of the ML-SROM, three dispersion hyperparameters $\delta_\mathcal{L}^A$, $\delta_\mathcal{M}^A$, and $\delta_\mathcal{H}^A$ are thus introduced (with $A = M, D, K$ referring to each deterministic matrix of the ML-NROM). For $\mathcal{I} = \mathcal{L}, \mathcal{M}, \mathcal{H}$ and $A = M, D, K$, let $[\mathbf{G}_\mathcal{I}^A]$ denote the random matrix with the same construction as $[\mathbf{G}]$ and verifying $(\delta_\mathcal{I}^A)^2 = \frac{1}{n_\mathcal{I}}\, E\{||[\mathbf{G}_\mathcal{I}^A] - [I_{n_\mathcal{I}}]||_F^2\}$, in which $n_\mathcal{I} = \dim(\mathcal{S}_\mathcal{I})$. Given the Cholesky factorization $[A] = [L_A]^T[L_A]$ of each deterministic matrix $[A]$ of the ML-NROM, each random matrix $[\mathbf{A}]$ of the ML-SROM is defined as

$$[\mathbf{A}] = [L_A]^T[\mathbf{G}^A][L_A]\,, \tag{25}$$

in which the $(n_g \times n_g)$ positive-definite symmetric real random matrix $[\mathbf{G}^A]$ is given by

$$[\mathbf{G}^A] = \begin{bmatrix} [\,\mathbf{G}_\mathcal{L}^A\,] & [\;0\;] & [\;0\;] \\ [\;0\;] & [\mathbf{G}_\mathcal{M}^A] & [\;0\;] \\ [\;0\;] & [\;0\;] & [\,\mathbf{G}_\mathcal{H}^A\,] \end{bmatrix}. \tag{26}$$

Denoting as $[\Psi] = [\,[\Phi^{\mathcal{L}}]\,[\Phi^{\mathcal{M}}]\,[\Phi^{\mathcal{H}}]\,]$ the ROB of the multilevel ROM and introducing the deterministic vector $\mathbf{f}(\omega) = [\Psi]^T \mathbb{F}(\omega)$ of generalized forces, the random generalized coordinates $\mathbf{Q}(\omega) = (Q_1(\omega) \ldots Q_{n_g}(\omega))$ of the ML-SROM are the solutions of the small-dimension matrix equation

$$(-\omega^2[\mathbf{M}] + i\omega[\mathbf{D}] + [\mathbf{K}])\mathbf{Q}(\omega) = \mathbf{f}(\omega)\,, \tag{27}$$

which is solved using the Monte-Carlo simulation method [12], and allow the random response $\mathbf{U}(\omega)$ associated with $\mathbb{U}(\omega)$ to be obtained from

$$\mathbf{U}(\omega) = [\Psi]\mathbf{Q}(\omega)\,. \tag{28}$$

6 Application to the complex computational model of a car

6.1 Nominal reduced-order models

The nominal finite element model is used for constructing the multilevel stochastic ROM. The finite element model has $m = 8,000,000$ DOF and the C-NROM is constructed using the first $n = 16,192$ elastic modes as a ROB (we have $f_n = 1,600$ Hz). Then, the global-displacements nominal ROM associated with subspace $\mathcal{S}_g$ is constructed choosing $\mathcal{D}_g = 31$, $\nu = 7,000$ and $f_g^c = 1,525$ Hz. Follow the construction of subspaces $\mathcal{S}_{\mathcal{LM}}$ and $\mathcal{S}_{\mathcal{L}}$ obtained choosing $\mathcal{D}_{\mathcal{LM}} = 15$, $\nu_{\mathcal{LM}} = 1,950$, $f_{\mathcal{LM}}^c = 1,000$ Hz and $\mathcal{D}_{\mathcal{L}} = 4$, $\nu_{\mathcal{L}} = 400$, $f_{\mathcal{LM}}^c = 300$ Hz. Dimensions n_g , $n_{\mathcal{LM}}$ and $n_{\mathcal{L}}$ of subspaces $\mathcal{S}_g$, $\mathcal{S}_{\mathcal{LM}}$, and $\mathcal{S}_{\mathcal{L}}$ are $n_g = 6,984$, $n_{\mathcal{LM}} = 1,919$, and $n_{\mathcal{L}} = 344$.

6.2 Multilevel stochastic reduced-order model

The objective of the stochastic model is to take into account the variability as well as the uncertainties in the computational model (due to both the model-parameter uncertainties and the modeling errors). The global displacements, which usually correspond to resonances in the low-frequency band, are more robust with respect to small design changes, variability, and model uncertainties. We recall the multilevel ROM to be constituted of the following three orthogonal subspaces:

- $\mathcal{S}_{\mathcal{L}}$, constituted of displacements obtained using degree $\mathcal{D}_{\mathcal{L}} = 4$ for the kinetic energy and associated with the frequencies below $f_{\mathcal{L}}^c = 300$ Hz, thus expected to consist in low-frequency global displacements.

- $\mathcal{S}_{\mathcal{M}}$, constituted of displacements obtained using degree $\mathcal{D}_{\mathcal{LM}} = 15$ for the kinetic energy, associated with the frequencies below $f_{\mathcal{LM}}^c = 1,000$ Hz and orthogonal to $\mathcal{S}_{\mathcal{L}}$, thus expected to consist in combinations of a few global displacements in presence of many local displacements in the low- and mid-frequency bands.

- $\mathcal{S}_{\mathcal{H}}$, constituted of displacements obtained using degree $\mathcal{D}_g = 31$ for the kinetic energy, associated with the frequencies below $f_g^c = 1,525$ Hz and orthogonal to both $\mathcal{S}_{\mathcal{L}}$ and $\mathcal{S}_{\mathcal{M}}$, thus expected to mainly consist in local displacements present

throughout the entire band with an increasing density towards higher frequencies.

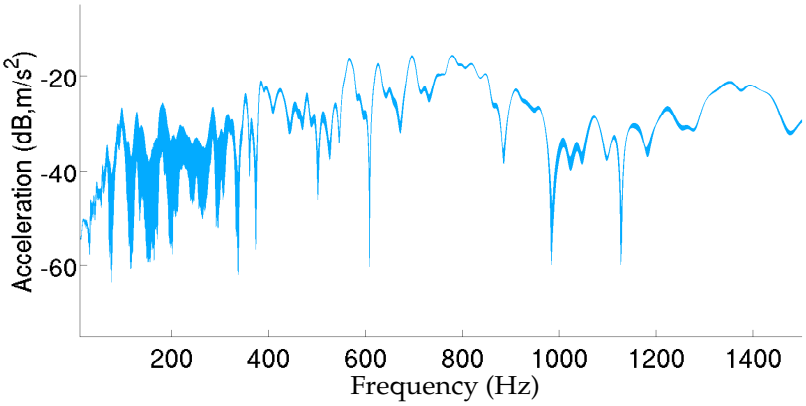

Figure 1: Random response using the ML-SROM with $\delta_{\mathcal{L}}^{M} = 0.1$ and for all other dispersion hyperparameters set to zero (95% confidence interval).

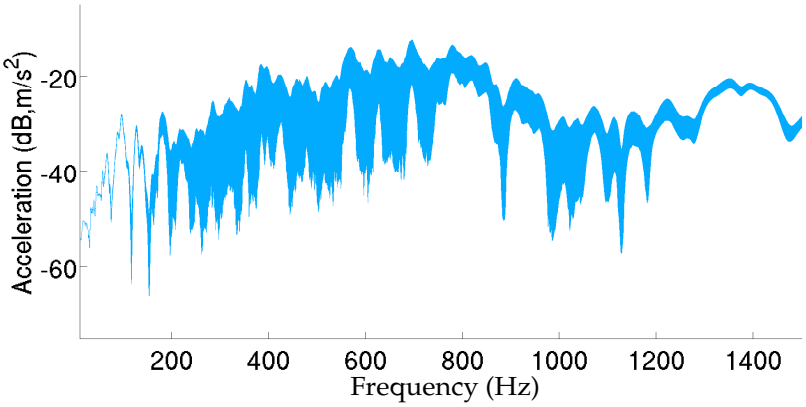

Figure 2: Random response using the ML-SROM with $\delta_{\mathcal{M}}^{M} = 0.1$ and for all other dispersion hyperparameters set to zero (95% confidence interval).

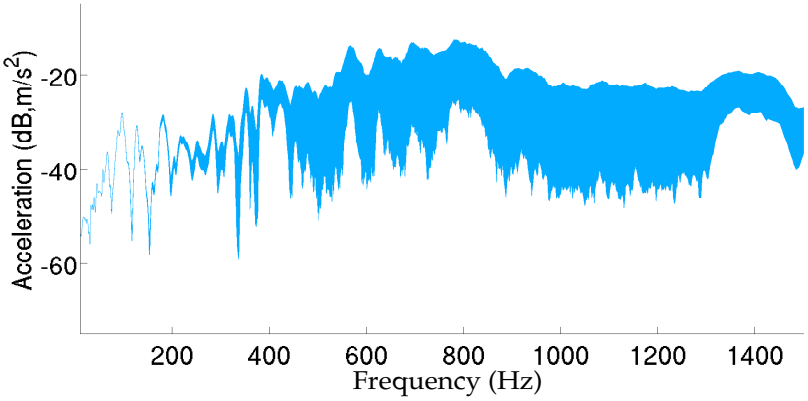

Figure 3: Random response using the ML-SROM with $\delta_{\mathcal{H}}^{M} = 0.1$ and all other dispersion hyperparameters set to zero (95% confidence interval).

The ML-SROM allows statistical dispersion levels to be controlled within each subspace. A sensitivity analysis of the ML-SROM with respect to the dispersion parameters is carried out. We are interested in performing a sensitivity analysis of frequency response functions for structural accelerations over the frequency band $\mathcal{B} = [10, 1500]$ Hz. To do so, the modulus in dB of the random normal acceleration in one point of the car (that is distant from the excitation point) is calculated using Eq. (28) with $n_{sim} = 300$ Monte-Carlo realizations. The 95% confidence intervals of the random response are plotted:

- in Fig. 1 for $\delta_{\mathcal{L}}^M = 0.1$ and for all other dispersion hyperparameters set to zero.
- in Fig. 2 for $\delta_{\mathcal{M}}^M = 0.1$ and for all other dispersion hyperparameters set to zero.
- in Fig. 3 for $\delta_{\mathcal{H}}^M = 0.1$ and for all other dispersion hyperparameters set to zero.

For only nonzero $\delta_{\mathcal{L}}^M$, the confidence interval is larger in the low-frequency band whereas it is very thin elsewhere. For only nonzero $\delta_{\mathcal{M}}^M$, the confidence interval is larger in the mid-frequencies although the dispersion also propagates around. For only nonzero $\delta_{\mathcal{H}}^M$, the confidence interval is larger in the high-frequency band although it is also large in the mid-frequency band. These results tend to agree with the qualitative expectations made hereinbefore. For $\delta_{\mathcal{M}}^M = 0.1$, the propagation of uncertainties in the high-frequency band is explained by the coupling between subspaces $\mathcal{S}_{\mathcal{M}}$ and $\mathcal{S}_{\mathcal{H}}$, which are not orthogonal with respect to the stiffness matrix.

7 Conclusions

A general method has been proposed for the construction of a multilevel stochastic reduced-order computational model devoted to the robust prediction of the frequency response functions of complex linear dynamical systems. The proposed multilevel ROM is based on the nonparametric probabilistic approach. The presence of several structural scales, characterized by the presence of more or less local displacements intertwined with the usual global displacements, and associated with the distinct low-, medium-, and high-frequency bands, induces a heterogeneous variability. Using several orthogonal subspaces each one composed of a particular type of displacements, the multilevel stochastic ROM allows for constructing a finer modeling of uncertainties. We have demonstrated the capability of the method proposed to adapt the stochastic modeling to the level of uncertainties as a function of the frequency bands that can be correlated to the scales of the global and of the local displacements.

8 Acknowledgements

This research was supported by Agence Nationale de la Recherche, Contract Hi-MoDe, ANR-2011-BLAN-00378. The authors thank PSA Peugeot Citroën for providing the car computational model.

REFERENCES

[1] R. Ohayon, C. Soize, *Advanced Computational Vibroacoustics - Reduced-Order Models and Uncertainty Quantification*. Cambridge University Press, 2014.

[2] L. Meirovitch, *Dynamics and Control of Structures*. Wiley, 1990.

[3] J. Argyris, H.P. Mlejnek, *Dynamics of Structures*. North-Holland, 1991.

[4] R.R. Craig, A.J. Kurdila, *Fundamentals of Structural Dynamics*. Wiley, 2nd Edition, John Wiley and Sons, 2006.

[5] C. Soize, A. Batou, Stochastic reduced-order model in low-frequency dynamics in presence of numerous local elastic modes. *Journal of Applied Mechanics - Transactions of the ASME*, **78**(6), 061003-1 to 9, 2011.

[6] A. Batou, C. Soize, Uncertainty quantification in low-frequency dynamics of complex beam-like structures having a high-modal density. *International Journal for Uncertainty Quantification*, **1**(1), 431–451, 2013.

[7] A. Arnoux, C. Soize, A. Batou, L. Gagliardini, Reduced-order computational model for low-frequency dynamics of automobiles. *Advances in Mechanical Engineering* **310362**, 1–12, 2013.

[8] O. Ezvan, A. Batou, C. Soize, Multilevel reduced-order computational model in structural dynamics for the low- and medium-frequency ranges. *Computer and Structures*, **160**, 111–125, 2015.

[9] C. Soize, Random matrix theory for modeling uncertainties in computational mechanics. *Computers Methods in Applied Mechanics and Engineering*, **194**(12-16), 1333-1366, 2005.

[10] C.E. Shannon, A Mathematical Theory of Communication. *Bell Syst. Tech. J.*, **27**, 379–423 and 623–659, 1948.

[11] E.T. Jaynes, Information Theory and Statistical Mechanics. *Phys. Rev.*, **106**(4), 620–630 and **108**(2), 171–190, 1957.

[12] R. Rubinstein, *Simulation and the Monte Carlo Method*. John Wiley and Sons, 1980.

ECCOMAS Congress 2016
VII European Congress on Computational Methods in Applied Sciences and Engineering
M. Papadrakakis, V. Papadopoulos, G. Stefanou, V. Plevris (eds.)
Crete Island, Greece, 5–10 June 2016

TO ESTIMATE NON-STATIONARY STOCHASTIC DISTRIBUTED LOAD ON A BEAM STRUCTURE FROM RESPONE SAMPLES

S.Q. Wu[1,2] **and J. Zhu**[1]

[1] Department of Engineering Mechanics, School of Civil Engineering, Southeast University, Nanjing, P.R. China
e-mail: cesqwu@seu.edu.cn

[2] Jiangsu Key Laboratory of Engineering Mechanics, Southeast University, Nanjing, P.R. China

Keywords: Spatially distributed load identification, Dynamic, Stochastic, non-stationary, Mode shape function.

Abstract. *A stochastic load identification approach is proposed based on a beam structure. The dynamic force is assumed as a non-stationary Gaussian random field varying with both time and space. The mode shape functions are selected as orthogonal basis for the projection of the distribution function of the stochastic dynamic force which enables the excitation force can be estimate from limit measurement response data. The statistics of the stochastic distributed force are estimated by the Mode Superposition Method (MSM) combined with the Monte Carlo Approach (MCA). A numerical example is studied. A trapezium-shaped function is assumed for the distribution of the stochastic dynamic force. The stochastic time history of the excitation forces at each location on beam is assumed to be Gaussian and have a time-varying mean value and power density function. Numerical simulations are conducted to verify the load identification algorithm. Results show that the proposed method is effective to identify the stochastic distributed load on the structure.*

1 INTRODUCTION

Dynamic load is one of the key factors in the design and condition assessment of various engineering structures. In the cases when the load information is difficult to be obtained by direct measurement, indirect approaches which noted as force identification techniques, are often adopted.

Numerous force identification approaches have been proposed in the past decades which can successfully estimate the dynamic excitation forces on engineering structure from measurement dynamic response. These methods can mainly be classified into two categories: frequency-domain method [1, 2] and time-domain method [3, 4], etc. Just as their name imply, the relationship between the measurement response and the dynamic force to be estimated are formulated in frequency domain and time domain respectively in the two kinds of method. Most of the aforementioned approaches are deterministic and focusing on the identification of concentrated force.

It is noted that various kinds of the dynamic load are spatially distributed along the structure. Two approaches namely the finite difference method and the modal method were proposed by Pezerat and Guyader [5] to estimate the spatially distributed dynamic force on structure and the regularization approach was adopted to solve the ill-posed problem [6]. In the modal method, when the force to be identified only spans over the contact region, a prohibitively large number of basis functions is often needed. An improved method was proposed by Liu and Shepard [7] in which new basis functions are introduced to overcome the drawback. A mode-selection method for distributed dynamic force was proposed by Jiang and Hu [8] and the optimal range of frequency and spatial modes was studied; to improve the accuracy on the identified force at fix boundary, the Legendre polynomials are used as the consistent orthogonal base functions to describe the distributed dynamic loads instead of the mode shape function, similar work was done by Li et al. [9] with the Chebyshev orthogonal polynomials. The temporal-dependent external forces for the cutting tools were estimated by Huang et al. [10] based on the conjugate gradient method. The acoustic holography and the force analysis technique were adopted by Pezerat et al. [11] to identify vibration sources from radiated noise measurements. The Virtual Fields Method was adopted by Berry et al. [12] to identify both mechanical point load excitation and distributed acoustic excitation of a bending panel.

Since randomness often exists in excitation forces due to the random nature, e.g. wind load, earthquake, excitation due to the road surface roughness, excitation from the ocean waves, etc. Stochastic force identification techniques have been developed. To identify the concentrated stochastic force on structure, the system uncertainty is not included at first, which can be divided into two kinds: frequency domain method [13] and time domain method [14, 15]; later, both the uncertainty in system parameters and excitation forces have been included [16, 17, 18]. These research work provide statistical estimations on the stochastic excitation forces on structure, however, stochastic excitation forces such as the wind load, load due to ocean waves, etc. are spatially distributed, new techniques should be developed to deal with the distributed stochastic dynamic force identification. A frequency domain method was proposed by Granger and Perotin [19] to identify the distributed random excitation acting on a vibrating structure and this method was further be adopted to a fluid-induced vibration problem [20]. The distributed random excitation is assumed as a stationary Gaussian random field and the mode method was adopted to identify the distribution and power spectrum density (PSD) function of the excitation force from the PSD of the measurement random response.

In this paper, a time domain approach is proposed in which a non-stationary stochastic distributed dynamical force is identified from the response sample sets from limit number of sensors under a beam structure. The mode shape functions are selected as orthogonal basis for the

projection of the stochastic distributed force. The statistics of the stochastic distributed force are estimated by the mode superposition technique combined with the MCA.

2 STOCHASTIC RESPONSE ANALYSIS OF A DYNAMICAL SYSTEM

2.1 Description of the dynamical system

A uniform simply supported Euler-Bernoulli beam subjected to a stochastic distributed dynamic force is shown in Figure 1 and this dynamic system will be adopted to demonstrate the new identification algorithm in this paper. It is noted that the proposed method may also be effective on other kinds of structure with different boundary conditions as long as the vibration modes are available.

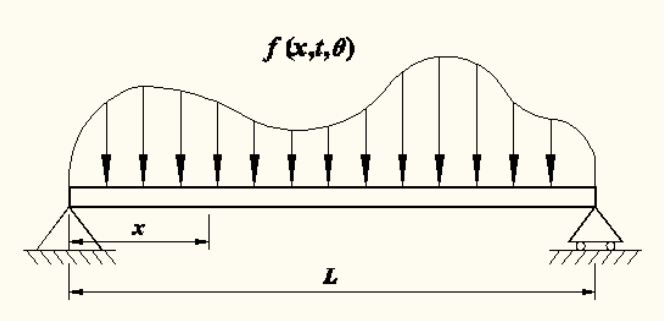

Figure 1: A simply supported beam subjected a stochastic distributed force

The equation of motion of the dynamical system is

$$\rho A\frac{\partial^2 w(x,t,\theta)}{\partial t^2}+c\frac{\partial w(x,t,\theta)}{\partial t}+EI\frac{\partial^4 w(x,t,\theta)}{\partial x^4}=f(x,t,\theta) \tag{1}$$

where ρ is the mass density and A is the cross-sectional area, therefore, ρA represents the mass per unit length. Symbols c and EI are the damping and the flexural rigidity of the beam, respectively. All the system parameters are assumed to be deterministic. $f(x,t,\theta)$ is a non-stationary Gaussian random field represents the stochastic distributed dynamic force; $w(x,t,\theta)$ is the stochastic displacement under the beam at location x and time t, and θ represents the random dimension.

2.2 Equation of motion in modal space

Though correlations may exist among the time, space and random dimension in stochastic excitations and random responses, in this research work, the distributed dynamic force is assumed as a non-stationary Gaussian random field and the distribution of the excitation is assumed to be independent of the other two dimensions and. With the ith mode shape function $\varphi_i(x)$, the stochastic distributed excitation $f(x,t,\theta)$ and the stochastic displacement under the beam $w(x,t,\theta)$ can respectively be expressed as

$$f(x,t,\theta)=\sum_{i=1}^{m}\varphi_i(x)F_i(t,\theta) \tag{2}$$

$$w(x,t,\theta)=\sum_{i=1}^{m}\varphi_i(x)q_i(t,\theta) \tag{3}$$

where the random processes $F_i(t,\theta)$ and $q_i(t,\theta)$ are the stochastic modal coordinates of the excitation and the displacement, respectively and m represents the number of modes adopted after truncation. When a simply supported Euler-Bernoulli beam is considered, the ith natural circular frequency ω_i and the mode shape $\varphi_i(x)$ have the following expressions respectively,

$$\omega_i=\left(\frac{i\pi}{L}\right)^2\sqrt{\frac{EI}{\rho A}} \quad i=1,2,\cdots,m$$
$$\varphi_i(x)=\sin\frac{i\pi x}{L} \tag{4}$$

where L is the length of the beam.

Substituting Eqs.(2) and (3) into Eq.(1), by employing the orthogonal property between the mode shape functions,

$$\int_0^L \rho A\varphi_i(x)\varphi_j(x)\mathrm{d}x=m_i\delta_{ij} \tag{5}$$

where δ_{ij} is the Kronecker delta and m_i represents the ith modal mass. In this case $m_i=\rho AL/2$. Then Eq.(1) can be rewritten as

$$\ddot{q}_i(t,\theta)+2\zeta_i\omega_i\dot{q}_i(t,\theta)+\omega_i^2q_i(t,\theta)=\frac{F_{mi}(t,\theta)}{m_i},\quad i=1,2,\cdots,m \tag{6}$$

where the over-dot represents the differentiation respect to time t. The symbol ζ_i denotes the damping ratio of the ith mode; $F_{mi}(t,\theta)$ is the ith modal force and

$$F_{mi}(t,\theta)=\int_0^L f(x,t,\theta)\varphi_i(x)\mathrm{d}x \tag{7}$$

The stochastic modal coordinates of excitation $F_i(t,\theta)$ can be calculated by

$$F_i(t,\theta)=\frac{F_{mi}(t,\theta)}{\int_0^L\varphi_i^2(x)\mathrm{d}x} \tag{8}$$

Eq.(6) is a set of stochastic ordinary differential equations which can be solved by numerical methods combined with statistical analysis tools such as the Monte Carlo simulation, the KL method, etc. and then the statistics of the random dynamical response under the beam can be obtained.

3 IDENTIFICATION OF THE DISTRIBUTED STOCHASTIC DYNAMIC FORCE

3.1 Projection scheme of the distributed excitation

When the distribution of the excitation is assumed to be independent of the other two dimensions, the stochastic distributed force $f(x,t,\theta)$ can be expressed in the follow form:

$$f(x,t,\theta)=T(x)\cdot P(t,\theta) \tag{9}$$

where $T(x)$ is a function represents the distribution pattern of the force and $P(t,\theta)$ is a random process represents the stochastic time history at each location x.

It is more difficult to estimate a distributed dynamic force $f(x,t)$ than a concentrate one since the unknown time histories of the force at each location x should be identified from limited measurement response data. The number of the unknowns tends to be infinite. In order to

reduce the unknowns in the identification process, a projection scheme is often adopted, e.g. to represent the distribution function $T(x)$ by a set of orthogonal bases $T_i(x)$,

$$f(x,t)=\sum_i T_i(x)d_i(t) \tag{10}$$

According to Eq.(10), once the coefficients $d_i(t)$ are estimated from limited measurement response data, the distributed dynamic force can be identified, which will significantly simplified the identification. With the projection scheme in Eq.(10), the ith modal force of a distributed dynamic force $f(x,t)$ gives,

$$F_{mi}(t)=\int_0^L f(x,t)\varphi_i(x)\mathrm{d}x=d_i(t)\int_0^L\sum_{ij}T_j(x)\varphi_i(x)\mathrm{d}x \tag{11}$$

When orthogonal property exists between $T_j(x)$ and $\varphi_i(x)$, the integration in Eq.(11) can be significantly simplified. Therefore, the mode shape function $\varphi_j(x)$ are adopted to replace $T_j(x)$ in Eq.(11) in this research work, according to Eq.(5), the expression of the ith modal force can be written as

$$F_{mi}(t)=d_i(t)\int_0^L\sum_{ij}\varphi_i(x)\varphi_j(x)\mathrm{d}x=\frac{m_i}{\rho A}d_i(t) \tag{12}$$

where

$$d_i(t)=\frac{\rho AF_{mi}(t)}{m_i} \tag{13}$$

Substituting Eq.(13) in to Eq.(10), according to Eqs.(5) and (8), the distributed dynamic force $f(x,t)$ can be represented by the mode shape functions as follows:

$$f(x,t)=\sum_i\varphi_i(x)d_i(t)=\sum_{i=1}^m\varphi_i(x)F_i(t) \tag{14}$$

It is noted that Eq.(14) will share the same expression with Eq.(2) when the random dimension θ is considered. To consider the random dimension θ in Eq.(12) and by substituting Eq.(12) into Eq.(6), we have

$$\ddot{q}_i(t,\theta)+2\zeta_i\omega_i\dot{q}_i(t,\theta)+\omega_i^2q_i(t,\theta)=\frac{1}{\rho A}d_i(t,\theta),\quad i=1,2,\cdots,m \tag{15}$$

Eq.(15) shows the relationship between the stochastic modal coordinates of the structural response and the stochastic coefficients of the distributed dynamic excitation force. The stochastic force identification algorithm can be formulated based on Eq.(15) with Monte Carlo approach.

3.2 Statistical force identification with MCA in modal space

Uncertainty in structural responses may originate from uncertainty in both the system parameters and excitation forces, in this research work, the system uncertainty is not addressed. The displacement measured at each location under the beam structure form a set of response sample and these sample sets belong to the population of the random displacement field $w(x,t,\theta)$. When the displacements at location $(x_1,x_2,\ldots x_n)$ are obtained from the rth measurement, these displacement data will form a vector as

$$\mathbf{W}_r = \begin{Bmatrix} w_r(x_1,t) & w_r(x_2,t) & \cdots & w_r(x_n,t) \end{Bmatrix}^{\mathrm{T}}, r = 1,\cdots,N_r \tag{16}$$

where N_r is the total number of the sample sets.

With the mode shape functions, the modal coordinates of each set of the dynamic response sample can be obtained from the following Equation,

$$\begin{Bmatrix} w_r(x_1,t) \\ w_r(x_2,t) \\ \vdots \\ w_r(x_n,t) \end{Bmatrix} = \begin{bmatrix} \varphi_1(x_1) & \varphi_2(x_1) & \cdots & \varphi_m(x_1) \\ \varphi_1(x_2) & \varphi_2(x_2) & \cdots & \varphi_m(x_2) \\ \vdots & \vdots & \ddots & \vdots \\ \varphi_1(x_n) & \varphi_2(x_2) & \cdots & \varphi_m(x_n) \end{bmatrix} \begin{Bmatrix} q_{1,r}(t) \\ q_{2,r}(t) \\ \vdots \\ q_{m,r}(t) \end{Bmatrix} + \begin{Bmatrix} \varepsilon_{1,r}(t) \\ \varepsilon_{2,r}(t) \\ \vdots \\ \varepsilon_{n,r}(t) \end{Bmatrix} \tag{17}$$

where $q_{i,r}(t)$ (i=1,⋯,m) is the modal coordinate of the ith mode and rth measurement and $\varepsilon_{j,r}(t)$ (j=1,⋯,n) is the error term of the jth location and rth measurement. The error term may include the measurement noise, model error, truncation of the higher order of modes and so on. Generally, the number of the modes m after truncation should be smaller than the number of the measurement locations n to avoid solving a set of underdetermined system of equations as shown in Eq.(17). When the rth sample of the coordinate of displacement $q_{i,r}(t)$ corresponding to the ith mode is obtained, the first and second derivatives of $q_{i,r}(t)$, which represent the coordinate of the velocity $\dot{q}_{i,r}(t)$ and acceleration $\ddot{q}_{i,r}(t)$, respectively, can be derived with differentiation. Therefore, the samples of the coefficient $d_{i,r}(t)$ for the distributed force can be calculated as

$$d_{i,r}(t) = \rho A\left[\ddot{q}_{i,r}(t) + 2\zeta_i\omega_i\dot{q}_{i,r}(t) + \omega_i^2 q_{i,r}(t)\right], \quad r = 1,2,\cdots,N_r \tag{18}$$

Finally, the statistics of the identified stochastic distributed force, i.e. the mean value $\mu_f(x,t)$ and the variance $Var_f(x,t)$ can respectively be derived as

$$\mu_f(x,t) = \frac{1}{N_r}\sum_{r=1}^{N_r}\sum_{i=1}^{m}\varphi_i(x)\,d_{i.r}(t) \tag{19}$$

$$Var_f(x,t) = \frac{1}{N_r - 1}\sum_{r=1}^{N_r}\left(\sum_{i=1}^{m}\varphi_i(x)\,d_{i.r}(t) - \mu_f(x,t)\right)^2 \tag{20}$$

4 NUMERICAL SIMULATIONS

To verify the effectiveness of the proposed method and investigate different factors which may influence the accuracy of this stochastic distributed dynamic force identification algorithm, numerical simulations are conducted. The following parameters of the beam structure are adopted.

Length of the beam L=40 m; Cross-sectional area A=4.8 m^2; Second moment of inertia of cross-section I=2.5498 m^4; Rayleigh damping is assumed for the structure with damping ratio ξ=0.02 for all vibration modes; Young's modulus E and mass density ρ of material are 5×10^{10} N/m^2 and 2.5×10^3 kg/m^3 respectively. The first five natural frequencies of the beam are 3.9, 15.6, 35.1, 62.5 and 97.6 Hz, respectively.

A trapezium-shaped distribution function of the stochastic dynamic force is assumed in this study which has the following expression,

$$T(x)=\begin{cases}4x/L & 0\le x<L/4\\ 1 & L/4\le x\le 3L/4\\ -4x/L+4 & 3L/4<x\le L\end{cases} \tag{21}$$

It should be noted that the selection of distribution function is arbitrary unless it is periodic. Theoretically, any periodical distribution functions $T(x)$ can be represented by the orthogonal modal shape function bases; therefore, it will not affect the investigation on the proposed method.

The stochastic time history of the excitation forces at each location x denoted by $P(t,\theta)$ is assumed with the following mean values,

$$P_{\mathrm{d}}(t)=20000\left(1+0.1\sin(2\pi t)\right)\ \mathrm{N} \tag{22}$$

where the subscript 'd' denotes the deterministic part. The random part of $P(t,\theta)$ is assumed as a zero-mean non-stationary Gaussian random process with a time-varying PSD function $S(\omega,t)$ as

$$S\left(\omega,t\right)=C_f P_{\mathrm{d}}(t)\Phi\left(\omega\right) \tag{23}$$

where C_f is a coefficient represents the level of randomness and $\Phi(\omega)$ is a two-sided PSD function of a zero-mean stationary Gaussian random process,

$$\Phi\left(\omega\right)=\frac{1}{2\pi}\frac{2}{\omega^2+1} \tag{24}$$

According to the spectral representation[21] for a Gaussian process, the rth sample of the stochastic distributed force $f(x,t,\theta)$ at location x can be simulated by the following series,

$$f_{\mathrm{r}}(x,t)=T\left(x\right)\left[P_{\mathrm{d}}(t)+C_f P_{\mathrm{d}}(t)\sum_{k=1}^{N_k}\sqrt{4\Delta\omega\Phi\left(\omega_k\right)}\cos(\omega_k t+\varphi_k)\right] \tag{25}$$

where

$$\omega_k=\omega_{\min}+\Delta\omega\left(k-1\right) \tag{26}$$

$$N_k=\left(\omega_{\max}-\omega_{\min}\right)/\Delta\omega \tag{27}$$

It should be noted that Eq. (25) is not unique and other forms of expansion can be adopted. The variable φ_k is a random phase angle uniformly distributed in the interval $[0, 2\pi]$. The constant $\Delta\omega$ denotes the frequency increment and N_k is the total number of frequency divisions in the interval $[\omega_{\min}, \omega_{\max}]$. In this study, $\omega_{\min}$=0 Hz, $\omega_{\max}$=200π Hz, N_k=512, therefore, $\Delta\omega$=1.227 Hz and the sampling frequency in all the simulations is 200Hz, the total time is 1s.

The relative errors between the referenced and calculated results, *RE*, is defined as

$$RE=\frac{\left\|R_{calculated}-R_{referenced}\right\|_2}{\left\|R_{referenced}\right\|_2}\times 100\% \tag{28}$$

where $\left\|\bullet\right\|_2$ denotes the 2-norm.

4.1 Verification of the Forward Problem

To verify the forward problem of the proposed algorithm, the response samples of the beam structure under a stochastic distributed dynamic force are calculated with two methods: Modal superposition method with MCA (MMA) and FEM with MCA (FMA).

The samples of the stochastic distributed dynamic force are calculated from Eq. (25) in which the random phase angle φ_k is generated by "rand" in MATLAB software. C_f which represents the level of randomness is set to 0.2. When the number of response samples is sufficient, accuracy of the proposed algorithm will not be affected by the level of randomness due to the characteristic of MCA. In MMA, the samples of the ith modal force $F_{mi}(t,\theta)$ is calculated according to Eq. (7) in which the integration is conducted using "trapz" in MATLAB software with a step of 0.4m. 30 vibrational modes are adopted and the samples of the modal coordinates of the structural response are calculated by solving Eq. (6) using Newmark-β method. Response statistics of both 5000 samples and 10000 samples from MCS are obtained. In FMA, the samples of the nodal forces are calculated by integrations between the samples of the stochastic distributed dynamic force and the Hermitian cubic interpolation shape functions and. eight beam elements are adopted in the finite element model. The response samples of the beam structure obtained in FMA is similar to that in MMA and the response statistics of 5000 samples from MCS are obtained.

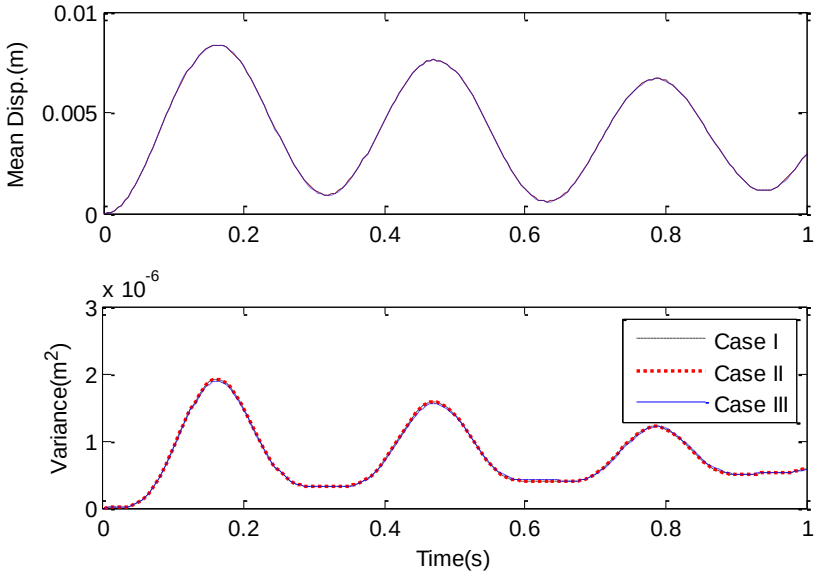

Figure 2. Response statistics of the mid-span displacement

Three sets of statistics of the mid-span displacement of the beam structure are demonstrated in Figure 2. They are from 5000 samples in MMA (Case I), 5000 samples in FMA (Case II) and 10000 samples in MMA (Case III), respectively. Results show that the time histories of mean value and covariance of the mid-span displacement from different simulations agree well with each other. If the response statistics of 10000 samples from MMA (Case III) is assumed as the "referenced" result, the relative errors of the mean value and variance between Case I and Case III according to Eq. (28) are 0.27% and 2.74%, respectively; the relative errors of the mean value and variance between Case II and Case III also equal to 2.85% and 5.82%, respectively. Results indicate that: (1) the time histories of response statistics in all Cases are agree well with each other; (2) 5000 runs in MCA are sufficient for obtaining accu-

rate response statistics; (3) Response statistics from FMA in this case is sightly smaller than that from MMA.

4.2 Verifications of the Inverse Problem

To verify the inverse problem of the proposed algorithm, i.e. to identify the statistics of the non-stationary stochastic distributed dynamic force from measurement response samples, 5000 sets of 19 displacements evenly distributed underneath the beam structure are adopted, i.e. N_r=5000 and n=19, the distance between two sensors in this case is 2m. It is noted that strain signals can also be adopted in the force identification, since strains have the following relationship with displacement for a beam structure,

$$\varepsilon(x,t) = -z\frac{\partial^2 w(x,t)}{\partial x^2} \tag{29}$$

where z represents the distance from the neutral axis of the beam to the strain gauge.

Nineteen modes are adopted in the inverse problem, i.e. m=19. When the number of the measurement locations n is not less than the number of the modes m, the modal coordinates for each set of displacement sample are calculated according to Eq. (17). The cubic spline interpolation is applied on the modal coordinates for each set of displacement sample $q_{i,r}(t)$, then the first and second derivatives of $q_{i,r}(t)$ are calculated which represent the modal coordinate of the velocity and acceleration, respectively. Therefore, the samples of the coefficient $d_{i,r}(t)$ for the distributed force can be calculated according to Eq.(18). Finally, the statistics of the identified stochastic distributed dynamic force can respectively be obtained from Eqs. (19) and (20). The "referenced" mean value and variance of the stochastic distributed dynamic force can respectively be estimated from the following Equations,

$$\tilde{\mu}_f(x,t) = \frac{1}{N_r}\sum_{r=1}^{N_r} f_r(x,t) \tag{30}$$

$$\tilde{Var}_f(x,t) = \frac{1}{N_r - 1}\sum_{r=1}^{N_r}\left(f_r(x,t) - \mu_f(x,t)\right)^2 \tag{31}$$

The identified and referenced statistics of the stochastic distributed dynamic force at the mid-span are shown in Figure 3. Results show that the time histories of two statistics agree well with each other, which indicates the statistics of the distributed non-stationary stochastic dynamic force can successfully be identified from response sample sets. The relative errors between the identified and the referenced mean value and variance are 4.55% and 7.08%, respectively.

Since the stochastic force is non-stationary, the distribution of the force will vary with respect to time. In order to demonstrate the accuracy on the identified distribution of the force, the identified distributions at different moments, e.g. at 0.25s, 0.5s and 0.75s, are normalized and compared with the referenced distribution function $T(x)$ in Eq. (21). Results are shown in Figure 4 in which the identified distributions of the mean force and the variance of the force at each moment are compared with $T(x)$ and $T(x)^2$, respectively. The distribution at each moment of the distributed non-stationary stochastic force can be successfully identified from limit number of measurement points. The relative errors between the identified and the referenced distribution for the mean value and variance of force at 0.5s are 0.57% and 0.92%, respectively. The relative errors among the identified distribution for the mean value and variance of force at different moments are smaller than 0.5%, i.e. the identification error is small and stable during the time history of the force.

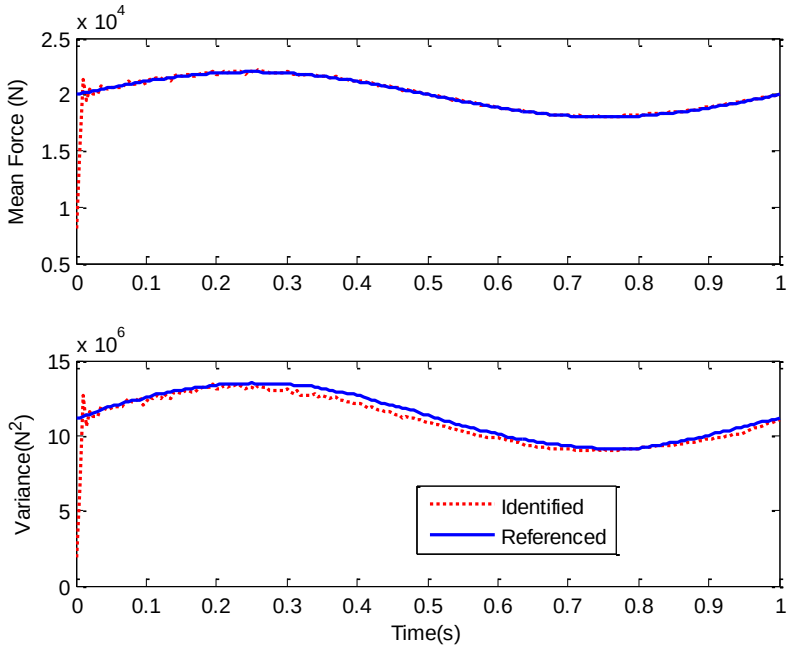

Figure 3. Comparison of the identified and referenced statistics of the distributed stochastic force at mid-span

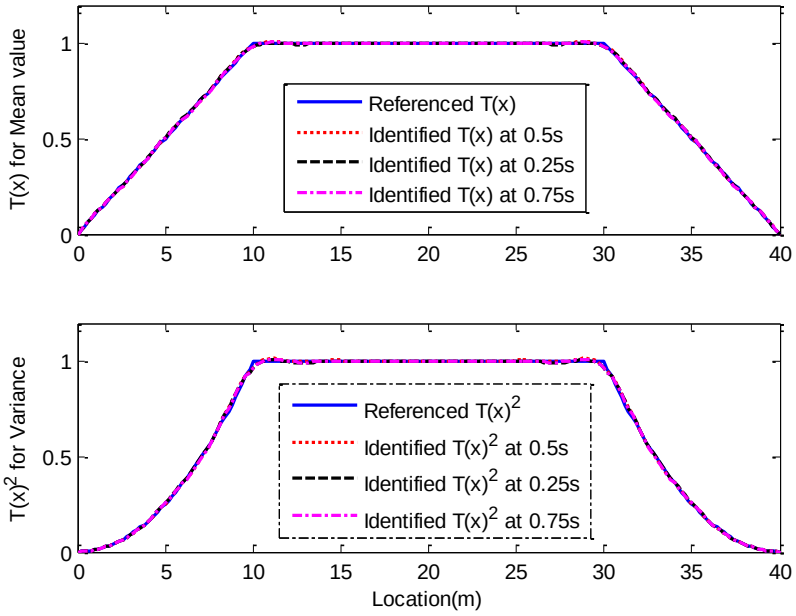

Figure 4. Comparison of the identified and referenced force distribution at different moments

5 CONCLUSIONS AND DISCUSSIONS

In order to estimate a distributed non-stationary random excitation on a vibrating structure, a time domain method is proposed and demonstrated on a beam structure. The dynamic force is assumed as a non-stationary Gaussian random field varying with both time and space. A trapezium-shaped distribution function is selected for the stochastic dynamic force in the numerical simulation. With a combination of MSM and MCA, both the distribution and the

time-varying statistics of the random excitation can be estimated from response sample sets with good accuracy.

Different factors such as the number of vibration modes, the installation of sensors, the noise pollution in the response samples, etc. which may affect the accuracy of the proposed method are need to be further investigated and since the mode shape function is adopted as the orthogonal basis, when the random excitation only applied on part of the structure, numerous mode shape function should be included to achieve accurate results, which will further require more measurement sensors to be installed to acquire response samples. For this statistical identification approach in time domain, sufficient number of sample sets is assumed to avoid the unexpected errors in variance identification, when the number of samples sets reduce, the errors in the identified statistics of the random forces will increase and tend to be unstable. Investigation on aspects mentioned above will improve this primary work and will be conducted in the future work.

REFERENCES

[1] S.S. Law, T.H.T. Chan, X.Q. Zhu, Q.H. Zeng, Regularization in moving force identification. *Journal of Engineering Mechanics-ASCE,* **127**, 136-148, 2001.

[2] Y. Liu, W.S. Shepard, Dynamic force identification based on enhanced least squares and total least-squares schemes in the frequency domain. *Journal of Sound and Vibration*, **282**, 37-60, 2005.

[3] Z.R. Lu, S.S. Law, Force identification based on sensitivity in time domain. *Journal of Engineering Mechanics-ASCE*, **132**, 1050- 1056, 2006.

[4] L.J.L. Nordstrom, A dynamic programming algorithm for input estimation on linear time-variant systems. *Computer Methods in Applied Mechanics and Engineering*, **195**, 6407-6427, 2006.

[5] C. Pezerat, J.L. Guyader, Two inverse methods for localization of external sources exciting a beam. *Acta Acustica*, **3**, 1-10,1995.

[6] C. Pezerat, J.L. Guyader, Force analysis technique: reconstruction of force distribution on plates, *Acustica*, **86**, 322-332, 2000.

[7] Y. Liu, W.S. Shepard, An improved method for the reconstruction of a distributed force acting on a vibrating structure. *Journal of Sound and Vibration*, **291**, 369-387, 2006.

[8] X.Q. Jiang, H.Y. Hu, Reconstruction of distributed dynamic loads on an Euler beam via mode-selection and consistent spatial expression. *Journal of Sound and Vibration*, **316**, 122-136, 2008.

[9] K. Li, J. Liu, X. Han, X. Sun, C. Jiang. A novel approach for distributed dynamic load reconstruction by space-time domain decoupling. *Journal of Sound and Vibration*, **348**, 137–148, 2015.

[10] C.H. Huang, C.C. Shih, S. Kim, An inverse vibration problem in estimating the spatial and temporal-dependent external forces for cutting tools. *Applied Mathematical Modelling*, **33**, 2683-2698, 2009.

[11] C. Pezerat, Q. Leclere, N. Totaro, M. Pachebat, Identification of vibration excitations from acoustic measurements using near field acoustic holography and the force analysis technique. *Journal of Sound and Vibration*, **326**, 540–556, 2009.

[12] A. Berry, O. Robin, F. Pierron, Identification of dynamic loading on a bending plate using the Virtual Fields Method. Journal of Sound and Vibration, **333**, 7151–7164, 2014.

[13] P.S. Varoto, K.G. Mcconnell, Predicting random excitation forces from acceleration response measurements. *Proceedings of SPIE, The International Society for Optical Engineering*, **3089**, 1-6, 1997.

[14] J.M. Angulo, M.D. Ruiz-Medina, Multi-resolution approximation to the stochastic inverse problem. *Advances in Applied Probability*, **31**, 1039-1057, 1999.

[15] S.Q. Wu, S.S. Law, Statistical moving load identification including uncertainties. *Probabilistic Engineering Mechanics*, **29**, 70-78, 2012.

[16] S.Q. Wu, S.S. Law, Moving force identification based on stochastic finite element model. *Engineering Structures*, **32**, 1016-1027, 2010.

[17] J. Liu, X. Han, C. Jiang, Dynamic load identification for uncertain structures based on interval analysis and regulation method. *International Journal of Computational Methods*, **8**, 667-683, 2011.

[18] J. Liu, X. Sun, X. Han, C. Jiang, D. Yu, Dynamic load identification for stochastic structures based on Gegenbauer polynomial approximation and regulation method. Mechanical Systems and Signal Processing, **56-57**, 35-54, 2015.

[19] S. Granger, L. Perotin, An inverse method for the identification of a distributed random excitation acting on a vibrating structure Part 1: Theory. *Mechanical Systems and Signal Processing*, **13**, 53-66, 1999.

[20] S. Granger, L. Perotin, An inverse method for the identification of a distributed random excitation acting on a vibrating structure Part 2: Flow-induced vibration application. *Mechanical Systems and Signal Processing*, **13**, 67-81, 1999.

[21] B. Hu, and W. Schiehlen, On the simulation of stochastic processes by spectral representation. *Probabilistic Engineering Mechanics*, **12**, 105-113, 1997.

ECCOMAS Congress 2016
VII European Congress on Computational Methods in Applied Sciences and Engineering
M. Papadrakakis, V. Papadopoulos, G. Stefanou, V. Plevris (eds.)
Crete Island, Greece, 5–10 June 2016

A ROBUST POLYNOMIAL CHAOS KALMAN FILTER FRAMEWORK FOR CORROSION DETECTION IN REINFORCED CONCRETE STRUCTURES

Wael G. Slika[1], **George A. Saad**[1]

[1] American University of Beirut
address
{wgs02, gs31}@aub.edu.lb

Keywords: Corrosion, Polynomial Chaos, Reinforced Concrete, Service Life prediction

Abstract. *A main reason behind reinforced concrete structural deterioration is chloride-induced corrosion. Once the critical chloride concentration is exceeded at the rebar level, the structure becomes susceptible to corrosion initiation. Corrosion propagates progressively, degrades the resistance capacity of the structure and decreases the design safety margin. To mitigate this risk, a stochastic sequential data assimilation technique based on chloride concentration measurements and the Polynomial Chaos Kalman Filter (PCKF) is presented.*
The Power of PCKF lies in its sampling free scheme and polynomial structure to represent uncertainty. In modeling chloride ingress mechanism, different independent sources of uncertainty should be incorporated in the system including, mathematical model simplification errors, parametric errors, boundary condition errors, and time independent sensors errors. In such circumstances, the curse of dimensionality hinders the efficiency and the applicability of PCKF, due to the exponential growth of the required bases to account for the added uncertainties. This study presents a practical framework to maintain an acceptable accuracy of PCKF without scarifying the computational efficiency of the filter. A one dimensional synthetic numerical example is presented to verify the efficiency of the proposed implementation scheme.

1 INTRODUCTION

Reinforced concrete (RC) structures, like buildings, bridges, dams, tunnels, pipelines, among others, are complex engineering systems, with long life expectancy, that serve society's industrial needs and guarantee economic prosperity. Labor force and financial assets are extensively invested in the design and construction stages of RC projects to achiever two-primer concerns, safety and serviceability through their lifetime. Research efforts and gained experience, influence design codes and governmental regulations to improve current practices in order minimize the risk of failure and loss of serviceability. However, structures might be exposed to different environmental conditions and severe loading that can lead to structural deterioration. Therefore, continuous monitoring of the changing environmental conditions and accurate prediction of response of structures under real conditions are becoming highly recommended in practice [1]. In technical terms, this process is known as Structural Health Monitoring (SHM). SHM relies on real time measurements, damage detection algorithm and data assimilation technique for early detection of risks and better assessment of the operating conditions. Consequently, early risk alerts are set and maintenance schedules and repair mechanisms are optimized for proactive measures.

Among these damage mechanisms, corrosion in reinforcement bars is recognized as a serious deterioration phenomenon that threatens structural integrity. It is usually referred to as the most common cause for structural deterioration, and it leads to major problems in maintenance and rehabilitation of RC structures. In practice, corrosion of RC can be understood as a two-stage process: the corrosion initiation stage and the propagation stage [2]. During the first stage, the pH of the pore solution is reduced, leading to the de-passivation of the protective film, and exposing the rebar to corrosion initiation. The most common cause of corrosion initiation is typically attributed to the presence of chloride ions; the de-passivation of the protective films occurs when their concentration at rebar level exceed a certain threshold. The source of chlorides may be admixtures, contaminants, marine environments, industrial brine and deicing salts. Once the corrosion is initiated, the steel starts to corrode generating iron oxides, which remarks the starting of the second stage. Corrosion then progressively propagates causing cracking, delamination and spalling of the concrete cover, thus threatening the structure and alerts serviceability failure.

Once the damage occurs, the process becomes irreversible and needs detailed inspections and may required complex repair strategies. This shifts the attention to proactive maintenance measures that includes treatment before any considerable damage. The application of this strategy needs adequate knowledge about the state of the structure and close monitoring of the corrosive species. Condition assessment of such structures is typically based on comparing the chloride content at steel level to the critical threshold chloride concentration.

For accurate prediction of corrosion initiation, Polynomial Chaos Kalman filter (PCKF) will be employed, in this study, for parametric identification of the quantities of interest in a probabilistic framework. Based on real time measurements and dynamic model predictions, the PCKF calibrates the chloride profile and model parameters to improve the prediction of the remaining corrosion free service life and to initiate proactive maintenance alert. This study will also suggest a practical implementation of PCKF, when time independent sources of uncertainties are incorporated in the system. The computational cost efficiency and the accuracy of the implementation will be compared to its closest descendent in the Kalman Filter family, the Ensemble Kalman filter (EnKF).

2 CHLORIDE INGRESS

Different phenomena govern the ingress of chloride ions into concrete pores depending on the state of the structure and the depths of concrete cover. In unsaturated medium, diffusion is the governing mechanism beyond the convection zone. However, in saturated and fully submerged concrete structures, the diffusion process is the governing mechanism after initial wetting [3, 4]. Since the principle objective is to estimate, the chloride concentration at rebar level, chloride ingress is typically modeled as a diffusion process according to Fick's second law and assuming constant boundary conditions. The general diffusion equation relates the diffusion coefficient and the gradient of the concentration as follows:

$$\frac{\partial C}{\partial t} = \nabla.(D(t)\nabla C) \tag{1}$$

where $C\ (kg/m^3)$ is the spatial chloride content at a certain location and time t. $D(t)$ is the diffusivity coefficient at t generally represented as a time decaying function:

$$D(t) = D_R\left(\frac{t_R}{t}\right)^m \tag{2}$$

where D_R is the reference diffusion coefficient at time t_R (usually$t_R = 28$ days) and m is a constant depending on concrete mix proportions. $D(t)$ should also account for the effects temperature and relative humidity [5].

An analytical solution, eq. 3, is derived from eq. 1 under several assumptions: 1-D diffusion process, constant surface chloride content, constant diffusion coefficient and infinite medium.

$$C(x,t) = C_s[1 - \mathrm{erf}\left(\frac{x}{2\sqrt{Dt}}\right)] \tag{3}$$

where C_s is the chloride surface concentration, x is the location away from the surface, and t is the time period.

To maintain generality and robustness, a numerical discrete solution for eq.1 will be implemented based on finite element/finite difference scheme rather than the solution presented in eq. 3 since the latter tends to lose its accuracy for varying environmental and parametric conditions. Moreover, using a numerical discretization scheme, spatial variability in the chloride profile can be updated and incorporated in the state vector for more accurate dynamic model propagation.

3 SOURCES OF UNCERTAINTY

Many sources of uncertainty are identified once developing an accurate mathematical model to simulate the chloride ingress process. First, the model input parameters have a wide margin of variability: the diffusion coefficient depends on the concrete mix and heterogeneous aging of concrete, concrete cover depends on the workmanship skills and on-site quality control, chloride surface concentration depends on type and severity of exposure, chloride concentration threshold values depend on steel bars and cementing material types and admixtures and method of measurement etc. [4]. Additional uncertainties can also be attributed to simplifications associated with the adopted mathematical model, measurement and human errors. To account for the effect of these uncertainties in modeling corrosion, probabilistic models can be used to estimate the probability of corrosion initiation, yet the quantification of

statistical input is usually very difficult and unfavorable in practice due to limited data and wide discrepancy [6].

Therefore, to identify accurately the corrosion initiation time, engineers are resorting to structural health monitoring (SHM). The process of monitoring the corrosion initiation time is theoretically tied to monitoring the free chloride ions in concrete and sometimes to total chloride content [7].

4 SERVICE LIFE PREDICTION

To guarantee safety and integrity of the structure, adequate maintenance is an essence. In the case of corrosion deterioration, the typical forms of repair are removing the concrete cover to clean the corroded steel and restoring the integrity of the formed cracks by certain injections. In some cases, additional structural support is necessary to rehabilitate the loss in designed structural capacity. This reactive maintenance practice is usually unfavorable for two main reasons: First, it pushes the structure to an extreme limit before interfering, which might lead to serviceability failure or even structural failure. Second, in case of corrosive deterioration, the later the maintenance is scheduled the more cost is associated with the repair mechanism. Therefore, pro-active maintenance is highly desirable in practice. The main strategy is to provide protection to reinforced concrete structures to either prevent or halt the problem of corrosion of the reinforcement before any considerable damage.

The probability of corrosion of the structure is computed as the probability of the chloride concentration exceeding the threshold value at the steel bar location. Typically, a reliability tolerance is selected based on the significance of the monitored structure, and accordingly, a maintenance plan is set and recurrently updated to prevent the structure from exceeding the designated probability of corrosion.

To represent the probability corrosion initiation, a limit state function relating the chloride threshold to chloride concentration at cover location is presented in equation 4. The limit state, g, is evaluated as the algebraic difference of the chloride critical threshold concentration and the predicted concentration at rebar level. A negative limit state indicates that corrosion has initiated while a positive outcome represents a safe un-corroded structure.

$$\mathrm{g}(\mathrm{C_{th}}, \mathrm{C_s}, \mathrm{D_R}, \mathrm{m}, \mathrm{x_r}) = \mathrm{C_{th}} - \mathrm{C}(\mathrm{C_s}, \mathrm{D_R}, \mathrm{m}, \mathrm{x_r}) \tag{4}$$

To quantify the uncertainties associated with modeling, parametric and boundary condition errors,C_{th},C_s,D_R, and x_r are modeled as lognormal random variables representing the chloride threshold concentration, chloride surface concentration, diffusion coefficient, and cover location respectively. The age factor m is best modeled as beta distribution between 0 and 1, to abide by the constraining physical behavior. The random process C is the numerical solution of the stochastic diffusion equation approximated using a finite elements/ finite difference scheme.

Thus, the probability of corrosion is theoretically represented as the integral of the joint probability density function, $\mathrm{f_x}$, of the outcome of g, over the negative domain or corrosion domain as shown in equation 5:

$$\mathrm{P_f} = \int_{\mathrm{g(C_{th},C_s,D_R,d,m)<0}} \mathrm{f_x}(\mathrm{C_{th}}, \mathrm{C_s}, \mathrm{D_R}, \mathrm{m}, \mathrm{x_r})\mathrm{dx} \tag{5}$$

The solution of the above integral is estimated using Monte Carlo simulation, which is simple and easy to implement; it consists of simulating the outcome using random samples of

the input parameter and repeating the process sufficiently enough times to represent the pdf of the outcome

5 SEQUENTIAL DATA ASSIMILATION

Sequential data assimilation techniques typically utilize the dynamics of a known process and set of observations of the outcome for improving the knowledge of unknown state model parameters and dynamic variables. A well-known sequential filter, in estimation theory, is Kalman filter, which gives unbiased estimate with a minimum error variance when the system has linear dynamics and Gaussian measurement errors. However, in a non-linear modeling framework and in non-Gaussian framework, the Kalman filter loses many of its pros. Extensions of Kalman filter have been suggested in literature for approximating the posterior measures in complex systems. To address this issue, this study proposes the use of polynomial chaos based Kalman filter for data assimilation purposes. PCKF was suggested as a sampling free alternative [8, 9, 10, 11]. A detailed explanation of its theoretical background and implementation is discussed below.

5.1 Polynomial Chaos Expansion (PCE)

PCE is a non sampling approach to represent uncertainty using deterministic orthogonal polynomials. Let $\xi(\theta)$ be a vector containing random independent variables, where θ is used as an index of the probabilistic character of the components of the vector (ξi). Each component of the vector denotes an independent source of uncertainty, where it's considered as a modeling decision to choose the length of the random variables vector or the contributing sources of uncertainty. Non-linear functional of ξ are expanded with respect to a basis in space of square integrable random variables. A suitable set of these bases is utilized by multidimensional polynomials, such that they are orthogonal to the joint probability measure of the random variables vector ξ. Therefore, in accordance with this formulation, if the random variable used is Gaussian, the orthogonal multidimensional basis is Hermite polynomials. Then accordingly, the deterministic coefficients of each basis are determined to parameterize the probabilistic distribution of the expanded function that uniquely represents its distribution and in an L2 sense. To elaborate the PCE more, consider a random process $u(x,\theta)$ that is expanded with respect to the vector ξ, with a finite covariance. Thus, its polynomial expansion is written with respect to multidimensional Hermite polynomials in Gaussian random variables arguments ($\xi i1, \xi i2 \dots \xi in$) as follows [12]:

$$u(x,\theta) = a_0(x)\Gamma_0 + \sum_{i_{1=1}}^{\infty} a_{i_1}(x)\Gamma_1\left(\xi_{i_1}(\theta)\right) + \sum_{i_{1=1}}^{\infty}\sum_{i_{2=1}}^{\infty} a_{i_1 i_2}(x)\Gamma_2\left(\xi_{i_1}(\theta)\xi_{i_2}(\theta)\right) + \cdots \quad (6)$$

Where Γ_n is the nth multidimensional Hermite polynomial, and a_{i_n} is its corresponding deterministic coefficient. The above series could be truncated by choosing a finite length independent random variable vector and an upper limit for the degree of the Hermite polynomial. By introducing a one to one mapping to a set of ordered indices, and truncating the series after the P^{th} term, the above expansion is rewritten as follow:

$$u(x,\theta) = \sum_{j=0}^{P} u_j(x)\psi_j(\theta) \tag{7}$$

The accuracy of the polynomial expansion is usually refined by increasing the M random dimension and/or the maximum order p of the expansion. The total number of terms, P+1, can be calculated as following:

$$P + 1 = \frac{(p + M)!}{M!\, p!} \tag{8}$$

5.2 Polynomial Chaos Kalman Filter (PCKF)

The PCKF consists of two stages: (1) a forecast stage and (2) an analysis stage if a measurement is present. The order and dimension of PC expansion are fixed from the beginning and throughout the processing for simplicity and computational purposes.

5.2.1. Forecast stage

Let A be the state matrix, which contains the vectors representing the deterministic coefficients of the PCE corresponding to model state and parameters at time t*:*

$$A = (u_0, u_1 \dots, u_p)\ \ u_i \in R^n, A \in R^{n\times(P+1)} \tag{9}$$

where u_i corresponds to the i^{th} component of the PCE expansion of the state vector u containing the chloride concentration at nodes, D, m and Cs. In the forecast stage, the uncertainty of the parameters and the dynamic state is propagated forward in time using stochastic Galerkin scheme. A process noise is added after forecast to represent the modeling error.

5.2.2. Analysis stage

This is a learning stage, where parameters and uncertainties are updated when a measurement is available. The measurement probabilistic representation, which is in this case the free chloride concentration at certain locations, is also expanded in a polynomial chaos form,

$$D = \sum_{j=0}^{P} d_j\psi_j \tag{10}$$

where dj is the deterministic coefficient of the jth basis. D is stored in a matrix form,

$$B = (d_0, d_1 \dots, d_p) \tag{11}$$

The filtering step relies on a minimum square error estimator of the coefficient of the polynomial chaos expansion. To evaluate the coefficient of the analysis step, the filtering step equation is projected on an approximating space by the basis of polynomial chaos $\{\psi_j\}_{j=0}^{P}$, this results in:

$$u_j^a = u_j^f + P^f H^T (H P^f H^T + R)^{-1} . (d_j - H u_j^f) \quad (12)$$

where f and a denote the forecast and analysis variables respectively, H acts as a linear measurement operator, to relate the true model state, to the measurements d and P ,with f or a indices, and R are the covariance error matrices of the forecast state and the measurements respectively

In a matrix form, it becomes [8],

$$A^a = A^f + P^f H^T (H P^f H^T + R)^{-1} . (B - H A^f) \quad (13)$$

5.3 Curse of Dimensionality and Suggested Implementation

When the process noises and measurement errors are considered in PCKF application as time independent variables, the PCE terms could increase beyond computational applicability. PCKF has gained a noticeable popularity since it was first used in 2007 [10], however, it was rarely applied with time independent process noises and model errors. Moreover, time independent measurements are usually approximated with a finite memory dimension with no clear methodology or error analysis for this representation. The theoretical necessity to add independent dimensions for every independent source of error discouraged researchers from applying polynomial chaos based filters to problems with high independent sources of errors. This issue could be the reason behind limiting the application of polynomial chaos based filters to problems with initial value errors and made the use of sampling filters advantageous for other applications.

Theoretically, each independent source of error will cost an increase in the dimensionality of the problem. However, this study will focus on keeping the computational cost minimal yet without scarifying the accuracy. The suggested approach to deal with increasing dimensionality of the PCE, due to incorporation of time independent errors, relies on limiting the PCE bases to finite terms, yet keeping an approximate same covariance. This strategy can be achieved by projecting the covariance matrix on a pre-specified number of first order terms when an additional basis is required beyond the fixed expansion length (P+1). This methodology maintains a good approximate propagation of the covariance and the mean of the parameters, and maintains a low-dimensional PCE. Thus, the unbearable cost of curse of dimensionality is shifted to the cost of projection the covariance matrix on first order terms, which is the solution of a system of non-linear equations, with, in most cases, a close initial guess. This approach is influenced by the characteristics of PCKF as being suited as an identification filter rather than inference method, since PCKF provides a good approximation of the posterior mean in Bayesian setting with a random priori estimation error [13]. In addition, it relies on the covariance matrices of the forecasted state vector and the covariance of the measurements, for an optimal identification of the state vector, i.e. maintaining a good estimate of the first two moments is the pillar for a successful implementation of PCKF.

6 NUMERICAL APPLICATION

The efficiency of the presented health-monitoring scheme is illustrated on 1-D diffusion example. The problem represents the chloride ingress in a near shore wall or an interior column exposed to a corrosive environment. A 50x25 cm reinforced concrete column with a 5 cm cover depth is used to demonstrate the efficacy of the presented framework. The sensors

are put in two locations in the zone of interest, near the rebar location, as shown in Table 1, and only one surface is assumed fully saturated.

Sensors	Location (m)
1	0.05 from surface
2	0.03 from surface

Table 1 Sensors' Locations

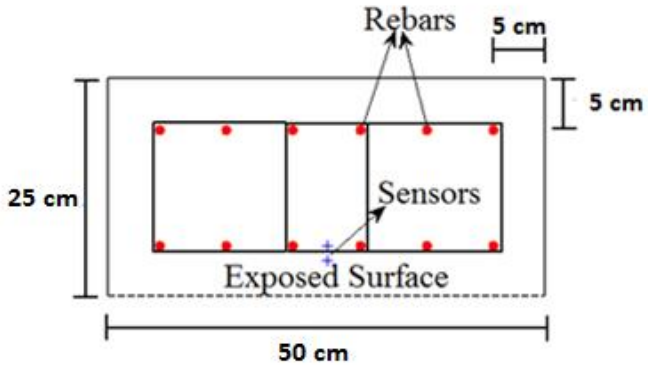

Figure 1 Schematic Drawing

6.1 Input Parameters

Table 2 presents the input parameters assumed for the base model. These parameters are used to simulate the measured chloride concentrations.

Parameter	Value	Comments
Surface Chloride Concentration, C_s	5 kg/m^3	High exposure
Reference Diffusion Rate, D_R	0.00015 $m^2/year$	At 28 days
Age factor, m	0.07	

Table 2 Base Model Input Parameters

The Crank solution eq. 3, with an average time varying diffusion rate Dm (t) [14], is used to generate the sensors' synthetic data. To represent measurement errors, an additive Gaussian white noise perturbation having a standard deviation equal to 2% of the actual data is added to the simulated chloride concentrations.

Starting with an initial assumption for the state of each parameter, the perturbed synthetic measurements are used to calibrate them as time progress. Table 3 presents the assumed initial probabilistic characteristics for the model parameters. Furthermore, it is assumed that the structures in both problems are chloride free at the beginning of the simulation time.

Parameter	Mean Value	cov	Distribution
Surface Chloride Concentration, C_s	4 kg/m^3	0.07	Lognormal
Reference Diffusion Rate, D_R	0.0001 $m^2/year$	0.07	Lognormal
Age factor, m	0.05	0.07	Beta

Table 3 Initial Model Parameters

Within the framework of the PCKF, a set of orthogonal polynomials are used to represent the uncertainty within the system. The initial PCE is propagated forward in time using finite element analysis with 0.025 years increment. The model error and parametric errors are represented via an additive Gaussian white noise with a standard deviation equals to 1.5% and 2.5% respectively of the forecasted mean. To represent the spatial variability in concrete, a spatial de-correlation length of 4 cm is assumed; thus a 6 i.d.d random variables are assigned to represent the uncertainty in the concentration profile grid each time model error is incorporated in the system. Whenever measurements are available, the model state vectors are updated using the analysis stage equations. With a real time sensor system, data availability is not a limitation since sensors typically give instantaneous measurements. However, due to the relatively slow nature of the chloride ingress, a one-year measurement interval is adopted.

6.2 Results

6.2.1. PCKF implementation

The benchmark for comparing the results of the suggested implementation will be an EnKF approach using theoretically sufficient ensembles representation, to eliminate sampling errors, that is in this case $5x10^5$ ensembles. To assess the effect of number of random variables and maximum order used in the PCE, the methodology will be applied to four independent formulations of PCE with: (1) 37 dimensions and order 1, (2) 37 dimensions and order 2 and (3) 37 dimensions and order 3 and (4) 45 dimensions and order 2. Note that the only constraint for applying the projection on the first order basis is that the number of first order basis (dimension) is at least equal to the length of the state vector, to be able to solve the non-linear system of equations. In addition, two EnKF formulations with $0.25\ x10^5$ and $1\ x10^5$ ensembles will be simulated for comparative purposes. The computational cost will be assessed based on the time (sec) needed to run the simulations for 20 years, or 800 time steps. However to assess the accuracy of the suggested scheme the average deviation, eq. 14, and the maximum deviation, eq. 15, of the first two order moments, from benchmark problem, of chloride concentration at rebar level and the time varying diffusion rate will be calculated for the simulated period, as follows:

Average deviation:

$$\%Ad = \sum_{n=0}^{800} \frac{|(\mathrm{u}^n - u^n_{benchmark})|}{800 \times u^n_{benchmark}} \times 100 \tag{14}$$

$$\%Maxd = Maximum\ (\frac{|(\mathrm{u}^n - u^n_{benchmark})|}{u^n_{benchmark}} \times 100)_0^{800} \tag{15}$$

Where u and $u_{bechmark}$ are first or second order moments of the studied sequential formulation and benchmark problem formulation respectively. The $\%Maxd$ of the studied parameters and the $\%Ad$, for the simulation period are presented in Tables 4 and 5 respectively. Table 6 presents the computational time, in seconds, required for the different sequential filters' formulations, to perform the forecast steps and the analysis steps for the 20 years. These tables reflect the power of the suggested scheme, where the PCKF with dimension 37 and order 2 rendered accurate results, with less than 0.35 $\%Maxd$ and less than 0.094 $\%Ad$ and with better accuracy and computational cost compared to EnKF formulations. Moreover, no significant improvement is shown in the PCE formulation beyond 37 dimensions and second

order. This can be attributed to the emphasize of the lower order terms due to the projection on the first order bases and to conservation of first two moments in all PCE expansions.

	$\%Ad$ for mean of C at x_r	$\%Ad$ for std of C at x_r	$\%Ad$ for mean of D	$\%Ad$ for std of D
EnKF: 10^5 Ensembles	0.180	0.571	0.061	0.446
EnKF: $0.25x10^5$ Ensembles	0.393	2.100	0.490	1.555
PCKF: Dimensions 37 Order 1	1.074	4.722	1.505	2.930
PCKF: Dimensions 37 Order 2	0.074	0.350	0.072	0.218
PCKF: Dimensions 37 Order 3	0.074	0.350	0.059	0.221
PCKF: Dimensions 45 Order 2	0.074	0.350	0.074	0.219

Table 4 Maximum percentage deviation from the benchmark problem for chloride concentration C at rebar level and diffusion rate D

	$\%Maxd$ for mean of C at x_r	$\%Maxd$ for std of C at x_r	$\%Maxd$ for mean of D	$\%Maxd$ for std of D
EnKF: 10^5 Ensembles	0.010	0.159	0.027	0.183
EnKF: $0.25x10^5$ Ensembles	0.039	0.346	0.129	0.421
PCKF: Dimensions 37 Order 1	0.106	0.249	0.387	0.506
PCKF: Dimensions 37 Order 2	0.007	0.084	0.024	0.094
PCKF: Dimensions 37 Order 3	0.006	0.082	0.020	0.094
PCKF: Dimensions 45 Order 2	0.007	0.084	0.024	0.094

Table 5 Average percentage deviation from the benchmark problem for chloride concentration C at rebar level and diffusion rate D

	Computational time (Sec)
Benchmark Problem	15168
EnKF: 10^5 Ensembles	3034
EnKF: $0.25x10^5$ Ensembles	751
PCKF: Dimensions 37 Order 1	230
PCKF: Dimensions 37 Order 2	372
PCKF: Dimensions 37 Order 3	24480
PCKF: Dimensions 45 Order 2	801

Table 6 Computational time in seconds for 20 years simulation period

6.2.2. Parametric identification

PCKF with 37 dimensions and second order PCE is used for health monitoring of chloride ingress in concrete. Figure 2 shows the mean prediction of chloride concentration at rebar level using PCKF calibration technique compared to using initial value parameters, and Figure 3 shows the mean and 1 std error bars of the calibrated time varying diffusion coefficient as compared to the base case model assumptions. A significant improvement in identifying the chloride concentration at rebar level and the diffusion parameter is reflected in these two figures. Consequently, a more accurate reliability assessment for corrosion initiation can be performed using the updated state vector parameters.

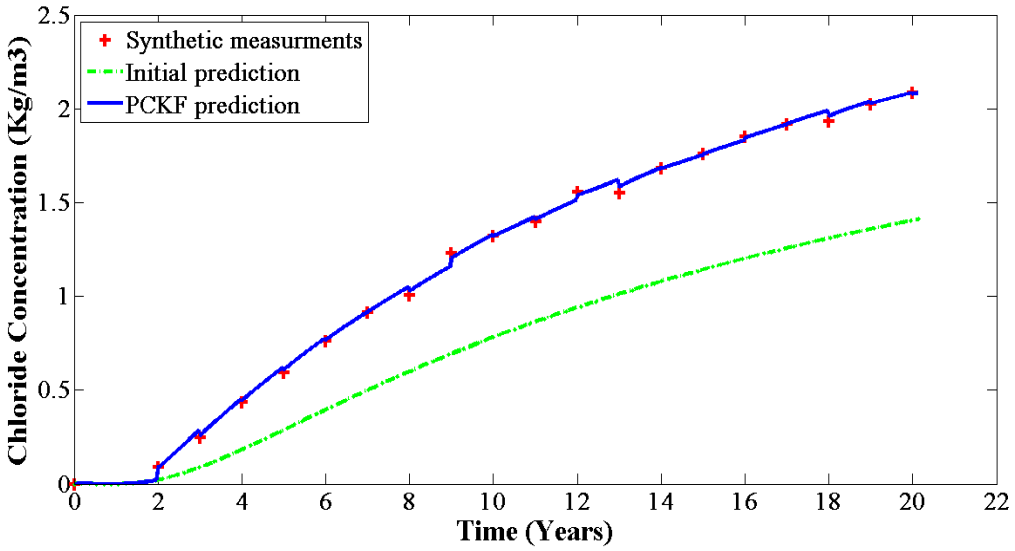

Figure 2 Measured Vs. Predicted chloride concentration chloride concentration using PCKF and initial parameters at rebar level

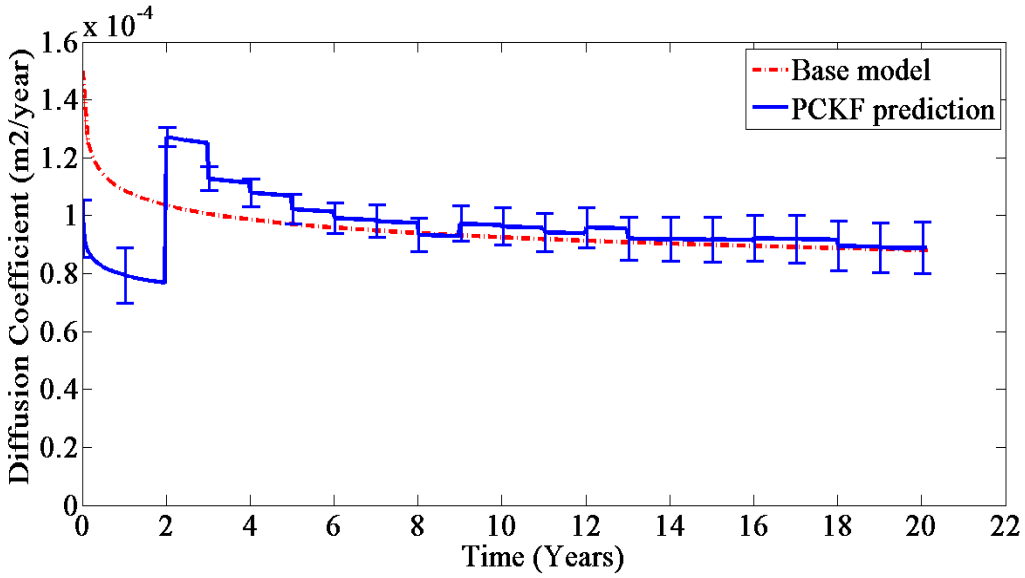

Figure 3 Base Case Vs. Mean calibrated time varying diffusion coefficient with 1 std error bars

7 CONCLUSIONS

In this study, PCKF was employed as a parametric identification tool using a suggested practical framework to mitigate the curse of the dimensionality. The power of the suggested scheme was reflected by comparing its accuracy and computational efficiency to the well - known EnKF. The suggested methodology was used for calibration of dynamic variables and model parameters of 1-D diffusion problem for better assessment of corrosion initiation time.

REFERENCES

[1] G. S. Duffó and S. B. Farina, "Development of an embeddable sensor to monitor the corrosion process of new and existing reinforced concrete structures," *Construction and Building Materials,* vol. 23, no. 8, pp. 2746-2751, 2009.

[2] D. Val, V. Trapper and A. Pavel, "Probabilistic evaluation of initiation time of chloride-induced corrosion," *Reliability Engineering and System Safety,* p. 364–372, 2008.

[3] B. Saassouh and Z. Lounis, "Probabilistic modeling of chloride-induced corrosion in concrete structures using first- and second-order reliability methods," *Cement & Concrete Composites,* p. 1082–1093, 2012.

[4] A. Ababneh, F. Benboudjema and Y. Xi, "Chloride Penetration in Nonsaturated Concrete," *J Mater Civ Eng,* vol. 15, pp. 189-191, 2003.

[5] A. V. Saetta, B. A. Schrefler and R. V. Vitaliani, "The carbonation of concrete and the mechanism of moisture, heat and carbon dioxide flow through porous materials," *Cement and Concrete Research,* vol. 23, no. 4, pp. 761-772, 1993.

[6] H.-W. Song, S.-W. Pack and K. Y. Ann, "Probabilistic assessment to predict the time to corrosion of steel in reinforced concrete tunnel box exposed to sea water," *Construction and Building Materials,* vol. 23, no. 10, pp. 3270-3278, 2009.

[7] G. Glass and N. Buenfield, "The presentation of chloride threshold level for corrosion of steel in concrete," *Corrosion Science,* vol. 39, pp. 1001-1013, 1997.

[8] G. Saad and R. Ghanem, "Characterization of reservoir simulation models using a polynomial chaos based ensemble Kalman Filter," *Water Resources Research,* vol. 45, p. W04417, 2009.

[9] J. Li and D. Xiu, "A generalized polynomial chaos based ensemble Kalman filter with high accuracy," *Journal of Computational Physics,* vol. 228, p. 5454–5469, 2009.

[10] G. Saad, Stochastic data assimilation with application to multi-phase flow and health monitoring problems, ProQuest, 2007.

[11] G. A. Saad and R. G. Ghanem, "Robust structural health monitoring using a polynomial chaos based sequential data assimilation technique," in *COMPDYN 2011*, Corfu, 2011.

[12] R. G. Ghanem and P. D. Spanos, Stochastic finite elements: a spectral approach, Courier Corporation, 2003.

[13] O. G. Ernst, B. Sprungk and H.-J. Starkloff, "Analysis of the Ensemble and Polynomial Chaos Kalman Filters in Bayesian Inverse Problems," *arXiv preprint arXiv,* p. 1504.03529, 2015.

[14] S.-W. a. J. M.-S. Pack, H.-W. Song, S.-H. Kim and K. Y. Ann, "Prediction of time dependent chloride transport in concrete structures exposed to a marine environment," *Cement and Concrete Research,* p. 302–312, 2010.

ECCOMAS Congress 2016
VII European Congress on Computational Methods in Applied Sciences and Engineering
M. Papadrakakis, V. Papadopoulos, G. Stefanou, V. Plevris (eds.)
Crete Island, Greece, 5–10 June 2016

ANALYSIS OF STOCHASTIC DYNAMIC SOIL-STRUCTURE INTERACTION PROBLEMS BY MEANS OF COUPLED FINITE ELEMENTS-PERFECTLY MATCHED LAYERS

Manthos Papadopoulos, Stijn François, Geert Degrande and Geert Lombaert

KU Leuven, Department of Civil Engineering, Structural Mechanics Section
Kasteelpark Arenberg 40, 3001 Leuven, Belgium
e-mail: {manthos.papadopoulos, stijn.francois, geert.degrande, geert.lombaert}@bwk.kuleuven.be

Keywords: Dynamic soil-structure interaction, stochastic analysis, perfectly matched layers, functionally graded finite elements.

Abstract. *This paper presents a probabilistic computational model for the dynamic soil-structure interaction problem. Specifically, the structure and a limited bounded volume of subsoil in its vicinity are modeled with functionally graded finite elements, allowing to consider heterogeneous local subsoil conditions. This part of subsoil is modeled as a three-dimensional constrained stochastic field. The unboundedness of the surrounding soil is accounted for by coupling the finite element model with perfectly matched layers. An incident wave field is incorporated in the finite element-perfectly matched layers model without explicitly including the source in the computational domain by decomposing the displacement field of the soil in accordance with the subdomain formulation developed for the soil-structure interaction problem. The proposed methodology is illustrated with a case study in which the overall uncertainty is propagated by means of Monte Carlo simulation. The analysis shows that the uncertainty of the structural response increases at specific frequency bands and generally for higher frequencies. These results illustrate how the stochastic variability of the subsoil properties affect both the incident wave field and the structural response in a wide frequency range, and sets the base for future investigations.*

1 INTRODUCTION

Dynamic soil-structure interaction (SSI) refers to the dynamic behavior of the coupled soil-structure system. This problem occurs in several applications from earthquake engineering to the prediction of traffic induced vibrations in the built environment. Pioneering work on the subject started in the nuclear industry for the design and construction of earthquake resistant nuclear reactors. More recently, the development of high-speed railway lines in Europe, east Asia and USA turned research interest also in the field of railway induced vibrations. Railway induced vibrations may lead to malfunctioning of sensitive equipment, discomfort to people and, at high vibration levels, damage to structures. The development of computational models that efficiently and effectively predict the dynamic response of structures excited by ground born vibrations is a matter of ongoing research.

When the knowledge of the subsoil properties is incomplete, the dynamic soil-structure interaction problem should be cast into a stochastic form. This can be done by considering parametric [14] and/or non-parametric uncertainty [3]. Most of the previously conducted work on the subject is mainly focused on earthquake engineering applications considering the very low frequency range (< 10 Hz). The present study considers parametric uncertainty and focuses on the prediction of vibrations in the built environment which makes the frequency range of interest much broader.

The remainder paper is organized as follows. First, the stochastic dynamic soil-structure interaction problem is introduced and the available modeling techniques are briefly discussed. Next, the particularities of modeling the stochastic subsoil are addressed. Finally, the results of a case study are presented, and conclusions are drawn.

2 THE STOCHASTIC DYNAMIC SSI

The soil immediately below the structure plays a dominant role in the structural response. In many cases, this soil is imperfectly known as it may have been perturbed during construction and its characteristics are likely to be different from those identified by geophysical tests on virgin land next to the structure. As discussed in the following, the use of finite elements (FE) provides a great flexibility that allows to incorporate heterogeneous properties in the modeling of this bounded volume of soil. The structure of interest and the limited bounded volume of soil in its vicinity will be denoted for convenience as the generalized structure (Figure 1).

The main difficulty in the modeling of dynamic soil-structure interaction stems from the semi-infinite extent of the soil surrounding the generalized structure, for which the radiation conditions of the elastodynamic waves to infinity should be satisfied. Generally, the dynamic soil-structure interaction problem can be formulated either directly or by following a domain decomposition technique [18]. In the direct approach, the unboundedness of the surrounding soil is accounted for by using appropriate absorbing boundaries in the limits of the regular domain (i.e. generalized structure). The use of perfectly matched layers (PML) [2] is a quite versatile solution to impose these boundary conditions. In the subdomain approach [1], the system is decomposed into two subsystems: the generalized structure and the soil. Both subsystems are analyzed separately and usually by a different computational method. The boundary element method can be used to simulate the unbounded soil domain of infinite extent, where the radiation conditions to infinity are implicitly satisfied, while the finite element method is typically used for the generalized structure.

Although the use of boundary elements entails the benefit of rendering three-dimensional problems in two-dimensional ones, the resulting boundary element system matrices are fully

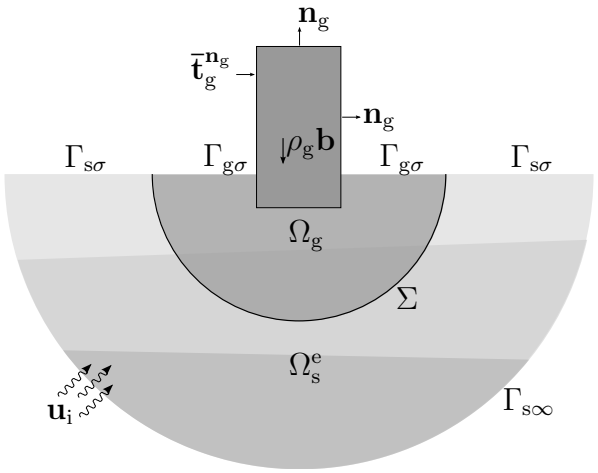

Figure 1: Dynamic soil-structure interaction problem. The interface Σ defines the physical boundary between the unbounded soil $\Omega_\mathrm{s}^\mathrm{e}$ and the generalized structure Ω_g.

populated as opposed to the sparse finite element matrices, leading to increased memory requirements and longer computer time for processing. This aggravates in the case of embedded or extended foundations where a large soil-foundation interface has to be considered. For these reasons, the direct formulation of the problem by means of FE-PML is advocated in this study.

The PML are non-physical absorbing layers that are placed at the exterior limits of the computational domain (Figure 2). Ideally, the waves that are outwardly propagating from the regular domain are fully attenuated inside the PML without any spurious reflections emerging [2]. The effectiveness of the PML strongly depends on the choice and parameterization of their stretch functions [8]. The bounded soil domain is modeled with finite elements: a distinction is made between heterogeneous functionally graded finite elements [13] with continuously varying properties and deterministic homogeneous finite elements. The former are used for the stochastic soil subdomain while the latter are used to enforce the perfectly matched conditions between the PML and the functionally graded FE. The resulting finite element system of equations of the total system is written in the frequency domain as:

$$\hat{\mathbf{K}}\hat{\mathbf{u}} = \hat{\mathbf{f}} \tag{1}$$

where $\hat{\mathbf{f}}$ is the load vector, $\hat{\mathbf{u}}$ is the displacement vector and $\hat{\mathbf{K}}$ is the dynamic stiffness matrix. The dynamic stiffness matrix $\hat{\mathbf{K}}$ can be subdivided into block matrices according to the degrees of freedom: $\hat{\mathbf{u}}_\mathrm{b}$ of the structure, $\hat{\mathbf{u}}_\mathrm{t}$ of the stochastic-heterogeneous soil, $\hat{\mathbf{u}}_\Sigma$ of the interface Σ delimiting the limits of the regular domain, $\hat{\mathbf{u}}_\mathrm{q}$ of the deterministic-homogeneous soil and $\hat{\mathbf{u}}_\mathrm{p}$ the non-physical degrees of freedom of the PML (Figure 2):

$$\begin{bmatrix} \hat{\mathbf{K}}_{\mathrm{bb}} & \hat{\mathbf{K}}_{\mathrm{bt}} & \mathbf{0} & \mathbf{0} & \mathbf{0} \\ \hat{\mathbf{K}}_{\mathrm{tb}} & \hat{\mathbf{K}}_{\mathrm{tt}} & \hat{\mathbf{K}}_{\mathrm{t}\Sigma} & \mathbf{0} & \mathbf{0} \\ \mathbf{0} & \hat{\mathbf{K}}_{\Sigma\mathrm{t}} & \hat{\mathbf{K}}_{\Sigma\Sigma} & \hat{\mathbf{K}}_{\Sigma\mathrm{q}} & \mathbf{0} \\ \mathbf{0} & \mathbf{0} & \hat{\mathbf{K}}_{\mathrm{q}\Sigma} & \hat{\mathbf{K}}_{\mathrm{qq}} & \hat{\mathbf{K}}_{\mathrm{qp}} \\ \mathbf{0} & \mathbf{0} & \mathbf{0} & \hat{\mathbf{K}}_{\mathrm{pq}} & \hat{\mathbf{K}}_{\mathrm{pp}} \end{bmatrix} \begin{bmatrix} \hat{\mathbf{u}}_\mathrm{b} \\ \hat{\mathbf{u}}_\mathrm{t} \\ \hat{\mathbf{u}}_\Sigma \\ \hat{\mathbf{u}}_\mathrm{q} \\ \hat{\mathbf{u}}_\mathrm{p} \end{bmatrix} = \begin{bmatrix} \hat{\mathbf{f}}_\mathrm{b} \\ \hat{\mathbf{f}}_\mathrm{t} \\ \hat{\mathbf{f}}_\Sigma \\ \mathbf{0} \\ \mathbf{0} \end{bmatrix} \tag{2}$$

Excitation sources can be located either close to the receiver like in the case of railway induced vibrations or far from the receiver like in case of an earthquake. If the interest of the analysis is limited only in the neighborhood of the receiver, a remote excitation source S

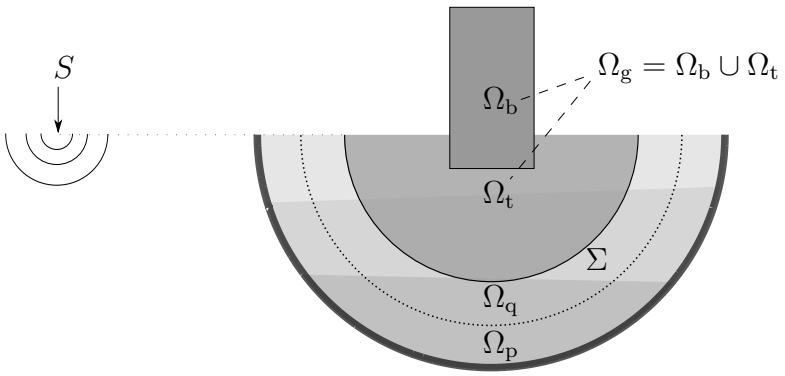

Figure 2: Formulation of the stochastic dynamic soil-structure interaction problem by means of FE-PML. The computational domain is subdivided into the structural Ω_{b}, stochastic soil Ω_{t}, deterministc soil Ω_{q} and PML Ω_{p} subdomains respectively. All but the last are modeled with finite elements. The interface Σ defines the limits of the regular computational domain.

(Figure 2) can be implicitly taken into account by decomposing the displacement field of the soil in accordance with the subdomain formulation developed for the soil-structure interaction problem [1]. This way, the computational cost decreases significantly as only the generalized structure has to be included in the regular domain. Specifically, the displacement field of the soil is decomposed as (Figure 3):

$$\hat{\mathbf{u}}_{\mathrm{s}} = \hat{\mathbf{u}}_{\mathrm{i}} + \hat{\mathbf{u}}_{\mathrm{d0}} + \hat{\mathbf{u}}_{\mathrm{d}} \tag{3}$$

where $\hat{\mathbf{u}}_{\mathrm{i}}$ are the free field displacements generated by the remote source S (Figure 3b). Generally, the free field displacements $\hat{\mathbf{u}}_{\mathrm{i}}$ (and tractions $\hat{\mathbf{t}}_{\mathrm{i}}$) can be computed by using the appropriate source model. The locally diffracted wave field $\hat{\mathbf{u}}_{\mathrm{d0}}$ is defined as the displacement field that is radiated in the soil with excavated the generalized structure for which applies $\hat{\mathbf{u}}_{\mathrm{d0}} = -\hat{\mathbf{u}}_{\mathrm{i}}$ on the interface Σ (Figure 3c). The wave field $\hat{\mathbf{u}}_{\mathrm{d}}$ corresponds to the displacement field radiated in the soil due to the generalized structure displacements $\hat{\mathbf{u}}_{\mathrm{g}}$ on the interface Σ (Figure 3d). Only the first and the second of the aforementioned displacement fields contribute to the equivalent loading vector $\hat{\mathbf{f}}_{\Sigma}$ on the interface Σ of the FE-PML model which represents excitation by a remote source.

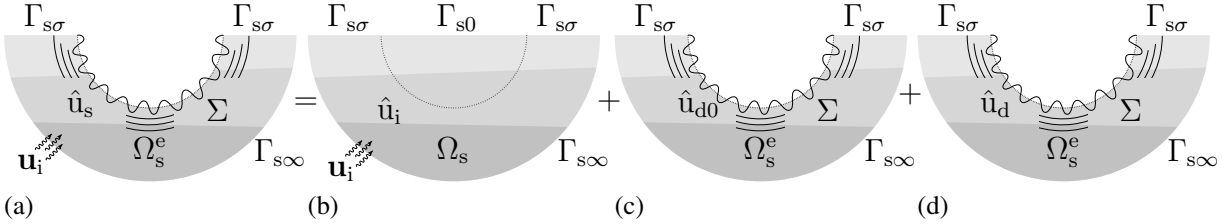

Figure 3: Decomposition of soil displacement field in accordance with the subdomain formulation of the dynamic soil-structure interaction problem. (a) The displacement field in the soil $\hat{\mathbf{u}}_{\mathrm{s}}$ is decomposed into: (b) free field $\hat{\mathbf{u}}_{\mathrm{i}}$, (c) locally diffracted $\hat{\mathbf{u}}_{\mathrm{d0}}$ (with $\hat{\mathbf{u}}_{\mathrm{d0}} = -\hat{\mathbf{u}}_{\mathrm{i}}$ on Σ) and (d) structurally radiated $\hat{\mathbf{u}}_{\mathrm{d}}$ (with $\hat{\mathbf{u}}_{\mathrm{d}} = \hat{\mathbf{u}}_{\mathrm{g}}$ on Σ).

Once the free field displacements $\hat{\mathbf{u}}_{\mathrm{i}}$ and tractions $\hat{\mathbf{t}}_{\mathrm{i}}$ have been evaluated on the interface Σ, the loading $\hat{\mathbf{f}}_{\Sigma}$ can be computed as:

$$\hat{\mathbf{f}}_{\Sigma} = -\int_{\Sigma} \mathbf{N}_{\boldsymbol{\Sigma}}^{\mathbf{T}} \hat{\mathbf{t}}_{\mathbf{i}}^{\mathbf{n_s^e}} d\Sigma - \hat{\mathbf{r}}_{\boldsymbol{\Sigma}}\left(\hat{\mathbf{u}}_{\mathbf{d0}}\right) = -\int_{\Sigma} \mathbf{N}_{\boldsymbol{\Sigma}}^{\mathbf{T}} \hat{\mathbf{t}}_{\mathbf{i}}^{\mathbf{n_s^e}} d\Sigma - \hat{\mathbf{r}}_{\boldsymbol{\Sigma}}\left(-\hat{\mathbf{u}}_{\mathbf{i}}\right) \tag{4}$$

where $\mathbf{N}_\Sigma$ is a matrix containing the shape functions of the finite element faces located on the interface Σ, $\hat{t}_i^{\mathbf{n_s^e}}$ are the free field tractions and $\hat{\mathbf{r}}_{\mathbf{\Sigma}}\left(-\hat{\mathbf{u}}_{\mathbf{i}}\right)$ is a vector of the reaction forces on the interface Σ of the FE-PML model with excavated the generalized structure due to the imposed displacements $-\hat{\mathbf{u}}_{\mathbf{i}}$ (figure 4). The reaction forces $\hat{\mathbf{r}}_{\mathbf{\Sigma}}\left(-\hat{\mathbf{u}}_{\mathbf{i}}\right)$ are computed as follows:

$$\hat{\mathbf{r}}_{\mathbf{\Sigma}}\left(-\hat{\mathbf{u}}_{\mathbf{i}}\right) = \left(\hat{\mathbf{K}}_{\Sigma \mathrm{r}} \hat{\mathbf{K}}_{\mathrm{rr}}^{-1} \hat{\mathbf{K}}_{\mathrm{r}\Sigma} - \hat{\mathbf{K}}_{\Sigma\Sigma}\right) \hat{\mathbf{u}}_{\mathbf{i}} \tag{5}$$

where the degrees of freedom of the deterministic soil $\hat{\mathbf{u}}_{\mathrm{q}}$ and the PML $\hat{\mathbf{u}}_{\mathrm{p}}$ have been grouped for clarity as $\hat{\mathbf{u}}_{\mathrm{r}} = \hat{\mathbf{u}}_{\mathrm{q}} \cup \hat{\mathbf{u}}_{\mathrm{p}}$. The stochastic variation of the soil properties inside the generalized structure does not affect the loading vector $\hat{\mathbf{f}}_\Sigma$ and as a result, in a Monte Carlo analysis it has to be computed only once.

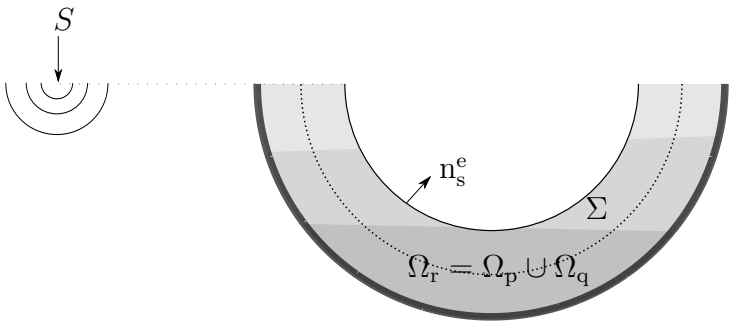

Figure 4: FE-PML model with excavated the stochastic soil subdomain. Auxiliary model for the incorporation of an incident wave field.

3 THE STOCHASTIC SUBSOIL MODELING

The imperfectly known subsoil is modeled as a stochastic field with given marginal probability distribution function (PDF) and correlation structure [17]. Usually, the mean value and the standard deviation are the only available information for the probabilistic characterization of the subsoil properties. In the absence of more detailed experimental results, a covariance function is assumed for the stochastic field. The covariance function is usually defined by the standard deviation function $\sigma_{\mathrm{G}}(s)$ and a correlation structure $\kappa_{\mathrm{G}}(s, s')$:

$$C_{\mathrm{G}}(s, s') = \sigma_{\mathrm{G}}(s)\sigma_{\mathrm{G}}(s')\kappa_{\mathrm{G}}(s, s') \tag{6}$$

This information is sufficient to generate realizations of Gaussian stochastic fields. In this study, non-Gaussian stochastic field realizations are generated by non-linear transformation of the underlying Gaussian. This is referred as translation process [7, 10]:

$$G(\theta, \boldsymbol{s}) = F_{\mathrm{G}}^{-1}\left(F_{\mathrm{Z}}\left(Z(\theta, \boldsymbol{s})\right)\right) \tag{7}$$

where F_{G}^{-1} is the inverse of the target non-Gaussian marginal cumulative probability distribution and Z is the standard normal cumulative probability distribution.

Furthermore, in order to avoid non-physical dynamic impedance contrasts, a conforming coupling between the stochastic and the deterministic subdomains of the soil is desirable. This is achieved by modeling a conditional (or constrained) stochastic field [17]. Conditional stochastic fields are necessarily heterogeneous as the mean value and standard deviation vary from location to location [11].

The Karhunen-Loève expansion can be employed to straightforwardly generate realizations of a heterogeneous Gaussian stochastic field [16]. Nevertheless, the computation of the Karhunen-Loève modes entails the solution of a Fredholm eigenvalue problem [6], which is computationally rather expensive and not trivial to implement in this case. Instead, the approach that is followed in this study is to directly discretize the stochastic field and its covariance matrix into a random vector and a covariance matrix respectively [9]. Subsequently, the random vector describing the Gaussian stochastic field is decorrelated by performing eigenvalue analysis to its covariance matrix:

$$\mathbf{\Lambda} = \mathbf{\Phi}^{\mathbf{T}} \mathbf{C}_{\mathrm{Z}} \mathbf{\Phi} \tag{8}$$

where $\mathbf{\Lambda}$ and $\mathbf{\Phi}$ are matrices containing the eigenvalues λ_{i} and the eigenvectors ϕ_{i} of the covariance matrix $\mathbf{C}_{\mathrm{Z}}$ respectively. The Gaussian realizations are computed as the superposition of the deterministic eigenvectors ϕ_{i} of the covariance matrix multiplied by random numbers ξ_{i} from the standard normal distribution. This corresponds to an equivalent discrete Karhunen-Loève expansion:

$$\mathbf{Z} = \mathbf{Z}_0 + \sum_{i=1}^{n_{\mathrm{m}}} \phi_{\mathrm{i}} Y_{\mathrm{i}} \quad = \mathbf{Z}_0 + \sum_{\mathbf{i}=1}^{\mathbf{n_m}} \phi_{\mathrm{i}} \sqrt{\lambda_{\mathrm{i}}} \xi_{\mathrm{i}} \tag{9}$$

Having generated the Gaussian realizations, the non-Gaussian are generated by following the translation process outlined previously. In Equation 9, the number of eigenvalues considered in the summation should be sufficiently large in order to capture the relevant information that is encoded in the covariance matrix. The first n_{m} largest magnitude eigenvalues, that result in normalized accumulated sum larger than a threshold value ϵ_{min} can be used as a selection criterion:

$$\epsilon(n_{\mathrm{m}}) = \frac{\sum_{i=1}^{n_{\mathrm{m}}} \lambda_i}{\mathrm{tr}(\mathbf{C}_{\mathrm{Z}})} \geq \epsilon_{\mathrm{min}} \tag{10}$$

where $\mathrm{tr}(\mathbf{C}_{\mathrm{Z}})$ is the trace of the covariance matrix.

In a Monte Carlo simulation, when random realizations are generated from the entire sampling space, clusters of realizations may form and as a result the space might not be equally explored. In order to improve the representativeness of the sampled pool of realizations, more sophisticated sampling techniques can be employed. Latin hypercube sampling with artificial correlation reduction is used in the present investigation [12].

4 CASE STUDY

The methodology is illustrated with a case study. A three story R/C office building with regular layout and slab foundation resting at the surface of a visco-elastic halfspace is studied (Figure 5). The characteristics of the building are summarized in Table 1, while the mean properties of the visco-elastic halfspace are shown in Table 2.

Figure 6 shows the FE-PML computational model. The subsoil domain is modeled with three-dimensional twenty-node finite elements. An element size of maximum 2.6 m is used for the mesh at the exterior limits of the computational domain, corresponding to 2.5 quadratic finite elements per shear wavelength λ_s at a frequency of 50 Hz, which is the upper limit considered in this work. The building is modeled with frame and eight-node shell elements. Standard

Story height h_s	3 m
Columns	0.35 m $\times$ 0.35 m
Beams	0.20 m $\times$ 0.50 m
x direction walls	0.20 m $\times$ 4 m
y direction walls	0.20 m $\times$ 2 m
Slab thickness t_s	0.15 m
Raft foundation thickness t_f	0.60 m
Young's modulus E_s	30 GPa
Material density ρ_s	2500 $\mathrm{kg/m^3}$

Table 1: R/C building characteristics.

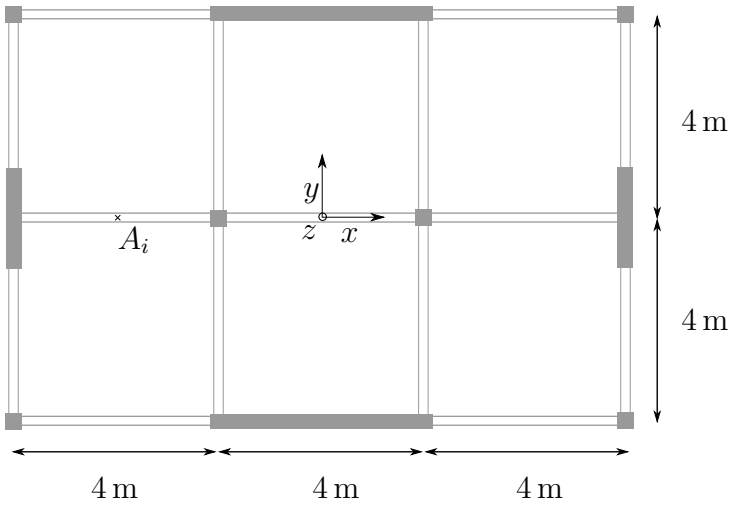

Figure 5: R/C building layout at floor i.

h	C_s	C_p	G	ν	ρ	β
[m]	[m/s]	[m/s]	[MPa]	[$-$]	[kg/m^3]	[$-$]
∞	300	600	162	1/3	1800	0.01

Table 2: Mean properties of the visco-elastic halfspace.

stretch functions are used for the formulation of the PML [8]. Because of the specifically employed FE discretization and PML parameterization, the model is appropiate for analysis in the frequency range between 10 Hz and 50 Hz. As the analysis is performed in the frequency domain, hysteretic damping is assumed for the R/C building with $\eta = 2\xi = 5\%$ [4].

First, the methodology for the incorporation of an incident wave field in the FE-PML model is verified. The homogeneous visco-elastic halfspace with the properties of Table 2 is used for this purpose. The visco-elastic halfspace is excited by a remote source S of unit amplitude located at (-34 m,-26 m,0 m) with respect to the origin of the reference system (Figure 6). The analysis is performed for the computation of the free field displacements without the presence of the R/C building. Figure 7 shows both the solutions obtained with the FE-PML model and the direct stiffness method [15]. The obtained results match perfectly for the frequencies at 10 Hz and 30 Hz, while small differences ($< 5\%$) are observed for the frequency at 50 Hz. This

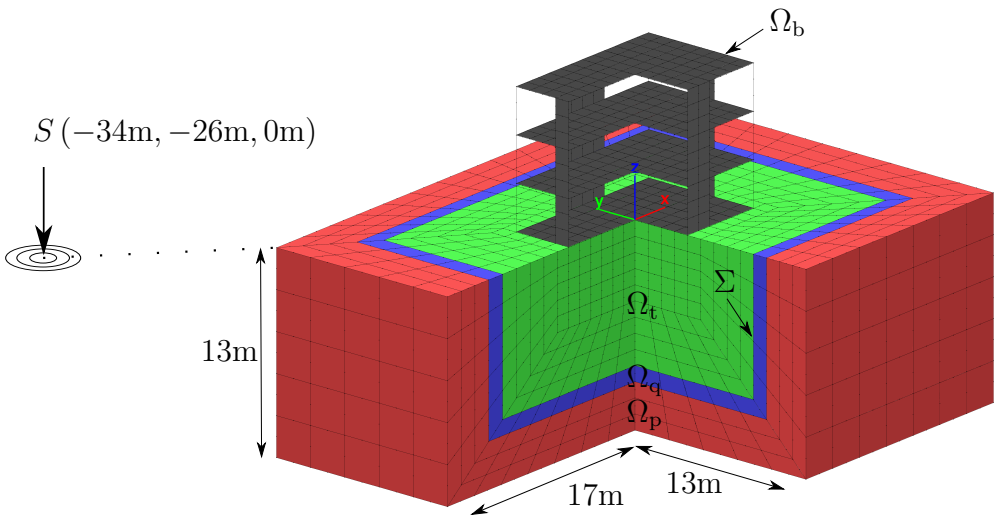

Figure 6: FE-PML model. Regular domain: heterogeneous functionally graded FE (green color) and homogeneous deterministic FE (grey and blue colors). PML domain (red color). Remote excitation source S located outside the limits of the computational domain.

difference can be mostly attributed to discretization error.

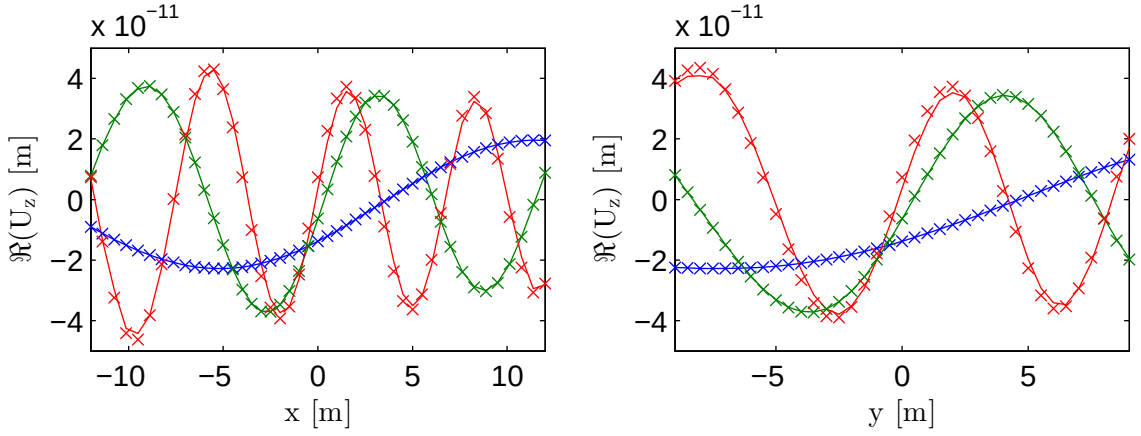

(a) (b)

Figure 7: Real part of vertical free field displacements along the (a) x and (b) y axes (z=0) of the FE-PML model. FE-PML model (solid lines) versus EDT solutions (x marks) [15]. Responses for 10 Hz (blue), 30 Hz (green) and 50 Hz (red).

Next, the R/C building is added at the surface of the stochastic soil. The soil has the mean properties of Table 2 and only the shear modulus is considered to be stochastic. The Gamma PDF is adopted for the shear modulus with a coefficient of variation of $\text{CoV} = 0.3$ (Figure 8). An exponential correlation structure with a correlation length of $l_c = 1.5$ is assumed for the

covariance function of the univariate stochastic field:

$$C_{\mathrm{G}}(s,s') = \sigma_{\mathrm{G}}^2 \exp\left(-\frac{|s-s'|^2}{l_{\mathrm{c}}^2}\right) \tag{11}$$

A threshold value $\epsilon_{\min} = 0.95$ (Equation 9) is used in the present work for the generation of the stochastic field realizations, resulting in $n_{\mathrm{m}} = 1000$ eigenvalues (figure 9). A large number of eigenvalues (and therefore random numbers) is generally required for an adequate representation of weakly correlated stochastic fields. Figure 10 shows a realization of the stochastic shear modulus of the soil mapped onto the finite element mesh. The stochastic shear modulus is constrained to take the deterministic value of the surrounding soil on the interface Σ.

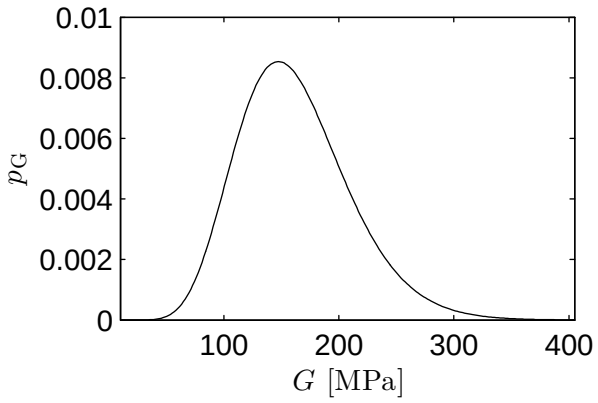

Figure 8: Marginal probability distribution function of soil's shrear modulus.

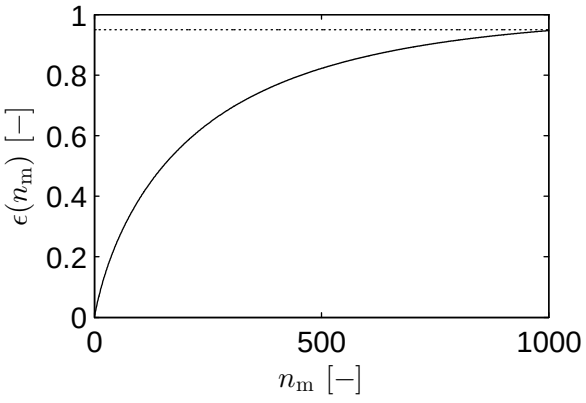

Figure 9: Normalized accumulated sum of Karhunen-Loève eigenvalues.

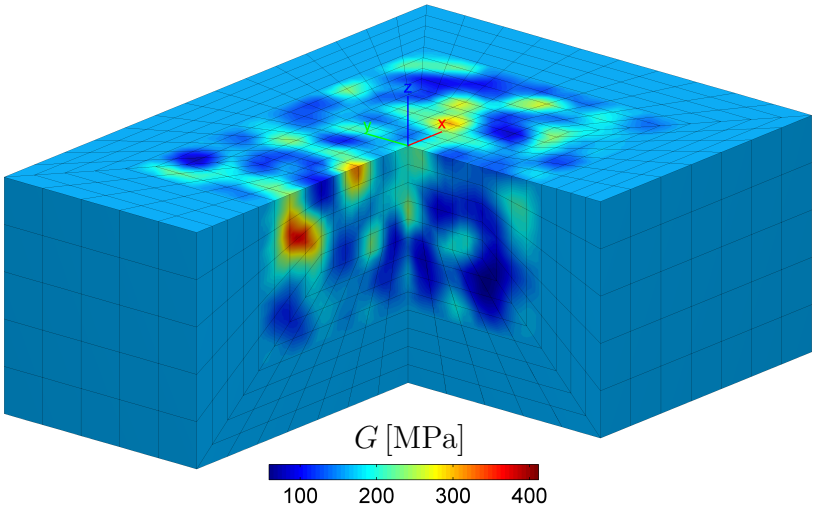

Figure 10: Realization of the stochastic shear modulus of the soil mapped onto the finite element mesh.

The uncertainty is propagated from the stochastic subsoil properties to the structural response quantities by means of Monte Carlo simulation. In total, $n_{\mathrm{R}} = 1001$ realizations are used for the

statistical estimation of the structural response quantities. Moreover, the quality of the estimated statistics is quantified by utilizing the bootstrap method [5]. The degree of uncertainty on the structural response is assessed by means of coefficients of variation and confidence regions. The former are defined as:

$$\mathrm{CoV}_{|\mathrm{U}|} = \frac{\sigma_{|\mathrm{U}|}}{\mu_{|\mathrm{U}|}} \tag{12}$$

where $|U|$ is the modulus of the response quantity U, and $\sigma_{|\mathrm{U}|}$ and $\mu_{|\mathrm{U}|}$ are the standard deviation and the mean value of $|U|$ respectively. Alternatively, a confidence region with a confidence level of $p_c = 90\%$ for the modulus of a response quantity $|U|$ can be defined such that:

$$P(|U_b| \leq |U| \leq |U_t|) \geq p_c \tag{13}$$

where the lower $|U_b|$ and the upper $|U_t|$ bounds can be obtained as the 5% and 95% percentiles of $|U|$ respectively from the Monte Carlo simulation results.

The (stochastic) spatial variability of the subsoil properties affects the structural response in two ways. First, the actual load that excites the structure is altered. Figure 11 shows the free field incident wave field that excites the R/C building in case of homogeneous subsoil conditions, and subsoil conditions as those depicted in Figure 10. Although the same excitation source S (Figure 6) is considered in both cases, the actual free field load that excites the building is different. This happens because, in the latter case, the spatial variability of the subsoil properties, with its inherent subsoil impedance contrasts (Equation 2), may give rise to constructive/destructive inference mechanisms that perturb the incident wave field.

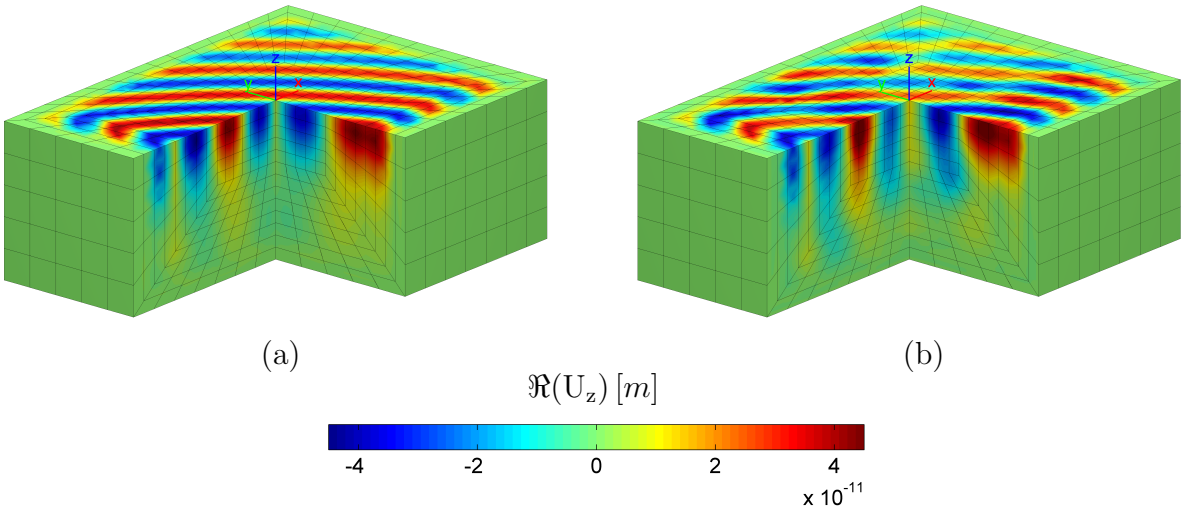

Figure 11: Free field displacements generated by the remote source S at 50 Hz. (a) Homogeneous subsoil conditions and (b) Stochastic realization with heterogeneous subsoil conditions.

Second, the modal characteristics of the coupled structure-soil system are modified. In the case where the loading on the structure is exactly the same for all stochastic subsoil realizations, any difference between the corresponding responses should be solely attributed to the influence that the spatial variability of the subsoil properties has on the modal characteristics of the system. This is demonstrated in Figure 12 which shows the response of node A_1 (Figure 5) in the

y direction in the case where the excitation is directly applied on the R/C building. Specifically, unit amplitude forces are simultaneously imposed on nodes A_1, A_2 and A_3 in the x, y and z directions (the subscripts of A stand for floor number). The mean value of $|U_{\mathrm{y}}|$ is plotted with the corresponding 90% confidence region as function of frequency. The response for five different stochastic subsoil realizations is also plotted. Figure 12b shows the CoV of $|U_{\mathrm{y}}|$ and the corresponding confidence 95% interval for this estimated statistics.

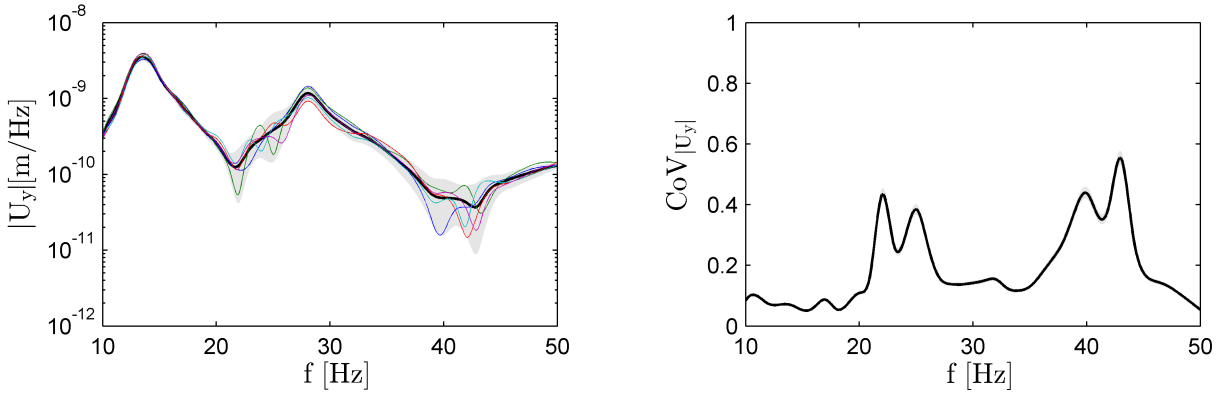

(a) (b)

Figure 12: Modulus of response of node A_1 in the y direction due to applied loading in the x, y and z directions on the nodes A_1, A_2 and A_3. (a) Mean value of response (solid line), the corresponding 90% confidence region of response (shaded area) and five realizations of response (colored lines). (b) Coefficient of variation of response (solid line) and 95% confidence interval for this statistical measure (shaded area).

In case the structure is excited by ground born vibrations, both of the aforementioned effects take place. Figures 13a and 14a show the responses of node A_1 (Figure 5) in the x and z direction, respectively, when the structure is excited by the remote source S (Figure 6). The mean value of $|U_{\mathrm{x}}|$ and $|U_{\mathrm{z}}|$ are plotted with the corresponding 90% confidence regions of response as functions of frequency. Additionally, Figures 13b and 14b show the CoV of $|U_{\mathrm{x}}|$ and $|U_{\mathrm{z}}|$ and the corresponding 95% confidence intervals for these estimated statistics.

A general trend observed in all figures, is that the structural response uncertainty increases at higher frequencies. However, there are certain frequency bands where the response of the coupled soil-structure system is found to be more sensitive to the subsoil properties. Similarly, there are other frequency bands in which the structural response is less sensitive. These frequency bands are not the same for every structural degree of freedom. From the mean response lines (Figures 13a, 14a and 12a), the uncertainty seems to increase at what looks to be the anti-resonance frequencies of the coupled structure-soil system. This can be misleading as these frequencies may correspond to eigenmodes of the coupled soil-structure system which are sensitive to the stochastic subsoil properties. This is demonstrated in Figure 12a, in which individual realization responses are plotted. Frequencies around 24Hz and 40Hz, which seem to be anti-resonance frequencies of the system in the mean response, are actually frequencies where the response of the coupled system is extremely sensitive to the subsoil properties.

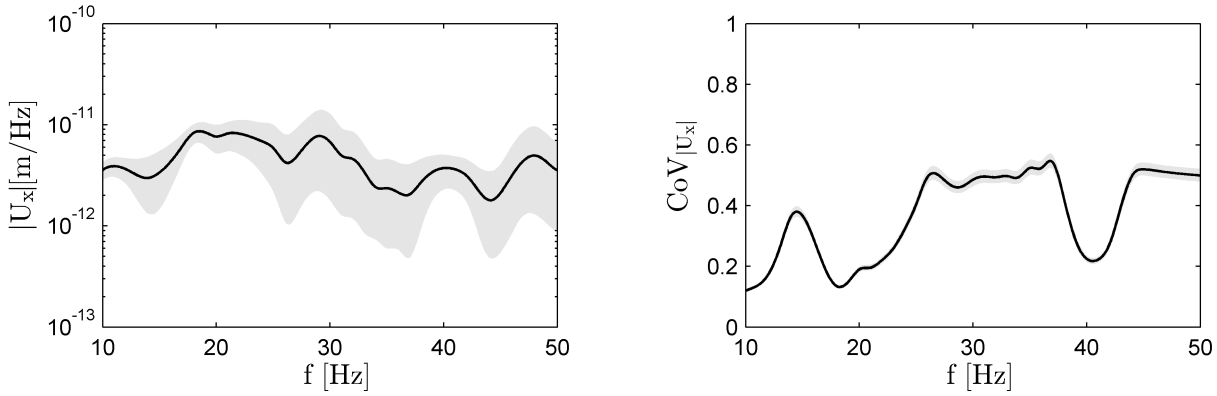

(a) (b)

Figure 13: Modulus of response of node A_1 in the x direction due to excitation by the remote source S. (a) Mean value of response (solid line) and the corresponding 90% confidence region of response (shaded area). (b) Coefficient of variation of response (solid line) and 95% confidence interval for this statistical measure (shaded area).

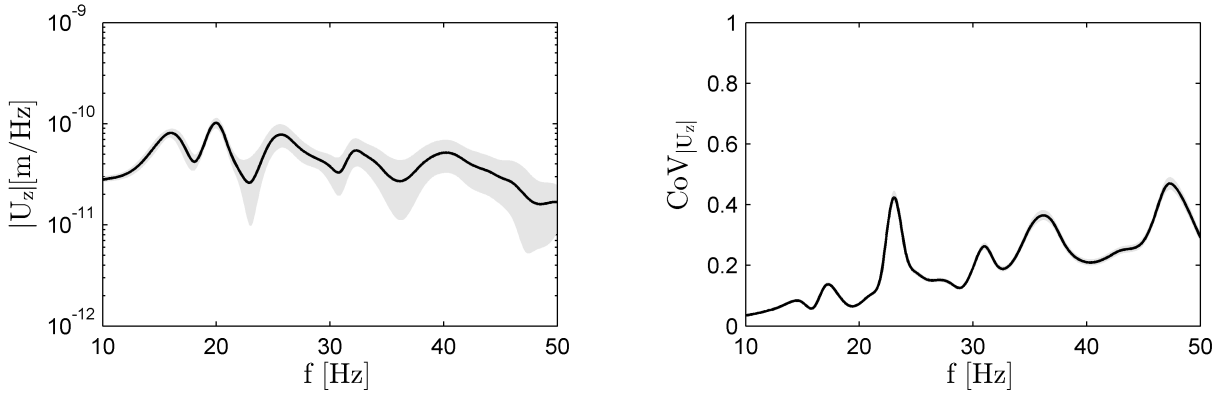

(a) (b)

Figure 14: Modulus of response of node A_1 in the z direction due to excitation by the remote source S. (a) Mean value of response (solid line) and the corresponding 90% confidence region of response (shaded area). (b) Coefficient of variation of response (solid line) and 95% confidence interval for this statistical measure (shaded area).

5 CONCLUSIONS

- A methodology is outlined for the direct formulation of the stochastic soil-structure interaction problem by means of coupled finite elements-perfectly matched layers. The model is suitable for analysis in a wide frequency range.
- The methodology is illustrated with a case study, the results of which set the base for future investigations. The two ways in which the stochastic spatial variability of the subsoil properties affects the structural response are, also, discussed.

- Generally, the structural response uncertainty increases at higher frequencies. However, the structural response sensitivity to the subsoil properties varies considerably over frequency bands.

REFERENCES

[1] D. Aubry, D. Clouteau, A subdomain approach to dynamic soil-structure interaction. In V. Davidovici , R.W. Clough editors, *Recent advances in earthquake engineering and structural dynamics*, p. 251-272, Ouest Editions/AFPS, Nantes, 1992.

[2] U. Basu, A.K. Chopra., Perfectly matched layers for time-harmonic elastodynamics of unbounded domains: theory and finite-element implementation. *Computer Methods in Applied Mechanics and Engineering*, **192(11-12)**, 13371375, 2003.

[3] R. Cottereau, D. Clouteau, C. Soize, S. Cambier Probabilistic nonparametric model of impedance matrices. Application to the seismic design of a structure. *European Journal of Computational Mechanics*, **15**, 131-142, 2006.

[4] R.W. Clough, J. Penzien, *Dynamics of structures*. Computers & Structures Inc., 2003.

[5] B. Efron, R. J. Tibshirani, *An Introduction to the Bootstrap*. Chapman & Hall, 1993.

[6] R.G. Ghanem, P.D. Spanos, *Stochastic Finite Elements: A Spectral Approach*. Springer-Verlag New York, 1991.

[7] M. Grigoriu, Crossings of non-Gaussian translation processes. *Journal of Engineering Mechanics*, **110(4)**, 610-620, 1984.

[8] S. Kucukcoban, L.F. Kallivokas, A symmetric hybrid formulation for transient wave simulations in PML-truncated heterogeneous media. *Wave Motion*, **50**, 57-79, 2013.

[9] C.C. Li, A. Der Kiureghian, Optimal discretization of random fields. *Journal of Engineering Mechanics*, **19(6)**, 11361154, 2003.

[10] P. Liu, A. Der Kiureghian, Multivariate distribution models with prescribed marginals and covariances. *Probabilistic Engineering Mechanics*, **1(2)**, 105-112, 1986.

[11] R.P Nordgren, J.P. Conte, On one-dimensional random fields with fixed end values. *Probabilistic Engineering Mechanics*, **14**, 301-310, 1999.

[12] A. M. J. Olsson, G. E. Sandberg, Latin hypercube sampling for stochastic finite element analysis. *Journal of Engineering Mechanics*, **128:(1)**, 121-125, 2002.

[13] M.H. Santare, P. Thamburaj, G.A. Gazonas, The use of graded finite elements in the study of elastic wave propagation in continuously nonhomogeneous materials. *International Journal of Solids and Structures*, **40**, 5621-5634, 2003.

[14] E. Savin, D. Clouteau, Elastic wave propagation in a 3D unbounded random heterogeneous medium coupled with a bounded medium. Application to seismic soilstructure interaction (SSSI). *International Journal for Numerical Methods in Engineering*, **54**, 607-630, 2002.

[15] M. Schevenels, G. Degrande, S. Francois, EDT: An ElastoDynamics Toolbox for MATLAB. *Computers & Geosciences*. In press. http://dx.doi.org/10.1016/j.cageo.2008.10.012

[16] G. Stefanou, The stochastic finite element method: Past, present and future. *Computational Methods in Applied Mechanics and Engineering*, **198**, 1031-1051, 2009.

[17] E. Vanmarcke, *Random Fields: Analysis and Synthesis*. MIT Press Classics, 1983.

[18] J.P. Wolf, *Dynamic soil-structure interaction*. Prentice-Hall, 1985.

ECCOMAS Congress 2016
VII European Congress on Computational Methods in Applied Sciences and Engineering
M. Papadrakakis, V. Papadopoulos, G. Stefanou, V. Plevris (eds.)
Crete Island, Greece, 5–10 June 2016

A MULTISCALE FRAMEWORK FOR THE STOCHASTIC ASSIMILATION AND MODELING OF UNCERTAINTY ASSOCIATED NCF COMPOSITE MATERIALS (ECCOMAS CONGRESS 2016)

Loujaine Mehrez[1], Roger Ghanem[1], Colin McAuliffe[2], William R Rodgers[3], and Venkat Aitharaju[3]

[1]Viterbi School of Engineering , University of Southern California,
210 KAP Hall, University of Southern California, Los Angeles, CA 90089, USA.
e-mail: {lmehrez,ghanem}@usc.edu

[2] Altair Engineering, Inc.
Altair Engineering, Inc, Troy MI 48083
e-mail: cmcauliffe@altair.com

[3] General Motors Company, GM R&D Technical Center
30500 Mound Rd, Warren, MI 48092, USA
e-mail: {william.r.rodgers,venkat.aitharaju}@gm.com

Keywords: multiscale homogenization, micro- meso- and macro-scales, stochastic assimilation, uncertainty propagation, NCF composite materials, polynomial chaos expansion.

Abstract. *A multiscale framework to construct stochastic macroscopic constitutive material models is proposed. A spectral projection approach, specifically polynomial chaos expansion, has been used to construct explicit functional relationships between the homogenized properties and input parameters from finer scales. A homogenization engine embedded in Multiscale Designer, software for composite materials, has been used for the upscaling process. The framework is demonstrated using non-crimp fabric composite materials by constructing probabilistic models of the homogenized properties of a non-crimp fabric laminate in terms of the input parameters together with the homogenized properties from finer scales.*

1 INTRODUCTION

Conventional approaches to perform multiscale designs have been to average over the fluctuations of the material properties throughout the scales. In these approaches it is possible to deduce the constitutive material properties at the macroscopic scale from information available at finer scales [1], where the properties are computed by averaging over fluctuations in the stress response of the material. For instance, to deduce the material properties of continuous non-crimp fabric (NCF) composite materials, the averaged homogenized properties of a unit cell of a unidirectional lamina (consisting of a tow surrounded by resin within a bounded volumetric unit), at the so-called meso-scale are required. These meso-scale properties of the tow are in turn homogenized properties from its constituents at a finer scale, i.e., micro- scale.

Robust designs for such complex systems, where properties across scales matter, require reliable accounting of the material features as well as the fluctuations and uncertainties associated with the description and the performance of the constitutive representations at the various scales of interest. The main objective of this work is to propose a multiscale framework that is able to account for uncertainties associated with finer scales explicitly. The multiscale framework is demonstrated by performing stochastic modeling of an NCF composite material across multiple scales. Specifically, the uncertainties associated with three hierarchical scales have been assimilated from available measurements and propagated throughout the scales. A Polynomial Chaos (PC) spectral projection approach [2] has been used to construct the hierarchical functional relationships throughout the scales. The hierarchy of the scales starts at the scale of the fibers and resin within the tows and goes upward to construct stochastic constitutive models of a laminate or a structure composed of composite laminates. A homogenization engine embedded in Multiscale Designer [3], software for composite materials, has been used for the upscaling process. The proposed framework (i) is suitable for the modeling and analysis of composite materials, (ii) can be generalized to account for the behavior of physical systems containing composite parts, and (iii) can be incorporated in inverse calibration frameworks.

2 DEFINITION OF THE COMPOSITE MATERIALS

The proposed multiscale framework is used to construct probabilistic models of composite laminates that are up-scaled across multiple scales. The composite laminates consist of eight laminae made of continuous non-crimp fabric (NCF). That is, each lamina is composed of continuous unidirectional tows and resin. The carbon fiber tows are made of 12K fibers (T700SC 12000 50C). The laminate is designed to be symmetric such that the laminae are oriented as $[0/45/-45/90/90/-45/45/0]$.

3 DEFINITION OF THE SCALES AND THE RESPECTIVE ASSOCIATED PARAMETERS

The NCF laminate, used in this study, is composed of 8 laminae. Each lamina is composed of unidirectional tows and resin. The tows are composed of fibers with resin filling the space between the fibers. Thus, the properties of the fibers and resin are required to predict the constitutive properties of the tows. Then, the properties of the composite tows and those of the resin again are required to predict the constitutive properties of the NCF unidirectional lamina, which in turn together with other laminae, being oriented according to a certain layout, are required to predict the constitutive properties of the eight-layer laminate. The chart depicted in Figure 1 defines the multiple scales involved in the aforementioned upscaling process.

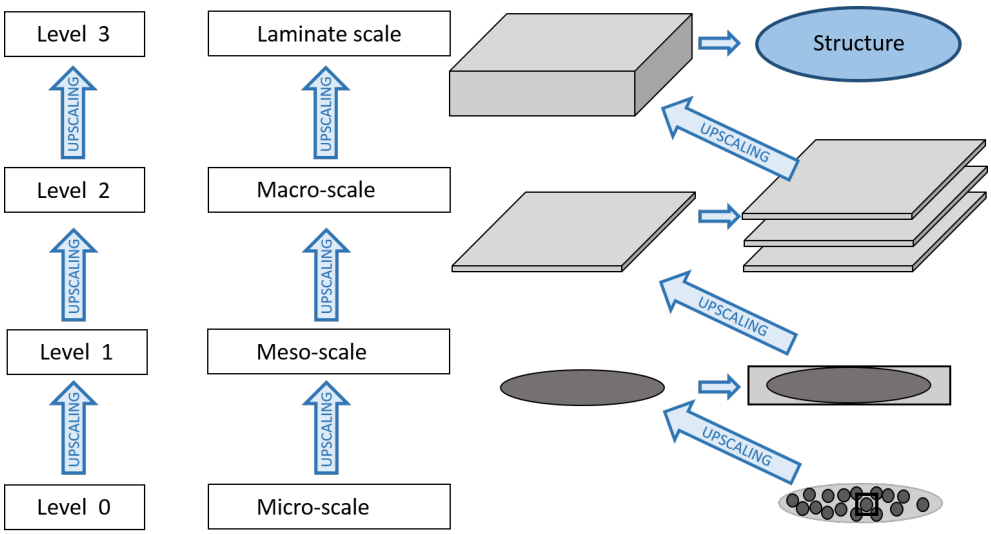

Figure 1: Schematic definition of the multiple scales.

The input parameters at each scale are grouped as (a) the parameters introduced at the scale (l) and which are characterized from available data at this scale, and (b) the parameters that are up-scaled from level ($l-1$). The parameters belonging to the first group are denoted by $\mathbf{P}^l$, where l refers to the respective scale. These groups are specific inputs to each level l; i.e., $\mathbf{P}^0$ is a group of inputs at level 0, and so on. The parameters belonging to the second group are denoted by $\mathbf{Q}^l$. The parameters from this group are input parameters at level l that have been obtained via an upscaling process from level $l-1$ to level l. The parameters from both groups are defined in the following subsections at each level.

3.1 Input parameters associated with level $l = 0$

The set of input parameters at level $l = 0$, $\mathbf{P}^0$, consists of three groups $\mathbf{P}^0_g$, $\mathbf{P}^0_f$,and $\mathbf{P}^0_m$ representing the parameters associated with the geometry of the unit cell, the material properties of transverse isotropic fibers, and the material properties of isotropic matrix, respectively.

Group	Parameter	Description
$\mathbf{P}^0_g$	$V_f^{F,T}$ %	Volume fraction of fiber within the tow
$\mathbf{P}^0_f$	$E_{f,A}$	Axial Young's modulus of fibers
	$E_{f,T}$	Transverse Young's modulus of fibers
	$G_{f,A}$	Axial shear modulus of fibers
	$\nu_{f,A}$	Axial Poisson's ratio of fibers
	$\nu_{f,T}$	Transverse Poisson's ratio of fibers
$\mathbf{P}^0_m$	E_m	Young's modulus of the matrix
	ν_m	Poisson's ratio of the matrix

Table 1: Input parameters $\mathbf{P}^0$ at level $l = 0$.

These parameters are modeled by uniform random variables. The volume fraction of fibers within the tow is denoted by $V_f^{F,T}$. The subscripts A and T, used with the tow material properties, denote the axial and transverse properties, respectively.

3.2 Input parameters associated with level $l = 1$

The set of input parameters at level $l = 1$, $\mathbf{P}^1$, consists of two groups $\mathbf{P}^1_g$ and $\mathbf{P}^1_m$ representing the parameters associated with the geometry of the unit cell in a NCF lamina and the material properties of an isotropic matrix, respectively. These parameters are modeled by uniform random variables.

Group	Parameter	Description
$\mathbf{P}^1_m$	E_m	Young's modulus of the matrix
	ν_m	Poisson's ratio of the matrix
$\mathbf{P}^1_g$	D_a	Major diameter of the tow
	d_a	Free distance along the major axis
	D_b	Minor diameter of the tow

Table 2: Input parameters $\mathbf{P}^1$ at level $l = 1$.

The geometry parameters define the dimensions of the unit cell of a NCF unidirectional lamina and are listed in Table 2. These are illustrated by the drawing in Figure 2, where D_a and D_b refer to the diameters of the tow along the major and minor directions, d_a and d_b refer to the gap between the tows along the major and minor directions, which are filled in by the matrix. Here, d_b is assumed to be constant and equal to $0.1\ mm$. The dimensions of the unit cell are denoted by $S_a = D_a + d_a$ and $S_b = D_b + d_b$.

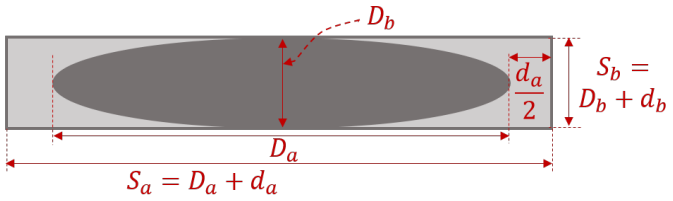

Figure 2: A schematic drawing of a unit cell in a NCF unidirectional lamina.

In addition, another set of input parameters at this scale is $\mathbf{Q}^1$, the set of homogenized material properties of the tow. These are the outcome of the homogenization H_1 associated with the upscaling process from level $l = 0$ to level $l = 1$.

Group	Parameter	Description
$\mathbf{Q}^1$	$E_{t,A}$	Axial Young's modulus of tow
	$E_{t,T}$	Transverse Young's modulus of tow
	$G_{t,A}$	Axial shear modulus of tow
	$\nu_{t,A}$	Axial Poisson's ratio of tow
	$\nu_{t,T}$	Transverse Poisson's ratio of tow

Table 3: Input parameters $\mathbf{Q}^1$ at level $l = 1$.

The material properties of the homogenized tow, which manifest a transverse isotropic symmetry, are denoted by $\mathbf{Q}^1 = (E_{t,A},\ E_{t,T},\ G_{t,A},\ \nu_{t,T},\ \nu_{t,A})$; where the subscript t refers to the tow and the subscripts A and T refer to the axial and transverse properties, respectively.

3.3 Input parameters associated with level $l = 2$

The input parameters at level $l = 2$, $\mathbf{P}^2$, consists of the geometry layout of the laminae within the eight-layer laminate, $\mathbf{P}^1_g$. The orientation of the unidirectional laminae is defined as $[0/45/-45/90]_s$, where the upper and lower laminae are oriented along the 0^o axis. The number of laminae is fixed for the laminate analyzed in this paper. The orientation of each lamina is also considered constant at this stage.

Moreover, the other set of input parameters at this scale, $\mathbf{Q}^2$, is the set of homogenized material properties of a unidirectional NCF lamina. These are the outcome of the homogenization H_2 associated with the upscaling process from level $l = 1$ to level $l = 2$. The material properties of the homogenized lamina, which are expected to manifest a transverse isotropic symmetry, are denoted by $\mathbf{Q}^2 = (E_{l,A},\ E_{l,T},\ G_{l,A},\ \nu_{l,T},\ \nu_{l,A})$; where the subscript l refers to the lamina and the subscripts A and T refer to the local axial and transverse properties, respectively.

Group	Parameter	Description
$\mathbf{Q}^2$	$E_{l,A}$	Axial Young's modulus of NCF lamina
	$E_{l,T}$	Transverse Young's modulus of NCF lamina
	$G_{l,A}$	Axial shear modulus of NCF lamina
	$\nu_{l,A}$	Axial Poisson's ratio of NCF lamina
	$\nu_{l,T}$	Transverse Poisson's ratio of NCF lamina

Table 4: Input parameters $\mathbf{Q}^2$ at level $l = 2$.

3.4 Output parameters associated with level 3

The layout of the laminate, $[0/45/-45/90]_s$, is designed to have quasi-isotropic material properties. These are grouped in $\mathbf{Q}^3$ and are: (1) $E_{xx} = E_{yy}$, (2) E_{zz} , (3) $G_{yz} = G_{xz}$, (4) G_{xy}, (5) $\nu_{xy} = \nu_{yx}$, (6) $\nu_{xz} = \nu_{yz}$, and (7) $\nu_{zx} = \nu_{zy}$.

4 HOMOGENIZATION APPROACH

A homogenization engine embedded in Multiscale Designer, software for composite materials, has been used for the upscaling process [3]. The multiscale design system enables the analysis and design of material systems, such as composite materials given their microstructure. An appropriate unit cell morphology is selected for each of the tow homogenization and the lamina homogenization, respectively.

5 MULTI-SCALE STOCHASTIC ASSIMILATION USING A SPECTRAL PROJECTION APPROACH

The homogenized properties of the laminate are obtained by upscaling the material and geometry parameters of the ordered laminae. The material properties of a lamina are obtained using a homogenization protocol that upscales the material and geometry parameters of a unit cell representing a lamina and consisting of a unidirectional tow. The homogenized material

properties of a tow are also obtained using a similar homogenization protocol that upscales the geometry and material properties of a unit cell of fibers and resin.

This hierarchy of upscaling processes is addressed in this current work by propagating uncertainties associated with parameters from each scale to construct probabilistic models of the homogenized material properties of the laminate. It is worth noting that the proposed hierarchical framework is not confined to the eight-layer laminate addressed in this paper. It is a general framework that can be applied to other composite materials or any heterogeneous material where fluctuations observed at coarse scales are influenced by fluctuations present at multiple finer scales.

The propagation of uncertainties across the scales has been carried out using a Non-Intrusive Spectral Projection (NISP) approach [4]. The NISP approach enables probabilistic models of the engineering constants representing the homogenized material properties of a laminate as well as the homogenized properties at lower levels. In other words, stochastic surrogate models could be constructed to approximate the functional relationship of the parameters $\mathbf{Q}^l$, l denotes the corresponding level, in terms of the input parameters at the finer scales (lower levels); i.e., $\mathbf{Q}^3$ can be expressed in terms of $\mathbf{P}^0$, $\mathbf{P}^1$, and $\mathbf{P}^2$ instead of $\mathbf{P}^2$ and $\mathbf{Q}^2$. This is achieved by projecting the stochastic properties $\mathbf{Q}^l$ on a finite-dimensional stochastic space, Θ, through an orthogonal projection. The dimension of this stochastic space equals the dimension of the grouped input variables $\mathbf{P} = \{\mathbf{P}^0,\ \mathbf{P}^1,\ \cdots,\ \mathbf{P}^{l-1}\}$. To do so, a mapping of $\mathbf{Q}^l$ to a probability space, Θ, can be expressed in terms of a truncated polynomial chaos (PC) expansion [2] as,

$$\mathbf{Q}^l\left(\xi\right) = \sum_{j=0}^{N_{pc}} \mathbf{q}_j^l\ \Psi_j(\xi), \tag{1}$$

where, $l = 1,\ 2,\ or\ 3$ refers to the level of upscaled parameters $\mathbf{Q}^l$, and $\Psi_j(\xi)$ is the PC basis which consists of a set of normalized multi-dimensional orthogonal polynomials in ξ; ξ is a vector grouping normalized standard variables. The mapping between ξ and the independently-assumed random variables $\mathbf{P}^i$, introduced in the previous sections at the finer scales i, is defined such that $\Phi^{\xi}\left(\boldsymbol{\xi}\right) = \Phi^{P}\left(\mathbf{P}\right)$. The parameters $\mathbf{q}_j^l$ are the projection coefficients and $N_{pc}+1$ is the dimension of the PC terms, which can be defined in terms of the PC order q and the stochastic dimension N_{rv} denoting the size of vector ξ.

The orthogonality condition can be expressed in terms of the inner product, defined on the stochastic space Θ, as,

$$\langle \Psi_i(\xi), \Psi_j(\xi) \rangle = \langle \Psi_j(\xi), \Psi_j(\xi) \rangle\ \delta_{ij}, \tag{2}$$

where,

$$\langle u, v \rangle = \int_{\Theta} u(\xi)\ v(\xi)\ p_{\xi}(\xi)\ d\xi, \tag{3}$$

The projection coefficients $\mathbf{q}_j^l$ at level l can be expressed, given the orthogonality of the basis, in terms of the following inner products,

$$\mathbf{q}_j^l = \frac{\left\langle \mathbf{Q}^l(\xi), \Psi_j(\xi) \right\rangle}{\left\langle \Psi_j(\xi), \Psi_j(\xi) \right\rangle},\ j = 0, 1, ..., N_{pc}. \tag{4}$$

To estimate $\left\langle \mathbf{Q}^l(\xi), \Psi_j(\xi) \right\rangle$, a sparse grid cubatures (SGC) approach could be used [4]. According to this approach, N_{sgc} sets of ξ realizations and associated weights are generated; $\xi^{(i)}$ and $w_i,\ i = 1,\ \cdots,\ N_{sgc}$ [5]. The dimension of each set N_{sgc} is a function of the stochastic dimension N_{rv} and the level of the sparse grid cubatures L. Thus,

$$q_j^l = \sum_{i=1}^{N_{sgc}} w_i\ \mathbf{Q}^l(\xi^{(i)})\ \Psi_j(\xi^{(i)})\ ,\ j = 1,\ \cdots,\ N_{pc}. \tag{5}$$

The spectral representation defined in eqation 1 is then fully identified in terms of the PC coefficients. The mean values, $\overline{\mathbf{Q}}^l$, and variances, $Var\left[\mathbf{Q}^l\left(\xi\right)\right]$, of the projected quantities of interest can be estimated, given the orthogonality of the basis, respectively, as,

$$\overline{\mathbf{Q}}^l = \mathbf{q}_j^0. \tag{6}$$

$$Var\left[\mathbf{Q}^l\left(\xi\right)\right] = \sum_{j=1}^{N_{pc}} {\mathbf{q}_j^l}^2. \tag{7}$$

6 EXAMPLE AND DISCUSSION

As explained in the previous section, it is possible to express the homogenization output at multiple scales ($\mathbf{Q}^l$, $\mathbf{Q}^2$, and $\mathbf{Q}^3$) using the same set of SGC nodes. First, the quantities of interest are computed at a set of SGC nodes, each of which consists of a combination of input parameters reported earlier for each scale. The process is repeated for increasing values of the SGC level in order to determine the appropriate SGC level. Second, at each of the given SGC levels, a set of respective polynomial chaos coefficients are estimated using equation 5. The estimated coefficients of (i) the axial modulus of a homogenized tow, $E_{t,A}$ from level $l = 1$, (ii) the axial modulus of a homogenized NCF lamina, $E_{l,A}$ from level $l = 2$, and (iii) the axial modulus of a homogenized NCF laminate E_{xx} from level $l = 3$ are plotted in Figures 3 to 5, respectively. The x-axis represents the index of the terms in the polynomial chaos expansion while the y-axis represents the value of the coefficients. The axial indices 1 to 11 correspond to the coefficients of the linear terms in the polynomial chaos representation. The coefficients are plotted for a set of polynomial chaos orders ranging from 1 to 3.

It is clearly shown that the nodes associated with SGC level 3 are sufficient to identify the coefficients $\mathbf{q}_j^l$. It can also be concluded that the contributions of some second order terms and possibly third order terms in the expansion are important for accurate representation of some homogenized properties at the different scales. To corroborate this conclusion, the probability density functions (PDFs) of the homogenized axial moduli at homogenization levels $l = 1$, $l = 2$, and $l = 3$ are plotted in Figure 6. The Figures show that the axial modulus of the homogenized tow at level $l = 1$ could be expressed as a linear combination of some of the input variables since the PDF curves associated with orders 1 to 3 are converged. However, the PDF curves of the axial moduli of the lamina, $l = 2$, and the laminate, $l = 3$, show that a second order polynomial chaos representation is appropriate, which indicates that some second order terms in the expansion contribute to these homogenized properties.

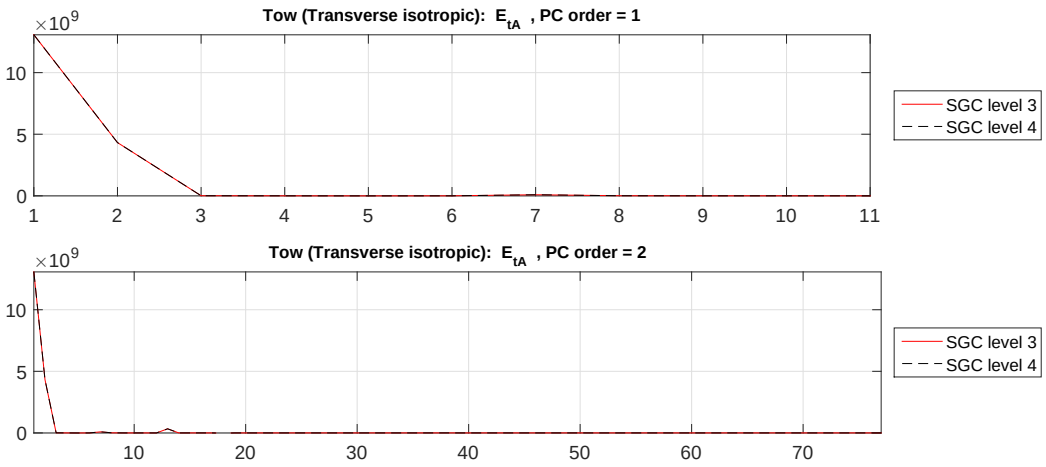

Figure 3: The PC coefficients q_j^1 for $E_{t,A}$.

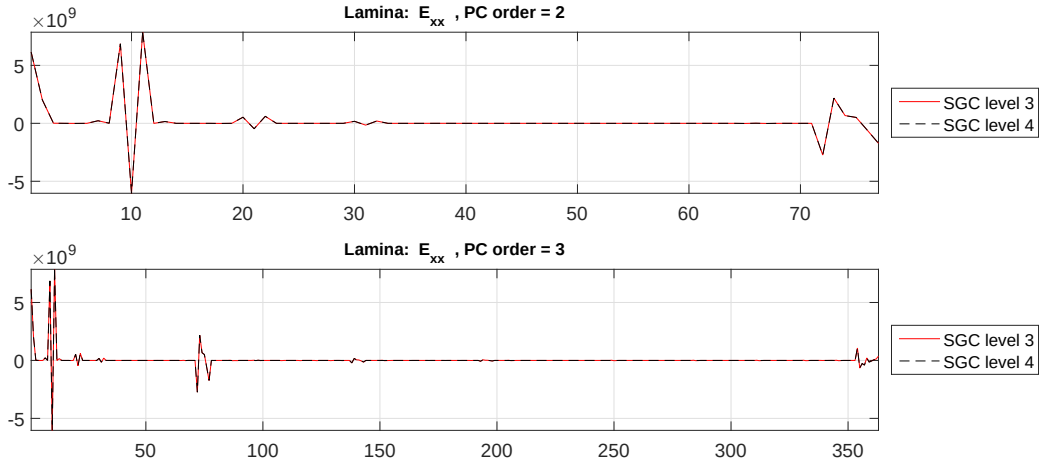

Figure 4: The PC coefficients q_j^2 for $E_{l,A}$.

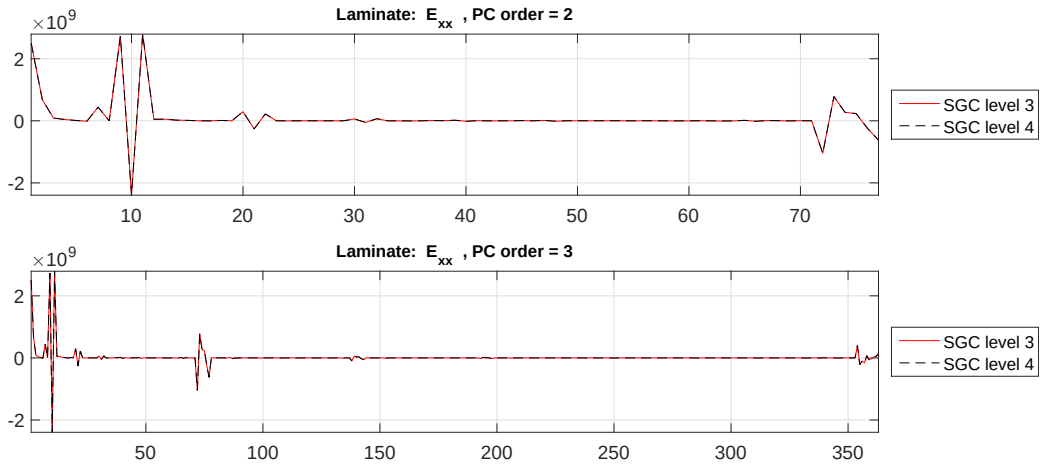

Figure 5: The PC coefficients q_j^3 for $E_{xx} = E_{yy}$.

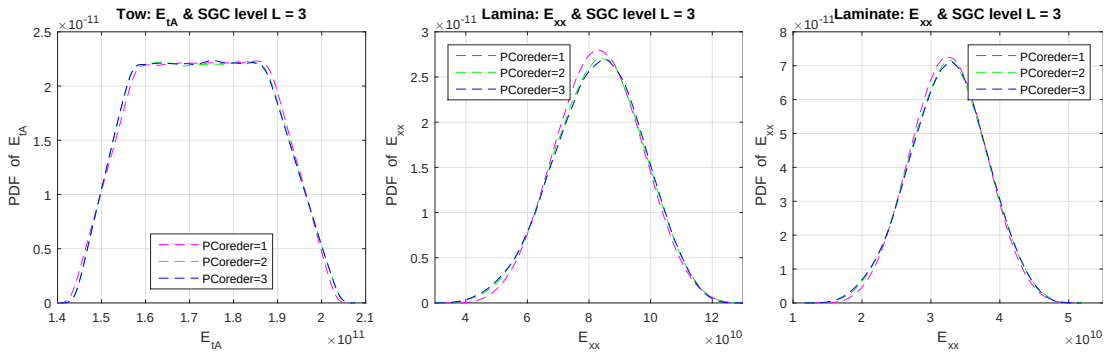

Figure 6: PDF curves for the axial elastic moduli: (left) $E_{tA} \in \mathbf{Q}^1$ (middle) $E_{lA} = E_{xx} \in \mathbf{Q}^2$ (right) $E_{xx} \in \mathbf{Q}^3$

7 CONCLUSIONS

It is shown that polynomial chaos expansion is able to characterize properties at a coarse scale in terms of fluctuations associated with properties from one or more finer scales. This characterization is achieved in terms of an analytical form of functional relationships with the underlying variables at the finer scales.

It is worth noting that the proposed hierarchical framework is not confined to the eight-layer laminate addressed in this paper. It is a general framework that can be applied to other composite materials or any heterogeneous material where fluctuations observed at coarse scales are influenced by fluctuations present at multiple finer scales.

The proposed framework (i) is suitable for the modeling and analysis of composite materials, (ii) can be generalized to account for the behavior of physical systems containing composite parts, (iii) enables analytical forms that can be readily used in sensitivity analyses, and (iv) can be incorporated in inverse calibration frameworks.

8 ACKNOWLEDGMENTS

The information, data, or work presented herein was funded in part by the Office of Energy Efficiency and Renewable Energy (EERE), U.S. Department of Energy, under Award Number DE-EE0006826. The information, data, or work presented herein was funded in part by an agency of the United States Government. Neither the United States Government nor any agency thereof, nor any of their employees, makes any warranty, express or implied, or assumes any legal liability or responsibility for the accuracy, completeness, or usefulness of any information, apparatus, product, or process disclosed, or represents that its use would not infringe privately owned rights. Reference herein to any specific commercial product, process, or service by trade name, trademark, manufacturer, or otherwise does not necessarily constitute or imply its endorsement, recommendation, or favoring by the United States Government or any agency thereof. The views and opinions of authors expressed herein do not necessarily state or reflect those of the United States Government or any agency thereof.

REFERENCES

[1] J. Fish, *Practical Multiscaling*. John Wiley & Sons, Ltd., 2014.

[2] R. Ghanem, and P. Spanos, *Stochastic Finite Elements: A Spectral Approach*. Springer Verlag, New York, 1991.

[3] Altair MDS, *http://www.altair.com/*. Altair, 2015.

[4] O.P. Le maitre, and O.M. Knio, *Spectral methods for Uncertainty Quantification*. Springer, New York, 2010.

[5] Dakota, *http://dakota.sandia.gov/*. Algorithms for design exploration and simulation credibility, 2016.

ECCOMAS Congress 2016
VII European Congress on Computational Methods in Applied Sciences and Engineering
M. Papadrakakis, V. Papadopoulos, G. Stefanou, V. Plevris (eds.)
Crete Island, Greece, 5–10 June 2016

A MULTI-FIDELITY ADAPTIVE SAMPLING METHOD FOR METAMODEL-BASED UNCERTAINTY QUANTIFICATION OF COMPUTER SIMULATIONS

Riccardo Pellegrini[1,2], Cecilia Leotardi[1], Umberto Iemma[2], Emilio F. Campana[1] and Matteo Diez[1]

[1]CNR-INSEAN, Natl. Research Council-Marine Technology Research Institute
Via di Vallerano 139, Rome, Italy
e-mail: c.leotardi@insean.it, {emiliofortunato.campana,matteo.diez}@cnr.it

[2] Roma Tre University, Dept. of Engineering
Via Vito Volterra 62, Rome, Italy
e-mail: {riccardo.pellegrini,umberto.iemma}@uniroma3.it

Keywords: Uncertainty Quantification, Multi-Fidelity Metamodel, Adaptive Sampling Method, Fluid-Structure Interaction.

Abstract. *A multi-fidelity global metamodel is presented for uncertainty quantification of computationally expensive simulations. The multi-fidelity approximation is built as the sum of a low-fidelity-trained metamodel and the metamodel of the difference (error) between high- and low-fidelity simulations. The metamodel is based on dynamic stochastic radial basis functions, which provide the prediction along with the associated uncertainty. New training points are added where the prediction uncertainty is largest, according to an adaptive sampling procedure. The prediction uncertainty of both the low-fidelity and the error metamodel are considered for the adaptive training of the low- and high-fidelity metamodels, respectively. The method is applied to a steady fluid-structure interaction (FSI) problem of a 3D NACA 0009 stainless steel hydrofoil. Two functions are considered simultaneously, namely lift and drag coefficients, versus angle of attack and Reynolds number. Two problems are presented: in the first problem the high-fidelity evaluations are obtained through steady FSI computer simulations, whereas in the second problem they are given by available experimental data from literature. Low-fidelity evaluations are provided in both cases by steady hydrodynamic simulations. The overall uncertainty of the multi-fidelity metamodel is used as a convergence criterion.*

1 INTRODUCTION

The simulation-based design (SBD) process of complex engineering systems (such as aerial, ground or maritime vehicles) requires computationally expensive physics-based solvers, in order to achieve accurate solutions. When dealing with real-world applications, most of the relevant inputs and outputs are affected by uncertainty, which stems from operational and environmental conditions, geometrical tolerances, numerical and/or modelling errors. Therefore, uncertainty quantification (UQ) methods are required, in order to assess the effects of uncertain parameters on the relevant outputs. Earlier uncertainty studies addressed deterministic uncertainty analysis (UA) for numerical and modelling errors [1, 2, 3]. More recently, the research moved to stochastic UQ for environmental and operating conditions. Stochastic UQ studies using high-fidelity simulations for ship hydrodynamic problems have been presented in [4, 5, 6, 7].

In design optimization, high-fidelity solvers and UQ methods are integrated with single/multi-objective local/global minimization/maximization algorithms, which may require a large number of computer simulations (and high computational cost) in order to converge to the final solution [7, 8, 9]. UQ and design optimization with high-fidelity solvers still represent a technological challenge and require efficient methods and implementations.

In order to reduce the computational cost, metamodelling methods have been developed and successfully applied in several engineering fields [10, 11, 12]. In addition to metamodels, multi-fidelity approximation methods have been developed with the aim of combining to some extent the accuracy of high-fidelity solvers with the computational cost of low-fidelity solvers [13, 14, 15], or the accuracy of experiments (high-fidelity data) and computer simulations (low-fidelity) [16]. Multi-fidelity approximations for uncertainty quantification have been successfully investigated in [17] and applied in maritime [18] and industrial problems [19]. Furthermore, multi-fidelity metamodels have been successfully used for design optimization [20, 21, 22].

The objective of the present work is to present a multi-fidelity global metamodel, which manages high- and low-fidelity solvers through a multi-fidelity adaptive sampling procedure. The method is developed as an essential part of efficient uncertainty quantification of computationally expensive computer simulations. The current method is an extension to multiple functions [23] of the work presented in [24].

The multi-fidelity approximation is built as the sum of a low-fidelity-trained metamodel and the metamodel of the difference (error) between high- and low-fidelity evaluations. The metamodel is based on the dynamic stochastic radial basis function (RBF) method, presented in [23] for uncertainty quantification and extended to design optimization in [25]. The method provides the prediction and the associated uncertainty. The adaptive sampling procedure is driven by the maximum absolute value of the uncertainty, evaluated for each multi-fidelity metamodel. The prediction uncertainty of both the low-fidelity and the error metamodel is used for the adaptive refinement of the low- and high-fidelity training sets. High- or low-fidelity simulations are computed, depending on the relative uncertainty of error and low-fidelity metamodels.

The method is applied to a steady fluid-structure interaction (FSI) problem, used as a benchmark both for experimental [26] and simulation-based shape design optimization studies, using high-fidelity solvers [27]. Herein, the performances of the 3D NACA 0009 stainless steel hydrofoil are addressed in terms of lift and drag coefficients versus the angle of attack (AoA) and the Reynolds number (Re). Two problems are presented. The first problem addresses lift and drag coefficients using high- and low-fidelity simulations. Specifically, high-fidelity evaluations are provided by steady FSI simulations and low-fidelity evaluations are given by

steady hydrodynamic simulations with fixed geometry. The second problem addresses the same functions using available experimental data [26] as high-fidelity evaluations. Both high- and low-fidelity simulations are performed by finite element method (FEM) using the commercial code COMSOL Multiphysics^{TM}. A preliminary structural and hydrodynamic characterization of the current hydrofoil has been provided in [28].

2 MULTI-FIDELITY ADAPTIVE METAMODEL

Considering n functions (relevant outputs), the multi-fidelity metamodel is defined as

$$\begin{aligned} \hat{f}_i(\mathbf{x}) &= \tilde{f}_{i,L}(\mathbf{x}) + \tilde{\delta}_i(\mathbf{x}),\ i = 1, \ldots, n \\ \delta_i(\mathbf{x}) &= f_{i,H}(\mathbf{x}) - f_{i,L}(\mathbf{x}),\ i = 1, \ldots, n \end{aligned} \tag{1}$$

where $\mathbf{x} \in \mathbb{R}^n$ is the independent variable (uncertain parameter), superscript $\sim$ denotes the RBF prediction, and δ_i is the difference (error) between high- and low-fidelity simulations (respectively, $f_{i,H}$ and $f_{i,L}$ with $i = 1, \ldots, n$).

The uncertainty associated with the prediction provided by the multi-fidelity metamodel of the i-th function is defined as

$$U_{\hat{f}_i}(\mathbf{x}) = \sqrt{U^2_{\tilde{f}_{i,L}}(\mathbf{x}) + U^2_{\tilde{\delta}_i}(\mathbf{x})} \tag{2}$$

where $U_{\tilde{f}_{i,L}}$ and $U_{\tilde{\delta}_i}$ are the uncertainties associated to the prediction of the i-th function, provided by the low-fidelity and error metamodels ($\tilde{f}_{i,L}$ and $\tilde{\delta}_i$), respectively [23].

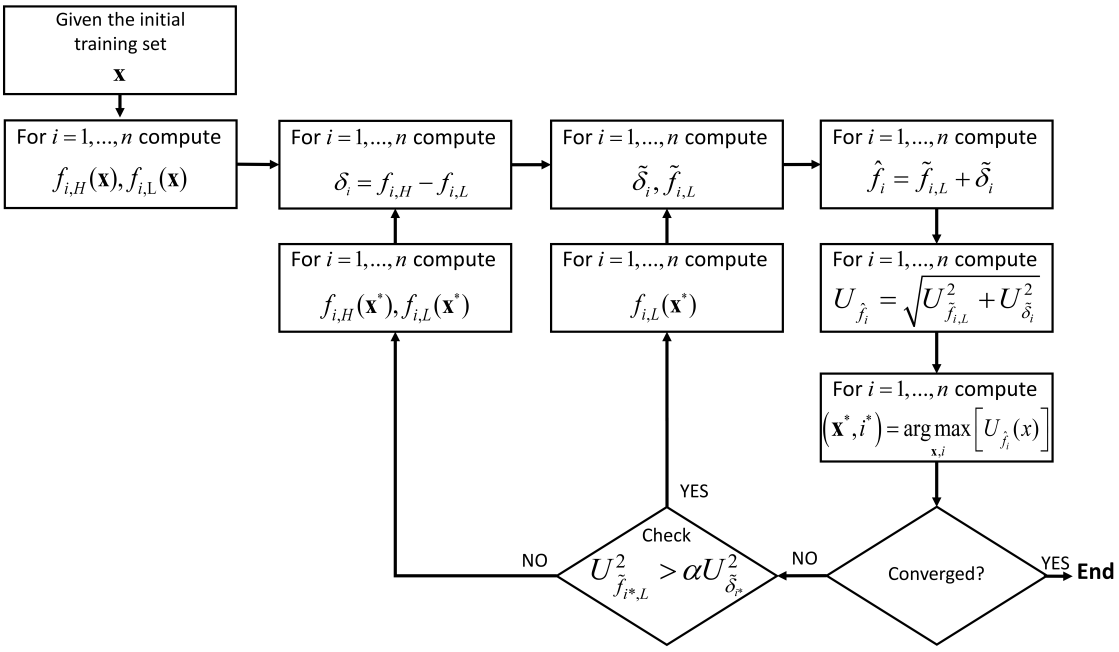

Figure 1: Multi-fidelity metamodel adaptive sampling procedure.

The multi-fidelity metamodel is trained using the adaptive procedure shown in Fig. 1. After initialization, a new sample is added to the training set at each iteration, solving the following

problem:

$$(\mathbf{x}^*, i^*) = \underset{\mathbf{x},i}{\operatorname{argmax}}[U_{\hat{f}_i}(\mathbf{x})] \tag{3}$$

Once $\mathbf{x}^*$ and i^* are evaluated, the training sets H and/or L (high- and low-fidelity, respectively) are updated as

$$\begin{cases} \text{If } U^2_{\tilde{f}_{i^*,L}}(\mathbf{x}^*) \geq \alpha U^2_{\tilde{\delta}_{i^*}}(\mathbf{x}^*), \text{ then add } \mathbf{x}^* \text{ to } L \\ \text{If } U^2_{\tilde{f}_{i^*,L}}(\mathbf{x}^*) < \alpha U^2_{\tilde{\delta}_{i^*}}(\mathbf{x}^*), \text{ then add } \mathbf{x}^* \text{ to } H \text{ and } L \end{cases} \tag{4}$$

where $\alpha \in$[0, 1] is an arbitrary tuning parameter, related to the ratio of the computational cost of the low- and high-fidelity simulations.

3 STOCHASTIC RADIAL BASIS FUNCTIONS

The prediction $\tilde{f}$ is evaluated as the expected value of a set of stochastic RBF predictions [23], which depend on the stochastic parameter $\epsilon \sim \text{unif}[1, 3]$:

$$\tilde{f}(\mathbf{x}) = E[g(\mathbf{x}, \epsilon)]_\epsilon \tag{5}$$

with

$$g(\mathbf{x}, \epsilon) = \sum_{i=1}^{m} w_i \, \varphi(\mathbf{x} - \mathbf{x}_i) \tag{6}$$

where m is the size of the training set, $\mathbf{x}_i$ are the training points, $\varphi(\cdot) = \|\cdot\|^\epsilon$, and $\|\cdot\|$ is the Euclidean norm. The coefficients w_i are obtained by the linear system $\mathbf{A}\mathbf{w} = \mathbf{y}$ with $\mathbf{w} = \{w_i\}$. The elements of the matrix $\mathbf{A}$ are $a_{ij} = \varphi(\mathbf{x}_i - \mathbf{x}_j)$ and the vector $\mathbf{y} = \{y_i\}$ collects the function evaluations at the training points, $y_i = f(\mathbf{x}_i)$.

The uncertainty associated to the metamodel prediction, $U(\mathbf{x})$, is quantified at each $\mathbf{x}$ as the 95%-confidence interval of $g(\mathbf{x}, \epsilon)$. This may be evaluated using a Monte Carlo sampling over ϵ, as shown in [23].

4 APPLICATION: NACA 0009 STAINLESS STEEL HYDROFOIL

The FSI problem presented by [26] is used herein to demonstrate the method. Specifically, the performances of a 3D NACA 0009 stainless steel hydrofoil are addressed in terms of lift and drag coefficients (C_L, C_D). C_L, C_D are evaluated versus AoA and Re (2D problem), respectively varying within [-1, 15] deg and [2E5, 6E5], which represent a subdomain of experimental data provided by [26] (AoA $\in$ [-15, 15] deg and Re $\in$ [2E5, 1E6]). Both the range of variation have been selected according to the outcomes provided by [26]. Specifically, it was observed that pre-stall forces are Re dependent only for Re$\leq$8E5 (although the dependence is weak).

The model main particulars are: root, mid and tip chords respectively equal to 0.12 m, 0.09 m and 0.06 m, and span length equal to 0.3 m. The resulting aspect ratio is 3.33. According to [26], a stainless steel with a density of 7900 kg/m^3, a Young modulus of 193 GPa and a Poisson modulus of 0.3 is chosen for the hydrofoil. Water density and dynamic viscosity are set equal to 999 kg/m^3 and 1.1545E–3 Pa·s, whereas the absolute pressure and temperature are set to 201.13 kPa and 293.15 K.

Figures 2(a) and 2(b) respectively show the experimental values of lift and drag coefficients, provided by [26], versus AoA for Re=$\{$2E5;4E5;6E5$\}$. The peak of the lift coefficient falls within 10 and 11 deg, showing stall for AoA$>$11 deg.

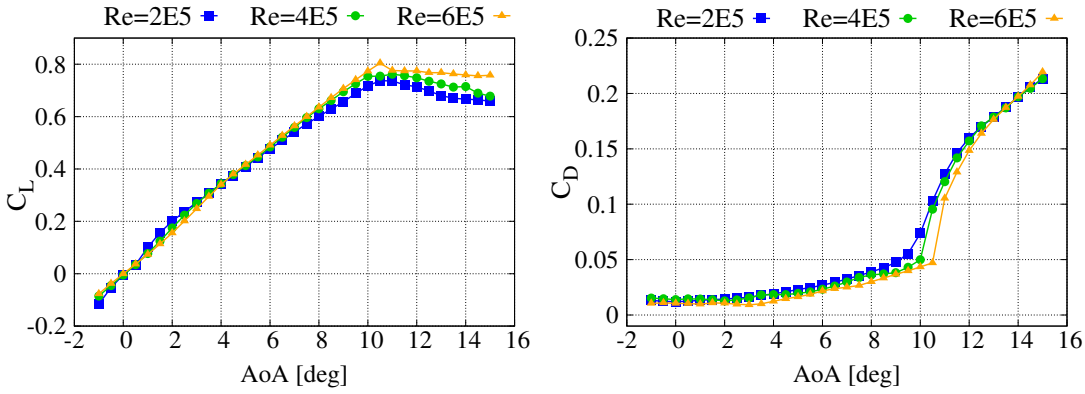

(a) Lift coefficient versus AoA

(b) Drag coefficient versus AoA

Figure 2: Experimental lift and drag coefficients for several Reynolds numbers [26].

Two problems are solved. In the first problem (namely problem 1) high-fidelity evaluations are provided by FSI simulations, performed with a two-way stationary coupling between hydrodynamic (steady incompressible Reynolds Averaged Navier-Stokes Equations, RANSE) and structural simulations. The low-fidelity evaluations are obtained through steady incompressible RANSE hydrodynamic simulations, with rigid hydrofoil. Both high- and low-fidelity simulations are performed using the commercial FEM-based code COMSOL Multiphysics^{TM} and the ratio between the computational time of the low- and the high-fidelity simulations is approximately equal to 0.2, see Tab. 1.

In the second problem (namely problem 2), the high-fidelity evaluations are provided by available experimental data from [26]. Therefore, the multi-fidelity metamodel is initially trained with experimental data and low-fidelity simulations. For this problem, the ratio between the computational time of the high-fidelity evaluations and the low-fidelity simulations is set to infinite, implying that only low-fidelity evaluations are used to update the multi-fidelity metamodel.

5 SIMULATION SETUP

FSI and hydrodynamic simulations share the same *C*-type domain for the hydrodynamics. A length equal to four mid-chords (C_m) is used as radius of the *C*, the total height of the domain is twice the span of the hydrofoil. Downstream, the domain extends ten times the mid-chord, see Fig. 3(a).

The domain is discretized with a structured mesh and the distribution of the elements in the downstream region is intentionally refined to guarantee the finest discretization of wake flow for each AoA of the hydrofoil. The grid is also refined in critical regions such as the root and the tip of the hydrofoil, Fig. 3(b). Parameters pertaining to the grid size used for high- and low-fidelity simulations are summarized in Tab. 1. Note that high-fidelity (FSI) simulations also include the structural grid (with coincident nodes) and associated degrees of freedom.

The $k-\epsilon$ turbulence model is used with standard coefficients [29] and wall function. The non-linear stationary problem is solved with a dumped Newton method through linear step [30]. A pseudo time-stepping is introduced to increase the simulation stability. The Courant-Friedrichs-Lewy (CFL) number adjusts the local time-step according to $\Delta t_{loc} = CFL_{loc}h/U$, where h is the longest cell edge, and U is the magnitude of the local fluid flow velocity. The

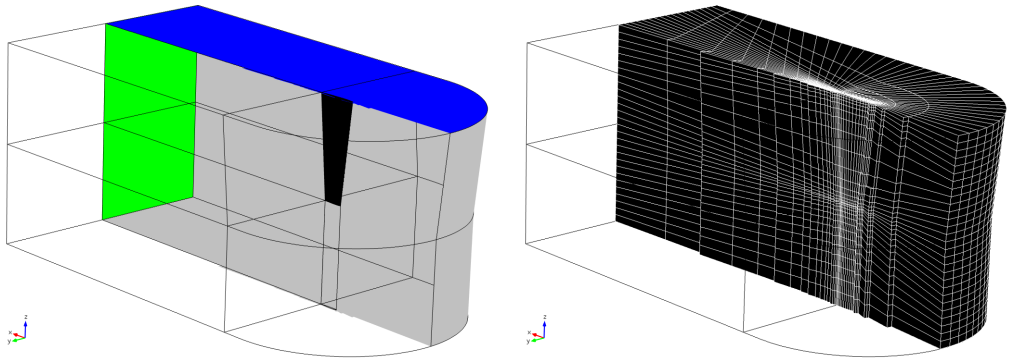

(a) Hydrodynamic domain and boundary conditions

(b) Meshed *C*-type domain

Figure 3: Hydrodynamic domain and grid.

Simulation	N. of elements	DoFs	Simulation time [h]
FSI	31.3k	2M	≈ 10
Hydrodynamic	29.7k	1.2M	≈ 2

Table 1: Summary of the simulation parameters.

CFL is decreased, proportionally with the increase of the AoA, starting from the value CFL=1.

Second order shape functions are used for the displacement vector, mesh deformation (if any), velocity, turbulent kinetic energy and turbulent dissipation rate. First order shape functions are used for the pressure.

The hydrodynamic boundary conditions are set considering an inlet/undisturbed flow on the gray face, a wall on the blue face and an outlet on the green face. The black faces represent the hydrofoil (elastic/rigid wall), see Fig. 3(a).

5.1 High-Fidelity Simulations: Fluid-Structure Interaction Solver

The structural boundary conditions include null displacement and rotation at the root section of the hydrofoil. The hydroelastic deformation of the hydrofoil implies the deformation of the mesh. In COMSOL Multiphysics^{TM} arbitrary Lagrangian-Euler (ALE) method is implemented. The Yeoh method is applied, with a stiffness factor equal to 150 [31].

A segregated iterative solver is applied in order to reduce the problem dimension. Specifically, three segregated groups are defined: the first for the displacement vector, the second for the spatial coordinates of the deformed mesh, and the third for the velocity, pressure, turbulent kinetic energy and turbulent dissipation rate.

The displacement vector is solved with a direct MUltifrontal Massively Parallel Solver (MUMPS) [31]. The others segregated groups are solved using the Flexible Generalized Minimal Residual Method (FGMRES) [32], preconditioned with Generalized Minimal Residual Method (GMRES) [33].

5.2 Low-Fidelity Simulations: Hydrodynamic Solver Only

Two segregated groups are solved: the first for velocity and pressure, and the second for turbulent kinetic energy and turbulent dissipation rate. Both segregated groups are solved using

the FGMRES, preconditioned with GMRES.

6 NUMERICAL RESULTS

The pressure contour on the hydrofoil and on the half-span plane are shown for both FSI and hydrodynamic-only simulations, for AoA=7 deg, Re=4E5, respectively in Figs. 4(a) and 4(b). In particular, the deflection of the tip of the hydrofoil is evident in Fig. 4(a).

Figure 5(a) shows for the FSI simulation the pressure contour on the hydrofoil and on the half-span plane, along with the streamlines deformed by the local velocity component (left color legend). Finally, Fig. 5(b) shows the pressure contour on the hydrofoil and the velocity contour on the half-span plane, along with the streamlines deformed by the local velocity component (left color legend).

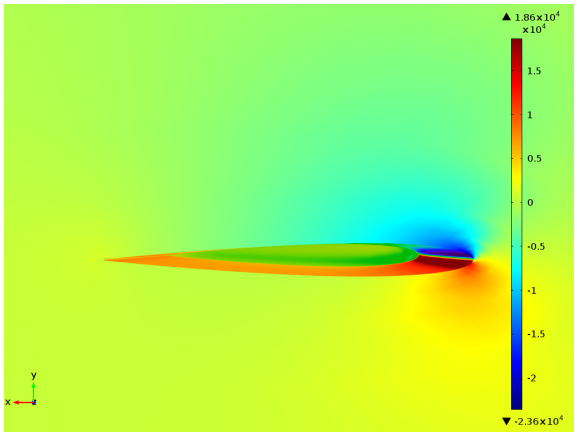

(a) FSI simulation. Pressure contour on hydrofoil and half-span plane

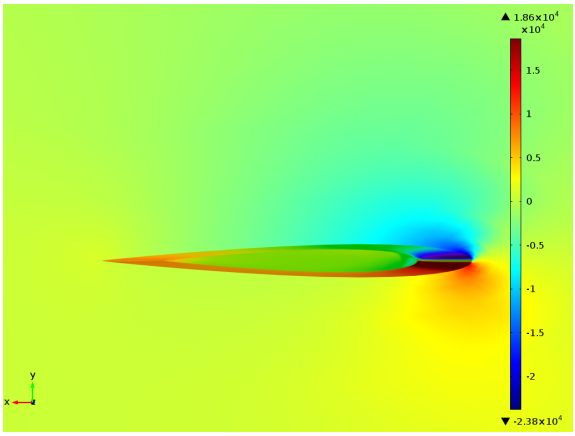

(b) Hydrodynamic-only simulation. Pressure contour on hydrofoil and half-span plane

Figure 4: High- and low-fidelity simulations, AoA=7 deg, Re=4E5.

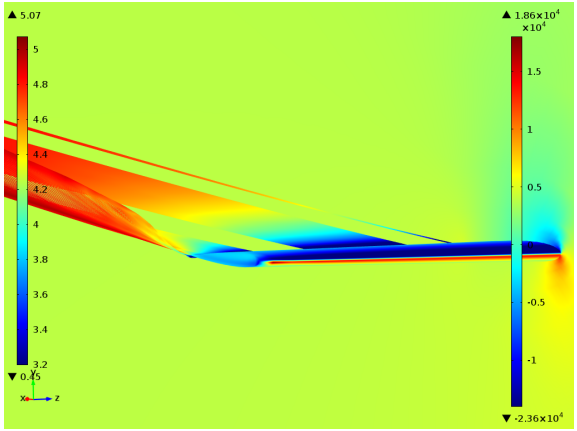

(a) FSI simulation. Pressure contour on hydrofoil and half-span plane

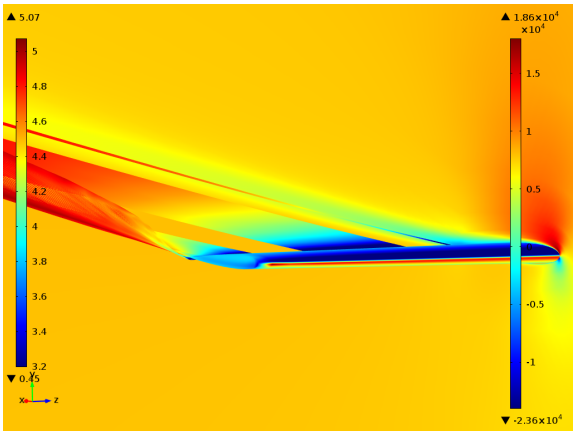

(b) FSI simulation. Pressure contour on hydrofoil and velocity contour on half-span plane

Figure 5: High-fidelity simulation, AoA=7 deg, Re=4E5.

The numerical results that follow are presented showing the maximum value of the uncertainty of the multi-fidelity metamodel, normalized with respect to the function range (R). The

adaptive sampling procedure is assumed at convergence when the maximum value of the uncertainty does not change significantly, if new simulations are added. Furthermore, the multi-fidelity metamodel, along with the uncertainty of the low-fidelity and error metamodels are shown at the initial and final iterations. Non-dimensional variables are used to build the metamodel. However, for the sake of clarity, dimensional results are shown. The initial training set is composed by the extreme values of the domain and the central point: AoA={-1;7;15} deg, permuted with Re={2E5;4E5;6E5}.

6.1 Problem 1

Figure 6 shows the maximum value of the normalized uncertainty of the multi-fidelity metamodel versus the computational cost. The maximum value of the uncertainty of the multi-fidelity metamodel of the lift coefficient shows a significant reduction during the iterative process, as shown in Fig. 6(a). The maximum value of the uncertainty of the multi-fidelity metamodel of the drag coefficient shows a quite sudden reduction after 4 iterations, as shown in Fig. 6(b). The convergence of the multi-fidelity metamodel is achieved after 13 iterations, corresponding to about 140 hours of simulation time (wall clock, using 1 Intel Xeon E5-1620 v2 3.9 GHz with 4 cores in parallel). A total of 9 high-fidelity and 20 low-fidelity simulations are used, as summarized in Tab. 2.

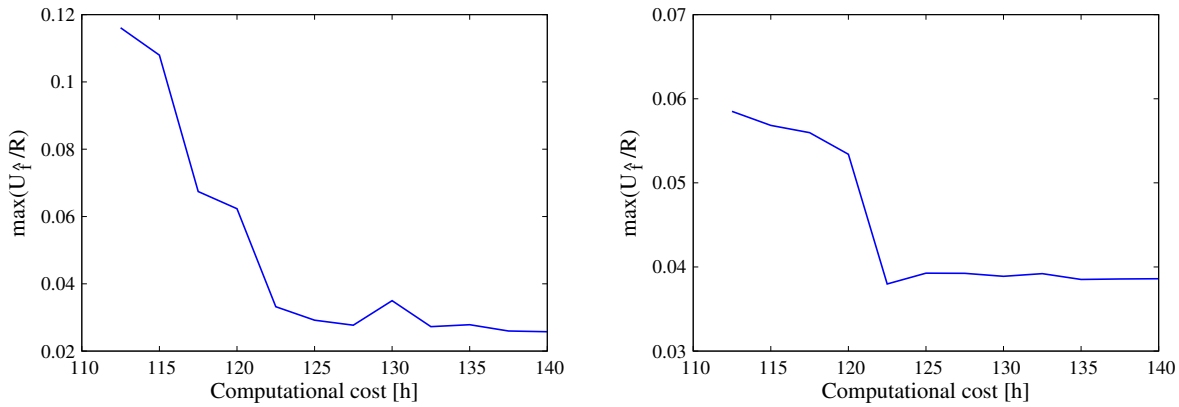

(a) Lift coefficient (b) Drag coefficient

Figure 6: Problem 1, maximum multi-fidelity metamodel uncertainty versus computational cost.

Figures 7(a)-(b), (c)-(d), and (e)-(f) show the initial multi-fidelity metamodel, the low-fidelity and error metamodel uncertainties, respectively for the lift and drag coefficients. The squares and triangles represent the points where the high- (H) and low-fidelity (L) simulations are computed.

Comparing Figs. 7(c) and 7(d) it is worth noting that the uncertainty associated to the low-fidelity metamodel of the lift coefficient is one order of magnitude greater than the uncertainty associated to the low-fidelity metamodel of the drag coefficient.

Figures 8(a)-(b), (c)-(d), and (e)-(f) show the multi-fidelity metamodel, the low-fidelity and error metamodel uncertainties, respectively for the lift and drag coefficients, corresponding to the final iteration (13-th iteration).

It should be noted that the uncertainty of the low-fidelity metamodel is significantly lower than in Figs. 7(c) and 7(d). Figures 8(e) and 8(f) show the uncertainty of the error metamodel, which is not changed, since high-fidelity simulations are not added to the original training set.

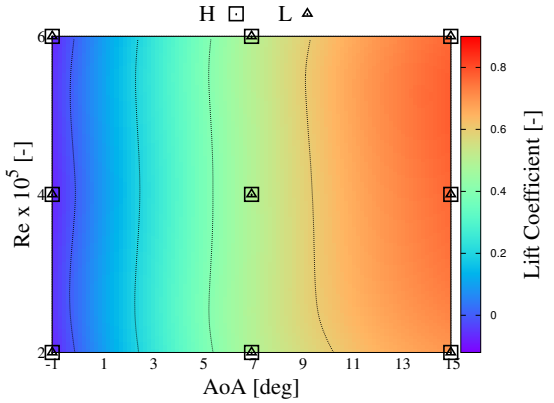

(a) Multi-fidelity metamodel of the lift coefficient

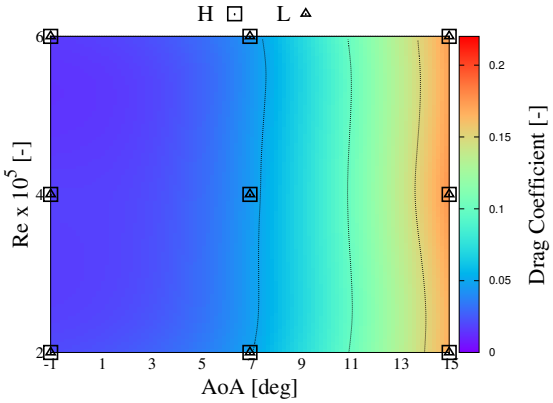

(b) Multi-fidelity metamodel of the drag coefficient

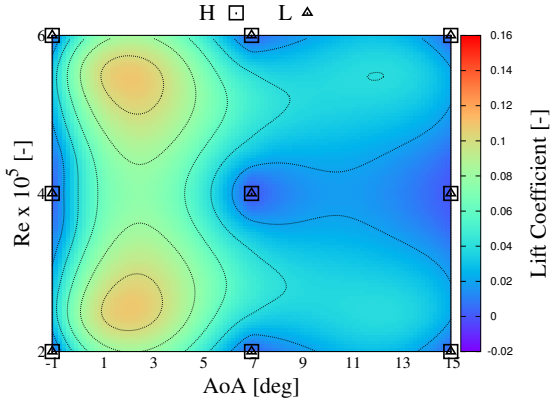

(c) Uncertainty of the low-fidelity metamodel of the lift coefficient

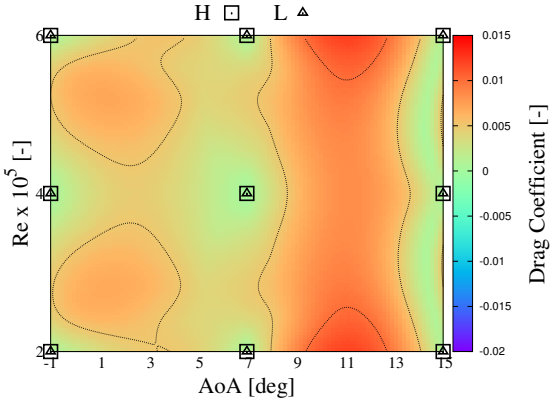

(d) Uncertainty of the low-fidelity metamodel of the drag coefficient

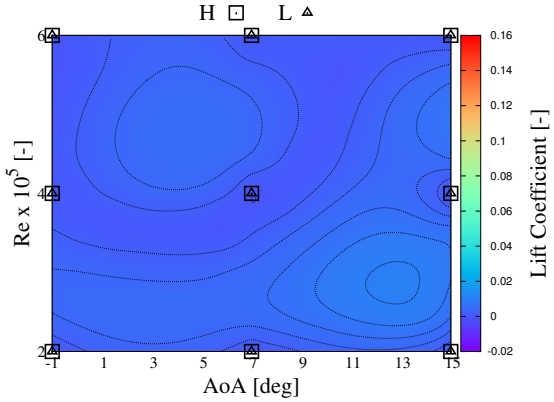

(e) Uncertainty of the error metamodel of the lift coefficient

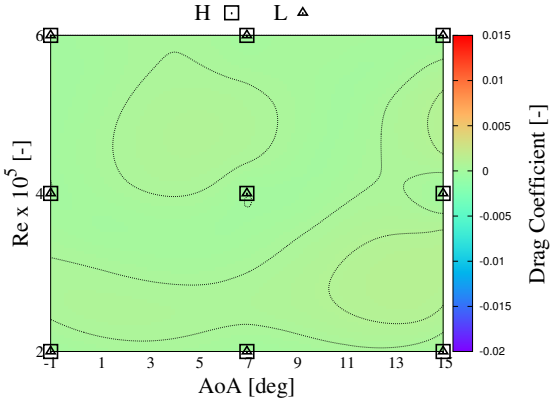

(f) Uncertainty of the error metamodel of the drag coefficient

Figure 7: Problem 1, initial iteration.

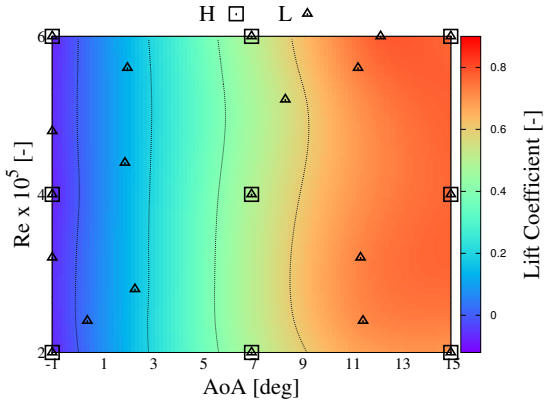

(a) Multi-fidelity metamodel of the lift coefficient

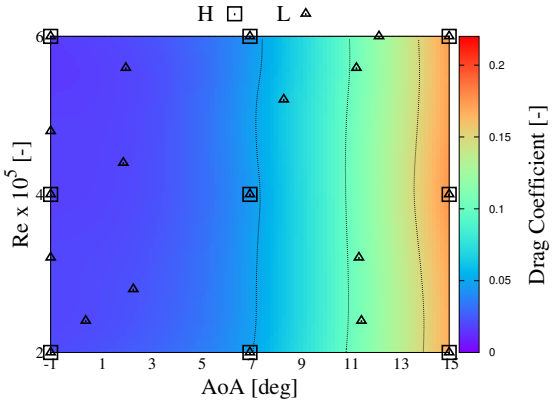

(b) Multi-fidelity metamodel of the drag coefficient

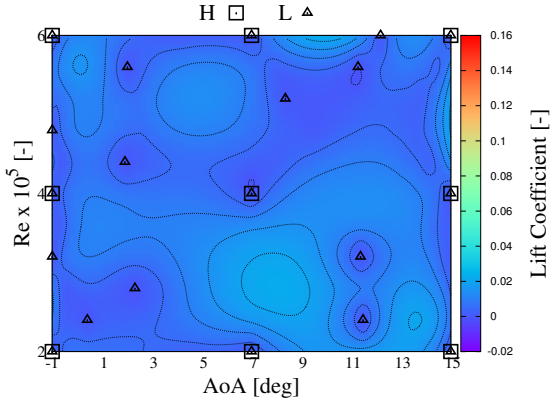

(c) Uncertainty of the low-fidelity metamodel of the lift coefficient

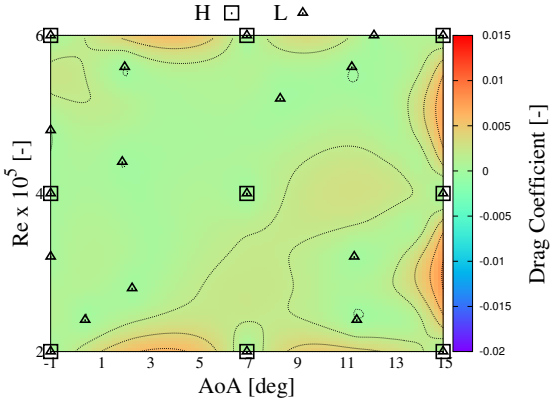

(d) Uncertainty of the low-fidelity metamodel of the drag coefficient

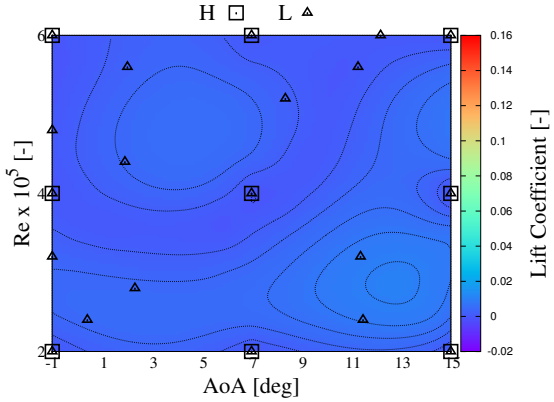

(e) Uncertainty of the error metamodel of the lift coefficient

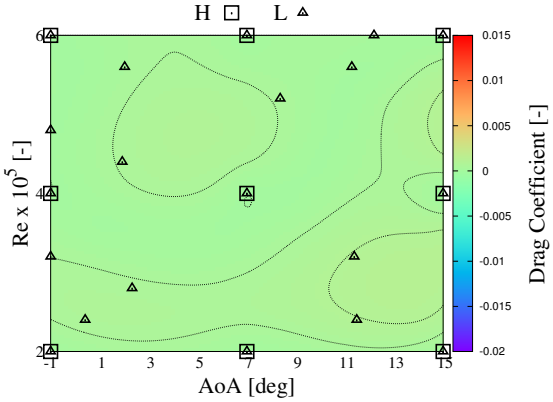

(f) Uncertainty of the error metamodel of the drag coefficient

Figure 8: Problem 1, final iteration.

6.2 Problem 2

Figure 9 shows the maximum value of the uncertainty of the multi-fidelity metamodel versus the computational cost. Figure 9(a) shows the reduction of the maximum value of the uncertainty of the multi-fidelity metamodel of the lift coefficient. The maximum value of the uncertainty of the multi-fidelity metamodel of the drag coefficient shows a quite sudden reduction after 3 iterations, see Fig. 9(b). The convergence of the multi-fidelity metamodel is achieved after 7 iterations, corresponding to about 130 hours of simulation time (wall clock, using 1 Intel Xeon E5-1620 v2 3.9 GHz with 4 cores in parallel). A total of 9 high-fidelity experimental data and 16 low-fidelity simulations are used, as summarized in Tab. 2.

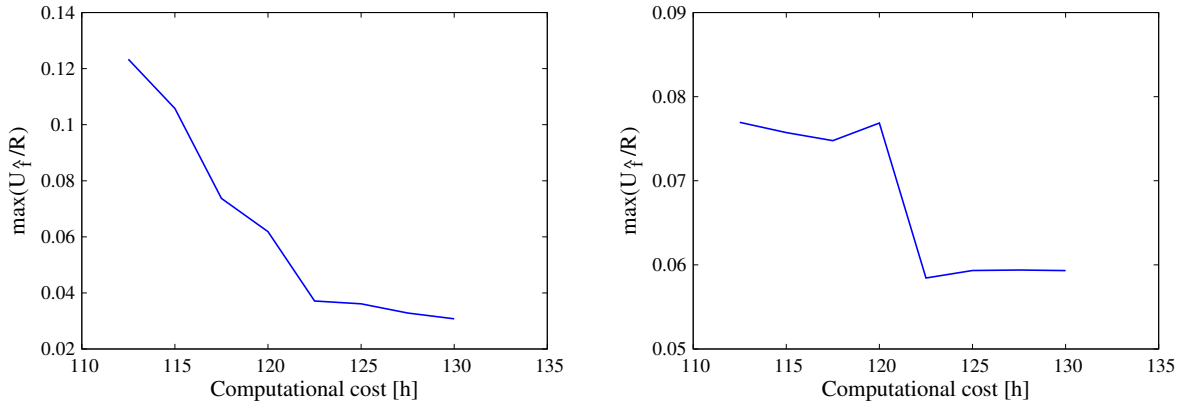

(a) Lift coefficient (b) Drag coefficient

Figure 9: Problem 2, maximum multi-fidelity metamodel uncertainty versus computational cost.

Figures 10(a)-(b), (c)-(d), and (e)-(f) show the initial multi-fidelity metamodel, the low-fidelity and error metamodel uncertainties, respectively for lift and drag coefficients. The squares represent high-fidelity experimental data (H) and the triangles represent the points where low-fidelity (L) simulations are computed.

Considering Figs. 10(c) and 10(d) it should be noted that the uncertainty associated to the low-fidelity metamodel of the lift coefficient is one order of magnitude greater than the uncertainty associated to the low-fidelity metamodel of the drag coefficient. Figures 10(e) and 10(f) show the uncertainty of the error metamodel, which is considerably greater than the corresponding uncertainties of Figs. 7(e) and 7(f). This effect is due to the difference between the simulations and the experiments, which is significantly greater than the difference between the high- and low-fidelity simulations.

Figures 11(a)-(b), (c)-(d), and (e)-(f) show the multi-fidelity metamodel, the low-fidelity and error metamodel uncertainties, respectively for lift and drag coefficients, at the final iteration (8-th iteration).

It is worth noting that the uncertainty of the low-fidelity metamodel, Figs. 11(c) and 11(d), is significantly lower than in Figs. 10(c) and 10(d), and that the uncertainty of the error metamodel is not changed, since no experimental data is added to the training set.

7 CONCLUSIONS

A multi-fidelity global metamodel has been presented for uncertainty quantification of computationally expensive computer simulations. High- and low-fidelity solvers are used for the metamodel training and managed through an adaptive sampling procedure. Multiple functions

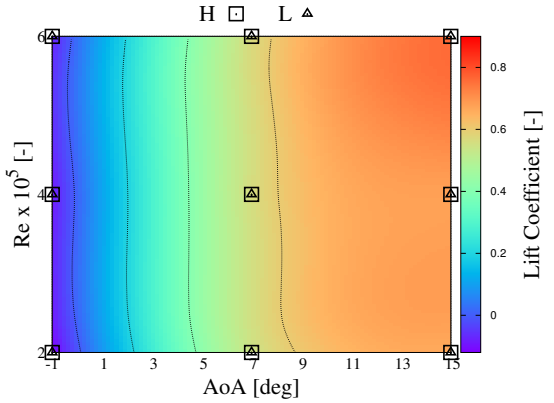

(a) Multi-fidelity metamodel of the lift coefficient

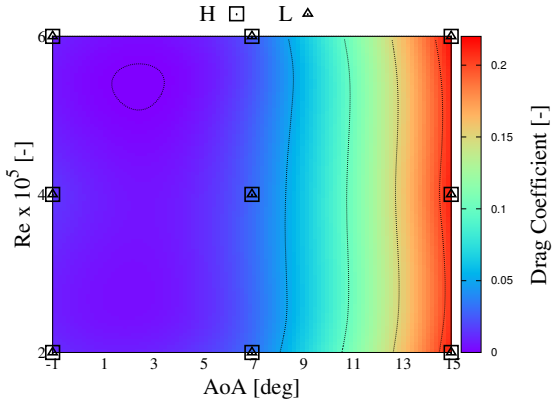

(b) Multi-fidelity metamodel of the drag coefficient

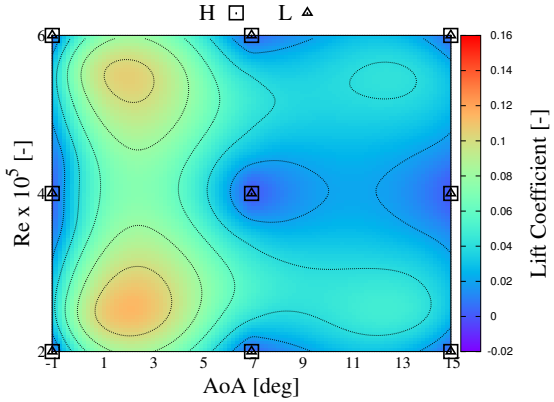

(c) Uncertainty of the low-fidelity metamodel of the lift coefficient

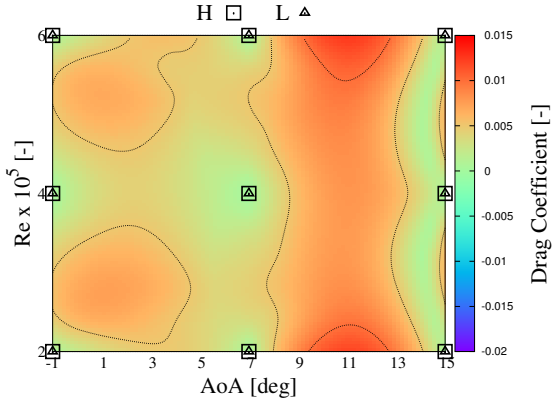

(d) Uncertainty of the low-fidelity metamodel of the drag coefficient

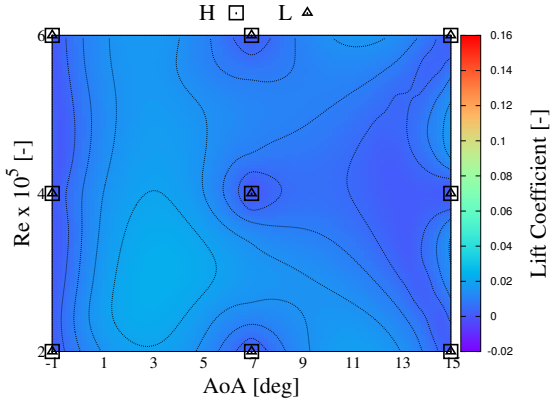

(e) Uncertainty of the error metamodel of the lift coefficient

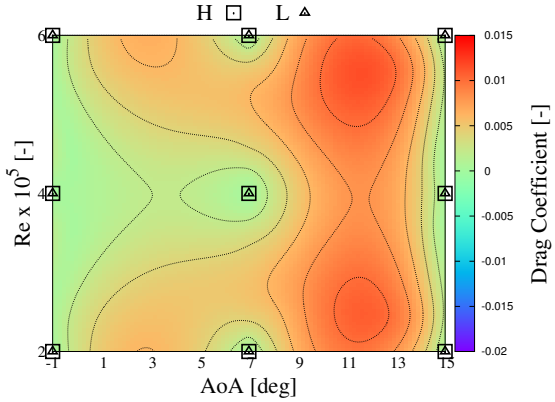

(f) Uncertainty of the error metamodel of the drag coefficient

Figure 10: Problem 2, initial iteration.

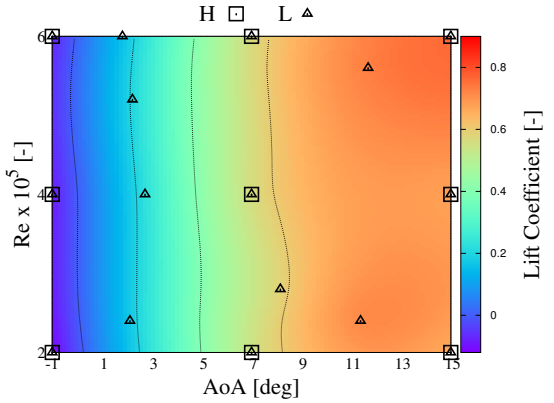

(a) Multi-fidelity metamodel of the lift coefficient

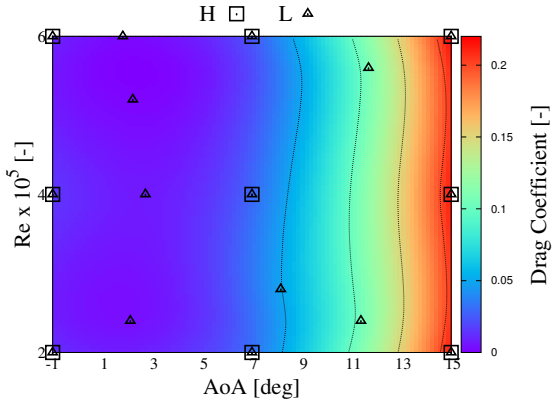

(b) Multi-fidelity metamodel of the drag coefficient

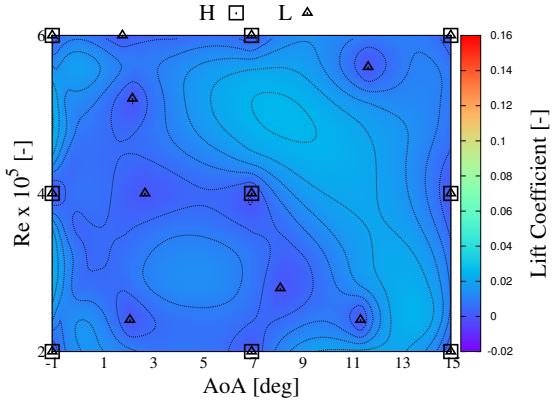

(c) Uncertainty of the low-fidelity metamodel of the lift coefficient

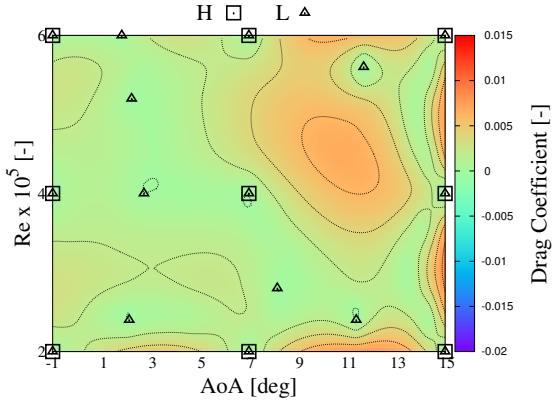

(d) Uncertainty of the low-fidelity metamodel of the drag coefficient

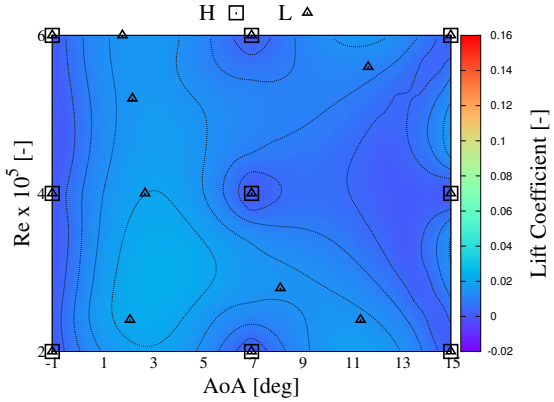

(e) Uncertainty of the error metamodel of the lift coefficient

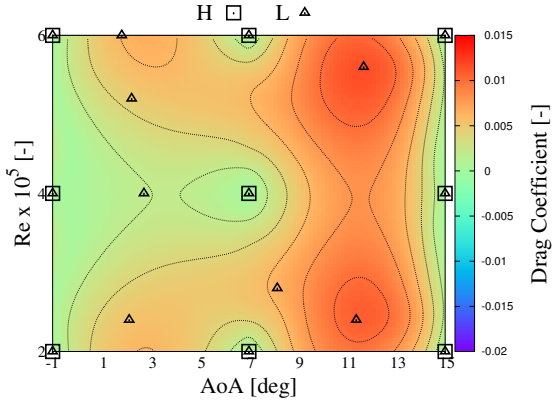

(f) Uncertainty of the error metamodel of the drag coefficient

Figure 11: Problem 2, final iteration.

Pr.			Initial iteration				Final iteration	
			C_L	C_D			C_L	C_D
#	H	L	$\max(U_{\hat{f}}/R)$	$\max(U_{\hat{f}}/R)$	H	L	$\max(U_{\hat{f}}/R)$	$\max(U_{\hat{f}}/R)$
1	9	9	0.1161	0.0585	9	20	0.0254	0.0386
2	9	9	0.1233	0.0769	9	16	0.0307	0.0593

Table 2: High (H) and low (L) fidelity evaluations and $\max(U_{\hat{f}}/R)$ at the initial and final iterations.

have been considered, simultaneously. The multi-fidelity approximation is obtained as the sum of a low-fidelity-trained metamodel and the metamodel of the difference (error) between high- and low-fidelity evaluations. The metamodel is based on the dynamic stochastic RBF method, which provides the prediction and the associated uncertainty. The prediction uncertainty of both the low-fidelity and the error metamodel is used for the adaptive refinement of the low- and high-fidelity training sets, respectively.

The method has been applied to a steady FSI problem addressing the lift and drag coefficients of a 3D NACA 0009 stainless steel hydrofoil. Two problems have been presented: the first with high-fidelity evaluations provided by steady FSI simulations and the second with high-fidelity evaluations provided by experimental data. Low-fidelity evaluations have been provided by hydrodynamic simulations for both problems.

For problem 1, the overall uncertainty of the multi-fidelity metamodels has been reduced achieving 2.5% and 3.8% (of the function range) for the lift and drag coefficient, respectively. For problem 2, an uncertainty of 3% and 5.9% for the lift and drag coefficient has been achieved, respectively. Although the overall uncertainty in Problem 1 is lower than in problem 2, a better agreement with the experimental results is obtained using experimental data in the initial training set as in problem 2. Furthermore, less iterations have been used for problem 2. For both problems 1 and 2, the adaptive sampling method always required low-fidelity evaluations and no high-fidelity information was added to the model after the initialization. This is due to the high cost of high-fidelity evaluations (simulations or experiments) and the small uncertainty associated to the error between low- and high-fidelity functions.

Future work will extend the current study to different (and more flexible) materials, such as aluminum and/or composite materials, and will also include the application of the method to separate and combined problems of uncertainty quantification and design optimization.

Acknowledgments

The present research is supported by the Italian Flagship Project RITMARE, coordinated by the Italian National Research Council and funded by the Italian Ministry of Education, University and Research, within the National Research Program 2011-2013. The authors are also grateful to Dr Woei-Min Lin and Dr Ki-Han Kim of the US Navy Office of Naval Research, for their support through NICOP grant N62909-15-1-2016.

REFERENCES

[1] F. Stern, R.V. Wilson, H.W. Coleman, E.G. Paterson, "Comprehensive approach to verification and validation of CFD simulations–Part 1: Methodology and Procedures," *ASME J. Fluids Eng.*, **123**(4), 793–802, 2001.

[2] F. Stern, R.V. Wilson, J. Shao, "Quantitative approach to V&V of CFD simulations and certification of CFD codes," *Int. J. Numer. Meth. Fluids*, **50**, 1335–1355, 2006.

[3] T. Xing, F. Stern, "Factors of safety for Richardson extrapolation," *ASME J. Fluids Eng.*, **132**(6), 2010.

[4] S.M. Mousaviraad, W. He, M. Diez, F. Stern, "Framework for convergence and validation of stochastic uncertainty quantification and relationship to deterministic verification and validation," *International Journal for Uncertainty Quantification*, **3**(5), 2013.

[5] M. Diez, W. He, E.F. Campana, F. Stern, "Uncertainty quantification of Delft catamaran resistance, sinkage and trim for variable Froude number and geometry using metamodels, quadrature and Karhunen-Loève expansion", *Journal of Marine Science and Technology*, **19**(2), 143–169, 2014.

[6] W. He, M. Diez, Z. Zou, E.F. Campana, F. Stern, "URANS study of Delft catamaran total/added resistance, motions and slamming loads in head sea including irregular wave and uncertainty quantification for variable regular wave and geometry", *Ocean Engineering*, **74**, 189–217, 2013.

[7] M. Diez, X. Chen, E.F. Campana, F. Stern, "Reliability-based robust design optimization for ships in real ocean environment", *Proc. 12th International Conference on Fast Sea Transportation, FAST*, Amsterdam, The Netherlands, December 2-5, 2013.

[8] M. Diez, E.F. Campana, F. Stern, "Development and evaluation of hull-form stochastic optimization methods for resistance and operability", *Proc. 13th International Conference on Fast Sea Transportation, FAST*, Washington D.C., USA, September 1-4, 2015.

[9] Y. Tahara, M. Diez, S. Volpi, X. Chen, E.F. Campana, F. Stern, "CFD-based multiobjective stochastic optimization of a waterjet propelled high speed ship", *Proc. 30th Symposium on Naval Hydrodynamics*, Hobart Tasmania, Australia, November 2-7, 2014.

[10] T. W. Simpson, J. Poplinski, P. N. Koch, J. K. Allen, "Metamodels for computer-based engineering design: survey and recommendations," *Engineering with computers*, **17**(2), 129–150, 2001.

[11] R. Jin, W. Chen, T. W. Simpson, "Comparative studies of metamodelling techniques under multiple modelling criteria," *Structural and Multidisciplinary Optimization*, **23**(1), 1–13, 2001.

[12] N. V. Queipo, R. T. Haftka, W. Shyy, T. Goel, R. Vaidyanathan,P. Kevin Tucker, "Surrogate-based analysis and optimization," *Progress in aerospace sciences*, **41**(1), 1–28, 2005.

[13] N. Alexandrov, E. Nielsen, R. Lewis, W. Anderson, "First-order model management with variable-fidelity physics applied to multi-element airfoil optimization," *AIAA paper*, 4886, 2000.

[14] N. M. Alexandrov, R. M. Lewis, C. R. Gumbert, L. L. Green, P. A. Newman, "Approximation and model management in aerodynamic optimization with variable-fidelity models," *Journal of Aircraft*, **38**(6), 1093–1101, 2001.

[15] T. W. Simpson, V. Toropov, V. Balabanov, F. A. Viana, "Design and analysis of computer experiments in multidisciplinary design optimization: a review of how far we have come or not," in *12th AIAA/ISSMO Multidisciplinary Analysis and Optimization Conference*, **5**(10), 10–12, 2008.

[16] Y. Kuya, K. Takeda, X. Zhang, A. I. J. Forrester, "Multifidelity Surrogate Model of Experimental and Computational Aerodynamic Data Sets," *AIAA Journal*, **49**(2), 289–298, 2011.

[17] L. W. T. Ng, M. Eldred, "Multifidelity uncertainty quantification using nonintrusive polynomial chaos and stochastic collocation," in *Proceedings of the 14th AIAA Non-Deterministic Approaches Conference, number AIAA-2012-1852*, Honolulu, HI, **43**, 2012.

[18] J. de Baar, S. Roberts, R. Dwight, B. Mallol, "Uncertainty quantification for a sailing yacht hull, using multi-fidelity kriging," *Computers & Fluids*, **123**, 185–201, 2015.

[19] A. S. Padrón, J. J. Alonso, F. Palacios, M. Barone, M. S. Eldred, "Multi-fidelity uncertainty quantification: application to a vertical axis wind turbine under an extreme gust," in *15th AIAA/ISSMO Multidisciplinary Analysis and Optimization Conference*, Atlanta, GA, USA, 2014.

[20] A. Nelson, J. J. Alonso, T. H. Pulliam, "Multi-fidelity aerodynamic optimization using treed meta-models," in *25th AIAA Applied Aerodynamics Conference*, Miami, 25–28, 2007.

[21] G. Sun, G. Li, S. Zhou, W. Xu, X. Yang, Q. Li, "Multi-fidelity optimization for sheet metal forming process," *Structural and Multidisciplinary Optimization*, **44**(1), 111–124, 2010.

[22] Q. Zhou, X. Shao, P. Jiang, H. Zhou, L. Shu, "An adaptive global variable fidelity metamodeling strategy using a support vector regression based scaling function," *Simulation Modelling Practice and Theory*, **59**, 18–35, 2015.

[23] S. Volpi, M. Diez, N. J. Gaul, H. Song, U. Iemma, K.K. Choi, E. F. Campana, F. Stern, "Development and validation of a dynamic metamodel based on stochastic radial basis functions and uncertainty quantification," *Structural and Multidisciplinary Optimization*, **51**, 347–368, 2015.

[24] R. Pellegrini, U. Iemma, C. Leotardi, E. F. Campana, M. Diez, "Multi-fidelity Adaptive Global Metamodel of Expensive Computer Simulations", Submitted to *2016 IEEE Congress on Evolutionary Computation*, July, Vancouver, Canada, 2016.

[25] M. Diez, S. Volpi, A. Serani, F. Stern, E. F. Campana, "Simulation-based design optimization by sequential multi-criterion adaptive sampling and dynamic radial basis functions," in *EUROGEN 2015, International Conference on Evolutionary and Deterministic Methods for Design, Optimization and Control with Applications to Industrial and Societal Problems*, Glasgow, UK, September, 2015.

[26] G. A. Zarruk, P. A. Brandner, B. W. Pearce, A. W. Phillips, "Experimental study of the steady fluid-structure interaction of flexible hydrofoils", *Journal of Fluids and Structures*, **51**, 326–343, 2014.

[27] N. Garg, G. K.W. Kenway, Z. Lyu, J. R.R.A. Martins, Y. L. Young "High-fidelity Hydrodynamic Shape Optimization of a 3-D Hydrofoil", *Journal of Ship Research*, **59**(4), 209–226, 2015.

[28] R. Pellegrini, C. Leotardi, U. Iemma, E. F. Campana, M. Diez, "Structural and Hydrodynamic Characterization of a NACA 0009 Hydrofoil by Finite Elements", *18th Numerical Towing Tank Symposium*, Cortona, Italy, September, 2015.

[29] W. Jones, B. Launder, "The prediction of laminarization with a two-equation model of turbulence". *International journal of heat and mass transfer*, **15**(2), 301–314, 1972.

[30] P. Deuflhard, "A modified newton method for the solution of ill-conditioned systems of nonlinear equations with application to multiple shooting", *Numerische Mathematik*, **22**(4), 289–315, 1974.

[31] COMSOL^{TM}, "COMSOL Multiphysics Reference Manual", 2014.

[32] Y. Saad, "A flexible inner-outer preconditioned GMRES algorithm", *SIAM Journal on Scientific Computing*, **14**(2), 461–469, 1993.

[33] Y. Saad, M. H. Schultz, "GMRES: A generalized minimal residual algorithm for solving nonsymmetric linear systems", *SIAM Journal on scientific and statistical computing*, **7**(3), 856–869, 1986.

ECCOMAS Congress 2016
VII European Congress on Computational Methods in Applied Sciences and Engineering
M. Papadrakakis, V. Papadopoulos, G. Stefanou, V. Plevris (eds.)
Crete Island, Greece, 5–10 June 2016

A LEAST-SQUARES, ADAPTIVE UNCERTAINTY PROPAGATION APPROACH FOR A PLASMA-COUPLED COMBUSTION SYSTEM

Kunkun Tang, Luca Massa, Jonathan Wang and Jonathan B. Freund

The Center for Exascale Simulation of Plasma-coupled Combustion (XPACC)
University of Illinois at Urbana-Champaign
1308 W Main St, Urbana IL 61801, USA
e-mail: {ktg,luca1,jmwang2,jbfreund}@illinois.edu

Keywords: Uncertainty quantification, Sensitivity analysis, Adaptive ANOVA, Polynomial dimensional decomposition (PDD), Combustion.

Abstract. *We employ a new stochastic methodology for the construction of surrogate models for uncertainty quantification (UQ) and sensitivity analysis (SA). It is based on polynomial dimensional decomposition (PDD), as are widely used in solving high-dimensional stochastic problems that arise in various applications. In our approach, the coefficients of the PDD expansion are determined by using a least-squares regression (LSR). Compared to a projection approach, the use of LSR not only avoids the computation of high-dimensional integrals, but also affords an attractive flexibility in choosing the sampling points, which facilitates importance sampling using a calibrated posterior distribution based on a Bayesian approach. LSR can be particularly advantageous in cases where the asymptotic convergence properties of polynomial expansions cannot be realized due to computation expense, focusing effort on efficient finite-resolution sampling. To efficiently include parameter spaces with a moderate number of uncertain parameters (up to 7 in this work), the PDD is coupled with an adaptive ANOVA (analysis of variance) decomposition. This provides an accurate surrogate as the union of several low-dimensional spaces, avoiding the typical computational overhead cost of a high-dimensional expansion. In addition, the PDD representation of the ANOVA component functions is further simplified in an adaptive way according to the relative contribution of the different polynomials to the variance. The overall methodology is demonstrated on plasma-mediated ignition simulations as part of a large predictive science effort in the Center for Exascale Simulation of Plasma-Coupled Combustion (XPACC). The specific configuration we study includes model parameters arising from reaction rates in a global chemical kinetics description, and a laser-induced breakdown ignition seed.*

1 INTRODUCTION

It is well-understood that global sensitivity analysis (GSA) has the advantage of taking into account the broad influence of input parameters over the ranges and their interactions onto the output quantity of interest, by considering the entire input space rather than a specific nominal point (see for example [6]). However, the main difficulty encountered when employing global methods is the high cost of Monte Carlo (MC) or a quasi Monte Carlo (QMC) methods. These can be prohibitively expensive.

The objective of this work consists of building an efficient Uncertainty Quantification (UQ) and GSA method featuring a surrogate model representation that is affordable for complex numerical simulation problems. To address the so-called curse of dimensionality, we employ the polynomial dimensional decomposition (PDD) (introduced and developed by Rahman and coworkers in e.g. [12, 13, 15, 21, 14]) and combine it with the Analysis of Variance (ANOVA) decomposition due to their direct link with each other. The least-squares regression (LSR) approach is an efficient tool to determine the expansion coefficients, by minimizing the error of the surrogate model representation in the mean square sense (see e.g. [7, 18, 3]). Compared to the projection approach (see e.g. [9, 11, 2]) where each polynomial coefficient is obtained by computing a multi-dimensional integral, the regression approach is more flexible (in choosing sampling points) for problems involving a moderate number of uncertain parameters. It is known that the number of ANOVA component functions increases exponentially with respect to the uncertain parameter dimensionality, and meanwhile the imposed polynomial order for the PDD expansion involves a polynomial increase of the number of PDD terms for each component function. This phenomenon causes one main limitation of the regression approach even for a truncated low-order ANOVA expansion, namely the high number of deterministic model evaluations for problems characterized by a moderate to large number of uncertainties; indeed, for the regression problem to be well posed, the number of deterministic model evaluations is necessary to be larger than the total polynomial expansion size [3, 4]. In this respect, this paper employs the approach proposed in [20] to combine the *active dimension* strategy and the *stepwise regression* technique [3, 4] to obtain an efficient sparse surrogate model representation.

In Section 2, we review basic concepts of ANOVA, Sobol' sensitivity indices and outline main idea of variance-based dimension reduction techniques. A 2-D axisymmetric application case is investigated in Section 3. Conclusions follow.

2 ANOVA AND VARIANCE-BASED DIMENSION REDUCTION

Let us suppose that the response of a given system of interest can be represented by a N-dimensional function $y = f(\boldsymbol{\xi})$

$$y = f(\boldsymbol{\xi}) = f(\xi_1, \xi_2, \cdots, \xi_N), \tag{1}$$

where $\boldsymbol{\xi}$ are independent input uncertain parameters.

An Analysis of Variance (ANOVA) [16, 8, 1, 17] decomposes $f(\boldsymbol{\xi})$ into a series of lower-dimentional component functions as

$$y = f_0 + \sum_{1 \leqslant i \leqslant N}^{N} f_i(\xi_i) + \sum_{1 \leqslant i < j \leqslant N}^{N} f_{ij}(\xi_i, \xi_j) + \cdots + f_{1,2,\cdots,N}(\xi_1, \xi_2, \cdots, \xi_N), \tag{2}$$

or in compact form

$$y = f_0 + \sum_{T=1}^{N} \sum_{i_1<\cdots<i_T}^{N} f_{i_1,\cdots,i_T}(\xi_{i_1}, \cdots, \xi_{i_T}). \tag{3}$$

Note in ANOVA component functions have zero mean and are orthogonal. For notational convenience in this section, we write a general T-dimensional component function ($1 \leq T \leq N$) of the ANOVA decomposition as

$$f_{\mathbf{i}_T}(\boldsymbol{\xi}_T) = f_{i_1,i_2,\cdots,i_T}(\xi_{i_1}, \xi_{i_2}, \cdots, \xi_{i_T}). \tag{4}$$

Keeping in mind its zero-mean property, the component function (4) can be expanded by employing Polynomial Dimensional Decomposition (PDD) using an infinite number of orthogonal basis functions (as done in [12]) by a tensor product for multi-indices $\mathbf{j}_T$:

$$f_{\mathbf{i}_T}(\boldsymbol{\xi}_T) = \sum_{j_T,\cdots,j_1}^{\infty} C_{\mathbf{i}_T}^{\mathbf{j}_T} \Psi_{\mathbf{i}_T}^{\mathbf{j}_T}. \tag{5}$$

Here $C_{\mathbf{i}_T}^{\mathbf{j}_T}$ is a coefficient, and $\Psi_{\mathbf{i}_T}^{\mathbf{j}_T}$ is a T-dimensional basis polynomial function.

In practice, the expansion with an infinite number of terms in (5) must be truncated. Following previous work [12], we truncate (5) by m terms for each dimension:

$$f_{\mathbf{i}_T}(\boldsymbol{\xi}_T) = \sum_{j_T,\cdots,j_1 \leq m} C_{\mathbf{i}_T}^{\mathbf{j}_T} \Psi_{\mathbf{i}_T}^{\mathbf{j}_T}. \tag{6}$$

In particular, the first-order, second-order, and third-order component functions are expressed as

$$\begin{aligned} f_i(\xi_i) &= \sum_{j=1}^{m} C_i^j \psi^j(\xi_i), \\ f_{\mathbf{i}_2}(\boldsymbol{\xi}_{\mathbf{i}_2}) &= \sum_{j_2=1}^{m} \sum_{j_1=1}^{m} C_{\mathbf{i}_2}^{\mathbf{j}_2} \psi^{j_1}(\xi_{i_1}) \psi^{j_2}(\xi_{i_2}), \\ f_{\mathbf{i}_3}(\boldsymbol{\xi}_{\mathbf{i}_3}) &= \sum_{j_3=1}^{m} \sum_{j_2=1}^{m} \sum_{j_1=1}^{m} C_{\mathbf{i}_3}^{\mathbf{j}_3} \psi^{j_1}(\xi_{i_1}) \psi^{j_2}(\xi_{i_2}) \psi^{j_3}(\xi_{i_3}). \end{aligned} \tag{7}$$

Least-squares regression (LSR) [5, 20] can be employed to determine the coefficients $\mathbf{C}_\alpha$ of (vector-form) PDD expansion

$$f(\boldsymbol{\xi}) = \mathbf{C}_\alpha^T \Phi_\alpha(\boldsymbol{\xi})$$

by using a suitable set of training points (i.e. experimental design) and model outputs. The second-order moment and the global sensitivity indices can be obtained in a straightforward way by post-processing.

Indeed, keeping in mind

$$E(f(\boldsymbol{\xi})) = C_{\alpha_0},$$

the approximated variance of the model output is then

$$\mathrm{Var}(f(\boldsymbol{\xi})) = \sum_{j=1}^{P-1} C_{\alpha_j}^2 \gamma_{\alpha_j},$$

with the multivariate normalization constant determined by

$$\gamma_{\alpha_j} = E\left[\Phi^2_{\alpha_j}(\boldsymbol{\xi})\right],$$

where P is the expansion size.

It is straightforward to write the variance-based global sensitivity indices (SI) by using the PDD expansion. Indeed,

$$\mathcal{S}_{i_1,\cdots,i_T} = \frac{\mathrm{Var}(f_{i_1,\cdots,i_T})}{\mathrm{Var}(f(\boldsymbol{\xi}))} = \frac{1}{\mathrm{Var}(f(\boldsymbol{\xi}))} \sum_{\alpha_j \subseteq (i_1,\cdots,i_T)} C^2_{\alpha_j} \gamma_{\alpha_j}. \tag{8}$$

The total sensitivity index $\mathcal{S}_i^T$ can be obtained simply by adding all the measures $\mathcal{S}_{i_1,\cdots,i_T}$ whose index involves the variable ξ_i.

For practical problems, in particular for the ones with a large number of stochastic parameters, the size of the PDD representation must be reduced to make the uncertainty analysis feasible.

A stepwise regression method has been proposed in [4, 3] using a generalized Polynomial Chaos (gPC) approach to build sparse polynomial representation of the model output. In order to efficiently represent a moderate to large dimensional parameter space, in addition to the stepwise regression technique proposed in [4, 3], the PDD approach used in this work is further coupled with an adaptive ANOVA decomposition, which allows to model a given number of low-dimensional spaces instead of a single high-dimensional one. The overall adaptive technique, as a variant of the one used in [4, 3], has been proposed in [20]. We summarize this LSR strategy as a set of coupled adaptive strategies as follows.

1. Set a truncation dimension ν (the maximum interaction order) in the ANOVA expansion. This follows the assumption that low-order interactions are of dominant importance compared to their high-order counterparts.

2. Solve the LSR system including only the PDD terms of the first-order ANOVA component functions, and a rank of importances can then be established quantitatively for all the input parameters. Hence, we retain only so-called active dimensions (the most influential parameters) for the PDD terms of the second- and higher-order ANOVA components. Let us use D_T to represent the active dimension for interaction order T.

3. Enrich the surrogate model representation by adding one-by-one significant polynomials of second- and higher-order interaction terms by keeping only the corresponding active dimensions. A variance-based selection criterion is used to retain only polynomials of significant importance to the total variance, which allows to build a very sparse model representation. We emphasize that recursive resolutions of regression problems are required for this task.

In next section, this adaptive LSR ANOVA approach is applied to an application case featuring input uncertainties arising from chemical kinetics and laser-induced breakdown ignition seed.

3 APPLICATION TO A 2-D COMBUSTION SYSTEM

The combustion in this work is modeled by multi-species Navier–Stokes equations involving source terms including contributions from a reduced chemical mechanism, and

a simplified laser-induced breakdown (LIB) plasma model. Both thermal and vortical contributions are modeled for LIB ignition seed [10]. The model parameter uncertainties considered in this work mainly come from these source terms.

Note the system of Navier–Stokes equations is discretized by finite difference methods on structured grids using the software *PlasComCM*. For details on numerical techniques, we refer to [10].

3.1 Source of uncertainties

The present combustion model featuring a Laser Induced Breakdown (LIB) ignition seed includes seven uncertain parameters, which are calibrated against low-dimensional computations or estimated based on experiments or previous literature data. We summarize these uncertain parameters in Table 1. Note A_3, b_3, and E_3 are calibrated Arrhenius

Combustion kinetics	A_3, b_3, E_3	Joint pdf_{post} calibrated
Laser Induced Breakdown	$L_{TW} \sim \mathcal{U}(0.993, 2.979)$	[mm]
	$R_{TW}(= D_{TW}/2) \sim \mathcal{U}(0.168, 0.504)$	[mm]
	$M_e \sim \mathcal{U}(1, 3)$	
	$E_{abs} \sim \mathcal{N}(17.642, 3.1157)$	[mJ]

Table 1: Summary of uncertain model parameters.

coefficients of the following reaction,

$$2H_2 + O_2 + H \rightarrow 2H_2O + H. \tag{9}$$

L_{TW} (resp. R_{TW}) represents the length (resp. radius) of the luminosity region measured by experiments (we assume the laser energy is spatially distributed over the luminosity region). M_e is the Mach number of LIB vorticity model, and finally, E_{abs} is the absorbed laser energy. The reader is refered to [10] for detailed physical modeling of LIB. Among the four parameters of LIB, the Gaussian distribution of E_{abs} is approximated using experimental results (3160 trials). However, we know significantly less about other three parameters. Thus, L_{TW} and R_{TW} are simply taken to follow a uniform distribution using an error bar of 50 % of their norminal value. The upper-bound value of $M_e = 3$ is the threshold with which our current numerical model becomes significantly unstable.

3.2 Axisymmetric 2-D test problem and quantity of interest (QoI)

An ignition case is computed on a 2-D rectangular domain (as shown in Fig. 1) discretized as a structured grid of size 501×503. The initial condition over the 2-D domain

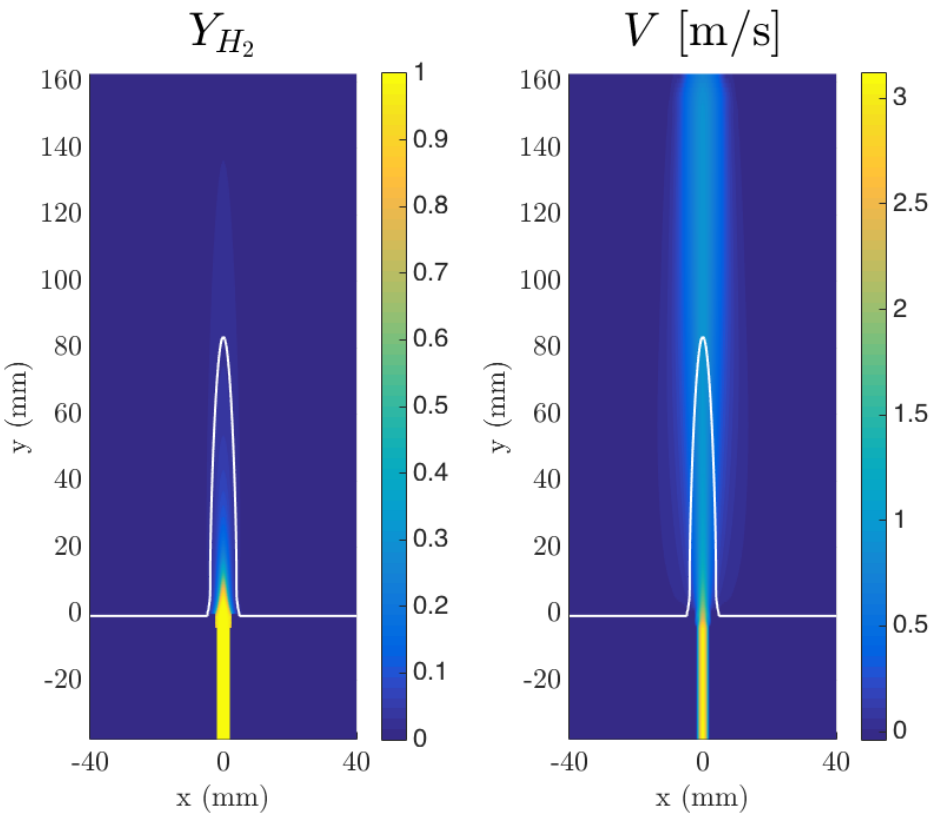

Figure 1: 2-D axisymmetric computational domain for the ignition case. Left: H_2 mass fraction at $t = 0$. Right: flow y velocity at $t = 0$.

is a stabilized cold hydrogen fuel jet (about 3 m/s) into a squared domain filled with air. The Fig. 1 illustrates this initial flow by showing the H_2 mass fraction and y-velocity.

Let

$$\boldsymbol{\zeta} = (\ln(A_3), b_3, \ln(E_3), L_{TW}, R_{TW}, M_e, E_{abs})^T$$

represent the random vector of uncertain model parameters, and $Q(\mathbf{x}, t; \boldsymbol{\zeta})$ be a quantity related to the solution of combustion system, and $Q_0(\mathbf{x})$ is its initial value. We can define the following quantity that links the mass fraction of fuel H_2 and oxidizer O_2 for the reaction (9),

$$\Phi(\mathbf{x}, t; \boldsymbol{\zeta}) = \frac{\nu'_{H_2,3} Y_{O_2}/W_{O_2}}{\nu'_{O_2,3} Y_{H_2}/W_{H_2}} = \frac{Y_{O_2}}{8 Y_{H_2}}.$$

Thus, the contour

$$\Phi(\mathbf{x}, t; \boldsymbol{\zeta}) = 1$$

defines the stoichiometric surface. E.g. the white contour in Fig. 1 represents the (stabilized) initial stoichiometric surface.

A spatial weighting function $w(\mathbf{x}, t; \boldsymbol{\zeta})$ can be defined following a Gaussian pdf with

respect to Φ,*

$$w(\mathbf{x}, t; \boldsymbol{\zeta}) = \frac{1}{\sigma\sqrt{2\pi}} \exp\left(-\frac{(\Phi - 1)^2}{2\sigma^2}\right),$$

where σ is a predefined deviation parameter; we use $\sigma = 0.001$ in this work. The spatial integral of weighting function is denoted by

$$\Omega(t; \boldsymbol{\zeta}) = \int w(\mathbf{x}, t; \boldsymbol{\zeta})\, \mathrm{d}\mathbf{x}.$$

The QoI used in this work is defined as a dimensionless average as follows

$$\mathcal{J}_Q(t; \boldsymbol{\zeta}) = \frac{\frac{1}{\Omega(t;\boldsymbol{\zeta})} \int Q(\mathbf{x}, t; \boldsymbol{\zeta}) w(\mathbf{x}, t; \boldsymbol{\zeta})\, \mathrm{d}\mathbf{x}}{\frac{1}{\Omega_0} \int Q_0(\mathbf{x}) w_0(\mathbf{x})\, \mathrm{d}\mathbf{x}} = \frac{\langle Q(t; \boldsymbol{\zeta}) \rangle}{\langle Q_0 \rangle}.$$

If $\mathcal{J}_Q(t \gg t_0; \boldsymbol{\zeta})$ is close to unity for a quantity such as temperature, it is obvious no ignition has appeared. Fig. 2 illustrates the temperature field of an ignited example, in which case the stoichiometric surface is heated by combustion and thus we have a high $\mathcal{J}_T$.

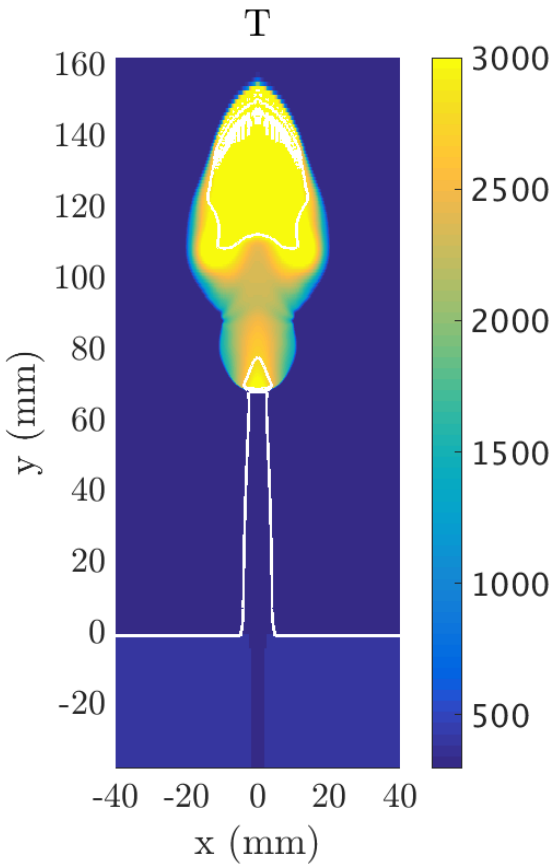

Figure 2: A successful ignition example. Compuational domain with a typical temperature field in [K]. Laser height: $y = 103.40$ mm.

*In present case where the stoichiometric surface under flame prpopagation does not change its form significantly in time, we can use a time-independent weighting function $w_0(\mathbf{x})$ for simplicity.

3.3 Uncertainty propagation and analysis

This section is devoted to the parameter sensitivity analysis for QoI $\mathcal{J}_T$. Let us analyze the case where the laser source is put at height $y = 103.40$ mm (with respect to experiments). We set the ANOVA interaction order $\nu = 3$ and size of experimental design $\mathcal{Q} = 100$.

The scatter plots of QoI with respect to each (tranformed) parameter are given in Fig. 3. Note here we employ the following isoprobabilistic tranform by using the cumulative distribution function (CDF) $\mathcal{F}$,

$$\xi_i = \mathcal{F}_{\zeta_i}(\zeta_i).$$

By definition $\mathcal{J}_T$ represents the dimensionless average temperature weighted on the initial-time stoichiometric surface. If we assume the raise of flame temperature in the vicinity of stoichiometric surface is mainly due to the release of enthalpy of formation of chemical reaction itself (not due to laser heat transfer), it is obvious that the greater the value of $\mathcal{J}_T$, the faster the flame propagates. Thus from Fig. 3 and as expected, we observe qualitatively

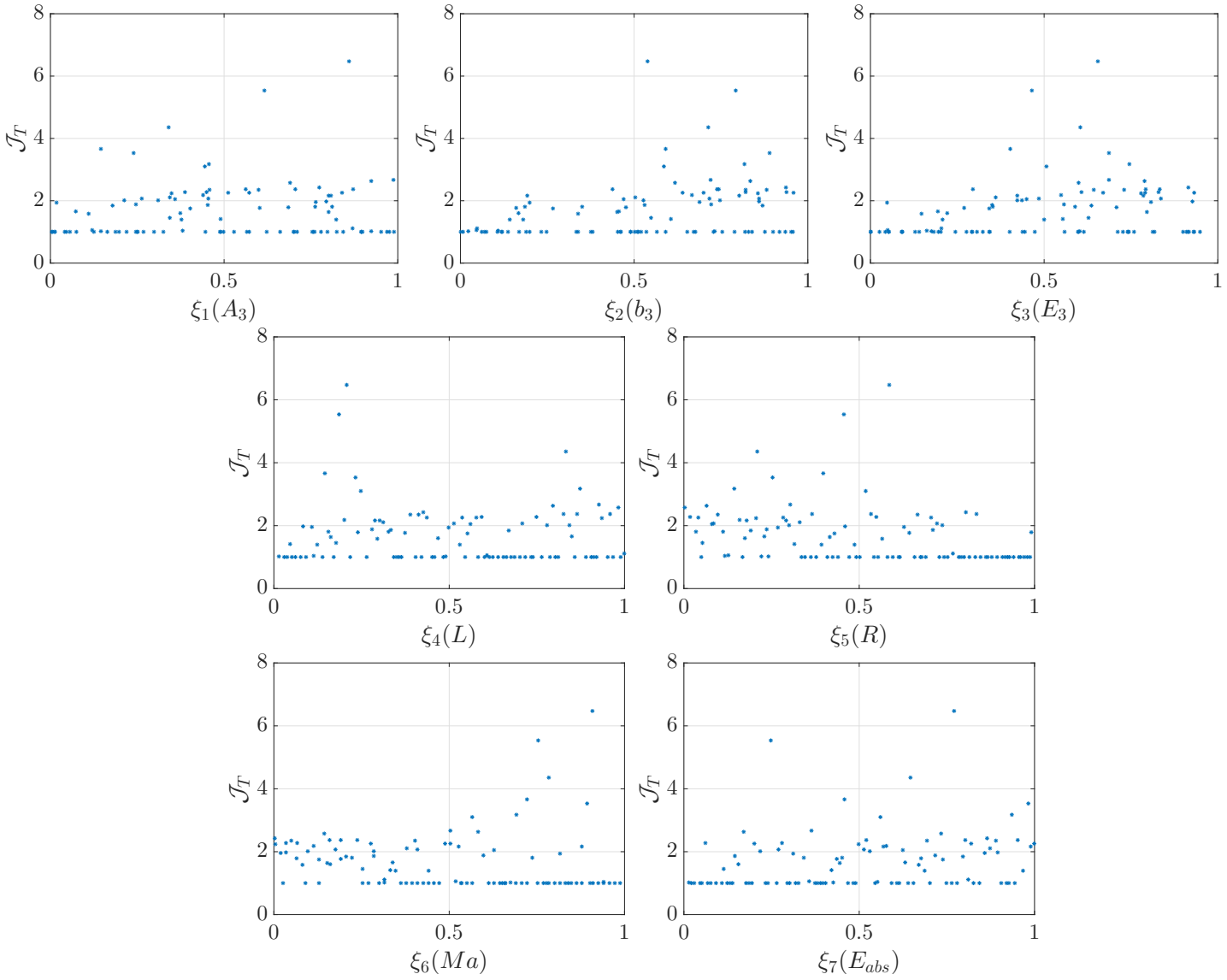

Figure 3: QoI vs. model parameters. Laser height: $y = 103.40$ mm.

with a stronger laser source (greater E_{abs} or smaller R_{TW} i.e. a more narrow region of high temperature), the more probably ignition occurs, and if this happens, the faster flame propagates. Also, a greater value of Mach number parameter M_e makes ignition more diffcult to happen because of the flow mixing; however, once ignited the flame is found to propagate considerably faster due to the vorticity. Concerning the remaining model parameters, we find it more difficult to draw a similar qualitative conclusion.

A procedure of parameter re-ordering is generally required (see end of Section 2) that depends upon their variance contribution of first-order ANOVA components.[†] Fig. 4 (top) presents the SI of input parameters, while the bottom figures illustrate the SI in the descending order together with the cumulated value. We denote the re-ordered input random vector for case $m = 4$ as,

$$\hat{\boldsymbol{\xi}}_{m=4} = (\xi_3, \xi_2, \xi_4, \xi_5, \xi_1, \xi_7, \xi_6)^T, \tag{10}$$

and for $m = 5$,

$$\hat{\boldsymbol{\xi}}_{m=5} = (\xi_2, \xi_3, \xi_4, \xi_5, \xi_1, \xi_7, \xi_6)^T. \tag{11}$$

Note they are slightly different about the relative importance of b_3 and E_3. In fact, the SI of b_3 and E_3 are very close in the case of $m = 5$.

Active dimension D_2 is evaluated using the sum of variances of first-order terms

$$\sum_{i=1}^{D_2} \mathrm{Var}(f_i) \geqslant p \sum_{i=1}^{N} \mathrm{Var}(f_i), \tag{12}$$

where p is a proportionality constant in $(0, 1)$, and is very close to 1. Thus we can conclude from Fig. 4 the following

$$\begin{aligned} D_2 &= 3, \quad \text{if } p = 0.7, \\ D_2 &= 4, \quad \text{if } p = 0.8, \\ D_2 &= 5, \quad \text{if } p = 0.9, \\ D_2 &= 6, \quad \text{if } p = 0.95, \\ D_2 &= 7, \quad \text{if } p = 0.999. \end{aligned}$$

We set $p = 0.999$ for this case, which results that all input parameters are taken into consideration for interaction calculations. In fact, the dimensionality of 7 is relatively low, and the proposed adaptive approach can handle this problem with an experimental design size $\mathcal{Q} = 100$ by setting this high active dimensionality at this stage. As a result, the ANOVA expansion has its size equal to

$$N + \binom{D_2}{2} + \binom{D_3}{3} = 63.$$

Fig. 5 illustrates the first-order SI together with total sensitivity indices (TSI). We observe that the kinetic parameters have a more significant variance contribution than their laser source counterparts in general. Meanwhile, both measures indicate the input parameter $\xi_3(E_3)$ is the most significant one, followed by $\xi_2(b_3)$. The TSI when setting $m = 5$ shows the variance contribution of the input $\xi_1(A_3)$ is more significant than all laser source parameters.

[†]We remind that this step involves a least-squares regression system that only contains polynomial bases of first-order.

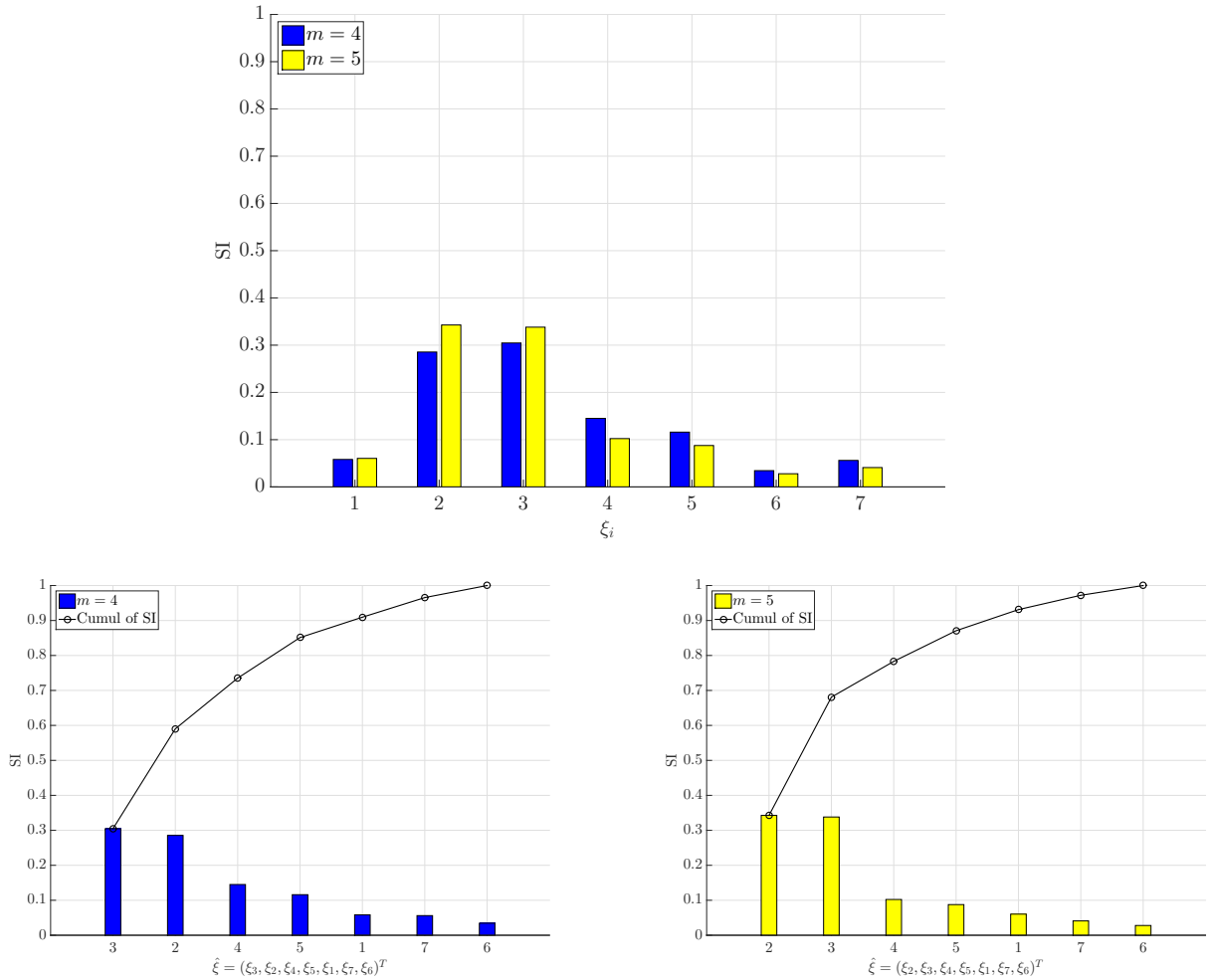

Figure 4: First-order SI for $m = 4$ and $m = 5$. x-axis indexing on the top figure is according to original random vector $\boldsymbol{\xi}$. $\hat{\boldsymbol{\xi}}$ on the bottom figures is the re-ordered input vector. $\nu = 3$. Experimental design size $\mathcal{Q} = 100$. $p = 0.999$. Laser height: $y = 103.40$ mm.

Fig. 6 illustrates the Sobol' sensitivity indices for both first- and higher-order ANOVA component functions. For the sake of clarity, we point out explicitly the following:

- $x-$axis indices $1-7$ represent first-order ANOVA components that are ordered according to the original random vector

$$\boldsymbol{\xi} \rightarrow \boldsymbol{\zeta} = (\ln(A_3), b_3, \ln(E_3), L_{TW}, R_{TW}, M_e, E_{abs})^T.$$

- $x-$axis indices $8-28$ represent second-order ANOVA components, while $29-63$ represent third-order ones. These indices are ordered following $\hat{\boldsymbol{\xi}}$ (10) or (11), and by using an ANOVA multi-index system presented in [19, page 1556].

We then mostly observe from Fig. 6 that the interaction between b_3 and $\ln(E_3)$ is significant compared to first-order and other interaction contributions. The third-order interactions are in general of less importance than second- and first-order components.

4 CONCLUSIONS AND FUTURE WORK

This paper aims to deal with Uncertainty Quantification of engineering and physical problems featuring a moderate to large number of uncertain input parameters. The purpose is to identify the relative importance of these uncertainties onto a given quantity of interest. This is achieved in this work by performing global sensitivity analysis, and in particular by combining the Analysis of Variance technique (ANOVA) and the polynomial dimensional decomposition approach (PDD). A set of coupled adaptivity strategies are futher employed and have been proved useful to identify important parameters in a simplified plasma-assisted combustion system.

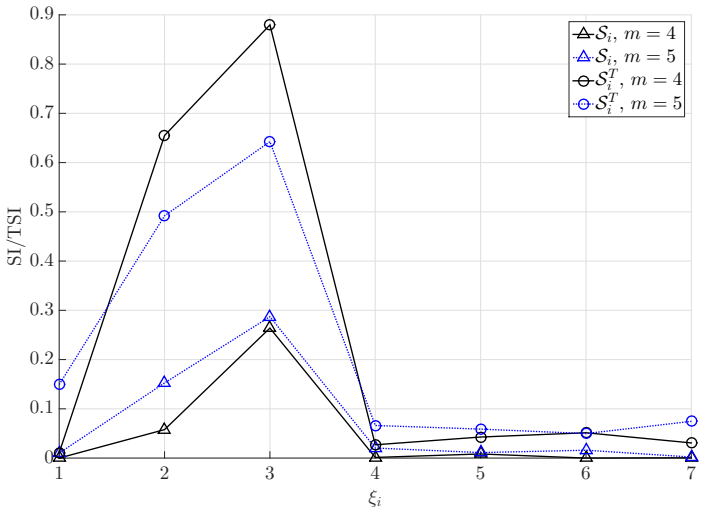

Figure 5: First-order Sobol' Sensitivity Indices (SI) and Total Sensitivity Indices (TSI). $\nu = 3$. $m = 4, 5$. Experimental design size $\mathcal{Q} = 100$. $p = 0.999$. All 7 parameters are considered in first- and higher-order ANOVA components. Laser height: $y = 103.40$ mm.

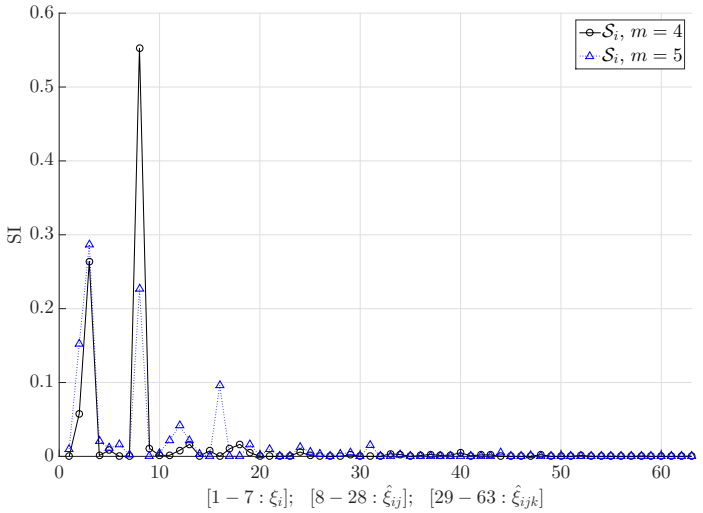

Figure 6: First-, second- and third-order Sobol' Sensitivity Indices (SI). The element indices of the original input vector $\boldsymbol{\xi}$ are used for first-order SI, while the ones of the re-ordered input vector $\hat{\boldsymbol{\xi}}$ are used for second- and third-order SI. $\nu = 3$. $m = 4, 5$. Experimental design size $\mathcal{Q} = 100$. $p = 0.999$. All 7 parameters are considered in first- and higher-order ANOVA components. Laser height: $y = 103.40$ mm.

The resulting surrogate polynomial approximation is a very sparse representation of the deterministic model. Since the surrogate model size is updated recursively in the stepwise regression procedure, the number of the required deterministic model evaluations is well controlled, and its final value is significantly smaller than when employing a standard Monte Carlo or quasi Monte Carlo method. Finally, the computation of the global sensitivity indices simply requires a post-processing of the polynomial coefficients.

More detailed models for Laser Induced Breakdown and Laser-Plasma Interaction are currently in development in XPACC, while we are also considering more detailed chemistry mechanism for future work. A dielectric-barrier discharge (DBD) force and radical generation model will also be included in our future parametric UQ study.

ACKNOWLEDGMENT

This material is based in part upon work supported by the Department of Energy, National Nuclear Security Administration, under Award Number DE-NA0002374.

References

[1] G. E. B. Archer, A. Saltelli, and I. M. Sobol'. Sensitivity measures, anova-like techniques and the use of bootstrap. *Journal of Statistical Computation and Simulation*, 58:99–120, 1997.

[2] Philip S. Beran, Chris L. Pettit, and Daniel R. Millman. Uncertainty quantification of limit-cycle oscillations. *Journal of Computational Physics*, 217(1):217–247, 2006.

[3] G. Blatman and B. Sudret. Efficient computation of global sensitivity indices using sparse polynomial chaos expansions. *Reliability Engineering and System Safety*, 95:1216–1229, 2010.

[4] Géraud Blatman and Bruno Sudret. An adaptive algorithm to build up sparse polynomial chaos expansions for stochastic finite element analysis. *Probabilistic Engineering Mechanics*, 25(2):183–197, April 2010.

[5] Géraud Blatman and Bruno Sudret. Adaptive sparse polynomial chaos expansion based on least angle regression. *Journal of Computational Physics*, 230(6):2345–2367, March 2011.

[6] E Borgonovo, G E Apostolakis, S Tarantola, and A Saltelli. Comparison of global sensitivity analysis techniques and importance measures in PSA. *Reliability Engineering & System Safety*, 79(2):175–185, 2003.

[7] Seung-Kyum Choi, Ramana V. Grandhi, Robert A. Canfield, and Chris L. Pettit. Polynomial Chaos Expansion with Latin Hypercube Sampling for Estimating Response Variability. *AIAA Journal*, 42(6):1191–1198, 2004.

[8] Toshimitsu Homma and Andrea Saltelli. Importance measures in global sensitivity analysis of nonlinear models. *Reliability Engineering & System Safety*, 52(1):1–17, 1996.

[9] O. Le Maître, M. T. Reagan, H. N. Najm, R. G. Ghanem, and O. M. Knio. A Stochastic Projection Method for Fluid Flow II. Random Process. *Journal of Computational Physics*, 181(1):9–44, September 2002.

[10] Luca L. Massa and Jonathan B Freund. An Integrated Predictive Simulation Model for the Plasma-Assisted Ignition of a Fuel Jet in a Turbulent Crossflow. In *54th AIAA Aerospace Sciences Meeting*, number January, pages 1–48, Reston, Virginia, jan 2016. American Institute of Aeronautics and Astronautics.

[11] Hermann G. Matthies and Andreas Keese. Galerkin methods for linear and nonlinear elliptic stochastic partial differential equations. *Computer Methods in Applied Mechanics and Engineering*, 194(12-16):1295–1331, 2005.

[12] Sharif Rahman. A polynomial dimensional decomposition for stochastic computing. *International Journal for Numerical Methods in Engineering*, 76:2091–2116, 2008.

[13] Sharif Rahman. Global sensitivity analysis by polynomial dimensional decomposition. *Reliability Engineering & System Safety*, 96(7):825–837, July 2011.

[14] Sharif Rahman and Xuchun Ren. Novel computational methods for high-dimensional stochastic sensitivity analysis. *International Journal for Numerical Methods in Engineering*, 2014.

[15] Sharif Rahman and Vaibhav Yadav. Orthogonal Polynomial Expansions for Solving Random Eigenvalue Problems. *International Journal for Uncertainty Quantification*, 1(2):163–187, 2011.

[16] I. M. Sobol'. Sensitivity estimates for nonlinear mathematical models. *Mathematical Modelling & Computational Experiments*, 1(4):407–414, 1993.

[17] I. M. Sobol'. Global sensitivity indices for nonlinear mathematical models and their Monte Carlo estimates. *Mathematics and Computers in Simulation*, 55(1-3):271–280, February 2001.

[18] B. Sudret. Global sensitivity analysis using polynomial chaos expansions. *Reliability Engineering & System Safety*, 93(7):964–979, July 2008.

[19] Kunkun Tang, Pietro M. Congedo, and Rémi Abgrall. Sensitivity analysis using anchored ANOVA expansion and high-order moments computation. *International Journal for Numerical Methods in Engineering*, 102(9):1554–1584, June 2015.

[20] Kunkun Tang, Pietro M. Congedo, and Rémi Abgrall. Adaptive surrogate modeling by ANOVA and sparse polynomial dimensional decomposition for global sensitivity analysis in fluid simulation. *Journal of Computational Physics*, 314:557–589, jun 2016.

[21] Vaibhav Yadav and Sharif Rahman. Adaptive-sparse polynomial dimensional decomposition methods for high-dimensional stochastic computing. *Computer Methods in Applied Mechanics and Engineering*, 274:56–83, June 2014.

ECCOMAS Congress 2016
VII European Congress on Computational Methods in Applied Sciences and Engineering
M. Papadrakakis, V. Papadopoulos, G. Stefanou, V. Plevris (eds.)
Crete Island, Greece, 5–10 June 2016

UNCERTAINTY QUANTIFICATION IN NUMERICAL SIMULATIONS OF THE FLOW IN THORACIC AORTIC ANEURYSMS

Alessandro Boccadifuoco[1], Alessandro Mariotti[2], Simona Celi[3], Nicola Martini [3] and Maria Vittoria Salvetti[2]

[1]Scuola Superiore Sant'Anna
Piazza Martiri della Libertà 33, 56127 Pisa, Italia
e-mail: alessandro.boccadifuoco@sssup.it

[2] Dipartimento di Ingegneria Civile e Industriale, Università di Pisa
Via G. Caruso 8, 56122 Pisa, Italia
e-mail: alessandro.mariotti@for.unipi.it, mv.salvetti@ing.unipi.it

[3] Fondazione CNR - Regione Toscana G. Monasterio,
Via Aurelia Sud, 54100 Massa, Italia
e-mail: s.celi@gmail.com, nicola.martini@gmail.com

Keywords: Ascending thoracic aortic aneurysms, CFD simulations, uncertainty quantification, polynomial chaos.

Abstract. *Numerical simulations of the flow in thoracic aortic aneurysms are carried out by using the open-source tool SimVascular and considering patient-specific geometries, obtained through in-vivo imaging. One of the main issues in these simulations is the choice of suitable boundary conditions, modeling the organs and vessels not included in the computational domain. The current practice is to use outflow conditions based on proximal resistance, capacitance and distal resistance (three-element Windkessel model), whose values are tuned to obtain a physiological behavior of the patient pressure. However, it is not known a priori how this choice affects the results of the simulation. A quantification of the impact on the numerical simulation results of uncertainties in the values of the Windkessel model parameters is carried out by using the generalized Polynomial Chaos approach. Different patient-specific geometries are considered, characterized by a different size of the aneurysms, and the effect of wall compliance is also investigated. We analyze the impact of the uncertainties in the selected outflow parameters on the time-averaged wall shear stress and on the oscillatory shear index, which are commonly used as hemodynamic descriptors.*

1 INTRODUCTION

The Ascending Thoracic Aortic Aneurysm (ATAA) is a life-threatening cardiovascular disease with remarkable morbidity and mortality. It is defined as a permanent and localized dilatation of the aorta, resulting from an irreversible loss of structural integrity of the aortic wall ([1, 2]), triggered by genetic mutations and/or mechanobiological aspects. Conventionally, an increase in diameter greater than 50% may be considered as evidence of an aneurysm ([3]). At the state of the art, clinical decisions on treatment strategies are currently based on empiric criteria, like the aortic diameter value or its growth rate.

From a biomechanical point of view, the aneurysmatic pathology has been investigated considering the structural change of the artery wall and its effects on the wall stress distribution, as well as performing fluid dynamical analyses in order to obtain the distribution of the wall shear stress. Biomechanical studies (see e.g. [4]) demonstrated that the criterion most widely used to predict the pathological state of ascending thoracic aortic aneurysms, i.e. the maximum aortic diameter, fails to predict rupture or dissection, especially in case of small-sized ascending thoracic aortic aneurysms and this means that other predictors are needed to understand and estimate the state of the aneurysm. Indeed, ATAAs are characterized by the presence of a complex hemodynamics, which could contribute to the onset/progression of the disease.

Advances in medical images provide not only accurate morphological features but also the non-invasive quantification of blood flow. In this context, the Phase Contrast Magnetic Resonance (PC-MRI) technique has become the prevalent imaging technique for non-invasive and detailed information due to its good spatial resolution with respect to hemodynamic quantities and due to the possibility of acquiring time-dependent data sets of the three-directional components of the blood flow velocity ([5, 6]).

In this scenario, CFD-based techniques are being used to build complex computer representations of the cardiovascular system in health and disease. CFD modeling enables investigation of pressure and flow fields at a temporal and spatial resolution unachievable by any clinical methodology, therefore allowing to easily quantify variables and indicators difficult to be obtained from *in-vivo* measurements. The main difficulty is represented by the assumptions made in CFD models, concerning, for instance, boundary conditions or the modeling of wall compliance and wall properties, which may affect the accuracy of CFD predictions. Thus, the combination between CFD simulation techniques and *in-vivo* and ex-vivo measurements is a key ingredient to set up reliable predictive tools. For instance, phase velocity and anatomic data ([7]) from PC-MRI have been used to perform patient-specific computational hemodynamics in healthy ([8, 9]) and diseased subjects ([10, 11]), in order to provide evidence of a possible relation of local wall shear stress with disease ([12, 13]), but, despite all those investigations, reliable patient-specific models are usually not easy to be obtained.

As previously mentioned, the accuracy of CFD predictions depends on the adopted modeling, but also on the quality of input data. For CFD applications it is unclear how detailed the clinical data needs to be in terms of geometry (segmented from medical images) and parametrization (variability described by the model and the tuning of patient-specific boundary conditions). In the present work we want to determine the impact of the uncertainties in the input data. This will provide further understanding of the relative importance of physiological parameters, determining those which are most influential, and those which can be assumed or averaged. In particular, we focused on the choice of suitable boundary conditions, modeling the organs and vessels not included in the computational domain. The current practice is to use outflow conditions based on proximal resistance, capacitance and distal resistance (three-element Windkessel model), whose

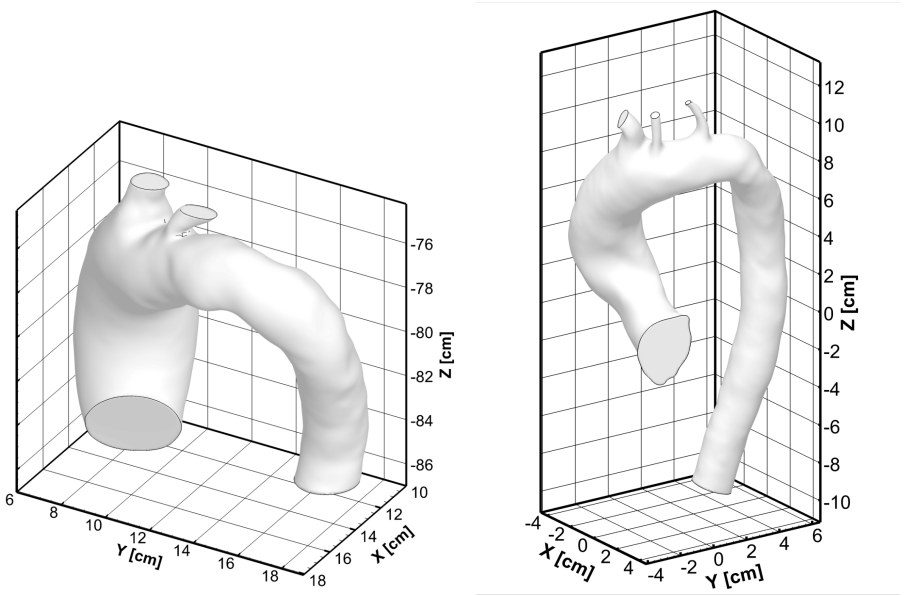

(a) Geometry A ($D_{r1} = 1.7$) (b) Geometry B ($D_{r2} = 1.5$)

Figure 1: Sketch of the considered geometries.

values are tuned to obtain a physiological behavior of the patient pressure. However, it is not known a priori how this choice affects the results of the simulation. Since a preliminary analysis showed that the proximal resistance and the capacitance are the main parameters affecting the pressure profile obtained in the Windkessel model, these two quantities were selected as uncertain parameters for the uncertainty quantification analysis, while a fixed reference value of the distal resistance was maintained.

This sensitivity was carried out through a stochastic approach, i.e. by modeling the unknown parameters as input random variables with a given probability distribution and propagating the uncertainties through the computational model to statistically quantify their effect on the results. The stochastic quantification was carried out by using the generalized Polynomial Chaos approach. Different patient-specific geometries were considered, characterized by a different size of the aneurysms, and the effect of wall compliance was also investigated. The impact of the uncertainties in the selected outflow parameters was investigated on the different quantities of interest; in particular, we analyzed the stochastic mean and standard deviation of the time-averaged wall shear stress and oscillatory shear index.

2 DEFINITION OF THE PROBLEM

2.1 Geometry definition

Two patient-specific geometries of thoracic aortas subjected to aneurysm in their ascending region were considered. Both cases were acquired by means of *in-vivo* imaging. The geometry A was reconstructed from Computed Tomography (CT), the geometry B by using Magnetic Resonance Imaging (MRI).

The two geometries are sketched in Figure 1. They differ in the severity of the disease, property quantified by the maximum diameter ratio $D_r = D_{\max}/D_{\text{healthy}}$, where $D_{\max}$ is the maximum transverse diameter (thus, obtained in correspondence of the widest section of the aneurysm) and D_{healthy} is the diameter of the healthy segment (measured in the descending region of the aorta). The two considered cases are characterized by $D_{r1} = 1.7$ and $D_{r2} = 1.5$,

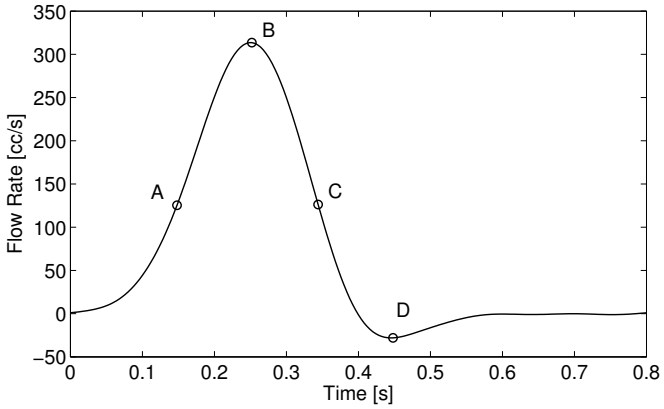

Figure 2: Flow rate profile imposed at the inlet section. The following characteristic time instants are highlighted: the maximum acceleration (A), the peak systole (B), the maximum deceleration (C) and early diastole (D).

respectively.

2.2 Simulation setup and numerical methodology

At the inlet section of the computational domain we imposed the physiological flow rate waveform of Figure 2 (see e.g. [14, 15]). The distribution of the velocity in the inlet section was assumed to be uniform.

The choice of outflow boundary conditions is more challenging, since they should accurately represent the effect of what happens outside the computational domain, modeling downstream organs and vessels (see e.g. [16] for a detailed overview). For this purpose, a three-element Windkessel model (also known as RCR model and sketched in Figure 3) was placed in correspondence of each outlet section, with a downstream pressure set to a constant reference value. Lumped parameter models are based on the analogy between electric circuits and hemodynamic problems: in particular, analogy is identified between the voltage difference and the drop in pressure, and between the current and the flow rate. In the presented scheme, the proximal and distal resistances (R_p and R_d) represent the viscous resistance the blood flow undergoes inside large and small vessels, respectively. The capacitance C quantifies the compliance, and thus the capability of storing fluid, of the major arteries. In the numerical deterministic computations used as a reference, these parameters were set in order to obtain a desired physiological behavior of the pressure profile ($125/80\,\mathrm{mmHg}$) in the simplified fully lumped model in which the contribution of the flow in the computational domain is not considered:

$$P(t) + R_d\, C \frac{dP(t)}{dt} = (R_p + R_d)Q(t) + R_p R_d\, C \frac{dQ(t)}{dt} \tag{1}$$

in which we imposed the inlet flow rate $Q(t)$ of Figure 2. Equation (1) was solved numerically. The resulting values are: $R_p = 106.5\,\mathrm{g\,cm^{-4}\,s^{-1}}$, $C = 10.4 \times 10^{-4}\,\mathrm{cm^4\,s^2\,g^{-1}}$ and $R_d = 1.67 \times 10^3\,\mathrm{g\,cm^{-4}\,s^{-1}}$.

Since descending from a fully lumped parameter model, the values of R_p, R_d and C were independent of the particular geometry considered. They were then distributed in the various

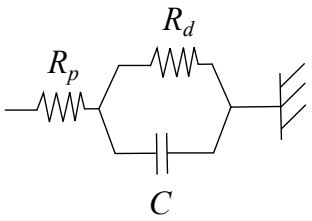

Figure 3: Scheme of a 3-Element Windkessel model.

Table 1: Summary of mechanical properties of the arterial wall used in the deformable simulations.

Quantity	Value
Density: ρ_{w} [$\mathrm{g\,cm^{-3}}$]	1.08
Young's Modulus: E_{w} [MPa]	3
Thickness: h_{w} [cm]	0.1
Poisson's Ratio: λ_{w}	0.499
Shear Correction Parameter: k_{w}	0.833

outlets as follows:

$$\begin{aligned} R_{p_i} &= R_p \frac{A_{\mathrm{tot}}}{A_i} \\ R_{d_i} &= R_d \frac{A_{\mathrm{tot}}}{A_i} \qquad \text{for } i = 1, \ldots, n_{\mathrm{outlets}} \\ C_i &= C \frac{A_i}{A_{\mathrm{tot}}} \end{aligned} \tag{2}$$

where n_{outlets} is the number of the outlets in the considered case (i.e., 3 in the first geometry and 4 in the second), A_i is the area of the outlet i and A_{tot} is the sum of the areas of all the outlets. The previous relations arise from the consideration that when increasing the vessel section the resistance opposed to the blood flow becomes smaller, while the wall compliance capability increases. Unlike R_p, R_d and C, the quantities obtained through Equation (2) are case-dependent.

On the arterial wall we imposed a no-slip condition. Both rigid and deformable simulations were performed. When considering the arterial wall compliance, for the sake of simplicity the aorta was assumed as an elastic, homogeneous and isotropic material, with a uniform wall thickness. The values of the mechanical properties chosen are reported in Table 1, where all dimensional properties, except for Young's Modulus, are expressed in *CGS* units.

The values of blood dynamic viscosity and density were specified as $\mu = 0.04\,\mathrm{g\,cm^{-1}\,s^{-1}}$ and $\rho = 1.06\,\mathrm{g\,cm^{-3}}$, respectively.

The hemodynamic simulations were performed with *SimVascular* (see [17]), an open-source comprehensive package specific for cardiovascular problems. The computational grid is unstructured and consists of tetrahedral elements, due to their adaptability to complex computational domains, like patient-specific geometries. The numerical code solves the three-dimensional incompressible Navier-Stokes equations by means of a stabilized finite element method, which makes it possible to choose linear shape functions for both velocity and pressure. For advancing in time, it uses the generalized α-method, which is an implicit technique that permits to achieve second order accuracy (see [18]).

The physical time step chosen for performing the numerical simulations was $0.001\,\mathrm{s}$ for both rigid and deformable cases, resulting in 800 time steps every cardiac cycle. After a grid sensitivity study, we chose a tetrahedral grid having approximately 2.2×10^5 for the geometry A and a tetrahedral grid with approximately 2.4×10^5 nodes for the geometry B.

Furthermore, each computation was run until the L_2 norms of the normalized differences between two successive pressure waveforms and between two successive flow rate waveforms were smaller than 10^{-5} (see [19]). These quantities were evaluated in correspondence of the descending aortic outlet section.

2.3 Quantities of interest and indicators

When considering the effects of the blood flow on the arterial wall, particular attention is given to the Wall Shear Stress (WSS), namely the modulus of the tangential stress $\boldsymbol{\tau}$ exerted by the flow on the arterial wall, i.e.

$$\mathrm{WSS}\left(\mathbf{x}, t\right) = \left|\boldsymbol{\tau}\left(\mathbf{x}, t\right)\right| \tag{3}$$

since it is thought to play an important role in the formation and growth of vascular diseases. Two additional parameters assume significant importance and are here used as hemodynamic descriptors: the Time-Averaged Wall Shear Stress (TAWSS), i.e. the wall shear stress throughout an entire cardiac cycle of period T, defined as:

$$\mathrm{TAWSS}\left(\mathbf{x}\right) = \frac{1}{T}\int_0^T \left|\boldsymbol{\tau}\left(\mathbf{x}, t\right)\right| \mathrm{d}t \tag{4}$$

and the Oscillatory Shear Index (OSI), which represents a measure of the deviation of the tangential stress from the predominant axial direction,

$$\mathrm{OSI}\left(\mathbf{x}\right) = \frac{1}{2}\left(1 - \frac{\left|\frac{1}{T}\int_0^T \boldsymbol{\tau}\left(\mathbf{x}, t\right) \mathrm{d}t\right|}{\frac{1}{T}\int_0^T \left|\boldsymbol{\tau}\left(\mathbf{x}, t\right)\right| \mathrm{d}t}\right) \tag{5}$$

This last indicator takes values in the range $[0, 0.5]$. Lower OSI values indicate that the tangential stresses at the wall are oriented predominately in the primary direction of the blood flow. On the other hand, high values indicate a very oscillatory behavior, 0.5 meaning that the instantaneous and the time-averaged vectors are never aligned.

3 RESULTS OF THE REFERENCE DETERMINISTIC SIMULATIONS

This section presents the results obtained for the reference deterministic simulations. For the geometry A (Figure 1(a)) simulations were carried out both for rigid and deformable walls, while for the geometry B (Figure 1(b)) only rigid walls were considered.

3.1 Geometry A with rigid walls

Figure 4 shows the instantaneous flow streamlines obtained in the simulation of the flow in the geometry A with rigid walls. The streamlines are colored according to the velocity magnitude. During systole they present a very regular behavior and the highest values of the velocity (Figure 4(a)), while recirculation areas occur in the diastolic phase (Figure 4(b)), which is characterized by reverse flow entering from the domain outlets.

In Figure 5 the WSS distributions at different time instants are shown. The four time instants marked in Figure 2 are considered. We selected the same WSS range in all the figures to highlight

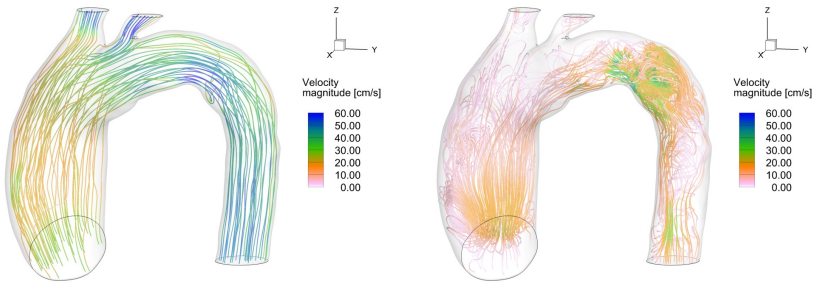

(a) Peak systole (b) Early diastole

Figure 4: Instantaneous flow streamlines for the geometry A with rigid walls. The streamlines are colored according to the velocity magnitude.

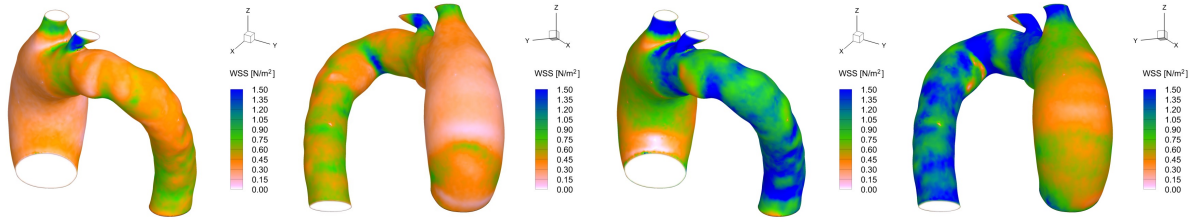

(a) Max acceleration (front) (b) Max acceleration (back) (c) Peak systole (front) (d) Peak systole (back)

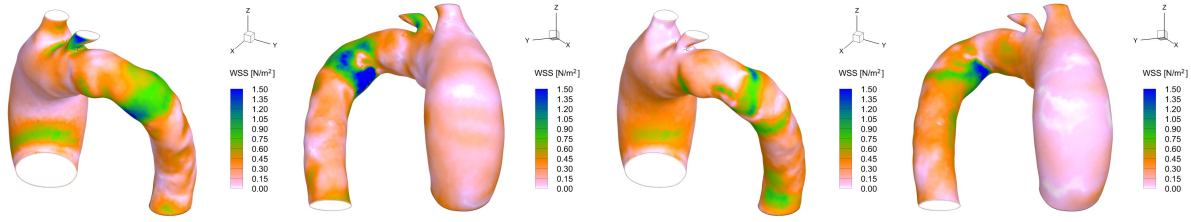

(e) Max deceleration (front) (f) Max deceleration (back) (g) Early diastole (front) (h) Early diastole (back)

Figure 5: WSS distribution for the geometry A with rigid walls.

the different magnitude of the tangential stresses along a cardiac cycle. The highest values of the stresses are found at peak systole in correspondence of the two small branches The stresses on the ascending region of the aorta are rather low during the whole cardiac cycle, possibly due to the large size of the aneurysm.

TAWSS and OSI are presented in Figures 6 and 7. The TAWSS distribution gives information on the mean behavior of WSS during the cardiac cycle, and it summarizes what found in the instantaneous maps: the most stressed regions are the areas with high curvature, while the aneurysm region is characterized by low stress. Since these mean stresses during a cardiac cycle are much smaller if compared with the maximum ones occurring during peak systole, a smaller TAWSS range was chosen.

High values of OSI (i.e., close to its maximum limit of 0.5) are associated to recirculation areas, see Figure 4(b) for comparison. Note that they occur also inside the aneurysm.

3.2 Effect of the wall compliance

In this section we evaluate the effect of the deformations of the arterial wall. The geometry A is considered.

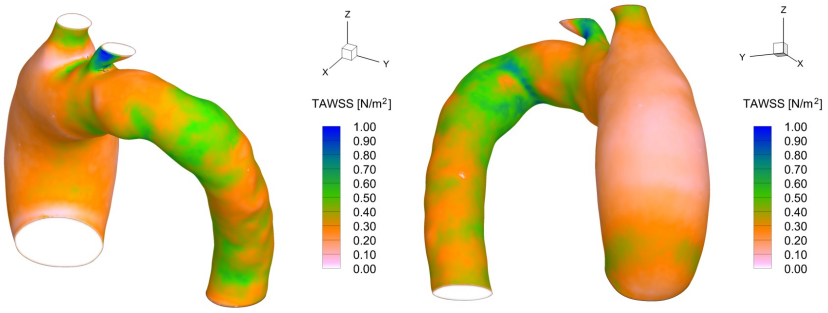

(a) Front view (b) Back view

Figure 6: TAWSS distribution for the geometry A with rigid walls.

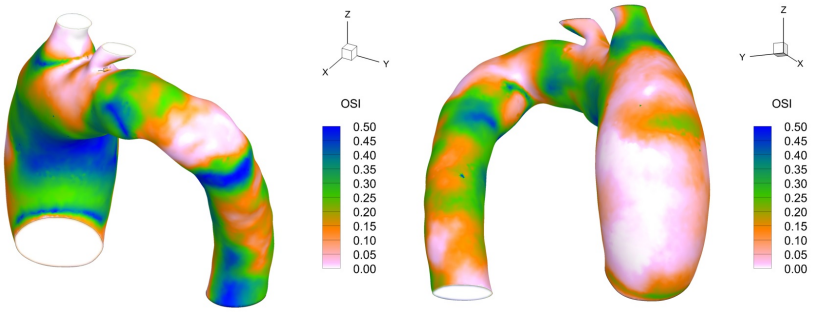

(a) Front view (b) Back view

Figure 7: OSI distribution for the geometry A with rigid walls.

The flow streamlines do not present significant differences if compared with the ones obtained with rigid walls, and thus they are not shown here. The only effect is a slight decrease of velocity magnitude, due to the widening of the vessel under the action of the blood flow.

The distributions of WSS and TAWSS are qualitatively very similar to the case of rigid walls, with only a variation in the quantitative values, which in the deformable case are lower (e.g., compare Figure 8 with Figure 6). This behavior could be expected given the possibility of the wall to move and relax.

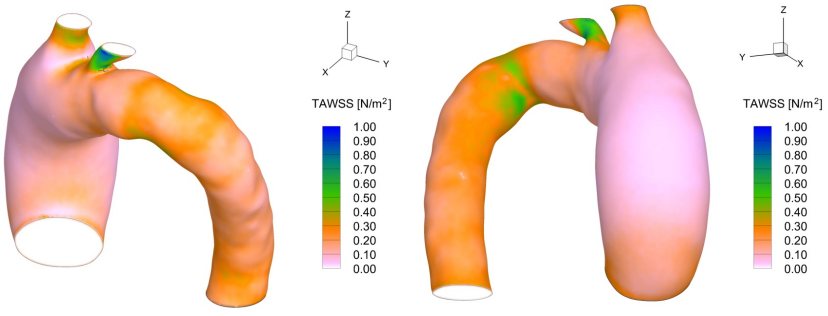

(a) Front view (b) Back view

Figure 8: TAWSS distribution for the geometry A with deformable walls.

The OSI distribution (Figure 9) does not present significant difference between deformable and rigid cases: this behavior is not surprising since this index is related to the velocity field,

which was found to be very similar in the two situations.

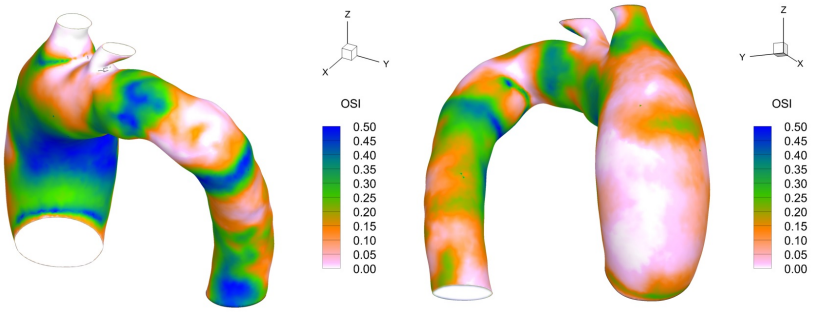

(a) Front view (b) Back view

Figure 9: OSI distribution for the geometry A with deformable walls.

3.3 Effect of the wall geometry

The effect of a different geometry and aneurysm size is evaluated by considering the geometry B (see Figure 1(b)). A simulation with rigid walls was performed with the same setup as for the geometry A.

Figure 10 shows the TAWSS distribution, and should be compared with Figure 6. The main effect of the geometry on TAWSS is the formation of areas of significant stress also in the ascending part of the aorta. This is due to the presence of a smaller aneurysm, and thus to the smaller size difference between the ascending and the descending regions.

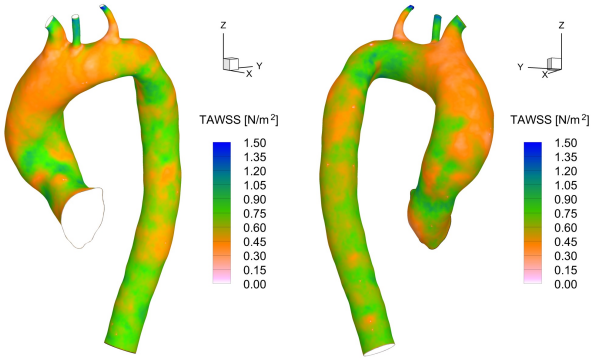

(a) Front view (b) Back view

Figure 10: TAWSS distribution for the geometry B with rigid walls.

High values of OSI can be found in the internal areas of both ascending and descending regions of the aorta, as shown in Figure 11, indicating thus that significant recirculation regions are present also inside the aneurysm.

4 UQ METHODOLOGY

The generalized Polynomial Chaos (gPC) approach, in its non-intrusive form, is an interpolant-type method, based on the projection of a given random process over an orthogonal known basis ([20]). The chaos expansion for a stochastic response output may be expressed as follows

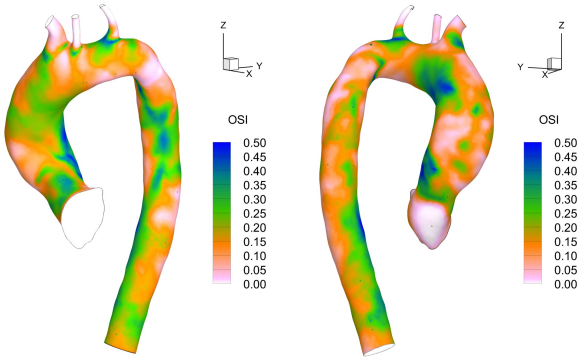

(a) Front view (b) Back view

Figure 11: OSI distribution for the geometry B with rigid walls.

(term-based indexing):

$$X(\omega) = \sum_{k=0}^{\infty} a_k \Phi_k(\boldsymbol{\xi}(\omega)) \tag{6}$$

where $X(\omega)$ is the random process, $\boldsymbol{\xi}(\omega)$ is the vector consisting of the independent random variables in the event space Ω, corresponding thus to the set of considered uncertain parameters, $\Phi_k(\boldsymbol{\xi})$ is the gPC polynomial of index k and a_k is the corresponding Galerkin projection coefficient.

The response surface is obtained by a truncation of the spectral decomposition (Equation (6)) to a finite limit T. Applying polynomial order bounds for all one-dimensional polynomials (tensor-product expansion), T is obtained as follows:

$$T = \prod_{i=1}^{M} (P_i + 1) - 1 \tag{7}$$

where M is the dimension of the random parameter space and P_i is the polynomial order bound for the i^{th} dimension.

Thanks to the orthogonality of the polynomial basis, the coefficient a_k can be computed as follows:

$$a_k = \frac{\langle X, \Phi_k \rangle}{\langle \Phi_k, \Phi_k \rangle} = \frac{1}{\langle \Phi_k, \Phi_k \rangle} \int_{\omega \epsilon \Omega} X \Phi_k \rho(\boldsymbol{\xi}) \, \mathrm{d}\xi \tag{8}$$

where $\rho(\boldsymbol{\xi})$ is the weight function associated with the chosen polynomial family. The integrals can be computed through different mathematical methods: Gaussian quadrature was used in the present work. The polynomial family to be used must be a priori specified. When dealing with Gaussian quadrature, an optimal family has a weight function similar to the probability measure, $W(\boldsymbol{\xi})$, of the random variables; it depends, thus, on the Probability Density Function (PDF) shape of the uncertain parameters.

As previously explained, the uncertain parameters in the Windkessel model are the proximal resistance, R_p, the capacitance, C, and the distal resistance, R_d. Since a UQ analysis with three uncertain parameters and 3D unsteady simulations is extremely expensive, a preliminary stochastic analysis was carried out to evaluate the single effect of R_p, C and R_d on the output pressure cycle in the 0D Windkessel model, i.e. neglecting the contribution of the 3D geometry of the aorta. This allowed to single out the effect of each uncertain parameter and, thus, to

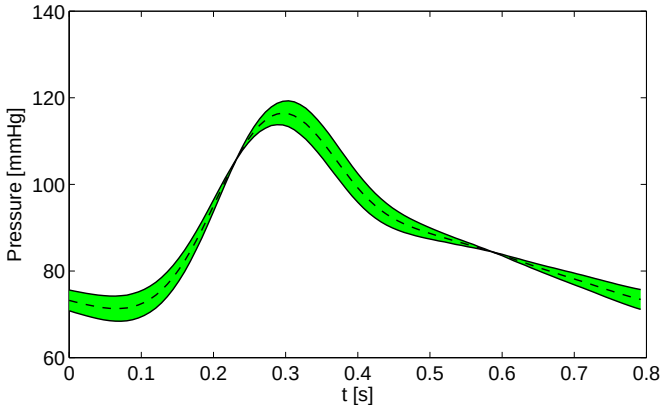

Figure 12: Effect of the variation of the capacitance C on the pressure waveform in correspondence of the descending aorta outlet section for the geometry A with rigid walls. The results are expressed in terms of stochastic mean (dashed line) $\pm$ stochastic standard deviation (continuous lines).

select the most important for the UQ analysis on 3D simulations, whose results are discussed in Sections 5 and 6.

After this 0D analysis, we selected R_p and C and allowed them to vary in the following ranges: $R_p \in [85.8, 148.4] \mathrm{g\,cm^{-4}\,s^{-1}}$ and $C \in [5.82 \times 10^{-4}, 12.6 \times 10^{-4}] \mathrm{cm^4\,s^2\,g^{-1}}$. First, we evaluated the effect of C alone: both rigid and deformable simulations were performed for the geometry A, while rigid walls were considered for the geometry B. Then, we investigated the combined effect of C and R_p: rigid simulations were performed for both the geometries.

The PDF of the input uncertain parameters is assumed to be uniform; this leads to the choice of Legendre polynomials for the gPC basis. The polynomial expansion is truncated to the third order for each dimension; hence, four quadrature points for each random variable are sufficient to compute the coefficients of the expansion. This leads to 4 or 16 hemodynamic simulations when considering one or two input parameters, respectively. These simulations were carried out for each quadrature point in the parameter space.

5 UQ ANALYSIS OF THE EFFECT OF UNCERTAINTIES IN THE VALUE OF C ON THE PRESSURE CYCLE AND ON THE FLOW FIELD

In this Section we evaluate how an uncertainty in the value of the capacitance C affects the quantities of interest reported in Section 2.3.

5.1 Geometry A with rigid walls

Figure 12 shows the output pressure waveform obtained in correspondence of the descending aorta outlet section. The results are presented in terms of the stochastic mean value $\pm$ the stochastic standard deviation. An increase of C leads to a reduction of the pulse pressure, as systolic and diastolic pressures become closer. On the other hand, the mean pressure P_{mean} is maintained practically constant.

The effect of the variation of C on TAWSS and OSI is evaluated in terms of the stochastic mean value and stochastic standard deviation, individually portrayed.

The stochastic mean distribution of TAWSS is almost equal to the reference deterministic result. The difference between the two TAWSS fields is shown in Figures 13(a) and 13(b) to allow a quantitative analysis. Differences are practically zero in most of the arterial lateral surface. Significant differences are found only in the upstream part of the descending aorta and

their absolute values are up to 10% of the corresponding stochastic mean values. In the same region we also find the largest stochastic variance of TAWSS (see Figures 13(c) and 13(d)). This means that this is the region in which TAWSS is most sensitive to the value of C.

Figures 14(a) and 14(b) report the difference between the stochastic mean distribution of OSI and the distribution obtained in the reference deterministic simulation. Again, differences are practically zero in the ascending aorta and in the two branches, independently of the value of OSI in those regions (note that in the reference deterministic simulation OSI assumes high values also in the internal part of the aneurysm, as shown in Figure 7(a)). On the other hand, significant positive and negative differences are found in localized regions of the aortic arch and of the descending aorta, where we also find the largest stochastic variance (see Figures 14(c) and 14(d)).

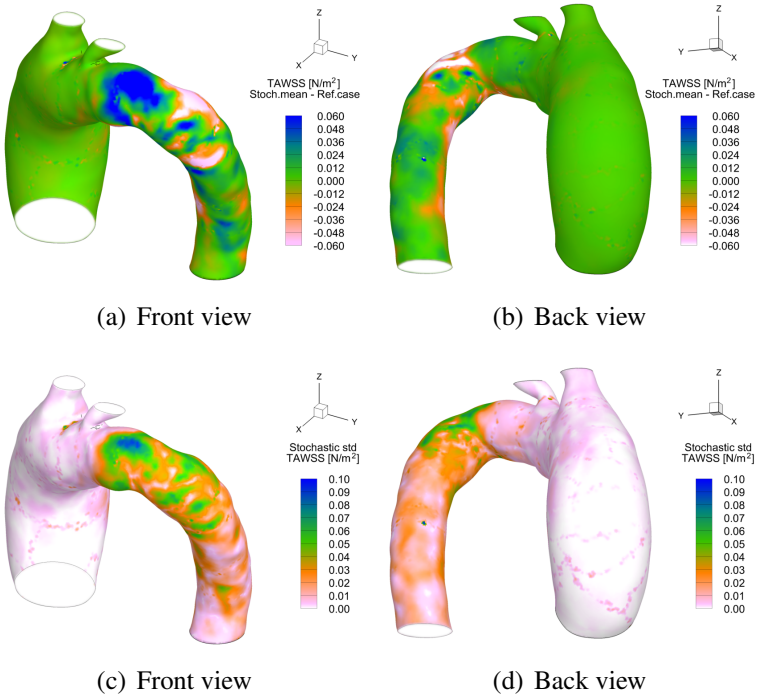

(a) Front view (b) Back view

(c) Front view (d) Back view

Figure 13: Difference between the stochastic mean value and the reference deterministic value of TAWSS (a-b), and stochastic standard deviation of TAWSS (c-d) for the geometry A with rigid walls. Effect of uncertainties in the value of the capacitance C.

5.2 Effect of the wall compliance

In this Section we repeat the same UQ analysis as in Section 5.1 but considering the wall compliance. As before, the pressure waveform is evaluated in correspondence of the outlet section of the descending aorta, and the results are presented in terms of the stochastic mean value $\pm$ the stochastic standard deviation in Figure 15. The results obtained by considering the walls rigid are also reported in the same figure for comparison. It is clear that taking into account wall deformations leads to a smaller pulse pressure. This result could be expected, since the wall compliance acts as a further capacitance contribution and in both cases an increase of C reduces the difference between systolic and diastolic pressures, the mean pressure value being almost constant. The stochastic variance with C is also slightly reduced in the compliant case.

The indicators quantifying the stress levels on the arterial wall are again presented in terms of

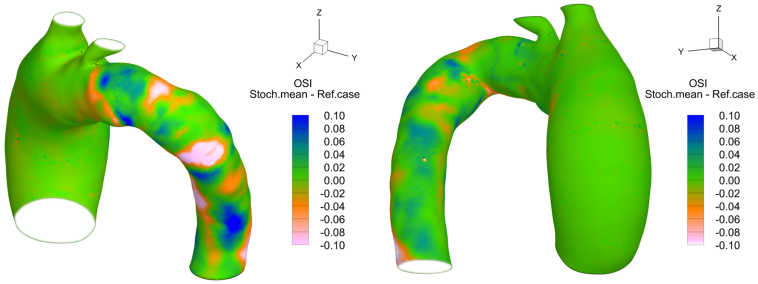

(a) Front view (b) Back view

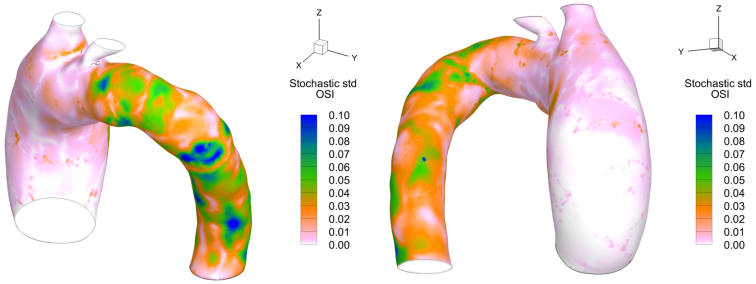

(c) Front view (d) Back view

Figure 14: Difference between the stochastic mean value and the reference deterministic value of OSI (a-b), and stochastic standard deviation of OSI (c-d) for the geometry A with rigid walls. Effect of uncertainties in the value of the capacitance C.

their stochastic mean value and of their stochastic standard deviation. As in the rigid case, for the sake of brevity we focus only on the cycle-averaged quantities.

Since the stochastic mean distribution of TAWSS is very close to the reference deterministic one, to allow a quantitative comparison in Figures 16(a) and 16(b) we present the difference between these two fields. As occurred in the rigid case, the differences are zero in most part of the aortic wall and are significant only in limited regions of the descending aorta. Their value never exceeds 10% of the corresponding stochastic mean. Figures 16(c) and 16(d) show the difference between the stochastic mean fields for deformable and rigid cases. This difference is uniform almost everywhere and negative in value, denoting that the arterial wall is subjected to smaller stresses when it has the possibility to expand and relax. However, the same qualitative behavior suggests that the flow topology does not significantly change.

The stochastic standard deviation of TAWSS is shown in Figures 16(e) and 16(f), while the difference between the deformable and the rigid cases is reported in Figures 16(g) and 16(h). The largest values of the stochastic standard deviation are found in the aortic arch and descending part (see Figures 16(e) and 16(f)) and they are smaller compared to the rigid case (see Figures 16(g) and 16(h)). As in the rigid case, the ascending region of the aorta presents no significant variability of the results.

Figures 17(a) and 17(b) show the difference between the stochastic mean distribution of OSI and the corresponding reference deterministic field. Again, most part of the aorta does not present significant differences. Differences can only be found in the distal aortic neck and in the descending region. However, they can reach about 30% of the corresponding stochastic mean value, thus being more important than the ones observed for TAWSS. Figures 17(c) and 17(d) highlight the difference between the OSI stochastic mean fields for deformable and rigid cases. Significant differences involve a larger portion of the aorta, mostly located at the aortic arch

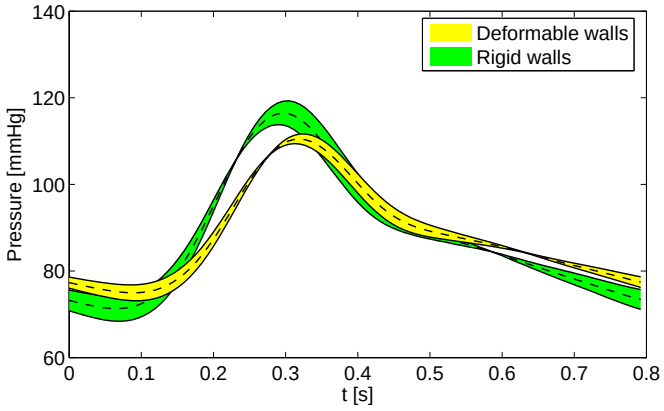

Figure 15: Effect of the variation of the capacitance C on the pressure waveform in correspondence of the descending aorta outlet section in the geometry A: comparison between deformable and rigid walls. The results are expressed in terms of stochastic mean (dashed line) $\pm$ stochastic standard deviation (continuous lines).

and descending part, but presenting some significant values also in the aneurysm region. This behavior can be related to the high sensitivity that OSI has to the flow field and to the locations of recirculation areas. A small variation in these locations can lead to a significant change in the OSI distribution. This can be deduced by analyzing the flow streamlines, here not shown for the sake of brevity.

Figures 17(e) and 17(f) show the stochastic standard deviation of OSI. Again, the descending aorta presents the largest variability, while the aneurysm region is characterized by small values of the stochastic variance. The comparison with the rigid case is evaluated in Figures 17(g) and 17(h), which illustrate the difference between the stochastic standard deviation of OSI for rigid and deformable walls. As observed for the stochastic mean distribution, the large differences in the descending aorta are possibly due to small changes in the flow field.

5.3 Effect of the wall geometry

In this Section we investigate the effect of the wall geometry by performing the UQ analysis on the geometry B with rigid walls. The output pressure waveform at the descending aorta outlet section is almost identical to the one obtained for geometry A with rigid walls (see Figure 12) and for sake of brevity is not shown.

The difference between the stochastic mean distribution of TAWSS and the corresponding reference deterministic distribution is presented in Figures 18(a) and 18(b). The effect of considering a smaller aneurysm is that the ascending and descending regions are closer in size. This produces a similar difference distribution in the whole aorta. These differences are not very high, except in some limited regions in which they reach 15% of the stochastic mean value at the same location.

Figures 18(c) and 18(d) show the stochastic standard deviation. Again, for the geometry B a significant variability is present also in the aneurysm region. The largest values of the stochastic standard deviation are about 25% of the corresponding stochastic mean value.

The difference between the stochastic mean value of OSI and the corresponding reference deterministic one is presented in Figures 19(a) and 19(b). Unlike what observed for the geometry A, differences affect not only the aortic arch and the descending aorta but also the aneurysm region. However, these differences may be again related to small changes in the flow field and small changes in location of recirculation areas.

Figures 19(c) and 19(d) illustrate the stochastic standard deviation obtained for OSI. High

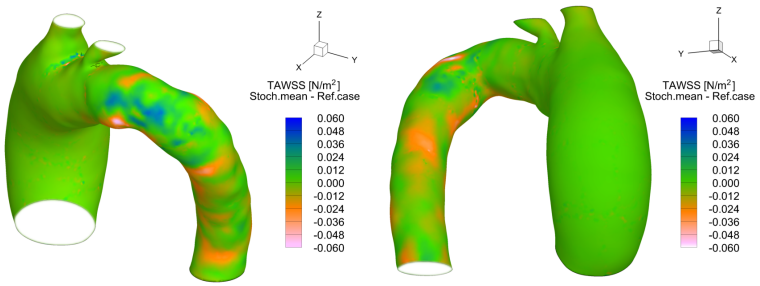

(a) Front view (b) Back view

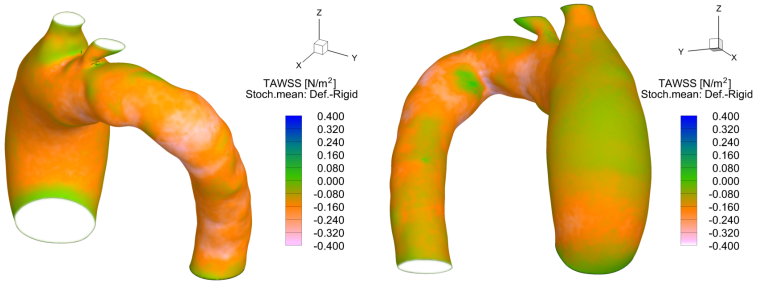

(c) Front view (d) Back view

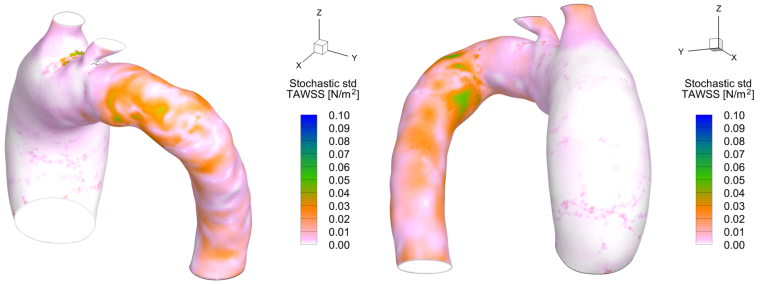

(e) Front view (f) Back view

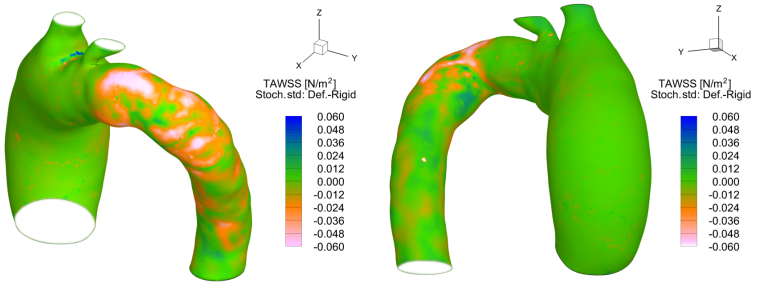

(g) Front view (h) Back view

Figure 16: Effect on the TAWSS distribution of uncertainties in the value of the capacitance C (geometry A with deformable walls): difference between the stochastic mean value and the reference deterministic value (a-b), difference between the stochastic mean values in deformable and rigid cases (c-d), stochastic standard deviation in the deformable case (e-f), and difference between the stochastic standard deviations in deformable and rigid cases (g-h).

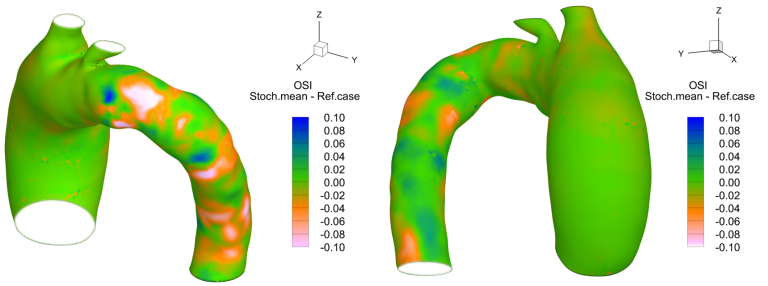

(a) Front view (b) Back view

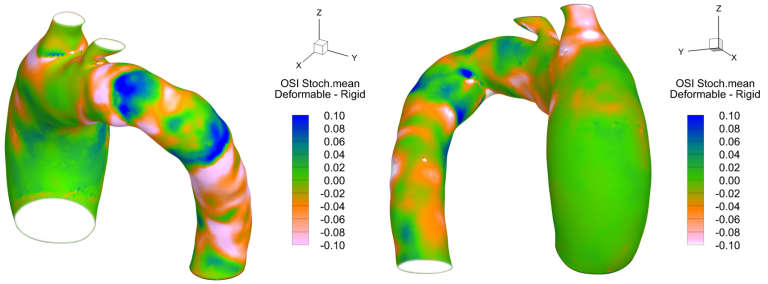

(c) Front view (d) Back view

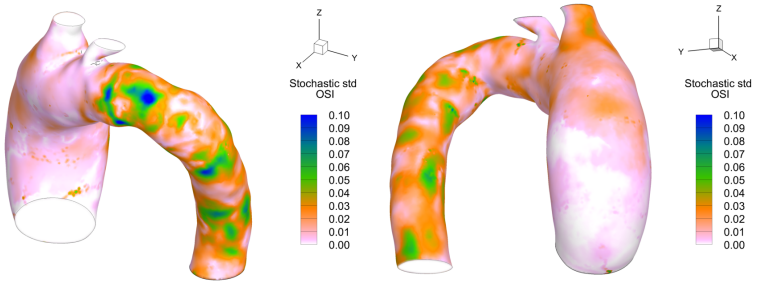

(e) Front view (f) Back view

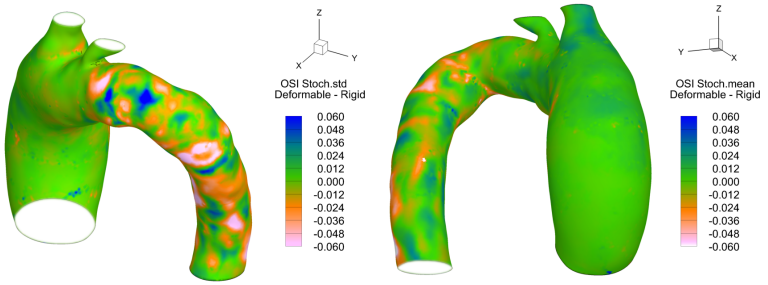

(g) Front view (h) Back view

Figure 17: Effect on the OSI distribution of uncertainties in the value of the capacitance C (geometry A with deformable walls): difference between the stochastic mean value and the reference deterministic value (a-b), difference between the stochastic mean values in deformable and rigid cases (c-d), stochastic standard deviation in the deformable case (e-f), and difference between the stochastic standard deviations in deformable and rigid cases (g-h).

variability is mostly found in the aneurysm region, where it can reach values about 35% of the stochastic mean value in the same location.

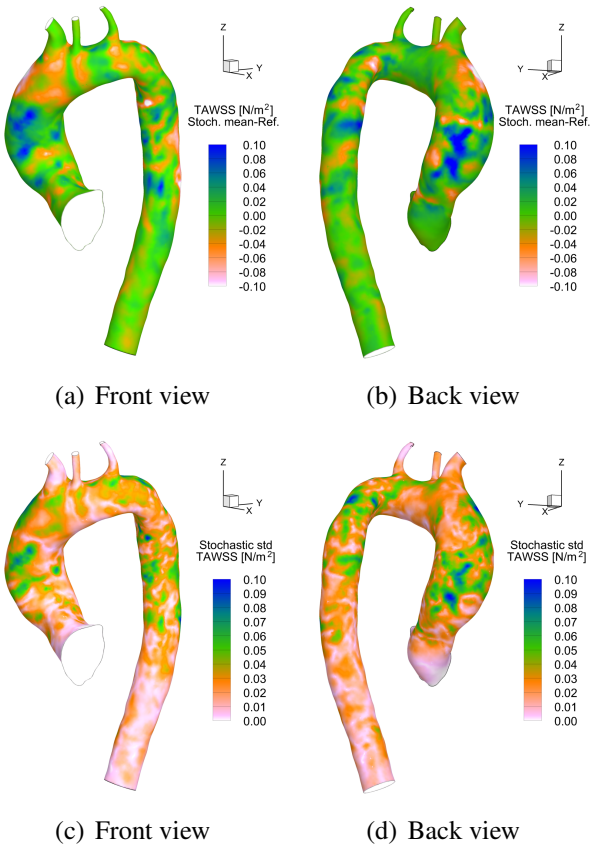

(a) Front view (b) Back view

(c) Front view (d) Back view

Figure 18: Difference between the stochastic mean value and the reference deterministic value of TAWSS (a-b), and stochastic standard deviation of TAWSS (c-d) for the geometry B with rigid walls. Effect of uncertainties in the value of the capacitance C.

6 UQ ANALYSIS OF THE EFFECT OF UNCERTAINTIES IN THE VALUES OF R_p AND C ON THE PRESSURE CYCLE AND ON THE FLOW FIELD

The aim of this Section is to assess the effect of uncertainties in the proximal resistance R_p and in the capacitance C on the quantities of interest reported in Section 2.3.

6.1 Geometry A with rigid walls

Figure 20(a) shows the output pressure waveform at the descending aorta outlet section, again in terms of the stochastic mean value $\pm$ the stochastic standard deviation. The main difference compared to the case in which only the capacitance C was allowed to vary is an increased variability of the results, especially in the region near the maximum pressure value (see Figure 12 for comparison). Figure 20(b) confirms this indication, illustrating the partial sensitivities to the two uncertain parameters alone and combined. For most part of the cardiac cycle the capacitance C is the main responsible of the variability of the results. In these regions the uncertainty in the proximal resistance R_p does not produce significant effects on the pressure profile, which thus maintains substantially the behavior of Figure 12. R_p becomes predominant in a small portion of the cycle, near peak systole. This explains why an increased stochastic standard deviation can be

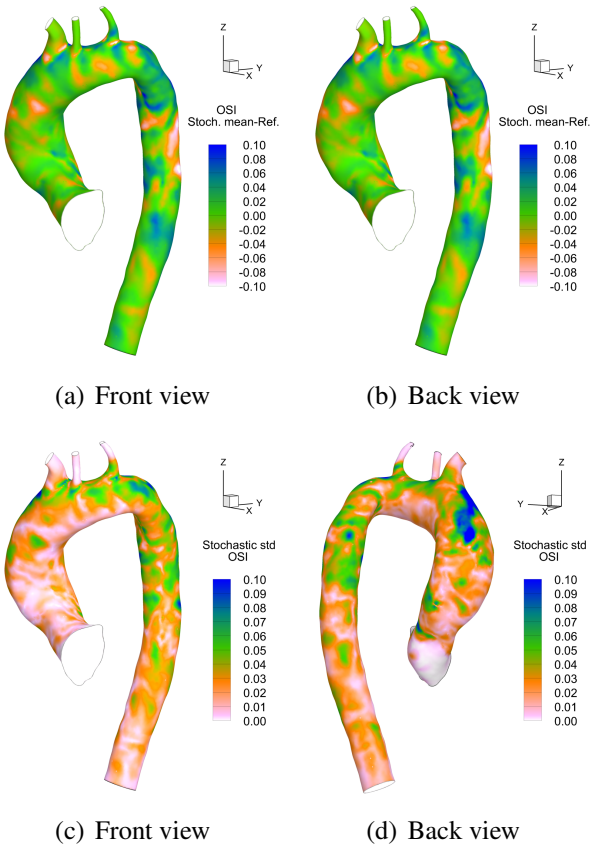

(a) Front view (b) Back view

(c) Front view (d) Back view

Figure 19: Difference between the stochastic mean value and the reference deterministic value of OSI, and stochastic standard deviation of OSI for the geometry B with rigid walls. Effect of uncertainties in the value of the capacitance C.

observed in the region near the maximum pressure value.

The effect of the second source of uncertainty (R_p) is evaluated considering the difference distributions between the stochastic outputs in the cases of two sources (C and R_p) and single source (C) of uncertainty. The averaged effect during a cardiac cycle of R_p on WSS is illustrated by the TAWSS distribution. Figures 21(a) and 21(b) show the difference distribution between the stochastic mean values of TAWSS in the two UQ analyses, while Figures 21(c) and 21(d) present the difference in the stochastic standard deviation. The effect of the second source of uncertainty on the stochastic mean value is very limited, with only small regions significantly affected. On the other side, its effect on the stochastic standard deviation is much more significant. The differences are mainly located in the region of the distal aortic neck and can reach 50% of the corresponding value obtained when considering only the variation of C.

Similar considerations apply also to OSI. The effect of considering R_p as an uncertain parameter has a limited effect on the stochastic mean value (see Figures 22(a) and 22(b)), while the stochastic standard deviation is in proportion much more affected (see Figures 22(c) and 22(d)). The difference respect to the case of single source of uncertainty is mainly located in the distal aortic neck. As found previously, this region presents again the highest sensitivity to the uncertain parameters.

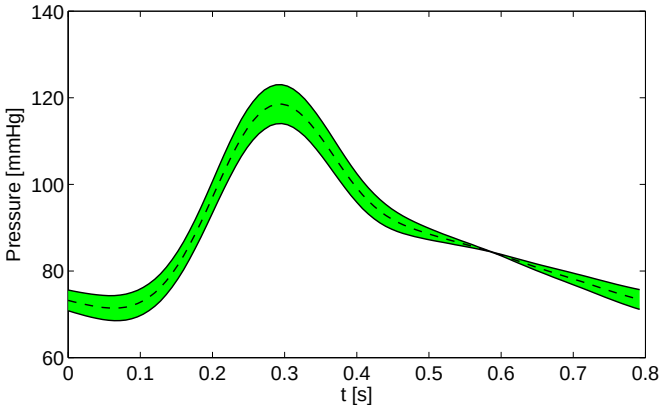

(a)

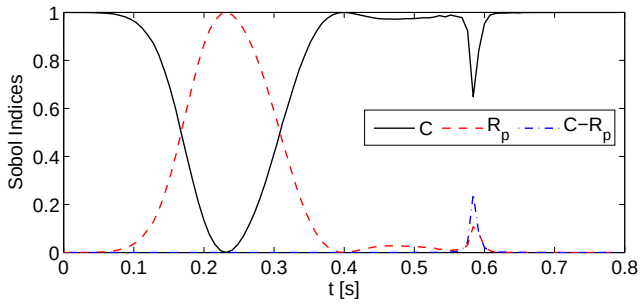

(b)

Figure 20: Effect of the variation of the capacitance C and proximal resistance R_p on the pressure profile in correspondence of the descending aorta outlet section (geometry A with rigid walls). The results are expressed in terms of stochastic mean $\pm$ stochastic standard deviation (a) and partial sensitivities to the two parameters (b).

6.2 Effect of the wall geometry

In this Section we investigate the effect of the geometry of the aorta. A UQ analysis with two uncertain parameters (C and R_p) was thus performed on the geometry B with rigid walls. The output pressure waveform at the descending aorta outlet section is almost identical to the one obtained for the geometry A (Figure 20) and for the sake of brevity is not shown here. This behavior suggests that the two geometries have basically the same resistance contribution on the flow, thus producing very small changes in the output pressure. This confirms what found in Section 5.3 for the case of only one source of uncertainty.

To isolate the effect of R_p on TAWSS and OSI, we again present for each stochastic output the difference field between the distribution obtained with two sources of uncertainty (C and R_p) and that obtained with a single source of uncertainty (C).

Figure 23 quantifies these differences for the stochastic mean value and stochastic standard deviation of TAWSS. As found for the geometry A, the second source of uncertainty R_p has a small effect on both the stochastic mean distribution (see Figures 23(a) and 23(b)) and the stochastic standard deviation (see Figures 23(c)), even if the variation of the stochastic standard deviation is in percentage terms again more significant. The effect of the geometry B is that these difference distributions are more uniform in the whole aorta, due to the similar size of the ascending and descending regions.

Considerations similar to those made for TAWSS also apply to OSI. Both the stochastic mean value (Figures 24(a) and 24(b)) and the stochastic standard deviation (Figures 24(c) and 24(d)) are little affected by the introduction of the second uncertain parameter R_p. However, 0.5 is the

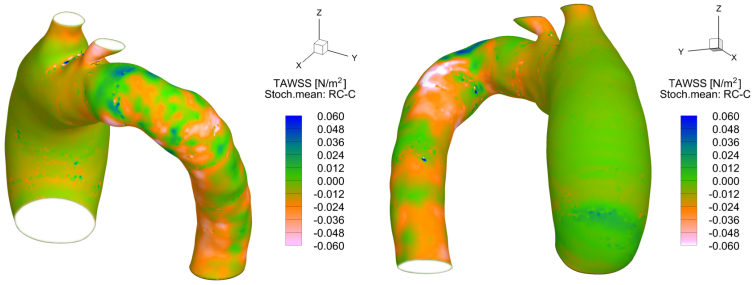

(a) Front view (b) Back view

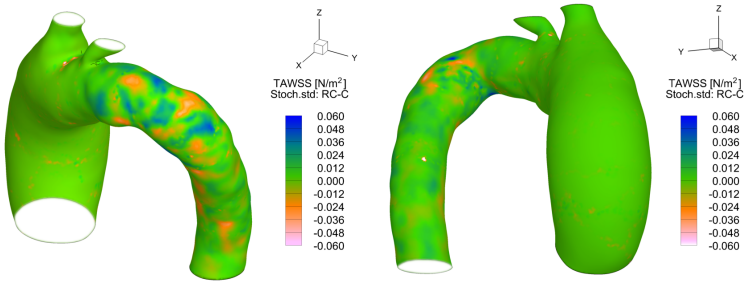

(c) Front view (d) Back view

Figure 21: Difference between the distributions of TAWSS obtained when considering both the uncertainties in C and R_p and the uncertainty in C alone. Stochastic mean (a-b) and stochastic standard deviation (c-d), geometry A with rigid walls.

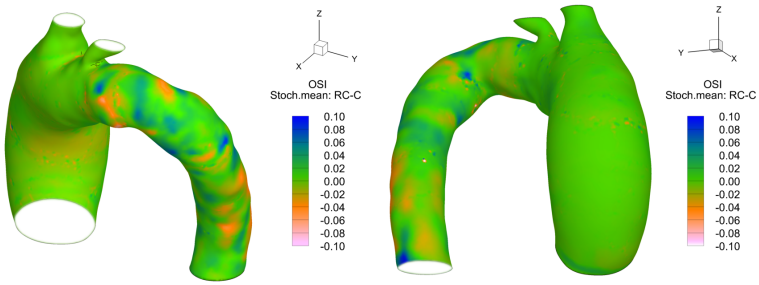

(a) Front view (b) Back view

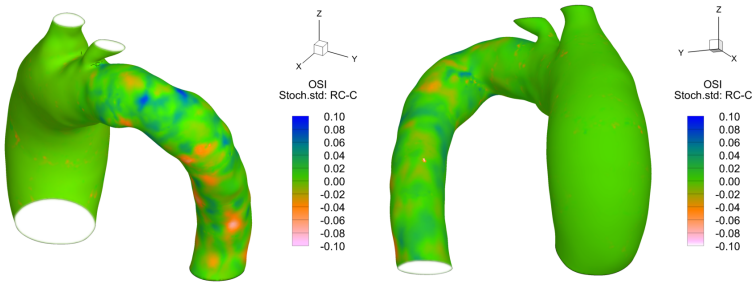

(c) Front view (d) Back view

Figure 22: Difference between the distributions of OSI obtained when considering both the uncertainties in C and R_p and the uncertainty in C alone. Stochastic mean (a-b) and stochastic standard deviation (c-d), geometry A with rigid walls.

maximum value that OSI can take, so even small differences in absolute terms can be relatively significant.

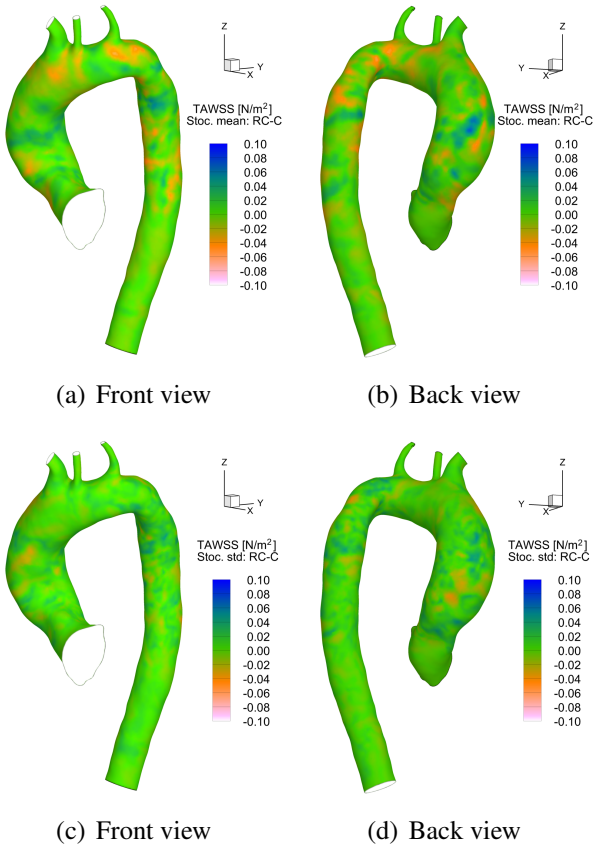

(a) Front view (b) Back view

(c) Front view (d) Back view

Figure 23: Difference between the distributions of TAWSS obtained when considering both the uncertainties in C and R_p and the uncertainty in C alone. Stochastic mean (a-b) and stochastic standard deviation (c-d), geometry B with rigid walls.

7 CONCLUDING REMARKS

The blood dynamics in two patient-specific ATAA geometries, characterized by different severity of the aneurysm pathology, was simulated. Deterministic simulations showed that the size of the aneurysm has a significant impact on the wall stress and flow feature, the smaller aneurysm being characterized by larger wall shear stresses and by a more recirculating flow. The wall compliance uniformly reduces the values of the shear stresses without changing their distribution, at least for the elastic, homogeneous, isotropic and constant thickness properties of the walls considered herein.

A stochastic sensitivity analysis to the uncertainties in the outflow boundary-condition parameters, namely the capacitance and the proximal resistance in the Winkdessel model, was also carried out. The mean stochastic values of TAWSS and OSI are very similar to those obtained in deterministic simulations carried out with values of the parameters guessed to obtain a desired physiological behavior of the pressure profile in a simplified fully lumped model. The stochastic variance of TAWSS and OSI was found to be very low inside the larger aneurysm, while more significant variations are present in localized regions of the aortic arch and of the descending aorta. For the geometry characterized by a smaller aneurysm, significant variability

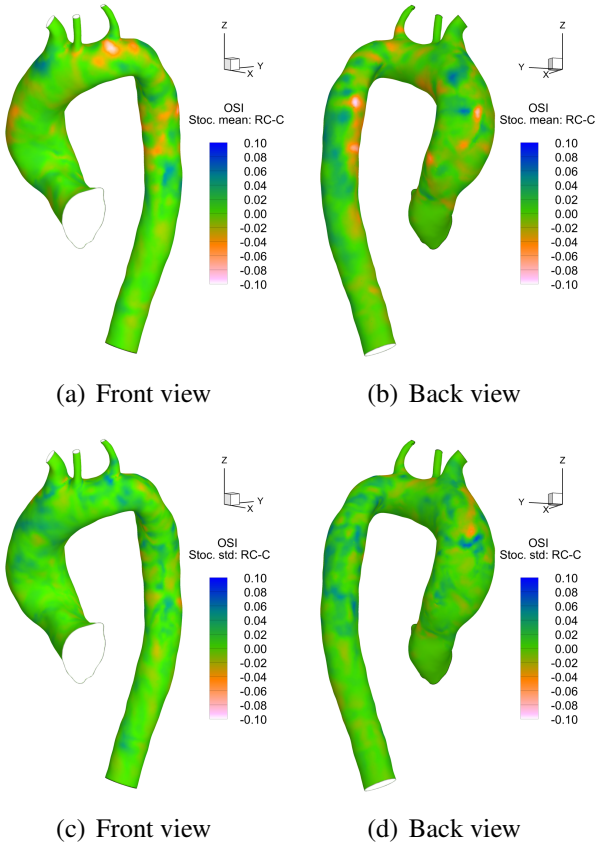

(a) Front view (b) Back view

(c) Front view (d) Back view

Figure 24: Difference between the distributions of OSI obtained when considering both the uncertainties in C and R_p and the uncertainty in C alone. Stochastic mean (a-b) and stochastic standard deviation (c-d), geometry B with rigid walls.

is present also inside the aneurysm, indicating that the stress numerical predictions inside small aneurysms are more sensitive to the outflow boundary conditions. The effects of wall compliance on the stochastic mean value of TAWSS are the same as those observed in the deterministic simulations, i.e. a uniform reduction of TAWSS. The variability of TAWSS with the considered boundary-condition parameters is also reduced in the case with compliant walls.

Finally, considering the uncertainties in the capacitance only and in both the capacitance and the proximal resistance leads to very similar distributions of the stochastic mean values of TAWSS and OSI for both geometries. This means that the effect of the proximal resistance on the stochastic mean distributions is very limited. Conversely, its effect on the stochastic variability of TAWSS and OSI is more significant, again for both considered geometries.

The proposed methodology permits to quantify the propagation of the uncertainties in input data on the output quantities of interest in patient-specific ATAA configurations. In the present case, we focused on uncertainties in the outflow parameters, but the same methodology could be applied to different types of uncertainties, as e.g. uncertainties in the geometry due to imaging/reconstruction errors or in the mechanical properties of the vessel walls. Finally, if *in-vivo* measured hemodynamic quantities are available, calibration of different simulation parameters could be carried out using a stochastic approach, providing thus a platform integrating CFD simulations and *in-vivo* measurements.

REFERENCES

[1] D. Botta and J.A. Elefteriades. Matrix metalloproteinases in thoracic aortic aneurysm disease. *International Journal of Angiology*, 15(1):1–8, 2006.

[2] J.S. Wilson and J.D. Humphrey. Evolving anisotropy and degree of elastolytic insult in abdominal aortic aneurysms: Potential clinical relevance? *Journal of Biomechanics*, 47(12):2995–3002, 2014.

[3] K.W. Johnston, R.B. Rutherford, M.D. Tilson, D.M. Shah, L. Hollier, and J.C. Stanley. Suggested standards for reporting on arterial aneurysms. *Journal of Vascular Surgery*, 13(3):452–458, 1991.

[4] S. Pasta, A. Rinaudo, A. Luca, M. Pilato, C. Scardulla, T.G. Gleason, and D.A. Vorp. Difference in hemodynamic and wall stress of ascending thoracic aortic aneurysms with bicuspid and tricuspid aortic valve. *Journal of Biomechanics*, 46(10):1729–1738, 2013.

[5] M. Markl, W. Wallis, and A. Harloff. Reproducibility of flow and wall shear stress analysis using flow-sensitive four-dimensional mri. *Journal of Magnetic Resonance Imaging*, 33(4):988–994, 2011.

[6] U. Morbiducci, R. Ponzini, G. Rizzo, M. Cadioli, A. Esposito, F.M. Montevecchi, and A. Redaelli. Mechanistic insight into the physiological relevance of helical blood flow in the human aorta: An in vivo study. *Biomechanics and Modeling in Mechanobiology*, 10(3):339–355, 2011.

[7] P. Volonghi, D. Tresoldi, M. Cadioli, A.M. Usuelli, R. Ponzini, U. Morbiducci, A. Esposito, and G. Rizzo. Automatic extraction of three-dimensional thoracic aorta geometric model from phase contrast mri for morphometric and hemodynamic characterization. *Magnetic Resonance in Medicine*, 2015.

[8] U. Morbiducci, R. Ponzini, D. Gallo, C. Bignardi, and G. Rizzo. Inflow boundary conditions for image-based computational hemodynamics: Impact of idealized versus measured velocity profiles in the human aorta. *Journal of Biomechanics*, 46(1):102–109, 2013.

[9] U. Morbiducci, D. Gallo, S. Cristofanelli, R. Ponzini, M.A. Deriu, G. Rizzo, and D.A. Steinman. A rational approach to defining principal axes of multidirectional wall shear stress in realistic vascular geometries, with application to the study of the influence of helical flow on wall shear stress directionality in aorta. *Journal of Biomechanics*, 48(6):899–906, 2015.

[10] S. Celi, F. Di Puccio, P. Forte, and L. Spadoni. Investigation on residual stress effects in fe simulations of balloon angioplasty. volume 2005, pages 249–250, 2005.

[11] S. Celi and S. Berti. Three-dimensional sensitivity assessment of thoracic aortic aneurysm wall stress: A probabilistic finite-element study. *European Journal of Cardio-thoracic Surgery*, 45(3):467–475, 2014.

[12] A. Frydrychowicz, A.F. Stalder, M.F. Russe, J. Bock, S. Bauer, A. Harloff, A. Berger, M. Langer, J. Hennig, and M. Markl. Three-dimensional analysis of segmental wall shear stress in the aorta by flow-sensitive four-dimensional-mri. *Journal of Magnetic Resonance Imaging*, 30(1):77–84, 2009.

[13] D.C. Wendell, M.M. Samyn, J.R. Cava, L.M. Ellwein, M.M. Krolikowski, K.L. Gandy, A.N. Pelech, S.C. Shadden, and J.F. LaDisa Jr. Including aortic valve morphology in computational fluid dynamics simulations: Initial findings and application to aortic coarctation. *Medical Engineering and Physics*, 35(6):723–735, 2013.

[14] D. Gallo, G. De Santis, F. Negri, D. Tresoldi, R. Ponzini, D. Massai, M.A. Deriu, P. Segers, B. Verhegghe, G. Rizzo, and U. Morbiducci. On the use of in vivo measured flow rates as boundary conditions for image-based hemodynamic models of the human aorta: Implications for indicators of abnormal flow. *Annals of Biomedical Engineering*, 40(3):729–741, 2012.

[15] J. Lantz, J. Renner, and M. Karlsson. Wall shear stress in a subject specific human aorta - influence of fluid-structure interaction. *International Journal of Applied Mechanics*, 3(4):759–778, 2011.

[16] A.D. Caballero and S. Laín. A review on computational fluid dynamics modelling in human thoracic aorta. *Cardiovascular Engineering and Technology*, 4(2):103–130, 2013.

[17] Alison Marsden and Shawn Shadden. SimVascular: Cardiovascular modeling and simulation. `http://simvascular.org`, 2015. Online; accessed 11-December-2015.

[18] Kenneth E. Jansen, Christian H. Whiting, and Gregory M. Hulbert. A generalized-α method for integrating the filtered Navier-Stokes equations with a stabilized finite element method. *Computer Methods in Applied Mechanics and Engineering*, 190(3-4):305 – 319, 2000.

[19] Lucian Itu, Puneet Sharma, Tiziano Passerini, Ali Kamen, Constantin Suciu, and Dorin Comaniciu. A parameter estimation framework for patient-specific hemodynamic computations. *Journal of Computational Physics*, 281(0):316 – 333, 2015.

[20] D. Xiu and G. Karniadakis. The Wiener-Askey polynomial chaos for stochastic differential equations. *SIAM Journal on Scientific Computing*, 24(2):619–644, 2003.

ECCOMAS Congress 2016
VII European Congress on Computational Methods in Applied Sciences and Engineering
M. Papadrakakis, V. Papadopoulos, G. Stefanou, V. Plevris (eds.)
Crete Island, Greece, 5–10 June 2016

OPTIMIZATION OF A PHOTOACOUSTIC GAS SENSOR USING MULTIFIDELITY RBF METAMODELING

Cédric Durantin[1,2], Justin Rouxel[1], Jean Antoine Désidéri[3] and Alain Glière [1]

[1]Univ. Grenoble Alpes, F-38000 Grenoble, France
CEA, LETI, MINATEC Campus, F-38054 Grenoble, France
e-mail: {cedric.durantin,justin.rouxel,alain.gliere}@cea.fr

[2] University Nice - Sophia Antipolis, 06108 Nice, France

[3] ACUMES Team
INRIA Sophia Antipolis Méditerranée, 06902, Sophia Antipolis,France
e-mail: jean-antoine.desideri@inria.fr

Keywords: Metamodel, Optimization, Multifidelity, Radial Basis Function

Abstract. *The numerical optimization of a photoacoustic gas sensor is a challenging problem in terms of computational time. The signal detected by the gas sensor is a non-linear function depending on several geometrical parameters. The optimization requires a very large number of function calls, thus an important simulation time. In the case of photoacoustics, two different numerical models with different fidelity levels are available to simulate the behavior of the component. In order to reduce the computational burden of optimizing the gas sensor, a new multifidelity metamodeling framework, based on Radial Basis Function, is proposed. The present method offers an alternative to co-kriging (a widely used multifidelity metamodel). This multifidelity model is then used in an optimization sequence to enrich a training database, via a strategy inspired by Gutmann [1]. The process is applied to the optimization of geometrical parameters in the gas sensor problem.*

1 INTRODUCTION

Numerical simulation is widely employed in engineering to study the behavior of future devices and optimize their design. Nevertheless, each computation is often time consuming and, during an optimization sequence, the simulation code is evaluated a large number of times. An interesting way to reduce the computational burden is to resort to a metamodel (or surrogate model) of the simulation code. The process of metamodeling successively implies creating a design of experiment (DOE), evaluating the numerical model response of the DOE and then training the metamodel on the dataset previously obtained. Once the metamodel is built, it can predict the response of the numerical model for a new evaluation point at an extremely reduced time. Thus it can be used in a costly procedure in terms of number of evaluations such as sensibility analysis or optimization. The prediction accuracy depends on the number of points in the dataset and the complexity of the function to replace. Sometimes, models having different levels of fidelity are available and can be hierarchically ranked in accuracy. In this case, multifidelity surrogate modeling aims at efficiently combining information from the different levels of approximation in order to build a metamodel at a reduced cost.

Here the focus is set on the design of a photoacoustic gas sensor. Two different simulation codes are used to describe the performance of the component. The linearized Navier-Stokes equations constitute the high fidelity model and the coarse model consists in the decomposition of the pressure field onto the acoustic modes basis, obtained by solving the homogeneous Helmholtz equation. The computational time for the high fidelity model exceeds one hour on a twenty-core cluster node cadenced at 3 GHz. For the coarse model, the computational time is reported on the same node at 3 minutes. There is a potential time saving in using as much as possible information obtained from the coarse model and still keep good prediction accuracy by also using the expensive model.

Among metamodeling approaches, kriging models [2, 3, 4] are well known in the metamodeling community. This method is attractive because of its capability to estimate a confidence interval of the predicted function. It has recently been revised in order to allow the use of both coarse and complex versions of the computer simulation. This multifidelity approach enhances the prediction accuracy at a reduced computational cost [5]. Then several studies dealing with co-kriging (multifidelity version of kriging) and its use in optimization have been exposed [6, 7, 8]. Radial Basis Functions (RBF) based interpolation method is another existing choice as surrogate model. The new method offers an alternative to co-kriging that might be superior in high dimensional optimization problem, as stated by Regis and Shoemaker on single fidelity problems [9]. To the best of our knowledge, no version of multifidelity RBF-based method has been published at the moment.

The present work offers a new possible way to solve the optimization problem of the photoacoustic gas sensor design via RBF multifidelity metamodeling method (co-RBF). Since some optimization algorithms are already developed for RBF-based optimization [9, 1], they could be extended to a multifidelity version. Here only the so-called Gutmann-RBF method improved by Regis and Shoemaker [9] is used for the multifidelity metamodel based optimization of the gas sensor.

The optimization problem of the photoacoustic gas sensor is described in section 2 and the methodology of the co-RBF metamodeling method is detailed in section 3. The extension of RBF-based optimization algorithm to co-RBF is presented in section 4, together with the result of the gas sensor optimization.

2 MINIATURIZED PHOTOACOUSTIC GAS SENSOR DESIGN

2.1 Physical principle and numerical models

Photoacoustic (PA) spectroscopy is employed to detect gas traces with a high sensitivity, often below the part per billion by volume (ppbv) level. The principle of PA spectroscopy relies on the excitation of a molecule of interest by a light source emitting at the wavelength of an absorption line of the molecule. The light source, usually a laser in the mid-infrared range, is modulated at the acoustic frequency of a resonant cell, containing the gas mixture. During the molecules relaxation, the kinetic energy exchange with the surrounding gas creates local temperature modulation, and thus acoustic waves in the chamber [10].
The cell used in this work is of the differential Helmholtz resonator (DHR) [11] type. It is composed of two chambers linked by two capillaries (Figure 1). The gas excitation is ensured by illuminating one chamber with a laser source. At the Helmholtz resonance of the cavity, acoustic signals in the two chambers are in phase opposition. The signals provided by two microphones measuring the pressure into each chamber are subtracted to provide the PA signal. As the PA signal is inversely proportional to the volume of the resonant cell [10], a trend towards the size reduction of PA cells has been initiated during the last decade [12], [13]. Assuming

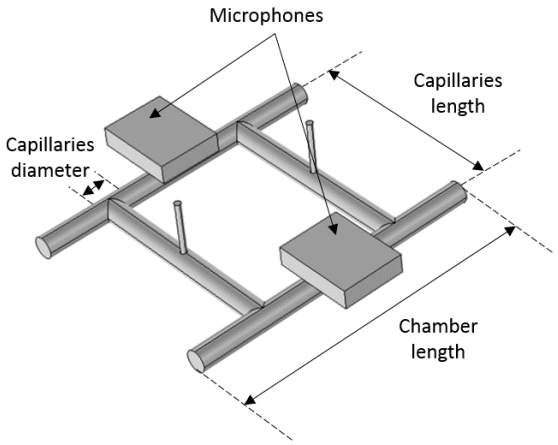

Figure 1: Geometry of a DHR cell.

no viscous and thermal losses and a harmonic heat source, the non-homogeneous Helmholtz equation can be used to compute the pressure field in the cell, and thus the differential PA signal:

$$\nabla^2 p + k^2 p = i\omega \frac{\gamma - 1}{c^2} \mathcal{H} \tag{1}$$

where ω is the modulation frequency, c the speed of sound, γ the Laplace coefficient of the gas, $k = \omega/c$ the wave number and $\mathcal{H}$ the Fourier transform of the power density of the heat source. This pressure acoustic model is computationally efficient and accurate at the macro-scale but fails at the micro-scale. In fact, various volume and surface dissipation processes, at work in the bulk of the propagation medium and close to the walls, cannot be neglected in miniaturized devices, where boundary layers occupy a non-negligible part of the overall cell volume. Numerous approximate models have been adapted from the pressure acoustic model to take into account the dissipation effects. For instance Kreuzer [14], rely on eigenmode expansion of the pressure field and a correction by quality factors. The latter model is fast and faithful enough to

constitute the coarse approximation used in our multifidelity approach.
The rigorous, but CPU time and memory consuming, model relies on the full linearized Navier-Stokes formulation (FLNS), that fully accounts for viscous and thermal dissipation effects. In that approach, small harmonic variations are assumed. The PDE equations system (2) is composed of the continuity equation, incorporating the ideal gas equation of state $p = \rho R_M T$, and the momentum and energy conservation laws:

$$\begin{aligned} i\omega\left(\frac{\tilde{p}}{p_0} - \frac{\tilde{T}}{T_0}\right) + \nabla\cdot\tilde{\mathbf{u}} &= 0 \\ i\omega\rho_0\tilde{\mathbf{u}} = -\nabla\tilde{p} + \nabla\cdot\left(\mu\left(\nabla\tilde{\mathbf{u}} + \nabla\tilde{\mathbf{u}}^T\right) + (\lambda - 2\mu/3)\left(\nabla\cdot\tilde{\mathbf{u}}\right)\mathbf{I}\right) \\ i\omega\rho_0 C_p\tilde{T} = -\nabla\cdot\left(-\kappa\nabla\tilde{T}\right) + i\omega\tilde{p} + Q \end{aligned} \tag{2}$$

where $\tilde{p}$, $\tilde{T}$ and $\tilde{\mathbf{u}}$ are respectively the pressure, temperature and velocity fields of the gas; p_0, T_0 and ρ_0 are the mean values of the pressure, temperature and density fields; λ and μ are the bulk viscosity and the shear viscosity. Q is the heat source.

2.2 Optimization problem

In the framework of the PA sensor case, the FLNS model represents the expensive code and the Kreuzer model the coarse version. The computational time for the FLNS model is actually around one hour and ten minutes on a twenty-core cluster node cadenced at 3 GHz. For the Kreuzer model, the computational time is reported on the same node at 3 minutes. Both models are solved using the commercial software COMSOL (COMSOL AB, Sweden), based on the finite element method.
The PA cell has a chamber diameter of 1 mm and three parameters are involved: chamber length, radius and length of capillaries. Parameters ranges are available in Table 1. The photoacoustic signal detected is the objective to maximize by varying the three geometrical parameters. The new metamodel developed to reduce the computational cost of model evaluations is described in the next section.

Input	Range (mm)
chamber length	[10,20]
capillaries radius	[0.3,0.5]
capillaries length	[5,20]

Table 1: Parameters and ranges of photoacoustic models.

3 MULTIFIDELITY RADIAL BASIS FUNCTION

The basics of RBF-based metamodelling [15, 16, 17, 18] are first briefly explained to introduce the derivation of the co-RBF method. The efficiency of the co-RBF method is not assessed here since it is out of the scope of this paper.

3.1 RBF interpolation model

Given a set of n distinct points $\mathcal{X} = \{\mathbf{x_1}, \ldots, \mathbf{x_n}\}(\mathbf{x_i} \in \mathbb{R}^\mathbf{d}, \mathbf{i} = \mathbf{1}, \ldots, \mathbf{n})$ where the corresponding function values $z_1, \ldots, z_n$ are known, the RBF approximation is defined as a linear combination of the radial basis function φ :

$$\hat{Y}(\mathbf{x}) = \sum_{i=1}^{n} \beta_i \varphi\left(\|\mathbf{x} - \mathbf{x}_i\|\right) + R(\mathbf{x}) \tag{3}$$

Where $\|\cdot\|$ denotes the Euclidean norm in $\mathbb{R}^d$, the coefficients β_i are real numbers and R belongs to the linear space of polynomials in d variables. The radial basis functions used in this paper and the corresponding polynomial forms are given in Table 2. Gaussian RBF gives more freedom to improve the generalization of Equation (3) at the expense of a more complex parameter estimation process. A procedure based on the minimization of the predict error is a possible way to estimate the Gaussian parameter. For a more complete list of available RBF, the reader is referred to Gutmann [1].

RBF	$\varphi(r),\ r>0$	$R(\mathbf{x})$
Cubic	r^3	$\mathbf{a}^T\mathbf{x}+b$
Gaussian	$\exp\left(-\sum_{i=1}^{d}\gamma_i {r_i}^2\right),\ \gamma_i>0$	0

Table 2: Different choices of radial basis functions.

Once a particular φ is selected, the interpolation condition rights:

$$\begin{gathered}\begin{pmatrix}\boldsymbol{\phi} & \mathbf{F}\\ \mathbf{F}^T & 0\end{pmatrix}\begin{pmatrix}\boldsymbol{\beta}\\ \mathbf{a}\\ b\end{pmatrix}=\begin{pmatrix}\mathbf{z}\\ 0\end{pmatrix}\\ \boldsymbol{\phi}_{ij}=\varphi\left(\|\mathbf{x}_i-\mathbf{x}_j\|\right),\ i=1,\dots,n\,,\ j=1,\dots,n\\ \mathbf{F}=\begin{pmatrix}\mathbf{x}_1^T & 1\\ \mathbf{x}_2^T & 1\\ \vdots & \vdots\\ \mathbf{x}_n^T & 1\end{pmatrix}\end{gathered}\tag{4}$$

In the Gaussian RBF case, the system is reduced to $\boldsymbol{\phi}\times\boldsymbol{\beta}=\mathbf{z}$. It can be shown that the system is invertible if and only if the data points are distinct. It is noteworthy that the inversion of this matrix is the most time demanding part of the training of the surrogate model and that, if points in $\mathcal{X}$ are close to each other, the matrix is ill-conditioned. An example of Gaussian and Cubic RBF for the approximation of the modified Branin function [19] is represented on Figure 2, where red dots are the training points and contour lines are the RBF-based metamodel. The training set is constructed with the Latin Hypercube Sampling method [20]. The third plot is the contour of the real Branin function. The Gaussian RBF emulates the Branin function better than the Cubic one because of the parameter $\boldsymbol{\gamma}$ that scales each inputs based on their impact on the output variance.

3.2 Co-RBF

In this work, a multifidelity version of RBF-based metamodel has been developed to solve the photoacoustic gas sensor optimization problem at a reduced computational time. It is now assumed that different levels of modeling in terms of accuracy are available for our physical problem. In the general context, it is possible to link multiple sets of data with different levels of fidelity, but, for sake of readability, the method description is limited here to two datasets. The more accurate set, which is also the more demanding in terms of computational time, is represented by training points $\mathcal{X}_e$ and their corresponding outputs $\mathbf{z}_e$. The coarse simulation model is represented by $\mathcal{X}_c$ and $\mathbf{z}_c$. These training sets can be obtained using the maximin optimized Nested Latin Hypercube designs [21] in order to improve prediction accuracy by better filling the whole input space.

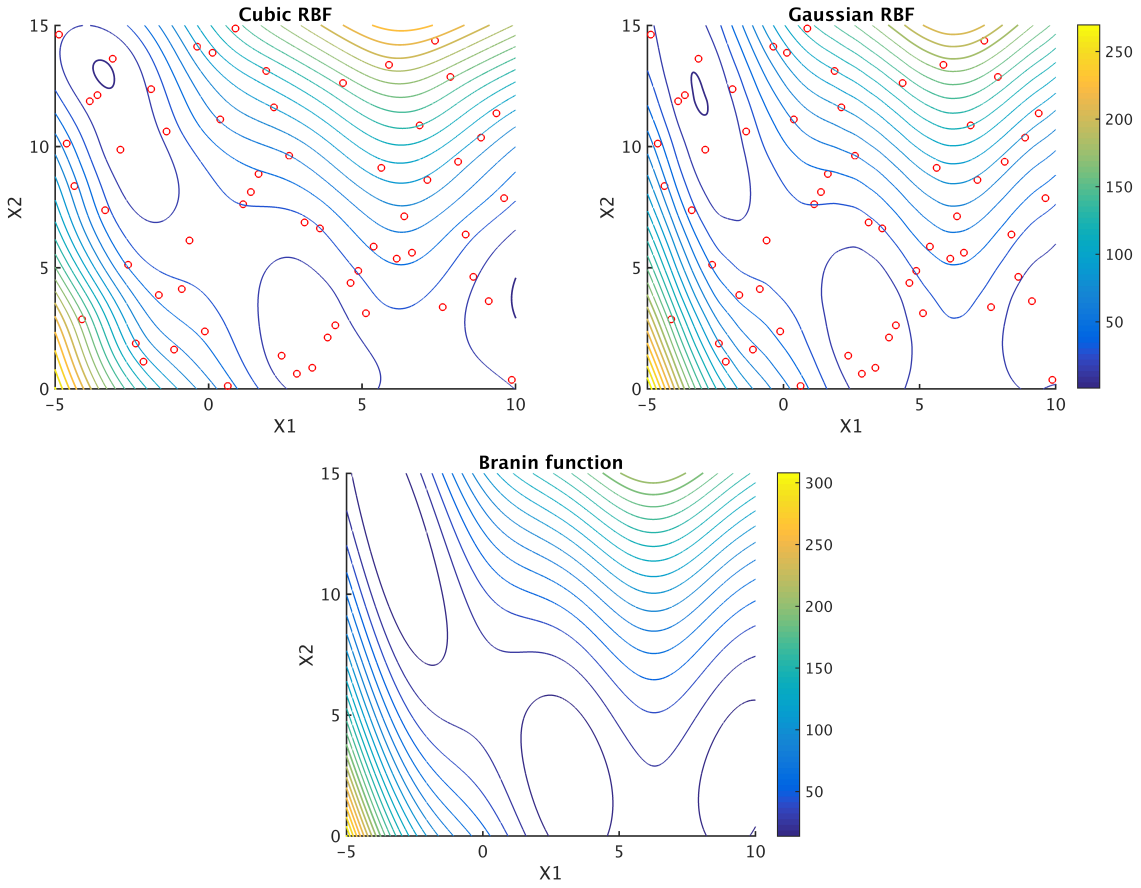

Figure 2: Cubic and Gaussian RBF-based metamodel of the modified Branin function.

The multifidelity approximation is built using the auto-regressive model of Kennedy and O'Hagan [5]:

$$\hat{y}_e(\mathbf{x}) = \rho \hat{y}_c(\mathbf{x}) + \hat{y}_d(\mathbf{x}) \tag{5}$$

where ρ is a scaling factor, y_c the RBF interpolant of the coarse model and y_d the RBF interpolant of the difference between the expensive process and the scaled coarse process. This formulation allows different levels of fidelity to have different correlation structures. The RBF parameters for the coarse and the difference model are not necessarily the same and are estimated separately. To build this multifidelity model, the coarse process is considered independently of the expensive one. Its parameters are estimated within the classical RBF framework described in section 3.1. Once $\begin{pmatrix} \boldsymbol{\beta}_c & \mathbf{a}_c & b_c \end{pmatrix}^T$ obtained, the RBF parameters of the difference function have to be estimated. The assumption is made that, given the point $\mathbf{x}_{c_i}$, no more information can be learnt about $\mathbf{z}_{e_i}$ from the coarse process. This Markov-like property implies that only $y_c(\mathbf{x}_e)$ is considered during the estimation of the difference model parameters. If the dataset $\mathcal{X}_e$ is not evaluated on the coarse model, his corresponding output is predicted by the previously built coarse model RBF. Then the following linear system has to be solved:

$$\begin{pmatrix} \boldsymbol{\phi}_d & \mathbf{F}_e \\ \mathbf{F}_e{}^T & 0 \end{pmatrix} \begin{pmatrix} \boldsymbol{\beta}_d \\ \mathbf{a}_d \\ b_d \end{pmatrix} = \begin{pmatrix} \mathbf{z}_e - \rho y_c(\mathbf{x}_e) \\ 0 \end{pmatrix} \tag{6}$$

The linear system, Equation 6, depends on the unknown scaling factor ρ. Rippa [22] derived a leave-one-out (LOO) formula that estimates the RBF model prediction error. This formula

was initially developed for calibrating the parameter of the Gaussian RBF by minimizing the LOO error. Here this method is used by adding the scaling factor ρ as a parameter to optimize. The LOO formula is given in Equation (7) and its optimization was solved using the covariance matrix adaptation evolution strategy (CMA-ES) [23]. In the Cubic RBF case, the LOO error depends only on the scaling factor:

$$LOO\left(\gamma,\rho\right)=\sum_{i=1}^{n}\left(\frac{\beta_{di}(\gamma)}{\phi_{d_{ii}}^{-1}(\rho)}\right)^{2} \tag{7}$$

An example of the evolution of the LOO depending on γ_d and ρ is available on Figure 3 left, in a test case defined by Forrester et al. [6]. The global minimum of the map is located at $\gamma_d = 1$ and $\rho = 1.74$. This map is obtained from a one-dimensional example displayed on the right plot. Four expensive points and eleven coarse points are evaluated to build the Gaussian co-RBF. The resulting interpolant is the red dashed line and it is close the real model (black solid line).

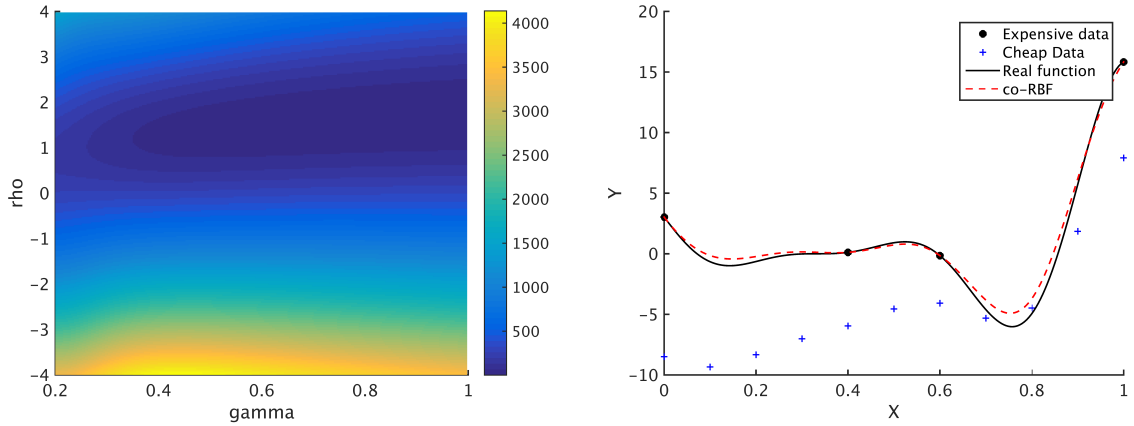

Figure 3: LOO cross-validation error on a one-dimensional example of co-RBF metamodeling.

4 OPTIMIZATION

4.1 Method

An optimization strategy has first been developed by Gutmann [1] in a single fidelity RBF metamodeling approach. It has then been improved by Regis and Shoemaker [9] and referred to as Controlled Gutmann RBF (CG-RBF). This method is an iterative algorithm similar to the Efficient Global Optimization (EGO) procedure derived by Jones [24] for kriging. A design of experiments of the function to optimize is first evaluated and interpolated by a RBF. At each optimization iteration, the RBF interpolant is updated with new evaluated points until the optimum is found. A criterion is defined to select the next infill points based on a measure of the bumpiness of the RBF interpolant [1]. A target value of the global minimum of the function to optimize is cyclically selected to orient the infill criterion toward global exploration or local refinement of the RBF. As a stopping criterion, the maximum number of evaluations is specified by the user.

Some assumptions are needed to transfer the CG-RBF method to the multifidelity framework. First we consider that only the expensive function is called to refine the prediction accuracy in

the vicinity of the global minimum. The evaluation time of the coarse model is considered to be so low that it can be evaluated a large number of time. The prediction accuracy on the coarse model is thus good enough and there is no need to add supplementary training points. Second, since the difference model is built using the expensive points, the infill criterion of the CG-RBF method is computed using the RBF function φ_d. As a result:

$$h_n(l) = \frac{(-1)^{m_\varphi+1}}{[\hat{y}_e(l) - f_n^*]} \times \left[\varphi_d(0) - \begin{pmatrix} u_n^T & F_l^T \end{pmatrix} \begin{pmatrix} \boldsymbol{\phi}_d & F_d \\ F_d{}^T & 0 \end{pmatrix}^{-1} \begin{pmatrix} u_n \\ F_l \end{pmatrix} \right] \tag{8}$$

where $u_n(l) := (\varphi(\|l - x_1\|), \ldots, \varphi(\|l - x_n\|))^T$, $F_l = \begin{bmatrix} l^T & 1 \end{bmatrix}$ and f_n^* corresponds to the targeted minimum value. The optimization of $\min_l - \log h_n(l)$ gives the next infill point.

4.2 Results of the optimization of the photoacoustic gas sensor

The photoacoustic signal detected is the objective to evaluate from simulation models, to surrogate with co-RBF and then to optimize with the CG-RBF-based procedure. The DOE of each model are first defined. For the coarse Kreuzer model, 100 points are evaluated and the RBF built on these data is assumed to be accurate enough. Then 5 points of the expensive FLNS model are evaluated. This allows the training of the co-RBF model in the Gutmann-RBF algorithm extension to multifidelity framework. Our stopping criterion is different from that described by Gutmann [1]. Here it is defined at the end of the target value cycle: once a cycle is over, the optimization stops if a better minimum value has not been evaluated compared to the previous cycle. Five different DOE are tested to check if the optimization leads to the same optimum. The number of evaluations needed to get the minimum location can also be assessed. The obtained results are summarized in Table 3. Two different areas are targeted at the end of the optimization algorithm. Parameters values are close to the upper bounds of the input space. This bound has been set up to fill some integration requirements of the gas sensor in a more complex system. It is either the capillaries length or the capillaries radius that is reduced to get an optimum value around 1.90 Pa. Both solutions provide an improved photoacoustic signal. Note that fabrication uncertainties have not been included yet in the design process but robustness could be a way to select one among the two solutions.

DOE	Optimum location	Optimum value	Number of function calls
1	[20 , 0.5 , 17.7]	1.90	18
2	[20 , 0.5 , 17.7]	1.90	24
3	[20 , 0.47 , 20]	1.90	18
4	[20 , 0.5 , 20]	1.88	12
5	[20 , 0.45 , 20]	1.91	24

Table 3: Results over five initial DOE of the optimization of the photoacoustic gas sensor.

The number of cycles needed to optimize the process is between 2 and 4. Each cycle has a cost of 6 calls to the expensive model. In a previous work, we used only the expensive model with the EGO procedure to get an optimal geometry. The algorithm converged after 40 function calls to a solution with an optimum value of 1.84 Pa and [20 , 0.36 , 19.6] as the optimum location. The benefit of the multifidelity approach developed in this work is clear, in terms of computational time and accuracy of the optimum obtained, when compared to this previous study.

5 CONCLUSIONS

A new multifidelity RBF-based metamodel has been proposed in this work. It is derived through the autoregressive model of Kennedy and O'Hagan [5] and combines the information from the coarse and the expensive numerical model of our design problem. An extension of the CG-RBF optimization algorithm is also suggested in the framework of the co-RBF. This allows the use of a complete multifidelity-based optimization procedure that is an alternative to the co-kriging method combined with EGO.
An optimal design of the photoacoustic gas sensor has been defined by to the new procedure. The extension of the CG-RBF optimization algorithm brings a way to refine the prediction accuracy toward the global optimum of our problem. The results obtained are superior than those obtained with a single fidelity approach in terms of accuracy and computational time.
This work in progress is a first step towards the creation of an efficient co-RBF based optimization algorithm. It has to be supplemented by a complete benchmark between this new procedure and the already existing co-kriging-based optimization method. Furthermore, other extension of already existing RBF-based optimization algorithms, such as the Constrained Optimization using Response Surfaces (CORS) algorithm [9] can be explored. The application of this method to the design of nanophotonic component is also considered.

REFERENCES

[1] H.-M. Gutmann, "A radial basis function method for global optimization," *Journal of Global Optimization*, vol. 19, no. 3, pp. 201–227, 2001.

[2] D. Krige, "A Statistical Approach to Some Basic Mine Valuation Problems on the Witwatersrand," 1951.

[3] C. E. Rasmussen and C. K. I. Williams, *Gaussian processes for machine learning*. Cambridge, Mass.: MIT Press, 2006.

[4] T. J. Santner, B. J. Williams, and W. I. Notz, *The Design and Analysis of Computer Experiments*. 2003.

[5] M. C. Kennedy and A. O'Hagan, "Predicting the Output from a Complex Computer Code When Fast Approximation are Available," *Biometrika*, vol. 87, pp. 1–13, Mar. 2000.

[6] A. I. Forrester, A. Sbester, and A. J. Keane, "Multi-fidelity optimization via surrogate modelling," *Proceedings of the Royal Society A: Mathematical, Physical and Engineering Sciences*, vol. 463, pp. 3251–3269, Dec. 2007.

[7] L. Le Gratiet and C. Cannamela, "Cokriging-based Sequential Design Strategies Using Fast Cross-Validation Techniques For Multi-Fidelity Computer Codes," *Technometrics,*, vol. 57, 2015.

[8] C. S. Reese, A. G. Wilson, M. Hamada, H. F. Martz, and K. J. Ryan, "Integrated Analysis of Computer and Physical Experiments," *Technometrics*, vol. 46, pp. 153–164, May 2004.

[9] R. G. Regis and C. A. Shoemaker, "Constrained global optimization of expensive black box functions using radial basis functions," *Journal of Global Optimization*, vol. 31, no. 1, pp. 153–171, 2005.

[10] A. Mikls, P. Hess, and Z. Bozki, "Application of acoustic resonators in photoacoustic trace gas analysis and metrology," *Review of Scientific Instruments*, vol. 72, pp. 1937–1955, Apr. 2001.

[11] V. Zeninari, V. A. Kapitanov, D. Courtois, and Y. N. Ponomarev, "Design and characteristics of a differential Helmholtz resonant photoacoustic cell for infrared gas detection," *Infrared physics & technology*, vol. 40, no. 1, pp. 1–23, 1999.

[12] R. Bauer, G. Stewart, W. Johnstone, E. Boyd, and M. Lengden, "3d-printed miniature gas cell for photoacoustic spectroscopy of trace gases," *Optics Letters*, vol. 39, pp. 4796–4799, Aug. 2014.

[13] J. Rouxel, J. G. Coutard, S. Gidon, O. Lartigue, S. Nicoletti, B. Parvitte, R. Vallon, V. Zninari, and A. Glire, "Development of a Miniaturized Differential Photoacoustic Gas Sensor," *Procedia Engineering*, vol. 120, pp. 396–399, 2015.

[14] L. B. Kreuzer, "The Physics of Signal Generation and Detection," in *Optoacoustic Spectroscopy and Detection* (Y.-H. PAO, ed.), pp. 1–25, Academic Press, 1977.

[15] M. J. D. Powell, "Radial basis function methods for interpolation to functions of many variables," in *HERCMA*, pp. 2–24, 2001.

[16] M. Buhmann, *Radial Basis Function : Theory and implementattions*. cambridge university press ed., 2003.

[17] N. Dyn, D. Levin, and S. Rippa, "Numerical Procedures for Surface Fitting of Scattered Data by Radial Functions," *SIAM Journal on Scientific and Statistical Computing*, vol. 7, pp. 639–659, Apr. 1986.

[18] R. L. Hardy, "Multiquadric equations of topography and other irregular surfaces," *Journal of Geophysical Research*, vol. 76, no. 8, 1971.

[19] A. I. J. Forrester, A. Sobester, and A. J. Keane, *Engineering design via surrogate modelling a practical guide*. Chichester, West Sussex, England; Hoboken, NJ: J. Wiley, 2008.

[20] M. D. Mckay, R. J. Beckman, and W. J. Conover, "A Comparison of Three Methods for Selecting Values of Input Variables in the Analysis of Output from a Computer Code," *Technometrics*, vol. 42, p. 55, Feb. 2000.

[21] G. Rennen, B. Husslage, E. R. Van Dam, and D. Den Hertog, "Nested maximin Latin hypercube designs," *Structural and Multidisciplinary Optimization*, vol. 41, pp. 371–395, Apr. 2010.

[22] S. Rippa, "An algorithm for selecting a good value for the parameter c in radial basis function interpolation," *Advances in Computational Mathematics*, vol. 11, no. 2-3, pp. 193–210, 1999.

[23] N. Hansen, "The CMA evolution strategy: A tutorial," vol. 29, 2005.

[24] D. R. Jones, M. Schonlau, and W. J. Welch, "Efficient global optimization of expensive black-box functions," *Journal of Global optimization*, vol. 13, no. 4, pp. 455–492, 1998.

ECCOMAS Congress 2016
VII European Congress on Computational Methods in Applied Sciences and Engineering
M. Papadrakakis, V. Papadopoulos, G. Stefanou, V. Plevris (eds.)
Crete Island, Greece, 5–10 June 2016

BEARING CAPACITY OF STRIP FOOTINGS ON SPATIALLY RANDOM SOILS USING KRIGING AND MONTE CARLO SIMULATION

Jawad Thajeel[1], Tamara Al-Bittar[2], Nour Issa[3] and Abdul Hamid Soubra[4]

[1] PhD student, University of Nantes, GeM, UMR CNRS 6183
Bd. de l'université, BP 152, 44603 Saint-Nazaire cedex, France
e-mail: Jawad.thajeel@etu.univ-nantes.fr

[2] Associate professor, Lebanese University, Faculty of Engineering
Tripoli, Al Kobeh, Liban
e-mail: Tamara.albittar@gmail.com

[3] Master student, Lebanese University, Faculty of Engineering
Tripoli, Al Kobeh, Liban
e-mail: noorissa_4@hotmail.com

[4]Professor, University of Nantes, GeM, UMR CNRS 6183
Bd. de l'université, BP 152, 44603 Saint-Nazaire cedex, France
e-mail: Abed.Soubra@univ-nantes.fr.

Keywords: probabilistic analysis, strip footing, bearing capacity, spatial variability, kriging, Monte Carlo simulation, probability of failure.

Abstract. *The probabilistic analysis of geotechnical structures presenting spatial variability in the soil properties is generally performed using Monte Carlo simulation (MCS) methodology. This methodology is not suitable for the computation of a small failure probability because it becomes very time-expensive in such a case due to the large number of simulations required to calculate the failure probability. For this reason, one needs to keep to a minimum the number of calls to the deterministic model when performing the probabilistic analyses. In order to overcome the shortcoming related to the excessive number of calls of the deterministic model when performing Monte Carlo simulations, Echard et al. (2011) proposed an Active learning reliability method (called AK-MCS) combining Kriging and Monte Carlo Simulation. The method was shown to be very efficient as the obtained probability of failure is very accurate needing only a small number of calls to the deterministic model. The probabilistic analyses presented in this paper were performed using AK-MCS methodology by Echard et al. (2011). The present study involves a probabilistic analysis at the ultimate limit state of a strip footing resting on a spatially varying soil using AK-MCS approach. The objective is the computation of the probability P_f of exceeding the ultimate bearing capacity of the footing under a prescribed footing load. The soil cohesion and angle of internal friction were considered as two non-isotropic non-Gaussian random fields. The deterministic model was based on numerical simulations using the finite difference code FLAC^{3D}. Some probabilistic results are presented and discussed.*

1 INTRODUCTION

The spatial variability of the soil properties affects the behavior of geotechnical structures (bearing capacity, foundation settlement, slope stability, etc.). Several authors have considered the effect of the spatial variability of the soil properties in their calculation models. For the bearing capacity of foundations which is the subject of the present paper, one may cite among others [1, 2].

It should be mentioned that when dealing with probabilistic studies that involve spatially varying soil properties, the classical Monte Carlo Simulation (MCS) methodology is generally used to determine the probability of failure P_f. This method is known to be very time-consuming. This is because (i) it generally makes use of finite element or finite difference models which are generally time-expensive and (ii) it requires a great number of calls of the deterministic model for the computation of the small failure probabilities encountered in practice. Thus, one needs to keep to a minimum the number of calls to the deterministic model when performing the probabilistic analyses.

In order to overcome the shortcoming related to the excessive number of calls of the deterministic model when performing Monte Carlo simulations, Echard et al. [3] proposed an active learning reliability method (called AK-MCS) combining Kriging and Monte Carlo Simulation. The method was shown to be very efficient as the obtained probability of failure is very accurate needing only a small number of calls to the deterministic model. The probabilistic analyses presented in this paper were performed using AK-MCS methodology by [3]. They involve the probabilistic analysis at the ultimate limit state of a strip footing resting on a spatially varying soil using AK-MCS approach. The objective is the computation of the probability P_f of exceeding the ultimate bearing capacity of the footing under a prescribed footing load. The soil cohesion and angle of internal friction were considered as two non-isotropic non-Gaussian random fields. They are characterized by two specified marginal distribution functions and a common autocorrelation function. The methodology proposed by [4] is used to generate these two random fields. The deterministic model is based on numerical simulations using FLAC^{3D} software. Some probabilistic results are presented and discussed.

The paper is organized as follows: The next section aims at presenting the probabilistic method used for the computation of the failure probability of a strip footing resting on a spatially varying soil. It is followed by some numerical results. The paper ends with a conclusion.

2 PROBABILISTIC MODELS

The aim of this section is to present the probabilistic model used in the present paper. The impact of the soil spatial variability on the ultimate bearing capacity was considered. It should be remembered here that the system response involves the ultimate bearing capacity (P_u) of a strip footing resting on a spatially varying soil. The soil cohesion c and friction angle φ were modeled as two non-isotropic non-Gaussian random fields. The EOLE methodology [4] was used to discretize the two random fields (i.e. to obtain realizations of the soil cohesion c and friction angle φ that respect the correlation structure of those fields). The performance function used to calculate the probability P_f of exceeding the ultimate bearing capacity was defined as follow:

$$G = \frac{P_u}{P_s} - 1 \tag{1}$$

Where P_s is the prescribed footing load. As for the probabilistic method used in this paper, the active learning reliability method combining kriging and Monte Carlo Simulation (called AK-MCS) was employed. This method combines both the classical crude Monte Carlo Simulation (MCS) methodology and the Kriging meta-model technique.

In this section, the EOLE method of discretization of random fields was firstly presented. It is followed by a brief presentation of the crude Monte Carlo method, the kriging metamodeling technique and the combined use of the kriging and the Monte Carlo Simulation (i.e. AK-MCS methodology) used for the probabilistic analysis.

2.1 Method of generation of anisotropic non-Gaussian random fields

Let us consider two anisotropic non-Gaussian random fields $Z_i^{NG}(x, y)(i = c, \varphi)$ described by: (i) constant means and standard deviations (μ_i, σ_i; $i = c, \varphi$), (ii) non-Gaussian marginal cumulative distribution functions G_i ($i = c, \varphi$), and (iii) a common square exponential autocorrelation function ρ_Z^{LN}[(x, y), (x', y')] which gives the values of the correlation between two arbitrary points (x, y) and (x', y'). This autocorrelation function is given as follows:

$$\rho_z^{LN}[(x, y), (x', y')] = \exp\left(-\left(\frac{|x - x'|}{a_x} \right)^2 - \left(\frac{|y - y'|}{a_y} \right)^2 \right) \tag{2}$$

where a_x and a_y are the autocorrelation distances along x and y respectively. The Expansion Optimal Linear Estimation method (EOLE) and its extension to cover the case of non-Gaussian random fields are used herein to generate the two random fields of c and φ. Notice that EOLE was first proposed by [4] for the case of uncorrelated Gaussian fields, and then extended by [5] to cover the case of correlated and uncorrelated non-Gaussian fields. In this method, one should first define a stochastic grid composed of q grid points (or nodes) $\{(x_1, y_1), ..., (x_q, y_q)\}$ for which the values of the field are assembled in a vector $\chi = \{Z(x_1, y_1), ..., Z(x_q, y_q)\}$. The number of grid points within the stochastic mesh is determined in such a manner that in each direction (x or y), there are five grid points within each autocorraltion distance. Secondly, one should determine the correlation matrix for which each element $\left(\Sigma_{\chi;\chi}\right)_{i,j}^{NG}$ is calculated as follows:

$$\left(\Sigma_{\chi;\chi}\right)_{i,j}^{NG} = \rho_z^{NG}\left[(x_i, y_i), (x_j, y_j)\right] \tag{3}$$

The common non-Gaussian autocorrelation matrix $\Sigma_{\chi;\chi}^{NG}$ should be transformed into the Gaussian space using Nataf model [6] since the discretization of the random fields using EOLE is done in the Gaussian space. As a result, one obtains two Gaussian autocorrelation matrices $\Sigma_{\chi;\chi}^{c}$ and $\Sigma_{\chi;\chi}^{\varphi}$ that can be used to discretize the two random fields as follows:

$$\tilde{Z}_i(x, y) = \mu_i + \sigma_i \sum_{j=1}^{N} \frac{\xi_{i,j}}{\sqrt{\lambda_j^i}} . \phi_j^i . \Sigma_{Z(x,y);\chi}^i \qquad i = c, \varphi \tag{4}$$

where $(\xi_{i,j}; i = c, \varphi)$ are two non-correlated blocks of independent standard normal random variables. Notice finally that $(\lambda_j^i, \phi_j^i; i = c, \varphi)$ in equation (4) are the eigenvalues and eigenvectors of the two Gaussian autocorrelation matrices $\Sigma_{\chi;\chi}^{c}$ and $\Sigma_{\chi;\chi}^{\varphi}$ respectively, and $\Sigma_{Z(x,y);\chi}$ is the correlation vector between the random vector χ and the value of the field at an

arbitrary point (x, y). Once the two Gaussian random fields are obtained, they should be transformed into the non-Gaussian space by applying the following formula:

$$\tilde{Z}_i^{NG}(x, y) = G_i^{-1}\left\{\Phi\left[\tilde{Z}_i(x, y)\right]\right\} \qquad i = c, \varphi \tag{5}$$

where $\Phi(.)$ is the standard normal cumulative density function.

2.2 Monte Carlo method

The Monte Carlo simulation method consists in generating *N* samples which respect the joint probability density function $f_X(X)$ of the *M* random variables ($X_1, \ldots, X_M$) gathered in a vector *X*. For each sample, the system response is calculated. Thus; for the *N* samples, one obtains *N* values of the system response gathered in a vector $\boldsymbol{G} = [G(\boldsymbol{x}_1), G(\boldsymbol{x}_2), \ldots, G(\boldsymbol{x}_N)]$ which may be used to determine the failure probability for a prescribed threshold of this system response. A very large number of realizations is required to obtain a rigorous value of the failure probability especially when computing small failure probabilities. It should be noted herein that the random variables considered in the present paper are the standard normal variables ξ_j ($j=1, \ldots, N$) that appear in Eq. (4) for the computation of a given realization of the cohesion c and the friction angle random fields.

2.3 Kriging metamodeling technique

The metamodeling technique aims at replacing the response (or the performance function in this paper) of a computationally-expensive mechanical model by a metamodel (i.e. a simple analytical equation). The kriging metamodeling technique is based on the idea that the performance function $G(\boldsymbol{x})$ is seen as a realization of a stochastic field $\hat{G}(\boldsymbol{x})$ [12]. The kriging metamodeling needs a design of experiments DoE of length *N* to define the stochastic parameters of this field and then, predictions of the response can be obtained on any unknown point. Let us define the design of experiments by the vector $\boldsymbol{X} = [\boldsymbol{x}_1, \boldsymbol{x}_2, \ldots, \boldsymbol{x}_N]$, with $\boldsymbol{x}_i$ the i[th] experiment, and $\boldsymbol{G} = [G(\boldsymbol{x}_1), G(\boldsymbol{x}_2), \ldots, G(\boldsymbol{x}_N)]$ the corresponding response vector. The approximate relationship between any experiment $\boldsymbol{x}$ and the response G($\boldsymbol{x}$) can be denoted as:

$$\hat{G}(\boldsymbol{x}) = \boldsymbol{F}(\boldsymbol{x}, \boldsymbol{\beta}) + \boldsymbol{Z}(\boldsymbol{x}) \tag{6}$$

Where:

- $\boldsymbol{F}(\boldsymbol{x}, \boldsymbol{\beta})$ is the deterministic part which gives an approximation of the mean value of the performance function. It corresponds to a regression model that can be written as:

$$\boldsymbol{F}(\boldsymbol{x}, \boldsymbol{\beta}) = \boldsymbol{f}^{\boldsymbol{T}}(\boldsymbol{x}).\boldsymbol{\beta} \tag{7}$$

Where $\boldsymbol{\beta}^T = [\beta_1, \ldots, \beta_p]$ is the vector of coefficients to be determined, $\boldsymbol{f}^T(\boldsymbol{x}) = [f_1(\boldsymbol{x}), f_2(\boldsymbol{x}), \ldots, f_p(\boldsymbol{x})]^T$ is a collection of regression functions (or regressors). The number *p* of regression functions is assumed to be less than or equal to the number *N* of observations so that the problem is not under-determined (i.e. it does not lack equations to compute the unknowns). In this paper, ordinary kriging is selected which means that $\boldsymbol{F}(\boldsymbol{x}, \boldsymbol{\beta})$ is a scalar to be determined [i.e. $\boldsymbol{F}(\boldsymbol{x}, \boldsymbol{\beta})=\beta$]. So the estimated $\hat{G}(\boldsymbol{x})$ can be simplified as:

$$\hat{G}(\boldsymbol{x}) = \boldsymbol{F}(\boldsymbol{x}, \boldsymbol{\beta}) + \boldsymbol{Z}(\boldsymbol{x}) = \beta + \boldsymbol{Z}(\boldsymbol{x}) \tag{8}$$

- $\boldsymbol{Z(x)}$ represents the fluctuation around the mean value. It is given by a Gaussian random process (or a random field) with zero mean and covariance defined by

$$Cov\left[Z(\boldsymbol{x_i}), Z(\boldsymbol{x_j})\right] = \sigma_z^2\, R(\boldsymbol{x_i}, \boldsymbol{x_j}) \tag{9}$$

where σ_z^2 is the process variance; $\boldsymbol{x}_i$, $\boldsymbol{x}_j$ are two points from the whole samples X and $R(\boldsymbol{x}_i, \boldsymbol{x}_j)$ is the correlation function between these two points with a correlation parameter vector $\boldsymbol{\theta}$. Several models exist to define the correlation function R. However, in this paper, the anisotropic squared-exponential function is selected. It is given by:

$$R(\boldsymbol{x_i}, \boldsymbol{x_j}) = \prod_{i=1}^{N} e^{\left(-\theta_i (x_i - x_j)^2\right)} \tag{10}$$

Where N is the number of random variables, x_i and x_j are the i[th] coordinates of the points $\boldsymbol{x}_i$ and $\boldsymbol{x}_j$ and θ_i is a scalar which is equal to the inverse of the correlation length in the i[th] direction.

As may be seen from equation (6), the kriging metamodel consists of a linear regression model $\boldsymbol{F(x, \beta)}$ and a stochastic process $\boldsymbol{Z(x)}$.

As $\boldsymbol{R}$ is a square matrix of dimension *N*x*N*, i.e. $\boldsymbol{R} = \left[R(\boldsymbol{x_i}, \boldsymbol{x_j})\right]_{N \times N}$ and **F** is a unit vector of dimension N, then β and σ_z^2 can be estimated as:

$$\hat{\beta} = (\boldsymbol{F}^T \boldsymbol{R}^{-1} \boldsymbol{F})^{-1}\, \boldsymbol{F}^T\, \boldsymbol{R}^{-1}\, \boldsymbol{G} \tag{11}$$

$$\hat{\sigma}_z^2 = \frac{1}{N} (\boldsymbol{G} - \beta \boldsymbol{F})^T\, \boldsymbol{R}^{-1} (\boldsymbol{G} - \beta \boldsymbol{F}) \tag{12}$$

The correlation parameter θ can be obtained through the maximum likelihood estimation:

$$\theta = arg_\theta \min(N \ln \sigma_z^2 + \ln|\boldsymbol{R}|) \tag{13}$$

Once the parameters $\hat{\beta}$, $\hat{\sigma}_z^2$ and θ are determined, the Best Linear Unbiased Predictor (BLUP) of the response $\hat{G}(\boldsymbol{x})$ at an unknown point $\boldsymbol{x}$ is shown to be a Gaussian random variate $\hat{G}(\boldsymbol{x}) \sim N\,(\mu_{\hat{G}(x)}, \sigma_{\hat{G}(x)})$ where

$$\mu_{\hat{G}(x)} = \beta + \boldsymbol{r}(\boldsymbol{x}) \boldsymbol{R}^{-1} (\boldsymbol{G} - \beta \boldsymbol{F}) \tag{14}$$

$$\sigma^2_{\hat{G}\,(x)} = \sigma_z^2(\boldsymbol{x})(\boldsymbol{1} + u^T(\boldsymbol{x})(\boldsymbol{F}^T \boldsymbol{R}^{-1} \boldsymbol{F})^{-1} u^T(\boldsymbol{x}) - \boldsymbol{r}^T(\boldsymbol{x}) R^{-1} \boldsymbol{r}(\boldsymbol{x})) \tag{15}$$

Where $\boldsymbol{r(x)}$= [**R**(**x, x**$_1$), **R**(**x, x**$_2$), . . . , **R**(**x, x**$_N$)], u(**x**) = $\boldsymbol{F}^T \boldsymbol{R}^{-1} \boldsymbol{r}(\boldsymbol{x}) - 1$. Notice that $\mu_{\hat{G}(x)}$ is usually taken as the estimated $\hat{G}(\boldsymbol{x})$ at point $\boldsymbol{x}$. The computation of $\mu_{\hat{G}(x)}$ and $\sigma^2_{\hat{G}\,(x)}$ can be obtained by MATLAB toolbox DACE [7].

Notice that the variance $\sigma^2_{\hat{G}\,(x)}$ is defined as the minimum of the mean squared error between $\hat{G}(\boldsymbol{x})$ and G(x). The variances of points in the initial DoE are zero, but the variances of the

other points are always not zero. A large value of $\sigma^2_{\hat{G}\ (x)}$ means that the prediction is not exact. Therefore, the variance prediction $\sigma^2_{\hat{G}\ (x)}$ is important in the unexplored areas and presents a good index to improve the initial DoE. This property is interesting and is used in the following paragraph.

2.4 AK-MCS methodology

In a first stage, a significant number of realizations (about 1 million) of the spatially varying soil medium were generated by MCS using the Expansion Optimal Linear Estimation (EOLE) method. The response of most of these realizations will not be computed from the original deterministic model; only a few numbers of realizations will be computed using this model depending on their corresponding learning function values. In a second stage, an initial small Design of Experiments (DoE) based on a random selection of some realizations among the MCS population was determined and employed to compute the Kriging model (based on the values of the responses obtained using the original deterministic model). In a third stage, the adopted learning function U (which makes use of the already-obtained kriging model) is employed to choose the best next realization (among all the realizations of the MCS population) to be used for the computation of the system response from the original deterministic model. This realization is the one that leads to the minimal value of the learning function U. In a final stage (stage 4), the response obtained from this realization is employed to update the kriging model with this new response value (only in case where the adopted stopping condition has not been reached). Notice that stages 3-4 should be repeated several times until reaching the adopted stopping condition. At the end, the surrogate kriging model is considered to be enough accurate for the estimation of the failure probability and the corresponding value of the coefficient of variation, for the prescribed number of simulations. If the coefficient of variation of the failure probability is found to be too high, the initial MCS population should be increased. A more comprehensive step-by-step procedure describing the implementation of the AK-MCS methodology for the computation of the failure probability may be given as follows:

1. Generate a population S of n_{MC} (say 1,000,000) realizations of the spatially varying soil parameters c and φ using Monte Carlo Simulation. It should be emphasized here that the computation of the performance function for these realizations (as defined in equation 1 based on the computationally-expensive $FLAC^{3D}$ model) is not required at this stage.
2. Randomly select from the S population a small number of realizations (called initial Design of Experiments DoE) containing N_1 realizations (say 20). For those N_1 realizations, one should evaluate the performance function given by equation (1) based on the computationally expensive $FLAC^{3D}$ model. The required initial DOE may be greater than 20 for a great number of random variables (i.e. for a spatially varying soil property with small values of the autocorrelation distances). This is because for high dimensional problems (i.e. when a large number of random variables is needed to discretize the c and φ random fields), the kriging model needs more points (i.e. realizations) in order to compute correlation parameters θ_i given by equation (10).
3. Compute the kriging model according to the small initial DoE containing the N_1 realizations. This kriging model is given by equation (14). It should be mentioned here that this stage was performed using the Matlab toolbox DACE [7]. In this paper,

ordinary kriging model was used (i.e. the regression model is considered to be constant) and a square exponential correlation function was adopted in the analysis.

4. By using DACE toolbox, compute (for the whole population S containing the n_{MC} realizations of the random field) both the kriging predictor values $\mu_{\hat{G}}$ of the performance function (based on equation 14) and their corresponding kriging variance values $\sigma_{\hat{G}}^2$ (based on equation 15). From the obtained values of the kriging predictors $\mu_{\hat{G}}$, obtain an estimation of the probability of failure $\hat{P}_f$ by counting the number of negative predictors $N_{\hat{G}\leq 0}$ and dividing it by the total number of samples in S as follows:

$$\hat{P}_f = \frac{N_{\hat{G}\leq 0}}{n_{MC}} \tag{16}$$

Also compute the coefficient of variation of $\hat{P}_f$ as follows:

$$\hat{COV}(\hat{P}_f) = \sqrt{\frac{1-\hat{P}_f}{\hat{P}_f n_{MC}}} \tag{17}$$

5. Identify the best next realization in S for which one will compute the performance function using FLAC^{3D}. This is performed by evaluating a learning function U for each realization in S. The learning function U is given by:

$$U(x_i) = \frac{\left|\mu_{\hat{G}(x_i)}\right|}{\sigma_{\hat{G}(x_i)}} \qquad i = 1, \ldots, n_{MC} \tag{18}$$

The best next candidate realization is the one with minimum value of U. If this minimum value of U is smaller than 2, the performance function based on FLAC^{3D} is evaluated for this best candidate and the initial DoE is updated. Thus one should go back to step 3 and evaluate a new kriging model based on the updated DoE. Steps 3, 4 and 5 are repeated until the minimum value of U becomes larger than 2. At this stage the learning stops and the metamodel is considered accurate enough based on the n_{MC} realizations.

6. When the learning stops, one must compute the estimated values of both the probability of failure $\hat{P}_f$ and the coefficient of variation $\hat{COV}\left(\hat{P}_f\right)$. The obtained value of $\hat{P}_f$ is considered to be accurate if $\hat{COV}\left(\hat{P}_f\right) \leq 5\%$. If the estimated coefficient of variation is larger than 5%, one must increase the population S in step 1 and repeat the procedure.

It should be emphasized herein that a small initial DoE is chosen within the present approach (see step 2) in order to keep to a minimum the number of calls to the deterministic model. This initial DoE is successively increased by a single realization at each time (see step 5). The chosen realization is the one that is improving the most the metamodel because equation (18) searches for the realization that has a small kriging predictor (i.e. a realization that is close to the limit state surface) and/or a high kriging variance (i.e. a high uncertainty in the sign of its performance function value). Notice that the realizations with high uncertainties in the sign of their performance function values (positive or negative) are those that are close to the limit state surface. Finally, notice that the stopping criterion min(U)>2 corresponds to a maximal probability of making a mistake

on the sign of the performance function of Φ(-2)=0.023. This means that the stopping criterion is relevant making use of the realizations with a small uncertainty in making a mistake in their performance functions' signs, the probability of making a mistake in the signs of their performance function values being negligible.

2.5 Probabilistic numerical results

The aim of this section is to present the probabilistic numerical results of a strip footing resting on a spatially varying soil and subjected to a vertical loading. The soil shear strength parameters (c and φ) were considered as anisotropic non-Gaussian random fields. The soil cohesion c was modeled by a lognormal distribution. Its mean value and its coefficient of variation (referred to in this paper as reference values) were taken as follows: $\mu_c = 20\ kPa$, $COV_c = 25\%$. On the other hand, the soil friction angle φ was assumed to be bounded (i.e $0 \leq \varphi \leq 45^{\circ}$). A beta distribution was selected for this parameter with a mean value and a coefficient of variation given as follows: $\mu_\varphi = 30^{\circ}$, $COV_\varphi = 10\%$. **.** The soil dilation angle ψ was considered to be related to the soil friction angle φ by $\psi = 2\varphi / 3$. This means that the soil dilation angle was implicitly assumed as a random field that is perfectly correlated to the soil friction angle random field. Notice that the same autocorrelation function (square exponential) was used for both c and φ.

As for the autocorrelation distances ax and ay of the two random fields c and φ, both cases of isotropic (i.e. ax=ay) and anisotropic (i.e. ax>ay) random fields will be treated although the soil is rarely isotropic in reality. In our study, the reference values adopted for ax and ay were ax=10m and ay=1m. For the considered soil domain and for the different values of the autocorrelation distances (ax, ay) used in the analysis, the total number N of random variables (or eigenmodes) that is used to discretize the two random fields c and φ is determined based on a variance of the error ≤10%. It should be mentioned here that the initial design of experiment (DoE) contain 20 samples.

2.5.1 Deterministic model

The deterministic model was based on numerical simulations using the finite difference code FLAC^{3D}. The soil behavior was modeled using a conventional elastic-perfectly plastic model based on Mohr-Coulomb failure criterion. Notice that the soil Young modulus E and Poisson ratio υ were assumed to be deterministic since the ultimate bearing capacity is not sensitive to these variables. Their corresponding values are respectively $E = 60MPa$ and $\nu = 0.3$. Finally, concerning the footing, a weightless strip foundation of 1m width and 0.25m height is used. It is assumed to follow an elastic linear model ($E = 25GPa, \nu = 0.4$). The connection between the footing and the soil mass is modeled by interface elements having the same mean values of the soil shear strength parameters in order to simulate a perfectly rough soil-footing interface. These parameters have been considered as deterministic in this study. Concerning the elastic properties of the interface, they also have been considered as deterministic and their values are as follows: $K_s = 1GPa$, $K_n = 1GPa$ where K_s and K_n are respectively the shear and normal stiffness of the interface.

As shown in Figure 1, a strip footing of width B=1m that rests on a soil domain of width 13B and depth 5B was considered in the analysis. For the displacement boundary conditions, the bottom boundary was assumed to be fixed and the vertical boundaries were constrained in motion in the horizontal direction. For the computation of the bearing capacity of the rigid rough strip footing subjected to a central vertical load using FLAC^{3D}, the following method is adopted: an optimal controlled downward vertical velocity of 5×10^{-6} m/timestep (i.e. displacement per timestep) was applied to the bottom central node of the footing. Damping of

the system is introduced by running several cycles until a steady state of plastic flow is developed in the soil underneath the footing. At each cycle, the vertical footing load is obtained by using a FISH function that calculates the integral of the normal stress components for all elements in contact with the footing. The value of the vertical footing load at the plastic steady state is the ultimate footing load.

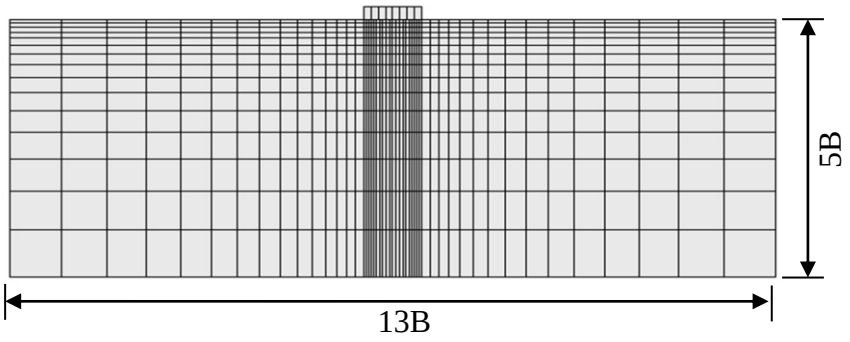

Figure 1. Soil domain and mesh in the FLAC^{3D}

2.5.2 Probabilistic results for the reference case

Figure (2) presents for the reference case (a_x=10m, a_y=1m) the failure probability P_f, the coefficient of variation COV_{Pf} and the learning function values U as function of the added points (i.e. added realizations) for a number of realizations n_{MC} equal to 500000. It should be mentioned here that 491 additional points were added to the initial DoE before the algorithm stops (U>2). The final obtained values of P_f and COV_{Pf} are respectively $1.408x10^{-3}$ and 3.766%. Figure (2) shows that the probability of failure starts to converge at about 480 calls to the deterministic model.

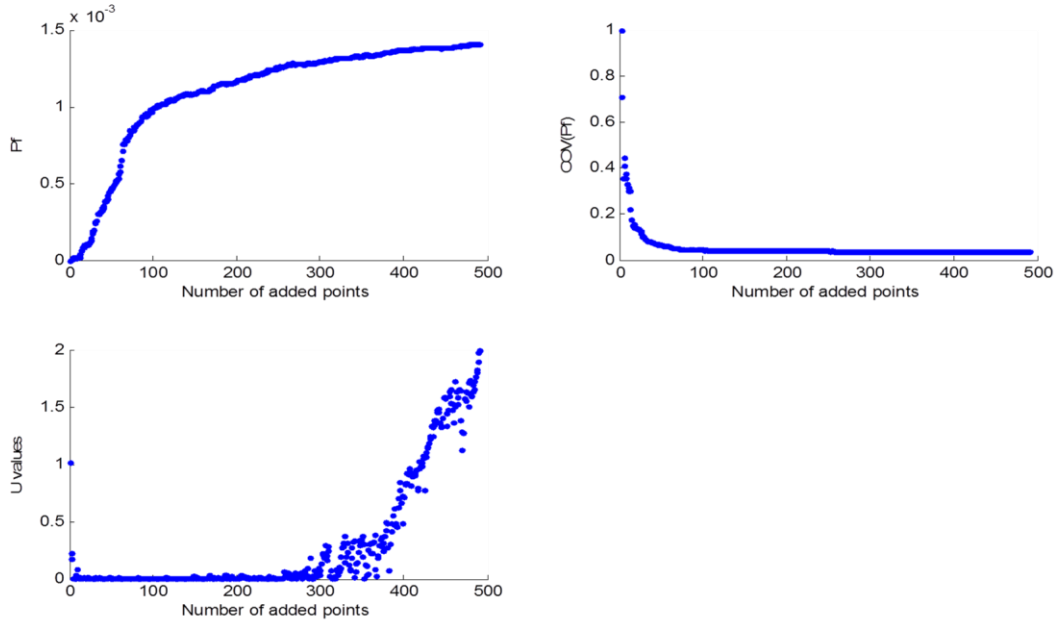

Figure 2. P_f, cov(P_f) and U values as function of the added points for the reference case

Figures (3) presents typical realizations and the corresponding velocity field of the random fields for the reference case. As may be seen from this figure, the spatial variability of the soil

properties can produce a non-symmetrical mechanism even though the footing is subjected to a symmetrical vertical load.

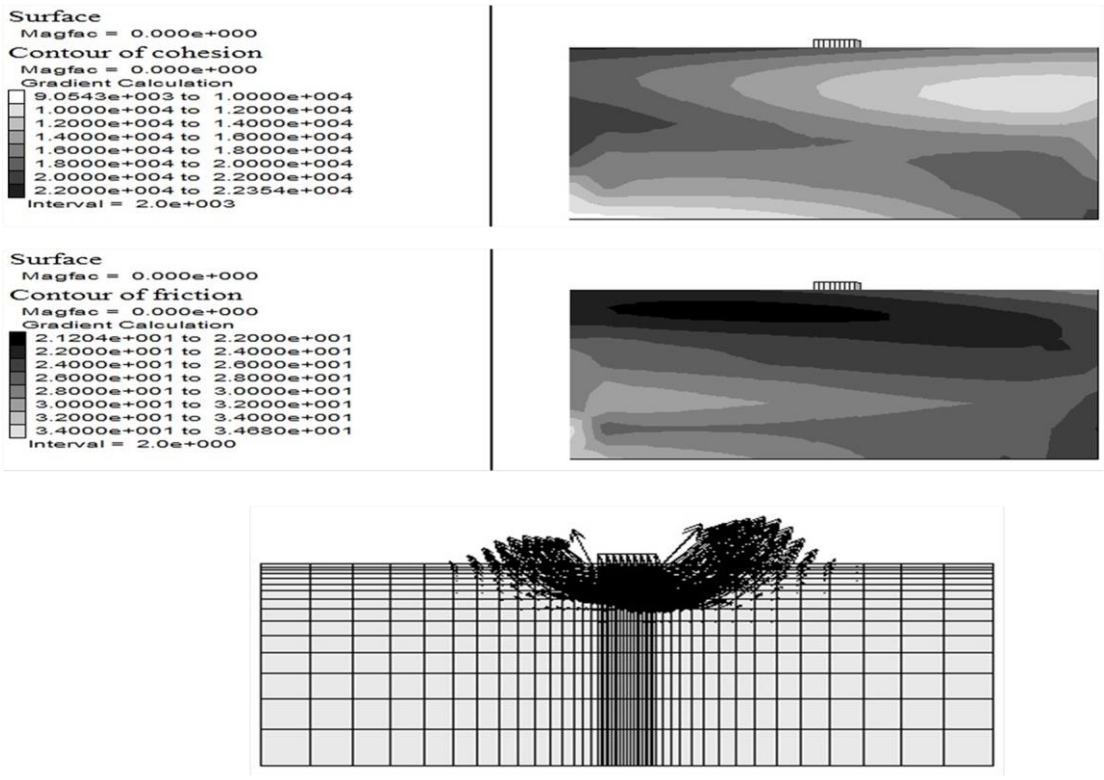

Figure 3. Typical realization and the corresponding velocity field of the random fields for the reference case (a_x=10m, a_y=1m) (n_{MC} = 500000)

2.5.3 Effect of the number of simulations on COV_{Pf}

To ensure a small uncertainty on the estimation of the failure probability, the number of realizations n_{MC} to be used must be sufficient to provide a small value of the coefficient of variation COV_{Pf} of this failure probability. Figure (4) shows for the reference case the variation of COV_{Pf} (as computed by AK-MCS methodology) with the number of realizations n_{MC}. As expected, Figure (4) shows that COV_{Pf} decreases (i.e. the accuracy of the failure probability increases) with the increase of n_{MC}.

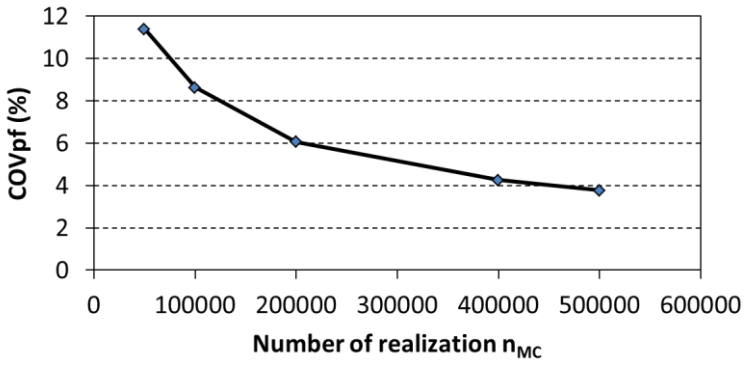

Figure 4. Coefficient of variation of P_f versus the number of realizations n_{MC}

2.5.4 Effect of the autocorrelation distance

Table 1 presents the effect of the isotropic autocorrelation distance (ax=ay) on the failure probability (P_f) and the corresponding coefficient of variation COV_{Pf} as computed by AK-MCS methodology using n_{MC}=1,000,000 realizations of the random field. This table also gives, for each autocorrelation distance, (i) the number of eigenmodes that is needed to satisfy the criterion imposed on the variance of the error of the random field (i.e. variance error<10%), (ii) the number of added points (i.e. the number of added realizations) and (iii) the obtained value of the learning function U for which the learning stops. As may be seen from this table, P_f increases with the increase in the autocorrelation distance. A small value of the coefficient of variation of the failure probability (smaller than 3%) was obtained for the adopted value of n_{MC}. The number of added realizations required to lead to a good approximation of the kriging model seems to be greater for the smaller values of the autocorrelation distance, although there is no regular increase in the number of added points with the decrease of the autocorrelation distance. Indeed, this number depends on the evolution of the learning function value to satisfy the stopping conditions.

Table 1. Number of random variables used to discretize the random field in EOLE method, P_f, COV_{Pf} and number of added points in the case of an isotropic case

ax=ay (m)	Number of needed random variables for the two random fields (c, φ)	$P_f \times 10^{-3}$	Cov_{pf} %	Number of added points	U
10	4	2.407	2.0358	243	2.033194
20	4	3.509	1.685	342	2.007373
50	4	3.824	1.614	65	2.292211
100	4	3.87	1.604	76	2.147826

3 CONCLUSION

The probabilistic analysis of shallow foundations resting on a spatially varying soil was generally performed in literature using MCS methodology. The mean value and the standard deviation of the system response were extensively investigated. This was not the case for the failure probability because MCS methodology requires a large number of calls of the deterministic model to accurately calculate a small failure probability. This paper mainly presented a probabilistic analysis at the ultimate limit state of a strip footing resting on a spatially varying soil using an active learning reliability method combining kriging and Monte Carlo Simulation (called AK-MCS). The method was shown to be very efficient as the obtained probability of failure is very accurate needing only a small number of calls to the deterministic model. Within this method, one performs a Monte Carlo simulation without evaluating the whole population using the original deterministic model. Indeed, the population is predicted using a kriging metamodel which is defined using only a few points of the population that are evaluated employing the original deterministic model. The objective of this paper is the computation of the probability P_f of exceeding the ultimate bearing capacity of the footing under a prescribed footing load. The soil cohesion and angle of internal friction were considered as two non-isotropic non-Gaussian random fields. The deterministic model

was based on numerical simulations using the finite difference code FLAC^{3D}. The main findings of this study can be summarized as follows:

1. The probabilistic analysis has shown that the small failure probability P_f was computed accurately (i.e. with a small COV_{Pf}) using only a small number of calls of the deterministic model.
2. The failure probability P_f increases with the increase in the autocorrelation distance. The number of added realizations required to lead to a good approximation of the kriging model seems to be greater for the smaller values of the autocorrelation distance.

REFERENCES

[1] Griffiths, D.V., and Fenton, G.A. (2001). "Bearing capacity of spatially random soil. The undrained clay Prandtl problem revisited." Géotechnique, 51(4): 351-359.

[2] Griffiths, D.V., Fenton, G.A., and Manoharan, N. (2002). "Bearing capacity of rough rigid strip footing on cohesive soil: Probabilistic study." Journal of Geotechnical and Geoenvironmental Engineering, ASCE, 128(9): 743-755.

[3] Echard B, Gayton N, Lemaire M. AK-MCS: an active learning reliability method combining Kriging and Monte Carlo simulation. Structural Safety 2011;33(2):145–54.

[4] Li, C.C., and Der Kiureghian, A. (1993). "Optimal discretization of random fields." Journal of Engineering Mechanics, 119(6): 1136-1154.

[5] Vorechovsky, M. (2008). "Simulation of simply cross correlated random fields by series expansion methods." Structural Safety, 30, 337-363.

[6] Nataf, A. (1962). "Détermination des distributions de probabilités dont les marges sont données." CR Acad Sci, 225: 42-3 (in French).

[7] Lophaven SN, Nielsen HB, Sondergaard J. DACE, a matlab Kriging toolbox, version 2.0. Tech. Rep. IMM-TR-2002-12; Technical University of Denmark; 2002a. <http://www2.imm.dtu.dk/hbn/dace/>.

ECCOMAS Congress 2016
VII European Congress on Computational Methods in Applied Sciences and Engineering
M. Papadrakakis, V. Papadopoulos, G. Stefanou, V. Plevris (eds.)
Crete Island, Greece, 5–10 June 2016

AN OPTIMAL SENSOR PLACEMENT METHOD FOR SHM BASED ON BAYESIAN EXPERIMENTAL DESIGN AND POLYNOMIAL CHAOS EXPANSION

Giovanni Capellari[1], Eleni Chatzi[2], and Stefano Mariani[1]

[1]Politecnico di Milano, Dipartimento di Ingegneria Civile e Ambientale
Piazza Leonardo da Vinci, 32, 20133 Milano (IT)
e-mail: giovanni.capellari, stefano.mariani@polimi.it

[2] ETH Zürich, Institut für Baustatik und Konstruktion
Stefano-Franscini-Platz, 5, 8093 Zürich (CH)
e-mail: chatzi@ibk.baug.ethz.ch

Keywords: Structural Health Monitoring, Damage Detection, Optimal Sensor Placement, Bayesian Inference, Uncertainty Quantification.

Abstract. *We present an optimal sensor placement methodology for structural health monitoring (SHM) purposes, relying on a Bayesian experimental design approach. The unknown structural properties, e.g. the residual strength and stiffness, are inferred from data collected through a network of sensors, whose architecture, i.e., type and position may largely affect the accuracy of the monitoring system. In tackling this issue, an optimal network configuration is herein sought by maximizing the expected information gain between prior and posterior probability distributions of the parameters to be estimated. Since the objective function linked to the network topology cannot be analytically computed, a numerical approximation is provided by means of a Monte Carlo analysis, wherein each realization is obtained via finite element modeling. Since the computational burden linked to this procedure often grows infeasible, a Polynomial Chaos Expansion (PCE) approach is adopted for accelerating the computation of the forward problem. The analysis expands over joint samples covering both structural state and design variables, i.e., sensor locations. Via increase of the number of deployed sensors in the network, the optimization procedure soon turns computationally costly due to the curse of dimensionality. To this end, a stochastic optimization method is adopted for accelerating the convergence of the optimization process and thereby the damage detection capability of the SHM system. The proposed method is applied to thin flexible structures, and the resulting optimal sensor configuration is shown. The effects of the number of training samples, the polynomial degree of the approximation expansion and the optimization settings are also discussed.*

1 INTRODUCTION

Let us consider a structural system, monitored through a network of sensors. The measured response of the system subjected to a set of given actions is collected in the vector $\mathbf{y} \in \mathbb{R}^{n_\mathbf{y}}$, where entries can be either displacements or rotations. Here $n_\mathbf{y}$ is the number of measurements, i.e., the number of sensors to be deployed multiplied by the number of physical quantities that can be measured by each sensor.
Let us define a set of mechanical properties like Young modulus, stiffness, modal parameters, collected in the vector $\boldsymbol{\theta} \in \mathbb{R}^{n_{\boldsymbol{\theta}}}$, to be identified using the measured data $\mathbf{y}$. The capability of a SHM system to detect and identify the said mechanical properties is basically affected by two aspects [1]: the mathematical tools exploited to estimate the parameters; and the experimental setting, i.e., the physical quantities to be measured and the procedure to measure them. Considering the experimental design alone, the estimation capability is affected by several aspect, including:

- sensor characteristics such as accuracy, resolution, sensitivity, noise, etc.;
- number of sensors;
- orientation and deployment of sensors;

which should be appropriately set to ensure high accuracy at a reduced cost.
Optimal sensor placement (OSP) forms a fundamental task for real SHM applications, as it can allow decreasing the cost and complexity of the SHM system. As summarized in [2, 3, 4], among the most commonly adopted OSP methods we find: the effective independence method (EFI); the driving-point residue method (EFI-DPR); the kinetic energy method (KEM); the modified variance method (MVM); methods based on topology optimization [5]. All aforementioned methods do not take into account that measurements are inevitably corrupted with errors, and hence they should be treated as stochastic quantities. The main goal of the present work is to determine the optimal configuration of sensors, that guarantees the best estimation of mechanical parameters or, in other words, the maximum amount of inferred information, under noise corrupted variables. The general purpose framework proposed in [6] is applied to the OSP problem, in order to find the sensor configuration guaranteeing a maximal amount of information, as already proposed in [7] and [8].
The remainders of the paper is organized as follows: in Section 2, the main theoretical aspects of the adopted methodology, such as the problem settings, the numerical solution of the problem and the optimization scheme, are described. In section 3, the framework is implemented on a simple benchmark problem consisting in a flexible simply supported plate. Finally, some concluding remarks and possible future developments are friefly summarized in Section 4.

2 BAYESIAN EXPERIMENTAL DESIGN FOR OPTIMAL SENSOR PLACEMENT

2.1 Problem settings

Moving from a space discretized system, the position of the sensors is defined through an appropriate design variable vector $\mathbf{d} \in \mathbb{R}^{n_\mathbf{d}}$, that can be set alternatively as:

- vector of spatial nodal coordinates

$$\mathbf{d} = \{x_1 \;\; y_1 \;\; z_1 \;\; \boldsymbol{\delta}_1 \;\; \ldots \;\; x_{n_{sens}} \;\; y_{n_{sens}} \;\; z_{n_{sens}} \;\; \boldsymbol{\delta}_{n_{sens}}\}^T \tag{1}$$

where $1 \leqslant n_{sens} \leqslant n_{nodes}$ is the number of sensors to be deployed; variable $\boldsymbol{\delta}_i = \{u_i, v_i, w_i\}^T$ identifies the orientation of the $i-$th sensor; the spatial coordinates x_i, y_i, z_i are defined in the discrete domain of all the nodes of the Finite Element (FE) model;

- vector of nodal labels
$$\mathbf{d} = \{d_1 \ \boldsymbol{\delta}_1 \ \ \ldots \ \ d_{n_{sens}} \ \boldsymbol{\delta}_{n_{sens}}\}^T \tag{2}$$
with d_i designating the FE model node where the $i-$th sensor is placed.

The measured quantities $\mathbf{y}$ are related to the model output $\mathbf{u} \in \mathbb{R}^{n_{nodes}n_{dof}}$, n_{dof} denoting the number of degrees of freedom of each node associated to the FE model, through the relation:

$$\mathbf{y} = \mathbf{L}\mathbf{u} + \boldsymbol{\epsilon} \tag{3}$$

where $\boldsymbol{\epsilon} \in \mathbb{R}^{n_{sens}}$ is the model prediction error, accounting for the modelling and measurement errors, and is therefore related to the type of sensors deployed. $p_{\boldsymbol{\epsilon}} = p(\boldsymbol{\epsilon})$ is defined as the probability density function associated with the model prediction error. $\mathbf{L} \in \mathbb{R}^{n_{sens} \times n_{nodes}n_{dof}}$ is a configuration matrix, linking the measurements $\mathbf{y}$ to the model response $\mathbf{u}$, defined as a boolean matrix, with 1 or 0 entries corresponding respectively to the measured and non-measured quantities. $\mathbf{L}$ depends both on the sensors positions, i.e., the nodes in which the sensors are placed, and the direction of the measured displacement or accelerations. Therefore, $\mathbf{L} = \mathbf{L(d)}$ is function of the experimental variable $\mathbf{d}$.
Since the structure is modeled through a FE model, the model response $\mathbf{u}$ depends on the meachanical properties of the system, according to:

$$\mathbf{u} = \mathbf{K}(\boldsymbol{\theta})^{-1}\mathbf{F} \tag{4}$$

where $\mathbf{K} \in \mathbb{R}^{n_{nodes}n_{dof} \times n_{nodes}n_{dof}}$ is the stiffness matrix associated with the discretized structure and $\mathbf{F} \in \mathbb{R}^{n_{nodes}n_{dof}}$ is the load vector. The load is assumed implemented as a quasi-static way and therefore any dynamic effect on the response is disregarded.
Eqs. (3) and (4) lead to:

$$\mathbf{y} = \mathbf{G}(\mathbf{d}, \boldsymbol{\theta}) + \boldsymbol{\epsilon} \tag{5}$$

where:

$$\mathbf{G}(\mathbf{d}, \boldsymbol{\theta}) = \mathbf{L(d)}\mathbf{K}(\boldsymbol{\theta})^{-1}\mathbf{F} \tag{6}$$

is the forward model operator $\mathbb{R}^{n_{\mathbf{d}}} \times \mathbb{R}^{n_{\boldsymbol{\theta}}} \to \mathbb{R}^{n_{\mathbf{u}}}$ that maps the design variable and the parameters to be estimated onto the response domain.
The main goal of the OSP problem is to determine the optimal sensor configuration $\mathbf{d}^*$, for the Bayesian inference of the mechanical parameters $\boldsymbol{\theta}$. Here we use the general framework proposed in [6, 9], which is applicable to any Bayesian inference problem; $\boldsymbol{\theta}$ and $\mathbf{y}$ are therefore treated as random variables, with their appropriate probability densities, accounting for their respective uncertainties.
Bayes' theorem allows to compute the conditional probability density of the parameters to be inferred, given the acquired data, i.e., the measurements. In the case of experimental design, the Bayes' rule can be specialized, taking also into account the design variable, as:

$$p(\boldsymbol{\theta}|\mathbf{y}, \mathbf{d}) = \frac{p(\mathbf{y}|\boldsymbol{\theta}, \mathbf{d})p(\boldsymbol{\theta}|\mathbf{d})}{p(\mathbf{y}|\mathbf{d})} \tag{7}$$

where $p(\boldsymbol{\theta}|\mathbf{y}, \mathbf{d})$ is the posterior distribution (probability density of $\boldsymbol{\theta}$, given $\mathbf{y}$ and $\mathbf{d}$), $p(\mathbf{y}|\boldsymbol{\theta}, \mathbf{d})$ is the likelihood, $p(\boldsymbol{\theta}|\mathbf{d})$ is the prior distribution and $p(\mathbf{y}|\mathbf{d})$ is the evidence. In the following, the

evidence is assumed to be independent of the design variable, therefore $p(\boldsymbol{\theta}|\mathbf{d}) = p(\boldsymbol{\theta})$. Hence, the prior knowledge of $\boldsymbol{\theta}$ is not affected by the experimental procedure.
Following [10], the optimal experimental design in a Bayesian sense can be obtained by maximizing the following expression:

$$\max_{\mathbf{d}\in\boldsymbol{\mathcal{D}}} \int_{\boldsymbol{\mathcal{Y}}} \int_{\boldsymbol{\Theta}} U(\mathbf{d},\mathbf{y},\boldsymbol{\theta}) p(\boldsymbol{\theta},\mathbf{y}|\mathbf{d}) d\boldsymbol{\theta} d\mathbf{y} \tag{8}$$

where $\boldsymbol{\mathcal{Y}}$ and $\boldsymbol{\Theta}$ respectively designate the supports of $p(\mathbf{y}|\mathbf{d})$ and $p(\boldsymbol{\theta})$. Within a decision theory formulation, $U(\mathbf{d},\mathbf{y},\boldsymbol{\theta})$ is a utility function defined in $(\boldsymbol{\mathcal{D}},\boldsymbol{\mathcal{Y}},\boldsymbol{\Theta}) \rightarrow \mathbb{R}$ that takes into account the usefulness of the experimental decision $\mathbf{d}$, given a particular value of $\boldsymbol{\theta}$ and $\mathbf{y}$. The optimal experimental design aims to maximize the expected utility function specified by Eq. (8). As summarized in [11], the choice of the utility function is strictly related to the type of problem, whether it is a prediction or an estimation one. As suggested in [7], the most common utility function for the inference problems is the expected Kullbach-Leibler divergence (also called expected gain in Shannon information [12] or relative entropy) between the posterior and the prior probability distributions [13]:

$$D_{KL}(p(\boldsymbol{\theta}|\mathbf{y},\mathbf{d})||p(\boldsymbol{\theta})) = \int_{\boldsymbol{\mathcal{Y}}} \int_{\boldsymbol{\Theta}} \log \frac{p(\boldsymbol{\theta}|\mathbf{y},\mathbf{d})}{p(\boldsymbol{\theta})} p(\mathbf{y},\boldsymbol{\theta}|\mathbf{d}) d\mathbf{y} d\boldsymbol{\theta} \tag{9}$$

The rationale behind this choice relies on the concept that the optimal configuration should yield the largest increase in information between the prior and the posterior.
Recasting Eq. (9) into the experimental design problem, the utility function becomes:

$$U(\mathbf{d},\mathbf{y},\boldsymbol{\theta}) = U(\mathbf{d},\mathbf{y}) = \int_{\boldsymbol{\Theta}} \log \frac{p(\bar{\boldsymbol{\theta}}|\mathbf{y},\mathbf{d})}{p(\bar{\boldsymbol{\theta}})} p(\bar{\boldsymbol{\theta}}|\mathbf{y},\mathbf{d}) d\bar{\boldsymbol{\theta}} \tag{10}$$

Remebering that $\bar{\boldsymbol{\theta}}$ is a dummy variable and using Eq. (10), the optimization statement of Eq. (8) becomes:

$$\max_{\mathbf{d}\in\boldsymbol{\mathcal{D}}} \int_{\boldsymbol{\mathcal{Y}}} \int_{\boldsymbol{\Theta}} p(\boldsymbol{\theta}|\mathbf{y},\mathbf{d}) \ln \frac{p(\boldsymbol{\theta}|\mathbf{y},\mathbf{d})}{p(\boldsymbol{\theta})} d\boldsymbol{\theta} p(\mathbf{y}|\mathbf{d}) d\mathbf{y} \tag{11}$$

Rearranging Eq. (11) using Eq. (7), we can rewrite the optimization problem as:

$$\begin{aligned} &\text{find} \quad \mathbf{d}^* = \arg\max_{\mathbf{d}\in\mathcal{D}} \bar{U}(\mathbf{d}) \\ &\text{such that} \quad \bar{U}(\mathbf{d}) = \int_{\boldsymbol{\mathcal{Y}}} \int_{\boldsymbol{\Theta}} \{\ln[p(\mathbf{y},\boldsymbol{\theta}|\mathbf{d})] - \ln[p(\mathbf{y}|\mathbf{d})]\} p(\mathbf{y},\boldsymbol{\theta}|\mathbf{d}) p(\boldsymbol{\theta}) d\boldsymbol{\theta} d\mathbf{y} \end{aligned} \tag{12}$$

where $\bar{U}(\mathbf{d})$ is the so-called expected information gain in $\boldsymbol{\theta}$.

2.2 Surrogate modeling

The optimization problem defined in Eq. (12) is handled through Monte Carlo sampling as:

$$\bar{U}(\mathbf{d}) \approx \frac{1}{N_{out}} \sum_{i=1}^{N_{out}} \left\{ \ln\left[p(\mathbf{y}^i|\boldsymbol{\theta}^i,\mathbf{d})\right] - \ln\left[p(\mathbf{y}^i|\mathbf{d})\right] \right\} \tag{13}$$

where N_{out} represents the number of samples $\boldsymbol{\theta}^i$ to be drawn in the outer Monte Carlo sum.
The evidence computed at $\mathbf{y}^{(i)}$ is approximated as:

$$p(\mathbf{y}^i|\mathbf{d}) \approx \frac{1}{N_{in}} \sum_{j=1}^{N_{in}} p(\mathbf{y}^i|\boldsymbol{\theta}^j,\mathbf{d}) \tag{14}$$

The samples $\boldsymbol{\theta}^i$ and $\boldsymbol{\theta}^j$ are drawn from the prior distribution $p(\boldsymbol{\theta})$, which is chosen a priori. In SHM applications, the main goal is to identify the mechanical properties of a damaged structure, and it is common to assume parameters $\boldsymbol{\theta}$ as drawn from a uniform distribution $\mathcal{U}(\boldsymbol{\Theta})$. In reducing the associated computational cost, the same set of samples $\boldsymbol{\theta}$ is used for both the inner and the outer sum, resulting in $N_{in} = N_{out}$; the computational complexity is thus reduced from $O(N_{out}N_{in})$ to $O(N_{out})$. For further details on the bias introduced by this assumption and on the numerical approximation, the interested reader is referred to [6].
The term $p(\mathbf{y}|\boldsymbol{\theta}, \mathbf{d})$ corresponds to the probability density of the measured data $\mathbf{y}$, given a specific set of mechanical parameters $\boldsymbol{\theta}$ and a specific sensor configuration $\mathbf{d}$. Using Eq. (5), we can conclude that:

$$p(\mathbf{y}|\boldsymbol{\theta}, \mathbf{d}) = p_{\boldsymbol{\epsilon}}(\boldsymbol{\epsilon}) = p_{\boldsymbol{\epsilon}}(\mathbf{y} - \mathbf{G}(\mathbf{d}, \boldsymbol{\theta})) \tag{15}$$

Hence, via use of Eqs. (6) and (15), Eq. (13) becomes:

$$\begin{aligned} \bar{U}(\mathbf{d}) &\approx \frac{1}{N_{out}} \sum_{i=1}^{N_{out}} \left\{ \ln \left[p_{\boldsymbol{\epsilon}}(\boldsymbol{\epsilon}^i) \right] - \ln \left[\frac{1}{N_{in}} \sum_{j=1}^{N_{in}} p_{\boldsymbol{\epsilon}}(\mathbf{G}(\mathbf{d}, \boldsymbol{\theta}^i) + \boldsymbol{\epsilon}^i - \mathbf{G}(\mathbf{d}, \boldsymbol{\theta}^j)) \right] \right\} = \\ &= \frac{1}{N_{out}} \sum_{i=1}^{N_{out}} \left\{ \ln \left[p_{\boldsymbol{\epsilon}}(\boldsymbol{\epsilon}^i) \right] - \ln \left[\frac{1}{N_{in}} \sum_{j=1}^{N_{in}} p_{\boldsymbol{\epsilon}}(\mathbf{L(d)}[\mathbf{K}^{i^{-1}} - \mathbf{K}^{j^{-1}}]\mathbf{F} + \boldsymbol{\epsilon}^i) \right] \right\} \end{aligned} \tag{16}$$

where $\mathbf{K}^{i,j} = \mathbf{K}(\boldsymbol{\theta}^{i,j})$. The samples $\boldsymbol{\epsilon}^i$ are drawn from the density distribution $p_{\boldsymbol{\epsilon}}$, that is chosen once again a priori.
From a computational point of view, the most time-consuming part of the procedure is the evaluation of the system response through the model mapping $\mathbf{G}(\mathbf{d}, \boldsymbol{\theta})$ of Eq. (6). Assuming that we use the same batch of samples $\boldsymbol{\theta}$ for both sums, the Monte Carlo approximation would require N_{out} evaluations of the system output, each one associated to a stiffness matrix inversions, rendering the computation practically infeasable. In order to overcome this problem, in [6] the adoption of a Polynomial Chaos Expansion (PCE) scheme has been proposed. Given an input random vector with independent components $\mathbf{x} \in \mathbb{R}^{n_{\mathbf{x}}}$, described by a joint probability density function $f_{\mathbf{x}}$, and an output random vector $\mathbf{y}$ calculated through a certain computational model $\mathcal{M}$, the PCE allows to build a map, or metamodel, relating the two spaces. Assuming that:

$$\mathbb{E}[\mathbf{y}^2] = \int_{\mathcal{D}_{\mathbf{x}}} \mathcal{M}^2(\mathbf{x}) f_{\mathbf{x}}(\mathbf{x}) d\mathbf{x} \; < \; \infty \tag{17}$$

it is possible to define (see [14]):

$$\mathbf{y} = \mathcal{M}(\mathbf{x}) = \sum_{\boldsymbol{\alpha} \in \mathbb{N}^M} y_{\boldsymbol{\alpha}} \boldsymbol{\psi}_{\boldsymbol{\alpha}}(\mathbf{x}) \tag{18}$$

where $\boldsymbol{\psi}_{\boldsymbol{\alpha}}$ are multivariate polynomials of order p orthonormal to $f_{\mathbf{x}}$, $\boldsymbol{\alpha} \in \mathbb{N}^M$ is a multi-index associated with $\boldsymbol{\psi}_{\boldsymbol{\alpha}}$, and $y_{\boldsymbol{\alpha}} \in \mathbb{R}$ are the corresponding coefficients. For practical purposes, the sum is truncated to a sub-set of the multi-indeces $\boldsymbol{\alpha} \in \mathcal{A} \subset \mathbb{N}^M$, according to:

$$\mathbf{y} \cong \mathbf{y}^{PCE} = \mathcal{M}^{PCE}(\mathbf{x}) = \sum_{\boldsymbol{\alpha} \in \mathcal{A}} y_{\boldsymbol{\alpha}} \boldsymbol{\psi}_{\boldsymbol{\alpha}}(\mathbf{x}) \tag{19}$$

where $\mathcal{M}^{PCE}$ stands for the surrogate model, and $\mathbf{y}^{PCE}$ is the approximated response computed through it.

Recalling Eq. (5), the forward model maps the design variable and the parameters into the measurement domain $(\boldsymbol{\mathcal{D}}, \boldsymbol{\Theta}) \rightarrow \boldsymbol{\mathcal{Y}}$ as:

$$\mathbf{y} = \mathcal{M}(\mathbf{x}) = \mathbf{G}(\mathbf{d}, \boldsymbol{\theta}) \tag{20}$$

As suggested in [6], the PCE is applied jointly as:

$$\mathbf{x} = \begin{bmatrix} \boldsymbol{\theta} \\ \mathbf{d} \end{bmatrix} \tag{21}$$

with $\mathbf{x} \in \mathbb{R}^{n_{\boldsymbol{\theta}}+n_{\mathbf{d}}}$. In this way, it is not necessary to build a different PCE for each possible design variable $\mathbf{d}$, which would lead to a larger computational cost. In order to compute the surrogate model, two sets of samples $\boldsymbol{\theta}_k$ and $\mathbf{d}_k$ with $k = 1, \cdots, N_{PCE}$ are drawn from the respective aforementioned probability densities; the output samples are then calculated through the complete model $\mathbf{y}_k = \mathcal{M}(\mathbf{x}_k)$. Once the input and output populations have been built, the truncated bases and the relative coefficients are computed through the Least Angle Regression (LAR) algorithm, as specified in [14, 15]. The accuracy of the surrogate model with respect to the complete one is affected by both the population size N_{PCE} and the poynomial degree p; these settings should be chosen so as to minimize the leave-one-out (LOO) cross-validation error, as defined in [16].

2.3 Optimization algorithm

The optimization statement summarized in Eq. (12) is herein solved by applying the Covariance Matrix Adaptation Evolution Strategy (CMA-ES) [17], which comprises a stochastic search algorithm for numerical optimization of non-linear non-convex functions. The basic idea is to sample the design variable $\mathbf{d}$ from a multivariate normal distribution, and produce a new mutation of the generated population that is closer to the maximum of the function $\bar{U}(\mathbf{d})$.
The algorithm can be summarized as follows:

1. for each iteration, a population of design points $\mathbf{d}$ is sampled from the Normal multivariate distribution $\mathbf{d}_i \sim \mathbf{m} + \sigma\mathcal{N}_i(\mathbf{0}, \mathbf{C})$ for $i = 1, \cdots, \lambda$, where $\mathbf{m} \in \mathbb{R}^{\mathbf{n_d}}$ is the mean vector, $\sigma \in \mathbb{R}$ is the step size and $\mathbf{C} \in \mathbb{R}^{\mathbf{n_d} \times \mathbf{n_d}}$ is the covariance matrix;

2. $\mathbf{m}$ and $\mathbf{C}$ are updated through cumulation, in order the likelihood of the successive iterations to be increased;

3. the previous steps are repeated until a certain tolerance on the function evaluation is attained.

Further details on the algorithm can be found in [18].

3 RESULTS

The method discussed in Section 2 is now applied to a simple SHM benchmark case; a square plate, simply supported at four edges and subjected to a static force applied at its centre point (see node 1 in Figure 1). The structure is ideally subdivided into four zones and the aim of the SHM system is the estimation of the Young modulus E_j, $j = 1, ..., 4$, of each zone. The sensors can be positioned at each node of the adopted 10x10 FE model and, for the sake of simplicity, only the out-of-plane deflections are assumed to be measured. The structure is discretized through conventional shell elements, with 6 degrees of freedom per node. The mechanical behaviour of the material is supposed to be linear elastic.
Two cases are considered herein:

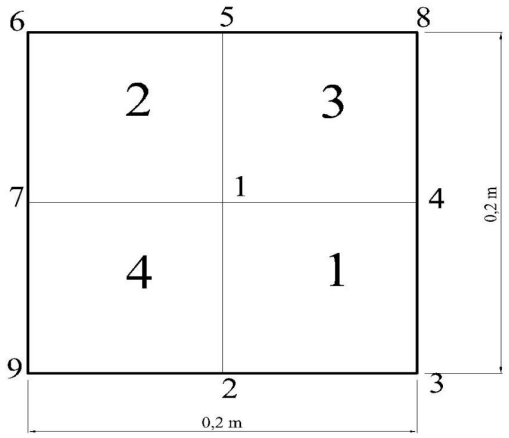

Figure 1: Benchmark structural case.

(a) the position of the damaged zone is known, therefore the input variables of the PCE surrogate model are summarized in vector:

$$\mathbf{x} = \{E_2 \;\; d_1 \;\; \cdots \;\; d_{n_{sens}}\}^T \tag{22}$$

(b) the position of the damaged zone is unknown:

$$\mathbf{x} = \{E_1 \;\; E_2 \;\; E_3 \;\; E_4 \;\; d_1 \;\; \cdots \;\; d_{n_{sens}}\}^T \tag{23}$$

Let us consider the simplest case: only one sensor is deployed. Figures 2 and 3 demonstrate the contour plot of the objective function defined by Eq. (12) computed on each node of the plate, respectively related to cases (a) and (b). The parameters to be estimated, aggregated in vector $\boldsymbol{\theta}$, are sampled from a uniform distribution $\mathcal{U}(0, E)$, where E is the Young modulus of the undamaged material. The probability distribution of the model prediction error ϵ is supposed to be Gaussian $\mathcal{N}(0, \sigma^2)$ with standard deviation $\sigma = 10^{-5}$ m. In order to compute the PCE coefficients and bases, the design variable **d** is sampled uniformly with coordinates defined over the interval $[0, 0.2]$, both along the width and the length of the plate.
The optimal configuration, i.e., maximizing the objective function, is determined at position $(x^*, y^*) = (0.08, 0.12)$ for case (a), i.e., as expected near the zone in which the damage will occur, see [5]. In case (b), the problem settings are perfectly symmetric and therefore the objective function as well: the optimal is determined in point $(x^*, y^*) = (0.10, 0.10)$. The figures show the optimization paths obtained through the CMA-ES algorithm: each path corresponds to a different initial condition, i.e., the four corner points, and the red circles identify the results reached after 25 objective function evaluations. It is demonstrated that, for both cases, the results are stable with respect to the initialization settings and they correspond to the maximum of the contour plot.
The accuracy of the optimization process is largely affected by the PCE approximation phase. The error introduced by the PCE surrogate model with respect to the FE model can be measured through the leave-one-out (LOO) error, as defined in [16]:

$$\epsilon_{LOO} = \frac{\sum_{i=1}^{N} \left(\mathcal{M}(\mathbf{x}^i) - \mathcal{M}^{PCE}(\mathbf{x}^i)\right)^2}{1 - h_i} \Bigg/ \left(\sum_{i=1}^{N} \left(\mathcal{M}(\mathbf{x}^i) - \hat{\mu}_Y\right)^2\right) \tag{24}$$

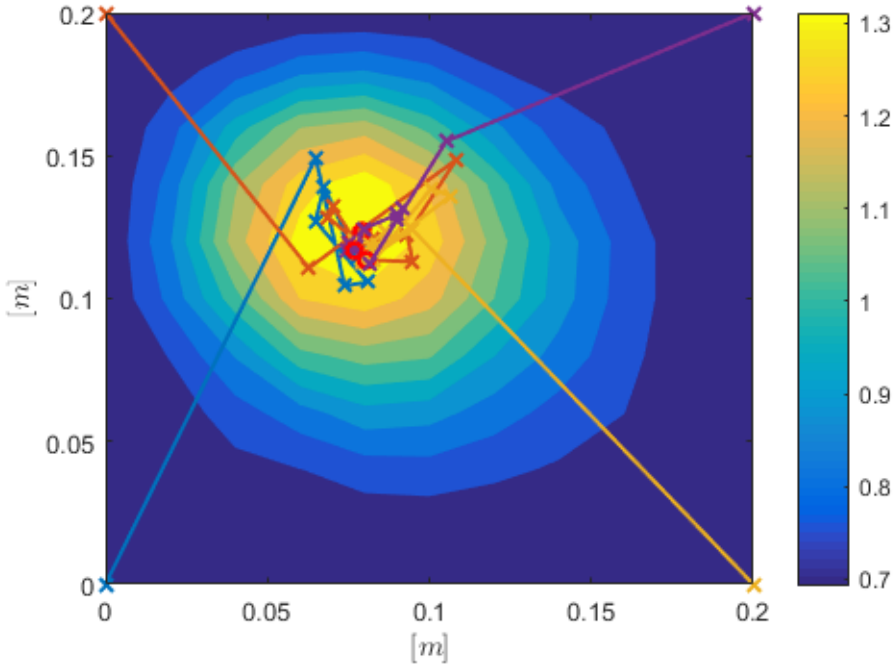

Figure 2: Contour plot of the objective function $\hat{U}(\mathbf{d})$ with one sensor for case (a) and CMA-ES optimization paths ($N^{PCE} = 10^4$, $p = 10$, $N^{MC} = 5 \cdot 10^3$).

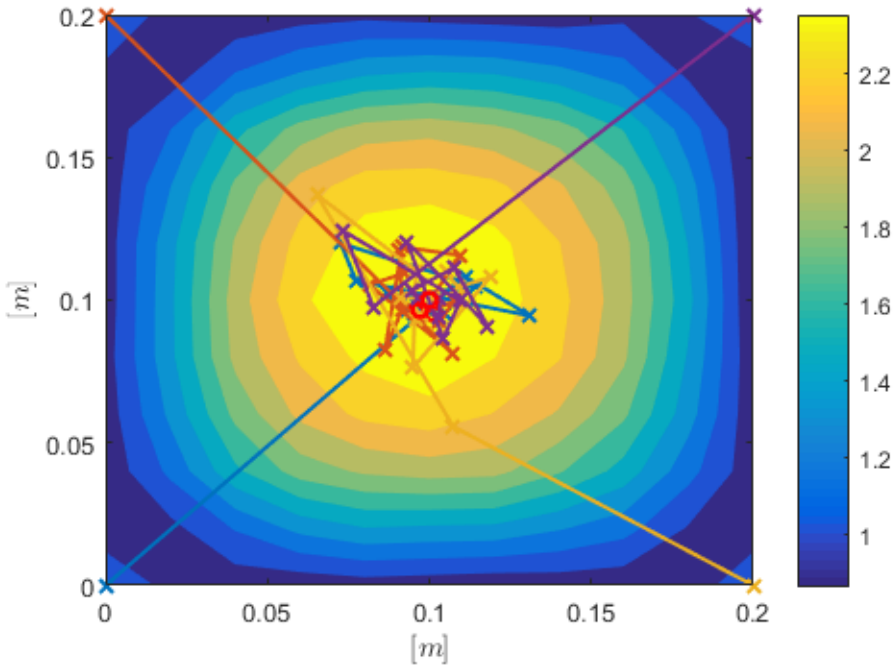

Figure 3: Contour plot of the objective function $\hat{U}(\mathbf{d})$ with one sensor for case (b) and CMA-ES optimization paths ($N^{PCE} = 10^4$, $p = 10$, $N^{MC} = 5 \cdot 10^3$).

where $\hat{\mu}_Y = \frac{1}{N} \sum_{i=1}^{N} \mathcal{M}(\mathbf{x}^i)$ is the sample mean of the set of quadrature points and h_i is the i^{th} component of the vector given by:

$$h = \text{diag}\left(\mathbf{A}(\mathbf{A}^T\mathbf{A})^{-1}\mathbf{A}^T\right) \tag{25}$$

where **A** is the experimental matrix that contains the values of all the basis polynomials in the experimental design points.
Figures 4 and 5 report the LOO error as a function of the polynomial order p and the number of samples N^{PCE} in a log-log plot. Figures show that, as expected, the error decreses as N^{PCE} and p increase; we can point out that for increase beyond a certain value of N^{PCE}, the error trend remains basically stable.

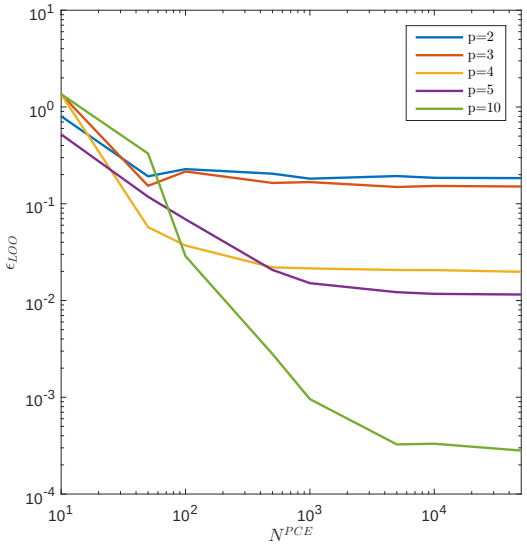

Figure 4: LOO error ϵ_{LOO} associated to the PCE surrogate model for case (a).

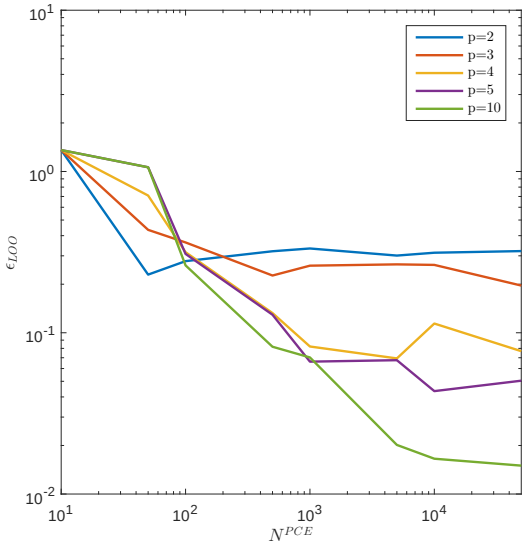

Figure 5: LOO error ϵ_{LOO} associated to the PCE surrogate model for case (b).

4 CONCLUSIONS

In the present paper, a new method has been proposed for optimal sensor placement in structural health monitoring applications, having supposed the measurements are noise-corrupted. The method is adapted from the general framework proposed in [6] for the optimal design of experiments; the procedure is coupled with a Covariance Matrix Adaptation Evolution Strategy optimization scheme, which allows for determining the optimal sensor configuration, associated with the maximum amount of information given by the measurements. In order to reduce the computational cost linked to the multiple forward problem simulations required, a Polynomial Chaos Expansion metamodeling scheme is adopted.
The method is herein applied to a simple benchmark problem of a simply supported plate under bending loads. It has been demonstrated that the optimization algorithm is able to find the optimal sensor configuration, further taking also into account measurement error. The method proves successful and yielding a design of experiments corresponding to reduced approximation error.
Further developments will concern the application to more complex structures, with multiple sensors configurations.

ACKNOWLEDGMENTS

G.C. and S.M. wish to acknowledge the financial support by Fondazione Cariplo through project Safer Helmets.

The authors wish to acknowledge the Chair of Risk, Safety and Uncertainty Quantification and the Computational Science and Engineering Laboratory at ETH Zürich for having provided the MATLAB-based softwares UQLab and CMA-ES used for the implementation of the method.

REFERENCES

[1] D. Balageas, C. P. Fritzen, A. Gemes, *Structural Health Monitoring*. Wiley-ISTE, 2006.

[2] C. Leyder, V. Ntertimanis, E. Chatzi, A. Frangi, Optimal Sensors Placement for the Modal Identification of an Innovative Timber Structure. *Proceedings of the 1st International Conference on Uncertainty Quantification in Computational Sciences and Engineering*, 467-476, 2015.

[3] M. Meo, G. Zumpano, On the optimal sensor placement techniques for a bridge structure. *Engineering Structures*, 27:14881497, 2005.

[4] M. Chang, S. Pakzad, Optimal Sensor Placement for Modal Identification of Bridge Systems Considering Number of Sensing Nodes. *Journal of Bridge Engineering*, 19(6):04014019, 2014.

[5] M. Bruggi, S. Mariani, Optimization of sensor placement to detect damage in flexible plates. *Engineering Optimization*, 45(6), 659-676, 2013.

[6] X. Huan, Y. M. Marzouk, Simulation-based optimal Bayesian experimental design for nonlinear systems. *Journal of Computational Physics*, 232(1):288-317, 2013.

[7] K. J. Ryan, Estimating Expected Information Gains for Experimental Designs with Application to the Random Fatigue-Limit Model. *Journal of Computational and Graphical Statistics*, 12(3):585-603, 2003.

[8] C. Papadimitriou, Optimal Sensor Placement Methodology for Parametric Identification of Structural Systems. *Journal of Sound and Vibration*, 278:923947, 2004.

[9] X. Huan, Y. M. Marzouk, Gradient-Based Stochastic Optimization Methods in Bayesian Experimental Design. *International Journal for Uncertainty Quantification*, 4(6):479-510, 2014.

[10] D. V. Lindley, *Bayesian Statistics, A Review*, Society for Industrial and Applied Mathematics (SIAM), 1972.

[11] K. Chaloner, I. Verdinelli, Bayesian Experimental Design: A Review. *Statistical Science*, 10(3):273-304, 1995.

[12] C. E. Shannon, A Mathematical Theory of Communication. *Bell System Technical Journal*, 27:379-423, 1948.

[13] D. V. Lindley, On a Measure of the Information Provided by an Experiment. *The Annals of Mathematical Statistics*, 27(4):986-1005, 1956.

[14] S. Marelli, B. Sudret, *UQLab User Manual*. Chair of Risk, Safety & Uncertainty Quantification, ETH Zürich, 2015.

[15] G. Blatman, B. Sudret, Adaptive Sparse Polynomial Chaos Expansion Based on Least Angle Regression. *Journal of Computational Physics* , 230:2345-2367, 2011.

[16] G. Blatman, *Adaptive Sparse Polynomial Chaos Expansion for Uncertainty Propagation and Sensitivity Analysis*. Ph.D. thesis, Blaise Pascal University, Clermont-Ferrand, 2009.

[17] N. Hansen, A. Ostermeier, Adapting arbitrary normal mutation distributions in evolution strategies: The covariance matrix adaptation. *Proceedings of the 1996 IEEE International Conference on Evolutionary Computation*, 312-317, 1996.

[18] N. Hansen, S. D. Müller, P. Koumoutsakos, Reducing the Time Complexity of the Derandomized Evolution Strategy with Covariance Matrix Adaptation (CMA-ES). *Evolutionary Computation*, 11(1):1-18, 2003.

ECCOMAS Congress 2016
VII European Congress on Computational Methods in Applied Sciences and Engineering
M. Papadrakakis, V. Papadopoulos, G. Stefanou, V. Plevris (eds.)
Crete Island, Greece, 5–10 June 2016

CALIBRATION OF NESTED COMPUTER MODELS

Sophie Marque-Pucheu[1], **Guillaume Perrin**[1], **and Josselin Garnier**[2]

[1]CEA DAM DIF
F-91297, Arpajon, France
e-mail: sophie.marque-pucheu@cea.fr, guillaume.PERRIN2@cea.fr

[2] Laboratoire de Probabilités et Modèles Aléatoires, Laboratoire Jacques-Louis Lions
Université Paris Diderot, 75205 Paris Cedex 13, France
e-mail: garnier@math.univ-paris-diderot.fr

Keywords: Nested computer models, metamodeling, Bayesian calibration, Gaussian process, uncertainity quantification.

Abstract. *Thanks to computing power increase, risk quantification relies more and more on computer modelling. Methods of risk quantification based on a fixed computational budget exist, but computer models are almost always considered as a single black box.*

In this paper, we are interested in analyzing the behavior of a complex phenomenon, whose evolution can be modelled via two nested parametrized computer models. By two nested computer models, we mean that some inputs of the second model are outputs of the first model. Based on series of observations of the considered phenomenon, the idea is, first, to calibrate the parameters of each model, and then, to construct a predictor for the output of the second model, which takes into account the fact that, on the first hand, the two models are not perfect, and on the other hand, there exist uncertainties in the parameters' calibration.

Concerning the calibration of the models' parameters we distinguish between the classic "black-box" method, parallel method and grouped method. In the case of a parallel calibration, each model is calibrated separately whereas in the case of a grouped calibration, the parameters of the two models are calibrated all together. In both cases, the extent to which the proposed predictor integrates the uncertainties of the nested system is demonstrated. The proposed methods are then applied to an example.

1 INTRODUCTION

In this paper, we are interested in analyzing the behavior of a complex phenomenon, whose evolution can be modeled by two nested parametrized computer models. By two nested computer models, we mean that some inputs of the second model are outputs of the first model. The computer models are assumed linear with respect to the models' parameters $\beta_{\mathbf{1}}$ and $\beta_{\mathbf{2}}$. Both models are supposed to be affected by model errors ϵ_1 and ϵ_2. These errors are assumed to be independent. So we have :

$$\begin{aligned} y_1(x_1) &= \mathbf{h_1}(x_1)^t \beta_{\mathbf{1}} + \epsilon_1(x_1) \\ y_2(x_2) &= \mathbf{h_2}(x_2)^t \beta_{\mathbf{2}} + \epsilon_2(x_2) \\ x_2 &= y_1 \end{aligned} \tag{1}$$

where :

- $x_1 \mapsto y_1$ and $x_2 \mapsto y_2$ are the considered phenomena, $x_1 \in \mathbb{R}$, $x_2 \in \mathbb{R}$, $y_1 \in \mathbb{R}$ and $y_2 \in \mathbb{R}$
- $\mathbf{h_1}(x_1)^t \beta_{\mathbf{1}}$ and $\mathbf{h_2}(x_2)^t \beta_{\mathbf{2}}$ the deterministic computer codes, $\mathbf{h_1}(x_1) \in \mathbb{R}^{p_1} \times 1$, $\mathbf{h_2}(x_2) \in \mathbb{R}^{p_2} \times 1$, $\beta_{\mathbf{1}} \in \mathbb{R}^{p_1} \times 1$, $\beta_{\mathbf{2}} \in \mathbb{R}^{p_2} \times 1$,
- ϵ_1 and ϵ_2 the real-valued models' errors. They are modelled by centered Gaussian processes.

The outline of this paper is the following. In section 2 is presented the general method to calibrate these two nested codes. We suppose we have access to observations of the phenomena $x_1 \mapsto y_1$, $x_2 \mapsto y_2$ and $x_1 \mapsto y_2$. In sections 3 to 5 three special cases of the general method are presented. These cases, depending on the available information, are the following :

- the parallel method. In this case, there are observations only for the phenomena $x_1 \mapsto y_1$ and $x_2 \mapsto y_2$ which are denoted by $\left(\mathbf{x_{1,obs}}^{(1)}, \mathbf{y_{1,obs}}^{(1)}\right)$ and $\left(\mathbf{x_{2,obs}}^{(2)}, \mathbf{y_{2,obs}}^{(2)}\right)$,
- the "black-box" method. In this case, there are observations only for the nested phenomenon ($x_1 \mapsto y_2$), which are denoted by $\left(\mathbf{x_{1,obs}}^{(3)}, \mathbf{y_{2,obs}}^{(3)}\right)$,
- the "grouped" method. In this case, there are observations for the phenomenon $x_1 \mapsto y_1 \mapsto y_2$, which are denoted by $\left(\mathbf{x_{1,obs}}^{(1)}, \mathbf{y_{1,obs}}^{(1)}\right)$, $\left(\mathbf{x_{2,obs}}^{(2)}, \mathbf{y_{2,obs}}^{(2)}\right)$ and $\left(\mathbf{x_{1,obs}}^{(3)}, \mathbf{y_{2,obs}}^{(3)}\right)$, where $\mathbf{y_{1,obs}}^{(1)} = \mathbf{x_{2,obs}}^{(2)}$, $\mathbf{x_{1,obs}}^{(3)} = \mathbf{x_{1,obs}}^{(1)}$ and $\mathbf{y_{2,obs}}^{(2)} = \mathbf{y_{2,obs}}^{(3)}$.

Note : notations $^{(1)}$, $^{(2)}$ and $^{(3)}$ correspond to first phenomenon, second phenomenon and nested phenomenon.
Finally in section 6 the three specific cases of the general method are applied on a numerical example.

2 THE GENERAL METHOD

In this section we propose a general framework to calibrate nested codes and build posterior predictors of these codes by taking into account observations of the three phenomena ($x_1 \mapsto y_1$, $x_2 \mapsto y_2$ and $x_1 \mapsto y_2$).

2.1 Nested model linearization

According to equation (1) the relation between y_2 and x_1 is given by :

$$y_2(x_1) = \mathbf{h_2}\left(\mathbf{h_1}(x_1)^t \beta_\mathbf{1} + \epsilon_1(x_1)\right)^t \beta_\mathbf{2} + \epsilon_2\left(\mathbf{h_1}(x_1)^t \beta_\mathbf{1} + \epsilon_1(x_1)\right), \tag{2}$$

Assuming that nominal values $\bar{\beta}_\mathbf{1}$ and $\bar{\beta}_\mathbf{2}$ of $\beta_\mathbf{1}$ and $\beta_\mathbf{2}$ are available such that in the vicinity of $\bar{\beta}_\mathbf{1}$, $\mathbf{h_1}(x_1)^t\left(\beta_\mathbf{1} - \bar{\beta}_\mathbf{1}\right) + \epsilon_1(x_1)$ is small, we get a linear approximation of the nested code and its error :

$$y_3(x_1) = \mathbf{h_3}(x_1)^t \beta_\mathbf{c} + \epsilon_3(x_1), \tag{3}$$

where $\epsilon_3(x_1)$ is the proposed model error :

$$\epsilon_3(x_1) = \Delta F_{2c}\left(x_1, \bar{\beta}_\mathbf{c}\right)\epsilon_1(x_1) + \epsilon_2\left(\mathbf{h_1}(x_1)^t \bar{\beta}_\mathbf{1}\right), \tag{4}$$

and :

$$\begin{aligned}
\mathbf{h_3}(x_1) &= \begin{bmatrix} \mathbf{h_{31}}(x_1) \\ \mathbf{h_{32}}(x_1) \end{bmatrix} \\
y_3(x_1) &= y_2(x_1) + \mathbf{h_{31}}(x_1)^t \bar{\beta}_\mathbf{1} \\
\mathbf{h_{31}}(x_1) &= \Delta F_{2c}\left(x_1, \bar{\beta}_\mathbf{c}\right)\mathbf{h_1}(x_1) \\
\mathbf{h_{32}}(x_1) &= \mathbf{h_2}\left(\mathbf{h_1}(x_1)^t \bar{\beta}_\mathbf{1}\right) \\
\Delta F_{2c}\left(x_1, \bar{\beta}_\mathbf{c}\right) &= \tfrac{\partial \mathbf{h_2}}{\partial x_2}\left(\mathbf{h_1}(x_1)^t \bar{\beta}_\mathbf{1}\right)^t \bar{\beta}_\mathbf{2} \\
\bar{\beta}_\mathbf{c} &= \begin{bmatrix} \bar{\beta}_\mathbf{1} \\ \bar{\beta}_\mathbf{2} \end{bmatrix}.
\end{aligned} \tag{5}$$

Given equations (1) and (3) a joint model for the three phenomena ($x_1 \mapsto y_1$, $x_2 \mapsto y_2$ and $x_1 \mapsto y_2$) is proposed :

$$\mathbf{y_{gp}}(\mathbf{x_{gp}})\,|\beta_\mathbf{c} \sim \mathcal{N}\left(\mathbf{h_{gp}}(\mathbf{x_{gp}})^t \beta_\mathbf{c},\ \mathbf{C_{gp}}\left(\mathbf{x_{gp}}; \mathbf{x'_{gp}}\right)\right) \tag{6}$$

where :

$$\beta_\mathbf{c} = \begin{bmatrix} \beta_\mathbf{1} \\ \beta_\mathbf{2} \end{bmatrix}, \tag{7}$$

$$\mathbf{x_{gp}} = \left(x_1^{(1)}, x_2^{(2)}, x_1^{(3)}\right), \tag{8}$$

$$\mathbf{y_{gp}}\left(\mathbf{x_{gp}}\right) = \begin{bmatrix} y_1\left(x_1^{(1)}\right) \\ y_2\left(x_2^{(2)}\right) \\ y_3\left(x_1^{(3)}\right) \end{bmatrix}, \tag{9}$$

$$\mathbf{h_{gp}}\left(\mathbf{x_{gp}}\right)^t = \begin{bmatrix} \mathbf{h_1}\left(x_1^{(1)}\right)^t & 0 \\ 0 & \mathbf{h_2}\left(x_2^{(2)}\right)^t \\ \mathbf{h_{31}}\left(x_1^{(3)}\right)^t & \mathbf{h_{32}}\left(x_1^{(3)}\right)^t \end{bmatrix}, \tag{10}$$

$$\mathbf{C_{gp}}\left(x_1^{(1)}, x_2^{(2)}, x_1^{(3)}; x_1^{'(1)}, x_2^{'(2)}, x_1^{'(3)}\right) = \tag{11}$$

$$\begin{bmatrix} C_1\left(x_1^{(1)}, x_1^{'(1)}\right) & 0 & C_1\left(x_1^{(1)}, x_1^{'(3)}\right)\Delta F_{2c}\left(x_1^{'(3)}, \bar{\beta}_{\mathbf{c}}\right) \\ 0 & C_2\left(x_2^{(2)}, x_2^{'(2)}\right) & C_2\left(x_2^{(2)}, \mathbf{h_1}\left(x_1^{'(3)}\right)^t \bar{\beta}_{\mathbf{1}}\right) \\ \Delta F_{2c}\left(x_1^{(3)}, \bar{\beta}_{\mathbf{c}}\right) C_1\left(x_1^{(3)}, x_1^{'(1)}\right) & C_2\left(\mathbf{h_1}\left(x_1^{(3)}\right)^t \bar{\beta}_{\mathbf{1}}, x_2^{'(2)}\right) & C_3\left(x_1^{(3)}, x_1^{'(3)}\right) \end{bmatrix},$$

and C_1, C_2 and C_3 are the covariance functions of ϵ_1, ϵ_2 and ϵ_3 errors.
Given equation (6), in the case of uninformative prior or Gaussian prior for $\beta_{\mathbf{c}}$, the parameters' distribution and the posterior predictive distribution given the observations, are Gaussian (see [1], [6], [7], [11] [12]).
The following sections present the parameters' calibration and the prediction given series of observations according to the model presented above.

2.2 Calibration of the codes' parameters and posterior predictive distributions

Given equation (6), we have :

$$\mathbf{y_{gp,obs}}|\beta_{\mathbf{c}} \sim \mathcal{N}\left(\mathbf{H_{gp}}\beta_{\mathbf{c}}\,,\,\mathbf{R_{gp}}\right), \tag{12}$$

where :

$$\mathbf{y_{gp,obs}} = \begin{bmatrix} \mathbf{y_{1,obs}}^{(1)} \\ \mathbf{y_{2,obs}}^{(2)} \\ \mathbf{y_{3,obs}}^{(3)} \end{bmatrix}, \tag{13}$$

$$\mathbf{y_{3,obs}}^{(3)} = \mathbf{y_{2,obs}}^{(3)} + \mathbf{h_{31}}\left(\mathbf{x_{1,obs}}^{(3)}\right)^t \bar{\beta}_{\mathbf{1}}, \tag{14}$$

$$\mathbf{x_{gp,obs}} = \begin{bmatrix} \mathbf{x_{1,obs}}^{(1)} \\ \mathbf{x_{2,obs}}^{(2)} \\ \mathbf{x_{1,obs}}^{(3)} \end{bmatrix}, \tag{15}$$

$$\mathbf{H_{gp}} = \mathbf{h_{gp}}\left(\mathbf{x_{gp,obs}}\right)^t, \tag{16}$$

$$\mathbf{R_{gp}} = \mathbf{C_{gp}}\left(\mathbf{x_{gp,obs}}; \mathbf{x_{gp,obs}}\right). \tag{17}$$

Given equation (12), the posterior distribution of $\beta_{\mathbf{c}}$ given the observations $\mathbf{y_{gp,obs}}$ can be modeled in a Bayesian framework. We distinguish two cases :

- No prior information case :
$$\pi^{prior}\left[\beta_{\mathbf{c}}\right] \sim 1 \tag{18}$$

- Gaussian prior case :
$$\pi^{prior}\left[\beta_{\mathbf{c}}\right] \sim \mathcal{N}\left(\ \widehat{\beta}_{\mathbf{c}}^{prior}\ ,\ {\mathbf{R}_{\beta_{\mathbf{c}}}}^{prior}\ \right) \tag{19}$$

In a Bayesian framework, in these two cases, the parameters' posterior distribution is Gaussian :

$$\beta_{\mathbf{c}} \mid \mathbf{y_{gp,obs}} \sim \mathcal{N}\left(\ \mathbb{E}\left(\beta_{\mathbf{c}} \mid \mathbf{y_{gp,obs}}\right)\ ,\ cov\left(\beta_{\mathbf{c}} \mid \mathbf{y_{gp,obs}}\right)\ \right) \tag{20}$$

where :

- in the no prior information case :
$$\begin{aligned} cov\left(\beta_{\mathbf{c}} \mid \mathbf{y_{gp,obs}}\right) &= \mathbf{R}_{\beta_{\mathbf{c}}} = \left(\mathbf{H_{gp}}^t {\mathbf{R_{gp}}}^{-1} \mathbf{H_{gp}}\right)^{-1} \\ \mathbb{E}\left(\beta_{\mathbf{c}} \mid \mathbf{y_{gp,obs}}\right) &= \widehat{\beta}_{\mathbf{c}} = \mathbf{R}_{\beta_{\mathbf{c}}} \mathbf{H_{gp}}^t {\mathbf{R_{gp}}}^{-1} \mathbf{y_{gp,obs}} \end{aligned} \tag{21}$$

- in the Gaussian prior case :
$$\begin{aligned} \left(\mathrm{cov}\left(\beta_{\mathbf{c}} \mid \mathbf{y_{gp,obs}}\right)\right)^{-1} &= \widetilde{\mathbf{R}}_{\beta_{\mathbf{c}}}^{-1} = {\mathbf{R}_{\beta_{\mathbf{c}}}}^{-1} + \left({\mathbf{R}_{\beta_{\mathbf{c}}}}^{prior}\right)^{-1} \\ \mathbb{E}\left(\beta_{\mathbf{c}} \mid \mathbf{y_{gp,obs}}\right) &= \widetilde{\beta}_{\mathbf{c}} = \widetilde{\mathbf{R}}_{\beta_{\mathbf{c}}} \left[{\mathbf{R}_{\beta_{\mathbf{c}}}}^{-1} \widehat{\beta}_{\mathbf{c}} + \left({\mathbf{R}_{\beta_{\mathbf{c}}}}^{prior}\right)^{-1} \widehat{\beta}_{\mathbf{c}}^{prior}\right] \end{aligned} \tag{22}$$

Given equations (6), (12) and (20), the posterior predictive distribution $\mathbf{y_{gp}}\left(\mathbf{x_{gp}}\right) | \mathbf{y_{gp,obs}}$ is Gaussian. Its properties are :

$$\mathbf{y_{gp}}\left(\mathbf{x_{gp}}\right)\ |\ \mathbf{y_{gp,obs}} \sim \mathcal{N}\left(\ \widehat{y}_{gp}\left(\mathbf{x_{gp}}, \mathbb{E}\left(\beta_{\mathbf{c}} \mid \mathbf{y_{gp,obs}}\right)\right)\ ,\ \widehat{\mathbf{C}}_{\mathbf{gp}}\left(\mathbf{x_{gp}}; \mathbf{x_{gp}}\right)\ \right) \tag{23}$$

where for all $\beta_{\mathbf{c}}$:

$$\widehat{y}_{gp}\left(\mathbf{x_{gp}}, \beta_{\mathbf{c}}\right) = \mathbf{h_{gp}}\left(\mathbf{x_{gp}}\right)^t \beta_{\mathbf{c}} + \mathbf{r_{gp}}\left(\mathbf{x_{gp}}\right)^t {\mathbf{R_{gp}}}^{-1} \left(\mathbf{y_{gp,obs}} - \mathbf{H_{gp}} \beta_{\mathbf{c}}\right) \tag{24}$$

$$\mathbf{r_{gp}}\left(\mathbf{x_{gp}}\right) = \mathbf{C_{gp}}\left(\mathbf{x_{gp,obs}}; \mathbf{x_{gp}}\right) \tag{25}$$

$$\begin{aligned} \widehat{\mathbf{C}}_{\mathbf{gp}}\left(\mathbf{x_{gp}}; \mathbf{x'_{gp}}\right) = \ & \mathbf{C_{gp}}\left(\mathbf{x_{gp}}; \mathbf{x'_{gp}}\right) - \mathbf{r_{gp}}\left(\mathbf{x_{gp}}\right)^t {\mathbf{R_{gp}}}^{-1} \mathbf{r_{gp}}\left(\mathbf{x'_{gp}}\right) \\ & + \mathbf{u_{gp}}\left(\mathbf{x_{gp}}\right)^t \mathrm{cov}\left(\beta_{\mathbf{c}} \mid \mathbf{y_{gp,obs}}\right) \mathbf{u_{gp}}\left(\mathbf{x'_{gp}}\right) \end{aligned} \tag{26}$$

$$\mathbf{u_{gp}}\left(\mathbf{x_{gp}}\right) = \mathbf{h_{gp}}\left(\mathbf{x_{gp}}\right) - \mathbf{H_{gp}}{\mathbf{R_{gp}}}^{-1}\mathbf{r_{gp}}\left(\mathbf{x_{gp}}\right) \tag{27}$$

In the following sections are presented three specific cases of the general method previously introduced. The cases are distinguished according to the type of available observations.

3 THE PARALLEL APPROACH

In this section we present a particular case of the previously presented general framework. The parallel method corresponds to the case where only observations of the phenomena $x_1 \mapsto y_1$ and $x_2 \mapsto y_2$ are available.

3.1 Key features of the approach

In the parallel approach, there is no observation for the nested phenomenon, that is : $\left({\mathbf{x_{1,obs}}}^{(3)}, {\mathbf{y_{2,obs}}}^{(3)}\right) = \emptyset$.
This method includes the following steps :

1. the parameters' calibration given the observations $\left({\mathbf{x_{1,obs}}}^{(1)}, {\mathbf{y_{1,obs}}}^{(1)}\right)$ and $\left({\mathbf{x_{2,obs}}}^{(2)}, {\mathbf{y_{2,obs}}}^{(2)}\right)$. Considering that the covariance matrix given by equation (11) is a block diagonal matrix, it is like $\beta_{\mathbf{1}}$ and $\beta_{\mathbf{2}}$ were calibrated separately given the observations $\left({\mathbf{x_{1,obs}}}^{(1)}, {\mathbf{y_{1,obs}}}^{(1)}\right)$ and $\left({\mathbf{x_{2,obs}}}^{(2)}, {\mathbf{y_{2,obs}}}^{(2)}\right)$.
2. the construction of the posterior predictors given the observations :
   (a) for the phenomenon 1 : the proposed predictor is an interpolating Gaussian predictor given the observations $\left({\mathbf{x_{1,obs}}}^{(1)}, {\mathbf{y_{1,obs}}}^{(1)}\right)$
   (b) for the phenomenon 2 : the proposed predictor is an interpolating Gaussian predictor given the observations $\left({\mathbf{x_{2,obs}}}^{(2)}, {\mathbf{y_{2,obs}}}^{(2)}\right)$
   (c) for the nested phenomenon : the proposed predictor is Gaussian thanks to a linearization of the coupling of the Gaussian predictors of the phenomena 1 and 2 (see 3.2).

The following section presents how the predictor of the nested code is built in the parallel approach.

3.2 Parallel predictor for the nested code

As shown above, we have two posterior Gaussian predictors given the observations :

$$y_{pred,i}\left(x_i\right) = y_i\left(x_i\right) \mid \left({\mathbf{x_{i,obs}}}^{(i)}, {\mathbf{y_{i,obs}}}^{(i)}\right) \sim \mathcal{N}\left(\, \widehat{y}_i\left(x_i, \beta_{\mathbf{i}}\right) \,,\, \widehat{C}_i\left(x_i, x_i\right) \right) \quad i = \{1, 2\} \tag{28}$$

where :

$$\widehat{y}_i\left(x_i, \beta_{\mathbf{i}}\right) = \mathbf{h_i}\left(x_i\right)^t \beta_{\mathbf{i}} + \mathbf{r_i}\left(x_i\right)^t {\mathbf{R_i}}^{-1}\left({\mathbf{y_{i,obs}}}^{(i)} - \mathbf{h_i}\left({\mathbf{x_{i,obs}}}^{(i)}\right)^t \beta_{\mathbf{i}}\right) \tag{29}$$

$$\mathbf{r_i}\left(x_i\right) = C_i\left(\mathbf{x_{i,obs}}^{(i)}; x_i\right) \tag{30}$$

$$\mathbf{R_i} = C_i\left(\mathbf{x_{i,obs}}^{(i)}; \mathbf{x_{i,obs}}^{(i)}\right) \tag{31}$$

$$\widehat{C}_i\left(x_i; x_i'\right) = C_i\left(x_i; x_i'\right) - \mathbf{r_i}\left(x_i\right)^t \mathbf{R_i}^{-1}\mathbf{r_i}\left(x_i'\right) - \mathbf{u_i}\left(x_i\right)^t \mathbf{R_{\beta_i}}^{-1}\mathbf{u_i}\left(x_i'\right) \tag{32}$$

$$\mathbf{u_i}\left(x_i\right) = \mathbf{h_i}\left(x_i\right) - \mathbf{h_i}\left(\mathbf{x_{i,obs}}^{(i)}\right)\mathbf{R_i}^{-1}\mathbf{r_i}\left(x_i\right) \tag{33}$$

Given equation (28) the posterior predictor for the nested phenomenon can be written :

$$y_{pred,3}\left(x_1, \beta_{\mathbf{c}}\right) = \widehat{y}_2\left(\widehat{y}_1\left(x_1, \beta_{\mathbf{1}}\right) + \delta\widehat{y}_1\left(x_1\right), \beta_{\mathbf{2}}\right) + \delta\widehat{y}_2\left(\widehat{y}_1\left(x_1, \beta_{\mathbf{1}}\right) + \delta\widehat{y}_1\left(x_1\right)\right) \tag{34}$$

where :

$$\delta\widehat{y}_i\left(x_i\right) \sim \mathscr{N}\left(0\ ,\ \widehat{C}_i\left(x_i; x_i\right)\right) \quad i = \{1, 2\} \tag{35}$$

Thanks to a first order Taylor series expansion and making the following approximation according to equation (29)

$$\frac{\partial\widehat{y}_2}{\partial x_2}\left(x, \beta\right) = \left[\frac{\partial\mathbf{h_2}}{\partial x_2}\left(x\right)\right]^t \beta \tag{36}$$

the posterior predictor for the nested code is :

$$y_{pred,3}\left(x_1, \widehat{\beta}_{\mathbf{c}}\right) \simeq \widehat{y}_2\left(\widehat{y}_1\left(x_1, \widehat{\beta}_{\mathbf{1}}\right), \widehat{\beta}_{\mathbf{2}}\right) + \left[\frac{\partial\mathbf{h_2}}{\partial x_2}\left(\widehat{y}_1\left(x_1, \widehat{\beta}_{\mathbf{1}}\right)\right)\right]^t \widehat{\beta}_{\mathbf{2}}\delta\widehat{y}_1\left(x_1\right) + \delta\widehat{y}_2\left(\widehat{y}_1\left(x_1, \widehat{\beta}_{\mathbf{1}}\right)\right) \tag{37}$$

It is a linear combination of the independent Gaussian processes $\delta\widehat{y}_1$ and $\delta\widehat{y}_2$, thus it is a Gaussian predictor.
Table 1 summarizes the 'parallel' method's characteristics.

Table 2 presents the MSE of the calibrated codes and predictors for the 'parallel' method.

4 THE 'BLACK-BOX' APPROACH

In this section we present a particular case of the previously presented general framework (see 2). The 'black-box' method corresponds to the case where only observations of the phenomenon $x_1 \mapsto y_2$ are available, that is $\left(\mathbf{x_{1,obs}}^{(1)}, \mathbf{y_{1,obs}}^{(1)}\right) = \emptyset$ and $\left(\mathbf{x_{2,obs}}^{(2)}, \mathbf{y_{2,obs}}^{(2)}\right) = \emptyset$.
About the nested model's error, the following cases are distinguished :

- ϵ_1 and ϵ_2, are known, so the error is given by equation (4),
- ϵ_1 and ϵ_2 are unknown, so a specific model error for the nested code is proposed (it is assumed to be a zero-mean stationary Gaussian process).

Nested model error	The nested model error is not used because there is no observation for the nested phenomenon.
Calibration of parameters $\beta_{\mathbf{c}} = (\beta_{\mathbf{1}}, \beta_{\mathbf{2}})$	• $\beta_{\mathbf{1}}$ is calibrated given the observations for $x_1 \mapsto y_1$, • $\beta_{\mathbf{2}}$ is calibrated given the observations for $x_2 \mapsto y_2$.
Posterior predictor for phenomenon $x_1 \mapsto y_1$	Gaussian predictor given the observations of the phenomenon $x_1 \mapsto y_1$
Posterior predictor for phenomenon $x_2 \mapsto y_2$	Gaussian predictor given the observations of the phenomenon $x_2 \mapsto y_2$
Posterior predictor for phenomenon $x_1 \mapsto y_2$	Gaussian predictor thanks to a linearization of the coupling of the Gaussian predictors of the phenomena $x_1 \mapsto y_1$ and $x_2 \mapsto y_2$.

Table 1: This table summarizes the 'parallel' method's characteristics

Phenomenon	Empirical normalized integrated squared error (Empirical MSE) of the calibrated codes	Empirical normalized integrated squared error (Empirical MSE) of the posterior predictors
$x_1 \mapsto y_1$	$\frac{\sum_{x_1}\left(y_1(x_1) - \mathbf{h_1}(x_1)^t \widehat{\beta}_{\mathbf{1}}\right)^2}{\sum_{x_1}(y_1(x_1))^2}$	$\frac{1}{\sum_{x_i}(y_i(x_i))^2}\sum_{x_i}(y_i(x_i) - \mathbf{h_i}(x_i)^t \widehat{\beta}_{\mathbf{i}} - \mathbf{r_i}(x_i)^t \mathbf{R_i}^{-1}\left(\mathbf{y_{i,obs}} - \mathbf{h_i}(\mathbf{x_{i,obs}})^t \widehat{\beta}_{\mathbf{i}}\right))^2$ $i = \{1, 2\}$
$x_2 \mapsto y_2$	$\frac{\sum_{x_2}\left(y_2(x_2) - \mathbf{h_2}(x_2)^t \widehat{\beta}_{\mathbf{2}}\right)^2}{\sum_{x_2}(y_2(x_2))^2}$	
$x_1 \mapsto y_2$	$\frac{1}{\sum_{x_1}(y_2(x_1))^2}\sum_{x_1}(y_2(x_1) - \mathbf{h_2}\left(\mathbf{h_1}(x_1)^t \widehat{\beta}_{\mathbf{1}}\right)^t \widehat{\beta}_{\mathbf{2}})^2$	$\frac{\sum_{x_1}\left(y_2(x_1) - \widehat{y}_2\left(\widehat{y}_1\left(x_1, \widehat{\beta}_{\mathbf{1}}\right), \widehat{\beta}_{\mathbf{2}}\right)\right)^2}{\sum_{x_1}(y_2(x_1))^2}$

Table 2: This table presents the normalized empirical integrated mean squared error of the calibrated codes and predictors for the 'parallel' method

Nested model error	Two cases are distinguished : • ϵ_1 and ϵ_2, are known, so the error is given by equation (4), • ϵ_1 and ϵ_2 are unknown, so a specific model error for the nested code is proposed (it is assumed to be a zero-mean stationary Gaussian process).
Calibration of parameters $\beta_{\mathbf{c}} = (\beta_{\mathbf{1}}, \beta_{\mathbf{2}})$	$\beta_{\mathbf{c}}$ is calibrated given the observations for $x_1 \mapsto y_2$
Posterior predictor for phenomenon $x_1 \mapsto y_1$	First code using the posterior distribution of $\beta_{\mathbf{1}}$
Posterior predictor for phenomenon $x_2 \mapsto y_2$	Second code using the posterior distribution of $\beta_{\mathbf{2}}$
Posterior predictor for phenomenon $x_1 \mapsto y_2$	Gaussian predictor given the observations of the phenomenon $x_1 \mapsto y_2$

Table 3: This table summarizes the 'black-box' method's characteristics

The method includes the following steps :

1. the parameters' calibration given the observations $\left({\mathbf{x}_{\mathbf{1},\mathbf{obs}}}^{(3)}, {\mathbf{y}_{\mathbf{2},\mathbf{obs}}}^{(3)}\right)$,
2. the construction of the posterior predictors given the observations :
   (a) for the phenomenon 1 : there is no observation $\left({\mathbf{x}_{\mathbf{1},\mathbf{obs}}}^{(1)}, {\mathbf{y}_{\mathbf{1},\mathbf{obs}}}^{(1)}\right)$, so the proposed predictor is the calibrated code. Thanks to the code's linearity and the parameters' Gaussian distribution the calibrated code's distribution is Gaussian with :
      - mean : $\mathbf{h_1}\left(x_1\right)^t \mathbb{E}\left(\beta_{\mathbf{1}} \mid \left({\mathbf{x}_{\mathbf{1},\mathbf{obs}}}^{(3)}, {\mathbf{y}_{\mathbf{2},\mathbf{obs}}}^{(3)}\right)\right)$
      - and variance : $\mathbf{h_1}\left(x_1\right)^t \mathrm{cov}\left(\beta_{\mathbf{1}} \mid \left({\mathbf{x}_{\mathbf{1},\mathbf{obs}}}^{(3)}, {\mathbf{y}_{\mathbf{2},\mathbf{obs}}}^{(3)}\right)\right) \mathbf{h_1}\left(x_1\right)$

   (b) for the phenomenon 2 : there is no observation $\left({\mathbf{x}_{\mathbf{2},\mathbf{obs}}}^{(2)}, {\mathbf{y}_{\mathbf{2},\mathbf{obs}}}^{(2)}\right)$, so the proposed predictor is the calibrated code. Thanks to the code's linearity and the parameters' Gaussian distribution the calibrated code's distribution is Gaussian with :
      - mean : $\mathbf{h_2}\left(x_2\right)^t \mathbb{E}\left(\beta_{\mathbf{2}} \mid {\mathbf{y}_{\mathbf{2},\mathbf{obs}}}^{(2)}\left({\mathbf{x}_{\mathbf{1},\mathbf{obs}}}^{(3)}\right)\right)$
      - and variance : $\mathbf{h_2}\left(x_2\right)^t \mathrm{cov}\left(\beta_{\mathbf{2}} \mid \left({\mathbf{x}_{\mathbf{1},\mathbf{obs}}}^{(3)}, {\mathbf{y}_{\mathbf{2},\mathbf{obs}}}^{(3)}\right)\right) \mathbf{h_2}\left(x_2\right)$

   (c) for the nested phenomenon : the proposed predictor is an interpolating Gaussian predictor given the observations $\left({\mathbf{x}_{\mathbf{1},\mathbf{obs}}}^{(3)}, {\mathbf{y}_{\mathbf{2},\mathbf{obs}}}^{(3)}\right)$

Table 3 summarizes the 'black-box' method's characteristics.
Table 4 presents the normalized empirical integrated mean squared error of the calibrated codes and predictors of this method.

Phenomenon	Empirical normalized integrated squared error (Empirical MSE) of the calibrated codes	Empirical normalized integrated squared error (Empirical MSE) of the posterior predictors
$x_1 \mapsto y_1$	$\frac{\sum_{x_1}\left(y_1(x_1)-\mathbf{h_1}(x_1)^t\widehat{\beta}_\mathbf{1}\right)^2}{\sum_{x_1}(y_1(x_1))^2}$	
$x_2 \mapsto y_2$	$\frac{\sum_{x_2}\left(y_2(x_2)-\mathbf{h_2}(x_2)^t\widehat{\beta}_\mathbf{2}\right)^2}{\sum_{x_2}(y_2(x_2))^2}$	
$x_1 \mapsto y_2$	$\frac{1}{\sum_{x_1}(y_2(x_1))^2}\sum_{x_1}(y_2(x_1) -\mathbf{h_2}\left(\mathbf{h_1}(x_1)^t\widehat{\beta}_\mathbf{1}\right)^t\widehat{\beta}_\mathbf{2})^2$	$\frac{1}{\sum_{x_1}(y_2(x_1))^2}\sum_{x_1}(y_3(x_1) - \mathbf{h_3}(x_1)^t\widehat{\beta}_\mathbf{c} -\mathbf{r_3}(x_1)^t\mathbf{R_3}^{-1}\left(\mathbf{y_{3,obs}} - \mathbf{h_3}(\mathbf{x_{1,obs}})^t\widehat{\beta}_\mathbf{c}\right))^2$ where : $\mathbf{r_3}(x_1)^t = C_3(x_1;\mathbf{x_{1,obs}})$ $\mathbf{R_3} = C_3(\mathbf{x_{1,obs}};\mathbf{x_{1,obs}})$

Table 4: This table presents the normalized empirical integrated mean squared error of the calibrated codes and predictors for the 'black-box' method

Nested model error	Zero-mean Gaussian process, combination of the propagation of the first phenomenon's uncertainty ϵ_1 and the second phenomenon's uncertainty ϵ_2 (ϵ_1 et ϵ_2 zero-mean Gaussian process with covariance function Matérn $\frac{5}{2}$), see equation (4)
Calibration of parameters $\beta_{\mathbf{c}} = (\beta_{\mathbf{1}}, \beta_{\mathbf{2}})$	$\beta_{\mathbf{c}}$ is calibrated given the observations of the three phenomena ($x_1 \mapsto y_1$, $x_2 \mapsto y_2$ and $x_1 \mapsto y_2$)
Posterior predictor for phenomenon $x_1 \mapsto y_1$	Gaussian predictor given the observations of the three phenomena ($x_1 \mapsto y_1$, $x_2 \mapsto y_2$ and $x_1 \mapsto y_2$)
Posterior predictor for phenomenon $x_2 \mapsto y_2$	Gaussian predictor given the observations of the three phenomena ($x_1 \mapsto y_1$, $x_2 \mapsto y_2$ and $x_1 \mapsto y_2$)
Posterior predictor for phenomenon $x_1 \mapsto y_2$	Gaussian predictor given the observations of the three phenomena ($x_1 \mapsto y_1$, $x_2 \mapsto y_2$ and $x_1 \mapsto y_2$)

Table 5: This table summarizes the 'grouped' method's characteristics

5 THE 'GROUPED' APPROACH

In this section we present a particular case of the previously presented general framework (see 2). The 'grouped' method corresponds to the case where observations are chosen for the phenomenon $x_1 \mapsto y_1 \mapsto y_2$. So we have ${\mathbf{x}_{\mathbf{1},\mathbf{obs}}}^{(1)} = {\mathbf{x}_{\mathbf{1},\mathbf{obs}}}^{(3)}$, ${\mathbf{x}_{\mathbf{2},\mathbf{obs}}}^{(2)} = {\mathbf{y}_{\mathbf{1},\mathbf{obs}}}^{(1)}$ and ${\mathbf{y}_{\mathbf{2},\mathbf{obs}}}^{(2)} = {\mathbf{y}_{\mathbf{2},\mathbf{obs}}}^{(3)}$.
The method includes the following steps :

1. the parameters' calibration given the observations $\left({\mathbf{x}_{\mathbf{1},\mathbf{obs}}}^{(1)}, {\mathbf{y}_{\mathbf{1},\mathbf{obs}}}^{(1)}\right)$, $\left({\mathbf{x}_{\mathbf{2},\mathbf{obs}}}^{(2)}, {\mathbf{y}_{\mathbf{2},\mathbf{obs}}}^{(2)}\right)$ and $\left({\mathbf{x}_{\mathbf{1},\mathbf{obs}}}^{(3)}, {\mathbf{y}_{\mathbf{2},\mathbf{obs}}}^{(3)}\right)$,
2. the construction of the posterior predictors given the observations :
   (a) for the phenomenon 1 : the proposed predictor is an interpolating Gaussian predictor given the observations $\left({\mathbf{x}_{\mathbf{1},\mathbf{obs}}}^{(1)}, {\mathbf{y}_{\mathbf{1},\mathbf{obs}}}^{(1)}\right)$, $\left({\mathbf{x}_{\mathbf{2},\mathbf{obs}}}^{(2)}, {\mathbf{y}_{\mathbf{2},\mathbf{obs}}}^{(2)}\right)$ and $\left({\mathbf{x}_{\mathbf{1},\mathbf{obs}}}^{(3)}, {\mathbf{y}_{\mathbf{2},\mathbf{obs}}}^{(3)}\right)$,
   (b) for the phenomenon 2 : the proposed predictor is an interpolating Gaussian predictor given the observations $\left({\mathbf{x}_{\mathbf{1},\mathbf{obs}}}^{(1)}, {\mathbf{y}_{\mathbf{1},\mathbf{obs}}}^{(1)}\right)$, $\left({\mathbf{x}_{\mathbf{2},\mathbf{obs}}}^{(2)}, {\mathbf{y}_{\mathbf{2},\mathbf{obs}}}^{(2)}\right)$ and $\left({\mathbf{x}_{\mathbf{1},\mathbf{obs}}}^{(3)}, {\mathbf{y}_{\mathbf{2},\mathbf{obs}}}^{(3)}\right)$,
   (c) for the nested phenomenon : the proposed predictor is an interpolating Gaussian predictor given the observations $\left({\mathbf{x}_{\mathbf{1},\mathbf{obs}}}^{(1)}, {\mathbf{y}_{\mathbf{1},\mathbf{obs}}}^{(1)}\right)$, $\left({\mathbf{x}_{\mathbf{2},\mathbf{obs}}}^{(2)}, {\mathbf{y}_{\mathbf{2},\mathbf{obs}}}^{(2)}\right)$ and $\left({\mathbf{x}_{\mathbf{1},\mathbf{obs}}}^{(3)}, {\mathbf{y}_{\mathbf{2},\mathbf{obs}}}^{(3)}\right)$.

Table 5 summarizes the 'grouped' method's characteristics. Table 6 presents the normalized empirical integrated mean squared error of the calibrated codes and predictors of this method.

6 NUMERICAL EXAMPLE

In this section we apply the previously presented particular cases of the general method on a numerical example. In this example we study a computer model coupled with itself.

Phenomenon	Empirical normalized integrated squared error (Empirical MSE) of the calibrated codes	Empirical normalized integrated squared error (Empirical MSE) of the posterior predictors
$x_1 \mapsto y_1$	$\frac{\sum_{x_1}\left(y_1(x_1) - \mathbf{h_1}(x_1)^t \widehat{\beta}_{\mathbf{1}}\right)^2}{\sum_{x_1}(y_1(x_1))^2}$	$\frac{1}{\sum_{x_1}(y_1(x_1))^2}\sum_{x_1}(y_1(x_1) - \mathbf{h_{gp}}(\mathbf{x_{gp,1}})^t \widehat{\beta}_{\mathbf{c}}$ $-\mathbf{r_{gp}}(\mathbf{x_{gp,1}})^t \mathbf{R_{gp}}^{-1}\left(\mathbf{y_{gp,obs}} - \mathbf{h_{gp}}(\mathbf{x_{gp,obs}})^t \widehat{\beta}_{\mathbf{c}}\right))^2$ where : $\mathbf{x_{gp,1}} = (x_1, \emptyset, \emptyset)$
$x_2 \mapsto y_2$	$\frac{\sum_{x_2}\left(y_2(x_2) - \mathbf{h_2}(x_2)^t \widehat{\beta}_{\mathbf{2}}\right)^2}{\sum_{x_2}(y_2(x_2))^2}$	$\frac{1}{\sum_{x_2}(y_2(x_2))^2}\sum_{x_2}(y_2(x_2) - \mathbf{h_{gp}}(\mathbf{x_{gp,2}})^t \widehat{\beta}_{\mathbf{c}}$ $-\mathbf{r_{gp}}(\mathbf{x_{gp,2}})^t \mathbf{R_{gp}}^{-1}\left(\mathbf{y_{gp,obs}} - \mathbf{h_{gp}}(\mathbf{x_{gp,obs}})^t \widehat{\beta}_{\mathbf{c}}\right))^2$ where : $\mathbf{x_{gp,2}} = (\emptyset, x_2, \emptyset)$
$x_1 \mapsto y_2$	$\frac{1}{\sum_{x_1}(y_2(x_1))^2}\sum_{x_1}(y_2(x_1)$ $-\mathbf{h_2}\left(\mathbf{h_1}(x_1)^t \widehat{\beta}_{\mathbf{1}}\right)^t \widehat{\beta}_{\mathbf{2}})^2$	$\frac{1}{\sum_{x_1}(y_2(x_1))^2}\sum_{x_1}(y_3(x_1) - \mathbf{h_{gp}}(\mathbf{x_{gp,3}})^t \widehat{\beta}_{\mathbf{c}}$ $-\mathbf{r_{gp}}(\mathbf{x_{gp,3}})^t \mathbf{R_{gp}}^{-1}\left(\mathbf{y_{gp,obs}} - \mathbf{h_{gp}}(\mathbf{x_{gp,obs}})^t \widehat{\beta}_{\mathbf{c}}\right))^2$ where : $\mathbf{x_{gp,3}} = (\emptyset, \emptyset, x_1)$

Table 6: This table presents the normalized empirical integrated mean squared error of the calibrated codes and predictors for the 'grouped' method

Method	Average variance over a test set according to the source of uncertainty
General method	$\epsilon_{cond} = \mathbb{E}_{\mathbf{x_{gp}}^{gal}=(\emptyset,\emptyset,x_1)}\left[\mathbf{C_{gp}}\left(\mathbf{x_{gp}}^{gal};\mathbf{x_{gp}}^{gal}\right) - \mathbf{r_{gp}}\left(\mathbf{x_{gp}}^{gal}\right)^t \mathbf{R_{gp}}^{-1}\mathbf{r_{gp}}\left(\mathbf{x_{gp}}^{gal}\right)\right]$ $\epsilon_{\beta} = \mathbb{E}_{\mathbf{x_{gp}}^{gal}=(\emptyset,\emptyset,x_1)}\left[\mathbf{u_{gp}}\left(\mathbf{x_{gp}}^{gal}\right)^t \text{cov}\left(\beta_{\mathbf{c}} \mid \mathbf{x_{gp,obs}}\right)\mathbf{u_{gp}}\left(\mathbf{x_{gp}}^{gal}\right)\right]$
Parallel method	$\epsilon_{cond} = \epsilon_{cond,1} + \epsilon_{cond,2}$ $\epsilon_{cond,1} = \mathbb{E}_{x_1}\left[\left[\frac{\partial \mathbf{h_2}}{\partial x_2}\left(\widehat{y}_1\left(x_1,\widehat{\beta}_{\mathbf{1}}\right)\right)\right]^t \widehat{\beta}_{\mathbf{2}}\left(\sigma_1^2 - \mathbf{r_1}\left(x_1\right)^t \mathbf{R_1}^{-1}\mathbf{r_1}\left(x_1\right)\right)\right]$ $\epsilon_{cond,2} = \mathbb{E}_{x_1}\left[\sigma_2^2 - \mathbf{r_2}\left(\widehat{y}_1\left(x_1,\widehat{\beta}_{\mathbf{1}}\right)\right)^t \mathbf{R_2}^{-1}\mathbf{r_2}\left(\widehat{y}_1\left(x_1,\widehat{\beta}_{\mathbf{1}}\right)\right)\right]$ $\epsilon_{\beta} = \epsilon_{\beta,1} + \epsilon_{\beta,2}$ $\epsilon_{\beta,1} = \mathbb{E}_{x_1}\left[\left[\frac{\partial \mathbf{h_2}}{\partial x_2}\left(\widehat{y}_1\left(x_1,\widehat{\beta}_{\mathbf{1}}\right)\right)\right]^t \widehat{\beta}_{\mathbf{2}}\mathbf{u_1}\left(x_1\right)^t \text{cov}\left(\beta_{\mathbf{1}} \mid \mathbf{y_{1,obs}}^{(1)}\right)\mathbf{u_1}\left(x_1\right)\right]$ $\epsilon_{\beta,2} = \mathbb{E}_{x_1}\left[\mathbf{u_2}\left(\widehat{y}_1\left(x_1,\widehat{\beta}_{\mathbf{1}}\right)\right)^t \text{cov}\left(\beta_{\mathbf{2}} \mid \mathbf{y_{2,obs}}^{(2)}\right)\mathbf{u_2}\left(\widehat{y}_1\left(x_1,\widehat{\beta}_{\mathbf{1}}\right)\right)\right]$
'Black-box' method	$\epsilon_{cond} = \mathbb{E}_{x_1}\left[C_3\left(x_1;x_1\right) - \mathbf{r_3}\left(x_1\right)^t \mathbf{R_3}^{-1}\mathbf{r_3}\left(x_1\right)\right]$ $\epsilon_{\beta} = \mathbb{E}_{x_1}\left[\mathbf{u_3}\left(x_1\right)^t \text{cov}\left(\beta_{\mathbf{c}} \mid \mathbf{y_{2,obs}}^{(3)}\right)\mathbf{u_3}\left(x_1\right)\right]$ $\mathbf{u_3}\left(x_1\right) = \mathbf{h_3}\left(x_1\right) - \mathbf{h_3}\left(\mathbf{x_{1,obs}}^{(3)}\right)\mathbf{R_3}^{-1}\mathbf{r_3}\left(x_1\right)$
Grouped method	see General method

Table 7: This table presents the sources of uncertainty of the nested phenomenon's predictors. We denote by ϵ_{cond} the part of variance coming from the conditional Gaussian process and by ϵ_{β} the part of variance coming from the parameters' posterior distribution.

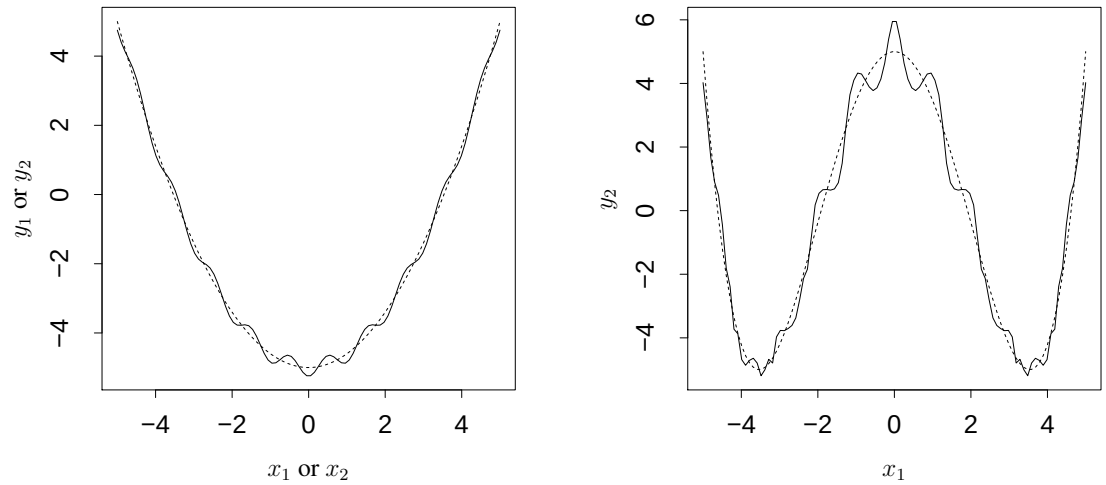

(a) Model (code 1 or 2) (b) Nested model

Figure 1: The continuous line corresponds to reality i.e. $y_1(x_1)$, $y_2(x_2)$ or $y_2(x_1)$ and the dashed line correspond to the codes $\mathbf{h_1}(x_1)^t \beta_\mathbf{1}$, $\mathbf{h_2}(x_2)^t \beta_\mathbf{2}$ or $\mathbf{h_2}\left(\mathbf{h_1}(x_1)^t \beta_\mathbf{1}\right)^t \beta_\mathbf{2}$. Figure 1a presents phenomena $x_1 \mapsto y_1$, $x_2 \mapsto y_2$ and figure 1b phenomenon $x_1 \mapsto y_2$.

This section is organised as follow. Firstly, the phenomenon and its associated computer code are introduced. Secondly, the way to choose the observations is presented. Thirdly, the method to estimate the hyperparameters of the model error is exposed. Fourthly, the test sets of the posterior predictors are presented. Finally the achieved results for the 'parallel', 'black-box' and 'grouped' methods on this example are showed.

6.1 Presentation of the phenomenon

The model properties of the numerical example are :

$$\mathbf{h_1}(x) = \mathbf{h_2}(x) = \begin{bmatrix} 1 \\ x^2 \end{bmatrix} \tag{38}$$

$$\begin{gathered} \beta_\mathbf{1} = \beta_\mathbf{2} = \begin{bmatrix} -5 \\ 0.4 \end{bmatrix} \\ y_1(x) = y_2(x) = \mathbf{h_1}(x)^t \beta_\mathbf{1} - \tfrac{1}{4}\cos(2\pi x) = \mathbf{h_2}(x)^t \beta_\mathbf{2} - \tfrac{1}{4}\cos(2\pi x) \end{gathered} \tag{39}$$

Figure 1 presents the model alone and the nested model. It can be seen that the errors of the phenomena $x_1 \mapsto y_1$ and $x_2 \mapsto y_2$ are regular. The error of the nested phenomenon is more chaotic.

The three previously presented methods are applied on this example.

6.2 Observations' choice

Regarding the number of observations three cases are studied : 4, 8 or 12 observations. The observations are generated given a maximin Latin Hypercube Sampling for $\mathbf{x_{1,obs}}^{(1)}$

and $\mathbf{x_{2,obs}}^{(2)}$ in the parallel method (in this example $\mathbf{x_{1,obs}}^{(1)} = \mathbf{x_{2,obs}}^{(2)}$), for $\mathbf{x_{1,obs}}^{(3)}$ for the 'black-box' method and for $\mathbf{x_{1,obs}}^{(1)}$ and $\mathbf{x_{1,obs}}^{(3)}$ for the grouped method (in this example $\mathbf{x_{1,obs}}^{(1)} = \mathbf{x_{1,obs}}^{(3)}$). The observations' sampling, the parameters' calibration and the posterior predictors' construction are repeated 50 times for each case.

6.3 Covariance functions' hyperparameters

The covariance functions' hyperparameters are assumed to be known before the parameters' calibration. In the parallel and the grouped methods the hyperparameters of the Matérn covariance functions of ϵ_1 and ϵ_2 are estimated by a Restricted Maximum Likelihood Estimator (see [1]). In the 'black-box' method, ϵ_3 is assumed to be a zero-mean stationary Gaussian process. The hyperparameters of its Matérn covariance function ϵ_3 are estimated by a Restricted Maximum Likelihood Estimator.

6.4 Analysis of the predictors' performances

Once the predictors are built, their performances are analyzed on 100 points' grids over the input space of each phenomenon. For the three phenomena the input space is $[-5, 5]$.

6.5 The parallel approach

In the parallel approach, there are observations for the phenomena $x_1 \mapsto y_1$ and $x_2 \mapsto y_2$ which are denoted by $\left(\mathbf{x_{1,obs}}^{(1)}, \mathbf{y_{1,obs}}^{(1)}\right)$ and $\left(\mathbf{x_{2,obs}}^{(2)}, \mathbf{y_{2,obs}}^{(2)}\right)$. Figure 2 presents for the phenomena $x_1 \mapsto y_1$, $x_2 \mapsto y_2$ and $x_1 \mapsto y_2$ the calibrated codes' and the predictors' accuracy for the 'parallel' method. Figure 3 presents an example of posterior predictor for each phenomenon (1, 2 and nested). Figure 4 presents the sources of uncertainty of the nested phenomenon's predictor. The findings are :

- The more observations there are, the more accurate predictions and the better calibrated codes are.
- The predictors' performance is less sensitive to the observations' choice when the number of observations increases.
- Both mean and confidence interval of 95% of all predictors are accurate.
- The predictors for the phenomena $x_1 \mapsto y_1$ and $x_2 \mapsto y_2$ are interpolating. The predictor for the phenomenon $x_1 \mapsto y_2$ is a linearization of coupling the predictors of the first and the second phenomena, thus it is not interpolating because there is no observation of phenomenon $x_1 \mapsto y_2$.
- When there are few observations, the uncertainty of the nested phenomenon's predictor mainly comes from the parameters' posterior distribution. The uncertainty lowers with the numbers of observations. This reduction with the number of observations is particularly significant for the uncertainty coming from the parameters' distribution.

6.6 The 'black-box' approach

In the 'black-box' approach there are observations for the nested phenomenon only, which are denoted by $\left(\mathbf{x_{1,obs}}^{(3)}, \mathbf{y_{2,obs}}^{(3)}\right)$. Figure 5 presents for the phenomena $x_1 \mapsto y_1$,

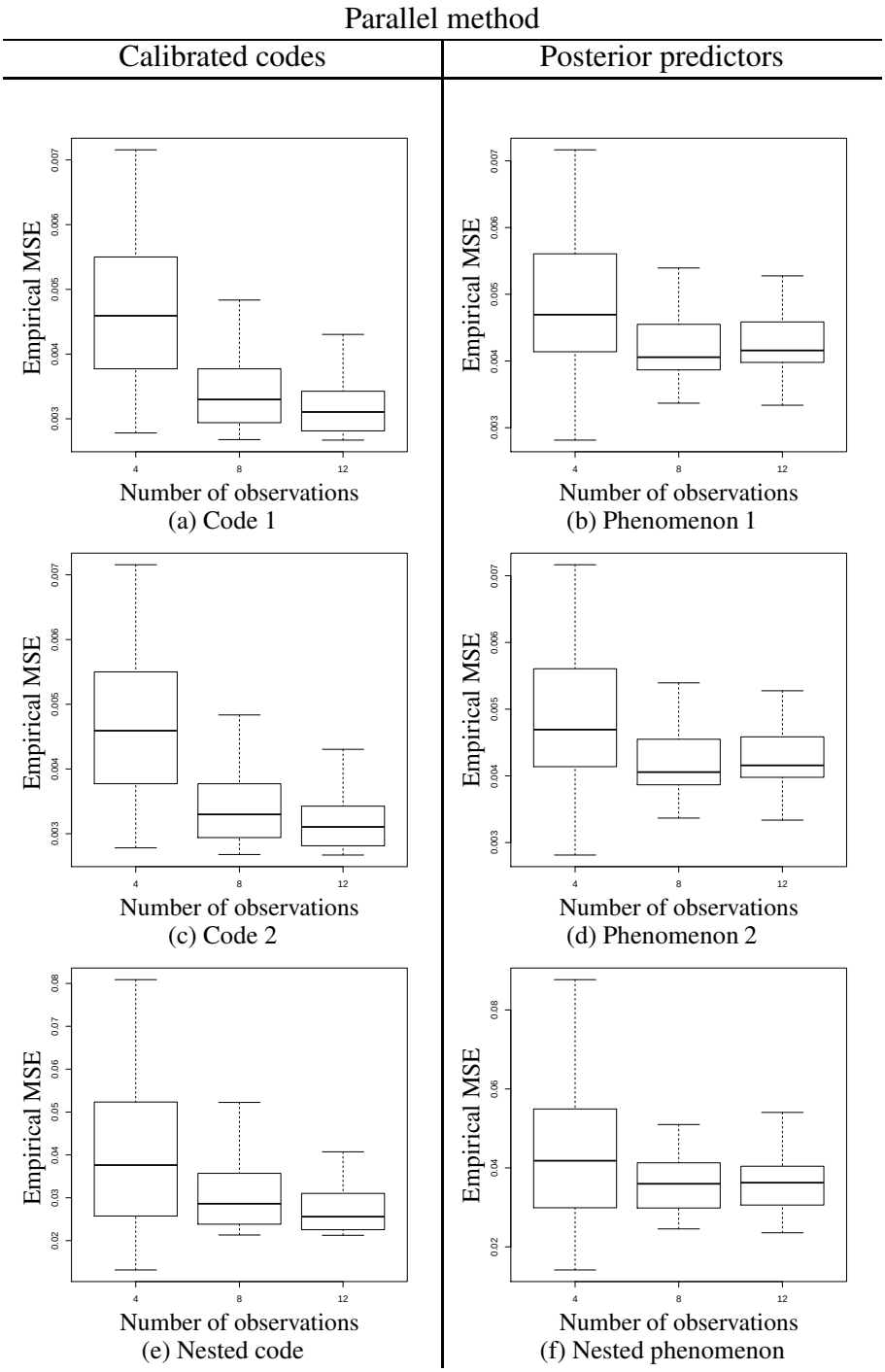

Figure 2: The figures present the empirical MSE (see table 2) of the calibrated codes (2a, 2c, 2e) and the predictors (2b, 2d, 2f) for the "parallel" method. The parameters' calibration and the posterior predictors' construction have been repeated with 50 series of observations. The same observations were used for both codes ($\mathbf{x_{1,obs}}^{(1)} = \mathbf{x_{2,obs}}^{(2)}$). The lower the empirical MSE is, the more accurate the calibrated code is. It can be seen that the accuracy of the predictors and calibrated codes increases with the number of observations and that all codes are well calibrated.

Parallel method : Posterior predictors' mean and confidence interval

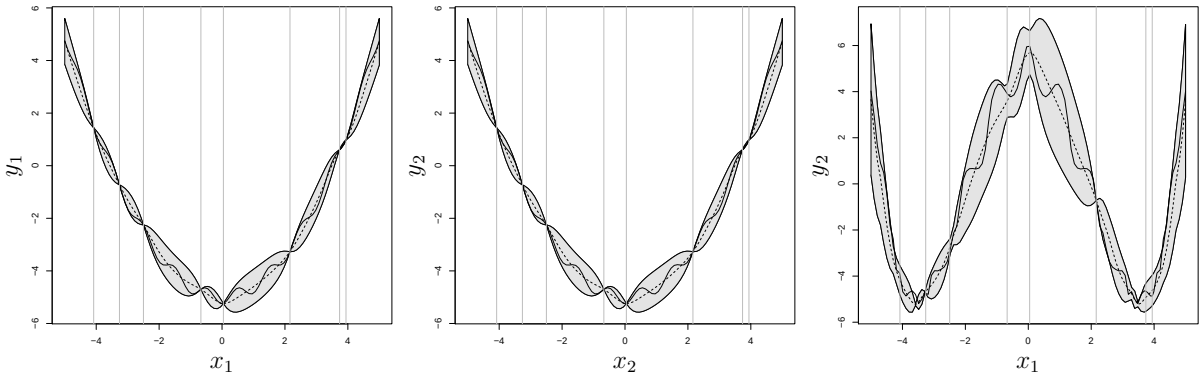

(a) Phenomenon 1 (b) Phenomenon 2 (c) Nested phenomenon

Figure 3: Each figure presents an example of posterior predictor for each phenomenon. The dotted line represents the predictor's mean, the continuous line the real phenomenon and the grey area the predictor's confidence interval of 95%. The predictors are built with the same 8-point LHS maximin designs for $x_1 \mapsto y_1$ and $x_2 \mapsto y_2$ phenomena ($\mathbf{x_{1,obs}}^{(1)}$=$\mathbf{x_{2,obs}}^{(2)}$). It can be seen that the predictors' means and confidence intervals of 95% are accurate. The predictor of the nested code is not an interpolating Gaussian predictor because there is no observation for the phenomenon $x_1 \mapsto y_2$.

Parallel method : sources of uncertainty of the nested phenomenon's predictor

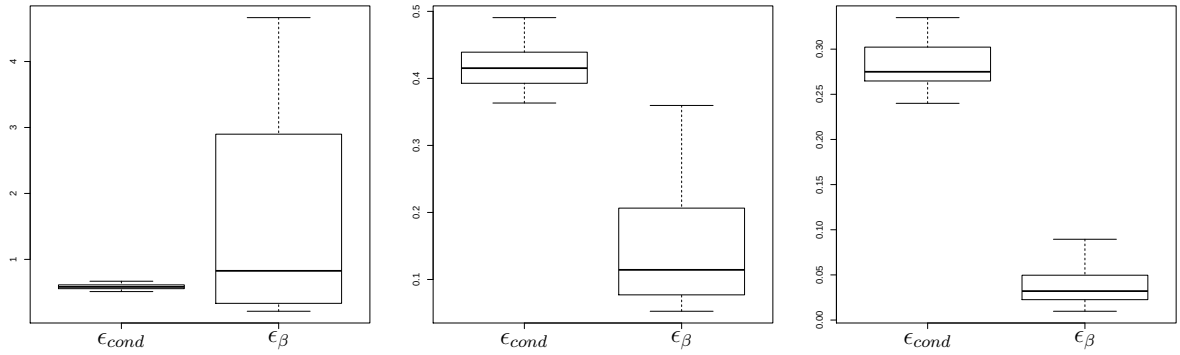

(a) 4 observations (b) 8 observations (c) 12 observations

Figure 4: The figures above present the distribution of the average variance of the nested phenomenon's predictor over a test set of 100 points. We denote by ϵ_{cond} the part of variance coming from the conditional Gaussian process and by ϵ_β the part of variance coming from the parameters' posterior distribution (see table 7). It can be seen that the variance lowers with the number of observations. This reduction is particularly significant for the uncertainty coming from the parameters' distribution.

$x_2 \mapsto y_2$ and $x_1 \mapsto y_2$ the calibrated codes' and predictors' accuracy for the 'black-box' method. Figure 6 presents an example of posterior predictor for each phenomenon (1, 2 and nested). Figure 7 presents the sources of uncertainty of the nested phenomenon's predictor. The findings are :

- The more observations there are, the more accurate the nested predictor is.
- When the number of observations increases, the parameters' calibration is less sensitive to the observations' choice.
- The second code is better calibrated than the first code.
- The nested code is never well calibrated.
- The mean of the nested phenomenon's predictor is accurate, but its variance is relatively high.
- The predictors of the first and the second phenomena are just calibrated codes. Their variances are relatively high.
- When there are few observations, the uncertainty of the nested phenomenon's predictor mainly comes from the parameters' posterior distribution. The uncertainty lowers with the number of observations. This reduction is particularly significant for the uncertainty coming from the parameters' distribution.

6.7 The 'grouped' approach

In this case observations of the three phenomena are available, which are denoted by $\left(\mathbf{x_{1,obs}}^{(1)}, \mathbf{y_{1,obs}}^{(1)}\right)$, $\left(\mathbf{x_{2,obs}}^{(2)}, \mathbf{y_{2,obs}}^{(2)}\right)$ and $\left(\mathbf{x_{1,obs}}^{(3)}, \mathbf{y_{2,obs}}^{(3)}\right)$. In this example we consider that $\mathbf{x_{1,obs}}^{(1)} = \mathbf{x_{1,obs}}^{(3)}$, $\mathbf{y_{1,obs}}^{(1)} = \mathbf{x_{2,obs}}^{(2)}$ and $\mathbf{y_{2,obs}}^{(2)} = \mathbf{y_{2,obs}}^{(3)}$. Figure 8 presents for the phenomena $x_1 \mapsto y_1$, $x_2 \mapsto y_2$ and $x_1 \mapsto y_2$ the calibrated codes' and the predictors' accuracy for the 'grouped' method. Figure 9 presents an example of the posterior predictors for each phenomenon (1, 2 and nested). Figure 10 presents the sources of uncertainty of the nested phenomenon's predictor. The findings are :

- Both codes are well calibrated,
- For the phenomenon $x_1 \mapsto y_1$, the accuracy of the calibrated code increases with the number of observations,
- For the phenomenon $x_2 \mapsto y_2$, the accuracy of the calibrated code decreases with the number of observations. This is probably due to an ill-conditioned problem. The space filling of the observations $\mathbf{x_{2,obs}}^{(2)}$ is not good.
- When there are few observations, the uncertainty of the nested phenomenon's predictor mainly comes from the parameters' posterior distribution. The uncertainty lowers with the number of observations. This reduction is particularly significant for the uncertainty coming from the parameters' distribution.

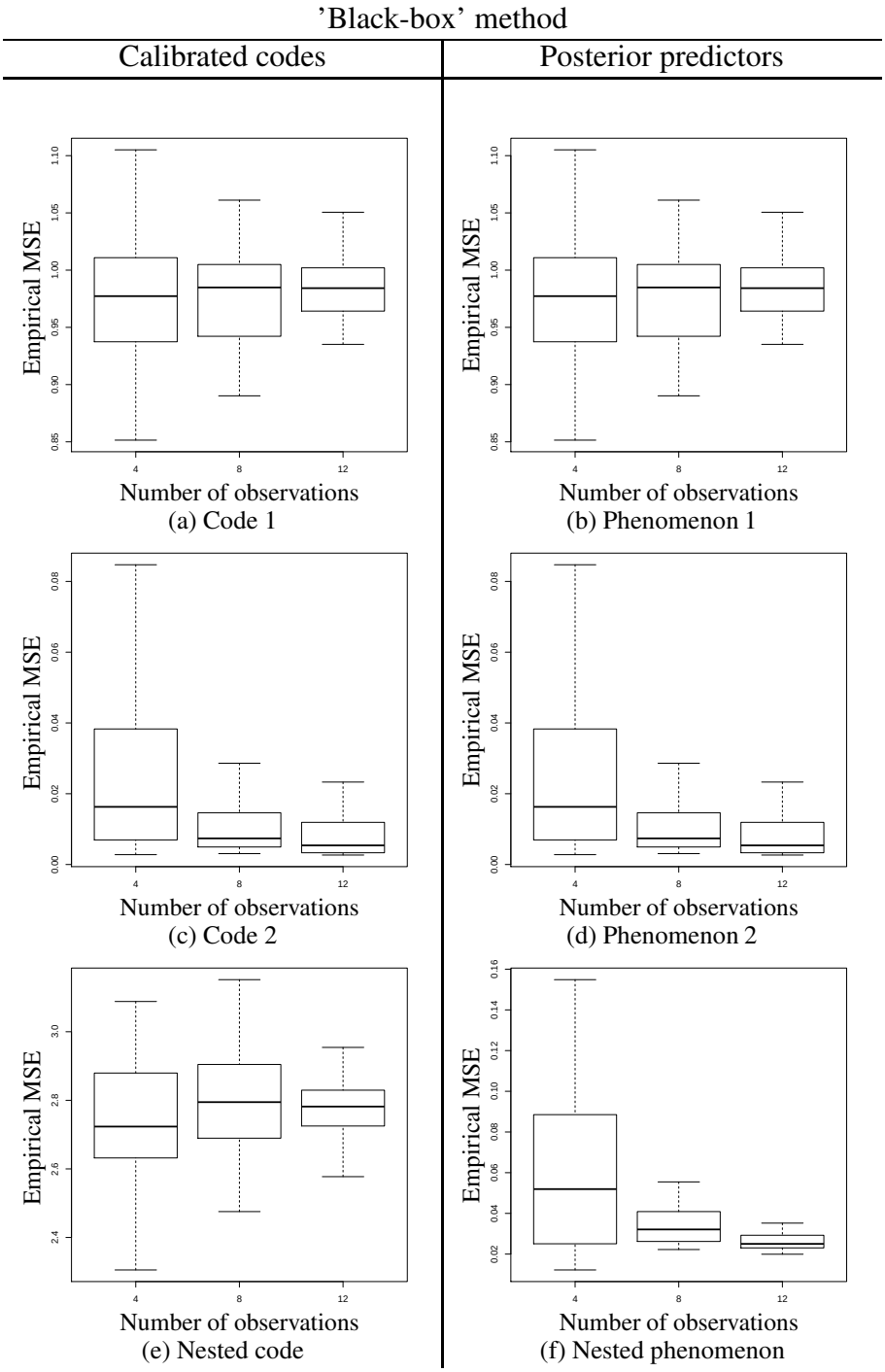

Figure 5: The figures present the empirical MSE (see table 4) of the calibrated codes (5a, 5c, 5e) and the predictors (5b, 5d, 5f) for the "black-box" method. The parameters' calibration and the posterior predictors' construction have been repeated for 50 series of observations. It can be seen that the second code is always better calibrated than the first code. When the number of observations increases, the empirical MSE lowers and is less sensitive to the observations' choice. So the calibrated codes' and predictors' robustness and accuracy increases with the number of observations.

'Black-box' method : Posterior predictors' mean and confidence interval

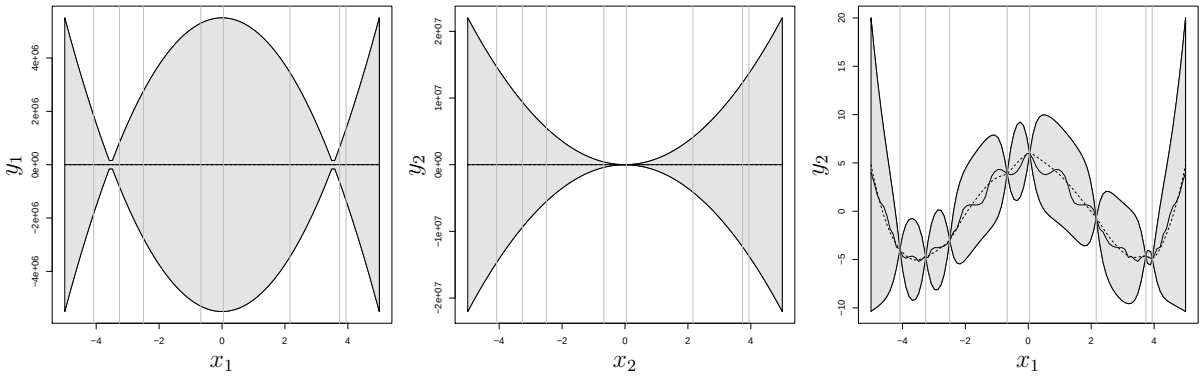

(a) Phenomenon 1 (b) Phenomenon 2 (c) Nested phenomenon

Figure 6: Each figure presents an example of posterior predictor for each phenomenon. The dotted line represents the predictors' mean, the continuous line the real phenomenon and the grey area the confidence interval of 95%. The predictors are built with a 8-point LHS maximin design. The confidence intervals are relatively high. The predictors of the first and the second phenomena are not interpolating because there is no observation for these phenomena ($\left(\mathbf{x_{1,obs}}^{(1)}, \mathbf{y_{1,obs}}^{(1)}\right) = \emptyset$ and $\left(\mathbf{x_{2,obs}}^{(2)}, \mathbf{y_{2,obs}}^{(2)}\right) = \emptyset$). The predictors for these phenomena are just calibrated codes integrating posterior parameters distribution.

'Black-box' method : sources of uncertainty of the nested phenomenon's predictor

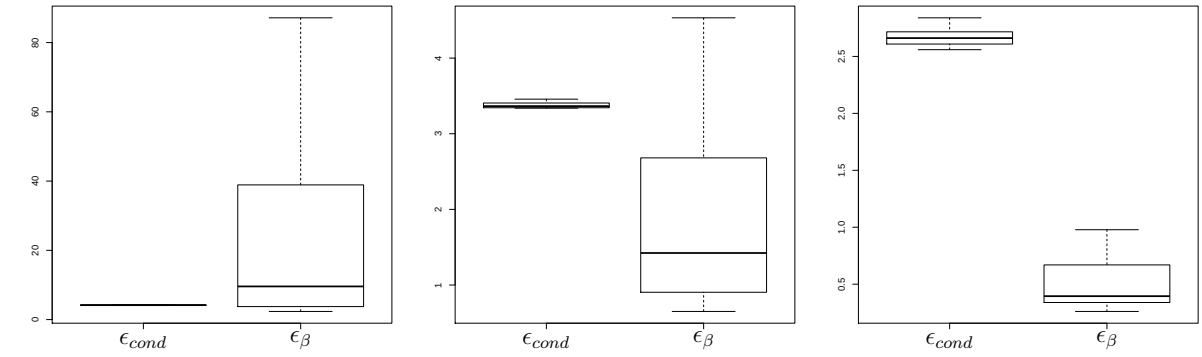

(a) 4 observations (b) 8 observations (c) 12 observations

Figure 7: The figures above present the distribution of the average variance of the nested phenomenon's predictor over a test set of 100 points. We denote by ϵ_{cond} the part of the variance coming from the conditional Gaussian process and by ϵ_β the part of the variance coming from the parameters' posterior distribution. The variance lowers with the number of observations, especially for the part coming from the parameters' distribution (see table 7). The variance coming from the conditional process is relatively high because the error of the nested model is chaotic (see figure 1)

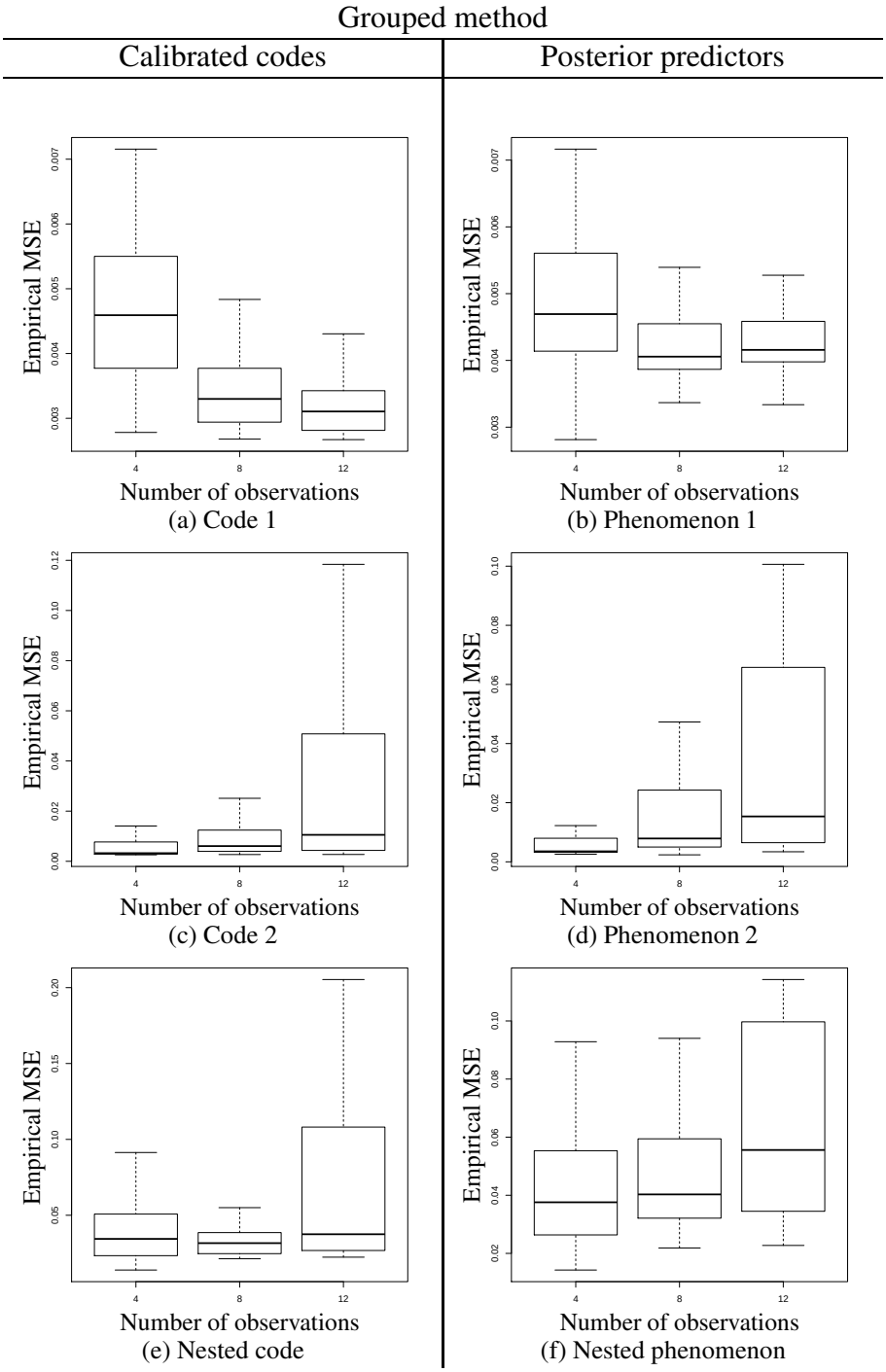

Figure 8: The figures present the empirical MSE (see table 6) of the calibrated codes (8a, 8c, 8e) and the predictors (8b, 8d, 8f) for the "grouped" method. The observations' sampling, the parameters' calibration and the posterior predictors' construction have been repeated 50 times. All codes are well calibrated. The calibrated code's and predictor's accuracy of the phenomenon 1 increases with the number of observations. The calibrated code's and predictor's accuracy of the phenomenon 2 is poorer than for the phenomenon 1 and decreases with the number of observations. This is due to the bad space filling of ${\mathbf{y}_{\mathbf{1},\mathbf{obs}}}^{(1)} = {\mathbf{x}_{\mathbf{2},\mathbf{obs}}}^{(2)}$. Indeed the observations are chosen for phenomenon $x_1 \mapsto x_2 \mapsto y_2$. So even if the observations ${\mathbf{x}_{\mathbf{1},\mathbf{obs}}}^{(1)}$ fill in well the space $[-5;5]$, the observations ${\mathbf{y}_{\mathbf{1},\mathbf{obs}}}^{(1)} = {\mathbf{x}_{\mathbf{2},\mathbf{obs}}}^{(2)}$ are not well distributed in $[-5;5]$. This leads to an ill-conditioned problem.

Grouped method : Posterior predictors' mean and confidence interval

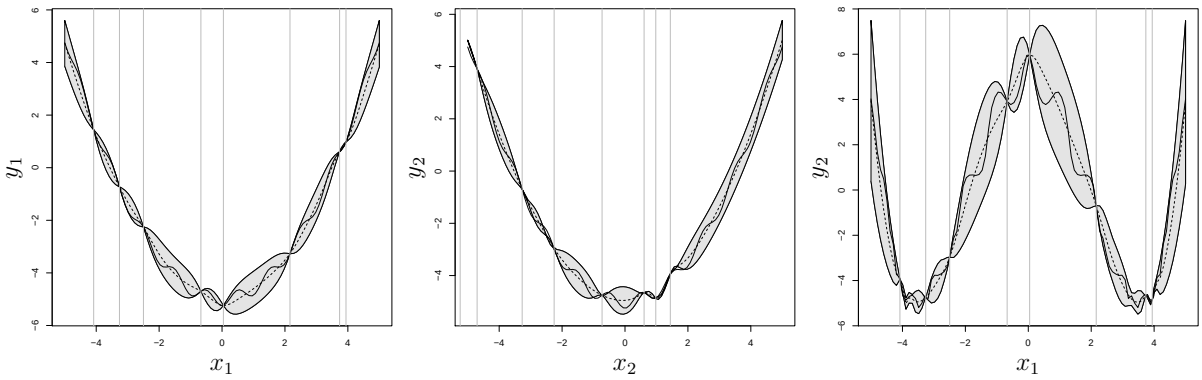

(a) Phenomenon 1 (b) Phenomenon 2 (c) Nested phenomenon

Figure 9: Each figure presents an example of posterior predictor for each phenomenon. The dotted line represents the predictors' mean, the continuous line the real phenomenon and the grey area the confidence interval of 95%. The predictors are built with a 8-point LHS maximin design $x_1 \mapsto x_2 \mapsto y_2$. It can be seen that both mean and confidence interval are well estimated. The observations of the phenomenon 2 are not well distributed in $[-5; 5]$. All the predictors are Gaussian and interpolating.

Grouped method : sources of uncertainty of the nested phenomenon's predictor

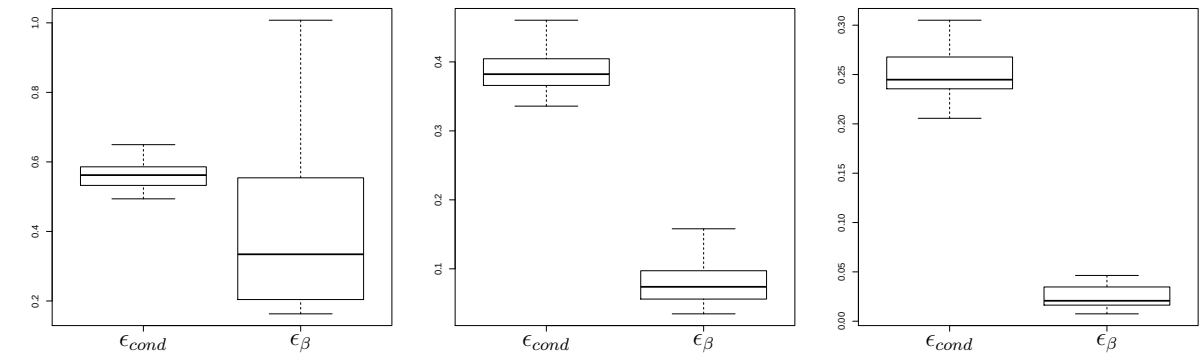

(a) 4 observations (b) 8 observations (c) 12 observations

Figure 10: The figures above present the distribution of the average variance of the nested phenomenon's predictor over a test set of 100 points. We denote by ϵ_{cond} the part of variance coming from the conditional Gaussian process and by ϵ_β the part of variance coming from the parameters' posterior distribution (see table 7). It can be seen that the variance lowers with the number of observations. This reduction is particularly significant for the uncertainty coming from the parameters' distribution. It can be seen that both part of variance are relatively low even when there are few observations.

7 CONCLUSIONS AND FURTHER WORK

A general framework has been proposed to calibrate nested computer models whatever the type of available observations among the three possibilities $\left(\mathbf{x_{1,obs}}^{(1)}, \mathbf{y_{1,obs}}^{(1)}\right)$, $\left(\mathbf{x_{2,obs}}^{(2)}, \mathbf{y_{2,obs}}^{(2)}\right)$ and $\left(\mathbf{x_{1,obs}}^{(3)}, \mathbf{y_{2,obs}}^{(3)}\right)$. Predictors for all phenomena have been proposed for all possibilities of available observations. Three specific cases of this general method have been presented depending on the available observations. The performance of the codes' calibration and the posterior predictors has been analyzed on a numerical example for these three specific cases.

Questions remain about the choice of the design points. In particular our general framework could enable designs where there are not the same number of observations for the first and the second phenomena. Thus parsimonious or sequential (see [2], [3], [4], [5], [8], [9], [10]) designs could be proposed in order to improve the accuracy of the nested phenomenon's predictor.

REFERENCES

[1] F. Bachoc. Calibration and improved prediction of computer models by universal kriging. *Nuclear Science and Engineering*, 176:81–97, 2014.

[2] J. Bect, D. Ginsbourger, L. Li, V. Picheny, and E. Vazquez. Sequential design of computer experiments for the estimation of a probability of failure. *Stat. Comput.*, 22:773–793, 2012.

[3] B. J. Bichon, M. S. Eldred, L. P. Swiler, S. Mahadevan, and J. M. Mcfarland. Efficient Global Reliability Analysis for Nonlinear Implicit Performance Functions. *AIAA J.*, 46:2459–2468, 2008.

[4] C. Chevalier, J. Bect, D. Ginsbourger, and E. Vazquez. Fast parallel kriging-based stepwise uncertainty reduction with application to the identification of an excursion set. *Technometrics*, 56(4):455–465, 2014.

[5] B. Echard, N. Gayton, and M. Lemaire. AK-MCS: An active learning reliability method combining Kriging and Monte Carlo Simulation. *Struct. Saf.*, 33:145–154, 2011.

[6] M. C. Kennedy and A. O'Hagan. Predicting the output from a complex computer code when fast approximations are avalaible. *Biometrika*, 87:1–13, 2000.

[7] M. C. Kennedy and A. O'Hagan. Bayesian Calibration of Computer Models. *J. R. Stat. Soc. . Ser. B (Statistical Methodol.*, 63(3):425–464, 2001.

[8] G. Perrin. Active learning surrogate models for the conception of systems with multiple failure modes. *Reliability Engineering and System Safety*, 149:130–136, 2016.

[9] V. Picheny, D. Ginsbourger, O. Roustant, R. T. Haftka, and N.-H. Kim. Adaptive Designs of Experiments for Accurate Approximation of a Target Region. *Am. Soc. Mech. Eng.*, 132(7), 2010.

[10] P. Ranjan, D. Bingham, and G. Michailidis. Sequential Experiment Design for Contour Estimation From Complex Computer Codes. *Technometrics*, 50(4):527–541, 2008.

[11] J. Sacks, W. Welch, T. J. Mitchell, and H. P. Wynn. Design and Analysis of Computer Experiments. *Stat. Sci.*, 4:409–435, 1989.

[12] T. J. Santner, B. J. Williams, and W. Notz. *The design and analysis of computer experiments*. Springer series in statistics. Springer, New York, 2003.

ECCOMAS Congress 2016
VII European Congress on Computational Methods in Applied Sciences and Engineering
M. Papadrakakis, V. Papadopoulos, G. Stefanou, V. Plevris (eds.)
Crete Island, Greece, 5–10 June 2016

A STATISTICAL APPROACH FOR BUILDING SPARSE POLYNOMIAL CHAOS EXPANSIONS

Simon Abraham, Ghader Ghorbaniasl, and Chris Lacor

Vrije Universiteit Brussel (VUB), Department of Mechanical Engineering Research Group Fluid Mechanics and Thermodynamics
Pleinlaan 2, 1050 Brussels
e-mail: Simon.Abraham@ulb.ac.be, Ghader.Ghorbaniasl@vub.ac.be, Chris.Lacor@vub.ac.be

Keywords: Sparse polynomial chaos expansion, Uncertainty quantification, Regression, Statistical inference, Curse of dimensionality, Compressive sampling

Abstract. *Over the last years, a lot of effort has been made to make existing uncertainty quantification techniques more efficient in high dimensions. An important class of methods relies on the assumption that the polynomial chaos representation of the model response is sparse. This paper contributes to the validation and assessment of an innovative basis selection technique for building sparse polynomial chaos expansions. A regression approach is used for computing the polynomial chaos coefficients. The technique is based on statistical inference theory which provides information about the true regression model from an estimated regression model based on samples. The latter information is used to build iteratively the sparse polynomial chaos expansion. Using the developed methodology, a more robust and efficient basis selection technique is obtained. For validation purpose, the methodology is applied to high dimensional analytical test cases, including the Oakley & O'Hagan function (d=15) and the Morris function (d=20). The results are compared with those obtained from two state-of-the-art techniques, namely the LARS-based algorithm and compressive sampling. As compared to previous work, more comparisons with the LARS-based method are provided, through the use of UQLab, a MATLAB-based uncertainty quantification framework developed by Sudret and Marelli [1]. It is shown that, with equal settings, the developed methodology results in a more accurate polynomial chaos expansion compared to the aforementioned technique. In addition, a new criterion for building an optimal polynomial chaos expansion is further investigated. The conclusions are in-line with previous findings, i.e. the present criterion always builds a sparser polynomial chaos expansion which is, in addition, at least as accurate as compared to the optimal polynomial chaos expansion obtained from the classical cross validation technique.*

1 INTRODUCTION

In recent years, due to the increase in computational power, the interest in uncertainty quantification (UQ) in computational fluid dynamics (CFD) has drastically increased. This has led to an extensive use of polynomial chaos (PC) methods, which are known for their ability to propagate efficiently uncertainties through complex engineering models.

Initially, the PC applications were highly intrusive in the sense that the PC expansion was inserted in the partial differential equations describing the problem. Some applications of intrusive PC are available in [2, 3]. Though, it turned out that, in addition to being error prone, a lot of effort was required to modify the CFD code. This made intrusive PC less attractive for industry who are relying on their own well-validated CFD code. It is for this reason that a focus was made on non-intrusive techniques, where no change to the CFD software is required.

In non-intrusive PC, the PC coefficients are computed using either a projection or a regression approach [4]. In both cases, the stochastic solution is calculated by running a series of deterministic simulations for different realization of the uncertain input parameters. The exact number of calls to the CFD software, also referred to as the number of samples, depends on the PC expansion order but also, and most importantly, on the number of input random variables. For a given PC order, the number of samples required grows exponentially with the number of dimension. In the literature, this exponential increase of computational cost with the number of random dimensions is often referred to as the *curse-of-dimensionality*. The latter issue constitutes a serious brake in the application of non-intrusive PC to relevant industrial applications, which are inherently characterized by many uncertainties, e.g. uncertainties on operational conditions, geometrical uncertainties, etc. Hence, in order to handle this issue, efficient non-intrusive techniques have been developed in the last few years.

To takle the curse of dimensionality, an important class of methods, which has been proven particularly effective, relies on the assumption that the PC solution is sparse. This means that only a limited number of features will contribute significantly to the modeling of the model response. The most famous techniques relying on such assumption are the sparse regression technique of [5, 6] and the compressive sampling technique [7, 8]. In the former approach, the PC coefficients are calculated using the LARS method while in the later approach, an underdetermined system of equations is solved using ℓ_1 regularization [7].

In this paper, an innovative basis selection technique for building sparse polynomial chaos expansion is further investigated. The methodology combines statistical inference theory with regression-based PC. The use of statistical inference will provide information about the true regression given an estimated regression model based on samples. The latter information is then used to build the sparse PC metamodel iteratively, following a forward-backward strategy. It follows that the developed methodology has two important features, i.e. (i) *robustness* as the dependency with respect to the sampling strategy is removed and (ii) *effectiveness* as most of the terms that are captured will contribute to the true regression model. An extensive comparison with state-of-the-art techniques such as the LARS-based method and the compressive sampling technique is provided.

2 REGRESSION-BASED POLYNOMIAL CHAOS

Suppose Y is the exact model response. Y is function of a set of random variables $\boldsymbol{\xi} = (\xi_1, ..., \xi_d)$, where d is the dimension of the random space. The polynomial chaos theory consists in expanding the exact model response into a series of orthogonal polynomials,

$$Y(\boldsymbol{\xi}) = \sum_{i=0}^{P} u_i \psi_i(\boldsymbol{\xi}) \tag{1}$$

where u_i are the PC coefficients and ψ_i are the PC basis, chosen in accordance with the probability density function of the input random variables following the so-called Askey scheme of polynomials [9]. As an example, if the random variables are uniformly distributed, then the Legendre polynomials are used.

The PC coefficients can be calculated using either a quadrature (projection) or a regression method. In the present work, we focused on the regression approach. The regression method consists in evaluating Equation (1) at different location in the stochastic space and solving the resulting system of equations, i.e.

$$Y\left(\boldsymbol{\xi}^{(j)}\right) = \sum_{i=0}^{P} u_i \psi_i\left(\boldsymbol{\xi}^{(j)}\right), \quad j = 1, ..., n \tag{2}$$

In practice, an overdetermined system of equations is built to avoid the overfitting phenomenon [10]. As a rule of thumb, the number of samples is often chosen as twice the number of PC terms and the system is solved in a least squared sense. The statistical moments are then derived by post-processing the estimated PC coefficients, as detailed in [11].

3 STATISTICAL INFERENCE IN REGRESSION ANALYSIS

In this work, a distinction is made between the population regression model, which is built based on an infinite number of samples, and the estimated regression model, based on a limited number of samples. A convention commonly used is to denote estimated parameters with a "hat" superscript. This convention will be followed throughout this paper. The population regression model is written as

$$Y = \sum_{i=0}^{P} u_i \psi_i + \varepsilon \tag{3}$$

where ε denote the error made by approximating the exact model by the population regression model. In the sequel, it will be assumed that the error is iid. with zero mean and constant variance σ^2. On the other hand, an estimated regression model is given by

$$Y = \sum_{i=0}^{P} \hat{u}_i \psi_i + \hat{\varepsilon} \tag{4}$$

where $\hat{\varepsilon}$, the difference between the exact model and an estimated regression model, is called residual. The primary goal of statistical inference is to derive information about the parameters of the true regression model given the parameters of the estimated regression model. In the following, statistical inference will be used for (i) building confidence intervals on the regression coefficients, (ii) testing the dependency between the exact model response and one specific predictor.

3.1 Confidence intervals

In this section, we build confidence intervals (CIs) on the regression coefficients. A CI always takes the same form, i.e. an estimate $\pm$ critical value $\times$ standard deviation of the estimate. The estimate $\hat{u}_j$ is provided by ordinary least squares (OLS) while it is possible to show that the variance of the regression coefficients can be calculated as [12]

$$\mathbb{V}[\hat{u}] = \sigma^2(\mathbf{\Psi}^T\mathbf{\Psi})^{-1} \tag{5}$$

where $\mathbf{\Psi}$ denotes the design matrix (matrix containing all the features). The variance σ^2 is a population parameter which can be estimated as follows [12]

$$\hat{\sigma}^2 = \frac{1}{\text{DOF}}\sum_{i=1}^{n}(Y_i - \hat{Y}_i)^2 \tag{6}$$

which is nothing else but the residual sum of squares (RSS) divided by the number of degrees of freedom (DOF) [12]. It turns out that the CIs for the regression coefficients can be built as

$$u_j \in \left[\hat{u}_j \pm t_{\text{DOF};\alpha/2}\sqrt{\mathbb{V}[\hat{u}_j]}\right] \tag{7}$$

where $t_{\text{DOF};\alpha/2}$ is the critical value.

3.2 Hypothesis testing

The goal of hypothesis testing in regression analysis is to test the dependency between the exact model response Y and a given predictor. Let consider the following estimated regression model

$$\hat{Y} = \sum_{i=1}^{P}\hat{u}_i\psi_i \tag{8}$$

In order to test the dependency between the response and one specific predictor ψ_i, the null and alternative hypotheses are stated as follows

$$\text{H}_0 : u_i = 0 \tag{9}$$
$$\text{H}_1 : u_i \neq 0 \tag{10}$$

To assess the veracity of H_0 a test statistic is defined

$$t_{\hat{u}_i} = \frac{\hat{u}_i}{\sqrt{\mathbb{V}[\hat{u}_i]}} \sim t_{\text{DOF}} \tag{11}$$

which means that the test statistic follows a Student-t-distribution with DOF degrees of freedom. The decision rule is

$$\text{RH}_0 \text{ : if } |t_{\hat{u}_i}| \geq t_{\text{DOF};1-\alpha/2} \tag{12}$$
$$\cancel{\text{RH}}_0 \text{ : if } |t_{\hat{u}_i}| < t_{\text{DOF};\alpha/2} \tag{13}$$

where RH_0 means the null hypothesis is rejected in favour of the alternative hypothesis and $\cancel{\text{RH}}_0$ the null hypothesis is not rejected. In other words, the test statistic is compared with a critical value. If the test statistic lies inside the critical region, then H_0 is rejected.

4 RESULTS AND DISCUSSION

4.1 Oakley & O'Hagan function (d=15)

First the Oakley & O'Hagan function [13] is considered:

$$Y = \mathbf{a_1}^T \boldsymbol{\xi} + \mathbf{a_2}^T \sin(\boldsymbol{\xi}) + \mathbf{a_3}^T \cos(\boldsymbol{\xi}) + \boldsymbol{\xi}^T \mathbf{M} \boldsymbol{\xi} \tag{14}$$

where $\boldsymbol{\xi} = \{\xi_1, ..., \xi_{15}\}$ are independent random variables, normally distributed with zero mean and variance equals one, i.e. $\xi_i \sim \mathcal{N}(0, 1)$, $i = 1, ..., 15$. The Oakley & O'Hagan function consists of 15 random dimensions, among which 5 variables contribute significantly to the variability of the output, 5 have a smaller effect and the remaining 5 input variables have almost no effect on the output of interest [14]. The vectors $\boldsymbol{a_j}$, $j = \{1, 2, 3\}$ and the matrix $\mathbf{M}$ are reported at `http://www.jeremy-oakley.staff.shef.ac.uk/psa_example.txt`.

The Oakley & O'Hagan function is seen as the expensive model, that will be modeled by a sparse PC expansion using Hermite polynomials. In the sequel, for the sake of comparison, two sparse PC metamodels will be built. The first one is built using the LARS-based method and the second one using the statistic-based approach. On the one hand, the LARS-based calculation of the PC coefficients is provided by UQLab, a MATLAB-based UQ framework developed by Sudret and Marelli [1]. Regarding the settings, the degree-adaptivity is activated, i.e. the calculation of the PCE coefficients is performed for a range of PC degree and the degree with the lowest leave-one-out (LOO) error is selected [REF]. In addition, no truncation to the set of candidates basis has been applied ($q = 1$). On the other hand, the STAT method is also run for a range of PC degree, among which the best PC metamodel is selected. A cut-off level of 20% is applied for the STAT-CI method. In all cases, the PCE-based methods are run with two quasi-random experimental designs of size $n = 500$ and $n = 750$ respectively. The relative ℓ_2 error is used to measure the accuracy of the resulting PC expansions.

Results are reported in Table 1. It turns out that, using the same experimental design, the STAT method results in a metamodel which is almost one order of magnitude more accurate as compared to the accuracy of the best metamodel calculated with the LARS method. Moreover, the level of sparsity of the resulting PCE is significantly much smaller when the STAT-CI method is used (almost 50% less terms are captured). This confirms that the statistic-based method selects the PC terms in a smarter way, which can result in large savings in terms of computational cost.

	LARS-MCV		**STAT-MCV**		**STAT-CI**	
	n=500	n=750	n=500	n=750	n=500	n=750
Relative ℓ_2 error	$2.0 \cdot 10^{-2}$	$4.6 \cdot 10^{-3}$	$3.8 \cdot 10^{-3}$	$7.3 \cdot 10^{-4}$	$3.4 \cdot 10^{-3}$	$4.9 \cdot 10^{-4}$
Level of sparsity	204	341	234	374	135	189
PC order	3	4	4	5	4	5

Table 1: Oakley function - Comparison of different adaptive methods for building sparse PC expansions.

More detailed comparisons are reported in Figure 1. In that Figure, the magnitude of the estimated PC coefficients is plotted against a reference solution. The reference solution is given by a full PCE of order 4 where PC coefficients are computed with regression (requiring 7752 samples). For the sake of comparison only, the LARS algorithm is run using a PC degree of 4 (which is not optimal as shown in Table 1). It is shown that, using only 500 samples, the STAT

method is able to capture exactly the most important contributions while the LARS method also captures lots of irrelevant contributions. It is therefore not surprizing that the STAT method results in better performance as compared to the LARS method.

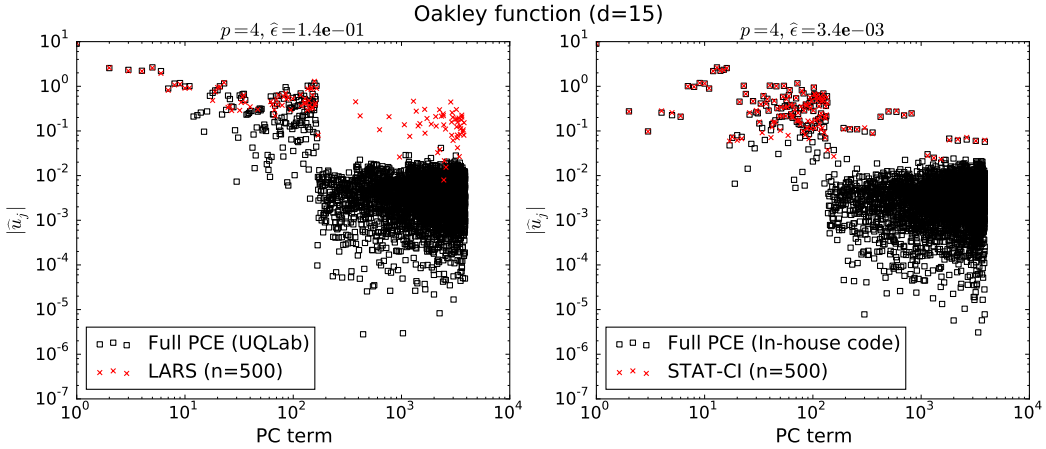

Figure 1: Oakley function - Magnitude of estimated regression coefficients versus a full PCE of order 4 (Left: LARS, Right: STAT)

Eventually, a comparison is made between the STAT method and compressive sampling, using the same experimental design (n=500). Results are reported in Figure 2. It is shown that the compressive sampling technique captures some important contributions. Roughly, the coefficients whose order of magnitude lies in the range $1-10$ are correctly captured. Though CS completely fails in capturing the PC coefficients with lower order of magnitude, resulting in a metamodel of poor quality compared to the one computed with the STAT-CI method.

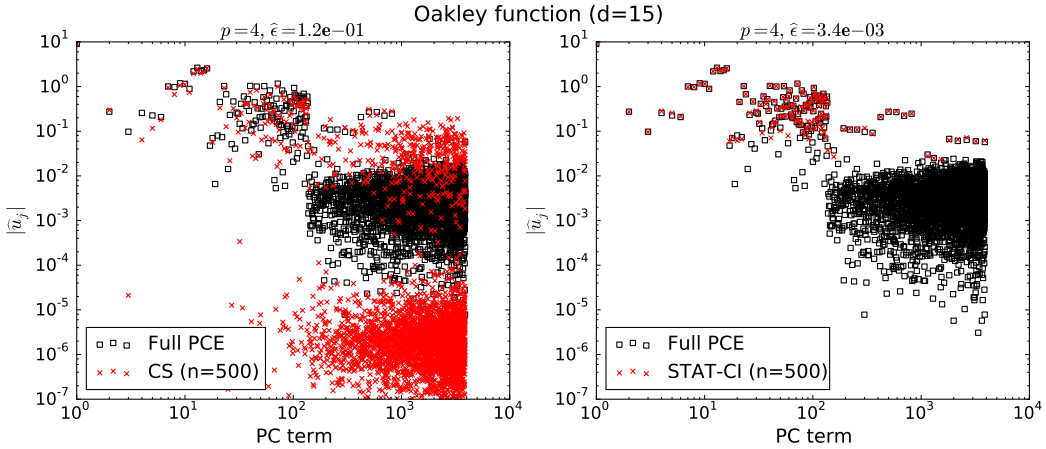

Figure 2: Oakley function - Comparison between the STAT-CI method and compressive sampling

4.2 Morris function (d=20)

The second function considered is another high dimensional function, namely the so-called Morris function [14]:

$$Y = \beta_0 + \sum_{i=1}^{20} \beta_i w_i + \sum_{i<j}^{20} \beta_{ij} w_i w_j + \sum_{i<j<k}^{20} \beta_{ijk} w_i w_j w_k + \sum_{i<j<k<\ell}^{20} \beta_{ijk\ell} w_i w_j w_k w_\ell \tag{15}$$

where

$$w_i = \begin{cases} 2\left(1.1\frac{\xi_i}{\xi_i+0.1} - 0.5\right) & \text{if } i = 3,5,7 \\ 2(\xi_i - 0.5) & \text{otherwise.} \end{cases} \qquad \xi_i \sim \mathcal{U}(0,1) \tag{16}$$

and

$$\begin{cases} \beta_i = 20 & \text{for } i = 1,...,10 & \text{and } \beta_i = (-1)^i & \text{otherwise} \\ \beta_{ij} = -15 & \text{for } i = 1,...,6 & \text{and } \beta_{ij} = (-1)^{i+j} & \text{otherwise} \\ \beta_{ijk} = -10 & \text{for } i = 1,...,5 & \text{and } \beta_{ijk} = 0 & \text{otherwise} \\ \beta_{ijk\ell} = 5 & \text{for } i = 1,...,4 & \text{and } \beta_{ijk\ell} = 0 & \text{otherwise} \end{cases} \tag{17}$$

The Morris function consists of 20 random dimensions, uniformly distributed over [0,1]. A detailed sensitivity analysis of the Morris function is available in [14]. The Morris function is seen as the expensive model which will be replaced by a sparse PC-based metamodel using Legendre polynomials. A similar study is performed as compared to the previous test case. The PC-based methods are run with two quasi random designs of experiments ($n = 500$, $n = 750$). Again, a cut-off level of 20% is applied for the STAT-CI method.

Results are shown in Table 2. In that case, the STAT-CI method still outperforms the LARS method but the gap between both approaches is less significant. The gain in terms of accuracy reaches 27% (resp. 34%) using a design of experiments made of 500 (resp. 750) individuals.

	LARS-MCV		**STAT-MCV**		**STAT-CI**	
	n=500	n=750	n=500	n=750	n=500	n=750
Relative ℓ_2 error	$8.4 \cdot 10^{-2}$	$5.9 \cdot 10^{-2}$	$1.1 \cdot 10^{-1}$	$5.7 \cdot 10^{-2}$	$6.1 \cdot 10^{-2}$	$3.9 \cdot 10^{-2}$
Level of sparsity	52	93	192	195	53	62
PC order	3	3	3	4	3	4

Table 2: Morris function - Comparison of different adaptive methods for building sparse PC expansions.

The resulting sparse PC expansions ($n = 500$) are now faced with a reference solution, namely a full PCE of order 3 whose PC coefficients were calculated with regression (see Figure 3). Those results are in-line with previous findings, i.e. in contrast with the STAT-based method, the terms captured by the LARS method do not exactly correspond to those calculated by the full PC solution. This will inevitably result in a deterioration in the estimation of the statistical moments.

Eventually, the performance of the STAT-CI method is compared with the compressive sampling technique (see Figure 4). Using the same design of experiments ($n = 500$), the performance of compressive sampling is comparable to the performance of the statistic-based method. The main difference with previous test case is that the order of magnitude of the PC coefficients

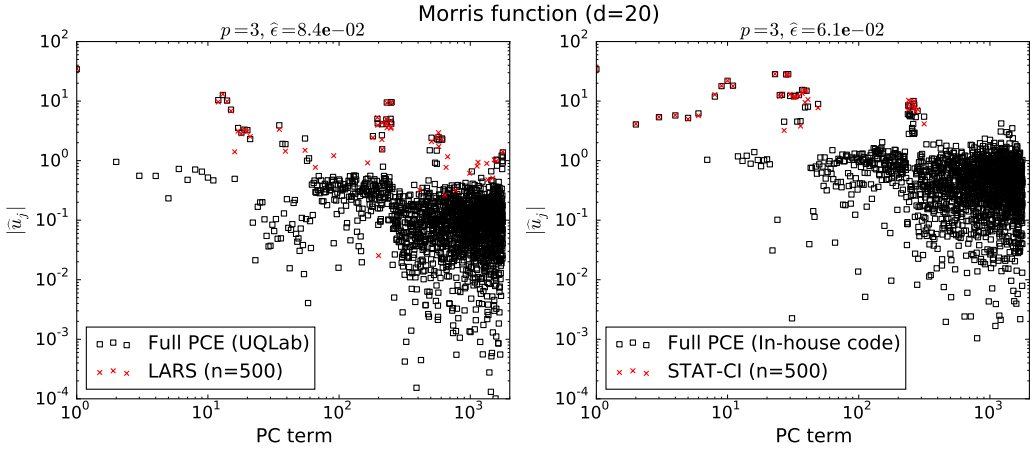

Figure 3: Morris function - Magnitude of estimated regression coefficients versus a full PCE of order 3 (Left: LARS, Right: STAT)

is greater than in the previous test case. Those terms are perfectly capture by the compressive sampling technique.

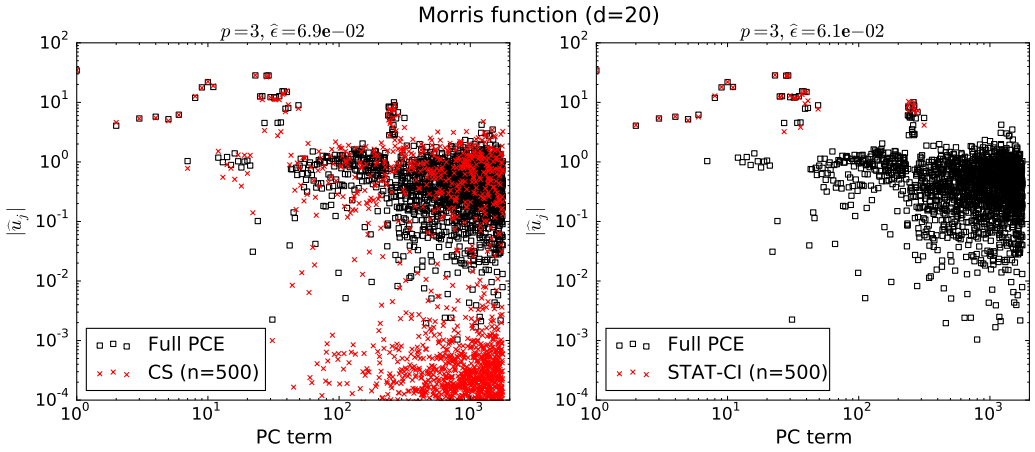

Figure 4: Morris function - Comparison between the STAT-CI method and compressive sampling

5 CONCLUSIONS

In this paper, the performance of a novel basis selection technique are further investigated. The developed methodology shows good potential in building sparse PC expansions at a reduced computational expense. Moreover, it has two essential features, i.e. (i) robustness with respect to the experimental design and (ii) effectiveness in the sense that only terms that truly contribute to the true regression model are captured.

In order to show the effectiveness of the proposed method, two high-dimensional analytical test cases are considered, namely the Oakley & O'Hagan function ($d = 15$) and the more challenging Morris function ($d = 20$). In each case, at equal settings, the accuracy of the sparse PC metamodel shows significant improvement as compared to existing state-of-the-art techniques. Particularly, the results confirm the superiority of the statistic-based approach over the

LARS-based approach. In addition, it is confirmed that the terms captured by the statistic-based method correspond exactly to the most important features calculated by a full PC expansion.

In the future, the method will be applied to relevant industrial applications.

REFERENCES

[1] S. Marelli, B. Sudret. UQLab, The framework for Uncertainty Quantification. Retrieved February 26, 2016, from `http://www.uqlab.com`

[2] C. Lacor, S. Smirnov. Uncertainty propagation in the solution of compressible Navier-Stokes equations using polynomial chaos decomposition. In *CD Rom Proc. of NATO AVT symposium*, page 13, Athens, December 2007.

[3] C. Lacor, S. Smirnov. Non-deterministic compressible Navier-Stokes simulations using polynomial chaos. In *Proc. ECCOMAS Conf*, Venice, July 2008.

[4] M.P. Petterssen, G. Iaccarino, J. Nordstrm. *Polynomial Chaos Methods for Hyperbolic Partial Differential Equations*. Springer 2015. ISBN 978-3-319-10714-1

[5] G. Blatman, B. Sudret. Sparse polynomial chaos expansions and adaptive stochastic finite elements using a regression approach. *C.R. Mecanique*, **336**:518523, 2008.

[6] G. Blatman, B. Sudret. Adaptive sparse polynomial chaos expansion based on Least Angle Regression. *J. Comput. Phys.*, **230**:23452367, 2011.

[7] A. Doostan, H. Owhadi. A non-adapted sparse approximation of PDEs with stochastic inputs. *J. of Comput. Phys.*, **230**(8):30153034, April 2011.

[8] J. Hampton, A. Doostan. Compressive sampling of polynomial chaos expansions: Convergence analysis and sampling strategies. *J. Comput. Phys.*, **280**:363386, 2015.

[9] R. Askey and J. Wilson. *Some Basic Hypergeometric Orthogonal Polynomials That Generalize Jacobi Polynomials*. AMS, 1985.

[10] G. Blatman. *Adaptive sparse polynomial chaos expansions for uncertainty propagation and sensitivity analysis*. PhD thesis, Universite Blaise Pascal, Clermont Ferrand, 2009.

[11] B. Sudret. Global sensitivity analysis using polynomial chaos expansions. *Reliab. Eng. Syst. Safe.*, **93**(7):964979, 2008.

[12] J.O. Rawlings, S.G. Pantula, D.A. Dickey. *Applied Regression Analysis: A Research Tool*. Springer Texts in Statistics. Springer, 2nd edition, 2001. ISBN: 978-0-387-98454-4.

[13] J. Oakley, A. OHagan. Probabilistic sensitivity analysis of complex models: a Bayesian approach. *J Royal Stat Soc*, Series B 2004;**66**:751 769.

[14] B. Sudret, C.V. Mai. Computing derivative-based global sensitivity measures using polynomial chaos expansions. *Reliab. Eng. Syst. Safe.*, **134**:241250, 2015.

ECCOMAS Congress 2016
VII European Congress on Computational Methods in Applied Sciences and Engineering
M. Papadrakakis, V. Papadopoulos, G. Stefanou, V. Plevris (eds.)
Crete Island, Greece, 5–10 June 2016

FINITE ELEMENT METAMODELING OF UNCERTAIN STRUCTURES

Vasilis K. Dertimanis[1], Dimitrios Giagopoulos[2], and Eleni N. Chatzi[1]

[1] ETH Zurich, Inst. of Structural Engineering, Department Of Civil, Environmental and Geomatic Engineering
Stefano-Franscini-Platz 5, 8093 Zurich, Switzerland
e-mail: {v.derti,chatzi}@ibk.baug.ethz.ch

[2] University of Western Macedonia, Department of Mechanical Engineering
Bakola & Sialvera Str., 501 00 Kozani, Greece
e-mail: dgiagopoulos@uowm.gr

Keywords: Substructuring, Metamodeling, Vehicle dynamics, Finite elements, Model reduction, Polynomial chaos, B–splines, ARX.

Abstract. *The necessity for more detailed descriptions of both structural geometry and mechanical properties, renders the use of highly detailed finite element (FE) models almost prohibitive for complex, large structures. This becomes even more challenging when taking into account that structural systems and their excitations are often characterized by parameter uncertainty. To this end, this study addresses the problem of estimating reduced order metamodels for the accurate representation of computationally costly numerical models. A substructuring approach is adopted for segregating the modeled system into a series of smaller components, by separating the parts with exclusively linear characteristics from the uncertain ones. Each of these components is then approximated by corresponding ARX representations, the parameters of which are functionally dependent on uncertain input parameters, also accounting for uncertainty propagation through the FE model. These functional models are coupled in the time domain to formulate a complete metamodel of the system. The effectiveness of the proposed method is illustrated through its application on the metamodeling of a vehicle frame with uncertain suspension. The results demonstrate the efficiency of the proposed methodology for accurate prediction and simulation of the numerical model dynamics.*

1 INTRODUCTION

FE modeling has nowadays become a standard tool for the numerical simulation of civil, mechanical and aeronautical engineering structures [1, 2, 3] and is extensively used for design optimization [4], reliability analysis [5, 6], as well as for the simulation of hysteretic behaviour [7, 8] and damage [9, 10]. When dynamic loading is involved, however, the increased complexity of FE models renders the efficient characterization of the structural response a quite difficult task, especially for large structures, despite the rapidly growing computational power and the continuous development of increasingly efficient algorithms [11, 12]. A common strategy in such cases is to apply less refined macro-models to the simulation of the global behaviour using, for example, model reduction methods [13], and then implement more detailed local FE micro-models for the description of complex parts of the structure.

Alternatively, substructuring techniques [14] can be considered, under which the total structure is disassembled into several subcomponents that can be analysed separately. This framework retains many advantages over other approaches, since it allows isolation of areas, in which more detail is required, it can be successfully implemented in parallel computing and software–in–the–loop schemes, while it allows for flexible usage of the subcomponents in other structures. This latter advantage is one of the most significant aspects of substructuring, taking under consideration modern challenges of production engineering [15], where coupling of numerical models with fabricated subcomponents (e.g., in the form of experimental prototypes [16]) is a common practice, using hybrid testing and hardware–in–the–loop methods [17].

Another important aspect that must be taken into consideration during the simulation process corresponds to the inherent uncertainty that characterizes critical parameters of the available FE model, such as its associated mechanical properties, the range of operational and environmental conditions under which the structure is designed to operate and, of course, the diverse nature and levels of all possible excitations. In dealing with this issue, Monte Carlo–based methods have been widely applied, despite the necessity for a large number of simulations, with each one demanding excessive computational cost. In contrast to these, simpler representations of the numerical model are formulated using metamodelling techniques, which essentially build a parametric model of the original FE one, termed as *metamodel* or *surrogate model* [18, 19]. This metamodel must be able to predict the dynamic response in a computationally inexpensive way and with sufficient accuracy [20, 21].

Under this perspective, the problem faced in the current study pertains to the determination of the structural response in critical points of the structure using a *small number* of *computationally inexpensive* simulations, which take into account the whole operational range of inherent uncertainties and provide a representative behavioral map of the structure. A special case to this problem corresponds to the availability of physically available parts of the structure, for which experimental data, rather than an analytical model, are available. To address this problem, a process that consists of three overlapping and interrelated stages, namely, (i) the *substructuring* stage, (ii) the *model reduction* stage and (iii) the *metamodeling* stage, is proposed and outlined in the following.

The paper is organized as follows: Section 2 outlines the proposed methodology and describes the associated substructuring, model reduction and metamodeling stages. Section 3 contains a numerical study pertaining to a "vehicle"–like prototype that consists of a frame substructure and one linear suspension with uncertain stiffness. Finally, in Section 4 the results are summarized and remarks for further research are given.

2 THE PROPOSED FRAMEWORK

2.1 Problem formulation

Let us consider an n–DOF FE model of a damped structural system that can be mathematically represented by a second–order vector differential equation of the form

$$\mathbf{M}(\boldsymbol{\xi})\ddot{\mathbf{q}}(t) + \mathbf{D}(\boldsymbol{\xi})\dot{\mathbf{q}}(t) + \mathbf{K}(\boldsymbol{\xi})\mathbf{q}(t) = \mathbf{f}(t) \tag{1}$$

where $\mathbf{M}(\boldsymbol{\xi})$, $\mathbf{D}(\boldsymbol{\xi})$ and $\mathbf{K}(\boldsymbol{\xi})$ are the real $[n \times n]$ mass, viscous damping and stiffness matrices, $\mathbf{q}(t)$ is the $[n \times 1]$ vibration displacement vector and $\mathbf{f}(t)$ is the $[n \times 1]$ vector of excitations.

The dependence of the structural matrices to $\boldsymbol{\xi}$ is herein used to notate their variability due to a number of uncertain parameters related with either inherent properties of the structure, or exogenous random variables, e.g. geometry, mass distribution, environmental conditions and so on. For a number of L such uncertain parameters it follows that $\boldsymbol{\xi}(t) = [\xi_1, \xi_2, \ldots, \xi_L]$. In its most general statistical representation, the parameter vector $\boldsymbol{\xi}$ may be considered as a realization of the vector random process $\boldsymbol{\Xi}$ with joint PDF $f_{\boldsymbol{\Xi}}(\boldsymbol{\xi})$. Simpler realizations are possible if it is assumed that each parameter ξ_k is a realization of an independent random process Ξ_k with PDF $f_{\Xi_k}(\xi_k)$.

In this setting, the problem addressed herein aims at simulating the structural response, in the form of vibration displacement, velocity, or acceleration, under the following conditions:

- The size n of the FE model of the structure is prohibitely large for computationally efficient direct simulation.
- The structure can be split into a number of smaller substructures and all the associated boundaries can be adequately described.
- A statistical description of the uncertain parameters and the excitations is available for the whole operating range of the structure.

2.2 Substructuring

Assume that the total structure, described by Eq. 1, is constructed by the proper assembly of two substructures, $A(\boldsymbol{\xi})$ and $B(\boldsymbol{\xi})$. Then, instead of attempting to simulate the whole structure, it is possible to carry out distributed simulations for each substructure, provided that the common interface among the subdomains is appropriately defined. Indeed, the equations of motion that describe each substructure are

$$\mathbf{M}_A(\boldsymbol{\xi})\ddot{\mathbf{q}}_A(t) + \mathbf{D}_A(\boldsymbol{\xi})\dot{\mathbf{q}}_A(t) + \mathbf{K}_A(\boldsymbol{\xi})\mathbf{q}_A(t) = \mathbf{f}_A(t) + \mathbf{h}_A(t) \tag{2}$$

and

$$\mathbf{M}_B(\boldsymbol{\xi})\ddot{\mathbf{q}}_B(t) + \mathbf{D}_B(\boldsymbol{\xi})\dot{\mathbf{q}}_B(t) + \mathbf{K}_B(\boldsymbol{\xi})\mathbf{q}_B(t) = \mathbf{f}_B(t) + \mathbf{h}_B(t) \tag{3}$$

with all the associated quantities previously defined, with the exception of $\mathbf{h}_*(t)$, which corresponds to the vector of connecting forces. Then, from de Klerk *et al.* [14], recovery of Eq. 1 proceeds by first stacking the substructures as

$$\underbrace{\begin{bmatrix}\mathbf{M}_A & \mathbf{O}\\ \mathbf{O} & \mathbf{M}_B\end{bmatrix}}_{\overline{\mathbf{M}}}\begin{bmatrix}\ddot{\mathbf{q}}_A(t)\\ \ddot{\mathbf{q}}_B(t)\end{bmatrix} + \underbrace{\begin{bmatrix}\mathbf{D}_A & \mathbf{O}\\ \mathbf{O} & \mathbf{D}_B\end{bmatrix}}_{\overline{\mathbf{D}}}\begin{bmatrix}\dot{\mathbf{q}}_A(t)\\ \dot{\mathbf{q}}_B(t)\end{bmatrix} + \underbrace{\begin{bmatrix}\mathbf{K}_A & \mathbf{O}\\ \mathbf{O} & \mathbf{K}_B\end{bmatrix}}_{\overline{\mathbf{K}}}\underbrace{\begin{bmatrix}\mathbf{q}_A(t)\\ \mathbf{q}_B(t)\end{bmatrix}}_{\overline{\mathbf{q}}(t)} = \underbrace{\begin{bmatrix}\mathbf{f}_A(t)\\ \mathbf{f}_B(t)\end{bmatrix}}_{\overline{\mathbf{f}}(t)} + \underbrace{\begin{bmatrix}\mathbf{h}_A(t)\\ \mathbf{h}_B(t)\end{bmatrix}}_{\overline{\mathbf{h}}(t)} \tag{4}$$

and then by specifying the compatibility (identical displacements of the coupled DOFs) and equilibrium (action–reaction forces) conditions as,

$$\mathbf{C}\overline{\mathbf{q}}(t) = \mathbf{0} \quad \text{and} \quad \mathbf{E}^T\overline{\mathbf{h}}(t) = \mathbf{0} \tag{5}$$

respectively, with $\mathbf{C}$ and $\mathbf{E}$ denoting signed Boolean and Boolean matrices, respectively. Accordingly, by defining a unique set of structural DOFs, $\mathbf{q}(t)$, through

$$\overline{\mathbf{q}}(t) = \mathbf{E}\mathbf{q}(t) \tag{6}$$

it follows from Eq. 5 that $\mathbf{C}\overline{\mathbf{q}}(t) = \mathbf{C}\mathbf{E}\mathbf{q}(t) = \mathbf{0}$, from which $\mathbf{E} = \text{null}\{\mathbf{C}\}$. Substituting Eq. 6 to Eq. 4 implies

$$\overline{\mathbf{M}}\mathbf{E}\ddot{\mathbf{q}}(t) + \overline{\mathbf{D}}\mathbf{E}\dot{\mathbf{q}}(t) + \overline{\mathbf{K}}\mathbf{E}\mathbf{q}(t) = \overline{\mathbf{f}}(t) + \overline{\mathbf{h}}(t) \tag{7}$$

thus, multiplication by $\mathbf{E}^T$ leads to the representation of the total structure by Eq. 1 with

$$\mathbf{M} = \mathbf{E}^T\overline{\mathbf{M}}\mathbf{E}, \;\; \mathbf{D} = \mathbf{E}^T\overline{\mathbf{D}}\mathbf{E}, \;\; \mathbf{K} = \mathbf{E}^T\overline{\mathbf{K}}\mathbf{E}, \;\; \mathbf{f}(t) = \mathbf{E}^T\overline{\mathbf{f}}(t) \tag{8}$$

2.3 Model reduction

When the substructures still retain a large number of DOFs, model reduction can be used to further suppress the DOFs. While several other alternatives are possible (the interested reader is referred to Antoulas [13] for an authoritative treatment) the Ritz transformation is currently implemented. Following the previous discussion and if only the substructure $A(\boldsymbol{\xi})$ requires reduction, a new set of coordinates is provided by

$$\mathbf{q}_A(t) = \boldsymbol{\Psi}_A\mathbf{q}_{AR}(t) \tag{9}$$

where $\boldsymbol{\Psi}_A$ is a subset of the normal modes of Eq. 2, the selection of which depends on the frequency range examined. Applying this transformation to Eq. 2 and pre–multiplying by $\boldsymbol{\Psi}_A^T$ implies

$$\mathbf{M}_{AR}(\boldsymbol{\xi})\ddot{\mathbf{q}}_{AR}(t) + \mathbf{D}_{AR}(\boldsymbol{\xi})\dot{\mathbf{q}}_{AR}(t) + \mathbf{K}_{AR}(\boldsymbol{\xi})\mathbf{q}_{AR}(t) = \mathbf{f}_{AR}(t) + \mathbf{h}_{AR}(t) \tag{10}$$

for

$$\begin{aligned} \mathbf{M}_{AR} = \boldsymbol{\Psi}^T\mathbf{M}_A\boldsymbol{\Psi}, \;\; \mathbf{D}_{AR} = \boldsymbol{\Psi}^T\mathbf{D}_A\boldsymbol{\Psi}, \;\; \mathbf{K}_{AR} = \boldsymbol{\Psi}^T\mathbf{K}_A\boldsymbol{\Psi} \\ \mathbf{f}_{AR}(t) = \boldsymbol{\Psi}^T\mathbf{f}_A(t), \;\; \mathbf{h}_{AR}(t) = \boldsymbol{\Psi}^T\mathbf{h}_A(t) \end{aligned} \tag{11}$$

and corresponds to a reduced representation of the substructure $A(\boldsymbol{\xi})$.

2.4 Metamodeling

The third stage of the proposed methodology aims at estimating a reduced model of Eq. 3. Consider the case where the substructure $B(\boldsymbol{\xi})$ contains one DOF, a single excitation and a single uncertain parameter, so that Eq. 3 corresponds to a scalar nonlinear differential equation and $\boldsymbol{\xi} = \xi$. Then the structural output can be approximated using Adaptable Functional Series Autoregressive with eXogenous input (AFS-ARX) models of the form [22]

$$y[t,\xi] + \sum_{i=1}^{na}\alpha_i(\xi)y[t-i] = \sum_{i=0}^{nb}\beta_i(\xi)u[t-i] + e[t] \tag{12}$$

where $y[t]$ and $u[t]$ denote the model's output and input, respectively, $\alpha_i(\xi)$ and $\beta_i(\xi)$ are the coefficients of the AR and exogenous polynomials, of orders na and nb, respectively, and $e[t] \sim \mathcal{N}(0, \sigma_e^2)$ is the model's zero-mean Gaussian residual sequence.

The AFS-ARX(na, nb) model of Eq. 12 accounts for the uncertainty of $B(\boldsymbol{\xi})$ through the regression parameters $\theta_i(\xi)$, which are currently admitting a representation based on B–spline functions

$$\alpha_i(\xi) = \sum_{j=1}^{p} \alpha_{ij} S_{j,k}(\xi, \boldsymbol{\delta}_\alpha) \tag{13a}$$

$$\beta_i(\xi) = \sum_{j=1}^{p} \beta_{ij} S_{j,k}(\xi, \boldsymbol{\delta}_\beta) \tag{13b}$$

with $S_{j,k}(\xi, \boldsymbol{\delta})$ denoting the sequence of B-splines of order k and of functional subspace parameter vector $\boldsymbol{\delta} \equiv [\tau_{k+1}, \dots, \tau_p]^T$, henceforth referred to as the vector of free knots, of dimension $\dim(\boldsymbol{\delta}) = p - k$, consisting of the non-decreasing sequence of the free internal knots. Given a realization ξ, a particularly convenient way for defining $S_{j,k}(\xi, \boldsymbol{\delta})$ is obtained by means of the Cox-de Boor recursion formula for the normalized B-splines [23, p. 90], according to which

$$S_{j,1}(\xi, \boldsymbol{\delta}) = \begin{cases} 1 & \text{if } \tau_j \leq \xi < \tau_{j+1} \\ 0 & \text{otherwise} \end{cases} \tag{14a}$$

$$S_{j,i}(\xi, \boldsymbol{\delta}) = w_{j,i}(\xi) S_{j,i-1}(\xi, \boldsymbol{\delta}) + (1 - w_{j,i}(\xi)) S_{j+1,i-1}(\xi, \boldsymbol{\delta}), \quad \text{for } 1 < i \leq k \tag{14b}$$

where

$$w_{j,i}(\xi) = \begin{cases} \frac{\xi - \tau_j}{\tau_{j+i-1} - \tau_j} & \text{if } \tau_j < \tau_{j+i-1}, \\ 0 & \text{otherwise.} \end{cases} \tag{14c}$$

It is noted that since the internal free knots form a non decreasing sequence of real numbers, they have to satisfy proper constraints in relation to their bounds and order [24].

The efficient representation of $B(\xi)$ through AFS-ARX(na, nb) models is succeeded through the establishment and the solution of an associated identification problem, in which all the unknown parameters of the model are estimated, that is, the integers na, nb, p and k, the parameters α_{ij} and β_{ij} in Eq. 13, the vectors of free knots $\boldsymbol{\delta}_\alpha$ and $\boldsymbol{\delta}_\beta$, as well as the residual variance σ_e^2. To this end, the original AFS-ARX(na, nb) model of Eq. 12 is transformed into a linear regression form as

$$y[t] = \boldsymbol{\phi}[t, \boldsymbol{\delta}]\boldsymbol{\theta} + e[t] \tag{15}$$

for $\boldsymbol{\delta} = [\boldsymbol{\delta}_\alpha \;\; \boldsymbol{\delta}_\beta]^T$ and

$$\boldsymbol{\phi}[t, \boldsymbol{\delta}] = \big[-y[t-1] S_{1,k}(\xi, \boldsymbol{\delta}_\alpha) \;\; -y[t-1] S_{2,k}(\xi, \boldsymbol{\delta}_\alpha) \;\; \dots \;\; x[t-nb] S_{p,k}(\xi, \boldsymbol{\delta}_\beta) \big] \tag{16}$$

and

$$\boldsymbol{\theta} = [\alpha_{1,1} \; \alpha_{1,2} \; \dots \; \alpha_{na,p}]^T \tag{17}$$

If input–output data are available over $t = 1, \dots, N$ then Eq. 15 yields

$$\mathbf{y} = \boldsymbol{\phi}(\boldsymbol{\delta})\boldsymbol{\theta} + \mathbf{e} \tag{18}$$

where $\mathbf{y} = [y[1] \ \dots \ y[N]]^T$, $\boldsymbol{\phi}(\boldsymbol{\delta}) = [\boldsymbol{\phi}[1,\boldsymbol{\delta}] \ \dots \ \boldsymbol{\phi}[N,\boldsymbol{\delta}]]^T$ and $\mathbf{y} = [e[1] \ \dots \ e[N]]^T$. Notice that the AFS-ARX(na, nb) model must include all available statistical information of ξ. Thus, a number of simulations (or experiments, if the substructure $B(\xi)$ is experimental) is performed, say L, given a set of uncertainty parameter realizations, ξ_l, and the corresponding input–output data sets are obtained, $\mathbf{x}_l = [x_l[1] \ \dots \ x_l[N]]^T$ and $\mathbf{y}_l = [y_l[1] \ \dots \ y_l[N]]^T$, respectively, for $l = 1, 2, \dots, L$. Each one of these sets must satisfy Eq. 18, so that

$$\mathbf{y}_l = \boldsymbol{\phi}_l(\boldsymbol{\delta})\boldsymbol{\theta} + \mathbf{e}_l \tag{19}$$

By pooling Eq. 19 for all available experiments it follows that

$$\begin{bmatrix} \mathbf{y}_1 \\ \vdots \\ \mathbf{y}_l \end{bmatrix} = \begin{bmatrix} \boldsymbol{\phi}_1(\boldsymbol{\delta}) \\ \vdots \\ \boldsymbol{\phi}_l(\boldsymbol{\delta}) \end{bmatrix} \theta + \begin{bmatrix} \mathbf{e}_1 \\ \vdots \\ \mathbf{e}_l \end{bmatrix} \Rightarrow \mathbf{Y} = \boldsymbol{\Phi}(\boldsymbol{\delta})\boldsymbol{\theta} + \mathbf{E} \tag{20}$$

and the parameter vector $\boldsymbol{\theta}$ can be recovered by the least squares estimate

$$\boldsymbol{\theta} = \left[\boldsymbol{\Phi}(\boldsymbol{\delta})^T\boldsymbol{\Phi}(\boldsymbol{\delta})\right]^{-1}\boldsymbol{\Phi}(\boldsymbol{\delta})^T\mathbf{Y} = \boldsymbol{\Phi}(\boldsymbol{\delta})^\dagger\mathbf{Y} \tag{21}$$

with $\boldsymbol{\Phi}(\boldsymbol{\delta})^\dagger$ denoting the pseudo-inverse of $\boldsymbol{\Phi}(\boldsymbol{\delta})$. Since the parameter vector $\boldsymbol{\theta}$ depends on the vector of free knots $\boldsymbol{\delta}$, the latter must be estimated prior to the implementation of Eq. 21. Notice that the prediction error sequence $\mathbf{E}$ can be expressed as

$$\begin{aligned} \mathbf{E} &= \mathbf{Y} - \boldsymbol{\Phi}(\boldsymbol{\delta})\boldsymbol{\theta} \Rightarrow \\ &= \mathbf{Y} - \boldsymbol{\Phi}(\boldsymbol{\delta})\boldsymbol{\Phi}(\boldsymbol{\delta})^\dagger\mathbf{Y} \Rightarrow \\ &= \left[\mathbf{I} - \boldsymbol{\Phi}(\boldsymbol{\delta})\boldsymbol{\Phi}(\boldsymbol{\delta})^\dagger\right]\mathbf{Y} \end{aligned} \tag{22}$$

Thus, $\boldsymbol{\delta}$ can be estimated by the solution of the following nonlinear optimization problem [24]

$$\hat{\boldsymbol{\delta}} = \arg\min_{\boldsymbol{\delta}} V_{\text{VP}}(\boldsymbol{\delta}) \doteq \arg\min_{\boldsymbol{\delta}} \|(\mathbf{I} - \boldsymbol{\Phi}(\boldsymbol{\delta})\boldsymbol{\Phi}(\boldsymbol{\delta})^\dagger)\mathbf{Y}\|^2 \tag{23}$$

A final note in metamodeling refers to the cases of large data: observe that from Eqs. 18–20 the involved matrices, $\mathbf{Y}$ and $\boldsymbol{\Phi}(\boldsymbol{\delta})$, can become quite large even for small values of na, nb, p, L and N. Indicatively, for an AFS-ARX(2,3) model with B–spline basis of second order, $p = 3$, $L = 20$ and $N = 500$, their sizes are $[10000 \times 1]$ and $[10000 \times 15]$, respectively. In such cases, and in order to avoid numerical inconsistencies, it may be preferable to model directly the parameters $\alpha_i(\xi)$ and $\beta_i(\xi)$ from Eq. 13, in a process that can be easily realized in parallel. Such an estimation problem turns out to be a typical data–driven uncertainty quantification one that can be solved using, for example, the method described in Spiridonakos *et al.* [24]. This alternative is adopted for the analysis presented in the next section.

3 IMPLEMENTATION

The method's performance and effectiveness is assessed via the metamodeling of a "vehicle"–like prototype that consists of a frame substructure, displayed in Fig. 1, which is connected to four wheelsets through corresponding primary linear suspensions. Each wheelset is modeled as a mass with one degree of freedom and with equivalent stiffness and damping, while all suspensions are identical, except from the front right one that is characterized by uncertain stiffness. The associated parameters of the model are displayed in Tab. 1.

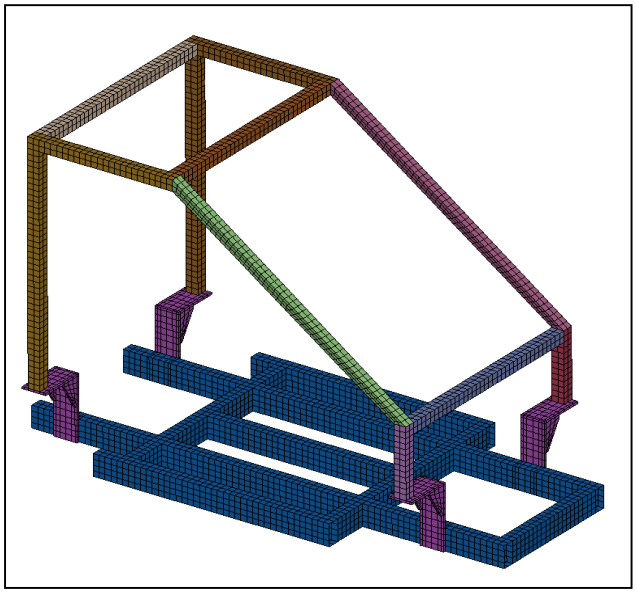

Figure 1: The frame substructure.

Quantity	**Symbol**	**Value**	**Unit**
Frame material density	E	2.1×10^{11}	N/m
Frame material modulus	ρ	7850	kg/m^3
Wheelset mass	m_w	16	kg
Wheelset stiffness	k_w	35	N/m
Wheelset damping	c_w	0	Ns/m
Suspension stiffness	k_s	22	N/m
Suspension damping	c_s	5	Ns/m
Uncertain stiffness	k_{fr}	$\sim \mathcal{N}(22, 6)$	N/m
Road profile	r_{fr}	$\sim \mathcal{N}(0, 7 \times 10^{-3})$	m

Table 1: Parameters of the simulated vehicle.

The FE model of the frame is constructed using quadrilateral shell and hexahedral solid elements, resulting in 45564 DOFs. Model reduction is accordingly applied using the method outlined in Section 2.3, leading to a reduced model of only 54 DOFs. The latter is then connected to the wheelset–suspension subsystems and the total structure is simulated by assuming excitation only in the front right position, which consists of a zero mean Gaussian process that is filtered using a 10th order digital Butterworth filter with low-pass frequency at 30 Hz. A number of $L = 50$ simulations is performed at a sampling period $T_s = 1$ ms and for $t = 5$ s, each one under a specific realization of k_{fr}, drawn using the latin hypercube sampling (LHS) method and illustrated in Fig. 2. The substructure $B(\xi)$ is herein selected to be the subsystem that has the road-induced force applied to the wheelset mass as an input and the vertical acceleration of the common boundary between the frame and the front right suspension as an output. Vibration excitation-response pairs of $N = 5000$ data are thus stored after every simulation. Figure 3 displays an indicative data pair that corresponds to $L = 20$.

To examine the consistency of the method under the availability of limited simulations and /or data, estimation of $B(\xi)$ is conducted using only simulations $\#$ 16 until $\#$ 30 (see Fig. 2). In

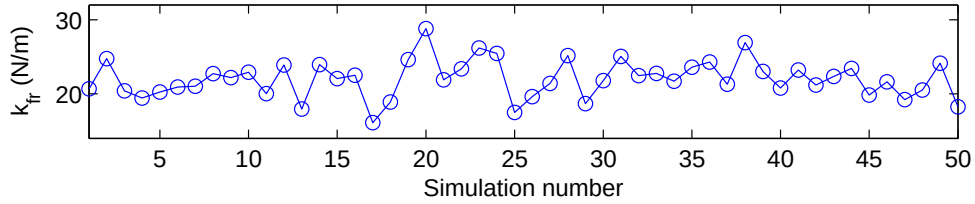

Figure 2: The uncertain stiffness k_{fr} for the 50 simulations conducted.

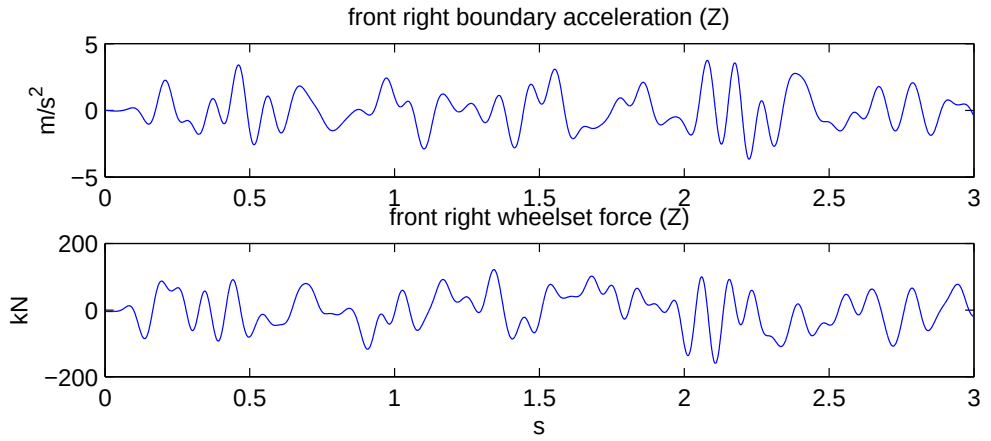

Figure 3: Vibration acceleration response at the front right boundary and road induced force for $L = 20$.

every case, the first 2000 values are extracted from the input–output data set, in order to avoid modeling transient effects, and the set used for identification consists of only the next 1000 data. In order to get an initial insight some initial trial-and-error modeling attempts were performed, revealing that AFS-ARX(2,3) are potentially adequate for representing the substructure $B(\xi)$. This results in five parameters, α_1, α_2, β_0, β_1 and β_2, which must be expressed in respect to the uncertain stiffness. A two–stage procedure is utilized to this purpose:

[S1] Simple ARX(2,3) models are estimated for every simulation and five new (compressed) data sets are formulated, with the uncertain stiffness as input and the AR/X parameter as output.

[S2] Models in the form of Eq. 13 are fitted to each parameter, for $p = 1, \ldots, 10$ and $k = 1, \ldots, 4$.

Figure 4 illustrates the results of this procedure. All examined models returned almost perfect match, as can be seen by the percentage fitness to the data, calculated by

$$\text{fit} = 100\left(1 - \frac{\|q - \hat{q}\|}{\|q - \bar{q}\|}\right)\ (\%) \tag{24}$$

where q and $\hat{q}$ denote true and estimated quantity, respectively, and $\bar{q}$ denotes mean value, with only $S_{j,1}$ exhibiting slightly lower performance. Thus, a model with B-spline basis functions of second order, $S_{j,2}$, and of $p = 3$ was selected for the uncertainty quantification of the AFS-ARX(3,2) parameters. For this model, Fig. 4 further displays the true (e.g., the ones estimated during step **[S1]** above) parameter values versus the model calculated ones.

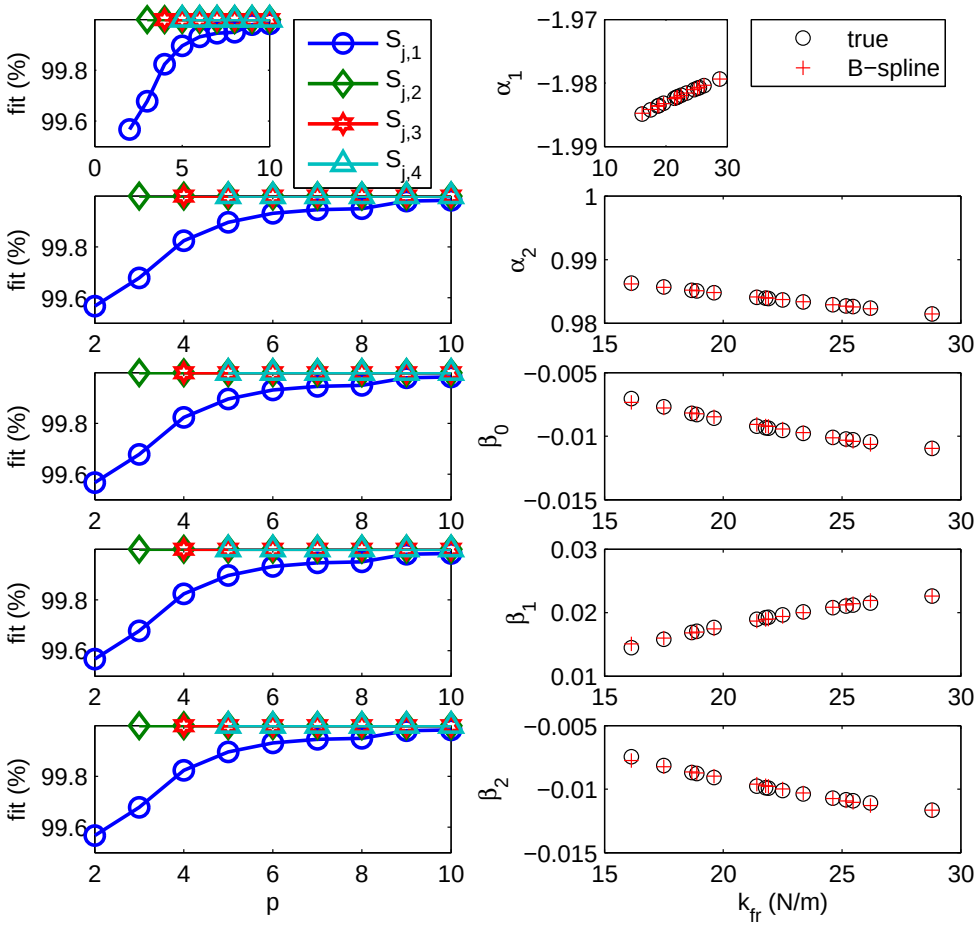

Figure 4: Results of the uncertainty quantification process for each parameter of the AFS-ARX(2,3) model. Left side: percentage fitness to data of every estimated model. Right side: true versus model-based outputs, using Eq. 13 with $p = 3$ and $k = 2$.

The identified AFS-ARX(3,2) model is finally validated against its applicability to the whole spectrum of possible uncertain values. To this end, the data from four simulations that were not used in the estimation process (randomly selected, with two realizations among $\#1, \ldots, \#15$ and two among $\#31, \ldots, \#50$) are forwarded into the model and the predicted output is plotted over the one simulated from the total structure in Fig. 5. Excellent matching is confirmed, implying that the AFS-ARX(3,2) model can adequately replace substructure $B(\xi)$.

4 CONCLUSION

A process for the effective simulation of large–scale, uncertain FE models was outlined in this study, consisting of three interrelated stages that take on the substructuring, the model reduction and the metamodeling steps. The illustrated results provide significant indication of effectiveness and suggest further investigation in this path, with respect to a number of issues that remain active challenges in the field of structural modeling and simulation. Automation of the proposed process, by focusing on the smart interpretation of boundary constraints, the extension to simultaneous substructuring and metamodeling of nonlinear models, as well as the implementation to real-time hybrid testing techniques are issues that are currently being investigated by the authors.

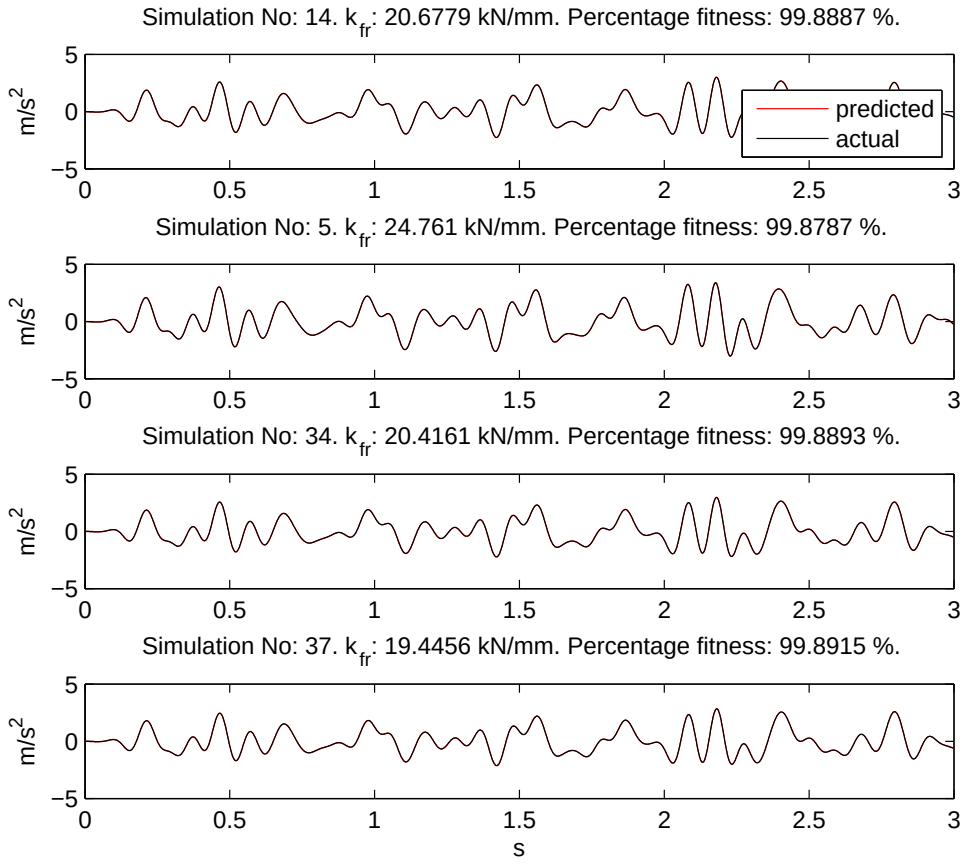

Figure 5: Validation of the AFS-ARX(2,3) model in for simulations not used for identification.

REFERENCES

[1] J. Argyris and S. Kelsey. Energy theorems and structural analysis. *Aircraft Engineering*, 26-27, 1954-1955.

[2] K.-J. Bathe. Finite element method. In B. Wah, editor, *Wiley Encyclopedia of Computer Science and Engineering*, pages 1253–1264. Wiley & Sons, Inc., 2009.

[3] R. Clough. The finite element method in plane stress analysis. In *2nd ASCE Conference on Electronic Computation, Pittsburgh, PA, USA, 1960 September 8-9*, pages 345–378, 1960.

[4] P. Chang and J. Perl. A finite element based approach to multi-objective structural optimization using goal programming. *Engineering Optimization*, 13(1):65–82, 1988.

[5] Armen Der Kiureghian and Jyh-Bin Ke. The stochastic finite element method in structural reliability. *Probabilistic Engineering Mechanics*, 3(2):83–91, 1988.

[6] Dian-Qing Li, Te Xiao, Zi-Jun Cao, Chuang-Bing Zhou, and Li-Min Zhang. Enhancement of random finite element method in reliability analysis and risk assessment of soil slopes using subset simulation. *Landslides*, pages 1–11, 2015.

[7] F. Taucer, E. Spacone, and F. Filippou. A fiber beam-column element for seismic response analysis of reinforced concrete structures. Technical Report UCB/EERC 91/17, Earthquake Engineering Research Center, Univ. of California, Berkeley, 1992.

[8] S. Triantafyllou and V. Koumousis. Bouc-wen type hysteretic plane stress element. *Journal of Engineering Mechanics*, 138(3):235–246, 2012.

[9] D. Rabinovich, D. Givoli, and S. Vigdergauz. Xfem-based crack detection scheme using a genetic algorithm. *International Journal for Numerical Methods in Engineering*, 71(9):1051–1080, 2007.

[10] H. Waisman, E. Chatzi, and S. Smyth. Detection and quantification of flaws in structures by the extended finite element method and genetic algorithms. *International Journal for Numerical Methods in Engineering*, 82(3):303–328, 2010.

[11] L. Pichler, A. Gallina, T. Uhl, and L.A. Bergman. A meta-modeling technique for the natural frequencies based on the approximation of the characteristic polynomial. *Computers and Structures*, 102-103:108–116, July 2012.

[12] S. Gholizadeh and E. Salajegheh. Optimal design of structures subjected to time history loading by swarm intelligence and an advanced metamodel. *Computer Methods in Applied Mechanics and Engineering*, 198:2936–2949, 2009.

[13] A.C. Antoulas. *Approximation of Large-Scale Dynamical Systems*. Society for Industrial and Applied Mathematics, Philadelphia, USA, 2005.

[14] D. de Klerk, D.J. Rixen, and S.N. Voormeeren. General framework for dynamic substructuring: History, review, and classification of techniques. *AIAA Journal*, 46(5):1169–1181, 2008.

[15] H. Van Der Auweraer, J. Anthonis, S. De Bruyne, and J. Leuridan. Virtual engineering at work: The challenges for designing mechatronic products. *Engineering with Computers*, 29(3):389–408, 2013.

[16] D. Giagopulos and S. Natsiavas. Hybrid (numerical-experimental) modeling of complex structures with linear and nonlinear components. *Nonlinear Dynamics*, 47(1-3):193–217, 2007.

[17] O.S. Bursi and D. Wagg, editors. *Modern Testing Techniques for Structural Systems*. Springer, Vienna, Austria, 2008.

[18] S. Yesilyurta and A. Patera. Surrogates for numerical simulations; optimization of eddy-promoter heat exchangers. *Computer Methods in Applied Mechanics and Engineering*, 121(1-4):231–257, 1995.

[19] F.A. Diazdelao, S. Adhikari, E.I. Saavedra Flores, and M.I. Friswell. Stochastic structural dynamic analysis using Bayesian emulators. *Computers & Structures*, 120:24–32, 2013.

[20] M.D. Spiridonakos and E.N. Chatzi. Metamodeling of dynamic nonlinear structural systems through polynomial chaos {NARX} models. *Computers & Structures*, 157:99 – 113, 2015.

[21] M.D. Spiridonakos and E.N Chatzi. Metamodeling of structural systems with parametric uncertainty subject to stochastic dynamic excitation. *Earthquakes and Structures/ An International Journal for Earthquake Engineering & Earthquake Effects on Structures*, 8(4):915–934, 2015. Special Issue on Structural Identification and Monitoring with Dynamic Data.

[22] M.D. Spiridonakos and S.D. Fassois. Adaptable functional series {TARMA} models for non-stationary signal representation and their application to mechanical random vibration modeling. *Signal Processing*, 96, Part A:63 – 79, 2014.

[23] C. de Boor. *A Practical Guide to Splines*. Springer-Verlag, Revised edition, 2001.

[24] M.D. Spiridonakos, V.K. Dertimanis, and E.N. Chatzi. Estimation of data-driven polynomial chaos using hybrid evolution strategies. In Y. Tsompanakis, J. Kruis, and B.H.V. Topping, editors, *Proceedings of the Fourth International Conference on Soft Computing Technology in Civil, Structural and Environmental Engineering*, Stirlingshire, UK, 2015. Civil-Comp Press. Paper 24.

ECCOMAS Congress 2016
VII European Congress on Computational Methods in Applied Sciences and Engineering
M. Papadrakakis, V. Papadopoulos, G. Stefanou, V. Plevris (eds.)
Crete Island, Greece, 5–10 June 2016

DYNAMICS OF MULTIBODY SYSTEMS SUBJECT TO UNILATERAL MOTION CONSTRAINTS USING A NEW NUMERICAL ALGORITHM FOR CONTACT DETECTION

Antonios Pournaras [1], **Fotios Karaoulanis** [1], **and Sotirios Natsiavas** [1]

[1]Department of Mechanical Engineering
Aristotle University
54 124 Thessaloniki, Greece

e-mail: anpourna@gmail.com, fotios.karaoulanis @gmail.com, natsiava@auth.gr

Keywords: Collision Detection, Unilateral Contact, Friction, Multibody Dynamics, Computational Methods.

Abstract. *In this work, some new results are presented on the dynamics of multibody mechanical systems involving contact and friction. The main contribution refers to the development of a new, systematic and accurate method for detecting contact among the components of the system. For simple geometries, this task is achieved by employing analytical means. For systems with components involving complex geometric shapes a more involved numerical methodology is developed. In both cases, once contact is detected, the common normal vector and the penetration depth is also calculated, leading to determination of the contact force and moment arising between the contacting bodies. This information is then passed to a solver, providing the full dynamic response of the system. The validity and numerical efficiency of the methodology developed is first demonstrated by considering a number of examples with relatively small geometric complexity but large traditional value and interesting dynamic response. Some new results are obtained on the dynamics of these systems. Finally, the same methodology is also tested and found to give more realistic results in more complicated mechanical applications.*

1. INTRODUCTION

Accurate and efficient prediction of dynamics of a multibody system subject to unilateral constraints is necessary in a large number of modern engineering applications [1-4]. This prediction is based heavily on suitable algorithms, leading to a fast and accurate prediction of the contact points and the forces developed there during motion. As a result, there is a continuous effort to improve the available techniques in both the contact detection and the prediction of the overall dynamics, as reflected by the vast amount of the literature devoted to the subject. The present research work belongs to this general category of investigations.

In general, the contact detection methods rely heavily on the type of geometric modeling. There are two major categories of geometric models employed currently, the polygonal and the non-polygonal. According to the first category, a solid body is divided into polygon soups (the solid is represented by a set of connected triangles) and conventional polyhedra (the geometry is represented with a polyhedron). These polyhedra may be convex or non-convex. In the category of the non-polygonal models, the body is divided into constructive solid geometry, implicit surfaces and parametric surfaces. Using the constructive solid geometry method, one can create objects from basic primitives such as spheres, blocks, cones and others, by combining them with set theoretical operations. The contact detection methods developed in the present research work use conventional convex polyhedra and basic primitives. These methods have found wide application in many diverse areas such as robotic simulations and computer games [5-8].

In particular, a two step approach has been developed in this work for the contact detection problem, referring to the computational problem of detecting intersection of two or more rigid bodies. In brief, a broad phase detection is considered first, which is typically a computationally efficient operation that yields pairs of objects that may intersect. This involves either the bounding volume approach (more specifically the axis aligned bounding boxes (AABB) for the cases of simple primitives) or the more elaborate approach of an AABB tree for the cases where a triamesh construction of a surface is involved. Next, a narrow phase detection is considered, where the individual pairs of bodies identified in the previous strep as potentially intersecting are checked in a more elaborate manner. This includes simple analytical relations (as in the case of sphere to sphere or sphere to box) or more complex approaches for the general convex polytope cases. In the latter case, intersection is tested using the Gilbert-Johnson-Keerthi's algorithm, which relies on support functions to measure the shortest directed distance for the two bodies of interest by creating and iteratively updating a simplex inside the Minkowski difference. As soon as contact is detected, the corresponding contact response is resolved. This includes evaluation of the penetration depth and the contact normal as well as identification of the contact manifold. For the non trivial cases, the penetration depth and the contact normal are resolved by employing the expanding polytope algorithm. According to this algorithm, a polytope is created inside the Minkowski difference and is iteratively expanded until an edge of the Minkowski difference is hit, thereby yielding the penetration depth and the contact normal vector. Finally, for the non trivial cases a clipping algorithm is used, where the two objects are clipped in the direction of the contact normal generating the contact manifold. The geometric center of the contact manifold is assumed to be the contact point.

In the present paper, a collection of contact detection methods between bodies of specific shape are presented. This includes a two part combination of canonical shapes, like a sphere, an orthogonal parallelepiped, an ellipsoid, a conical frustum and a triangle. The algorithms used are analytical in some cases and numerical in others. In all cases, the algorithm comprises of three parts. At first, it is determined whether there is contact between two bodies. Then, the contact point, the common normal vector and the penetration depth are calculated. Finally, the contact force and moment are applied on both bodies taking into account the penetration depth,

the relative velocities of the bodies and the contact point. The last part of the algorithm is the same for all the above cases. The first two parts are different for each case and they are presented thoroughly in Sections 2 and 3 below.

Employing the aforementioned contact detection algorithm, a number of characteristic example problems was solved by using existing numerical codes for predicting the dynamic response [9, 10]. The first set of examples chosen are of academic interest and well-known in previous literature [4, 11-17]. This includes the rattleback, the Euler disk, the sphere on a turntable, the tippe–top and the woodpecker toy. A selected set of numerical results are first presented for these systems, throwing some new light into special features of their dynamics, which were not examined before. In addition, results for a more involved mechanical system [18-20], taken from an industrial application, are also obtained by using the same methodology and presented.

The organization of this paper is as follows. First, in Section 2, some simple cases of contact detection are briefly summarized. In particular, these cases refer to contact of bodies with a canonical geometric shape, which can be solved in an analytical manner,. Then, in Section 3, a general contact detection methodology is presented, referring to bodies with arbitrary geometrical shapes. Next, in Section 4 some numerical results are presented for two selected mechanical systems. Finally, the most important findings of this work are summarized in the last section.

2. CONTACT DETECTION BETWEEN BODIES OF CANONICAL SHAPE

In the present section, a collection of results on contact detection between bodies with a specific canonical shape are presented. These shape combinations include the following: sphere to sphere, sphere to orthogonal parallelepiped (or simply box), sphere to ellipsoid, sphere to conical frustum and sphere to triangle.

2.1 Sphere to Sphere

This case is trivial. Let $\mathbf{c}_1$ and $\mathbf{c}_2$ be the position vectors of the two spheres' centers, while r_1 and r_2 are the corresponding radii. Then, the two spheres intersect when the distance between their centers is less than or equal to the sum of the radii. This means that $\|\mathbf{c}_1-\mathbf{c}_2\| \leq r_1+r_2$. In addition, the penetration depth is $d = (r_1+r_2) - \|\mathbf{c}_1-\mathbf{c}_2\|$, as shown in Fig. 1. Moreover, the contact point $\mathbf{x}$ is defined by the intersection of the line that connects the centers and an arbitrarily chosen sphere. The common normal vector $\mathbf{n}$ defines the line of impact and its direction is defined from the contact point to the sphere's center which was arbitrarily chosen.

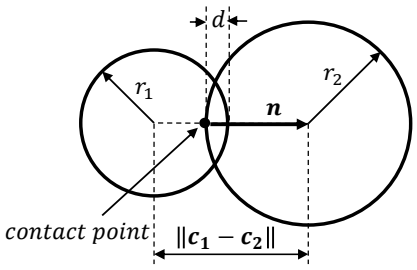

Fig. 1. Geometry of sphere to sphere contact.

2.2 Sphere to box

The intersection test is done by computing the point in the parallelepiped (or box, for brevity) which is closest to the sphere. Let the box be centered at the origin and aligned with the axes,

as shown in Fig. 2. The dimensions of the box in the x, y and z axes are $2n_1$, $2n_2$ and $2n_3$, respectively. The sphere's center is at $\mathbf{c} = (c_1 , c_2 , c_3)$. The point in the box closest to the sphere's center is given by

$$\mathbf{x} = (\text{clamp}(c_1,-n_1,n_1),\text{clamp}(c_2,-n_2,n_2),\text{clamp}(c_3,-n_3,n_3)) \quad (1)$$

where

$$\text{clamp}(c,a,b)=\begin{cases} a, \text{ if } c<a \\ b, \text{ if } c>b \\ c, \text{ otherwise} \end{cases} \quad (2)$$

The sphere intersects the box if the point **x** is contained in the sphere $\|\mathbf{x}-\mathbf{c}\| \leq r$, where r is the sphere's radius. The contact point is **x**. The penetration depth is given by $d = r - \|\mathbf{x}-\mathbf{c}\|$. The common normal vector **n** is a vector starting from the contact point **x** and ending at the sphere's center **c**.

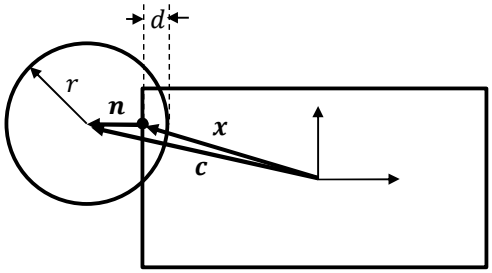

Fig. 2. Geometry of sphere to orthogonal parallelepiped contact.

2.3 Sphere to ellipsoid

For testing the intersection of a sphere with radius R and an ellipsoid with semi–principal axes a, b and c, the point of the ellipsoid closest to the sphere is calculated. Let the axes' origin be centered at the ellipsoid center, as depicted in Fig. 3. Also, let $\mathbf{p} = (p_x , p_y, p_z)$ be the sphere's center and $\mathbf{r} = (x, y, z)$ be the point in the ellipsoid closest to the sphere. In order to determine this point, the following constrained minimization problem needs to be solved

$$\min \ (p_x - x)^2 + \left(p_y - y\right)^2 + (p_z - z)^2 \quad (3)$$

such that

$$\left(\frac{x}{a}\right)^2 + \left(\frac{y}{b}\right)^2 + \left(\frac{z}{c}\right)^2 - 1 = 0. \quad (4)$$

For this, a Lagrange multiplier λ and a function L(x,y,z,λ) are introduced by

$$L(x, y, z, \lambda) = (p_x - x)^2 + \left(p_y - y\right)^2 + (p_z - z)^2 + \lambda\left(\left(\frac{x}{a}\right)^2 + \left(\frac{y}{b}\right)^2 + \left(\frac{z}{c}\right)^2 - 1\right). \quad (5)$$

Then, the minimum of the above function is calculated by solving the following equations

$$\frac{\partial L}{\partial x} = 0, \frac{\partial L}{\partial y} = 0, \frac{\partial L}{\partial z} = 0, \frac{\partial L}{\partial \lambda} = 0 \quad (6)$$

The resulting set of nonlinear algebraic equations is solved with the Newton–Raphson method.

The sphere intersects the ellipsoid if the point **r** is contained in the sphere $\|\mathbf{r}-\mathbf{p}\| \leq R$. The contact point is **r**. The penetration depth is given by $d = R - \|\mathbf{r}-\mathbf{p}\|$. The common normal **n** vector is a vector starting from the contact point **r** and ending to the sphere's center **p**.

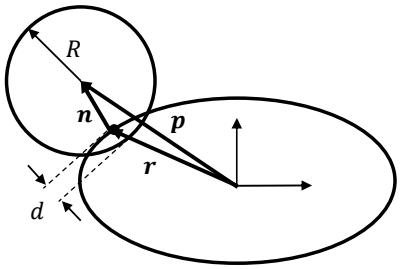

Fig. 3. Geometry of sphere to ellipsoid contact.

2.4 Sphere to conical frustum

This case leads to an axisymmetric problem with axis being the frustum's axis, as shown in Fig. 4. By taking the plane which is defined by the frustum's axis and the sphere's center, the problem becomes equivalent to determining the intersection between a trapezoid and a circle. The coordinate system origin is placed at the center of the bottom face of the frustum. For testing the intersection, a point **x** in the trapezoid which is closest to the sphere is calculated. The space outside the trapezoid is divided into five sections and according to which section the sphere's center **p** belongs to, a different analytical method of calculating the closest point is applied. Then, the sphere intersects the frustum if the point **x** is contained within the sphere $\|\mathbf{x}-\mathbf{c}\| \leq r$, where r is the sphere's radius. The contact point is **x**. The penetration depth is given by $d = r - \|\mathbf{x}-\mathbf{c}\|$. The common normal vector **n** is a vector starting from the contact point **x** and ending to the sphere's center **c**.

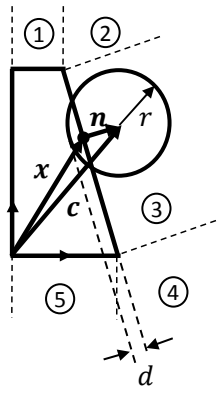

Fig. 4. Geometry of sphere to conical frustum contact.

2.5 Sphere to triangle

The intersection test is done by computing the point **x** in the triangle which is closest to the sphere. Let the coordinate system origin be placed at the center of the sphere, as shown in Fig. 5. Let $\mathbf{p}_0$, $\mathbf{p}_1$ and $\mathbf{p}_2$ be the vertices of the triangle. The sphere's center is projected on the triangle's plane. This plane is divided into seven sections and according to which section the sphere's projected center belongs to, a different analytical method of calculating the closest point is applied. Then, the sphere intersects the triangle if the point **x** is contained in the sphere

$||\mathbf{x}|| \leq r$, where r is the sphere's radius. The contact point is **x**. The penetration depth is given by $d = r - ||\mathbf{x}||$. The common normal vector **n** is a vector starting from the contact point **x** and ending to the sphere's center.

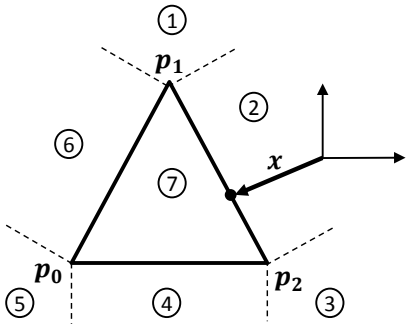

Fig. 5. Geometry of sphere to triangle contact.

3. CONTACT DETECTION BETWEEN BODIES OF GENERAL SHAPE

For the general case of two convex polytopes, the contact detection problem is resolved by following the algorithmic treatment presented in this section. The computational problem is assumed to be defined given a pair of convex shapes and the spatial relation between them. The above treatment is currently employed for cases including the rectangular cuboid (or simply box), the conical frustum and the ellipsoid, giving a total of six different contact combinations. The proposed approach is split into the following three steps.

1. The *intersection testing*, which refers to a Boolean query that is true if and only if the intersection of two shapes is nonempty [8]. The intersection is tested within this work, using the Gilbert-Johnson-Keerthi's algorithm [5, 6].
2. The *evaluation of the penetration depth and the contact normal*. As soon as the intersection testing query yields true, the corresponding penetration depth and the contact normal are evaluated using the Expanding Polytope Algorithm (EPA) [5]. The penetration depth and the contact normal can then be used for the estimation of the corresponding contact force/moment vector.
3. The generation of the contact manifold, i.e., the set of contacting points [6], which can be used for the contact force/moment vector application. An implementation based on clipping is proposed for all cases except those employing an ellipsoid. For the latter, the geometric properties of the ellipsoid are exploited.

3.1 Intersection testing

The intersection is tested using the Gilbert-Johnson-Keerthi's (GJK) algorithm. GJK is an iterative method, initially proposed for computing the distance between complex objects in three-dimensional space [5]. It can, however, be also employed to solve different proximity queries including ones that are of interest in the collision detection problem. GJK is quite popular in this field, mainly because it is very versatile (only a set of vertices describing the convex polytope can be used) and is extremely efficient [6].

Overall, GJK relies on support functions to measure the shortest directed distance between the two convex polytopes of interest, say A and B. It does so, by creating and iteratively updating a simplex inside the Minkowski difference set A–B, with $A–B=\{\mathbf{a}–\mathbf{b} \mid \mathbf{a} \in A, \mathbf{b} \in B\}$. A simplex is defined as the convex hull of an affinely independent set of vertices. Up to four vertices can be employed, so a simplex can be a single point, a line, a triangle or a tetrahedron.

In each iteration, the updated simplex lies closer to the origin than the previous one. When the origin of the Minkowski difference is included in the simplex, the two shapes are determined to intersect.

```
function EPA:
  D ← arbitrary vector
  v ← A.Support(d) – B.Support(-d)
  W ←{v}
  do:
    w ← A.Support(v) – B.Support(-v)
    if v·w > 0:
      return false
    W ←ProjectOrigin(W ∪ v)
  until |W| = 4 or ||v|| < tol
  return true
```

Table 1. The basic steps of the GJK algorithm

In the above, `Support` provides the support mapping

$$S_A(\boldsymbol{v}) = \{\mathbf{p}: \max\{\boldsymbol{v}\cdot\boldsymbol{a}: \boldsymbol{a} \in A = \boldsymbol{v}\cdot\boldsymbol{p}, \boldsymbol{p} \in A\}\}.$$

Given a direction $\boldsymbol{v}$ this returns the points $\mathbf{p}$ in the shape A that would be the first to come in contact with a plane with normal $\boldsymbol{v}$ that moves from infinitely far away towards the center of A. Furthermore, `ProjectOrigin` returns the point on a point (obvious solution), line or triangle which is the closest to the origin.

3.2 Penetration depth and contact normal

The penetration depth and the contact normal are found using the Expanding Polytope Algorithm (EPA). EPA is an accurate algorithm used for computing the penetration depth between a pair of shapes A and B, having a non-empty intersection. Similar to the GJK, EPA employs only the support mappings of the corresponding shapes, further contributing to the versatility of the overall approach.

Starting point for the EPA is a polytope that contains the origin of the Minkowski difference. The simplex provided by GJK is used to generate the polytope required. The GJK may consist of only a point, a line or a triangle. In this case, proper initialization of the polytope is performed, following the approach described in [6].

As soon as a valid simplex is build inside the Minkowski difference set, then this is iteratively expanded into a convex polytope. The algorithm proceeds in each step so that the face closest to the origin is the one that is expanded. The iterations stop when an edge of the Minkowski difference is recovered during expansion (within some numerical accuracy), thereby yielding the penetration depth (and the corresponding normal vector), as equal to the distance from the origin to this face.

```
function EPA:
  P ← A convex polytope containing the origin
  Q ← ∅
  for each face f in P:
    e ← construct(f)
    if e.closest_internal():
      Q.push(e)
```

```
    μ ← infinity
    do:
      e = Q.pop()
      if not e.obsolete:
        v ← e.v
        w ← A.Support(v) – B.Support(-v)
        μ ← min(μ, (v·w)² / ||v||²)
        close_enough ← μ ≤ (1 + tol)²||v||²
        if not close_enough:
          e.obsolete = true
          E ← ∅
          for i ← 0, 1, 2:
            sihlouette(e.adjᵢ, e.jᵢ, w, E)
            for se, i ∈ E:
              ne ← construct(se.yᵢ⊕₁, se.yᵢ, w)
              if ne.affinely_dependent:
                return ||v||
              if ne.closest_internal()
                 and ||v||²≤|ne· v|≤μ:
                   Q.push(ne)
    until close_enough or Q.empty() or ||Q.pop().v||² > μ
    return ||v||
```

Table 2. The algorithm in [6]

In the above `Q` is a priority list and μ is an upper bound for the squared penetration depth. Entry is a structure for the polytope face, that holds the vertices (`y`), the adjacent entries (`adj`), the indices of the corresponding adjoining edges (`j`) and `obsolete` which is a boolean that identifies if this face has become obsolete during a previous iteration. Furthermore $\oplus$ denotes the addition modulo 3.

Once an entry `e` that contains the point closest to the origin, point `w` is calculated as described above. The front side of entry `e` can always be seen from the `w`, so that `e` is marked `obsolete`. Then, the polytope is recursively traversed starting with each entry adjacent to `e`. All the entries that can be seen from e are further marked as `obsolete`. This procedure is provided by function `sihlouette`, which is based on a recursive flood filling algorithm.

```
function sihlouette(e, i, w, E):
  if not e.obsolete:
    if e.v·w < ||e.v||²:
      E ← {E, (e, i)}
    else:
      e.obsolete ← true
      sihlouette(e.adji⊕1, e.ji⊕1, w, E)
      sihlouette(e.adji⊕2, e.ji⊕2, w, E)
```

Table 3. Pseudocode for function `sihlouette`

3.3 Contact manifold generation

The contact manifold, which usually is further reduced to a single point where the contact force is to be applied, is generated using a clipping algorithm. For this case, the faces of the shapes A and B should be explicitly defined. This is a major difference from the algorithmic

treatment described so far, that required only the corresponding support mappings. Furthermore, this procedure may introduce accuracy issues when the shape is not defined from flat faces only. This is the reason why the contact point in the ellipsoid is not generated by this method, but by exploiting its geometric property of the normal uniqueness.

As a first step, the reference face is identified, which is the face normal to the contact vector (or its opposite), as returned by the EPA. An incident face is then identified on the other shape, which is the one that is closer to the opposite of the vector used for the reference face. Then, a set of clippings is performed between the incident face and the faces that are adjacent to the reference one. Each clipping reduces the size of the contact manifold, which is initially set equal to the incident face. A final clipping is performed in the remaining area by the reference face.

```
function clipping:
  reference ← A.find_reference(v)
  incidence ← B.find_incidence(v)
  if not reference:
    reference ← B.find_reference(-v)
    incidence ← A.find_incidence(-v)
  manifold ← incidence.vertices()
  for f ← reference.faces():
    manifold ← manifold.clip(f)
  manifold ← manifold.translate(||v||)
  manifold ← manifold.clip(reference)
```

Table 4. Pseudocode for the clipping function

The contact point can then be assumed as the geometrical center of the contact manifold.

4. NUMERICAL RESULTS

Employing the aforementioned contact detection algorithms, a number of characteristic example problems was solved by using an existing numerical codes for predicting the dynamic response [9]. The first example chosen is of academic interest and is known in literature as the woodpecker toy [15-17]. In addition, results for a more complex mechanical system, involving ball bearings, were also obtained by using the same methodology [18-20].

4.1 Results for the woodpecker toy

The woodpecker toy shown in Fig. 6 consists of a pole fixed to the ground, a sleeve, a torsional spring and a woodpecker. The sleeve and the woodpecker are connected with a revolute joint and a torsional spring. The hole in the sleeve is slightly larger than the diameter of the pole. The toy's response is heavily affected by friction and impact phenomena. The woodpecker moves down due to gravity with a pitching motion and impacts the pole while the sleeve acts as a jamming mechanism with the presence of friction. The system oscillates and may end up in a stable limit cycle.

The first scientific studies on the dynamics of this toy, based on application of non–smooth and contact mechanics theory, was presented in [15-17]. The model is planar and consists of three rigid bodies: the woodpecker, the sleeve and the pole. The sleeve's lateral movement is small so it is neglected. Another major assumption is that both the woodpecker and the sleeve rotate with small angle, so the gap functions are calculated with linearized kinematics.

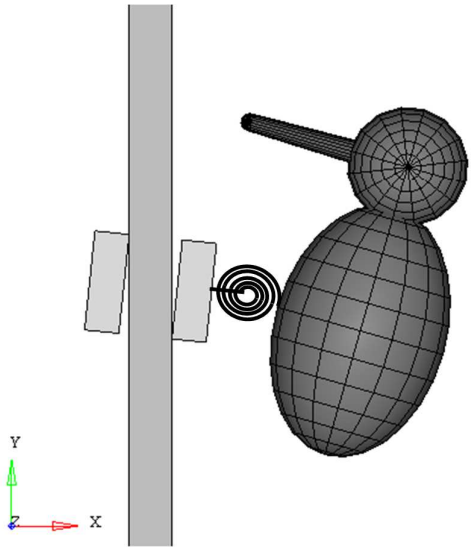

Fig. 6. The woodpecker toy.

In the present paper, the model is created using basic solids. Specifically, the pole is represented by an orthogonal parallelepiped, the sleeve by two orthogonal parallelepipeds, the body of the woodpecker by an ellipsoid, its head by a sphere, its beak by a conical frustum and a sphere at the tip (see Fig. 6). There exist also a revolute joint and a torsional spring between the sleeve and the woodpecker. Contact is taken into account between the beak's tip and the pole (sphere to box) and between the sleeve and the pole (box to box). Values for the geometry, masses, moments of inertia and contact parameters are taken from [16]. Here, the model is also planar. However, the sleeve's lateral movement is taken into account, although it does not make any significant difference. The major difference with [16] is that the rotations of both the sleeve and the woodpecker are not assumed to be small, hence the kinematics is nonlinear. The above assumptions are critical and play a significant role to the system's response. By examining the results of [5], it can be seen that the woodpecker's and sleeve's extremum angles are 30 and 6 degrees respectively. The woodpecker's rotation is far too large to be linearized, whereas the sleeve's angle just passes the limit.

Comparing the results obtained here with those presented in [16] it is concluded that the linearization based on small rotations influences the results especially in the woodpecker's angle where the upper and lower limits are slightly greater and smaller respectively (see Fig. 7a). Regarding the sleeve's angle there are no significant differences because for such an angle range the linearization is a good approximation (Fig. 7d). Similar bevahior is evident concerning the angular velocities. Examining these quantities, it is evident that a slight variation appears at the upper and lower limits for both the woodpecker and the sleeve (Figs. 7c and 7d).

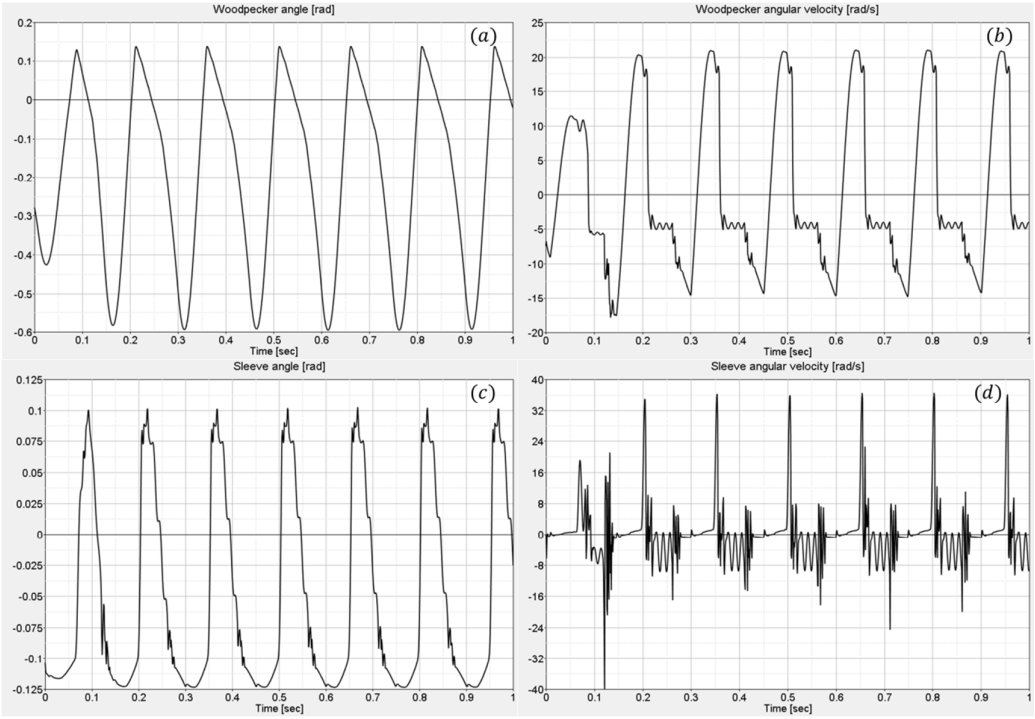

Fig. 7. Numerical results for the woodpecker toy. Time history of the woodpecker: (a) rocking angle, (b) angular speed, (c) sleave angle and (d) sleave angular speed.

4.2 Results for a mechanism with a rolling bearing

Dynamics of ball bearings has been studied from many different angles of view, including lubrication, wear, vibration and sound. In some cases, a multibody model was used. The most preferred modeling assumptions are the following: no slipping of the balls during rolling on the surface (the ball motion is defined by a kinematic constraint), no friction between the balls and the bearing's rings, planar motion and negligible mass of the balls [18, 19]. To investigate whether these assumptions are reasonable, development and consideration of more realistic models that remove the above assumptions is needed.

In the present paper, a model for a ball bearing (SKF BB1B420205) is first developed. Then, this is used in a crank-rod-slider mechanism to represent the revolute joint between the crank and the rod, as shown in Fig. 8a. Regarding the ball bearing modeling, the balls are modeled by eight spheres, while the inner and outer rings and the cage are modeled by triangle meshed solids (see Fig. 8b). Moreover, contact is enabled between each sphere and both rings, while sphere to sphere and inner to outer ring contact is not taken into account. Although contact between the cage and the balls could also be studied, it was choosen not to do it here because the loads arising between the cage and the balls are not significant. Another reason for this is that the model becomes much more complicated, resulting in additional computer simulation time with no significant gain. To prevent the balls from coming into contact, eight inline constraints are added between each ball's center and a specific coordinate system on the cage (see Fig. 8c). Concerning other major connections, the cage is connected to the inner ring's center with a revolute joint, the outer ring is fixed to the crank, while the inner ring is fixed to the rod. Values for the geometry, masses, moments of inertia and contact parameters are taken from [19]. The evaluation of the contact forces is based on Herzian contact deformation theory that

takes into account the geometry and the material properties. The methodology for calculating the stiffness values for the contact is described thoroughly in [20].

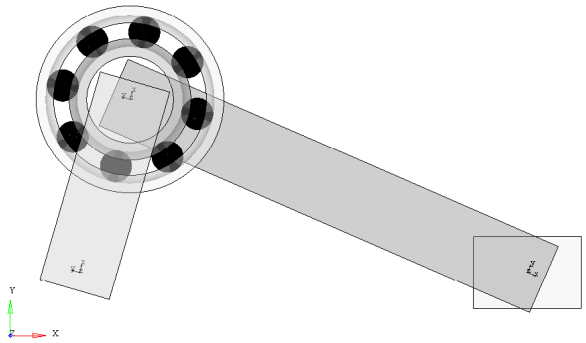

Fig. 8a. Mechanism

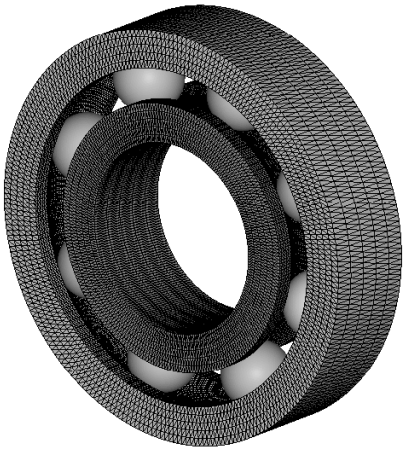

Fig. 8b. Ball bearing model

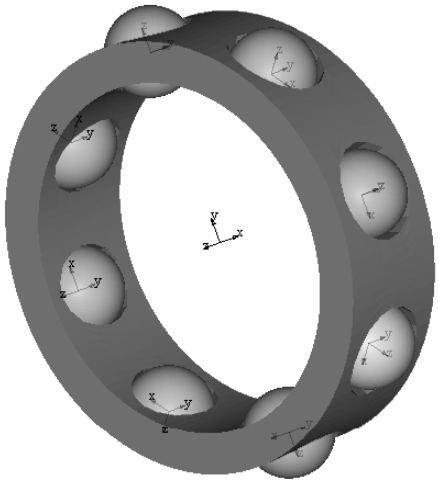

Fig. 8c. Cage model

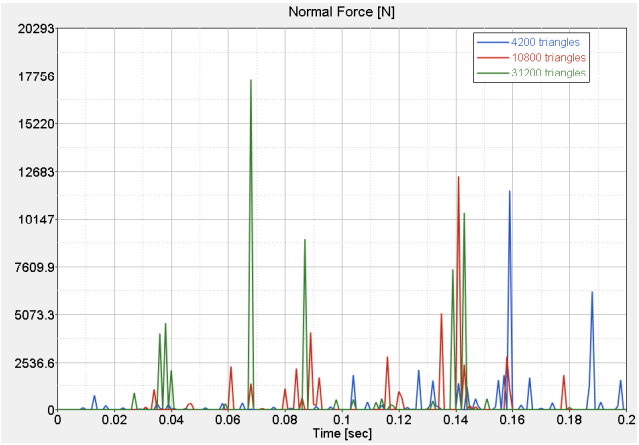

Fig. 8d. Normal force on a ball

By implementing the contact detection algorithm between sphere and triangle presented in Section 2, the mechanical model developed was simulated, assuming that the crank rotates with a constant angular speed of 300 rpm. In Fig. 8d is depicted the normal force acting from the outer ring to a ball for three different meshes. Although the maximum force is congruent with that presented in [19], the time history is completely different. This is believed to be due to the lack of friction in the model employed in [19], where the balls movement is induced by imposing a kinematic constraint, taking into account that the balls roll without sliding. In reality, this is not true and causes the balls to be at a different position.

5. SYNOPSIS

A new contact detection methodology was presented, leading to an accurate and numerically efficient determination of the dynamic response of a class of multibody engineering systems involving contacts and friction. The methodology developed allows solution to general

mechanical problems, without having to formulate the equations of motion and the gap functions in each case, separately. Furthermore, the new algorithm takes into account large relative rotations between two solid bodies and does not suffer from restrictions caused by kimenatic linearization. In particular, the contact detection algorithm between a sphere and a triangle allows to create more detailed and realistic models for ball bearings or any machine element involving contact between a sphere and a general surface (e.g., constant velocity joint). Furthermore, it allows incorporation of friction using either Amontons–Coulomb or even more sophisticated friction laws. Therefore, it is expected that this tool can prove usefull to engineers who want to study various phenomena arising in complex mechanical systems with components involving contact and friction. Some of these advantages were illustrated in this work by presenting results for the classical woodpecker toy and a more complex systems involving ball bearings.

REFERENCES

[1] M. Geradin, A. Cardona, Flexible Multibody Dynamics: A Finite Element Approach, John Wiley & Sons, New York, 2001.

[2] O.A. Bauchau, Flexible Multibody Dynamics, Springer Science+Business Media B.V., London, 2011.

[3] B. Brogliato, Nonsmooth Mechanics (2nd edition), Springer-Verlag, London, 1999.

[4] C. Glocker, Set-Valued Force Laws, Dynamics of Non-Smooth Systems, Springer, Berlin, 2001.

[5] E. Gilbert, D. Johnson, S. Keerthi, A fast procedure for computing the distance between complex objects in three-dimensional space, IEEE Journal of Robotics and Automation 4 (1988) 193–203.

[6] G. van den Bergen, Collision Detection in Interactive 3D Environments, Morgan Kaufmann Publishers,San Francisco, 2004.

[7] C. Ericson, Real-Time Collision Detection, Morgan Kaufmann Publishers,San Francisco, 2005.

[8] L. Olvång. Real-Time Collision Detection with Implicit Objects, Department of Information Technology, Uppsala University, Sweeden, 2010.

[9] MotionSolve v11.0, User Guide, Altair Engineering Inc., Irvine, California, USA.

[10] MSC ADAMS, User Guide, MSC Software Corporation, California, USA.

[11] C. Studer, Numerics of Unilateral Contacts and Friction, Springer-Verlag, Berlin, 2009.

[12] R.I. Leine, C. Glocker, A set-valued force law for spatial Coulomb-Contensou friction, European Journal of Mechanics A/Solids 22 (2003) 193-216.

[13] K. Weltner, Stable circular orbits of freely moving balls on rotating discs, Am. J. Phys. 47 (1979), 984-986.

[14] F. Pfeiffer, C. Glocker, Multibody Dynamics with Unilateral Contacts, Wiley-VCH, Weinheim, 2004.

[15] C. Glocker, C. Studer, Formulation and preparation for numerical evaluation of linear complementarity systems in dynamics, Multibody System Dynamics 13 (2005) 447-463.

[16] R.I. Leine, D.H. van Campen, C. Glocker, Nonlinear dynamics and modeling of various wooden toys with impact and friction, Journal of Vibration and Control 9 (2003) 25-78.

[17] P. Kessler, O. M. O' Reilly, The ringing of Euler's disk. Regural and Chaotic Dynamics 7 (2002) 49-60.

[18] V.N. Patel, N. Tandon, R.K. Pandey, A dynamic model for vibration studies of deep groove ball bearings considering single and multiple defects in races. Journal of Tribology 132 (2010) 1193-1201.

[19] L.X. Xu, Y.H. Yang, Y.G. Li, C.N. Li, S.Y. Wang, Modeling and analysis of planar multibody systems containing deep groove ball bearing with clearance, Mechanism and Machine Theory 56 (2012) 69-88.

[20] T.A. Harris, Rolling Bearing Analysis, Wiley, New York, 2001.

ECCOMAS Congress 2016
VII European Congress on Computational Methods in Applied Sciences and Engineering
M. Papadrakakis, V. Papadopoulos, G. Stefanou, V. Plevris (eds.)
Crete Island, Greece, 5–10 June 2016

EQUATIONS OF MOTION FOR MECHANICAL SYSTEMS SUBJECT TO ACATASTATIC CONSTRAINTS

Elias Paraskevopoulos[1], **Sotirios Natsiavas**[2]

[1] Department of Mechanical Engineering, Aristotle University
Thessaloniki, Greece
e-mail: eapcivil@gmail.com

[2] Department of Mechanical Engineering, Aristotle University
Thessaloniki, Greece
e-mail: natsiava@auth.gr

Keywords: Analytical dynamics; Newton's law of motion; Rheonomic constraint; Acatastatic constraint; Foliated manifold; Scleronomic manifold.

Abstract. *This study is focused on a class of discrete mechanical systems subject to equality motion constraints involving time and acatastatic terms. In addition, their original configuration manifold possesses time dependent geometric properties. The emphasis is placed on a proper application of Newton's law of motion. A first step is to consider the corresponding event manifold by adding time to the set of coordinates and then determine its geometric properties. Next, the way of introducing time dependence in these properties through a coordinate transformation in the event manifold or the motion constraints is also investigated. Also, foliation theory is used to clarify some key concepts and provide an accurate definition of a scleronomic manifold, leading to a set of coordinate invariant conditions. The analysis is completed by an appropriate set of equations of motion on the original configuration manifold, appearing as a system of second order ordinary differential equations. Finally, the analytical findings are enhanced and illustrated further by considering selected examples.*

1 INTRODUCTION

Among the many subjects of analytical dynamics, a central place is occupied by those referring to the derivation of the equations of motion of systems subject to equality constraints (e.g., [8, 21, 23]). Over the last decades, it has become apparent that many of the theoretical questions in this area of dynamics can be answered in an illustrative and complete way by employing fundamental concepts of differential geometry [4, 17, 18]. This in turn provides a stronger foundation in solving difficult engineering problems by employing new, more accurate and robust numerical techniques (e.g., [2, 6, 11]). Based on these observations, the main objective of this work is to use such concepts in order to treat a class of mechanical systems. These systems are described by configuration manifolds possessing time dependent geometric properties (i.e., metric and connection) and are subject to equality motion constraints involving an explicit time dependence and acatastatic terms. Besides providing a new and clear interpretation of the key concepts, the theoretic framework chosen allows a systematic derivation of the equations of motion for the class of systems examined.

The present study is an extension of recent work of the authors on scleronomic systems [15, 19]. Again, the emphasis is put on explaining several demanding theoretical aspects, which are of keen interest to the engineering community. In addition, the main philosophical approach adopted is that the safest and deepest principle of Mechanics is Newton's law of motion [7, 9]. Specifically, the new contributions of this work can be summarized as follows. First, the central issue is the consistent application of Newton's law to the class of mechanical systems examined. Due to the presence of time in the properties of the configuration manifold, the need to express Newton's law in an invariant form leads naturally to its application to the event configuration manifold of the system [12, 23]. This step is performed first in a geometrically consistent manner. Moreover, another issue clarified in this work is the way time effects are introduced into the properties of a configuration manifold in an explicit manner. It is shown that these effects appear either by performing a time dependent transformation in the event manifold or by enforcing additional time dependent motion constraints. In addition, it is demonstrated that the former effects are in fact removable. Furthermore, the geometrical picture built by employing the classical engineering approach is enhanced in a remarkable way by utilizing some ideas of foliation theory [3, 14, 22]. Among other things, this theory provides a coordinate invariant way of stating the conditions for a configuration manifold to be scleronomic, even though its geometric properties may exhibit a spurious time dependence. Another important new contribution of the present work is the derivation of the equations of motion for the class of systems examined as a set of second order ordinary differential equations in the original configuration manifold. This presents certain advantages when compared to classical approaches leading to a set of differential algebraic equations, instead. It also exhibits better characteristics than previous methods leading to sets of ordinary differential equations through elimination of motion constraints or Lagrange multipliers [2, 15]. Finally, for the special case of scleronomic systems, the equations of motion derived are shown to become identical with a similar set of equations obtained earlier [15].

The organization of this paper is as follows. First, some useful concepts of differential geometry are briefly summarized in Section 2. In Section 3, the idea of the event manifold is employed and its geometric properties are set up. Then, the equations of motion are derived, firstly on the event and subsequently on the configuration manifold. In Section 4 are discussed effects caused by a special change of coordinates in the event manifold. Likewise, in Section 5 is investigated the effect caused by the presence of time dependent and acatastatic terms in the motion constraints. The results of these effects are identified and separated in Section 6, where a set of scleronomicity conditions is presented by employing basic ideas of

foliation theory on manifolds. Then, the equations of motion for the general class of systems examined are derived and presented in Section 7. Finally, results are presented for two mechanical examples, illustrating basic features of the class of systems examined.

2 SOME GEOMETRIC PRELIMINARIES

This work focuses on the dynamics of mechanical systems, whose spatial configuration can be determined at any time by a finite set of local coordinates, say $q^1,\ldots,q^n$ [12, 21]. The motion of such a system can be represented by the motion of a fictitious point p moving along a curve $\gamma=\gamma(s)$ on an n-dimensional manifold M, the configuration space of the system [23]. Then, if φ is a coordinate map acting from a neighborhood of point p to the classical space $\mathbb{R}^n$, the coordinates of p are

$$q=\varphi(p), \tag{1}$$

with $q=(q^1,\ldots,q^n)$. Usually, the parameter s coincides with time t and the quantity $\underline{v}=d\gamma/dt$ represents the velocity vector at p. This vector is tangent to γ and belongs to an n-dimensional vector space T_pM, the tangent space of the manifold at p [4, 10], with components $v^i=\dot{q}^i$ in the holonomic basis $\mathfrak{B}_g=\{\underline{g}_1 \ \ldots \ \underline{g}_n\}$ [5]. Adopting the usual summation convention for repeated indices [24], the velocity vector can be written as

$$\underline{v}=\sum_{i=1}^{n} v^i \underline{g}_i = v^i \underline{g}_i .$$

In general, any element $\underline{u}$ of the vector space T_pM can be expressed in the form $\underline{u}=u^i \underline{e}_i$, where $\mathfrak{B}_e=\{\underline{e}_1 \ \ldots \ \underline{e}_n\}$ is an arbitrary basis of T_pM. Also, one needs often to establish a relation between two different bases, say between $\mathfrak{B}_g$ and $\mathfrak{B}_e$, through equations of the form

$$\underline{e}_i=A_i^j \underline{g}_j \quad \text{or} \quad \underline{g}_i=B_i^j \underline{e}_j \quad (i,j=1,\ldots,n), \tag{2}$$

where A_i^j and B_i^j are elements of $n\times n$ matrices, satisfying the conditions

$$A_i^j B_k^i = A_k^i B_i^j = \delta_k^j , \tag{3}$$

which involve Kronecker's delta δ_k^j [17]. Moreover, any basis of T_pM is characterized by its structure constants c_{jk}^i, defined through the Lie bracket in the form

$$[\underline{e}_j,\underline{e}_k]=c_{jk}^i \underline{e}_i .$$

A complete description of the motion of a dynamical system can be achieved by introducing the dual space to T_pM at any point of the manifold, denoted by T_p^*M. Its elements are called convectors. Then, for any vector $\underline{u}$, a covector $\underset{\sim}{u}^*$ may be found through the dual product. For example, to each basis $\mathfrak{B}_e$ of T_pM, a dual basis $\mathfrak{B}_e^*$ can be constructed for T_p^*M, with elements $\{\underset{\sim}{e}^i\}$ satisfying

$$\underset{\sim}{e}^i(\underline{e}_j)=\delta_j^i , \tag{4}$$

Apart from the set of points, a manifold used in dynamics should possess two additional geometrical objects. One of them is the metric tensor, with components in the basis $\mathfrak{B}_e^*$ given by

$$g_{ij} = \langle \underline{e}_i, \underline{e}_j \rangle \,, \tag{5}$$

where $\langle \cdot, \cdot \rangle$ denotes the inner product of the tangent space $T_p M$. This provides a dual product by

$$\underset{\sim}{u}^*(\underline{w}) \equiv \langle \underline{u}, \underline{w} \rangle, \quad \forall \underline{w} \in T_p M \,. \tag{6}$$

If the components of the metric tensor are identified with those of mass matrix, through the kinetic energy, then the covector corresponding to the velocity vector $\underline{v}$ is the generalized momentum $\underset{\sim}{p}^*$.

Another geometrical tool which is essential in dynamics is the affine connection, represented by symbol ∇ . Its components Λ^i_{jk} in a basis $\mathfrak{B}_e$ of space $T_p M$, known as affinities, are defined by

$$\nabla_{\underline{e}_j} \underline{e}_k = \Lambda^i_{jk} \underline{e}_i \,. \tag{7}$$

Then, the covariant differential of a covector $\underset{\sim}{u}^*$ along a curve on M with tangent vector $\underline{v}$ is

$$\nabla_{\underline{v}} \underset{\sim}{u}^* = (u_{i,j} - \Lambda^{\ell}_{ji} u_{\ell}) v^j \underset{\sim}{e}^i \,, \tag{8}$$

with $u_{i,j} = \partial u_i / \partial q^j$. Then, M is a Newton manifold if determination of the true path of motion on M due to a given set of applied forces $\underset{\sim}{f}^*$ is based on application of Newton's second law with form

$$\nabla_{\underline{v}} \underset{\sim}{p}^* = \underset{\sim}{f}^* , \tag{9}$$

Next, consider a new manifold M_A, with a dimension m smaller than n, generated after imposing a set of motion constraints on M , which are eventually cast in the form

$$v^i = N^i_{\alpha} v^{\alpha} \quad (i = 1, \ldots, n \,;\; \alpha = 1, \ldots, m), \tag{10}$$

where $\underline{v}_A = v^{\alpha} \underline{e}_{\alpha}$ is a vector of $T_{p_A} M_A$ and $\underline{v} = v^i \underline{e}_i$ is an element of $T_p M$. Then, it was shown in a previous study that if the original manifold M is Newtonian, the new manifold M_A remains Newtonian, provided that the metric and connection on M_A satisfy the compatibility conditions

$$g_{\alpha\beta} = N^i_{\alpha} g_{ij} N^j_{\beta} \tag{11}$$

and

$$(\Lambda^{\lambda}_{\beta\alpha} g_{\lambda\gamma} - N^i_{\alpha,\gamma} N^j_{\beta} g_{ij} - N^i_{\alpha} N^j_{\beta} N^k_{\gamma} \Lambda^{\ell}_{ji} g_{\ell k}) v^{\beta} v^{\gamma} = 0 \,, \tag{12}$$

with $N^i_{\alpha,\gamma} = \partial N^i_{\alpha} / \partial q^{\gamma}$ [26]. Using Eq. (8), the last condition yields

$$\Lambda^{\lambda}_{\beta\alpha} = g^{\lambda\gamma} [N^j_{\beta} (N^i_{\alpha,\gamma} g_{ij} + N^i_{\alpha} N^k_{\gamma} \Lambda^{\ell}_{ji} g_{\ell k}) + \sigma_{\alpha\beta\gamma}] \,,$$

where $\sigma_{\alpha\beta\gamma} = -\sigma_{\alpha\gamma\beta}$ and the remaining part corresponds to what is known in the literature as "the metric compatibility condition" [4, 24].

3 GEOMETRIC PROPERTIES OF EVENT MANIFOLD - APPLICATION OF NEWTON'S LAW

For a mechanical system, the geometric properties of the configuration manifold M can be determined through enforcement of a set of constraints on the motion of a system of N unconstrained particles, taking place within an archetypal Euclidean manifold E^{3N}, with dimension $3N$ [9, 17]. When inertial Cartesian coordinates are used, the metric of this space involves only constant diagonal elements, while all the affinities vanish [19]. Furthermore, even when general curvilinear coordinates are used, the geometric properties of this manifold may depend on the position on the manifold but they do not depend on time explicitly. In this way, E^{3N} presents a raw model for a scleronomic manifold. Then, for a general scleronomic manifold M, it is true that

$$g_{ij} = g_{ij}(q) \quad \text{and} \quad \Lambda_{ij}^{k} = \Lambda_{ij}^{k}(q)\,, \tag{13}$$

where the coordinates q are related to position on the manifold through Eq. (1). However, in several cases, the motion constraints imposed on the original system of particles or the transformations performed are such that the geometric properties of a configuration manifold M appear in the form

$$g_{ij} = g_{ij}(q(t),t) \quad \text{and} \quad \Lambda_{ij}^{k} = \Lambda_{ij}^{k}(q(t),t) \tag{14}$$

and the manifold is rheonomic. In fact, this can occur artificially, even in the archetypal scleronomic manifold E^{3N}, by performing a velocity transformation like that of Eq. (2), with elements $A_i^j(q,t)$, depending on time [9, 16]. Another way to introduce time dependence is through enforcement of a set of motion constraints. These ideas will become more concrete in Sections 4 and 5, respectively.

When the geometric properties of a manifold M are time dependent, the need to keep the form invariance of Newton's law, as expressed by Eq. (9) through the covariant derivative of momentum, makes it convenient to perform the analysis of the motion on the so called event or extended configuration manifold, denoted by $\bar{M}$, with dimension $n+1$ [12, 23]. A natural way to introduce this manifold is through coordinate maps. Specifically, if $\bar{\varphi}$ is a coordinate map of $\bar{M}$, corresponding to a coordinate map φ on M, then the coordinates of point p of $\bar{M}$ can be selected by

$$\bar{q} = \bar{\varphi}(p) = (q,\tau)\,,$$

where τ is a new coordinate, introduced for accommodating time. This means that

$$\bar{q}^{i} = q^{i} \quad (i=1,\ldots,n) \quad \text{and} \quad \bar{q}^{n+1} \equiv \bar{q}^{0} = \tau\,. \tag{16}$$

Consequently, the tangent vector $\underline{\bar{v}}$ to the image curve $\bar{\gamma}(s)$ on $\bar{M}$ of a curve $\gamma(s)$ on M at point p belongs to an $(n+1)$-dimensional vector space $T_p\bar{M}$, with components

$$\bar{v}^{i} = \tfrac{d}{ds}(\bar{\varphi}\circ\bar{\gamma})^{i} \quad (i=1,\ldots,n) \quad \text{and} \quad \bar{v}^{n+1} \equiv \bar{v}^{0} = d\tau/ds \tag{17}$$

in the natural basis $\mathfrak{B}_{\bar{g}} = \{\underline{\bar{g}}_1 \quad \cdots \quad \underline{\bar{g}}_n \quad \underline{\bar{g}}_0\}$ of $T_p\bar{M}$, created by the tangent vectors to the coordinate lines corresponding to the coordinate map defined by Eq. (15). The last result can be put in the form

$$\underline{\bar{v}} = \bar{v}^I \underline{\bar{g}}_I = \bar{v}^i \underline{\bar{g}}_i + \bar{v}^0 \underline{\bar{g}}_0 \quad (I = 1,\ldots,n+1;\ i = 1,\ldots,n). \tag{18}$$

Similar expressions can also be obtained for bases $\mathfrak{B}_{\bar{e}}$ of $T_p\bar{M}$ other than the natural basis $\mathfrak{B}_{\bar{g}}$ but respecting the separation of the temporal from the spatial coordinates induced by Eq. (19). Such bases will be referred to as separable bases of $T_p\bar{M}$ (or $\bar{M}$, for simplicity) in the sequel.

In essence, incorporation of time into the set of coordinates helps in converting the original manifold M into an extended configuration manifold $\bar{M}$, which is scleronomic [17]. Then, a linear velocity transformation similar to that of Eq. (10) can always be established between the two scleronomic manifolds $\bar{E}^{3N} \equiv E^{3N} \times \mathbb{R}$ and $\bar{M}$. Before employing this transformation, it is first necessary to determine the geometric properties of $\bar{E}^{3N}$ and $\bar{M}$. Based on the definition of the former manifold as a Cartesian product of E^{3N} and $\mathbb{R}$, its metric matrix appears in the form

$$\bar{G} = [\bar{G}_{IJ}] = \begin{bmatrix} G(q) & \underline{0} \\ \underline{0}^T & G_{00}(\tau) \end{bmatrix}, \tag{19}$$

where the $n \times n$ submatrix $G = [G_{ij}]$ includes the components of the metric tensor on E^{3N}, while $G_{00}(\tau)$ is a non-negative scalar, which may be a function of the temporal coordinate. In addition, the set of affinities on $\bar{E}^{3N}$, say $\bar{\Gamma}^K_{IJ}$ (with $I,J,K = 1,\ldots,n+1$), includes the following elements

$$\bar{\Gamma}^k_{ij} = \Gamma^k_{ij}(q) \quad (i,j,k = 1,\ldots,n) \quad \text{and} \quad \bar{\Gamma}^0_{00} = \Gamma^0_{00}(\tau), \tag{20}$$

where Γ^k_{ij} are the affinities on E^{3N}, while all the remaining mixed type affinities (involving any combination of the spatial coordinates and the temporal coordinate) are zero.

Next, knowledge of the set of motion constraints imposed on $\bar{E}^{3N}$ in order to get the motion on $\bar{M}$ permits evaluation of the velocity transformation matrix between the tangent spaces of these manifolds, expressed by Eq. (10) (see Section 5). Then, the geometric properties of $\bar{M}$ can be determined by application of Eqs. (11) and (12). First, the metric matrix on $\bar{M}$ is obtained in the form

$$\bar{g}(\bar{q}) = [\bar{g}_{IJ}] = \begin{bmatrix} \hat{g}(q,\tau) & \underline{\bar{g}}_0(q,\tau) \\ \underline{\bar{g}}_0^T(q,\tau) & \bar{g}_{00}(q,\tau) \end{bmatrix}, \tag{21}$$

where $\hat{g} = [\hat{g}_{ij}]$ is an $n \times n$ matrix, while $\underline{\bar{g}}_0$ is an n-vector and $\bar{g}_{00}$ is a scalar quantity. In addition, the set of affinities becomes complete, in the sense

$$\bar{\Lambda}^K_{IJ}(\bar{q}) = [\bar{\Lambda}^k_{ij}, \bar{\Lambda}^k_{i0}, \bar{\Lambda}^k_{0j}, \bar{\Lambda}^k_{00}, \bar{\Lambda}^0_{ij}, \bar{\Lambda}^0_{i0}, \bar{\Lambda}^0_{0j}, \bar{\Lambda}^0_{00}]. \tag{22}$$

Taking into account the qualitative difference in the role of the temporal and the spatial coordinates and Eq. (19), it is frequently advantageous to select a special basis in $T_p\bar{M}$, in which

$$\bar{g}_0(q,\tau) = \underline{0}\,.$$

Such a basis will be called a standard basis of $\bar{M}$ in the sequel. Based on Eq. (5), this means that standard is a special separable basis, with base vector corresponding to the temporal coordinate being normal to the base vectors associated with the subspace of $T_p\bar{M}$ spanned by the spatial coordinates. Then, it is easy to show that in a standard basis of $T_p\bar{M}$ it is true that

$$\bar{v}^i = v^i \quad (i = 1,\ldots,n), \tag{23}$$

where v^i represents velocity components in the corresponding basis of T_pM. Due to the symmetry of the metric matrix, this choice is always possible through a transformation.

For the problem at hand, the communication between the configuration manifold M and the event manifold $\bar{M}$, after selecting $s = \tau$, is achieved by imposing the single holonomic constraint

$$\bar{q}^0 - \tau = 0 \quad \Rightarrow \quad \bar{v}^0 - 1 = 0\,. \tag{24}$$

Moreover, Eqs. (17) and (23) define an $(n+1)\times n$ transformation between the spaces T_pM and $T_p\bar{M}$. By employing a standard basis in $T_p\bar{M}$, it can be put in the following compact form

$$\bar{v}^I = \delta_i^I v^i + \delta_0^I \bar{v}^0 \quad (I = 1,\ldots,n+1;\ i = 1,\ldots,n). \tag{25}$$

Based on this transformation, the components g_{ij} and Λ_{ij}^k of the metric and the affinities on manifold M can be related to the components $\bar{g}_{IJ}$ and $\bar{\Lambda}_{IJ}^K$ of the metric and the affinities on manifold $\bar{M}$ through the compatibility conditions (11) and (12). More specifically, employing a separable basis on $\bar{M}$, the linear part of the velocity transformation expressed by Eq. (10) is given in the present case by

$$N_i^I = \delta_i^I\,. \tag{26}$$

Therefore, it is straightforward to verify that Eq. (11) is satisfied when

$$g_{ij} = \bar{g}_{ij} \quad (i, j = 1,\ldots,n), \tag{27}$$

while application of Eq. (14) yields the following condition on the affinities

$$(\Lambda_{ji}^{\ell} g_{\ell k} - \bar{\Lambda}_{ji}^{\ell} \bar{g}_{\ell k} - \bar{\Lambda}_{ji}^{0} \bar{g}_{0k}) v^j v^k = 0 \quad (i, j, k, \ell = 1,\ldots,n). \tag{28}$$

In a standard basis, the last condition is satisfied by the simpler choice $\bar{\Lambda}_{ij}^k = \Lambda_{ij}^k$.

The above help in establishing the interrelation between manifolds M and E^{3N}, through the interrelation between the event manifolds $\bar{M}$ and $\bar{E}^{3N}$, as shown schematically in Fig. 1.

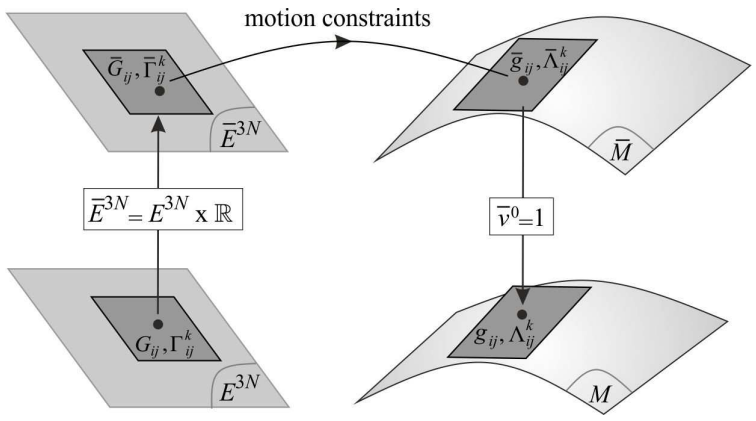

Fig. 1 Relation between manifolds M and E^{3N}, through their relation to $\bar{M}$ and $\bar{E}^{3N}$

Using the metric matrix in the form of Eq. (21), the kinetic energy of the system on the extended configuration manifold $\bar{M}$ can be put in the form

$$\bar{T} = \tfrac{1}{2}\bar{v}^I \bar{g}_{IJ} \bar{v}^J \equiv \bar{T}_2 + \bar{T}_1 + \bar{T}_0 \quad (I, J = 1, \ldots, n+1),$$

where, using Eqs. (18) and (27), the three individual terms are found in a separable basis as follows

$$\bar{T}_2 = \tfrac{1}{2}\bar{v}^i g_{ij} \bar{v}^j, \quad \bar{T}_1 = \bar{v}^i \bar{g}_{i0} \bar{v}^0 \quad \text{and} \quad \bar{T}_0 = \tfrac{1}{2}\bar{v}^0 \bar{g}_{00} \bar{v}^0 .$$

Therefore, all these terms are in fact quadratic in velocity. Moreover, the generalized momenta in the event manifold $\bar{M}$ can be determined in the form

$$\bar{p}_I = \bar{g}_{IJ} \bar{v}^J \quad (I, J = 1, \ldots, n+1),$$

with

$$\bar{p}_i = \bar{g}_{iJ} \bar{v}^J = g_{ij} \bar{v}^j + \bar{g}_{i0} \bar{v}^0 \quad (i = 1, \ldots, n) \quad \text{and} \quad \bar{p}_{n+1} \equiv \bar{p}_0 = \bar{g}_{0J} \bar{v}^J = \bar{g}_{0j} \bar{v}^j + \bar{g}_{00} \bar{v}^0 .$$

Finally, since the extended configuration manifold $\bar{M}$ is scleronomic, the true path of motion on it can be determined by application of Newton's second law in the generalized form

$$\nabla_{\underset{\sim}{\bar{v}}} \underset{\sim}{p}^*_{\bar{M}} = \underset{\sim}{f}^*_{\bar{M}}, \tag{29}$$

where $\underset{\sim}{f}^*_{\bar{M}}$ represents the applied forces on $\bar{M}$, while

$$\nabla_{\underset{\sim}{\bar{v}}} \underset{\sim}{p}^*_{\bar{M}} = (\bar{p}_{I,K} \bar{v}^K - \bar{\Lambda}^L_{JI} \bar{p}_L \bar{v}^J) \underset{\sim}{\bar{e}}^I, \tag{30}$$

where $\bar{p}_{I,J} \equiv \partial \bar{p}_I / \partial \bar{q}^J$ [10, 19].

Then, a special class of covectors, known as Newton covectors[21], can be defined on manifold $\bar{M}$ by

$$\underset{\sim}{h}^*_{\bar{M}} \equiv \nabla_{\underline{\bar{v}}} \underset{\sim}{p}^*_{\bar{M}} - \underset{\sim}{f}^*_{\bar{M}}, \tag{31}$$

with components in a general basis of $T_p^*\bar{M}$ given by

$$\bar{h}_I = (\bar{g}_{IJ}\bar{v}^J)_{,K}\bar{v}^K - \bar{\Lambda}^L_{JI}\bar{g}_{LK}\bar{v}^J\bar{v}^K - \bar{f}_I. \tag{32}$$

By definition of these covectors, the law of motion on manifold $\bar{M}$ is expressed in the form

$$\underset{\sim}{h}^*_{\bar{M}} = \underset{\sim}{0} \quad \Rightarrow \quad \bar{h}_I = 0, \tag{33}$$

in the absence of any motion constraints.

Next, based on Eq. (26), the components of the Newton covectors on the original manifold M are found by employing the following mapping from a separable basis of $T_p^*\bar{M}$ to T_p^*M

$$h_i = \delta_i^I \bar{h}_I. \tag{34}$$

Using Eqs. (32), (27) and performing simple mathematical operations, it eventually turns out that

$$h_i = (g_{ij}\bar{v}^j + \bar{g}_{i0})_{,k}\bar{v}^k + (g_{ij}\bar{v}^j + \bar{g}_{i0})_{,0} - \bar{\Lambda}^L_{Ji}\bar{g}_{LK}\bar{v}^J\bar{v}^K - f_i, \tag{35}$$

with

$$\begin{aligned}\bar{\Lambda}^L_{Ji}\bar{g}_{LK}\bar{v}^J\bar{v}^K = {} & (\bar{\Lambda}^\ell_{ji}g_{\ell k} + \bar{\Lambda}^0_{ji}\bar{g}_{0k})\bar{v}^j\bar{v}^k \\ & + (\bar{\Lambda}^\ell_{ji}\bar{g}_{\ell 0} + \bar{\Lambda}^0_{ji}\bar{g}_{00} + \bar{\Lambda}^\ell_{0i}g_{\ell j} + \bar{\Lambda}^0_{0i}\bar{g}_{0j})\bar{v}^j + (\bar{\Lambda}^\ell_{0i}\bar{g}_{\ell 0} + \bar{\Lambda}^0_{0i}\bar{g}_{00}).\end{aligned} \tag{36}$$

Again, in the special case of a standard basis of $\bar{M}$, the last expression is simplified considerably to

$$\bar{\Lambda}^L_{Ji}\bar{g}_{LK}\bar{v}^J\bar{v}^K = \Lambda^\ell_{ji}g_{\ell k}v^jv^k + (\bar{\Lambda}^\ell_{0i}g_{\ell j} + \bar{\Lambda}^0_{ji}\bar{g}_{00})v^j + \bar{\Lambda}^0_{0i}\bar{g}_{00}. \tag{37}$$

Furthermore, more terms disappear for scleronomic systems, since then all the mixed affinities vanish. Then, Newton's law on manifold M is written in the simpler form

$$h_i = (g_{ij}v^j)_{,k}v^k - \Lambda^\ell_{ji}g_{\ell k}v^jv^k - f_i = 0, \tag{38}$$

resembling fully that of Eq. (32) on $\bar{M}$. The extra terms in Eq. (35) are inertial and come either from terms involving the off-diagonal components $\bar{g}_{i0}$ of the metric of a non-standard basis or by mixed affinities, defined on the event manifold only and related to differentiation with respect to time.

4 APPLICATION OF A SPECIAL COORDINATE TRANSFORMATION ON THE EVENT MANIFOLD

Next, let ψ be an alternate coordinate map in the vicinity of point p on M, similar to that

defined by Eq. (1). Then, the corresponding set of coordinates of p on $\bar{M}$ can be selected by

$$\bar{x} = \bar{\psi}(p) = (x, \omega),$$

through a new coordinate map $\bar{\psi}$. The last equation can be combined with Eq. (15) to yield

$$\bar{x} = \bar{\chi}(\bar{q}) = (x(q,\tau), \omega(q,\tau)), \tag{39}$$

with composite map $\bar{\chi} = \bar{\psi} \circ \bar{\varphi}^{-1}$, so that

$$\bar{x}^i = x^i(q,\tau) \quad (i = 1,\ldots,n) \quad \text{and} \quad \bar{x}^{n+1} \equiv \bar{x}^0 = \omega(q,\tau). \tag{40}$$

In fact, for the purposes of the present study, the last coordinate can be selected by

$$\omega(q,\tau) = \tau. \tag{41}$$

Then, the Jacobian matrix $\bar{J} = [\bar{J}^I_{\hat{I}}]$ (with $I, \hat{I} = 1,\ldots,n+1$) corresponding to this particular type of coordinate transformation is given by

$$\bar{J}(\bar{q}) = \frac{\partial \bar{x}}{\partial \bar{q}} = \begin{bmatrix} J(q,\tau) & \underline{c}(q,\tau) \\ \underline{0}^T & 1 \end{bmatrix}, \tag{42}$$

where the $n \times n$ matrix $J = [J^i_{\hat{i}}]$ and the n-vector $\underline{c}$ are determined by

$$J(q,\tau) = \partial x / \partial q \quad \text{and} \quad \underline{c}(q,\tau) = \partial x / \partial \tau. \tag{43}$$

Based on the above, the class of transformations considered are similar to Eq. (2), but have the special structure exhibited by Eq. (42). Then, the new and old base vectors in the corresponding bases of $T_p\bar{M}$ and $T^*_p\bar{M}$ are related by

$$\underline{\bar{e}}_{\hat{I}} = \bar{J}^I_{\hat{I}}(\bar{q})\underline{\bar{e}}_I \quad \text{and} \quad \underline{\bar{e}}^I = \bar{J}^I_{\hat{I}}(\bar{q})\underline{\bar{e}}^{\hat{I}}, \tag{44}$$

while the components of the vectors and covectors in these bases are related by

$$\bar{v}^I = \bar{J}^I_{\hat{I}}(\bar{q})\bar{v}^{\hat{I}} \quad \text{and} \quad \bar{v}_{\hat{I}} = \bar{J}^I_{\hat{I}}(\bar{q})\bar{v}_I, \tag{45}$$

respectively [17]. Finally, the components of the metric tensor and the affinities in the new basis of $T_p\bar{M}$ are found by

$$\bar{g}_{\hat{I}\hat{J}} = \bar{J}^I_{\hat{I}}\bar{g}_{IJ}\bar{J}^J_{\hat{J}} \quad \text{and} \quad \bar{\Lambda}^{\hat{K}}_{\hat{I}\hat{J}} = \bar{J}^I_{\hat{I}}\bar{J}^J_{\hat{J}}\bar{B}^{\hat{K}}_K\bar{\Lambda}^K_{IJ} + \bar{J}^K_{\hat{J},\hat{I}}\bar{B}^{\hat{K}}_K,$$

respectively. These relations demonstrate that the new metric components and affinities are time dependent, when at least one element of matrix J or vector $\underline{c}$ is time dependent, even if the original components do not depend on time. Specifically, the new metric matrix appears in the form

$$\hat{\bar{g}} = [\bar{g}_{\hat{I}\hat{J}}] = \bar{J}^T\bar{g}\bar{J} = \begin{bmatrix} \hat{g} & \underline{g}_{\hat{0}} \\ \underline{g}^T_{\hat{0}} & g_{\hat{0}\hat{0}} \end{bmatrix} \tag{47}$$

on the extended configuration manifold $\bar{M}$. Taking Eq. (21) into account, it turns out that

$$\hat{g} = [g_{\hat{i}\hat{j}}] = J^T\hat{g}J, \quad \underline{g}_{\hat{0}} = J^T\hat{g}\underline{c} + J^T\underline{\bar{g}}_0 \quad \text{and} \quad g_{\hat{0}\hat{0}} = \underline{c}^T\hat{g}\underline{c} + 2\underline{c}^T\underline{\bar{g}}_0 + \bar{g}_{00}. \tag{48}$$

The above results hold even in cases where the elements of matrix J and vector $\underline{c}$ in Eq. (42) do not satisfy Eq. (43). Then, the new basis, defined by Eq. (44), will be anholonomic in general. However, it is easy to verify that it will remain separable. In this respect, it is noteworthy that the set of matrices expressed by Eq. (42) presents similarities with the Galilean group of transformations applied to a particle in order to preserve the form of Newton's law in Cartesian coordinate systems [1, 23]. Also, even when a standard basis is employed in $T_p\bar{M}$ originally (i.e., when $\underline{\bar{g}}_0 = \underline{0}$), the new basis will turn into a separable basis eventually, if $\underline{c} \neq \underline{0}$. Finally, when the transformation is such that $\underline{c} = \underline{0}$, a standard basis yields a new standard basis, since then Eqs. (47) and (48) lead to

$$\hat{\bar{g}} = \begin{bmatrix} J^T \bar{g} J & \underline{0} \\ \underline{0}^T & \bar{g}_{00} \end{bmatrix}. \tag{49}$$

Now, based on Eq. (45b), the components of the Newton covectors in the new basis of $T_p^*\bar{M}$ are

$$\bar{h}_{\hat{I}} = \bar{J}^I_{\hat{I}}\, \bar{h}_I \,. \tag{50}$$

Substituting Eq. (32) in the right hand side of the last equation and performing simple operations leads to

$$\bar{h}_{\hat{I}} = (\bar{J}^I_{\hat{I}}\, \bar{g}_{IJ} \bar{J}^J_{\hat{J}} \bar{v}^{\hat{J}})_{,\hat{K}}\, \bar{v}^{\hat{K}} - (\bar{J}^I_{\hat{I},\hat{K}} \bar{J}^J_{\hat{J}}\, \bar{g}_{IJ} + \bar{J}^I_{\hat{I}} \bar{J}^J_{\hat{J}} \bar{J}^K_{\hat{K}} \bar{\Lambda}^L_{JI} \bar{g}_{LK}) \bar{v}^{\hat{J}} \bar{v}^{\hat{K}} - \bar{J}^I_{\hat{I}}\, \bar{f}_I \,. \tag{51}$$

Next, following an application of the compatibility conditions expressed by Eqs. (11) and (12) in the more appropriate form

$$\bar{g}_{\hat{I}\hat{J}} = \bar{J}^I_{\hat{I}} \bar{g}_{IJ} \bar{J}^J_{\hat{J}} \quad \text{and} \quad (\bar{\Lambda}^{\hat{L}}_{\hat{J}\hat{I}} \bar{g}_{\hat{L}\hat{K}} - \bar{J}^I_{\hat{I},\hat{K}} \bar{J}^J_{\hat{J}}\, \bar{g}_{IJ} - \bar{J}^I_{\hat{I}} \bar{J}^J_{\hat{J}} \bar{J}^K_{\hat{K}} \bar{\Lambda}^L_{JI} \bar{g}_{LK}) \bar{v}^{\hat{J}} \bar{v}^{\hat{K}} = 0 \,, \tag{52}$$

it eventually turns out that

$$\bar{h}_{\hat{I}} = (\bar{g}_{\hat{I}\hat{J}} \bar{v}^{\hat{J}})_{,\hat{K}}\, \bar{v}^{\hat{K}} - \bar{\Lambda}^{\hat{L}}_{\hat{J}\hat{I}} \bar{g}_{\hat{L}\hat{K}} \bar{v}^{\hat{J}} \bar{v}^{\hat{K}} - \bar{f}_{\hat{I}} \,. \tag{53}$$

Note that the form of the last equation is identical to the fundamental form of Eq. (32). Finally, by employing the mapping from a separable basis of $T_p^*\bar{M}$ to T_p^*M defined by

$$h_i = \delta^{\hat{I}}_i \bar{h}_{\hat{I}} \tag{54}$$

and performing simple mathematical operations it eventually turns out that

$$h_i = (g_{i\hat{j}} \bar{v}^{\hat{j}} + \bar{g}_{i\hat{0}})_{,\hat{k}}\, \bar{v}^{\hat{k}} + (g_{i\hat{j}} \bar{v}^{\hat{j}} + \bar{g}_{i\hat{0}})_{,\hat{0}} - \bar{\Lambda}^{\hat{L}}_{\hat{J}\hat{I}} \bar{g}_{\hat{L}\hat{K}} \bar{v}^{\hat{J}} \bar{v}^{\hat{K}} - f_i \,, \tag{55}$$

with

$$\begin{aligned} \bar{\Lambda}^{\hat{L}}_{\hat{j}\hat{i}} \bar{g}_{\hat{L}\hat{K}} \bar{v}^{\hat{j}} \bar{v}^{\hat{K}} = {} & (\bar{\Lambda}^{\hat{\ell}}_{\hat{j}\hat{i}} \bar{g}_{\hat{\ell}\hat{k}} + \bar{\Lambda}^{\hat{0}}_{\hat{j}\hat{i}} \bar{g}_{\hat{0}\hat{k}}) \bar{v}^{\hat{j}} \bar{v}^{\hat{k}} \\ & + (\bar{\Lambda}^{\hat{\ell}}_{\hat{j}\hat{i}} \bar{g}_{\hat{\ell}\hat{0}} + \bar{\Lambda}^{\hat{0}}_{\hat{j}\hat{i}} \bar{g}_{\hat{0}\hat{0}} + \bar{\Lambda}^{\hat{\ell}}_{\hat{0}\hat{i}} \bar{g}_{\hat{\ell}\hat{j}} + \bar{\Lambda}^{\hat{0}}_{\hat{0}\hat{i}} \bar{g}_{\hat{0}\hat{j}}) \bar{v}^{\hat{j}} + (\bar{\Lambda}^{\hat{\ell}}_{\hat{0}\hat{i}} \bar{g}_{\hat{\ell}\hat{0}} + \bar{\Lambda}^{\hat{0}}_{\hat{0}\hat{i}} \bar{g}_{\hat{0}\hat{0}}). \end{aligned} \tag{56}$$

Eq. (55) is similar to Eq. (35), while Eq. (56) is similar to Eq. (36). Moreover, in a standard basis, the last equation can be put in a form similar to Eq. (37). Obviously, the last observations reveal that the form of the components of the Newton covectors remains invariant under the special transformation performed. This confirms the form invariance of Newton's law when expressed in different bases.

To complete the picture, consider a companion change of basis in the configuration manifold M, relating the new and old base vectors in T_pM and T_p^*M by

$$\underline{e}_{\hat{i}} = J_{\hat{i}}^{i}(q,t)\underline{e}_i \quad \text{and} \quad \underline{\bar{e}}^{i} = J_{\hat{i}}^{i}(q,\tau)\underline{\bar{e}}^{\hat{i}},$$

respectively, where matrix $J=[J_{\hat{i}}^{i}]$ is selected to coincide with the $n\times n$ matrix covering the upper left part of matrix $\bar{J}$ defined by Eq. (42). Then, the components of the vectors and covectors in T_pM and T_p^*M are related by

$$v^i = J_{\hat{i}}^{i}(q,t)v^{\hat{i}} \quad \text{and} \quad v_{\hat{i}} = J_{\hat{i}}^{i}(q,t)v_i, \tag{57}$$

respectively, while the components of the metric and the affinities in the new basis of M are given by

$$g_{\hat{i}\hat{j}} = J_{\hat{i}}^{i}g_{ij}J_{\hat{j}}^{j} \quad \text{and} \quad \Lambda_{\hat{i}\hat{j}}^{\hat{k}} = J_{\hat{i}}^{i}J_{\hat{j}}^{j}B_{k}^{\hat{k}}\Lambda_{ij}^{k} + J_{\hat{j},\hat{i}}^{k}B_{k}^{\hat{k}}, \tag{58}$$

respectively, with

$$J_{\hat{i}}^{i}B_{j}^{\hat{i}} = \delta_j^i \quad \text{and} \quad B_i^{\hat{j}}J_{\hat{i}}^{i} = \delta_{\hat{i}}^{\hat{j}}. \tag{59}$$

Consequently, the components of the Newton covectors in the transformed basis of the original manifold M are found in the form

$$h_{\hat{i}} = J_{\hat{i}}^{i}h_i. \tag{60}$$

Employing Eq. (35) and performing lengthy but simple mathematical operations in the right hand side of the last equation, which are similar to those involved in Eqs. (51) and (52), it eventually turns out that $h_{\hat{i}}$ regains the form of Eq. (55). This verifies the existence of commutativity between the special type of coordinate transformation examined and the transformation between the original manifold M and the extended manifold $\bar{M}$.

Finally, using Eq. (23) in conjunction with Eq. (57a) yields

$$\bar{v}^i = v^i = J_{\hat{i}}^{i}(q,t)v^{\hat{i}} \quad (i,\hat{i}=1,\ldots,n),$$

where $\bar{v}^i$ is the velocity component in the corresponding standard basis of $\bar{M}$. Taking into account Eq. (59), the last equation leads to

$$v^{\hat{i}} = \bar{v}^{\hat{i}} + \hat{v}^{\hat{i}}, \tag{61}$$

with

$$\hat{v}^{\hat{i}} = B_i^{\hat{i}}J_{\hat{0}}^{i}\bar{v}^{\hat{0}} = B_i^{\hat{i}}c^i. \tag{62}$$

Eq. (61) shows that $v^{\hat{i}} \neq \bar{v}^{\hat{i}}$, in general, even when $v^i = \bar{v}^i$. Substitution of the term $\bar{v}^{\hat{i}}$ from Eq. (61) into Eq. (55) yields the equations of motion on manifold M in terms of the velocity components $v^{\hat{i}}$ in T_pM and $\hat{v}^{\hat{i}}$. By their definition, Eq. (62), the terms $\hat{v}^{\hat{i}}$ are known and due to the presence of the n-vector $\underline{c}$ in the Jacobian $\bar{J}(\bar{q})$, defined by Eq. (42). Based on Eq. (43), it is clear that this vector becomes zero when a time independent chart (i.e., coordinate system) is selected on $\bar{M}$, defined by

$$x = x(q). \tag{63}$$

This means that the terms $\hat{v}^{\hat{i}}$ can be eliminated by a proper selection of the chart on manifold $\bar{M}$. Therefore, only such charts may have meaningful counterparts on M, which clarifies some of the terminology employed in the literature on "time dependent" charts.

5 APPLICATION OF A SPECIAL COORDINATE TRANSFORMATION ON THE EVENT MANIFOLD

In the present section, it is assumed that the motion of the system examined on configuration manifold M is subject to an additional set of k constraints with form

$$A(q,t)\underline{v} + \underline{a}(q,t) = \underline{0}\,, \tag{64}$$

where $A=[a_i^R]$ is a known $k\times n$ matrix. Then, the motion of the system takes place on a curve $\gamma_A(t)$ of another manifold M_A, with dimension $m=n-k$ [19]. Next, let $\{\theta^\alpha\}$ ($\alpha=1,\ldots,m$) be a set of generalized coordinates in a neighborhood of a point p_A of M_A, related to point p of M through Eq. (64). Furthermore, let $\{\underline{e}_\alpha\}$ and and $\{\underline{e}^\alpha\}$ be a basis of $T_{p_A}M_A$ and $T^*_{p_A}M_A$, respectively.

The new fundamental item in Eq. (64) is not so much the explicit appearance of time but rather the acatastatic term $\underline{a}$ [21]. This term destroys the linearity and provides an affine nature to the constraint equations. In principle, Eq. (64) can be used in order to establish a mapping between the tangent spaces $T_{p_A}M_A$ and T_pM. Namely, Eq. (64) can easily be recast in the form

$$\underline{v} = N(q,t)\dot{\underline{\theta}} + \underline{\upsilon}(q,t)\,, \tag{65}$$

where the $n\times m$ matrix N and the n-vector $\underline{\upsilon}$ are determined in terms of the elements of the $k\times n$ matrix A and the k-vector $\underline{a}$ [12, 19]. To overcome the loss of linearity, due to the presence of the term $\underline{\upsilon}$, the last equation is put in the form of a linear transformation between the tangent spaces $T_{p_A}\bar{M}_A$ and $T_p\bar{M}$ of the corresponding event manifolds. This permits conversion of Eq. (65) into the following linear relation between the components of tangent vectors

$$\bar{v}^I = \bar{N}^I_\Phi(\bar{q})\bar{v}^\Phi\,, \tag{66}$$

with $\Phi=1,\ldots,m+1$ and $I=1,\ldots,n+1$, where the extended matrix $\bar{N}$ appears in the form

$$\bar{N}=[\bar{N}^I_\Phi(\bar{q})]=\begin{bmatrix} N(q,\tau) & \underline{\upsilon}(q,\tau) \\ \underline{0}^T & 1 \end{bmatrix}. \tag{67}$$

This $(n+1)\times(m+1)$ matrix has a similar structure with the Jacobian matrix defined by Eq. (42).

Next, the metric matrix on manifold $\bar{M}$ is assumed to have the general form expressed by Eq. (21), while the set of affinities is complete, in the sense of Eq. (22). Then, based on the velocity transformation represented by Eq. (66), the components of the metric matrix and the affinities on the new manifold are determined by employing Eqs. (11) and (12) in the form

$$\bar{g}_{\Phi\Psi} = \bar{N}^I_\Phi \bar{g}_{IJ}\bar{N}^J_\Psi \quad \text{and} \quad (\bar{\Lambda}^{\mathrm{X}}_{\Psi\Phi}\bar{g}_{\mathrm{X}\Omega} - \bar{N}^I_{\Phi,\Omega}\bar{N}^J_\Psi\bar{g}_{IJ} - \bar{N}^I_\Phi\bar{N}^J_\Psi\bar{N}^K_\Omega\bar{\Lambda}^L_{JI}\bar{g}_{LK})\bar{v}^\Psi\bar{v}^\Omega = 0\,. \tag{68}$$

Obviously, any time dependence of matrix N and vector $\underline{\upsilon}$ is transferred into the geometric properties of manifold $\bar{M}_A$. In particular, the metric matrix on the new Newtonian manifold $\bar{M}_A$ is

$$\bar{g}_A = [\bar{g}_{\Phi X}] = \bar{N}^T \bar{g} \bar{N} = \begin{bmatrix} N^T \hat{g} N & N^T (\hat{g}\underline{\upsilon} + \underline{\bar{g}}_0) \\ (\underline{\upsilon}^T \hat{g} + \underline{\bar{g}}_0^T) N & \underline{\upsilon}^T \hat{g} \underline{\upsilon} + 2\underline{\upsilon}^T \underline{\bar{g}}_0 + \bar{g}_{00} \end{bmatrix}.$$

In general, this $(m+1)\times(m+1)$ matrix is full. Therefore, unless

$$N^T (\hat{g}\underline{\upsilon} + \underline{\bar{g}}_0) = \underline{0}, \tag{70}$$

the new basis obtained in $T_{p_A}\bar{M}_A$ is not standard, even when the basis of $T_p\bar{M}$ is standard.

As usual, application of Eq. (66) means that the base vectors in $T_{p_A}\bar{M}_A$ and $T_p\bar{M}$ are related by

$$\underline{e}_\Phi = \bar{N}^I_\Phi(\bar{q})\underline{e}_I \quad (\Phi = 1,\ldots,m+1;\ I = 1,\ldots,n+1),$$

while the components of the covectors are related by

$$\bar{v}_\Phi = \bar{N}^I_\Phi(\bar{q})\bar{v}_I . \tag{71}$$

Therefore, the components of the Newton covectors in the basis of $T^*_{p_A}\bar{M}_A$ are found through

$$\bar{h}_\Phi = \bar{N}^I_\Phi \bar{h}_I . \tag{72}$$

Substituting Eq. (32) in the right hand side of the last equation and performing simple operations yields first the following relation

$$\bar{h}_\Phi = (\bar{N}^I_\Phi \bar{g}_{IJ} \bar{N}^J_\Psi \bar{v}^\Psi)_{,\Omega}\bar{v}^\Omega - (\bar{N}^I_{\Phi,\Omega}\bar{N}^J_\Psi \bar{g}_{IJ} + \bar{N}^I_\Phi \bar{N}^J_\Psi \bar{N}^K_\Omega \bar{\Lambda}^L_{JI}\bar{g}_{LK})\bar{v}^\Psi \bar{v}^\Omega - \bar{N}^I_\Phi \bar{f}_I . \tag{73}$$

Next, application of the compatibility conditions expressed by Eqs. (68), leads to the final form

$$\bar{h}_\Phi = (\bar{g}_{\Phi\Psi}\bar{v}^\Psi)_{,\Omega}\bar{v}^\Omega - \bar{\Lambda}^X_{\Psi\Phi}\bar{g}_{X\Omega}\bar{v}^\Psi\bar{v}^\Omega - \bar{f}_\Phi . \tag{74}$$

Once again, the form of the last equation is similar to Eq. (32). Also, in accordance with Eq. (34), the transformation between separable bases from $T^*_{p_A}M_A$ to $T^*_p\bar{M}$ appears in the form

$$h_\alpha = \delta^\Phi_\alpha \bar{h}_\Phi . \tag{75}$$

Consequently, by performing simple mathematical operations one can originally obtain the components of the Newton covectors on the manifold M_A in the form

$$\begin{aligned} h_\alpha = {} & (\bar{g}_{\alpha\beta}\bar{v}^\beta + \bar{g}_{\alpha 0})_{,\gamma}\bar{v}^\gamma + (\bar{g}_{\alpha\beta}\bar{v}^\beta + \bar{g}_{\alpha 0})_{,0} - (\bar{\Lambda}^\gamma_{\beta\alpha}\bar{g}_{\gamma\delta} + \bar{\Lambda}^0_{\beta\alpha}\bar{g}_{0\delta})\bar{v}^\beta\bar{v}^\delta \\ & - (\bar{\Lambda}^\gamma_{\beta\alpha}\bar{g}_{\gamma 0} + \bar{\Lambda}^0_{\beta\alpha}\bar{g}_{00} + \bar{\Lambda}^\gamma_{0\alpha}\bar{g}_{\gamma\beta} + \bar{\Lambda}^0_{0\alpha}\bar{g}_{0\beta})\bar{v}^\beta - (\bar{\Lambda}^\gamma_{0\alpha}\bar{g}_{\gamma 0} + \bar{\Lambda}^0_{0\alpha}\bar{g}_{00}) - f_\alpha = 0. \end{aligned} \tag{76}$$

Some simplifications apply to the last equation when the transition from manifold $\bar{M}_A$ to M_A is performed by using a standard basis in $T_{p_A}\bar{M}_A$, so that

$$\bar{v}^\alpha = v^\alpha, \quad \bar{g}_{\alpha\beta} = g_{\alpha\beta}, \quad \bar{\Lambda}^\gamma_{\alpha\beta} = \Lambda^\gamma_{\alpha\beta} \quad (\alpha,\beta,\gamma = 1,\ldots,m)$$

and the new metric matrix is block diagonal. In addition, some more terms drop out when the system is scleronomic. Then, Eq. (76) can eventually be put in the form

$$h_\alpha = (g_{\alpha\beta} v^\beta)_{,\gamma} v^\gamma - \Lambda^\gamma_{\beta\alpha} g_{\gamma\delta} v^\beta v^\delta - f_\alpha ,$$

which is identical to that of Eq. (38), obtained for the original manifold M in Section 3.

6 APPLICATION OF FOLIATION THEORY AND DEFINITION OF A SCLERONOMIC MANIFOLD

The material presented in this section completes the geometrical picture created in Section 3 for the event manifold $\bar{M}$. First, the attention is focused on creating the extended configuration manifold $\bar{M}$ based on the configuration manifold M at a fixed time $\tau = t$. This is done by considering the flow

$$p = \psi(p_0, t; \tau) \equiv \psi_{\tau,t} p_0 , \tag{77}$$

taking points $p_0 \in M \subset \bar{M}$ at time t to points $p \in \bar{M}$ at a later time τ, as shown in Fig. 2, so that a local coordinate chart on M and a time independent chart on $\bar{M}$ share the same spatial coordinates at each point. Using terminology of foliation theory, the local coordinates (q, τ) on $\bar{M}$, where q are also coordinates on manifold M for each τ, are called distinguished coordinates, while the temporal coordinate τ is known as a transverse coordinate [14]. In this setting, the chart corresponding to Eqs. (39) and (41) is a foliated or distinguished chart, while manifold M is considered to be a leaf of $\bar{M}$ through point p under this foliation. The specific foliation examined here has codimension 1 and partitions the event manifold $\bar{M}$ into manifolds M of dimension n, one at each time τ. Moreover, T denotes a transverse submanifold of $\bar{M}$, which is single dimensional and is described by the temporal coordinate. In fact, it is a total transversal since it meets all the leaves of the foliation, by construction [22]. In addition, the collection of the subspaces of $T_p\bar{M}$ possessing vectors with projection on T_pM only, at all points of $\bar{M}$, forms the special distribution D_M on $\bar{M}$. This is known as the structural distribution of $\bar{M}$, while its complement D_T is called the transversal distribution on $\bar{M}$ [3]. Finally, the tangent space of the event manifold $\bar{M}$ at point p can be split in the form

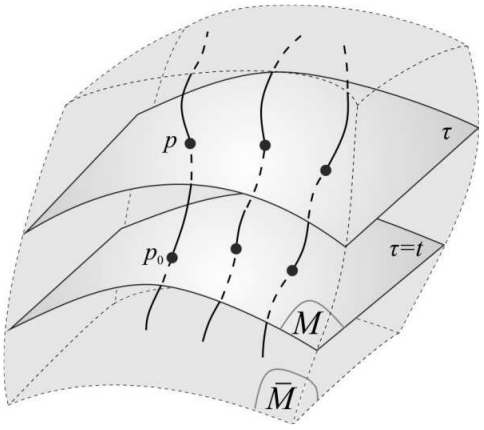

Fig. 2 Construction of manifold $\bar{M}$ by M and the time flow

$$T_p\bar{M} = H_p \oplus V_p , \tag{78}$$

where H_p and V_p are subspaces of $T_p\bar{M}$, forming the distribution D_M and D_T, respectively. Among other things, Eq. (78) implies that any vector of $T_p\bar{M}$ can be split uniquely in the form

$$\underline{u} = \underline{h} + \underline{v}, \tag{79}$$

with $\underline{h} \in H_p$ and $\underline{v} \in V_p$, where $\underline{v}$ is a tangent vector along the time flow defined by Eq. (77).

Next, it is assumed that manifold M is a fixed set of points but its metric components and affinities may depend on time. The objective is to provide conditions for M to be scleronomic. To achieve this goal, it is first necessary to define two special sets of curves on $\bar{M}$. The first set includes "leaf curves" $\gamma_M(\tau; s)$, lying entirely on M for each fixed τ, with tangent vector $\underline{h} = d\gamma_M / ds$ belonging to D_M, as depicted in Fig. 3. Likewise, the second set includes "transverse curves" $\gamma_T(q; \sigma)$, with tangent vector $\underline{v} = d\gamma_T / d\sigma$ belonging entirely to the transversal distribution D_T.

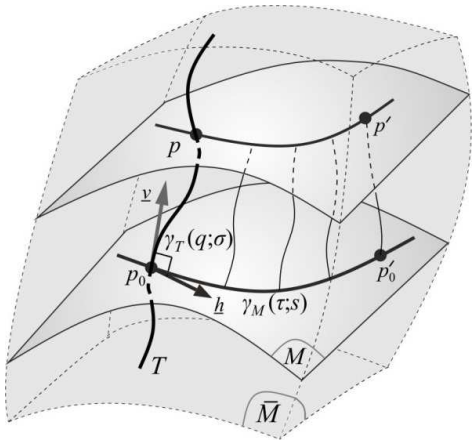

Fig. 3 Definition of two special families of curves on $\bar{M}$

By definition, a scleronomic manifold M can be viewed as a fixed surface within a Euclidean space of a bigger dimension [7, 23]. This means that its geometric properties may depend on its position in M but not on time. Then, the corresponding event manifold $\bar{M}$ can be seen as a product

$$\bar{M} = M \times T. \tag{80}$$

When a manifold possesses properties depending on time in an explicit manner, it can be viewed as a surface varying with time within a Euclidean space possessing a sufficiently bigger dimension [4, 17]. However, time dependence may also be introduced in the geometric properties by performing a transformation in $\bar{M}$ even in inherently scleronomic manifolds, as was shown in Section 4. The key to resolving this problem comes from the product form expressed by Eq. (80), which is true for a scleronomic manifold only. This is crucial in revealing and stating its geometric properties, since it implies that the event manifold $\bar{M}$ carries two complementary foliations [3]. Specifically, in such a case, a second foliation exists, which has codimension n and partitions the event manifold $\bar{M}$ into manifolds T of dimension 1, one for each combination of the spatial coordinates q. Based on this, for a configuration manifold M to be scleronomic, it is required that an autoparallel curve starting at a point of M and

ending on another point of M, for a fixed τ, should always remain on M. Likewise, an autoparallel curve starting on T and ending on T, for a fixed set of spatial coordinates q, should always remain on T. Taking into account the definition of the special families of curves γ_M and γ_T, these statements are expressed by the following mathematical conditions

$$\nabla_{\underline{h}}\underline{h} \in D_M \quad \text{and} \quad \nabla_{\underline{v}}\underline{v} \in D_T \,. \tag{81}$$

Furthermore, the Lie derivative of the vector fields created by extending the vector $\nabla_{\underline{h}}\underline{h}$ on all of $\bar{M}$, along a vector field on $\bar{M}$ with tangent vector $\underline{v}$ (i.e., the time flow represented by Eq. (77)), should be zero. Likewise, the Lie derivative of the vector fields created by extending the vector $\nabla_{\underline{v}}\underline{v}$ on all of $\bar{M}$, along a vector field on $\bar{M}$ with tangent vector $\underline{h}$, should also be zero. Mathematically, these statements are equivalent to

$$L_{\underline{v}}(\nabla_{\underline{h}}\underline{h}) = \underline{0} \quad \text{and} \quad L_{\underline{h}}(\nabla_{\underline{v}}\underline{v}) = \underline{0} \,, \tag{82}$$

where the above Lie derivatives can be determined through the corresponding Lie brackets by

$$L_{\underline{v}}(\nabla_{\underline{h}}\underline{h}) = [\underline{v}, \nabla_{\underline{h}}\underline{h}] \quad \text{and} \quad L_{\underline{h}}(\nabla_{\underline{v}}\underline{v}) = [\underline{h}, \nabla_{\underline{v}}\underline{v}] \,,$$

respectively. Moreover, the parallel transfer of the tangent vector $\underline{h}$ of a leaf curve $\gamma_M(\tau; s)$ along a transverse curve $\gamma_T(q; \sigma)$ and vice versa is preserved on a scleronomic manifold. This means that

$$\nabla_{\underline{v}}\underline{h} = \underline{0} \quad \text{and} \quad \nabla_{\underline{h}}\underline{v} = \underline{0} \,.$$

On a scleronomic manifold M, conditions should also be imposed on the metric tensor of $\bar{M}$. First, based on the product form of $\bar{M}$, expressed by Eq. (80), its metric matrix in the holonomic basis defined by the foliated coordinates can be decomposed in the special form

$$\bar{g} = \begin{bmatrix} g_M(q) & \underline{0} \\ \underline{0}^T & g_T(\tau) \end{bmatrix} .$$

Then, the following conditions must also be true for preserving the form of the metric tensor along the vector fields created by the special vectors $\underline{v}$ and $\underline{h}$ on a scleronomic manifold

$$L_{\underline{v}}\bar{g}_M = 0 \quad \text{and} \quad L_{\underline{h}}\bar{g}_T = 0 \,, \tag{84}$$

where $\bar{g}_M$ and $\bar{g}_T$ represent the restriction of metric $\bar{g}$ on the structural and transverse distribution of $\bar{M}$, respectively. Among other things, the last conditions guarantee that the metric $\bar{g}$ is bundle-like and any autoparallel of $\bar{M}$, which is orthogonal to a leaf of the foliation, is also orthogonal to every other leaf it meets [22].

In summary, the manifold scleronomicity conditions are expressed by Eqs. (81)-(84). These conditions do not depend on the basis selected on $T_p\bar{M}$. However, they take a very explicit and useful form when they are expressed in the special coordinate basis corresponding to the foliated coordinates of $\bar{M}$. In fact, taking into account that the metric is Riemannian, the two complementary foliations of $\bar{M}$ are now orthogonal, that is $D_T = D_M^{\perp}$ [3]. Therefore, the base vector $\underline{\bar{g}}_0$, corresponding to the temporal coordinate, is orthogonal to all the base vectors $\underline{\bar{g}}_i$ ($i = 1, \ldots, n$), corresponding to the spatial coordinates. At this point, it is clear that a foliated basis is a holonomic separable basis, while a foliated basis with $\underline{\bar{g}}_0$ orthogonal to $\underline{\bar{g}}_i$

corresponds to a holonomic standard basis. Also, the special vectors which are tangent to the leaf and transverse family of curves can be expressed in the form

$$\underline{h} = h^i(q)\underline{\overline{g}}_i \quad \text{and} \quad \underline{v} = v^0(\tau)\underline{\overline{g}}_0 ,$$

respectively, in a holonomic standard basis. Next, employing the first of Eqs. (81) and performing the necessary mathematical operations it turns out originally that

$$\nabla_{\underline{h}}\underline{h} = (h^K_{,I} + \overline{\Lambda}^K_{IJ}h^J)h^I\,\underline{\overline{g}}_K = (h^k_{,i} + \overline{\Lambda}^k_{ij}h^j)h^i\,\underline{\overline{g}}_k + \overline{\Lambda}^0_{ij}h^ih^j\,\underline{\overline{g}}_0 .$$

Then, a simultaneous application of Eq. (82a) leads eventually to the conditions

$$\overline{\Lambda}^k_{ij} = \overline{\Lambda}^k_{ij}(q) \quad \text{and} \quad \overline{\Lambda}^0_{ij} = 0 . \tag{85}$$

Treating Eqs. (81b) and (82b) in a similar manner yields

$$\overline{\Lambda}^0_{00} = \overline{\Lambda}^0_{00}(\tau) \quad \text{and} \quad \overline{\Lambda}^i_{00} = 0 . \tag{86}$$

Likewise, application of the two conditions in Eq. (83) leads to

$$\overline{\Lambda}^K_{0j} = 0 \;\Rightarrow\; \overline{\Lambda}^k_{0j} = \overline{\Lambda}^0_{0j} = 0 \quad \text{and} \quad \overline{\Lambda}^K_{i0} = 0 \;\Rightarrow\; \overline{\Lambda}^k_{i0} = \overline{\Lambda}^0_{i0} = 0 , \tag{87}$$

respectively. Finally, substituting the appropriate vector and tensor quantities in Eqs. (84) and performing the necessary mathematical operations, taking into account that the Lie derivative of the metric tensor along the flow defined by Eq. (77) is given by

$$L_{\underline{v}}g = [v^I g_{JK,I} + (v^I_{,J} - c^I_{LJ}v^L)g_{IK} + (v^I_{,K} - c^I_{LK}v^L)g_{IJ}]\underline{e}^J \otimes \underline{e}^K ,$$

leads eventually to

$$\tfrac{\partial}{\partial t}(g_M)_{ij} = 0 \;\Rightarrow\; g_M = g_M(q) \quad \text{and} \quad \tfrac{\partial}{\partial q}g_T = 0 \;\Rightarrow\; g_T = g_T(\tau) . \tag{88}$$

Thus, Eqs. (85)-(88) provide a set of scleronomicity conditions in component form, with respect to a standard basis. Obviously, these conditions are identical to the conditions stated earlier in the form of Eq. (13) or, alternatively, Eqs. (19) and (20).

7 EQUATIONS OF MOTION ON THE CONFIGURATION MANIFOLD

In Section 5, a set of equations of motion was derived on the constrained manifold M_A, with respect to a minimal set of coordinates. Such an approach is inconvenient to apply, especially for complex systems, since it requires the selection of a specific set of independent coordinates and elimination of the dependent coordinates through the constraint equations at every time instant. In general, this is not an easy task to achieve. Moreover, it requires differentiation of the constraint equations, leading to their violation at the lower kinematic level [2, 11]. In addition, the geometric properties of the constrained manifold need to be redetermined at every step, through Eqs. (11) and (12). For these reasons, it is frequently advantageous to derive the equations of motion on the original manifold M, for which the geometric properties are known and not affected by the additional constraints.

Next, it is assumed that the original configuration manifold M of the class of systems examined possesses time dependent geometric properties. Moreover, the system is subject to an additional set of k time dependent acatastatic motion constraints, in the form of Eq. (64), or equivalently in the form

$$\dot{\psi}^R(q,\underline{v},t) \equiv a^R_i(q,t)v^i + a^R_0(q,t) = 0 \quad (R = 1,\ldots,k). \tag{89}$$

When a constraint is holonomic, Eq. (89) can be integrated and cast in the form

$$\phi^R(q,t)=0\,.$$

The derivation of the equations of motion is based on a consistent application of Newton's law of motion, similar to that performed in an earlier study [15]. One of the basic ideas in that study was to consider the configuration manifold M as the total space of a fiber bundle with base space M_A and fibers consisting of the Cartesian product manifold $M_C=M_1\times\cdots\times M_k$, where the single dimensional manifolds M_R, $R=1,\ldots,k$, are related to the action of the R-th motion constraint. Since that study is applicable to scleronomic systems, some modifications are necessary before applying it here. First, based on Eq. (89), the velocity components of a vector in $T_p\bar{M}$ and $T_{p_R}\bar{M}_R$ are related by

$$\bar{v}^i=c_R^i\bar{v}^R+c_{R0}^i\bar{v}_R^0\quad(i=1,\ldots,n)\quad\text{and}\quad\bar{v}^0=\bar{v}_R^0\,,$$

which can be combined and put in the form of Eq. (65). Moreover, the components c_R^i and c_{R0}^i correspond to special vectors of $T_p\bar{M}$, for each constraint R, satisfying the conditions

$$a_i^R c_R^i=1\quad\text{and}\quad a_i^R c_{R0}^i=-a_0^R\quad(R=1,\ldots,k;\ i=1,\ldots,n).\tag{90}$$

In addition, a transformation similar to that represented by Eqs. (66) and (67) can be established between $T\bar{M}$ and $T\bar{M}_R$, through the $(n+1)\times 2$ matrix

$$\bar{N}_R=\begin{bmatrix}\underset{\sim}{c}_R(q,\tau) & \underset{\sim}{c}_{R0}(q,\tau)\\ 0 & 1\end{bmatrix}.$$

Therefore, the components of the metric and the affinities on the event manifold $\bar{M}_R$ can be determined by an equation similar to Eq. (68), while the Newton covectors on the dual space $T^*_{p_R}M_R$ are obtained by application of an equation similar to Eq. (76), with form

$$\begin{aligned}h_R=&(g_{RR}\bar{v}^R+\bar{g}_{R0})_{,R}\bar{v}^R+(g_{RR}\bar{v}^R+\bar{g}_{R0})_{,0}-(\bar{\Lambda}^R_{RR}g_{RR}+\bar{\Lambda}^0_{RR}\bar{g}_{0R})\bar{v}^R\bar{v}^R\\&-(\bar{\Lambda}^R_{RR}\bar{g}_{R0}+\bar{\Lambda}^0_{RR}\bar{g}_{00}+\bar{\Lambda}^R_{0R}g_{RR}+\bar{\Lambda}^0_{0R}g_{0R})\bar{v}^R-\bar{\Lambda}^R_{0R}\bar{g}_{R0}-\bar{\Lambda}^0_{0R}\bar{g}_{00}-f_R.\end{aligned}$$

Employing the connection compatibility condition and performing simple mathematical operations, the last expression can eventually be put in the form

$$h_R=(\bar{m}_{RR}\dot{\bar{\lambda}}^R+\bar{m}_{R0})^{\cdot}+\bar{c}_{RR}\dot{\bar{\lambda}}^R+\bar{k}_{RR}\bar{\lambda}^R-\bar{f}_R\,.\tag{91}$$

The quantity $\bar{\lambda}^R$ represents the spatial coordinate of the two dimensional manifold $\bar{M}_R$. Also, in the last equation and in the sequel, the convention on repeated indices does not apply to index R, while

$$\bar{m}_{RR}\equiv g_{RR}=c_R^i g_{ij}c_R^j\,,\quad \bar{m}_{R0}\equiv\bar{g}_{R0}=c_R^i(g_{ij}c_{R0}^j+\bar{g}_{i0})\,,\quad \bar{c}_{RR}=-c_R^i\frac{\partial f_i}{\partial v^j}c_R^j-c_{R,0}^i g_{ij}c_R^j\,,\quad \bar{k}_{RR}=-c_R^i f_{i,j}c_R^j$$

and

$$\bar{f}_R=c_R^i f_i+c_{R,0}^i(g_{ij}c_{R0}^j+\bar{g}_{i0})\,.\tag{92}$$

Following the analysis presented in [15], by incorporating the above modifications into the constraint equations and omitting the details, the equations of motion can be put in the form

$$\underset{\sim}{h}^*_M=\underset{\sim}{h}^*_C\tag{93}$$

on manifold M, with

$$\underset{\sim}{h}_M^* = h_i \, \underset{\sim}{e}^i \,,$$

where h_i is given by Eqs. (35) and (36), while

$$\underset{\sim}{h}_C^* = \sum\nolimits_{R=1}^{k} h_R \, a_i^R \underset{\sim}{e}^i \,,$$

with h_R given by Eq. (91). Next, substitution of the last two equations in Eq. (93) leads eventually to the following set of equations of motion on the original configuration manifold M

$$\begin{aligned}(g_{ij}\overline{v}^j + \overline{g}_{i0})^{\cdot} - (\overline{\Lambda}^{\ell}_{ji}\overline{g}_{\ell k} + \overline{\Lambda}^{0}_{ji}\overline{g}_{0k})\overline{v}^j\overline{v}^k + (\overline{\Lambda}^{\ell}_{ji}\overline{g}_{\ell 0} + \overline{\Lambda}^{0}_{ji}\overline{g}_{00} + \overline{\Lambda}^{\ell}_{0i}\overline{g}_{\ell j} + \overline{\Lambda}^{0}_{0i}\overline{g}_{0j})\overline{v}^j \\ + \overline{\Lambda}^{\ell}_{0i}\overline{g}_{\ell 0} + \overline{\Lambda}^{0}_{0i}\overline{g}_{00} - f_i = \sum\nolimits_{R=1}^{k} a_i^R[(\overline{m}_{RR}\dot{\overline{\lambda}}^R + \overline{m}_{R0})^{\cdot} + \overline{c}_{RR}\dot{\overline{\lambda}}^R + \overline{k}_{RR}\overline{\lambda}^R - \overline{f}_R],\end{aligned} \tag{94}$$

where

$(g_{ij}\overline{v}^j)^{\cdot} = (g_{ij}\overline{v}^j)_{,\ell}\,\overline{v}^{\ell} + (g_{ij}\overline{v}^j)_{,0}$ and $(\overline{m}_{RR}\dot{\overline{\lambda}}^R)^{\cdot} = (\overline{m}_{RR}\dot{\overline{\lambda}}^R)_{,R}\,\dot{\overline{\lambda}}^R + (\overline{m}_{RR}\dot{\overline{\lambda}}^R)_{,0}$.

The additional information needed for a complete mathematical formulation is obtained by incorporating an appropriate form of the k equations of the constraints. In particular, proceeding in a manner similar to that followed in previous work [15], a second order ordinary differential equation (ODE) is obtained for each holonomic constraint, with form

$$(\overline{m}_{RR}\dot{\phi}^R)^{\cdot} + \overline{c}_{RR}\dot{\phi}^R + \overline{k}_{RR}\phi^R = 0 \,, \tag{95}$$

which forces both $\dot{\phi}^R$ and ϕ^R to become zero eventually. Likewise, each nonholonomic constraint gives rise to a scalar ODE with form

$$(\overline{m}_{RR}\dot{\psi}^R)^{\cdot} + \overline{c}_{RR}\dot{\psi}^R = 0 \,, \tag{96}$$

causing $\dot{\psi}^R$ to become zero.

Next, by introducing the matrix notation

$\underline{\overline{q}} = (\overline{q}^1 \;\; \cdots \;\; \overline{q}^n)^T$, $\underline{\dot{\overline{\lambda}}} = (\dot{\overline{\lambda}}^1 \;\; \cdots \;\; \dot{\overline{\lambda}}^k)^T$, $\underline{\overline{v}} = (\overline{v}^1 \;\; \cdots \;\; \overline{v}^n)^T$ and $M = [g_{ij}]$,

Eq. (94) can be put in the following general form

$$(M(\underline{\overline{q}},t)\underline{\overline{v}})^{\cdot} + \underline{h}(\underline{\overline{q}},\underline{\overline{v}},t) = A^T(\underline{\overline{q}},t)[(\overline{M}\,\underline{\dot{\overline{\lambda}}})^{\cdot} + \underline{\overline{h}}(\underline{\overline{\lambda}},\underline{\dot{\overline{\lambda}}},t)] \,. \tag{97}$$

The array $\underline{h}(\underline{\overline{q}},\underline{\overline{v}},t)$ includes all the terms in Eq. (94) multiplied by the affinities or originating from the components $\overline{g}_{i0}$ of the metric on the event manifold $\overline{M}$, together with the applied forces f_i. Likewise, the elements of the diagonal matrix $\overline{M} = diag(\overline{m}_{11} \;\; \cdots \;\; \overline{m}_{kk})$ and the array $\underline{\overline{h}} \equiv \overline{C}\,\underline{\dot{\overline{\lambda}}} + \overline{K}\,\underline{\overline{\lambda}} + \underline{\dot{\overline{m}}}_0 - \underline{\overline{f}}$,

including the diagonal matrices $\overline{C} = diag(\overline{c}_{11} \;\; \cdots \;\; \overline{c}_{kk})$ and $\overline{K} = diag(\overline{k}_{11} \;\; \cdots \;\; \overline{k}_{kk})$ and the arrays $\underline{\dot{\overline{m}}}_0 = (\dot{\overline{m}}_{10} \;\; \cdots \;\; \dot{\overline{m}}_{k0})^T$ and $\underline{\overline{f}} = (\overline{f}_1 \;\; \cdots \;\; \overline{f}_k)^T$, are determined through application of Eq. (92).

In summary, Eq. (94) furnishes a set of n second order ODEs. These equations together with Eqs. (95) and (96) form a set of $n+k$ second order ODEs in the $n+k$ unknown coordinates q^i and λ^R, describing the behavior of mechanical systems with an arbitrary (but finite) number of coordinates, possessing a time dependent original configuration manifold and being subject to time dependent and acatastatic motion constraints. In general, solution of these equations can only be achieved by numerical means, after applying a suitable numerical discretization [20, 25]. For the scleronomic case, it is easy to verify that these equations are simplified considerably and become identical with those presented in [15]. The ODE form of the

set of equations derived is associated with several advantages over formulations leading to sets of algebraic-differential equations (DAEs) [2, 11]. It also presents advantages over previous formulations leading to an ODE form after elimination of the redundant coordinates or the Lagrange multipliers from the equations of motion, since this is done at the expense of violating the motion constraints at the lower kinematical levels [2, 15]. Finally, another advantage of the present approach is that the affinities are independent and not derived from the metric components (i.e., the connection is not necessarily metric compatible). This allows for the most general and consistent derivation of the equations of motion [19].

8 EXAMPLES

Two examples are presented in this section, illustrating theoretical aspects investigated in the previous sections. The first refers to motion of a constrained particle, with attention on recognizing when a constraint is scleronomic or rheonomic. Then, the problem of the rolling motion of a sphere over a rotating table is re-examined, by employing the scleronomicity conditions developed in Section 6.

8.1 Spherical pendulum with a moving end

Consider the spatial motion of a particle with mass m. The unconstrained motion is described by three coordinates x^i with respect to an inertial Cartesian coordinate frame $\mathbb{X}$. Then, the components of the metric tensor and the affinities can be easily determined for both the configuration manifold $M = E^3$ and the corresponding event manifold $\bar{E}^3 = E^3 \times \mathbb{R}$. The particle motion is constrained by a rigid bar with negligible mass and length L, as shown in Fig. 5. The particle is located at one end of the bar, while the other end (point P) moves along the axis Ox^3 with a known displacement history

$$x_P(t) = \hat{x}_P \cos \omega t \, .$$

This is represented by a holonomic constraint with equation

$$\phi^1(x,t) = (x^1)^2 + (x^2)^2 + (x^3 - x_P(t))^2 - L^2 = 0 \, , \tag{98}$$

which by differentiation with respect to time can be put in the general form of Eq. (89), with

$$\underset{\sim}{a}^1(x,t) = (2x^1 \quad 2x^2 \quad 2(x^3 - x_P(t))) \quad \text{and} \quad a_0^1(x,t) = -2(x^3 - x_P(t))\dot{x}_P(t) \, .$$

Next, consider the motion of the particle with respect to a new set of coordinates, corresponding to a new frame $\mathbb{S}$. This frame has origin at point P and axes remaining parallel to the axes of frame $\mathbb{X}$. Due to the constraint by Eq. (98), the position of the particle can be fully determined by the angular spherical coordinates θ^1 and θ^2, as depicted in Fig. 5. Specifically, the following relations are established between the original Cartesian coordinates and these spherical coordinates

$$x^1 = L \sin\theta^1 \cos\theta^2 \, , \quad x^2 = L \sin\theta^1 \sin\theta^2 \quad \text{and} \quad x^3 = L \cos\theta^1 + \hat{x}_P \cos \omega t \, . \tag{99}$$

Then, the velocity transformation (66) is set up with extended matrix $\bar{N}$ in the form of Eq. (67), with

$$N = \begin{bmatrix} L\cos\theta^1 \cos\theta^2 & -L\sin\theta^1 \sin\theta^2 \\ L\cos\theta^1 \sin\theta^2 & L\sin\theta^1 \cos\theta^2 \\ -L\sin\theta^1 & 0 \end{bmatrix} \quad \text{and} \quad \underline{v} = \begin{pmatrix} 0 \\ 0 \\ -\omega \hat{x}_P \sin \omega t \end{pmatrix} .$$

Substituting the above into Eq. (69), the metric matrix is determined in the form

$$\bar{g}_A = \begin{bmatrix} mL^2 & 0 & m\omega L\hat{x}_P \sin\theta^1 \sin\omega t \\ 0 & mL^2 \sin^2\theta^1 & 0 \\ m\omega L\hat{x}_P \sin\theta^1 \sin\omega t & 0 & g_{00} + m(\omega\hat{x}_P \sin\omega t)^2 \end{bmatrix}.$$

This result shows that the basis obtained in $\bar{M}_A$ is not standard. In addition, it is found that there exist both pure and mixed affinities, which are expressions of coordinates θ^1, θ^2 and t.

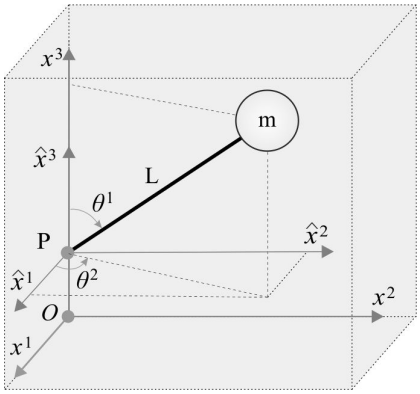

Fig. 5 A spherical pendulum with a translating end

Next, the emphasis was placed in investigating whether these effects are removable by a change of basis in $\bar{M}_A$. Using integrability conditions, the following change of coordinates

$$\theta^1 = 2\tan^{-1}(e^{\hat{\theta}^1 + \cos\omega\hat{\tau}}), \quad \theta^2 = \hat{\theta}^2 \quad \text{and} \quad \tau = \hat{\tau}, \tag{100}$$

was found to lead to a coordinate basis where the new metric matrix is block diagonal. In fact, the metric matrix in the new coordinate system is obtained in the 3×3 diagonal form

$$\hat{\bar{g}}_A = diag(mL^2 \sin\eta(\hat{\theta}^1,\hat{\tau}) \quad mL^2 \sin\eta(\hat{\theta}^1,\hat{\tau}) \quad g_{00} + m[\omega\hat{x}_P \cos\eta(\hat{\theta}^1,\hat{\tau})\sin\omega t]^2),$$

with

$$\eta(\hat{\theta}^1,\hat{\tau}) = 2\tan^{-1}(e^{\hat{\theta}^1 + \cos\omega\hat{\tau}}).$$

However, all its elements have a mixed dependence on both the spatial coordinate $\hat{\theta}^1$ and the temporal coordinate $\hat{\tau}$. Similar findings resulted in evaluating the corresponding affinities. These imply that conditions (13), or alternatively Eqs. (85)-(88), do not hold in the case examined. Therefore, the manifold M_A is rheonomic. Since the original manifold M is scleronomic, the motion constraint expressed by Eq. (98) is rheonomic, in accordance with the classical definitions [12].

Next, consider the motion of the particle with respect to a new Cartesian coordinate frame $\mathbb{Y}$, with coordinates y^i $(i=1,2,3)$, in the same configuration manifold M. In particular, the origin of this frame is point P, while its axes remain parallel to the corresponding axes of frame $\mathbb{X}$, as shown in Fig. 5. Then, the two sets of coordinates are related by

$$x^1 = y^1, \quad x^2 = y^2 \quad \text{and} \quad x^3 = y^3 + \hat{x}_P \cos\omega t. \tag{101}$$

In the new coordinate system, the motion constraint appears also in a holonomic form

$$\phi^1(y,t) = (y^1)^2 + (y^2)^2 + (y^3)^2 - L^2 = 0. \tag{102}$$

However, in contrast to Eq. (98), this now appears in a scleronomic catastatic form, according to common terminology [12, 23]. In order to explain the discrepancy with Eq. (98), it is useful to view Eq. (101), together with $t = \hat{t}$, as a coordinate transformation in the original event manifold $\bar{M} = \bar{E}^3$, similar to that expressed by Eq. (39). Then, the Jacobian is obtained in the form of Eq. (42), with

$$J = I_3 \quad \text{and} \quad \underline{c} = (0 \quad 0 \quad -\omega \hat{x}_P \sin \omega t)^T .$$

Consequently, evaluation of the metric in the new basis of $\bar{E}^3$ through Eq. (48) yields

$$\hat{g} = g = mI_3 , \quad \underline{g}_{\hat{0}} = (0 \quad 0 \quad -m\omega \hat{x}_P \sin \omega t)^T \quad \text{and} \quad g_{\hat{0}\hat{0}} = g_{00} + m(\omega \hat{x}_P \sin \omega t)^2 .$$

As expected, based on the fact that $\underline{c} \neq \underline{0}$, the new basis in $T_p \bar{M}$ is not standard, since $\underline{g}_{\hat{0}} \neq \underline{0}$ for $\omega \hat{x}_P \neq 0$. Moreover, all the affinities on $\bar{M}$ are found to be equal to zero, exception for

$$\bar{\Lambda}^{\hat{3}}_{\hat{0}\hat{0}} = \omega^2 \hat{x}_P \cos \omega t .$$

Therefore, despite the fact that it does not involve time in an explicit manner, the motion constraint expressed by Eq. (102) is in fact rheonomic, since the configuration manifold M is scleronomic, while the constrained manifold M_A is rheonomic, as shown above. This result resolves the difference observed in the time dependence appearing in the constraint equations (98) and (102). Furthermore, it demonstrates that the classical classification of constraints on a mechanical system with configuration manifold possessing time dependent geometric properties is accurate only when the components involved in the constraint equations are expressed with respect to standard bases in both $\bar{M}$ and $\bar{M}_A$.

8.2 Rolling of a sphere on a rotating table

Next, consider the motion of a rigid sphere, rolling without slipping on a horizontal table [9]. This table rotates with an angular speed $\Omega(t)$ with respect to a fixed vertical axis Ox^3, as shown in Fig. 6. The sphere has radius r, mass m and a known mass moment of inertia J with respect to any axis passing through its center of mass C. The coordinate system $\mathbb{F}$, shown in Fig. 6, is fixed (inertial) and the angular velocity of the table is

$$\underline{\omega}_T(t) = \Omega(t)\underline{e}_3 . \tag{103}$$

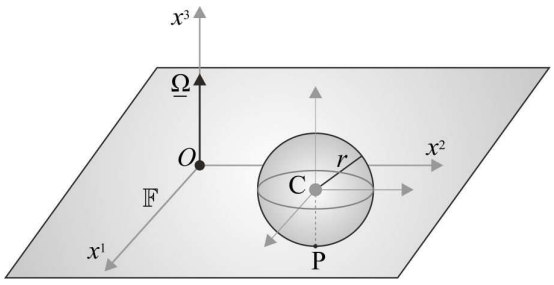

Fig. 6 Rigid sphere rolling over a rotating table

First, the position of the sphere is determined at any time t by the generalized coordinates

$$\underline{q}(t) = (\underline{x}_C^T \quad \underline{\theta}^T)^T , \tag{104}$$

where the arrays

$$\underline{x}_C = (x^1 \quad x^2 \quad x^3)^T \quad \text{and} \quad \underline{\theta} = (\theta^1 \quad \theta^2 \quad \theta^3)^T$$

represent the position of the center of mass and the orientation of the sphere, respectively, with respect to the inertial reference frame $\mathbb{F}$. Due to the symmetry of the sphere, the classical Cartesian rotation vector is selected for the description of its rotational motion [11]. The coordinates $\underline{q}(t)$ represent a point on a product configuration manifold $M = \mathbb{R}^3 \times M(3)$, with dimension n=6 [18]. Then, the motion of the system can be viewed as the motion of a point along a specific path $\gamma(t)$ on manifold M, with tangent vector given by

$$\underline{v}(t) = (\underline{v}_C^T \quad \underline{\omega}^T)^T,$$

where

$$\underline{v}_C = (v^1 \quad v^2 \quad v^3)^T \quad \text{and} \quad \underline{\omega} = (\omega^1 \quad \omega^2 \quad \omega^3)^T,$$

with $v^i = \dot{x}^i$ $(i = 1,2,3)$. Moreover, the quasi-velocities $\underline{\omega}$ are related to the true angular velocities $\dot{\underline{\theta}}$ through the corresponding tangent operator $T(\underline{\theta})$ at $\underline{\theta}$ [11], by

$$\underline{\omega} = T^T(\underline{\theta})\dot{\underline{\theta}}.$$

Then, based on the kinetic energy of the sphere, the metric of M is found in the block diagonal form

$$g = [g_{ij}] = \begin{bmatrix} mI_3 & 0 \\ 0 & JI_3 \end{bmatrix}. \tag{105}$$

Moreover, since the manifold M examined is a product manifold, its affinities appear in product form as well. In particular, all the affinities related to the translational part can be selected to be zero, while the non-zero affinities related to the rotational part of the motion can be chosen to take the following constant values in a body frame

$${}_R\Lambda^1_{23} = -{}_R\Lambda^1_{32} = {}_R\Lambda^2_{31} = -{}_R\Lambda^2_{13} = {}_R\Lambda^3_{12} = -{}_R\Lambda^3_{21} = 1. \tag{106}$$

Moreover, all the mixed affinities are zero [18]. Then, the affinities can be evaluated in the coordinate system used by employing the rotation matrix $R = \exp(\tilde{\theta})$ as a transformation matrix in Eq. (46).

Next, due to the constraints imposed on the motion of the sphere, there appear $k = 3$ constraint equations, so that the dimension of manifold M_A is just $m = 3$. Specifically, the first constraint is holonomic and guarantees that the center of the sphere stays on a constant height

$$\phi^1 = x^3 - r = 0 \quad \Rightarrow \quad \dot{\phi}^1 = v^3 = 0. \tag{107}$$

In addition, the rolling condition of the sphere leads to two more constraints, namely

$$\psi^2 = \dot{x}^1 - r\omega^2 + \Omega x^2 = 0 \quad \text{and} \quad \psi^3 = \dot{x}^2 + r\omega^1 - \Omega x^1 = 0, \tag{108}$$

which are nonholonomic and acatastatic. Therefore, the 3×6 matrix of constraints A and the vector $\underline{a}$ appearing in Eq. (64) take the form

$$A = \begin{bmatrix} 0 & 0 & 1 & 0 & 0 & 0 \\ 1 & 0 & 0 & 0 & -r & 0 \\ 0 & 1 & 0 & r & 0 & 0 \end{bmatrix} \quad \text{and} \quad \underline{a}(\underline{q},t) = \begin{pmatrix} 0 \\ \Omega x^2 \\ -\Omega x^1 \end{pmatrix}. \tag{109}$$

Based on these results, one can determine the components of the special constraint vectors $\underline{c}_R$ and $\underline{c}_{R0}$ by Eq. (90). For instance, a possible choice for these vectors is the following

$$\underline{c}_1 = (0 \quad 0 \quad 1 \quad 0 \quad 0 \quad 0)^T, \quad \underline{c}_2 = (0 \quad 0 \quad 0 \quad 0 \quad -1/r \quad 0)^T, \quad \underline{c}_3 = (0 \quad 0 \quad 0 \quad 1/r \quad 0 \quad 0)^T,$$

$$\underline{c}_{10} = \underline{0}, \quad \underline{c}_{20} = (0 \quad 0 \quad 0 \quad 0 \quad \Omega x^2/r \quad 0)^T \quad \text{and} \quad \underline{c}_{30} = (0 \quad 0 \quad 0 \quad \Omega x^1/r \quad 0 \quad 0)^T.$$

Consequently, application of the first two relations in Eq. (92) leads to determination of the elements of the diagonal mass matrix $\bar{M}$ and the vector $\bar{\underline{m}}_0$ in the form

$$\bar{m}_{11} = m, \quad \bar{m}_{22} = \bar{m}_{33} = J/r^2, \quad \bar{m}_{10} = 0, \quad \bar{m}_{20} = -\Omega x^2 J/r^2 \quad \text{and} \quad \bar{m}_{30} = \Omega x^1 J/r^2.$$

Likewise, given a set of applied forces acting on the sphere, which can be represented by a resultant force $\underline{f}(\underline{q}, \underline{\dot{q}}, t)$ and moment $\underline{m}_C(\underline{q}, \underline{\dot{q}}, t)$ with respect to its center C [21], the elements $\bar{c}_{RR}$ and $\bar{k}_{RR}$ of the diagonal damping and stiffness matrices $\bar{C}$ and $\bar{K}$, as well as the corresponding forcing terms $\bar{f}_R$ ($R = 1, \ldots, 3$) are also evaluated by applying Eq. (92).

Collecting all the above and substituting in Eq. (94) leads to the equations of motion of the constrained system examined on the original configuration manifold in matrix form. The set of coordinates $\underline{q}$ is given by Eq. (104), while the Lagrange multipliers $\underline{\lambda} = (\lambda^1 \quad \lambda^2 \quad \lambda^3)^T$ correspond to the set of constraints (107) and (108). In the present formulation, the six ODEs represented by Eq. (97) are accompanied by a constraint equation in the form of Eq. (95) and two constraint equations in the form of Eq. (96), where the terms ϕ^1, $\dot{\phi}^1$, ψ^2 and $\dot{\psi}^3$ are taken from Eqs. (107) and (108). This leads to a system of 9 second order ODEs for the 9 unknowns, $\underline{q}$ and $\underline{\lambda}$, of the problem.

Finally, a simple inspection of Eqs. (105) and (106) reveals that the original configuration manifold M is scleronomic. Moreover, based on Eq. (109), an appropriate 7×4 transformation matrix $\bar{N}$ is first determined in the form of Eq. (67), so that the 4×4 metric matrix corresponding to the event constrained manifold $\bar{M}_A$ is determined by application of Eq. (69) in the diagonal form

$$\bar{g}_A = diag((m + J/r^2) \quad (m + J/r^2) \quad J \quad g_{00} + mJ\Omega^2[(\theta^1)^2 + (\theta^2)^2]/(mr^2 + J)),$$

where θ^α (with $\alpha = 1, \ldots, 4$) is a coordinate set on $\bar{M}_A$. This corresponds to a standard basis. Evaluation of the corresponding structure constants shows that they are all zero, except for

$$c^1_{02} = -c^1_{20} = J\Omega/(mr^2 + J) = c^2_{10} = -c^2_{01}.$$

This indicates that the basis selected in $\bar{M}_A$ is not holonomic. Therefore, it is more convenient here to apply the scleronomicity checks in the coordinate invariant form presented in Section 6 in order to judge safely whether the constrained manifold is rheonomic or not. Indeed, application of Eq. (84) to the example considered reveals that the first condition on the metric is satisfied identically. However, evaluation of the Lie derivative required by the second condition in the same equation shows that there appears the following non-zero term

$$(L_{\underline{h}} \bar{g}_T)_{00} = 2mJ\Omega^2/(mr^2 + J),$$

which becomes zero only when $\Omega = 0$, corresponding to a stationary table. This demonstrates that Eq. (84) is violated when $\Omega \neq 0$ and reveals that manifold M_A is rheonomic, indeed.

9 SYNOPSIS

This study was devoted to mechanical systems possessing configuration manifolds with time dependent geometric properties and being subject to additional acatastatic equality motion constraints involving time explicitly. This time dependence, in conjunction with the need to keep invariant the form of Newton's law in different manifolds, led to an introduction and consideration of the corresponding event manifold. These time dependent terms were shown to be introduced by either a basis transformation in the event manifold or by additional motion constraints. Moreover, the time terms introduced by a basis transformation are artificial and can be removed from the equations of motion. These results were reinforced and enhanced further by exploiting some concepts of foliation theory. Apart from providing useful clarifications on the geometry of the motion, this theory was also employed in establishing a set of coordinate invariant conditions for judging whether a configuration manifold is scleronomic. Finally, the equations of motion were obtained in the original configuration manifold, in the presence of constraints. Also, some of the analytical findings were illustrated by examining two systems exhibiting basic features of the class of systems examined.

The results presented in this work are applicable and cover a wide range of engineering systems. To obtain them, some useful tools from differential geometry were employed. In return, apart from providing a nice interpretation of the key concepts, these tools helped in performing a consistent application of Newton's law to manifolds with general time dependent geometric properties. Eventually, this led to a system of second order ODEs, which are much easier to handle than sets of DAEs [2, 11]. In addition, the final set of equations of motion was obtained on the original configuration manifold, whose geometric properties are not affected by the presence of the additional motion constraints. Also, these equations involve properties of the corresponding event manifold. These provide fertile ground for developing new advanced formulations, leading to more accurate, effective and robust numerical methods for solving these equations, by enhancing available techniques [6, 13, 20].

REFERENCES

[1] Arnold, V.I.: *Mathematical Methods of Classical Mechanics, second ed*. Springer-Verlag, Berlin, 1989.

[2] Bauchau, O.A.: *Flexible Multibody Dynamics*. Springer Science+Business Media B.V., London, 2011.

[3] Bejancu, A., Farran, H.R.: *Foliations and Geometric Structures*. Springer, Netherlands, 2006.

[4] Bloch, A.M.: *Nonholonomic Mechanics and Control*. Springer-Verlag, New York, 2003.

[5] Bowen, R.M., Wang, C.-C.: *Introduction to Vectors and Tensors, second ed*. Dover Publications, Mineola, New York, 2008.

[6] Brüls, O., Cardona, A., Arnold, M.: Lie group generalized-α time integration of constrained flexible multibody systems. *Mechanism and Machine Theory* **48**, 121-137, 2012.

[7] Casey, J.: Geometrical derivation of Lagrange's equations for a system of particles. *Am. J. Phys.* **62**, 836–847, 1994.

[8] Chetaev, N.G.: *Theoretical Mechanics*. Mir Publishers, Moscow, 1989.

[9] Essen, H.: On the geometry of nonholonomic dynamics. *ASME J. Appl. Mech.* **61**, 689-694, 1994.

[10] Frankel, T.: *The Geometry of Physics: An Introduction*. Cambridge University Press, New York, 1997.

[11] Geradin, M., Cardona, A.: *Flexible Multibody Dynamics*. John Wiley & Sons, New York, 2001.

[12] Greenwood, D.T.: *Classical Dynamics*. Dover Publications, New York, 1977.

[13] Lew, A., Marsden, J.E., Ortiz, M., West, M.: Asynchronous variational integrators. *Arch. Rational Mech. Anal.* **167**, 85-146, 2003.

[14] Molino, P.: *Riemannian Foliations*, Progress in Math. **73**, Birkhauser, Boston, 1988.

[15] Natsiavas, S., Paraskevopoulos, E.: A set of ordinary differential equations of motion for constrained mechanical systems. *Nonlinear Dyn.* ***79***, 1911-1938, 2015.

[16] Neimark, J.I., Fufaev, N.A.: *Dynamics of Nonholonomic Systems*, Translations of Mathematical Monographs, American Mathematical Society **33**, 1972.

[17] Papastavridis, J.G.: *Tensor Calculus and Analytical Dynamics*. CRC Press, Boca Raton, 1999.

[18] Paraskevopoulos, E., Natsiavas, S.: A new look into the kinematics and dynamics of finite rigid body rotations using Lie group theory. *Int. J. Solids Struct.* **50**, 57-72, 2013.

[19] Paraskevopoulos, E., Natsiavas, S.: On application of Newton's law to mechanical systems with motion constraints. *Nonlinear Dyn.* **72**, 455-475, 2013.

[20] Paraskevopoulos, E., Natsiavas, S.: Weak formulation and first order form of the equations of motion for a class of constrained mechanical systems. *Int. J. Non-linear Mech.* 77, 208-222, 2015.

[21] Pars, L.A.: *A Treatise on Analytical Dynamics*. Heinemann Educational Books, London, 1965.

[22] Reinhart, B.L.: *Differential Geometry of Foliations*. Springer–Verlag, Berlin, 1983.

[23] Rosenberg, R.M.: *Analytical Dynamics of Discrete Systems*. Plenum Press, New York 1977.

[24] Shabanov, S.V.: Constrained systems and analytical mechanics in spaces with torsion. J. *Phys. A: Mathematical and General* **31**, 5177-5190, 1998.

[25] Simo, J.C., Tarnow, N., Wong, K.K.: Exact energy-momentum conserving algorithms and symplectic schemes for nonlinear dynamics. *Comp. Meth. Appl. Mech. Eng.* **100**, 63-116, 1992.

[26] Udwadia, F.E., Kalaba, R.E.: *Analytical Dynamics a New Approach*. Cambridge University Press, Cambridge, 1996.

ECCOMAS Congress 2016
VII European Congress on Computational Methods in Applied Sciences and Engineering
M. Papadrakakis, V. Papadopoulos, G. Stefanou, V. Plevris (eds.)
Crete Island, Greece, 5–10 June 2016

Parameter Estimation of Nonlinear Large Scale Systems through Stochastic Methods and Measurement of its Dynamic Response

Dimitrios Giagopoulos[1], Alexandros Arailopoulos[1]

[1] Department of Mechanical Engineering, University of Western Macedonia
Kozani 50100, Greece
e-mail: dgiagopoulos@uowm.gr, aarailopoulos@uowm.gr

Keywords: Large Scale Models, Nonlinear Dynamics, System Identification, Substructuring.

Abstract. *In this work, a computational framework is presented in order to estimate the optimal values of the linear and nonlinear components of large scale dynamical systems using vibration measurements. An extensible framework for Bayesian Uncertainty Quantification and Propagation of complex and computationally demanding physical models, was connected in an efficient way with a numerical code leading to an automated determination of dynamic response of linear and nonlinear mechanical systems. The effect of correlation in the prediction error models postulated in the Bayesian model selection and parameter estimation technique is investigated. The measurements are taken to be either response time histories or frequency response functions. The framework was applied in two complex mechanical systems. First examined a lightweight bicycle frame with the nonlinear front suspension component. In this system uncertainty models of the linear and nonlinear suspension components are identified using the experimentally obtained transmissibility functions. These uncertainties, integrated with uncertainties in the linear frame of the bicycle, are propagated in order to estimate the uncertainties for the combined system. The second system examined include a two stage gear transmission system. In this model the housing of the gearbox is modeled by using finite elements, while the essential effects of the gear-pair, the bearings and the shafts are taken into account via a lumped nonlinear mathematical model. This model possesses strongly nonlinear characteristics, accounting for gear backlash, meshing stiffness, transmission error properties and bearing stiffness nonlinearities. In order to identify the values of the parameters, accelerations time histories are used, obtained during various operating conditions of the gearbox. These measurements are recorded from a special experimental device (Drivetrain Prognostics Simulator). The computational challenges are outlined and the effectiveness of the framework on these two complex mechanical systems is demonstrated.*

1 INTRODUCTION

The main objective of the present work is to demonstrate the advantages of applying appropriate numerical and experimental methodologies in order to identify, update and optimize the model parameters and develop a high fidelity finite element model of both linear and non-linear components, comprising the whole assembly of the examined structure. In this process, many issues are taken into account, related to the development of FE model, the experimental modal analysis procedure and the development of effective computational model updating techniques.

The equations of motion of mechanical systems with complex geometry are first set up, applying classical finite element techniques. As the order of these models increases, the existing numerical and experimental methodologies for a systematic determination of their dynamic response become inefficient to apply. Therefore, there is a need for the development, improvement and application of new suitable methodologies for investigating dynamics of large-scale mechanical models in a systematic and efficient way. Moreover, in order to optimize the FE model of a structure, structural model updating methods [11], have been proposed in order to reconcile the numerical (FE) model, with experimental data. Structural model parameter estimation based on measured modal data (e.g. [4-10]) are often formulated as weighted least-squares estimation problems in which metrics, measuring the residuals between measured and model predicted modal characteristics, are build up into a single weighted residuals metric formed as a weighted average of the multiple individual metrics using weighting factors. Standard gradient-based optimization techniques are then used to find the optimal values of the structural parameters that minimize the single weighted residuals metric representing an overall measure of fit between measured and model predicted modal characteristics. Due to model error and measurement noise, the results of the optimization are affected by the values assumed for the weighting factors.

In this work, the applicability and effectiveness of the updating methods, coupled with robust, accurate and efficient finite element analysis software are applied on linear and non-linear components of a whole structure using experimentally identified modal data. The framework was applied in two complex mechanical systems. First examined a lightweight bicycle frame with the nonlinear front suspension component. The second system examined include a two stage gear transmission system. In this work was selected to be presented in detail only the results of the first system. More specifically, a lightweight and geometrically complex bicycle frame as well as the suspension-fork subassembly of a real bicycle are examined, comprising the linear and nonlinear subsystems of the whole bike assembly. Furthermore, the suspension-fork subassembly is consisted of two linear parts (upper and lower fork part) connected with two springs and two seals which impose strong nonlinearity in the system. Issues related to estimating unidentifiable solutions [12-15] arising in FE model updating formulations are also addressed. A systematic study is carried out to demonstrate the effect of model error, finite element model parameterization, number of measured modes and number of mode shape components on the optimal models and their variability. It is demonstrated that the updated finite element models obtained using measured modal data may vary considerably.

The organization of this paper is as follows. First in the first section, the theoretical formulation of finite element model updating based on modal characteristics and frequency response functions is briefly presented. In the second section, the experimental device is introduced. First, a quick presentation of the digitization of the bicycle components leading to the final parametric CAD model is shown with the corresponding detailed FE models. Next presented the experimental modal analysis procedure followed in order to identify the modal

characteristics and the FRF's. Finally, the parametric studies on updating the linear and nonlinear FE models of the bicycle components, with the predictions of frequency response functions and time histories, based on the optimal models, are presented in the fourth section. Conclusions are summarized in the fifth section.

2 FINITE ELEMENT MODEL UPDATING METHODS

2.1 Modal Residuals

Let $D=\{\hat{\omega}_r,\hat{\underline{\phi}}_r \in R^{N_o}, r=1,\cdots,m\}$ be the measured modal data from a structure, consisting of modal frequencies $\hat{\omega}_r$ and mode shape components $\hat{\underline{\phi}}_r$ at N_o measured DOFs, where m is the number of observed modes. Consider a parameterized class of linear structural models used to model the dynamic behavior of the structure and let $\underline{\theta}\in R^{N\theta}$ be the set of free structural model parameters to be identified using the measured modal data. The objective in a modal-based structural identification methodology is to estimate the values of the parameter set $\underline{\theta}$ so that the modal data $\{\omega_r(\underline{\theta}),\ \underline{\phi}_r(\underline{\theta})\in R^{N_0}, r=1,\cdots,m\}$ predicted by the linear class of models at the corresponding N_0 measured DOFs best matches the experimentally obtained modal data in D. For this, let

$$\varepsilon_{\omega_r}(\underline{\theta})=\frac{\omega_r^2(\underline{\theta})-\hat{\omega}_r^2}{\hat{\omega}_r^2} \quad \text{and} \quad \varepsilon_{\underline{\phi}}(\underline{\theta})=\frac{\left\|\beta_r(\underline{\theta})\underline{\phi}_r(\underline{\theta})-\hat{\underline{\phi}}_r\right\|}{\left\|\hat{\underline{\phi}}_r\right\|} \tag{1}$$

be the measures of fit or residuals [16] between the measured modal data and the model predicted modal data for the r-th modal frequency and mode shape components, respectively, where $\|\underline{z}\|^2=\underline{z}^{\mathrm{T}}\underline{z}$ is the usual Euclidean norm, and $\beta_r(\underline{\theta})=\hat{\underline{\phi}}_r^T\underline{\phi}_r(\underline{\theta})/\left\|\underline{\phi}_r(\underline{\theta})\right\|^2$ is a normalization constant that guaranties that the measured mode shape $\hat{\underline{\phi}}_r$ at the measured DOFs is closest to the model mode shape $\beta_r(\underline{\theta})\underline{\phi}_r(\underline{\theta})$ predicted by the particular value of $\underline{\theta}$. To proceed with the model updating formulation, the measured modal properties are grouped into two groups. The first group contains the modal frequencies while the second group includes the mode shape components for all modes. For each group, a norm is introduced to measure the residuals of the difference between the measured values of the modal properties involved in the group and the corresponding modal values predicted from the model class for a particular value of the parameter set $\underline{\theta}$. For the first group, the measure of fit $J_1(\underline{\theta})$ is selected to represent the difference between the measured and the model predicted frequencies for all modes. For the second group, the measure of fit $J_2(\underline{\theta})$ is selected to represent the difference between the measured and the model predicted mode shape components for all modes. Specifically, the two measures of fit are given by

$$J_1(\underline{\theta})=\sum_{r=1}^{m}\varepsilon_{\omega_r}^2(\underline{\theta}) \quad \text{and} \quad J_2(\underline{\theta})=\sum_{r=1}^{m}\varepsilon_{\underline{\phi}_r}^2(\underline{\theta})=\sum_{r=1}^{m}\left[1-MAC_r^2(\underline{\theta})\right] \tag{2}$$

where $MAC_r(\underline{\theta})=\underline{\phi}_r{}^T\hat{\underline{\phi}}_r(\underline{\theta})/\left\|\underline{\phi}_r\right\|\left\|\hat{\underline{\phi}}_r\right\|$ is the Modal Assurance Criterion [23] between experimentally identified and estimated mode shapes for the r-th mode. Alternative measures of fit can easily be used and found in literature [18-22].

2.2 Response Residuals

Derived from the MAC for any measured frequency point, ω_k a global correlation coefficient may be used [17, 24]:

$$x_s(\omega_k)=\frac{\left|\{H_X(\omega_k)\}^H\{H_A(\omega_k)\}\right|^2}{\left(\{H_X(\omega_k)\}^H\{H_X(\omega_k)\}\right)\left(\{H_A(\omega_k)\}^H\{H_A(\omega_k)\}\right)} \tag{3}$$

where $\{H_X(\omega_k)\}$ and $\{H_A(\omega_k)\}$ are the experimental (measured) and the analytical (predicted) response vectors at matching excitation - response locations. As the MAC value, $x_s(\omega_k)$ assumes a value between zero and unity and indicates perfect correlation with $x_s(\omega_k)=1$. For $x_s(\omega_k)=0$, no correlation exists. Similar to the MAC, $x_s(\omega_k)$ is unable to detect scaling errors and is only sensitive to discrepancies in the overall deflection shape of the structure. To emphasis this characteristic, $x_s(\omega_k)$ is accordingly called the shape correlation coefficient [24].

The lack of sensitivity to scaling of the shape correlation coefficient does not allow the identification of identical FRFs. This insufficiency becomes even more dramatic if just one measurement and its corresponding prediction are correlated. In this case, the column vectors reduce to scalars and $\{H_A(\omega_k)\}=k\{H_X(\omega_k)\}$ is always satisfied (constant k may be complex), therefore leading to $x_s=1$ across the full frequency spectrum for uncorrelated FRFs.

As a result, a supplementary correlation coefficient $x_a(\omega_k)$ is proposed by targeting the discrepancies in amplitude. The amplitude correlation coefficient is defined as:

$$x_a(\omega_k)=\frac{2\left|\{H_X(\omega_k)\}^H\{H_A(\omega_k)\}\right|}{\left(\{H_X(\omega_k)\}^H\{H_X(\omega_k)\}\right)+\left(\{H_A(\omega_k)\}^H\{H_A(\omega_k)\}\right)} \tag{4}$$

where the response vectors are identical to those used for $x_s(\omega_k)$. As for the shape correlation coefficient, $x_a(\omega_k)$ is defined to lie between zero and unity. This time, however, the correlation measure is more stringent and only becomes unity if $\{H_A(\omega_k)\}=\{H_X(\omega_k)\}$. That is to say, all elements of the response vectors must be identical in both phase and amplitude even if only one measurement is considered. Similarly to modal residuals, two measures of fit are proposed using $x_s(\hat{\omega}_r)$ and $x_a(\hat{\omega}_r)$ which correspond to the identified resonant frequencies of the system:

$$J_3(\underline{\theta})=\sum_{r=1}^{m}\left[1-x_s(\hat{\omega}_r,\underline{\theta})^2\right] \text{ and } J_4(\underline{\theta})=\sum_{r=1}^{m}\left[1-x_a(\hat{\omega}_r,\underline{\theta})^2\right] \tag{5}$$

2.3 Weighting Residuals Method

Minimizing at global minimum the following single objective, traditionally solves the parameter estimation problem:

$$J(\underline{\theta};\underline{w})=w_1J_1(\underline{\theta})+w_2J_2(\underline{\theta})+w_3J_3(\underline{\theta})+w_4J_4(\underline{\theta}) \tag{6}$$

formed by the four objectives $J_i(\underline{\theta})$, using the weighting factors $w_i\geq 0$, $i=1,2,3,4$, with $w_1+w_2+w_3+w_4=1$. The objective function $J(\underline{\theta};\underline{w})$ represents an overall measure of fit between the measured and the model predicted characteristics. The relative importance of the residual errors in the selection of the optimal model is reflected in the choice of the weights. The

results of the identification depend on the weight values used. The optimal solutions for the parameter set $\underline{\theta}$ for given $\underline{w}$ are denoted by $\underline{\hat{\theta}}(\underline{w})$ [12-15].

3 EXPERIMENTAL APPLICATION

The model updating methodologies are applied in order to update the FE model of a real bicycle. The bicycle consisted of the main frame, which presented in Figure 1 and is made of aluminum and from the front suspension which also consisted of two main parts which are presented respectively in Figures 3 and 4. The lower part of the fork, has the same material properties with the bicycle frame, while the upper fork part, consisted of steel tubes which are connected with a solid aluminum part. The thicknesses of the cross sections of the main frame as long as the lower part of the fork can vary along their length.

3.1 Digitization and FE Models

First, using a 3D Laser Scanner in order to collect, process and design the CAD model. Next, the geometry of the bicycle frame is discretized mainly by shell elements (triangular) and solid elements (tetrahedral). The total number of DOFs was 1,000,000. Similarly, the upper part of the fork was modeled with shell (triangular and quadrilateral) and solid (tetrahedral) elements resulting to 125,000 DOFs and the lower part of the fork was modeled only with solid (tetrahedral) elements resulting to 205,000 DOFs. The detailed FE models are presented in Figures 2, 3 and 4. For the development and solution of the finite element models appropriate software was used [25, 26].

Figure 1: Bicycle frame

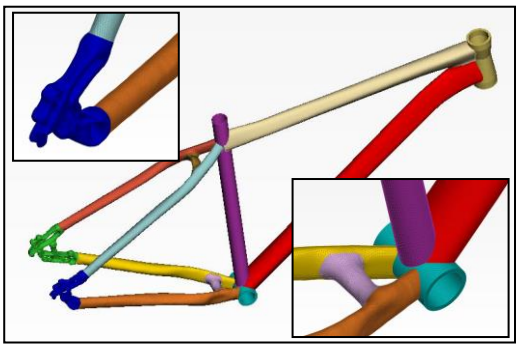

Figure 2: Finite element model of the frame

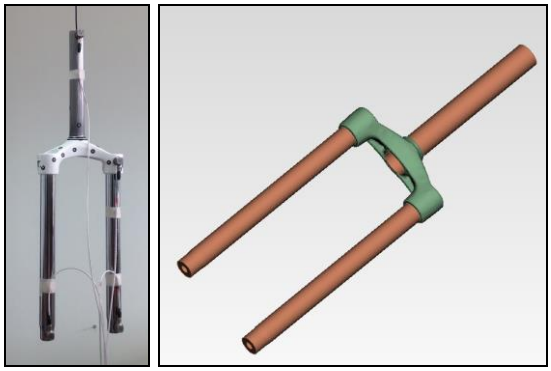

Figure 3: Upper (part 1) of the suspension-fork

Figure 4: Lower (part 2) of the suspension-fork

3.2 Experimental Modal Analysis

After developing the nominal finite element models, an experimental modal analysis of the frame and fork parts, was performed to quantify its dynamic characteristics. The frame and fork parts were hung up using a crane and straps, to approximate free-free boundary conditions for the test. First, all the necessary elements of the FRF matrix required for determining the response of the substructures were determined by imposing impulsive loading [5-9]. The measured frequency range was 0-2048 Hz, which includes the analytical frequency range of interest for the frame, 0-600 Hz, as well as for the fork parts, 0-500 Hz. An initial investigation indicated eleven natural frequencies for the frame and four for the fork parts, in this frequency range. A schematic illustration of the experimental arrangement is presented in Figure 5. In these figures, the locations and directions of acceleration measurements are presented, applying an impulsive load in all directions and at several locations. Based on the measured FR functions, the natural frequencies and the damping ratios of the substructures were estimated [10, 11, 15]. The identified mode shapes have also been recorded so that they can be used for updating the finite element models.

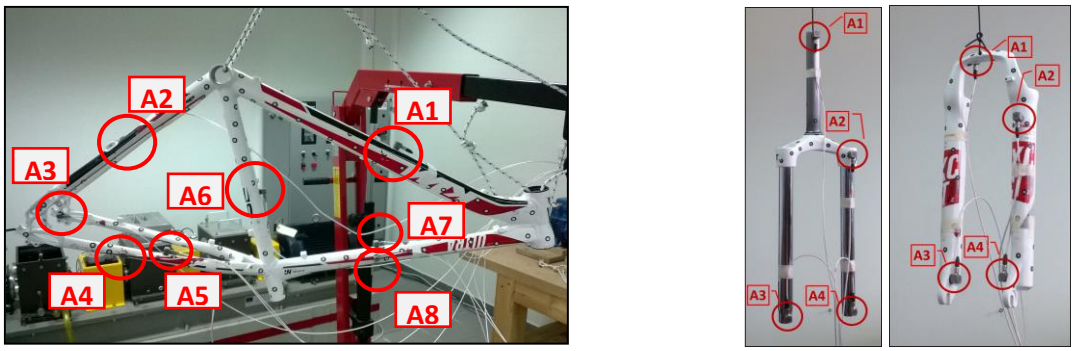

Figure 5: Accelerometer locations on main frame and fork parts 1 and 2

As an outcome of the above two procedures, in the Table 1 summarized the modal analysis results for the main frame, while similar results presented for the fork parts 1 and 2 in the Table 2.

Mode	Identified Modal Frequency	Nominal FE Predicted Modal Frequency	Difference between Identified and FE Predicted Modal Frequencies	Identified Modal Damping Ratio
	$\omega_{rE}\,[Hz]$	$\omega_{rN_{FE}}[Hz]$	$\frac{\omega_{rN_{FE}}-\omega_{rE}}{\omega_{rN_{FE}}}100\%$	$\zeta_{rE}\,(\%)$
1	84.88	96.46	12.01	0.21
2	108.29	118.72	8.78	0.19
3	270.69	319.15	15.19	0.12
4	311.96	357.30	12.69	0.08
5	315.15	358.72	12.15	0.13
6	368.01	414.69	11.26	0.13
7	425.73	491.11	13.31	0.12
8	450.25	494.05	8.87	0.16
9	465.19	530.79	12.36	0.16
10	484.45	545.44	11.18	0.35
11	504.86	575.88	12.33	0.23

Table 1: Modal frequencies and modal damping ratios of the frame

Mode	Identified Modal Frequency	Nominal FE Predicted Modal Frequency	Difference between Identified and FE Predicted Modal Frequencies	Identified Modal Damping Ratio
	$\omega_{rE}\,[Hz]$	$\omega_{rN_{FE}}[Hz]$	$\frac{\omega_{rN_{FE}}-\omega_{rE}}{\omega_{rN_{FE}}}100\%$	$\zeta_{rE}\,(\%)$
FORK PART 1				
1	188.26	168.18	11.94	0.15
2	268.79	259.38	3.63	0.11
3	419.36	453.39	7.51	0.39
4	452.13	499.42	9.47	0.43
FORK PART 2				
1	79.65	80.88	1.51	0.48
2	86.21	94.45	8.72	0.15
3	425.04	429.20	0.97	0.12
4	497.25	553.03	10.09	0.11

Table 2: Modal frequencies and modal damping ratios of the two parts of the suspension-fork

More specifically, the first column of Table 1 presents the values of the lowest natural frequencies (ω_{rE}), while the corresponding damping ratios are included in the fourth column. In the same table, the second column presents the values of the natural frequencies obtained from the analysis of the nominal finite element model ($\omega_{rN_{FE}}$) and the third column compares these frequencies with the corresponding frequencies obtained by the experimental data. The errors determined between the nominal FE model and the experimental measurements are not insignificant, indicating that the FE model updating process is necessary.

4 FINITE ELEMENT MODEL UPDATING

4.1 Linear FE model parameterization

The parameterization of the finite element models is introduced in order to demonstrate the applicability of the proposed finite element model updating method. The parameterized models are consisted of thirteen, two and four parts, for the frame, fork part 1 and fork part 2, respectively, as shown in Figure 6. The first four parts (P1, P2, P3 and P4) of the frame are modeled with solid elements, while the remaining nine parts (P5-P13) are modeled with shell elements. Fork part 1 is modeled with shell and solid elements for P1 and P2 respectively and fork part 2 is modeled solely with solid elements. The thickness of the shell elements, the Young's modulus and the density are used as design variables. Thus, the final numbers of the design parameters are thirty-five (35), five (5) and eight (8) variables for the frame, fork part 1 and part 2 respectively.

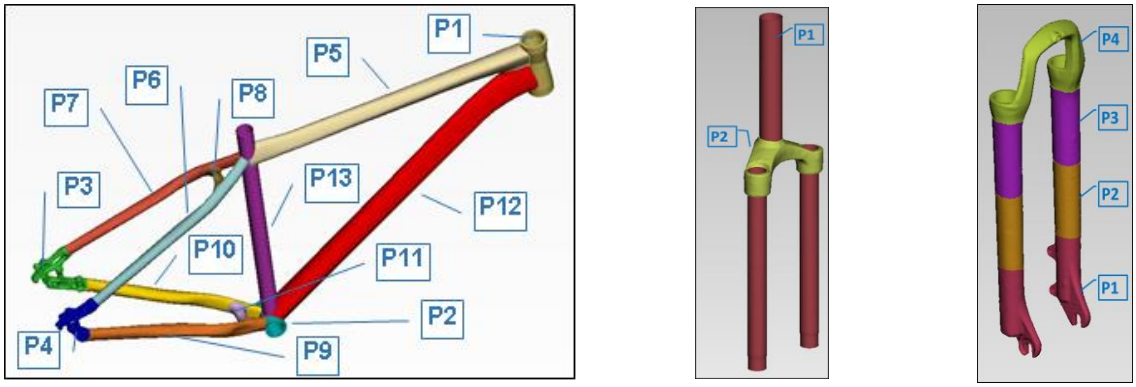

Figure 6: Parts of the parameterized FE Models of the frame and suspension- fork parts

The FE models of the main frame and the fork parts are updated using the identified modal frequencies and mode shapes shown in Tables 1 and 2. The identified mode shapes include components at all sensor locations. Additionally, we define as design response the total weight of the model, in order to be taken into consideration during the optimization process.

4.2 Linear FE Model Updating Results

The results from the FE model updating method are shown in Tables 3 and 4 for the frame and fork parts respectively. A comparison between identified (ω_{rE}) and optimal FE predicted modal frequencies ($\omega_{rO_{FE}}$) is also presented.

The FRF predicted by the optimal FE model (black dashed line) for the frame are compared in Figure 7 with the FRF computed directly from the measured data (red continuous line) at two indicative measurement locations in the frequency range [50Hz, 550Hz]. The FRF of the initial nominal model (blue dashed dot line) is also shown in these

figures to be inadequate to represent the measured FRF. Compared to the FRF of the initial nominal model, it is observed that the updated optimal model tend to considerably improve the fit between the model predicted and the experimentally obtained FRF close to the resonance peaks.

Mode	Identified Modal Frequency	Optimal FE Predicted Modal Frequency	Difference between Identified and FE Predicted Modal Frequencies
	$\omega_{rE}[Hz]$	$\omega_{rO_{FE}}[Hz]$	$\frac{\omega_{rO_{FE}}-\omega_{rE}}{\omega_{rO_{FE}}}100\%$
1	84.88	84.89	0.01
2	108.29	108.29	0.00
3	270.69	270.61	0.03
4	311.96	312.16	0.06
5	315.15	315.47	0.10
6	368.01	368.01	0.00
7	425.73	426.01	0.07
8	450.25	449.51	0.17
9	465.19	465.59	0.09
10	484.45	484.38	0.02
11	504.86	505.23	0.07

Table 3: Comparison between identified and optimal FE predicted modal frequencies for the main frame.

Mode	Identified Modal Frequency	Optimal FE Predicted Modal Frequency	Difference between Identified and FE Predicted Modal Frequencies
	$\omega_{rE}[Hz]$	$\omega_{rO_{FE}}[Hz]$	$\frac{\omega_{rO_{FE}}-\omega_{rE}}{\omega_{rO_{FE}}}100\%$
FORK PART 1			
1	188.26	188.53	0.14
2	268.79	267.86	0.35
3	419.36	420.83	0.35
4	452.13	452.10	0.01
FORK PART 2			
1	79.65	79.65	0.00
2	86.21	86.21	0.00
3	425.04	425.04	0.00
4	497.25	497.25	0.00

Table 4: Comparison between identified and optimal FE predicted modal frequencies for the fork parts 1 & 2.

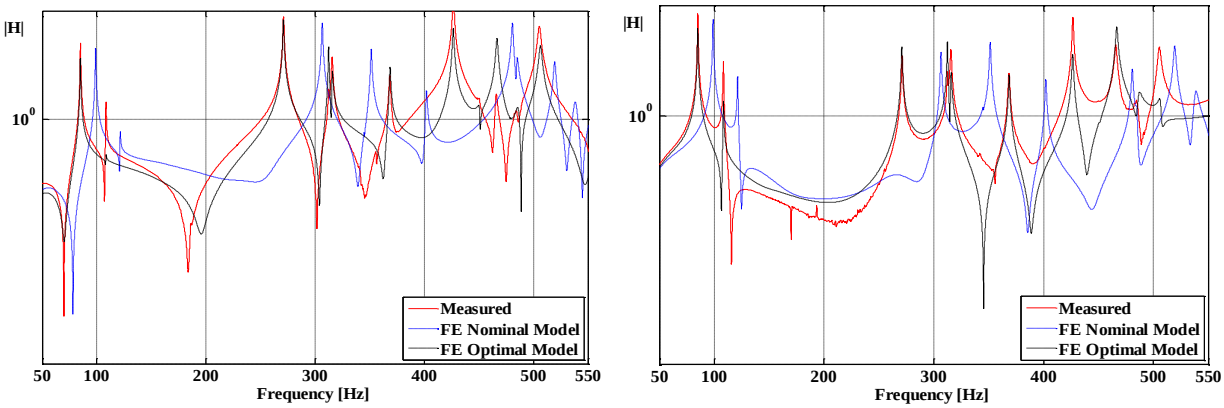

Figure 7: Comparison between measured, nominal and optimal FRF in two typical elements of the FRF matrix

5 ANALYSIS OF NON-LINEAR SYSTEM

The FE model, of the nonlinear subassembly of the suspension-fork, was created connecting fork part 1 and 2 with two springs simulating the restoring force $f_r(x)$ and two non-linear bushing elements simulating the damping force $f_d(\dot{x})$. The final nonlinear suspension FE model with the corresponding lumped model presented in Figure 8.

In order to identify the parameters of the subsystem, which exhibit strongly nonlinear characteristics, a series of experimental trials was performed. In the experimental device

shown in Figure 9 two electromagnetic devices are used, at the top and at the bottom of the suspension, imposing harmonic excitation with $\pi/2$ rad phase difference using 0.2 Hz frequency step for three different forcing levels.

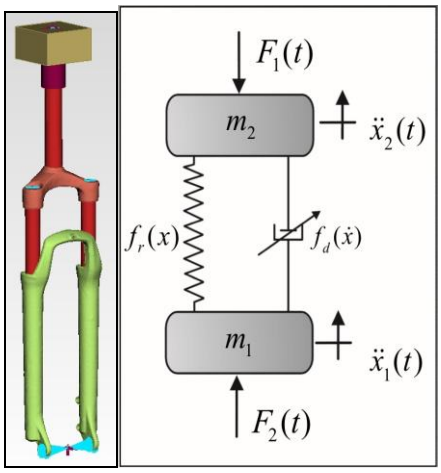

Figure 8: FE model of the suspension-fork and theoretical lumped model

Figure 9: Schematic illustration and experimental arrangement of suspension sub-assembly

In Figure 10 depicted the imposed forces $F_1(t)$ and $F_2(t)$ for the three different forcing levels at $\omega = 6Hz$ which is approximately the resonant frequency of the system, while in Figure 11 depicted the acceleration transmissibility functions of measurement location 2, for the three different forcing levels. A number of models of the restoring and damping forces, say f_r and f_d, respectively, were tried for modeling the action of the supports and compared with the experimental results. The classic linear dependence of the restoring force on the displacement and of the damping forces on the velocity of the support unit was first assumed. However, critical comparison with the experimental results using the Bayesian model selection framework demonstrated that the outcome was unacceptable in terms of accuracy. Eventually it was found that an acceptable form of the restoring forces is the one where they remain virtually in a linear relation with the extension of the spring, namely

$$f_r(x) = kx \tag{7}$$

while the damping force was best approximated by the following formula

$$f_d(\dot{x}) = c_1\dot{x} + \frac{c_2\dot{x}}{c_3 + |\dot{x}|} \tag{8}$$

As usual, the linear term in the last expression is related to internal friction at the support, while the nonlinear part is related to the existence and activation of dry friction. More specifically, in the limit $c_3 \to 0$, the second term in the right hand side of Equation (8) represents energy dissipation action corresponding to dry friction. On the other side, in the limit $c_3 \to \infty$ this term represents classical viscous action and can actually be absorbed in the first term.

The results for k, c_1, c_2 and c_3 are obtained based on the experimental response spectra values for the accelerations of the two suspension components, using the parameters of the updated linear parts (1 and 2) of the suspension fork subassembly and the transmissibility functions of the support system for three different forcing levels. Let $S = \{\hat{s}_r(\omega_r) \in R^{N_r}, r = 1,\cdots,n\}$

be the measured transmissibility functions at N_r measured frequencies where n is the number of involved frequencies. Let $\underline{\theta}=(k_1,c_1,c_2,c_3\in R^{N_\theta})$ be a parameter space, corresponding to the linear and nonlinear coefficients of the restoring and damping forces respectively.

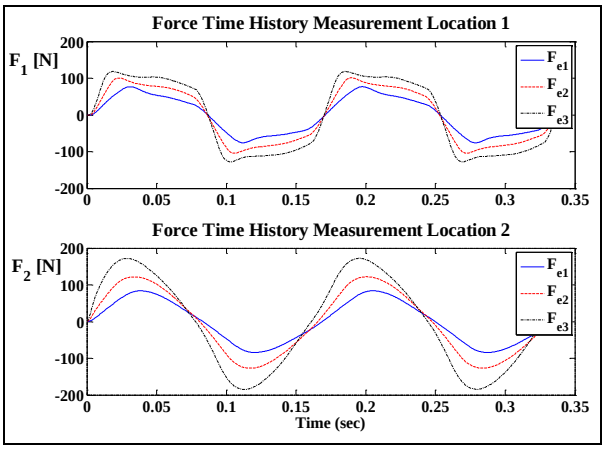

Figure 10: Time-history of the external forces applied at a fundamental harmonic frequency $\omega=6Hz$

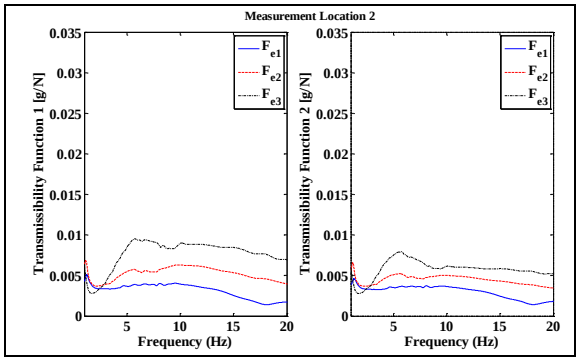

Figure 11: Transmissibility functions of the support system for three different forcing levels

The results for k, c_1, c_2 and c_3 are obtained based on the experimental response spectra values for the accelerations of the two suspension components, using the parameters of the updated linear parts (1 and 2) of the suspension fork subassembly and the transmissibility functions of the support system for three different forcing levels. Let $S=\{\hat{s}_r(\omega_r)\in R^{N_r}, r=1,\cdots,n\}$ be the measured transmissibility functions at N_r measured frequencies where n is the number of involved frequencies. Let $\underline{\theta}=(k_1,c_1,c_2,c_3\in R^{N_\theta})$ be a parameter space, corresponding to the linear and nonlinear coefficients of the restoring and damping forces respectively. Similarly to the linear model, the objective is to estimate the values of the parameter set $\underline{\theta}$ so that the analytical response spectra values, namely the transmissibility functions match the experimentally obtained functions estimated in S. In Figure 12, presented a comparison in two measured locations, between the numerical nonlinear FE model (red line), with the experimental measurements (black line), in harmonic excitation with forcing frequency of $\omega=6Hz$. More specifically, the nonlinear FE model with the estimated values of the stiffness and damping properties, was solved with nonlinear transient response analysis. The blue line was derived using the equivalent theoretical linear model and is presented also for comparison purposes.

From these results, it arises that the estimation of the values of the parameters is very close to the real values, since the theoretical nonlinear model is very close to those of the experimental results.

Finally, in order to test the reliability of the applied methodology, we examine the full bicycle model (Fork and frame). More specifically, with the use of two electrodynamic shakers imposing base excitation at the wheels locations and measuring the dynamic response in several locations in the frame and suspension substructures in the three directions.

An illustration of the fixed-free arrangement of the bike on the shakers with acceleration measurement locations is presented in Figure 14, while in Figure 13 the finite element model of the whole bike assembly is shown.

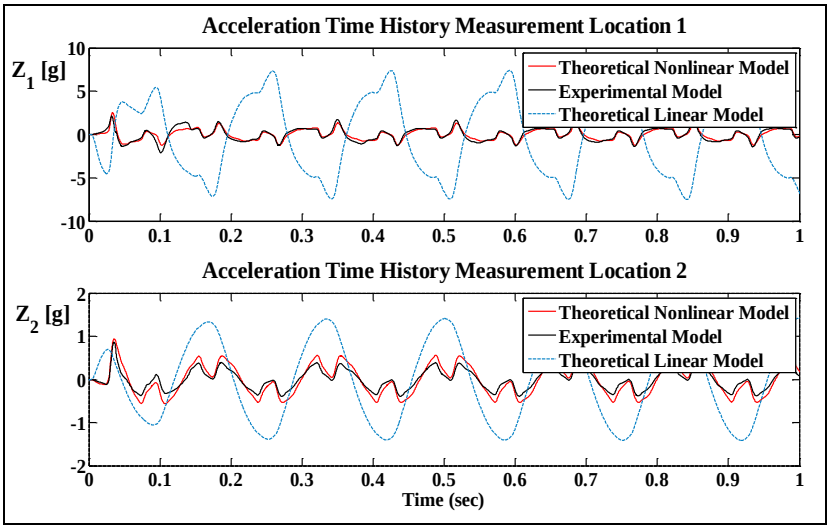

Figure 12: Acceleration time histories at two measured locations in harmonic excitation with frequency $\omega = 6Hz$

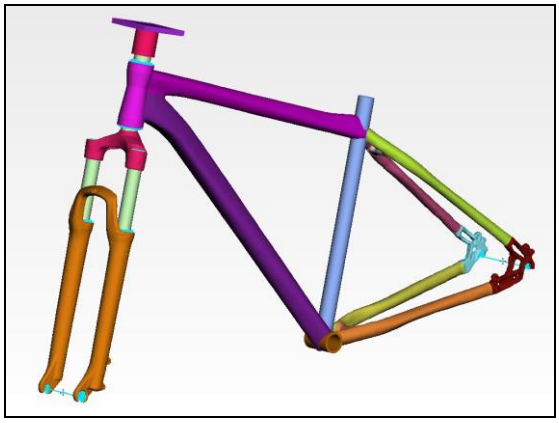

Figure 13: FE model of the bike assembly.

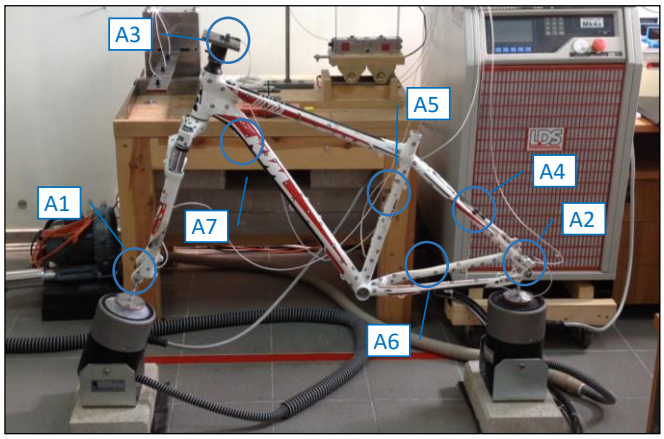

Figure 14: Fixed-free arrangement on electrodynamic shakers

The measured acceleration time histories in the three directions in the locations 1 and 2, were imported as base excitation in the finite element model of the system. In Figure 15, presented a comparison in three measured locations in the vertical direction, between the numerical nonlinear FE model (red line), with the experimental measurements (black line), in harmonic excitation with forcing frequency of $\omega = 6Hz$. The blue line was derived using the equivalent theoretical linear model and is presented again for comparison purposes.

From these results, it arises that the full bicycle theoretical nonlinear FE model is very close to those of the experimental results.

Also, in Figure 16, is shown an indicative point of time, of the dynamic response of the full nonlinear system.

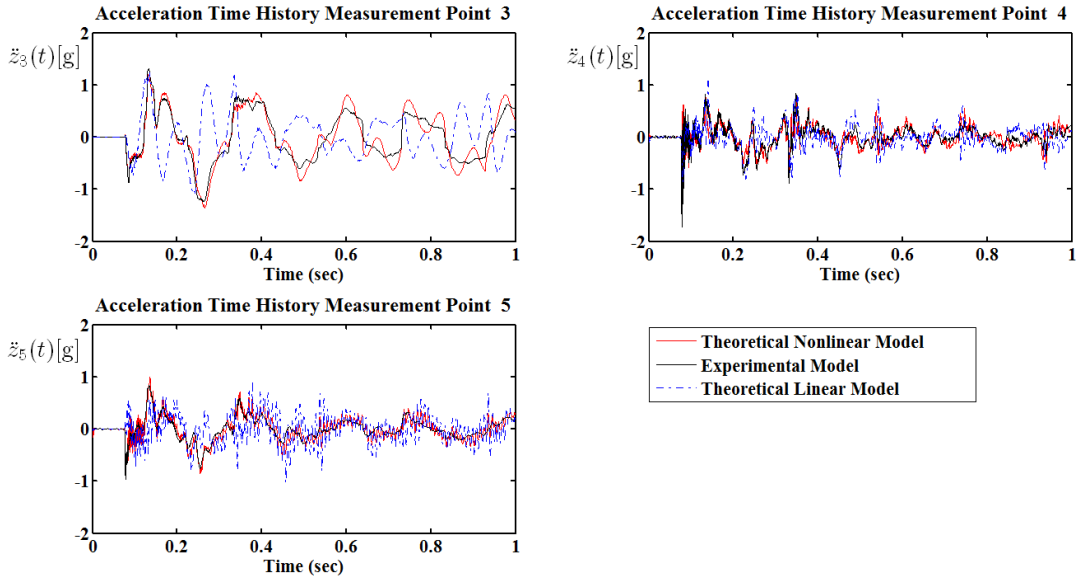

Figure 15: Acceleration time histories at three measured locations in harmonic excitation with frequency $\omega = 6Hz$

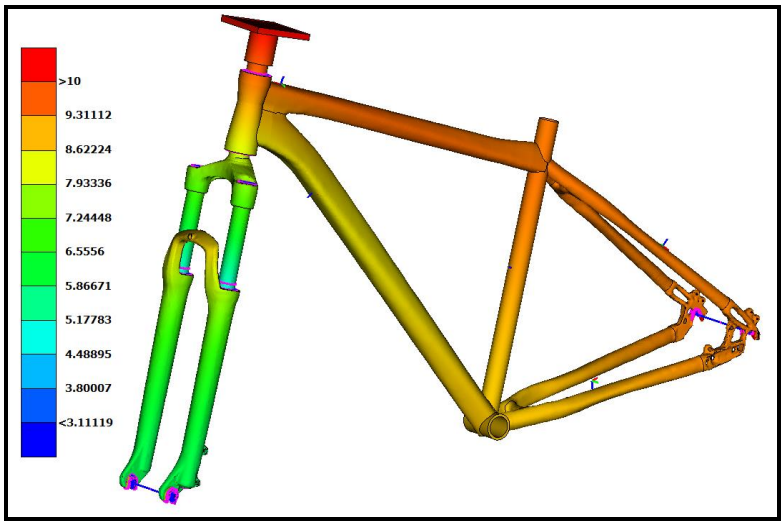

Figure 16: Dynamic response of the nonlinear full FE model in harmonic excitation with frequency $\omega = 6Hz$

6 SUMMARY

A computational framework is presented in order to estimate the optimal values of the linear and nonlinear components of large scale dynamical systems using vibration measurements. An extensible framework for Bayesian Uncertainty Quantification and Propagation of complex and computationally demanding physical models, was connected in an efficient way with a numerical code leading to an automated determination of dynamic response of linear and nonlinear mechanical systems. Numerical and experimental methodologies were applied in order to identify the model parameters and develop a high fidelity finite element model of the structure examined. The applicability and effectiveness of

the methods applied, is explored by updating finite element model of a lightweight and geometrically complex bicycle assembly, using experimentally identified modal data. Direct comparison of the numerical and experimental data verified the reliability and accuracy of the methodology applied.

REFERENCES

[1] D. Rypl, Z. B. (2005). Generation of computational surface meshes of STL models. Prague, Czech Republic: Faculty of Civil Engineering, Department of Structural Mechanics, Czech Technical University.

[2] E. Bechét, J. C. (2002). Generation of a finite element MESH from stereolitography (STL) files. Paris, France: Computer-Aided Design

[3] Bianconi, F. (2002). Bridging the gap between CAD and CAE using STL files. Perugia, Italy: Department of Industrial Engineering, University of Perugia.

[4] Cuppens, K., Sas, P. and Hermans, L., Evaluation of FRF based substructuring and modal synthesis technique applied to vehicle FE data, ISMA 2000, K.U. Leuven, Belgium, pp. 1143-1150, 2000.

[5] Giagopoulos, D. and Natsiavas, S., Hybrid (numerical-experimental) modeling of complex structures with linear and nonlinear components, Nonlinear Dynamics, Vol. 47, pp. 193-217, 2007.

[6] Giagopoulos, D. and Natsiavas, S., Dynamic Response and Identification of Critical Points in the Superstructure of a Vehicle using a Combination of Numerical and Experimental Methods, Experimental Mechanics, DOI 10.1007/s11340-014-9966-z, 2014.

[7] Ewins, D.J., 1984, Modal Testing: Theory and Practice, Research Studies Press, Somerset, England.

[8] Mohanty, P. and Rixen, D.J., Identifying mode shapes and modal frequencies by operational modal analysis in the presence of harmonic excitation, Experimental Mechanics, Vol. 45, pp. 213-220, 2005.

[9] Spottswood, S.M. and Allemang, R.J., On the investigation of some parameter identification and experimental modal filtering issues for nonlinear reduced order models, Experimental Mechanics, Vol. 47, pp. 511-521, 2007.

[10] Richardson, M.H. and Formenti, D.L., Global curve fitting of frequency response measurements using the rational fraction polynomial method, Third IMAC Conference, Orlando, Florida, 1985.

[11] Mottershead, J.E. and Friswell, M.I., Model updating in structural dynamics: A survey, Journal of Sound and Vibration, Vol. 167, pp. 347-375, 1997.

[12] Papadimitriou, C., Ntotsios, E., Giagopoulos, D. and Natsiavas, S., Variability of updated finite element models and their predictions consistent with vibration measurements, Structural Control and Health Monitoring, Vol. 19, pp. 630-654, 2012.

[13] Giagopoulos, D., Papadioti, D.-Ch., Papadimitriou, C. and Natsiavas, S., Bayesian uncertainty quantification and propagation in nonlinear structural dynamics, Proceedings of the IMAC-XXXI 2013, Garden Grove, California, USA, 2013.

[14] Christodoulou K, Ntotsios E, Papadimitriou C, Panetsos P. Structural model updating and prediction variability using Pareto optimal models. Computer Methods in Applied Mechanics and Engineering 2008; 198 (1):138-149.

[15] Ntotsios E, Papadimitriou C. Multi-objective optimization algorithms for finite element model updating. International Conference on Noise and Vibration Engineering (ISMA2008); Katholieke Universiteit Leuven, Leuven, Belgium, September 15-17, 2008.

[16] Mottershead J, Link M, Friswell M. The sensitivity method in finite element model updating: A tutorial. Mechanical Systems and Signal Processing. DOI 10.1016/j.ymssp.2010.10.012, 2010

[17] Grafe H Model Updating of Large Structural Dynamics Models Usong Measured Response Functions. Imperial College of Science, Department of Mechanical Engineering, Dynamics Section, Phd Thesis, 1998

[18] Fritzen CP, Jennewein D, Kiefer T. Damage detection based on model updating methods. Mechanical Systems and Signal Processing 1998; 12(1):163–186.

[19] Moaveni B, He X, Conte JP, Restrepo JI. Damage identification study of a seven-story full-scale building slice tested on the UCSD-NEES shake table. Structural Safety 2010; 32(5):347–356.

[20] Moaveni B, He X, Conte JP, De Callafon RA. Damage identification of a composite beam using finite element model updating. Computer-Aided Civil and Infrastructure Engineering 2008; 23(5):339–359.

[21] Weber B, Paultre P, Proulx J. Structural damage detection using nonlinear parameter identification with Tikhonov regularization. Structural Control and Health Monitoring 2007; 14:406–427.

[22] Yuen K-V, Beck JL, Katafygiotis LS. Efficient model updating and health monitoring methodology using incomplete modal data without mode matching. Structural Control and Health Monitoring 2006; 13:91–107.

[23] Allemang, R. and D. Brown (1982). A correlation coefficient for modal vector analysis. In 1st International Modal Analysis Conference, Orlando, USA.

[24] Grafe, H. (1995, May). Review of frequency response function updating methods. Technical report no. 1.01, BRITE-URANUS BRE2-CT94-0946.

[25] DYNAMIS 3.1.1, Solver Reference Guide, DTECH, Thessaloniki, Greece, 2013.

[26] ANSA and META-Post, BETA CAE Systems S.A., Thessaloniki, Greece.

ECCOMAS Congress 2016
VII European Congress on Computational Methods in Applied Sciences and Engineering
M. Papadrakakis, V. Papadopoulos, G. Stefanou, V. Plevris (eds.)
Crete Island, Greece, 5–10 June 2016

VARIABLE FIDELITY MODELLING IN MODERN AIRCRAFT DESIGN

Marian A. Zastawny[1]

[1] Aircraft Research Association Ltd.
Manton Lane, Bedford, MK41 7PF, UK
e-mail: mzastawny@ara.co.uk

Keywords: Aircraft Design, Set-Based Design, Surrogate Modelling, Variable-Fidelity Modelling, Krigging

Abstract. *The key to successful application of surrogate modelling is the ability to quickly generate high quality data over a large parameter space. This can be achieved through application of Variable Fidelity Modelling (VFM), which is a data fusion technique that allows data from different sources to be combined. VFM can be used to correct a dataset obtained by a simple and fast method with a small number of high quality samples in order to generate a high-fidelity surrogate at a marginal cost.*

This paper presents the results of a feasibility study of a VFM technique based on Hierarchical Kriging in the context of aerospace applications. A generic process for generation of a high quality surrogate using VFM and assessment of its accuracy is presented and validated for a number of realistic use case scenarios. Investigation of the impact of various parameters of the method is conducted, highlighting the importance of selection of the appropriate data correlation functions.

The potential of VFM to significantly reduce the computational cost required for generation of a high-fidelity surrogate is demonstrated for the case of a parametric study of wing cruise performance used at the early stages of the aircraft design process. In addition, an application where the VFM method is used to predict the effects of wing section optimization is shown. The VFM approach presented in this paper can be implemented in a number of different scenarios and can offer significant improvements for the surrogate generation process by quickly generating high-fidelity response surfaces.

1 INTRODUCTION

Due to the high costs involved, aircraft designers have to ensure that every new aircraft meets the required safety and performance standards long before it enters service. In practice, this is achieved during a long development process, which involves intensive calculations, tests and numerical simulations. Modern design offices make extensive use of computers, simulating almost every aspect of the aircraft system.

In practice, a significant number of important decisions, which have substantial impact on the design of a new aircraft, are taken at the preliminary design stage when the amount of available information is usually small and a large number of possible configuration variants are still considered. In a conventional approach, the so-called Point-Based Design (PBD), a baseline concept is developed at an early design stage and is subsequently modified to achieve a feasibility, and ideally, optimal design during the design process. Usually, this involves a number of iterations during which the aircraft can undergo significant modifications as more information becomes available. This means that a wrong decision taken at the beginning of the project can lead to problems downstream, once more information becomes available.

An alternative approach, using the Set-Based Design (SBD) paradigm, was proposed in the CONGA (Configuration Optimisation for Next Generation Aircraft) programme [1]. In this methodology, a number of designs are developed concurrently and, as more information becomes available, the unfeasible concepts are removed from the set. By keeping the design space open and reducing the number of additional iterations, SBD enables fast convergence on the designs which satisfy all constraints [2].

The main challenge of SBD is the fact that a large amount of data has to be developed at the early stage of the project. This can prove problematic, especially for a novel aircraft configuration, for which the amount of empirical, legacy data is limited. Even despite the continuous improvements in simulation algorithms and speed of computers, performing extensive simulations of large data sets is still not feasible in practice. A promising alternative is the use of surrogates generated from a reduced number of data points to explore the design space. This can considerably reduce the computational costs; however, a large number of simulations may still be necessary.

A further reduction of the effort required to generate an appropriate surrogate can be achieved if a low-fidelity method is used for its construction. This, however, may result in a loss of data quality. The Variable Fidelity Method (VFM) explored in this paper attempts to take advantage of speed offered by application of the low-fidelity methods, without compromising the accuracy of the final surrogate, by correcting it with a limited set of high-fidelity data points.

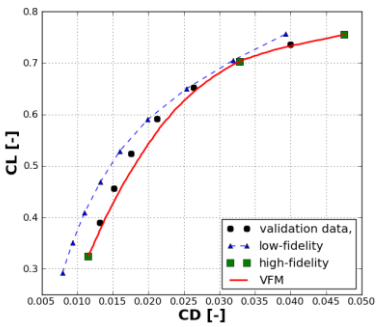

Figure 1: Illustration of the VFM concept.

The concept of VFM is illustrated in Figure 1. In principle, the VFM uses a simple fast method to construct a response surface that characterises the overall trends in the dataset. This is then corrected by a small set of high-fidelity data allowing a high-quality response surface to be obtained at a fraction of the cost required to generate it only from the high-fidelity data.

This paper evaluates the potential applications of VFM in the context of aerodynamic aircraft design. First, the VFM concept developed by DLR [3], which is used in this study, is briefly presented and discussed. This is followed by analysis of the results for four test cases aimed at the investigation of different features of the method. Next, a short discussion on possible application of the VFM approach is given. The paper finishes with short summary and main conclusions.

2 VARIABLE FIDELITY MODELLING

As described in the introduction, the VFM is a data fusion technique that allows the data with different levels of fidelity to be combined in order to generate a high-fidelity surrogate with a limited number of high-fidelity data points. The method discussed in this paper has been introduced in [3] and expanded further in [4]-[6]. This section provides an overview of the technique and outlines the main ideas used.

2.1 Method description

The VFM method discussed in this paper is based on the concept of Hierarchical Kriging (HK). Kriging is a statistical interpolation method introduced by Krige in [7], which models the interpolated variables by a Gaussian process and allows for their prediction based on covariance between the known samples. HK extends this concept to different levels of sample fidelities by adding the next step during which the low-fidelity surrogate is corrected by the high-fidelity data [4].

A low-fidelity surrogate is constructed during the first stage of the HK process. The values predicted by the surrogate can be calculated as:

$$\hat{y}_{lf}(\boldsymbol{x}) = \beta_{0,lf} + \boldsymbol{r}_{lf}^{T}(\boldsymbol{x})\boldsymbol{R}_{lf}^{-1}\left(\boldsymbol{y}_{S,lf} - \beta_{0,lf}\mathbf{1}\right) \tag{1}$$

where $\boldsymbol{y}_{,lf}$ are the low fidelity samples, $\boldsymbol{R}_{lf}$ is the correlation matrix representing the correlation between the available samples, $\boldsymbol{r}_{lf}$ is the correlation vector representing the correlation between the untried point, and the available samples and $\mathbf{1}$ is the identity matrix**.** $\beta_{0,lf}$ is an unknown constant calculated as $\beta_{0,lf} = \left(\mathbf{1}^{T}\boldsymbol{R}_{lf}^{-1}\mathbf{1}\right)^{-1}\mathbf{1}^{T}\boldsymbol{R}_{lf}^{-1}\boldsymbol{y}_{s,lf}$.

The VFM response surface, which corrects the low-fidelity surrogate with high-fidelity samples, is calculated in the second stage of the process. The resulting high-fidelity predictions are evaluated as:

$$\hat{y}(\boldsymbol{x}) = \beta_0\,\hat{y}_{lf}(\boldsymbol{x}) + \boldsymbol{r}^{T}(\boldsymbol{x})\boldsymbol{R}^{-1}(\boldsymbol{y}_S - \beta_0\boldsymbol{F}) \tag{2}$$

where $\boldsymbol{y}_S$ are the high fidelity samples, $F = \left[\hat{y}_{lf}\left(\boldsymbol{x}^{(1)}\right), \ldots, \hat{y}_{lf}\left(\boldsymbol{x}^{(n)}\right)\right]^{T}$, and $\beta_0 = (\boldsymbol{F}^{T}\boldsymbol{R}^{-1}\boldsymbol{F})^{-1}\,\boldsymbol{F}^{T}\boldsymbol{R}^{-1}\boldsymbol{y}_S$ is the scaling factor, indicating the correlation of the low- and high-fidelity functions.

It is quite clear that the generated response surface will strongly depend on the chosen correlation model, that has an impact on both high- and low-fidelity correlation matrices $\boldsymbol{R}$ and

$\boldsymbol{R}_{lf}$ as well as on the correlation vectors $\boldsymbol{r}$ and $\boldsymbol{r}_{lf}$. The most common correlation model is the Gaussian exponential function which can be written as:

$$\boldsymbol{R}(\boldsymbol{\theta}, \boldsymbol{x}, \boldsymbol{x}') = \prod_{k=1}^{m} \exp(-\theta_k |x_k - x_k'|^{p_k}), \qquad 1 < p_k \leq 2 \tag{3}$$

where θ are unknown hyper-parameters which need to be calculated. Different correlation models, such as Gauss correlation function, cubic splines or radial-basis-functions are also available.

Although the scaling factors β can be determined analytically, they depend on the θ hyper-parameters, which are obtained during surrogate construction process by maximum likelihood estimation. This essentially requires optimisation of the hyper-parameter values in a way that leads to minimising the variances in the surrogate. More information on the process can be found in [4].

2.2 Error estimation

One of the main advantages of the applied method is that it provides an estimate for the root mean-square error (RSME), which can be used to assess the quality of the generated surrogate. The RSME estimate can be used not only to evaluate the statistical accuracy of the generated response surface (e.g. max, mean), but also to highlight the surrogate regions with highest uncertainty in the results. This can be applied for adaptive surrogate refinement, as will be shown later.

It has to be noted, however, that the RSME estimate is based on the mathematical formulation and depends on the chosen correlation model, therefore it might not be accurate. In fact, it is generally found that, although it correctly highlights the surrogate regions with least confidence, the prediction is generally too optimistic when compared to true errors [4]. Hence, an additional test is required to validate the accuracy of the obtained response surface.

Different techniques for surrogate error analysis are available. If a sufficient number of high-fidelity data points is available, a cross-validation can be performed. In such a scenario, a subset of high-fidelity data is identified and removed from the set of points used for the generation of the VFM surrogate. The surrogate prediction can be then compared to the available high-fidelity data in order to determine the values of true errors.

Most often, however, the amount of high-fidelity data is so small that it is desirable to use all available data for generation of the surrogate. In those circumstances the so-called "leave-one-out test" [8] can be adopted. The principle of this technique is to generate several variants of the response surface. For each variant a single high-fidelity point is randomly removed and the true error is calculated by comparison of the surrogate prediction with the high-fidelity data. If the true error remains small for all tested variants, the surrogate can be considered as saturated, i.e. sufficiently accurate so that addition of new high-fidelity points will not lead to significant improvement in the quality of the generated response surface.

2.3 VFM process at ARA

This section describes how the VFM procedure, suggested in [6], was implemented at ARA. Figure 2 illustrates various steps of the process. First, Design of Experiment (DoE) techniques are used to define the samples for low- and high-fidelity data used to generate the VFM surrogate. The aim is to ensure that the entire design space is covered with as few data-points as possible. Usually the number of high-fidelity points is between 5-10% of the number of low-fidelity samples.

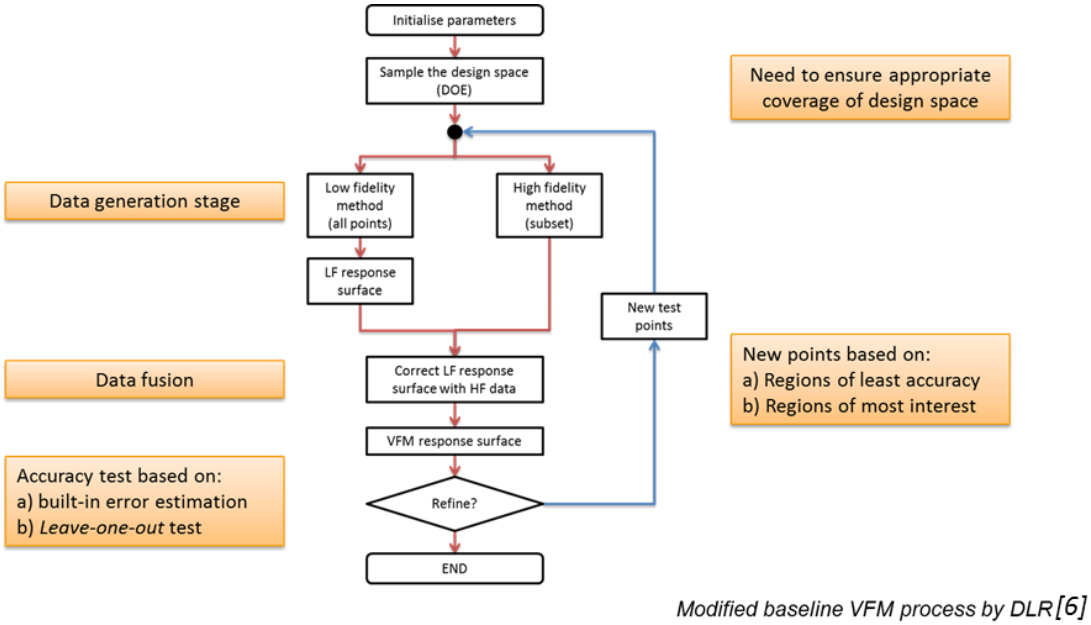

Figure 2: VFM process implemented at ARA.

Next, data for both sets of samples is generated either by simulation or through experiments. In fact, the source of data is irrelevant, as long as the fidelities of different data sets can be easily identified. Once the data are available, a low-fidelity response surface is generated and corrected with the high-fidelity data using the process described above.

The quality of the obtained surface is evaluated based on the VFM RSME prediction. If the estimated accuracy is sufficient, the surrogate is validated using either reference high-fidelity data or by means of the leave-one-out test. If this test is passed as well, the surrogate generation finishes, otherwise additional refinement is performed.

The choice of refinement points depends on the purpose of the generated surrogate, and weighting of errors in different regions of the surrogate. Either way, the new high-fidelity points are generated based on the RSME estimate, usually more than one at a time. Occasionally, if the RSME error prediction is small but the true errors are considerable, additional points can be added based on the true error values. The process concludes once a VFM model of sufficient accuracy is obtained.

3 FEASIBILITY STUDY

This section presents the results of the VFM feasibility study conducted at ARA in order to evaluate potential applications of this technique and offer a better understanding of its limitations. The tests described here focus on VFM applications in the field of aerodynamics and each of them aims at evaluation of a specific feature of the VFM approach.

3.1 Choice of the low-fidelity model

One of the obvious applications of the VFM is to combine the data obtained with methods characterized by different levels of fidelity. In general, the low-fidelity method allows for the results to be obtained quickly, but with a limited level of accuracy. The high-fidelity data, on the other hand, offers a greater accuracy, but requires more effort to be obtained. This test addresses the impact of the choice of the low-fidelity method on the resulting VFM surrogate and how the low-fidelity data affects the required number of high-fidelity correction data points.

The example presented here covers 2D simulations of the flow over a NACA 63_2-215 aerofoil resolved using the BVGK code [9] in two variants:

- low-fidelity – inviscid
- high-fidelity – inviscid with coupled boundary layer

Two scenarios are investigated. First, a lift polar at Mach number $M = 0.5$ is simulated over a linear incidence (α) range from 0 to 5 degrees. Figure 3 shows the lift coefficient as the function of the incidence angle for different levels of fidelity, along with the high-fidelity points used for generation of the VFM. It can be observed that although the low-fidelity data predicts higher values of the lift coefficient Cl, it predicts the same trend as the reference high-fidelity results. A VFM surrogate of a sufficient accuracy is be obtained for all investigated high-fidelity points configurations.

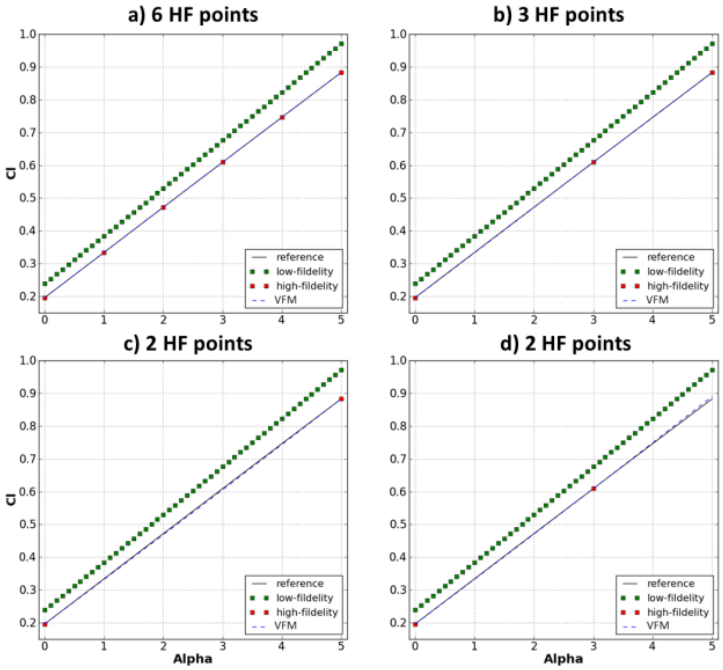

Figure 3: VFM of lift coefficient obtained with different high-fidelity points.

A comparison of error estimation obtained during the VFM generation with the 'true' error calculated as the difference between the lift coefficient predicted by the VFM and the reference high-fidelity data is shown in Figure 4. The figure demonstrates that reducing the number of high-fidelity points used to generate the VFM surrogate leads to higher errors. Also, apart from case (c), with 3 high-fidelity points, the error prediction has a similar behaviour to the 'true' error although they differ in magnitude.

The second scenario considered during this test was an investigation of a drag polar at $M = 0.6$ over a similar incidence range from 0 to 5 degrees. The resulting drag polars along with the used high-fidelity points are illustrated in Figure 5. Again, a sufficient number of high-fidelity points allows for a VFM surrogate of a reasonable quality to be obtained. On the other hand, using 3 high-fidelity points, which was sufficient in the previous scenario, now results in a VFM of a very poor accuracy. This can be explained by inspection of the low-fidelity data behaviour shown in Figure 6a. Since the low-fidelity model is inviscid, the resulting drag coefficient will be zero everywhere, apart from high incidences where wave drag effects are observed. The low-fidelity prediction of the drag coefficient has therefore

a completely different behaviour to the trends observed in the high-fidelity model, thus it actually impacts the VFM surrogate generation in a negative way. In fact, for this scenario, generation of a response surface from high-fidelity points only would result in a better prediction.

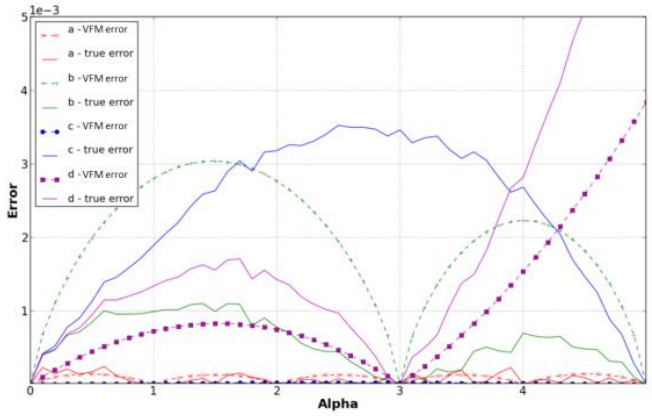

Figure 4: Comparison of errors for the lift coefficient prediction.

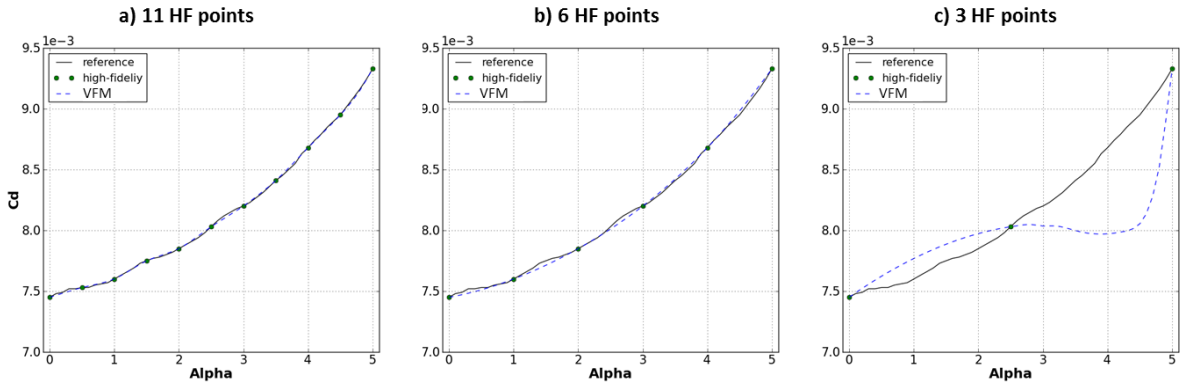

Figure 5: VFM of drag coefficient obtained with different high-fidelity points.

What is encouraging, however, is that the model errors, shown in Figure 6b, illustrate that the built-in VFM error prediction is capable of capturing the poor quality of the generated surrogate and highlighting the areas where improvement is required.

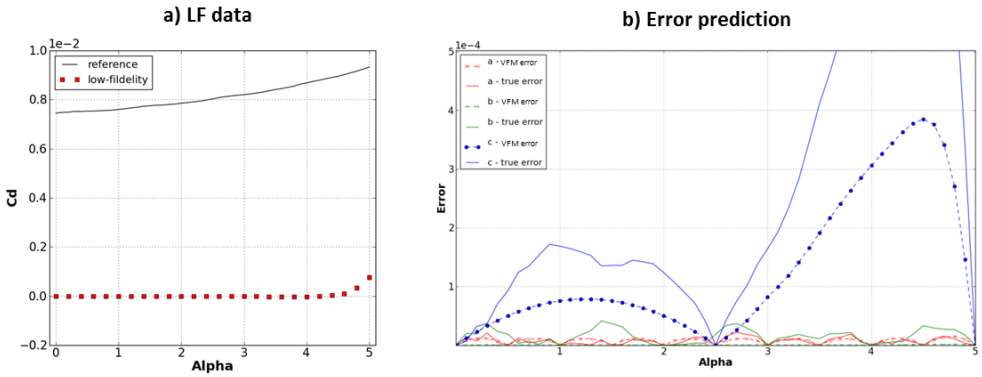

Figure 6: Comparison of errors of lift coefficient predictions.

The main conclusion from this test is that the choice of adequate low-fidelity data is critical to successful application of the VFM. The low-fidelity data should be characterised by a similar behaviour to the trends observed in the high-fidelity model. The second conclusion is that the error estimates obtained using the VFM, although not precisely correct, allow for the assessment of the quality of the surrogate and indicate the parameters for which more high-fidelity information should be provided.

3.2 VFM accuracy and surrogate refinement process

The second feasibility test focused on investigation of the accuracy improvement offered by adoption of the VFM when compared to a response surface generated only from the high-fidelity data points and on the impact of surrogate refinement process on the accuracy of the obtained data.

In this case, the drag coefficient dependency over a range of Mach numbers and incidences for a civil airliner wing was studied. The high-fidelity data was generated from the results of 3D simulations of the wing using the TAU RANS solver [10]. The low-fidelity data was obtained by spanwise integration of the results obtained for 2D simulations of the sections of the investigated wing. The concept of the process is illustrated in Figure 7.

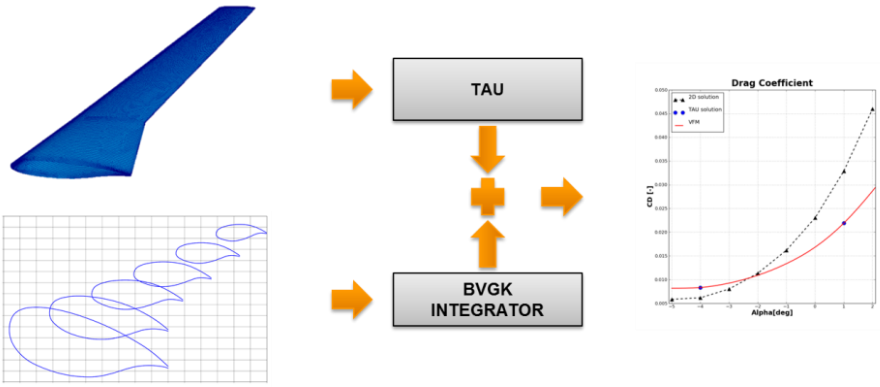

Figure 7: Illustration of the process used for surrogate refinement test.

Figure 8 shows the surrogates of the drag coefficient as a function of incidence angle at various Mach numbers obtained using VFM and by fitting a response surface (RSM) for high-fidelity points only. The initial surrogates were generated with 5 high-fidelity data points obtained by DoE (see highlighted circles in Figure 8a). The surrogates were subsequently refined by addition of new high-fidelity data points in the regions where VFM error prediction indicated the largest values of the relative error (ratio between error and drag coefficient value). The use of relative error was motivated by the fact that, in practice, the low drag coefficient values are of most interest. The surrogates were deemed as saturated, i.e. addition of new high-fidelity points resulted in a little difference in estimated errors, when 19 high-fidelity data points were used. The final surrogates are compared to each other and to the reference data (TAU) in Figure 8b.

The convergence of statistical characteristics (maximum, average, median) of the VFM error estimates is illustrated in Figure 9. A rapid, although non-monotonic, reduction in all statistical values describing the error estimates is observed at the beginning of the refinement process. Change in the relative error remains relatively small when 11 high-fidelity points are used and decreases monotonically when more than 15 points are available. Similar behaviour is observed for the absolute error values, although here, the maximum error remains relatively high.

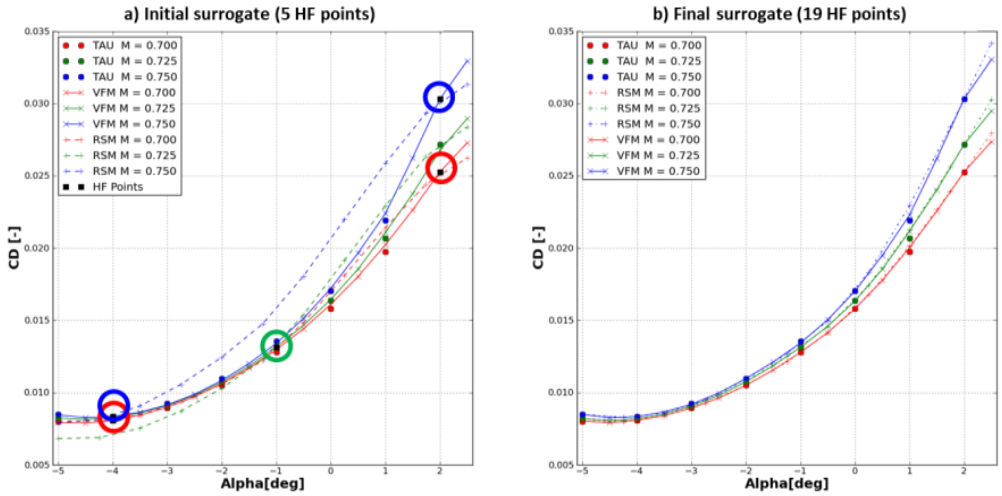

Figure 8: Surrogates of the drag coefficient polars at various Mach numbers obtained using VFM and fitting a response surface (RSM) from high-fidelity points only.

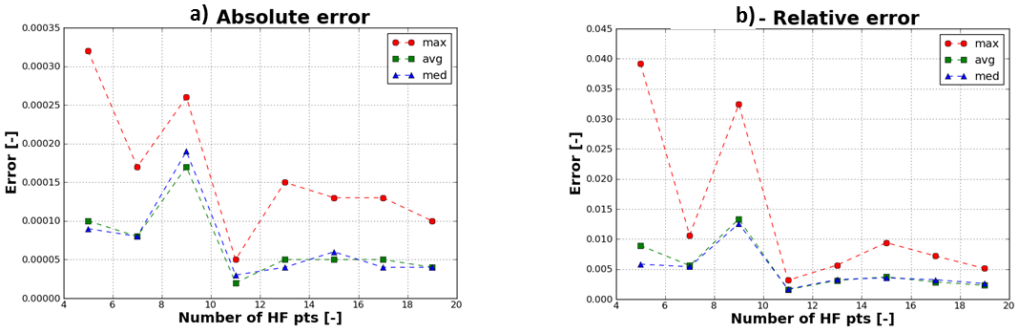

Figure 9: Convergence of the error estimates.

Figure 10: Comparison of absolute and relative error prediction for VFM and RSM.

A comparison of the statistics of the error predictions before and after the refinement process for the VFM and high-fidelity only surrogate (RSM) is shown in Figure 10. Although the error reduction for the RSM is considerably more pronounced, the RSM prediction remains

inferior to the VFM. Moreover, the VFM surrogate obtained with 5 high-fidelity data points offers similar accuracy as the refined RSM both in terms of absolute and relative errors. The refinement process, driven by the requirement to minimise the maximum relative error, allowed both the maximum absolute error and maximum relative error to be reduced by a factor of 3. In general the improvement in relative errors is stronger than for absolute errors.

High-fidelity solutions for a number of additional points, not used for surrogate refinement, were obtained for an additional validation stage. This allowed for the real errors, i.e. the difference between VFM prediction of the drag coefficient and the actual simulated value, to be calculated. The results of this validation for the initial and saturated surrogates are demonstrated in Figure 11.

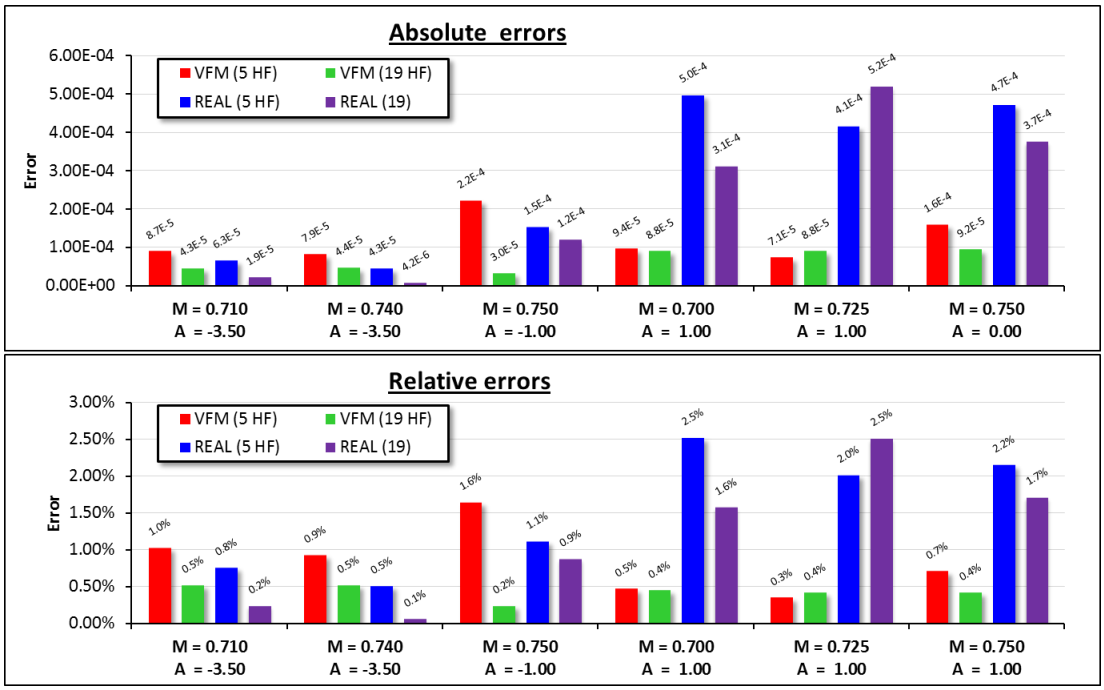

Figure 11: Comparison of the VFM error estimates and the actual prediction errors.

Both absolute and relative errors remain small for the low drag coefficient values, but the real errors are considerably larger in the high incidence range. Although in general, the surrogate refinement led to reduction of both estimated and actual errors, in some cases, i.e. $M = 0.725$ and $A = 1.0$, the errors have increased. No direct correlation between the errors predicted by the VFM and the actual errors can be identified. Nevertheless, the same trends can be observed, i.e. reduction in error estimate corresponds to the reduction of the actual inaccuracy of the prediction.

This test clearly demonstrates that given an appropriate low-fidelity model, VFM can be used to generate a surrogate of a superior quality to a response surface generated from high-fidelity data only. In practice, this means that by adopting the VFM technique the number of required high-fidelity data points can be significantly reduced or the quality of the surrogate can be improved.

The analysis of the error estimates shows how it can be used to drive the refinement process in the desired way (local vs. global, absolute vs. relative). Although the error estimates generally give a reasonable prediction of the surrogate accuracy, additional tests, using high-fidelity data, are required in order to ensure the quality of the obtained response surface.

3.3 Time benefits enabled by application of VFM

One of the main motivations for application of the VFM technique is to enable generation of a high-quality surrogate at a fraction of the cost required to generate the same surrogate based only on high-fidelity points. One of the main ARA requirements in the CONGA project was to construct a dataset with wing cruise performance (lift and drag coefficients) for a wing family with varying planform areas and spans at a range of incidences (see Figure 12 for illustration).

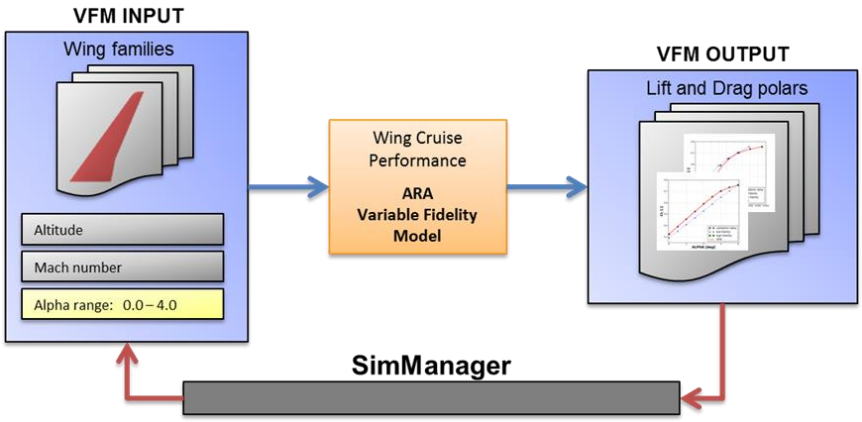

Figure 12: Illustration of the process adopted in CONGA project.

The required dataset was constructed from 108 points over a three-dimensional design space with 3 values of span, 4 values of wing surface area and 9 incidences. The low-fidelity data was computed with the Viscous Full-Potential method (VFP) [11], whereas the high-fidelity results were extracted from the results of TAU simulations. A surrogate refinement process, similar to the one described in previous section was adopted, with lift coefficient surrogate refinement driven by reduction of absolute error estimates, and drag coefficient surrogate driven by the relative error reduction. The leave-one-out test has been applied to ensure a sufficient quality of the obtained surrogates. The final VFM surrogate was constructed from 108 low-fidelity points and 20 high-fidelity results.

On average, 15 minutes were required to generate a single data point with VFP compared to 4 hours on a 20-core cluster needed for a single TAU solution. A comparison of the time needed to generate the VFM surrogate with the time required for 108 TAU simulations is shown in Figure 13. Application of VFM allowed the surrogate of appropriate quality to be obtained in 25% of the time necessary to simulate all 108 data points. In theory, it could be possible to construct a surrogate from a smaller number of high-fidelity data points, but, as already demonstrated in the previous example, it is unlikely that it would have similar quality and would still require significant computational effort.

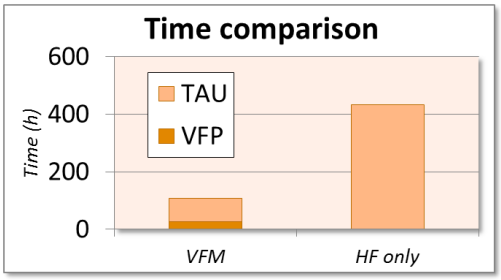

Figure 13: Comparison of the time required to generate the final data set.

This test case clearly demonstrates the time benefits of the application of the VFM technique. Generation of a surrogate has an additional advantage in that it can be used to examine the drag and lift coefficients at intermediate values of the design parameters, at virtually no cost, since the generated VFM response surface is continuous. Moreover, it is easily possible to extend the surrogate by increasing the range of parameters or by addition of new dimensions.

3.4 Impact of the correlation function

The final test presented in this paper investigates the impact of one of the most important parameters of the VFM technique, i.e. the choice of correlation function used to generate the response surface.

In order to assess the impact of the correlation function, surrogates with dependence of the aerofoil performance (L/D) on its thickness-to-chord ration (t/c) are analysed. Unlike in the previous examples, where two different methods were used to generate the solutions, here both low- and high-fidelity data are generated using the same 2D solver – BVGK. The difference in the level of data fidelity is attributed to the different means of obtaining the geometry. The high-fidelity data consists of 3 aerofoils of different thicknesses designed for optimum performance, while the low-fidelity geometries are generated by scaling the baseline section thickness while maintaining a fixed camber line (see Figure 14 for illustration).

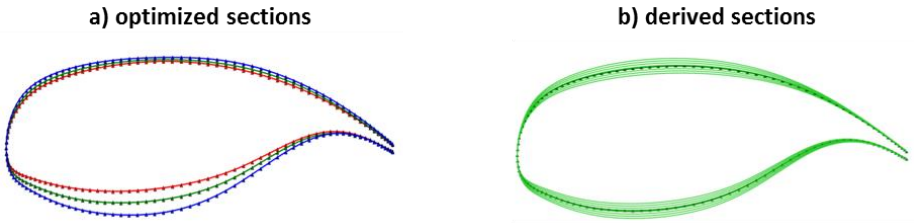

Figure 14: Sections used for generation of VFM surrogate.

This exercise is motivated by the fact that it is not normally possible, due to the time constraints, to optimise sections during the preliminary aircraft design stage. In fact, the wing sections probably do not exist at this point in time and even if some legacy data are available, this might not be suitable for the new aircraft model. Still, ability to predict the potential optimum aerodynamic performance would allow realistic performance targets to be set when sizing the aircraft, without actually performing the time and resource intensive optimisation.

The VFM surrogates generated with two different correlation functions, i.e. Gaussian Exponential function (GEXP) and Multi-Quadratic (MQ) Radial Basis Function (RBD), are shown in Figure 15. Both surrogates use the same low-fidelity data – performance (L/D) characteristics of the varying thickness sections are derived from the optimised baseline aerofoil. Two high-fidelity data points, corresponding to the baseline and thick sections, are used in both scenarios. The thin optimised aerofoil is used as a reference point for validation.

The data presented in Figure 15 highlight significant differences not only in the obtained VFM surrogates but also differences in the low-fidelity response surfaces constructed during the process. While the GEXP low-fidelity response surface closely follows the supplied data points, the MQ surface is smoother and follows the general trend rather than the actual data. Similar behaviour is observed for the generated VFM surrogates, i.e. in the extrapolation region the GEXP surrogate follows the low-fidelity data, whereas the MQ extends the original data trend. The magnitude of estimated errors is also smaller for the case of the MQ correlation function.

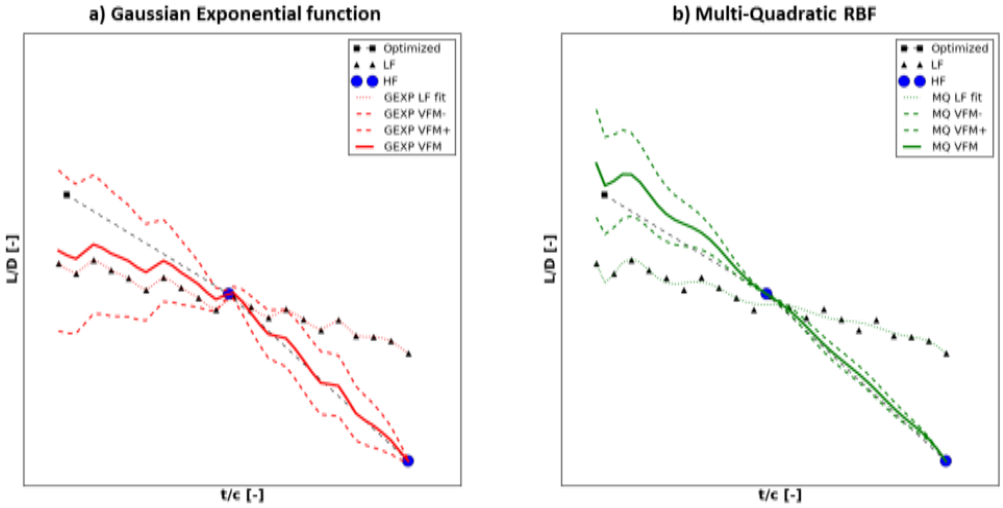

Figure 15: Comparison of the VFM surrogates obtained with different correlation functions.

The results presented for this test case show the importance of the choice of an appropriate correlation function. If the input data is characterised by a high level of noise it is beneficial to use RFB-based correlation functions, as they allow for a smooth surrogate to be generated. On the other hand, GEXP is more localised, so it is a more appropriate choice for data where the general behaviour is not necessarily smooth and local effects need to be considered. In all cases, however, care needs to be taken when extrapolating the data beyond the available high-fidelity data boundaries.

4 POSSIBLE APPLICATIONS OF VFM

The VFM technique has a range of possible applications in the context of modern aircraft design. This section attempts to summarise the various ways in which this method can be adopted. It is suggested to divide the range of possible VFM applications into two main groups, namely data fusion and local surrogate refinement.

The objective of data fusion is to combine two or more datasets with different level of fidelity into a single high-quality response surface. As demonstrated in previous sections, using the VFM not only offers significant reduction of the time needed to generate high quality surrogates from sparse datasets, but also allows for efficient assessment of the surrogate accuracy.

Below is a non-exhaustive list of possible scenarios for data fusion:

- Correcting low-fidelity code with high-fidelity code (e.g. EULER + RANS)
- Correcting partially converged CFD results with fully converged ones
- Combining results with different mesh refinement levels
- Combining wind tunnel data with CFD data
- Correcting CFD for aeroelasticity effects
- Combining results with different levels of geometry maturity

An alternative application of the VFM is to locally refine the surrogate during the optimisation process. Combined with an optimisation algorithm, VFM can be applied to find function minima efficiently (see Figure 16 for illustration). In such a case, the design space is

explored with the low-fidelity response surface, while high-fidelity results are used for local refinement of the surrogate. An example process is described below:

1. Find the function minimum with the low-fidelity response surface
2. Run the high-fidelity code on the optimum point
3. Generate the VFM surrogate with the addition of high-fidelity data
4. Use the VFM as response surface in step 1

It is believed that the approach presented above could significantly reduce the time required for optimisation, as only a few high-fidelity simulations would be necessary.

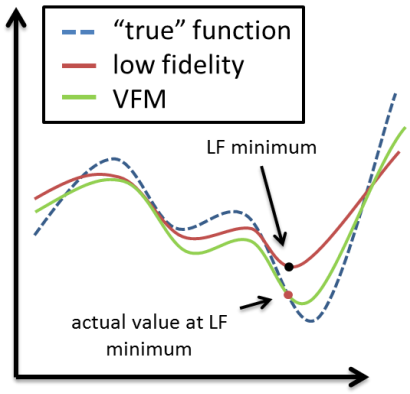

Figure 16: Illustration of VFM used for optimisation.

5 CONCLUSIONS

This paper explored the applicability of using the Variable Fidelity Modelling (VFM) in the context of aerodynamic analysis of modern aircraft designs. The VFM can be used for rapid generation of high-quality surrogate models by combining the results obtained from a low-fidelity method with a limited number of high-fidelity data points. By reducing the number of high-fidelity points required for generation of the surrogate, VFM enables the overall cost of creating the response surface to be significantly reduced.

A wide range of possible applications has been identified, which include, but are not limited to, combining results from simulations at different levels of fidelity, using different levels of input fidelities, as well as using the method to increase efficiency during an optimisation process. The studied examples have clearly demonstrated that applying VFM can offer significant time reduction without loss of surrogate quality, or can be applied to enhance the quality of an existing dataset.

Examination of the presented test cases allowed for the best practice for VFM application to be developed:

- The quality of VFM strongly depends on the trends observed in low-fidelity data
- VFM results are sensitive to the chosen correlation function. Gaussian Exponential Function is generally more robust, however Multi-Quadratic Radial Basis Function can be used to obtain smooth data and is more suitable for extrapolation

- The error estimates returned by the VFM can be used to indicate the error magnitudes and areas of poor surrogate quality, however, they do not offer accurate error values
- The best practice for surrogate construction is to drive the refinement process using the built-in error estimator and use additional techniques (e.g. leave-one-out test) for results verification

REFERENCES

[1] Al-Ashaab, A., Golob, M., Noriega, P., Torriani, F., Alvarez, P., Beltran, A., Busachi, A., Ex-Ignotis, L., Rigatti, C. and Sharma, S. (2013), "Capturing the Industrial Requirements of Set-Based Design for CONGA Framework", Proceedings of the 11th International Conference on Manufacturing Research (ICMR2013), Cranfield University, Cranfield, UK

[2] Sobek II, Durward K., Allen C. Ward, and Jeffrey K. Liker. "Toyota's principles of set-based concurrent engineering." *MIT Sloan Management Review* 40.2 (1999): 67.

[3] Han, Z-H., S. Görtz, and R. Hain. "A variable-fidelity modeling method for aero-loads prediction." *New Results in Numerical and Experimental Fluid Mechanics VII*. Springer Berlin Heidelberg, 2010. 17-25.

[4] Han, Zhong-Hua, and Stefan Görtz. "Hierarchical kriging model for variable-fidelity surrogate modeling." *AIAA journal* 50.9 (2012): 1885-1896.

[5] Han, Zhong-Hua, Ralf Zimmermann, and Stefan Görtz. "A new cokriging method for variable-fidelity surrogate modeling of aerodynamic data." *AIAA Paper* 1225 (2010): 2010.

[6] Han, Zhong-Hua, Stefan Görtz, and Ralf Zimmermann. "Improving variable-fidelity surrogate modeling via gradient-enhanced kriging and a generalized hybrid bridge function." *Aerospace Science and Technology* 25.1 (2013): 177-189.

[7] Krige, D. G. "A statistical approach to some basic mine valuation problems on the Witwatersrand." *Journal of the South African Institute of Mining and Metallurgy* 94.3 (1994): 95-112.

[8] Keane, Andy, and Prasanth Nair. Computational approaches for aerospace design: the pursuit of excellence. John Wiley & Sons, 2005.

[9] Ashill, P. R., Wood R. F., and D. J. Weeks. "An improved semi-inverse version of the Viscous Garabedian and Korn method (VGK)." *RAE TR* 87002 (1987).

[10] Schwamborn, D., Gerhold, T., and Heinrich R.. "The DLR TAU-code: Recent applications in research and industry." ECCOMAS CFD 2006: Proceedings of the European Conference on Computational Fluid Dynamics, Egmond aan Zee, The Netherlands, September 5-8, 2006. Delft University of Technology; European Community on Computational Methods in Applied Sciences (ECCOMAS), 2006.

[11] Arthur M. "A method for calculating subsonic and transonic flows over wings or wing-fuselage combinations with an allowance for viscous effects", 22nd Aerospace Sciences Meeting, Aerospace Sciences Meetings,.

ECCOMAS Congress 2016
VII European Congress on Computational Methods in Applied Sciences and Engineering
M. Papadrakakis, V. Papadopoulos, G. Stefanou, V. Plevris (eds.)
Crete Island, Greece, 5–10 June 2016

FOUR-DIMENSIONAL PATH INTEGRATION METHOD FOR ESTIMATING THE STOCHASTIC ROLL RESPONSE

Wei Chai[1], **Arvid Naess**[2, 3], **and Bernt J. Leira**[1]

[1] Department of Marine Technology, Norwegian University of Science and Technology
Otto Nielsens veg 10, Department of Marine Technology, NTNU, 7491 Trondheim, Norway
{chai.wei, bernt.leira}@ntnu.no

[2] Centre for Ships and Ocean Structures, Norwegian University of Science and Technology
Otto Nielsens veg 10, Department of Marine Technology, NTNU, 7491 Trondheim, Norway
{arvid.naess}@math.ntnu.no

[3] Department of Mathematical Sciences, Norwegian University of Science and Technology
Sentralbygg 2, 11th floor, room 1144, Gløshaugen, 7491 Trondheim, Norway
{arvid.naess}@math.ntnu.no

Keywords: Path integration method, nonlinear ship rolling, stochastic response.

Abstract. *In this paper, the Markov theory is introduced in order to model the roll motion excited by random wave excitation. Specifically, a four-dimensional (4D) Markov dynamic system is established by combing the single-degree-of-freedom (SDOF) model used to represent the ship rolling behavior in random beam seas with a second-order linear filter used to approximate the stationary wave excitation moment. Based on the Markov property of the 4D coupled dynamic system, a 4D path integration (PI) method is applied in order to solve the Fokker-Planck equation, which governs the probabilistic properties of the coupled dynamic system. The theoretical principle and numerical implementation of the current state of the art 4D PI method are presented. Furthermore, the numerical robustness and accuracy of the 4D PI method are evaluated by means of the versatile Monte Carlo simulation (MCS) technique.*

1 INTRODUCTION

The challenge to calculate the response statistics of nonlinear, marine structures subjected to a random seaway is still substantial. In this work, the rolling behavior of a vessel in random beam seas is to be studied since the associated high-level responses with low probability levels are important for reliability based ship design and operation in practice.

For the cases of beam seas, the roll motion is assumed to be decoupled from other motions and governed by a single-degree-of-freedom (SDOF) equation [1], which is also a second order differential equation. In the SDOF model, the nonlinearities associated with damping and restoring terms as well as the randomness of the wave excitation term are all incorporated.

Various probabilistic approaches have been proposed to analyze the stochastic response of the roll motion in random seas [2-4]. Among these strategies, the methodology based on the Markov diffusion theory is attractive because the probabilistic properties of the roll motion is governed by the Fokker-Planck (FP) equation. In order to build a Markov system for describing the random roll motion, a second order linear filter is applied in order to approximate the stationary wave excitation moment as a filtered white noise. Subsequently, a four-dimensional (4D) coupled system is generated but the corresponding high-dimensional FP equation leads to another challenge.

Analytical solutions of the FP equations are only available for some linear systems and a very limited class if nonlinear systems. Direct numerical methods aiming to solve the low-dimensional FP equations, such as the finite element method [5] and the finite difference method [6], are hardly feasible because for the high-dimensional FP equations. In this regard, the so-called "curse of dimension" problem comes into play, which means that difficulties arise due to the processing capacity as well as the storage needed for the computation increases dramatically with the dimension of the FP equation.

The path integration (PI) method is an efficient approximation for solving the FP equation and providing the stationary or non-stationary response probability density function (PDF) of the dynamic system [7-9]. The evolution of the response PDF is computed in short time steps via a step-by-step solution technique. Specifically, the based on the Chapman-Kolmogorov equation, the response PDF at a given time instant can be obtained when the response PDF at an earlier close time as well as the conditional PDF are already known. In this work, a 4D PI procedure is developed to address the challenge of determining the response statistics of the roll motion in random beam seas. The feasibility and reliability of the PI technique will be demonstrated by comparing with the Monte Carlo simulation.

2 MATHEMATICAL MODEL

When the ship is excited by beam wave loads, the roll motion is described by the following SDOF equation [10]:

$$\ddot{\theta}(t)+b_{44}\dot{\theta}(t)+b_{44q}\dot{\theta}(t)\,|\,\dot{\theta}(t)\,|+c_1\theta(t)-c_3\theta^3(t)=m(t) \tag{1}$$

where $\theta(t)$ and $\dot{\theta}(t)$ are the roll angle and the roll velocity, respectively. b_{44} and b_{44q} are the relative linear and quadratic damping coefficients, c_1 and c_3 are the relative linear and nonlinear roll restoring coefficients. m(t) is the relative roll excitation moment, it is a stationary Gaussian process and described by the spectrum $S_{mm}(\omega)$. The SDOF model (1) can be transformed into the following state-space equation which is written as:

$$\begin{cases} dx_1 = x_2 dt \\ dx_2 = (-b_{44}x_2 - b_{44q}x_2\,|\,x_2\,| - c_1x_1 + c_3x_1^3 + x_3)dt \end{cases} \tag{2}$$

where $x_1=\theta(t)$, $x_2=\dot{\theta}(t)$ and $x_3=m(t)$ is the driving process for the dynamic system (2).

The linear filter technique is widely used in the engineering community due to its simplicity and practicality. The driving process $m(t)$ is a stationary Gaussian process with appropriate spectral density, it can approximated quite satisfactorily by a suitable linear filter. In this work, a second-order linear is applied in order to approximate the desired spectrum, $S_{mm}(\omega)$.

The second-order linear filter is expressed by the following differential equation:

$$\begin{cases} dx_3 = (x_4 - \beta x_3)dt + \gamma dW \\ dx_4 = -\alpha x_3 dt \end{cases} \tag{3}$$

where x_3 and x_4 are the state variables in the filter equation with x_3 representing the output $m(t)$. $dW(t)=W(t+dt)-W(t)$ represents an infinitesimal increment of a standard Wiener process with $E\{dW(t)\}=0$ and $E\{dW(t)dW(s)\}=0$ for $t \neq s$ and $E\{dW(t)^2\}=0$. The spectrum generated by the second-order linear filter (3) is denoted as $S_{Filter}(\omega)$ and given as:

$$S_{Filter}(\omega)=\frac{1}{2\pi}\frac{\gamma^2\omega^2}{(\alpha-\omega^2)^2+(\beta\omega)^2} \tag{4}$$

where α, β, γ are the parameters of the linear filter and they are determined by minimizing the least square error between the spectral density of the filtered spectrum $S_{Filter}(\omega)$ and the spectral density of the target spectrum, $S_{mm}(\omega)$. It is worth emphasizing that the filtered spectrum (4) is double-sided, while the relative roll excitation spectrum $S_{mm}(\omega)$ is physically single-sided. This difference needs to be reflected when performing the simulation itself.

By combining the equation (2) with equation (3), the extended dynamic system is formed. Therefore, the roll motion in random beam seas can be described by the following 4D state space equation:

$$\begin{cases} dx_1 = x_2 dt \\ dx_2 = (-b_{44}x_2 - b_{44q}x_2 \mid x_2 \mid -c_1x_1 + c_3x_1^3 + x_3)dt \\ dx_3 = (x_4 - \beta x_3)dt + \gamma dW \\ dx_4 = -\alpha x_3 dt \end{cases} \tag{5}$$

3 4D PATH INTEGRATION METHOD

3.1 Main principle

The dynamic system represented by equation (5) is a Markov diffusion process and it can be expressed as the following stochastic differential equation:

$$d\mathbf{x} = \mathbf{a}(\mathbf{x},t)dt + \mathbf{b}(t)d\mathbf{W}(t) \tag{6}$$

where $\mathbf{x}(t)=(x_1(t),\ldots, x_4(t))^T$ is a 4D state space vector process, the vector $\mathbf{a}(\mathbf{x},t)$ is the drift term and $\mathbf{b}(t)d\mathrm{W}(t)$ represents the diffusive term. The vector $d\mathbf{W}(t)=\mathbf{W}(t+dt)-\mathbf{W}(t)$ denotes independent increments of a standard Wiener process.

For the Markov process $\mathbf{x}(t)$, its transition probability density, $p(\mathbf{x},t|\mathbf{x}',t')$, also known as the conditional PDF is governed by the FP equation, which is expressed as:

$$\frac{\partial}{\partial t}p(\mathbf{x},t\mid\mathbf{x}',t') = -\sum_{i=1}^{4}\frac{\partial}{\partial x_i}a_i(\mathbf{x},t)\,p(\mathbf{x},t\mid\mathbf{x}',t') + \frac{1}{2}\sum_{i=1}^{4}\sum_{j=1}^{4}\frac{\partial^2}{\partial x_i\partial x_j}(b(t)\cdot b^T(t))_{ij}\,p(\mathbf{x},t\mid\mathbf{x}',t') \tag{7}$$

where $\mathbf{x}'$ denotes the state space vector at time t' and $t'< t$.

For numerical solution of the time continuous stochastic differential equation (SDE) (6), discretization of the equation with respect to time t is essential. In this regard, Naess and Moe propose a fourth-order Runge-Kutta-Maruyama approximation:

$$\mathbf{x}(t) = \mathbf{x}(t') + \mathbf{r}(\mathbf{x}(t'), t')\Delta t + b(t')\Delta \mathbf{W}(t') \tag{8}$$

where $\Delta t = t - t'$ is the time increment and the vector $\mathbf{r}(\mathbf{x}(t'), t')$ denotes the explicit fourth-order Runge-Kutta (RK4) increment or RK4 approximation. Since $\mathbf{W}(t)$ is a Wiener process, for short time increment Δt, the independent increment $\Delta\mathbf{W}(t') = \mathbf{W}(t) - \mathbf{W}(t')$ is a Gaussian variable for every t' (a constant is considered to be a Gaussian variable with zero standard deviation).

With the introduction of the time discrete approximation, the time sequence $\{\mathbf{x}(i \cdot \Delta t)\}_{i=0}^{\infty}$ is a Markov chain and it can approximate the time-continuous Markov solution of the SDE (6) with satisfactory accuracy when the time increment Δt is sufficiently small [8].

For a time increment $\Delta t = t - t'$, the transition probability density of equation (8), $p(\mathbf{x}, t | \mathbf{x}', t')$, is given as a (degenerate) Gaussian distribution, which is written as:

$$\begin{aligned} p(\mathbf{x}, t \mid \mathbf{x}', t') = {} & \delta(x_1 - x_1' - r_1(\mathbf{x}', t', \Delta t)) \cdot \delta(x_2 - x_2' - r_2(\mathbf{x}', t', \Delta t)) \\ & \cdot \tilde{p}(x_3, t \mid x_3', t') \cdot \delta(x_4 - x_4' - r_4(\mathbf{x}', t', \Delta t)) \end{aligned} \tag{9}$$

where $\tilde{p}(x_3, t \mid x_3', t')$ is given by the relation:

$$\tilde{p}(x_3, t \mid x_3', t') = \frac{1}{\sqrt{2\pi\gamma^2 \Delta t}} \cdot \exp\left\{ -\frac{(x_3 - x_3' - r_3(\mathbf{x}', t', \Delta t))^2}{2\gamma^2 \Delta t} \right\} \tag{10}$$

in which $r_i(\mathbf{x}', t', \Delta t) = r_i(\mathbf{x}(t'), t', \Delta t)$, $i = 1,2,3,4$ are the Runge-Kutta increments for the state space variables.

For the PI method, the evolution of the response statistics, such as the PDF of the random process $\mathbf{x}$ at time t can be obtained by the following basic equation:

$$p(\mathbf{x}, t) = \int_{R^4} p(\mathbf{x}, t \mid \mathbf{x}', t') p(\mathbf{x}', t') d\mathbf{x}' \tag{11}$$

where $d\mathbf{x}' = \prod_{i=1}^{4} dx_i'$.

Since the expression for the transition probability density is obtained (i.e., the equations (9) and (10)), the PDF of $\mathbf{x}(t)$ can be obtained by the following iterative algorithm if an initial PDF (i.e. at time t_0) is given:

$$p(\mathbf{x}, t) = \int_{R^4} \cdots \int_{R^4} \prod_{s=1}^{n} p(\mathbf{x}^{(s)}, t_s \mid \mathbf{x}^{(s-1)}, t_{s-1}) \cdot p(\mathbf{x}^{(0)}, t_0) d\mathbf{x}^{(0)} \ldots d\mathbf{x}^{(n-1)} \tag{12}$$

where $\mathbf{x} = \mathbf{x}^{(n)} = \mathbf{x}(t_n)$, $t = t_n = t_0 + n \cdot \Delta t$, $\mathbf{x}^{(s)} = \mathbf{x}(t_s)$ and $t_s = t_0 + s \cdot \Delta t$.

3.2 Numerical implementation

Equation (12) describes the mathematical principle of the PI approach. For numerical implementation of the 4D PI method, a reasonable computational domain and the corresponding computational grid have to be determined at first. In this work, the initial PDF $p(\mathbf{x}^{(0)}, t_0)$ is chosen as a 4D Gaussian PDF in four dimensions with zero mean and variances evaluated by a simple Monte Carlo simulation [8]. The straightforward Monte Carlo simulation (MCS) ensures that the initial 4D Gaussian PDF includes all the information corresponding to the selected parameters of the dynamic system, and it also provides a rational computational domain and computational grid for the subsequent simulation.

As for the numerical implementation of the iterative algorithm (12) for each grid point, it represents the PDF at the previous time t' as an interpolating spline surface via Parabolic B-spline. Then, the RK4 approximation scheme is applied to calculate the deterministic trajectories backwards for each grid point. Therefore, each grid point at time t is mapped backwards with the corresponding starting point at the previous time t' and the PDF values at the backward-mapped points, i.e. the starting points, can be given by using the spline surface. Finally, the PDF at time t, i.e. the new PDF, is calculated by substituting the transition probability density given in terms of equations (9) and (10) into the integral equation (11). The flowchart of the numerical implementation of the 4D PI method with the iterative algorithm described above is shown in Figure 1.

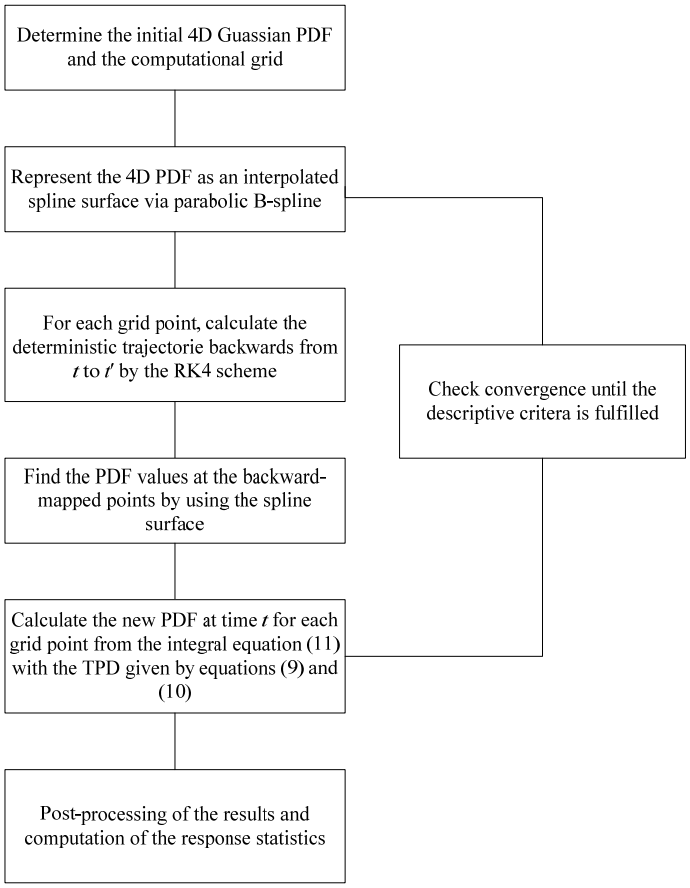

Figure 1: Flowchart of the numerical implementation of the 4D PI method

4 NUMERICAL RESULTS

In this Section, an ocean surveillance ship is selected in order to study the stochastic roll response. The parameters for this parameters are given in Ref. [11]. The relative roll excitation moment spectrum $S_{mm}(\omega)$ for a given sea state [10] is presented in Figure 2.

As mentioned above, the parameters α, β, γ in the second-order filter (4) are determined by minimizing the square errors between the filtered spectrum and the target spectrum, S_{mm}. It can be readily seen that the filtered spectrum is reasonable in terms of bandwidth, peak frequency and peak value. However, there is a slight discrepancy between the two spectra in the critical region near the natural roll frequency ω_0. This discrepancy should not be neglected since the distribution of high level response is sensitive to the variation of the external excitation in this frequency region [12]. Therefore, a constant, c, should be introduced as a correc-

tion factor for the filtered spectrum in order to decrease the discrepancy in the critical frequency region. The filtered spectrum (4) can then be changed into:

$$S_{Filter}(\omega)=\frac{1}{2\pi}\frac{(c\cdot\gamma)^2\omega^2}{(\alpha-\omega^2)^2+(\beta\omega)^2} \tag{13}$$

and the corrected (or modified) spectrum in the critical region is also presented in Figure 2.

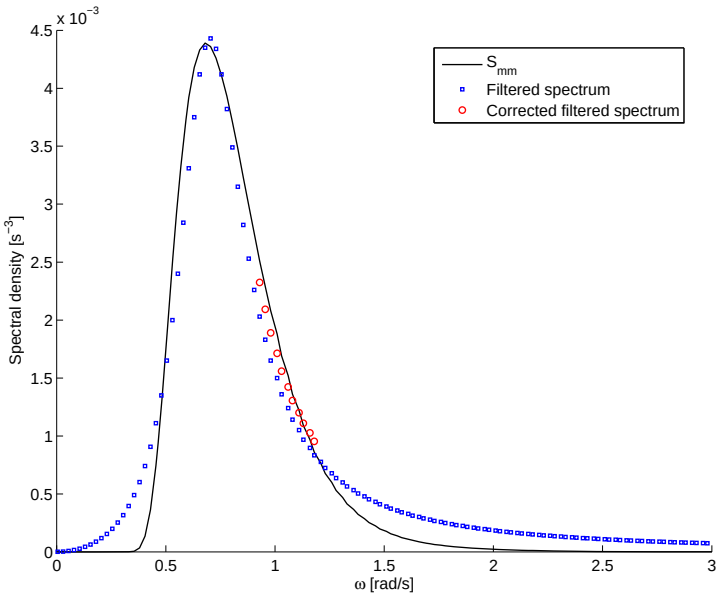

Figure 2: Relative roll excitation moment spectrum and the filtered spectrum, the corrected filtered spectrum (part) for a given sea state.

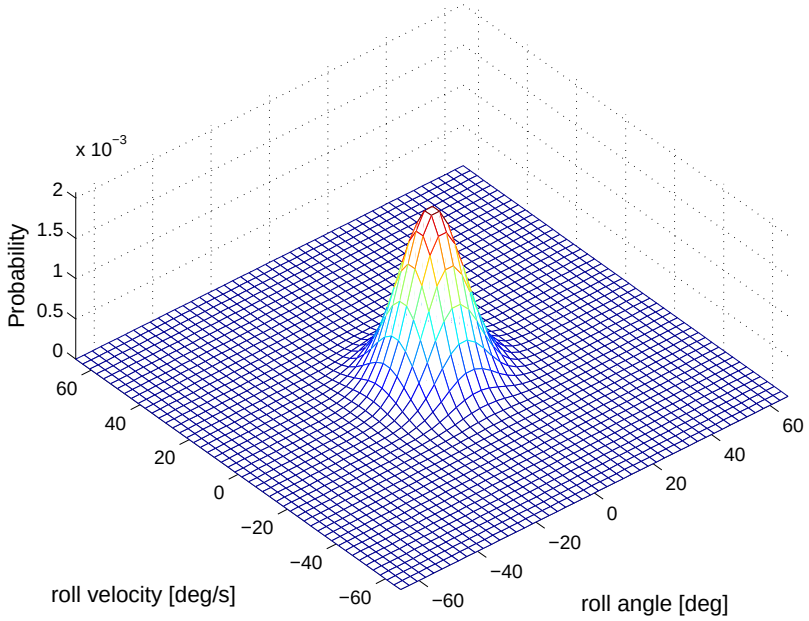

Figure 3: Joint PDF of the roll response obtained by the 4D PI method.

As mentioned in Section 3, the joint PDF of the roll angle process and the roll velocity process can be obtained directly by the 4D PI method. The joint PDF of the roll response yielded by the 4D PI method for the selected sea state is presented in Figure 3 and the mar-

ginal PDFs of the roll angle process and the roll velocity process are shown in Figure 4 and Figure 5, respectively.

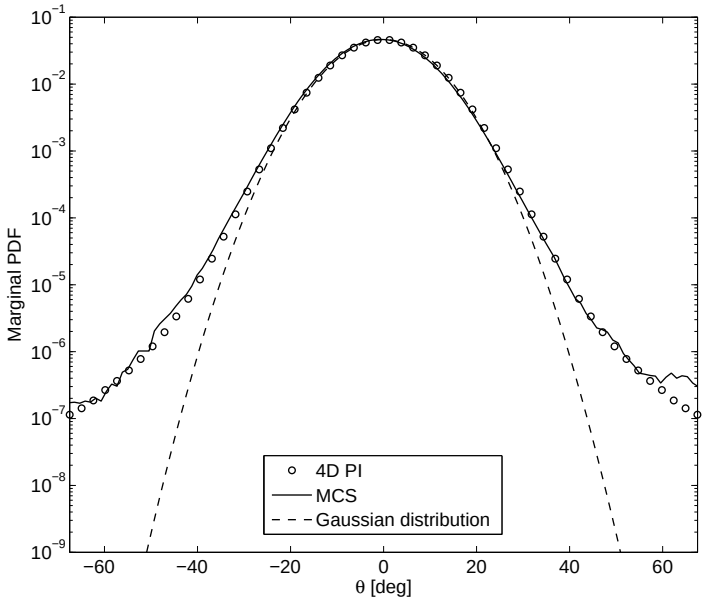

Figure 4: Marginal PDF of the roll angle process.

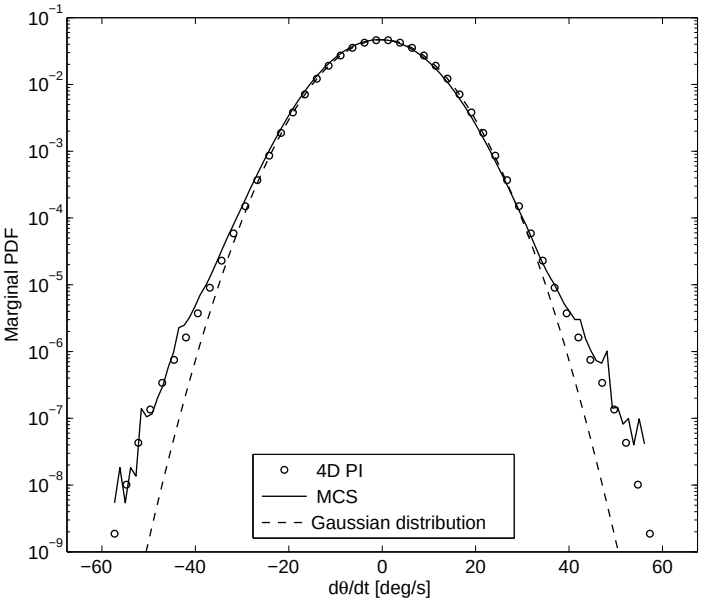

Figure 5: Marginal PDF of the roll velocity process.

In Figures 4 and 5, it is observed that the comparisons of the marginal PDFs obtained by the 4D PI method and the corresponding empirical estimations obtained by MCS demonstrate the high-level accuracy of the 4D PI method. Furthermore, the 4D PI method provides nice results for the low probabilities, but the distribution obtained by MCS are suffering from uncertainties. The Gaussian distributions of the marginal PDFs in Figures 4 and 5 are obtained by using the variances evaluated by the straightforward MCS technique mentioned in Section 3. Actually, they are the marginal PDFs of the 4D Gaussian PDF, $p(\mathbf{x}^{(0)}, t_0)$, which serves as the initial PDF in the 4D PI procedure. It is shown that the Gaussian distributions in Figures 4 and 5 provide reasonable approximations of the statistics of small amplitude roll motions.

However, for the high-level responses, the distributions of the roll angle process and the roll velocity process are very different from the normal distribution, which underestimates the corresponding low levels in this region.

The mean upcrossing rate is a key parameter for estimation of the large and extreme response statistics as well as for evaluation of the associated reliability of marine structures subjected to random external excitations. The calculation of the mean upcrossing rate of the roll angle process $\theta(t)$ is usually based on the Rice formula (14) and the joint PDF of the roll response, which can be obtained directly by the 4D PI technique. The mean upcrossing rate $v^+(\zeta)$ is given as follows:

$$\begin{aligned} v^+(\zeta) &= \lim_{t\to\infty} v^+(\zeta;t) \\ v^+(\zeta;t) &= \int_0^\infty \dot{\theta} f_{\theta\dot{\theta}}(\zeta,\dot{\theta};t)d\dot{\theta} \end{aligned} \tag{14}$$

where $v^+(\zeta;t)$ denotes the expected number of upcrossings for the ζ-level per unit time at time t by the roll angle process $\theta(t)$, $f_{\theta\dot{\theta}}(\theta,\dot{\theta};t)$ is the joint PDF of the roll angle process and the roll velocity process at the time instant t.

The upcrossing rate for the selected sea state calculated by application of the 4D PI approach and the corresponding empirical estimation of the upcrossing rate as well as the 95% confidence interval (CI) obtained by MCS are shown in Figure 6. It can be readily seen that the 4D PI technique yields quite accurate and reliable result, even in the high roll response region. Hence, the 4D PI method is suitable for evaluation of the response statistics with low probability levels.

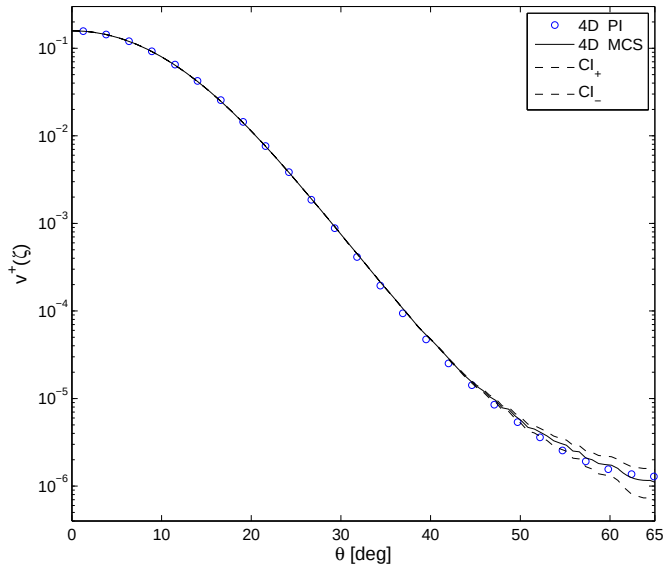

Figure 6: Upcrossing rates obtained by the 4D PI method and MCS.

5 CONCLUSIONS

In this work, a 4D Markov dynamic system is generated in order to describe the rolling behavior of a vessel subjected to random wave excitation. Based on the Markov property of the dynamic system, a 4D PI scheme is introduced to solve the high-dimensional FP equation. Comparisons of the response statistics obtained by the 4D PI method and MCS demonstrate the numerical robustness and accuracy of the 4D PI in calculating the statistics of the high roll response levels when subjected to random wave excitation.

REFERENCES

[1] J. Roberts, M. Vasta, Markov modelling and stochastic identification for nonlinear ship rolling in random waves. *Philosophical Transactions of the Royal Society of London. Series A: Mathematical, Physical and Engineering Sciences*, **358**, 1917-1941, 2000.

[2] W. Chai, J. Fan, R. Zhu, X. Huang, G. Miao, Calculation of Ship Rolling Capsizing Probability by Path Integral Solution. *Journal of Shanghai Jiaotong University*, **28**, 317-322, 2013.

[3] L. Dostal, E. Kreuzer, Probabilistic approach to large amplitude ship rolling in random seas. *Proceedings of the Institution of Mechanical Engineers, Part C: Journal of Mechanical Engineering Science*, **225**, 2464-2476, 2011.

[4] Z. Su, J.M. Falzarano, Markov and Melnikov based methods for vessel capsizing criteria. *Ocean Engineering*, **64**, 146-152, 2013.

[5] Jr, B. Spencer, L. Bergman, On the numerical solution of the Fokker-Planck equation for nonlinear stochastic systems. *Nonlinear Dynamics*, **4**, 357-372, 1993.

[6] S.F. Wojtkiewicz, E.A. Johnson, L.A. Bergman, M. Grigoriu, Jr, B.F. Spencer, Response of stochastic dynamical systems driven by additive Gaussian and Poisson white noise: Solution of a forward generalized Kolmogorov equation by a spectral finite difference method. *Computer methods in applied mechanics and engineering*, **168**, 73-89, 1999.

[7] W. Chai, A. Naess, B.J. Leira, Filter models for prediction of stochastic ship roll response. *Probabilistic Engineering Mechanics*, **41**, 104-114, 2015.

[8] E. Mo, Nonlinear stochastic dynamics and chaos by numerical path integration. Norwegian University of Science and Technology, *PhD Thesis*, 2008.

[9] A. Naess, J. Johnsen, Response statistics of nonlinear, compliant offshore structures by the path integral solution method. *Probabilistic Engineering Mechanics*, **8**, 91-106, 1993.

[10] W. Chai, A. Naess, B.J. Leira, Stochastic Dynamic Analysis and Reliability of a Vessel Rolling in Random Beam Seas. *Journal of Ship Research*, **59**, 113-131, 2015.

[11] Z. Su, Nonlinear response and stability analysis of vessel rolling motion in random waves using stochastic dynamical systems. Texas A&M University, *PhD Thesis*, 2012.

[12] W. Chai, A. Naess, B.J. Leira, Stochastic nonlinear ship rolling in random beam seas by the path integration method. *Probabilistic Engineering Mechanics*, in press, 2015.

ECCOMAS Congress 2016
VII European Congress on Computational Methods in Applied Sciences and Engineering
M. Papadrakakis, V. Papadopoulos, G. Stefanou, V. Plevris (eds.)
Crete Island, Greece, 5–10 June 2016

SEISMIC RELIABILITY ASSESSMENT OF FRAME STRUCTURES WITH FLEXIBILITY-BASED STOCHASTIC BEAM-COLUMN ELEMENTS

Georgios Balokas[1,2] **and Michalis Fragiadakis**[1]

[1] Laboratory for Earthquake Engineering, School of Civil Engineering,
National Technical University of Athens, Athens, GR-15773, Greece
e-mail: Georgios.Balokas@elan-ausy.com, mfrag@mail.ntua.gr

[2] Structure Development Department, ELAN-AUSY GmbH,
Harburger Schloßstr. 24, Hamburg, Germany

Keywords: Non-Gaussian translation fields, Fiber-approach, Distributed plasticity, Stochastic analysis.

Abstract. *We study the nonlinear static and dynamic analysis of problems with uncertain, spatially variable material properties using specifically tailored flexibility-based fiber elements. For deterministic problems, flexibility, or force-based, fiber elements have been proven able to provide accurate response estimates using a single beam element per structural member. We extent this formulation for the probabilistic assessment of structures whose properties are described by homogeneous non-Gaussian translation stochastic fields. The proposed modeling allows the use of different integration schemes, depending on the correlation length parameter of the stochastic field. This element formulation, contrary to ordinary displacement-based elements, allows to overcome the need for a very dense mesh of beam elements, which depends on the stochastic field and the regions where plastic rotations will occur. The performance of the proposed modeling approach is demonstrated on a steel portal frame. Considerable reduction of the computing effort is achieved in all cases. The paper underlines the importance of realistic uncertainty quantification and is expected to provide valuable guidance for the structural analysis and the design of systems with uncertain properties.*

1 INTRODUCTION

The stochastic approach continuously gains acceptance as a reliable and valuable tool for the calculation of the response variability of structures. The inherent randomness of certain systems in terms of material, geometry and loads prohibits deterministic treatment of the problem. Over the past 20 years the seismic reliability assessment of structures including uncertainties, has received considerable attention. The spatial variability of material and geometrical properties [1] along with the uncertainty of seismic excitation [2] and the coupling of stochasticity and nonlinearity [3], have been thoroughly investigated with various approaches.

Fiber elements have been used on many occasions for the reliability assessment of frame structures. Contrary to the deterministic problem where inelastic deformations are lumped at the beam ends, in stochastic analysis we need distributed plasticity elements so that our calculations consider the variation of system properties along the member [4]. The use of force-based fiber beam-column elements allows to consistently integrate the spatial variability of inelastic systems with uncertain system properties. For deterministic problems these elements are able to provide accurate response estimates using a single beam element per member. The use of force-based elements for the stochastic assessment of steel frames was first presented in [5] where the seismic capacity of a steel frame subjected to natural ground motion records was examined. In [6] the force-based formulation for the reliability assessment of bridges was used under moving loads, while [7] used force-based fiber elements for the nonlinear static assessment of a simple two-bay frame. Their numerical results are based on a series of measurements of the system properties [8].

2 INELASTIC FIBER BEAM-COLUMN ELEMENTS

2.1 Distributed plasticity elements

Distributed plasticity beam-column elements allow yielding to occur at any location along the element as opposed to plastic-hinge elements, where inelastic demand is lumped at the beam ends. The two most common formulations of distributed plasticity elements are the displacement-based (DB) and the force-based (FB) approach.

Displacement-based elements, also known as stiffness-based elements, follow the classical finite element theory and use cubic Hermitian shape functions to interpolate the displacement field. These elements require a fine mesh at the regions where inelastic deformations are expected to be high, e.g. the beam ends. On the other hand, force-based elements [9,10,11] use force interpolation functions to overcome the problem of the unknown curvature distribution once yielding occurs. This approach always maintains equilibrium of both forces and deformations and converges to a state that satisfies the constitutive laws within a specified tolerance. As a result, for deterministic problems a single force-based element per member is sufficient for accurately predicting the nonlinear behavior, provided that no element loads are present.

Nonlinear beam-column elements are usually based on the "natural" coordinate system (also known as "basic" or "corotational" system) which is a system that translates and rotates following the motion of the element. The beam elements have three degrees-of-freedom (Figure 1), the axial displacement u_1 and two rotations θ_1 and θ_2 which fully describe the inelastic demand and are grouped in $\mathbf{v} = [u_1, \theta_1, \theta_2]^T$. Following the Euler-Bernoulli beam theory, the strain $\varepsilon_x(x,y)$ is obtained as:

$$\varepsilon_x(x,y) = \begin{bmatrix} 1 & -y \end{bmatrix} \begin{bmatrix} \varepsilon_0(x) \\ k(x) \end{bmatrix} = \mathbf{a}_S(y)\,\mathbf{d}_{\text{sec}}(x) \tag{1}$$

where $\mathbf{a}_s(y)$ is the section kinematic matrix and $\mathbf{d}_{sec}$ (x) is the section deformation vector. The section stiffness matrix is calculated as the derivative of the section forces $\mathbf{D}_{sec}$ with respect to the section deformations $\mathbf{d}_{sec}$:

$$\mathbf{k}_{sec} = \frac{\partial \mathbf{D}_{sec}}{\partial \mathbf{d}_{sec}} = \frac{\partial \mathbf{D}_{sec}}{\partial \sigma}\frac{\partial \sigma}{\partial \varepsilon}\frac{\partial \varepsilon}{\partial \mathbf{d}_{sec}} = \int_A \mathbf{a}_S \frac{\partial \sigma}{\partial \varepsilon}\mathbf{a}_S^{\mathrm{T}} dA = \int_A \frac{\partial \sigma}{\partial \varepsilon}\begin{bmatrix} 1 & -y \\ -y & y^2 \end{bmatrix} dA \tag{2}$$

where $\partial\sigma/\partial\varepsilon$ is the tangent of the nonlinear uniaxial constitutive law and y is the distance from the neutral axis. Distributed plasticity elements are also known as "fiber" elements, since each section is discretized to a finite number of fibers which are used to numerically calculate the section stiffness $\mathbf{k}_{sec}$ of Eq. (2). If N is the axial force and M is the bending moment of a cross-section, the section forces are calculated by integrating the stress over the height of the cross-section as follows:

$$\mathbf{D}_{sec} = \begin{bmatrix} N \\ M \end{bmatrix} = \int_A \begin{bmatrix} 1 \\ -y \end{bmatrix} \sigma_x dA = \int_A \mathbf{a}_S^{\mathrm{T}} \sigma_x dA \tag{3}$$

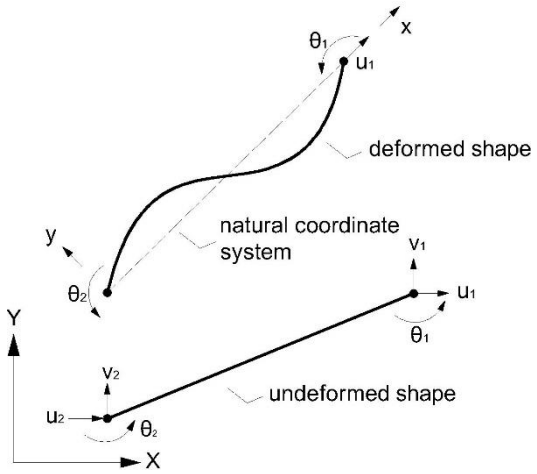

Figure 1: Cartesian and natural coordinates of a plane beam-column element.

2.2 Displacement-based elements

The displacement-based (DB) method uses the element interpolation functions and its derivatives in order to calculate section deformations and strains from the nodal displacements. The relationship of section and element deformations is given by:

$$\mathbf{d}_{sec} = \mathbf{B}_N(x)\mathbf{v} = \frac{1}{L}\begin{bmatrix} 1 & 0 & 0 \\ 0 & 2(3x/L-2) & 2(3x/L-1) \end{bmatrix}\mathbf{v} \tag{4}$$

$\mathbf{B}_N(x)$ is the strain-displacement transformation matrix of the element. The element stiffness matrix is calculated in the natural system as:

$$\mathbf{K}_N = \int_L \mathbf{B}_N^{\mathrm{T}} \mathbf{k}_{sec} \mathbf{B}_N dL \tag{5}$$

The Cartesian element stiffness is obtained from $\mathbf{K}_N$ with the aid of simple algebraic transformations [12].

2.3 Force-based elements

The force-based (FB) method uses force interpolation functions, which are always exact since the distribution of bending moments remains linear after element yielding. The force interpolation matrix $\mathbf{b}_s$ relates section forces with the natural forces **S**, thus:

$$\mathbf{D}_{\text{sec}} = \mathbf{b}_S \mathbf{S} \Leftrightarrow \mathbf{D}_{\text{sec}} = \begin{bmatrix} 1 & 0 & 0 \\ 0 & x/L-1 & x/L \end{bmatrix} \mathbf{S} \tag{6}$$

The natural stiffness matrix is calculated as the inverse of the element flexibility matrix as:

$$\mathbf{K}_N^{-1} = \mathbf{F}_N = \int_L \mathbf{b}_S^T \left(\mathbf{k}_{\text{sec}}\right)^{-1} \mathbf{b}_S \, dL \tag{7}$$

For both displacement and force-based elements, the element stiffness matrix is calculated numerically using Gauss integration. For the case of force-based elements, Gauss-Lobatto integration is preferred which is a variation of Gauss integration that considers the beam ends as integration sections. This rule is preferred since the bending moment receives its maximum values at the beam ends.

3 THE STOCHASTIC FINITE ELEMENT METHOD

3.1 Stochastic field discretization

For nonlinear inelastic problems the discretization of the stochastic field requires special attention. A stochastic (or random) field $H(\mathbf{x},\omega)$ is a mapping from a random outcome ω to a function of space (or time) of a random variable x. It is usually called "field" when it varies in space and "process" when it varies in time. The statistical properties of stochastic fields (e.g. probability distribution and correlation structure) are either assumed or obtained from experimental measurements. In the stochastic finite element method the choice of the FE mesh size is critical, since this decision affects also the discretization of the stochastic field. In principle, the FE mesh size is controlled by the geometry and the expected gradient of the stress field, which in nonlinear problems is not constant during analysis, while the variation of the stochastic field is a property of the structure. The variation of the stochastic field is usually measured using the correlation length parameter b, which is the distance over which significant loss of correlation occurs. Therefore, the FE mesh should be short enough in order to capture the essential features of the random field and avoid loss of information.

3.2 Simulation of non-Gaussian stochastic fields

Non-Gaussian stochastic fields are suitable for the description of many practical engineering parameters, such as material properties, geometric characteristics, soil properties, waves, wind loads, etc. In order to simulate a non-Gaussian stochastic field, a transformation of a Gaussian field with known second-order statistics needs to be performed. The spectral representation method [13] is a direct method for the simulation of Gaussian stochastic fields. The method calculates the stochastic field as the sum of cosine functions with random phase angles and amplitudes. It is based on the power spectrum concept, which is a real, non-negative function that describes how the variance of the stochastic field data is distributed over the frequency domain. Spectral density functions include the variance and the correlation scale characteristics of the stochastic field and usually are functions of exponential or square exponential type.

A power spectrum of square exponential type is shown in Figure 2a for different values of the correlation length b, while the influence of the correlation length parameter to the sample

functions of a Gaussian stochastic field, generated by the spectral representation method, is shown in Figure 2b.

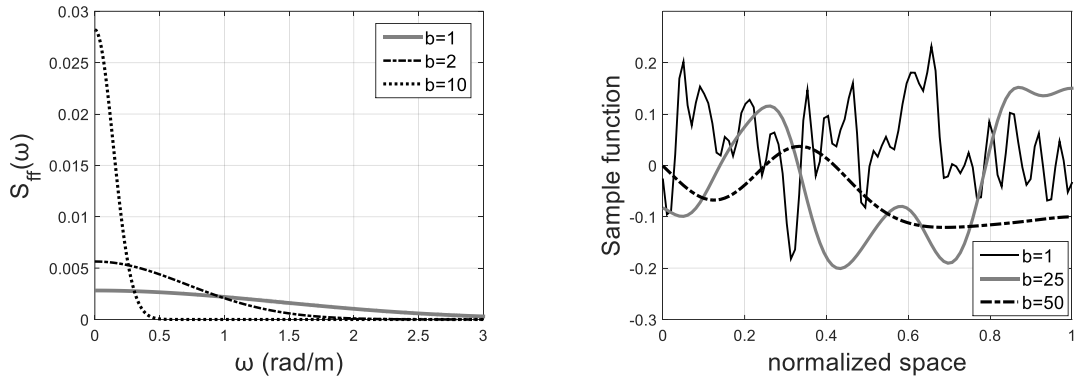

Figure 2: (a) Sample spectral density function $S_{ff}(\omega)$ of square exponential type with standard deviation σ_{ff}=0.1 and different correlation length values, (b) sample functions of a Gaussian stochastic field for different values of the correlation length parameter b.

A non-Gaussian stochastic field can be obtained as a translation field by properly transforming a Gaussian field. Specifically, a zero-mean homogeneous non-Gaussian stochastic field $f(\mathbf{x})$ with spectral density function $S_{ff}(\omega)$, can be obtained with the aid of a nonlinear monotonic transformation of a zero-mean Gaussian field $H(\mathbf{x})$ as:

$$f(\mathbf{x}) = F^{-1}\Phi\left[H(\mathbf{x})\right] \tag{8}$$

where F is the non-Gaussian marginal cumulative distribution function (CDF) of $f(\mathbf{x})$ and Φ is the standard Gaussian CDF. The above transformation is a memory-less translation of every space coordinate x_i. However, the choice of the marginal distribution for the translation field $f(x)$ imposes constraints to its correlation structure [14]. For non-Gaussian translation fields whose autocorrelation function has some inadmissible values, or is not positive-definite, the approximation error should be also taken into consideration [15].

4 PROPOSED METHODOLOGY

We propose the use of flexibility-based elements for the seismic probabilistic assessment of nonlinear frame structures with stochastic properties. For the deterministic analysis of inelastic frame structures, flexibility-based elements are able to capture the response using a single element per member. When stochastic problems are considered, the frame properties vary along the length of every member. Most FE types require appropriately modifying the FE mesh depending on the properties of the stochastic field and also on the regions where concentration of inelastic demand is expected, i.e. beam ends, region of concentrated forces etc. However, for stochastic problems the critical locations are not known a priori since the structural properties vary. We show that force-based elements, if combined with a pertinent numerical integration scheme, offer accurate estimates of the response variability, maintaining the advantage of a single element per member. The resulting FE scheme is suitable for full-scale frame structures with affordable computing cost and accuracy.

We use stochastic non-Gaussian fields to simulate the material properties. Constitutive laws typically depend on several parameters. A simple bilinear model depends on two parameters: the elastic modulus E and the yield stress f_y, while more parameters may be required for other materials, e.g. reinforced concrete. The material parameters may be denoted as D_i and

are here assumed uncorrelated. If $H(\mathbf{x})$ is the zero-mean stochastic field, each material property is distributed along each member. If $D_{0,i}$ is the expected value of each parameter the material property is described as $D_i(\mathbf{x}) = D_{0,i}(1 + H_i(\mathbf{x}))$. The section stiffness $\mathbf{k}_{sec}$ is calculated with the aid of Eq. (2), where the material properties are a function of $\mathbf{D} = [D_1, D_2, \ldots, D_N]^T$. For example for a bilinear steel material $\mathbf{D} = [E, f_y,]^T$ and the section stiffness is obtained with the aid of Eq. (2):

$$\mathbf{k}_{\text{sec}} = \int_A \mathbf{a}_S^T \frac{\partial \sigma(\mathbf{D})}{\partial \varepsilon} \mathbf{a}_S^T dA \tag{9}$$

The element stiffness matrix is calculated at the Gauss-Lobatto integration sections as:

$$\begin{aligned} &\mathbf{K}_N = \int_L \mathbf{b}^T \mathbf{k}_{\text{sec}}^{-1} \mathbf{b}^T dL \Leftrightarrow \\ &\mathbf{K}_N = w_1 \mathbf{b}^T(x_1)\mathbf{k}_{\text{sec}}^{-1}(x_1)\mathbf{b}(x_1) + w_{NIP}\mathbf{b}^T(x_{NIP})\mathbf{k}_{\text{sec}}^{-1}(x_{NIP})\mathbf{b}(x_{NIP}) + \\ &+ \sum_{i=2}^{NIP-1} w_i \mathbf{b}^T(x_i)\mathbf{k}_{\text{sec}}^{-1}(x_i)\mathbf{b}(x_i) \end{aligned} \tag{10}$$

where NIP is the number of integration points, w_i and x_i are the weights and the location of Gauss-Lobatto integration sections. Note that x_1 and x_{NIP} refer always to the two ends of the beam element. A similar integration is also adopted for the element internal forces. The above methodology is implemented with the aid of OpenSees [16]. OpenSees is an open-source structural analysis software that allows the user to define any numerical integration scheme. The pre and post processing of our results are performed with the aid of customized in-house software.

We first generate zero-mean Gaussian stochastic fields using the spectral representation method. These fields have a spectral density function of square exponential type:

$$S_{HH}(\omega) = \frac{\sigma^2 b}{2\sqrt{\pi}} \exp\left(-\frac{b^2\omega^2}{4}\right) \tag{11}$$

where σ is the standard deviation of the stochastic field and b is the correlation length parameter. The lognormal fields are subsequently obtained using Eq. (8). The spectral density function is expected to be slightly different from $S_{HH}(\omega)$, since the translation to the lognormal CDF adds a small approximation error.

5 STEEL PORTAL FRAME EXAMPLE

We consider the steel portal frame of Figure 3 as a case study. All the members of the frame have HEB 200 wide flange cross-sections and are modeled with a single force-based beam-column element. A distributed load q=40kN/m is applied at the bay and remains constant throughout the loading history. The uncertain material properties are the Young's modulus E and the yield stress f_y, both assumed to vary stochastically along each member. The material properties are described by the following expressions:

$$\begin{aligned} E(x) &= E_0\left[1 + H_1(x)\right] \\ f_y(x) &= f_{y0}\left[1 + H_2(x)\right] \end{aligned} \tag{12}$$

where $H_1(x)$, $H_2(x)$ are two zero-mean 1D-1V homogeneous lognormal stochastic fields with COV equal to 10% as indicated by the Joint Committee for Structural Safety [17]. Different values of the correlation length parameter b are considered in order to investigate the sensitiv-

ity of the response to the correlation scale of the stochastic fields. In order to validate the proposed method, we consider as reference solution FE models that use a very dense mesh of 50 displacement-based fiber elements per member. Such a dense mesh is expected to accurately describe randomness for any correlation length.

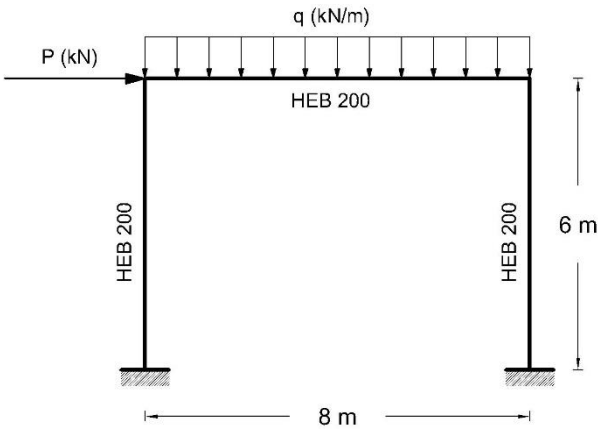

Figure 3: One-storey steel frame.

5.1 Nonlinear static analysis

The response variability of the steel frame is calculated through nonlinear static analysis for a sample size of 500 crude Monte Carlo simulations. For every simulation we obtain the capacity curve in terms of roof drift versus applied load. The mean capacity curve of the frame is shown in Figure 4a, together with the mean plus and minus one standard deviation curves. The vertical dashed line is used in order to separate the pre-yielding from the post-yielding phase of loading. Figure 4a clearly shows that the effect of E is rather small (pre-yielding phase), while considerable variability is observed after yielding where f_y comes into play.

According to Figure 4b the calculation of the mean capacity is not sensitive to the number of integration sections even for a small correlation length (b=0.1). On the other hand, Figure 5 examines the necessary number of integration points in order to capture the response variability defined as the COV (standard deviation divided by the mean value) conditional on the roof drift. As a reference solution we use the red solid curve obtained with the aid of a very dense mesh of 50 displacement-based elements per member. For four correlation length values, we compare the COV estimates using force-based elements of 5, 10, 15 and 20 integration sections. All four plots of Figure 5 show that increasing the number of integration points offers a better description of the random fields, since the COV values converge to the exact solution. The convergence is faster as the correlation length b becomes larger (e.g. compare Figure 5a and Figure 5d). The vertical dashed line (defined in Figure 4) provides the threshold between linear elastic and inelastic response. In the elastic regions the COV is practically constant and very low (2-6%). When the frame starts to yield, the COV increases almost monotonically as the roof drift also increases.

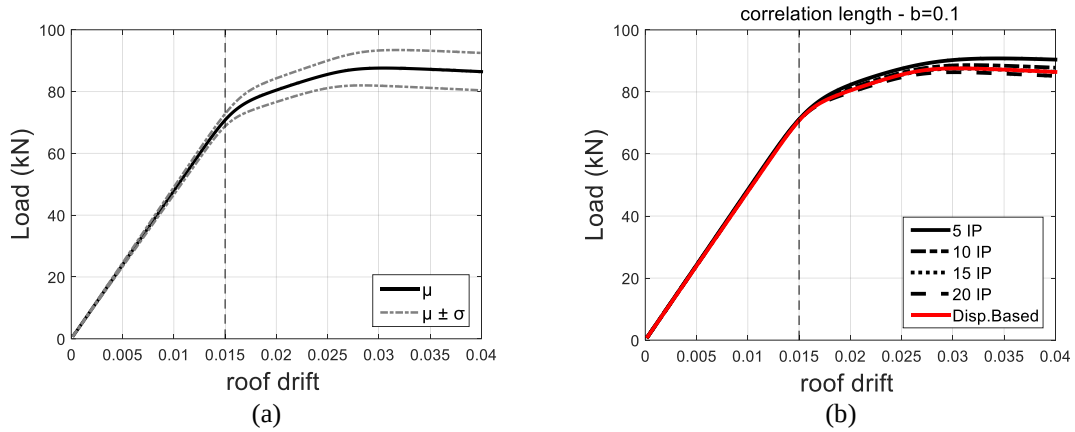

Figure 4: (a) Mean and mean ± one sigma capacity curves of the portal frame, (b) mean capacity curves for ranging number of integration points.

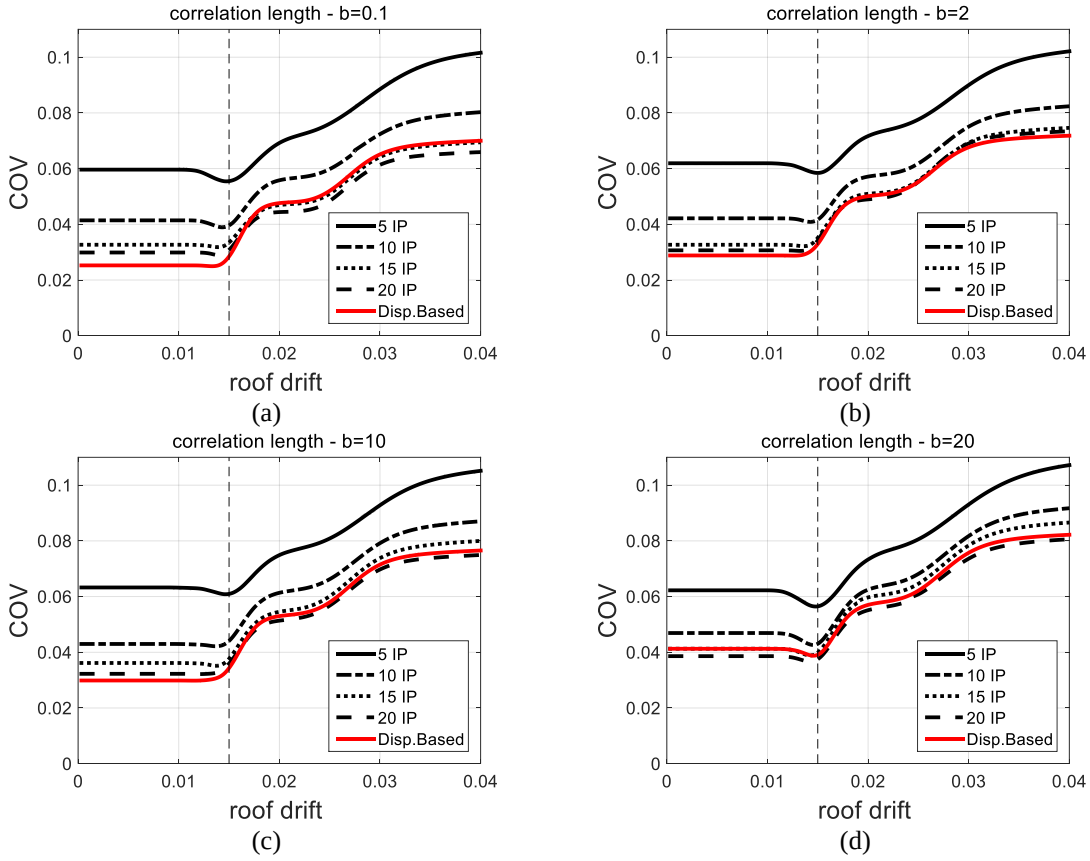

Figure 5: Sensitivity of response variability (COV) to the number of integration points for different correlation lengths.

5.2 Nonlinear response history analysis

The seismic performance of the steel portal frame is also studied using nonlinear response history analysis. Seismic demand is measured with the aid of the maximum roof drift ratio (θ_{max}). A lumped mass matrix is formed in agreement to the distributed load q (Figure 3). The fundamental mode of the frame was found equal to T_1=1.24sec when the mean value of the Young's modulus E is used, while the damping matrix was obtained assuming 5%-Rayleigh

damping on the first and the second mode. All response history analyses were performed using a single force-based beam-column element per member with 20 Gauss-Lobatto integration sections. Again we assume that the correct solution is that of a very dense mesh of displacement-based elements.

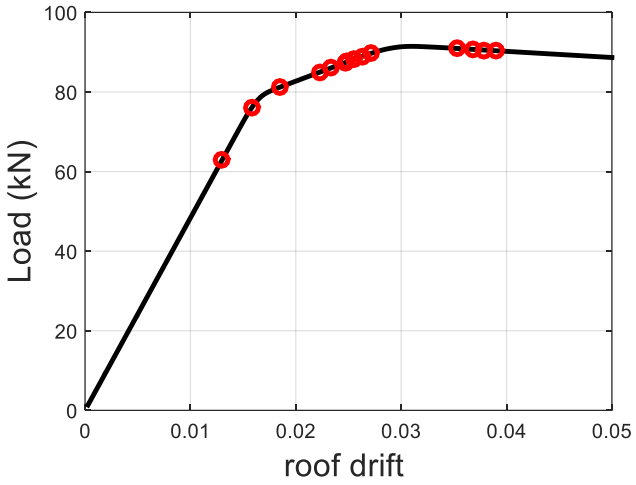

Figure 6: Roof drift demand of the natural ground motion records (red circles) plotted on the capacity curve of the frame (solid line).

All response history analyses are performed with fifteen ground motion records. The records cover a broad spectrum of seismic intensities in order to evaluate the structural behavior at different levels of seismic demand. All records are scaled with a uniform scaling factor equal to 2, to guarantee that some of them will yield the frame. Figure 6 shows the maximum drifts demand for every record plotted against the capacity curve of the frame, assuming the mean value of every random parameter. Significant record-to-record variability is expected due to the different frequency content and duration of the ground motions.

The accuracy of the proposed method is examined considering the first three statistical moments. Figure 7 shows the mean storey drift (θ_{max}) for four values of the correlation length. The proposed force-based modeling provides results that are practically identical to the "correct" solution. Note that in Figure 7, the records are sorted from left to right according to the maximum expected drift demand of Figure 6.

Figure 8 shows the effect of stochastic material properties on the COV of θ_{max} demand. For all b values considered, the accuracy of the force-based formulation is again very close to the correct solution. The errors observed are small proving that the discretization with 20 sections is sufficient. Furthermore, records that do not cause large inelastic displacement demand (records on the left) have smaller COV values than records that caused inelastic damage on the building (records towards the right). Still, the COV values are very sensitive to the record characteristics while, for most ground motions, the COV of the response is lower than the variance of the stochastic input parameters. The effect of the correlation length is small compared to the significance of the ground motion properties, while large correlation lengths tend to increase the COV.

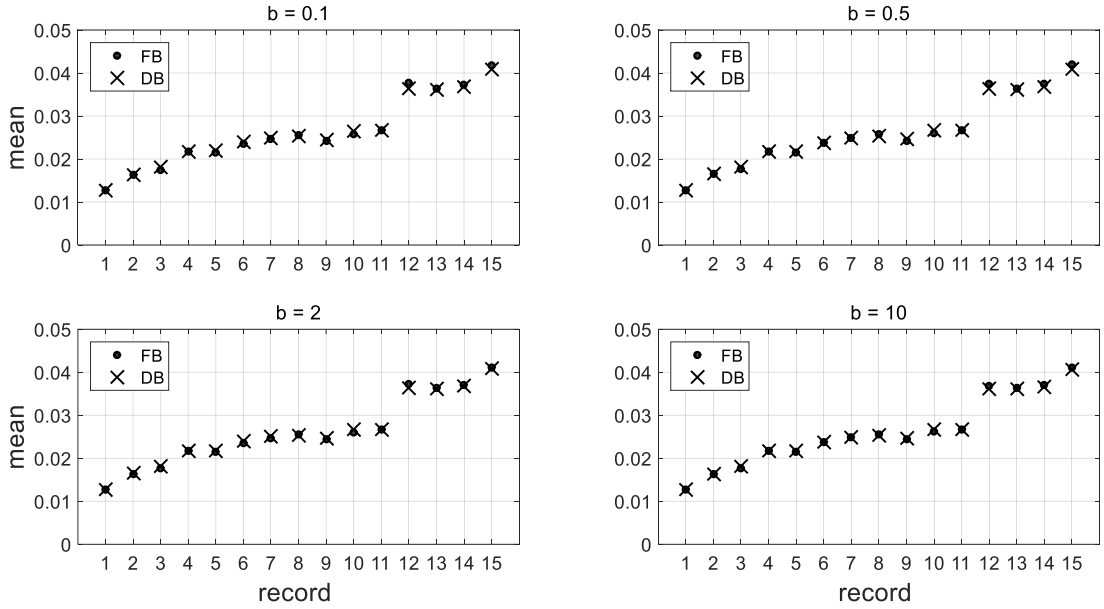

Figure 7: Mean drift demand for correlation values equal to *b*=0.1, 0.5, 2 and 10.

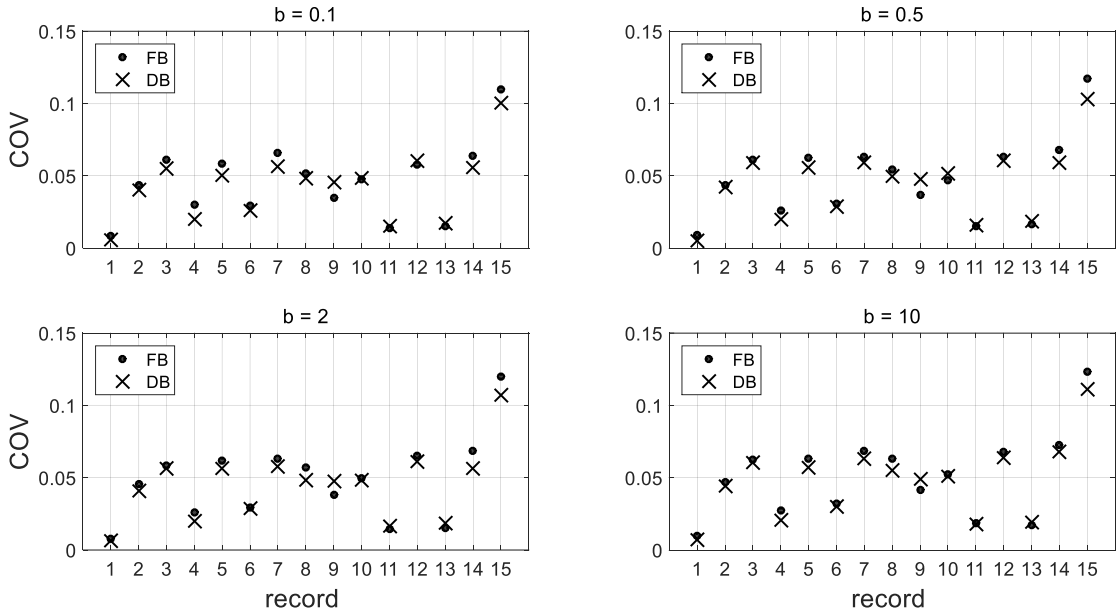

Figure 8: COV of drift demand for correlation values equal to *b*=0.1, 0.5, 2 and 10.

Figure 9 shows the skewness (third statistical moment). The skewness provides a measure of the asymmetry of the sample's cumulative distribution function. Contrary to the COV, the skewness is quite sensitive to the correlation length and varies with the record properties. For many records the skewness differs considerably for different *b* values and doesn't follow the properties of the lognormal material/input properties. Furthermore, samples of opposite skewness for the same natural record, e.g. records 11 and 15, were found. In all cases, the proposed modeling gave excellent estimates of the skewness.

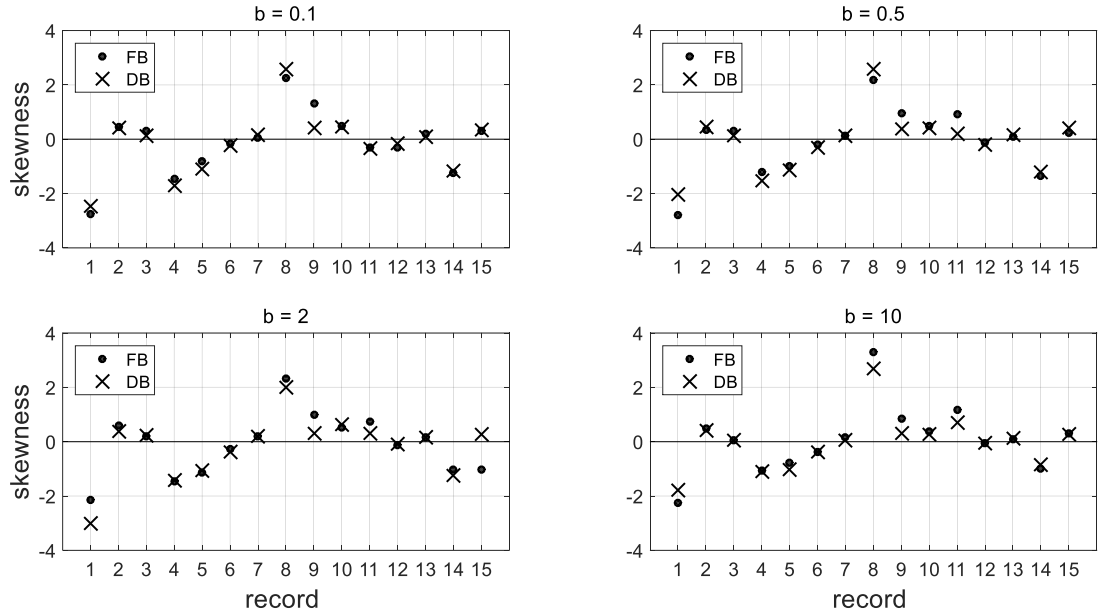

Figure 9: Skewness of drift demand for correlation values equal to *b*=0.1, 0.5, 2 and 10.

Apart from accuracy, the proposed method also reduces considerably the computing cost. Figure 10 compares the computational cost of the proposed element to that of the displacement-based formulation for both static and dynamic analysis. An Intel Core 2 Duo processor required more than double time to run 500 Monte Carlo simulations for the nonlinear static case. For the response history analysis of a single record, the proposed methodology required approximately 10% of the time of the displacement-based element for the same number of simulations. Although the computational effort of the displacement-based element can be reduced using a more coarse mesh, Figure 10 provides a clear indication of the exceptional performance of the force-based element which can be therefore adopted for the simulation of real-scale problems without having to modify the mesh of fiber elements.

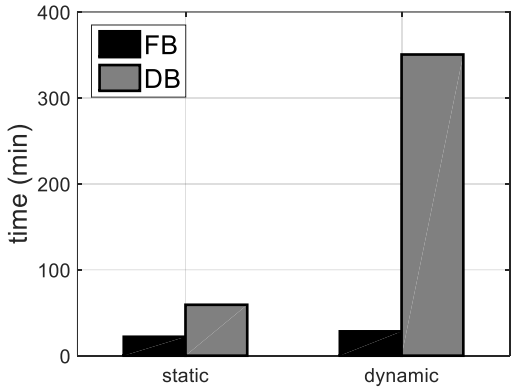

Figure 10: Computing cost of 500 Monte Carlo simulations of the portal frame for the force-based and the displacement-based formulation.

6 CONCLUSIONS

A novel modeling approach for the probabilistic seismic assessment of frame structures with stochastic system properties is proposed. The proposed method extends the use of flexi-

bility-based fiber elements to the stochastic finite element method, offering the possibility of applications to real-scale problems due to the remarkable computational performance and stability of these elements. The performance of the proposed modeling is demonstrated on a one-storey steel portal frame. The study provides a valuable guidance for the analysis and the design of structures with non-Gaussian system properties and its main conclusions are here summarized:

- The choice of the number of integration points is essential. The integration should be able to capture the spectral characteristics of the input stochastic field.
- The proposed modeling offers remarkable accuracy and reduced computing numerical effort, even for very small values of the correlation length parameter (highly uncorrelated stochastic fields).
- The computational performance was exceptional, especially for the case of response history analysis where the proposed modeling reduced the required computing effort by 90%. This allows the implementation of the method to real-scale problems.

REFERENCES

[1] S. Chakraborty, S.S. Dey, Stochastic finite element method for spatial distribution of material properties and external loading. *Computers and Structures*, **55**, 41-45, 1995.

[2] I.A. Kougioumtzoglou, P.D. Spanos, An approximate approach for nonlinear system response determination under evolutionary stochastic excitation. *Current Science*, **97**(8), 1203-1211, 2009.

[3] J-B. Chen, J. Li, Stochastic seismic response analysis of structures exhibiting high nonlinearity. *Computers and Structures*, **88**, 395-412, 2010.

[4] T-H. Lee, M. Mosalam, Probabilistic fiber element modeling of reinforced concrete structures. *Computers and Structures*, **82**, 2285-2299, 2004.

[5] G. Stefanou, M. Fragiadakis, Nonlinear dynamic analysis of frames with stochastic non-Gaussian material properties. *Engineering Structures*, **31**, 1841-1850, 2009.

[6] O.M. Hamutcuoglu, M.H. Scott, Finite element reliability analysis of bridge girders considering moment-shear interaction. *Structural Safety*, **31**, 356-362, 2009.

[7] D. Feng, J. Li, Stochastic nonlinear behaviour of reinforced concrete frames. II: Numerical Simulation. *Journal of Structural Engineering*, DOI: 10.1061/(ASCE)ST.1943-541X.0001443, 2015.

[8] J. Li, D. Feng, X. Gao, Y. Zhang, Stochastic nonlinear behaviour of reinforced concrete frames. I: Experimental investigation. *Journal of Structural Engineering*, DOI: 10.1061/(ASCE)ST.1943-541X.0001442, 2015.

[9] C. Zeris, S.A. Mahin, Analysis of reinforced concrete beam-columns under uniaxial excitation. *Journal of Structural Engineering*, **114**(4), 804-820, 1988.

[10] E. Spacone, V. Ciampi, F. Filippou, Mixed formulation of nonlinear beam element. *Computers and Structures*, **58**(1), 71-83, 1996.

[11] A. Neuenhofer, F. Filippou, Geometrically nonlinear flexibility-based frame finite element. *Journal of Structural Engineering*, **124**(6), 704-711, 1998.

[12] M. Fragiadakis, *Nonlinear analysis of steel and RC frame structures.* Laboratory for Earthquake Engineering, Class notes, Athens, Greece, 2016.

[13] M. Shinozuka, G. Deodatis, Simulation of stochastic processes by spectral representation. *Applied Mechanics Reviews*, **44**(4), 191-203, 1991.

[14] M. Grigoriu, Simulation of stationary non-Gaussian translation processes. *Journal of Engineering Mechanics*, **124**(2), 121-126, 1998.

[15] P. Bocchini, G. Deodatis, Critical review and latest developments of a class of simulation algorithms for strongly non-Gaussian random fields. *Probabilistic Engineering Mechanics*, **23**, 393-407, 2008.

[16] F. McKenna, G.L. Fenves, *The OpenSees command language manual version 1.2.* Pacific Earthquake Engineering Research Centre, University of California, Berkeley, 2001.

[17] Joint Committee for Structural Safety. *Probabilistic Model Code. Part 3: Resistance Models*, 2001.

ECCOMAS Congress 2016
VII European Congress on Computational Methods in Applied Sciences and Engineering
M. Papadrakakis, V. Papadopoulos, G. Stefanou, V. Plevris (eds.)
Crete Island, Greece, 5–10 June 2016

THERMAL TRADE OFF SUSTAINED BY MULTI DISCIPLINARY AND MULTI LEVEL OPTIMIZATION

Olivier Tabaste[1], **Cedric Campguilhem**[2]

[1] MSC Software
3 Ave du Canada, 91978 Courtabœuf Cedex, France
e-mail: olivier.tabaste@mscsoftware.com

[2] Airbus Operations
316 Rte de Bayonne, 31060 Toulouse Cedex 9, France
cedric.campguilhem@airbus.com

Keywords: Architecture Trade-Off, Collaborative Simulation, Multidisciplinary and Multi-Level optimization, TOICA EU FP7 Project.

Abstract. *Evolution toward more complex electrical systems on board of commercial aircrafts to be fitted in smaller containment areas of composite lightweight structures have raised challenges in respect of thermal optimization in a multi-disciplinary context. It is so crucial to OEMs that it motivated the assembly of a consortium from 32 companies around an R&D project, named "Thermal Overall Integrated Conception of Aircraft" under the umbrella for Framework Program 7 with a focus on:*

- *Closing the gap between architectural view and domain specific simulations*
- *Enabling multi-level, multi-disciplinary approach for flexible architecture trade-offs*
- *Developing new integrated architecture aiming to thermally optimize aircraft*

Among others activities along this project, MSC is engaged to sustain one of the selected use cases conducted by Airbus and referenced here as new power plant integration.
Specifically, an environment enabling architects to conduct a trade-off study collaboratively with domain specialists has been developed. It is tightly integrated with Airbus simulation environment built on the top of heterogeneous solutions from Siemens, Cenaero and MSC. TOICA outcome so far have focused on:

- *Trade Study Process Management capitalizing on former projects developments like the "Modeling and Simulation information in a collaborative Systems Engineering Context" (MoSSEC) introduced in Crescendo*
- *Multi-Level and Multi-Disciplinary Optimization tightly linked to the concept of agile behavioral model generation*

This paper exposes maturity of the proposed solution validated by real plateaus execution involving all actors of the targeted study.

1 INTRODUCTION

Among critical capabilities required by architects and chief engineers, managing efficient trade-off studies of thermal energy has become a number one priority. The efficiency and management are needed because the aircraft manufacturers work collaboratively with their extended enterprise to propose competitive solutions.

Indeed, if early evaluation of more alternatives is key to avoid late recognition of "low-performing" design solution and facilitate faster time to market demands, then better understanding of the thermal behaviour has emerged because of the growth of inter-related challenges at sub-component level:

- Shift from hydraulic and pneumatic systems to more electrical ones in modern aircrafts has highly affected the overall thermal load; the thermal load has increased five-fold over the two last decades. No reduction in such a trend being expected for the foreseeable future.
- Further, confinement of equipment to address payload increase (cargo and passengers) has raised issues related to sensitivity of new generation batteries to ambient temperature.
- Effort to lighten Aircraft Structures through use of composite materials, whose insulation power is higher by 2 orders of magnitude, created more thermal constraints. However, the mechanical properties of composites might also drop drastically beyond their glass transition temperature. The gap between composite and thermal expansion coefficients can also induce critical constraints at the junctions of some components assembly.

To overcome these thermal challenges, it is key that the aerospace industry performs thermal trade management as early as possible in the development process. Therefore, a consortium of 32 companies, coordinated by Airbus, launched an R&D project, named "Thermal Overall Integrated Conception of Aircraft" (TOICA [8]) that has been awarded for funding by the European Community's Seventh Framework Programme (FP7/2007-2013, under grant agreement n°604981).

The focus of this project is on:

- Closing the gap between architectural view and domain specific simulations validation
- Enabling multi-level, multi-disciplinary approach for preforming flexible architecture trade-off analyses.
- Developing new integrated architecture/solutions aiming to thermally optimize aircraft

Among the partners and their associated contributions:

- Airbus leads several Use Cases and drive their implementation through "plateaus". Plateaus are technical working sessions where thermal trade-off studies are operated using the TOICA capabilities and where business benefits are assessed.
- MSC contributes to the development of TOICA capabilities like:
    - Specific Aircraft Architect Environment to empower the architects with means of assessing their architectures in early design phases, through trade-off studies and reviews.
    - Collaborative data and process management capitalizing on previous project outcomes like Behavioural Digital Aircraft matured by CRESCENDO.
    - Parametric Model Generation to enable end users to build objects serving as inputs in studies of configurations and their evaluations along trade off process.

- Coupling simulation approaches in Multi Discipline and Multi-level context.

This paper intends:

- To share the status of the proposed methods, elaborated with partners using Technology Readiness Level, reviewing Airbus's use case relative to Pylon Architecture trade-off for new power plant integration.

  Specifically, the TOICA collaborative richness will be described showing how the Flexible Model Generation capability, capitalizing on Pyramid of Model and Super Integration concepts, is used either to address needs of the simulation experts or as a trade-off generator engine serving the architect platform.

  MSC, as work package leader, is coordinating the Flexible Model Generation capability; Siemens/LMS is orchestrating the Pyramid of Model concept.

- To map the proposed methods to TOICA use case driven by Airbus and focusing on management of power plant integration trade off from a multi-disciplinary perspective.

2 TOICA AT A GLANCE

TOICA is a 3-year European project, coordinated by Airbus that was launched in 2013. Its contributors comprise a consortium of 32 partners from 8 countries associated with a budget of nearly 30M€.

R&D effort is balanced amongst eleven industrial companies, seven IT vendors, five small and medium enterprises, four research centers, and five universities.

Capitalizing on results (Figure 1) of the CRESCENDO European project (2009-2012), where the concept of the Behavioural Digital Aircraft (BDA, now referred to as the MoSSEC standard [7]) architecture was specified, developed and validated, TOICA aims to introduce the next generation approach to sustain aircraft thermal studies throughout the design cycle. The proposed path is to develop simultaneously the systems, equipment and components by utilising the exchange of their behavioural representations amongst the stakeholders.

In that respect, the TOICA members have agreed on four High Level Objectives (HLO):

- HLO1: Develop customized collaborative simulation capabilities improving the generation, management, and maturity of the BDA dataset.
- HLO2: Develop new concepts for improved thermal load management within aircraft components, systems and equipment, which will integrate innovative cooling technologies and products.
- HLO3: Assess and validate the developed capabilities and technology concepts against different common reference aircraft targeting both "Enter into Service (EIS) 2020" and EIS 2030+ Thermal Concept Aircraft".
- HLO4: Optimise aircraft design by enabling highly dynamic allocation and association between requirements, functions and product elements (Super integration) for product innovations.

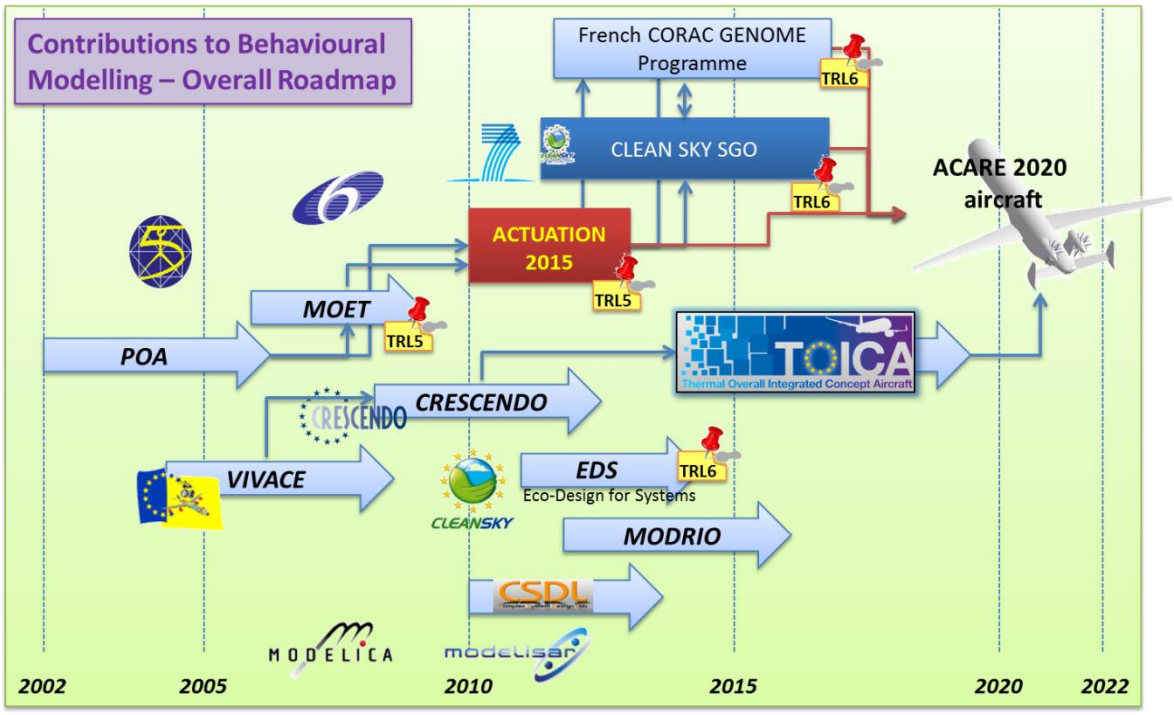

Figure 1: TOICA History

In order to deliver applicable results on time, TOICA relies on its Use Case driven organization; with a progress monitoring scheme derived from a realistic aircraft design cycle that is drum beat by regular Milestone plateaus (MSP). In other words, real actors, in the context of their design activity, test any capability developed, which allows them to check a proposed method and review its Technology Readiness Level (TRL) validation. Further, it allows them to evaluate the gap between the expectations and the evidence produced.

Six main use cases, illustrated in Figure 2, have been retained:

- Manage Future Aircraft Architecture
- Integrate Equipment Thermal
- Research new cooling Technologies
- Manage Aircraft Heat Load via Heat Sink
- Optimize Overall Thermal (Energy) for Systems
- Integrate Power plant

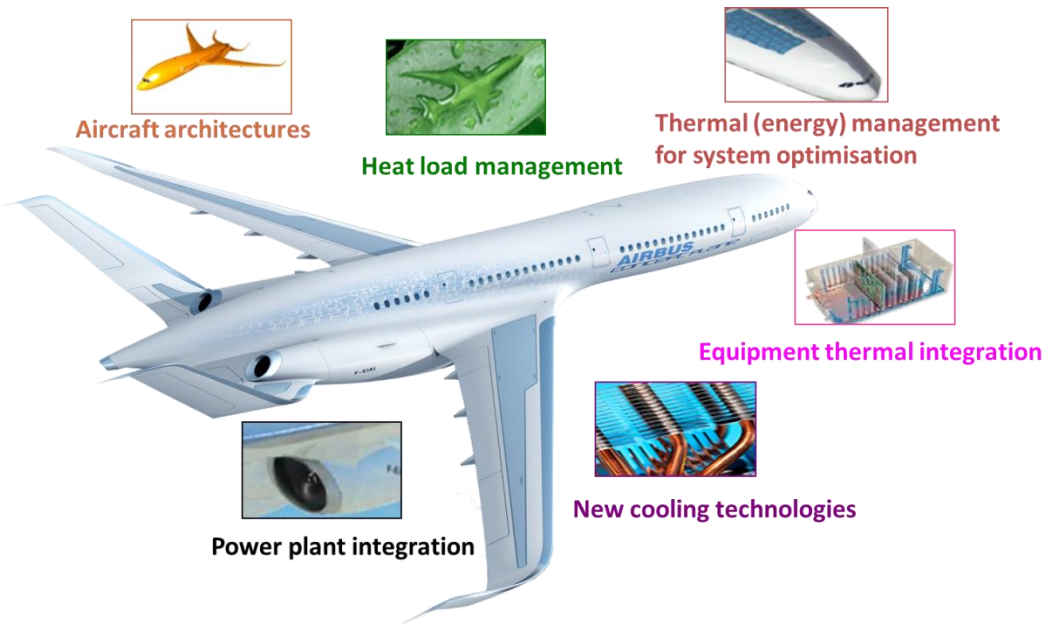

Figure 2: TOICA Use Cases

TOICA partners target to contribute to "Challenge 3 – Competitiveness through innovation" of the ACARE SRA2 High Level Target Concept (HLTC) "High Efficient Air Transport System", enhancing:

- Aircraft development cost
    - Reducing by 10% equipment development impact via a more robust specification process allowing equipment supplier, or risk-sharing partners, to design systems and equipment according to more realistic margins.
    - Reduce the costs and time associated with integration and installation of systems and equipment in aircraft by strongly reducing the need for late rework
- Supply chain efficiency
    - Reduce by 50% the lead time of an aircraft thermal architecture assessment.
    - Shorten by 6 months the equipment development process by improving the exchanges of thermal requirements with the suppliers and sharing the overall thermal view information across the supply chain.
- Aircraft operational costs:
    - Reduce by 5% the energy/power consumption used for active cooling or controlling (heating) of systems
    - Increase the Mean Time Between Failure (MTBF) by 15% as the direct impact of more equipment-dedicated specifications

In the following chapter, we focus on a specific study related to the future architecture associated to Airbus New Engine Option (NEO). For the sake of this study, we will pay special attention to TOICA developed capabilities: Architects' Cockpit, and Flexible Model Generation. We will highlight how the overall study is already benefiting from the MoSSEC standard [7] and the multi-level coupling, mechanisms. Finally we will elaborate on how it will be fully delivered using additional TOICA developed capabilities like Super Integration.

3 NEO USE CASE

3.1 Business Challenges and benefits

Maximum re-use of equipment is expected in order drastically reduce program development costs.

However, for various reasons like hotter engine and reduced space allocation the thermal environment of equipment, thermal constraints on new configuration raise. This trend is even accentuated by new nacelles and engines design orientations like:

- Increase of the engine by-pass ratio impacting cooling efficiency
- Shorter nacelles impacting space allocation
- More electrical function generating more heat sources.

This leads to a strong need for efficient thermal trade-off means of equipment, required to face such an emergence of thermal challenges.

The required capabilities to be delivered by TOICA should:

- Enable early trades on power plant and pylon integration considering thermal integration & ventilation as well as re-use of constrains.
- Enable trade on bleed architecture that includes all the driving parameters: ventilation, thermal impact and exhaust section, bleed performance, etc…
- Analyze the close aero-mechanical-thermal coupling impact to pylon design.

3.2 Trade off scenario

In this case, the evolution of the aircraft configuration follows a process composed of the following key steps:

- Define Top level aircraft requirement;
- Define Mission;
- Derive Neo Power Plant architecture constraints from aircraft baseline including
    - Aircraft level requirements
    - System level design requirements
    - Functional definition
    - Baseline architecture definition
- Analysis at aircraft and system level of the baseline configuration
- Review and challenge of the baseline configuration
- Evolve the configuration in a iterative process

In particular, the introduction of baseline variants or alternatives hypothetically takes place during the review and leads to the evolution of the configuration.

The evolution of the configuration will generate a variant dataset, linked to the baseline dataset to ensure traceability of the entire evolution process. This is because the dataset is linked to the configuration

Specifically, as shown in the workflow views reported above, the main actors' interactions with the dataset can be summarized as follows:

- Power Plant Architect: Defines the trade-off study He specifies the study objectives and populates the dataset by creating/importing the
    - TLAR
    - Operational definition
    - Aircraft configuration and zoning
    - Objectives
- Thermal Expert: Receives the study request from the Power Plant Architect and enriches the dataset by defining the thermal objectives and constraints before to split the request in two branches:
    - The first one, the analysis of cooling and packing of engine integration compartments
        - In turn this sub-study will involve additional actors like the Engine Architect and his thermal team, at integrator partner's level.
    - The second one, relative to pylon thermally constrained design trade off
        - Equally to the previous one, this branch will grow into a distributed and collaborative study coordinated by a thermal leader

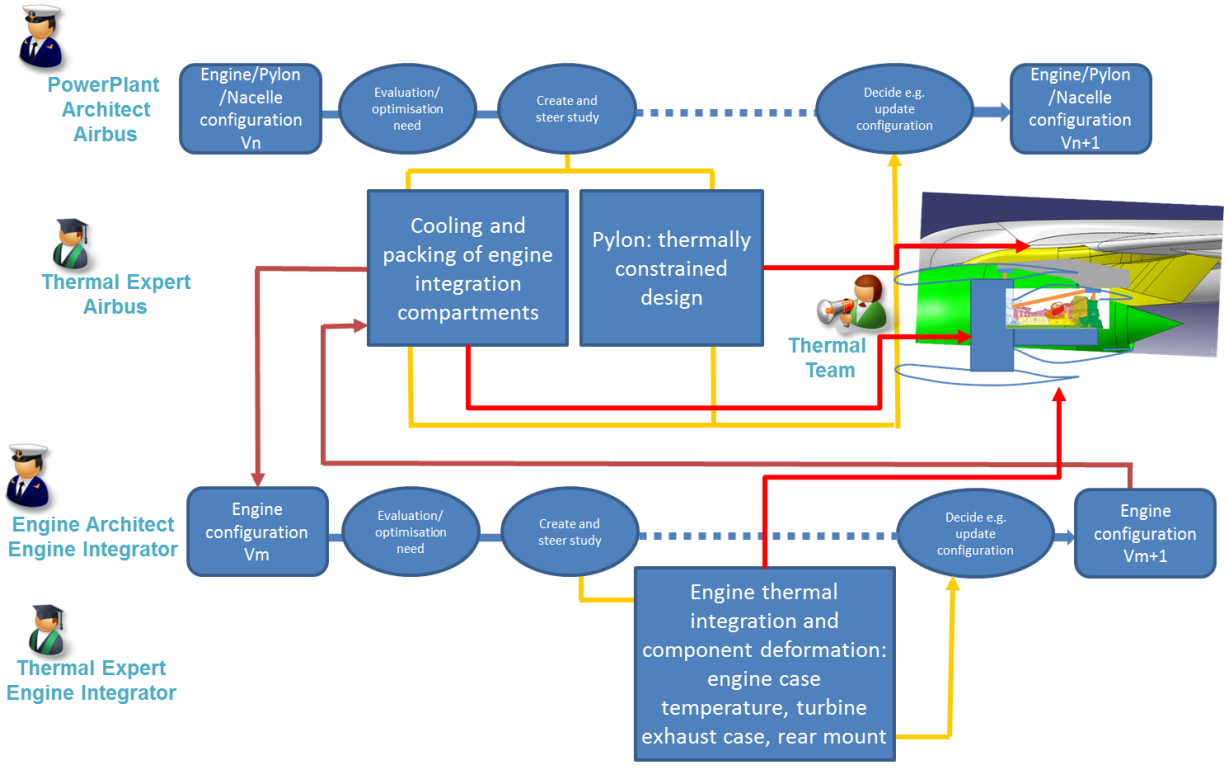

Figure 3: TOICA Neo Use Case Scenario

The sub-study dedicated to pylon trade-off will be detailed along the next paragraph to illustrate how thermal expert will leverage most of the TOICA developed capabilities to col-

laborate with the architect. This expert will orchestrate a multidisciplinary and multi-level optimization process for the engine pylon, where this process takes into account thermal, flutter and detailed stress constraints (Figure 4).

The goal in that case being to assess the sensitivity of the main performance indicators with respect to variations of the pylon width along three different of its sections. The considered performance indicators will be mass of the pylon and the drag coefficient; proposing a set of design solutions that are optimal in the sense of both aerodynamics and structure disciplines.

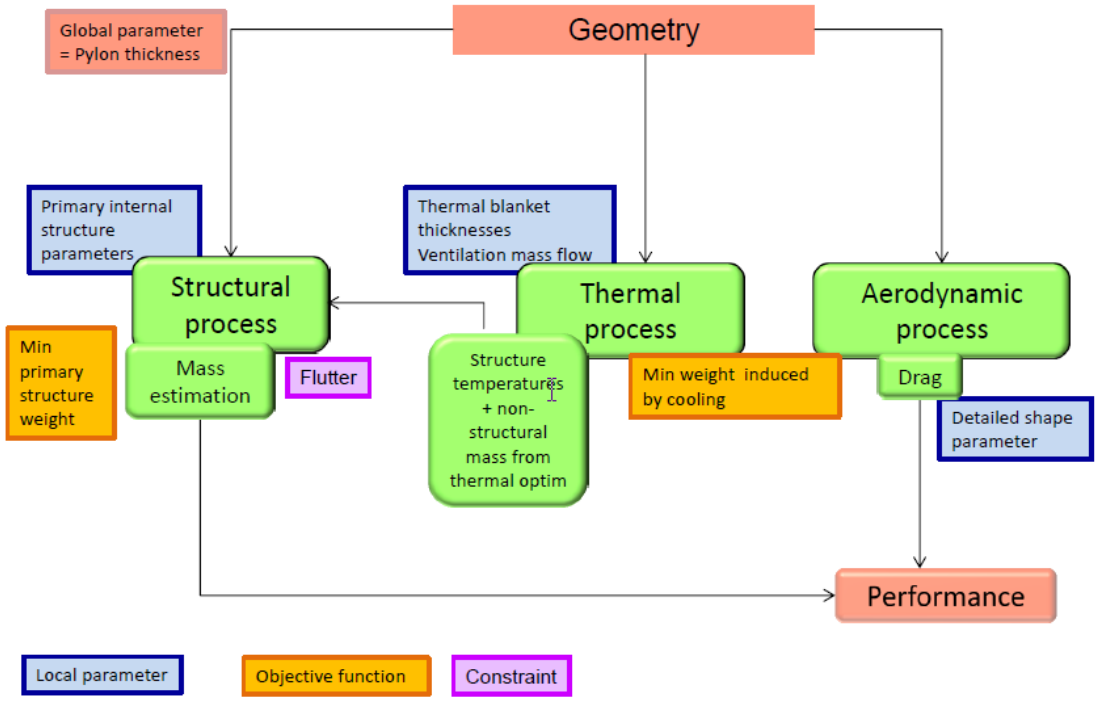

Figure 4: Multi-Disciplinary scenario overview

Technically this will be reached by leveraging a bi-level approach:

- At global level: each discipline feeds the global process with shared parameters (pylon width, material choice…), constraints and objectives (minimum drag and mass).
- At local level: specific parameters and constraints for each discipline are addressed, and are not shared among the disciplines.

3.3 To-Be process requirements mapping to TOICA capabilities

In order to address the business objectives defined in 3.1, the "As-Is" process needs to be enhanced in a way that the workflow, highlighted by Figure 3, can be executed by the actors.

Initial requirements direct us to an environment where the architects can (Figure 5)

- Define their domain architecture at aircraft level, (the Power Plant level in the specific case of TOICA), or at Engine Integrator level. Forthwith these objects are called models because:
    - Conceptually they are supported by the idealization from various perspectives, being for instance functional; logical, 1D to 3D views.

- Such models are essentially assembly of sub-models: from the requirements and objectives within an operational scenario to physical representations that can co-exist at different levels.

- Edit/Author the architecture model, meaning:
  - Populating datasets for a certain view
  - Updating view representation while development matures
  - Deriving alternatives from a baseline, or an existing library of architectures. At this stage, it corresponds to trade variable definition converted to parameters of the architecture model, where a parameter can encompass many representations like
    - Geometrical (change of a dimension or a zone)
    - Functional (choice in function to perform)
    - Architectural (requirements & objectives balance scope)
    - Behavioural (selection of Idealization level & method to assemble possible components of overall object)
- Explore a proposed architecture through visualization of the
  - Requirements space (requirements, objectives, constraints)
  - Alternatives, as an initial means of comparison
- Instantiate and manage trade off request from previous variants:
    - Defining and distributing tasks to various stakeholders across the extended enterprise; while retaining Intellectual Property Rights in the context of heterogeneous domain tools and infrastructures.
    - Monitoring based on selected key indicators throughout the project by tracing
    - Assumptions
    - Uncertainties
    - Results
    - Decisions

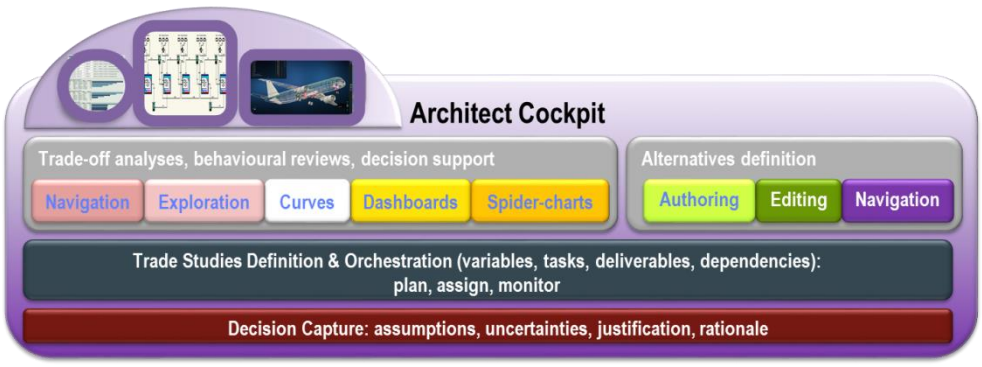

Figure 5: Architects' Cockpit functional scope

Beyond natural interest into an Architects' Cockpit from the NEO scenario, two additional TOICA developed capabilities will consolidate the benefits delivered to the end users. In the latter scenario, many stakeholders are engaged in a collaborative effort. The foreseen deployment does anticipate multiple lifecycle management platforms (Airbus legacy and /or partner's heterogeneous infrastructure constraints). Therefore, the communication and exchange scheme with the extended enterprise require some level of standard format and services to work collaboratively with them. In that respect, TOICA contributes to the MoSSEC [7] standard, by working on necessary BDA objects expanding the thermal collaborative scenario that were already validated during CRESCENDO project [1].

Keeping in mind the Architects' Cockpit requirements, and switching to the Modeling and Simulation (M&S) toolbox, it is now easy to understand why and how it has to be "powered inside" with Flexible Model Generation technology. Indeed, its purpose is to enable the assembly of componentized models: what an architecture definition is; and to introduce parameters to enable creation of variant models: what a tradeoff requires.

At such a stage, we do not even need to know what the sub-model components will be. Their representation will be populated with richer models while the development cycle of the aircraft progresses. In paragraph 3.4, we will show examples like top-level aircraft requirements (TLAR); operational scenarios, functional or system models and surrogate simulation models or 3D CAD models. However, at this stage it is important to emphasize that if Flexible Model Generation allows you to select a sub component and/or parameterized it along the global model assembly, it does not affect the possible choices among level representations.

Indeed, if a choice does not exist at the start of the aircraft project it is important to organize the way we make a particular choice when several options become available. Do I select a surrogate representation of the structure, or a full 3D model? Does a 3D model derives from a preliminary simplified representation, or vice versa: surrogate versus 3D is not only a difference in the maturity of the study; it can be a preference in respect of the analysis performance associated with the precision on the expected result. The M&S workgroup in charge of this capability has developed the Pyramid of Models organization that can be seen at process-oriented libraries of models that the Flexible Generation aspect will query when a possible choice occurs.(Figure 6)

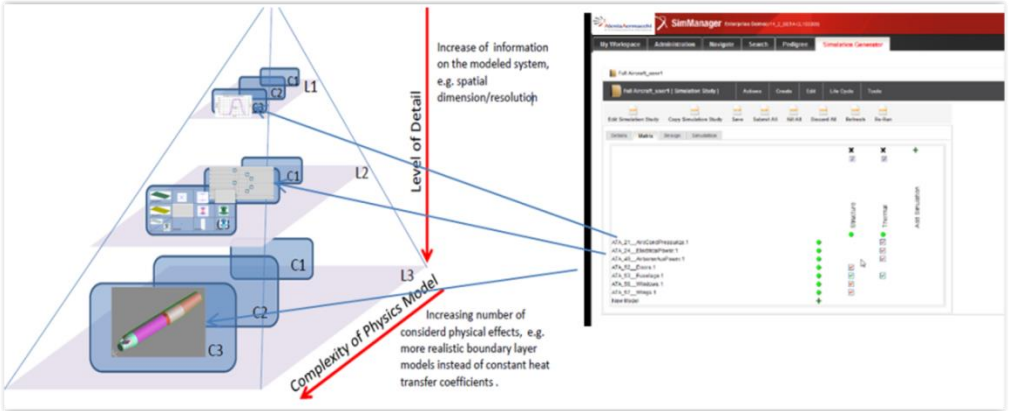

Figure 6: Pyramid of Models Serving the Flexible Model Assembly Generation

This coupled solution enables framework of model usage to sustain NEO scenario with the Multi-Disciplinary architectural/behavioral representation of the complete aircraft, in any operating conditions.

During the implementation of NEO use case detailed in this paper, we will see a second aspect of Flexible Model Generation directly applied to a more commonly understood geometry parameterization, driving a parametric simulation model. In that respect TOICA has capitalized on methodology introduced by Airbus and enhanced in a European project from framework program seven named MAAXIMUS [3].This approach is to use external shapes and add Design Parametric Objects (DPOs) of structural components like, ribs, holes, stiffeners or corners piece reinforcements

Then for each DPO an excel design table (DT) is created with associated parameters and each parameter of the DTs can be linked through excel with others if needed, or with parameters associated to an external shape and logged into an xml format.

Diving more into the details: we know that the scenario has to be driven by a Multi-Disciplinary Optimization (MDO) and Multi-Level as well as accounting for optimization and coupling aspects, using the TOICA M&S capabilities. We will not elaborate this optimization method because it is covered by a "conventional" Design of Experiment approach. Therefore, we focus attention to the fashion in which simulations are coupled.

Indeed, we have already described benefits of Flexible Model, assembling components from libraries organized as a Pyramid of Models. What we have dropped so far was the magic to make dissimilar idealization components compatible for the execution of a coupled run. In the context of NEO such integration has been performed by the creation of behavioural libraries and surrogate models that will enable exchange though "MoSSEC" connectors. This "interface" component, in the generation of the model, becomes one of the possible "variability" or parameter of the Flexible Model. It means here that if Architect view of the aircraft is:

- Pylon Structure +Interfaces+ Equipment + Operational Scenario

The representation for a simulation of a trade study can be for instance upon choice of equipment partner's CAE preferred domain tools:

- Pylon Structure(Solver A) + Interface (Solver A to B) + Equipment(Solver B) + Loads &Boundary Conditions
- Pylon Structure (Solver A) + Interface (Solver A to C) + Equipment(Solver C) + Loads & Boundary Conditions

As we need to enlarge Flexible Model to the concept of Architectural Model, the method needs to sustain not only coupling of models via an "interface component" but also functional models for which one change is going to impact more than, for instance the definition of model itself (more electrical components…) . Flexible Model will then be supported by Super Integration, which will be demonstrated in future TOICA plateaus.

Finally, we will close this presentation of TOICA capabilities complementarity, as well as their mapping to the use case needs pointing onto risk reduction one. It is the final touch to empower stakeholders and ultimately architects to trace information and decision associated with the KPIs.

3.4 Scenario implementation example

Consistently with capability mapping, the cornerstone component of the scenario implementation has been the Architects' Cockpit. Choice has been made on MSC SimManager interacting with SimManager as the SLM for the pylon multi-disciplinary trade-off and another PLM technologies representing legacy or extended enterprise platforms. This will enable the demonstration of TOICA collaborative philosophy, throughout the exposure of a communication to a SimManager server across APIs that are MoSSEC compliant, as demonstrated in CRESENDO [2]. Then a key core product functionality known as "Assemble&Simulate" that

enables in the simulation context to glue model components together for a particular simulation scheme(parts idealization, connectors ,loads, constrains, materials, solver parameters, key results to extract, report to generate) before to automatically submit a job and retrieve the outputs, has been extended to an "Assemble&WorkRequest". As such it is behaving in the same way in respect of an architecture model to define, populate with datasets and associate to a trade study, requests to be sent to other actors.

Knowing that SimManager work request are by design mapped to MoSSEC model network representation, the solution can be implemented in a context of the extended enterprise for which the trade study demand is conveyed then to the partner by a MoSSEC web service.

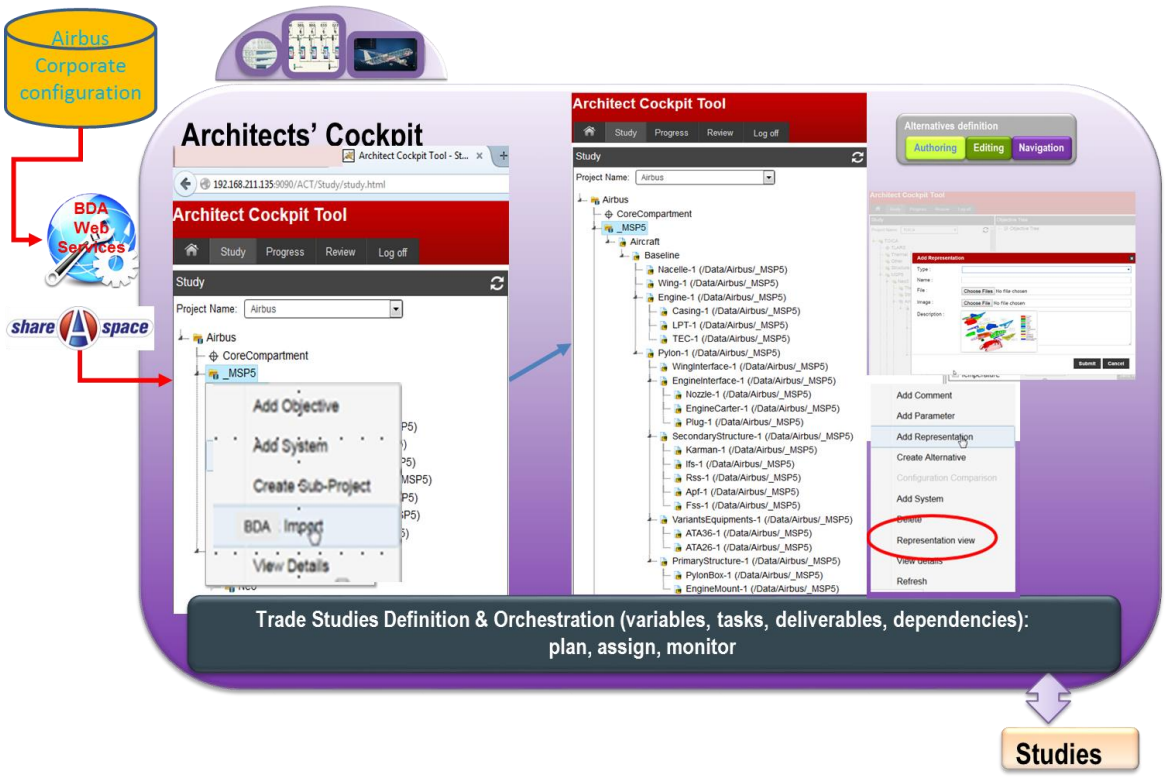

Figure 7: Illustration of Architects' Cockpit leveraging Flexible Model Assembly from functional architecture vs scenario

Representation can be updated by right clicking on a model component in order to browse the "MoSSEC" libraries (Pyramid of Model & Super Integration) and select the preferred available level to be used in the study. User interface also allows for variant generation for instance by dragging and dropping an existing instance prior to define the variable parameters and update the master consequently. (Figure 7)

Same kind of sequence is applicable to any layer of architects in the scenario, knowing that each time a request is made to actors, a notification is send which allows next stake holder to update the detail of the model in respect of its domain of concerns.

And finally, Architects' Cockpit will monitor study request execution, checking each task status (pending, running, completed, aborted…) in respect of planning. Each task can report objects, returned to the requester by the actor in charge of a particular aspect of the study. Of course, a result (temperature, width impact…), or a report of combined information can help to sustain a documented decision, in between additional milestone feedback like validation gates can also be controlled. Knowing that communication here again is managed by

MoSSEC associative model network (AMN) [2], it is possible to sink two activities with a filter on the granularity of details, and the representation of information exchanged.

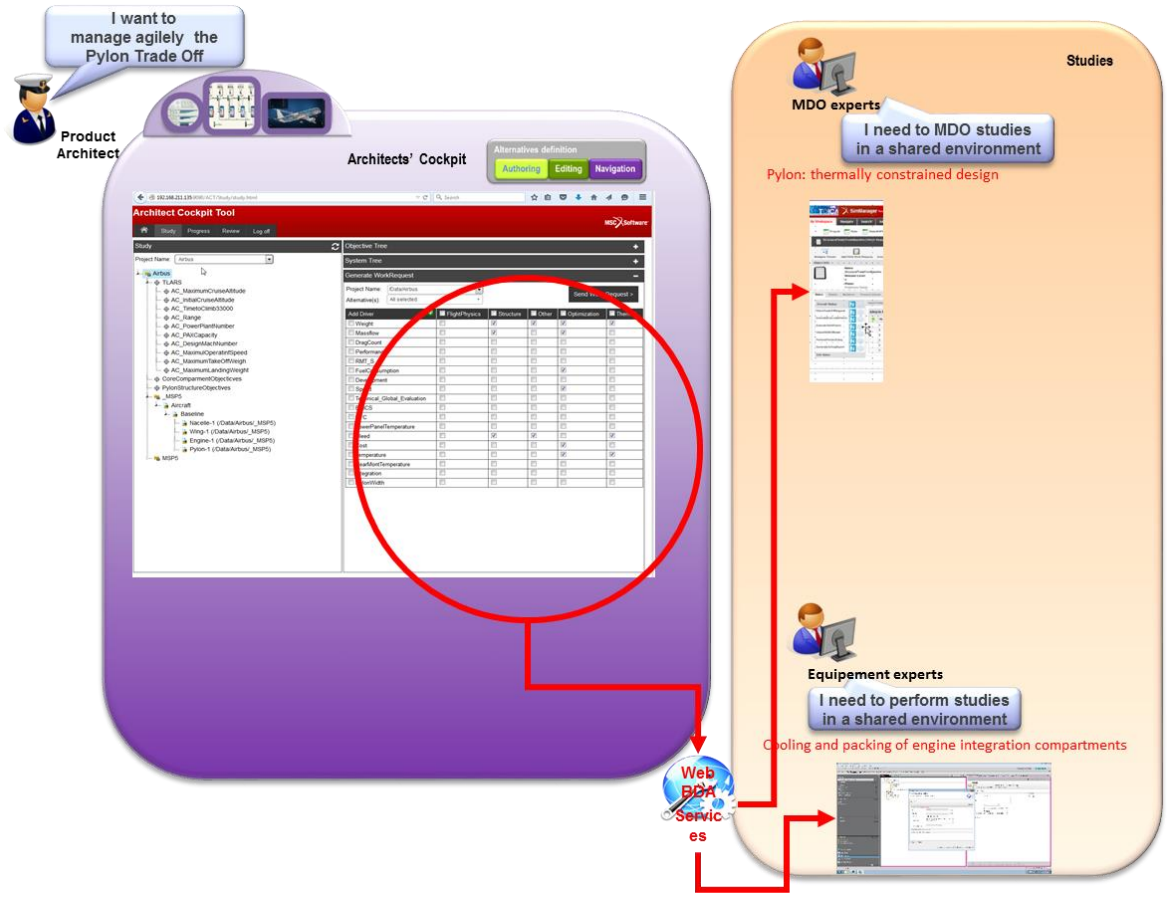

Figure 8: Multi-Level process granularity from Architects' Cockpit to SLM

The first use of AMN allows architect to safely trace simulation expert answers without any burden on CAE domain know how has shown in Figure 8, while the second way of use empowers Intellectual Property Right preservation by the mean of behavioral representation along the collaboration.

The second enabler, we will detail is the Flexible Model Generation applied this time to Simulation domain. In order here to address need for multiple variant on a geometrically parameterized model, we have developed around MSC SimXpert, a tool that can (Figure 9):

- Read an aircraft geometry and associated parametrization relying on DPOs as introduced in chapter 3.3
- Leverage the Airbus patented ways in associating them to Parameterized Geometric Support (PGS): a child CAD model of the DMU associated to DTs representing part of the physics [5].

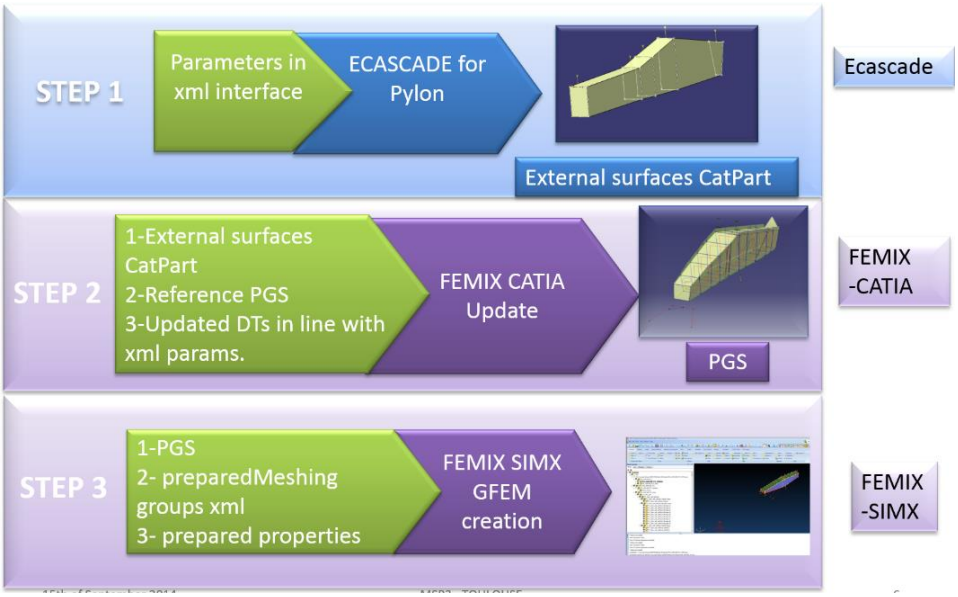

Figure 9: Airbus FEMIX based Flexible Model Generation

Multi-Level Coupling is managed then by an extension of FEMIX capabilities to the DPOs relevant to the various additional domains like thermal one (by the way FEMIX for non-purely structural solution has been demonstrated as well in CRESCENDO for Acoustics), and the optimization "block" is implemented by coupling a Nastran SOL200 Finite Element Model run to the Sizing process (second level of optimization) within Airbus Sizing legacy environment by the mean of Nastran DRESP3.

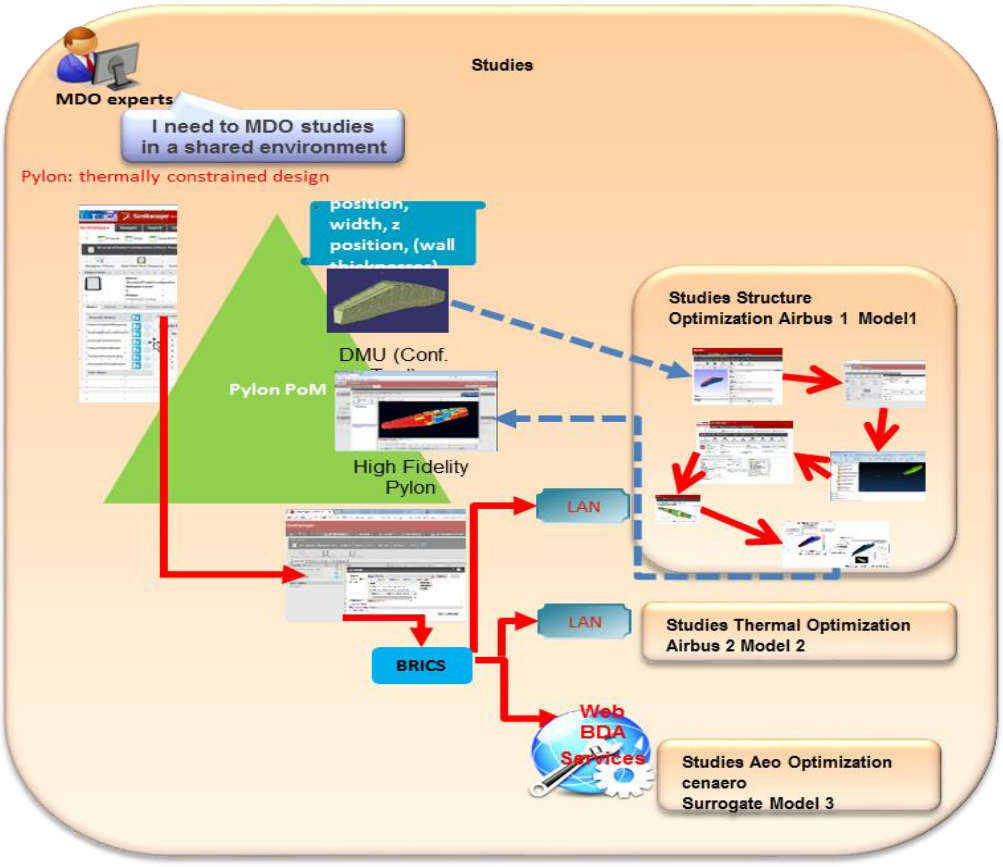

Figure 10: Multi-Level Multi-Disciplinary process

Along the 5th plateau (MSP5) execution, SimManager took into account the collaborative MDO distribution of surrogate models for the structural, thermal and aero domains in one hand, while it was driving on the other hand, the structural optimization to sizing process. As illustrated in Figure10. This was achieved with support from NLR's tool named BRICS [6] and Cenaero's platform known as MINAMO. The flexible model capability from SimXpert has matured and will execute a full automatic coupling of the structural optimization process with thermal and aero surrogate models at horizon of 6th plateau.

In that scenario, the post processing with architects' cockpit and risk reduction associated to value assessment were also demonstrated for MSP5. (Figure 11)

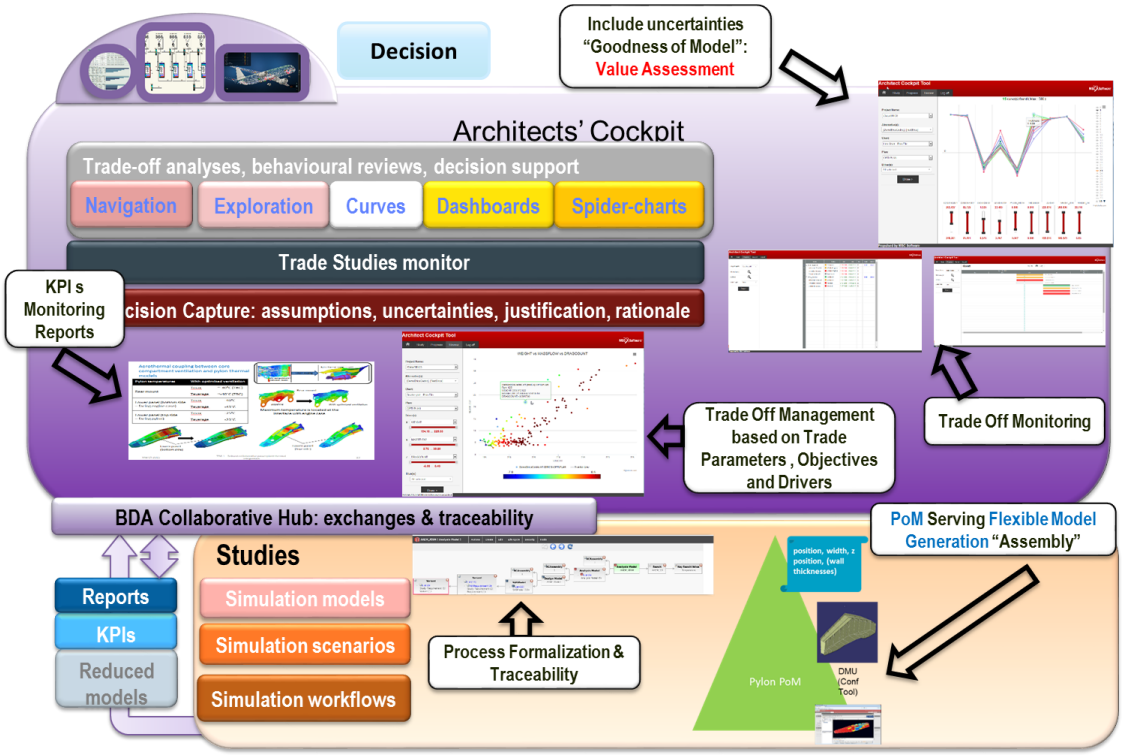

Figure 11: Trade-off decision and value assessment interaction

4 CONCLUSIONS

Through the review of one of the Airbus Use Cases, we have illustrated the relevance and benefit of TOICA capabilities, whether it relates to their interactions through MoSSEC as a standard for collaboration, or independently operating as M&S innovations.

A strong point has been made on the fact that TOICA capabilities, though split by project WBS to optimize consortium knowhow and resources, are not totally independent and conjointly contribute to TOICA high-level objectives.

In particular Flexible Model associated to Pyramid of Models and Coupling in the simulation world; as well as Super Integration from Architecture perspective is a Key enabler of Architects' Cockpit: a pillar of TOICA.

It is important to notice that between mid-term project presented in previous papers [9] and outcome of 5th plateau detailed in chapter 3, the solutions have matured to higher level of maturity. Indeed the referenced demonstration executed by end users themselves, within an IT infrastructure exact image of their industrial working environment, enabled validation of a

TLR4, for Architect's Cockpit and Flexible Model capabilities acting here in a tight interaction. This trend is expected to mature even more for the last plateau to be held just before this paper is publicly presented.

5 ACKNOWLEDGEMENT

The authors from Airbus and MSC thank their colleagues and partners involved in the use cases described, for their contribution to this work. Namely we were able to capitalize on NLR's technology for the distribution of MDO request, while Design of Experiment was conducted by Cenaero's framework.

We also would like to show our gratitude to Sanjiv Sharma (Airbus Operations Limited), Jean-Claude Dunyach and Pierre Arbez (Airbus Operations SAS) for their contribution to the project description within this paper.

REFERENCES

[1] Olivier Tabaste (MSC Software, France), Pierre Arbez, Stéphane Grihon, Timo Laudan, Matthieu Thomas (Airbus, France), "Illustration of Comprehensive Behavioural Digital Aircraft Enablement trough Use Cases", Nafems 2013 World Congres-incorporating 1st SPDM worldwide conference,

[2] Pierre Arbez, (Airbus, France) June 2012, "Developing the thermal aircraft along the lifecycle", Crescendo Forum Presentation 230; Toulouse France

[3] Olivier Tabaste (MSC Software France), Patrick Sarouille (Airbus France), "Engineering Process Capture and Automation to sustain Aircraft Composite Structure Optimization", 3rd ECCOMAS Thematic Conference on the Mechanical Response of Composites, Hannover, Germany, September, 2011,

[4] Olivier Tabaste (MSC Software, France), Dr Pierre Arbez, Dr Stéphane Grihon, Dr Timo Laudan, (Airbus, France), "Being prepared for the future: trade-off management technology for architects within designing the robust virtual aircraft", GPDIS 2012

[5] Dominique Barthe, Jean-Christophe Bonnet (Airbus France), "Virtual Aircraft Development in Airbus Engineering Structure", MSC European Aerospace Summit 2008

[6] E.H. Baalbergen, J. Kos and W.F. Lammen, (NLR), "Collaborative multi-partner modelling & simulation processes to improve aeronautical product design", 4th CEAS Air & Space Conference, Linköping, Sweden, September 2013

[7] MoSSEC page on ASD SSG website: www.asd-ssg.org/mossec

[8] TOICA website: www.toica-fp7.eu

[9] Olivier Tabaste (MSC Software, France); PierPaolo Borrelli (Alenia Aermacchi, Italy); Anne Gazaix (Airbus Operations S.A.S, France); Yves Baudier (Airbus Group Innovation, France), Congress "Aircraft Thermal Architecture Trade Off Management Use Case", Nafems 2015 World

ECCOMAS Congress 2016
VII European Congress on Computational Methods in Applied Sciences and Engineering
M. Papadrakakis, V. Papadopoulos, G. Stefanou, V. Plevris (eds.)
Crete Island, Greece, 5–10 June 2016

COLLABORATIVE ENGINEERING TECHNOLOGIES ENABLING MULTI-PARTNER THERMAL ANALYSIS IN EARLY DESIGN STAGES OF AIRCRAFT

Erik H. Baalbergen[1], Willem F. Lammen[1], Albert J. de Wit[1], Robert Maas[1], S. Maryam Moghadasi[1], Johan Kos[1], and Fabio Chiacchio[2]

[1] Netherlands Aerospace Centre NLR
Anthony Fokkerweg 2, 1059 CM Amsterdam, The Netherlands
{Erik.Baalbergen,Wim.Lammen,Bert.de.Wit,Robert.Maas,Marie.Moghadasi,Johan.Kos}@nlr.nl

[2] Finmeccanica S.p.A.
Viale dell'Aeronautica, Pomigliano d'Arco, 80038, Italy
fabio.chiacchio@finmeccanica.com

Keywords: Collaborative Simulation, Thermal Analysis, TOICA EU FP7 Project, Cross-Organisation Workflow, Surrogate Modelling, Fuel Tank Thermal Modelling.

Abstract. *The TOICA EU FP7 project focuses on developing capabilities that support aircraft manufacturers and their supply chain in jointly performing thermal analyses of aircraft architectures. Collaboration capabilities and related multi-disciplinary modelling and simulation technologies are key pillars for joint thermal analyses. The paper describes two such capabilities: surrogate modelling and smooth cross-organisation workflow execution. These capabilities have been further developed based on TOICA needs. The integrated application of the capabilities is illustrated in the context of an aircraft wing fuel tank thermal analysis conducted in TOICA.*

1 INTRODUCTION

Aeronautics research and technology development programs generally involve collaboration among different organisations, in order to include all required skills from the supply chain, to share risks and costs and to timely and efficiently develop innovative products. To achieve the challenging objectives of contemporary and future aeronautics, and to maintain global industrial leadership [1], a high level of integrated system design of the aircraft and its subsystems is needed. This requires a continuously increased level of collaborative engineering through modelling and simulation along the supply chain in order to improve cost and time efficiency and to reduce the integration risk in later phases. Teams of engineers from various disciplines and organisations are supposed to collaborate across organisational and geographical boundaries. The size and complexity of aircraft programs, the market demands, and the competition in the market require the collaboration to be effective and efficient, while obeying security constraints and preserving the intellectual property of the supply chain members.

To achieve a step change in the way multi-disciplinary teams in an extended enterprise carry out modelling and simulation processes, several capabilities that support collaboration and multi-disciplinary modelling and simulation were developed in the context of the TOICA EU FP7 project. TOICA develops these capabilities for application in the thermal analysis of aircraft architectures and validates them on realistic thermal use cases. The need for thermal analysis of aircraft architectures has emerged from the increased application in aircraft of technologies that strongly impact the thermal behaviour of the aircraft.

Collaborative engineering through modelling and simulation along the supply chain has to deal with two opposite goals. Firstly, the supply members want to protect their intellectual property rights (IPR) amongst each other, whereas more integrated simulation may ask for more and agile exchange of data among the supply chain. Secondly, security policies at the supply chain members limit access to simulation resources, whereas increased collaboration asks for well-established simulation workflows across the supply chain that support reproducibility and traceability of simulation data and processes.

In the TOICA project, the Netherlands Aerospace Centre NLR developed and applied two innovative technologies that enable collaborative engineering through modelling and simulation, while respecting IPR and security policies among the supply chain: the Brics capability and surrogate modelling. Brics enables multi-disciplinary and multi-partner engineering teams achieving cross-organisational simulation workflows while dealing with security constraints and measures of the involved organisations. Surrogate modelling is an effective method for reducing a complex simulation model to a ‘light’ version, which may respect IPR policies and can be exchanged easily among the supply chain. A surrogate model is specifically useful for extensive trade-off studies at aircraft level during conceptual design (as in TOICA), since a surrogate model requires low computational efforts.

The two innovative technologies are illustrated on the realistic use case of fuel tank thermal modelling, which was set up in the abovementioned TOICA project. This use case is driven by the needs to investigate the potential of fuel as heat sink and to support certification of a wing fuel tank that is made from non-aluminium materials. The potential of fuel as heat sink is limited by thermal constraints due to certification requirements. In case of novel materials for the fuel tank extensive testing and/or detailed thermal analysis is necessary to determine the bulk fuel tank thermal behaviour for different flight cases.

Section 2 will introduce the TOICA project, the fuel tank thermal modelling use case, and the problems and challenges that have led to the development of the Brics and surrogate modelling technologies. Sections 3 and 4 describe the backgrounds, details, and realistic example

applications of Brics and surrogate modelling, respectively. Section 5 describes the integrated application of the two technologies to the fuel tank thermal modelling use case. Section 6 presents conclusions.

2 OUTLINING THE CONTEXT

This section describes the context and rationale of the study of which the results are presented in this paper. Subsection 2.1 introduces the TOICA project. Subsection 2.2 introduces the fuel tank thermal modelling use case. Subsection 2.3 describes the problems and challenges that have led to the development of the two innovative capabilities addressed in this paper.

2.1 Introduction to TOICA

Thermal behaviour has become a crucial topic in the development of modern aircraft. This is due to the increasing number of complex systems required by modern, more electric commercial aircraft, the introduction of hotter engines with higher by-pass ratios, the increased use of composite material in aircraft structures, and the confinement of highly dissipative equipment and systems in smaller areas, to save space for passengers and cargo. New advanced techniques to manage the aircraft thermal behaviour at the early stages of development are essential to take the right configuration decisions while meeting market demands.

The 'Thermal Overall Integrated Conception of Aircraft' (TOICA) EU FP7 project intends to change the way thermal studies are performed within the aircraft design processes [2]. The project focuses on the creation and management of new aircraft architectures, including thermal analysis and trade-off studies of such architectures, via a so-called "Architect's Cockpit" as depicted in Figure 1. The thermal analyses require collaborative effort from the supply chain involved in the development of modern aircraft. The TOICA project develops advanced capabilities to support the collaborative analyses.

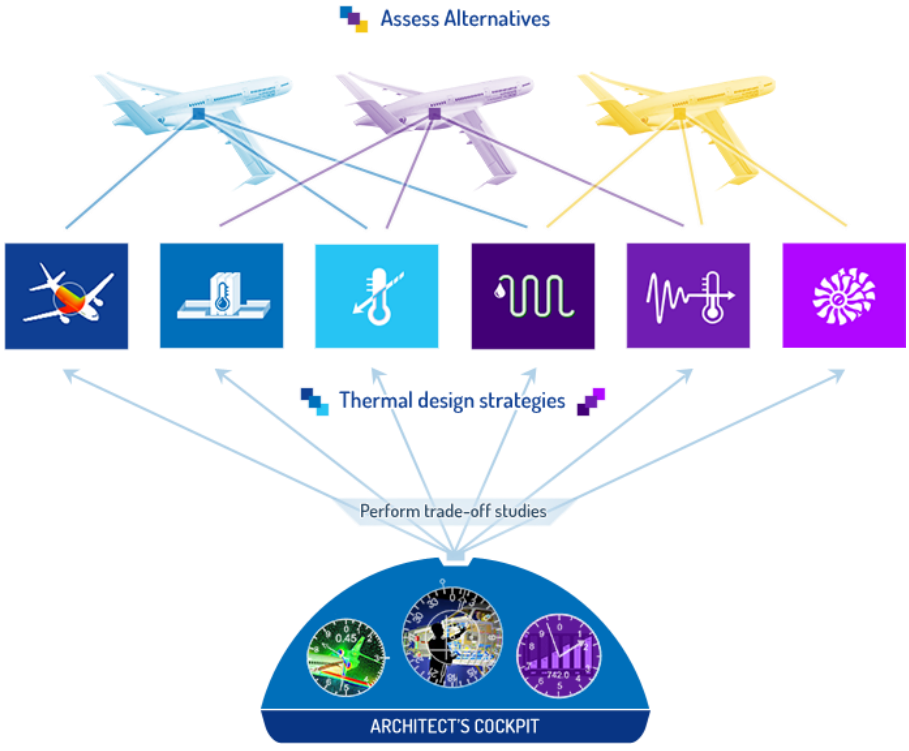

Figure 1: Depiction of the TOICA Thermal Architect's Cockpit that enables collaborative thermal trade-off studies (source: [2])

2.2 The fuel tank leading edge case

The use case addressed in this paper is related to one of the use cases of the TOICA project: using fuel as a heat sink for waste heat from other systems. This may raise certification issues with regards to the fuel tank, especially if innovative, non-aluminium materials are involved. Therefore, part of the TOICA use case is dedicated to the integrated analysis of the thermal behaviour of a wing fuel tank. The applicable wing fuel tank thermal model is part of the Alenia Thermal Aircraft Model lead by Finmeccanica's Aircraft Division. To comply with certification standards of a wing fuel tank that is made from non-aluminium materials, extensive testing and/or detailed thermal analysis is necessary to determine the bulk fuel tank thermal behaviour for different flight cases. The methodology for the fuel tank thermal characteristics evaluation shall indicate - during the aircraft preliminary design phase – whether or not a flammability reduction means (FRM) is needed.

Figure 2 depicts a 3D schematic view of a wing fuel tank and leading edge. The tank is filled with fuel up to a certain level. Consequently, there remains a part of the tank that is not filled with fuel, but which may contain fuel vapour. This part is called the 'ullage'. The tank compartment is separated from the leading edge compartment by a spar. Within the leading edge compartment a bleed pipe resides that transports hot air from the engine. The bleed pipe causes the fuel and the ullage to heat up when the engine is switched on. Furthermore, other heat sources such as solar radiation on the wing may cause the fuel and the ullage to heat up. All such heat sources need to be taken into account into the integrated thermal analysis of the wing fuel tank.

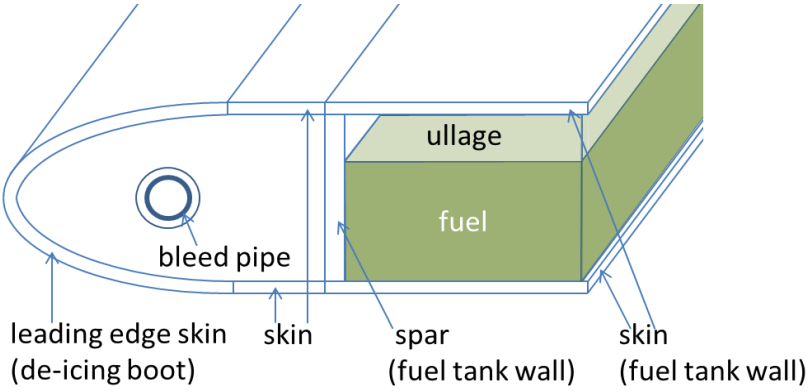

Figure 2: Schematic of the wing fuel tank. The bleed pipe is located in front of the wing fuel tank. The bleed pipe causes the fuel and ullage, i.e., the unfilled part of the tank, inside the tank to heat up.

The thermal analyses are performed at two levels:

- Detailed thermal analysis by calculating the three-dimensional temperature profiles via structural Finite Element Analysis (FEA) and Computational Fluid Dynamics (CFD).
- Quick thermal analysis and prediction of the bulk temperature via a nodal model, applying a thermal network approach. The nodal model must be validated by the detailed thermal analysis. An efficient and sufficiently accurate model is needed for applying the analysis during the aircraft predesign phase.

Both analysis levels rely on accurate boundary condition estimations for the fuel tank structure. Therefore, the effect of heat sources that are located close to the tank (e.g. the bleed pipe) is modelled to identify hot spots on the boundary of the fuel tank due to external heat sources.

On the detailed level this estimation is supported by a model of the wing leading edge. This model is described in further detail in subsection 5.1. On the quick analysis level the estimation is performed by a surrogate model of the wing leading edge. The derivation of the surrogate model is described in subsection 5.2.

Figure 3 provides a scheme of simulation models that are involved in the fuel tank thermal analysis together with their interrelations and thermal coupling. The different simulation models depicted in Figure 3 have been developed by different partners with different tooling: University of Padova using StarCCM+ for the fuel tank CFD model, Siemens Industry Software using LMS Imagine.Lab Amesim™ for the fuel tank nodal model, and NLR using Abaqus for the fuel tank structure FEA model and for the leading edge FEA/CFD model. The latter model is addressed in this paper. In the ideal situation these models run all at one physical location: at the aircraft manufacturer. However, if this is not the case, collaborative engineering technologies can facilitate an efficient integration workflow/process. Various reasons for such collaborative multi-partner approach will be explained for the general case in the next section.

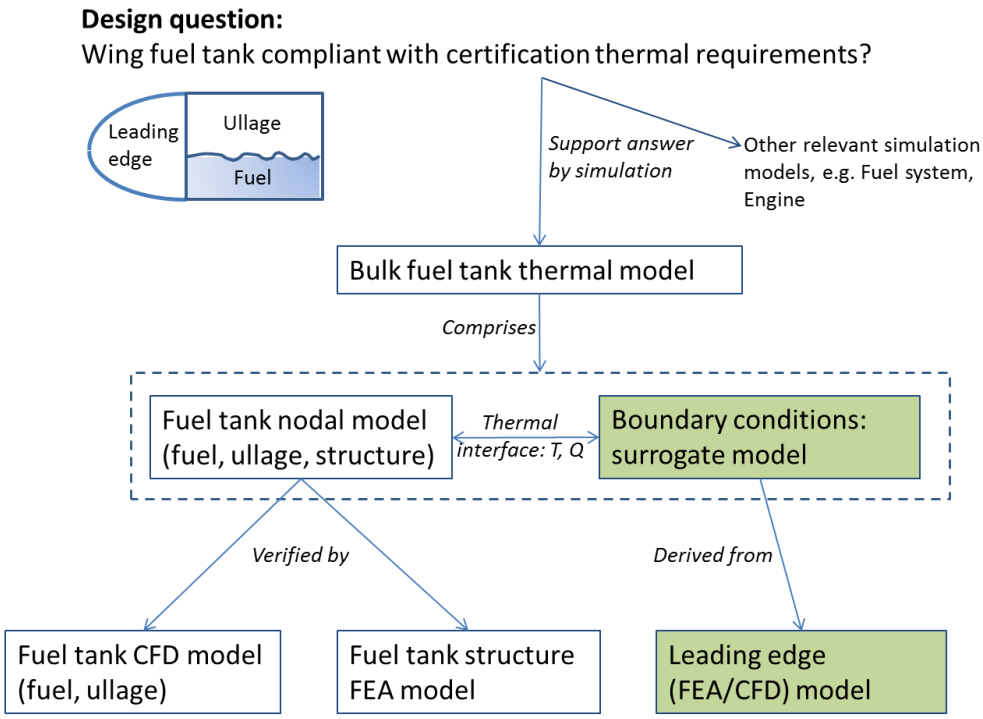

Figure 3: Model coupling and relation scheme of the fuel tank thermal analysis. The models in the green blocks will be further detailed in this paper (see section 5).

2.3 Problem description and challenge

Collaborative modelling and simulation in aeronautical industry with a multi-disciplinary, multi-organisational and multi-site engineering team are commonly hampered by security constraints, protection of intellectual property, and dependency on simulation tools and complex simulation models that are expensive to run. Several research projects in the EU framework programmes, such as VIVACE, CESAR, and CRESCENDO have been dedicated to development of innovative concepts and technologies that support collaborative engineering processes in the aerospace context. In the context of TOICA, NLR addressed two particular aspects: distributed collaboration technologies and cost and time efficient simulation technologies.

With respect to distributed collaboration, NLR investigated the limitations of cross-organisation collaborative engineering resulting from the fact that organisations are protective with respect to access to their own assets. Due to a variety of security constraints imposed by the connected organisations, running a simulation workflow that comprises tools at the different organisations is not obvious. Organisational rules and fire wall settings seem to make participation of a partner in a cross-organisation simulation workflow difficult or even impossible. NLR's challenge in this respect is to facilitate and smoothen the execution of cross-organisation workflows while dealing and complying with the policy and rules of the involved organisations. The approach is outlined in section 3.

NLR also focussed on cost and time efficient simulation technologies. These are often a challenge within aeronautic design. Models that describe the behaviour of an aircraft component in detail are usually expensive to run. They may be dependent on specific simulation tools and difficult to interface with other models. This makes it difficult to apply them in trade-off studies on aircraft level. Furthermore, they may not be shared with partners in order to protect the company's knowledge that lies behind the model. Surrogate modelling can provide a solution to these challenges. In order to achieve cost and time efficient simulation technologies NLR's objective is to develop surrogate models in such way that:

- the generated models have an appropriate accuracy (fit for purpose),
- the generated models are efficient (computationally cheap),
- intellectual property of the detailed model owner is protected,
- integration and model derivation effort is minimal, and
- both transient and steady-state thermal behaviour can be simulated.

This capability is presented in section 4.

Both capabilities will be illustrated by separate application examples in the frame of TOICA. Furthermore, their integrated application in the context of the fuel tank leading edge use case is described in subsection 5.3.

3 SMOOTH EXECUTION OF CROSS-ORGANISATION WORKFLOWS

This section introduces Brics as capability for the support of smooth execution of cross-organisation workflows. A quick, high-level introduction to Brics, describing its rationale and a global overview is given in subsection 3.1. A more detailed description of Brics is given in subsection 3.2. Implementation aspects of Brics are described in subsection 3.3. A first realistic example application of Brics in the context of a distributed MDO study is briefly presented in subsection 3.4. The application of Brics in the context of fuel tank thermal modelling is described in subsection 5.3.

3.1 Cross-organisation collaboration challenges

Collaborative engineering activities and simulation workflows are largely supported by information and communication technology and software tools. But making cross-organisation collaborative engineering efficient and effective in practice requires a step change. For example, collaborative workflows typically span the networks of the collaborating organisations. The workflows would ideally run seamlessly across the networks of these organisations. However, with the current complexity of design, analysis and simulation tools and workflows it is difficult to be compatible with the varying security settings and the variety thereof. Engineers are facing unintended security restrictions due to security rules, fire walls and proxy servers. These restrictions help organisations protecting their assets and intellectual properties and obeying legislation and regulations. In practice, aircraft collaborative design teams end up in using standard facilities, such as e-mail and FTP servers, and in dealing with IT depart-

ments and security officers that seem unwilling to cooperate. From an aircraft program technical point of view, effective and efficient collaboration in the jungle of security rules, measures and technologies is a big challenge. This challenge has been the point of departure for the development of Brics.

NLR has long history of experiences in supporting the realisation of cross-organisation workflows. The knowledge, expertise and reusable solutions have been collected in, and are being deployed through Brics. In a nutshell, Brics targets to achieve smooth and secure execution of cross-organisational multi-partner collaborative workflows. It enables all engineering partners to participate, even if they are "network access restricted" because of security measures [3]. At the same time, Brics complies with the security constraints of the organisations involved. Brics also aims to allow each partner to have full control over its own resources, including computing resources, on-line data, and software tools. This means that organisations do not have to put their resources under management of Brics, any cross-organisation workflow nor any umbrella authority. The resources may be deployed on behalf of cross-organisation workflows only under full control of the organisation's own employees. Brics caters for a "man-in-the-loop", as is shown in Figure 4.

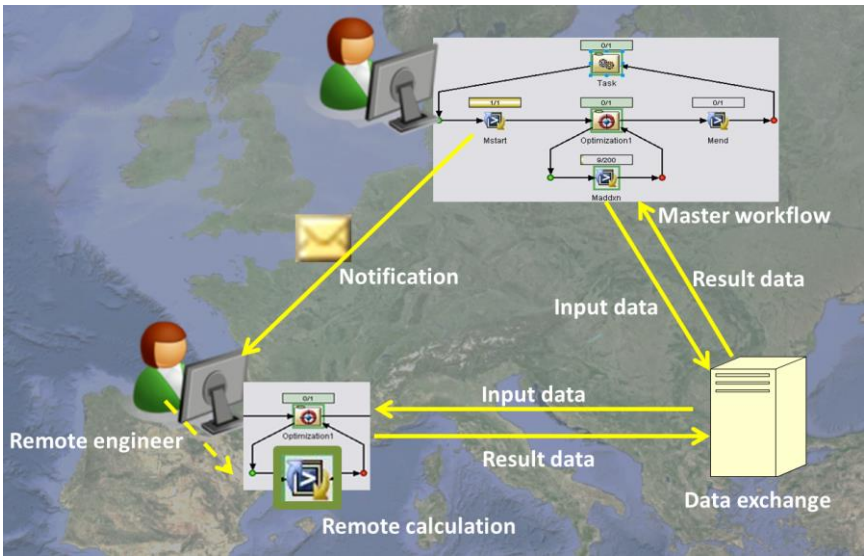

Figure 4: Schematic overview of the basic idea behind Brics: performing a remote calculation from within a "master" workflow by sending a notification to a remote engineer, who may decide on whether or not perform an action or a series of similar actions. Brics in addition facilitates the orchestration of the remote job and the data exchanges involved.

The "evolution" of Brics started more than ten years ago, in research projects aimed at establishing virtual or extended enterprises in the support of collaborative engineering activities (VIVACE[4], CESAR[5], CRESCENDO[6]). Cross-organisation collaboration used to be mainly based on the exchange of data files via e-mail, FTP servers, websites for information exchange and collaboration (e.g., SharePoint), product lifecycle management and support systems, telecon and videoconference systems. In some cases it involved the shared use of tools, workflows and data on centralised systems. Commercial workflow management tools are available to support cross-organisation workflows but generally put heavy demands on the interconnectivity of the systems and organisation networks involved. They usually enforce the collaborating partners to install and use the same tool.

Brics has evolved and still is evolving "on the job". This means that it is being developed in projects that target or apply collaborative engineering activities and workflows. Its devel-

opment is fed by needs and requirements that come from projects, use cases, and engineering teams that involve more and more cross-organisation collaborative engineering while facing ever increasing security constraints. Through the years, the security rules and mechanisms have become and still are becoming stricter. At the same time, partners in collaborations want to persist using their own processes, methods and tools, even while fulfilling their role in collaborations and collaborative workflows. This will enable them to fully exploit their own expertise and to pursue their own way of working, but on the other hand leads to more and more heterogeneous environments to be dealt with in collaborations. The two growing barriers of security and heterogeneity have fed and still feed the ongoing evolution of Brics.

3.2 Brics technology to support cross-organisation collaborative workflows

Brics comprises protocols and supporting middleware that facilitate remote execution of tools and workflows. The remote execution involves sending of notifications to remote engineers, exchange of data, and synchronisation of distributed activities. Brics is based on default and standard network protocols, tools and facilities. Application of Brics has minimum "connectivity" requirements: being able to send and receive e-mail messages and to upload and download files to a file or data server that is accessible to at least one other partner. To avoid misunderstandings, Brics does not "penetrate" fire walls nor rely on known bugs in networking software or in other security means. The communication related to Brics-enabled cross-organisation workflows is fully transparent and can be explained easily to the involved IT departments and security officers upon request. Brics respects the security rules of the collaborating partners. It supports the application of secure communication technologies, it involves remote engineers explicitly and it enables the collaboration partners to have full control over their own resources. Brics can be used complementary to existing engineering tools and workflows, and does not require changes of tools, methods, and processes in organisations. These properties contribute to the possible deployment of Brics with minimum impact on the business of the connected organisations.

Brics is based on a simple protocol that arranges the execution and data flow between an orchestrating (or "master") workflow in one organisation and a remote engineer in another organisation who is assigned to execute a tool or a part of the workflow. The protocol comprises the uploading of data files that are input for a remote process, sending a notification to a remote engineer requesting the execution of a task, the synchronisation with the remote task, and the downloading of the data files that are output of the remote task; cf. Figure 5. The 'single-task' protocol is suitable for the execution of a single remote task. If the same protocol were applied in a loop, the remote engineer would repeatedly be notified to execute the same task again with slightly different input data. The handling of a consecutive series of similar notifications is cumbersome, time consuming and error prone. Brics has an extended protocol for gracefully dealing with such multi-task jobs. The 'multi-task' protocol centralises the triggering of the remote engineering into a single notification, requesting the remote engineer to execute a series of equal tasks. The protocol furthermore deals with handling the series of equal tasks and the graceful termination thereof. The protocols are described in detail in [7].

The middleware provide software methods to support the protocols. The methods can be plugged in easily as commands in scripts and tools in workflows and hence enable the use of the protocols from within scripts and workflows. The middleware supports the use of various existing mechanisms for notifications and data exchanges. It includes mechanisms to deal with proxy servers and to use permitted communication channels with the required level of security. It also includes mechanisms for relaying data files and notifications, to cater for situations in which partners have no access to particular data, file or e-mail services. The middle-

ware furthermore supports engineers in providing specific parametric calculations "as a service", for use by (possibly remote) engineers and workflows [8].

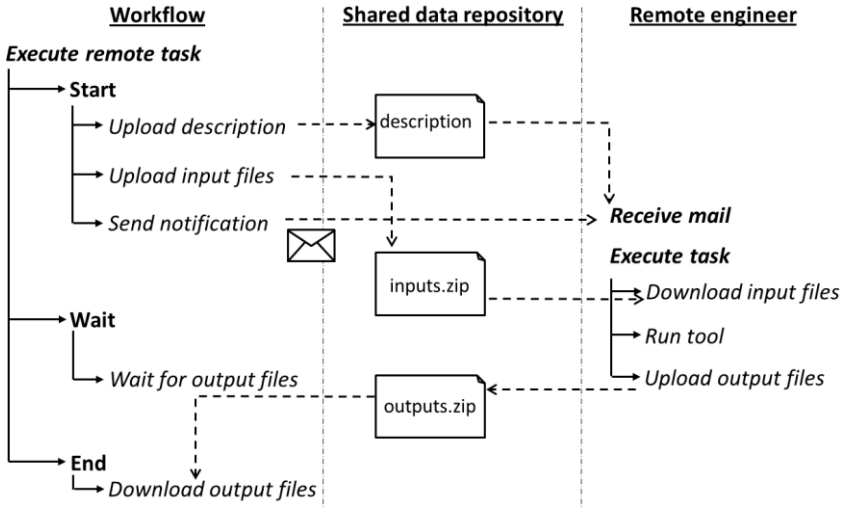

Figure 5: Simplified sequence diagram of the Brics single-task protocol.

3.3 Implementation

The Brics middleware comprises a set of Java packages with a small number of 'main' programs and interfaces. As such, Brics is operational on a variety of operating systems, including Windows, Linux, and UNIX. The Java packages enable easy integration of the middleware in Java applications and existing products. Brics has been successfully integrated in COTS and open-source workflow management and optimisation tools such as Boss Quattro, Isight/FIPER, RCE, and Optimus. The main programs include simple command interpreters that cater for interactive use of Brics as well as use of Brics from within script languages such as UNIX and Linux command scripts, Windows BAT scripts, Python, and Matlab.

To support data exchange, Brics is capable of interacting with a variety of data and file servers. Examples are FTP, MS SharePoint, Share-A-space, and shared file systems. Interfaces to other, including new and organisation-specific data exchange services, such as Airbus' FTS+ service, can be added easily at the Brics developer's level. Brics' default mechanism for notifications is e-mail. Brics has also provisions for dealing with product-specific notification mechanisms.

As might be clear from the above, Brics includes many interfaces. The middleware is also capable of communicating through a variety of – secure as well as insecure – internet communication channels. Use of Brics requires some configuration, which includes the specification of what data server and e-mail interfaces to use, web addresses and authentication information for the services, and proxy servers to deal with. The configuration information can be provided as parameters at the Java level as well as via environment variables and configuration files for the main programs and interfaces. The light-weight configuration means makes Brics an agile tool in the various collaboration settings.

3.4 Example application in a distributed MDO process

Brics has been installed in industry, research institutes, software vendors, and SMEs. It has been, and still is being applied for the implementation of cross-organisation distributed workflows in several EU and national research projects (VIVACE, CRESCENDO, CESAR, TOICA). In these projects, Brics has proven to be a valuable tool through which partners can

experience collaborative working in a flexible and easily accessible way, even in an early stage of the development of multi-partner scenarios and workflows.

Brics facilitates the transformation and integration of local workflows into cross-organisation collaborative engineering workflows, by supporting the replacement of a tool by a 'stub' that handles the remote execution of the tool as if it runs locally. Section 5.3 describes the application of Brics in thermal analysis of an aircraft wing fuel tank. A realistic example application was set up and demonstrated live in the context of TOICA [9]. In this use case, Brics has been used for the realisation of an automated multi-partner and cross-organisation distributed multidisciplinary design optimisation (MDO) workflow; see Figure 6.

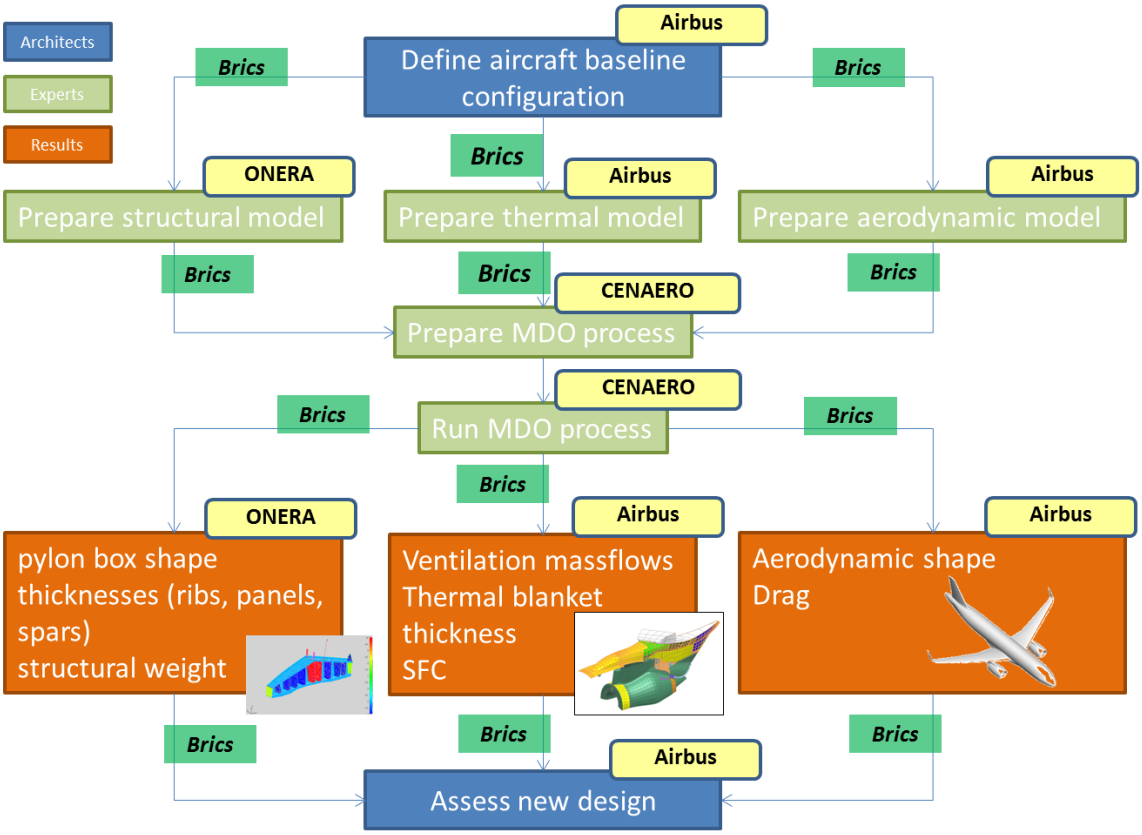

Figure 6: Overall process of preliminary design of power plant structures under thermal constraints. The process includes a distributed cross-organisation MDO workflow. The yellow boxes indicate the different partners. Note that different departments from Airbus were involved. The small green boxes indicate the role of Brics for orchestration and data exchange.

The MDO workflow serves to support the preliminary design of aircraft power plant structures under thermal conditions. The optimisation requires multiple disciplines and tools available from the aircraft OEM as well as the suppliers. The MDO workflow concerns the optimisation of an aircraft pylon design using structural, thermal as well as aerodynamic simulations. The so-called "master" workflow drives the MDO process and is operated from the OEM's site by a simulation expert. The progress of the optimisation process can be monitored by the simulation expert as well as the architect. The master workflow uses Brics to initialise the optimisation and simulation processes (tools and workflows) at the different partners. The optimisation process uses Brics to orchestrate the simulations and to manage the data exchanges in between. The remote partners use Brics to respond to the series of simulation re-

quests and to manipulate the data to be exchanged. Notifications are sent by e-mail messages, and data exchanges take place via a single shared data server located at the OEM.

Subsection 5.3 describes the application of Brics in the fuel tank modelling case introduced in section 2.2. In that case, Brics has been used in combination with the surrogate modelling techniques that are discussed in the next section.

4 SURROGATE MODELLING

This section describes the details of NLR's surrogate modelling capability. An introduction is provided in subsection 4.1. The general surrogate modelling process is presented in subsection 4.2. Subsection 4.3 focusses on surrogate modelling of time-dependent models. A first realistic TOICA application of the surrogate modelling capability is discussed briefly in subsection 4.4. The application of the capability in the context of fuel tank thermal modelling is described in subsection 5.2.

4.1 Capability introduction

A surrogate model is an approximating model that replaces a more complex simulation model. The terminology "surrogate model" is used in the context of behavioural models. It is also referred to as "reduced model". Similarly to the complex simulation model the surrogate model is a representation of the behaviour of a system. The surrogate model however aims at reducing the complexity needed to compute the system behaviour. There are several possible reasons for creating a surrogate model from a complex model:

- Numerical efficiency – A surrogate model requires less computational power than the complex model. This is specifically useful in case the model needs to be used in an optimisation loop and therefor executed many times
- Protection of intellectual property (IP) – The complex model may not be distributed to other parties because of the protection of IP. A surrogate model may be an alternative for this as it can be implemented as a black-box. The contents of the original complex model are not visible anymore.
- Ease of integration – Running a complex model may require the specific tool, which it was developed with. In several cases the model needs to be integrated with other models, developed with other tools at other organisations. These tools do not necessarily interface with each other. A surrogate model – being a simplified representation of the original complex model – can usually be integrated more easily into other tools.

One can consider two broad families of surrogate/ reduced models. First, data-fitted surrogate models are data-driven models that emulate the responses of a complex simulation model (see Figure 7). This type is applicable to this paper. Second, simulation models can also be reduced in a physics-based way. This type is not treated in detail in this paper, but is considered in TOICA e.g.:

- Model reduction by means of geometry simplification of the original CAD model; see [10] and [11].
- Model reduction by means of thermal nodal modelling; see [12] for an explanation.

In aeronautic design surrogate models are usually applied as part of a design optimisation loop. In some cases the surrogate models are adapted on the fly as part of the optimisation algorithm: so-called adaptive surrogate models. Another frequent application is the creation of surrogate models as part of data analysis and statistics. A surrogate model is then directly derived from experimental data in order to predict a certain behaviour that is under investigation [13].

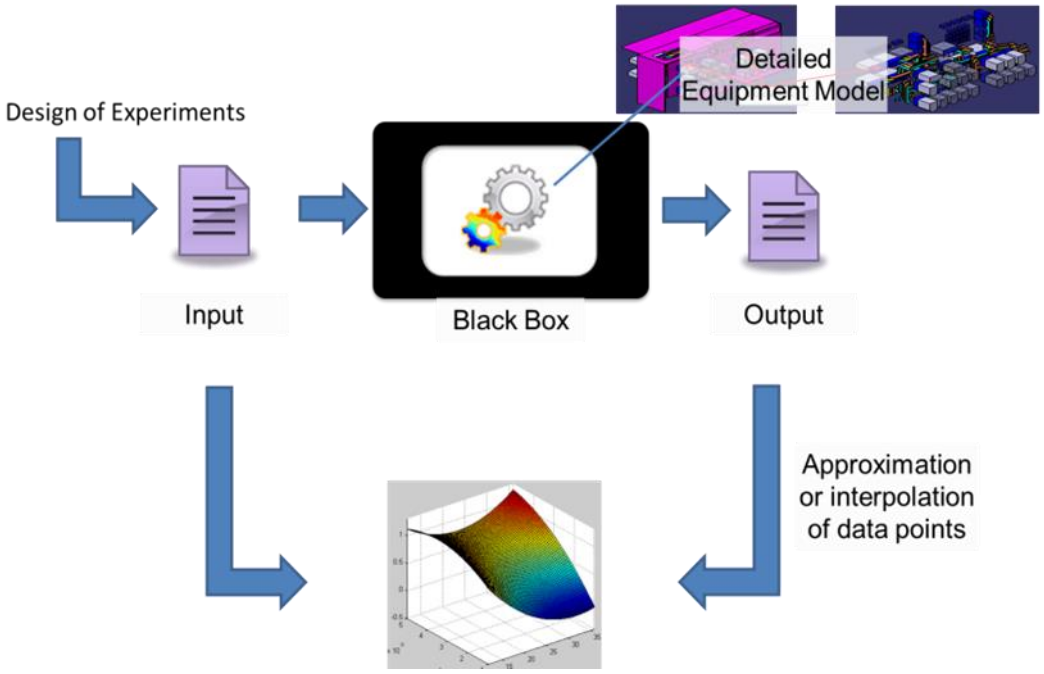

Figure 7: Illustration of data-fitted surrogate model derived from a detailed model of an equipment behaviour.

Organisations that need to create surrogate models develop their own tools for it or use commercial-off-the-shelf (COTS) software packages. Several steps in the surrogate modelling process can indeed be performed automatically (see also subsection 4.2), but to derive a surrogate model that is fit for purpose the involvement of experts is still essential. Expert judgment is needed as the choice for the most appropriate data fitting method depends very much on the data set that is to be fitted. NLR has long experience in developing and applying surrogate models based on data fitting from various EU research projects (e.g., POA[14], ICE[13], VIVACE[15], CRESCENDO[16], MAAXIMUS[17]).

4.2 Workflow for surrogate model derivation

The derivation of a surrogate model comprises several steps. When a surrogate model is derived from a set of input/output data of the complex model, the sampling of the data points is based on a so called Design of Experiments (DoE). The DoE is a crucial ingredient of the surrogate generation process, especially when the function evaluations are expensive. It should provide sufficient variation in the input values to cover the desired input range because it must contain as much information as possible. Examples of DoE methods are full or fractional factorial designs, Latin Hypercube Sampling (LHS) or D-optimal methods. Based on the DoE a database is derived that contains the results (input and output data) of the sequence of simulations with the complex model.

The surrogate model itself is derived by fitting the set of input-output data. For this several fitting techniques exist. The most common is polynomial regression, also referred to as response surface method. Other methods have been developed with more complicated analytical expressions like artificial neural networks, kriging, radial basis functions, splines, etc. The methods can be divided in *interpolation* and *approximation* methods. In case of interpolation the resulting surrogate model exactly matches the data points from which it was created with estimations in between those data points. In case of approximation the surrogate model does not exactly match the data points but approximates them as well as the space in between. The feasibility of a fit method depends on the nature of the data set: high or low dimensional,

sampled in a grid or scattered, noisy or clean, sampled in a sparse or dense manner (referring to the DoE), etc.

The fitting process is usually supported by dedicated software tools that statistically analyse and pre-process the data set, provide multiple fit methods and facilitate a fit assessment to select the best method with the appropriate settings. At NLR the MATLAB based in-house fitting tool MultiFit[15] is used. The assessment of a candidate surrogate model is performed by excluding a number of points of the data set from the fit and reserving them for validation afterwards by comparing the surrogate prediction in these points with the true values. This validation data set can be shifted across the complete data set to have a better validation range: cross-validation Several error metrics are available to represent the validation, e.g. Root Mean Square Error (RMSE), Mean Absolute Percentage Error (MAPE), R-squared test and quantile tests.

Figure 8 shows the identified steps that constitute the generic surrogate modelling workflow. Almost all steps are implemented using MATLAB. Only the runs with the high-fidelity model depend on its particular enabler (e.g. CFD or FEA computations). These runs can be orchestrated and linked into the surrogate modelling workflow using Brics. Such integration is detailed in subsection 5.3.

The resulting surrogate models are represented with analytical functions, calculating an output prediction in one step. As such they require very low computational effort.

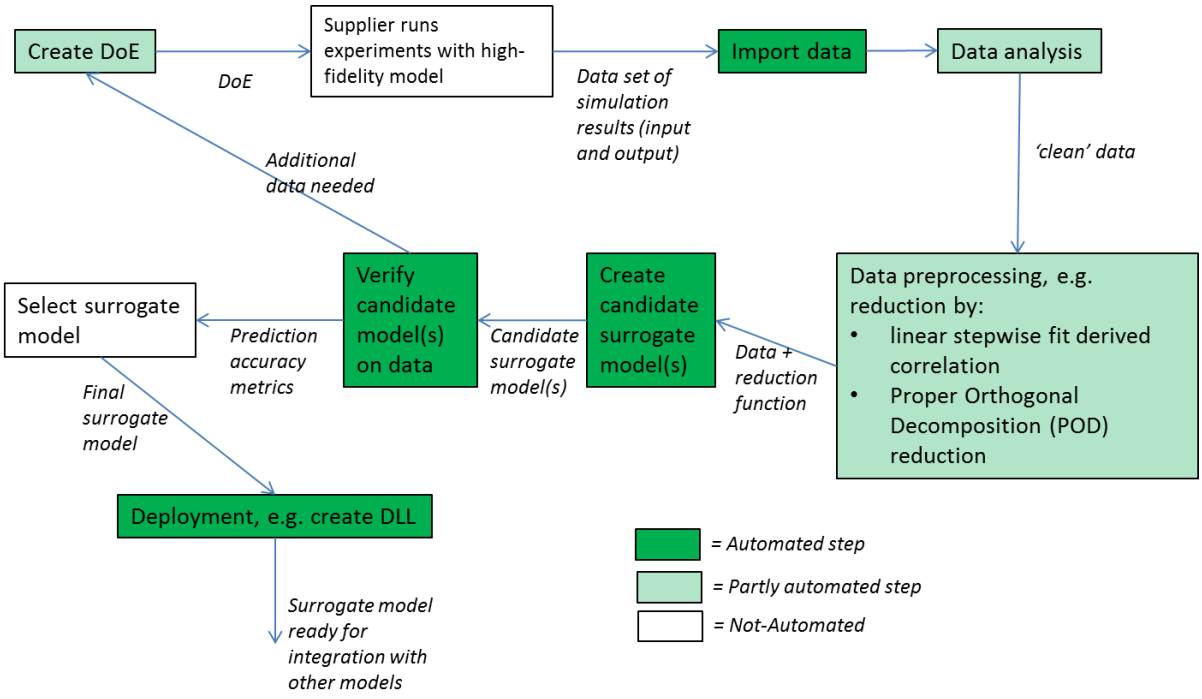

Figure 8: Generic workflow for deriving a surrogate model.

The surrogate models are by default available as MATLAB analytical functions, since they were created in the MATLAB environment. They have been exported as C type DLL or executable file using the MATLAB Coder. The export makes the model a black box and easy to integrate with other simulation tools, e.g. as Functional Mock-up Unit [18].

4.3 Transient surrogate modelling

In most cases data-based surrogate models are applied in the context of a steady-state analysis of system behaviour. During TOICA a method has been developed for creating transient surrogate models. This means that the surrogate model is able to capture time-dependent behaviour, specifically in short intervals of time (dynamic behaviour). The transient surrogate modelling problem is formulated as follows. Derive a function *f* such that

$$y(t) \approx f(y(t-\Delta t), u(t), u(t-\Delta t), \Delta t), \tag{1}$$

with *y* the vector of output variables, *u* the vector of input variables, *t* the simulation time and Δt a time step. For simplicity reasons only one time delay Δt of *u* and *y* is added in equation 1 but one could also consider multiple time delays here. In the context of thermal analysis *y* usually represents a temperature field whereas *u* represents boundary temperatures and/or heat flows.

The creation of a transient surrogate model gives rise to a significant increase of data, because complete time histories of the model inputs and outputs are needed to derive a surrogate model. Furthermore the dimensions of *u* and *y* may be very high, e.g. if complete temperature fields on a structure are to be predicted. In general, the more input dependencies need to be taken into account by the surrogate model, the more data points are needed. In many cases a large number of simulations is not feasible, because of the computational cost (e.g. CFD runs). In such cases it is useful to analyse whether the dimensionality of the inputs and outputs can be reduced. In the context of a thermal analysis this reduction can be applied to the temperature field y. As such a data pre-processing step is performed in which a transformation of the data is created that affects the eventual surrogate model. The transformation function will become part of the final surrogate model. The data pre-processing step has been performed using Proper Orthogonal Decomposition (POD) [19]. With this method the dimension of the data is reduced by finding the (spatial) coherence in the simulated time histories of *y* by performing a singular value decomposition of the snapshot matrix and retaining the singular vectors that correspond with largest singular values. These POD vectors derived from the simulation results form a reduced basis for *y*. Then a function *g* is to be fitted such that

$$c(t) \approx g(c(t-\Delta t), u(t), u(t-\Delta t), \Delta t), \tag{2}$$

with *c* the predictions of the POD coefficients (i.e., the representation of *y* in the new basis), *u* the vector of input variables, *t* the simulation time and Δt a time step. Typically *c* has a dimension that is orders of magnitude smaller than *y*.

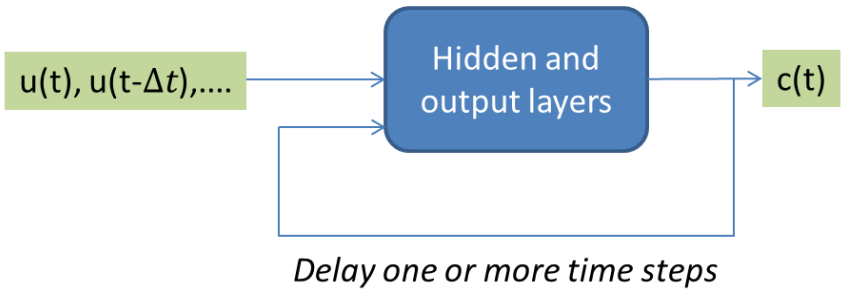

Figure 9: Top-level view of a recurrent artificial neural network that fits the POD coefficients *c(t)*.

A suitable method for deriving the function *g* is a recurrent artificial neural network (ANN). This method supports fitting of time series [20]. The recurrent ANN fits the values *c(t)* of the POD coefficient matrix as a function of the inputs *u(t)* -including a number of time delays of

u(t) - and it feeds the predictions of *c(t)* back into the network with one or multiple time delays. This is illustrated in Figure 9. A recurrent ANN is applied as surrogate modelling method in the fuel tank use case described in subsection 5.2.

With a recurrent ANN the time step Δt is assumed to be fixed. In some cases the data set may contain time series with different time step values, e.g. when the data set is assembled from other data sets. In those cases a feed-forward ANN can be used instead, in which the histories of *c(t)* and the time step Δt are to be treated as inputs as well. Such ANN is illustrated in Figure 10, and has been applied in the example described in subsection 4.4.

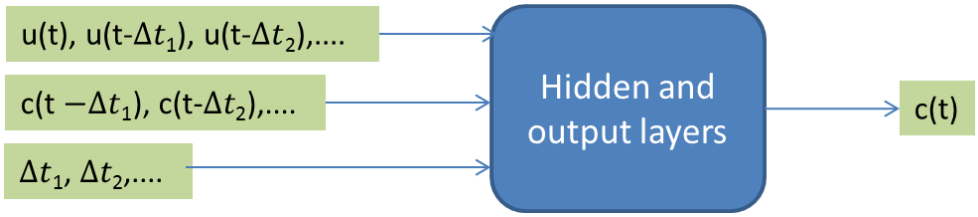

Figure 10: Top-level view of a feed-forward artificial neural network that fits the POD coefficients *c(t)*, for time histories with variable time steps

The steps for creating transient surrogate models have been automated as much as possible using the generic workflow depicted in Figure 8.

4.4 Example application in equipment thermal integration

The application of the transient surrogate modelling method to the fuel tank analysis use case is detailed in subsection 5.2. Earlier during TOICA, the method has been applied in the context of equipment thermal integration. That realistic application is summarised in this subsection.

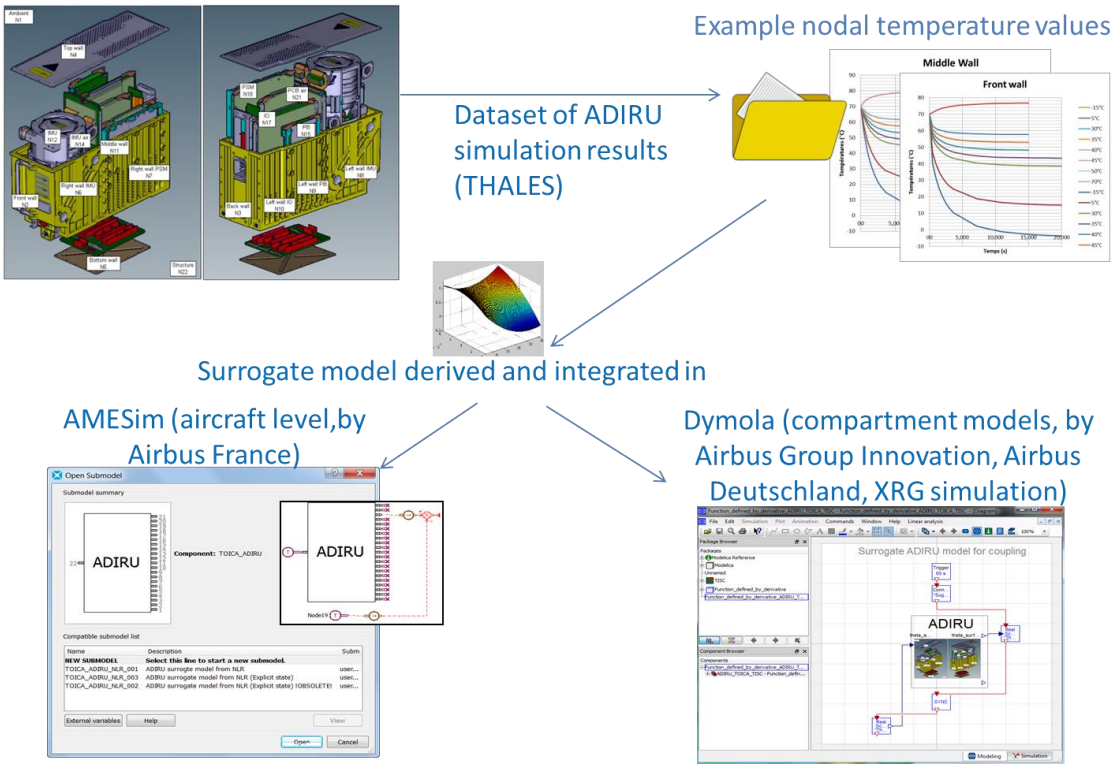

Figure 11: Illustration of surrogate modelling in the context of equipment thermal integration.

A data set has been provided of the transient thermal behaviour of the Air Data Inertial Reference Unit (ADIRU), by Thales (see Figure 11). The data set contains a number of time histories of 21 nodal temperatures on the equipment with varied initial conditions and a varied ambient temperature. The nodal temperatures represent the vector of output variables *y* to be predicted and the ambient temperature represents the input variable *u* (see equation 1). The data set consists of 5448 records in total. The dimensions of the data set have been reduced using POD. Five singular vectors have been retained. The POD coefficients have been predicted by a feed-forward ANN, taking the time history of the POD coefficients at the previous time step, the ambient temperature and the time step as input (see also Figure 10). The ANN consists of 2 hidden layers of size 12 and 8 respectively. Training has been performed using Bayesian regularisation. The resulting surrogate model has a temperature prediction error of order 1-2 ^{o}C (measured on the full data set used for fitting).

The surrogate model has been exported as a C type DLL which has been integrated with the system simulation tools (representing equipment thermal integration, see Figure 11):

- Amesim, used for integration of the surrogate ADIRU model on aircraft level.
- Dymola, used for integration of the surrogate ADIRU model on avionics compartment level.

5 THERMAL SIMULATION OF A FUEL TANK LEADING EDGE

This section details the case of thermal simulation of a fuel tank leading edge, which is related to one of the use cases of the TOICA project: using fuel as a heat sink for waste heat from other systems. Part of the TOICA use case is dedicated to the integrated analysis of the thermal behaviour of a wing fuel tank. The applicable wing fuel tank model is part of the Alenia Thermal Aircraft Model lead by Finmeccanica's Aircraft Division.

In subsection 5.1 the thermal model of a hot spot close to the fuel tank is described. The model is used to simulate the thermal effect of a bleed pipe on the tank wall. Furthermore, in subsection 5.2 a surrogate model is created from the results obtained in subsection 5.1. This surrogate model is then shown to produce comparable results of thermal history as the original model of subsection 5.1. Finally, in subsection 5.3, the simulation and surrogate creation steps are integrated into the collaborative engineering chain. All simulations have been performed by NLR.

5.1 Thermal modelling

Thermal analysis of an aircraft wing fuel tank consists of an internal and external temperature simulation. External temperature analysis covers the wing structure and structural heat sources, e.g. bleed pipe. Internal temperature covers the fluid and ullage (cf. Figure 2).

To identify the effect of heat sources external to the wing tank, a thermal model is necessary that is able to capture convection, conduction and radiation effects of these heat sources. Such heat sources are typically components that are running through the wing where the fuel tank is located. These components may not be directly in contact with the wing fuel tank. However, their supports are typically connected to the wing spar that is part of the fuel tank structure, causing the wing spar to locally heat up. Furthermore, the air inside the bay where the heat source is located is heated up. Therefore, a fluid-structure model is created that models the effect of heat sources and e.g. cooling effects of vents that are present in front of the fuel tank wall. The present case consists of a hot spot in the form of a bleed pipe located in the wing leading edge in front of the fuel tank; see Figure 2.

The thermal model for fuel tank external heat sources consists of two individual models that are coupled. The first model is a structural thermal model using a Finite Element ap-

proach and simulates the structural thermal loading. The second model consists of a fluid thermal model using a Finite Volume approach and models thermal behaviour of the air inside the leading edge. The two models are coupled to exchange temperature and heat flux values. These models are simulated in Abaqus standard (Finite Element) and Abaqus CFD (Finite Volume), and are coupled through Abaqus co-simulation engine [21].

In Figure 2, an overview is given of the wing structure consisting of skin, spar, and bleed pipe. The fluid model consists of the air inside the wing leading edge bounded by skin, spar and bleed pipe. Hence, the hot air inside the bleed pipe is not part of the CFD model but modelled as boundary conditions for the structural FE model. Furthermore, the front spar is the boundary of the structure model. The fuel and ullage section is not modelled in this fluid-structure model and is taken into account via a boundary condition. Modelling of the fuel and ullage are carried out by another TOICA partner, the University of Padova, using a CFD program.

Structural model

The upper and lower skins as well as the wing spar are made of composite material with different thermal properties in plane 6.7 W/mK and out of plane 0.7 W/mK, a density of 1.60 g/cm^3 and specific heat of 1.4 J/gK. The curved part of the leading edge consists of a de-icing boot. Inside the leading edge is a bleed pipe made of aluminium. The structure model is shown in Figure 12.

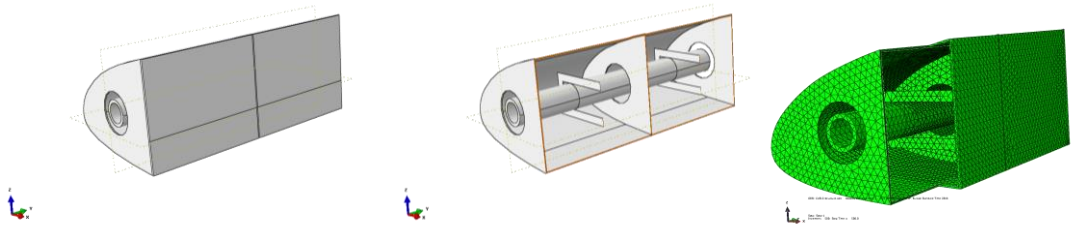

Figure 12: Wing structure part for which an FEA model is created. Left: the closed wing leading edge. Middle: a cut-out to show the internal structure showing the ribs, bleed pipe and bleed pipe supports. Right: the finite element mesh of the leading edge structure, bleed pipe and supports. Via a cut-out the internals are shown.

Hot air coming from the engine is running through the bleed pipe. This bleed pipe is then heated up and releases its heat via radiation to the surrounding walls. Additionally, via convection with the air inside the leading edge and finally via conduction with the bleed pipe supports, the walls are heated up. Air is running through the wing leading edge via ventilation holes. As can be seen in Figure 12 the bleed pipe radius is smaller than the hole in the rib section. Through this open area air is entering the wing leading edge in the model. On the opposite side air is leaving the wing leading edge via the space between the rib and the bleed pipe.

For meshing the structural model, linear tetrahedron elements are used and mesh seeding is chosen such that it more or less corresponds to the mesh seed that is used for the fluid domain. Boundary conditions are fixed temperatures on the wing top and bottom skin (including the de-icing boot). Thermal interaction of the front wing spar with the fuel is modelled via a heat transfer coefficient that was obtained from a CFD analysis conducted by the University of Padova for the fuel tank internals, i.e. ullage and fuel. The interaction with the air inside the leading edge is modelled via a fluid-structure interaction. Calculated wall temperatures on the FEA nodes are transmitted to the fluid calculations and the fluid calculations return heat trans-

fer coefficients on the CFD nodes. Interpolation of the calculated values is used to map results of the FEA onto the CFD and vice versa.

Fluid (air) model

To model the thermal interaction via convection of the wing leading edge structure and the air inside the leading edge, a fluid (air) model is created of the leading edge internals. In Figure 13 the geometry is shown. To summarise, all the empty space inside the leading edge is used for the volume mesh.

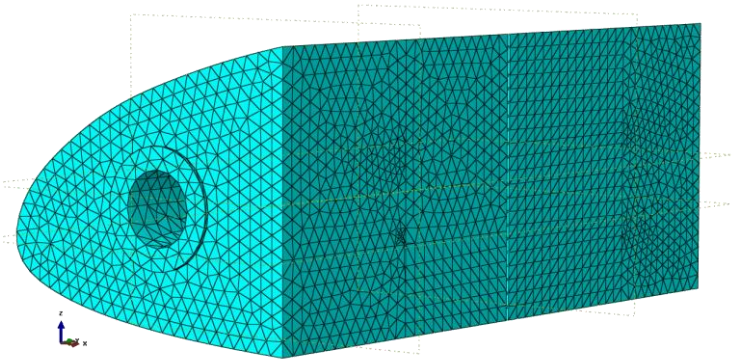

Figure 13: Wing leading edge air model showing the mesh of the air inside the wing leading edge that is modelled via a finite volume approach.

The fluid model is meshed using fluid linear tetrahedron elements. The mesh seed is chosen such that it more or less corresponds to the mesh seed that is used for the structure domain. The Spalart-Allmaras turbulence model is applied that uses wall functions to avoid very fine meshes near the walls. Boundary conditions are no slip conditions where the air touches the structure. Furthermore, a constant fluid flow is prescribed on one side of the leading edge.

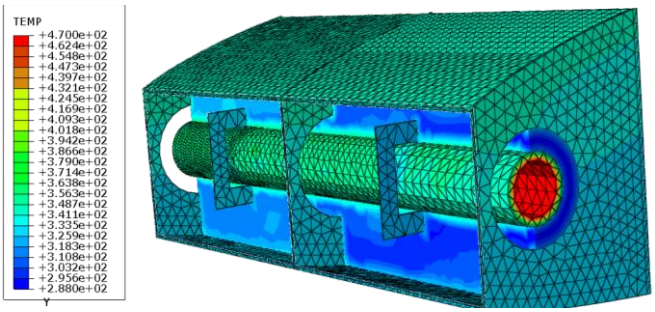

Figure 14: Temperature plot in degrees Kelvin of a cut-out of the Finite Element model for the structure filled up with a cut-out of the Finite Volume model for the fluid (air) in the leading edge.

The air intake is located on the front side of the leading edge shown in Figure 14. The ventilation is taken into account in the model using a constant 1kg/s airflow running from left to right through the ribs. There is an opening in the rib that is larger than the size of the bleed pipe. On the back side of the leading edge the rib has an opening and here a constant pressure of 1 bar is applied. The result is a flow of air that cools the leading edge and prevents the leading edge internal from heating up too much by the bleed pipe.

Co-simulation approach

A transient analysis is carried out with an initial time step of 1 for both FEA and CFD. For the CFD model an automatic time stepping scheme is used called Courant-Friedrichs-Lewy

(CFL) time increment method and the time integration method is Galerkin. The numerical procedure to solve the pressure equation is using Bi-Conjugate Gradient, stabilised with a pre-conditioner algebraic multigrid. Furthermore, the inflow of air is smoothly introduced over a period of ten seconds.

The FEA model uses a fixed time increment, a direct solver and Full Newton. The maximum allowable temperature change per increment is 10 degrees and the maximum allowable emissivity change per increment is 0.1.

The Co-simulation agent uses a Gauss-Seidel coupling algorithm (FEA and CFD are solved sequentially). The target time step for both analyses is the FEA time step. The FEA uses so-called fixed time stepping, i.e. lockstep, and the CFD uses so-called subcycling, i.e. multiple time stepping within a targeted time step.

Main results

The heat flow in the leading edge is simulated for a situation where the aircraft is on ground with engine on. Several ambient temperatures are chosen as starting condition. Furthermore, cooling of the leading edge is accomplished via a constant mass flow of ambient air into the leading edge. The top part of the leading edge is heated up by a constant solar radiation that leads to a 344K temperature of upper skin. The bottom part of the leading edge is heated via reflection of solar radiation from the ground leading to a 327K temperature of lower skin. Hot air (473K) is heating up the bleed pipe which is modelled via sink temperature and convection coefficient. The right tank compartment is full of fuel at a temperature of 324K while in the left tank compartment the fuel has a temperature of 321K. In addition, the left tank compartment has a fuel level of 12cm from the tank bottom. The ullage space in the left tank compartment has a temperature of 326K.

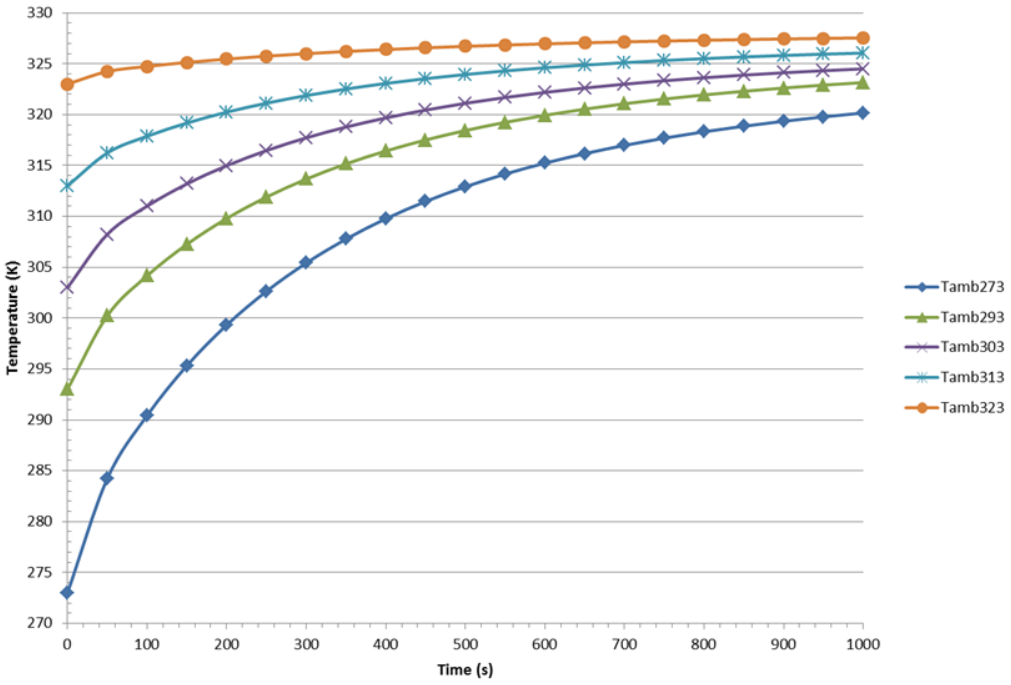

Figure 15: Temperature history of the front spar for different ambient starting conditions. The average temperature of the entire front spar is plotted.

Figure 15 shows the temperature history of the average temperature of the front spar with an output time step of 50 seconds. For different ambient starting conditions the final tempera-

ture approaches a value between 320K and 327K. Hence the effect of the hot bleed pipe is sufficiently compensated for by the cooling effect from outside venting air. Not all transient simulations have reached a final steady-state within 1000 seconds, but for all cases the steady-state temperature of the front spar is not expected to be significantly higher than that of the fuel inside the tank. Nevertheless, Figure 15 shows that the time it takes to reach the steady-state temperature depends on the ambient temperature, ranging from approximately 700 seconds for an ambient temperature of 323K more than 1000 seconds for 273K. The simulations are time consuming. A single analysis can take up to 2 days to run on a single cluster node with 20 cores. Application of such simulations is not practical for long transient simulations and in case the transient behaviour is to be predicted for ambient starting conditions additional to the ones depicted in Figure 15, e.g. during extensive trade-off studies at aircraft level in the early design stages. This is where a surrogate model of the transient behaviour is an added value.

5.2 Surrogate model

With the thermal model of the leading edge transient simulations can be performed. However the calculation time of one transient simulation is very long, e.g. up to 2 days for a simulation of 1000 seconds. The high computational effort makes it difficult to apply such simulation as part of efficient thermal analysis during the early design stage. Therefore a surrogate model has been derived using the transient surrogate modelling capability as described in subsection 4.3. The surrogate model of the leading edge predicts the wing spar temperature field at a certain time as a function of the wing spar temperature field during the previous time step and of the ambient air temperature. Equation 1 has been adapted to:

$$\vec{T}(t) \approx f\left(\vec{T}(t-\Delta t), T_{ambient}(t), \Delta t\right), \tag{3}$$

with $\vec{T}$ the temperature field in K, $T_{ambient}$ in K, t the simulation time, Δt the time step and f the analytical function representing the surrogate model. The ambient temperature remains constant during one transient simulation. Therefore a time delay of $T_{ambient}$ – like applied in equation 1 on the input u – is not considered relevant here.

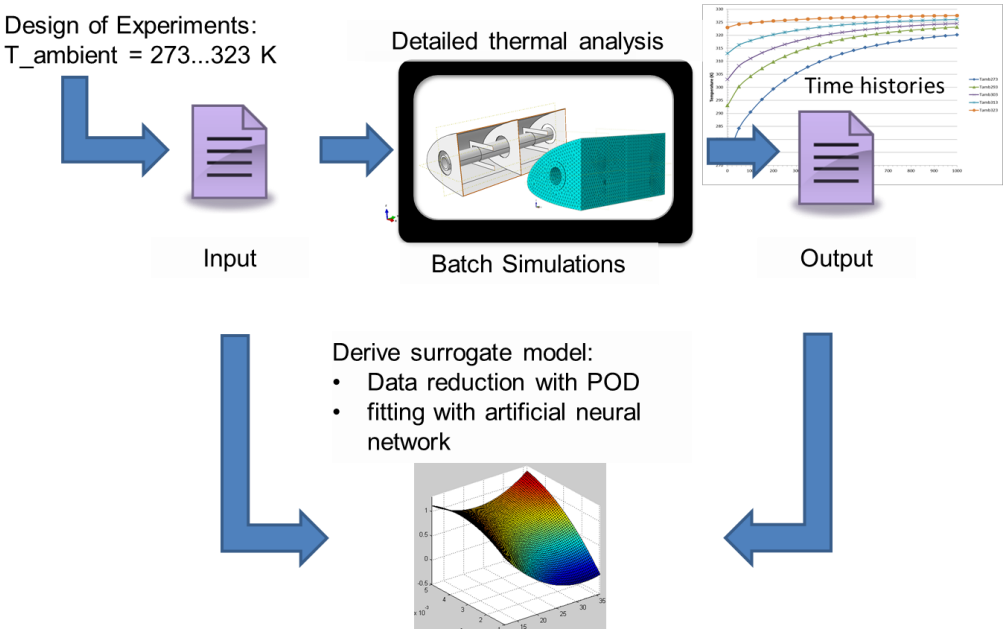

Figure 16: Surrogate modelling process scheme of the leading edge model.

Figure 16 illustrates the process of deriving the surrogate model. Five transient simulations have been performed, starting at different ambient temperatures. The ambient temperature has been varied between 273K and 323K. It is assumed that the temperature of the ventilation air through the leading edge is equal to the ambient temperature. Each transient simulation runs for 1000 seconds with an output time step of 50 seconds (cf. Figure 15). The resulting data represents the temperature field on the wing spar, calculated by the FEA analysis on 2700 nodes.

The spatial dimension of the data has been reduced using POD. The dimensionality has been reduced from 2700 nodes to 5 POD vectors that represent the relevant spatial behaviour over time. The data fitting problem is now reduced to fitting the time history of the POD coefficients, see also equation 2. A recurrent artificial neural network has been applied using a hidden layer of 5 nodes (see also Figure 9). The POD transformation functions have been integrated into the surrogate model such that the surrogate model predicts the complete temperature field at the 2700 spatial nodes. The predictions have a maximum error of 1.6K measured over the full data set of nodal temperatures.

Figure 17 depicts the surrogate model predictions over time together with the FEA data points compared by their spatial mean values. The transient predictions by the surrogate model have been extended to 2000 seconds in order to test the prediction of the steady-states. Within the time interval between 1000 and 2000 seconds the results have been compared with a number of simulation results from additional transient runs with the detailed FEA/CFD model, with output time step 250 seconds. Figure 17 shows that the predictions by the surrogate model between 1000 and 2000 seconds are close to the FEA data points, even though the surrogate model is extrapolating in this region. Close to 2000 seconds the extrapolation starts to give undesired effects: the curves bend downwards again. However, the surrogate model provides a useful means to estimate the steady-state temperatures and the times when they have been reached.

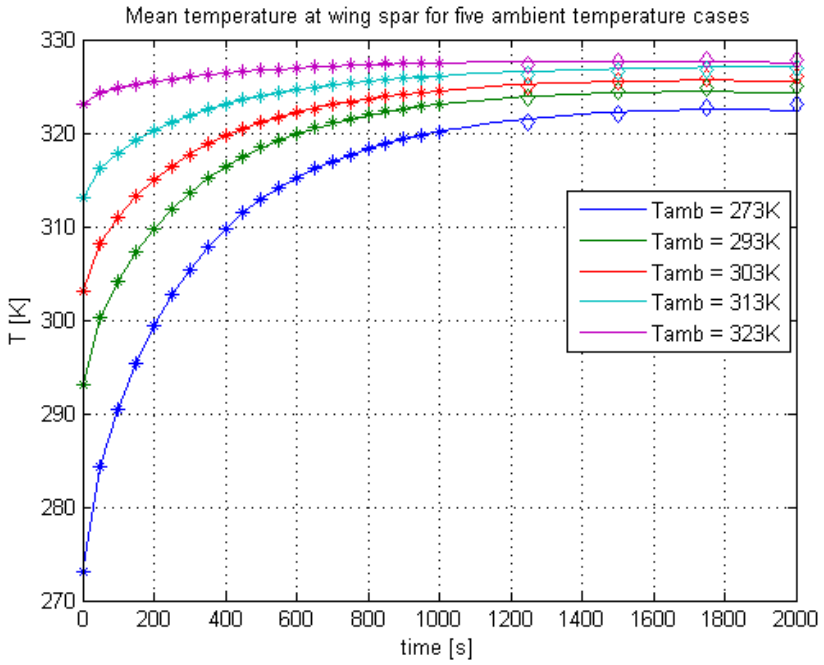

Figure 17: Spatial mean values of the surrogate model predictions (solid lines), fit data points provided by FEA (stars) and additional verification data points provided by FEA (diamonds) for the five simulation cases with ambient temperature variations.

5.3 Integrating the collaborative engineering capabilities

The integrated thermal analysis of a wing fuel tank usually involves experts from different disciplines and possibly different departments and organisations. Disciplines involved could concern fuel systems, wing structure, pylon, fuselage, and thermal analysis (FEA/CFD and systems). Organisations involved could be aircraft manufacturers, system and component suppliers, and simulation solution providers. This distributed process can be performed as a collaborative workflow, using Brics for orchestration and data exchange, and using surrogate modelling to bridge the gaps between different simulation tools of the disciplines and organisations. To demonstrate such distributed process a part of it has been realised, namely the derivation of the leading edge surrogate model as described in the previous section.

The calculation of the simulation FEA/CFD data set for creation of the leading surrogate model is a time-consuming process. Furthermore it may be challenging to obtain time slots and permissions for performing the simulation on appropriate computer hardware while using the specific software licenses that are needed. And when all simulations have been performed the generated data may be contained in very large files which are difficult to handle and access. Extraction of the relevant data needed for fitting is still to be performed in a post-processing step. It has been experienced that structuring the whole data calculation process into a workflow improves the efficiency of deriving the surrogate model. Brics supports the implementation of such a workflow, especially when the FEA/CFD thermal simulations are to be calculated by another partner than the one who derives the surrogate model. Figure 18 illustrates the implementation of the workflow. The detailed thermal analysis by means of batch simulations as illustrated in the upper part of Figure 16 is now realised through a distributed process with Brics. This process results in a data set from which the surrogate model can be derived.

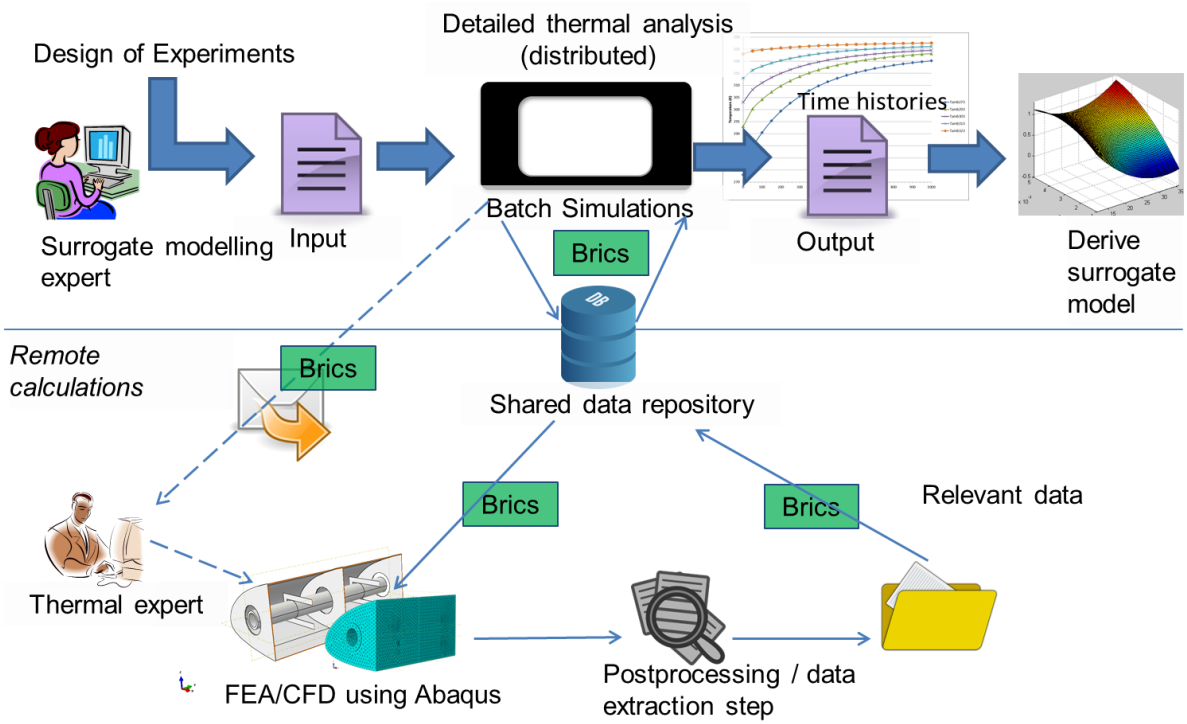

Figure 18: Distributed process for obtaining the data for a surrogate model of the leading edge. The upper half covers Figure 16, while in this figure the detailed thermal analysis is performed in a distributed way.

The surrogate modelling expert does not need to worry about how the data set of thermal behaviour of the leading edge is derived (and how the relevant parts are accessed). This is being performed by a thermal expert who may be part of another organisation or another department. The orchestration of the distributed calculation process and the exchange of the data is performed by Brics. At NLR thermal analysis, surrogate modelling, and distributed collaboration with Brics have been combined in order to derive a surrogate model of the leading edge thermal behaviour in an efficient way.

6 CONCLUSIONS

In the paper, we presented two collaborative engineering capabilities that support the need for high level of integrated system design of the aircraft and its subsystems: surrogate modelling and smooth cross-organisation workflow execution. The development of the capabilities took place in past projects, driven by needs and requirements from and discussions with stakeholders, and based on experiences gained with collaborative engineering and simulation solutions built. The capabilities have been further developed based on needs and distributed multi-partner simulation scenarios in the TOICA project. The application of the technologies has been illustrated by realistic examples of collaborative thermal analysis conducted in TOICA. An integrated application of the technologies has been demonstrated in a specific use case: wing leading edge thermal simulation for the thermal analysis of fuel tank.

Based on the experiences with solutions for distributed multi-partner scenarios based on Brics, and successful demonstrations thereof, we conclude that Brics enables the smooth cross-organisation execution of engineering workflows in a world full of security rules and measures, while still complying with the overall and organisation-specific security policies. Through its flexible integration with a variety of standard and COTS software, Brics also demonstrated to be applicable through the various organisations with minimum effort. The impact on the business of the individual organisations is kept to a minimum, apart from the ability to connect to extra-organisation workflows. As such, we conclude that Brics responds to the challenges of distributed cross-organisation collaboration, and hence contributes to effective and efficient collaboration among aircraft manufacturers and their supply chains.

As demonstrated in the fuel tank thermal modelling case, surrogate modelling has proven to make expensive, time-consuming and typically complex simulations of aircraft component behaviour available for quick thermal analysis. In collaborative simulations, it also caters for use of models that may not or cannot be shared with partners for intellectual property preservation reasons or that are restricted by their implementation tools. As such, surrogate modelling has proven providing valuable technology for cost and time efficient simulation during the preliminary design phase.

Furthermore, the detailed modelling of the thermal behaviour of a wing leading edge, based on FEA and CFD analysis, has been described. Such thermal modelling capability caters for detailed analysis of aircraft components that are to be manufactured with innovative materials, such as composites, in order to support certification of these components.

The capabilities have been further developed and demonstrated in the context of collaborative thermal analyses orchestrated by the aircraft manufacturer and performed throughout the supply chain, including small to medium enterprises. More generally, the capabilities can be applied beyond thermal analysis to support modelling and simulation for high level of integrated aircraft design in general, which increases the competitiveness of the European aeronautics industry. The generic character of the capabilities suggests investigating the applicability in other areas, such as automotive and ship-building.

The research leading to the results described in this paper has received funding from the European Community Seventh Framework Programme (FP7/2013-2016) under grant agree-

ment no. 604981 (TOICA, [2]). The authors would like to acknowledge all colleagues from the TOICA project partners who contributed to the success of the collaborative engineering and simulation studies that provided valuable input for the research described in this paper.

REFERENCES

[1] Advisory Council for Aviation Research and Innovation in Europe (ACARE), *Realising Europe's vision for aviation. Strategic Research & Innovation Agenda*, September 2012.

[2] EU FP7 TOICA Project public web page, http://www.toica-fp7.eu/. Last visited 4 February 2016.

[3] E.H. Baalbergen, W.F. Lammen, J. Kos, Mastering Restricted Network Access in Aeronautic Collaborative Engineering across Organizational Boundaries. *PDT Europe 2012*, The Hague, the Netherlands, 25-26 September 2012.

[4] E. Kesseler, M. Guenov eds. *Advances in Collaborative Civil Aeronautical Multidisciplinary Design Optimization.* Progress in Astronautics and Aeronautics Series, Vol. 233, American Institute of Aeronautics and Astronautics, Reston, VA, 2010.

[5] E.H. Baalbergen, W.J. Vankan, A. Kanakis, A practical approach for coordination of multi-partner engineering jobs in the design of small aircraft. CESAR Special Issue of *Journal Czech Aerospace Proceedings / Letecký zpravodaj, Journal for Czech Aerospace Research*, No. 3, p. 5-9, November 2009.

[6] P. Coleman, CRESCENDO consortium partners, *Innovations in collaborative modelling and simulation to deliver the Behavioural Digital Aircraft*. CRESCENDO Forum Participants Handbook, Toulouse, France, June 2012.

[7] E.H. Baalbergen, J. Kos, W.F. Lammen, Collaborative multi-partner modelling & simulation processes to improve aeronautical product design. T. Melin, P. Krus, E. Vinterhav, K. Övrebö eds. *4th CEAS Air & Space Conference*, Linköping, Sweden, September 2013.

[8] B.I. Soemarwoto, A. Nugroho, E.H. Baalbergen and A. Aribowo, CFD-based collaborative design optimization using eCFD. *29th Congress of the International Council of the Aeronautical Sciences*, St. Petersburg, Russia, September 7-12, 2014.

[9] Olivier Tabaste, Cedric Campguilhem, Thermal Trade off sustained by multi disciplinary and multi level optimization. Submitted to ECCOMAS 2016, 5-10 June 2016 Crete Island, Greece, 2016.

[10] Declan C. Nolan, Chris M. Tierney, Cecil G. Armstrong, Trevor T. Robinson, Jonathan E. Makem, Automatic dimensional reduction and meshing of stiffened thin-wall structures. *Engineering with Computers*, Volume 30, Issue 4, pp 689-701, October 2014.

[11] Jorge Camacho Camasero, Automatic generation of 2D axisymmetric finite element models from 3D quasi-axisymmetric components. Submitted to ECCOMAS 2016, 5-10 June 2016 Crete Island, Greece, 2016.

[12] *Thermal Modeling Handbook*, K&K Associates 1999-2000, Version 97.003.

[13] W.J. Vankan, Predicting well-being in aircraft cabins, Results from the ICE project, NLR Technical Publication, NLR-TP-2009-048, 2009.

[14] W.J. Vankan, W.F. Lammen, J. Kos and R. Maas, Complementary approximate modeling in Matlab and Modelica. *5th EUROSIM Congress on Modelling and Simulation*, 2004.

[15] W.J. Vankan, W.F. Lammen, and R. Maas, Meta-modeling and multi-objective optimization in aircraft Design. E. Kesseler, M. Guenov eds. *Advances in collaborative civil aeronautical multidisciplinary design optimization. Progress in Astronautics and Aeronautics*, Vol. 233, chapter 6, American Institute of Aeronautics and Astronautics, Reston, VA, 2010.

[16] Wim Lammen, Philipp Kupijai, Daniel Kickenweitz, Timo Laudan, Integrate engine manufacturer's knowledge into the preliminary aircraft sizing process. *Aircraft Engineering and Aerospace Technology: An International Journal*, Vol. 86, Iss. 4, pp. 336-344, 2014.

[17] W.J. Vankan, R. Maas, Surrogate modelling for efficient design optimisation of composite aircraft fuselage panels. *27th International Congress of the Aeronautical Sciences (ICAS 2010)*, Nice, France, 2010.

[18] Partners of the Modelica Association Project "Functional Mock-up Interface", *Functional Mock-up Interface*, https://www.fmi-standard.org/, last visited 4 February 2016.

[19] S. Volkwein, Model reduction using proper orthogonal decomposition. Lecture Notes, Institute of Mathematics and Scientific Computing, University of Graz, Austria, 2011. See http://www.uni-graz.at/imawww/volkwein/POD.pdf, last visited 4 February 2016.

[20] MATLAB Neural Networks Toolbox User's Guide, http://www.mathworks.com, last visited 4 February 2016.

[21] Abaqus documentation, Dassault Systèmes, release 6.14, 2014.

ECCOMAS Congress 2016
VII European Congress on Computational Methods in Applied Sciences and Engineering
M. Papadrakakis, V. Papadopoulos, G. Stefanou, V. Plevris (eds.)
Crete Island, Greece, 5–10 June 2016

VISUAL ANALYTICS FOR EVALUATION OF VALUE IMPACT IN ENGINEERING DESIGN

Timoleon Kipouros[1] **and Ola Isaksson**[2]

[1] University of Cambridge, Department of Engineering,
Trumpington Street, Cambridge, CB2 1PZ, UK
tk291@eng.cam.ac.uk

[2] GKN Aerospace Engine Systems, R&T,
46181, Trollhättan, Sweden
ola.isaksson@gknaerospace.com

Keywords: Engineering Design, Computational Design, Interactivity, Parallel Coordinates, Aerospace, Decision Making, Value Assessment, Value Driven Design, Visual Analytics.

Abstract. *Many traditional engineering design processes in industry have evolved, and nowadays they are supported by computational tools and methods. As a consequence, apart from the quantity of information and data, a network of simulation methods produces information at various level of detail and nature. Furthermore, human interactivity is an essential consideration when building and designing such computational systems, simply because there is a requirement to process and understand this information that is produced during an engineering project effectively in real time.*

We introduce here a Visual Analytics perspective in computational engineering design process, as well as tightening the interactive analysis of engineering data with Parallel Coordinates and Scatter plots. To demonstrate the benefits of the proposed approach we use a case study that describes the design of an aero engine component critically suffering from the operating conditions but at the same time from the change of specifications and customer requirements.

Some of the benefits include minimisation of rework through early identification of behaviour in selected Value Dimensions, as well as the ability to trade product performance (e.g. weight, minimum expected life) with internal stakeholder expectations (e.g. higher overall productivity of aircraft, low degree of aircraft modifications, faster design convergence). Furthermore, the proposed method develops the ability to identify architectural options that align with Value Creation Strategies, but also the evaluation of design options in advance of physical trade studies.

1 INTRODUCTION

These days, people perceive for granted complex engineering products, such as an aircraft, and most importantly use them in their daily routine. As a result, the requirements and specifications should meet the expectations of the customers and stakeholders simultaneously. In other words, the technical and engineering objectives that usually drive a design process, should now reflect the impact of customer satisfaction. In our example, a passenger would wish to have more leg space for comfort, better quality of air in the cabin, and cheap ticket price, and expect to be able to reach at the airport and spend minimum amount of time during security control and boarding. But how do these expectations translate to engineering performance indicators? How these metrics can be modelled? What are the relationships between such properties? We believe Visual Analytics and Big Data management can assist towards finding answers to these questions, and perhaps more importantly to create new questions that weren't thought before, but will further support the human imagination and creativity.

In an engineering design process, as illustrated in Figure 1, we start with the description of a problem, which we then need to formulate and model, often, in a computational/simulation environment. The same problem can have many model instances depending on the level of detail that is described, or even the point of view of the analysis. Each of these problem formulations are then explored, almost simultaneously through design optimisation studies, simulation and analysis tools, or similar. Before we are able to cascade this information downstream in the process for decision making, we need to collect, synthesise, and process the data.

The process to collect this data, most of the times, has a complex structure, since many different analysis and simulation tools are used during an engineering design project. Furthermore, in many cases they are located in geographically different sources.

The mere amount of aspects that need to be considered simultaneously when making decisions during product development is one of the main reasons why synthesis in engineering design relies on experienced and advanced human cognitive skills. Since the introduction of computational support, the ability to design and optimise products have made several leaps forward. As one example, the actual definition and representation of a compressor, or turbine blade is no longer possible to be defined by hand. Advances in Computational Fluid Dynamics and the following ability to optimise such designs have enabled efficiency of compressor design to advance from 9X% to over 99% in just a couple of decades. A second aspect is that to differentiate on the marketplace, success is increasingly determined by how well the product performs from multiple perspectives.

From an industrialist's perspective, we are now at a point where we no longer create a single concept with small variations of forthcoming products, but rather exploring entire design spaces using advanced computer tools. Engineers have the capability to produce more data per instance, for more variants and for more situations than ever before.

There is a need to visualise the data and more importantly to be able to interpret and understand what these data mean in a sensible way. Traditional ways of the representation of the behaviour of a design solution include the use of animations of e.g. deflection and distortion of a product (modal analysis, stress plots, etc.). Where the engineer could display results of one, or few alternatives, now is no longer feasible due to the multitude of variants and circumstances (loads) that the product is exposed to. Many aspects need to be explored for a range of alternative solutions. As a consequence, even if it is possible to generate such information, the analysis of a multi-parameter design space for many alternatives drive the need to interact and understand much richer and more complex dataset.

Hence, we need to complement other visualisation techniques to enable rich understanding of many alternatives subject to variation to many variables or aspects. This is also another major contribution of this paper.

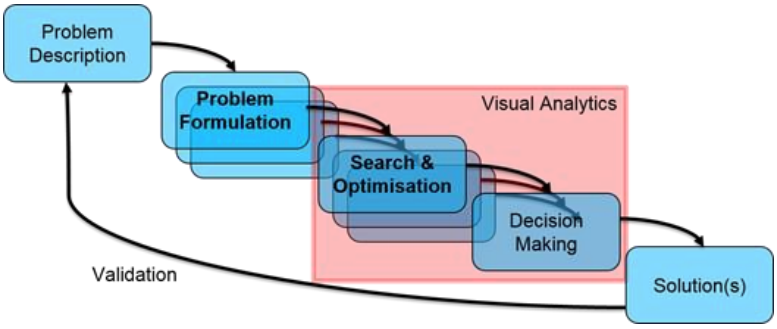

Figure 1: High level view of an engineering design process supported by visual analytics tools and methods.

2 BACKGROUND AND LITERATURE

Decision making during development is by nature multi-disciplinary, and several authors have proposed ways on how to explore design spaces in many dimensions. The MOVA framework by Woodruff et.al. [6] extended a finite dimensional design strategy to a more general framework to include multiple objectives, and compared the approach with alternative decision making strategies. Keim et al [15] summarised the area of Visual Analytics as a result from a three year European project, and concluded that assisting designers using visual analytic systems was one of the key challenges for the future.

In Figure 2 it is shown a schematic representation of a concept of how to facilitate human interactivity within the automated computational engineering design cycle.

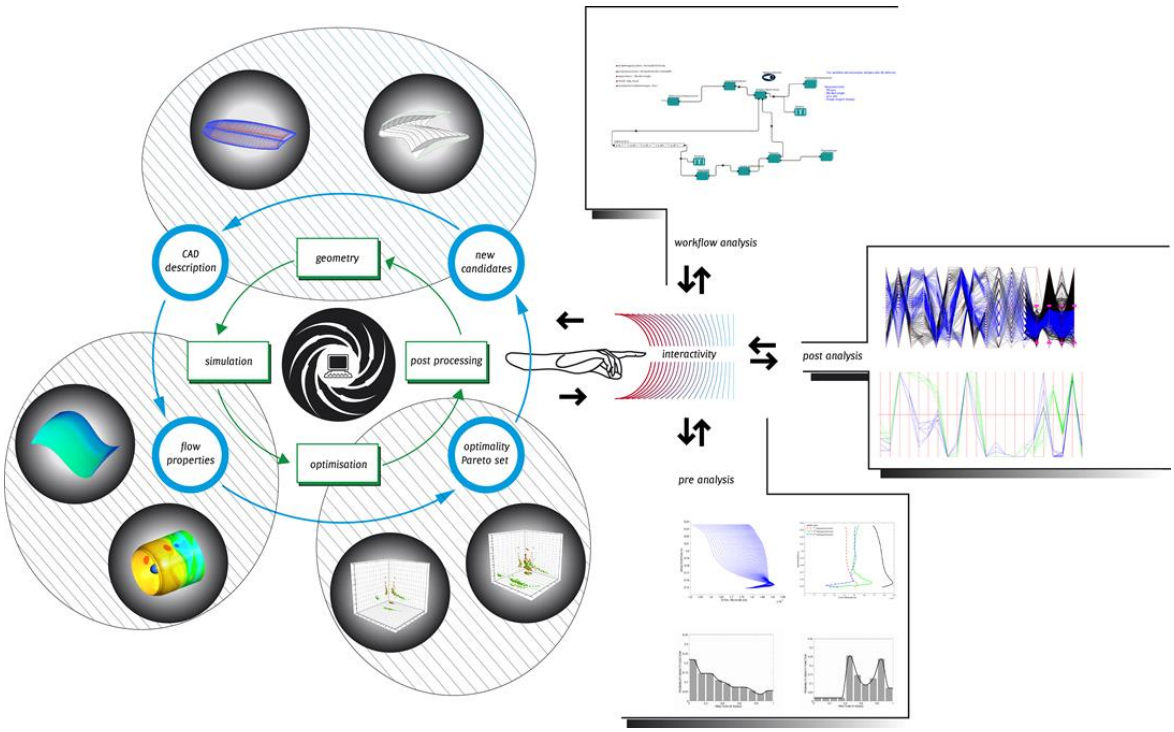

Figure 2: Schematic representation of an interactive optimisation engineering design process [10].

The automated computational design cycle is shown on the left, and at the heart of the overall process is the human, who interactively analyses the results of the process, understands the complexities and infuses this knowledge in real-time into the automated process.

Although engineering design largely relies on the use of numerical and computational analysis tools, the synthesis and insights enabling design decisions still expect design engineers to understand the breadth of the design problem. There is a human aspect on decision making where the influence of appearance and visualisation has been shown to affect decision making in design situations. The influence of colours in visualising results has been previously applied in the area of Value Driven Design [16]. It has further been demonstrated the effect of contextual information of product oriented data and observed the effect on engineering team attention to how data was visualised [14]. The ability to interact with alternatives and changing conditions, such as product requirements changes and/or preference changes are clearly emphasised.

Engineering Design is a highly iterative activity, where the definition of forthcoming products is typically matured through managing iteration and changes. Any decision support method needs to facilitate the study of variation, trading, etc. Data is typically produced in engineering tools, but also in less quantitative manner. Subjective metrics such as confidence, appearance, risk, etc co-exist with quantifiable aspects such as stresses, strains etc.

Parallel coordinates (||-coords) can support and facilitate the possibility to identify trends and relationships between technical properties and specification characteristics when these are simultaneously represented in a multi-dimensional domain.

There are platforms and frameworks under investigation and development that facilitate the human interaction and drive/guide optimisation studies. But also offer visual representation of the product in an auxiliary engineering analysis environment (i.e. Workways [12]).

3 AN ENGINEERING EXAMPLE

The initial aim and objective of this work was to identify the means to connect high level stakeholder and customer expectations and requirements to actual technical key performance characteristics and indicators. We use the Value Assessment method as introduced in [2] and expanded in [1]. Here, we only provide a brief description of the main stages of the Value Assessment process. For more details the reader should refer to [1] and [2].

3.1 Value Driven Design Methodology

A Value Assessment process can be best described within the Value Driven Design process as shown in Figure 3.

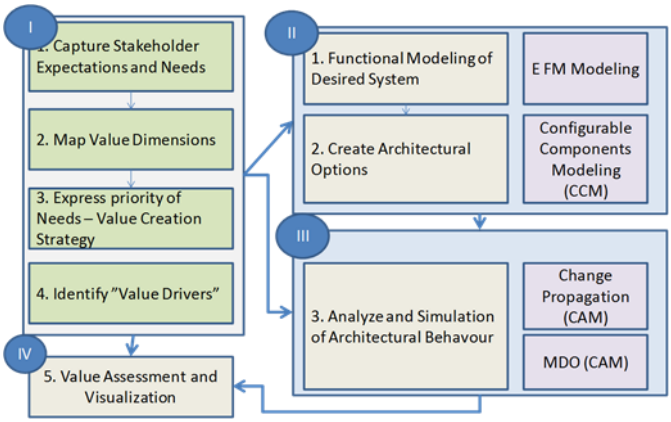

Figure 3: The four phases of the Value Driven Design methodology.

In phase I the stakeholder expectations and needs are captured and linked with Value Dimensions and Value Drivers. The often tacitly expressed expectations are organised into a Value Creation Strategy (VCS), this is the prioritised set of stakeholder needs that can be influenced in design via the Value Drivers. The Value Drivers are consequently aspects wherein it is possible to define the design parameters to explore. Typically, the breadth of information in phase I is vast. Explicit and numerically defined expectations, such as expected range or target weights are mixed with tacit and ill-defined expectations, such as being "sustainable" or "easily maintainable", "easy to integrate into a system" etc. Explicit and quantifiable modeling may not be feasible, not at least in early phases, but may still be necessary to include in decision making.

The second phase takes the VCS as input and serves to support the design synthesis stage. Searching for solutions in the design space is divided into an architectural modeling phase, in this case using an extended function means modeling approach, where the functionality of the systems is modeled and the alternative design solutions are defined. At this phase, the characteristics of the forthcoming design is modeled for all relevant candidate design solutions. One way of representing an architectural option is via Design Structure Matrices (DSM's), where the pattern of internal dependencies of design objects provides a quantifiable pattern of the architectural option (Figure 4).

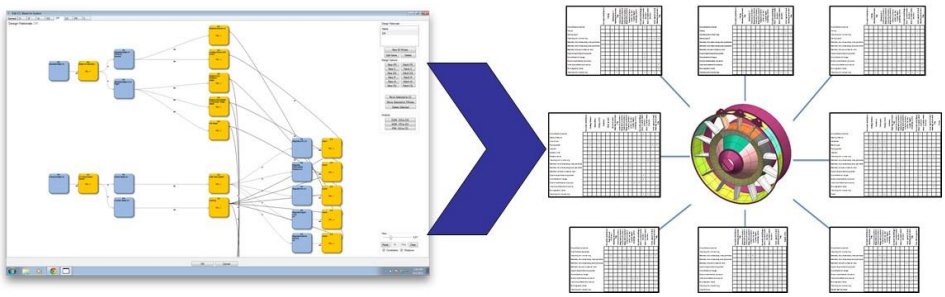

Figure 4: Through Function-Means modeling in CCM (Configurable Components Model) environment [17], alternative architectures of a RTS engine component are exported as DSM's.

The third phase introduces analytical tools that analyse the behaviour of the alternative architectures along with the evaluation of the properties identified as Value Dimensions in phase I. One efficient method to understand and explore the behaviour of the product is the Change Propagation Method (CPM) [18], where dependencies between the architectural objects are assigned with probability and impact information. Change propagation analysis then generate information of how an architectural definition reacts to changes and perturbations (Figure 5). It has been demonstrated that it is possible to define first order relations to several stakeholder needs, such as "integration ability" and "development process efficiency" [1]. Of course, more traditional methods such as Finite Element Analysis (FEA) and Computational Fluid Dynamics (CFD) are also possible to be applied at this stage of the Value Driven Design methodology.

The focus of this paper is the fourth phase where the results from the simulated behaviour of all alternative architectural studies are collected and organised. Using ||-coords as a means of visualisation, the experience and intuition of the designer can be combined with the patterns discovered using analytical methods. Since multiple aspects and multiple architectural options are studied, the pattern recognition abilities of humans is used to facilitate interactive exploration and search for suitable combinations of input and output.

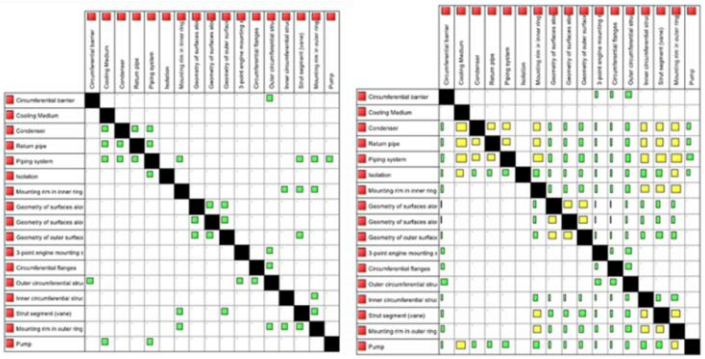

Figure 5: A DSM representation of the product and the combined risk matrix as calculated in CAM (Cambridge Advanced Modeller) environment.

3.2 A Brief Description of the Case Study

The method using visual analytics is applied onto a case study. The product studied is a sub system of an aircraft jet-engine, a rear turbine structure (RTS) as shown in Figure 6. From an applied perspective, the RTS is a tightly integrated structural component of the jet engine used to propel the aircraft and provide power to the aircraft also for other purposes. A re-engine scenario where the aircraft manufacturer wishes to upgrade the performance of the aircraft by replacing and/or upgrading the existing engine type is considered here. The engine manufacturing consortia consisting of the jet engine OEM and its design partners need to understand the new consequences and assess what design options exist that are necessary to satisfy the ambitions of the re-engine scenario.

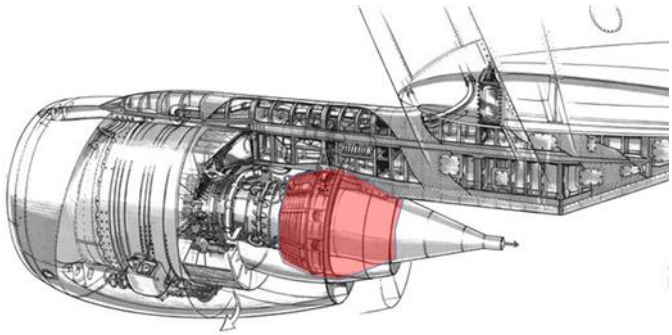

Figure 6: Re-engine scenario: turbine exit structure (*illustration from Flight Magazine).*

In the European project TOICA, the scenario is defined as a context, wherein the Value Assessment Methodology, described in [1] and introduced above has been followed. In this paper we focus on phase IV but capture portions of the dataset for clarification and to present the sources of information used when assessing value in the interactive way using ||-coords. From phase I, a range of Value information is captured, each linking Stakeholder Expectations to Value Drivers. In Figure 7 this is illustrated for the "Higher Productivity of Aircraft" Stakeholder Expectations. This expectation eventually is influenced by weight since this has a first order influence on payload, and on minimum expected life which has an equal direct influence in the operating cost of an aircraft.

Stakeholder Expectations	Stakeholder Needs	Value Dimensions	Value Drivers
Higher productivity of aircraft	Increased payload	Mission performance	Weight
	Reduced operating cost		Minimum expected life

Figure 7: Expression of generic stakeholder expectations and needs, and the mapping to value dimensions and value drivers.

Since the stakeholder expectation of "Higher productivity of Aircraft" and both of its Stakeholder Needs are attributed to the operation of the aircraft, the property of "Mission Performance" was the right classification of value dimension. Notably, there are other Value Dimensions, addressing other aspects of stakeholders, such as how costly the products are to integrate into a system etc.

The weight of a component is a good example of a Value Driver that can be assigned as a firm and quantifiable target. It can equally be related to the impact on productivity of the aircraft, since frequently is the case in aerospace that weight is given a direct relation to productivity of the aircraft. In design phases, it is equally common to formulate penalty relations in monetary terms if target weights are not met.

In a similar manner, there are relations with the expected life and the productivity of operating the aircraft. Maintenance schedules, repair and inspection costs are directly related to the satisfaction of a minimum expected life.

Both minimum expected life and weight of components are examples of quantifiable value drivers. To evaluate weight and expected life, there is effectively no mature way of analysing this impact for new alternative designs without modeling the CAD definition (calculation of volume) and making physics based evaluations using computational techniques such as finite element analysis (calculation of the stresses and strains) and some life analysis technique (such as crack propagation and/or fatigue analysis).

The actual relations between weight and performance, or minimal life and operating cost are business sensitive data and not disclosed explicitly in this paper.

4 INTERACTIVE ANALYSIS WITH PARALLEL COORDINATES

4.1 Methodology

The inputs to the interactive analysis for Value Assessment are initially the results from the functional analysis and CPM analyses, as well FEA and CFD analyses. Parallel coordinates are used to display simultaneously the results onto each value dimension in the same plot as the design variables. The architect can work interactively with the data set, and filter out architectures in several ways, either via filters on the parameters or via a graphical plot in 2D where two selected parameters are compared to each other. As the concepts are refined, more advanced modeling and analysis tools can be used to predict the behaviour or the concept.

The first step (to the left below) operate on the pre-embodiment DSM data. In this step alternative variants are down-selected, and the most promising variants are selected for further refinement. Selection of variants allow physical and parametric geometrical modeling and finite element analyses to be conducted. The same tool and interactive analysis is re-used with a richer data set. This is described to the left in Figure 8.

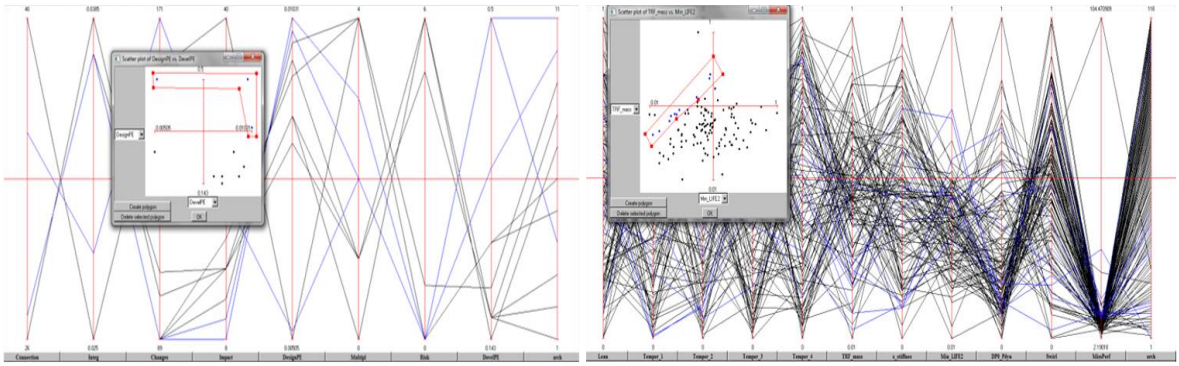

Figure 8: Parallel coordinates and interactive analysis and visualisation of impact of stakeholder needs and value dimensions enabled using multi-disciplinary analysis and design tools.

Similar examples and methods of interactive analysis can be found in [7], [8], [9], [10], [11], [12], and [13].

5 FUTURE WORK AND CONCLUSIONS

The approach presented, and the interactive way of analysing datasets was used to assess initial architectural descriptions based on DSM representations and CPM as analysis method. The same visual analytics tools is re-used as the data set is enriched through more detailed and refined models of the architectures. In particular, the visual and interactive tool has been demonstrated effective as a means to facilitate the communication between architects and different engineering design teams. The ability to link "high level" objectives through the Value Creation Strategy, to the design variables characterising the various architectures has been demonstrated successfully. Since information in complex product development typically engage many disparate competences and specialist teams, the value of communicating the expectations and technical results are decisive. The Visual Analytics methods and tools are highly suitable to combine data from different sources and of different nature.

In particular, the ability to analyse the often extensive data sets by filtering, selecting and searching for combinations of parameter values is an important feature. This is typically the task for multidisciplinary optimisation specialists, whereas through the visual analytics approach different stakeholders can analyse the datasets simultaneously. Based on this type of interaction during the development of the methods and tools in the TOICA project, engagement and critical understanding were aspects that were significantly improved.

Here we also list the identified benefits so far, and emphasis is given on further potentials and contributions in the engineering design field.

These include:

- Ability to represent many design alternatives that were evaluated simultaneously for many variables
- Aggregation of information, where dynamic navigation in resolution and underlying assumptions can be done interactively
- Analysis supported by the ability to search for better and more suitable solution areas
- Describe the logic-disciplinary development via computational tools
- Ability to combine disciplines (multi-physics)
- Ability to process large amount of data (computational power)

- Ability to automatically generate the necessary designs and their variation (design automation, KBE, etc)
- Differentiation in business by tailoring and customising products and services (i.e. more variations and aspects ageing)

But also other enabling means to support decision making:

- Impact of component performance to global performance
- Identify meaningful trade-offs between requirements and design parameters
- Understand the design space and find answers to the questions:
    - What are the important parameters?
    - How the requirements compete?
    - Where are the most promising solutions?
- Manage risk

For further work there are several directions of interest. One is to further strengthen the interaction with different scientific communities, such as the engineering disciplines, computer science, visual analytics communities, mathematics and cognitive decision making specialists.

Secondly, already in its current state of maturity, there is an exploitation track to explore. The needs and contexts prevailing in decision making situations during product development can already now benefit from the ability to bring in complex data sets, link them to high level objectives and increase interaction with specialists. There is a route to more clearly understand, demonstrate and implement support for decision making in complex product and production development situations. The ability to represent and characterise architectures via internal and external dependencies is a promising area, where research is needed to enhance representation, definition and evaluation methods and tools. It is likely that the actual decision making process throughout a development project will continue to develop new practices. One of which is the facilitation of more interactive, visual and analytical tools.

Acknowledgements

The research leading to these results has received funding from the European Seventh Framework Programme (FP7/2007-2013) under grant agreement n^{o}604981, TOICA (www.toica-fp7.eu).

REFERENCES

[1] T. Kipouros, O. Isaksson, Integrating value assessment into the computational engineering design cycle, *in OPT-i 2014: International Conference on Engineering and Applied Sciences Optimization*, Kos Island, Greece, Paper 3620, 2014.

[2] O. Isaksson, M. Kossmann, M. Bertoni, H. Eres, A. Monceaux, A. Bertoni, S. Wiseall, X. Zhang, Value-driven design: a methodology to link expectations to technical requirements in the extended enterprise, *in INCOSE International Symposium*, Philadelphia, PA, 2013.

[3] J.T. Oden, T. Belytschko, I. Babuska, T.J.R. Hughes, Research directions in computational mechanics. *Computer Methods in Applied Mechanics and Engineering*, **192**, 913-922, 2003.

[4] R.C Basole, A. Qamar, H. Park, C.J.J. Paredis and L.F. McGinnis, "Visual analytics for early-phase complex engineered system design support," *IEEE Computer Graphics and Application*, vol. 35, pp. 41-51, 2015.

[5] X. Yan, M. Qiao, J. Li, T.W. Simpson, G.M. Stump and X. Zhang, "A work-centered visual analytics model to support engineering design with interactive visualization and data-mining," in *45th Hawaii International Conference on System Sciences*, IEEE, pp. 1845-1854, 2012.

[6] M.J. Woodruff, P.M. Reed and T.W. Simpson, "Many objective visual analytics: rethinking the design of complex engineered systems," *Struct Multidisc Optim*, vol. 48, pp. 201-219, 2013.

[7] A. Inselberg, "Parallel coordinates: visual multidimensional geometry and its applications," *Springer*, New York, 2009.

[8] D-H. Ham, "The state of the art of visual analytics," *Springer Proceedings in Physics*, vol. 135, pp. 213-222, 2010.

[9] S.D. Scott, N. Lesh and G.W. Klau, "Investigating human-computer optimization," *Mitsubishi Electric Research Laboratories*, TR2001-39, 2001.

[10] T. Kipouros, "Human-in-the-loop computational engineering design," in *EVOLVE International Conference*, 2014.

[11] A. Lewis and T. Kipouros, "Methods of interactive optimisation in engineering design," in *13th International Conference on Computer Applications*, 2015.

[12] H.A. Nguyen, D. Abramson, T. Kipouros, A. Janke and G. Galloway, "Workways: interacting with scientific workflows," *Concurrency and Computation: Practice and Experience*, 2015. DOI: 10.1002/cpe.3525.

[13] J. Heinrich, "Visualization techniques for parallel coordinates," *PhD Thesis*, University of Stuttgart, 2013.

[14] M. H. Eres, M. Bertoni, M. Kossmann, J. P. Scanlan, "Mapping customer needs to engineering characteristics: an aerospace perspective for conceptual design". *Journal of Engineering Design*, DOI: 10.1080/09544828.2014.903387, 2014.

[15] D.A. Keim, J. Kohlhammer, G. Ellis, F. Mansmann (eds) (2010) "Mastering the information age - solving problems with visual analytics" *Eurographics*, available at http://www.vismaster.eu/wp-content/uploads/2010/11/VisMaster-book-lowres.pdf

[16] A. Bertoni, M. Bertoni, O. Isaksson, , "Communicating the Value of PSS Design Alternatives using Color-Coded CAD Models", in J. Hesselbach and C. Herrmann (eds.), *Functional Thinking for Value Creation: Proceedings of the 3rd CIRP International Conference on Industrial Product Service Systems*, Technische Universität Braunschweig, Braunschweig, Germany, May 5th - 6th, 2011

[17] D. Raudberget, C. Levandowski, O., Isaksson, T. Kipouros, H. Johannesson, J. Clarkson, "Modelling and assessing platform architectures in pre-embodiment phases through set-based evaluation and change propagation", *Journal of Aerospace Operations*, vol. 3, no. 3,4, pp. 203-221, 2015

[18] P. Clarkson, C. Simons and C. Eckert, "Predicting change propagation in complex design," *J Mech Des* 126, (2004), pp. 788-797

ECCOMAS Congress 2016
VII European Congress on Computational Methods in Applied Sciences and Engineering
M. Papadrakakis, V. Papadopoulos, G. Stefanou, V. Plevris (eds.)
Crete Island, Greece, 5–10 June 2016

COMBINING AN RBF-BASED MORPHER WITH CONTINUOUS ADJOINT FOR LOW-SPEED AERONAUTICAL OPTIMIZATION APPLICATIONS

E.M. Papoutsis-Kiachagias[1], M. Andrejašič[2], S. Porziani[3], C. Groth[4], D. Eržen[2], M.E. Biancolini[4], E. Costa[3], and K.C. Giannakoglou[1]

[1] National Technical University of Athens (NTUA), School of Mechanical Engineering,
Parallel CFD & Optimization Unit, Greece,
e-mail: vaggelisp@gmail.com, kgianna@central.ntua.gr
[2] PIPISTREL d.o.o. Ajdovščina, R&D, Department of Aerodynamics, Slovenia,
e-mail: matej.andrejasic@pipistrel.si, david@pipistrel.si
[3] D'Appolonia S.p.A. Italy,
e-mail: stefano.porziani@dappolonia.it, emiliano.costa@dappolonia.it,
[4] University of Rome Tor Vergata (UTV), Italy,
e-mail: Corrado.Groth@uniroma2.it, biancolini@ing.uniroma2.it

Keywords: Continuous Adjoint, RBF Morphing, Aeronautical Optimization

Abstract. *In this paper, the continuous adjoint method, developed by NTUA in the OpenFOAM® environment, is coupled with an RBF-based morpher developed by UTV to tackle optimization problems in low-speed aeronautics. The adjoint method provides a fast and accurate way for computing the sensitivity derivatives of the objective functions (here, drag, lift and losses) with respect to the design variables. The latter are defined as a set of variables controlling a group of RBF control points used to deform both the surface and volume mesh of the computational domain. The use of the RBF-based morpher provides a fast and robust way of handling mesh and geometry deformations, facing two challenging tasks related to shape optimization with the same tool. The coupling of the above-mentioned tools is used to tackle (a) the minimization of the cooling losses for an electric motor installed on a lightweight aircraft, by controlling the cooling air intake shape and (b) the shape optimization of a glider geometry targeting maximum lift-to-drag ratio by mainly optimizing the wing-fuselage junction. Regarding problem (a), a porous media is utilized to simulate the pressure drop caused by the radiator; the adjoint to this porosity model is developed and presented. This work was carried out in the framework of the EU-funded RBF4AERO project and the presented methods are available through the RBF4AERO platform (www.rbf4aero.eu).*

1 INTRODUCTION

During the last years, CFD-based aerodynamic shape optimization has been attracting the interest of both academia and industry. The constituents needed for executing an automated shape optimization loop include the flow solver, the geometry parameterization (the parameters of which act as the design variables), an optimization method capable of computing the optimal values of the design variables and a way to adapt (or regenerate) the computational mesh to each candidate solution.

Nowadays, a great variety of in-house and commercial flow solvers exist. In the study presented in this paper, the steady-state flow solver of the open-source CFD toolbox, OpenFOAM®, is used to numerically solve the Navier-Stokes equations for incompressible, turbulent flows.

Shape parameterization techniques can be divided into two categories, i.e. those parameterizing only the surface to be optimized and those which also deform the surrounding mesh nodes. In the context of an optimization method, the former rely on, among others, the normal displacement of surface wall nodes [14], the displacement of control points of Bézier–Bernstein or NURBS curves or surfaces and the variation in CAD parameters [15, 17]. The latter include volumetric B-splines or NURBS [9], Radial Basis Functions (RBFs) [6, 4], the harmonic coordinates method, etc. The great advantage of this category is that the interior of the computational mesh is also deformed, avoiding, thus, costly re-meshing and allowing the initialization of the flow field from the solution obtained in the previous optimization cycle, since the mesh topology is preserved. In this paper, a number of parameters controlling the positions of groups of RBF control points are used as the design variables, using technology and methods developed in the context of the RBF Morph software [3].

Gradient-based optimization methods require a high effort to develop and maintain but can have a cost per optimization cycle that does not scale with the number of design variables, when the adjoint method is used to compute the gradients of the objective function. Both discrete and continuous adjoint methods, [5, 12], have been developed. In this work, a continuous adjoint method implemented on the NTUA in-house version of the OpenFOAM® software is used.

The above-mentioned tools are combined in order to form an automated optimization loop, targeting the maximization of the lift-to-drag ratio for a glider plane and the cooling losses minimization caused by the cooling system of a small electric airplane.

The work presented in this paper was carried out in the framework of the RBF4AERO Project which aims at developing the RBF4AERO Benchmark Technology, namely a numerical platform conceived to face the requirements of top-level aeronautical design studies such as multi-physics and multi-objective optimization, fluid-structure interaction (FSI), adjoint-driven optimization and ice accretion simulation. Based on the RBF mesh morphing technique, the platform allows to significantly boost the aerodynamic design process and a relevant impact is then expected in the ever-growing technological demand posed by aeronautical manufacturers in relation to the performance and reliability of aircraft components.

2 THE CONTINUOUS ADJOINT METHOD

In this section, the formulation of the continuous adjoint PDEs, their boundary conditions and the sensitivity derivatives (gradient) expression are presented in brief. The interested reader could find more about the adjoint method used in [18, 19, 13]. Since both geometries to be studied operate at low air speeds, the development is based on the incompressible RANS equations.

2.1 Flow equations

The mean flow equations read

$$R^p = -\frac{\partial v_i}{\partial x_i} = 0 \tag{1a}$$

$$R_i^w = v_j \frac{\partial v_i}{\partial x_j} + \frac{\partial p}{\partial x_i} - \frac{\partial \tau_{ij}}{\partial x_j} + f_i = 0 \tag{1b}$$

where v_i are the velocity components, p is the static pressure divided by the constant density, $\tau_{ij} = (\nu + \nu_t)\left(\frac{\partial v_i}{\partial x_j} + \frac{\partial v_j}{\partial x_i}\right)$ are the components of the stress tensor, ν and ν_t the kinematic and turbulent viscosity, respectively. In eq. 1b, term f_i stands for any external force acting on the fluid. In one of the applications studied in section 5, a non-linear, anisotropic porosity model is used based on the Darcy-Forchheimer law, [1]. In this case, f_i reads

$$f_i = r_{ij} v_j \quad , \quad r_{ij} = \nu D_{ij} + \sqrt{v_k^2} E_{ij} \tag{2}$$

where D_{ij} and E_{ij} are constant Darcy and Forchheimer tensorial coefficients.

Eqs. 1 along with the turbulence model PDE(s) comprise the primal or state equations. In the applications presented in section 5, the Spalart-Allmaras, [16], and k-ω SST, [10], models are used. Though the continuous adjoint to both turbulence models has been developed by some of the authors, [18, 13, 8], the remainder of the continuous adjoint formulation will neglect their differentiation in the interest of space.

2.2 General objective function

Let F be the objective function to be minimized by computing the optimal values of the design variables $b_n, n \in [1, N]$. A general expression for an objective function defined on (parts of) the boundary S and the computational domain Ω is given by

$$F = \int_S F_{S_i} n_i dS + \int_\Omega F_\Omega d\Omega \tag{3}$$

where $\mathbf{n}$ is the outward facing normal unit vector.

Differentiating eq. 3 w.r.t. to b_n and applying the chain rule yields

$$\begin{aligned}\frac{\delta F}{\delta b_n} = &\int_S \left(\frac{\partial F_{S_k}}{\partial v_i} n_k + \acute{F}^v_{S,i}\right) \frac{\partial v_i}{\partial b_n} dS + \int_S \left(\frac{\partial F_{S_i}}{\partial p} n_i + \acute{F}^p_S\right) \frac{\partial p}{\partial b_n} dS + \int_S \frac{\partial F_{S_k}}{\partial \tau_{ij}} n_k \frac{\partial \tau_{ij}}{\partial b_n} dS \\ &+ \int_{S_W} n_i \frac{\partial F_{S_i}}{\partial x_k} \frac{\delta x_k}{\delta b_n} dS + \int_{S_W} F_{S_i} \frac{\delta (n_i dS)}{\delta b_n} + \int_{S_W} F_\Omega n_k \frac{\delta x_k}{\delta b_n} dS + \int_\Omega \acute{F}^v_{\Omega,i} \frac{\partial v_i}{\partial b_n} d\Omega + \int_\Omega \acute{F}^p_\Omega \frac{\partial p}{\partial b_n} d\Omega\end{aligned} \tag{4}$$

where S_W is the parameterized part of the solid wall boundaries and $\acute{F}^\Phi_\Omega$ includes the partial derivative $\partial F_\Omega / \partial \Phi$ plus any term resulting from the use of the Green-Gauss theorem for integrals of the form $\int_\Omega \frac{\partial}{\partial b_n}\left(\frac{\partial \Phi}{\partial x_j}\right) d\Omega$. Terms $\acute{F}^v_{S,i}$ and $\acute{F}^p_S$ are non-zero only if F_Ω includes differential operators of v_i or p. In eq. 4, $\delta\Phi/\delta b_n$ is the total derivative of any quantity Φ while $\partial\Phi/\partial b_n$ is its partial derivative. These are related by

$$\frac{\delta \Phi}{\delta b_n} = \frac{\partial \Phi}{\partial b_n} + \frac{\partial \Phi}{\partial x_k} \frac{\delta x_k}{\delta b_n} \tag{5}$$

To avoid computing variations in the flow variables, the adjoint method as presented in the next subsection, is used.

2.3 Continuous adjoint formulation

Starting point of the continuous adjoint formulation is the introduction of the augmented objective function

$$F_{aug} = F + \int_{\Omega} u_i R_i^v d\Omega + \int_{\Omega} q R^p d\Omega \tag{6}$$

where u_i are the components of the adjoint velocity vector and q is the adjoint pressure. For the development of the adjoint to the turbulence model PDEs, the reader is referred to [13]. The differentiation of eq. 6, based on the Leibniz theorem, yields

$$\frac{\delta F_{aug}}{\delta b_n} = \frac{\delta F}{\delta b_n} + \int_{\Omega} u_i \frac{\partial R_i^v}{\partial b_n} d\Omega + \int_{\Omega} q \frac{\partial R^p}{\partial b_n} d\Omega + \int_{S_W} (u_i R_i^v + q R^p) n_k \frac{\delta x_k}{\delta b_n} dS \tag{7}$$

Then, the derivatives of the flow residuals in the volume integrals on the r.h.s. of eq. 7 are developed by differentiating eqs. 1 and applying the Green-Gauss theorem, where necessary. This development can be found in [18, 8, 13].

In order to obtain a gradient expression which does not depend on the partial derivatives of the flow variables w.r.t. b_n, their multipliers in (the developed form of) eq. 7 are set to zero, giving rise to the field adjoint equations

$$R^q = -\frac{\partial u_j}{\partial x_j} + \acute{F}_{\Omega}^p = 0 \tag{8a}$$

$$R_i^v = u_j \frac{\partial v_j}{\partial x_i} - \frac{\partial (v_j u_i)}{\partial x_j} - \frac{\partial \tau_{ij}^a}{\partial x_j} + \frac{\partial q}{\partial x_i} + \acute{F}_{\Omega,i}^v + f_i^a = 0 \tag{8b}$$

where $\tau_{ij}^a = (\nu + \nu_t)\left(\frac{\partial u_i}{\partial x_j} + \frac{\partial u_j}{\partial x_i}\right)$ are the components of the adjoint stress tensor and f_i^a is the adjoint to the external force term. The adjoint to the Darcy-Forchheimer porosity force term reads

$$f_i^a = u_k (r_{ki} + E_{kj} v_j v_i) \tag{9}$$

The adjoint boundary conditions are derived by treating the flow variations in the boundary integrals (of the developed form of) eq. 7. This development is presented in detail in [13].

In industrial applications, the wall function technique is used routinely in analysis and design. When the design is based on the adjoint method, considering the adjoint to the wall function model becomes necessary. The continuous adjoint method in problems governed by the RANS turbulence models with wall functions was initially presented in [19], where the adjoint wall function technique was introduced for the $k-\varepsilon$ model and a vertex–centered finite volume method with slip velocity at the wall. The proposed formulation led to a new concept: the "adjoint law of the wall". This bridges the gap between the solid wall and the first node off the wall during the solution of the adjoint equations. The adjoint wall function technique has also been implemented in flow solvers based on cell-centered finite-volume schemes, for the Spalart–Allmaras , [18], and $k-\omega$ *SST*, [8], models.

After satisfying the adjoint PDEs and their boundary conditions, the remaining terms in eq. 7

yield the sensitivity derivatives

$$\begin{aligned}\frac{\delta F_{aug}}{\delta b_n} = &-\int_{S_W}\left[(\nu+\nu_t)\left(\frac{\partial u_i}{\partial x_j}+\frac{\partial u_j}{\partial x_i}\right)n_j - qn_i + \frac{\partial F_{S_{W,l}}}{\partial v_i}n_l + \acute{F}^v_{S_{W,i}}\right]\frac{\partial v_i}{\partial x_k}\frac{\delta x_k}{\delta b_n}dS \\ &+\int_{S_W} n_i\frac{\partial F_{S_{W,i}}}{\partial x_k}\frac{\delta x_k}{\delta b_n}dS + \int_{S_W} F_{S_{W,i}}\frac{\delta(n_i dS)}{\delta b_n}dS + \int_{S_W}(u_i R^v_i + qR^p + F_\Omega)\frac{\delta x_k}{\delta b_n}n_k dS \\ &-\int_{S_W}\left[\left(-u_{\langle n\rangle}+\frac{\partial F_{S_{W,k}}}{\partial \tau_{lm}}n_k n_l n_m\right)\left(\tau_{ij}\frac{\delta(n_i n_j)}{\delta b_n}+\frac{\partial \tau_{ij}}{\partial x_m}n_m\frac{\delta x_k}{\delta b_n}n_k n_i n_j\right)\right]dS \\ &-\int_{S_W}\left[\frac{\partial F_{S_{W,k}}}{\partial \tau_{lm}}n_k t^I_l t^I_m\left(\tau_{ij}\frac{\delta(t^I_i t^I_j)}{\delta b_n}+\frac{\partial \tau_{ij}}{\partial x_m}n_m\frac{\delta x_k}{\delta b_n}n_k t^I_i t^I_j\right)\right]dS \\ &-\int_{S_W}\left[\left(\frac{\partial F_{S_{W,k}}}{\partial \tau_{lm}}n_k(t^{II}_l t^I_m + t^I_l t^{II}_m)\right)\left(\tau_{ij}\frac{\delta(t^{II}_i t^I_j)}{\delta b_n}+\frac{\partial \tau_{ij}}{\partial x_m}n_m\frac{\delta x_k}{\delta b_n}n_k t^{II}_i t^I_j\right)\right]dS \\ &-\int_{S_W}\left[\frac{\partial F_{S_{W,k}}}{\partial \tau_{lm}}n_k t^{II}_l t^{II}_m\left(\tau_{ij}\frac{\delta(t^{II}_i t^{II}_j)}{\delta b_n}+\frac{\partial \tau_{ij}}{\partial x_m}n_m\frac{\delta x_k}{\delta b_n}n_k t^{II}_i t^{II}_j\right)\right]dS \end{aligned} \tag{10}$$

New symbols appearing in eq. 10 are explained in [13]. The deformation velocities, $\delta x_k/\delta b_n$, included in eq. 10 express the dependency of the boundary wall nodes on the shape modification parameters. This can be computed by differentiating the surface parameterization scheme presented in the next section.

3 RBF-BASED MORPHING

In this section the mesh morphing algorithm based on RBFs is described. The background theory of RBFs and details of its application in the mesh morphing field are presented; the industrial implementation of the method, as provided by the stand alone version of the software RBF Morph, is then described; finally, the coupling of the mesh morphing tool with adjoint-based sensitivities is explained.

3.1 RBFs background

RBFs are mathematical functions able to interpolate data defined at discrete points only (source points) in an n-dimensional environment. The interpolation quality and its behavior depends on the chosen radial basis function.

In general, the solution of the RBF mathematical problem consists on the computation of the scalar parameters of a linear system of order equal to the number of considered source points. The RBF system solution, determined after defining a set of source points with their displacement, is employed to operate mesh morphing to the discretized domain of the computational model. Operatively, once the RBF system coefficients have been computed, the displacement of an arbitrary node of the mesh, either inside (interpolation) or outside (extrapolation) the domain, can be expressed as the sum of the radial contribution of each source point (if the point falls inside the influence domain). In such a way, a desired modification of the mesh nodes position (smoothing) can be rapidly applied preserving mesh topology.

RBFs can be classified on the basis of the type of support (global or compact) they have, meaning the domain where the chosen RBF is non zero-valued.

An interpolation function composed of a radial basis function φ and a polynomial h of order $m-1$, where m is the order of φ, introduced with the aim to guarantee the compatibility with

rigid motions, is defined as follows

$$s(x) = \sum_{i=1}^{N} \gamma_i \varphi \left(\| x - x_{k_i} \| \right) + h(x) \tag{11}$$

where N is the total number of contributing source points. The degree of the polynomial has to be chosen depending on the kind of RBF adopted. A radial basis fit exists if the coefficients γ_i and the weights of the polynomial can be found such that the desired function values are obtained at source points and the polynomial terms gives no contributions at source points, i.e.

$$s(x_{k_i}) = g_i, 1 \leq i \leq N \ , \ \sum_{i=1}^{N} \gamma_i q(x_{k_i}) = 0 \tag{12}$$

for all polynomials q with a degree less or equal to that of polynomial h. The minimal degree of polynomial h depends on the choice of the RBF. A unique interpolant exists if the basis function is a conditionally positive definite function [11]. If the RBFs are conditionally positive definite of order $m \leq 2$ [2], a linear polynomial can be used

$$h(x) = \beta_1 + \beta_2 x + \beta_3 y + \beta_4 z \tag{13}$$

The subsequent development will assume that the aforementioned hypothesis is valid. The values for the coefficients γ_i of RBF and the coefficients β of the linear polynomial can be obtained by solving the system

$$\begin{pmatrix} \mathbf{M} & \mathbf{P} \\ \mathbf{P^T} & \mathbf{0} \end{pmatrix} \begin{pmatrix} \gamma \\ \beta \end{pmatrix} = \begin{pmatrix} \mathbf{g} \\ \mathbf{0} \end{pmatrix} \tag{14}$$

where g are the known values at the source points and $\mathbf{M}$ is the interpolation matrix defined by calculating all the radial interactions between source points

$$M_{ij} = \varphi \left(\left\| x_{k_i} - x_{k_j} \right\| \right), 1 \leq i \leq N, 1 \leq j \leq N \tag{15}$$

P is a constraint matrix that arises to balance the polynomial contribution and contains a column of "1" and the x, y, z positions of the source points in the other three columns

$$\mathbf{P} = \begin{pmatrix} 1 & x_{k_1} & y_{k_1} & z_{k_1} \\ 1 & x_{k_2} & y_{k_2} & z_{k_2} \\ \vdots & \vdots & \vdots & \vdots \\ 1 & x_{k_N} & y_{k_N} & z_{k_N} \end{pmatrix} \tag{16}$$

RBF interpolation works for scalar fields, hence a system of the form of eq. 14 has to be solved for each of the three spatial directions.

The RBF method has several advantages that make it very attractive for mesh smoothing. The key point is that being a meshless method only grid points are moved regardless of which elements are connected to them; this make the method suitable for parallel implementation. In fact, once the solution is known and shared in the memory of each processing node of the cluster, each partition has the ability to smooth its nodes without taking care of what happens outside, because the smoother is a global point function and the continuity at interfaces is implicitly guaranteed. Though meshless, the method is able to exactly prescribe known deformations onto the surface mesh: this effect is achieved by using all the mesh nodes as RBF centres with prescribed displacements, including the simple zero field to guarantee that a surface is left untouched by the morphing action.

3.2 RBF Morph tool

The industrial implementation of the RBF mesh morphing poses two challenges: the numerical complexity related to the solution of the RBF problem for a large number of centers and the definition of suitable paradigms to effectively control shapes using RBF. The software RBF Morph allows to deal with both as it comes with a fast RBF solver capable to fit large datasets (hundreds of thousands of RBF points can be fitted in a few minutes) and with a suite of modeling tools that allows the user to set-up each shape modification in an expressive an flexible way.

RBF Morph allows to extract and control points from surfaces and edges, to put points on primitive shapes (boxes, spheres and cylinders) or to specify them directly by individual coordinates and displacements. Primitive shapes can be combined in a Boolean fashion and allow to limit the action of the morpher itself. Two shape modifications used in this study are represented in fig. 1. It is worth noticing that the shape information coming from an individual RBF set-up are generated interactively with the help of the GUI and are used subsequently in batch commands that allows to combine many shape modifications in a non linear fashion (non linearity occurs when rotation axes are present in the RBF set-up).

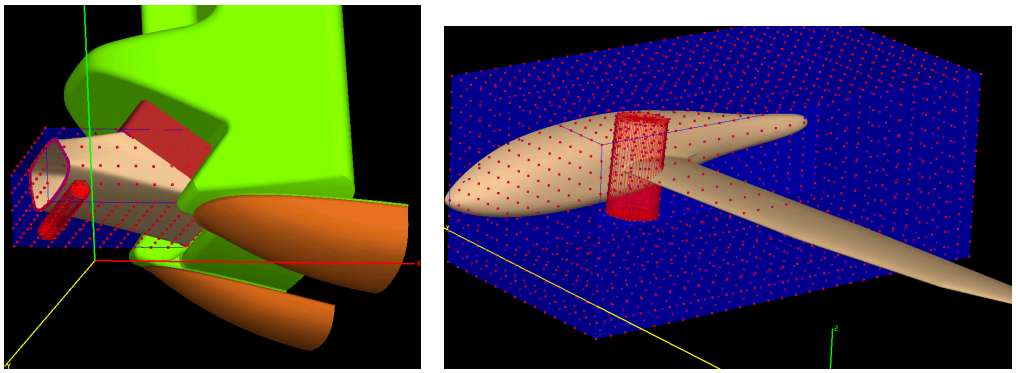

(a) cooling system diffuser (b) wing-fuselage junction

Figure 1: Example of RBF points arrangement for the definition of two shape parameters, (a) the lower wall of the cooling system diffuser is parameterized using a cluster of RBF control points forming a cylinder. A Box Encapsulation is used to limit the effect of the movement in the vicinity of the diffuser, also making sure that the edge forming the diffuser inlet will not be deformed, since it is defined by the fuselage shape which needs to remain intact, (b) a similar setup is used to define the deformation of the wing-fuselage junction close to the leading edge.

3.3 Coupling of RBF mesh morphing with adjoint sensitivities

Once the adjoint-based sensitivities are available, it is possible to easily compute the sensitivities w.r.t. shape parameters exploiting the parametric mesh available using the mesh morphing tool. In order to take into account the non-linear fashion of the morphing field, the mesh deformation velocities are generated by numerical differentiation of the morphing field around the current design point in the parametric space. For a given set of shape parameters, the morpher is capable to update the baseline mesh into the current one. A perturbed mesh, w.r.t. the current one, can then be obtained for each shape parameter, computing the mesh resulting from its perturbation while keeping all the other constant. The sensitivity w.r.t. each given parameter is then obtained by multiplying the surface perturbation field by the surface sensitivities, eq. 10. It is worth noting that the aforementioned coupling works not just at the origin of the parametric space (baseline model) but at any given design point; adjoint data need to be recomputed for

each design point for which local sensitivities are required.

4 OPTIMIZATION ALGORITHM

The gradient-based algorithm used to minimize the objective function is described in brief below:

1. Define the shape modification parameters, section 3.
2. Solve the flow equations, eqs. 1.
3. Compute F.
4. Solve the adjoint equations, eqs. 8.
5. Compute the deformation velocities and through them, the sensitivity derivatives, eq. 10.
6. Update the design variables by using a descent method.
7. Morph the parameterized surface and displace the interior mesh nodes.
8. Unless the stopping criterion is met, go to step 2.

5 APPLICATIONS

5.1 Cooling losses minimization for an electric aircraft

The first application of the automated optimization loop presented in section 4 deals with the minimization of the fluid power dissipation within the cooling system of the electric engine mounted on a lightweight aircraft. The RANS equations are solved around a simplified fuselage geometry which includes the cooling system configuration, fig. 2; a hex-dominated mesh consisting of about 2.1 million cells is utilized. The flow Reynolds number is $Re = 1.22 \times 10^5$ based on the hydraulic diameter of the cooling system inlet and the k-ω SST turbulence model is used. To avoid simulating the flow within the heat exchanger, its impact on the flow is modeled through the addition of a non-isotropic porosity term, eqs. 1b and 2. The objective function to be minimized reads

$$F = \frac{F_1}{F_2}, \quad F_1 = \int_{\Omega_c} \left[\frac{(\nu + \nu_t)}{2} \left(\frac{\partial v_i}{\partial x_j} + \frac{\partial v_j}{\partial x_i} \right)^2 + r_{ij} v_i v_j \right] d\Omega, \quad F_2 = \int_{S_{I_C}} v_i n_i dS \tag{17}$$

In eq. 17, F_1 expresses the fluid power dissipation within the cooling system domain Ω_c, fig. 2, in the presence of an anisotropic porous medium. Since the flow rate through the cooling system is not fixed, the denominator F_2, quantifying the volume flow rate through the cooling system inlet S_{I_C}, is included in F in order to prevent the optimization algorithm from reducing the power dissipation by dramatically reducing the flow through the radiator. The latter is important since the cooling capacity directly depends on the flow mass passing through the cooling configuration.

Since S_{I_C} is not a mesh boundary, computing the appropriate contributions from the differentiation of F_2 to the adjoint flow is not a trivial task. In order to facilitate the imposition of the adjoint boundary conditions, a couple of coinciding boundaries are defined at S_{I_C}, abbreviated as $S_{I_C}^L$ and $S_{I_C}^R$; flow variables are equated in the corresponding faces of $S_{I_C}^L$ and $S_{I_C}^R$. Due to the

applied boundary conditions, $S_{I_C}^L$ and $S_{I_C}^R$ practically act as internal mesh faces during the solution of the flow equations. Then, for the solution of the adjoint equations, F_2 is defined along only one of these boundaries, say $S_{I_C}^L$. Developing the adjoint to the aforementioned objective function and taking into consideration the primal boundary conditions, the following adjoint boundary conditions are derived along $S_{I_C}^L$ and $S_{I_C}^R$

$$u_i^L = u_i^R \quad , \quad q^L = q^R + \frac{F_1}{F_2^2} \tag{18}$$

Only the shape of the diffuser of the cooling system, located directly downstream of its inlet, fig. 2(a) is allowed to vary in this optimization study. Eight RBF-based design variables are defined, controlling the upper, lower and side walls of the diffuser, fig. 3. The CG method is used to update the design variables and a 5% reduction in F is obtained within 4 optimization cycles, caused by an 8% reduction in fluid power dissipation and a slight reduction of the volume flow rate by 3%. The optimized diffuser geometry along with the cumulative surface displacement is depicted in fig. 2(c). In fig. 4, the flow streamlines inside the initial and optimized cooling system geometries are presented. The reduction in the objective value can be attributed to the fact that the flow recirculation present close to the upper diffuser wall has practically vanished in the optimized geometry.

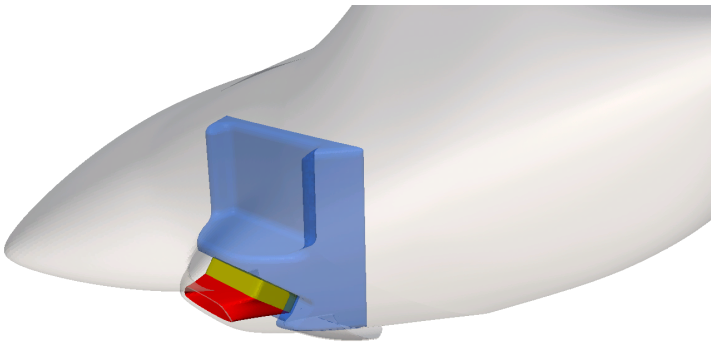

(a)

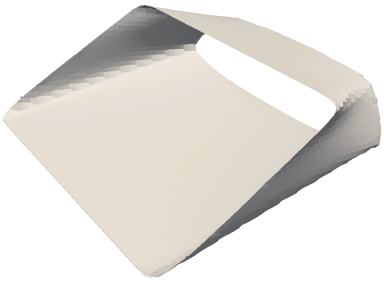

(b)

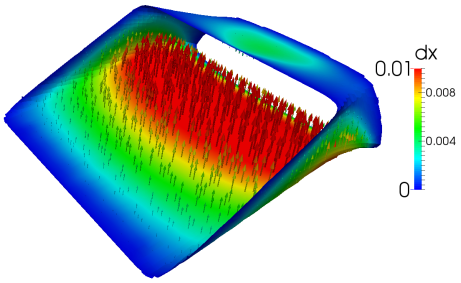

(c)

Figure 2: Cooling system optimization: (a) the cooling system and its position in the airplane geometry. The diffuser is coloured in red and is the only part of the geometry that is allowed to vary during the optimization. The yellow area is where the actual cooling takes place and is modeled by adding an anisotropic porosity term in the momentum equations. The combination of the red, yellow and blue parts comprises Ω_c, (b) the initial diffuser geometry (flow from right to left) and (c) the optimized diffuser geometry, colored based on the cumulative (after four optimization cycles) surface displacement; the maximum displacement is located at the lower diffuser wall.

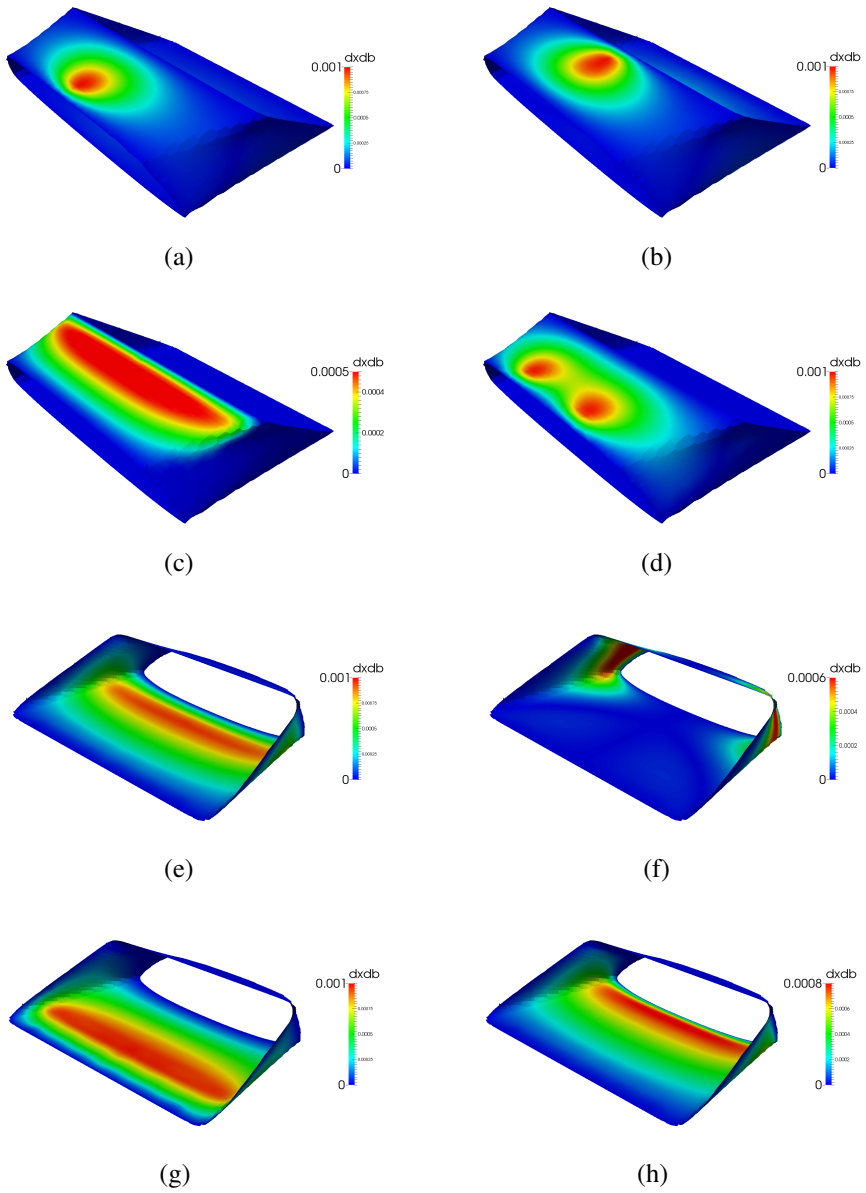

Figure 3: Cooling system optimization: deformation velocity ($\delta x_k/\delta b_m$) for the eight design variables parameterizing the diffuser shape. Design variables (a)-(d) parameterize the upper diffuser wall while those shown in (e)-(h) the side and lower walls.

5.2 Lift-to-drag ratio maximization for a glider plane

This section is concerned with the shape optimization of a glider plane targeting the maximization of the lift-to-drag ratio or, equivalently, the minimization of

$$F = -\frac{\int_{S_W} \left(-\tau_{ij} n_j + p n_i\right) r_i^L dS}{\int_{S_W} \left(-\tau_{ij} n_j + p n_i\right) r_i^D dS} \tag{19}$$

where $\mathbf{r^L}$ and $\mathbf{r^D}$ are the lift and drag force projection (unit) directions, respectively. The flow Reynolds number is $Re = 1.55 \times 10^6$ based on the wing chord, the Spalart–Allmaras turbulence model is used, the mesh consists of about 4.7 million cells and the far-field flow angle is 10^o. The geometry is parameterized using four RBF-based design variables depicted in fig. 5, controlling the wing-fuselage junction close to the leading and trailing edges as well as parts of the

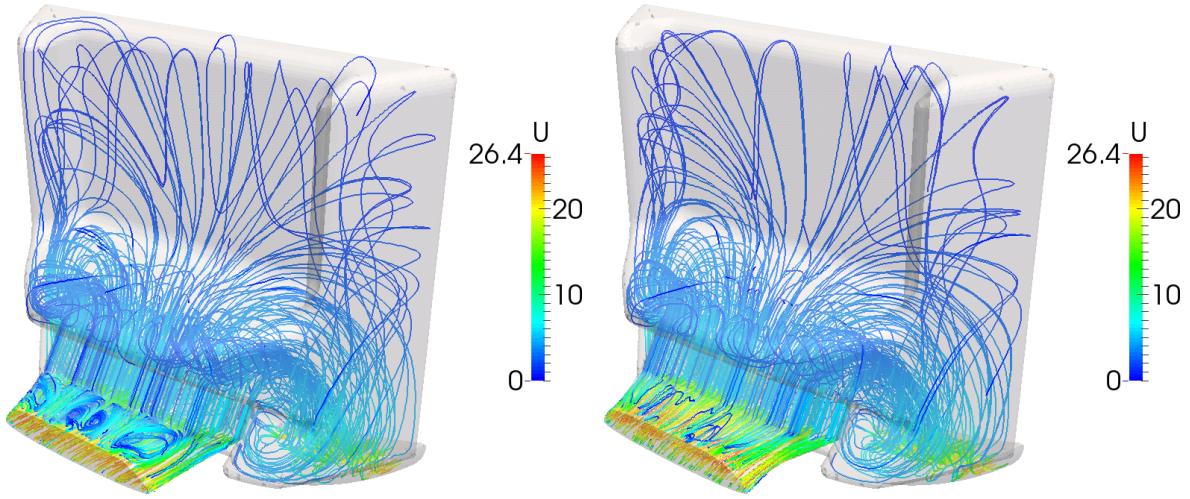

(a) initial, $\|v\|$ (b) optimized, $\|v\|$

Figure 4: Cooling system optimization: streamlines plotted through the initial (left) and optimized (right) geometries, coloured based on the flow velocity. The intense flow recirculation present close to the upper diffuser wall has practically disappeared.

upper fuselage surface. The convergence of the steepest descent-driven algorithm presented in section 4 is showcased in fig. 6(a). It can be observed that the lift-to-drag ratio has increased by 15%, caused by 10% drag reduction and a 4% lift increase. The optimized geometry is illustrated in fig. 6(b). In fig. 7, the near-wall velocity isolines are plotted on the glider surface for the initial and optimized geometries. It can be observed that the flow recirculation formed close to the trailing edge-fuselage junction has been significantly reduced.

6 CONCLUSIONS

The continuous adjoint method and an RBF-based morpher, combined into an automated optimization software were used to build a gradient-based optimization algorithm, applied to two low-speed aeronautical applications; the first targeted the losses minimization within the cooling system of a small electric airplane while the second one the increase of the lift-to-drag ratio for a glider plane. The first application required the differentiation of a non-linear, anisotropic porosity model, used to simulate the flow resistance within the radiator of the cooling system. In both cases, the optimized solution was achieved within very few optimization cycles, leading to a small optimization turnaround time. The coupling of the adjoint-based optimization software and the RBF-based morpher is part of the RBF4AERO platform. In a companion paper, [7], the part of RBFAERO platform which combines the RBF-based morpher with an Evolutionary Algorithm-based optimization strategy is also presented.

ACKNOWLEDGMENT

This work was funded by the RBF4AERO ”Innovative benchmark technology for aircraft engineering design and efficient design phase optimisation” project funded in the Aeronautics and Air Transport (AAT) research thematic area of the EUs 7th Framework Programme (FP7-AAT, 2007-2013) under Grant Agreement no. 605396.

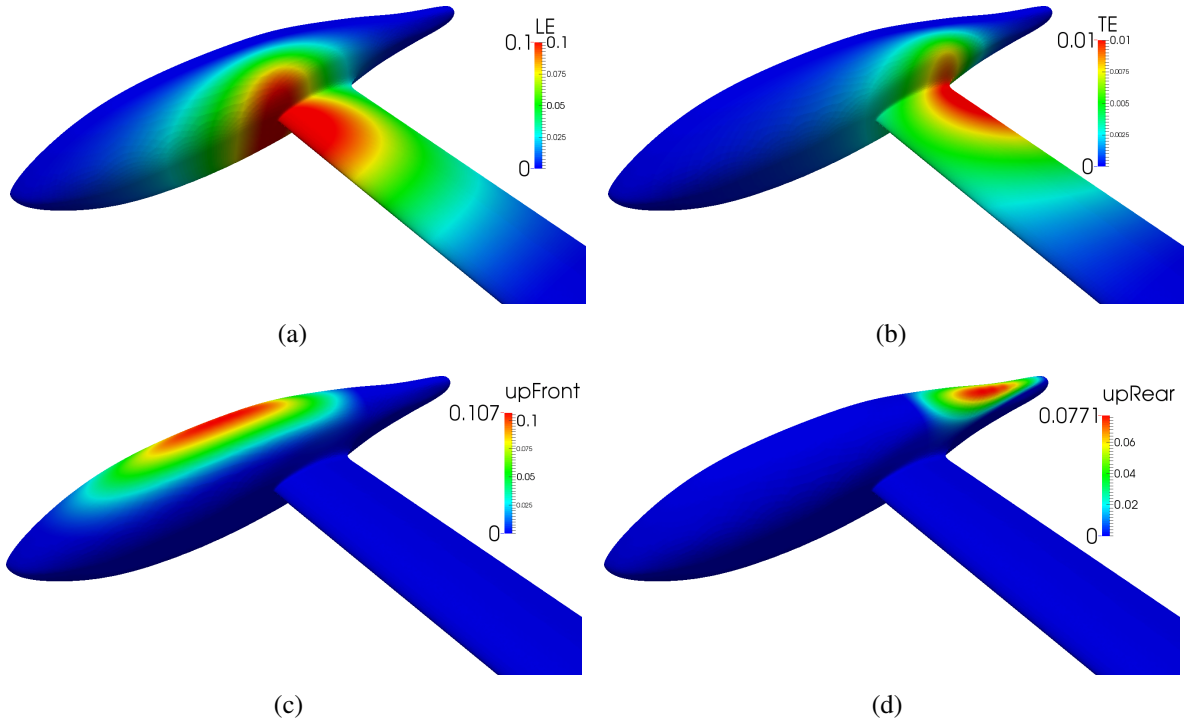

Figure 5: Glider shape optimization: the magnitude of the parametric velocity ($\delta x_k / \delta b_m$) for the four design variables parameterizing the glider shape. The first two parameterize the wing-fuselage junction close to the leading and trailing edges, while the second two affect parts of the upper glider surface. All design variables are allowed to vary within certain limits in order to prevent the generation of non-manufacturable solutions.

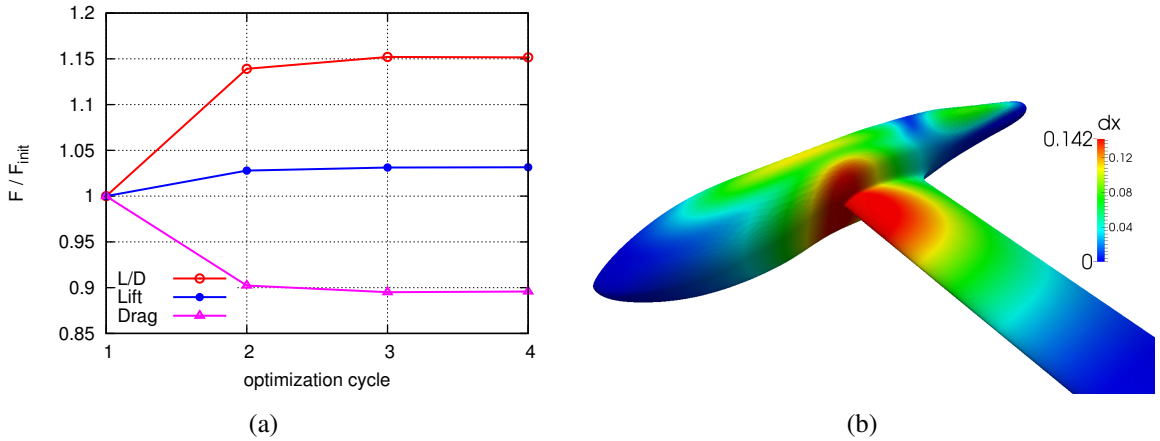

Figure 6: Glider shape optimization: (a) convergence of the lift-to-drag ratio (L/D), along with the lift and drag values. All values plotted w.r.t. the ones obtained using the initial geometry. A 15% lift-to-drag increase is observed in 4 optimization cycles by mainly reducing the drag value and slightly increasing lift, (b) the optimized glider geometry, coloured based on the cumulative surface displacement. A maximum displacement of 14.2 *cm* is observed close to the leading-edge and fuselage junction.

REFERENCES

[1] JS. Andrade, UMS. Costa, MP. Almeida, HA. Makse, and HE. Stanley. Inertial effects on fluid flow through disordered porous media. *Physical Review Letters*, 82(26):5249–5252, 1999.

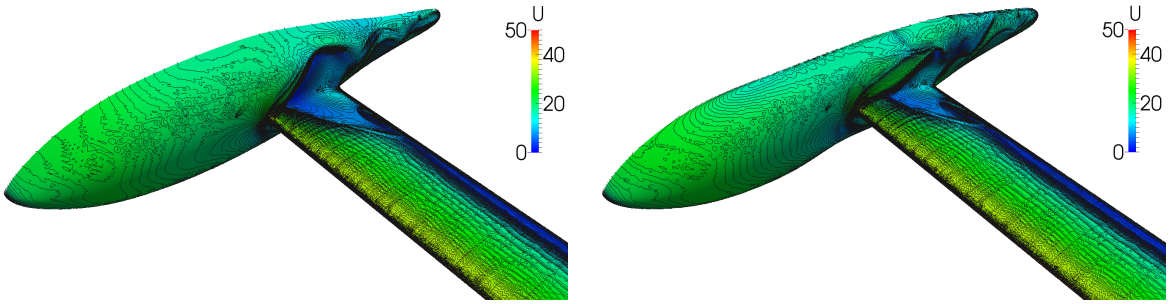

(a) (b)

Figure 7: Glider shape optimization: near wall velocity isolines, plotted on the glider surface for the (a) initial and (b) optimized geometries. It can be observed that the low velocity area close to the trailing edge has been considerably reduced.

[2] A. Beckert and H. Wendland. Multivariate interpolation for fluid-structure-interaction problems using radial basis functions. *Constructive Approximation*, 5(2):125–134, 2011.

[3] ME. Biancolini. Mesh morphing and smoothing by means of radial basis functions (RBF): A practical example using Fluent and RBF Morph. In *Handbook of Research on Computational Science and Engineering: Theory and Practice (2 vol)*, pages 347–380, 2011.

[4] ME. Biancolini, IM. Viola, and M. Riotte. Sails trim optimisation using CFD and RBF mesh morphing. *Computers & Fluids*, 93:46–60, 2014.

[5] M. Giles and N. Pierce. An introduction to the adjoint approach to design. *Flow, Turbulence and Combustion*, 65:393–415, 2000.

[6] S. Jakobsson and O. Amoignon. Mesh deformation using radial basis functions for gradient-based aerodynamic shape optimization. *Computers & Fluids*, 36:1119–1136, 2007.

[7] DH. Kapsoulis, VG. Asouti, KC. Giannakoglou, E. Costa S. Porziani, C. Groth, U. Cella, and ME. Biancolini. Evolutionary aerodynamic shape optimization through the RBF4AERO platform. In *ECCOMAS Congress 2016, VII European Congress on Computational Methods in Applied Sciences and Engineering*, Greece, 5-10 June 2016.

[8] IS. Kavvadias, EM. Papoutsis-Kiachagias, G. Dimitrakopoulos, and KC. Giannakoglou. The continuous adjoint approach to the $k-\omega$ SST turbulence model with applications in shape optimization. *Engineering Optimization*, 47(11):1523–1542, 2015.

[9] MJ. Martin, E. Andres, C. Lozano, and E. Valero. Volumetric B-splines shape parametrization for aerodynamic shape design. *Aerospace Science and Technology*, 37:26–36, 2014.

[10] FR. Menter, M. Kuntz, and R. Langtry. Ten years of industrial experience with the SST turbulence model. *Turbulence, Heat and Mass Transfer*, 4:625–632, 2003.

[11] C. Micchelli. Interpolation of scattered data: Distance matrices and conditionally positive definite functions. *Constructive Approximation*, 2(1):11–22, 1986.

[12] S. Nadarajah and A. Jameson. Studies of the continuous and discrete adjoint approaches to viscous automatic aerodynamic shape optimization. In *AIAA Paper 2001-2530, 15th Computational Fluid Dynamics Conference*, Anaheim, CA, 2001.

[13] EM. Papoutsis-Kiachagias and KC. Giannakoglou. Continuous adjoint methods for turbulent flows, applied to shape and topology optimization: Industrial applications. *Archives of Computational Methods in Engineering, DOI 10.1007/s11831-014-9141-9*, 2014.

[14] EM. Papoutsis-Kiachagias, SA. Kyriacou, and KC. Giannakoglou. The continuous adjoint method for the design of hydraulic turbomachines. *Computer Methods in Applied Mechanics and Engineering*, 278:621–639, 2014.

[15] TT. Robinson, CG. Armstrong, HS. Chua, C. Othmer, and T. Grahs. Optimizing parameterized CAD geometries using sensitivities based on adjoint functions. *Computer-Aided Design & Applications*, 9(3):253–268, 2012.

[16] P. Spalart and S. Allmaras. A one-equation turbulence model for aerodynamic flows. In *AIAA Paper 1992-0439, 30th Aerospace Sciences Meeting and Exhibit*, Reno, Nevada, 6-9 January 1992.

[17] PM. Thompson, TT. Robinson, and CG. Armstrong. Efficient CAD-based aerodynamic design optimization with adjoint CFD data. In *21st AIAA Computational Fluid Dynamics Conference, Fluid Dynamics and Co-located Conferences*, June 2013.

[18] AS. Zymaris, DI. Papadimitriou, KC. Giannakoglou, and C. Othmer. Continuous adjoint approach to the Spalart-Allmaras turbulence model for incompressible flows. *Computers & Fluids*, 38(8):1528–1538, 2009.

[19] AS. Zymaris, DI. Papadimitriou, KC. Giannakoglou, and C. Othmer. Adjoint wall functions: A new concept for use in aerodynamic shape optimization. *Journal of Computational Physics*, 229(13):5228–5245, 2010.

ECCOMAS Congress 2016
VII European Congress on Computational Methods in Applied Sciences and Engineering
M. Papadrakakis, V. Papadopoulos, G. Stefanou, V. Plevris (eds.)
Crete Island, Greece, 5–10 June 2016

LOAD CONTROL OF NATURAL-LAMINAR-FLOW WING VIA BOUNDARY LAYER CONTROL

Wienczyslaw Stalewski[1], **Janusz Sznajder**[2]

[1] Institute of Aviation
Aleja Krakowska, 110/114, 02-256 Warsaw, Poland
e-mail: wienczyslaw.stalewski@ilot.edu.pl

[2] Institute of Aviation
Aleja Krakowska, 110/114, 02-256 Warsaw, Poland
e-mail: janusz.sznajder@ilot.edu.pl

Keywords: flow control, wing-load control, Natural-Laminar-Flow Wing, Transonic wing, Computational Fluid Dynamics

Abstract. *The concept of Smart Micro Vanes (SMV) has been developed and investigated through computational simulations. The concept may significantly extend the applicability of natural-laminar-flow-and-high-aspect-ratio wing for modern, low-cost transport aircraft. The proposed device is an array of deployable micro-vanes (turbulators) located at a front part of the suction side of the wing. In nominal, cruise flight conditions the SMV are hidden in order not to trip the laminar boundary layer. In transonic flow, in extraordinary conditions of sudden gust the SMV are deployed to force laminar-turbulent transition of boundary layer on the suction side of the wing. This causes sudden drop of lift force acting on the wing and significant reduction of a danger of buffet onset. Both these phenomena are beneficial and desirable in the context of active control of aerodynamic loads acting on the wing structure. The paper presents results of computational simulations of transonic flight of simplified model of natural-laminar-flow wing in conditions of sudden-gust appearance. The simulations have been conducted for the case of clean model wing as well as for the same wing equipped with Smart Micro Vanes, deployed automatically (simulation of simple close-loop control) to protect the wing structure against excessive aerodynamic loads.*

1 INTRODUCTION

Reduction of operational costs of modern transport airplanes is one of key goals of contemporary Aeronautical Engineering. The goal is trying to be achieved by reduction of both the aerodynamic drag and weight of aircraft [1]. For transport airplanes operating at transonic air speeds, the main drag components are: induced drag, friction drag and wave drag. Reduction of each of the drag components is achieved by different means. Reduction of induced drag can be achieved by application of higher-aspect ratio wing, but this leads to increased aircraft weight. For this reason a design solution based on active flow control that make it possible to build lighter high-aspect-ratio wings are in demand. On the other hand the known solution for reduction of friction and wave drag is transonic, natural-laminar-flow wing. This solution has, however, significant drawbacks in unsteady flow. In cases of rapid changes of flight conditions, as in sudden gusts the loads on laminar wing grow more rapidly than on turbulent wing and buffet oscillations leading to structural damage of wing may appear earlier than for turbulent wing.

Taking into account all above pros and cons concerning application of Natural Laminar Flow (NLF) technology for wings of low-cost transport airplanes operating at transonic speeds, one may conclude, that such approach needs application of smart devices controlling the flow on the wing and loads acting on the wing in extraordinary flight conditions. In contrast to classic wing-load-control systems protecting the wing structure against excessive loads, such a system for the NLF wing should also protect the transonic flow on the wing against the buffet onset.

The interaction between boundary layer and transonic effects on the NLF wing has been investigated within the FP7 project TFAST (Transition Location Effect on Shock Wave Boundary Layer Interaction). Based on results of computational investigations conducted within the project [2], the authors of the paper have developed concept of Smart Micro Vanes (SMV). This concept may significantly extend the applicability of natural-laminar-flow-and-high-aspect-ratio wing for modern, low-cost transport aircraft. The proposed smart device is an array of deployable micro-vanes (small, thin plates) located at a front part of the suction side of the wing. In nominal, cruise flight conditions the SMV are hidden inside the wing in order not to trip the laminar boundary layer. It is assumed that the SMV are deployed to force laminar-turbulent transition of boundary layer generally in two situations:

1. In extraordinary conditions of sudden gust in transonic flow:
    - to alleviate growing aerodynamic load acting on the wing
    - to reduce a danger of buffet onset (as well as wing buffeting)
2. Optionally, in takeoff-and-landing conditions (low speed, high lift) to avoid a danger of laminar-stall appearance at high angles of attack (which is well known drawback of laminar airfoils and wings).

The paper presents results of computational simulations of transonic flight of simplified model of NLF wing in conditions of sudden-gust appearance. The simulations have been conducted for the case of clean NLF wing as well as for the same wing equipped with Smart Micro Vanes, activated (deployed) to protect the wing structure against excessive aerodynamic loads.

2 RESEARCH SUBJECT AND METHODOLOGY

The computational investigations of SMV applied for wing-load control via boundary-layer control were conducted for the case of simplified model of wing segment presented in Figure 1. The segment was built based on V2C laminar airfoil designed by Dassault Aviations especially for investigations of SWBLI in the TFAST project. Two configurations of the wing

have been investigated: the clean wing (with fully retracted micro vanes) shown on the left side of Figure 1 and the wing equipped with SMV, which were retracted or deployed depending on current flight conditions. The latter configuration in nominal cruise flight conditions looked exactly the same as clean-wing configuration. In sudden-gust conditions, when aerodynamic loads exceeded given threshold, the SMV were deployed and investigated configuration looked as it is shown on the right side of Figure 1.

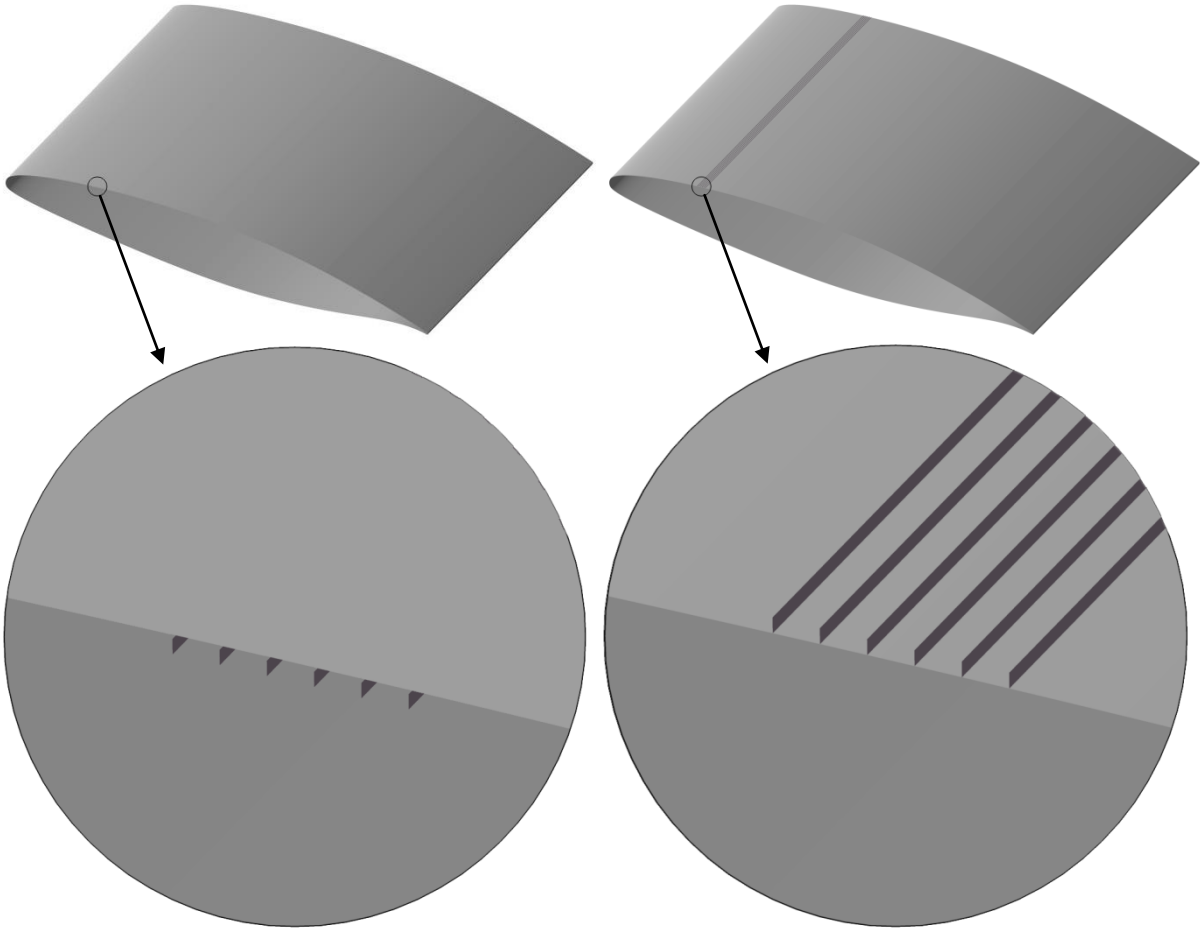

Figure 1: Investigated model of NLF-Transonic Wing equipped with Smart Micro Vanes.
Left side: Clean NLF Wing with retracted SMV. Right side: Wing with fully deployed SMV.

The wing-flight simulations were conducted through solution of Unsteady Reynolds-Averaged Navier-Stokes Equations (URANS) using ANSYS FLUENT solver [3]. For the modelling of investigated phenomena the four-equation Transition SST turbulence model was applied. This model solves additional four equations on four unknown variables: k – turbulent kinetic energy, ω - specific dissipation rate of k, γ - intermittency (probability of boundary layer being turbulent) and Re_θ - Reynolds number based on boundary layer momentum thickness. Second-order spatial and temporal discretisation of URANS equations was applied.

In conducted simulations, instead of finite-span wing segment, the infinite-span wing was investigated, utilising periodicity conditions at the ends of wing segment. The chord of the wing was C=0.2m.

During the wing-flight simulations, the effect of sudden gust was modelled by sudden growth of angle of attack, which was achieved by physical rotation of computational mesh.

The effect of deployment of SMV was realised through a change of status of cell walls modelling physical surfaces of deployed vanes. In case when the vanes were retracted, the surfaces had status "interior" while for fully deployed vanes they had status "wall".

In conducted CFD simulations, a simple Closed-Loop Control (CLC) of wing loads was introduced. It was assumed that during the flight, the control system is monitoring current values of load factor (n), defined as the ratio:

$$n = L / W \tag{1}$$

where L is a current lift force acting on the wing and W is a weight of aircraft. According to assumed CLC algorithm: the load/flow control system was activated (SMV were deployed) when for increasing load factor it exceeded the assumed activation threshold n=1.3.

Similar approach using time-accurate solution of URANS equations was already applied for analysis of reduction of aerodynamic loads in gust as an effect of fluidic wing-load-control devices [4],[5].

3 SIMULATION OF TRANSONIC FLIGHT OF NLF WING IN SUDDEN-GUST CONDITIONS

3.1 Flight Conditions

In conducted computational simulations, the nominal, cruise flight conditions were assumed as follows:

- Mach number: M=0.7
- Reynolds number: $Re=2.67 \cdot 10^6$
- Lift coefficient: $C_L = 0.76$

The assumed sudden-gust model was realised through change of current angle of attack - physical rotation of computational mesh with angular speed 5deg/s. As a result, the gust velocity profile presented in Figure 2 was applied in the conducted simulations. In presented results, only the gust-velocity-growth phase was taken into consideration.

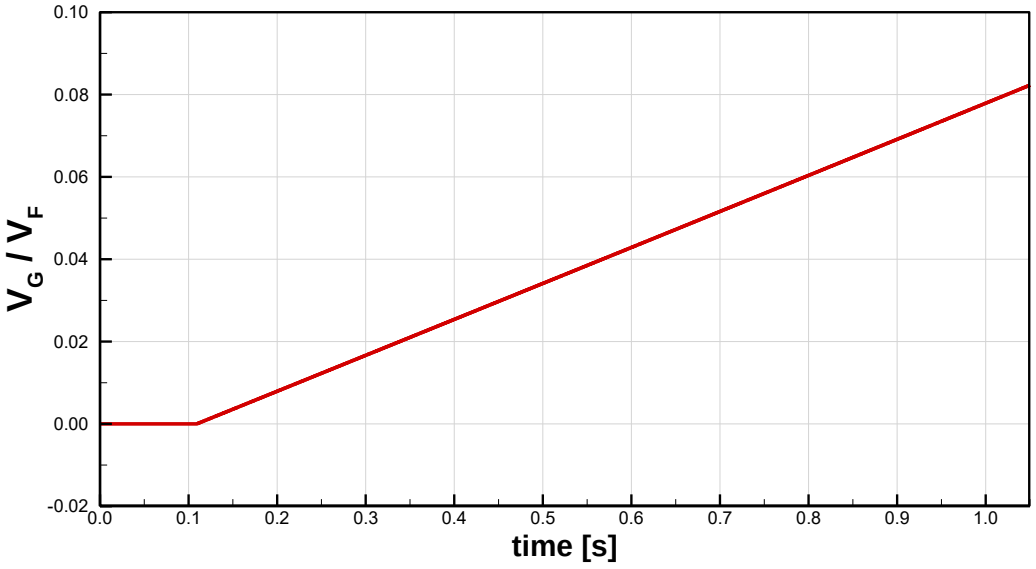

Figure 2: Assumed model of sudden-gust conditions. Time-variable gust velocity (V_G) related to flight velocity (V_F) during the gust-velocity-growth phase.

Within the TFAST project, several different positions and heights of SMV were investigated from point of view of their effectiveness and suitability for wing-load-control purposes. In the presented simulations only the configuration of six rows of SMV of height of 0.125% of wing chord, located at 20% of wing chord (see Figure 1) was investigated, because such configuration seemed to be optimal based on previously conducted research [2].

3.2 Results of Simulations

Time history of flight in sudden gust conditions of two compared configurations: clean wing and wing equipped with SMV, in synthetic form is presented in Figure 3.

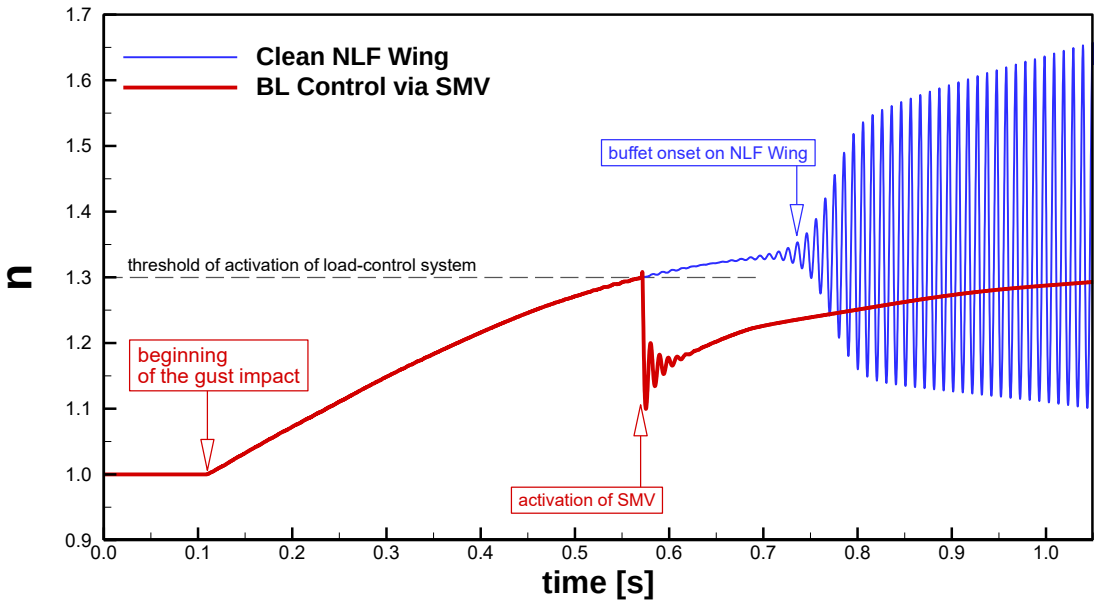

Figure 3: Comparison of time histories of load factor (n) during the sudden, growing gust, for two configurations: 1) Clean NLF Wing and 2) the Laminar Wing equipped with SMV controlling the flow inside the boundary layer.

According to assumed gust profile (Figure 2) the gust started influencing the wing loads at the moment t≈0.11s of simulation. The load factor started growing from this moment, and it exceeded the threshold 1.3 at the moment t≈0.57s. For the clean-wing configuration, the load factor continued growing smoothly until the moment t≈0.70s. Starting from this moment, the load factor for the clean-wing configuration indicated oscillations of quickly growing amplitude. These oscillations were effect of buffet onset on the suction side of the wing, due to a strong, unsteady flow separation behind the shock wave. Frequency of the observed buffet was approximately 98 Hz.

For the configuration of wing equipped with SMV, the simulation of unsteady gust load was the same as for the clean wing until the moment t≈0.57s when the load factor exceeded assumed threshold 1.3. At the moment, the SMV were fully deployed. Figure 3 shows that activation of SMV caused sudden drop of load factor of nearly 0.2. Next, for a moment, the load factor indicated some diminishing oscillations and after it continued smooth, mild increase. For the conditions, where the flow around clean wing indicated strong buffet, the flow around the wing with deployed SMV was free of any instabilities.

The same qualitative differences in the transonic flow around two compared configurations are visible in Figure 4, where the time histories of wing pitching-moment coefficient are compared.

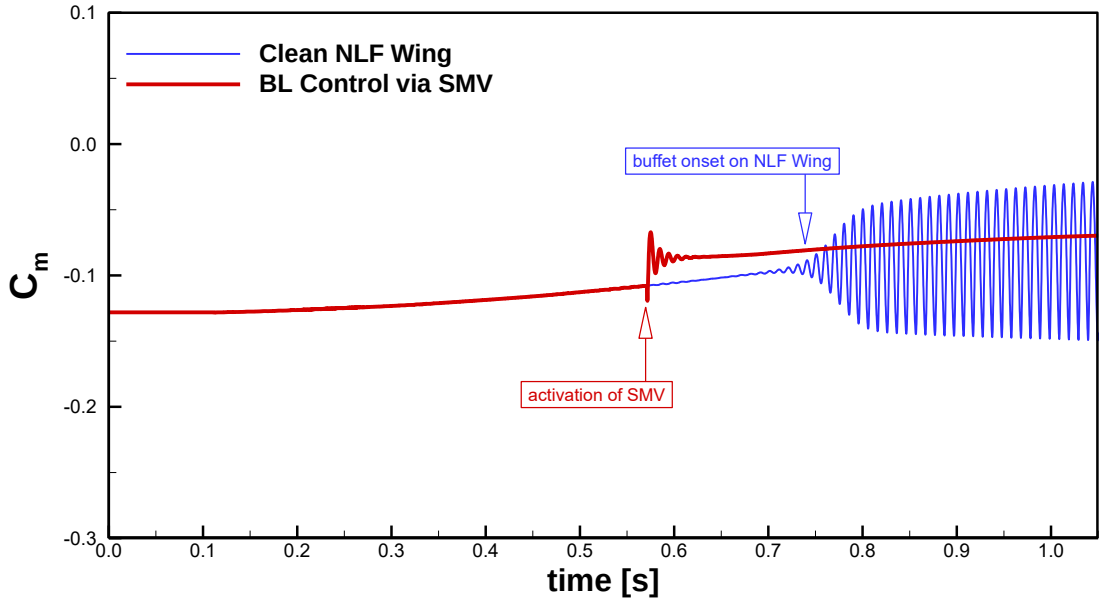

Figure 4: Comparison of time histories of pitching-moment coefficient (C_m) during the sudden, growing gust, for two configurations: 1) Clean NLF Wing and 2) the Laminar Wing equipped with SMV controlling the flow inside the boundary layer.

Figure 5, Figure 6 and Figure 7 present numerical Schlieren visualisations (contours of gradient of air density projected on appropriate direction) of shock waves in the flow around two compared configuration captured in selected moments of wing-flight computational simulations. For the moments t=0.6172 (Figure 5) and t=0.7072 (Figure 6) the visualisations show that in turbulent flow forced by the deployed SMV the shock waves are slightly weaker and located nearer the leading edge of the wing than in purely laminar flow.

Figure 7 presents Schlieren visualisations of shock waves in the flow around two compared configuration captured at the moment, when for the clean wing the strong buffet is observed. In this case the shock wave is extremely unsteady and it quickly changes its position causing quick changes of flow parameters. Extreme-front and extreme-back positions of the shock wave during the buffet observed for the clean wing are shown in upper and middle part of Figure 7. For the configuration of wing with deployed SMV, the shock wave does not indicate any instabilities.

Figure 8, Figure 9 and Figure 10 present distribution of pressure coefficient (C_P) in selected cross-section of the wing, captured for two compared configuration in selected moments of simulations. The C_P distributions presented in Figure 8 are captured at a moment shortly after achieving by the load factor (n) the threshold 1.3 and after deployment of SMV. The differences in C_P distribution clearly explain significant drop of aerodynamic load concerning the configuration with deployed SMV. For this configuration, the observed decrease in pressure difference between upper and lower surfaces of the wing is a result of deceleration of the flow on the upper surface caused by both the deployed SMV and induced by them turbulent boundary layer which is much thicker than laminar boundary layer.

In Figure 10 the unsteady C_P distributions on the clean wing captured during the strong buffet are compared with C_P distribution on the wing with deployed SMV, which does not indicate any instabilities.

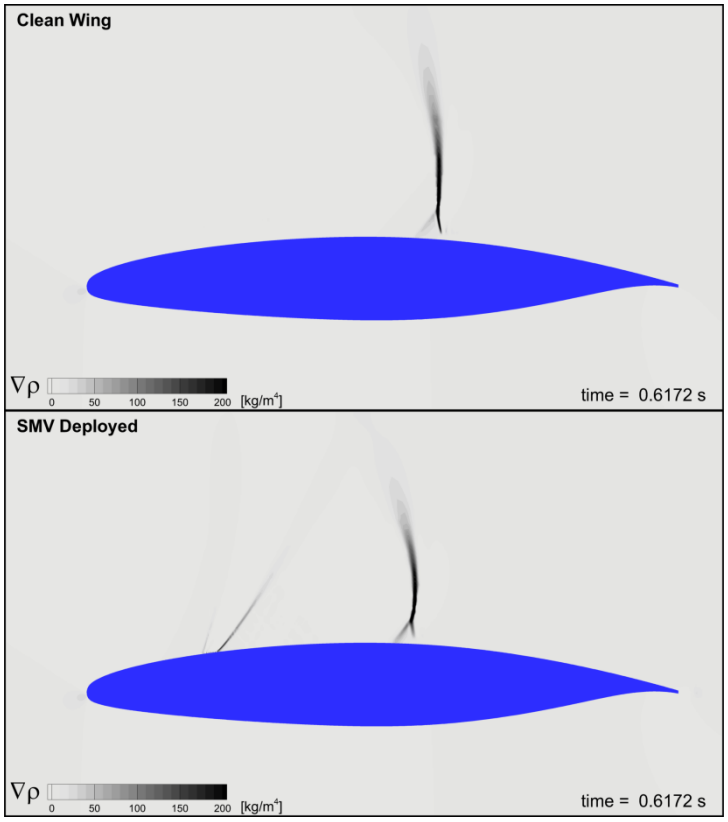

Figure 5: Schlieren visualisation of shock waves at a moment shortly after deployment of SMV. Upper graph: clean-wing configuration. Lower graph: configuration with fully deployed SMV.

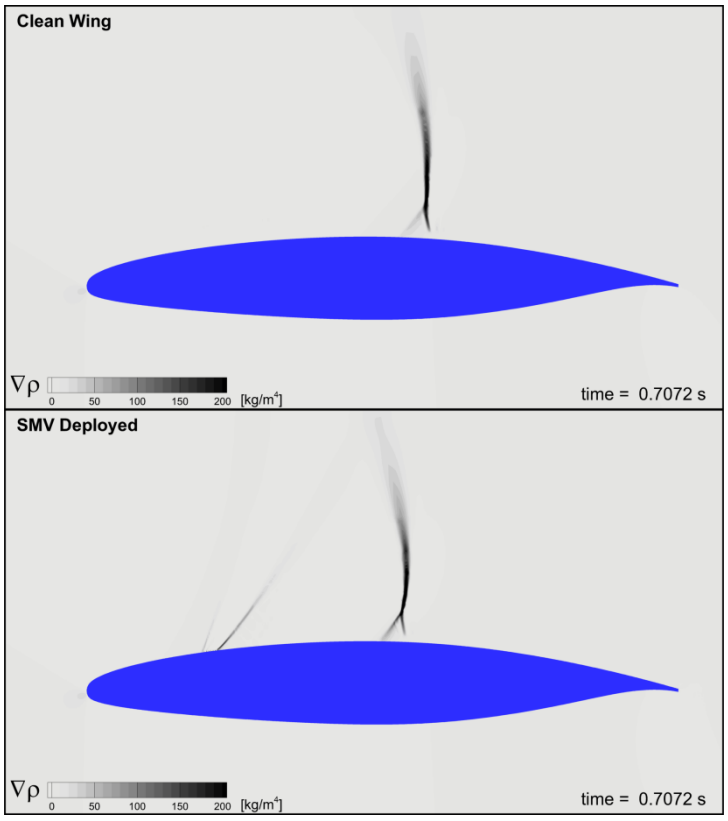

Figure 6: Schlieren visualisation of shock waves at a moment shortly before the buffet onset on the clean wing. Upper graph: clean-wing configuration. Lower graph: configuration with fully deployed SMV.

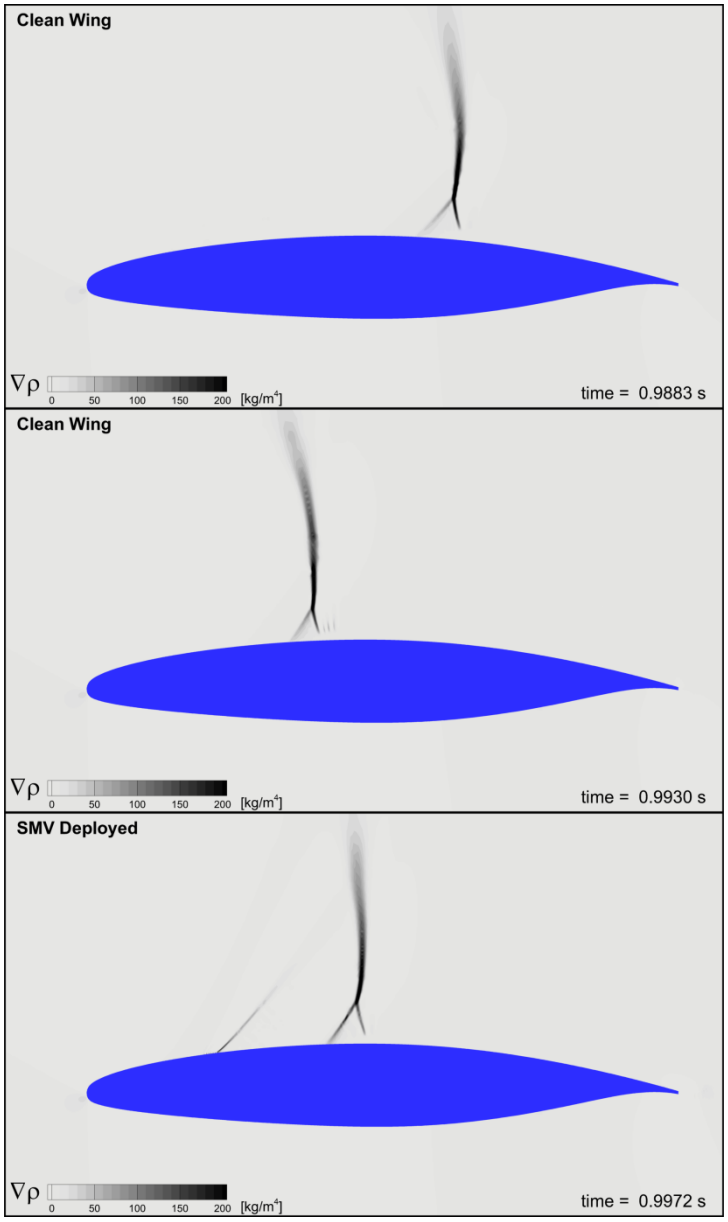

Figure 7: Schlieren visualisation of shock waves during a strong buffet on the clean wing. Upper and middle graphs: clean-wing configuration for extreme-back and extreme-front positions of the shock waves. Lower graph: configuration with fully deployed SMV and steady position of the shock wave.

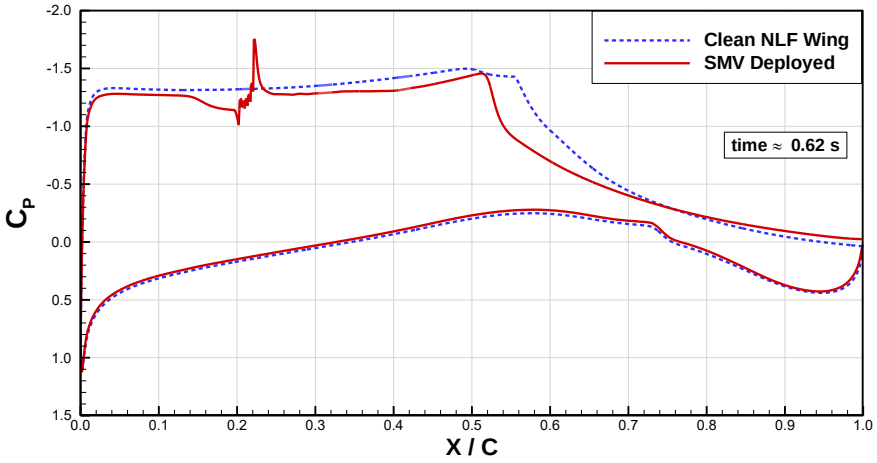

Figure 8: Comparison of pressure-coefficient (C_P) distribution on the wing at a moment shortly after deployment of SMV, for two configurations: 1) Clean NLF Wing and 2) the Laminar Wing with fully deployed SMV.

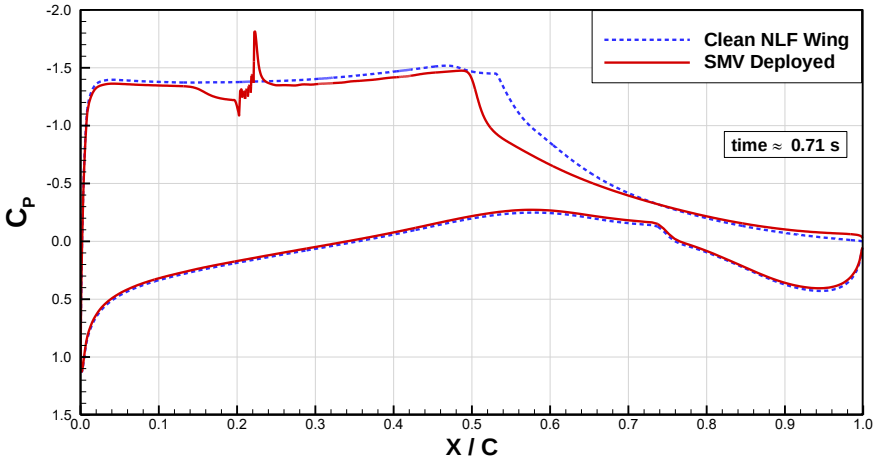

Figure 9: Comparison of pressure-coefficient (C_P) distribution on the wing at a moment shortly before the buffet onset on the clean NLF wing, for two configurations: 1) Clean NLF Wing and 2) the Laminar Wing with fully deployed SMV.

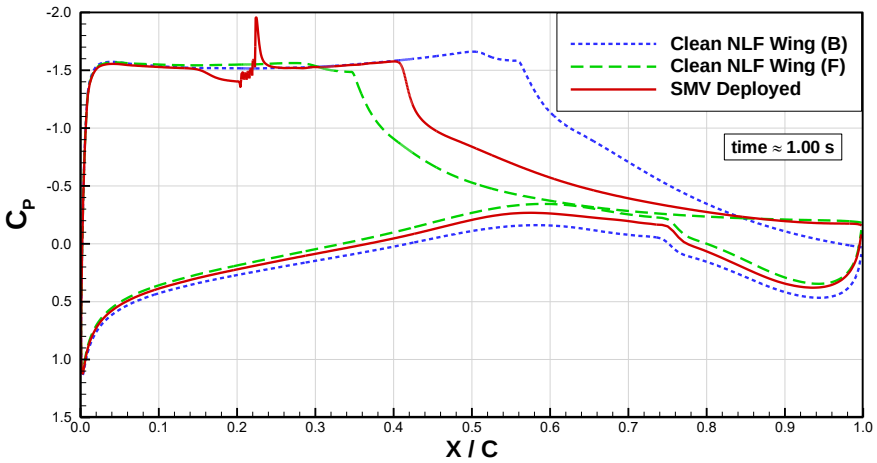

Figure 10: Comparison of pressure-coefficient (C_P) distribution on the wing during a strong buffet on the clean NLF wing, for two configurations: 1) Clean NLF Wing, two cases of extreme-front (F) and extreme-back (B) positions of shock waves and 2) the Laminar Wing with fully deployed SMV and steady position of the shock wave.

4 CONCLUSIONS

- The concept of Smart Micro Vanes has been developed and investigated through computational simulations so as to prove its potential advantages which may significantly extend the applicability of natural-laminar-flow-and-high-aspect-ratio wings for modern, low-cost transport aircraft operating at transonic air speeds.
- The proposed device is an array of micro-vanes which in extraordinary, high-aerodynamic-load flight conditions are deployed to force laminar-turbulent transition which leads to immediate drop of excessive wing load as well as to reduction of danger of transonic buffet onset.
- Conducted simulations showed that effective flow control and wing-load control may be ensured by Smart Micro Vanes of height at least 0.125% of wing chord, preferably located at 20% of wing chord.
- For the investigated configuration of wing equipped with Smart Micro Vanes, in sudden-gust conditions, observed reduction of load factor, being the effect of activation of the device, was approximately 0.2 shortly after activation and 0.1 in a further phase of the gust.
- For the investigated configuration of wing equipped with Smart Micro Vanes, in sudden-gust conditions, in contrast to the clean-wing configuration, the transonic-buffet phenomenon was not observed.

5 ACKNOWLEDGEMENTS

The research leading to these results has received funding from the European Union's Seventh Framework Programme **(FP7/2007-2013)** within the project TFAST (Transition Location Effect on Shock Wave Boundary Layer Interaction), under Grant Agreement No. 265455.
The project was also co-financed by the ministry of science of Poland from the funds dedicated to scientific research in 2012-2015, agreement no. **2641/7.PR/12/2013/2** and by Institute of Aviation.
Computational support was obtained from university of Warsaw Interdisciplinary Centre for Mathematical and Computational Modelling, in the computational grant no. G57-2.

NOMENCLUATURE

C	- wing chord
C_L	- lift coefficient
C_m	- pitching moment coefficient
C_P	- pressure coefficient
L	- lift force
M	- Mach number
n	- load factor – def. (1)
t	- time
V_G	- gust velocity (normal to flight direction)
V_F	- flight velocity
W	- weight of aircraft
Re	- Reynolds number
ρ	- density

BL - Boundary Layer
NLF - Natural Laminar Flow
SMV - Smart Micro Vanes
SST - Shear Stress Transport
URANS - Unsteady Reynolds-Averaged Navier-Stokes Equations

REFERENCES

[1] Rokicki, J., Stalewski W., Żółtak J, Multi-Disciplinary Optimisation of the Forward Swept Wing; in Evolutionary and Deterministic Methods for Design, Optimisation and Control with Applications to Industrial and Societal Problems (A Series of Handbooks on Theory and Engineering Applications of Computational Methods), editors: Burczynski T., Périaux J., Barcelona, CIMNE, 2011.

[2] Kwiatkowski T., Stalewski, W., Surmacz K., Sznajder J., Numerical simulation of laminar-turbulent transition and investigation of its influence on basic aerodynamic characteristics of laminar airfoil, TFAST D5.2.3 Deliverable Report, Institute of Aviation, Warsaw, 2016.

[3] ANSYS FLUENT Theory Guide, Release 14.5, Ansys.Inc, 2012.

[4] Stalewski W., Sznajder J., Wing Load Control via Fluidic Devices, Final Proceedings of 4-th EASN Workshop on Aircraft Design, 27-29 Oct. 2014, Aachen, Germany, pp. 319-333.

[5] Stalewski W., Wing-Load Control Based On The "Leaky Wing" Concept, Proceedings of ICAS 2014 Congress, St. Petersburg, Russia, 2014.

ECCOMAS Congress 2016
VII European Congress on Computational Methods in Applied Sciences and Engineering
M. Papadrakakis, V. Papadopoulos, G. Stefanou, V. Plevris (eds.)
Crete Island, Greece, 5–10 June 2016

AN ADAPTIVE TRAILING EDGE FOR LARGE COMMERCIAL AIRCRAFT

A. Concilio[1], I. Dimino[1], and R. Pecora[2]

[1] CIRA, The Italian Aerospace Research Centre, Adaptive Structures Division,
Via Maiorise, 81043, Capua (CE), Italy
e-mail: a.concilio@cira.it, i.dimino@cira.it

[2]University of Naples "Federico II", Industrial Engineering Dept. Aerospace Division,
Via Claudio, 21, 80125, Naples, Italy,
e-mail: rosario.pecora@unina.it

Keywords: Morphing, Adaptive Trailing Edge Device, Actuation system, Flutter Analysis

Abstract. *This paper deals with the design of an adaptive trailing edge aimed at increasing the range capacity of a large commercial aircraft. Moving from the requisites, a brief discussion about the expected performance will be introduced together with a suitable layout. Then, the design of the structural system able to guarantee both the deformability and the structural resistance will be presented. The next step is devote to the actuation system design, able to be integrate din the structural body and bear the external aerodynamic load. The external skin contributes to load bearing but also to the actuation effort required. Details refer to other publications while here it is considered though its effect only. An aeroelastic study, ensuring the stability of the proposed device over the whole wing system will be finally dealt with. A discussion on the real applicability in the aeronautics will conclude the work, pointing out at the necessary improvement required. Other work on the same subject, but referring to other design and implementation aspect will be fully referred to.*

1 INTRODUCTION

Conventional high lift systems, such as flaps or slats, are the common way to modify aircraft wing geometry during take-off and landing in order to provide additional lift at low speed. However, they have limited efficiency due to the geometric discontinuities, require high installation efforts and offer no functional flexibility in cruise, as, for instance, differential surface deflection. For some last-generation aircraft as B787 and A350, additional functions, such as differential flap settings are ensured by innovative flap actuation system concepts.

In the framework of SARISTU project, research was conducted to develop an adaptive trailing edge device aiming at maximizing wing aerodynamic performance in cruise. Wing shape is controlled during flight in order to compensate the weight reduction following the fuel burning, by allowing the trimmed configuration to remain optimal in terms of efficiency (Lift to Drag ratio) or minimal drag. Trailing edge adaptations were investigated to achieve significant benefits in aircraft fuel consumption whose reduction ranges from 3% to 5% depending on flight mission. Target morphed shapes - to be reproduced in flight - were determined through CFD-based optimization analyses; the same applies to the overall dimensions of the morph-able trailing edge (chord/span, see Figure 1). In order to assure the necessary figures for the aerodynamic efficiency of the reference A/C wing, it was found that the morphable trailing edge portion should have spanned 3.0 meters along the inner wing (kink) and 9.6 meters along the outer wing region; the required chordwise extensions should have been equal to the 20% and to the 10% of the wing MAC (nearly 3.5 meters) respectively for the inner and the outer segments.

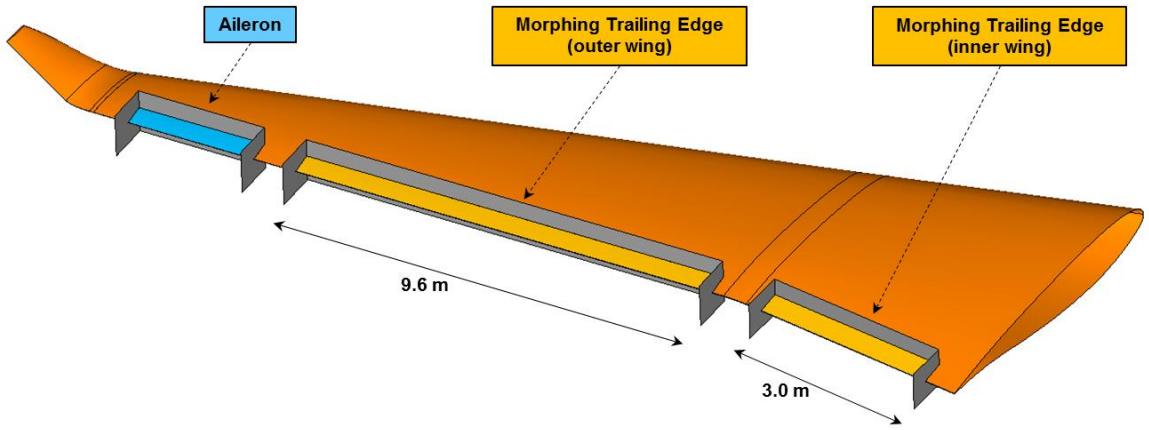

Figure 1: Morphing trailing edge regions [1].

Morphing is enabled by a multi-finger architecture driven by load-bearing actuators systems (hidden in Figure 2), designed to work synchronously to provide camber variation. After information gained from a widely distributed strain sensor network, the control system drives actuators movement. An adaptive, highly deformable skin, (shown in Figure 3), consisting of hard and soft segments, absorbs part of the external loads and insures a smooth profile. While the soft skin segments release a smooth, gapless transition between movable and fixed parts of the underlying kinematic structure, the hard skin segments compensate deformations due to air pressure gradients. The soft segments are based on elastomer foam while the hard segments consist of aluminum profiles. Both segments are covered by a thin layer to ensure a smooth surface. The system keeps its structural properties while actuated, then allowing the

preservation of a specific target shape regardless the action of the operational loads. The soft segments are located above and under the rib hinges while the hard segments are connected to the rib structure.

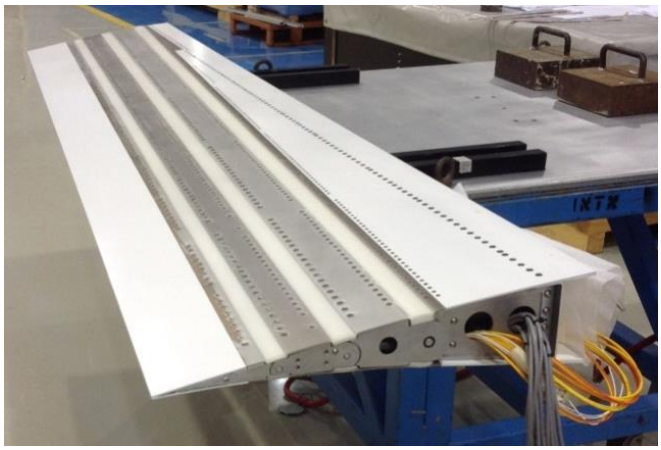

Figure 2: The Adaptive Trailing Edge (ATED) device [5].

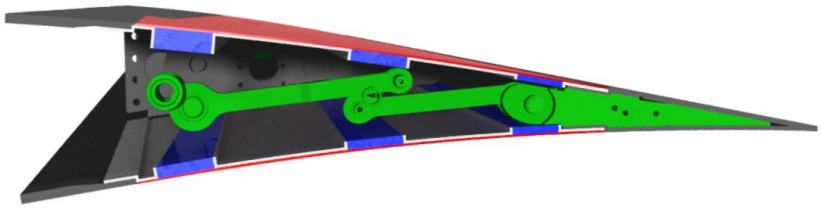

Figure 3: The morphing skin consists of hard and soft segments. Elastomer foam is used for soft segments which are located above and under the rib hinges. Hard segments are alumium profiles (grey). Hard and soft segments are covered with a thin elastomer layer [5].

These geometrical parameters were used as input for the definition of the structural concept enabling the transition from the baseline trailing edge configuration to the morphed one. The structural sizing of the concept was addressed while considering the effective operative loads expected in service and the applicable airworthiness requirements; nevertheless, for the economy of the project, detailed design activities were carried out with reference to the installation on wind tunnel demonstrator only. On the other side, the wind tunnel demonstrator replicated the last eight bays of the wing in full-scale size; the morphing trailing edge layout pertinent to the outer wing segment of the reference aircraft was then simply relocated along the wing span and supposed to be installed in the region usually occupied by the aileron (Figure 4). Its overall dimensions remained therefore unchanged with respect to real aircraft installation.

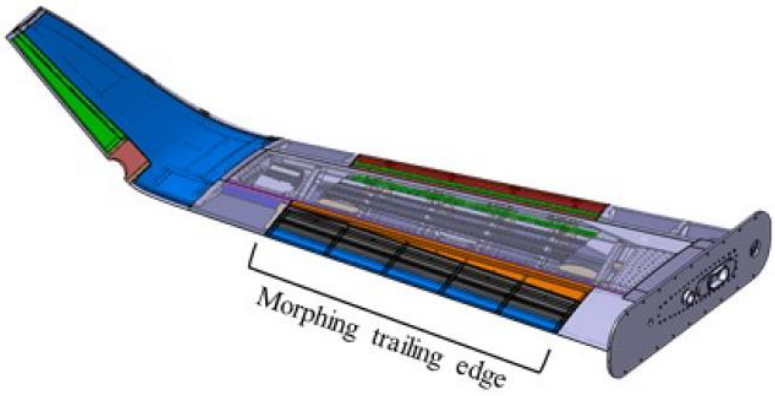

Figure 4: Wind Tunnel Demonstrator.

2 MORPHING TRAILING EDGE CONCEPT

In order to enable the transition of the trailing edge sections from the reference (baseline) shape to the target ones, a morphing structural concept was developed for ribs. Each rib (Figure 5) was assumed to be segmented into four consecutive blocks (B0, B1, B2, B3) connected to each other by means of hinges located on the airfoil camber line (A, B, C). Block B0 is rigidly connected to the rest of the wing structure, while all the other blocks are free to rotate around the hinges on the camber line, thus physically turning the camber line into an articulated chain of consecutive segments. Linking rod elements (L1, L2) - hinged on not adjacent blocks - force the camber line segments to rotate according to specific gear ratios compliant with the shapes to be achieved

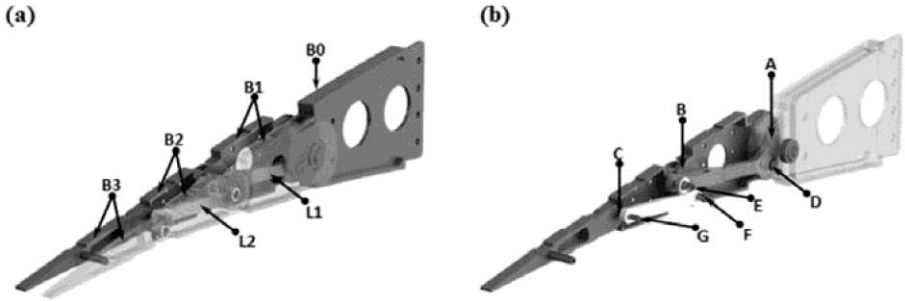

Figure 5: Morphing rib layout: (a) blocks and links, (b) hinges

These elements make each rib equivalent to a single-DOF mechanism: if the rotation of any of the blocks is prevented, no change in shape can be obtained; on the other hand, if an actuator moves any of the blocks, all the other blocks follow the movement accordingly. The rib mechanism uses a three segment polygonal line to approximate the camber of the ATED airfoil and to morph it into the desired configuration while keeping approximately unchanged the airfoil thickness distribution.

The ribs' kinematic was transferred to the overall trailing edge structure by means of a multi-box arrangement (Figure 6(a)). Each box of the structural arrangement was assumed to be characterized by a single-cell configuration delimited along the span by homologue blocks of consecutive ribs, and along the chord by longitudinal stiffening elements (spars and/or stringers).

Servo rotary load-bearing actuators coupled to quick-return mechanisms were adopted for the independent control of each rib of the device. An FBG-based system based on sensing

elastic beams located at the middle of each bay was used to detect shape configurations and to generate the information for appropriate open- and closed-loop control actions.

The structural concept herein described resulted from an iterative design process consisting of three main loops; the executive layout was obtained by progressively updating a preliminary assessed configuration on the base of feasibility considerations and stress analyses outcomes. The updating process followed the design progress of the ATED main equipment (basically actuation/sensing system) and structural interfaces with the rest of the wing (dead box). Finally, in order to assure the safety of the wind tunnel test, aeroelastic investigations on wind tunnel demonstrator were carried out in order to show the clearance of the device installation from any flutter up to three times the maximum airspeed to be tested (80 m/s).

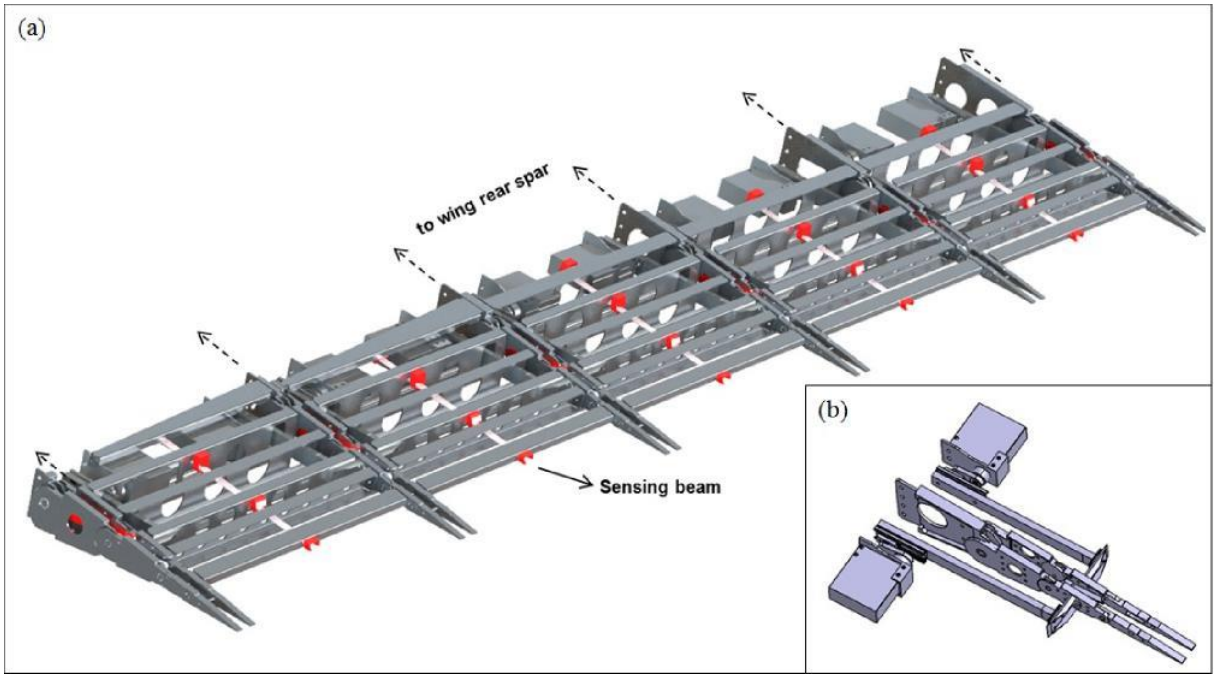

Figure 6: Morphing box architecture (a) and actuation system (b).

3 ACTUATION SYSTEM

Contrary to flexural joints-based compliant morphing mechanisms, the morphing trailing edge device combines a rigid-body mechanical system with a compliant adaptive skin. The actuation kinematics is based on a "direct-drive" actuation consisting of an arm (actuation beam) that is rigidly connected to the B2 block shown in Figure 6 (b). This arm rotates the resulting 1-DOF-based mechanical system and transmits the actuation torque from the actuator to the adaptive rib.

In order to minimize the actuation torque necessary to hold and move the ATE device, different actuation kinematics were assessed during the design phase. The size and shape of a suitable actuator were in turn estimated taking into account weight and safety constraints. The torque needed to activate the device is generated by an actuation force acting perpendicularly to this arm (if the friction can be considered equal to zero) resulting from the contact between a carriage and a linear guide. This force is generated by a rotational actuator via a crank rotating with the actuator shaft. A simplified sketch of the mechanism is shown in Figure 7. The actuation arm rotates around the "virtual hinge" (the point around which the second rib block rotates during the movement of the ATE device) and transmits the actuation load (torque) from the actuator to the second rib block. As shown in Figure 8, the mechanical advantage

increases with the morphing angle and this is much more evident as higher is the ratio between the arm length L (distance between the second rib block virtual hinge) and the actuation crank radius R. However, the higher the L/R ratio is, the higher the actuator rotation angle has to be. This limits the palette of Commercial Off-The-Shelf (COTS) servo actuators suitable for the actual application.

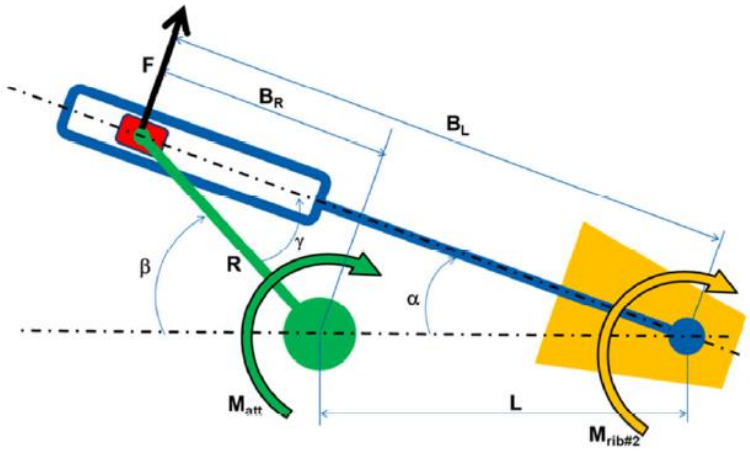

Figure 7: The actuation system layout [6].

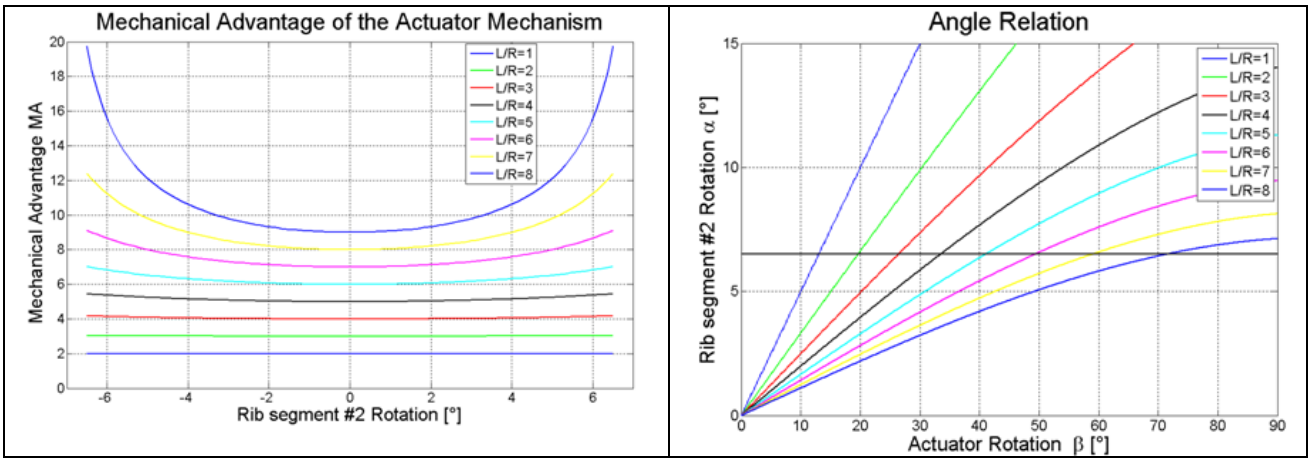

Figure 8: Mechanical advantage and actuator shaft angles of the actuation system.

4 FLUTTER ANALYSIS

In order to assure the safety of wind tunnel tests, flutter analyses were carried by considering the morphing trailing edge device integrated into the full-scale SARISTU wind tunnel demonstrator. The finite element used for static analyses was condensed into a dynamically equivalent one characterized by a reduced number of degrees of freedom. Dynamic condensation was based on the generation of direct input matrices at grids [7] to capture both inertial and stiffness properties of the device.

Reduction grids were rationally selected to get optimal modes shape resolution. The condensed dynamic model was then assembled to the FEM of the test article (Figure 9) and the overall system modes were evaluated.

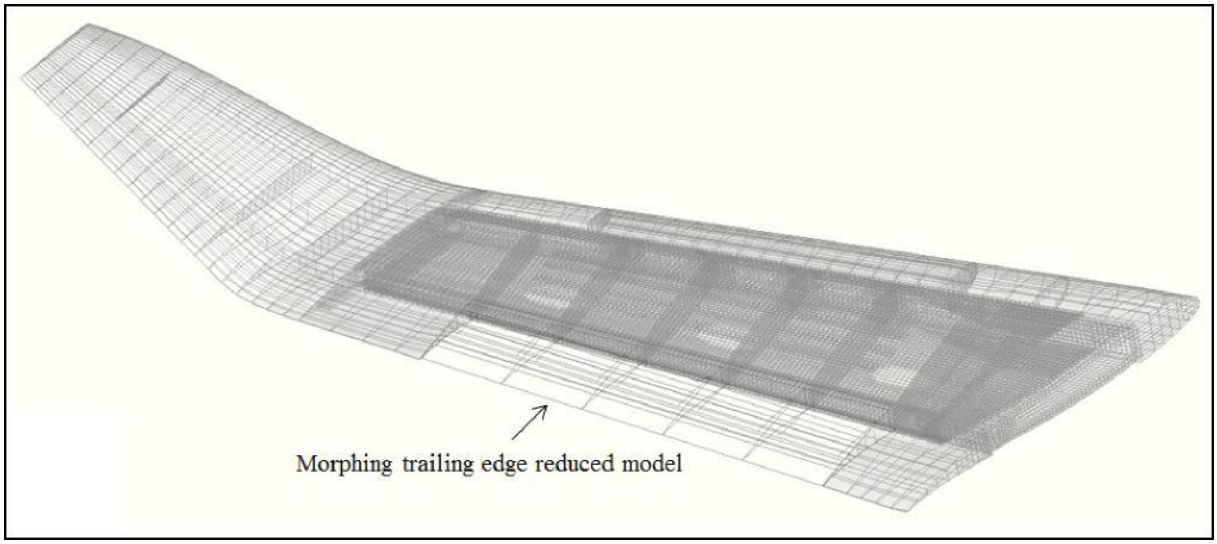

Figure 9: Structural model used for aeroelastic computations.

Doublet lattice method was adopted for the evaluation of the unsteady aerodynamic coefficients; a suitable 3D paneling was implemented for such a purpose (Figure 10). Surface splines were used to interpolate modal displacements along the centers of the aerodynamic panels and generalized aerodynamic forces were evaluated with reference to the airflow conditions expected during tests.

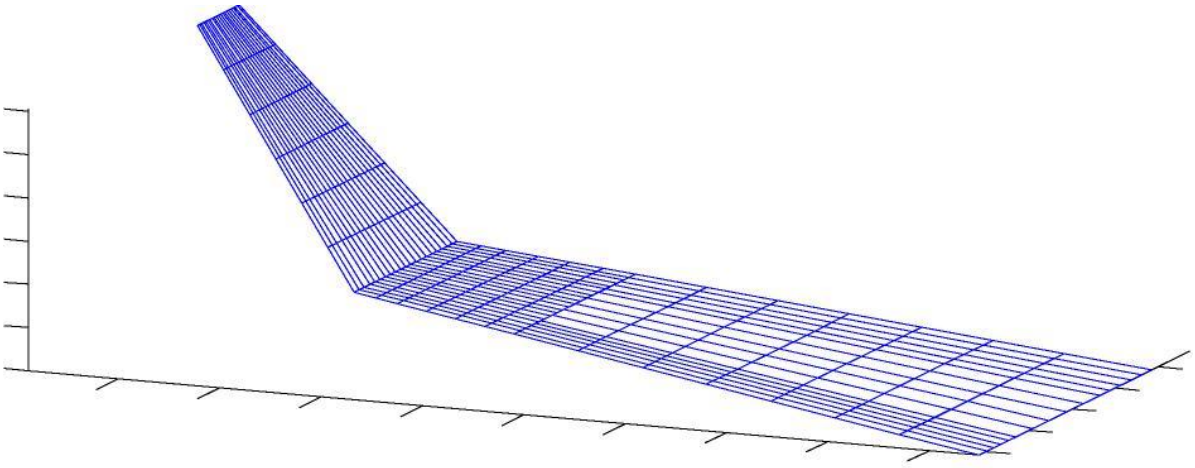

Figure 10: Test article aerodynamic model.

PK method [9] was adopted to investigate the occurrence of flutter in the speed range 0-3*Vmax, being Vmax the maximum speed expected during tests (=80 m/s). 1% critical damping was conservatively assumed for all elastic modes. No flutter was detected up to 240 m/s (Figure 11); a first instability was found at 250 m/s and essentially due to the coupling of test article bending and trailing edge elastic deflection (Figure 12).

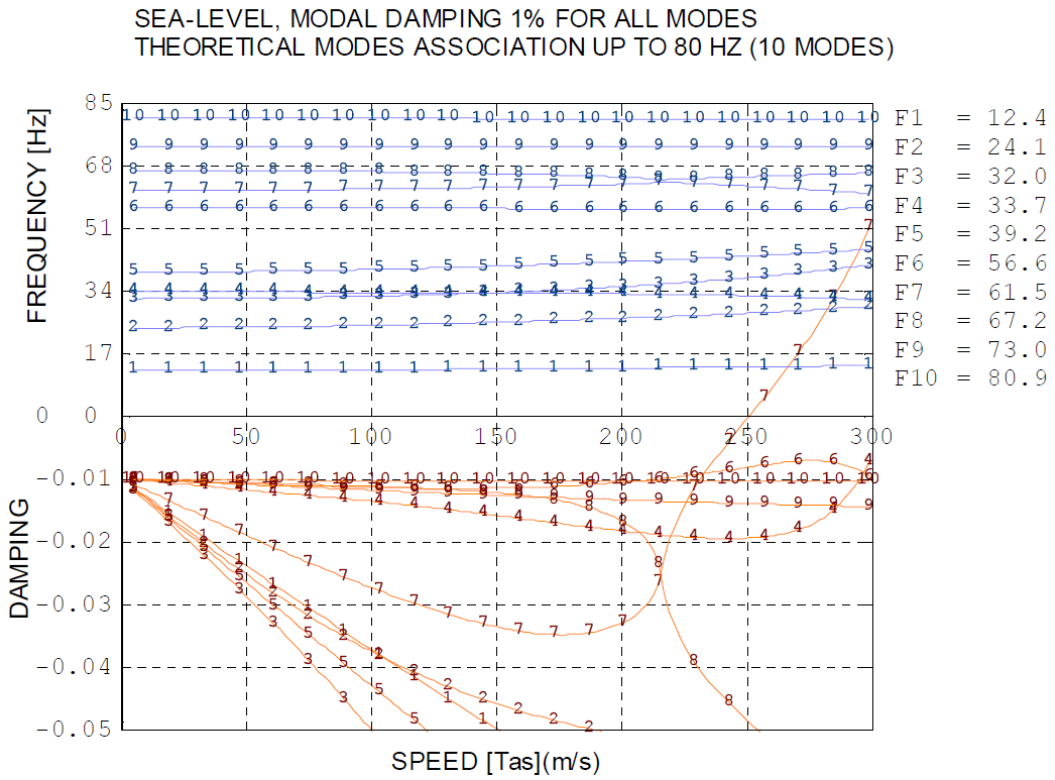

Figure 11: Flutter Vg plot.

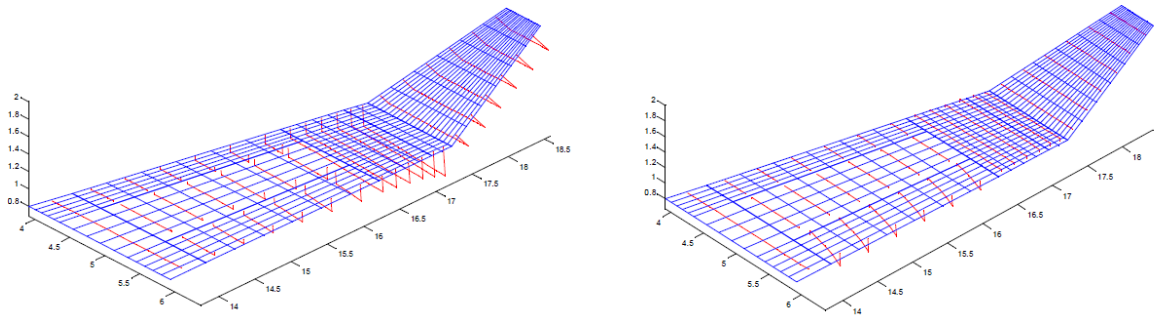

Figure 12: Modes highly participating into flutter dynamic : test article bending (left), trailing edge elastic deflection (right).

5 CONCLUSIONS

A novel architecture enabling wing trailing edge camber morphing was addressed with reference to large aircraft end-applications (EASA CS-25 category). The conventional monolithic box arrangement was replaced by a multi-box solution characterized by conventional spars and segmented adaptive ribs. Single-degree-of-freedom mechanisms, driven by load-bearing electro-mechanical actuators, were implemented to change the wing trailing edge shape by controlling the adaptive ribs individually. A compliant multi-material skin was used to accommodate the large deformation induced by ribs kinematics while providing enough stiffness to properly withstand external aerodynamic loads.

A brief and general description of the approaches and methodologies followed for the structural assessment of the overall device was presented; design strategies and consequent

results were outlined. Some open issues still remain on the developed architecture, installation aspects and implementation strategy. The specifications should be improved by considering a complete aircraft, so to compute the overall effect of the trailing edge device on the overall aircraft aerodynamic polar. The layout of the device shall also derive from the global reference geometry, so to find the best arrangement along the wing span and its chord. Further complications are also expected, following the implementation of a complex kinematic system on a movable surface such as a flap. On the other hand, the available room should be far more adequate to host the innovative components with respect to the wing tip zone. Indeed, studies to verify the possibility of inserting such systems in the aileron are currently performed by this same team and other researchers.
The actuator system design shall be integrated within the structural design, so to come to a unique active structural, load-bearing system, instead of merging to components, separately developed. Finally, control system capability, not addressed in this paper, should move from adaptive feedforward architectures, based on pre-built strain maps, to real-time feedback systems, sensible to the selected objective parameter; therefore included into the overall aircraft avionics.

REFERENCES

[1] R. Pecora, F. Amoroso, M. Magnifico, I. Dimino, A. Concilio, KRISTINA: Kinematic Rib based Structural system for Innovative Adaptive trailing edge, SPIE Smart Structures/NDE, Las Vegas, Nevada (USA) March 2016.

[2] Pecora, R., Barbarino, S., Concilio, A., Lecce, L. and Russo, S., "Design and functional test of a morphing high-lift device for a regional aircraft", J. Intel. Mat. Syst. Str., 22, 1005-1023, 2011.

[3] Monner, H.P., Sachau, D. and Brietbach, E., "Design aspects of the elastic trailing edge for an adaptive wing", Proceedings of the RTO AVT Specialists' Meeting on Structural Aspects of Flexible Aircraft Control, Ottawa (Canada), October, 1999.

[4] I. Dimino, A. Concilio and R. Pecora, "Safety and Reliability Aspects of an Adaptive Trailing Edge Device (ATED)", 24th AIAA/AHS Adaptive Structures Conference, AIAA SciTech, 4-8 Jan 2016.

[5] O. Schorsch, A. Lühring, C. Nagel, R. Pecora, I. Dimino, Polymer based morphing skin for adaptive wings, , Proceedings of the 7th ECCOMAS Conference on Smart Structures and Materials – SMART2015, 3-6 June 2015, Azores.

[6] I. Dimino, D. Flauto, G. Diodati, A. Concilio, R. Pecora, Actuation System Design for a Morphing Wing Trailing Edge, Recent Patents on Mechanical Engineering, Volume 7, pp 138-148, 2014.

[7] MSC-MD NASTRAN®, Software Package, Ver. R1-2012, MSC Software Corporation, Santa Ana, CA, 2012.

[8] Pecora, R., Magnifico, M., Amoroso, F., Monaco, E., "Multi-parametric flutter analysis of a morphing wing trailing edge", Aeronautical Journal, Vol. 118, Issue 1207, 2014, pp. 1063-1078.

[9] Broadbent, E. G., Flutter and Response Calculations in Practice, AGARD Manual on Aeroelasticity, Vol. 3, NASA, February 1963.

ECCOMAS Congress 2016
VII European Congress on Computational Methods in Applied Sciences and Engineering
M. Papadrakakis, V. Papadopoulos, G. Stefanou, V. Plevris (eds.)
Crete Island, Greece, 5–10 June 2016

APPLICATION OF SYNTHETIC JETS ACTUATORS IN WING-PYLON JUNCTION AREA TO IMPROVE THE HIGH LIFT PERFORMANCES

P. Vrchota[1]

[1] VZLU, Vyzkumny a zkusebni letecky ustav a.s., Czech Republic
address
e-mail: vrchota@vzlu.cz

Keywords: high-lift, Synthetic Jet Actuator, Computational Methods.

Abstract. *Synthetic jets actuators that produce a zero net mass flow rate have been locally applied at the pylon-wing junction to suppress the high-lift penalties caused by the closely coupled engine integration. The high fidelity numerical simulations utilizing unsteady Reynolds-averaged Navier-Stokes have been performed to simulate this problem. A wind tunnel model representing a 2,5D wing with pylon, nacelle and deployed high-lift devices is used for this study. Active flow control applied at the wing-pylon junction area can prevent the larger flow separation on the wing behind the nacelle caused by the slat cutback, increase the lift and to postpone the stall angle by interaction of the vortices from the SJA with vortices dominating this region. The performed unsteady CFD simulations demonstrate the possibility locally affect the flow by utilization of AFC. The geometrical setup of the actuators and the flow variables (blowing coefficient, actuation frequency) have been varied, as well. Two different shapes and positions of the nacelle's strike have also been considered during the simulations. The positive effect of the application of the SJA on maximum lift and stall angle has been observed.*

1 INTRODUCTION

Utilization of the Ultra-High Bypass Ration (UHBR) engine in air transport is driven by ecological and economical aspects. These new engines have lower emissions of CO2 and NOx, higher efficiency and smaller fuel consumption. On the other hand the integration of UHBR engine is very challenging part from two aspects, at least. The first one is the high-lift conditions at high angles of attack and low-speeds and the second one is connected with the clearance between the runway surface and the nacelle. To avoid longer landing gear struts suffering from weight and space penalties, the nacelle should closely-coupled to the wing. This closely-coupled integration causes the high-lift penalties due to the high-lift devices cut-back to prevent clashes with the nacelle or thrust reverser [1]. Among other techniques the Active Flow Control (AFC) can be successfully applied to remedy this lift lost due to the high-lift devices cut-back.

Within the European project AFLoNext [2] one of the main goals is the application of Active Flow Control (AFC) techniques, like pulsed jet blowing and Synthetic Jet Actuators (SJA), on wing/pylon junction to remedy the lift losses caused by in closely-coupled engine integration. A significant effort of experimental and numerical investigation of the application of the passive and AFC techniques to locally suppress the flow separation or improve the high-lift performances at the wing-pylon area, outer-wing or applied to high-lift devices has been done [3-7]. This paper summarized the results of the SJA of the high-lift configuration using the CFD simulation by means of URANS approach. The effect of the momentum coefficient $C\mu$ and actuation frequency f is discussed.

2 GEOMETRICAL SET-UP

2.1 Wind tunnel model

Model used for CFD studies is based on a wing section of a generic high-lift wing, the DLR-F15 [8], which is representative for today's transport aircraft high-lift system layout. It is equipped with a slat and a single-slotted Fowler flap. Because of the AFLoNext project this model was modified to integrate pylon and nacelle. It represents 2,5D wing with sweep angle 28deg equipped with the side plates.

2.2 Strake configurations

Two different strake's configurations were used during this study. They differ in the shape and location on the nacelle. Both strakes are depicted in Figure 1. The new strake is located closer to the wing to be more effective and creates stronger strake's vortex. The effect of the original and new strake on baseline flowfield is described in subsequent section.

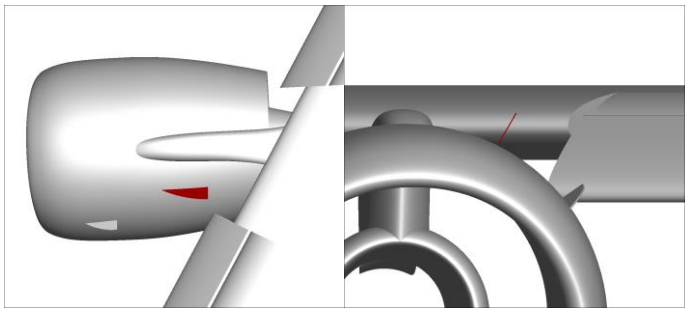

Figure 1 Position of old (grey) and new strake (red) on nacelle

2.3 Actuator's geometry and position

The circular actuator with area $5mm^2$ was used for simulation of the synthetic jet. Two configurations of the actuators were used during this study. They differ in the location and number of actuators. The first configuration is characterized by two rows of actuators located at 0.01% and 0.021% of the chord of the wing. The spanwise position of this configuration with two rows of actuators is limited by the inner slat-end on one side and the pylon's axis on the other side. The actuators in the second row are placed in cascade regarding the actuators in the first row. The second configuration was created from the first one by omitting the second row of actuator. One halve of actuators is considered in comparison with the first configuration. The spanwise location remained the same. The spanwise spacing between the actuators is 0.01m.

Actuators of both configurations were placed parallel with the leading edge and inclined 30deg towards the wing's surface. The actuators' cavities were physically modeled to enable the development of boundary layer inside them.

3 NUMERICAL METHODS

3.1 Grid creation

All grids used during this study were created in Pointwise grid generation software. The grids are unstructured with rectangular elements on the model surfaces and with tetrahedral elements in the volume. The boundary layer is simulated by prismatic elements and the condition of y+ bellow 1 was fulfilled. The region of interest was refined to capture all flow phenomena (interaction of the vortices, flow separation,…). In case that the modification of the strake or actuator's positions was considered, the same grid topology was used. Only the blocking of the surface grid on the nacelle and in the region of actuators was modified due to new strake and different actuators locations, the number of nodes remained the same. The grid in the region of interest was not changed.

3.2 Boundary conditions and CFD solver

Mass flow inlet/outlet boundary conditions (BC) were used to simulate the flow from SJA. The mass flow, total temperature and flow direction are defined at these BC. The adjusted mass flow corresponds to the required blowing velocity at the cavity's outlet. The simulation of the synthetic jet is done by switching between the mass flow inlet and mass flow outlet boundary condition controlled by harmonic (or step) function. It is possible to define the desired peak velocity and frequency of the synthetic jet using the harmonic function. In case that the step function is used, the duty cycle can be also controlled. The typical course of the mass flow in time for synthetic jet actuator is depicted in Figure 2. The cavities of the actuators were physically modeled during the mesh generation process to enable the development of boundary layer velocity profile inside them. The boundary conditions were applied at the bottom part of these cavities. The fully modeled cavities have some drawback in terms of the grid creation, number of cells etc., but the flow at the cavities' outlets is more realistic. On the other hand same effort has been devoted to applying the surface boundary conditions simulating the flow from actuators and actuation models in the past [7, 9-11].

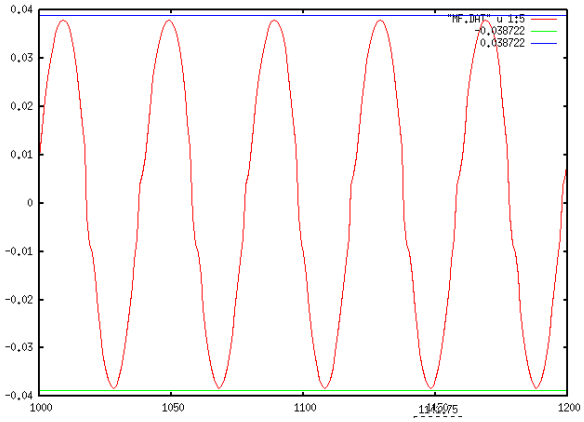

Figure 2 Typical course of the mass flow during the simulation of synthetic jet

3.3 Flow conditions

All of the computations were performed at a chord-based Reynolds number of $Re=4.65 \cdot 10^6$, the freestream Mach number 0.2 and freestream pressure corresponded to the 0m International Standard Atmosphere. These flow conditions correspond to the landing conditions of the characteristic airliner.

3.4 Baseline configuration – strake effect

The effect of the strake on the local flowfield has been experimentally and numerically investigated in the past [12]. It is usually used to remedy the lift losses due to the slat cut-back. During this study it was found that the original strake did not affect the flow as it was expected. The strake's vortex was too high above the wing and applying the AFC it transported low momentum flow towards the wing. It was the main reason to use a new strake design by DLR during the AFLoNext project. The new strake has been moved towards the wing's leading edge and it is slightly larger than the original one. The position of this strake was verified by numerical simulations performed also by DLR.

The comparison of the lift curves of the original and new strake configurations is depicted in Figure 3. It can be seen that the new strake has a significant effect on the local flowfied behind the nacelle at stall condition and it is able to improve the lift more effectively than the original one. The new strake creates stronger vortex which is closer to the wing and more interacts with the vortices dominating this region.

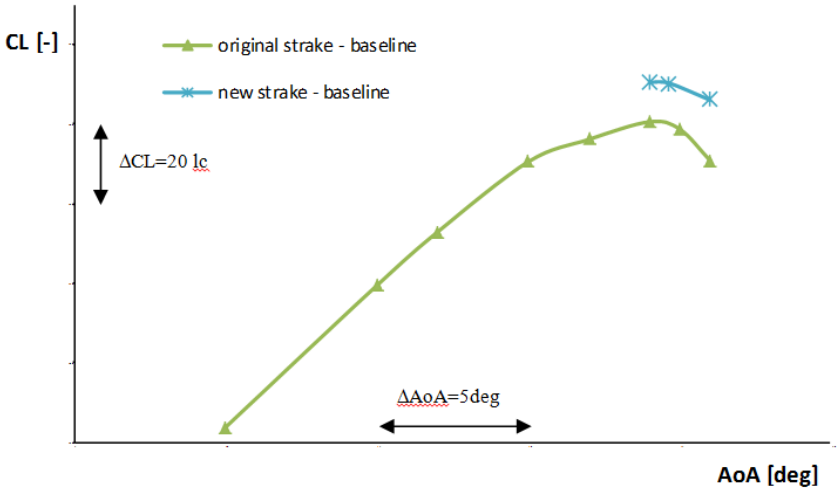

Figure 3 Effect of strakes on baseline flow

The surface streamlines together with the area of separated flow (visualized by negative x component of the skin friction coefficient) of the baseline flow with original strake are depicted in Figure 4. It is possible to see the development of the separated area with increasing AoA (depicted by the arrow). The surface streamlines and flow separation areas of the baseline flow corresponding to the configuration with the new strake is depicted in Figure 5. It is possible to see that for the same AoAs, the flow separation area is smaller in comparison with the configuration with original strake. No flow separation has been observed in the outer part of the wing (behind the pylon's axis in spanwise direction) for the simulated AoAs.

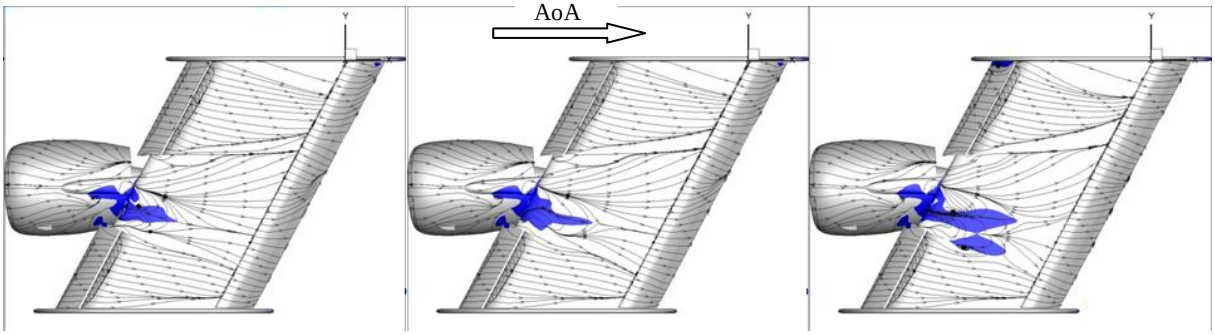

Figure 4 Surface streamlines and flow separation area (visualized by negative Cfx in blue) for baseline configuration – original strake

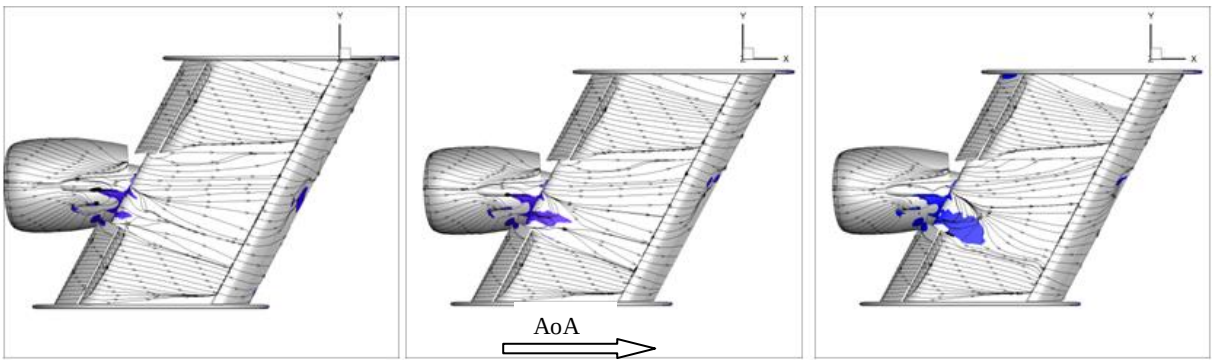

Figure 5 Surface streamlines and flow separation area for baseline configuration with new strake

The location of the flow separated area between the inner slat-end and pylon's axis was the main reason for creation of the configuration of the circular actuators with limited span wise position between the inner slat-end and pylon's axis. The configuration with the new strake was used during the CFD simulations of the SJA.

3.5 Synthetic Jet simulations

The boundary condition described in 3.2 was used for simulating of the Synthetic Jet (SJ) by means of URANS approach. A harmonic function with defined frequency and amplitude, representing the desired mass flow, was used for SJA. The frequency was limited by the limit of 100 Hz at first. A more realistic actuation frequency 1kHz has been simulated consequently. Due to extremely high time consuming simulation of the higher actuation frequency, only one post stall AoA was simulated for the configuration of the actuators in one row. The adjusted mass flow corresponded to the peak velocity 150m/s.

The configurations with one and two rows of actuators have been used to evaluate the effect of Cμ on aerodynamic performances. The frequency effect was evaluated on the configuration with one row of actuators using different actuation frequency.

From lift curves depicted in Figure 6 it is possible to see the effect of SJA with actuation frequency 100Hz (red curve) and the effect of different Cμ and f, as well. The stall angle was delayed by about 2deg in comparison with the baseline configuration. The C_{LMAX} was improved by about 8 lc according to the baseline C_{LMAX} and by about 14 lc at the same post stall AoA of the baseline configuration.

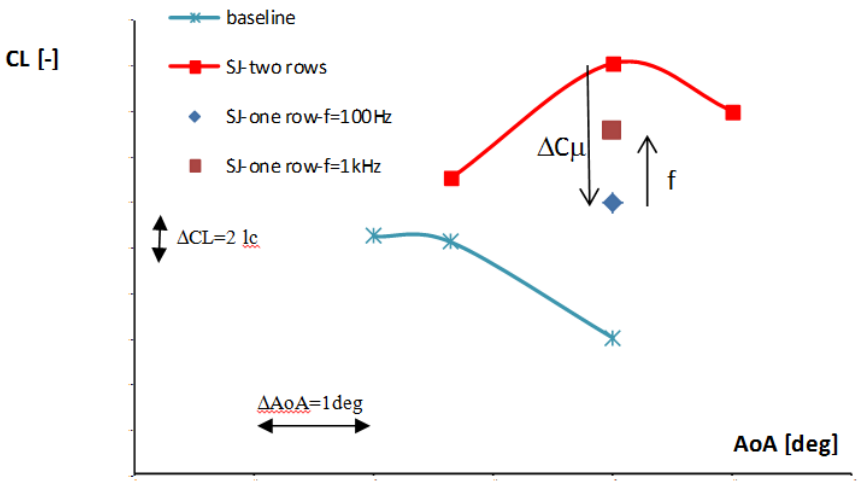

Figure 6 Lift curves and CL values of bsl and SJA of both configurations of actuators

The surface streamlines and separated areas of the configuration of two rows of SJA working with frequency 100Hz at simulated AoAs are depicted in Figure 7. It is possible to see that the separated area at stall angle is almost the same as at lower AoA due to the interaction of the synthetic jet with the inboard LE-step and slat-end vortices (see Figure 8). With increasing AoA the SJA is not able to effectively control the vortices and inboard LE-step vortex bursts and it causes the large flow separation area (see Figure 7 and Figure 8, right). The vortices for simulated AoAs are depicted in Figure 8. It is possible to see the interaction of the flow from SJA with the inboard LE-step and slat-end vortices and the discontinuity of the slat-end vortex and slightly reduced inboard LE-step vortex at post stall AoA. These vortices cannot af-

fect the flow in close vicinity of the wing and the flow separates. It has to be emphasized that these surface streamlines and vortices correspond to the last iteration of the simulations.

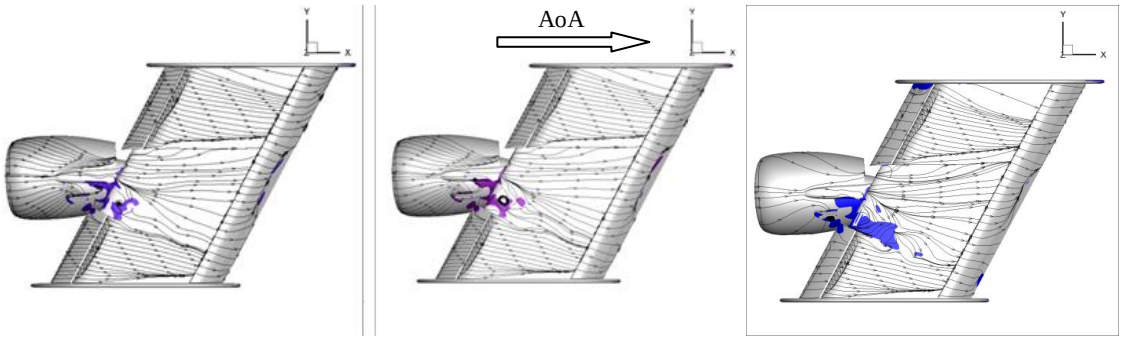

Figure 7 - Surface streamlines and flow separation area for two rows of SJA

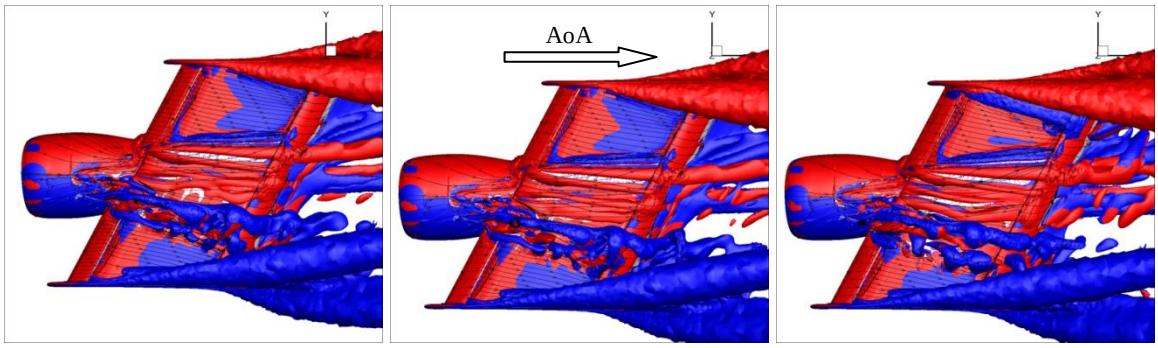

Figure 8 Vortex structures for two rows of SJA, pre-stall AoA (left), stall AoA (middle) and post stall AoA (right)

The effects of Cμ and actuation frequency on C_L at stall AoA are also depicted in Figure 6. The Cμ is decreased from 0.0252% to 0.0127% by using one row of actuators instead of two rows. The effect of reduced Cμ on the C_L is depicted in Figure 6 by the left arrow. The value of C_L is decreased by about 6 lc. The vortex structures for both values of Cμ are depicted in Figure 9 (left and middle figures). It is possible to see the positive effect of higher Cμ on the structure of the inboard LE-step and slat-end vortices. These vortices are more continuous in comparison with the vortices corresponding to the lower Cμ (one row of actuators). For the smaller Cμ the slat-end vortex is more discontinuous and the inboard LE-step vortex is slightly weaker and not so much affects the local flow close to the wing's surface.

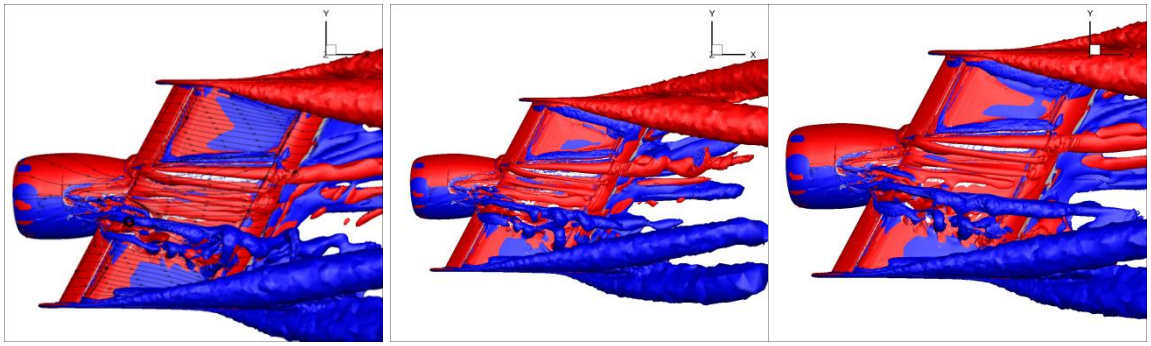

Figure 9 Effects of Cμ and actuation frequency on vortex structures, two rows of actuators (left), one row (middle) and one row of actuators with f=1000Hz (right)

In case that the one row of actuators is used (smaller Cμ) and the actuation frequency is increased from 100Hz to 1000Hz, the CL is increased by about 3 lc (see Figure 6). The right black arrow indicates the change of C_L with the change of actuation frequency. The dimensionless frequencies F^+ corresponding to the 100Hz and 1000Hz are increased from 4.79 to 47.9, respectively. The effect of actuation frequency on forming the vortex structure is depicted in Figure 9 (middle and right figures). In comparison with the lower Cμ and lower frequency (vortices in the middle), the slat-end and also the strake's vortex are more affected by SJA with higher actuation frequency. Especially the LE-step vortex is stronger.
Comparison of the flow separation areas for particular cases with SJA are depicted in Figure 10. It is possible to see that the flow separation area is increased by using smaller Cμ and on the contrary the higher actuation frequency slightly reduce it.

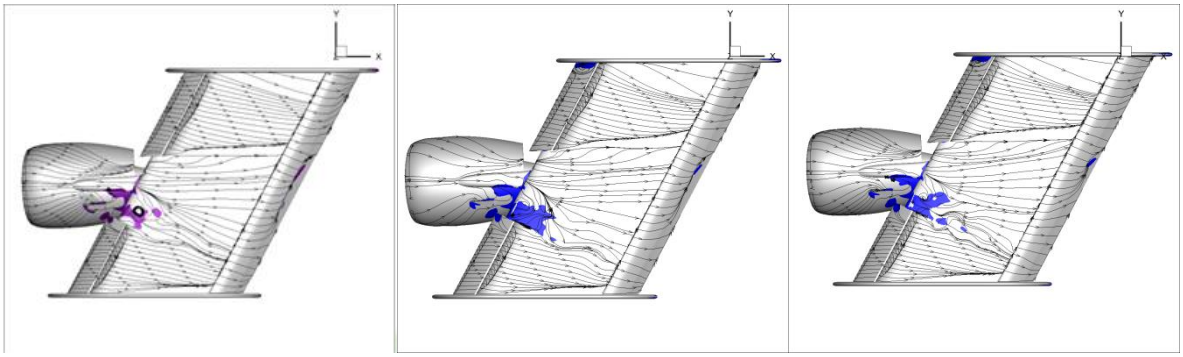

Figure 10 Surface streamlines and flow separation area of two rows of actuator (left), one row of actuator (middle) and one row of actuator with actuation frequency 1000Hz (right)

4 CONCLUSIONS

No flow separation was observed in the outboard part of the wing for the baseline and controlled flows for both strakes configurations. It was the main reason for the location of the actuators between the inner slat-end and pylon's axis.

The strake's shape and its position have a significant effect on the C_L and local flowfield without AFC. The new strake increases the C_{LMAX} by about 9 lc in comparison with the original one.

The stability and vertical position of the vortices forming behind the slat-end and inboard LE-step vortex have a significant effect on local flow separation on the wing-pylon area. If these vortices are "continuous" (not bursting or discontinuous) and closer to the wing's surface, the flow separation is usually suppressed. The structures and positions of these vortices can be, to a certain degree, maintained by a local application of AFC like SJA.

The effect of Cμ and the actuation frequency of SJA was considered and evaluated on the configuration with the new strake. The C_{LMAX} can be increased by about 8 lc by means of applying of two rows of SJ actuators with actuation frequency 100Hz. The Cμ has been changed from 0.0252% to 0.0127% by considering two rows or one row of actuators, respectively. In case that the Cμ is reduced to one half, the C_L is decreased by about 6 lc. But utilizing higher actuation frequency, the C_L can be increased again by about 3 lc. The overall drop of C_L by means of smaller value of Cμ and higher actuation frequency is only 3 lc in comparison with the value of C_L obtained using SJA in two rows and actuation frequency 100Hz.

Due to the very high time consuming of the simulations of the SJA especially with the higher actuation frequency (1000Hz), the effect of the Cμ and f was evaluated only for one post stall AoA.

The simulated high actuation frequency 1000Hz is still approximately one half of the working frequency of the real SJA. The simulation of the working frequency of SJ should be done using large eddy simulation (LES) instead of URANS, but for our target large Reynolds number it is not feasible today.

ACKNOWLEDGEMENT

These activities were done under FP7-AAT-2013-RTD-1 in the frame of AFLoNext, which is gratefully acknowledged.

Access to computing and storage facilities owned by parties and projects contributing to the National Grid Infrastructure MetaCentrum, provided under the programme "Projects of Large Infrastructure for Research, Development, and Innovations" (LM2010005), is greatly appreciated.

This work was supported by The Ministry of Education, Youth and Sports from the Large Infrastructures for Research, Experimental Development and Innovations project „IT4Innovations National Supercomputing Center – LM2015070“.

REFERENCES

[1] M. Lengers, Industrial Assessment of Overall Aircraft Driven Local Active Flow Control, *29th Congress of the International Council of the Aeronautical Sciences*, St. Petersburg, Russia, September 7-12, 2014

[2] AFLoNext project website: aflonext.eu

[3] V. Ciobaca, T. Kühn und R. Rudnik, „Active Flow Separation Control on a High-Lift Wing-Body Configuration. Part 2: The Pulsed Blowing Application,“ *29th AIAA Applied Aerodynamics Conference*, Honolulu, Hawaii, 2011.

[4] V. Ciobaca, J. Wild: Active Flow Control for an Outer Wing Model of a Take-off Transport Aircraft Configuration - A Numerical Study, *AIAA Paper 2014-2403*

[5] S. Fricke, V. Ciobaca, J. Wild, D. Norman: Numerical Studies of Active Flow Control Applied at the Engine-Wing Junction, *Advances in Simulation of Wing and Nacelle Stall Volume 131 of the series Notes on Numerical Fluid Mechanics and Multidisciplinary Design* pp 397-411

[6] M. Meunier und J. Dandois, „Simulations of Novel High-Lift Configurations Equipped with Passive and Active Means of Separation Control,“ *4th Flow Control Conference*, Seatle, Washington State, 2008-4080.

[7] P. Vrchota, P. Hospodář: Response Surface Method Application to High-Lift Configuration with Active Flow Control, Journal of Aircraft, Vol. 49, No. 6, pp. 1796-1802, 2012

[8] J. Wild, Experimental investigation of Mach- and Reynolds-number dependencies of the stall behavior of 2-element and 3-element high-lift wing sections. *AIAA-Paper 2012-0108*, 50th AIAA Aerospace Science Meeting, Nashville, 9-12 Jan. 2012.

[9] M.C. Galbraith, Numerical Simulation of a High-Lift Airfoil Employing Active Flow Control, *AIAA Paper 2006-147*

[10] R. Chow, K. Chu, G. Carpenter, Navier-Stokes Simulations of the Flow Field Around a Blown-Flap High-Lift System, *AGARD CP 515*, Sept.1993

[11] L.D. Kral, J.F. Donovan, A.B. Cain, A.W. Cary, Numerical Simulation of Synthetic Jet Actuators, AIAA Paper 1997-1834

[12] H. Frhr. v. Geyr, N. Schade: Prediction of Maximum Lift Effects on Realistic High-Lift-Commercial-Arcraft-Configurations within the European project EUROLIFT II, *Second symposium "Simulation of Wing Nacelle Stall"*, June 22-23, 2010, Braunschweig, Germany

ECCOMAS Congress 2016
VII European Congress on Computational Methods in Applied Sciences and Engineering
M. Papadrakakis, V. Papadopoulos, G. Stefanou, V. Plevris (eds.)
Crete Island, Greece, 5–10 June 2016

A NANO-MACRO BOTTOM-UP APPROACH TOWARDS BRITTLE FRACTURE

Sandeep P. Patil[1], Yousef Heider[2], Carlos Alberto Hernandez Padilla[3], Eduardo R. Cruz-Chú[4], and Bernd Markert[5]

[1 2 3 5]Institute of General Mechanics, RWTH Aachen University, Templergraben 64, 52062 Aachen, Germany
e-mail: {patil,heider,chernandez,markert}@iam.rwth-aachen.de

[2]Heidelberg Institute for Theoretical Studies, Schloss-Wolfsbrunnenweg 35, 69118 Heidelberg, Germany
e-mail: Eduardo.CruzChu@h-its.org

Keywords: Argonite, Fracture, Molecular Dynamics, Phase-Field Modeling.

Abstract. *A novel combined method for highly brittle materials, which provides an efficient and accurate insight into multi-scale fracture modeling, is proposed. In particular, physically-motivated molecular dynamics simulations are performed to predict crack propagation, in the nanoscale, and therewith determine material and other parameters required for the macroscale modeling under a phase-field continuum approach. The proposed computational approach, which does not require any empirical parameters, contributes towards an improved understanding of mechanics at all length-scale levels.*

1 INTRODUCTION

Molecular Dynamics (MD) simulations are considered new computational methods, employed to describe the time evolution of a system of interacting particles. They require the numerical solution of Newton's equations for every particle governed by an interatomic potential, i. e., bonded and non-bonded potentials, keeping track of the evolution of the system in space. Due to their real time scales (pico seconds), MD methods are perfectly suited to study the high-speed crack propagation of brittle materials, as demonstrated in the work of Rountree et al. [30]. Additionally, there have also been some applications of the method for a variety of inorganic crystals, such as Si_3N_4 [16], SiO_2 [31], 3C-SiC [17], and GaAs [34]. Although these studies have provided valuable in-sights into crack dynamics, a systematic analysis of mechanical properties at an atomistic scale, as well as a link to the macroscopic continuum mechanical approaches are still not well established.

Nowadays, typical MD simulations can be performed on systems containing hundreds of thousands, or perhaps, a few millions of atoms for simulation times ranging from a few hundred nanoseconds up to a millisecond. These numbers are certainly respectable, but one may run into conditions, where size and/or time limitations become important. The challenges related to the limited dimensions or time scales can be tackled by upscaling MD parameters and frameworks through continuum models. In fact, as it has been shown in numerous other studies, i. e., [5, 26, 27, 28], the mechanical behavior of a given continuous material can be reproduced in a different scale by using mechanical parameters derived directly from atomistic MD simulations.

In what numerical modeling regards, phase-field modeling (PFM) has emerged as a powerful tool to model brittle fracture under a macroscopic continuum approach, offering a good accordance between numerical treatment, accuracy, and computational costs. The pioneering works related to an elastic energy-based approach to describe brittle fracture, namely the works of Griffith [9] and Irwin [15], as well as the variational formulations presented in [4, 8], can be considered as the pillars of a well-established energy-based framework for brittle fracture. In the past decades, many PFMs, which approximate the sharp edges of the crack by a diffusive interface, have been developed. Due to their simple implementation, these models are able to predict quasi-static and dynamic cases of brittle and ductile fracture, considering diferent fracture modes and loadings, under several discretization schemes [4, 8, 3, 11, 22, 35, 19, 21].

Consequently, this research work pursues to establish a link between the understanding of brittle fracture of a material at an atomistic scale and its macroscopic mechanical features. To this end, an aragonite ($CaCO_3$) tablet undergoing fracture is studied using both, MD and PFM. Herein, the key mechanical properties (e. g., Young's modulus, Poisson's ratio), as well as the phase-field transition width (ϵ) and the mechanical energy release rate (G) of an aragonite crystal are obtained *ab initio*. These physical properties are subsequently employed to reproduce a nanoscale model under a continuous PFM approach.

Given that PFM and MD are relatively new topics in the realm of mechanics, the second and third sections of this work will briefly introduce the implementation of both methods. In the fourth section, a thorough description and brief evaluation of the numerical experiments in MD, as well as PFM are presented. The last section is dedicated to the conclusion and outlook of the present work.

2 MATERIALS AND MD SIMULATIONS

In the present work, MD and PFM simulations are employed to describe the behavior under fracture of Aragonite ($CaCO_3$), a highly brittle ceramic and major constituent of nacre (95 % vol.).

Tablets of this material were modeled, as seen in Fig. 1, by using the software Visual Molecular Dynamics (VMD) [14]. One double-notched tablet model was built with length (l), width (w) and height (h) of $15.38 \times 11.12 \times 4.30$ nm^3, respectively. The pulling layer thicknesses (pt) was considered to be three atomic layers wide. For the subsequent MD simulations, the molecular dynamics program GROMACS 5.0.4 package [33] was used. For aragonite interactions, newly-developed $CaCO_3$ forcefield [36], that describes angle, planar, dihedral, electrostatic and van der Waals interactions, was implemented.

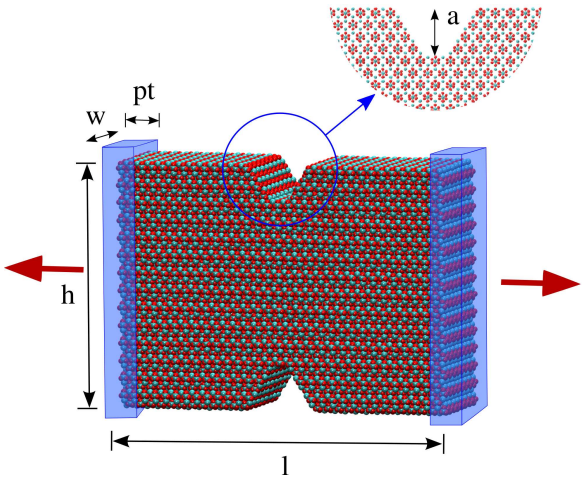

Figure 1: Double-notched all-atom model of an aragonite tablet. Oxygen and carbon atoms of carbonate groups are shown in cyan and red beads, respectively. Calcium atoms are shown with green beads. The dimension a (center) denotes the notch depth, while h, l, w and pt represent the height, length, width and pulling layer thickness, respectively. Pulling directions are perpendicular to the notch depth, which is marked by red arrows. Inset: enlargement of the front view of v-notch region.

The model in question was minimized and equilibrated in the NPT (isothermal-isobaric) ensemble for 10 ns at 300 K and 1.013 bar. The tablet did not show any significant changes neither in structural ordering nor in cell dimensions. The last frames were used to create notched systems as follows: The simulation boxes were extended 12 nm along l and h, leaving as much empty space as required to allow the tablet extension during pulling simulations. The periodic vector through the width w was not extended, resulting in tablets of infinite length along w-direction. Then, the v-shaped notches were introduced by removing atoms. The cut lines followed the (101) and ($\bar{1}$01) lattice planes, which resulted in an opening angle of 84.4 °. Such cut lines impose the removal of one calcium atom per carbonate group, preserving the electroneutrality of the systems.

In the MD calculations, the simulation box, in which the aragonite tablets were pulled, was repeated periodically in all three dimensions using 2 fs time steps. Van der Waals interactions were calculated using a cutoff of 1.0 nm. The Particle Mesh Ewald (PME) method [6] was chosen to account for long-range electrostatic interactions. To increase the simulation time step, a linear constraint solver for molecular simulations (LINCS) [12] was used to constrain all bond vibrations. The Nosé-Hoover [24, 13] temperature coupling was applied with a coupling time constant of 0.1 ps.

Fig. 1 shows an aragonite notched model with loading conditions and representative dimensions. The aragonite tablet model was not constrained at any point (which allows for rigid body motions) to capture a natural behavior in the simulations. The system was further equilibrated in the NVT (canonical ensemble, amount of substance N, volume V and temperature T

are conserved) for 10 ns at 300 K. To avoid tablet drifting, two cuboid volumes parallel to the (100) lattice plane were restrained, each cuboid volume containing the three outermost layers of $CaCO_3$ atoms. This resulted in a system of 66,720 atoms.
Once the equilibration of the system was achieved, a force-probe Molecular Dynamics (FPMD) simulation [10] was employed to enforce an external load. The restrained layers were released and pulled axially outwards with a spring-like force applied to the outer surfaces, with a constant velocity of 10 nm ns^{-1} and a spring constant of 1000 kJ mol^{-1} nm^{-2}. FPMD simulations were performed until tablet rupture, which usually occurred within 13 ns. Altogether, five FPMD simulations were performed. The obtained results were later post-processed to obtain critical material parameters, as well as the phase-field transition width and crack resistance energy.
Postulated in 1920, though still in force, the Griffith's energy-based analysis of cracks [9] states that the fracture strength is always lower than theoretical cohesive strength and attributes this discrepancy to the inherent defects in brittle materials, leading to stress concentration.
One of the underlying principles of fracture mechanics is that crack propagation occurs when the released elastic strain energy is at least equal to the energy required to generate new crack surface. The Griffith's energy criterion for fracture of brittle materials can then be written as

$$\sigma_f = \frac{1}{\alpha}\left[\frac{2E\gamma}{\pi a}\right]^{1/2} \quad , \tag{1}$$

where σ_f is the rupture strength, a is the notch depth, γ is the surface energy, E is the Young's modulus, and α is a geometry correction factor. For double edge notched tension of a semi-infinite tablet with notch depth a and tablet height h, α reads [29]

$$\alpha = 1.12 + 0.43\left[\frac{a}{h}\right] - 4.79\left[\frac{a}{h}\right]^2 + 15.46\left[\frac{a}{h}\right]^3. \tag{2}$$

It is now assumed that the available external and internal energy is transferred into surface energy. In what brittle fracture regards, dissipation and kinetic energy are neglected. This results in the so-called Griffith energy balance where the energy release rate G is equal to 2γ in J/m^2. The mechanical energy release rate in the $CaCO_3$ geometry is the amount of energy per unit area that is supplied by the elastic energy stored in the system.
The energy release rate can alternatively be calculated by integrating the stress-strain curve with respect to strain [20, 17]

$$G = l\int_0^{\varepsilon} \sigma(\varepsilon')d\varepsilon', \tag{3}$$

where l is the model width in the loading direction, see Fig. 1, and σ is the loading direction component of the stress well ahead of the crack tip. At a strain above ε_c, crack propagation at constant velocity is achieved after an initial transient [20].

3 BRITTLE FRACTURE MODELING USING THE PFM APPROACH

The macroscopic modeling of brittle fracture is based on the PFM approach, which has been widely discussed in several research works, see, e.g. [3, 22, 35] for an overview. In this, a phenomenological phase-field variable ϕ is introduced, which approximates the sharp interface of the crack by a diffusive transition zone. Thus, the global potential energy function $\mathscr{F}$ can be written with the help of ϕ and its gradient as an integral over the whole body ([4, 8, 19, 21]) as

$$\mathscr{F}(\phi, \operatorname{grad}\phi, \boldsymbol{\varepsilon}) = \int_V \left[\Psi_{elast}\left(\phi, \boldsymbol{\varepsilon}\right) + \Psi_{crack}(\phi, \operatorname{grad}\phi)\right] \mathrm{d}v \tag{4}$$

with $\boldsymbol{\varepsilon}$ being the linear strain tensor. The phase-field variable $\phi \in [0,1]$, in the sense of an indicator function, represents the crack state, where $\phi = 0$ for a cracked state and $\phi = 1$ for an undamaged state. The fracture energy Ψ_{crack} is defined as

$$\Psi_{crack}\left(\phi, \operatorname{grad}\phi\right) = \frac{G}{4\epsilon}(1-\phi)^2 + G\,\epsilon\,|\operatorname{grad}\phi|^2, \tag{5}$$

where ϵ is an internal length related to the width of the diffusive crack transition zone. As the degradation of the material is assumed to occur only under tension or shear, one applies an additive splitting of the linear elastic energy into a positive part Ψ^{+}_{elast}, that considers the tension and shear responses, and a negative part Ψ^{-}_{elast}, that considers the compression response. Moreover, the degradation function $g(\phi)$ can simply be defined in a quadratic form as $g(\phi) = [(1-\eta)(\phi)^2 + \eta]$ to obtain

$$\Psi_{elast}\left(\phi, \boldsymbol{\varepsilon}\right) = g(\phi)\ \Psi^{+}_{elast} + \Psi^{-}_{elast}\,. \tag{6}$$

Here, η is a residual stiffness added for numerical stability purpose. The linear elastic stress $\boldsymbol{\sigma}$ is obtained through the derivation of the phase-field potential with respect to the strain tensor, see [23].

$$\boldsymbol{\sigma}(\phi, \boldsymbol{\varepsilon}) = \frac{\partial \mathscr{F}}{\partial \boldsymbol{\varepsilon}} = g(\phi)\ \frac{\partial\, \Psi^{+}_{elast}}{\partial \boldsymbol{\varepsilon}} + \frac{\partial\, \Psi^{-}_{elast}}{\partial \boldsymbol{\varepsilon}}\,. \tag{7}$$

Furthermore, the momentum balance equation under the assumptions of a quasi-static state and neglecting the body forces can be expressed as

$$\operatorname{div}\boldsymbol{\sigma} = \mathbf{0}\,, \tag{8}$$

allowing the computation of displacement field $\mathbf{u}$. To this end, the evolution of the phase field is derived using the Allen-Cahn model,which describes the process of crack evolution via a reaction-diffusion equation as

$$\begin{aligned} \dot{\phi} &= \frac{\partial \phi}{\partial t} = -M \frac{\partial \mathscr{F}}{\delta \phi} \\ &= -M \left[2\,(1-\eta)\phi\ \Psi^{+}_{elast} - \frac{G}{2\epsilon}(1-\phi) - 2\,G\,\epsilon \operatorname{div}\operatorname{grad}\phi \right], \end{aligned} \tag{9}$$

where $M \geq 0$ represents a mobility constant.

For the numerical implementation of the PFM problem, an initial boundary-value problem of mode-I fracture, illustrated in Figure 2, is solved using the finite element package FlexPDE.

The numerical solution is computed considering quadratic shape functions for the displacement and the phase-field variable, and the time integration is applied using the 2^{nd}-order backward difference formula (BDF2), where a time-step automatic adaptivity is also employed. Moreover, a fixed mesh, refined in the area between the notches, is implemented. A plane stress, linear elastic model is used to reproduce the MD simulation. Under this setup, the stress is applied until instantaneous rupture of the plate takes place.

The material parameters, E, ϵ and G, for the PFM of the aragonite plate were directly derived from the outcomes of the MD simulations as will be discussed in the next section. Therewith, the obtained values were $E = 126$ GPa for the Young's modulus. The crack resistance (or energy release rate) was found to be $G = 2.091$ J/m^2 and the internal length scale $\epsilon = 0.05$ nm. The values of the mobility and the residual stiffness parameters were set to $M = 10{\times}10^9$nm^2/Ns

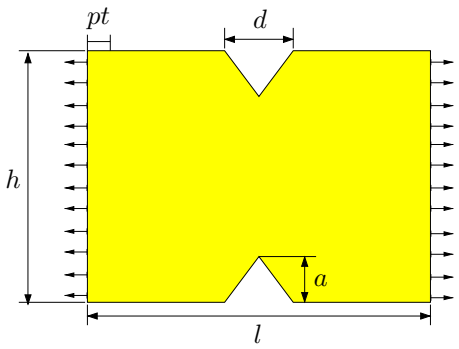

Figure 2: Boundary conditions of the IBVP (load-controlled). For the boundary layers with width pt, $\nu = 0$ and zero-stress in vertical direction. In the middle of the extreme edges (left and right), two points are fixed in the vertical direction to prevent a rigid body motion. The dimensions here are h=11.2 nm, l=15.3 nm, d=3.08 nm, and a=1.84 nm.

and $\eta = 10^{-5}$, respectively, whereas the applied Poisson's ratio is $\nu = 0.44$. The material properties such as Possion's ratio ν and the density ρ were benchmarked with the aragonite-related literature ([1, 2, 7, 25]), whereas the mobility parameter M and the residual stiffness parameter η are in good agreement with the ranges proposed in, e.g., [18, 23].

4 RESULTS AND DISCUSSION

As stated previously, to examine the fracture behavior at atomistic scale of aragonite, monotonic tension tests were performed by means of FPMD. The molecular system was loaded by moving virtual springs applied to the outer surfaces of the tablets with constant velocity. The force is obtained directly from the resultant spring force at the boundaries. Accordingly, the stress is computed by dividing the spring force by the cross sectional area comprehended between two notches. Moreover, the relative displacement of atoms was measured between the center of mass of both pulling layers. Here, the engineering strain is obtained by dividing the total displacement of the center of mass of any pulling layer by the original distance between this layer and the center of specimen. The crystals deformed during the FPMD simulations until the externally applied stress reached the ultimate tensile strength σ_f, resulting in a sudden rupture. Due to the chemical structure of calcium carbonate $[Ca^{2+}][CO_3^{2-}]$, and its arrangement in compact crystal, it is not always possible to have symmetric notches on both edges as well as notches at the exact center of all tablets of $CaCO_3$ models. Therefore, the v-notches in the tablets are not sharp, and the notch tips can have, either, single or double $CaCO_3$ units (enlarged view in Fig. 1). Thus, different crack propagations were observed in the tablet models, e. g., the crack starts at the top edge, bottom edge or at both edges simultaneously (shown in Fig. 3). For all simulations, the cracks propagated with an s-shape along the (101) and ($\bar{1}$01) lattice planes, as expected.

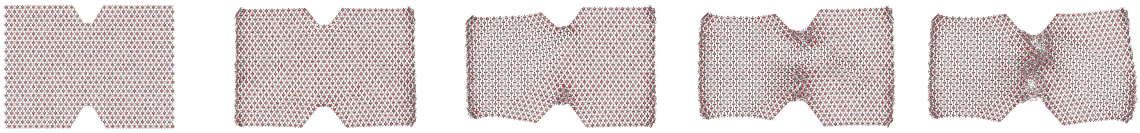

Figure 3: Rupture of the double-notched aragonite tablets. The snapshots show the fracture of the aragonite tablets under constant pulling velocity. As the two atom groups at the ends are pulled, the tablets slightly stretch and break abruptly around the notch. Here, the crack initiates at the bottom, though, is propagated from both sides and with an s-shape.

Fig. 3 shows snapshots of the rupture processes observed in the $CaCO_3$ tablet models. The model was loaded with a constant velocity for 12.88 to 13.056 ns, without observing crack initiation. However, the crack initiation took place during the following 0.012 ns, inducing an instantaneous total failure.

The results describe a good agreement with the expectations. First of, the energy release rate G can be calculated using the MD results together with either Griffith's criterion given in Eq. (1) or by use of Eq. (3). Both equations confirm that the fracture of the $CaCO_3$ tablet occurs at a value $G \approx 2.091$ J/m^2. This value is slightly lower than the theoretical values of G for $CaCO_3$ (2.10 – 3.74 J/m^2), which can be found in the literature [1, 2, 7], though this difference is merely negligible. Therefore, $G = 2.091$ J/m^2 is adopted for the PFM.

To avoid model dependency in MD simulations, five different aragonite tablet models were considered, and the stress-strain curves were jointly analyzed. The recovered elasticity modulus E of aragonite ranges between 106 to 148 GPa, which is in the range of experimental and theoretical studies, see [1, 2, 7]. With regard to the ultimate tensile strength, the resulting MD simulations value of the aragonite notched samples is 4.6 GPa. This value is slightly lower than the theoretical strength of flawless minerals, which was estimated to lie in the range of 5 to 10 GPa [32].

Fig. 4 shows the force-displacement curves of the continuous PFM (considering a Young's modulus of $E = 126$ GPa) and all-atom simulations. With regard to the force at failure, the resulting MD simulations value of the aragonite notched samples is 47 μN and the nonlinear behavior, which is due to the potential energy non-linearities, is clearly observed. Although, a linear elastic model was considered for the PFM, an outstanding correlation of the results is observed.

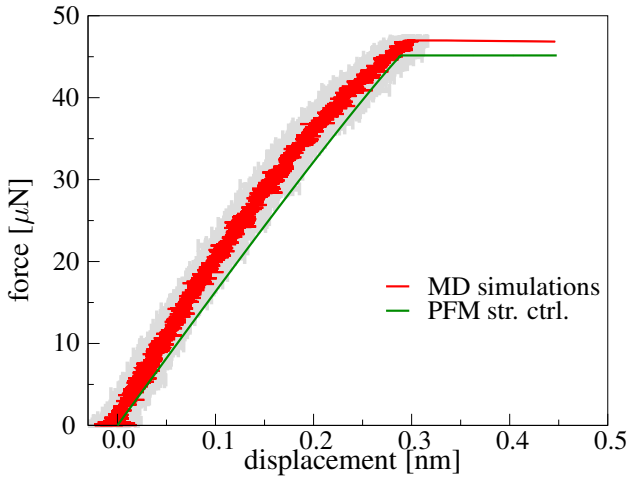

Figure 4: Force-displacement curves for the aragonite tablet models. The red line is the averaged force-displacement curve from the MD simulations, and the gray shaded area indicates the standard error deviation. The green line indicate the force-displacement curves obtained from the PFM stress-controlled simulation.

Phenomenologically, the s-shaped crack propagation (along the (101) and ($\bar{1}$01) lattice planes) is obtained in both MD and PFM approaches. Moreover, the ultimate tensile strength obtained in the PFM simulations falls perfectly into the ranges described in the all-atom simulations. Nevertheless, a discrepancy between the two schemes can be seen which can be traced to two main reasons: On the one side, the boundary conditions in the MD simulation allow for rigid body rotations and translations, which are constrained in the continuum model by fixing the vertical displacement of two points. This fixation causes an artificial symmetry and simultaneously

stiffens the material. On the other side, the PFM considers a linear elastic material response, which is not able to account for the inherent material non-linearities. As seen in Fig. 4, these non-linearities are naturally captured in the atomistic simulations.
An important outcome, particularly for the phase-field parameters, is the theoretical and numerical consistency of the critical energy release rate G, and a potential relationship between the molecular transition (distortion) zone and the phase-field transition width governed by the internal length parameter ϵ. The former can be estimated by means of the Griffith's theory or by integration of the stress-strain curve, yielding a value within the literature range (approximately 2.1 J/m^2). The latter can be obtained by measuring the cracked surfaces in a straightforward post-processing step. The results of the MD and PFM simulations are shown in Fig. 5. Taking into account the density plot of the MD and overlapping it with the resultant intact-to-cracked material transition of the PFM, as seen in Fig. 5, the phenomenological correlation is evident.

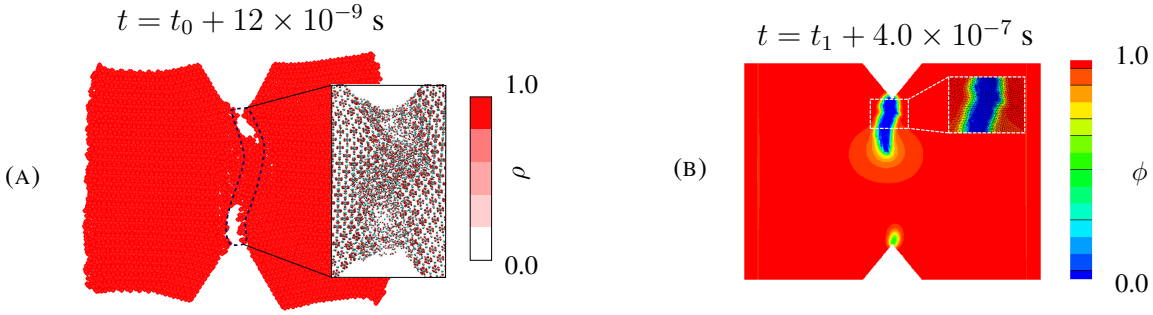

Figure 5: Crack initiation and propagation comparison: (A) Density plots of atoms in MD simulations (ρ stands for density). The s-shaped crack is illustrated with a dotted line, and the inset shows an all-atom simulation snapshot of the crack propagated area. (B) PFM results for stress-controlled simulations (ϕ stands for the damage phase-field, blue corresponds to cracked material, and red refers to undamaged material). The times t0 and t1 are the total loading times before crack initiation in MD (t0 = 13056 ps) and PFM stress-controlled (t1 = 0.0403089 s) respectively.

5 CONCLUSIONS

As shown in this work, the efficiency of continuum mechanics allows to infer mechanical properties from the molecular scale, which is the key to understand a material's interplay of the atomic structure and its overall performance. Through an atomistic obtention of the material parameters, the PFM presented in this work observes a fair convergence, and more important remains qualitatively and quantitatively within the outcomes of MD simulations and the benchmarked literature. Moreover, a correlation between the phase-field parameter ϵ (which is of extreme importance for convergence) and an MD transition zone was captured for the first time. Through further study, this could result in a physical meaning and obtention of the parameter value, which is up to date "fitted́ according to each model. Moreover, the observed molecular dissipative zone between the undamaged and cracked material allows to think that in fact, brittle fracture observe a transition zone, under a purely atomistic standpoint.
As part of a novel approach, this work remains to have improvement areas. The outlook of this research will firstly consist of implementing a non-linear elastic model in order to better capture the material behavior from all-atom simulations. Moreover, further MD as well as PFM simulations under different setups (shear, combined loadings, dynamic case, different

geometries, etc.) are required. Deeper and extensive studies of the molecular dissipative zone observed in the simulations of this work, are also to be carried over.

REFERENCES

[1] F. Barthelat and H. D. Espinoza. Elastic properties of nacre aragonite tablets. In *In SEM Annual Conference and Exposition on Experimental and Applied Mechanics*, page 187, 2003.

[2] F. Barthelat, C. M. Li, C. Comi, and H. D. Espinosa. Mechanical properties of nacre constituents and their impact on mechanical performance. *J. Mater. Res.*, 21:1977–1986, 2006.

[3] M. J. Borden, C. V. Verhoosel, M. A. Scott, T. J. R. Hughes, and C. M. Landis. A phase-field description of dynamic brittle fracture. *Comput. Method. Appl. M.*, 217–220:77–95, 2012.

[4] B. Bourdin, G.A. Francfort, and J.J. Marigo. The variational approach to fracture. *J. Elasticity*, 91:5–148, 2008.

[5] Murat Cetinkaya, Senbo Xiao, Bernd Markert, Wolfram Stacklies, and Frauke Gräter. Silk fiber mechanics from multiscale force distribution analysis. *Biophys J*, 100(5):1298–1305, Mar 2011.

[6] T. Darden, D. York, and L. Pedersen. Particle mesh ewald: An n log (n) method for ewald sums in large systems. *J. Chem. Phys.*, 98:10089–10092, 1993.

[7] T. Z. Forbes, A. V. Radha, and A. Navrotsky. The energetics of nanophase calcite. *GeoChim. Cosmochim. Ac.*, 75:7893–7905, 2011.

[8] G.A. Francfort and J.-J. Marigo. Revisiting brittle fracture as an energy minimization problem. *J. Mechan. and Phys. Solids.*, 46:1319–1342, 1998.

[9] A. A. Griffith. The phenomena of rupture and flow in solids. *Phil. Trans. Roy. Soc. Lond. A*, 221:163–198, 1921.

[10] H. Grubmüller, B. Heymann, and P. Tavan. Ligand binding: molecular mechanics calculation of the streptavidin-biotin rupture force. *Science*, 271(5251):997–999, Feb 1996.

[11] C. A. Hernandez Padilla and B. Markert. A coupled ductile fracture phase-field model for crystal plasticity. *Continuum Mech. Thermodyn. DOI:10.1007/s00161-015-0471-0*, pages 1–10, 2015.

[12] B. Hess, H. Bekker, H. J. C. Berendsen, and J. G. E. M. Fraaije. Lincs: a linear constraint solver for molecular simulations. *J. Comput. Chem.*, 18(12):1463–1472, 1997.

[13] W. G. Hoover. Canonical dynamics: Equilibrium phase-space distributions. *Phys. Rev. A*, 31(3):1695–1697, 1985.

[14] W. Humphrey, A. Dalke, and K. Schulten. Vmd: visual molecular dynamics. *J. Mol. Graph.*, 14(1):33–38, 1996.

[15] G. R. Irwin. Analysis of stresses and strains near the end of a crack traversing a plate. *J Appl Mech*, 24:361–364, 1957.

[16] R. K. Kalia, A. Nakano, A. Omeltchenko, K. Tsuruta, and P. Vashishta. Role of ultrafine microstructures in dynamic fracture in nanophase silicon nitride. *Phys. Rev. Lett.*, 78:2144, 1997.

[17] H. Kikuchi, R. K. Kalia, A. Nakano, P. Vashishta, P. S. Branicio, and F. Shimojo. Brittle dynamic fracture of crystalline cubic silicon carbide (3c-sic) via molecular dynamics simulation. *J. Appl. Phys*, 98:103524, 2005.

[18] C. Kuhn and R. Müller. A continuum phase field model for fracture. *Eng. Fract. Mech.*, 77:3625 –3634, 2010.

[19] C. Kuhn, A. Schlüter, and R. Müller. A phase field approach for dynamic fracture. *PAMM*, 13(1):87–88, 2013.

[20] B. Lawn. *Fracture of Brittle Solids*. Cambridge University Press, Cambridge, 1993.

[21] B. Markert and Y. Heider. Coupled multi-field continuum methods for porous media fracture. In Miriam Mehl, Manfred Bischoff, and Michael Schäfer, editors, *Recent Trends in Computational Engineering - CE2014*, volume 105 of *Lecture Notes in Computational Science and Engineering*, pages 167–180. Springer International Publishing, 2015.

[22] C. Miehe, M. Hofacker, and F. Welschinger. A phase field model for rate-independent crack propagation: Robust algorithmic implementation based on operator splits. *Comput. Method. Appl. M.*, 199:2765 –2778, 2010.

[23] C. Miehe, F. Welschinger, and M. Hofacker. Thermodynamically consistent phase-field models of fracture: Variational principles and multi-field fe implementations. *Int. J. Numer. Meth. Eng.*, 83:1273–1311, 2010.

[24] S. Nosé. A molecular dynamics method for simulations in the canonical ensemble. *Mol. Phys.*, 52(2):255–268, 1984.

[25] S. P. Patil, Y. Heider, C.A. Hernandez-Padilla, E.R. Cruz-Chú, and B. Markert. A combined molecular dynamics-phase-field modeling approach to fracture. *Comput. Methods Appl. Mech. Engrg.*, page submitted, 2015.

[26] S. P. Patil, B. Markert, and F. Gräter. Refining a bottom-up computational approach for spider silk fibre mechanics. *Proceedings of the 3rd GAMM Seminar on Continuums Biomechanics*, II-21:75–87, 2012.

[27] Sandeep P. Patil, Bernd Markert, and Frauke Gräter. Rate-dependent behavior of the amorphous phase of spider dragline silk. *Biophys J*, 106(11):2511–2518, Jun 2014.

[28] Sandeep P. Patil, Senbo Xiao, Konstantinos Gkagkas, Bernd Markert, and Frauke Gräter. Viscous friction between crystalline and amorphous phase of dragline silk. *PLoS One*, 9(8):DOI: 10.1371/journal.pone.0104832, 2014.

[29] N. Perez. *Fracture Mechanics*. Kluwer Academic Publisher Group, 2004.

[30] C. L. Rountree, R. K. Kalia, E. Lidorikis, A. Nakano, L. van Brutzel, and P. Vashishta. Atomistic aspects of crack propagation in brittle materials: Multimillion atom molecular dynamics simulations. *Annu. Rev. Matter. Res.*, 32:377–400, 2002.

[31] C. L. Rountree, S. Prades, D. Bonamy, E. Bouchaud, R. Kalia, and C. Guillot. A unified study of crack propagation in amorphous silica: Using experiments and simulations. *J. Alloy. Comp.*, 434–435:60–63, 2007.

[32] C. H. Scholz. *The Mechanics of Earthquakes and Faulting*. Cambridge University Press, 2^{nd} edition, 2002.

[33] D. van der Spoel, E. Lindahl, B. Hess, G. Groenhof, A. E. Mark, and H. J. Berendsen. Gromacs: fast, flexible, and free. *J. Comput. Chem.*, 26(16):1701–1718, 2005.

[34] P. Vashishta, M. E. Bachlechner, T. Campbell, R. K. Kalia, H. Kikuchi, S. Kodiyalam, A. Nakano, S. Ogata, F. Shimojo, and P. Walsh. Multimillion atom simulation of nanostructured materials on parallel computers. *Prog. Theor. Phys. Supplement*, 138:135–170, 2000.

[35] J. Vignollet, S. May, R. de Borst, and C. V. Verhoosel. Phase-field models for brittle and cohesive fracture. *Meccanica*, 49:2587–2601, 2014.

[36] S. Xiao, S. A. Edwards, and F. Gräter. A new transferable forcefield for simulating the mechanics of $caco_3$ crystals. *J. Phys. Chem. C*, 115:20067–20075, 2011.

ECCOMAS Congress 2016
VII European Congress on Computational Methods in Applied Sciences and Engineering
M. Papadrakakis, V. Papadopoulos, G. Stefanou, V. Plevris (eds.)
Crete Island, Greece, 5–10 June 2016

INTEGRATION OF DESIGN AND ANALYSIS THROUGH BOUNDARY INTEGRAL EQUATIONS

Benjamin Marussig[1], Jürgen Zechner[1], Gernot Beer[1,2], and Thomas-Peter Fries[1]

[1]Institute of Structural Analysis
Graz University of Technology
Lessingstraße 25/II, 8010 Graz, Austria
e-mail: {marussig,juergen.zechner,fries}@tugraz.at

[2] Centre for Geotechnical and Materials Modeling
University of Newcastle Callaghan, NSW 2308, Australia
e-mail: gernot.beer@tugraz.at

Keywords: Isogeometric Analysis, Boundary Element Method, Trimmed NURBS, Independent Field Approximation, Extended B-splines.

Abstract. *The direct integration of Computer Aided Geometric Design (CAGD) models into a numerical simulation improves the accuracy of the geometrical representation of the problem as well as the efficiency of the overall analysis process.*

In this work, the complementary features of isogeometric analysis and boundary integral equations are combined to obtain a coalescence of design and analysis which is based on a boundary-only discretization. Following the isogeometric concept, the functions used by CAGD are employed for the simulation. An independent field approximation is applied to obtain a more flexible and efficient formulation. In addition, a procedure is presented which allows a stable analysis of trimmed geometries and a straightforward positioning of collocation points.

Several numerical examples demonstrate the characteristics and benefits of the proposed approach. In particular, the independent field approximation improves the computational efficiency and reduces the storage requirements without any loss of accuracy. The proposed methodology permits a seamless integration of the most common design models into an analysis of linear elasticity problems.

1 INTRODUCTION

Isogeometric analysis aims to close the existing gap between the design process and analysis such that a simulation can be performed without generating a mesh. Consequently, the accuracy and efficiency of the overall simulation process is improved, since meshing is time-consuming [1, 2] and introduces additional (geometrical) approximation errors. In addition, the basis functions used by design models, i.e. NURBS, provide further benefits such as high continuity [3, 4].

However, during the last years, it has become clear that a true integration of design and analysis is far from trivial due to several reasons: first of all, most engineering design models are based on a *boundary representation* (B-Rep) rather than a volume description. Secondly, three dimensional B-Rep models are usually defined by a *non-conforming* partition of NURBS surfaces, i.e. their mathematical parametrizations have no explicit relation to each other. Thirdly, each boundary surface is based on a tensor product structure which is a very efficient representation but has limitations due to its four sided nature. As a result, almost all NURBS based design models use *trimming* procedures to increase the flexibility of tensor product surfaces. This means that only a certain area of a surface is visualized while the underlying mathematical parametrization remains unchanged.

In this work, a coherent framework is presented which allows a seamless integration of trimmed NURBS models into an analysis. In general, the governing equations of the problem are expressed by means of boundary integral equations which are discretized by a numerical approximation method. Here, the *boundary element method* (BEM) is used since it is the most versatile approach. However, it should be pointed out that other schemes like the Nyström method can be applied as well [5, 6]. An *independent field approximation* concept is introduced in order to obtain a flexible BEM formulation. Furthermore, this allows the stabilization of trimmed NURBS geometries by the application of *extended B-splines*. The following sections provide an overview of the proposed methodology. They actually recap and unify the main features presented in [6–8]. Hence, the interested reader is particularly referred to the first one of these references for an in-depth discussion.

2 METHODOLOGY

2.1 Isogeometric Boundary Element Method

A linear elastic body Ω subject to external loading without body forces is considered. The closed boundary of the domain is denoted by Γ and the surface normal $\mathbf{n}$ points outside. Using Betti's or Green's theorem the following integral equation also known as *Somigliana's identity* is obtained

$$\mathbf{u}(\boldsymbol{x}) = \int_\Gamma \mathsf{U}(\boldsymbol{x},\boldsymbol{y})\,\mathbf{t}(\boldsymbol{y})\,\mathrm{ds}_{\boldsymbol{y}} - \int_\Gamma \mathsf{T}(\boldsymbol{x},\boldsymbol{y})\,\mathbf{u}(\boldsymbol{y})\,\mathrm{ds}_{\boldsymbol{y}} \qquad \forall \boldsymbol{x} \in \Omega,\ \forall \boldsymbol{y} \in \Gamma \tag{1}$$

where U and T are fundamental solutions for displacement and traction, respectively [9]. In general, a fundamental solution $\mathsf{U}(\boldsymbol{x},\boldsymbol{y})$ provides the response at a *field point* $\boldsymbol{y}$ due to a unit point source applied at $\boldsymbol{x}$, which is denoted as *source point*. It should be noted that once the Cauchy data, i.e. displacement $\mathbf{u}(\boldsymbol{y})$ and traction $\mathbf{t}(\boldsymbol{y})$, are known on the entire boundary Γ, the representation formula (1) describes the displacement $\mathbf{u}(\boldsymbol{x})$ within the whole domain Ω. In order to solve for unknown boundary values, the source points $\boldsymbol{x}$ are shifted to Γ leading to the

boundary integral equation

$$\mathbf{c}(\boldsymbol{x})\mathbf{u}(\boldsymbol{x}) = \int_\Gamma \mathsf{U}(\boldsymbol{x},\boldsymbol{y})\,\mathbf{t}(\boldsymbol{y})\,\mathrm{ds}_{\boldsymbol{y}} - \int_\Gamma \mathsf{T}(\boldsymbol{x},\boldsymbol{y})\,\mathbf{u}(\boldsymbol{y})\,\mathrm{ds}_{\boldsymbol{y}} \qquad \forall \boldsymbol{x},\boldsymbol{y} \in \Gamma \tag{2}$$

in which the coefficient $\mathbf{c}(\boldsymbol{x})$ depends on the geometrical angle of Γ at $\boldsymbol{x}$ and the Poisson's ratio [10]. Equation (2) represents the governing equations of the problem by means of an integral over the boundary of the computational domain. Hence, corresponding numerical approximation methods like the BEM do not require a domain discretization.

In isogeometric boundary element formulations, the geometry as well as the boundary data are represented by B-spline or NURBS basis functions. The boundary Γ of the computational domain is specified by a disjoint set of patches (curves or surfaces) γ such that

$$\Gamma = \bigcup_{i=1}^{I} \gamma_i \tag{3}$$

which is equivalent to the representation of design models. Since this is the best geometry representation available the computational boundary is described as accurate as possible.

Within each γ, the geometry $\boldsymbol{x}(\xi)$ is defined by a set of basis functions $B_{i,p}$ of degree p with corresponding coefficients in physical space $\boldsymbol{c}_i$ which are denoted as control points. The geometrical mapping χ from parameter space ξ to physical space is given by

$$\chi(\xi) \coloneqq \boldsymbol{x}(\xi) = \sum_{i=0}^{I-1} B_{i,p}(\xi)\,\boldsymbol{c}_i \tag{4}$$

with I representing the total number of basis functions. The main advantages of these patches are that their continuity is directly controlled by the applied basis functions. The parameter space ξ as well as the properties of this basis functions are determined by a knot vector Ξ which is a non-decreasing sequence of parametric coordinates ξ_i. For more detailed information on B-splines and NURBS the interested reader is referred to [2, 11]. Similar to the geometric mapping (4), displacements and tractions of each γ are discretized by

$$\mathcal{Y}_u(\xi) := \mathbf{u}(\xi) = \sum_{i=0}^{I-1} B_i(\xi)\,\tilde{\mathbf{u}}_i \qquad \text{and} \qquad \mathcal{Y}_t(\xi) := \mathbf{t}(\xi) = \sum_{j=0}^{J-1} B_j(\xi)\,\tilde{\mathbf{t}}_j. \tag{5}$$

The coefficients $\tilde{\mathbf{u}}_i$ and $\tilde{\mathbf{t}}_j$ are control parameters of the corresponding field and the related basis functions are denoted by B_i and B_j.

The system of equations is set up using a collocation approach where the boundary integral equation is enforced in a set of *collocation points* $\boldsymbol{x}^c$. In particular, each basis function B_i of the unknown field is related to a certain $\boldsymbol{x}_i^c$. It has been demonstrated by several authors [7, 12, 13] that the Greville abscissae

$$\bar{\xi}_i = \frac{\xi_{i+1} + \xi_{i+2} + \cdots + \xi_{i+p}}{p} \tag{6}$$

are a robust and accurate choice for the location of the collocation points, i.e. $\boldsymbol{x}_i^c = \chi(\bar{\xi}_i)$. For each $\boldsymbol{x}_i^c$, the integrals of the boundary integral equation (2) with $\boldsymbol{x} = \boldsymbol{x}_i^c$ are evaluated using numerical integration. Since each γ may contain non-smooth regions, it has to be subdivided

into integration elements. Within those integration elements, the integrand is smooth and hence numerical integration can be performed properly.

Usually, equation (6) leads to some collocation points located on the boundary of each γ. Hence, they should be considered during the integration of adjacent γ as well. For two dimensional problems, i.e. boundary curves, this is not challenging. However, in case of boundary surfaces, detection of adjacent surfaces and determination of the collocation points' intrinsic coordinates within them may be very involved. Especially, if non-conforming partitions of trimmed surfaces are considered. The application of discontinuous collocation is an elegant remedy to this issue [6, 7]. Using such schemes, collocation points along the boundary of γ are slightly shifted inside, thereby abolishing the link to adjacent surfaces. In general, this is possible since interelement continuity is not necessarily required in BEM [14].

2.2 Independent Field Approximation

In the context of isogeometric BEM, the Cauchy data are discretized by means of B-splines or NURBS. The related mappings (5) are denoted by $\mathcal{Y}_u(\xi)$ and $\mathcal{Y}_t(\xi)$ for displacements $\mathbf{u}$ and traction $\mathbf{t}$, respectively. In the following, the distinction between *isoparametric* and *subparametric* patches is introduced. The former employs the isoparametric paradigm, i.e. all fields are represented by the same basis functions, as it is generally the case in isogeometric analysis. The latter utilizes the proposed independent field approximation. The term subparametric indicates that less parameters are used for the description of the geometry than for the Cauchy data.

2.2.1 Isoparametric Patches

In an isoparametric discretization, the mappings $\mathcal{Y}_u(\xi)$ and $\mathcal{Y}_t(\xi)$ are equal to the geometrical one $\chi(\xi)$. This implies some compromises. First of all, the same refinement is applied to all fields. On the one hand, refinement of the unknown field is mandatory to improve the solution. But as a consequence, the geometry and the known field are refined even though they may be exactly represented by the initial basis functions. In addition to refinement aspects, the fields have different continuity requirements along corners and edges. In particular, discontinuous basis functions are required to describe traction jumps. However, they are not optimal for representing the displacement field, which should be continuous according to the physical constraint. Furthermore, the number of basis functions would be increasing unnecessarily.

Thus, a preliminary conclusion is that an isoparametric discretization introduces superfluous control variables. This increases the numerical effort and storage requirements for setting up the system of equations, particularly for its right hand side. Moreover, refinement of CAGD models affects the efficiency of all geometry evaluations performed during the analysis. These points motivate the application of the proposed subparametric approach presented next.

2.2.2 Subparametric Patches

In this section, subparametric patches are introduced. The key idea is to treat each field separately in order to fulfill their individual needs. In particular, the concept of a subparametric element is adopted, i.e. more basis functions will be used to represent the field variables than for the geometry representation. The basis functions of the geometry, the displacements, and the tractions are defined by the knot vector Ξ_g, Ξ_u, and Ξ_t, respectively. Without loss of generality, basis functions of the Cauchy data are defined as an extended version of Ξ_g, so that $\Xi_g \subset \Xi_u$ and $\Xi_g \subset \Xi_t$. This definition guarantees a proper partition of integration elements. It should,

however, be noted that it allows the variation of basis functions types. For instance, the Cauchy data over a NURBS patch may be approximated by B-splines. The resulting benefits are that the evaluation of Cauchy data becomes more efficient and the refinement procedure is simplified. Moreover, it has been demonstrated that the approximation quality is hardly effected by such a combination [7, 13].

In the present implementation the geometry knot vector Ξ_g provides the initial basis for all fields. Subsequently, basis functions are refined only if it is necessary. Discontinuous basis functions are introduced only for the traction field at non-smooth boundaries. The known Cauchy data are classified as *simple* or *complex* boundary conditions as indicated in Figure 1. The former can be exactly represented by Ξ_g, hence the corresponding discretization does not need to be refined. Homogeneous boundary conditions or constant loading are examples for such boundary conditions. The latter can only be approximated and the corresponding basis functions have to be refined to improve the representation of the known Cauchy data. In such a case, refinement is performed equally to the one for the approximation of the unknown field.

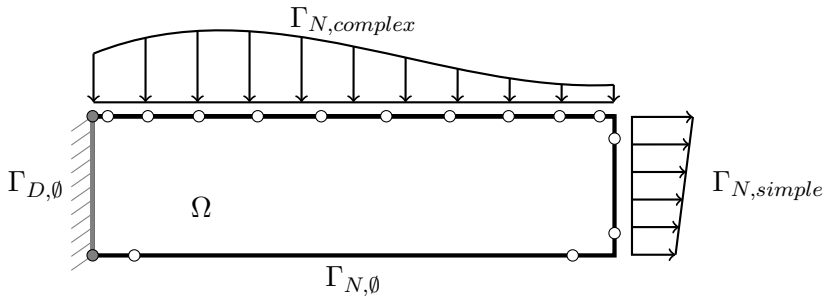

Figure 1: Examples of simple and complex boundary conditions applied to a cantilever beam. Homogeneous boundary condition are denoted by the subscript $\emptyset$. Circles indicate the related Greville abscissae of the basis functions which represent the known data.

To sum up, the main aim of independent field approximation is to avoid redundancies in the discretization, leading to an enhanced isogeometric BEM formulation. At the same time, no discretization errors are introduced and the initial design model remains unchanged during the simulation which simplifies the interaction with CAGD software.

2.3 Stable Basis for Trimmed Geometries

In general, a trimmed parameter space has only a certain area which represents the part of an object that is visualized. This part is denoted as valid domain Ω^{v} for the remainder of this paper. Usually, trimming is used for surfaces and in this case Ω^{v} is determined by so-called trimming curves which are defined within the parameter space of the surface.

There are two main aspects that have to be considered if trimmed geometries are integrated into a numerical simulation: firstly, only the visualized part has to be considered for the analysis. Secondly, the trimmed parameter space has to be stabilized, because basis functions with small support occur which may lead to ill-conditioned system matrices. Several different approaches [15–20] have been proposed to address the former issue. However, the latter has hardly been considered in the literature so far. Hence, the current section focuses on this aspect. In particular, it is proposed to stabilize trimmed parameter spaces by using so-called *extended B-splines* which have been originally introduced in the context of fictitious domain – finite element methods [21–24].

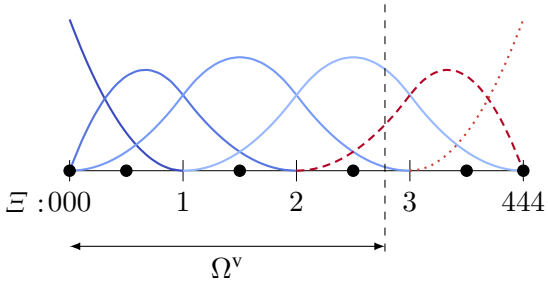

Figure 2: Classification of basis function types in case of a trimmed parameter space: stable (continuous), degenerated (dashed), and exterior (dotted). The related Greville abscissae are illustrated by circles.

The basic idea of extended B-splines is to replace basis functions which may cause instabilities by extrapolations of neighboring ones which have a sufficient large support. In order to classify the B-splines of a trimmed parameter space, three types are introduced: stable, degenerated, and exterior. We propose to label B-splines $B_{i,p}$ as stable if their corresponding Greville abscissae is within the valid domain, i.e. $\bar{\xi}_i \in \Omega^{\mathrm{v}}$. The support of exterior B-splines, on the other hand, is entirely outside of Ω^{v}. The remaining degenerated basis functions are partially inside of Ω^{v} but their Greville abscissae is outside, i.e. $\bar{\xi}_i \notin \Omega^{\mathrm{v}}$. These various types are shown for an univariate parameter space in Figure 2. Once the degenerated B-splines are detected, the functions within their support are substituted by extensions of the closest stable segments as illustrated in Figure 3. The resulting extended B-splines $B^e_{i,p}$ are defined by a linear combination of the original ones

$$B^e_{i,p} = B_{i,p} + \sum_{j \in \mathbb{J}_i} e_{i,j} B_{j,p} \tag{7}$$

where $\mathbb{J}_i$ is an index-set of all degenerated B-splines $B_{j,p}$ related to the current $B^e_{i,p}$. For univariate basis functions, the corresponding extrapolation weights $e_{i,j}$ are generally defined by the so-called *de Boor–Fix* or dual functional (see e.g. [6, 23, 25]). In addition, a simplified formula can be derived for uniform parameter spaces [22, 24]. In the bivariate case, the extrapolation weights are simply determined by the tensor product of univariate values.

Extended B-splines inherit most properties of conventional B-splines and provide a stable basis for the analysis of trimmed geometries. The proposed strategy for detecting degenerated basis functions is particularly beneficial for collocation schemes, because the definition of the collocation point locations within Ω^{v} is straightforward, i.e. equal to the non-trimmed situation.

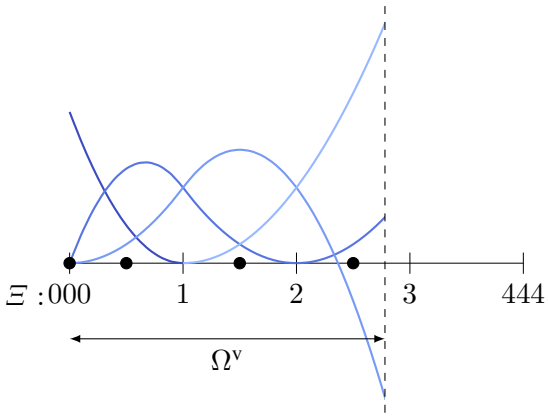

Figure 3: Extended B-splines

The presented concept focuses on B-spline basis functions. However, if the geometry is defined by trimmed NURBS, we take advantage of the independent field approximation and simply approximate the Cauchy data by B-splines without modifying the geometrical representation.

3 NUMERICAL RESULTS

The following examples emphasize the benefits of the proposed methodology. Firstly, the advantage of accurate geometry models is investigated. Secondly, the performance of isogeometric and subparametric patches is compared. Finally, the approximation quality of extended B-splines is studied.

3.1 Sphere

The excavation of a spherical cavity with radius $r_s = 5.0\,\mathrm{m}$ is investigated. An isotropic elastic material is considered with Poisson's ratio $\nu = 0.3$ and Young's modulus $E = 1000\,\mathrm{MPa}$. Hydrostatic stress $\sigma_0 = 1.0\,\mathrm{MPa}$ is applied as loading which leads to a uniform internal pressure along the excavation surface. The resulting radial displacement u_r can be determined analytically by

$$u_r = \sigma_0 \frac{1+\nu}{2\,E} \frac{r_s^3}{r^2} \tag{8}$$

where r denotes the distance of the point observed to the center of the sphere. Hence, the reference solution for u_r along the boundary, i.e. $r = r_s$, is $3.25 \times 10^{-3}\,\mathrm{m}$.

The problem is solved by conventional and isogeometric BEM simulations. Both approaches employ quadratic basis functions. The conventional BEM meshes approximate the boundary of the computation domain with quadratic Serendipity elements. In the isogeometric case, NURBS basis function of degree $p = 2$ are used. In fact, the geometry can be represented exactly by a single NURBS patch which has degenerated edges at each pole of the sphere. This model has been exported from the CAGD software Rhinoceros, where the precision of the exported data was set to $\epsilon_e = 10^{-8}$. Discontinuous collocation is applied in order to deal with the degenerated edges of the model.

The relative error of the radial displacement ϵ_{u_r} as well as the relative deviation of the geometry representation to an analytical sphere ϵ_{geo} are summarized for various degrees of freedom n in Table 1. Further, three numerical results and their corresponding discretizations are illustrated in Figure 5 and Figure 4, respectively.

Isogeometric BEM			Conventional BEM		
n	ϵ_{u_r}	ϵ_{geo}	n	ϵ_{u_r}	ϵ_{geo}
216	1.74×10^{-5}	3.42×10^{-8}	483	1.61×10^{-2}	4.76×10^{-1}
288	2.65×10^{-6}	3.42×10^{-8}	2436	1.27×10^{-3}	1.53×10^{-2}
			9312	5.58×10^{-4}	1.81×10^{-3}
			12 120	4.42×10^{-4}	1.10×10^{-3}
			21 858	1.49×10^{-4}	3.21×10^{-4}
			38 886	7.52×10^{-5}	1.08×10^{-4}

Table 1: Relative error of solution ϵ_{u_r} and geometry representation ϵ_{geo} of the spherical excavation measured in L_2-norm due to an isogeometric and conventional BEM analysis with quadratic basis functions.

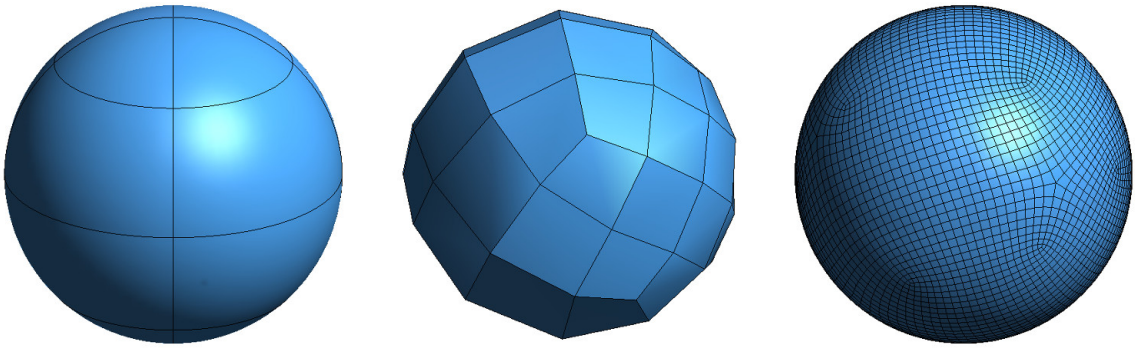

(a) $n = 288$ (b) $n = 483$ (c) $n = 38\,886$

Figure 4: Various unknown field discretizations of the spherical cavity with different degrees of freedom n: (a) finest isogeometric BEM, (b) coarsest, and (c) finest conventional BEM analysis.

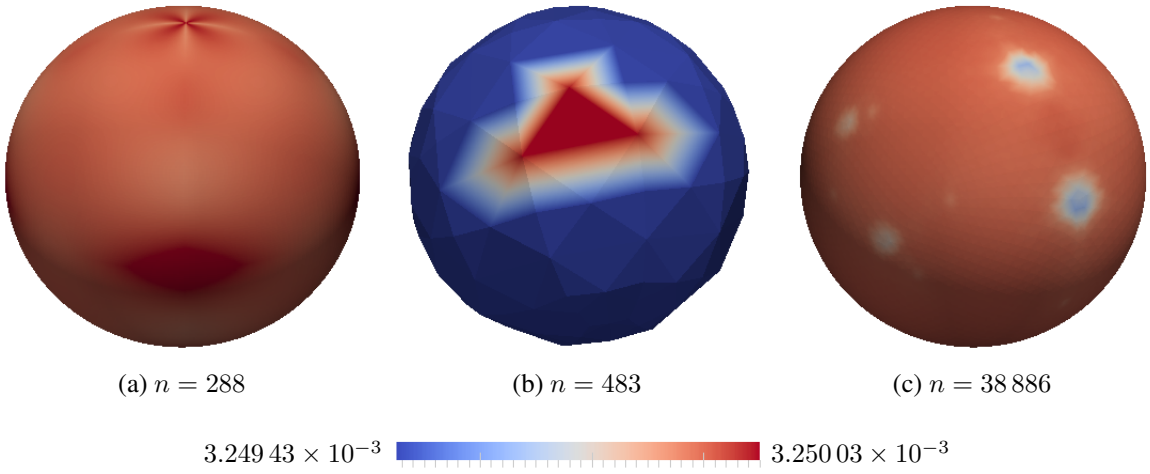

(a) $n = 288$ (b) $n = 483$ (c) $n = 38\,886$

Figure 5: Radial displacement u_r of various spherical excavation discretizations: (a) finest isogeometric BEM, (b) coarsest, and (c) finest conventional BEM analysis.

The error ϵ_{geo} demonstrates clearly the superiority of the isogeometric concept concerning accurate geometry representations. The unrefined NURBS patch provides already a precise geometric model, while a large number of Serendipity elements is required for an adequate approximation. Note that ϵ_{geo} correlates to the accuracy of the input data ϵ_e in the isogeometric case, hence it can be controlled by the user. Moreover, the isogeometric solution provides excellent results for u_r despite of the low number of degrees of freedom n. It should, however, be noted that the example suits NURBS basis functions ideally. Such remarkable differences between isogeometric and conventional BEM solutions can not be expected in general. Nevertheless, conic sections and their three dimensional counterparts, e.g. spheres and cylinders, are very common design elements for which NURBS surpass the approximation quality of conventional basis functions.

3.2 Crankshaft

The concept of independent field approximation is applied to a crankshaft example. The geometry is defined by several regular NURBS patches and illustrated in Figure 6. Displacements are fixed at the axle and flywheel, while the crank pins are subjected to vertical loading. These boundary conditions are exactly represented by the initial discretization and do not require re-

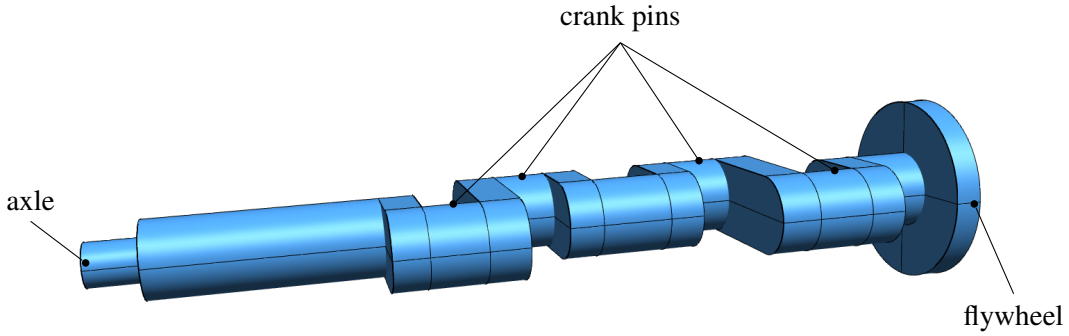

Figure 6: Geometry model of the crankshaft.

finement. The material property is specified by $E = 210\,\mathrm{GPa}$ and $\nu = 0.25$.

Subparametric and isoparametric discretizations are applied to the problem. They differ not only in the refinement procedure, but the type of basis function used for representing the Cauchy data. In particular, B-splines are employed in the subparametric case. The degree of the basis functions related to Cauchy data p_c is either equal to the one of the geometry representation p_g or increased by means of degree elevation, i.e. $p_c = p_g + 1$. Subsequently, knot insertion is used to improve the results, which is the equivalent to h-refinement in conventional analysis. For each simulation, the analysis time t_i and t_s of the isoparametric and subparametric discretization are compared. To be precise, the runtime for setting up the left hand side matrix $\mathbf{L}$ and the right hand side matrix $\mathbf{R}$ of the system of equations is measured. Each analysis has been performed single-threaded, concurrently for each t_i and t_s, and repeated several times.

The resulting speedup factors t_i/t_s are summarized in Figure 7. In addition, the displacements corresponding to the third h-refinement step of the case where $p_c = p_g$ are exemplarily shown in Figure 8.

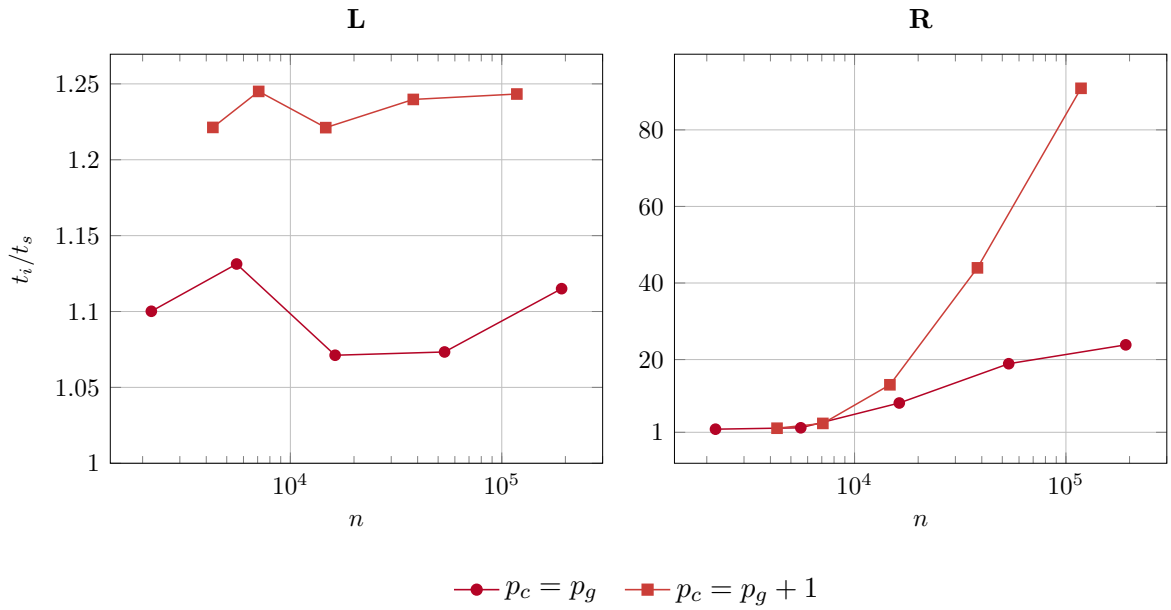

Figure 7: Computational time for the set up of $\mathbf{L}$ and $\mathbf{R}$ related to various discretization of the crankshaft example as a function of the degrees of freedom n. The runtime of the isoparametric discretization t_i is related to the subparametric one t_s.

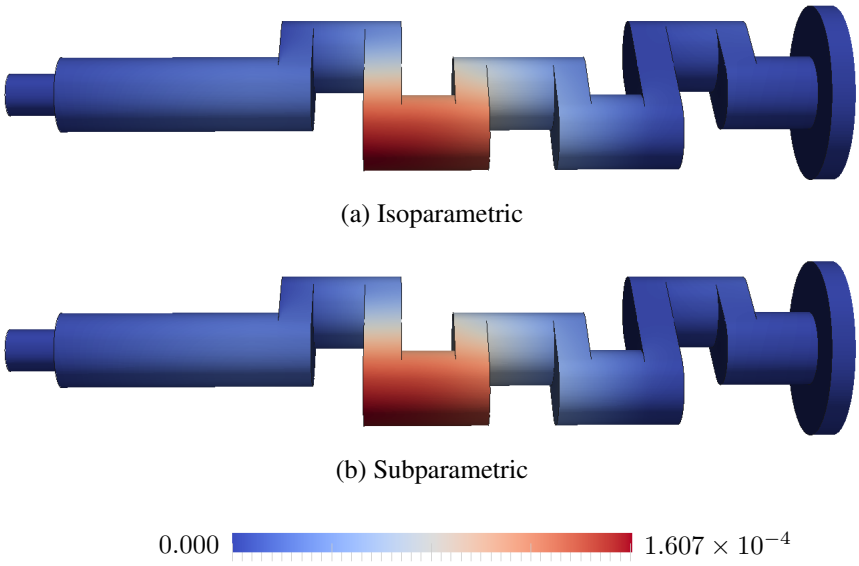

(a) Isoparametric

(b) Subparametric

Figure 8: The absolute displacement $|\mathbf{u}|$ of the crankshaft example without degree elevation and three h-refinement steps due to an (a) isoparametric BEM and (b) subparametric BEM discretization.

The shown results indicate that independent field approximation reduces the computational effort, especially for the right hand side of the system of equations. The number of columns of $\mathbf{R}$ is constant for all subparametric discretizations, because known Cauchy data do not need to be refined. Hence, its storage requirement is linear with respect to the degrees of freedom n which is the driving force for the enormous speedup with respect to $\mathbf{R}$. The efficient geometry evaluation as well as the substitution of NURBS by B-splines are the key factor regarding the faster computation of $\mathbf{L}$ in the subparametric case. The former impact is clearly indicated by the additional offset between the graphs related to $p_c = p_g$ and $p_c = p_g + 1$ on the left hand side of Figure 7.

3.3 Trimmed Cube

In order to investigate the approximation quality of extended B-splines in the context of an isogeometric BEM analysis a unit cube is analyzed. The geometry is discretized by two different models as illustrated in Figure 9. One is described by 6 regular patches, whereas 4 trimmed patches are included in the other. Both represent the same geometry, i.e. $\ell_x = \ell_y = \ell_z = 1.0$,

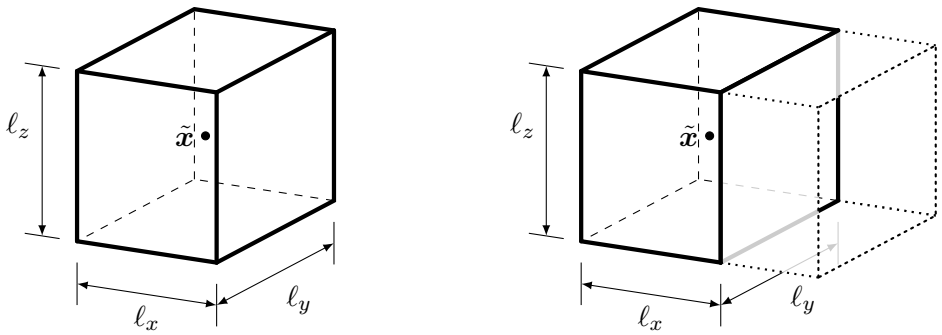

(a) Untrimmed

(b) Trimmed

Figure 9: Discretization of a unit cube by (a) regular patches and (b) trimmed patches.

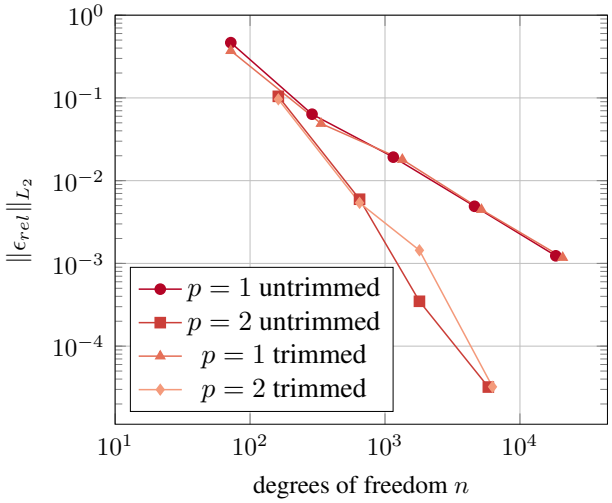

Figure 10: Relative L_2-error of an exterior Neumann problem on the (trimmed) cube example with respect to the number of degrees of freedom n.

which defines the boundary Γ of an infinite domain Ω. The boundary condition is given by

$$\mathbf{t}(\boldsymbol{y}) = \mathsf{T}(\tilde{\boldsymbol{x}}, \boldsymbol{y}) \qquad \boldsymbol{y} \in \Gamma,\ \tilde{\boldsymbol{x}} \in \Omega^- \tag{9}$$

with Ω^- denoting the void, i.e. $\tilde{\boldsymbol{x}} \notin \Omega$. In particular, a source point $\tilde{\boldsymbol{x}}$ in the center of the cube defines the boundary conditions for the exterior Neumann problem. The discretizations are set up for different degrees $p = \{1, 2\}$ and knot insertion is applied to improve the solutions. The relative approximation error is determined by

$$\epsilon_{rel} = \frac{\mathbf{u}(\boldsymbol{y}) - \mathsf{U}(\tilde{\boldsymbol{x}}, \boldsymbol{y})}{\mathsf{U}(\tilde{\boldsymbol{x}}, \boldsymbol{y})} \qquad \forall \boldsymbol{y} \in \Gamma,\ \tilde{\boldsymbol{x}} \in \Omega^- \tag{10}$$

where $\mathbf{u}(\boldsymbol{y})$ is the obtained solution along the boundary. In Figure 10, the results measured with respect to the L_2-norm, i.e. $\|\epsilon_{rel}\|_{L_2}$, are shown. It can be observed that the trimmed model shows very good agreement with the untrimmed case.

4 CONCLUSIONS

A comprehensive concept for integrating design models into a numerical simulation has been presented. The essential ingredient is that the isogeometric method applied is based on boundary integral equations. This allows to overcome the challenge of deriving a volume discretization from a design model, in a simple and elegant manner. In addition, no connectivity information is required between adjacent patches. The proposed concept is completed by an independent field approximation paradigm allowing a more flexible interaction with the design model and a technique which stabilizes trimmed parameter space. These enhancements are by no means restricted to the boundary element method used in this work.

The presented results demonstrate the superiority of isogeometric schemes regarding accurate geometry description, the computational advantage of independent field approximation related to conventional isoparametric formulations, and the suitability of the proposed stabilization. The latter results are indeed very promising and deserves to be investigated in more detail. For instance, the behavior for higher degree approximations has been neglected in the present work and is of particular interest for further research.

REFERENCES

[1] M. F. Hardwick, R. L. Clay, P. T. Boggs, E. J. Walsh, A. R. Larzelere, A. Altshuler. DART system analysis. Technical Report SAND2005-4647, *Sandia National Laboratories*, 2005.

[2] J. A. Cottrell, T. J. R. Hughes, Y. Bazilevs, *Isogeometric analysis: Toward integration of CAD and FEA*. John Wiley & Sons, Chichester, England, 2009.

[3] J. A. Cottrell, A. Reali, Y. Bazilevs, T. J. R. Hughes, Isogeometric analysis of structural vibrations. *Computer Methods in Applied Mechanics and Engineering*, **195**(41-43), 5257–5296, 2006.

[4] J. A. Cottrell, T. J. R. Hughes, A. Reali, Studies of refinement and continuity in isogeometric structural analysis. *Computer Methods in Applied Mechanics and Engineering*, **196**(41–44), 4160–4183, 2007.

[5] J. Zechner, B. Marussig, G. Beer, T.-P. Fries, The isogeometric Nyström method. *Computer Methods in Applied Mechanics and Engineering*, submitted. available as preprint:http://arxiv.org/abs/1506.03914.

[6] B. Marussig. *Seamless integration of design and analysis through boundary integral equations*. PhD thesis, Graz University of Technology, 2015.

[7] B. Marussig, J. Zechner, G. Beer, T.-P. Fries, Fast isogeometric boundary element method based on independent field approximation. *Computer Methods in Applied Mechanics and Engineering*, **284**, 458–488, 2015.

[8] G. Beer, B. Marussig, C. Duenser, Isogeometric boundary element method for the simulation of underground excavations. *Géotechnique Letters*, **3**, 108–111, 2013.

[9] G. Beer, I. M. Smith, C. Duenser, *The boundary element method with programming*. Springer Wien - New York, 2008.

[10] V. Mantic, A new formula for the C-matrix in the Somigliana identity. *Journal of Elasticity*, **33**, 191–201, 1993.

[11] L. Piegl, W. Tiller, *The NURBS book*. Springer, New York, 2 edition, 1997.

[12] F. Auricchio, L. Beirão Da Veiga, T. J. R. Hughes, A. Reali, G. Sangalli, Isogeometric collocation methods. *Mathematical Models and Methods in Applied Sciences*, **20**(11), 2075–2107, 2010.

[13] K. Li, X. Qian, Isogeometric analysis and shape optimization via boundary integral. *Computer-Aided Design*, **43**(11), 1427–1437, 2011.

[14] C. Patterson, M. Sheikh, Interelement continuity in the boundary element method. In C. Brebbia, editor, *Topics in Boundary Element Research*, 123–141. Springer US, 1984.

[15] G. Beer, B. Marussig, J. Zechner, A simple approach to the numerical simulation with trimmed CAD surfaces. *Computer Methods in Applied Mechanics and Engineering*, **285**, 776–790, 2015.

[16] H. Harbrecht, M. Randrianarivony, From Computer Aided Design to wavelet BEM. *Computing and Visualization in Science*, **13**(2), 69–82, 2010.

[17] H.-J. Kim, Y.-D. Seo, S.-K. Youn, Isogeometric analysis for trimmed CAD surfaces. *Computer Methods in Applied Mechanics and Engineering*, **198**(37-40), 2982–2995, 2009.

[18] H.-J. Kim, Y.-D. Seo, S.-K. Youn, Isogeometric analysis with trimming technique for problems of arbitrary complex topology. *Computer Methods in Applied Mechanics and Engineering*, **199**(45–48), 2796–2812, 2010.

[19] R. Schmidt, R. Wüchner, K.-U. Bletzinger, Isogeometric analysis of trimmed NURBS geometries. *Computer Methods in Applied Mechanics and Engineering*, **241–244**, 93–111, 2012.

[20] Y.-W. Wang, Z.-D. Huang, Y. Zheng, S.-G. Zhang, Isogeometric analysis for compound B-spline surfaces. *Computer Methods in Applied Mechanics and Engineering*, **261–262**, 1–15, 2013.

[21] K. Höllig, U. Reif, J. Wipper, Weighted extended B-spline approximation of Dirichlet problems. *SIAM Journal on Numerical Analysis*, **39**(2), 442–462, 2002.

[22] K. Höllig, *Finite element methods with B-splines*, Vol. 26 of *Frontiers in Applied Mathematics*. SIAM, 2003.

[23] K. Höllig, U. Reif, Nonuniform web-splines. *Computer Aided Geometric Design*, **20**(5), 277–294, 2003.

[24] T. Rüberg, F. Cirak, Subdivision-stabilised immersed b-spline finite elements for moving boundary flows. *Computer Methods in Applied Mechanics and Engineering*, **209–212**(0), 266–283, 2012.

[25] C. de Boor, *A practical guide to splines*, Vol. 27 of *Applied Mathematical Sciences*. Springer, New York, 2001.

ECCOMAS Congress 2016

VII European Congress on Computational Methods in Applied Sciences and Engineering

ECCOMAS Congress 2016

Proceedings of the VII European Congress on Computational Methods in Applied Sciences and Engineering

M. Papadrakakis, V. Papadopoulos, G. Stefanou, V. Plevris (Eds)

First Edition, September 2016

ISBN: 978-618-82844-0-1

Institute of Structural Analysis and Antiseismic Research
National Technical University of Athens, Greece